Flourishing on a Foundation of Strength and Depth

In 1997 the emergence of the European Journals was heralded in an editorial (En Route to European Journals of Inorganic and Organic Chemistry). The importance of a good foundation was emphasized. On that foundation the journals were established seven years ago. These years have been a time of consolidation to fuse the group of owner societies into the Editorial Union of Chemical Societies (EUChemSoc), to expand this union, and to achieve its challenging aims explicitly stated in the editorial (1999) of the European Journal of Inorganic Chemistry: "It is our most dedicated goal to reach the level of the top-3 Inorganic Chemistry journals on a world wide scale within three to five years". Where does the EurJIC stand five years down the road? With an Impact Factor of 2.482 the journal certainly has reached this level. The first boards have attained their goals admirably. The phase of consolidation is over − it is time to press on!

From the same editorial I quote: "We expect gradually to move to a system where a limited number (of Editorial Board members) each cover a certain subfield within … Inorganic Chemistry." This change has been realised from 2005. The Editorial Board has been expanded to include experts in coordination and supramolecular chemistry; organometallic chemistry and catalysis; bioinorganic chemistry and metal ions in biology; main-group chemistry; solid-state and materials chemistry; and physical and theoetical inorganic chemistry. Although the Editorial Board members primarily advise on matters in their field of competence, one Editorial Board member representing the chemical societies of France, Germany, Italy, the Netherlands, and Spain is responsible to the EUChemSoc who owns the journal. These are the countries in EUChemSoc from which we receive the largest number of manuscripts. The smaller chemical societies involved − those of Belgium, Greece, Hungary, and Portugal − shall supply one member in turn. An interesting statistic in this regard is the source of the submitted manuscripts. More than 60% come from other countries. EurJIC is indeed "made in Europe for the world".

Expertise in the Editorial Board

Two of the original members have retired to make way for members in new fields. Jaume Casabó has dedicated many years to publishing. Since 1994 he has been Editor of the Spanish Chemical Society (RSEQ) and prepared the way for the amalgamation of its journal into EurJIC. In addition to his work as Editorial Board member of EurJIC from 1999, he initiated the Spanish membership journal and was its first editor until 2000. Bernard Meunier took on the position in the Board for France in 1998. Although his recent prestigious appointment as President of the CNRS will leave him little time for editorial duties, he remains faithful to the concept of European publishing as member of the Editorial Advisory Board of *ChemBioChem*. On behalf of the Editorial Board and the Editorial Office of EurJIC I warmly thank both of them for their invaluable work at a crucial period for the journal and wish them every success in the future. I enjoyed the close cooperation and very much appreciated their advice.

We welcome three new members, Pablo Espinet, Rinaldo Poli and João Rocha. Their expertise in all aspects of organometallics, catalysis, materials and theoretical chemistry comes at the right time as EurJIC is expanding into these important areas of inorganic chemistry. I look forward to working with them more closely and hope that they will enjoy being ambassadors for the journal.

Simultaneously, the regular rotation in the Advisory Board has begun. About one-third of the Board have retired and eleven new members join this month. There is not enough space to mention the contributions of all whose term of office has now ended, but I thank all of them for their part in the development of the journal. When we pondered the new composition of the International Advisory Board we recognised that Austria, the Czech Republic, and Sweden − the Associate

Thanks to outgoing International Advisory Board Members

 © 2005 Wiley-VCH Verlag GmbH & Co. KGaA, Weinheim

Member countries, who actively support the journal but for one reason or another could not merge a journal − should also be represented. The names of all current members are given on the second masthead page. With these advisors your interests in inorganic chemistry, whatever they are, will receive expert attention.

Applications and basic research

Table 1 shows a selection of papers published in 2004 that have already been multiply cited. First it is clear that our authors come from all over the world. Second the papers cover the wide range of the fields mentioned above. perties all get a They focus on the structure and reactivity of inorganic compounds. Applications are clearly very important. Luminescent, photoluminescent, magnetic and electrochemical properties all get a look in. Bioinorganic, supramolecular and cluster chemistry, coordination polymers and main-group chemistry are all there. Ionic liquids and theoretical modelling also get a mention. And finally, international cooperations are a strength of the journal. EurJIC is indeed international and covers all aspects of modern Inorganic Chemistry.

Change characterises life, so it is unremarkable that scientific publishing, too, faces new challenges. The most controversial discussions on open access will continue in 2005, debating the issues of "Who pays?" and "Can we maintain the quality if an author pays?" The progress I wish to highlight here has been achieved: the standardisation of the measures for quoting the number of downloads. Without standards, usage figures could and did look good, but very often the highest figures were not the best and com-

Table 1. A selection of the most cited EurJIC Papers published in 2004

Title	Authors
The "Rebound Controversy": An Overview and Theoretical Modeling of the Rebound Step in C −-H Hydroxylation by Cytochrome P450	S. Shaik,* S. Cohen, S. P. de Visser, P. K. Sharma, D. Kumar, S. Kozuch, F. Ogliaro, D. Danovic
The Dynamic Status Quo of Polyhedral Silsesquioxane Coordination Chemistry	R. W. J. M. Hanssen, R. A. van Santen, H. C. L. Abbenhuis*
Eu^{III} Luminescence in a Hygroscopic Ionic Liquid: Effect of Water and Evidence for a Complexation Process	I. Billard, S. Mekki, C. Gaillard, P. Hesemann, G. Moutiers, C. Mariet, A. Labet, J.-C. G. Bünzli*
A Blue Photoluminescent 2-D Coordination Polymer Constructed by Dinuclear Zinc(II) Subunits $[Zn_2(oz)_2]$ [Hoz = 2-(2-Hydroxyphenyl)-2-oxazoline] and Dicyanamide	J. Zhang, S. Gao, C.-M. Che*
Determination of the Solvothermal Synthesis Mechanism of Metal Imidazolates by X-ray Single-Crystal Studies of a Photoluminescent Cadmium(II) Imidazolate and Its Intermediate Involving Piperazine	Y.-Q. Tian*, L. Xu, C.-X. Cai, J.-C. Wei, Y.-Z. Li, X.-Z. You
Supramolecular Host−Guest Systems in Zeolites Prepared by Ship-in-a-Bottle Synthesis	A. Corma*, H. Garcia*
Metal-Directed Self-Assembly: Two New Metal-Binicotinate Grid Polymeric Networks and Their Fluorescence Emission Tuned by Ligand Configuration	B.-L. Wu, D.-Q. Yuan, F.-L. Jiang, R.-H. Wang, L. Han, Y.-F. Zhou, M.-C. Hong*
Reactivity of Organoelement Subhalides of Gallium and Indium − Ga−Ga and In−In Bonds Bridged by Carboxylato Ligands	W. Uhl*, A. El-Hamdan
Structural Snapshots of a Dynamic Coordination Sphere in Model Complexes for Catechol 1,2-Dioxygenases	M. Merkel, D. Schnieders, S. M. Baldeau, B. Krebs*
Synthesis, Crystal Structures, and Magnetic Properties of a Mono- and a Dinuclear Copper(II) Complex of the 2,4,6-Tris(2-pyridyl)-1,3,5-triazine Ligand	T. Glaser*, T. Lügger, R. Fröhlich
Synthesis, Characterization and Electrochemistry of the Novel Dawson-Type Tungstophosphate $[H_4PW_{18}O_{62}]^{7-}$ and First Transition Metal Ions Derivatives	I.-M. Mbomekalle, B. Keita, Y. W. Lu, L. Nadjo*, R. Contant, N. Belai, M. T. Pope
The Construction of $(N_2S_2)Ni-Pd$ Clusters: A Slant-Chair, a Basket and a C_4-Paddlewheel Structure	M. L. Golden, S. P. Jeffery, M. L. Miller, J. H. Reibenspies, M. Y. Darensbourg*

 © 2005 Wiley-VCH Verlag GmbH & Co. KGaA, Weinheim

parisons were meaningless. Since January 2004, *Wiley InterScience* usage statistics have been COUNTER-compliant. What lies behind this new standard statistic?

COUNTER stands for Counting Online Usage of NeTworked Electronic Resources and "has been developed to provide a single, international, extendible Code of Practice that allows the usage of online information products and services to be measured in a credible, consistent and compatible way using vendor-generated data." Comparisons can now be reliably made between all COUNTER-compliant statistics. You can find out more about COUNTER under http://www.projectcounter.org/.

I wish all our readers and authors a Happy New Year. May the year 2005 bring you peace and prosperity, and success in all your endeavours.

Karen Hindson
Editor, EurJIC

 © 2005 Wiley-VCH Verlag GmbH & Co. KGaA, Weinheim

EurJIC
European Journal of Inorganic Chemistry

Issue 1/2005

Pages 1–228

Papers available ahead of print in Early View at www.interscience.wiley.com

Earliest available Table of Contents:
Automatically, free of charge by e-mail through
www.interscience.wiley.com/alerts

COVER PICTURE

The cover picture shows the hexagonal 2:4 coordination complex formed between 1,3-bis(3′-pyridylethynyl)benzene and copper(II) acetate. The ligand, synthesized by the Sonagashira coupling of 1,3-ethynylbenzene with 3-bromopyridine, was designed to form hexagonal coordination complexes with metals that favor linear coordination geometry. In this example the dimeric copper(II) acetate paddlewheel forms an almost linear connection between a pair of dipyridyl ligands. Details are discussed in the Short Communication by E. Bosch et al. on p. 45 ff.

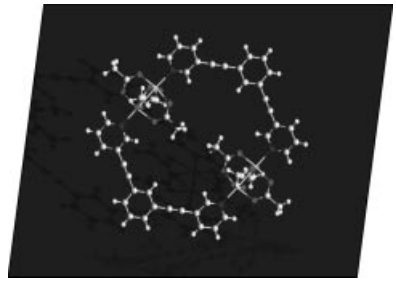

MICROREVIEW

Contents

27 **M. A. Carreon, V. Guliants***

Ordered Meso- and Macroporous Binary and Mixed Metal Oxides

Keywords: Mesoporous / Macroporous / Transition metal oxides / Catalytic applications

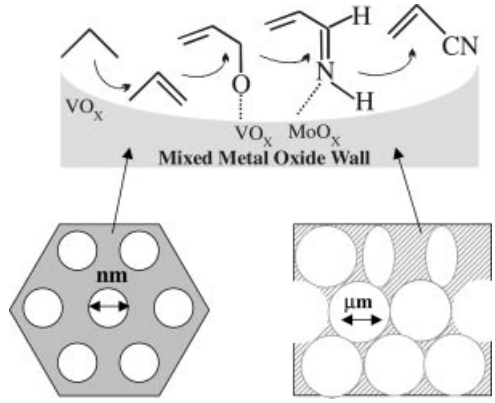

 © 2005 Wiley-VCH Verlag GmbH & Co. KGaA, Weinheim

SHORT COMMUNICATIONS

45 **N. Schultheiss, J. M. Ellsworth, E. Bosch,* C. L. Barnes**

Formation of Hexagonal Coordination Complexes

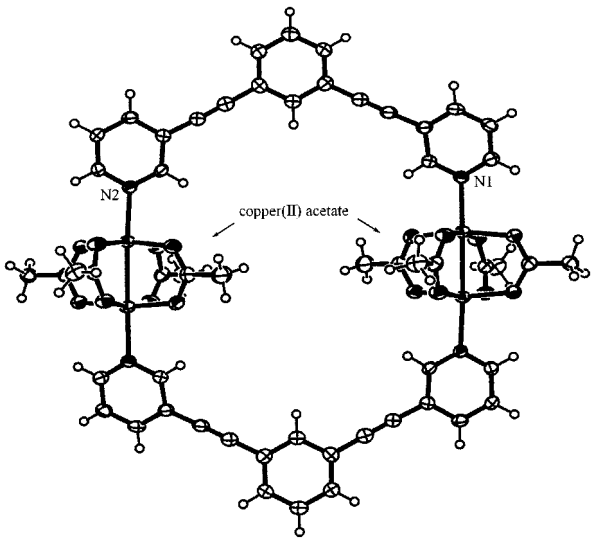

Keywords: Crystal engineering / N ligands / Metallacycles / Microporous materials

47 **H. Zhang, S. Zhang,* M. Zuo, G. Li, J. Hou**

Synthesis of ZnS Nanowires and Assemblies by Carbothermal Chemical Vapor Deposition and Their Photoluminescence

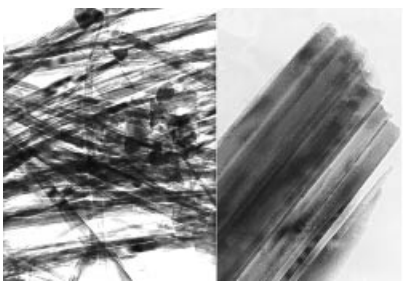

Keywords: Chemical vapor deposition / Luminescence / Nanostructures / Self-assembly / Zinc

51 **R. P. Davies,* S. Hornauer**

Lithium Cyanocuprates: Structural Studies of a Phosphane Adduct of a "Lower-Order" Lithium Cyanocuprate

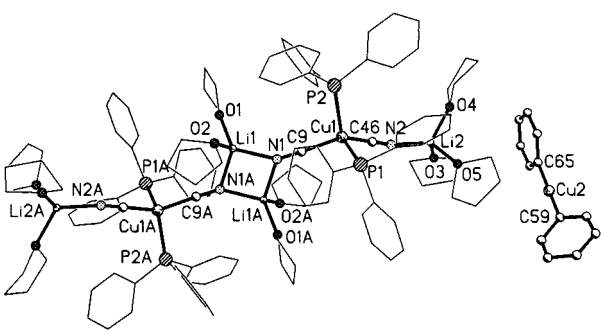

Keywords: Cuprates / Lithium / Reaction intermediates / Michael addition

55 **J.-M. Shi,* W. Xu, B. Zhao, P. Cheng, D.-Z. Liao, X.-Y. Chen**

A 2D Thiocyanato-Bridged Copper(II)-Manganese(II) Bimetallic Coordination Polymer with Ferromagnetic Interactions

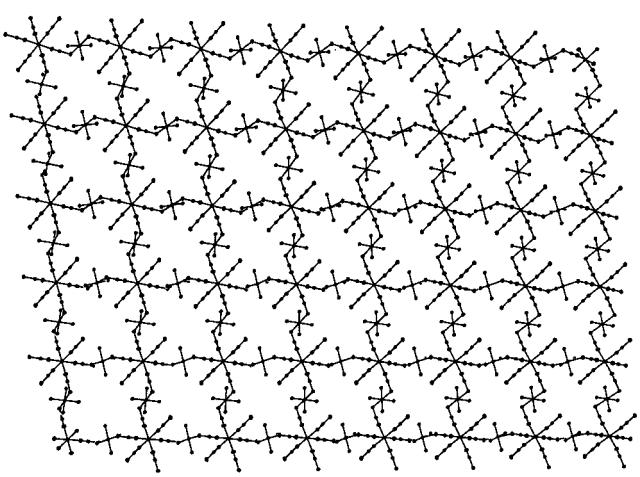

Keywords: Structure elucidation / Magnetic properties / Bridging ligands / Manganese

 © 2005 Wiley-VCH Verlag GmbH & Co. KGaA, Weinheim

59 **D. Fenske,* A. Rothenberger, M. S. Fallah**

Oxidation of a One-Dimensional Coordination Polymer and Synthesis of the Macrocyclic Silver Complex $[Ag_{12}(PhS_2P{-}PS_2Ph)_6(dppeS)_6]$

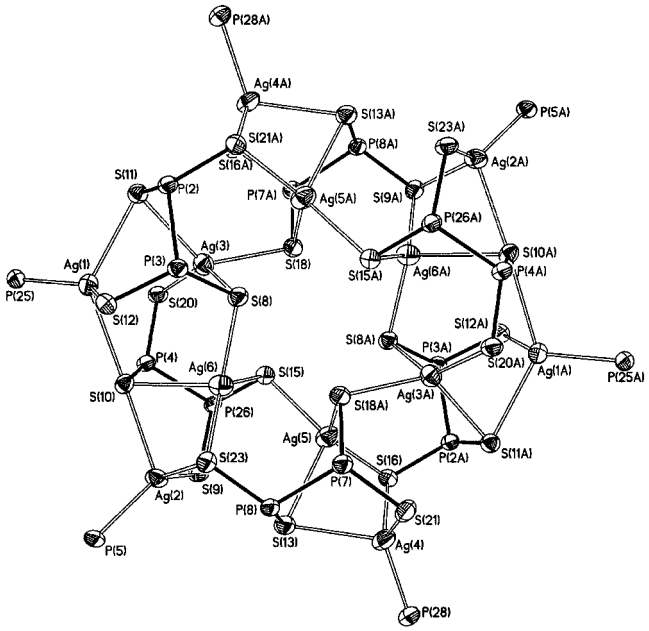

Keywords: Silver / Chalcogenides / Macrocycle / P ligands / S ligands

63 **J. Dou,* L. Wu, Q. Guo, D. Li, D. Wang**

A New Strategy for the Preparation of Metallaboranes − Solvothermal Synthesis and Structural Characterisation of Two Nido 11-vertex Diplatinaundecaborane Clusters

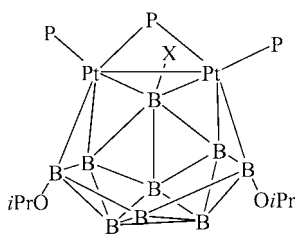

X = Cl, O*i*Pr

Keywords: Diplatinaundecaborane / Deboronation / Hydrothermal synthesis

66 **K. Heinze,* M. Schlenker**

Anion-Induced Motion in a Ferrocene Diamide

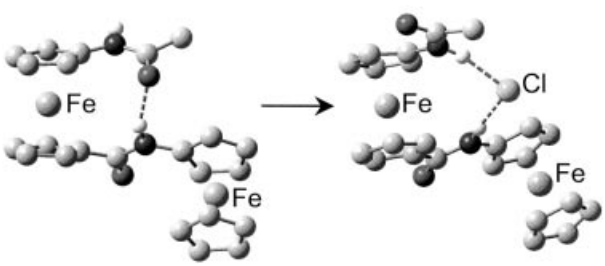

Keywords: Anion recognition / Anion sensing / Hydrogen bonds / Metallocenes / Receptors

72 **K. P. Bryliakov,* E. A. Duban, E. P. Talsi**

The Nature of the Spin-State Variation of $[Fe^{II}(BPMEN)(CH_3CN)_2](ClO_4)_2$ in Solution

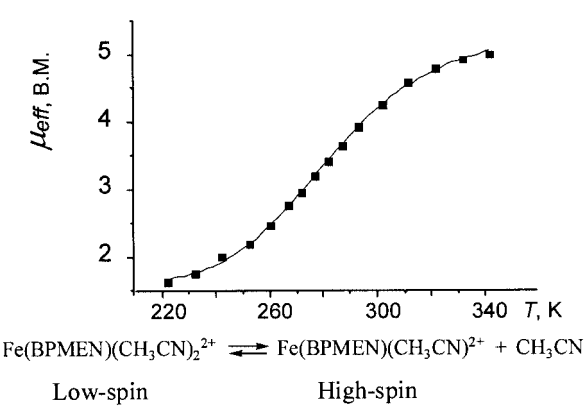

Keywords: Magnetic properties / Iron(II) complexes / Spin crossover / Liquid state / Solvent effects

 © 2005 Wiley-VCH Verlag GmbH & Co. KGaA, Weinheim

77 **Z.-Z. Lin, F.-L. Jiang, L. Chen, D.-Q. Yuan, Y.-F. Zhou, M.-C. Hong***

Two Novel Inorganic-Organic Hybrid Frameworks Based on In^{III}-BTC and In^{III}-BTEC

Keywords: Indium(III) / Benzenemulticarboxylate

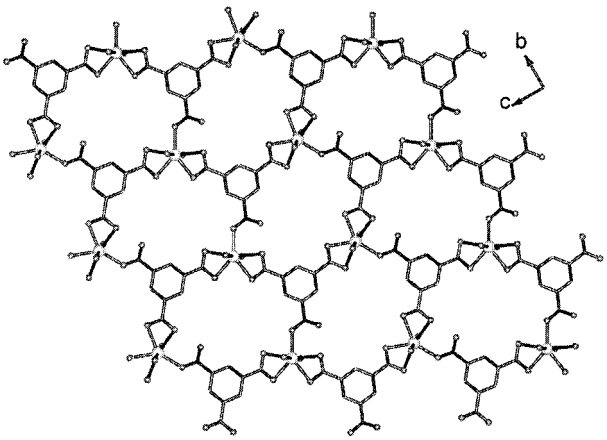

82 **I.-P. Lorenz,* S. Rudolph, H. Piotrowski, K. Polborn**

Reactions of $K_2[Fe(CO)_3(PPh_3)]$: Reductive Sb−Sb Coupling with Ph_2SbCl To Form *trans*-$[Fe(CO)_3(PPh_3)(Sb_2Ph_4)]$ and Salt Metathesis with Me_3SbCl_2 To Yield *trans*-$[Fe(CO)_3(PPh_3)(SbMe_3)]$

Keywords: Antimony / Coupling reactions / Iron / Metathesis

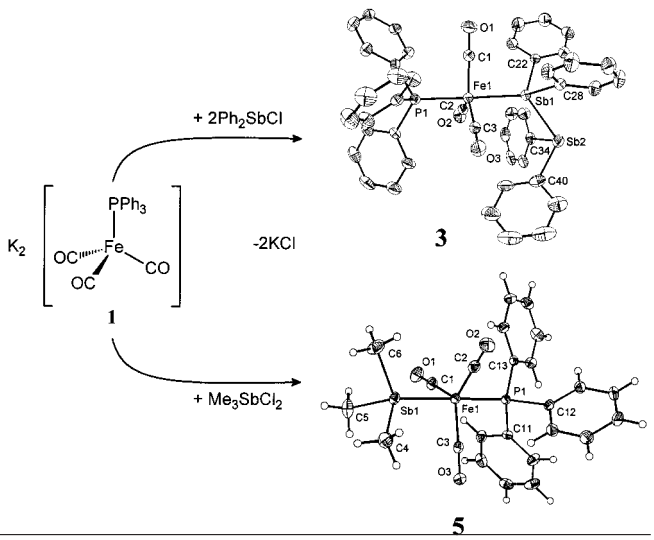

FULL PAPERS

87 **I. Levin,* Q. Z. Huang, L. P. Cook, W. Wong-Ng**

Nonquenchable Chemical Order−Disorder Phase Transition in Yttrium Oxyfluoride

Keywords: Phase transitions / Yttrium / X-ray diffraction / Order−disorder transitions

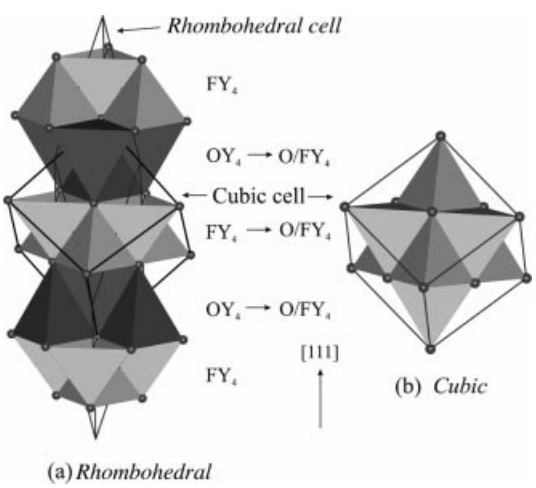

92

B. Meyer zu Berstenhorst, G. Erker,* G. Kehr, J.-C. Wasilke, J. Müller, H. Redlich, J. Pyplo-Schnieders

Bioorganometallic Chemistry: Reactions of Methyltitanocene Cation Complexes with a Singly Deprotected Methyl Glucopyranoside

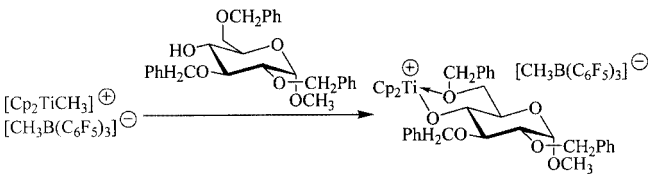

Keywords: Carbohydrate complexes / Titanocene / Zirconocene / Lewis acid / Chelate complexes / Bioorganometallic chemistry

100

F. A. Jalón, B. R. Manzano,* B. Moreno-Lara

Apparent Allyl Rotation and Pd−N Bond Rupture in Allylpalladium Complexes with N-Donor Ligands − Evidence of an Associative Mechanism

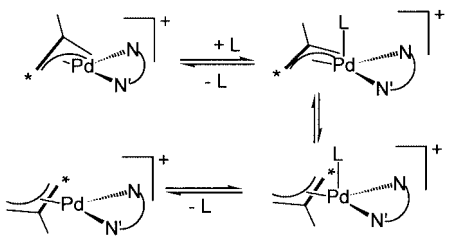

Keywords: Allyl ligands / Fluxionality / N ligands / Palladium

110

M. Lepeltier, T. Kwonk-Ming Lee, K. Kam-Wing Lo,* L. Toupet, H. Le Bozec, V. Guerchais*

Synthesis, Structure, and Photophysical and Electrochemical Properties of Cyclometallated Iridium(III) Complexes with Phenylated Bipyridine Ligands

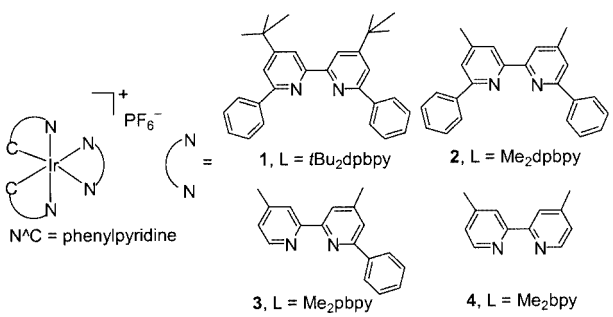

Keywords: Electrochemistry / Iridium / N ligands / Photochemistry

118

A. A. Martí, G. Mezei, L. Maldonado, G. Paralitici, R. G. Raptis, J. L. Colón*

Structural and Photophysical Characterisation of *fac*-[Tricarbonyl(chloro)(5,6-epoxy-1,10-phenanthroline)rhenium(I)]

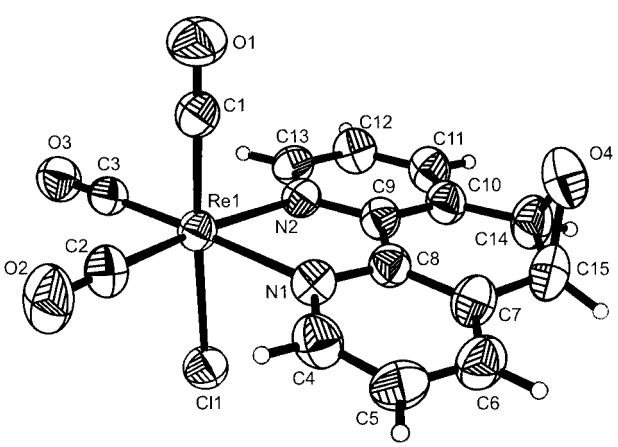

Keywords: Carbonyl ligands / Coincidental resonances / Facial isomers / Energy gap law / Rhenium

 © 2005 Wiley-VCH Verlag GmbH & Co. KGaA, Weinheim

125 **M. Dochnahl, M. Doux, E. Faillard, L. Ricard, P. Le Floch***

A New Mixed P,S-Bidentate Ligand Featuring a λ^4-Phosphinine Anion and a Phosphanyl Sulfide Group − Synthesis, X-ray Crystal Structures and Catalytic Properties of Its Chloro(cymene)ruthenium and Allylpalladium Complexes

Keywords: Density functional calculations / Homogeneous catalysis / P ligands / Ruthenium / Palladium / S ligands

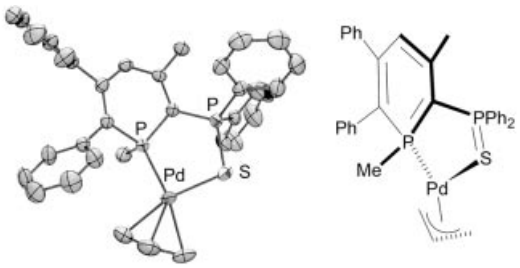

135 **M. Scheer,* U. Vogel, U. Becker, G. Balazs, P. Scheer, W. Hönle, M. Becker, M. Jansen**

Synthesis and Characterisation of Novel Complexes Containing Group 15 Elements and Their Potential Use as Molecular Precursors for the Formation of Transition Metal Pnictides

Keywords: Cobalt / Cluster compounds / Phosphorus / Thermochemistry / Tungsten

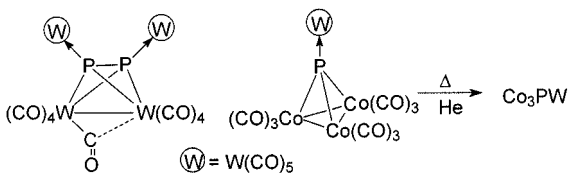

142 **S. B. Artemkina, N. G. Naumov,* A. V. Virovets, V. E. Fedorov**

3D-Coordination Cluster Polymers $[Ln(H_2O)_3Re_6Te_8(CN)_6]\cdot nH_2O$ (Ln = La^{3+}, Nd^{3+}): Direct Structural Analogy with the Mononuclear $LnM(CN)_6\cdot nH_2O$ Family

Keywords: Rhenium / Cluster compounds / Structure elucidation / Cyanide ligand / Lanthanides

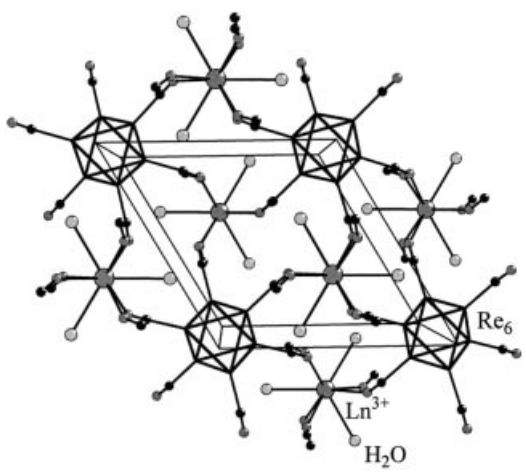

147 **M. R. Maurya,* S. Agarwal, C. Bader, D. Rehder***

Dioxovanadium(V) Complexes of ONO Donor Ligands Derived from Pyridoxal and Hydrazides: Models of Vanadate-Dependent Haloperoxidases

Keywords: Vanadium / Hydrazones / Catalytic bromination / Pyridoxal

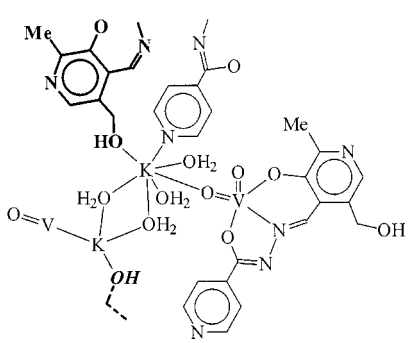

 © 2005 Wiley-VCH Verlag GmbH & Co. KGaA, Weinheim

158 **A. Machkour, D. Mandon,* M. Lachkar, R. Welter**

Oxidative Dehydrogenation of Secondary Amines: The Case of the *N*,*N*,*N*′-Tris(2-pyridylmethyl)-*o*-phenylenediamine Ligand when Coordinated to Iron Dichloride

Keywords: Ferrous complexes / Dioxygen activation / Oxidative dehydrogenation

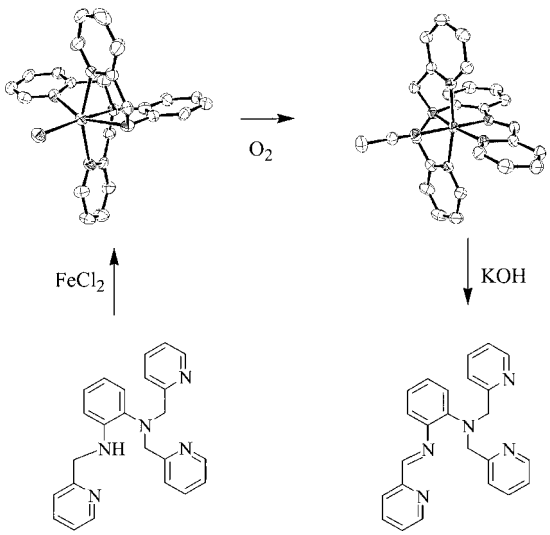

162 **G. Falini,* S. Fermani, S. Vanzo, M. Miletic, G. Zaffino**

Influence on the Formation of Aragonite or Vaterite by Otolith Macromolecules

Keywords: Biomineralization / Otoliths / Vaterite / Aragonite / Calcium carbonate / Polymorphism / Bioinorganic chemistry

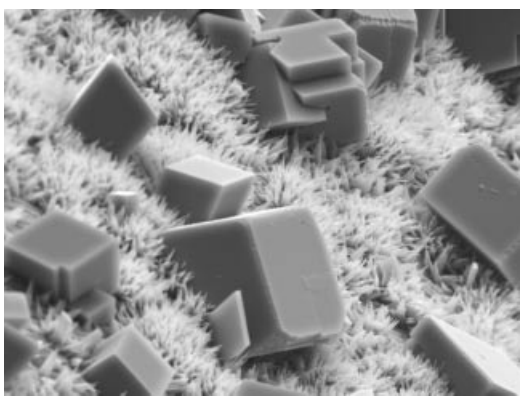

168 **K.-P. Zeller,* P. Schuler, P. Haiss**

The Hidden Equilibrium in Aqueous Sodium Carbonate Solutions − Evidence for the Formation of the Dicarbonate Anion

Keywords: Dicarbonate anion / Isotopic labeling / NMR spectroscopy / Oxygen transfer

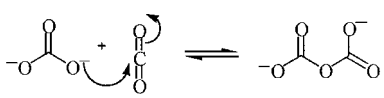

173 **K. A. Mahmoud, Y.-T. Long, G. Schatte, H.-B. Kraatz***

Rearrangement of the Active Ester Intermediate During HOBt/EDC Amide Coupling

Keywords: Ferrocene / Hydroxybenzotriazole / Amide coupling / Amino acid / Electrochemistry

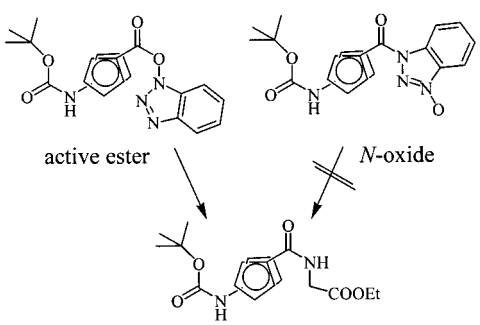

 © 2005 Wiley-VCH Verlag GmbH & Co. KGaA, Weinheim

181 **G. Barberio, A. Bellusci, A. Crispini, M. Ghedini, A. Golemme, P. Prus, D. Pucci***

Columnar Mesomorphism in Hexacatenar Tetrahedral (2,2′-Bipyridine)zinc Complexes and Homologous Palladium Derivatives

Keywords: Bipyridine ligands / Zinc / Palladium / Metallomesogens / Columnar structures

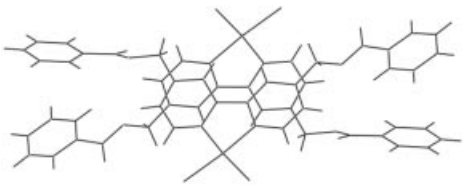

189 **C. Miranda, F. Escartí, L. Lamarque, E. García-España,* P. Navarro,* J. Latorre, F. Lloret, H. R. Jiménez, M. J. R. Yunta**

Cu^{II} and Zn^{II} Coordination Chemistry of Pyrazole-Containing Polyamine Receptors − Influence of the Hydrocarbon Side Chain Length on the Metal Coordination

Keywords: Pyrazole macrocycles / Copper and zinc coordination / Acid-base and metal formation equilibria / Polyamine ligands / Paramagnetic NMR

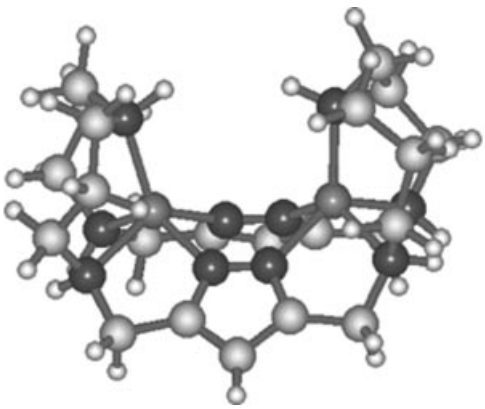

209 **C. J. Burchell, S. M. Aucott, A. M. Z. Slawin, J. D. Woollins***

Synthesis and Characterisation of the First Cyanodiselenoimidocarbonate $[C_2N_2Se_2]^{2-}$ Complexes

Keywords: Selenium / Platinum / Coordination modes

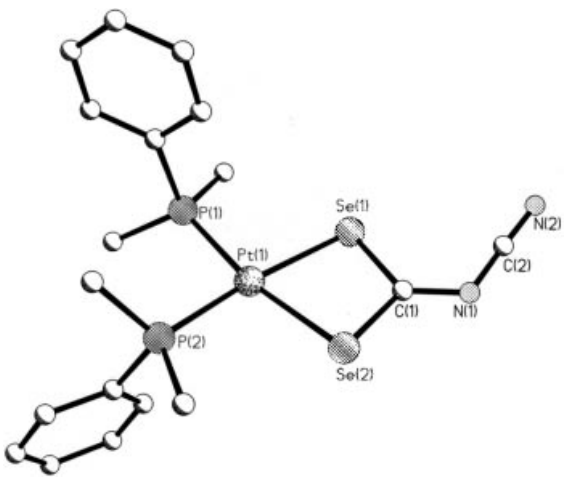

214 **Y. V. Mironov, V. N. Ikorskii, V. E. Fedorov, J. A. Ibers***

Octahedral Molybdenum Cluster Cyanide Complexes with Selenide and Halide Ligands in the Cluster Core

Keywords: Molybdenum / Clusters / Chalcohalide / Cyanide / Solid-state structures

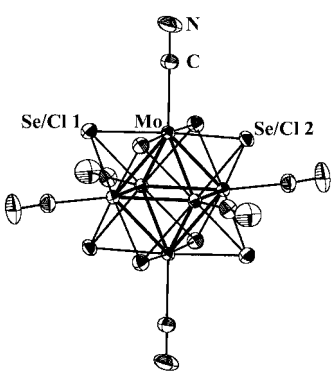

 © 2005 Wiley-VCH Verlag GmbH & Co. KGaA, Weinheim

218 **Z.-Y. Cheng, B.-L. Shi, B.-X. Gao, M.-L. Pang, S.-Y. Wang, Y.-C. Han, J. Lin***

Spin-Coating Preparation of Highly Ordered Photoluminescent Films of Layered PbI_2-Aminoalkyloxysilane Perovskites

Keywords: Layered perovskite / Sol-gel / Films / Photoluminescence

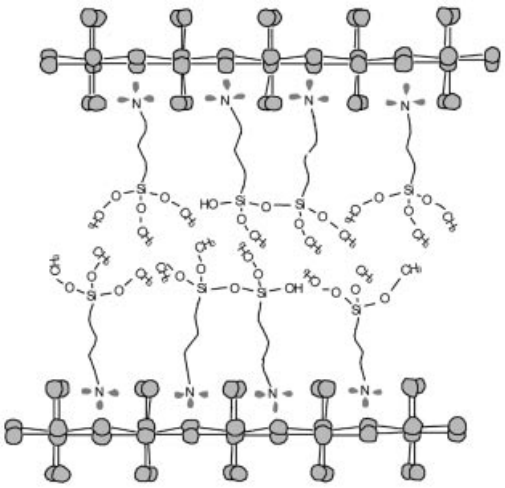

 © 2005 Wiley-VCH Verlag GmbH & Co. KGaA, Weinheim

EurJIC
European Journal of Inorganic Chemistry

1. General Information

The *European Journal of Inorganic Chemistry* (*EurJIC*) is published twice monthly.

Manuscripts should be submitted online using our online submission service at http://www.manuscriptXpress.org. You should prepare a **single file containing all tables, graphics, supporting information (where appropriate) etc.** Acceptable file formats are **Microsoft Word, Rich Text Format, Postscript and PDF**. Avoid the use of page breaks even between the title page and the introduction. If graphics are included at the end of the manuscript, try to fit as many as possible onto a single page. The file should have margins of 2 cm and be 1.5-line spaced.

Authors can follow the progress of their manuscript on their **personal homepage**, which is created automatically upon initial registration. This homepage is the same for the family of Wiley-VCH European journals and can be used to **store the latest version of a submitted paper** and to **upload the document file after acceptance**. Your referee reports for the family of Wiley-VCH European journals are also archived here.

No paper copies of the manuscript are required when using this system.

- The author must inform the editor of all manuscripts submitted, soon to be submitted, or in press at other journals that have a bearing on the manuscript being submitted.
- The correspondence author of a Microreview will receive a complimentary copy of the journal along with a PDF file of his/her paper restricted to 50 printouts; the correspondence author of other articles will receive a PDF file restricted to 25 printouts. Colour figures can be reproduced. Unless essential for the understanding of a paper, authors will be requested to make a contribution towards the costs of colour reproduction. Details will be provided after acceptance of the manuscript.
- We encourage authors to submit pictures for the cover page. A template of our cover page, **eurjiccover.pdf**, can be reached by clicking the link "For Authors" on our journal homepage (http://www.eurjic.org), to help you visualize the final effect of your design.

IMPORTANT: Any manuscript already available on personal/group web pages will be considered by the editors as already published and will not be accepted.

2. Types of Contributions

EurJIC publishes articles on inorganic, organometallic, bioinorganic, physical inorganic and solid-state chemistry. All contributions undergo peer review. An author may appeal against the decision on his/her manuscript, in writing. Three types of contributions are accepted for publication:

- **Full Papers** are articles with an Experimental Section that describe a significant contribution to the development of an area of research of importance. There are no restrictions placed on the length of a Full Paper.
- **Short Communications** are brief reports on results of high significance and urgency. Generally, they are no longer than 12−16 double-spaced pages or 3−4 typeset pages. An Experimental Section (as a separate paragraph or as part of the references) is desirable; if it is not included in the paper, the experimental data should be submitted as Supporting Information for refereeing purposes, and marked as such. A justification for urgent publication should accompany submission.
- **A Microreview** introduces the reader to a particular area of an author's research through a concise overview of a selected topic. As a rule, Microreviews are written on invitation, although unsolicited articles are also welcome. It is recommended, however, to contact the editor before submitting an unsolicited Microreview. The content should balance scope with depth; it should be a focused review of 25−30 double-spaced pages or 6−8 typeset pages. Reference to important work from others that is significant to the topic should be included. Microreviews will be refereed but will have no Experimental Section.

3. Manuscript Preparation

3.1 General

The whole of the manuscript should be 1.5-line spaced and in a large script (Times New Roman, 12 pt). We recommend that you prepare your text with **Microsoft Word (PC or Macintosh versions)** (see Section 3.2). Use the automatic pagination function incorporated in your word processor to number the pages; do not insert page numbers by hand. Leave a 2-cm margin around the perimeter of each page. **The figures, schemes and graphical abstract in the accepted version should be camera-ready**. Consult a current issue of the journal for an overview of the format. A manuscript should comprise: □ Title Page □ Keywords □ Abstract □ Main Text including Introduction, Results and Discussion etc. □ Experimental Section □ Acknowledgments (optional) □ Captions □ Tables □ References □ Schemes and Figures □ Graphical Abstract. □ For Microreviews only: Biographical sketches and a portrait-quality photograph of all authors.

3.2 Text

The text should be typed with carriage returns (hard returns) only at the end of a paragraph, title, heading and similar features. Avoid end-of-line word divisions.

Abbreviations and acronyms should be used sparingly and consistently. Where they first appear in the text, the complete term — apart from the most common ones such as NMR, IR, THF, *t*Bu etc. — should also be given.

 © 2005 Wiley-VCH Verlag GmbH & Co. KGaA, Weinheim

In the Experimental Section, quantities of reactants, solvents etc. should be included in parentheses [e.g. A solution of triphenylphosphane (500 mg, 1.91 mmol) in dichloromethane (15 mL) was added to.....].

NMR spectroscopic data should be quoted as in the following example: ^{1}H NMR (300 MHz, C_6D_6, 25 °C): δ = 1.3 (s, 18 H, $SiMe_3$), 0.9 (d, $^3J_{H,H}$ = 5.7 Hz, 2 H, 2-H) ppm. For each chemical shift, additional information should be given in the order: multiplicity, coupling constant, number of protons, assignment. The NMR data of different nuclei should be listed in ascending order of atomic weight (e.g. ^{1}H, ^{13}C, ^{19}F, ^{29}Si.....).

The purity of all new compounds should be verified by elemental analysis to an accuracy within ±0.4%. In special cases, for instance when the compound is unstable or not available in sufficient quantities for complete analysis, the exact relative molecular mass obtained from a high-resolution mass spectrum and a clean ^{13}C NMR spectrum (as additional material for inspection by the referees) should be supplied.

Symbols of physical quantities, but not their units (e.g. *T* for temperature, *J*, *a*), stereochemical information (*cis*, *trans*, *Z*, *R*), locants (*N*-methyl), symmetry and space groups ($P2_1/c$), and prefixes in formulas or compound names (*t*Bu, *tert*-butyl) **must be in italics**. Latin phrases, such as "in situ", should not.

Stereochemical descriptors, such as D- and L-, and molar (M) or normal (N) should be in **small capitals**.

Use character formatting for italic and bold characters. Avoid any *special style sheets* to format these features. Write *capital letters* using the keyboard (shift + letter key), **not** the format "Capital letter" in Word.

Use only characters from the Symbol and Normal Text character sets, especially when inserting Greek letters and characters with umlauts, accents, tildes, etc.: α, Å, ã, ä, à.

There are three types of hyphens: normal dashes (-), en dashes (−), and em dashes (—). Use these as illustrated — spacing is important too — in the following examples:

well-known reaction	C−H bond
six-membered ring	Tables 2−4
3-position of the ring	carbon−oxygen bond
signal-to-noise ratio	C−N stretch
Mo-K_α	Diels−Alder reaction
1,2-dicyanobutane	structure−activity relationship
p-*tert*-butylphenol	80−100 mg
(−)-tartaric acid	carried out at −10°C
$[M^+ - CH_3]$	cm^{-1}

Use the symbol × where appropriate, rather than the letter x:
... washed with water (2 × 150 mL) ...
Use the double quotation marks "..." rather than „...“, "..." or «...»

Graphics (including structural formulas, schemes, figures, equations and small graphical items that appear in captions) must be submitted camera-ready on separate pages after acceptance of the manuscript (see Section 3.5).

Lines or **arcs**, for example to indicate ring compounds, cannot be used within the text. Another method for indicating such compounds must be devised. Please contact the Editorial Office if any help is needed.

If practical, authors should use a systematic name (IUPAC or Chemical Abstracts) for each title compound in the Experimental Section. Please try to avoid complicated, multi-line names if a simpler version (e.g. alcohol **4**, ketone **5**, compound **6**) could be used instead.

3.3 Tables

Use the Insert Table command from the Table menu or use the Insert Table button on the Standard toolbar for creating tables, and use tabs ONLY to move between cells.

3.4 References

We strongly recommend the use of the Endnotes feature of Word. If you prefer not to use this function, references should be indicated by numbers in square brackets as superscripts and, if applicable, after punctuation (example: text.[1]). Use the Format Font menu.

Journal titles should be abbreviated according to the Chemical Abstracts Service Source Index (CASSI).

The Author is responsible for correct citations. The *European Journal of Inorganic Chemistry* is a member of Cross Ref. (http://www.crossref.org), a service which links reference citations to the online content that those references cite. This can only function if the citations are accurate. Please ensure that only one reference is cited under each reference number or that a composite reference is subdivided into parts a), b) etc. For example:

[1] A. Einstein, A. N. Other, *Eur. J. Inorg. Chem.* **2003**, 1−15.
[2] R. Schoenfeld, *The Chemist's English*, 3rd ed., VCH, Weinheim, **1990**, p. 111.

or

[1] a) A. Einstein, A. N. Other, *Eur. J. Inorg. Chem.* **2003**, 1−15; b) R. Schoenfeld, *The Chemist's English*, 3rd ed., VCH, Weinheim, **1990**, p. 111.

but not

[1] a) A. Einstein, A. N. Other, *Eur. J. Inorg. Chem.* **2003**, 1−15; R. Schoenfeld, *The Chemist's English*, 3rd ed., VCH, Weinheim, **1990**, p. 111.

3.5 Graphics

Graphics are schemes, figures, equations and small graphical items that appear in captions. Graphics differ fundamentally from the text portion of your manuscript in that they must be scanned or electronically processed.

In the revised version please submit **each graphic in its own file** within a graphic folder. The following formats are preferred: *.cdr, *.cdx, *.wmf (windows metafile), *.pct, *.tif, *.eps. For good reproduction the resolution should be a minimum of 300 dpi.
Consult the following table for the appropriate size of lettering. Lettering smaller than 3.0 mm will reproduce poorly. Please use only one size of lettering per graphic and a font like Times New Roman, which distinguishes between l (small L) as in HCl (hydrochloric acid) and I (capital i) as in HCI (iodocarbene).

Table 1. Guide for preparing graphics

Letter Size	Font	Maximum Graphic Width[a] 1-Column Format	2-Column Format
	Times New Roman		
3.0 mm	12	13 cm	26 cm
3.5 mm	**14**	**15 cm**[b]	–
4.0 mm	**16**	**17 cm**[b]	–
4.5 mm	18	19 cm	–

[a] Most graphics are in 1-column format. [b] We prefer lettering of 3.5 or 4.0 mm with maximum graphic widths of 15 or 17 cm, respectively.

The settings for one-column graphics constructed with Chem Draw can be found in the template **eurjourn.zip**, which can be reached by clicking the link "For Authors" on our journal homepage (http://www.eurjic.org). These settings are: Print Setup: Orientation Portrait. Caption and Label Settings: Font Times New Roman, Font Style Standard, Size 12.

Note that the graphical abstract must be in one-column format and in black-and-white.

 © 2005 Wiley-VCH Verlag GmbH & Co. KGaA, Weinheim

These settings help ensure the correct letter-size-to-graphic-width ratio for best reproduction.
Use abbreviations such as R^1, R^2 (not R_2), R′, R″, Ph, Me, Et, *i*Pr, *t*Bu, Ph, Bn (benzyl), Bz (benzoyl), Hal, L, M (metal), X (heteroatom).

4. Crystallographic Data

Authors must deposit the data of X-ray structure analyses in a crystallographic database before submitting their manuscript, so that referees can access the information electronically. The two databases, the Cambridge Crystallographic Data Centre (CCDC) and the Fachinformationszentrum Karlsruhe (FIZ) have the same procedure for the deposition of data and both will be pleased to provide help. In general, you will receive a depository number from the database two working days after electronic deposition. Send your data to the appropriate address below and quote the standard text, including the depository number, in your manuscript.

- **For all compounds without C−H bonds:**

Fachinformationszentrum Karlsruhe (FIZ)
76344 Eggenstein-Leopoldshafen, Germany
Phone: +49-(0)7247/808-205
Fax: +49-(0)7247/808-666
E-mail: crysdata@fiz-karlsruhe.de
FTP: ftp.fiz-karlsruhe.de (under path /pub/csd)
WWW: http://www.fiz-karlsruhe.de (under "Products and Services ")

Further details of the crystal-structure investigation(s) may be obtained from the Fachinformationszentrum Karlsruhe, 76344 Eggenstein-Leopoldshafen, Germany, on quoting the depository number(s) CSD-....

- **For all compounds with at least one C−H bond:**

Cambridge Crystallographic Data Centre (CCDC)
12 Union Road, Cambridge CB2 1EZ, UK
Phone: +44-(0)1223/336-408
Fax: +44-(0)1223/336-033
E-mail: deposit@ccdc.cam.ac.uk
WWW: http://www.ccdc.cam.ac.uk

CCDC-****** contains the supplementary crystallographic data for this paper. These data can be obtained free of charge from The Cambridge Crystallographic Data Centre via www.ccdc.cam.ac.uk/data_request/cif.

NOTE: Please use the free online **Checkcif** service provided by the International Union of Crystallography and submit the Checkcif report along with your manuscript: http://journals.iucr.org/services/cif/checkcif.html.

Finally, before you return your revised manuscript, please update your database entry if necessary.

5. Electronic Supporting Information

A manuscript may include Electronic Supporting Information which will be accessible only on the WWW. Authors must keep a copy to make available to readers who do not have access to the internet. As this material [text, tables, schemes, figures **but not crystallographic (CIF) data**, which must be submitted to either the FIZ or the CCDC] undergoes the peer review process, it must be included, clearly marked as "Supporting Information to be published electronically", when the paper is submitted. The following file formats are accepted: MS Winword or ASCII (*.doc, *.txt), MS Excel (*.xls), Encapsulated Postscript (*.eps), Portable Document Format (*.pdf), graphics embedded in MS Winword; if you wish to submit other formats, please consult the Editorial Office. When preparing such material, authors should keep in mind that — once accepted — it will be made available as provided by the author and not edited. Material accepted for electronic publication will be available mostly as PDF files (Adobe Acrobat Reader required) by following the Table of Contents link of EurJIC's WWW home page. A standard text will be added on the first page of the article in the printed version:

- Supporting information for this article is available on the WWW under http://www.eurjic.org or from the author.

The supporting information file must start with the title of the paper, the authors and the CASSI abbreviation of the journal to which it was submitted (e.g. *Eur. J. Inorg. Chem.*).

6. Basic Keyword List

To increase the relevance of articles found by search engines of Wiley InterScience, we have compiled a keyword catalogue common to our chemistry journals that is printed here and is also available online (http://www.eurjic.org).

To assist you in finding keywords they are listed according to categories. You may choose keywords from any category. As with all such records, a few guidelines facilitate the catalogue's use, and these are briefly explained below:
1. As many as possible, but at least two, of the maximum of five keywords assigned to an article must come from this list.
2. Named reactions will be incorporated only in exceptional cases. Generally the reaction type is selected instead. For example, Diels−Alder reactions will be found under "Cycloadditions" and Claisen rearrangements under "Rearrangements".
3. Heteroanalogues of compounds are mainly classified under the C variants, for example, (hetero)cumulenes, (hetero)dienes. A few aza and phospha derivatives are exceptions.
4. Compounds with inorganic components that are central to the article are listed under the element, for instance, iron complexes under "Iron". Some group names like "Alkali metals" exist alongside the names of important members of the group like "Lithium". In such cases the group name is used for these members only when comparative studies are described. The members not appearing separately are also categorised under the group name.
5. A keyword in the form "N ligand" is only chosen if a considerable portion of the paper deals with the coordination of any ligand ligating through the atom concerned.
6. Spectroscopic methods are assigned as keywords only if the article is about the method itself, or if the spectroscopic technique has made an important contribution to the problem under investigation.
7. "Structure elucidation" is intended only if the crux of the paper is a structural elucidation or if a combination of several spectroscopic techniques were needed for conclusive solution of the structure.
8. An attempt has been made to avoid synonyms and to select more general concepts rather than specialized terms. Thus, the term "Double-decker complexes" is excluded in favour of "Sandwich complexes".

This list will be a "living" catalogue to be flexible enough to absorb the new developments in chemistry. We therefore welcome all suggestions from our authors that might improve its user-friendliness.

 © 2005 Wiley-VCH Verlag GmbH & Co. KGaA, Weinheim

Guidelines for Authors

Analytical Chemistry and Spectroscopic Methods

Analytical methods
Circular dichroism
Cyclic voltammetry
Electron diffraction
Electron microscopy
Electrophoresis
ENDOR spectroscopy
EPR spectroscopy
EXAFS spectroscopy
Fluorescence spectroscopy
Gas chromatography
High-throughput screening
Ion chromatography
Ion exchange
IR spectroscopy
Isotopic labeling
Laser spectroscopy
Liquid chromatography
Luminescence
Mass spectrometry
Moessbauer spectroscopy
Neutron diffraction
NMR spectroscopy
Photoelectron spectroscopy
Plasma chemistry
Raman spectroscopy
Rotational spectroscopy
Scanning probe microscopy
Sensors
Surface analysis
Surface plasmon resonance
Trace analysis
UV/Vis spectroscopy
Vibrational spectroscopy
Water chemistry
X-ray absorption spectroscopy
X-ray diffraction
ZEKE spectroscopy

Biological Chemistry and Chemical Biology (including Biochemistry, Bioinorganic Chemistry, Bioorganic Chemistry, Medicinal Chemistry and Molecular and Cell Biology)

Allosterism
Amino acids
Angiogenesis
Antibiotics
Antibodies
Antifungal agents
Antigens
Antisense agents
Antitumor agents
Antiviral agents
Azapeptides
Azasugars
Bioinformatics
Bioinorganic chemistry
Biological activity
Biomimetic synthesis
Bioorganic chemistry
Biophysics
Biosensors
Biosynthesis
Biotransformations
C-Glycosides
Carbohydrates
Carbon dioxide fixation
Carotenoids
Cell adhesion
Cell recognition
Cerebrosides
Chaperone proteins
Cobalamines
Cofactors
Combinatorial chemistry
Cyclitols
Cyclodextrins
Cytokines
DNA
DNA cleavage
DNA damage
DNA methylation
DNA recognition
DNA replication
DNA structures
Dopamines
Drug delivery
Drug design
Electron transport
Enzyme models
Enzymes
Fibrous proteins
Fluorescent probes
Gene expression
Gene sequencing
Gene technology
Genomics
Glycoconjugates
Glycolipids
Glycopeptides
Glycoproteins
Glycosides
Glycosylation
Growth factors
Helical structures
Heme proteins
Hormones
Hydrolases
Immobilization
Immunoassays
Immunochemistry
Immunology
Inhibitors
Ion channels
Ionophores
Isomerases
Ligases
Lipids
Lipophilicity
Lipoproteins
Liposomes
Lyases
Medicinal chemistry
Membrane proteins
Membranes
Metabolism
Metalloenzymes
Metalloproteins
Micelles
Molecular evolution
mRNA
Mutagenesis
Natural products
Neurochemistry
Neurotransmitters
Nitrogen fixation
Nitrogenases
Nucleic acids
Nucleobases
Nucleosides
Nucleotides
Oligonucleotides
Oligosaccharides
Oxidoreductases
Peptide nucleic acids
Peptides
Peptidomimetics
Pheromones
Phospholipids
Photoaffinity labeling
Photosynthesis
Phytochemistry
Polyketides
Polymerase chain reaction
Prodrugs
Prostaglandins
Protein design
Protein engineering
Protein folding
Protein models
Protein modifications
Protein structures
Proteins
Proteomics
Proton transport
Radiopharmaceuticals
Receptors
Redox chemistry
Ribonucleosides
Ribozymes
RNA
RNA recognition
RNA structures
Sensitizers
Sequence determination
Sialic acids
Siderophores
Signal transduction
Sphingolipids
Steroids
Structure−activity relationships
Terpenoids
Toxicology
Transferases
tRNA
Vesicles
Vitamins

Catalysis

Asymmetric catalysis
Autocatalysis
Biphasic catalysis
Catalytic antibodies
Enzyme catalysis
Heterogeneous catalysis
Homogeneous catalysis
Phase-transfer catalysis
Supported catalysts

 © 2005 Wiley-VCH Verlag GmbH & Co. KGaA, Weinheim

Coordination Chemistry: Compound Classes

Cage compounds
Chelates
Clathrates
Cluster compounds
Cuprates
Dendrimers
Heterometallic complexes
Metallacycles
Metallocenes
Nitrogen oxides
Polyoxometalates
Sandwich complexes
Ylides

Coordination Chemistry: Ligand Classes

Alkene ligands
Alkyne ligands
Allyl ligands
Arene ligands
As ligands
Bridging ligands
Carbene ligands
Carbonyl ligands
Carboxylate ligands
Carbyne ligands
Cyclopentadienyl ligands
Diene ligands
Dioxygen ligands
Fluorinated ligands
Hydride ligands
Isocyanide ligands
Macrocyclic ligands
N ligands
N,O ligands
N,P ligands
O ligands
Oxo ligands
Peroxo ligands
Phosphane ligands
P ligands
S ligands
Si ligands
Tridentate ligands
Tripodal ligands
Vinylidene ligands

Coordination Chemistry: Methodology and Reactions

Carbon dioxide fixation
Chemical vapor deposition
Chiral resolution
Crystal engineering
Ligand design
Matrix isolation
Metathesis
Neighboring-group effects
Nitrogen fixation
O−O activation
Oxidation
Radical reactions
Reduction
Ring-opening polymerization
Solvent effects
Solvolysis
Substituent effects
Template synthesis

Coordination Chemistry: Structure

Agostic interactions
Aurophilicity
Charge transfer
Cooperative effects
Coordination modes
Donor−acceptor systems
Electron-deficient compounds
Electronic structure
Electrostatic interactions
Fluxionality
Helical structures
Host−guest systems
Hydrogen bonds
Inclusion compounds
Isolobal relationship
Jahn−Teller distortion
Ligand effects
Metal−metal interactions
Multiple bonds
Noncovalent interactions
Pi interactions
Stacking interactions
Structure elucidation
Through-bond interactions
Through-space interactions

Elements and Element Groups

Actinides
Alkali metals
Alkaline earth metals
Aluminum
Antimony
Argon
Arsenic
Barium
Beryllium
Bismuth
Boron
Bromine
Cadmium
Calcium
Carbon
Cerium
Cesium
Chalcogens
Chlorine
Chromium
Cobalt
Copper
Deuterium
Fluorine
Gallium
Germanium
Gold
Group 13 elements
Group 14 elements
Hafnium
Halogens
Helium
Hydrogen
Indium
Iodine
Iridium
Iron
Krypton
Lanthanides
Lanthanum
Lead
Lithium
Magnesium
Manganese
Mercury
Molybdenum
Neon
Nickel
Niobium
Nitrogen
Noble gases
Osmium
Oxygen
Palladium
Phosphorus
Platinum
Pnicogens
Potassium
Rare earths
Rhenium
Rhodium
Rubidium
Ruthenium
Samarium
Scandium
Selenium
Silicon
Silver
Sodium
Strontium
Sulfur
Tantalum

 © 2005 Wiley-VCH Verlag GmbH & Co. KGaA, Weinheim

Technetium
Tellurium
Thallium
Tin
Titanium
Tungsten
Uranium
Vanadium
Xenon
Ytterbium
Yttrium
Zinc
Zirconium

Environmental and Atmospheric Chemistry

Anions
Atmospheric chemistry
Cations
Chlorine
Computer chemistry
Crop protection agents
Cycloaddition
Denitrification
Desulfurization
Environmental chemistry
Fluorine
Gas-phase reactions
Green chemistry
Halogenation
Kinetics
Molecular dynamics
Molecular modeling
Nitrogen oxides
Oxidation
Ozone
Peroxides
Photochemistry
Photolysis
Photooxidation
Radical ions
Radical reactions
Radicals
Reaction mechanisms
Reactive intermediates
Sensors
Toxicology
Trace analysis
Waste prevention
Water chemistry

Inorganic Chemistry

Alanes
Allotropy
Alloys
Aluminosilicates
Amalgams
Amorphous materials
Anions
Automerization
Autoxidation
Azides
Bond theory
Boranes
Borates
Carbene homologues
Carbides
Carboranes
Cations
Chain structures
Chromates
Clathrates
Cluster compounds
Cyanides
Electron-deficient compounds
Fluorides
Halides
High-pressure chemistry
Host–guest systems
Hydrates
Hydrides
Hypervalent compounds
Inclusion compounds
Intercalations
Intermetallic phases
Isoelectronic analogues
Isomers
Layered compounds
Lewis acids
Lewis bases
Main group elements
Metal–metal interactions
Mixed-valent compounds
Nitrides
Nonstoichiometric compounds
Organic–inorganic hybrid composites
Perovskite phases
Peroxides
Phosphaalkenes
Phosphaalkynes
Phosphanes
Phosphazenes
Platinates
Pnictides
Polyanions
Polycations
Polychalcogenides
Polyhalides
Polymorphism
Polyoxometalates
Radical ions
Radicals
Silanes
Silicates
Sol–gel processes
Solid-phase synthesis
Solid-state reactions
Solid-state structures
Solvothermal synthesis
Spinel phases
Stannanes
Subvalent compounds
Synthesis design
Titanates
Topochemistry
Transition metals
Transuranium elements
Valence isomerization
Vanadates
Zeolite analogues
Zeolites
Zincates
Zintl anions
Zintl phases

Materials Science: General

Alloys
Amorphous materials
Automerization
Block copolymers
Ceramics
Charge-carrier injection
Chemical vapor deposition
Chemical vapor transport
Clays
Cluster compounds
Colloids
Conducting materials
Copolymerization
Crystal engineering
Crystal growth
Cyclooligomerization
Cyclotrimerization
Dendrimers
Doping
Energy conversion
Fullerenes
Gels
Glasses
Holography
Imprinting
Intercalations
Interfaces
Intermetallic phases
Ladder polymers
Layered compounds
Liquid crystals
Materials science
Mechanical properties
Membranes
Mesophases
Mesoporous materials
Metal–metal interactions
Metallomesogens
Micelles
Microporous materials
Monolayers
Nanostructures
Nanotechnology
Nanotubes
Nonlinear optics
Polymerization
Polymers
Ring-opening polymerization
Scanning probe microscopy
Semiconductors
Sensitizers
Sensors

 © 2005 Wiley-VCH Verlag GmbH & Co. KGaA, Weinheim

Superconductors
Surface chemistry
Thin films
Vesicles
Zeolite analogues
Zeolites

Miscellaneous

History of science

Organic Chemistry: Compound Classes

Alcohols
Aldehydes
Alkaloids
Alkanes
Alkenes
Alkynes
Allenes
Allylic compounds
Amides
Amines
Amino acids
Amino alcohols
Amino aldehydes
Amphiphiles
Anhydrides
Anions
Annulenes
Arenes
Arynes
Azides
Azo compounds
Azomethine ylides
Betaines
Biaryls
Calixarenes
Carbanions
Carbenes
Carbenoids
Carbocations
Carbocycles
Carbohydrates
Carboxylic acids
Carotenoids
Catenanes
Cations
Cavitands
Crown compounds
Cryptands
Cumulenes
Cyanides
Cyanines
Cyclodextrins
Cyclophanes
Dendrimers
Diazo compounds
Dyes/Pigments
Enols
Enones
Enynes
Fatty acids
Fragrances
Fullerenes
Fused-ring systems
Heterocycles
Hydrazones
Hydrides
Hydrocarbons
Ketones
Lactams
Lactones
Ladder polymers
Macrocycles
Mannich bases
Medium-ring compounds
Metallacycles
Natural products
Nitrogen heterocycles
Oxygen heterocycles
Peroxides
Pheromones
Phosphorus heterocycles
Phthalocyanines
Polycycles
Polymethines
Porphyrinoids
Quinodimethanes
Quinones
Radical ions
Radicals
Rotaxanes
Schiff bases
Small ring systems
Spiro compounds
Steroids
Sulfonamides
Sulfur heterocycles
Surfactants
Terpenoids
Ylides
Zwitterions

Organic Chemistry: Methodology and Reactions

Acylation
Aldol reactions
Alkylation
Allylation
Amination
Annulation
Aromatic substitution
Aromaticity
Asymmetric amplification
Asymmetric catalysis
Asymmetric synthesis
Automerization
Autoxidation
Biomimetic synthesis
C−C activation
C−C coupling
C−H activation
C1 building blocks
Carbonylation
Carboxylation
Chiral auxiliaries
Chiral pool
Cleavage reactions
Combinatorial chemistry
Cracking
Cross-coupling
Cyclization
Cycloaddition
Cyclotrimerization
Dehydrogenation
Dihydroxylation
Dimerization
Domino reactions
Electrocyclic reactions
Electrophilic addition
Electrophilic substitution
Elimination
Ene reaction
Epoxidation
Flash pyrolysis
Glycosylation
Grignard reaction
Halogenation
Heck reaction
High-pressure chemistry
Hydroamination
Hydroboration
Hydroformylation
Hydrogen transfer
Hydrogenation
Hydrolysis
Hydrosilylation
Hydrostannation
Hydroxylation
Immobilization
Insertion
Ionic liquids
Isomerization
Lithiation
Metalation
Michael addition
Molecular diversity
Multicomponent reactions
Nucleophilic addition
Nucleophilic substitution
Olefination
Oligomerization
Oxidation
Oxygenation
Ozonolysis
Perfluorinated solvents
Pericyclic reaction
Phosphorylation
Photooxidation
Polymerization
Protecting groups
Protonation
Radical reactions
Rearrangement
Reduction
Retro reactions
Ring contraction
Ring expansion
Sigmatropic rearrangement
Solid-phase synthesis
Solvent effects
Solvolysis
Steric hindrance

 © 2005 Wiley-VCH Verlag GmbH & Co. KGaA, Weinheim

Substituent effects
Synthesis design
Synthetic methods
Template synthesis
Topochemistry
Total synthesis
Transesterification
Umpolung
Wittig reactions

Organic Chemistry: Stereochemistry and Structures

Atropisomerism
Chemoselectivity
Chiral resolution
Chirality
Configuration determination
Conformation analysis
Conjugation
Diastereoselectivity
Enantioselectivity
Hyperconjugation
Kinetic resolution
Regioselectivity
Strained molecules
Structure elucidation
Tautomerism
Valence isomerization

Physical Chemistry and Chemical Physics (including Electrochemistry, Kinetics, Photochemistry, Radiochemistry, Thermodynamics and Theoretical Chemistry)

Ab initio calculations
Absorption
Acidity
Adsorption
Basicity
Biophysics
Bond energy
Bond theory
Calorimetry
CARS (Coherent Anti-Stokes Raman Scattering)
Charge-carrier injection
Charge transfer
Chemisorption
Chromophores
Colloids
Computer chemistry
Conducting materials
Conical intersections
Crystal engineering
Crystal growth
Cyclic voltammetry
Density functional calculations
Donor–acceptor systems
Doping
Electrochemistry
Electron microscopy
Electron transfer
ELF (Electron Localization Function)
Energy conversion
Exchange interactions
Femtochemistry
Fluorescence
Fluorescent probes
Fractals
FRET (Fluorescence Resonance Energy Transfer)
Gas-phase reactions
Gels
Glasses
Group theory
Heats of formation
High-pressure chemistry
High-temperature chemistry
Hot-atom chemistry
Hydrophobic effect
Imaging agents
Ion pairs
Ion–molecule reactions
Ionization potentials
Isotope effects
Isotopes
Kinetics
Langmuir–Blodgett films
Laser chemistry
Lewis acids
Lewis bases
Linear free energy relationships
Liquid crystals
Liquids
Low-temperature studies
Magnetic properties
Matrix isolation
Mesophases
Metallomesogens
Metastable compounds
Microreactors
Molecular dynamics
Molecular electronics
Molecular modeling
Monolayers
Nanotechnology
Neighboring-group effects
Nonequilibrium processes
Phase diagrams
Phase transitions
Photochemistry
Photochromism
Photolysis
Physisorption
Plasma chemistry
Polarized spectroscopy
Quantum chemistry
Radiochemistry
Radiopharmaceuticals
Reaction mechanisms
Reactive intermediates
Redox chemistry
Salt effect
Semiempirical calculations
Single-molecule studies
Singlet oxygen
Sol–gel processes
Solvatochromism
Spin crossover
Statistical mechanics
Statistical thermodynamics
Structure–activity relationships
Superacidic systems
Supercritical fluids
Thermochemistry
Thermodynamics
Time-resolved spectroscopy
Transition states
Viruses
Voltammetry

Supramolecular Chemistry

Aggregation
Host–guest systems
Molecular devices
Molecular evolution
Molecular recognition
Nanostructures
Pi interactions
Receptors
Self-assembly
Supramolecular chemistry

 © 2005 Wiley-VCH Verlag GmbH & Co. KGaA, Weinheim

Ordered Meso- and Macroporous Binary and Mixed Metal Oxides

Moises A. Carreon[a,b] and Vadim V. Guliants*[a]

Keywords: Mesoporous / Macroporous / Transition metal oxides / Catalytic applications

A critical review is provided of the principles guiding the synthesis of meso- and macroporous metal oxides on multiple length scales in the presence of surfactant mesophases and colloidal arrays of monodisperse spheres, and correlations between the synthesis conditions and the properties of the resulting meso- and macroporous oxides, such as thermal stability, pore structure, elemental and nanophase compositions of the inorganic wall, etc. The thermal stability of mesostructured metal-oxide phases, in particular, is discussed in terms of charge-matching at the organic–inorganic interface, the strength of interactions between inorganic species and surfactant headgroups, the flexibility of the M–O–M bond angles in the constituent metal oxides, the Tammann temperature of the metal oxide, and the occurrence of redox reactions in the metal-oxide wall. The ordered meso- and macroporous transition-metal-oxide phases are highly promising for a range of potential applications in separations, chemical sensing, heterogeneous catalysis, microelectronics, and photonics as, respectively, insulating layers of low-dielectric-constant and photonic-bandgap materials. Furthermore, the functionalization of the internal pore surfaces in these materials and deposition of functional nanoparticles within the pores offer numerous new possibilities for molecular engineering of catalytic and other advanced nanostructured materials displaying quantum-confinement effects. The emerging catalytic applications of these novel metal-oxide phases are discussed in particular detail.

(© Wiley-VCH Verlag GmbH & Co. KGaA, 69451 Weinheim, Germany, 2005)

1. Introduction

Highly ordered mesoporous inorganic oxides were first reported by the researchers at Mobil Research and Development Corporation over a decade ago.[1–3] These materials, with well-defined pores up to about 3 nm in diameter, belong to the novel family of so-called M41S aluminosilicate molecular sieves[1–3] that break past the pore-size constraints of largely microporous zeotypes. Extremely high surface areas (>1000 m^2/g), finely tuned pore sizes, and flexible wall-compositions are among the many desirable properties that have made such mesoporous materials the focus of great interest for applications in heterogeneous catalysis. The preparation of the M41S phases represents a

[a] Department of Chemical and Materials Engineering, University of Cincinnati,
Cincinnati, OH 45221-0012, USA
E-Mail: Vadim.Guliants@uc.edu
[b] Current address: Materials Chemistry Research Group, Chemistry Department, University of Toronto,
80 Saint George Street, Toronto, Ontario, Canada M5S 3H6

Vadim V. Guliants was born in Baku, USSR. He studied Chemistry and obtained a Diploma with Highest Honors at Moscow State University in 1987. He received his Ph.D. in Chemistry at Princeton University in 1995 with Profs. J. B. Benziger and S. Sundaresan in the area of materials chemistry of catalytic vanadium-phosphorus oxides. After holding a research position in the area of molecular modeling, synthesis and physico-chemical characterization of crystalline microporous oxides at Praxair Inc. (Tonawanda, NY), he joined the Chemical Engineering Faculty at the University of Cincinnati in 1999. He is currently Associate Professor and Associate Head of the Department of Chemical and Materials Engineering at the University of Cincinnati. His current research is focused on the self-assembly of ordered meso- and macroporous metal oxides for applications in heterogeneous catalysis, biocatalysis and separations.

Moises A. Carreon was born in Morelia, Mexico, in 1974. He received his Bachelor's degree in Chemical Engineering at the Universidad Michoacana (UMSNH) in 1996, where he also received his Master's degree in Materials Science and Engineering in 1999. He obtained his Ph.D. degree in the Department of Chemical and Materials Engineering at the University of Cincinnati in 2003 under the supervision of Professor Vadim V. Guliants working on the hierarchical design of novel macro- and mesoporous vanadium-phosphorus-oxide phases for the selective oxidation of lower hydrocarbons. Currently he is a post-doctoral fellow in the Materials Chemistry Research Group, Chemistry Department at University of Toronto. His research centers on the molecular engineering of ordered periodic mesoporous transition metal oxides for nanotechnological applications.

MICROREVIEWS: This feature introduces the readers to the authors' research through a concise overview of the selected topic. Reference to important work from others in the field is included.

 DOI: 10.1002/ejic.200400675 © 2005 Wiley-VCH Verlag GmbH & Co. KGaA, Weinheim

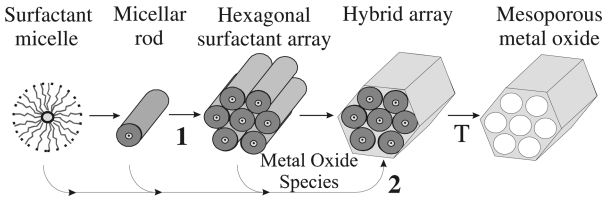

Figure 1. Self-assembly of mesoporous metal oxides possessing a 2D hexagonal pore structure.

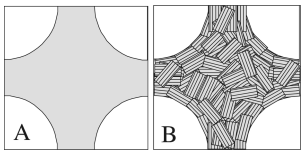

Figure 2. Mesoporous structures with (A) amorphous and (B) nanocrystalline walls.

new approach in organic-template-assisted synthesis, where, instead of individual organic molecules (as in the case of zeotypes), self-assembled molecular aggregates or supramolecular assemblies are employed as the structure-directing agents.

The discovery of M41S silicas has stimulated the search for other ordered mesostructured materials with non-silicate compositions over the last decade.[4] The general self-assembly pathway for mesostructured metal oxides is illustrated in Figure 1. Mesoporous *mixed* metal oxides are particularly promising as heterogeneous catalysts because of their tunable surface compositions, metal oxidation states (via organic-inorganic interfacial chemistry), and wall structures − amorphous or nanocrystalline (Figure 2). Furthermore, their electronic properties and the surface structure, which are critical parameters for the catalytic performance of any catalyst, are expected to change greatly in the nano regime,[5] thereby offering new, exciting possibilities for the molecular engineering of mixed metal oxides with unique catalytic, optical, and electrical properties. Ordered macroporous materials templated by ordered arrays of colloidal spheres and other shapes have recently attracted considerable attention from the scientific community.[6] The macroscale templating approach consists of the three distinct processing steps shown in Figure 3. First, the interstitial voids of the monodisperse colloidal latex sphere (approx. 100 nm to 50 μm in diameter) arrays are filled with precursors of various classes of materials, such as ceramics, semiconductors, metals, monomers, etc. In the second step, the precursors condense around the spheres and form a solid framework. Finally, the spheres are removed by either calcination or solvent extraction to form the 3D ordered macroporous structures. In this paper we critically review the current state of the art for the synthesis and emerging catalytic applications of meso- and macroporous *binary* and *mixed* metal oxides. We first discuss the structures and self-assembly mechanisms of mesoporous oxides for *silicate* compositions, since these compositions have been investigated in much greater detail than structurally similar metal oxides. We then outline synthesis guidelines for the novel

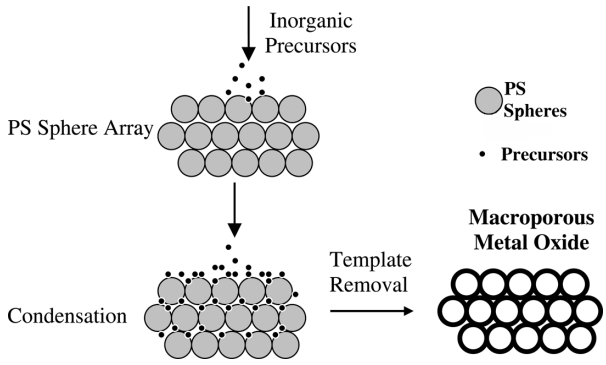

Figure 3. General procedure for the synthesis of highly ordered *macroporous* mixed-metal oxide phases employing polystyrene (PS) spheres.

mesoporous metal oxides with flexible compositions and improved thermal stability that are desirable for applications in heterogeneous catalysis. Finally, we discuss recent advances in the macroscale self-assembly of mixed metal oxides and their emerging catalytic applications.

2. Ordered Mesostructured Oxides

2.1. Structural Characteristics

Several common ordered pore-structures encountered in the M41S family are shown in Figure 4. The 2D hexagonal phase with *P6mm* symmetry, templated by hexagonal close-packed cylindrical arrays of surfactants, is the most common ordered structure. Lamellar phases are unstable upon surfactant removal, which causes the collapse of the expanded layered structures. Various cubic phases have also been reported. In the case of mesoporous silica, the bicontinuous cubic gyroid phase with *Ia3d* symmetry is found in alkali-catalyzed syntheses. This phase, with its system of interconnected pores, is much more attractive than the 2D hexagonal phase for applications requiring diffusion of species into and out of the pore network. The *Pm3n* phase templated by spherical surfactant micelles in a cubic close-packed arrangement is found in both acid- and alkaline-catalyzed syntheses of mesoporous silica.[1–3]

Figure 4. Representative members of the M41S family.

 © 2005 Wiley-VCH Verlag GmbH & Co. KGaA, Weinheim

The pioneering work of Kresge et al.[1,3] and Beck et al.[2] involved only alkaline-catalyzed syntheses, and the silicates reported in their papers are referred to as MCM-41 (*P6mm*, the 2D hexagonal phase), MCM-48 (*Ia3d*, the cubic phase), and MCM-50 (the lamellar phase). The 2D hexagonal mesoporous silicas prepared by Inagaki et al.[7] from surfactant-intercalated kanemite are referred to as FSM-16. Subsequent reaction in an acidic medium led to ordered mesoporous silicas with similar pore symmetries but distinct wall properties: SBA-1 (*Pm3n*, the cubic phase), SBA-2 ($P6_3/mmc$, the 3D hexagonally packed spherical micelle phase), and SBA-3 (*P6mm*, the 2D hexagonally packed cylinders).[8] Other surfactant-templated phases include disordered materials with a wormhole network of channels, such as KIT-1[9] and MSU-1,[10] a well-defined intergrown cubic hexagonal phase STAC-1,[11] and ordered nonionic alkyl-EO_x-templated materials, for example the cubic SBA-11 (*Pm-3m*) and 3D hexagonal SBA-12 ($P6_3/mmc$).[12] Using the same methodology, triblock-copolymer-templated materials with much larger pores have also been synthesized in acidic systems, for example the 2D hexagonal (*P6mm*) SBA-15[13] and cubic cage (*Im-3m*) SBA-16 structures.[12]

Several aspects of the ordered mesoporous oxides have been reviewed by Brinker (recent advances in porous inorganic materials),[14] Vartuli et al. (synthesis of the M41S family),[15] Stucky et al. (biomimetic synthesis of mesoporous materials),[16] Raman et al. (porous silicates templated by surfactants and organosilicate precursors),[17] and Guliants et al. (mesoporous inorganic films and membranes).[18] Several synthetic strategies for the molecular design of mesoporous oxides, including those with non-siliceous compositions, have been recently reviewed by Soler-Illia et al.[19] However, thermal stability considerations for mesostructured metal oxides were not discussed in those reviews.

2.2. Self-Assembly Mechanisms And Stability Considerations

2.2.1. Liquid Crystal Templating Mechanism

A "liquid crystal templating" (LCT) mechanism of formation was proposed by the Mobil researchers, based on the similarity between liquid crystalline surfactant assemblies (i.e. lyotropic phases) and M41S.[1–3] Two mechanistic pathways were proposed to explain formation of MCM-41 containing 2D hexagonal arrays of cylindrical mesopores: 1) condensation and cross-linking of the inorganic species at the interface with a pre-existing hexagonal lyotropic liquid crystal (LC) phase, and 2) ordering of the surfactant molecules into the 2D hexagonal mesophase mediated by the inorganic species, followed by their condensation and cross-linking.

In both pathways the inorganic species, which are negatively charged at the high synthesis pH, preferentially interact with the positively charged alkylammonium headgroups of the surfactants and condense into a solid, continuous framework. The resulting organic-inorganic mesostructure could be alternatively viewed as a hexagonal array of surfactant micellar rods embedded in a silica matrix. Removal of the surfactant produces an open mesoporous MCM-41 framework. These mesophases, with pore diameters greater than 2.5 nm, generally display type IV nitrogen adsorption–desorption isotherms at 77 K, which are characteristic of mesoporous materials with an ordered, unimodal pore-size distribution. The second mechanistic pathway of LCT was proposed as a cooperative self-assembly of the alkylammonium surfactant and the silicate precursor species below the critical micelle concentration (CMC).[1–3] It is well established that no preformed LC phase is necessary for the MCM-41 formation, but, to date, the mechanistic details of the MCM-41 synthesis have not yet been fully agreed upon. Several mechanistic models have been advanced, although all share the basic idea that the silicate species promote LC phase formation below the CMC.[1–3]

2.2.2. Inorganic-Species-Driven Self-Assembly

Davis et al.[20] found that a hexagonal LC phase does not develop during the MCM-41 synthesis, based on an in situ ^{14}N NMR spectroscopic study. They proposed that, under the synthesis conditions reported by Mobil, the formation of MCM-41 begins with the deposition of two to three monolayers of silicate precursors onto isolated surfactant micellar rods. The silicate-encapsulated rods are randomly ordered, and eventually pack into a hexagonal mesostructure. Heating and aging completes the condensation of the silicates into the obtained MCM-41 mesostructure.

Steel et al.[21] postulated that surfactant molecules assemble directly into the hexagonal LC phase upon addition of the silicate species, based on their ^{14}N NMR spectroscopic data. The silicates organize into layers, with rows of cylindrical rods intercalated between the layers. Aging the mixture causes the layers to pucker and collapse around the rods, which then transform into the surfactant-containing 2D hexagonal MCM-41 structure.

The "charge density matching" mechanistic model proposed by Monnier et al.[22] and Stucky et al.[23] suggests that MCM-41 could be derived from a lamellar phase. The initial phase of the synthesis mixture is layered, as detected by X-ray diffractometry (XRD), due to the electrostatic attraction between the anionic silicates and the cationic surfactant head-groups. As the silicate species begin to condense, the charge density is reduced. Accompanying this process, a curvature is introduced into the layers to maintain the charge-density balance with the surfactant headgroups, which transforms the lamellar phase into a hexagonal mesostructure.

Under synthesis conditions that prevent condensation of the silicate species, such as low temperatures and high pH (ca. 14), a truly cooperative self-assembly of the silicates and surfactants was found to be possible. Firouzi et al.[24] showed, through ^{2}H and ^{29}Si NMR spectroscopy and neutron scattering, that a micellar solution of CTAB (cetyltrimethylammonium bromide) transforms into a hexagonal phase in the presence of silicate anions. This is consistent with the effect of electrolytes on micellar phase-transi-

 © 2005 Wiley-VCH Verlag GmbH & Co. KGaA, Weinheim

tions.[25] The silicate anions ion-exchange with the surfactant halide counterions to form a "silicatropic liquid crystal" (SLC) phase that involves silicate-encrusted cylindrical micelles. This SLC phase exhibited behavior very similar to typical lyotropic systems, except that the surfactant concentrations were much lower and the silicate counterions were reactive.[26] Heating the SLC phase caused the silicates to condense irreversibly into MCM-41. Firouzi et al.[24,26] also demonstrated that, in addition to the charge-balance requirement (i.e. electrostatic interaction), there was preferential bonding of the alkylammonium head-groups to multi-charged D4R (double four-ring, $[Si_8O_{20}]^{8-}$) silicate anions under the high pH conditions.

All these previous theories have regarded the formation of MCM-41 as a series of events that occur homogeneously throughout an aqueous solution. Recent work has shown, however, that MCM-41 might be formed heterogeneously. Regev,[27] for example, has found evidence for MCM-41 intermediate structures in the form of clusters of rod-like micelles "wrapped" by a coating of silicate from low-temperature transmission electron microscopy (TEM) and small-angle X-ray scattering. These clusters of elongated micelles were found before precipitation occurred. According to Regev,[27] as the reaction progresses, the silicate species diffuse to, and deposit on, the individual surfaces of the micelles within the cluster. The clusters of elongated micelles therefore eventually become clusters of silicate-covered micelles. Thus, the clusters of micelles serve as nucleation sites for MCM-41 formation.

Frasch et al. have proposed a modified mechanism for the formation of 2D hexagonal silica.[28] The silicate–counterion exchange at the micellar surface was followed by fluorescence techniques using pyrene or dipyrenylpropane as fluorescent probes. The variation of the properties of CTAB and CTACl (cetyltrimethylammonium chloride) micelles upon the successive addition of a large excess of base [NaOH or TMAOH (tetramethylammonium hydroxide)] and silicate species was studied. Their results showed that, prior to the formation of the ordered mesophase, the interactions between the silicate species and surfactant micelles are weak. They therefore proposed a new model for the formation of mesostructured silica in which the key step is the formation of siliceous pre-polymers. According to this model, the growing pre-polymers interact with an increasing number of surfactant molecules to form hybrid silica-surfactant micellar aggregates. Further polymerization of these complexes takes place during the precipitation/aging process to give ordered mesostructured silica. The formation of mesoscopically ordered silica/surfactant composites under acidic synthesis conditions was studied by time-resolved in situ small-angle X-ray scattering (SAXS) using synchrotron radiation.[29] The various proposed mechanisms of formation of ordered mesostructured phases have been recently reviewed by Zana et al.[30] Recently, Linden et al.[31] have followed the initial stages of the formation of SBA-15 by in situ SAXS/XRD using synchrotron radiation. The authors proposed that the first step in the formation of an SBA-15 mesostructure is the liquid–liquid phase separation of spherical P123-silicate hybrid micelles; nucleation and growth of the 2D hexagonal phase then takes place.

2.3. Thermal Stability of Mesostructured Phases

The high thermal stability of mesostructured phases is perhaps the most critical requirement for their applications in heterogeneous catalysis. In general, the thermal stability of mesostructured metal-oxide phases depends on: (1) the degree of charge-matching at the organic–inorganic interface, (2) the strength of interactions between inorganic species and surfactant head-groups, (3) the flexibility of the M–O–M bond angles in the constituent metal oxides, (4) the Tammann temperature of the metal oxide, and (5) the occurrence of redox reactions in the metal-oxide wall.

The *charge-matching* at the organic–inorganic interface enables control over the wall composition and facilitates cross-linking of the inorganic species into a robust mesostructured network. A knowledge of the electrokinetic behavior (i.e. the isoelectric points) of the inorganic species in solution is required for fine-tuning electrostatic and other interactions at the inorganic–organic interface in order to obtain thermally stable mesoporous phases.[32] The isoelectric points of common transition-metal solid oxides and hydroxides are shown in Table 1.[32,33] The presence of strong *covalent bonds* between metal-oxide species and surfactant head-groups, for example metal–N bonds, means that harsh conditions, such as combustion, are required for surfactant

Table 1. Isoelectric points of common transition metal oxides.[28,29]

Metal oxide	Isoelectric point	General comments
V_2O_5	0.5	oxovanadium(v) species
MoO_3	<0.5	NA
Nb_2O_5	<0.5	NA
TiO_2	4.7	natural rutile
TiO_2	6.2	synthetic rutile, anatase
ZrO_2	4.0	natural mineral
ZrO_2	6.7	$Zr(NO_3)_4$ + NaOH
Y_2O_3 (hydrous)	8.95	$Y(NO_3)_3$ + NaOH
NiO	10.3 ± 0.4	NiO
WO_3 (hydrous)	0.5	Na_2WO_4 + HCl
MgO	12.4 ± 0.3	MgO
MnO_2	4.0–4.5	$Mn(NO_3)_2$ + HCl
α-Fe_2O_3	8.7	hydrolysis of $Fe(NO_3)_3$ solution
γ-Fe_2O_3	6.7 ± 0.2	precipitation of FeOOH
Fe_3O_4	6.5 ± 0.2	natural magnetite

Table 2. Tammann temperatures of some common transition-metal oxides.[5,34]

Metal oxide	M. p. (K)	Tammann temp. (K)
V_2O_5	943	472
MoO_3	1068	534
Nb_2O_5	1784	892
TiO_2	2128	1064
ZrO_2	2983	1492
NiO	2257	1129
WO_3	1745	873
MgO	3125	1563
MnO	1923	962
Fe_2O_3	1838	919

 © 2005 Wiley-VCH Verlag GmbH & Co. KGaA, Weinheim

removal, and these may lead to collapse of the mesostructure. Similarly, *rigid M–O–M bond angles* that are unable to accommodate the curvature of the inorganic–organic interface may result in the formation of only lamellar or dense metal-oxide phases. On the other hand, metal-oxide species should possess low lattice mobility at elevated temperatures in order to prevent transformation of the mesostructured metal oxides into more thermodynamically stable dense phases. The mobility of metal ions or atoms in a crystalline metal oxide increases rapidly in the vicinity of its *Tammann temperature*, defined as $0.5–0.52T_m$, where T_m is the melting point in Kelvin.[34] Therefore, it is not surprising that the low Tamman temperature of some transition- metal oxides[5,35] translates into a limited thermal stability of the corresponding mesostructures (Table 2). Finally, the structural collapse of mesophases may be caused by *redox reac-*

Table 3. Mesostructured and mesoporous *binary* metal oxides.

Framework composition	Precursors	Mesophase and unit cell parameter (Å)	Ref.
Vanadium oxide[c]	ammonium vanadate, CTACl, H_2O	lamellar (c = 27) hexagonal (a = 39)	[56]
Vanadium oxide[a]	V_2O_5, DTABr, H_2O	lamellar (c = 21.6)	[57]
Vanadium oxide[a]	oxovanadium triisopropoxide, dodecylamine, ethanol/H_2O	lamellar (c = 23–28) hexagonal (a = 34.6)	[58]
Vanadium oxide[a]	VCl_4, triblock copolymers, ethanol	mesostructured (lack of long-range order) (maximum d-spacing 111)	[59]
Vanadium oxide[c]	$VOSO_4$, P123, ethanol/H_2O	wormhole like (channel spacing 30–40)	[60]
Molybdenum oxide[a]	Na_2MoO_4, H_2MoO_4, DTABr, H_2O	lamellar (c = 22.9)	[57]
Molybdenum oxide[a]	$MoCl_5$, triblock copolymers, ethanol	mesostructured (lack of long-range order) (maximum d-spacing 100)	[59]
Niobium oxide[b]	niobium ethoxide, sodium dodecyl sulfate, sodium dodecyl phosphonate, primary alkylamines	lamellar (c = 25) hexagonal (a = 32–52), cubic (d-spacing 48)	[61,62]
Niobium oxide[b]	$NbCl_5$, tribolck copolymers, ethanol	hexagonal (a = 32–52)	[59,63]
Titanium oxide[b]	$TiCl_4$, triblock copolymers, ethanol	hexagonal (a = 117) cubic (a = 107)	[59,63]
Titanium oxide[c]	peroxytitanates, CTACl, H_2O	lamellar (c = 31) hexagonal (d-spacing 41)	[69]
Titanium oxide[a]	titanium isopropoxide, CTABr, ethylene glycol, NaOH,	mesostructured (lack of long-range order) (channel spacings 50)	[70]
Zirconium oxide[b]	zirconium n-propoxide, H_2O, carboxylates, alkyl sulfonates, dodecyl sulfate, primary alkylamines	lamellar, hexagonal, mesostructured (lack of long-range order) (maximum d-spacings = 16–40)	[80]
Zirconium oxide[b]	$ZrCl_4$, triblock copolymers, ethanol	hexagonal (a = 122)	[59,63]
Zirconium oxide[a]	$Zr(OC_2H_5)_4$, CTABr, ethylene glycol, NaOH	mesostructured (lack of long-range order) (channel spacings = 31–37)	[70]
Hafnium oxide[b]	$HfCl_4$, H_2O, CTABr	wormhole-like (channel spacings 40)	[82]
Hafnium oxide[b]	$HfCl_4$, triblock copolymers, ethanol	mesostructured (lack of long-range order) (maximum d-spacing 124)	[59,63]
Tantalum oxide[b]	tantalum ethoxide, octadecylamine, H_2O	hexagonal (a = 33–50)	[86]
Tantalum oxide[b]	$TaCl_5$, triblock copolymers, ethanol	hexagonal (a = 78)	[59,63]
Nickel oxide[a]	$NiSO_4$ $6H_2O$, CTABr, H_2O	disoredered + lamellar (channel spacings = 46)	[89]
Yttrium oxide[a]	$Y(NO_3)_3$ $6H_2O$, dodecylsulfate, H_2O, urea	lamellar (c = 40), hexagonal (a = 62)	[91]
Rhenium oxide[a]	methyltrioxo-rhenium, primary alkylamines, H_2O	disordered + lamellar (channel spacings = 25–33)	[92]
Manganese oxide[c]	$MnCl_2$ $4H_2O$, H_2O, $C_{12}H_{25}NMe_3OH$	lamellar, disordered (d-spacing 42)	[90]
Tungsten oxide[a]	H_2WO_4, DTABr, H_2O	Keggin-type structure	[57]
Tungsten oxide[b]	WCl_6, triblock-copolymers, ethanol	mesostructured (lack of long-range order) (maximum d-spacing 126)	[59,63]
Iron oxide	iron(III) ethoxide, CTAB	mesoporous and lamellar	[96,97]

[a] Thermally unstable. [b] Thermally stable. [c] Partially stable (up to 625 K) or after solvent extraction.

 © 2005 Wiley-VCH Verlag GmbH & Co. KGaA, Weinheim

tions occurring in the metal-oxide wall during surfactant removal or catalytic reaction.

Accordingly, we review below the synthesis, pore structures, elemental and nanophase compositions, thermal stability, and emerging applications of mesoporous metal oxides in heterogeneous catalysis.

2.4. Binary Mesostructured Metal Oxides

The mesostructured binary transition metal oxides that are promising for applications in heterogeneous catalysis are summarized in Table 3. High-resolution TEM images of the three most-common porous structures observed in mesostructured metal oxides − lamellar, hexagonal, and cubic − are illustrated in Figure 5, Figure 6 and Figure 7, respectively. Metal oxides containing 2D hexagonal and cubic mesopore structures are characterized by the unimodal pore-size distributions and type IV adsorption–desorption isotherms typical of mesoporous materials (Figure 8).

Vanadium-, molybdenum-, and niobium-based mixed metal oxides are particularly promising as catalysts or catalytic supports for selective oxidation reactions.[36–50] For example, supported vanadium oxide catalysts are widely used for the partial oxidation of olefins,[51] aromatics,[52] and methanol,[53] the selective catalytic reduction of NO_x,[54] and ammoxidation of aromatics.[55] Molybdenum- and niobium-based oxides are catalytically active in the selective oxidation and reduction of hydrocarbons.[39] Mesostructured vanadium oxide was reported for the first time by Luca et al.[56] They suggested that anionic vanadate species self-assemble with the cationic head-group of cetyltrialkylammonium chloride surfactant (CTACl) in alcoholic media to produce the mesostructure. Although the structural order was retained after low-temperature calcination, both porosity studies and thermogravimetric analysis indicated that the surfactant was only partially removed, thus leading to thermally unstable phases. Other attempts to prepare mesoporous vanadium oxide have been reported. Whittingham et al.[57] have prepared a mesostructured, layered vanadium oxide by hydrothermal treatment of V_2O_5 in the presence of dodecyltrimethylammonium bromide (DTAB). However, the DTAB surfactant was not removed upon cation exchange. Sayari et al.[58] have synthesized lamellar and hexagonal mesostructured vanadium oxide by hydrolyzing oxovanadium triisopropoxide in the presence of dodecylamine, although no attempt was made to remove the surfactant. A mesostructured vanadium oxide obtained from the assembly of triblock copolymers with VCl_4 has been re-

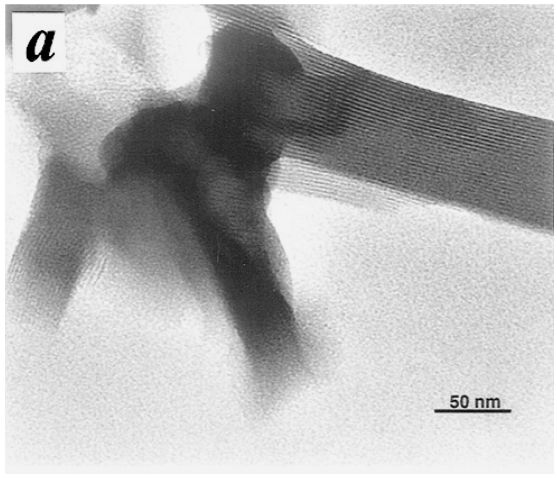

Figure 5. TEM of *lamellar* mesostructured vanadium oxide.[58]

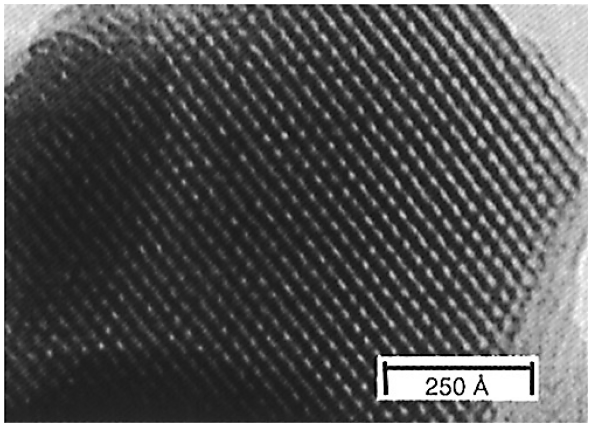

Figure 6. TEM of *hexagonal* mesoporous niobium oxide.[61]

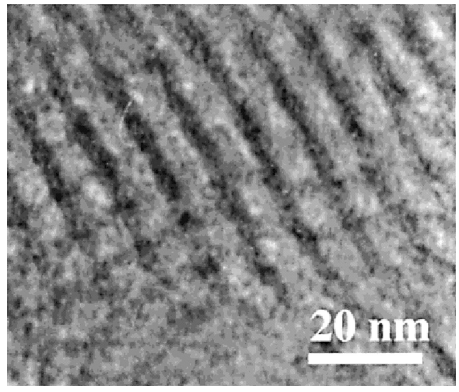

Figure 7. TEM image of *cubic* mesoporous zirconium oxide.[59]

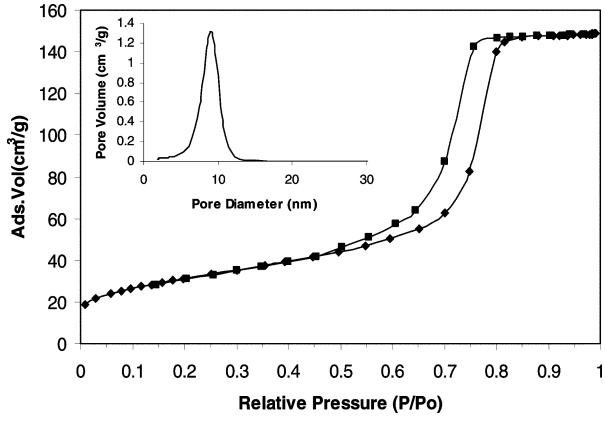

Figure 8. Nitrogen adsorption–desorption isotherms and BJH pore-size distribution plot (inset) for mesoporous niobium.

 © 2005 Wiley-VCH Verlag GmbH & Co. KGaA, Weinheim

ported by Stucky et al.,[59] although it lost its mesoscopic order upon calcination. Liu et al.[60] have reported the synthesis of mesostructured V_2O_5 by electrochemical deposition using nonionic surfactants. The final wormhole mesostructure was found to contain 3–4 nm pores. Although the complete removal of the surfactant was reported by the authors, no surface area or pore data were provided. The low Tammann temperature of V_2O_5 (472 K), as well as the cycles of redox reactions during surfactant combustion, account for the poor thermal stability of this oxide system.

Mesostructured molybdenum oxides have also been reported by Whittingham et al.[57] and Stucky et al.[59] A layered structure with a repetitive interplanar distance of 22 Å was prepared by hydrothermal reaction of molybdic acid with DTAB.[57] A mesostructured molybdenum oxide with larger ordering lengths (100 Å) was successfully synthesized by the assembly of triblock copolymers with $MoCl_5$. However, the obtained mesostructured materials were unstable upon calcination.[57,59] Incomplete condensation of the inorganic frameworks, the cycles of redox reactions during surfactant combustion, as well as the low Tammann temperature of the constituent metal oxides, are mainly responsible for the poor thermal stability of these metal-oxide mesophases. On the other hand, thermally stable mesoporous Nb_2O_5 has been obtained by Ying et al.[61,62] in the presence of amines as structure-directing agents. They proposed a ligand-assisted liquid-templating mechanism for the formation of thermally stable mesoporous Nb and Ta oxides. The formation of covalent bonds between Nb and the N-atom of the amine template directs the interaction between the organic and inorganic species. The improved thermal stability of mesoporous niobium oxide is probably due to the relatively high Tammann temperature of niobium oxide (892 K). High specific surface areas (approx. 600 m^2/g) were observed for these mesophases after template removal by acid/solvent extraction with triflic acid. In a different approach, Stucky et al.[59,63] have prepared mesoporous niobium oxide with pores of about 50 Å and a surface area of about 190 m^2/g using triblock copolymers as structure-directing agents. The improved thermal stability of these phases was attributed to weak H-bonding interactions between the template and inorganic walls, making the template removal possible without damaging the inorganic framework.

Titania possesses very interesting catalytic, photochemical, and electrical properties, which make it an attractive system for several applications. For instance, TiO_2 is commonly used as a photocatalyst.[64,65] Crystalline titania modified with sulfate ions is an active catalyst for low-temperature esterification, isomerization, alkylation, and cracking of hydrocarbons.[66,67] Other applications of titania are as an electrode material in electrochemistry, a capacitor in electronics, in humidity and gas sensors, and in photovoltaic solar cells.[68]

Mesoporous TiO_2 has been obtained using different synthetic approaches.[59,63,69,70] Stucky et al.[59,63] have employed hydrogen bonding to direct the synthesis and obtained large-pore (ca. 65 Å) hexagonal and cubic mesoporous TiO_2 with a specific surface area of 200 m^2/g. Interestingly, the walls of the TiO_2 mesostructure were built of nanocrystalline anatase, which is promising for potential applications in photocatalysis, since anatase is the most photocatalytically active crystalline phase of TiO_2.[65] In a different approach, charge matching between cationic surfactants and anionic peroxytitanates was used to produce mesoporous TiO_2 [69] with a surface area of 310 m^2/g and a pore size of about 36 Å. The final mesostructure, however, was found to lack long-range order, thus suggesting the formation of a wormhole pore network. A nonaqueous route for the preparation of mesostructured titania was studied by Kuperman et al.[70] The final mesoporous structures, with surface areas of up to 420 m^2/g, were thermally stable only when silanol groups were incorporated into the inorganic framework by the gradual exposure of the inorganic framework to 7–15 wt.-% of Si_2H_6. The composite was then heated to 125 °C and the excess of unreacted Si_2H_6 was removed under vacuum.

Zirconium oxide is a particularly interesting catalytic system, and has found many uses in chemical and petrochemical processes because it possesses acidic, basic, and redox properties. For example, it is an effective catalyst for the selective formation of isobutane and isobutene from synthesis gas,[71,72] and acts as a superacid (sulfated ZrO_2) in the isomerization and cracking of paraffins and alkylation and acylation of aromatics.[73–76] Crystalline *stable* tetragonal or cubic zirconia is required in most catalytic applications. For example, the tetragonal ZrO_2 phase has been claimed as the active phase in *n*-butane isomerization[76,77] and alkylation and acylation of aromatic compounds.[78,79]

Wong and Ying[80] have studied the formation of mesostructured ZrO_2 directed by anionic and nonionic surfactants. High-surface-area (360 m^2/g), mesoporous ZrO_2 was obtained only when alkyl phosphate surfactants were used. They associated the enhanced thermal stability of the final mesoporous structure with the presence of the phosphate groups on the ZrO_2 surface after the surfactant removal. However, no specific details were provided for the role of phosphate in stabilizing the ZrO_2 mesostructure.

Other mesoporous zirconia with pore sizes between 58 and 62 Å[59,63] and wormlike zirconia[70] have been also reported. For instance, thermally stable mesoporous zirconia with a surface area of about 280 m^2/g has been prepared,[59] although the mesostructure was only stable when SiO_2 was incorporated into the zirconia wall during synthesis. Mesoporous zirconia with both amorphous[70] and tetragonal nanocrystalline[59,63] walls has also been prepared, thus allowing an exploration of the role of the extended crystal structure on the catalytic properties of this metal oxide.

Sulfated hafnium oxide is another attractive superacid system for selective alkane isomerization.[81] The thermally stable hafnium oxide reported by Sayari et al.[82] exhibits a high surface area (ca. 200 m^2/g) and a wormhole pore-structure without long-range structural order. The pore diameter evaluated by the Horvath–Kawazoe method was only 11 Å, thus indicating the formation of a microporous phase. Mesoporous HfO_2 with large pores (70 Å) has also been

 © 2005 Wiley-VCH Verlag GmbH & Co. KGaA, Weinheim

prepared by a neutral self-assembly approach employing Pluronic P-123 as a structure-directing agent.[59,63]

Tantalum oxide is yet another interesting metal-oxide system with potential applications in photocatalysis, such as photocatalytic water splitting.[83–85] Hexagonal mesoporous Ta_2O_5 with pore sizes in the 20–40 Å range and specific surface areas of up to 500 m^2/g was reported for the first time by Antonelli and Ying.[86] The synthesis was directed by covalent bonding between the primary alkylamine headgroups and Ta atoms in a ligand-assisted liquid-templating mechanism. Similar to the synthesis of mesoporous Nb_2O_5, mesoporous Ta_2O_5 has also been obtained in the presence of nonionic surfactants (Pluronic P-123) by neutral self-assembly directed by hydrogen-bonding interactions.[59,63]

Other reported mesostructured binary oxides with potential applications in catalysis are NiO and MnO_2. Nickel-oxide-based catalysts have been used successfully in the partial oxidation of olefins, nitroxidation of hydrocarbons into nitriles, and partial oxidation of isobutylene into methylacrolein.[87] Manganese oxides show catalytic activity in the oxidation of alkanes.[88] Shih et al.[89] have investigated the synthesis of mesostructured nickel oxide in the presence of CTAB. The NiO mesostructure was thermally unstable and collapsed upon thermal treatment. Since NiO exhibits a high Tammann temperature (1129 K), the limited stability of this mesostructured oxide may be associated with a low degree of cross-linking, redox reactions, and rigidity of the Ni–O–Ni framework. However, the addition of sodium silicate during the NiO synthesis produced a thermally stable mesostructure with a surface area of 530 m^2/g. The addition of silicate (Si/Ni = 0.2–0.5) is believed to strengthen the inorganic mesostructure. It was suggested that the resultant mesophase had a structure of SiO_4 tetrahedra linked together by Ni atoms on every corner to produce a robust mesostructure. Mesostructured lamellar manganese oxide has been prepared by Suib et al.[90] by employing $(C_{12}H_{25})NMe_3OH$ as a surfactant. However, no information was provided on the surfactant removal from these lamellar manganese oxides.

Other reported mesostructured transition-metal oxides include Y_2O_3, WO_3, and ReO_2: yttrium oxide is used as a matrix for solid-state lasers and luminescent systems,[91] rhenium oxides exhibit interesting electrical conductivity properties,[92] while tungsten oxides have found applications as semiconductor materials.[59,63] Lamellar and hexagonal mesostructured yttrium oxides have been prepared by employing anionic surfactants, such as sodium dodecylsulfate.[91] In this case, removal of the surfactant led to high surface areas (ca. 550 m^2/g) and mesoporous structures with pores of about 30 Å. Mesostructured rhenium oxide exhibiting wormhole channels occupied by surfactant molecules has been prepared employing dodecylamine as a surfactant.[92] However, no porosity was observed after the surfactant removal, indicating that the mesostructure collapses under oxidizing conditions, while the pores were blocked with residual pyrolyzed carbon after a thermal treatment in an inert atmosphere. Mesostructured tungsten oxide has been prepared in the presence of DTAB; however, DTAB removal by cation exchange was not successful.[57] High surface area WO_3 (125 m^2/g) displaying pores of about 50 Å has also been prepared by employing Pluronic P-123 as a structure-directing agent.[59,63]

Iron oxide is another interesting catalytic system that has been used to catalyze the oxidative dehydrogenation of hydrocarbons. For example, hematite is an active catalyst for transforming butane[93,94] and ethylbenzene.[95] High-surface-area (274 m^2/g) mesoporous iron oxides have been synthesized by sonochemical synthesis.[96,97] Iron(III) ethoxide was used as the inorganic precursor and CTAB as surfactant. Since the self-assembly process is directed by strong coulombic interactions, the improved thermal stability of mesostructured iron oxide may be associated with its relatively high Tamman temperature (919 K).

In addition to the above-mentioned applications in catalysis, these metal oxides (Table 3) may also be used as mesoporous hosts for the growth of functional nanoparticles, such as supported metals for applications in catalysis and semiconductor nanoparticles for electronic and optical applications.[98–100]

2.5. Mesostructured Mixed-Metal Oxides

Mixed-metal oxides are particularly attractive as catalysts for the selective oxidation of lower alkanes. For example, vanadium-phosphorus oxides are highly active and selective for the oxidation of *n*-butane to maleic anhydride.[101–105] The recently reported bulk mixed Mo-V-Sb-Nb oxides[101–104] are active and selective for the oxidation of propane to acrylic acid, and it is well known that the most efficient catalysts for propane ammoxidation are based on bulk mixed-metal oxides (i.e. vanadium antimonates or promoted molybdates).[110,111] V-Mg oxides are very active in the oxidative dehydrogenation of light alkanes to alkenes.[112,113] Mesostructuring of these complex metal-oxide systems offers the possibility to design novel catalytic materials with high surface areas, controlled porosities, tunable surface compositions, and improved catalytic performance. Examples of mesostructured mixed-metal oxides most relevant to applications in catalysis are summarized in Table 4.

One of the most remarkable mixed-metal oxide systems is the vanadium-phosphorus-oxide (VPO) system for the oxidation of *n*-butane to maleic anhydride, which is the only industrial vapor-phase oxidation of an alkane.[101–105] Few reports exist on the synthesis of mesostructured VPO materials. Iwamoto et al.[114] have reported the synthesis of mesostructured hexagonal vanadium-phosphorus oxide materials using alkyltrimethylammonium surfactants (C_{12}–C_{16}). However, the mesostructure in these materials was lost upon calcination. Doi and Miyake[115] have reported the synthesis of a novel hexagonal mesostructured VPO compound from the VPO catalyst precursor $VOHPO_4 \cdot 0.5H_2O$ by surfactant intercalation and subsequent hydrothermal treatment. However, these materials suffer from poor thermal stability and low phosphorus content that are detri-

 © 2005 Wiley-VCH Verlag GmbH & Co. KGaA, Weinheim

Table 4. Mesostructured and mesoporous *mixed* metal oxides.

Framework composition	Precursors	Mesophase and unit cell parameter (Å)	Ref.
VPO[a]	$VOSO_4$, H_3PO_4, C_nTACl, H_2O, n = 12,14,16	hexagonal (maximum d-spacing 33–40)	[114]
VPO[a]	$VOHPO_4$ 0.5 H_2O, C_{14}TAMCl, H_2O	lamellar (channel spacing 30) and hexagonal (NA)	[115]
VPO[a]	V_2O_5, H_3PO_4, CTABr, H_2O, V metal	hexagonal (ICMUV-2) (a = 42–46)	[116]
VPO[a]	V_2O_5, H_3PO_4, CTAOH, CTACl, H_2O, V metal	lamellar (c = 32.2), hexagonal (a = 50.5), cubic (a = 85.4)	[117]
VPO[a]	$VOSO_4$, $VO(acac)_2$, H_3PO_3, H_3PO_4, H_2O, alkylamines, sulfonates, phosphonates, alkyltrimethylammonium bromide	lamellar (c = 23–32), hexagonal (a = 40–44), cubic (a = 92–99)	[118–121]
Nb-Ta oxide[b]	$NbCl_5$, $TaCl_5$, P123, MeOH, EtOH, ButOH, HexOH	disordered mesoporous structure (channel spacings 30–40)	[122]
Nb-V oxide[b]	vanadium triisopropoxy oxide, niobium ethoxide, octadecylamine, ethanol/H_2O	wormhole pore structure (maximum d-spacing 40)	[123]
Mg-V oxide[b]	$V(acac)_3$, $MgCl_2$, DTABr, MTABr, CPBr, CTABr, SDS, SDBS, BTABr, H_2O	lamellar (c = 35), wormlike channel spacing 38), hexagonal (a = 36)	[112,113]
TiO_2-PO_4 [b]	titanium methoxide, H_3PO_4, dodecanol + 5 EO tenside, H_2O	disordered hexagonal (maximum d-spacing 62)	[124]
TiO_2-PO_4 [b]	titanium propoxide, H_3PO_4, H_2O $CH_3(CH_2)_n$ $N(CH_3)_3Br$, n = 7,11,15,17,	hexagonal (a = 33–55) lamellar	[125]
TiO_2-PO_4 [b]	titanium isopropoxide, H_3PO_4, C $_n$ TABr (n = 16, 18, 20), H_2O	hexagonal (d-spacing 27–36)	[126]
ZrO_2-SO_4, ZrO_2-PO_4 [b]	zirconium propoxide, ammonium sulfate, H_3PO_4, CTABr, OTABr, H_2O	hexagonal (a = 30–51)	[127]
Y_2O_3-ZrO_2 [b]	zirconium ethoxide, ethylene glycol, yttrium acetate, CTABr, H_2O	wormhole (d-spacings 42–46)	[138]
Y_2O_3-ZrO_2 [a]	$ZrO(NO_3)_2$, Y_2O_3, SDS, urea, H_2O	lamellar (c = 32–35) and hexagonal (a = 44)	[139]
Zr-Ti oxide[b]	$ZrCl_4$/$TiCl_4$, triblock copolymers, ethanol	NA (d-spacing 103)	[59,63]
Zr-W oxide[b]	$ZrCl_4$/WCl_4, triblock copolymers, ethanol	NA (d-spacing 100)	[59,63]

[a] Thermally unstable. [b] Thermally stable.

mental for their use as heterogeneous catalysts. Amoros et al.[116] have described the synthesis of hexagonal mesostructured oxovanadium phosphates, denoted as ICMUV-2. However, the removal of surfactant from their vanadium phosphates resulted in the collapse of the mesostructure. Mizuno et al.[117] have described the synthesis of hexagonal, cubic, and lamellar mesostructured vanadium-phosphorus-oxides that lose their structural order upon calcination. We recently reported novel hexagonal, cubic, and lamellar VPO phases, which displayed improved thermal stability, desirable chemistries (i.e. the P/V ratios and vanadium oxidation states), and pore structures for the partial oxidation of lower alkanes.[118–120] We demonstrated in these studies that the V oxidation state and the surface P/V ratios can be tuned, respectively, by post-synthesis thermal treatment (i.e., oxidizing vs. reducing atmosphere) and inorganic–organic interfacial chemistry (i.e., the surfactant functionality).[118,121] The N_2 adsorption–desorption isotherm measurements indicated that these novel VPO phases have a broad size-distribution in the micropore range. However, complete removal of the surfactant and achievement of thermal stability for the mesoporous VPO system still represents a major challenge.[121] The incomplete cross-linking of the VPO framework, its redox properties, and the low Tammann temperature of the constituent oxides have so far prevented the preparation of thermally stable mesoporous VPO phases.

The Nb and Ta oxides possess moderately strong Lewis and Brønsted acidity and are promising as solid-acid catalysts and catalytic supports.[50] The mesoporous mixed Nb/Ta (ca. 1:1) oxide displaying a wormhole pore structure was prepared by a neutral templating method.[122] Interestingly, the resultant mesostructure displayed not only high thermal stability, but also the presence of nanocrystalline walls. However, as the crystallinity of the mesostructure increased with calcination time, the BET surface areas decreased from 168 to 22 m^2/g, suggesting the densification of the final mesostructure. In order to prevent this decrease in surface area, Antonelli et al.[123] have employed the ligand-assisted method to prepare mesoporous V-Nb oxides (5–15 mol.-% V in mesoporous niobium oxide). Although high-surface-area composites (500–830 m^2/g) were reported, only disordered wormhole pore structures were obtained, with walls about 2.0–2.3 nm thick. Chao and Ruckenstein have succeeded in the preparation of mesoporous Mg-V oxides (Mg/V = 0.5–10) with relatively high surface areas (i.e. 70–250 m^2/g) and wormhole-like pores that are promising for the oxidative dehydrogenation of alkanes.[112–113] The pore size of these composites could be fine-tuned by changing the pH. They proposed a self-assembly mechanism in which anionic polyvanadate species associated with an Mg^{2+} cation condense around positively charged surfactant micelles. The thermal stability of this system was attributed to the incorporation of Mg cations into the inorganic oxovanadium

 © 2005 Wiley-VCH Verlag GmbH & Co. KGaA, Weinheim

framework. Figure 9 shows the typical wormhole-like mesoporous structure of mixed transition-metal oxides.

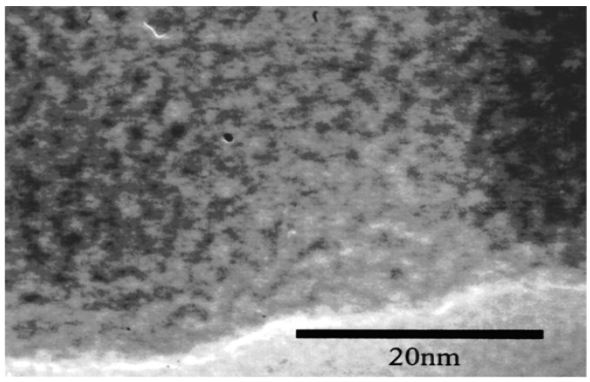

Figure 9. TEM of mesostructured vanadium-magnesium oxide exhibiting wormhole channels occupied by surfactant molecules.[112]

Mesoporous titanium phosphate is another example of a mixed-metal oxide obtained by a templated self-assembly approach.[124–126] Crystalline phosphated titania is catalytically active in the isomerization and alkylation of hydrocarbons.[66–67] Mesoporous titanium phosphate was prepared by a neutral templating route employing poly(ethylene oxide)s as surfactants.[124] The final mesostructure displayed thermal stability and high surface area (≈ 350 m^2/g). The relatively high thermal stability of mesoporous titanium phosphate was associated with a high degree of condensation of the amorphous titanium phosphate framework, which prevents crystallization and densification of the mesostructure. However, the obtained mesostructures were highly disordered, suggesting that weak hydrogen-bonding interactions between the surfactant and inorganic species lead to a decrease in the structural order. The synthesis of mesoporous phosphated titania (P/Ti = 1 and 2) has also been directed by electrostatic interactions.[125] In this case, disordered mesostructures with much higher surface areas (up to 740 m^2/g) and wormhole-like pores were obtained after surfactant extraction. However, the surface area decreased by about 60 % upon calcination. Titanium phosphates possessing ordered hexagonal mesostructure have been obtained by Schüth et al. in the presence of alkyltrimethylammonium bromides.[126] Interestingly, the pore analysis showed a type-I isotherm that is characteristic of microporous materials after surfactant removal by calcination, which suggests the formation of a hierarchical porous structure in which the micropores are most likely incorporated in the walls of the mesostructure.

Low-temperature alkane isomerization is of great interest to the petrochemical industry since branched alkanes are important gasoline products and additives.[104] Superacids, such as ZrO_2-SO_4 and ZrO_2-PO_4, catalyze alkane isomerization and other reactions demanding high acidity.[73–75] Highly ordered and thermally stable hexagonal mesoporous ZrO_2-SO_4 and ZrO_2-PO_4 have been reported by Schüth et al.[127] In these studies, the improved thermal stability was associated with the presence of the sulfate and phosphate groups, which strengthen the walls of ZrO_2. The authors proposed that uncondensed ZrOH groups bond with phosphate groups, thereby increasing the extent of cross-linking and enhancing the stability of the mesophase upon surfactant removal.

Mixed yttrium-zirconium oxide is an example of a catalytic system that is promising for the Fischer–Tropsch synthesis.[128] Yttria is commonly used to stabilize the tetragonal or cubic ZrO_2 phase.[129,130] When Y is incorporated into the ZrO_2 lattice, oxygen vacancies are created to preserve the lattice neutrality. It has been suggested that the active sites for CO hydrogenation are these oxygen vacancies.[128] Mesoporous yttria-zirconia with nanocrystalline walls, wormhole pore channels of about 20 Å, and 100–250 m^2/g BET surface areas has been reported by Ozin et al.,[131] whereas Gedanken et al.[132] have prepared lamellar and hexagonal Y/Zr (1:1) oxide mesostructures by a sonochemical method employing sodium dodecyl sulfate as the surfactant. Mesoporous structures with surface areas of about 245 m^2/g were obtained after surfactant extraction with sodium acetate. However, a nonuniform pore-size distribution was observed, and the mesoporous mixed-metal oxide collapsed upon thermal treatment due to poor cross-linking of the inorganic framework and its redox properties.

The use of nanoparticles as building blocks instead of molecular precursors is an attractive route to mesoporous metal oxides with nanocrystalline walls that display improved thermal stability and show significant promise for structure-sensitive catalytic reactions. Ying et al.[133] have employed colloidal ZrO_2 nanocrystals to prepare mesoporous mixed tungsten-zirconium oxide. They proposed that this self-assembly process is driven by attractive forces between negatively charged metatungstate ions (I^-), positively charged ZrO_2 nanoparticles (C^+), and hydrogen-bonded polymer surfactants (S^0H^+). The same synthesis pathway has been used successfully to prepare mesoporous tungsten-titanium oxide. Honma et al. have reported a novel methodology to prepare ordered mesoporous nanocomposites with crystalline oxide frameworks employing functional nanocrystals as the building blocks.[134] Ordered mesoporous nanocomposites consisting of electrochemically active nanocrystals and semiconductive glass in the TiO_2-P_2O_5-M_xO_y systems (where M is a metal ion) were formed. Other mesoporous mixed-metal oxides, such as Zr-Ti and Zr-W oxides, have also been reported by Stucky et al.[59,63]

3. Ordered Macroporous Oxides

3.1. Structural Characteristics

Colloidal crystals consisting of three-dimensional ordered arrays of monodispersed spheres can be used as novel templates for the preparation of highly ordered macroporous inorganic solids that exhibit precisely controlled pore sizes and highly ordered 3D porous structures. The macroscale templating approach typically consists of three steps. First, the interstitial voids of the monodisperse sphere arrays are filled with precursors of various classes of materials, such as ceramics, semiconductors, metals, monomers,

 © 2005 Wiley-VCH Verlag GmbH & Co. KGaA, Weinheim

etc. In the second step, the precursors condense and form a solid framework around the spheres. Finally, the spheres are removed by either calcination or solvent extraction.

The success of forming macroporous ordered structures is mainly determined by van der Waals interactions, wetting of the template surface, filling of the voids between the spheres, and volume shrinkage of the precursors during the solidification process. The colloidal crystal templating method may be used in combination with sol-gel, salt solution, nanocrystalline, and other precursors to produce the inorganic 3D macrostructures.[6] The colloidal-crystal templates used to prepare 3D macroporous materials include monodisperse polystyrene (PS), poly(methyl methacrylate) (PMMA), and silica spheres. A typical SEM image of a colloidal array of polystyrene spheres used as a template in the synthesis of macroporous inorganic materials is shown in Figure 10. Prior to precursor infiltration, these monodisperse spheres are ordered into close-packed arrays by sedimentation, centrifugation, vertical deposition, or electrophoresis.[135] The final inorganic macroporous structure after the removal of spheres contains the ordered interconnected pore structure shown in Figure 11.

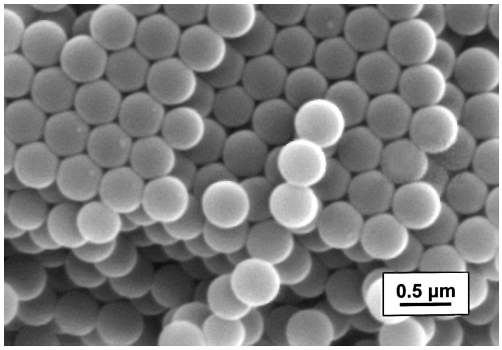

Figure 10. SEM image of an ordered array of ~400 nm polystyrene spheres.[173]

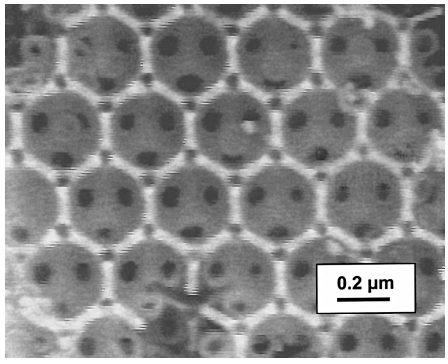

Figure 11. SEM image of a macroporous inorganic material. The walls consist of ~20 nm $(VO)_2P_2O_7$ crystals (modified from ref.[173]).

3.2. Macroporous Binary and Mixed-Metal Oxides

Several synthesis methods have been used in the past to prepare 3D macroporous inorganic materials. These include sol-gel, salt precipitation, nanocrystal infiltration, and polymerization. All these synthesis methods rely on the use of a polymeric or inorganic template, usually in a form of spheres packed in a periodic fashion. Bulk ordered transition metal macroporous oxides prepared by the sol-gel[136–145] and other methods[146–158] are summarized in Table 5 and Table 6, respectively. The most representative methods to prepare inorganic macrostructures are briefly discussed below.

Macroporous inorganic frameworks have been successfully prepared using the sol-gel method, in which metal alkoxides dissolved in alcohol are impregnated into the voids of the colloidal (polymer) sphere arrays. Hydrolysis and condensation take place at the sphere surface to form the inorganic framework. Subsequent heat treatment to remove the polymer spheres results in an ordered macroporous metal oxide. The final macropore dimensions are about 15–30 % smaller than those of the original spheres due to the shrinkage of the inorganic framework. This is caused by a large volume loss during the sol-gel process as the alcohol is evaporated. Significant shrinkage of the inorganic framework during template removal by heat treatment results in severe cracking and loss of long-range order. Therefore the sol-gel method, in combination with heat treatment to remove polymer spheres, has not resulted to date in highly ordered macroporous materials for photonic bandgap applications, for which long-range order is required. Several single, binary, and tertiary oxides have been prepared using sol-gel chemistry: SiO_2;[136] TiO_2, ZrO_2, SiO_2;[137] TiO_2, ZrO_2, Al_2O_3;[138] SiO_2, TiO_2, ZrO_2, Al_2O_3, Fe_2O_3, Sb_4O_6,

Table 5. Macroporous transition-metal oxides prepared using colloidal sphere templates by a sol-gel method.

Colloidal template	Macroporous framework	Pore structure	Ref.
ca. 0.35 µm oil microemulsion droplets	TiO_2, ZrO_2	> 50 nm hcp	Imhof and Pine 1997[137]
ca. 0.47 µm ps	TiO_2, ZrO_2	320–360 nm hcp	Holland et al. 1998[138]
0.4–0.7 µm ps	TiO_2, ZrO_2, Fe_2O_3, Sb_4O_6, WO_3, $YZrO_2$	250–500 nm ffc/hcp	Holland et al. 1999[139]
ca. 0.4 µm ps	vanadium phosphorus oxides	300–400 nm hcp	Carreon and Guliants 2001[141] 2002[142]
ca. 1 µm ps	TiO_2, ZrO_2, $PbTiO_3$, $Pb(ZrTi)O_3$	disordered hcp 800–1000 nm	Gundiah and Rao 2000[143]
0.64 µm ps	TiO_2, ZrO_2	disordered hcp ~400 nm	Wang et al. 2001[145]

 © 2005 Wiley-VCH Verlag GmbH & Co. KGaA, Weinheim

Table 6. Macroporous transition metal oxides prepared using colloidal sphere templates by other synthesis methods.

Colloidal template	Macroporous framework	Pore structure	Synthesis method	Ref.
0.36–2.92 μm ps	TiO_2	240–2000 nm hcp	liquid phase chemical reaction	Wijnhoven and Vos 1998[146]
ca. 0.4–0.7 μm ps	NiO	250–500 nm hcp	salt precipitation and chemical conversion	Yan et al. 1999[147]
0.6–0.8 μm ps	MgO, NiO, Cr_2O_3, Mn_2O_3, Fe_2O_3, Co_3O_4,	380–550 nm hcp	salt precipitation and chemical conversion	Yan et al. 2000[148]
0.56 μm ps	TiO_2	320–525 nm fcc	nanocrystal incorporation	Subramanian et al. 1999[149]
0.33 μm ps/0.336 μm silica spheres 0.33 μm pmma/0.336 μm silica spheres	TiO_2, ZrO_2	ca. 270–330 nm hcp	inverse opal templating	Colvin et al. 2001[158]

WO_3, $YZrO_2$;[139] SiO_2;[140] V-P-O;[141,142] SiO_2, TiO_2, ZrO_2, $PbTiO_3$, $Pb(ZrTi)O_3$;[143] Eu_2O_3, Nd_2O_3, Sm_2O_3;[144] TiO_2, TiO_2/SiO_2;[145] TiO_2.[146]

Precipitation of metal salts, such as acetates and oxalates, and oxides within the colloidal polymer-sphere arrays, and subsequent chemical conversion of the inorganic precursors, is an alternative method to prepare ordered macroporous structures. This procedure is less sensitive to atmospheric humidity and allows the formation of ordered 3D macroporous structures for compositions difficult to prepare by sol-gel techniques. Yan et al.[147] have reported the synthesis of macroporous NiO with 250–500 nm voids by templated precipitation and subsequent chemical conversion of the inorganic precursors. The metal salt solution (acetates or nitrates) penetrates the void spaces between the spheres, and subsequent calcination of the macrocomposite removes the spheres and produces the desired metal oxide. A number of ordered macroporous inorganic oxides have been prepared by the salt precipitation method: MgO, Cr_2O_3, Mn_2O_3, Fe_2O_3, Co_3O_4.[148]

Ordered macroporous materials may be prepared by filling the void spaces of colloidal sphere arrays with nanoparticles. This method offers the great advantage of incorporating specific nanoparticles of desirable crystalline phases into the wall structure of the macroporous framework. Another major advantage of this method is that it results in very little shrinking and cracking of the 3D framework during template removal. Typically, the pore shrinkage is limited to 5–10 %. Subramania et al.[149] have used monodisperse PS spheres to template colloidal dispersions of silica and titania and form 3D structures with 320–525 nm macropores. Vlasov et al.[150] have used CdSe nanocrystals templated against monodisperse silica spheres to synthesize macroporous CdSe semiconductors.

Polymerization of organic precursors around colloidal silica-sphere arrays is a common method to produce ordered macroporous polymeric materials. The colloidal arrays of spheres are filled with a liquid monomer, which is subsequently polymerized by heat treatment or UV irradiation. Macroporous polyurethane, poly(acrylate/methacrylate), PMMA, polystyrene, epoxy, and poly(methyl acrylate) have been prepared using this methodology.[151–153]

Other miscellaneous techniques for the preparation of inorganic macrostructures include spraying techniques,[154,159] electrodeposition,[155–157,160] and inverse opal templating.[152,158] Spraying techniques have been used mainly in the preparation of macroporous films. Macroporous TiO_2, for example, has been prepared by spray pyrolysis by depositing titanyl acetylacetonate onto silica spheres,[154] and macroporous Au has been synthesized by ion spraying.[159] Electrodeposition techniques offer excellent control over the degree of filling and wall thickness. Growth of the desirable macrostructure occurs galvanostatically or potentiostatically. Macrostructures of CdS, CdSe,[155,156] ZnO,[160] polypyrrole, polyaniline, and poly(bithiophene)[157] have been successfully prepared by electrodeposition. In the inverse opal templating method, 3D macroporous structures prepared by templating with opal structures can be subsequently used to form another opal replica. A wide range of compositions, (TiO_2, ZrO_2, Al_2O_3, polypyrrole, PPV (polyphenylene-vinylene), CdS, AgCl, Au, Ni) [158] have been prepared by this method.

Macroporous vanadium-phosphorus-oxide (VPO) phases with remarkable compositional, structural, and morphological properties have been synthesized by employing monodisperse polystyrene sphere arrays as a template.[141,142] Colloidal polystyrene spheres were ordered into closed-packed arrays by sedimentation or centrifugation. Depending on the choice of VPO source and template-removal method, various crystalline VPO phases were obtained. The macroscale-templated synthesis produced VPO phases with unprecedentedly high surface areas (75 m^2/g), desirable macroporous architectures, optimal bulk compositions (P/V ≈ 1.1), desirable vanadium oxidation states (+4.1 to +4.4), and preferential exposure of the surface (100) planes of vanadyl(IV) pyrophosphate, $VO_2P_2O_7$, which is the proposed active and selective phase for *n*-butane oxidation to maleic anhydride.

The ability to control wall thickness, pore size, and elemental and phase compositions makes colloidal sphere array templating a versatile, attractive, and flexible route for the synthesis of highly ordered macroporous materials with fine-tuned pore and framework architectures. The wall thickness of macroporous structures can be controlled by the hydrolysis/condensation rates of the inorganic precursors,[139] the packing of the PS spheres,[142] and by forming core-shell structures at the sphere surface (i.e. deposition of polyelectrolyte multilayers at the sphere surface).[145] The pore size can be easily manipulated in the range of the sphere sizes, which are typically between 100 nm and 50 μm

 © 2005 Wiley-VCH Verlag GmbH & Co. KGaA, Weinheim

in diameter. Even smaller spheres (20 nm) can be prepared and used to template small-pore materials.[6] Furthermore, it is possible to build macroporous structures containing a specific crystalline phase by incorporating nanoparticles of desired phases in the voids of sphere arrays.[149,150] Depending on the choice of the inorganic sources and template-removal method, various crystalline phases can be obtained.[142] This suggests that the most critical aspects in the preparation of these macroporous structures are the ability of the precursors to infiltrate and condense between the spaces of the colloidal spheres without swelling or destroying the template, as well as the ability to avoid excessive grain growth, as this leads to a decrease in macroporosity and structural order.

4. Emerging Catalytic Applications

4.1. Mesoporous Metal Oxides

Finely tuned pore sizes, metal oxide wall structures and compositions, high surface areas, and enhanced accessibility of the active surface sites in ordered mesoporous metal oxides are highly attractive for diverse catalytic applications. A thorough review of emerging applications of mesoporous transition metal oxides in catalysis is given here. Reported examples of catalytic mesoporous metal oxides are summarized in Table 7.

Some early examples of catalytic mesoporous silicates have been reviewed by Sayari.[159] More recently, Ogawa et al.[160] have reported the use of Al-containing mesoporous silica films as nanoreactors for organic photochemical reactions. An adsorbed azobenzene derivative incorporated in the film exhibited photochemical isomerization upon UV/Vis irradiation at temperatures as low as 80–300 K. However, no comparison with conventional nonmesoporous systems was conducted. Ikeue et al.[161] have reported Ti-containing porous silica films that exhibit high photocatalytic activity in the reaction of CO_2 with H_2O to produce CH_4 and CH_3OH as the main products. The quantum yield of these mesoporous Ti-silica films was 0.28 %, which is significantly higher than the value of 0.02 % obtained with titanium oxides anchored on a transparent porous silica glass (PVG). Such improvement in the reactivity may be attributed to the higher surface area and ordered pore structure of the mesoporous Ti-silica films. Soga et al.[162] have prepared aluminoxanes adsorbed on mesoporous silica that display ethylene polymerization activity in a catalytic system containing bis(cyclopentadienyl)zirconium dichloride. Furuya et al.[163] have used Ti-mesoporous silica to oxidize cyclohexene to cyclohexene oxide with *t*BuOOH in the presence of benzene and cyclohexane with 99 % selectivity at 98 % conversion. Methanol oxidation over Nb_2O_5/SiO_2 and Nb/MCM-41 has been studied by Wachs et al.[164] Although their results showed that the dispersed Nb species in both catalysts were the active and selective sites for methanol oxidation, Nb/MCM-41 displayed higher overall activity due to a better dispersion of isolated NbO_4 species per unit mass of this catalyst.

Only a few reports exist on catalytic applications of mesoporous transition metal oxides. Yussuf et al.[165] have reported the photocatalytic behavior of mesoporous titania films. They found that the photocatalytic activity of the films for the oxidation of NO_x was higher for the mesoporous films than for conventional gel films, probably due to

Table 7. Emerging catalytic applications of mesoporous metal oxides.

Oxide system[a]	Reaction	Product	Reaction conditions	Activity/ selectivity	Ref.
TiO_2	NO photooxidation	NO_2	black light intensity 10 mW/m^2 (λ = 365 nm), 1 ppm NO in 50 % rel. humidity air at 3.0 L/min	15 % NO removal, 10 % NO_2 generation	[165]
NiO-Ta_2O_5	photocatalytic water decomposition	$H_2 + O_2$	0.5 g 4 wt.-% NiO/Ta_2O_5 in 400 mL H_2O, irradiated by high pressure Hg lamp (450 W)	515 μmol/h H_2, 272 μmol/h O_2	[166]
PO_3-TiO_2-Nb_2O_5	2-propanol dehydrogenation	acetone	0.4 g catalyst in 50 mL 1:1 2-propanol/H_2O mixture sparged by 2 mL/min O_2 and irradiated by 150 W Xe lamp	quantum yields[b]: 0.0089 (**TiO_2**) 0.45 (Degussa P25) 0.0041 (**Nb_2O_5**) 0.217 (Nb_2O_5)	[167]
Fe_2O_3-TiO_2	cyclohexane oxidation	cyclohexanol, cyclohexanone, isobutyraldehyde, acetic acid	T = 343 K p = 1 atm time = 15–17 h	conversion = 25.8 % selectivity to cyclohexanol and cyclohexanone = 90 %	[168]
VO_x -TiO_2	propene oxidation	CO + CO_2	T = 500 K p_{O_2} = 6.6 kPa $p_{C_3H_6}$ = 2.4 kPa	activity (min^{-1}) CO = 0.091 CO_2 = 0.279 select. to CO_2 = 75 %	[169]
VPO	*n*-butane oxidation	maleic anhydride	T = 673 K 1.7 % *n*-butane in air space velocity F/V = 55 min^{-1}	*n*-butane conversion = 10 % selectivity to maleic anhydride = 40 %	[121]

[a] Letters in bold refer to the mesoporous oxides. [b] Quantum yield is defined as the molecules of acetone formed per incident photon.

 © 2005 Wiley-VCH Verlag GmbH & Co. KGaA, Weinheim

the higher surface areas of the mesoporous films. In a different study,[166] mesoporous Ta_2O_5 doped with NiO was found to display higher photocatalytic activity than nonporous amorphous and crystalline NiO-Ta_2O_5. It was claimed that the higher surface areas and better NiO dispersion over the mesoporous Ta_2O_5 host were responsible for the superior catalytic performance of these materials. The photocatalytic activity of mesoporous phosphated titanium and niobium oxide catalysts has been studied in the dehydrogenation of 2-propanol to acetone.[167] Surprisingly, a lower activity of the mesoporous Ti and Nb oxides was observed than for the bulk anatase phase. The amorphous nature of the mesoporous walls and the surface defects in these mesoporous oxides are probably responsible for the recombination of photogenerated electron-hole pairs and the poor catalytic performance.

Gedanken et al.[168] have studied the oxidation of cyclohexane to cyclohexanol and cyclohexanone over a mesoporous Fe_2O_3-TiO_2 catalyst. The mesoporous catalysts displayed about a 5 % higher cyclohexane conversion under the same conditions as compared to catalysts in which Fe_2O_3 was incorporated into nonporous TiO_2. Yoshitake and Tatsumi[169] have incorporated vanadium oxide into mesoporous TiO_2 and studied these novel catalysts in propene oxidation reaction. They found that the rate of propane oxidation to CO and CO_2 was about 18 times higher with mesoporous VO_x-TiO_2 catalysts than with conventional VO_x-TiO_2 (i.e. a nonporous TiO_2 matrix). The high surface areas displayed by these mesoporous catalysts and improved dispersion of active surface sites in the mesoporous hosts are responsible for their enhanced catalytic performance.

The catalytic performance of ordered mesostructured vanadium-phosphorus-oxides in selective *n*-butane oxidation has been studied by Carreon and Guliants.[121] Mesostructured VPO was evaluated in the oxidation of *n*-butane to maleic anhydride. Selectivities to maleic anhydride of up to 40 mol-% were observed at 673 K at about 10 % *n*-butane conversion. A conventional organic VPO catalyst containing well-crystallized vanadyl(IV) pyrophosphate, the proposed active and selective phase for *n*-butane oxidation to maleic anhydride, displayed selectivities to maleic anhydride of 50 mol-% under the same reaction conditions. The limited thermal stability of mesostructured VPO during *n*-butane oxidation led to the gradual loss of the structural order and poor catalytic performance. These results further suggested that crystalline vanadyl(IV) pyrophosphate is required for this alkane oxidation reaction.

Other potential applications of mesoporous metal oxides, such as in fuel cells, as semiconductors, cathode materials, superparamagnets, etc., have been discussed recently by He and Antonelli[170] and are outside the scope of this review.

4.2. Macroporous Metal Oxides

Ordered macroporous films and membranes are novel monolithic materials with potential applications in heterogeneous catalysis, bioseparations, as well as membrane supports for the separation of small molecules. Due to their high surface area (up to 230 m^2/g) and unimodal large pores, these macroporous structures are highly attractive for a variety of separation and catalytic applications involving large molecules.

Only a few examples of catalytic applications have been reported for bulk macroporous solids. Stein et al.[171,172] have used ordered macroporous silica as a support for catalytically active species. For instance, they found that γ-$SiW_{10}O_{36}$ polyoxometalate clusters incorporated into the walls of macroporous silica exhibit catalytic activity for the epoxidation of cyclooctene.[171] In another study, they[172] compared different pore structures (macro, meso and nonporous silica surfaces) with the activity of silica samples doped with transition-metal-substituted polyoxometalates (TMSPs). Although the three types of catalysts showed comparable conversions in the epoxidation of cyclohexene to cyclohexene oxide, the open macroporous structure supported a greater number of TMSP clusters at its surface, thus leading to improved cluster retention during the catalytic reaction. The recently reported macroporous VPO represents the first example of a macroporous transition mixed-metal oxide employed in the selective oxidation of lower alkanes.[173] The catalytic performance of this VPO phase was evaluated in the partial oxidation of *n*-butane to maleic anhydride. The observed yield of maleic anhydride was greater than 50 % for macroporous VPO.[173] Under similar reaction conditions, the yield of maleic anhydride was about 40 % for the conventional organic VPO catalyst. The ordered open-pore structures, the high surface areas (>40 m^2/g), and the presence of nanocrystalline $(VO)_2P_2O_7$ in macroporous VPO resulted in improved catalytic performance. The successful preparation of these catalytically active bulk phases ushers in new and exciting opportunities for the design of macroporous films and membranes for various applications in biocatalysis and bioseparations. Other nanotechnological applications of these novel meso- and macroporous metal-oxide phases have been recently reviewed.[18]

5. Concluding Remarks

The present review of mesostructured binary and mixed-metal oxides demonstrates that complete surfactant removal and the attainment of high thermal stability are some of the critical challenges in the synthesis of mesoporous metal oxides. Incomplete cross-linking of the inorganic frameworks, strong covalent bonds between the inorganic species and surfactant molecules, the rigidity of the M–O–M bond angles, the low Tammann temperature of the constituent metal oxides, and bulk redox reactions are among the most notable causes of the limited thermal stability of mesoporous binary and mixed-metal oxides.

Several synthetic strategies are promising to overcome the limited thermal stability of mesostructured transition metal oxides. One proposed strategy is to strengthen the

 © 2005 Wiley-VCH Verlag GmbH & Co. KGaA, Weinheim

inorganic framework by increasing cross-linking with silicate[89] and phosphate[174] species prior to surfactant removal. Another strategy consists in avoiding strong electrostatic interactions at the organic–inorganic interface, instead directing the synthesis through weak hydrogen-bonding interactions, and consequently improving the thermal stability of the final mesostructure.[59,63]

Furthermore, the lattice oxygen mobility during surfactant combustion may be lowered and, as a result, the thermal stability of the mesostructure improved by employing oxides with high Tammann temperatures (Table 1). For example, Nb_2O_5 [61,62] and ZrO_2 [80] mesostructures with relatively high Tammann temperatures (Table 1) display good thermal stability. Similarly, thermally stable mesoporous mixed-metal oxides may be obtained by employing oxides with a high Tammann temperature as the major structural component. For instance, thermally stable mesoporous V-Mg oxide,[112,113] V-Nb oxide,[123] and Y_2O_3-ZrO_2 [138] have been successfully prepared. In all these cases oxides with high Tammann temperature (i.e. Mg, Nb, and Zr oxides) were used as the major component in the mixed-metal oxide system.

The use of a liquid crystalline L_3 phase represents another attractive alternative for the preparation of mesoscopic mixed-metal oxides with open-pore structures without the need for surfactant removal. The L_3 phase consists of a surfactant bilayer forming a sponge-like structure with randomly distributed mesopores interconnected in all three dimensions.[175,176] The pore diameter in the L_3 phase increases with increasing solvent content, thus providing a procedure by which the pore diameter can be tuned to a specific size. Only the solvent, rather than the surfactant molecules, occupies the primary pore volume. Therefore, the void space is immediately available for the condensation of an inorganic framework without the need to remove the surfactant. The only limitation of this approach is that the resultant mesostructures must be used at temperatures below the surfactant decomposition temperature (i.e. about 600 K) to avoid the collapse of the mesostructure.

For many structure-sensitive catalytic applications, such as the selective oxidation of lower alkanes over bulk mixed-metal oxides, it is highly desirable to have a well-defined crystalline catalytic phase. Therefore, the self-assembly of nanocrystalline building blocks into mesostructured metal-oxide phases represents a highly promising method to prepare mesoporous metal oxides with nanocrystalline walls.[140] In this respect, the macroscale-templated synthesis of nanocrystalline mixed-metal oxides is an attractive approach for the design of catalytic phases that possess remarkable ordering on the macroscale (>50 nm for pore architectures) displaying nanocrystalline walls.

Meso- and macroscale self-assembly approaches are particularly attractive for the design of novel catalytic phases on multiple length-scales that possess unique pore structures, flexible compositions, and tunable surface active sites. These unique porous structures with finely tuned surface active sites are highly promising as improved catalysts for a variety of selective alkane oxidation reactions. Moreover, it is expected that these novel model catalytic systems would lead to an improved fundamental understanding of the relationships between the molecular structure and catalytic properties of a broad range of industrially relevant catalytic systems.

[1] C. T. Kresge, M. E. Leonowicz, W. J. Roth, J. C. Vartuli, J. S. Beck, *Natur e* **1992**, *359*, 710.
[2] J. S. Beck, J. C. Vartuli, W. J. Roth, M. E. Leonowicz, C. T. Kresge, K. D. Schmitt, C. T.-W. Chu, D. H. Olson, E. W. Sheppard, S. B. McCullen, J. B. Higgins, J. L. Schlenker, *J. Am. Chem. Soc.* **1992**, *114*, 10834.
[3] C. T. Kresge, M. E. Leonowicz, W. J. Roth, J. C. Vartulli J. C. (Mobil Oil Corp.) US Patent 5098684, **1992**.
[4] F. Schüth, *Chem. Mater.* **2001**, *13*, 3184.
[5] A. T. Bell, *Science* **2003**, *299*,1688.
[6] A. Stein, R. C. Schroden, *Curr. Opin. Solid State Mater. Sci.* **2001**, *65*, 553.
[7] S. Inagaki, Y. Fukushima, K. Kuroda, *J. Chem. Soc. Chem. Commun.* **1993**, 680.
[8] Q. Huo, D. I. Margolese, G. D. Stucky, *Chem. Mater.* **1996**, *8*, 1147.
[9] R. Ryoo, J. M. Kim, C. H. Ko, C. H. Shin, *J. Phys. Chem.* **1996**, *100*, 17718.
[10] S. A. Bagshaw, E. Prouzet, T. J. Pinnavaia, *Scienc e* **1995**, *269*, 1242.
[11] W. Zhou, J. Klinowski, *Chem. Phys. Lett.* **1998**, *292*, 207.
[12] D. Zhao, Q. Huo, J. Feng, B. F. Chmelka, G. D. Stucky, *J. Am. Chem. Soc.* **1998**, *120*, 6024.
[13] D. Zhao, J. Feng, Q. Huo, N. Melosh, G. H. Fredickson, B. F. Chmelka, G. D. Stucky, *Scienc e* **1998**, *279*, 548.
[14] C. J. Brinker, *Curr. Opin. Solid State. Mater. Sci* . **1996**, *1*, 798.
[15] J. C. Vartuli, C. T. Kresge, W. J. Roth, S. B. McCullen, J. S. Beck, K. D. Schmitt, M. E. Leonowicz, J. D. Lutner, E. W. Sheppard, in Advanced Catalysts and Nanostructured Materials: Modern Synthesis Methods (Ed.: W. R. Moser), Academic Press, New York, **1996**.
[16] G. D. Stucky, Q. Huo, A. Firouzi, B. F. Chmelka, S. Schacht, I. G. Voigt-Martin, F. Schüth, *Studies in Surface Science and Catalysis* **1997**, *105*, 3.
[17] N. K. Raman, M. T. Anderson, C. J. Brinker, *Chem. Mater.* **1996**, *8*, 1682.
[18] V. V. Guliants, M. A. Carreon, Y. S. Lin, *J. Membr. Sci.* **2004**, *235*, 53.
[19] G. J. de A. A. Soler-Illia, C. Sanchez, B. Lebeau, J. Patarin, *Chem. Rev.* **2002**, *102*, 4093.
[20] C. Y. Chen, S. L. Burkett, H. X. Li, M. E. Davis, *Microlithogr. World Micropor. Mater.* **1993**, *2*, 27.
[21] A. Steel, S. W. Carr, M. W. Anderson, *J. Chem. Soc. Chem. Commun.* **1994**, 1571.
[22] A. Monnier, F. Schüth, Q. Huo, D. Kumar, D. Margolese, R. S. Maxwell, G. D. Stucky, M. Krishnamurty, P. Petroff, A. Firouzi, M. Janicke, B. F. Chmelka, *Scienc e* **1993**, *261*, 1299.
[23] G. D. Stucky, A. Monnier, F. Schüth, Q. Huo, D. Margolese, D. Kumar, M. Krishnamurty, P. Petroff, A. Firouzi, M. Janicke, B. F. Chmelka, *Mol. Cryst. Liq. Cryst.* **1994**, *240*, 187**.**
[24] A. Firouzi, D. Kumar, L. M. Bull, T. Besier, R. Sieger, Q. Huo, S. A. Walker, J. A. Zasadzinski, C. Glinka, J. Nicol, D. Margolese, G. D. Stucky, B. F. Chmelka, *Scienc e* **1995**, *267*, 1138.
[25] S. Ikeda, in Surfactants in Solution, vol. 2 (Eds.: K. L. Mittal, B. Lindman), Plenum, New York, **1984**, 825.
[26] A. Firouzi, F. Atef, A. G. Oertli, G. D. Stucky, B. F. Chmelka, *J. Am. Chem. Soc.* **1997**, *119*, 3596.
[27] O. Regev, *Langmui r* **1996**, *12*, 4940.
[28] J. Frasch, B. Lebeau, M. Soulard, L. Patarin, R. Zana, *Langmuir* **2000**, *16*, 9049.
[29] M. Tiemann, V. Goletto, R. Blum, F. Babonneau, H. Amenitsch, M. Linden, *Langmui r* **2002**, *18*, 1005.

 © 2005 Wiley-VCH Verlag GmbH & Co. KGaA, Weinheim

[30] J. Patarin, B. Lebeau, R. Zana, *Current Opinion in Colloids & Interface Science* **2002**, *7*, 107.
[31] K. Flodstroem, C. V. Teixeira, H. Amenitsch, V. Alfredsson, M. Linden, *Langmuir* **2004**, *20*, 12, 4885.
[32] R. J. Hunter, *Zeta potential in colloid science: principles and applications*, Academic Press, London, New York, **1981**.
[33] G. A. Parks, *Chem. Rev.* **1965**, *65*, *2*, 17.
[34] T. J. Gray, D. P. Detwiler, D. E. Rase, W. G. Lawrence, R. R. West, T. J. Jennings, *The Defect Solid State*, Interscience, New York, **1957**, p. 96.
[35] *CRC Handbook of Chemistry and Physics: A Ready-Reference Book of Chemical and Physical Data* (Ed.-in-Chief: R. C. Weast; Associate Eds.: M. J. Astle, W. H. Beyer), 67th ed., CRC Press, Boca Raton, FL, **1986**.
[36] M. M. Lin, *Appl. Catal.* **2001**, *207*(1–2), 1.
[37] G. Centi, *Catal. Today* **1993**, *16–18*, 16.
[38] M. Hatano, A. Kayo, EP Patent 318,295 A1, **1988**.
[39] T. Ushikubo, K. Oshima, T. Umezawa, K. Kiyono, EP Patent 512,846 A1, **1992**.
[40] K. Oshima, A. Kayo, T. Umezawa, K. Kiyono, I. Sawaki, EP Patent 529, 853 A2, **1992**.
[41] G. Centi, F. Trifiro, *Catal. Rev. Sci. Eng.* **1986**, *28*, 165.
[42] R. K. Grasselli, *Catal. Today* **1999**, *49*, 141.
[43] P. Concepcion, J. M. Lopez Nieto, J. Perez-Pariente, *J. Mol. Catal. A: Chem.* **1995**, *99*, 173.
[44] E. A. Mamedov, V. C. Corberan, *Appl. Catal. A* **1995**, *127*, 1.
[45] R. Catani, G. Centi, F. Trifiro, R. K. Grasselli, *Ind. Eng. Chem. Res.* **1992**, *31*, 107.
[46] M. Bettahar, G. Costentin, L. Savary, J. Lavalley, *Appl. Catal. A* **1996**, *145*, 1.
[47] D. J. Hucknall, Selective Oxidation of Hydrocarbons, Academic Press, London **1974**.
[48] S. T. Oyama, A. N. Desikan, J. W. Hightower, Catalytic Selective Oxidation, ACS Symposium Series 523, American Chemical Society: Washington DC **1993**.
[49] J. Haber, *Stud. Surf. Science Catal*. **1997**, *110*, 1; (3rd World Congress on Oxidation Catalysis).
[50] G. Centi, F. Cavani, F. Trifiro, Selective Oxidation by Heterogeneous Catalysis. Fundamental and Applied Catalysis, Kluwer Academic/Plenum Publishers, New York, **2001**.
[51] J. L. G. Fierro, L. A. Arrua, J. M. Lopez Nieto, G. Kremenic, *Appl. Catal.* **1988**, *37*, 323.
[52] D. A. Bulushev, L. Kiwi-Minsker, V. I. Zaikovskii, A. Renken, *J. Catal.* **2000**, *193*,145.
[53] G. S. Wong, D. D. Kragten, J. M. Vohs, *J. Phys. Chem. B* **2001**, *105*, 1366.
[54] N.-Y. Topsoe, H. Topsoe, J. A. Dumesic, *J. Catal.* **1995**, *151*, 226.
[55] H. Roussel, B. Mehlomakulu, F. Belhadj, E. Van Steen, J. M. Millet, *J. Catal.* **2002**, *205*, 97.
[56] V. Luca, D. J. MacLachlan, J. M. Hook, R. Withers, *Chem. Mater.* **1995**, *7*, 2220.
[57] G. G. Janauer, A. Dobley, J. Guo, P. Zavalij, M. S. Whittingham, *Chem. Mater.* **1996**, *8*, 2096.
[58] P. Liu, I. L. Moudrakouski, J. Liu, A. Sayari, *Chem. Mater.* **1997**, *9*, 2513.
[59] P. Yang, D. Zhao, D. I. Margolese, B. F. Chmelka, G. D. Stucky, *Chem. Mater.* **1999**, *11*, 2813.
[60] P. Liu, S.-H. Lee, C. E. Tracy, Y. Yan, J. A. Turner, *Adv. Mater.* **2002**, *14*, *1*, 27.
[61] D. M. Antonelli, A. Nakahira, J. Y. Ying, *Inorg. Chem.* **1996**, *35*, 3126.
[62] D. M. Antonelli, J. Y. Ying, *Angew. Chem. Int. Ed. Engl.* **1996**, *35*, *4*, 426.
[63] P. Yang, D. Zhao, D. I. Margolese, B. F. Chmelka, G. D. Stucky, *Natur e* **1998**, *396*, 152.
[64] A. Fujishima, K. Hinda, *Natur e* **1972**, *238*, 37.
[65] Z. B. Zhang, C. C. Wang, R. Zakaria, J. Y. Ying, *J. Phys. Chem. B* **1998**, *102*, 10871.
[66] F. Lonyi, J. Valyon, J. Engelhardt, F. Mizukami, *J. Catal.* **1996**, *160*, 279.
[67] T. Yamaguchi, *Appl. Catal.* **1990**, *61*, 1.
[68] X. Bokhimi, A. Morales, O. Novaro, T. Lopez, E. Sanchez, R. Gomez, *J. Mater. Res.* **1995**, *10*,*11*, 2788.
[69] D. T. On, *Langmui r* **1999**, *15*, 8561.
[70] D. Khushalani, G. A. Ozin, A. Kuperman, *J. Mater. Chem.* **1999**, *9*, 1491.
[71] W. S. Postula, Z. Feng, C. V. Philip, A. Akgerman, R. G. Anthony, *J. Catal.* **1994**, *145*, 126.
[72] Z. Feng, W. S. Postula, C. V. Philip, R. G. Anthony, *J. Catal.* **1994**, *148*, 84.
[73] A. F. Bedilo, K. J. Klabunde, *J. Catal.* **1998**, *176*, 448.
[74] C. Morterra, G. Cerrato, F. Pinna, M. Signoretto, G. Strukul, *J. Catal.* **1994**, *149*,181.
[75] F. R. Chen, G. Coudurier, J. F. Joly, J. C. Vedrine, *J. Catal.* **1993**, *143*, 616.
[76] M. A. Risch, E. E. Wolf, *Appl. Catal. A* **1998**, *172*, L1.
[77] C. Morterra, G. Cerrato, F. Pinna, M. Signoretto, *J. Catal.* **1995**, *157*, 109.
[78] K. Arata, *Adv. Catal.* **1990**, *37*, 165.
[79] C. Morterra, G. Cerrato, C. Emanuel, V. Bolis, *J. Catal.* **1993**, *142*, 349.
[80] M. S. Wong, J. Y. Ying, *Chem. Mater.* **1998**, *10*, 2067.
[81] X. Song, A. Sayari, *Catal. Rev. Sci. Eng.* **1996**, *38*, 329.
[82] P. Liu, J. Liu, A. Sayari, *Chem. Commun.* **1997**, 577.
[83] I. E. Wachs, Y. Chen, J.-M. Jehng, L. E. Briand, T. Tanaka, *Catal. Today* **2003**, *78*, 13.
[84] M. Hara, G. Hitoki, T. Takata, J. N. Kondo, H. Kobayashi, K. Domen, *Catal. Today* **2003**, *78*, 555.
[85] H. Kato, A. Kudo, *Catal. Today* **2003**, *78*, 561.
[86] D. M. Antonelli, J. Y. Ying, *Chem. Mater.* **1996**, *8*, 874.
[87] G. M. Panjok, *Appl. Catal.* **1991**, *72*, 217.
[88] Z. R. Tian, W. Tong, J. Y. Wang, N. G. Duan, V. V. Krishnan, S. L. Suib, *Scienc e* **1997**, *276*, 926.
[89] X. Liu, C.-M. Chun, I. A. Aksay, W.-H. Shih, *Ind. Eng. Chem. Res.* **2000**, *39*, 684.
[90] J. Luo, S. L. Siub, *Chem. Commun.* **1997**, 1031.
[91] M. Yada, H. Kitamura, M. Machida, T. Kijima, *Inorg. Chem.* **1998**, *37*, 6470.
[92] M. Froba, O. Muth, *Adv. Mater.* **1999**, *11*, *7*, 564.
[93] B. J. Liaw, D. S. Cheng, B. L. Yang, *J. Catal.* **1989**, *118*, 312.
[94] B. L. Yang, M. C. Kung, H. H. Kung, *J. Catal.* **1984**, *89*, 172.
[95] F. Hong, B. L. Yang, L. H. Schwartz, H. H. Kung, *J. Phys. Chem.* **1984**, *88*, 2525.
[96] D. N. Srivastava, N. Perkas, A. Gedanken, I. Felner, *J. Phys. Chem. B* **2002**, *106*, *8*, 1878.
[97] Y. Wang, L. Yin, A. Gedanken, *Ultrason. Sonochem.* **2002**, *9*,*6*, 285.
[98] P. Yang, *J. Chromatogr. Libr. Monolith. Mater.* **2003**, *67*, 301.
[99] S. Polarz, B. Smarsly, *J. Nanosci. Nanotech.* **2002**, *2*,*6*, 581.
[100] K. Moller, T. Bein, *Chem. Mater.* **1998**, *10*, 2950.
[101] V. V. Guliants, J. B. Benziger, S. Sundaresan, I. E. Wachs, J. M. Jehng, J. E. Roberts, *Catal. Today* **1996**, *28*, 275.
[102] R. M. Contractor, US Patent 4 668 802 to E. I. DuPont de Nemours and Company **1987**.
[103] R. M. Contractor, H. S. Horowitz, G. S. Patience, J. D. Sullivan, US Patent 5 895 821 to E. I. DuPont de Nemours and Company **1999**.
[104] U. Rodemerck, B. Kubias, H. W. Zanthoff, G. U. Wolf, M. Baerns, *Appl. Catal. A* **1997**, *153*, 217.
[105] G. Centi, F. Trifirò, J. R. Ebner, V. M. Franchetti, *Chem. Rev.* **1988**, *88*, 55.
[106] E. M. Thornsteinson, T. P. Wilson, F. G. Young, P. H. Kasai, *J. Catal.* **1978**, *52*, 116.
[107] K. Ruth, R. Burch, R. Kieffer, *J. Catal.* **1998**, *175*, 27.
[108] M. Takahashi, X. Tu, T. Hirose, M. Ishii, M. US Patent 5994580, assigned to Toagosei Co. Ltd., Japan **1999**.
[109] J. N. Al-Saeedi, V. V. Guliants, *Appl. Catal. A* **2002**, *237*, *1–2*, 111.

 © 2005 Wiley-VCH Verlag GmbH & Co. KGaA, Weinheim

[110] M. O. Guerrero-Perez, J. L. G. Fierro, M. A. Vicente, M. A. Bañares, *J. Catal.* **2002**, *206*, 339.
[111] M. O. Guerrero-Perez, J. L. G. Fierro, M. A. Bañares, *Catal. Today* **2003**, *78*, *1–4*, 387.
[112] Z-S.Chao, E. Ruckenstein, *Langmui r* **2002**, *18*, 734.
[113] Z-S. Chao, E. Ruckenstein, *Langmui r* **2002**, *18*, 8535.
[114] T. Abe, A. Taguchi, M. Iwamoto, *Chem. Mater.* **1995**, *7*, 1429.
[115] T. Doi, T. Miyake, *Chem. Commun.* **1996**, 1635.
[116] J. E. Haskouri, M. Roca, S. Cabrera, J. Alamo, A. Beltran-Porter, D. Beltran-Porter, M. D. Marco, P. Amoros, *Chem. Mater.* **1999**, *11*, 1446.
[117] N. Mizuno, H. Hatayama, S. Uchida, A. Taguchi, *Chem. Mater.* **2001**, *13*, 179.
[118] M. A. Carreon, V. V. Guliants, *Microporous Mesoporous Mater.* **2002**, *55*, *3*, 297.
[119] M. A. Carreon, V. V. Guliants, *Stud. Surf. Sci. Catal.* **2002**, *141*, 301.
[120] M. A. Carreon, V. V. Guliants, *Catal. Today* **2003**, *78*, 303.
[121] M. A.Carreon, V. V. Guliants, F. Pierelli, F. Cavani, *Catal. Lett.* **2004**, *92*, *1–2*, 11.
[122] B. Lee, T. Yamashita, D. Lu, J. N. Kondo, K. Domen, *Chem. Mater.* **2002**, *14*, 867.
[123] X. He, A. Y. H. Lo, M. Trudeau, R. W. Schurko, D. Antonelli, *Inorg. Chem.* **2003**, *42*, 335.
[124] M. Thieme, F. Schüth, *Microporous Mesoporous Mater.* **1999**, *27*, 193.
[125] D. J. Jones,G. Aptel, M. Brandhorst, M. Jacquin, J. J. Jimenez, A. J. Lopez, P. M. Torres, I. Piwonski, E. R. Castellon, J. Zajac, J. Roziere, *J. Mater. Chem.* **2000**, *10*, 1957.
[126] J. Blanchard, F. Schüth, P. Thens, M. Hudson, *Microporous Mesoporous Mater.* **2000**, *39*,163.
[127] U. Ciesla, M. Froba, G. D. Stucky, F. Schuth, *Chem. Mater.* **1999**, *11*, 227.
[128] R. G. Silver, C. J. Huo, J. G. Ekerdt, *J. Catal.* **1989**, *118*, 400.
[129] C. D. Sagel-Ransijn, A. J. A. Winnubst, B. Kerkwijk, A. J. Burggraaf, H. Verweij, *J. Eur. Ceram. Soc.* **1997**, *17*, *6*, 831.
[130] P. Waldemar, *J. Eur. Ceram. Soc.* **1997**, *17*, *2–3*, 121
[131] M. Mamak, N. Coombs, G. Ozin, *J. Am. Chem. Soc.* **2000**, *122*, 8932.
[132] Y. Wang, L. Yin, O. Palchik, Y. R. Hacohen, Y. Koltypin, A. Gedanken, *Chem. Mater.* **2001**, *13*, 1248.
[133] M. S. Wong, E. S. Jeng, J. Y. Ying, *Nanoletter s* **2001**, *1*, *11*, 637.
[134] D. Li, H. Zhou, I. Honma, *Nature Mater.* **2004**, *3*,*1*, 65.
[135] Y. Xia, B. Gates, Y. Yin, Y. Lu, *Adv. Mater.* **2000**, *12*, *10*, 693
[136] a) O. D. Velev, T. A. Jede, R. F. Lobo, A. M. Lenhoff, *Natur e* **1997**, *389*, 447; b) O. D. Velev, T. A. Jede, R. F. Lobo, A. M. Lenhoff, *Chem. Mater.* **1998**, *10*, 3597.
[137] A. Imhof, D. J. Pine, *Natur e* **1997**, *389*, 948.
[138] B. T. Holland, C. F. Blanford, A. Stein, *Scienc e* **1998**, *281*, 538.
[139] B. T. Holland, C. F. Blanford, T. Do, A. Stein, *Chem. Mater.* **1999**, *11*, 795.
[140] B. T. Holland, L. Abrams, A. Stein, *J. Am. Chem. Soc.* **1999**, *121*, 4308.
[141] M. A. Carreon, V. V. Guliants, *Chem. Commun.* **2001**, 1438.
[142] M. A. Carreon, V. V. Guliants, *Chem. Mater.* **2002**, *14*, *6*, 2670.
[143] G. Gundiah, C. N. R. Rao, *Sol. State Sc.* **2000**, *2*, 877.
[144] Y. Zhang, Z. Lein, J. Li, S. Lu, *New J. Chem.* **2001**, *25*, 1118.
[145] D. Wang, R. A. Caruso, F. Caruso, *Chem. Mater.* **2001**, *13*, 364.
[146] J. E. G. Wijnhoven, W. L. Vos, *Scienc e* **1998**, *281*, 802.
[147] H. Yan, C. F. Blanford, B. T. Holland, M. Parent, W. H. Smyrl, A. Stein, *Adv. Mater.* **1999**, *11*, *12*, 1003.
[148] H. Yan, C. F. Blanford, B. T. Holland, W. H. Smyrl, A. Stein, *Chem. Mater.* **2000**, *12*, 1134.
[149] G. Subramanian, V. N. Manoharan, J. D. Thorne, D. J. Pine, *Adv. Mater.* **1999**, *11*, *15*, 1261.
[150] Y. A. Vlasov, N. Yao, D. J. Norris, *Adv. Mater.* **1999**, *11*, *2*, 165.
[151] S. H. Park, Y. Xia, *Adv. Mater.* **1998**, *10*, 1045.
[152] B. Gates, Y. Yin, Y. Xia, *Chem. Mater.* **1999**, *11*, 2827.
[153] P. Jiang, K. S. Hwang, D. M. Mittleman, J. F. Bertone, V. L. Colvin, *J. Am. Chem. Soc.* **1999**, *121*, 11630.
[154] Q. Luo, Z. Liu, L.Li, S. Xie, J. Kong, D. Zhao, *Adv. Mater.* **2001**, *13*, 286.
[155] P. V. Braun, P. Wiltzius, *Natur e* **1999**, *402*, 603.
[156] P. V. Braun, P. Wiltzius, *Adv. Mater.* **2001**, *13*, 482.
[157] P. N. Bartlett, P. R. Birkin, M. A. Ghanem, C. S. Toh, *J. Mater. Chem.* **2001**, *11*, 849.
[158] P. Jian, J. F. Bertone, V. L. Colvin, *Scienc e* **2001**, *291*, 453.
[159] A. Sayari, *Chem. Mater.* **1996**, *8*, 1840.
[160] M. Ogawa, K. Kuroda, J. Mori, *Chem. Commun.* **2000**, 241.
[161] K. Ikeue, S. Nozaki, M. Ogawa, M. Anpo, *Catal. Lett.* **2002**, *80*, 3.
[162] K. Soga, Y. Sano, T. Uozumi, Patent No. JP 2000063387, **2000**.
[163] M. Furuya, S. Riku, Patent No. JP 2002069015, **2002**.
[164] X. Gao, I. E. Wachs, MS Wong, J. Y. Ying, *J. Catal.* **2001**, *203*, 18.
[165] M. M. Yusuf, H. Imai, H. Hirashima, *J. Sol-Gel Sci. Technol.* **2002**, *25*, 65.
[166] Y. Takahara, J. N. Kondo, T. Takata, D. Lu, K. Domen, *Chem. Mater.* **2001**, *13*, 1194.
[167] V. F. Stone Jr., R. J. Davis, *Chem. Mater.* **1998**, *10*, 1468.
[168] N. Perkas, Y. Wang, Y. Koltypin, A. Gedanken, S. Chandrasekaran, *Chem. Commun.* **2001**, *11*, 988.
[169] H. Yoshitake T. Tatsumi, *Chem. Mater.* **2003**, *15*, 1695.
[170] X. He, D. Antonelli, *Angew. Chem. Int. Ed.* **2002**, *41*, 214.
[171] R. C. Schroden, C. F. Blanford, B. J. Melde, B. J. S. Johnson, A. Stein, *Chem. Mater.* **2001**, *13*, 1074.
[172] B. J. S. Johnson, A. Stein, *Inorg. Chem.* **2001**, *40*, 801.
[173] M. A. Carreon, PhD Thesis, University of Cincinnati, **2003**.
[174] A. Sayari, P. Liu, J. S. Reddy, *Mater. Res. Soc. Symp. Proc.* **1996**, *431*, 101.
[175] K. M. McGrath, D. M. Dabbs, N. Yao, K. J. Edler, I. A. Aksay, S. M. Gruner, *Langmui r* **2000**, *16*, 398.
[176] A. S. Malik, D. M. Dabbs, I. A. Aksay, H. E. Katz, *Mater. Res. Soc. Symp. Proc.* **2001**, 658.

Received August 3, 2004

 © 2005 Wiley-VCH Verlag GmbH & Co. KGaA, Weinheim

Formation of Hexagonal Coordination Complexes

Nate Schultheiss,[a] Joseph M. Ellsworth,[a] Eric Bosch,*[a] and Charles L. Barnes[b]

Keywords: Crystal engineering / N ligands / Metallacycles / Microporous materials

The synthesis of the ligand 1,3-bis(3′-pyridylethynyl)benzene and the coordination complex formed with copper(II) acetate is described. The complex is hexagonal with two ligands bridged by paddlewheel-shaped dimeric copper(II) acetate moieties. The complexes are packed in such a way that the benzene rings from two separate complexes penetrate into the central cavity.

(© Wiley-VCH Verlag GmbH & Co. KGaA, 69451 Weinheim, Germany, 2005)

Introduction

The synthesis of porous solids is a research area of current interest.[1−4] For example solids that contain channel-like void spaces are attractive goals with potential applications in molecular adsorption, ion exchange, and also heterogeneous catalysis. Hexagonal channels and cavities are often found in nature, and several approaches to the synthesis of hexagonal channels have been reported. Moore, for example, reported the formation of a purely organic porous solid with wide channels based on the π-stacking and hydrogen bonding of a planar hexagonal macrocycle comprising six phenols linked by *meta*-ethynyl groups.[5] Robson reported a coordination chemistry approach and characterized a large hexagonal complex on self-assembly of 2,4,6-tris(4′-pyridyl)-1,3,5-triazine with copper(II) acetate.[6] That coordination network did not contain channels because of the offset packing of adjacent sheets of the coordination network. In this report we describe a different coordination chemistry approach to the preparation of hexagonal channels.

Results and Discussion

As ligand we chose to prepare the bidentate ligand 1,3-bis(3′-pyridylethynyl)benzene, **1**, and to self-assemble this with metals that favor linear coordination as shown in Equation (1). Sonagashira coupling[7] of 3-bromopyridine with 1,3-diethynylbenzene yielded the ligand **1** in good yield as shown in Equation (2).[8] We then allowed the ligand **1** to self assemble with copper(II) acetate in acetonitrile solution and obtained green diamond-shaped crystals.[9] Elemental analysis of the bulk solid indicated that a 1:2 ligand/Cu^{II} complex was formed. Single-crystal X-ray analysis revealed this to be a hexagonal 2:4 coordination complex as shown in Figure 1.[10]

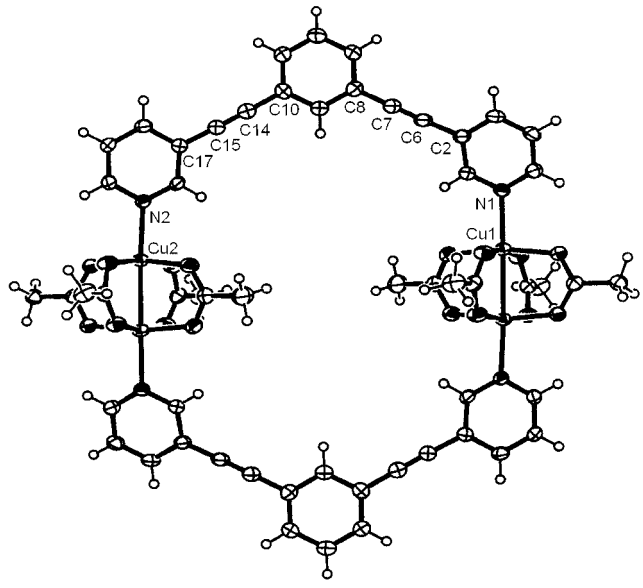

Figure 1. Ortep view of the 2:4 complex formed between **1** and copper(II) acetate; ellipsoids drawn at the 50% probability level

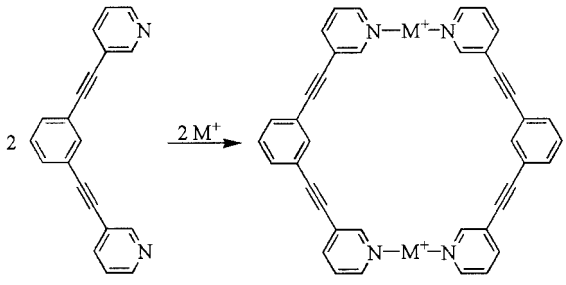

(1)

[a] Department of Chemistry, Southwest Missouri State University,
Springfield, MO 65804, USA
[b] Department of Chemistry, University of Missouri,
Columbia, MO 65211, USA

 DOI: 10.1002/ejic.200400722 © 2005 Wiley-VCH Verlag GmbH & Co. KGaA, Weinheim

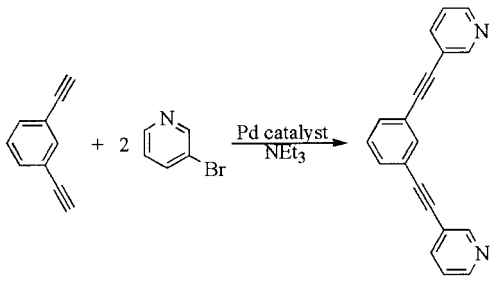

(2)

The complex between two ligands and two copper(II) acetate dimeric units forms a slightly irregular hexagon as shown in Figure 1. The copper(II) acetate linkage gives longer sides with a N(1)−N(2) distance of 6.957 Å, while the C(2)−C(8) and C(10)−C(17) distances are 4.067 and 4.065 Å, respectively. The copper acetate paddlewheel forms an almost linear connection between the pair of ligand molecules with nitrogen−copper−copper angles of 174.82(6) and 177.43(7)°. The copper−nitrogen bond lengths of 2.185(2) and 2.175(2) Å and the copper−copper bond length of 2.6053(5) Å are normal. The copper−oxygen bond lengths range from 1.959(2) Å to 1.987(2) Å, and the oxygen−copper−oxygen bond angles on each side of the paddlewheel range from 87.56(9) to 92.32(9)°. The alkynes are undistorted with normal triple bond lengths of 1.190(4) and 1.191(4) Å and angles about the sp C atoms between 177.3(4) and 179.3(4)°. The pyridyl rings are slightly twisted with respect to the central benzene ring with torsional angles of approximately 28 and 13°.

Unfortunately, the hexagonal complexes do not stack on top of each other to form porous materials − instead individual complexes stack in an offset manner with the end of two complexes partially penetrating the central cavity of a third complex. This is shown in Figure 2.

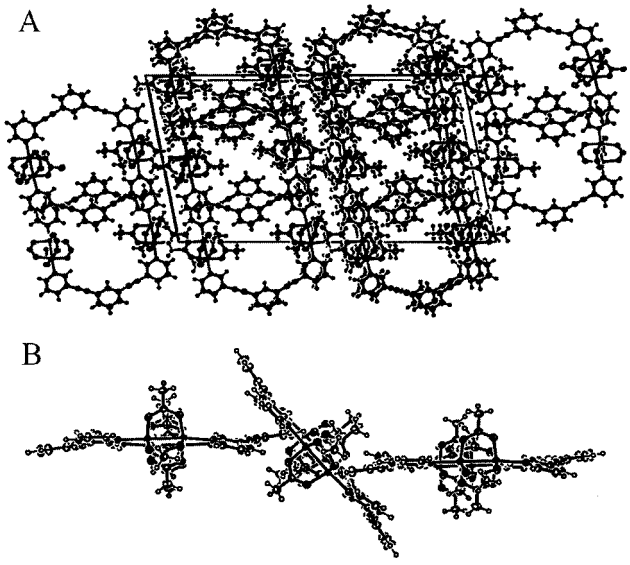

Figure 2. **A:** The packing in the unit cell viewed along the a axis; **B:** view showing the partial penetration of two complexes into a central tilted complex.

Acknowledgments

We thank the Petroleum Research Fund administered by the ACS (Grant # 37506-B3) and the Graduate College at SMSU for partial funding of this research.

[1] M. J. Zaworotko, *Angew. Chem. Int. Ed.* **2000**, *39*, 3052−3054.
[2] P. H Dinolfo, J. T. Hupp, *Chem. Mater.* **2001**, *13*, 3113−3125.
[3] O. M. Yaghi, H. Li, C. Davis, D. Richardson, T. L. Groy, *Acc. Chem. Res.* **1998**, *31*, 474−484.
[4] M. Eddaoudi, D. B. Moler, H. Li, B. Chen, T. M. Reineke, M. O′Keeffe, O. M. Yaghi, *Acc. Chem. Res.* **2001**, *34*, 319−330.
[5] D. Venkataraman, S. Lee, J. Zhang, J. S. Moore, *Nature* **1994**, *371*, 591−593.
[6] S. R. Batten, B. F. Hoskins, B. Moubaraki, K. S. Murray, R. Robson, *Chem. Commun.* **2000**, 1095−1096.
[7] K. Sonogashira, *Metal-Catalyzed Cross-Coupling Reactions* (Eds.: F. Diederich, P. J. Stang), Wiley-VCH, New York, **1998**, pp. 203−229.
[8] 1,3-Diethynylbenzene (1.26 g, 10 mmol) was added with the aid of a syringe to a mixture of 3-bromopyridine (3.26 g, 20.6 mmol), bis(triphenylphosphane)palladium(II) dichloride (150 mg), CuI (15 mng), and triphenylphosphane (150 mg) in diethylamine (25 mL). Nitrogen was bubbled though the mixture for 10 minutes, and the reaction was heated to 60 °C under nitrogen for 16 h. The crude product was purified, by precipitation from ethyl acetate with hexanes, as a white powder in 64% yield (1.02 g). ^{1}H NMR ($CDCl_3$): δ = 7.38−7.26 (m, 3 H, ArH), 7.56−7.52 (m, 2 H, ArH), 7.75 (t, J = 1.5 Hz, 1 H, ArH), 7.81 (td, J = 1.8, 8.0 Hz, 2 H, ArH), 8.57 (dd, J = 1.8, 5.2 Hz, 2 H, ArH), 8.78 (dd, J = 0.8, 2.0 Hz, 2 H, ArH) ppm. ^{13}C NMR: δ = 86.7, 91.5, 120.1, 123.0, 128.6, 131.8, 134.7, 138.4, 148.7, 152.3 ppm. $C_{20}H_{12}N_2$ (280.32): calcd. C 85.71, H 4.29, N 10.00; found C 85.55, H 4.32, N 9.90.
[9] A mixture of acetonitrile (2 mL) and dichloromethane (2 mL) was layered over a solution of 1,3-bis(3′-pyridylethynyl)benzene (11.0 mg, 0.04 mmol) in dichloromethane (2 mL). A solution of copper(II) acetate monohydrate (16.0 mg, 0.08 mmol) in acetonitrile (2 mL) was carefully layered over that. The vial was capped and placed in the dark. Green diamond-shaped crystals formed after 2 days (14.7 mg, 59%). m.p. 222 °C. $C_{28}H_{24}N_2Cu_2O_8$ (643.6): calcd. C 52.25, H 3.76, N 4.35; found C 52.32, H 3.68, N 4.37.
[10] Crystal size 0.40 × 0.25 × 0.05 mm, $C_{28}H_{24}Cu_2N_2O_8$, mol. mass 643.57; monoclinic, $C2/c$, a = 36.5577(17) Å, b = 7.8999(4) Å, c = 21.4256(11) Å; β = 100.3440(10)°; V = 6087.2(5) Å^3; Z = 8; ρ (calculated) = 1.404 Mg/m^3; reflections collected = 21246 (6700 unique); F(000) = 2624; Absorption coefficient = 1.445 mm^{-1}; 1.93 < θ < 27.14 ; max. and min. transmission = 0.93 and 0.59; final R indices [$I > 2\sigma(I)$], $R1$ = 0.0440, $wR2$ = 0.1005; largest diff. peak and hole = 0.660 and −0.382 e·Å^{-3}. CCDC-246104 contains the supplementary crystallographic data for this paper. These data can be obtained free of charge at www.ccdc.cam.ac.uk/conts/retrieving.html [or from the Cambridge Crystallographic Data Centre, 12 Union Road, Cambridge CB2 1EZ, UK; Fax: +44-1223-336-033; E-mail: deposit@ccdc.cam.ac.uk].

Received August 25, 2004

 © 2005 Wiley-VCH Verlag GmbH & Co. KGaA, Weinheim

Synthesis of ZnS Nanowires and Assemblies by Carbothermal Chemical Vapor Deposition and Their Photoluminescence

Hua Zhang,[a] Shuyuan Zhang,*[a] Ming Zuo,[a] Gongpu Li,[a] and Jianguo Hou[a]

Keywords: Chemical vapor deposition / Luminescence / Nanostructures / Self-assembly / Zinc

A carbothermal method combined with CVD has been developed to synthesize ZnS nanowires and their self-assemblies at low temperatures. In this process, active carbon serves as reductant to react with sulfur, which then goes on to form ZnS nanowires. X-ray diffraction and X-ray photoelectron spectroscopy studies indicate that the samples are single-crystal wurtzite ZnS and are rich in sulfur. The nanowires have diameters ranging from 20 to 60 nm. High-resolution electron microscopy shows the [100] growth direction for the monodispersed nanowires and the different crystal orientation for the nanowires constituting the assembly. The photoluminescence (PL) peak is located at 490 nm. A vapor-solid (VS) mechanism might explain the formation of ZnS nanowires.

(© Wiley-VCH Verlag GmbH & Co. KGaA, 69451 Weinheim, Germany, 2005)

Introduction

Recently, there has been considerable interest in well-arranged nanostructures prepared by various methods, including template synthesis[1] and electrochemical deposition,[2] as they have potential applications in many areas, such as infrared photo detectors,[2] field emissions,[3] and as substrates for photocatalysis and photovoltaics.[4] As they are probably building blocks for well-ordered nanostructures and nanodevices,[5−7] one-dimensional nanomaterials have recently attracted much attention.[8−11] ZnS is an important II-VI semiconductor that possesses unique properties and has potential applications in numerous areas like optics,[12] electronics,[13] photocatalysis,[14] etc., and is especially promising in electric nanodevices. Except for our previously prepared ordered constructions[15] like flowers and sheets, only nanocombs[16] and microrods[17] composed of regularly arranged ZnS nanowires have been reported. ZnS nanowires and their assemblies have often been prepared by both solution methods[18] and thermal evaporation.[19] For the latter, ZnS powder precursors have generally been thermally evaporated under at 900−1600 °C. For example, ZnS-Si-ZnS triaxial nanowires[20] have been prepared by heating a mixture of SiO and ZnS powders to 1300 °C for 1 h and then to 1600 °C for 1.5 h. The obtained product was a composite material containing cubic Si and zincblende-structured ZnS. Wang's group[21] has employed a silicon wafer and Au films as substrate and catalyst, respectively. Wurtzite phase ZnS nanowires were successfully prepared by heating ZnS powders to 900 °C for 2 h,. According to Li and co-workers,[22] Zn/ZnS nanocables can be fabricated by thermal evaporation of ZnS and a graphite-powder mixture at 1300 °C for 5 h. In spite of these reports it is still a challenge to explore other new and versatile alternatives for the synthesis of pure ZnS nanowires and their assemblies at lower temperatures.

Here, we demonstrate that pure, wurtzite-phase ZnS nanowires can be prepared by a carbothermal, chemical-vapor-deposition method (CVD) by heating a mixture of activated carbon, sublimed sulfur and anhydrous $ZnCl_2$ powders to 500 °C. In addition, we have found that some self-assembled structures composed of ZnS nanowires coexist in the samples. Because of its lower temperature and versatility, this new fabrication method might present a new and easy way to form various kinds of sulfides. The green-blue emission of the as-grown ZnS nanowires and their assemblies may have potential applications in electronic/optical nanodevices.

Results and Discussion

The X-ray diffraction (XRD) pattern (see Supporting Information) of the as-prepared samples shows that the samples are well crystallized. All the peaks can be indexed as (100), (002), (101), (110), (103) and (112) crystal planes corresponding to JCPDS card 36-1450, which suggests that the samples are pure, wurtzite-phase, structured ZnS with lattice parameters $a = 3.820$ Å and $c = 6.257$ Å.

The Zn and S content in the ZnS nanowires was obtained from the X-ray photoelecton spectroscopy (XPS) patterns (Figure 1). No impurities, such as trace metals and other

[a] Structure Research Laboratory, University of Science and Technology of China
Hefei, Anhui 230026, People's Republic of China
Fax: + 86-0551-360-2803
E-mail: zhangsy@ustc.edu.cn

Supporting information for this article is available on the WWW under http://www.eurjic.org or from the author.

sulfides, are observed in the complete spectrum (see Supporting Information). The binding energy for Zn $2p^3$ (Figure 1a) is 1023.25 eV, which is a slight increase compared with that reported in the database[23] compiled and evaluated by Wagner, thus indicating a small difference in the chemical state of zinc in our samples. Curve 1 in Figure 1b shows the pattern of S $2p^3$ with two shoulders at about 162 and 164 eV. In order to determine the chemical states of sulfur, curves 2, 3 and 4, centered at 162.40, 163.40 and 164.60 eV, respectively, were fitted accompanied by their combined curve 5. Curves 2 and 3 represent the sulfur in ZnS; a small amount of elemental sulfur is responsible for curve 4. Therefore, the ratio of S to Zn in ZnS is about 1.077:1, which shows the richness of S instead of the sulfur deficiency generally found in previous papers.[24]

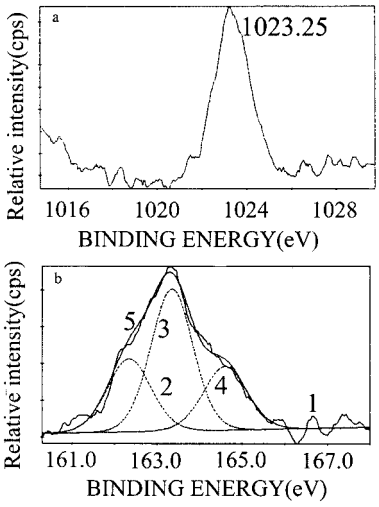

Figure 1. XPS patterns of the ZnS sample: (a) Zn $2p^3$ (b) S $2p^3$

Figure 2a displays a typical low-magnification transmission electron microscopy (TEM) image, which shows that the products consist of nanowires with uniform diameters ranging from 20 to 60 nm. The wires are long, straight and smooth with few other particles present. The electron diffraction (ED) pattern (inset) taken from a single nanowire (Figure 2b) can be indexed as the (100) and (001) planes of wurtzite-phase ZnS. Figure 2c shows a high-resolution electron microscopy (HREM) image, with a measured spacing of about 0.626 nm corresponding to the (001) plane. It can be clearly observed that the growth direction of the wire is perpendicular to [001], i.e. the [100] direction. The inset in the HREM image of another wire shows the two-dimensional lattice spacing, from which the (101) crystal plane, with a measured spacing of 0.293 nm, can clearly be seen.

Some regularly assembled structures, shown in Figures 3a and b, have been found in the as-prepared samples. From the high-magnification TEM image (Figure 3b) the characteristics of the wires can clearly be seen, especially from the different contrast and the places indicated by the arrows. These nanowires, with smooth surfaces and diameters in the range of 10−60 nm, are self-organized in the radial direction and are nearly parallel to each other, while in the thickness direction the self-organization can't be comfirmed from the contrast; this is different to the case of microrods,[17] where the assembly happens in two dimensions. The (001) and (002) crystal planes of the wurtzite phase can be identified in the ED pattern. The HREM image taken from the frame-labeled area is shown in Figure 3c. There are two different lattice spacings related to the two neighboring single nanowires. One is 0.313 nm, corresponding to the (002) plane, and the other is 0.227 nm, corresponding to the (102) plane. This indicates that not all the nanowires making up the assembly grow along the same crystal orientation.

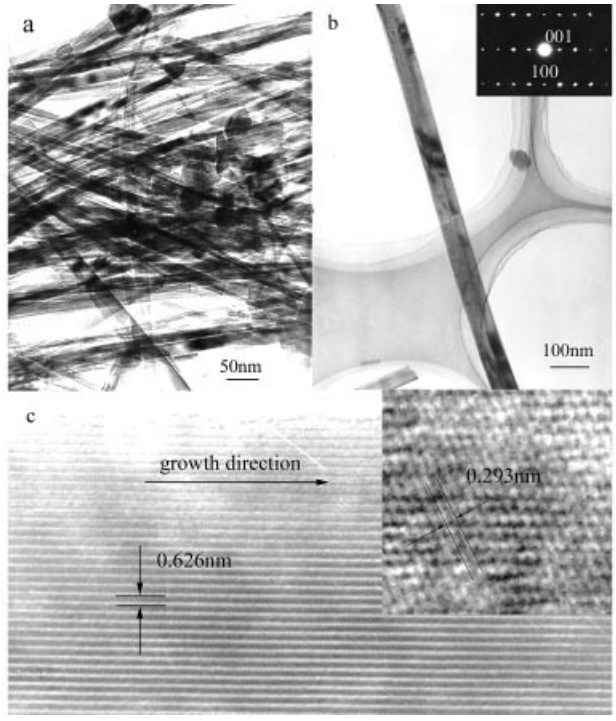

Figure 2. (a) TEM image of ZnS nanowires; (b) TEM image of a single ZnS nanowire and its ED pattern (inset); (c) one-dimensional and (inset) two-dimensional HREM images of a ZnS nanowire

The room-temperature photoluminescence (PL) spectrum of the as-synthesized ZnS nanowires and assemblies was measured with excitation and filter wavelengths of 313 nm and 350 nm, respectively. As shown in Figure 4, a strong emission peak is located at 490 nm, which is similar to that of the well-known ZnS-related luminescence (at about 480 nm) produced by zinc vacancies.[25] The ZnS nanomaterials reported previously have ultra-violet emission with bands in the range 400−450 nm[26−27] associated with the sulfur vacancy. It has been reported in previous work on ZnS that the vacancy states lie deeper in the gap than the interstitial states.[28] Therefore, in the case of the sulfur-rich nanowires containing no impurities reported here, we reasonably believe that the green-blue luminescence is attributed to zinc vacancies rather than the vacancy and interstitial sites of sulfur.

 © 2005 Wiley-VCH Verlag GmbH & Co. KGaA, Weinheim

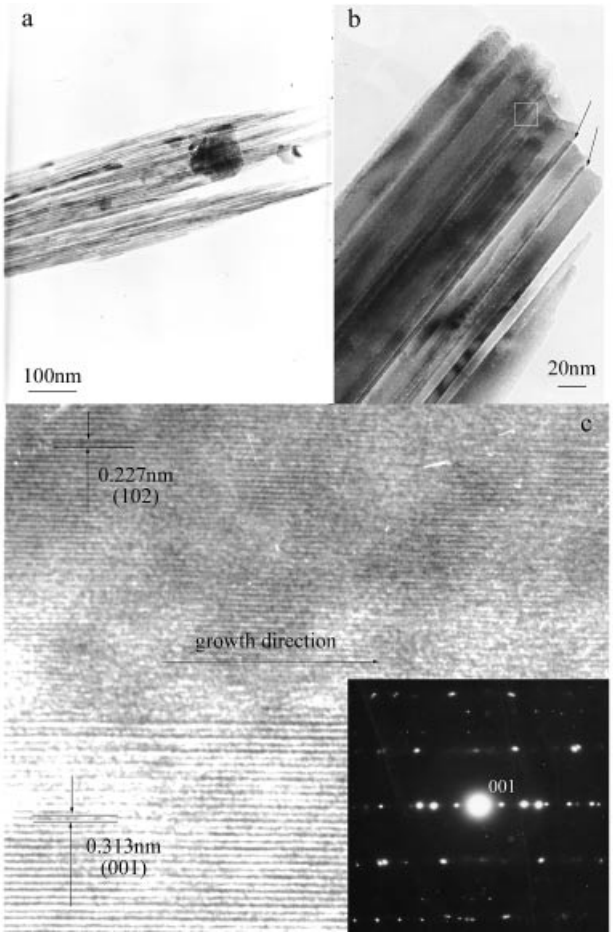

Figure 3. (a) and (b) TEM images of self-assembled ZnS nanowires and (inset) their ED pattern; (c) HREM image taken from the two, neighboring, frame-labeled single nanowires with two different lattice spacings: one is 0.313 nm corresponding to the (002) crystal plane, and the other is 0.227 nm corresponding to the (102) crystal plane: this indicates the different growth direction of the constituent nanowires

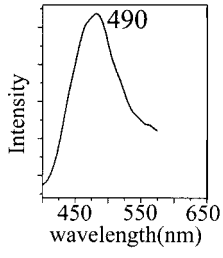

Figure 4. Room-temperature PL spectrum of the as-synthesized ZnS sample with excitation at 313 nm and a filter at 350 nm; the green-blue emission peak is located at 490 nm

To the best of our knowledge, the carbothermal reduction method is usually used to fabricate oxides,[29] carbides[30] and nitrides,[31] in which active carbon or graphite generally reacts with source chemicals containing O or N to generate intermediate compounds. It is well known that active carbon can serve as a reductant and react in a furnace with sulfur to generate CS_2, which can act as a sulfur source in the fabrication of sulfides.[32] Due to the low boiling point of CS_2 (b.p. 46.26 °C) and low melting point of $ZnCl_2$ (m.p. 318 °C),[33] there is enough vapor to react and the one-dimensional characteristic of CS_2 could contribute to the formation of ZnS nanowires. According to these ideas, we designed the above-described experiments and found that ZnS nanowires were synthesized successfully. In the absence of active carbon we only obtained nanoparticles. This synthesis method can be understood in terms of carbothermal CVD. The growth of one-dimensional nanomaterials by thermal evaporation is often explained by a vapor-liquid-solid (VLS)[34] or vapor-solid (VS)[35] growth mechanism. For example, the silicon nanowires reported by Yu[36] were synthesized on solid substrates by the VLS mechanism using Au or Zn nucleation catalysts. In this case, the presence of a big particle at the tip of the nanowire is commonly considered to be evidence for the operation of the VLS mechanism. Jiang's group has fabricated ZnS nanoribbons[37] by a VS mechanism through hydrogen-assisted thermal evaporation. Comparing the features of these two mechanisms, and with no tip-located particles present, the VS explanation may be operative in the formation process of our ZnS nanowires. The experimental conditions and the anisotropy might provide the external and internal driving forces for the crystal growth. Once the nucleation starts, the crystal grow in the preferential orientation of the ZnS crystal planes.

Conclusion

In summary, ZnS nanowires and their self-assemblies have been successfully prepared for the first time by a carbothermal CVD method at low temperature. The as-prepared samples are wurtzite-phase, single nanocrystals with uniform morphology. The mono-dispersed nanowires grow along the [100] direction and those nanowires constituting the self-assemblies grow in different crystal orientation. Possibly due to their sulfur-rich nature, the samples show strong green-blue emission at room temperature, which is consistent with the luminescence of the zinc vacancy. The growth of our ZnS nanowires can be explained by a VS mechanism. Because of its easy operation and versatility, this carbothermal CVD route may be extended to the synthesis of other kinds of sulfide semiconductor nanowires. Further improvements of the equipment and studies on the application of ZnS nanowires and their self-organized structures are in progress.

Experimental Section

All the employed reactants were commercial and analytical grade without any further purification. A thoroughly blended powder mixture of sublimed sulfur (S), active carbon (C), and anhydrous zinc chloride ($ZnCl_2$) with a molar ratio of 4:1:2 was put into a porcelain boat which was placed in the bottom of a short quartz tube (approx. 25 mm diameter and 10 cm length) closed at one end. The short tube was placed with the open end downstream in the

 © 2005 Wiley-VCH Verlag GmbH & Co. KGaA, Weinheim

center of a long quartz tube (approx. 50 mm diameter and 1 m length) mounted in a horizontal furnace, which was sealed and high-purity nitrogen was passed through it for 2 h to purge the air from the system. After heating to 500 °C for 2 h, the tube furnace was allowed to cool to room temperature in a constant flow of nitrogen. White samples were collected from the inner wall of the short tube, and then washed with distilled water and absolute ethanol several times. The purity and phase structure of the products were obtained by X-ray powder diffraction (XRD) analysis, which was performed with a D/max-γA X-ray diffractometer (λ = 0.15405 nm). The composition of the samples was determined by XPS with an ESCALAB MKII electron spectrometer using Mg-K_α radiation as the source. The morphologies and microstructure were observed and analyzed by TEM and HREM with a JEOL-2010 transmission electron microscope using an acceleration voltage of 200 kV. The PL measurements were carried out with a HITACHI850-type visible-ultraviolet spectrophotometer with a 313 nm excitation and a 350 nm filter at room temperature. The XRD pattern and the complete XPS spectrum of our sample are available as Supporting Information.

Acknowledgments

This work was supported by the National Natural Science Foundation of China (grant no. 50132030).

[1] S. Han, X. Y. Shi, F. M. Zhou, *Nano Lett.* **2002**, *2*, 97−100.
[2] N. Kouklin, L. Menon, A. Z. Wong, D. W. Thompson, J. A. Woollam, P. F. Williams, S. Bandyopadhyay, *Appl. Phys. Lett.* **2001**, *79*, 4423−4425.
[3] J. Chen, S. Z. Deng, N. S. Xu, *Appl. Phys. Lett.* **2002**, *80*, 3620−3622.
[4] Y. Y. Wu, H. Q. Yan, P. D. Yang, *Top. Catal.* **2002**, *19*, 197−202.
[5] Y. Cui, C. M. Lieber, *Science* **2001**, *291*, 851−853.
[6] T. Rueckes, K. Kim, E. Joselerich, G. Y. Tseng, C. Cheung, C. M. Lieber, *Science* **2000**, *289*, 94−97.
[7] S. Noda, K. Tomoda, N. Yamamoto, A. Chutinan, *Science* **2000**, *289*, 604−606.
[8] S. M. Zhou, Y. S. Feng, L. D. Zhang, *Eur. J. Inorg. Chem.* **2003**, 1794−1797.
[9] X. D. Wang, P. X. Gao, J. Li, C. J. Summers, Z. L. Wang, *Adv. Mater.* **2002**, *14*, 1732−1735.
[10] J. W. Liu, M. W. Shao, Q. Tang, S. Y. Zhang, Y. T. Qian, *J. Phys. Chem. B* **2003**, *107*, 6329−6332.
[11] A. Govindaraj, F. L. Deepak, N. A. Gunari, C. N. R. Rao, *Isr. J. Chem.* **2001**, *41*, 23−30.
[12] L. V. Zavyalova, A. K. Savin, G. S. Svechnikov, *Displays* **1997**, *18*, 73−78.
[13] X. J. Liu, X. Cai, J. F. Mao, C. Y. Jin, *Appl. Surf. Sci.* **2001**, *183*, 103−110.
[14] H. Fujiwara, H. Hosokawa, K. Murakoshi, Y. Wada, S. Yanagida, *Langmuir* **1998**, *14*, 5154−5159.
[15] H. Zhang, S. Y. Zhang, D. Y. Pan, G. P. Li, S. Pan, J. G. Hou, *J. Nanosci. Nanotech.* **2004**, *4*, 209−213.
[16] C. Ma, D. Moore, J. Li, Z. L. Wang, *Adv. Mater.* **2003**, *15*, 228−231.
[17] Y. C. Zhu, Y. Bando, D. F. Xue, D. Golberg, *Adv. Mater.* **2004**, *16*, 831−834.
[18] Q. T. Zhao, L. S. Hou, R. Huang, *Chem. Commun.* **2003**, *6*, 971−972.
[19] Y. Jiang, X. M. Meng, J. Liu, Z. R. Hong, C. S. Lee, S. T. Lee, *Adv. Mater.* **2003**, *15*, 1195−1198.
[20] J. Q. Hu, Y. Bando, Z. W. Liu, T. Sekiguchi, D. Golberg, J. H. Zhan, *J. Am. Chem. Soc.* **2003**, *125*, 11306−11313.
[21] Y. W. Wang, L. D. Zhang, C. H. Liang, G. Z. Wang, X. S. Peng, *Chem. Phys. Lett.* **2002**, *357*, 314−316.
[22] Q. Li, C. R. Wang, *Appl. Phys. Lett.* **2003**, *82*, 1398−1400.
[23] C. D. Wagner, A. V. Naumkin, A. K. Vass, J. W. Allison, C. J. Powell, J. R. Rumble, Jr., *NIST X-ray Photoelectron Spectroscopy Database*, version 3.4, NIST Standard Reference Database 20 (web version).
[24] K. Manzoor, S. R. Vadera, N. Kumar, T. R. N. Kutty, *Mater. Chem. Phys.* **2003**, *82*, 718−725.
[25] S. Oda, H. Kukimoto, *J. Lumin.* **1979**, *18/19*, 829−835.
[26] J. F. Suyver, S. F. Wuister, J. J. Kelly, A. Meijerink, *Nano Lett.* **2001**, *1*, 429−433.
[27] W. G. Becker, A. J. Bard, *J. Phys. Chem.* **1983**, *87*, 4888−4893.
[28] D. Denzler, M. Olschewski, K. Sattler, *J. Appl. Phys.* **1998**, *84*, 2841−2845.
[29] H. T. Ng, B. Chen, J. Li, J. Han, M. Meyyappan, J. Wu, S. X. Li, E. E. Haller, *Appl. Phys. Lett.* **2003**, *82*, 2023−2025.
[30] J. A. Johnson, C. M. Hrenya, A. W. Weimer, *J. Am. Ceram. Soc.* **2002**, *85*, 2273−2280.
[31] H. Arik, *J. Eur. Ceram. Soc.* **2003**, *23*, 2005−2014.
[32] X. C. Jiang, Y. Xie, J. Lu, L. Y. Zhu, W. He, Y. T. Qian, *Chem. Mater.* **2001**, *13*, 1213−1218.
[33] J. A. Jean, *Lange's Handbook of Chemistry*, 13th ed., McGraw-Hill, New York, **1985**, p 4−34.
[34] C. Kawai, A. Yamakawa, *Ceram. Int.* **1998**, *24*, 135−138.
[35] Y. C. Zhu, Y. Bando, D. F. Xue, *Appl. Phys. Lett.* **2003**, *82*, 1769−1771.
[36] J. Y. Yu, S. W. Chung, J. R. Heath, *J. Phys. Chem. B* **2000**, *104*, 11864−11870.
[37] Y. Jiang, X. M. Meng, J. Liu, Z. Y. Xie, C. S. Lee, S. T. Lee, *Adv. Mater.* **2003**, *15*, 323−327.

Received August 1, 2004

 © 2005 Wiley-VCH Verlag GmbH & Co. KGaA, Weinheim

Lithium Cyanocuprates: Structural Studies of a Phosphane Adduct of a "Lower-Order" Lithium Cyanocuprate

Robert P. Davies*[a] and Stefan Hornauer[a]

Keywords: Cuprates / Lithium / Reaction intermediates / Michael addition

Addition of PPh_3 to the "lower-order" cyanocuprate PhCuCNLi results in a significant increase in reactivity in 1,4-Michael addition reactions. This is explained by a marked structural change in the cyanocuprate reagent, observed in both THF solution and the solid state, to give $[Ph_2Cu]^-$ cuprate anions and a $[Cu_2Li_4(CN)_4(PPh_3)_4(THF)_{10}]^{2+}$ dication.

(© Wiley-VCH Verlag GmbH & Co. KGaA, 69451 Weinheim, Germany, 2005)

Introduction

Lithium cyanocuprates are commonly used in the regioselective formation of new carbon−carbon bonds, and have been shown to have significant advantages for certain reactions over classical Gilman reagents prepared from copper(I) halides.[1,2] Cyanocuprates can conveniently be divided into two distinct groups based upon their composition and reactivity: "*lower order*" cyanocuprates formed from the 1:1 reaction of CuCN and LiR (R = organo group) to give species of the general formula RCu(CN)Li; and "*higher order*" species from the 1:2 reaction of CuCN and LiR and hence with the formulation $R_2Cu(CN)Li_2$. Spectroscopic studies of lower-order cyanocuprates both in solution[3] and the solid state[4−7] have shown **1**, or aggregates of **1** such as **2**, to be the most likely structural motif for these species (Scheme 1). Hence $[(Me_2PhSi)_3C-Cu(CN)Li(THF)_3]$[4] is a monomer (**1**) in the solid state, whilst $[(Me_2PhSi)_3CCu(CN)Li(THF)_2]_2$,[4] $[(C_6H_3_2,6\text{-}Trip_2)Cu(CN)Li(THF)_2]_2$ [5] (Trip = $-C_6H_2$-2,4,6-iPr$_3$), $[Me_3SiCH_2CuCNLi(OEt_2)_2]_2$,[6] and $[t\text{BuCu(CN)Li-}(Et_2O)_2]_\infty$ [7] are all dimers (**2**). However, the structure of higher-order cyanocuprates has been the subject of much more controversy with arguments centering on whether the cyanide group remains bound to the copper or not. Again recent crystallographic studies have played a major part in this discussion with structural characterization of the higher order cyanocuprates $[t\text{Bu}_2\text{Cu}\{\text{Li(THF)-(pmdeta)}\}_2\text{CN}]$[7] and $[(2\text{-}C_6H_4CH_2NMe_2)_2Cu\{Li-(THF)_2\}_2CN]_\infty$ [8] both revealing ionic compounds consisting of $[R_2Cu]^-$ cuprate anions and $[Li-CN-Li]^+$ cations (**3**). In contrast, infrared spectroscopic,[9] NMR spectroscopic,[10−13] cryoscopic,[14] and kinetic reactivity[15,16] studies of these higher-order cuprates have been less conclusive predicting several possible solution structures. However, the current consensus as laid out by Krause in a recent review,[17] is that the reactive solution species consists of a cuprate anion $[R_2Cu]^-$ and a $[Li-CN-Li]^+$ cation, either as a solvent-separated ion pair (SSIP), such as **3**, and similar to the structures observed in the solid-state characterizations, or possibly as some form of contact-ion pair (CIP).

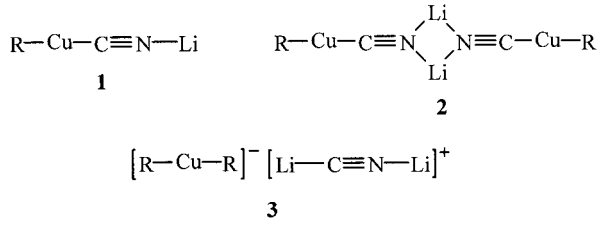

Scheme 1. Solid-state structural motifs for lower-order (**1**, **2**) and higher-order (**3**) lithium cyanocuprates

Despite these recent advances, there are still many gaps in our knowledge of cyanocuprates, and this is particularly true when we consider the use of additives. Boron trifluoride, alkali-metal halides and phosphanes amongst others have all been employed as additives for lithium cyanocuprates in order to enhance the stability, selectivity and/or reactivity of these species.[1] Despite their reported success in this field, little is know about their mode of operation and the effect they have upon the molecular structure of the organocopper reagents. This paper reports on the first structural characterization of a phosphane adduct of a lithium cyanocuprate and discusses its reactivity in Michael addition reactions.

Results and Discussion

Addition of triphenylphosphane to a THF/toluene solution of the lower-order cyanocuprate PhCuCNLi (formed

[a] Dept. of Chemistry, Imperial College London, South Kensington, London, SW7 2AZ, UK
Fax: (internat.) +44-870-1300438
E-mail: r.davies@imperial.ac.uk

from the 1:1 reaction of CuCN and LiPh) at 0 °C gave a clear yellow solution from which crystals of **4** were grown at −30 °C (Scheme 2). X-ray structural studies show **4** to be an ionic species comprising a centrosymmetric $[Cu_2Li_4(CN)_4(PPh_3)_4(THF)_{10}]^{2+}$ dication and two symmetry-related $[CuPh_2]^-$ cuprate anions (Figure 1).

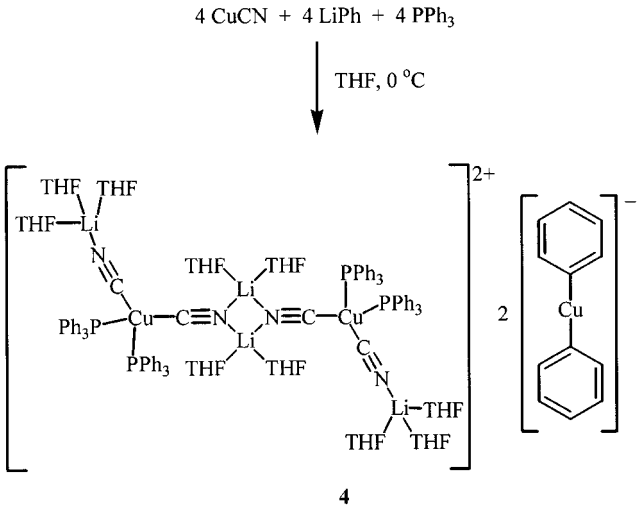

Scheme 2. Synthesis of **4**

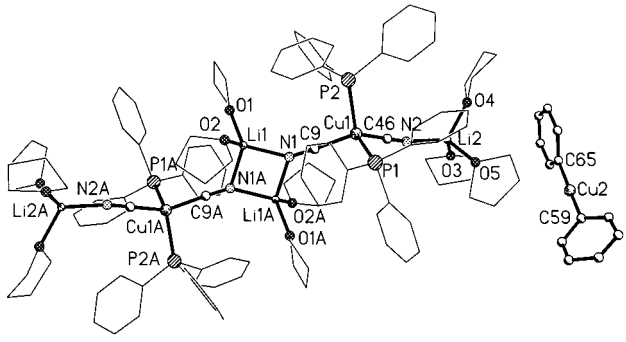

Figure 1. Molecular structure of **4**; only one of the two symmetry-related $[CuPh_2]^-$ cuprate anions is shown for clarity

The dication in **4** is unprecedented, containing both Li^+ and Cu^I ions linked together through cyanide groups, and can perhaps best be thought of as two PPh_3-complexed $[Cu(CN)_2]^-$ anions aggregated with four THF-solvated Li^+ cations. The copper atoms in the dication are approximately tetrahedral, and bond to two PPh_3 groups [Cu(1)−P(1) 2.294(2) Å; Cu(1)−P(2) 2.299(2) Å] and to the carbon atoms of two cyanide groups [Cu(1)−C(9) 1.944(6) Å; Cu(1)−C(46) 1.952(9) Å]. These Cu−CN distances are therefore longer than those observed in previously reported lower-order cyanocuprates (mean, 1.906 Å),[4−7] but are similar to the Cu−CN distances of 1.964(4) and 1.948(5) Å reported for $[Cu_2(CN)_2(PPh_3)_4(hppH)]$ (hppH = 1,3,4,6,7,8-hexahydro-2*H*-pyrimido[1,2-*a*]pyrimidine), which also contains a $Cu^I(CN)_2(PPh_3)_2$ metal center.[18] Two different lithium ions are observed in the asymmetric unit of **4**: Li(1) bridges two cyanide groups at their nitrogen ends [Li(1)−N(1) 2.036(12) Å; Li(1)−N(1A) 2.095(12) Å] and is solvated by two THF molecules [mean Li−O, 1.919 Å], whereas Li(2) is terminally bound to just one cyanide group [Li(2)−N(2) 1.90(4) Å] and has its quadruplet completed by three THF molecules [mean Li−O, 1.87 Å]. In keeping with all previously reported lithium cyanocuprates,[4−7] the cyanide carbon atoms in **4** are essentially linear [Cu(1)−C(9)−N(1), 175.5(6); Cu(1)−C(46)−N(2), 176.2(8)°] and the CN unit is bent out of the plane of the central Li_2N_2 ring (by 12.6°).

The $[Ph_2Cu]^-$ cuprate anions in **4** contain close to linear Cu^I centers [C(59)−Cu(2)−C(65), 174.8(4)°] with C−Cu bond lengths of 1.900(11) Å [Cu(2)−C(59)] and 1.931(11) Å [Cu(2)−C(65)]. The dihedral angle between the phenyl rings is 59.1°. These units are therefore structurally very similar to the $[R_2Cu]^-$ cuprate anions observed in the higher-order cyanocuprates $[tBu_2CuLi_2(CN)(THF)_2(pmdeta)_2]$[7] and $[(2\text{-}C_6H_4CH_2NMe_2)_2Cu\{Li(THF)_2\}_2CN]_\infty$.[8]

Low temperature (−100 °C) ^1H-decoupled ^{13}C NMR spectroscopy carried out on an aliquot of the CuCN + PhLi + PPh_3 reaction mix after stirring for 10 min at 0 °C in toluene/THF solution shows singlets at δ = 174.20 and 144.27 ppm for the phenyl *ipso* carbon and the cyanide carbon resonances, respectively. The chemical shift of the *ipso* carbon is therefore downfield from the value observed for PhCuCNLi in the absence of phosphane (δ = 166.05 ppm),[3] indicating some structural change has occurred. Bertz has previously reported the chemical shifts of the *ipso* carbon atoms of the higher-order cyanocuprate formed from CuCN +2 PhLi and also of the Gilman reagent from CuI +2 PhLi as 174.33 and 174.13 ppm, respectively (in $[D_8]$THF at −78 °C).[10] Based on these almost identical NMR shifts, he was able to argue that $[CuPh_2]^-$ cuprate subunits were present in each case. The fact that we observe the *ipso* carbon shift to be of an almost identical value to those observed by Bertz confirms that diphenylcuprate anions are present in solution for **4** as well as in the solid state. The cyanide ^{13}C NMR resonance (δ = 144.27 ppm) differs from that observed for PhCuCNLi in the absence of PPh_3 (δ =148.50 ppm)[3] and is significantly upfield from the $[Li_2CN]^+$ cation cyanide resonance reported for higher-order cyanocuprates (mean, δ = 158.80 ppm).[10] However, the resonance is close to the range of reported values for lower-order cyanocuprates (δ = 45.51−151.20 ppm),[3−7] suggesting that "CuCNLi" units, similar or identical to those observed in the cation of **4**, are present in solution.

Infrared spectroscopic characterization of the addition product of PhLi and CuCN (PhCuCNLi) gave a cyanide stretch in THF solution at 2137 cm^{-1} (cf. 2133 cm^{-1} previously reported for MeCuCNLi).[9] On addition of PPh_3, this peak decreases significantly in size and a new peak is observed at 2120 cm^{-1}. This new absorption differs in frequency from the cyanide stretch reported for the higher-order cyanocuprate formed from CuCN + 2MeLi (2115 cm^{-1}), attributable to $[Li{-}CN{-}Li]^+$,[9] and instead can be

 © 2005 Wiley-VCH Verlag GmbH & Co. KGaA, Weinheim

assigned to a cyanide stretch in a $[Cu(PPh_3)_2CNLi]^+$ unit, which is also in agreement with the ^{13}C NMR spectroscopic and X-ray crystallographic observations (vide supra).

^{31}P NMR spectroscopy on the reaction mixture in THF containing excess triphenylphosphane (CuCN + PhLi +1.5 PPh_3) reveals one peak ($\delta = -2.54$ ppm) at room temperature. On cooling to −100 °C, this peak splits into two new resonances: a broad peak at $\delta = 0.04$ ppm and a sharp peak at $\delta = -7.76$ ppm. These resonances can be assigned to $[Cu(CN)_2]^-$-complexed PPh_3 and free PPh_3, respectively, and interchange of the two types of PPh_3 occurs at room temperature on the NMR time scale. ^7Li NMR spectroscopy on the same reaction mixture reveals two resonances ($\delta = -2.44$ and -3.37 ppm), consistent with the bridging and terminal lithium atoms present in the cation of **4**.

The addition of the phosphane therefore results in a considerably different structural motif for **4** relative to all previously reported lower-order cyanocuprates (**1**, **2**), and the most significant difference, in terms of its effect on the reactivity, undoubtedly is the generation of $[Ph_2Cu]^-$ cuprate anions. The observed increased reactivity of higher- than lower order cyanocuprates has previously been attributed to the presence of such $[R_2Cu]^-$ cuprate units,[17] and it seems likely that any increase in reactivity for PhCuCNLi on addition of PPh_3 is due to the generation of these anions. However, although it has previously been suggested that addition of PPh_3 to cuprates does indeed increase their reactivity,[1] no systematic studies have been reported. We therefore obtained logarithmic reactivity profiles (LRPs)[15] to compare the rates of reaction of (a) PhCuCNLi, (b) PhCuCNLi + PPh_3 (**4**), and (c) $Ph_2CuCNLi_2$ in Michael addition reactions with 2-cyclohexanone (Table 1). The LRP was generated by quenching the reaction after a series of times spanning several orders of magnitude, and measuring the yields of 3-phenylcyclohexanone using GLC and the internal standard method.[15] The lower order cyanocuprate PhCuCNLi is very unreactive under these conditions with no product formation observed even after 1 h. However, addition of PPh_3 increases the yields significantly to 29% after 1 h. The yields are larger still for the higher order cyanocuprate and this can be explained by double the concentration of cuprate anions in solution for $Ph_2CuCNLi_2$ than **4**, and also by the differing nature of the cations in the two reagents, with the larger more sterically hindered cations in **4** likely to favor the formation of SSIPs rather than the more reactive CIP species.[16]

Table 1. LRP data for reactions of (a) PhCuCNLi, (b) **4** and (c) $Ph_2CuCNLi_2$ with 2-cyclohexanone in THF, showing the yields (%) of 3-phenylcyclohexanone

Reagent[a]	Time [h]			
	0.001	0.01	0.1	1
(a) PhCuCNLi	0	0	0	0
(b) PhCuCNLi + PPh_3 (**4**)	1	3	22	29
(c) $Ph_2CuCNLi_2$	19	53	66	70

[a] Reactions were carried out at −78 °C on a 1 mmol scale at 0.1 M in THF. Quench: 6 mL of saturated aqueous ammonium chloride/ammonia (90:10).

Conclusion

Addition of PPh_3 to the "lower-order" cyanocuprate PhCuCNLi drastically alters its structure by promoting the formation of $[CuPh_2]^-$ cuprate units both in THF solution (observed using multi-nuclear and variable temperature NMR spectroscopy) and in the solid state (observed using single-crystal X-ray diffraction). Such cuprate units have been previously reported in "higher-order" cyanocuprates and Gilman cuprates, but this is this first time they have been observed in a formally "lower-order" cyanocuprate. The addition of PPh_3 is also shown to increase the reactivity of PhCuCNLi in Michael addition reactions with 2-cyclohexanone, and this increase in reactivity can be explained by the observed structural changes in the reagent on addition of phosphane, in particular the generation of the anionic $[R_2Cu]^-$ cuprate units.

Experimental Section

General Remarks: CuCN (Fluka > 99%), PPh_3 (Aldrich 99%) and 2-cyclohexene-1-one (Lancaster Synthesis 97%) were used without further purification. Pure, halogen-free PhLi was synthesized prior to use by reaction of equimolar amounts of PhI with *n*BuLi in hexane at 0 °C.[19] THF and diethyl ether were distilled from over sodium wire/benzophenone. Unless otherwise stated, all manipulations were carried out under nitrogen using either a glove box or double-manifold vacuum line. Dry ice/2-propanol baths were used for reactions at −78 °C. GC analyses were performed with an Agilent GC4890 gas chromatograph equipped with FID detector and a 25-m SGE BPX5 capillary column [0.22 mm i.d., 0.25 micron film, cross-linked 5% phenyl (equiv.) polysilphenylene-siloxane]. The GC was calibrated with authentic product (3-phenylcyclohexanone) and dodecane (Aldrich 99%) as internal standard. NMR spectra were recorded on a Jeol EX270 Delta Upgrade or a Bruker AM-500 spectrometer. External standards used were TMS (^1H, ^{13}C) 85% H_3PO_4 (^{31}P) and LiCl/D_2O (^7Li).

Synthesis of $[Cu_2Li_4(CN)_4(PPh_3)_4(THF)_{10}]\cdot 2[Ph_2Cu]$ (4): A solution of PhLi (1.8 M in cyclohexane/diethyl ether; 1.1 mL, 2.0 mmol) was added to a suspension of CuCN (0.180 g; 2.0 mmol) in THF (10 mL) at −78 °C followed by dropwise addition of PPh_3 (0.577 g; 2.2 mmol) in THF (5 mL). The resulting clear yellow solution was warmed to 0 °C, filtered through celite and reduced in vacuo to 10 mL. On storage for 72 h at −30 °C, crystals of **4** were obtained in 46% yield (0.57 g). M.p. 118−122 °C (dec.). Note that NMR studies on the reaction mix, as detailed in the main text, indicate a near quantitative yield based on PhLi and CuCN consumption. Due to the extreme air and moisture sensitive nature of **4** we were unable to obtain satisfactory elemental analyses. ^1H NMR spectroscopy (270 MHz, [D$_6$]DMSO, 298 K): $\delta = 7.09-7.44$ (m, 70 H, P*Ph*$_3$, Cu*Ph*$_2$), 3.58 (m, 20 H, THF), 1.72 (m, 20 H, THF) ppm − note that some THF was lost during the isolation procedure. ^{13}C NMR spectroscopy (101 MHz, THF, 173 K): $\delta = 174.20$ (CN), 141.33 (Cu-*ipso*-Ph), 137.49−124.97 (Cu-*o*/*m*/*p*-*Ph*, P*Ph*$_3$), 67.57 (THF), 25.84 (THF) ppm. ^{31}P NMR spectroscopy (109.38 MHz, THF, 298 K): $\delta = -2.54$ ppm. ^7Li NMR spectroscopy

 © 2005 Wiley-VCH Verlag GmbH & Co. KGaA, Weinheim

(194.31 MHz, THF, 298 K): $\delta = -2.44, -3.36$ ppm. IR (THF, 25 °C): $\tilde{\nu} = 2120$ (s) cm^{-1} (C≡N).

Logarithmic Reactivity Profiles (LRPs): The three cuprate reagents used were prepared as follows: (a) PhCuCNLi. CuCN (4 mmol, 358 mg) and PhLi (4 mmol, 336 mg) were weighed out into a 250 mL Schlenk flask equipped with a stirrer bar, and cold THF (40 mL, −78 °C) was added, and the flask was maintained at a temperature of −78 °C. The reaction mixture was stirred for 6 min and then warmed up to 0 °C for 6 min to anneal the reagent before it was cooled back to −78 °C; (b) PhCuCNLi + PPh_3 (**4**). CuCN (4 mmol, 358 mg) and PPh_3 (4 mmol, 336 mg) were weighed out into a 250 mL Schlenk flask equipped with a stirrer bar. PhLi (4 mmol, 336 mg) was weighed out into a separate Schlenk flask equipped with a stirrer bar. Cold THF (20 mL, −78 °C) was added with a syringe into each Schlenk flask, and both solutions were stirred for 10 min at room temperature making sure that the PhLi had completely dissolved. Both Schlenk flasks were then immersed in a cooling bath (−78 °C), and the PhLi solution was transferred with a cannula into the THF suspension of $CuCN/PPh_3$. The reaction mixture was stirred for 6 min and then warmed up to 0 °C for 6 min to anneal the reagent before it was cooled back to −78 °C; (c) $Ph_2CuCNLi_2$. CuCN (4 mmol, 358 mg) and PhLi (8 mmol, 672 mg) were weighed out into a 250 mL Schlenk flask equipped with a stirrer bar. Cold THF (40 mL, −78 °C) was added, and the flask was maintained at a temperature of −78 °C. The resulting cloudy suspension was stirred at −78 °C for 18 min to give a clear yellow solution.

For all cuprates (a)−(c): After a further 6 min of stirring at −78 °C, 10 mL of the reagent was transferred with a syringe into each of four 25 mL flasks. The flasks were predried overnight in an oven at 120 °C and taken into the glove box where they were equipped with a stirrer bar and a rubber septum. They were kept under a positive nitrogen pressure throughout the experiment. A solution of 2-cyclohexene-1-one (96 mg, 1 mmol) in THF (1 mL) was added to the flask with a syringe. The stopwatch was started when the plunger was pushed. After the appropriate LRP time, a quench solution consisting of 6 mL of saturated aqueous ammonium chloride/ammonia (90:10) was injected. The LRP times used were 1 h = 60 min, 0.1 h = 6 min, 0.01 h = 36 s, 0.001 h = 4 s. After quenching the reaction, the flask was removed from the dry ice/2-propanol bath and warmed in warm water until it reached room temperature. The internal GC standard (dodecane, 227 μL, 1 mmol) was then added. The aqueous layer was removed using a pipette, and the organic layer filtered into a vial. The flask and residue were rinsed with diethyl ether (5 mL), and the combined organic layer and ether extract were dried over $MgSO_4$. A sample of the quenched reaction mixture was then run on the GC to ascertain the percentage yield of 3-phenylcyclohexanone. Repeat experiments indicated an experimental error of up to a maximum of ±10% (see reference 15 for a thorough discussion of experimental errors in LRP studies of cuprates).

X-ray Crystallographic Data for 4: $C_{147}H_{168}Cu_4Li_4N_4O_{10}P_4$, $M_r = 2556.65$, monoclinic, space group $P2_1/c$, $a = 20.240(2)$, $b = 16.112(3)$, $c = 24.575(3)$ Å, $\beta = 113.37(2)°$, $V = 7356.6(18)$ Å^3, $Z = 2$ (C_i symmetry), $\rho_{calcd.} = 1.154$ g·cm^{-3}, Mo-K_α radiation, $\lambda = 0.71069$ Å, $\mu = 0.668$ mm^{-1}, $T = 230(2)$ K. 14981 unique data ($R_{int} = 0.1147$, $\theta < 27.24°$) were collected on a Nonius Kappa CCD diffractometer. The structure was solved by direct methods and refined by full-matrix least-squares on F^2 values of all data using the SHELXTL and SHELX-97 program systems,[20] to give $wR2 = 0.3492$, conventional $R = 0.1069$ for 7011 observed absorption-corrected reflections with $F^2 > 2\sigma(F^2)$, $S = 1.035$, 667 parameters. Residual electron density extrema ±1.165 e·Å^{-3}. Since it proved impossible to differentiate between the cyanide carbon and nitrogen atoms crystallographically, these atoms have been assigned based on previously reported structural characterizations of cyanocuprates, all of which contain the cyanide unit attached to the copper through the carbon end and linear carbon atoms.[4,7] CCDC-226575 contains the supplementary crystallographic data for this paper. These data can be obtained free of charge at www.ccdc.cam.ac.uk/conts/retrieving.html [or from the Cambridge Crystallographic Data Centre, 12 Union Road, Cambridge CB2 1EZ, UK; Fax: (internat.): +44-1223-336-033; E-mail: deposit@ccdc.cam.ac.uk].

Acknowledgments

We thank the donors of the American Chemical Society Petroleum Research Fund for support of this research.

[1] [1a] R. J. K. Taylor, *Organocopper Reagents* (Series Eds.: L. M. Harwood, C. J. Moody), Oxford University Press, **1994**. [1b] J. A. Kozlowski, in *Comprehensive Organic Synthesis* (Eds.: B. M. Trost, I. Fleming), Pergamon, Oxford, **1991**, vol. 4, pp. 169−198. [1c] B. H. Lipshutz, in *Comprehensive Organometallic Chemistry II* (Eds.: E. W. Abel, F. G. A. Stone, G. Wilkinson), Pergamon, Oxford, **1995**, vol. 12, pp. 194−213. [1d]N. Krause, A. Gerold, *Angew. Chem. Int. Ed. Engl.* **1997**, *36*, 186−204. [1e] N. Krause, *Modern Organocopper Chemistry*, Wiley-VCH, Weinheim, **2002**.
[2] B. H. Lipshutz, *Synlett* **1990**, 119−128.
[3] S. H. Bertz, *J. Am. Chem. Soc.* **1991**, *113*, 5470−5471.
[4] C. Eaborn, M. S. Hill, P. B. Hitchcock, J. D. Smith, *Organometallics* **2000**, *19*, 5780−5783.
[5] C.-S. Hwang, P. P. Power, *J. Am. Chem. Soc.* **1998**, *120*, 6409−6410.
[6] F. Bosold, M. Marsch, K. Harms, G. Boche, *Z. Kristallogr. New Cryst. Struct.* **2001**, *216*, 143−144.
[7] G. Boche, F. Bosold, M. Marsch, K. Harms, *Angew. Chem. Int. Ed.* **1998**, *37*, 1684−1685.
[8] C. M. P. Kronenburg, J. T. B. H. Jastzebski, A. L. Spek, G. van Koten, *J. Am. Chem. Soc.* **1998**, *120*, 9688−9689.
[9] H. Huang, K. Alvarez, Q. Lui, T. M. Branhart, J. P. Snyder, J. E. Penner-Hahn, *J. Am. Chem. Soc.* **1996**, *118*, 8808−8816.
[10] S. H. Bertz, *J. Am. Chem. Soc.* **1990**, *112*, 4031−4032.
[11] B. H. Lipshutz, B. James, *J. Org. Chem.* **1994**, *59*, 7585−7587.
[12] S. H. Bertz, G. Miao, M. Eriksson, *Chem. Commun.* **1996**, 815−816.
[13] X. Xie, C. Auel, W. Henze, R. M. Gschwind, *J. Am. Chem. Soc.* **2003**, *125*, 1595−1601.
[14] A. Gerold, J. T. B. H. Jastrzebski, C. M. P. Kronenburg, N. Krause, G. van Koten, *Angew. Chem. Int. Ed. Engl.* **1997**, *36*, 755−757.
[15] S. H. Bertz, A. Chopra, M. Eriksson, C. A. Ogle, P. Seagle, *Chem. Eur. J.* **1999**, *5*, 2680−2691.
[16] M. John, C. Auel, C. Behrens, M. Marsch, K. Harms, F. Bosold, R. M. Gschwind, P. R. Rajamohanan, G. Boche, *Chem. Eur. J.* **2000**, *6*, 3060−3068.
[17] N. Krause, *Angew. Chem. Int. Ed.* **1999**, *38*, 79−81.
[18] M. P. Coles, P. B. Hitchcock, *Polyhedron* **2001**, *20*, 3027−3032.
[19] E. Wehman, J. T. B. H. Jastrzebski, J.-M. Ernsting, D. M. Grove, G. van Koten, *J. Organomet. Chem.* **1988**, *353*, 133−143.
[20] G. Sheldrick, SHELXTL PC version 5.1, Bruker AXS, Madison, WI, **1997** and SHELX-97, Institut Anorg. Chemie, Tammannstr. 4, 37077 Göttingen, Germany, **1998**.

Received August 9, 2004

 © 2005 Wiley-VCH Verlag GmbH & Co. KGaA, Weinheim

A 2D Thiocyanato-Bridged Copper(II)-Manganese(II) Bimetallic Coordination Polymer with Ferromagnetic Interactions

Jing-Min Shi,*[a] Wei Xu,[a] Bin Zhao,[b] Peng Cheng,*[b] Dai-Zheng Liao,[b] and Xiao-Yan Chen[b]

Keywords: Structure elucidation / Magnetic properties / Bridging ligands / Manganese

The first ferromagnetic coupled, thiocyanato-bridged copper(II)-manganese(II) bimetallic 2D polymer $\{[Cu(ipa)_2]_2Mn(NCS)_6\cdot 2H_2O\}_n$ (ipa = 1,2-propanediamine) has been synthesised and characterised by a single-crystal X-ray structure determination and variable temperature magnetic susceptibility studies.
(© Wiley-VCH Verlag GmbH & Co. KGaA, 69451 Weinheim, Germany, 2005)

Introduction

Recently, the field of molecular magnetism has attracted considerable attention and major advances have been made both in the theoretical description and applications of new molecular-based materials.[1] In particular, special attention has been paid to the design and construction of multi-dimensional homo- and heterometallic coordination polymers in order to undertake theoretical studies of their magnetic properties and develop high *T*c molecular-based magnets.[2] The thiocyanate anion, which exhibits an ambidentate character with end-to-end or end-on coordination modes, can be expected to play a key role in the design of polymetallic coupling systems. A certain number of polynuclear complexes have been synthesised with discrete 1-, 2- and 3D crystal structures and some of them exhibit interesting ferromagnetic coupling properties, e.g. the 1D uniform chain complexes[3] $Co(NCS)_2(Hlm)_2$ and $Ni(NCS)_2(Hlm)_2$. The heterometallic species, however, are quite limited and show low-dimensional structures,[4−8] whereas large numbers of cyanato-bridged analogues have been reported and some exhibit interesting magnetic properties. The 1D copper(II)-manganese(II) heterometallic compound $[Cu(en)_2Mn(NCS)_4(H_2O)_2]_n$ [4] derived from $K_2[Mn(NCS)_4(H_2O)_2]$ as a precursor has also been described. The chains of Mn^{II} (S = 5/2) and Cu^{II} (S = 1/2) ions structurally ordered in an alternating manner are of intense interest as potential building blocks in the synthesis of molecular-based ferromagnetic materials.[9] In this area, the novel 2D complex $\{[Cu(ipa)_2]_2Mn(NCS)_6\cdot 2H_2O\}_n$ was successfully constructed from a heterometallic octanuclear square lattice as a subunit and it exhibits interesting ferromagnetic coupling between adjacent Mn and Cu ions. In this species, the Cu and Mn atoms are alternately arrayed and are connected by thiocyanate bridges. To the best of our knowledge, in the reported compounds comprising SCN^- bridges, this is the first time that the octanuclear lattice of $Cu_4Mn_4C_8N_8S_8$ has been fabricated from SCN^- bridges and further assembled into a fascinating 2D structure. Remarkably, this ferromagnetic behaviour is absent for the systems containing Cu and Mn ions.

Figure 1 shows the coordination diagram for the complex with the atom numbering scheme. It indicates that the complex consists of two types of distinct building blocks, namely $Mn(NCS)_6$ and $Cu(ipa)_2(SCN)_2$. Each copper atom exhibits an elongated octahedral coordination environment: the equatorial plane is formed from four nitrogen atoms of two ipa ligands with Cu−N distances of 1.988(3) to 2.024(3) Å and the axial positions are occupied by the sulfur atoms of the thiocyanate bridges. The Cu-S separations are not identical and the two types of Cu1−S1 bonds have distances of 2.9635(16) and Cu2−S2 3.0214(16) Å which are shorter than those of other reported complexes.[10] The coordination sphere around the Mn^{2+} centre displays octahedral geometry and is completed by six N atoms from the thiocyanate ions. Four of the N atoms are from four bridging SCN^- anions with Mn−N distances of 2.185(4) to 2.218(4) Å and the other two come from two terminal SCN^- anions which occupy the remaining apical positions of the Mn centre with the Mn−N distances of 2.275(4) Å being longer than those in the equatorial plane. The symmetry elements of the crystal, namely the inversion centres, are located on the Mn and Cu atoms. This is shown clearly in Figure 1 and Figure 2. Interestingly, the equatorial planes of the Cu1 and Cu2 ions run almost parallel to that of the Mn ion with dihedral angles of 9.7°. The

[a] Department of Chemistry, Shandong Normal University, Jinan 250014, P. R. China
Fax: (internat.) +86-531-6948773
E-mail: shijingmin@beelink.com
[b] Department of Chemistry, Nankai University, Tianjin 300071, P. R. China

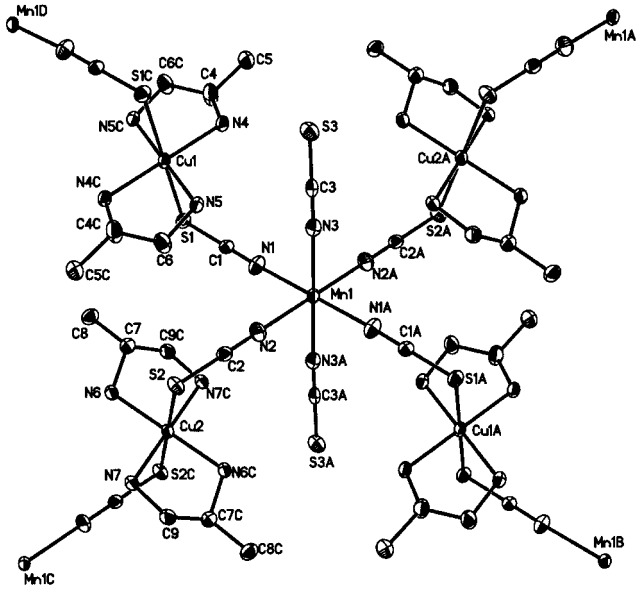

Figure 1. Diagram of the title complex with the atom numbering scheme; H atoms and water molecules are omitted for clarity

S(SCN)−Cu−N(ipa) angles, which are between 82.61(10)° and 95.99(12)°, indicate that the Cu−S bond is nearly perpendicular to the equatorial plane of the Cu ion. Each Mn ion has four Cu ions as the nearest metal centers, while the Cu ion has two Mn ions in its vicinity which is consistent with the Mn:Cu molar ratio. Adjacent Cu and Mn ions are connected through SCN^- bridges to form a 32-membered $Cu_4Mn_4C_8N_8S_8$ square lattice subunit of dimensions 9.118×10.089 Å. Mn atoms are located on the vertexes of squares and Cu atoms lie on the middle points of the edges. Importantly, the square subunits are further assembled into a 2D polymer. The distances between the neighbouring Mn···Cu pairs are 5.683 Å for Mn1···Cu1 and 5.717 Å for Mn1···Cu2.

The plot of μ_{eff} versus T is shown in Figure 3. At room temperature μ_{eff} is 7.00 μ_B which is slightly greater than the expected value for an isolated Mn ion and four Cu ions (6.86 μ_B for $g_{av} = 2$). The μ_{eff} value increases gradually with decreasing temperature from 7.00 μ_B at 300 K, reaching a maximum value of 7.32 μ_B at 5 K. This magnetic behaviour indicates ferromagnetic interactions between the $\mu_{1,3}$-NCS-bridged Mn^{II} ion and the Cu^{II} ion which is supported by the fact that the magnetic susceptibility values obey the Curie−Weiss law with a positive Weiss constant $\theta = 1.36$ K.

Theoretically, the exchange interaction between Mn^{II} and Cu^{II} is most likely antiferromagnetic in nature because it is extremely difficult to reach strict orthogonality between the magnetic orbitals for a M(high-spin d^5)-M′(d^1) pair irrespective of the local symmetry of each.[11] Also, to the best of our knowledge, this concept has been somewhat confirmed by previously reported Mn^{II}-Cu^{II} couplings. Unexpectedly, the title compound exhibits ferromagnetic interactions and represents the first example of a Mn^{II}-Cu^{II} system. Indeed, as mentioned in the description of the structure, all the Mn−NCS−Cu angles are close to 90 degree

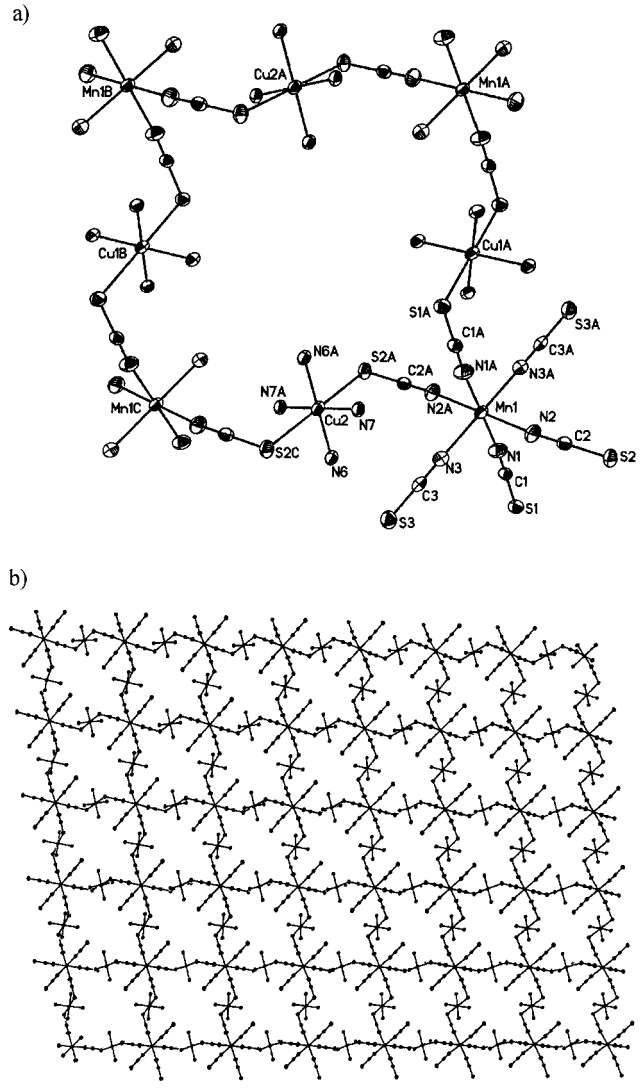

Figure 2. a) 32-membered square lattice motif of $Cu_4Mn_4C_8N_8S_8$; b) view along the [001] direction showing the 2D structure; the H atoms, C atoms in the ipa ligand and solvent molecules are omitted for clarity

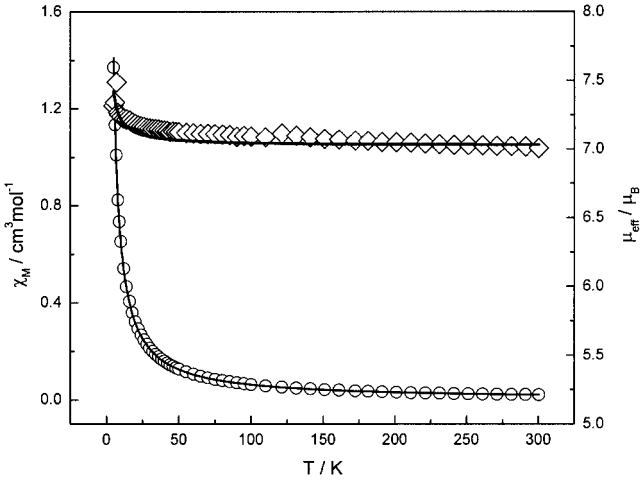

Figure 3. Plots of χ_M (diamonds) and μ_{eff} (circles) versus T

 © 2005 Wiley-VCH Verlag GmbH & Co. KGaA, Weinheim

and the S atom is in the apical position of the Cu^{II} centre. Therefore, the small spin density of the d_{z^2} type orbital of the Cu^{II} centre interacts with that of the $d_{x^2-y^2}$ type magnetic orbital of the Mn^{II}. This situation occurs because of strict orthogonality and results in a ferromagnetic contribution. On the other hand, the $3d^5$ electrons of the Mn^{II} display a sphere-type distribution, thus partial overlapping of the magnetic orbitals of the Cu^{II} and Mn^{II} ions inevitably occurs which causes an antiferromagnetic contribution to the Cu^{II} and Mn^{II} system. The two kinds of interactions conflict in an antagonistic process but the ferromagnetic contribution may predominate, however, and this should be responsible for the ferromagnetic coupling between Cu^{II} and Mn^{II}.

Taking into account the complex magnetic treatment for multi-dimensional systems containing paramagnetic centres, only approximate models were employed to fit the experimental data so far obtained. In this context, the pentanuclear Mn-Cu_4 system was considered as the smallest repeat unit in order to analyse the magnetic properties of the 2D structure. Equation (2) was obtained based on an isotropic Hamiltonian presented as in Equation (1) with interactions between Cu ions neglected due to the long distance between them.

$$\hat{H} = -2J\hat{S}_{Mn}(\hat{S}_{Cu1} + \hat{S}_{Cu2} + \hat{S}_{Cu3} + \hat{S}_{Cu4}) \quad (1)$$

$$\chi_M = Ng^2\beta^2A/4k_BT + TIP \quad (2)$$

$A = 165 + 84\exp(-9J/kT) + 35\exp(-16J/kT) + 10\exp(-21J/kT) + 252\exp(-5J/kT) + 105\exp(-12J/kT) + 30\exp(-17J/kT) + 70\exp(-10J/kT)$

$B = 5 + 4\exp(-9J/kT) + 3\exp(-16J/kT) + 2\exp(-21J/kT) + \exp(-24J/kT) + 12\exp(-5J/kT) + 9\exp(-12J/kT) + 6\exp(-17J/kT) + 6\exp(-10J/kT)$

where J is the Heisenberg exchange constant between adjacent Mn^{II} and Cu^{II} ions, S_{Mn} and S_{Cu} are spin operators corresponding to Mn and Cu, respectively, and the temperature-independent paramagnetism TIP = 3.0×10^{-4}. The theoretical model gave a good fitting of the experimental results. The agreement factor $R = 5.8\times10^{-4}$ [R was defined as $R = \Sigma(\chi_{obsd.} - \chi_{calcd.})^2/(\chi_{obsd.})^2$], $g = 2.04$ and $J = 0.13\ cm^{-1}$. The sign and magnitude of the J value suggest that weaker ferromagnetic coupling exists between adjacent Cu^{II} and Mn^{II} centres bridged by SCN^- anions.

To further support the nature of the interaction provided by the temperature dependence of the magnetisation, the field dependence of the magnetisation for the complex was measured in a field of 0−50 kOe at 7 K. The experimental values of M for the title compound were compared with those calculated by the Brillouin function corresponding to an $S = 9/2$ spin state with $g = 2$ (Figure 4). The plot of M vs. H approaches the Brillouin curve based on $S = 9/2$, although experimental values do not reach a magnetic saturation value of 9. This behaviour confirms that the ground state of $S = 9/2$ results from ferromagnetic interactions between the Mn and Cu ions of the pentanuclear system.

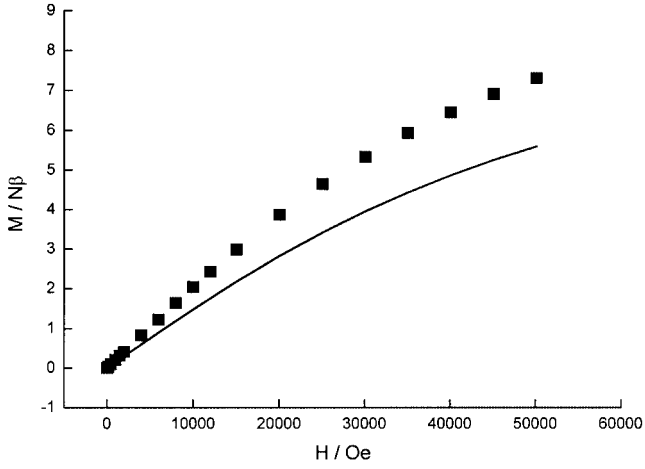

Figure 4. Plot of M versus H (squares) and the Brillouin curve for four independent Cu^{II} ions and one Mn^{II} ion

In conclusion, a novel 2D heterometallic polymer has been assembled from 32-membered $Cu_4Mn_4C_8N_8S_8$ square lattices as subunits fabricated from SCN anions bridges. It shows a fascinating topological motif which is relatively rare in SCN-bridged complexes. Magnetic studies revealed intriguing ferromagnetic couplings between adjacent Cu^{II} and Mn^{II} ions which is the first report of such a phenomenon in Cu^{II}-Mn^{II} systems.

Experimental Section

General: Infrared spectra were recorded with a Bruker Tensor 27 infrared spectrometer in the 4000−500 cm^{-1} region using KBr discs. C, H and N elemental analyses were carried out on a Perkin−Elmer 240 instrument. Variable-temperature magnetic susceptibilities of microcrystalline powder samples were measured in a magnetic field of 1 kOe in the temperature range of 5−300 K on a SQUID magnetometer. The data were corrected for magnetisation of the sample holder and for diamagnetic contributions which were estimated from Pascal's constants.

Synthesis of the Complex: All chemicals were of analytical grade and were used without further purification. $Cu(ipa)_2(ClO_4)_2$ (ipa = 1,2-propanediamine) (0.1949 g, 0.58 mmol) and $Na_4Mn(NCS)_6\cdot9H_2O$ (0.4199 g, 0.64 mmol) were each dissolved in H_2O (10 mL), the two solutions were mixed together and the resultant mixture stirred for a few minutes. Purple single crystals were obtained after the resultant solution was allowed to stand at room temperature for several days. Yield: 0.2027 g (81%). $C_{18}H_{44}Cu_2MnN_{14}O_2S_6$ (863.05): calcd. Cu, 14.73, Mn, 6.37, C 25.05, H 5.14, N 22.73; found Cu, 14.28, Mn, 5.93, C 25.37, H 5.58, N 23.15%. The IR spectrum shows a characteristic strong and sharp absorption peak for the NCS^- groups at 2084 cm^{-1} and the sharp peaks due to the NH and NH_2 groups appear at 3462, 3305 and 1583 cm^{-1}.

X-ray Crystallographic Analysis of the Complex:[12] A single-crystal of dimensions 0.15 × 0.12 × 0.08 mm was selected and subsequently glued to the tip of a glass fibre. The determination of the

 © 2005 Wiley-VCH Verlag GmbH & Co. KGaA, Weinheim

crystal structure at 25 °C was carried out on a Bruker Smart-1000 CCD X-ray diffractometer using graphite-monochromated Mo-K_α radiation (λ = 0.71073 Å). Corrections for *Lp* factors were applied and all nonhydrogen atoms were refined with anisotropic thermal parameters. Hydrogen atoms were located from a difference Fourier map and refined isotropically using a riding model with displacement parameters. The programs for structure solution and refinement were SHELXS-97[13] (Sheldrick, 1990) and SHELXL-97[14] (Sheldrick, 1997), respectively. The crystal belongs to the triclinic space group $P\bar{1}$ with a = 9.118(5), b = 10.089(5), c = 11.434(6) Å, α = 74.652(7), β = 66.775(7), γ = 72.358(8)°, V = 908.4(8) Å^3, Z = 1, empirical formula $C_{18}H_{44}Cu_2MnN_{14}O_2S_6$, molecular mass 863.05, D_c = 1.578 g·cm^{-3}, $F(000)$ = 445, θ range 2.49−26.36°, index ranges $-11 \le h \le 11$, $-12 \le k \le 8$, $-14 \le l \le 14$. A total of 5076 reflections were collected, 3574 were independent (R_{int} = 0.0238) and 2422 observed reflections with $I > 2\sigma(I)$ were used in the succeeding refinement. The final refinement including hydrogen atoms converged to R = 0.0453, wR = 0.0979, $(\Delta\rho)_{max.}$ = 0.644 eÅ^{-3}, $(\Delta\rho)_{min}$ = −0.579 eÅ^{-3}.

Acknowledgments

This work was supported by the National Natural Science Foundation of China (Nos. 20271043, 90101028), the Natural Science Foundation of Shandong Province (No. Y2002B10) and the TRAPOYT of MOE, P. R. C.

[1] [1a] J. R. Friedman, M. P. Sarachik, J. Tejada, R. Ziolo, *Phys. Rev. Lett.* **1996**, *76*, 3830−3833. [1b] W. Wernsdorfer, R. Sessoli, *Science* **1999**, *284*, 133−135. [1c] G. L. J. A. Rickken, E. Raupack, *Nature* **2000**, *405*, 932−935. [1d] R. Lescouëzec, J. Vaissermann, C. R. Pérez, F. Lloret, R. Carrasco, M. Julve, M. Verdaguer, Y. Dromzee; D. Gatteschi, W. Wernsdorfer, *Angew. Chem. Int. Ed.* **2003**, *42*, 1483−1486. [1e] E. Q. Gao, S. Q. Bai, Z. M. Wang, C. H. Yan, *J. Am. Chem. Soc.* **2003**, *125*, 4984−4985. [1f] C. Janiak, *Dalton Trans.* **2003**, 2881−2804.

[2] [2a] K. Nakatani, P. Bergerat, E. Codjovi, C. Mathoniere, Y. Pei, O. Kahn, *Inorg. Chem.* **1991**, *30*, 3977−3978. [2b] S. Tanase, F. Tuna, P. Guionneau, T. Maris, G. Rombaut, C. Mathonière, M. Andruh, O. Kahn, J. P. Sutter, *Inorg. Chem.* **2003**, *42*, 1625−1631. [2c] S. M. Holmes, G. S. Girolami, *J. Am. Chem. Soc.* **1999**, *121*, 5593−5594. [2d] "*Molecule-Based Materials*", (J. S. Miller, M. Drillon, Eds.), Wiley-VCH: Weinheim, Germany, **2001**, vol. 2. [2e]M. Ohbn, H. Okawa, *Coord. Chem. Rev.* **2000**, *198*, 313−328. [2f] R. Sessoli, D. Gatteschi, A. Caneschi, M. A. Novak, *Nature* **1993**, *365*, 141−143. [2g] Y. Liao, W. W. Shum, J. S. Miller, *J. Am. Chem. Soc.* **2002**, *124*, 9336−9337. [2h] S. L. James, *Chem. Soc., Rev.* **2003**, *32*, 276−288.

[3] B. Zurowska, J. Mrozinski, M. Julve, F. Lloret, A. Maslejova, W. Sawka-Dobrowolska, *Inorg. Chem.* **2002**, *41*, 1771−1777.

[4] H. Z. Kou, D. Z. Liao, P. Cheng, Z. H. Jiang, S. P. Yan, G. L. Wang, X. K. Yao, H. G. Wang, *Can. J. Chem.* **1998**, *76*, 1102−1107.

[5] K. L. Zhang, W. Chen, Y. Xu, Z. Wang, Z. J. Zhong, X. Z. You, *Polyhedron* **2001**, *20*, 2033−2036.

[6] A. Skorupa, B. Korybut-Daszkiewicz, J. Mrozinski, *Inorg. Chim. Acta* **2001**, *324*, 286−292.

[7] G. Francese, S. Ferlay, H. W. Schmalle, S. Decurtins, *New J. Chem.* **1999**, 267−269.

[8] G. Wrzeszcz, L. Dobrzanska, A. Wojtczak, A. Grodzicki, *Dalton Trans.* **2002**, 2862−2867.

[9] B. Chiari, A. Cinti, O. Piovesana, P. F. Zanazzi, *Inorg. Chem.* **1995**, *34*, 2652−2657.

[10] L. Shen, Y. Z. Xu, *J. Chem. Soc., Dalton Trans.* **2001**, 3413−3414.

[11] O. Kahn, *Struct. Bonding (Berlin)* **1987**, 68, 89−167.

[12] CCDC-199138 contains the supplementary crystallographic data for this paper. These data can be obtained free of charge at www.ccdc.cam.ac.uk/conts/retrieving.html [or from the Cambridge Crystallographic Data Centre, 12, Union Road, Cambridge CB2 1EZ, UK; Fax: +44-1223-336-033; E-mail: deposit@ccdc.cam.ac.uk].

[13] G. M. Sheldrick, *SHELXS-97*, University of Göttingen, Göttingen, Germany, **1997**.

[14] G. M. Sheldrick, *SHELXL-97*, Univeristy of Göttingen, Göttingen, Germany, **1997**.

Received April 27, 2004

 © 2005 Wiley-VCH Verlag GmbH & Co. KGaA, Weinheim

Oxidation of a One-Dimensional Coordination Polymer and Synthesis of the Macrocyclic Silver Complex $[Ag_{12}(PhS_2P-PS_2Ph)_6(dppeS)_6]$

Dieter Fenske,*[a] Alexander Rothenberger,[a] and Maryam Shafaei Fallah[a]

Keywords: Silver / Chalcogenides / Macrocycle / P ligands / S ligands

The cluster chemistry with functionalised trimethylsilyl reagents was investigated. The oxidation of the one-dimensional coordination polymer $1/_\infty[\{Ag_2(PhS_2P–PS_2Ph)\text{-}dppe\}\cdot dppe]_\infty$ leads to the formation of $[Ag_{12}(PhS_2\text{-}P–PS_2Ph)_6(dppeS)_6]$ (dppeS = $Ph_2P(CH_2)_2P(S)Ph_2$]. The dianionic ligand $[PhPS_2–PS_2Ph]^{2-}$ could possibly give rise to a new class of macrocyclic transition-metal chalcogenides.

(© Wiley-VCH Verlag GmbH & Co. KGaA, 69451 Weinheim, Germany, 2005)

Introduction

Over the last few years we have been investigating the syntheses, structures and properties of a variety of silver-chalcogen clusters including the phosphane-stabilised nanoparticle $[Ag_{262}S_{100}(StBu)_{62}(dppb)_6]$ [dppb = 1,4-bis(diphenylphosphanyl)butane], which can be regarded as the largest ligand-protected silver sulfide complex characterised so far.[1] The general synthetic route to these species involves the reaction of AgX (X = halide, carboxylate) salts with tertiary phosphanes and subsequent reaction with trimethylsilyl chalcogenides.[1] Recently, we continued with earlier work where we investigated the potential of reactions between the sulfur-functionalised phosphane $P(S)(SSiMe_3)_3$ and late transition metal salts for the building up of transition metal clusters with functionalised phosphane ligands.[2] A discovery made during these investigations was that $P(S)(SSiMe_3)_3$ cannot be used as a source of $[PS_4]^{3-}$ anions. Instead a hexathiodiphosphonato tetraanion $[S_3P-PS_3]^{4-}$ is formed in reactions with late transition metal salts and this indicates that $P(S)(SSiMe_3)_3$ possibly undergoes disproportionation into $[(Me_3SiS)_2(S)P-P(S)(SSiMe_3)_2]$, elemental sulfur and $S(SiMe_3)_2$.[2d,2e] This reactivity prompted us to prepare new families of metal aggregates, which are accessible by the reaction of Ag_2S with P_2S_5 or by heating mixtures of elemental Ag, P and S.[3,4] Research in this area was motivated by the interest in sulfide-based glasses and their use as solid electrolytes.[3] For a wet-chemistry approach to these compounds, however, the use of solubilising organic groups is particularly promising. We therefore chose the related silylated reagent $PhP(S)(SSiMe_3)_2$, tertiary phosphanes and silver acetate (AgOAc) as starting materials. Here we wish to report the first result of these efforts and demonstrate the versatility of the P−S ligand $[PhS_2P-PS_2Ph]^{2-}$ generated in the reaction.

Results and Discussion

By the reaction of AgOAc with dppe [dppe = 1,2-bis(diphenylphosphanyl)ethane] and $PhP(S)(SSiMe_3)_2$ (Scheme 1), the one-dimensional coordination polymer $1/_\infty[\{Ag_2(PhS_2P-PS_2Ph)dppe\}\cdot dppe]_\infty$ (**1**) was obtained, and it was characterised by X-ray crystallography and ^{31}P NMR spectroscopy (Figure 1).

Analogous to the previously described reaction of $P(S)(SSiMe_3)_3$, the formation of a P−P bond was observed in reactions of AgOAc with $PhP(S)(SSiMe_3)_2$. In the solid-state structure of **1**, the dianion $[PhS_2P-PS_2Ph]^{2-}$ and one molecule of the neutral phosphane ligand dppe hold together a tricyclic arrangement of two tetrahedrally coordinated Ag^+ ions. An additional molecule of dppe completes the coordination sphere of the Ag atoms and acts as a bridging ligand between the $[Ag_2(dppe)(PhS_2P-PS_2Ph)]$ units (Figure 1). Bond lengths in **1** are within the range of commonly observed values.[4] S−Ag−S bond angles in **1** [96.20(5) and 96.88(5)°] are similar to those observed in a bis(diphenylphosphanyl)methane adduct of a silver thiocarboxylate {S−Ag−S [99.67(5)°]}.[5] It is worth noting that each S atom in **1** (coordination number: 2) coordinates one Ag atom only, and the C−P−P−C torsion angle in the $[PhS_2P-PS_2Ph]^{2-}$ ligand is 50.2(4)°. A change of this torsion angle means alternative orientations of the S-donor centres in the ligand $[PhS_2P-PS_2Ph]^{2-}$, and this might therefore result in different coordination modes of this ligand. Higher coordination numbers for the S-donor centres were found in the related complex $[Cu_6(P_2S_6)Cl_2(PPh_3)_6]$.[2b] X-ray structures of the closest related complexes of **1**,

[a] Institut für Anorganische Chemie, Universität Karlsruhe, Engesserstraße 15, Germany
Fax: (internat.) +49-(0)721-6088440
E-mail: dieter.fenske@chemie.uni-karlsruhe.de

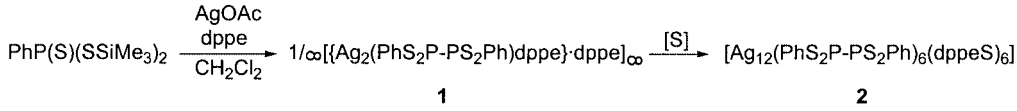

Scheme 1. Synthesis of **1** and oxidation leading to the formation of **2**

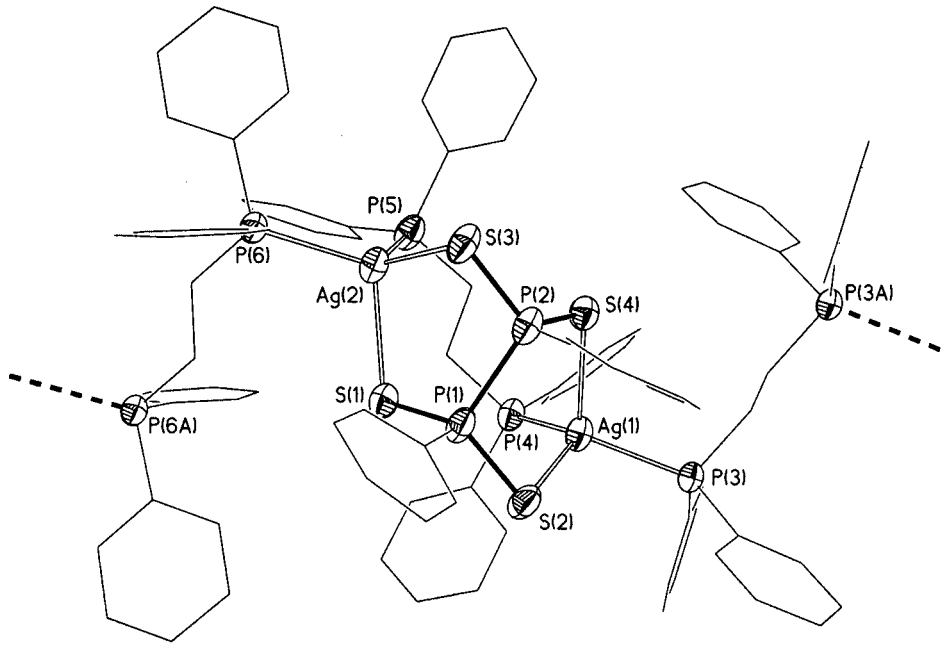

Figure 1. Structure of a dppe-bridged [{$PhPS_2$}$_2Ag_2$·dppe] unit in polymeric **1** (ellipsoids at 50%; connections to adjacent units are indicated; H atoms are omitted); selected bond lengths (Å) and angles (°): Ag−S 2.556(2)−2.631(2), Ag−P 2.475(2)−2.510(2), P−S 1.981(2)−1.992(2), P(1)−P(2) 2.262(3); C−P(1)−P(2)−C 50.2(4), S(2)−Ag(1)−S(4) 96.88(5), S(3)−Ag(2)−S(1) 96.20(5), S−Ag−P 103.89(6)−117.66(6), P−P−S 108.1(1)−108.8(1), S(1)−P(1)−S(2) 117.3(1), S(4)−P(2)−S(3) 116.0(1)

[$M_2(PhS_2P-PS_2Ph)$] (M = Li, K), have to the best of our knowledge not yet been determined.[6]

In solutions of **1**, two species, possibly rotamers, containing P−P bonds are present, which show two singlet resonances at δ = 84.4 and 81.2 ppm. A similar value (δ = 85.4 ppm) is observed in the ^{31}P NMR spectrum of [$Li_2(PhS_2P-PS_2Ph)$].[6b] The P−P bond formation during the preparation of **1** could be rationalized by the disproportion of $PhP(S)(SSiMe_3)_2$ into [$Ph(S)(SSiMe_3)P-P(S)(SSiMe_3)Ph$], which instantly reacts with AgOAc, elemental sulfur and $S(SiMe_3)_2$. The dppe ligands present in solution were oxidised to $Ph_2P(CH_2)_2P(S)Ph_2$ ($\delta_{P=S}$ = 45.6 ppm, $^3J_{P,P}$ = 58 Hz).[7] In **1**, the P^{III} centres of the dppe ligands and $Ph_2P(CH_2)_2P(S)Ph_2$ are identified by a broad singlet resonance (δ = 0.6 ppm) (P−Ag coupling has not been resolved).[7,5] In order to gain further mechanistic insight and to understand the formation of the $[PhS_2P-PS_2Ph]^{2-}$ dianion we tried to synthesise the postulated intermediate diphenyltetrathiodiphosphonic acid trimethylsilyl ester [$Ph(S)(SSiMe_3)P-P(S)(SSiMe_3)Ph$] in the absence of AgOAc by the reaction of $PhP(S)(SSiMe_3)_2$ with dppe. However, these attempts failed, and this indicates that P−P bond formation only occurs in the presence of AgOAc.

Storage of a reaction mixture containing crystals of **1** at room temperature for approximately three weeks produced colourless crystals of [$Ag_{12}(PhS_2P-PS_2Ph)_6(dppeS)_6$] (**2**) [dppeS = $Ph_2P(CH_2)_2P(S)Ph_2$] (Scheme 1). Initially, this was realised because the amount of crystalline precipitate in the reaction mixtures containing crystals of **1** increased, and a closer look revealed that only crystalline blocks of **2** were present. Further experiments have shown that **2** can also be obtained by filtering off crystals of **1** and storage of the filtrate for several weeks. Mixtures of both **1** and **2** were not observed. An X-ray analysis of **2** confirms the results from the ^{31}P NMR spectra, in which indication for the formation of dppeS is found. As a consequence, oxidation-induced fragmentation of polymeric arrangements of **1** gives rise to the macrocyclic complex **2** (Figure 2).

Complex **2** crystallizes in the space group $P\bar{1}$ with the inversion centre located in the middle of the molecule. Complex **2** is constructed from six corner-sharing distorted AgS_4 tetrahedra [Ag−S 2.553(3)−2.767(3)Å, S−Ag−S 89.4(1)−139.9(1)°] and forms a twelve-membered $[AgS]_6$ ring (Figure 2). The six S atoms of the ring are located on the corners of an octahedron with nonbonding S−S distances of about 3.64−4.04 Å. In the periphery, Ag(1) is co-

 © 2005 Wiley-VCH Verlag GmbH & Co. KGaA, Weinheim

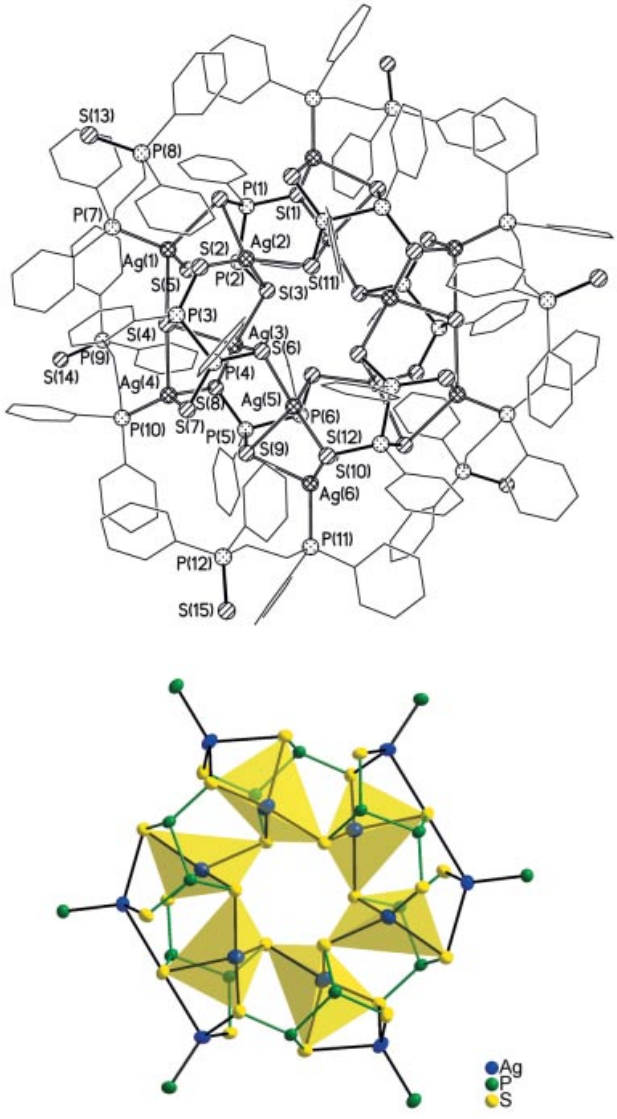

Figure 2. Molecular structure of **2** (H atoms are omitted) and structure of the core of **2** (C atoms and peripheral P and S atoms are omitted; ellipsoids at 50%;); selected ranges of bond lengths (Å) and angles (°): Ag−S 2.535(3)−2.952(4), Ag−P 2.430(3)−2.449(3), P−P 2.261(4)−2.275(5), P−S 1.988(4)−2.020(4), P−S_{dppeS} 1.955(5)−1.966(4); S−Ag−S 87.5(1)−139.9(1), S−Ag−P 91.1(1)−132.6(1), P−P−S 104.1(2)−110.7(2), S−P−S 119.1(2)−120.0(2)

ordinated by S atoms of two different AgS_4 tetrahedra, whilst Ag(4) and Ag(6) are located over the edges of the central AgS_4 units. One S atom of each $[PhS_2P-PS_2Ph]^{2-}$ ligand is not part of the $[Ag_6S_{18}]$ core and completes the tetrahedral coordination sphere of the outer Ag atoms, together with one P atom of the monodentate dppeS ligands (Figure 2). Signals for the chemically non-equivalent P atoms in the $[PhS_2P-PS_2Ph]^{2-}$ ligand in **2** can be observed in the ^{31}P NMR spectrum (AB spin system; two doublet resonances at δ = 82.0 and 79.4 ppm, $^1J_{P,P}$ = 56 Hz). In the Maldi TOF-MS the ions $[Ag(dppeS)]^+$, $[dppe]^+$ and $[dppeS]^+$ were detected. The coordination numbers of the S atoms in **2** are greater than those in the solid-state structure of **1**, and also the C−P−P−C torsion angle in **2** [55.45(5)−58.59(5)°] is about 5−8° wider than that observed in **1**.

Conclusion

The ability of the $[PhS_2P-PS_2Ph]^{2-}$ ligand to coordinate in a variety of modes is demonstrated. Slight changes in the C−P−P−C torsion angle should allow access to a range of new coordination modes with different arrangements of polyhedral building blocks, for example, MS_4 tetrahedra (M = Cu, Ag).[8] Further reactions currently under investigation include metathesis reactions of **1** with metal halides and the oxidation of **1** with elemental sulfur.

Experimental Section

General Remarks: All operations were carried out under purified nitrogen. Dichloromethane was refluxed over calcium hydride, heptane was dried with Na/benzophenone and freshly distilled. AgOAc and dppe were purchased from Aldrich and used without further purification. $PhP(S)(SSiMe)_2$ was prepared by a published method.[9]

1: $PhP(S)(SSiMe_3)_2$ (0.50 g, 1.44 mmol) was added to a pale yellow solution of AgOAc (0.24 g, 1.44 mmol) and dppe (0.57 g, 1.44 mmol) in dichloromethane (20 mL) at −40 °C. The solution instantly became colourless, and the mixture was stirred for 2 h and then warmed up to −10 °C. The reaction was kept at 0 °C for two days. The solvent was then reduced to about 15 mL. Upon addition of heptane (approximately 0.7 mL), a colourless precipitate was formed, which redissolved when the mixture was shaken. After storage of the solution at 0 °C for three weeks, colourless cuboctahedral crystals of **1** were isolated. ^{31}P NMR (101.256 MHz, $CDCl_3$, 25 °C, 65%H_3PO_4) δ = 84.4, 81.2 (s, PhS_2P-PS_2Ph), 0.8 ppm (br. s, Ph_2P-), an additional resonance was observed at δ = 45.0 ppm (d, $^3J_{P,P}$ = 60 Hz, $Ph_2P(CH_2)_2P(S)Ph_2$]. $C_{384}H_{348}Ag_{12}P_{36}S_{24}$: calcd. C 56.65, H 4.31; found C 57.03, H 3.92.

2: After formation of **1** (this was checked by determination of unit-cell dimensions of a small sample), the reaction was stored for four more weeks at 0 °C, and only blocks of **2** were isolated. Yield 0.41 g, 58% (based on AgOAc supplied; **2**, excluding lattice-bound CH_2Cl_2). M.p. 166−168 °C (decomposition into brown melt >172 °C). ^{31}P NMR (121.485 MHz, $CDCl_3$, 25 °C, 65% H_3PO_4): δ = 93.2, 89.4 (s, PhS_2P-PS_2Ph), 82.0 and 79.4 (dd, $^1J_{P,P}$ = 56 Hz, PhS_2P-PS_2Ph), 45.2 [br. m, $Ph_2P(CH_2)_2P(S)Ph_2$], 28.3 ppm [m, $^3J_{P,P}$ = 59 Hz, $Ph_2P(CH_2)_2P(S)Ph_2$] coupling to $^{107/109}Ag$ could not be identified unequivocally, $Ph_2P(CH_2)_2P(S)Ph_2$. IR (CsI, Nujol): $\tilde{\nu}$ = 1439 (P−Ph), 690, 612 (P=S), 579, 508, 466 cm^{-1} (tentatively assigned as P−P and P−S). MS (Maldi TOF), *m*/*z* (%) = 538.39 (30) [dppeSAg$^+$], 430.61 (100) [dppeS$^+$], 398.69 (8) [dppe$^+$]. $C_{228}H_{204}Ag_{12}P_{24}S_{30}$ (5943.7): calcd. C 46.07, H 3.46; found C 46.05, H 3.50.

X-ray Crystallography: Data were collected with a STOE STADI 4 diffractometer equipped with a CCD detector (**1**) and with a Stoe IPDS II diffractometer (**2**) using graphite-monochromated Mo-K_α radiation (λ = 0.71073 Å). The structures were solved by direct methods and refined by full-matrix least-squares on F^2 (all data) with the SHELXTL program package.[10] Hydrogen atoms were placed in calculated positions, non-hydrogen atoms were assigned

 © 2005 Wiley-VCH Verlag GmbH & Co. KGaA, Weinheim

anisotropic thermal parameters, atoms of lattice-bound solvent molecules were refined with isotropic thermal parameters. In order to identify further possible by-products unit-cell dimensions of crystals from different samples were repeatedly determined, and in each case, at first **1** and then **2**, were obtained as the only products that we were able to characterise.

Crystal Data for $1{\cdot}8C_7H_{16}{\cdot}6CH_2Cl_2$: $C_{384}H_{348}Ag_{12}P_{36}S_{24}$ (eight heptane and six CH_2Cl_2 solvent molecules per formula unit), M = 8141.93; trigonal, space group $R\bar{3}$; Z = 3; a = b = 31.214(4), c = 40.099(8) Å; V = 33835(10) Å^3; T = 197(2) K; $F(000)$ = 14568; $D_{calcd.}$ = 1.392 gcm^{-3}. 59537 reflections collected, of which 19049 were unique (R_{int} = 0.0615). 771 parameters; final wR_2 = 0.2367 (all data); R_1 = 0.0727 {$I > 2\sigma(I)$}; largest difference peak and hole 2.834, −0.947 e·Å^{-3}.

Crystal Data for $2{\cdot}18CH_2Cl_2$: $C_{228}H_{204}Ag_{12}P_{24}S_{30}$ (eighteen CH_2Cl_2 solvent molecules per formula unit) M = 5943.83; triclinic, space group $P\bar{1}$; Z = 1; a = 19.281(4), b = 20.329(4), c = 22.806(5) Å; α = 96.20(3), β = 114.11(3), γ = 108.83(3)°; V = 7419(3) Å^3; T = 130(2) K; $F(000)$ = 3732; $D_{calcd.}$ = 1.672 gcm^{-3}. 43858 reflections measured, of which 24516 were unique (R_{int} = 0.0860). 1432 parameters; final wR_2 = 0.2395 (all data); R_1 = 0.0859 {$I > 2\sigma(I)$}; largest difference peak and hole 2.457, -2.055 e·Å^{-3}.

CCDC-243898 and CCDC-243899 contain the supplementary crystallographic data for this paper. These data can be obtained free of charge at www.ccdc.cam.ac.uk/conts/retrieving.html [or from the Cambridge Crystallographic Data Centre, 12 Union Road, Cambridge CB2 1EZ, UK; Fax: (internat.) +44-1223-336-033; E-mail: deposit@ccdc.cam.ac.uk].

Acknowledgments

We gratefully acknowledge the DFG (Zentrum für funktionelle Nanostrukturen) and the Fonds der Chemischen Industrie for financial support. Thanks are also due to Dr. O. Fuhr (Forschungszentrum Karlsruhe) for recording MALDI-TOF spectra.

[1] D. Fenske, C. Persau, S. Dehnen, C. E. Anson, *Angew. Chem.* **2004**, *116*, 309−313 and references cited therein.
[2] For transition metal clusters containing P−P bonded P−S/Se ligands see, for example. [2a] C. W. Liu, C.-M. Hung, B. K. Santra, J.-C. Wang, H.-M. Kao, Z. Lin, *Inorg. Chem.* **2003**, *42*, 8551−8556. [2b] C. W. Liu, H.-C. Chen, J.-C. Wang, T.-C. Keng, *Angew. Chem.* **2001**, *113*, 2404−2406, *Angew. Chem. Int. Ed.* **2001**, *40*, 2342−2344. [2c] K. Chondroudis, D. Chakrabarty, E. A. Axtell, M. G. Kanatzidis, *Z. Anorg. Allg. Chem.* **1998**, *624*, 975−979. [2d] S. Wirth, D. Fenske, *Z. Anorg. Allg. Chem.* **1999**, *625*, 2064−2070. [2e] F. Weigend, S. Wirth, R. Ahlrichs, D. Fenske, *Chem. Eur. J.* **2000**, *6*, 545−551.
[3] Z. Zhang, J. H. Kennedy, H. Eckert, *J. Am. Chem. Soc.* **1992**, *114*, 5775−5784 and references cited therein.
[4] P−P 2.267(5) Å, P−S ca. 2.0 Å, Ag−S 2.528(5)−2.942(5) Å in $Ag_4P_2S_6$: P. Toffoli, P. Khodadad, N. Rodier, *Acta Crystallogr., Sect. C* **1983**, *39*, 1485−1488.
[5] T. C. Deivaraj, J. J. Vittal, *J. Chem. Soc., Dalton Trans.* **2001**, 322−328.
[6] [6a] E. Fluck, H. Binder, *Angew. Chem.* **1967**, *79*, 903. [6b] A. Schmidpeter, K.-H. Zirkow, *Phosphorus and Sulfur* **1988**, *36*, 15−21.
[7] E. I. Matrosov, Z. A. Starikova, A. I. Yanovsky, D. I. Lobanov, I. M. Aladzheva, O. V. Bykhovskaya, Y. T. Struchkov, T. A. Mastryukova, M. I. Kabachnik, *J. Organomet. Chem.* **1997**, *535*, 121−127.
[8] S. Dehnen, A. Eichhöfer, D. Fenske, *Eur. J. Inorg. Chem.* **2002**, 279−317.
[9] J. Hahn, T. Nataniel, *Z. Anorg. Allg. Chem.* **1986**, *543*, 7−21.
[10] G. M. Sheldrick, SHELXTL-97, *Program for Crystal Structure Determination*, University of Göttingen, Germany, **1997**.

Received September 2, 2004

 © 2005 Wiley-VCH Verlag GmbH & Co. KGaA, Weinheim

A New Strategy for the Preparation of Metallaboranes − Solvothermal Synthesis and Structural Characterisation of Two Nido 11-vertex Diplatinaundecaborane Clusters

Jianmin Dou,*[a] Libin Wu,[a] Qingliang Guo,[a] Dacheng Li,[a] and Daqi Wang[a]

Keywords: Diplatinaundecaborane / Deboronation / Hydrothermal synthesis

Two novel nido 11-vertex diplatinaundecaborane clusters $[(\mu\text{-}PPh_2)(PPh_3)_2Pt_2B_9H_6Cl(O\textit{i}Pr)_2]$ (**1**) and $[(\mu\text{-}PPh_2)(PPh_3)_2Pt_2B_9H_6(O\textit{i}Pr)_3]$ (**2**) have been solvothermally synthesised and characterised by elemental analysis, IR, Raman, ^1H and ^{13}C NMR spectroscopy and single-crystal X-ray diffraction. The latter analysis revealed that two Pt atoms remain in neighbouring positions of the open Pt_2B_3 face in both clusters which were markedly different from the products obtained from the identical starting mixture under refluxing conditions.
(© Wiley-VCH Verlag GmbH & Co. KGaA, 69451 Weinheim, Germany, 2005)

Introduction

Hydro(solvo)thermal techniques were originally developed by geochemists to mimic the conditions of mineral growth. They involve heating reaction mixtures in a sealed vessel such that reaction temperatures greater than the boiling point of the solvent can be reached, typically under autogenous pressure. The temperature regime available in hydro(solvo)thermal techniques, intermediate between low-temperature solution chemistry and high-temperature solid-state chemistry, can favour the formation of metastable kinetic rather than thermodynamic products. Recently, hydro(solvo)thermal techniques have attracted much attention in preparative chemistry[1] and have been employed extensively in the preparation of zeolites,[2] oxide and chalcogenide nanoparticles[3] as well as in the synthesis of molecular magnets[4] and coordination polymers.[5]

On the other hand, boron cluster chemistry has progressed considerably and developed into a fruitful area that includes boranes, carboranes, main group heteroboranes, metallaboranes, metallacarboranes and metallaheteroboranes. It has provided a lot of potentially useful applications, including boron neutron capture treatment (BNCT) of tumours, in solvent extractions, material science as well as in catalytic and host-guest chemistry.[6−8] The synthetic methods used to prepare metal-boron clusters are mostly conventional reactions at reflux temperature or cluster fusion processes.[9] To the best of our knowledge, there are no reports on the preparation of metallaboranes using hydro(solvo)thermal techniques in boron cluster chemistry. We have been exploring hydro(solvo)thermal techniques and introducing the strategy into the synthesis of metallaboranes. We now report two nido 11-vertex diplatinaundecaborane clusters $[(\mu\text{-}PPh_2)(PPh_3)_2Pt_2B_9H_6Cl(O\textit{i}Pr)_2]$ (**1**) and $[(\mu\text{-}PPh_2)(PPh_3)_2Pt_2B_9H_6(O\textit{i}Pr)_3]$ (**2**) prepared from the reaction of $[PtCl_2(PPh_3)_2]$ with $[B_{10}H_{10}]^{2-}$ in *i*PrOH under solvothermal conditions.

[a] Department of Chemistry, Liaocheng University, Liaocheng 252059, P. R. China

Results and Discussion

X-ray structural analyses revealed that the structures of these two clusters are very similar except for the substituent groups at position 11 in each case. They both have a *nido*-eleven-vertex $\{Pt_2B_9\}$ polyhedral skeleton with two Pt atoms in neighbouring positions of the open Pt_2B_3 face. These are the first examples of nido 11-vertex diplatinaundecaborane clusters in metallaborane chemistry characterised by X-ray diffraction. There is a PPh_2 group bridging two Pt atoms and the Pt−Pt distances [2.6672(11) Å for **1**, 2.6357(8)Å for **2**] are shorter than the Pt−Pt distances in the diplatinaborane $[(PMe_2Ph)_3ClPt_2B_{10}H_9(PMe_2Ph)]$ (2.863Å)[10] and considerably shorter than the Pt−Pt distances in $[Pt_3(\mu\text{-}PPh_2)_3Ph(PPh_3)_2]$[11] (average 3.0744Å) which also has a PPh_2 group as a bridging ligand. The Pt(7)−P(1) and Pt(8)−P(1) bond lengths are 2.314(4) Å in **1** and 2.2992(10) Å in **2**, and 2.299(4) Å in **1** and 2.3013(13) Å in **2**, respectively. The Pt(7)−P(1)−Pt(8) angle is 70.65(10)° in **1** and 69.91(3)° in **2**, values which are smaller than that in $[Pt_3(\mu\text{-}PPh_2)_3Ph(PPh_3)_2]$[11] [average 86.1(1)°]. Each Pt atom is also connected to one PPh_3 group and three B atoms. The Pt−P bond lengths [2.298(4)−2.3208(10) Å] are similar to the reported Pt−P bond distances in $[(PMe_2Ph)_2PtB_{10}H_{12}]$[12] and $[(PMe_2Ph)_2PtB_{10}H_{11}Cl]$[13] [2.309(1)−2.354(3)Å]. The Pt−B bond lengths are consistent with the corresponding distances found in the related compound $[(PPh_3)(PhCOS)PtB_{10}H_{11}]$

 DOI: 10.1002/ejic.200400731 © 2005 Wiley-VCH Verlag GmbH & Co. KGaA, Weinheim

[2.263(19) Å].[14] A Cl atom remains at vertex 11 in cluster **1**, whereas a O*i*Pr group occupies the same position in cluster **2**. Both have two O*i*Pr group at positions 3 and 9. The bond lengths B−Cl [1.80(2) Å] and B−O [1.359(4)−1.393(4)Å] are in the ranges of the corresponding values in metallaborane clusters.[15]

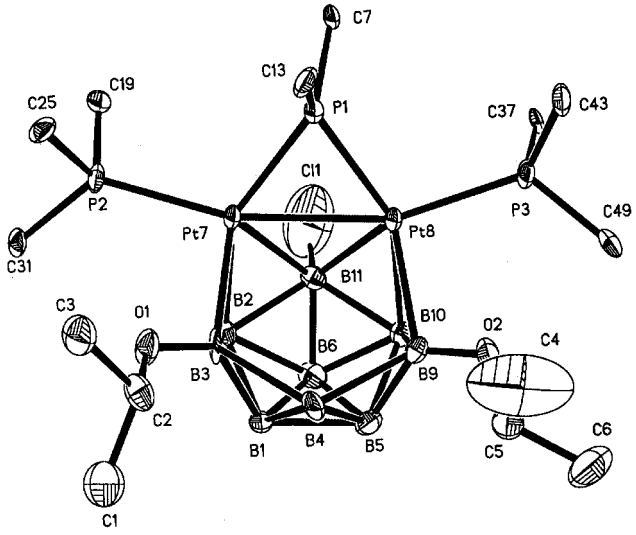

Figure 1. Molecular structure of **1** (H atoms omitted for clarity); selected bond lengths (Å) and angles (°): Pt(7)−Pt(8) 2.6672(11), Pt(7)−P(1) 2.314(4), Pt(8)−P(1) 2.298(4), Pt(7)−P(2) 2.319(4), Pt(8)−P(3) 2.299(4), Pt(7)−B(2) 2.242(16), Pt(7)−B(3) 2.258(19), Pt(7)−B(11) 2.244(16), Pt(8)−B(9) 2.248(18), Pt(8)−B(10) 2.260(15), Pt(8)−B(11) 2.252(16), B(3)−O(1) 1.355(18), B(9)−O(2) 1.38(2), B(11)−Cl(1) 1.80(2); Pt(8)−P(1)−Pt(7) 70.67(10), B(2)−Pt(7)−B(11) 48.4(6), B(2)−Pt(7)−B(3) 47.5(6), B(3)−Pt(7)−B(11) 81.7(6), B(9)−Pt(8)−B(10) 45.7(6), B(9)−Pt(8)−B(11) 82.0(7), B(11)−Pt(8)−B(10) 48.1(6).

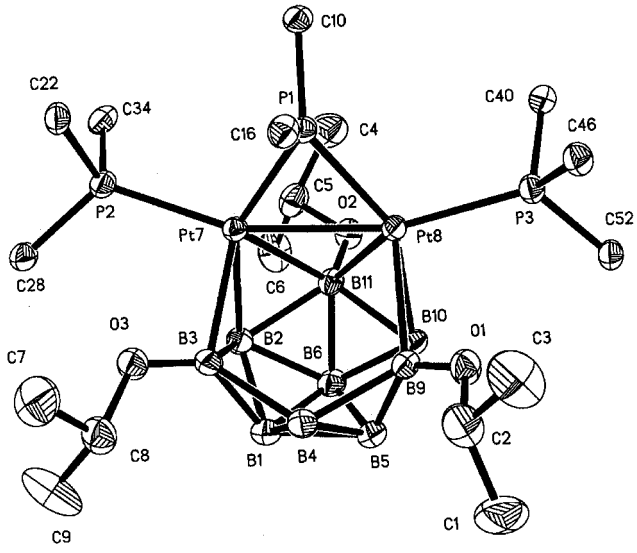

Figure 2. Molecular structure of **2** (H atoms omitted for clarity). Selected bond lengths (Å) and angles (°): Pt(7)−Pt(8) 2.6357(8), Pt(7)−P(1) 2.2992(10), Pt(8)−P(1) 2.3013(13), Pt(7)−P(2) 2.3208(10), Pt(8)−P(3) 2.3081(12), Pt(7)−B(2) 2.260(4), Pt(7)−B(3) 2.261(4), Pt(7)−B(11) 2.301(4), Pt(8)−B(9) 2.293(4), Pt(8)−B(10) 2.242(4), Pt(8)−B(11) 2.277(4), B(3)−O(3) 1.359(4), B(9)−O(1) 1.371(4), B(11)−O(2) 1.393(4); Pt(8)−P(1)−Pt(7) 69.91(3), B(2)−Pt(7)−B(11) 48.31(13), B(2)−Pt(7)−B(3) 46.44(14), B(3)−Pt(7)−B(11) 83.29(14), B(9)−Pt(8)−B(10) 46.37(15), B(9)−Pt(8)−B(11) 83.25(14), B(11)−Pt(8)−B(10) 49.03(13).

When the reaction of $[PtCl_2(PPh_3)_2]$ with $[B_{10}H_{10}]^{2-}$ in *i*PrOH takes place under conventional reflux conditions under a dry N_2 atmosphere, three nido 11-vertex platinaundecaborane clusters $[(PPh_3)_2PtB_{10}H_{10}$-8-O*i*Pr], $[(PPh_3)_2PtB_{10}H_{10}$-9-O*i*Pr] and $\{(PPh_3)_2PtB_{10}H_{10}$–8, 10-$(OiPr)_2\}$ are obtained.[16] These species are markedly different from the products obtained under solvothermal conditions. The reason for this may be attributed to the high temperature of the solvothermal reaction. Another example is that the reaction of $[RuCl_2(PPh_3)_3]$ with $[B_{10}H_{10}]^{2-}$ in glycol also yield two deboronated clusters $[(PPh_3)ClHRuB_9H_6(PPh_3)_2(OCH_2CH_2OH)]$ and $[(PPh_3)$-$ClHRuB_9H_5(OCH_2CH_2OH)_2(PPh_3)_2]$.[17] This illustrates that deboronation can be occur easily at high temperature. Another case of deboronation of $[B_{10}H_{10}]^{2-}$ can be included: trans-$[Ir(CO)Cl(PPh_3)_2]$ reacts with $[B_{10}H_{10}]^{2-}$ in methanol at reflux to yield $[\{IrC(OH)B_8H_6(OMe)\}$-$(C_6H_4PPh_2)(PPh_3)]$, $[(MeCOO)(PPh_3)\{HIrCB_8H_7(PPh_3)\}]$ and $[1,1,2$-$(CO)_3$-1-(PPh_3)-2,2-$(Ph_2P$-*ortho*-$C_6H_4)_2$-*closo*-$(1,2$-$Ir_2B_4H_2)]$.[18]

Conclusion

We have introduced solvothermal techniques into the preparation of metallaborane clusters for the first time and obtained two novel nido 11-vertex diplatinaundecaborane clusters, in which one boron atom was deboronated and two Pt atoms remain in neighbouring positions of the open Pt_2B_3 face in both clusters. The isolation of these two clusters suggests that temperature can control the result of the reaction.

Experimental Section

Materials and General Methods: All chemicals were commercially purchased and used without further purification except *i*PrOH which was dried with CaH_2. Elemental analyses (C, H and N) were performed with a Perkin−Elmer 2400 II Elemental Analyser. IR spectra were recorded in the range 400−4000cm^{-1} with an Nicolet-460 FT-IR spectrophotometer using KBr pellets. Raman spectra were acquired on a Renshaw RM2000 spectrophotometer. ^{1}H NMR and ^{13}C NMR spectra were recorded using a Varian Mercury 400 (400 MHz) nuclear magnetic resonance instrument.

Synthesis of $[(\mu$-$PPh_2)(PPh_3)_2Pt_2B_9H_6Cl(OiPr)_2]$ (1) and $[(\mu$-$PPh_2)(PPh_3)_2Pt_2B_9H_6(OiPr)_3]$ (2): $(NEt_4)_2[B_{10}H_{10}]$ (303 mg, 8 mmol), $[PtCl_2(PPh_3)_2]$ (317 mg, 4 mmol) and distilled *i*PrOH (25 mL) were mixed in a Telfon lined autoclave under a dry N_2 atmosphere. The mixture was maintained at 170 °C for 96 h then slowly cooled to room temperature. TLC separation (silica G, CH_2Cl_2/light petroleum, 4:1) gave clusters **1** (R_f = 0.54, 18 mg, 2.9%) and **2** (R_f = 0.24, 77 mg, 12.4%). The single-crystals were obtained from an *n*-pentane/dichloromethane solution.

Cluster 1: $C_{54}H_{60}B_9ClO_2P_3Pt_2$ (M = 1356.85): calcd. C 47.80, H 4.42, found C 47.68, H 4.33. FT-IR (KBr): 3054 (m), 2970 (m), 2507 (vs), 1633 (s), 1434 (vs), 1234 (s), 1109 (s), 1095 (vs), 691 (s), 528 cm^{-1} (s).

 © 2005 Wiley-VCH Verlag GmbH & Co. KGaA, Weinheim

Cluster 2: $C_{57}H_{67}B_9O_3P_3Pt_2$ (M = 1380.49): calcd. C 49.55, H 4.85, found C 49.13, H 4.56. FT-IR (KBr): 3050 (m), 2963 (m), 2509 (vs), 1634 (m), 1433 (s), 1382 (m), 1108 (vs), 691 cm^{-1} (vs); Raman: 3052.5 (m), 2513.8 (vs), 1583 (m), 1097 (m), 1000 (vs), 215 cm^{-1} (w). ^1H NMR (400.15 MHz, $CDCl_3$): δ = 0.659 (d, J = 6.0 Hz, 6 H, CH_3), 0.822 (d, J = 6.0 Hz, 6 H, CH_3), 1.101 (d, J = 6.4 Hz, 6 H, CH_3), 4.181 (7, J = 6.4 Hz, 1 H, CH), 4.462 ppm (7, J = 6.0 Hz, 2 H, CH). ^{13}C NMR (100.63 MHz, $CDCl_3$): δ = 23.452, 23.766, 25.475, (6 C, CH_3), 73.781 ppm (3 C, CH).

X-ray Crystallography: Data were collected on a Bruker SMART 1000 CCD diffractometer using Mo-K_α radiation. Both structures were solved by direct methods and subsequent Fourier difference techniques and then refined anisotropically for all nonhydrogen atoms by full-matrix least-squares calculations on F^2 using the SHELXTL program package. CCDC-245790 and -245791 contain the supplementary crystallographic data for this paper. These data can be obtained free of charge at www.ccdc.cam.ac.uk/conts/retrieving.html [or from the Cambridge Crystallographic Data Centre, 12 Union Road, Cambridge CB2 1EZ, UK; Fax: +44-1223-336-033; E-mail: deposit@ccdc.cam.ac.uk].

Crystal Data for 1: $C_{54}H_{60}B_9ClO_2P_3Pt_2$, M = 1356.85, triclinic, space group $P\bar{1}$, a = 12.611(5), b = 13.469(5), c = 17.930(7) Å, α = 83.357(6), β = 75.989(6), γ = 67.832(5)°, V = 2735.40(18) Å^3, T = 293(2) K, Z = 2, $D_{calcd.}$ = 1.647 g/cm^3, crystal dimensions 0.38 × 0.27 × 0.17 mm, Mo-K_α radiation, λ = 0.71073 Å, R_1 = 0.0675, wR_2 = 0.1471 for 5531 reflections with $I > 2\sigma(I)$, and R_1 = 0.1197, wR_2 = 0.1675 for all 14090 reflections.

Crystal Data for 2: $C_{57}H_{67}B_9O_3P_3Pt_2$, M = 1380.49, monoclinic, space group $P2_1/c$, a = 14.104(6), b = 16.846(7), c = 24.842(11) Å, β = 99.021(9)°, V = 5829(4) Å^3, T = 298(2) K, Z = 4, $D_{calcd.}$ = 1.573 g/cm^3, crystal dimensions 0.45 × 0.41 × 0.29 mm, Mo-K_α radiation, λ = 0.71073 Å, R_1 = 0.0195, wR_2 = 0.0473 for 8792 reflections with $I > 2\ \sigma(I)$, and R_1 = 0.0279, wR_2 = 0.0504 for all 30174 reflections.

Acknowledgments

This work was financially supported by the National Natural Science Foundation of China (Project No. 20371025).

[1] A. Rabenau, *Angew. Chem. Int. Ed. Engl.* **1985**, *24*, 1026−1040.
[2] [2a] J. Livage, *Coord. Chem. Rev.* **1998**, 178−180, 999−1018. [2b] R. I. Walton, *Chem. Soc., Rev.* **2002**, *31*, 230−238.
[3] [3a] M. Rajamathi, R. Seshadri, *Currt. Opin. Solid State Mater. Sci.* **2002**, *6*, 337−345. [3b] J. Li, Z. Chen, R.-J. Wang, D. M. Proserpio, *Coord. Chem. Rev.* **1999**, 190−192, 707−735.
[4] R. H. Laye, E. J. L. Mclnnes, *Eur. J. Inorg. Chem.* **2004**, *14*, 2811−2818.
[5] J. Y. Lu, *Coord. Chem. Rev.* **2003**, *246*, 327−347.
[6] M. F. Hawthorne, *Angew. Chem. Int. Ed. Engl.* **1993**, *32*, 950−984.
[7] [7a] J. Plesek, *Chem. Rev.* **1992**, *92*, 269−278. [7b] R. N. Grimes, *J. Chem. Ed.* **2004**, *81*, 658−672.
[8] [8a] M. F. Hawthorne, X. G. Yang, Z. Zheng, *Pure Appl. Chem.* **1994**, *66*, 245−254. [8b] M. F Hawthorne, Z. Zheng, *Acc. Chem. Res.* **1997**, *30*, 267−276. [8c] M. J. Hardie, C. L. Raston, *Angew. Chem. Int. Ed.* **2000**, *39*, 3835−3839. [8d] M. J. Hardie, C. L. Raston, *Chem. Commun.* **2001**, 905−906. [8e] N. Malic, P. J. Nichols, C. L. Raston, *Chem. Commun.* **2002**, 16−17. [8f] S. L. Shea, J. Bould, M. G. S. Londesborough, S. D. Perera, A. Franken, D. L. Ormsby, T. Jelínek, B. Stíbr, J. Holub, C. M. Thornton-Pett, J. D. Kennedy, *Pure Appl. Chem.* **2003**, *75*, 1239−1248.
[9] [9a] N. N. Greenwood, *Chem. Soc., Rev.* **1973**, *2*, 231−271. [9b] N. N. Greenwood, *Pure Appl. Chem.* **1983**, *55*, 1415−1430. [9c] N. N. Greenwood, *Nova. Acta Leopold.* **1985**, *59*, 291−304. [9d] N. N. Greenwood, J. D. Kennedy, *Pure Appl. Chem.* **1991**, *63*, 317−326. [9e] A. K. Hughes, *J. Organomet. Chem.* **2002**, *657*, 9−19. [9f] Z. W. Xie, *Coord. Chem. Rev.* **2002**, *231*, 23−46. [9g] R. N. Grimes, *Coord. Chem. Rev.* **2002**, 200−202, 773−811. [9h] A. K. Saxena, N. S. Hosmane, *Chem. Rev.* **1993**, *93*, 1081−1124. [9i] A. K. Saxena, J. A. Maguire, N. S. Hosmane, *Chem. Rev.* **1997**, *97*, 2421−2462. [9j] J. D. Kennedy, *Royal Chem. Soc.* **1997**, *201*, 451−462. [9k] J. Bould, W. Clegg, S. J. Teat, L. Barton, N. P. Rath, M. Thornton-Pett, J. D. Kennedy, *Inorg. Chim. Acta* **1999**, *289*, 95−124.
[10] D. M. P. Mingos, *J. Chem. Soc., Dalton Trans.* **1977**, 602−610.
[11] R. Bender, P. Braunstein, A. Dedieu, P. D. Ellis, B. Huggins, P. D. Harvey, E. Sappa, A. Tirepicchio, *Inorg. Chem.* **1996**, *35*, 1223−1234.
[12] S. K. Boocock, N. N. Greenwood, J. D. Kennedy, W. S. McDonald, J. Staves, *J. Chem. Soc., Dalton Trans.* **1981**, 2573−2584.
[13] J. E. Crook, N. N. Greenwood, J. D. Kennedy, W. S. McDonald, *J. Chem. Soc., Dalton Trans.* **1984**, 2487−2495.
[14] C.-H. Hu, J.-M. Dou, J. Sun, H.-J. Yao, J.-D. Wei, R.-S. Jin, P.-J. Zheng, *Acta Crystallogr., Sect. C* **1998**, *54*, 1089−1091.
[15] [15a] J. D. Kennedy, *Prog. Inorg. Chem.* **1984**, *32*, 519−679. [15b] J. D. Kennedy, *Prog. Inorg. Chem.* **1986**, *34*, 211−434.
[16] [16a] Y. Nie, C.-H. Hu, X. Li, W. Yong, J.-M. Dou, J. Sun, R.-S. Jin, P.-J. Zheng, *Acta Crystallogr., Sect. C* **2001**, *57*, 897−899. [16b] W. Yong, C.-H. Hu, J.-M. Dou, J. Sun, K.-J. Hu, R.-S. Jin, P.-J. Zheng, *Chin. J. Chem.* **2001**, *19*, 1162−1164.
[17] H.-J. Yao, C.-H. Hu, J.-M. Dou, J. Sun, J.-D. Wei, R.-S. Jin, P.-J. Zheng, *Acta Crystallogr., Sect. C* **1999**, *55*, 337−339.
[18] [18a] J. E. Crook, N. N. Greenwood, J. D. Kennedy, W. S. McDonald, *J. Chem. Soc., Chem. Commun.* **1981**, 933−934. [18b] J. E. Crook, N. N. Greenwood, J. D. Kennedy, W. S. McDonald, *J. Chem. Soc., Chem. Commun.* **1982**, 383−384. [18c] J. E. Crook, N. N. Greenwood, J. D. Kennedy, W. S. McDonald, *J. Chem. Soc., Chem. Commun.* **1983**, 83−84.

Received August 30, 2004

 © 2005 Wiley-VCH Verlag GmbH & Co. KGaA, Weinheim

Anion-Induced Motion in a Ferrocene Diamide

Katja Heinze*[a] and Manuela Schlenker[a]

Keywords: Anion recognition / Anion sensing / Hydrogen bonds / Metallocenes / Receptors

An unsymmetrical diferrocene diamide has been reacted with chloride ions. The anion splits the intramolecular hydrogen bond of the receptor and is coordinated simultaneously by both amide groups of the receptor via hydrogen bonds. Chloride coordination changes the relative angular position of the cyclopentadienyl rings and the potential of the ferrocene/ferricinium redox couple.

(© Wiley-VCH Verlag GmbH & Co. KGaA, 69451 Weinheim, Germany, 2005)

Introduction

Control of mechanical motions of single molecules by external stimuli has attracted great attention in relation to biological machines such as muscles and for the development of artificial molecular machines and devices. Various molecular machines have been reported, such as motors, shuttles, switches and tweezers that respond to stimuli such as protons (pH), electrons (redox processes) and light.[1−3] Here we describe an anion-driven molecular hinge where the opening of an intramolecular lock is transformed into an angular motion. Examples of such an interlocking mechanical motion are still rare;[4] most precedent machines, based on rotaxanes or catenanes, operate by individual motions of driving parts.

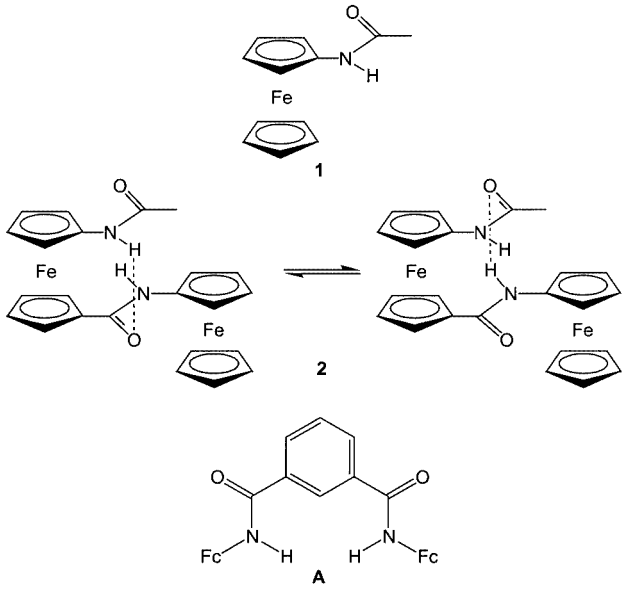

Scheme 1. Ferrocene amides **1**, **2** and Crabtree's receptor **A**[6] (Fc = ferrocenyl)

Results and Discussion

Recently, we prepared the unsymmetrical diferrocene diamide **2**, which possesses a dynamic intramolecular hydrogen bond in solution (Scheme 1, middle).[5] This dynamic bridge remains intact up to 55 °C, as shown by NMR and IR spectroscopy and corroborated by DFT calculations.[5] The amide protons of **2** do not undergo H/D exchange with D_2O in CH_2Cl_2, underlining this stability. Thus, the hydrogen-bond lock hinders the normally free rotation of the cyclopentadienyl rings of the disubstituted ferrocene.

Conversely, external hydrogen acceptors such as anions bind to amide groups.[7] This could, presumably, affect the internal hydrogen bond. Thus ferrocene amides **1**, which represents "one half" of **2** (Scheme 1), and **2** were treated with chloride ions in the non-coordinating solvent dichloromethane.

Addition of chloride ions as their tetra-*n*-butyl ammonium salts to the receptors **1** and **2** leads to the disappearance of the signal of the "free" NH groups (**1**: 3435 cm^{-1}; **2**: 3430 cm^{-1}) from the IR spectra (Figure 1, left) and a shift of the CO stretching signals to lower energy (Figure 1, right: **1**: 1685 → 1666 cm^{-1}; **2**: 1679/1660 → 1659 cm^{-1}) for both ferrocene amides, indicating that the chloride ions interact with the amide groups. As the strong signals of the CH vibrations of the tetra-*n*-butyl ammonium

[a] Anorganisch-Chemisches Institut der Universität Heidelberg
Im Neuenheimer Feld 270, 69120 Heidelberg, Germany
Fax: (internat.) + 49-(0)6221-545707
E-mail: katja.heinze@urz.uni-heidelberg.de

Supporting information for this article is available on the WWW under http://www.eurjic.org or from the author.

 © 2005 Wiley-VCH Verlag GmbH & Co. KGaA, Weinheim DOI: 10.1002/ejic.200400726

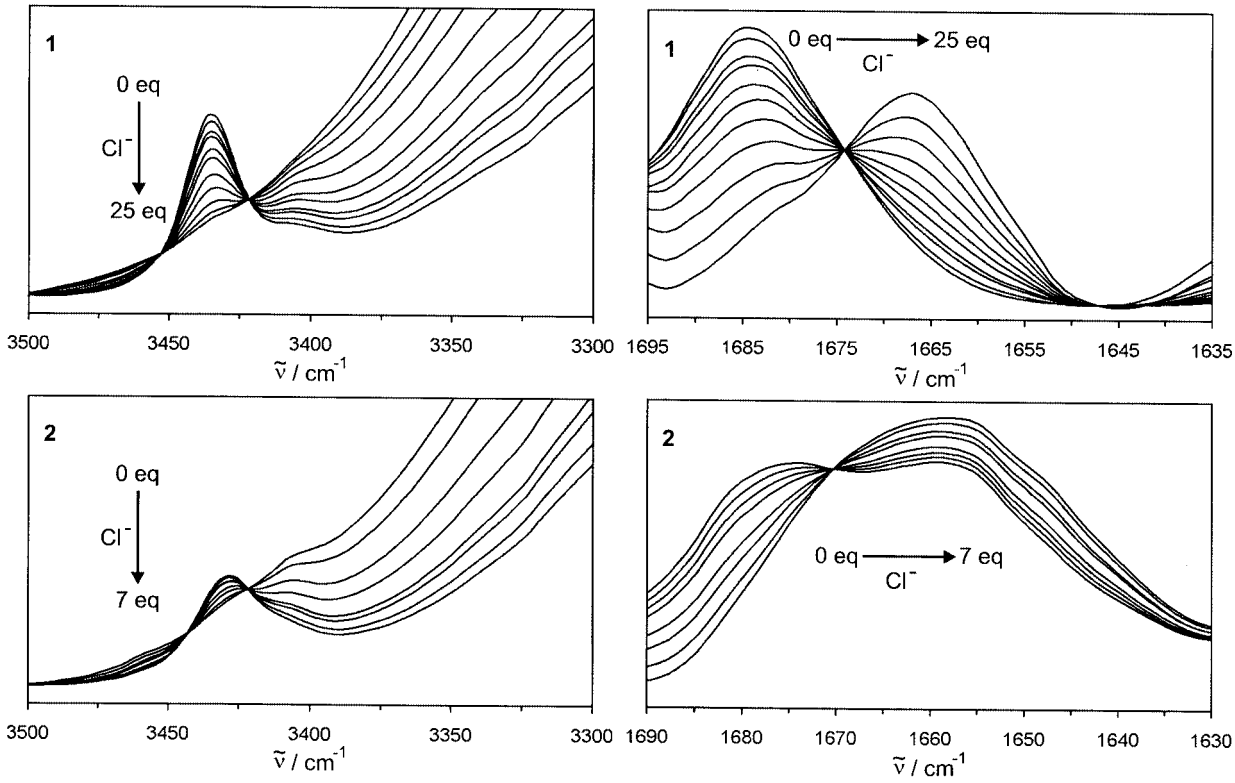

Figure 1. IR spectra of **1** (top) and **2** (bottom) during addition of $(n\text{Bu})_4\text{NCl}$ in CH_2Cl_2 at 300 K (0.0036 M)

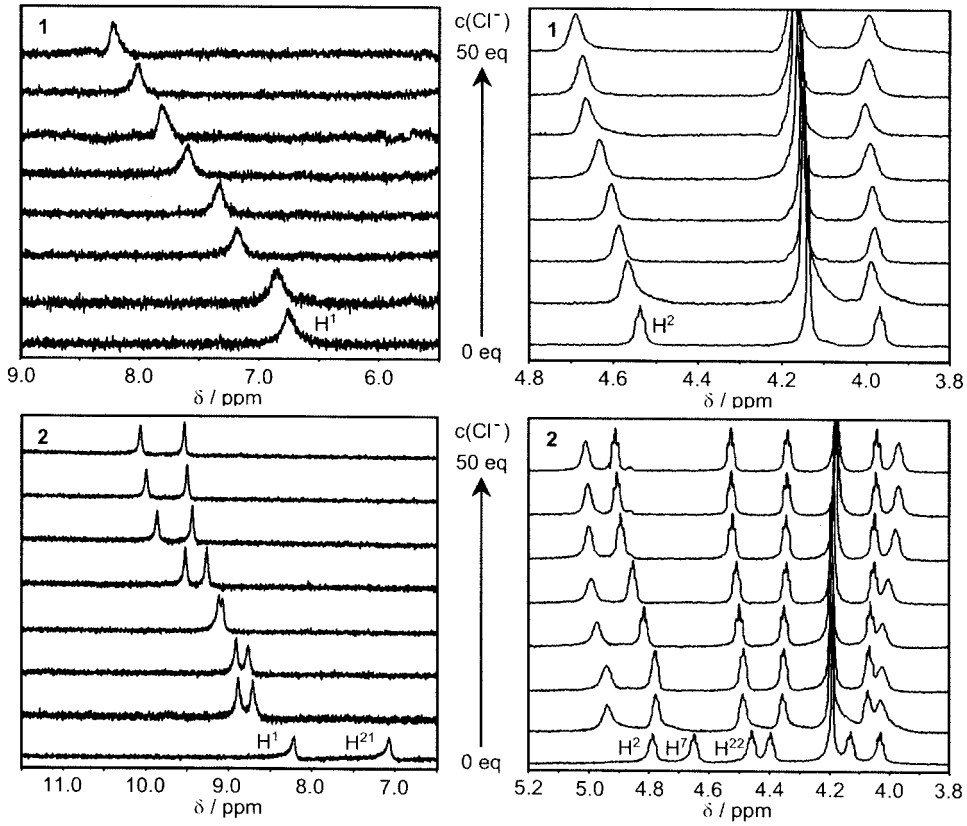

Figure 2. ^{1}H NMR spectra of **1** (top) and **2** (bottom) (NH and Cp-H region) during addition of $(n\text{Bu})_4\text{NCl}$ at 300 K (0.005 M)

 © 2005 Wiley-VCH Verlag GmbH & Co. KGaA, Weinheim

cation strongly modify the baseline, integration of the NH stretching vibration signals proved unreliable. However, receptor **1** requires more chloride ions than receptor **2** to reach saturation − as seen qualitatively from the IR spectra (Figure 1).

To obtain deeper insight into the association process proton NMR spectra[8] were recorded during the addition of chloride ions (Figure 2). Several proton signals of the ferrocene amides are shifted significantly to lower field upon increasing chloride concentration. The shift is especially pronounced for signals of the amide protons H^1 and H^{21} and the neighboring cyclopentadienyl protons H^2 ("upper" cyclopentadienyl ring), H^{22} and H^7 ("middle" cyclopentadienyl rings) (see Figure 4 for atom numbering).

Saturation is reached at relative concentrations of approximately 1:50 (**1**:Cl^-) and 1:20 (**2**:Cl^-), respectively (Figure 3), which is in qualitative agreement with the IR data. Thus, diamide **2** has a much larger affinity to chloride ions than monoamide **1**. If the amide groups of **2** behaved independently the amount of anion needed to satisfy both groups of **2** should be about twice that needed for monoamide **1**, i.e. saturation would be expected at a **2**:Cl^- ratio of ca. 1:100. As this is obviously not the case the two amide groups of **2** bind chloride ions in a cooperative way.

Thorough investigation of the CIS (chemically induced shift) values of **2** revealed that the two NH groups, with their neighboring CH groups, display different affinity towards chloride ions, with H^1 and its neighboring H^2 having a stronger affinity than H^{21} and its neighboring H^{22} and H^7 (Figure 3, bottom). This finding is in contrast to observations made for the symmetrical diferrocene diamide **A** prepared by Crabtree[6] (Scheme 1, bottom) as the protons of the two amides of **A** are spectroscopically indistinguishable. The strongly shifted amide protons H^1 and H^{21} and the Cp protons H^2, H^7 and H^{22} allow us to map the sites of receptor **2** where anion coordination takes place (Figure 4). According to Figure 4, the chloride ion can approach the receptor at the "upper" amide group (H^1, H^2), at the "lower" amide group (H^{21}, H^7, H^{22}) or at both NH groups simultaneously in a different conformation of **2**. To prove that both amide groups are accessible for chemical attack, **2** has been reacted with excess sodium amide and

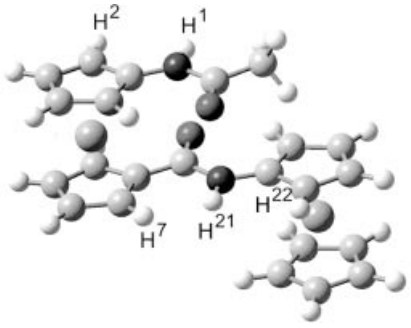

Figure 4. Protons of **2** affected by anion coordination

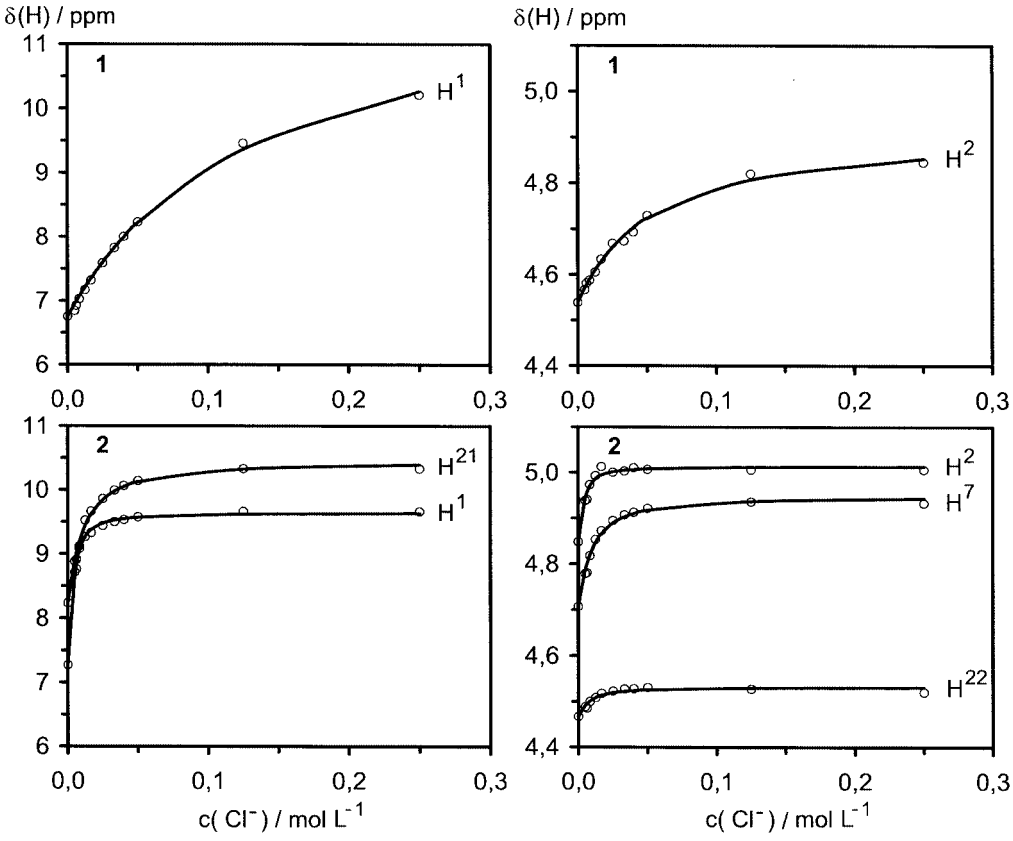

Figure 3. ^1H NMR titration plots of **1** (top) and **2** (bottom) with $(n\text{Bu})_4NCl$ in CD_2Cl_2 at 300 K (0.005 M)

 © 2005 Wiley-VCH Verlag GmbH & Co. KGaA, Weinheim

quenched with D_2O. Proton NMR and IR spectra of the final product (see Supporting Information) show that **2** can be deprotonated either at H^1 or at H^{21} with equal probability.[9] Thus, sterically, H^1 and H^{21} are equally accessible.

The much stronger binding capability of **2** as compared to that of **1** is certainly due to a chelate effect, which has numerous precedents in anion recognition chemistry.[10] However, the cooperative binding of the two amide groups is much less pronounced for **2** than for the "unlocked" preorganised receptor **A** (Scheme 1, bottom).[6] Thus, we propose a stepwise mechanism of anion association to **2** (Figure 5).

According to DFT calculations (B3LYP, LanL2DZ; see Supporting Information), the chloride ion can associate to H^1 (Figure 5, structure **I**), to H^2 (Figure 5, structure **II**) or to both amide protons simultaneously (Figure 5, structure **III**).[11] This accords with the NMR spectroscopic data, which show that both amide protons interact with the chloride ion, and with the IR data, which show the disappearance of "free" NH groups upon chloride addition. All three minimum structures **I**−**III** possess two hydrogen bonds: structure **I** displays a hydrogen bond from H^1 to chloride and an intramolecular hydrogen bond from H^2 to O^1; **II** shows a hydrogen bond from H^2 to chloride and an intramolecular hydrogen bond from H^1 to O^2; and in structure **III** the chloride ion is attached to H^1 and H^2 simultaneously, which corresponds to the most stable structure. The loss of the intramolecular NH···O hydrogen bond in **III** explains the lower affinity of **2** compared to the preorganised receptor **A**.[6]

All the structures can be interconverted by hydrogen bond-making/breaking processes and concomitant relative rotation of the cyclopentadienyl rings. As the equilibria could not be frozen out down to 190 K on the NMR time scale (500 MHz), intermolecular[11] low-energy pathways should exist that easily interconvert **I**, **II** and **III** and their respective enantiomers.

For the lowest energy structure **III** the two cyclopentadienyl rings of the 1,1′-disubstituted ferrocene are rotated against each other by 95°, which is about twice the angle calculated for a light-driven ferrocene-based "molecular scissor" (49°).[4]

The native "locked" state of **2**, i.e. the intramolecular hydrogen bond, can be restored by removal of the chloride ions through the addition of excess thallium cations.[12] Angular motion of the cyclopentadienyl rings of **2** can thus be triggered by the presence or absence of chloride ions (Scheme 2, a). Thus the anion-based system presented resembles Lehn's cation-induced dynamic chemical device based on a *transoid/cisoid* rearrangement of terpyridines (Scheme 2, b).[3]

In addition to the angular motion induced by anion binding, the ferrocene moieties provide the electrochemical response expected for amide substituted ferrocenes.[10] Figure 6 shows the cyclic voltammograms of receptors **1** and **2** during the addition of chloride ions. For receptor **2**, the second oxidation becomes irreversible at higher chloride concentrations, probably due to the coordination of another anion to the charged receptor.

The anion-induced cathodic shift of the ferrocene/ferricinium oxidation wave is linear up to two equivalents of chloride ions for monoamide **1** (Figure 7). Due to the larger anion affinity of **2**, saturation is reached at 1.2 equivalents of chloride (Figure 7). As the maximum cathodic shifts $\Delta E_{1/2}$ are equal for both amidoferrocenes (30 mV within the linear range[13]), the slope of the $\Delta E_{1/2}$ vs. $[Cl^-]$ plot,

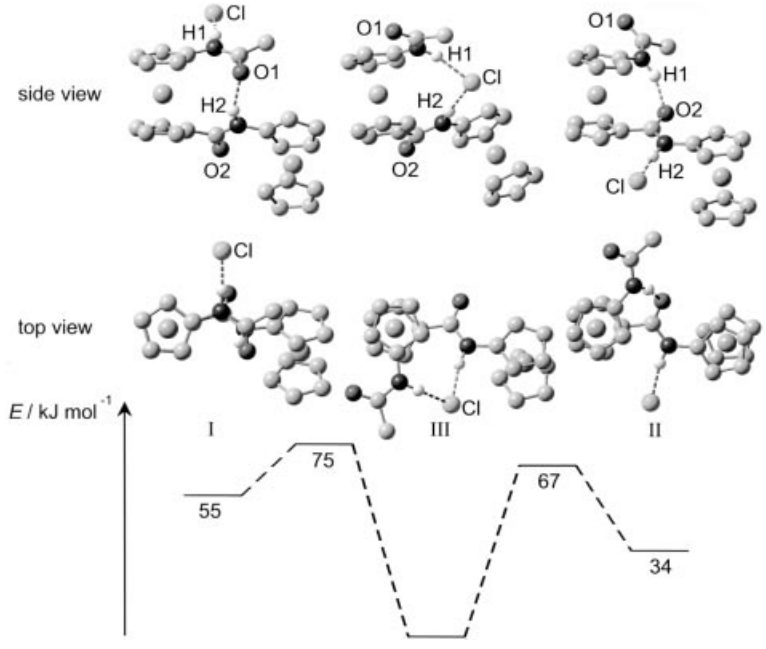

Figure 5. DFT calculated minimum structures **I**−**III** for chloride association to **2** (C−H protons not shown)

 © 2005 Wiley-VCH Verlag GmbH & Co. KGaA, Weinheim

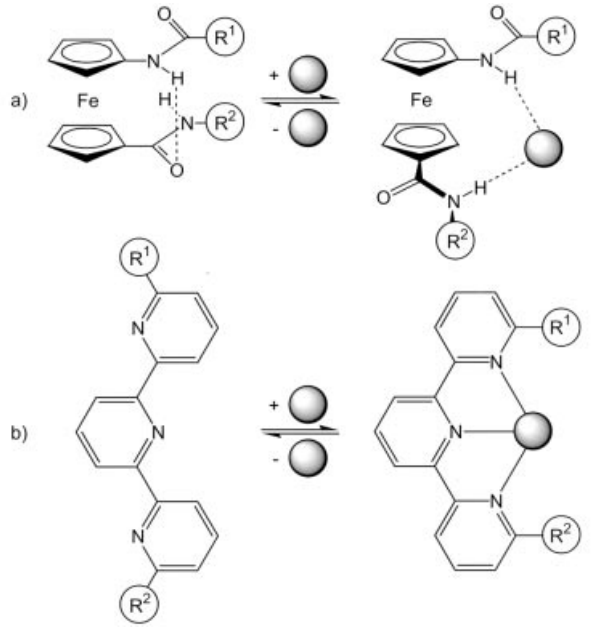

Scheme 2. (a) $R^1 = CH_3$, R^2 = ferrocenyl, grey circle: chloride anion; (b) $R^1 = R^2$ = pyrenyl, grey circle: zinc cation

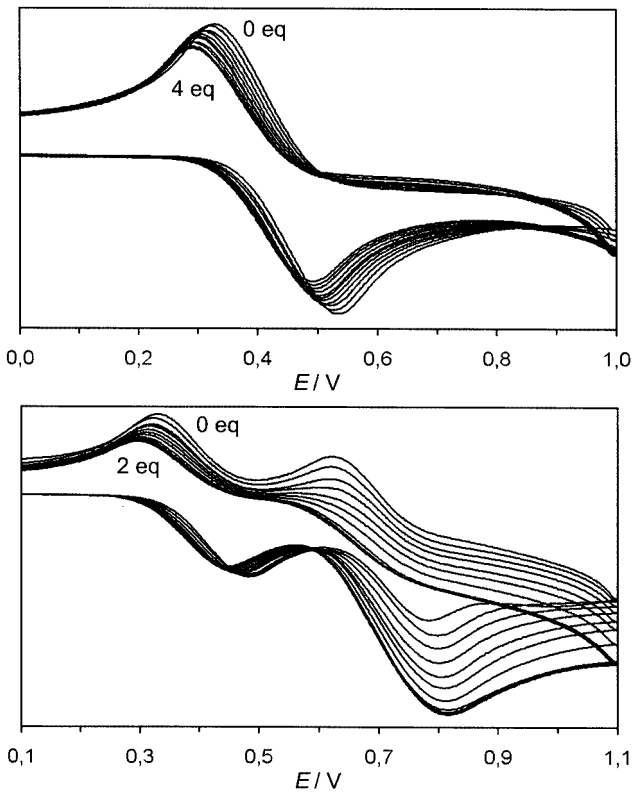

Figure 6. Cyclic voltammograms of **1** (top) and **2** (bottom) in the presence of $(n\text{Bu})_4\text{NCl}$ in 0.1 M $(n\text{Bu})_4\text{NBF}_4/CH_2Cl_2$ vs. SCE at 300 K (scan rate 200 mV s^{-1})

and thus the sensitivity as anion sensor, is enhanced for receptor **2** relative to **1** (Figure 7).

Consequently, **2** is a "dual-functional molecular machine", giving a mechanical and an electrochemical output upon a simple chemical input. Incorporation of this flexible

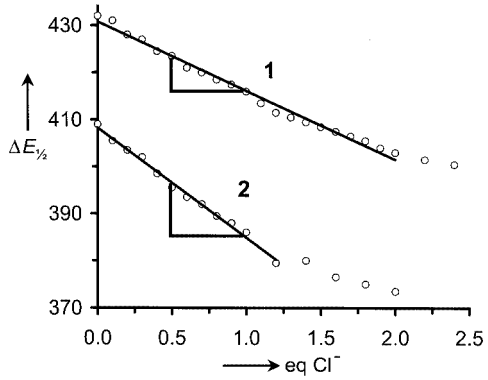

Figure 7. ΔE vs. eq Cl^- plots for receptors **1** and **2**

but controllable building block into larger arrays, e.g. in the backbone of peptides (R^1, R^2 = peptides in Scheme 2, a), or between fluorescent reporter groups may lead to novel hybrid (bio)materials with unconventional dynamics and (redox) functions.[14–16] Work in this direction is currently in progress.

Experimental Section

Compounds **1** and **2** were prepared by published procedures.[5] NMR: Bruker Avance DPX 200 at 200.15 MHz (^1H) at 303 K; chemical shifts (δ) in ppm with respect to residual solvent peaks as internal standard: CD_2Cl_2 (^1H: δ = 5.32 ppm). IR spectra were recorded on a BioRad Excalibur FTS 3000 spectrometer using CaF_2 cells in CH_2Cl_2. Cyclic voltammetry was performed using a glassy carbon electrode, a platinum electrode and a SCE electrode, 10^{-3} M in 0.1 M $n\text{Bu}_4\text{NBF}_4/CH_2Cl_2$; potentials are given relative to SCE. Computational method: density functional calculations were carried out with the Gaussian03/DFT[17] series of programs. B3LYP formulation of density functional theory was used employing the LanL2DZ basis set.[17] Harmonic vibrational frequencies and infrared intensities were calculated by numerical second derivatives using analytically calculated first derivatives. All points were characterised as minima or first-order saddle points by frequency analysis.

Acknowledgments

This work was supported by the Deutsche Forschungsgemeinschaft and the Fonds der Chemischen Industrie. The generous support of Professor G. Huttner is gratefully acknowledged. We thank Simone Leingang for preparative and Sven Reinhardt for theoretical assistance.

[1] Special issue on Molecular Machines: *Acc. Chem. Res.* **2001**, *34*.
[2] C. P. Mandl, B. König, *Angew. Chem.* **2004**, *116*, 1650–1652; *Angew. Chem. Int. Ed.* **2004**, *43*, 1622–1624.
[3] M. Barboiu, L. Prodi, M. Montalti, N. Zaccheroni, N. Kyritsakas, J.-M. Lehn, *Chem. Eur. J.* **2004**, *10*, 2953–2959.
[4] Recently, a light-induced "molecular scissor" has been reported: T. Muraoka, K. Kinbara, Y. Kobayashi, T. Aida, *J. Am. Chem. Soc.* **2003**, *125*, 5612–5613.
[5] K. Heinze, M. Schlenker, *Eur. J. Inorg. Chem.* **2004**, 2974–2988.

 © 2005 Wiley-VCH Verlag GmbH & Co. KGaA, Weinheim

[6] K. Kavallieratos, S. Hwang, R. H. Crabtree, *Inorg. Chem.* **1999**, *38*, 5184−5186.

[7] Many studies have been devoted to monosubstituted and symmetrically 1,1′-disubstituted amido ferrocenes derived from ferrocenecarboxylic acid, ferrocenyl alanine and ferrocenedicarboxylic acid. For ferrocenecarboxylic acid derived amides see: [7a] Y. Xu, H.-B. Kraatz, *Tetrahedron Lett.* **2001**, *42*, 2601−2603. [7b] M. V. Baker, H.-B. Kraatz, J. W. Quail, *New. J. Chem.* **2001**, *25*, 427−433. [7c] P. Saweczko, G. D. Enright, H.-B. Kraatz, *Inorg. Chem.* **2001**, *40*, 4409−4419. [7d] J. C. Verheijen, G. A. van der Marel, J. H. van Boom, N. Metzler-Nolte, *Bioconjugate Chem.* **2000**, *11*, 741−743. [7e] O. Brosch, T. Weyhermüller, N. Metzler-Nolte, *Inorg. Chem.* **1999**, *38*, 5308−5313. [7f] J. F. Gallagher, P. T. M. Kenny, M. J. Sheehy, *Inorg. Chem. Commun.* **1999**, *2*, 327−330. [7g] H.-B. Kraatz, J. Lusztyk, G. D. Enright, *Inorg. Chem.* **1997**, *36*, 2400−2405. For ferrocenyl alanine derived amides see: [7h] K. Severin, R. Bergs, W. Beck, *Angew. Chem.* **1998**, *110*, 1722−1743; *Angew. Chem. Int. Ed.* **1998**, *37*, 1634−1654. For ferrocenedicarboxylic acid derived amides see: [7i] D. R. van Staveren, T. Weyhermüller, N. Metzler-Nolte, *Dalton Trans.* **2003**, 210−220. [7j] T. Moriuchi, A. Nomoto, K. Yoshida, A. Ogawa, T. Hirao, *J. Am. Chem. Soc.* **2001**, *123*, 68−75. [7k] T. Moriuchi, A. Nomoto, K. Yoshida, T. Hirao, *Organometallics* **2001**, *20*, 1008−1013. [7l] P. D. Beer, A. R. Graydon, A. O. M. Johnson, D. K. Smith, *Inorg. Chem.* **1997**, *36*, 2112−2118.

[8] 2D NMR experiments allowed assignment of all proton signals (see ref. 5).

[9] In the IR spectrum deuterated **2** shows an ND stretching absorption at 2451 cm^{-1} and an NH stretching absorption at 3316−3327 cm^{-1} with equal intensity. In the ^1H NMR spectrum of deuterated **2**, H^1 and H^{21} signals display only half of the original intensity. See Supporting Information.

[10] For transition metal receptor systems and the sensing of anionic guests see (and cit. lit.): [10a] P. D. Beer, *Acc. Chem. Res.* **1998**, *31*, 71−80. [10b] P. D. Beer, P. A. Gale, *Angew. Chem.* **2001**, *113*, 502−532; *Angew. Chem. Int. Ed.* **2001**, *40*, 486−516.

[11] Job Plots reveal that the receptor:chloride binding stoichiometry is 2:1 for both complexes (see Supporting Information), showing that the chloride ion is associated to two receptor molecules. This stoichiometry does not affect the dynamic behavior of the system as all calculated minimum structures (**I**−**III**) with 1:1 stoichiometry can form the corresponding 2:1 complexes. The 2:1 stoichiometry and the narrow solubility window of **1** and **2** prevented the determination of 2:1 binding constants $K^{21} = [(\mathbf{1})_2Cl^-]/[\mathbf{1}]^2[Cl^-]$ and $K^{21} = [(\mathbf{2})_2Cl^-]/[\mathbf{2}]^2[Cl^-]$, respectively. This prevented direct comparison with literature data on 1:1 binding constants of receptor/anion complexes (e.g. refs. 6 and 7). However, NMR spectroscopic data (at 0.005 M concentrations of **1** and **2**) can be fitted to 1:1 binding isotherms, giving $K^{11} = 7.8\ M^{-1}$ (**1**; based on H^1; $R^2 = 0.9976$), $K^{11} = 630\ M^{-1}$ (**2**; based on H^1; $R^2 = 0.9963$) and $K^{11} = 120\ M^{-1}$ (**2**; based on H^{21}; $R^2 = 0.9938$); which can be compared qualitatively to those measured for Fc-CO-NH-*n*Bu ($K^{11} = 4.7\ M^{-1}$ in $CDCl_3$ at 0.01 M[7l]) and for **A** ($K^{11} = 9500\ M^{-1}$ in CD_2Cl_2 at 0.001 M[6]). In addition, 2:1 complexes have been observed between Fc-CO-NH-py and the neutral guest glutaric acid: [11a] J. D. Carr, L. Lambert, D. E. Hibbs, M. B. Hursthouse, K. M. Abdul Malik, J. H. R. Tucker, *Chem. Commun.* **1997**, 1649−1650.

[12] Addition of solid $Tl(PF_6)$ to the chloride-loaded receptor **2** restores the original (chloride-free) ^1H NMR spectrum. Recharging with chloride anions again results in downfield shifts of the proton signals.

[13] Similar shifts were observed for the receptor **A**[6] and $(Cp\text{-}NHCOR)_2Fe$ in the presence of chloride: P. D. Beer, J. J. Davis, D. A. Drillsma-Milgrom, F. Szemes, *Chem. Commun.* **2002**, 1716−1717.

[14] H.-A. Klok, *Angew. Chem.* **2002**, *114*, 1579−1583; *Angew. Chem. Int. Ed.* **2002**, *41*, 1509−1513.

[15] M. Rueping, Y. R. Mahajan, B. Jaun, D. Seebach, *Chem. Eur. J.* **2004**, *10*, 1608−1615.

[16] L. Alfonta, Z. Zhag, S. Uryu, J. A. Loo, P. G. Schultz, *J. Am. Chem. Soc.* **2003**, *125*, 14662−14663.

[17] Gaussian 03, Revision B.03, M. J. Frisch, G. W. Trucks, H. B. Schlegel, G. E. Scuseria, M. A. Robb, J. R. Cheeseman, J. A. Montgomery, Jr., T. Vreven, K. N. Kudin, J. C. Burant, J. M. Millam, S. S. Iyengar, J. Tomasi, V. Barone, B. Mennucci, M. Cossi, G. Scalmani, N. Rega, G. A. Petersson, H. Nakatsuji, M. Hada, M. Ehara, K. Toyota, R. Fukuda, J. Hasegawa, M. Ishida, T. Nakajima, Y. Honda, O. Kitao, H. Nakai, M. Klene, X. Li, J. E. Knox, H. P. Hratchian, J. B. Cross, C. Adamo, J. Jaramillo, R. Gomperts, R. E. Stratmann, O. Yazyev, A. J. Austin, R. Cammi, C. Pomelli, J. W. Ochterski, P. Y. Ayala, K. Morokuma, G. A. Voth, P. Salvador, J. J. Dannenberg, V. G. Zakrzewski, S. Dapprich, A. D. Daniels, M. C. Strain, O. Farkas, D. K. Malick, A. D. Rabuck, K. Raghavachari, J. B. Foresman, J. V. Ortiz, Q. Cui, A. G. Baboul, S. Clifford, J. Cioslowski, B. B. Stefanov, G. Liu, A. Liashenko, P. Piskorz, I. Komaromi, R. L. Martin, D. J. Fox, T. Keith, M. A. Al-Laham, C. Y. Peng, A. Nanayakkara, M. Challacombe, P. M. W. Gill, B. Johnson, W. Chen, M. W. Wong, C. Gonzalez, J. A. Pople, Gaussian, Inc., Pittsburgh PA, **2003**.

Received August 26, 2004

 © 2005 Wiley-VCH Verlag GmbH & Co. KGaA, Weinheim

The Nature of the Spin-State Variation of $[Fe^{II}(BPMEN)(CH_3CN)_2](ClO_4)_2$ in Solution

Konstantin P. Bryliakov,*[a] Eduard A. Duban,[a] and Evgenii P. Talsi[a]

Keywords: Magnetic properties / Iron(II) complexes / Spin crossover / Liquid state / Solvent effects

Thermally-induced spin variation behavior of $[Fe^{II}(BPMEN)(CH_3CN)_2](ClO_4)_2$ in CD_3CN solution [low spin (LS)–high spin (HS)] was investigated. Variable temperature solution magnetic susceptibility measurements gave $\Delta H°_{LS-HS}$ = 39.7 ± 2.0 kJ·mol^{-1} and $\Delta S°_{LS-HS}$ = 135 ± 9 J·mol^{-1} K^{-1} values. These values are too high for a pure spin transition and reflect a significant contribution of chemical processes to the spin transition, namely, the detected dissociation of one bound acetonitrile molecule. Thus, LS–HS conversion should be regarded as a chemical equilibrium overlapped with a thermal spin crossover. The thermodynamic parameters for the overall process estimated from the variation of the NMR shifts with temperature ($\Delta H°$ = 40 ± 3 kJ·mol^{-1}, $\Delta S°$ = 137 ± 10 J·mol^{-1} K^{-1}) are in perfect agreement with those obtained by magnetic susceptibility measurements.

(© Wiley-VCH Verlag GmbH & Co. KGaA, 69451 Weinheim, Germany, 2005)

Introduction

In recent years, Que and co-workers reported a series of non-heme Fe^{II}(BPMEN)- and Fe^{II}(TPA)-type catalysts for stereospecific oxidation of hydrocarbons with H_2O_2 [TPA is tris(2-pyridylmethyl)amine ligand and BPMEN is *N*,*N*′-dimethyl-*N*,*N*′-bis(2-pyridylmethyl)-1,2-diaminoethane ligand].[1−4] These species can be functional models for non-heme iron oxygenases, such as Rieske dioxygenases capable of olefin *cis*-dihydroxylation.[3] The catalysts reported were either diamagnetic or paramagnetic complexes, depending on the substituent at the 6-position of the pyridine rings. Interestingly, the parent $[Fe^{II}(BPMEN)(CH_3CN)_2](ClO_4)_2$ complex displayed solution spin-transition behavior in the temperature range −40 to +30 °C. However, the authors only mentioned this phenomenon and did not report a detailed spectroscopic/magnetic susceptibility investigation. Recently, a theoretical study appeared where the structure and spin states of Fe-BPMEN complexes were evaluated by DFT.[5] Apparently, knowledge on the nature of this low-to-high spin transition could be of help in understanding the reactivity of these systems.

The temperature-induced LS−HS transitions in Fe^{II} complexes[6−8] have been extensively studied over the last few years, mostly in the solid state; however, variable-temperature studies in solution have also appeared.[8−10] Solid-state spin equilibria in some diisothiocyanato iron(II) complexes with BPMEN type ligands were studied by Toftlund et al.[11] In this paper, we present a detailed magnetic susceptibility and ^{1}H NMR study of $[Fe^{II}(BPMEN)(CH_3CN)_2](ClO_4)_2$ in solution (**I**, Scheme 1) spin variation in [D_3]acetonitrile and the thermodynamic parameters of this reaction. The results of magnetic susceptibility measurements on solutions are compared with those obtained by a paramagnetic ^{1}H NMR study.

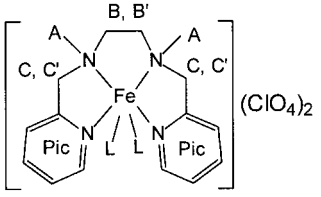

I, L= CH_3CN

Scheme 1. Complex **I**

Results and Discussion

At room temperature, complex **I** exhibits a magnetic moment of 4.1 μ_B in acetonitrile solutions, which is indicative of a spin-crossover system. Temperature-dependent magnetic susceptibility measurements were carried out to explore the equilibria that occur in acetonitrile solutions of complex **I** (see a in Figure 1, trace 1). Fitting the observed magnetic moment dependencies μ_{eff} versus T to Equation (5) (see Exp. Sect.) gave the limiting magnetic moment values μ_{LS} = 1.30 ± 0.1 μ_B and μ_{HS} = 5.45 ± 0.1 μ_B, which are higher than the spin-only values 0 and 4.90 μ_B, thus suggesting significant orbital contributions to the observed

[a] G. K. Boreskov Institute of Catalysis, Siberian Branch of the Russian Academy of Sciences,
630090 Novosibirsk, Russian Federation
Fax: (internat.) + 7-3832-308766
E-mail: bryliako@catalysis.nsk.su

Supporting information for this article is available on the WWW under http://www.eurjic.org or from the author.

 © 2005 Wiley-VCH Verlag GmbH & Co. KGaA, Weinheim DOI: 10.1002/ejic.200400429

magnetic moments (see ref.[8,11]). Spin transition is accomplished within the temperatures accessible for acetonitrile: the $\mu_{eff}(T)$ values practically level off in the higher and lower limits of the temperature range considered. The μ_{LS} value is in good agreement with the solid-state magnetic moment 1.40 μ_B (T = 294 K).

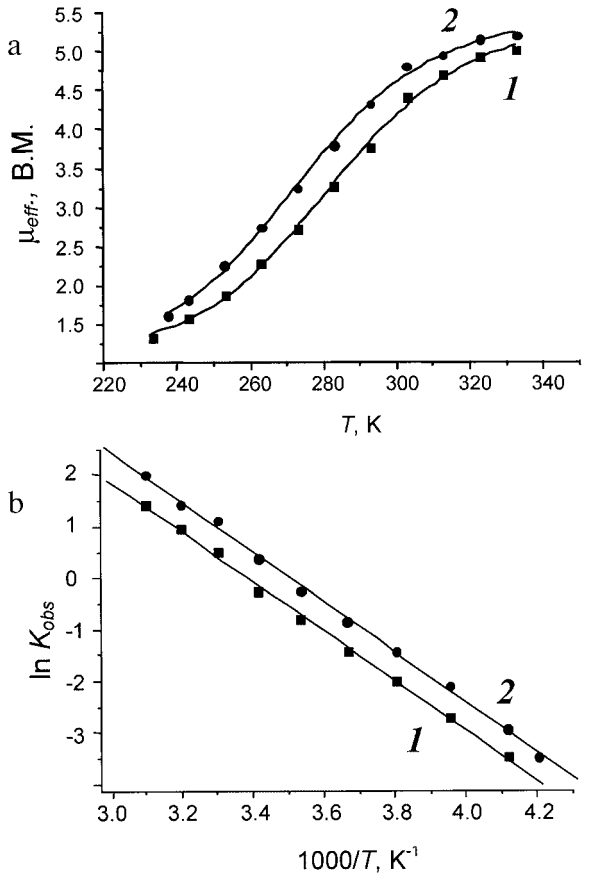

Figure 1. Fits of $\mu_{eff}(T)$ to Equation (5) for complex **I** (a) and linear fits of ln K_{obs} versus 1000/T (b) in [D_3]acetonitrile - trace 1 (■) and in [D_3]acetonitrile/[D_6]acetone - trace 2 (•) (in Table 1, see entries 1 and 7, respectively)

The equilibrium parameters $\Delta S°$ and $\Delta H°$ (see b in Figure 1, trace 1) measured in [D_3]acetonitrile gave $\Delta S°$ = 135 ± 9 J mol^{-1} K^{-1} (in which the contribution of R ln 5 arises from spin degeneracy of the HS state) and $\Delta H°$ = 39.7 ± 2.0 kJ mol^{-1}. Both values are substantially higher than those reported in the literature for solution spin-crossover systems.[7,10,12] This lead us to suggest that spin change in this system could overlap with other (chemical) processes. The fact that in other solvents (e.g. [D_6]acetone, see Supporting Information) a conventional Curie dependence of ^{1}H paramagnetic shifts is observed is in favor of dissociation of bound acetonitrile molecules at elevated temperatures, see Equation (1).

$$[Fe^{II}(BPMEN)(CH_3CN)_2]^{2+} \underset{}{\overset{K}{\rightleftharpoons}} [Fe^{II}(BPMEN)(CH_3CN)_{2-n}]^{2+} + n\,CH_3CN \quad (1)$$

LS HS

A similar behavior was previously proposed to describe the spin-state variation of $[Fe(Me_3tacn)(MeCN)_3]$ in solution.[9] The observed equilibrium constant [$K_{obs}(T) = C_{HS}/C_{LS}$] values should be related to the thermodynamic equilibrium constant as shown in Equation (2).

$$K_{obs}(T) = K/[L]^n \quad (2)$$

[L] is the concentration of acetonitrile in solution. Dilution of acetonitrile with a noncoordinating solvent would result in higher K_{obs} values, so that $K_{obs}([L_o])/K_{obs}([L_1]) = ([L_1]/[L_o])^n$. Also, taking the logarithm of Equation (2) and assuming that $\Delta H°$ is independent of acetonitrile concentration, one obtains Equation (3).

$$\Delta S°_{obs} = \Delta S° - nR \ln [L] \quad (3)$$

$\Delta S°_{obs}$ and $\Delta S°$ correspond to K_{obs} and K (i.e. ΔS related at some standard conditions), respectively, and R is the gas constant. Thus, the 1.63-fold decrease in CD_3CN concentration would result in a $(1.63)^n$-fold increase in the K_{obs} value and an nR ln(1.63) = 4n J mol^{-1} K^{-1} increase in $\Delta S°_{obs}$. Unfortunately, the low precision of μ_{eff} measurements did not allow reliable detection of these small effects. In the temperature range considered, such experiments with combined $CD_3CN/CDCl_3$, CD_3CN/CCl_4, CD_3CN/[D_6]acetone solvents (Table 1, Figure 1) showed a 1.3-fold increase in the value of K_{obs} with a 1.63-fold decrease in CD_3CN concentration and a 1.7-fold increase in the value of K_{obs} with a 2.65-fold decrease in [CD_3CN] (these values are lower than those expected, indicating that $\Delta H°$ also changes with changing CD_3CN concentration). In the $\mu_{eff}(T)$ – T diagram, this resulted in a $T_{1/2}$ change from 284 to 275 K (see a in Figure 1). The question, what is n in Equation (3), could be answered as follows: if both acetonitrile molecules dissociated at high temperatures, we should observe similar high-temperature spectra in [D_6]acetone and in [D_3]acetonitrile/[D_6]acetone combined solvent. However, the spectra are substantially different (Supporting Information), indicating, apparently, the existence of $[Fe^{II}(BPMEN)]^{2+}$ in the first case and $[Fe^{II}(BPMEN)(CD_3CN)]^{2+}$ in the second case. We conclude that the experimentally observed picture is consistent with dissociation of one acetonitrile molecule, therefore leading to a weaker ligand field.

^{1}H NMR spectra of complex **I** in [D_3]acetonitrile gradually change from diamagnetic at −40 °C to paramagnetic at +60 °C (see a in Figure 2), indicating that the process in Equation (1) is fast on the NMR timescale. At high temperatures the spectrum is typical for high-spin Fe^{II} complexes,[9,13–14] and the peaks can be assigned unambiguously based on the relative intensities and linewidths of the peaks by assuming a dipolar line broadening mechanism.[15] The thermodynamic parameters estimated from NMR shifts according to Equation (9): $\Delta S°$ = 137 ± 10 J·mol^{-1} K^{-1} and $\Delta H°$ = 40 ± 3 kJ·mol^{-1} (see b in Figure 2), do not differ from those obtained by magnetic

 © 2005 Wiley-VCH Verlag GmbH & Co. KGaA, Weinheim

Table 1. Thermodynamic parameters for $[Fe^{II}(BPMEN)(CH_3CN)_2](ClO_4)_2$ (**I**) spin crossover in different solutions

Entry	Solvent	$c^0(D_3CN/CCD_3CN)$	$T_{1/2}$, K	K_{obs}/K[a]	$\Delta H°$ (±2.0), kJ mol^{-1}	$\Delta S°$ (±9.0), J mol^{-1} K^{-1}
1	CD_3CN	1	284	1.0	40.6	138
2	CD_3CN	1	284.5	0.96	38.7	131
3	CD_3CN/[D_6]acetone	1.63	279	1.2	38.5	132
4	$CD_3CN/CDCl_3$	1.63	280.5	1.3	36.0	124
5	CD_3CN/CCl_4	2.0	280	1.1	40.5	139
6	$CD_3CN/CDCl_3$	2.65	277	1.2	40.3	138
7	CD_3CN/[D_6]acetone	2.65	275	1.7	39.5	139

[a] Average values over the temperature range −40 to +60 °C.

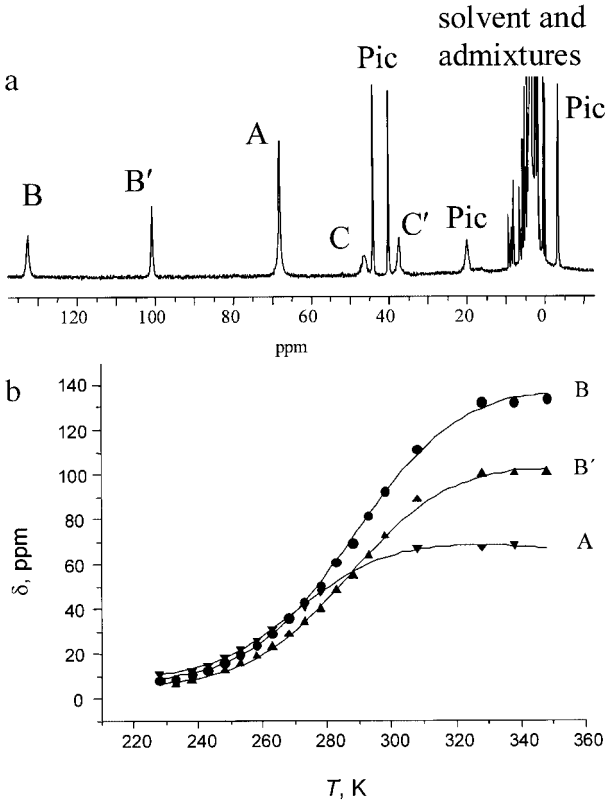

Figure 2. ^{1}H NMR spectrum (0.01 M solution in [D_3]acetonitrile, 60 °C) of complex **I** (a); plot of variation of chemical shifts with temperature for ^{1}H resonances of **I** (b); symbols A, B, B′ and Pic mark the same protons as in Scheme 1; "solvent and admixtures" stands for residual protons of [D_3]acetonitrile and unidentified proton-containing admixtures

measurements. In weaker coordinating solvents (e.g. [D_6]-acetone), **I** displays a paramagnetic spectrum from 130 to −10 ppm, which is indicative of loss of both coordinated CH_3CN molecules.

The phenomenon of ligand dissociation induced spin transition has a nice interpretation in terms of crystal field theory. If one looks at the Tanabe−Sugano diagram for the d^6 configuration (Figure 3), one can see that a conventional spin equilibrium $^1A_1(LS) \rightleftarrows {}^5T_2(HS)$ should be represented by the vertical arrow, which indicates gradual population of the higher lying $^5T_2$ HS state with increasing temperature. On the contrary, the spin conversion caused by ligand dissociation could be associated with the *horizontal* arrow, which represents the dislocation from the high-field region to the low-field one. In our case, an intermediate process seems to take place: an attempt to split the spin interconversion and ligand dissociation processes was made (see Supporting Information), and this revealed comparable contributions of both processes to the observed equilibrium.

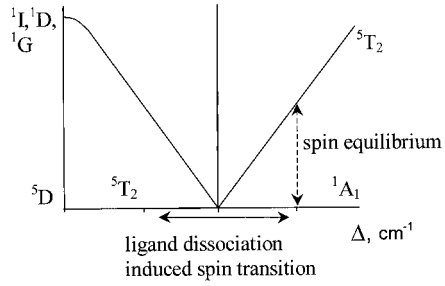

Figure 3. Schematic representation of the Tanabe−Sugano diagram (fragment) for d^6 configuration; the abscissa and ordinate are the crystal field parameter Δ and energy, respectively

In a series of works on bis(benzimidazole)pyridine iron(II) and other iron(II) complexes, it was shown that solvent effects can overlap with the true spin crossover,[16−22] so that substitution or dissociation of coordinated ligands lead to the change in spin state. As Toftlund mentioned, phenomena like these should not be considered as true spin-crossover interconversions.[23] LS/HS transition systems like the one presented (where the spin transition is due to the substantial contribution of the ligand dissociation, and thus weakening the ligand field splitting) seem to be fairly rare in the literature. In this paper we have reported the first measurements of thermodynamic parameters defining the LS/HS transition in $[Fe^{II}(BPMEN)(CH_3CN)_2](ClO_4)_2$ in solution, and demonstrated the high utility of the combined solution magnetic susceptibility/^{1}H NMR spectroscopic measurements for the detailed physico-chemical investigations of one of the few systems of this type documented so far.

Experimental Section

Materials: BPMEN[11] and **I**[1] were prepared as described. For solution magnetic susceptibility measurements, **I** was recrystallized

 © 2005 Wiley-VCH Verlag GmbH & Co. KGaA, Weinheim

from CH_3CN/Et_2O at +4 °C.[1] Deuterated solvents ([D_3]acetonitrile, [D]chloroform) were dried with molecular sieves prior to use.

Physical Measurements: ^1H NMR spectra were recorded in standard 5-mm cylindrical glass tubes on a Bruker DPX-250 NMR spectrometer at 250.13 MHz and referenced to TMS (samples volume 0.50 cm^3 at 298 K). Operating conditions for ^1H NMR measurements: high temperature, spectral width 50 kHz, spectrum accumulation frequency 5 Hz; low temperature, spectral width 5 kHz, spectrum accumulation frequency 0.5 Hz; 90° pulse at 8.2 μs.

Solid state magnetic susceptibility was measured by the Faraday method, with $(NH_4)_2Fe(SO_4)_2{\cdot}6H_2O$ as calibrant. Solution magnetic susceptibility measurements were measured as a function of temperature (−50 to +70 °C) in deuterated solvents CD_3CN, CD_3CN/[D_6]acetone, CD_3CN/CCl_4 and $CD_3CN/CDCl_3$ by the Evans method,[24] with TMS as an internal reference. To prepare the "1.63-fold diluted" CD_3CN solutions, $CDCl_3$ was added to CD_3CN (0.61 mL) to make the volume 1.00 mL. To prepare the "2.65-fold diluted" CD_3CN solutions, [D_6]acetone was added to CD_3CN (0.375 mL) to make the volume 1.00 mL. To prepare the "2-fold diluted" CCl_4 solutions, CCl_4 was added to CD_3CN (0.500 mL) to make the volume 1.00 mL. Temperature uncertainty was ±1 °C. Special stem coaxial insert tubes (203 mm × 4 mm o.d.) with a capillary reference volume of 60 μL (50 mm × 2 mm o.d.) were purchased from Wilmad Glass Co. Mass magnetic susceptibilities χ_g ($cm^3\ g^{-1}$), were calculated from Equation (4).

$$\chi_g = -3\Delta f/4\pi f m + [\chi_o + \chi_o(d_o - d_s)/m] \quad (4)$$

Δf is the frequency shift in Hz of the reference compound, f is the spectrometer frequency in Hz, m is the mass in g of the complex in 1 cm^3 of the solution, χ_o is the mass susceptibility of the solvent in $cm^3\ g^{-1}$, and d_o and d_s are the densities of the solvent and solution, respectively. The term in square brackets disappears, because at the concentrations used (10−15 mM), the solution density was approximated as $d_s = d_o + m$. We note that the original Evans technique[24] was developed for the cylindrical sample axis perpendicular to the magnetic field, whereas for the sample axis parallel to the magnetic field, a factor of 3/4π rather than 3/2π[1,25] should be applied in Equation (4).[10,26] To take into account the solution volume changes with temperature, a correction was introduced in the m values so that $m = m_o h_o/h$, where m_o is the mass in g of the complex in 1 cm^3 of the solution at 298 K, and h_o and h are sample heights at 298 K and at the given temperature, respectively.
Multiplying the χ_g values by the molecular weight, the molar susceptibility χ_M was obtained. The latter was corrected for the diamagnetic contributions of BPMEN ligands, counteranions and Fe^{II} core electrons using Pascal's constants to give the corrected molar susceptibility χ_M'.[25] The latter was used to calculate the effective magnetic moment $\mu_{eff} = 2.828(\chi_M'T)^{1/2}$ (μ_B), where T is temperature in K.[26] μ_{eff} was fit to Equation (5) in a manner similar to that applied in ref.[10]

$$\mu_{eff}(T) = \{\mu_{LS}^2 + \mu_{HS}^2\,[\exp(\Delta S°/R)\exp(-\Delta H°/RT)]\}^{1/2} \{1 + \exp(\Delta S°/R)\exp(-\Delta H°/RT)\}^{-1/2} \quad (5)$$

μ_{LS} and μ_{HS} are the limiting magnetic moments of the low-spin and high-spin states, and $\exp(\Delta S°/R)\exp(-\Delta H°/RT)$ is the observed equilibrium constant $K_{obs} = [HS\text{-}Fe^{II}]/[LS\text{-}Fe^{II}]$.

Calculation of Observed Equilibrium Constant Values K_{obs}: Equation (5) implies a four-parameter fit that gives significant uncertainties for $\Delta S°$ and $\Delta H°$. For more precise $\Delta S°$ and $\Delta H°$ measurements, the solution equilibrium treatment of Crawford and Swanson was applied.[27] Namely, after μ_{LS} and μ_{HS} were obtained from Equation (5) (and averaged over all experiments), the probabilities of Fe^{II} to be in LS and HS forms were calculated as according to Equation (6) and $K_{obs}(T) = P_{HS}(T)/P_{LS}(T)$. Then, $\Delta S°$ and $\Delta H°$ were obtained from linear logarithmic plots of ln K_{obs} versus $1/T$.

$$P_{LS}(T) = (\mu_{HS}^2 - \mu_{eff}(T)^2)/(\mu_{HS}^2 - \mu_{LS}^2)$$
$$P_{HS}(T) = 1 - P_{LS}(T) \quad (6)$$

Calculation of $\Delta H°$ and $\Delta S°$ from the Temperature Dependence of the Observed ^1H NMR Chemical Shifts: For LS and HS forms in fast equilibrium, a single paramagnetically broadened ^1H resonance was observed, see Equation (7).

$$\delta_{obs} = \delta_{LS}P_{LS} + \delta_{HS}P_{HS} \quad (7)$$

δ_{LS} is the chemical shift for the diamagnetic state,

$$P_{LS}(T) = 1/(1 + K_{obs}).$$

$$P_{HS}(T) = K_{obs}/(1 + K_{obs}) \quad (8)$$

δ_{HS} stands for the chemical shift of the HS (paramagnetic) state. According to ref.[28−29] $\delta_{HS} = \delta_{dia} + \delta_{hf}$, where δ_{hf} is the hyperfine (contact + pseudocontact) contribution and diamagnetic contribution δ_{dia} is the same as δ_{LS}. Assuming that δ_{hf} has the theoretically expected Curie temperature dependence (C/T), one could calculate δ_{obs} according to Equation (9).

$$\delta_{obs} = \{\delta_{LS} + (\delta_{LS} + C/T)[\exp(\Delta S°/R)\exp(-\Delta H°/RT)]\}/\{1 + \exp(\Delta S°/R)\exp(-\Delta H°/RT)\} \quad (9)$$

C is a constant and $\exp(\Delta S°/R)\exp(-\Delta H°/RT) = K_{obs}$. Thus, $\Delta S°$ and $\Delta H°$ were obtained from the plots of δ_{obs} versus T.

Supporting Information (see also the footnote on the first page of this article): ^1H NMR spectroscopic data, spectra, chemical shift plots for complex **I** in different solvents.

Acknowledgments

This work was supported by the Russian Foundation for basic research, grant 03-03-32009.

[1] K. Chen, L. Que, *Chem. Commun.* **1999**, 1375−1376.
[2] M. Costas, A. K. Tipton, K. Chen, D.-H. Jo, L. Que, *J. Am. Chem. Soc.* **2001**, *123*, 6722−6723.
[3] K. Chen, M. Costas, J. Kim, A. Tipton, L. Que, *J. Am. Chem. Soc.* **2002**, *124*, 3026−3035.
[4] K. Chen, M. Costas, L. Que, *J. Chem. Soc., Dalton Trans.* **2002**, 672−679.
[5] D. Quiñonero, D. G. Musaev, K. Morokuma, *Inorg. Chem.* **2003**, *42*, 8449−8455.
[6] [6a] P. Gütlich, Y. Garcia, H. A. Goodwin, *Chem. Soc., Rev.* **2002**, *29*, 419−427. [6b] P. Gütlich, H. Spiering, A. Hauser, Spin Transitions in Iron(II) Compounds, in *Inorganic Electronic Structure and Spectroscopy*, vol. II; John Wiley & Sons, **1999**, 575−622.

 © 2005 Wiley-VCH Verlag GmbH & Co. KGaA, Weinheim

[7] E. König, *Struct. Bonding* **1991**, *76*, 51−152.
[8] J. W. Turner, F. A. Schultz, *Coord. Chem. Rev.* **2001**, *219−221*, 81−97.
[9] D. W. Blakesley, S. C. Payne, K. S. Hagen, *Inorg. Chem.* **2000**, *39*, 1979−1989.
[10] J. W. Turner, F. A. Schultz, *Inorg. Chem.* **2001**, *40*, 5296−5298.
[11] H. Toftlund, E. Pedersen, S. Yde-Adersen, *Acta Chem. Scand., Ser. A* **1984**, *38*, 693−697.
[12] G. Lemercier, A. Bousseksou, M. Verlst, F. Varret, J. P. Tuchagues, *J. Magn. Magn. Materials* **1995**, *150*, 227−230.
[13] E. P. Talsi, D. E. Babushkin, N. V. Semikolenova, V. N. Zudin, V. N. Panchenko, V. A. Zakharov, *Macromol. Chem. Phys.* **2001**, *202*, 2046−2051.
[14] R. H. Holm, C. J. Hawkins, Stereochemistry and Structural and Electronic Equilibria, in *NMR of Paramagnetic Molecules* (Eds.: G. N. LaMar, W. D. Horrocs, R. H. Holm), Academic Press Inc.: New York, **1973**, 243−332.
[15] T. J. Swift, The Paramagnetic Linewidth, in *NMR of Paramagnetic Molecules* (Eds.: G. N. LaMar, W. D. Horrocs, R. H. Holm), Academic Press Inc.: New York, **1973**, 53−83.
[16] B. Strauss, V. Gutmann, W. Linert, *Monatsh. Chem.* **1993**, *124*, 515−522.
[17] W. Linert, M. Enamullah, V. Gutmann, R. F. Jameson, *Monatsh. Chem.* **1994**, *125*, 661−670.
[18] M. Enamullah, W. Linert, *J. Coord. Chem.* **1996**, *40*, 193−346.
[19] R. Boca, P. Baran, L. Dlhán, J. Sima, G. Wiesinger, F. Renz, U. El-Ayaan, W. Linert, *Polyhedron* **1997**, *16*, 47−55.
[20] M. Enamullah, W. Linert, *Thermochim. Acta* **2002**, *388*, 401−406.
[21] W. Linert, M. Konecny, F. Renz, *J. Chem. Soc., Dalton Trans.* **1994**, 1523−1531.
[22] A. W. Addison, S. Burman, C. G. Wahkgren, O. A. Rajan, T. M. Rowe, E. Sinn, *J. Chem. Soc., Dalton Trans.* **1987**, 2621−2630.
[23] H. Toftlund, *Monatsh. Chem.* **2001**, *132*, 1269−1277.
[24] D. F. Evans, *J. Chem. Soc.* **1959**, 2003−2005.
[25] R. S. Drago, *Physical Methods for Chemists*, 2nd ed.; Surfside Scientific Publishers: Gainesville, FL, **1992**, chapter 11.
[26] M. L. Naklicki, C. A. White, L. L. Plante, C. E. B. Evans, R. J. Crutchley, *Inorg. Chem.* **1998**, *37*, 1880−1885.
[27] T. H. Crawford, J. Swanson, *J. Chem. Educ.* **1971**, *48*, 382−386.
[28] J. P. Jesson, The Paramagnetic Shift, in *NMR of Paramagnetic Molecules* (Eds.: G. N. LaMar, W. D. Horrocs, R. H. Holm), Academic Press Inc.: New York, **1973**, 2−52.
[29] F. A. Walker, *Inorg. Chem.* **2003**, *42*, 4526−4544.

Received May 24, 2004

 © 2005 Wiley-VCH Verlag GmbH & Co. KGaA, Weinheim

Two Novel Inorganic-Organic Hybrid Frameworks Based on In^{III}-BTC and In^{III}-BTEC

Zheng-Zhong Lin,[a] Fei-Long Jiang,[a] Lian Chen,[a] Da-Qiang Yuan,[a] You-Fu Zhou,[a] and Mao-Chun Hong*[a]

Keywords: Indium(III) / Benzenemulticarboxylate

Hydrothermal reactions of $InCl_3$ with 1,3,5-benzenetricarboxylic acid (H_3BTC) or pyromellitic dianhydride produced $[In_2(BTC)_2(H_2O)_2]_n \cdot 2nH_2O$ (**1**) and $[In_2(H_2BTEC)_2(OH)_2]_n \cdot 2nH_2O$ (**2**), respectively (H_4BTEC = 1,2,4,5-benzenetetracarboxylic acid). The structure of **1** is a 2D double-layer network, while that of **2** is a 3D framework constructed from chains of corner-linked octahedra. Intense greenish-blue emissions at 494 nm (λ_{ex} = 325 nm) for **1** and 489 nm (λ_{ex} = 337 nm) for **2** were observed in the solid state.

(© Wiley-VCH Verlag GmbH & Co. KGaA, 69451 Weinheim, Germany, 2005)

Introduction

The development of organic-inorganic hybrid compounds constructed by the deliberate selection of metals and multifunctional exodentate ligands represents one of the most active research area in chemistry. The fascinating structures of these complexes together with their functional properties makes them highly prospective as a new class of materials.[1−4] 1,3,5-benzenetricarboxylic acid (H_3BTC) and 1,2,4,5-benzenetetracarboxylic acid (H_4BTEC) are two promising ligands which provide high symmetry, diverse charge and a multi-connecting ability which has been applied in the design of hybrid complexes exploiting both the diversity of metal coordination geometries and weak intermolecular forces such as π−π interactions and hydrogen bonding. The rigid conformation and strong coordinating ability of the carboxylate groups bestows excellent thermal properties on the resultant hybrid complexes. The use of H_3BTC and divalent metal ions has led to the generation of products consisting 1D chains,[5,6] 2D layers[7−11] and 3D structural frameworks.[12−16] H_4BTEC is a building block that has been commonly adopted in the design of hybrids in connection with transition[17−21] and rare earth metal elements.[22−24] In the search for a further class of hybrid materials we have introduced a trivalent metal, namely indium(iii), in order to investigate the influence of a change in the metal centre on the coordination architecture during the course of the assembly of the metal centres with H_3BTC or H_4BTEC. It was postulated that the incorporation of trivalent metal ions might create diverse structures different from those containing divalent metal ions because of the increased valence charge. Furthermore, compared with the systematic and extensive studies on M^{II}-BTC complexes, reports of M^{III}-BTC complexes are rare.[25,26] Although some literature reports concerning M^{III}-BTEC complexes have recently appeared, the metal centres incorporated were mostly confined to the rare earth metal elements,[23,24] Fe^{III} [27] or V^{III}.[28] There is a deficiency of the selection of the ^{III}A group elements as inorganic linkers. We addressed this situation by choosing In^{III} as the metal and a series of 3D In^{III}-BTC and 3D In^{III}-BTEC complexes with protonated pyridine or pyridine derivatives as templates and counter anions have been synthesised. Herein we describe a 2D double-layered In^{III}-BTC compound $[In_2(BTC)_2(H_2O)_2]_n \cdot 2nH_2O$ (**1**) and a 3D In^{III}-BTEC compound $[In_2(H_2BTEC)_2(OH)_2]_n \cdot 2nH_2O$ (**2**) showing characteristic $In^{III}O_4(OH)_2$ octahedral chains.

Results and Discussion

The formation of compounds **1** and **2** was found to be extremely sensitive to the pH value of the reaction mixture. Synthetic studies were carried out using pyridine as a basic reagent to adjust the pH value in the reaction system. In both systems, a pH value between 2 and 3 is an essential condition for the formation of **1** and **2**. For the preparation of In^{III}-BTC, a pH value ranging from 3 to 4 produces a mixture of **1** and a 3D porous coordination polymeric compound.[29] Likewise, two phases (compound **2** and a 3D porous In^{III}-BTEC framework[30]) also crystallise concurrently from the reaction system of **2** when a pH value of 3−4 is maintained. In both reaction systems, more basic pH values led to predominant formation of the 3D porous by-prod-

[a] State Key Laboratory of Structural Chemistry, Fujian Institute of Research on the Structure of Matter, Chinese Academy of Sciences, Graduate School of the Chinese Academy of Sciences, Fujian, Fuzhou, 350002, China
Fax: (internat.) +86-591-3714946
E-mail: hmc@ms.fjirsm.ac.cn, zzlin@ms.fjirsm.ac.cn

ucts. Furthermore, when the reactions were carried out without pyridine as a basic reagent, the yields of **1** and **2** were very low. Thus, to ensure a high yield of **1** and **2**, an appropriate amount of pyridine is needed to adjust the pH value around 3.

Compound **1** exhibits a double-layer sheet configuration (Figure 1) generated from the interconnection of two single-layers which are produced from the extension of honeycomb-like grids along the (100) plane. Three In^{III} centres and three BTC trianions form such a 6-membered grid with dimensions of about 7.4 Å × 9.2 Å. Inside the grids, each indium atom binds to six carboxylate oxygen atoms from four BTC groups and one water oxygen atom (O7) to form a slightly distorted pentagonal bipyramidal motif. The dihedral angle between the benzene plane of the BTC group and the plane defined by In, InA, and InB is about 12.6°. Consequently, the sheet adopts a slightly wavy configuration. A bidentate carboxylate arm (C9−O5−O6) lies out of the BTC benzene ring plane with a dihedral angle as high as 26° such that the carboxylate arms act as the bridges linking two single-layers into a double-layer. The other two carboxylate arms bond in a chelating bidentate mode and participate in the propagation of the grids. The two single-layers are related to each other through the twofold screw symmetry operation and the distance between them is about 3.8 Å. Because of the translation operation of the screw axis, the available sizes of honeycomb-like grids are significantly reduced. This explains the fact that **1** absorbs little nitrogen gas even after dehydration.[31] To balance the charge, O7 can be considered to be a coordinated water oxygen atom. This assumption is confirmed by bond valence calculations for O7 which give a result of 0.5.[32] The

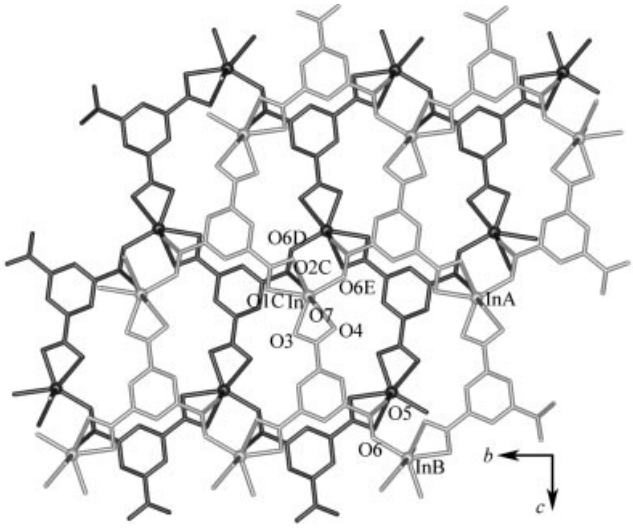

Figure 1. View of the double-layer in **1** interlinked by two single-layers displayed in black and light grey, respectively; free water and coordinated water molecules are not shown for clarity; selected bond lengths (Å): In−InA 8.979(1); In−InB 10.288(1); InA−InB 9.468(1); In−O7 2.167(3); In−O3 2.198(1); In−O4 2.292(1); In−O1C 2.271(3); In−O2C 2.304(4); In−O5D 2.138(5); In−O6E 2.144(3); selected bond angles (°): O7−In−O5D 178.0(1); O3−In−O7 89.0(1); O1C−In−O7 95.6(1); symmetry code: (A) x, $1 + y$, z (B) x, $1.5 - y$, $0.5 + z$ (C) x, $0.5 - y$, $-0.5 + z$ (D) $-x$, $-0.5 + y$, $0.5 - z$ (E) x, $1.5 - y$, $-0.5 + z$

In−O7 vectors are perpendicular to the double-layer plane and point towards the extra double-layer region. Furthermore, the double-layers are stacked in parallel separated by about 4 Å. This is sufficiently close such that the In−O7 vectors on the double-layers are interdigitated. Coordinated water oxygen atoms form strong hydrogen bonds with carboxylate oxygen atoms from adjacent double-layers [O7···O2A, 2.775(4) Å, (A):$1 - x$, $0.5 + y$, $0.5 - z$]. The free water molecules included in the honeycomb-like grids also form hydrogen bonds with the above coordinated water pendants of the double-layers [O8···O7, 2.679(7) Å]. Although some honeycomb structures have been found,[7,14,33] compound **1** is, to the best of our knowledge, unprecedented because of the double-layer conformation.

Compound **2** exhibits a 3D hybrid framework constructed from chains of corner-linked octahedra connected by carboxylate linkers (Figure 2). Each indium atom binds to four carboxylate oxygen atoms from four H_2BTEC groups and two other bridging oxygen atoms (O17 and O18) to form an octahedron. Bond valence calculations for O17 and O18 give a value of 1.3. Thus, the oxygen atoms (O17 and O18) can be considered to be μ-OH functions thereby balancing the negative charge in **2**. The octahedra are linked into infinite chains running along the [010] direction via μ-OH functions. Furthermore, two adjacent octahedra in one chain are bridged by two carboxylate arms from two different organic linkers. The octahedra are severely tilted and this is reflected by angles of 122.1(5)° (In1−O17−In1) and 122.2(5)° (In2−O18−In2), both being very far from the value 180° which would be expected if the chains of octahedra were perfectly linear. Each H_2BTEC group binds to four indium atoms, in a bidentate mode, situated in two different chains through the 1,5-carboxylate arms. The other two carboxylate arms are uncoordinated and protonated. Geometrically, the latter two carboxylate arms are coplanar with the phenyl ring whereas the other two are perpendicular to the phenyl rings. All phenyl rings are perpendicular to the directions of the chains. The chains are interweaved by organic linkers in such a way that the

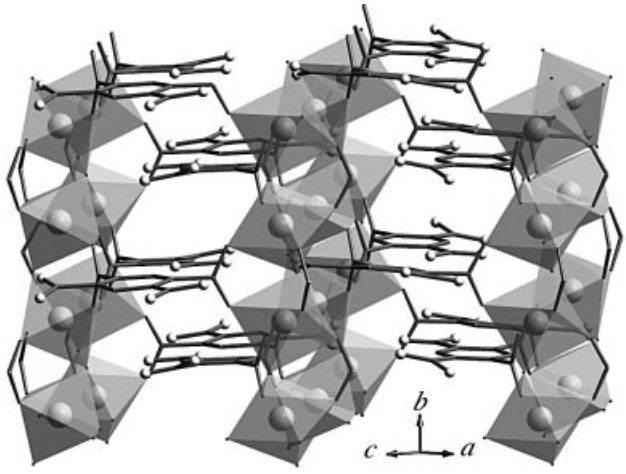

Figure 2. View of the interconnection between polyhedral chains and H_2BTEC groups in **2**; free water oxygen atoms are omitted for clarity

 © 2005 Wiley-VCH Verlag GmbH & Co. KGaA, Weinheim

adjacent indium atoms in any chain are situated at approximately $y = 0$ and $y = 1/2$ while the phenyl rings located between two indium atoms are at approximately $y = 1/4$ on one side of the chain and $y = 3/4$ on the other side of the same chain (Figure 3). Such arrangement of metal and organic moieties is similar to that of the compound MIL-61.[28] These types of connections between the organic and inorganic moieties result in 1D polygonal tunnels. However, the uncoordinated carboxylic functions point towards these tunnels and reduce the effective sizes of the cavities. This helps understand why **2** absorbs little nitrogen gas even after dehydration.[31] Water molecules reside in the tunnels and give rise to hydrogen bonds with uncoordinated carboxylic functions [O19···O14 2.65(2) Å, O20···O5 2.629(8) Å, O19···O8A 2.859(4) Å, O20···O12B 2.915(3) Å. Symmetry code: (A) $-x$, $-0.5 + y$, $0.5 - z$; (B) $1 - x$, $1 - y$, $1 - z$].

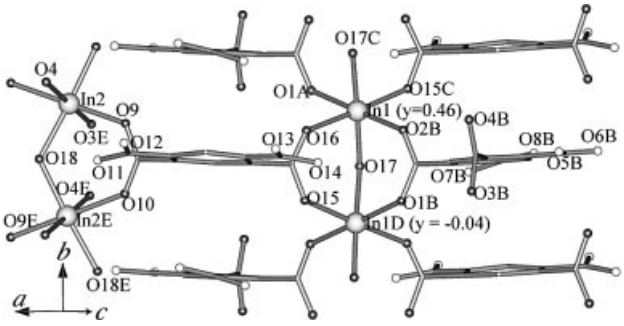

Figure 3. Diagram showing the relative positions of indium atoms and H2BTEC groups in **2**; selected bond lengths (Å): In1−O1A 2.19(1), In1−O2B 2.16(1), In1−O15C 2.18(1), In1−O16 2.20(1), In1−O17 2.00(1), In1−O17C 2.12(1); In2−O3E 2.16(1); In2−O4 2.17(1); In2−O9 2.16(1); In2−O18 2.06(1); In2E−O18 2.07(1); In2E−O10 2.21(1); selected bond angles (°): O1A−In1−O2B 179.3(4); O1A−In1−O16 89.2(5); O16−In1−O2B 91.2(5); O17−In1−O5C 90.0(5); In1−O17−In1D 122.1(5); O3E−In2−O4 178.6(6); O4−In2−O9 89.0(5); In2−O18−In2E 122.2(5); symmetry code: (A) x, $1.5 - y$, $0.5 + z$; (B) $-x$, $1 - y$, $1 - z$; (C) $-x$, $0.5 + y$, $1.5 - z$; (D) $-x$, $-0.5 + y$, $1.5-z$; (E) $1 - x$, $-0.5 + y$, $1.5 - z$

The homogeneous nature of compounds **1** and **2** was shown by X-ray powder diffraction (XRPD) patterns (Figure 4). The powder patterns obtained experimentally for **1** (b) and **2** (e) are in agreement with the calculated patterns for **1** (a) and **2** (d), respectively. The exceptions are the lines at $2\theta = 16.5$ and 20.5° in **2** which are too intense in the experimental pattern. This phenomenon is a result of the preferred orientation of the crystallites.

The infrared absorption bands of **1** and **2** are listed in Table 1. In **1**, the absence of the characteristic bands at 1730−1690 cm^{-1} due to the protonated carboxylate groups indicates that complete deprotonation of H_3BTC occurs upon reaction with indium ions.[34] A strong absorption at 1731 cm^{-1} in **2** confirms the presence of the carboxylic acid function. Both results are in agreement with the crystallographic data.

Thermogravimetric (TG) analyses were carried out under air. The TG diagram (Figure 5) of **1** shows that the first weight loss of 10.1% occurring from about 50 °C to 167 °C

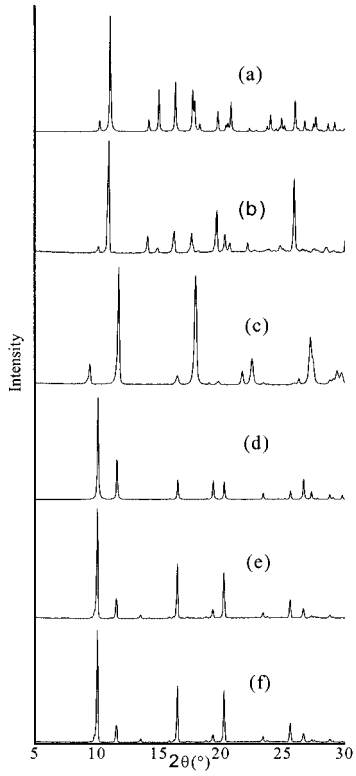

Figure 4. The calculated (a) and experimental (b) XRPD patterns for **1** and the calculated (d) and experimental (e) XRPD patterns for **2**; the patterns (c) and (f) correspond to the sintered samples at 180 °C for **1** and **2**, respectively

Table 1. Characteristic IR absorption bands for **1** and **2** (cm^{-1})

	$\upsilon_{as}(CO_2^-)$	$\upsilon_s(CO_2^-)$	$\upsilon(CO_2H)$	$\upsilon(H_2O)$	$\upsilon(OH)$
1	1619 (s)	1441 (s)		3420 (s)	
	1583 (m)	1384 (s)			
2	1579 (vs)	1444 (s)	1731 (s)	3489 (s)	3127 (s)
	1495 (m)	1400 (vs)			

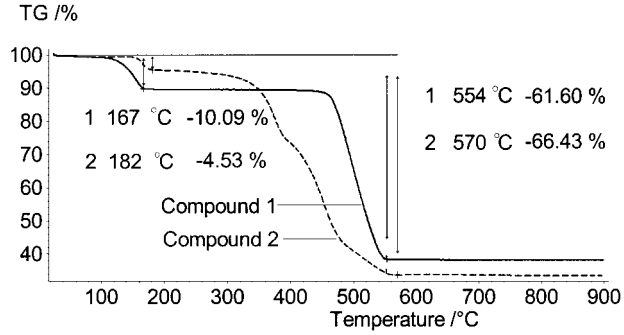

Figure 5. TG curves for **1** and **2**

corresponds to the complete loss of free and coordinated water molecules (calculated: 10.1%), accompanied by the transformation of the framework of **1** indicated by the XRD pattern (see c in Figure 4). The second weight loss, occurring from about 424 °C to 554 °C, is the stage at which **1** dramatically loses its organic component. The light yellow

 © 2005 Wiley-VCH Verlag GmbH & Co. KGaA, Weinheim

residue is In_2O_3 with a residual weight fraction of 38.4% (calculated: 38.8%). This was confirmed by XRD analysis.

Compound **2** also undergoes a two-step weight loss (Figure 5). The first weight loss of 4.53% from about 50 °C to 182 °C can be attributed to the loss of free water molecules (calculated: 4.48%). In contrast to compound **1**, XRD studies show that the framework of **2** remains intact after the loss of water molecules (see f in Figure 4). The second weight loss occurs in the temperature range of 380 to 570 °C, in which **2** dramatically loses weight and begins decomposing due to the loss of organic matter. The residue at 570 °C weighing 33.6% of the total is In_2O_3 (calculated: 34.53%). This was confirmed by XRD analysis.

Compounds **1** and **2** exhibit intense greenish-blue emissions in the solid state at 494 nm (λ_{ex} = 325 nm) for **1** and 489 nm (λ_{ex} = 337 nm) for **2**. Compared with the fluorescent analysis of other metal-BTC compounds,[33] we can assign the 494 and 489 nm emission bands to ligand-to-metal charge-transfer (LMCT) processes.

Experimental Section

Synthesis of $[In_2(BTC)_2(H_2O)_2]_n \cdot 2nH_2O$ (1): Compound **1** was synthesised hydrothermally from the reaction of $InCl_3$ (221 mg, 1 mmol), H_3BTC(210 mg, 1 mmol), pyridine (0.3 mL, 3.7 mmol) and H_2O (5 mL) (pH value 2−3) in a 30-mL Teflon-lined stainless steel vessel at 120 °C for 85 h. The reaction mixture was then cooled at a rate of 6 °C·h^{-1} to give the only product, namely colourless crystals of **1**. The crystals were collected and washed with *N*,*N*-dimethylformamide and distilled water. The yield was 85% (302 mg) based on $InCl_3$. Elemental analysis calcd. (found) for $C_9H_7InO_8$ (*fw* = 357.97): calcd. C 30.20 (30.17), H 1.97 (1.93). IR (KBr pellet [cm^{-1}]): $\tilde{\nu}$ = 3420 (vs, br), 3090 (m), 1619 (vs), 1583 (m), 1548 (s), 1441 (vs), 1384 (vs), 1114 (w), 1061 (w), 757 (s), 715 (m).

Synthesis of $[In_2(H_2BTEC)_2(OH)_2]_n \cdot 2nH_2O$ (2): Compound **2** was synthesised hydrothermally from the reaction of $InCl_3$ (221 mg, 1 mmol), pyromellitic dianhydride (218 mg, 1 mmol), pyridine (0.3 mL, 3.7 mmol) and H_2O (6 mL) (pH value = 2−3) in a 30-mL Teflon-lined stainless steel vessel at 160 °C for 85 h. The reaction mixture was then cooled at a rate of 6 °C·h^{-1} to give the only product, namely colourless crystals of **2**. The crystals were collected and washed with *N*,*N*-dimethylformamide and distilled water. The yield was 70% (280 mg) based on $InCl_3$. Elemental analysis calcd. (found) for $C_{20}H_{14}In_2O_{20}$ (*fw* = 803.95): calcd. C 29.88 (30.10), H 1.76 (1.80). IR (KBr pellet [cm^{-1}]): $\tilde{\nu}$ = 3489 (m, br), 3127 (m), 1731 (s), 1579 (vs), 1495 (m), 1444 (s), 1400 (vs), 1345 (m), 1275 (s), 1210 (s), 1047 (m), 796 (m).

Crystallographic Studies: The crystal data and structure determination parameters for **1** and **2** are listed in the Table 2.[35] Intensity data were collected on a Rigaku−Mercury CCD diffractometer with graphite-monochromated Mo-K_α (λ = 0.71073 Å) radiation using the ω-2θ scan method at room temperature. The structures were solved by direct methods and all calculations were performed using the SHELXL-97 PC program. All nonhydrogen atoms were refined anisotropically. All hydrogen atoms were calculated in the ideal positions and refined isotropically. The structures were refined on F^2 using full-matrix least-squares methods.

Table 2. Crystallographic data for **1** and **2**.

	1	**2**
Empirical formula	$C_9H_7InO_8$	$C_{20}H_{14}In_2O_{20}$
Molecular mass	357.97	803.95
Crystal system	monoclinic	monoclinic
Space group	$P2_1/c$	$P2_1/c$
a (Å)	6.9532(7)	18.5774(19)
b (Å)	8.9789(8)	7.2222(0)
c (Å)	17.525(2)	21.4155(15)
β (°)	100.153(6)	125.187(6)
V (Å^3)	1077.0(1)	2348.3(3)
Z	4	4
D_c (g cm^{-3})	2.208	2.274
μ (mm^{-1})	2.228	2.069
Data collection (°)	$2.36 \le \theta \le 25.02$	$1.34 \le \theta \le 25.02$
Reflns. collected	6442	13746
Indep. reflns.	1901	4141
Reflns. with $I > 2\sigma(I)$	1661	3525
$R_{int.}$	0.0339	0.0414
Restrains/parameters	0/163	0/388
$(\Delta\rho)_{max}/(\Delta\rho)_{min}$, e/Å^3	0.804/−0.510	2.481/−3.795
R_1[a] [$I > 2\sigma(I)$]	0.0312	0.0940
wR[b] (all data)	0.0681	0.2344

[a] $R = \Sigma(||F_o| - |F_c||)/\Sigma|F_o|$. [b] $wR = \{\Sigma w[(F_o^2 - F_c^2)^2]/\Sigma w[(F_o^2)^2]\}^{1/2}$.

Acknowledgments

This work was supported by the National Nature Science Foundation of China (No. 20231020) and the Nature Science Foundation of Fujian Province.

[1] K. S. Min, M. P. Suh, *J. Am. Chem. Soc.* **2000**, *122*, 6834−6840.
[2] S. Noro, S. Kitagawa, M. Kondo, K. Seki, *Angew. Chem. Int. Ed.* **2000**, *39*, 2081−2084.
[3] M. Eddaoudi, D. B. Moler, H. Li, B. Chen, T. M. Reineke, M. O′Keeffe, O. M. Yaghi, *Acc. Chem. Res.* **2001**, *34*, 319−330.
[4] B. Moulton, M. J. Zaworotko, *Chem. Rev.* **2001**, *101*, 1629−1658.
[5] M. J. Plater, M. R. S. E. Foreman, C. J. Gomez-Garcia Coronado, A. M. Z. Slawin, *J. Chem. Soc., Dalton Trans.* **1999**, *23*, 4209−4216.
[6] M. Yaghi, H. L. Li, T. L. Groy, *J. Am. Chem. Soc.* **1996**, *118*, 9096−9101.
[7] H. J. Choi, M. P. Suh, *J. Am. Chem. Soc.* **1998**, *120*, 10622−10628.
[8] M. J. Plater, R. A. Howie, A. J. Roberts, *Chem. Commun.* **1997**, 893−894.
[9] C. J. Kepert, T. J. Prior, M. J. Rosseinsky, *J. Solid State Chem.* **2000**, *152*, 261−270.
[10] D. P. Cheng, M. A. Khan, R. P. Houser, *Inorg. Chem.* **2001**, *40*, 6858−6859.
[11] M. P. Suh, J. W. Ko, H. J. Choi, *J. Am. Chem. Soc.* **2002**, *124*, 10976−10977.
[12] T. J. Prior, M. J. Rosseinsky, *Chem. Commun.* **2001**, 1222−1223.
[13] W. Chen, J. Y. Wang, C. Chen, Q. Yue, H. M. Yuan, J. S. Chen, S. N. Wang, *Inorg. Chem.* **2003**, *42*, 944−946.
[14] T. J. Prior, M. J. Rosseinsky, *Chem. Commun.* **2001**, 495−496.
[15] J. R. Su, K. L. Yin, D. J. Xu, *Chin. J. Struct. Chem.* **2004**, *23*, 399−402.
[16] T. J. Prior, M. J. Rosseinsky, *Inorg. Chem.* **2003**, *42*, 1564−1575.
[17] H. Kumagai, C. J. Kepert, M. Kurmoo, *Inorg. Chem.* **2002**, *41*, 3410−3422.
[18] F. D. Rochon, G. Massarweh, *Inorg. Chim. Acta* **2001**, *314*, 163−171.

 © 2005 Wiley-VCH Verlag GmbH & Co. KGaA, Weinheim

[19] R. Murugavel, D. Krishnamurthy, M. Sathiyendiran, *Dalton Trans.* **2002**, 34−39.
[20] R. Diniz, H. A. de Abreu, W. B. de Almeida, M. T. C. Sansiviero, N. G. Fernandes, *Eur. J. Inorg. Chem.* **2002**, 1115−1123.
[21] M. Sanselme, J. M. Greneche, M. Riou-Cavellec, G. Ferey, *Chem. Commun.* **2002**, 2172−2173.
[22] D. F. Sun, R. Cao, Y. C. Liang, Q. Shi, M. C. Hong, *Dalton Trans.* **2002**, 1847−1851.
[23] C. D. Wu, C. Z. Lu, W. B. Yang, S. F. Lu, H. H. Zhuang, J. S. Huang, *Eur. J. Inorg. Chem.* **2002**, 797−800.
[24] R. Cao, D. F. Sun, Y. C. Liang, M. C. Hong, K. Tatsumi, Q. Shi, *Inorg. Chem.* **2002**, *41*, 2087−2094.
[25] C. Daiguebonne, O. Guilloa, Y. Gerault, A. Lecerf, K. Boubekeur, *Inorg. Chim. Acta* **1999**, *284*, 139−145.
[26] Z. Z. Lin, J. H. Luo, M. C. Hong, R. H. Wang, L. Han, Y. Xu, R. Cao, *J. Solid State Chem.* **2004**, *177*, 2494−2498.
[27] D. Q. Chu, C. L. Pan, L. M. Wang, J. Q. Xu, *Mendeleev Commun.* **2002**, 207−209.
[28] K. Barthelet, D. Riou, M. Nogues, G. Ferey, *Inorg. Chem.* **2003**, *42*, 1739−1743.
[29] Manuscript in preparation. Crystallographic data for $[In_4(BTC)_3(OH)_4]_n \cdot 3nH_2O \cdot nHpy\cdot n$py: *C*2/*c*, a = 18.664 Å, b = 14.4433 Å, c = 17.573 Å, β = 114.680°, V = 4304.3 Å^3, Z = 4, Dc = 1.916, R_1 = 0.0665, wR = 0.1160.
[30] Manuscript in preparation. Molecular formula may be $[In_3(BTEC)_2(OH)_2]_n \cdot nHpy\cdot n$py.
[31] Nitrogen adsorption and desorption isotherms were measured at 77 K on a Micromeritics ASAP 2010 Micropore Analyser for **1** and **2**. Before the measurements, the samples were degassed at 523 K for 6 hours and then at room temperature for 16 hours. Both title compounds exhibit a type III isotherm, indicating weak adsorption or no adsorption.
[32] N. E. Brese, M. O′keeffe, *Acta Crystallogr., Sect. B* **1991**, *47*, 192.
[33] J. C. Dai, X. T. Wu, Z. Y. Fu, C. P. Cui, S. M. Hu, W. X. Du, L. M. Wu, H. H. Zhang, R. Q. Sun, *Inorg. Chem.* **2002**, *41*, 1391−1396.
[34] L. J. Bellamy, *The Infrared Spectra of Complex Molecules*; Wiley: New York, **1958**.
[35] CCDC-251131 and -251132 contain the supplementary crystallographic data for this paper. These data can be obtained free of charge at www.ccdc.cam.ac.uk/conts/retrieving.html [or from the Cambridge Crystallographic Data Centre, 12 Union Road, Cambridge CB2 1EZ, UK; Fax: +44-1223-336-033; E-mail: deposit@ccdc.cam.ac.uk].

Received July 9, 2004

 © 2005 Wiley-VCH Verlag GmbH & Co. KGaA, Weinheim

Reactions of $K_2[Fe(CO)_3(PPh_3)]$: Reductive Sb−Sb Coupling with Ph_2SbCl To Form *trans*-$[Fe(CO)_3(PPh_3)(Sb_2Ph_4)]$ and Salt Metathesis with Me_3SbCl_2 To Yield *trans*-$[Fe(CO)_3(PPh_3)(SbMe_3)]$

Ingo-Peter Lorenz,*[a] Stefan Rudolph,[a] Holger Piotrowski,[a] and Kurt Polborn[a]

Dedicated to Professor Dr. Hubert Schmidbaur on the occasion of his 70th birthday

Keywords: Antimony / Coupling reactions / Iron / Metathesis

In contrast to the ferrate $K_2[Fe(CO)_4]$, the phosphane-substituted ferrate $K_2[Fe(CO)_3(PPh_3)]$ (**1**) reacts with the stibane derivative Ph_2SbCl by metal-assisted reductive Sb–Sb coupling to give the distibane complex *trans*-$[Fe(CO)_3(PPh_3)(Sb_2Ph_4)]$ (**3**). The distibane ligand in **3** is terminally η^1-coordinated *trans* to the phosphane ligand. However, the stiborane derivative Me_3SbCl_2 reacts with **1** in a metathetical substitution reaction to form the monostibane complex *trans*-$[Fe(CO)_3(PPh_3)(SbMe_3)]$ (**5**). Both compounds have been characterized by spectroscopic (IR, NMR, MS), analytical (C, H) and X-ray diffraction analyses.

(© Wiley-VCH Verlag GmbH & Co. KGaA, 69451 Weinheim, Germany, 2005)

Introduction

Molecules containing transition metal−phosphorus frameworks are among the most frequently reported in coordination and cluster chemistry. The most common examples show terminal metal−PR_3, -PR_2- and -PR- modular systems, as well as their metal-bridging analogs.[1] Simple diphosphanes of the type $R_2X-X-PR_2$ (X = CH_2, NH, O) considerably increase the potential variety and applicability of these compounds. While the analogous arsane and diarsane homologues exist in great numbers with similar structural motifs, analogous examples of antimony and bismuth species are much less common.[2,3] Weaker σ-donor and π-acceptor interactions in antimony and bismuth compounds may be a reason for this. Therefore, only monostibane and methylidene-bridged distibane complexes (X = CH_2) obtained by substitution reactions, as in the case of phosphorus and arsenic compounds, have been structurally characterized. Mixed bispentelane complexes with Sb participation are not, to the best of our knowledge, known.

We report here the synthesis and structural characterization of the distibane ligand Sb_2Ph_4 bound to iron; it is produced by a metal-assisted reductive Sb−Sb coupling reaction in the presence of a coordinated phosphane ligand (PPh_3). Thus, we have successfully synthesized the first η^1-(Sb_2Ph_4)-coordinated complex as well as a very rare example of a mixed bispentelane complex. We also report the synthesis of a second mixed bispentelane complex by the metathetical reaction of $K_2[Fe(CO)_3(PPh_3)]$ with Me_3SbCl_2.

[a] Ludwig-Maximilians University Munich, Department of Chemistry,
Butenandtstraße 5−13, 81377 München, Germany
Fax: (internat.) +49 89-2180-77867
E-mail: ipl@cup.uni-muenchen.de

Results and Discussion

One synthetic route to pentelane complexes of iron(0) is the catalytic reaction of $Fe(CO)_5$ with the pentelanes ER_3 (E = P, As, Sb).[4−6] A similar route is the reaction of $Na_2[Fe(CO)_4]$ with one equivalent of Ph_2ECl (E = P, As), which gives first the monosubstituted ferrate $Na[Fe(CO)_4(EPh_2)]$ and then, upon reaction with a second equivalent of Ph_2ECl, the neutral dipentelane complex $[Fe(CO)_4(E_2Ph_4)]$ by E−E coupling.[7] Thus, mixed phosphanylarsane complexes can be obtained. Attempts to form distibane complexes of iron(0) have thus far been unsuccessful. Similarly, the reaction of the phosphane-substituted ferrate $K_2[Fe(CO)_3(PPh_3)]$ (**1**) with two equivalents of Ph_2SbCl proceeds with elimination of KCl to yield the first η^1-coordinated tetraphenyldistibane ligand by ferrate-assisted reductive Sb−Sb coupling of two Ph_2SbCl molecules. The resulting complex, *trans*-$[Fe(CO)_3(PPh_3)(Sb_2Ph_4)]$ (**3**), was structurally characterized by X-ray analysis.

The first mononuclear distibane complexes of the type $[M(CO)_5(Sb_2R_4)]$ (M = Cr, W; R = CH_3, C_2H_5, C_6H_5) were synthesized by photochemically induced substitution of $M(CO)_6$ (in THF) with the intact distibanes, but were only spectroscopically characterized.[8] The analogous diphosphane complexes, however, have already been synthesized and structurally characterized by Vahrenkamp et al.[9,10]

 © 2005 Wiley-VCH Verlag GmbH & Co. KGaA, Weinheim DOI: 10.1002/ejic.200400683

In our case, the distibane molecule is synthesized from monostibane derivatives bound to a metal by template-control and is incorporated as an η^1-bound ligand *trans* to the PPh_3 ligand (see a in Scheme 1). Attempts to obtain mixed bispentelane complexes of the type $R_3EFe(CO)_3E'R_3$ were previously unsuccessful because of symmetrization reactions.

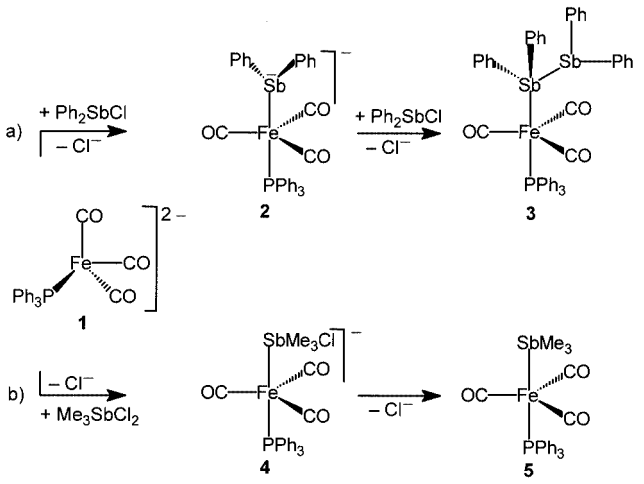

Scheme 1. Synthesis of **3** and **5**

The reductive Sb−Sb coupling reaction of **1** is similar to the Wurtz reaction and proceeds by two steps: electrophilic attack on the iron(II−) center of **1** by the first stibane (Sb^{3+}), followed by elimination of KCl. The monoanionic stibane complex **2**, with the negative charge located mainly on antimony, may be formed as an intermediate. As a result, the electrophilic attack of the second stibane occurs at the coordinated antimony, and leads to the formation of a neutral tetraphenyldistibane complex, **3**, with one Fe(0) and two Sb^{II} centers, and thus the formal redox reaction is completed.

The energy (1883 cm^{-1}) of the single ν(CO) absorption in the IR spectrum of **3** (*E′* symmetry) is similar to the single ν(CO) absorption of the symmetrical species *trans*-$[Fe(CO)_3(PPh_3)_2]$ (1886 cm^{-1}).[11] The signal in the $^{31}P\{^1H\}$ NMR spectrum of **3** is found at δ = 86.4 ppm. The ^1H and $^{13}C\{^1H\}$ NMR spectra show only the multiplets due to the phenyl protons (δ = 7.26−7.59 ppm) and phenyl-C atoms (δ = 126−131 ppm), in addition to one signal for the CO ligand (δ = 212 ppm).

If the ferrate **1** is treated with an excess of the stiborane derivative Me_3SbCl_2 no coupling reaction occurs; instead, a simple salt-metathesis reaction results in the formation of the novel mixed-dipentelane complex *trans*-$[Fe(CO)_3(PPh_3)(SbMe_3)]$ (**5**). As in the case of **3**, the formation of **5** can also occur via the intermediate **4**, which is formed by an electrophilic attack of Me_3SbCl^+ on the nucleophilic ferrate dianion (Scheme 1b).

The spectroscopic data of **5** (IR: ν(CO) = 1877 cm^{-1}; $^{31}P\{^1H\}$ NMR: δ = 85.5 ppm) are similar to those of **3**, except for the methyl-group signals in the NMR spectra (^1H NMR: δ = 1.31 ppm; $^{13}C\{^1H\}$ NMR: δ = 40.1 ppm).

Comparison of **3** and **5** is best achieved by single-crystal X-ray diffraction analysis.[12] Relevant bond lengths and angles are tabulated in the legends of the corresponding figures. As expected, the Fe center is trigonal-bipyramidally configured with the phosphane and distibane ligands in *trans*-axial positions. The Fe1−P1 and Fe1−Sb1 bond lengths are 2.188(2) and 2.457(1) Å, respectively, and the P1−Fe1−Sb1 bond angle of 177.99(6)° indicates a nearly linear P1−Fe−Sb1 arrangement (Figure 1). The three CO ligands surround the central iron in a trigonal planar grouping with the sum of angles at Fe(1) being exactly 360°. As Figure 2 shows, the Sb_2Ph_4 ligand exists in the gauche conformation, and differs by approximately 4° from the *trans* conformation. The Sb1−Sb2 bond length of 2.828 Å is slightly shorter than that of the free stibane Sb_2Ph_4 (2.844 Å).[13] The $Sb-C_{Ph}$ bond lengths around the two Sb centers are quite different. The bonds to Sb1 are 2.130(6) and 2.132(7) Å, whereas bonds to Sb2 are distinctly longer [2.138(9) and 2.145(7) Å], although both pairs are shorter than those in free tetraphenyldistibane (2.16 and 2.18 Å). Both Sb centers show a strongly distorted tetrahedral configuration. The steric demand of the nonbonding Sb2 MO

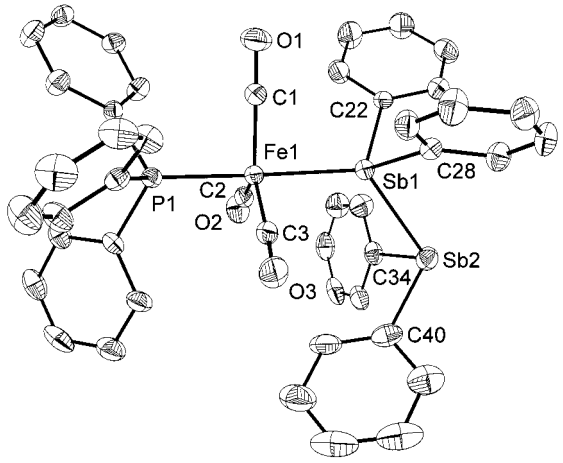

Figure 1. Molecular structure of **3** in the solid state; selected bond lengths (Å) and angles (°): Fe1−P1 2.188(2), Fe1−Sb1 2.457(1), Sb1−Sb2 2.8282(7), Fe1−C1 1.752(7), Fe1−C2 1.758(7), Fe1−C3 1.776(8), Sb1−C22 2.130(6), Sb1−C28 2.132(7), Sb2−C40 2.138(9), Sb2−C34 2.145(7); P1−Fe1−Sb1 177.99(6), Fe1−Sb1−Sb2 125.62(3), C1−Fe1−C2 119.6(3), C1−Fe1−C3 118.3(3), C2−Fe1−C3 122.1(3), C22−Sb1−C28 100.5(2), C22−Sb1−Sb2 98.6(2), C22−Sb1−Fe1 113.7(2), C28−Sb1−Fe1 114.5(2), C28−Sb1−Sb2 100.0(2), C40−Sb2−C34 98.4(3), C40−Sb2−Sb1 94.9(2), C34−Sb2−Sb1 98.1(2)

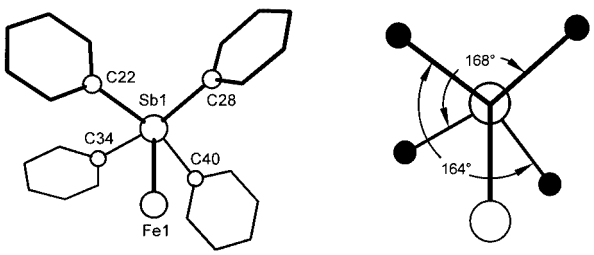

Figure 2. Conformation of the Sb_2Ph_4 ligand in **3** [Newman projection along the Sb1−Sb2 axis with dihedral angles (°)]

 © 2005 Wiley-VCH Verlag GmbH & Co. KGaA, Weinheim

leads to an 11−14° reduction of the bond angles compared to those of coordinated Sb1. In the same fashion, the Fe(CO)$_3$(PPh$_3$) group bound to Sb1 forces a greater deformation from an ideal tetrahedral configuration about Sb1, with the Fe1−Sb1−Sb2 angle of 126° differing most of all.

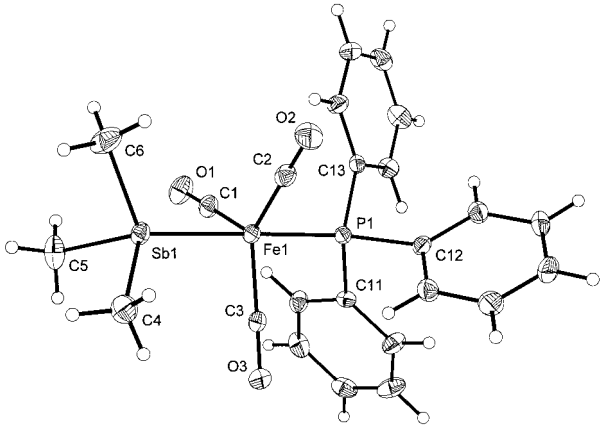

Figure 3. Molecular structure of **5** in the solid state; selected bond lengths (Å) and angles (°): Fe1−P1 2.199(1), Fe1−Sb1 2.463(6), Fe1−C1 1.769(5), Fe1−C2 1.778(5), Fe1−C3 1.778(4), Sb1−C4 2.094(5), Sb1−C5 2.118(5), Sb1−C6 2.114(5), P1−C_{Ph} 1.835(4); P1−Fe1−Sb1 177.56(4), C1−Fe1−C2 121.8(2), C1−Fe1−C3 119.5(2), C2−Fe1−C3 118.4(2), C4−Sb1−Fe1 116.62(15), C5−Sb1−Fe1 117.54(15), C6−Sb1−Fe1 118.46(16), C_{Ph}−P1−Fe1 ca. 115.7, C_{Ph}−Fe1−C5 ca. 102.6

The molecular structure of **5** (Figure 3) is similar to that of **3**; the analogous bond lengths and angles at the central iron are practically identical. The Newman projection of **5** shows the almost perfectly staggered conformation of the Me, CO, and Ph substituents along the Sb1−Fe1−P1 axis (Figure 4).

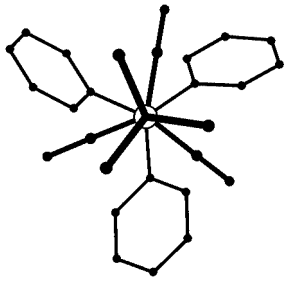

Figure 4. Newman projection of **5** along the Sb1−Fe1−P1 axis

Our new reductive Sb−Sb coupling reaction of two molecules of Ph$_2$SbCl to give the η^1-ligand Sb$_2$Ph$_4$ in **3** is explained by the presence of [Fe(CO)$_3$(PPh$_3$)]$^{2-}$ (**1**) (as suitable reducing agent) and by the activating and at the same time stabilizing effect of the complex fragment Fe(CO)$_3$(PPh$_3$). The *trans*-directing influence of PPh$_3$ may also play a positive role in the formation of the mixed dipentelane complex **3**. An analogous effect is also found in the reaction of **1** with the stiborane Me$_3$SbCl$_2$ to give **5**. However, in the case of the nonsubstituted ferrate Na$_2$[Fe(CO)$_4$], the corresponding Sb−Sb coupling reaction and distibane formation, as well as Fe−Sb bond formation, are not possible. When the monoanionic metalates [CpM(CO)$_n$]$^-$ (M = Fe, n = 2; M = Mo, W, n = 3) are reacted with Me$_2$SbBr, for example, a simple salt-metathesis reaction to form the metallostibanes [{Cp(CO)$_n$M}SbMe$_2$] is observed.[14] An Sb−Sb coupling reaction similar to the Wurtz reaction was recently reported in the reaction of Ph$_2$SbI with the metals Sm or Y in THF.[15] Further investigations with respect to the general application of this simple and elegant synthesis using other substituted phosphanes (PR$_3$ where R ≠ Ph) or coupling different pentelanes [e.g. Sb−E (E = P, As)] are in progress.

Experimental Section

All operations were carried out under an Argon atmosphere with complete exclusion of oxygen and moisture (Schlenk techniques). Solvents were dried and then saturated with argon. The following instruments were used for the spectroscopic and analytical measurements: IR: Nicolet 520 FT-IR spectrometer. ^{31}P NMR: Jeol 6SX

Table 1. X-ray structure analysis of **3** and **5**[12]

	3	**5**
Empirical formula	$C_{45}H_{35}FeO_3Sb_2$	$C_{24}H_{24}FeO_3PSb$
Molecular weight (g mol^{-1})	1038.98	569.024
Crystal size (mm)	0.37 × 0.33 × 0.10	0.34 × 0.23 × 0.14
Crystal color, habit	yellow-brown	red-brown prism
Crystal system	monoclinic	orthorhombic
Space group	$P2_1/c$ (No. 14)	Pbca
a (Å)	12.999(2)	10.897(1)
b (Å)	10.462(2)	16.6396(1)
c (Å)	32.805(4)	26.7645(2)
α (°)	90	90
β (°)	98.274(2)	90
γ (°)	90	90
Volume (Å^3)	4412.5(12)	4853.30(6)
Z	4	8
Density calcd. (g cm^{-3})	1.564	1.558
Absorption coefficient (mm^{-1})	1.736	1.798
F(000)	2056	
Index ranges	$-14 \le h \le 0$ $-11 \le k \le 0$ $-37 \le l \le 37$	$-14 \le h \le 11$ $-21 \le k \le 21$ $-34 \le l \le 34$
θ Range (°)	2.51−23.98	1.52−27.49
Reflections collected	7221	70393
Independent reflections	6885	5563
Observed reflections	5081	3959
Parameter/restraints	525/42	274/0
$R1/wR2$ (all data)	0.0745/0.1077	0.0747/0.1418
$R1/wR2$ (final)	0.0467/0.0928	0.0402/0.1004
GOOF	1.133	1.173
Min./max. ρ_e (e Å^3)	0.7242/0.9995	−1.184/1.404
Temperature (K)	293(2)	200(2)
Diffractometer	ENRAF Nonius CAD-4	Nonius Kappa CCD
Radiation	Mo-K_α, λ = 0.71073	Mo-K_α, λ = 0.71073
Scan type	ω-scan	area detection
Solution	SHELXS 86	SIR 97, direct methods
Refinement	SHELXL-93	SHELXL-97

 © 2005 Wiley-VCH Verlag GmbH & Co. KGaA, Weinheim

270 (85% H_3PO_4 as standard). X-ray analysis: ENRAF-Nonius CAD 4-diffractometer and Nonius Kappa CCD-diffractometer. Elemental analysis: Elementar vario EL (W. C. Heraeus). Melting Print: Büchi-510 (m.p. were not corrected).

Synthesis of 3: $K_2[Fe(CO)_3(PPh_3)]$ (**1**; 124 mg, 0.259 mmol) and Ph_2SbCl (353 mg, 0.518 mmol) were dissolved in 10 mL of THF, upon which the solution immediately turned deep red. After stirring for 2 h and filtering, the solvent was distilled off in vacuo to yield a viscous brownish oil. Repeated recrystallization from CH_2Cl_2/*n*-hexane resulted in a microcrystalline solid, which was dried in vacuo. Yield: 154 mg (63%), orange brown crystals, m.p. 137 °C. IR (KBr): ν(CO) = 1883 cm^{-1}. ^{13}C NMR ([D_6]acetone): δ = 126−131 (Ph), 212 (CO) ppm. $^{31}P\{^1H\}$ NMR: δ = 86.4 ppm. $C_{46}H_{37}FeO_3PSb_2$ (954.09): calcd. C 57.9, H 3.9; found C 57.9, H 3.8.

Synthesis of 5: $K_2[Fe(CO)_3(PPh_3)]$ (**1**; 275 mg, 0.573 mmol) was dissolved in 20 mL of THF containing Me_3SbCl_2 (136 mg, 0.573 mmol). The color of the solution changed to red, and a fine, light-colored precipitate of KCl formed. After stirring for 2 h and careful decantation, the solvent was distilled off in vacuo. The red-brown residue was recrystallized several times to give analytically pure **5**. Yield: 179 mg (55%), red-brown crystals, m.p. 121 °C. IR (KBr): ν(CO) = 1877 cm^{-1}. ^1H NMR ([D_6]acetone): δ = 1.31 (s, 9 H, Me), 7.22−7.63 (m, 15 H, Ph) ppm. $^{13}C\{^1H\}$ NMR ([D_6]acetone): δ = 40.1 (s, Me), 126−131 (m, Ph), 209 (s, CO) ppm. $^{31}P\{^1H\}$ NMR ([D_6]acetone): δ = 85.5 ppm. $C_{24}H_{24}FeO_3PSb$ (567.99): calcd. C 50.7, H 4.3; found C 51.6, H 3.7.

[1] C. A. McAuliffe, W. Levason, *Phosphine, Arsine and Stibine Complexes of the Transition Elements*, Elsevier **1979**.
[2] N. R. Champness, W. Levason, *Coord. Chem. Rev.* **1994**, *133*, 115−217.
[3] H. J. Breunig, I. Ghesner, *Adv. Organomet. Chem.* **2003**, 95−131.
[4] M. O. Albers, E. Singleton, N. J. Coville, *Inorg. Synth.* **1990**, *28*, 168−173.
[5] M. O. Albers, N. J. Coville, T. V. Ashworth, E. Singleton, *J. Organomet. Chem.* **1981**, *217*, 385−390.
[6] M. O. Albers, N. J. Coville, E. Singleton, *J. Organomet. Chem.* **1982**, *232*, 261−266.
[7] J. P. Collmann, R. G. Komoto, W. O. Siegl, *J. Am. Chem. Soc.* **1973**, *95*, 2389−2390.
[8] H. J. Breunig, W. Fichtner, *Z. Anorg. Allg. Chem.* **1979**, *454*, 167−174.
[9] M. Brockhaus, F. Staudacher, H. Vahrenkamp, *Chem. Ber.* **1972**, *105*, 3716−3725.
[10] L. Staudacher, H. Vahrenkamp, *Chem. Ber.* **1976**, *109*, 218−228.
[11] A. F. Clifford, A. K. Mukherjee, *Inorg. Synth.* **1966**, *8*, 185−189.
[12] CCDC-246697 (for **3**) and -246325 (for **5**) contain the supplementary crystallographic data for this paper. These data can be obtained free of charge from The Cambridge Crystallographic Data Centre via www.ccdc.cam.ac.uk/data request/cif.
[13] G. Becker, H. Freudenkamp, C. Witthauer, *Z. Anorg. Allg. Chem.* **1982**, *492*, 37−51.
[14] W. Malisch, P. Panster, *J. Organomet. Chem.* **1974**, *76*, C7−C10.
[15] E. A. Fedorova, O. A. Trokhaeva, G. S. Kalinina, M. W. Bochkarev, G. A. Razuvaev, *Metallorg. Khim.* **1988**, *1*, 397−399.
[16] Organikum, VEB Deutscher Verlag der Wissenschaften, Berlin, **1988**.
[17] J. E. Ellis, Y.-S. Chen, *Organometallics* **1989**, *8*, 1350−1361.
[18] M. Nunn, D. B. Sowerby, D. M. Wesolek, *J. Organomet. Chem.* **1983**, *251*, C45−C46.

Received August 6, 2004

 © 2005 Wiley-VCH Verlag GmbH & Co. KGaA, Weinheim

Nonquenchable Chemical Order−Disorder Phase Transition in Yttrium Oxyfluoride

Igor Levin,*[a] Qing Z. Huang,[a] Lawrence P. Cook,[a] and Winnie Wong-Ng[a]

Keywords: Phase transitions / Yttrium / X-ray diffraction / Order−disorder transitions

A chemical order–disorder polymorphic phase transition in yttrium oxyfluoride (YOF) was studied in situ by X-ray and neutron powder diffraction. The high-temperature form of YOF crystallizes with a cubic $Fm\bar{3}m$ fluorite structure in which the O and F atoms are disordered among the tetrahedrally coordinated sites. The low-temperature form of YOF exhibits rhombohedral $R\bar{3}m$ symmetry and evolves from the high-temperature form by the phase transition associated with the ordering of the O and F atoms. The transition occurs around 560 °C. The superstructure contains layers of $[OY_4]$ and $[FY_4]$ tetrahedra alternating along the *c*-axis of the trigonal cell (parallel to the <111> direction of the parent cubic structure). The ordering of the O and F atoms is accompanied by the significant displacements of the Y, O, and F atoms from their ideal positions in the cubic phase. Bond valence sum calculations indicate considerable bond strain for both O and F in the cubic structure; the strain is relieved in the ordered low-temperature phase. The order–disorder transition in YOF is completely reversible and exhibits fast nonquenchable kinetics.
(© Wiley-VCH Verlag GmbH & Co. KGaA, 69451 Weinheim, Germany, 2005)

Introduction

Phase equilibria in the Ba−Cu−Y−F−O system have become the subject of intensive investigation after the BaF_2−Cu−Y precursor films, deposited on RABiTS and annealed in water vapor, demonstrated the potential for producing high quality $Ba_2YCu_3O_{6+x}$ (Y-213) superconductor tapes.[1] One of the critical questions in studies of phase equilibria in this system concerns the existence of the transient fluorine-containing low-temperature melts, which could control formation of the Y-213 phase. Recent systematic studies of melting temperatures in the $BaF_2-YF_3-Y_2O_3-CuO_x$ subsystem using differential thermal analysis (DTA) showed a peak at T = 560 °C that could be attributed to such a transient melt.[2] However, subsequent analyses of these samples using variable-temperature X-ray powder diffraction demonstrated that this DTA event is associated with a nonquenchable phase transition in the stoichiometric yttrium oxyfluoride.[2] The crystal structure of YOF has been studied previously.[3,4] Zachariasen[3] reported both rhombohedral and tetragonal room-temperature forms of YOF. The tetragonal form is stabilized by the excess fluorine and occurs for the compositions YO_nF_{3-2n} with $0.7 < n < 1.0$, whereas the rhombohedral structure is stable for the stoichiometric composition with n = 1. Both structures have been described as derivatives of the cubic fluorite archetype with the ordering of oxygen and fluorine atoms into distinct tetrahedrally coordinated sites. Later X-ray diffraction studies by Bevan and Mann[4] confirmed the rhombohedral structure of stoichiometric YOF with the space group $R\bar{3}m$ (a = 3.797 Å, c = 18.89 Å). Zachariasen[2] has alluded to the potential existence of the disordered high-temperature cubic fluorite phase; however, all attempts to quench the cubic form were unsuccessful. Later studies[3−7] confirmed the existence of the rhombohedral ⇄ cubic phase transition in YOF at 560−570 °C, but provided few details on the evolution of structural parameters upon this phase change. In the present contribution, we report a detailed study of such nonquenchable order−disorder phase transition in stoichiometric YOF as analyzed in situ by variable-temperature X-ray and neutron powder diffraction.

[a] Materials Science and Engineering Laboratory, National Institute of Standards and Technology, Gaithersburg, MD 20899, USA

Results and Discussion

The room temperature X-ray powder diffraction patterns of YOF, both slowly cooled and quenched from 600 °C, were completely indexable according to the rhombohedral (R) unit cell with lattice parameters a_R = 3.800(5) Å and c_R = 18.863(9) Å. In addition to the major YOF phase, the sample contained small amounts of Y_2O_3. As the Y_2O_3 reflections do not overlap with those of YOF, they do not affect the refinement of the YOF structure and were excluded from the analysis. In situ studies of the YOF sample with high-temperature X-ray diffraction revealed a reversible phase transformation to a cubic (C) structure as inferred from the disappearance of the rhombohedral reflec-

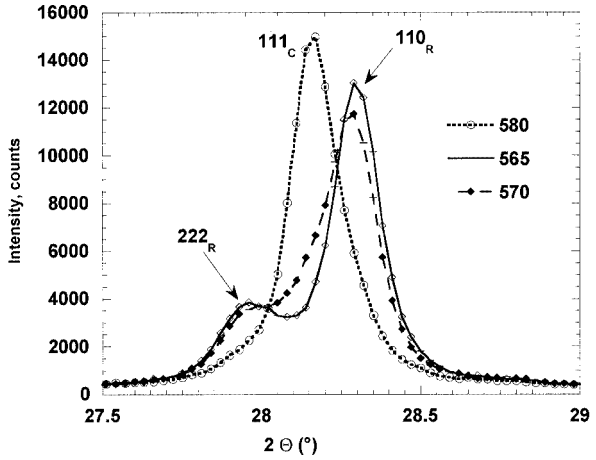

Figure 1. Evolution of the $222_R/110_R$ and 111_c reflections upon heating/cooling across the rhombohedral ⇄ cubic transition during in situ X-ray powder diffraction measurements

tion splitting (Figure 1). The transition occurred at $T_0 \approx$ 575 °C, which is in reasonable agreement with T_0 = 565 °C deduced from the DTA measurements (Figure 2).

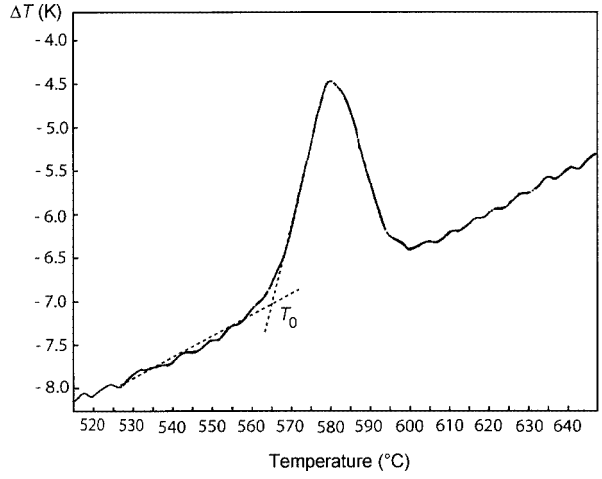

Figure 2. DTA plot for YOF; the transition temperature was determined from the extrapolated intersection of the baseline with the linear portion of the rising peak

Structural refinements using neutron powder diffraction data (Table 1, Figure 3, a) and the initial atomic positional parameters from ref.[4] confirmed that the low-temperature

Table 1. Refined structural parameters for the rhombohedral and cubic YOF polymorphs

Atom	x	y	z	$U_{iso}\times100$ Å^2
T = 514 °C K, $R\bar{3}m$, a = 3.8205(2) Å, c = 19.019(1) Å				
Y	0	0	0.2418(1)	1.40(4)
F	0	0	0.3698(1)	2.61(7)
O	0	0	0.1211(1)	1.89(6)
T = 613 °C, $Fm\bar{3}m$, a = 5.4527(2) Å				
Y	0	0	0	2.99(4)
O/F	1/4	1/4	1/4	3.51(4)

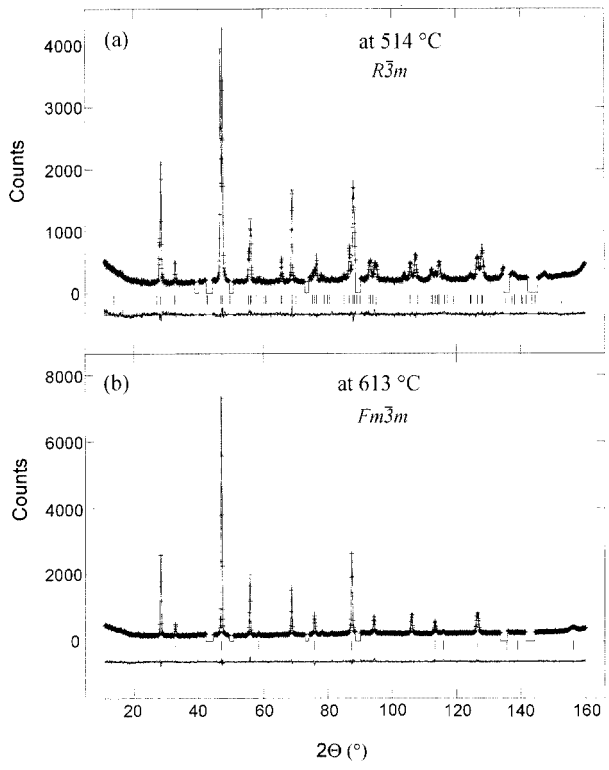

Figure 3. (Upper) Experimental (crosses) and calculated (line) neutron powder diffraction profiles of YOF acquired at a) 514 °C (rhombohedral phase), and b) 613 °C (cubic phase); regions containing reflections of the impurity phase were excluded from the fit; (lower) residual; the fitting reliability parameters are R_{wp} = 6.22%, χ = 1.18 for T = 514 °C, and R_{wp} = 6.32, χ = 1.20 for T = 613 °C

YOF polymorph crystallizes with a rhombohedral $R\bar{3}m$ superstructure. The superstructure features layers of [FY_4] and [OY_4] tetrahedra alternating along the c_R-axis (Figure 4). The atomic positional and displacement parameters refined for T = 514 °C are summarized in Table 2. In the rhombohedral structure, all three species, Y, O, and F, exhibit appreciable displacements (v_Y = 0.0082c_R, v_F =

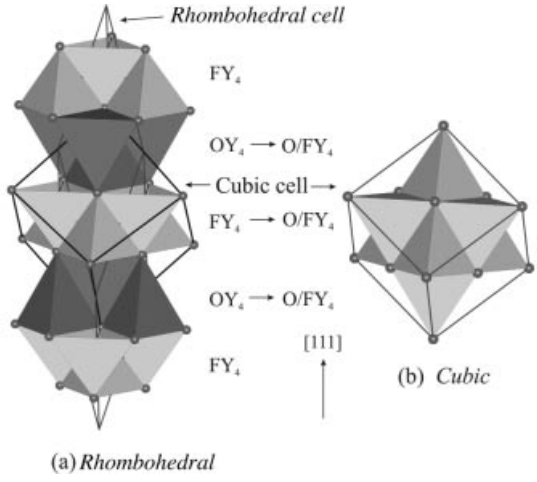

Figure 4. Schematic representation of the refined YOF rhombohedral (left) and cubic fluorite (right) structures

 © 2005 Wiley-VCH Verlag GmbH & Co. KGaA, Weinheim

$0.0052c_R$, $v_O = 0.0039c_R$) from the ideal positions in the cubic fluorite; the displacements occur along the *c*-axis, which is parallel to the $<111>_c$ direction of the cubic fluorite. The resulting Y−F bond distances (2.435 Å and 2.4412 Å) are significantly longer than the corresponding Y−O distances (2.297 Å and 2.2763 Å). Refinements of anisotropic temperature parameters did not reveal any significant anisotropy of displacements and produced little effect on the quality of the fit; therefore, in the final refinement run, the temperature parameters were assumed to be isotropic. As the site occupancies refined for the O and F positions were within the estimated standard uncertainties (2%) from the ideal values of unity, both positions were assumed to be fully occupied. Both $[FY_4]$ and $[OY_4]$ tetrahedra are appreciably distorted (Figure 5) as seen from comparison of both Y−F−Y (115.4°/103.0°) and O−Y−O (114.1°/104.3°) angles with a value of 109.47° in a perfect tetrahedron.

Table 2. Selected bond distances, and calculated BVS values for the YOF polymorphs

F−Y (Å)	O−Y (Å)
Rhombohedral (T = 514 °C)	
2.435(4)	2.297(4)
2.4412(9) ×3	2.2763(5)
BVS = 0.94 v.u.	*BVS* = 1.94 v.u .
Cubic (T = 613 °C)	
2.3611(1)	2.3611(10)
BVS = 1.16 v.u.	*BVS* = 1.57 v.u.
Average *BVS* = 1.37 v.u.	

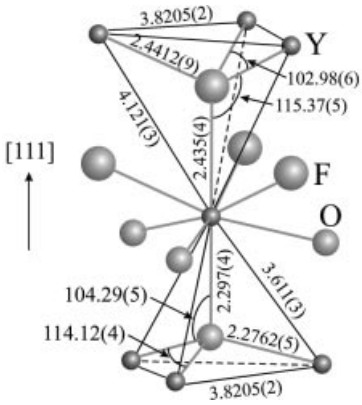

Figure 5. Coordination environment of the Y atoms in the YOF rhombohedral structure at 514 °C; selected bond distances and angles are indicated

Heating the YOF sample in situ during the neutron diffraction measurements caused a reversible phase transition to the cubic structure (Figure 6); the transition temperature T = 520 °C in the neutron experiments is lower than that determined with both DTA and X-ray diffraction. The lower value of T_0 from the neutron measurements was attributed to the temperature gradient in the furnace (up to 10 °C) combined with slow conduction of heat from the vacuum of the furnace through the container wall to the YOF powder. The neutron diffraction patterns recorded at T = 500 °C and T = 540 °C (on the thermocouple) contained single rhombohedral and cubic phases, respectively. In contrast, the neutron diffraction pattern recorded at 520 °C contained a two-phase mixture. Given the nonquenchable kinetics of the rhombohedral ⇄ cubic phase transition, the coexistence of these two phases at T = 520 °C for a prolonged time was attributed to thermal gradients across the relatively large neutron sample. The temperature dependence of the lattice parameters refined for the YOF polymorphs is summarized in Figure 7. The rhombohedral ⇄ cubic transition appears to be a first-order transition and is accompanied by a volume change of about 0.6%.

A structural model based on the ideal cubic fluorite structure (space group $Fm\bar{3}m$) with a disordered mixture of F and O atoms on the fourfold coordinated sites (Table 2) provided a satisfactory fit to the experimental data at T =

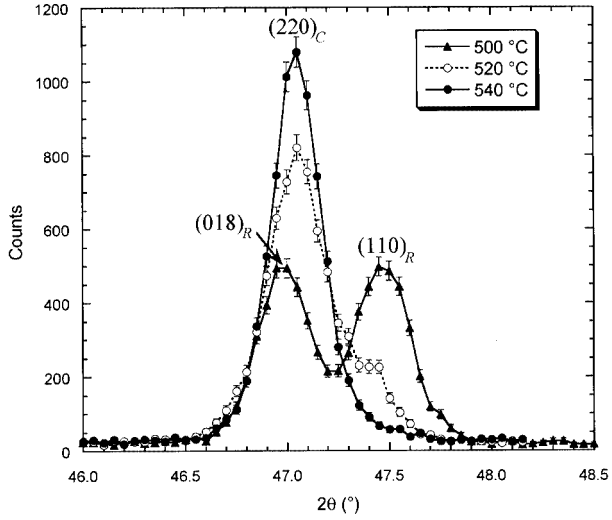

Figure 6. Evolution of the $110_R/108_R$ and 220_c neutron reflections upon heating/cooling across the rhombohedral ⇄ cubic transition; at T = 520 °C (on the thermocouple) a two-phase mixture is observed, presumably due to the thermal gradients in the sample

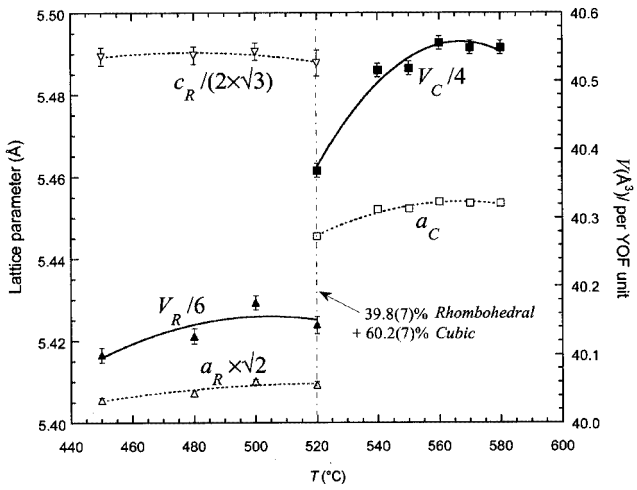

Figure 7. Temperature dependence of the lattice parameters for the rhombohedral and cubic phase; a significant volume change upon the rhombohedral ⇄ cubic transition is observed

 © 2005 Wiley-VCH Verlag GmbH & Co. KGaA, Weinheim

613 °C (see b in Figure 3). The symmetries of the high-temperature cubic and low-temperature rhombohedral phases obey a group−subgroup relation.

Bond valence sum (BVS) calculations for this cubic structure indicate strong under- and over-bonding for the O and F atoms, respectively, whereas the bond requirements for Y are closely satisfied. Such strong deviations from the ideal BVS values suggest the existence of *local* atomic displacements in the cubic structure aimed to accommodate the bonding requirements of the O and F atoms. Indeed, values of the temperature/displacement parameters for the Y and O atoms increased discontinuously upon transition to the cubic phase (Figure 8), which can be attributed to disordered local displacements of these atoms from their ideal positions in the cubic structure. Interestingly, temperature parameters for the over-bonded F atoms displayed no evidence for such local displacements. In contrast to the cubic phase, the low-temperature rhombohedral phase features nearly ideal BVS values for both O and F atoms. The BVS analyses suggest that simultaneous satisfaction of the bonding requirements for the O and F atoms, which cannot be achieved in the ideal cubic fluorite arrangement, provides a driving force for the O/F ordering and the associated ion displacements. Fast nonquenchable kinetics for the O/F order−disorder transition in YOF can be attributed to the high anion mobility often observed in fluorite-based ion conductors.

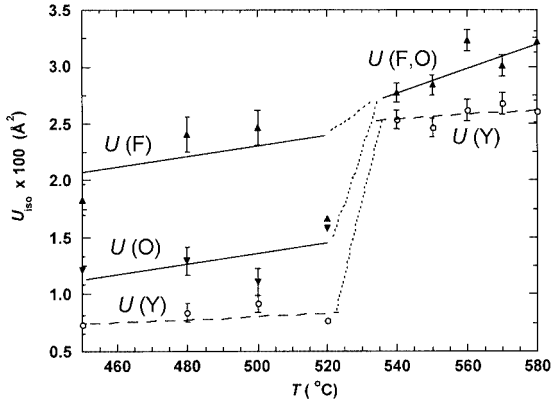

Figure 8. Temperature dependence of the isotropic temperature/displacement parameters, U_{iso}, for the Y, O, and F atoms in the YOF polymorphs; the U_{iso} parameters for both Y and O, but not F, exhibit a discontinuous increase upon the rhombohedral ⇄ cubic transition; such an abrupt increase in the magnitude of U_{iso} suggests the presence of local disordered displacements of both Y and O atoms in the cubic phase

Conclusions

YOF crystallizes with two polymorphs separated by the F/O order−disorder phase transition at T = 560 °C. The high-temperature form features a cubic $Fm\bar{3}m$ fluorite structure − the O and F atoms are disordered on the tetrahedrally coordinated sites. The ordering of F and O atoms upon transition to the low-temperature phase yields rhombohedral $R\bar{3}m$ symmetry and the lattice parameters $a_R \approx a_C/\nu 2$, $c_R \approx 2a_C\nu 3$. This fluorite-based superstructure contains layers of $[OY_4]$ and $[FY_4]$ tetrahedra alternating along the *c*-axis of the trigonal cell (parallel to the <111> direction of the parent cubic structure). The ordering of the O and F atoms is accompanied by the displacements of the Y, O, and F atoms from their ideal positions in the cubic phase. Bond valence sum calculations indicate considerable bond strain for both O and F in the cubic structure. The refinements suggest significant local displacements for the O and Y atoms (but not F), which are likely aimed to satisfy the bonding requirements of the anions. The bond strain about both O and F is relieved in the ordered low-temperature phase. The order−disorder transition in YOF is reversible and exhibits fast nonquenchable kinetics.

Experimental Section

Polycrystalline samples of YOF were prepared using powders of Y_2O_3 (Alfa Industries, lot # 093080, 99.999% purity, metals basis) and anhydrous YF_3 packed under Ar (Alfa Aesar lot # D10 K11, 99.9% purity, metals basis). Prior to use, the Y_2O_3 was preheated at 600 °C for 1 h to remove moisture. A 5-g mixture of Y_2O_3 and YF_3 in equimolar proportion was weighed in an Ar-filled glovebox with a continuously recirculating purifier, which removed contaminants to <1 ppm by volume. The powder mixture was transferred to a thermoanalyzer and annealed overnight at 500 °C in flowing Ar; the powder was contained in a platinum-lined crucible to prevent any reaction of YF_3 with the ceramic crucible. This procedure was repeated with intermediate grindings five times. The total mass lost during synthesis was 0.4 wt.-%.

Simultaneous differential thermal analysis/thermogravimetric analysis (DTA/TGA) experiments were completed in a Mettler TA1 thermoanalyzer outfitted with Anatech digital control and data acquisition electronics. DTA crucibles were fabricated from high purity Pt tubing, and experiments were conducted at a ramp rate of 10 °C/min. Phase-transition onset temperatures during heating were determined from extrapolated intersection of the baseline with the linear portion of the rising peak. The DTA apparatus was calibrated against the α→b quartz transition (571 °C) and the NaCl melting point (801 °C); DTA temperatures were estimated to have < ±3 °C standard uncertainty.

High-temperature X-ray diffraction (HTXRD) measurements were conducted in a Siemens 5000 θ−θ diffractometer equipped with a high-temperature furnace and a position sensitive detector. Cu-K_α radiation was used. The samples were prepared by applying a thin layer of powder (finely ground as an ethanol slurry) to a Pt heating band. The X-ray diffraction experiments were conducted under He gas flow.

Neutron powder diffraction data for Rietveld analysis were collected on the BT1 diffractometer at the Center for Neutron Research at the National Institute of Standards and Technology, using a Cu(311) monochromator with a wavelength of 1.5402(2) Å, and an array of 32 He-3 detectors at 5° intervals. Collimation of 15′, 20′, and 7′ arc were used before and after the monochromator, and after the sample, respectively. The YOF sample was held in a vanadium cylindrical sample container and heated in a furnace under vacuum. The data were collected over the 2θ range 3−168 ° at 11 temperatures between 450 °C and 613 °C. The GSAS package[8] was used for Rietveld structural refinements.

 © 2005 Wiley-VCH Verlag GmbH & Co. KGaA, Weinheim

[1] R. Feenstra, T. B. Lindemer, J. D. Budai, M. D. Galloway, *J. Appl. Phys.* **1991**, *69*, 6569.
[2] W. Wong-Ng, L. P. Cook, I. Levin, M. Vaudin, J. Suh, and R. Feenstra, *J. Mater. Res.,* to be submitted.
[3] W. H. Zachariasen, *Acta Crystallogr.* **1957**, *4*, 231−236.
[4] A. W. Mann, D. J. M. Bevan, *Acta Crystallogr., Sect. B* **1970**, *26*, 2129−2131.
[5] J. H. Miller, T. Petzel, *J. Alloys and Comp.* **1995**, *224*, 18−21.
[6] T. Petzel, V. Marx, B. Hormann, *J. Alloys and Comp.* **1993**, *200*, 27−31.
[7] K. Niihara, S. Yajima, *Bull. Chem. Soc. Jpn.* **1972**, *44 (3)*, 20−23.
[8] A. C. Larson and R. B. Von Dreele, "*General Structure Analysis System*", Los Alamos National Laboratory Report, LAUR 86−748, **1994**.

Received April 14, 2004
Early View Article
Published Online November 10, 2004

 © 2005 Wiley-VCH Verlag GmbH & Co. KGaA, Weinheim

Bioorganometallic Chemistry: Reactions of Methyltitanocene Cation Complexes with a Singly Deprotected Methyl Glucopyranoside

Birgit Meyer zu Berstenhorst,[a] Gerhard Erker,*[a] Gerald Kehr,[a] Julia-Christina Wasilke,[a] Jens Müller,[a] Hartmut Redlich,[a] and Jutta Pyplo-Schnieders[a]

Keywords: Carbohydrate complexes / Titanocene / Zirconocene / Lewis acid / Chelate complexes / Bioorganometallic chemistry

The dimethyltitanocene/$B(C_6F_5)_3$ system reacts with the 4-unprotected methyl α-D-glucopyranoside derivative **5** ("HO-carb.") to yield the ionic complex $[Cp_2Ti(O\text{-carb.})]^+[MeB(C_6F_5)_3]^-$ (**10a**). Spectroscopic studies have led us to believe that **10a** is characterized by an internal ether-chelate structure in solution that involves coordination of the 6-OCH_2Ph oxygen atom. Treatment of **10a** with trimethylphosphane gives the open, non-chelated complex **11a**, in which the phosphane coordinates to the metal center. Reaction of the THF-stabilized salt $[Cp_2TiCH_3(THF)]^+[BPh_4]^-$ (**12a**) with **5** gave complex **13a**, with coordinated THF. Experiments with bis(methylcyclopentadienyl)titanium systems gave analogous results (complexes **10b**, **11b** and **13b**). Zirconocenes react differently. Addition of dimethylzirconocene (**14a**) or dimethylbis(methylcyclopentadienyl)zirconium (**14b**) to **5** gave the neutral complexes **15a**, **15b** and methane. Treatment of **15a** (**15b**) with $B(C_6F_5)_3$ again resulted in the formation of an ionic chelate complex **16a** (**16b**). A non-chelated complex **18** was formed by treating the THF-stabilized salt $[Cp_2ZrCH_3(THF)]^+[BPh_4]^-$ (**17**) with **5**.
(© Wiley-VCH Verlag GmbH & Co. KGaA, 69451 Weinheim, Germany, 2005)

Introduction

Titanocene dichloride is a potent anti-cancer agent.[1,2] In contrast to other metal-containing anti-cancer drugs, such as, for example, the "cisplatinum" derivatives, the mechanism of the biological action of $[Cp_2TiCl_2]$ and its congeners has remained less understood,[3a,3b] but it seems to be different from that of the cisplatinum cancerostatica.[3c−3f] Therefore, it is of interest to learn about the chemistry that titanocene derivatives and similar compounds undergo with typical "bio-molecules".[4] For carrying out such model reactions and for monitoring their mechanistic course, the use of the corresponding methyl-Group 4 metallocene derivatives have been of advantage, although they are not the actual biologically active in vivo species.

We have recently shown that, e.g., methyltitanocene cation reacts quite selectively with a variety of oligopeptide derivatives.[5,6] The $[Cp_2TiMe]^+$ molecule was shown to add preferentially to specific internal carbonyl positions of, e.g., a tripeptide under kinetic control (see Scheme 1). Under thermodynamic control it then migrates along the peptide chain. Eventually, it binds to specific favored positions at the chain by means of deprotonation with evolution of methane.[5]

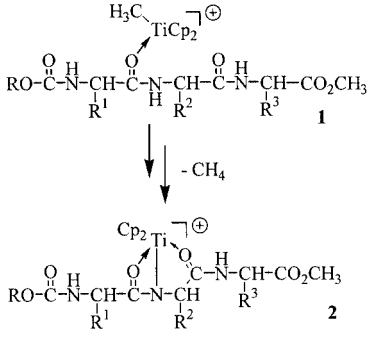

Scheme 1

We have now begun to carry out similar studies on the reactions of methyl titanocenes and related compounds with another important class of biomolecules, the carbohydrates.[7] In an initial series of experiments we have treated a variety of methyltitanocene complexes with a suitably protected glucopyranoside derivative that contained a single active −OH group. Reactions were carried out with titanocene and zirconocene derivatives and were shown to feature some remarkable differences.

Results and Discussion

We have employed methyl 2,3,6-tri-*O*-benzyl-α-D-glucopyranoside (**5**) as the carbohydrate reagent for this study.

[a] Organisch-Chemisches Institut der Universität Münster, Corrensstr. 40, 48149 Münster, Germany
E-mail: erker@uni-muenster.de
Supporting information for this article is available on the WWW under http://www.eurjoc.eurjic.org or from the author.

 © 2005 Wiley-VCH Verlag GmbH & Co. KGaA, Weinheim DOI: 10.1002/ejic.200400387

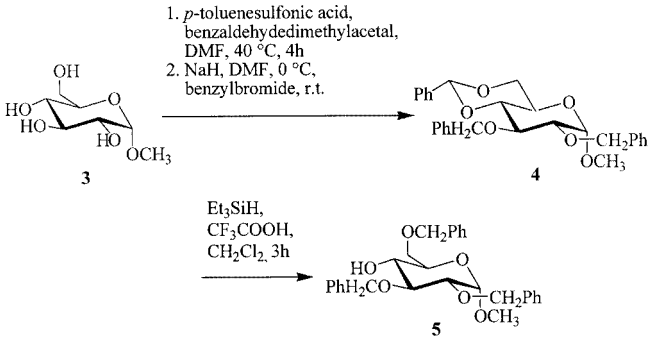

Scheme 2

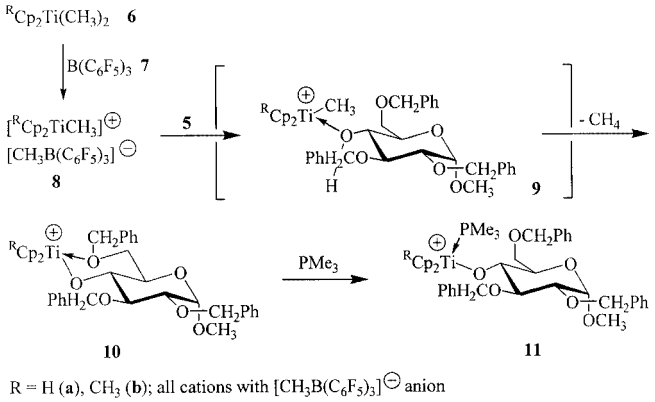

R = H (**a**), CH_3 (**b**); all cations with $[CH_3B(C_6F_5)_3]^{\ominus}$ anion

Scheme 3

It was synthesized as depicted in Scheme 2.[8] Treatment of methyl α-D-glucopyranoside (**3**) with 2 equiv. of benzaldehyde dimethyl acetal and 0.2 equiv. of *p*-toluenesulfonic acid led to the 4,6-*O*-benzylidene acetal of glucose. The raw product was deprotonated by using sodium hydride in mineral oil at 0 °C for 2 h. Reaction with benzyl bromide, overnight at room temperature, gave the methyl 2,3-di-*O*-benzyl-α-D-glucopyranoside **4**. Regioselective reductive cleavage of the acetal function to generate the 4-unprotected carbohydrate derivative was carried out by using triethylsilane in the presence of trifluoroacetic acid. Chromatographic workup eventually gave methyl 2,3,6-tri-*O*-benzyl-α-D-glucopyranoside (**5**) with an unprotected hydroxy group at C-4.

We used two pairs of titanocene and zirconocene reagents, namely the parent $[Cp_2M]$ derived compounds and their $[(MeC_5H_4)_2M]$ analogues, to ensure general reproducibility of our results. We first treated dimethyltitanocene (**6a**) with the carbohydrate derivative **5**. It turned out, however, that $[Cp_2TiMe_2]$ (**6a**) proved to be unreactive towards the free "4-OH sugar derivative" **5** in dichloromethane at room temperature. Similarly, the carbohydrate derivative **5** was recovered unchanged from the solution upon its attempted reaction with $[(CH_3-C_5H_4)_2TiMe_2]$ (**6b**).

The reaction conditions were, therefore, changed as follows: a solution containing **5** and 1 mol-equiv. of the strong Lewis acid $B(C_6F_5)_3$ (**7**)[9] was added dropwise to a dichloromethane solution of $[Cp_2TiMe_2]$ (**6a**). A rapid methane evolution was observed. Workup after 2 h at ambient temperature gave the salt $[Cp_2Ti(O\text{-carb.})]^+[MeB(C_6F_5)_3]^-$ (**10a**) as a red-brown solid in a yield of 70%. Under these conditions it can safely be assumed that the reagent $[Cp_2TiCH_3]^+[MeB(C_6F_5)_3]^-$ (**8a**) is generated in situ.[10] This is much more reactive than its neutral 16-electron precursor **6a** and is rapidly attacked by the free −OH group of **5**, potentially by involvement of a reactive coordinated intermediate **9a** to yield the product **10a** with liberation of 1 mol-equiv. of methane (see Scheme 3).

Complex **10a** features an optical rotation of $[\alpha]_D^{25} = +210$. It shows three separate ^1H NMR AB spin systems of the $-OCH_2Ph$ benzyl protective groups, and an AB part of an ABM spin system of the 6-H/H′ methylene hydrogen atoms (for the respective ^1H NMR chemical shifts see Table 1). The cyclopentadienyl groups at the titanium atom in **10a** are diastereotopic; they give rise to equal-intensity pairs of ^1H (δ = 6.60, 6.62 ppm) and ^{13}C (δ = 118.6, 121.4 ppm) NMR signals. This means that the titanium center in **10a** is pseudo-tetrahedrally coordinated by two η^5-Cp ligands, the carbohydrate 4-O oxygen atom and a fourth neutral donor ligand. In principle this could be the methyl group of the $[MeB(C_6F_5)_3]^-$ counteranion {tight ion pair formation between Group 4 metallocene $[Cp_2MR]^+$ cations and the $[MeB(C_6F_5)_3]^-$ anion is frequently observed}[11,12] or alternatively an internal ether oxygen coordination involving either the 3-OCH_2Ph or the 6-OCH_2Ph oxygen atom. A comparison with some typical ^{13}C NMR chemical shifts of related complexes (see below) enables us to assume that **10a** is characterized by an internal ether-chelate structure in solution that involves coordination of the 6-OCH_2Ph oxygen atom. The reaction between **5** and the in situ generated methylbis(methylcyclopentadienyl)titanium cation system **8a** gave analogous results (see Scheme 3 and Tables 1 and 2).

In order to answer this structural question, we treated both the complexes **10a** (R = H) and **10b** (R = CH_3) with PMe_3. It is known that trimethylphosphane serves as a stronger donor towards titanocene cation complexes than ethers. Thus, the formation of an open, non-chelate adduct is expected. The reaction of complex **10a** with PMe_3 in toluene at room temperature is instantaneous. The PMe_3 adduct **11a** was isolated as a brown solid in 67% yield ($[\alpha]_D^{25} = -44$). The ^1H NMR resonance of the PMe_3 ligand of **11a** occurs at δ = 0.78 ppm (d, $^2J_{H,P}$ = 9.1 Hz). Complex **11a** shows a pair of Cp resonances at δ = 5.31 and δ = 5.39 ppm, each of them is split into a doublet ($^3J_{H,P}$ = 2.8 Hz) by the *Ti*-coordinated PMe_3 ligand. The ^{31}P NMR resonance of the [Ti]−PMe_3 unit in **11a** was located at δ = 4.2 ppm. Complex **10b** reacts analogously with PMe_3 to yield the 1:1 addition product **11b** (63% isolated; $[\alpha]_D^{25} = -58$; ^{31}P NMR: δ = 3.2 ppm).[13]

For comparison we have also treated the THF-stabilized salt $[Cp_2TiCH_3(THF)]^+[BPh_4]^-$ (**12a**)[14] with **5**. This reaction does not proceed below room temperature. At room temperature evolution of methane is observed. The reaction is not as clean as the systems described above. Formation of a mixture of two major products in a 5:1 ratio is observed plus several minor components. Some further de-

 © 2005 Wiley-VCH Verlag GmbH & Co. KGaA, Weinheim

Table 1. Selected ^{1}H NMR spectroscopic data of the benzyl-protected titanocene- and zirconocene−*O*-glucopyranoside systems

	10a	**10b**	**11a**	**11b**	**13a**	**13b**	**15a**	**15b**	**16a**	**16b**	**18a**
1-*H*	4.67	4.70	4.59	4.59	4.85	4.77	4.70	4.71	4.66	4.62	4.81
2-*H*	3.58	3.66	3.42	3.44	3.76	3.71	3.51	3.50	3.49	3.50	3.68
3-*H*	3.79	3.93	3.54	3.61	3.70	3.67	3.45	3.51	3.69	3.73	3.65
4-*H*	4.88	4.94	4.34	4.51	4.89	4.68	3.84	3.84	4.19	4.26	4.28
5-*H*	3.58	3.65	3.38	3.48	3.56	3.50	3.37	3.51	3.51	3.52	3.51
6-*H*/6-H_a	3.52	3.65	3.14	3.20	3.29	3.57	3.43	3.41	3.74	3.77	3.40
6-*H′*/6-H_e	4.01	4.01	3.27	3.31	3.44	3.84	3.44	3.46	4.04	4.04	3.47
OCH_3	3.28	3.30	3.19	3.18	3.39	3.37	3.34	3.35	3.24	3.22	3.38
2-OCH_2	4.66, 4.75	4.65, 4.74	4.23, 4.29	4.18, 4.25	4.63, 4.63	4.65, 4.91	4.60, 4.64	4.60, 4.64	4.66, 4.74	4.59, 4.69	4.59, 4.61
3-OCH_2	4.56, 4.84	4.59, 4.92	4.03, 5.14	4.06, 5.08	4.34, 5.32	4.50, 5.24	4.57, 5.12	4.58, 5.08	4.66, 4.90	4.63, 4.85	4.39, 5.30
6-OCH_2	4.04, 4.40	4.07, 4.36	4.46, 4.58	4.53, 4.61	4.44, 4.76	4.47, 4.69	4.45, 4.53	4.42, 4.55	4.50, 4.67	4.48, 4.62	4.48, 4.69
Cp_A-*H*	6.60		5.31		5.93		5.86		6.53		6.03
Cp_B-*H*	6.62		5.39		5.99		5.89		6.67		6.03
Cp_A-CH_3		2.00		1.35		2.01		1.95		2.09	
α1-Cp_A-*H*		6.75		4.94		5.51		5.64		6.59	
α2-Cp_A-*H*		6.84		5.30		6.11		5.75		6.69	
β1-Cp_A-*H*		6.74		5.52		6.01		5.47		6.08	
β2-Cp_A-*H*		6.09		5.63		5.63		5.61		6.78	
Cp_B-CH_3		2.17		1.60		2.10		2.00		2.18	
α1-Cp_B-*H*		5.92		5.10		5.62		5.79		6.10	
α2-Cp_B-*H*		6.39		5.79		6.04		5.82		6.45	
β1-Cp_B-*H*		7.33		5.43		5.90		5.47		7.05	
β2-Cp_B-*H*		6.12		4.66		6.34		5.72		6.03	
Zr-CH_3							−0.08	−0.16			
α-THF-*H*					3.14	3.71					3.31
β-THF-*H*					1.63	1.82					1.66
P(CH_3)$_3$			0.78	0.77							
CH_3-BCF	0.48	0.52	1.37	1.39					0.56	0.45	

Table 2. Selected ^{13}C NMR spectroscopic data of the titanocene- and zirconocene-*O*-glucopyranoside complexes

	10a	**10b**	**11a**	**11b**	**13a**	**13b**	**15a**	**15b**	**16a**	**16b**	**18a**
C-1	98.6	98.6	97.1	97.2	96.3	97.3	97.4	97.3	98.3	98.1	96.6
C-2	78.9	80.5	80.7	80.7	80.0	80.6	80.1	80.2	78.5	79.0	79.6
C-3	81.1	82.5	81.1	81.5	80.7	83.1	82.4	82.6	80.3	81.1	80.2
C-4	95.2	93.7	88.4	88.4	89.2	86.0	79.0	79.2	87.1	85.7	82.5
C-5	66.8	67.4	71.9	72.2	69.2	71.4	71.3	71.5	67.2	67.1	69.6
C-6	73.8	74.1	68.7	68.6	67.9	68.8	68.9	69.0	74.8	74.7	68.1
OCH_3	55.9	56.0	55.3	55.3	55.2	55.0	54.9	54.9	55.5	55.5	55.3
2-OCH_2	73.4	73.5	72.2	72.1	72.2	72.5	72.4	72.4	74.8	73.0	71.6
3-OCH_2	75.2	75.8	73.7	73.3	73.3	75.2	75.1	75.1	73.1	75.4	73.0
6-OCH_2	79.7	80.1	74.7	74.8	73.9	72.3	73.2	73.1	80.0	80.0	73.9
Cp_A-*C*	121.4		113.9		118.1		110.3		118.0		115.2
Cp_B-*C*	118.6		114.0		118.5		110.4		116.5		115.2
Cp_A-*C*H_3		15.4		14.7		16.2		14.5		14.4	
ipso-Cp_A-*C*		139.2		129.2		131.3		122.6		137.3	
α1-Cp_A-*C*		115.6		114.4		116.6		112.4		111.9	
α2-Cp_A-*C*		117.0		114.8		123.4		108.0		113.0	
β1-Cp_A-*C*		116.0		111.8		113.2		106.0		118.4	
β2-Cp_A-*C*		123.0		115.4		107.9		112.0		114.6	
Cp_B-*C*H_3		16.6		14.8		15.7		14.7		15.3	
ipso-Cp_B-*C*		142.4		131.3		133.5		123.1		137.0	
α1-Cp_B-*C*		116.3		115.3		113.1		107.6		113.4	
α2-Cp_B-*C*		127.2		117.0		117.3		114.3		120.3	
β1-Cp_B-*C*		117.7		112.8		111.1		105.9		115.5	
β2-Cp_B-*C*		116.5		108.2		118.0		111.0		114.6	
Zr-*C*H_3							19.6	20.5			
α-THF-*C*					76.9	68.0					77.9
β-THF-*C*					24.4	25.5					25.4
P(*C*H_3)$_3$			15.4	16.2							
CH_3-BCF	9.9	10.4	11.4	11.6					9.9	9.8	

 © 2005 Wiley-VCH Verlag GmbH & Co. KGaA, Weinheim

composition took place with time at ambient temperature. From the spectroscopic features we assign the structure of the "open" THF adduct **13a** to the main product of the reaction [^{1}H NMR: δ = 5.93/5.98 (Cp) ppm] (see Scheme 4 and Tables 1 and 2). It may be that the minor component [^{1}H NMR: δ = 5.76/5.79 (Cp) ppm] features an internal chelate, but this remains inconclusive at this time. The corresponding reaction of $[(MeC_5H_4)_2TiCH_3(THF)]^+[BPh_4]^-$ (**12b**) with **5** was only slightly cleaner. It gave the THF-stabilized product **13b**, which was characterized spectroscopically.

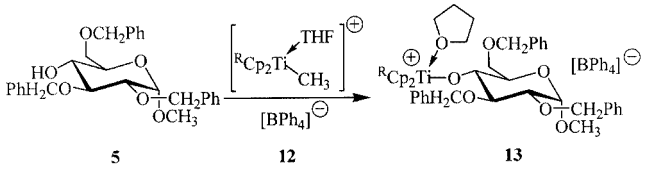

5 **12** **13**

R = H (**a**), CH_3 (**b**)

Scheme 4

One obtains an indication of the essential structural differences between the (internal chelate) complexes **10** and their open counterparts **11/13** upon inspection of some of their characteristic spectroscopic data (see Tables 1 and 2). The ^{13}C NMR chemical shifts are especially useful for this structural assignment (see Table 2). As can be seen from the compilation of data in Table 2, the ^{13}C NMR chemical shifts of the core carbon atoms C-1, C-2 and C-3 are within a close range in the series of the complexes **10a**,**b**, **11a**,**b**, and **13a**,**b**. This also extends to the ^{13}C NMR shifts of the benzyl-CH_2 groups of the 2-OCH_2Ph units. The 3-OCH_2Ph ^{13}C NMR resonance shows a small, but unsystematic variation in this series. However, we note a marked shift ($\Delta\delta \approx 5-7$ ppm) to smaller δ values for the 6-OCH_2Ph resonance on going from the (chelate) **10a**,**b** systems to their (open) counterparts **11a**,**b** or **13a**,**b**. At the same time this change of the coordination pattern is revealed at the C-4 ($\Delta\delta \approx 5-6$ ppm) and the C-6 ($\Delta\delta \approx 5$ ppm) ^{13}C NMR chemical shifts. The C-5 ^{13}C NMR resonance actually features the reverse chemical shift variation ($\Delta\delta \approx -4$ to -5 ppm). Also an additional indication is given by the change of the magnitude of the 6/6′-H, 5-H coupling constants from $^3J_{ae}$ = 10.1 Hz and $^3J_{aa}$ = 3.9 Hz (**10a**) to $^3J_{H,H}$ = 3.8 Hz and 1.5 Hz in **11a**.

Similar structural and spectroscopic effects are noticed in the related zirconocene series. However, some of the chemistry of the reactions of **5** with the methylzirconocene derivatives is markedly different. The zirconocene−*O*-glucopyranoside complexes were much more sensitive than their titanocene analogues. In most cases they decomposed when kept above −10 °C. This severely hampered their isolation but some of these compounds could be characterized spectroscopically in solution at low temperatures.

In contrast to the titanocene system, dimethylzirconocene (**14a**) reacted readily with **5** to give the neutral system **15a** and methane. Complex **15a** shows the typical set of an open metallocene−*O*-glucopyranoside complex (e.g. ^{13}C NMR signals of the glucopyranoside atoms C-4 at δ = 79.5 ppm, C-5 at δ = 71.3, C-6 at δ = 68.9 and of the 6-OCH_2 group at δ = 73.2 ppm). Subsequent treatment of **15a** with $B(C_6F_5)_3$ (**7**) resulted in the abstraction of the σ-methyl group at the zirconium atom[10] with formation of the cation complex **16a** {with $[MeB(C_6F_5)_3]^-$ anion}. The cation of **16a** features a shifting of the respective ^{13}C NMR resonances that again indicates internal coordination of the oxygen atom from the 6-*O*-benzyl group to the now strongly electrophilic zirconium center [**16a**: ^{13}C NMR signals of C-4 at δ = 87.1 ppm ($\Delta\delta$ = +7.6 ppm), of C-5 at δ = 67.2 ppm ($\Delta\delta$ = −4.1 ppm), of C-6 at δ = 74.8 ppm ($\Delta\delta$ = +5.9 ppm) and 6-OCH_2−Ph at δ = 80.0 ppm ($\Delta\delta$ = +6.8 ppm)]. The reaction of $[(MeC_5H_4)_2Zr(CH_3)_2]$ (**14b**) with **5** proceeded analogously to generate **15b**, which was subsequently converted into the salt **16b** by treatment with $B(C_6F_5)_3$. The complexes **15b** and **16b** exhibit similar NMR features (see Scheme 5 and Tables 1 and 2). The [Zr]−*O*-glucopyranoside series was complemented by the in situ generation of (the very sensitive) complex **18a** by treatment of $[Cp_2ZrCH_3(THF)]^+[BPh_4]^-$ (**17a**) with **5**. It shows the typical NMR spectra of an open, THF-stabilized zirconocene−*O*-glucopyranoside cation complex (see Scheme 5, and Tables 1 and 2).

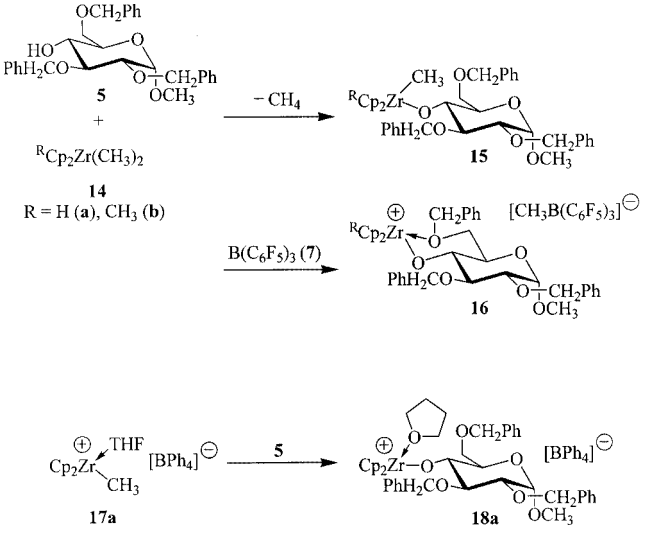

Scheme 5

Our study shows that titanocene cation complexes that bear an *O*-bonded carbohydrate σ-ligand seem to be rather robust molecules (as opposed to their very sensitive zirconium analogues). These titanocene cations are rather straightforwardly formed by our convenient one-pot synthesis using an in situ generated methyltitanocene cation. With the weakly coordinating $[CH_3B(C_6F_5)_3]^-$ counterion we obtained evidence for internal chelate coordination by the 6-*O*-benzyl group, but slightly stronger donors seem to very effectively compete with this internal ether coordination and add to the electrophilic titanocene cation.[15] This observation probably leaves some room for speculations about the potential use of carbohydrate-derived titanocene cation complexes as agents in medicinal chemis-

 © 2005 Wiley-VCH Verlag GmbH & Co. KGaA, Weinheim

try.[2] Such systems might offer some advantages by adding transporting or target donor ligands to the titanocene unit in vivo, and one might envisage that suitably attached carbohydrate moieties might help to guide the titanocene towards its target structures.[16] We shall try to develop biocompatible derivatives of the titanocene systems presented in this paper in order to test their medicinal properties.

Experimental Section

General: All reactions were carried out under dry argon in Schlenk-type glassware or in a glove box. Solvents, including deuterated solvents used for NMR spectroscopy, were dried and distilled prior to use. NMR spectra were measured using a Bruker AC 200 P, a Varian Inova 500 or a Varian Unity Plus 600 NMR spectrometer. Most NMR assignments were made by carrying out a variety of 2D NMR experiments.[17] The coupling constants between vicinal hydrogen atoms at the carbohydrate moiety are designated as J_{aa} (i.e. axial-axial) and J_{ae} (axial-equatorial), respectively. The following instruments were used for additional physical characterization: IR spectroscopy: Nicolet 5DXC FT-IR spectrometer; melting points: DSC 2010 (TA instruments); elemental analyses: Foss Heraeus CHN-O-Rapid; mass spectrometry: Mircomass-Quatro LC-Z-electrospray mass spectrometer; optical rotation: Perkin−Elmer polarimeter 351.

Preparation of $[Cp_2Ti(O\text{-carb.})]^+[MeB(C_6F_5)_3]^-$ (10a): The carbohydrate **5** (464 mg, 1.00 mmol) and $B(C_6F_5)_3$ (**7**) (512 mg, 1.00 mmol) were dissolved in dichloromethane and added dropwise to a solution of dimethyltitanocene (**6a**) (208 mg, 1.00 mmol) in dichloromethane (25 mL). A change in the reaction color to deep red occurred and a gas was released. The reaction mixture was stirred for 2 h, the volatiles were removed in vacuo and the residue was washed with pentane resulting in 814 mg (70%) of the product as red-brown solid. M.p. (DSC): 131 °C (dec.). $[\alpha]_D^{25} = +210$ (c = 0.53, CH_2Cl_2). MS [ESI$^+$, $C_{38}H_{41}O_6Ti^+$ (641)]: m/z = 641 $[M]^+$, 209 $[Cp_2TiOMe]^+$. $C_{57}H_{44}BF_{15}O_6Ti$ (1168.7): calcd. C 58.58, H 3.80; found C 58.15, H 3.75. IR (KBr): $\tilde{\nu}$ = 3118, 2912, 1642, 1511, 1458, 1366, 1266, 1086, 952, 823, 738, 699 cm^{-1}. ^{1}H NMR (CD_2Cl_2, 253 K, 600 MHz): δ = 0.48 (br. s, 3 H, CH_3−B$(C_6F_5)_3$], 3.28 (s, 3 H, OCH_3), 3.52 (t, $^2J = {}^3J_{aa}$ = 10.1 Hz, 1 H, 6-H$_a$), 3.58 (m, 2 H, 2-H, 5-H), 3.79 (t, $^3J_{aa}$ = 8.9 Hz, 1 H, 3-H), 4.01 (dd, ^2J = 10.1, $^3J_{ae}$ = 3.9 Hz, 1 H, 6-H$_e$), 4.04 (d, ^2J = 13.8 Hz, 1 H, 6-OCH_2Ph), 4.40 (d, ^2J = 13.8 Hz, 1 H, 6-OCH_2Ph), 4.56 (d, ^2J = 12.2 Hz, 1 H, 3-OCH_2Ph), 4.66 (d, ^2J = 11.7 Hz, 1 H, 2-OCH_2Ph), 4.67 (d, $^3J_{ae}$ = 3.5 Hz, 1 H, 1-H), 4.75 (d, ^2J = 11.7 Hz, 1 H, 2-OCH_2Ph), 4.84 (d, ^2J = 12.2 Hz, 1 H, 3-OCH_2Ph), 4.88 (t, $^3J_{aa}$ = 8.7 Hz, 1 H, 4-H), 6.60 (s, 5 H, Cp$_A$), 6.62 (s, 5 H, Cp$_B$), 7.22, 7.27, 7.32−7.39, 7.47 (each m, 15 H, Ph) ppm. ^{13}C{^{1}H} NMR (CD_2Cl_2, 253 K, 151 MHz): δ = 9.9 [CH_3−B$(C_6F_5)_3$], 55.9 (OCH_3), 66.8 (C-5), 73.4 (2-OCH_2Ph), 73.8 (C-6), 75.2 (3-OCH_2Ph), 78.9 (C-2), 79.7 (6-OCH_2Ph), 81.1 (C-3), 95.2 (C-4), 98.6 (C-1), 118.6 (Cp$_B$), 121.4 (Cp$_A$), 127.9−130.0 (Ph), 130.9, 138.0, 138.9 (*ipso*-Ph), 136.3 [dm, $^1J_{C,F}$ = 247 Hz, *meta*-B$(C_6F_5)_3$], 137.4 [dm, $^1J_{C,F}$ = 243 Hz, *ortho*-B$(C_6F_5)_3$], 148.1 [dm, $^1J_{C,F}$ = 234 Hz, *para*-B$(C_6F_5)_3$] ppm [*ipso*-B$(C_6F_5)_3$ signal not observed]. ^{11}B{^{1}H} NMR (CD_2Cl_2, 298 K, 64 MHz): $\delta = -15$ ($\nu_{1/2}$ = 38.8 Hz) ppm.

Preparation of $[(MeC_5H_4)_2Ti(O\text{-carb.})]^+[MeB(C_6F_5)_3]^-$ (10b): Carbohydrate **5** (464 mg, 1.00 mmol) and $B(C_6F_5)_3$ (512 mg, 1.00 mmol) (**7**) were dissolved in dichloromethane and added dropwise to a solution of $[(MeC_5H_4)TiMe_2]$ (**6b**) (236 mg, 1.00 mmol) in dichloromethane (25 mL). A change in the reaction color to deep red occurred and a gas was released. The reaction mixture was stirred for 2 h, the volatiles were removed in vacuo and the residue was washed with pentane resulting in 1.09 g (91%) of the product as a brown solid. M.p. (DSC): 129 °C (dec.). $[\alpha]_D^{25} = +308$ (c = 0.53, CH_2Cl_2). MS [ESI$^+$, $C_{40}H_{45}O_6Ti^+$ (669)]: m/z = 669 $[M]^+$. $C_{59}H_{48}BF_{15}O_6Ti$ (1196.7): calcd. C 59.22, H 4.04; found C 58.86, H 3.91. IR (KBr): $\tilde{\nu}$ = 3450, 2908, 1642, 1511, 1458, 1367, 1267, 1086, 952, 832, 746, 699 cm^{-1}. ^{1}H NMR (CD_2Cl_2, 298 K, 600 MHz): δ = 0.52 [s, 3 H, CH_3−B$(C_6F_5)_3$], 2.00 (s, 3 H, Cp$_A$−CH_3), 2.17 (s, 3 H, Cp$_B$−CH_3), 3.30 (s, 3 H, OCH_3), 3.65 (m, 2 H, 5-H, 6-H$_a$*), 3.66 (dd, $^3J_{ae}$ = 3.6, $^3J_{aa}$ = 9.4 Hz, 1 H, 2-H), 3.93 (dd, $^3J_{aa}$ = 9.4, $^3J_{aa}$ = 8.7 Hz, 1 H, 3-H), 4.01 (m, 1 H, 6-H$_e$*), 4.07 (d, ^2J = 13.6 Hz, 1 H, 6-OCH_2Ph), 4.36 (d, ^2J = 13.6 Hz, 1 H, 6-OCH_2Ph), 4.59 (d, ^2J = 11.3 Hz, 1 H, 3-OCH_2Ph), 4.65 (d, ^2J = 11.7 Hz, 1 H, 2-OCH_2Ph), 4.70 (d, $^3J_{aa}$ = 3.6 Hz, 1 H, 1-H), 4.74 (d, ^2J = 11.7 Hz, 1 H, 2-OCH_2Ph), 4.92 (d, ^2J = 11.3 Hz, 1 H, 3-OCH_2Ph), 4.94 (t, $^3J_{aa}$ = 8.7 Hz, 1 H, 4-H), 5.92 (m, 1 H, α1-Cp$_B$), 6.09 (m, 1 H, β2-Cp$_A$*), 6.12 (m, 1 H, β2-Cp$_B$), 6.39 (m, 1 H, α2-Cp$_B$), 6.74 (m, 1 H, β1-Cp$_A$*), 6.75 (m, 1 H, α1-Cp$_A$), 6.84 (m, 1 H, α2-Cp$_A$), 7.33 (m, 1 H, β1-Cp$_B$), 7.25, 7.34, 7.51 (m, 15 H, Ph) ppm (* denotes a tentative assignment). ^{13}C{^{1}H} NMR CD_2Cl_2, 298 K, 151 MHz): δ = 10.4 [CH_3−B$(C_6F_5)_3$], 15.4 (Cp$_A$−CH_3), 16.6 (Cp$_B$−CH_3), 56.0 (OCH_3), 67.4 (C-5), 73.5 (2-OCH_2Ph), 74.1 (C-6), 75.8 (3-OCH_2Ph), 80.1 (6-OCH_2Ph), 80.5 (C-2), 82.5 (C-3), 93.7 (C-4), 98.6 (C-1), 115.6 (α1-Cp$_A$), 116.0 (β1-Cp$_A$), 116.3 (α1-Cp$_B$), 116.5 (β2-Cp$_B$), 117.0 (α2-Cp$_A$), 117.7 (β1-Cp$_B$), 123.0 (β2-Cp$_A$), 127.2 (α2-Cp$_B$), 128.1−128.9, 130.2, 130.6 (Ph), 129.8 [*ipso*-B$(C_6F_5)_3$], 131.3 (*ipso*-Ph), 136.8 [dm, $^1J_{C,F}$ = 246 Hz, *meta*-B$(C_6F_5)_3$], 137.8 [dm, $^1J_{C,F}$ = 243 Hz, *ortho*-B$(C_6F_5)_3$], 138.3, 138.8 (*ipso*-Ph), 139.2 (*ipso*-Cp$_A$), 142.4 (*ipso*-Cp$_B$), 148.6 [dm, $^1J_{C,F}$ = 241 Hz, *para*-B$(C_6F_5)_3$] ppm. ^{11}B{^{1}H} NMR (CD_2Cl_2, 298 K, 64 MHz): $\delta = -15$ ($\nu_{1/2}$ = 36 Hz) ppm.

Preparation of $[Cp_2Ti(O\text{-carb.})(PMe_3)]^+[MeB(C_6F_5)_3]^-$ (11a): Addition of 3 drops of trimethylphosphane to a solution of $[Cp_2Ti(O\text{-carb.})]^+[MeB(C_6F_5)_3]^-$ (**10a**) (250 mg, 0.214 mmol) in toluene (10 mL) led immediately to a yellow liquid. After removal of the volatiles in vacuo, the residue was washed twice with pentane resulting in 176 mg (66%) of the product as a dark brown solid. M.p. (DSC): 217 °C (dec.). $[\alpha]_D^{25} = -44.0$ (c = 0.59, CH_2Cl_2). MS [ESI$^+$, $C_{41}H_{50}O_6PTi^+$ (717)]: m/z = 717 $[M]^+$, 641 $[M - P(CH_3)_3]^+$. $C_{60}H_{53}BF_{15}O_6PTi$ (1244.7): calcd. C 57.90, H 4.29; found C 58.04, H 4.74. IR (KBr): $\tilde{\nu}$ = 3065, 2919, 1642, 1511, 1458, 1369, 1264, 1087, 952, 804, 736, 698 cm^{-1}. ^{1}H NMR (C_6D_6, 298 K, 600 MHz): δ = 0.78 [d, $^2J_{H,P}$ = 9.1 Hz, 9 H, P(CH_3)$_3$], 1.37 [br. s, 3 H, CH_3−B$(C_6F_5)_3$], 3.14 (dd, ^2J = 11.9, ^3J = 3.8 Hz, 1 H, 6-H), 3.19 (s, 3 H, OCH_3), 3.27 (dd, ^2J = 11.9, ^3J = 1.5 Hz, 1 H, 6-H′), 3.38 (ddd, ^3J = 1.5, ^3J = 3.8, $^3J_{aa}$ = 9.3 Hz, 1 H, 5-H), 3.42 (dd, $^3J_{aa}$ = 9.0, $^3J_{ae}$ = 3.7 Hz, 1 H, 2-H), 3.54 (dd, $^3J_{aa}$ = 8.4, $^3J_{aa}$ = 9.0 Hz, 1 H, 3-H), 4.03 (d, ^2J = 12.0 Hz, 1 H, 3-OCH_2Ph), 4.23 (d, ^2J = 11.6 Hz, 1 H, 2-OCH_2Ph), 4.29 (d, ^2J = 11.6 Hz, 1 H, 2-OCH_2Ph), 4.34 (dd, $^3J_{aa}$ = 8.4, $^3J_{aa}$ = 9.3 Hz, 1 H, 4-H), 4.46 (d, ^2J = 11.4 Hz, 1 H, 6-OCH_2Ph), 4.58 (d, ^2J = 11.4 Hz, 1 H, 6-OCH_2Ph), 4.59 (d, $^3J_{ae}$ = 3.7 Hz, 1 H, 1-H), 5.14 (d, ^2J = 12.0 Hz, 1 H, 3-OCH_2Ph), 5.31 (d, $^3J_{H,P}$ = 2.8 Hz, 5 H, Cp$_A$), 5.39 (d, $^3J_{H,P}$ = 2.8 Hz, 5 H, Cp$_B$), 7.07, 7.11−7.21, 7.24−7.28, 7.31, 7.32 (each m, 15 H, Ph) ppm. ^{13}C{^{1}H} NMR (C_6D_6, 298 K, 151 MHz): δ = 11.4 [br. s, CH_3−B$(C_6F_5)_3$], 15.4 [d, $^1J_{C,P}$ = 24.5 Hz, P(CH_3)$_3$], 55.3 (OCH_3), 68.7 (C-6), 71.9 (C-5), 72.2 (2-OCH_2Ph), 73.7 (3-OCH_2Ph), 74.4 (6-OCH_2Ph), 80.7 (C-2), 81.1 (C-3), 88.4 (C-4), 97.3 (C-1), 113.9 (Cp$_A$), 114.0 (Cp$_B$), 127.7−128.9 (Ph), 137.2 [dm, $^1J_{C,F}$ = 247 Hz, *meta*-B$(C_6F_5)_3$], 138.2 [dm, $^1J_{C,F}$ = 239 Hz, *ortho*-B$(C_6F_5)_3$], 138.2, 138.2, 139.0 (*ipso*-Ph), 139.0 [*ipso*-B$(C_6F_5)_3$], 149.3 [dm, $^1J_{C,F}$ =

 © 2005 Wiley-VCH Verlag GmbH & Co. KGaA, Weinheim

235 Hz, *para*-$B(C_6F_5)_3$] ppm. $^{11}B\{^1H\}$ NMR (CD_2Cl_2, 298 K, 64 MHz): $\delta = -15$ ($\nu_{1/2} = 33$ Hz) ppm. $^{31}P\{^1H\}$ NMR (CD_2Cl_2, 298 K, 81 MHz): $\delta = 4.2$ (s) ppm.

Preparation of $[(MeC_5H_4)_2Ti(O\text{-carb.})(PMe_3)]^+[MeB(C_6F_5)_3]^-$ (11b): Addition of 3 drops of trimethylphosphane to a solution of $[(MeC_5H_4)_2Ti(O\text{-carb.})]^+[MeB(C_6F_5)_3]^-$ (**10b**) (250 mg, 0.209 mmol) in toluene (10 mL) led immediately to a yellow liquid. After removal of the volatiles in vacuo, the residue was washed twice with pentane resulting in 168 mg (63%) of the product as an orange solid. M.p. (DSC): 218 °C (dec.). $[\alpha]_D^{25} = -58$ ($c = 0.56$, CH_2Cl_2). MS [ESI$^+$, $C_{43}H_{54}O_6PTi^+$ (745)]: $m/z = 745$ $[M]^+$, 670 $[M - P(CH_3)_3]^+$. $C_{62}H_{57}BF_{15}O_6PTi$ (1272.7): calcd. C 58.51, H 4.51; found C 58.35, H 4.89. IR (KBr): $\tilde{\nu} = 3015, 2911, 1642, 1511, 1460, 1370, 1265, 1088, 953, 821, 738, 698$ cm^{-1}. ^1H NMR (C_6D_6, 298 K, 600 MHz): $\delta = 0.77$ [d, $^2J_{PH} = 2.3$ Hz, 9 H, $P(CH_3)_3$], 1.35 (s, 3 H, Cp_A-CH_3), 1.39 [s, 3 H, $CH_3-B(C_6F_5)_3$], 1.60 (s, 3 H, Cp_B-CH_3), 3.18 (s, 3 H, OCH_3), 3.20 (dd, $^2J = 11.8$, $^3J = 3.9$ Hz, 1 H, 6-H), 3.31 (dd, $^2J = 11.8$, $^3J = 1.5$ Hz, 1 H, 6-H′), 3.44 (dd, $^3J_{aa} = 9.1$, $^3J_{ae} = 3.4$ Hz, 1 H, 2-H), 3.48 (ddd, $^3J_{aa} = 9.4$, $^3J = 3.9$, $^3J = 1.5$ Hz, 1 H, 5-H), 3.61 (dd, $^3J_{aa} = 8.3$, $^3J_{aa} = 9.1$ Hz, 1 H, 3-H), 4.06 (d, $^2J = 11.9$ Hz, 1 H, 3-OCH_2Ph), 4.18 (d, $^2J = 11.5$ Hz, 1 H, 2-OCH_2Ph), 4.25 (d, $^2J = 11.5$ Hz, 1 H, 2-OCH_2Ph), 4.51 (dd, $^3J_{aa} = 8.3$, $^3J_{aa} = 9.4$ Hz, 1 H, 4-H), 4.53 (d, $^2J = 11.8$ Hz, 1 H, 6-OCH_2Ph), 4.59 (dd, $^3J_{ae} = 3.4$ Hz, 1 H, 1-H), 4.61 (d, $^2J = 11.8$ Hz, 1 H, 6-OCH_2Ph), 4.66 (m, 1 H, β2-Cp_B), 4.94 (m, 1 H, α1-Cp_A), 5.08 (d, $^2J = 11.9$ Hz, 1 H, 3-OCH_2Ph), 5.10 (m, 1 H, α1-Cp_B), 5.30 (m, 1 H, α2-Cp_A), 5.43 (m, 1 H, β1-Cp_B), 5.52 (m, 1 H, β1-Cp_A), 5.63 (m, 1 H, β2-Cp_A), 5.79 (m, 1 H, α2-Cp_B), 7.07, 7.12, 7.15, 7.26, 7.34 (m, 15 H, Ph) ppm. $^{13}C\{^1H\}$ NMR (C_6D_6, 298 K, 151 MHz): $\delta = 11.6$ [$CH_3-B(C_6F_5)_3$], 14.7 (Cp_A-CH_3), 14.8 (Cp_B-CH_3), 16.2 [br. s, $P(CH_3)_3$], 55.3 (OCH_3), 68.6 (C-6), 72.1 (2-OCH_2Ph), 72.2 (C-5), 73.3 (3-OCH_2Ph), 74.8 (6-OCH_2Ph), 80.7 (C-2), 81.5 (C-3), 88.4 (C-4), 97.2 (C-1), 108.2 (β2-Cp_B), 111.8 (β1-Cp_A), 112.8 (β1-Cp_B), 114.4 (α1-Cp_A), 114.8 (α2-Cp_A), 115.3 (α1-Cp_B), 115.4 (β2-Cp_A), 117.0 (α2-Cp_B), 127.3−128.8 (Ph), 129.2 (*ispo*-Cp_A), 131.3 (*ispo*-Cp_B), 137.2 [dm, $^1J_{C,F} = 245$ Hz, *meta*-$B(C_6F_5)_3$], 138.1, 138.2, 139.0 (*ipso*-Ph), 138.2 [dm, $^1J_{C,F} = 247$ Hz, *ortho*-$B(C_6F_5)_3$], 149.3 [dm, $^1J_{C,F} = 240$ Hz, *para*-$B(C_6F_5)_3$] ppm [*ipso*-$B(C_6F_5)_3$ not observed]. $^{11}B\{^1H\}$ NMR (CD_2Cl_2, 298 K, 64 MHz): $\delta = -15$ ($\nu_{1/2} = 31$ Hz) ppm. ^{31}P NMR (CD_2Cl_2, 298 K, 81 MHz): $\delta = 3.2$ (s) ppm.

Preparation of $[Cp_2Ti(O\text{-carb.})(THF)]^+[BPh_4]^-$ (13a): NMR spectroscopic experiment: A solution of $[Cp_2TiMe(THF)]^+[BPh_4]^-$ (**12a**) (47 mg, 0.08 mmol) in [D_2]dichloromethane was combined with the carbohydrate **5** (37 mg, 0.08 mmol) at −60 °C. The reaction was warmed to room temperature resulting in a red color. NMR spectroscopic studies showed that the reaction started at room temperature but the start of decomposition was also noticed, hence the solution was immediately cooled to −40 °C. The product obtained was a mixture of 5:1. Main product: ^1H NMR (CD_2Cl_2, 243 K, 600 MHz): $\delta = 1.52$ (m, 2 H, β-THF), 1.63 (m, 2 H, β′-THF), 1.81 (m, 4 H, β-THF_{free}), 3.09 (m, 2 H, α-THF), 3.14 (m, 2 H, α′-THF), 3.29 (dd, $^2J = 10.9$, $^3J = 2.6$ Hz, 1 H, 6-H), 3.39 (s, 3 H, OCH_3), 3.44 (dd, $^2J = 10.4$, $^3J = 1.9$ Hz, 1 H, 6-H′), 3.56 (m, 1 H, 5-H), 3.69 (m, 4 H, α-THF_{free}), 3.70 (m, 1 H, 3-H), 3.76 (dd, $^3J_{aa} = 9.2$, $^3J_{ae} = 3.3$ Hz, 1 H, 2-H), 4.34 (d, $^2J = 12.3$ Hz, 1 H, 3-OCH_2Ph), 4.44 (d, $^2J = 11.8$ Hz, 1 H, 6-OCH_2Ph), 4.63 (m, 2 H, 2-OCH_2Ph), 4.76 (d, $^2J = 11.8$ Hz, 1 H, 6-OCH_2Ph), 4.85 (d, $^3J_{ae} = 3.3$ Hz, 1 H, 1-H), 4.89 (dd, $^3J_{aa} = 8.4$, $^3J_{aa} = 9.7$ Hz, 1 H, 4-H), 5.32 (d, $^2J = 12.3$ Hz, 1 H, 3-OCH_2Ph), 5.93 (s, 5 H, Cp_A), 5.99 (s, 5 H, Cp_B), 6.21, 6.93, 7.07, 7.32 −7.50, 7.62 (each m, 35 H, Ph, BPh_4) ppm. $^{13}C\{^1H\}$ NMR (from ghsqc[17]) (CD_2Cl_2, 243 K, 151 MHz): $\delta = 24.4$ (β-THF, β′-THF), 25.1 (β-THF_{free}), 55.2 (OCH_3), 67.8 (α-THF_{free}), 67.9 (C-6), 69.2 (C-5), 72.2 (2-OCH_2Ph), 73.3 (3-OCH_2Ph), 73.9 (6-OCH_2Ph), 76.9 (α-THF, α′-THF), 80.0 (C-2), 80.7 (C-3), 89.2 (C-4), 96.3 (C-1), 118.1 (Cp_A), 118.5 (Cp_B), 125.2 −139.1 (Ph, BPh_4), 137.7, 137.8, 138.4 (*ipso*-Ph), 163.7 (1:1:1:1 q, $^1J_{CB} = 44$ Hz, *ipso*-BPh_4) ppm. Due to the ratio of the isomers the minor product was determined by the Cp resonances. Minor product: ^1H NMR (CD_2Cl_2, 243 K, 600 MHz): $\delta = 5.76$ (s, 5 H, Cp_A), 5.79 (s, 5 H, Cp_B) ppm.

Preparation of $[(MeC_5H_4)_2Ti(O\text{-carb.})(THF)]^+[BPh_4]^-$ (13b): $[(MeC_5H_4)_2TiMe(THF)]^+[BPh_4]^-$ (**12b**) (337 mg, 0.550 mmol) and the carbohydrate **5** (255 mg, 0.549 mmol) were each dissolved in dichloromethane (25 mL) and then combined in a flask at room temperature. The reaction mixture was stirred for 2 h, the volatiles were removed in vacuo and the residue was washed with pentane resulting in 512 mg (88%) of the product as an ocher solid, obtained in 95% purity. M.p. (DSC): 161 °C (dec.). MS [ESI$^+$, $C_{44}H_{53}O_7Ti^+$ (741)]: $m/z = 669$ $[M - THF]^+$, 237 $[(MeC_5H_4)_2TiOMe]^+$, 186 $[C_9H_{14}O_4]^+$. ^1H NMR (CD_2Cl_2, 243 K, 600 MHz): $\delta = 1.82$ (m, 4 H, β-THF), 2.01 (s, 3 H, Cp_A-CH_3), 2.10 (s, 3 H, Cp_B-CH_3), 3.37 (s, 3 H, OCH_3), 3.50 (dd, $^3J_{aa} = 9.6$, $^3J = 2.6$ Hz, 1 H, 5-H), 3.57 (m, 1 H, 6-H), 3.67 (d, $^3J_{aa} = 9.0$ Hz, 1 H, 3-H), 3.71 (m, 1 H, 2-H), 3.71 (m, 4 H, α-THF), 3.84 (dd, $^2J = 10.3$, $^3J = 2.6$ Hz, 1 H, 6-H′), 4.47 (d, $^2J = 11.4$ Hz, 1 H, 6-OCH_2Ph), 4.50 (d, $^2J = 11.5$ Hz, 1 H, 3-OCH_2Ph), 4.65 (d, $^2J = 11.4$ Hz, 1 H, 2-OCH_2Ph), 4.68 (m, 1 H, 4-H), 4.69 (d, $^2J = 11.4$ Hz, 1 H, 6-OCH_2Ph), 4.77 (d, $^3J_{ae} = 2.4$ Hz, 1 H, 1-H), 4.91 (d, $^2J = 11.4$ Hz, 1 H, 2-OCH_2Ph), 5.24 (d, $^2J = 11.5$ Hz, 1 H, 3-OCH_2Ph), 5.51 (m, 1 H, α1-Cp_A), 5.62 (m, 1 H, α1-Cp_B), 5.63 (m, 1 H, β2-Cp_A), 5.90 (m, 1 H, β1-Cp_B), 6.01 (m, 1 H, β1-Cp_A), 6.04 (m, 1 H, α2-Cp_B), 6.11 (m, 1 H, α2-Cp_A), 6.34 (m, 1 H, β2-Cp_B), 7.08, 7.26−7.49, 7.58, 7.62 (m, 35 H, Ph, BPh_4) ppm. $^{13}C\{^1H\}$ NMR (*ipso*-C of BPh_4^- not found) (CD_2Cl_2, 243 K, 151 MHz): $\delta = 15.7$ (Cp_B-CH_3), 16.2 (Cp_A-CH_3), 25.5 (β-THF), 55.0 (OCH_3), 68.0 (α-THF), 68.8 (C-6), 71.4 (C-5), 72.3 (6-OCH_2Ph), 72.5 (2-OCH_2Ph), 75.2 (3-OCH_2Ph), 80.6 (C-2), 83.1 (C-3), 86.0 (C-4), 97.3 (C-1), 107.9 (β2-Cp_A), 111.1 (β1-Cp_B), 113.1 (α1-Cp_B), 113.2 (β1-Cp_A), 116.6 (α1-Cp_A), 117.3 (α2-Cp_B), 118.0 (β2-Cp_B), 123.4 (α2-Cp_A), 127.0−128.8, 135.7−142.8 (m, Ph, BPh_4), 131.3 (*ipso*-Cp_A), 133.5 (*ipso*-Cp_B), 138.2, 138.7, 139.4 (*ipso*-Ph), 164.4 (1:1:1:1 q, $^1J_{CB} = 49$ Hz, *ipso*-BPh_4) ppm. $^{11}B\{^1H\}$ NMR (CD_2Cl_2, 298 K, 64 MHz): $\delta = -7$ ($\nu_{1/2} = 12.5$ Hz) ppm.

Preparation of $[Cp_2Zr(O\text{-carb.})Me]$ (15a): Dimethylzirconocene (**14a**) (540 mg, 2.15 mmol) and the carbohydrate **5** (1.00 g, 2.15 mmol) were both dissolved in dichloromethane (25 mL) and then combined in a flask, after which methane immediately evolved. The volatiles were removed in vacuo and the residue was twice washed with pentane resulting in 1.02 g (68%) of the product as a viscous yellow solid. $[\alpha]_D^{25} = +9$ ($c = 0.46$, CH_2Cl_2). IR (film, CH_2Cl_2): $\tilde{\nu} = 3062, 2987, 2928, 2690, 2306, 1422, 1368, 1249, 1156, 1086, 1048, 896, 804, 782, 713, 693$ cm^{-1}. ^1H NMR (CH_2Cl_2, 243 K, 600 MHz): $\delta = -0.08$ (s, 3 H, $Zr-CH_3$), 3.34 (s, 3 H, OCH_3), 3.37 (ddd, $^3J_{aa} = 8.8$, $^3J = 3.8$, $^3J = 1.8$ Hz, 1 H, 5-H), 3.43 (dd, $^2J = 10.2$, $^3J = 3.8$ Hz, 1 H, 6-H), 3.44 (dd, $^2J = 10.2$, $^3J = 1.8$ Hz, 1 H, 6-H′), 3.45 (t, $^3J_{aa} = 9.6$ Hz, 1 H, 3-H), 3.51 (dd, $^3J_{aa} = 9.6$, $^3J_{ae} = 3.4$ Hz, 1 H, 2-H), 3.84 (dd, $^3J_{aa} = 9.6$, $^3J_{aa} = 8.8$ Hz, 1 H, 4-H), 4.45 (d, $^2J = 11.5$ Hz, 1 H, 6-OCH_2Ph), 4.53 (d, $^2J = 11.5$ Hz, 1 H, 6-OCH_2Ph), 4.57 (d, $^2J = 11.5$ Hz, 1 H, 3-OCH_2Ph), 4.60 (d, $^2J = 11.7$ Hz, 1 H, 2-OCH_2Ph), 4.64 (d, $^2J = 11.7$ Hz, 1 H, 2-OCH_2Ph), 4.70 (d, $^3J_{ae} = 3.4$ Hz, 1 H, 1-H), 5.12 (d, $^2J = 11.5$ Hz, 1 H, 3-OCH_2Ph), 5.86 (s, 5 H, Cp_A), 5.89 (s, 5 H, Cp_B), 7.27−7.48 (m, 15 H, Ph) ppm. $^{13}C\{^1H\}$ NMR

 © 2005 Wiley-VCH Verlag GmbH & Co. KGaA, Weinheim

(CD_2Cl_2, 243 K, 151 MHz): δ = 19.6 (Zr−*C*H_3), 54.9 (O*C*H_3), 68.9 (C-6), 71.3 (C-5), 72.4 (2-O*C*H_2Ph), 73.2 (6-O*C*H_2Ph), 75.1 (3-O*C*H_2Ph), 79.5 (C-4), 80.1 (C-2), 82.4 (C-3), 97.4 (C-1), 110.3 (Cp_A), 110.4 (Cp_B), 111.4, 112.0, 127.0−128.4 (Ph), 138.1, 138.2, 139.5 (*ipso*-Ph) ppm.

Preparation of [(MeC_5H_4)$_2$Zr(O-carb.)Me] (15b): (MeC_5H_4)$_2$ZrMe_2 (**14b**) (559 mg, 2.00 mmol) and the carbohydrate **5** (929 mg, 2.00 mmol) were both dissolved in dichloromethane (20 mL) and then combined in a flask, after which methane immediately evolved. A color change of the solution from colorless to yellow was noticed. The volatiles were removed in vacuo and the residue was washed twice with pentane resulting in 1.15 g (79%) of the product as a viscous light yellow solid. $[\alpha]_D^{25}$ = +49 (*c* = 0.53, CH_2Cl_2). IR (film, CH_2Cl_2): $\tilde{\nu}$ = 3067, 2983, 2932, 2690, 2303, 1420, 1366, 1244, 1158, 1084, 1047, 894, 802, 785, 716, 691 cm^{-1}. ^{1}H NMR (CD_2Cl_2, 243 K, 600 MHz): δ = −0.16 (s, 3 H, C*H*$_3$−Zr), 1.95 (s, 3 H, Cp_A−C*H*$_3$), 2.00 (s, 3 H, Cp_B−C*H*$_3$), 3.35 (s, 3 H, OC*H*$_3$), 3.41 (dd, ^2J = 10.4, ^3J = 4.8 Hz, 1 H, 6-H), 3.44 (m, 1 H, 5-H), 3.46 (dd, ^2J = 10.4, ^3J = 1.5 Hz, 1 H, 6-H′), 3.50 (m, 1 H, 2-H), 3.51 (m, 1 H, 3-H), 3.84 (dd, $^3J_{aa}$ = 8.6, $^3J_{aa}$ = 9.4 Hz, 1 H, 4-H), 4.42 (d, ^2J = 11.6 Hz, 1 H, 6-OC*H*$_2$Ph), 4.55 (d, ^2J = 11.6 Hz, 1 H, 6-OC*H*$_2$Ph), 4.58 (d, ^2J = 11.3 Hz, 1 H, 3-OC*H*$_2$Ph), 4.60 (d, ^2J = 11.7 Hz, 1 H, 2-OC*H*$_2$Ph), 4.64 (d, ^2J = 11.7 Hz, 1 H, 2-OC*H*$_2$Ph), 4.71 (d, $^3J_{ae}$ = 2.4 Hz, 1 H, 1-H), 5.08 (d, ^2J = 11.3 Hz, 1 H, 3-OC*H*$_2$Ph), 5.47 (m, 2 H, β1-Cp_A, β1-Cp_B), 5.61 (m, 1 H, β2-Cp_A), 5.72 (m, 2 H, α1-Cp_A, β2-Cp_B), 5.75 (m, 1 H, α2-Cp_A), 5.79 (m, 1 H, α1-Cp_B), 5.82 (m, 1 H, α2-Cp_B), 7.30, 7.36, 7.42, 7.45 (m, 15 H, Ph) ppm. ^{13}C{^{1}H} NMR (CD_2Cl_2, 243 K, 151 MHz): δ = 14.5 (Cp_A−*C*H_3), 14.7 (Cp_B−*C*H_3), 20.5 (*C*H_3−Zr), 54.9 (O*C*H_3), 69.0 (C-6), 71.5 (C-5), 72.4 (2-O*C*H_2Ph), 73.1 (6-O*C*H_2Ph), 75.1 (3-O*C*H_2Ph), 79.0 (C-4), 80.2 (C-2), 82.6 (C-3), 97.3 (C-1), 105.9 (β1-Cp_B), 106.0 (β1-Cp_A), 107.6 (α1-Cp_B), 108.0 (α2-Cp_A), 111.0 (β2-Cp_B), 112.0 (β2-Cp_A), 112.4 (α1-Cp_A), 114.3 (α2-Cp_B), 122.6 (*ipso*-Cp_A), 123.1 (*ipso*-Cp_B), 127.2−128.3 (Ph), 138.2, 138.2, 139.4 (*ipso*-Ph) ppm.

Preparation of [Cp_2Zr(O-carb.)]$^+$[$MeB(C_6F_5)_3$]$^-$ (16a): NMR spectroscopic experiment: Complex **15a** (21 mg, 0.029 mmol) and $B(C_6F_5)_3$ (**7**) (15 mg, 0.03 mmol) were each dissolved in [D_2]dichloromethane (0.5 mL) and combined at −78 °C. The reaction color changed from colorless to yellow. NMR studies showed that the product is stable up to 10 °C. ^{1}H NMR (CD_2Cl_2, 233 K, 600 MHz): δ = 0.56 [s, 3 H, C*H*$_3$−$B(C_6F_5)_3$], 3.24 (s, 3 H, OC*H*$_3$), 3.49 (m, 1 H, 2-H), 3.51 (m, 1 H, 5-H), 3.69 (t, $^3J_{aa}$ = 8.9 Hz, 1 H, 3-H), 3.74 (t, ^2J = $^3J_{aa}$ = 10.2 Hz, 1 H, 6-H_a), 4.04 (d, ^2J = 10.2 Hz, 1 H, 6-H_e), 4.19 (t, $^3J_{aa}$ = 8.9 Hz, 1 H, 4-H), 4.50 (d, ^2J = 13.2 Hz, 1 H, 6-OC*H*$_2$Ph), 4.66 (d, ^2J = 12.1 Hz, 1 H, 2-OC*H*$_2$Ph), 4.66 (d, ^2J = 11.8 Hz, 1 H, 3-OC*H*$_2$Ph), 4.66 (d, $^3J_{ae}$ = 3.4 Hz, 1 H, 1-H), 4.67 (d, ^2J = 13.2 Hz, 1 H, 6-OC*H*$_2$Ph), 4.74 (d, ^2J = 12.1 Hz, 1 H, 2-OC*H*$_2$Ph), 4.90 (d, ^2J = 11.8 Hz, 1 H, 3-OC*H*$_2$Ph), 6.53 (Cp_A), 6.67 (Cp_B), 7.23−7.44, 7.52 (m, 15 H, Ph) ppm. ^{13}C{^{1}H} NMR (CD_2Cl_2, 233 K, 151 MHz): δ = 9.9 [*C*H_3−$B(C_6F_5)_3$], 55.5 (O*C*H_3), 67.2 (C-5), 73.1 (3-O*C*H_2Ph), 74.8 (C-6, 2-O*C*H_2Ph), 78.5 (C-2), 80.0 (6-O*C*H_2Ph), 80.3 (C-3), 87.1 (C-4), 98.3 (C-1), 116.5 (Cp_B), 118.0 (Cp_A), 126.9−128.3, 130.6 (Ph), 129.7 (*ipso*-Ph), 136.1 [dm, $^1J_{C,F}$ = 246 Hz, *meta*-$B(C_6F_5)_3$], 137.2 [dm, $^2J_{C,F}$ = 245 Hz, *ortho*-$B(C_6F_5)_3$], 137.8, 139.0 (*ipso*-Ph), 147.9 [dm, $^1J_{C,F}$ = 238 Hz, *para*-$B(C_6F_5)_3$] ppm [*ipso*-$B(C_6F_5)_3$ not observed].

Preparation of [(MeC_5H_4)Zr(O-carb.)]$^+$[$MeB(C_6F_5)_3$]$^-$ (16b): NMR spectroscopic experiment: Complex **15b** (73 mg, 0.100 mmol) and $B(C_6F_5)_3$ (**7**) (51 mg, 0.100 mmol) were each dissolved in [D_2]dichloromethane (0.5 mL), combined at −78 °C and warmed to room temperature. A change of the reaction color from colorless to yellow was noticed. ^{1}H NMR (CD_2Cl_2, 233 K, 600 MHz): δ = 0.45 [s, 3 H, C*H*$_3$−$B(C_6F_5)_3$], 2.09 (s, 3 H, Cp_A−C*H*$_3$), 2.18 (s, 3 H, Cp_B−C*H*$_3$), 3.22 (s, 3 H, OC*H*$_3$), 3.50 (dd, $^3J_{aa}$ = 9.2, $^3J_{ae}$ = 3.5 Hz, 1 H, 2-H), 3.52 (m, 1 H, 5-H), 3.73 (dd, $^3J_{aa}$ = 8.9, $^3J_{aa}$ = 9.2 Hz, 1 H, 3-H), 3.77 (t, ^2J = 10.5, $^3J_{aa}$ = 9.9 Hz, 1 H, 6-H_a), 4.04 (dd, ^2J = 10.5, $^3J_{ae}$ = 2.7 Hz, 1 H, 6-H_e), 4.26 (t, $^3J_{aa}$ = 8.9 Hz, 1 H, 4-H), 4.48 (d, ^2J = 13.1 Hz, 1 H, 6-OC*H*$_2$Ph), 4.59 (d, ^2J = 11.4 Hz, 1 H, 2-OC*H*$_2$Ph), 4.62 (d, $^3J_{ae}$ = 3.5 Hz, 1 H, 1-H), 4.62 (d, ^2J = 13.1 Hz, 1 H, 6-OC*H*$_2$Ph), 4.63 (d, ^2J = 11.0 Hz, 1 H, 3-OC*H*$_2$Ph), 4.69 (d, ^2J = 11.4 Hz, 1 H, 2-OC*H*$_2$Ph), 4.85 (d, ^2J = 11.0 Hz, 1 H, 3-OC*H*$_2$Ph), 6.03 (m, 1 H, β2-Cp_B), 6.08 (m, 1 H, β1-Cp_A*), 6.10 (m, 1 H, α1-Cp_B), 6.45 (m, 1 H, α2-Cp_B), 6.59 (m, 1 H, α1-Cp_A), 6.69 (m, 1 H, α2-Cp_A), 6.78 (m, 1 H, β2-Cp_A*), 7.05 (m, 1 H, β1-Cp_B), 7.26−7.35, 7.51 (each m, 15 H, Ph) (* denotes a tentative assignment). ^{13}C{^{1}H} NMR (CD_2Cl_2, 233 K, 151 MHz): δ = 9.8 [*C*H_3−$B(C_6F_5)_3$], 14.4 (Cp_A−*C*H_3), 15.3 (Cp_B−*C*H_3), 55.5 (O*C*H_3), 67.1 (C-5), 73.0 (2-O*C*H_2Ph), 74.7 (C-6), 75.4 (3-O*C*H_2Ph), 79.0 (C-2), 80.0 (6-O*C*H_2Ph), 81.1 (C-3), 85.7 (C-4), 98.1 (C-1), 111.9 (α1-Cp_A), 113.0 (α2-Cp_A), 113.4 (α1-Cp_B), 114.6 (β2-Cp_A, β2-Cp_B), 115.5 (β1-Cp_B), 118.4 (β1-Cp_A), 120.3 (α2-Cp_B), 127.2−128.3, 129.8, 130.7 (Ph), 129.6 (*ipso*-Ph), 136.0 [dm, $^1J_{C,F}$ = 249 Hz, *meta*-$B(C_6F_5)_3$], 137.0 (*ipso*-Cp_B), 137.2 [dm, $^1J_{C,F}$ = 245 Hz, *ortho*-$B(C_6F_5)_3$], 137.3 (*ipso*-Cp_A), 137.7, 138.2 (*ipso*-Ph), 147.8 [dm, $^1J_{C,F}$ = 236 Hz, *para*-$B(C_6F_5)_3$] ppm [*ipso*- $B(C_6F_5)_3$ not observed].

Preparation of [Cp_2Zr(O-carb.)(THF)]$^+$[BPh_4]$^-$ (18): NMR spectroscopic experiment: A solution of [Cp_2ZrMe(THF)]$^+$[BPh_4]$^-$ (**17**) (31 mg, 0.05 mmol) in [D_2]dichloromethane was combined with the carbohydrate **5** (23 mg, 0.05 mmol) at −60 °C resulting in a yellow color. The reaction mixture was warmed to room temperature. ^{1}H NMR (CD_2Cl_2, 233 K, 600 MHz): δ = 1.66 (br. s, 4 H, β-THF), 3.31 (br. s, 4 H, α-THF), 3.38 (s, 3 H, OC*H*$_3$), 3.40 (dd, ^2J = 10.9, ^3J = 3.4 Hz, 1 H, 6-H), 3.47 (dd, ^2J = 10.9, ^3J = 1.5 Hz, 1 H, 6-H′), 3.51 (ddd, $^3J_{aa}$ = 9.6, ^3J = 3.4, ^3J = 1.5 Hz, 1 H, 5-H), 3.65 (dd, $^3J_{aa}$ = 9.0, $^3J_{aa}$ = 8.0 Hz, 1 H, 3-H), 3.68 (dd, $^3J_{aa}$ = 9.0, $^3J_{ae}$ = 3.0 Hz, 1 H, 2-H), 4.28 (dd, $^3J_{aa}$ = 9.6, $^3J_{aa}$ = 8.0 Hz, 1 H, 4-H), 4.39 (d, ^2J = 12.2 Hz, 1 H, 3-OC*H*$_2$Ph), 4.48 (d, ^2J = 11.8 Hz, 1 H, 6-OC*H*$_2$Ph), 4.59 (d, ^2J = 11.8 Hz, 1 H, 2-OC*H*$_2$Ph), 4.61 (d, ^2J = 11.8 Hz, 1 H, 2-OC*H*$_2$Ph), 4.69 (d, ^2J = 11.8 Hz, 1 H, 6-OC*H*$_2$Ph), 4.81 (d, $^3J_{aa}$ = 3.0 Hz, 1 H, 1-H), 5.30 (d, ^2J = 12.2 Hz, 1 H, 3-OC*H*$_2$Ph), 6.03 (s, 10 H, Cp), 6.91, 7.06, 7.32−7.44 (each m, 35 H, Ph, BPh_4) ppm. ^{13}C{^{1}H} NMR (CD_2Cl_2, 233 K, 151 MHz): δ = 25.4 (β-THF), 55.3 (O*C*H_3), 68.1 (C-6), 69.6 (C-5), 71.6 (2-O*C*H_2Ph), 73.0 (3-O*C*H_2Ph), 73.9 (6-O*C*H_2Ph), 77.9 (α-THF), 79.6 (C-2), 80.2 (C-3), 82.5 (C-4), 96.6 (C-1), 115.2 (Cp), 121.8, 126.6−128.8, 131.0, 135.5, 138.5 (Ph, BPh_4), 137.0, 137.4, 138.8 (*ipso*-Ph), 163.6 (1:1:1:1 q, $^1J_{CB}$ = 49 Hz, *ipso*-BPh_4) ppm.

Acknowledgments

Financial support from the Deutsche Forschungsgemeinschaft and the Fonds der Chemischen Industrie is gratefully acknowledged.

[1] [1a] H. Köpf, P. Köpf-Maier, *Angew. Chem.* **1979**, *91*, 509; *Angew. Chem. Int. Ed. Engl.* **1979**, *18*, 477−488. [1b] P. Köpf-Maier, W. Wagner, H. Köpf, *Cancer Chemother. Pharmacol.* **1981**, *5*, 237−241. [1c] M. M. Harding, G. Mokdsi, *Curr. Med. Chem.* **2000**, *7*, 1289−1303.

[2] [2a] B. K. Keppler, *Metal Complexes in Cancer Chemotherapy*, Wiley-VCH, Weinheim, **1993**, p. 260−323.

[3] [3a] B. Rosenberg, L. VanCamp, J. E. Troska, V. H. Mansour, *Nature (London)* **1969**, *222*, 385−392. [3b] M. Rozencweig, D. D. von Hoff, M. Slavik, F. M. Muggia, *Ann. Intern. Med.* **1977**,

 © 2005 Wiley-VCH Verlag GmbH & Co. KGaA, Weinheim

86, 803−812. [3c] H. Sun, H. Li, R. A. Weir, P. J. Sadler, *Angew. Chem.* **1998**, *110*, 1622−1625; *Angew. Chem. Int. Ed.* **1998**, *37*, 1577−1579. [3d] M. Guo, P. J. Sadler, *J. Chem. Soc., Dalton Trans.* **2000**, 7−9. [3e] M. Guo, Z. Guo, P. J. Sadler, *J. Biol. Inorg. Chem.* **2001**, *6*, 698−707. [3f] S. Top, E. B. Kaloun, A. Vessières, I. Laios, G. Leclercq, G. Jaouen, *J. Organomet. Chem.* **2002**, *643*/*644*, 350−356.

[4] [4a] A. D. Ryabov, *Angew. Chem.* **1991**, *103*, 945−955; *Angew. Chem. Int. Ed. Engl.* **1991**, *30*, 931−941. [4b] K. Severin, R. Bergs, W. Beck, *Angew. Chem.* **1998**, *110*, 1722−1743; *Angew. Chem. Int. Ed.* **1998**, *37*, 1653−1654. [4c] K. Haas, W. Ponikwar, H. Nöth, W. Beck, *Angew. Chem.* **1998**, *110*, 1200−1203, *Angew. Chem. Int. Ed.* **1998**, *37*, 1086−1089.

[5] D. Harmsen, G. Erker, R. Fröhlich, G. Kehr, *Eur. J. Inorg. Chem.* **2002**, *1*, 3156−3171.

[6] J. Wonnemann, M. Oberhoff, G. Erker, R. Fröhlich, K. Bergander, *Eur. J. Inorg. Chem.* **1999**, *584*, 318−322.

[7] [7a] M. Riediker, P. Herold, S. Wyler-Helfer, R. O. Duthaler, *Helv. Chim. Acta* **1990**, *73*, 659−73. [7b] M. Riediker, A. Hafner, U. Piantini, G. Rihs, A. Togni, *Angew. Chem.* **1989**, *101*, 493−495; *Angew. Chem. Int. Ed. Engl.* **1989**, *28*, 494−500. [7c] L. Jessen, E. T. K. Haupt, J. Heck, *Chem. Eur. J.* **2001**, *7*, 3791−3797. [7d] C. Gack, P. Klüfers, *Acta Crystallogr., Sect. C* **1996**, *52*, 2972−2975. [7e] P. Klüfers, T. Kunte, *Angew. Chem.* **2001**, *113*, 4356−4358; *Angew. Chem. Int. Ed.* **2001**, *40*, 4210−4212. [7f] S. Herdin, G. Kettenbach, P. Klüfers, *Z. Naturforsch., Teil B* **2004**, *59*, 134−139. [7g] T. Matsumoto, H. Maeta, K. Suzuki, *Tetrahedron Lett.* **1988**, *29*, 3567−3570.

[8] [8a] J. J. Patroni, R. V. Stick, B. W. Skelton, A. H. White, *Austral. J. Chem.* **1988**, *41*, 91−102. [8b] R. C. Bernotas, *Tetrahedron Lett.* **1990**, *31*, 469−472. [8c] M. P. DeNinno, J. B. Etienne, K. C. Duplantier, *Tetrahedron Lett.* **1995**, *36*, 669−672.

[9] [9a] A. G. Massey, A. J. Park, F. G. A. Stone, *Proc. Chem. Soc.* **1963**, 212. [9b]A. G. Massey, A. J. Park, *J. Organomet. Chem.* **1964**, *2*, 245−250.

[10] [10a] X. Yang, C. L. Stern, J. T. Marks, *J. Am. Chem. Soc.* **1991**, *113*, 3623−3625. [10b] M. S. W. Chan, K. Vanka, C. C. Pye, T. Ziegler, *Organometallics* **1999**, *18*, 4624−4636.

[11] [11a] S. H. Strauss, *Chem. Rev.* **1993**, *93*, 927. [11b] S. Beck, M. H. Prosenc, H. H. Brintzinger, R. Goretzki, N. Herfert, G. Fink, *J. Mol. Catal. A: Chem.* **1996**, *111*, 67−79. [11c] P. A. Deck, C. L. Beswick, T. J. Marks, *J. Am. Chem. Soc.* **1998**, *120*, 1772−1784. [11d] I. A. Guzei, R. A. Stockland, Jr., R. F. Jordan, *Acta Crystallogr., Sect. C: Cryst. Struct. Commun.* **2000**, *C56*, 635−636. [11e] M.-C. Chen, J. A. S. Roberts, T. J. Marks, *J. Am. Chem. Soc.* **2004**, *126*, 4605−4625. [11f] C. Zuccaccia, N. G. Stahl, A. Macchioni, M.-C. Chen, J. A. Roberts, T. J. Marks, *J. Am. Chem. Soc.* **2004**, *126*, 1448−1464.

[12] [12a] J. Zhou, S. J. Lancester, D. A. Walker, S. Beck, M. Thornton-Pett, M. Bochmann, *J. Am. Chem. Soc.* **2001**, *123*, 233−237. [12b] F. Song, R. D. Cannon, M. Bochmann, *Chem. Commun.* **2003**, 542−543. [12c] A. Rodriguez-Delgado, M. D. Hannant, S. J. Lancaster, M. Bochmann, *Macromol. Chem. Phy.* **2004**, *205*, 334−346. [12d] V. Busico, V. Van Axel Castelli, P. Aprea, R. Cipullo, A. Segre, G. Talarico, M. Vacatello, *J. Am. Chem. Soc.* **2003**, *125*, 5451−5460. [12e] J. W. Strauch, J.-L. Fauré, S. Bredeau, C. Wang, G. Kehr, R. Fröhlich, H. Luftmann, G. Erker, *J. Am. Chem. Soc.* **2004**, *126*, 2089−2104.

[13] [13a] L. B. Kool, M. D. Rausch, *J. Organomet. Chem.* **1985**, *297*, 159−169. [13b] M. Bochmann, L. M. Wilson, M. B. Hursthouse, R. L. Short, *Organometallics* **1987**, *6*, 2556−2563. [13c] J. C. Green, M. L. H. Green, G. C. Taylor, J. Saunders, *J. Chem. Soc., Dalton Trans.* **2000**, 317−327. [13d] M. Dahlmann, R. Fröhlich, G. Erker, *Eur. J. Inorg. Chem.* **2000**, *8*, 1789−1793.

[14] [14a] R. F. Jordan, *Adv. Organomet. Chem.* **1991**, *32*, 325−387. [14b] R. Taube, L. Krukowka, *J. Organomet. Chem.* **1988**, *347*, C9−C11. [14c] S. L. Borkowsky, R. F. Jordan, G. D. Hinch, *Organometallics* **1991**, *10*, 1268−1274.

[15] [15a] K. Döppert, *J. Organomet. Chem.* **1987**, *319*, 351−354. [15b] J. H. Toney, T. J. Marks, *J. Am. Chem. Soc.* **1985**, *107*, 947−953. [15c] U. Thewalt, G. Schleußner, *Angew. Chem.* **1978**, *90*, 559−560; *Angew. Chem. Int. Ed. Engl.* **1978**, *17*, 531.

[16] M. Guo, H. Sun, H. J. McArdle, L. Gambling, P. J. Sadler, *Biochemistry* **2000**, *39*, 10023−10033.

[17] S. Braun, H.-O. Kalinowski, S. Berger, *150 and More NMR Experiments*, Wiley-VCH, Weinheim, **1995**.

Received May 11, 2004
Early View Article
Published Online November 10, 2004

 © 2005 Wiley-VCH Verlag GmbH & Co. KGaA, Weinheim

Apparent Allyl Rotation and Pd−N Bond Rupture in Allylpalladium Complexes with N-Donor Ligands − Evidence of an Associative Mechanism

Félix A. Jalón,[a] Blanca R. Manzano,*[a] and Belén Moreno-Lara[a]

Keywords: Allyl ligands / Fluxionality / N ligands / Palladium

The new didentate N-donor ligands 2-(4-methyl-1*H*-pyrazol-1-yl)pyrimidine (4Me-pzpm, **1**) and 2-(4-bromo-1*H*-pyrazol-1-yl)pyrimidine (4Br-pzpm, **2**) have been synthesised and used to obtain the allylpalladium derivatives [Pd(η^3-2Me-C_3H_4)(NN′)]X [X = BAr'_4^-, NN′ = **1** (**3**), NN′ = **2** (**4**); X = $CF_3SO_3^-$, NN′ = **1** (**5**), NN′ = **2** (**6**)]. In complexes **3**–**6** two types of fluxional process have been found: apparent allyl rotation that is observed as H_{syn}–H_{syn}, H_{anti}–H_{anti} interconversions and H^4–H^6 interchange of the pyrimidine protons that must involve Pd–N(pm) bond rupture. The influence of different factors on both processes — such as the nature of the N-donor ligand, counterion, solvent, complex concentration and addition of water — has been studied. It has been concluded that the apparent allyl rotation has a lower free energy of activation and in both cases the presence of a species with coordinating ability favours the process. Negative entropies of activation have been found. Associative mechanisms involving participation of five-coordinate intermediates have been proposed.

(© Wiley-VCH Verlag GmbH & Co. KGaA, 69451 Weinheim, Germany, 2005)

Introduction

The chemistry of (η^3-allyl)palladium complexes has received a great deal of attention because these derivatives can act as precursors or intermediates in different catalytic processes.[1] The fluxional behaviour of these systems, either directly related to the allyl group or to the ancillary ligands, has also been widely studied.[2] Besides the fundamental interest in these studies, the fluxional behaviour of allylpalladium derivatives has important implications in a variety of catalytic processes, especially those involving nucleophilic attack on (η^3-allyl)palladium intermediates in enantioselective synthesis.[3] One process frequently encountered in allylpalladium complexes is a mutual exchange of *syn* and *anti* groups.[4−12] This process is believed to occur through an η^3-η^1-η^3 pathway that in some cases is selective[6a,9a,10,13−16] due to steric or electronic factors. On the basis of theoretical calculations concerning the mechanism of the η^3-η^1-η^3 isomerisation in (η^3-allyl)palladium complexes, it has been proposed that the process involves tetracoordinate (η^1-allyl)palladium intermediates with coordination of a solvent molecule or an ancillary ligand.[17] A second dynamic process that is frequently observed in complexes with N-donor ligands is the apparent rotation of the allyl group.[18−28] In certain examples both of the aforementioned processes have been observed.[16,29−35] The apparent rotation is observed as a *syn-syn*, *anti-anti* exchange and/or an isomerisation process, depending on the molecular symmetry. Two main mechanisms have been proposed for the apparent allyl rotation: (i) associative mechanisms[20,28,29,32,35] that involve five-coordinate intermediates (coordination of the solvent, the anion or other molecules) that can undergo allyl pseudorotation, and (ii) dissociative mechanisms[18,19,21−23,25,26,31,33] with formation of T-shaped three-coordinate intermediates after dissociation of monodentate or didentate (partial dissociation) ligands. Consequently, one question that is open to debate is whether the apparent allyl rotation in derivatives with N-donor ligands involves Pd−N bond breaking or not. In the case of didentate ligands this question is interesting because it would involve the dissociation of one arm of a chelate, a subject of potential interest, especially in relation to catalytic processes. In some examples it has been reported that a ligand of higher basicity makes the apparent rotation more difficult,[21] while increased steric hindrance of the N-donor ligand can facilitate[20,29] or slow down[21] the process. Negative entropies of activation have been found in some cases[29,32] and it has been reported that the process takes place more easily with coordinating anions[19,29,31] or solvents such as DMSO.[20b] It has also been reported that the addition of ligand or water has a negligible effect on the process in a number of examples;[18,21] other examples have been described where the effect of adding ligand or chlorides is accelerative.[19,28,29] The effect of the anion has also been analysed.[29,31a] As far as the effect of the complex concentration is concerned, positive effects,[28,20b] at least to a limiting value, have been described but in some cases it has been found that this factor has no influence.[31a,35] In recent years we have been interested in the synthesis, structural characterisation and dynamic behaviour of allylpal-

[a] Departamento de Química Inorgánica, Orgánica y Bioquímica, Universidad de Castilla-La Mancha,
Avda. C. J. Cela, 10, 13071 Ciudad Real, Spain
E-mail: Blanca.Manzano@uclm.es

 © 2005 Wiley-VCH Verlag GmbH & Co. KGaA, Weinheim **DOI: 10.1002/ejic.200400412**

ladium(II) complexes with N-donor ligands containing pyrazolyl groups.[23−28,35] We have described the synthesis and fluxional behaviour of the complexes $[Pd(\eta^3\text{-}2Me\text{-}C_3H_4)(NN')]CF_3SO_3$ [NN′ = 2-(1*H*-pyrazol-1-yl)pyrimidine = pzpm (**I**); NN′ = 2-(1*H*-pyrazol-1-yl)pyridine = pzpy (**II**)][23] (see Scheme 1) where the *syn-syn*, *anti-anti* interconversion was detected along with an interchange process between the H^4 and H^6 protons of the pyrimidine ring in complex **I**. This last interchange is only possible through Pd−N(pm) bond rupture. Moreover, an NOE between the allylic H_{syn} and H_{anti} protons and $H^{5'}$ of the pyrazole ring was also detected in the case of complex **II** and this can only be explained through Pd−N(pz) bond rupture (see Scheme 1). Considering these facts, and given the similarities between our work and other results reported previously,[19] we proposed that it was possible that the apparent allyl rotation could also take place through an initial Pd−N bond rupture. In the work described here we have attempted to gain a further insight into these processes by looking for more data concerning the free energies of activation. More precisely, we were interested in determining whether or not the apparent allyl rotation processes and the H^4-H^6 pyrimidine proton interconversion have the same energy barrier and a common mechanism. Given that the H^4-H^6 interconversion must involve a Pd−N bond-breaking step, comparison of the free energies of activation for the two processes could provide information about the participation of Pd−N bond rupture in the apparent allyl rotation. As stated above, this aspect is now a matter of debate. We also decided to explore the influence on the processes of several factors such as the type of ligand, counterion, solvent, complex concentration and addition of water. These studies may prove useful in elucidating the type of mechanism (associative or dissociative) operating in the apparent allyl rotation process.

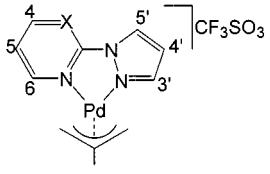

Scheme 1

Results and Discussion

Synthesis of the New Ligands and Complexes

We decided to prepare allylpalladium complexes with two different ligands containing a pyrimidine ring (in order to study the H^4-H^6 interconversion process) and different 4-substituted pyrazole groups: 2-(4-methyl-1*H*-pyrazol-1-yl)-pyrimidine (4Me-pzpm, **1**) and 2-(4-bromo-1*H*-pyrazol-1-yl)pyrimidine (4Br-pzpm, **2**; Scheme 2). The results obtained on these complexes could be compared with those obtained with pzpm. The differences in the three ligands are limited to the substituent in the 4-position of the pyrazole, and so it is foreseeable that, if any influence exists, it will be only electronic in nature. The pK_a values for the three pyrazole heterocycles are as follows: 4-methylpyrazole 3.04; pyrazole 2.48; 4-bromopyrazole 0.63.[36] The new ligands were prepared by reaction of the deprotonated pyrazole rings with 2-chloropyrimidine (see Scheme 2 and Exp. Sect.).

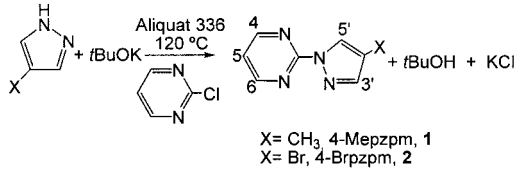

Scheme 2

We synthesised allyl derivatives with two types of counterion: triflate (OTf), which has coordinative ability, and the voluminous tetrakis(3,5-trifluoromethylphenyl)-borate ($BAr'_4{}^-$), which is non-coordinating. In both cases the starting material was $[Pd(\eta^3\text{-}2Me\text{-}C_3H_4)Cl]_2$ and this was allowed to react in one step with a stoichiometric amount of the nitrogen ligands and $TlBAr'_4$ or, alternatively, in two steps with prior elimination of the chlorides with $AgCF_3SO_3$ and addition of the nitrogen ligands after the AgCl had been filtered off (see Scheme 3).

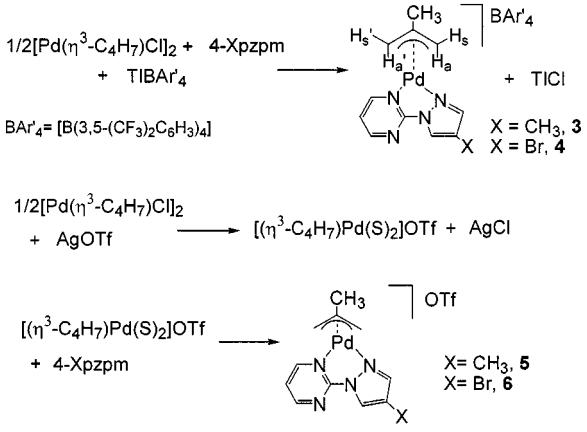

Scheme 3

The products are soluble in polar solvents such as acetone, dichloromethane and THF but are insoluble in hexane, pentane and diethyl ether.

Structural Characterisation

The new ligands and products were characterised by elemental analysis, and IR, ^1H and ^{13}C NMR spectroscopy. For the majority of the derivatives, HSQC experiments were also performed and, in some cases, NOE experiments were carried out.

The IR spectra of the ligands and complexes exhibit the stretching vibration bands for ν(C=N) (see Exp. Sect.). The

 © 2005 Wiley-VCH Verlag GmbH & Co. KGaA, Weinheim

Table 1. ^{1}H NMR spectroscopic data for ligands **1** and **2** and complexes **3**−**6**[a]

	Pyrazole			Pyrimidine		Allyl		
	$H^{5'}$	CH_3	$H^{3'}$	H^5	H^4/H^6	H_{syn}	H_{anti}	CH_3
1	8.38 (s)	2.14 (s)	7.62 (s)	7.36 (t), $J_{5,4/5,6}$ = 4.8	8.78 (d) $J_{4,5/6,5}$ = 4.8	–	–	–
2	8.73 (s)	–	7.84 (s)	7.48 (t), $J_{5,4/5,6}$ = 4.8	8.85 (d) $J_{4,5/6,5}$ = 4.8	–	–	–
3	8.72 (s)	2.27 (s)	8.28 (s)	[b]	9.20 (bs)	4.49 (s)	3.44 (s)	2.25 (s)
3[c]	8.90 (s)	2.22 (s)	8.33 (s)	[b]	9.25 (bs)	4.49 (s)	3.46 (s)	2.18 (s)
							3.32 (s)	
4	9.12 (s)	–	8.53 (s)	7.91 (bs)	9.51 (bs)	4.57 (s)	3.49 (s)	2.27 (s)
4[c]	9.41(s)	–	8.69 (s)	7.93 (t), $J_{5,4/5,6}$ = 4.9	9.32 (d)	4.54 (s)	3.49 (s)	2.17 (s)
					9.27 (d)	4.51 (s)	3.34 (s)	
4[d]	8.57 (s)	–	7.93 (s)	7.14 (t), $J_{5,4/5,6}$ = 5.1	8.56 (d)	3.93 (s)	2.91 (s)	2.05 (s)
					8.70 (d)	4.16 (s)	3.05 (s)	
5	8.67 (s)	2.27 (s)	8.22 (s)	7.75 (bs)	9.19 (bs)	4.49 (s)	3.43 (s)	2.25 (s)
5[c]	8.88 (s)	2.23 (s)	8.33 (s)	7.85 (t), $J_{5,4/5,6}$ = 5.1	9.31 (d)	4.50 (s)	3.48 (s)	2.20 (s)
					9.25 (d)		3.34 (s)	
6	9.14 (s)	–	8.56 (s)	7.86 (t), $J_{5,4/5,6}$ = 5.3	9.32 (bs)	4.58 (s)	3.49 (s)	2.27 (s)
					9.25 (bs)			
6[c]	9.45 (s)	–	8.73 (s)	7.95 (t), $J_{5,4/5,6}$ = 5.1	9.36 (d)	4.59 (s)	3.55 (s)	2.22 (s)
					9.31 (d)	4.57 (s)	3.40 (s)	
6[e]	8.71 (s)	–	8.04 (s)	7.72 (bs)	9.15 (bs)	4.35 (s)	3.39 (s)	2.17 (s)
					8.99 (bs)	4.29 (s)	3.20 (s)	

[a] Unless otherwise specified, room temperature and [D_6]acetone as solvent; s: singlet; d: doublet; bs: broad singlet; t: triplet. See Scheme 2 for the atom numbering. [b] Resonance under $BAr'_4{}^-$ signals. [c] −90 °C. [d] −60 °C, $CDCl_3$. [e] −80 °C, CD_2Cl_2. The resonances for the $BAr'_4{}^-$ anion are for **3**: δ = 7.79 (s, H*o*) and 7.68 (H*p*) ppm; for **4**: δ = 7.78 (s, H*o*) and 7.66 (H*p*) ppm.

allyl ligand gives rise to a band at 838 cm^{-1} in all the complexes due to the $\nu(C-CH_3)$ vibration. The presence of the corresponding counterions was confirmed by the presence of the expected bands (see Exp. Sect.).

The ^{1}H NMR spectroscopic data for the ligands and complexes are collected in Table 1. In the cases of derivatives **3** and **4**, due to some overlap with the resonances of the counterion, the spectra were recorded both in $CDCl_3$ and [D_6]acetone. The assignment for the nitrogen-ligand resonances was made on the basis of previous studies with similar ligands.[23,37] The $H^{3'}$ and $H^{5'}$ protons of the pyrazolyl rings appear as singlets both in the ligands and complexes as a result of the presence of the substituent in the 4-position. In the free ligands the H^5 proton of the pyrimidine ring appears as a triplet coupled to H^4 and H^6, which are equivalent. In the complexes the protons H^4 and H^6 are inequivalent due to coordination. However, signals for the two protons are only observed separately at room temperature in complex **6**. In the other cases these protons give rise to a single broad signal at this temperature. This phenomenon clearly indicates that the H^4-H^6 interconversion process previously detected in [Pd(η^3-2Me-C_3H_4)(pzpm)]CF_3SO_3 (**I**)[23] is also operating (see section on fluxional behaviour). In general, a shift towards higher frequency is observed for the corresponding resonances of the complexes with respect to the free ligands due to the ligand-to-metal σ-donation. As far as the allylic signals are concerned, a single resonance is observed at room temperature for the H_{syn} and also for the H_{anti} protons. This observation is not in accordance with a static situation of the complexes, where two different terminal allylic carbons would be expected due to the asymmetry of the nitrogen ligands. This constitutes a clear indication of a dynamic situation that involves a *syn-syn*, *anti-anti* interconversion, such as an apparent allyl rotation process, which will be analysed in the section on fluxional behaviour. The differentiation between the two methyl resonances of complex **3** [D_6]acetone was achieved with the help of NOE experiments. When $H^{5'}$ of the pyrazole ring was irradiated an NOE was found for the resonance at δ = 2.27 ppm. An NOE for the resonance at δ = 2.25 ppm and for the H_{anti} signal was also found when the H_{syn} resonance was irradiated.

The corresponding $^{13}C\{^1H\}$ NMR spectroscopic data are gathered in Table 2. The assignment for the nitrogen ligands was made on the basis of literature data[23,26,37−39] and HSQC experiments. In a similar way to the ^{1}H NMR spectra, a single signal was observed for the C^4 and C^6 pyrimidine carbons (in complex **4** this signal was not observed). A signal shift towards higher frequency with respect to the

Table 2. $^{13}C\{^1H\}$ NMR spectroscopic data for ligands **1** and **2** and complexes **3**−**6**[a]

	Pyrazole				Pyrimidine			η^3-Allyl		
	$C^{3'}$	$C^{4'}$	$C^{5'}$	CH_3	C^2	C^5	C^4/C^6	CH_2	C_{quat}	CH_3
1[b]	145.1	119.5	127.5	9.2	156.1	118.3	158.9			
1[c]	145.2	119.8	128.2	9.3	157.0	119.7	159.8			
2[b]	144.3	97.6	129.4	–	155.3	119.4	159.2			
2[c]	143.9	97.0	129.9	–	156.0	120.4	159.7			
3[b]	148.4	[d]	[e]	9.0	154.1	120.4	161.3	61.2 (bs)	136.3	23.4
4[b]	147.9	[d]	131.3	–	[d]	121.3	[e]	61.9 (bs)	137.1	23.4
5[c]	148.1	122.5	129.4	8.3	154.8	121.0	162.2	61.2 (bs)	135.5	22.7
6[c]	147.8	99.4	131.7	–	153.9	121.9	162.3	61.9 (bs)	136.0	22.7

[a] Unless specified, the signals are singlets; bs = broad singlet. See Scheme 2 for the atom numbering. [b] In $CDCl_3$. [c] In [D_6]acetone. [d] Not observed. [e] Resonances under $BAr'_4{}^-$ signals. The resonances of the anions are given in the Exp. Sect.

 © 2005 Wiley-VCH Verlag GmbH & Co. KGaA, Weinheim

free ligands is also seen. The allylic carbon resonances also reflect the apparent allyl rotation process as a single broad signal appears for the terminal carbons. The expected coupling with boron or fluorine is observed for the C_{ipso} and CF_3 carbons, respectively, of the BAr'_4 anion.[40]

Fluxional Behaviour

As stated previously, with these new allyl complexes we tried to obtain sufficient information concerning their fluxional behaviour to draw a conclusion as to whether the apparent allyl rotation process and the H^4-H^6 interconversion have the same energy barrier and follow a common mechanism. This information and the study of the influence of different factors could also shed light on the controversy surrounding mechanisms (associative or dissociative). In the case of derivative **I**,[23] the corresponding representation of free energy of activation versus coalescence temperature did not allow a conclusion to be drawn as to whether the two points for the apparent allyl rotation and the one for the H^4-H^6 interconversion were in a straight line — the information was insufficient to conclude, with certainty, whether the two process have the same energy barrier.

In order to analyse the dynamic behaviour of complexes **3**−**6** we performed variable temperature ^1H NMR studies under different conditions in order to obtain the coalescence temperatures (T_c) of the interconversion processes $H_{syn}-H_{syn}$, $H_{anti}-H_{anti}$ and H^4-H^6. For the majority of the complexes, two H_{syn} signals, two H_{anti} signals and separate signals for H^4 and H^6 were observed at low temperature, as one would expect for a static situation (see Table 1). An increase in the temperature allowed the corresponding coalescence temperatures to be determined. These values are given in Table 3 along with the δν values and the calculated free energies of activation.[41] However, in some cases it was not possible to determine the $\Delta G_c^{\ddagger}$ values. The reasons for this are that either the signals were not split at the minimum experimental temperature or the coalescence was not reached at the maximum temperature allowed by the solvent (in this case it is indicated that the T_c values are higher than the maximum temperature registered and the $\Delta G_c^{\ddagger}$ values

Table 3. δν, T_c and $\Delta G_c^{\ddagger}$ data for complexes **3**−**6** and **I**[a]

Entry	Complex	Anion	Solvent	Interchanging groups	ν_c (Hz)	T_c (K)	$\Delta G_c^{\ddagger}$ (kJ/mol)
1	**3**	BAr'_4	[D$_6$]acetone	$H_{anti}-H_{anti}$	39.8	213	43.6
2[b]	**4**	BAr'_4	[D$_6$]acetone	$H_{anti}-H_{anti}$	74.7	244	48.9
3[b]	**4**	BAr'_4	[D$_6$]acetone	$H_{syn}-H_{syn}$	2.0	204	46.7
4[b]	**4**	BAr'_4	[D$_6$]acetone	H^4-H^6	45.3	303	62.6
5	**5**	OTf	[D$_6$]acetone	$H_{anti}-H_{anti}$	41.5	237	48.6
6	**5**	OTf	[D$_6$]acetone	H^4-H^6	14.7	217	46.3
7	**6**	OTf	[D$_6$]acetone	$H_{anti}-H_{anti}$	48.1	246	50.4
8	**6**	OTf	[D$_6$]acetone	$H_{syn}-H_{syn}$	1.8	208	47.8
9	**6**	OTf	[D$_6$]acetone	H^4-H^6	28.5	300	63.2
10[b]	**6**	OTf	[D$_6$]acetone	$H_{anti}-H_{anti}$	73.2	250	50.3
11[b]	**6**	OTf	[D$_6$]acetone	$H_{syn}-H_{syn}$	1.9	205	47.1
12[b]	**6**	OTf	[D$_6$]acetone	H^4-H^6	51.2	304	62.5
13	**I**	OTf	[D$_6$]acetone	$H_{anti}-H_{anti}$	40.9	230	47.3
14	**I**	OTf	[D$_6$]acetone	$H_{syn}-H_{syn}$	10.3	216	47.8
15	**I**	OTf	[D$_6$]acetone	H^4-H^6	26.6	268	55.4
16	**4**	BAr'_4	$CDCl_3$	$H_{anti}-H_{anti}$	13.8	252	54.2
17	**4**	BAr'_4	$CDCl_3$	$H_{syn}-H_{syn}$	60.3	284	57.9
18	**4**	BAr'_4	$CDCl_3$	H^4-H^6	74.1	>331	>67.1
19	**6**	OTf	CD_2Cl_2	$H_{anti}-H_{anti}$	51.1	245	49.9
20	**6**	OTf	CD_2Cl_2	$H_{syn}-H_{syn}$	18.5	221	48.9
21	**6**	OTf	CD_2Cl_2	H^4-H^6	29.7	311	65.4
22[c]	**6**	OTf	CD_2Cl_2	$H_{anti}-H_{anti}$	71.3	251	50.5
23[c]	**6**	OTf	CD_2Cl_2	$H_{syn}-H_{syn}$	29.0	229	47.6
24[c]	**6**	OTf	CD_2Cl_2	H^4-H^6	54.8	>311	>63.8
25[c]	**6**	OTf	[D$_6$]acetone	$H_{anti}-H_{anti}$	56.3	246	49.9
26[c]	**6**	OTf	[D$_6$]acetone	$H_{syn}-H_{syn}$	1.7	209	48.2
27[c]	**6**	OTf	[D$_6$]acetone	H^4-H^6	28.5	303	63.8
28[c]	**4**	BAr'_4	$CDCl_3$	$H_{anti}-H_{anti}$	20.3	233	49.2
29[c]	**4**	BAr'_4	$CDCl_3$	$H_{syn}-H_{syn}$	63.7	263	53.3
30[c]	**4**	BAr'_4	$CDCl_3$	H^4-H^6	79.1	>330	>66.9
31[d]	**4**	BAr'_4	$CDCl_3$	$H_{syn}-H_{syn}$	62.3	226	45.6
32[d]	**4**	BAr'_4	$CDCl_3$	H^4-H^6	46.0	290	59.8
33[e]	**6**	OTf	[D$_6$]acetone	$H_{anti}-H_{anti}$	45.7	244	49.9
34[e]	**6**	OTf	[D$_6$]acetone	$H_{syn}-H_{syn}$	5.9	205	45.2
35[e]	**6**	OTf	[D$_6$]acetone	H^4-H^6	16.3	298	64.1

[a] Unless specified the complex concentration is 1.41×10^{-2} M and a 300 MHz spectrometer is used. [b] At 500 MHz. [c] Complex concentration of 7.05×10^{-3} M. [d] With addition of water (5.60×10^{-2} M in water; H_2O:complex = 4:1). [e] With addition of water (3.52×10^{-2} M in water; H_2O:complex = 2.5:1).

 © 2005 Wiley-VCH Verlag GmbH & Co. KGaA, Weinheim

are higher than those calculated for these temperatures). In the following discussion we will detail our conclusions concerning the influence of different factors on the fluxional behaviour of our allyl complexes.

Effect of the Ligand

Comparison of the data for complexes **3** and **4** (Entries 1−4) on the one hand and for **5** and **6** on the other, as well as those for complex **I**[23] (Entries 5−9 and 13−15), gives an indication of the influence of the ligand. Unfortunately, in the case of complexes with the 4-Mepzpm ligand it was not possible to determine all the coalescence temperatures and obtain the corresponding data. In the case of complex **3** it was only possible to detect the $H_{anti}-H_{anti}$ interconversion process while for **5** the splitting of the H_{syn} signals was not achieved. As far as the allylic interconversions are concerned, and although it would be desirable to have more data, it seems that the type of ligand does not have a clear influence, especially concerning the type of pyrazole ring. With respect to the H^4-H^6 interchange, three sets of data are available in the case of compounds containing the triflate anion. In these compounds there is an increase in the coalescence temperature and in the free energy of activation on changing from 4Me-pzpm to pzpm to 4Br-pzpm, but the three points fit reasonably well ($R^2 = 0.9924$) to a straight line (with positive slope), which might again indicate the lack of influence of the type of pyrazole in the ligand on the process. It is possible that the electronic differences between the three ligands are not sufficient to clearly influence the processes under investigation. In any case, it is necessary to bear in mind that for the H^4-H^6 interchange process the bond that must be broken is between the palladium and the pyrimidine ring, not the pyrazole heterocycle.

Type of Interchange

Before analyzing the influence of other factors, it is important to consider carefully the data for complex **6**. Although the δν value for the $H_{anti}-H_{anti}$ interconversion (48.1 Hz, Entry 7) is clearly higher than that for the H^4-H^6 interchange (28.5 Hz, Entry 9), the T_c and $\Delta G_c^{\ddagger}$ values are markedly higher in the latter case. This clearly indicates that the H^4-H^6 interchange has a higher energy barrier and will also have a different mechanism than the apparent allyl rotation. In order to obtain more data for this complex, we decided to perform the same study with an NMR spectrometer of different magnetic field (500 MHz as opposed to 300 MHz). In this way, we could obtain four data points for the allylic interconversions (Entries 7, 8, 10 and 11) and two for the H^4-H^6 interchange (Entries 9 and 12). The corresponding data are represented in Figure 1. The points for the allylic interconversions fit very well to a straight line ($R^2 = 0.9985$) while the other two values have free energies of activation that are clearly higher (7.9−8.9 kJ·mol^{-1}). This trend is consistent with our previous conclusion that the H^4-H^6 interchange has a higher energy barrier than the apparent allyl rotation. The difference in free energy of activation between the two processes will also be clear in other plots presented in this paper aimed at evaluating the influence of other factors (see below).

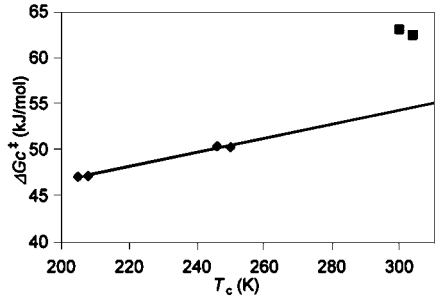

Figure 1. Linear plot of $\Delta G_c^{\ddagger}$ (kJ/mol) versus T_c (K) for complex **6** in [D$_6$]acetone (1.41×10^{-2} M) using data from 300 and 500 MHz NMR spectrometers (see Table 3): allylic interchange (diamonds, −−); ($R^2 = 0.9985$); H^4-H^6 interchange (squares)

Effect of the Counteranion

A comparison of Entries 1, 5 and 6 for the complexes with the 4-Mepzpm ligand and Entries 2−4 and 7−12 for those with the 4-Brpzpm ligand should give an indication of the influence of the counteranion on the processes in question. However, the lack of data for the 4-Mepzpm complexes precludes a clear conclusion from being drawn. However, with the 4-Brpzpm complexes (see Figure 2) it is possible to conclude that, at least in [D$_6$]acetone solution, there is a negligible influence of the anion on both the apparent allyl rotation and the H^4-H^6 interconversion. The data represented in Figure 2 also confirm the previous conclusion that the apparent allyl rotation has a lower free energy of activation than the H^4-H^6 interconversion.

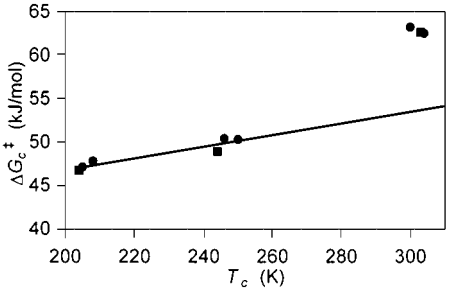

Figure 2. Linear plot of $\Delta G_c^{\ddagger}$ (kJ/mol) versus T_c (K) for complexes **4** and **6** in [D$_6$]acetone (1.41×10^{-2} M; see Table 3): **4** (squares); **6** (circles); allylic interchange (−−); $R^2 = 0.9706$

Effect of the Solvent

The studies described below are centred on complexes **4** and **6**, which contain the ligand 4-Brpzpm, because more coalescence points can usually be measured than for the 4-Mepzpm derivatives. For complex **4**, the data previously obtained in [D$_6$]acetone solution (Entries 2−4) were compared with those obtained in $CDCl_3$ at the same concentration (Entries 16−18). These data are represented in Fig-

 © 2005 Wiley-VCH Verlag GmbH & Co. KGaA, Weinheim

ure 3. The coalescence temperature for the H^4-H^6 interchange in $CDCl_3$ was not reached and this is indicated by an arrow in the figure to reflect the fact that the actual value is higher than the one indicated. As far as the apparent allyl rotation process is concerned, higher $\Delta G_c^{\ddagger}$ values are obtained when the solvent is $CDCl_3$ and the same seems to apply to the H^4-H^6 interchange. Consequently, for this complex, which contains a counteranion (BAr'_4^-) that does not have coordinating ability, the presence of a solvent that it is able to coordinate has a positive effect on the processes.

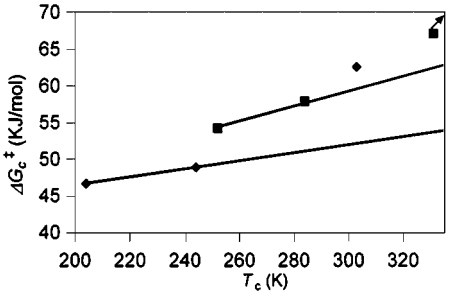

Figure 3. Linear plot of $\Delta G_c^{\ddagger}$ (kJ/mol) versus T_c (K) for complex **4** (1.41×10^{-2} M; see Table 3): $CDCl_3$ (squares); [D_6]acetone (diamonds); allylic interchange (−−)

A similar solvent effect is not observed in complex **6** where the anion (OTf^-) has coordinating ability. In this case the comparison is made between the [D_6]acetone (Entries 7−12) and CD_2Cl_2 (Entries 19−21) data. It can clearly be seen from Figure 4 that the solvent does not have any influence on the apparent allyl rotation, while for the H^4-H^6 interchange the conclusion is not as straightforward. Once again, this figure demonstrates the difference in free energy of activation between the apparent allyl rotation and the H^4-H^6 interchange.

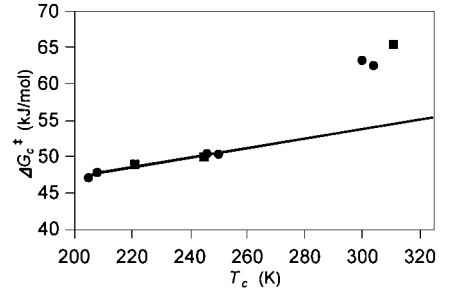

Figure 4. Linear plot of $\Delta Gc^{\ddagger}$ (kJ/mol) versus T_c (K) for complex **6** (1.41×10^{-2} M; see Table 3): CD_2Cl_2 (squares); [D_6]acetone (circles); allylic interchange (−−); $R^2 = 0.9914$

Effect of the Complex Concentration

In order to obtain information about the possible participation of bimolecular species in these processes, we carried out several variable temperature ^1H NMR studies with two different concentrations (1.41×10^{-2} and 7.05×10^{-3} M). For complex **6**, we performed the studies both in [D_6]acetone (Entries 7−12 and 25−27) and in CD_2Cl_2 solutions (Entries 19−24) and for complex **4** in $CDCl_3$ solutions (Entries 16−18 and 28−30). The coalescence of the H^4 and H^6 resonances was not reached up to the maximum temperature allowed by the solvent for complex **6** in CD_2Cl_2 or complex **4** in $CDCl_3$. When the results at the two concentrations are compared, it is possible to conclude that in the case of **6** in [D_6]acetone the three pairs of data are practically identical — the concentration does not influence either of the two processes. In the other two studies, there is insufficient information about the H^4-H^6 interchange and for the apparent allyl rotation the influence, if it exists, is very small (at least in the range of concentrations used).

Effect of the Addition of Water

The study of the influence of the addition of water was performed with complex **4** in $CDCl_3$ (Entries 16−18 and 31−32) in order to have a counterion and a solvent without coordinating ability. The data were obtained for a water-free $CDCl_3$ solution and after the addition of four mol of water per mol of product in this solution. The addition of water induces a general lowering of the coalescence temperatures, and the splitting of the H_{anti} resonances is not observed even down to −60 °C. However, the coalescence of the H^4-H^6 resonances, which was not achieved in the water-free solution, was observed at 17 °C after the addition of water. When the data for the allylic interconversions are taken into amount, it is concluded that the value obtained after the addition of water is 4.9 kJ·mol^{-1} below the straight line obtained with the data for the water-free solution. Consequently, at least in the situation where the counteranion and solvent are non-coordinating, the addition of water favours the apparent allyl rotation. We also studied the effect of the addition of water when there are species of coordinating ability in the reaction medium, for example for complex **6** in [D_6]acetone solution (comparison of Entries 7−9 with 33−35). In this case, there is no appreciable effect observed in the values of free energy of activation after the addition of water.

When the different plots for the apparent allyl rotation process are considered, a positive slope in the straight line obtained is observed. Although we do not believe that it is possible to give accurate data for the entropy of activation, it is clear that this parameter is negative.

It must be emphasised that our results indicate that care must be taken when studying these types of process in solvents that do not have coordinating ability. In solvents such as acetone, as observed previously,[35] the presence of small amounts of water does not influence the energy barrier of the process.

Conclusions of the ^1H NMR Variable Temperature Studies

We deduced that there is a lower energy barrier for the apparent allyl rotation process than for the H^4-H^6 interconversion and, consequently, the two processes follow different mechanisms. In the case of the apparent allyl rotation process, and concerning the effect of different factors

 © 2005 Wiley-VCH Verlag GmbH & Co. KGaA, Weinheim

on this phenomenon, we can state the following: (i) a clear influence of the type of pyrazole present in the nitrogen-containing ligand is not found; (ii) the results are the same when, in [D_6]acetone solutions, the counterion is changed (cf. $BAr'_4{}^-$ versus OTf^-) or when, for the complexes with the OTf^- anion, two different solvents are used ([D_6]acetone and CD_2Cl_2); (iii) in the complex with the $BAr'_4{}^-$ anion, the free energy of activation values are higher in a non-coordinating solvent such as $CDCl_3$ than in [D_6]acetone; (iv) the complex concentration does not affect the process in the range studied; (v) when the complex contains a non-coordinating anion and the study is carried out in $CDCl_3$, the addition of water decreases the free energy of activation. However, the addition of water does not affect the dynamic behaviour in [D_6]acetone when the counterion present is OTf^-; (vi) the entropy of activation is negative.

In the case of the H^4-H^6 interconversion process it is more difficult to draw conclusions because only one $\Delta G_c^{\ddagger}$ data point could be obtained for each study. Despite this, we believe that the following general points can be made: (i) the type of anion, ligand or complex concentration does not have any influence when the solvent is [D_6]acetone; (ii) when both the solvent ($CDCl_3$) and anion ($BAr'_4{}^-$) are non-coordinating, the addition of water reduces the free energy of activation but this addition does not affect the values of $\Delta G_c^{\ddagger}$ in [D_6]acetone when the counterion is OTf^-; (iii) the entropy of activation is negative.

During the studies described here, broadening of the H_{syn} or H_{anti} resonances was not observed in any case after coalescence was achieved. This fact indicates that if the $H_{syn}-H_{anti}$ interconversion process (usually proposed to occur through an η^3-η^1-η^3 mechanism) exists, it must be of higher energy and is therefore not observed under the conditions used here.

Mechanistic Proposal

Apparent Allyl Rotation

The negative sign of the entropy of activation points to an associative process with the formation of five-coordinate intermediates. On the basis of some of the conclusions outlined above (ii, iii and v), it is possible to state that a species with coordinating ability (counteranion, solvent or water) clearly favours the process. We must consider that when the counterion is $BAr'_4{}^-$, the solvents are CD_2Cl_2 or $CDCl_3$ and water is not added, the two processes, although with higher energies of activation, do take place. It is possible that in these cases traces of water or Cl^- in the solvents (decomposition of CD_2Cl_2 or $CDCl_3$), or the low coordinating ability of the solvents, allows the process to occur. Conclusion iv indicates that bimolecular species are not formed and that the free nitrogen of the pyrimidine ring does not participate in the formation of the five-coordinate intermediates. It is necessary to consider that the formation of an "ion pair" between the cation and the anion should be favoured in concentrated solutions. This would be particularly true in the case of a non-coordinating solvent, such as complex **6** in CD_2Cl_2. This phenomenon has been found by other authors[20b] but, depending on the temperature and the concentration range, the effect can be rather small because of the existence of a limiting constant value.

It is also important to consider that the energy barrier for the apparent allyl rotation is lower than for the H^4-H^6 interconversion process. This latter process necessarily involves a Pd−N(pm) bond rupture, probably as the limiting step. Consequently, the apparent allyl rotation process should occur through a path that does not involve Pd−N(pm) bond rupture and has a lower energy of activation. The breaking of the Pd−N(pyrazole) bond is less likely because of the higher basicity of this heterocycle (except for the case of 4-Br-pyrazole) with respect to the pyrimidine ring [pK_a(pyrimidine) = 1.1]. This again makes a dissociative mechanism less likely and points to an associative pathway. The partial dissociation of the didentate N-donor ligand in the five-coordinate intermediate has sometimes been considered.[20b] In our case, however, this possibility can be excluded. Consequently, the associative mechanism[20,28,29,32,35] we propose would have the following steps (see Scheme 4): (i) formation of a five-coordinate intermediate through coordination of the anion, solvent or water (L); (ii) pseudorotation of the allyl group in the intermediate formed, which interchanges the two allylic terminals; and (iii) decoordination of the L group, leading to the final product in which the observed $H_{syn}-H_{syn}$, $H_{anti}-H_{anti}$ interchange has taken place.

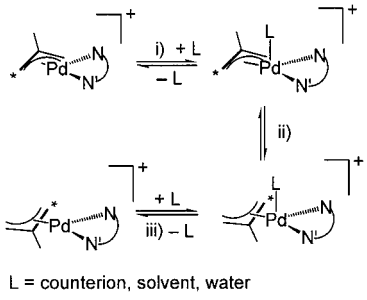

Scheme 4

H^4-H^6 Interconversion

The negative entropy of activation, the positive effect of the addition of water when both the solvent and the anion are non-coordinating, and the absence of other effects when the solvent is [D_6]acetone all indicate that, in this case, an associative mechanism is in operation. The mechanism should involve the following steps (see Scheme 5): (i) formation of the five-coordinate intermediate through coordination of the solvent, anion or water (L); (ii) Pd−N(pm) bond rupture; (iii) internal rotation of the ligand[19] through the C−N bond that links the two heterocycles in the tetracoordinate intermediate formed; (iv) recoordination of the pyrimidine ring through the other nitrogen atom; and (v) decoordination of the L group, leading to the final species

 © 2005 Wiley-VCH Verlag GmbH & Co. KGaA, Weinheim

in which the interchange between the positions of the H^4 and H^6 pyrimidine protons has taken place.

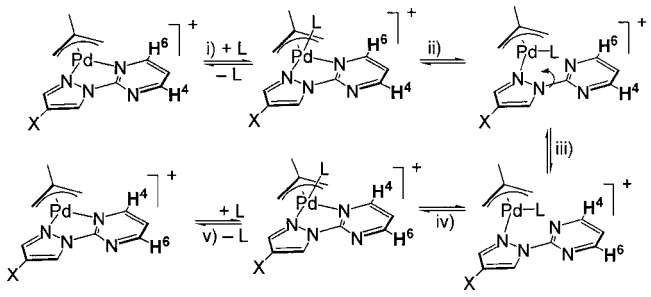

Scheme 5

Conclusions

New allylpalladium derivatives with N-donor ligands have been obtained and their fluxional behaviour studied. Two processes of apparent allyl rotation (observed as $H_{syn}-H_{syn}$, $H_{anti}-H_{anti}$ interconversions) and also H^4-H^6 interconversion of the pyrimidine protons have been observed. This last process must involve, probably as the limiting step, Pd−N(pyrimidine) bond rupture. It has been concluded that the apparent allyl rotation process has a lower free energy of activation. Consequently, this allyl rotation must not involve Pd−N bond rupture. The influence of factors such as counterion, solvent and addition of water has been studied and it is possible to conclude that the presence of a species with coordinating ability clearly favours both processes. A bimolecular mechanism can be excluded in both cases because the complex concentration does not affect the free energy of activation. Negative entropies of activation were obtained. Associative mechanisms with participation of five-coordinate intermediates have been proposed for both processes, with a step involving Pd−N(pyrimidine) bond rupture in the case of the H^4-H^6 interconversion.

On the basis of our studies it is possible to conclude that, for these types of process, the presence of traces of water in coordinating solvents like acetone does not affect the free energy of activation. However, this is not the case for non-coordinating solvents and great care must be taken in studies involving such solvents.

Experimental Section

General Comments: All manipulations were carried out under dry, oxygen-free nitrogen using standard Schlenk techniques. Solvents were distilled from the appropriate drying agents and degassed before use. The derivative $[Pd(\eta^3\text{-}C_4H_7)(\mu\text{-}Cl)]_2$ was synthesised according to a literature procedure.[42] Elemental analyses were performed with a Carlo Erba Instruments EA 1108 CHNS/O microanalyser (University of La Coruña). IR spectra were recorded as nujol mulls with a Perkin−Elmer PE 883 IR spectrometer. ^1H and $^{13}C\{^1H\}$ NMR spectra were recorded with a Varian Unity 300 and an Innova 500 spectrometer using $CDCl_3$, CD_2Cl_2 and $(CD_3)_2CO$ as solvents; the chemical shifts are given in ppm. Standard experimental conditions were employed.[25,26] The NOE difference spectra were recorded with the following acquisition parameters: spectral width 5000 Hz, acquisition time 3.27 s, pulse width 18 ms, relaxation delay 4 s, irradiation power 5−10 dB, number of scans 240. For ^1H-^{13}C g-HSQC spectra the standard Varian pulse sequences were used (V NMR 6.1 C software). The spectra were acquired using 7996 Hz (^1H) and 30154 Hz (^{13}C) spectral widths; 16 transients of 2048 data points were collected for each 256 increments. For variable-temperature spectra the probe temperature (±1 K) was controlled by a standard unit calibrated with a methanol reference. Free energies of activation (kJ·mol^{-1}) were calculated[41] from the coalescence temperature (T_c) and the frequency difference between the coalescing signals (extrapolated at the coalescence temperature) with the formula $\Delta G_c^{\ddagger} = a \cdot T \cdot [9.972 + \log(T/\delta\nu)]$, where $a = 1.914 \times 10^{-2}$. The estimated error in the calculated free energies of activation is ±1.1 kJ·mol^{-1}. *o* = *ortho*, *m* = *meta*, *p* = *para*.

2-(4-Methyl-1*H*-pyrazol-1-yl)pyrimidine (1): A mixture of 4-methylpyrazole (0.248 mL, 3 mmol), potassium *tert*-butoxide (600 mg, 6 mmol) and aliquat 336 (80 mg, 10%) was stirred at 120 °C for 30 min. 2-Chloropyrimidine (515 mg, 4.5 mmol) was then added at 120 °C and the reaction mixture was stirred at this temperature for 1 h. Extraction with dichloromethane (50 mL), removal of the solvent from the extract and flash chromatography of the residue on silica gel using ethyl acetate as the eluent allowed the isolation of **1**. Yield: 62% (298 mg). IR: $\tilde{\nu}$ = 1573 cm^{-1} [ν(C−N)]. $C_8H_8N_4$ (160.18): calcd. C 59.99, H 5.03, N 34.98; found C 59.70, H 5.29, N 34.62.

2-(4-Bromo-1*H*-pyrazol-1-yl)pyrimidine (2): A similar procedure to that used for **1** was applied for **2**. Amounts were as follows: 4-bromopyrazole (440.8 mg, 3 mmol), potassium *tert*-butoxide (600 mg, 6 mmol), aliquat 336 (80 mg, 10%) and 2-chloropyrimidine (515 mg, 4.5 mmol). Yield 60% (405.1 mg). IR: $\tilde{\nu}$ = 1570 cm^{-1} [ν(C−N)]. $C_7H_5BrN_4$ (225.05): calcd. C 37.36, H 24.89, N 2.24; found C 37.25, H 24.99, N 2.18.

$[Pd(\eta^3\text{-}C_4H_7)(4\text{-Mepzpm})]BAr'_4$ (3): 4-Mepzpm (24.3 mg, 0.152 mmol) and $TlBAr'_4$ (162.3 mg, 0.152 mmol) were added to a solution of $[Pd(\eta^3\text{-}C_4H_7)(\mu\text{-}Cl)]_2$ (30 mg, 0.076 mmol) in 10 mL of toluene. The mixture was stirred at room temperature for 1 h. The resulting suspension was filtered off. The solid was then extracted with dichloromethane (40 mL) and the solution was evaporated to dryness. The light-brown solid was washed with hexane and dried. Yield: 66% (119.1 mg). IR: $\tilde{\nu}$ = 1598 and 1566 [ν(C−N)], 1275, 890 (BAr'_4), 839 cm^{-1} ν[(C−CH_3), allyl]. $C_{44}H_{27}BF_{24}N_4Pd$ (1184.9): calcd. C 44.60, H 2.30, N 4.73; found C 44.52, H 2.44, N 4.69. $^{13}C\{^1H\}$ NMR (125 MHz, $CDCl_3$, 298 K; BAr'_4 resonances): δ = 161.9 (q, $^1J_{B,C}$ = 50.0 Hz, 4 C, C_{ipso}), 135.0 (s, 8 C, C_o), 129.2 (m, 8 C, C_m), 124.7 (q, $^1J_{C,F}$ = 272.6 Hz, 8 C, CF_3), 117.7 (s, 4 C, C_p) ppm.

$[Pd(\eta^3\text{-}C_4H_7)(4\text{-Brpzpm})]BAr'_4$ (4): A similar procedure to that used for **3** was applied for **4**. Amounts were as follows: $[Pd(\eta^3\text{-}C_4H_7)(\mu\text{-}Cl)]_2$ (20 mg, 0.051 mmol), 4-Brpzpm (22.9 mg, 0.102 mmol) and $TlBAr'_4$ (108.9 mg, 0.102 mmol). The solid was pale brown in colour. Yield: 66% (83.7 mg). IR: $\tilde{\nu}$ = 1599 and 1568 [ν(C−N)], 1279, 890 (BAr'_4), 838 cm^{-1} ν[(C−CH_3), allyl]. $C_{43}H_{24}BBrF_{24}N_4Pd$ (1249.8): calcd. C 41.32, H 1.94, N 4.48; found C 41.67, H 2.19, N 4.49. $^{13}C\{^1H\}$ NMR (75 MHz, $CDCl_3$, 298 K; BAr'_4 resonances): δ = 161.9 (q, $^1J_{B,C}$ = 49.3 Hz, 4 C, C_{ipso}), 134.9 (s, 8 C, C_o), 129.8 (m, 8 C, C_m), 124.7 (q, $^1J_{C,F}$ = 272.2 Hz, 8 C, CF_3), 117.7 (s, 4 C, C_p) ppm.

 © 2005 Wiley-VCH Verlag GmbH & Co. KGaA, Weinheim

[Pd(η^3-C_4H_7)(4-Mepzpm)]OTf (5): $AgCF_3SO_3$ (104.3 mg, 0.406 mmol) was added to a solution of [Pd(η^3-C_4H_7)(μ-Cl)]$_2$ (80 mg, 0.203 mmol) in THF (20 mL). The mixture was stirred for 1 h and protected from light. The solution was filtered through Celite to eliminate AgCl. The ligand 4-Mepzpm (65 mg, 0.406 mmol) was then added and the mixture was stirred for 1 h. The solvent was evaporated to dryness and the pale-yellow residue was washed with diethyl ether. Yield 70% (133.7 mg). IR: $\tilde{\nu}$ = 1596 and 1565 [ν(C−N)], 1266, 1154, 1032, 784 and 639 (OTf^-), 839 cm^{-1} ν[(C−CH_3), allyl]. $C_{13}H_{15}F_3N_4O_3PdS$ (470.75): calcd. C 33.17, H 3.21, N 11.90; found C 33.46, H 3.11, N 12.23. $^{13}C\{^1H\}$ NMR (125 MHz, [D_6]acetone, 298 K): δ = 121.7 (q, $^1J_{C,F}$ = 322.2 Hz, 1 C, CF_3) ppm.

[Pd(η^3-C_4H_7)(4-Brpzpm)]OTf (6): A similar procedure to that used for **5** was applied for **6**. Amounts were as follows: Ag CF_3SO_3 (78.1 mg, 0.304 mmol), [Pd(η^3-C_4H_7)(μ-Cl)]$_2$ (60 mg, 0.152 mmol), 4-Brpzpm (68.4 mg, 0.304 mmol). The solid was white in colour. Yield: 80% (126.6 mg). IR: $\tilde{\nu}$ = 1597 and 1566 [ν(C−N)], 1269, 1147, 1034, 785 and 639 (OTf^-), 838 cm^{-1} ν[(C−CH_3), allyl]. $C_{12}H_{12}BrF_3N_4O_3PdS$ (535.62): calcd. C 26.91, H 2.26, N 10.46; found C 27.01, H 2.11, N 10.27. $^{13}C\{^1H\}$ NMR (125 MHz, [D_6]-acetone, 298 K): δ = 121.8 (q, $^1J_{C,F}$ = 322.2 Hz, 1 C, CF_3) ppm.

Preparation of NMR Spectroscopic Samples: Samples with a concentration of 1.41 × 10^{-2} M were prepared by dissolving the corresponding amount of the complex in 0.5 mL of the deuterated solvent. Samples with a concentration of 7.05 × 10^{-3} M were prepared by adding 0.5 mL of the corresponding deuterated solvent to the previous sample. Samples for the studies of Entries 31 and 32 (Table 3) were prepared by adding 0.510 μL (2.8 × 10^{-2} mmol) of water to the original solution. Samples for the studies of Entries 33−35 were prepared by adding 0.320 μL (1.76 × 10^{-2} mmol) of water to the original sample.

Acknowledgments

We are grateful to the Spanish DGES/MCyT (Project N. BQU-2002-00286) and the Consejería de Ciencia y Tecnología de la Junta de Comunidades de Castilla-La Mancha (PBI-02-002) for financial support.

[1] [1a] J. Tsuji, *Palladium Reagents and Catalysts, Innovation in Organic Synthesis*, J. Wiley & Sons, Chichester, **1996**. [1b] S. A. Godleski, in *Comprehensive Organic Synthesis* (Eds.: B. M. Trost, I. Fleming), Pergamon Press: New York, **1991**, vol. 4, chapter 3.3. [1c] P. J. Harrington, in *Comprehensive Organometallic Chemistry II* (Eds.: E. W. Abel, F. G. A. Stone, G. Wilkinson, R. J. Puddephatt), Elsevier, New York, **1995**, vol. 12, p.797. [1d] J.-E. Bäckvall, *Metal-Catalysed Cross Coupling Reactions*, VCH, Weinheim, Germany, **1998**, p. 339. [1e] B. M. Trost, C. Lee, in *Catalytic Asymmetric Synthesis*, 2nd ed. (Ed.: I. Ojima), Wiley-VCH, New York, **2000**, p. 593−649. [1f] A. Pfaltz, M. Lautens, in *Comprehensive Asymmetric Catalysis* (Eds.: E. N. Jacobsen, A. Pfaltz, H. Yamamoto), Springer, Heidelberg, **1999**, p.833−886.

[2] [2a] K. Vrieze, *Dynamic Nuclear Magnetic Resonance Spectroscopy* (Eds.: L. M. Jackman, F. A. Cotton), Academic Press, New York, **1975**, chapter 11, p. 441. [2b] P. S. Pregosin, R. Salzmann, *Coord. Chem. Rev.* **1996**, *155*, 35−68. [2c] J. W. Faller, in *Encyclopedia of Inorganic Chemistry* (Ed.: R. B. King), John Wiley and Sons, Chichester, **1994**, vol. 7, p. 3925−3926. [2d] F. A. Jalón, B. R. Manzano, F. Gómez-de la Torre, A. M. Guerrero, A. M. Rodríguez, *Targets in Heterocyclic Systems, Chemistry and Properties* (Eds.: O. A. Attanasi, D. Spinelli), Roma, **1999**, vol. 3, p. 399−438.

[3] [3a] B. M. Trost, D. L. Van Vranken, *Chem. Rev.* **1996**, *96*, 395−422. [3b] B. M. Trost, *Pure Appl. Chem.* **1996**, *68*, 779−784. [3c] J. D. Oslob, B. Åkermark, P. Helquist, P. O. Norrby, *Organometallics* **1997**, *16*, 3015−3021. [3d] C. Larksarp, H. Alper, *J. Am. Chem. Soc.* **1997**, *119*, 3709−3715. [3e] H. Hagelin, B. Åkermark, P.-O. Norrby, *Organometallics* **1999**, *18*, 2884−2895. [3f] J. C. Anderson, R. J. Cubbon, J. D. Harling, *Tetrahedron: Asymmetry* **2001**, *12*, 923−935. [3g] P. J. Harrington, in *Comprehensive Organometallic Chemistry* (Eds.: E. W. Abel, F. G. A. Stone, G. Wilkinson, L. S. Hegedus), Pergamon, Oxford, **1995**, vol. 12, p. 882−894 and references cited therein.

[4] [4a] P. W. N. M. van Leeuwen, P. W. Praat, *J. Chem. Soc., Chem. Commun.* **1970**, 365−366. [4b] F. G. A. Stone, N. M. Boag, M. Green, J. L. Spencer, *J. Organomet. Chem.* **1977**, *127*, C51−C54. [4c] R. E. Rülke, V. E. Raasjager, P. Wehman, C. J. Elsevier, P. W. N. M. van Leeuwen, K. Vrieze, J. Fraanje, K. Boubitz, A. L. Spek, *Organometallics* **1996**, *15*, 3022−3031.

[5] [5a] J. M. Brown, D. I. Hulmes, P. J. Guiry, *Tetrahedron* **1994**, *50*, 4493−4506. [5b] T. D. W. Claridge, J. M. Long, J. M. Brown, D. Hibbs, M. B. Hursthouse, *Tetrahedron* **1997**, *53*, 4035−4050.

[6] [6a] P. Barbaro, P. S. Pregosin, R. Salzmann, A. Albinati, R. W. Kunz, *Organometallics* **1995**, *14*, 5160−5170. [6b] T. Hosokawa, Y. Wakabayashi, K. Hosokawa, T. Tsuji, S. I. Murahashi, *Chem. Commun.* **1996**, 859−860. [6c] S. Ramdeehul, L. Barloy, J. A. Osborn, A. De Cian, J. Fischer, *Organometallics* **1996**, *15*, 5442−5444. [6d] H. A. Ankersmit, N. Veldman, A. L. Spek, K. Vrieze, G. Van Koten, *Inorg. Chim. Acta* **1996**, *252*, 339−354. [6e] L. Barloy, S. Ramdeehul, J. A. Osborn, C. Carlotti, F. Taulelle, A. De Cian, J. Fisher, *Eur. J. Inorg. Chem.* **2000**, *12*, 2523−2532.

[7] L. Canovese, F. Visentin, P. Uguagliati, V. Lucchini, G. Bandoli, *Inorg. Chim. Acta* **1998**, *277*, 247−252.

[8] [8a] I. Schwarz, J. Rust, C. W. Lehmann, M. Braun, *J. Organomet. Chem.* **2000**, *605*, 109−116. [8b] F. Gómez-de la Torre, Y. Gutiérrez, F. A. Jalón, B. R. Manzano, A. Rodríguez, *Monatsh. Chem.* **2000**, *131*, 1267−1280.

[9] [9a] J. Krause, R. Goddard, R. Mynott, K.-R. Pörschke, *Organometallics* **2001**, *20*, 1992−1999. [9b] P. Braunstein, F. Naud, A. Dedieu, M. M. Rohmer, A. De Cian, S. J. Rettig, *Organometallics* **2001**, *20*, 2966−2981.

[10] M. Kollmar, B. Goldfuss, M. Reggelin, F. Rominger, G. Helmchen, *Chem. Eur. J.* **2001**, *7*, 4913−4927.

[11] L. Canovese, G. Chessa, C. Santo, F. Visentin, P. Uguagliati, *Organometallics* **2002**, *21*, 4342−4349.

[12] M. Ogasawara, K. Takizawa, T. Hayashi, *Organometallics* **2002**, *21*, 4853−4861.

[13] [13a] C. Breutel, P. S. Pregosin, R. Salzmann, A. Togni, *J. Am. Chem. Soc.* **1994**, *116*, 4067−4068. [13b] P. S. Pregosin, R. Salzmann, A. Togni, *Organometallics* **1995**, *14*, 842−847. [13c] J. Herrmann, P. S. Pregosin, R. Salzmann, A. Albinati, *Organometallics* **1995**, *14*, 3311−3318.

[14] R. Fernández-Galán, F. Jalón, B. R. Manzano, J. Rodríguez de la Fuente, M. Vrahami, B. Jedlicka, W. Weissensteiner, *Organometallics* **1997**, *16*, 3758−3768.

[15] P. Dotta, P. G. A. Kumar, P. S. Pregosin, *Magn. Reson. Chem.* **2002**, *40*, 653−658.

[16] B. Crociani, S. Antonaroli, G. Bandoli, L. Canovese, F. Visentin, P. Uguagliati, *Organometallics* **1999**, *18*, 1137−1147.

[17] N. Solin, K. J. Szabó, *Organometallics* **2001**, *20*, 5464−5471.

[18] A. Albinati, R. W. Kunz, C. J. Ammann, P. S. Pregosin, *Organometallics* **1991**, *10*, 1800−1806.

[19] A. Gogoll, J. Örnebro, H. Grennberg, J.-E. Bäckvall, *J. Am. Chem. Soc.* **1994**, *116*, 3631−3632.

[20] [20a] B. Crociani, F. Di Bianca, A. Giovenco, T. Boschi, *Inorg. Chim. Acta* **1987**, *127*, 169−182. [20b] B. Crociani, S. Antonaroli, M. Paci, F. Di Bianca, L. Canovese, *Organometallics* **1997**, *16*, 384−391.

[21] A. Gogoll, H. Grennberg, A. Axén, *Organometallics* **1997**, *16*, 1167−1178.

 © 2005 Wiley-VCH Verlag GmbH & Co. KGaA, Weinheim

[22] Y. Takao, T. Takeda, J. Watanabe, J. Setsune, *Organometallics* **1999**, *18*, 2936−2938.
[23] J. Elguero, A. Fruchier, A. de la Hoz, F. A. Jalón, B. R. Manzano, A. Otero, F. Gómez-de la Torre, *Chem. Ber.* **1996**, *129*, 589−594.
[24] F. A. Jalón, B. R. Manzano, A. Otero, M. C. Rodríguez, *J. Organomet. Chem.* **1995**, *494*, 179−185.
[25] F. Gómez-de la Torre, A. de la Hoz, F. A. Jalón, B. R. Manzano, A. Otero, A. M. Rodríguez, M. C. Rodríguez-Pérez, A. Echevarría, J. Elguero, *Inorg. Chem.* **1998**, *37*, 6606−6614.
[26] F. Gómez-de la Torre, A. de la Hoz, F. A. Jalón, B. R. Manzano, A. M. Rodríguez, J. Elguero, M. Martínez-Ripoll, *Inorg. Chem.* **2000**, *39*, 1152−1162.
[27] N. Arroyo, F. Gómez-de la Torre, F. A. Jalón, B. R. Manzano, B. Moreno-Lara, A. M. Rodríguez, *J. Organomet. Chem.* **2000**, *603*, 174−184.
[28] M. C. Carrión, A. Díaz, A. Guerrero, F. A. Jalón, B. R. Manzano, A. Rodríguez, R. L. Paul, J. C. Jeffery, *J. Organomet. Chem.* **2002**, *650*, 210−222.
[29] S. Hansson, P-O. Norrby, M. P. T. Sjögren, B. Åkermark, M. E. Cucciolito, F. Giordano, A. Vitagliano, *Organometallics* **1993**, *12*, 4940−4948.
[30] J. Sprinz, M. Kiefer, G. Helmchen, M. Reggelin, G. Huttner, O. Walter, L. Zsolnai, *Tetrahedron Let.* **1994**, *35*, 1523−1526.
[31] [31a] J. G. P. Delis, J. H. Groeen, K. Vrieze, P. W. N. M. van Leeuwen, N. Veldman, A. L. Spek, *Organometallics* **1997**, *16*, 551−562. [31b] L. Canovese, F. Visentin, P. Uguagliati, G. Chessa, V. Lucchini, G. Bandoli, *Inorg. Chim. Acta* **1998**, *275/276*, 385−394.
[32] R. J. van Haaren, K. Goubitz, J. Fraanje, G. P. F. Van Strijdonck, H. Oevering, B. Coussens, J. N. H. Reek, P. C. J. Kamer, P. W. N. M. van Leeuwen, *Inorg. Chem.* **2001**, *40*, 3363−3372.
[33] J. W. Faller, H. L. Stokes-Huby, M. A. Albrizzio, *Helv. Chim. Acta* **2001**, *84*, 3031−3042.
[34] M. A. Pericàs, C. Puigjaner, A. Riera, A. Vidal-Ferran, M. Gómez, F. Jiménez, G. Muller, M. Rocamora, *Chem. Eur. J.* **2002**, *8*, 4164−4178.
[35] A. M. Guerrero, F. A. Jalón, B. R. Manzano, R. M. Claramunt, M. D. Santa María, C. Escolástico, J. Elguero, A. M. Rodríguez, M. A. Maestro, J. Mahía, *Eur. J. Inorg. Chem.* **2002**, 3178−3189.
[36] J. Catalán, J.-L. M. Abboud, J. Elguero, *Adv. Heterocycl. Chem.* **1987**, *41* 187−274.
[37] J. Elguero, A. Guerrero, F. Gómez de la Torre, A. de la Hoz, F. A. Jalón, B. R. Manzano, A. Rodríguez, *New. J. Chem.* **2001**, *25*, 1050−1060.
[38] [38a] L. A. Oro, M. Esteban, R. M. Claramunt, J. Elguero, C. Foces-Foces, F. H. Cano, *J. Organomet. Chem.* **1984**, *276*, 79−97. [38b] M. A. Esteruelas, L. A. Oro, M. C. Apreda, C. Foces-Foces, F. H. Cano, R. M. Claramunt, C. López, J. Elguero, M. Begtrup, *J. Organomet. Chem.* **1988**, *344*, 93−108.
[39] [39a] M. Fajardo, A. de la Hoz, E. Díez-Barra, F. A. Jalón, A. Otero, A. Rodríguez, J. Tejeda, D. Belletti, M. Lanfranchi, M. A. Pellinghelli, *J. Chem. Soc., Dalton Trans.* **1993**, 1935−1939. [39b] F. A. Jalón, B. R. Manzano, A. Otero, M. C. Rodríguez-Pérez, *J. Organomet. Chem.* **1995**, *494*, 179−185.
[40] M. Brookhart, B. Grant, A. F. Volpe Jr., *Organometallics* **1992**, *11*, 3920−3922.
[41] J. Sandström, *Dynamic NMR Spectroscopy*, Academic Press, London, **1982**.
[42] W. T. Dent, R. Long, G. Wilkinson, *J. Chem. Soc.* **1964**, 1585−1588.

Received May 19, 2004
Early View Article
Published Online November 10, 2004

 © 2005 Wiley-VCH Verlag GmbH & Co. KGaA, Weinheim

Synthesis, Structure, and Photophysical and Electrochemical Properties of Cyclometallated Iridium(III) Complexes with Phenylated Bipyridine Ligands

Marc Lepeltier,[a] Terence Kwok-Ming Lee,[b] Kenneth Kam-Wing Lo,*[b] Loic Toupet,[c] Hubert Le Bozec,[a] and Véronique Guerchais*[a]

Dedicated to Professor David Carillo on the occasion of his 65th birthday

Keywords: Electrochemistry / Iridium / N ligands / Photochemistry

A series of cationic diiminoiridium(III) complexes [Ir(ppy-*N*,*C*)$_2$(L-*N*,*N*)](PF$_6$) has been prepared [Hppy = 2-phenylpyridine; L = 4,4′-*t*Bu$_2$dpbpy (**1**), 4,4′-Me$_2$dpbpy (**2**), 4,4′-Me$_2$pbpy (**3**), 4,4′-Me$_2$bpy (**4**)] and their photophysical and electrochemical properties studied. X-ray diffraction studies of complex **1** reveal a dihedral angle of about 33° between the pyridine rings, and that the two phenyl groups are also tilted with respect to the adjacent pyridine rings. All the complexes exhibit moderately intense and long-lived emission. The origin of the emission is tentatively assigned to a triplet metal-to-ligand charge-transfer ^{3}MLCT [dπ(Ir) → π*(diimine)] excited state, although the possibility of a triplet σ-bond-to-ligand charge transfer ^{3}SBLCT [σ(Ir–C) → π*(diimine)] cannot be excluded. The luminescence properties of the complexes are dependent on the substituents on the diimine ligands. Selective *N*-methylation of the diimine ligands has been achieved and their *N*,*C*-coordination to the Ir centre has been attempted.
(© Wiley-VCH Verlag GmbH & Co. KGaA, 69451 Weinheim, Germany, 2005)

Introduction

Cyclometallated polypyridineiridium(III) complexes have attracted a great deal of interest due to their photophysical properties.[1−8] These systems exhibit luminescence emitted predominantly from triplet MLCT excited states with high quantum yields. Another interesting feature of these compounds is the possibility to tune the emission energy by simply modifying the cyclometallating and/or polypyridine ligands. One class of compounds that has been particularly well investigated for their photophysical properties and their use as dopants in organic light-emitting diode (OLED) devices are homoleptic neutral tris(cyclometallated) Ir^{III} complexes and related complexes.[2−4] The design of cationic cyclometalled Ir^{III} complexes [Ir(ppy-*N*,*C*)$_2$(bpy-*N*,*N*)]$^+$ (where bpy is 2,2′-bipyridine and Hppy is 2-phenylpyridine) has also been reported and their use as biological labelling reagents has been described recently.[5−8] A wide range of substituted 2,2′-bipyridines are now available, and, in particular, aromatic substituents can be introduced in the 6- and 6′-positions.[9,10] Such ligands are particularly attractive since they could adopt both *N*,*N* and *N*,*C* coordination. The latter coordination mode, involving orthometallation of the aryl group, requires prior *N*-protection of one pyridine ring in order to avoid the more facile *N*,*N*-coordination. It is anticipated that sequential *N*,*C*-coordination would allow access to polymetallic systems. We report herein the preparation, molecular structure, and photophysical and electrochemical properties of a series of cyclometallated diiminoiridium(III) complexes [Ir(ppy-*N*,*C*)$_2$(L-*N*,*N*)](PF$_6$) containing phenyl, methyl and/or *tert*-butyl substituents at various locations of the diimine ligands L. The effects of these different substituents on the luminescence properties of the complexes are discussed. We also describe here the selective *N*-methylation reactions of these ligands and attempts to coordinate them in an *N*,*C*-mode to the Ir centre.

[a] Institut de Chimie de Rennes, UMR CNRS-Université de Rennes 1 6509, "Organométalliques et Catalyse"
Campus de Beaulieu, 35042 Rennes Cedex, France
E-mail: veronique.guerchais@univ-rennes1.fr
[b] Department of Biology and Chemistry,
City University of Hong Kong,
Tat Chee Avenue, Kowloon, Hong Kong, P. R. China
[c] Groupe Matière Condensée, UMR CNRS-Université de Rennes 1 6626, Campus de Beaulieu,
35042 Rennes Cedex, France

Results and Discussion

Synthesis and Characterization

The phenylated bipyridine ligands were prepared by classical procedures.[9,10] The phenylation reaction of 4,4′-dimethyl-2,2′-bipyridine (Me$_2$bpy) affords a mixture of monophenylated (Me$_2$pbpy) and diphenylated (Me$_2$dpbpy)

 © 2005 Wiley-VCH Verlag GmbH & Co. KGaA, Weinheim DOI: 10.1002/ejic.200400418

derivatives. They are readily separated by column chromatography and were isolated in 46% and 25% yield, respectively. Diphenylation of 4,4′-di-*tert*-butyl-2,2′-bipyridine (*t*Bu_2bpy) is similar to that of Me_2bpy.[10] The reaction is performed in refluxing THF, followed by hydrolysis and oxidation by manganese dioxide. After chromatographic purification, the diphenylated derivative *t*Bu_2dpbpy was isolated as a white solid in 84% yield; formation of the monophenylated product was not observed in this case.

The corresponding complexes [Ir(ppy-*N*,*C*)$_2$(L-*N*,*N*)](PF_6) [L = 4,4′-*t*Bu_2dpbpy (**1**), 4,4′-Me_2dpbpy (**2**), 4,4′-Me_2pbpy (**3**)] were then obtained from the reaction of the *ortho*-metallated dimer [Ir(ppy-*N*,*C*)$_2$(μ-Cl)]$_2$ and the appropriate diimine ligand L (Scheme 1). For comparison, the non-phenylated complex [Ir(ppy-*N*,*C*)$_2$(Me_2bpy-*N*,*N*)](PF_6) (**4**) was also prepared. The chloro-bridged dimer was synthesized following the procedure of Nonoyoma.[11] The coordination reactions of the diimine ligands to the Ir centre were performed in refluxing 1,2-dichloroethane; the use of methanol was avoided due to a protonation side-reaction of the diimine ligand. The presence of a silver salt is required, otherwise the starting material is recovered. All the complexes were crystallized from CH_2Cl_2/Et_2O and isolated as yellow crystals (yield: 70−80%). Complexes **1**−**4** were characterized by ^{1}H and ^{13}C NMR spectroscopy, and assignments were made on the basis of HMBC, HMQC, and COSY spectra. The heterocycles of the ppy ligands remain in a *trans* configuration as in the precursor dimer. Complexes **1**−**4** were formed as one isomer of low symmetry, as indicated by the NMR spectroscopic data. No *N*,*C*-chelation was thus observed under the reaction conditions used.

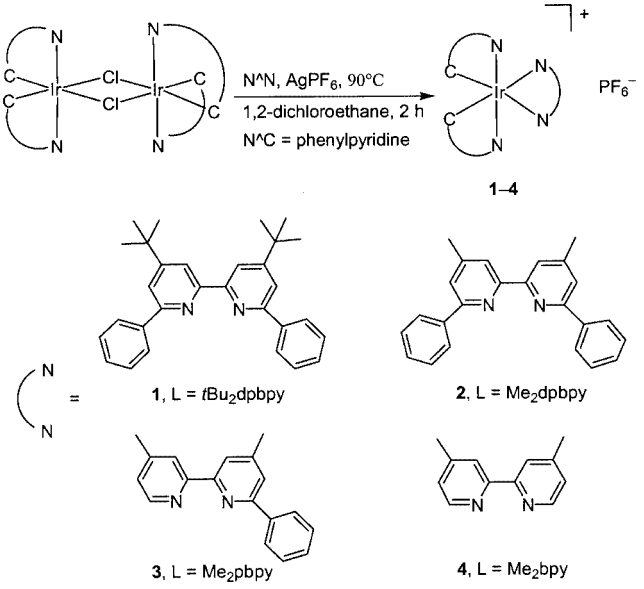

Scheme 1

The ^{1}H NMR spectrum of complex **3** shows two different sets of signals for the phenylpyridine ligands. In addition, the two N-heterocycles of the unsymmetric Me_2pbpy ligand are clearly distinguishable.

X-ray Crystal Structure of Complex 1

Crystals were obtained by slow diffusion of diethyl ether into a CH_2Cl_2 solution of **1**. The ORTEP diagram is depicted in Figure 1. Selected bond lengths and angles are listed in Table 1. Complex **1** (containing 1.5 H_2O molecules) exhibits a pseudo-octahedral geometry around the iridium centre, the two Ir−C bonds being in a *cis* position as in the precursor dimer. The Ir−N distances of the diimine ligand are similar to those of related complexes, and they are in accordance with a *trans* influence of the *C*-cyclometallating ligands. The slight lengthening of the Ir−N bond is similar to that observed for related cationic complexes.[5d,5g,6,12] The bite angle of the *t*Bu_2dpbpy ligand is similar to that of [Ir(ppy-*N*,*C*)$_2$(4′-R-6′-phenyl-2,2′-bipyridine-*N*,*N*)](PF_6) (R = $OCOC_6H_4OCOC_6H_4OC_6H_{13}$) [75.2(4)°].[5g] The bipyridine rings are not coplanar (dihedral angle 32.97°) and the 6,6′-diphenyl groups are also tilted with respect to the adjacent pyridine rings (dihedral angles 45.27° and 93.85°). This is probably due to steric reasons. Moreover, the phenyl rings are almost coplanar with the phenyl groups of the ppy

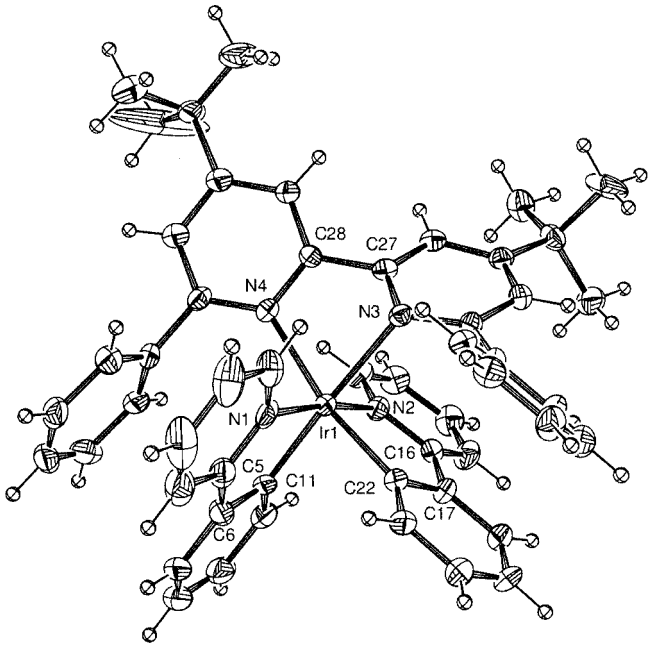

Figure 1. ORTEP representation of complex **1**; the unit cell contains 1.5 molecules of H_2O, which have been omitted for clarity, as has the PF_6^- counteranion

Table 1. Selected bond lengths [Å] and angles [°] for complex **1**

Ir−N(1)	2.057(6)	Ir−C(11)	1.997(6)
Ir−N(2)	2.056(5)	Ir−C(22)	2.014(6)
Ir−N(3)	2.262(5)	C(22)−Ir−N(1)	95.5(2)
Ir−N(4)	2.217(5)	C(22)−Ir−N(2)	80.7(2)
N(1)−Ir−N(4)	90.53(19)	C(22)−Ir−N(3)	93.7(2)
N(1)−Ir−N(3)	104.3(2)	C(22)−Ir−N(4)	168.6(2)
N(3)−Ir−N(4)	75.44(18)	C(11)−Ir−N(1)	80.5(3)
N(2)−Ir−N(4)	94.22(19)	C(11)−Ir−N(2)	93.4(3)
N(2)−Ir−N(3)	81.69(19)	C(11)−Ir−N(3)	175.0(3)
C(11)−Ir−C(22)	84.6(2)	C(11)−Ir−N(4)	168.6(2)

 © 2005 Wiley-VCH Verlag GmbH & Co. KGaA, Weinheim

ligands. This feature has been previously reported for the above-mentioned monophenylated derivative.[5g]

Electronic Absorption Spectroscopy

The electronic absorption spectral data for complexes **1**−**4** in CH_2Cl_2 are summarized in Table 2. All complexes display intense absorption bands in the ultraviolet region at about 250−300 nm, which are assigned to spin-allowed intraligand ^{1}IL [$\pi \rightarrow \pi^*$(ppy and diimine)] transitions. In the visible region, weak absorption bands at about 345−445 nm are observed; these bands are attributed to spin-allowed ^{1}MLCT [$d\pi(Ir) \rightarrow \pi^*$(ppy and diimine)] transitions. In addition, weaker absorption bands and tailing at lower energy, corresponding to spin-forbidden ^{3}MLCT [$d\pi(Ir) \rightarrow \pi^*$(ppy and diimine)] transitions, are also observed. The absorption characteristics of these complexes are similar to those of related cyclometallated polypyridineiridium complexes.[1,5−8]

Table 2. Electronic absorption spectral data for complexes **1**−**4** at 298 K[a]

Complex	λ_{abs} [nm] (ε [M^{-1} cm^{-1}])
1	260 (49000), 300 (32000), 345sh (12000), 385sh (5200), 445sh (1600), 480sh (1000)
2	260 (48000), 300sh (29000), 345sh (12000), 385sh (5600), 445sh (1600), 475sh (900)
3	260 (32000), 300sh (21000), 335sh (9400), 370sh (6300), 410sh (3700), 465sh (740)
4	260 (42000), 300sh (21000), 345sh (12000), 380 (6900), 420 (4100), 470 (1000)

[a] Data for deoxygenated CH_2Cl_2 solutions.

Luminescence Properties

Upon photoexcitation, complexes **1**−**4** display moderately intense and long-lived orange-yellow to greenish-yellow emission under ambient conditions and in low-temperature glass. The emission spectra of complexes **1**−**4** in CH_3CN at 298 K and alcohol glass at 77 K are shown in Figures 2−5. The photophysical data are listed in Table 3. The observed emission lifetimes in the microsecond and sub-microsecond time scales indicate the phosphorescent nature of the emission. The emission maxima occur at higher energy in less-polar CH_2Cl_2 than in more-polar CH_3CN. This observation is commonly made in other luminescent cyclometallated diiminoiridium systems.[1,5−8] In view of the low-lying π^*-orbitals of the diimine ligands, the emission is assigned to an emissive state of predominately ^{3}MLCT [$d\pi(Ir) \rightarrow \pi^*$(diimine)] character. However, the low reversibility of the oxidation waves of the complexes (see below) suggests the involvement of covalent Ir−C bond character in the HOMOs of the complexes. The possibility of a triplet σ-bond-to-ligand ^{3}SBLCT [$\sigma(Ir-C) \rightarrow \pi^*$(diimine)] emissive state thus cannot be totally ignored.[5a,7b,7c]

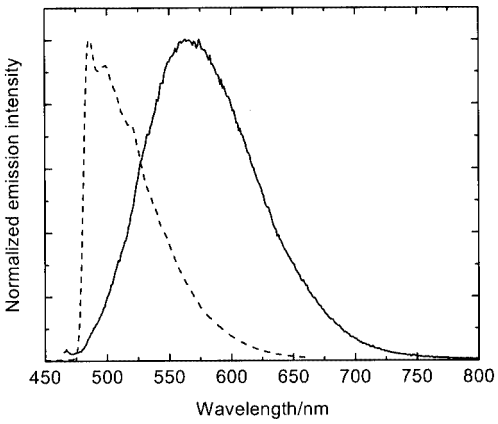

Figure 2. Emission spectra of complex **1** in CH_3CN at 298 K (− − −) and EtOH/MeOH (4:1, v/v) at 77 K (------)

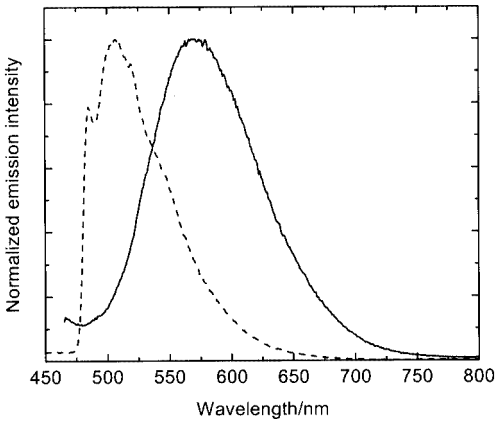

Figure 3. Emission spectra of complex **2** in CH_3CN at 298 K (− − −) and EtOH/MeOH (4:1, v/v) at 77 K (------)

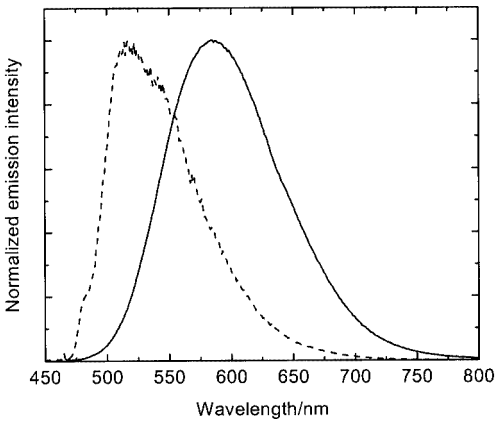

Figure 4. Emission spectra of complex **3** in CH_3CN at 298 K (− − −) and EtOH/MeOH (4:1, v/v) at 77 K (------)

Nevertheless, more detailed studies such as MO calculations are required to obtain a clearer picture of the electronic structures and excited-state nature of the complexes.

 © 2005 Wiley-VCH Verlag GmbH & Co. KGaA, Weinheim

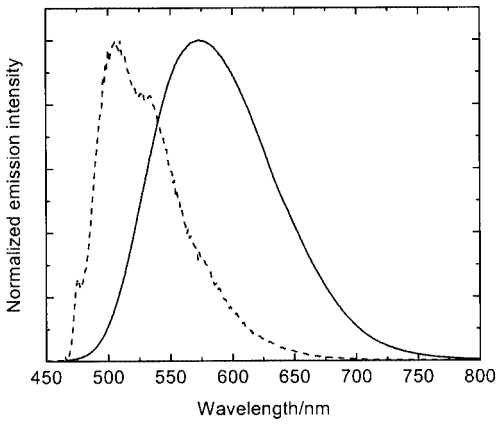

Figure 5. Emission spectra of complex **4** in CH_3CN at 298 K (– – –) and EtOH/MeOH (4:1, v/v) at 77 K (------)

The assignment of a ^{3}MLCT/^{3}SBLCT excited state is supported by the observation that the dimethyl complex **4** (λ_{em} = 573 nm in CH_3CN at 298 K) emits at noticeably higher energy than the non-substituted bipyridine analogue $[Ir(ppy\text{-}N,C)_2(bpy\text{-}N,N)]^+$ (λ_{em} = 606 nm).[1d] It is likely that the dimethyl substituents of complex **4** destablize the π*-orbitals of the Me_2bpy ligand, and thereby increase the ^{3}MLCT emission energy. The observation that the dimethylphenyl complex **3** (λ_{em} = 585 nm in CH_3CN at 298 K) emits at lower energy than complex **4** suggests that the phenyl ring at the 6-position of the bipyridine ligand of complex **3** lowers the energy level of the π*-orbitals due to electronic effects. Interestingly, the emission of the dimethyldiphenyl complex **2** occurs at almost the same energy as the dimethyl complex **4**, even though the former has two additional phenyl rings. The presence of two phenyl substituents in the 6- and 6′-positions does not lead to a bathochromic shift as would be expected for a more extended π-conjugated diimine ligand. A possible explanation is that in complex **2**, due to steric reasons, the two phenyl rings are not coplanar with the bpy moiety, and the degree of coplanarity of the bipyridine rings is also substantially reduced, as observed in the solid-state structure of complex **1** (see above). Thus, the lack of extensive π-conjugation raises the π*-level, and the ^{3}MLCT/^{3}SBLCT emission occurs at higher energy than expected. On the other hand, the di-*tert*-butyldiphenyl complex **1** (λ_{em} = 566 nm) emits at slightly higher energy than complex **2** (λ_{em} = 571 nm), probably due to the stronger electron-donating properties of the two *tert*-butyl substituents on the bipyridine ligand.

It is noteworthy that complex **1** (λ_{em} = 566 nm) emits at significantly higher energy than its phenyl-free counterpart $[Ir(ppy\text{-}C,N)_2(t\text{Bu}_2bpy\text{-}N,N)]^+$ (581 nm in CH_3CN).[8] This observation is in line with the crystal structure of complex **1**, which reveals that the two additional phenyl rings lower the π-conjugation between the two pyridine rings, and thereby destabilize the π*-orbitals of the diimine ligand, and increase the ^{3}MLCT/^{3}SBLCT emissive energy.

Upon cooling to 77 K, all four complexes display structural spectra and hypsochromic shifts in their emission maxima. These findings are commonly observed in other related luminescent cyclometallated polypyridineiridium complexes.[1,5–8] The emission decay is strictly single-exponential, with a lifetime of about 4–5 μs. In general, the emission is tentatively assigned to an excited state of predominantly ^{3}MLCT/^{3}SBLCT character.

Electrochemical Properties

The electrochemical data for complexes **1**–**4** are reported in Table 4. The cyclic voltammograms of the complexes in CH_3CN solution exhibit a reversible reduction at about −1.90 V vs. Fc/Fc^+. These waves can be assigned to the reduction of the bipyridine ligand as the cyclometallating ppy ligand is known to be reduced at much lower potential.[5d,6d] The cyclic voltammograms also exhibit an irreversible oxidation wave at a potential between 0.82 and 0.87 V vs. Fc/Fc^+. According to previous electrochemical studies on related complexes, these waves are attributed to metal-centered Ir^{III}/Ir^{IV} oxidation processes.[5a,7b,7c] The irreversible nature of this process suggests that the HOMOs may involve some covalent σ(Ir–C) character.[5a,7b,7c] By contrast, a quasi-reversible oxidation is observed for complex **4** containing the non-phenylated 4,4′-dimethyl-2,2′-bipyridine ligand. It is noteworthy that the same reversible oxi-

Table 3. Photophysical data for complexes **1**–**4**

Complex[a]	Medium (T [K])	λ_{em} [nm]	τ_o [μs]	Φ_{em}	k_r [s^{-1}]	k_{nr} [s^{-1}]
1	CH_3CN (298)	566	0.69	0.0038	3.9×10^4	7.9×10^5
	CH_2Cl_2 (298)	555	0.52	0.0070	9.0×10^4	1.1×10^6
	glass (77)[b]	485, 499, 520 sh, 537 sh	4.44			
2	CH_3CN (298)	571	0.12	0.0076	6.3×10^4	8.3×10^6
	CH_2Cl_2 (298)	564	0.15	0.012	8.0×10^4	6.6×10^6
	glass (77)[b]	485, 507, 520 sh 547 sh	4.48			
3	CH_3CN (298)	585	0.18	0.039	2.2×10^5	5.3×10^6
	CH_2Cl_2 (298)	576	0.32	0.12	3.8×10^5	2.8×10^6
	glass (77)[b]	482 sh, 517, 547 sh	3.95	–	–	–
4	CH_3CN (298)	573	0.49	0.16	3.3×10^5	1.7×10^6
	CH_2Cl_2 (298)	563	0.78	0.31	4.0×10^5	8.8×10^5
	glass (77)[b]	476 sh, 506, 534 sh, 580 sh	4.83			

[a] Data for deoxygenated solutions. [b] EtOH/MeOH (4:1, v/v).

 © 2005 Wiley-VCH Verlag GmbH & Co. KGaA, Weinheim

Table 4. Electrochemical data for complexes **1**−**4** in CH_3CN (0.1 M nBu_4NPF_6, Pt electrode, scan rate 100 mV·s^{-1})

Complex	E_p [V] vs. Fc/Fc^+	$E_{1/2}$ [V] vs. Fc/Fc^+
1	0.83[a]	−1.91[b]
2	0.82[a]	−1.8[b]
3	0.87[a]	−1.89[b]
4	0.86[c]	−1.90[b]

[a] Irreversible process. [b] Quasi-reversible wave. [c] Reversible wave.

dation process has recently been reported for the related complex $[Ir(ppy\text{-}N,C)_2(t\text{Bu}_2\text{bpy-}N,N)]^+$.[8]

N-Alkylation Reactions and Attempts to Enforce N,C-Coordination of the Diimine Ligands

N-Protection by methylation of one pyridine ring of the above diimine ligands was performed in order to avoid *N*,*N*-coordination. The methylation reactions were performed with either MeOTf or $(Me_3O)(BF_4)$ as alkylating reagents in a chlorinated solvent. In the case of $t\text{Bu}_2$dpbpy, the reaction gives the dialkylated product. The desired monoprotected cations were obtained in a pure form after recrystallisation from a CH_2Cl_2/diethyl ether mixture as a white powder in moderate to good yield (36−56%). It is noteworthy that the monophenylated derivative Me_2pbpy undergoes selective methylation at the non-phenylated pyridine ring, probably due to steric reasons (Scheme 2). Thus, the phenylpyridine fragment of this compound is accessible for *N*,*C*-coordination. In addition, the *N*-methyl group can be readily removed in the presence of DABCO. A second *N*,*C*-coordination could be subsequently envisaged in the case of the diphenylated derivatives.

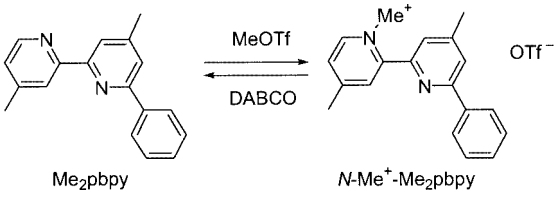

Scheme 2

It is noteworthy that the coordination of pyridinium ligands has not been reported for Ir so far, whereas examples are known for Ru, Rh, Pt and Pd complexes.[13,14] The classical procedures reported for the preparation of *fac*-tris-(cyclometallated) complexes have been applied for the cationic ligands.[2] The dimer $[Ir(ppy\text{-}N,C)_2(\mu\text{-Cl})]_2$ and [*N*-Me^+-Me_2pbpy](OTf) were refluxed at 200°C in glycerol in the presence of Na_2CO_3 (Scheme 3). However, this route

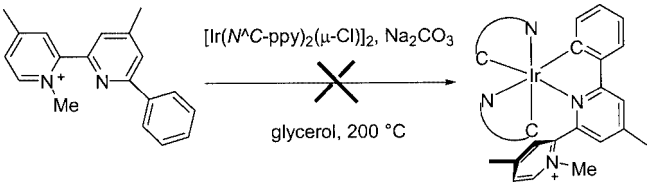

Scheme 3

was found to be inefficient, and the precursor dimer was partially recovered. Moreover, syntheses starting directly from $IrCl_3{\cdot}nH_2O$ to prepare the homoleptic complexes were also unsuccessful whatever the nature of the ligand. The fact that the bipyridine ligand may adopt a *transoid* conformation could induce a steric hindrance due to the presence of a substituent in the 4-position, especially in the case of the *t*Bu-substituted derivative.

Concluding Remarks

In conclusion, we have isolated a new series of luminescent cyclometallated diiminoiridium(III) complexes containing substituted bipyridine ligands. Upon photoexcitation, all the complexes are emissive in fluid solutions under ambient conditions and in low-temperature glass. The emission originates from an excited state of ^{3}MLCT [$d\pi(Ir) \rightarrow \pi^*$(diimine)] character, perhaps with some ^{3}SBLCT [$\sigma(Ir-C) \rightarrow \pi^*$(diimine)] character. Interestingly, instead of lowering the emission energy, addition of two phenyl substituents at the 6- and 6′-positions of the bipyridine ligand increases the emission energy of the complex. It is likely that the presence of the phenyl rings significantly lowers the degree of coplanarity of the bipyridine ligand, and thereby destabilizes the ^{3}MLCT emissive state. This is in line with the tilting of the two pyridine rings observed in the crystal structure of complex **1**. Our next target is to functionalize the 4,4′-dimethyl groups of the bipyridine ligand so that the complexes can be immobilized on a solid support. Related work is in progress.

Experimental Section

General Procedures: All manipulations were performed using Schlenk techniques under Ar. All solvents were dried and purified by standard procedures. All starting materials were used as received, MnO_2 was purchased from Merck. 6,6′-Diphenyl-2,2′-bipyridine (dpbpy), 6,6′-diphenyl-4,4′-dimethyl-2,2′-bipyridine (Me_2dpbpy) and 4,4′-di-*tert*-butyl-6,6′-diphenyl-2,2′-bipyridine ($t\text{Bu}_2$dpbpy) were prepared according to literature methods.[9,10] NMR spectra were recorded with Bruker DPX-200, AV 300 or AV 500 MHz spectrometers. ^{1}H and ^{13}C NMR chemical shifts are given versus $SiMe_4$ and were determined by reference to residual ^{1}H and ^{13}C solvent signals. Attribution of carbon atoms was based on HMBC, HMQC and COSY experiments. UV/Vis absorption spectra were recorded using a UVIKON 9413 spectrophotometer, and emission spectra were measured with a PTI C 60 fluorescence spectrophotometer. High-resolution mass spectra (HRMS) were performed with an MS/MS ZABSpec TOF at the CRMPO (Centre de Mesures Physiques de l'Ouest) in Rennes. Elemental analyses were performed by the Service central d'analyse du CNRS at Vernaison. Cyclic voltammograms were recorded using a PAR model 273 Autolab. The working electrode was polished Pt, the counter-electrode was a Pt wire, and a saturated calomel electrode (SCE) was used as the reference electrode. The Cp_2Fe/Cp_2Fe^+ redox couple was used as a secondary internal reference. Luminescence quantum yields were measured by the optically dilute method[15] using an aerated aqueous solution of $[Ru(bpy)_3]Cl_2$ (Φ_{em} = 0.028)[16] as the standard solution. Low-temperature (77 K) glass photophysical measurements were performed with the sample loaded in a quartz

 © 2005 Wiley-VCH Verlag GmbH & Co. KGaA, Weinheim

tube inside a quartz-walled Dewar flask filled with liquid nitrogen. The excitation source for emission lifetime measurements was the 355 nm output (third harmonic) of a Quanta-Ray Q-switched GCR-150-10 pulsed Nd-YAG laser. Luminescence decay signals from a Hamamatsu R928 photomultiplier tube were converted into potential changes by a 50 Ω load resistor and then recorded with a Tektronix Model TDS 620A digital oscilloscope.

4,4′-Di-*tert*-butyl-6,6′-diphenyl-2,2′bipyridine (*t*Bu$_2$dpbpy): PhLi (11 mL, 20 mmol; 1.8 M, cyclohexane/diethyl ether) was added to a solution of 4,4′-di-*tert*-butyl-2,2′-bipyridine (1.34 g, 5 mmol) in 20 mL of THF. After stirring at room temperature for 30 min, the reaction medium was refluxed for 12 h. The reaction mixture was then hydrolysed at 0°C and the residue extracted with CH_2Cl_2 (3 × 150 mL). The organic phase was dried with $MgSO_4$ and MnO_2 (12.5 g, 144 mmol) was added. The reaction medium was stirred for 12 h and then filtered through Celite. Chromatography on silica gel (heptane/ethyl acetate, 95:5) afforded a white powder (1.34 g, 84%). ^{1}H NMR (200 MHz, $CDCl_3$): δ = 8.61 (d, ^4J = 1.8 Hz, 2 H, H$^{3/5}$-Py), 8.17 (m, 4 H, Ph *ortho*), 7.78 (d, ^4J = 1.8 Hz, 2 H, H$^{3/5}$-Py), 7.50 (m, 6 H, Ph *meta* and *para*), 1.47 (s, 18 H, *t*Bu) ppm. ^{13}C {^{1}H} NMR (75.4 MHz, $CDCl_3$): δ = 162.0 (C$^{2/6}$-Py), 156.9 (C$^{2/6}$-Py), 140.6 (C^4-Py), 129.2 (Ph), 128.8 (Ph), 127.6 (Ph), 127.0 (Ph), 118.0 (C$^{3/5}$-Py), 117.4 (C$^{3/5}$-Py), 35.7 (*t*Bu), 31.2 (*t*Bu). HRMS: *m*/*z* = 420.2563 [M]$^+$; calcd. for $C_{30}H_{32}N_2$ 420.25655. $C_{30}H_{32}N_2$ (420.6): calcd. C 85.67, H 7.67, N 6.66; found C 85.05, H 7.94, N 6.27.

4,4′-Dimethyl-6-phenyl-2,2′-bipyridine (Me$_2$pbpy): The monophenylated derivative 4,4′-dimethyl-6-phenyl-2,2′-bipyridine was obtained during the preparation of Me$_2$dpbpy.[9] Chromatography on silica gel using ethyl acetate as eluent gave pure Me$_2$pbpy as a white powder. Yield: 46%. ^{1}H NMR (200 MHz, CD_3COCD_3): δ = 8.51 (d, ^3J = 4.8 Hz, 1 H, H^6-Py), 8.49 (d, ^4J = 1.2 Hz, 1 H, H^3-Py), 8.22 (m, 3 H, H$^{3/5}$-Py* and Ph *ortho*), 7.79 (d, ^4J = 1.8 Hz, 1 H, H$^{3/5}$-Py*), 7.52 (m, 3 H, Ph), 7.22 (dd, ^3J = 4.8, ^4J = 1.2 Hz, 1 H, H^5-Py), 2.50 (s, 3 H, MePy*), 2.48 (s, 3 H, MePy) ppm; (Py* = Ph-Py). HRMS: *m*/*z* = 260.1328 [M]$^+$; calcd. for $C_{18}H_{16}N_2$ 260.13135. $C_{18}H_{16}N_2$ (260.3): calcd. C 83.04, H 6.19, N 10.76; found C 82.93, H 6.33, N 10.10.

Synthesis of [Ir(ppy-*N*,*C*)$_2$(L-*N*,*N*)](PF$_6$) (1−4): The chloride-bridged dimer [Ir(ppy-*N*,*C*)$_2$(μ-Cl)]$_2$ (0.1 mmol), the appropriate bipyridine derivative L (0.2 mmol), and $AgPF_6$ (0.2 mmol) were mixed in 1,2-dichloroethane (10 mL). The reaction mixture was refluxed under Ar for 2 h. The solution was then concentrated to dryness and the product was extracted with CH_2Cl_2 (3 × 5 mL). Crystallisation from a CH_2Cl_2/diethyl ether mixture gave a yellow-green powder.

[Ir(ppy-*N*,*C*)$_2$(*t*Bu$_2$dpbpy-*N*,*N*)](PF$_6$) (1): Yield 76%. ^{1}H NMR (300 MHz, CD_3COCD_3): δ = 8.65 (dd, ^3J = 5.8, ^4J = 1.4 Hz, 2 H, H^6-Py), 8.60 (d, ^4J = 2.0 Hz, 2 H, H^3-Py*), 7.96 (td, ^3J = 8.2, ^4J = 1.4 Hz, 2 H, H^4-Py), 7.86 (dd, ^3J = 8.2, ^4J = 1.5 Hz, 2 H, H^3-Py), 7.42 (d, ^4J = 2.0 Hz, 2 H, H^5-Py*), 7.26 (td, ^3J = 8.2, ^3J = 5.8, ^4J = 1.5 Hz, 2 H, H^5-Py), 7.21 (dd, ^3J = 7.7, ^4J = 1.2 Hz, 2 H, H^3-Ph), 6.99 (m, 2 H, Ph* *para*), 6.76 (m, 8 H, Ph* *meta* and *ortho*), 6.48 (td, ^3J = 7.7, ^4J = 0.8 Hz, 2 H, H^4-Ph), 6.13 (td, ^3J = 7.7, ^4J = 1.2 Hz, 2 H, H^5-Ph), 5.29 (dd, ^3J = 7.7, ^4J = 0.8 Hz, 2 H, H^6-Ph), 1.43 (s, 18 H, *t*Bu) ppm. ^{13}C {^{1}H} NMR (75.4 MHz, CD_3COCD_3): δ = 168.0 (C^2-Py), 163.9 (C^4-Py*, C^6-Py*), 160.1 (C^2-Py*), 150.8 (C^6-Py), 146.8 (C^1-Ph), 141.9 (C^2-Ph), 138.6 (Ph* *ipso*), 138.1 (C^4-Py), 130.8 (C^6-Ph), 129.1 (C^5-Ph), 128.0 (Ph* *para*), 127.4 (Ph* *ortho* and *meta*), 125.8 (C^5-Py*), 124.1 (C^3-Ph), 121.7 (C^5-Py, C^3-Py*), 120.5 (C^4-Ph), 119.1 (C^3-Py), 35.4 (*t*Bu), 29.4 (*t*Bu) ppm; Py* = Ph-Py. HRMS: *m*/*z* = 921.3510 [M]$^+$; calcd. for $C_{52}H_{48}N_4{}^{193}$Ir 921.3512.

[Ir(ppy-*N*,*C*)$_2$(Me$_2$dpbpy-*N*,*N*)](PF$_6$) (2): Yield 80%. ^{1}H NMR (300 MHz, CD_3COCD_3): δ = 8.61 (dd, ^3J = 5.8, ^4J = 0.6 Hz, 2 H, H^6-Py), 8.57 (d, ^4J = 1 Hz, 2 H, H^3-Py*), 7.95 (td, ^3J = 8.3, ^3J = 7.6, ^4J = 0.6 Hz, 2 H, H^4-Py), 7.85 (dd, ^3J = 7.6, ^4J = 1.5 Hz, 2 H, H^3-Py), 7.28 (td, ^3J = 8.3, ^3J = 5.8, ^4J = 1.5 Hz, 2 H, H^5-Py), 7.25 (d, ^4J = 1 Hz, 2 H, H^5-Py*), 7.19 (dd, ^3J = 7.8, ^4J = 1.3 Hz, 2 H, H^3-Ph), 6.98 (m, 2 H, Ph* *para*), 6.71 (m, 4 H, Ph* *ortho* and *meta*), 6.45 (td, ^3J = 7.8, ^4J = 0.7 Hz, 2 H, H^4-Ph), 6.11 (td, ^3J = 7.8, ^4J = 1.3 Hz, 2 H, H^5-Ph), 5.25 (dd, ^3J = 7.8, ^4J = 0.7 Hz, 2 H, H^6-Ph), 2.57 (s, 6 H, Me) ppm. ^{13}C {^{1}H} NMR (75.4 MHz, CD_3COCD_3): 168.1 (C^2-Py), 164.4 (C^6-Py*), 159.1 (C^2-Py*), 151.5 (C^4-Py*), 150.9 (C^6-Py), 147.2 (C^1-Ph), 141.9 (C^2-Ph), 138.6 (Ph* *ipso*), 138.0 (C^4-Py), 130.7 (C^6-Ph), 130.1 (C^5-Py*), 129.1 (C^5-Ph), 127.9 (Ph *para*), 127.4 (Ph* *ortho*/*meta*), 127.3 (Ph* *ortho*/*meta*), 125.2 (C^3-Py*), 123.9 (C^3-Ph), 122.1 (C^5-Py), 120.4 (C^4-Ph), 119.3 (C^3-Py). 20.9 (Me) ppm; Py* = Ph-Py. HRMS: *m*/*z* = 837.2574 [M]$^+$; calcd. for $C_{46}H_{36}N_4{}^{193}$Ir 837.2572. $C_{46}H_{36}F_6IrN_4P$ (982.0): calcd. C 56.26, H 3.70, N 5.71; found C 56.32, H 4.06, N 5.62.

[Ir(ppy-*N*,*C*)$_2$(Me$_2$pbpy-*N*,*N*)](PF$_6$) (3): Yield 80%. ^{1}H NMR (300 MHz, CD_3COCD_3): δ = 8.78 (s, 1 H, H^3-Py*), 8.75 (s, 1 H, H^3-Py), 8.09 (m, 2 H, H^3-PyA, H^3-PyB), 8.00 (m, 2 H, H$^{4/6}$-PyB), 7.91 (m, 2 H, H$^{4/6}$-PyA), 7.76 (d, ^3J = 5.7 Hz, 1 H, H^6-Py), 7.68 (dd, ^3J = 7.8, ^4J = 1.2 Hz, 1 H, H^3-PhA), 7.41 (m, 2 H, H^5-Py, H^5-Py*), 7.37 (dd, ^4J = 1.3, ^3J = 7.8 Hz, 1 H, H^3-PhB), 7.26 (td, ^3J = 5.9, ^3J = 7.8, ^4J = 1.4 Hz, 1 H, H^5-PyA), 7.19 (td, ^4J = 1.6, ^3J = 5.9, ^3J = 7.8 Hz, 1 H, H^5-PyB), 6.92 (m, ^4J = 1.2, ^3J = 7.8 Hz, 2H, H^4-PhA, Ph *para*), 6.78 (m, 3 H, H^5-PhA, Ph *meta*), 6.66 (m, 2 H, Ph *ortho*), 6.54 (td, ^3J = 7.6, ^4J = 1.2 Hz, 2 H, H^4-PhB), 6.33 (td, ^3J = 7.6, ^4J = 1.3 Hz, 1 H, H^5-PhB), 6.00 (dd, ^4J = 1.2, ^3J = 7.6 Hz, 1 H, H^6-PhA), 5.63 (dd, ^3J = 7.7, ^4J = 1.2 Hz, 1 H, H^6-PhB), 2.67 (s, 3 H, Me-Py*), 2.57 (s, 3 H, Me-Py) ppm. ^{13}C {^{1}H} NMR (75.4 MHz, CD_3COCD_3): 169.0 (C^2-PyB), 167.2 (C^2-PyA), 164.9 (C^6-Py*), 156.9 (C^2-Py), 156.7 (C^2-Py*), 152.0 (C^4-Py*), 151.7 (C^4-Py, C^1-PhB), 149.8 (C^6-PyA), 149.3 (C^6-PyB, C^6-Py), 147.3 (C^1-PhA), 143.4 (C^2-PhA), 143.2 (C^2-PyB), 138.5 (C^4-PyA), 138.3 (Ph *ipso*), 138.2 (C^4-PyB), 131.4 (C^6-PhB), 130.5 (C^5-Py*), 130.3 (C^5-PhA), 130.2 (C^6-PhA), 129.0 (C^5-PyB), 128.6 (Ph *para*), 128.4 (C^5-Py), 127.6 (Ph *meta*), 127.4 (Ph *ortho*), 125.9 (C^3-Py), 124.6 (C^3-Py*), 124.5 (C^3-PhA), 124.4 (C^3-PhB), 123.6 (C^5-PyA), 122.5 (C^5-PyB), 120.2 (C^4-PhB), 119.9 (C^3-PyB), 119.7 (C^3-PyA), 20.4 (Me-Py), 20.1 (Me-Py*) ppm; Py* = Ph-Py. HRMS: *m*/*z* = 761.2268 [M]$^+$; calcd. for $C_{40}H_{32}N_4{}^{193}$Ir 761.2259.

[Ir(ppy-*N*,*C*)$_2$(Me$_2$bpy-*N*,*N*)](PF$_6$) (4): Yield 80%. ^{1}H NMR (300 MHz, CD_3COCD_3): δ = 8.74 (s, 2 H, H^3-Py*), 8.27 (d, ^3J = 8.1 Hz, 2 H, H^3-Py*), 7.97 (m, 4 H, H^3-Ph, H^4-Py), 7.86 (m, 4 H, H^6-Py*, H^6-Py), 7.50 (d, ^3J = 6.2 Hz, 2 H, H^5-Py*), 7.19 (td, ^3J = 5.8, ^3J = 7.2, ^4J = 1.1 Hz, 2 H, H^5-Py), 7.05 (td, ^3J = 7.4, ^4J = 0.8 Hz, 2 H, H^4-Ph), 6.94 (td, ^3J = 7.4, ^4J = 1.2 Hz, 2 H, H^5-Ph), 6.38 (dd, ^3J = 7.4, ^4J = 0.8 Hz, 2 H, H^6-Ph), 2.59 (s, 6 H, Me) ppm. ^{13}C {^{1}H} NMR (75.4 MHz, CD_3COCD_3): δ = 167.6 (C^2-Py), 155.7 (C^2-Py*), 152.1 (C^4-Py*), 149.8 (C^1-Ph), 149.7 (C^6-Py*), 149.2 (C^6-Py), 144.3 (C^2-Ph), 138.7 (C^4-Py), 131.0 (C^6-Ph), 130.4 (C^5-Ph), 129.1 (C^5-Py*), 125.6 (C^3-Py*), 125.1 (C^3-Ph), 123.7 (C^5-Py), 122.6 (C^4-Ph),120.0 (C^3-Py), 20.4 (Me) ppm. HRMS: *m*/*z* = 685.1939 [M]$^+$; calcd. for $C_{34}H_{28}N_4{}^{193}$Ir 685.1945. $C_{34}H_{28}F_6IrN_4P$ (829.8): calcd. C 49.50, H 3.68, N 6.64; found C 49.21, H 3.40, N 6.75.

4,4′-Di-*tert*-butyl-1-methyl-6,6′-diphenyl-2,2′-bipyridinium Tetrafluoroborate: [Me$_3$O][BF$_4$] (97 mg, 0.66 mmol) was added to a solu-

 © 2005 Wiley-VCH Verlag GmbH & Co. KGaA, Weinheim

tion of tBu$_2$dpbpy (250 mg, 0.60 mmol) in 10 mL of $ClCH_2CH_2Cl$. After refluxing for 15 h, the solution was concentrated to dryness. The residue was crystallized from a CH_2Cl_2/diethyl ether mixture in order to separate the *N,N*-dimethyl adduct and the diimine precursor. The product was isolated as a white powder by concentration of the resulting solution (112 mg, 36%). ^{1}H NMR (300 MHz, CD_3COCD_3): δ = 8.40 (d, ^4J = 2.3 Hz, 1 H, H^3-Py*), 8.28−8.22 (m, 4 H, H^5-Py*, H^5-Py, Ph *ortho*), 8.05 (d, ^4J = 1.4 Hz, 1 H, H^3-Py), 7.90−7.85 (m, 2 H, Ph* *ortho*), 7.76−7.66 (m, 3 H, Ph* *meta* and *para*), 7.59−7.50 (m, 3 H, Ph *meta* and *para*), 4.13 (s, 3 H, *N*-Me), 1.57 (s, 9 H, *t*Bu*), 1.50 (s, 9 H, *t*Bu) ppm. ^{13}C {^{1}H} NMR (75.4 MHz, CD_3COCD_3): δ = 170.6 (C^4-Py*), 163.4 (C^4-Py), 157.4 (C^6-Py), 156.9 (C^6-Py*), 154.7 (C^2-Py*), 151.3 (C^2-Py), 138.4 (Ph *ipso*), 133.3 (Ph* *ipso*), 131.2 (Ph*), 129.8 (Ph), 129.6 (Ph*), 129.4 (Ph*), 128.9 (Ph), 127.3 (Ph), 126.8 (C^5-Py*), 126.1 (C^3-Py*), 121.8 (C^3-Py), 119.1 (C^5-Py), 45.0 (*N*-Me), 36.6 (*t*Bu*), 35.4 (*t*Bu), 29.8 (*t*Bu), 29.2 (*t*Bu*) ppm; Py* = *N*-MePy. HRMS: *m*/*z* = 435.2784 [M]$^+$; calcd. for $C_{31}H_{35}N_2$ 435.2800.

1,4,4′-Trimethyl-6,6′-diphenyl-2,2′-bipyridinium Triflate: Me$_2$dpbpy (0.25 g, 0.74 mmol) was dissolved in 5 mL of $ClCH_2CH_2Cl$ in a Schlenk tube and MeOTf (83 μL, 0.74 mmol) was then added. The reaction mixture was stirred overnight and the solvent evaporated. The residue was extracted with 5 mL of CH_2Cl_2. Addition of diethyl ether precipitated the precursor compound; the monocation was then recovered as a white powder (176 mg, 48%) upon evaporation of the resulting solution. ^{1}H NMR (300 MHz, CD_3COCD_3): δ = 8.27 (d, ^4J = 1.9 Hz, 1 H, H^3-Py*), 8.22 (m, 2 H, Ph*), 8.13 (m, 2 H, H^5-Py, H^5-Py*), 7.88 (m, 3 H, Ph *ortho*, H^3-Py), 7.75 (m, 3 H, Ph *meta* and *para*), 7.55 (m, 3 H, Ph* *meta* and *para*), 4.22 (s, 3 H, *N*-Me), 2.85 (s, 3 H, Me*), 2.62 (s, 3 H, Me) ppm. ^{13}C {^{1}H} NMR (75.4 MHz, CD_3COCD_3): δ = 159.4 (C^4-Py*), 156.7 (C^6-Py*), 154.0 (C^2-Py*), 150.8 (C^2-Py, C^4-Py), 150.4 (C^6-Py), 138.9 (Ph* *ipso*), 133.0 (Ph *ipso*), 131.4 (Ph *para*), 130.3 (C^5-Py*), 129.8 (Ph*), 129.6 (C^3-Py*), 129.4 (Ph), 129.2 (Ph), 128.9 (Ph*), 127.1 (Ph*), 125.3 (C^3-Py), 122.8 (C^5-Py), 45.2 (*N*-Me), 20.9 (Me*), 20.4 (Me) ppm; Py* = *N*-MePy. HRMS: *m*/*z* = 351.1858 [M]$^+$; calcd. for $C_{25}H_{23}N_2$ 351.18612.

1,4,4′-Trimethyl-6′-phenyl-2,2′-bipyridinium Triflate: Me$_2$pbpy (0.10 g, 0.38 mmol) was dissolved in 5 mL of $CHCl_3$ in a Schlenk tube. The solution was cooled to −30°C and MeOTf (43 μL, 0.38 mmol) was then added. The reaction mixture was warmed up to room temperature and the solvent evaporated. The residue was washed with toluene (2 × 3 mL) and the residue extracted with 5 mL of $CHCl_3$. The solution was cooled to −20°C, filtered, and then concentrated to afford a white powder (90 mg, 56%). ^{1}H NMR (200 MHz, CD_3COCD_3): δ = 9.05 (d, ^3J = 6.6 Hz, 1 H, H^6-Py), 8.24 (d, ^4J = 1.8 Hz, 1 H, H^3-Py), 8.17 (d, ^4J = 1.6 Hz, 1 H, H$^{3/5}$-Py*), 8.16 (t, ^3J = 6.0 Hz, 2 H, Ph^3), 8.12 (dd, ^3J = 6.6, ^4J = 1.8 Hz, 1 H, H^5-Py), 7.78 (d, ^4J = 1.6 Hz, 1 H, H$^{3/5}$-Py*), 7.52 (td, ^3J = 6.0, ^4J = 1.8 Hz, 1 H, Ph^4), 7.49 (dd, ^3J = 6.0, ^4J = 1.8 Hz, 1 H, Ph^2), 4.52 (s, 3 H, *N*-Me), 2.80 (s, 3 H, MePy), 2.60 (s, 3 H, MePy*) ppm; Py* = *N*-MePy. HRMS: *m*/*z* = 275.1553 [M]$^+$; calcd. for $C_{19}H_{19}N_2$ 275.1548.

Deprotection of 1,4,4′-Trimethyl-6,6′-diphenyl-2,2′-bipyridinium Triflate: A solution of the salt (120 mg, 0.18 mmol) and DABCO (20 mg, 0.18 mmol) in 20 mL of DMF was refluxed for 2 h. After addition of 30 mL of water, the product was extracted with CH_2Cl_2 (2 × 20 mL). The organic phase was dried with $MgSO_4$. Evaporation of the solvent gave a white powder (50 mg, 82%) which was identified by ^{1}H NMR spectroscopy as Me$_2$dpbpy.

Attempts at *N,C*-Coordination: 1,4,4′-Trimethyl-6′-phenyl-2,2′-bipyridinium triflate (49 mg, 0.116 mmol) and Na_2CO_3 (49 mg, 0.46 mmol) were added to a solution of [Ir(ppy-*N,C*)$_2$(μ-Cl)]$_2$ (50 mg, 0.046 mmol) in 10 mL of glycerol. The reaction mixture was then heated to 200 °C for 24 h. Addition of water (10 mL) gave a brown precipitate, which was washed with diethyl ether (2 × 5 mL) and methanol (5 mL). ^{1}H NMR studies of the crude product showed the presence of the dimer precursor and an unidentified product.

Structural Determination of Complex 1: Single crystals for X-ray diffraction studies were grown by slow diffusion of diethyl ether into a CH_2Cl_2 solution of complex **1** at 20 °C. The samples were studied with a NONIUS Kappa CCD with graphite-monochromated Mo-K_α radiation. The data collection and refinement parameters are presented in Table 5. The structures were solved with SIR-97,[17a] which reveals the non-hydrogen atoms of the molecules. The whole structures were refined by full-matrix, least-squares techniques on F^2, with hydrogen atoms refined using the riding mode. Structures were solved by Patterson or direct methods. The structures were completed by subsequent difference Fourier techniques and refined by full-matrix least squares on F^2 (SHELXL-97) with initial isotropic parameters.[17] CCDC-225743 contains the supplementary crystallographic data for this paper. These data can be obtained free of charge at www.ccdc.cam.ac.uk/conts/retrieving.html [of from Cambridge Crystallographic Data Centre, 12 Union Road, Cambridge CB2 1EZ; Fax: + 44-1223-336-033; E-mail: deposit@ccdc.cam.ac.uk].

Table 5. Crystallographic data and refinement for complex **1**

Empirical formula	$C_{52}H_{51}F_6N_4IrO_{1.5}P$
Formula mass	1093.14
Crystal system	orthorhombic
Space group	$P2_12_12_1$
a [Å]	13.3214(2)
b [Å]	17.4083(3)
c [Å]	25.0454(3)
V [Å^3]	4936.1(1)
Z	4
$D_{calcd.}$ [g/cm^3]	1.471
F(000)	2196
λ(Mo-K_α) [Å]	0.71073
θ range [°]	2.48−27.50
No. of reflections collected	11257
No. of unique reflections	11257
No. of observed reflections [$I > 2\sigma(I)$]	9931
No. of parameters	596
Goodness of fit on F^2	1.023
Final R, Rw	0.044, 0.112
$\Delta\rho_{max,min}$ [e•Å^{-3}]	2.4, −1.126

Acknowledgments

M. L. thanks the Région Bretagne for a grant. We also thank Prof. Vivian W. W. Yam of the University of Hong Kong for access to equipment for photophysical measurements.

[1] [1a] R. J. Watts, *Inorg. Chem.* **1981**, *20*, 2302. [1b] S. Sprouse, K. A. King, P. J. Spellane, R. J. Watts, *J. Am. Chem. Soc.* **1984**, *106*, 6647. [1c] Y. Ohsawa, S. Sprouse, K. A. King, M. K. DeArmond, K. W. Hanck, R. J. Watts, *J. Phys. Chem.* **1987**, *91*, 1047. [1d] F. O. Garces, K. A. King, R. J. Watts, *Inorg. Chem.* **1988**, *27*, 3464. [1e] A. P. Wilde, R. J. Watts, *J. Phys. Chem.* **1991**, *95*, 622. [1f] A. P. Wilde, K. A. King, R. J. Watts, *J. Phys. Chem.* **1991**, *95*, 629. [1g] K. Dedeian, P. I. Djurovich, F. O. Garces, G. Carslon, R. J. Watts, *Inorg. Chem.* **1991**, *30*, 1685. [1h] P. I.

 © 2005 Wiley-VCH Verlag GmbH & Co. KGaA, Weinheim

Djurovich, R. J. Watts, *Inorg. Chem.* **1993**, *32*, 4681. [1i] B. Schmid, F. O. Garces, R. J. Watts, *Inorg. Chem.* **1994**, *33*, 9. [1j] M. G. Colombo, T. C. Brunold, T. Riedner, H. U. Güdel, M. Förtsch, H.-B. Bürgi, *Inorg. Chem.* **1994**, *33*, 545.

[2] [2a] S. Lamansky, P. Djurovich, D. Murphy, F. Abdel-Razzaq, H. E. Lee, C. Adachi, P. E. Burrows, S. R. Forrest, M. E. Thompson, *J. Am. Chem. Soc.* **2001**, *123*, 4304. [2b] S. Lamansky, P. Djurovich, D. Murphy, F. Abdel-Razzaq, R. Kwong, I. Tsyba, M. Bortz, B. Mui, R. Bau, M. E. Thompson, *Inorg. Chem.* **2001**, *40*, 1704. [2c] R. Gao, D. G. Ho, B. Hernandez, M. Selke, D. Murphy, P. L. Djurovich, *J. Am. Chem. Soc.* **2002**, *124*, 14828.

[3] [3a] M. A. Baldo, M. E. Thompson, S. R. Forrest, *Nature* **2000**, 403. [3b] T. Watanabe, K. Nakamura, S. Kawami, Y. Fukuda, T. Tsuji, T. Wakimoto, S. Miyaguchi, M. Yahiro, M. J. Yang, T. Tsutsui, *Synth. Met.* **2001**, *122*, 203. [3c] J. C. Ostrowski, M. R. Robinson, A. J. Heeger, G. C. Bazan, *Chem. Commun.* **2002**, 784.

[4] [4a] V. V. Grushin, N. Herron, D. D. LeCloux, W. J. Marshall, A. Petrov, Y. Wang, *Chem. Commun.* **2001**, 1494. [4b] H. Z. Xie, M. W. Liu, O. Y. Wang, X. H. Zhang, C. S. Lee, L. S. Hung, S. T. Lee, P. F. Teng, H. L. Kwong, H. Zhen, C. M. Che, *Adv. Mater.* **2001**, *13*, 1245. [4c] J.-P. Duan, P.-P. Sun, C.-H. Cheng, *Adv. Mater.* **2003**, *15*, 224. [4d] T. Tsuzuki, N. Shirasawa, T. Suzuki, S. Tokito, *Adv. Mater.* **2003**, *15*, 1455. [4e] I. R. Laskar, T.-M. Chen, *Chem. Mater.* **2004**, *16*, 111.

[5] [5a] S. Serroni, A. Juris, S. Campagna, M. Venturi, G. Denti, V. Balzani, *J. Am. Chem. Soc.* **1994**, *116*, 9086. [5b] G. Calogero, G. Giuffrida, S. Serroni, V. Ricevuto, S. Campagna, *Inorg. Chem.* **1995**, *34*, 541. [5c] A. Mamo, I. Stefio, M. F. Parisi, A. Credi, M. Venturi, C. Di Pietro, S. Campagna, *Inorg. Chem.* **1997**, *36*, 5947. [5d] F. Neve, A. Crispini, S. Campagna, S. Serroni, *Inorg. Chem.* **1999**, *38*, 2250. [5e] P. M. Griffiths, F. Loiseau, F. Puntoriero, S. Serroni, S. Campagna, *Chem. Commun.* **2000**, 2297. [5f] F. Neve, A. Crispini, F. Loiseau, S. Campagna, *J. Chem. Soc., Dalton Trans.* **2000**, 1399. [5g] F. Neve, A. Crispini, *Eur. J. Inorg. Chem.* **2000**, 1039. [5h] F. Neve, A. Crispini, S. Serroni, F. Loiseau, S. Campagna, *Inorg. Chem.* **2001**, *40*, 1093.

[6] [6a] K. K.-W. Lo, D. C.-M. Ng, C.-K. Chung, *Organometallics* **2001**, *20*, 4999. [6b] K. K.-W. Lo, C.-K. Chung, D. C.-M. Ng, N. Zhu, *New J. Chem.* **2002**, *26*, 81. [6c] K. K.-W. Lo, C.-K. Chung, D. C.-M. Ng, N. Zhu, *Chem. Eur. J.* **2003**, *9*, 475. [6d] K. K.-W. Lo, C.-K. Chung, T. K.-M. Lee, L.-H. Lui, K. H.-K. Tsang, N. Zhu, *Inorg. Chem.* **2003**, *42*, 6886.

[7] [7a] E. A. Plummer, J. W. Hofstraat, L. De Cola, *Dalton Trans.* **2003**, 2080. [7b] P. Didier, I. Ortmans, A. Kirsh-De Mesmaeker, R. J. Watts, *Inorg. Chem.* **1993**, *32*, 5239. [7c] M. Polson, S. Fracasso, V. Bertolasi, M. Ravaglia, F. Scandola, *Inorg. Chem.* **2004**, *43*, 1950.

[8] Such a cationic *N*,*N*-complex was used recently as a multifunctional chromophore for single-layer electroluminescent devices: J. D. Slinker, A. A. Gorodetsky, M. S. Lowry, J. Wang, S. Parker, R. Rohl, S. Bernhard, G. G. Malliaras, *J. Am. Chem. Soc.* **2004**, *126*, 2763.

[9] [9a] C. O. Dietrich-Buchecker, P. A. Marnot, J. P. Sauvage, *Tetrahedron Lett.* **1982**, *23*, 5291. [9b] C. Kaes, M. W. Hosseini, A. De Cian, J. Fisher, *Tetrahedron Lett.* **1997**, *38*, 4389.

[10] [10a] T. Ben Hadda, I. Zidane, S. A. M. Moya, H. Le Bozec, *Polyhedron* **1996**, *15*, 1571. [10b] T. Ben Hadda, State Doctorate, University of Mohamed 1st, Oujda, Morocco, **1995**.

[11] M. Nonoyama, *Bull. Chem. Soc. Jpn.* **1974**, *47*, 767.

[12] [12a] R. Urban, R. Krämer, S. Mihan, K. Polborn, B. Wagner, W. Beck, *J. Organomet. Chem.* **1996**, *517*, 191. [12b] J. H. van Diemen, J. G. Haasnoot, R. Hage, E. Müller, J. Reedjik, *Inorg. Chim. Acta* **1991**, *181*, 245.

[13] For examples of *N*-methylation of nitrogen ligands, see, inter alia: [13a] S. Serroni, G. Denti, *Inorg. Chem.* **1992**, *31*, 4251. [13b] J.-M. Lehn, J.-P. Sauvage, J. Simon, R. Ziessel, C. Piccini-Leopardi, G. Germain, J.-P. Declercq, M. Van Meerssche, *Nouv. J. Chim.* **1983**, *7*, 413. [13c] F. L. Wimmer, S. Wimmer, *Polyhedron* **1985**, *4*, 1665. [13d] F. L. Wimmer, S. Wimmer, *J. Chem. Soc., Dalton Trans.* **1994**, 879.

[14] S. Campagna, G. Denti, S. Serroni, A. Juris, M. Venturi, V. Ricetto, V. Balzani, *Chem. Eur. J.* **1995**, *1*, 211.

[15] J. N. Demas, G. A. Crosby, *J. Phys. Chem.* **1971**, *75*, 991.

[16] K. Nakamaru, *Bull. Chem. Soc. Jpn.* **1982**, *55*, 2697.

[17] [17a] A. Altomare, M. C Burla, M. Camalli, G. Cascarano, C. Giacovazzo, A. Guagliardi, A. G. G Moliterni, G. Polidori, R. Spagna, *J. Appl. Crystallogr.* **1998**, *31*, 74−77. [17b] G. Sheldrick, *SHELX97-2, Program for Crystal Structure Refinement*, Göttingen, Germany, **1997**. [17c] *International Tables for X-ray Crystallography*, vol. C (Ed.: A. J. C. Wilson), Kluwer Academic Publishers, Dordrecht, **1992**. [17d] A. Spek, L. *PLATON, A Multipurpose Crystallographic Tool*, Utrecht University, Utrecht, The Netherlands. **1998**.

Received May 19, 2004
Early View Article
Published Online November 10, 2004

 © 2005 Wiley-VCH Verlag GmbH & Co. KGaA, Weinheim

Structural and Photophysical Characterisation of *fac*-[Tricarbonyl(chloro)-(5,6-epoxy-1,10-phenanthroline)rhenium(I)]

Angel A. Martí,[a] Gellert Mezei,[a] Lorena Maldonado,[a] Giovanni Paralitici,[a] Raphael G. Raptis,[a] and Jorge L. Colón*[a]

Keywords: Carbonyl ligands / Coincidental resonances / Facial isomers / Energy gap law / Rhenium

The structural and spectroscopic characterisations of *fac*-[Re(phen)$(CO)_3$Cl] (**1**) (phen = 1,10-phenanthroline), *fac*-[Re(ephen)$(CO)_3$Cl] (**3**) [ephen = 5,6-epoxy-1,10-phenanthroline (**2**)] and ephen are reported. The appearance of weak hydrogen bond networks in the crystal lattice of [Re(ephen)$(CO)_3$Cl] and ephen are discussed. Two different isomers of [Re(ephen)$(CO)_3$Cl] were identified by IR and NMR spectroscopy. Coincidental resonances were differentiated for these complexes by temperature-dependent NMR spectroscopy. Recrystallisation of the crude material allowed the separation of the two isomers. The spectroscopic data permitted the calculation of radiative and nonradiative luminescence rate constants which are consistent with the energy gap law.

(© Wiley-VCH Verlag GmbH & Co. KGaA, 69451 Weinheim, Germany, 2005)

Introduction

The first observation of electronically excited luminescence in carbonylmetal compounds at room temperature was reported by Wrighton and Morse in 1974 for [ReX$(CO)_3$Cl], where X is 1,10-phenanthroline and its derivatives.[1] Since then, a great variety of luminescent carbonylmetal complexes have emerged with applications in areas ranging from electronic and energy transfer to catalysis.[2] In the last few years, self-assembled multinuclear carbonylrhenium complexes have been prepared with interesting photophysical and photochemical properties.[3] In addition, carbonylrhenium compounds have been used to modify proteins with the aim of studying biological electron transfer pathways.[4]

Tricarbonylrhenium(I) complexes are d^6 species which undergo spin-forbidden charge transfer emissions after photoexcitation.[5] Excitation promotes an electron from rhenium-centred orbitals to π* ligand localised orbitals, whereupon internal conversion occurs to the triplet state (or mixed singlet-triplet state) followed by subsequent relaxation into the ground state with the emission of a photon.[1] These d^6 complexes are isoelectronic with tris(2,2′-bipyridine)ruthenium(II) and their emission properties are similar to other d^6 metal complexes which undergo electron transfer reactions from their excited states.[6]

The construction of supramolecular assemblies of photoactive metal complexes requires the availability of well-characterised and preferably easily synthesised moieties with functionalities that allow their attachment to other parts of the framework. Among the possibilities, epoxy group containing molecules are good candidates because they enable the easy formation of covalent bonds between a carbon atom and a specific anchoring group. This possibility has been explored by Shen and Sullivan who used an epoxidised phenanthroline for the attachment of a crown ether.[7] The phenanthroline was then coordinated to a tricarbonylrhenium centre to complete the photoluminescent system. These authors reported that treatment of [Re$(CO)_5$Cl] with 5,6-epoxy-1,10-phenanthroline (ephen, **2**) produced *fac*-[tricarbonyl(chloro)(5,6-epoxy-1,10-phenanthroline)rhenium(I)] {*fac*-[Re(ephen)$(CO)_3$Cl], **3**}. However, no detailed synthetic scheme or characterisation of this complex was reported. As stated above, detailed structural and photophysical characterisation of this complex is necessary if the intention is to use it as part of photoactive molecular frameworks. Here, we report the complete structural and photophysical characterisation of *fac*-[Re(ephen)$(CO)_3$Cl]. In addition, for comparison, we have determined the crystal structure of *fac*-[tricarbonyl(chloro)(1,10-phenanthroline)rhenium(I)] {*fac*-[Re(phen)$(CO)_3$Cl], **1**}. We also report the crystal structure of the ephen ligand.

[a] University of Puerto Rico, Río Piedras,
Department of Chemistry,
P. O. Box 23346, Río Piedras, Puerto Rico, 00931
Fax: (internat.) + 1-787-756-8242
E-mail: jorgecr@caribe.net

Supporting information for this article is available on the WWW under http://www.eurjic.org or from the author.

 © 2005 Wiley-VCH Verlag GmbH & Co. KGaA, Weinheim **DOI: 10.1002/ejic.200400531**

Results and Discussion

Crystal Structure Description

The structure of **1** consists of a rhenium(I) atom octahedrally coordinated by a chelating phenanthroline ligand, a chloride ion and three carbonyl groups in a facial conformation (Figure 1 and Supporting Information; for Supporting Informations see also the footnote on the first page of this article). Selected bond lengths and bond angles are listed in Table 1. Although this molecule was prepared by Wrighton et. al ca. 30 years ago, this is the first time that its crystal structure has been reported.

The bond lengths in **1** agree with those in similar *fac*-(tricarbonylrhenium) compounds.[4,8] The average Re−N bond length is 2.179(3) Å which is shorter than the Re−N bond length of 2.211(3) Å for *fac*-[tricarbonyl(chloro)bis-(pyridine)rhenium] [$Re(py)_2(CO)_3Cl$], and 2.218(6) and 2.200(6) Å for *fac*-[tricarbonyl(chloro)bis(4,4′-bipyridine)-rhenium] [$Re(4,4'\text{-bpy})_2(CO)_3Cl$].[9]

Figure 2 shows an ORTEP representation of **2**·$CHCl_3$. The structure of **2**·$CHCl_3$ is similar to that of the parent ligand 1,10-phenanthroline with some evident exceptions (Supporting Information, Figure S1).[10] The insertion of oxygen atoms at positions 5 and 6 of the phenanthroline ligand disrupts the delocalised π-system aromaticity in the ligand. The effect of this disruption is that the two pyridine rings rotate relative to each other by ca. 6° (rotation about the C11−C12 axis).

The X-ray crystal structure of **2**·$CHCl_3$ shows a chloroform solvent molecule hydrogen-bonded to the nitrogen atoms of the ephen ligand. However, this bifurcated hydrogen bond is weak (H···N distances of 2.41 Å and 2.30 Å) and the crystals of **2**·$CHCl_3$ loses the chloroform molecule easily. This type of weak hydrogen bond has been well documented in the literature.[11] Mascal presented statistical evidence of C−H···N hydrogen bonding in a variety of crystal structures with H···N distances ranging from 2.05 to 2.45 Å.[12] An additional hydrogen bond between C1−H and the epoxy oxygen atom of a nearby **2**·$CHCl_3$ molecule (H···O 2.64 Å) adds stability to the crystal lattice (see Supporting Information, Figure S2).

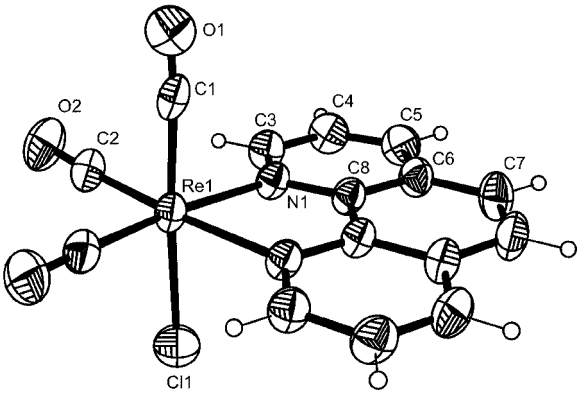

Figure 1. ORTEP representation of **1**; ellipsoids are shown at the 50% probability level

Table 1. Selected bond lengths [Å] and angles [°] for **1**

Re−N1	2.179(3)	Re−C2	1.917(4)
Re−C1	1.973(6)	Re−Cl1	2.4688(17)
N1−Re−N1	75.77(17)	C1−Re−Cl1	176.33(14)
N1−Re−Cl1	84.93(9)	C1−Re−N1	92.18(14)
C2−Re−Cl1	93.79(13)	C2−Re−C2	91.1(3) 6
C2−Re−C1	88.77(16)	Re−C1−O1	176.2(5)
C2−Re−N1	172.33(15)	Re−C2−O2	176.6(4)

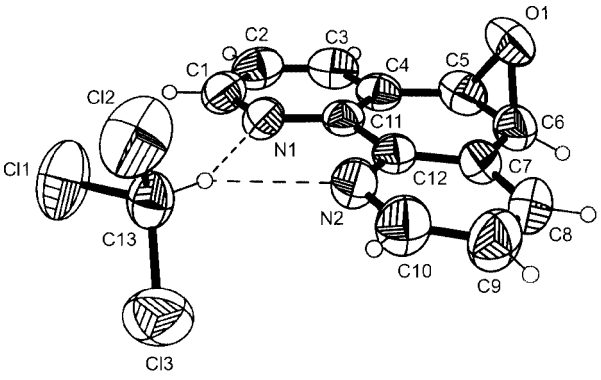

Figure 2. ORTEP representation of **2**·$CHCl_3$; ellipsoids are shown at the 50% probability level

Figure 3 shows an ORTEP representation of **3a**. For *fac*-[$Re(ephen)(CO)_3Cl$] we found two polymorphs, **3a** and **3b**, in which the chloride ion is *trans* to the chloro ligand in both forms (Supporting Information, Figure S1). There are no significant differences between the bond lengths and angles in **3a** and **3b**. The Re atom is in a distorted octahedral environment with the carbonyl groups in a facial arrangement as in the parent compound **1**. The most significant deviation from octahedral geometry can be seen for the chloride ion where C1−Re−Cl1 is 176.58(16)°

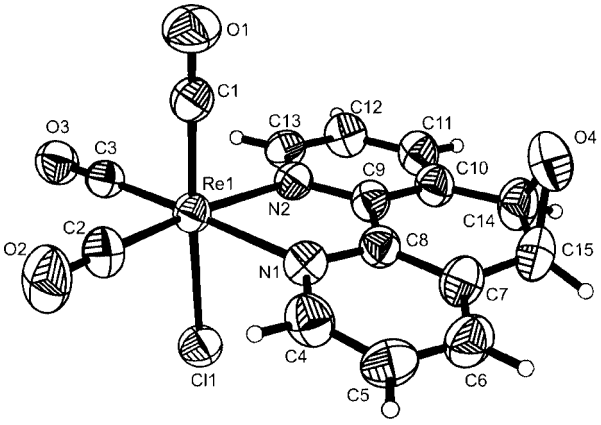

Figure 3. ORTEP representation of **3a**; ellipsoids are shown at the 50% probability level

 © 2005 Wiley-VCH Verlag GmbH & Co. KGaA, Weinheim

Table 2. Selected bond lengths [Å] and angles [°] for **3a**

Re−N1	2.172(4)	Re−C3	1.928(5)
Re−N2	2.171(4)	Re−Cl1	2.4600(16)
Re−C1	1.915(6)	O4−C14	1.456(7)
Re−C2	1.918(5)	O4−C15	1.471(8)
N1−Re−N2	75.48(15)	C1−Re−N2	91.87(19)
N1−Re−Cl1	82.18(13)	C1−Re−C2	89.4(2)
N2−Re−Cl1	84.88(11)	Re−C1−O1	179.6(5)
C1−Re−Cl1	176.58(16)	Re−C2−O2	178.8(5)
C2−Re−Cl1	93.64(18)	Re−C3−O3	177.5(4)
C3−Re−Cl1	91.24(13)	C2−Re−C3	88.8(2)
C2−Re−N1	96.89(18)	C14−O4−C15	61.0(4)
C3−Re−N2	98.72(17)	O4−C14−C10	115.5(4)
C1−Re−N1	95.99(19)	O4−C15−C7	114.5(5)

(Table 2). This angle is similar to that of 176.33(14)° in **1**. The bonds lengths and angles are similar to those of **1**, differing only in the ephen ligand. The distinguishing feature between the structures of the polymorphs **3a** and **3b** is the number of weak C−H···O hydrogen bonds (H···O < 2.67 Å) between adjacent molecules of **3a** and **3b**, respectively, with there being one for **3a** and three for **3b** (Supporting Information, Figures S3 and S4).

Infrared Spectroscopy

The IR spectrum of **1** (Figure 4) shows three bands in the 2100−1800 cm^{-1} region which can be attributed to the vibrations of the carbonyl groups in the facial conformation. Group theory predicts that a molecule with C_{3v} point group symmetry must possess two fundamental vibrational modes (both IR- and Raman-active), i.e. an A_1 symmetric stretching mode and a degenerate E stretching mode.[13] Since the symmetry of **3** is C_s, the local C_{3v} symmetry of the carbonyl groups is perturbed. Thus, changing the symmetry from C_{3v} to C_s causes the A_1 mode to become A′ and the degenerate E mode to split into A′ and A″.The carbonyl region of **1** was used to identify the facial isomer and exclude the presence of the meridional isomer.[14] A facial isomer must possess three intense bands in the carbonyl region {e.g., *fac*-[Re(phen)$(CO)_3$Cl] shows three intense bands at 2015, 1912 and 1890 cm^{-1}},[1] while the meridional isomer must possess two intense bands and one weak band at higher wavenumber[15] {e.g., *mer*-[Re$(CO)_3(PPh_3)_2$Cl] shows two intense bands at 1944 and 1894 cm^{-1}, while the weak band expected at ca. 2050 cm^{-1} was not observed}.[16] Figure 4 shows that the IR spectrum of molecule **1** exhibits three intense bands that characterise it as a facial isomer. Staal et al. studied the carbonyl vibrations in analogous complexes [M$(CO)_3$X(DBA)] (M = Mn, Re; X = Cl, Br, I; DBA = 1,4-diazabutadiene) with different substitutions on the DBA ligand.[15] These authors assigned the band above 2000 cm^{-1} to the symmetric stretching mode A′ of the carbonyl groups adjacent to the halogen atom. The next band at higher wavenumber was assigned to the asymmetric A″ mode of the carbonyl groups adjacent to the halogen atom and the last one at the highest wavenumber was assigned to the stretching mode of the carbonyl group *trans* to the halogen atom. Because of the analogy of this system with **1** and **3** we have based our assignment of the vibrational modes on that previous work.

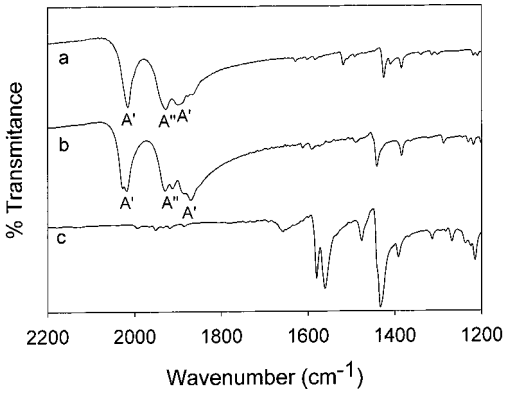

Figure 4. Infrared spectra including the carbonyl region for **1** (a), **3** (crude material) (b) and **2** (c)

In contrast, the spectrum of **3** is more complicated. Each band is split into two (see b in Figure 4), whereas **2** does not show any transition in this region (see c in Figure 4). The splitting of the carbonyl bands observed in the spectrum of **3** will be discussed in the next section along with the NMR spectroscopic results which shed light on the origin of this splitting.

NMR Spectroscopy

^{1}H NMR studies in DMF indicate that **2** possesses three signals in the aromatic region (doublets of doublets) attributable to the pyridine hydrogen atoms (the corresponding atoms in each pyridine ring are equivalent) and an upfield signal attributable to the aliphatic epoxide hydrogen atoms (singlet). ^{13}C NMR spectroscopy shows the signals of the five pyridine carbon atoms in the aromatic region and the epoxide carbon atoms upfield in the hydrocarbon region. These studies confirm that the solution structure of **2** is consistent with its crystal structure (see Supporting Information, Figure S5).

^{1}H NMR spectroscopy of **1** shows four signals in the aromatic region as expected. Six signals in the aromatic region of the ^{13}C NMR spectrum are consistent with the presence of the phenanthroline ligand. The CO carbon signals appear at δ = 190.69 and 198.63 ppm, the latter being assigned to the carbonyl group *trans* to the chloride ion (based on the *trans* effect).

The ^{1}H and ^{13}C NMR spectra of crude **3** are more complicated than would be expected based on the close similarity between **3** and **1** (Figure 5). The most distinctive feature of these spectra compared with those of **1** is that each peak is split. This is especially notable in the ^{13}C NMR spectrum which shows two close sets of resonances when only one is to be expected. Another intriguing finding is that the epoxide resonance in the ^{1}H NMR spectrum (δ = 5.17 ppm) is not split like the rest of the resonances. There are three possible explanations for these observations: (a) there is differentiation of the otherwise equivalent protons of the ephen ligand due to the loss of planarity, (b) there is a mixture of the *fac* and *mer* isomers, or (c) there is a mix-

 © 2005 Wiley-VCH Verlag GmbH & Co. KGaA, Weinheim

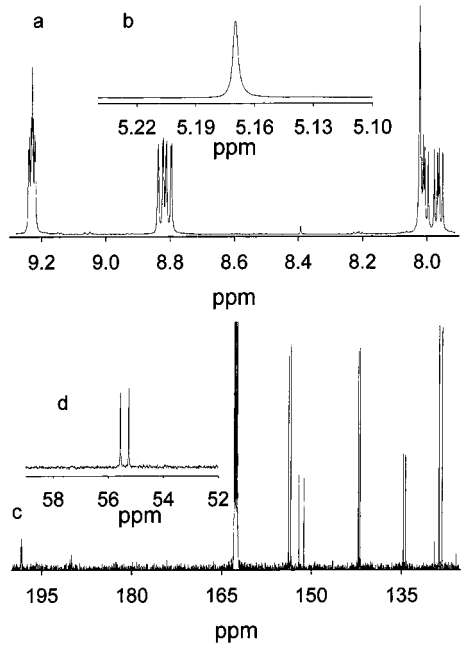

Figure 5. ^{1}H NMR spectrum of **3** (a); ^{1}H NMR high-field ephen hydrogen signals of **3** (crude material) (b); ^{13}C NMR spectrum of **3** (c); ^{13}C NMR high-field ephen carbon signals of **3** (d)

ture of *fac* isomers with the epoxide group of the ephen ligand oriented on different sides of the plane passing through the equatorial carbonyl groups (see Supporting Information, Figure S6).

The first explanation requires that the chemical environment around the protons and carbon atoms on different sides of the mirror plane bisecting the phenanthroline ligand be different enough to show different signals in NMR spectroscopy. The crystal structure shows only subtle differences which can be expected to be normalised by the dynamic environment of the solvent. In addition, this explanation does not account for the splitting of the carbonyl bands in the IR spectra. The splitting of the carbonyl bands appears to be consistent with the existence of two different isomers which leads us to favour either explanation (b) or (c).

In the case of explanation (b), the occurrence of *mer* and *fac* isomers would produce splitting of the bands in the ^{13}C NMR and ^{1}H NMR spectra and the occurrence of new bands in the IR spectroscopic carbonyl region compared with **1**. However, close inspection of the carbonyl region in the ^{13}C NMR spectrum indicates that these resonances are very close to those observed for *fac*-[Re(phen)(CO)$_3$Cl] (**1**). Because the carbonyl groups assume a very different orientation in the *mer* isomer than in the *fac* isomer, one would expect differentiation of the carbonyl signals. However, the spectra suggest that the carbonyl chemical environments of these two isomers are very similar (by the similarity of their carbonyl signals) which is inconsistent with the assignment of a mixture of *fac* and *mer* isomers. Moreover, the synthesis used for **3** is very similar to the one used for **1**, the latter being obtained with a 100% yield of the *fac* isomer.[16] Because of the similarity of these compounds we would expect the synthesis of **3** to also produce only the *fac* isomer. Finally, an octahedral complex with three carbonyl groups in the *fac* conformation would exhibit three intense bands in the carbonyl region (ca. 1900 to 2050 cm^{-1}) while a *mer* isomer must show two intense bands between 2000 and 1900 cm^{-1} and a weak band at ca. 2015 cm^{-1} which on some occasions is even absent.[14,16] As it is evident from Figure 4, the presence of two sets of three intense bands is consistent with the existence of two *fac* isomers.

Explanation (c) requires that the epoxy group has little or no influence on the coordination of the ephen ligand to the rhenium centre. If this is true, it could explain the presence of two closely spaced sets of resonances in both the ^{1}H and ^{13}C NMR spectra and also the observed 1:1 signal intensity ratio. However, only the isomer with the epoxy group *trans* to the chloride ion could be characterised by single-crystal X-ray diffraction. Attempts to crystallise the second isomer were unsuccessful. The structure of the isomer with the epoxy group *trans* to the chloride ion and the proposed structure of the isomer with the epoxy group *cis* to the chloride ion are presented in the Supporting Information (Figure S6).

The unexpected fact that the epoxide proton resonance is not split, prompted us to perform NMR measurements at a higher temperature (60 °C). The most significant difference is the splitting of the epoxide hydrogen resonance at 60 °C (Figure 6) compared with that at 25 °C. These resonances collapse into a single peak when cooled again to 25 °C. Previous studies of this complex at low temperature by Shen and Sullivan indicated that this signal also splits when the material is cooled to −60 °C.[7] This observation led the authors to conclude that a relatively low exchange barrier exists between the *trans* and *cis* isomers. However, the new temperature-dependent data we are presenting indicate that this is not the case. A low isomerisation barrier for this ligand would not produce a splitting of the epoxide signal upon a rise in temperature. Rather, an increase in temperature would increase the rate of isomerisation producing a single peak within the time of measurement of the instrument. Therefore, the appearance of two resonances at 60 °C is consistent with the existence of two *fac* isomers. An explanation could be that the factors which account for the chemical shift of these hydrogen atoms in both isomers cancel out to yield a single resonance at room temperature.

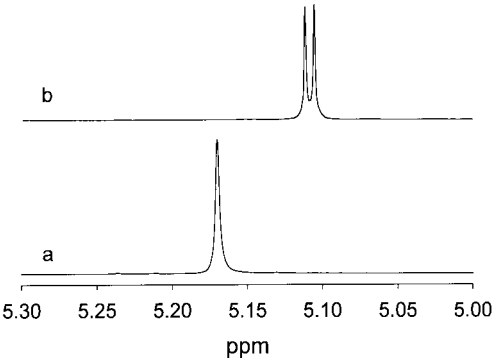

Figure 6. ^{1}H NMR spectrum of crude **3** showing the resonance signals for the hydrogen atoms attributed to the epoxide in the ephen ligand at 25 °C (a) and 60 °C (b)

 © 2005 Wiley-VCH Verlag GmbH & Co. KGaA, Weinheim

These coincidental resonances can be differentiated at higher temperature because of the variation of the solvent's physical properties at those temperatures (e.g., density, viscosity, dielectric constant). The other peaks in both the ^{13}C and ^{1}H NMR spectra at 25 °C and 60 °C are very similar, with some minor displacements due to the change in temperature.

Finally, there is still the question of why we observe only one isomer in the crystal structure. We propose that the isomer with the epoxy group *trans* to the chloride ion is preferred during crystallisation because of a more favourable hydrogen bonding network. We also observed that along with the crystals, a yellow powder also precipitates and this could be the other isomer. Infrared spectra of the crystals and the powder (see Supporting Information, Figure S7) correlate exactly except for the carbonyl region which is consistent with the presence of two different isomers. In order to unequivocally assign the NMR spectra of both isomers we determined the ^{1}H NMR spectra of both the crystals and the yellow powder resulting from the recrystallisation of the crude material (see Supporting Information, Figure S8). The ^{1}H NMR spectrum of the crystals exhibit signals which are shifted downfield relative to those of the powder, again supporting our assignment of two different isomers.

Electronic Absorption and Luminescence Characterisation

One of the most distinctive features in the UV/Vis absorption spectrum of **3** is the presence of a peak near 385 nm corresponding to the MLCT band which can be assigned by analogy with its parent compound **1**. As is evident from Figure 7, this band is not present in the spectrum of **2** or that of the phenanthroline ligand (phen). The MLCT absorption maximum of **3** is red-shifted with respect to **1** which suggests that the epoxy oxygen atom draws electron density from the phenanthroline ring, facilitating the photoinduced metal-to-ligand charge transfer.[17]

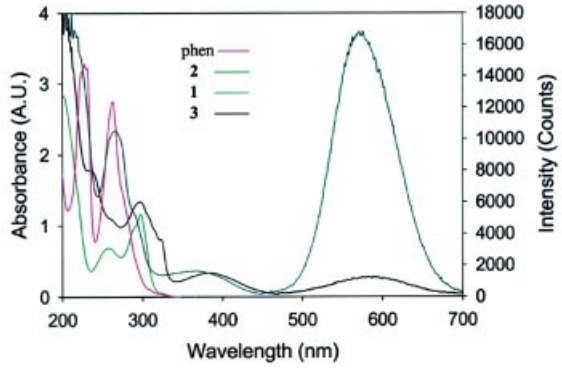

Figure 7. UV/Vis spectra of phen, **2**, **1** and **3**; luminescence spectra are shown for **1** and **3** in the region of 470−700 nm

Studies of **1** by Wrighton et al. indicated that upon absorption this complex undergoes intersystem crossing to the triplet state (or the mixed singlet-triplet state) with nearly 100% efficiency.[1] Luminescence measurements show a red shift in the emission band from 573 nm (**1**) to 585 nm (**3**) as shown in Figure 7.[18] This behaviour is consistent with previous studies using substituted phenanthrolines.[1,19] Quantum yield results (Table 3) indicate that the emission efficiency of **3** is less than that of **1**. In addition, the luminescence lifetime of **3** (15.1 ns) is also less than that of **1** (183 ns). To better understand the relaxation processes of the excited states of these two complexes we determined the radiative and nonradiative decay rate constants. Table 3 shows that the radiative decay rate constants remains basically unaffected while the nonradiative decay rate constant increases by a factor of 10 for **3** compared with that of **1**. Previous studies indicated that the nonradiative decay rate constant is affected by the energy gap.[20] The energy gap law states that the coupling between the vibrational levels of the ground and the excited state increases as the energy gap decreases.[21] A large coupling between the excited- and ground-state vibrational levels will increase the nonradiative decay rate constant. The increase in the nonradiative decay rate constant upon a decrease in the energy gap (as indicated in the red shift from 573 to 585 nm) is consistent with the energy gap law. However, because the aromaticity of the phenanthroline group is affected by the epoxye substitution in positions 5 and 6 a better comparison might be made with [Re(bpy)(CO)$_3$Cl] (**4**) in which the bpy (2,2′-bipyridine) ligand lacks the extensive aromatic delocalisation of phenanthroline. Also, **4** (similar to **3**) displays a lower emission energy and a shorter lifetime than **1**. Table 3 indicates that the energy gap of **3** is smaller than that in **4** while the nonradiative rate constant is larger for **4** than for **3**. The decrease in the energy gap (comparing **3** with **4**) can cause an increase in the coupling between the ground- and excited-state levels increasing the nonradiative pathways and hence the nonradiative rate constant. This behaviour is also consistent with the energy gap law. In addition, the increase in the nonradiative decay rate constant can also be attributed to new deactivation pathways available for the epoxidated phenanthroline ligand in comparison with the unmodified phenanthroline (e.g. thermal deactivation by vibrations of the epoxy oxygen atom and dipole coupling by hydrogen bonds to the epoxide). Tricarbonylrhenium complexes with substituted phenanthrolines like 5-nitro-1,10-phenanthroline and 1,10-phenanthroline-5,6-dione do not exhibit luminescence in dichloromethane at room temperature[1] and this can also be attributed to deactivation pathways due to phenanthroline substitution.

Table 3. Radiative and nonradiative decay rate constant for **1** and **3** in acetonitrile

	Emission $\lambda_{max.}$ [nm]	τ [ns]	φ	k_R [s^{-1}]	k_{NR} [s^{-1}]
1	573	183 ± 5	0.0177	9.67×10^4	5.37×10^6
3	585	15.1 ± 0.8	0.0013	8.61×10^4	6.61×10^7
4	580	25.6 ± 0.9	0.0039	1.56×10^5	3.89×10^7

Conclusion

The crystal structures of *fac*-[Re(phen)(CO)$_3$Cl], ephen and *fac*-[Re(ephen)(CO)$_3$Cl] have been reported. An exten-

 © 2005 Wiley-VCH Verlag GmbH & Co. KGaA, Weinheim

sive hydrogen bonding network has been identified in the crystal lattices of **2** and **3**. IR and NMR spectroscopic studies allow the identification of two isomers of **3**. These isomers differ in the orientation of the epoxy oxygen atom relative to the chlorine atom and are nearly equally abundant. Luminescence experiments show an increase in the nonradiative decay rate constant for **3** consistent with the energy gap law. This increase can also arise due to new deactivation pathways available for **3** but not for **1** and **4**. Molecule **3** is potentially useful in synthesising donor-bridge-acceptor systems, photoactive polymers, modified surfaces and a variety of photoactive molecular frameworks involving rhenium centres since the epoxy functionality provides an easy way of forming covalent bonds. The photophysical and structural characterisation of **3** presented in this article is important for the synthesis and study of more complex structures involving this building block. Future studies will include the modification of layered zirconium phosphates using epoxyphenanthroline-based ligands for the covalent attachment of metal complexes to this material.

Experimental Section

Materials: All chemicals were purchased from Aldrich Chemical Co. and used as received. Acetonitrile was of spectrophotometric quality.

Syntheses: The syntheses of *fac*-[Re(phen)$(CO)_3$Cl] (**1**)[1] and ephen (**2**)[7] are described elsewhere. The published procedure for the synthesis of **1** was adopted for the synthesis of *fac*-[Re(ephen)$(CO)_3$Cl] (**3**). In a typical procedure, **2** (0.1068 g) and [Re$(CO)_5$Cl] (0.2001 g) were dissolved in toluene (30 mL). The solution was heated to reflux under N_2 for 1 h and the precipitate obtained was filtered and washed with diethyl ether. The yields were typically ca. 0.2116 g (ca. 80%). ^{1}H NMR of the crude material (DMF, 500 MHz): δ = 5.15 (s, 2 H), 7.97 (m, 2 H), 8.80 (m, 2 H), 9.22 (m, 2 H) ppm. ^{13}C NMR (DMF, 125 MHz): δ = 55.29, 55.59, 128.30, 128.80, 134.40, 134.74, 141.94, 142.21, 151.30, 152.12, 153.46, 153.82, 190.08, 190.31, 198.40, 198.50 ppm.

X-ray Crystal Structure Determinations: Crystals of **1** were grown by slow concentration of a saturated acetonitrile solution at 4 °C. Crystals of **2** were obtained by slow diffusion of hexanes into a saturated chloroform solution. For the crystal structure determination, a crystal of **2**·$CHCl_3$ was sealed in a quartz capillary in order to prevent solvent loss. Two polymorphs of **3** were obtained: **3a** by slow concentration of a saturated acetonitrile solution at 4 °C and **3b** by concentration of a saturated DMF solution at room temperature. X-ray diffraction data, collected from a single crystal in each case mounted atop a glass fibre with a Siemens SMART-CCD diffractometer,[22] were corrected for Lorentz and polarisation effects.[23] The structures were solved by direct methods using the SHELXTL program and refined by full-matrix least-squares methods on F^2.[24] Crystallographic details are summarised in Table 4. CCDC-239409 (**1**), -239410 (**2**), -239411 (**3a**) and -239412 (**3b**) contain the supplementary crystallographic data for this paper. These data can be obtained free of charge at www.ccdc.cam.ac.uk/conts/retrieving.html [or from the Cambridge Crystallographic Data Centre, 12 Union Road, Cambridge CB2 1EZ, UK; Fax: (internat.) + 44-1223-336-033; E-mail: deposit@ccdc.cam.ac.uk].

Spectroscopic Characterisation: UV/Vis absorption measurements were performed with an HP-8453 diode array spectrophotometer. Luminescence measurements were performed with an SE-900 spectrofluorimeter (Photon Technology International, PTI) using a 150-W xenon lamp as the excitation source and a PTI Model 710 photon counting detector with a Hamamatsu R1527P photomultiplier. The bandpass of the emission monochromator was 8.75 nm for the steady-state luminescence experiments at 384 nm and the spectra presented are uncorrected for the photomultiplier efficiency and lamp output. Time domain luminescence measurements were performed using a PTI GL-3300 N_2 pulsed laser coupled with a PTI 5020-ELT stroboscopic detector with a Hamamatsu R1527P photomultiplier. The excitation wavelength was 337 nm while emission was detected at 573 and 585 nm for **1** and **3**, respectively. The iterative reconvolution of the decay transients was performed using PTI Time Master 1.2 software. Quantum yields were determined using [Ru$(bpy)_3$]$(PF_6)_2$ in acetonitrile as a standard (φ = 0.062),[25] using the following formula:[26]

$$\phi = \phi_R \frac{I}{I_R} \frac{OD_R}{OD}$$

Table 4. Crystallographic data for **1**, **2**·$CHCl_3$, and **3**

	1	**2**·$CHCl_3$	**3a**	**3b**
Empirical formula	$C_{15}H_8ClN_2O_3Re$	$C_{13}H_9Cl_3N_2O$	$C_{15}H_8ClN_2O_4Re$	$C_{15}H_8ClN_2O_4Re$
Formula mass	485.88	315.57	501.88	501.88
Space group	*C*2/*m* (No. 12)	*Pbca* (No. 61)	$Pca2_1$ (No. 29)	$P2_1/n$ (No. 14)
a [Å]	15.8686(19)	12.146(3)	15.812(2)	8.2761(11)
b [Å]	11.8859(14)	11.619(2)	10.4330(15)	12.7831(18)
c [Å]	8.0134(10)	19.741(4)	9.1023(13)	13.9959(19)
β [°]	107.154(2)	90	90	92.197(2)
V [Å^3]	1444.2(3)	2785.8(10)	1501.6(4)	1479.6(3)
Z	4	8	4	4
$\rho_{calcd.}$ [g/cm^{-3}]	2.235	1.505	2.220	2.253
μ [mm^{-1}]	8.612	0.649	8.291	8.414
$R1$[a], $wR2$[b] [$I > 2\sigma(I)$]	0.0231, 0.0584	0.0458, 0.0992	0.0177, 0.0445	0.0185, 0.0476
$R1$[a], $wR2$[b] (all data)	0.0243, 0.0591	0.0753, 0.1123	0.0190, 0.0452	0.0209, 0.0489
Goodness-of-fit	1.094	1.019	1.073	1.083

[a] $R_1 = \Sigma||F_o| - |F_c||/\Sigma|F_o|$. [b] $wR_2 = [\Sigma w(F_o^2 - F_c^2)^2/\Sigma w(F_o^2)^2]^{1/2}$.

 © 2005 Wiley-VCH Verlag GmbH & Co. KGaA, Weinheim

where φ_R is the quantum yield of the reference standard, I and I_R are the integrated intensities for the luminescent molecule and the standard, respectively. OD and OD_R are the optical densities for the luminescent molecule and the standard solution, respectively. Both quantum yield and lifetime measurements were performed in solutions purged with N_2 (99.9%) for 15 min. Knowledge of the quantum yield and luminescence lifetime allows the determination of the radiative and nonradiative rate constants as follows:

$$k_r = \frac{\phi}{\tau}$$

$$k_{nr} = \frac{(1-\phi)}{\tau}$$

NMR experiments were performed in [D_6]DMF with a Bruker-Advance DRX-500 spectrometer. IR spectra were recorded in KBr pellets with a Nicolet Magna 750 FTIR spectrometer or directly on the sample with a Bruker Tensor 27 FTIR spectrometer.

Acknowledgments

We thank Joe Martinez for his help with the NMR measurements and Dr. Antonio Prieto for helpful discussions. A. A. M. acknowledges NIH-RISE (grant R25GM061151) and NSF Graduate Teaching Fellows in K-12 Education (Award 9979566) for financial support.

[1] M. Wrighton, D. L. Morse, *J. Am. Chem. Soc.* **1974**, *96*, 998−1003.
[2] [2a] P. A. Mabrouk, M. S. Wrighton, *Chem. Phys. Lett.* **1984**, *103*, 332−335. [2b] P. J. Giordano, M. S. Wrighton, *J. Am. Chem. Soc.* **1979**, *101*, 2888−2897. [2c] Y. Yang, J. Chen, Y. Lin, M. Cheng, Y. Wang, *J. Organomet. Chem.* **1994**, *467*, C6−C8.
[3] [3a] S. Sun, D. T. Tran, O. S. Odongo, A. J. Lees, *Inorg. Chem.* **2002**, *41*, 132−135. [3b] S. Sun, A. S. Silva, I. M. Brinn, A. J. Lees, *Inorg. Chem.* **2000**, *39*, 1344−1345. [3c] J. A. Baiano, D. L. Carlson, G. M. Wolosh, D. E. DeJesus, C. F. Knowles, E. G. Szabo, W. R. Murphy, *Inorg. Chem.* **1990**, *29*, 2327−2332.
[4] [4a] W. B. Connick, A. J. Di Billio, W. P. Schaefer, H. B. Gray, *Acta Crystallogr., Sect. B* **1999**, *55*, 913−916. [4b] W. B. Connick, A. J. Di Billio, M. G. Hill, J. R. Winkler, H. B. Gray, *Inorg. Chim. Acta* **1995**, *240*, 169−173.
[5] M. Wrighton, *Chem. Rev.* **1974**, *74*, 401−429.
[6] W. K. Smothers, M. S. Wrighton, *J. Am. Chem. Soc.* **1983**, *105*, 1067−1069.
[7] Y. Shen, P. Sullivan, *Inorg. Chem.* **1995**, *34*, 6235−6236.
[8] [8a] O. S. Wenger, L. M. Henling, M. W. Day, J. R. Winkler, H. B. Gray, *Inorg. Chem.* **2004**, *43*, 2043−2048. [8b] M. Bakir, *Acta Crystallogr., Sect. B* **2002**, *58*, m74−m76. [8c] K. Wang, L. Huang, L. Gao, C. Huang, *Inorg. Chem.* **2002**, *41*, 3353−3358. [8d] D. H. Gilbson, B. A. Sleadd, A. Vij, *J. Chem. Crystallogr.* **1999**, *29*, 619−622. [8e] R. N. Dominey, B. Hauser, J. Hubbard, J. Dunham, *Inorg. Chem.* **1991**, *30*, 4754−4758.
[9] S. Belanger, J. T. Hupp, C. L. Stern, *Acta Crystallogr., Sect. B* **1998**, *54*, 1596−1600.
[10] S. Nishigaki, H. Yoshioka, K. Nakatsu, *Acta Crystallogr., Sect. B* **1978**, *34*, 875−879.
[11] [11a] A. N. M. M. Rahman, R. Bishop, D. C. Craig, M. L. Scudder, *Eur. J. Org. Chem.* **2003**, 72−81. [11b] G. R. Desiraju, T. Steiner, *The Weak Hydrogen Bond*, Oxford University Press, New York, **1999**, p. 4. [11c] G. A. Jeffrey, *An Introduction to Hydrogen Bond*, Oxford University Press, New York, **1997**, chapter 5. [11d]F. H. Allen, J. A. K. Howard, V. J. Hoy, G. R. Desiraju, D. S. Reddy, C. C. Wilson, *J. Am. Chem. Soc.* **1996**, *118*, 4081−4084. [11e] T. Steiner, J. A. Kanters, J. Kroon, *Chem. Commun.* **1996**, 1277−1278. [11f] G. P. A. Yap, A. L. Rheingold, P. Das, R. H. Crabtree, *Inorg. Chem.* **1995**, *34*, 3474−3476. [11g] P. Behrens, G. van de Goor, C. C. Freyhardt, *Angew. Chem. Int. Ed. Engl.* **1995**, *34*, 2680−2682. [11h] T. Steiner, *Chem. Commun.* **1994**, 2341−2342.
[12] M. Mascal, *Chem. Commun.* **1998**, 303−304.
[13] F. A. Cotton, *Chemical Applications of Group Theory*, John Wiley & Sons, New York, **1990**, chapter 10.
[14] B. J. Brisdon, D. A. Edwards, J. W. White, *J. Organomet. Chem.* **1978**, *156*, 427−437.
[15] L. H. Staal, A. Oskam, K. Vrieze, *J. Organomet. Chem.* **1979**, *170*, 235−245.
[16] A. M. Bond, R. Colton, M. E. McDonald, *Inorg. Chem.* **1978**, *17*, 2842−2847.
[17] H. Kunley, A. Vogler, *Inorg. Chim. Acta* **2003**, *343*, 357−360.
[18] The luminescence spectra for the tricarbonylrhenium complexes are uncorrected. Although the $\lambda_{max.}$ values are blue-shifted compared with previously reported values using corrected spectra (K. Kalyanasundaram, *Inorg. Chem. Commun.* **2000**, *188*, 323) we are only comparing uncorrected spectra recorded in our laboratory under different chemical micro-environments.
[19] D. R. Striplin, G. A. Crosby, *Coord. Chem. Rev.* **2001**, *211*, 163−175.
[20] J. V. Caspar, T. J. Meyer, *J. Phys. Chem.* **1983**, *87*, 952−957.
[21] T. J. Meyer, *Pure Appl. Chem.* **1986**, *58*, 1193−1206.
[22] Data Collection: *SMART-NT Software Reference Manual*, version 5.0, Bruker AXS, Inc., Madison, WI 53719-1173, **1998**.
[23] Data Reduction: *SAINT-NT Software Reference Manual*, version 4.0, Bruker AXS, Inc., Madison, WI 53719-1173, **1996**.
[24] G. M. Sheldrick, *SHELXTL-NT*, version 5.1, Bruker AXS, Inc., Madison, WI 53719-1173, **1999**.
[25] R. Alarcon, *Synthesis and characterisation of Re^{I} complexes used for protein modification and intercalation in zirconium layered materials*, Masters Degree, University of Puerto Rico, Río Piedras P.R., February **1997**, p. 62.
[26] [26a] J. R. Lakowicz, *Principles of Fluorescence Spectroscopy*, Kluwer Academics/Plenum Publisher, New York, **1999**, pp. 52−53. [26b] C. A. Parker, W. T. Rees, *Analyst (Cambridge, U. K.)* **1960**, *85*, 587−600.

Received June 17, 2004
Early View Article
Published Online November 10, 2004
Minor changes have been made to the manuscript since it's publication in *Eur. J. Inorg. Chem.* Early View. *The Editors*

A New Mixed P,S-Bidentate Ligand Featuring a λ^4-Phosphinine Anion and a Phosphanyl Sulfide Group − Synthesis, X-ray Crystal Structures and Catalytic Properties of Its Chloro(cymene)ruthenium and Allylpalladium Complexes

Maximilian Dochnahl,[a] Marjolaine Doux,[a] Emilie Faillard,[a] Louis Ricard,[a] and Pascal Le Floch*[a]

Keywords: Density functional calculations / Homogeneous catalysis / P ligands / Ruthenium / Palladium / S ligands

1,3,2-Diazaphosphinine (**1**) reacts successively with diphenylacetylene and diphenyl(1-propynyl)phosphane sulfide to afford the P,S-bidentate phosphinine **3**. Reaction of *n*BuLi with **3** followed by complexation with $[RuCl_2(C_{10}H_{14})]_2$ gave two diastereoisomers **5a**,**b**. Variable-temperature NMR spectroscopy and ONIOM DFT calculations were carried out to rationalize their formation. Complexes **5a**,**b** were used as catalysts in hydrogen-transfer hydrogenation (TON up to 200). Reaction of MeLi with **3** followed by complexation with $[PdCl_2(\eta^3\text{-}C_3H_5)]_2$ yielded two diastereomers **7a**,**b**, which were used as catalysts in the Suzuki–Miyaura cross-coupling reaction of aryl bromides with pinacolborane to yield the corresponding arylboronic esters (TON up to 799000).

(© Wiley-VCH Verlag GmbH & Co. KGaA, 69451 Weinheim, Germany, 2005)

Introduction

Since the pioneering work of Grim and co-workers in the mid-1970s,[1] there has been a continuing interest in the chemistry of mixed tertiary phosphane/monochalcogenide (λ^3,σ^3)P−X (X = O, S) ligands.[2−7] These systems, which combine soft σ-donor (P) and good π-donor (O, S) binding sites, display very unique steric and electronic properties that differ markedly from those of classical bidentate phosphorus ligands. Most importantly, in some cases, these compounds have been employed to build very active catalysts. For example, in 1995 it was shown that a rhodium(I) complex of the monosulfide of dppm (dppm = $Ph_2PCH_2PPh_2$) could efficiently catalyze the carbonylation of methanol.[8] Later on, palladium(II) complexes of the same ligands were shown to be active catalysts for the ethylene/CO copolymerization.[9] On the other hand, P,O-mixed ligands, such as monoxides of dppm and dppe ($Ph_2PCH_2CH_2PPh_2$) and dppp ($Ph_2PCH_2CH_2CH_2PPh_2$), give better results than classical bidentate phosphanes in the cobalt-catalyzed hydroformylation of epoxides due to their hemilability.[10]

In 2002 we reported the synthesis of a new type of S,P,S-pincer ligand that incorporates a pseudo-ylidic λ^4-phosphorus atom as the central binding site (Scheme 1).[11,12] These tridentate ligands, which are readily available from the reaction of nucleophiles with phosphinines, were found to exhibit very specific electronic properties. Thus, their rhodium(I) complexes show a high reactivity towards small molecules such as O_2, CO_2, CS_2 and SO_2.[13] Furthermore, their palladium(II) complexes proved to be active catalysts in the Miyaura cross-coupling reaction that allows the synthesis of arylboronic esters from pinacolborane and haloarenes.[14]

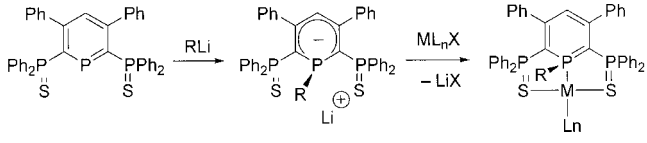

Scheme 1

Exploiting the same strategy, Yoshifuji et al. reported this year on the synthesis of mixed P,S-systems of the type (RP=C−P=S) featuring a kinetically stabilized phosphaalkene (λ^3,σ^2-phosphorus atom) and a phosphane sulfide group.[15,16] A cationic palladium(II) complex of these new low-coordinate, phosphorus-based ligands was employed as a catalyst in the direct conversion of allyl alcohol to allylaniline.[17]

Initially, we postulated that the presence of two ancillary phosphane sulfide groups was a prerequisite for the stabilization of these new types of σ complexes. Indeed, it is well-known that 1-alkylphosphininyllithium salts usually react

[a] Laboratoire "Hétéroéléments et Coordination", UMR CNRS 7653 (DCPH), Département de Chimie, Ecole Polytechnique, 92128 Palaiseau Cédex, France
Fax: + 33-1-69333990
E-mail: lefloch@poly.polytechnique.fr

Supporting information for this article is available on the WWW under http://www.eurjic.org or from the author.

through their π-system with metal fragments to yield the corresponding η^5-coordinated complexes.[18−23] In this article, we show that anionic bidentate P,S-ligands featuring a pseudo-ylidic λ^4-phosphorus atom can be easily assembled from a diphenyl(2-phosphininyl)phosphane sulfide.

Results and Discussion

The synthetic strategy used for the synthesis of these new systems relies on the reactivity of 4,6-di-*tert*-butyl-1,3,2-diazaphosphinine (**1**) towards functionalised alkynes.[24,25] This precursor proved to be a very efficient source of tetrafunctionalised phosphinines through successive [4 + 2] cycloaddition/cycloreversion processes with functionalised alkynes. We first focused our work on the synthesis of diphenyl(3-R-5,6-diphenylphosphinin-2-yl)phosphane sulfide derivatives. Azaphosphinine **2**, which was only used as a transient species, was readily formed by warming equimolar amounts of **1** and diphenylacetylene at 60 °C in toluene for 3 d (Scheme 2).

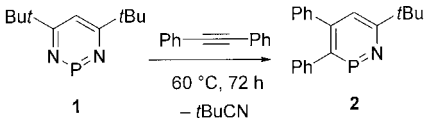

Scheme 2

Compound **2** proved to be sufficiently reactive to undergo a second [4 + 2] cycloaddition/cycloreversion process with 1 equiv. of alkynyl-substituted diphenylphosphane sulfides in toluene at reflux. We chose Me−C≡C−P(S)Ph_2 for this reaction in order to increase the solubility of the ligand. We found that the reaction with diphenyl(1-propynyl)phosphane sulfide only yielded phosphinine **3**, which was isolated as an air-stable, white solid and was fully characterized by NMR techniques and elemental analysis. The presence of the diphenylphosphane sulfide group at the α-position of the phosphorus atom was evidenced in the ^{31}P NMR spectrum by a large $^2J_{P,P}$ coupling constant of 108.2 Hz (in $CDCl_3$ at 25 °C) (Scheme 3). The formulation proposed on the basis of NMR spectroscopic data was confirmed by an X-ray crystal structure analysis. A view of a molecule of **3** is presented in Figure 1; crystal data are summarized in the Exp. Sect. This structure deserves no particular comments as the metric parameters fall in the usual range for λ^3-phosphinines.

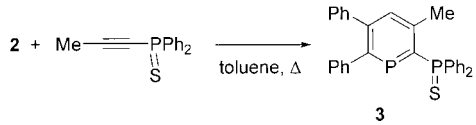

Scheme 3

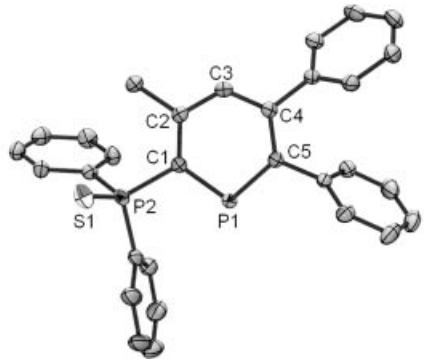

Figure 1. ORTEP view of a molecule of ligand **3**; ellipsoids are scaled to enclose 50% of the electron density; the numbering is arbitrary and different from that used in the assignment of the NMR spectra; selected distances [Å] and bond angles [°]: P1−C1 1.739(2), C1−C2 1.406(2), C2−C3 1.395(2), C3−C4 1.392(2), C4−C5 1.404(2), C5−P1 1.736(2), C1−P2 1.824(2), P2−S1 1.954(1); P1−C1−C2 124.4(1), C1−C2−C3 120.8(2), C2−C3−C4 126.6(2), C3−C4−C5 121.7(2), C4−C5−P1 123.9(1), C5−P1−C1 102.60(7), P1−C1−P2 115.1(1); (mean plane C1−C2−C4−C5)−P1 0.45, (mean plane C1−C2−C4−C5)−C3 0.8

As previously explained, the synthesis of the corresponding 1-alkylphosphininyllithium salts can be conventionally achieved by treating equimolar amounts of phosphinines with nucleophiles. Thus, **3** was treated with *n*-butyllithium in THF at −78 °C to afford the lithium salt **4**, which was identified by ^{31}P NMR spectroscopy. The lithium salt **4** appears as an AB system [δ = −37.6 (P−Bu) and 42.4 ppm (PPh_2) in THF at 25 °C; $^2J_{P,P}$ = 151.9 Hz]. The chemical shift of the ring phosphorus atom (δ = −37.6 ppm) is similar to those of other 1-alkylphosphininyllithium salts.[14,23]

Reaction of **4** with the dimer [Ru(η^6-$C_{10}H_{14}$)Cl_2]$_2$ was carried out in THF at low temperature. After warming to room temperature, the ^{31}P NMR spectrum of the crude mixture indicated that two complexes **5a** and **5b** had formed in a 3:1 ratio (Scheme 4).

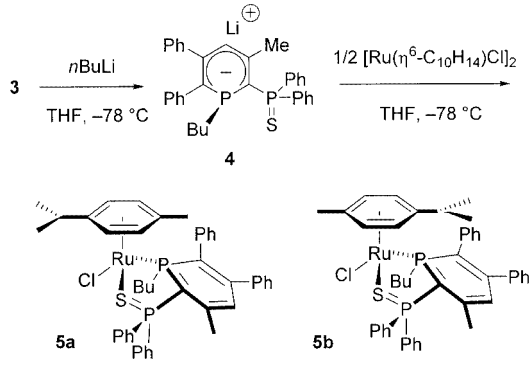

Scheme 4

Both complexes appear as an AB spin-system with close chemical shifts (δ = 40.7 and 44.3 ppm for **5a** and δ = 43.4 and 45.9 ppm for **5b**) and $^2J_{P,P}$ coupling constants (115.5 Hz for **5a** and 97.2 Hz for **5b**). The only major difference between **5a** and **5b** in the ^1H NMR spectra arises from

 © 2005 Wiley-VCH Verlag GmbH & Co. KGaA, Weinheim

the chemical shifts of the aromatic protons of the cymene ligand: in **5a** two hydrogen signals are shifted to high field (doublets at δ = 3.17 and 3.69 ppm with $^3J_{H,H}$ = 5.5 and 6.1 Hz, respectively) compared with those of **5b** (doublets at δ = 4.13 and 4.17 ppm with $^3J_{H,H}$ = 6.0 and 5.6 Hz, respectively) and other reported complexes.[26] Fortunately, complex **5a** proved to be insoluble in diethyl ether, thus allowing the separation of the two diastereomers. Single crystals of complex **5a** were obtained at room temperature from C_6D_6 as solvent (crystals deposited during the recording of the NMR spectra). An ORTEP view of a molecule of **5a** is presented in Figure 2; crystal data are presented in the Exp. Sect. As can be seen, the complex adopts a classical pianostool structure with the *n*-butyl substituent at the phosphorus atom pointing backwards probably to avoid steric congestion with the cymene ligand. The most interesting finding is related to the external P−C and P=S bond lengths. The shortening of the C1−P2 bond from 1.824(2) in **3** to 1.745(2) Å in **5a** and the elongation of the P2=S1 bond from 1.954(1) in **3** to 2.0283(7) Å in **5a** suggests a slight delocalization over the P1−C1−P2−S1−Ru1 skeleton. This induces a relocalization of the internal P−C and C−C bonds within the phosphinine ring: for instance, C2−C3 and C4−C5 shorten [1.372(3) and 1.376(3) Å, respectively] with respect to the free ligand [1.395(2) and 1.404(2) Å] whereas C1−C2, C3−C4 and C5−P1 lengthen [1.422(3), 1.435(2) and 1.805(2) Å in **5a** compared with 1.404(2), 1.394(2) and 1.736(2) Å in **3**]. The S−Ru bond [2.4239(5) Å] falls in the usual range of P=S−Ru bond lengths.[27,28] As previously noted in the structures of Ni, Pd, Pt and Rh complexes,[12,13] the phosphorus atom and the C3 carbon atom lie out of the plane defined by the C1, C2, C4 and C5 atoms by 12.6° and 1.8°, respectively, to yield a boat-like conformation. The phosphorus atom is now pyramidal (sum of angles at P1 = 313.8°) and compares well with classical tertiary phosphanes.

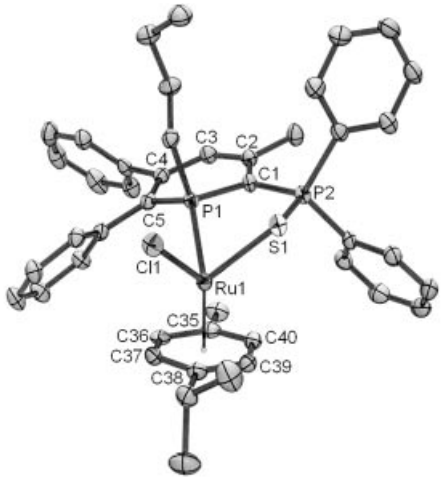

Figure 2. ORTEP view of a molecule of complex **5a**; ellipsoids are scaled to enclose 50% of the electron density; the numbering is arbitrary and different from that used in the assignment of the NMR spectra; selected distances [Å] and bond angles [°]: P1−C1 1.790(2), C1−C2 1.422(3), C2−C3 1.372(3), C3−C4 1.435(2), C4−C5 1.376(3), C5−P1 1.805(2), P1−Bu 1.852(2), C1−P2 1.745(2), P2−S1 2.0283(7), Ru1−P1 2.3351(5), Ru1−S1 2.4239(5), Ru1−Cl1 2.4186(5), Ru1−C35 2.237(2), Ru1−C36 2.239(2), Ru1−C37 2.196(2), Ru1−C38 2.276(2), Ru1−C39 2.257(2), Ru1−C40 2.189(2), Ru1−Ct 1.725, C35−C36 1.442(3), C36−C37 1.401(3), C37−C38 1.420(3), C38−C39 1.408(3), C39−C40 1.430(3), C40−C35 1.402(3); P1−C1−C2 121.1(1), C1−C2−C3 122.5(2), C2−C3−C4 125.3(2), C3−C4−C5 125.1(2), C4−C5−P1 119.2(1), C5−P1−C1 102.82(8), P1−C1−P2 111.9(1); (mean plane C1−C2−C4−C5)−P1 12.55, (mean plane C1−C2−C4−C5)−C3 1.75

Additional experiments were carried out in order to see which factors control the ratio between **5a** and **5b**. However, whatever the experimental conditions used (concentration and reaction temperature) the 3:1 ratio initially obtained could not be significantly modified. Variable-temperature NMR experiments were also carried out on the mixture of **5a** and **5b** but, even under reflux in THF, no interconversion could be observed. The stereochemistry of **5a** could not be established on the sole basis of its NMR spectroscopic data. In theory, four diastereomers can be formed (**5a**,**b**,**c**,**d**; Scheme 5) depending on the orientation of the substituent at the phosphorus atom (backwards in **5a** and **5b**, inwards in **5c** and **5d**) and on the orientation of the methyl and isopropyl groups of the cymene ligand. Although simple molecular modelling strongly suggests that diastereomers **5c** and **5d** could not be formed because of the important steric congestion between the cymene ligand and both the substituent at the phosphorus atom and one of the phenyl groups of the diphenylphosphane sulfide group, the four diastereomers were computed using the ONIOM method at the B3LYP/UFF level (see Exp. Sect. for details on basis sets and partition of the molecule into QM and MM shells). In these calculations the *n*-butyl group at the phosphorus atom was replaced by a methyl group to minimize the degrees of freedom. Optimizations of the theoretical complexes **5c** and **5d** failed and no minima could be located, the ligand being displaced away from the Ru−Cl fragment during the optimization. The introduction of an *n*-butyl group at the phosphorus atom would not yield a different result due to the bulkiness generated by the alkyl chain. However, two minima could be located for structures **Ia** (model of **5a**) and **Ib** (model of **5b**). Two views of these theoretical structures are presented in Fig-

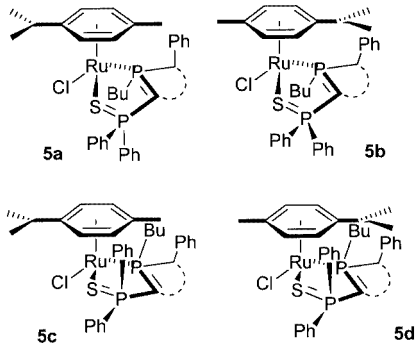

Scheme 5

 © 2005 Wiley-VCH Verlag GmbH & Co. KGaA, Weinheim

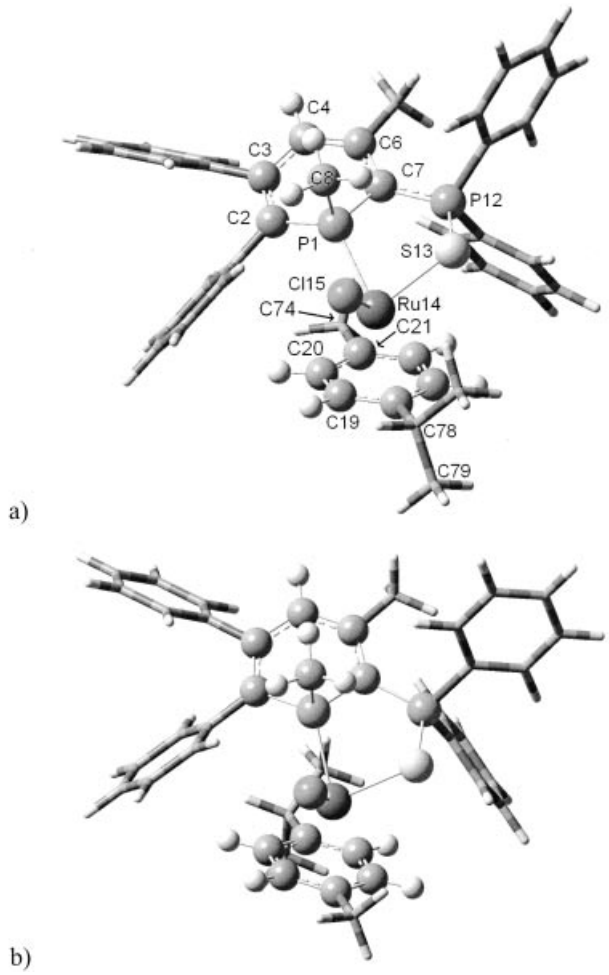

Figure 3. Optimized structures of model complexes **Ia** (a) and **Ib** (b) obtained at the ONIOM(B3LYP/UFF) level of theory; atoms included in the QM part are shown in ball-and-stick format and atoms included in the MM part are represented by tubes; the numbering is the same for **Ia** and **Ib**

ure 3; fully labelled molecules of **Ia**,**b** are presented in the Supporting Information. The most significant bond lengths and bond angles of **Ia,b** are reported in Table 1. As can be seen by examining these data, there is an acceptable fit between theoretical and experimental parameters. In **Ia** the P,S-ligand and the Ru−Cl, Ru−S and Ru−P bond lengths are very close to those of the X-ray structure of **5a**: for instance, in **Ia** the P1−C2, C7−P12, P12−S13, Ru14−S13 and Ru14−P1 bond lengths are 1.812, 1.757, 2.061, 2.449 and 2.385 Å, respectively, versus 1.805, 1.745, 2.028, 2.424 and 2.335 Å in **5a**. The only discrepancies arise in the cymene ring. Despite excellent agreement between the C−C bond lengths (for example C19−C20, C74−C21, C78−C79 are 1.407, 1.511 and 1.534 Å, respectively, in **Ia** versus 1.401, 1.511 and 1.534 Å in **5a**), the cymene ring is too far away from the ruthenium atom (the C16−Ru14 distance is 2.328 Å in **Ia** compared to 2.189 Å in **5a**). Modification of the basis set for Ru (all-electron basis sets rather than ECP) was not performed due to the already long computational time. The same trends are observed between **Ia** and **Ib** and deserve no other comment.

Table 1. Selected bond lengths [Å] for calculated structures **Ia**,**b**

	Ia	**Ib**
P1−C2	1.812	1.810
C2−C3	1.388	1.387
C3−C4	1.440	1.439
C4−C6	1.386	1.386
C6−C7	1.429	1.431
C7−P1	1.806	1.814
P1−R8	1.851	1.851
C26−C2	1.492	1.491
C37−C3	1.491	1.491
C48−C6	1.512	1.513
C7−P12	1.757	1.759
P12−S13	2.061	2.059
P1−Ru14	2.385	2.391
S13−Ru14	2.449	2.432
Cl15−Ru14	2.443	3.329
C16−Ru14	2.328	2.407
C17−Ru14	2.391	2.357
C18−Ru14	2.385	2.349
C19−Ru14	2.228	2.291
C20−Ru14	2.327	2.361
C21−Ru14	2.321	2.442
C74-cycle	1.499	1.499
C78-cycle	1.517	1.519
C79−C78	1.531	1.532
C80−C78	1.536	1.530

Single-point calculations at the B3LYP level of theory carried out on both optimized ONIOM structures revealed that the model complex **Ia** is more stable than the isomer **Ib** ($\Delta\Delta H = -4.8$ kcal/mol), thus confirming the experimental results. Most importantly, no transition state could be located between **Ia** and **Ib**, the rotation of the cymene ligand around its centroid−ruthenium axis being completely blocked by the two peripheral phenyl groups. This result allows us to rationalize why no interconversion between **5a** and **5b** is observed, even under heating.

The catalytic activity of complexes **5a,b** in the transfer hydrogenation of ketones was tested (Scheme 6).[29−34] Reactions were conducted in 2-propanol as a proton source and solvent and KOH as base using 0.5 mol % of catalysts in most cases. The results are summarized in Table 2. As can be seen, although conversion is acceptable, long reaction times are needed to achieve complete conversions. It must be noted that no efforts have been made, so far, to improve these figures (solvents, role of the base, amount of catalyst).

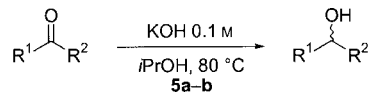

Scheme 6

The synthesis of a $[Pd(\eta^3\text{-}C_3H_5)]^+$ complex of the lithium salt **4** was also investigated. As previously reported for the synthesis of **5a**,**b**, reaction of phosphinine **3** with methyllithium in THF at −78 °C afforded the lithium salt **6**, which was identified by ^{31}P NMR spectroscopy. Like **4**, the lith-

 © 2005 Wiley-VCH Verlag GmbH & Co. KGaA, Weinheim

Table 2. Transfer hydrogenation of ketones using complex **5a**,**b** as catalyst; conditions: substrate (2 mmol), catalyst **5a**,**b** (0.5 mol %, unless stated otherwise), 10 mL of 0.1 M KOH in *i*PrOH, 80 °C, 2.5 d.

Entry	Substrate	Yield (%)[a]	Time[b]	TON
1	4-heptanone	91.6	2.5	183.2
2	1,3-diphenylacetone	100	2.5	200
3	cyclohexanone	100	2.5	200
4	2,6-dimethylcyclohexanone	100	2.5	200
5	acetophenone	82.1[c]	0.5	82.1
6	acetophenone	97.6	2.5	195.2
9	4-Br-acetophenone	96.6	2.5	193.2
10	4-F-acetophenone	100	2.5	200
11	4-methyl-acetophenone	94.1	2.5	182.8
12	benzophenone	98.5	2.5	197
13	4,4′-dimethoxy-benzophenone	72.1[d]	2.5	90.1
14	transchalcone	100	2.5	200

[a] Yields were determined by ^{1}H NMR spectroscopy, mass spectrometry or GC. [b] In days. [c] 1 mol % of catalyst. [d] 0.8 mol % of catalyst.

ium salt **6** appears as an AB system with comparable chemical shifts [δ = −40.7 (P−Me) and 42.5 ppm (PPh_2) in THF at 25 °C; $^2J_{P,P}$ = 156.7 Hz]. Reaction of **6** with the dimer [Pd(η^3-C_3H_5)Cl]$_2$ was carried out in THF at low temperature. After warming to room temperature, the ^{31}P NMR spectrum of the crude mixture indicated that complexes **7a** and **7b** had formed in a 3:1 ratio (Scheme 7). Complexes **7a** (major isomer) and **7b** (minor isomer) appear as an AB spin-system with very similar chemical shifts (δ = 24.6 and 52.4 ppm for **7a** and δ = 23.4 and 52.0 ppm for **7b**) and $^2J_{P,P}$ coupling constants (135.8 Hz for **7a** and 132.7 Hz for **7b**). Separation of complexes **7a** and **7b** could not be achieved despite many attempts. These complexes were, however, fully characterized by ^{1}H and ^{13}C NMR spectroscopy, and elemental analysis. In the ^{1}H NMR spectrum of **7**, two sets of five non-equivalent η^3-allyl proton resonances are observed. One of the signals of the minor isomer **7b** overlaps with those of the major isomer **7a**.

Isomer interconversion was investigated by variable-temperature NMR experiments but no conversion was observed. We suppose that the rotation of the allyl moiety is disfavoured by a repulsive interaction between the CH_2 allyl

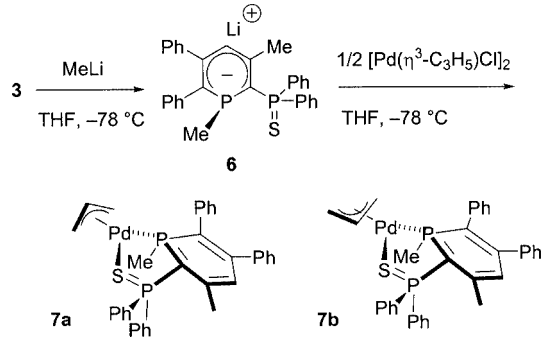

Scheme 7

group and the phenyl group in the C6 position of the phosphinine ring. A similar phenomenon has already been reported for other complexes.[35,36]

Crystals of **7a** suitable for X-ray analysis were obtained by slow diffusion of hexanes into a solution of complexes **7a**,**b** in $CDCl_3$. An ORTEP view of **7a** is presented in Figure 4 and the refinement parameters are given in the Exp. Sect. This structure confirms the η^3-coordination of the allyl moiety and also that the geometry around the palladium atom is trigonal-planar. The P1−Pd [2.2778(6) Å] and the S1−Pd [2.3371(6) Å] bond lengths are similar to classical phosphane−palladium and P=S−Pd bond lengths,[36] although the P1−Pd distance is greater than in previously reported tridentate palladium complexes.[12] The Pd−C32, Pd−C33, Pd−C34 [2.138(3), 2.137(3), 2.199(3) Å] and C32−C33 and C33−C34 [1.359(4) and 1.383(5) Å] bond lengths and the C32−C33−C34 angle [123.8(3)°] are in the typical range of η^3-allylpalladium complexes.[37−40] The geometry of the phosphinine moiety is similar to that in complex **5a** and deserves no further comment. In the major isomer an H,C-HSQC NMR experiment showed that the signals of the two hydrogen atoms of the CH_2 allyl fragments at δ = 2.16 and 2.52 ppm are connected, as are those at δ = 3.00 and 4.21 ppm. An H,H-NOESY experiment also revealed that, in this same isomer, the P−Me group (C6 in the ORTEP view) is in the spatial neighbourhood of only two hydrogen atoms of the CH_2 allyl fragments (at δ = 2.16 and 2.52 ppm) and is far from the CH and the other CH_2 fragments (at δ = 4.89, 3.00 and 4.21 ppm, respectively). The major isomer is therefore complex **7a**.

The catalytic activity of complexes **7a**,**b** was tested in the Suzuki−Miyaura cross-coupling reaction, which allows the synthesis of arylboronic esters from haloarenes and phenylboronic acid (Scheme 8).[41−49] The reactions were conduc-

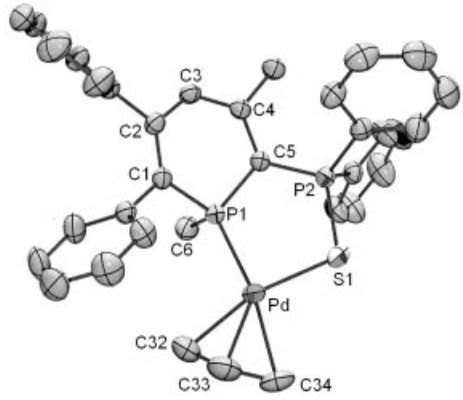

Figure 4. ORTEP view of one molecule of complex **7a**; ellipsoids are scaled to enclose 50% of the electron density; the numbering is arbitrary and different from that used in the assignment of the NMR spectra; selected distances [Å] and bond angles [°]: P1−C1 1.802(2); C1−C2 1.360(3), C2−C3 1.444(3), C3−C4 1.378(3), C4−C5 1.422(3), C5−P1 1.756(2), P1−C6 1.828(2), C5−P2 1.733(2), P2−S1 2.0288(8), Pd1−P1 2.2778(6), Pd−S1 2.3371(6), Pd−C32 2.138(3), Pd−C33 2.137(3), Pd−C34 2.199(3), C32−C33 1.359(4), C33−C34 1.383(5); P1−C1−C2 117.2(2), C1−C2−C3 123.4(2), C2−C3−C4 124.5(2), C3−C4−C5 121.0(2), C4−C5−P1 117.5(2), C5−P1−C1 101.7(1), P1−C5−P2 117.8(1), C32−C33−C34 123.8(3); (mean plane C1−C2−C4−C5)−P1 21.7; (mean plane C1−C2−C4−C5)−C3 7.3

 © 2005 Wiley-VCH Verlag GmbH & Co. KGaA, Weinheim

ted in toluene in the presence of K_2CO_3 using 0.0001 mol % of catalyst in most cases. The results are summarized in Table 3. As can be seen, the conversions obtained in the transformation of aryl bromides are acceptable: turnover numbers (TONs) fall in the range of 242000 for electron-rich arenes (4-bromoanisole) to 799000 for electron-deficient species (4-bromoacetophenone). It must be noted that no efforts were made to improve these results (solvents, role of the base). However, under the same experimental conditions (toluene at reflux), no reaction was observed with the less-reactive aryl chlorides, even when using 2.0 mol % of catalyst.

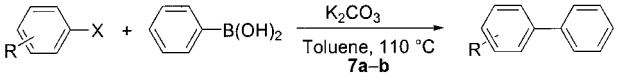

Scheme 8

Table 3. Suzuki−Miyaura reaction of aryl halides using complex **7** as catalyst; conditions: aryl bromide (1.0 mmol), phenylboronic acid (1.5 mmol), K_2CO_3 (2.0 mmol) catalyst **7** (0.0001 mol % unless stated otherwise), 10 mL of toluene, 110 °C, 24 h

Entry	Substrate	Yield (%)[a]	Benzene (%)[a]	TON
1	bromobenzene	80.9[b]	5.6	80 900
2	bromobenzene	50.0	5.4	500 000
3	4-bromoanisole	43.2	8.6	432 000
4	4-bromotoluene	24.4	9.8	244 000
5	4-bromoacetophenone	79.9	9.4	799 000

[a] Yields were determined by GC. [b] 0.01 mol % of catalyst.

Conclusion

We have developed an access to a new class of ligands that features a pseudo-ylidic phosphorus atom and a P=S ancillary arm. Interestingly, this allows to show that coordination through the phosphorus atom in 1-alkylphosphininyllithium salts does not require the presence of two pendant ancillary P=S ligands. Although the catalytic activity of the (cymene)Ru derivatives in the transfer hydrogenation of ketones was found to be modest, interesting conversion yields were obtained in the Pd-catalysed synthesis of arylboronic esters from bromoarenes and phenylboronic acid. Further studies are now focusing on the synthesis of other transition-metal complexes and investigation of their catalytic properties.

Experimental Section

General Remarks: All reactions were routinely performed under argon or nitrogen with Schlenk and glove-box techniques and dry deoxygenated solvents. Dry THF and hexanes were obtained by distillation from Na/benzophenone, dry diethyl ether from $CaCl_2$ and then NaH, and dry CH_2Cl_2 from P_2O_5. $CDCl_3$ was dried with P_2O_5 and stored over Linde molecular sieves (4 Å). C_6D_6 was used as purchased and stored in the glovebox. $[PdCl(C_3H_5)]_2$ was purchased from Fluka. NMR spectra were recorded with a Bruker Avance 300 spectrometer operating at 300.0 MHz for ^1H, 75.5 MHz for ^{13}C and 121.5 MHz for ^{31}P. Solvent peaks are used as internal reference relative to $SiMe_4$ for ^1H and ^{13}C chemical shifts (ppm); ^{31}P chemical shifts are quoted relative to an 85% H_3PO_4 external reference. Coupling constants are given in Hz. Mass spectra were obtained at 70 eV with an HP 5989B spectrometer coupled to an HP 5980 chromatograph by the direct inlet method. Elemental analyses were performed by the "Service d'analyse du CNRS", at Gif sur Yvette, France. Diazaphosphinine **1**,[24] diphenyl(1-propynyl)phosphane sulfide[50] and $[RuCl_2(\eta^6\text{-}C_{10}H_{14})]_2$ [51] were prepared according to reported procedures.

Phosphinine 3: Diphenylacetylene (3.79 g, 21 mmol) was added to a solution of diazaphosphinine **1** in toluene (8×10^{-5} mol/mL, 20 mmol) and the mixture was stirred at 60 °C for 72 h. Consumption of **1** (δ = 269.0 ppm) and formation of the 5,6-diphenyl-1,2-azaphosphinine **2** (δ = 267.4 ppm) was checked by ^{31}P NMR spectroscopy. Diphenyl(1-propynyl)phosphane sulfide (3.44 g, 22 mmol) (δ = 18.8 ppm) was then added and the solution was stirred at 120 °C for 96 h. After evaporation of the solvent, the solid was washed with hexanes (3 × 20 mL) and MeOH (20 mL) and the resulting solid was dissolved in hot MeOH and stored at 0 °C. The white solid that separated was washed several times with cold MeOH (3 × 30 mL). After drying, **3** was recovered as a white solid. Yield: 6.0 g (62%). Crystals suitable for X-ray crystallography were obtained by slow diffusion of hexanes into a solution of **3** in CH_2Cl_2. ^1H NMR (300 MHz, $CDCl_3$, 25 °C): δ = 2.67 (s, CH_3), 7.00−7.98 (m, 21 H, CH of Ph and H4) ppm. ^{13}C NMR (75.5 MHz, $CDCl_3$, 25 °C): δ = 25.4 (d, $^3J_{C,P_B}$ = 8.2, CH_3), 127.2−133.5 (m, CH of Ph), 132.9 (dd, J_{C,P_B} = 84.6, J_{C,P_A} = 5.3, C), 138.6 (vt, $^3J_{C,P_A}$ = $^3J_{C,P_B}$ = 12.8, C4H), 141.3 (s, C), 141.7 (s, C), 148.0 (dd, J_{C,P_B} = 9.1, J_{C,P_A} = 3.8, C), 149.0 (dd, J_{C,P_B} = 12.8, J_{C,P_A} = 4.5, C), 159.4 (dd, J_{C,P_B} = 76.3, J_{C,P_A} = 67.2, C), 166.2 (dd, J_{C,P_B} = 58.9, J_{C,P_A} = 14.3, C) ppm. ^{31}P NMR (121.5 MHz, $CDCl_3$, 25 °C): δ = 42.6 (d, $^2J_{P_A,P_B}$ = 108.1, P_BPh_2), 226.7 (d, $^2J_{P_A,P_B}$ = 108.1, P_A) ppm. MS (CH_2Cl_2): *m/z* = 479 [M^+], 447 [M − S]$^+$, 416 [M − PS]. $C_{30}H_{24}P_2S$ (478.49): calcd. C 75.30, H 5.06; found C 74.97, H 4.72.

Lithium Salt 4: A solution of BuLi (0.235 mL, 1.6 M, 0.38 mmol) was added through a syringe into a solution of **3** (180 mg, 0.38 mmol) in THF (6 mL) at −78 °C. The solution was warmed to room temperature and stirred for 20 min. After evaporation of the solvent, the solid was washed several times with hexanes (3 × 2 mL). After drying, **4** was recovered as a red solid. Yield: 100%.^{31}P NMR (121.5 MHz, THF, 25 °C): δ = −37.6 (d, $^2J_{P_A,P_B}$ = 151.9, P_A−Bu), 42.4 (d, $^2J_{P_A,P_B}$ = 151.9, P_BPh_2).

Ruthenium Complexes 5a,b: A solution of BuLi (0.235 mL, 1.6 M, 0.38 mmol) was syringed into a solution of **3** (180 mg, 0.38 mmol) in THF (6 mL) at −78 °C. The solution was warmed to room temperature and stirred for 20 min. Complete formation of the lithium salt **4** was checked by ^{31}P NMR spectroscopy. In a glovebox, $[RuCl_2(cymene)]_2$ (115 mg, 0.19 mmol) was added to the solution and the solution was stirred for 1 h. After removing the solvent,

 © 2005 Wiley-VCH Verlag GmbH & Co. KGaA, Weinheim

the resulting solid was dissolved in toluene and filtered through Celite. After drying, **5** was recovered as a red solid containing a mixture of two diastereoisomers (25:75). Yield: 242 mg (80%). The major diastereoisomer, which is insoluble in diethyl ether, could be obtained by washing the red solid several times with diethyl ether (3 × 10 mL). The resulting filtrate was kept at 0 °C overnight during which time the minor diastereoisomer separated as a red solution.

Major Diastereoisomer 5a: Yield: 150 mg (49%). Crystals suitable for X-ray crystallography were deposited from a solution of **5a** in C_6D_6. ^{1}H NMR (300 MHz, C_6D_6, 25 °C): δ = 0.97 (d, $^3J_{H,H}$ = 7.0, 3 H, *CH*$_3$−CH of cymene), 0.97 (t, $^3J_{H,H}$ = 7.2, 3 H, CH_3 of *n*Bu), 1.17 (d, $^3J_{H,H}$ = 6.7, 3 H, *CH*$_3$−CH of cymene), 1.50−1.58 (m, 2 H, CH_2 of *n*Bu), 1.72 (s, 3 H, CH_3 of phosphinine), 1.95 (s, 3 H, Ar−*CH*$_3$ of cymene), 2.14−2.28 (m, 1 H, CH_2 of *n*Bu), 2.32−2.50 (m, 1 H, CH_2 of *n*Bu), 2.52−2.69 (m, 1 H, CH_2 of *n*Bu), 2.99−3.09 (m, 2 H, Ar−*CH* of cymene and CH_2 of *n*Bu), 3.17 (d, $^3J_{H,H}$ = 5.5, Ar−H of cymene), 3.69 (d, $^3J_{H,H}$ = 6.1, Ar−H of cymene), 4.67 (d, $^3J_{H,H}$ = 6.1, Ar−H of cymene), 5.06 (d, $^3J_{H,H}$ = 5.5, Ar−H of cymene), 5.43 (d, $^4J_{H,P}$ = 6.3, H4), 6.88−7.12 (m, 12 H, H of Ph), 7.55−7.58 (m, 2 H, H of Ph), 7.69−7.80 (m, 4 H, H of Ph), 7.88−7.95 (m, 2 H, H of Ph) ppm. ^{13}C NMR (75.5.5 MHz, C_6D_6, 25 °C): δ = 13.2 (s, CH_3 of *n*Bu), 15.4 (s, Ar−CH_3 of cymene), 18.2 (s, CH_3 of isopropyl), 22.9 (vt, $\Sigma J_{C,P}$ = 5.1, CH_3 of isopropyl), 23.6 (d, $^3J_{C,P_A}$ = 11.6, CH_2 of *n*Bu), 24.5 (s, CH_3 of phosphinine), 25.9 (d, $^2J_{C,P_A}$ = 7.5, CH_2 of *n*Bu), 29.1 (s, CH of isopropyl), 42.5 (d, $^1J_{C,P_A}$ = 19.8, P_A−CH_2), 60.0 (dd, $^1J_{C,P_A}$ = 104.9, $^1J_{C,P_B}$ = 55.9, C2), 67.5 (s, C of cymene), 75.1 (s, CH of cymene), 87.1 (s, CH of cymene), 89.1 (s, CH of cymene), 90.4 (d, $^2J_{C,P_A}$ = 9.1, CH of cymene), 94.4 (s, C of cymene), 99.3 (dd, $^1J_{C,P_A}$ = 43.8, $^3J_{C,P_B}$ = 7.6, C6), 112.6 (dd, $J_{C,P}$ = 12.8, $J_{C,P}$ = 6.8, C4H), 114.8 (d, $J_{C,P}$ = 9.1, C), 123.3−132.8 (m, CH of Ph), 134.1 (m, C), 134.7 (m, C), 141.8 (dd, $J_{C,P}$ = 15.9, $J_{C,P}$ = 2.3, C), 144.2 (d, $J_{C,P}$ = 5.3, C3), 145.1 (d, $J_{C,P}$ = 7.6, C5), 150.2 (d, $J_{C,P}$ = 1.5, C) ppm. ^{31}P NMR (121.5 MHz, C_6D_6, 25 °C): δ = 40.7 (d, $^2J_{P_A,P_B}$ = 115.5, P), 44.3 (d, $^2J_{P_A,P_B}$ = 115.5, P) ppm.

Minor Diastereoisomer 5b: Yield: 33 mg (11%). ^{1}H NMR (121.5 MHz, C_6D_6, 25 °C; selected data): δ = 0.88−2.44 (m, 25 H, Bu, *i*Pr, 3 × Me), 4.13 (d, $^3J_{H,H}$ = 6.0, Ar−H of cymene), 4.17 (d, $^3J_{H,H}$ = 5.6, Ar−H of cymene), 4.91 (d, $^3J_{H,H}$ = 6.0, Ar−H of cymene), 4.96 (d, $^3J_{H,H}$ = 5.7, Ar−H of cymene), 5.31 (d, $^4J_{H,P}$ = 5.5, H_4), 6.70−8.25 (m, 20 H, H of Ph) ppm. ^{31}P NMR (121.5 MHz, C_6D_6, 25 °C): δ = 43.4 (d, $^2J_{P_A,P_B}$ = 97.2, P), 45.9 (d, $^2J_{P_A,P_B}$ = 97.2, P). $C_{44}H_{47}ClP_2RuS$ (806.34): calcd. C 65.54, H 5.87; found C 65.22, H 5.48.

Hydrogenation of Ketones: A mixture of complexes **5a**,**b** (8 mg, 0.01 mmol, 0.5 mol %) was added to a solution of ketone (2 mmol, 1 equiv.) in KOH/2-propanol (0.1 M, 10 mL). The mixture was stirred at 80 °C for 2.5 d. The progress of the reaction was monitored by GC, mass spectrometry or ^{1}H NMR spectroscopy. The mixture was then neutralized with a saturated solution of 3 M HCl (3 mL) and $NaHCO_3$ (15 mL), and it was then extracted with dichloromethane (3 × 15 mL). The organic layers were collected and dried with $MgSO_4$ and the solvents evaporated to yield the corresponding alcohol. The alcohols were characterised by comparing their ^{1}H and ^{13}C NMR spectra with reported NMR spectroscopic data and by mass spectrometry.

Characterization of Secondary Alcohols: 4-Heptanol,[52] 1,3-diphenyl-2-propanol,[53] *syn*-2,5-dimethylcyclohexanol,[54] 1-phenylethanol,[55] diphenylmethanol,[56] 1-(*p*-bromophenyl)ethanol,[57] bis(*p*-methoxyphenyl)methanol.[58]

Lithium Salt 6: A solution of MeLi (0.235 mL, 1.6 M, 0.38 mmol) was added through a syringe into a solution of **3** (180 mg, 0.38 mmol) in THF (6 mL) at −78 °C. The solution was warmed to room temperature and stirred for 20 min. After evaporation of the solvent, the solid was washed several times with hexanes (3 × 2 mL). After drying, **6** was recovered as a red solid. Yield: 100%.^{31}P NMR (121.5 MHz, THF, 25 °C): δ = −46.7 (d, $^2J_{P_A,P_B}$ = 156.7, P_A−Me), 42.5 (d, $^2J_{P_A,P_B}$ = 156.7, P_BPh$_2$) ppm.

Palladium Complexes 7a,**b:** A solution of MeLi (0.156 mL, 1.6 M, 0.25 mmol) was added through a syringe into a solution of **3** (120 mg, 0.25 mmol) in THF (5 mL) at −78 °C. The solution was warmed to room temperature and stirred for 20 min. Complete formation of the lithium salt **6** was checked by ^{31}P NMR spectroscopy. In a glovebox, $[PdCl(C_3H_5)]_2$ (44 mg, 0.12 mmol) was added to the solution and the mixture stirred for 1 h. After removing the solvent, the resulting solid was dissolved in CH_2Cl_2 and filtered through Celite. After drying, **7** was recovered as a brown solid containing a mixture of two diastereoisomers (25:75). No further purification was carried out to separate the two diastereoisomers. Crystals of **7a** suitable for X-ray diffraction were obtained by slow diffusion of hexane into a CH_2Cl_2 solution of **7a**,**b** Yield: 123 mg (77%).

Major Diastereoisomer 7a: ^{1}H NMR (300 MHz, $CDCl_3$, 25 °C): δ = 1.19 (d, $^2J_{H,P_A}$ = 8.1, 3 H, P_AMe), 1.65 (s, 3 H, Me), 2.16 (d, $^2J_{H,H}$ = 13.2, 1 H, CH_2 allyl), 2.52 (d, $^3J_{H,H}$ = 6.4, 1 H, CH_2 allyl), 3.00 (dd, $^2J_{H,H}$ = 13.2, $^3J_{H,H}$ = 10.4, 1 H, CH_2 allyl), 4.21 (vt, $^2J_{H,H}$ = $^3J_{H,H}$ = 6.5, 1 H, CH_2 allyl), 4.89 (m, CH allyl), 5.57 (d, $^4J_{H,P_A}$ = 5.9, H4), 7.04−8.09 (m, 20 H, H of Ph) ppm. ^{13}C NMR (75.5.5 MHz, $CDCl_3$, 25 °C): δ = 17.1 (dd, $^1J_{C,P}$ = 20.6, $^3J_{C,P}$ = 2.7, P_AMe), 25.9 (dd, $^3J_{C,P}$ = 4.2, $^3J_{C,P}$ = 3.1, Me), 55.0 (dd, $J_{C,P}$ = 111.7, $J_{C,P}$ = 54.2, C2/6), 59.6 (d, $^2J_{C,P}$ = 5.7, CH_2 allyl), 69.1 (dd, $^2J_{C,P}$ = 32.4, $^4J_{C,P}$ = 4.5, CH_2 allyl), 109.8 (dd, $J_{C,P}$ = 47.9, $J_{C,P}$ = 5.1, C2/6), 113.4 (dd, $J_{C,P}$ = 12.6, $J_{C,P}$ = 10.1, C4), 117.0 (d, $^2J_{C,P}$ = 6.4, CH allyl), 125.1−133.1 (m, CH and C of Ph), 136.9 (dd, $J_{C,P}$ = 78.1, $J_{C,P}$ = 7.2, C3/5), 143.5 (dd, $J_{C,P}$ = 8.8, $J_{C,P}$ = 2.9, C3/5), 144.4 (d, $J_{C,P}$ = 15.6, C of Ph), 145.4 (d, $J_{C,P}$ = 1.9, C of Ph) ppm. ^{31}P NMR (121.5 MHz, $CDCl_3$, 25 °C): δ = 24.6 (d, $^2J_{P,P}$ = 135.8, P_A), 52.4 (d, $^2J_{P,P}$ = 135.8, P_BPh$_2$).

Minor Diastereoisomer 7b: ^{1}H NMR (300 MHz, $CDCl_3$, 25 °C): δ = 1.16 (br. s, 3 H, PMe), 1.65 (s, 3 H, Me), 1.72 (d, $^2J_{H,H}$ = 13.3, 1 H, CH_2 allyl), 2.90 (d, $^2J_{H,H}$ = 13.4, 1 H, CH_2 allyl), 3.18 (d, $^2J_{H,H}$ = 7.0, 1 H, CH_2 allyl), 5.01 (m, 1 H, CH allyl), 7.04−8.09 (m, 20 H, H of Ph) ppm; signals of 1 H of CH_2 allyl and H4 were not observed. ^{13}C NMR (75.5.5 MHz, $CDCl_3$, 25 °C): δ = 18.2 (dd, $^1J_{C,P}$ = 20.0, $^3J_{C,P}$ = 2.7, P_AMe), 25.9 (m, Me), 55.0 (m, C2/6), 59.1 (d, $^2J_{C,P}$ = 5.1, CH_2 allyl), 70.0 (m, CH_2 allyl), 108.7 (m, C2/6), 113.6 (dd, $J_{C,P}$ = 12.8, $J_{C,P}$ = 9.5, C4), 116.8 (d, $^2J_{C,P}$ = 6.3, CH allyl), 124.4−133.5 (m, CH and C_q of Ph), 136.2 (d, $J_{C,P}$ = 83.9, $C_{3/5}$), 143.2 (dd, $J_{C,P}$ = 11.7, $J_{C,P}$ = 3.0, C3/5), 144.2 (d, $J_{C,P}$ = 8.8, C of Ph), 145.7 (d, $J_{C,P}$ = 2.1, C of Ph) ppm. ^{31}P NMR (121.5 MHz, $CDCl_3$, 25 °C): δ = 23.4 (d, $^2J_{P,P}$ = 132.7, P−Me), 52.0 (d, $^2J_{P,P}$ = 132.7, PPh_2) ppm. $C_{34}H_{32}P_2PdS$ (641.00): calcd. C 63.70, H 5.03; found C 63.46, H 4.81.

Suzuki−Miyaura Reaction of Aryl Halides: Catalyst **7** as a toluene solution (1.00 mL), made up to the correct concentration by multiple volumetric dilutions of a stock solution, was added to a mixture of the aryl halide (1.0 mmol), $PhB(OH)_2$ (0.183 g, 1.5 mmol) and K_2CO_3 (0.276 g, 2.0 mmol) in toluene (10 mL). The resultant mixture was then heated at 110 °C for 24 h, cooled and quenched with HCl(aq) (2 M, 40 mL). The organic layer was removed and the aqueous layer was extracted with toluene (3 × 50 mL). The combined organic layers were washed with water, dried ($MgSO_4$), fil-

 © 2005 Wiley-VCH Verlag GmbH & Co. KGaA, Weinheim

Table 4. Crystal data and structural refinement details for **3**, **5a** and **7a**

	3	**5a**	**7a**
Empirical formula	$C_{30}H_{24}P_2S$	$C_{44}H_{47}ClP_2RuS$	$C_{34}H_{32}P_2PdS$
M_r	478.49	806.34	641.00
Crystal system	monoclinic	monoclinic	triclinic
Space group	$P2_1/c$	$P2_1/n$	$P\bar{1}$
a [Å]	6.611(5)	11.3830(10)	11.2180(10)
b [Å]	42.648(5)	22.7280(10)	12.0220(10)
c [Å]	17.464(5)	14.6770(10)	12.7300(10)
α [°]	90	90	67.8200(10)
β [°]	92.430(5)	91.5450(10)	77.4300(10)
γ [°]	90	90	69.3200(10)
V [Å^3]	4919(4)	3795.7(5)	1480.3(2)
Z	8	4	2
ρ [g cm^{-3}]	1.292	1.411	1.438
μ [cm^{-1}]	0.278	0.654	0.827
Crystal size [mm]	0.20 × 0.20 × 0.20	0.18 × 0.14 × 0.10	0.22 × 0.18 × 0.05
F(000)	2000	1672	656
Index ranges	$-8 \le h \le 8$	$-16 \le h \le 16$	$-15 \le h \le 15$
	$-55 \le k \le 57$	$-29 \le k \le 31$	$-16 \le k \le 15$
	$-23 \le l \le 23$	$-20 \le l \le 20$	$-17 \le l \le 17$
$2\Theta_{max}$ [°]	28.70	30.03	30.03
Parameters refined	597	447	360
Data/parameters	16	18	17
Reflections collected	22198	18845	18500
Independent reflections	12430	11031	8591
Reflections used	9562	8413	6275
$wR2$	0.1143	0.1046	0.0790
$R1$	0.0414	0.0377	0.0344
Goodness of fit	1.054	1.007	1.018
Largest diff peak/hole [e·Å^{-3}]	0.352(0.060)/−0.404(0.060)	0.983(0.084)/−0.932(0.084)	0.853(0.072)/−0.750(0.072)

tered and the solvent removed under reduced pressure. The residue was dissolved in toluene (6 mL), hexadecane (0.068 M in CH_2Cl_2, 1.00 mL, internal standard) was added and the conversion into product determined by GC.

Characterizations of Suzuki−Miyaura Coupling Products: The NMR spectra of the biphenyl compounds were compared with those of commercial products (Aldrich); 4-methylbiphenyl,[59] 4-methoxybiphenyl,[59] 4-acetylbiphenyl.[60]

X-ray Crystallographic Study: Crystals of **3** and **7a** suitable for X-ray diffraction were obtained by slow diffusion of hexane into a CH_2Cl_2 solution of **3** and **7a**. Crystals of **5a** suitable for X-ray diffraction deposited overnight from a solution in C_6D_6. Data were collected at 150.0(1) K with a Nonius Kappa CCD diffractometer equipped with an Mo-K_α (λ = 0.71070 Å) X-ray source and a graphite monochromator, using φ and ω scans. The crystal structures were solved by using SIR 97[61] and SHELXL-97.[62] For ORTEP drawings ORTEP III for Windows was used.[63] Further details can be found in Table 4. CCDC-242764 to -242766 (for **3**, **5a** and **7a**) contain the supplementary crystallographic data for this paper. These data can be obtained free of charge at www.ccdc.cam.ac.uk/conts/retrieving.html [or from the Cambridge Crystallographic Data Centre, 12 Union Road, Cambridge CB2 1EZ, UK; Fax: + 44-1223-336-033; E-mail: deposit@ccdc.cam.ac.uk].

Theoretical Mmethods: All calculations were performed with the Gaussian 03 set of programs using the ONIOM method.[64] The two complexes were optimized at the ONIOM(B3LYP/UFF) level,[65] where the QM part was treated within the framework of density functional theory at the B3LYP level (B3 for Becke's three-parameter exchange functional[66] and LYP for the Lee−Yang−Parr non-local correlation functional[67]) and the UFF force field[68] was used for the molecular mechanic calculations. In all calculations (QM and QM/MM), the lanl2dz basis set was used for the ruthenium atom.[69] The 6-31+G(d) basis set was used for all atoms directly bound to the ruthenium centre (P, S, Cl atoms as well as the C atoms of the aromatic part of the cymene ligand). The C and H atoms of the phosphinine ring were calculated using the 6-31G(d) basis set. Full optimizations were realized at the ONIOM level, followed by analytical computation of the Hessian matrix to confirm the nature of the located minima on the potential energy surface. A single-point calculation was performed on the ONIOM optimized structures at the B3LYP level of theory using the 6-31G(d) basis sets for C, H, P, S, and Cl atoms and the lanl2dz basis set for Ru.

Supporting Information: See footnote on the first page of this article. Fully labelled structures of **Ia** and **Ib** and the geometrical parameters of the theoretical structures.

Acknowledgments

This work was supported by the CNRS, the Ecole Polytechnique and the DGA. M. D. thanks the DGA for financial support. The authors would like to thank IDRIS (Paris XI Orsay University) for the allocation of computer time.

[1] S. O. Grim, J. D. Mitchell, *Synth. React. Met. Org. Chem.* **1974**, *4*, 221−230.

[2] S. M. Aucott, A. M. Z. Slawin, J. D. Woolins, *Eur. J. Inorg. Chem.* **2002**, 2408−2418.
[3] L. Gonsalvi, H. Adams, G. J. Sunley, E. Ditzel, A. Haynes, *J. Am. Chem. Soc.* **2002**, *124*, 13597−13612.
[4] T. C. Blagborough, R. Davis, P. Ivison, *J. Organomet. Chem.* **1994**, *467*, 85−94.
[5] K. M. Pietrusiewicz, M. Kuznikowski, *Heterocycl. Chem.* **1991**, *3*, 37−40.
[6] T. Mizuta, Y. Imamura, K. Miyoshi, *J. Am. Chem. Soc.* **2003**, *125*, 2068−2069.
[7] P. Mastrorilli, C. F. Nobile, G. P. Suranna, F. P. Fanizzi, G. Ciccarella, U. Englert, Q. Li, *Eur. J. Inorg. Chem.* **2004**, 1234−1242.
[8] M. J. Baker, M. F. Giles, A. G. Orpen, M. J. Taylor, R. J. Watt, *J. Chem. Soc., Chem. Commun.* **1995**, 197−198.
[9] G. P. Suranna, P. Mastrorilli, C. F. Nobile, W. Keim, *Inorg. Chim. Acta* **2000**, *305*, 151−156.
[10] R. Weber, U. Englert, B. Ganter, W. Keim, M. Möthrath, *Chem. Commun.* **2000**, 1419−1420.
[11] M. Doux, C. Bouet, N. Mézailles, L. Ricard, P. Le Floch, *Organometallics* **2002**, *21*, 2785−2788.
[12] M. Doux, N. Mézailles, L. Ricard, P. Le Floch, *Eur. J. Inorg. Chem.* **2003**, 3878−3894.
[13] M. Doux, N. Mézailles, L. Ricard, P. Le Floch, *Organometallics* **2003**, *22*, 4624−4626.
[14] M. Doux, N. Mézailles, M. Melaimi, L. Ricard, P. Le Floch, *Chem. Commun.* **2002**, 1566−1567.
[15] S. Ito, H. Liang, M. Yoshifuji, *Chem. Commun.* **2003**, 398−399.
[16] H. Liang, K. Nishide, S. Ito, M. Yoshifuji, *Tetrahedron Lett.* **2003**, *44*, 8297−8300.
[17] H. Liang, S. Ito, M. Yoshifuji, *Org. Lett.* **2004**, *6*, 425−427.
[18] K. Dimroth, H. Kaletsch, *J. Organomet. Chem.* **1983**, *247*, 271−285.
[19] G. Baum, W. Massa, *Organometallics* **1985**, *4*, 1572−1574.
[20] T. Dave, S. Berger, E. Bilger, H. Kaletsch, J. Pebler, J. Knecht, K. Dimroth, *Organometallics* **1985**, *4*, 1565−1572.
[21] G. Märkl, C. Martin, *Angew. Chem. Int. Ed. Engl.* **1972**, *13*, 408−409.
[22] F. Nief, J. Fischer, *Organometallics* **1986**, *5*, 877−883.
[23] A. Moores, L. Ricard, P. Le Floch, N. Mezailles, *Organometallics* **2003**, *22*, 1960−1966.
[24] N. Avarvari, P. Le Floch, F. Mathey, *J. Am. Chem. Soc.* **1996**, *118*, 11978−11979.
[25] N. Avarvari, P. Le Floch, L. Ricard, F. Mathey, *Organometallics* **1997**, *16*, 4089−4098.
[26] V. Cadierno, P. Crochet, J. Josefina Díez, J. García-Álvarez, S. E. García-Garrido, S. García-Granda, J. Gimeno, M. A. Rodríguez, *Dalton Trans.* **2003**, 3240−3249.
[27] M. Valderrama, R. Contreras, V. Arancibia, P. Munoz, D. Boys, M. P. Lamata, F. Viguri, D. Carmona, F. J. Lahoz, J. A. Lopez, L. A. Oro, *J. Organomet. Chem.* **1997**, *546*, 507−517.
[28] Q. F. Zhang, H. G. Zheng, W. Y. Wong, W. T. Wong, W. H. Leung, *Inorg. Chem.* **2000**, *39*, 5255−5264.
[29] M. Albrecht, R. H. Crabtree, J. Mata, E. Peris, *Chem. Commun.* **2002**, 32−33.
[30] M. Albrecht, J. R. Miecznikowski, A. Samuel, J. W. Faller, R. H. Crabtree, *Organometallics* **2002**, *21*, 3596−3604.
[31] A. Fujii, S. Hashiguchi, N. Uematsu, T. Ikariya, R. Noyori, *J. Am. Chem. Soc.* **1996**, *118*, 2521−2522.
[32] R. Noyori, S. Hashiguchi, *Acc. Chem. Res.* **1997**, *30*, 97−102.
[33] R. Noyori, T. Ohkuma, *Angew. Chem. Int. Ed.* **2001**, *40*, 40−73.
[34] C. Thoumazet, M.-A. Melaimi, L. Ricard, F. Mathey, P. Le Floch, *Organometallics* **2003**, *22*, 1580−1581.
[35] M. Kollmar, H. Steinhagen, J. P. Janssen, B. Goldfuss, S. A. Malinovskaya, J. Vázquez, F. Rominger, G. Helmchen, *Chem. Eur. J.* **2002**, *8*, 3103−3114.
[36] S. K. Mandal, G. A. N. Gowda, S. S. Krishnamurthy, M. Nethaji, *Dalton Trans.* **2003**, 1016−1027.
[37] K. Boog-Wick, P. S. Pregosin, M. Worle, A. Albernati, *Helv. Chim. Acta* **2002**, *81*, 1622−1633.
[38] D. A. Evans, K. R. Campos, J. S. Tedrow, F. E. Michael, M. R. Gagne, *J. Org. Chem.* **1999**, *64*, 2994−2995.
[39] A. L. Rheingold, L. M. Liable-Sands, S. Trofimenko, *Inorg. Chim. Acta* **2002**, *330*, 38−43.
[40] J. Spencer, V. Gramlich, R. Hausel, A. Togni, *Tetrahedron: Asymmetry* **1996**, *7*, 41−45.
[41] A. Suzuki, *J. Organomet. Chem.* **1999**, *576*, 147−168.
[42] N. Miyaura, *Top. Curr. Chem.* **2002**, *219*, 11−59.
[43] N. Miyaura, *Angew. Chem. Int. Ed.* **2004**, *43*, 2201−2203.
[44] N. Miyaura, A. Suzuki, *Chem. Rev.* **1995**, *95*, 2457−2483.
[45] I. Kondolff, H. Doucet, M. Santelli, *Tetrahedron* **2004**, *60*, 3813−3818.
[46] R. B. Bedford, C. S. J. Cazin, S. J. Coles, T. Gelbrich, M. B. Hursthouse, V. J. M. Scordia, *Dalton Trans.* **2003**, 3350−3356.
[47] M. van der Heiden, H. Plenio, *Chem. Eur. J.* **2004**, *10*, 1789−1797.
[48] S. D. Walker, T. E. Barder, J. R. Martinelli, S. L. Buchwald, *Angew. Chem. Int. Ed.* **2004**, *43*, 1871−1876.
[49] O. Navarro, R. A. Kelly, S. P. Nolan, *J. Am. Chem. Soc.* **2003**, *125*, 16194−16195.
[50] A. M. Aguiar, J. R. Smiley Irelan, N. S. Bhacca, *J. Org. Chem.* **1969**, *34*, 3349−3352.
[51] M. A. Bennett, T. N. Huang, T. W. Matheson, A. K. Smith, *Inorg. Synth.* **1982**, *21*, 74−78.
[52] J. D. Roberts, F. J. Weigert, J. I. Kroschwitz, H. J. Reich, *J. Am. Chem. Soc.* **1970**, *92*, 1338−1347.
[53] D. H. R. Barton, D. Crich, W. B. Motherwell, *Tetrahedron* **1985**, *41*, 3901−3924.
[54] M. Raban, S. K. Lauderback, D. Kost, *J. Am. Chem. Soc.* **1975**, *97*, 5178−5183.
[55] P. L. Rinaldi, N. J. Baldwin, *J. Am. Chem. Soc.* **1983**, *105*, 7523−7527.
[56] C. G. Screttas, M. Micha-Screttas, *J. Org. Chem.* **1982**, *47*, 3008−3011.
[57] C. H. Wang, C. A. Kingsbury, *J. Org. Chem.* **1972**, *37*, 2489−2494.
[58] T. Ohwada, K. Shudo, *J. Am. Chem. Soc.* **1988**, *110*, 1862−1870.
[59] D. W. Old, J. P. Wolfe, S. L. Buchwald, *J. Am. Chem. Soc.* **1998**, *120*, 9722−9723.
[60] G. Häfelinger, M. Beyer, P. Burry, B. Eberle, G. Ritter, G. Westermayer, M. Westermayer, *Chem. Ber.* **1984**, *117*, 895−903.
[61] A. Altomare, M. C. Burla, M. Camalli, G. Cascarano, C. Giacovazzo, A. Guagliardi, A. G. G. Moliterni, G. Polidori, R. Spagna, *SIR97, an integrated package of computer programs for the solution and refinement of crystal structures using single crystal data*.
[62] G. M. Sheldrick, *SHELXL-97*, Universität Göttingen, Göttingen, Germany, **1997**.
[63] L. J. Farrugia, *ORTEP-3*, Department of Chemistry, University of Glasgow, **2000**.
[64] M. J. Frisch, G. W. Trucks, H. B. Schlegel, G. E. Scuseria, M. A. Robb, J. R. Cheeseman, J. J. A. Montgomery, T. Vreven, K. N. Kudin, J. C. Burant, J. M. Millam, S. S. Iyengar, J. Tomasi, V. Barone, B. Mennucci, M. Cossi, G. Scalmani, N. Rega, G. A. Petersson, H. Nakatsuji, M. Hada, M. Ehara, K. Toyota, R. Fukuda, J. Hasegawa, M. Ishida, T. Nakajima, Y. Honda, O. Kitao, H. Nakai, M. Klene, X. Li, J. E. Knox, H. P. Hratchian, J. B. Cross, C. Adamo, J. Jaramillo, R. Gomperts, R. E. Stratmann, O. Yazyev, A. J. Austin, R. Cammi, C. Pomelli, J. W. Ochterski, P. Y. Ayala, K. Morokuma, G. A. Voth, P. Salvador, J. J. Dannenberg, V. G. Zakrzewski, S. Dapprich, A. D. Daniels, M. C. Strain, O. Farkas, D. K. Malick, A. D. Rabuck, K. Raghavachari, J. B. Foresman, J. V. Ortiz, Q. Cui, A. G. Baboul, S. Clifford, J. Cioslowski, B. B. Stefanov, G. Liu, A.

 © 2005 Wiley-VCH Verlag GmbH & Co. KGaA, Weinheim

Liashenko, P. Piskorz, I. Komaromi, R. L. Martin, D. J. Fox, T. Keith, M. A. Al-Laham, C. Y. Peng, A. Nanayakkara, M. Challacombe, P. M. W. Gill, B. Johnson, W. Chen, M. W. Wong, C. Gonzalez, J. A. Pople, *Gaussian 03*, Revision B.04 ed., Gaussian, Inc., Pittsburgh PA, **2003**.
[65] M. Svensson, S. Humbel, R. D. J. Froese, T. Matsubara, S. Sieber, K. J. Morokuma, *J. Phys. Chem.* **1996**, *100*, 19357−19363.
[66] A. D. Becke, *J. Chem. Phys.* **1993**, *98*, 5648−5662.
[67] C. Lee, W. Yang, R. G. Parr, *Phys. Rev. B* **1988**, *37*, 785−789.
[68] A. K. Rappé, C. J. Casewitt, K. S. Colwell, W. A. Goddard, W. M. Skiff, *J. Am. Chem. Soc.* **1992**, *114*, 10024−10035.
[69] P. J. Hay, R. L. Martin, *J. Am. Chem. Soc.* **1992**, *114*, 2736−2737.

Received June 25, 2004
Early View Article
Published Online November 10, 2004

 © 2005 Wiley-VCH Verlag GmbH & Co. KGaA, Weinheim

Synthesis and Characterisation of Novel Complexes Containing Group 15 Elements and Their Potential Use as Molecular Precursors for the Formation of Transition Metal Pnictides

Manfred Scheer,*[a] Ulf Vogel,[a] Uta Becker,[a] Gabor Balazs,[a] Petra Scheer,[b] Wolfgang Hönle,[c] Michael Becker,[d] and Martin Jansen[d]

Dedicated to Prof. Dr. M. Veith on the occasion of his 60th birthday

Keywords: Cobalt / Cluster compounds / Phosphorus / Thermochemistry / Tungsten

The reaction of $[\{W(CO)_5\}_2PCl]$ with $K[Co(CO)_4]$ yields the novel compounds $[\{W(CO)_4Co_2(CO)_6\}\{\mu_3\text{-}PW(CO)_5\}_2]$ (**3**) and $[\{(CO)_4WCo_3(CO)_6\}\{\mu_3\text{-}PW(CO)_5\}_3]$ (**4**) along with known derivatives $[Co_2(CO)_6\{\mu,\eta^2\text{-}PW(CO)_5\}_2]$ (**1**) and $[Co_3(CO)_9\{\mu_3\text{-}PW(CO)_5\}]$ (**2**). The complex $[\{W_2(CO)_8(\mu\text{-}CO)\}\{\mu,\eta^2{:}\eta^1{:}\eta^1\text{-}PW(CO)_5\}_2)]$ (**5**) was synthesised by treating $Na_2[W_2(CO)_{10}]$ with PBr_3. Reaction of $K[Mn(CO)_5]$ with $SbCl_3$ affords $[Sb\{Mn(CO)_5\}_3]$ (**6**) in high yields. The spectroscopic and structural characterisation of the novel products is discussed, as well as the thermolytic behaviour of **2**, **3** and **6** for the potential formation of novel phases of transition metal pnictides.

(© Wiley-VCH Verlag GmbH & Co. KGaA, 69451 Weinheim, Germany, 2005)

Introduction

One of our research interests is focused on the synthesis of P_n ligand complexes[1] starting from P_1-containing compounds. The use of $[(CO)_5CrPCl_3]$ or L_nMPCl_2 in the reaction with transition-metal metalates leads to novel as well as known P_n ligand ($n \geq 2$) complexes under special conditions in low-temperature reactions.[2] However, the use of complexes of the type $[(L_nM)_2PX]$ [$L_nM = M(CO)_5$; M = Cr, W] in these reactions gives the formation of only P_2-ligand complexes that are probably formed via an intermediate of the composition $[L_nM{\equiv}P{\rightarrow}M(CO)_5]$.[3]

In continuation of these investigations we have focussed our interests particularly on products containing, besides the transition metal and the group 15 element ligand, only CO. The general interest in this type of complex is the challenge of their use as molecular precursors for the generation of novel, metastable phases[4] of transition metal pnictides by eliminating CO ligands quantitatively at moderate temperatures and ending up with a solid of a given non-metal/metal composition. Transition metal pnictides were usually obtained by high-temperature routes.[5] This idea was supported by a previous report by Gladfelter et al. on the use of $[\{Co(CO)_3\}_2(\mu,\eta^2\text{-}E_2)]$ (E = P, As) as molecular precursors for the generation of CoE layers by CVD techniques.[6]

We describe here the synthesis of novel E_1 ligand complexes starting from different E_1 sources and the first investigations of the thermolysis behaviour of selected products under high vacuum as well as inert gas atmosphere conditions with MS control.

Results and Discussion

Looking into the details of existing Co/P complexes one example for these potential precursor compounds is $[Co_2(CO)_6(\mu,\eta^2\text{-}P_2\{W(CO)_5\}_2)]$ (**1**), which was described by Huttner et al. as a product of the reaction between the chlorophosphinidene complex $[\{W(CO)_5\}_2PCl]$ and $K[Co(CO)_4]$.[7] They observed **1** as the only product if the reaction is carried out at room temperature. In agreement with our general reaction methodology we found that, by carrying out this reaction at low temperature, it is possible to isolate three further products.

[a] Institut für Anorganische Chemie der Universität Regensburg, 93040 Regensburg, Germany
Fax: + 49-941-943-4441
E-mail: mascheer@chemie.uni-regensburg.de
[b] Forschungszentrum Karlsruhe, Institut für Nanotechnologie, PF 3640,
76021 Karlsruhe, Germany
Fax: + 49-7247-82-6368
E-mail: petra.scheer@int.fzk.de
[c] Max Planck Institut für Chemische Physik fester Stoffe, Nöthnitzer Str. 40, 01187 Dresden, Germany
Fax: + 49-351-4646-4611
E-mail: hoenle@cpfs.mpg.de
[d] Max Planck Institut für Festkörperforschung Stuttgart, 70569 Stuttgart, Germany
Fax: + 49-711-689-1502
E-mail: M.Jansen@fkf.mpg.de

Reaction between the chlorophosphinidene complex [{W(CO)$_5$}$_2$PCl] and K[Co(CO)$_4$] in THF at −78 °C yields the novel products **3** and **4** as well as the previously described complexes **1**[7] and **2** [Equation (1)].[8] Vahrenkamp has obtained the latter product from the reaction of [(CO)$_5$WPH$_3$] with Co$_2$(CO)$_8$.[8] Complexes **1** and **2** can also be obtained by the reaction of [Cl$_3$PW(CO)$_5$] with K[Co(CO)$_4$] in THF at −78 °C [Equation (2)]. Column chromatographic workup was necessary for the separation of the products, leading to reduced yields.

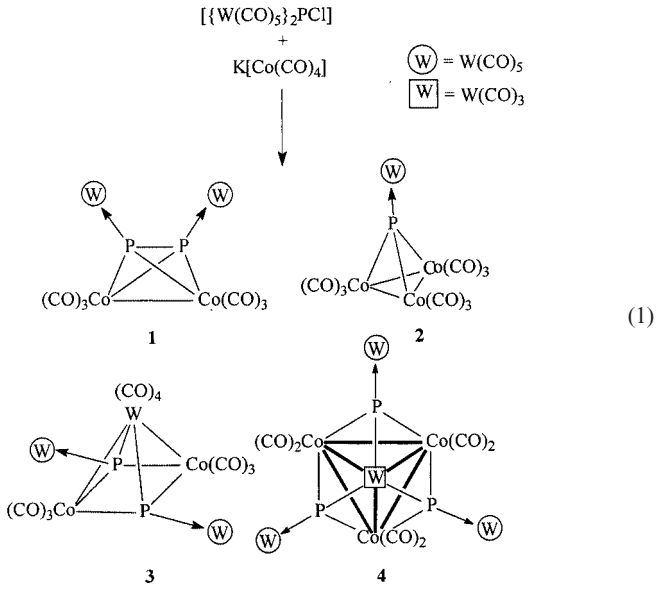

(1)

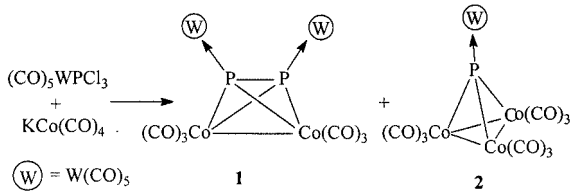

(2)

Other P_1 starting materials are the non-coordinated phosphorus trihalides. We recently found that the reaction of PCl$_3$ with Na$_2$[W$_2$(CO)$_{10}$] at ambient temperature leads to the formation of [{W(CO)$_5$}$_2$PCl], [W(CO)$_5$PCl$_3$] and [(CO)$_5$W(μ,η^2:η^1:η^1-P$_2$Cl$_2${W(CO)$_5$}$_2$)], the latter complex containing a novel ClP=PCl ligand.[9] We have found that with a different stoichiometric ratio (1:1.5) the reaction of PBr$_3$ with Na$_2$[W$_2$(CO)$_{10}$] in toluene results in the formation of **5** [Equation (3)]. Complex **5** is the first homoleptic complex of phosphorus and carbonyltungsten.

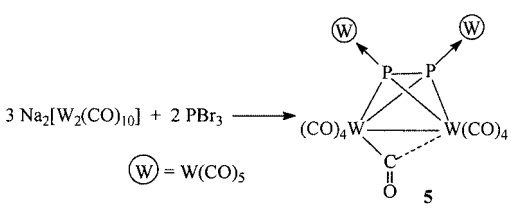

(3)

Furthermore, the reaction of SbCl$_3$ with K[Mn(CO)$_5$] in THF at low temperatures leads to the homoleptic metallostibane **6** [Equation (4)], which was obtained in 52% yield. Complex **6** has been described previously in the literature, but the authors only characterised it at low temperature and found that the compound decomposes at room temperature.[10] However, by performing the workup of the reaction mixture very rapidly at room temperature, we were able to isolate **6** in high yields as a crystalline solid that can be stored under inert gas for months at room temperature without decomposition.

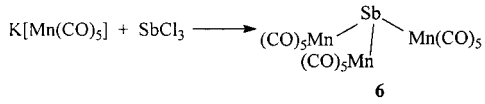

(4)

All compounds were characterised by IR, and ^{31}P NMR spectroscopy and mass spectrometry. The data for **1** and **2** were found to be identical with the values described in the literature. An X-ray structure analysis was carried out for **2**, which, due to a lower measurement temperature, resulted in slightly better *R* values than the previously described measurement[8] and is therefore included in this paper.

Complex **3** forms red crystals and compound **4** forms black crystals that are slightly soluble in hexane and readily soluble in toluene and CH_2Cl_2. The black crystals of **5** are only slightly soluble in toluene and CH_2Cl_2. The black, crystalline complex **6** is soluble in hydrocarbons and other organic solvents, but solutions must be kept at low temperature to avoid decomposition. The IR spectra of the products show various absorptions in the region of terminal carbonyl ligands. In the mass spectra of **3**, **4** and **5** only fragments were observed, whereas for **6** the appropriate molecular-ion peak and peaks for subsequent loss of all CO ligands were detected.

The ^{31}P NMR spectrum of **3** shows a broad signal at δ = −40 ppm which is probably due to the quadrupole moment of the ^{59}Co nuclei. Compound **4** reveals a singlet at δ = −135 ppm in the ^{31}P NMR spectrum, which shows two tungsten satellites ($J_{P,W}$ = 87.2 and 131.2 Hz). The larger coupling constant can be assigned to the coordinative bonding to the [W(CO)$_5$] moiety, while the smaller one reflects the coupling to the central cluster atom W4 (see below). This assignment is supported by the intensity ratio of the satellites, which is almost 3:1. The ^{31}P NMR spectrum of **5** shows a singlet at δ = −123 ppm, which exhibits only one pair of tungsten satellites ($^1J_{P,W}$ = 116 Hz), which can be assigned to the coupling to the coordinatively bound [W(CO)$_5$] moieties. The expected second pair of satellites should possess a smaller coupling constant and therefore seems to be hidden in the broadening of the signal.

The novel products were also characterized by single-crystal X-ray diffraction. The molecular structure of **3** (Figure 1) reveals a *cyclo*-Co$_2$P$_2$ moiety — the torsion angle Co−P−P−Co is 16.52(7)° — that is capped by a W(CO)$_4$ group. This *nido* structure is expected for this 14-skeletal -

 © 2005 Wiley-VCH Verlag GmbH & Co. KGaA, Weinheim

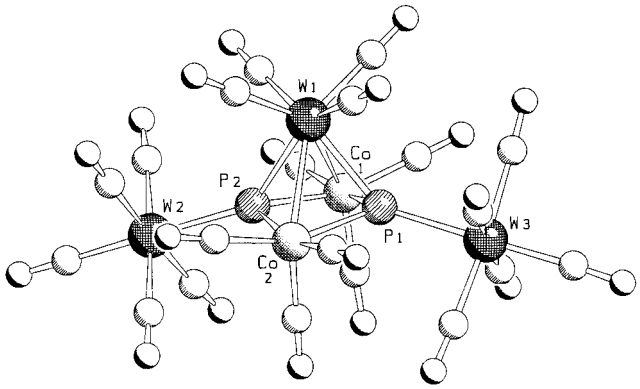

Figure 1. Molecular structure of **3** in the crystal; selected bond lengths [Å] and angles [°]: W1−P1 2.471(3), W2−P1 2.430(3), W2−P2 2.439(3), W2−Co1 2.787(2), W2−Co1 2.807(2), W3−P2 2.471(3), Co1−P1 2.271(3), Co1−P2 2.266(3), Co2−P1 2.261(3), Co2−P2 2.263(3); P1−W2−P2 73.19(9), P1−W2−Co1 51.06(7), P2−W2−Co1 50.86(7), P1−W2−Co2 50.54(7), P2−W2−Co2 50.53(7), Co1−W2−Co2 75.98(5), P1−Co1−P2 79.53(11), P1−Co1−W2 56.31(7), P2−Co1−W2 56.59(7), P1−Co2−P2 79.81(11), P1−Co2−W2 56.07(7), P2−Co2−W2 56.29(7), Co1−P1−Co2 98.87(12), Co1−P1−W2 72.63(8), Co2−P1−W2 73.40(9), Co1−P2−Co2 98.96(12), Co1−P2−W2 72.55(9), Co2−P1−W2 73.19(8)

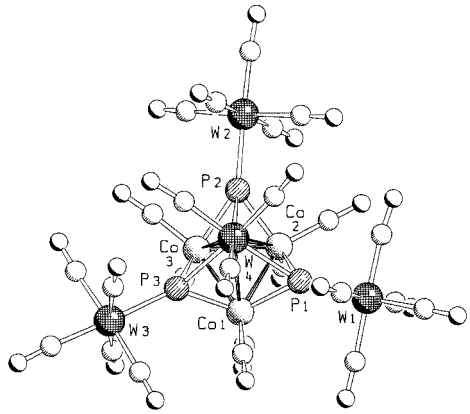

Figure 2. Molecular structure of **4** in the crystal; selected bond lengths [Å] and angles [°]: W1−P1 2.406(6), W2−P2 2.407(7), W3−P3 2.412(7), W4−P1 2.496(6), W4−P2 2.467(7), W4−P3 2.442(6), W4−Co1 2.638(3), W4−Co2 2.695(3), W4−Co3 2.652(3), Co1−P1 2.229(7), Co1−P3 2.197(7), Co2−P1 2.189(7), Co2−P2 2.186(7), Co3−P2 2.264(7), Co3−P3 2.200(7), Co1−Co2 2.549(5), Co1−Co3 2.580(5), Co2−Co3 2.545(5); Co1−W4−Co2 57.10(10), Co1−W4−Co3 58.38(10), Co2−W4−Co3 56.85(10), Co2−Co1−Co3 59.49(13), Co2−Co1−W4 62.56(10), Co3−Co1−W4 61.07(10), Co1−Co2−Co3 60.86(13), Co1−Co2−W4 60.34(10), Co3−Co2−W4 60.73(10), Co1−Co3−Co2 59.65(13), Co1−Co3−W4 60.55(10), Co2−Co3−W4 62.42(10)

electron compound. The lone pair of each phosphorus atom is further coordinated to a $[W(CO)_5]$ fragment. The carbonyl ligands of the atom W1 are in eclipsed positions to the ring atoms resulting in a quadratic antiprismatic coordination pattern around the atom W1, which is unusual for tungsten. The same structural arrangement has been found for the capping Cr atom in the isostructural complex $[(CO)_4CrCo_2(CO)_6\{\mu_3\text{-}AsCr(CO)_5\}_2]$.[11] The average Co−P bond length (2.265 Å) is within the usual range. The bond lengths from phosphorus to the capping tungsten atom are 2.430(3) and 2.439(3) Å, respectively. They are surprisingly short in comparison to $[W(CO)_4\{\eta^4\text{-}P_4\langle W(CO)_5\rangle_4\}]$,[12] where the average W−P distance within the cluster core is found to be 2.604 Å. In contrast, the Co−W bond lengths with [2.807(2) and 2.787(2) Å] are unusually long compared, for example, with the bond lengths in the cluster $[\{Co(CO)_2(\mu\text{-}CO)\}_3W(CO)_2Cp]$ [2.715 Å (av)].[13]

The molecular structure of **4** (Figure 2) shows a distorted tetrahedral WCo_3 cluster core (angles between 58° and 62°), in which each of the Co_2W faces is bridged by one phosphorus atom. The lone pairs of these three P atoms are additionally coordinated to $[W(CO)_5]$ fragments. This structure is in agreement with the EAN rule,[14] which predicts a tetrahedral geometry for a 60-valence-electron cluster. A comparison of the average Co−Co bond lengths of **4** with those of the compound $[Co_4(\mu_3\text{-}PPh)_4(PPh_3)_4]$,[15] which also possesses phosphorus-capped Co_3 faces, shows similar values (2.558 Å vs. 2.578 Å). However, the Co−W bond lengths of **4** [2.662 Å (av)] are slightly shorter than in $[\{Co(CO)_2(\mu\text{-}CO)\}_3W(CO)_2Cp]$[13] [2.715 Å (av)], which has a similar cluster core. This longer Co−W bond length is attributed to the absence of capping P atoms in the latter compound.

The central structural feature of the molecular structure of **5** (Figure 3) is a distorted tetrahedral W_2P_2 core, where the lone pairs of each phosphorus atom coordinate to a $[W(CO)_5]$ moiety. The two phosphorus atoms are shifted significantly towards the atom W2 [W1−P1 2.610(2), W1−P2 2.636(2), W2−P1 2.500(2), W2−P2 2.514(2) Å]. This asymmetry is electronically compensated for by the semibridging CO ligand between the two W atoms (W1−C5 2.086(6) Å, W2···C5 2.750 Å). The P1−P2 distance [2.062(2) Å] is slightly shorter than in the tetrahedral complexes $[\{Cp(CO)_2W\}_2(\mu,\eta^2\text{-}P_2)]$ [2.104(4) Å][16] and

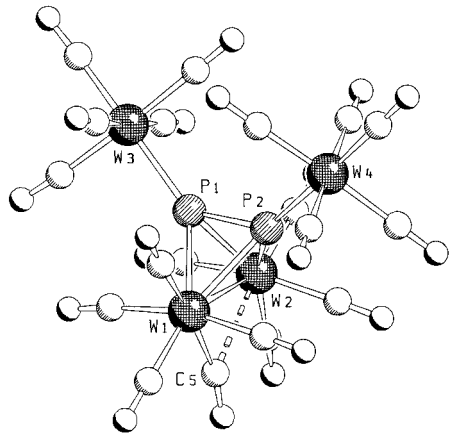

Figure 3. Molecular structure of **5** in the crystal; selected bond lengths [Å] and angles [°]: W1−W1 3.0819(6), W1−P1 2.610(2), W1−P2 2.636(2), W2−P1 2.500(2), W2−P2 2.514(2), W3−P1 2.484(2), W4−P2 2.477(2), P1−P2 2.062(2), W1−C5 2.086(6), W2···C5 2.750; P1−W1−P2 46.29(5), P1−W1−W2 51.29(4), P2−W1−W2 51.45(4), P1−W2−P2 48.58(5), P1−W2−W1 54.57(4), P2−W2−W1 55.08(4), P2−P1−W1 67.50(7), P2−P1−W2 66.07(7), P2−P1−W3 137.00(9), P1−P2−W1 66.20(6), P1−P2−W2 65.36(7), P1−P2−W4 133.70(9)

 © 2005 Wiley-VCH Verlag GmbH & Co. KGaA, Weinheim

[{Cp*(CO)$_2$W}$_2$(μ,η^2:η^1-P$_2$){W(CO)$_5$}] [2.092(4) Å].[17] The W1−W2 bond length [3.082(1) Å] is similar to that in the latter complex [3.092(1) Å].

The X-ray structure analysis of **6** reveals two independent molecules in the unit cell with similar bond lengths and angles (Figure 4 shows molecule A). The central antimony atom is surrounded by three Mn(CO)$_5$ moieties and adopts a trigonal pyramidal geometry with Mn−Sb−Mn angles ranging from 107.91(2)° to 111.00(2)°. The average Mn−Sb bond length [2.808(1) Å] is significantly longer than in other complexes with a similar bonding situation (cf. [(F$_3$C)$_2$SbMn(CO)$_5$] 2.663(1) Å[18]); these long bonds reflect the steric crowding of the antimony atom by the bulky pentacarbonylmanganese groups, which themselves show a slightly distorted octahedral coordination.

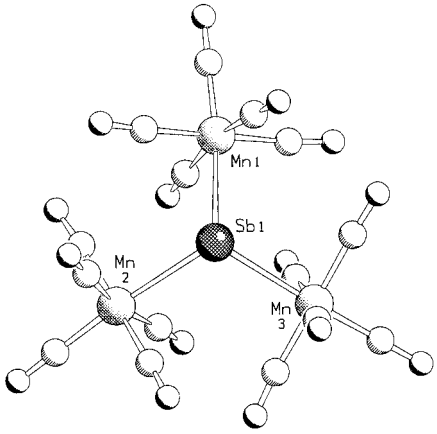

Figure 4. Molecular structure of **6** in the crystal (molecule A); selected bond lengths [Å] and angles [°]: Sb1−Mn1 2.8135(8), Sb1−Mn2 2.8027(7), Sb1−Mn3 2.7928(8); Mn1−Sb1−Mn2 110.02(2), Mn1−Sb1−Mn3 108.22(2), Mn2−Sb1−Mn3 109.71(2)

Thermogravimetric measurements were carried out on the clusters **2**, **3** and **6** under high vacuum as well as on **3** and **6** under inert gas flow conditions, and were combined with MS control of the volatile products in the temperature range up to 1000 °C. Thermogravimetric analysis of **3** under vacuum conditions shows that it decomposes in two steps: between 90 and 130 °C with a mass loss of about 39%, and between 540 and 640 °C with a further mass loss of about 11%, both of which are accompanied by W(CO)$_6$ elimination.[19] The second step also occurs with elimination of Co- and P-containing moieties.

The thermogravimetric analysis of **2** in high vacuum shows a two-step decomposition in the temperature range of 65 to 165 °C (first step 65−134 °C, second step 134−165 °C), with a mass loss of about 62% due to the elimination of CO and W(CO)$_6$,(Figure 5)[19] that leaves a CO-containing sample with the formal composition Co$_3$P(CO)$_3$.[20] In contrast, complex **6** decomposes by Mn(CO)$_n$ elimination in two steps (between 65−120 °C and 120−180 °C) with an overall mass loss of about 67% that leaves a nearly C-free sample with the composition Mn$_2$Sb.[21] However, if the thermogravimetric experiments are carried out under a flow of an inert gas (Ar or He) there is a significant change in the decomposition behaviour, which is characterised mainly by CO elimination. For **2** the only detectable volatile material is CO, leading to a mass loss of about 50% in the temperature range 120−180 °C (Figure 5). For **6**, CO and Mn(CO)$_n$ fragments are eliminated in two steps between 100 °C and 200 °C, and this is accompanied by a weight loss of 56%. The remaining amorphous solids have the compositions Co$_3$WP and SbMn$_{2.6}$, respectively,[22] and are very sensitive to oxygen.

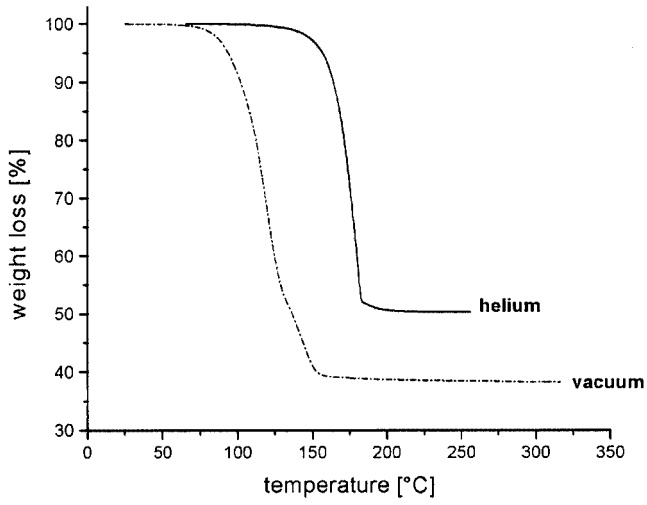

Figure 5. Thermogravimetric analysis of **2** in helium gas (solid line) and in vacuo (dashed line)

Initial attempts to obtain crystalline materials suitable for powder XRD characterisation were carried out by heating the remaining solids at 550 °C for 500 h. While no novel phase could be observed for the compound generated from **2**, reflections of a hexagonal phase could be indexed for the solid originating from **6**, with $a = b = 5.139$, $c = 13.017$ Å; and $V = 297.7$ Å^3.[23]

Conclusion

Our results have shown that novel cluster complexes of naked group-15 elements can be obtained by reacting pnicogen halide complexes with transition metal metalates at low temperature. These cluster compounds with naked group-15 elements and CO as the only ligands can be used as potential precursors for the generation of novel solids. Their decomposition occurs at relatively low temperatures of up to 200 °C, and the composition of the remaining amorphous solids is partially controlled by the composition of the metals of the employed cluster core. Whereas the thermolysis under high-vacuum conditions leads partially to the elimination of CO and metalcarbonyl fragments, the better way to obtain non-metal/metal materials from single-source precursors is to carry out the thermal decomposition under a flow of inert gas. There are some indications that the presence of bonds between the transition metals in the

 © 2005 Wiley-VCH Verlag GmbH & Co. KGaA, Weinheim

molecular precursor compound is one precondition for the exclusive elimination of CO. Thus, for cluster **2** only CO elimination occurs under the latter conditions, whereas the Sb-linked complex **6**, which possesses only Sb−Mn bonds loses $Mn(CO)_n$ units. Furthermore, the stability and the vapour pressure of the eliminated moieties also influence the decomposition behaviour.

The preliminary results presented in this paper show that the use of CO-containing molecular precursors for the preparation of novel transition metal pnictides seems to be of substantial potential. Nevertheless, further research is necessary to obtain more information about the structure and the properties of these novel compounds.

Experimental Section

General Remarks: All manipulations were performed under dry nitrogen using standard glove-box and Schlenk techniques. All solvents were freshly distilled from appropriate drying reagents immediately prior to use. IR spectra were obtained with a Bruker IFS280 spectrometer, and ^{31}P NMR spectra were recorded at room temperature with a Bruker AMX 300 spectrometer (^{31}P: 121.49 MHz) using 85% H_3PO_4 as an external standard; mass spectra were recorded with a Varian MAT-711 spectrometer. $[\{W(CO)_5\}_2PCl]$,[7] $[Cl_3PW(CO)_5]$[24] and $K[Co(CO)_4]$[25] were synthesised according to literature procedures.

Reaction of $[\{W(CO)_5\}_2PCl]$ with $K[Co(CO)_4]$: $K[Co(CO)_4]$ (0.33 g, 1.55 mmol) was added to a solution of $[\{W(CO)_5\}_2PCl]$ (1.11 g, 1.55 mmol) in 20 mL of THF at −78 °C. After stirring for 30 min, the mixture was allowed to reach room temperature within 1 h and was stirred for an additional 1 h. The reaction mixture was filtered through Celite, 5 mL of silica gel was added and all solvents were removed in vacuo. Products **1**, **2**, **3** and **4** were separated by column chromatography on silica gel.

$[Co_2(CO)_6(\mu,\eta^2\text{-}P_2\{W(CO)_5\}_2)]$ (1): After elution of a purple fraction with hexane/toluene (10:1) crystals of **1** were obtained by recrystallisation from CH_2Cl_2 (0.11 g, 15% based on P). The analytical data agreed with the literature values.[7]

$[Co_3(CO)_9(\mu_3\text{-}P\{W(CO)_5\})]$ (2): This compound was eluted with hexane as a yellowish-brown fraction and obtained as brown platelets after recrystallisation from CH_2Cl_2 (0.036 g, 3% based on P). $^{31}P\{^1H\}$ NMR (C_6D_6): δ = 41.0 ppm (s, br). The analytical data agreed with the literature values.[8]

$[(CO)_4WCo_2(CO)_6\{\mu_3\text{-}PW(CO)_5\}_2]$ (3): Elution of a brown fraction with hexane/toluene (5:1) and recrystallisation from CH_2Cl_2 yielded **3** as black, metallic crystals (0.07 g, 7% based on P). IR (KBr): ν(CO) = 2090 (sh), 2064 (s, br), 2046 (sh), 2014 (w), 2007 (w), 1991 (sh), 1960 (sh), 1947 (vs, br), 1932 (sh) cm^{-1}. $^{31}P\{^1H\}$ NMR (C_6D_6): δ = −40.0 (s, $w_{1/2}$ = 500 Hz) ppm. EI-MS: *m*/*z* (%) = 821.3 (0.6) $[(CO)_{13}PCoW_2]^+$, 457.5 (3.6) $[PCoW_2]^+$. $C_{20}Co_2O_{20}P_2W_3$ (1291.57): calcd. C 18.60; found C 18.09.

$[WCo_3(CO)_{12}\{\mu_3\text{-}PW(CO)_5\}_3]$ (4): A brown fraction eluted with hexane/toluene (2:1) yielded a small amount of **4** after recrystallisation from CH_2Cl_2 (0.015 g, 2% based on P). IR (KBr): ν(CO) = 2076 (s), 2070 (sh), 2017 (sh), 2003 (sh), 1984 (sh), 1943 (vs, br), 1919 (sh), 1891 (sh) cm^{-1}. $^{31}P\{^1H\}$ NMR (C_6D_6): δ = −135.3 ppm (s, $J_{P,W}$ = 87.2, 131.2 Hz) cm^{-1}. $C_{24}Co_3O_{24}P_3W_3$ (1493.52): calcd. C 19.30; found C 19.01.

Reaction of $[Cl_3PW(CO)_5]$ with $K[Co(CO)_4]$: A solution of $K[Co(CO)_4]$ (1.26 g, 6.00 mmol) in 40 mL of THF was added dropwise to a solution of $[Cl_3PW(CO)_5]$ (0.922 g, 2.00 mmol) in 40 mL of THF at −78 °C. After 30 min, the reaction mixture was allowed to warm to room temperature and stirred for an additional 14 h. All volatiles were removed in vacuo and $[W(CO)_6]$ was removed by sublimation under high vacuum at 50 °C. The residue was dissolved in CH_2Cl_2, 5 mL of silica gel was added, and the solution was reduced to dryness. Compounds **1** and **2** were separated by column chromatography. Compound **1** was eluted with hexane (yellow-brown fraction) and obtained by recrystallisation from CH_2Cl_2 (0.12 g, 12% based on P). Elution with hexane/toluene (10:1) yielded a purple fraction from which **2** could be isolated after recrystallisation from CH_2Cl_2 (0.16 g, 10.2% based on P).

$[W_2(CO)_9(\mu,\eta^2\text{:}\eta^1\text{:}\eta^1\text{-}P_2\{W(CO)_5\}_2]$ (5): Solid $Na_2[W_2(CO)_{10}]$ (0.768 g, 1.11 mmol) was added at room temperature to a solution of PBr_3 (0.2 g, 0.74 mmol) in 50 mL of toluene, which immediately became purple. The solution was stirred for 3 hours and the solvent removed in vacuo. Extraction of the remaining solid twice with 10 mL of CH_2Cl_2 and reduction of the solvent volume to about 10 mL yielded black crystals of **5** after one day at 4 °C (0.15 g, 30%). Further reduction of the solvent volume gave more product. The ^{31}P NMR spectrum of the crude reaction mixture in $[D_8]THF$ shows singlets at δ = 103.5 and −90.8 ppm besides the major singlet at δ = −122.7 ppm for **5**. IR (CH_2Cl_2): ν(CO) = 2051 (vs), 2035 (s), 1999 (m), 1956 (s, br) cm^{-1}. $^{31}P\{^1H\}$ NMR ($CDCl_3$): δ = −122.6 (s, $^1J_{P,W}$ = 116 Hz) cm^{-1}. $C_{19}O_{19}P_2W_4$ (1329.55): calcd. C 17.16; found C 17.23.

$[\{(CO)_5Mn\}_3Sb]$ (6): A solution of $K[Mn(CO)_5]$ (2.20 g, 9.40 mmol) in 50 mL of THF was added to a solution of $SbCl_3$ (715 mg, 3.13 mmol) in 50 mL of THF at −78 °C over a period of 1 h. The reaction mixture was stirred at low temperature for an additional 1 h before the cold bath was removed and the solution warmed to room temperature. All solvents were evaporated in vacuo and the remaining residue was extracted with pentane. Filtration through Celite and storage at −30 °C yielded **6** as black needles (1.16 g, 52%). *Note:* Care has to be taken that the operations carried out at room temperature are performed as quickly as possible to avoid decomposition. IR (KBr): ν(CO) = 2105 (m), 2071 (s), 1980 (vs, br) cm^{-1}. EI-MS: *m*/*z* (%) = 706.7 (20) $[M^+]$, 678.7 (22) $[M^+ - CO]$, 594.7 (2) $[M^+ - 4\ CO]$, 566.7 (7) $[M^+ - 5\ CO]$, 538.7 (20) $[M^+ - 6\ CO]$, 510.7 (43) $[M^+ - 7\ CO]$, 482.6 (3) $[M^+ - 8\ CO]$, 454.6 (9) $[M^+ - 9\ CO]$, 426.6 (21) $[M^+ - 10\ CO]$, 398.6 (19) $[M^+ - 11\ CO]$, 370.6 (17) $[M^+ - 12\ CO]$, 342.6 (9) $[M^+ - 13\ CO]$, 314.6 (8) $[M^+ - 14\ CO]$, 286.6 (27) $[M^+ - 15\ CO]$. $C_{15}Mn_3O_{15}Sb$ (706.72): calcd. C 25.49; found C 25.34.

Thermogravimetric Analysis: Thermogravimetric analyses were carried out with a thermobalance STA 409 from Netzsch either in vacuo or with a dynamic helium gas flow (70 mL/min) at a heating rate of 5 K/min. The balance was coupled to a quadrupole mass spectrometer QMG 422 (Balzers) that includes a skimmer system for measurements under normal pressure.

X-ray Structure Determination and Details of Refinement: Data were collected with a STOE STADI4 four-cycle diffractometer for complexes **2**, **3** and **4** and for complexes **5** and **6** on an IPDS area-detector diffractometer using Mo-K_α (λ = 0.71069 Å) radiation. Machine parameters, crystal data and data collection parameters are summarised in Table 1. The structures were solved by direct methods using SHELXS-86,[26a] with full-matrix least-squares refinement on F^2 in SHELXL-93[26b] with anisotropic displacement for non-H atoms. Hydrogen atoms were placed in idealised posi-

 © 2005 Wiley-VCH Verlag GmbH & Co. KGaA, Weinheim

Table 1. Crystallographic data for **2**−**6**

	2	**3**	**4**	**5**	**6**
Empirical formula	$C_{14}Co_3O_{14}PW$	$C_{20}Co_2O_{20}P_2W_3$	$C_{24}Co_3O_{24}P_3W_4$	$C_{19}O_{19}P_2W_4$	$C_{15}Mn_3O_{15}Sb$
M_r	783.75	1291.55	1677.34	1329.53	706.72
T [K]	200(2)	200(2)	200(2)	210(2)	200(1)
Crystal size	0.95 × 0.38 × 0.24	0.38 × 0.23 × 0.02	0.15 × 0.08 × 0.04	0.22 × 0.08 × 0.04	0.30 × 0.15 × 0.02
Space group	$P\bar{1}$	$P\bar{1}$	$P\bar{1}$	$P2_1/c$	$P\bar{1}$
Crystal system	triclinic	triclinic	triclinic	monoclinic	triclinic
a [Å]	8.746(2)	8.959(2)	9.735(2)	11.944(2)	6.744(1)
b [Å]	9.052(2)	9.202(2)	10.060(2)	12.786(2)	16.208(3)
c [Å]	14.989(3)	21.800(4)	20.688(4)	19.717(4)	20.389(4)
α [°]	73.22(3)	79.07(3)	100.40(3)	90	90.31(2)
β [°]	83.97(3)	81.50(3)	93.07(3)	101.17(3)	99.55(2)
γ [°]	71.01(3)	61.52(3)	98.91(3)	90	90.07(2)
V [Å^{-3}]	1074.2(4)	1547.6(5)	1961.8(7)	2954.0(10)	2086.7(7)
Z	2	2	2	4	4
D_c [g cm^{-3}]	2.423	2.722	2.840	2.989	2.136
μ_c [mm^{-1}]	7.755	12.244	13.122	15.715	2.974
2θ range [°]	$4.92 \le 2\theta \le 55.00$	$3.82 \le 2\theta \le 50.00$	$1.00 \le 2\theta \le 48.02$	$3.48 \le 2\theta \le 51.76$	$4.06 \le 2\theta \le 51.70$
hkl range	$-11 \le h \le 10$ $-11 \le k \le 11$ $-0 \le l \le 19$	$-10 \le h \le 10$ $-10 \le k \le 10$ $0 \le l \le 25$	$-11 \le h \le 11$ $-11 \le k \le 11$ $-0 \le l \le 23$	$-14 \le h \le 14$ $-15 \le k \le 15$ $-22 \le l \le 22$	$-7 \le h \le 7$ $-19 \le k \le 19$ $-24 \le l \le 24$
Data/restraints/parameters	4874/0/298	5401/0/424	6136/0/283	5343/0/397	7877/0/613
No. of unique data	4876 (R_{int} = 0.0000)[a]	5422 (R_{int} = 0.0000)[a]	6168 (R_{int} = 0.0000)[a]	5343 (R_{int} = 0.1232)	7877 (R_{int} = 0.0480)
Reflections collected	4876	5422	6168	20649	15901
Independent reflections [$I > 2\sigma(I)$]	4759	4562	4579	4772	6978
Goodness-of fit on F^2	1.139	1.112	1.570	1.071	0.990
R_1,[b] wR_2[c] [$I > 2\sigma(I)$]	0.0224, 0.0586	0.0405, 0.1006	0.0630, 0.1427	0.0277, 0.0758	0.0282, 0.0695
R_1,[b] wR_2 [c] (all data)	0.0232, 0.0596	0.0540, 0.1203	0.1001, 0.1635	0.0319, 0.0807	0.0318, 0.0709
Largest diff. peak/hole [e·Å^{-3}]	1.699, −1.605	1.453, −2.823	2.335, −2.992	1.491, −1.014	0.898, −0.816

[a] Four-circle diffractometer. [b] $R = ||F_o| - |F_c||/|F_o|$. [c] $wR_2 = [\omega(F_o^2 - F_c^2)^2]/[(F_o^2)^2]^{1/2}$.

tions and refined isotropically according to the riding model. Due to the low crystal quality of **4**, only the heavy atoms W, Co and P were anisotropically refined, leaving a relatively large residual electron density. The two independent molecules of the molecular structure of **6** were tested to be identical, but this resulted in noteworthy differences in angles and bond lengths. Attempts to refine the data set of **6** in the higher monoclinic space group resulted in a R_{int} value greater than 0.50. Thus, it can be concluded that the two molecules are independent in the triclinic unit cell. CCDC-245196 to -245200 (**2**−**6**) contain the supplementary crystallographic data for this paper. These data can be obtained free of charge at www.ccdc.cam.ac.uk/conts/retrieving.html [or from the Cambridge Crystallographic Data Centre, 12 Union Road, Cambridge CB2 1EZ, UK; Fax: + 44-1223-336-033; E-mail: deposit@ccdc.cam.ac.uk].

Acknowledgments

The authors thank the Deutsche Forschungsgemeinschaft and the Fonds der Chemischen Industrie for comprehensive financial support.

[1] For reviews, see: M. Scheer, E. Herrmann, *Z. Chem.* **1990**, *29*, 41. O. J. Scherer, *Angew. Chem. Int. Ed. Engl.* **1990**, *29*, 1104. K. H. Whitmire, *Adv. Organomet. Chem.* **1998**, *42*, 1. M. Ehses, A. Romerosa, M. Peruzzini, *Top. Curr. Chem.* **2002**, *220*, 107−140.

[2] Selected publications: [2a] M. Scheer, K. Schuster, G. Friedrich, *Angew. Chem.* **1993**, *105*, 641; *Angew. Chem. Int. Ed. Engl.* **1993**, *32*, 593. [2b] M. Scheer, K. Schuster, A. Krug, H. Hartung, *Chem. Ber./Recueil* **1997**, *130*, 1299. [2c] M. Scheer, K. Schuster, A. Krug, H. Hartung, *Chem. Ber.* **1996**, *129*, 973. [2d] T. Gröer, M. Scheer, *Z. Anorg. Allg. Chem.* **2000**, *626*, 1211−1216.

[3] M. Scheer, *Coord. Chem. Rev.* **1997**, *163*, 271−286. B. P. Johnson, G. Balazs, M. Scheer, *Top. Curr. Chem.* **2004**, *232*, 1−23.

[4] Generated at lower temperatures than solid state reactions normally proceed.

[5] H. G. von Schnering, W. Hönle, *Encyclopedia of Inorganic Chemistry* (Ed.: B. King), John Wiley & Sons, Ltd., London **1994**, p. 3106−3143.

[6] Y. Senzaki, W. L. Gladfelter, *Polyhedron* **1994**, *13*, 1159−1167.

[7] H. Lang, L. Zsolnai, G. Huttner, *Angew. Chem. Suppl.* **1983**, 1463−1476.

[8] R. Lal De, H. Vahrenkamp, *Z. Naturforsch., Teil B* **1985**, *40*, 1250−1257.

[9] U. Vogel, G. Stößer, M. Scheer, *Angew. Chem.* **2001**, *113*, 1476−1478; *Angew. Chem. Int. Ed.* **2001**, *40*, 1443−1445.

[10] V. Grossbruchhaus, D. Rehder, *Inorg. Chim. Acta* **1990**, *172*, 141−145.

[11] H. Lang, G. Huttner, B. Sigwarth, I. Jibril, L. Zsolnai, O. Orama, *J. Organomet. Chem.* **1986**, *304*, 137−155.

[12] M. Scheer, E. Herrmann, J. Sieler, M. Oehme, *Angew. Chem.* **1991**, *103*, 1023−1025; *Angew. Chem. Int. Ed. Engl.* **1991**, *30*, 969−971.

[13] H. Vahrenkamp, H. T. Schacht, *J. Organomet. Chem.* **1990**, *381*, 261.

[14] S. M. Owen, *Polyhedron* **1988**, *7*, 253.

 © 2005 Wiley-VCH Verlag GmbH & Co. KGaA, Weinheim

[15] D. Fenske, R. Basoglu, J. Hachgenei, F. Rogel, *Angew. Chem.* **1984**, *96*, 160−162; *Angew. Chem. Int. Ed. Engl.* **1984**, *23*, 160−162.
[16] J. E. Davies, M. C. Klunduk, M. J. Mays, P. R. Raithby, G. P. Shields, P. K. Tompkins, *J. Chem. Soc., Dalton Trans.* **1997**, 715.
[17] M. Scheer, E. Leiner, P. Kramkowski, M. Schiffer, G. Baum, *Chem. Eur. J.* **1998**, *4*, 1917.
[18] J. Grobe, W. Golla, D. Le Van, B. Krebs, M. Lage, *Organometallics* **1998**, *17*, 5717.
[19] Observable as fragmentation peaks of $[W(CO)_n]^+$ ($n = 1-6$) in the mass spectra.
[20] Based on the TG/MS results.
[21] C content <2%. Annealing at a temperature of 800 °C gives only traces of the known phase Mn_2Sb, accompanied by oxides of Mn and Sb.
[22] Based on the found metal ratio.
[23] Furthermore, CoP, Co_2P and also Mn_2Sb, Sb and Mn could be assigned to the crystalline part of the annealed samples.
[24] W. Strohmeier, F.-J. Müller, *Chem. Ber.* **1969**, *102*, 3608−3612.
[25] W. L. Gladfelter, P. C. Steinhardt, *Inorg. Chem.* **1980**, *19*, 332.
[26] [26a] G. M. Sheldrick, *SHELXS-86*, University of Göttingen, **1986**. [26b] G. M. Sheldrick, *SHELXL-93*, University of Göttingen, **1993**.

Received July 21, 2004
Early View Article
Published Online November 18, 2004

 © 2005 Wiley-VCH Verlag GmbH & Co. KGaA, Weinheim

3D-Coordination Cluster Polymers $[Ln(H_2O)_3Re_6Te_8(CN)_6]\cdot nH_2O$ (Ln = La^{3+}, Nd^{3+}): Direct Structural Analogy with the Mononuclear $LnM(CN)_6\cdot nH_2O$ Family

Sofia B. Artemkina,[a] Nikolai G. Naumov,*[a] Alexander V. Virovets,[a] and Vladimir E. Fedorov[a]

Keywords: Rhenium / Cluster compounds / Structure elucidation / Cyanide ligand / Lanthanides

Using the hydrothermal method two novel 3D-coordination complexes $[Ln(H_2O)_3Re_6Te_8(CN)_6]\cdot nH_2O$ (Ln = La^{3+}, Nd^{3+}) have been synthesised and structurally characterised. For compound $[La(H_2O)_3Re_6Te_8(CN)_6]\cdot 4H_2O$ (**1**) the unit cell parameters are: Space group $P6_3/m$, a = 9.3060(13), c = 20.528(4) Å, V = 1539.6(4) Å^3, R_f = 0.0597. For compound $[Nd(H_2O)_3Re_6Te_8(CN)_6]\cdot H_2O$ (**2**) the unit cell parameters are: Space group $P6_3/m$, a = 9.3030(10), c = 20.222(4) Å, V = 1515.7(4) Å^3, R_f = 0.0226. The structures of the cluster compounds are topologically analogous to the mononuclear polymeric complex $LaCr(CN)_6\cdot 5H_2O$.

(© Wiley-VCH Verlag GmbH & Co. KGaA, 69451 Weinheim, Germany, 2005)

Introduction

Octahedral cluster cyano complexes of transition metals have been intensively studied during the past decade (selected references: $[Re_6Q_8(CN)_6]^{4-}$ [1−3], $[Mo_6Q_8(CN)_6]^{7-}$ [4,5], $[W_6Q_8(CN)_6]^{6-}$ [6], $[Nb_6Cl_{12}(CN)_6]^{4-}$ [7,8] and heterometallic $[Re_{6-x}Mo_xS_8(CN)_6]^{5-}$ [9]). These anions are topological analogues of hexacyanometalate ions $[M(CN)_6]^{n-}$ and the anions can form polymeric arrays based on covalent cyano-bridged interactions with transition metals, for instance ···−Re_6−C≡N−M−N≡C−Re_6−··· (selected references: Re:[10−13], W:[14], Nb:[8]). Despite the equivalent disposition of terminal cyano groups in $[M(CN)_6]^{n-}$ and $[M_6Q_8(CN)_6]^{n-}$, it is difficult to expect isotypical structures when $[M(CN)_6]^{n-}$ is changed to $[M_6Q_8(CN)_6]^{n-}$. The reason is the larger size of cluster cyanides compared with mononuclear ones. This increase of linear size leads to a corresponding increase in pore volume, hence the network has a tendency to distort, collapse or to be interpenetrated.

Indeed, from the widely diverse family of cluster cyano-bridged polymers, only three compounds exhibit a direct structural analogy with mononuclear cyanometallates, namely: $Fe_4[Re_6Te_8(CN)_6]_3\cdot 27H_2O$, $Ga_4[Re_6Se_8(CN)_6]_3\cdot 38H_2O$,[15] and $(Me_4N)_2Mn[Nb_6Cl_{12}(CN)_6]$ [16] which crystallises in the highly symmetrical space group $Fm\bar{3}m$ and has an ordinary six-connected network equivalent to the well-known Prussian Blue net.[8] All other reported cluster networks have no examples in the family of mononuclear cyanometallates.

In this paper we report the synthesis and structures of two new coordination compounds based on the cluster complexes $[Re_6Te_8(CN)_6]^{3-}$ and Ln^{3+} (La^{3+}, Nd^{3+}).These compounds demonstrate another example of the direct structural analogy between compounds built from mononuclear $[M(CN)_6]^{n-}$ and cluster expanded $[M_6Q_8(CN)_6]^{n-}$ anions.

Results and Discussion

Syntheses of 1 and 2: The interaction of $K_4Re_6Te_8(CN)_6$ with $LnCl_3\cdot nH_2O$ under hydrothermal conditions described in the Exp. Sect. gave solid products which consisted of thin dark hexagonal plates of compounds **1** and **2**. X-ray diffraction patterns showed that the bulk samples were single phases with unit cell parameters as follows: **1**: a = 9.316(3), c = 20.521(4); **2**: a = 9.307(3), c = 20.213(4) Å. Chemical analysis (EDAX) of the crystals showed that they contained no potassium. The magnetic susceptibility of **1** is μ_{eff} (298) = 1.81 μ_B which corresponds to one unpaired electron per formula unit $[La(H_2O)_3Re_6Te_8(CN)_6]\cdot 4H_2O$. The magnetic susceptibility of **2** is μ_{eff} (298) = 4.18 μ_B. This value is very close to μ_{eff} = 4.24 μ_B calculated using the equation $\mu^2_{eff} = \mu^2(Nd^{3+}) + \mu^2([Re_6Te_8(CN)_6]^{3-})$ and corresponds to the presence of two noninteracting paramagnetic centres in the structure, namely Nd^{3+} and $[Re_6Te_8(CN)_6]^{3-}$. Based on magnetic and stoichiometric considerations, we postulate that the cluster complex $[Re_6Te_8(CN)_6]^{4-}$ has undergone one-electron oxidation during the reaction. Redox transformations of $[Re_6Te_8(CN)_6]^{4-}$ have been studied pre-

[a] Nikolaev Institute of Inorganic Chemistry SB RAS,
3, Akad. Lavrentiev Avenue, Novosibirsk 630090, Russia,
Fax: (internat.) +7-3832-344489
E-mail: naumov@che.nsk.su

Supporting information for this article is available on the WWW under http://www.eurjic.org or from the author.

 © 2005 Wiley-VCH Verlag GmbH & Co. KGaA, Weinheim DOI: 10.1002/ejic.200400139

viously[17] and it was found that the cluster complex is characterised by an oxidation potential low enough to be oxidised with oxygen dissolved in an aqueous solution. In fact, $[Re_6Te_8(CN)_6]^{4-}$ can lose one electron and the resultant $[Re_6Te_8(CN)_6]^{3-}$ can be isolated as a salt with an organic cation, i.e. $(Et_4N)_2(H)[Re_6Te_8(CN)_6]\cdot 2H_2O$.[18]

Structures of Compounds 1 and 2: Compounds **1** and **2** crystallise in the hexagonal space group $P6_3/m$ and they have identical coordination networks, i.e. $[Ln(H_2O)_3Re_6Te_8(CN)_6]_{3\infty}$. Structure **1** contains one rhenium atom (Re1), two tellurium atoms (Te1, Te2), one cyano group (C1, N1), Ln1, and O1 (coordinated water) in its asymmetric unit (Figure 1). The centre of the cyanocluster is located in the special position *2a* of the $P6_3/m$ space group and has $\bar{6}$ crystallographic symmetry close to the ideal O_h. Each rhenium atom is coordinated to one cyano group forming an almost linear Re−C−N fragment. Selected bond distances of structures **1**, **2** and other related complexes are listed in Table 1 for comparison. Comparing the bond lengths Re−Re, Re−Te, Re−C and C−N in $[Re_6Te_8(CN)_6]$ we can say that the oxidation does not significantly affect these distances (within the limits of the errors obtained).

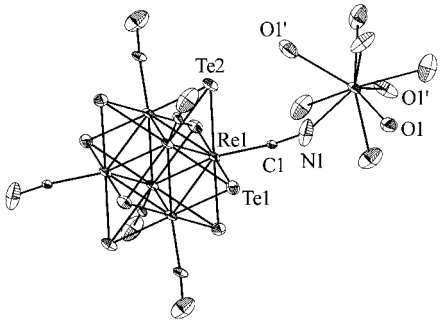

Figure 1. Asymmetric unit of the coordination network of $[Ln(H_2O)_3Re_6Te_8(CN)_6]_{3\infty}$ in the crystal structures of **1** and **2**; the atoms are shown at the 50% probability level

The lanthanide atom Ln1 (La^{3+} as well as Nd^{3+}) is located in the special position *2c* (1/3, 2/3, 1/4) with $\bar{6}$ symmetry. It is coordinated by six nitrogen atoms from the CN groups of different cluster anions and three water molecules. The coordination polyhedron of Ln1 is a regular tricapped trigonal prism (Figure 2) with bond lengths La−O 2.63(3), La−N 2.57(3) Å for **1** and Nd−O 2.645(15), Nd−N 2.537(11) Å for **2**.

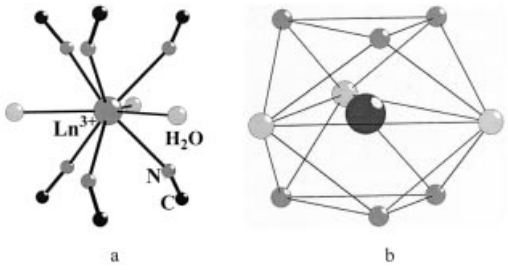

Figure 2. Coordination environments of Ln^{3+} in the crystal structures of **1** and **2** (a); coordination polyhedron around the Ln^{3+} cations (b)

The cluster complex $[Re_6Te_8(CN)_6]^{3-}$ is linked via lanthanide cations to produce a 3D-coordination network $[Ln(H_2O)_3Re_6Te_8(CN)_6]_{3\infty}$. Cluster complexes form six bridging cyano groups with Ln^{3+}. Six nitrogen atoms and three water molecules constitute the coordination sphere of the lanthanide cations as shown in Figure 2. In the network, the cluster complexes and Ln^{3+} cations are arranged in layers (Figure 3, *a*) parallel to the crystallographic *ab* plane and their packing can be presented as a sequence ···ABAC··· (A = cluster complex; B and C = lanthanide cations). For polymeric compounds based on octahedral cluster complexes, this kind of network has a sufficiently high packing coefficient of 69% (i.e. the coordination network occupies 69% of the cell volume).[19]

The connectivity of the network can be described as a (6,6)-connected net according to the nomenclature detailed in a review.[20] The nodes are Ln^{3+} lanthanide cations in a regular triangular prismatic environment of six nitrogen atoms belonging to the cluster complexes, the cluster complexes being coordinated to Ln^{3+} cations via six octahedrally arranged cyano groups. Rare earth cations have larger ionic radii than *3d* transition metals which drives the formation of the new type of network of octahedral cluster cyanometallates.

In compounds **1** and **2**, the coordination networks are isostructural while the total amount and locations of solvent water molecules in **1** and **2** are different. In the final difference electron density map of **1**, two peaks were found. One of them, assigned to O(1 W), is located on a mirror plane (position *6h*). In the unit cell, these atoms form an equilateral triangle with O···O distances of 3.02 Å around a special point of $\bar{6}$. The U_{eq} parameter is quite high (0.21

Table 1. Bond lengths in the cluster complexes $[Re_6Te_8(CN)_6]^{4-}$, $[Re_6Te_8(CN)_6]^{3-}$ and other selected compounds

Formula	Re−Re	Re−Te	Re−C	C−N
$[La(H_2O)_3Re_6Te_8(CN)_6]\cdot 4H_2O$ (**1**)	2.6780(19), 2.6814(18), av. 2.6797	2.683(3)−2.704(2), av. 2.694	2.05(3)	1.24(4)
$[Nd(H_2O)_3Re_6Te_8(CN)_6]\cdot H_2O$ (**2**)	2.6813(10), 2.6834(9), av. 2.6824	2.6749(16)−2.7065(11), av. 2.6915	2.095(15)	1.149(18)
$(Et_4N)_2(H)[Re_6Te_8(CN)_6]\cdot 2H_2O$[18]	2.676(1), 2.677(2)	2.682(2)−2.708(2); av. 2.691	2.09(5)	1.15(3), 1.19(5); av. 1.16
$Cs_4[Re_6Te_8(CN)_6]\cdot 2H_2O$[3]	2,674(1)−2.698(1); av. 2.684	2.691(1)−2.708(1); av. 2.698	2.09(2)−2.10(2); av. 2.10	1.12(2) − 1.17(2); av. 1.14
$Ba_2[Re_6Te_8(CN)_6]\cdot 12H_2O$[3]	2.671(2)−2.691(2); av. 2.681	2.695(2)−2.713(2); av. 2.702	2.09(2)−2.10(2); av. 2.10	1.14(3)−1.16(3); av. 1.15

 © 2005 Wiley-VCH Verlag GmbH & Co. KGaA, Weinheim

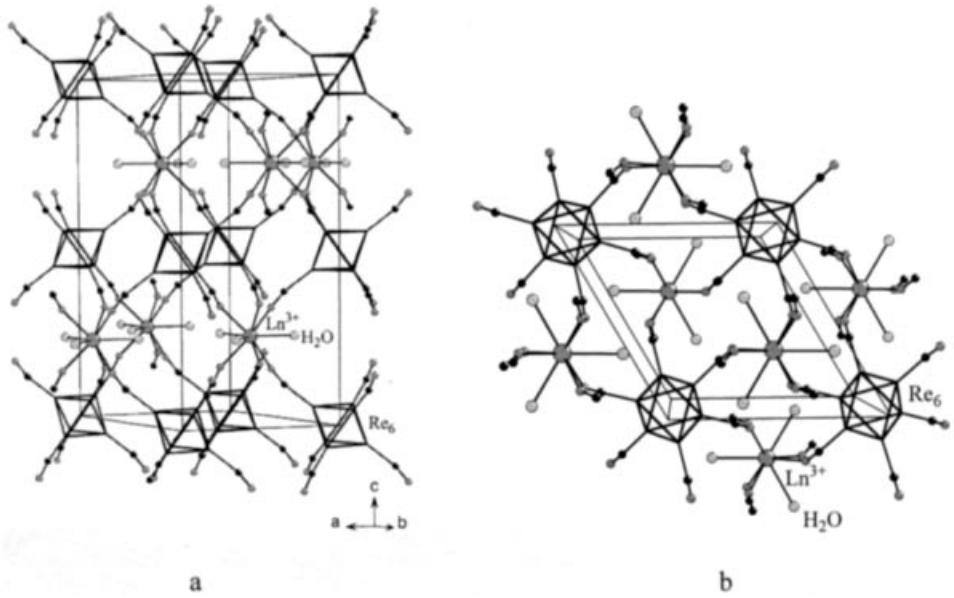

Figure 3. Coordination networks in the structures of **1** and **2** showing the layers of the cluster cores of $\{Re_6Te_8\}$ and the Ln^{3+} cations (a); view along the *c* direction (b)

$Å^{-2}$) but our attempt to refine the site occupancy factor (s. o. f.) did not give any improvement in the residuals. The second peak, assigned to O(2 W), was found in a *4f* special position (1/3, 2/3, *z*). This atom is located between three nitrogen atoms of the CN groups with O···N distances equal to 2.60 Å. The refinement of its s. o. f. resulted in a value of 0.5 with $U_{eq} = 0.085$ $Å^{-2}$.

In **2**, the final difference electron density map contained only one suitable peak which was assigned to an oxygen atom disordered over three positions around the special point of a $\bar{6}$ axis forming a triangle on a mirror plane. The O···O distances in the triangle of 1.34 Å are short, indicating that only one of three symmetrically related positions is actually occupied. Therefore, the s. o. f. was set to 33%. The resultant $U_{eq} = 0.079$ $Å^{-2}$ is as expected for solvent water molecules.

Structural Analogy with Mononuclear Compounds: Compounds **1** and **2** possess symmetry and a packing motif equivalent to mononuclear complexes with the general formula $LnM(CN)_6{\cdot}nH_2O$ or $ALnM(CN)_6{\cdot}nH_2O$. Indeed, compounds **1**, **2**, $[La(H_2O)_3Cr(CN)_6]{\cdot}2H_2O$[21], $[La(H_2O)_2Fe(CN)_6]{\cdot}2H_2O$[22] and $Cs[Ce(H_2O)_3Fe(CN)_6]{\cdot}H_2O$[23] crystallise in the space group $P6_3/m$. The cell parameters as well as the bond distances Ln−O(H_2O) and Ln−N(CN) are listed in Table 2. The packing of the cluster cores in **1** and **2** mimics the packing of the cations Cr^{3+}, Fe^{3+} and Fe^{2+} (Figure 4), as well as the packing motives of the lanthanide cations La^{3+}, Ce^{3+} and Nd^{3+}. A comparison of the angles in the coordination networks of **1**, **2** and $[La(H_2O)_3Cr(CN)_6]{\cdot}2H_2O$ revealed a moderate variation.

In these five structures, the coordination sphere of the lanthanide cation is tricapped trigonal prismatic containing six nitrogen atoms and three water molecules (Figure 2), except for $[La(H_2O)_2Fe(CN)_6]{\cdot}2H_2O$ in which one water molecule is absent and a two-capped trigonal prism (hendecahedron) is formed. Other known Ln−$[M(CN)_6]$ compounds crystallising in the orthorhombic system include[23−27] ($TlTmRu(CN)_6{\cdot}3H_2O$, $ErFe(CN)_6{\cdot}4H_2O$, $NdCo(CN)_6{\cdot}4H_2O$, $GdKFe(CN)_6{\cdot}3H_2O$, $YbKFe(CN)_6{\cdot}3.5H_2O$) and examples in the monoclinic system include[23,28−30] $CsLnFe(CN)_6{\cdot}5H_2O$ (Ln = Ce, Pr, Nd), $SmFe(CN)_6{\cdot}4H_2O$, $SmKFe(CN)_6{\cdot}3H_2O$ and $SmCo(CN)_6{\cdot}4H_2O$. However, their crystal structures exhibit similar packings of the building blocks and motives to those seen in coordination networks.[31]

In conclusion, we have prepared two new coordination compounds based on the cluster complexes $[Re_6Te_8(CN)_6]^{3-}$ and Ln^{3+} (La^{3+}, Nd^{3+}). These com-

Table 2. Selected bond lengths and cell parameters in compounds **1**, **2** and some mononuclear cyanometallates

Formula	Ln−O(H_2O) (Å)	Ln−N(CN) (Å)	Cell parameters (Å)
$[La(H_2O)_3Re_6Te_8(CN)_6]{\cdot}4H_2O$ (**1**)	2.63(3)	2.57(3)	$a = 9.3060(13)$, $c = 20.528(4)$
$[Nd(H_2O)_3Re_6Te_8(CN)_6]{\cdot}H_2O$ (**2**)	2.645(15)	2.537(11)	$a = 9.303(10)$, $c = 20.222(4)$
$[La(H_2O)_3Cr(CN)_6]{\cdot}2H_2O$[21]	2.591(5)	2.619(5)	$a = 7.7053(4)$, $c = 14.8155(9)$
$[La(H_2O)_2Fe(CN)_6]{\cdot}2H_2O$[22]	2.50(6)	2.56(3)	$a = 7.541(3)$, $c = 13.955(9)$
$Cs[Ce(H_2O)_3Fe(CN)_6]{\cdot}H_2O$[23]	2.682(4)	2.575(3)	$a = 7.4415(5)$, $c = 14.129(1)$

 © 2005 Wiley-VCH Verlag GmbH & Co. KGaA, Weinheim

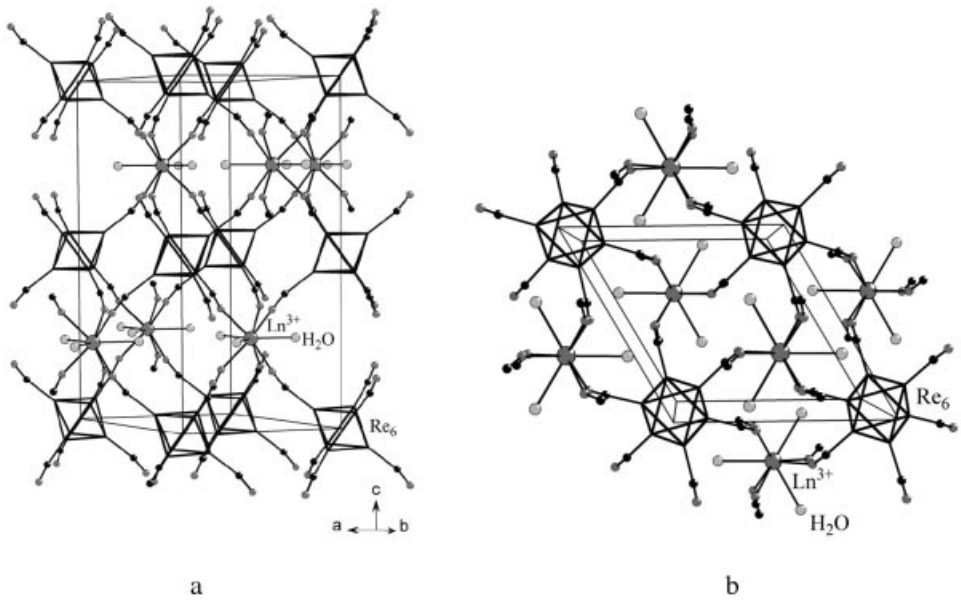

Figure 4. Coordination network in $[La(H_2O)_3Cr(CN)_6]\cdot 2H_2O$ showing layers of Cr^{3+} and La^{3+} cations (a); view along the *c* direction (b)

pounds exhibit a direct structural analogy with the $LnM(CN)_6\cdot nH_2O$ family.

Experimental Section

General: $K_4[Re_6Te_8(CN)_6]$[3] was prepared from polymeric Re_6Te_{15}.[32] All other reagents were used as purchased. Infrared spectra were measured in KBr disks with a Bruker IFS-85 spectrometer. X-ray powder diffraction data (XPD) were obtained with a Philips APD 1700 powder diffractometer using Cu-K_α radiation. Magnetic measurements were performed with a Quantum Design SQUID magnetometer, field 5 kOe.

X-ray Structural Studies: The diffraction measurements were performed by standard techniques at 298(2) K with an Enraf−Nonius CAD4 diffractometer (graphite-monochromated Mo-K_α radiation). Face-indexed absorption corrections were applied. The crystal structures were solved by direct methods and refined by full-matrix least-squares methods using SHELX-97.[33] Hydrogen atoms of the water molecules were not located. Dark hexagonal plates of **1** and **2** were selected from the reaction products.

Crystallographic Data for 1: $C_6H_{14}La_1N_6O_7Re_6Te_8$, FW = 2559.16, hexagonal crystal system, space group $P6_3/m$, a = 9.3060(13), c = 20.528(4) Å, V = 1539.6(4) Å^3, Z = 2, $D_{calcd.}$ = 5.443 g·cm^{-3}, μ = 32.299 mm^{-1}. Total 2416 reflections were collected up to $\theta_{max.}$ = 24.97°, of which 939 independent (R_{int} = 0.1394). Final residuals are: $R1$ = 0.0597, $wR2$ = 0.1339 for 493 $F_{hkl}(4\sigma)$, $R1$ = 0.0941, $wR2$ = 0.1578 for all unique reflections.

Crystallographic Data for 2: $C_6H_8N_6NdO_4Re_6Te_8$, FW = 2510.45, crystal system is hexagonal, space group $P6_3/m$, a = 9.3030(10), c = 20.222(4) Å, V = 1515.7(4) Å^3, Z = 2, $D_{calcd.}$ = 5.501 g·cm^{-3}, μ = 33.108 mm^{-1}. Total 3537 reflections were collected up to $\theta_{max.}$ = 27.46°, of which 1196 independent (R_{int} = 0.0633). Final residuals are: $R1$ = 0.0226, $wR2$ = 0.0441 for 616 $F_{hkl}(4\sigma)$, $R1$ = 0.0606, $wR2$ = 0.0585 for all unique reflections.

Further details of the crystal-structure investigation(s) may be obtained from the Fachinformationszentrum Karlsruhe, 76344 Eggenstein-Leopoldshafen, Germany, on quoting the depository number(s) CSD-413628 (for **1**) and CSD-413629 (for **2**). X-ray powder patterns of samples **1** and **2** are also included.

Preparation of $[La(H_2O)_3Re_6Te_8(CN)_6]\cdot 4H_2O$ (1): A mixture of $LaCl_3\cdot 7H_2O$ (0.033 g, 0.09 mmol) and $K_4Re_6Te_8(CN)_6$ (0.050 g, 0.02 mmol) was placed in a glass ampoule (15 mL) and an aqueous solution of ammonia was added to the mixture to adjust the pH to 9. The ampoule was sealed and heated at 140 °C for two days. The ampoule was then gradually cooled. The product consisted of dark hexagonal plates and a thin light precipitate as well as a reasonable quantity of a dark crystalline powder. The dark plates were selected, washed with water and dried in air. Yield ca. 0.020 g (39%). In our opinion, the presence of ammonia in the reaction solution results in better crystallisation. IR: ν_{CN} 2098−2085 (broad), ν_{OH} 1610; δ_{HOH} 3572 (broad); ν_{Re-C} 453 cm^{-1}. μ_{eff} (298 K) = 1.81 μ_B.

Preparation of $[Nd(H_2O)_3Re_6Te_8(CN)_6]\cdot H_2O$ (2): The same method was used to prepare **2**, $NdCl_3\cdot 6H_2O$ (0.040 g, 0.10 mmol) being the source of Nd^{3+}. Yield ca. 0.015 g (30%). IR: δ_{HOH} 3559, 3521; ν_{CN} 2081; ν_{OH} 1566; ν_{Re-C} 454 cm^{-1}. μ_{eff} (298 K) = 4.18 μ_B.

Acknowledgments

This work was supported by the Russian Foundation for Basic Research (Grant No. 02−03−32264) and an INTAS grant (number 2000−0651). The authors thank Prof. V. N. Ikorskii (Nikolaev Institute of Inorganic Chemistry) for magnetic measurements.

[1] Y. V. Mironov, A. V. Virovets, V. E. Fedorov, N. V. Podberezskaya, O. V. Shishkin, Y. T. Struchkov, *Polyhedron* **1995**, *14*, 3171−3173.
[2] A. Slougui, Y. V. Mironov, A. Perrin, V. E. Fedorov, *Croat. Chem. Acta* **1995**, *68*, 885−890.
[3] H. Imoto, N. G. Naumov, A. V. Virovets, T. Saito, V. E. Fedorov, *J. Struct. Chem. Engl. Tr.* **1998**, *39*, 720−727.

 © 2005 Wiley-VCH Verlag GmbH & Co. KGaA, Weinheim

[4] Y. V. Mironov, A. V. Virovets, N. G. Naumov, V. N. Ikorskii, V. E. Fedorov, *Chem. Eur. J.* **2000**, *6*, 1361−1365.
[5] K. A. Brylev, A. V. Virovets, N. G. Naumov, Y. V. Mironov, D. Fenske, V. E. Fedorov, *Russ. Chem. Bull.* **2001**, *50*, 1140−1143.
[6] S. Jin, F. J. DiSalvo, *Chem. Commun.* **2001**, 1586−1587.
[7] N. G. Naumov, S. Cordier, C. Perrin, *Solid State Sci.* **2003**, *5*, 1359−1367.
[8] B. Yan, H. Zhou, A. Lachgar, *Inorg. Chem.* **2003**, *42*, 8818−8822.
[9] N. G. Naumov, K. A. Brylev, Y. V. Mironov, A. V. Virovets, D. Fenske, V. E. Fedorov, *Polyhedron* **2004**, manuscript accepted.
[10] N. G. Naumov, A. V. Virovets, M. N. Sokolov, S. B. Artemkina, V. E. Fedorov, *Angew. Chem. Int. Ed.* **1998**, *37*, 1943−1945.
[11] N. G. Naumov, A. V. Virovets, V. E. Fedorov, *J. Struct. Chem. Engl. Tr.* **2000**, *41*, 499−520.
[12] M. V. Bennett, L. G. Beauvais, M. P. Shores, J. R. Long, *J. Am. Chem. Soc.* **2001**, *123*, 8022−8032.
[13] Y. Kim, S. M. Park, W. Nam, S. J. Kim, *Chem. Commun.* **2001**, 1470−1471.
[14] S. Jin, F. J. DiSalvo, *Chem. Mater.* **2002**, *14*, 3448−3457.
[15] M. P. Shores, L. G. Beauvais, J. R. Long, *J. Am. Chem. Soc.* **1999**, *121*, 775−779.
[16] The compound $K_7[Mo_6Se_8(CN)_6]\cdot 8H_2O$ (ref.[4]) could be formally attributed to this structural type by considering K1 in the structure as a node of a net instead of a transition metal.
[17] T. Yoshimura, S. Ishizaka, Y. Sasaki, H.-B. Kim, N. Kitamura, N. G. Naumov, M. N. Sokolov, V. E. Fedorov, *Chem. Lett.* **1999**, 1121−1122.
[18] N. G. Naumov, E. V. Ostanina, A. V. Virovets, M. Schmidtmann, A. Müller, V. E. Fedorov, *Russ. Chem. Bull., Int. Ed.* **2002**, *51*, 866−871.
[19] The packing coefficient was calculated using the program KPACK. The KPACK calculating method is similar to that used in OPEC (Gavezzotti, 1983) and is based on equidistant distribution of testing points (200 points/Å^3). The crystal structure is supposed to be a superposition of atomic spheres of van der Waals radii. The packing coefficient is equal to the ratio of the number of testing points belonging to one or more atomic spheres and the total number of points. The procedure was described in detail in A. V. Virovets, N. V. Podberezskaya, *Kristallografiya* **1992**, *37*, 1017−1019 (in Russian).
[20] M. O'Keeffe, M. Eddaoudi, H. Li, T. Reineke, O. M. Yaghi, *J. Solid State Chem.* **2000**, *152*, 3−20.
[21] A. Dommann, H. Vetsch, F. Hulliger, *Acta Crystallogr., Sect. C* **1990**, *46*, 1994−1996.
[22] D. F. Mullica, W. O. Milligan, R. L. Garner, *Acta Crystallogr., Sect. B* **1980**, *36*, 2561−2564.
[23] T. Siegrist, C. Besnard, C. Svensson, *Solid State Sci.* **2000**, *2*, 607−614.
[24] A. Dommann, H. Vetsch, F. Hulliger, W. Petter, *Acta Crystallogr., Sect. C* **1990**, *46*, 1992−1994.
[25] D. F. Mullica, P. K. Hayward, E. L. Sappenfield, *Acta Crystallogr., Sect. C* **1996**, *52*, 61−63.
[26] D. F. Mullica, J. L. Ward, E. L. Sappenfield, *Acta Crystallogr., Sect. C* **1996**, *52*, 2956−2959.
[27] D. F. Mullica, E. L. Sappenfield, T. A. Cunningham, *J. Solid State Chem.* **1991**, *91*, 98−104.
[28] D. F. Mullica, H. O. Perkins, E. L. Sappenfield, D. A. Grossie, *J. Solid State Chem.* **1988**, *74*, 9−15.
[29] D. F. Mullica, E. L. Sappenfield, H. O. Perkins, *J. Solid State Chem.* **1989**, *78*, 301−306.
[30] F. Mullica, H. O. Perkins, E. L. Sappenfield, *J. Solid State Chem.* **1988**, *74*, 419−423.
[31] Vector equations between monoclinic and hexagonal cells are: $a_{hex} \approx a_{monocl}$, $b_{hex} \approx c_{monocl}$, $c_{hex} \approx -b_{monocl}$, $\beta_{monocl} \approx 120°$. Vector Equations between orthorhombic (*C*-centered, *Cmcm*, primitive, *Pnma)* and hexagonal unit cell: $a_{hex} \approx (a_{orth} + b_{orth})/2$, $b_{hex} \approx -a_{orth}$, $c_{hex} \approx c_{orth.}$
[32] V. E. Fedorov, N. V. Podberezskaya, A. V. Mischenko, G. F. Khudorozko, I. P. Asanov, *Mater. Res. Bull.* **1986**, *21*, 1335−1342.
[33] G. M. Sheldrick, **1997**. SHELX97 release 97−2, University of Göttingen, Germany.

Received February 19, 2004
Early View Article
Published Online November 18, 2004

 © 2005 Wiley-VCH Verlag GmbH & Co. KGaA, Weinheim

Dioxovanadium(V) Complexes of ONO Donor Ligands Derived from Pyridoxal and Hydrazides: Models of Vanadate-Dependent Haloperoxidases

Mannar R. Maurya,*[a] Shalu Agarwal,[a] Cerstin Bader,[b] and Dieter Rehder*[b]

Keywords: Vanadium / Hydrazones / Catalytic bromination / Pyridoxal

[$VO(acac)_2$] reacts with H_2L [H_2L are the hydrazones H_2pydx-inh (**I**), H_2pydx-nh (**II**), or H_2pydx-bhz (**III**); pydx = pyridoxal, inh = isonicotinohydrazide, nh = nicotinohydrazide, bhz = benzohydrazide] in dry methanol to yield the oxovanadium(IV) complexes [VOL] (H_2L = **I**: **1**; H_2L = **II**: **4**) or [VO(pydx-bhz)]. These complexes, when exposed to air, convert into the corresponding dioxovanadium(V) complexes [VO_2HL] (H_2L = **I**: **2**; H_2L = **II**: **5**; H_2L = **III**: **7**). Aqueous solutions of vanadate and the ligands at pH = 7.5 give rise to the formation of [$K(H_2O)_3$][VO_2(pydx-inh)] (**3**), [$K(H_2O)_2$][VO_2-(pydx-nh)] (**6**) and [$K(H_2O)_2$][VO_2(pydx-bhz)] (**8**). Treatment of **6** and **8** with H_2O_2 generates the oxo(peroxo)vanadium complexes [$VO(O_2)L$] (H_2L = **II**: **9**; H_2L = **III**: **10**). Complexes **9** and **10** are capable of transferring an oxo group to PPh_3. Acidification of **8** with HCl afforded a hydroxo(oxo) complex. The crystal and molecular structures of ligand **I** and complex **3** have been solved by single-crystal X-ray diffraction. In the anion **3**, the vanadium atom is in a distorted tetragonal-pyramidal environment (τ = 0.23). The K^+ ion is coordinated to four water molecules (two of which bridge to a neighbouring K^+ ion), the pyridine nitrogen atom of an isonicotinic moiety, the equatorial oxo group of the VO_2^+ fragment, and the alcoholic group of the pyridoxal moiety, which links adjacent layers in the three-dimensional lattice network. In the presence of KBr/H_2O_2, the anionic complexes **3**, **6** and **8** catalyse the oxidative bromination of salicylaldehyde in water to 5-bromosalicylaldehyde in ca. 40% yields with ca. 87% selectivity.
(© Wiley-VCH Verlag GmbH & Co. KGaA, 69451 Weinheim, Germany, 2005)

Introduction

Recent interest in vanadium coordination chemistry[1,2] with *ON* oligodentate ligands arises from the potential of these complexes as insulin-enhancing or insulin-mimetic agents,[3] their model character for vanadate-dependent haloperoxidases occurring in fungi and marine algae[4] and, in relation to these enzymes, their use in oxo-transfer catalysis and oxidative halogenation. Vanadate-dependent haloperoxidases contain $VO(OH)O_2^{2-}$ (HVO_4^{2-}) coordinated to the N^{ε} of a histidine in an overall trigonal-bipyramidal coordination.[5] These enzymes, and models of their active centre, catalyse the oxidation of halides by peroxide to hypohalous acid [which further halogenate non-enzymatically hydrocarbons; Equation (1)],[6] and the oxidation of organic (prochiral) sulfides to (chiral) sulfoxides.[7,8] Peroxo and hydroperoxo complexes have been proposed to act as the active intermediates.[6,9] The peroxo form, containing peroxovanadate $HVO_3(O_2)^{2-}$ attached to histidine, and in a tetragonal-pyramidal geometry, has been structurally characterised.[10]

$$Hal^- + H_2O_2 + RH + H^+ \rightarrow RHal + 2\,H_2O \quad (1)$$

We have previously reported on dioxovanadium(V) complexes with *ONO*, *NNO* and *NNS* functional ligands, derived from hydrazones based on the carbonyl components salicylaldehyde or 2-acetylpyridine, and the hydrazides of isonicotinic or benzoic acid, or *S*-benzyldithiocarbazate,[11] and reduced Schiff bases derived from salicylaldehyde and various amino acids.[12] Anionic and neutral *cis*-dioxovanadium(V) complexes with tridentate (*ONO*) *N*-salicylidenehydrazide ligand systems as models for vanadate-dependent haloperoxidases have recently been reviewed by Plass.[13] The present work is an extension to hydrazones formed from the biogenic carbonyl constituents pyridoxal (vitamin B_6; HpydxOH), and the hydrazides of nicotinic acid (H_2nh), isonicotinic acid (H_2inh) or benzoic acid (H_2bhz; see Scheme 1), which reveals novel structural features, and reactivity patterns that model the haloperoxidase activity.

Results and Discussion

Scheme 2 provides an overview of the complexes reported in this contribution. Structures of these complexes are based on spectroscopic (IR, UV/Vis, EPR, ^{1}H and ^{51}V NMR) data, thermogravimetric studies, elemental analyses and X-ray diffraction analyses of the ligand H_2pydx-inh (**I**) and complex **3**.

[a] Department of Chemistry, Indian Institute of Technology Roorkee,
Roorkee 247667, India
E-mail: rkmanfcy@iitr.ernet.in
[b] Institut für Anorganische und Angewandte Chemie, Universität Hamburg,
Martin-Luther-King-Platz 6, 20146 Hamburg, Germany
E-mail: dieter.rehder@chemie.uni-hamburg.de

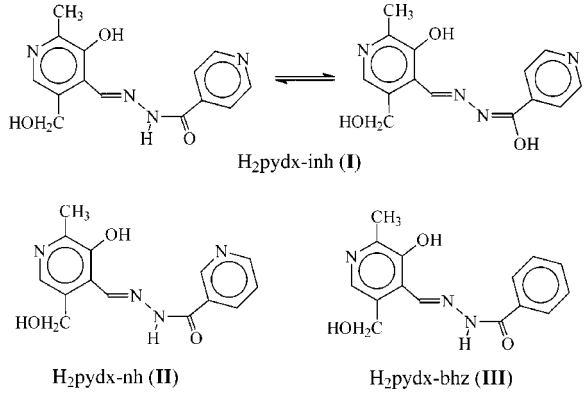

Scheme 1. Tautomerism shown for **I** only

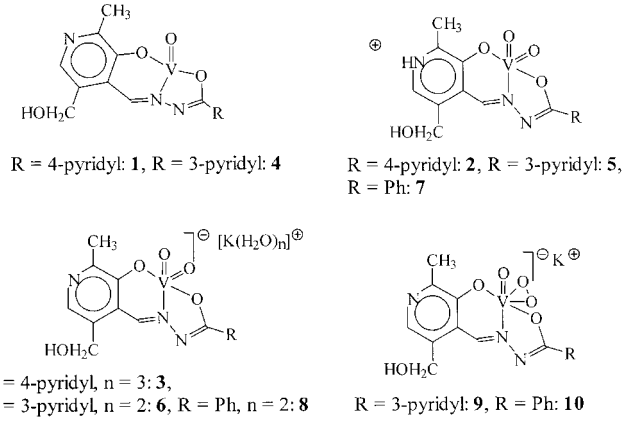

Scheme 2. **1** and **4** are idealised structural units; cf. text

Synthesis and General Characteristics

Reaction between equimolar amounts of $[VO(acac)_2]$ and ligand **I** or **II** (Scheme 1) in dry, refluxing methanol gave the oxovanadium(IV) complex [VO(pdyx-inh)] (**1**) or [VO(pdyx-nh)] (**4**), respectively. According to elemental analyses and thermogravimetric studies, there is no coordinated additional ligand such as water or methanol present in the isolated, solid compounds; **1** and **4** exhibit a magnetic moment, at ambient temperature of 1.32 and 1.41 μ_B, respectively; the spin-only value for a d^1 system is 1.73 μ_B. The magnetic data can be interpreted in terms of antiferromagnetic exchange interaction,[14] implying close contacts between the monomers or the formation of dinuclear complexes such as $[\{VO(L)\}_2\mu\text{-}O]$. Although dinuclear complexes of this type are well documented,[15] the size of the magnetic moments and the low wave number for the V=O stretch (888 cm^{-1}) suggest intermolecular interactions of the kind (L)V=O···VO(L),[16] and thus an effective coordination number of 5. Anisotropic EPR data of DMSO solutions (see Exp. Sect.) correspond to those expected for the equatorial donor set shown for **1** and **4** in Scheme 2, i.e. $O_{phenolate}N_{imine}O_{enolate}$, plus a relatively weakly bonding equatorial ligand such as water or DMSO.[17]

On aerial oxidation of **1** in methanol, the dioxovanadium(V) complex $[VO_2(Hpdyx\text{-}inh)]$ (**2**) was obtained. The intermediate complex **1** can be isolated from the methanolic solution prior to aeration. Equations (2) and (3) represent the synthetic procedures.

$$\underset{\mathbf{I}}{[VO(acac)_2]} + H_2pydx\text{-}inh \rightarrow \underset{\mathbf{1}}{[V^{IV}O(pydx\text{-}inh)]} + 2\ Hacac \quad (2)$$

$$2\ \underset{\mathbf{1}}{[VO(pydx\text{-}inh)]} + H_2O + 1/2\ O_2 \rightarrow 2\ \underset{\mathbf{2}}{[V^{V}O_2(Hpydx\text{-}inh)]} \quad (3)$$

Similarly, the complex [VO(pydx-nh)] (**4**), can be oxidised in methanol to $[VO_2(Hpydx\text{-}nh)]$ (**5**). Further, complexes **2** and **5** were obtained from the reaction of potassium vanadate (which, at ambient pH, is actually present as a mixture of vanadates; vide infra), generated in situ by dissolving V_2O_5 in an aqueous solution of KOH, with solutions of the potassium salts of ligands **I** or **II** and adjustment of the pH of the reaction mixture to 6.0. Adjustment of the pH of these solutions to 7.5 results in the formation of a mixture of $[K(H_2O)_3][VO_2(pydx\text{-}inh)]$ (**3**) and **2** [Equation (4)], or $[K(H_2O)_2][VO_2(pydx\text{-}nh)]$ (**6**) and **5**, respectively. The final pH of the reaction mixture plays an important role in that a decrease in pH (e.g. to pH = 6.5) increases the yield of the neutral complexes **2** or **5**. This pH dependence is possibly due to the actual vanadate species present in solution: At pH = 6, $H_2VO_4^-$ is in equilibrium with $H_2V_2O_7^{2-}$, $V_4O_{12}^{4-}$(dominant species), $V_5O_{15}^{5-}$ and $V_{10}O_{28}^{6-}$; at pH = 7.5, decavanadate disappears, and monovanadate (again in equilibrium with divanadate, tetravanadate as the main species, and pentavanadate) is present in the mono- and diprotonated forms (the pK_a for $H_2VO_4^-$ is around 8.1).[18] The two complexes **2** and **3**, or **5** and **6**, can be separated by fractional crystallisation from methanol, where the neutral complex crystallises first. Complexes **7** and **8** were prepared similarly from $[VO(acac)_2]$ and "KVO_3", respectively. Addition of H_2O_2 to the methanolic solution of **6** and **7** yields the oxomono(peroxo)vanadium(V) complexes **9** and **10** [Equation (5)].

$$K_{3-x}H_xVO_4 + K_2pydx\text{-}inh \rightarrow \underset{\mathbf{2}}{[VO_2(Hpydx\text{-}inh)]} + \underset{\mathbf{3}}{[K(H_2O)_3][VO_2(pydx\text{-}inh)]}\ (x = 1, 2) \quad (4)$$

$$[VO_2L]^- + H_2O_2 \rightarrow [VO(O_2)L]^- + H_2O \quad (H_2L = \mathbf{II}\text{: }\mathbf{9};\ H_2L = \mathbf{III}\text{: }\mathbf{10}) \quad (5)$$

Potassium vanadate reacts with 30% aqueous H_2O_2 to generate $K[VO(O_2)_2(OH/H_2O)_x]^{n-}$. In the presence of the potassium salt of ligand **III**, the peroxo complex $K[VO(O_2)(pydx\text{-}bhz)]$ (**10**) forms; see idealised Equation (6).

$$KH_2VO_4 + K_2pydx\text{-}bhz + H_2O_2 \rightarrow K[VO(O_2)(pydx\text{-}bhz)] + 2\ KOH + H_2O \quad (6)$$

The peroxo complex of ligand **I** could not be isolated in the solid state by any of the above methods due to its instability at ambient temperature. The formation of a peroxo complex in solution by treatment of **8** with H_2O_2 has also

 © 2005 Wiley-VCH Verlag GmbH & Co. KGaA, Weinheim

been established by electronic absorption spectroscopy. The spectral changes are depicted in Figure 1. The band for $[VO_2(pydx\text{-}bhz]^-$ (**8**) at 404.5 nm shifts to 424 nm along with an increase in intensity on dropwise addition of H_2O_2, while the band at 329 nm only marginally shifts to 333 nm with partial reduction in intensity. The amount of peroxo complex formed depends upon the amount of H_2O_2 added. The final spectral pattern is similar to that obtained for the isolated peroxo complex **10** in methanol.

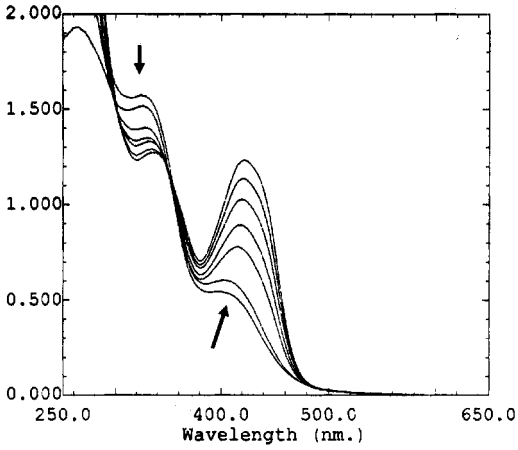

Figure 1. Titration of $[K(H_2O)_2][VO_2(pydx\text{-}bhz)]$ (**8**) with 30% H_2O_2; the spectra were recorded after successive addition of 2-drop portions of H_2O_2 to 10 mL of a ca. 10^{-4} M solution of **8** in MeOH

The peroxo complexes **9** and **10** undergo oxygen transfer reactions with PPh_3 in methanol to give the corresponding dioxovanadium(V) complexes **6** and **8** [Equation (7)].

$$[VO(O_2)L]^- + PPh_3 \rightarrow [VO_2L]^- + OPPh_3;\ (H_2L = \mathbf{I} \text{ or } \mathbf{III}) \quad (7)$$

Structure Description

An ORTEP plot and cell drawing of the ligand H_2pydx-inh (**I**) along with the atom-labelling scheme is presented in Figure 2 and selected structure parameters in Table 1. The bond parameters are well within the expected range. From the bond lengths *d*(C6−O1) [1.223(2) Å] and *d*(C6−N2) [1.363(3) Å], and the angles at C6 (av.120.0°) and N2 [116.0(2)°] it is clear that in the free ligand the ketonic form

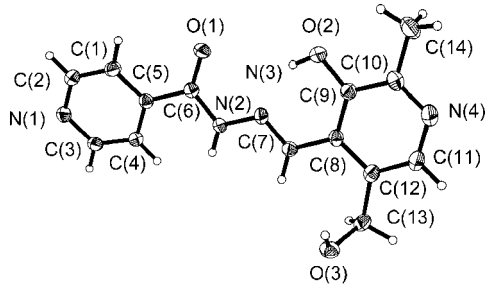

Figure 2. ORTEP plot (at the 50% probability level) of the ligand H_2pydx-inh (**I**)

Table 1. Bond lengths [Å] and angles [°] for **I** and **3** (symmetry transformations used to generate equivalent atoms: #1: $-x, -y+1, -z$; #2: $x, y+1, z$; #3: $x, y-1, z$; #4: $x, y, z+1$)

I		**3**	
		V1−O1	1.6318(12)
		V1−O2	1.6332(12)
		V1−O3	1.9906(11)
		V1−O4	1.8886(11)
		V1−N3	2.1233(13)
		K1−O2	2.8309(12)
		K1−O5	2.7184(13)
		K1−O6	2.8867(13)
		K1−O7	2.9463(13)
		K1−O8	2.7893
		K1−O8#	2.8444(14)
		K1−N1	2.8076(14)
		K1···K1#	3.8176
O1−C6	1.223(3)	O3−C6	1.3053(18)
N2−C6	1.363(3)	N2−C6	1.302(2)
N2−N3	1.362(3)	N2−N3	1.3969(18)
N3−C7	1.281(3)	N3−C7	1.2984(19)
O2−C9	1.354(3)	O4−C12	1.3185(18)
C12−C13	1.506(3)	C9−C14	1.510(2)
O3−C13	1.428(3)	O5−C14	1.427(2)
		O2−V1−N3	138.99(6)
		O3−V1−O4	152.65(5)
		O3−V1−N3	73.91(5)
		O4−V1−N3	82.40(5)
		V1−O2−K1	133.64(7)
		O2−K1−O5	156.19(4)
		K1−O5−C14	128.30(10)
		K1−O8−K1#	85.31(4)
C12−C13−O3	113.5(2)	C9−C14−O5	110.29(13)
O1−C6−N2	122.7(2)	O3−C6−N2	123.48(14)
C6−N2−N3	116.0(2)	C6−N2−N3	108.45(12)
N3−C7−C8	117.7(2)	N3−C7−C8	124.02(14)

prevails. This is further confirmed by an intermolecular hydrogen bond N2H···O3HCH$_2$ (1.970 Å). Additional close intermolecular contacts exist between adjacent molecules via C3H and O1 (2.575 Å) of the isonicotinic acid moieties, as well as isonicotinic N1 and pyridoxal O3HCH$_2$ (2.749 Å).

Figure 3 shows an ORTEP plot and a schematic drawing for the vanadium and potassium coordination environments of **3**; Figure 4 is a representation of the 3D arrangement of the molecular units. Selected structure parameters are collated in Table 1. The geometry of the anion can be described in terms of a tetragonal pyramid, distorted towards a trigonal bipyramid. The τ value {[∠(O3−V−O4) − ∠(O2−V−N3)]/60} is 0.23 (τ = 0 vs. 1 for ideal tetragonal-pyramidal vs. trigonal-bipyramidal arrangements), reflecting a common situation encountered with pentacoordinate oxovanadium complexes. For rare examples of a distorted trigonal-bipyramidal arrangement, see ref.[19] The *cis*-dioxovanadium unit is coordinated through the phenolate oxygen atom O4 of pyridoxal, the imine nitrogen atom N3, and the enolate oxygen atom O3 of the isonicotinic acid hydrazone. Together with the doubly bonded O2, bridging to the potassium ion, these functions form the tetragonal plane. The angle at O2 is 133.67(7)°. The bond lengths

 © 2005 Wiley-VCH Verlag GmbH & Co. KGaA, Weinheim

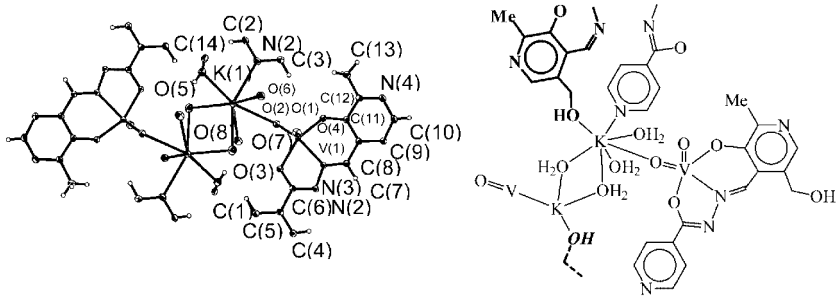

Figure 3. ORTEP plot (30% probability level) of $[K(H_2O)_3](VO_2(pydx\text{-}inh)]$ (**3**), and a schematic drawing of the vanadium and potassium environments; bold parts refer (to connections) to planes above and below

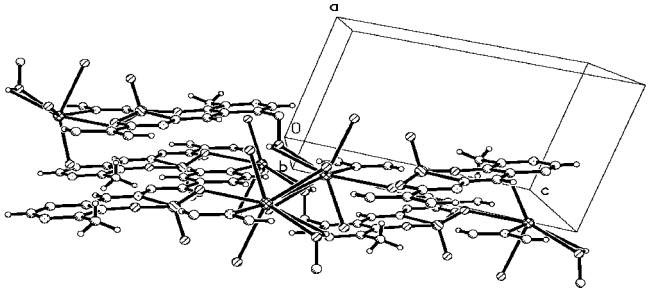

Figure 4. Section from the crystal lattice of **3**, showing the supramolecular arrangement

d(V−N3) [2.1233(13)], *d*(V−O3) [1.9906(11)] and *d*(V−O4) [1.8886(11) Å] are in agreement with literature values for imine, enolate and phenolate coordinating to the vanadium centre. Further, the bond lengths *d*(N2−N3) [1.3969(18)], *d*(N2−C6) [1.302(17)] and *d*(O3−C6) [1.3053(18) Å] are consistent with the enolate mode of coordination, supported by a comparison with the respective parameters for the free ligand (Table 1), in which the carbonyl form is present. The apical V=O bond, *d*(V−O1) = 1.6318(12) is in the expected range, while the basal V=O bond, *d*(V−O2) = 1.66332(12) Å, is slightly elongated as a consequence of covalent bonding contact to the K^+ ion.

The K^+ ion links three complex anions through the basal oxo group of VO_2^+ (O2), the pyridine nitrogen atom of an isonicotinic acid moiety (N1) and the alcoholic oxygen atom of a pyridoxal moiety (O5). In addition, four water molecules (three per molecular unit) are coordinated to K^+, resulting in the coordination number 7 for each potassium ion. In the dinuclear rhombohedral $\{K_2(\mu\text{-}OH_2)_2\}$ core, the angles are 85.31(4) at O8 and 94.69(4)° at K1; *d*(K1···K1#) amounts to 3.818 Å. O5 on K1 and O5# on K1# link to adjacent planes. Supramolecular links are further established by one of the terminal water molecules, which is hydrogen-bonded to the ring nitrogen atom of the pyridoxal moiety, N4···H_2O6 = 2.848 Å.

For the structures of the related complexes **2**, **5** and **7**, **6** and **8**, and the peroxo complexes **9** and **10**, we assume a ligand arrangement corresponding to that in **3**; cf. Scheme 2.

Thermal Studies

The complexes [VO(pydx-inh)] (**1**) and [VO(pydx-nh)] (**4**) lose about 75% of their mass between 250 and 450 °C in two overlapping steps, which corresponds to the loss of the organic components minus 1.5 oxygen atoms per molecule (3 per two molecules) (calculated mass loss: 74.1%). Consequently, the remaining product is V_2O_5. The TGA profiles of the dioxovanadium(v) complexes $[K(H_2O)_3][VO_2(pydx\text{-}inh)]$ (**3**), $[K(H_2O)_3][VO_2(pydx\text{-}nh)]$ (**6**) and $[K(H_2O)_3][VO_2(pydx\text{-}bhz)]$ (**8**) show that these complexes contain three (**3**) or two (**6** and **8**) water molecules per formula unit. The loss of this water in the temperature range 95−220 °C is indicative of coordinated water. On further increasing the temperature, the water-free species $K[VO_2(pydx\text{-}inh)]$ and $K[VO_2(pydx\text{-}nh)]$ decompose in one step between 220 and 350 °C to form KVO_3. The total loss corresponds to the loss of ligand minus 1 oxygen atom. A mass loss of 8.6%, equivalent to two water molecules (calcd. 8.93%) for **7** in the temperature range 80−135 °C, suggests that this is just water of crystallisation. Complexes **2**, **5** and the water-free form of **7** have decomposition patterns similar to those of the respective forms of **3**, **6**, and **8** after loss of water. They all yield V_2O_5 as the final product.

IR Spectroscopic Studies

The IR spectra of the ligands exhibit two bands at 3230 and 1678 [H_2pydx-inh (**I**)], 3250 and 1673 [H_2pydx-nh (**II**)] and 3210 and 1677 cm^{-1} [H_2pydx-bhz (**III**)] due to ν(NH) and ν(C=O) stretches, respectively, indicative of their ketonic nature in the solid state; cf. also Figure 1. The absence of these bands in the spectra of all complexes is consistent with enolisation and replacement of H by the metal ion. A new band appearing in the region 1220−1262 cm^{-1} is assigned to the $\nu(C-O_{enolic})$ mode. The $\nu(C=N_{azomethine})$ stretch of the free ligands appears as a weak band at 1617−1637 cm^{-1} along with the ν(C=N) stretches of the pyridine rings. A very sharp band at 1596−1608 cm^{-1} in the complexes is indicative of the coordination of the azomethine nitrogen atom. A ligand band appearing at 1017 (**I**), 1010 (**II**) and 1028 cm^{-1} (**III**) due to ν(N−N) undergoes a shift to higher wave numbers by 5−45 cm^{-1} upon complex formation. The high frequency shift of the ν(N−N)

 © 2005 Wiley-VCH Verlag GmbH & Co. KGaA, Weinheim

band is expected because of diminished repulsion between the lone pairs of adjacent nitrogen atoms.[20] The ligands exhibit a medium-intensity ν(OH) band covering the region 2300−2700 cm^{-1}, which is due to intramolecular hydrogen bonds. On complexation, this band broadens and gains intensity due to the involvement of the CH_2OH group in hydrogen bonding. All of the dioxovanadium(v) complexes exhibit two or three sharp bands in the 885−950 cm^{-1} region, corresponding to the *cis*-$[VO_2]^+$ structural unit. The peroxo complexes **9** and **10** show three IR-active vibration modes associated with the peroxo moiety $[V(O_2)^{3+}]$ at 894−917, 707−717 and 553−574 cm^{-1}, which are assigned to the O−O intra-stretch (ν_1), the antisymmetric $V(O_2)$ stretch (ν_3), and the symmetric $V(O_2)$ stretch (ν_2).[21] The presence of these bands confirms the common η^2-coordination of the peroxo group.[21] In addition, both peroxo complexes exhibit an intense ν(V=O) at 946−970 cm^{-1}.

Electronic Spectra

The absorption maxima of the ligands and complexes along with their extinction coefficients are listed in Table 2. The UV spectra of H_2pydx-inh (**I**) shows three absorption bands at 216, 285.5 and 342 nm, while H_2pydx-bhz (**III**) displays four bands at 206, 296.5, 306 and 335 nm, probably belonging to the transitions φ → φ*, π → π* and *n* → π*, with the π → π* band split into two components in the case of **III**. A weak shoulder associated with the second band is traced back to association by hydrogen bonding. All of the complexes invariably showed this band, indicating the existence of hydrogen bonding in these complexes in solution as well.[22] The φ → φ* transition is only observed in the

Table 2. Electronic absorption spectra (in methanol, if not indicated otherwise)

Compound	$\lambda_{max.}$ [nm] (ε [$M^{-1}\cdot cm^{-1}$])
H_2pydx-inh (**I**)	216 (18541), 285.5 (18010), 342 (8270), 411.5 (2085)
$[VO_2$(Hpydx-inh)] (**2**) in DMF	272 (8881), 340 (7659), 421 (5769)
$[VO_2$(Hpydx-inh)] (**2**)	273 (19403), 308 (16178), 343 (16704), 416 (5073)
$[K(H_2O)_3][VO_2$(pydx-inh)] (**3**)	269.5 (18115), 337 (15146), 418 (11475)
H_2pydx-nh (**II**)	211 (23417), 307 (23898), 342 (17817)
$[VO_2$(Hpydx-nh)] (**5**)	235 (23118), 279 (16339), 328 (16322), 415 (4644)
$[K(H_2O)_2][VO_2$(pydx-nh)] (**6**)	234 (21351), 280 (16569), 326 (4384), 416 (4453)
$K[VO(O_2)$(pydx-nh)]·H_2O (**9**)	225 (19005), 297 (15205), 308 (14622), 407 (8579)
H_2pydx-bhz (**III**)	206 (20330), 296.5 (18113), 306 (17616), 335 (11085), 406 (2106)
$[VO_2$(Hpydx-bhz)] (**4**) in DMF	270 (31939), 337 (26968), 414 (18638)
$[VO_2$(Hpydx-bhz)] (**4**)	272 (9358), 334 (5324), 407 (3164)
$[K(H_2O)_2][VO_2$(pydx-bhz)] (**8**)	237 (18304), 265 (19310), 333 (15110), 404.5 (5381)
$K[VO(O_2)$(pydx-bhz)]·H_2O (**10**)	266 (15573), 329 (11810), 424 (10282)

Table 3. ^{1}H NMR spectroscopic data

Compound[a][b]	OH (phenolic)	−CH=N−	$-CH_2-$	$-CH_3$	Aromatic H
H_2pydx-inh (**I**)	13.40 (br, 1 H)	8.15 (s,1 H)	4.76 (s, 2 H)	2.60 (s, 3 H)	9.13 (s, 1 H), 8.83 (d, 2 H), 7.99 (d, 2 H)
$[VO_2$(Hpydx-inh)] (**2**)		9.48 (s, 1 H)	4.93 (s, 2 H)	2.63 (s, 3 H)	8.90 (br, 2 H), 8.28 (s, 1 H), 8.07 (d, 2 H)
(*Δ*δ)		(1.33)			
$[K(H_2O)_3][VO_2$(pydx-inh)] (**3**)		9.10 (s, 1 H)	4.58 (s, 2 H)	2.30 (s, 3 H)	8.52 (br, 2 H), 7.91 (s, 1 H), 7.75 (d, 2 H)
(*Δ*δ)		(0.95)			
H_2pydx-nh (**II**)	13.29 (br, 1 H)	8.15 (s, 1 H)	4.76 (s, 2 H)	2.60 (s, 3 H)	9.17 (s, 1 H), 9.07 (s, 1 H), 8.81 (d, 1 H), 8.42 (d, 1 H), 7.63 (m, 1 H)
$[VO_2$(Hpydx-nh)] (**5**)		9.32 (s, 1 H)	4.83 (s, 2 H)	2.51 (s, 3 H)	8.74 (br, 1 H), 8.38 (d, 1 H), 7.89 (s, 1 H), 7.55 (m, 1 H)
(*Δ*δ)		(1.17)			
$[K(H_2O)_2][VO_2$(pydx-nh)] (**6**)		9.33 (s, 1 H)	4.89 (s, 2 H)	2.57 (s, 3 H)	9.22 (s, 1 H), 8.74 (d, 1 H), 8.40 (d, 1 H), 7.97 (s, 1 H), 7.56 (m, 1 H)
(*Δ*δ)		(1.18)			
H_2pydx-bhz (**III**)	13.14 (br, 1 H)	8.14 (s, 1 H)	4.76 (s, 2 H)	2.60 (s, 3 H)	9.09 (s, 1 H), 8.04 (d, 2 H), 7.54 (m, 3 H)
$[VO_2$(Hpydx-bhz)] (**7**)		9.28 (s, 1 H)	4.85 (s, 2 H)	2.56 (s, 3 H)	8.04 (m, 3 H), 7.49 (m, 3 H)
(*Δ*δ)	−	(1.14)			
$[K(H_2O)_2][VO_2$(pydx-bhz)] (**8**)		9.29 (s, 1 H)	4.90 (s, 2 H)	2.58 (s, 3 H)	8.10 (m, 3 H), 7.50 (m, 3 H)
(*Δ*δ)	−	(1.15)			
$K[VO(O_2)$(pydx-bhz)$H_2O]$ (**10**)		9.28 (s, 1 H)	4.89 (s, 2 H)	2.55 (s, 3 H)	8.14 (m, 3 H), 7.52 (m, 3 H)
(*Δ*δ)	−	(1.14)			

[a] Letters given in parentheses indicate the signal structure: s = singlet, d = doublet, br = broad (unresolved), m = multiplet. [b] $\Delta\delta$ = δ(complex) − δ(ligand).

 © 2005 Wiley-VCH Verlag GmbH & Co. KGaA, Weinheim

oxovanadium(IV) complexes; the two other bands are significantly shifted towards lower wavelengths with respect to the uncoordinated ligands. The dioxovanadium(V) complexes are dominated by an intense band at 404.5−421 nm, which is assigned to a ligand-to-metal charge transfer (LMCT) from the phenolate oxygen atom to an empty d-orbital of the vanadium ion.

NMR Spectroscopic Studies

The coordinating modes of the ligands were confirmed by comparing ^{1}H NMR patterns of the ligands and the complexes. The relevant spectroscopic data are collected in Table 3. The broad signal appearing at δ = 13.14−13.29 ppm, due to the phenolic OH group, disappears in the spectra of the complexes. A significant downfield shift ($\Delta\delta$ = 0.84−1.33 ppm) of the signal for the azomethine (−CH=N−) proton in the complexes relative to the corresponding ligands demonstrates the coordination of the azomethine nitrogen atom. The signals due to the NH group (which is hydrogen-bonded to the alcoholic pyridoxal OH group, viz. NH···OHCH$_2$; see the structure description for **I** above) and OH protons could not be located in the δ = 0−15 ppm region in the spectra of the ligands. However, appearance of a broad signal at $\delta \approx$ 5.8 ppm in all complexes, which we allocate to CH$_2$O*H*, suggests the breaking down of hydrogen bonding and coordination of the enolate oxygen atom of the hydrazone moiety, further supported by the absence of the NH proton signal in the complexes. The methylene and methyl protons of the pyridoxal moiety of the ligands resonate at δ = 4.76 and 2.60 ppm, and these signals appear in the complexes with slight shifts in their positions. Aromatic protons appear in the expected regions in the spectra of the ligands as well as of the complexes with minor variations in their positions. All these data are consistent with the conclusions drawn from the IR spectral studies and support the dibasic, tridentate *ONO* coordination mode.

Further characterisation of the complexes was obtained from ^{51}V NMR spectra; values of specific compounds, where solubility permitted data to be recorded, are presented in the Exp. Sect.. The resonances are somewhat broadened due to quadrupolar interaction (^{51}V: nuclear spin = 7/2, quadrupole moment = -0.05×10^{-28} m^2); the line widths at half-height are approximately 200 Hz, which is still considered comparatively narrow in ^{51}V NMR spectroscopy.[23] The dioxovanadium(V) complexes **3**, **6** and **8** show one strong resonance between δ = −532 and −534 ppm in [D$_6$]DMSO, an expected value for dioxovanadium(V) complexes having a mixed *O*/*N* donor set.[23,24] Complex **8** exhibits distinct solvent dependence. In [D$_6$]DMSO, the ^{51}V NMR signal appears at δ = −534.2 ppm, while in CH$_3$OH/CD$_3$OD it appears at δ = −546.8, possibly indicating the participation of the solvent in coordination. Similarly, the neutral dioxovanadium(V) complex **7** gives rise to a signal at δ = −535.7 ppm in [D$_6$]DMSO and at δ = −546.7 ppm in CH$_3$OH/CD$_3$OD. The peroxo complex **10** displays a ^{51}V NMR signal at δ = −586.0 ppm in [D$_6$]DMSO. This upfield shift with respect to the dioxo complexes **7** and **8** is commonly observed as an oxo group is replaced by the side-on coordinated peroxo group.[23,25]

Reaction with HCl

For the catalytic activity of vanadate-dependent haloperoxidases, the presence of a coordinated hydroxo ligand has been proposed on the basis of kinetic investigations.[6] The generation of hydroxo(oxo) species has been accomplished for [K(H$_2$O)$_2$][VO$_2$(pydx-bhz)]·H$_2$O (**8**) on reaction with HCl: Addition of HCl-saturated methanol to a methanolic solution of **8** results in a colour change from yellow to orange with gradual shift of the 404.5-nm band in the electronic absorption spectrum to 420 nm, along with a slight broadening and decrease in intensity of the absorption maximum (Figure 5). Addition of further HCl results in an increase in intensity of the 333-nm band, disappearance of the 265-nm band, and appearance of two new bands at 317 and 308 nm. In addition, a shoulder starts to appear at ca. 360 nm. The intensity and position of the 237-nm band remain constant. Corresponding results have been obtained with HClO$_4$ (dissolved in a minimum amount of methanol and added dropwise to a methanolic solution of **8**). We interpret this result in terms of the formation of an hydroxo(oxo) complex of composition [VO(OH)(H$_2$pydx-bhz)]$^{2+}$ via [VO$_2$(Hpydx-bhz)] and [VO$_2$(H$_2$pydx-bhz)]$^+$ on acidification as shown in Equation (8). The formation of the intermediate species, protonated at the pyridine nitrogen atom, viz. [VO$_2$(Hpydx-bhz)], is based on the fact that the electronic absorption spectrum of a solution of **8** obtained after addition of 4 drops of HCl nearly matches the spectrum of authentic complex **7**. The protonation of the N atom of the hydrazide moiety not involved in coordination is documented by a newly arising medium-intensity band in the IR at 3205 cm^{-1} (free Schiff base: 3210 cm^{-1}) on acidification of **8**. A comparable protonated Schiff-base complex, viz. [VO$_2$(Hsal-bhz)] (where H$_2$sal-bhz is the hydrazone derived from salicylaldehyde and benzohydrazide) has been structurally characterised.[26]

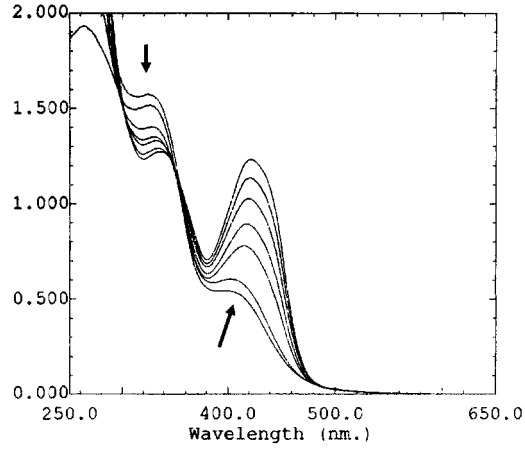

Figure 5. Titration of [K(H$_2$O)$_2$][VO$_2$(pydx-bhz)] (**8**) with a saturated solution of HCl in MeOH; the spectra were recorded after addition of 2-drops portions of MeOH/HCl to 10 mL of ca. 10^{-4} M solution of **8** in MeOH

 © 2005 Wiley-VCH Verlag GmbH & Co. KGaA, Weinheim

$$[VO_2(pydx\text{-}bhz)] \xrightarrow{H^+} [VO_2(Hpydx\text{-}bhz)] \xrightarrow{H^+} [VO_2(H_2pydx\text{-}bhz)]^+ \rightarrow [VO(OH)(H_2pydx\text{-}bhz)]^{2+} \quad (8)$$

8 **7**

Hydroxo(oxo)vanadium complexes have previously been generated on acidification of $K[VO_2(sal\text{-}inh)H_2O]$ and $[K(H_2O)_2][VO_2(Clsal\text{-}sbdt)]$ ($H_2Clsal\text{-}sbdt$ = ligand derived from salicylaldehyde and *S*-benzyldithiocarbazate).[11] An hydroxo(oxo) complex, $[VO(OH)(LH)]^+$ {where LH = *N*-(2-hydroxyethyl)-*N*′-[(*o*-hydroxyphenyl)methyl]ethylenediamine}, has been reported to form from a dinuclear dioxovanadium(v) precursor in a similar manner.[27] $[V^VO(OH)(8\text{-oxyquinolinate})_2]$[28a] and $[V^{IV}O(OH)Tp(H_2O)]$ [Tp = tris(3,5-diisopropyl-1-pyrazolyl)borate(1−)][28b] have been characterised in the solid state. On addition of a methanolic solution of KOH to $[VO(OH)(H_2pydx\text{-}bhz)]^{2+}$, the solution acquired the original spectrum of **8**; the reaction is thus reversible. This reversibility is an important observation in the context of the active-site structure and the catalytic activity of vanadate-dependent haloperoxidases, for which a hydroxo ligand at the vanadium centre has also been made plausible on the basis of X-ray diffraction data.[29]

Oxidative Bromination of Salicylaldehyde

Oxidative bromination catalysed by V_2O_5 and oxovanadium(v) complexes has been reported earlier using H_2O_2/Br^-.[30] During this process, vanadium reacts with 1 or 2 equiv. of H_2O_2, forming mono(peroxo) $[VO(O_2)^+]$ or bis(peroxo) $[VO(O_2)_2^-]$ species, which ultimately oxidise bromide, possibly by formation of a hydroperoxo intermediate. The oxidised bromine species (Br_2, Br_3^- or, most likely, HOBr) then brominates the substrate.[4,31]

We have observed that the complexes **3**, **6** and **8** satisfactorily catalyse the oxidative bromination of salicylaldehyde, using H_2O_2/KBr in the presence of $HClO_4$ in aqueous solution; cf. Equation (9). A maximum conversion of 40−46% of salicylaldehyde was found. In the case of **3** as the catalyst, GC analysis revealed the presence of three products in the ratio 8.8:86.6:4.3%, with 5-bromosalicylaldehyde being the major product. Thus, based on GC, the selectivity of the formation of 5-bromosalicylaldehyde is 86.6% with respect to salicylaldehyde conversion. On purification of the crude product by column chromatography, 5-bromosalicylaldehyde was obtained in 40% yield (related to salicylaldehyde). The average yields of pure 5-bromosalicylaldehyde for **6** and **8** as catalysts were 34.7% and 36.5%, respectively; the selectivity of formation of 5-bromosalicylaldehyde was again about 87%. In the absence of the catalyst, the reaction mixture did not produce any brominated product. Similarly, acid (here $HClO_4$) was found to be essential to carry out catalytic bromination. The complexes slowly decompose during the reaction; decomposition is slowed down, if $HClO_4$ is successively added in portions (see Exp. Sect.). Using CH_3COOH as solvent as well as the acid supplier, efficiently produced 5-bromosalicylaldehyde within 2 h of reaction time, but relatively fast decomposition of the complexes took place.

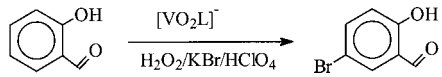

(9)

As hydroxo(oxo) species such as $[VO(OH)(H_2pydx\text{-}bhz)]^{2+}$ very likely form upon acidification of $[K(H_2O)_2][VO_2(pydx\text{-}bhz)]$ (**8**), and oxo(peroxo) species **10** are obtained upon treatment with H_2O_2 in methanol, the formation of an active oxo(peroxo) via a hydroxo(oxo) complex is likely to occur in the presence of acid as well as H_2O_2 during the catalytic reaction.[4] Activation of peroxide by coordination to vanadium may then be succeeded by formation of an intermediate hydroperoxo complex, which allows nucleophilic attack of the bromide,[21] followed by release of hypobromous acid which then brominates salicylaldehyde. A catalytic cycle is proposed in Scheme 3. It should be noted here that recent electrospray ionisation MS studies in the peroxovanadium/bromide system indicated the formation of a hypobromite species, $[VO(OH)(H_2O)_3OBr]^+$, the stability of which is supported by ab initio calculations.[32]

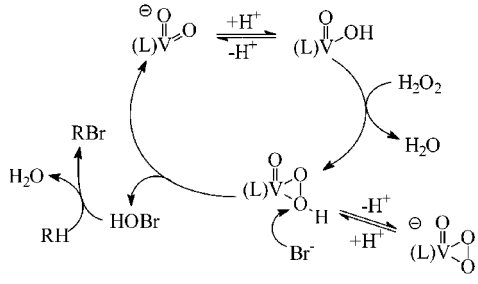

Scheme 3

Conclusion

Pentacoordinated neutral and cationic dioxovanadium complexes containing a ligand system providing a dianionic *ONO* donor set and thus modelling the active site of vanadate-dependent haloperoxidases have been synthesised and characterised. The cationic complexes of the general composition $[K(H_2O)_n][VO_2(ONO)]$ can be converted in situ on acidification to hydroxo(oxo) complexes $[VO(OH)(H_2ONO)]^{2+}$ and to the peroxo complexes $K[VO(O_2)(ONO)]$, and thus to species assumed to be intermediates in the bromoperoxidase activity of the enzymes. The complexes are in fact active in bromination of salicylaldehyde in the presence of H_2O_2, Br^- and acid, and hence may also be considered *functional* models. The *ONO* ligands employed are hydrazones containing pyridoxal (vitamin B_6) and nicotinohydrazides as components, and thus biogenic molecular moieties.

The complex $[K(H_2O)_3][VO_2(pydx\text{-}inh)]$ (where pydx-inh is the doubly deprotonated condensation product from

 © 2005 Wiley-VCH Verlag GmbH & Co. KGaA, Weinheim

pyridoxal and isonicotinohydrazide), which has been structurally characterised, contains the ligand in the enolate form (the free ligand constitutes the ketonic form). The seven-coordinate potassium ion links to three different $[VO_2(pydx\text{-}inh)]^-$ anions and thus generates, together with hydrogen bonds, a complex supramolecular, three-dimensional network.

Experimental Section

Materials and Instrumentation: V_2O_5, NH_4VO_3, isonicotinohydrazide, benzoyl chloride, hydrazine hydrate (Loba Chemie, India), pyridoxal hydrochloride (Fluka Chemie, GmbH, Switzerland), acetylacetone (Hacac) (Aldrich, U.S.A.), and 30% aqueous H_2O_2 (Qualigens, India) were used as obtained. Other chemicals and solvents were of analytical reagent grade. Benzohyrazide was prepared by the reaction of a twofold excess of hydrazine hydrate with ethyl benzoate, which in turn was obtained by refluxing benzoyl chloride in an excess of absolute ethanol. $[VO(acac)_2]$ was prepared according to the method reported in the literature.[33] The microanalytical section of the Central Drug Research Institute, Lucknow, India, performed elemental analyses of the ligands and complexes. IR spectra were recorded as KBr pellets with a Perkin−Elmer model 1600 FT-IR spectrometer. Electronic absorption spectra were measured in methanol or DMF with a UV-1601 PC UV/Vis spectrophotometer. ^{1}H NMR spectra were obtained with a Bruker 200, and ^{51}V NMR spectra with a Bruker Avance 400 MHz spectrometer at 94.73 MHz with the common parameter settings. NMR spectra were usually recorded in $[D_6]$DMSO, and $\delta(^{51}V)$ values are quoted relative to $VOCl_3$ as external standard. Selected ^{51}V NMR spectroscopic results have also been obtained in CD_3OD. Thermogravimetric analyses of the complexes were carried out under oxygen using a TG Stanton Redcroft STA 780 instrument. Magnetic susceptibility measurements of oxovanadium(IV) complexes were carried out at room temperature by the Scientific Instrumentation Centre of the Indian Institute of Technology in Roorkee. EPR spectra were recorded with a Bruker ESP 300E spectrometer between 9.42 and 9.47 GHz, and EPR parameters were adjusted by simulation with the Bruker program system SimFonia. All reaction products obtained from the catalytically conducted reactions were identified by recording their m.p., ^{1}H NMR and IR spectra after purification and separation by column chromatography on silica gel using CH_2Cl_2 as an eluant. The product mixture obtained before purification was additionally analysed with a Shimadzu 14B gas chromatograph, fitted with an SE-52 packed column, coupled with an FID detector, and the identity of the products confirmed by checking against the GC-MS reference system Shimadzu QP-5000. Crystal structure data were collected with a Bruker SMART Apex CCD diffractometer, using graphite-monochromated Mo-K_α radiation (λ = 0.71073 Å) at 153(2) K. In the case of ligand **I**, all hydrogen atoms (except H3A) were placed into calculated positions and included in the last cycles of refinement. H3A of ligand **I** and all H atoms of complex **3** were found. The program systems SHELXS 86 and SHELXL 93 were used throughout. Crystal data and details of the data collection and refinement are collated in Table 4. CCDC-233587 (**I**) and −233586 (**3**) contain the supplementary crystallographic data of this paper. These data can be obtained free of charge at www.ccdc.cam.ac.uk/conts/retrieving/

Table 4. Crystal and refinement data for complex **3** and ligand **I**

	3	**I**
Empirical formula	$C_{14}H_{10}KN_4O_8V$	$C_{14}H_{15}N_4O_3$
Formula mass [g·mol^{-1}]	452.30	287.30
Crystal system	triclinic	monoclinic
Space group	*Pi*	*P*21/*n*
Unit cell dimensions:		
a [Å]	7.3320(4)	8.0828(5)
b [Å]	10.9605(6)	12.9614(9)
c [Å]	12.6229(7)	12.9926(8)
α [°]	64.7210(10)	90
β [°]	81.113(2)	90.5000(10)
γ [°]	89.366(2)	90
V [Å^3]	904.54(9)	1361.11(15)
Z	2	3
Calculated density [g·cm^{-3}]	1.661	1.397
Absorption coefficient [mm^{-1}]	0.830	0.102
F(000)	456	600
Crystal size [mm]	0.80 × 0.22 × 0.12	0.43 × 0.29 × 0.19
θ range for data collection [°]	2.06 to 32.56	2.22 to 28.00
Index ranges	$-10 \le h \le 10$	$-10 \le h \le 10$
	$-16 \le k \le 16$	$-16 \le k \le 17$
	$-19 \le l \le 19$	$-17 \le l \le 16$
Reflections collected	24828	16031
Independent reflections	6380 [*R*(int) = 0.0435]	3182 [*R*(int) = 0.0409]
Completeness to θ [°]	97.0%	96.6%
Data/restraints/parameters	6380/0/293	3182/0/192
Goodness-of-fit on F^2	1.052	1.111
Final *R* indices [$I > 2\sigma(I_0)$]	*R*1 = 0.0400, *wR*2 = 0.1178	*R*1 = 0.0608, *wR*2 = 0.1330
R indices (all data)	*R*1 = 0.0453, *wR*2 = 0.1206	*R*1 = 0.0818, *wR*2 = 0.1523
Largest difference peak/hole [e Å^{-3}]	0.936/−0.439	0.631/−0.623

 © 2005 Wiley-VCH Verlag GmbH & Co. KGaA, Weinheim

html or from the Cambridge Crystallographic Data Centre, 12 Union Road, Cambridge CB2 1EZ, UK [Fax: (internat.) + 44-1223-336-033; E-mail: deposit@ccdc.cam.ac.uk].

Preparation of Ligands

H_2pydx-inh (I): A mixture of pyridoxal hydrochloride (1.02 g, 5 mmol) and isonicotinohydrazide (0.685 g, 5 mmol) in 50 mL of methanol was refluxed using a water bath for 4 h. After reducing the solvent volume to ca. 15 mL, the mixture was cooled to room temperature within 3 h. During this time, a light orange solid of **I** precipitated, which was filtered off, washed with methanol and dried. **I** was recrystallised from methanol to give a crystalline solid. Yield 1.15 g (81%). $C_{14}H_{14}N_4O_3$ (286.3): calcd. C 58.74, H 4.90, N 19.58; found C 58.69, H. 4.82, N 19.41. IR (KBr): $\tilde{\nu}_{max.}$ = 3230 (NH), 1678 (C=O), 1620, 1600 (ring C=N and C=N), 1017 (N−N) cm^{-1}.

H_2pydx-nh (II) and H_2pydx-bhz (III): These ligands were prepared according to the procedure outlined for **I**.

II: Yield 1.12 g (78%). $C_{14}H_{14}N_4O_3$ (286.3): calcd. C 58.74, H 4.90, N 19.58; found C 58.82, H 4.85, N 19.48. IR (KBr): $\tilde{\nu}_{max.}$ = 3250 (NH), 1673 (C=O), 1617 (ring C=N, C=N), 1025 (N−N) cm^{-1}.

III: Yield 1.07 g (75%). $C_{15}H_{15}N_3O_3$ (285.3): calcd. C 63.18, H 5.26, N 14.74; found C 63.00, H, 5.34, N 14.68. IR (KBr): $\tilde{\nu}_{max.}$ = 3210 (NH), 1677 (C=O), 1637, 1624 (ring C=N, C=N), 1045 (N−N) cm^{-1}.

Preparation of Complexes

[VO(pydx-inh)] (1) and [VO_2(Hpydx-inh)] (2): A stirred solution of H_2pydx-inh (0.570 g, 0.002 mol) in dry methanol (20 mL) was treated with [$VO(acac)_2$] (0.530 g, 0.002 mol), dissolved in dry methanol (10 mL), and the resulting reaction mixture was refluxed using a water bath for 5 h. After cooling to room temperature, a brown precipitate of **1** was filtered off, washed with methanol and dried. Compound **1** was suspended in methanol (50 mL), and air was slowly passed through the suspension at ca. 40 °C for ca. 24 h with occasional shaking. During this period of time, the brown suspension slowly disappeared and crystalline orange-red solid **2** separated. This was filtered off, washed with methanol and dried in vacuo. For the direct preparation of **2**, it is not necessary to isolate **1**.

Data for 1: Yield 0.35 g (50%). $C_{14}H_{12}N_4O_4V$ (351.2): calcd. C 47.86, H 3.42, N 15.95; found C 47.43, H 3.61, N 15.86. IR (KBr): $\tilde{\nu}_{max.}$ = 1601 (C=N), 1262 (C−O, enolate), 1060 (N−N), 888 (V=O) cm^{-1}. EPR (DMSO, 98 K): g_{xy} = 1.984, g_z = 1.949; A_{xy} = 55.1, $A_z = 159.7 \times 10^{-4}$ cm^{-1}.

Data for 2: Yield 0.48 g (65%) based on [$VO(acac)_2$]. $C_{14}H_{13}N_4O_5V$ (368.2): calcd. C 45.65, H 3.53, N 15.22; found C 45.39, H 3.72, N 15.44. IR (KBr): $\tilde{\nu}_{max.}$ = 1599 (C=N), 1257 (C-O, enolate), 1055 (N−N), 956, 908 (sym. and antisym. VO_2^+) cm^{-1}.

[$K(H_2O)_3$][VO_2(pydx-inh)] (3): Vanadium(V) oxide (0.91 g, 0.005 mol) was suspended in aqueous KOH (0.30 g, 0.005 mol in 10 mL H_2O) and stirred with occasional heating at 50 °C for 2 h. The potassium vanadate solution thus generated was filtered. A filtered solution of H_2pydx-inh (1.42 g, 0.005 mol), dissolved in 20 mL of aqueous KOH (0.56 g, 0.010 mol), was added with stirring, and the pH of the reaction mixture was cautiously adjusted to 7.5 with 4 M HCl. After 2 h of stirring, the precipitated yellow solid was filtered off, washed with water followed by acetone, and dried. On crystallisation from ca. 50 mL of methanol, **2** precipitated as an orange-red solid, which was filtered off and dried in vacuo over silica gel. For the data of **2**, see above. After reducing the volume of the filtrate to ca. 15 mL and keeping it at ca. 10 °C, yellow crystalline **3** slowly precipitated within 2 d. This was filtered off, washed with cold methanol and dried. Yield 1.58 g (68%). $C_{14}H_{18}KN_4O_8V$ (460.4): calcd. C 36.52, H 3.91, N 12.17; found C 36.33, H 3.85, N 12.26. IR (KBr): $\tilde{\nu}_{max.}$ = 1596 (C=N), 1257 (C−O, enolate), 1055 (N−N), 955, 909 (sym. and antisym. VO_2^+) cm^{-1}. ^{51}V NMR ([D_6]DMSO): δ = −532.0 ppm.

[VO(pydx-nh)] (4) and [VO_2(Hpydx-nh)] (5): Complex **4** was prepared analogously to **1**, replacing H_2pydx-inh for H_2pydx-nh. Air was slowly passed through the methanolic suspension (50 mL) of **4** at ca. 40 °C for ca. 24 h with occasional shaking. After cooling to ca. 10 °C for 2 d, yellow crystalline **5** slowly preciptated, which was filtered, washed with methanol and dried in vacuo.

Data for 4: Yield 0.61 g (86.8%). $C_{14}H_{12}N_4O_4V$ (351.2): calcd. C 47.86, H 3.42, N 15.95; found C 47.94, H 3.31, N 15.98. IR (KBr): $\tilde{\nu}_{max.}$ = 1608 (C=N), 1248 (C−O, enolate), 1050 (N−N), 888 (V=O) cm^{-1}. EPR (DMSO, 98 K): g_{xy} = 1.984, g_z = 1.942; A_{xy} = 56.7, $A_z = 161.2 \times 10^{-4}$ cm^{-1}.

Data for 5: Yield 0.40 g (54%) based on $VO(acac)_2$. $C_{14}H_{13}N_4O_5V$ (368.2): calcd. C 45.65, H 3.53, N 15.22; found C 45.83, H 3.36, N 15.17. IR (KBr): $\tilde{\nu}_{max.}$ = 1597 (C=N), 1234(C−O, enolate), 1064 (N−N), 961, 942, 884 (sym. and antisym. VO_2^+) cm^{-1}.

[$K(H_2O)_2$][VO_2(pydx-nh)] (6): This complex was prepared from KVO_3 and H_2pydx-nh by the method outlined for **3**. The crude mass obtained on crystallisation from methanol gave a 1.45 g (66%) yield of **6**. $C_{14}H_{16}KN_4O_7V$ (417.3): calcd. C 38.01, H 3.65, N 12.67; found C 38.20, H 3.74, N 12.56. IR (KBr): $\tilde{\nu}_{max.}$ = 1606 (C=N), 1258 (C−O, enolate), 1042 (N−N), 940, 923 (sym. and antisym. VO_2^+) cm^{-1}. ^{51}V NMR ([D_6]DMSO): δ = −532.0 ppm.

[VO_2(Hpydx-bhz)]·2H_2O (7): A stirred solution of H_2pydx-bhz (0.570 g, 2 mmol) in methanol (20 mL) was treated with [$VO(acac)_2$] (0.530 g, 2 mmol), and the reaction mixture was refluxed using a water bath for 5 h to give a brown solution. After cooling to ambient temperature, a current of air was passed through this solution for ca. 20 h; during this procedure, yellow complex **7** slowly precipitated. This was filtered off, washed with methanol and dried in vacuo. Yield 0.68 g (84%) based on [$VO(acac)_2$]. $C_{15}H_{18}N_3O_7V$ (403.3): calcd. C 44.66, H 4.47, N 10.42; found C 44.75, H 4.36, N 10.28. IR (KBr): $\tilde{\nu}_{max.}$ = 1599 (C=N), 1220 (C−O, enolate), 1063 (N−N), 940, 918, 888 (sym. and antisym. VO_2^+) cm^{-1}. ^{51}V NMR: δ: −535.7 ppm ([D_6]DMSO); −546.4 ppm (MeOH/CD_3OD).

[$K(H_2O)_2$][VO_2(pydx-bhz)] (8): Complex **8** was prepared from KVO_3 (generated in solution from V_2O_5 and KOH) according to the procedure outlined for **3**. Recrystallisation from methanol gave **8** in pure form as a yellow crystalline material. Yield 1.48 g (66%). $C_{15}H_{17}KN_3O_7V$ (441.4): 40.82, C 3.88, N 9.52; found C 40.73, H 3.97, N 9.41. IR (KBr): $\tilde{\nu}_{max.}$ = 1597 (C=N), 1222 (C−O, enolate), 1063 (N−N), 938, 915, 888 (sym. and antisym. VO_2^+) cm^{-1}. ^{51}V NMR: δ = −534.2 ppm ([D_6]DMSO); −546.9 ppm (MeOH/CD_3OD).

K[$VO(O_2)$(pydx-nh)]·H_2O (9): Complex **6** (900 mg, 2 mmol), dissolved in 20 mL of MeOH, was treated with 30% aqueous H_2O_2 (3 mL, 26.5 mmol) while stirring the reaction mixture at 10 °C, which caused darkening of the solution. After 2 h of stirring, the volume was reduced to ca. 10 mL and the solution was kept at 10 °C overnight. Yellow crystals precipitated, which were filtered off and dried in vacuo. Yield 0.30 g (34%). $C_{14}H_{14}KN_4O_7V$ (440.33): calcd. C 38.19, H 3.20, N 12.72; found C 38.0, H 3.33, N 12.61. IR (KBr): $\tilde{\nu}_{max.}$ = 1603 (C=N), 1250 (C−O, enolate), 1043 (N−N),

 © 2005 Wiley-VCH Verlag GmbH & Co. KGaA, Weinheim

946 (V=O), 894 (O−O), 707 [$V(O_2)$ antisym.], 574 [$V(O_2)$ sym.] cm^{-1}.

K[VO(O$_2$)(pydx-bhz)]·H$_2$O (10). Method 1: A 30% aqueous solution of H_2O_2 (2 mL, 17.6 mmol) was added to an aqueous solution of KVO_3 (2 mmol), prepared as outlined above. The potassium salt of H_2pydx-bhz was prepared separately by treating **III** (0.570 g, 2 mmol) with KOH (0.168 g, 3 mmol) in water (10 mL) followed by filtration. This solution was added dropwise to the above solution with constant stirring. After 2 h of stirring, the orange solid that had precipitated was filtered, washed with water and dried. The crude mass was recrystallised from methanol. Yield 0.14 g (16%). **Method 2:** This method parallels the one adopted for **9**, using **8** and H_2O_2. Yield 0.48 g (22%). $C_{15}H_{15}KN_3O_7V$ (439.3): calcd. 41.01, H 3.44, N 9.56; found C 40.87, H 3.41, N 9.45. IR (KBr): $\tilde{\nu}_{max.}$ = 1596 (C=N), 1246 (C−O, enolate), 1033 (N−N), 970 (V=O), 917 (O−O), 717 [$V(O)_2$ antisym.], 553 [$V(O)_2$ sym.] cm^{-1}. ^{51}V NMR ([D$_6$]DMSO): δ = −536.0 ppm.

Reactions of 9 and 10 with PPh$_3$: PPh_3 (0.39 g, 1.5 mmol) was added to complex **9** or **10** (1 mmol), dissolved in dry methanol (20 mL), and the reaction mixture heated under reflux for 8 h. After reduction of the volume to ca. 10 mL, the solution was kept at 10 °C to yield a yellow precipitate. This was filtered, washed with methanol and dried in vacuo. Yield ca. 50%. The analytical and spectroscopic data of the complexes thus obtained match well with those of **6** and **8**, respectively. The formation of $OPPh_3$ was documented by ^{31}P NMR spectroscopy.

Catalytic Oxidative Bromination of Salicylaldehyde: In a typical reaction, salicylaldehyde (0.244 g, 2 mmol) was added to an aqueous solution of KBr (0.5 g, 4 mmol, in 4 mL H_2O), followed by addition of aqueous 30% H_2O_2 (1.93 g, 15 mmol). This mixture was treated whilst stirring with the catalyst (0.02 g) and 70% $HClO_4$ (1 mmol). Addiditional 1-mmol portions of $HClO_4$ were added during the course of the reaction every hour. After 4 h of reaction time, the white precipitate that had formed was filtered off, washed with water followed by diethyl ether, and dried. The crude mass was dissolved in CH_2Cl_2, and insoluble material, if any, was removed by filtration. The filtrate was concentrated to ca. 5 mL and chromatographed on silica gel (column dimensions 30 × 2.5 cm) with CH_2Cl_2 as eluant. The first fraction was collected and the solvents were evaporated to dryness to give 5-bromosalicylaldehyde. Alternatively, the filtered dichloromethane solution of the crude material was analysed by GC-MS.

Acknowledgments

We acknowledge the performance of the microanalyses by the Regional Sophisticated Instrumental Centre, CDRI, Lucknow, and financial assistance from the Department of Science and Technology, Government of India (Grant No. SP/S1/F-07/2001), New Delhi, and the Deutsche Forschungsgemeinschaft (grant RE 431/13-4).

[1] M. R. Maurya, *Coord. Chem. Rev.* **2003**, *237*, 163−181.
[2] D. Rehder, *Inorg. Chem. Commun.* **2003**, *6*, 604−617.
[3] [3a] K. H. Thompson, J. H. McNeill, C. Orvig, *Chem. Rev.* **1999**, *99*, 2561−2571. [3b] H. Sakurai, Y. Kojima, Y. Yoshikawa, K. Kawabe, H. Yasui, *Coord. Chem. Rev.* **2002**, *226*, 187−198. [3c] D. Rehder, J. Costa Pessoa, C. F. G. C. Geraldes, M. M. C. A. Castro, T. Kabanos, T. Kiss, B. Meier, G. Micera, L. Pettersson, M. Rangel, A. Salifoglou, I. Turel, D. Wang, *J. Biol. Inorg. Chem.* **2002**, *7*, 384−396.
[4] A. Butler, *Coord. Chem. Rev.* **1999**, *187*, 17−25.
[5] [5a] M. Weyand, H.-J. Hecht, M. Kieß, M.-F. Liaud, H. Vilter, D. Schomburg, *J. Mol. Biol.* **1999**, *293*, 595−611. [5b] M. I. Isupov, A. R. Dalby, A. A. Brindley, Y. Izumi, T. Tanabe, G. N. Murshudov, J. A. Littlechild, *J. Mol. Biol.* **2000**, *299*, 1035−1049. [5c] A. Messerschmidt, R. Wever, *Proc. Natl. Acad. Sci. U. S. A.* **1996**, *93*, 392−396.
[6] [6a] G. J. Colpas, B. J. Hamstra, J. W. Kampf, V. L. Pecoraro, *J. Am. Chem. Soc.* **1996**, *118*, 3469−3478. [6b] B. J. Hamstra, G. J. Colpas, V. L. Pecoraro, *Inorg. Chem.* **1998**, *37*, 949−955.
[7] H. B. ten Brink, H. E. Schoemaker, R. Wever, *Eur. J. Biochem.* **2001**, *268*, 132−138.
[8] [8a] C. Bolm, F. Bienewald, *Angew. Chem. Int. Ed. Engl.* **1996**, *34*, 2640−2642. [8b] G. Santoni, G. M. Licini, D. Rehder, *Chem. Eur. J.* **2003**, *9*, 4700−4708. [8c] T. S. Smith II, V. L. Pecoraro, *Inorg. Chem.* **2002**, *41*, 6750−6760.
[9] [9a] K. Kimplin, X. Bu, A. Butler, *Inorg. Chem.* **2002**, *41*, 161−163. [9b] M. Časný, D. Rehder, *Chem. Commun.* **2001**, 921−922.
[10] A. Messerschmidt, L. Prade, R. Wever, *Biol. Chem.* **1997**, *378*, 309−315.
[11] [11a] M. R. Maurya, S. Khurana, C. Schulzke, D. Rehder, *Eur. J. Inorg. Chem.* **2001**, 779−787. [11b] M. R. Maurya, S. Khurana, W. Zhang, D. Rehder, *J. Chem. Soc., Dalton Trans.* **2002**, 3015−3023. [11c] M. R. Maurya, S. Khurana, W. Zhang, D. Rehder, *Eur. J. Inorg. Chem.* **2002**, 1749−1760.
[12] M. R. Maurya, S. Khurana, D. Rehder, *Trans. Met. Chem.* **2003**, *28*, 511−517.
[13] W. Plass, *Coord. Chem. Rev.* **2003**, *237*, 205−212.
[14] C. C. Lee, A. Syamal, L. J. Theriot, *Inorg. Chem.* **1971**, *10*, 1669−1672.
[15] [15a] C. J. Carrano, C. M. Nun, R. Quan, J. A. Bonadies, V. L. Pecoraro, *Inorg. Chem.* **1990**, *29*, 944−951. [15b] D. Schulz, T. Weyhermüller, K. Wieghardt, B. Nuber, *Inorg. Chim. Acta* **1995**, *240*, 217−229. [15c] J. Costa Pessoa, J. A. L. Silva, A. L. Vieira, L. Vilas-Boas, P. O'Brien, P. Thornton, *J. Chem. Soc., Dalton Trans.* **1992**, 1745−1749. [15d] S. Mondal, P. Ghosh, A. Chakravorty, *Inorg. Chem.* **1997**, *36*, 59−63. [15e] C. Grüning, H. Schmidt, D. Rehder, *Inorg. Chem. Commun.* **1999**, *2*, 57−59.
[16] N. Julien-Cailhol, E. Rose, J. Vaisserman, D. Rehder, *J. Chem. Soc., Dalton Trans.* **1996**, 2111−2121.
[17] [17a] A. J. Tasiopoulos, A. N. Troganis, A. Evangelou, C. P. Raptopoulos, A. Terzis, Y. Deligiannakis, T. A. Kabanos, *Chem. Eur. J.* **1999**, 910−921. [17b] T. S. Smith II, R. LoBrutto, V. L. Pecoraro, *Coord. Chem. Rev.* **2002**, *228*, 1−18.
[18] K. Elvingson, A. Gonzáles-Baró, L. Pettersson, *Inorg. Chem.* **1996**, *35*, 3388−3393.
[19] [19a] C. R. Cornman, K. M. Geiser-Bush, S. P. Rowley, P. D. Boyle, *Inorg. Chem.* **1997**, *36*, 6401−6408. [19b] G. Santoni, G. Licini, D. Rehder, *Chem. Eur. J.* **2003**, *9*, 4700−4708.
[20] S. P. Perlepes, D. Nicholls, M. R. Harison, *Inorg. Chim. Acta* **1985**, *102*, 137−143.
[21] [21a] A. D. Westland, F. Haque, J.-M. Bouchard, *Inorg. Chem.* **1980**, *19*, 2255−2259. [21b] M. Časný, D. Rehder, *Dalton Trans.* **2004**, 839−846. [21c] M. Sivák, M. Mad'orová, J. Taatiersky, J. Marek, *Eur. J. Inorg. Chem.* **2003**, 2075−2081.
[22] A. T. T. Hsieh, R. M. Sheahan, B. O. West, *Aust. J. Chem.* **1975**, *28*, 885−891.
[23] [23a] D. Rehder, C. Weidemann, A. Duch, W. Priebsch, *Inorg. Chem.* **1988**, *27*, 584−587. [23b] D. Rehder, *Transition Metal Nuclear Magnetic Resonance* (Ed.: P. S. Pregosin), Elsevier, New York **1991**, pp. 1−58.
[24] O. W. Howarth, *Progr. Magn. Reson. Spetrosc.* **1990**, *22*, 453−485.
[25] I. Andersson, S. Angus-Dunne, O. Howarth, L. Pettersson, *J. Inorg. Biochem.* **2000**, *80*, 51−58.
[26] W. Plass, A. Pohlmann, H.-K. Yozgatli, *J. Inorg. Biochem.* **2000**, *80*, 181−183.
[27] G. J. Colpas, B. J. Hamstra, J. W. Kampf, V. L. Pecoraro, *Inorg.*

 © 2005 Wiley-VCH Verlag GmbH & Co. KGaA, Weinheim

Chem. **1994**, *33*, 4669−4675.
[28] [28a] A. Giacomelli, C. Floriani, A. O. De Souza Duarte, A. Chiesi-Villa, C. Guastino, *Inorg. Chem.* **1982**, *21*, 3310−3316. [28b] M. Kosugi, S. Hikichi, M. Akita, Y. Moro-oka, *Inorg. Chem.* **1999**, *38*, 2567−2578.
[29] [29a] A. Messerschmidt, L. Prade, R. Wever, *Biol. Chem.* **1997**, *378*, 309−315. [29b] S. Macedo-Ribeiro, W. Hemrika, R. Renirie, R. Wever, A. Messerschmidt, *J. Biol. Inorg. Chem.* **1999**, *4*, 209−219.
[30] A. G. J. Ligtenbarg, R. Hage, B. L. Feringa, *Coord. Chem. Rev.* **2003**, *237*, 89−101.
[31] [31a] A. Butler, in *Bioinorganic Catalysis* (Eds.: J. Reedijk, E. Bouwman), 2nd ed., Marcel Dekker, New York **1999**, chapter 5. [31b] V. L. Pecoraro, C. Slebodnick, B. Hamstra, in *Vanadium Compounds: Chemistry, Biochemistry and Therapeutic Applications* (Eds.: D. C. Crans, A. S. Tracy), ACS Symposium Series, American Chemical Society, Washington, **1998**, chapter 12.
[32] O. Bortolini, M. Carrano, V. Conte, S. Moro, *Eur. J. Inorg. Chem.* **2003**, 42−46.
[33] R. A. Row, M. M. Jones, *Inorg. Synth.* **1957**, *5*, 113−116.

Received March 15, 2004
Early View Article
Published Online November 4, 2004

 © 2005 Wiley-VCH Verlag GmbH & Co. KGaA, Weinheim

Oxidative Dehydrogenation of Secondary Amines: The Case of the *N*,*N*,*N*′-Tris(2-pyridylmethyl)-*o*-phenylenediamine Ligand when Coordinated to Iron Dichloride

Ahmed Machkour,[a] Dominique Mandon,*[a] Mohammed Lachkar,[b] and Richard Welter[c]

Keywords: Ferrous complexes / Dioxygen activation / Oxidative dehydrogenation

We report the preparation and the X-ray crystal structure of the iron complex [Fe(L^1)Cl][Cl] [L^1 = *N*,*N*,*N*′-tris(2-pyridylmethyl)-*o*-phenylenediamine], and its reactivity towards molecular dioxygen. Upon exposure to dry O_2, coordinated L^1 is oxidatively dehydrogenated to the aldimine ligand L^2. The ferric cation [Fe(L^2)(CH_3CN)]$^{3+}$ is thus obtained, and characterized by UV/Vis and EPR spectroscopy, and X-ray diffraction analysis. The free L^2 ligand can be recovered after decomplexation.

(© Wiley-VCH Verlag GmbH & Co. KGaA, 69451 Weinheim, Germany, 2005)

Modelling of the active site of non-heme iron-containing oxygenases is one of the main reasons that led to the important development of the chemistry of iron complexes with (aminomethyl)pyridyl-containing ligands.[1−4] Oxygen-atom-transfer processes, however, and all their related chemistry, represent only a part of what Nature is able to carry out. Oxidative dehydrogenation of amines under aerobic conditions is another important process encountered in biochemistry — it is suspected to be one of the possible reasons for cell ageing, and is believed to be catalysed, in some cases, by iron-containing sites.[5] A search of the chemical literature reveals that most of the related published work involves Ni, Ru, Os and Cu complexes, only a limited number of studies being available in the chemistry of iron.[6] Examples taken from the chemistry of iron complexes with (aminomethyl)pyridyl-containing ligands include disproportionation of anionic species under strongly oxidizing conditions, to yield the corresponding coordinated imine as one of the reaction products,[7,8] or, more recently, the indirect demonstration that a tetrapyridine ligand can be desaturated under oxidative conditions.[9] In these cases, however, we could not find any direct evidence that molecular dioxygen is involved during these desaturation process, although O_2 is postulated as one of the key reagents in biologically occurring processes.[5] In the course of our investigations on the biomimetic use of molecular dioxygen with simple iron complexes,[10,11,13] we prepared the new compound [Fe(L^1)Cl][Cl] [L^1 = *N*,*N*,*N*′-tris(2-pyridylmethyl)-*o*-phenylenediamine] and found that, upon exposure to dry dioxygen, [Fe(L^1)Cl][Cl] in solution in acetonitrile smoothly converts to the ferric complex [Fe(L^2)(CH_3CN)][OH][Cl]$_2$, where L^2 is a dehydrogenated form of L^1, i.e. the corresponding imine. This clean reaction, together with the crystal structures of the two new complexes, is reported in this article. This work directly illustrates the fact that molecular dioxygen, as is believed to be the case in natural systems, can, at least at an early stage, induce a clean process of desaturation of acyclic amines by reaction with aferrous complex.

Ligand L^1 was prepared according to a published procedure.[14] The metallation by iron dichloride was carried out anaerobically according to a standard method,[11] and afforded [Fe(L^1)Cl][Cl] almost quantitatively as a stable greenish-yellow solid, as indicated in Scheme 1.[12] The UV/Vis spectrum of [Fe(L^1)Cl][Cl] in an acetonitrile solution displays three maxima {λ (ε [10^3 mmol·cm^2]) = 258 (10.24), 306 (sh.) and 407 (2.67) nm}.

Single crystals could be obtained by slow diffusion of diethyl ether into an acetonitrile solution of [Fe(L^1)Cl][Cl].[15] An ORTEP diagram of the cation [Fe(L^1)Cl]$^+$ is shown in Figure 1. The X-ray structure analysis reveals that the iron atom is coordinated in a distorted octahedral fashion. The metal−nitrogen distances are all above 2.19 Å, which is indicative of a high-spin state for the metal atom, and are

[a] Laboratoire de Chimie Biomimétique des Métaux de Transition, UMR CNRS no. 7513, Université Louis Pasteur, Institut Le Bel,
4 rue Blaise Pascal, 67070 Strasbourg cedex, France
Fax: + 33-3-90245001
E-mail: mandon@chimie.u-strasbg.fr
[b] Laboratoire d'Analyses, d'Essais et d'Environnement (LAEE), Département de Chimie, Faculté des Sciences Dhar Mehraz, Université Sidi Mohamed Ben Abdellah,
1796 Atlas, 30000 Fès, Morocco
[c] Laboratoire DECMET, UMR CNRS no. 7513, Université Louis Pasteur, Institut Le Bel,
4 rue Blaise Pascal, 67070 Strasbourg cedex, France
Supporting information for this article is available on the WWW under http://www.eurjic.org or from the author.

 © 2005 Wiley-VCH Verlag GmbH & Co. KGaA, Weinheim DOI: 10.1002/ejic.200400373

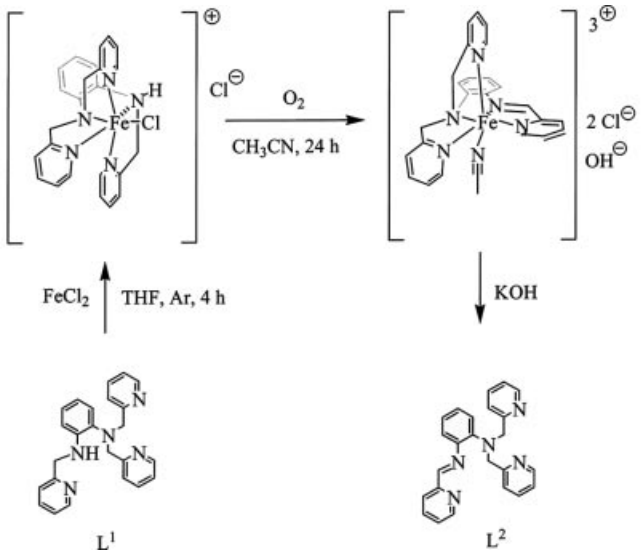

Scheme 1

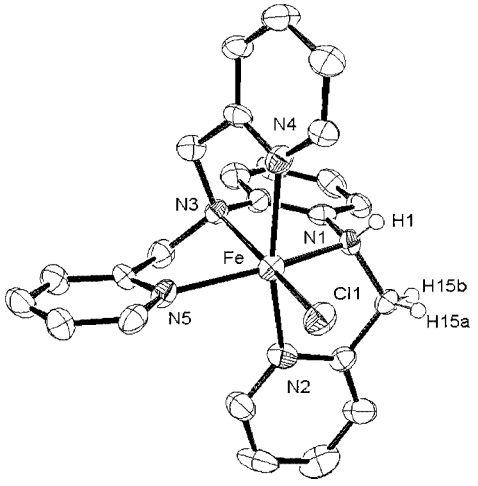

Figure 1. ORTEP diagram of the cation $[Fe(L^1)Cl]^+$ with a partial numbering scheme; all hydrogen atoms except the amine and the H15 methylene ones have been removed for clarity; selected bond lengths [Å] and angles [°]: Fe−Cl1 2.332(2), Fe−N1 2.196(6), Fe−N2 2.238(6), Fe−N3 2.240(6), Fe−N4 2.212(6), Fe−N5 2.195(6); N3−Fe−Cl1 167.83(17), N1−Fe−N5 149.0(2), N4−Fe−N2 159.0(2)

comparable to those reported in another complex with a more flexible pentadentate ligand.[16] The angles belonging to the five-membered metallacycle are found in the range 74−79°, the others being between 93° and 109°.

The addition of dry dioxygen to a solution of $[Fe(L^1)Cl][Cl]$ in acetonitrile resulted in a progressive darkening of its colour, which turned slightly green. Figure 2 displays the spectral variations observed by UV/Vis spectroscopy. A new intense absorption at $\lambda = 322$ nm is detected, and a weak and broader one at $\lambda = 694$ nm, whose intensities stabilised 24 h after the beginning of the reaction.

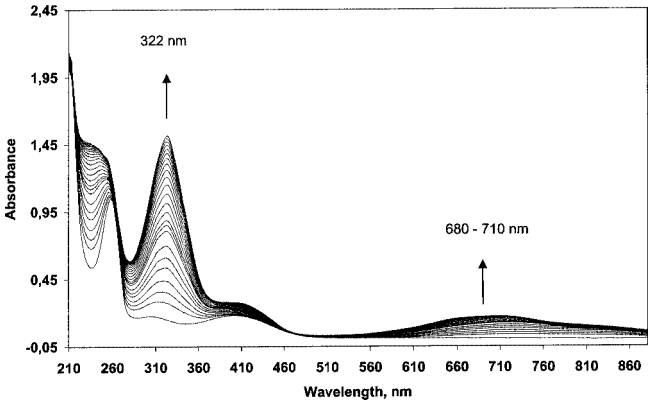

Figure 2. UV/Vis spectral changes observed upon oxygenation of $[Fe(L^1)Cl][Cl]$ at room temperature in acetonitrile solution (one trace per hour over 24 h)

The same experiment was carried out on a preparative scale, and a new complex, formulated as $[Fe(L^2)(CH_3CN)][OH][Cl]_2$, was obtained. The UV/Vis spectrum of this dark-green material in an acetonitrile solution displays several maxima {λ (ε [10^3 mmol·cm^2]) = 252 (sh. in solvent), 322 (17.36), 404 (3.23) and 694 (br., 1.59) nm}. The intensity of the new UV absorption suggested the presence of a new conjugated π system. In the IR spectrum, the ν_{O-H} vibration appears at 3418 cm^{-1}, and the band at 1651 cm^{-1} is assigned to the $\nu_{C=N}$ vibration. The EPR spectrum of an acetonitrile solution recorded at 90 K displays signals at $g_x = 2.460$, $g_y = 2.244$ and $g_z = 1.874$, indicating the presence of a rhombic low-spin iron species. The ^{1}H NMR spectrum displays a complex set of broad and paramagnetically shifted peaks lying between $\delta = 120$ and -15 ppm, consistent with the EPR data.

Attempts to crystallise this new compound as obtained directly after oxygenation were unsuccessful. However, single crystals could be obtained from a solution of the complex to which a small amount of $FeCl_2$ had been added.[17] All spectroscopic data remained unaffected by the presence of $FeCl_2$, whose only function was to help in obtaining single crystals by allowing the formation of the $FeCl_4^{2-}$ counteranion. An ORTEP diagram of the cation $[Fe(L^2)(CH_3CN)]^{3+}$ is shown in Figure 3.

The main feature of this structure is the modification of the ligand: the N7−C6 distance [1.294(4) Å] indicates the presence of an imine bond. Moreover, an almost planar conjugated pyridinyl-*o*-phenylenediamine system is formed, which is responsible for the intense absorption at $\lambda = 322$ nm in the UV/Vis spectrum. As expected from the EPR spectrum, the metal−ligand distances are all short (< 1.96 Å), which is consistent with a low-spin state for the metal atom in the solid state. The short N7−Fe distance [1.883(3) Å] corresponds to a strong coordination of the imine to the metal atom. We suggest that the new broad absorption at $\lambda = 694$ nm is due to an Fe→N=C metal-to-ligand charge transfer (MLCT) transition. It is noteworthy that the hydroxide is not coordinated to the iron atom — the acetonitrile ligand is preferred by the trication. This preference

 © 2005 Wiley-VCH Verlag GmbH & Co. KGaA, Weinheim

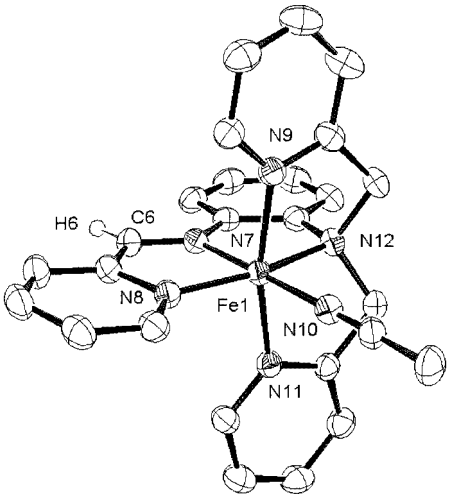

Figure 3. ORTEP diagram of the cation $[Fe(L^2)(CH_3CN)s]^{3+}$ with a partial numbering scheme; all hydrogen atoms except the aldimine one have been removed for clarity; selected bond lengths [Å] and angles [°]: Fe1−N7 1.881(3), Fe1−N8 1.955(3), Fe1−N9 1.972(3), Fe1−N10 1.951(3), Fe1−N11 1.960(3), Fe1−N12 1.989(4), N7−C6 1.294(4); N7−Fe1−N10 178.68(13), N8−Fe1−N12 166.82(14), N9−Fe1−N11 166.17(13)

may derive from the *trans* effect of the strong imine−Fe^{III} bond.[18]

Decoordination of the ligand could be achieved by treatment of a solution of $[Fe(L^2)(CH_3CN)][OH][Cl]_2$ with potassium hydroxide; L^2, obtained as a reddish oil, was characterised by ^{1}H NMR spectroscopy and mass spectrometry.

Iron complexes with the related pentadentate imine ligand *N*,*N*-bis(pyridin-2-ylmethyl)-*N*′-[(1*E*)-pyridin-2-ylmethylene]ethane-1,2-diamine ($SBPy_3$) have been previously obtained by direct reaction of iron salts with the stable free ligand.[19] In this case the iron(III) state was reported to be unstable, and only the diamagnetic iron(II) complex was fully characterized. At first glance, $SBPy_3$ looks similar to L^2. Thus, $[Fe(L^2)(CH_3CN)][OH][Cl]_2$ might be expected to be unstable. However, this is definitely not the case. This behaviour must be due to a major difference in the structure of $SBPy_3$ and L^2. The presence in the latter of a conjugation between the pyridyl, the imine and the aromatic moieties (from the *o*-phenylenediamine skeleton, absent in $SBPy_3$) seems to be crucial. This obviously provides both a different rigidity of the ligand and modified electronic properties, and, as a consequence, very different spectroscopic properties and stability patterns.

In summary, we provide in this article the first direct evidence for desaturation of a coordinated acyclic secondary amine initiated by the reaction of molecular dioxygen with a stable iron(II) complex. This reaction is certainly related to the peculiar structure of the ligand, and especially the presence of both a secondary amine and a non-innocent benzylic position close to the metal center. From a mechanistic point of view, oxidation of the iron(II) center to iron(III) by molecular dioxygen has been reported in the chemistry of dichlorotris[(2-pyridylmethyl)amino]iron(II) complexes,[13] and seems also to be a reasonable starting hypothesis here. However, the role of dioxygen in the overall reaction is, at present, not completely established. Mechanistic investigations are currently being carried out in our laboratory.

Experimental Section

Metallation of L^1: This reaction was carried out with 100 mg of L^1 according to the procedure detailed in ref.[14] The desired iron complex (130 mg, 90% yield) was obtained in microcrystalline form after workup. $C_{26}H_{26}Cl_2FeN_6$ (549): calcd. C 56.83, H 4.73; found C 57.01, H 4.82. The ^{1}H NMR spectrum displays a complex set of broad and paramagnetically shifted peaks lying between δ = 170 and −40 ppm. It is provided as Supporting Information.

Oxygenation of $[Fe(L^1)Cl][Cl]$ on a Preparative Scale: After addition of dry dioxygen by syringe to a solution of 100 mg of $[Fe(L^1)Cl][Cl]\cdot CH_3CN$ in acetonitrile, the medium was allowed to stand for 24 h. It was then concentrated and a dark compound precipitated by addition of diethyl ether. The dark-green solid was recrystallised from acetonitrile/diethyl ether, washed with diethyl ether and dried under vacuum (90 mg, 88% yield). $C_{26}H_{25}Cl_2FeN_6O$ $\{[Fe(L^2)(CH_3CN)][OH][Cl]_2\}$ (564): calcd. C 55.32, H 4.43; found C 55.19, H 4.28. The compound was also characterised by ES mass spectrometry. The spectra were recorded in the positive mode without addition of any acidic source because the compounds are somehow sensitive to protonation. High-power conditions were therefore used, and *m*/*z* values differing by −1 unit were generally observed. The traces are provided as Supporting Information. *m*/*z* (%) = 492 (100) $[\{Fe(L^2)(CH_3CN)\}\{OH\}]^{2+}$, 450 (5) $[\{Fe(L^2)\}\{OH\}]^{2+}$, 378 (6) $[L^2 - H]^+$. The EPR spectrum was recorded in solution (CH_3CN) at 30 K (power: 20.2 mW; modulation amplitude: 5.01G; modulation frequency: 100.00 kHz). The ^{1}H NMR spectrum displays a complex set of broad and paramagnetically shifted peaks lying between δ = 120 and −15 ppm. It is provided as Supporting Information.

Decomplexation: A green acetonitrile solution of $[Fe(L^2)(CH_3CN)][OH][Cl]_2$ (100 mg in 100 mL) was treated with an aqueous solution of KOH. The medium was extracted with dichloromethane, which was subsequently washed, dried and concentrated. The free imine (50 mg) was recovered as a light reddish-brown oil after addition of pentane. We could not avoid the presence of impurities in the decomplexation medium, detected by ^{1}H NMR as weak signals in the aromatic region. Attempts to purify L^2 by chromatography were unsuccessful, the imine being unstable on the stationary phases. For this reason we could not obtain any satisfactory elemental analysis. ^{1}H NMR ($CDCl_3$): δ = 8.56, 8.52, 8.44 (broadened doublets, 1 H each, α-pyridyl), 7.80−7.10 (m, 13 H, aromatic), 6.55 (s, 1 H, *H*C=N), 4.46 (s, 4 H, CH_2) ppm; additional weak signals were also present in the aromatic region. ES/MS: *m*/*z* = 378 $[L^2 - H^+]$ ($C_{24}H_{21}N_5$).

X-ray Crystallography: For details, see refs.[15,17]; CCDC-224186 and -224187 contain the supplementary crystallographic data for this paper. These data can be obtained free of charge via www.ccdc.cam.ac.uk/conts/retrieving.html (or from the Cambridge Crystallographic Data Centre, 12 Union Road, Cambridge CB2 1EZ, UK; Fax: + 44-1223-336-033; E-mail: deposit@ccdc.cam.ac.uk).

Acknowledgments

The authors thank the CNRS and ULP for financial support.

[1] E. I. Solomon, T. C. Brunold, M. I. Davis, J. M. Kensley, S.-K. Lee, N. Lehnert, F. Neese, A. J. Skulan, Y. S. Yang, J. Zhou, *Chem. Rev.* **2000**, *100*, 235−349.
[2] J. Du Bois, T. J. Mizogushi, S. J. Lippard, *Coord. Chem. Rev.* **2000**, *200−202*, 443−485.
[3] M. Costas, K. Chen, L. Que Jr., *Coord. Chem. Rev.* **2000**, *200−202*, 517−544.
[4] M. Costas, M. P. Mehn, M. P. Jensen, L. Que Jr., *Chem. Rev.* **2004**, *104*, 939−986.
[5] E. R. Stadtman, *Science* **1992**, *257*, 1220−1224.
[6] F. R. Keene, *Coord. Chem. Rev.* **1999**, *187*, 121−149.
[7] M. Goto, N. Koga, Y. Ohse, H. Kurosaki, T. Komatsu, Y. Kuroda, *J. Chem. Soc., Chem. Commun.* **1994**, 2015−2016.
[8] M. Goto, M. Takeshita, N. Kanda, T. Sakai, V. L. Goedken, *Inorg. Chem.* **1985**, *24*, 582−587.
[9] M. Renz, C. Hemmert, B. Donnadieu, B. Meunier, *Chem. Commun.* **1998**, 1635−1636.
[10] D. Mandon, A. Nopper, T. Litrol, S. Goetz, *Inorg. Chem.* **2001**, *40*, 4803−4806.
[11] D. Mandon, A. Machkour, S. Goetz, R. Welter, *Inorg. Chem.* **2002**, *41*, 5363−5372.
[12] Systematically, dichloroiron(II) complexes are obtained from $FeCl_2$ and ligands in anhydrous conditions, with dried solvents.[11,13] However, a general feature in this kind of chemistry is that, provided the reaction medium is kept under strictly anaerobic conditions, the presence of noticeable amounts of water in the solvent (up to 5% in technical grade CH_3CN for instance) does not induce significant changes in preparation, structure or stability of the complexes. The same observation accounts for complex $[Fe(L^1)Cl][Cl]$.
[13] A. Machkour, D. Mandon, M. Lachkar, R. Welter, *Inorg. Chem.* **2004**, *43*, 1545−1550.
[14] M. Sato, Y. Mori, T. Iida, *Synthesis* **1992**, *6*, 539−540.
[15] Crystal data for $[Fe(L^1)Cl][Cl]\cdot CH_3CN$: yellow crystals, $C_{26}H_{26}Cl_2FeN_6$ (549.28), tetragonal, $P4_3$, $a = b = 9.378(1)$, $c = 29.134(2)$ Å, $V = 2562.2(4)$ Å^3, $Z = 4$, $R = 0.061$, $Rw = 0.120$.
[16] V. Balland, F. Banse, E. Anxolabehere-Mallart, M. Ghiladi, T. Mattioli, C. Philouze, G. Blondin, J.-J. Girerd, *Inorg. Chem.* **2003**, *42*, 2470−2477.
[17] Crystal data for $[Fe(L^2)(CH_3CN)][OH][FeCl_4]\cdot(CH_3CN)_2$: dark green crystals, $C_{30}H_{30}Cl_4Fe_2N_8O$ (772.12), triclinic, $P\bar{1}$, $a = 12.415(1)$, $b = 12.520(1)$, $c = 13.261(1)$ Å, $V = 1662.5(2)$ Å^3, $Z = 2$, $R = 0.056$, $Rw = 0.174$.
[18] The hydroxide anion lies between one chloride ion of the $FeCl_4^{2-}$ anion and the nitrogen atom of one of the CH_3CN molecules present as solvate in the unit cell. Short contacts are found and support stabilization of OH^- in this position by hydrogen bonding.
[19] A. K. Patra, R. Afshar, M. M. Olmstead, P. K. Masharak, *Angew. Chem. Int. Ed.* **2002**, *41*, 2512−2515.

Received May 6, 2004
Early View Article
Published Online November 4, 2004

 © 2005 Wiley-VCH Verlag GmbH & Co. KGaA, Weinheim

Influence on the Formation of Aragonite or Vaterite by Otolith Macromolecules

Giuseppe Falini,*[a,b] Simona Fermani,[b] Silvia Vanzo,[c] Marin Miletic,[c] and Giulia Zaffino[b]

Keywords: Biomineralization / Otoliths / Vaterite / Aragonite / Calcium carbonate / Polymorphism / Bioinorganic chemistry

Calcium carbonate polymorphism is one of the most challenging problems in biomineralization. Calcium carbonate exists in three crystalline forms: calcite, aragonite and vaterite. Otoliths of teleost fishes are made of vaterite and aragonite, located in different sacs and never mixed together. This paper presents a biochemical characterization of the intracrystalline macromolecules associated to the vateritic and aragonitic phases of otoliths. Experimental evidences from calcium carbonate overgrowth on the surface of otoliths and in vitro crystallization on the chitin-silk fibroin assembly organic matrix suggest that the intracrystalline macromolecules associated to the otolith influence the aragonite–vaterite polymorphism.

(© Wiley-VCH Verlag GmbH & Co. KGaA, 69451 Weinheim, Germany, 2005)

Introduction

The term otolith refers to the ear bone of teleost fishes. These carbonatic structures are a part of the stato-acustical organ of advanced fishes that corresponds to the inner ear (labyrinth) and is responsible for the ability to hear and the equilibrium sense. The labyrinth includes three connected semicircular canals and three otolithic organs consisting of the sacculus, utricle and lagena,[1−3] each of which contains an otolith called sagitta, asteriscus and lapillus respectively. The asteriscus and lapillus are usually millimetre sized, but the sagitta can range from millimetre to centimetre size.[1] As sagittae are the largest otolith, they have been widely utilized in teleost growth rate and age assessment studies.[1]

Crystals of otoliths, once deposited, are metabolically inert, except under extreme stress. Thus, the otolith can potentially retain the variation in crystalline structure due to variation in the organic matrix or in the crystallization environment.[1]

Biomineralization of otoliths differs from that of vertebrate bone, molluscan shell and coral skeleton since the otolith epithelium is not in direct contact with the region of calcification. As a result, the calcification is heavily dependent upon the composition of the endolymphatic fluid surrounding the otolith.[4−6] However, the mineral crystalline units are associated with an organic matrix. Approximately half of the otolith matrix macromolecules are water insoluble[7] and, presumably, make up the structural framework for subsequent calcification. The soluble proteins are characterized by a high abundance of acidic amino acids, and are termed "otolin".[8] The most recently elucidated otolith water-soluble protein is characterized by a high content of acidic amino acids and can control the calcium carbonate morphology and polymorphism.[9]

Different polymorphs of calcium carbonate are linked to the different otolith organs. While aragonite is normal in sagittae and lapillus, most asteriscus are made of vaterite.[10,11] Vaterite is also the principal polymorph in many abnormal otoliths.[12] There is no accepted explanation for the formation of vateritic otoliths together with aragonitic ones.[13] Vaterite precipitates in supersaturated solutions that are far from equilibrium;[14] alternatively, matrix proteins may mediate vaterite formation, similarly as described for calcite and aragonite in mollusc shells.[15]

We present here a characterization of the intracrystalline acidic macromolecules associated to aragonitic and vateritic otoliths. The influence of such macromolecules on calcium carbonate polymorphism in fish otoliths is also analyzed and discussed.

Results

General Description

Figure 1 (a, b) gives a view of the otoliths lapillus and asteriscus of *Chondrostoma nasus nasus*. In the family of

[a] Environmental Chemistry Laboratory, University of Bologna, Via dell'Agricoltura 5, 48100 Ravenna, Italy
[b] Department of Chemistry "G. Ciamician", Alma Mater Studiorum University of Bologna, Via Selmi 2, 40126 Bologna, Italy
Fax: (internat.) + 39-051-2099456
E-mail: giuseppe.falini@unibo.it
[c] Department of Biology, University of Trieste, Via Weiss 2, Trieste, Italy

 © 2005 Wiley-VCH Verlag GmbH & Co. KGaA, Weinheim DOI: 10.1002/ejic.200400419

Ciprinidi, sagitta is the smallest otolith, while lapillus and asteriscus can reach the size of millimetres. Their morphology has been well described.[13]

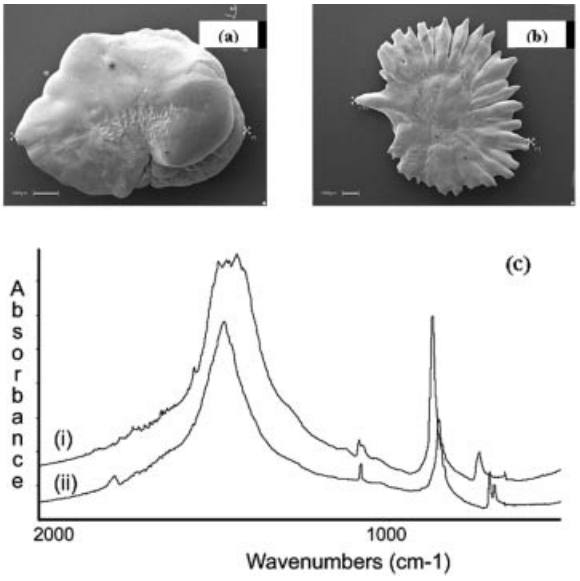

Figure 1. Scanning electron microscopy images of the anti-sulcal surface of otoliths lapillus (a) and asteriscus (b) from *Chondrostoma nasus nasus*; (c) FTIR spectra of asteriscus (i) and lapillus (ii) show the characteristic absorption peaks of vaterite and aragonite respectively[18]

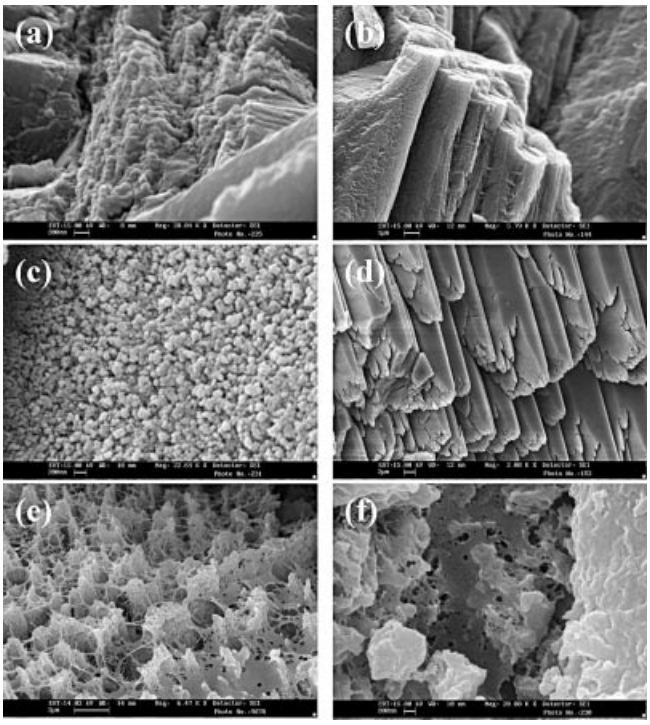

Figure 2. Scanning electron microscopy images of the textural organization of crystalline units in asteriscus (a) and (c) and lapillus (b) and (d); in (e) and (f) the insoluble organic matrix after fixation associated to asteriscus and lapillus respectively is shown

Lapillus and asteriscus were used as sources of aragonitic and vateritic associated intracrystalline macromolecules, respectively (see c in Figure 1). The textural organization in lapillus and asteriscus (Figure 2) has locally radial oriented crystalline units that change in size as a function of the polymorph. Those of aragonite appear as a long prism with an average thickness of about 5 μm (see a in Figure 2). Interestingly, this is the thickness of the crystalline units in the nacre of the shells.[3] Vaterite crystalline units in the asteriscus appear as small needles locally oriented (see b in Figure 2). Each crystalline unit, of either aragonite or vaterite, is embedded completely in an organic matrix (Figure 2, c and d). This organic matrix is partially water insoluble and its structure is observable after decalcification in the presence of fixatives. It makes a continuous network that can bridge all the crystalline units (Figure 2, e and f). In the pictures the fixed organic matrix appears to be full of holes and small fragments; we cannot exclude that this is an artifact of the drying process, as has been shown for others organic matrices.[16]

Acidic Macromolecules Associated to Aragonite and Vaterite

Cation exchange resin was used to extract the acidic intracrystalline macromolecules from the otoliths.[17] SDS-PAGE, amino acid analysis and FTIR spectroscopy were used to characterize the soluble macromolecules extracted from lapillus and asteriscus.

Figure 3 compares the major otoliths proteins of the two calcium carbonate polymorphs, aragonite and vaterite. In lines numbered 1 the molecular weight markers are reported, while lines 2−4 show the running gels of the soluble macromolecular assembly extracted from asteriscus (2), and lapillus (3, 4) at different concentrations. In the macromolecular gel lines some material was retained close to the top and a main band at about 67000 was observed. Other weak bands at higher molecular weight are present. However, there are differences between the macromolecules associated to aragonite (lines 3 and 4) and those associated to vaterite (line 2). Those associated to aragonite show a second main band at about 30000 while those of vaterite show a strong at about 40000. Many other minor bands are present in both the aragonitic- and vateritic-soluble macromolecular assemblies. Table 1 gives the amino acid composition of the proteic part of the soluble macromolecular assembly associated with aragonite (lapillus) and vaterite (asteriscus) in the otoliths. The total amino acid composition is quite similar; the main difference is a higher content of Glx in the macromolecules associated to vaterite. Figure 4 reports the FTIR spectra of intracrystalline soluble macromolecules associated to lapillus (aragonitic) and asteriscus (vateritic).

A protein amide I absorption band at 1654 cm^{-1} and a large absorption band at around 1100 cm^{-1} dominate the infrared spectrum of the ensemble of macromolecules from asteriscus (Figure 4).[18]

 © 2005 Wiley-VCH Verlag GmbH & Co. KGaA, Weinheim

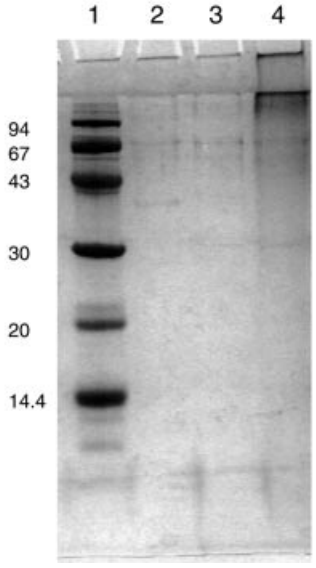

Figure 3. SDS-PAGE of acidic macromolecules extracted from *Chondrostoma nasus nasus* aragonitic (line 3, 4) or vateritic (50 ng, line 2) otoliths; concentrations of aragonitic acidic macromolecules of 10 and 50 ng were used in lines 3 and 4 respectively; in line 1, hmw markers are reported

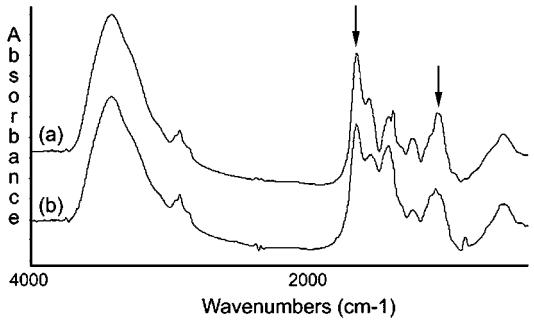

Figure 4. FTIR spectra of ground samples (tens of micrograms) in KBr pellets of acidic macromolecules extracted from *Chondrostoma nasus nasus* vateritic (a) or aragonitic (b) otoliths; arrows indicate the main absorption bands associated with the proteic and glycosidic regions of the acidic macromolecules

Table 1. Amino acid composition of the proteic parts associated with the soluble macromolecules extracted from the otoliths asteriscus and lapillus; the last row gives the proteic concentration in the mineral phase

	Otoliths	
	Asteriscus	Lapillus
Asx	19.34	19.24
Thr	7.84	8.50
Ser	12.92	11.69
Glx	14.29	10.06
Pro	6.13	5.55
Gly	9.18	10.06
Ala	8.82	7.85
Cys	0.19	0.00
Val	4.95	4.84
Met	1.34	1.30
Ile	1.72	2.11
Leu	3.77	3.99
Tyr	0.80	1.13
Phe	1.73	1.87
Lys	4.04	4.56
His	1.87	2.65
Arg	1.08	1.25
ppm	427	474

The IR spectrum of the lapillus macromolecules shows bands at 1100 and 1255 cm^{-1}, protein amide I absorption at 1653 cm^{-1}, and relatively strong carboxylate absorption bands at around 1575 and 1417 cm^{-1}.

In vitro Crystal Growth

SEM images of the mineral phases obtained from the overgrowth experiments are shown in Figure 5. Large rhombohedral crystals, along with many small needle-like ones, form on the surface of lapillus (Figure 5, b). The latter crystals almost completely cover the surface, with a few big rhombohedral crystals grown among them (Figure 5, d). Comparison with known morphologies of calcium carbonate polymorphs indicates that the rhombohedral ones are calcite while the needle-like ones are aragonite[3] (Figure 5, e).

On the asteriscus surface, however, the overgrowth of calcium carbonate produced different results. The calcite crystals are no longer well separated and grow in clusters on small regions of the asteriscus surface (Figure 5, a). Together with the typical {104} rhombohedral faces, the crystals show specific additional faces (Figure 5, c) that are more pronounced in the centre of the otoliths than on the edge. These additional faces are almost parallel to the calcite *c* axis. In some surface regions, aggregates of plate-like crystals were seen (Figure 5, e) that show a similar morphology to that of synthetic vaterite.[3]

Crystallization experiments of calcium carbonate were also carried out on a silk-fibroin/β chitin assembly in which the soluble macromolecules extracted from lapillus and asteriscus were adsorbed (Table 2). In all crystallization experiments, a mixture of calcite and vaterite was obtained. Calcite was observed on the substrate surface as small single crystals, with a rhombohedral appearance, while vaterite crystallized as crystalline aggregated spherulites (Figure 6, a and b). The mineral phase was identified by an FTIR technique (Figure 6, c).[18]

In the controls system, where no acidic macromolecules were adsorbed, calcite, as the main phase, and vaterite were formed. The pH at the end of the crystallization experiment was 7.8 and the average number of crystals (calcite plus vaterite) was about 9.6 per cm^2. In the presence of adsorbed acidic macromolecules extracted from lapillus, both calcite and vaterite were observed. However, with respect to the control, a higher density of crystallization was observed (about 26.6 crystal per cm^2), even if the average size, the polymorphic distribution and the final pH of the crystallization media were almost the same. A different scenario

 © 2005 Wiley-VCH Verlag GmbH & Co. KGaA, Weinheim

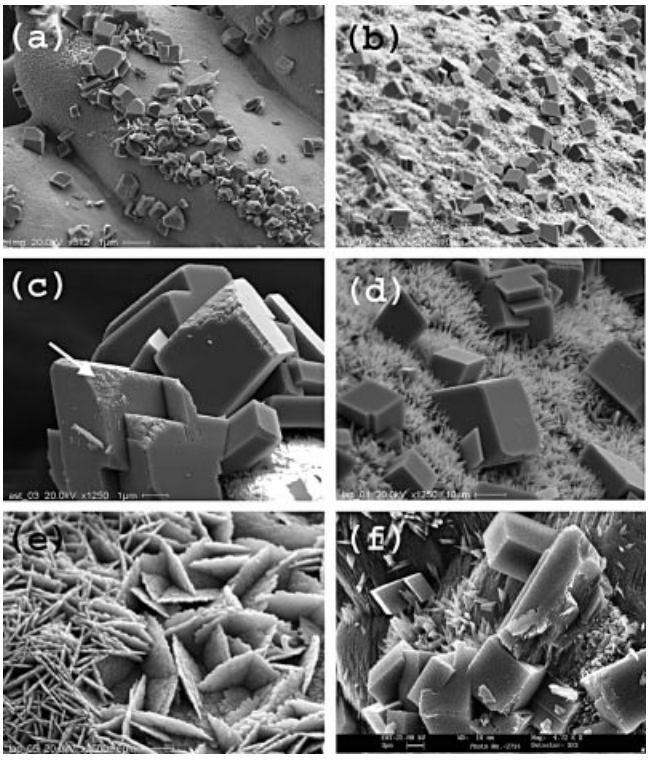

Figure 5. Scanning electron microscopy images of calcium carbonate crystal overgrown on the surface of otoliths asteriscus (a, c, e) and lapillus (b, d, f). (a) and (b); general overview of the calcium carbonate overgrown on the otoliths surface; (c) and (d) show calcite crystals; note the different morphology; calcite crystal overgrown on the asteriscus surface shows an additional face (marked by an arrow and indexed {*hk*0}) with respect to those overgrown on lapillus surface, which show only the typical {104} rhombohedral faces; (e) vaterite plate-like crystals overgrown on asteriscus surfaces; (f) aragonite needle-like crystals overgrown on the lapillus surface

Table 2. Calcium carbonate polymorphs obtained on the silk fibroin β-chitin assembly in the presence of soluble acidic macromolecules extracted from aragonitic (lapillus) or vateritic (asteriscus) otoliths

Mineral phase[b]	Control[a] **C** + V	Lapillus **C** + V	Asteriscus C + **V**
Longest crystal axis[c] [mm]	0.05 0.08	0.05 0.08	0.05 0.23
Crystals density[d] [*n*/cm^2]	9.6	26.6	26.6
Final pH[e]	7.8	7.8	8.2

[a] No additives added to the silk fibroin β-chitin assembly in the control experiment. [b] Main calcium carbonate polymorph in bold. [c] Average longest axis of the calcite crystals (first row) and average diameter of the spherulite of vaterite (second row). [d] Crystal density measured by counting crystalline units under an optical microscope. [e] Final pH of the aqueous media in which the crystallization process took place.

occurred in the presence of acidic macromolecules extracted from asteriscus. The spherulites of vaterite appeared bigger than those formed on the control, and the final pH of the crystallization media increased with respect to the control, from 7.8 to 8.2.

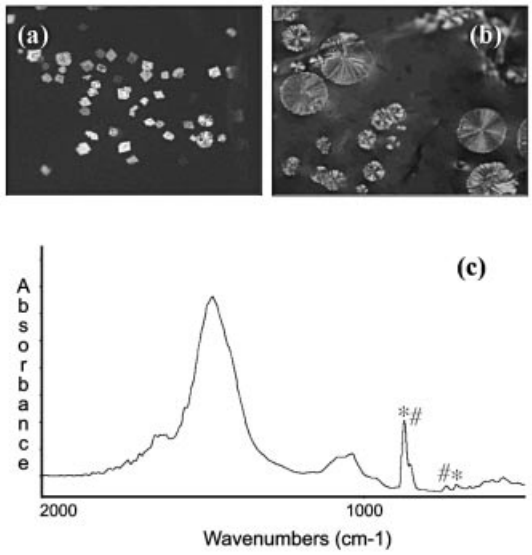

Figure 6. Optical micrographs in cross polar of calcium carbonate aggregates grown in the β-chitin/silk fibroin assembly with or with out acidic macromolecules extracted from *Chondrostoma nasus nasus* aragonitic or vateritic otoliths; (a) calcite crystals and a few vaterite spherulites formed in the presence of aragonite associated acidic macromolecules; (b) vaterite spherulites and a few calcite crystals formed in the presence of vaterite associated acidic macromolecules; magnification 40×; (c) FTIR spectrum of the mineral phases associated to the β-chitin/silk fibroin assembly, showing absorption peaks characteristic of vaterite (*) and calcite (#)[18]

Discussion

Otoliths of the teleost fish *Chondrostoma nasus nasus* are deposits of calcium carbonate formed of aragonite and vaterite. Intracrystalline acid macromolecules associated at these two mineral phases have been studied. They are an assembly of proteins and glycoproteins with a wide range of molecular weights. A main band at about 67 000 seems to be common to both mineralized tissues. Differences are present in minor bands. A band at about 30 000 seems to be characteristic of lapillus macromolecules while one at about 40 000 is observed only in asteriscus macromolecules. This latter band has been reported previously.[19] The amino acid composition shows no strong, significant differences between the proteic regions of the acidic macromolecules extracted from aragonitic and vateritic otoliths. However, vateritic ones have a higher Glx content. High Glx contents have also been observed in acidic macromolecules associated to amorphous calcium carbonate.[20] If we consider that amorphous calcium carbonate has the highest solubility among calcium carbonates, and that vaterite is the most soluble calcium carbonate crystalline phase, we could speculate that a high Glx content may be associated with highly soluble calcium carbonate mineral phases.

FTIR spectra of the two families of acidic macromolecules show different absorptions in the region typical of carbohydrates (around 1000 cm^{-1}), suggesting a different degree of glycosilation. These differences may be correlated with the SDS-PAGE bands.

 © 2005 Wiley-VCH Verlag GmbH & Co. KGaA, Weinheim

The control of acidic macromolecules over the mineral deposition was tested using two crystallization systems. Overgrowth experiments are a powerful tool to evaluate the effect of acidic macromolecules on mineral deposition since they are in a conformation that in many aspects is the closest to the native one. Two different families of mineral grew on the surface of the aragonitic lapillus. Calcite crystals grew with a regular rhombohedral habit, suggesting that no macromolecules interacted with them. These crystals do not show a preferential direction of growth, although this is not easy to state since the lapillus surface is quite rough. Together with the calcite crystals, many much smaller platelike crystals of aragonite were observed (ca. 1 μm versus more than 20 μm for calcite). These crystals almost completely covered the surface and gathered in clusters with no preferential orientation.

A different scenario appears on the asteriscus surface after the overgrowth experiments. The calcite crystals show a new crystalline face with respect to the regular rhombohedral calcite. This new face, almost parallel to the calcite *c* axis, has been observed previously by Albeck et al.[21] It was associated to a specific interaction of one (or more) soluble macromolecule(s) on a specific crystalline plane, stabilizing it and producing its appearance. This new face on the calcite crystals is more evident in the central part of the asteriscus than on the edges. This may be explained in terms of a higher concentration of the released macromolecules in the surrounding media of those regions.

On the surface of asteriscus, in regions distant from the calcitic one, vaterite was also observed. This polymorphic spatial specification could be associated to a different etching and hence to a different release of acidic macromolecules.

These observations indirectly confirm the SDS-PAGE and FTIR observations. The two families of acidic macromolecules associated to the aragonitic and vateritic otoliths are composed of different macromolecules, and they can interact with growing calcium carbonate in different ways.

Aragonite forms on the surface of aragonitic biomaterial[22] but, to our knowledge, this is the first example of the overgrowth of vaterite on a vateritic biomineral, under conditions where calcite precipitation is favored.

The ability of the acidic macromolecules to influence calcium carbonate polymorphism has also been tested using an artificial assembly made of silk fibroin and β-chitin. The silk-fibroin/β chitin assembly is not strictly relevant in otolith biomineralization, since neither β-chitin nor silk fibroin-like proteins has been shown to be present in the otolith insoluble matrix. However, this artificial assembly has been used successfully to verify the nucleating properties of acidic macromolecules extracted from mollusc shells. In search of an analogy between these two mineralized tissues, we used it to run crystallization experiments. Calcite and vaterite were observed in all crystallization experiments, irrespective of the presence of the acidic macromolecules. However, some interesting features arise from the crystallization results (Table 2). The substrate in which acidic macromolecules extracted from the lapillus were adsorbed showed no differences to the control in terms of polymorph distribution, crystal size and final chemical properties of the surrounding media. Calcite was the main crystalline phase, with few vaterite spherulites. The density of crystallization on the surface increased, suggesting that these charged macromolecules, once adsorbed on a substrate, favor the nucleation and growth of calcium carbonate.[23] No evidence for aragonite was obtained. This indicates that the artificial assembly does not cover the requirement for the acidic macromolecules' polymorphic control, or that these proteins are unable to control aragonite formation. In this case, a pure physical control should be addressed. In the presence of the acidic macromolecules extracted from the asteriscus the final pH of the crystallization media increased with respect to those of the control and lapillus (Table 2) and larger spherulites of vaterite made up the main phase on the matrix surface. This means that the system reached equilibrium at a higher supersaturation than did the control, justifying the formation of vaterite in the matrix.[24] Vaterite is metastable in water solution and spontaneously transforms into calcite;[25] the presence of large vaterite spherulites suggests that the system acidic macromolecules from asteriscus−artificial assembly favors and stabilizes vaterite formation.

Conclusion

Intracrystalline acidic macromolecules of otoliths influence calcium carbonate polymorphism. A preliminary characterization of these acidic macromolecules has been carried out, and their calcium carbonate nucleating properties have been tested using overgrowth and substrate-mediated approaches.

Experimental Section

Materials: Otoliths for this study were taken from the head of the fish *Chondrostoma nasus nasus* collected from the Isonzo river (Italy). After dissecting them from the fish ears, they were washed with sodium hypochlorite for 1 h to remove any organic superficial contaminant, then with Milli-Q water, and finally air-dried. No distinction was made between sex and left or right ear otoliths.

Morphological Investigations: Scanning electron microscopy (SEM) images were obtained by means of a Philips XL20 electron microscope on samples glued on an aluminium stub and gold sputtered. Prior to observations some otolith samples were mechanically broken to observe the inner morphology or decalcified in the presence of fixative to observe the insoluble organic matrix.[11]

Protein Extraction: Proteins were extracted using the cation exchange resin procedure.[24] Specifically, ground otoliths powder was poured into dialysis tubes and suspended in water (20 mL per 1.5 g of otolith). The sealed dialysis tube was then placed in a plastic cylinder. About one quarter of the cylinder, outside the dialysis tube, was filled with prewashed cation exchange resin and water was added to fill the cylinder. The cylinder was then closed with a stopper and rotated slowly and continuously in a propeller-like mode at room temperature to keep the powder and the resin in

 © 2005 Wiley-VCH Verlag GmbH & Co. KGaA, Weinheim

suspension. The water outside the dialysis tube was changed twice per day. Decalcification was complete in about three days, and the absence of mineral was checked by IR spectroscopy. The content of the dialysis tube was then dialyzed against water for two days. The resulting soluble and insoluble material inside the dialysis tube was subsequently separated by centrifugation. The final soluble material was then concentrated by lyophilization.

Polyacrylamide Gel Electrophoresis of Proteins: Tris-tricine ready-to-use Minigels of 15% polyacrylamide were employed. The gel ran at 100 V for 1.5−2 h and was developed with Blue Coomassie.

FTIR Spectrometry: IR analyses were carried out on dried soluble and insoluble matrices. Calcium carbonate formed in the chitin−silk fibroin assembly was removed mechanically before analysis. All spectra were recorded at 4 cm^{-1} resolution with a 32 scan with a Perkin-Elmer Model 1600 Fourier Transform Infrared Spectrometer (FTIR) from 4000 to 450 cm^{-1}. Powder sample and KBr were dried under a red lamp, careful mixed in a mortar, and pelleted with a press. A background spectrum was measured for pure KBr.

In vitro Crystal Growth: Two types of crystallization experiments were performed. Calcium carbonate crystals were overgrown on cleaned otoliths, or crystals were grown *de novo* in the presence of the soluble total macromolecular assemblage extracted from lapillus or asteriscus adsorbed on β-chitin and silk fibroin substrate.[15] The crystal growth procedure has been detailed previously.[26,27] Briefly, synthetic calcium carbonate crystals were grown for four days in a closed box, by slow diffusion of ammonium carbonate vapor into plastic Petri dishes containing the otoliths, or the nucleating substrate, overlaid by a 10 mM $CaCl_2$ solution. The obtained calcium carbonate crystals were rinsed with Milli-Q water, observed under optical microscope, and successively air-dried. For detailed morphological analysis, the crystals were gold coated and observed by SEM

Acknowledgments

This work was supported by MIUR (Cofin 2003), CNR and the University of Bologna (Funds for Selected Research Topics).

[1] S. E. Campana, *Mar. Ecol.: Prog. Ser.* **1999**, *188*, 263−297.
[2] O. Lowenstain, *Br. Med. Bull.* **1956**, *12*, 110−4.
[3] H. A. Lowenstam, S. Weiner, *On Biomineralization*, Oxford University, Press New York, **1989**.
[4] P. Payan, H. Kossmann, A. Watrin, N. Mayer-Gostan, G. Boeuf, *J. Exp. Biol.* **1997**, *200*, 1905−1912.
[5] P. Payan, G. Borelli, G. Boeuf, N. Mayer-Gostan, *Fish Physiol. Biochem.* **1998**, *19*, 35−41.
[6] L. Addadi, S. Weiner, *Angew. Chem.* **1992**, *31*, 153−169; *Angew. Chem. Int. Ed. Engl.* **1992**, *31*, 153−169.
[7] M. Asano, Y. Mugiya, *Comp. Biochem. Physiol., Part B: Biochem. Mol. Biol.* **1993**, *104*, 201−205.
[8] T. E. Degens, W. G. Deuser, R. L. Haedrich, *Mar. Biol.* **1969**, *2*, 105−13.
[9] C. Soellner, M. Burghammer, E. Busch-Nentwich, J. Berger, H. Schwarz, C. Riekel, T. Nicolson, *Science* **2003**, *302*, 282−286.
[10] A. M. Oliveira, M. Farina, I. P. Ludka, B. Kachar, *Naturwissenschaften* **1996**, *83*, 133−135.
[11] D. Lenaz, M. Miletic, *Neues Jahrb. Mineral., Monatsh.* **2000**, *11*, 522−528.
[12] R. W. Gauldie, S. K. Sharma, E. Volk, *Comp. Biochem. Physiol., Part A: Mol. Integr. Physiol.* **1997**, *118*, 167−194.
[13] R. W. Gauldie, *J. Morphol.* **1993**, *218*, 1−28.
[14] D. Kralj, L. Brecevic, A. E. Nielsen, *J. Cryst. Growth* **1990**, *104*, 793−800.
[15] G. Falini, S. Albeck, S. Weiner, L. Addadi, *Science* **1996**, *271*, 67−9.
[16] Y. Levi-Kalisman, G. Falini, L. Addadi, S. Weiner, *J. Struct. Biol.* **2001**, *135*, 8−17.
[17] D. Worms, S. Weiner, *J. Exp. Zool.* **1986**, *237*, 11−20.
[18] W. B. White in *Infrared Spectra of Minerals* (Ed.: V. C. Farmer), Mineralogical Society, London, **1974**, pp. 227−284.
[19] B. A. Gotliv, L. Addadi, S. Weiner, *ChemBioChem.* **2003**, *4*, 522−529.
[20] J. Aizenberg, G. Lambert, L. Addadi, S. Weiner, *Adv. Mater.* **1996**, *8*, 222−6.
[21] S. Albeck, S. Weiner, L. Addadi, *Chem. Eur. J.* **1996**, *2*, 278−84.
[22] S. Blank, M. Arnoldi, S. Khoshnavaz, L. Treccani, M. Kuntz, K. Mann, G. Grathwohl, M. Fritz, *J. Microsc. (Oxford, U.K.)* **2003**, *212*, 280−291.
[23] L. Addadi, S. Weiner, *Proc. Natl. Acad. Sci. U. S. A.* **1985**, *82*, 4110−14.
[24] G. Falini, S. Fermani, M. Gazzano, A. Ripamonti, *Chem. Eur. J.* **1998**, *4*, 1048−1052.
[25] D. Kralj, L. Brecevic, J. Kontrec, *J. Cryst. Growth* **1997**, *177*, 248−257.
[26] S. Albeck, L. Addadi, S. Weiner, *Connect. Tissue Res.* **1996**, *35*, 365−370.
[27] J. Aizenberg, S. Albeck, S. Weiner, L. Addadi, *J. Cryst. Growth* **1994**, *142*, 156−64.

Received May 20, 2004
Early View Article
Published Online November 18, 2004

 © 2005 Wiley-VCH Verlag GmbH & Co. KGaA, Weinheim

The Hidden Equilibrium in Aqueous Sodium Carbonate Solutions − Evidence for the Formation of the Dicarbonate Anion

Klaus-Peter Zeller,*[a] Paul Schuler,[a] and Peter Haiss[a]

Keywords: Dicarbonate anion / Isotopic labeling / NMR spectroscopy / Oxygen transfer

Crossover ^{13}C NMR experiments between [^{13}C]carbonate and [^{18}O]carbonate in aqueous solution confirm the combined action of two oxygen-exchange modes. The isotopomeric carbon dioxides formed in the hydrolysis equilibrium of the labeled carbonate anions react with hydroxide with formation of hydrogencarbonate and with isotopomeric carbonate anions yielding the corresponding dicarbonate species, which, in the back reaction, form carbon dioxide and carbonate anions with distributed oxygen.

(© Wiley-VCH Verlag GmbH & Co. KGaA, 69451 Weinheim, Germany, 2005)

Introduction

In aqueous solutions of metal carbonates the carbonate ion suffers from partial hydrolysis into hydrogencarbonate, carbonic acid and dissolved carbon dioxide [reactions (1)−(4)]. An impressive number of techniques have been applied to determine the rate and equilibrium constants of the reaction steps involved. Much of this data has been collected.[1] Because of its kinetic instability in the presence of water,[2] the fraction of the solvated carbon dioxide present as carbonic acid is less than 1%.[3] From the first (apparent) and the second dissociation constant of "carbonic acid", and the ion product of water, the dependence of the composition of the $CO_2/HCO_3^-/CO_3^{2-}$ system on the pH value can be calculated. For example, a 0.01 M solution of sodium carbonate exhibits a pH value of 11.16 and the molar fractions of carbonic species are $x_{CO_3^{2-}} = 0.86$, $x_{HCO_3^-} = 0.14$ and $x_{CO_2} = 3 \times 10^{-6}$.

$$(1)\quad CO_3^{2-} + H_2O \rightleftharpoons HCO_3^- + OH^-$$

$$(2)\quad HCO_3^- + H_2O \rightleftharpoons H_2CO_3 + OH^-$$

$$(3)\quad H_2CO_3 \rightleftharpoons CO_2 + H_2O$$

$$(4)\quad HCO_3^- \rightleftharpoons CO_2 + OH^-$$

As shown in the pioneering work of Mills and Urey,[4] carbonate dissolved in ^{18}O-enriched water slowly exchanges its oxygen atoms with the oxygen atoms of the water. The rate of this oxygen exchange is mainly governed by the addition of hydroxide to carbon dioxide.[4,5] Himmelblau and Babb[6] have studied the rate of this reaction step by adding ^{14}C-labeled hydrogencarbonate to unlabeled hydrogencarbonate/CO_2 solutions and observing the appearance of $^{14}CO_2$. The values obtained by this method for the hydroxylation of carbon dioxide are much higher than those found by other techniques. This discrepancy points to a superimposition of an oxygen-exchange process between carbonic species.[7,8] A kind of molecular complex, written as $CO_2{\cdot}OH^-$ and supposed to be distinctly separated from HCO_3^- and $CO_2 + OH^-$, has been suggested for this purpose.[7] It is assumed that this complex is able to transfer OH^- to a second CO_2 molecule. The occurrence of cyclic oligomeric orthocarbonic acid was also proposed to account for the oxygen-transfer process.[8]

Tu and Silverman[9] have studied the kinetics of the oxygen exchange by adding ^{18}O-labeled carbonate to solutions containing ^{13}C-enriched carbonate. The rate of appearance of ^{18}O in the ^{13}C-enriched species was measured by mass spectrometry at pH values ranging from 8 to 10. A kinetic analysis revealed that the oxygen transfer can be described by the overall reaction (5).

$$(5)\quad {}^{13}CO_2 + C^{18}O_3^{2-} \rightleftharpoons {}^{13}CO_2{}^{18}O^{2-} + C^{18}O_2$$

The rate of the second-order reaction (5) was found to be competitive with the rate of the back-reaction (4). Therefore, the carbonate oxygen atoms are simultaneously exchanged between carbonic species [reaction (5)] and with the solvent water [reaction (4)].

In this contribution the parallel occurrence of two oxygen-exchange modes is directly observed by NMR spectroscopy and explained by a competitive addition of hydroxide and carbonate ions to carbon dioxide.

[a] Institut für Organische Chemie, Universität Tübingen, Auf der Morgenstelle 18, 72076 Tübingen, Germany
Fax: + 49-7071-295-076
E-mail: kpz@uni-tuebingen.de

Supporting information for this article is available on the WWW under http://www.eurjic.org or from the author.

 © 2005 Wiley-VCH Verlag GmbH & Co. KGaA, Weinheim **DOI: 10.1002/ejic.200400445**

Results

Sodium [$^{18}O_3$]carbonate was prepared from tetraethyl orthocarbonate by stepwise hydrolysis with [^{18}O]water. The first acid-catalyzed step yields diethyl [carbonyl-^{18}O]carbonate, which was further transformed into sodium [^{18}O]carbonate by saponification. According to ^{13}C NMR measurements the sodium carbonate obtained consists of about 46% [$^{18}O_3$], 41% [$^{18}O_2$], 12% [^{18}O] and 1% unlabeled carbonate. This corresponds to an ^{18}O content in the water of 77%. The isotopic enrichment of the water used for hydrolysis was determined to be 80% ^{18}O. The somewhat lower value in the reaction product results from the presence of traces of [^{16}O]water during the synthetic procedure.

The distribution of the isotopomeric carbonate species could be established by ^{13}C NMR spectroscopy. The ^{18}O isotope bound to C causes a small high-field shift of the ^{13}C resonance frequency relative to the ^{16}O compound.[10] The ^{18}O isotope effect on the ^{13}C chemical shift is additive. Therefore, the four isotopomeric species $C^{18}O_{3-n}O_n^{2-}$ (n = 0, 1, 2, 3) should produce four equidistantly separated signals. The carbonyl-^{13}C resonances in ketones, aldehydes, esters and carboxylic acids are shifted up-field by about 0.05,[10b] 0.04,[10b] 0.04,[10b] and 0.03 ppm,[10b] respectively, when replacing ^{16}O by ^{18}O. Because of the lower double-bond character in the carbonate ion, a value of $\Delta\delta$ = 0.02 ppm per ^{18}O is expected (see Supporting Information for more details).

The ^{13}C NMR spectrum was measured in D_2O containing 1 equiv. of NaOD per ^{18}O-labeled Na_2CO_3. Under these conditions the relative amount of ^{18}O-labeled CO_2, formed according to the hydrolysis equilibrium in reactions (1)−(4), is suppressed by about two orders of magnitude and, thus, the oxygen exchange is slowed down. Indeed, repeated measurements within 12 h produced spectra with four signals separated by 0.016 ppm, with no detectable changes in their relative intensities.

In contrast, the ^{13}C NMR spectra of a 0.44 M solution in pure D_2O measured over several weeks showed an exchange of the oxygen atoms of the carbonate ion with the oxygen atoms of the solvent D_2O. Some selected examples are presented in Figure 1. It becomes evident that the carbonate species, separated by 0.018 ppm according to the number of incorporated ^{18}O atoms, lose the heavier oxygen atoms successively. After standing at 20 °C for 100 d, the carbonate consists of about 92% $C^{16}O_3^{2-}$. This is near the calculated end-point for statistical distribution of oxygen atoms from the labeled carbonate and the solvent D_2O (93.28% $^{16}O_3$, 6.59% $^{16}O_2{}^{18}O$, 0.15% $^{16}O^{18}O_2$, 0.001% $^{18}O_3$).

The intermolecular oxygen transfer between carbonic species was examined by means of a crossover experiment. A solution of 1 mg of sodium [^{13}C]carbonate (99% ^{13}C) and 31 mg of the ^{18}O-labeled sodium carbonate in 600 μL of D_2O was subjected to ^{13}C NMR spectroscopy. At t = 0 this solution is composed of 43.49% $Na_2C^{18}O_3$, 39.46% $Na_2C^{18}O_2{}^{16}O$, 11.75% $Na_2C^{18}O^{16}O_2$, 1.04% $Na_2C^{16}O_3$, 0.48% $Na_2{}^{13}C^{18}O_3$, 0.43% $Na_2{}^{13}C^{18}O_2{}^{16}O$, 0.13% $Na_2{}^{13}C^{18}O^{16}O_2$, and 3.19% $Na_2{}^{13}C^{16}O_3$. The total carbonate concentration

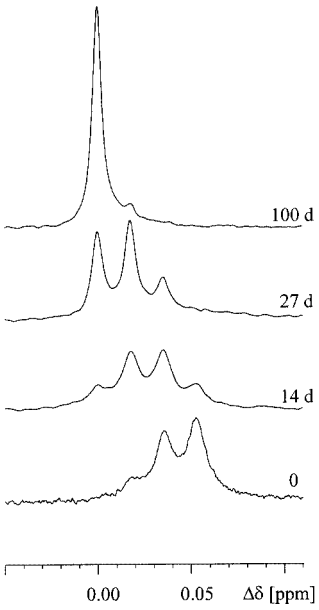

Figure 1. Time-dependent ^{13}C NMR spectra of a 0.44 M solution of $Na_2C^{18}O_{3-n}O_n^{2-}$ in D_2O at 20 °C

is 0.48 M. The ^{13}C,^{18}O-containing species result from the natural ^{13}C content in the ^{18}O-labeled carbonate. The ^{13}C-labeled isotopomers of this mixture amount to 4.23% of total carbonate and contribute to the ^{13}C NMR spectrum. The calculated ratio of the NMR-active isotopomers at t = 0 is: $^{13}C^{16}O_3^{2-}/^{13}C^{16}O_2{}^{18}O^{2-}/^{13}C^{16}O^{18}O_2{}^{2-}/^{13}C^{18}O_3{}^{2-}$ = 74.3:3.1:10.6:12.0. After infinite time, the total amount of ^{18}O and ^{16}O incorporated in the solution by the isotopomeric carbonates and D_2O should be statistically distributed. The resulting ratio of $^{13}C^{16}O_3{}^{2-}/^{13}C^{16}O_2{}^{18}O^{2-}/^{13}C^{16}O^{18}O_2{}^{2-}$ was calculated to be 94.1:5.8:0.1.

Provided that the statistical distribution is caused only by oxygen exchange between carbonic species and D_2O, this end-point should be approached in a monotonic manner. Inspection of the ^{13}C NMR measurements over a period of 154 d obviously reveals that this is not the case. Some representative measurements are given in Figure 2 (the complete set of data in form of schematic diagrams showing the relative amounts of $^{13}C^{16}O_{3-n}{}^{18}O_n^{2-}$ isotopomers as a function of time can be found in the Supporting Information).

The relative amounts of the four isotopomers $^{13}C^{16}O_{3-n}{}^{18}O_n^{2-}$ (n = 0−3) are plotted against time in Figure 3. It can be seen that the relative amount of $^{13}C^{16}O_3{}^{2-}$ decreases from 74% to a minimum of about 25% within 16 d. It then steadily increases again and slowly approaches the calculated end-point. On the other hand the curve representing $^{13}C^{16}O_2{}^{18}O^{2-}$ increases at the beginning and then reaches a plateau before slowly declining after about 25 d. The relative amount of $^{13}C^{16}O^{18}O_2{}^{2-}$ also passes through a maximum after about 15 d.

 © 2005 Wiley-VCH Verlag GmbH & Co. KGaA, Weinheim

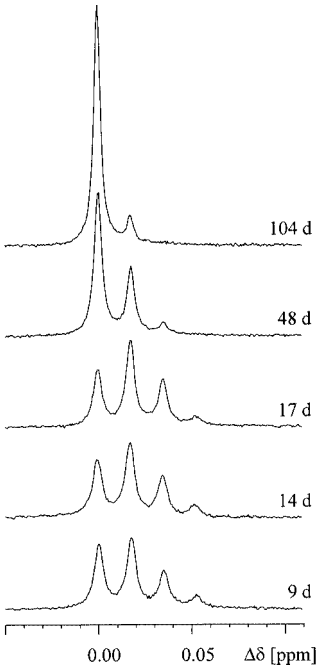

Figure 2. Time-dependent ^{13}C NMR spectra of a 0.48 M solution of a mixture (initial composition see text) of ^{13}C- and ^{18}O-labeled sodium carbonate in D_2O

Discussion

The change of the relative intensities of the $^{13}C^{16}O_{3-n}{}^{18}O_n{}^{2-}$ species present in the carbonate mixture prepared from [^{13}C]- and [^{18}O]-labeled sodium carbonate indicates the parallel operation of two oxygen-exchange modes. At the beginning the vast majority of the carbonate consists of $^{12}C^{18}O_3{}^{2-}$ and $^{12}C^{16}O^{18}O_2{}^{2-}$. At this stage the overall reactions (5) and (5′) contribute mainly to the appearance of the ^{13}C NMR spectra.

(1′) $^{13}CO_3{}^{2-} + D_2O \rightleftharpoons D^{13}CO_3{}^- + OD^-$

(4′) $D^{13}CO_3{}^- \rightleftharpoons {}^{13}CO_2 + OD^-$

(5) $^{13}CO_2 + C^{18}O_3{}^{2-} \rightleftharpoons {}^{13}C^{18}O_2O^{2-} + C^{18}O_2$

(5′) $^{13}CO_2 + CO^{18}O_2{}^{2-} \rightleftharpoons {}^{13}CO_2{}^{18}O^{2-} + CO^{18}O$

Parallel to these exchange processes the ^{18}O-labeled carbonates, added as $^{12}C^{18}O_{3-n}{}^{16}O_n{}^{2-}$ or formed in the meantime as $^{13}C^{16}O_{3-n}{}^{18}O_n{}^{2-}$, lose ^{18}O as the result of the hydrolysis sequence [reactions (1′′) and (4′′)]. The [^{18}O]hydroxide ions expelled rapidly equilibrate with the large ^{16}O stock of the solvent D_2O [reaction (6)]; thus, in the back-reaction (hydroxylation of isotopomeric carbon dioxides) mainly ^{16}O is introduced. Therefore, the carbonic species are continuously depleted of their ^{18}O labeling. This reduces the amount of $^{12}C^{18}O_{3-n}{}^{16}O_n{}^{2-}$ species capable of transferring ^{18}O to $^{13}CO_2$, and the $^{13}C^{16}O_{3-n}{}^{18}O_n{}^{2-}$ species produced in the meantime will be degraded again. Therefore, as the reaction progresses the intensity of $^{13}C^{16}O_3{}^{2-}$ passes through a minimum before it steadily increases towards the value of about 94% calculated for the statistical distribution.

The direct observation of the oxygen-exchange processes in aqueous carbonate solution by ^{13}C NMR spectroscopy confirm the conclusion of Tu and Silverman.[9] The well-established up-take of oxygen atoms from water has to be combined with a process of transferring oxygen atoms be-

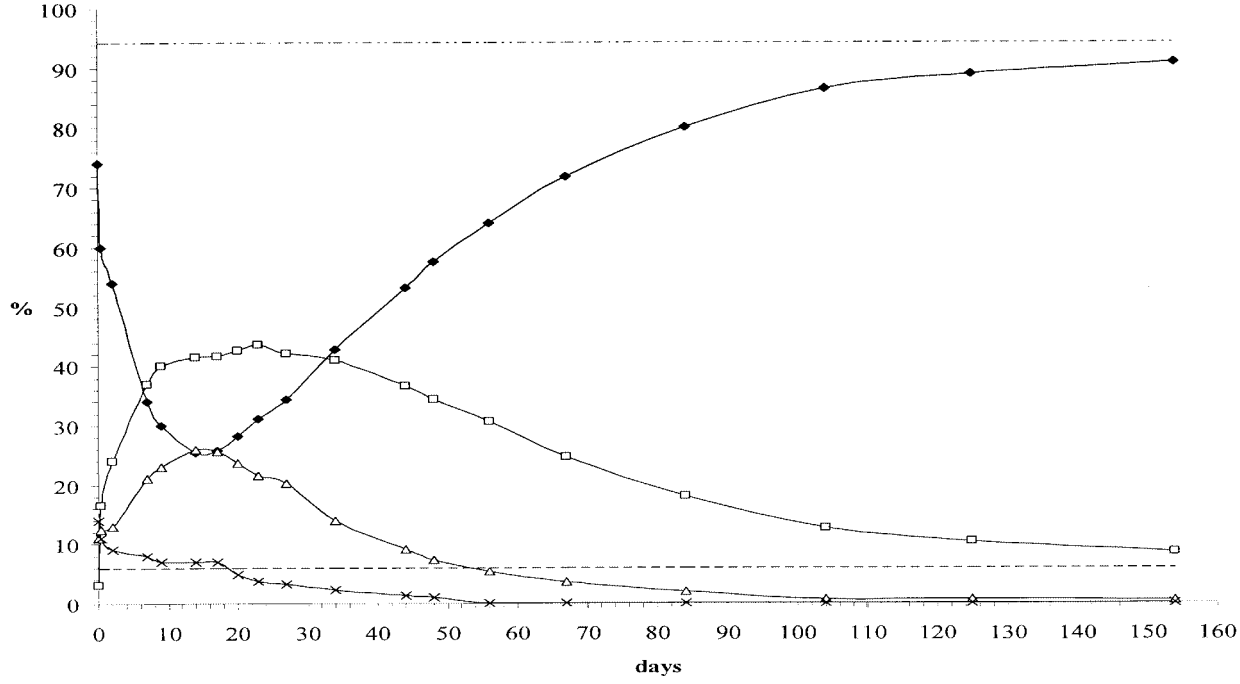

Figure 3. Change of the concentration of [^{13}C]carbonate species as a function of time (black diamonds: $^{13}C^{16}O_3{}^{2-}$; squares: $^{13}C^{16}O_2{}^{18}O^{2-}$; triangles: $^{13}C^{16}O^{18}O_2{}^{2-}$; X: $^{13}C^{18}O_3{}^{2-}$; – - - – : calculated end-point for $^{13}C^{16}O_3{}^{2-}$; – – – : calculated end-point for $^{13}C^{16}O_2{}^{18}O^{2-}$

 © 2005 Wiley-VCH Verlag GmbH & Co. KGaA, Weinheim

tween carbonic species. The latter process remains hidden unless crossover experiments between carbon- and oxygen-labeled isotopomers of carbonate are performed.

(1") $^{13}CO_2{}^{18}O^{2-} + D_2O \rightleftharpoons D^{13}CO_2{}^{18}O^- + OD^-$

(4") $D^{13}CO_2{}^{18}O^- \rightleftharpoons {}^{13}CO_2 + {}^{18}OD^-$

(4''') $D^{13}CO_2{}^{18}O^- \rightleftharpoons {}^{13}CO{}^{18}O + OD^-$

(6) $^{18}OD^- + D_2O \rightleftharpoons D_2{}^{18}O + OD^-$

In terms of reaction mechanisms the hydroxylation of carbon dioxide is a nucleophilic addition of hydroxide to a carbonyl group, as shown in reaction (7). For reactions of this type the basicity is a main factor for determining the nucleophilic power of the nucleophiles.[11] From the nucleophiles present in an aqueous carbonate solution the CO_3^{2-} anion (pK_a = 10.33) is nearest to the OH^- ion (pK_a = 15.74) in its basicity. The addition of carbonate to CO_2 would lead to the dicarbonate anion [reaction (8)], which is the first member of the series of hypothetical oligomeric carbonate ions of the general formula $C_nO_{2n+1}{}^{2-}$.

(7) 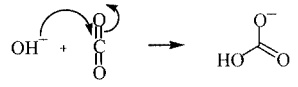

(8) 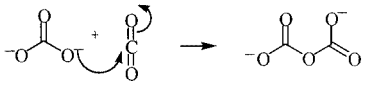

Assuming a linear structure-reactivity relationship, the rate constant of reaction (8) can be roughly estimated as 54 $mol^{-1}\cdot L\cdot s^{-1}$ (see Supporting Information). This is in acceptable agreement with the rate constant of 114 ± 11 $mol^{-1}\cdot L\cdot s^{-1}$ [9] for the overall reaction (5) describing the oxygen exchange between carbonic species. Thus, the dicarbonate anion is a likely intermediate for this process.

Reaction (8) has also been proposed to account for the experimental finding that the solubility of CO_2 in a ternary, eutectic melt of Li_2CO_3, Na_2CO_3 and K_2CO_3 is 50 times higher than deduced from the electrochemical reduction of "free" CO_2.[12] In a theoretical investigation of the structure and stability of the dicarbonate ion at the HF MP2 and QCISD levels a remarkably high free enthalpy of reaction for process (8) in the gas phase could be derived (ΔG = −44 to −48 $kcal\cdot mol^{-1}$ at 298 K).[13] If, in aqueous solution, reaction (8) was similarly exergonic, the hydrolysis of CO_3^{2-} followed by reaction (8) should result in almost complete conversion of carbonate into dicarbonate according to the overall reaction (9).

(9) $2\,CO_3^{2-} + H_2O \rightleftharpoons C_2O_5^{2-} + 2\,OH^-$

However, because of solvation effects in aqueous solution the free enthalpies of the left-hand side and the right-hand side of reaction (8) are leveled. The free enthalpies of solvation of the carbonate ion and CO_2 in water are −314[14] and −4 $kcal\cdot mol^{-1}$,[15] respectively. The solvation effect for the $C_2O_5^{2-}$ ion in water can be estimated, on the basis of an electrostatic model,[14] as $\Delta G_{hyd.} \approx -220$ $kcal\cdot mol^{-1}$. An ionic radius, $r(C_2O_5^{2-})$, of 0.326 nm derived from the geometry-optimized structure[13] has been assumed for this purpose. From this it follows that, in water, reaction (8) is no longer exergonic and only small stationary concentrations of the dicarbonate ion are built up in a reversible reaction.

As briefly addressed in the introductory section a molecular complex between CO_2 and OH^- [7] and oligomeric cyclic orthocarbonates[8] have been discussed in the earlier literature as intermediates to explain the oxygen transfer between carbonic species. This hypothetical molecular complex is supposed to be able to exchange its CO_2 very rapidly with surrounding CO_2. This could offer an alternative rationalization for intermolecular oxygen transfer [reaction (10)].

(10) $HC^*O_3^- \rightleftharpoons C^*O_2\cdot{}^*OH^- \overset{{}^*CO_2\ C^*O_2}{\rightleftharpoons} {}^*CO_2\cdot{}^*OH^- \rightleftharpoons H^*CO_2{}^*O^-$

The suggested linear arrangement of the carbon and oxygen atoms[7] to describe the molecular complex is problematic. A hydrogen-bonded structure, which is essentially a hydroxide ion solvated by carbon dioxide, would be a representation in better agreement with structural theory. However, it is difficult to see how this mode of solvation can compete with the very strong hydration of OH^- in aqueous solution. Thus, it seems unlikely that a species like $CO_2\cdot OH^-$ can exist in water with a sufficiently long lifetime to react with CO_2 present in very low concentration.

The involvement of intermediate cyclic oligomeric orthocarbonates as species responsible for oxygen exchange between the carbonic species of a carbonate solution would require the formation of new C−O bonds between carbonate and/or hydrogencarbonate units. This is rather unlikely due to the low carbonyl activity of these ions. Indeed, the negatively charged oxygen atoms of carbonate coordinate with the proton of hydrogencarbonate rather than with the much less electrophilic carbon atom. The resulting hydrogen-bridged dimeric anion $[H(CO_3)_2]^{3-}$ is well known as a structural unit in the mineral trona.[16] Higher oligomeric hydrogen-bridged carbonates of the general formula $[H_{n-1}(CO_3)_n]^{(n+1)-}$ are also known.[17,18] Of course, in this type of oligomeric carbonate oxygen transfer from carbon to carbon is not possible.

In summary, both, the involvement of a molecular complex $CO_2\cdot OH^-$ and the intermediate formation of cyclic oligomeric orthocarbonates as rationalization of the observed oxygen transfer between carbonic species in aqueous carbonate solution can be excluded. However, the reversible formation of the dicarbonate anion $C_2O_5^{2-}$ readily explains this process. The corresponding dicarbonic acid is un-

 © 2005 Wiley-VCH Verlag GmbH & Co. KGaA, Weinheim

known, although its dialkyl esters are well characterized and are widely used as reagents in synthetic chemistry.[19]

Experimental Section

General Remarks: The ^{13}C NMR spectroscopic data were obtained with a Bruker AMX 600 spectrometer by single-pulse excitation without proton decoupling (flip angle 30°, delay time 10 s, acquisition time 5 s). During the intervals between the measurements of the crossover experiment the tightly closed NMR tube was stored at 20 ± 0.5 °C. Sodium [^{13}C]carbonate (99% ^{13}C) was purchased from Aldrich. [^{18}O]Water recycled from ^{18}F production in the PET center, University Hospital, Tübingen, with an ^{18}O enrichment of 80% was used in the synthesis of ^{18}O-labeled sodium carbonate.

Sodium [^{18}O]Carbonate: The ^{18}O-labeled carbonate was prepared according to the method of Hutchinson and Mabuni[20] for the synthesis of sodium [^{18}O]acetate. A rigorously dried flask equipped with a septum was charged with tetraethyl orthocarbonate (5 mL, 23.8 mmol) and dehydrated 4-toluenesulfonic acid (1−2 mg). [^{18}O]Water (200 μL, 9.1 mmol, 80% ^{18}O) was then injected under magnetic stirring. After a few minutes of exothermic reaction, the mixture became homogeneous. A 0.5 M solution of sodium methoxide in dry methanol (30 mL, 15 mmol) and [^{18}O]water (350 μL, 15.9 mmol) was added to the resulting ^{18}O-labeled ethyl carbonate and the mixture heated to 70−75 °C for 30 h. A white crystalline mass precipitated. The reaction mixture was dried first in a rotary evaporator (70 °C/30 Torr) and then with an oil pump (160 °C/10^{-3} Torr); yield 1 g (98%). The degree of ^{18}O-enrichment was determined by ^{13}C NMR spectroscopy of a 0.5 M solution in D_2O containing 1 equiv. of NaOD to suppress oxygen exchange with the solvent D_2O. Four equidistantly separated signals ($\Delta\delta$ = 0.016 ppm) could be detected for the carbonate ion in an intensity ratio of 46:41:12:1 caused by $^{18}O_3$, $^{18}O_2{}^{16}O$, $^{18}O^{16}O_2$ and $^{16}O_3$ species.

Measurements of the dependence of the isotopic effect on the ^{13}C chemical shift of aqueous sodium carbonate are given in the Supporting Information. In addition to Figures 2 and 3 of the main text the full set of time-dependent intensity distributions of the $^{13}C^{16}O_{3-n}{}^{18}O_n{}^{2-}$ ions (n = 0−3) are presented as schematic diagrams. The rate constant for the addition of $CO_3{}^{2-}$ to CO_2 is estimated based on a linear relation between log k and pK_a.

Acknowledgments

We thank Prof. Dr. H.-J. Machulla, Abt. Radiopharmazie, Universitätsklinikum Tübingen, for a generous gift of [^{18}O]water.

[1] Gmelin, *Handbuch der Anorganischen Chemie*, 8th ed., "Kohlenstoff", part C3, **1973**, pp. 117−137.
[2] T. Loerting, C. Tautermann, R. T. Kroemer, I. Kohl, H. Hallbrucker, E. Mayer, K. R. Liedl, *Angew. Chem.* **2000**, *112*, 920−922; *Angew. Chem. Int. Ed.* **2000**, *39*, 891−894.
[3] R. Ludwig, A. Kornath, *Angew. Chem.* **2000**, *112*, 1479−1481; *Angew. Chem. Int. Ed.* **2000**, *39*, 1421−1423.
[4] G. A. Mills, H. C. Urey, *J. Am. Chem. Soc.* **1940**, *62*, 1019−1026.
[5] D. J. Poulton, H. W. Baldwin, *Can. J. Chem.* **1967**, *45*, 1045−1050.
[6] D. M. Himmelblau, A. L. Babb, *AIChE J.* **1958**, *4*, 143−152.
[7] J. Koefoed, K. Engel, *Acta Chem. Scand.* **1961**, *15*, 1319−1326.
[8] P. V. Danckwerts, K.-A. Melkersson, *Trans. Faraday Soc.* **1962**, *58*, 1832−1838.
[9] C. K. Tu, D. N. Silverman, *J. Phys. Chem.* **1975**, *79*, 1647−1651.
[10] [10a] J. M. Risley, R. L. Van Etten, *J. Am. Chem. Soc.* **1979**, *101*, 252−253. [10b] J. M. Risley, R. L. Van Etten, *J. Am. Chem. Soc.* **1980**, *102*, 4609−4614. [10c] J. M. Risley, R. L. Van Etten, *J. Am. Chem. Soc.* **1980**, *102*, 6699−6702. [10d] J. M. Risley, S. A. DeFrees, R. L. Van Etten, *Org. Magn. Reson.* **1983**, *21*, 2835. [10e] T. L. Mega, R. L. Van Etten, *J. Am. Chem. Soc.* **1993**, *115*, 12056−12059.
[11] R. W. Alder, R. Baker, J. M. Brown, *Mechanisms in Organic Chemistry*, Wiley-Interscience, London, New York, Sidney, Toronto, **1975**, p. 312.
[12] P. Claes, D. Moyaux, D. Peeters, *Eur. J. Inorg. Chem.* **1999**, 583−598.
[13] D. Peeters, D. Moyaux, P. Claes, *Eur. J. Inorg. Chem.* **1999**, 589−592.
[14] Y. Marcus, *J. Chem. Soc., Faraday Trans.* **1991**, *87*, 2995−2999.
[15] N. Brückl, J. I. Kim, *Z. Phys. Chem. (Muenchen, Ger.)* **1981**, *126*, 133−150.
[16] C. S. Choi, A. D. Mighell, *Acta Crystallogr., Sect. B* **1982**, *38*, 2874−2876.
[17] V. Cirpus, A. Arnold, *Z. Anorg. Allg. Chem.* **1995**, *621*, 1197−1204.
[18] N. G. Fernandez, R. Tellgren, I. Olovsson, *Acta Crystallogr., Sect. B* **1990**, *46*, 466−474.
[19] U. Kraatz, in Houben-Weyl, *Methoden der Organischen Chemie* (Ed.: H. Hagemann), Thieme-Verlag Stuttgart, **1983**, vol. E4, p. 1000.
[20] R. Hutchinson, C. T. Mabuni, *J. Labelled Compd. Radiopharm.* **1977**, *13*, 571−574.

Received May 27, 2004
Early View Article
Published Online November 10, 2004

 © 2005 Wiley-VCH Verlag GmbH & Co. KGaA, Weinheim

Rearrangement of the Active Ester Intermediate During HOBt/EDC Amide Coupling

Khaled A. Mahmoud,[a] Yi-Tao Long,[a] Gabriele Schatte,[b] and Heinz-Bernhard Kraatz*[a]

Keywords: Ferrocene / Hydroxybenzotriazole / Amide coupling / Amino acid / Electrochemistry

3-{[1′-(*tert*-Butyloxycarbonylamino)ferrocen-1-yl]carbonyl}-benzotriazole 1-oxide (**3**) has been successfully separated during the synthesis of benzotriazol-1-yl 1′-(*tert*-butyloxycarbonylamino)ferrocene-1-carboxylate (**2**) as an active ester for peptide coupling. The yield of **3** increased by using polar, rather than nonpolar solvents. The two compounds have been fully characterized and studied by X-ray crystallography and spectroscopic methods. The active ester derivative 2 formed a urethane bond with the glycine ethyl ester while the *N*-oxide **3** did not react. The X-ray structural analysis of **3** shows strong intermolecular hydrogen bonding involving the urethane group and the *N*-oxide of an adjacent molecule [N–O···H–N = 2.859(2) Å]. No hydrogen bonding is present in the solid state for compound **2**, while solution studies indicate the presence of intramolecular hydrogen bonding. Both complexes display a quasi-reversible single one-electron oxidation, the halfwave potentials $E_{1/2}$ for **2** and **3** were 672 ± 5 and 591 ± 5 mV, respectively.
(© Wiley-VCH Verlag GmbH & Co. KGaA, 69451 Weinheim, Germany, 2005)

Introduction

1-Hydroxybenzotriazole (HOBt) is widely used in peptide synthesis as an activating agent for the acid component and for its ability to suppress racemization. The intermediate benzotriazole active ester **A** then reacts with an amino group to form the urethane bond.[1] The conversion of **A** into the *N*-oxide isomer **B** was reported.[2,3]

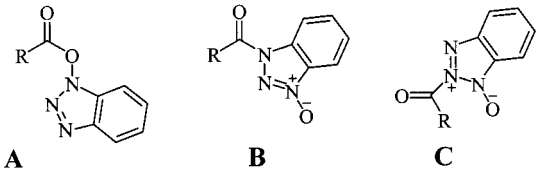

A **B** **C**

The *N*-oxide is favored in polar solvents, while the desired active ester **A** predominates in less-polar solvents.[4] It appears that the active ester **A** is the kinetic product, which is reactive towards rearrangement to the corresponding urethane form **B**.[5] In addition, Davies et al. proposed the intermediacy of isomer **C** to explain enhanced racemization rates for certain amino acid esters.[6] Formation of the *N*-oxide under mild conditions was reported by Lu and coworkers by reacting Os_3 clusters with HOBt.[7] ^{13}C NMR spectroscopy, used to identify the different isomers, confirmed the predominance of the active ester form **A** in DMSO,[8] while acetone stabilized the more polar zwitterionic *N*-oxide.[9] More recently, Carpino reported a detailed investigation into the reactivity of the guanidinium salts HBTU and HATU. It was shown that the *O*-substituted uronium salt is significantly more reactive in peptide coupling reactions than the *N*-substituted guanidinium salt.[10]

In the context of organometallic peptide conjugates, OBt-active esters provide a convenient route to labeling peptides under very mild conditions, which are also readily automated for solid-phase peptide synthesis (SPPS). This was shown by the use of benzotriazolyl ferrocenecarboxylate as a stoichiometric delivery reagent for the redox active ferrocene (Fc) group, or more recently by the use of one-pot reactions involving cobaltocenium carboxylic acid and TBTU and HATU.[11] Whether the active ester is used stoichiometrically or used as an intermediate in a one-pot reaction or during SPPS, there is the potential for lowered incorporation of the organometallic label due to different reaction kinetics. During the preparation and column separation of Fc-peptide conjugates, we along with other groups noticed the appearance of a red Fc-containing material, which also appears to possess an OBt substituent. However, it was not possible to properly identify this material. Given that the main role of OBt active ester intermediates is the preparation of organometallic peptide conjugates, we decided to investigate this in more detail. Here we describe our results of the study into the preparation of the OBt active ester **2** of 1′-(*tert*-butyloxycarbonylamino)ferro-

[a] Department of Chemistry, University of Saskatchewan,
110 Science Place, Saskatoon, SK S7N 5C9, Canada
Fax: (internat.) + 1-306-966-4660
E-mail: kraatz@skyway.usask.ca
[b] Saskatchewan Structural Science Centre, University of Saskatchewan,
Saskatoon, SK S7N 5C9, Canada

cene-1-carboxylic acid and its isomer 3-{[1′-(*tert*-butyloxycarbonylamino)ferrocen-1-yl]carbonyl}benzotriazole 1-oxide (**3**).

Results and Discussion

During the synthesis of the active ester **2**, from 1′-(*tert*-butyloxycarbonylamino)ferrocene-1-carboxylic acid (**1**), in the presence of HOBt and EDC, we prepared and isolated in addition to the desired product **2**, the zwitterionic *N*-oxide **3** (Scheme 1). We have no indication of the formation of the 2-ferrocenylated product.

The two forms are readily separated from each other by chromatography, giving **2** as an orange-red compound and compound **3** as a dark red crystalline compound. The experimental results show that the active ester **2** is the kinetic product, which undergoes rearrangement to the corresponding urethane form.[5] The rearrangement process is phase dependant; in dry dichloromethane the product **3** is obtained in 4% yield while in aqueous acetone the rearrangement is faster producing 11% yield of **3**. Although, we expected higher reactivity according to earlier reports,[10] the electron-withdrawing effect of the *N*-oxide group most likely deactivates **3** with respect to its reactivity with the amino acids. Thus, we did not observe any reactivity with glycine.

Compounds **2** and **3** were characterized by NMR spectroscopy ^{1}H, $^{13}C\{^{1}H\}$, DEPT-135 NMR, HMQC (Heteronuclear Multiple Quantum Correlation), and HMBC (Heteronuclear Multiple Bond Correlation). Table 1 summarizes the complete assignment of the NMR signals for compounds **2** and **3**. It is interesting to note that the signals due to H2, H5 and H2′, H5′ are observed at significantly different chemical shifts, indicating changes in the local environment due to the change in the substituent, which undoubtedly affects both C rings. Changes are also significant in the ^{13}C chemical shifts of the *ipso*-carbon atoms indicating that electronic differences due to the substituents are "seen" by the Fc system. C1 is affected more by the change from ester to amide *N*-oxide than C1′, the *ipso*-C to which the different substituent is attached. Comparing the chemical shifts for the proton H11 in **2** and **3**, this proton is particularly deshielded due to the proximity to the *N*-oxide group in **3**. The NH proton showed broad singlets at $\delta = 6.42$ and 5.75 ppm for **2** and **3**, respectively.

Table 1. Spectroscopic characterization of compounds **2** and **3**

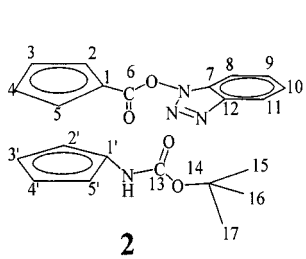

2

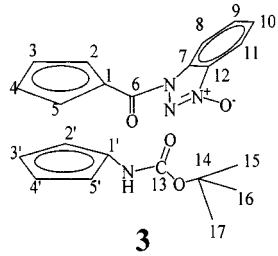

3

Site	^{1}H	^{13}C	HMQC	HMBC	^{1}H	^{13}C	HMQC	HMBC
1′				100.2				98.9
1				65.2				71.6
2′, **5′**	4.71		62.9		4.52		62.7	
2, **5**	5.00		72.3		5.36		74.1	
3′, **4′**	4.08		55.9		3.94		67.0	
3, **4**	4.62		74.7		4.63		74.8	
6		167.5				168.0		
7				129.5				132.4
8	8.02		120.8		7.97		115.7	
9	7.38		125.2		7.49		127.0	
10	7.49		129.1		7.72		133.2	
11	7.45		109.1		8.46		117.3	
12				143.9				133.82
13		153.5				153.5		
14				80.6				80.5
15−**17**	1.27		28.5		1.26		28.5	

Both compounds exhibit a single broad absorbance in the visible region. For compound **2**, $\lambda_{max.} = 453$ nm, while for **3** the band is observed at $\lambda_{max.} = 484$ nm. This bathochromic shift clearly shows electronic coupling of the *N*-oxide OBt with the Fc group. Shifts were also observed for pyridine *N*-oxides (305−333 nm) and quinoline *N*-oxides (> 320 nm) with substituents that are in direct conjugation with the *N*-oxide group, and rationalized in terms of tautomer and resonance contributions. In quinoxaline di-*N*,*N*-oxide shifts are due to intramolecular charge transfer.[12]

The IR spectra of both compounds show two carbonyl bands. For compound **2** a band due to the active ester is observed at 1788 cm^{-1}. This band is absent in compound **3** and is replaced by an amide band at 1688 cm^{-1}. Both compounds exhibit a strong absorption around 1722 cm^{-1}, due to the carbamate carbonyl group on the other Cp ring.

Crystal Structures of 2 and 3: Selected bond lengths and angles for **2** and **3** are given in Table 2. ORTEP views of

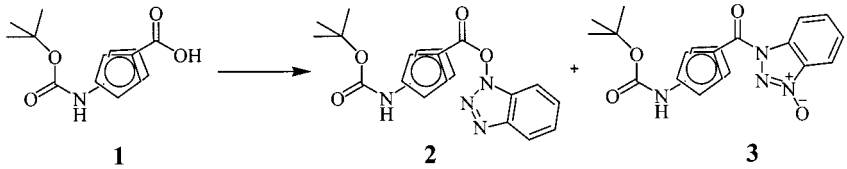

1 **2** **3**

Scheme 1

 © 2005 Wiley-VCH Verlag GmbH & Co. KGaA, Weinheim

Table 2. Relevant bond lengths (Å) and angles (°) for **2** and **3**

	2	**3**
av. Fe(1)−C(Cp1)	2.038(14)	2.039(13)
av. Fe(1)−C(Cp2)	2.043(16)	2.047(12)
C(10)−C(15A)/ C(10)−C(15A)	1.489(9)	1.459(2)
C(15A)−O(11A)/ C(15)−O(11)	1.172(9)	1.210(2)
C(15A)−O(12A)/C(15)−N(11)	1.429(8)	1.426(2)
O(12A)−N(11)	1.358(3)	
N(11)−N(12)	1.342(2)	1.364(2)
N(12)−N(13)	1.302(4)	1.308(2)
N(13)−O(12)		1.2699(19)
C(20)−N(21)	1.411(4)	1.401(2)
N(21)−C(25)	1.349(4)	1.366(2)
C(25)−O(22)	1.350(3)	1.348(2)
C(25)−O(21)	1.207(3)	1.206(2)
C(10)−C(15A)−O(12A)/C(10)−C(15)−N(11)	106.6(6)	119.2(1)
C(10)−C(15)−O(11A)/C(10)−C(15)−O(11)	131.7(6)	125.4(2)
C(20)−N(21)−C(25)	123.7(2)	124.9(1)
N(11)−N(12)−N(13)	106.4(3)	105.5(1)
N(21)−C(25)−O(22)	109.6(2)	107.3(1)
N(21)−C(25)−O(21)	124.8(3)	126.0(1)

these complexes are presented in Figures 1 and 2, respectively.

Compound **2** crystallizes in the polar orthorhombic space group $Pna2_1$ as a twinned racemic crystal, whereas compound **3** crystallizes in the monoclinic space group $P2_1/c$. In both complexes, the Cp rings are virtually parallel to each other [Cp−Fe−Cp angles: **2**: 2.1(3)°; **3:** 2.98(14)°]. The distances of the Fe atoms to the carbon atoms of the Cp rings are in the expected range in comparison to other ferrocene structures.[13]

For compound **2**, the bond lengths and angles of the Cp-ester-benzotriazole moiety are almost identical to those reported for Fc−CO−OBt.[14,15] The ester bond to the benzotriazole moiety in **2** is long [1.429(8) Å], as expected. The benzotriazole (Bt) substituent is rotated out of the ester plane by only 80.8(2)°, compared to 96.56(6)° in Fc−CO−OBt.[15] In the case of Fc−CO−OBt, this does not permit the efficient interaction between the two π-systems,[15] but increases reactivity of the carbonyl C atom towards external nucleophiles and therefore allows a faster reaction of the ester. A similar observation was made for (*S*)-3-(O^{γ}-methyl,N^{α}-triphenylmethylglutamyl)benzotriazole 1-oxide,[16] which bears the acyl and OBt groups on the same plane, resulting in a slower reactivity towards amines compared to the OBt active ester.[17] 3-(N^{α}-Tritylmethionyl)benzotriazole 1-oxide also exhibits the same structural features with coplanar OBt and acyl groups.[18] The geometry and conformation for a variety of ester and amide derivatives of HOBt and HOAt have been reported.[19,20] A more recent investigation into the reactivity of HATU showed that the *O*-substituted uronium salt is significantly more reactive in peptide coupling reactions than the *N*-substituted guanidinium salt,[10] in line with earlier investigations on OBt derivatives. In compound **3**, the planar OBt *N*-oxide, the urethane and the Cp ring to which it is attached are not coplanar [OBt *N*-oxide/Cp, 16.5(1)°; amide/Cp, 18.9(1)°]. Just like the parent benzotriazole-1-oxide and hydroxybenzotriazole, the heterocycle in compound **3** is essentially flat. In the *N*-oxide, the N−N bond lengths are shortened compared to hydroxybenzotriazole. For compound **3**, the N−N bond lengths in the heterocycle are non-equidistant. The distance between the N(O)−N are shorter and the distance N(12)−N(13) of 1.3084(19) Å indicates significant double bond character between the two nitrogen atoms. Similar observations were made have been made for (*S*)-3-(O^{γ}-methyl,N^{α}-triphenylmethylglutamyl)benzotriazole 1-oxide and 3-(N^{α}-tritylmethionyl)benzotriazole 1-oxide. As seen from Table 3, the urethane moieties in **2** and **3** are not coplanar with the Cp rings. The observed ω angle for **2** is close to the ideal value for a 1,2′ conformation (−72°), while **3** crystallizes in the 1,1′-conformation with $\omega = 13.3(8)°$.

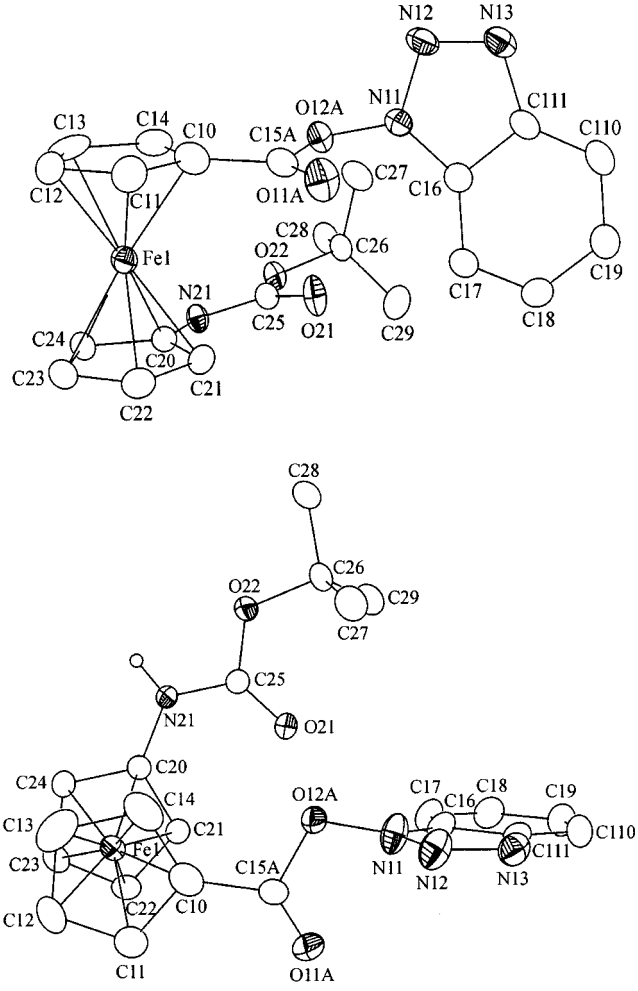

Figure 1. ORTEP drawing of compound **2** (30% probability); H atoms omitted for clarity; side-on view and view down the Cp−Fe−Cp axis to visualize the 1,2′-conformation of the Fc group

There is no hydrogen bonding present between adjacent molecules of **2**. The amide proton does not point towards the Bt substituent. In contrast, hydrogen bonding is observed in the structure of compound **3** between the oxygen

 © 2005 Wiley-VCH Verlag GmbH & Co. KGaA, Weinheim

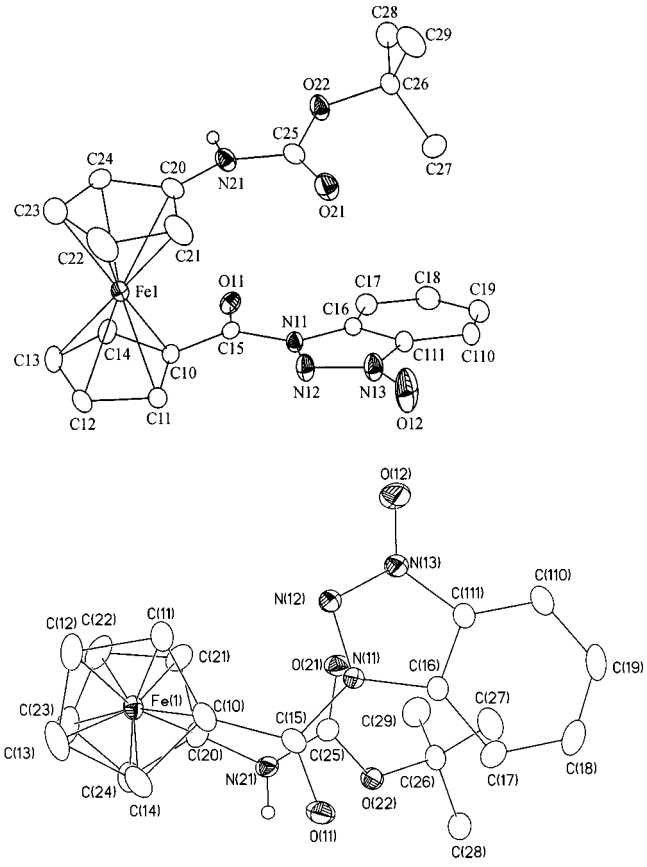

Figure 2. ORTEP drawing of compound **3** (30% probability); H atoms omitted for clarity; side-view and view down the Cp−Fe−Cp axis to show the 1,1′-conformation of the Fc system

Table 3. Torsions angles (°) for **2** and **3**

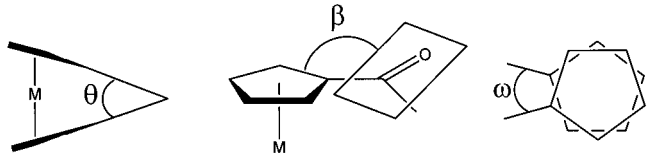

Angle	**2**	**3**
θ[a]	2.1(3)	2.98(14)
β[b]	5.0(7) [C(*ipso*)−C=O] / 12.3(2) [N−C=O]	18.8(2) [C(*ipso*)-C=O] / 18.9(1) [N−C=O]
ω[c]	−70.8(8)	13.3(8)

[a] The dihedral angle between two Cp rings. [b] The dihedral angle between the plane of the Cp ring and the C(*ipso*)C=O bond or between the plane of the Cp ring and the N−C=O bond. [c] The torsion angle is defined as C(*ipso*)−Cp(centroid)−C(*ipso*).

atom attached to one of the nitrogen atoms of the Bt substituent, carrying a partial negative charge, and the amide proton in an adjacent molecule. The O(12)···N(21)* bond lengths of 2.859(2) Å indicates the presence of strong hydrogen bonding in the solid state.

The packing arrangements in **2** and **3** are very different (Figure 3). In compound **3**, the Fc groups are aligned with the NO groups of the Bt group in the adjacent molecules forming strands along the *c*-axis. In **2**, the molecules form a strand-like arrangement along the 2_1-axis with the Fc groups adjacent to each other.

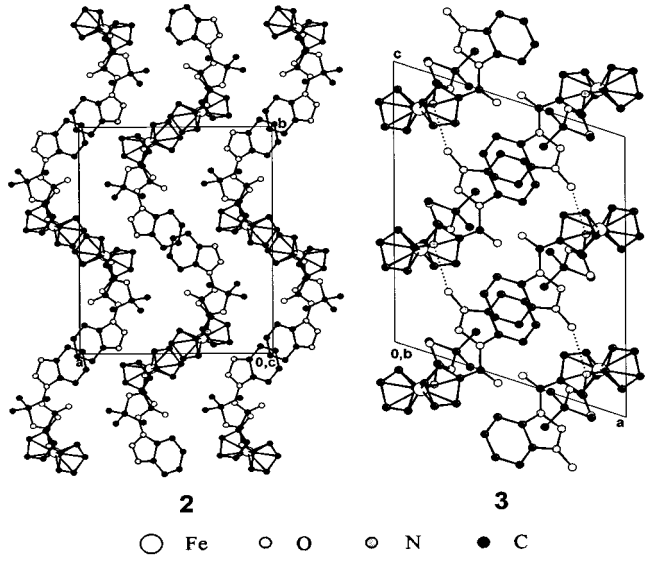

Figure 3. Packing diagrams for compounds **2** and **3**

Heinze recently[14] reported the structural properties of the acetylamino-analogue of compound **2**. In the solid state, the molecule displayed significant intramolecular hydrogen bonding. The Boc derivative **2** on the other hand, does not display any intramolecular hydrogen bonding involving the urethane NH group. Compound **3** on the other hand displays intermolecular hydrogen bonding in the solid state. This raises the question whether the presence of the Boc-

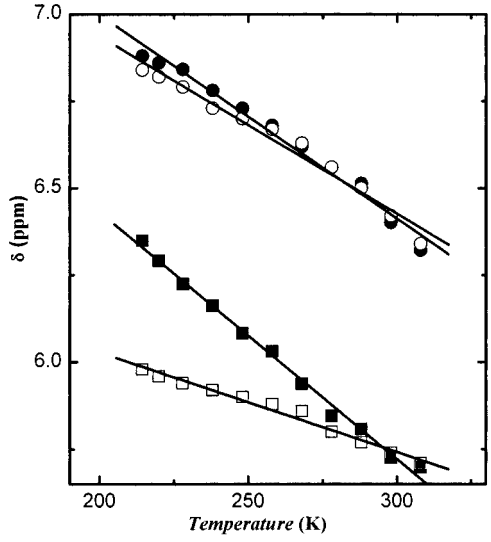

Figure 4. Temperature dependence of the chemical shifts for NH signals of compounds **2** (circles), **3** (squares) in $CDCl_3$ [open symbols indicate 1 mM; solid symbols indicate 50 mM]

 © 2005 Wiley-VCH Verlag GmbH & Co. KGaA, Weinheim

protecting group can account for the differences in H-bonding behavior in the solid-state structures. Is the lack of intramolecular hydrogen bonding in compound **2** due to the spatial requirement of the bulky Boc carbamate group? In order to answer these questions, we decided to investigate the hydrogen-bonding behavior of compounds **2** and **3** in solution. Variable-temperature ^{1}H NMR studies of compounds **2** and **3**, recorded at 1 and 50 mM in $CDCl_3$ in the temperature range 215 and 308 K, showed a significant difference in the NH chemical shift between the two compounds with the temperature variation. A plot of $\Delta\delta$ versus T is shown in Figure 4. For compound **2**, the chemical shift of the amide NH was affected by temperature but the temperature dependence was independent of concentration (1 mM: -5.1 ppb K^{-1}; 50 mM: -6.4 ppb K^{-1}).

In contrast, compound **3** displayed a concentration dependent temperature behavior (1 mM: -2.8 ppb K^{-1}; 50 mM: -7.1 ppb K^{-1}), indicating the presence of intermolecular hydrogen bonding in compound **3** in solution. The temperature behavior of the NH chemical shift indicates the presence of intramolecular hydrogen bonding in compound **2** in solution.[11,21] However, the crystal structure does not show any hydrogen bonding, presumably as a result of crystal packing. Interestingly, the Cp protons in compound **2** undergo some temperature dependent changes, as is shown in Figure 5. The signals due to H2 and H5 in compound **2** are very broad at low temperatures (215−220 K) but appear at 228 K, and gradually sharpen. Heinze's Ac derivative displays a similar temperature behavior, which was interpreted as a possible interconversion between two ferrocenyl rotamers of the molecule. Our results suggest that a similar equilibrium may also exist for compound **2**. The Cp region of compound **3** does not change with temperature (Figure 6).

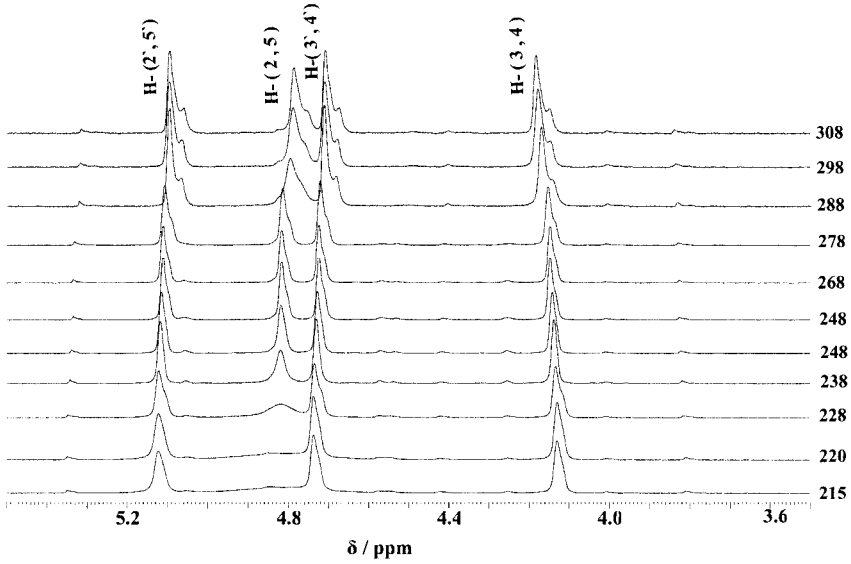

Figure 5. Variable temperature ^{1}H NMR spectra of **2** (50 mM, $CHCl_3$) in a region of 215−308 K

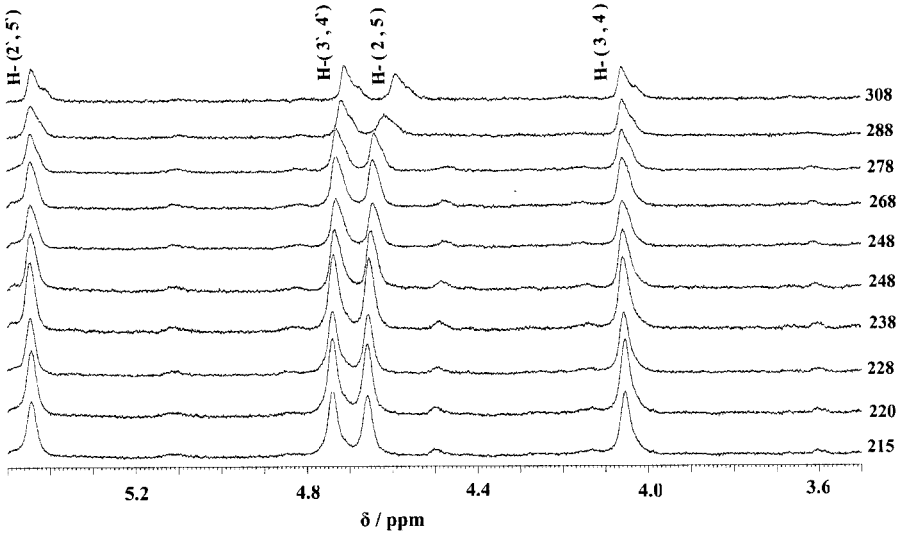

Figure 6. Variable temperature ^{1}H NMR spectra of **3** (50 mM, $CHCl_3$) in a region of 215−308 K

 © 2005 Wiley-VCH Verlag GmbH & Co. KGaA, Weinheim

Figure 7 shows the electrochemical behavior of compounds **2** and **3**. Both compounds show a quasi-reversible single one-electron oxidation. The separation between oxidative and reductive peak potentials ΔE_p is about 96±5 mV for **2** (87±5 mV for **3**). The ratio of peak currents is close to unity for both compounds (**2**: $i_c/i_a = 1$; **3**: $i_c/i_a = 1.05$). As expected for *N*- and *O*-ferrocenylated systems, the halfwave potentials $E_{1/2}$ for **2** and **3** are significantly different. While $E_{1/2}$ = 672 ± 5 mV for the active ester **2**, the $E_{1/2}$ = 591 ± 5 mV for the *N*-oxide **3**.

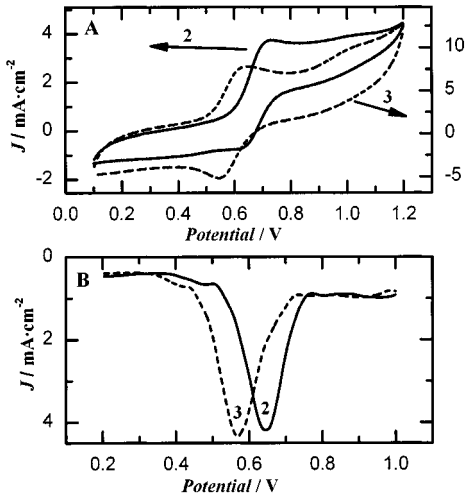

Figure 7. Electrochemical study of compounds **2** and **3** in CH_3CN/0.1 M TBAP: **A** shows the cyclic voltammetry at a scan rate of 100 mV/s (ΔE_p for the Fc/Fc^+ couple under identical conditions was 68 ±5 mV); **B** shows the differential pulse voltammetry at a scan rate 10 mV/s; for **2**: DPV, E_p = 643 ± 5 mV; for **3**, E_p = 566 ± 5 mV

Conclusion

In summary, we have prepared the two ferrocene−amino acid derivatives **2** and **3** and report their full characterization. Initially, compound **3** was obtained as a by-product in the preparation of the desired active ester. Reports on HATU active esters show this to be a common reaction in peptide synthesis. Importantly, this by-product was not reported in ferrocene chemistry. Given the importance of the Fc-OBt active ester intermediates in the preparation of Fc-bioconjugates and as a potential intermediate for the stepwise synthesis of ferrocenamide-based polymers, our finding is significant. Importantly, the reactivity towards peptide coupling is different. Whereas, the active ester derivative **2** undergoes amide bond formation with glycine ethyl ester and other amino acids and peptides,[22] the *N*-oxide **3** does not react. This is in contrast with earlier reports on the reactivity of HATU *N*-oxide derivatives, which were shown to undergo a slow conversion into the desired amide.

Experimental Section

General Procedure: The syntheses of 1′-(*tert*-butyloxycarbonylamino)ferrocene-1-carboxylic acid (**1**) was carried out using the published procedure.[23] All syntheses were carried out in air unless otherwise indicated. CH_2Cl_2 (BDH; ACS grade) used for synthesis was dried (CaH_2) and distilled prior to use. $CDCl_3$ (Aldrich) was dried (CaH_2), and stored over molecular sieves (8−12 mesh; 4 Å effective pore size; Fisher) before use. EDC·HCl, HOBt (Quantum), $MgSO_4$, and $NaHCO_3$ (VWR) were used as received. For column chromatography, a column with a width of 2.7 cm (ID) and a length of 45 cm was packed 18−22 cm high with 230−400 mesh silica gel (VWR). For TLC, aluminum plates coated with silica gel 60 F_{254} (EM Science) were used. NMR spectra were recorded with a Bruker Avance-500 spectrometer using a 5-mm broadband probe operating at 500.134 MHz (^1H) and 125.766 MHz ($^{13}C\{^1H\}$). Peak positions in both ^1H and ^{13}C spectra are reported in ppm relative to TMS. The ^1H NMR spectra are referenced to the residual $CHCl_3$ signal at δ 7.27. All $^{13}C\{^1H\}$ spectra are referenced to the $CDCl_3$ signal at δ = 77.23 ppm. Mass spectrometry was carried out with a VG Analytical 70/20 VSE instrument. Infrared spectra were obtained with a Perkin−Elmer model 1605 FT-IR.

Preparation of (Benzotriazol-1-yl) 1′-(*tert*-Butyloxycarbonylamino)-ferrocene-1-carboxylate (2) and 3-{[1′-(*tert*-Butyloxycarbonylamino)ferrocen-1-yl]carbonyl}benzotriazole 1-Oxide (3). Procedure A: Solid HOBt (4.05 mmol, 0.62 g) and EDC·HCl (4.05 mmol, 0.78 g) were added to a solution of 1′-(*tert*-butyloxycarbonyamino)-ferrocene-1-carboxylic acid (**1**) (3.68 mmol, 1.27 g) in CH_2Cl_2 (40 mL),. The reaction mixture was stirred at room temperature (20 °C) for 2 h and then treated with an aqueous solution of saturated $NaHCO_3$, citric acid (10%), and water. The organic phase was separated and dried with Na_2SO_4, and evaporated to dryness under reduced pressure. The crude product was purified by flash column chromatography (SiO_2, EthOAc/hexanes, 1:2) to give dark orange crystals of compound **2** (1.32 g, 78%) (R_f = 0.74), followed by red crystals of compound **3** (68 mg, 4%) (R_f = 0.42). **Procedure B:** The same mixture as described under **A** was stirred at room temperature for two hours in aqueous acetone (30 mL). The reaction mixture was dried under reduced pressure and redissolved in CH_2Cl_2. After the purification (vide supra), compounds **2** and **3** were obtained in yields of (1.15 g, 64%) and (180 mg, 11%), respectively.

Characterization of 2: FAB-MS (*m*/*z*): calcd. for $C_{22}H_{22}FeN_4O_4$ [M + 1]$^+$: 463.2; found 463.1. FT-IR (KBr (cm^{-1}): $\tilde{\nu}$ = 3322 (m, N−H), 1788, 1723 (s, C=O). UV/Vis (MeCN): λ (ε, $L\cdot mol^{-1}\cdot cm^{-1}$) = 453 nm (706). ^1H NMR ($CDCl_3$): δ = 8.02 (d, $J_{H,H}$ = 8.5 Hz, 1 H, *Bt*-ArH), 7.49 (t, $J_{H,H}$ = 15.0 Hz, 1 H, *Bt*-ArH), 7.45 (d, $J_{H,H}$ = 8.2 Hz, 1 H, *Bt*-ArH), 7.38 (t, $J_{H,H}$ = 15.2 Hz, 1 H, *Bt*-ArH), 6.42 (br. s, 1 H, NH), 5.00 (s, 2 H, H-2 and H-5, Fc), 4.71 (s, 2 H, H-2′ and H-5′, Fc), 4.62 (s, 2 H, H-3 and H-4, Fc), 4.08 (s, 2 H, H-3′ and H-4′, Fc), 1.27 [s, 9 H, $C(CH_3)_3$] ppm. $^{13}C\{^1H\}$ NMR ($CDCl_3$): δ = 167.5 (s, *C*OON-Bt), 153.5 [s, $COOC(CH_3)_3$], 143.9, 129.5 (quaternary C of Ar Bt), 129.1, 125.2, 120.8, 109.1 (s, Ar Bt), 100.2 (C-1′, Fc), 80.58 [$C(CH_3)_3$], 74.7 (C-3 and C-4, Fc), 72.3 (C-2 and C-5, Fc), 66.9 (C-3′ and C-4′, Fc), 65.2 (C-1, Fc), 62.3 (C-2′ and C-5′, Fc), 28.5 [$C(CH_3)_3$] ppm.

Characterization of 3: FAB-MS (*m*/*z*): calcd. for $C_{22}H_{22}FeN_4O_4$ [M + 1]$^+$: 463.2; found 463.1. FT-IR (KBr (cm^{-1}): $\tilde{\nu}$ = 3310 (m, N−H), 1721, 1688 (s, C=O). UV/Vis (MeCN): λ (ε, $L\cdot mol^{-1}\cdot cm^{-1}$) = 484 nm (1200). ^1H NMR ($CDCl_3$): δ = 8.46 (d, $J_{H,H}$ = 8.5 Hz, 1 H, *Bt*-ArH), 7.97 (d, $J_{H,H}$ = 8.4 Hz, 1 H, *Bt*-ArH), 7.72 (t, $J_{H,H}$ = 15.5 Hz, 1 H, *Bt*-ArH), 7.49 (t, $J_{H,H}$ = 17.3 Hz, 1 H, *Bt*-ArH), 5.75 (br. s, 1 H, NH), 5.36 (s, 2 H, H-2 and H-5, Fc), 4.63 (s, 2 H, H-3and H-4, Fc), 4.52 (s, 2 H, H-2′ and H-5′, Fc), 3.94 (s, 2 H, H-3′ and H-4′, Fc), 1.26 [s, 9 H, $C(CH_3)_3$] ppm. $^{13}C\{^1H\}$ NMR ($CDCl_3$): δ = 168.0 (s, *C*ON-Bt), 153.5 [s, $COO(CH_3)_3$], 133.8, 132.4 (quaternary C of Ar Bt), 133.2, 127.0,

 © 2005 Wiley-VCH Verlag GmbH & Co. KGaA, Weinheim

Table 4. X-ray crystallographic data of complexes **2** and **3**

	2	**3**
Formula	$C_{22}H_{22}FeN_4O_4$	$C_{22}H_{22}FeN_4O_4$
Molecular mass	462.29	462.29
Crystal dimensions (mm)	0.15 × 0.15 × 0.10	0.25 × 0.20 × 0.13
Crystal system	Orthorhombic	monoclinic
Space group (no.)	$Pna2_1$	$P2_1/c$ (14)
a (Å)	12.6580(2)	11.8140(2)
b (Å)	17.2760(3)	12.0982(2)
c (Å)	9.7170(5)	15.4850(3)
β (Å)	90	110.9844(8)
Cell volume (Å^3)	2124.91(2)	2066.45(6)
Molecular units per cell	4	4
μ (mm^{-1})	0.746	0.768
Density (calcd.) (g·cm^{-3})	1.445	1.486
T (K)	173	173
Scan range (2θ)	1.99−24.70	3.28−30.06
Scan speed (s frame^{-1})	135	40
Measured reflections	3462	11239
Unique reflections	3462	6005
Obsd. reflections ($I = 2\sigma$)	3187	4632
Parameters refined	312	286
Max. residual electron density (Å^{-3})	0.297 / −0.211	0.357/-0.374
Agreement factors[a][b] (F^2 refinement)	R_1 = 3.27%; R_w = 6.87%	R_1 = 3.90%; R_w = 9.05%

[a] $R_1 = [\Sigma||F_o| - |F_c||]/[\Sigma|F_o|]$ for $[I > 2\sigma(I)]$. [b] $wR_2 = \{[\Sigma w(F_o^2 - F_c^2)^2]/[\Sigma w(F_o^2)^2]\}^{1/2}$.

117.3, 115.7 (Ar Bt), 98.9 (C-1′, Fc), 80.5 [$C(CH_3)_3$], 74.8 (C-3 and C-4, Fc), 74.1 (C-2 and C-5, Fc), 71.6 (C-1, Fc), 67.0 (C-3′ and C-4′, Fc), 62.7 (C-2′ and C-5′, Fc), 28.5 [$C(CH_3)_3$] ppm.

Attempted Coupling of 3: A solution of H-Gly-OEt·HCl (0.24 mmol, 0.03 g) and Et_3N (0.4 mL) in dry CH_2Cl_2 (5 mL) was added to a stirring solution of **3** (0.22 mmol, 0.10 g) in dry CH_2Cl_2 (10 mL). The progress of the reaction was followed by TLC (EtOAc/hexanes/MeOH, 4:5:1). No product was observed after 24 h.

Electrochemical Measurements: The electrochemical experiments were carried out at room temperature using a CV-50 W voltammetric analyzer. A gold electrode (diameter 50 μm) was used as working electrode. 1 mM solutions of compounds **2** and **3** were prepared in 0.1 M tetrabutylammonium perchlorate (TBAP) solution in a CH_3CN. The measurements carried out at a low scan rate of 100, 10 mV/s for cyclic voltammetry (CV) and differential pulse voltammetry (DPV), respectively. A platinum wire (1 mm) was used as the counter electrode and a Ag/AgCl (BAS) was used a the reference electrode. The $E_{1/2}$ of the Fc/Fc^+ couple under the experimental conditions is 448(±5) mV (vs. Ag/AgCl).

X-ray Crystallography: Suitable crystals of compounds **2** (orange plate-like crystal; 0.15 × 0.15 × 0.10 mm) were obtained from an ether-layered solution of the compounds in chloroform, while **3** (dark red plate-like crystal; 0.25 × 0.20 × 0.13 mm) was obtained by slow evaporation from an ethyl acetate/hexane(3:1) solvent mixture. All measurements were made with a Nonius KappaCCD 4-Circle Kappa FR540C diffractometer using graphite-monochromated Mo-K_α radiation (λ = 0.71073 Å) at −100 °C. An initial orientation matrix and cell was determined from 10 frames using φ scans.[24] Data were measured using φ- and ω-scans.[24] The data were processed using the standard Nonius software.[25] The structures were solved by direct methods (**2**: SIR-97; **3**: SHELXS-97)[26,27] and refined by full-matrix least-squares methods on F^2 with SHELXL-97−2.[28] The non-hydrogen atoms were refined anisotropically. Hydrogen atoms were included at geometrically idealized positions (C−H bond lengths 0.95/0.99 Å; N−H bond lengths 0.88 Å) and were not refined. The isotropic thermal parameters of the hydrogen atoms were fixed at 1.2 times that of the preceding carbon or nitrogen atom. The carbon and oxygen atoms of one −C(O)O unit [labeled as C(15A), O(11A), O(12A), C(15B), O(11B), O(12B)] in **2** were disordered over two positions with site occupancy factors of 0.825(5) and 0.175(5). The refined absolute structure parameter [0.552(18)] for **2** was neither unity nor nil and was used as the scale parameter in the racemic twin refinement. The hydrogen atom at nitrogen atom N(21) in **3** was located from the Fourier difference map. Its coordinates were allowed to refine, whereas its isotropic thermal parameter was fixed at 1.2 times that of the preceding nitrogen atom. Data relating to the structure determination are presented in Table 4. CCDC-241248 (**2**), -236850 (**3**) contains the supplementary crystallographic data for this paper. These data can be obtained free of charge at www.ccdc.cam.ac.uk/conts/retrieving.html [or from the Cambridge Crystallographic Data Centre, 12 Union Road, Cambridge CB2 1EZ, UK; Fax: (internat.) + 44-1223-336-033; E-mail: deposit@ccdc.cam.ac.uk].

Acknowledgments

Financial support from NSERC, CFI and SIF is gratefully acknowledged. H.-B. K. is the Canada Research Chair in Biomaterials. We are grateful to the Saskatchewan Structure Science Center (SSSC) for providing access to all necessary instrumentation. Ken Thoms, Department of Chemistry, University of Saskatchewan, is also acknowledged for carrying out the MS experiments.

[1] W. Konig, R. Geiger, *Chem. Ber.* **1970**, *103*, 788.
[2] S. I. Murahashi, H. Mitsui, T. Watanabe, S. I. Zenki, *Tetrahedron Lett.* **1983**, *24*, 1049.

 © 2005 Wiley-VCH Verlag GmbH & Co. KGaA, Weinheim

[3] R. Bosch, G. Jung, W. Winter, *Acta Chyst.* **1983**, *C39*, 1089.
[4] F. T. Boyle, R. A. Y. Jones, *J. Chem. Soc., Perkin Trans.* **1973**, *2*, 160.
[5] J. Singh, R. Fox, M. Wong, T. P. Kissick, J. l. Moniot, *J. Org. Chem.* **1988**, *53*, 205.
[6] J. S. Davies, A. K. Mohammed, *J. Chem. Soc., Perkin Trans.* **1981**, *1*, 2982.
[7] K. Lu, S. Kumaresan, Y. Wen, J. R. Hwu, *Organometallics* **1994**, *13*, 3170.
[8] F. Alain, J. Elguero, A. F. Hegarty, D. G. McCarthy, *Org. Magn. Reson.* **1980**, *13*, 339.
[9] E. Anders, A. R. Katritzky, N. Malhotra, J. Stevens, *J. Org. Chem.* **1992**, *57*, 3698.
[10] L. A. Carpino, H. Imazumi, A. El-Faham, *Angew. Chem. Int. Ed.* **2002**, *41*, 441.
[11] D. R. v. Staveren, T. Weyhermuller, N. Metzler-Nolte, *Dalton Trans.* **2003**, 210.
[12] V. P. Andreev, A. V. Ryzhakov, *Khim. Geterotsikl. Soedin.* **1993**, *12*, 1662.
[13] T. Okamura, K. Sakauye, N. Ueyama, A. Nakamura, *Inorg. Chem.* **1998**, *37*, 6731.
[14] K. Heinze, M. Schlenker, *Eur. J. Inorg. Chem.* **2004**, 2053.
[15] H.-B. Kraatz, J. Lusztyk, G. D. Enright, *Inorg. Chem.* **1997**, *36*, 2400.
[16] P. Mamos, D. Papaioannou, C. Kavounis, V. Nastopoulos, *Acta Crystallogr., Sect. B* **1997**, *53*, 1973.
[17] K. Barlos, D. Papaioannou, D. Theodoropoulos, *Int. J. Peptide Protein Res.* **1984**, *23*, 300.
[18] K. Barlos, D. Papaioannou, S. Voliotis, R. Prewo, J. Bieri, *J. Org. Chem.* **1985**, *50*, 696.
[19] M. Crisma, G. Valle, V. Moretto, F. Formaggio, C. Toniolo, *Lett. Pept. Sci.* **1998**, *5*, 247.
[20] C. Toniolo, M. Crisma, F. Formaggio, *Biopolymers (Pept. Sci.)* **1996**, *40*, 627.
[21] E. S. Stevens, N. Sugawara, G. M. Bonora, C. Toniolo, *J. Am. Chem. Soc.* **1980**, *102*, 7048.
[22] N. Metzler-Nolte, private communication.
[23] L. Barisic, V. Kovac, *Croat. Chem. Acta* **2002**, *75*, 199.
[24] COLLECT data collection software, N. B.V., **1998**.
[25] H. D. SCALEPACK, W. M. v1.96: Z. Otwinowski, *Processing of X-ray Diffraction Data Collected in Oscillation Mode, Methods in Enzymology*, vol. 276 (Macromolecular Crystallography, part A) (Eds.: C. W. Carter, Jr., R. M., Sweet); Academic Press, San Diego, CA, **1997**.
[26] A. Alatomare, M. C. Burla, M. Camalli, G. L. Cascarano, C. Giacovazzo, A. Guagliardi, A. G. G. Moliterni, G. Polidori, R. Spagna, *J. Appl. Crystallogr.* **1999**, *32*, 115.
[27] G. M. Sheldrick, *SHELXS-97*, University of Göttingen, Göttingen, Germany, **1997**.
[28] G. M. Sheldrick, Program for the Solution of Crystal Structures; University of Göttingen, Göttingen, Germany, **1997**.

Received June 10, 2004
Early View Article
Published Online November 10, 2004

Columnar Mesomorphism in Hexacatenar Tetrahedral (2,2′-Bipyridine)zinc Complexes and Homologous Palladium Derivatives

Giovanna Barberio,[a] Anna Bellusci,[a] Alessandra Crispini,[a] Mauro Ghedini,[a] Attilio Golemme,[a] Piotr Prus,[a] and Daniela Pucci*[a]

Keywords: Bipyridine ligands / Zinc / Palladium / Metallomesogens / Columnar structures

The synthesis and characterisation of novel liquid crystals which display columnar mesomorphism induced upon complexation of a series of nonmesomorphic hexacatenar 4,4′-disubstituted 2,2′-bipyridines (**L^n**) are reported. The introduction of different metal centres (Zn, Pd) causes the appearance of mesomorphism in all complexes regardless of the geometry around the metal ion. We therefore report the first examples of mesomorphism in tetrahedral zinc derivatives. The nature of the columnar phases is related to the self-assembly of the half-disc shaped [**L^{n}MCl$_2$**] (M = Zn, Pd) complexes into full disc-shaped supramolecules. The molecular organisation in the mesophase is mainly driven by intermolecular attractive interactions, as shown by the crystal structure of the model compound [**LPdCl$_2$**]. Preliminary measurements of photoconductivity have been performed on samples of [**L^{n}MCl$_2$**] complexes doped with C_{60} to increase absorption. Promising results were obtained.

(© Wiley-VCH Verlag GmbH & Co. KGaA, 69451 Weinheim, Germany, 2005)

Introduction

The role of metal ions in the formation of molecular motifs and intermolecular interactions, which are unapproachable for organic liquid crystals and promote mesomorphism in nonmesogenic ligands, continues to make metallomesogens promising materials with novel and interesting properties.[1−6] In particular, the design of suitable metal-ligand combinations represents a challenge for obtaining new functional liquid crystalline materials by molecular self-assemblies.[7]

In this context, we recently reported[8] the synthesis of a series of nonmesomorphic dialkyl 2,2′-bipyridine-4,4′-dicarboxylates for which the complexation with various metal salts resulted in [(Bipy)MX$_2$] (M = Pd, Pt, Ni, Zn) species which self-assemble in dimers built up from attractive intermolecular interactions. This is described by the complementary shape approach.[9]

Due to the overall shape of the stacked units, these complexes exhibit lamellar mesomorphism which depends mostly on the geometry of the metal centre. In fact, the zinc homologues do not exhibit liquid crystalline properties due to their tetrahedral coordination. In continuation of our previous studies on the relationship between molecular structures, symmetry prerequisites and mesomorphism, we have been interested in the design of a further class of 4,4′-disubstituted 2,2′-bipyridines in order to induce, upon complexation, a molecular disc shape and columnar mesomorphism in the corresponding supramolecular metal aggregates. Moreover, since discotic liquid crystal systems have recently gained interest because of new applications in molecular electronics and optoelectronics,[10−12] we wanted to investigate if the design of supramolecular disc-like metallomesogens, with a long-range molecular order, would be advantageous for the enhancement of pre-selected properties such as charge transport or luminescence. The attractiveness of these systems is also demonstrated by the fact that during the preparation of the current article an apparently similar study was reported.[13] However, although the same methodology was used for inducing columnar mesophases in hemi-disc like complexes, Donnio et al. carried out their studies on terdentate ligands such as the 2,6-bis[3′,4′,5′-tri(alkoxy)phenyliminomethyl]pyridines and consequently the discrete building blocks show very different geometric features.

In the present work we report the synthesis of a series of hexacatenar 4,4′-disubstituted 2,2′-bipyridine ligands and related *cis*-dichloro zinc and palladium derivatives. The single-crystal X-ray structure of the palladium model complex [**LPdCl$_2$**] is also reported and discussed. The liquid crystalline properties of all [**L^{n}MCl$_2$**] (M = Zn, Pd) complexes which, in contrast to the free ligands, exhibit columnar mesomorphism are also described. It should be noted that rigid tetrahedral molecules usually seem to prevent mesophase formation[14] and the only examples of mesomorphic zinc derivatives to date exhibit either a trigonal-bipyramidal geometry with dithiobenzoate[1] or terpyridine

[a] LASCAMM, Unità INSTM della Calabria, Dipartimento di Chimica, Università della Calabria,
87030, Arcavacata (CS), Italy
Fax: (internat.) + 39-0984-492066
E-mail: d.pucci@unical.it

ligands[13,15] or a square-planar geometry when the metal centre is incorporated in a porphyrin or a phthalocyanine core.[1,16] Moreover, preliminary measurements of photoconductivity have been performed on samples of [$\mathbf{L^nMCl_2}$] doped with C_{60} to increase absorption. Promising results were obtained.

Results and Discussion

Synthesis and Characterisation

The hexacatenar $\mathbf{L^n}$ ligands (where n denotes the number of carbon atoms in the alkoxy chains) were prepared as white solids, in high yields, from the reaction of the 4,4′-bis(hydroxymethyl)-2,2′-bipyridine with the appropriate 3,4,5-trialkoxy-substituted benzoic acid using a DCC-PPY esterification (Scheme 1). The model ligand **L**, without the six alkoxy chains grafted on the peripherical phenyl rings, has been synthesised in an analogous manner by treating the 4,4′-bis(hydroxymethyl)-2,2′-bipyridine with benzoic acid.

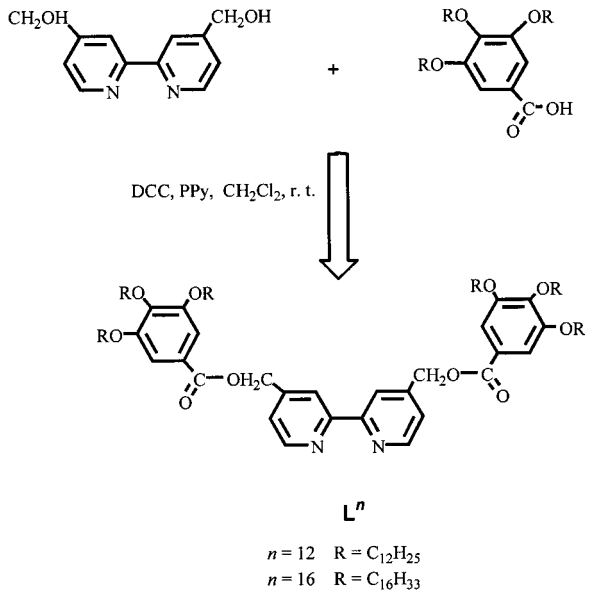

Scheme 1. Synthetic route to the hexacatenar $\mathbf{L^n}$ ligands

The hexacatenar complexes [$\mathbf{L^nMCl_2}$] as well as the model complexes [$\mathbf{LMCl_2}$], were prepared by treatment of an equimolar amount of the appropriate ligand with $ZnCl_2$ (in dichloromethane at room temperature) or $[Pd(PhCN)_2Cl_2]$ (in chloroform at reflux), respectively.

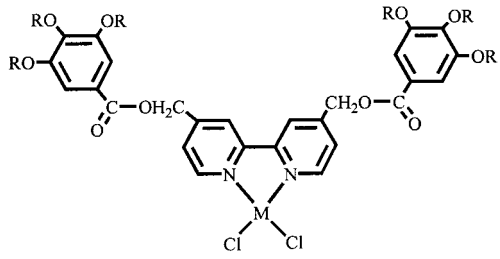

[$\mathbf{L^nMCl_2}$]
M = Zn, Pd

The structures and purities of all the ligands and complexes were confirmed by IR and ^{1}H NMR spectroscopy and elemental analyses. In the ^{1}H NMR spectra of these complexes the H3 and H6 bipyridinic proton resonances shifted (by about 0.3 ppm) up and down field with respect to their organic precursors. These observations confirmed the coordination of the bipyridines to the metal fragments.

Single-Crystal X-ray Diffraction of [$\mathbf{LPdCl_2}$]

The [$\mathbf{LPdCl_2}$] complex was synthesised and then structurally characterised with the explicit intention of giving more insight into the molecular organisation in the 3D space of these new (2,2′-bipyridine)metal complexes in which the 4,4′-disubstituents are now different from the carboxylates with long alkyl chains already discussed in a previous paper.[8b] Moreover, in the absence of diffraction-quality crystals for any of the long-chain homologues, [$\mathbf{LPdCl_2}$] could be considered as a model compound and its molecular organisation taken as being representative for the discussion of the liquid-crystalline states of similar mesogenic complexes. The structure of [$\mathbf{LPdCl_2}$] is shown in Figure 1 and a selection of bond lengths and angles is reported in Table 1.

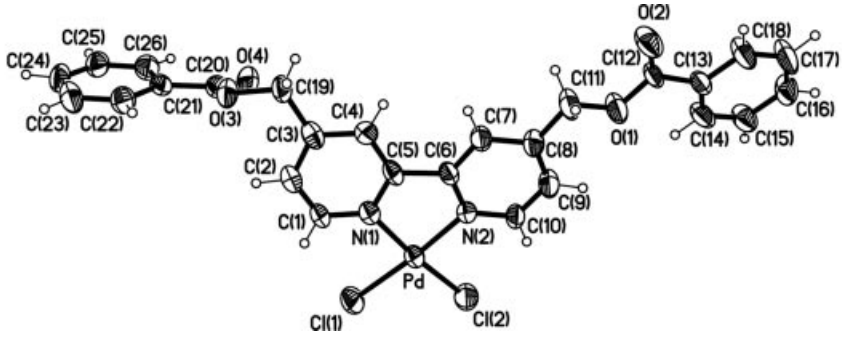

Figure 1. Molecular structure and atomic labelling scheme (50% probability thermal ellipsoids) of complex [$\mathbf{LPdCl_2}$]

 © 2005 Wiley-VCH Verlag GmbH & Co. KGaA, Weinheim

Table 1. Selected bond lengths (Å) and angles (°) for complex **[LPdCl$_2$]**

Pd−N(1)	2.023(5)	Pd−N(2)	2.034(4)
Pd−Cl(1)	2.283(2)	Pd−Cl(2)	2.283(2)
N(1)−Pd−N(2)	80.9(2)	Cl(1)−Pd−Cl(2)	90.0(7)
N(1)−Pd−Cl(1)	94.0(1)	N(1)−Pd−Cl(2)	174.4(1)
N(2)−Pd−Cl(1)	174.9(2)	N(2)−Pd−Cl(2)	95.0(1)

The palladium atom has a distorted square-planar geometry and the bond lengths and angles around the metal ion and within the five-membered chelate ring are similar to those recently reported by us for the complex (dihexadecyl 2,2′-bipyridyl-4,4′-dicarboxylate)palladium(II) chloride.[8b] The two substituents on the 2,2′-bipyridine ligand run in opposite directions as shown by the dihedral angles C(4)−C(3)−C(19)−O(3) and C(7)−C(8)−C(11)−O(1) of 171.6(5) and −162.5(5)°, respectively. While the carboxylic oxygen atom O(2) points toward the internal part of the bipyridine ligand [C(12)−O(1)−C(11)−C(8) 180.0(5)°], O(4) shows a very different orientation [C(20)−O(3)−C(19)−C(3) −76.2(6)°]. The asymmetry in the conformation around the "CH_2−O" bond of the two substituents can be clarified by considering the crystal packing of molecules of the **[LPdCl$_2$]** complex.

The molecular organisation is dominated by intermolecular interactions of two main types: i) hydrogen bonds (C−H···O and "aromatic hydrogen bonds" C−H···π[17]) and ii) π−π contacts (Figure 2 a).

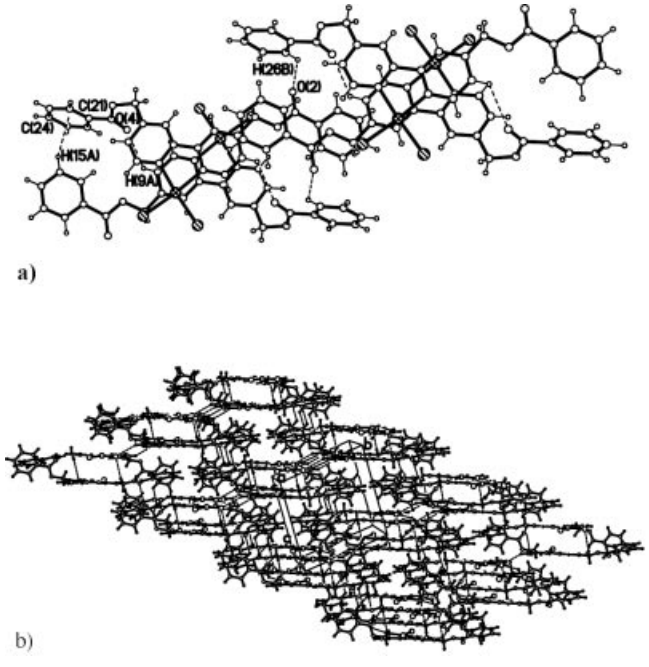

Figure 2. Ball and stick representation of interacting dimers of **[LPdCl$_2$]** viewed approximately down the *c* axis (top view) and repetition of dimers in 3D space with generation of a columnar arrangement (bottom view)

The association of molecules into dimers (superimposed approximately along the c axis) related by an inversion centre is characterised by the presence of hydrogen bonds between the carboxylic oxygen atoms and one of the pyridine hydrogen atoms [C(9a)···O(4) = 3.17(1) Å, H(9a)···O(4) 2.54(1) Å, C(9a)−H(9a)···O(4) 124.8(5)°, a = $-x$, $-y$, $-z$]. The reciprocal orientation of the C(21)/C(26) phenyl ring with respect to the centrosymmetric C(13)/C(18) ring with a dihedral angle of 66° is able to create an interesting intermolecular contact of the C−H/Ph type, for which the distance between H(15a) and the aromatic centroid X of the C(21)/C(26) ring (2.68 Å) and the C(15a)−H(15a)···X angle (147°) are indicative of the presence of a weak hydrogen C−H-π bond.[17] Moreover, the disposition of the pyridinic aromatic rings gives rise to a parallel displaced π−π stacking arrangement characterised by a centroid contact of 3.52 Å, an angle of 18° between the ring normal and the centroid vector and a corresponding horizontal displacement of 1.20 Å.[18] The M···M intermolecular separation of 5.6 Å within the dimer is significantly different from any weak Pd···Pd attractive interaction. The carboxylic oxygen atom O(2) which is not involved in any significant interaction within the dimer, assists in holding dimers together through the formation of hydrogen bonds with one of the hydrogen atoms of the peripheral phenyl rings (see a in Figure 2). In 3D space, the repetition of dimers which are stacked along the c direction and separated by layers of interacting aromatic rings (see b in Figure 2) is of particular interest in the discussion of the columnar organisation found for the analogous complexes **[L^{n}MCl$_2$]** with long alkoxy chains on the peripheral aromatic rings in the liquid crystalline state. Moreover, the absence of solvent molecules in the crystal packing enables us to view this molecular arrangement as a fingerprint for identification of future columnar liquid crystalline organisations.

Thermal Behaviour of [L^{n}MCl$_2$] Complexes

Although hexacatenar 2,2′-bipyridine ligands are not liquid crystals, all **[L^{n}MCl$_2$]** complexes show enantiotropic columnar mesomorphism which was investigated using polarised optical microscopy (POM), differential scanning calorimetry (DSC) and temperature dependent powder X-ray diffraction (PXRD) measurements. The thermal data of the **[L^{n}MCl$_2$]** series are summarised in Table 2.

For all **[L^{n}MCl$_2$]** complexes the results from POM suggested the presence of a columnar hexagonal mesophase, as indicated by the typical pseudo-focal-conics and areas of homeotropic orientation (Figure 3).

The dodecyloxy homologues feature two mesophases as shown by DSC and confirmed by subtle textural changes, such as the appearance in POM of fine disclination lines and deeper colours at the second order transition. This could indicate a transition between two hexagonal phases with different degrees of order within the columns. In the case of the palladium complexes, cooling from the isotropic liquid did not lead to crystallization but instead to solidification into a glassy state retaining the structure of the hexagonal mesophase.

 © 2005 Wiley-VCH Verlag GmbH & Co. KGaA, Weinheim

Table 2. Optical and thermal data of [L^nMCl_2] complexes

Compound	Transition[a]	T/°C[b]	ΔH/kJ·mol^{-1}
	Cr − Col_{h1}	46.2	24.5
	Col_{h1} − Col_{h2}	122.6	15.0
[$L^{12}ZnCl_2$]	Col_{h2} − I	132.1	2.7
	I − Col_{h2}	131.0	2.1
	Col_{h2} − Col_{h1}	110.6	15.2
	Col_{h1} − Cr	56.7	30.0
	Cr − Cr′	58.5	73.7
	Cr′ − Col_h	90.6	37.7
[$L^{16}ZnCl_2$]	Col_h − I	111.4	8.0
	I − Col_h	111.1	1.3
	Col_{h1} − Cr′	59.3	24.7
	Cr − Col_{h1} [c]	76.0	102.5
[$L^{12}PdCl_2$]	Col_{h1} − Col_{h2}	136.4	30.0
	Col_{h2} − I	145.3	1.26
	I − Col_{h2}	145.2	2.5
	Cr − Col_h	48.6	20.8
[$L^{16}PdCl_2$]	Col_h − I	127.5	20.9
	I − Col_h	112.5	9.4

[a] Cr: crystal; Col_h: columnar hexagonal; I: isotropic liquid. [b] Temperature data as peak onset.[c] Microscopy data.

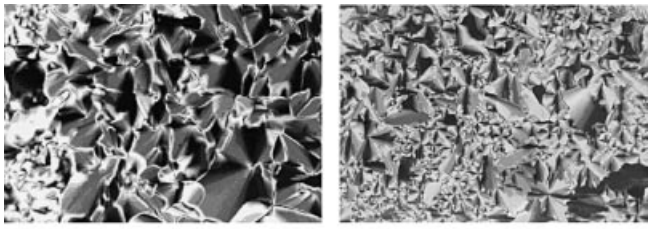

Plate 1 *Plate 2*

Figure 3. Polarised light optical photomicrograph of the texture exhibited by [L^nMCl_2] complexes; plate 1: texture of the hexagonal columnar mesophase of [$L^{12}ZnCl_2$] at 128 °C; plate 2: texture of the hexagonal columnar mesophase Col_{hd1} of [$L^{12}PdCl_2$] at 135 °C

The mesophases were also identified by temperature-dependent powder-XRD experiments. The X-ray diffraction patterns confirmed the results of optical microscopy. In all cases, in the small angle region a sharp high intensity peak and two lower intensity peaks at wider angles were indexed to the (1 0), (1 1) and (2 0) reflections. This is typical of a 2D hexagonal lattice (Table 3).

Moreover, in the case of [L^nMCl_2], a transition between hexagonal phases was observed. As shown in Figure 4 for [$L^{12}ZnCl_2$], in the wide angle region of the XRD spectrum recorded at 90 °C, the pattern consists of a broad diffuse scattering halo (B in Figure 4) at ca. 4.6 Å, corresponding to the liquid-like disorder of the aliphatic chains. Also observed was another broad diffuse band (C in Figure 4) at ca. 4.1 Å which is characteristic of the distance between adjacent cores (also definable as the stacking period in a column)[19] and, finally, a third less intense broad band (A in Figure 4) at ca. 8 Å possibly indicating a perpendicular stacking of the hemi-disc shaped molecules which is necessary to produce a disc-shaped dimer for the formation of the columnar phase.[20]

The proposed model of organisation in the hexagonal phase is in accordance with the calculated number of molecules in the cross section of the columns. This value, which was found to be around 2, was estimated by assuming a density of 1 g·cm^{-3} and a height for the columnar slice of 4.1 or 4.7 Å for M = Zn and 3.8 or 4.6 Å for M = Pd (Table 3). The transition Col_{h1} − Col_{h2} is accompanied by a decrease in the hexagonal lattice constant and a loss of the broad diffuse band centred at 4.1 or 3.8 Å (Table 3). These differences may characterise Col_{h2} as a more disordered hexagonal phase than Col_{h1}. Within the temperature range in which the first hexagonal phase may be observed, the lattice parameter was found to be temperature dependent. In fact, the low angle reflection shifted to a larger d spacing with decreasing temperature indicating a lattice expansion.[21]

A further increase in the number of carbon atoms in the side chains was not accompanied by any change of sym-

Table 3. X-ray diffraction data of [[L^nMCl_2] complexes

Compound	Mesophase Lattice constants/Å	$d_{obsd.}$/Å (d_{calcd}/Å)	Miller indices
[$L^{12}ZnCl_2$]	Col_{h1} at 90 °C	35.3 (35.3)	(1 0)
	a = 40.6	20.0 (20.5)	(1 1)
	h = 4.1	17.7 (17.7)	(2 0)
		11.5 (11.8)	(3 0)
	n = 2.1[a]	8.2	halo
		ca. 4.6	broad
		ca. 4.1	"
	Col_{h2} at 130 °C	32.6 (32.6)	(1 0)
	a = 37.5	18.9 (18.8)	(1 1)
		16.1 (16.3)	(2 0)
	n = 2.1[b]	ca. 4.7	halo
[$L^{16}ZnCl_2$]	Col_h at 100 °C	37.0 (37.0)	(1 0)
	a = 42.7	21.5 (21.4)	(1 1)
		18.4 (18.5)	(2 0)
	n= 2.2[b]	17.5 (16.6)	(3 0)
		ca. 4.6	halo
[$L^{12}PdCl_2$]	Col_{h1} at 90 °C	35.0 (35.0)	(1 0)
	a = 40.3	20.1 (20.2)	(1 1)
	h = 3.8	17.4 (17.5)	(2 0)
		11.5 (11.8)	(3 0)
		8.0	halo
	n = 1.9[a]	ca. 4.6	"
		ca. 3.8	"
	Col_{h2} at 141 °C	32.7 (32.7)	(1 0)
	a = 38.0	18.8 (18.9)	(1 1)
		16.7 (16.4)	(2 0)
	n = 2.0[b]	7.3	halo
		ca. *4.8*	"
[$L^{16}PdCl_2$]	Col_h at 60 °C	43.6 (43.6)	(1 0)
		25.6 (25.2)	(1 1)
	a = 50.6	21.8 (21.8)	(2 0)
	h = 3.6	14.7 (14.5)	(3 0)
	n = 2.3[a]	ca. 4.6	halo
		ca. 3.6	"

[a] Number of molecules in each segment of the columns calculated with h = 4.1 and 3.6 Å. [b] Number of molecules in each segment of the columns calculated with h in the range 4.7−4.8 Å.

 © 2005 Wiley-VCH Verlag GmbH & Co. KGaA, Weinheim

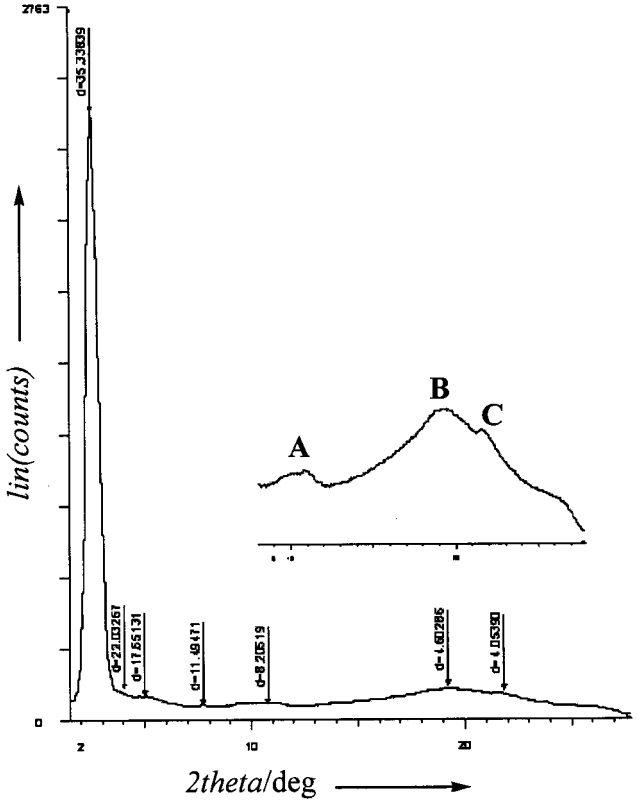

Figure 4. Powder X-ray diffraction pattern of the columnar hexagonal phase (Col_{h1}) at 90 °C for complex [$\mathbf{L^{12}ZnCl_2}$]

metry but a significant difference of the lattice parameter between [$\mathbf{L^{16}ZnCl_2}$] and [$\mathbf{L^{16}PdCl_2}$] was observed (Table 3). In fact, the noteworthy increase of *a* from 42.7 to 50.6 Å on going from the Zn^{II} to the Pd^{II} derivative is indicative of an increase of the size of the disk formed by the association of two molecules into a dimeric unit. At this particular length of the side chains, the geometry around the metal ion clearly plays an important role in the association of molecules into dimers. The flatness of the molecules in the case of the square planar Pd^{II} complex compared with the distorted tetrahedral Zn^{II} derivative encourages close proximity between the cores within the dimer (broad diffuse band in the XRD spectra at ca. 3.6 Å which corresponds to the distance between adjacent cores). In consequence, a larger horizontal displacement and an overall rise of the radius of the disk can be observed.

In both cases, a slight change of the position of the first peak in the low angle region was observed on increasing the temperature. A corresponding decrease in the intecolumnar distance to less than 1 Å was also observed. This slow change corresponds to a very low enthalpy (3.3 and 0.6 kJ/mol) and the absence of important optical textural changes.

Photoconductivity Measurements

Because of the incremental charge mobility induced by molecular self-assembling,[12] columnar mesophases have recently become attractive for their potential applications in organic photovoltaic and electroluminescent devices in which high conduction is required. In order to probe the effectiveness of our materials as photoconductors, we selected the longer chain length palladium and zinc derivatives and performed standard measurements as described in the Exp. Sect. Since pure samples show no absorption in the visible region, photogeneration was induced by doping with a small amount (0.05%) of C_{60} which is known as a good acceptor thereby promoting the formation of hole carriers. Phase transitions were not affected by the small amount of this dopant. Within our cells, it was not possible to obtain a homogeneous alignment of the mesophases using standard techniques and all the measurements were performed on unaligned samples. Figure 5 shows the ratio of the light and dark conductivities for [$\mathbf{L^{16}PdCl_2}$] at 633 nm over a temperature range which incorporates solid, columnar and isotropic phases.

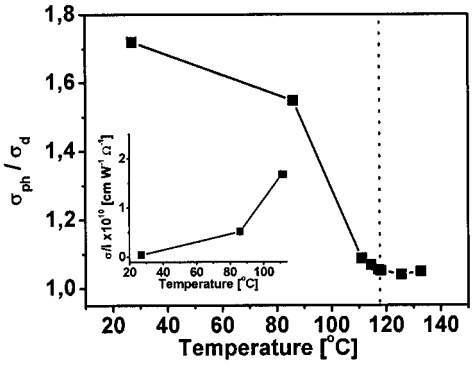

Figure 5. Ratio between the photoconductivity σ_{ph} and the conductivity in the dark σ_d for a 40 μm thick sample of complex [$\mathbf{L^{16}PdCl_2}$] doped with C_{60} as a function of temperature; the vertical line marks the I − Col_h transition; inset: normalised photoconduction measured as a function of temperature for the same sample; data were collected in an applied field of 8 V/μm and a wavelength λ = 633 nm

It is clearly visible that with decreasing temperature such a ratio starts to increase at the I-Col_h transition and keeps increasing upon further decreases in temperature. This is a signature of the reduced contribution of ionic (impurities) conduction at low temperatures compared with the contribution of electron (hole) hopping. The temperature dependence of the photoconductivity, normalised to the power density of the incident radiation, is shown in the inset of Figure 5, while its applied field dependence is shown in Figure 6. A proper comparison of conductivity with similar compounds would require mobility measurements which have not been yet carried out. Nevertheless, although the ratio of photo-conductivity to dark-conductivity is rather low, the measured values of the absolute photoconductivity are quite good, especially considering that the absorption coefficient for these samples at 633 nm is rather low ($\alpha \approx 16\ cm^{-1}$) and that for the relatively low values of the applied fields used, the photogeneration quantum efficiency should also be low.

The data in Figure 6 in fact show photoconductivity which is orders of magnitude higher than that measured for

 © 2005 Wiley-VCH Verlag GmbH & Co. KGaA, Weinheim

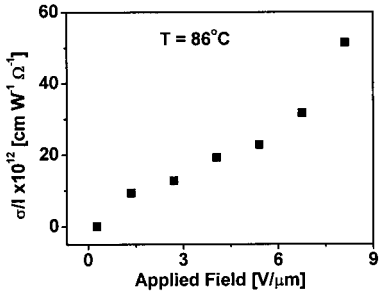

Figure 6. Normalised photoconduction at $\lambda = 633$ nm measured as a function of applied field for complex [$\mathbf{L^{16}PdCl_2}$] doped with C_{60}

standard photoconductors such as polyvinylcarbazole at the same applied field and with the same absorption coefficients. As a consequence, these results indicate that charge mobility in [$\mathbf{L^{16}PdCl_2}$] could be high and measurements are in progress to confirm this hypothesis. In the case of the related [$\mathbf{L^{16}ZnCl_2}$] complex, the measured photoconductivity is about two orders of magnitude lower. Since the measurements are in a preliminary stage, it is not possible at the moment to rationalise this behaviour.

Conclusions

A series of hexacatenar 4,4′-disubstituted 2,2′-bipyridines (**L″**) and the corresponding zinc(II) and palladium(II) complexes [$\mathbf{L''MCl_2}$] have been synthesised and characterised. Although the ligands are not mesomorphic, the association of the hemi-disc shaped molecules in face-to-face disc-shaped dimers induces columnar mesogenic properties for all the metal derivatives, regardless of the nature of metal atom. In fact, liquid crystal properties were also induced for the first time on tetrahedrally coordinated zinc complexes while for the palladium derivatives [$\mathbf{L''PdCl_2}$], the lamellar mesophases observed in dialkyl 2,2′-bipyridine-4,4′-dicarboxylate compounds[8a] are replaced by hexagonal columnar mesomorphism. Hence, it can be suggested that for all the new [$\mathbf{L''MCl_2}$] complexes in which the organic parts of the molecules have been modified through the introduction of further aromatic rings, the driving force in producing a supramolecular columnar arrangement is the existence of intermolecular interactions (hydrogen bonds, C−H−π and π−π contacts) between the large flat aromatic cores rather than dipolar or metal-metal interactions. The analysis of the crystal packing in the solid state of the model compound [$\mathbf{LPdCl_2}$] has given excellent insight into the future arrangements of the mesophases of the corresponding long chain derivatives, at least as far as the polar fragments of the molecules are concerned. The presence of long alkoxy chains in the [$\mathbf{L''MCl_2}$] derivatives gives rise to mesomorphism without interfering with the promesogenic columnar arrangement of the aromatic cores of the molecules.

Moreover, the thermal behaviour in each series was found to be insensitive to the nature of the metal atom and slightly decreases in the order Zn < Pd. This can be correlated with the overall supramolecular organisation rather than with the segregation effects of the simple molecular units.

These results show that by a careful choice of molecular building blocks, it is possible to finely modulate the interactions which determine the organisation of single molecules (association into dimers) in supramolecular architectures, giving rise to the desired functionalised metallomesogenic materials. For this class of derivatives, our goal was the design of metal-containing columnar liquid crystals in which the pre-selected property for improvement was the charge carrier mobility for charge transport. Preliminary measurements of photoconductivity, in samples of [$\mathbf{L''MCl_2}$] complexes doped with C_{60} to increase absorption in the visible, have given excellent results and further experiments are in progress.

Experimental Section

Materials and Measurements: All reagents were purchased from the following and used as received: 4,4′-Dimethyl-2,2′-bipyridine, benzoic acid, 1-bromododecane, 1-bromohexadecane, zinc chloride, 4-pyrrolidinopyridine (PPY) from Aldrich, methyl 3,4,5-trihydroxybenzoate from Lancaster and *N*,*N*′-dicyclohexylcarbodiimide (DCC) from Fluka. The solvents were used as received from commercial sources without further purification and were dried using standard methods when required. *cis*-Bis(benzonitrile)dichloropalladium,[22] 4,4′-bis(hydroxymethyl)-2,2′-bipyridine[23] and 3,4,5-trialkoxybenzoic acids[24] were prepared with slight changes following the methods described in the literature. Infrared spectra were recorded with a Spectrum One FT-IR Perkin−Elmer spectrometer and ^{1}H NMR spectra with a Bruker WH-300 spectrometer in [D_6]DMSO, $CDCl_3$ or CD_3OD with TMS as an internal standard. Elemental analyses were performed with a Perkin−Elmer 2400 analyser. The textures of the mesophases were examined with a Zeiss Axioscope polarising microscope equipped with a Linkam CO 600 heating stage. The transition temperatures and enthalpies were measured on a Perkin−Elmer Pyris1 Differential Scanning Calorimeter with a heating and cooling rate of 10 °C/min. The apparatus was calibrated with indium. Two or more heating/cooling cycles were performed on each sample. Spectrofluorimetric grade dichloromethane (Acros Organics) was used for the photophysical investigations in solution at room temperature. Absorption spectra were recorded with a Perkin−Elmer Lambda 900 spectrophotometer. The experimental uncertainty of the band maximum for the absorption spectra was 2 nm. The ligands and the complexes are stable in CH_2Cl_2 as demonstrated by the constancy of their absorption spectra over a week. The powder X-ray diffraction patterns were obtained using a Bruker AXS General Area Detector Diffraction System (D8 Discover with GADDS) with Cu-K_α radiation. The highly sensitive area detector was placed at a distance of 10 cm from the sample and equipped with a CalCTec (Italy) heating stage. The samples were heated at a rate of 5.0 °C min^{-1} to the appropriate temperature. Measurements were performed by placing samples in Lindemann capillary tubes with an inner diameter of 0.05 mm. Samples for photoconductivity measurements were prepared by mixing the complex [$\mathbf{L^{16}MCl_2}$] and 0.05% C_{60} in toluene and then evaporating the solvent. The resultant material was then transferred between two ITO-covered conducting glass slides by using the effect of capillarity within the isotropic phase. The thickness was controlled with glass spacers. The conductivity was measured by monitoring the voltage drop across a resistor in

 © 2005 Wiley-VCH Verlag GmbH & Co. KGaA, Weinheim

series with the sample cell. For temperature dependent measurements, a CalCTec (Italy) hot stage was used. For photoconductivity observations, an approximately 10^{-2} cm^2 sample was illuminated with 5 mW of light from a He-Ne laser at 633 nm.

X-ray Crystallographic Data Collection and Refinement of the [LPdCl$_2$] Structure: Orange crystals of [**LPdCl$_2$**] were formed at room temperature from a DMSO/ethanol mixture. Diffraction measurements were carried out at room temperature on a Siemens *R*3*m*/*V* automated four-circle diffractometer equipped with graphite-monochromated Mo-K_α radiation (λ = 0.71073 Å). The data were corrected for Lorentz, polarisation and X-ray absorption effects using the XABS2 program.[25] Details of the crystal data collection are listed in Table 4. Structure solution (Patterson method) and full-matrix least-squares refinements based on F^2 were performed with the SHELXS/L programs of the SHELXTL-NT software package (Version 5.10).[26] All nonhydrogen atoms were refined anisotropically. The hydrogen atoms were included in the refinement in their observed positions and then fixed as idealised atoms riding on the respective carbon atom. CCDC-241996 contains the supplementary crystallographic data for this paper. These data can be obtained free of charge at www.ccdc.cam.ac.uk/conts/retrieving.html or from the Cambridge Crystallographic Data Centre, 12 Union Road, Cambridge CB2 1EZ, UK; Fax: (internat.) + 44-1223-336-033; E-mail: deposit@ccdc.cam.ac.uk].

Table 4. Crystal and structure refinements for complex [**LPdCl$_2$**]

Formula	$C_{26}H_{20}Cl_2N_2O_4Pd$
M_r	601.7
Crystal system	triclinic
Space group	$P\bar{1}$
a (Å)	9.671(2)
b (Å)	11.329(3)
c (Å)	11.484(3)
α (°)	99.06(2)
β (°)	95.20(2)
γ (°)	105.48(2)
V (Å^3)	1185.7(4)
T (K)	298
Z	2
Density (Mg/m^{-3})	1.685
Absorption coefficient (mm^{-1})	1.045
F(000)	604
Reflections collected	4483
Unique reflections [$I > 2\sigma(I)$]	4213 (2447)
R(int)	0.037
Parameters	314
R_1[a] [$I > 2\sigma(I)$]	0.0486
wR_2[b] (all data)	0.1006
GOF on F^2	0.825

[a] $R1 = \Sigma(|F_o| - |F_c|)/\Sigma|F_o|$. [b] $wR2 = \{\Sigma[w(F_o^2 - F_c^2)^2]/\Sigma[w(F_o^2)^2]\}^{1/2}$.

Synthesis

Model Ligand: 4,4′-Bis(benzoyloxymethyl)-2,2′-bipyridine (L): 4,4′-Bis(hydroxymethyl)-2,2′-bipyridine (0.099 mg, 0.46 mmol), benzoic acid (0.112 g, 0.92 mmol) and DCC (0.208 g, 1.01 mmol) were suspended in dry dichloromethane (20 mL). PPY (0.013 g, 0.09 mmol) was added and the reaction was stirred at room temperature and under N_2 for a week. The colourless precipitate was removed by filtration and the solvent was evaporated. The crude product was recrystallised from chloroform/methanol giving a colourless solid. Yield 0.161 g (82%); m.p. 179 °C. ^{1}H NMR (300 MHz, $CDCl_3$, 25 °C, TMS): δ = 5.47 (s, 4 H, CH_2), 7.49 (m, 2 H, CH), 7.58 (m, 4 H, CH), 7.61 (m, 4 H, CH), 8.13 (dd, $^3J_{H,H}$ = 8.5, $^4J_{H,H}$ = 2.4 Hz, 2 H, H-5 bpy), 8.48 (s, 2 H, H-3 bpy), 8.70 (d, $^3J_{H,H}$ = 8.5 Hz, 2 H, H-6 bpy) ppm. IR (KBr): $\tilde{\nu}$ = 1723 cm^{-1} (C=O). UV/Vis (dichloromethane): $\lambda_{max.}$ (ε, mol^{-1}·dm^3·cm^{-1}) = 282 nm (17800). $C_{26}H_{20}N_2O_4$ (424.46): calcd. C 73.57, H 4.57, N 6.60; found C 73.44, H 4.62, N 6.76. All **L^n** ligands were prepared similarly starting from 4,4′-bis(hydroxymethyl)-2,2′-bipyridine and the appropriate 3,4,5-trialkoxy-substituted benzoic acid. Therefore only yields, melting points, ^{1}H NMR data, IR data and elemental analyses are reported below.

4,4′-Bis[3,4,5-(tridodecyloxy)benzoyloxymethyl]-2,2′-bipyridine (L^{12}): Yield 0.62 g (78%); m.p. 73 °C. ^{1}H NMR (300 MHz, $CDCl_3$, 25 °C, TMS): δ = 0.88 (t, $^3J_{H,H}$ = 6.6 Hz, 18 H, CH_3), 1.26 [m, 108 H, $(CH_2)_5CH_3$], 1.78 [m, 12 H, $CH_2(CH_2)_5CH_3$], 4.03 (t, $^3J_{H,H}$ = 6.3 Hz, 12 H, OCH_2), 5.44 (s, 4 H, CH_2), 7.33 (s, 4 H, CH), 7.37 (d, $^3J_{H,H}$ = 4.7 Hz, 2 H, H-5 bpy), 8.49 (s, 2 H, H-3 bpy), 8.67 (d, $^3J_{H,H}$ = 4.7 Hz 2 H, H-6 bpy) ppm. IR (KBr): $\tilde{\nu}$ = 1720 cm^{-1} (C=O). UV/Vis (dichloromethane): $\lambda_{max.}$ (ε, mol^{-1}·dm^3·cm^{-1}) = 277 nm (39100). $C_{98}H_{164}N_2O_{10}$ (1530.39): calcd. C 76.91, H 10.80, N 1.83; found C 76.72, H 11.00, N 2.01.

4,4′-Bis[3,4,5-(trihexadecyloxy)benzoyloxymethyl]-2,2′-bipyridine (L^{16}): Yield 0.35 g (63%); m.p. 90 °C. ^{1}H NMR (300 MHz, $CDCl_3$, 25 °C, TMS): δ = (t, $^3J_{H,H}$ = 6.6 Hz, 18 H, CH_3), 1.25 [m, 156 H, $(CH_2)_5CH_3$], 1.77 [m, 12 H, $CH_2(CH_2)_5CH_3$], 4.02 (m, 12 H, OCH_2), 5.44 (s, 4 H, CH_2), 7.33 (s, 4 H, CH), 7.37 (d, $^3J_{H,H}$ = 5.0 Hz, 2 H, H-5 bpy), 8.49 (s, 2 H, H-3 bpy), 8.68 (d, $^3J_{H,H}$ = 5.0 Hz, 2 H, H-6 bpy) ppm. IR (KBr): $\tilde{\nu}$ = 1704 cm^{-1} (C=O). UV/Vis (dichloromethane): $\lambda_{max.}$ (ε, mol^{-1}·dm^3·cm^{-1}) = 278 nm (88700). $C_{122}H_{212}N_2O_{10}$ (1867.02): calcd. C 78.48, H 11.44, N 1.50; found C 78.55, H 11.50, N 1.70.

Zinc Complexes: All zinc complexes were prepared in a similar manner. The synthesis of [**LZnCl$_2$**] is described in detail below and for all other homologues only yields, ^{1}H NMR and IR data and elemental analyses are reported.

[4,4′-Bis(benzoyloxymethyl) 2,2′-bipyridyl]zinc(II) Chloride [LZnCl$_2$]: A suspension of $ZnCl_2$ (0.013 g, 0.094 mmol) and **L** (0.040 g, 0.094 mmol) in dichloromethane (10 mL) was stirred at room temperature for four days. By filtration through Celite and evaporation the final product was obtained as a colourless solid after recrystallisation from methanol. Yield 0.37 g (70%); m.p. 260 °C. ^{1}H NMR (300 MHz, CD_3OD, 25 °C, TMS): δ = 5.61 (s, 4 H, CH_2), 7.51 (m, 4 H, CH), 7.65 (m, 2 H, CH), 7.83 (m, 4 H, CH), 8.12 (d, $^3J_{H,H}$ = 7.3 Hz, 2 H, H-5 bpy), 8.75−8.68 (m, 4 H, H-3,6 bpy) ppm. IR (KBr): $\tilde{\nu}$ = 1720 cm^{-1} (C=O). $C_{26}H_{20}Cl_2N_2O_4Zn$ (560.74): calcd. C 55.69, H 3.60, N 5.00; found C 55.48, H 3.58, N 4.74.

{4,4′-Bis[3,4,5-tridodecyloxy)benzoyloxymethyl]-2,2′-bipyridyl}-zinc(II) Chloride [L^{12}ZnCl$_2$]: Recrystallisation from dichloromethane/diethyl ether. Yield 0.160 g (86%); thermotropic behaviour in Table 2. ^{1}H NMR (300 MHz, $CDCl_3$, 25 °C, TMS): δ = 0.88 (t, $^3J_{H,H}$ = 6.4 Hz, 18 H, CH_3), 1.26 [m, 108 H, $(CH_2)_5CH_3$], 1.79 [m, 12 H, $CH_2(CH_2)_5CH_3$], 4.03 (m, 12 H, OCH_2), 5.52 (s, 4 H, CH_2), 7.29 (s, 4 H, CH), 7.78 (d, $^3J_{H,H}$ = 5.3 Hz, 2 H, H-5 bpy), 8.24 (s, 2 H, H-3 bpy), 8.85 (d, $^3J_{H,H}$ = 5.3 Hz, 2 H, H-6 bpy) ppm. IR (KBr): $\tilde{\nu}$ = 1718 cm^{-1} (C=O). UV/Vis (dichloromethane): $\lambda_{max.}$ (ε, mol^{-1}·dm^3·cm^{-1}) = 282 (30500), 297 (31400), 307 nm (27700). $C_{98}H_{164}Cl_2N_2O_{10}Zn$ (1666.67): calcd. C 70.62, H 9.92, N 1.68; found C 70.31, H 9.63, N 1.90.

 © 2005 Wiley-VCH Verlag GmbH & Co. KGaA, Weinheim

{4,4′-Bis(3,4,5-tris[hexadecyloxy)benzoyloxymethyl]-2,2′-bipyridyl}-zinc(II) Chloride [$L^{16}ZnCl_2$]: Recrystallisation by chloroform/acetone. Yield 0.12 g (91%); thermotropic behaviour in Table 2. ^{1}H NMR (300 MHz, $CDCl_3$, 25 °C, TMS): δ = 0.87 (t, $^3J_{H,H}$ = 6.7 Hz, 18 H, CH_3), 1.25 [m, 156 H, $(CH_2)_5CH_3$], 1.80 [m, 12 H, $CH_2(CH_2)_5CH_3$], 4.03 (m, 12 H, OCH_2), 5.52 (s, 4 H, CH_2), 7.28 (s, 4 H, CH), 7.77 (d, $^3J_{H,H}$ = 5.1 Hz, 2 H, H-5 bpy), 8.24 (s, 2 H, H-3 bpy), 8.86 (d, $^3J_{H,H}$ = 5.1 Hz, 2 H, H-6 bpy) ppm. IR (KBr): $\tilde{\nu}$ = 1720 cm^{-1} (C=O). UV/Vis (dichloromethane): $\lambda_{max.}$ (ε, $mol^{-1}\cdot dm^3\cdot cm^{-1}$) = 282 (25600), 296 (27400), 307 nm (24600). $C_{122}H_{212}Cl_2N_2O_{10}Zn$ (2003.32): calcd. C 73.15, H 10.67, N 1.40; found C 73.38, H 10.90, N 1.48.

Palladium Complexes: All palladium complexes were prepared in a similar manner. The synthesis of **[$LPdCl_2$]** is described in detail below. For all other homologues only yields, ^{1}H NMR and IR data and elemental analyses are reported.

[4,4′-Bis(benzoyloxymethyl)-2,2′-bipyridyl]palladium(II) Chloride [$LPdCl_2$]: A solution of $[Pd(PhCN)_2Cl_2]$ (0.045 g, 0.12 mmol) and **L** (0.20 g, 0.17 mmol) in chloroform (10 mL) was heated to reflux for 7 h. Filtration and washing with methanol gave the final product as a pale yellow solid. Yield 0.08 g (80%); m.p. 322 °C. ^{1}H NMR (300 MHz, [D$_6$]DMSO, 25 °C, TMS): δ = 5.59 (s, 4 H, CH_2), 7.56 (m, 4 H, CH), 7.70 (m, 2 H, CH), 7.90 (d, 4 H, CH), 8.105 (dd, $^3J_{H,H}$ = 6.85, $^4J_{H,H}$ = 1.4 Hz, 2 H, H-5 bpy), 8.68 (s, 2 H, H-3 bpy), 9.075 (d, $^3J_{H,H}$ = 6.85 Hz, 2 H, H-6 bpy) ppm. IR (KBr): $\tilde{\nu}$ = 1720 cm^{-1} (C=O). $C_{26}H_{20}Cl_2N_2O_4Pd$ (601.78): calcd. C 51.89, H 3.35, N 4.66; found C 51.63, H 3.35, N 4.62.

{4,4′-Bis[3,4,5-tri(dodecyloxy)benzoyloxymethyl]-2,2′-bipyridyl}-palladium(II) Chloride [$L^{12}PdCl_2$]: Recrystallisation from chloroform/methanol. Yield 0.21 g (93%); thermotropic behaviour in Table 2. ^{1}H NMR (300 MHz, $CDCl_3$, 25 °C, TMS): δ = 0.87 (m, 18 H, CH_3), 1.26 (m, 108 H, $(CH_2)_5CH_3$], 1.78 (m, 12 H, $CH_2(CH_2)_5CH_3$], 4.02 (m, 12 H, OCH_2), 5.52 (s, 4 H, CH_2), 7.29 (s, 4 H, CH), 7.48 (d, $^3J_{H,H}$ = 5.2 Hz, 2 H, H-5 bpy), 8.18 (s, 2 H, H-3 bpy), 9.10 (d, $^3J_{H,H}$ = 5.2 Hz, 2 H, H-6 bpy) ppm. IR (KBr): $\tilde{\nu}$ = 1723 cm^{-1} (C=O). UV/Vis (dichloromethane): $\lambda_{max.}$ (ε, $mol^{-1}\cdot dm^3\cdot cm^{-1}$) = 268 (36600), 304 (24700) 314 nm (23000). $C_{98}H_{164}Cl_2N_2O_{10}Pd$ (1707.71): calcd. C 68.93, H 9.68, N 1.64; found C 69.15, H 9.50, N 1.37.

{4,4′-Bis[3,4,5-tri(hexadecyloxy)benzoyloxymethyl]-2,2′-bipyridyl}-palladium(II) Chloride [$L^{16}PdCl_2$]: Yield 0.20 g (91%); thermotropic behaviour in Table 2. ^{1}H NMR (300 MHz, $CDCl_3$, 25 °C, TMS): δ = 0.87 (t, $^3J_{H,H}$ = 6.5 Hz, 18 H, CH_3), 1.25 [m, 156 H, $(CH_2)_5CH_3$], 1.78 [m, 12 H, $CH_2(CH_2)_5CH_3$], 4.02 (m, 12 H, OCH_2), 5.52 (s, 4 H, CH_2), 7.29 (s, 4 H, CH), 7.49 (d, $^3J_{H,H}$ = 5.8 Hz, 2 H, H-5 bpy), 8.16 (s, 2 H, H-3 bpy), 9.11 (d, $^3J_{H,H}$ = 5.8 Hz, 2 H, H-6 bpy) ppm. IR (KBr): $\tilde{\nu}$ = 1721 cm^{-1} (C=O). UV/Vis (dichloromethane): $\lambda_{max.}$ (ε, $mol^{-1}\cdot dm^3\cdot cm^{-1}$) = 268 (43900), 304 (26400), 314 nm (22800). $C_{122}H_{212}Cl_2N_2O_{10}Pd$ (2044.35): calcd. C 71.68, H 10.45, N 1.37; found C 71.83, H 10.22, N 1.65.

Acknowledgments

This work was partly supported by CIPE grants (Clusters 14 and 26) from the Ministero dell'Istruzione, dell'Università e della Ricerca. P. P. is pleased to acknowledge the Marie Curie development host fellowship Contract HPMD-CT-2001-00073 for financial support.

[1] J. L. Serrano, *Metallomesogens*, Wiley-VCH, Weinheim, **1996**.
[2] B. Donnio, D. W. Bruce, in *Structure and Bonding* (Ed.: D. M. P. Mingos), Springer, Berlin, **1999**, vol. 95.
[3] R. W. Date, E. F. Iglesias, K. E. Rowe, J. M. Elliott, D. W. Bruce, *Dalton Trans.* **2003**, 1914−1932.
[4] R. Giménez, D. P. Lydon, J. L. Serrano, *Curr. Opin. Sol. State Mat. Sci.* **2002**, *6*, 527−535.
[5] [5a] I. Aiello, M. Ghedini, M. La Deda, D. Pucci, O. Francescangeli, *Eur. J. Inorg. Chem.* **1999**, 1367−1372. [5b] C. Tschierske, *Angew. Chem. Int. Ed.* **2000**, *39*, 2454−2458. [5c] H. Richtzenhain, A. J. Blake, D. W. Bruce, I. A. Fallis, W-S. Li, M. Schröder, *Chem. Commun.* **2001**, 2580−2581. [5d] M. Benouazzane, S. Coco, P. Espinet, J.-M. Martin-Alvarez, J. Barbera, *J. Mater. Chem.* **2002**, *12*, 691−696. [5e] L. Plasseraud, L. Gonzales Cuervo, D. Guillon, G. Suss-Fink, R. Deschenaux, D. W. Bruce, B. Donnio, *J. Mater. Chem.* **2002**, *12*, 2653−2658. [5f] D. M. Huck, H. Loc Nguyen, H. Coles, M. Hursthouse, B. Donnio, D. W. Bruce, *J. Mater. Chem.* **2002**, *12*, 2879−2886. [5g] L. Douce, T.-H. Diep, R. Ziessel, A. Skoulios, M. Césario, *J. Mater. Chem.* **2003**, *13*, 1533−1539.
[6] J. L. Serrano, T. Sierra, *Chem. Eur. J.* **2000**, *6*, 759−766.
[7] T. Kato, N. Mizoshita, *Curr. Opin. Sol. State Mat. Sci.* **2002**, *6*, 579−587.
[8] [8a] D. Pucci, G. Barberio, A. Crispini, O. Francescangeli, M. Ghedini, *Mol. Cryst. Liq. Cryst.* **2003**, *395*, 325−335. [8b] D. Pucci, G. Barberio, A. Crispini, O. Francescangeli, M. Ghedini, M. La Deda, *Eur. J. Inorg. Chem.* **2003**, *19*, 3649−3661.
[9] A. G. Serrette, T. M. Swager, *J. Am. Chem. Soc.* **1993**, *115*, 8879−8880.
[10] J. Bushby, O. R. Lozman, *Curr. Opin. Coll. Interf. Sci.* **2002**, *7*, 343−354.
[11] R. J. Busby, O. R. Lozman, *Curr. Opin. Sol. State Mat. Sci.* **2002**, *6*, 569−578.
[12] M. O'Neill, S. M. Kelly, *Adv. Mater.* **2003**, *15*, 1135−1146.
[13] F. Morale, R. W. Date, D. Guillon, D. W. Bruce, R. L. Finn, C. Wilson, A. J. Blake, M. Schroder, B. Donnio, *Chem. Eur. J.* **2003**, *9*, 2484−2501.
[14] A. Pegenau, T. Hegmann, C. Tschierske, S. Diele, *Chem. Eur. J.* **1999**, *5*, 1643−1660.
[15] E. Terazzi, J.-M. Bénech, J.-P. Rivera, G. Bernardinelli, B. Donnio, D. Guillon, C. Piguet, *Dalton Trans.* **2003**, 769−772.
[16] A. N. Cammidge; H. Gopee, *Chem. Commun.* **2002**, 966−967.
[17] G. R. Desiraju, T. Steiner, in *The Weak Hydrogen Bond* (IUCr Monograph on Crystallography 9), Oxford Science Publ., **1999**.
[18] C. Janiak, *J. Chem. Soc., Dalton Trans.* **2000**, 3885−3896.
[19] A.-J. Attias, C. Cavalli, B. Donnio, D. Guillon, P. Hapiot, J. Malthête, *Chem. Mater.* **2002**, *14*, 375−384.
[20] [20a] S. T. Trzaska, T. M. Swager, *Chem. Mater.* **1998**, *10*, 438−443. [20b] T. Hegmann, J. Kain, S. Diele, B. Schubert, H. Bögel, C. Tschierske, *J. Mater. Chem.* **2003**, *13*, 991−1003.
[21] H. Zheng, C. K. Lai, T. M. Swager, *Chem. Mater.* **1995**, *7*, 2067−2077.
[22] M. S. Karash, R. C. Seyler, F. R. Mayo, *J. Am. Chem. Soc.* **1938**, *60*, 882−885.
[23] G. Will, G. Boschloo, S. Nagaraja Rao, D. Fitzmaurice, *J. Phys. Chem. B* **1999**, *103*, 8067−8079.
[24] K.E. Rowe, D.W. Bruce, *J. Mater. Chem.* **1998**, *8*, 331−341.
[25] S. Parkin, B. Moezzi, H. J. Hope, *Appl. Crystallogr.* **1995**, *28*, 53−56.
[26] *SHELXTL/NT* crystal structure analysis package, Bruker AXS, Inc.: Madison, WI, **1999**.

Received June 17, 2004
Early View Article
Published Online November 10, 2004

 © 2005 Wiley-VCH Verlag GmbH & Co. KGaA, Weinheim

Cu^{II} and Zn^{II} Coordination Chemistry of Pyrazole-Containing Polyamine Receptors − Influence of the Hydrocarbon Side Chain Length on the Metal Coordination

Carlos Miranda,[a] Francisco Escartí,[b] Laurent Lamarque,[a] Enrique García-España,*[b] Pilar Navarro,*[a] Julio Latorre,[b] Francisco Lloret,[b] Hermás R. Jiménez,[b] and María J. R. Yunta[c]

Dedicated to Prof. Dr. José Elguero

Keywords: Pyrazole macrocycles / Copper and zinc coordination / Acid-base and metal formation equilibria / Polyamine ligands / Paramagnetic NMR

The synthesis of a new macrocyclic receptor (**L⁴**) containing two 3,5-dimethylpyrazole units connected by dipropylenetriamine bridges is reported for the first time; pH-metric titrations indicate that **L⁴** shows six protonation steps in the pH range 2–11. In the absence of metal ions, the pyrazole moieties are not involved in acid-base processes in this pH range. Addition of Cu^{II} and Zn^{II} results in deprotonation of the pyrazole moieties which act as bis(monodentate) η^1:η^1 ligands. This induced deprotonation occurs at higher pH values than in the complexes of the analogous ligand containing diethylenetriamine bridges (**L¹**). The crystal structures of $[Cu_2(H_{-2}\mathbf{L^4})](ClO_4)_2$ and $[Zn_2(H_{-2}\mathbf{L^4})](ClO_4)_2$ obtained by treatment of $Na_2[H_{-2}\mathbf{L^4}]$ with either $Cu(ClO_4)_2{\cdot}6H_2O$ or $Zn(ClO_4)_2{\cdot}6H_2O$ in methanol followed by recrystallisation from water/methanol also show the deprotonation of the pyrazole moieties. The coordination geometry around each metal ion is square-pyramidal and involves all nitrogen atoms of the macrocycle. The crystal structure of $[Zn_2(H_{-2}\mathbf{L^1})](ClO_4)_2$ shows full involvement of all the nitrogen atoms of the macrocycle in the coordination to the metal ions. The coordination geometry can be defined as midway between a square pyramid and an irregular trigonal bipyramid. Treatment of neutral **L⁴** in methanol with $Cu(ClO_4)_2{\cdot}6H_2O$ yields a blue complex which, after heating in boiling water, crystallises as a red compound. Elemental microanalyses, ESI-MS and FAB-MS data of both forms of this complex are consistent with the formula $[Cu_2\mathbf{L^4}](ClO_4)_4{\cdot}2H_2O$. Furthermore, these data along with the paramagnetic ^1H NMR spectrum of the red form of the compound suggest a structure in which the pyrazole rings are deprotonated while the central nitrogen atoms of the bridging chains are protonated and consequently uncoordinated. The change from the blue (square-pyramidal) to the red form (square-planar) can be ascribed to dissociation of the water molecules which occupy the axial positions in the Cu^{II} coordination spheres of the blue form. The variation of the magnetic susceptibility of the red complex $[Cu_2\mathbf{L^4}](ClO_4)_4{\cdot}2H_2O$ and the complex $[Cu_2(H_{-2}\mathbf{L^4})](ClO_4)_2$ with temperature has been studied in the 2–300 K temperature range. Fitting of the experimental data provides J values which are among the highest found for doubly pyrazolate-bridged dicopper(II) complexes {J = −299 cm^{-1} for red-$[Cu_2\mathbf{L^4}](ClO_4)_4{\cdot}2H_2O$ and J = −286 cm^{-1} for $[Cu_2(H_{-2}\mathbf{L^4})](ClO_4)_2$}. A trinuclear Cu^{II} complex of formula $[Cu_3(H_{-2}\mathbf{L^4})](ClO_4)_4{\cdot}2MeOH$ was also isolated after treatment of **L⁴** with $Cu(ClO_4)_2{\cdot}6H_2O$ solutions of higher concentration.
(© Wiley-VCH Verlag GmbH & Co. KGaA, 69451 Weinheim, Germany, 2005)

[a] Instituto de Química Médica, Centro de Química Orgánica Manuel Lora Tamayo, CSIC,
c/ Juan de la Cierva 3, 28006 Madrid, Spain
E-mail: iqmnt38@iqm.csic.es
[b] Departamento de Química Inorgánica, Facultad de Química, Universidad de Valencia,
c/ Doctor Moliner 50, 46100 Burjassot (Valencia), Spain
Fax: (internat.) + 34-96-3864322
E-mail: enrique.garcia-es@uv.es
[c] Departamento de Química Orgánica, Facultad de Química, Universidad Complutense de Madrid,
Avda. Complutense s/n, 28040 Madrid, Spain
Supporting information for this article is available on the WWW under http://www.eurjic.org or from the author.

Introduction

Over the last decades a large amount of research effort has been devoted to identifying the biological roles of metal ions such as Cu^{II} and Zn^{II}. In order to achieve such a goal, different parallel approaches have been followed. The most straightforward consists of directly studying the active site in the metalloenzymes. A second approach, which has proved very useful in some instances,[1−3] has been to mimic the chemical features of the metal sites using smaller sized coordination compounds as models. The knowledge ob-

tained from the way in which metalloenzymes activate small molecules like H_2, N_2, CO_2, etc. has also resulted in considerable interest in the development of catalysts for industrial purposes.

A second biological aspect of metal complexes that has to be taken into account is their implications in pharmacology. For instance, complexes of macrocyclic ligands such as bicyclams and their Zn^{II} complexes have shown useful applications as potent anti-HIV-1 agents and several Mn^{II} and Cu^{II} complexes of hexaazamacrocycles have found applications as SOD mimics.[4] Another point of interest concerns the use of chelate ligands for selectively complexing and removing excess amounts of metal ions from which arise undesirable effects such as the oxidative damage detected in several neurodegenerative disorders.[5] An illustrative example comes from the use of the ligand PBT1 (clioquinol) for removing excess Cu^{II} which accumulates in the neocortex following the oxidative damage produced in Alzheimer disease.[6]

Therefore, the preparation and study of the coordination chemistry of ligands featuring new characteristics in their interaction with metal ions represents a challenge in coordination and biomedical chemistry. Ligands including 1*H*-pyrazole fragments offer a wealth of possibilities in this respect. The pyrazole unit can behave as a monodentate ligand through its sp^2 nitrogen atom or, upon deprotonation, as an $\eta^1{:}\eta^1$ bis(monodentate) bridging ligand (Scheme 1).[7,8]

Recently, we have examined the acid-base behaviour, Cu^{II} coordination chemistry and dopamine recognition capabilities of a series of pyrazole-containing polyamine macrocycles of different topologies [see ligands **1** (**L**^{1}) to **3** (**L**^{3}) in Scheme 2].[9−11] Here we extend these studies to the metal ion Zn^{II}. Additionally, we report on the synthesis of the pyrazole-containing macrocycle 3,7,11,14,15,18,22,26,29,30-decaazatricyclo[26.2.1.1^{13,16}]dotriacontane-1(31),13,16(32),28-tetraene (**4**) (**L**^{4}) (see Scheme 2) which has only propylenic chains and the preparation of its disodium dipyrazolate salt **4′** [$Na_2(H_{-2}$**L**^{4})]. We discuss the effect of the propylenic chains on the acid-base behaviour and on the Cu^{II} and Zn^{II} coordination chemistry in aqueous solution. We also report different Cu^{II} and Zn^{II} complexes prepared either from **4** and **4′** or from the ligands **1**−**3** and we discuss the influence of the hydrocarbon chain length on the coordination features of these new complexes.

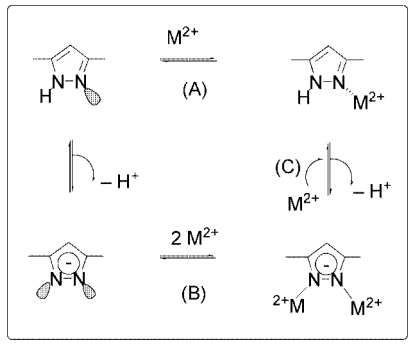

Scheme 1

Results and Discussion

Synthesis of 4 and 4′

The preparation of **4** was performed by a [2+2] dipodal condensation of 3,5-pyrazoledicarbaldehyde with *N*-(3-aminopropyl)-1,3-propanediamine in methanol at room temperature, followed by in situ reduction of the resultant Schiff base with $NaBH_4$. After careful purification firstly by chromatography and then by crystallisation from toluene, **4** (**L**^{4}) was isolated as a pure solid of melting point 154−156 °C in 49% yield. Compound **4** and its hydrochloride **4**·6HCl

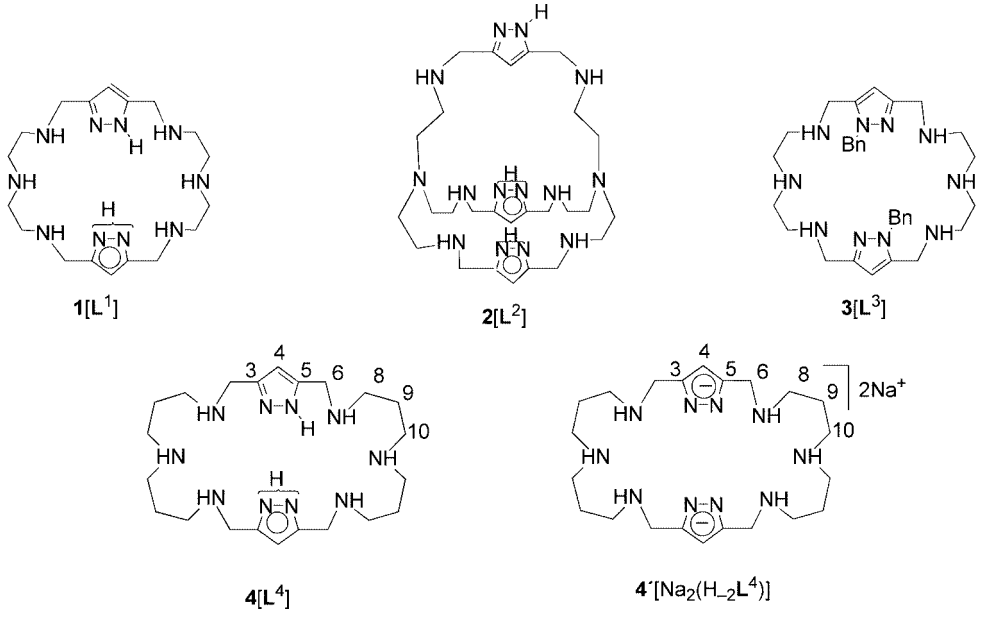

Scheme 2

Table 1. Comparison of ^1H and ^{13}C NMR spectroscopic data (δ [ppm], D_2O) of **4** recorded at pH = 10.5 and 8.0 and **4**·6HCl recorded at pH = 3.7

	4 (1) pH = 10.5	**4** (2) pH = 8.0	**4**·6HCl (3) pH = 3.7	Δδ (2−1)	Δδ (3−2)
4-H	6.07 (s, 2 H)	6.22 (s, 2 H)	6.63 (s, 2 H)	0.15	0.41
6-H	3.53 (s, 8 H)	3.71 (s, 8 H)	4.26 (s, 8 H)	0.18	0.55
8-H	2.26 (t. 8 H)[a]	2.61 (t, 8 H)[a]	3.05 (m, 8 H)	0.35	0.44
9-H	1.37 (m, 8 H)	1.70 (m, 8 H)	2.01 (m, 8 H)	0.33	0.31
10-H	2.26 (t. 8 H)[a]	2.87 (t, 8 H)[a]	3.05 (m, 8 H)	0.61	0.18
	4 (1) pH = 10.5	**4** (2) pH = 8.0	**4**·6HCl (3) pH = 3.7	Δδ (2−1)	Δδ (3−2)
C-3,5	147.71	145.40[b]	139.20	−2.31	−6.20
C-4	103.68	104.52	109.01	0.84	4.58
C-6	43.79	43.64	42.68	−0.15	−0.96
C-8	45.34	45.26	43.83	−0.08	−1.43
C-9	28.40	24.79	22.81	−3.61	−1.98
C-10	46.55	45.96	44.65	−0.59	−1.31

[a] J = 7 Hz. [b] Broad signal.

(m.p. 265−268 °C) have been fully characterised by elemental analyses and NMR spectroscopy.

Table 1 shows a comparison of the ^1H and ^{13}C NMR spectroscopic data of the new ligand **4**, recorded in D_2O at pH = 10.5 and 8.0, with those of its hexahydrochloride **4**·6HCl recorded at pH = 3.7. The signals have been analysed on the basis of their HMQC and multiple-bond HMBC 2D NMR heteronuclear correlation spectra. The above ^1H NMR spectra are graphically compared in the Supporting Information [Figure 1S (A−C)] (for Supporting Information see also the footnote on the first page of this article).

As usually occurs for 3,5-disubstituted 1*H*-pyrazole derivatives, at pH = 10.5 (where the nonprotonated species predominates) **4** shows a very simple pattern of signals which indicates that because of the fast prototropic equilibrium of the pyrazole ring, the compound exhibits an average fourfold symmetry on the NMR time scale. The carbon atoms labelled C-3 and C-5 (for the labelling see Scheme 2) appear together as a sharp signal and the pairs of methylene carbon atoms C-6, C-8, C-9 and C-10 are magnetically equivalent.

In general, the pH-dependent variation of the NMR resonances of the β-carbon atoms and of the hydrogen atoms bound to the α-carbon atoms with respect to the protonated nitrogen atoms are of great help in establishing protonation sequences of polyamine molecules.[9] As can be derived from the basicity constants, the two first protonations of $\mathbf{L^4}$ occur in the pH range of 11−8. Thus, in the NMR spectra of **4** recorded at pH = 8.0 (Table 1), the carbon signal shifted the most upfield is that of carbon atoms C-9 ($\Delta\delta$ = −3.61 ppm), whereas the signal of carbon atoms C-8 and that of the quaternary carbon atoms C-3,5 do not experience significant shifts in this pH region. In the same way, the most downfield shifted ^1H signal is that of 10-H ($\Delta\delta$ = 0.61 ppm), clearly indicating that **4** is protonated firstly at the centre nitrogen atoms of the bridging chains. On the other hand, by comparing the NMR signals of **4** at pH = 8 and those of **4**·6HCl at pH = 3.7 (Table 1) it can be observed that after protonation of the aliphatic nitrogen atoms closer to the pyrazole rings, the most downfield shifted hydrogen signals are those of 6-H and 8-H ($\Delta\delta$ = 0.55 and 0.44 ppm, respectively) and that the signals of the methylene carbon atoms which experience the largest upfield variations are C-9 = −1.98 ppm) which are located in the β-position with respect to the above-mentioned nitrogen atoms.

Furthermore, in **4**·6HCl, the signals of the pyrazole carbon atoms C-3,5 and C-4 (located in the β- and γ-positions, respectively, in relation to the closer protonated aliphatic nitrogen atoms) also experience large upfield ($\Delta\delta$ = 6.20 ppm for C-3,5) and downfield ($\Delta\delta$ = 4.58 ppm for C-4) shifts. These variations are of a similar order to those previously reported for $\mathbf{L^1}$.[9] It is important to point out that such variations do not reflect any particular implication of the pyrazole subunits in the protonation process, since it is well known that β- and γ-aromatic carbon atoms belonging to polyamine-bridged cyclophanes containing benzene units also bear similar chemical shifts upon protonation.[12,13] Finally, we also obtained the disodium dipyrazolate salt **4′** [$Na_2(H_{-2}\mathbf{L^4})$] as a pure solid (m.p. 208−210 °C) in 98% yield, by heating the free ligand **4** to reflux with 2 equiv. of NaOH in MeOH.

Acid-Base Behaviour

Table 2 includes the stepwise protonation constants of the new receptor $\mathbf{L^4}$ and those previously reported for compounds **1** ($\mathbf{L^1}$) to **3** ($\mathbf{L^3}$).[9−11] The basicity constants of **4** ($\mathbf{L^4}$), with only propylenic chains are higher than those of $\mathbf{L^1}$ containing only ethylenic chains and are also higher than those of the compound with ethylenic chains and *N*-benzylpyrazole spacers ($\mathbf{L^3}$). The differences between the stepwise constants of $\mathbf{L^4}$ and those of $\mathbf{L^1}$ and $\mathbf{L^3}$ are particularly large for the fifth and sixth protonation steps (Table 2). The fifth and six protonations occur at the central nitrogen atoms of the polyamine chains of the macrocycle. Therefore, at this stage, the incoming proton will notice a lower elec-

 © 2005 Wiley-VCH Verlag GmbH & Co. KGaA, Weinheim

Table 2. Protonation constants of the receptors **L¹** to **L⁴** determined in 0.15 mol·dm^{-3} NaCl at 298.1 K

Reaction[a]	**L¹** [b]	**L²** [c]	**L³** [b]	**L⁴** [d]
H + **L** = H**L**	9.74	9.54	8.90	10.05(2)[e]
H + H**L** = H_2**L**	8.86	8.71	8.27	9.34 (2)
H + H_2**L** = H_3**L**	7.96	7.72	6.62	7.63 (3)
H + H_3**L** = H_4**L**	6.83	6.55	5.85	7.07 (3)
H + H_4**L** = H_5**L**	4.57	6.52	3.37	6.45 (3)
H + H_5**L** = H_6**L**	3.19	5.22	2.27	5.55 (4)
log β[f]	41.1	44.3	35.3	46.1

[a] Charges omitted for clarity. [b] Taken from ref.[9] [c] Taken from ref.[11] [d] This work. [e] Values in parentheses are standard deviations in the last significant figure. [f] log $\beta = \Sigma \log K_{HjL}$.

trostatic repulsion from the adjacent polyammonium sites in **L⁴** than in **L¹** or in **L³** due to the presence of the larger propylenic chains.[14] Curiously, the basicities displayed by **L⁴** and the cryptand **L²** are rather similar even if their structures and numbers of nitrogen atoms are different.

The high degree of protonation that **L⁴** presents at physiological pH values (mean number of protons at pH = 7.4 is 3.02) makes this receptor a promising candidate for the coordination of anionic or polar species.

Metal Coordination in Aqueous Solution

The stability constants for the formation of Cu^{II} complexes of **4** (**L⁴**) together with those previously reported for the related receptors **1** (**L¹**) to **3** (**L³**) under the same experimental conditions are shown in Table 3.[11] The stability constants for the interaction of Zn^{II} with **L¹** to **L⁴** determined in this work are presented in Table 4.

With Cu^{II}, **L⁴** forms mononuclear $[Cu(H_xL)]^{(x+2)}$ complexes with $x = 0$, 1, 2 and 3 and dinuclear $[Cu_2(H_xL)]^{(x+4)}$ species with $x = -1$, -2 and -3. The extent of formation of each one of these complexes depends on pH, M/L molar ratio and concentration as can be seen in Figure 1 which shows the distribution diagrams for the Cu^{II} complexes of **L⁴** in molar ratios of 1:1 (Figure 1, A) and 2:1 (Figure 1, B), complexes of **L¹** in a molar ratio of 2:1 (Figure 1, C) and for the Zn^{II} complexes of **L⁴** and **L¹** in a molar ratio 2:1 (Figure 1, D and E, respectively).

The stability constant for the species $[Cu\mathbf{L^4}]^{2+}$ is intermediate between that found for $[Cu\mathbf{L^1}]^{2+}$ (**L¹** is the analogous macrocycle with ethylenic chains) and that of $[Cu\mathbf{L^3}]^{2+}$ (**L³** being the compound with ethylenic chains and *N*-benzylated pyrazole spacers) (Entry 4 in Table 3). The same situation occurs for the dinuclear $[Cu_2\mathbf{L}]^{4+}$ complexes (Entry 7). The sequence of five-membered chelate rings present in **L¹** leads to a stronger coordination to Cu^{II} than the sequence of six-membered rings present in **L⁴**. The situation for **L³** is different since the substituted spacers cannot be deprotonated and each one provides only an sp^2 nitrogen donor over all the pH ranges studied.

Deprotonation of the pyrazole spacers induced by coordination to metal ions is a characteristic feature of this heterocycle.[8,11,15–17] The structure of **L⁴** enables an analysis of the influence of the length of the hydrocarbon chain and thereby of the denticity of the chelate rings on such deprotonation processes. The distribution diagrams calculated for an M/L ratio of 2:1 shown in Figure 1 indicate that while the species $[Cu_2(H_{-2}L)]^{2+}$ with both pyrazole moieties deprotonated is already predominant in solution at pH ≈ 4.3 for **L¹**, a similar species is produced only at pH

Table 3. Stability constants for the formation of Cu^{II} complexes of the receptors **L¹**, **L²**, **L³** and **L⁴** determined in 0.15 mol·dm^{-3} NaCl at 298.1 K

Entry	Reaction[a]	**L¹** [b]	**L²** [b]	**L³** [b]	**L⁴** [c]
1	Cu + L + 3 H = CuH_3L				37.68(9)
2	Cu + L + 2 H = CuH_2L	35.05(2)[d]	35.42(8)	27.9(1)	32.64(6)
3	Cu + L + H = CuHL	30.82(2)	28.85(7)	22.12(8)	25.91(4)
4	Cu + L = CuL	23.48(3)	21.76(6)	13.60(7)	17.83(8)
5	Cu + L = $CuH_{-1}L$ + H		13.05(3)		
6	2 Cu + L + H = Cu_2HL		39.04(7)	29.37(5)	
7	2 Cu + L = Cu_2L	34.45(3)	36.72(3)	26.27(3)	28.72(2)
8	2 Cu + L = $Cu_2H_{-1}L$ + H		31.31(5)	16.85(4)	23.62(3)
9	2 Cu + L = $Cu_2H_{-2}L$ + 2 H	26.56(3)	24.13(5)	7.06(3)	15.69(8)
10	2 Cu + L = $Cu_2H_{-3}L$ + 3 H				5.87(7)
11	CuH_2L + H = CuH_3L				5.04
12	CuHL + H = CuH_2L	4.23	6.57	5.78	6.73
13	CuL + H = CuHL		7.09	8.52	8.08
14	CuL = $CuH_{-1}L$ + H	7.34	8.71		
15	CuL+Cu = Cu_2L	10.97	12.67		10.89
16	Cu_2L + H = Cu_2HL		2.32	3.1	
17	Cu_2L = $Cu_2H_{-1}L$ + H		−5.41	−9.42	−5.1
18	$Cu_2H_{-1}L$ = $Cu_2H_{-2}L$ + H		−7.18	−9.79	−8.07
19	Cu_2L = $Cu_2H_{-2}L$ + 2 H	−7.89	−12.59	−19.21	−13.03
20	$Cu_2H_{-2}L$ = $Cu_2H_{-3}L$ + H				−9.72

[a] Charges omitted for clarity. [b] Taken from ref.[11] [c] This work. [d] Values in parentheses are standard deviations in the last significant figure.

Table 4. Stability constants for the formation of Zn^{II} complexes of the receptors **L¹**, **L²**, **L³** and **L⁴** determined in 0.15 mol·dm^{-3} NaCl at 298.1 K

Entry	Reaction[a]	**L¹**	**L²**	**L³**	**L⁴**
1	$Zn + L + 3\,H = ZnH_3L$	32.26(7)[b]	32.72(2)		
2	$Zn + L + 2\,H = ZnH_2L$	26.4(2)	27.42(3)		
3	$Zn + L + H = ZnHL$	22.26(4)	22.227(9)	16.67(2)	17.54(3)
4	$Zn + L = ZnL$	15.74(4)	14.12(2)	8.53(4)	8.8(1)
5	$Zn + L = ZnH_{-1}L + H$	7.21(4)	3.91(2)	−0.43(4)	−1.0(1)
6	$2\,Zn + L + H = Zn_2HL$				
7	$2\,Zn + L = Zn_2L$		20.19(3)	14.40(2)	14.42(3)
8	$2\,Zn + L = Zn_2H_{-1}L + H$	14.63(5)	14.71(1)	6.04(4)	8.22(1)
9	$2\,Zn + L = Zn_2H_{-2}L + 2\,H$	8.94(4)	4.75(2)	−2.71(3)	−1.50(3)
10	$2\,Zn + L = Zn_2H_{-3}L + 3\,H$			−12.81(3)	
11	$3\,Zn + L = Zn_3H_{-3}L + 3\,H$		1.80(4)		
12	$ZnH_2L + H = ZnH_3L$	5.9	5.30		
13	$ZnHL + H = ZnH_2L$	4.1	5.19		
14	$ZnL + H = ZnHL$	6.52	8.11	8.14	8.7
15	$ZnL = ZnH_{-1}L + H$	−8.53	−10.21	−8.96	−9.8
16	$ZnL + Zn = Zn_2L$		6.07	5.87	5.62
17	$Zn_2L + H = Zn_2HL$				
18	$Zn_2L = Zn_2H_{-1}L + H$		−5.48	−8.36	−6.2
19	$Zn_2H\text{-}_1L = Zn_2H_{-2}L + H$	−5.69	−9.96	−8.75	−9.72
20	$Zn_2L = Zn_2H_{-2}L + 2\,H$		−15.44	−17.11	−15.92
21	$Zn_2H_{-2}L = Zn_2H_{-3}L + H$				

[a] Charges omitted for clarity. [b] Values in parentheses are standard deviations in the last significant figure.

> 8 for **L⁴** (Figure 1, B). The first average deprotonation of $[Cu_2\mathbf{L^4}]^{2+}$ gives $pK_{a1} = 5.1$ and the second one $pK_{a2} = 8.1$.

However, care has to be taken in drawing such a conclusion since in the red solid red-$[Cu_2\mathbf{L^4}](ClO_4)_4\cdot 2H_2O$ {red-[**13**]$(ClO_4)_4\cdot 2H_2O$}, prepared from neutral **L⁴** and $Cu(ClO_4)_2\cdot 6H_2O$ (vide infra), the two pyrazole units are deprotonated while the central amino groups of both chains are protonated giving the ligand an overall charge of zero (see **13** in Scheme 3). Therefore, Cu^{II} coordination induces the ready deprotonation of the pyrazole nitrogen atoms which, in this complex, occurs at a lower pH than the deprotonation of the central propylenic chain. This is a particular feature of **L⁴** not observed in the related ligand **L¹** with ethylenic chains. The higher basicity of **L⁴** in its two first protonation steps should facilitate this situation. Such behaviour contrasts with that of the free ligands, for which neither deprotonation nor protonation processes occur at the pyrazole rings throughout the pH range of 2−11.[9,11] On the other hand, all the dinuclear Cu^{II} complexes are EPR-silent.

The stability constants gathered in Table 4 show that, as expected, the Zn^{II} complexes display remarkably lower stabilities than the Cu^{II} analogues (see for instance, Entries 4 in Table 3 and 4 for the $[M\mathbf{L}]^{2+}$ complexes). In all the Zn/L systems, formation of mono- and dinuclear complexes can be observed and for the Zn/**L²** system even a trinuclear species $[Zn_3(H_{-3}\mathbf{L^2})]^{4+}$ was detected. The degree of protonation of the mononuclear complexes reaches a value of 3 for **L¹** and **L²** {$[Zn(H_3\mathbf{L})]^{5+}$ species} and only of 1 for the systems Zn/**L³** and Zn/**L⁴** {i.e. $[Zn(H\mathbf{L})]^{3+}$ species}. The degree of protonation of the dinuclear Zn^{II} complexes varies between 0 and −3. In the case of the Zn/**L¹** system, it has not been possible to identify any nondeprotonated dinuclear species (see distribution diagram in Figure 1). A comparison with Cu^{II} shows that for Zn^{II}, the deprotonation of pyrazole is shifted approximately two units to higher pH values as a result of the poorer inductive effect exerted by this metal ion. Taking into account the crystal structure of $[Zn_2(H_{-2}\mathbf{L^4})](ClO_4)_2$ and the spectroscopic data (vide infra) it is likely, that in the two species $[Zn_2(H_{-1}\mathbf{L^4})]^{3+}$ and $[Zn_2(H_{-2}\mathbf{L^4})]^{2+}$, both pyrazole groups are deprotonated. In $[Zn_2(H_{-1}\mathbf{L^4})]^{3+}$ one of the central nitrogen atoms of the bridging chain will be protonated. In the case of **L¹** the species $[Zn_2(H_{-1}\mathbf{L^1})]^{3+}$ cannot be detected and the only dinuclear species found in solution is $[Zn_2(H_{-2}\mathbf{L^1})]^{2+}$ (Figure 1, D and E). For the cryptand **L²** the situation is analogous to that of **L¹** and the species $[Zn_2(H_{-1}\mathbf{L^2})]^{3+}$ can be postulated as having the two pyrazole moieties involved in coordination to Zn^{II} being deprotonated, while the pyrazole in the noncoordinating bridge will be nondeprotonated and one of the amino groups in this region will be protonated. Such a situation has already been observed in the crystal structure of the analogous Cu^{II} complex of **L²**.[11] Finally, in the ligand with *N*-benzylated pyrazole spacers, the main species in solution at neutral pH, is $[Zn_2\mathbf{L^3}]^{4+}$. Deprotonation of the coordinated water molecules to give hydroxo species requires higher pH values.

Synthesis of Solid Zn^{II} Dinuclear Complexes from Polyamine Receptors with Ethylenic Chains 1 (L¹) to 3 (L³)

Some time ago the in situ deprotonation of ligands **1** (**L¹**) and **2** (**L²**) upon addition of NaOH, as well as the formation of Zn^{II} pyrazolate complexes was observed using NMR techniques in $[D_6]DMSO/D_2O$ mixtures.[18,19] However,

 © 2005 Wiley-VCH Verlag GmbH & Co. KGaA, Weinheim

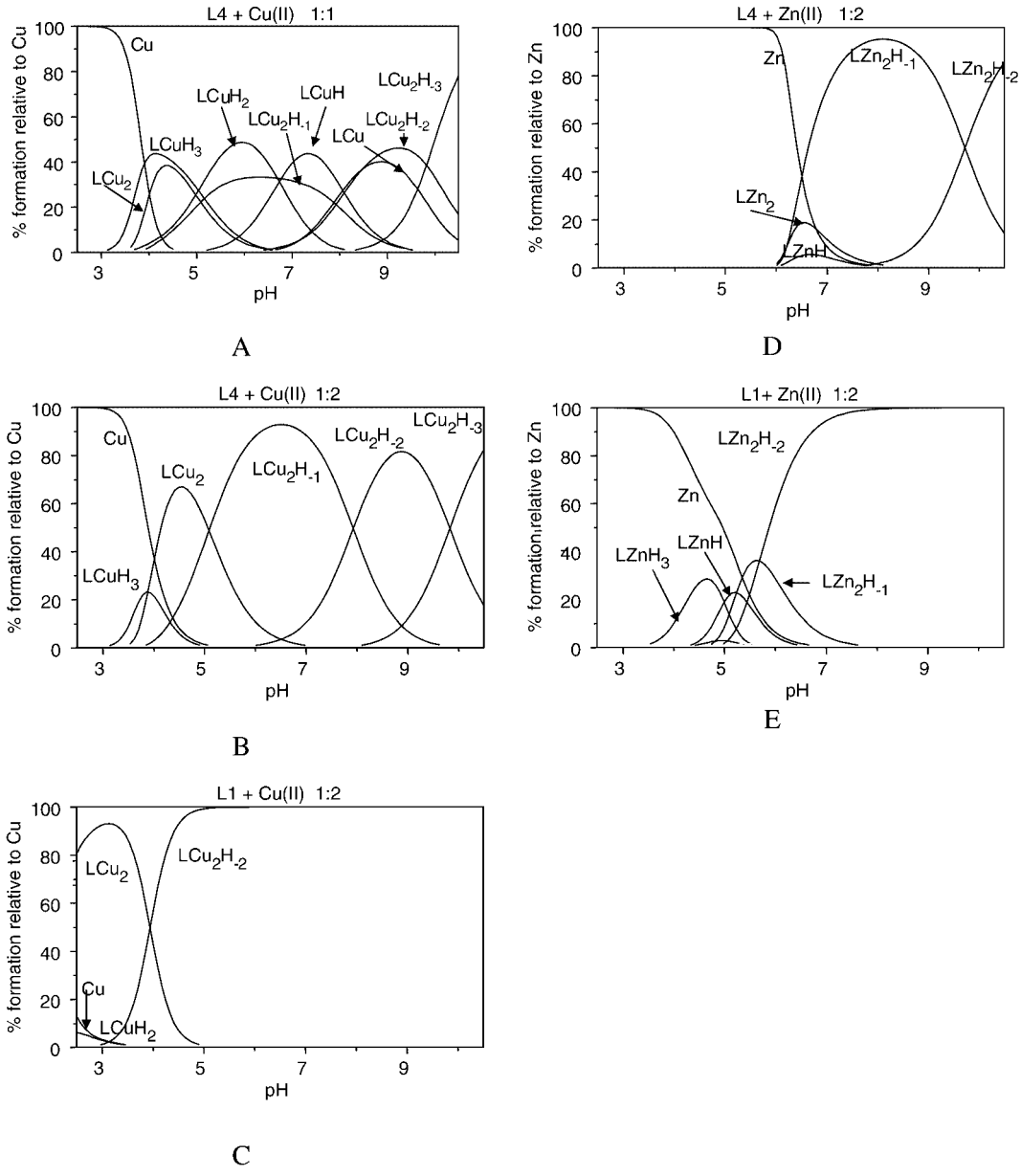

Figure 1. Distribution diagrams for the species existing in equilibrium in the systems: A) Cu^{II}/**L**^{4} molar ratio 1:1, B) Cu^{II}/**L**^{4} molar ratio 2:1, C) Cu^{II}/**L**^{1} molar ratio 2:1, D) Zn^{II}/**L**^{4} molar ratio 2:1, E) Zn^{II}/**L**^{1} molar ratio 2:1; the concentration of ligand is 1×10^{-3} M in all systems

none of the latter mentioned complexes were either isolated or structurally characterised as solid compounds. However, by treating the neutral ligands **L**^{1} to **L**^{3} with $Zn(ClO_4)_2 \cdot 6H_2O$ in methanol (molar ratio M/L = 2:1) we have now isolated three new solid complexes which were recrystallised from water. The analytical and MS data of these compounds are consistent with the formulae $[Zn_2(H_{-2}\mathbf{L}^{1})](ClO_4)_2$ {[**8**]$(ClO_4)_2$}, $[Zn_2(H_{-2}\mathbf{L}^{2})](ClO_4)_2 \cdot 4H_2O$ {[**9**]$(ClO_4)_2 \cdot 4H_2O$} and $[Zn_2\mathbf{L}^{3}](ClO_4)_4 \cdot 6H_2O$ {[**10**]$(ClO_4)_4 \cdot 6H_2O$} (Scheme 3). Electrospray ionisation (ESI-MS) and fast atom bombardment (FAB-MS) mass spectrometry have been used for the characterisation of all the new Zn^{II} complexes.[20] Besides, in the case of [**8**]$(ClO_4)_2$, suitable crystals for X-ray analysis were grown from the aqueous solution (vide infra).

The above data support the fact that in the case of **L**^{1} and **L**^{2}, Zn^{II} coordination induces the deprotonation of the pyrazole rings to afford the pyrazolate bridging ligand without the need to add a base. On the other hand, considering that the structure of the starting ligand **L**^{3} corresponds to a constitutional isomer in which the 1-benzylpyrazole substituents are in positions opposite each other displaying C_2 symmetry[9] and taking into account the crystal structure of the analogous Cu^{II} complex [**7**]$(ClO_4)_4 \cdot 4H_2O$,[11] it is reasonable to assume that in the Zn^{II} complex [**10**]$(ClO_4)_4 \cdot 6H_2O$ the sp^2 nitrogen atoms of the pyrazole rings are also involved in the coordination to the metal ions.

The ESI (positive mode) and FAB mass spectra of complex {[**8**]$\cdot(ClO_4)_2$} show common peaks at *m*/*z* (%) = 615.1 (10) and 615.4 (10), respectively, which confirm the presence

 © 2005 Wiley-VCH Verlag GmbH & Co. KGaA, Weinheim

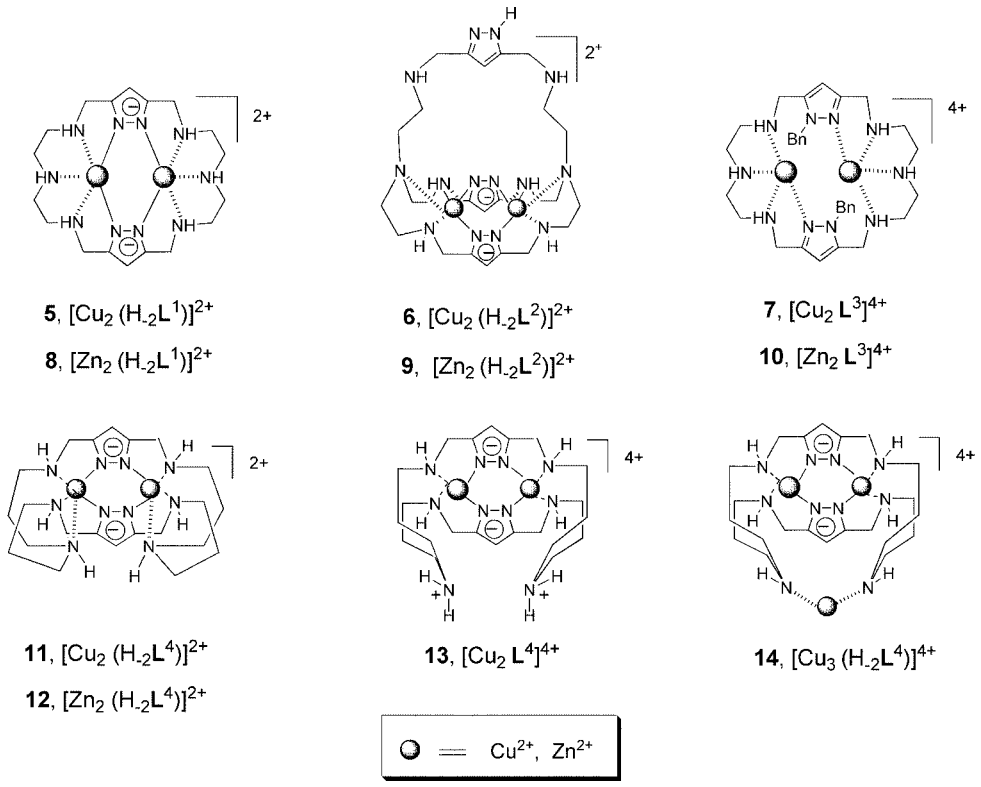

Scheme 3

of the dinuclear $[Zn_2(H_{-2}\mathbf{L^1})(ClO_4)]^+$ species, as well as intense peaks at *m*/*z* (%) = 453.4 (100) and 453.2 (47), respectively, corresponding to the species $[Zn(H_{-1}\mathbf{L^1})]^+$ generated by loss of $Zn(ClO_4)_2$.

Similarly, in both the ESI and FAB mass spectra of $[\mathbf{9}](ClO_4)_2{\cdot}4H_2O$, the protonated molecular ion $[Zn_2(H_{-2}\mathbf{L^2})(ClO_4)_2]H^+$ appears at *m*/*z* (%) = 893.2 (2) and 893.1 (23), respectively, and the ionic species $[Zn_2(H_{-2}\mathbf{L^2})(ClO_4)]^+$ is confirmed by the presence of intense peaks at *m*/*z* (%) = 793.2 (73) and 793.3 (63), respectively.

Finally, in the ESI (positive mode) and the FAB mass spectra of complex $[Zn_2\mathbf{L^3}](ClO_4)_4{\cdot}6H_2O$ appear common peaks which clearly support the proposed structure. At *m*/*z* (%) = 995.1 (5 and 44, respectively) appears a peak corresponding to the dinuclear $[Zn_2\mathbf{L^3}(ClO_4)_3]^+$ species formed from the molecular ion by loss of perchlorate and at *m*/*z* (%) = 733.5 (54) and 733.3 (23), respectively, a peak attributable to the ionic species $[Zn\mathbf{L^3}(ClO_4)]^+$ formed by successive loss of $Zn(ClO_4)_2$ and ClO_4^- can be observed.

Crystal Structure of $[Zn_2(H_{-2}L^1)](ClO_4)_2$ {[8](ClO4)2}

Crystals of $[Zn_2(H_{-2}\mathbf{L^1})](ClO_4)_2$ suitable for X-ray analysis were obtained by concentrating aqueous solutions containing $\mathbf{L^1}$ and $Zn(ClO_4)_2$ at pH = 9. The structure consists of $[Zn_2(H_{-2}\mathbf{L^1})]^{2+}$ cations and perchlorate anions. Each Zn^{II} is coordinated by the three nitrogen atoms from one of the polyamine bridges and by one sp^2 nitrogen atom from each one of the pyrazole units which are deprotonated

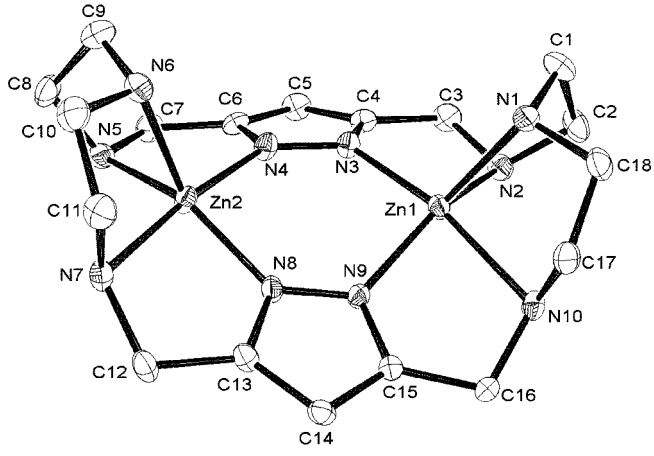

Figure 2. ORTEP drawing for the cation $[Zn_2(H_{-2}\mathbf{L^1})]^{2+}$ (**8**); thermal ellipsoids are drawn at the 30% probability level

and behave as bridging $\eta^1{:}\eta^1$-bis(monodentate) pyrazolate ligands (see Figure 2). The coordination geometry around each one of the metal ions can be defined as midway between a strongly distorted square pyramid and a trigonal bipyramid. The percentage of trigonal-bipyramidal units calculated by means of the facial planes[21] is 44.5% for the Zn1 site and 50.7% for the Zn2 site.

The shorter distances in the coordination spheres of both metal ions are those involving the pyrazolate sp^2 nitrogen atoms (see Table 5) and the largest ones are those of the amino groups adjacent to the pyrazole fragments. In order

 © 2005 Wiley-VCH Verlag GmbH & Co. KGaA, Weinheim

to achieve such a coordination geometry the central part of the chains are forced to move in the same direction giving something of a boat-like shape (Figure 2).

Table 5. Selected bonds lengths [Å] and angles [°] of [**8**]$(ClO_4)_2$

Parameter	Length/angle
Zn1−N1	2.110(5)
Zn1−N2	2.212(5)
Zn1−N3	2.037(4)
Zn1−N9	2.027(4)
Zn1−N10	2.267(5)
Zn2−N4	2.027(4)
Zn2−N5	2.181(5)
Zn2−N6	2.109(5)
Zn2−N7	2.235(5)
Zn2−N8	2.005(4)
N1−Zn1−N2	83.3(2)
N1−Zn1−N3	110.4(2)
N1−Zn1−N9	128.7(2)
N1−Zn1−N10	81.1(2)
N2−Zn1−N3	78.3(2)
N2−Zn1−N10	103.9(2)
N3−Zn1−N9	95.4(2)
N9−Zn1−N10	76.6(2)
N4−Zn2−N5	79.5(2)
N4−Zn2−N6	101.6(2)
N4−Zn2−N8	94.9(2)
N5−Zn2−N6	83.8(2)
N5−Zn2−N7	106.8(2)
N6−Zn2−N7	82.0(2)
N6−Zn2−N8	125.2(2)
N7−Zn1−N8	78.3(2)

The Zn−Zn distance (3.99 Å) is close to those found for the analogous Cu^{II} complexes of $\mathbf{L^1}$ and $\mathbf{L^2}$, implying that the rigidity of the pyrazole spacer is the main factor controlling this parameter. It is interesting to remark that, as already observed in the systems Cu/$\mathbf{L^1}$ and Cu/$\mathbf{L^2}$,[11,17] Cu^{II} coordination causes the ready deprotonation of the pyrazole moieties without requiring any addition of base.

Synthesis of Cu^{II} and/or Zn^{II} Dipyrazolate Complexes $[Cu_2(H_{-2}L^4)](ClO_4)_2$ {[**11**]$(ClO_4)_2$} and $[Zn_2(H_{-2}L^4)](ClO_4)_2$ {[**12**]$(ClO_4)_2$} from **4′**

Synthesis and Spectroscopic Characterisation

In order to unequivocally obtain Cu^{II} and Zn^{II} dipyrazolate complexes we first used the disodium dipyrazolate salt **4′** (Scheme 2) as a starting material. Treatment of **4′** with $Cu(ClO_4)_2{\cdot}6H_2O$ (2 equiv.) in MeOH afforded a blue solid which, after being crystallized from a 2:3 water/MeOH mixture, gave the Cu^{II} dipyrazolate complex $[Cu_2(H_{-2}L^4)](ClO_4)_2$ {[**11**]$(ClO_4)_2$}.

The ESI (positive mode) mass spectrum of [**11**]$(ClO_4)_2$ in MeOH shows two intense peaks at *m*/*z* (%) = 671.0 (100) and 571.2 (58) which are assignable to the molecular species $[Cu_2(H_{-2}L^4)(ClO_4)]^+$ and $[Cu_2(H_{-3}L^4)]^+$, respectively. These confirm that the compound is a dinuclear Cu^{II} dipyrazolate complex. There also appears a fairly weak peak at *m*/*z* = 508.1 corresponding to the mononuclear $[Cu(H_{-1}L^4)]^+$ species which may be formed from the monoprotonated molecular ion $[Cu_2(H_{-1}L^4)(ClO_4)_2]^+$ by loss of $Cu(ClO_4)_2$.

The Zn^{II} dinuclear complex $[Zn_2(H_{-2}L^4)](ClO_4)_2$ {[**12**]$(ClO_4)_2$} (Scheme 3) was obtained by treatment of the sodium salt **4′** with 2 equiv. of $Zn(ClO_4)_2{\cdot}6H_2O$ according to a similar procedure to that previously mentioned. After crystallisation from a water/methanol mixture, the analytical and spectroscopic data of the white solid obtained were consistent with formula $[Zn_2(H_{-2}L^4)](ClO_4)_2$ {[**12**]$(ClO_4)_2$}. In its ESI (positive mode) mass spectrum, three main peaks detected at *m*/*z* (%) = 671.2 (32), 609.3 (27) and 509.4 (100) are attributable to the ionic species $[Zn_2(H_{-2}L^4)ClO_4]^+$, $[Zn(L^4)ClO_4]^+$ and $[Zn(H_{-1}L^4)]^+$, respectively.

The structure of $[Zn_2(H_{-2}L^4)](ClO_4)_2$ {[**12**]$(ClO_4)_2$} in solution was also fully characterised by NMR spectroscopy. In Tables 6 and 7 are gathered the respective ^1H and ^{13}C NMR spectroscopic data of this compound recorded in [D_6]DMSO together with those of the dipyrazolate salt **4′** and those of the free ligand **4**. Table 6 verifies that the ^1H NMR spectroscopic data of **4** and **4′** are similar. Each shows a single set of signals for all the methylene protons, the chemical shift differences between **4** and **4′** being lower than 0.2 ppm. However, in the ^1H NMR spectrum of $[Zn_2(H_{-2}L^4)]^{2+}$ (**12**) (Figure 3, A), the methylene protons 6-H_2, 8-H_2 and 9-H_2 which are neighbours of the pyrazole

Table 6. Comparison of the ^1H NMR spectra (δ [ppm], [D_6]DMSO) of the free ligand **4**, its sodium dipyrazolate salt **4′** and the Zn^{II} dipyrazolate complex [**12**]$(ClO_4)_2$

	4	**4′**	[**12**]$(ClO_4)_2$
4-H	5.99 (s, 2 H)	5.82 (s, 2 H)	5.77 (s, 2 H)
6-H_A	3.56 (s, 4 H)	3.56 (s, 4 H)	4.02 (dd, 4 H)[a]
6-H_B	3.56 (s, 4 H)	3.56 (s, 4 H)	3.50 (dd, 4 H)[b]
8-H_A	2.48 (m, 4 H)	2.53 (m, 4 H)	3.09 (m, 4 H)
8-H_B	2.48 (m, 4 H)	2.53 (m, 4 H)	2.71 (m, 4 H)
9-H_A	1.49 (m, 4 H)	1.49 (m, 4 H)	1.93 (m, 4 H)
9-H_B	1.49 (m, 4 H)	1.49 (m, 4 H)	1.69 (m, 4 H)
10-H	2.48 (m, 8 H)	2.47 (m, 8 H)	2.96 (m, 8 H)
7-H	−	−	4.77 [m (t), 4H]
11-H	−	−	5.03 [m (t), 2H]

[a] ^1J = 16 Hz; ^2J = 7 Hz. [b] ^1J = 16 Hz; ^2J = 3 Hz.

Table 7. Comparison of the ^{13}C NMR spectra (δ [ppm], [D_6]DMSO) of the free ligand **4**, its sodium dipyrazolate salt **4′** and the Zn^{II} dipyrazolate complex [**12**]$(ClO_4)_2$

	4 (1)	**4′** (2)	Δδ (2−1)	{[**12**]$(ClO_4)_2$} (3)	Δδ (3−2)
C-3,5	146.97[a]	147.31[b]	0.34	151.12[b]	3.81
C-4	101.71	100.58	−1.13	96.88	−3.70
C-6	45.27	46.26	0.99	45.90	−0.36
C-8	47.02	47.14	0.12	50.67	3.56
C-9	29.22	29.26	0.04	23.72	−5.94
C-10	47.67	47.78	0.11	49.96	2.18

[a] Broad signal. [b] Sharp singlet.

 © 2005 Wiley-VCH Verlag GmbH & Co. KGaA, Weinheim

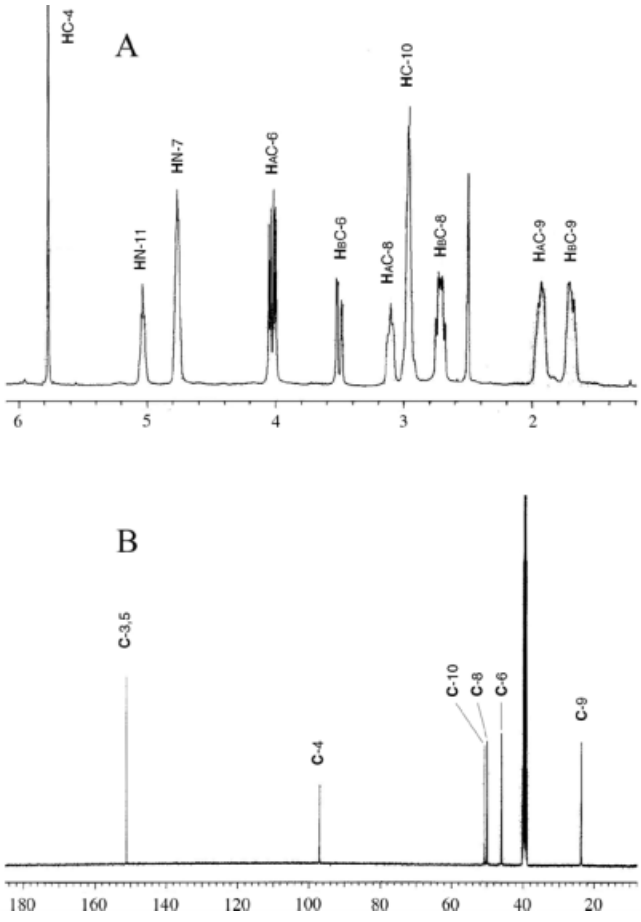

Figure 3. ^1H (A) and ^{13}C (B) NMR spectra of the Zn^{II} complex {[**12**]$(ClO_4)_2$} in [D_6]DMSO solution

moieties, appear in the spectrum as an AB spin system (Figure 3) suggesting that Zn^{II} coordination confers a rigid structure on the complex. Except for the 4-H pyrazole proton, all the other protons belonging to the macrocyclic cavity of **12** exhibit a generalised downfield chemical shift of their signals. It is interesting to note that in the ^1H NMR spectrum appear two signals at $\delta = 4.77$ and $\delta = 5.03$ ppm, which are attributable to the protons of the amino groups 7-H and 11-H, respectively. The triplet-like shape of these signals can be ascribed to their coupling with the neighbour methylene groups.

Table 7 shows the ^{13}C NMR signals of **4**, **4′** and [**12**]$(ClO_4)_2$ as well as the variations in the chemical shifts due to deprotonation of the pyrazole moieties which leads to **4′** [$\Delta\delta$ (2−1)] and the formation of the dinuclear Zn^{II} complex **12** [$\Delta\delta$ (3−2)].

In [D_6]DMSO, the C-3,5 quaternary carbon atoms of the free ligand **4** appear in the spectrum as a broad signal, while in the spectrum of **4′** this signal changes to a sharp singlet indicating that the slow prototropic equilibrium of the pyrazole rings has disappeared. Furthermore, as can be expected, upfield (δ =1.13 ppm for C-4) and downfield (δ = 0.34 ppm for C-3,5) variations of the pyrazole carbon signals confirm the formation of pyrazolate anions (Table 7).

Taking the ^{13}C NMR signals of **4′** as a reference, it can be observed that formation of the Zn^{II} dipyrazolate complex **12** induces strong downfield shifts in the signals of all the carbon atoms located in the α- positions to the nitrogen atoms involved in the complexation of the Zn^{II} ions. It also exerts strong upfield shifts on the signals of those located in the β- positions (Table 7).

*Crystal Structure of [$Cu_2(H_{-2}L^4)$]$(ClO_4)_2$ {[**11**]$(ClO_4)_2$}*

The crystallographic data were recorded at 150 K because some disorder found within the propylenic chains of the bridges and in the perchlorate counter anions prevented a satisfactory solution of the crystal structure from data collected at room temperature. Although even at low temperature some disorder persists, the solution is good enough for unequivocally identifying the structural characteristics of the coordination sites.

Crystals of [**11**]$(ClO_4)_2$ consist of $[Cu_2(H_{-2}\mathbf{L^4})]^{2+}$ cations and perchlorate anions. The coordination geometry around each copper atom is an irregular, axially elongated square pyramid. The base of the pyramid is formed by the two secondary nitrogen atoms of the polyamine bridge closer to the heterocycle and by two nitrogen atoms of two different pyrazolate units which act as $\eta^1{:}\eta^1$ bis(monodentate) anionic bridging ligands (Figure 4). The displacements of the metal ions from the plane of the nitrogen donors are 0.322(2) Å for Cu1 and 0.303(2) Å for Cu2. The central nitrogen atoms of the bridges occupy the axial positions. In both coordination sites, the Cu−N distances involving the sp^2 pyrazolate nitrogen atoms [Cu(1)−N(3) = 1.963(9) Å, Cu(2)−N(4) = 1.94(1) Å; Table 8] are much shorter than those of the secondary nitrogen atoms [Cu(1)−N(2) = 2.10(1) Å, Cu(2)−N(5) = 2.11(1) Å]. The Cu(1)−Cu(2) distance is 3.96 Å which is almost identical to those found in the crystal structures of $[Cu_2(H_{-2}\mathbf{L^1})](ClO_4)_2$ {[**5**]$(ClO_4)_2$}[17,11] and $[Cu_2(H_{-1}\mathbf{L^2})](ClO_4)_3{\cdot}2H_2O$ {[**6**]$(ClO_4)_2(HClO_4){\cdot}2H_2O$}[11] as well as in several crystal structures of other pyrazole-containing complexes in which the pyrazolate anions exhibit the same coordination mode.[8,15,16] However, such a distance is not so fixed in some complexes of podand ligands containing pyrazole bridges.[22] It is also interesting to point out that the axial

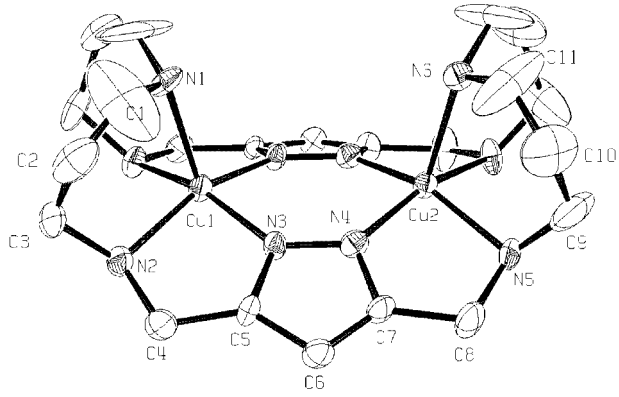

Figure 4. ORTEP drawing for the cation $[Cu_2(H_{-2}\mathbf{L^4})]^{2+}$ (**11**); thermal ellipsoids are drawn at the 30% probability level

 © 2005 Wiley-VCH Verlag GmbH & Co. KGaA, Weinheim

Table 8. Selected bonds lengths [Å] and angles [°] of [**11**]$(ClO_4)_2$

Parameter	Length/angle
Cu1−N1	2.20(2)
Cu1−N2	2.1(1)
Cu1−N3	1.963(9)
Cu2−N4	1.94(1)
Cu2−N5	2.11(1)
Cu2−N6	2.24(2)
N1−Cu1−N2	92.6(5)
N1−Cu1−N3	106.8(5)
N2−Cu1−N3	80.5(4)
N4−Cu2−N5	81.1(4)
N4−Cu2−N6	106.4(4)
N5−Cu2−N6	91.7(5)

elongation observed in this complex is much smaller than those previously reported for $[Cu_2(H_{-2}\mathbf{L^1})](ClO_4)_2$ and $[Cu_2(H_{-1}\mathbf{L^2})](ClO_4)_3{\cdot}2H_2O$.[11] The complex again adopts a boat-shaped conformation with the side-chains folded towards the same side of the macrocyclic cavity.

Crystal Structure of [$Zn_2(H_{-2}L^4)$]$(ClO_4)_2$ {[12]$(ClO_4)_2$}

The crystallographic data were also recorded at 150 K because similar disorder to that found in the previous case was observed and this prevented a satisfactory solution from data recorded at room temperature. Crystals of [**12**]$(ClO_4)_2$ consist of $[Zn_2(H_{-2}\mathbf{L^4})]^{2+}$ cations and perchlorate anions. The coordination geometry around each Zn^{II} atom is very irregular and can be defined as a distorted square pyramid. Analogous to the previous structure, the base of the pyramid is formed by the two secondary nitrogen atoms of the polyamine bridge closer to the heterocycle and by two nitrogen atoms of two different pyrazolate units which act as $\eta^1{:}\eta^1$ bis(monodentate) anionic bridging ligands (Figure 5). The displacements of the metal atoms above the plane defined by the nitrogen donors are 0.595(2) Å for Zn1 and 0.554(2) Å for Zn2. The central nitrogen atoms of the polyamine bridges occupy the axial positions which in this case do not show any distortion. In contrast to the analogous Cu^{II} complex, the Zn−N distances of the sp^2 pyrazole nitrogen atoms in this case [Zn(1)−N(3) = 2.037(9) Å, Zn(2)−N(4) = 2.040(8) Å; Table 9] are close to those of their secondary nitrogen atoms in the centre of the bridge [Zn(1)−N(1) = 2.08(1) Å, Zn(1)−N(2) = 2.09(1) Å]. The largest M−N distances are found for the secondary nitrogen atom adjacent to the heterocycle. The Zn(1)−Zn(2) distance is again 3.96 Å confirming that it is fixed by the pyrazolate bridge. The conformation of the whole molecule is again boat-shaped with the central part of both chains folded towards the same side of the macrocyclic plane (Figure 5).

Table 9. Selected bonds lengths [Å] and angles [°] of [**12**]$(ClO_4)_2$

Parameter	Length/angle
Zn1−N1	2.08(1)
Zn1−N2	2.206(8)
Zn1−N3	2.037(9)
Zn2−N4	2.040(8)
Zn2−N5	2.196(8)
Zn2−N6	2.09(1)
N1−Zn1−N2	99.5(4)
N1−Zn1−N3	114.3(4)
N2−Zn1−N3	77.4(3)
N4−Zn2−N5	77.38(3)
N4−Zn2−N6	112.7(3)
N5−Zn2−N6	98.1(3)

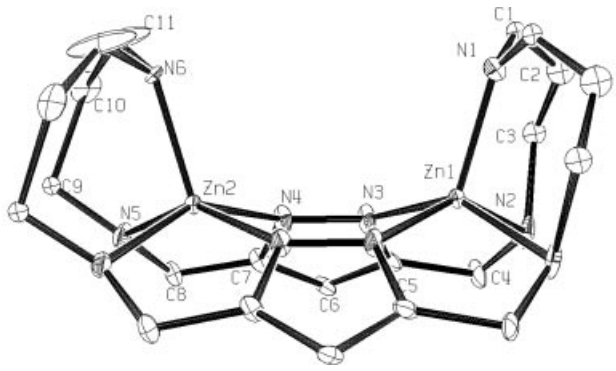

Figure 5. ORTEP drawing for the cation $[Zn_2(H_{-2}\mathbf{L^4})]^{2+}$ (**12**); thermal ellipsoids are drawn at the 30% probability level

Synthesis of Cu^{II} Dipyrazolate Complexes[$Cu_2(L^4)$]$(ClO_4)_4{\cdot}2H_2O$ {[13]$(ClO_4)_4{\cdot}2H_2O$} and [$Cu_3(H_{-2}L^4)$]$(ClO_4)_4{\cdot}2MeOH$ {[14]$(ClO_4)_4{\cdot}2MeOH$} from L^4

Synthesis and Spectroscopic Characterisation

It is interesting to point out that when we tried to obtain the dipyrazolate complexes $[Cu_2(H_{-2}\mathbf{L^4})](ClO_4)_2$ {[**11**]$(ClO_4)_2$} by direct treatment of the neutral ligand **4** with $Cu(ClO_4)_2{\cdot}6H_2O$ in methanol, we observed very different behaviour to that previously described using the disodium dipyrazolate salt **4′** as a starting material. Thus, treatment of a methanolic solution of **4** (2.5×10^{-2} M) with $Cu(ClO_4)_2{\cdot}6H_2O$ (2 equiv.) at room temperature gave a blue precipitate which, after being vacuum-dried at 100 °C, afforded a blue solid of formula $[Cu_2\mathbf{L^4}](ClO_4)_4{\cdot}2H_2O$ in 71% yield. After redissolving this blue solid in boiling water for 5 min, a red solid slowly and unexpectedly crystallised. After being vacuum-dried at 100 °C, this resulted in a reddish-brown complex of formula $[Cu_2\mathbf{L^4}](ClO_4)_4{\cdot}2H_2O$ {[**13**]$(ClO_4)_4{\cdot}2H_2O$} (Scheme 3) in 61% yield. Surprisingly, this red complex had identical analytical data to the blue precursor mentioned above. Microanalysis performed by X-ray energy dispersive spectrometry confirmed the proposed Cu/Cl ratio. This can be explained if both the blue and the red forms of this complex correspond to dinuclear Cu^{II} dipyrazolate species which share the characteristic feature of having the two sp^3 nitrogen atoms located at the centre of the side chains protonated and, in contrast to $[Cu_2(H_{-2}\mathbf{L^4})](ClO_4)_2$ {[**11**]$(ClO_4)_2$}, thereby not directly coordinated to the metal atoms (Scheme 3). The coordination

 © 2005 Wiley-VCH Verlag GmbH & Co. KGaA, Weinheim

of the metal ion causes the release of the protons from the pyrazole fragments which are captured by the basic central nitrogen atoms of the bridges.

Furthermore, the ESI-MS data of either the precursor blue form or the red final form show identical peaks which appear with different relative abundances as shown in Table 10. In the negative mode, the molecular ion $[M - H]^-$, corresponding to $[Cu_2(H_{-1}\mathbf{L^4})(ClO_4)_4]^-$ appears at m/z = 969.4 with low relative abundance (see Table 10), together with a more intense peak at m/z = 1071.4 and the base peak at m/z = 869.4 assignable to the species $[M + ClO_4]^-$ and $[(M - ClO_4 - 2\ H]^-$, respectively, which agree with the proposed structure. Moreover, in the positive mode, two characteristic peaks appear at m/z = 871 and 771, assignable to the $[Cu_2(\mathbf{L^4})(ClO_4)_3]^+$ and $[Cu_2(H_{-1}\mathbf{L^4})(ClO_4)_2]^+$ species which correspond to dinuclear Cu^{II} dipyrazolate fragments containing partly protonated polyamine chains. On the other hand, in addition to the expected peak at m/z = 671 assignable to the most abundant fragment $[(H_{-2}\mathbf{L^4})Cu_2(ClO_4)]^+$, both the precursor blue and the final red forms of $[\mathbf{13}](ClO_4)_2(H_2O)_2$ show a characteristic peak at m/z = 547 attributable to $[(H_2\mathbf{L^4})(ClO_4)]^+$ which demonstrates the presence of protonated nitrogen atoms in the ligand structure.

Table 10. Comparison of the most significant peaks recorded in the ESI-MS data of the dinuclear Cu^{II} complex $\{[\mathbf{13}](ClO_4)_4{\cdot}2(H_2O)\}$ (1007.6) in both its blue and red forms

m/z	Composition	% blue	% red
Negative mode			
1071	$\{[Cu_2\mathbf{L^4}](ClO_4)_5\}^-$	35	14
969	$\{[Cu_2(H_{-1}\mathbf{L^4})](ClO_4)_4\}^-$	6	8
869	$\{[Cu_2(H_{-2}\mathbf{L^4})](ClO_4)_3\}^-$	100	100
Positive mode			
871	$\{[Cu_2\mathbf{L^4}](ClO_4)_3\}^+$	10	3
771	$\{[Cu_2(H_{-1}\mathbf{L^4})](ClO_4)_2\}^+$	10	4
671	$\{[Cu_2(H_{-2}\mathbf{L^4})](ClO_4)\}^+$	100	59
569	$[Cu_2(H_{-3}\mathbf{L^4})]^+$	3	4
547	$\{[H_2\mathbf{L^4}](ClO_4)\}^+$	51	33
447	$[H\mathbf{L^4}]^+$	–	41
224	$[(\mathbf{L^4}/2)+H]^+$	–	100

Unfortunately, up to now, it has not been possible to obtain adequate crystals of either the precursor blue form or the red form suitable for X-ray analysis.

However, on the basis of the above observations, the colour changes observed can be tentatively attributed to the presence of the two water molecules which are bound in a different manner in both complexes. In the blue form they would be coordinated to the metal ion occupying the axial positions of the pentacoordinate environment (see Scheme 4, blue-[**13**]). In the red form the coordination environment around each Cu^{II} will be square-planar and the water molecules would not occupy the first coordination sphere of the metal ion (Scheme 4, red-[**13**]). In both cases the water molecules might be stabilised through $^+NH\cdots OH_2$ hydrogen bonds with the two protonated sp^3 nitrogen atoms located in the centre of the side chains. We previously reported these types of monohydrated ammonium groups in the crystalline structure of the dinuclear Cu^{II} complex $[\mathbf{6}](HClO_4)(ClO_4)_2{\cdot}2H_2O$[11] where one of the aliphatic nitrogen atoms of the noncoordinated bridge is protonated and hydrogen-bonded to a water molecule.

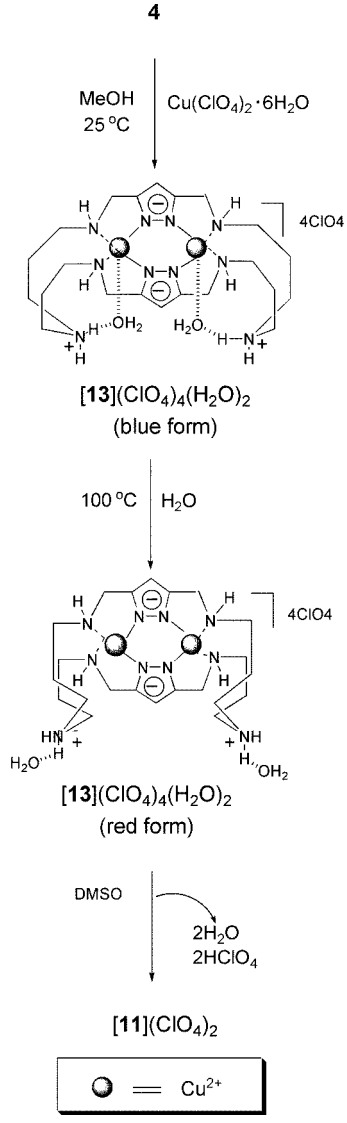

Scheme 4

In the complex $\{\text{red-}[\mathbf{13}](ClO_4)_2{\cdot}2H_2O\}$, the conformational change produced would be induced by the treatment of the starting precursor blue form with boiling water.

Finally, when we tried to obtain similar dinuclear complexes starting from a more concentrated solution of ligand $\mathbf{L^4}$ (**4**) (6.0×10^{-2} M) under similar reaction conditions [2 equiv. of $Cu(ClO_4)_2{\cdot}6H_2O$ at room temp.], we obtained another unexpected result. A bright green solid precipitated from the methanol solution which, after being vacuum-dried at 100 °C, gave a new trinuclear copper complex in low yield (28%). The analytical and MS data of this new complex are consistent with the formula $[Cu_3(H_{-2}\mathbf{L^4})](ClO_4)_4{\cdot}2MeOH$ $\{[\mathbf{14}](ClO_4)_4{\cdot}2MeOH\}$

 © 2005 Wiley-VCH Verlag GmbH & Co. KGaA, Weinheim

(Scheme 3). The Cu/Cl (3:4) molar ratio was confirmed by X-ray energy dispersive spectrometry.

Since matrix-assisted laser desorption/ionisation (MALDI-TOF) mass spectrometry is actually among the most important ionisation methods for strong metal-ion complexes,[23] we used this technique in order to confirm the structure of the trinuclear complex. Table 11 shows the most significant trinuclear copper ions detected in the MALDI-TOF mass spectrum of {[**14**]$(ClO_4)_4$·2MeOH} using 2,5-dihydroxybenzoic acid (DHB) as a matrix. In a similar way as has already been observed in other MALDI-TOF mass spectra of copper complexes in which Cu^{II} ions are apparently simply reduced,[24,25] the composition of most of the ionic fragments gathered in Table 11 agree with different copper oxidation states due to partial or total copper reduction processes for which the source of the electrons may be the photoionised DHB matrix. Thus, at *m*/*z* = 635 appears the base peak corresponding to the skeletal trinuclear copper fragment $[Cu_3(H_{-2}\mathbf{L^4})]^+$ in which the three Cu^{II} atoms are reduced to Cu^{I}. Other characteristic ions which correspond to the proposed structure appear at *m*/*z* (%) = 734.3 (78) and 797.2 (27). Both peaks are attributable to the ionic species $[Cu_3(H_{-2}\mathbf{L^4})(ClO_4)]^+$ and $[Cu_3(H_{-2}\mathbf{L^4})(MeO)(MeOH)]^+$, respectively, in which two of the three Cu^{II} atoms have been reduced to Cu^{I}. The last mentioned species (*m*/*z* = 797.2) confirms the presence of two MeOH molecules in the complex and simultaneously suggests that one of these molecules may be acting as a bridge between two copper ions.

Table 11. Most significant peaks recorded in the MALDI-TOF-MS of [**14**]$(ClO_4)_4$·2MeOH corresponding to trinuclear copper fragments

m/*z* (%)	Composition[a]	Oxidation state
797.2 (27)	$\{[Cu_3(H_{-2}\mathbf{L})](MeO)(MeOH)\}^+$	2 Cu^+ + Cu^{2+}
750.3 (7)	$\{[Cu_3(H_{-2}\mathbf{L})](ClO_4)+(O)\}^+$	3 Cu^{2+}
734.3 (78)	$\{[Cu_3(H_{-2}\mathbf{L})](ClO_4)\}^+$	2 Cu^+ + Cu^{2+}
649.4 (26)	$\{[Cu_3(H_{-4}\mathbf{L}) +(O)]\}^{\cdot+}$	3 Cu^{2+}
635.4 (100)	$[Cu_3(H_{-2}\mathbf{L})]^+$	3 Cu^+

[a] [$(H_{-2}\mathbf{L})$ = ($C_{22}H_{40}N_{10}$) and $(H_{-4}\mathbf{L})$=($C_{22}H_{38}N_{10}$)].

Finally, at *m*/*z* = 750.3 and 649.4 are two peaks assignable to ionic fragments containing oxygen in which the Cu^{II} initial oxidation state has not changed. However, it is difficult to be certain if these ions are truly formed or are the result of secondary oxidation reactions in the matrix as was previously observed in other MALDI-TOF mass spectra of metallic complexes.[25]

Molecular Modelling Studies

In order to gain further insight into the molecular structures of both the dinuclear Cu^{II} [**13**]$(ClO_4)_4$·$2H_2O$ and the trinuclear Cu^{II} complex {[**14**]$(ClO_4)_4$·2MeOH}, we performed some modelling studies. Molecular mechanics models of complexes of a variety of metal ions have been recently developed[26] and have proved useful for ligand design. Use of a well-established biochemically oriented force field with specific metal parameters would allow the interactions of metal complexes and biological molecules to be studied and modelled. Among the well-established force-fields, AMBER[27] has found widespread use in the modelling of biological molecules and the development of suitable parameter sets which allows the modelling of metal complexes. This has produced results in good agreement with experimental observations without requiring additional changes.[28] For those reasons, in this work, molecular modelling studies were carried out using the AMBER method modified by the inclusion of appropriate parameters.

To check the consistency of the calculations we modelled the complex [**11**]$(ClO_4)_2$ (which has a known X-ray structure) according to the same procedure detailed in the Exp. Sect. with no restraints. Data obtained in this modelling study agree quite well with the crystallographic results, although the calculated Cu−Cu distances are shorter than the experimentally measured ones (0.12 Å, similar to maximum deviation obtained by Comba et al.).[29]

To study the copper complexes [**13**]$(ClO_4)_4$·$2H_2O$ and [**14**]$(ClO_4)_4$·MeOH, coordination numbers and geometries were selected according to the preferences of copper(II) and, taking into account all the experimental data for the synthesised complexes, red-[**13**] was assumed to be square-planar while blue-[**13**] and green [**14**] were assumed to be pyramidal. Thus, we modelled the blue and red forms of the dihydrated complex [**13**]$(ClO_4)_4$·$2H_2O$ with the results given in Figure 6 (A).

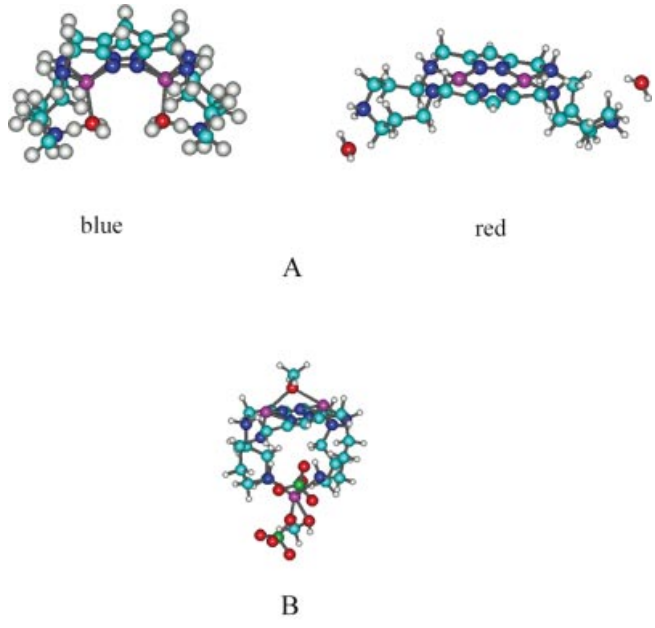

Figure 6. A) Molecular models of the blue and red forms of the complex [**13**]$(ClO_4)_4(H_2O)_2$; B) molecular model for the trinuclear complex [**14**]$(ClO_4)_4(MeOH)_2$

In the above complexes, the calculated Cu−Cu distance between the two metal ions coordinated with pyrazole ni-

 © 2005 Wiley-VCH Verlag GmbH & Co. KGaA, Weinheim

trogen atoms is 3.52 Å for the red form of [**13**], denoting the rigidity of the bridge, and 4.03Å for its blue form which is more similar to the values found for [**11**] (calculated 3.84 Å, X-ray data 3.96 Å).

Since they have different connectivities, no attempt was made to compare the calculated molecular mechanics strain energies of the different coordination complexes since each one needs a different parameter set. PM3 calculations of the corresponding heats of formation, however, suggests that the red form of {[**13**]$(ClO_4)_4$·$2H_2O$} is more stable than the blue one.

Finally, a model for the green trinuclear Cu^{II} complex [**14**]$(ClO_4)_4$·2MeOH is given in Figure 6 (B). Coordination of the metal centres to the pyrazole sp^2 nitrogen atoms and the adjacent nitrogen atoms forces the central parts of both bridges to move upwards in the same direction thereby enabling the central nitrogen atoms to coordinate to a further metal ion provided there are other ancillary ligands that can assist the processes. In this case the methanol molecules could complete the coordination spheres. In [**14**], the calculated Cu−Cu distances between the third metal ion and the pyrazole-coordinated metal ion are 5.89 Å and 6.41 Å, respectively, while the distance between these two remains quite similar to that of 3.83 Å in the blue form of [**13**].

^{1}H NMR Spectra of {red-[13]$(ClO_4)_4$·$2H_2O$}

In order to obtain further information about the nature of the red complex $[Cu_2\mathbf{L^4}](ClO_4)_4$·$2H_2O$ {red-[**13**]$(ClO_4)_4$·$2H_2O$} (Scheme 3), we performed paramagnetic ^{1}H NMR spectroscopy. This technique is very useful for the study of magnetically coupled systems such as dinuclear Cu^{II}−Cu^{II} complexes.[30,31] However, in the case of mononuclear Cu^{II} complexes its usefulness is rather limited due to the large electronic relaxation time of Cu^{II} which consequently produces a large broadening of the signals. The information that this technique provides refers to the electronic properties, coordination geometry and conformational changes in solution.

The ^{1}H NMR spectrum of the red $[Cu_2\mathbf{L^4}](ClO_4)_4$·$2H_2O$ complex in $(CD_3)_2SO$ is shown in Figure 7 (A). It displays, in the downfield region, nine hyperfine-shifted signals (a−i) and four other signals (j−m) which are shifted upfield. When the temperature is raised up to 45 °C, the broad signals a−c and e move upfield, Figure 7 (B, C). This change is irreversible and at the same time the colour of solution changes from red-violet to blue, indicating a conformational change. The isotropically shifted resonances, longitudinal relaxation times (T_1) and line widths at half-height are reported in Table 12 for the red complex $[Cu_2\mathbf{L^4}](ClO_4)_4$·$2H_2O$ {red-[**13**]$(ClO_4)_4$·$2H_2O$}. The above-mentioned signals (a−c) display short T_1 values (< 1 ms) and broad line widths at half-height of around 2000 Hz. This, together with the proton integrations, permits the assignment of these signals to the protons of the CH_2 groups located α to the coordinated nitrogen atoms nearest to the Cu^{II} ion (see Scheme 5). When the temperature is raised up to 45 °C (see Figure 7, C), the broad signals which move upfield integrate for eight more protons, indicating an increase in the coordination number of the copper ion. In this sense, signal (e) which integrates for eight protons and can

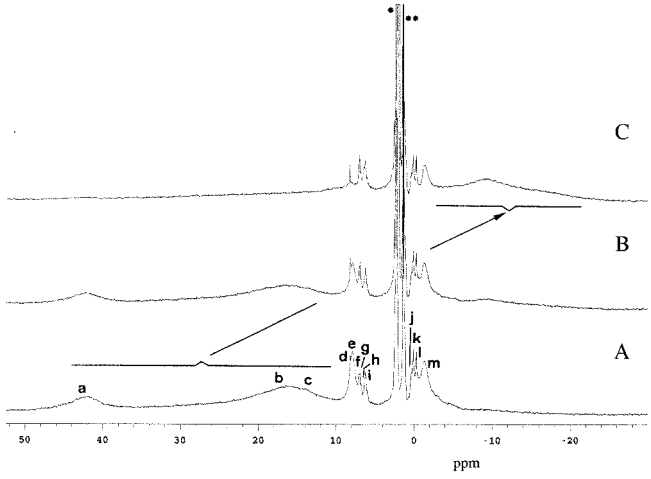

Figure 7. 400 MHz ^{1}H NMR spectra of $[Cu_2\mathbf{L^4}](ClO_4)_4(H_2O)_2$ in $(CD_3)_2SO$ at different temperatures: 298 K (A); 313 K (B); 323 K (C); the asterisks mark the residual solvent and impurity signals [* $(CH_3)_2SO$; ** HOD]

Table 12. ^{1}H NMR hyperfine-shifted resonances of red-[**13**]$(ClO_4)_4$·$2H_2O$ in $(CD_3)_2SO$ at 298 K

Signal	δ [ppm]	Assignments	Number of protons	T_1 [ms]	$\Delta\nu_{1/2}$ [Hz]	T_2 [ms][a]
a	42.3	α-CH_2		< 1	1740	0.18
b	15.8	α-CH_2	16	< 1	2128	0.15
c	14.2	α-CH_2		< 1	[b]	[b]
d	8.2	$H_{pyrazole}$[c]	1	138	52[d]	6.1[d]
e	7.8	γ-CH_2	8	108	[b]	[b]
f	7.1	$H_{pyrazole}$[c]	1	146	[b]	[b]
g	6.9	β-CH_2		146	[b]	[b]
h	6.4	β-CH_2		150	[b]	[b]
i	6.2	β-CH_2		152	[b]	[b]
j	0.27	β-CH_2	8	130	[b]	[b]
k	0.05	β-CH_2		158	[b]	[b]
l	−0.32	β-CH_2		158	65[d]	4.9[d]
m	−1.4	β-CH_2		114	322[d]	1.0[d]

[a] Measured from the line width at half-height. [b] Overlap prevents measurement of this value. [c] Tentative assignments. [d] Measured at 323 K (blue complex).

 © 2005 Wiley-VCH Verlag GmbH & Co. KGaA, Weinheim

be assigned to CH_2 groups located γ to the coordinated nitrogen atoms in the red-violet $[Cu_2\mathbf{L^4}](ClO_4)_4{\cdot}2H_2O$ {red-[**13**]$(ClO_4)_4{\cdot}2H_2O$} complex, disappears completely in the ^{1}H NMR spectrum of the blue complex **13**. These results clearly illustrate a change in the coordination geometry from square-planar in the red form to pyramidal or five-coordinate in the blue form. The data also suggest that in the blue form, the nitrogen atoms in the centre of the bridges are coordinated to the metal ion. Therefore, in the weakly acidic solvent $(CD_3)_2SO$, the centre nitrogen atoms are deprotonated and the red complex gradually transforms to $[Cu_2(H_{-2}\mathbf{L^4})]^{2+}$ (**11**) (see Scheme 5). Indeed, this spectrum is identical to that obtained of a solution formed by directly dissolving $[Cu_2(H_{-2}\mathbf{L^4})](ClO_4)_2$ ([**11**]$(ClO_4)_2$] in the same solvent. The other signals (d and f−m), which correspond to the CH_2 groups β to the coordinated nitrogen atoms and to the pyrazole protons, display large T_1 values (100−150 ms). As described previously,[31] dinuclear Cu^{II} complexes have similar T_1 values and broad line widths.

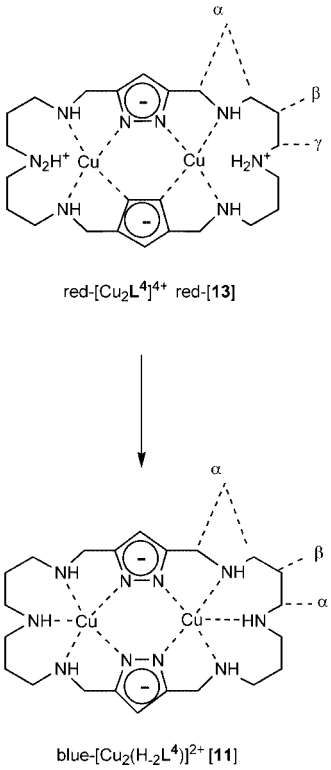

Scheme 5

In addition, variable-temperature ^{1}H NMR spectra of red-$[Cu_2\mathbf{L^4}](ClO_4)_4{\cdot}2H_2O$ were recorded from 293 to 323 K. The representation of the temperature dependence of the paramagnetic hyperfine-shifted resonances for some protons is shown in Figure 8. All signals are temperature-independent except for signals (a) and (b). Only signal (a) exhibits anti-Curie behaviour and furthermore signal (b) shows Curie behaviour. Extrapolated values at infinite temperatures for signal (a) indicate the existence of magnetic coupling.[31]

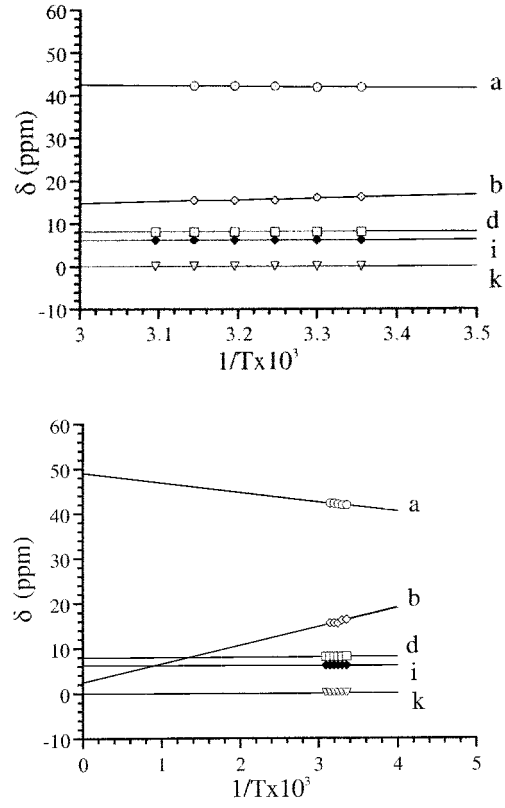

Figure 8. Temperature dependence of the isotropically shifted resonances of red-[**13**]$(ClO_4)_4{\cdot}2H_2O$; the insert shows the plot with the $1/T$ coordinate expanded

Magnetic Measurements of {red-[13] $(ClO_4)_4{\cdot}2H_2O$} and {[11] $(ClO_4)_2$}

The magnetic properties of $[Cu_2(H_{-2}\mathbf{L^4})](ClO_4)_2$ {[**11**]$(ClO_4)_2$} and $[Cu_2(\mathbf{L^4})](ClO_4)_4{\cdot}2H_2O$ {red-[**13**]$(ClO_4)_4{\cdot}2H_2O$} are shown in Figure 9 in the form of $\chi_M T$ versus T, χ_M being the magnetic susceptibility per two copper(II) ions. The value of $\chi_M T$ at room temperature is 0.46 $cm^3{\cdot}mol^{-1}$ K for $[Cu_2\mathbf{L^4}](ClO_4)_4{\cdot}2H_2O$ and $[Cu_2(H_{-2}\mathbf{L^4})](ClO_4)_2$, a value which is significantly lower than that expected for two uncoupled Cu^{II} ions. Upon cool-

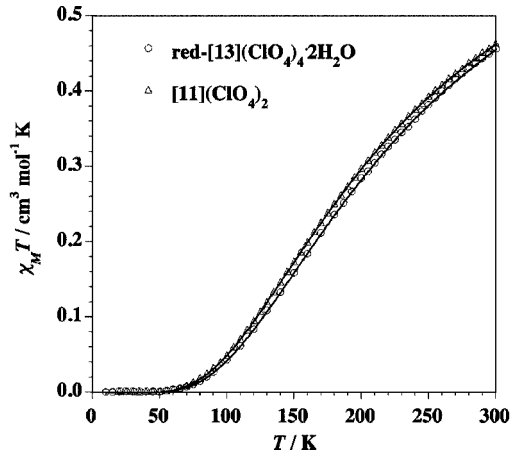

Figure 9. Plot of $\chi_M T$ vs. T for the complexes red-[**13**]$(ClO_4)_4{\cdot}2H_2O$ and [**11**]$(ClO_4)_2$

 © 2005 Wiley-VCH Verlag GmbH & Co. KGaA, Weinheim

ing $\chi_M T$ continuously decreases, vanishing at around 70 K. Moreover, the corresponding χ_M curves show maxima at 270 K (for $[Cu_2\mathbf{L^4}](ClO_4)_4{\cdot}2H_2O$) and 255 K (for $[Cu_2(H_{-2}\mathbf{L^4})](ClO_4)_2$] (see Supporting Information, Figure S2). This magnetic behaviour is characteristic of an important antiferromagnetic interaction between the Cu^{II} ions with singlet spin ground states.

We have interpreted the magnetic data according to the actual dinuclear nature of the complexes with the spin Hamiltonian $\mathbf{H} = -J\mathbf{S_1S_2}$. The fit of the magnetic data to the appropriate susceptibility expression derived from the van Vleck formula and assuming that the *g* factors for both Cu^{II} ions are identical, leads to $J = -299(7)$ cm^{-1} and $g = 2.09(1)$ for red-$[Cu_2\mathbf{L^4}](ClO_4)_4{\cdot}2H_2O$ {red-**[13]**$(ClO_4)_2{\cdot}2H_2O$}, and $J = -286(6)$ cm^{-1} and $g = 2.07(1)$ for $[Cu_2(H_{-2}\mathbf{L^4})](ClO_4)_2$ {**[11]**$(ClO_4)_2$}.

The observed *J* values lie in the upper range of the magnetic interactions found for related bis(μ-pyrazolato)-bridged dinuclear complexes. In fact, to the best of our knowledge, the highest *J* value observed for this family is $J = -412$ cm^{-1} for the compound $[Cu_2\mathbf{L^2}](BF_4)_2$ where L = 3,5-bis(*i*PrSCH$_2$)pyz.[32] The existence of σ-donor atoms as peripheral ligands may be responsible for these strong interactions.[33] However, the number of structurally characterised examples reported in the literature is still limited.[34]

The pathway for magnetic exchange is propagated through the bridging pyrazolate ligands. From the molecular structure of $[Cu_2(H_{-2}\mathbf{L^4})](ClO_4)_2$ {**[11]**$(ClO_4)_2$} one can conclude that the unpaired electron in each metal centre is clearly described by a $d_{x^2-y^2}$ magnetic orbital which is coplanar with the pyrazolate skeleton. The significant overlap between these magnetic orbitals accounts for the strong antiferromagnetic coupling observed. Although the crystal structure of $[Cu_2\mathbf{L^4}](ClO_4)_4{\cdot}2H_2O$ is not available, the very close magnetic behaviour of the complexes $[Cu_2\mathbf{L^4}](ClO_4)_4{\cdot}2H_2O$ {red-**[13]**$(ClO_4)_4{\cdot}2H_2O$} and $[Cu_2(H_{-2}\mathbf{L^4})](ClO_4)_2$ allows us to predict a similar exchange pathway. This again supports the suggestion that deprotonation of the pyrazole rings has occurred in both structures.

Conclusions

The synthesis of a 2+2 polyamine macrocycle containing pyrazole spacers connected through methylene groups to dipropylenetriamine bridges (**L^4**) has been described here for the first time. The acid-base behaviour of **L^4** in water reveals that, like the analogous macrocycle containing diethylenetriamine bridges (**L^1**), the pyrazole spacers do not participate in any net protonation step in the pH range of 2−11. The number of protonation steps observed is equal to the number of amino groups in the bridges. ^{1}H and ^{13}C NMR spectroscopy support this conclusion. The overall basicity of **L^4** is, on the other hand, five orders of magnitude greater than that of **L^1**. The deprotonation of the pyrazole moieties can, however, be readily achieved in the presence of coordinated metal ions. Cu^{II} induces the deprotonation of the pyrazole rings at lower pH values than Zn^{II} due to its much stronger interaction with the ligand. On the other hand, pyrazole deprotonation is more readily achieved (at more acidic pH values) with the ligand **L^1** bearing ethylenic chains in the bridges with five-membered chelates than in **L^4** containing six-membered chelates and a higher overall basicity.

The higher basicity of **L^4** is also reflected in the different syntheses of the dinuclear solid complexes which we have carried out. In the case of **L^1**, treatment of $Cu(ClO_4)_2{\cdot}6H_2O$ with either neutral **L^1** or with its disodium salt $Na_2[H_{-2}\mathbf{L^1}]$ in ethanol followed by crystallisation from water leads to the formation of the same dinuclear complex $[Cu_2(H_{-2}\mathbf{L^1})](ClO_4)_2$ in which the pyrazole groups are deprotonated thereby behaving as $\eta^1{:}\eta^1$ monodentate bridging ligands and the polyamine bridges are completely deprotonated. In the case of **L^4** the situation is different. Treatment of neutral **L^4** with $Cu(ClO_4)_2{\cdot}6H_2O$ in MeOH gives a blue solid complex which by heating in boiling water (for 5 min) followed by slow crystallisation leads to a red compound. The elemental analyses of both the blue and the red forms of this complex are consistent with the same empirical formula, i.e. $[Cu_2\mathbf{L^4}](ClO_4)_4{\cdot}2(H_2O)$. The ESI-MS and ^{1}H NMR paramagnetic data of the red complex clearly indicates that it is a dinuclear square-planar Cu^{II} complex in which the central nitrogen atoms of the bridging chains are not involved in the coordination to the metal ions and are therefore protonated. On the basis of both the elemental analysis of {red-**[13]**$(ClO_4)_4{\cdot}2H_2O$} and crystallographic data of polyamine receptors previously reported, it seems reasonable to suppose that the above-mentioned protonated nitrogen atoms may be hydrogen-bonded to water molecules [Scheme 4, **13** (red form)]. The blue form shows the same feature but in this case the coordination geometry should be pyramidal with the water molecules occupying the axial positions. The exchange between the two forms depends on both the temperature and the solvent. Therefore, the marked basicity of the propylamine chains facilitates the capture of the protons released from the pyrazole rings.

However, if $Cu(ClO_4)_2{\cdot}6H_2O$ is treated with the sodium salt $Na_2[H_{-2}\mathbf{L^4}]$ in methanol followed by crystallisation from water, the complex obtained is $[Cu_2(H_{-2}\mathbf{L^4})](ClO_4)_2$ {**[11]**$(ClO_4)_2$} which is analogous to that obtained with **L^1** (Scheme 3). The crystal structure of $[Cu_2(H_{-2}\mathbf{L^4})](ClO_4)_2$ shows a very irregular square-pyramidal coordination geometry in which the shorter distances are those involving the pyrazole nitrogen atoms and the axial ones are involved in both coordination sites by the central nitrogen atoms of the propylenic chains. Analogously, in the case of Zn^{II}, the crystal structures of $[Zn_2(H_{-2}\mathbf{L^1})](ClO_4)_2$ {**[8]**$(ClO_4)_2$} and $[Zn_2(H_{-2}\mathbf{L^4})](ClO_4)_2$ {**[12]**$(ClO_4)_2$} also reveal similar coordination arrangements. In the three structures, the overall shape of the complex cations is boat-like with the central parts of the polyamine bridges displaced towards the same side of the macrocyclic ring.

 © 2005 Wiley-VCH Verlag GmbH & Co. KGaA, Weinheim

Finally, treatment of concentrated solutions of **L⁴** with $Cu(ClO_4)_2 \cdot 6H_2O$ gives a trinuclear complex of stoichiometry $[Cu_3(H_{-2}\mathbf{L^4})](ClO_4)_4 \cdot 2MeOH$ in low yield which has been characterised by MALDI-TOF mass spectrometry. The boat-like arrangement of the macrocycle in the dinuclear complex seems to facilitate the process.

Experimental Section

General: All starting materials were purchased from commercial sources (Aldrich) and used without further purification. Solvents were dried using standard techniques.[35] The organic reactions were monitored by thin layer chromatography (TLC) on precoated aluminium sheets of silica gel. Compounds were detected with iodine and/or with phosphomolybdic acid. Flash column chromatography was performed in the indicated solvent system on silica gel (particle size 0.040−0.063 mm). Melting points were determined with a Reichert-Jung hot-stage microscope. ^1H and ^{13}C NMR spectra were recorded with Varian Unity Inova-300, Varian Unity Inova-400 or Varian Unity 500 spectrometers at room temperature, employing D_2O or [D_6]DMSO as solvents. The pH was calculated from the measured pD values using the correlation pH = pD − 0.4.[36] Chemical shifts are reported in parts per million (ppm) from tetramethylsilane but were measured against the solvent signals. Dioxane (δ = 67.4 ppm) was used as reference for the ^{13}C NMR spectra in D_2O. All assignments were performed on the basis of ^1H-^{13}C heteronuclear multiple quantum coherence experiments (gHSQC and gHMBC). IR spectra were recorded with a Perkin−Elmer 681 spectrometer. EI mass spectra were recorded with a Hewlett Packard 5973 spectrometer with a direct insertion probe (70 eV). Electrospray mass spectra were obtained with a Hewlett Packard 1100 MSD and FAB mass spectra with a VG AutoSpec spectrometer using an *m*-nitrobenzyl alcohol (NBA) matrix. Elemental analyses were provided by the Departamento de Análisis, Centro de Química Orgánica "Manuel Lora Tamayo", CSIC, Madrid, Spain. Cu−Cl ratios were provided by the SCSIE (University of Valencia) using X-ray energy dispersive spectroscopy with an EDAX DX4 detector and a Philips XL30 ESEM electronic microscope.

Synthesis of Ligands: Ligands **L¹** (**1**), **L²** (**2**) and **L³** (**3**) were prepared by treatment of the corresponding 3,5-pyrazoledicarbaldehydes with diethylenetriamine [**L¹** (**1**) and **L³** (**3**)] or tris(2-aminoethyl)amine **L²** (**2**) as reported previously in refs.[10,11], respectively.

3,7,11,14,15,18,22,26,29,30-Decaazatricyclo[26.2.1.1^{13,16}]dotriaconta-1(31),13,16(32),28-tetraene [L⁴ (4)]: 3,5-Pyrazoledicarbaldehyde (496 mg, 4.0 mmol) was dissolved in hot dry methanol (200 mL). The solution was then cooled to room temperature and added dropwise under argon to a stirred solution of *N*-(3-aminopropyl)-1,3-propanediamine (525 mg, 4 mmol) in dry methanol (120 mL) over 2.5 h. The reaction was monitored by TLC ($CHCl_3$/MeOH, 10:1) and when it was complete (ca. 12 h), $NaBH_4$ (912 mg, 24.0 mmol) was added portionwise over 15 min. The mixture was stirred for 2 h and the solvent removed in vacuo. The residue was purified by flash column chromatography (MeOH/30% aqueous NH_4OH, 49:1 to 45:5 mixtures). The fractions containing the product of R_f = 0.65 (TLC, MeOH/30% aqueous NH_4OH, 1:1) were concentrated to dryness. The residue was then extracted with boiling toluene and on concentration and cooling gave **L⁴** (**4**) as an oil which was crystallised from toluene to give a white solid (443 mg, 49%) m.p. 154−156 °C. IR (KBr): $\tilde{\nu}$ = 3500−3300 cm^{-1} (NH). MS (FAB$^+$, 3-nitrobenzyl alcohol matrix): *m*/*z* (%) = 447 (100) [MH^+]. $C_{22}H_{42}N_{10}$ (446.6): calcd. C 59.16, H 9.48, N 31.36; found C 58.92, H 9.62, N 31.11.

Preparation of L⁴·6HCl (4·6HCl): A mixture of **L⁴** (**4**) (223 mg, 0.5 mmol) and 1 M aqueous hydrochloric acid (4 mL) was stirred for 12 h. After addition of EtOH (50 mL), a white precipitate formed which was filtered off and dried under reduced pressure for 48 h to give a white solid (319 mg, 91%); m.p. 265−268 °C. MS (ESI positive mode, H_2O): *m*/*z* (%) = 447 (100) [(M − 6 HCl)H$^+$]. $C_{22}H_{42}N_{10} \cdot 6HCl \cdot 2H_2O$ (701.4): calcd. C 37.67, H 7.47, N 19.97; found C 38.05, H 7.70, N 19.78.

Preparation of 4′ [Na₂(H₋₂L⁴)]: To a stirred solution of **4** (45 mg, 0.1 mmol) in dry MeOH (2 mL), was added NaOH (8 mg, 0.2 mmol), previously dissolved in MeOH (1 mL). The mixture was stirred at room temperature for 12 h. The solvent was then evaporated and the residue dried under reduced pressure for 48 h to give **4′** as a white solid (48 mg, 98%); m.p. 208−210 °C. MS (ESI positive mode, H_2O/MeOH): *m*/*z* (%) = 491.2 (10) [M + H]$^+$, 469.3 (76) [M + 2 H − Na]$^+$, 447.3 (100) [M + 3 H − 2 Na]$^+$. $C_{22}H_{40}N_{10}Na_2$ (490.6): calcd. C 53.86, H 8.21, N 28.54; found C 53.87, H 8.16, N 28.57.

Syntheses of $[Zn_2(H_{-2}L^1)](ClO_4)_2$ {[8](ClO₄)₂}, $[Zn_2(H_{-2}L^2)](ClO_4)_2 \cdot 4H_2O$ {[9](ClO₄)₂·4H₂O} and $[Zn_2(L^3)](ClO_4)_4 \cdot 6H_2O$ {[10](ClO₄)₄·6H₂O} from Ligands L¹−L³ (1−3). General Procedure: Working under argon, a solution of $Zn(ClO_4)_2 \cdot 6H_2O$ (74 mg, 0.2 mmol) in dry MeOH (1 mL) was added with stirring to a solution of the polyamine ligand L¹−L³ (0.1 mmol), dissolved in 2 mL of the same solvent. After 12 h, the precipitate was collected by filtration and vacuum-dried at 100 °C over phosphorus pentoxide for 24 h. In all cases, the white solid thus obtained was crystallised from water.

{[8](ClO₄)₂}: Yield 55 mg, 77%. M.p. > 350 °C. MS (ESI positive mode, H_2O): *m*/*z* (%) = 615.1 (10) [M − ClO_4]$^+$, 453.4 (100) [M + H − $Zn(ClO_4)_2$]$^+$, 391.4 (75) [M + 3 H − 2 $ZnClO_4$]$^+$. MS (FAB$^+$, 3-nitrobenzyl alcohol matrix): *m*/*z* (%) = 616.9 (20) [(M + 2 H)$^+$ − ClO_4], 615.4 (12) [M$^+$ − ClO_4], 553.2 (100) [(M + 2 H)$^+$ − $ZnClO_4$], 453.2 (47) [(M + H)$^+$ − $Zn(ClO_4)_2$]. $C_{18}H_{32}N_{10}Zn_2(ClO_4)_2$ (718.2): calcd. C 30.16, H 4.47, N 19.55; found C 30.39, H 4.77, N 19.73.

{[9](ClO₄)₂·4H₂O}: Yield 78 mg, 80%. M.p. > 350 °C. MS (ESI positive mode, MeOH/H_2O): *m*/*z* (%) = 893.2 (2) [M + H]$^+$, 793.2 (73) [M − ClO_4]$^+$, 731.4 (58) [M + 2 H − $ZnClO_4$]$^+$, 631.4 (50) [M + H − $ZnClO_4$ − ClO_4]$^+$, 569.5 (100) [M + 3 H − 2 $ZnClO_4$]$^+$. MS (FAB$^+$, 3-nitrobenzyl alcohol matrix): *m*/*z* (%) = 893.1 (23) [M + H]$^+$, 793.2 (63) [M$^+$ − ClO_4], 695 (100) [(M + H)$^+$ − 2 ClO_4], 731.3 (56) [M + H − $Zn(ClO_4)$]$^+$, 631.3 (77) [M + H − $Zn(ClO_4)_2$]$^+$. $C_{27}H_{46}N_{14}Zn_2(ClO_4)_2 \cdot 4H_2O$ (968.5): calcd. C 33.48, H 5.62, N 20.24; found C 33.26, H 5.40, N 20.46.

{[10](ClO₄)₂·6H₂O}: Yield 91 mg, 75%. M.p. > 350 °C. MS (ESI positive mode, MeOH/H_2O): *m*/*z* (%) = 995.1 (5) [(M − ClO_4]$^+$, 833.0 (31) [M + H − $Zn(ClO_4)_2$]$^+$, 733.5 (54) [M − Zn − 3 ClO_4]$^+$, 671.2 (100) [M + 2 H − 2 Zn − 3 ClO_4]$^+$, 571.6 (91) [M + H − 2 $Zn(ClO_4)_2$]$^+$. MS (FAB$^+$, 3-nitrobenzyl alcohol matrix): *m*/*z* (%) = 996.1 (20) [(M + H)$^+$ − ClO_4], 995.1 (44) [M$^+$ − ClO_4], 897 (33) [(M + 2 H)$^+$ − 2 ClO_4], 895 (21) [M$^+$ − 2 ClO_4], 733.3 (23) [M$^+$ − $Zn(ClO_4)_2$ − ClO_4], 633.3 (30) [M$^+$ − $Zn(ClO_4)_2$ − $HClO_4$]. $C_{32}H_{46}N_{10}Zn_2(ClO_4)_4 \cdot 6H_2O$ (1207.5): calcd. C 31.84, H 4.81, N 11.61; found C 31.91, H 5.17, N 11.69.

 © 2005 Wiley-VCH Verlag GmbH & Co. KGaA, Weinheim

Synthesis of M^{II} Dinuclear Complexes from the Disodium Dipyrazolate Salt 4′

Preparation of $[Cu_2(H_{-2}L^4)](ClO_4)_2$ {[11]$(ClO_4)_2$}: To a stirred solution of the sodium dipyrazolate salt **4′** (53 mg, 0.1 mmol) in MeOH (2 mL) was added a solution of $Cu(ClO_4)_2·6H_2O$ (74 mg, 0.2 mmol) in 2 mL of the same solvent dropwise under argon. The mixture was stirred at room temperature overnight and the desired complex $[Cu_2(H_{-2}L^4)](ClO_4)_2$ {[**11**]$(ClO_4)_2$} separated as a blue precipitate. This was isolated by filtration, dried under vacuum and crystallised from a water/methanol mixture (2:3) (16 mg, 21%); m.p. > 350 °C. MS (ESI positive mode, H_2O/MeOH): *m/z* (%) = 671.0 (100) $[M - ClO_4]^+$, 571.2 (58) $[M - ClO_4 - HClO_4]^+$, 508.1 (9) $[M + H - Cu(ClO_4)_2]^+$. $C_{22}H_{40}Cu_2N_{10}(ClO_4)_2$ (770.61): calcd. C 34.28, H 5.23, N 18.17; found C 34.05, H 4.98, N 17.96.

Preparation of Zn^{II} Dinuclear Complex $[Zn_2(H_{-2}L^4)](ClO_4)_2$ {[12]$(ClO_4)_2$}: To a stirred solution of the sodium dipyrazolate salt of **4′** (53 mg, 0.1 mmol) in MeOH (2 mL) was added a solution of $Zn(ClO_4)_2·6H_2O$ (74 mg, 0.2 mmol) in 2 mL of the same solvent dropwise under argon. The mixture was stirred at room temperature overnight and the title complex precipitated. It was then isolated by filtration, dried under vacuum and crystallised from a water/methanol mixture (2:3) to afford $[Zn_2(H_{-2}L^4)](ClO_4)_2$ {[**12**]$(ClO_4)_2$} as a white solid (27 mg, 35%); m.p. > 350 °C. MS (ESI positive mode, H_2O/MeOH): *m/z* (%) = 671.2 (32) $[M - ClO_4]^+$, 609.3 (27) $[M + 2\,H - Zn - ClO_4]^+$, 575.2 (51) $[M + H - 2\,ClO_4H]^+$, 509.4 (100) $[M + H - Zn(ClO_4)_2]^+$, 447.4 (64) $[M + 3\,H - Zn(ClO_4)_2 - Zn]^+$. $C_{22}H_{40}N_{10}Zn_2(ClO_4)_2$ (774.3): calcd. C 34.13, H 5.21, N 18.09; found C 33.99, H 5.24, N 17.97.

Synthesis of Cu^{II} Dinuclear Complexes from Ligand 4

Preparation of Cu^{II} Dinuclear Complex $[Cu_2L^4](ClO_4)_4·2H_2O$ {[13]$(ClO_4)_4·2H_2O$} (Blue and Red Forms): Working under argon, a solution of $Cu(ClO_4)_2·6H_2O$ (74 mg, 0.2 mmol) in dry MeOH (2 mL) was added with stirring to a solution of the polyamine ligand **4** (45 mg, 0.1 mmol) in 2 mL of same solvent. After 4 h, a blue precipitate had formed. This was filtered off and vacuum-dried at 100 °C over phosphorus pentoxide for 24 h to give a blue solid (72 mg, 71%); m.p. > 350 °C. MS (ESI negative mode, H_2O/MeOH): *m/z* (%) = 1070.9 (35) $[M + ClO_4]^-$, 968.8 (6) $[M - H]^-$, 869.0 (100) $[M - (HClO_4 + H)]^-$. MS (ESI positive mode, H_2O/MeOH): *m/z* (%) = 871.0 (10) $[(M - ClO_4]^+$, 771.0 (10) $[(M - (HClO_4 + ClO_4)]^+$, 710.2 (30) $[M - Cu(ClO_4)_2 + H]^+$, 671.1 (100) $[M - (2\,HClO_4 + ClO_4)]^+$, 608.1 (5) $[M - \{Cu(ClO_4)_2 + ClO_4\}]^+$, 547.3 (51) $[M - \{Cu(ClO_4)_2 + CuClO_4\} + 2\,H]^+$. $C_{22}H_{40}Cu_2N_{10}(ClO_4)_2(HClO_4)_2(H_2O)_2$ (1007.56): calcd. C 26.23, H 4.60, N 13.90; found C 26.21, H 4.54, N 13.69. When the above blue solid was heated to reflux in water (5 mL) for 5 min and the resultant blue aqueous solution allowed to stand at room temperature, a red precipitate was unexpectedly obtained upon slow evaporation of the solvent. This was filtered off, washed with methanol and vacuum-dried at 100 °C over phosphorus pentoxide for 24 h to give the complex {red-[**13**]$(ClO_4)_4·2H_2O$} as a brown-reddish solid (61 mg, 60%); m.p. > 350 °C. MS (ESI negative mode, H_2O/MeOH): *m/z* (%) = 1071.4 (100) $[M + ClO_4]^-$, 969.4 (15) $[M - H]^-$, 869.4 (83) $[M - (HClO_4 + H)]^-$. MS (ESI positive mode, H_2O/MeOH): *m/z* (%) = 871.0 (3) $[M - ClO_4]^+$, 771.0 (4) $[M - (HClO_4 + ClO_4)]^+$, 710.1 (22) $[M - Cu(ClO_4)_2 + H]^+$, 671.1 (59) $[M - (2\,HClO_4 + ClO_4)]^+$, 608.1 (23) $[M - \{Cu(ClO_4)_2 - ClO_4\}]^+$, 547.3 (33) $[M - \{Cu(ClO_4)_2 + CuClO_4\} + 2\,H]^+$, 447.4 (41) $[M - 2\,Cu(ClO_4)_2 + H]^+$, 224.3 (100) $[\{M - 2\,Cu(ClO_4)_2\}/2 + H]^+$. MS ($FAB^+$, 3-nitrobenzyl alcohol matrix): *m/z* (%) = 871.1 (3) $[M - ClO_4]^+$, 771.2 (12) $[M - (HClO_4 + ClO_4)]^+$, 710.3 (7) $[M - Cu(ClO_4)_2 + H]^+$, 671.2 (100) $[M - (2\,HClO_4 + ClO_4)]^+$, 608.3 (5) $[M - \{Cu(ClO_4)_2 - ClO_4\}]^+$, 659.2 (44) $[M - \{3\,HClO_4 + ClO_4\}]^+$, 507.3 (7) $[M - \{Cu(ClO_4)_2 + 2\,HClO_4\}^{·+}]$. $C_{22}H_{42}Cu_2N_{10}(ClO_4)_4·2H_2O$ (1007.56): calcd. C 26.23, H 4.60, N 13.90; found C 26.31, H 4.77, N 13.86.

Preparation of the Green Cu^{II} Trinuclear Complex $[Cu_3(H_{-2}L^4)](ClO_4)_4·2MeOH$ {[14]$(ClO_4)_4·2MeOH$}: Basic anion-exchange resin (DOWEX, 550A OH) was added in portions to a stirred solution of [**4**]·6HCl (100 mg, 0.14 mmol) in H_2O (20 mL) until a pH of 11−12 was reached. The resin was then filtered off and the solvent removed under reduced pressure. The resultant solid was crystallised from toluene to give **4** as a white solid of m.p. 154−156 °C. Then, working under argon, a solution of $Cu(ClO_4)_2·6H_2O$ (93 mg, 0.24 mmol) in dry MeOH (1 mL) was added with stirring to a solution of the above polyamine $\mathbf{L^4}$ (**4**) (56 mg, 0.12 mmol) in 1 mL of the same solvent. After 4 h, a green precipitate was formed. This was filtered off and vacuum-dried at 100 °C over phosphorus pentoxide for 24 h to afford compound [**14**]$(ClO_4)_4·2MeOH$ as a green solid; m.p. > 350. MS (FAB^+, 3-nitrobenzyl alcohol matrix): *m/z* (%) = 927.7 (6) $[M - (2\,MeOH + ClO_4H + 4\,H)]^+$, 867.7 (14) $[M - (2\,Me + 2\,ClO_4)]^+$, 827.7 (80) $[M - (2\,MeOH + 2\,ClO_4H + 4\,H)]^+$, 732.1 (59) $[M - (2\,MeOH + 2\,ClO_4H + ClO_4)]^+$, 671.3 (51) $[M - \{2\,MeOH + Cu(ClO_4)_2 + ClO_4\}]^+$, 633.2 (100) $[M - (2\,MeOH + 2\,ClO_4H + ClO_4)]^+$, 569.3 (37) $[M - \{2\,MeOH + Cu(ClO_4)_2 + HClO_4H + ClO_4\}]^+$. MS (MALDI-TOF, 2,5-dihydroxybenzoic acid matrix): *m/z* (%) = 851.2 (16) $[(M - (Me + MeO + 2\,ClO_4)]^+$, 797.2 (27) $[M - 3\,ClO_4 + ClO_4H]^+$, 750.3 (7) $[M - (MeOH + Me + 3\,ClO_4)]^+$, 734.3 (78) $[M - (2\,MeOH + 3\,ClO_4)]^+$, 672.3 (69) $[M - \{2\,MeOH + Cu(ClO_4)_2 + ClO_4\}]^+$, 649.4 (26) $[M - (MeOH + Me + 4\,ClO_4)]^+$, 635.4 (100) $[M - 2\,MeOH + 4\,ClO_4]^+$. $C_{22}H_{40}Cu_3N_{10}(ClO_4)_4·2MeOH$ (1097.14): calcd. C 26.27, H 4.41, N 12.77; found C 26.06, H 4.08, N 12.38.

X-ray Crystallography: Crystal data and details of the data collection for the complexes $[Zn_2(H_{-2}\mathbf{L^1})](ClO_4)_2$ {[**8**]$(ClO_4)_2$}, $[Cu_2(H_{-2}L^4)](ClO_4)_2$ {[**11**]$(ClO_4)_2$} and $[Zn_2(H_{-2}L^4)](ClO_4)_2$ {[**12**]$(ClO_4)_2$} are given in Table 13. The crystal data were collected with a Nonius Kappa CCD instrument (λ = 0.71073 Å). In the case of [**11**]$(ClO_4)_2$ and [**12**]$(ClO_4)_2$ the data were collected at 120 K. The crystals were monitored for decay during data collection and appropriate corrections were made where necessary. A profile analysis was performed on every reflection.[37] A semiempirical absorption correction, Ψ-scan based, was performed in each case.[38] Lorentz and polarisation corrections were applied and the data were reduced to F_o^2 values. The structures were solved by Patterson methods using SHELXS-86 with an IBM PENTIUM II 300 computer.[39] Isotropic least-squares refinements were performed using SHELXL-93.[40] The hydrogen atoms were placed in calculated positions. All non-hydrogen atoms were refined anisotropically. The hydrogen atoms were refined with a common thermal parameter. Atomic scattering factors were taken from the International Tables for X-ray Crystallography.[41] The molecular plots were produced using ORTEP.[42] CCDC-240640, -240641 and -240642 contain the supplementary crystallographic data for structures [**8**]$(ClO_4)_2$, [**11**]$(ClO_4)_2$ and [**12**]$(ClO_4)_2$, respectively. These data can be obtained free of charge via www.ccdc.cam.ac.uk/const/retrieving.html [or from the Cambridge Crystallographic Data Centre, 12 Union Road, Cambridge CB2 1EZ, UK; Fax: (internat.) + 44-1223-336-033; or E-mail: deposit@ccdc.cam.ac.uk].

Electromotive Force (emf) Measurements: The potentiometric titrations were carried out in 0.15 M NaCl at 298.1 ± 0.1 K using the experimental procedure (burette, potentiometer, cell, stirrer,

 © 2005 Wiley-VCH Verlag GmbH & Co. KGaA, Weinheim

Table 13. Crystallographic data for [**8**]$(ClO_4)_2$, [**11**]$(ClO_4)_2$ and [**12**]$(ClO_4)_2$

	[**8**]$(ClO_4)_2$	[**11**]$(ClO_4)_2$	[**12**]$(ClO_4)_2$
Empirical formula	$C_{19}H_{26}N_6O_8CL^2Zn_2$	$C_{21}H_{36}N_{10}O_8CL^2Cu_2$	$C_{21}H_{36}N_{10}O_8CL^2Zn_2$
M	668.1706	754.5724	758.2984
T [K]	293	293	293
Crystal system	triclinic	orthorhombic	orthorhombic
Colour	colourless	blue	colourless
Space group	$P\bar{1}$	*Pmcn*	*Pmcn*
a [Å]	10.4570(2)	13.762(1)	13.5330(7)
b [Å]	11.7980(2)	15.393(1)	15.3960(8)
c [Å]	13.3670(4)	15.524(2)	16.098(1)
α [°]	111.624(1)	90	90
β [°]	107.061(1)	90	90
γ [°]	100.304(2)	90	90
V [Å^3]	1387.06(5)	3288.6(5)	3354.1(3)
Z	2	4	4
$D_{calcd.}$ [g·cm^{-3}]	1.60	1.524	1.502
λ [Å]	0.7103	0.7103	0.7103
μ [mm^{-1}]	1.974	1.513	1.645
$F(000)$	680	1552	1560
θ range of data collection [°]	$1.83 < \theta < 27.39$	$1.86 < \theta < 21.76$	$1.83 < \theta < 27.39$
Index ranges	$-13 < h < 12$	$-13 < h < 13$	$-17 < h < 17$
	$-15 < k < 14$	$-16 < k < 16$	$-19 < k < 18$
	$0 < l < 17$	$-16 < l < 16$	$-19 < l < 20$
Number of reflections measured	6230	13525	5893
Unique reflections	630	2031	3348
Number of reflections observed [$I > 2\sigma(I)$]	3995	1133	1424
Parameters/restraints	393/0	245/0	261/0
Goodness of fit/Goof	1.051	0.944	1.049
R factor all reflections ωR_2	0.135	0.151	0.2087
R factor ωR_1	0.055	0.078	0.080
Max./min. nonassigned density [e/Å^3]	1.645/−0.742	0.919/−0.678	1.76/−1.49

Weighting details: $\omega = 1/[\sigma^2(F_o^2) + (0.1000P)^2 + 0.0000P]$ where $P = (F_o^2 + 2F_c^2)^{1/3}$

microcomputer, etc.) fully described elsewhere.[43] The acquisition of the emf data was performed with the computer program PASAT.[44] The reference electrode was an Ag/AgCl electrode in a saturated KCl solution. The glass electrode was calibrated as a hydrogen ion concentration probe by titration of known amounts of HCl with CO_2-free NaOH solutions[45] and determination of the equivalent point by Gran's method[46] which gives the standard potential $E^{\circ\prime}$ and the ionic product of water [pK_w = 13.73(1)]. The computer program HYPERQUAD[47] was used to calculate the protonation and stability constants and the DISPO[48] program was used to obtain the distribution diagrams. The titration curves for each system (ca. 200 experimental points corresponding to at least three measurements, pH = 2−11, concentration of ligands 1×10^{-3} to 5×10^{-3} M) were treated either as a single set or as separated curves without significant variations in the values of the stability constants. Finally, the sets of data were merged and treated simultaneously to give the final stability constants.

Magnetic Measurements: Magnetic susceptibility measurements of polycrystalline samples were measured over the temperature range 2−300 K with a Quantum Design SQUID magnetometer using an applied magnetic field of 1 T. Diamagnetic corrections of the constituents atoms were estimated from Pascal's constants and a value of 60×10^{-6} cm^3·mol^{-1} was used for the temperature-independent paramagnetism of each copper(II) ion.

Paramagnetic ^{1}H NMR Spectroscopy: Paramagnetic ^{1}H NMR spectra were recorded with a Varian Unity 400 spectrometer operating at 400 MHz. 1D spectra were recorded in $(CD_3)_2SO$ with presaturation of the $(CH_3)_2SO$ signal during part of the relaxation delay. Because the relaxation times were diverse, a variety of NMR parameters were utilised. Acquisition times from 40 to 80 ms, relaxation delay times from 50 to 200 ms, presaturation times from 50 to 200 ms, spectral widths of 40 to 100 kHz and 256 to 1024 of scans were used. 1D spectra were processed using exponential line-broadening weighting functions as apodisation with values of 20−40 Hz. Chemical shifts were referenced to the residual solvent protons of $(CD_3)_2SO$ resonating at δ = 2.50 ppm relative to $SiMe_4$. ^{1}H longitudinal relaxation times were calculated using the inversion recovery pulse sequence[49] (d_1 − 180° − τ − 90° − acq), 18 values of τ were selected, (d_1 + acq) values were 200 ms and the number of scans was 512. The T_1 values were calculated from the inversion-recovery equation. Transversal relaxation times were obtained by measuring the line broadening of the isotropically shifted signals at half-height with the equation $T_2^{-1} = \pi \Delta\nu_{1/2}$.

Molecular Modelling: Molecular modelling studies were carried out using the AMBER method implemented in the Hyperchem 6.0 package[50] and modified by the inclusion of appropriate parameters. Where available, the parameters were analogous to those reported in the literature.[29,50] All others, namely those regarding the particular atomic connections of our ligands with the metal ion, were developed according to the Norrby procedures[28,51] in a similar way to the ones used in the MOMEC program.[52] The equilibrium bond lengths and angles were derived from experimental values on reasonable reference compounds. All additional parameters are given in the Supporting Information (Table S1). The starting structures were built using Hyperchem capabilities and geometries were minimised to a maximum energy gradient of 0.1 kcal/(Å mol) using the Polak−Ribiere (conjugate gradient) algorithm.

 © 2005 Wiley-VCH Verlag GmbH & Co. KGaA, Weinheim

Supporting Information: Table S1 includes nonstandard force field parameters used in the modelling. Figures S1 (A−C) show the ^1H NMR spectra of **L⁴** at pH values 10.5, 8 and 3.7. Figure S2 represents χ_M vs. T for compounds red-[**13**]$(ClO_4)_4 \cdot 2H_2O$ and [**11**]$(ClO_4)_2$.

Acknowledgments

Financial support by the Spanish "Comisión Interministerial de Ciencia y Tecnología" (CICYT, SAF-99-0063 and BQU2003-09215-CO3-01) and Generalitat Valenciana (CTIDIB/2002/244 and Grupos03/196) is gratefully acknowledged.

[1] [1a] W. Kaim, B. Schwederski, *Bioinorganic Chemistry: Inorganic Elements in the Chemistry of Life, An Introduction and Guide*, John Wiley & Sons, Chichester, **1995**. [1b]R. H. Holm, E. I. Solomon, *Chem. Rev.* **1996**, *96*, 2237−3042. [1c] I. Bertini, H. B. Gray, S. J. Lippard, J. S. Valentine, *Bioinorganic Chemistry*, University Science Books, Mill Valley, California, **1994**.

[2] [2a] J. P. Collman, *Acc. Chem. Res.* **1977**, *10*, 265−272. [2b] G. Feher, J. P. Allen, M. Y. Okamura, D. C. Rees, *Nature (London)* **1989**, *339*, 111−116. [2c] N. Kitajima, Y. Moro-oka, *J. Chem. Soc., Dalton Trans.* **1993**, 2665−2671. [2d] P. Woolley, *Nature (London)* **1975**, *258*, 677−682. [2e] S. H. Gellman, R. Petter, R. Breslow, *J. Am. Chem. Soc.* **1986**, *108*, 2388−2394. [2f] T. Koike, S. Kajitani, I. Nakamura, E. Kimura, M. Shiro, *J. Am. Chem. Soc.* **1995**, *117*, 1210−1219. [2g] R. Breslow, *Acc. Chem. Res.* **1995**, *28*, 146−153.

[3] [3a] R. H. Holm, E. I. Solomon, *Chem. Rev.* **1996**, *96*, 2237−3042. [3b] B. A. Mackay, M. D. Fryzuk, *Chem. Rev.* **2004**, *104*, 385−401. [3c] T. Nakamura, Y. Yammamoto, *Chem. Rev.* **2004**, *104*, 2127−2198.

[4] [4a] B. Rosenberg, L. Van Camp, K. Trigas, *Nature (London)* **1965**, *205*, 698−699. [4b] B. Rosenberg, L. Van Camp, J. E. Trosko, V. H. Mansour, *Nature (London)* **1969**, *222*, 385−386. [4c] C. Orvig, M. J. Abrams, *Chem. Rev.* **1999**, *99*, 2201−2842.

[5] [5a] D. Parker, *Chem. Soc. Rev.* **1990**, *19*, 271−291. [5b] M. J. Abrahams, B. A. Murrer, *Science* **1993**, *261*, 725−730. [5c] S. Jurisson, D. Berning, W. Jia, D. Ma, *Chem. Rev.* **1993**, *93*, 1137−1156. [5d] M. J. Heeg, S. S. Jurisson, *Acc. Chem. Res.* **1999**, *32*, 1053−1060. [5e] S. Kobayashi, H. Uyama, S. Kimura, *Chem. Rev.* **2001**, *101*, 398−3818.

[6] X. Huang, M. P. Cuajungco, C. S. Atwood, M. A. Hartshorn, J. D. A. Tyndall, G. R. Hanson, K. C. Stokes, M. Leopold, G. Multhaup, L. E. Goldstein, R. C. Scarpa, A. J. Saunders, J. Lim, R. D. Moir, C. Glabe, E. F. Bowden, C. L. Masters, D. P. Fairlie, R. E. Tanzi, A. I. Bush, *J. Biol. Chem.* **1999**, *274*, 37111−37116.

[7] J. Elguero, "Pyrazoles" in *Comprehensive Heterocyclic Chemistry II, A Review of the Literature 1982−1995* (Eds.: A. R. Katritzky, C. V. Rees, E. F. V. Scriven), Elsevier Science Ltd., Oxford, **1996**, vol. 3.

[8] R. Mukherjee, *Coord. Chem. Rev.* **2000**, *203*, 151−218.

[9] V. J. Arán, M. Kumar, J. Molina, L. Lamarque, P. Navarro, E. García-España, J. A. Ramirez, S. V. Luis, B. Escuder, *J. Org. Chem.* **1999**, *64*, 6135−6146.

[10] L. Lamarque, C. Miranda, P. Navarro, F. Escartí, E. García-España, J. Latorre, J. A. Ramirez, *Chem. Commun.* **2000**, 1337−1338.

[11] L. Lamarque, P. Navarro, C. Miranda, V. J. Arán, C. Ochoa, F. Escartí, E. García-España, J. Latorre, S. V. Luis, J. F. Miravet, *J. Am. Chem. Soc.* **2001**, *123*, 10560−10570.

[12] [12a] A. Andrés, M. I. Burguete, E. García-España, S. V. Luis, J. F. Miravet, C. Soriano, *J. Chem. Soc., Perkin Trans. 2* **1993**, 749−755. [12b] A. Bianchi, B. Escuder, E. García-España, S. V. Luis, V. Marcelino, J. F. Miravet, J. A. Ramírez, *J. Chem. Soc., Perkin Trans. 2* **1994**, 1253−1259. [12c] A. Andrés, C. Bazzicaluppi, A. Bianchi, E. García-España, S. V. Luis, J. F. Miravet, J. A. Ramírez, *J. Chem. Soc., Dalton Trans.* **1994**, 2995−3004.

[13] J. A. Aguilar, E. García-España, J. A. Guerrero, J. M. Llinares, J. A. Ramírez, C. Soriano, S. V. Luis, A. Bianchi, L. Ferrini, V. Fusi, *J. Chem. Soc., Dalton Trans.* **1996**, 239−246.

[14] A. Bencini, A. Bianchi, E. García-España, M. Micheloni, J. A. Ramírez, *Coord. Chem. Rev.* **1999**, *188*, 97−156.

[15] L. Behle, M. Neuburger, M. Zehnder, T. A. Kaden, *Helv. Chim. Acta* **1995**, *78*, 693−702.

[16] H. Weller, L. Siegfried, M. Neuburger, M. Zehnder, T. A. Kaden, *Helv. Chim. Acta* **1997**, *80*, 2315−2328.

[17] M. Kumar, V. J. Arán, P. Navarro, A. Ramos-Gallardo, A. Vegas, *Tetrahedron Lett.* **1994**, *35*, 5723−5726.

[18] M. Kumar, V. J. Arán, P. Navarro, *Tetrahedron Lett.* **1993**, *34*, 3159−3162.

[19] M. Kumar, V. J. Arán, P. Navarro, *Tetrahedron Lett.* **1995**, *36*, 2161−2164.

[20] [20a] S. F. Ralph, M. M. Sheil, L. A. Hick, R. J. Geue, A. M. Sargeson, *J. Chem. Soc., Dalton Trans.* **1996**, 4417−4424. [20b] A. Matsumoto, T. Fukumoto, H. Adachi, H. Watarai, *Anal. Chim. Acta* **1999**, *390*, 193−199 and references contained therein. [20c] N. Yoshida, K. Ichikawaa, M. Shirob, *J. Chem. Soc., Perkin Trans. 2* **2000**, 17−26.

[21] E. L. Muetterties, L. J. Guggenberger, *J. Am. Chem. Soc.* **1974**, *96*, 1748−1756.

[22] [22a] J. Ackermann, F. Meyer, E. Kaifer, H. Pritzkow, *Chem. Eur. J.* **2002**, *8*, 247−258. [22b] F. Meyer, A. Jacobi, B. Nuber, P. Rutsch, L. Zsolnai, *Inorg. Chem.* **1998**, *37*, 1213−1218.

[23] R. Zenobi, R. Knochenmuss, *Mass Spectrom. Rev.* **1998**, *17*, 337−366.

[24] [24a] E. Lehmann, R. Knochenmuss, R. Zenobi, *Rapid Commun. Mass Spectrom.* **1997**, *11*, 1483−1492. [24b] R. Zenobi, *Chimia* **1997**, *51*, 801−803.

[25] P. Siemsen, U. Gubler, C. Bosshard, P. Guenter, F. Diederich, *Chem. Eur. J.* **2001**, *7*, 1333−1341.

[26] [26a] P. Comba, T. W. Hambley, *Molecular Modelling of Inorganic Compounds*, VCH Publishers, New Cork, **1995**. [26b] C. R. Landis, D. M. Root, T. Cleveland, *Reviews in Computational Chemistry* (Eds.: K. B. Lipkowitz, D. B. Boyd), VCH Publishers, New York, **1995**, vol. 6, pp. 73−148. [26c] M. Zimmer, *Chem. Rev.* **1995**, *95*, 2629−2649.

[27] W. D. Cornell, P. Cieplak, C. I. Bayly, I. R. Gould, K. M. J. Merz, D. M. Ferguson, D. C. Spelmeyer, T. Fox, J. W. Caldwell, P. A. Kollman, *J. Am. Chem. Soc.* **1995**, *117*, 5179−5197.

[28] D. E. Reichert, P.-O. Norrby, M. J. Welch, *Inorg. Chem.* **2001**, *40*, 5223−5230.

[29] P. Comba, R. Remenyi, *Coord. Chem. Rev.* **2003**, *238−239*, 9−20.

[30] I. Bertini, C. Luchinat, "NMR of paramagnetic substances", in *Coord. Chem. Rev.* **1996**, *150*.

[31] N. N. Murthy, K. D. Karlin, I. Bertini, C. Luchinat, *J. Am. Chem. Soc.* **1997**, *119*, 2156−2162.

[32] [32a] F. Meyer, S. Beyreuther, K. Heinze, L. Zsolnai, *Chem. Ber./Recl.* **1997**, *130*, 605−614. [32b] F. Meyer, A. Jacobi, L. Zsolnai, *Chem. Ber./Recl.* **1997**, *130*, 1441−1448.

[33] [33a] T. Kamiusuki, H. Okawa, N. Matsumoto, S. Kida, *J. Chem. Soc., Dalton Trans.* **1990**, 195−198. [33b] V. P. Hanot, T. D. Robert, J. Kolnaar, J. G. Haasnoot, J. Reedijk, H. Kooijman, A. L. Spek, *J. Chem. Soc., Dalton Trans.* **1996**, 4275−4281. [33c] J. Pons, X. López, J. Casabo, F. Teixidor, A. Caubet, J. Rius, C. Miravitlles, *Inorg. Chim. Acta* **1992**, *195*, 61−66. [33d] R. Gupta, R. Hotchandani, R. Mukherjee, *Polyhedron* **2000**, *19*, 1429−1435. [33e] A. M. Schuitema, M. Engelen, I. A. Koval, S. Gorter, W. L. Driessen, J. Reedijk, *Inorg. Chim. Acta* **2001**, *324*, 57−64.

[34] P. Román, C. Guzmán-Miralles, A. Luque, J. I. Beitia, J. Cano, F. Lloret, M. Julve, S. Alvarez, *Inorg. Chem.* **1996**, *35*, 3741−3751.

[35] D. D. Perrin, W. L. F. Armarego, D. R. Perrin, *Purification of Laboratory Chemicals*, Pergamon Press, Oxford, **1980**.

 © 2005 Wiley-VCH Verlag GmbH & Co. KGaA, Weinheim

[36] A. K. Covington, M. Paabo, R. A. Robinson, R. G. Bates, *Anal. Chem.* **1968**, *40*, 700−706.
[37] [37a] M. S. Lehmann, F. K. Larsen, *Acta Crystallogr., Sect. A* **1978**, *30*, 580−584. [37b] D. F. Grant, E. J. Gabe, *J. Appl. Crystallogr.* **1978**, *11*, 114−120.
[38] A. C. T. Nort, D. C. Phillips, F. S. Mathews, *Acta Crystallogr., Sect. A* **1968**, *24*, 351−359.
[39] G. M. Sheldrick, C. Kruger, R. Goddard, Editors, *Crystallographic Computing*, Clarendon Press, Oxford, England, **1985**, p. 175.
[40] G. M. Sheldrick, *SHELXL-93: Program for Crystal Structure Refinement*, Institut für Anorganische Chemie, University of Göttingen, Germany, **1993**.
[41] *International Tables for X-ray Crystallography*, The Kynoch Press: Birmingham, England, **1974**, vol. IV.
[42] C. K. Johnson, ORTEP; Report ORNL-3794, Oak Ridge National Laboratory, Oak Ridge, TN, **1971**.
[43] E. García-España, M.-J. Ballester, F. Lloret, J. M. Moratal, J. Faus, A. Bianchi, *J. Chem. Soc., Dalton Trans.* **1988**, 101−104.
[44] M. Fontanelli, M. Micheloni, *Proc. 1st Spanish-Italian Congr. Thermodynamics of Metal Complexes*, Peñíscola, Castellón (Spain), June 3−6, **1990**.
[45] M. Micheloni, A. Sabatini, A. Vacca, *Inorg. Chim. Acta* **1977**, *25*, 41.
[46] [46a] G. Gran, *Analyst (London)* **1952**, *77*, 661−671. [46b] F. J. C. Rossoti, H. Rossoti, *J. Chem. Educ.* **1965**, *42*, 375−378.
[47] P. Gans, A. Sabatini, A. Vacca, *Talanta* **1996**, *43*, 1739−1753.
[48] A. Vacca, *FORTRAN program for the determination of species distribution in multicomponent systems*, Florence, **1977**.
[49] A. E. Derome, *Modern NMR Techniques for Chemistry Research*, Pergamon Press, Oxford, **1987**.
[50] Hyperchem 6.0 (Hypercube Inc), Scientific Software, USA, **2000**.
[51] [51a] P. V. Bernhardt, P. Comba, *Inorg. Chem.* **1992**, *31*, 2638−2644. [51b] J. E. Bol, C. Buning, P. Comba, J. Reedijk, M. Ströhle, *J. Comput. Chem.* **1998**, *19*, 512−523. [51c] P.-O. Norrby, P. Brandt, *Coord. Chem. Rev.* **2001**, *212*, 79−109. [51d] C. Miranda, F. Escartí, L. Lamarque, M. J. R. Yunta, P. Navarro, E. García-España, M. L. Jimeno, *J. Am. Chem. Soc.* **2004**, *126*, 823−833.
[52] T. W. Hambley, G. Laur, N Okon, *MOMEC 97*, Heidelberg, Germany, **1997**.

Received August 2, 2004
Early View Article
Published Online November 18, 2004

Synthesis and Characterisation of the First Cyanodiselenoimidocarbonate $[C_2N_2Se_2]^{2-}$ Complexes

Colin J. Burchell,[a] Stephen M. Aucott,[a] Alexandra M. Z. Slawin,[a] and J. Derek Woollins*[a]

Keywords: Selenium / Platinum / Coordination modes

$[Pt(C_2N_2Se_2)(PR_3)_2]$ (PR_3 = PMe_2Ph, PPh_3) and $[Pt(C_2N_2Se_2)(PP)]$ (PP = dppe, dppm, dppf) were obtained by the reaction of the appropriate metal halide containing complex with potassium cyanodiselenoimidocarbonate. The dimeric cyanodiselenoimidocarbonate complexes $[M\{(C_2N_2Se_2)(\eta^5\text{-}C_5Me_5)\}_2]$ (M = Rh Ir)] were synthesised from the appropriate transition metal dimer starting material. The cyanodiselenoimidocarbonate ligand is *Se*,*Se*-bidentate in the monomeric complexes – the terminal CN group is approximately coplanar with the CSe_2 group, and the nitrogen atom is trigonal therefore reducing the planar symmetry of the ligands.
(© Wiley-VCH Verlag GmbH & Co. KGaA, 69451 Weinheim, Germany, 2005)

Introduction

The coordination of chalcogen donor ligands is an important area.[1−12] Sulfur-based ligands, especially *S*,*S*-bidentate ligands, have a variety of industrial applications.[9−12] Relative to the significant interest in sulfur donor ligands, the selenium analogues are a rather understudied area. Metal selenides and metal polyselenides are well known and are readily prepared by direct reaction of the elements. There has been significant interest in ZnSe and CdSe semiconductors in photovoltaic devices because of their intermediate energy bandgap.[13] Hence organometallic compounds such as cadmium and zinc diselenocarbamato complexes[14] and selenoimidophosphonates[13] have been investigated as single-source precursors for deposition of these semiconductor materials. Other well-established selenium donor ligands include the selenoethers[15−18] and the pseudohalide selenocyanate.[19,20] However, there are very few *Se*,*Se*-bidentate ligands reported in the literature, which include a series of (diselenothiocarbonato)bis(phosphane)platinum compounds,[21] two triselenocarbonate complexes $[(\eta\text{-}^5C_5H_5)Co(CSe_3)(PMe_3)]$[22] and $[Ba(CSe_3)]$,[23] a (2,4-dioxo-3,3-pentanediselenolato)bis(phosphane)platinum complex,[24] two diselenocarbonimidato compounds,[25,26] $[\{CH[Si(CH_3)_3]_2\}_2Sn(SeSe)PC_6H_2[C(CH_3)_3]_3]$[27] and a series of $[Pt\{Se_2P(Se)(C_6H_5)\}(PR_3)_2]$ complexes.[28] As part of our program studying the properties of chalcogen donor systems we have recently reported a series of cyanodithioimidocarbonate complexes.[29] Here we describe the synthesis of the corresponding cyanodiselenoimidocarbonate complexes. Selected examples have been chosen for crystallographic study.

Results and Discussion

The synthesis of dipotassium cyanodiselenoimidocarbonate was reported by Jensen and Henriksen in 1970.[30] The original synthesis involved the dropwise addition of potassium hydroxide in water to cyanamide and carbon diselenide in dioxane at 0 °C. Our synthesis is essentially the same [Equation (1)], except the reaction was carried out in ethanol and potassium ethoxide was used in place of potassium hydroxide to prevent the generation of water during the reaction.

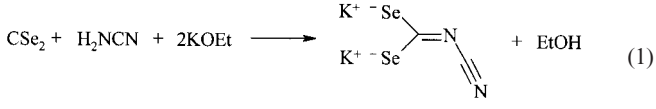

(1)

After suction filtration under nitrogen, the product was obtained as an impure off-yellow solid. In the IR spectrum, a strong ν(C≡N) band at 2127 cm^{-1} and a strong band at 1347 cm^{-1} assigned as ν(C=N) are observed. Purification proved unsuccessful, hence the dipotassium cyanodiselenoimidocarbonate was used as obtained for subsequent reaction.

The bis(phosphane)platinum complexes $[Pt(C_2N_2Se_2)(PR_3)_2]$ (PR_3 = PMe_2Ph, PPh_3) and $[Pt(C_2N_2Se_2)(PP)]$ (PP = dppe, dppm, dppf) were obtained by reaction of the appropriate $[PtCl_2(PR_3)_2]$ or $[PtCl_2(PP)]$ complex with excess potassium cyanodiselenoimidocarbonate in tetrahydrofuran. A large excess of the dipotassium salt was used as

[a] School of Chemistry, University of St. Andrews, St. Andrews, Fife KY16 9ST, UK
E-mail: jdw3@st-andrews.ac.uk

this gave a cleaner reaction. The solvent was evaporated under reduced pressure, and dichloromethane was added. The mixture was filtered through a Celite pad to remove precipitated KCl and any residual dipotassium cyanodiselenoimidocarbonate, and the filtrate was then concentrated to dryness to give the product [Equation (2)].

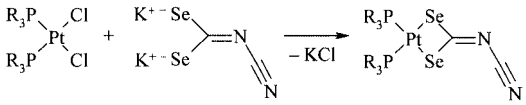

1 PR_3 = PMe_2Ph
2 PR_3 = PPh_3
3 PR_3 = 1/2dppe
4 PR_3 = 1/2dppm
5 PR_3 = 1/2dppf (2)

The microanalyses of all compounds were satisfactory, and all compounds showed the anticipated [M^+] peak in their mass spectra (Table 1). The ν(C≡N) vibrations are observed in the range 2174−2179 cm^{-1}, and the ν(C=N) vibrations can be seen in the region of 1492−1495 cm^{-1} (Table 2); these values are comparable with the corresponding (cyanodithioimidocarbonate)bis(phosphane)platinum complexes.[29] The ν(Pt−Se) bands all lie within the range 246−294 cm^{-1} (Table 2). The (cyanodiselenoimidocarbonate)bis(phosphane)platinum complexes **1**−**5** (Table 2) all show sharp singlets with platinum and selenium satellites in their $^{31}P\{^1H\}$ NMR spectra, and have similar δ values to the sulfur analogues.[29] The $^1J(^{195}Pt-^{31}P)$ coupling constants lie in the range 2620−3263 Hz, and the variations reflect the nature of the phosphane group. In all the complexes, *cis* and *trans* $^2J(^{31}P-^{77}Se)$ couplings can be observed (Table 2). The values noted are of similar magnitude to those found in the literature for bis(phosphane)platinum complexes containing selenium donor ligands. Some comparable examples are $[PtSe_2C_2(CO_2CH_3)_2(PPh_3)_2]$[31] [$^2J(^{31}P-^{77}Se)$ 52 Hz], $[Pt\{C_6H_2(CF_3)_3\}Se]_2(PPh_3)_2]$[32] [$^2J(^{31}P-^{77}Se)$ 47 Hz] and $[(CO)_6Fe_2(\mu_3\text{-}Se)_2Pt(PPh_3)_2]$[33] [$^2J(^{31}P-^{77}Se)$ 24 Hz]. The X-ray crystal structures of both **1** (Table 3, Figure 1) and **3** (Table , Figure 2) were obtained. In both examples, the X-ray analysis shows that the platinum core lies at the centre of a distorted square-planar coordination sphere. The distortion from idealised square-planar geometry (90°) can be illustrated by the P(1)−Pt(1)−P(2) bond angle of 94.46(9)° in **1** and 86.64(8)° in **3**. The corresponding Se(1)−Pt(1)−Se(2) bite angles in **1** and **3** are 77.37(4)° and 77.81(3)°, respectively. In the $PtSe_2C$ ring for **1**, the Pt−Se−C angles are 86.1(3)° and 86.9(3)°. The Se(1)−C(1)−Se(2) angle is 109.5(5)°. In compound **3**, the Pt−Se−C angles are 86.1(2)° and 85.9(2)°. The Se(1)−C(1)−Se(2) angle is 110.2(4)°. The nonbonded selenium distance is 3.08 Å and 3.09 Å for **1** and **3**, respectively, and both these values correspond to about 81% of the van der Waals radii of selenium, which implies that there is a significant interaction between the two selenium atoms. As observed in the sulfur analogues, N(1) is trigonal therefore reducing the planar symmetry of the ligand in both **1** and **3**. In **1**, the cyanodiselenoimidocarbonate ligand lies within the coordination plane with the exception of C(1)−N(1)−C(2)−N(2), which is hinged at an angle of 9° to the plane. In **3**, the whole complex is almost planar, however, there is a small hinge angle of 2° with respect to the coordination plane.

The dimeric cyanodiselenoimidocarbonate complexes $[M\{(C_2N_2Se_2)(\eta^5\text{-}C_5Me_5)\}_2]$ [M = Rh (**6**), Ir (**7**)] were synthesised and isolated in a similar manner to the (cyanodiselenoimidocarbonate)bis(phosphane)platinum complexes **1**−**5** by reaction of excess dipotassium salt with the appropriate transition metal dimer starting material [Equation (3)].Compounds **6** and **7** both gave satisfactory microanalyses and show the anticipated [M^+] peak in their mass spectra (Table 1). The ν(C≡N) vibrations are observed at

Table 1. Microanalytical (calculated values in parentheses) and mass spectrometric data for complexes **1**−**7**

Complex	C	H	N	*m/z*
1 $[Pt(C_2N_2Se_2)(PMe_2Ph)_2]$	31.60 (31.73)	3.01 (3.25)	3.83 (4.11)	682
2 $[Pt(C_2N_2Se_2)(PPh_3)_2]$	49.41 (49.10)	2.85 (3.25)	2.76 (3.01)	931
3 $[Pt(C_2N_2Se_2)(dppe)]$	41.88 (41.86)	2.79 (3.01)	3.29 (3.49)	804
4 $[Pt(C_2N_2Se_2)(dppm)]\cdot CH_2Cl_2$	38.89 (38.46)	2.68 (2.77)	3.13 (3.20)	791
5 $[Pt(C_2N_2Se_2)(dppf)]\cdot CH_2Cl_2$	42.83 (42.55)	2.64 (2.69)	2.37(2.68)	960
6 $[\{Rh(C_2N_2Se_2)(\eta^5\text{-}C_5Me_5)\}_2]$	32.44 (32.17)	3.77 (3.37)	5.76 (6.25)	898
7 $[\{Ir(C_2N_2Se_2)(\eta^5\text{-}C_5Me_5)\}_2]$	27.21 (26.82)	2.39 (2.81)	5.65 (5.21)	1077

Table 2. $^{31}P\{^1H\}$ NMR (109.4 MHz) and selected IR data for complexes **1**−**5**

Complex	δ(P) [ppm]	$^1J(^{195}Pt-^{31}P)$ [Hz]	$^2J(^{77}Se-^{31}P)$ [Hz]	ν(C≡N) [cm^{-1}]	ν(C=N) [cm^{-1}]	ν(Pt-Se) [cm^{-1}]
1 $[Pt(C_2N_2Se_2)(PMe_2Ph)_2]$	−19.6	3063	42, 23	2179	1494	294, 254
2 $[Pt(C_2N_2Se_2)(PPh_3)_2]$	17.3	3190	68, 42	2177	1497	282, 246
3 $[Pt(C_2N_2Se_2)(dppe)]$	44.8	3049	73, 49	2178	1492	280, 246
4 $[Pt(C_2N_2Se_2)(dppm)]$	−54.2	2620	40, 19	2175	1492	282, 258
5 $[Pt(C_2N_2Se_2)(dppf)]$	16.4	3263	47, 28	2174	1495	279, 252

 © 2005 Wiley-VCH Verlag GmbH & Co. KGaA, Weinheim

Table 3. Selected bond lengths [Å] and angles [°] for compounds **1** and **3**

Compound	**1**	**3**
Pt(1)−P(1)	2.271(2)	2.245(2)
Pt(1)−P(2)	2.266(3)	2.236(2)
Pt(1)−Se(1)	2.4570(12)	2.4577(9)
Pt(1)−Se(2)	2.4725(11)	2.4617(9)
Se(1)−C(1)	1.916(9)	1.880(8)
Se2)−C(1)	1.856(10)	1.886(7)
C(1)−N(1)	1.305(13)	1.333(9)
N(1)−C(2)	1.329(13)	1.350(10)
C(2)−N(2)	1.184(12)	1.167(10)
Se(1)−Pt(1)−Se(2)	77.37(4)	77.81(3)
P(1)−Pt(1)−P(2)	94.46(9)	86.64(8)
Se(1)−C(1)−N(1)	126.6(7)	127.9(6)
Se(2)−C(1)−N(1)	123.9(7)	121.8(6)
Pt(1)−Se(1)−C(1)	86.1(3)	86.1(2)
Pt(1)−Se(2)−C(1)	86.9(3)	85.9(2)
P(1)−Pt(1)−Se(1)	92.96(7)	95.71(6)
P(2)−Pt(1)−Se(2)	95.11(7)	99.83(6)
C(1)−N(1)−C(2)	119.1(8)	115.0(6)
N(1)−C(2)−N(2)	175.9(12)	175.8(9)

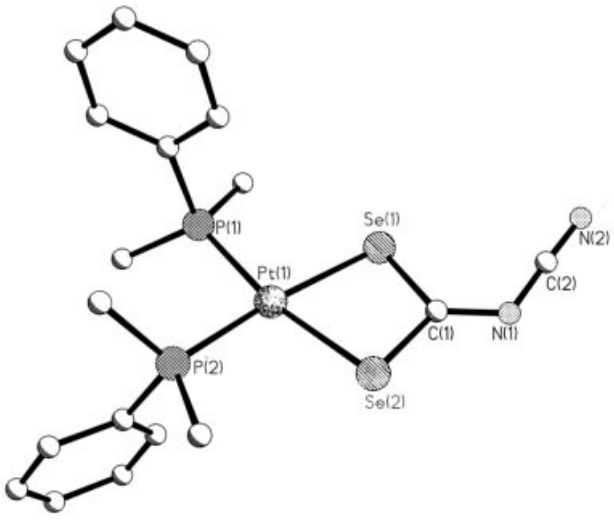

Figure 1. Crystal structure of **1**

approximately 2180 cm^{-1}, and the ν(C=N) vibrations can be seen in the region of 1459−1492 cm^{-1}. The bands for ν(M−Se) are all observed in the range 240−282 cm^{-1}.

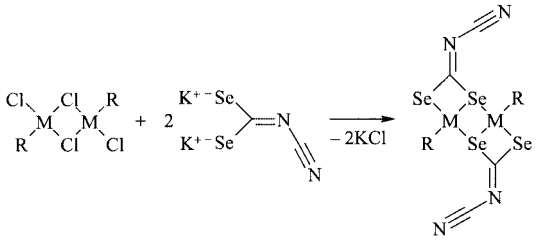

(3)

6 M = Rh, R = η^5-C_5Me_5
7 M = Ir, R = η^5-C_5Me_5

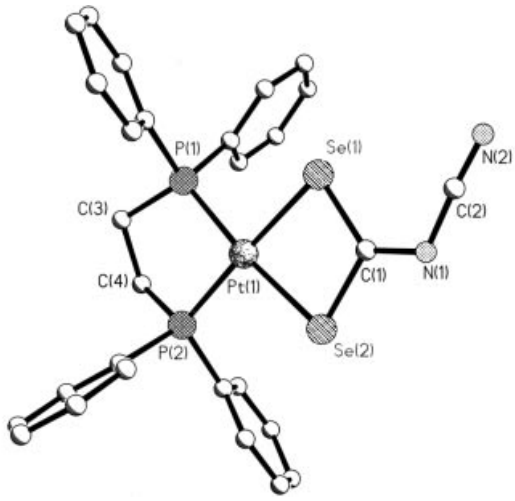

Figure 2. Crystal structure of **3**

Experimental Section

General: Unless otherwise stated, operations were carried out under oxygen-free nitrogen by using standard Schlenk techniques. All solvents and reagents were purchased from Aldrich, Alfa Aesar, BDH, Fisons and Strem and used as received. We are grateful to Johnson Matthey PLC for the loan of the precious metal salts. Diethyl ether and tetrahydrofuran were purified by reflux in the presence of sodium/benzophenone and by distillation under nitrogen. Hexane was purified by reflux in the presence of sodium and by distillation under nitrogen. Dichloromethane was heated to reflux in the presence of powdered calcium hydride and distilled under nitrogen. CD_2Cl_2 (99.6+ atom D) was used as received. Carbon diselenide was prepared as a dichloromethane solution by passing dichloromethane over elemental selenium at 600 °C.[34,35] The metal complexes $[\{RhCl(\mu\text{-}Cl)(\eta^5\text{-}C_5Me_5)\}_2]$[36] and $[\{IrCl(\mu\text{-}Cl)(\eta^5\text{-}C_5Me_5)\}_2]$[36] were prepared according to literature procedures. The complexes $[PtCl_2(PMe_2Ph)_2]$, $[PtCl_2(PPh_3)_2]$, $[PtCl_2(dppe)]$ [dppe = bis(diphenylphosphanyl)ethane], $[PtCl_2(dppm)]$ and $[PtCl_2(dppf)]$ [dppf = bis(diphenylphosphanyl)ferrocene] were prepared by the addition of stoichiometric quantities of the appropriate free phosphane or diphosphane to a dichloromethane solution of $[PtCl_2(cod)]$ (cod = cycloocta-1,5-diene). Infrared spectra were recorded (IR spectra as KBr discs, unless otherwise stated) with a Perkin−Elmer System 2000 FT/IR/Raman spectrometer. ^{31}P, ^{13}C and ^1H NMR spectra were recorded with a JEOL DELTA GSX 270 FT NMR spectrometer. Microanalysis was performed by the University of St. Andrews service. Fast atom bombardment (FAB) and electron ionisation (EI) mass spectra were performed by the EPSRC National Mass Spectrometer service.

$[Pt(C_2N_2Se_2)(PMe_2Ph)_2]$ (1): $[PtCl_2(PMe_2Ph)_2]$ (0.050 g, 0.0769 mmol) was dissolved in THF (20 mL), and potassium cyanodiselenoimidocarbonate (0.167 g, 0.580 mmol) was added as a solid in one portion. The resulting orange solution was stirred in the absence of light for 48 h. The solvent was evaporated in vacuo, and the remaining solid was extracted with dichloromethane (20 mL). The mixture was filtered through a Celite pad to remove precipitated KCl and washed with additional dichloromethane (30 mL). The filtrate was concentrated to dryness in vacuo to give a pale orange powder. The following compounds **2**−**7** were prepared and worked up in the same manner as platinum complex **1**. The product was recrystallised by vapour diffusion from chloroform/hexane to give X-ray quality crystals. Yield 0.027 g (52%). ^1H NMR

 © 2005 Wiley-VCH Verlag GmbH & Co. KGaA, Weinheim

Table 4. Details of the X-ray data collections and refinements for compounds **1** and **3**

Compound	**1**	**3**
Empirical formula	$C_{18}H_{22}N_2P_2PtSe_2$	$C_{28}H_{24}N_2P_2PtSe_2$
Crystal dimensions [mm]	0.1 × 0.03 × 0.03	0.13 × 0.05 × 0.05
Crystal system	monoclinic	monoclinic
Space group	*C*2/*c*	$P2_1/n$
a [Å]	33.596(8)	12.1941(18)
b [Å]	11.542(3)	18.081(3)
c [Å]	10.974(3)	12.6978(19)
β [°]	91.536(5)	105.898(3)
V [Å^3]	4253.5(19)	2692.6(7)
Z	8	4
M	681.33	803.44
D_c [g·cm^{-3}]	2.128	1.982
μ [mm^{-1}]	10.175	8.054
Measured reflections	13027	11392
Independent reflections (R_{int})	3804 (0.0937)	3816 (0.0613)
Final *R*1, *wR*2 [$I > 2\sigma(I)$]	0.0426, 0.0687	0.0314, 0.0533

(CD_2Cl_2): δ = 1.63 [d, $^3J(^{195}Pt-^1H)$ = 36 Hz, $^2J(^{31}P-^1H)$ = 10 Hz, 12 H, PMe], 7.48−7.69 (m, 10 H, aromatic H) ppm.

[Pt($C_2N_2Se_2$)(PPh_3)$_2$] (2): [$PtCl_2(PPh_3)_2$] (0.050 g, 0.0632 mmol) and potassium cyanodiselenoimidocarbonate (0.208 g, 0.722 mmol) gave the product as a beige powder. Yield 0.029 g (49%). ^{1}H NMR (CD_2Cl_2): δ = 7.24−7.52 (m, 30 H, aromatic H).

[Pt($C_2N_2Se_2$)(dppe)] (3): [$PtCl_2$(dppe)] (0.060 g, 0.0903 mmol) and potassium cyanodiselenoimidocarbonate (0.227 g, 0.788 mmol) gave the product as an orange powder. The product was recrystallised by vapour diffusion from chloroform/hexane to give X-ray quality crystals. Yield 0.049 g (67%). ^{1}H NMR (CD_2Cl_2): δ = 2.40−2.59 (m, 4 H, PCH_2CH_2P), 7.48−7.69 (m, 20 H, aromatic H) ppm.

[Pt($C_2N_2Se_2$)(dppm)] (4): [$PtCl_2$(dppm)] (0.060 g, 0.0923 mmol) and potassium cyanodiselenoimidocarbonate (0.211 g, 0.732 mmol) gave the product as a yellow powder. Yield 0.022 g (30%). ^{1}H NMR (CD_2Cl_2): δ = 3.89−4.18 (m, 2 H, PCH_2P), 7.25−7.71 (m, 20 H, aromatic H) ppm.

[Pt($C_2N_2Se_2$)(dppf)] (5): [$PtCl_2$(dppf)] (0.080 g, 0.0975 mmol) and potassium cyanodiselenoimidocarbonate (0.085 g, 0.295 mmol) gave the product as a yellow powder. Yield 0.044 g (45%). ^{1}H NMR (CD_2Cl_2): δ = 4.36 [br. m, 4 H, β-CH (C_5H_4)], 4.44 [br. m, 4 H, α-CH (C_5H_4)], 7.36−7.88 (m, 20 H, aromatic) ppm.

[{Rh($C_2N_2Se_2$)(η^5-C_5Me_5)}$_2$] (6): [{RhCl(μ-Cl)(η^5-C_5Me_5)}$_2$] (0.060 g, 0.0971 mmol) and potassium cyanodiselenoimidocarbonate (0.359 g, 1.246 mmol) gave a very dark red powder. Yield 0.037 g (42%). ^{1}H NMR (CD_2Cl_2): δ = 1.54−1.89(m, 30 H, η^5-C_5Me_5) ppm. Selected IR data (KBr): $\tilde{\nu}$ = 2162 [s, ν(C≡N)], 1492 [br., s, ν(C=N)], 279 (w), 259 [w, ν(Rh−S)] cm^{-1}.

[{Ir($C_2N_2Se_2$)(η^5-C_5Me_5)}$_2$] (7): [{IrCl(μ-Cl)(η^5-C_5Me_5)}$_2$] (0.040 g, 0.0502 mmol) and potassium cyanodiselenoimidocarbonate (0.268 g, 0.9308 mmol) gave an orange powder. Yield 0.021 g (39%). ^{1}H NMR (CD_2Cl_2): δ = 1.57−1.86 (m, 30 H, η^5-C_5Me_5) ppm. Selected IR data (KBr): $\tilde{\nu}$ = 2192 [s, ν(C≡N)], 1459 [br., s, ν(C=N)], 282 (w), 240 [w, ν(Ir−S)] cm^{-1}.

X-ray Crystallography: Tables 3 and 4 list details of data collections and refinements. For **1** and **3**, data were collected at 125 K with a Bruker SMART system. Intensities were corrected for Lorentz polarisation and for absorption. The structures were solved by the heavy atom method or by direct methods. The positions of the hydrogen atoms were idealised. Refinements were by full-matrix least squares based on F^2 using SHELXTL.[37] CCDC-233740 and -233741 contain the supplementary crystallographic data for this paper. These data can be obtained free of charge at www.ccdc.cam.ac.uk/conts/retrieving.html [or from the Cambridge Crystallographic Data Centre, 12 Union Road, Cambridge CB2 1EZ, UK; Fax: (internat.) + 44-1223-336-033; E-mail: deposit@ccdc.cam.ac.uk].

[1] S. M. Aucott, A. M. Z. Slawin, J. D Woollins, *Polyhedron* **2003**, *22*, 361−368.
[2] C. Gimenez Saiz, J. D. Woollins, A. M. Z. Slawin, *Cryst. Struct. Eng.* **2002**, 15−24.
[3] D. J. Birdsall, J. Novosad, A. M. Z. Slawin, J. D. Woollins, *J. Chem. Soc., Dalton. Trans.* **2000**, 435−439.
[4] D. J. Birdsall, A. M. Z. Slawin, J. D. Woollins, *Inorg. Chem.* **1999**, *38*, 4152−4154.
[5] T. Q. Ly, A. M. Z. Slawin, J. D. Woollins, *Angew. Chem. Int. Ed.* **1998**, *37*, 2501−2502.
[6] J. Arnold, *Prog. Inorg. Chem.* **1995**, *43*, 353−417.
[7] D. Corillo, *Coord. Chem. Rev.* **1992**, *119*, 137−169.
[8] M. G. Kanatzideo, S. J. Huang, *Coord. Chem. Rev.* **1994**, *130*, 509−621.
[9] A. M. Bond, R. L. Martin, *Coord. Chem. Rev.* **1984**, *54*, 23−98.
[10] R. P. Burns, F. P. McCullough, C. A. McAuliffe, *Adv. Inorg. Chem. Radiochem.* **1980**, *23*, 211−280.
[11] R. P. Burns, C. A. McAuliffe, *Adv. Inorg. Chem. Radiochem.* **1979**, *22*, 308−348.
[12] R. Eisenberg, *Prog. Inorg. Chem.* **1970**, *12*, 295−369.
[13] M. Afzaal, D. Crouch, P. O'Brien, J.-H. Park, S. M. Aucott, J. D. Woollins, *Chem. Vap. Deposition* **2002**, *8*, 187−189.
[14] M. Chunggaze, M. A. Malik, P. O'Brien, *J. Mater. Chem.* **1999**, *9*, 2433−2437.
[15] E. W. Abel, S. K. Bhargava, K. G. Orrell, *Progr. Inorg. Chem.* **1984**, *32*, 1−118.
[16] N. J. Hill, W. Levason, M. E. Light, G. Reid, *Chem. Commun.* **2003**, 110−111.
[17] W. Levason, G. Reid,, *Chem. Res. S* **2002**, 467−472.
[18] R. Hart, W. Levason, B. Patel, G. Reid, *J. Chem. Soc., Dalton Trans.* **2002**, 3153−3159.
[19] N. N. Greenwood, A. Earnshaw, *Chemistry of the Elements*, 2nd ed., Butterworth Heinman, Oxford, **1997**, p. 324−327.
[20] A. M. Golub, H. Kohler, V. V. Skopenko, *Chemistry of Pseudohalides*, Elsevier, Berlin, **1986**, p. 364−406.

 © 2005 Wiley-VCH Verlag GmbH & Co. KGaA, Weinheim

[21] M. Ebner, H. Werner, *Chem. Ber.* **1986**, *119*, 482−487.
[22] O. Kolb, H. Werner, *J. Organomet. Chem.* **1984**, *268*, 49−62.
[23] G. Gattow, M. Drager, *Z. Anorg. Allgem. Chem.* **1966**, *348*, 229−237.
[24] S. Yamazaki, T. Ueno, M. Hojo, *Bull. Chem. Soc. Jpn.* **1991**, *64*, 1404−1406.
[25] M. Saito, N. Tokitoh, R. Okazaki, *J. Organomet. Chem.* **1995**, *499*, 43−48.
[26] P. Haw, A. Walker, M. A. Woitzik, *J. Organomet. Chem.* **1981**, *212*, 419−423.
[27] J. Escudie, C. Couret, A. Raharinirina, J. Satge, *New J. Chem.* **1987**, *11*, 627−632.
[28] I. P. Parkin, M. J. Pilkington, A. M. Z. Slawin, D. J. Williams, J. D. Woollins, *Polyhedron* **1990**, *9*, 987−990.
[29] C. J. Burchell, S. M. Aucott, H. L. Milton, A. M. Z. Slawin, J. D. Woollins, *Dalton Trans.* **2004**, 369−374.
[30] K. Jensen, L. Henriksen, *Acta Chem. Scand.* **1970**, *24*, 3213−3229.
[31] C. M. Bolinger, T. B. Rauchfuss, *Inorg. Chem.* **1982**, *21*, 3947−3954.
[32] N. Bertel, H. W. Roesky, F. T. Edelmann, M. Noltmeyer, H. G. Schmidt, *Z. Anorg. Allg. Chem.* **1990**, *586*, 7−18.
[33] D. A. Lesch, T. B. Rauchfuss, *J. Organomet. Chem.* **1980**, *199*, C6−C8.
[34] W.-H. Pan, J. P. Fackler Jr., H.-W. Chen, *Inorg. Chem.* **1981**, *20*, 856−863.
[35] D. Ives, R. W. Pittman, W. J. Wardlaw, *J. Chem. Soc.* **1947**, 1080−1083.
[36] C. White, A. Yates, P. M. Maitlis, *Inorg. Synth.* **1992**, *29*, 228−230.
[37] *SHELXTL*, Bruker AXS, Madison, **1999**.

Received April 8, 2004
Early View Article
Published Online November 18, 2004

 © 2005 Wiley-VCH Verlag GmbH & Co. KGaA, Weinheim

Octahedral Molybdenum Cluster Cyanide Complexes with Selenide and Halide Ligands in the Cluster Core

Yuri V. Mironov,[a] Vladimir N. Ikorskii,[b] Vladimir E. Fedorov,[b] and James A. Ibers*[a]

Keywords: Molybdenum / Clusters / Chalcohalide / Cyanide / Solid-state structures

Two new octahedral molybdenum cluster cyanide complexes with mixed selenide/halide ligands in the cluster core, $Cs_5[Mo_6Se_{3.6}Cl_{4.4}(CN)_6]$ (**1**) and $Cs_5[Mo_6Se_{3.4}Br_{4.6}(CN)_6]$ (**2**), have been synthesized by the reaction of Mo_6Cl_{12} or Mo_6Br_{12} with an aqueous solution of Cs_2Se_3, and then with an aqueous solution of KCN. Both compounds have been characterized by single-crystal X-ray diffraction methods. The compounds are isostructural and crystallize in the trigonal space group $P\bar{3}c1$ with two formula units per unit cell. The unit cell dimensions at 153 K are a = 9.8895(9) Å, c = 19.395(3) Å, V = 1642.7(3) Å^3 (**1**) and a = 9.9805(9) Å, c = 19.763(2) Å, V = 1704.9(3) Å^3 (**2**).
(© Wiley-VCH Verlag GmbH & Co. KGaA, 69451 Weinheim, Germany, 2005)

Introduction

Molybdenum(II) chloride comprising a Mo_6Cl_8 cluster core was discovered over 100 years ago. Complexes with the cluster cores Mo_6Q_8 (Q = S, Se, Te) and Mo_6Y_8 (Y = Cl, Br, I) are now well known,[1−4] and include anionic cyanide complexes.[5−8] Nevertheless, only limited number of complexes with the mixed chalcohalide core $Mo_6Q_xY_{8-x}$ are known. The first such cluster anion, $[(Mo_6SCl_7)Cl_6]^{3-}$, was obtained in 1982.[9] Since then other complexes with one or two halogen atoms substituted by chalcogen atoms have been synthesized. These include the species $[(Mo_6QY_7)Y'_6]^{3-}$ (VEC = 24) and $[(Mo_6QY_7)Y'_6]^{2-}$ (VEC = 23) (Y, Y′ = Cl, Br; Q = S, Se),[10,11] $[Et_4N]_3[(Mo_6TeCl_7)Cl_6]$ (VEC = 24),[12] $[Et_4N]_3[(Mo_6Se_2Cl_6)Cl_6]$ (VEC = 23), $[Ph_4P]_2[H_3O]_2[(Mo_6Se_2Cl_6)Cl_6]$ (VEC = 24),[13] $Cs_4[(Mo_6Q_2Br_6)Br_6]$ (VEC = 24),[14] and $Cs_{0.4}K_{0.6}[Et_4N]_{11}[(Mo_6Q_2Br_6)(CN)_6]_3\cdot 16H_2O$ (VEC = 24) (Q = S, Se).[14]

Herein we present the syntheses and structure determinations of two new Mo_6 cyanide complexes that possess mixed chalcohalide cluster cores.

Results

Syntheses

The Mo_6S_8 cluster unit may be synthesized from Mo_6Cl_{12} by its reaction with NaSH and NaOBu in refluxing *n*BuOH/pyridine.[15] This synthesis demonstrates that in solution the μ_3-halide ligands in the cluster core may be easily substituted by chalcogen ligands. Recently we found that the reaction in water of Mo_6Br_{12} with Cs_2S_3 leads to the formation of the tetrahedral molybdenum polysulfide $Cs_6[Mo_4S_{23.6}]$.[16] However, we find that the reaction of Mo_6Y_{12} (Y = Cl, Br) with Cs_2Se_3 leads to amorphous products that are different from those from the reaction with Cs_2S_3. To discover the structure of these products, we have "excised" the cluster core by treating these solids with KCN in boiling water, and then letting the resultant solutions evaporate. In this way, crystals in the form of hexagonal plates were obtained, and their structures have been determined by X-ray diffraction methods. These reactions take place without cluster decomposition, but with partial substitution of the Y ligands by Se to form $Cs_5[Mo_6Se_{3.6}Cl_{4.4}(CN)_6]$ (**1**) and $Cs_5[Mo_6Se_{3.4}Br_{4.6}(CN)_6]$ (**2**), both of which contain the cluster core $Mo_6Se_xY_{8-x}$. Both compounds are soluble in water, but the resulting solutions are not stable in air. Partial stabilization may be achieved by the addition of KCN to the solutions. Such differences in behavior of S and Se octahedral complexes were recently observed for Mo_6 chalcocyanide complexes. Whereas Mo_6Se_8 reacts with KCN to afford the octahedral $[Mo_6Se_8(CN)_6]^{7-}$ cluster anion,[6] in a similar reaction Mo_6S_8 affords the tetrahedral $[Mo_4S_4(CN)_{12}]^{6-}$ cluster anion.[7]

Structures

The structures of the compounds $Cs_5[Mo_6Se_{3.6}Cl_{4.4}(CN)_6]$ (**1**) and $Cs_5[Mo_6Se_{3.4}Br_{4.6}(CN)_6]$ (**2**) comprise a Mo_6 octahedron residing inside an $(SeY)_8$ pseudocube (Figure 1). Packing of the cluster anions in the unit cell is shown in Figure 2. The anions have crystallographically imposed $\bar{3}$ symmetry. As such, Se and Y atoms are disordered over the corners of the cube in an overall ratio

[a] Department of Chemistry, Northwestern University, Evanston, Illinois 60208-3113, USA
Fax: (internat.) + 1-847-491-2976
[b] Nikolaev Institute of Inorganic Chemistry, 3 Acad. Lavrentiev pr., 630090 Novosibirsk, Russia

 © 2005 Wiley-VCH Verlag GmbH & Co. KGaA, Weinheim **DOI: 10.1002/ejic.200400497**

of 3.6:4.4 for Y = Cl, and 3.4:4.6 for Y = Br. Such disorder is common in $Mo_6Q_xY_{8-x}$ cluster complexes. Important distances are: Mo−Mo, 2.642(1) Å and 2.647(1) Å (**1**), 2.656(1) Å and 2.658(1) Å (**2**); Mo−(Se/Cl), 2.534(2)−2.553(1) Å (**1**); Mo−(Se/Br), 2.595(1)−2.607(1) (**2**) Å. Each Mo atom is further ligated with a terminal cyano ligand; the Mo−C distances are 2.196(9) Å (**1**) and 2.213(7) Å (**2**). The Cs atoms in both structures are surrounded by N and Se/Y atoms, as shown in Figure 3 for compound **1**.

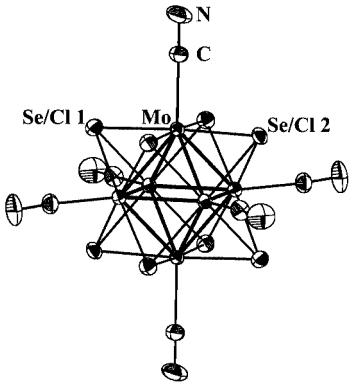

Figure 1. View of the $[Mo_6Se_{3.6}Cl_{4.4}(CN)_6]^{5-}$ anion in **1**; displacement ellipsoids are drawn at the 50% probability level

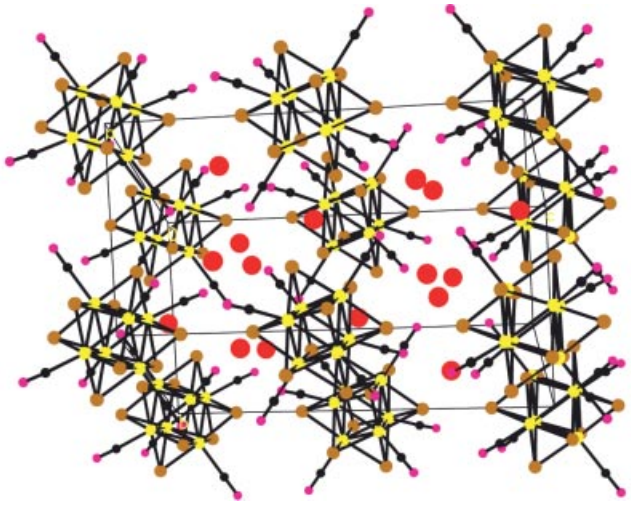

Figure 2. A view of the unit cell of $Cs_5[Mo_6Se_{3.6}Cl_{4.4}(CN)_6]$ (**1**); the yellow circles are Mo, the brown circles are Se/Cl, the black circles are C, the small red circles are N, and the large red circles are Cs atoms

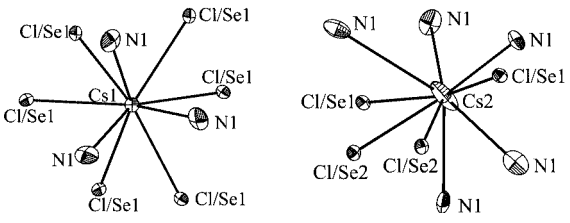

Figure 3. The coordination environments of atoms Cs1 and Cs2 in $Cs_5[Mo_6Se_{3.6}Cl_{4.4}(CN)_6]$ (**1**); displacement ellipsoids are drawn at the 50% probability level

It is useful to compare metrical data as a function of VEC numbers for these complexes. For example, the average Mo−Mo distance is equal to 2.651(1) Å for $Cs_{0.4}K_{0.6}[Et_4N]_{11}[(Mo_6Se_2Br_6)(CN)_6]_3\cdot 16H_2O$ (VEC = 24),[14] 2.657(1) Å for compound **2** (VEC = 23.5), 2.700(3) Å for $K_7[(Mo_6Se_8)(CN)_6]\cdot H_2O$ (VEC = 21),[6] and 2.711(2) Å for $(Me_4N)_4K_2[(Mo_6Se_8)(CN)_6]\cdot 10H_2O$ (VEC = 20).[6] Although the differences are small, it is clear that the average Mo−Mo distance increases as the VEC value decreases.

Magnetism

Figure 4 displays the temperature dependence of the inverse magnetic susceptibilities of $Cs_5[Mo_6Se_{3.6}Cl_{4.4}(CN)_6]$ (**1**) and $Cs_5[Mo_6Se_{3.4}Br_{4.6}(CN)_6]$ (**2**). Both compounds are paramagnetic. Over the temperature range 78−300 K, the magnetic susceptibility data are well described by the Curie−Weiss law together with a temperature-independent term $N\alpha$ [Equation (1)] where $C = N\beta^2\mu_B^2/3k$.

$$\chi = C^*(T - \theta)^{-1} + N\alpha \quad (1)$$

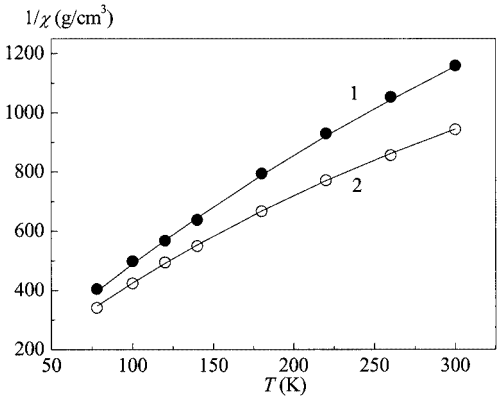

Figure 4. The temperature dependence of the inverse magnetic susceptibility of $Cs_5Mo_6Se_{3.6}Cl_{4.4}(CN)_6$ (**1**) and $Cs_5Mo_6Se_{3.4}Br_{4.6}(CN)_6$ (**2**); the solid curves were calculated from Equation (1)

Table 1 presents the parameters derived from the magnetic data. The effective magnetic moments of these complexes of 1.24 μ_B (**1**) and 1.27 μ_B (**2**) are less than the spin-only value of 1.73 μ_B. Hence, only part of the cluster complexes contains unpaired electrons. To estimate the number of clusters, *n* (Table 1), containing one unpaired electron (% per mol) we used the ratio $n = \mu_{eff}^2/[4S(S + 1)]\cdot 100\% = \mu_{eff}^2/3\cdot 100\%$, where $[4S(S + 1)]^{1/2}$ is the electron spin magnetic moment.

Discussion

As we noted previously,[17] crystal-structure determinations provide limited insight into the true nature of the cluster core in compounds such as the present ones in which Q/Y disorder at the cube corners of the $Mo_6Q_xY_{8-x}$ core

 © 2005 Wiley-VCH Verlag GmbH & Co. KGaA, Weinheim

Table 1. Magnetic data

	C [cm^3·K/mol]	$-\theta$ [K]	$N\alpha$ [cm^3/mol]	μ_{eff} [μ_B]	n[a] (%)
$Cs_5Mo_6Se_{3.6}Cl_{4.4}(CN)_6$ (**1**)	0.191	6	$0.24\cdot10^{-3}$	1.24	51
$Cs_5Mo_6Se_{3.4}Br_{4.6}(CN)_6$ (**2**)	0.203	3	$0.39\cdot10^{-3}$	1.27	54

[a] Contents of paramagnetic components in **1** and **2**.

can arise in diverse ways. These include cocrystallization of different compounds, geometric disorder, orientational disorder, or a combination of these. Given the magnetic measurements, the simplest, but by no means unique interpretation, is that the compounds $Cs_5[Mo_6Se_{3.6}Cl_{4.4}(CN)_6]$ (**1**) and $Cs_5[Mo_6Se_{3.4}Br_{4.6}(CN)_6]$ (**2**) comprise solid solutions of $Cs_5[Mo_6Se_3Y_5(CN)_6]$ and $Cs_5[Mo_6Se_4Y_4(CN)_6]$ (Y = Cl or Br) in an approximate 1:1 ratio.

The substitution of inner halogen ligands by chalcogens in Mo_6 cluster complexes drastically decreases oxidation potentials [for example, +1.38 V for (Mo_6Br_8), +0.55 V for (Mo_6SBr_7), −0.056 V for ($Mo_6S_2Br_6$)].[14] For clusters that have VEC = 24, additional substitution of inner halogen atoms must lead to a similar cathodic shift because stabilization of species with a lower number of valence electrons occurs. Examples include the present $[Mo_6Se_4Y_4(CN)_6]^{5-}$ cluster anions (VEC = 23) and complexes with Mo_6Q_8 cores (VEC = 21, 20).[6,7]

Experimental Section

General: All reagents were used as purchased. Mo_6Br_{12} was synthesized by the reaction of Mo with Br_2 at 750 °C.[18] Mo_6Cl_{12} was synthesized by the reaction of Mo with $MoCl_5$ at 650 °C.[19] Cs_2Se_3 was synthesized by the reaction of Cs with Se in liquid ammonia. FT-IR data were collected with a Bio-Rad Digilab FTS-60 instrument. Microanalyses for C, H, and N were performed by Oneida Research Services, Whitesboro, NY, USA.

Synthesis of $Cs_5[Mo_6Se_{3.6}Cl_{4.4}(CN)_6]$ (1): Mo_6Cl_{12} (0.2 g, 0.2 mmol) and Cs_2Se_3 (0.8 g, 1.6 mmol) were placed in degassed boiling water (20 mL) for 1 h. KCN (0.5 g, 7.7 mmol) was then added to the mixture, which was boiled for another hour before filtering. The dark red-brown filtrate was evaporated to a volume of 5 mL and then cooled to room temperature. The dark crystalline product was filtered off, and was washed twice with cold water (2 mL) until the solution turned violet. The crystals were then washed twice with ethanol (10 mL) and then dried. Yield: 0.25 g (68% based on Mo). Semi-quantitative analysis of the crystals with an EDX-equipped Hitachi S-3500 SEM gave Cs:Mo:Se:Cl = 4.7:6:3.8:4.3. $C_6Cl_{4.4}Cs_5Mo_6N_6Se_{3.6}$ (derived from X-ray data) calcd. C 3.9, N 4.6; found C 4.1, N 4.8. IR (KBr): $\tilde{\nu}$ = 2085 s (ν_{CN}) cm^{-1}.

Synthesis of $Cs_5Mo_6Se_{3.4}Br_{4.6}(CN)_6$ (2): The synthesis above was followed with Mo_6Br_{12} substituted for Mo_6Cl_{12}. Yield: 0.28 g (69%). Examination of the crystals with an EDX-equipped Hitachi S-3500 SEM gave the ratio Cs:Mo:Se:Br = 5.2:6:3.5:4.7. $C_6Br_{4.6}Cs_5N_6Mo_6Se_{3.4}$ calcd. C 3.5, N 4.1; found C 3.5, N 4.5. IR (KBr): $\tilde{\nu}$ = 2092 s (ν_{CN}) (cm^{-1}).

X-ray Crystallography: Single-crystal X-ray diffraction data were collected on $Cs_5[Mo_6Se_{3.6}Cl_{4.4}(CN)_6]$ (**1**) and $Cs_5[Mo_6Se_{3.4}Br_{4.6}(CN)_6]$ (**2**) with the use of graphite-monochromotized MoK_α radiation (λ = 0.71073 Å) at 153 K with a Bruker Smart-1000 CCD diffractometer with the operating program SMART.[20] The crystal-to-detector distance was 5.023 cm. Crystal decay was monitored by recollecting 50 initial frames at the end of the data collection. Data were collected in groups of 606 frames, with a scan step of 0.3° in ω and with φ settings of 0°, 90°, 180°, and 270°. The exposure time was 15 s/frame. Cell refinement and data reduction were carried out with the program SAINT.[20] A face-indexed absorption correction was performed numerically with the use of XPREP.[21] The program SADABS[20] was then employed to make incident beam and decay corrections. Both structures were solved by direct methods, by means of SHELXS of the SHELXL[21] suite of programs, and were refined by full-matrix least-squares techniques.[21] Both structures were standardized through the use of the program TIDY.[22] $Cs_5[Mo_6Se_{3.6}Cl_{4.4}(CN)_6]$ (**1**) displays Se:Cl disorder. The Se:Cl occupancy values at each of the two crystallo-

Table 2. Crystal data and structure refinement details for $Cs_5[Mo_6Se_{3.6}Cl_{4.4}(CN)_6$ (**1**) and $Cs_5Mo_6Se_{3.4}Br_{4.6}(CN)_6$ (**2**)

	1	**2**
Empirical formula	$C_6Cl_{4.4}Cs_5Mo_6N_6Se_{3.6}$	$C_6Br_{4.6}Cs_5N_6Mo_6Se_{3.4}$
Formula mass [g/mol]	1837.42	2032.36
a [Å]	9.8895(9)	9.9805(9)
c [Å]	19.395(3)	19.763(3)
V [Å^3]	1642.7(3)	1704.9(3)
$\rho_{calcd.}$ [g/cm^3]	3.715	3.959
Space group	$P\bar{3}c1$	$P\bar{3}c1$
Z	2	2
μ [cm^{-1}]	120.57	164.31
T [K]	153	153
$R_1(F)$ [$F_o^2 > 2\sigma(F_o^2)$][a]	0.0466	0.0467
$R_w(F^2)$[b]	0.1114	0.106

[a] $R_1(F) = \Sigma||F_o| - |F_c||/\Sigma|F_o|$. [b] $Rw(F_o^2) = [\Sigma w(F_o^2 - F_c^2)^2/\Sigma wF_o^4]^{1/2}$; $w^{-1} = \sigma^2(F_o^2) + (0.04F_o^2)^2$ for $F_o^2 > 0$; $w^{-1} = \sigma^2(F_o^2)$ for $F_o^2 \leq 0$.

 © 2005 Wiley-VCH Verlag GmbH & Co. KGaA, Weinheim

graphically independent sites were refined. The results were: Se(1):Cl(1) = 0.472(8):0.528(8); Se(2):Cl(2) = 0.393(14):0.607(14). The position of the Cs2 atom in **2** is disordered over two symmetry-equivalent positions, the refinement of the occupancy value converged to 0.456(4). These occupancy values lead to the composition $Cs_{4.74(9)}[Mo_6Se_{3.62(3)}Cl_{4.38(3)}(CN)_6]$. The occupancy of atom Cs2 was set to 0.5 in subsequent refinements; this had no significant effect on the final metrical data. Given the hazards of establishing compositions through the refinement of X-ray data[23] we adopt the formula $Cs_5[Mo_6Se_{3.6}Cl_{4.4}(CN)_6]$ for compound **1**. $Cs_5[Mo_6Se_{3.4}Br_{4.6}(CN)_6]$ (**2**) displays Se/Br disorder, but owing to the very similar X-ray scattering powers of Se and Br, no site occupancy refinement was possible. Rather, each site was assumed to contain Se:Br in the ratio 0.425:0.575, as determined from the EDX results. The final results are essentially independent of this ratio. The positions of the Cs1 atoms are well defined in both structures. The disorder of the Cs2 position in compound **2** has been modeled in a somewhat unsatisfactory way by the introduction of atoms Cs2 and "Cs3". Their combined occupancy values converged to 0.49(1) and were set at 0.5. Despite the differences in the Cs occupancy values, we consider the two compounds to be isostructural. Additional experimental details are given in Table 2, and in the crystallographic data files, which have been deposited with FIZ Karlsruhe.[24]

Magnetic Measurements: The magnetic susceptibility measurements on $Cs_5[Mo_6Se_{3.6}Cl_{4.4}(CN)_6]$ (**1**) and $Cs_5[Mo_6Se_{3.4}Br_{4.6}(CN)_6]$ (**2**) were carried out by the Faraday method at 10 kOe over the temperature range 78−300 K. Data were corrected for the diamagnetic contributions of -696×10^{-6} and -737×10^{-6} cm^3/mol for **1** and **2**, respectively.

Acknowledgments

This work was supported by the National Science Foundation under Grant No. CHE98-19385 and by INTAS-00-00689.

[1] M. N. Sokolov, V. P. Fedin, A. G. Sykes, in *Comprehensive Coordination. Chemistry II* (Eds: J. A. McCleverty, T. J. Meyer), Elsevier Pergamon, **2004**, vol. 4, p. 761−823.
[2] T. G. Gray, *Coord. Chem. Rev.* **2003**, *243*, 213−235.
[3] M. H. Chisholm (Ed.), *Early transition metal clusters with π-donor ligands*, VCH Publishers, New York, **1995**.
[4] N. Prokopuk, D. F. Shriver, *Adv. Inorg. Chem.* **1998**, *46*, 1−49.
[5] M. K. Simsek, D. Bublitz, W. Preetz, *Z. Anorg. Allg. Chem.* **1997**, *623*, 1885−1891.
[6] Y. V. Mironov, A. V. Virovets, N. G. Naumov, V. N. Ikorskii, V. E. Fedorov, *Chem. Eur. J.* **2000**, *6*, 1361−1365.
[7] K. A. Brylev, A. V. Virovets, N. G. Naumov, Y. V. Mironov, D. Fenske, V. E. Fedorov, *Russ. Chem. Bull., Int. Ed.* **2001**, *50*, 1140−1143.
[8] C. Magliocchi, X. Xie, T. Hughbanks, *Inorg. Chem.* **2000**, *39*, 5000−5001.
[9] J. B. Michel, R.E. McCarley, *Inorg. Chem.* **1982**, *21*, 1864−1872.
[10] M. Ebihara, K. Toriumi, K. Saito, *Inorg. Chem.* **1988**, *27*, 13−18.
[11] M. Ebihara, K. Isobe, Y. Sasaki, K. Saito, *Inorg. Chem.* **1992**, *31*, 1644−1649.
[12] M. Ebihara, T. Imai, T. Kawamura, *Acta Crystallogr., Sect. B* **1995**, *51*, 1743−1745.
[13] M. Ebihara, K. Toriumi, Y. Sasaki, K. Saito, *Gazz. Chim. Ital.* **1995**, *125*, 87−94.
[14] S. Cordier, N. G. Naumov, D. Salloum, F. Paul, C. Perrin, *Inorg. Chem.* **2004**, *43*, 219−226.
[15] S. J. Hilsenbeck, V. G. Young, R. E. McCarley, *Inorg. Chem.* **1994**, *33*, 1822−1832.
[16] Y. V. Mironov, A. S. Gardberg, J. A. Ibers, *Inorg. Chem.* **2002**, *41*, 1333−1334.
[17] Y. V. Mironov, J. A. Cody, T. E. Albrecht-Schmitt, J. A. Ibers, *J. Am. Chem. Soc.* **1997**, *119*, 493−498.
[18] V.A. Khutornoi, N. G. Naumov, Y. V. Mironov, O. Oeckler, A. Simon, V. E. Fedorov, *Russ. J. Coord. Chem.* **2002**, *28*, 183−190.
[19] H. Schäfer, H.-G. Schnering, J. Tillack, F. Kuhnen, H. Wöhrle, H. Baumann, *Z. Anorg. Allg. Chem.* **1967**, *353*, 281−310.
[20] *SMART*, Version 5.054 (Data Collection), and *SAINT-PLUS*, Version 6.19 (Data Processing), Software for the SMART System, Bruker Analytical X-ray Instruments, Inc., Madison, WI, **1999**.
[21] G. M. Sheldrick, *SHELXTL*, DOS/Windows/NT, Version 5.10, Bruker Analytical X-ray Instruments, Inc., Madison, WI, **1997**.
[22] L. M. Gelato, E. Parthé, *J. Appl. Crystallogr.* **1987**, *20*, 139−143.
[23] J. F. Mitchell, J. K. Burdett, P. M. Keane, J. A. Ibers, D. C. DeGroot, T. P. Hogan, J. L. Schlinder, C. R. Kannewurf, *J. Solid State Chem.* **1992**, *99*, 103−109.
[24] Crystallographic data in CIF format for $Cs_5[Mo_6Se_{3.6}Cl_{4.4}(CN)_6]$ (**1**) and $Cs_5[Mo_6Se_{3.4}Br_{4.6}(CN)_6]$ (**2**) have been deposited with FIZ Karlsruhe. Further details of the crystal-structure investigation(s) may be obtained from the Fachinformationszentrum Karlsruhe, 76344 Eggenstein-Leopoldshafen, Germany (Fax: + 49-7247-808-666; E-mail: crysdata@fiz-karlsruhe.de), on quoting the depository numbers CSD-414112 (**1**) and -414113 (**2**).

Received June 9, 2004
Early View Article
Published Online November 18, 2004

 © 2005 Wiley-VCH Verlag GmbH & Co. KGaA, Weinheim

Spin-Coating Preparation of Highly Ordered Photoluminescent Films of Layered PbI_2-Aminoalkyloxysilane Perovskites

Zi-Yong Cheng,[a] Bao-Li Shi,[a] Bao-Xiang Gao,[a] Mao-Lin Pang,[b] Shu-Yun Wang,[a] Yan-Chun Han,*[a] and Jun Lin*[b]

Keywords: Layered perovskite / Sol-gel / Films / Photoluminescence

By utilising 3-aminopropyltrimethoxysilane (APTMOS) cations and PbI_2 as the organic and inorganic precursors, respectively, a spin-coated film of a layered perovskite-type organic/inorganic derivative of APTMOS-PbI_4 was prepared. The structure of APTMOS-PbI_4 was characterised by X-ray diffraction (XRD), UV/Vis absorption and infrared red spectroscopy (IR). The film showed green emission from the excitons of the inorganic layers and a weak blue emission related to the small amount of gel of adjacent APTMOS cations. Furthermore, the significant effect of the size of the inorganic framework on the cross-linking degree of APTMOS molecules is discussed.
(© Wiley-VCH Verlag GmbH & Co. KGaA, 69451 Weinheim, Germany, 2005)

Introduction

The self-organisation of molecules into highly ordered architectures with layered structures has attracted a wide range of scientific and practical interest. The perfect combination of the organic and inorganic components provides tremendous mechanical strength and toughness that is not possessed by a single phase alone. To date, the most frequently used method for the synthesis of 2D nanostructured hybrids is the sol-gel process, employing organic silane molecules in the presence of surfactants which are used as structure directors due to their amphiphilic nature in a selective solution.[1a−1g] On the other hand, the layered compounds can also be obtained by intercalating the guest molecules, generally organic species such as alkylammonium salts, into the interlayer spaces of a pre-existing inorganic layered structure.[2a−2c] Recently, layered polysiloxane containing alkylammonium groups has been prepared by the sol-gel reaction of 3-aminopropyltrimethoxysilane (APTMOS) with hydrochloric acid, without using any surfactants or long-chain alkyl groups in the monomers.[3] Similarly, we reported a simple method of preparing a layered nanocomposite containing a silica network by a perovskite-type self-organisation.[4] Lead(II) chloride was employed as the inorganic layer in this superlattice material and photoluminescence in the ultraviolet region was observed due to the nature of the low-dimensional structure. In order to further explore the feasibility of this method and obtain luminescence in the visible region, lead(II) iodide (with a smaller band-gap and a larger "footprint" of the inorganic framework) and APTMOS cations were used in this study. It was observed that these materials can also be self-organised into a perovskite-type layered structure which shows green luminescence arising from the inorganic semiconductor of the lead(II) iodide layers. The expected structure of PbI_2-based perovskite and the simulated structure of the APTMOS molecule are shown in Figure 1.

[a] State key Laboratory of polymer physics and Chemistry, Changchun Institute of Applied Chemistry, Chinese Academy of Sciences,
Changchun, 130022, P. R. China
E-mail: ychan@ciac.jl.cn
[b] Key Laboratory of Rare Earth Chemistry and Physics, Changchun Institute of Applied Chemistry, Chinese Academy of Sciences,
Changchun, 130022, P. R. China
E-mail: jlin@ciac.jl.cn

Results and Discussion

Synthesis and Film Preparation

At the beginning of the experiment for the preparation of APTMOS·HI, we tried to simply mix the APTMOS with PbI_2 in a dilute hydroiodic acid solution but we were unable to obtain the final product as expected. HI is a very strong acid and a nucleophile and APTMOS is very susceptible to hydrolysis and polycondensation in an acidic environment. The Si−O, C−O and Si−C bonds are broken upon nucleophilic attack by I^-. Thus, a rigorous procedure for removing water and a low temperature bath of diethyl ether/dry ice were applied in order to avoid the occurrence of the above reactions. In spite of these precautions, the acid-base reaction between the head of the amine group of APTMOS and HI was not be impeded at low temperature.

The molecular formula $[(CH_3O)_3Si-CH_2-CH_2-CH_2-NH_3]_2PbI_4$ (APTMOS-PbI_4 for short) was defined by the single layers of the <100> oriented perovskite sheets which

 © 2005 Wiley-VCH Verlag GmbH & Co. KGaA, Weinheim DOI: 10.1002/ejic.200400501

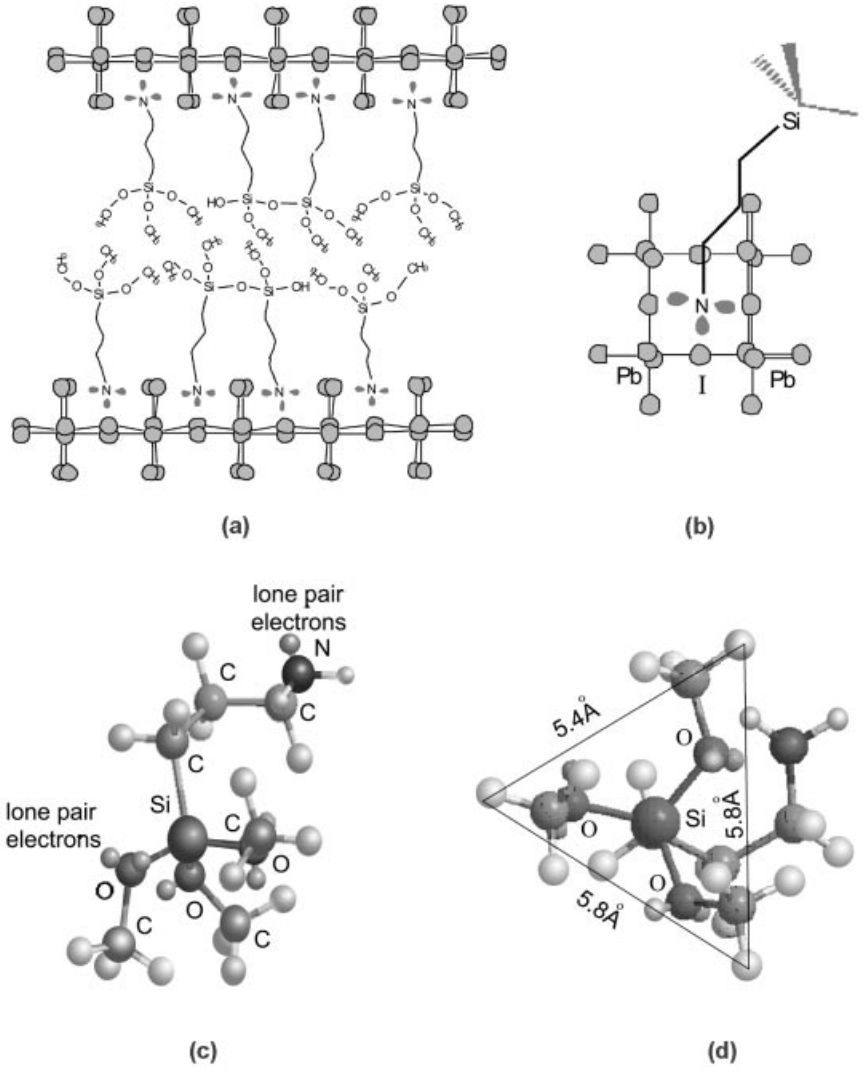

Figure 1. Schematic representation of the expected structure for APTMOS-PbI_4 perovskite and the simulated results of the dimensions of the APTMOS molecules; the APTMOS-PbI_4 layered superlattice consists of an extended framework of corner-sharing lead iodide octahedra alternating with a bilayer of APTMOS cations; (a) view parallel to the perovskite sheet of the APTMOS-PbI_4 structure, (b) view perpendicular to the perovskite sheet of the APTMOS-PbI_4 structure, (c) the profile of the APTMOS molecule, (d) the dimensions of the cross-section of the APTMOS molecule; the ball-and-stick model of the APTMOS molecule represents a favourable energy state

consist of corner-sharing metal halide octahedra, alternating with the ATMOS cation bilayers. Each octahedron has a Pb^{2+} cation in the centre and six I^- units as coordination anions. The four bridging I^- ions are shared by the two adjacent octahedra. Figure 1 (a and b) shows the model of the layered perovskite structure. From a view perpendicular to the perovskite sheets in the APTMOS-PbI_4 structures, each APTMOS cation is nominally located in a square defined by the four neighbouring Pb atoms and the Pb−I−Pb linkages can be regarded as the sides of the square (see b in Figure 1).[5] In contrast to the length of about 5.6 Å in Pb−Cl−Pb based structures,[6a] the PbI_2-based perovskite exhibits a larger framework of 6.4 Å for the Pb−I−Pb unit according to the single-crystal structure.[6b] The shape and relevant molecular dimensions of the APTMOS molecule are shown in parts c and d of Figure 1. These results were calculated using the MM2 force field with the Chem3D program (CambridgeSoft Corp.). The lengths of the sides of the silicon tetrahedra in an unhydrolysed APTMOS molecule are in a range of 5.4−5.8 Å. Thus, the PbI_2-based perovskites have enough space to accommodate the unhydrolysed APTMOS molecules in the self-assembly process. In contrast, in the preparation of the APTMOS-$PbCl_4$ perovskite, an intentional hydrolysis was applied before the film deposition for reducing the cross-sectional area of the APTMOS cations.[4]

Infrared Spectroscopy

The FT-IR spectra of APTMOS (a), APTMOS·HI (b) and the perovskite structure of APTMOS-PbI_4 (c) are given in Figure 2. In Figure 2 (see a), for APTMOS, the weak peaks at 3376 and 3298 cm^{-1} are due to asymmetric/symmetric N−H stretching vibrations of primary amine ($-NH_2$) groups. The locations and assignments of the other

 © 2005 Wiley-VCH Verlag GmbH & Co. KGaA, Weinheim

absorption peaks are 2938 (ν_{as}, CH_2), 2832 (ν_s, CH_2), 1576 (δ, NH_2), 1469 (δ, CH_2), 1190 (ν_{as}, Si−CH_2), 1085 (ν_{as}, Si−OCH_3), 815 (ν_s, Si−OCH_3) and 450 cm^{-1}(δ, Si−OCH_3) (where ν_{as} stands for asymmetric stretching, ν_s for symmetric stretching, and δ for bending).[7a−7c] After treatment with dry HI gas, as shown in part b of Figure 2, the N−H stretching at 3298 and 3376 cm^{-1} disappeared. Instead, a broad band centred at 2900 cm^{-1} and a series of overtone peaks from 2000 to 2705 cm^{-1} were observed which are typical characteristics of organic amine salts. The weak absorptions at 3450 and 920 cm^{-1} due to silanols of hydrolysed APTMOS molecules could be observed, despite a rigorous procedure for removing water and the application of a low temperature during the preparation of the amine salt. Other than the absorption of the silanols at 3430 cm^{-1} becoming more strong, there were no great differences between the FT-IR spectrum of APTMOS-PbI_4 (see c in Figure 2) and that of APTMOS·HI (b in Figure 2). Note that the asymmetric stretching mode at 1085 cm^{-1} and the symmetric stretching mode at 817 cm^{-1} corresponding to the Si−OCH_3 group also remained as shown in Figure 2 (see c), indicating that a large amount of unhydrolysed APTMOS cations remained in the perovskite structure. The Si−O−Si bond also gives at least one very intense band in the 1100−1000 cm^{-1} region due to the asymmetric stretching mode. Thus, the mode corresponding to Si−O−Si or Si−O−C appearing in this region cannot be easily distinguished. As for the short open-chain alkylpolysiloxanes or small cyclic polysiolxanes, the asymmetric stretching of Si−O−Si shows a characteristic single band at 1000−1100 cm^{-1}.[1b] With progressively longer linear alkylpolysiloxanes or larger cyclic polysiloxanes, the band in this region splits into two or more overlapping components and becomes broader.[8a−8b] Base on this fact, the appearance of only a singlet absorption band at 1079 cm^{-1} for APTMOS-PbI_4 perovskite is consistent with the formation of a mixture which is composed largely of Si−OCH_3 functionalities, silanol groups and perhaps a small amount of short-chain polysiloxanes/small cyclic polysiloxanes. In contrast to the FT-IR spectrum of APTMOS-$PbCl_4$, where the Si−O−Si asymmetric stretching band is characteristic of long-chain linear siloxanes with two broad doublet peaks at 1107 and 1037 cm^{-1},[4] the APTMOS cations in the APTMOS-PbI_4 perovskite have less cross-linking because only one band is present in this region. This can be attributed to the fact that the space provided by the PbI_2-based framework is too large for the perpendicular APTMOS cations to form long Si−O−Si chains. The films of APTMOS-PbI_4 have poor stability compared with the APTMOS-$PbCl_4$ films and traditional organic/inorganic perovskites such as $(C_4H_9NH_3)_2PbI_4$. The APTMOS-PbI_4 films usually decomposed in air over several days and became colourless. The instability of the APTMOS-PbI_4 films may be ascribed to the large spaces in the PbI_2-based framework and the strong propensity for polycondensation between the adjacent APTMOS cations confined in the perovskite structure. These factors cause the layered perovskite structure to eventually collapse.

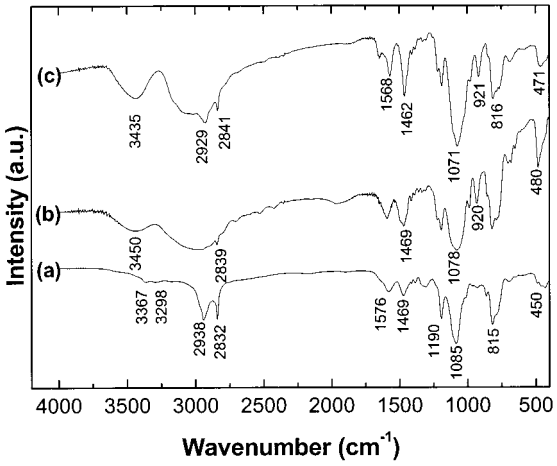

Figure 2. FT-IR spectra for 3-aminopropyltrimethoxysilane (APTMOS, a: using liquid film on KBr crystal disk), the amine salt of APTMOS (APTMOS·HI, b: KBr pellet) and the layered perovskite with a silica network (APTMOS-PbI_4, c: KBr pellet)

XRD

X-ray diffraction (XRD) is the most useful tool for the structural characterisation of a crystalline material. From the XRD pattern (Figure 3) of an APTMOS-PbI_4 film spin-coated on a fused silica plate, only 00*l* diffraction peaks were detected due to the extremely high degree of preferential orientation arising from the manner in which the sample was mounted. The 00*l* reflections can be counted as corresponding to $l = 1, 2, 3...$ or $l = 2, 4, 6...$ and we chose the latter based on previous literature for the layered perovskite-type organic/inorganic $(C_4H_9NH_3)_2PbI_4$ structure.[6b] The observation of these multiple order diffraction peaks supports the formation of a PbI_2-based perovskite structure in the films and the alternating layers stack perpendicularly to the substrate surface. The 00*l* reflections correspond to an extended network of corner-sharing metal halide octahedra with an interlayer distance of 1.91 nm separating the inorganic sheets. According to the structural properties of the general hybrid perovskites, the interlayer space decreases from Pb−Cl to Pb−Br and to Pb−I.[9] This can be attributed to the larger space provided by the inorganic frame and the alkyl chains can tilt or interdigitate. Compared with the APTMOS-$PbCl_4$ perovskite structure which has an interlayer space of 1.83 nm,[4] a small increase of 0.08 nm in APTMOS-PbI_4 was observed by XRD, rather than a decrease. This abnormal increase may be due to the unhydrolysed APTMOS molecules which have a longer chain and a larger silane tail which hinders the APTMOS molecules from tilting/interdigitation.

UV/Vis Absorption Spectroscopy

A simple way to confirm the formation of the layered perovskite structure is using UV/Vis absorption spectroscopy since exciton absorption can be observed at room temperature due to the quantum confinement effect.[10a−10c] Figure 4 shows the UV/Vis absorption spectrum of

 © 2005 Wiley-VCH Verlag GmbH & Co. KGaA, Weinheim

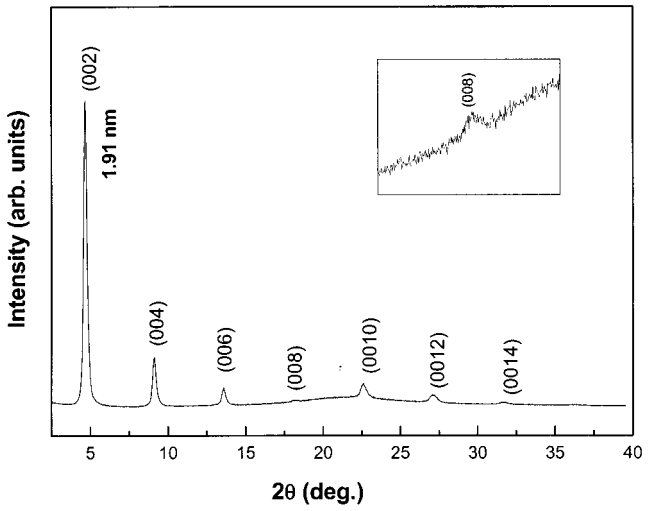

Figure 3. X-ray diffraction profiles for a spin-coated film of APTMOS-PbI_4 on a quartz plate; the inset is an enlarged figure for clarity

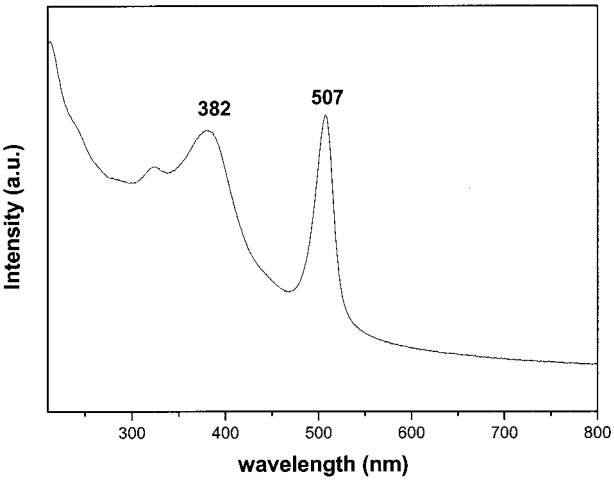

Figure 4. UV/Vis absorption spectrum for an APTMOS-PbI_4 spin-coated film on a quartz plate

APTMOS-PbI_4 films on a fused silica plate. Two strong absorption bands at 382 and 507 nm can be observed. The former is due to the band-gap absorption of the PbI_2-based perovskite structure with one layer of inorganic sheets. Generally, the top of the valence-band of this class of material consists primarily of a mixture of I ($5P_{xy}$), Pb (6s) and I ($5P_z$), whereas the bottom of the conduction-band consists primarily of the Pb ($6P_{xy}$) state.[10] Note that a strong and sharp absorption peak at 507 nm is present which is similar to the previously reported PbI_2-based perovskite structure with a single-layer inorganic sheet.[6b] This suggests that the extended 2D PbI_4^{2-} frameworks are sandwiched on both sides by the APTMOS cations with alkyl chains which have a much lower dielectric constant compared with the inorganic component. The two dimensionality of the layered structure combined with the dielectric confinement effect enables the formation of a stable exciton with a large binding energy in the PbI_4^{2-} semiconductor layer. As a result, the feature of the sharp absorption of excitons can be observed even at room temperature. This generally cannot be observed in bulk PbI_2. This is also the reason that the colour of the APTMOS-PbI_4 films is somewhat different from PbI_2. The difference in colour can be simply used to judge the formation of a layered perovskite structure in the spin-coating procedure.

Photoluminescence

From the photoluminescence spectra (Figure 5), a dominant emission of an exciton state at 518 nm was observed. In contrast to the $PbCl_2$-based perovskite, the band-gap of PbI_2-based perovskite is reduced and the luminescence absorption red-shifted from the ultraviolet to the visible region.[6b] As a result, the green luminescence could be seen when the spin-coated APTMOS-PbI_4 films were exposed to a hand-held UV lamp at room temperature. The photoluminescent properties of the $PbCl_2$-based layered perovskite structure incorporated with APTMOS cations have the features of a weak emission in the ultraviolet region originating from the exciton state and a strong blue emission at 440 nm which corresponds to the highly condensed siloxane network of the tails of the APTMOS cations.[4] Interestingly in Figure 5 one can see, apart from the strong emission of the exciton at 518 nm, that there is a strong background emission between 425 and 600 nm with a maximum at 456 nm. This should come from the organic component and is related to the photoluminescence of the sol-gel derived silica gel of the APTMOS cations.[8a,11a–11c] The weak intensity can be attributed to the reduced cross-linking between the APTMOS cations in the APTMOS-PbI_4 film. This result is consistent with the FT-IR spectrum (see c in Figure 2) which only demonstrates the existence of short Si–O–Si chains (one peak at 1071 cm^{-1}). Note that the shoulder emission analogues were generally observed at higher wavelengths in the previously reported organic-inorganic perovskites and were explained as being due to degradation or the presence of impurities.[6b,12]

Formation of the Perovskite Structure

We propose that the formation of the layered APTMOS-PbI_4 superlattice occurs mainly by an organic/inorganic perovskite-type self-organisation.[9] Such behaviour is different from that of long-chain amphiphiles because there are no strong interactions between the short alkyl chains of the APTMOS cations. The main driving force is the propensity of metal halides to format the extended corner-sharing networks of MX_6 octahedra. The ammonium "heads" of the organic cations interact with the halogens of the inorganic sheets in an ionic or hydrogen bonding manner and then hydrolysis and condensation may occur between some adjacent APTMOS molecules, leading to an alternating layered structure. Thus, the inorganic framework plays an important templating role for the APTMOS cations. In ad-

 © 2005 Wiley-VCH Verlag GmbH & Co. KGaA, Weinheim

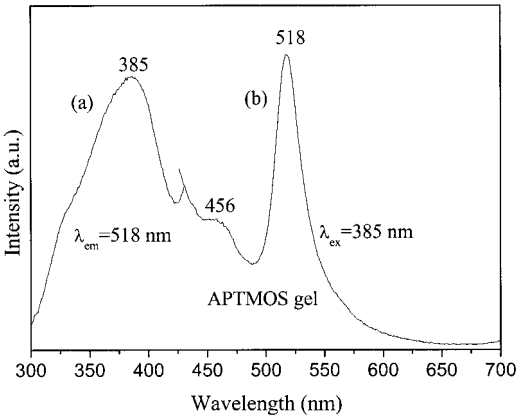

Figure 5. Photoluminescence excitation (a) and emission (b) spectra for an APTMOS-PbI_4 film on a quartz substrate

dition, the H-bonds between silanols have the effect of forming a tail-to-tail arrangement of the APTMOS cations.[13]

Conclusions

In this study, the spin-coating method was successfully used to prepare highly ordered perovskite-type films with a layered structure in which the lead iodide inorganic layer was sandwiched by the APTMOS cations. The films show strong green luminescence arising from the excitons of the inorganic semiconductor lead iodide layers and the weak blue emission relates to the hydrolysed APTMOS cations. The large framework provided by the inorganic layer impedes the APTMOS cations from forming a network with a high degree of cross-linking. This kind of self-organising system offers a potential method for the preparation of nano- and mesoporous silica films after the lead iodide template has been removed.

Experimental Section

Syntheses: The starting materials used in the synthesis were PbI_2 (99.999%, Aldrich) and 3-aminopropyltrimethoxysilane (>97%, Aldrich). HI gas was obtained by dropwise addition of water into a Schlenk tube containing an iodine-red phosphorus mixture. The liberated HI gas was dried using a $CaCl_2/P_2O_5$ mixture packed into the drying towers and collected by condensing into a liquid nitrogen trap. APTMOS (10 mL) was dissolved in absolute diethyl ether (150 mL, refined by heating to reflux for 12 h over sodium) and the solution was maintained at −78 °C in an acetone/dry-ice bath. The trap containing the solid hydrogen iodide was then removed from the liquid nitrogen and dipped into a bath with a K_2CO_3/ice mixture (−30 °C) to release the HI gas slowly. The small steam of HI gas was directed to flow into the APTMOS/diethyl ether solution, resulting in the formation of an APTMOS salt (APTMOS·HI, white precipitate). Note that the excess noxious HI gas was collected in a vacuum desiccator containing sodium hydroxide. The powder of APTMOS·HI was obtained after removal of the diethyl ether by evaporation in a vacuum at room temperature. The final APTMOS·HI powder was stored in an evacuated desiccator using $P_2O_5/CaCl_2$ as the desiccant at −25 °C.

Film Preparation: Dimethylformamide (DMF) was dried over calcium hydride for two days with stirring and was then distilled under reduced pressure. PbI_2 and APTMOS·HI (1:2 molar ratio) were dissolved in the dry DMF to form a clear solution (2.5 wt%). The solution was spin-coated on fused silica plates at 700 rpm for 3s and then 1500 rpm for 45s at room temperature in air. After drying at 70 °C under vacuum for 6 h, continuous and crack-free films of the PbI_2-based layered perovskite $[(CH_3O)_3Si-CH_2-CH_2-CH_2-NH_3]_2PbI_4$ were obtained. A small amount of APTMOS-PbI_4 powder was scraped off the substrates for FT-IR measurements.

Characterisations: The FT-IR spectra were recorded on a Bio-rad FTS 135 spectrometer with a nominal resolution of 4 cm^{-1}. The X-ray diffraction (XRD) of film samples was examined on a Rigaku-Dmax 2500 diffractometer using Cu-K_α radiation (λ = 0.15405 nm). The UV/Vis absorption spectrum was measured on a TU-1901 spectrophotometer. The photoluminescence excitation and emission spectra were recorded on a Hitachi F-4500 spectrofluorimeter equipped with a 150-w xenon lamp as the excitation source.

Acknowledgments

This work was subsidised by the National Natural Science Foundation of China (50125311, 20334010, 20274050, 50390090, 50373041, 20490220, 20474065, 20431030, 50403007), the Ministry of Science and Technology of China (2003CB615601), and the Chinese Academy of Sciences (Distinguished Talents Program, KJCX2-SW-H07).

[1] [1a] M. Ogawa, *J. Am. Chem. Soc.* **1994**, *116*, 7941−7942. [1b] A. N. Parikh, M. A. Schivley, E. Koo, K. Seshadri, D. Aurentz, K. Mueller, D. L. Allara, *J. Am. Chem. Soc.* **1997**, *119*, 3135−3143. [1c] A. Shimojima, Y. Sugahara, K. Kuroda, *J. Am. Chem. Soc.* **1998**, *120*, 4528−4529. [1d] M. Ogawa, *Langmuir* **1997**, *13*, 1853−1855. [1e] K. Sakata, T. Kunitake, *J. Chem. Soc., Chem. Commun.* **1990**, 504−505. [1f] Y. Zhou, J. H. Schattka, M. Antonietti, *Nano Lett.* **2004**, *4*, 477−481. [1g] Y. Fujimoto, A. Shimojima, K. Kuroda, *Chem. Mater.* **2003**, *15*, 4768−4774.
[2] [2a] Z. Zhong, W. Ding, W. Hou, Y. Chen, X. Chen, Y. Zhu, N. Min, *Chem. Mater.* **2001**, *13*, 538−542. [2b] R. A. Vaia, R. K. Teukolsky, E. P. Giannelis, *Chem. Mater.* **1994**, *6*, 1017−1022. [2c] A. Matsumoto, S. Oshita, D. Fujioka, *J. Am. Chem. Soc.* **2002**, *124*, 13749−13756.
[3] Y. Kaneko, N. Iyi, T. Matsumoto, K. Fujii, K. Kurashima, T. Fujita, *J. Mater. Chem.* **2003**, *13*, 2058−2060.
[4] Z. Y. Cheng, B. X. Gao, M. L. Pang, S. Y. Wang, Y. C. Han, J. Lin, *Chem. Mater.* **2003**, *15*, 4705−4708.
[5] D. B. Mitzi, *J. Chem. Soc., Dalton Trans.* **2001**, 1−12.
[6] [6a] D. B. Mitzi, *J. Solid State Chem.* **1999**, *145*, 694−704. [6b] D. B. Mitzi, *Chem. Mater.* **1996**, *8*, 791−800.
[7] [7a] J. Lin, J. A. Siddiqui, R. M. Ottenbrite, *Polym. Adv. Technol.* **2001**, *12*, 285−292. [7b] N. V. Venkataraman, S. Bhagyalakshmi, S. Vasudevan, R. Seshadri, *Phys. Chem. Chem. Phys.* **2002**, *4*, 4533−4538. [7c] H. T. Tang, *Spectroscopic Identification of Organic Compounds* (in Chinese), Beijing University Press, **1992**.
[8] [8a] W. H. Green, K. P. Le, J. Grey, T. T. Au, M. J. Sailor, *Science* **1997**, *276*, 1826−1828. [8b] P. J. Launer, in *Silicon, Germanium, Tin and Lead Compounds, Metal Alkoxides, Diketonates and Carboxylates, A Survey of Properties and Chemistry* (Ed.: B. Arkles), Gelest Inc., U. S. A., **1998**, p. 100.
[9] D. B. Mitzi, *Prog. Inorg. Chem.* **1999**, *48*, 1−121.

 © 2005 Wiley-VCH Verlag GmbH & Co. KGaA, Weinheim

[10] [10a] T. Ishihara, *Optical Properties of Low-Dimensional Materials* (Eds.: T. Ogawa, Y. Kanemitsu), World Scientific, Singapore, **1995**, p. 288−339. [10b]X. Hong, T. Ishihara, A. V. Nurmikko, *Phys. Rev. B* **1992**, *45*, 6961−6964. [10c] M. Era, S. Morimoto, T. Tsutsui, S. Saito, *Appl. Phys. Lett.* **1994**, *65*, 676−678.
[11] [11a] V. Bekiari, P. Lianos, *Chem. Mater.* **1998**, *10*, 3777−3779. [11b] T. Brankova, V. Bekiari, P. Lianos, *Chem. Mater.* **2003**, *15*, 1855−1859. [11c] B. E. Yodas, *J. Mater. Res.* **1990**, *5*, 1157−1158.
[12] M. Era, S. Morimoto, T. Tsutsui, S. Saito, *Synth. Metals* **1995**, *71*, 2013−2014.
[13] [13a] Z. Xu, D. B. Mitzi, *Chem. Mater.* **2003**, *15*, 3632−3637. [13b] G. Cerveau, R. J. P. Corriu, B. Dabiens, J. Le Bideau, *Angew. Chem. Int. Ed.* **2000**, *39*, 4533−4537.

Received June 10, 2004
Early View Article
Published Online November 24, 2004

 © 2005 Wiley-VCH Verlag GmbH & Co. KGaA, Weinheim

EurJIC
European Journal of Inorganic Chemistry

Issue 2/2005

Pages 229–432

Papers available ahead of print in Early View at www.interscience.wiley.com

Earliest available Table of Contents:
Automatically, free of charge by e-mail through
www.interscience.wiley.com/alerts

COVER PICTURE

The cover picture shows the pH dependency of the geometry of the tris(5-bromo-2-hydroxybenzyl)triaminoguanidinium cation $[H_6Br_3L]^+$. In the solid state, a conformation which is less favourable for the coordination of metal centres is predominant. In the presence of a basic metal salt, a partial change in the conformation can be observed, whereas in the presence of base even in the absence of metal ions, a complete conformation change takes place. In this way, the reaction of $[H_6Br_3L]^+$ with metal salts can be easily controlled. The formation of an $[M_3Br_3L]^{(3n-5)+}$ species as a triangular building block for use in supramolecular chemistry is also described in the article by I. M. Müller and D. Möller on p. 257 ff.

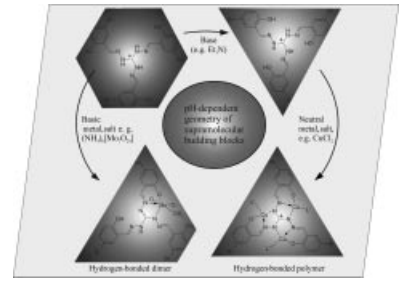

MICROREVIEW

Contents

245 **V. I. Bakhmutov***

Proton Transfer to Hydride Ligands with Formation of Dihydrogen Complexes: A Physicochemical View

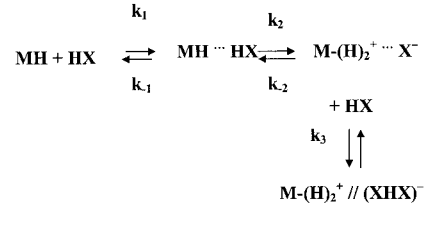

Keywords: Hydrogen bonding / Dihydrogen bonding / Proton transfer / Dihydrogen complexes / Metal hydrides / Kinetics

 © 2005 Wiley-VCH Verlag GmbH & Co. KGaA, Weinheim

FULL PAPERS

257 **I. M. Müller,* D. Möller**

A New Ligand for the Formation of Triangular Building Blocks in Supramolecular Chemistry

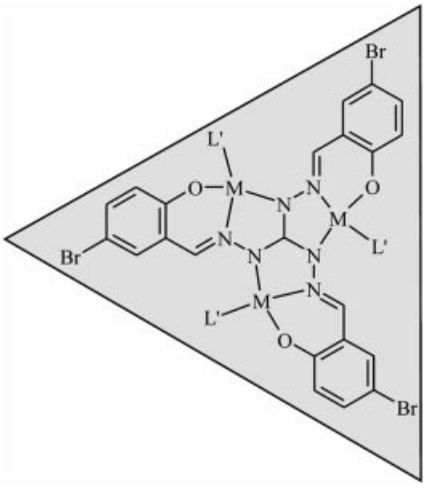

Keywords: Tridentate ligands / Copper / Molybdenum

264 **Z. Han, Y. Zhao, J. Peng,* H. Ma, Q. Liu, E. Wang, N. Hu, H. Jia**

Directed Synthesis of a 1D Double-Chain Polyoxometalate Assembly: $\{[Ag_2(bppy)_3][Ag(bppy)_2][Ag(bppy)]_2PW_{11}Co(bppy)O_{39}\}\cdot 2H_2O$

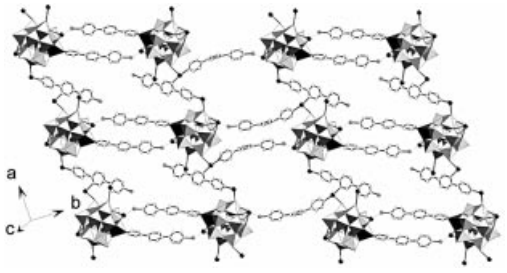

Keywords: Polyoxometalates / N ligands / Silver / Organic-inorganic hybrids / Supramolecular chemistry

272 **N. E. Katz,* I. Romero, A. Llobet, T. Parella, J. Benet-Buchholz**

Fine Tuning of MLCT States in New Mononuclear Complexes of Ruthenium(II) Containing Tris(1-pyrazolyl)methane, 2,2′-Bipyridine and Aromatic Nitrogen Heterocycles

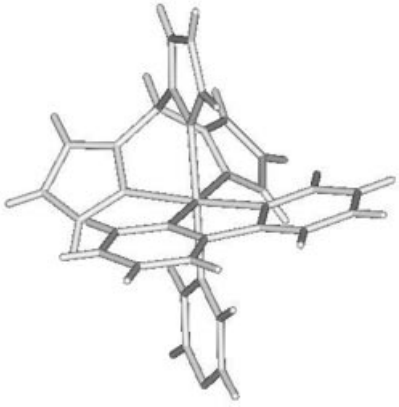

Keywords: Charge transfer / Ruthenium / N ligands / Scorpionate ligands

278 **M. Cusumano,* M. L. Di Pietro, A. Giannetto, P. A. Vainiglia**

The Reaction of (Bipyridyl)palladium(II) Complexes with Thiourea − Influence of DNA and Other Polyanions on the Rate of Reaction

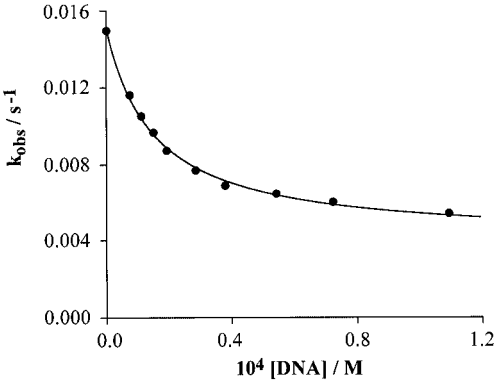

Keywords: Intercalation with DNA / Inhibition of ligand substitution

 © 2005 Wiley-VCH Verlag GmbH & Co. KGaA, Weinheim

285 **T. Tomon, T. Koizumi, K. Tanaka***

Stabilization and Destabilization of the Ru−CO Bond During the 2,2′-Bipyridin-6-onato (bpyO)-Localized Redox Reaction of [Ru(terpy)(bpyO)-(CO)](PF_6)

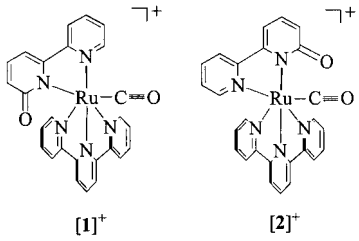

[1]$^+$ [2]$^+$

Keywords: Carbonyl complex / Electrochemistry / IR spectroscopy / Ruthenium

294 **M. Du,* X.-J. Zhao, J.-H. Guo, X.-H. Bu,* J. Ribas***

Towards the Design of Linear Homo-Trinuclear Metal Complexes Based on a New Phenol-Functionalised Diazamesocyclic Ligand: Structural Analysis and Magnetism

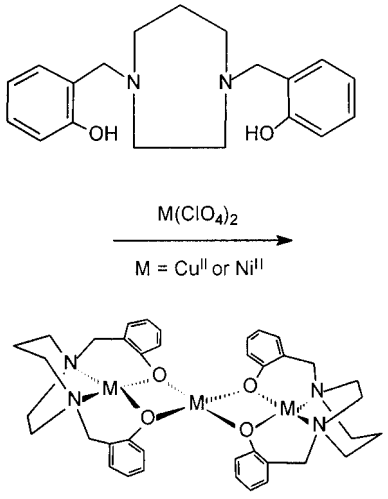

Keywords: Functionalised diazamesocyclic ligand / Copper(II) and Nickel(II) / Crystal structures / Magnetochemistry / Trinuclear complexes

305 **M. D. Godbole, M. Kloskowski, R. Hage, A. Rompel, A. M. Mills, A. L. Spek, E. Bouwman***

Highly Efficient Disproportionation of Dihydrogen Peroxide: Synthesis, Structure, and Catalase Activity of Manganese Complexes of the Salicylimidate Ligand

Keywords: Catalase / Michaelis−Menten kinetics / Hydrogen peroxide disproportionation / Enzyme mimics / Manganese / Kinetics

314 **B. Ronig, H. Schulze, I. Pantenburg, L. Wesemann***

Anionic Phosphane − A New Ligand with a Phosphane and a Weakly Coordinating Heteroborate Moiety

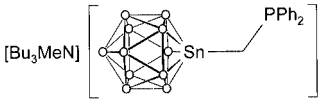

Keywords: Boranes / Cluster compounds / Phosphane ligands / Tin

 © 2005 Wiley-VCH Verlag GmbH & Co. KGaA, Weinheim

321 **X. Li, R. Cao,* Y. Sun, W. Bi, X. Li, Y. Wang**

Syntheses and Characterizations of Multidimensional Metal-Organic Frameworks Based on Rings and 1D Chains

Keywords: Bridging ligand / Polymers / Hydrothermal reaction / Hydrogen bonds

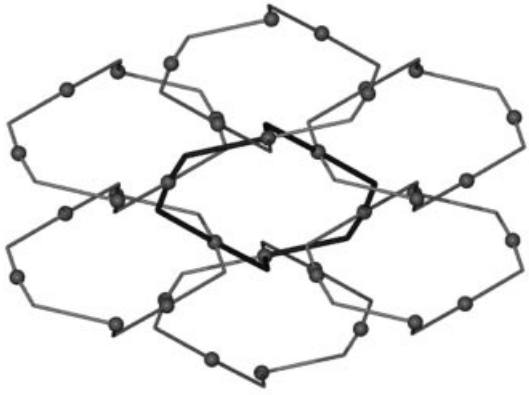

330 **Z. Yu, J. E. Knox, A. V. Korolev, M. J. Heeg, H. B. Schlegel, C. H. Winter***

Synthesis, Characterization, and Hydrolysis Products of $(\eta^2\text{-}t\text{Bu}_2\text{pz})\text{AlH}(\mu\text{:}\eta^1,\eta^1\text{-}t\text{Bu}_2\text{pz})_2\text{AlH}_2$ − Structural Characterization of a Complex Containing η^1-, η^2-, and $\mu\text{:}\eta^1,\eta^1$-Pyrazolato Ligands and a Complex Containing a Terminal Hydroxo Ligand

Keywords: Hydrogen bond / N ligands / Aluminum / Pyrazolato ligands / Molecular orbital calculations

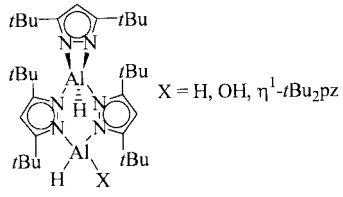

338 **V. Tabernero, T. Cuenca***

Studies of the Nature of the Catalytic Species in the α-Olefin Polymerisation Processes Generated by the Reaction of Diamido(cyclopentadienyl)-titanium Complexes with Aluminium Reagents as Cocatalysts

Keywords: Titanium / Diamido ligands / Olefin polymerisation / Trimethylaluminium / Methylaluminoxane

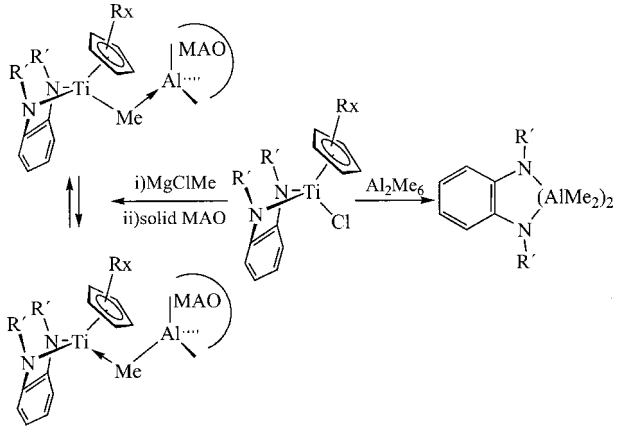

347 **A. Bertogg, F. Camponovo, A. Togni***

N-Ferrocenyl-Substituted Planar-Chiral N-Heterocyclic Carbenes and Their Pd^{II} Complexes

Keywords: Carbene ligands / Chirality / Ferrocenes / Nitrogen heterocycles / Palladium

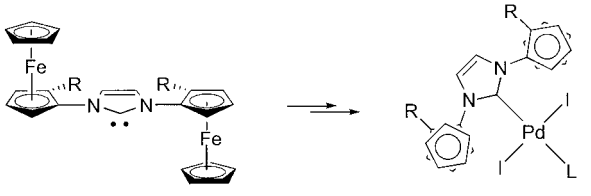

R = H, Me

a: R = Me; L = py
b: R = H; L = py
c: R = Me; L = PPh_3
d: R = H; L = PPh_3

 © 2005 Wiley-VCH Verlag GmbH & Co. KGaA, Weinheim

357 S. Supriya, K. S. Latha, S. K. Das*

A New Type of Supramolecular Assembly by Hydrogen Bond Templating: Identification of Rare Monodentate Acetate Coordination in $[Fe_3(\mu_3\text{-}O)(\mu_2\text{-}CH_3COO)_6(H_2O)_2(CH_3COO)]\cdot T\cdot ClO_4$ (T = 2,6-Diaminopyridinium Cation, $C_5H_8N_3$ and 2-Aminopyridinium Cation, $C_5H_7N_2$)

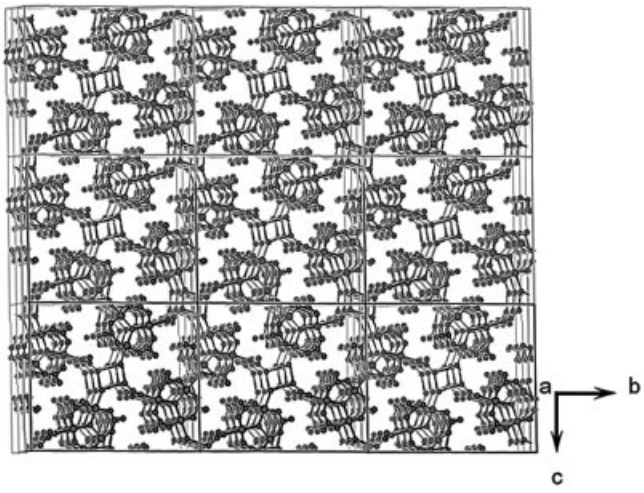

Keywords: Iron trinuclear cluster / Hydrogen bond templating / Monodentate acetate / Supramolecular assembly

364 I. P.-Y. Shek, W.-F. Yeung, T.-C. Lau,* J. Zhang, S. Gao,* L. Szeto, W.-T. Wong

$Ni^{II}Ru^{II}$ and $Cu^{II}Ru^{II}$ Coordination Polymers Constructed from $[Ru(CN)_6]^{4-}$

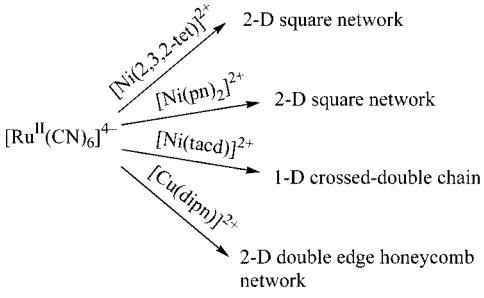

Keywords: Coordination polymers / Cyanides / Magnetic properties / Ruthenium

371 D. Sellmann, F. Lauderbach,* F. W. Heinemann

Trinuclear [NiFe] Clusters as Structural Models for [NiFe] Hydrogenase Active Sites

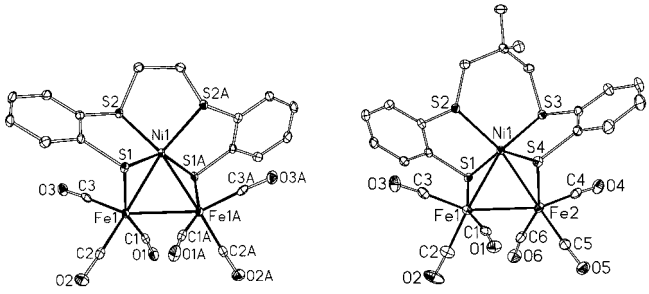

Keywords: Nickel / Iron / Cluster compounds / Carbonyl ligands / S ligands

378 D. Nikolova, C. von Hänisch*

Novel Binary Compounds of Group 15 Elements: Synthesis and Characterisation of $[Sb_4(PSiMe_2Thex)_4]$, $[Sb_4(AsSi\mathit{i}Pr_3)_4]$ and $[Sb_2(PSiPh_2\mathit{t}Bu)_4]$

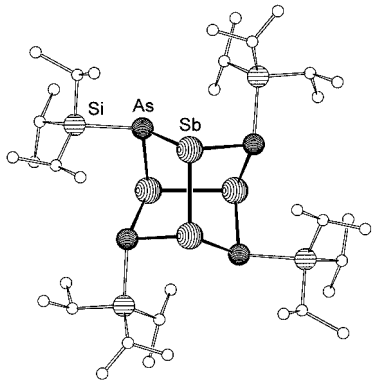

Keywords: Arsenic / Antimony / Cage compounds / Phosphorus

 © 2005 Wiley-VCH Verlag GmbH & Co. KGaA, Weinheim

383 **P. Comba,* G. Linti, K. Merz, H. Pritzkow, F. Renz**

Electronic Interactions in Ferrocene- and Ruthenocene-Functionalized Tetraazamacrcocyclic Ligand Complexes of $Fe^{II/III}$, Co^{II}, Ni^{II}, Cu^{II} and Zn^{II}

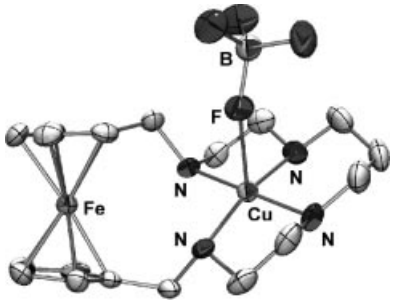

Keywords: Macrocyclic ligands / Transition metals / Ferrocene / Ruthenocene

389 **A. Alberola, E. Coronado, C. Giménez-Saiz, C. J. Gómez-García, F. M. Romero,* A. Tarazón**

Hybrid Magnetic Materials Based on Nitroxide Free Radicals and Extended Oxalato-Bridged Bimetallic Networks

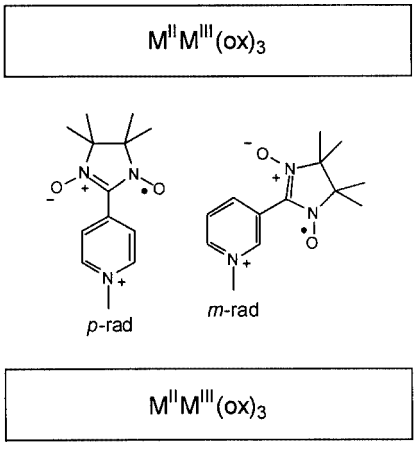

Keywords: Magnetic properties / Heterometallic complexes / Hybrid materials / Radicals / Layered compounds

401 **M. Asnani, S. Sharma, S. E. Lofland, K. V. Ramanujachary, P. A. Buffat, A. Ramanan***

Novel Topotactic Conversion of an Organically Templated Vanadyl Phosphate Framework into Layered Structures

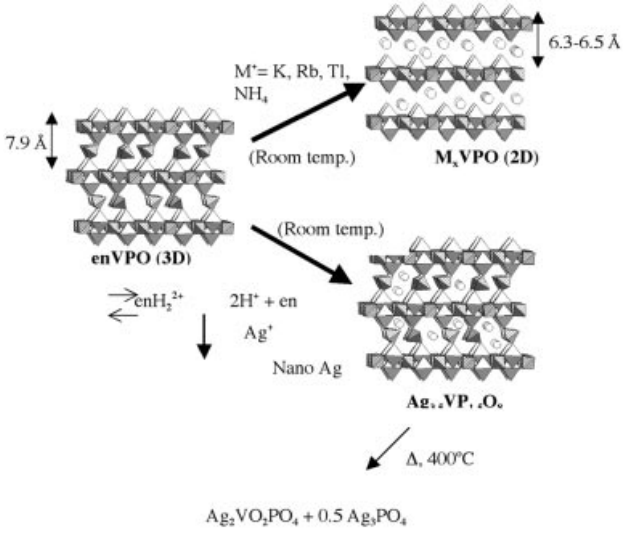

Keywords: Vanadyl phosphate / Topotactic / Intercalation / Ion exchange

410 **G. Barone, G. La Manna, D. Duca***

X-ray Absorption Spectra of Cu^{II} and Cu^{III} Complexes of *N*,*N*′-1,2-Phenylenebis(2-mercapto-2-methylpropionamide)

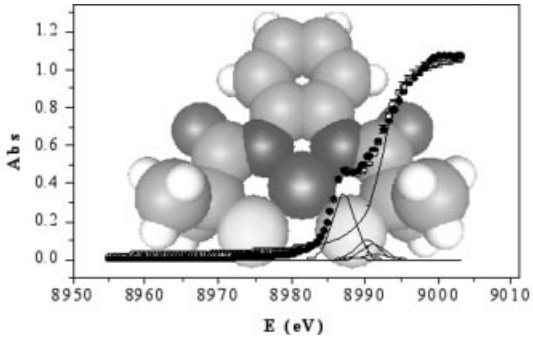

Keywords: Copper / N,S ligands / X-ray absorption spectroscopy / Density functional calculations / Ab initio molecular orbital calculations

 © 2005 Wiley-VCH Verlag GmbH & Co. KGaA, Weinheim

416

V. G. Albano,* V. De Felice, M. Monari, G. Roviello, F. Ruffo*

Oxidative Addition of Phenylselenyl Halides to Platinum(0) Complexes: Characterisation and Reactivity of the Products [PtX(SePh)(*N,N*-chelate)(olefin)] (X = Cl, Br, I)

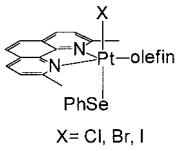

Keywords: Isomers / Oxidative addition / Platinum / Selenium

423

S.-M. Chen, C.-Z. Lu,* Q.-Z. Zhang, J.-H. Liu, X.-Y. Wu

Temperature-Controlled Solvothermal Syntheses, Structures and Characterizations of a Novel Class of Zn Complexes Constructed from 1,4-Bis[2-(5-phenyloxazolyl)]benzene

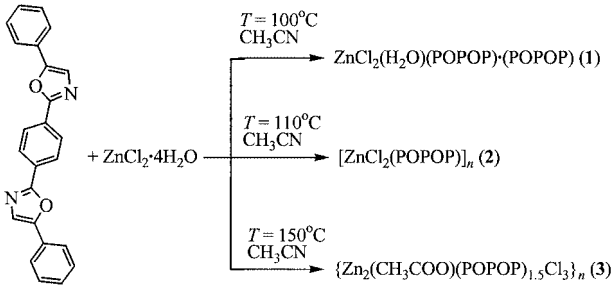

Keywords: Complexes / N ligands / Crystal engineering / Coordination modes / Properties

 © 2005 Wiley-VCH Verlag GmbH & Co. KGaA, Weinheim

Proton Transfer to Hydride Ligands with Formation of Dihydrogen Complexes: A Physicochemical View

Vladimir I. Bakhmutov*[a]

Keywords: Hydrogen bonding / Dihydrogen bonding / Proton transfer / Dihydrogen complexes / Metal hydrides /Kinetics

Protonation of hydridic hydrogens has attracted increasing interest from chemists over the past decade. This review, focusing on key physicochemical data, describes general rules governing proton transfer to hydride ligands and discusses kinetic schemes for the protonation as a process starting from dihydrogen-bonded adducts and H-bonded contact ion pairs and ending in dihydrogen complexes as solvent-separated ion pairs or free ions. It has been shown that the particulars of proton transfer to hydride ligands and to conventional organic bases are similar. The difference between them is apparent in the contact ion pair formation step.

(© Wiley-VCH Verlag GmbH & Co. KGaA, 69451 Weinheim, Germany, 2005)

1. Introduction

Proton transfer to hydridic hydrogens with H_2 elimination, which has attracted great interest from chemists, plays a key role in various chemical and biochemical processes[1] occurring in solution and the solid state.[2] In the case of transition metal hydrides this reaction gives dihydrogen complexes[3] which can initiate, for example, catalytic ionic hydrogenation of unsaturated compounds.[4] The elucidation of the mechanism of proton transfer to hydride ligands has been a main goal from the beginning of the interest in the chemistry of dihydrogen complexes. Important aspects of acid-base reactivity, protonation and hydrogen bonding of transition metal hydride systems have already been the subject of several reviews.[5a–5d] Nevertheless, it seems to the author that a reader who is not familiar with transition metal hydride chemistry in particular, still needs a general physicochemical view on this important topic. This approach does not go into the details of hydride chemistry but provides (i) analysis of key results (earlier and recent) from the studies of the spectroscopic, kinetic and thermodynamic parameters which vary with the nature of the metal hydrides, acids and solvents used (ii) a description of the energy profile of proton transfer occurring via a chain of H-bonded intermediates and transition states (iii) a discussion of the driving force in each step of the overall process and also (iv) a comparison of the mechanism of proton transfer to hydride ligands with that operating in proton transfer to conventional organic bases.

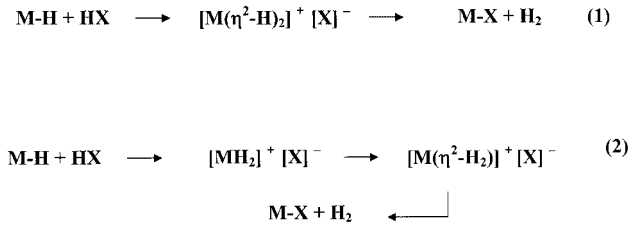

Scheme 1

Dihydrogen complexes can be generated through direct proton attack on hydride ligands or an initial protonation of the metal centre[3] (Scheme 1) leading to classical hydrides $[MH_2]^+$ which then convert to dihydrogen complexes

[a] Department of Chemistry, Texas A&M University, College Station,
Texas 77843-3255, USA

Vladimir I. Bakhmutov (born in 1948 in Moscow, Russia) obtained his Ph.D in 1974 at the Moscow State University and Doctor of Science Degree in 1984 at the Institute of Organo-Element Compounds of the Russian Science Academy (INEOS). He became a Head of the NMR department at INEOS in 1994. Currently he is an NMR spectroscopist at Texas A&M University, USA. He has authored or co-authored more than 220 research and review papers. He is author of the book "Practical NMR Relaxation for Chemists" (John Wiley & Sons) and contributor to two books. His research interests are in the field of NMR spectroscopy and transition metal hydride chemistry.

MICROREVIEWS: This feature introduces the readers to the authors' research through a concise overview of the selected topic. Reference to important work from others in the field is included.

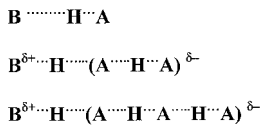

Scheme 2

$[M(\eta^2\text{-}H_2)]^+$ as the thermodynamic products of the reaction. Since protonation of hydride sites is kinetically preferable,[6] the second pathway (rather rare and resulting from a unique combination of steric and electronic features of the initial hydrides) has not been considered in this paper. For the same reason, we have not discussed H-bonded species H–M···H–X as intermediates in proton transfer to metal centres.[7a,7b] Finally, we have also not discussed H_2 elimination from dihydrogen complexes, the species being considered stable under the experimental conditions.

2. Reaction Intermediates: Spectroscopic (IR, NMR) and DFT Studies

Strong hydrogen bonds dominate in the protonation of usual organic bases.[8] For example, proton transfer from acetic acid, (H-A), to pyridine, (B), occurs via the H-bonded complexes in Scheme 2 which can be directly observed by ^1H and ^{15}N NMR spectroscopy in $CDClF_2/CDF_3$ at low temperatures.[8a] It is known now that the hydrogen bond strength increases with a partial proton transfer. For this reason, if the proton overcomes an energy barrier due only to its motion, this barrier must be very small.[8a] In full agreement with this statement, protonation of common organic bases is a very fast process. According to recent DFT calculations, a similar situation takes place for transition metal hydrides in the gas phase. When a strong acid, H_3O^+, is placed near a hydride molecule, for example $[CpRuH(CO)(PH_3)]$[9] or $[Cp_2NbH_3]$,[10] the proton is transferred directly to the negatively charged hydride ligand *without* an energy barrier. However such a single-step process is not realistic in solvents with a relatively small polarity such as THF, toluene and CH_2Cl_2 which are usually used for the protonation of transition metal hydrides. Under these conditions, even strong acids (HCl, HBr, CF_3COOH or CF_3SO_3H) become weak and attack hydride ligands in a molecular form.[11] For this reason, various unusual H-bonded intermediates can be located on the reaction coordinate of the proton transfer to the hydride ligand, leading to a relatively high energy barrier for the process.

Dihydrogen Bonding

The interaction between hydrogen atoms carrying opposite charges, known as dihydrogen bonding,[12] is a common phenomenon in modern chemistry. H···H bonds play an important role in crystal packing and molecular aggregation in the solid state[13a,13b] and also in the stabilisation of conformational molecular states in solution.[13c] The X–H···H–Y binding energy depends on the nature of the electropositive

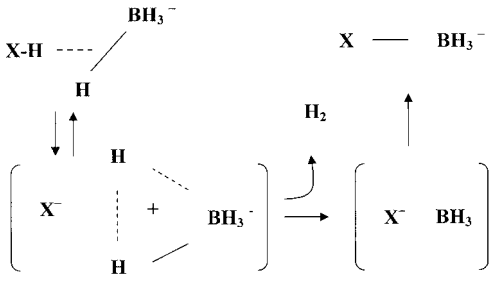

Figure 1. Schematic representation of the solid-state proton transfer to a hydridic hydrogen of the BH_4^- group via the dihydrogen bond[2]

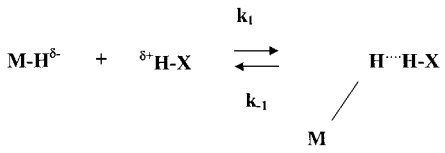

Scheme 3

and electronegative elements X and Y and covers the $-\Delta H^0$ region from 1[13b] to 7 kcal/mol.[2] Recent data [2,14] have demonstrated that dihydrogen bonding is an important preorganising factor in solid-state proton transfer. In fact, heating the solid complex, $NaBH_4$·triethanolamine, containing B–H···H–X bonds, results in loss of H_2 (Figure 1). Subsequently, the Lewis acidic and basic subunits, remaining in close proximity, combine to form new strong covalent bonds.[2] Likewise, dihydrogen-bonded adducts formed in solution by HX protons and negatively charged hydride ligands[15] (Scheme 3) may participate in the first step of proton transfer. In fact, such aggregates formed by $[CpRuH(CO)(PH_3)]$ or $[Cp_2NbH_3]$ and the relatively weak proton donors CF_3COOH and $(CF_3)_3COH$ have recently been located at energy minima in DFT calculations, even in the gas phase.[9,10]

Both IR and NMR techniques can be used to detect M–H···HX bonds. A combination of the two spectroscopic methods is best.[5c,5d] In the IR spectra, commonly recorded at low temperatures to avoid H_2 elimination, dihydrogen bonding is indicated by the new lower-frequency ν_{M-H} bands (or shoulders) which are shifted by 20–40 cm^{-1} from the corresponding values in the initial hydrides. The timescale of IR spectroscopy allows observation of both the free and H-bonded hydride molecules. In contrast, resonances from the free and coordinated hydrides in the ^1H NMR spectra are usually averaged even at low temperatures. However, upon dihydrogen bond formation, the signals of initial hydrides undergo remarkable high-field shifts (≈ 0.5–1 ppm) and their spin-lattice relaxation times (^1H T_1) are diminished due to additional proton-hydride dipole-dipole interactions.[16] It should be emphasised that the concurrent observation of both the effects is required for establishing a reliable NMR criterion for the presence of dihydrogen bonds. In rare cases, the application of Freon solvents "stops" the MH···HX bond formation even on the ^1H NMR timescale. For example, the ReH resonance of

 © 2005 Wiley-VCH Verlag GmbH & Co. KGaA, Weinheim

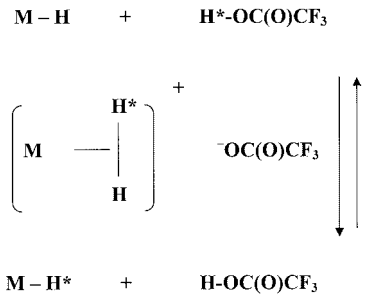

Figure 2. Schematic representation of a proton/hydride exchange occurring via a short-lived dihydrogen complex

[Cp*ReH(CO)(NO)] decoalesces in the presence of acidic alcohols at 96 K giving two resolved lines at –7.54 and –8.87 ppm, assignable to the free and dihydrogen bonded hydride, respectively.[17] A similar difference in the chemical shifts of M–H and M–H···HX has been reported for the [(triphos)Ru(CO)H_2]/$(CF_3)_2$CHOH system in TDF.[18] The difference in the chemical shifts is not as big as in the case of systems with classical hydrogen bonds, possibly due to insignificant electronic perturbations on the target nuclei. However more theoretical investigations of this NMR effect are needed.

According to DFT calculations,[9,10,15] dihydrogen bonding leads to slight elongations of M–H and X–H bonds in proportion to the acidity of the proton donors. For example, the M–H bond length in [M(NO)$(CO)_2(PH_3)_2$H···HX] adducts (M = Mo, W) increases by 0.04 Å. H···H distances in dihydrogen bonded species have been determined as 1.6–2.2 Å by ^{1}H T_1 relaxation time measurements in solution[5c,5d,16,18] and DFT calculations in the gas phase.[9,10,15] The $H^{\delta+}\cdots^{\delta-}$H–M angles have been calculated to be between 130° and 180°. Finally, polyhydride molecules such as [Cp_2NbH_3] can form bifurcated dihydrogen bonds[10] where coordination of HX molecules to the central and lateral hydride ligands occurs.

An unusually short H···H distance of 1.43 has been recently reported for the H-bonded complex [CpRu($PP^{Ph}PF$)H···HO_2CCF_3] which has been proposed as a new intermediate in proton transfer.[19] The H···H value has been determined by ^{1}H T_1 time measurements in [D_6]acetone. However, the ^{1}H and ^{31}P NMR spectra of the initial hydride [CpRuH($PP^{Ph}PF$)] in the absence and in the presence of the acid were indistinguishable. Therefore, the short ^{1}H T_1 relaxation times measured for the hydride (RuH) and proton (CF_3COOH) resonances (49 ms, 234 K, 300 MHz), are rather due to proton/hydride exchange occurring on the NMR timescale via a short-lived dihydrogen complex (Figure 2). Note that the same relaxation effect has previously been observed in a CD_2Cl_2 solution of the dihydride [ReH_2(CO)(NO)($POiPr_3)_2$] with CF_3COOH in which the dihydrogen complex was invisible.[20] However, this complex, with a very short ^{1}H T_1 time (5 ms, 200 MHz, 193 K), can be clearly detected by ^{1}H and ^{31}P NMR spectroscopy in the presence of a twentyfold excess of CF_3COOH.

The driving force for the formation of MH···HX bonds is the electrostatic attraction between the electrons of the polar M–H σ-bonds and H^+ from the proton donors. As in the case of classical H-bonds, the electrostatic component provides a dominant contribution to the total dihydrogen bonding energy[15,21] which depends on the nature of the transition metal hydrides, acids and solvents used. Enthalpies ($-\Delta H^0$), measured for the formation of MH···HX bonds in solution, vary between 2.0[22] and 7.6 kcal/mol.[5d] The influence of hydrides on dihydrogen bonding can be quantitatively scaled in terms of the basicity factor, E_j, determined via Equation (1)

$$E_j = \Delta H_{ij}/\Delta H_{11} P_i \quad (1)$$

where ΔH_{ij} are bond energies determined by IR spectroscopy, P_i is the proton donor ability of the OH acids and ΔH_{11} is the enthalpy of the standard H-bonded phenol complex.[5d] On this scale, the E_j factor varies in the range between 0.54 and 1.67. Effects of the metal are expressed, for example, as E_j = 1.09, 1.32 and 1.67 as recently obtained for PP_3FeH_2, PP_3RuH_2 and PP_3OsH_2, respectively.[23]

A good illustration of the solvent influence on dihydrogen bond formation is provided by the $-\Delta H^0$ values of 6.2, 5.8 and 3.1 kcal/mol for the interaction of [ReH_2(CO)(NO)$(PMe_3)_2$] with $(CF_3)_3COH$ in C_7D_{14}, hexane and [D_8]toluene, respectively.[7a,22b,22c] A similar trend was reported for the [CpRuH(CO)(PCy_3)]/$(CF_3)_2$CHOH system showing $-\Delta H^0$ values of 6.3 and 5.1 kcal/mol in hexane and the more polar CH_2Cl_2, respectively.[5d,9] The effects of the acidic component are demonstrated by the $-\Delta H^0$ values calculated as 8.4 and 9.7 kcal/mol for the interaction of [CpRu(CO)(PH_3)] with CF_3COOH and $(CF_3)_3COH$, respectively.[9]

Data on H···H bond formation rates is rather limited since the process is usually too fast for studies by standard kinetic techniques. Nevertheless, some estimations are possible from the low-temperature ^{1}H NMR experiments in Freon solutions.[17] As mentioned above, the Re–H signal of [Cp*ReH(CO)(NO)] decoalesces in the presence of acidic alcohols at 94 K. Under these conditions, the life time of the MH···HX complexes, τ, can be calculated via Equation (2)

$$\tau = 1/k_1 = \sqrt{2}/\pi\cdot\Delta\nu \quad (2)$$

where Δν is the chemical shift difference for the free and bonded state expressed in Hz.[24] The calculation gives $\tau \approx 10^{-3}$ s, corresponding to the rate constant, k_1, of ca. 10^4 L/mol·s for concentrations of acidic alcohols of $< 10^{-1}$ mol/L.

Regioselective Dihydrogen Bonding

The location of the spectroscopically observed MH···HX adducts on the reaction coordinate of the proton transfer process is well supported by the variable-temperature IR and NMR spectra of the hydrides [$RuH_2(dppm)_2$], [$MeC(CH_2PPh_2)_3Re(CO)_2H$], [Cp*Ru($PCy_3$)$H_3$] and [(Cp-N)RuH($PPh_3)_2$] in acidic solution in which MH···HX species and dihydrogen complexes $[M(\eta^2\text{-}H_2)]^+$ $[X]^-$ coexist

 © 2005 Wiley-VCH Verlag GmbH & Co. KGaA, Weinheim

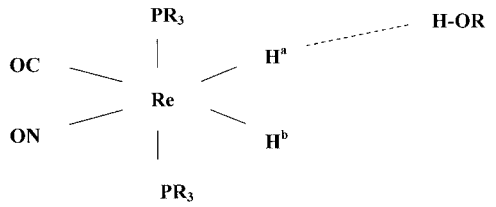

Scheme 4

in a slow equilibrium.[5d,22a] An additional possibility is that of a regioselective attack on a hydride ligand with the formation of MH···HX bonds, ending in a proton/hydride exchange (see below).

Regioselective dihydrogen bonding has been observed for $[ReH_2(CO)(NO)(PR_3)_2]$ (R = Me, Et) in the presence of $(CF_3)_2CH\text{-}OH$ or $(CF_3)_3COH$ by variable-temperature ^1H NMR spectroscopy in $[D_8]$toluene or $[D_{14}]$methylcyclohexane.[22b] A fivefold excess of $(CF_3)_3COH$ causes a high-field shift of the ReH^a resonance (Scheme 4) by 1.24 ppm (193 K) while the ReH^b resonance is shifted by 0.04 ppm only. The same spectroscopic behaviour can be observed for the trihydride $[Cp_2NbH_3]$ upon addition of $(CF_3)_2CH\text{-}OH$. The central hydride ligand acts as a proton acceptor.[10]

Scheme 4 shows the $(CF_3)_3COH$ attack on the H^a ligand located trans to NO in $[Re(CO)H_2(NO)(PR_3)_2]$ ending in the formation of $H\cdots H^a$ bonds with $-\Delta H^0$ values of 6.2 and 3 kcal/mol in $[D_{14}]$methylcyclohexane and $[D_8]$toluene, respectively. In contrast, the weaker proton donor, $(CF_3)_2\text{-}CH\text{-}OH$, binds to both the hydride ligands. Nevertheless, even in this case, the $H\cdots H^a$ bonds are more preferable: $-\Delta H^0(H\cdots H^a) = 2.1$ kcal/mol and $-\Delta H^0(H\cdots H^b) = 1.7$ kcal/mol. All these effects, not explainable in steric terms, are directly associated with different electronic properties (hydridicity) of the hydride ligands. Finally, it should be pointed out that the oxygen atoms of the NO groups in $[Re(CO)\text{-}H_2(NO)(PR_3)_2]$ can accept a proton while no Re···H bonds have been found for these hydrides.[22c]

Contact H-bonded Ion Pairs

Protonation of the heteroatom Y of an organic base consists of a proton shift along a linear H-bond, O–H···Y, with the formation of an intimate ion pair, $O^-\cdots H\text{-}Y^+$, as the product of partial proton transfer. This H-bonded ion pair then converts to a solvent-separated ion pair to finally give free ions when the solvent polarity is sufficient for full proton transfer. In the limits of this concept, proton transfer to hydride ligands can be represented by Figure 3 where the reaction ends with the formation of solvent-separated ion pairs due to the relatively small permittivities of the solvents (THF, toluene, CH_2Cl_2) usually applied for protonation of transition metal hydrides.

The best experimental method for observing intimate ion pairs, $M(\eta^2\text{-}H_2)^+\cdots X^-$, is IR spectroscopy in which the positions of indicator bands (for example, ν_{MH} or ν_{CO}) attributable to contact ion pairs markedly depend on the nature of the proton donor HX, i.e. on H-bonded anions X^-.[5d]

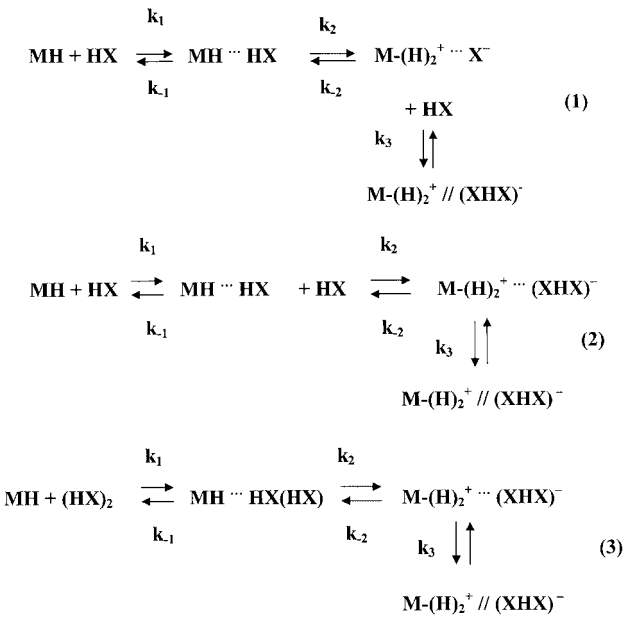

Figure 3. The schemes illustrating proton transfer to a hydride ligand via dihydrogen bonds with participation of two proton donor HX molecules: dimer $(HX)_2$ forms the dihydrogen bond (pathway 3); the second HX molecule initiates the formation of the solvent-separated or contact ion pair [pathway (1) or (2), respectively]

Such pairs have been found in hexane solutions of the hydride $[CpRuH(CO)(PCy_3)]$ protonated with $(CF_3)_2CHOH$, $(CF_3)_3COH$ and CF_3COOH, the IR spectra of which have shown ν_{CO} bands at 1972, 1978 and 2004 cm^{-1}, respectively.[9] In addition, the ν_{CO} frequencies of MH···HX complexes, simultaneously detected in these solutions, also depend reasonably on X^- (1931, 1935 and 1940 cm^{-1}) whereas the ν_{CO} bands of the solvent-separated ion pairs $[CpRu(H_2)(CO)(PCy_3)]^+//CF_3COO^-$ and $[CpRu(H_2)(CO)\text{-}(PCy_3)]^+//BF_4^-$ cannot be distinguished (2020 cm^{-1}, CH_2Cl_2).

As expected, increasing the solvent polarity from hexane to CD_2Cl_2 should lead to displacement of the positions of the equilibria in Figure 3 towards contact ion pairs due to stabilisation of species with a larger charge separation. In accord with this, the CH_2Cl_2 IR spectra of $[CpRuH(CO)(PCy_3)]$ in the presence of $(CF_3)_3COH$ exhibit ν_{CO} bands belonging only to contact ion pairs. In addition, the $[CpRuH(CO)(PCy_3)]/CF_3COOH$ system can show only intimate ion pairs, only solvent-separated ion pairs or both species simultaneously as a function of the CF_3COOH/hydride ratio.[5d,9] Unfortunately, thermodynamic aspects of conversions of H···H complexes to contact ion pairs remain unstudied. However, according to preliminary data,[7c] contact ion pairs are energetically preferable by only 0.2 kcal/mol, for example in CH_2Cl_2 solutions of the $[CpRuH(CO)(PCy_3)]/(CF_3)_3COH$ system.

In spite of reliable experiments concerning observations of contact ion pairs, the gas-phase DFT calculations[9,10] of the ion-pair structures $[CpRu(CO)(PH_3)(H_2)]^+\cdots OC(CF_3)_3^-$ and $[CpRu(CO)(PH_3)(H_2)]^+\cdots OCOCF_3^-$ or $[Cp_2NbH_2\text{-}(H_2)]^+\cdots OC(CF_3)_3^-$ and $[Cp_2NbH_2(H_2)]^+\cdots OCOCF_3^-$ have

 © 2005 Wiley-VCH Verlag GmbH & Co. KGaA, Weinheim

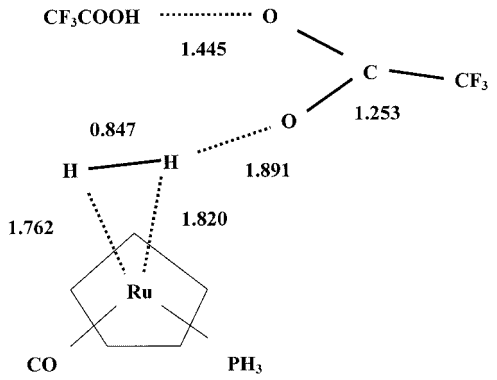

Figure 4. The DFT-optimised geometry of the hydrogen-bonded contact ion pair, $[CpRu(CO)(PH_3)(H_2)]^+\cdots[CF_3C(O)O\cdots H\cdots O(O)CCF_3]^-$ stabilised by the $[CF_3C(O)O\cdots H\cdots O(O)CCF_3]^-$ anion in the gas phase; the distances are given in Å

ended up in the initial dihydrogen-bonded complexes. In addition, the products of full proton transfer, i.e. free ions, were thermodynamically unstable and their energies were higher with respect to the reagents by 100 kcal/mol. Polar solvents could stabilise the charged species. In fact, calculations modelling CH_2Cl_2 led to reduced energies of the systems containing free ions. Nevertheless, the products of proton transfer remained 22 kcal/mol above the initial compounds. Again, no energy minima have been located for contact ion pairs. However, these intermediates have been calculated with minimal energies even in the gas phase if homoconjugated anions, $[RO\cdots H\cdots OR]^-$, are taken into consideration as an additional factor for charge stabilisation. Note that this factor has been well demonstrated by kinetic experiments on the protonation of transition metal hydrides in solution.[6] The calculations led to the structures $[CpRu(CO)(PH_3)(H_2)]^+\cdots[RO\cdots H\cdots OR]^-$ and $[Cp_2NbH_2(H_2)]^+\cdots[RO\cdots H\cdots OR]^-$, the optimised geometries of the former are shown in Figure 4. As can be seen, one of the dihydrogen atoms in $[CpRu(CO)(PH_3)(H_2)]^+\cdots[CF_3C(O)O\cdots H\cdots O(O)CCF_3]^-$ acts as a proton donor forming the H-bond with a length of 1.891 Å.[9] The corresponding Ru–H distance (1.820 Å) is slightly longer with respect to the free cationic dihydrogen complex (1.765 and 1.775 Å) while the H···H separations in the (H_2) ligands are very similar in both the species (0.847 Å). Finally the H–O bond in the ion pair involved into H-bonding is significantly elongated with respect to that in the free proton donor (1.253 Å and 0.98 Å, respectively).

Hartree–Fock calculations of the dihydrogen-bonded $Li-H^{\delta-}\cdots{}^{\delta+}H-F$ complex have shown that an electric field, applied along the molecular axis, leads to transfer of H atoms between two heavy atoms to give the dihydrogen $Li^+\cdots H-H\cdots F^-$ system.[25] Thus the transformation of the M–H···HX species to contact ion pairs can be interpreted as movement of two hydrogen atoms, under the field due to the charges, towards the state with a larger charge separation if the latter can be stabilised by a polar solvent and/or by homoconjugated anions. In contrast to proton transfer to usual organic bases, these movements require strong electronic perturbations. A priori, this circumstance should lead to significant energy barriers, separating dihydrogen-bonded complexes and contact ion pairs.

3. Kinetic Experiments

Table 1 lists kinetic data for the protonation of transition metal hydrides, obtained by the spectroscopic (NMR, UV, IR) and electrochemical methods with the application of usual or stopped-flow mixing techniques. The kinetic experiments have mostly been performed under pseudofirst-order conditions in which acids have been added in large excess.[11,26a–26d] The $[ReH_2(NO)(CO)(PR_3)_2]/CF_3COOH$ systems have been studied with comparable concentrations of the reagents.[26e] In all cases, the overall kinetic order has been found to be close to 2.

The data in Table 1 illustrate the dependences of the rate constants on the nature of the acid used. For example, the rate of proton transfer to [Cp*Fe(dppe)H] strongly increases with the acidity of the proton donor as $CF_3CH_2OH < (CF_3)_2CHOH < (CF_3)_3COH < CF_3COOH$.[26d] At the same time, the *cis*-hydride $[FeH_2PPh_3]$ shows very insignificant changes in the k values in the order $CF_3COOH < HCl < HBr$.[11] In addition, the rate constants are smaller for the stronger acids HBF_4 and CF_3SO_3H. The same effect has been reported for $[RuH_2(dppe)_2]$[26a] and $[ReH_2(NO)(CO)(PMe_3)_2]$ protonated with CF_3COOH and $[\{3,5\text{-}(CF_3)_2C_6H_3\}_4B]^-[H(OEt_2)]^+$.[26e] Thus, in common cases, the rate of proton transfer and the acid strength do not correlate. This result can be explained by the relatively small permittivities of the solvents (THF, toluene, CH_2Cl_2) where even strong acids exist in an equilibrium between molecular forms, ion pairs and free ions (Scheme 5). If free H^+ attacks a hydride, then proton transfer should be suppressed by the addition of X^- ions. However, NBu_4BF_4 does not affect protonation rates of *cis*-$[FeH_2PPh_3]$ by the action of HBF_4 in THF. This is good evidence for the parallel attack of the molecular form HX and the ion pair where ion pairs react slower than HX.[11]

Kinetic experiments on the acids HX and DX, carried out under pseudofirst-order conditions, have revealed inverse kinetic isotope effects, k_H/k_D (Table 2). The results can be interpreted either as the kinetic effects measured for a single-step proton transfer or as the inverse thermodynamic isotope effects in fast preequilibria.[11] In contrast to the effects on usual H-bonds,[27] the effects of deuterium on the thermodynamics of dihydrogen bonding are unknown. On the other hand, under pseudofirst-order conditions, the position of the kinetic preequilibrium should be completely shifted towards the dihydrogen bonds. Therefore, the hypothesis of a single-step proton transfer via a late transition state could be successful for interpreting the observed isotopic effects. A structure, similar to that of the contact ion pairs in Figure 4 with almost complete formation of new bonds, could represent such a transition state. The k_H/k_D values can then be calculated by Equation (3),[11] where $\nu_i(H)$ and $\nu_i^{\neq}(H)$ are the stretching frequencies in the

 © 2005 Wiley-VCH Verlag GmbH & Co. KGaA, Weinheim

Table 1. The second-order rate constants (k, 25 °C) for protonation of transition metal hydrides with formations of dihydrogen complexes in solution

Complex	HX	k L/mol·s	Solvent	Ref.
$[FeH_2PPh_3]$	HBF_4	1.7×10^{-4}	THF	[11]
	CF_3COOH	0.112×10^{-2}		
	CF_3SO_3H	0.176×10^{-2}		
	HCl	1.32×10^{-2}		
	HBr	3.4×10^{-2}		
$[FeH_2(dppe)_2]$	HBF_4	9.7×10^{-3}	THF	[26b]
	CF_3COOH	1.39×10^{-2}		
	CF_3SO_3H	2.1×10^{-2}		
	HCl	4.8×10^{-2}		
$[CpW(CO)_2(PMe_3)H]$	$[Me_2NHC_6H_4C(Me_3)]^+[BF_4]^-$	2.7×10^{-3} (a)	CD_2Cl_2	[6]
[CpRuH(dppm)]	HBF_4	1.86×10^{2}	THF	[26c]
[CpRuH(dppe)]	HBF_4	0.70×10^{2}	THF	[26c]
$[CpRuH(PPh_3)_2]$	HBF_4	1.69×10^{2}	THF	[26c]
$[RuH_2(dppe)_2]$	HBF_4	1.1×10^{3}	THF	[26a]
	CF_3COOH	9.2×10^{4}		
	HCl	$1.7\ 10^{6}$		
$[ReH_2(NO)(CO)(PiPr_3)_2]$	CF_3COOH	4.4×10^{2} (b)	CD_2Cl_2	[26e]
$[ReH_2(NO)(CO)(PMe_3)_2]$	CF_3COOH	192×10^{2} (c)	CD_2Cl_2	[26e]
[Cp*Fe(dppe)H]	CF_3COOH	very fast	CH_2Cl_2	[26d]
	PFTB	1.56×10^{2}	CH_2Cl_2	
	HFIP	5.4	CH_2Cl_2	
	CF_3CH_2OH	1.5×10^{-3}	CH_2Cl_2	

[a] At –10 °C. [b] At –80 °C. [c] At –90 °C.

$$\mathbf{H\text{-}X} \rightleftharpoons \mathbf{H^+ / X^-} \rightleftharpoons \mathbf{H^+ + X^-}$$

Scheme 5

Table 2. Kinetic isotope effects [k(H)/k(D)] measured for protonation of transition metal hydrides in solution

Complex	HX	Solvent	k(H)/k(D) (T °C)	k(H)/k(D) calcd.	Ref.
$[FeH_2(dppe)_2]$	CF_3SO_3H	THF	0.21 (25)	0.87	[26b]
	HCl		0.36 (25)	0.47	
	HBr		0.55 (25)	0.39	
$[FeH_2PPh_3]$	CF_3SO_3H	THF	0.45 (25)	0.87	[11]
	HCl		0.62 (25)	0.47	
	HBr		0.64 (25)	0.39	
$[RuH_2(dppe)_2]$	CF_3COOH	THF	0.80 (25)	0.87	[26a]
	HCl		0.38 (25)	0.47	
$[ReH_2(NO)(CO)(PiPr_3)_2]$	CF_3COOH	CD_2Cl_2	1.4 (–80)	0.87	[26e]

fundamental and transition states, respectively. As can be seen, Table 2 shows good agreements between the theoretical and experimental k_H/k_D values.

$$k(H)/k(D) = \exp\{7.06\ 10^{-4}[\textstyle\sum_i \nu_i(H) - \sum_i \nu_i^{\neq}(H)]\} \quad (3)$$

As in the case of classical organic bases, proton transfer to a hydride ligand is not a single-step process and occurs via dihydrogen-bonded intermediates. It follows from the previous section that the factor of the basicity, E_j, characterising the formation of H···H bonds, changes from 0.54 to 1.67. The effects of solvents on dihydrogen bonding are also insignificant. Thus dihydrogen bonding is a weak preorganising interaction which cannot be responsible for very big variations in rate constants of proton transfers (Table 1). For example, the k constant, measured for proton transfer from CF_3COOH to $[FeH_2PPh_3]$, $[ReH_2(NO)(CO)(PMe_3)_2]$ and $[RuH_2(dppe)_2]$, increases by six orders from $0.112\ 10^{-2}$ (25 °C) to $192\ 10^{2}$ (–90 °C) to $9.2\ 10^{4}$ (25 °C) l/mol.

IR monitoring of the $[CpRuH(CO)(PCy_3)]/(CF_3)_3COH$ (1:2) system has directly shown a slow (≈30 min) conversion of H···H complexes to intimate H-bonded ion pairs in nonpolar hexane.[9] The ^1H NMR spectra, recorded for the same hydride in the presence of 12 and 100 equivalents of $(CF_3)_3COH$ in $CDClF_2/CDF_3$ (2:1),[7c] support this observation. It is important to emphasise that the formation of H···H bonds is very fast on the NMR timescale even at 120 K. In contrast, the hydride signal, averaged between the intimate and solvent-separated ion pairs, is strongly broadened at 120 K, indicating retardation of ionpair transformations on the NMR timescale.

The schemes in Figure 3 represent proton transfers to hydride ligands with the participation of two proton donor molecules, emphasising the role of homoconjugated $[X\cdots H\cdots X]^-$ species in the kinetics of the process. Note that the second HX molecule initiates the formation of the solvent-separated or contact ion pair, corresponding to pathway (1) or (2).

Formally pathway (1) can be expressed via Equation (4). Since the formation of contact ion pairs is rate-determining (i.e. $k_2 << k_{-1}$ and $k_3[HX] >> k_{-2}$), the equation becomes

 © 2005 Wiley-VCH Verlag GmbH & Co. KGaA, Weinheim

Table 3. Activation parameters for proton transfer to hydride ligands in solution

System	$\Delta H^{\neq}$ kcal/mol	$\Delta S^{\neq}$ e.u.	Solvent	Ref.
$CpRuH(CO)(PCy_3)$/PFTB (1:2)	11.0	–19	hexane	[9]
$ReH_2(NO)(CO)(PiPr_3)_2$/CF_3COOH (1:1)	11.1	12.0	CD_2Cl_2	[26e]
$ReH_2(NO)(CO)(PMe_3)_2$/CF_3COOH (1:1)	13.5	36.8	CD_2Cl_2	[26e]
$ReD(PMe_3)_4(CO)$/CF_3COOD (1:1)	14.4	14.8	CH_2Cl_2	[26e]

Equation (5) and thus the reaction represents a first-order process with respect to the acid. It is easy to show that under the pseudofirst-order conditions (when the preequilibrium is shifted completely to H···H complexes) the measured rates become independent of HX concentration.

$$d[MH]/dt = -\{k_1k_2k_3[MH][HX]^2\}/\{k_{-1}k_{-2} + k_{-1}k_3[HX]\} + k_2k_3[HX] \quad (4)$$

$$d[MH]/dt = -(k_1/k_{-1})\cdot k_2[MH][HX] \quad (5)$$

Experimentally, this pathway has been well established from the IR spectra of the $[CpRuH(CO)(PCy_3)]/(CF_3)_3OH$ system in CH_2Cl_2 in which large variations in hydride/alcohol ratios did not affect a slow transformation of H···H complexes to H-bonded ion pairs with k values between 1.4 10^{-3} and 1.6 10^{-3} s^{-1}.[7a] Activation parameters for this step (Table 3) have been determined in hexane.[9] It is probable that such a mechanism operates for the protonation of the hydrides $[ReH_2(NO)(CO)(PR_3)_2]$ with CF_3COOH (Table 3) in CD_2Cl_2 where the reaction corresponds to first order kinetics on the acid at hydride/acid ratios ≥ 1.[26e]

In contrast, UV monitoring of the hydride [Cp*Fe(dppe)-H] protonated with a 30–200 fold excess of $(CF_3)_3COH$ or $(CF_3)_2CHOH$ (CH_2Cl_2) (pseudofirst-order conditions) led to the first-order dependence of the measured rates on the alcohol concentration.[26d] In the framework of pathway (1) the result can be interpreted according to Equation (6) obtained from equation (5) by assuming $k_3[HX] << k_{-2}$. It is clear that under the pseudofirst-order kinetic measurement conditions, this equation will show a first order dependence on the acid concentration.

$$d[MH]/dt = -(k_1/k_{-1})(k_2/k_{-2})k_3[MH][HX]^2 \quad (6)$$

On the other hand, the above data can be rationalised in the context of pathway (2) where a slow transformation of the H···H complexes to contact ion pairs is accompanied by the second HX molecule [Equation (7)].

$$d[MH]/dt = -\{k_1k_2k_3[MH][HX]^2\}/\{k_{-1}k_{-2} + k_{-1}k_3 + k_2k_3[HX]\} \quad (7)$$

Then, at $k_2[HX] << k_{-1}$, Equation (7) converts to Equation (8).

$$d[MH]/dt = -\{k_1k_2k_3[MH][HX]^2\}/k_{-1}(k_{-2} + k_3) \quad (8)$$

The latter will correspond to the first-order process under the pseudofirst-order kinetic measurement conditions. Finally, the gas-phase and solution DFT calculations have revealed that proton transfer in the $[CpRu(CO)(PH_3)H]/CF_3COOH$ system is energetically preferable if the second HX molecule participates in each step of the process.[9] When the acid is initially a dimer, this situation corresponds, in kinetic terms, to Equation (9) [$(HX)_2$ = DM] showing first order kinetics for the DM acid.

$$d[MH]/dt = -k_1k_2k_3[MH][DM]/\{k_{-1}k_{-2} + k_{-1}k_3 + k_2k_3\} \quad (9)$$

To account for the dimerisation of CF_3COOH,[28] this scheme cannot be excluded when interpreting the kinetic data collected for the $[ReH_2(NO)(CO)(PR_3)_2]/CF_3COOH$ (1:1) system in CD_2Cl_2.[26e] It is clear that only detailed kinetic measurements for large variations in reagent concentrations can distinguish pathways 1–3. For obvious reasons, such experiments are often impossible. However, on the basis of the data presented in this section, pathway (1) can be taken as a general mechanism of proton transfer.

4. Proton/ HydrideExchange as a Measure of Proton Transfer

Intra- and intermolecular positional exchanges with the participation of hydride ligands are widely known.[6,29] Proton/hydride exchanges similar to those in Figure 2 are manifested in the ^1H NMR spectra as broadenings and coalescences of the hydride and HX resonances upon heating and can be quantitatively characterised with the help of a lineshape analysis or saturation transfer experiments.[24] As in the case of proton transfer, the exchange rates in Table 4 strongly depend on the nature of the hydrides and are sensitive to isotope displacements. The overall kinetic order of the exchanges is also equal to 2[6,26e] in agreement with almost negative activation entropies. The nature of the acids also has a significant influence on exchange rates: the exchange is faster when the anion of HX is capable of assistance.[26e]

According to the ^1H NMR spectroscopic data collected for an isomeric mixture of the hydride $[CpW(CO)_2(PMe_3)-H]$ in the presence of $[PhNH_3(OEt_2)]^+_{1-2}[B(Ar^f)_4]^-$, the proton/hydride exchange is fast only for the *trans* isomer.[6] It is obvious that this selective proton/hydride exchange is a good test for a proton attack on the hydride ligand.

The exchanges are highly regioselective in [D_8]toluene solutions of the $[ReH_2(NO)(CO)(PR_3)_2]/CF_3COOH$ system where only the H ligands, located *trans* to NO, are involved in the exchange (Table 4).[26e] Since this effect correlates

 © 2005 Wiley-VCH Verlag GmbH & Co. KGaA, Weinheim

Table 4. Kinetic parameters of proton/hydride exchanges, determined by ^{1}H NMR in solution[6,26e]

System	k(exch) (T, °C) (L/mol·s)	$\Delta H^{\neq}$ (kcal/mol)	$\Delta S^{\neq}$ e.u.	Solvent
$[CpW(CO)_2(PMe_3)H]/[(CH_3)_3C_6H_4N(CH_3)_2D]^+$	1.8×10^{-4} (–10)	10.7	–35.2	CD_2Cl_2
$[CpW(CO)_2(PMe_3)D]/[(CH_3)_3C_6H_4N(CH_3)_2H]^+$	8.9×10^{-4} (–10)	11.2	–30.2	CD_2Cl_2
$[ReH_2(NO)(CO)(PiPr_3)_2]/CF_3COOH$	33.7×10^2 (–70)[a]	7.7	–2.3	$[D_8]$toluene
$[ReD_2(NO)(CO)(PiPr_3)_3]/CF_3COOD$	16.0×10^2 (–70)[a]	–	–	toluene
$[ReH_2(NO)(CO)(POiPr_3)_2]/CF_3COOH$	20.7×10^2 (–66) [a,b]	7.4	–5.5	CD_2Cl_2
$[ReD_2(NO)(CO)(POiPr_3)_2]/CF_3COOD$	4.6×10^2 (–70)[a]	7.1	–10.3	toluene
$[ReD_2(NO)(CO)(POiPr_3)_2]/CF_3COOD$	3.6×10^2 (–70)[a]	6.0	–16.6	CD_2Cl_2/toluene (1:1)
	0.93×10^2 (–60)[b]	7.7	–13.9	CD_2Cl_2/toluene (1:1)
$[ReH_2(NO)(CO)(PMe_3)_2]/CF_3COOH$	250×10^2 (–73)[a]	7.8	0	$[D_8]$toluene
$[ReD(PMe_3)_4(CO)]/CF_3COOD$ (1:1)	0.92×10^2 (–60)	6.3	–19.2	CH_2Cl_2

[a] *trans* to the NO group. [b] *cis* to the NO group.

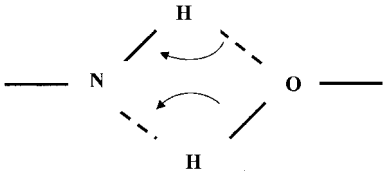

Scheme 6

with the regioselective dihydrogen bonding and Re···HOR bonds are not observed, the dihydrogen-bonded adducts can be taken as a starting point for the proton/hydride exchange process.

A priori, a hydride atom and an acidic proton can exchange their positions if both H atoms are bound to a metal centre in a transition state or an intermediate. It is clear that the solvent-separated ion pairs, $M(H_2)^+//X^-$, could play the roles of such states. Experimentally this statement can be supported by the equal rates measured for the proton/hydride exchange and the formation of dihydrogen complexes. This case is documented for the $[ReH_2(NO)(CO)(PiPr_3)_2]/CF_3COOH$ system in the relatively polar CD_2Cl_2:[26e] a line-shape analysis of the hydride resonances (a test for the exchange) and the ^{31}P NMR signals of $[ReH_2(NO)(CO)(PiPr_3)_2]$ and $[ReH(H_2)(NO)(CO)(PiPr_3)_2]^+$ $[CF_3COO]^-$ (a test for the formation of dihydrogen complexes) gave very similar rate constants (15–20 10^2 L/mol·s, –70 °C). In is clear that under these conditions, the proton/hydride exchange is a good probe for full proton transfer to a hydride ligand.

However, as in the case of usual organic bases, the situation can change. In fact, proton exchanges in organic acid/base pairs can occur without charge separation via the cyclic nonpolar transition states in Scheme 6 where N-H is a base and H-O is an acid. As a result, for example, the dihydrogen complexes $[ReH(H_2)(CO)(NO)(PR_3)_2]^+$ $[CF_3COO]^-$ are formed *slowly* in nonpolar toluene on the ^{31}P NMR timescale while *fast* proton/hydride exchanges still occur on the ^{1}H NMR timescale.[26e] The same effect can be observed in a CH_2Cl_2 solution of $[ReD(PMe_3)_4(CO)]$ and CF_3COOD. As follows from Table 4, the activation energies $\Delta H^{\ddagger}$ necessary for the exchanges are remarkably smaller than those for the formation of dihydrogen complexes (Table 3). In contrast, the isotopic effect k_H/k_D for the

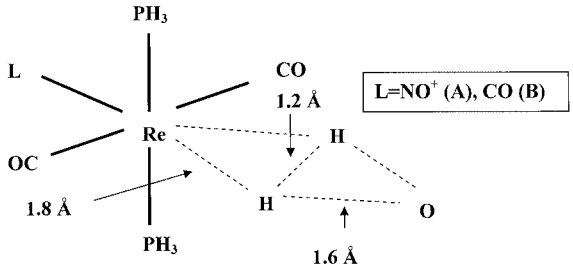

Figure 5. The models of the transition states **A** and **B**, suitable for proton/hydride exchange processes, obtained by EHT calculations on the basis of symmetrical pseudooctahedral geometry (H^+ and O^{2-} represent the acid)[26e]

exchange is larger. It becomes obvious, that in spite of the same starting point (dihydrogen bonded complexes), both processes occur via different transition states and thus such a type of exchange is not a measure of proton transfer and only accompanies the latter. Structures **A** and **B** in Figure 5 could be models of exchange transition states for the Re hydrides, where H^+ and O^{2-} represent the acid.[26e] The structures obtained by EHT calculations are not optimised but they do exhibit feasible features for the orbital interactions and explain the selectivity of the exchanges. For example, state **A** with a *trans* NO has a reasonable HOMO/LUMO gap (≈2.5 eV) and crucial participation of the oxygen orbitals in the binding of the H_2 unit to the metal centre. The orbital interactions are built up from d_{XY} and σ-type functions on the Re centre by the two s_H hydrogen orbitals and s, p_X and p_Y orbitals from the oxygen atom. Thus the appearance of H···H bonding is a main feature of the exchange transition state with participation of hydride ligands in contrast to the transition state in Scheme 6 which is typical of usual organic bases.

5. Energy Profile of Proton Transfer to Hydride Ligands

The discussed spectroscopic, kinetic and thermodynamic data are quite sufficient to describe, semiquantitatively, the energy profile of proton transfer to a hydride ligand in solution.[5c,5d,30] Figure 6 shows the energy as a function of the proton–hydride distance varying from an initial state to a

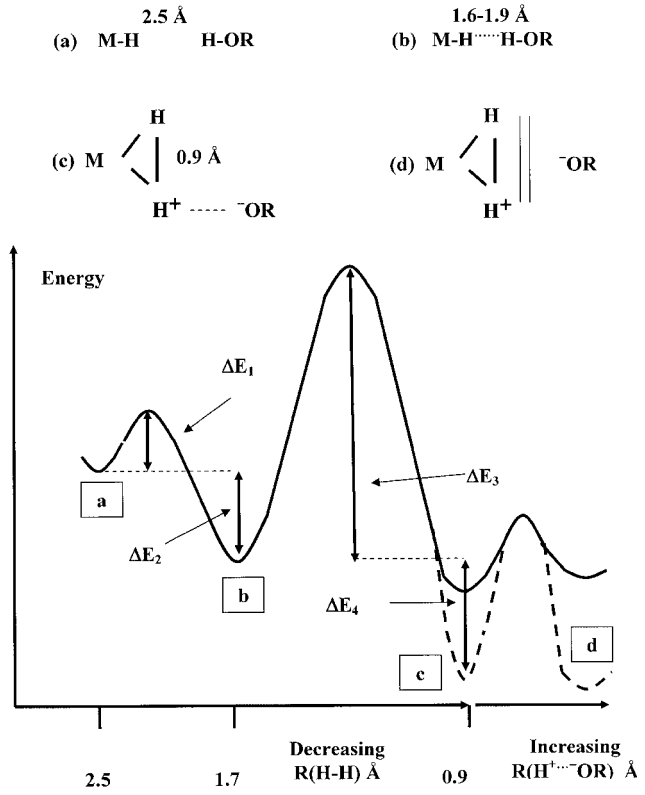

Figure 6. Energy profiles of proton transfer to a hydride ligand of a transition metal complex in solution: ΔE_1 = +3–4 kcal/mol, ΔE_2 = –5 to –7 kcal/mol, ΔE_3 = +10–14 kcal/mol and ΔE_4 = –7 kcal/mol, respectively; the energy is a function of the proton–hydride distance varying from an initial state (2.5 Å) to the final product (0.9 Å); conversion of the intimate ion pair to the solvent/separated ion pair is shown as a function of the $H^+\cdots O^-$ distance

final product. The averaged structural parameters of the initial hydrides and intermediates have been taken from the experimental measurements and DFT calculations. Since proton-hydride contacts of ≤ 2.4 Å, found for different compounds in the solid state, correspond to the appearance of weak bonding interactions,[13b] the H···H distance of 2.5 can be regarded as the starting point with zero energy. The proton transfer process ends with a structure in which the $H^{\delta+}\cdots^{\delta-}H$ distance becomes 0.9 Å, a typical value for dihydrogen ligands.[3]

The pattern in Figure 6 contains four energy minima occupied by the initial hydride, the dihydrogen-bonded complex, the intimate ion pair and the solvent-separated ion pair as a final product of the reaction. For simplicity, homoconjugated species, $[RO\cdots H\cdots OR]^-$, assisting proton transfer and stabilising the protonated products can be ruled out.

Usually, the formation of the H-bonded complexes is regarded as a very fast and diffusion-controlled process with no energy barrier.[5d] On the other hand, even ultra fast molecular reorientations in solution require energy for reorganisation of molecular environments. Since transition metal complexes reorient in solutions with energies of 3.0–4.5 kcal/mol, this magnitude can be taken as a reasonable first barrier, separating the free hydride molecules and the H···H complexes. Dihydrogen bonding results in systems with H···H separations between 1.6 and 1.9 Å. The energy of these systems is reduced by 2.0–7.6 kcal/mol. Note that the latter remarkably depends on the nature of hydrides and acids while the solvent influence is insignificant. The M–H and H–O bonds in the dihydrogen bonded adduct are only slightly elongated with respect to the initial hydride and the acid. The electronic perturbations are minimal and do not require significant energies. The next energy minimum is populated by contact ion pairs and stabilised by H-bonds with anions. This intermediate has the H···H separation very close to that in the dihydrogen complex and its H···O bond is strongly elongated. In spite of the significant structural changes, the depths of the energy minima occupied by dihydrogen- bonded complexes and contact ion pairs are very similar. Since the ion pair species were not localised in the gas-phase DFT calculations, the effect is certainly consistent with their stabilisation by polar solvents or homoconjugated anions $[RO\cdots H\cdots OR]^-$.

As in the case of classical acid/base pairs, the formation of contact ion pairs $M(H_2)^+\cdots X^-$ is the step of proton transfer. However, for transition metal hydrides this step requires significant changes in the M–H–H–X geometry and the H···H and X–H bond lengths. For this reason, the energy barrier separating the M–H···H–X and $M(H_2)^+\cdots X^-$ species increases to 11–13 kcal/mol (Table 3) in very good agreements with the DFT calculations[9] modelling proton transfer in the $[CpRuH(CO)PH_3]/CF_3COOH$ and $[CpRuH(CO)PH_3]/(CF_3)_3COH$ systems (heptane, CH_2Cl_2). Note that this step is responsible for the total kinetics of proton transfer and the large variation in the *k* constants in Table 1. The solvent-separated ion pair finishes the process with enthalpy changes between –2.4 and –9 kcal/mol.[7,5d,30] The NMR experiments on the $[CpRuH(CO)(PCy_3)]/(CF_3)_3COH$ system in $CDClF_2/CDF_3$ (2:1)[17] showed a low energy barrier separating the contact and solvent-separated ion pairs. Therefore, in the absence of quantitative kinetic data on the last step, the barrier between $M(H_2)^+\cdots X^-$ and $M(H_2)^+//X^-$ can be taken to be small.

6. Conclusion

The concept of hydrogen bonding, known since the beginning of the 20 century, has played a very important role in the understanding of the nature and properties of chemical compounds. The problem of dihydrogen bonding, as an interaction between oppositely charged hydrogen atoms, is significantly younger.[12a,13c,31] In spite of this, its fundamental significance in catalysis, bio-organic and supramolecular chemistry has been well recognised.

This microreview, ignoring details of hydride chemistry and focusing on key physicochemical data, discusses possible kinetic schemes for the protonation process and formulates a general mechanism whereby dihydrogen bonding is the preorganising interaction in proton transfer and proton/hydride exchanges. Protonation of hydride ligands occurs via intermediates, H···H complexes and H-bonded con-

 © 2005 Wiley-VCH Verlag GmbH & Co. KGaA, Weinheim

tact ion pairs, and ends in dihydrogen complexes as solvent-separated ion pairs or free ions. General rules governing proton transfer to hydride ligands and conventional organic bases are very similar. The difference between the two is quantitative rather than qualitative in character and is apparent in the contact ion pair formation step. In the case of transition metal hydrides, this step, which determines the kinetics of the process, requires significantly larger activation energies and for this reason the total rate of proton transfer is remarkably slower.

In spite of the numerous studies considered in this article, some important mechanistic details of proton transfer are still unclear and could be the subject of further investigations, one of these being the regularity governing the participation of homoconjugated $[X\cdots H\cdots X]^-$ species. For example, it remains uncertain as to which intermediate step needs such $[X\cdots H\cdots X]^-$ assistance for dictating the total kinetic order of the process. Thermodynamic aspects of conversions of H···H complexes to contact ion pairs are also practically unstudied. To answer these fundamental questions, additional experimental and theoretical investigations are needed. Among various experimental approaches, NMR experiments at extremely low temperatures[8] seem to be very appropriate.

As in the case of conventional organic bases, proton/hydride exchanges in transition metal hydrides can be considered as a probe for full proton transfer. In this context, further theoretical work investigating models of transition states for both processes will be most interesting.

[1] a) X. Zhao, I. P. Georgakaki, M. L. Miller, J. C. Yarbourh, M. Y. Darensbourg, *J. Am. Chem. Soc.* **2001**, *123*, 9710; b) J. W. Peters, *Curr. Opin. Struct. Biol.* **1999**, *9*, 670; c) M. W. Adams, *Biochim. Biophys. Acta* **1990**, *1020*, 115.

[2] R. Custelcean, J. E. Jackson, *J. Am. Chem. Soc.* **1998**, *120*, 12935.

[3] G. J. Kubas, *Metal Dihydrogen and s-Bond Complexes*, Kluwer Academic/Plenum, New York, **2001**.

[4] R. M. Bullock, *Chem. Eur. J.* **2004**, *10*, 2366.

[5] a) R. H. Morris, *Nonclassical Hydrogen Bonding along the Pathway to the Heterolytic Splitting of Dihydrogen*, in: *Recent Advances in Hydride Chemistry* (Eds.: R. Poli, M. Peruzzini), Elsevier, Amsterdam, London, New York, Paris, Tokyo, **2001**, pp. 1–38; b) E. T. Papish, M. P. Magee, J. R. Norton, *Protonation of Transition Metal Hydrides to Give Dihydrogen Complexes: Mechanistic Implications and Catalytic Applications*, in: *Recent Advances in Hydride Chemistry* (Eds.: R. Poli, M. Peruzzini), Elsevier, Amsterdam, London, New York, Paris, Tokyo, **2001**, pp. 39–74; c) L. M. Epstein, N. V. Belkova, E. S. Shubina, *Dihydrogen Bonded Complexes and Proton Transfer to Hydride Ligands by Spectral (IR, NMR) Studies*, in: *Recent Advances in Hydride Chemistry* (Eds.: R. Poli, M. Peruzzini), Elsevier, Amsterdam, London, New York, Paris, Tokyo, **2001**, pp. 391–418; d) L. M. Epstein, E. S. Shubina, *Coord. Chem. Rev.* **2002**, *231*, 165.

[6] E. T. Papish, F. C. Rix, N. Spetseris, J. R. Norton, R. D. Williams, *J. Am. Chem. Soc.* **2000**, *122*, 12235.

[7] a) N. V. Belkova, E. I. Gutsul, E. S. Shubina, L. M. Epstein, *Z. Phys. Chem. (Muenchen Ger.)* **2003**, *217*, 1525; b) G. Orlova, S. Scheiner, *J. Phys. Chem. A.* **1998**, *102*, 4813; c) N. V. Belkova, A. V. Ionidis, L. M. Epstein, E. S. Shubina, S. Gruendemann, N. S. Golubev, H. H. Limbach, *Eur. J. Inorg. Chem.* **2001**, 1753.

[8] a) N. S. Golubev, S. N. Smirnov, V. A. Gindin, G. S. Denisov, H. Benedict, H. H. Limbach, *J. Am. Chem. Soc.* **1994**, *116*, 12055; b) G. S. Denisov, N. G. Golubev, V. A. Gindin, H. H. Limbach, S. S. Ligay, S. N. Smirnov, *J. Mol. Struct.* **1994**, *322*, 83.

[9] N. V. Belkova, M. Besora, L. Epstein, A. Lledos, F. Maseras, E. S. Shubina, *J. Am. Chem. Soc.* **2003**, *125*, 7715.

[10] E. V. Bakhmutova, V. I. Bakhmutov, N. V. Belkova, M. Besora, L. Epstein, A. Lledos, G. I. Nikonov, E. S. Shubina, J. Tomas, E. V. Vorontsov, *Chem. Eur. J.* **2004**, *10*, 661.

[11] M. G. Basallote, J. Duran, J. Fernandez-Trujillo, M. A. Manez, J. R. Torre, *J. Chem. Soc. Dalton Trans.* **1998**, 745.

[12] a) R. H. Crabtree, P. E. M. Siegbahn, O. Eisenstein, A. L. Rheingold, T. F. Koetzle, *Acc. Chem. Res.* **1996**, *29*, 348; b) A. J. Lough, S. Park, R. Ramachandran, R. H. Morris, *J. Am. Chem. Soc.* **1994**, *116*, 8356.

[13] a) R. Custelcean, J. E. Jackson, *Chem. Rev.* **2001**, *101*, 1963; b) K. N. Robertson, O. Knop, T. S. Cameron, *Can. J. Chem.* **2003**, *81*, 727; c) M. Guizado-Rodriguez, A. Ariza-Castolo, G. Merino, A. Vela, H. Noth, V. I. Bakhmutov, R. Contreras, *J. Am. Chem. Soc.* **2001**, *123*, 9144.

[14] a) R. Custelcean, M. Vlassa, J. E. Jackson, *Chem. Eur. J.* **2002**, *8*, 302; b) R. Custelcean, J. E. Jackson, *Angew. Chem. Int. Ed.* **1999**, *38*, 1661.

[15] a) G. Orlova, S. Scheiner, *J. Phys. Chem. A.* **1998**, *102*, 260; b) G. Orlova, S. Scheiner, *J. Phys. Chem. A.* **1999**, *103*, 514.

[16] E. S. Shubina, N. V. Belkova, A. N. Krylov, E. V. Vorontsov, L. M. Epstein, D. G. Gusev, M. Niedermann, H. Berke, *J. Am. Chem. Soc.* **1996**, *118*, 1105.

[17] E. S. Shubina, N. V. Belkova, A. V. Ionidis, N. S. Golubev, L. M. Epstein, *Russ. Chem. Bull.* **1997**, *44*, 1349.

[18] V. I. Bakhmutov, E. V. Bakhmutova, N. V. Belkova, C. Bianchini, L. M. Epstein, D. Masi, M. Peruzzini, E. S. Shubina, E. V. Vorontsov, F. Zanobini, *Can. J. Chem.* **2001**, *79*, 479.

[19] E. Cayuela, F. A. Jalon, B. R. Manzano, G. Espino, W. Weissensteiner, K. Mereiter, *J. Am. Chem. Soc.* **2004**, *126*, 7049.

[20] V. I. Bakhmutov, E. V. Vorontsov, D. Y. Antonov, *Inorg. Chim. Acta* **1998**, *278*, 122.

[21] a) I. Alkorta, J. Elguero, O. Mo, M. Yanez, J. E. D. Bene, *J. Phys. Chem. A.* **2002**, *106*, 9325; b) G. Merino, V. I. Bakhmutov, A. Vela, *J. Phys. Chem. A.* **2002**, *106*, 8491.

[22] a) J. A. Ayllon, S. F. Sayers, S. Sabo-Etienne, B. Donnadieu, B. Chaudret, E. Clot, *Organometallics* **1999**, *18*, 3981; b) A. Messmer, H. Jacobsen, H. Berke, *Chem. Eur. J.* **1999**, *5*, 3341; c) N. V. Belkova, E. S. Shubina, A. V. Ionidis, L. M. Epstein, H. Jacobsen, A. Messmer, H. Berke, *Inorg. Chem.* **1997**, *36*, 1522.

[23] E. I. Gutsul, N. V. Belkova, M. S. Sverdlov, E. S. Shubina, L. Epstein, V. I. Bakhmutov, M. Perruzzini, C. Binachini, F. Zanobini, T. N. Gribanova, R. M. Minyaev, *Chem. Eur. J.* **2003**, *9*, 2219.

[24] R. K. Harris, *Nuclear Magnetic Resonance Spectroscopy. A Physicochemical View*, Longman Scientific&Technical, UK, **1986**, pp. 119–126.

[25] I. Rozas, I. Alkorta, J. Elguero, *Chem. Phys. Letters* **1997**, *275*, 423.

[26] a) M. G. Basallote, J. Duran, M. J. Fernandez-Ttujillo, M. A. Manez, *Inorg. Chem.* **1999**, *38*, 5067; b) M. G. Basallote, J. Duran, M. J. Fernandez-Ttujillo, M. A. Manez, *J. Chem. Soc. Dalton Trans.* **1998**, 2205; c) M. G. Basallote, J. Duran, M. J. Fernandez-Ttujillo, M. A. Manez, *Organometallics* **2000**, *19*, 695; d) N. V. Belkova, P. O. Revin, L. Epstein, E. V. Vorontsov, V. I. Bakhmutov, E. S. Shubina, E. Collange, R. Poli, *J. Am. Chem. Soc.* **2003**, *125*, 11106; e) S. Feracin, T. Burgi, V. I. Bakhmutov, I. Eremenko, E. V. Vorontsov, A. B. Vimenits, H. Berke, *Organometallics* **1994**, *13*, 4194.

[27] P. Schah-Mohammedi, I. G. Shenderovich, C. Detering, H. H. Limbach, P. M. Tolstoy, S. N. Smirnov, G. S. Denisov, N. S. Golubev, *J. Am. Chem. Soc.* **2000**, *122*, 128787.

[28] a) N. S. Golubev, G. S. Denisov, *Zhur. Prikl. Spectr.* **1982**, *37*, 265; b) V. V. Myasoedova, O. A. Abramova, G. A. Krestov, *Vysokomol. Siedin. Ser B.* **1984**, *26*, 215.

 © 2005 Wiley-VCH Verlag GmbH & Co. KGaA, Weinheim

[29] a) S. S. Kristjansdottir, J. R. Norton, *Acidity of Hydrido Transition Metal Complexes in Solution*, in: *Transition Metal Hydrides* (Ed.: A. Dedieu), VCH, Weinheim, Germany, **1992**, pp 309–351; b) P. L. Gaus, S. C. Kao, M. Y. Darensbourg, L. W. Arndt, *J. Am. Chem. Soc.* **1984**, *106*, 4752.
[30] N. V. Belkova, E. V. Bakhmutova, E. S. Shubina, C. Bianchini, M. Peruzzini, V. I. Bakhmutov, L. M. Epstein, *Eur. J. Inorg. Chem.* **2001**, 2163.
[31] For example: a) P. L. A. Popelier, *J. Phys. Chem. A.* **1998**, *102*, 1873; b) Alkota, I. Rozas, J. Elguero, *Chem. Soc. Rev.* **1998**, *27*, 163; c) L. M. Epstein, E. S. Shubina, E. V. Bakhmutova, L. N. Saikulova, V. I. Bakhmutov, A. L. Chistyakov, I. V. Stankevich, *Inorg. Chem.* **1998**, *37*, 3013; d) M. J. Calhorda, *Chem. Commun.* **2000**, 801; e) S. A. Kulkarni, A. K. Srivastava, *J. Phys. Chem. A.* **1999**, *103*, 2836; f) T. Kar, S. Scheiner, *J. Chem. Phys.* **2003**, *119*, 1473.

Received August 13, 2004

 © 2005 Wiley-VCH Verlag GmbH & Co. KGaA, Weinheim

A New Ligand for the Formation of Triangular Building Blocks in Supramolecular Chemistry

Iris M. Müller*[a] and Daniela Möller[a]

Keywords: Tridentate ligands / Copper / Molybdenum

In this article we describe the synthesis, characterisation and metal binding properties of tris(5-bromo-2-hydroxybenzylidene)triaminoguanidinium chloride $[H_6Br_3L]Cl$ (**1**), which can be seen as a triangular building block for supramolecular chemistry. **1** crystallises either in a triclinic (**1a**) or a rhombohedral (**1b**) system depending on the used solvent . The pure ligand adopts a conformation unfavourable for the coordination of metal centres, but in the presence of a base or a basic metal salt, a change in the conformation can be observed. The reaction of **1** with $(NH_4)_6[Mo_7O_{24}]$ in the absence of further base results in the formation of small, red crystal needles with the formula $[Mo(O)_2(OH_2)(H_3Br_3L)]\cdot 2$ DMF (**2**), while the reaction of **1** with $CuCl_2$, sodium 5,5-diethylbarbiturate (NaH*bar*) and Et_3N leads to the formation of dark red-black crystals with the formula $(Et_4N)_2[\{Cu(Hbar)\}_3Br_3L]$ (**3**).

(© Wiley-VCH Verlag GmbH & Co. KGaA, 69451 Weinheim, Germany, 2005)

Introduction

There are two different ways of subdividing the rapidly growing field of supramolecular chemistry. One is by classifying the products that can be formed, namely polymers [1] or discrete cages and helical molecules.[2] The other way is based on the molecular building units, especially on the properties of the participating ligands. Up to now, the use of asymmetric or C_2 symmetric ligands has predominated, and despite their potential, far fewer C_3 symmetric ligands or ligands of higher symmetry have been employed for supramolecular coordination chemistry.[2] In particular, the C_3-symmetric ligands can be regarded as triangular building blocks, which should be suitable for the construction of most of the Platonic and Archimedic bodies. The smallest conceivable C_3 symmetric ligand is the carbonate dianion (Scheme 1, a). The guanidinium cation, which is isoelectronic with carbonic acid (Scheme 1, b; R = H), is known to be able to form metal complexes and can be modified chemically.[3]

A possible way of designing more stable products is to put the stabilizing chelate effect to use as in the case of the triaminoguanidinium cation (Scheme 1, c). Due to its character as a reducing agent, the introduction of protection groups is necessary, and if these also contain a donor atom, a tris(chelating) ligand with threefold symmetry will be formed (Scheme 1, d), which can be used to bind three metal centres as shown in Scheme 1 (e). The preferred coordination geometry of the metal centres determines the number and position of additional ligands. With the use of this strategy, different types of complexes, from monomeric species[4] to cage-like compounds with the outer shape of a doughnut,[4] a rectangular box,[5] a tetrahedron[6] and an octahedron,[5] can be prepared as described previously. The structural characterisation of large cage compounds by X-ray crystallography is often difficult due to rapid solvent loss and a typical high degree of disorder of both the counter ions and solvent molecules. The introduction of heavy atoms into the ligand should increase the scattering power of such oligomeric complexes and therefore improve the resolution and quality of the experimental X-ray data. With

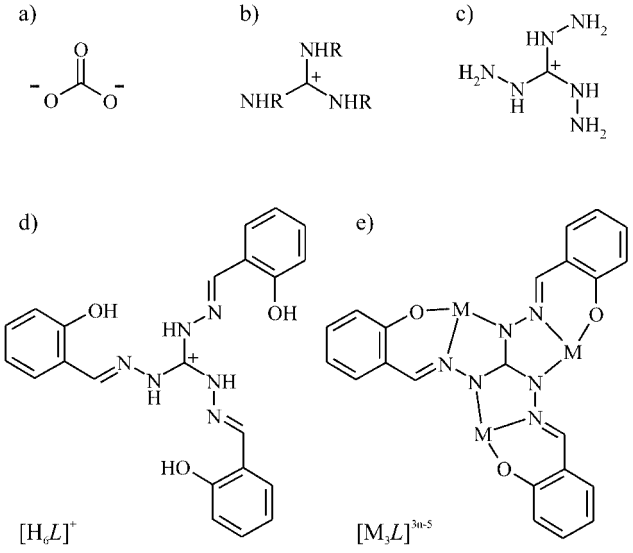

Scheme 1

[a] Lehrstuhl für Analytische Chemie, NC 4 / 27,
Ruhr-Universität Bochum
44780 Bochum, Germany
Fax: (internat.) + 49-(0)234-321-4420
E-mail: iris.m.mueller@rub.de

this goal in mind, we present here the synthesis and characterisation of tris(5-bromo-2-hydroxybenzylidene)triaminoguanidinium chloride and report on its metal binding properties.

Results and Discussion

Tris(5-bromo-2-hydroxybenzylidene)triaminoguanidinium chloride $[H_6Br_3L]Cl$ (**1**), can be easily obtained from triaminoguanidinium chloride and 5-bromosalicylaldehyde (Scheme 2).

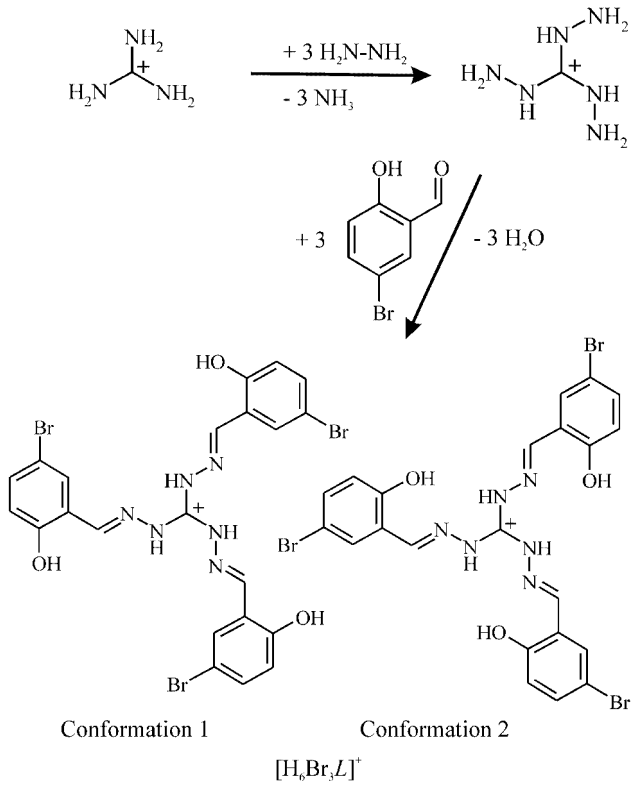

Scheme 2

Diffusion of HCl into an aqueous solution of **1** leads to triclinic pale yellow crystals of **1a**, whose molecular structure (space group $P\bar{1}$) is shown in Figure 1 (a).[7] In the solid state, **1** adopts conformation 1 (Scheme 2), which is stabilized by close contacts between the hydroxy groups and the Cl^- anions (Table 1). This results in the formation of a two-dimensional hydrogen-bonded network.

Diffusion of HCl into a solution of **1** in DMF leads to rhombohedral pale yellow crystals of **1b** (space group $R\bar{3}$).[8] The conformation of the $[H_6Br_3L]^+$ cation is the same as that observed in **1a** (Figure 1, b). However, hydrogen bonds lead, in this case, to the formation of double layers, which enclose a layer of DMF molecules. The bond length and angles observed in **1a** and **1b** fall in the expected ranges. All carbon and nitrogen atoms show sp^2-hybridisation with the distance between the central carbon and the nitrogen atoms exhibiting an average value of 1.327(7) Å,

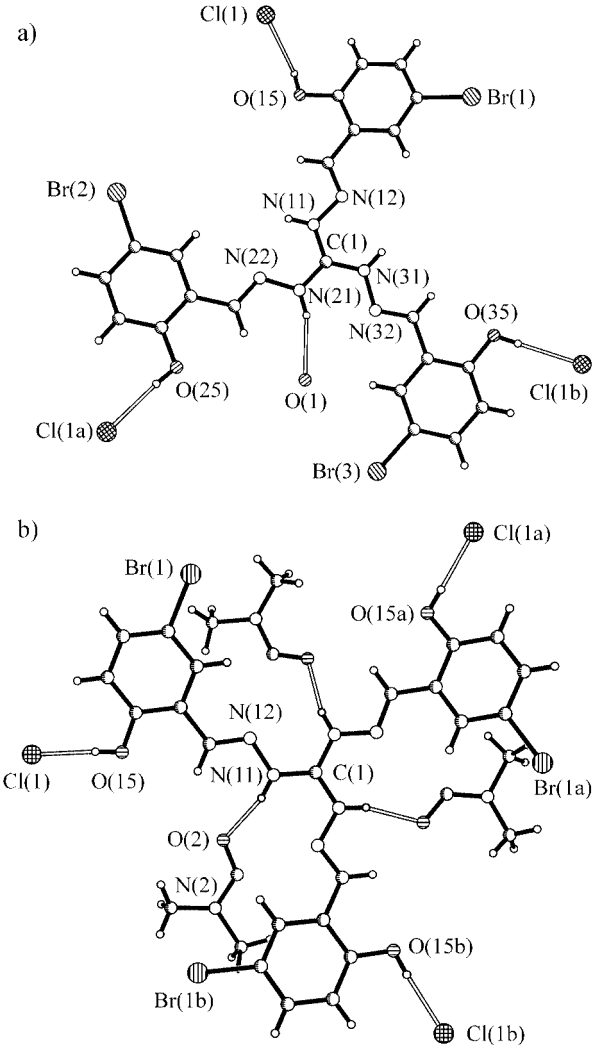

Figure 1. Crystal structures of **1**; a) **1a**; b) **1b**

Table 1. Hydrogen bonds (* = intramolecular)

	Proton	Bond to	Distance	Angle at H
1a	H15	Cl	2.49 Å	126°
	H25	Cl	2.27 Å	163°
	H35	Cl	2.30 Å	168°
	H21	O (H_2O)	2.19 Å	160°
	H11	N	2.31 Å*	101°*
	H21	N	2.33 Å*	101°*
	H31	N	2.32 Å*	102°*
1b	H15	Cl	2.15 Å	173°
	H11	O (DMF)	1.94 Å	165°
	H11	N	2.45 Å*	95°*
2	H25	O (DMF)	1.87 Å	160°
	H35	N	2.13 Å*	142°*
	H31	N	2.13 Å*	106°*
	H3a	O (DMF)	2.35 Å	123°
	H3b	N11	1.89 Å	175°
3	H43	O (*bar*)	2.04 Å	172°
	H53	O (*bar*)	1.98 Å	173°
	H63	N (CH_3CN)	2.24 Å	161°

 © 2005 Wiley-VCH Verlag GmbH & Co. KGaA, Weinheim

in accordance with a partial double-bond character. A propeller-like distortion can be observed, and the dihedral angles between the central CN_6 core and the aromatic systems adopt values between 1.5° and 22.3°. The ^1H NMR spectrum of **1** contains only a few sharp signals. This suggests that in solution one conformation must be dominant (Figure 2, a). The very weak interaction between H3 and H4 seen in the H,H-NOESY experiment suggests that in solution only conformation 1 will be of importance. It therefore appeared interesting to determine how readily conformation 1 can be transformed into conformation 2, which is the required conformation for the coordination of metal centres. In high-temperature ^1H NMR experiments (up to 80 °C), a shift of the signals can be observed, but no line-broadening can be seen. This indicates that no change in the conformation takes place within this temperature range.

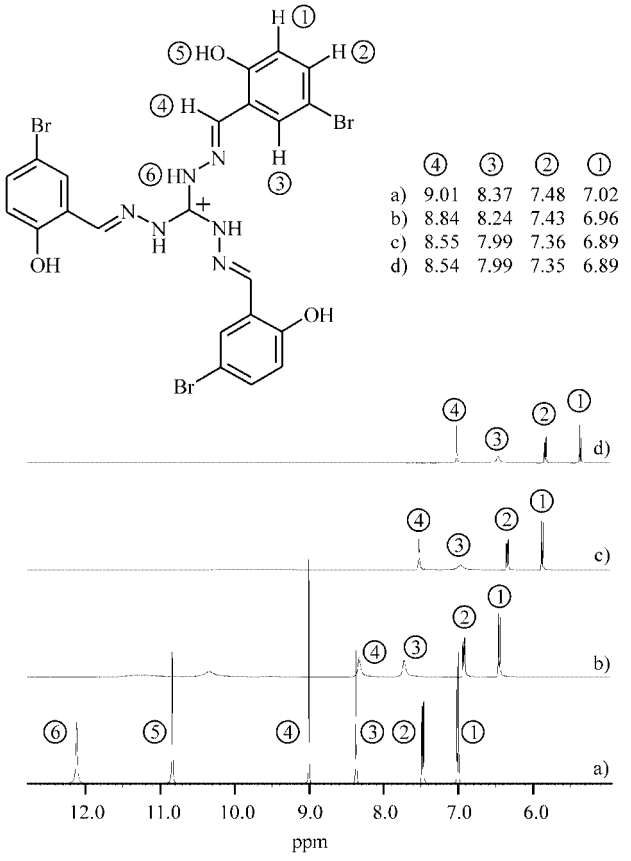

Figure 2. ^1H NMR in $[D_6]$DMSO and chemical shifts in ppm of **1**; a) pure solution; b) + 1 equivalent Et_3N; c) + 3 equivalents Et_3N; d) + 6 equivalents Et_3N

In contrast, the addition of one to six equivalents of base (triethylamine) to a solution of **1** leads to the upfield shift of the signals for H1−H4 and the broadening of the signals for H3 and H4 as depicted in Figure 2 (b−d). This phenomenon can be explained by the transformation of conformation 1 into conformation 2 upon deprotonation, with resulting long-range coupling between the affected protons, whose proximity is confirmed by the observed strengthening of their cross peak in the H,H-NOESY spectrum. In solution a base is able to transform the conformation of **1**, but can a metal ion achieve the same result by metalating its N and O atoms? The reaction of $[H_6Br_3L]Cl$ with neutral $CdCl_2$ in acetone leads, for instance, even at higher temperatures, only to the formation of crystals with the formula $[H_6Br_3L]_2[CdCl_4]$, in which the ligand still adopts conformation 1.[9]

The reaction of **1** with $(NH_4)_6[Mo_7O_{24}]$ as a basic metal salt results in the formation of small, red crystal needles. The X-ray structure shows a complex with the formula $[Mo(O)_2(OH_2)(H_3Br_3L)]\cdot 2DMF$ (**2**), whose asymmetric unit is shown in Figure 3 (a).[10]

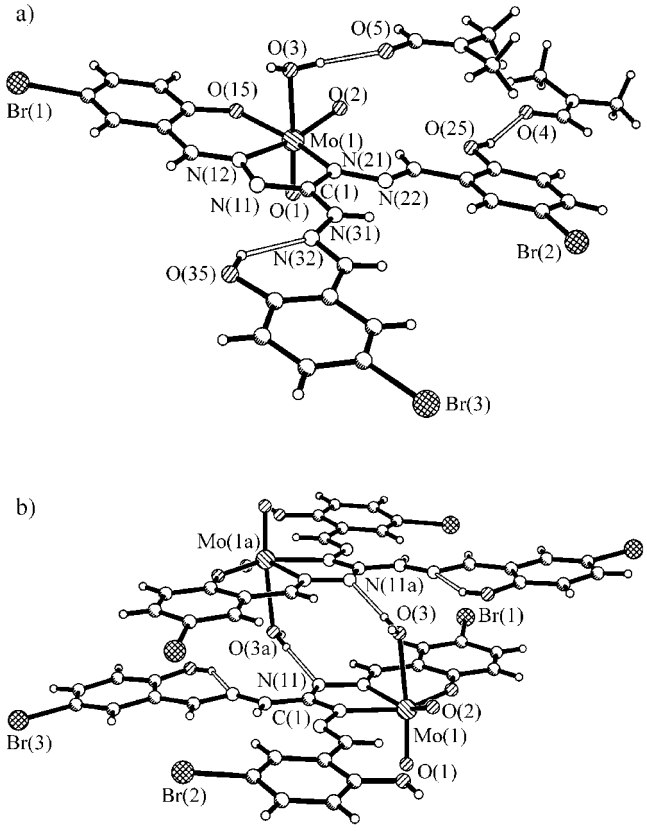

Figure 3. Crystal structure of **2**; a) asymmetric unit; b) hydrogen-bonded dimer

In **2** the ligand is partially deprotonated, and N12, N21 and O15 participate in the Mo(VI) coordination sphere. Two of the three arms of **1** (starting with N11 and N31) are transformed into conformation 2, the third arm (starting with N21) remains in conformation 1 and is stabilized by a strong hydrogen bond with a DMF molecule [*d*(H25···O4) = 1.87 Å, Table 1]. In this complex, $[H_3Br_3L]^{2-}$ coordinates to a Mo(VI) centre with a distorted octahedral geometry. Three of the four equatorial positions are occupied by the ligand, the fourth by a doubly bonded oxygen atom (O2). The two axial coordination sites contain a second oxygen atom (O1) and a water molecule (O3). Due to the relatively rigid geometry of the ligand, the distortion

 © 2005 Wiley-VCH Verlag GmbH & Co. KGaA, Weinheim

Table 2. Selected bond lengths and angles (ϕ = average value, Σ = angle sum, ^{c} = coordinating atom, ^{nc} = noncoordinating atom)

	1a (213 K)	**1b** (213 K)	**2** (100 K)	**3** (100 K)
C−N [Å]	1.327(7)	1.336(2)	N11: 1.323(8) 1.360(8)	1.350(7)
N−N [Å]	1.380(5)	1.389(3)	1.395(7)^{c} 1.362(8)^{nc}	1.390(6)
N=C [Å]	1.279(5)	1.278(3)	1.293(8)^{c} 1.287(8)^{nc}	1.294(6)
C−Br [Å]	1.896(6)	1.906(3)	1.905(7)	1.904(6)
Angle at C1	ϕ 120.4(4)° Σ 360.0°	ϕ 120.0(1)° Σ 360.0°	123.6(6)° ^{c} 118.2(6)° ^{nc} Σ 360.0°	ϕ 120.0(5)° Σ 360.0°
Angle at N1	ϕ 117.6(4)°	ϕ 117.4(2)°	113(2)° − 130.0(5)° Σ 359.7°	110.9(8)° − 135(1)° Σ 356.8°
Angle at N2	ϕ 115.3(4)°	ϕ 115.1(2)°	116(3)° − 128.2(4)° Σ 360.0°	116.0(9)° − 126.2(4)° Σ 359.7°
Angle at O	−	−	138.3(4)°	127.9(7)°
Average deviation from CN_6 plane	± 0.03(2) Å	± 0.19(2) Å	± 0.014(5) Å	± 0.04(1) Å
Torsion angle CN_6 vs. phenyl	1.5° − 22.3°	18.8°	3.5° − 7.1°	9.9° − 31.3°

at the metal centre can clearly be seen at the angles along the N21−Mo1−O15 [152.1(2)°] and N12−Mo1−O2 axes [153.8(2)°, Table 3]. The Mo atom is displaced at a distance of 0.32(1) Å from the O1/N21/O3/O15 equatorial plane towards the doubly bonded oxygen atom (O1). The $[H_3Br_3L]^{2-}$ ligand itself shows no further distortion due to the coordination. The observed bond lengths (Table 2) are within the tolerance of 3σ, similar to those in the isolated $[H_6Br_3L]^{+}$ cation. The propeller-like distortion of the ligand (dihedral angles of 3.5° to 7.1°) in **2** is lower or similar to that in **1a** and **1b**. Due to the chelation, the angles observed in the central part of the ligand in **2** are markedly different from those in **1**.

2 is electronically neutral; the ligand nitrogen N11 is deprotonated and stabilized by a strong hydrogen bond from the coordinated water molecule of a neighbouring complex [*d*(N11···H3b) = 1.89 Å, angle at H3b: 175°). This and a symmetry-related bridge results in the formation of dimers as shown in Figure 3 (b).

The reaction of $[H_6Br_3L]Cl$ with $CuCl_2$, sodium 5,5-diethylbarbiturate (NaH*bar*) and Et_3N at room temperature leads to the formation of dark red-black crystals with the formula $(Et_4N)_2[\{Cu(Hbar)\}_3Br_3L]$ (**3**).[11] The X-ray structure shows that the ligand is now fully deprotonated and coordinated to three Cu(II) centres (Figure 4).

The metal atoms exhibit square-planar coordination spheres, in which three positions are occupied by the ligand, the fourth by a partly deprotonated diethylbarbiturate anion ($Hbar^{-}$). The copper centres show only minor distortions from the idealised coordination geometry, with observed *trans* angles of 168(2)° and 171(5)° (Table 3). The metals lie almost in the ideal plane formed by the ligand, with a deviation of only 0.03(1) Å. Furthermore, the distortion of the ligand is limited despite the fact that it is involved in the coordination with three metal atoms. The bond lengths observed in **3** are similar to those in **1a** and **1b**. Only the first nitrogen atom in each arm is twisted slightly out of plane, which can clearly be seen in the sum of the observed angles (Table 2). The propeller like distor-

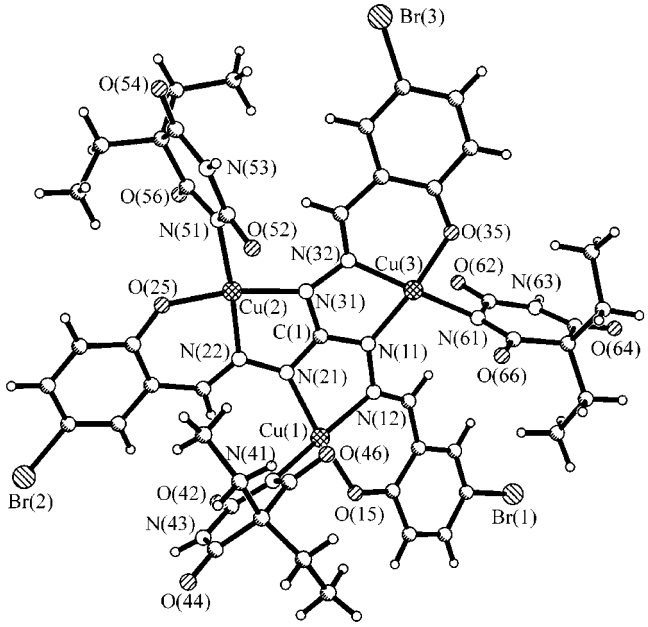

Figure 4. Crystal structure of **3** (countercations omitted for clarity)

Table 3. Bond lengths and angles at the metal centres in **2** and **3**

	2 (100 K)	**3** (100 K)
M−N(1)	2.115(5) Å	1.98(1) Å
M−N(2)	2.235(5) Å	1.959(6) Å
M−O	1.933(4) Å	1.906(5) Å
M−L′(eq)	1.717(4) Å	−
M−L′′(ax)	1.701(5) Å (=O) 2.325(5) Å ($-OH_2$)	−
N(1)−M−N(2)	71.2(2)°	79.4(4)°
N(2)−M−O	82.1(2)°	92.3(4)°
N(1)−M−O	152.1(2)°	168(2)°
N(2)−M−L′(eq)	153.8(2)°	171(5)°
L′′(ax)−M−L′′(ax)	173.1(2)°	−

 © 2005 Wiley-VCH Verlag GmbH & Co. KGaA, Weinheim

tion as gauged by its dihedral angle of 31.3° is significantly more pronounced for one of the phenyl groups than in previously reported compounds. The other two angles are 9.9° and 13.2°. This once again emphasises the high degree of flexibility of the $[Br_3L]^{5-}$ ligand. The H*bar*$^-$ ligands in **3** are still protonated at the second nitrogen atom. Two of the three *bar* ligands form hydrogen bonds with the carbonyl oxygen atom of an adjacent H*bar*$^-$ ligand (Figure 5, a), the third shows a close contact to a neighbouring acetonitrile molecule (Table 1). This results in the formation of the infinite chains depicted in Figure 5, b.

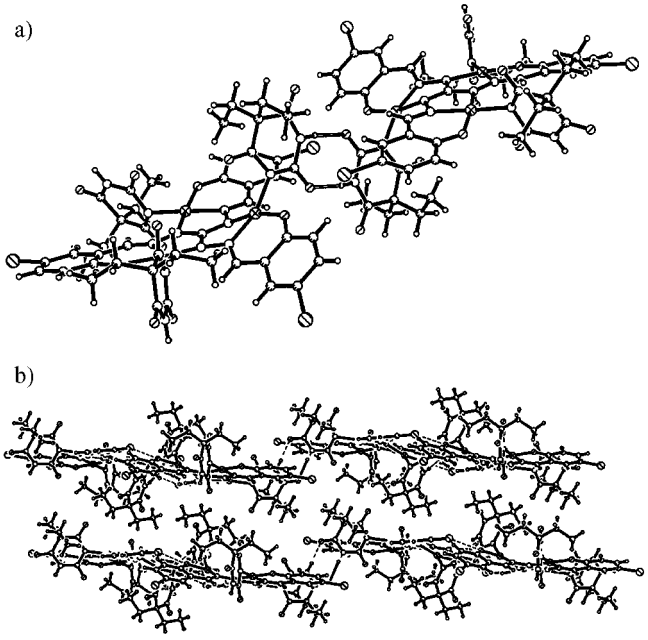

Figure 5. Packing diagram of **3** (countercations omitted for clarity); a) hydrogen-bonded dimer; b) stacking of two chains

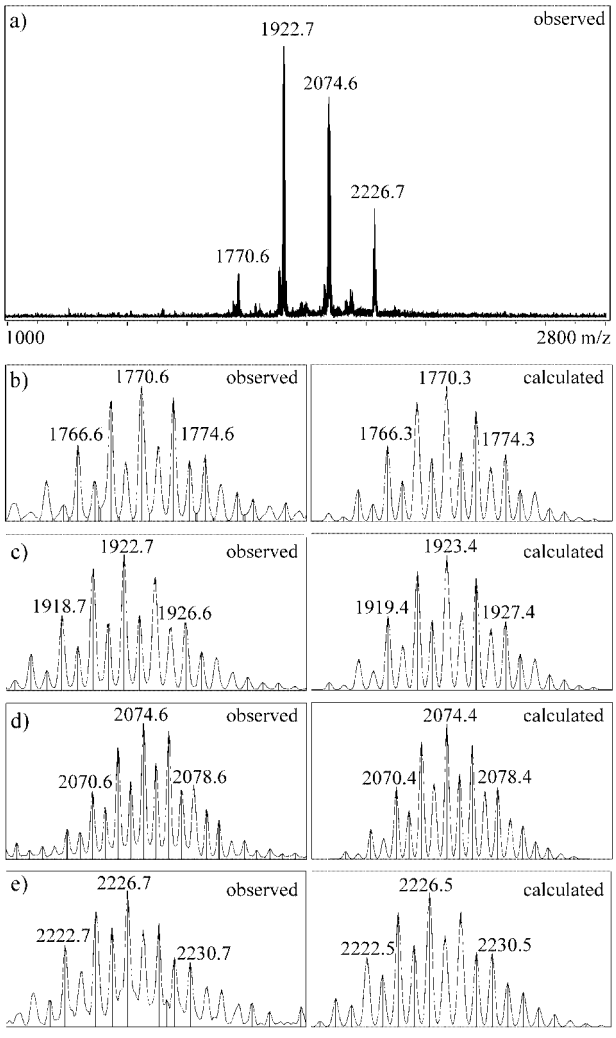

Figure 6. a) ESI mass spectrum for **3** in MeOH; b)−e) observed and calculated isotope pattern for the peaks observed in a).

The structure of **3** demonstrates that it is possible to bind three ligands, with a steric demand as high as that of H*bar*$^-$, to a M_3Br_3L unit. This is an important requirement when employing $[M_3Br_3L]^{3n-5}$ units for the construction of coordination polymers and cages. In fact, in the ESI mass spectrum of **3** in methanol, the only observed molecular ions can be explained by the formation of a dimeric species (Figure 6, a). Two $[Cu_3Br_3L]^+$ units are bridged by three monoanionic coligands: three OCH_3^-, $[C_{47}H_{33}N_{12}O_9Cu_6Br_6]^-$ (Figure 6, b); two CH_3O^-, one H*bar*$^-$, $[C_{54}H_{42}N_{14}O_{11}Cu_6Br_6]^-$ (Figure 6, c); one CH_3O^-, two H*bar*$^-$, $[C_{61}H_{49}N_{16}O_{13}Cu_6Br_6]^-$ (Figure 6, d); three H*bar*$^-$, $[C_{68}H_{57}N_{18}O_{15}Cu_6Br_6]^-$ (Figure 6, e).

In summary, we are able to show that $[H_6Br_3L]^+$ should be a suitable C_3-symmetric ligand for the formation of coordination cages and polymers. The free coordination sites at the metal centres bound by $[Br_3L]^{5-}$ can be occupied by a coligand with high steric demands, without the distortion of the $[M_3Br_3L]^{3n-5}$ unit or the C_3 symmetry. In the solid state, $[H_6Br_3L]^+$ adopts a conformation that is disadvantageous for the coordination of metal centres. Deprotonation by adding a base enables the transformation into the more favourable conformation. In this way, the reaction with metal ions can easily be controlled.

Experimental Section

Triaminoguanidinium chloride was prepared by literature methods.[12] 5-Bromosalicylaldehyde and sodium 5,5-diethylbarbiturate were purchased and used without further purification.

$[C_{22}H_{18}N_6O_3Br_3]Cl$ (1): Triaminoguanidinium chloride (4.681 g, 33.3 mmol) was dissolved in a hot mixture of H_2O (50 mL) and ethanol (100 mL). A solution of 5-bromosalicylaldehyde (20.0392 g, 99.7 mmol) in ethanol (140 mL) was slowly added. The resulting suspension was cooled to room temperature. **1** was crystallised from acetone (400 mL). Yield: 22.2691 g (32.3 mmol, 97%). $C_{22}H_{18}Br_3ClN_6O_3$ (689.58), calcd. values are given in parentheses, based on M + 1 H_2O: C 37.42 (37.34), H 2.57 (2.85), N 11.77 (11.88). ^{1}H NMR (400 MHz, [D$_6$]DMSO, 25 °C): δ = 12.12 (s, 1 H, NH), 10.83 (s, 1 H, OH), 9.01 (s, 1 H, N=CH−), 8.37 [s(d), ^4J = 2.52 Hz, 1 H, C(6)−H], 7.48 [d(d), ^3J = 9.04, ^4J = 2.52 Hz, 1 H, C(4)−H], 7.01 [d, ^3J = 9.04 Hz, 1 H, C(3)−H] ppm. ^{13}C

 © 2005 Wiley-VCH Verlag GmbH & Co. KGaA, Weinheim

NMR (100 MHz, [D$_6$]DMSO, 25°C): δ = 156.38 (C2), 148.79 (C$^+$), 145.92 (C=N), 135.70 (C4), 128.70 (C6), 121.55 (C1), 118.50 (C3), 110.95 (C5) ppm. Crystals suitable for X-ray crystallography were grown by slow diffusion of HCl gas into a solution of **1** in water with Et_3N (pH 8−9, resulting in **1a**) or into a solution of **1** in DMF (resulting in **1b**).

[Mo(O)$_2$(OH$_2$)(C$_{22}$H$_{15}$N$_6$O$_3$Br$_3$)]·2(C$_3$H$_7$NO) (2): Solutions of tris(5-bromo-2-hydroxybenzylidene)triamminoguanidinium chloride (69.2 mg, 0.1 mmol) and ammonium heptamolybdate tetrahydrate (52.0 mg, 0.042 mmol) in DMF (1 mL each) were mixed. Water (1 mL) was added. Red crystals of **2** were formed after a couple of days. Yield: 28.0 mg (0.0297 mmol, 30%). $C_{28}H_{31}Br_3MoN_8O_8$ (943.3), calcd. values are given in parentheses, based on M + 1 H_2O: C 35.27 (34.99), H 3.68 (3.46), N 11.53 (11.66). ^{1}H NMR (400 MHz, [D$_6$]acetone, 25°C): δ = 11.67 (s, 1 H, N−H), 10.40 (s, 1 H, O−H), 9.69 (s, 1 H, O−H), 8.72 (s, 1 H, N=C−H), 8.54 (s, 1 H, N=C−H), 8.41 (s, 1 H, N=C−H), 7.84 [s(d), ^4J = 2.48 Hz, 1 H, C(6)−H], 7.52 [d(d), ^3J = 8.52, ^4J = 2.52 Hz, 1 H, C(4)−H], 7.51 [s(d), ^4J = 2.52 Hz, 1 H, C(6)−H], 7.36 [d(d), ^3J = 8.52, ^4J = 2.48 Hz, 1 H, C(4)−H], 7.35 [s(d), ^4J = 2.48 Hz, 1 H, C(6)−H], 7.34 [d(d), ^3J = 9.04, ^4J = 2.48 Hz, 1 H, C(4)−H], 6.90 [d, ^3J = 8.52 Hz, 1 H, C(3)−H], 6.88 [d, ^3J = 9.04 Hz, 1 H, C(3)−H], 6.83 [d, ^3J = 8.52 Hz, 1 H, C(3)−H] ppm.

[(C$_2$H$_5$)$_4$N]$_2$[{Cu(C$_8$H$_{11}$N$_2$O$_3$)}$_3$C$_{22}$H$_{12}$N$_6$O$_3$Br$_3$] (3): Tris(5-bromo-2-hydroxybenzylidene)triaminoguanidinium chloride (34.6 mg, 0.05 mmol), copper(II) chloride (20.24 mg, 0.15 mmol), sodium 5,5-diethylbarbiturate (20.9 mg, 0.10 mmol) and tetraethylammonium chloride (14.5 mg, 0.088 mmol) were dissolved in acetonitrile (2 mL) and triethylamine (1 mL). More triethylamine (1 mL) was slowly diffused into the reaction mixture. After three weeks dark red−black crystals of **2** were formed. Yield: 36.0 mg (0.022 mmol, 65.5%). $C_{62}H_{85}Br_3Cu_3N_{14}O_{12}$ (1648.78), calcd. values are given in parentheses, based on M + 2 CH_3CN + 2 H_2O: C 44.75 (44.86), H 5.10 (5.42), N 12.66 (12.68), Cu 11.2 (10.8).

X-ray Analysis: Intensity data for **1a** and **1b** were collected with an AXS Smart/CCD diffractometer (Mo-K_α radiation) and for **2** and **3** with a Nonius Kappa CCD (Mo-K_α rotating anode) always employing the ω scan method. All data were corrected for Lorentz and polarisation effects. Absorption corrections were performed for **1a** and **1b** by SADABS and for **2** and **3** by the Gauss method. **1a**−**3** were solved by using direct methods (SHELXS-97)[13] and refined by using a full-matrix least-squares refinement procedure (SHELXL-97).[14] The protons were placed at geometrically estimated positions. CCDC-241614 to -241617 contain the supplementary crystallographic data for this paper. These data can be obtained free of charge at www.ccdc.cam.ac.uk/conts/retrieving.html [or from the Cambridge Crystallographic Data Centre, 12 Union Road, Cambridge CB2 1EZ, UK; Fax: (internat.) +44-1223-336-033; E-mail: deposit@ccdc.cam.ac.uk].

Acknowledgments

The authors would like to thank Manuela Winter (Anorganische Chemie II, Ruhr-Universität Bochum) for the data collection of **1a** and **1b**, Heike Schucht (Max Planck Institut für Bioanorganische Chemie, Mülheim) for the data collection of **2** and **3** and Robert Schoenen (Anorganische Chemie I, Ruhr-Universität Bochum) for the ESI spectrum.

[1] [1a] S. Kitagawa, R. Kitaura, S. Noro, *Angew. Chem.* **2004**, *116*, 2388−2430, *Angew. Chem. Int. Ed.* **2004**, *43*, 2334−2375. [1b] C. Janiak, *J. Chem. Soc., Dalton Trans.* **2003**, 2781−2804. [1c] B. Moulton, M. J. Zaworotko, *Chem. Rev.* **2001**, *101*, 1629−1658. [1d] S. R. Batten, *CrystEngComm* **2001**, *18*, 1−7. [1e] M. J. Zaworotko, *Angew. Chem.* **2000**, *112*, 3180−3182, *Angew. Chem. Int. Ed.* **2000**, *39*, 3052−3054. [1f] R. Robson, *J. Chem. Soc., Dalton Trans.* **2000**, 3735−3744.

[2] [2a] R. W. Saalfrank, B. Demleitner, H. Glaser, H. Maid, S. Reihs, W. Bauer, M. Maluenga, F. Hampel, M. Teichert, H. Krautscheid, *Eur. J. Inorg. Chem.* **2003**, 822−829. [2b] G. F. Swiegers, T. J. Malefetse, *Coord. Chem. Rev.* **2002**, *225*, 91−121. [2c] D. L. Caulder, C. Brückner, R. E. Powers, S. König, T. N. Parac, J. A. Leary, K. N. Raymond, *J. Am. Chem. Soc.* **2001**, *123*, 8923−8938. [2d] M. Fujita, K. Umemoto, M. Yoshizawa, N. Fujita, T. Kusukawa, K. Biradha, *J. Chem. Soc., Chem. Commun.* **2001**, 509−518. [2e] G. F. Swiegers, T. J. Malefetse, *Chem. Rev.* **2000**, *100*, 3483−3537. [2f] S. Leininger, B. Olenyuk, P. J. Stang, *Chem. Rev.* **2000**, *100*, 853−908. [2g] L. R. MacGillivray, J. L. Atwood, *Angew. Chem.* **1999**, *111*, 1080−1096, *Angew. Chem. Int. Ed.* **1999**, *38*, 1018−1033. [2h] D. L. Caulder, K. N. Raymond, *J. Chem. Soc., Dalton Trans.* **1999**, 1185−1200. [2i] D. L. Caulder, K. N. Raymond, *Acc. Chem. Res.* **1999**, *32*, 975−982.

[3] [3a] S. R. Foley, G. P. A. Yap, D. S. Richeson, *Inorg. Chem.* **2002**, *41*, 4149−4157. [3b] P. J. Bailey, K. J. Grant, L. A. Mitchell, S. Pace, A. Parkin, S. Parsons, *J. Chem. Soc., Dalton Trans.* **2000**, 1887−1891. [3c] N. Thirupathi, G. P. A. Yap, D. S. Richeson, *J. Chem. Soc., Chem. Commun.* **1999**, 2483−2484. [3d] G. R. Giesbrecht, A. Shafir, J. Arnold, *J. Chem. Soc., Dalton Trans.* **1999**, 3601−3604. [3e] T. Chivers, M. Parvez, G. Schatte, *J. Organomet. Chem.* **1998**, *550*, 213−220. [3f] P. J. Bailey, R. O. Gould, C. N. Harmer, S. Pace, A. Steiner, D. S. Wright, *J. Chem. Soc., Chem. Commun.* **1997**, 1161−1162. [3g] P. J. Bailey, L. A. Mitchell, P. R. Raithby, M.-A. Rennie, K. Verhorevoort, D. S. Wright, *J. Chem. Soc., Chem. Commun.* **1996**, 1351−1352. [3h] P. J. Bailey, A. J. Blake, M. Kryszczuk, S. Parsons, D. Reed, *J. Chem. Soc., Chem. Commun.* **1995**, 1647−1648.

[4] I. M. Müller, R. Robson, *Angew. Chem.* **2000**, *112*, 4527−4530, *Angew. Chem. Int. Ed.* **2000**, *39*, 4357−4359.

[5] I. M. Müller, S. Spillmann, H. Franck, R. Pietschnig, *Chem. Eur. J.* **2004**, *10*, 2207−2213.

[6] I. M. Müller, R. Robson, F. Separovic, *Angew. Chem.* **2001**, *113*, 4519−4520, *Angew. Chem. Int. Ed.* **2001**, *40*, 4385−4386.

[7] **1a**: 0.12 × 0.20 × 0.22 mm^3, triclinic, $P\bar{1}$, a = 7.488(2) Å, b = 12.889(3) Å, c = 14.489(3) Å, α = 109.735(5)°, β = 102.471(5)°, γ = 96.972(5)°, V = 1256.1(4) Å^3, $\rho_{calcd.}$ = 1.871 g·cm^{-3}, $2\theta_{max.}$ = 50.16°, λ = 0.71073 Å, T = 213 K, 7057 measured reflections, 4334 independent reflections (R_{int} = 0.0308), 3133 observed reflections ($I > 2\sigma(I)$), μ = 4.966 mm^{-1}, empirical absorption correction, $T_{min.}$ = 0.383, $T_{max.}$ = 0.551, 325 parameters, $R_1(I > 2\sigma(I))$ = 0.0396, wR_2 (all data) = 0.0986, max./min. residual electron density 0.652/−0.737 e·Å^{-3}.

[8] **1b**: 0.27 × 0.51 × 0.51 mm^3, trigonal, $R\bar{3}$, a = 15.576(2) Å, b = 15.576(2) Å, c = 28.452(5) Å, V = 5978(1) Å^3, $\rho_{calcd.}$ = 1.515 g·cm^{-3}, $2\theta_{max.}$ = 58.14°, λ = 0.71073 Å, T = 213 K, 4419 measured reflections, 3107 independent reflections (R_{int} = 0.0772), 2290 observed reflections ($I > 2\sigma(I)$), μ = 3.155 mm^{-1}, empirical absorption correction, $T_{min.}$ = 0.221, $T_{max.}$ = 0.429, 156 parameters, $R_1(I > 2\sigma(I))$ = 0.0486, wR_2(all data) = 0.1440, max./min. residual electron density 0.563/−0.907 e·Å^{-3}.

[9] I. M. Müller, D. Möller, C. Schalley, *Angew. Chem.*, in press.

[10] **2**: 0.015 × 0.035 × 0.13 mm^3, triclinic, $P\bar{1}$, a = 9.7149(5) Å, b = 13.1846(6) Å, c = 15.0352(7) Å, α = 71.394(2)°, β = 82.217(2)°, γ = 71.008(2)°, V = 1724.7(1) Å^3, $\rho_{calcd.}$ = 1.816 g·cm^{-3}, $2\theta_{max.}$ = 56.82°, λ = 0.71073 Å, T = 100 K, 14140 measured reflections, 8219 independent reflections (R_{int} = 0.0659), 4923 observed reflections ($I > 2\sigma(I)$), μ = 3.915

 © 2005 Wiley-VCH Verlag GmbH & Co. KGaA, Weinheim

mm^{-1}, numerical absorption correction, $T_{min.} = 0.630$, $T_{max.} = 0.944$, 444 parameters, $R_1(I > 2\sigma(I)) = 0.0695$, wR_2(all data) = 0.1377, max./min. residual electron density 1.141/−0.728 e·Å^{-3}.

[11] **3**: 0.03 × 0.04 × 0.20 mm^3, triclinic, $P\bar{1}$, $a = 9.683(2)$ Å, $b = 17.576(4)$ Å, $c = 23.238(5)$ Å, $\alpha = 82.83(3)°$, $\beta = 81.41(3)°$, $\gamma = 81.66(3)°$, $V = 3847(1)$ Å^3, $\rho_{calcd.} = 1.530$ g·cm^{-3}, $2\theta_{max.} = 50.50°$, $\lambda = 0.71073$ Å, $T = 100$ K, 44104 measured reflections, 13909 independent reflections ($R_{int} = 0.0978$), 8964 observed reflections ($I > 2\sigma(I)$), $\mu = 2.449$ mm^{-1}, numerical absorption correction, $T_{min.} = 0.748$, $T_{max.} = 0.937$, 1022 parameters, $R_1(I > 2\sigma(I)) = 0.0613$, wR_2(all data) = 0.1166, max./min. residual electron density 0.679/−0.752 eÅ^{-3}.

[12] S. Weiss, H. Krommer (SKW Trostberg AG, Germany) DE 83−3341645 [*Chem. Abstr.* **1986**, *104*, 206730].

[13] G. M. Sheldrick, SHELXS-97, *Program for Crystal Structure Solution*, University of Göttingen, **1997**.

[14] G. M. Sheldrick, SHELXL-97, *Program for Crystal Structure Refinement*, University of Göttingen, **1997**.

Received June 16, 2004
Early View Article
Published Online October 1, 2004

 © 2005 Wiley-VCH Verlag GmbH & Co. KGaA, Weinheim

Directed Synthesis of a 1D Double-Chain Polyoxometalate Assembly: $\{[Ag_2(bppy)_3][Ag(bppy)_2][Ag(bppy)]_2PW_{11}Co(bppy)O_{39}\}\cdot 2H_2O$

Zhangang Han,[a] Yulong Zhao,[a] Jun Peng,*[a] Huiyuan Ma,[a] Qun Liu,[a] Enbo Wang,[a] Ninghai Hu,[b] and Hengqing Jia[b]

Keywords: Polyoxometalates / N ligands / Silver / Organic-inorganic hybrids / Supramolecular chemistry

A 1D double-chain assembly based on the monosubstituted Keggin polyoxometalate (POM) with pendant ligands and of formula $\{[Ag_2(bppy)_3][Ag(bppy)_2][Ag(bppy)]_2PW_{11}Co(bppy)O_{39}\}\cdot 2H_2O$ (**1**) [bppy = 5-(4-bromophenyl)-2-(4-pyridinyl)pyridine] has been synthesised and characterised. The crystals of **1** belong to the space group $P\bar{1}$, $Mr = 5801.06$, $a = 18.720(4)$ Å, $b = 19.474(4)$ Å, $c = 19.815(4)$ Å, $\alpha = 96.30(3)$, $\beta = 96.07(3)$, $\gamma = 90.12(3)°$, $V = 7139(2)$ Å^3, $Z = 2$, $D_{calcd.} = 2.699$ Mg·m^{-3}. The final statistics based on F^2 are $GOF = 1.007$, $R_1 = 0.0620$ and $wR_2 = 0.1346$ for $I > 2\sigma(I)$. X-ray diffraction analysis revealed that the structure of **1** contains a 1D chain constructed from a monosubstituted tungstophosphate with one pendant conjugated ligand, five silver–bppy groups and two water molecules. The periphery of the Keggin cluster consists of five Ag–bppy groups so that a bicapped trisupporting Keggin structure is obtained. It is rare that a Keggin anion cluster is simultaneously coordinated to five transition metal atoms.

(© Wiley-VCH Verlag GmbH & Co. KGaA, 69451 Weinheim, Germany, 2005)

Introduction

The construction of various intriguing molecular frameworks based on inorganic polyoxometalates (POMs) and organic species with delocalised π systems is of significant contemporary interest owing to their interesting electrical and optical properties such as electrochromism, photochromism, conductivity and redox activity.[1−11] In recent years, research in this field has focused on functionalisation and immobilisation of POMs.[12−20] In addition, conjugated organic molecules and polymers are electrically active organic materials.[21] Thus, these hybrids should offer the potential for broadening the application of POMs in the field of material science.

Despite the deficient charge density on the surface oxygen atoms of many Keggin- and Dawson-type POMs, these oxygen atoms may nevertheless still be involved in more distant bonding with other cations. According to a basic concept, as the charge density on the surface oxygen atoms of the POM increases there should appear a significant affinity for the polyoxoanions to coordinate to transition metal complex cations. A frequent and effective method for obtaining such highly negative polyoxoanions is to substitute the six valent metal centres of W^{VI} and Mo^{VI} with lower valent metal atoms such as V^V and Nb^V. However, we noticed that the number of transition metal complexes supported by these kinds of POMs rarely exceeds two.[22−24] We previously reported a polyoxoanion coordinated to four transition metal complex moieties, i.e. $\{PW_9V_3O_{40}[Ag(2,2'\text{-bipy})]_2[Ag_2(2,2'\text{-bipy})_3]_2\}$ which contains a discrete, neutral molecular unit.[25]

In our ongoing efforts to develop synthetic and functional analogues of large inorganic clusters, we have explored an approach to the synthesis of POMs with covalently bonded pendant ligands which, as mentioned in our prior study on the interactions of adenosine triphosphate (ATP) and adenosine monophosphate (AMP) with 3d transition metal complexes in the presence of the monovacant polyoxotungstate anion α-$[SiW_{11}O_{39}]^{8-}$, leads to metal-substituted tungstosilicates and simultaneously increases the charge density on the surface oxygen atoms of POMs.[26−27] The strategy is to cross-link the inorganic clusters and to anchor the clusters via terminal ligand-support linkages and perhaps through H-bonding interactions thereby avoiding structural collapse.

Recently, the secondary metal coordination groups (SMGs) have been widely used to put POM clusters into high dimensional framework structures which has proved helpful in directing the formation of a given structure.[28−30] Hence, the synthetic strategy here starts firstly by generating a metal-substituted Keggin POM with a pendant-conjugated organic ligand as a building block. A suitable SMG as a connector must then be found in order to assemble the

[a] Faculty of Chemistry, Northeast Normal University, Changchun, 130024, P. R. China
E-mail: jpeng@nenu.edu.cn
[b] Changchun Institute of Applied Chemistry, Chinese Academy of Sciences, Changchun, 130022, P. R. China
Supporting information for this article is available on the WWW under http://www.eurjic.org or from the author.

 © 2005 Wiley-VCH Verlag GmbH & Co. KGaA, Weinheim **DOI: 10.1002/ejic.200400471**

inorganic clusters into a high-dimensional network. Through this route, directed synthesis of a 1D double chain complex $\{[Ag_2(bppy)_3][Ag(bppy)_2][Ag(bppy)]_2PW_{11}Co(bppy)O_{39}\}\cdot 2H_2O$ (**1**) [bppy = 5-(4-bromophenyl)-2-(4-pyridinyl)pyridine] has been obtained. Compound **1** contains a chain structure constructed from a monosubstituted tungstophosphate with one pendant conjugated ligand, five silver-bppy groups and two water molecules. To the best of our knowledge, it is rare to observe a Keggin anion cluster simultaneously coordinated to five metal atoms, let alone extended into a 1D array.

Results and Discussion

Organic Ligand and Silver(I): Combining known transition-metal coordination environments with multifunctional multidentate ligands can generate interesting crystallographic architectures with implications for the rational design of functional solids. Linear bifunctional "spacer" or "rod" ligands have been used to propagate a number of motifs.[33−35] In this experiment, we chose bppy (see Scheme 1) as the organic ligand based on the following considerations: (i) One terminal N site in this molecule is advantageous for forming polyoxometalate complexes with pendant ligands. The middle N atom and the terminal Br atom are potential coordination sites which may help to extend the linkage into an unprecedented high-dimensional structure. (ii) The length of the linear molecule bppy (ca.13.2 Å) is sufficient to overcome the disadvantage of the repulsion of adjacent polyanions.

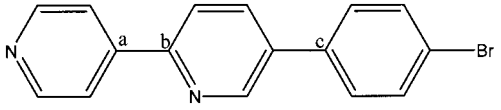

Scheme 1. The molecular structure of the organic ligand bppy; the angle $a-b\cdots c$ is ca. 180°, the length $N_t\cdots Br$ is ca.13.2 Å (N_t = terminal N)

Silver(I) exists in the following possible coordination environments: linear, T-shaped and tetrahedral. In its complexes, silver also displays an ability to coordinate readily to both hard and soft donor centers.[36−40] Considering that the coordination positions of two N atoms in a bppy ligand are similar to those in 2,4′-bipyridine, we anticipated that treatment of Ag with bppy would afford linear, T-shaped or diamond shaped structural subunits with the potential to link POMs into high-dimensional crystallographic architectures.

Synthesis: Compound **1** was synthesised by hydrothermal methods. The pH of the solution plays an important role in the isolation of phases of a given composition and structure. The starting material H_3PO_4 not only plays a central atom role but also adjusts the pH of the reaction mixture. When the pH value is beyond the range of 4.5−4.9 (values prone to the formation of mono-vacant polyoxometalates) the isolation of **1** was unsuccessful affording only amorphous powders. During the course of our reiterative experiments, a yellow crystalline phase besides compound **1** was observed when the reaction was allowed to proceed for three days but this disappeared upon prolonging the reaction time to four days. The material was identified as a salt of $[PW_{12}O_{40}]^{3-}$ by its IR spectrum (see Supporting information Figure S1(b); For Supporting Information see also the footnote on the first page of this article). This may indicate that $[PW_{12}O_{40}]^{3-}$ may initially form and then change to other species, e.g. compound **1**. The mechanism needs to be studied further.

Structure Description: Single-crystal X-ray diffraction analysis revealed that **1** consists of $\{[Ag(bppy)_2][Ag(bppy)]_2PW_{11}Co(bppy)O_{39}\}$ clusters linked by $Ag_2(bppy)_3$ units into an infinite 1D arrangement along the direction of the *a* axis (see Figure 1). The periphery of the Keggin cluster consists of five Ag-bppy groups and a bicapped tri-supporting Keggin structure is thus obtained (see Figure 2). Two adjacent chains form a double-stranded structure via Ag−Br linkages which further extends into a 3D framework via hydrogen bonding and π-π stacking interactions.

The monosubstituted tungstophosphate anion contains a paramagnetic Co^{II} centre covalently linked by a rigid, π-conjugated organic ligand on a peripheral octahedral site of the Keggin core. The P−O bond lengths range from 1.525(8) to 1.534(9) Å. The W−O_d (O_d = terminal oxygen) bonds are in the usual range of 1.669(11)−1.737(8) Å. All W−W distances are nearly equal, ranging from 3.412 to 3.488 Å (mean value: 3.440 Å) in each triplet except for the triplet substituted with a Co atom [W(1)−W(9): 3.382 Å]. The octahedral coordination Co is defined by one quadruple (bridging) oxygen atom (O_q), four triply bridging oxygens and one terminal N atom from the bppy ligand with the following bond lengths: Co(1)−O(25): 2.018(9), Co(1)−O(35): 2.049(8), Co(1)−O(13): 2.056(9), Co(1)−O(38): 2.087(10), Co(1)−O(3): 2.310(8) and Co(1)−N(1): 2.081(11) Å. The distance P(1)−O(3) is the longest of all the P−O bonds, whereas the distance Co(1)−O(3) is the shortest of all M−O_q linkages (M = W or Co). The most unusual structural feature of compound **1** is that nine surface bridging oxygen atoms of the Keggin anion $[PW_{11}O_{39}Co(bppy)]^{5-}$ are coordinated to five silver-bppy complex cations. To the best of our knowledge, such types of monosubstituted Keggin anions simultaneously supporting so many transition metal complexes has not been reported.

Another remarkable aspect of **1** is that the five silver atoms have different coordination environments: four-coordinate Ag(1) and Ag(2) and three-coordinate Ag(3), Ag(4) and Ag(5). The Ag(1) and Ag(2) atoms are defined by one terminal nitrogen atom of the bppy ligand and three bridging oxygen atoms of the pseudo-Keggin anion, respectively. The distances Ag(1)−O(15), Ag(1)−O(23), Ag(1)−O(21) are 2.402(8), 2.520(9) and 2.603(8) Å, respectively, while the distance Ag(1)−N(3) is 2.152(16) Å. The Ag(2) atom lies in the opposite position to Ag(1) in the POM cluster with the bond lengths of 2.337(8), 2.526(9), 2.684(47) and 2.181(13)

 © 2005 Wiley-VCH Verlag GmbH & Co. KGaA, Weinheim

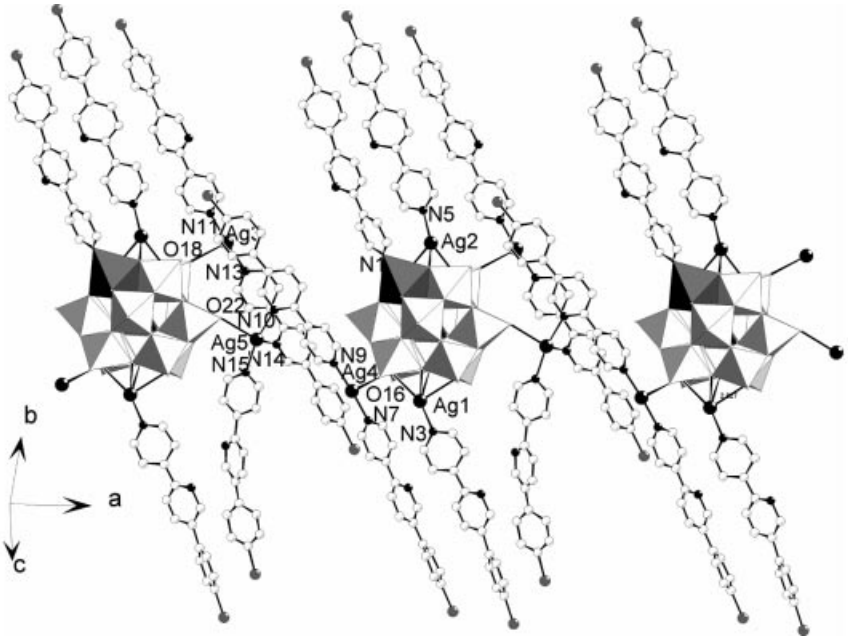

Figure 1. Polyhedral representation of the 1D chain structure of **1**; dark octahedra: {$Co^{II}O_4N$}; light octahedra: {$W^{VI}O_6$} and {PO_4}

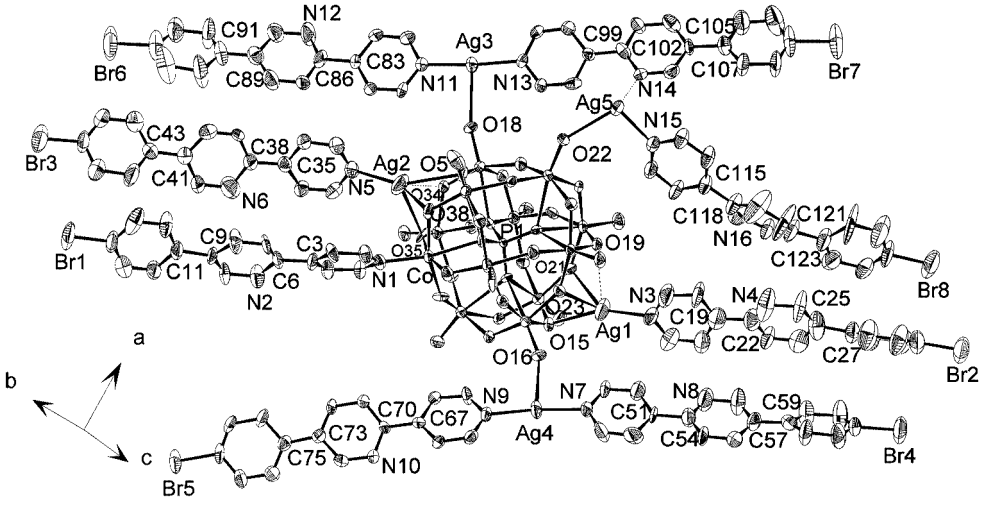

Figure 2. ORTEP view of the building block unit of the 1D chain of **1** showing the linkage mode of the polyanion and the silver-bppy fragments; ellipsoids are drawn at the 50% probability level

Å for Ag(2)−O(38), Ag(2)−O(35), Ag(2)−O(5) and Ag(2)−N(5), respectively. The proximity of the fourth oxygen atom O(19) to Ag(1), [Ag(1)−O(19): 2.823(41) Å] (the sum of the van der Waals radii of Ag and O is 3.20 Å),[41] implies a weak binding and leads to the coordination geometry around Ag(1) being a distorted square pyramid. Similarly, there is a weak interaction between Ag(2) and O(34) with a distance of 3.015(34) Å. The significant variation in the Ag(1) and Ag(2) − oxygen bond lengths may be due to the effect of the coordination environment described below. Ag(1) and Ag(2) cover two opposite faces of the polyanion to form a bicapped α-Keggin-type structure. As is known, in fully oxidised POMs (all W or Mo atoms in the VI oxidation state), terminal oxygen atoms are weakly basic and nonreactive. However, in compound **1**, three terminal oxygen atoms O(18), O(16) and O(22) further extend their linkages via Ag−bppy groups with distances of 2.627(32) Å for Ag(3)−O(18), 2.665(38) Å for Ag(4)−O(16) and 2.644(38) Å for Ag(5)−O(22). For the three-coordinate "T-shaped" Ag(3), Ag(4) and Ag(5) atoms, the other two coordination sites are occupied by N atoms from two bppy ligands with Ag−N distances in the range of 2.116(11)−2.227(12) Å. The bond angles are 175.0(4)°for N(11)−Ag(3)−N(13), 173.2(5)° for N(9)−Ag(4)−N(7) and 166.3(4)° for N(15)−Ag(5)−N(10). A longer distance of 2.839(51) Å between Ag(5) and a N donor atom of another bppy ligand is beyond the usual limits of covalent bonding and may be considered as a weak interaction. Therefore, the Ag(5) atom exhibits a coordination environment which is intermediate between "T-shaped' and tetragonal. Ag(4)

 © 2005 Wiley-VCH Verlag GmbH & Co. KGaA, Weinheim

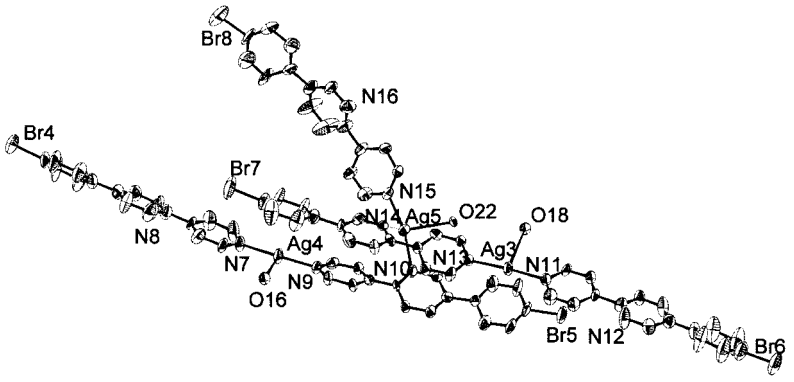

Figure 3. Coordination environments of the Ag(3), Ag(4) and Ag(5) atoms in **1**

and Ag(5) share three bppy molecules to form $[Ag_2(bppy)_3]^{2+}$ which connects adjacent polyanion clusters via Ag−O linkages into a chain structure (see Figure 3). Compound **1** shows that the charge deficient monosubstituted tungstophosphate is capable of bonding with transition metal complexes to form a high-dimensional structure. Compound **1** also shows the flexible coordination mode of silver(I) and provides a good prototype between polyoxoanions with surface-bound inorganic moieties and actually extended polyoxoanion-coordination compound assemblies.

In the crystal structure of **1**, an additional noteworthy fact is that the Br(8) atom lies significantly within the coordination sphere of Ag(1) at a distance of 3.179(51) Å in terms of the sum of the van der Waals radii (1.72 Å for Ag and 1.85 Å for Br).[42] Severe bending of the originally linear bppy containing Br(8) also reflects this interaction with a C(115)−C(118)···C(123) angle of 167.54° and a N(15)···Br(8) length of 12.95 Å (see Figure 2). Thus, taking the Ag(1)−Br(8) into account, a double-strand ladder structure is formed (see Figure 4). Additionally, the distance Ag(2)···Br(1) of 3.726(58) Å, which is beyond the sum of the van der Waals radii of Ag and Br, is too long to be considered as a significant interaction. For comparison, the ligand containing Br(1) is almost linear with the C3−C6···C11 angle being 176.73° and the N(1)···Br(1) length being 13.21 Å. These different interactions between Ag and Br may explain the above mentioned differences of the Ag(1) and Ag(2) − oxygen bond lengths. The two adjacent silver-silver distances of Ag(3)···Ag(3): 3.849(40) Å and Ag(4)···Ag(4): 3.598(34) Å are longer than the van der Waals contact distance (3.44 Å) of silver.[42] As shown in Figure 5, there are significant π-stacking interactions of ligands linked to Ag(3) or Ag(4) (the centre-to-centre and interplane distances are 3.849 and 3.598 Å, respectively.) which implies the formation of a 3D structure in compound **1**. However, ligand packing effects are not responsible for the pairing as is demonstrated by the crystal structure of $[3,5\text{-}Me_2pzH]_3$ which exhibits a planar trimeric association rather than a dimeric "packing".[43] On the contrary, ligand repulsion may actually prevent the silver atoms from fully eclipsing to give Ag−Ag contacts.[44]

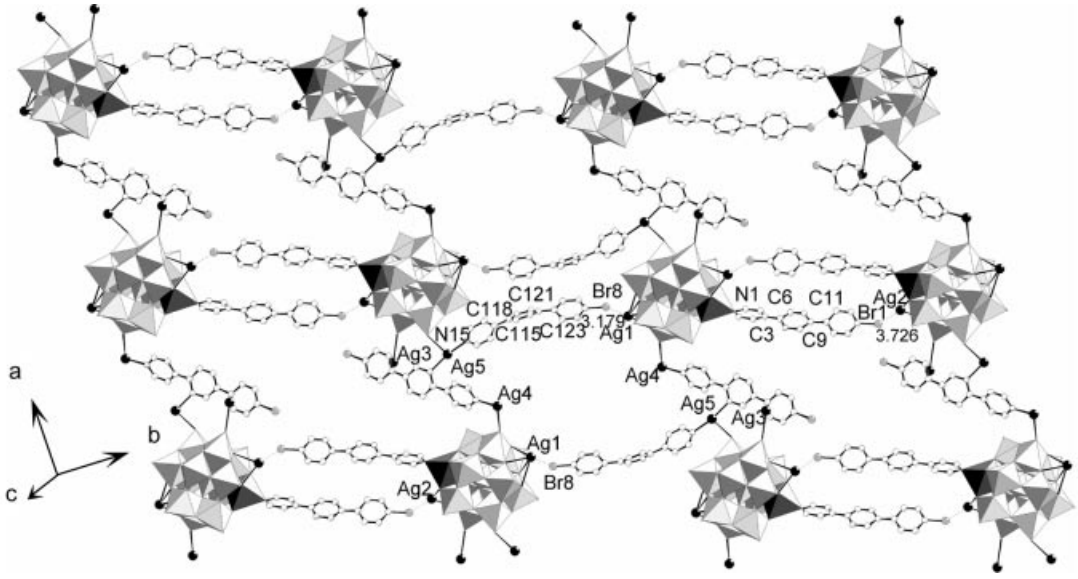

Figure 4. View of the 1D double-chain structure of **1** based on the interaction Ag(1)−Br(8); distances [Å]: Ag(1)···Br(8) 3.179(51), Ag(2)···Br(1) 3.726(58); some bppy groups are omitted for clarity; dark octahedra: $\{Co^{II}O_4N\}$; light octahedra: $\{W^{VI}O_6\}$

 © 2005 Wiley-VCH Verlag GmbH & Co. KGaA, Weinheim

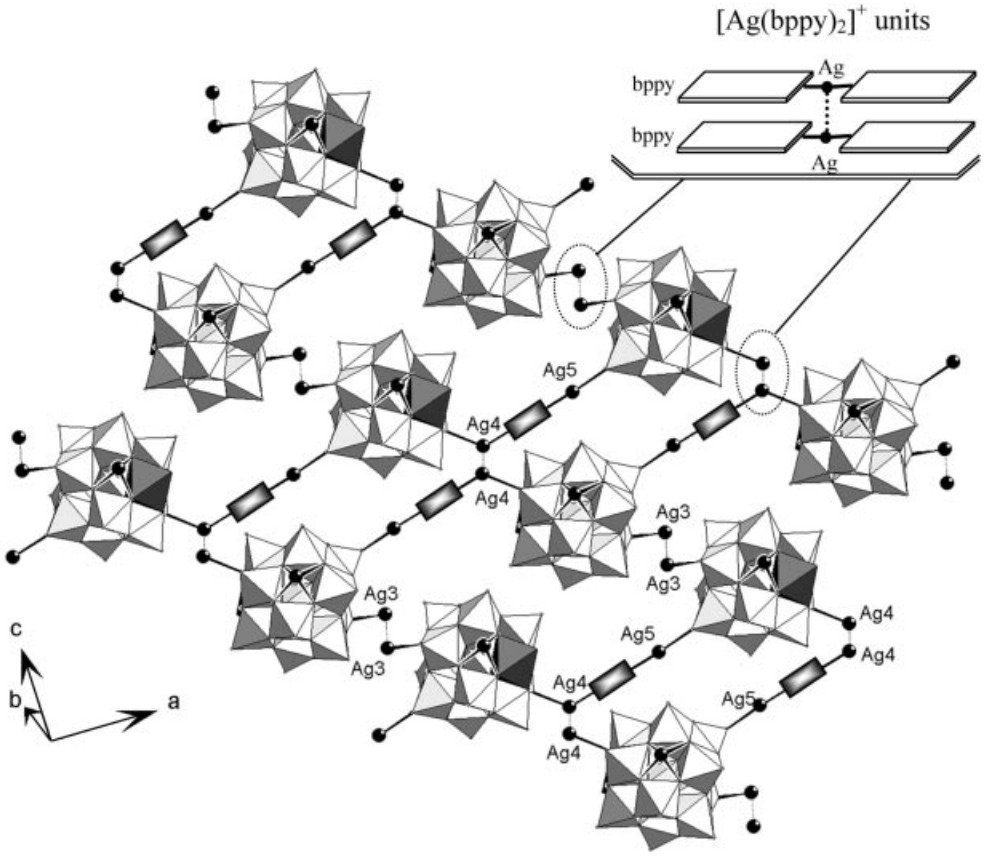

Figure 5. A schematic diagram of **1** showing the extension of 1D chains into a 3D sturctrure via π-stacking interactions of the ligands (see the inset) bonded to Ag(3) and Ag(4); Ag(3)···Ag(3) 3.849(40), Ag(4)···Ag(4) 3.598(34) Å; the dark rectangle blocks represent the covalent linkage of Ag(4) and Ag(5) via bppy groups; organic ligands are omitted for clarity; dark octahedra: $\{Co^{II}O_4N\}$; light octahedra: $\{W^{VI}O_6\}$

The interesting aspect of this structure is the multiple role of the conjugated organic bppy: its first function is to act as a pendant ligand to functionalise the polyanions. The second is to form SMG groups linking the polyanions into chains and the third function is to produce strong aromatic-aromatic interactions giving a 3D structure. 3D supramolecular architectures fabricated from layers by means of hydrogen bonds or π-stacking are common in coordination polymers.[45−46] However, such 3D supramolecular architectures constructed from 1D chains are rare.

The crystal structure of **1** is further strengthened by hydrogen bonding. Two waters of crystallisation have multipoint hydrogen bonding interactions with the organic ligands and the surface oxygen atoms of the POM. The short distances [Å] are (see Figure 6): Ow(1)···Ow(2) 3.070, Ow(1)···O(12) 2.949, Ow(1)···O(25) 3.018, Ow(2)···O(17) 2.902, Ow(2)···C(72) 3.146, Ow(2)···C(4) 3.195, Ow(3)···Ow(3) 2.779, Ow(3)···O(26) 3.057 and Ow(3)···O(7) 2.724.

In summary, the structure of **1** can be described as a monosubstituted tungstophosphate anion $[PW_{11}Co(bppy)O_{39}]^{5-}$ linked by Ag-bppy units into a 1D chain structure running along the direction of the *a* axis. The chains further extend into a double-strand structure based on the interaction of Ag(1) with Br(8) and the π-π interactions of the bppy ligands. These double-strand structures then form a 3D framework structure by hydrogen bonding and a number of π-π interactions of the bppy groups.

Bond valence sum calculations (BVS)[47] indicate that the W centres are in the highest oxidation state and that the Co atom possesses 2.223 of its formal oxidation state in compound **1**. The calculated valence sums for Ag(1) to Ag(5) are 0.902, 0.789, 0.895, 0.960 and 0.792, respectively, indicating the oxidation state of the Ag atoms is +1. The ESR spectrum at room temperature shows the paramagnetic signal of Co^{2+} with $g = 2.258$ which is consistent with the calculation result.[48]

FT-IR Spectrum, XPS Spectrum and TG-DTA Analysis: The IR spectrum [see Supporting Information Figure S1(a)] of **1** exhibits characteristic peaks of the Keggin anion at 999, 953, 885 and 814 cm^{-1}, attributable to ν (W−O_c−W), ν(W−O_b−W) and ν(W−O_d) (O_d = terminal oxygen, O_b = bridged oxygen of two octahedral sharing a corner, O_c = bridged oxygen of two octahedral sharing an edge), respectively. The informative bands at 1080 and 1048 cm^{-1} can be assigned to the P−O stretching vibrations in **1**. Compared with a typical value of about 1067 cm^{-1} for the Keggin anion,[49−50] the P−O stretch of the mono-substituted Keggin tungstophosphate ion splits into two bands because of the lower symmetry than that in the T_d parent Keggin

 © 2005 Wiley-VCH Verlag GmbH & Co. KGaA, Weinheim

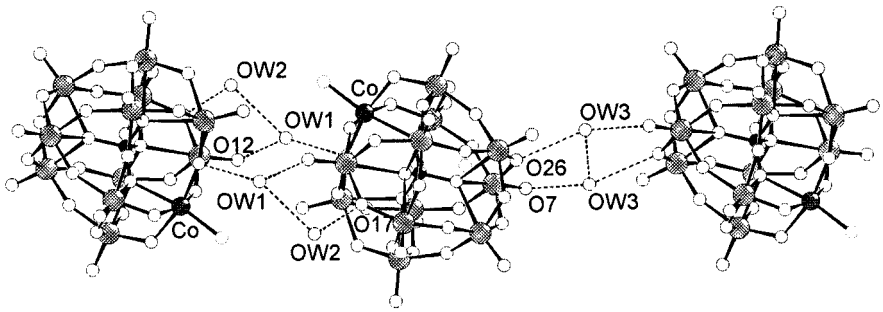

Figure 6. Hydrogen bonds between water and the POM (the silver atoms and organic ligands are omitted for clarity)

anion. The bands in the 3000−1080 cm^{-1} region can be attributed to characteristic vibrations of bppy. Comparatively, the P−O stretch of the by-product salt of $[PW_{12}O_{40}]^{3-}$ does not split into two bands but shows a peak at 1090 cm^{-1} [see Supporting Information Figure S1(b)].

The XPS spectrum (see Supporting Information Figure S2) shows a peak at 368.3 eV, attributable to Ag^{+}, a peak at 70.2 eV attributable to Br^{-} and a peak at 35.2 eV attributable to W^{6+}. These results further confirm the composition of compound **1**.

The TG curve (see Figure 7) shows that compound **1** is stable below 368 °C. A noteworthy finding is that there is still weight loss above 800 °C, indicating that organic material is still being lost even at the upper limit of measurement range. In this range, the DTA curve reveals three exothermic peaks at 396, 510 and 720 °C which correspond to the oxidation of the bppy ligands and/or a phase transformations of inorganic components, respectively. The thermal behaviour of **1** may be largely attributed to the effect of the pendant surface ligand, H-bonding and strong π-π stacking interactions.

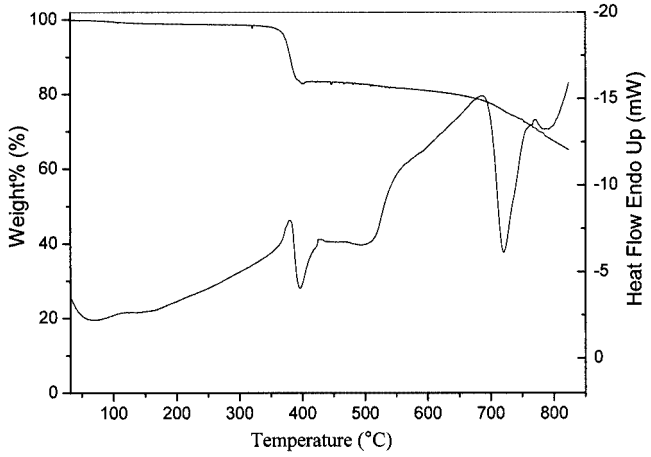

Figure 7. TG and DTA curves of compound **1**

Conclusion

A 1D double chain assembly based on the monosubstituted Keggin POM with pendant ligands has been synthesised and structurally characterised. The successful isolation of crystalline **1** suggests a promising approach for preparing extend arrays of polyoxometalate clusters. By generating metal-substituted polyoxometalates with increased negative charge density on the surface oxygen atoms of the POMs and introducing suitable structure-directing linkages via the secondary metal-ligand complex, rational design and synthesis of a target structure may be achieved, to a certain degree, under hydrothermal conditions. The conjugated organic bppy plays several roles in the structural formation. In particular, the 2′ N-donor is involved in forming a 1D chain through binding to the transition metal. Work on further extending these kind of linkages into 2 or 3D frameworks by this route is underway.

Experimental Section

Materials and Methods: All reagents were purchased and used without further purification; bppy was synthesised and identified by IR and ^{1}H NMR spectroscopy. Elemental analyses were carried out with an MOD 1106 elemental analyser. The infrared spectrum was recorded with an Alpha Centaur FT/IR spectrometer with a KBr pellet in the 4000−400 cm^{-1} region. XPS analysis was performed with a VGESCALAB MK II spectrometer with a Mg-K_{α} (1253.6 eV) achromatic X-ray source. The vacuum inside the analysis chamber was maintained at 6.2×10^{-6} Pa during analysis. The EPR spectrum was recorded with a Bruker ER 200D EPR spectrometer at 293 K. The thermal gravimetric analysis (TGA) and the differential thermal analysis (DTA) were carried out under N_2 with a Perkin−Elmer DTA 1700 differential thermal analyser at a rate of 10.00 °C /min in the range 30−800 °C.

Preparation of Compound 1: A mixture of $Na_2WO_4{\cdot}2H_2O$ (660 mg, 2 mmol), $Co(NO_3)_2{\cdot}6H_2O$ (291 mg, 1 mmol), $AgNO_3$ (213 mg, 1.3 mmol), bppy (62 mg, 0.2 mmol) and H_2O (10 mL) was adjusted to pH = 4.7 with dilute H_3PO_4 solution. The resultant mixture was sealed in a 25 mL Teflon-lined autoclave (70% full) and heated at 170 °C for 96 h. The autoclave was then cooled at 10 °C·per hour to room temperature. Pink crystals of **1** were obtained (yield: 82% based on bppy) along with an amorphous powder which was characterised as a simple compound by its IR spectrum [see Supporting Information Figure S1(c)]. The crystals were washed with water and dried in a desiccator at ambient temperature. The final pH value of the filtrate was 3.6. $C_{128}H_{92}Ag_5Br_8CoN_{16}O_{41}PW_{11}$: calcd. C 26.48, H 1.59, N 3.86; found C 26.51, H 1.63, N 3.82. IR (cm^{-1}): $\tilde{\nu}$ = 1610 (s), 1590 (m), 1540 (w), 1470 (s), 1420 (m), 1370 (w), 1080 (s), 1048 (s), 999 (m), 953 (s), 885 (s) 814 (s), 750 (m), 656 (w), 515 (w) and 417 (w).

 © 2005 Wiley-VCH Verlag GmbH & Co. KGaA, Weinheim

Table 1. Selected bond lengths [Å] and angles [°] for compound **1**

W(1)−O(11)	1.686(9)	Co(1)−O(3)	2.310(8)	Ag(5)−N(10)	2.227(12)
W(1)−O(13)	1.765(9)	Ag(1)−N(3)	2.152(16)	Ag(5)−O(22)	2.644(38)
W(1)−O(10)	1.935(9)	Ag(1)−O(15)	2.402(8)	C(14)−Br(1)	1.879(18)
W(1)−O(39)	1.947(10)	Ag(1)−O(23)	2.520(9)	C(30)−Br(2)	1.91(2)
W(1)−O(8)	2.036(9)	Ag(1)−O(21)	2.603(8)	C(46)−Br(3)	1.854(17)
W(1)−O(3)	2.429(8)	Ag(2)−N(5)	2.181(13)	C(62)−Br(4)	1.907(17)
P(1)−O(4)	1.525(8)	Ag(2)−O(38)	2.337(8)	C(78)−Br(5)	1.892(14)
P(1)−O(1)	1.531(9)	Ag(2)−O(35)	2.526(9)	C(94)−Br(6)	1.92(2)
P(1)−O(3)	1.534(9)	Ag(3)−N(11)	2.132(11)	C(110)−Br(7)	1.962(17)
P(1)−O(2)	1.532(8)	Ag(3)−N(13)	2.164(11)	C(126)−Br(8)	1.905(19)
Co(1)−O(25)	2.018(9)	Ag(3)−O(18)	2.627(32)	Ag(1)···O(19)	2.823(41)
Co(1)−O(35)	2.049(8)	Ag(4)−N(9)	2.116(11)	Ag(2)···O(34)	3.015(34)
Co(1)−O(13)	2.056(9)	Ag(4)−N(7)	2.127(12)	Ag(1)···Br(8)	3.179(51)
Co(1)−N(1)	2.081(11)	Ag(4)−O(16)	2.665(38)	Ag(2)···Br(1)	3.726(58)
Co(1)−O(38)	2.087(10)	Ag(5)−N(15)	2.161(12)		
Angles					
O(11)−W(1)−O(13)	104.1(4)	N(3)−Ag(1)−O(23)	122.7(5)		
O(11)−W(1)−O(10)	100.3(5)	O(15)−Ag(1)−O(23)	63.7(3)		
O(13)−W(1)−O(10)	93.5(4)	N(3)−Ag(1)−O(21)	136.9(4)		
O(11)−W(1)−O(39)	102.3(5)	O(15)−Ag(1)−O(21)	63.5(3)		
O(13)−W(1)−O(39)	93.1(4)	O(23)−Ag(1)−O(21)	76.9(3)		
O(10)−W(1)−O(39)	154.2(3)	N(5)−Ag(2)−O(38)	141.8(4)		
O(11)−W(1)−O(8)	97.6(4)	N(5)−Ag(2)−O(35)	118.9(4)		
O(13)−W(1)−O(8)	158.1(4)	O(38)−Ag(2)−O(35)	72.3(3)		
O(10)−W(1)−O(8)	85.2(4)	N(11)−Ag(3)−N(13)	175.0(4)		
O(39)−W(1)−O(8)	79.5(4)	N(9)−Ag(4)−N(7)	173.2(5)		
O(11)−W(1)−O(3)	173.8(5)	N(15)−Ag(5)−N(10)	166.3(4)		
O(13)−W(1)−O(3)	77.8(3)	O(25)−Co(1)−O(38)	163.9(4)		
O(10)−W(1)−O(3)	73.6(3)	O(35)−Co(1)−O(38)	88.0(4)		
O(39)−W(1)−O(3)	83.4(3)	O(13)−Co(1)−O(38)	87.9(4)		
O(8)−W(1)−O(3)	80.9(3)	N(1)−Co(1)−O(38)	93.4(4)		
O(25)−Co(1)−O(35)	87.5(3)	O(25)−Co(1)−O(3)	90.0(3)		
O(25)−Co(1)−O(13)	92.4(4)	N(13)−Ag(3)−O(18)	95.56(36)		
O(35)−Co(1)−O(13)	164.6(4)	N(11)−Ag(3)−O(18)	89.39(37)		
O(25)−Co(1)−N(1)	102.0(4)	Ag(3)−O(18)−W(3)	163.93(51)		
O(35)−Co(1)−N(1)	90.7(4)	N(7)−Ag(4)−O(16)	89.18(38)		
O(13)−Co(1)−N(1)	104.3(4)	N(9)−Ag(4)−O(16)	97.58(38)		
O(35)−Co(1)−O(3)	89.0(3)	Ag(4)−O(16)−W(2)	158.51(52)		
O(13)−Co(1)−O(3)	75.6(3)	N(15)−Ag(5)−O(22)	103.09(38)		
N(1)−Co(1)−O(3)	168.0(4)	N(10)−Ag(5)−O(22)	89.46(36)		
O(38)−Co(1)−O(3)	74.5(3)	Ag(5)−O(22)−W(6)	142.72(42)		
N(3)−Ag(1)−O(15)	157.8(5)				

X-ray Crystallographic Study: A single crystal of **1** with dimensions 0.18 × 0.10 × 0.08 mm was glued on a glass fibre. Data were collected on a CCD diffractometer with graphite-monochromated Mo-K_α radiation (λ = 0.71703 Å) at 293 K. Semi-empirical from equivalents were applied. The structure was refined by the full-matrix least-squares method on F^2 using the SHELXTL crystallographic software package.[31−32] Anisotropic thermal parameters were used to refine all nonhydrogen atoms. Hydrogen atoms were located in idealised positions. Selected bond lengths (Å) and angles (°) for compound **1** are listed in Table 1. Crystal data: $C_{128}H_{92}Ag_5Br_8CoN_{16}O_{41}PW_{11}$, triclinic, $P\bar{1}$, Mr = 5801.06, a = 18.720(4) Å, b = 19.474(4) Å, c = 19.815(4) Å, α = 96.30(3)°, β = 96.07(3)°, γ = 90.12(3)°, V = 7139(2) Å^3, Z = 2, $D_{calcd.}$ = 2.699 Mg·m^{-3}, μ = 11.935 mm^{-1}, crystal size: 0.18 × 0.10 × 0.08 mm. The final statistics based on F^2 are GOF = 1.007, R_1 = 0.0620 and wR_2 = 0.1346 for $I > 2\sigma(I)$. CCDC-238955 contains the supplementary crystallographic data for this paper. These data can be obtained free of charge at www.ccdc.cam.ac.uk/conts/retrieving.html [or from the Cambridge Crystallographic Data Centre, 12 Union Road, Cambridge CB2 1EZ, UK; Fax: (internat.) + 44-1223-336-033; E-mail: deposit@ccdc.cam.ac.uk].

Supporting Information Available (see also footnote on the first page of this article): IR and XPS spectra for **1**.

Acknowledgments

This work was financially supported by the National Natural Science Foundation of China (20271001).

[1] M. T. Pope, A. Müller, *Polyoxometalates: from Platonic Solids to Anti-Retroviral Activity*, Kluwer, Dordrecht, The Netherlands, **1994**.
[2] Special issue on polyoxometalates; Guest Editor: C. Hill, *Chem. Rev.* **1998**, *98*, 1−2, and references cited therein.
[3] M. T. Pope, T. Yamase, *Polyoxometalate Chemistry for Nano-Composite Design*, Kluwer Academic/Plenum Publishers, **2002**.
[4] J. M. Clemente-Juan, E. Coronado, *Coord. Chem. Rev.* **1999**, *193−195*, 361−394.
[5] E. Coronado, C. Mingotaud, *Adv. Mater.* **1999**, *11*, 869−872.
[6] M. Clemente-León, E. Coronado, P. Delhaes, C. J. Gómez-García, C. Mingotaud, *Adv. Mater.* **2001**, *13*, 574−577.
[7] M. Clemente-León, H. Soyer, E. Coronado, C. Mingotaud, C. J. Gómez-García, P. Delhaès, *Angew. Chem. Int. Ed.* **1998**, *37*, 2842−2845.

 © 2005 Wiley-VCH Verlag GmbH & Co. KGaA, Weinheim

[8] X. H. Wang, J. F. Liu, M. T. Pope, *Dalton Trans.* **2003**, 957−960.
[9] U. Kortz, M. G. Savelie, F. Y. A. Ghali, L. M. Khalil, S. A. Maalouf, D. I. Sinno, *Angew. Chem. Int. Ed.* **2002**, *41*, 4070−4073.
[10] Y. G. Wei, W. Lu, C. F. Cheung, C. L. Barnes, Z. H. Peng, *Inorg. Chem.* **2001**, *40*, 5489−5490.
[11] L. Xu, M. Lu, B. B. Xu, Y. G. Wei, Z. H. Peng, D. R. Powell, *Angew. Chem. Int. Ed.* **2002**, *41*, 4129−4132.
[12] P. Gouzerh, A. Proust, *Chem. Rev.* **1998**, *98*, 77−112.
[13] Z. H. Peng, *Angew. Chem. Int. Ed.* **2004**, *43*, 930−935.
[14] B. B. Xu, Z. H. Peng, Y. G. Wei, D. R. Powell, *Chem. Commun.* **2003**, 2562−2563.
[15] R. D. Gall, C. L. Hill, J. E. Walker, *Chem. Mater.* **1996**, *8*, 2523−2527.
[16] S. Q. Liu, Z. Y. Tang, Z. X. Wang, Z. Q. Peng, E. K. Wang, S. J. Dong, *J. Mater. Chem.* **2000**, 2727−2733.
[17] Y. H. Guo, Y. H. Wang, C. W. Hu, Y. H. Wang, E. B. Wang, Y. C. Zhou, S.H. Feng, *Chem. Mater.* **2000**, *12*, 3501−3508.
[18] M. R. Weir, J. Moore, R. A. Kydd, *Chem. Mater.* **1997**, *9*, 1686−1690.
[19] S. Damyanova, J. L. G. Fierro, *Chem. Mater.* **1998**, *10*, 871−879.
[20] Y. Yoshinaga, K. Seki, T. Nakato, T. Okuhara, *Angew. Chem. Int. Ed. Engl.* **1997**, *36*, 2833−2835.
[21] *Handbook of Organic Conductive Molecules and Polymers I−IV* (Ed.: H. S. Nalwa), Wiley, Chichester, England, **1997**.
[22] Y. Xu, J. Q. Xu, K. L. Zhang, Y. Zhang, X. Z. You, *Chem. Commun.* **2000**, 153−154.
[23] R. G. Finke, M. W. Droege, *J. Am. Chem. Soc.* **1984**, *106*, 7274−7277.
[24] M. Pohl, Y. Lin, T. J. R. Weakley, K. Nomiya, M. Kaneko, H. Weiner, R. G. Finke, *Inorg. Chem.* **1995**, *34*, 767−777.
[25] G. Y. Luan, Y. G. Li, S. T. Wang, E. B. Wang, Z. B. Han, C. W. Hu, N. H. Hu, H. Q. Jia, *Dalton Trans.* **2003**, 233−235.
[26] J. Peng, W. Z. Li, E. B. Wang, Q. L. Bai, *J. Chem. Soc., Dalton Trans.* **2001**, 3668−3671.
[27] J. Peng, H. Y. Ma, Z. G. Han, B. X. Dong, W. Z. Li, J. Lu, E. B. Wang, *Dalton Trans.* **2003**, 3850−3855.
[28] P. J. Hagrman, D. Hagrman, J. Zubieta, *Angew. Chem. Int. Ed.* **1999**, *38*, 2638−2684.
[29] Z. G. Han, H. Y. Ma, J. Peng, Y. H. Chen, E. B. Wang, N. H. Hu, *Inorg. Chem. Commun.* **2004**, *7*, 182−185.
[30] S. Reinoso, P. Vitoria, L. Lezama, A. Luque, J.M. Gutiérrez-Zorrilla, *Inorg. Chem.* **2003**, *42*, 3709−3711.
[31] G. M. Sheldrick, *SHELXS-97, Program for Crystal Structure Solution*, University of Göttingen, Germany, **1997**.
[32] G. M. Sheldrick, *SHELXL-97, Program for Crystal Structure Refinement*, University of Göttingen, Germany, **1997**.
[33] Y. G. Wei, B. B. Xu, C. L. Barnes, Z. H. Peng, *J. Am. Chem. Soc.* **2001**, *123*, 4083−4084.
[34] M. Lu, Y. G. Wei, B. B. Xu, C. F. C. Cheung, Z. H. Peng, D. R. Powell, *Angew. Chem. Int. Ed.* **2002**, *41*, 1566−1568.
[35] J. L. Samonte, M. T. Pope, *Can. J. Chem.* **2001**, *79*, 802−808.
[36] R. Q. Zou, J. R. Li, Y. B. Xie, R. H. Zhang, X. H. Bu, *Crystal Growth Design* **2004**, *4*, 79−84.
[37] C. M. Hartshorn, P. J. Steel, *J. Chem. Soc., Dalton Trans.* **1998**, 3935−3940.
[38] F. Robinson, M. J. Zaworotko, *J. Chem. Soc., Chem. Commun.* **1995**, 2413−2414.
[39] M. A. Withersby, A. J. Blake, N. R. Champness, P. Hubberstey, W. S. Li, M. Schröder, *Angew. Chem. Int. Ed. Engl.* **1997**, *36*, 2327−2329.
[40] O. S. Jung, Y. J. Kim, Y. A. Lee, K. M. Park, S. S. Lee, *Inorg. Chem.* **2003**, *42*, 844−850.
[41] J. E. Huheey, *Inorganic Chemistry, Principles of Structure and Reactivity*, 2nd ed., Harper & Row, New York, **1978**, pp. 230−236.
[42] A. Bondi, *J. Phys. Chem.* **1964**, *68*, 441−451.
[43] J. A. S. Smith, B. Wehrle, F. Aguilar-Parrilla, H. H. Limbach, M. d. l. C. Foces-Foces, F. H. Cano, J. Elguero, A. Baldy, M. Pierrot, M. M. T. Khurshid, J. B. Larcombe-McDouall, *J. Am. Chem. Soc.* **1989**, *111*, 7304−7312.
[44] K. Singh, J. R. Long, P. Stavropoulos, *J. Am. Chem. Soc.* **1997**, *119*, 2942−2943.
[45] S. Subramanian, M. J. Zaworotko, *Angew. Chem. Int. Ed. Engl.* **1995**, *34*, 2127−2129.
[46] S. Noro, S. Kitagawa, M. Kondo, K. Seki, *Angew. Chem. Int. Ed.* **2000**, *39*, 2081−2084.
[47] I. D. Brown, D. Altermatt, *Acta Crystallogr., Sect. B* **1985**, *41*, 244−247.
[48] S. van Doorslaer, R. Bachmann, A. Schweiger, *J. Phys. Chem. A* **1999**, *103*, 5446−5455.
[49] C. Rocchiccioli-Deltcheff, M. Fournier, R. Franck, R. Thouvenot, *Inorg. Chem.* **1983**, *22*, 207−216.
[50] R. Massart, R. Contant, J. M. Fruchart, J. P. Ciabrini, M. Fournier, *Inorg. Chem.* **1977**, *16*, 2916−2921.

Received June 4, 2004
Early View Article
Published Online November 18, 2004

 © 2005 Wiley-VCH Verlag GmbH & Co. KGaA, Weinheim

Fine Tuning of MLCT States in New Mononuclear Complexes of Ruthenium(II) Containing Tris(1-pyrazolyl)methane, 2,2′-Bipyridine and Aromatic Nitrogen Heterocycles

Néstor E. Katz,*[a] Isabel Romero,[b] Antoni Llobet,*[b] Teodor Parella,[c] and Jordi Benet-Buchholz[d]

Keywords: Charge transfer / Ruthenium / N ligands / Scorpionate ligands

The syntheses of new mononuclear ruthenium(II) complexes of the type: [Ru(bpy)(L)(tpm)]$(PF_6)_2$ {tpm = tris(1-pyrazolyl)-methane; bpy = 2,2′-bipyridine; L = pz (pyrazine; **1**), 4,4′-bpy (4,4′-bipyridine; **2**), and bpe [*trans*-1,2-bis(4-pyridyl)ethylene; **3**]} are described, together with their spectroscopic, electrochemical, and photophysical properties. A complete assignment of the NMR resonances of the three species could be made in CD_3CN by bidimensional techniques. A fine tuning of the energies of MLCT (metal-to-ligand charge transfer) states in these complexes is disclosed when comparing, in CH_3CN, the values of their maximum absorption wavelengths for the most intense visible bands (λ_{max}) and their redox potentials for the Ru^{III}/Ru^{II} couples; this effect, relevant to the design of efficient photocatalysts, can be attributed to a decreasing order of $d_\pi(Ru) \rightarrow \pi^*(2,2'\text{-bpy})$ backbonding when decreasing the distance between both N atoms in the aromatic nitrogen heterocycle L that acts in a monodentate manner. Only the species with L = bpe emits at room temperature, pointing to the conclusion that MLCT excited states in this series become higher in energy than dd excited states when the value of λ_{max} is lower than 400 nm. These species are also useful building blocks for new dinuclear mixed-valent complexes.

(© Wiley-VCH Verlag GmbH & Co. KGaA, 69451 Weinheim, Germany, 2005)

Introduction

Polypyridylruthenium(II) complexes represent a keystone in the development of photochemistry and electron- and energy-transfer disciplines,[1] and, among other applications, have led to the design of molecular electronic devices,[2] including wires and switches.[3] Furthermore, polypyridylruthenium(II) complexes are often used as building blocks for the development of macromolecular assemblies of interest in biochemistry and clinical diagnosis,[4] as well as for the design of molecular machines.[5] In most of these areas, the synthetic strategy followed to obtain the desired compounds is by Ru^{II} substitution chemistry.[6] Unfortunately, full mechanistic studies on these reactions are scarce and, in many cases, incomplete.[7] As a result of these two factors, it is of primary importance to understand and control the electronic and steric factors exerted by different types of ligands in order to properly monitor their substitution processes.

Ruthenium(II) complexes of the type $[Ru(bpy)(L)(tpm)]^{2+}$ with the tripodal ligand tpm [tris(1-pyrazolyl)methane], the bidentate ligand bpy (2,2′-bipyridine), and monodentate ligands L (Cl^-, H_2O, O^{2-} or py) are well known.[8,9] A coarse control of MLCT (metal-to-ligand charge transfer) excited states can be achieved by changing substituents in the 4,4′-positions of bpy.[9–11] In this work, we report on the fine tuning of the energies of $d_\pi(Ru) \rightarrow \pi^*(bpy)$ MLCT states introduced by changing the nature of the ligand L in $[Ru(bpy)(L)(tpm)]^{2+}$ complexes with L = pz (pyrazine), 4,4′-bpy (4,4′-bipyridine), and bpe [*trans*-1,2-bis(4-pyridyl)ethylene]. These changes can be compared to the variations observed in the analogous series $[Ru(bpy)(L)(trpy)]^{2+}$ (trpy = 2,2′:6′,2″-terpyridine),[12–16] and can be related to the electronic and structural variations induced when going from a meridional (trpy) to a facial (tpm) coordination.[17] The control of MLCT excited sates is relevant in photocatalysis, as demonstrated by the extensive literature concerning artificial photosynthesis based on transition-metal complexes.[18–22] On the other hand, scorpionate ligands, like tpm, can be

[a] Instituto de Química Física, Facultad de Bioquímica, Química y Farmacia, Universidad Nacional de Tucumán,
Ayacucho 491, T4000INI San Miguel de Tucumán, Argentina
E-mail: nkatz@arnet.com.ar
[b] Departament de Química, Universitat de Girona,
Campus de Montilivi, 17071 Girona, Spain
Fax: + 34 972-41-81-50
E-mail: antoni.llobet@udg.es
[c] Servei de RMN, Universitat Autònoma de Barcelona,
Bellaterra 08193, Barcelona, Spain
Fax: + 34 93-581-22-91
E-mail: teodor.parella@uab.es
[d] Bayer Industry Services SUA-SPA X-ray Laboratory, Geb. Q18, Raum 490, Bayer AG,
51368 Leverkusen, Germany
E-mail: jbenet@iciq.es
Supporting information for this article is available on the WWW under http://www.eurjic.org or from the author.

 © 2005 Wiley-VCH Verlag GmbH & Co. KGaA, Weinheim **DOI: 10.1002/ejic.200400487**

used for obtaining luminescent supramolecular complexes.[23] The new complexes studied here are also useful building blocks for new, dinuclear, mixed-valent species, some of which will be reported in a subsequent paper. The structures of the ligands are shown in Scheme 1.

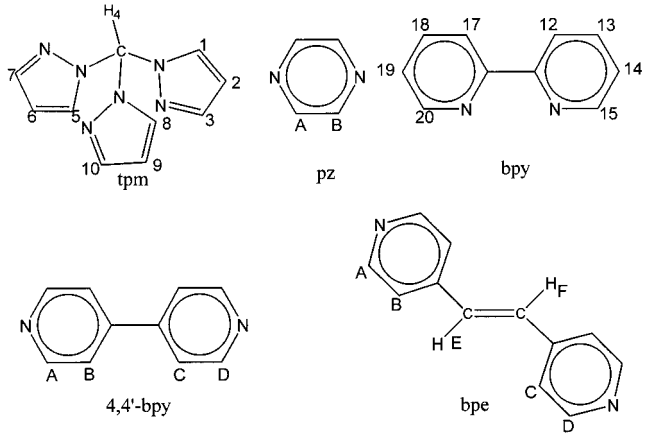

Scheme 1

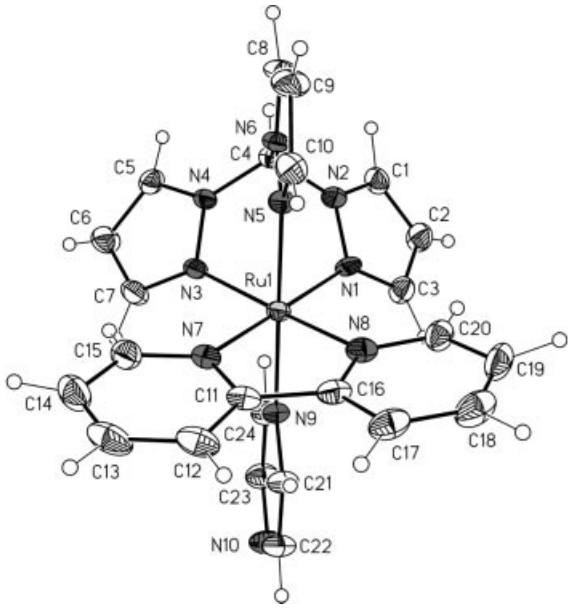

Figure 1. ORTEP plot (ellipsoids drawn at 50% probability) of the cationic moiety of complex **1** together with its labeling scheme; selected bond lengths [Å] and angles [°]: Ru(1)−N(1) 2.082(2), Ru(1)−N(3) 2.083(3), Ru(1)−N(5) 2.060(2), Ru(1)−N(7) 2.049(2), Ru(1)−N(8) 2.049(3), Ru(1)−N(9) 2.079(2); N(1)−Ru(1)−N(3) 83.13(16), N(1)−Ru(1)−N(5) 85.95(9), N(5)−Ru(1)−N(3) 86.80(15), N(7)−Ru(1)−N(8) 79.04(18), N(1)−Ru(1)−N(8) 99.69(17), N(5)−Ru(1)−N(8) 89.13(16), N(5)−Ru(1)−N(7) 92.54(9), N(3)−Ru(1)−N(7) 98.02(17), N(7)−Ru(1)−N(9) 90.18(9), N(8)−Ru(1)−N(9) 92.91(15), N(9)−Ru(1)−N(1) 91.35(9), N(9)−Ru(1)−N(3) 91.28(14), N(1)−Ru(1)−N(7) 178.06(17), N(3)−Ru(1)−N(8) 174.88(13), N(5)−Ru(1)−N(9) 176.86(13)

Results and Discussion

Synthesis and Solid-State Structures

The synthetic procedures followed to obtain complexes **1**−**3** are straightforward and involve the substitution of the anionic Cl^- ligand in the complex $[Ru^{II}Cl(bpy)(tpm)]^+$ by the desired monodentate ligand L (pz, 4,4′-bpy or bpe), as shown below.

$$[Ru^{II}Cl(tpm)(bpy)]^+ + L \xrightarrow[\text{reflux}]{MeOH/H_2O} [Ru^{II}(L)(tpm)(bpy)]^{2+} + Cl^-$$

The crystal structure of complex **1** was solved by means of a single-crystal X-ray diffraction analysis. Figure 1 shows the ORTEP diagram of the molecule along with the corresponding labeling scheme. The Ru center adopts a pseudo-octahedral type of geometry with three N atoms (N1, N3, N5) from the tpm ligand coordinated in a facial fashion. Two other positions are occupied by the 2,2′-bpy ligand (N7, N8), which acts in chelate manner, while the sixth one is occupied by the nitrogen atom, N9, of the monodentate pz ligand. The Ru−N bond lengths are within the range found for similar complexes previously described in the literature.[24,25] The bonding angles are also within the ranges found in the literature[24,25] and reflect the nature of the different ligands.

Complex **1** has a local pseudo-C_m symmetry with the mirror plane located in the plane formed by the pyrazine ring and the pyrazolyl group of tmp *trans* to the pyrazine. This symmetry is slightly disturbed by a 4.3° rotation of the bpy out of the mirror plane. The local C_m symmetry of the molecule is broken by the location of the anions in the crystal packing. These are arranged around the complex and together they form a one-dimensional 2_1 screw axis which gives the chirality to the crystal.

Spectroscopic and Redox Properties

Complexes of the type $[Ru(bpy)(L)(tpm)]^{2+}$ are well known in relation to catalysis.[8] However, the influence of slight variations in the structure of the ligands L on the spectral, electrochemical, and photophysical properties of these species has not been much studied; besides, there are no examples so far of mixed-valent species that incorporate tpm in their coordination sphere. As noted before,[9] the simplification introduced by having a poor π-backbonding ligand such as tpm would, in principle, disclose the role of the chromophoric ligands in controlling the spectroscopic, electrochemical, and photophysical properties of MLCT excited states.

NMR Spectroscopy

Figure 2 shows the aromatic region of the ^1H NMR spectrum of complex **1** in $[D]_3$acetonitrile, as a representative example; the COSY, NOESY and HSQC spectra together with all the NMR spectra for complexes **2** and **3** are provided as Supporting Information. The spectra can be unambiguously assigned thanks to molecular symmetry, the smaller coupling constants of five-membered pyrazolyl rings with regard to six-membered pyridyl and pyrazinyl

 © 2005 Wiley-VCH Verlag GmbH & Co. KGaA, Weinheim

rings, and with the aid of 2D NMR spectra. The symmetry lost in the solid state is recovered in solution and thus the two pyrazolyl rings *cis* to the pyrazine ligand become magnetically equivalent, as do the pyridyl moieties of bpy. Two intraligand NOE effects are observed for tpm between H4 and H1 and H8, together with a third interligand NOE between H3 of tpm and H20 of bpy (d_{H3-H20} = 2.46 Å); the latter is a key feature that allows us to assign the NMR resonances with total confidence. The pyrazine and the other ligands acting in a monodentate fashion — 4,4′-bpy and bpe — lose their symmetry upon coordination, a fact that is clearly manifested in their NMR spectra.

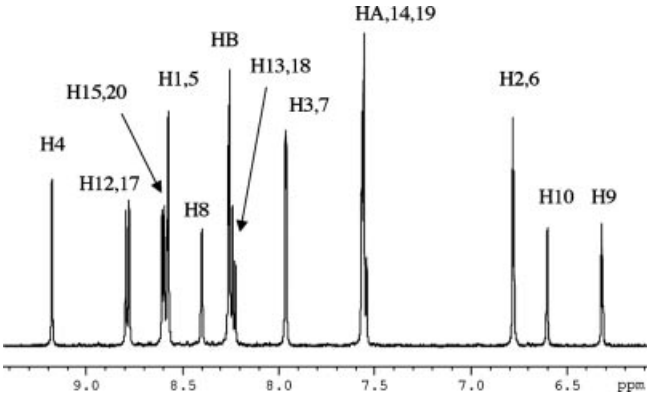

Figure 2. ^{1}H NMR spectrum showing the aromatic region of $[Ru(bpy)(pz)(tpm)]^{2+}$ in CD_3CN

UV/Vis Spectra

Table 1 shows the UV/Vis spectroscopic data of the three new complexes in CH_3CN together with that of $[Ru(bpy)(py)(tpm)]^{2+}$ for comparison purposes. Figure 3 shows the electronic spectrum of complex **1**, as a representative example. Bands between 200 and 300 nm are assigned to the $\pi-\pi^*$ transitions of tpm and bpy.[9] In the visible region, characteristic bands of $d_\pi(Ru) \rightarrow \pi^*(2,2'\text{-bpy})$ and $d_\pi(Ru) \rightarrow \pi^*(L)$ MLCT transitions are observed. Gaussian deconvolution of the spectrum of **1** (see Supporting Information) allows the assignment of the bands at 457 and 392 nm to the former MLCT, while the intermediate one at 418 nm corresponds to the latter MLCT. When the deconvoluted maxima of the $d_\pi(Ru) \rightarrow \pi^*(2,2'\text{-bpy})$ MLCT bands are compared in the series, a decreasing order of energies of the MLCT excited states is disclosed as follows: $[Ru(bpy)(pz)(tpm)]^{2+} > [Ru(4,4'\text{-bpy})(bpy)(tpm)]^{2+} > [Ru(bpe)(bpy)(tpm)]^{2+}$.

This fine tuning is consistent with the backbonding capabilities of the L ligands. As the second (uncoordinated) nitrogen of the aromatic heterocycle L is further away from the Ru center, the total backbonding effect from Ru to L is diminished, thus increasing the backbonding from Ru to the 2,2′-bpy ligand. This effect was not so evident in the series $[Ru(bpy)(L)(trpy)]^{2+}$,[12,13] due to the complications in the spectra produced by the presence of a second chromophoric ligand (trpy).

Electrochemistry

Table 1 includes the values for the redox potentials of the Ru^{III}/Ru^{II} and the $bpy^{0/-}$ couples present in the three complexes; the cyclic voltammogram for **1** is shown in the Supporting Information. The order disclosed by the MLCT bands is also shown in the decreasing values of $E_{1/2}(Ru^{III}/Ru^{II})$ redox potentials in the series: pz > 4,4′-bpy > bpe. The Ru^{II} state is stabilized when the total π-backbonding effects are maximized. The reduction potentials, $E_{1/2}(bpy^{0/-})$, of the ligand bpy are almost unchanged in this series.

Photophysical Properties

Figure 4 shows the emission spectrum of complex **3**, which is the only complex of this series that emits at room temperature in CH_3CN (λ_{em} = 606 nm at λ_{exc} = 400 nm). This value is consistent with the photophysical data of $[Ru(bpy)(py)(tpm)]^{2+}$ (py = pyridine).[9] Complexes **1** and **2** do not emit at room temperature and rearrange with loss of ligand L to give $[Ru(bpy)(CH_3CN)(tpm)]^{2+}$ as the final product. We thus conclude that the dd states become lower in energy than the MLCT states when the absorption maximum corresponding to the $d_\pi(Ru) \rightarrow \pi^*(bpy)$ transition is lower than 400 nm, with subsequent labilization of the ligand L. This result is consistent with that found before[9] when changing the substituents X in complexes of the type $[Ru(py)(tpm)(X_2bpy)]^{2+}$; in this case, changing the nature of X exerts a coarse control over the energies of the Ru → bpy MLCT excited states.

Dinuclear Species

Preliminary experiments indicated the formation of dinuclear species when reacting the mononuclear complexes described here with equimolar amounts of $[Ru(NH_3)_5(H_2O)](PF_6)_2$ under an Ar atmosphere. Oxidation of these new complexes with Br_2 gave the corresponding mixed-valent complexes $[Ru(bpy)(L)(tpm)Ru(NH_3)_5]^{5+}$ (L = pz, 4,4′-bpy, and bpe). They all show MMCT (metal-to-metal charge transfer) bands near 700 nm, as expected because of the high redox asymmetry between both metallic centers.[26] The properties of these species will be presented in a subsequent paper.[27] There are no reports of mixed-valent complexes that include tpm in their coordination spheres.

Conclusions

The spectroscopic and electrochemical properties of the new complexes described in this work disclose the following order of decreasing energies of Ru → bpy MLCT states: $[Ru(bpy)(pz)(tpm)]^{2+} > [Ru(4,4'\text{-bpy})(bpy)(tpm)]^{2+} > [Ru(bpe)(bpy)(tpm)]^{2+}$. This can be accounted for by the decreasing π-backbonding effects along the series. While a coarse control of the energies of the MLCT states in com-

 © 2005 Wiley-VCH Verlag GmbH & Co. KGaA, Weinheim

Table 1. Electrochemical and absorption spectroscopic data of complexes of the type $[Ru(bpy)(L)(tpm)]^{2+}$ in CH_3CN at room temperature

Complex[a]	$E_{1/2}(Ru^{III}/Ru^{II})$[b]	$E_{1/2}(bpy^{0/-})$[b]	λ_{max} ($10^{-3}\varepsilon$)[c]	Assignment
$[Ru(bpy)(pz)(tpm)]^{2+}$	1.26	−1.41	457 sh (2.0)	$d_\pi\rightarrow\pi^*$ (bpy)
			418 sh (2.0)	$d_\pi\rightarrow\pi^*$ (pz)
			392 (8.4)	$d_\pi\rightarrow\pi^*$ (bpy)
			327 (6.8)	$d_\pi\rightarrow\pi^*$ (bpy)
			294(19)	$\pi\rightarrow\pi^*$
			286(22)	$\pi\rightarrow\pi^*$
			254(15)	$\pi\rightarrow\pi^*$
			227(14)	$\pi\rightarrow\pi^*$
			210 (24)	$\pi\rightarrow\pi^*$
$[Ru(4,4'\text{-bpy})(bpy)(tpm)]^{2+}$	1.21	−1.41	464 sh (2.3)	$d_\pi\rightarrow\pi^*$(bpy)
			424 sh (5.7)	$d_\pi\rightarrow\pi^*$(4,4′-bpy)
			395 (11)	$d_\pi\rightarrow\pi^*$(bpy)
			339 (6.8)	$d_\pi\rightarrow\pi^*$(bpy)
			290 sh (17)	$\pi\rightarrow\pi^*$
			286 (22)	$\pi\rightarrow\pi^*$
			254 sh (19)	$\pi\rightarrow\pi^*$
			237 (22)	$\pi\rightarrow\pi^*$
			210 (26)	$\pi\rightarrow\pi^*$
$[Ru(bpe)(bpy)(tpm)]^{2+}$	1.15	−1.39	466 sh (4.6)	$d_\pi\rightarrow\pi^*$ (bpy)
			426 sh (4.6)	$d_\pi\rightarrow\pi^*$ (bpe)
			410 (13)	$d_\pi\rightarrow\pi^*$ (bpy)
			343 sh (6.7)	$d_\pi\rightarrow\pi^*$ (bpy)
			294 sh (32)	$\pi\rightarrow\pi^*$
			285 (35)	$\pi\rightarrow\pi^*$
			254 (27)	$\pi\rightarrow\pi^*$
$[Ru(bpy)(py)(tpm)]^{2+}$ [d]	1.15	−1.39	466 sh (1.8)	$d_\pi\rightarrow\pi^*$ (bpy)
			416 sh (4.2)	$d_\pi\rightarrow\pi^*$ (bpy)
			343 sh (12.5)	$d_\pi\rightarrow\pi^*$ (bpy)
			287 (26)	$\pi\rightarrow\pi^*$
			244 (15)	$\pi\rightarrow\pi^*$

[a] As their PF_6^- salts. [b] V vs. SCCE, with 0.1 M TBAH as supporting electrolyte. [c] λ_{max} in nm, ε values in $M^{-1}\cdot cm^{-1}$. [d] From ref.[2]

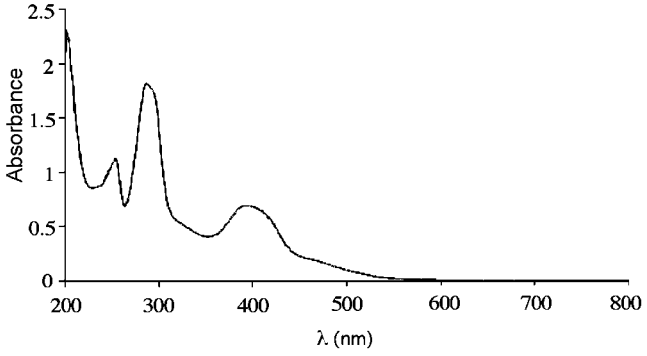

Figure 3. UV/Vis spectrum of $[Ru(bpy)(pz)(tpm)]^{2+}$ in CH_3CN at room temperature ($C = 9.5 \times 10^{-5}$ M)

plexes of the type $[Ru(py)(tpm)(X_2bpy)]^{2+}$ has been reported[9] by changing the nature of the substituents X on the 2,2′-bipyridine unit, a much finer control can be exerted by changing the π-backbonding abilities of the ligand L. Therefore, a whole range of Ru-bpy excited states can be finally obtained, which is relevant for the development of efficient photocatalysts.[18] Furthermore, these mononuclear species are useful building blocks for new mixed-valent

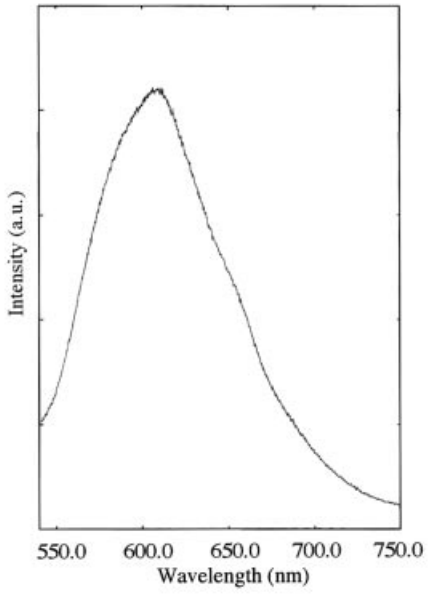

Figure 4. Emission spectrum, at room temperature, of $[Ru(bpy)(bpe)(tpm)]^{2+}$ in CH_3CN (λ_{exc} = 400 nm)

 © 2005 Wiley-VCH Verlag GmbH & Co. KGaA, Weinheim

species that incorporate tpm in their coordination spheres.[27]

Experimental Section

Materials: All reagents were obtained from Aldrich Chemical Co. and used without further purification. CH_3CN was freshly distilled for electrochemical measurements.

Preparations: All synthetic manipulations were routinely performed under nitrogen using Schlenk tubes and vacuum-line techniques. Electrochemical experiments were performed in the dark under N_2 or Ar with degassed solvents. IR spectra were recorded with an FT Nicolet 205 spectrophotometer with a reflectance accessory. UV/Vis spectra were recorded with a Cary 50 Scan (Varian) spectrophotometer, with 1-cm quartz cells. Cyclic voltammetry (CV) measurements were carried out with an IJ-Cambria IH-660 equipment with a three-electrode cell. A glassy carbon disk electrode (3 mm diameter) from BAS was used as working electrode, platinum wire as auxiliary electrode, and SSCE as reference electrode. All CV experiments were recorded at a 200 $mV \cdot s^{-1}$ scan rate under nitrogen purging, in pure CH_3CN containing 0.1 M tetrakis(*n*-butyl)ammonium hexafluorophosphate (TBAH). The values for the redox potentials, $E_{1/2}$, were estimated from cyclic voltammetry as the average of oxidative and reductive peak potentials $(E_{p,a} + E_{p,c})/2$. NMR spectra were recorded in CD_3CN with a Bruker 500 MHz spectrometer. Elemental analyses were carried out using a CHNS-O Elemental Analyser EA-1108 from Fisons. Luminiscence spectra were recorded with a Shimadzu RF-5301 PC spectrofluorometer, provided with 1-cm fluorescence cells. Argon was bubbled through the solutions prior to the photophysical measurements.

Synthesis of [Ru(tpm)(bpy)(pz)](PF$_6$)$_2$ (1): A sample of $[RuCl(bpy)(tpm)]Cl \cdot 2H_2O$ (80 mg, 0.14 mmol), prepared as described before,[8] was added to a solution of pz (0.6 g, 7 mmol) in ethanol/water (1:1, 25 mL) and the mixture heated at reflux for 6 h. After cooling, the ethanol was evaporated and the remaining aqueous solution was loaded onto a Sephadex C-25 column. The unchanged chloro complex was eluted with 0.2 M LiCl, while the pz complex was eluted with 0.3 M LiCl. This last eluate was concentrated to 5 mL and then a concentrated solution of NH_4PF_6 (1 g in 2 mL of water) was added. After cooling, the precipitate was filtered and washed with cold water. It was then redissolved in acetone (5 mL), re-precipitated with diethyl ether (50 mL), washed with diethyl ether, and dried in vacuo over KOH. Yield: 38 mg (32%). $C_{24}H_{22}F_{12}N_{10}P_2Ru$ (841.07): calcd. C 34.30, H 2.63, N 16.60; found C 34.20, H 2.70, N 16.20. ^{1}H NMR (500 MHz, CD_3CN, 25 °C): δ = 6.32 (dd, 1 H, H9), 6.60 (d, 1 H, J_{10-9} = 2.3 Hz, H10), 6.78 (dd, 2 H, H2), 7.56 (dd, 2 H, H14), 7.56 (d, 2 H, HA), 7.96 (d, J_{3-2} = 2.1 Hz, 2 H, H3), 8.24 (dd, 2 H, H13), 8.26 (dd, 2 H, HB), 8.40 (d, $J_{8,9}$ = 2.9 Hz, 1 H, H8), 8.57 (d, $J_{1,2}$ = 3.0 Hz, 2 H, H1), 8.60 (br. d, $J_{15,14}$ = 5.4 Hz, 2 H, H15), 8.78 (br. d, $J_{12,13}$ = 8.1 Hz, 2 H, H12), 9.18 (s, 1 H, H4), ppm. ^{13}C NMR (500 MHz, CD_3CN, 25 °C): δ = 76.0 (C4), 108.8 (C9), 110.3 (C2), 125.6 (C12), 126.5 (C14), 135.8 (C8), 135.9 (C1), 138.6 (C13), 144.3 (C10), 145.5 (CB), 147.4 (C3), 148.5 (CA), 153 (C15) ppm. NOEs: H4 with H1 and H8; H3 with H15.

Synthesis of [Ru(4,4′-bpy)(bpy)(tpm)](PF$_6$)$_2$·2H$_2$0 (2): A sample of $[RuCl(bpy)(tpm)]Cl \cdot 2H_2O$ (70 mg, 0.12 mmol) was added to a solution of 4,4′-bpy (1 g, 6.4 mmol) in ethanol/water (1:1, 25 mL) and the mixture heated at reflux for 6 h. After cooling, the ethanol was evaporated and the remaining aqueous solution was filtered to eliminate excess 4,4′-bpy. The filtrate was loaded onto a Sephadex C-25 column. The unchanged chloro complex was eluted with 0.2 M LiCl, while the 4,4′-bpy complex was eluted with 0.3 M LiCl. This last eluate was concentrated to 5 mL and then a concentrated solution of NH_4PF_6 (1 g in 2 mL of water) was added. After cooling, the precipitate was filtered, washed thoroughly with cold water, dried in vacuo over KOH, and recrystallized from acetone/diethyl ether. Yield: 37 mg (33%). $C_{30}H_{30}N_{10}O_2P_2F_{12}Ru$ (953.07): calcd. C 37.8, H 3.2, N 14.7; found C 38.1, H 2.7, N 14.1. ^{1}H NMR (500 MHz, CD_3CN, 25 °C): δ = 6.30 (dd, 1 H, H9), 6.58 (d, $J_{9,10}$ = 2.2 Hz, 1 H, H10), 7.47 (dd, 2 H, HB), 7.55 (dd, 2 H, H14), 7.64 (dd, $J_{A,B}$ = 5.7, $J_{A,D}$ = 1.3 Hz, 2 H, HA), 7.82 (dd, $J_{C,D}$ = 5.1, $J_{C,B}$ = 1.4 Hz, 2 H, HC), 7.95 (d, $J_{3,2}$ = 1.9 Hz, 2 H, H3), 8.22 (ddd, $J_{12,14}$ = 8.5, $J_{12,13}$ = 7.7 Hz, 2 H, H13), 8.63 (d, $J_{8,9}$ = 2.8 Hz, 1 H, H8), 8.67 (dd, $J_{15,14}$ = 5.6, $J_{15,13}$ = 1.2 Hz, 2 H, H15), 8.73 (dd, $J_{D,C}$ = 5.1, $J_{D,A}$ = 1.3 Hz, 2 H, HD), 8.79 (d, $J_{12,13}$ = 7.7 Hz, 2 H, H12), 8.86 (d, $J_{1,2}$ = 2.6 Hz, 2 H, H1), 10.96 (s, 1 H, H4) ppm. ^{13}C NMR (500 MHz CD_3CN, 25 °C): δ = 74.9 (C4), 108.8 (C9), 110(C2), 122.8 (CC), 125.5 (C12), 126.8 (C14), 135.7 (C8), 136 (C1), 138.3 (C13), 144 (C10), 147.6 (C3, CD), 153.6 (C15), 154.2 (CA) ppm. NOEs: H4 with H1 and H8; H3 with H15 and HA.

Synthesis of [Ru(bpe)(bpy)(tpm)](PF$_6$)$_2$ (CH$_3$)$_2$CO (3): A sample of $[RuCl(bpy)(tpm)]Cl \cdot 2H_2O$ (100 mg, 0.17 mmol) was added to a solution of bpe (0.6 g, 3.3 mmol) in ethanol/water (1:1, 25 mL) and the mixture heated at reflux for 6 h. After cooling, the ethanol was evaporated and the remaining aqueous solution was filtered to eliminate excess bpe. The filtrate was loaded onto a Sephadex C-25 column. The unchanged chloro complex was eluted with 0.2 M LiCl, while the bpe complex was eluted with 0.3 M LiCl. This last eluate was concentrated to 5 mL and then a concentrated solution of NH_4PF_6 (1 g in 2 mL of water) was added. After cooling, the precipitate was filtered, washed thoroughly with cold water, dried in vacuo over KOH, and then recrystallized from acetone/diethyl ether. Yield: 29 mg (33%). $C_{35}H_{34}F_{12}N_{10}OP_2Ru$ (1001.1): calcd. C 42.0, H 3.4, N 14.0; found C 42.1, H 3.0, N 13.6. ^{1}H NMR (500 MHz, CD_3CN, 25 °C): δ = 6.31 (dd, 1 H, H9), 6.59 (d, 1 H, H10), 6.77 (dd, 2 H, H2), 7.30 (d, 2 H, HB), 7.40(d, 1 H, HE), 7.49 (d, 2 H, H15), 7.50 (d, 1 H, HF), 7.55 (dd, 2 H, H14), 7.80 (d, $J_{C,D}$ = 5.8 Hz, 2 H, HC), 7.96 (d, 2 H, H3), 8.22 (ddd, 2 H, H13), 8.40 (d, 1 H, H8), 8.58 (d, 2 H, H1), 8.65 (dd, 2 H, H15), 8.78 (d, 2 H, H12), 9.18 (s, 1 H, H4) ppm. ^{13}C NMR (500 MHz, CD_3CN, 25 °C): δ = 76.3 (C4), 108.8 (C9), 110.1 (C2), 122.7 (CB), 123.2 (C13), 125.3 (C12), 126.7 (C14), 130.9 (CE), 133 (CF), 135.8 (C8), 136 (C1), 138.2 (C13), 144.2 (C10), 145.4 (CD), 147.7 (C3), 153.2 (C15), 153.7(CA) ppm. NOEs: H4 with H1 and H8; H3 with H8 and HA.

X-ray Structure Determination for 1: Yellow, needle-shaped crystals of **1** were grown by slow diffusion of diethyl ether into a concentrated acetone solution of the complex at room temperature. The crystal to be measured (700 × 40 × 20 μm) was isolated under inert conditions and immersed in perfluoropolyether as protection. Empirical formula $C_{24}H_{22}F_{12}N_{10}P_2Ru$, M = 841.53, monoclinic, space group $P2_1$, a = 10.3101(7) Å, b = 14.5022(10) Å, c = 11.1954(7) Å, β = 117.021(2)°, V = 1491.20(17) Å^3, Z = 2, μ = 0.746 mm^{-1}, $d_{calcd.}$ = 1.874 g/cm^3. The measurement was carried out with a Siemens P4 diffractometer equipped with a SMART-CCD-1000 area detector, a MACScience Co. rotating anode with Mo-K_α radiation, a graphite monochromator and a Siemens low-temperature device LT2 (T = −120 °C). The measurement range was 2.04−31.52°; 23212 reflections were collected of which 9439 were unique (R_{int} = 0.0574) and 8449 observed [$F > 4\sigma(F_o)$]. Full-

 © 2005 Wiley-VCH Verlag GmbH & Co. KGaA, Weinheim

sphere data collection ω and φ scans. Programs used: Data collection Smart V. 5.060 (Bruker AXS, **1999**), data reduction Saint+ Version 6.02 (Bruker AXS, **1999**) and absorption correction SADABS (max/min transmission: 1.000000/0.490397, Bruker AXS, **1999**). Structure solution and refinement were performed using SHELXTL Version 5.10 (Sheldrick, Universtität Göttingen, Göttingen, Germany, **1998**). The structure was solved by direct methods and refined by full-matrix least-squares against F^2. All calculated hydrogen positions were refined as constrained. Final R_1 [$I > 2\sigma(I)$] = 0.0449 and wR(F^2) [$I > 2\sigma(I)$] = 0.1045. The number of refined parameters was 564. Absolute structure parameter −0.03(2). CCDC-230222 contains the supplementary crystallographic data for this paper. These data can be obtained free of charge at www.ccdc.cam.ac.uk/conts/retrieving.html [or from the Cambridge Crystallographic Data Centre, 12 Union Road, Cambridge CB2 1EZ, UK; Fax: + 44-1223-336-033; E-mail: deposit@ccdc.cam.ac.uk].

Supporting Information Available: Additional spectroscopic and electrochemical data (see also footnote on the first page of this article).

Acknowledgments

We thank the "Ministerio de Educación, Cultura y Deporte" of Spain for a fellowship awarded to N. E. K. We also thank CIUNT ("Consejo de Investigaciones de la Universidad Nacional de Tucumán") and CONICET for financial support. N. E. K. is a Member of the Research Career of CONICET ("Consejo Nacional de Investigaciones Científicas y Técnicas") Argentina. This research has also been financed by MCYT of Spain through projects BQU2000-0458, BQU2003-02884, and BQU2003-01677. We would also like to thank the CIRIT Generalitat de Catalunya (Spain) for a Distinction award and the aid SGR2001-UG-291.

[1] [1a] *Organic and Inorganic Photochemistry* (Eds.: V. Ramamurthy, K. S. Schanze), Marcel Dekker, New York, **1998**. [1b] D. W. Thompson, J. R. Schoonover, D. K. Graff, C. N. Fleming, T. J. Meyer, *J. Photochem. Photobiol. A: Chem.* **2000**, *137*, 131−134. [1c] H. E. Toma, R. M. Serrasqueiro, R. C. Rocha, G. J. F. Demets, H. Winnischofer, K. Araki, P. E. A. Ribeiro, C. L. Donnici, *J. Photochem. Photobiol. A: Chem.* **2000**, *135*, 185−191. [1d] M. H. Keefe, K. D. Benkstein, J. T. Hupp, *Coord. Chem. Rev.* **2000**, *205*, 201−228. [1e] M. I. Romero, M. Rodríguez, A. Llobet, M. N. Collomb-Dunand-Sauthier, A. Deronzier, T. Parella, H. Stoeckli-Evans, *J. Chem. Soc., Dalton Trans.* **2000**, 1689−1694. [1f] D. S. Tyson, C. R. Luman, X. Zhou, F. N. Castellano, *Inorg. Chem.* **2001**, *40*, 4063−4071. [1g] V. Balzani, A. Juris, *Coord. Chem. Rev.* **2001**, *211*, 97−115. [1h] D. M Dattelbaum, C. M. Hartshorn, T. J. Meyer, *J. Am. Chem. Soc.* **2002**, *124*, 4938−4939. [1i] S. Nikolau, H. E. Toma, *J. Chem. Soc., Dalton Trans.* **2002**, 352−359.

[2] [2a] A. Hatzidimitriou, A. Gourdon, J. Devillers, J. P. Launay, E. Mena, E. Amouyal, *Inorg. Chem.* **1996**, *35*, 2212−2219. [2b] V. Balzani, A. Credi, M. Venturi, *Chem. Eur. J.* **2002**, *8*, 5524−5532. [2c] S. G. Camera, H. E. Toma, *J. Photochem. Photobiol. A: Chem.* **2002**, *151*, 57−65.

[3] [3a] J. P. Sauvage, J. P. Collin, J. C. Chambron, S. Guillerez, C. Coudret, *Chem. Rev.* **1994**, *94*, 993−1019. [3b] M. K. Brennaman, J. H. Alstrumacevedo, C. N. Fleming, P. Jang, T. J. Meyer, J. M. Papanikolas, *J. Am. Chem. Soc.* **2002**, *124*, 15094−15098.

[4] [4a] A. E. Friedman, J. C. Cambrón, J. P. Sauvague, N. J. Turro, J. K. Barton, *J. Am. Chem. Soc.* **1990**, *112*, 4960−4962. [4b] Y. Jenkis, A. E. Friedman, N. J. Turro, J. K. Barton, *Biochemistry* **1992**, *21*, 809−816. [4c] R. E. Holmlin, E. D. A. Stemp, J. K. Barton, *Inorg. Chem.* **1998**, *37*, 29−34. [4d] L. Li, H. Szmacinski, J. R. Lakowicz, *Biospectroscopy* **1997**, *3*, 155−159. [4e] L. Li, H. Szmacinski, J. R. Lakowicz, *Anal. Biochem.* **1997**, *244*, 80−85. [4f] E. Terpetschnig, H. Szmacinski, J. R. Lakowicz, *Anal. Biochem.* **1995**, *227*, 140−147. [4g] H. Youn, E. Terpetschnig, H. Szmacinski, J. R. Lakowicz, *Anal. Biochem.* **1995**, *232*, 24−30. [4h] Z. Murtaza, Q. Chang, G. Rao, H. Lin, J. R. Lakowicz, *Anal. Biochem.* **1997**, *247*, 216−222. [4i] T. M. Santos, B. J. Goodfellow, M. G. B. Drew, J. Pedrosa de Jesus, V. Félix, *Metal-Based Drugs* **2001**, *8*, 125−136.

[5] [5a] J. P. Sauvage, *Acc. Chem. Res.* **1998**, *31*, 611−619. [5b] V. Balzani, M. Gomez-López, J. F. Stoddart, *Acc. Chem. Res.* **1998**, *31*, 405−414. [5c] *Struct. Bonding (Berlin)* **2001**, *99*, 1−281: Special volume on "Molecular Machines and Motors". [5d] V. Balzani, A. Credi, F. M. Raymo, J. F. Stoddart, *Angew. Chem. Int. Ed.* **2000**, *39*, 3349−3391. [5e] J. P. Collin, C. Dietrich-Buchecker, P. Gaviña, M. C. Jiménez-Molero, J. P. Sauvage, *Acc. Chem. Res.* **2001**, *34*, 477−487.

[6] [6a] B. P. Sullivan, J. M. Calvert, T. J. Meyer, *Inorg. Chem.* **1980**, *19*, 1404−1407. [6b] M. Silva, E. Tfouni, *Inorg. Chem.* **1997**, *36*, 274−277. [6c] G. Malouf, P. C. Ford, *J. Am. Chem. Soc.* **1977**, *26*, 7213−7221. [6d] A. C. Laemmel, J. P. Collin, J. P. Sauvage, *R. Acad. Sci. Paris, Sér. IIc, Chim./Chem.* **2000**, *3*, 43−49. [6e] T. Matsubara, C. J. Creutz, *Am. Chem. Soc.* **1979**, *18*, 1956−1966.

[7] [7a] R. Arakawa, K. Abe, T. Abura, Y. Nakabayashi, *Bull. Chem. Soc. Jpn.* **2002**, *75*, 1983−1989. [7b] C. A. Bessel, J. A. Margarucci, J. H. Acquaye, R. S. Rubino, J. Crandall, A. J. Jircitano, K. J. Takeuchi, *Inorg. Chem.* **1993**, *32*, 5779−5784.

[8] A. Llobet, P. Doppelt, T. J. Meyer, *Inorg. Chem.* **1988**, *27*, 514−520.

[9] K. R. Barqawi, A. Llobet, T. J. Meyer, *J. Am. Chem. Soc.* **1988**, *110*, 7751−7759.

[10] P. A. Anderson, F. R. Keene, T. J. Meyer, J. A. Moss, G. F. Strouse, J. A. Treadway, *J. Chem. Soc., Dalton Trans.* **2002**, *20*, 3820−3831.

[11] A. Llobet, *Inorg. Chim. Acta* **1994**, *221*, 125−131.

[12] F. Fagalde, N. E. Katz, *J. Chem. Soc., Dalton Trans.* **1993**, 571−575.

[13] F. Fagalde, N. E. Katz, *Polyhedron* **1995**, *14*, 1213−1220.

[14] D. Szalda, F. Fagalde, N. E. Katz, *Acta Crystallogr., Sect. C* **1996**, *52*, 3013−3016.

[15] M. E. García Posse, M. M. Vergara, F. Fagalde, N. E. Katz, *Polyhedron* **2003**, *22*, 465−471.

[16] N. C. Fletcher, F. R. Keene, *J. Chem. Soc., Dalton Trans.* **1998**, *14*, 2293−2302.

[17] F. Laurent, E. Plantalech, B. Donnadieu, A. Jiménez, F. Hernández, M. Martínez-Ripoll, M. Biner, A. Llobet, *Polyhedron* **1999**, *18*, 3321−3331.

[18] N. Sutin, C. Creutz, *Pure Appl. Chem.* **1980**, *52*, 2717−2738.

[19] T. J. Meyer, *Acc. Chem. Res.* **1989**, *22*, 163−170.

[20] V. Balzani, F. Scandola, *Supramolecular Photochemistry*, Ellis Horwood, Chichester, **1991**.

[21] V. Balzani, A. Juris, M. Venturi, S. Campagna, S. Serroni, *Chem. Rev.* **1996**, *96*, 759−834.

[22] V. Balzani, S. Campagna, G. Denti, A. Juris, S. Serroni, M. Venturi, *Acc. Chem. Res.* **1998**, *31*, 26−34.

[23] L. Huang, K. J. Seward, B. P. Sullivan, W. E. Jones, J. J. Mecholsky, W. J. Dressick, *Inorg. Chim. Acta* **2000**, *310*, 227−236.

[24] M. Rodríguez, I. Romero, A. Llobet, A. Deronzier, M. Biner, T. Parella, H. Stoeckli-Evans, *Inorg. Chem.* **2001**, *40*, 4150−4156.

[25] C. Sens, M. Rodríguez, I. Romero, A. Llobet, T. Parella, J. Benet-Buchholz, *Inorg. Chem.* **2003**, *42*, 8385−8394.

[26] N. E. Katz, C. Creutz, N. Sutin, *Inorg. Chem.* **1988**, *27*, 1687−1694.

[27] N. E. Katz, F. Fagalde, M. I. Romero, A. Llobet, work in progress.

Received June 8, 2004
Early View Article
Published Online November 18, 2004

 © 2005 Wiley-VCH Verlag GmbH & Co. KGaA, Weinheim

The Reaction of (Bipyridyl)palladium(II) Complexes with Thiourea − Influence of DNA and Other Polyanions on the Rate of Reaction

Matteo Cusumano,*[a] Maria Letizia Di Pietro,[a] Antonino Giannetto,[a] and Pasquale Antonio Vainiglia[a]

Keywords: Intercalation with DNA / Inhibition of ligand substitution

$[Pd(bipy)(py)_2](PF_6)_2$ reacts stepwise with excess thiourea to give $[Pd(tu)_4](PF_6)_2$. The kinetics of the second step, which refers to the replacement of bipyridyl in $[Pd(bipy)(tu)_2](PF_6)_2$, have been studied in water and in the presence of calf thymus DNA, sodium polyriboadenylate, sodium polyvinylsulfonate or sodium polymetaphosphate at 25 °C and pH = 7 and a fixed sodium chloride concentration. The reaction follows a first order course and a plot of k_{obs} against [thiourea]^2 affords a straight line with a small intercept. DNA inhibits the process without altering the rate law. The k_{obs} values decrease systematically on increasing the DNA concentration eventually tending to a limiting value. The values are larger at higher ionic strengths and the other polyanions show similar behaviour. The influence of DNA on the kinetics can be related to steric inhibition caused by noncovalent binding with the complex. Upon interaction with DNA, $[Pd(bipy)(tu)_2]^{2+}$ gives rise to immediate spectroscopic changes in the UV/Vis region as well as induced circular dichroism suggesting that the complex, like similar platinum(II) and palladium(II) species of bipyridyl, intercalates with the double helix. Such a type of interaction hampers the attack of the nucleophile at the metal centre inhibiting the reaction. The decrease in the rate of ligand substitution upon decreasing salt concentration but at a given DNA concentration is due to the influence of ionic strength on the complex–DNA interaction. The reactivity inhibition by single-stranded poly(A), polyvinylsulfonate or polymetaphosphate can be accounted for in terms of self-aggregation of the complex induced by the polyanion.

(© Wiley-VCH Verlag GmbH & Co. KGaA, 69451 Weinheim, Germany, 2005)

Introduction

Since the discovery that square-planar complexes can intercalate[1] with DNA, many platinum(II) compounds containing aromatic ligands have been used[2] to study the basic features of this type of noncovalent interaction. These substances are thermodynamically stable and, furthermore, their kinetic inertness prevents undesired covalent interactions with the DNA nucleobases within the time needed for the experiments. The geometry and the ease of which their steric and electronic properties can be tuned by an appropriate choice of the ligands, renders platinum(II) complexes very suitable for studying intercalation with the DNA double helix. Palladium(II) complexes can also be used to study this type of noncovalent interaction with nucleic acids.[3] These substances share the thermodynamic stability and other chemicophysical properties of platinum(II) complexes but are less inert[4] and this feature makes them more amenable to study from a kinetic point of view. Various investigations have shown that the reactivity of a small molecule can be altered upon noncovalent interaction with DNA and RNA. Both inhibition[5] and enhancement[6] of reactivity of metal complexes have been observed. The influence on the kinetics may be related to the particular type of noncovalent interaction and, therefore, the study of the reactivity of a metal complex in the absence and in the presence of DNA or RNA can give interesting information about the interaction itself. In this paper we report the results of a kinetic investigation of the reaction between the palladium(II) complex $[Pd(bipy)(py)_2](PF_6)_2$ (bipy = 2,2′-bipyridyl; py = pyridine) and thiourea in water in the presence of double-helical DNA. The investigation was carried out at 25 °C and pH 7 at two different sodium chloride concentrations. In order to compare the influence of double stranded polyanions with single stranded, helical and random coiled polyanions, the reactions were studied in the presence of sodium polyriboadenylate [poly(A)], sodium polyvinylsulfonate (PVS) and sodium polymetaphosphate (PMP). In addition, the interaction of the complex with the polyanions has been studied by absorption and circular dichroism.

Results and Discussion

The electronic spectrum of $[Pd(bipy)(py)_2]^{2+}$ in water does not change over time although fast reversible spectro-

[a] Dipartimento di Chimica Inorganica, Chimica Analitica e Chimica Fisica, University of Messina,
Salita Sperone 31, 98166 Vill. S. Agata − Messina, Italy
Fax: (internat.) + 39-090393756
E-mail: cusumano@chem.unime.it

Supporting information for this article is available on the WWW under http://www.eurjic.org or from the author.

 © 2005 Wiley-VCH Verlag GmbH & Co. KGaA, Weinheim DOI: 10.1002/ejic.200400509

scopic variations can be observed on changing the pH of the solution. Such variations are not expected on the basis of the nature of the complex. Accordingly, ^{1}H NMR experiments show the presence of signals due to free pyridine in D_2O solutions of $[Pd(bipy)(py)_2]^{2+}$. These signals are not present if the spectrum is run in a poorly coordinating solvent such as deuterated acetone. It appears, therefore, that the complex undergoes hydrolysis within the preparation times of the solutions. Hydrolytic equilibria are common for square-planar complexes and lead to a wide range of products. In the present case, precise indications of the nature of the products are difficult to obtain either by UV/Vis or NMR spectroscopic measurements. However, previous studies on platinum(II) and palladium(II) complexes have shown[7] that hydrolysis produces monomeric aqua and hydroxo species as well as oligomeric species with bridging hydroxo or aqua groups.

Addition of sodium chloride, even in a large excess, to aqueous solutions of $[Pd(bipy)(py)_2]^{2+}$ alters the nature of the hydrolytic species in equilibrium without exchanging coordinated bipyridyl. However when thiourea is used, a bipyridyl is also replaced as well as the monodentate ligands coordinated to palladium. NMR spectra of the reaction mixtures in D_2O unambiguously show the signal corresponding to the released bipyridyl.

The rate of this process, which can be easily obtained by kinetic analysis of the spectroscopic variations over time (Figure 1), is largely independent of chloride and hydrogen ion concentration. Such independence suggests that the monitored process corresponds to the substitution of bipy in $[Pd(bipy)(tu)_2]^{2+}$ formed by the action of thiourea on the hydrolysis products [Equation (1)].

$$[Pd(bipy)(tu)_2]^{2+} + 2\,tu \rightarrow [Pd(tu)_4]^{2+} + bipy \quad (1)$$

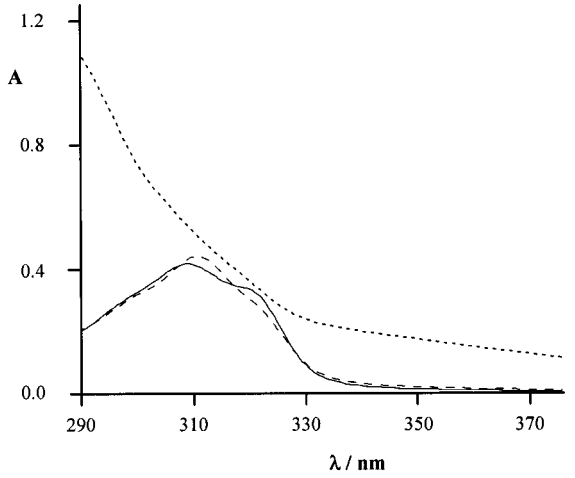

Figure 1. Spectroscopic changes at 25 °C and pH = 7 for the reaction of $[Pd(bipy)(py)_2]^{2+}$ in water (−), in the presence of Cl^- (− −) and with tu (···); $[Pd(bipy)]_{tot} = 3.75 \times 10^{-5}$ M

Thiourea, one of the strongest nucleophiles towards square-planar complexes,[4,8] replaces the monodentate ligands of the hydrolytic complexes in a fast step prior to substitution of bipy. In agreement with this observation, both the spectroscopic variations and the k_{obs} values are almost identical to those obtained upon treatment of a sample of independently synthesised $[Pd(bipy)(tu)_2]^{2+}$ with thiourea, under the same experimental conditions.

Under pseudo first-order conditions the reaction follows a first order course with respect to the complex. Plotting k_{obs} against $[tu]^2$ results in a straight line with a small intercept [Equation (2), Figure 2].

$$k_{obs} = k_1 + k_2 \cdot [tu]^2 \quad (2)$$

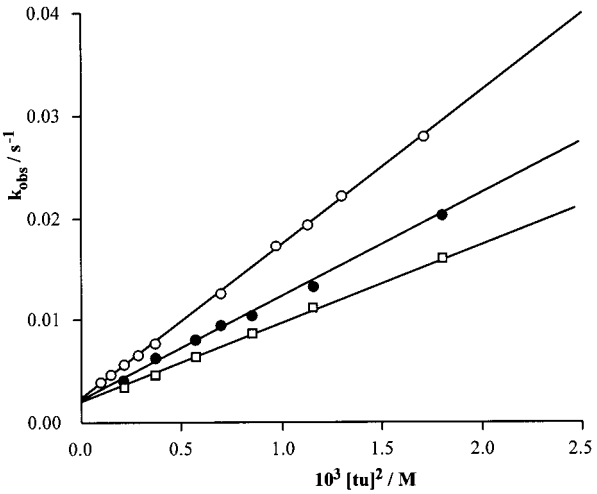

Figure 2. Plot of k_{obs} vs. $[tu]^2$ for reaction (1) [Equation (1)] at 25 °C and pH = 7; without DNA (open circles), in the presence of DNA at $I = 5.0 \times 10^{-2}$ M (filled circles), in the presence of DNA at $I = 2.2 \times 10^{-2}$ M, (squares) $[Pd(bipy)]_{tot} = 3.75 \times 10^{-5}$ M ; [DNA]/[complex] = 0.5

A possible mechanism that accounts for the experimental kinetic values is depicted below in Scheme 1.

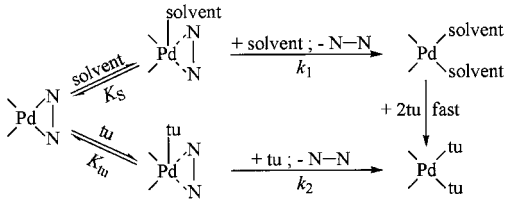

Scheme 1

This scheme implies the attack of a first thiourea molecule at the palladium atom with formation of an intermediate which leads to the product upon interaction with another thiourea molecule. $[Pd(tu)_4]^{2+}$ also forms through the customary solvolytic pathway.[8] The intermediates can be described as having a structure in which the ligand is monodentate but rapidly exchanging its point of attachment with the central atom.[9] From this scheme the following Equation (3) can be postulated.

 © 2005 Wiley-VCH Verlag GmbH & Co. KGaA, Weinheim

$$k_{obs} = \frac{k_1 K_S^{''} + k_2 [tu]^2 K_{tu}}{(1 + K_S^{'} + [tu] K_{tu})} \quad (3)$$

K'_S = [solvent]·K_S and K''_S = [solvent]^2·K_S. Taking into account that the intermediates could not be detected even using a large thiourea concentration, both K_{tu} and K_S should be very small and (K_{tu}·[tu] + K'_S) < 1. Therefore, rate law (3) is very similar to experimental rate law (2). When the reactions are conducted in the presence of DNA, no change in the rate law is observed and this suggests that the mechanism is the same as it is in water. However DNA influences the rate of reaction which becomes lower with respect to that in water (Figure 2).

In addition, the presence of DNA induces dependence of the kinetics on the ionic strength. Thus, when DNA is present, the kinetic values become significantly lower as the salt concentration decreases (Table 1).

Table 1. Values of rate constants for reaction (1) [Equation (1)] at 25 °C and pH = 7; $[Pd(bipy)]_{tot} = 3.75 \times 10^{-5}$ M

$10^3 k_1$ [s^{-1}]	k_2 [$M^{-2} \times s^{-1}$]
3.4 ± 0.3	15.1 ± 0.3[a]
2.0 ± 0.2	10.3 ± 0.7[b]
2.0 ± 0.3	7.6 ±0.5[c]

[a] Without DNA. [b] With DNA 1.87×10^{-5} M; $I = 5.0 \times 10^{-2}$ M. [c] With DNA 1.87×10^{-5} M; $I = 2.2 \times 10^{-2}$ M.

The inhibition caused by DNA depends on its concentration. In Figure 3 the k_{obs} values at fixed ionic strength and at a given thiourea concentration are plotted against the concentration of DNA.

On increasing the DNA concentration, there is a systematic decrease in the rate constants which tend to a limiting value. In addition, the sensitivity of the k_{obs} values to the DNA concentration change increases as the ionic strength is lowered. The presence of other polyanions also inhibits reaction (1) and again the presence of polymetaphosphate, poly(A) or polyvinylsulfonate does not change the rate law but the k_{obs} values become lower in all cases compared with those of the reaction in water. For these polyanions (Figure 4) the kinetic values are also less sensitive to their concentrations at higher ionic strengths.

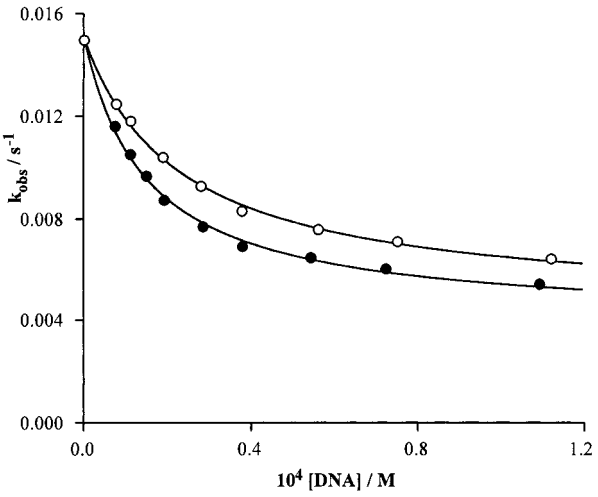

Figure 3. Plot of k_{obs} vs. [DNA] for reaction (1) [Equation (1)] at 25 °C and pH = 7; $[Pd(bipy)]_{tot} = 3.75 \times 10^{-5}$ M; [tu] = 2.91×10^{-2} M; $I = 5.0 \times 10^{-2}$ M (open circles); $I = 2.2 \times 10^{-2}$ M (filled circles)

The influence of the polyanion on the rate of bipyridyl substitution cannot be explained on the basis of concentration effects[10] arising from a particular distribution of the reactants driven by electrostatic interactions. While the dicationic complex tends to concentrate around the polyanion, the uncharged thiourea has no preference for any particular region of the solution. The inhibiting effect seems to be steric in origin and can be interpreted on the basis of noncovalent interactions between the complex and the

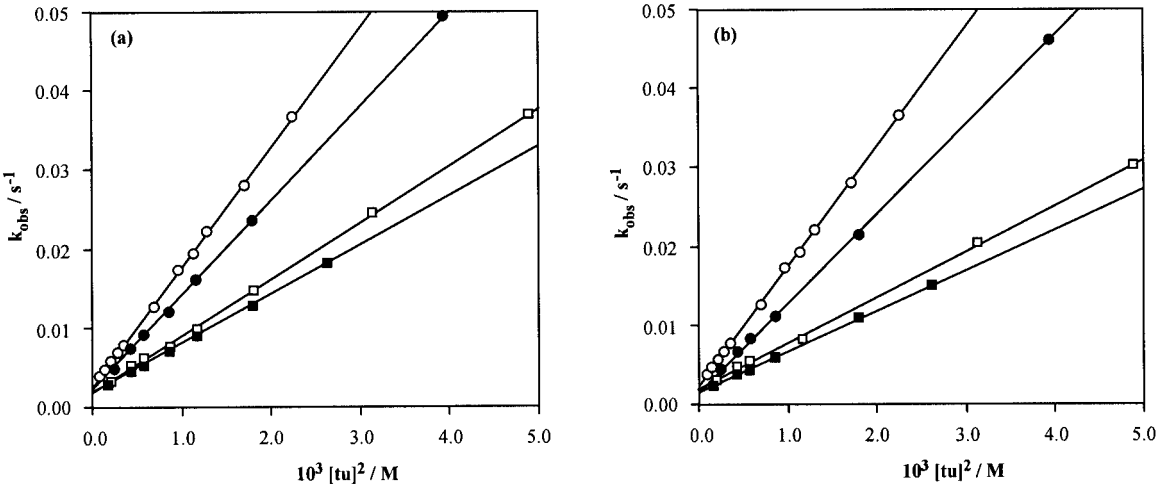

Figure 4. Plot of k_{obs} vs. [tu]^2 for reaction (1) [Equation (1)], at 25 °C and pH = 7, in water (open circles) and in the presence of polyanions (a) at $I = 5.0 \times 10^{-2}$ M and (b) at $I = 2.2 \times 10^{-2}$ M; $[Pd(bipy)]_{tot} = 3.75 \times 10^{-5}$ M, [PMP] = 7.50×10^{-5} M (filled circles), [Poly(A)] = 3.75×10^{-5} M (open squares), [PVS] = 1.87×10^{-5} M (filled squares)

 © 2005 Wiley-VCH Verlag GmbH & Co. KGaA, Weinheim

polyanions. In principle, due to the lability of palladium(II) complexes, covalent binding could also occur with the DNA nucleobases. However, under our experimental conditions, the complex and the DNA are initially separate. The biopolymer is then added together with thiourea in a large excess. Thiourea is a much stronger nucleophile than the nucleobases and competition between the two nucleophiles is, therefore, highly unlikely.

In the absence of thiourea, addition of any of the polyanions to $[Pd(bipy)(tu)_2]^{2+}$(the actual chemical species involved in the process studied) produces immediate spectroscopic variations characterised by hypochromism (Figure 5 and 6).

The presence of noncovalent interactions between a small molecule and a chiral polyanion such as DNA or poly(A) is also indicated by the appearance of a CD signal in the spectroscopic region where the bound molecule absorbs. This CD signal is due to induced circular dichroism as a result of the rigid orientation assumed by the bound substance with respect to the helical axis of the polyanion. Figure 7 shows the CD spectra of the complex in the presence of increasing amounts of DNA and poly(A).

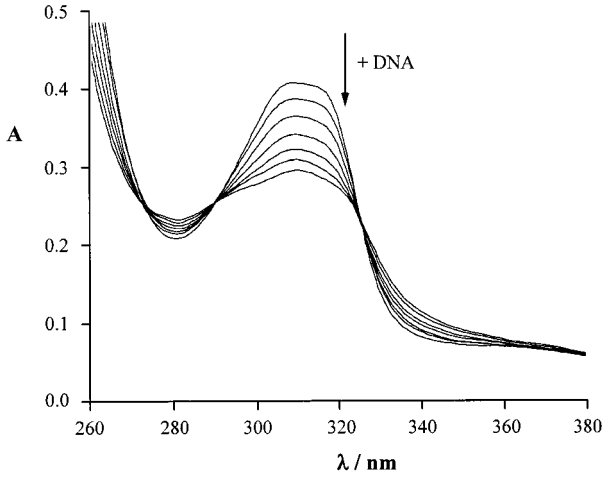

Figure 5. Spectroscopic changes for the interaction of $[Pd(bipy)(tu)_2]^{2+}$ (3.75×10^{-5} M) with DNA, at 25 °C and pH = 7; $I = 2.2 \times 10^{-2}$ M; [DNA]/[complex] = 0, 0.27, 0.52, 0.84, 1.14, 1.55, 2.03

As is well known, small molecules can interact noncovalently with double stranded DNA[11] either by surface binding or by intercalation. Both binding modes and especially intercalation imply shielding of the reaction centre, reducing the effectiveness of the incoming ligand and lowering the rate of substitution. Though neither absorption nor circular dichroism experiments can establish the type of noncovalent interaction between a small molecule and the DNA double helix, previous investigations[2d] have shown that $[Pt(bipy)(py)_2]^{2+}$, as well as many other dicationic platinum(II) and palladium(II) complexes of bipyridyl, intercalate with DNA. Similar conclusions can also be drawn for $[Pd(bipy)(tu)_2]^{2+}$ and its precursor $[Pd(bipy)(py)_2]^{2+}$. The binding constant for the interaction of $[Pd(bipy)(tu)_2]^{2+}$ with DNA at 25 °C and $I = 2.2 \times 10^{-2}$ M, obtained by the analysis of the spectrophotometric titration data via the McGhee von Hippel[12] equation is $(1.0 \pm 0.1) \times 10^5$ M^{-1}. Such a value is of the same order of magnitude as other similar platinum(II) and palladium(II) complexes.[2b,2d,3]

Intercalation may well account for the observed rate effect. Shielding of both sides of the square plane by the nucleobases hampers the attack of the incoming nucleophile thus inhibiting the substitution process. The decrease in the rate of ligand substitution at a given DNA concentration, as the salt concentration is reduced, is due to the influence[13] of ionic strength on the complex-DNA interaction. Due to competition of the interacting small molecule and the other cations present in solution for the anionic phosphate groups of DNA, ionic strength destabilises any type of noncovalent interaction between cationic species and this biopolymer. In addition, ionic strength influences DNA conformation. Increasing ionic strength reduces repulsion between phosphate groups allowing adjacent base pairs to get closer thus disfavouring intercalation. For the other polyanions, where intercalation is not possible, the reactivity inhibition can be interpreted on the basis of self-aggregation of the complex. Stacking of aromatic rings produces hypochromism[14] as experimentally observed upon interac-

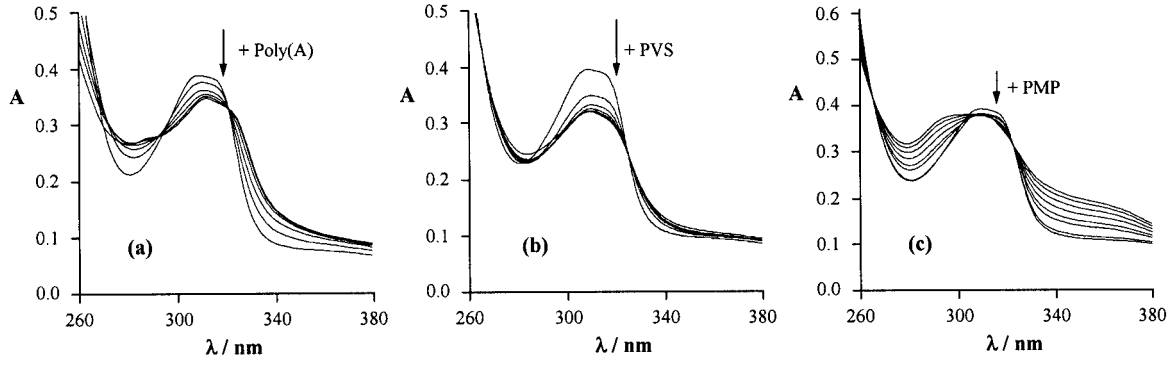

Figure 6. Spectrophotometric titration of $[Pd(bipy)(tu)_2]^{2+}$ (3.75×10^{-5} M), at 25 °C and pH = 7, with (a) poly(A) ([poly(A)]/[complex] = 0, 0.55, 1.02, 1.43, 1.79, 2.11), (b) PVS ([PVS]/[complex] = 0, 0.007, 0.014, 0.020, 0.027, 0.033), and (c) PMP ([PMP]/[complex] = 0, 5.8, 11.5, 22.5, 43.4, 80.9, 113.5, 142.2, 167.6); $I = 2.2 \times 10^{-2}$ M

 © 2005 Wiley-VCH Verlag GmbH & Co. KGaA, Weinheim

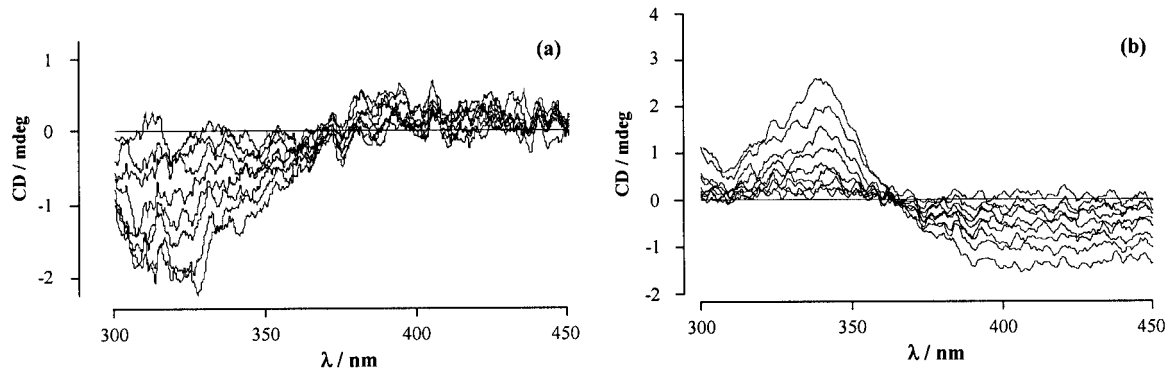

Figure 7. CD spectroscopic titration of $[Pd(bipy)(tu)_2]^{2+}$ (3.75×10^{-5} M) with (a) DNA and (b) poly(A) at 25 °C and pH = 7; $I = 2.2 \times 10^{-2}$ M

tion with the polyanions, while for poly(A) the observed hypochromism could be caused either by interaction of the adenine rings with the bipyridyl rings or by self stacking of the bipyridyl rings. Only the latter type of interaction is conceivable for PVS and PMP. In both cases, however, the interaction shields the reaction centre thus hampering attack of the nucleophile at palladium and so lowering the rate of reaction. Rate effects of other palladium(II) complexes upon the reaction with thiourea in the presence of polyvinylsulfonate have been previously reported.[6b] The observed acceleration of the rate of ethylenediamine substitution both for complexes of the type $[Pd(N-N)_2]^{2+}$ (N−N = ethylenediamine or *N*,*N*-substituted ethylenediamine) and $[Pd(bipy)(en)]^{2+}$ has been accounted for in terms of the enhanced acidity of the surfaces of the polyanions. These processes are acid catalysed and proceed faster in the proximity of a polyanion where the pH is lower than in the bulk.[15] In the case of $[Pd(bipy)(en)]^{2+}$, catalysis is observed even though the bipyridyl moieties undergo stacking and slow down the process. The accelerating effect, due to polyanion local acidity, probably prevails over the inhibition caused by stacking. The rate of bipyridyl replacement in $[Pd(bipy)(tu)_2]^{2+}$ is independent of the solution acidity and only inhibition, most likely due to self-stacking of the complexes, can occur as experimentally observed. The influence of the ionic strength on the rate of the reaction is similar to that observed for DNA and is again due to competition between the complex and the other cations present in solution for the negative charges of the polyanion.

The dependence of the k_{obs} values on the DNA concentration can be reasonably interpreted by assuming that the dicationic complex is partitioned between the DNA pseudo-phase and the bulk solution (Scheme 2). The DNA pseudo-phase includes the double helix itself, in which the complex is intercalated, and its electrostatic environment.

Taking into account that noncovalent interactions are much faster than the covalent steps involved in the scheme, the rate law according to Equation (4) may be deduced, where $K'_{S,W} = K_{S,W}\cdot[solvent]$, $K''_{S,W} = K_{S,W}\cdot[solvent]^2$, $K'_{S,DNA} = K_{S,DNA}\cdot[solvent]$, $K''_{S,DNA} = K_{S,DNA}\cdot[solvent]^2$; $k_{1,W}$ and $k_{1,DNA}$ are, respectively, the rate constants for replacement of monocoordinated bipyridyl by water in the

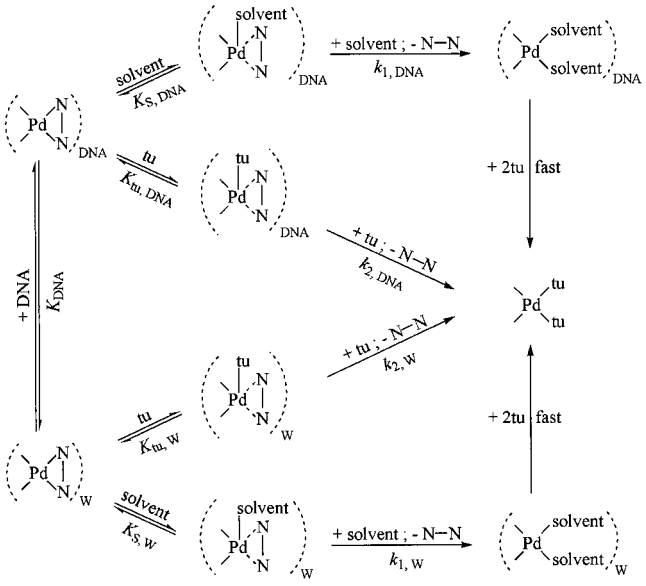

Scheme 2

bulk phase and in the DNA pseudophase, while $k_{2,W}$ and $k_{2,DNA}$ are the rate constants for replacement of monocoordinated bipyridyl by thiourea in the bulk phase and in the DNA pseudophase. $K_{S,W}$ and $K_{S,DNA}$ are, respectively, the equilibrium constants for formation of the monosubstituted solvo-intermediate in water and in the DNA pseudophase, while $K_{tu,W}$ and $K_{tu,DNA}$ are the equilibrium constants for formation of the monosubstituted thiourea-intermediate in water and in DNA pseudophase, respectively. K_{DNA} is the equilibrium constant for partitioning of the complex in water and in the DNA pseudophase.

$$k_{obs} = \frac{k_{1,W}K''_{S,W} + k_{2,W}K_{tu,W}[tu]^2 + [DNA]\left(k_{1,DNA}K''_{S,DNA}K_{DNA} + k_{2,DNA}K_{tu,DNA}K_{DNA}[tu]^2\right)}{1 + [DNA]\left(K_{DNA} + K_{DNA}K'_{S,DNA} + K_{DNA}K_{tu,DNA}[tu]\right) + K'_{S,W} + K_{tu,W}[tu]} \quad (4)$$

In the absence of DNA Equation (4) coincides with Equation (3). When the concentration of DNA is large enough, for a given thiourea concentration, the rate constant

 © 2005 Wiley-VCH Verlag GmbH & Co. KGaA, Weinheim

k_{obs} assumes a constant value which is lower than that in water [Equation (5)].[16]

$$k_{obs} = \frac{k_{1,DNA}K^{''}_{S,DNA} + k_{2,DNA}K_{tu,DNA}[tu]^2}{1 + K^{'}_{S,DNA} + K_{tu,DNA}[tu]} \quad (5)$$

The good agreement between the experimental plot of k_{obs} against [DNA] and that obtained by fitting the data in accordance with Equation (4) supports the proposed scheme. In addition, the value of the binding constant of 6.5×10^4 M^{-1}, obtained from the fitting of the kinetic data[17] to the same equation at $I = 2.2 \times 10^{-2}$ M, is in fair agreement with that of $(1.0 \pm 0.1) \times 10^5$ M^{-1} determined spectrophotometrically under the same experimental conditions.

Experimental Section

Synthesis. [Pd(bipy)(py)$_2$](PF$_6$)$_2$: The compound was prepared according to a general procedure previously described[3,4] by heating an aqueous suspension of [Pd(bipy)Cl$_2$] with an excess of pyridine to reflux. After dissolution of the solid, NH_4PF_6 was added and the resultant complex precipitated as a pale yellow substance which was recrystallised from water-acetone. **[Pd(bipy)(tu)$_2$](PF$_6$)$_2$:** The compound was prepared in a similar way by treating [Pd(bipy)Cl$_2$] with thiourea in a ratio of 1:2. Both complexes were characterised by elemental analysis and ^{1}H NMR spectroscopy in [D$_6$]acetone.

DNA: Calf thymus DNA was purchased from Sigma Chemical Co. and purified as described previously.[18] DNA concentration, expressed in base pairs, was calculated spectrophotometrically using an ε_{260} value of 1.31×10^4 M^{-1}·cm^{-1}.[19] NaCl and other chemicals were of reagent grade and were used without further purification.

Poly(A): Polyadenylic acid was purchased from Pharmacia Co. and used as received. The Poly(A) concentration was calculated spectrophotometrically using an ε_{258} value of 9.8×10^3 M^{-1}·cm^{-1}.[20]

PVS and PMP: Sodium polyvinylsulfonate and sodium polymetaphosphate were also of reagent grade (Aldrich).

Methods: All experiments were carried out at 25 °C in a phosphate buffer 1×10^{-3} M ([KH$_2$PO$_4$]/[Na$_2$HPO$_4$] = 1.61) to maintain pH = 7 and sufficient NaCl to give the desired ionic strength. The pH was measured with a Radiometer PHM 62 instrument. Absorption spectra were recorded using a Lambda 5 Perkin–Elmer spectrophotometer. ^{1}H NMR spectra were recorded with a Bruker ARX-300 spectrometer. CD spectra were recorded with a J-810 Jasco polarimeter.

Kinetics: The kinetics of ligand substitution were followed spectrophotometrically in the range of 320–400 nm at 25 °C. In order to avoid competing covalent binding of the complex to the DNA nucleobases, the biopolymer was added to the complex and placed in a cuvette preheated to 25 °C together with thiourea. The concentration of the latter was at least twenty times larger than that of the DNA and the complex. A Perkin–Elmer Lambda 5 spectrophotometer was used to monitor the process. The absorbance changes were displayed on a PC interfaced with the spectrophotometer and pseudo first-order rate constants k_{obs} were obtained from nonlinear least-squares fits of the experimental data to $A_t = A_\infty + (A_0 - A_\infty)\exp(-k_{obs}t)$, where A_0, A_∞ and k_{obs} are the parameters to be optimised (A_0 = absorbance after mixing of the reagents, A_∞ = absorbance at completion of reaction). The k_{obs} values were reproducible to better than ±5%.

Binding Constant Determination: To a solution of complex (3.75×10^{-5} M) were added successive aliquots of DNA, also containing the complex, in a 10-mm stoppered quartz cell and a spectrum was recorded after each addition. The spectrophotometric data were analysed by a non least-squares fitting program using the McGhee and von Hippel equation.[12] The binding constant K_B was determined by the program using the extinction coefficient, the free complex concentration and the ratio of bound complex per mole of DNA. The extinction coefficient for the bound complex was determined by Beer's law plots in the presence of a large excess of DNA.

Supporting Information: All the kinetic data are available (see also footnote on the first page of this article).

Acknowledgments

This work was supported by funds from PRA (Progetto di Ricerca d'Ateneo) of the University of Messina.

[1] S. J. Lippard, *Acc. Chem. Res.* **1978**, *11*, 211–217.
[2] [2a] W. I. Sundquist, S. J. Lippard, *Coord. Chem. Rev.* **1990**, *100*, 293–322. [2b] C. M. Che, *J. Chem. Soc., Chem. Commun.* **1995**, 509–510. [2c] A. McCoubrey, H. C. Latham, P. R. Cook, A. Rodger, G. Lowe, *FEBS Lett.* **1996**, *380*, 73–78. [2d] M. Cusumano, M. L. Di Pietro, A. Giannetto, F. Nicolò, E. Rotondo, *Inorg. Chem.* **1998**, *37*, 563–568. [2e] M. Cusumano, M. L. Di Pietro, A. Giannetto, *Inorg. Chem.* **1999**, *38*, 1754–1758.
[3] M. Cusumano, A. Giannetto, *J. Inorg. Biochem.* **1997**, *65*, 137–144.
[4] L. Cattalini ("Reaction Mechanism Inorganic Chemistry"), in *M.T.P. Internat. Rev. Sci.*, ser. 1, vol. 9 (Ed.: M. L. Tobe), Butterworths, London, **1972**.
[5] [5a] R. F. Pasternack, E. J. Gibbs, R. Santucci, S. Shaertel, P. Ellinas, S. C. Sah, *J. Chem. Soc., Chem. Commun.* **1987**, 1771–1774. [5b] M. Cusumano, M. L. Di Pietro, A. Giannetto, M. A. Messina, F. Romano, *J. Chem. Soc., Chem. Commun.* **1999**, 1495–1496.
[6] [6a] T. W. Welch, S. A. Ciftan, P. S. White, H. H. Thorp, *Inorg. Chem.* **1997**, *36*, 4812–4821. [6b] M. Cusumano, M. L. Di Pietro, A. Giannetto, M. A. Messina, F. Romano, *J. Am. Chem. Soc.* **2001**, *123*, 1914–1919.
[7] [7a] G. Anderegg, H. Wanner, *Inorg. Chim. Acta* **1986**, *113*, 101–108. [7b] R. Faggiani, B. Lippert, C. J. Lock, B. Rosenberg, *J. Am. Chem. Soc.* **1977**, *99*, 777–781.
[8] [8a] F. Basolo, R. G. Pearson in *Mechanisms of Inorganic Reactions*, John Wiley, New York, **1968**. [8b] R. G. Wilkins in *Kinetics and Mechanisms of Reactions of Transition Metal Complexes*, VCH Weinheim, Germany, **1991**.
[9] K. R. Dixon, *Inorg. Chem.* **1977**, *16*, 2618–2624.
[10] E. U. Cordes, R. B. Dunlap, *Acc. Chem. Res.* **1969**, *2*, 329–337.
[11] I. Blackburn, M. J. Gait in *Nucleic Acids in Chemistry and Biology*, 2nd ed., Oxford University Press, Oxford, **1996**.
[12] J. D. McGhee, P. H. von Hippel, *J. Mol. Biol.* **1974**, *86*, 469–489.
[13] G. S. Manning, *Q. Rev. Biophys.* **1978**, *11*, 179–266.
[14] [14a] O. Yamauchi, A. Odani, R. Shimata, Y. Kosaka, *Inorg. Chem.* **1986**, *25*, 3337–3339. [14b] A. Odani, R. Shimata, H. Masuda, O. Yamauchi, *Inorg. Chem.* **1991**, *30*, 2133–2138. [14c] A. Odani, R. Masuda, O. Yamauchi, S. Ishiguro, *Inorg. Chem.* **1991**, *30*, 4484–4486.

 © 2005 Wiley-VCH Verlag GmbH & Co. KGaA, Weinheim

[15] [15a] G. Lamm, G.R. Pack, *Proc. Natl. Acad. Sci. U. S. A.* **1990**, *87*, 9033−9036. [15b] G. Lamm, L. Wong, G. R. Pack, *J. Am. Chem. Soc.* **1996**, *18*, 3325−3331.
[16] K_{DNA} is expected to be very large as experimentally found for many (bipyridine)platinum(II) and -palladium(II) complexes. Therefore, the values in parentheses both in the numerator and the denominator of Equation (4) should be much larger than the other terms.
[17] Owing to the large value of K_{DNA} the denominator of Equation (4) is approximately equal to K_{DNA}[DNA]. Thus, the value of the parameter P_3 obtained from the fitting of the kinetic data to $k_{obs} = (P_1 + P_2[DNA])/(1 + P_3[DNA])$ corresponds essentially to the value of K_{DNA}.
[18] R. F. Pasternack, E. J. Gibbs, J. J. Villafranca, *Biochemistry* **1983**, *22*, 2406−2414.
[19] R. D. Wells, J. E. Larson, R. C. Grant, B. E. Shortle, C. R. Cantor, *J. Mol. Biol.* **1970**, *54*, 465−497.
[20] Amersham Pharmacia Biotech, unpublished results.

Received June 11, 2004
Early View Article
Published Online November 18, 2004

Stabilization and Destabilization of the Ru−CO Bond During the 2,2′-Bipyridin-6-onato (bpyO)-Localized Redox Reaction of [Ru(terpy)(bpyO)(CO)](PF_6)

Takashi Tomon,[a] Take-aki Koizumi,[a] and Koji Tanaka*[a]

Keywords: Carbonyl complex / Electrochemistry / IR spectroscopy / Ruthenium

Two stereoisomers of [Ru(terpy)(bpyO)(CO)](PF_6) ([**1**]$^+$ and [**2**]$^+$; terpy = 2,2′:6′,2′′-terpyridine, bpyO = 2,2′-bipyridin-6-onato) were prepared. The pyridonato moiety in the bpyO ligand of [**1**]$^+$ and [**2**]$^+$ is located *trans* and *cis*, respectively, to CO. Treatment of [**1**]$^+$ and [**2**]$^+$ with HPF_6 produced [**1**H]$^{2+}$ and [**2**H]$^{2+}$, both of which contain bpyOH (bpyOH = 6-hydroxy-2,2′-bipyridine). The difference in the pK_a values of [**1**H]$^{2+}$ (3.5) and [**2**H]$^{2+}$ (3.9) reflects the stronger electronic interaction between CO and the pyridonato moiety in the bpyO ligand in the *trans* position compared with that in the *cis* position. The molecular structures of [**1**](PF_6), [**2**](PF_6)·H_2O and [**2**H](PF_6)$_2$·2H_2O were determined by X-ray structure analyses. [**1**]$^+$ and [**2**]$^+$ undergo one, reversible reduction at $E_{1/2}$ = −1.65 V and −1.51 V, respectively, and one irreversible reduction at $E_{p,c}$ = −2.07 and $E_{p,c}$ = −2.13 V, respectively. Both reductions are assigned to redox reactions localized at the terpy and bpyO ligands. Irreversible reduction of [**1**]^0 results from reductive cleavage of the Ru–CO bond of [**1**]$^-$. On the other hand, a two-electron oxidation of [**2**]$^-$ almost regenerates [**2**]$^+$ because of the depression of the reductive Ru–CO bond cleavage of [**2**]$^-$ due to cyclometalation formed by an attack of oxygen of bpyO to the carbon of the Ru–CO bond. An unusually large shift of the ν(C≡O) band on going from [**2**]^0 (1950 cm^{-1}) to [**2**]$^-$ (1587 cm^{-1}) also supports a reversible cyclometalation driven by the bpyO-localized redox reaction.
(© Wiley-VCH Verlag GmbH & Co. KGaA, 69451 Weinheim, Germany, 2005)

Introduction

Polypyridylruthenium complexes exhibit a unique electrochemical behavior[1] because of the low energy level of the π*-orbitals of the ligands. For example, redox reactions of polypyridyl ligands can be utilized as electron pools in photo-[2] and electrochemical[3] reduction of CO_2 catalyzed by polypyridylruthenium complexes. Modification of polypyridyl ligands may create new functionalities in addition to the role of the redox centers of ruthenium complexes. For example, a keto-enol tautomerism between 6-hydroxy-2,2′-bipyridine (bpyOH) and 2,2′-bipyridin-6(1*H*)-one (bpyO) [Equation (1)] would induce the acid-base equilibrium of bpyOH ligated to Ru [Equation (2)], followed by resonance between (2,2′-bipyridin-6-onato)- and (2,2′-bipyridin-6-olato)ruthenium complexes [Equation (3)].

(1)

(2)

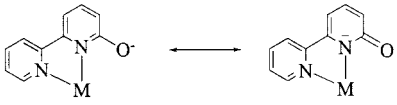

(3)

A few metal complexes with bpyO have been reported to date,[4] but neither the equilibrium of Equation (2) nor the resonance of Equation (3) has been discussed. The acid-base equilibrium of Ru(bpyOH) complexes [Equation (2)] and the subsequent resonance of Ru(bpyO) ones [Equation (3)] may allow these complexes to undergo proton-coupled electron transfer. The ligand-localized redox reaction of metal−bpyO(H) complexes would influence the equilibrium of Equation (2) and the resonance of Equation (3). In connection with this, a drastic change of basicity of the free nitrogen of the 1,8-naphthyridine ligand of [Ru(bpy)$_2$(napy-κ*N*)(CO)]$^{2+}$ (napy = 1,8-naphthyridine) has been reported. One-electron reduction of napy resulted in an attack of the free nitrogen at the carbon atom of the Ru−CO bond to form a metallacyclic ring, which smoothly opened upon oxidation of the napy ligand.[5] Such reversible cyclometalation driven by ligand-localized redox reactions falls

[a] Institute for Molecular Science and CREST, Japan Science and Technology Agency (JST),
5-1 Higashiyama, Myodaiji, Okazaki, Aichi 444-8787, Japan
Fax: + 81-564-59-5582
E-mail: ktanaka@ims.ac.jp
Supporting information for this article is available on the WWW under http://www.eurjic.org or from the author.

into a new category in a number of metallacyclic complexes bearing five-[6] and six- membered[7] rings and containing CO as a cycle component.

In this work, we have prepared two geometrical isomers of $[Ru(terpy)(bpyO)(CO)]^+$ with regard to the orientation of bpyO ($[\mathbf{1}]^+$ and $[\mathbf{2}]^+$) and determined the pK_a values of their protonated complexes ($[\mathbf{1H}]^{2+}$ and $[\mathbf{2H}]^{2+}$). Two-electron reduction of $[\mathbf{1}]^+$, which has the pyridonato moiety of the bpyO ligand *trans* to CO, caused reductive cleavage of the Ru−CO bond, while two-electron reduction of $[\mathbf{2}]^+$, which has the pyridonato moiety of the bpyO ligand *cis* to CO, formed a metallacyclic ring due to an attack of the oxygen of bpyO at the carbon of the Ru−CO bond.

Results and Discussion

Syntheses and Structures of $[\mathbf{1}]^+$, $[\mathbf{1H}]^{2+}$, $[\mathbf{2}]^+$, and $[\mathbf{2H}]^{2+}$

There are two possible orientations of the pyridonato ring of bpyO in $[Ru(terpy)(bpyO)(CO)]^+$ (vide infra): one is in a position *trans* to CO ($[\mathbf{1}]^+$) and the other is in a position *cis* to CO ($[\mathbf{2}]^+$). The preparative pathways of $[\mathbf{1}]^+$ and $[\mathbf{2}]^+$ are depicted in Scheme 1. Treatment of $[RuCl(terpy)(bpyOH)]^+$ with $AgPF_6$ under CO (15 atm) in 2-methoxyethanol produced $[Ru(terpy)(bpyO)(CO)]^+$ ($[\mathbf{1}]^+$).

The ^{1}H NMR spectra of the PF_6 salt of $[\mathbf{1}]^+$ clearly show the selective formation of one of the two isomers under these reaction conditions. X-ray analysis of $[\mathbf{1}](PF_6)$ demonstrated coordination of CO to Ru in the position *trans* to the pyridonato ring of bpyO (vide infra). On the other hand, the substitution reaction of an aqua ligand of $[Ru(terpy)(bpyO)(OH_2)]^+$ by CO (20 atm) in 2-methoxyethanol selectively produced the other isomer of $[Ru(terpy)(bpyO)(CO)]^+$ with CO in the position *cis* to the pyridonato ring of bpyO ($[\mathbf{2}]^+$). The ^{1}H NMR spectra of the crude product of $[\mathbf{2}](PF_6)$ did not show any contamination by $[\mathbf{1}](PF_6)$. It is worthwhile to note that the orientation of bpyOH in $[Ru(terpy)(bpyOH)Cl]^+$ is inverted in $[\mathbf{1}]^+$, whereas that in $[Ru(terpy)(bpyO)(OH_2)]$ is maintained in $[\mathbf{2}]^+$. Such a difference may result from an involvement of an attack of CO to pentacoordinate $[Ru(terpy)(bpyOH)]^+$ that would be produced in the reaction of $[Ru(terpy)(bpyOH)Cl]^+$ with Ag^+.

Treatment of $[\mathbf{1}]^+$ and $[\mathbf{2}]^+$ with one equivalent of HPF_6 produced $[\mathbf{1H}]^{2+}$ and $[\mathbf{2H}]^{2+}$, respectively, in CH_3CN. The addition of one equivalent of Et_3N to $[\mathbf{1H}]^{2+}$ and $[\mathbf{2H}]^{2+}$ completely regenerated $[\mathbf{1}]^+$ and $[\mathbf{2}]^+$, respectively, in CH_3CN [Equation (4)].

$$\underset{[\mathbf{1}]^+ \text{ and } [\mathbf{2}]^+}{[Ru(trpy)(bpy\text{-}O)(CO)]^+} + H^+ \rightleftharpoons \underset{[\mathbf{1H}]^{2+} \text{ and } [\mathbf{2H}]^{2+}}{[Ru(trpy)(bpy\text{-}OH)(CO)]^{2+}} \quad (4)$$

The ^{1}H NMR spectra of $[\mathbf{1}]^+$ and $[\mathbf{2}]^+$ clearly confirm the protonation of the oxygen atom of the bpyO ligand, since treatment of $[\mathbf{1}]^+$ and $[\mathbf{2}]^+$ with HPF_6 in CD_3CN shifts the pyridonate ring protons to lower magnetic field by 0.65−1.3 ppm, while the terpy and pyridine protons of bpyO shift by only 0.1−0.25 ppm upon protonation of $[\mathbf{1}]^+$ and $[\mathbf{2}]^+$. The pK_a values of hydroxypyridine in $[\mathbf{1H}](PF_6)_2$ and $[\mathbf{2H}](PF_6)_2$ were determined to be 3.5 and 3.9, respectively, by pH titrations in H_2O at 25 °C. The difference in the pK_a values of $[\mathbf{1H}]^{2+}$ and $[\mathbf{2H}]^{2+}$ can reasonably be ascribed to the stronger electronic interaction between CO and the pyridonato moiety in the bpyO ligand in the *trans* position compared with that in the *cis* position.

The crystal structures of the cations of complexes $[Ru(terpy)(bpyO)(OH_2)](PF_6)$ and $[Ru(terpy)(bpyOH)Cl](PF_6)$[8] are depicted in Figure 1 and the Supporting Information, respectively. The bond lengths and angles of $[Ru(terpy)(bpyO)(OH_2)]^+$ are listed in Table 1. The pyridonato ring of $[Ru(terpy)(bpyO)(OH_2)]^+$ and the hydroxypyridine ring of $[Ru(terpy)(bpyOH)Cl]^+$ are situated *cis* to the H_2O and Cl ligands, respectively. The C1−O1 and C−C bonds lengths of the pyridonato ring of bpyO in $[Ru(terpy)(bpyO)(OH_2)]^+$ are 1.288(5) Å and 1.368(7)−1.417(7) Å, and are similar to those in the 2-pyridonato ligands of $[Ru(terpy)(NC_5H_4O\text{-}\kappa N)_2(OH_2)]$[9] and *mer*-$[Pt(NH_3)_2(NC_5H_4O\text{-}\kappa N)Cl_3]$[10] ($NC_5H_4O\text{-}\kappa N$ = 2-pyridonato). The Ru1−O2 bond length is 2.152(3) Å, which is quite close to that in $[Ru(terpy)(NC_5H_4O\text{-}\kappa N)_2(OH_2)]$ (2.160 Å).[9] The interatomic O1···O2 distance [2.533(5) Å] be-

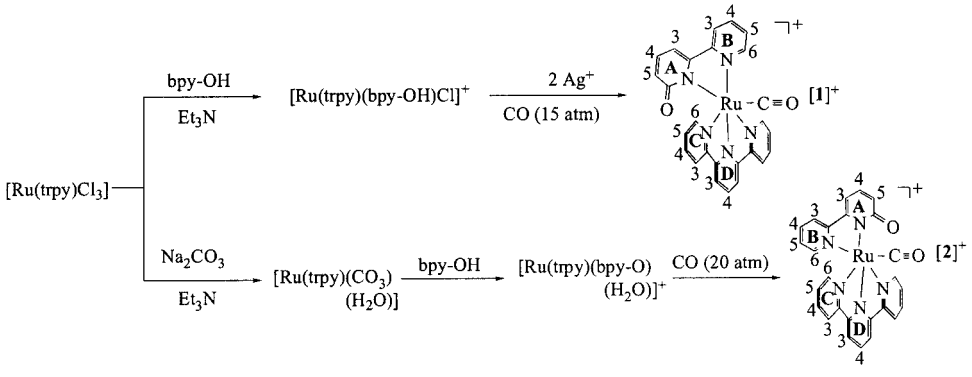

Scheme 1. Synthetic routes to the carbonyl complexes $[\mathbf{1}]^+$ and $[\mathbf{2}]^+$

 © 2005 Wiley-VCH Verlag GmbH & Co. KGaA, Weinheim

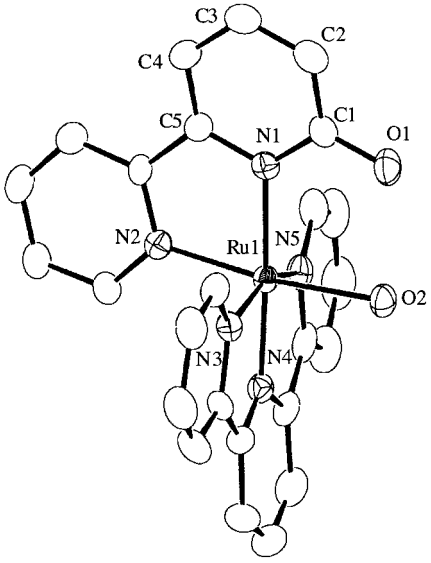

Figure 1. Molecular structure of $[Ru(terpy)(bpyO)(OH_2)]^+$ with atom labeling; hydrogen atoms are omitted for simplicity

Table 1. Selected bond lengths [Å] and angles [°] for $[Ru(terpy)(bpyO)(OH_2)](PF_6)$

Ru1−N1	2.089(4)	Ru1−N2	2.036(4)
Ru1−N3	2.062(4)	Ru1−N4	1.957(4)
Ru1−N5	2.081(4)	Ru1−O2	2.152(3)
N1−C1	1.370(6)	N1−C5	1.358(6)
C1−O1	1.288(5)	C1−C2	1.417(7)
C2−C3	1.368(7)	C3−C4	1.399(7)
C4−C5	1.375(6)		
N1−Ru1−N2	78.7(1)	N1−Ru1−N4	175.8(1)
N1−Ru1−O2	94.5(1)	N3−Ru1−N4	80.0(2)
N4−Ru1−N5	79.6(2)		
O1−C1−N1	120.1(4)	O1−C1−C2	120.8(4)
N1−C1−C2	119.1(4)		

tween the pyridonato and the aqua ligands suggests hydrogen-bond formation between them.

The molecular structures of the ruthenium carbonyl complexes bearing bpyO ($[\mathbf{1}]^+$ and $[\mathbf{2}]^+$) and bpyOH ($[\mathbf{2H}]^{2+}$) were determined by X-ray crystal structure analysis. The crystal structures of the cations of these complexes are shown in Figure 2; selected bond lengths and angles are listed in Table 2. The pyridonato group of the bpyO ligand in $[\mathbf{1}]^+$ and $[\mathbf{2}]^+$ is situated *trans* and *cis,* respectively, to the CO ligand (Figure 2a and 2b). The orientation of bpyOH in $[\mathbf{2H}]^{2+}$ is the same as that in $[\mathbf{2}]^+$ (Figure 2c). The Ru1−N bond lengths of terpy in the carbonyl complexes are 1.989(3)−2.100(3) for $[\mathbf{1}]^+$, 2.006(9)−2.09(1) for $[\mathbf{2}]^+$, and 1.983(4)−2.098(4) for $[\mathbf{2H}]^{2+}$. These bond lengths are close to those of similar ruthenium carbonyl complexes such as $[Ru(terpy)(bpy)(CO)]^{2+}$ (1.989−2.086 Å)[3e] and $[Ru(terpy)(bpy)(py)]^{2+}$ (1.963−2.078 Å; py = pyridine).[11] The C1−O1 bond lengths of bpyO in $[\mathbf{1}]^+$ [1.250(4) Å] and $[\mathbf{2}]^+$ [1.26(1) Å] are in the range of a normal C=O double bond. It is worthwhile to note that the C1−O1 bond length in $[\mathbf{2H}]^{2+}$ [1.326(7) Å] is much longer than those in $[\mathbf{1}]^+$ and $[\mathbf{2}]^+$, and is close to that of a C−O single bond. Furthermore, elongation of the Ru1−N1 bond length [2.112(4) Å], as well as the C1−O1 bond length of $[\mathbf{2H}]^{2+}$, compared with that of $[\mathbf{2}]^+$ [2.087(9) Å] demonstrates the decrease of the covalency of the Ru−N1 bond due to the protonation of the oxygen atom of bpyO in $[\mathbf{2}]^+$ [Equation (2)]. There seems to be a substantial strain in the coordination of bpyO to Ru in $[\mathbf{1}]^+$ because the C1−N1−Ru1−N4 dihedral angle [15.6(3)°] in $[\mathbf{1}]^+$ is much larger than the corresponding angle (C1−N1−Ru1−C26) in $[\mathbf{2}]^+$ [7(1)°]. This may be caused by repulsion between the lone-pair electrons of the bpyO oxygen atom and the π-electrons of the central pyridine ring of terpy. The shift of the oxygen atom of bpyO near the pyridyl ring of terpy in $[\mathbf{1}]^+$ to the position *cis* to the CO ligand of $[\mathbf{2}]^+$ will release the strain in the coordination of bpyO to Ru. A relatively short interatomic distance between

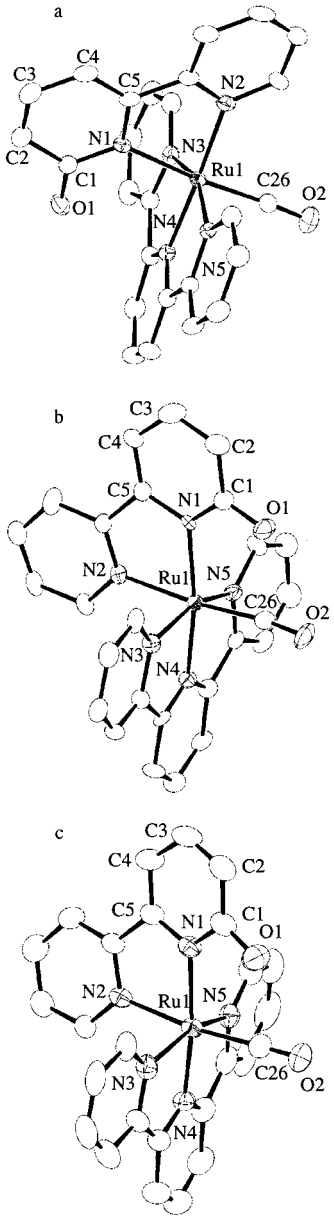

Figure 2. Molecular structures of $[\mathbf{1}]^+$ (a), $[\mathbf{2}]^+$ (b) and $[\mathbf{2H}]^{2+}$ (c) with atom labeling; hydrogen atoms are omitted for simplicity

 © 2005 Wiley-VCH Verlag GmbH & Co. KGaA, Weinheim

Table 2. Selected bond lengths [Å] and angles [°] for [1](PF$_6$), [2](PF$_6$)·H$_2$O, and [2H](PF$_6$)$_2$·2H$_2$O

	[1]$^+$		
Ru1−N1	2.118(3)	R1−N2	2.086(3)
Ru1−N3	2.085(3)	Ru1−N4	1.989(3)
Ru1−N5	2.100(3)	Ru1−C26	1.868(3)
N1−C1	1.382(4)	N1−C5	1.373(4)
C1−O1	1.250(4)	C1−C2	1.441(5)
C2−C3	1.355(5)	C3−C4	1.404(5)
C4−C5	1.376(5)	C26−O2	1.137(4)
N1−Ru1−N2	77.6(1)	N1−Ru1−N4	98.6(1)
N2−Ru1−C26	97.2(1)	N3−Ru1−N4	79.7(1)
N4−Ru1−N5	79.3(1)	Ru1−C26−O2	176.0(3)
O1−C1−N1	120.4(3)	O1−C1−C2	122.3(3)
N1−C1−C2	117.2(3)		
	[2]$^+$		
Ru1−N1	2.087(9)	R1−N2	2.13(1)
Ru1−N3	2.08(1)	Ru1−N4	2.006(9)
Ru1−N5	2.09(1)	Ru1−C26	1.90(1)
N1−C1	1.33(1)	N1−C5	1.40(1)
C1−O1	1.26(1)	C1−C2	1.40(2)
C2−C3	1.39(2)	C3−C4	1.40(2)
C4−C5	1.35(2)	C26−O2	1.12(1)
N1−Ru1−N2	78.3(4)	N1−Ru1−C26	96.2(4)
N2−Ru1−N4	93.6(4)	N3−Ru1−N4	79.1(4)
N4−Ru1−N5	78.4(4)	Ru1−C26−O2	173(1)
O1−C1−N1	120(1)	O1−C1−C2	120(1)
N1−C1−C2	120(1)		
	[2H]$^{2+}$		
Ru1−N1	2.112(4)	R1−N2	2.117(5)
Ru1−N3	2.098(4)	Ru1−N4	1.983(4)
Ru1−N5	2.094(4)	Ru1−C26	1.909(6)
N1−C1	1.345(7)	N1−C5	1.366(7)
C1−O1	1.326(7)	C1−C2	1.410(8)
C2−C3	1.344(9)	C3−C4	1.399(9)
C4−C5	1.366(7)	C26−O2	1.115(7)
N1−Ru1−N2	77.3(2)	N1−Ru1−C26	96.6(2)
N2−Ru1−N4	93.8(2)	N3−Ru1−N4	79.2(2)
N4−Ru1−N5	79.1(2)	Ru1−C26−O2	177.5(5)
O1−C1−N1	116.5(5)	O1−C1−C2	122.0(5)
N1−C1−C2	121.4(5)		

the oxygen atom of bpyO and the carbon atom of CO in [2]$^+$ of 2.55 Å implies a donor−acceptor interaction between them. An increase of the distance between the oxygen atom of bpyOH and the carbon atom of CO (O1···C26 = 2.62 Å) in [2H]$^{2+}$ is therefore explained by the decrease in the basicity of the oxygen atom of bpyO upon protonation.

Cyclic Voltammetry of [1](PF$_6$), [2](PF$_6$), [1H](PF$_6$)$_2$ and [2H](PF$_6$)$_2$

The cyclic voltammograms (CVs) of [1](PF$_6$) and [2](PF$_6$) were measured in CH$_3$CN (Figure 3). The CV of [1]$^+$ shows a nearly reversible redox couple at $E_{1/2}$ = −1.65 V ($E_{p,c}$ = −1.70, $E_{p,a}$ = −1.61 V) and a subsequent irreversible cathodic wave at $E_{p,c}$ = −2.07 V (Figure 3a), both of which are assigned to terpy- and bpyO-ligand-based redox reactions[12] by analogy with the redox behavior of

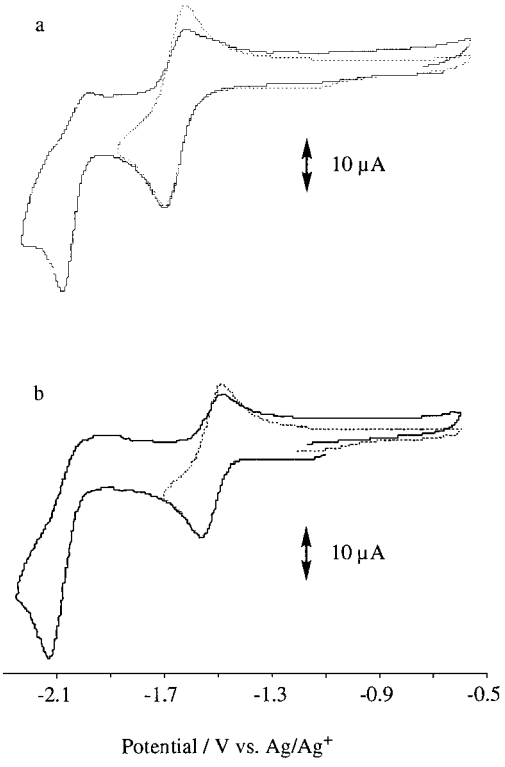

Figure 3. Cyclic voltammograms of [1](PF$_6$) (a) and [2](PF$_6$) (b) in CH$_3$CN under N$_2$; dE/dt = 100 mV·s^{-1}

[Ru(terpy)$_2$]$^{2+}$.[13] The irreversible reduction of [1]^0 probably results from a partial Ru−CO bond cleavage of [1]$^-$ (vide infra), because two-electron reduction of [Ru(terpy)(bpy)(CO)]$^{2+}$ leads to reductive Ru−CO bond cleavage (CO evolution), which is a key process in the electrochemical reduction of CO$_2$ catalyzed by this complex.[3e] The CV of [2]$^+$ also shows an almost reversible [2]$^+$/[2]^0 redox couple at $E_{1/2}$ = −1.51 V ($E_{p,c}$ = −1.55 and $E_{p,a}$ = −1.47 V) and an irreversible cathodic wave at $E_{p,c}$ = −2.13 V (Figure 3b). In contrast to the reductive cleavage of the Ru−CO bond of [1]$^-$, the irreversible reduction of [2]^0 is due to a cyclometalation caused by an intramolecular attack of the pyridonato oxygen at the carbonyl carbon atom (vide infra). The oxidation processes of [1]$^+$ and [2]$^+$ were also examined, but both complexes were not oxidized up to +1.0 V.

The CV of [1H]$^{2+}$ in CH$_3$CN displays four cathodic waves at $E_{p,c}$ = −1.40, −1.69, −1.85, and −2.05 V in the first potential sweep (Figure 4a).[14] The cathodic wave at $E_{p,c}$ = −1.40 V completely disappeared in the second potential sweep, while the other three cathodic waves at $E_{p,c}$ = −1.69, −1.85, and −2.05 V remained at almost the same potentials in multiscanning potential sweeps. The addition of one equivalent of Et$_3$N to the solution also caused the disappearance of the cathodic wave at $E_{p,c}$ = −1.40 V in the first potential sweep. However, the second cathodic wave became broad. Based on the fact that Et$_3$NH$^+$ undergoes an irreversible reduction at −1.75 V in CH$_3$CN on a glassy carbon electrode, the broad cathodic wave at $E_{p,c}$ = −1.69 V apparently results from overlapping of the terpy-

 © 2005 Wiley-VCH Verlag GmbH & Co. KGaA, Weinheim

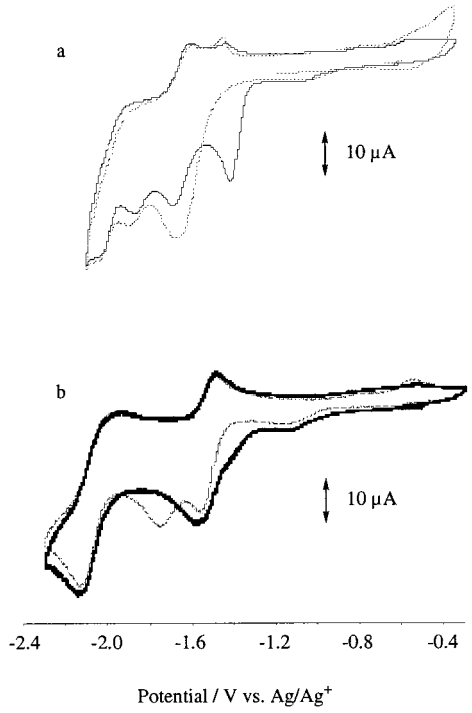

Figure 4. Cyclic voltammograms of $[\mathbf{1}H](PF_6)_2$ (a) and $[\mathbf{2}H](PF_6)_2$ (b) in the absence (−) and the presence (---) of 1.0 equiv. of Et_3N under N_2; $dE/dt = 100\ mV{\cdot}s^{-1}$

based reduction and an irreversible reduction of Et_3NH^+ produced in the reaction of $[\mathbf{1}H]^+$ with Et_3N. The CV of $[\mathbf{2}H]^{2+}$ displays a broad cathodic wave at $E_{p,c} = -1.58$ V and a subsequent irreversible cathodic wave at $E_{p,c} = -2.14$ V (Figure 4b).[15] Addition of one equivalent of Et_3N to the solution sharpened the cathodic wave at $E_{p,c} = -1.58$ V and resulted in an irreversible cathodic wave at −1.75 V due to the reduction of Et_3NH^+. These results indicate that the proton of the bpyOH ligand of $[\mathbf{1}H]^{2+}$ and $[\mathbf{2}H]^{2+}$ undergoes irreversible reduction at $E_{p,c} = -1.40$ and −1.58 V, respectively, to form $[\mathbf{1}]^+$ and $[\mathbf{2}]^+$ [Equation (5)].

$$\underset{[\mathbf{1}H]^{2+}\text{ and }[\mathbf{2}H]^{2+}}{[Ru(trpy)(bpy\text{-}OH)(CO)]^{2+}} + e^- \longrightarrow \underset{[\mathbf{1}]^+\text{ and }[\mathbf{2}]^+}{[Ru(trpy)(bpy\text{-}O)(CO)]^+} \quad (5)$$

IR Spectroscopy of $[\mathbf{1}]^+$ and $[\mathbf{2}]^+$ under the Electrolysis Conditions

The IR spectra of $[\mathbf{1}](PF_6)$ show the ν(C≡O) band and the ν(C=O) band of bpyO at 1979 and 1620 cm^{-1}, respectively, in CD_3CN. The appearance of those bands at 1996 and 1612 cm^{-1} in the IR spectrum of $[\mathbf{2}](PF_6)$ is ascribed to the stronger electron-donor ability of bpyO located *trans* to CO compared to when it is *cis* to CO (the redox potentials of the reversible $[\mathbf{1}]^{+/0}$ and $[\mathbf{2}]^{+/0}$ couples were observed at −1.65 and −1.51 V, respectively, in CH_3CN). In other words, the resonance between metal pyridinolate and pyridonate forms of $[\mathbf{1}]^+$ [Equation (3)] is shifted more towards the pyridonato than in $[\mathbf{2}]^+$. It is worthwhile to note that the redox behaviors of $[\mathbf{1}]^+$ and $[\mathbf{2}]^+$ are similar (one reversible and one irreversible reduction). However, there is a distinct difference between the IR spectra during the reduction and oxidation cycles of the two complexes. The ν(C≡O) band of $[\mathbf{1}]^+$ at 1979 cm^{-1} disappears completely during the controlled potential electrolysis of the complex at −1.70 V in CH_3CN, and a new ν(C≡O) band appears at 1932 cm^{-1} (Figure 5a). The 1932 cm^{-1} band is further shifted to 1853 cm^{-1}, with a lower peak intensity, when the electrolysis potential is changed from −1.70 V to −2.0 V (Figure 5b). The decrease of the peak intensity of the 1853 cm^{-1} band compared with those of the 1979 and 1932 cm^{-1} bands probably results from a gradual Ru−CO bond cleavage of $[\mathbf{1}]^-$; reoxidation of the solution at 0 V did not recover the peak intensity of the ν(C≡O) band of $[\mathbf{1}]^+$ at 1979 cm^{-1}. Besides the change of the ν(C≡O) band, two bands at 1605 and 1620 cm^{-1}, assigned to the stretching modes of the pyridine rings and the C=O group of the bpyO ligand of $[\mathbf{1}]^+$, respectively, moved to 1602 and 1618 cm^{-1}, and then to 1595 and 1581 cm^{-1} in the electrochemical reduction at −1.70 and −2.0 V. The red-shift of the band of the pyridonato ring of bpyO from 1620 to 1581 cm^{-1} upon two-electron reduction could be associated with a shift of the resonance of Equation (3) towards the pyridonato form.

The ν(C≡O) band at 1996 cm^{-1} of $[\mathbf{2}]^+$ shifts to 1950 cm^{-1} upon one-electron reduction of the complex at −1.70 V (Figure 5c). The 1950 cm^{-1} band of $[\mathbf{2}]^0$ vanishes completely under electrolysis at −2.05 V. Although no new bands assignable to ν(C≡O) were detected in the region 1800−1900 cm^{-1}, a new band emerged at 1587 cm^{-1} (Figure 5d). Re-oxidation of the resultant solution at 0 V almost recovered the IR spectrum of $[\mathbf{2}]^+$ [ν(C≡O) band at 1996 cm^{-1}].[16] Thus, the conversion between $[\mathbf{2}]^+$ and $[\mathbf{2}]^-$ in CH_3CN is a chemically reversible process, although $[\mathbf{2}]^0$ undergoes an irreversible reduction at −2.05 V. The 1587 cm^{-1} band of $[\mathbf{2}]^-$ is therefore assigned to the stretching mode of the O−C=O moiety of the five-membered metallacycle formed by the attack of the pyridonato oxygen at the carbonyl atom of the CO ligand [Equation (6)].

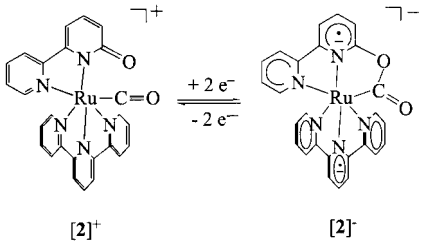

$[\mathbf{2}]^+$ $[\mathbf{2}]^-$ (6)

This reversible ring-closing and -opening [Equation (6)] is also supported by the IR spectra of $[\mathbf{2}^*]^+$, which contains a $C^{18}O$ ligand. The ν(C≡^{18}O) band at 1946 cm^{-1} of $[\mathbf{2}^*]^+$ shifts to 1907 cm^{-1} and then to 1562 cm^{-1} upon electrolysis at −1.70 and −2.00 V, respectively (Figure 6). Thus, the 1562 cm^{-1} band of $[\mathbf{2}^*]^-$ can reasonably be associated with the isotropic shift of the 1587 cm^{-1} band of $[\mathbf{2}]^-$. Both $[\mathbf{2}]^-$

 © 2005 Wiley-VCH Verlag GmbH & Co. KGaA, Weinheim

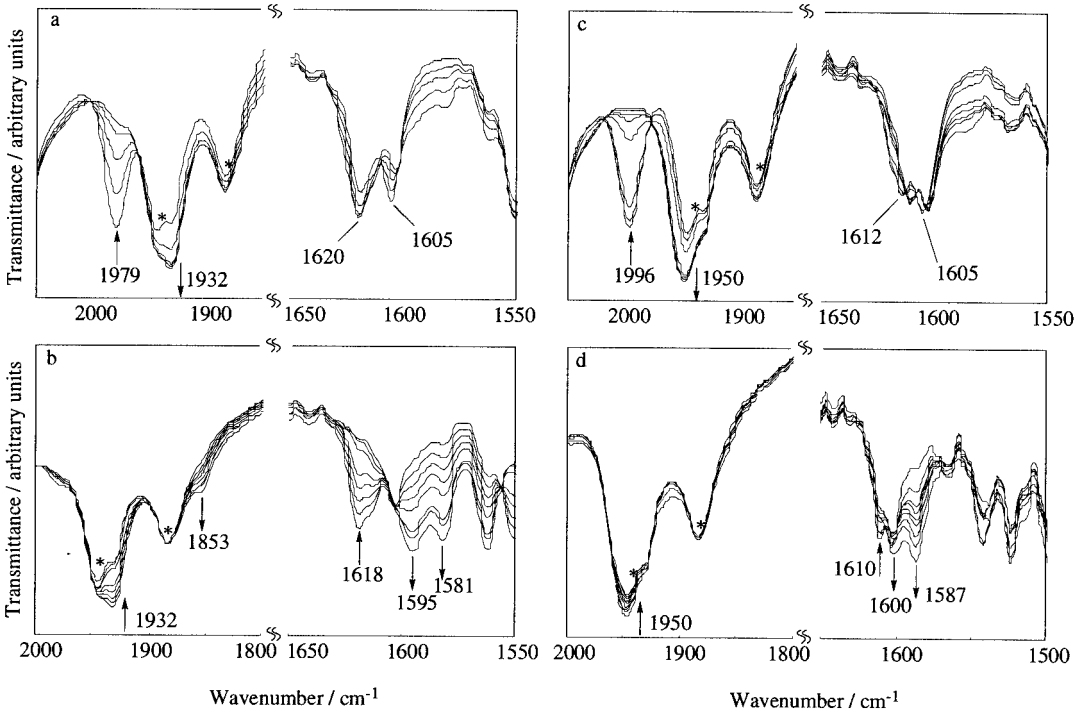

Figure 5. IR spectra of [**1**](PF_6) (a and b) and [**2**](PF_6) (c and d) under controlled-potential electrolyses at −1.70 V (a and c) and −2.00 V (b and d) in CD_3CN under N_2; * denotes CD_3CN peaks

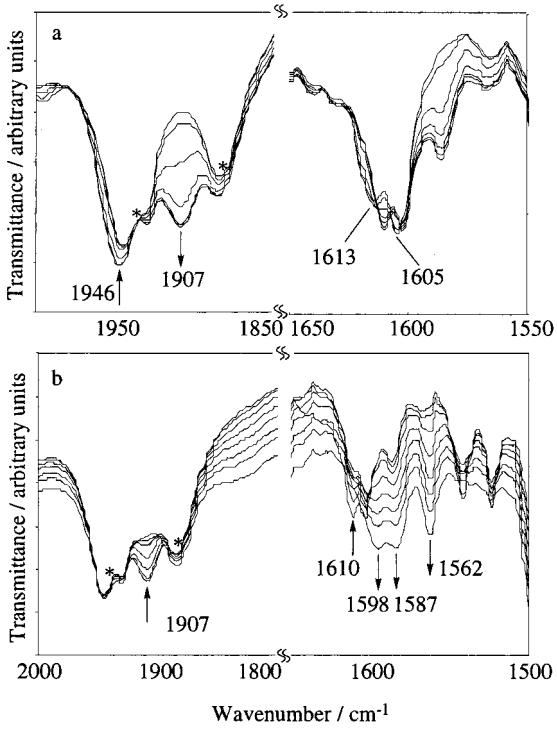

Figure 6. IR spectra of [**2***](PF_6) under controlled potential electrolysis at −1.70 V (a) and −2.00 V (b) in CD_3CN under N_2; * denotes CD_3CN peaks

and [**2***]$^-$ exhibit a band at 1587 cm^{-1}. This observation indicates the overlapping of the ring vibration mode of the bpyO moiety of [**2**]$^-$ with the stretching mode of the O−C=^{16}O group.

As described above, the hydroxyl proton of the bpyOH ligand of [**1**H]$^{2+}$ and [**2**H]$^{2+}$ undergoes irreversible reduction at around −1.50 V to form [**1**]$^+$ and [**2**]$^+$ in CH_3CN [Equation (5)]. In fact, the electrolysis of [**1**H]$^{2+}$ and [**2**H]$^{2+}$ in CH_3CN at −1.40 V causes the disappearance of the ν(C≡O) bands at 1992 and 2005 cm^{-1} of these complexes, and the appearance of the ν(C≡O) bands at 1979 and 1996 cm^{-1} of [**1**]$^+$ and [**2**]$^+$, respectively. Although the redox potentials of [**1**]$^+$ and [**2**]$^+$ are too negative to evaluate whether the pK_a values of the bpyOH ligand depend on the oxidation states of the complexes, the distinct difference in the Ru−CO bond stability between [**1**]$^-$ and [**2**]$^-$ is explained by the cyclometallation due to the intramolecular attack of the oxygen of bpyO at CO in the latter.

Conclusion

We succeeded in selectively synthesizing two isomers ([**1**]$^+$ and [**2**]$^+$) with a different orientation of bpyO at the ruthenium center. The hydrogen bond between the pyridonate oxygen and H_2O in [Ru(terpy)(bpyO)(OH_2)]$^+$ may play an important role in the preparation of [**2**]$^+$. [**1**]$^+$ and [**2**]$^+$ can be reversibly converted into [**1**H]$^{2+}$ and [**2**H]$^{2+}$ by the protonation of the oxygen atom of bpyO. Based on their pK_a's, CVs and IR spectra, the electron density at the ruthenium center of [**1**]$^+$ is higher than that of [**2**]$^+$. Such a difference is associated with the stronger *trans* influence of CO compared with the central pyridine of terpy, because the electron-withdrawing ability of CO induces the pyridonato

 © 2005 Wiley-VCH Verlag GmbH & Co. KGaA, Weinheim

structure of the resonance between metal-pyridinolate and -pyridonate forms [Equation (3)]. The CVs of $[\mathbf{1}]^+$ and $[\mathbf{2}]^+$ show one reversible and one irreversible redox wave due to terpy- and bpyO-based redox reactions. The two-electron reduction of $[\mathbf{1}]^+$ is followed by a partial Ru−CO bond cleavage. On the other hand, the bpyO-based reduction of $[\mathbf{2}]^+$ causes cyclometalation by an attack of the pyridonato oxygen at the carbonyl carbon; re-oxidation of the resultant $[\mathbf{2}]^-$ almost recovers $[\mathbf{2}]^+$. Thus, cyclometallation caused by a bpyO-based reduction effectively supresses the reductive cleavage of a Ru−CO bond.

Experimental Section

Reagents: 2-Bromo-6-methoxypyridine, 2,2′:6′,2″-terpyridine and $AgPF_6$ were purchased from Aldrich Chemical Co., Inc. 2-(Tri-*n*-butylstannyl)pyridine was purchased from Lancaster Synthesis, pyridine hydrochloride from Kanto Chemical Co., Inc., NH_4PF_6 from Wako Pure Chemical Industries, Ltd., and Me_4NBF_4 from Nacalai Tesque. CD_3CN was purchased from Merck (for IR measurements) and Isotec (for NMR measurements). All solvents used for preparations were reagent grade and used without further purification. $[Ru(terpy)Cl_3]$ was prepared according to the literature method.[17]

Physical Methods: ^1H and ^1H-^1H-COSY NMR experiments were performed with a JEOL LA-500 spectrometer. IR spectra were recorded with a Shimadzu FTIR-8300 spectrophotometer. ESI-MS spectra were measured with a Shimadzu LCMS-2010 liquid chromatograph mass spectrometer. pH titrations were performed with a Hiranuma automatic titrator COM-980 Win. Aqueous solutions (3 mL) of $[\mathbf{1}H](PF_6)_2$ (1.0−1.5 mM) or $[\mathbf{2}H](PF_6)_2$ (1.0−1.5 mM) were titrated with an aqueous NaOH solution (0.1 N, f = 1.04) at 25 °C. Cyclic voltammograms were obtained in a one-compartment cell consisting of a glassy carbon working electrode, a platinum counterelectrode and an $Ag/AgNO_3$ (10 mM) reference electrode in CH_3CN containing Me_4NBF_4 (50 mM) and the complex (1 mM). The cyclic voltammetric data were collected with an ALS/Chi model 1660A electrochemical analyzer. IR spectra under controlled-potential electrolysis conditions were obtained using a thin-layer cell sandwiched between two KBr crystals with an Au mesh working electrode, a platinum wire counterelectrode, and an $Ag/AgNO_3$ (10 mM) reference electrode.[3d] The measurements were conducted in CD_3CN or CH_3CN containing the sample complex (10 mM) and Me_4NBF_4 (50 mM) as an electrolyte.

Preparation of 6-Methoxy-2,2′-bipyridine: A toluene solution (35 mL) containing 2-bromo-6-methoxypyridine (1.0 g, 5.32 mmol), 2-(tri-*n*-butylstannyl)pyridine (3.0 g), LiCl (2.2 g, 53 mmol), and $[PdCl_2(PPh_3)_2]$ (290 mg, 0.42 mmol) was deaerated by bubbling N_2 throug it. The mixture was then refluxed under N_2 for 18 h, and an aqueous solution (10 mL) of NaF (2.2 g, 53 mmol) was added to the solution at room temperature. The resultant solution was further stirred at ambient temperature for 30 min. An insoluble solid was filtered off, and the filtrate was treated with a 5% Na_2CO_3 aqueous solution in a separating funnel. The organic layer was dried with anhydrous sodium sulfate, and the solvents were evaporated to dryness under reduced pressure. The obtained oil was dissolved in $CHCl_3$/EtOAc (95:5, v/v), and purified on a silica gel column. Yield: 830 mg (83.7%). The identification of the compound was performed according to the literature (^1H NMR).[18]

Preparation of 6-Hydroxy-2,2′-bipyridine (bpyOH): A mixture of 6-methoxy-2,2′-bipyridine (700 mg, 3.76 mmol) and pyridine hydrochloride (10 g) was heated under N_2 at 210 °C for 90 min. After the reaction mixture had cooled to ambient temperature, the white solid that appeared was dissolved in H_2O (50 mL). The crude product was extracted from the aqueous solution with dichloromethane. The dichloromethane layer was further treated with a saturated aqueous $NaHCO_3$ solution. The organic layer was dried with anhydrous sodium sulfate, and the solvents were evaporated to dryness under reduced pressure. Recrystallization from CH_2Cl_2/hexane (1:1, v/v) gave a pale-yellow solid. Yield 520 mg (80.4%). The identification of the compound was performed according to the literature (^1H NMR).[19]

Preparation of $[Ru(terpy)(bpyOH)Cl]Cl\cdot H_2O$: BpyOH (40 mg, 0.23 mmol) and Et_3N (120 mg, 1.18 mmol) were added to a suspension of $[Ru(terpy)Cl_3]$ (100 mg, 0.22 mmol) in 2-methoxyethanol. The mixture was stirred under N_2 at 85 °C for 3 h, during which time the suspension gradually changed to a deep purple solution. After an insoluble solid was filtered off, the filtrate was concentrated to about 5 mL under reduced pressure. The resultant precipitate was separated by filtration and recrystallized from methanol. Yield 65 mg (49.6%). $C_{25}H_{21}Cl_2N_5O_2Ru$: calcd. C 50.42, H 3.55, N 11.76; found C 49.98, H 3.47, N 11.60. ESI-MS: m/z = 542 $[Ru(terpy)(bpyOH)Cl]^+$.

Preparation of $[Ru(terpy)(bpyO)(CO)](PF_6)$ {$[\mathbf{1}](PF_6)$}: A mixture of $[Ru(terpy)(bpyOH)Cl]Cl\cdot H_2O$ (90 mg, 0.15 mmol) and $AgPF_6$ (81 mg, 0.32 mmol) in 2-methoxyethanol was stirred under CO pressure (15 atm) at 85 °C for 24 h. After the solution had cooled to room temperature, the solution was filtered through a Celite layer to remove the AgCl precipitate and then concentrated to about 5 mL. Addition of an excess amount of an aqueous NH_4PF_6 solution gave a yellow precipitate, which was separated by filtration. The resultant product was recrystallized from acetone/ethanol (2:1, v/v) containing Et_3N (30 μL). Yield 100 mg (53.6%). ^1H NMR (500 MHz, CD_3CN): δ = 5.65 (d, 1 H, H^{A3}), 6.98 (d, 1 H, H^{A5}), 7.08 (dd, 1 H, H^{A4}), 7.39 (ddd, 2 H, H^{C4}), 7.61 (ddd, 1 H, H^{B5}), 7.69 (d, 2 H, H^{C3}), 8.05 (td, 2 H, H^{C5}), 8.09 (td, 1 H, H^{B4}), 8.21 (t, 1 H, H^{D4}), 8.26 (d, 1 H, H^{B3}), 8.31 (m, 4 H, H^{C6} and H^{D3}), 9.35 (d, 1 H, H^{B6}) ppm. $C_{26}H_{18}F_6N_5O_2PRu$: calcd. C 46.03, H 2.67, N 10.32; found C 45.86, H 2.79, N 10.33. ESI-MS: m/z = 534 $[Ru(terpy)(bpyO)(CO)]^+$.

Preparation of $[Ru(terpy)(bpyOH)(CO)](PF_6)_2$ {$[\mathbf{1}H](PF_6)_2$}: Yellow crystals of $[\mathbf{1}H](PF_6)_2$ were obtained by crystallization of $[\mathbf{1}](PF_6)$ from CH_3CN/H_2O (1:1, v/v) containing 1.5 equiv. of an aqueous HPF_6 solution (1 M). ^1H NMR (500 MHz, CD_3CN): δ = 6.97 (d, 1 H, H^{A3}), 7.41 (ddd, 2 H, H^{C4}), 7.68 (d, 2 H, H^{C3}), 7.76 (dd, 1 H, H^{A4}), 7.79 (ddd, 1 H, H^{B5}), 7.90 (d, 1 H, H^{A5}), 8.11 (td, 2 H, H^{C5}), 8.26 (td, 1 H, H^{B4}), 8.38 (t, 1 H, H^{D4}), 8.43 (d, 2 H, H^{C6}), 8.47 (d, 2 H, H^{D3}), 8.51 (d, 1 H, H^{B3}), 9.45 (d, 1 H, H^{B6}) ppm. ESI-MS: m/z = 267.5 $[Ru(terpy)(bpyOH)(CO)]^{2+}$.

Preparation of $[Ru(terpy)(bpyO)(OH_2)](PF_6)$: Na_2CO_3 (91 mg, 0.86 mmol) and Et_3N (0.4 mL) were added to a suspension of $[Ru(terpy)Cl_3]$ (250 mg, 0.57 mmol) in $MeOH/H_2O$ (1:2 v/v, 80 mL), and then the suspension was refluxed under N_2 for 150 min. The resultant solution was cooled to room temperature, filtered, and the filtrate was concentrated to dryness under reduced pressure. The resulting solid was dissolved in ethanol and any insoluble salt was removed by filtration. Then, the solution was concentrated to dryness, and the solid was purified by column chromatography on a Cosmosil column, with MeOH as eluent. An aqueous solution

 © 2005 Wiley-VCH Verlag GmbH & Co. KGaA, Weinheim

(5 mL) of [Ru(terpy)(CO_3)(OH_2)] (60 mg) and bpyOH (30 mg, 0.17 mmol) was stirred at ambient temperature for 2−3 d, and the solution was then filtered. Addition of an excess amount of NH_4PF_6 to the filtrate gave [Ru(terpy)(bpyO)(OH_2)](PF_6) as a red-purple powder which was isolated by filtration, and recrystallized from acetone/H_2O (4:1, v/v). Yield 45 mg (11.8%). ^{1}H NMR (500 MHz, [D_6]acetone): δ = 6.71 (d, 1 H, H^{A3}), 6.89 (ddd, 1 H, H^{B4}), 7.30 (d, 1 H, H^{B3}), 7.56 (ddd, 2 H, H^{C4}), 7.62 (td, 1 H, H^{B5}), 7.67 (d, 1 H, H^{A5}), 7.79 (t, 1 H, H^{A4}), 8.05 (td, 2 H, H^{C5}), 8.11 (d, 2 H, H^{C3}), 8.20−8.25 (m, 2 H, H^{B6} and H^{D4}), 8.64 (d, 2 H, H^{C6}), 8.76 (d, 2 H, H^{D3}) ppm. $C_{25}H_{20}F_6N_5O_2PRu$: calcd. C 44.92, H 3.01, N 10.48; found C 45.16, H 3.20, N 10.44. ESI-MS: *m*/*z* = 524 [Ru(terpy)(bpyO)(OH_2)]$^+$.

Preparation of [Ru(terpy)(bpyO)(CO)](PF_6)·H_2O {[2](PF_6)·H_2O}: A 2-methoxyethanol solution of [Ru(terpy)(bpyO)(OH_2)](PF_6) (45 mg, 0.07 mmol) was stirred under CO pressure (20 atm) at 90 °C for 12 h. The reaction mixture was then concentrated to about 5 mL under reduced pressure. Addition of an excess amount of an aqueous NH_4PF_6 solution to the solution gave an orange precipitate, which was separated by filtration. Orange crystals were obtained by vapor diffusion of diethyl ether into an EtOH solution containing Et_3N (15 μL). Yield 22 mg (44.9%). ^{1}H NMR (500 MHz, CD_3CN): δ = 6.60 (d, 1 H, H^{A3}), 7.00 (d, 1 H, H^{B3}), 7.05 (ddd, 1 H, H^{B4}), 7.24 (d, 1 H, H^{A5}), 7.45 (ddd, 2 H, H^{C4}), 7.54 (dd, 1 H, H^{A4}), 7.81 (td, 1 H, H^{B5}), 7.90 (d, 2 H, H^{C3}), 8.07 (td, 2 H, H^{C5}), 8.12 (d, 1 H, H^{B6}), 8.39 (d, 2 H, H^{C6}), 8.42 (t, 1 H, H^{D4}), 8.54 (d, 2 H, H^{D3}) ppm. $C_{26}H_{20}F_6N_5O_3PRu$: calcd. C 44.83, H 2.89, N 10.05; found C 44.71, H 2.93, N 10.09. ESI-MS: *m*/*z* = 534 [Ru(terpy)(bpyO)(CO)]$^+$.

Preparation of [Ru(terpy)(bpyOH)(CO)](PF_6)$_2$·$2H_2O$ {[2H](PF_6)$_2$·$2H_2O$}: Orange crystals of [2H](PF_6)$_2$·$2H_2O$ were obtained by crystallization of [2](PF_6) from CH_3CN/H_2O (1:1, v/v) containing 1.5 equiv. of an aqueous HPF_6 solution (1 M). ^{1}H NMR (500 MHz, CD_3CN): δ = 7.14 (d, 1 H, H^{B3}), 7.27 (ddd, 1 H, H^{B4}), 7.42−7.45 (m, 3 H, H^{A3} and H^{C4}), 7.80 (d, 2 H, H^{C3}), 8.01 (td, 1 H, H^{B5}), 8.10−8.20 (m, 4 H, H^{A4}, H^{A5} and H^{C5}), 8.38 (d, 1 H, H^{B6}), 8.43 (d, 2 H, H^{C6}), 8.51 (t, 1 H, H^{D4}), 8.58 (d, 2 H, H^{D3}) ppm. $C_{26}H_{23}F_{12}N_5O_4P_2Ru$: calcd. C 36.29, H 2.69, N 8.14; found C 36.26, H 2.80, N 8.13. ESI-MS: *m*/*z* = 267.5 [Ru(terpy)(bpyOH)(CO)]$^{2+}$.

Preparation of [Ru(terpy)(bpyO)($C^{18}O$)](PF_6) {[2*](PF_6)}: Et_3N (0.1 equiv.) was added to a $CH_3CN/H_2{}^{18}O$ (4:1, v/v, 1 mL) solution of [2](PF_6) (40 mg) and the mixture was heated at 50 °C for 2 d. After the solution had cooled to room temperature, the solvent was removed completely. The orange solid thus obtained was recrystallized from CH_3CN/EtOH (1:4, v/v). The purity of the complex was checked by comparison of the parent peaks of *m*/*z* = 534 ([2]$^+$) and 536 ([2*]$^+$) in the ESI-MS, and of the ν($C^{16}O$) and ν($C^{18}O$) bands at 1996 and 1946 cm^{-1} in the IR spectra. Based on these results, the sample used in the experiments contained about 80% [2*](PF_6) and 20% [2](PF_6). Yield 18 mg. ESI-MS: *m*/*z* = 536 [Ru(terpy)(bpyO)($C^{18}O$)]$^+$.

Crystallographic Study of [Ru(terpy)(bpyO)(OH_2)](PF_6), [1](PF_6), [2](PF_6)·H_2O, and [2H](PF_6)$_2$·$2H_2O$: Crystals for X-ray analyses of the complexes were obtained as described above. A suitable single crystal for the measurement was mounted on a glass fiber. Data were collected at −100 °C on a Rigaku/MSC Mercury CCD diffractometer with graphite-monochromated Mo-K_α radiation (λ = 0.71070 Å). All data were collected and processed using the Crystal Clear program (Rigaku). All the calculations were carried out with the teXsan software package.[20] All structures were solved by direct methods and expanded using Fourier techniques. Refinements were performed anisotropically for all non-hydrogen atoms by the full-matrix least-squares method. Hydrogen atoms were placed at the calculated positions and were included in the structure calculation without further refinement of the parameters. Crystal data and processing parameters are summarized in Table 3. CCDC-240927 for [Ru(terpy)(bpyO)(OH_2)](PF_6), -217817 for [1](PF_6), -217818 for [2](PF_6)·H_2O and -217819 for [2H](PF_6)$_2$·$2H_2O$ contain the supplementary crystallographic data for this paper. These data can be obtained free of charge at www.ccdc.cam.ac.uk/conts/retrieving.html [or from the Cambridge Crystallographic Data Centre, 12 Union Road, Cambridge CB2 1EZ, UK; Fax: + 44-1223-336-033; E-mail: deposit@ccdc.cam.ac.uk].

Table 3. Crystallographic data for [Ru(terpy)(bpyO)(OH_2)](PF_6), [1](PF_6), [2](PF_6)·H_2O and [2H](PF_6)$_2$·$2H_2O$

	[Ru(terpy)(bpyO)(OH_2)](PF_6)	[1](PF_6)	[2](PF_6)·H_2O	[2H](PF_6)$_2$·$2H_2O$
Empirical formula	$C_{25}H_{20}F_6N_5O_2PRu$	$C_{26}H_{18}F_6N_5O_2PRu$	$C_{26}H_{20}F_6N_5O_3PRu$	$C_{26}H_{23}F_{12}N_5O_4P_2Ru$
Formula mass	668.50	678.49	696.51	860.50
Crystal system	monoclinic	monoclinic	orthorhombic	triclinic
Space group	$P2_1/n$	$C2/c$	$Pca2_1$	$P\bar{1}$
Color	red purple	orange	orange	orange
a [Å]	10.413(1)	41.034(3)	15.457(1)	8.6983(4)
b [Å]	14.505(1)	8.5910(5)	16.176(1)	14.0966(1)
c [Å]	16.601(1)	14.349(1)	11.3332(8)	14.8504(2)
α [°]				62.952(9)
β [°]	98.593(4)	95.404(3)		78.28(1)
γ [°]				84.67(1)
V [Å^3]	2479.3(4)	5036.0(6)	2833.7(6)	1587.9(2)
Z	4	8	4	2
D_{calcd} [g·cm^{-3}]	1.791	1.790	1.623	1.80
Crystal size [mm]	0.30 × 0.15 × 0.10	0.20 × 0.20 × 0.10	0.25 × 0.13 × 0.06	0.40 × 0.20 × 0.10
T [K]	173	173	173	173
λ [Å]	0.71070	0.71070	0.71070	0.71070
μ [mm^{-1}]	0.778	0.768	0.687	0.708
R_1 [a]	0.067	0.048	0.070	0.079
R_w [b]	0.153	0.108	0.176	0.201

[a] $R_1 = \Sigma||F_o| - |F_c||/\Sigma|F_o|$ for $I > 2.0\sigma(I)$ data. [b] $Rw = \Sigma[w(F_o^2 - F_c^2)^2/\Sigma w(F_o^2)^2]^{1/2}$.

 © 2005 Wiley-VCH Verlag GmbH & Co. KGaA, Weinheim

[1] [1a] M. Suzuki, C. C. Waraksa, T. E. Mallouk, H. Nakayama, K. Hanabusa, *J. Phys. Chem. B* **2002**, *106*, 4227. [1b] M. Osawa, M. Hoshino, Y. Wakatsuki, *Angew. Chem. Int. Ed.* **2001**, *40*, 3472. [1c] S. Fanni, F. M. Weldon, L. Hammarström, E. Mukhtar, W. R. Browne, T. E. Keyes, J. G. Vos, *Eur. J. Inorg. Chem.* **2001**, 529. [1d] B. Saha, D. M. Stanbury, *Inorg. Chem.* **2000**, *39*, 1294. [1e] C. Nasr, S. Hotchandani, P. V. Kamat, *J. Phys. Chem. B* **1998**, *102*, 4944. [1f] T. Rajendran, S. Rajagopal, C. Srinivasan, P. Ramamurthy, *J. Chem. Soc., Faraday Trans.* **1997**, *93*, 3155. [1g] J.-P. Sauvage, J.-P. Collin, J.-C. Chambron, S. Guillerez, C. Coudret, *Chem. Rev.* **1994**, *94*, 993. [1h] R. Argazzi, C. A. Bignozzi, T. A. Heimer, F. N. Castellano, G. J. Meyer, *Inorg. Chem.* **1994**, *33*, 5741. [1i] Y. I. Kim, S. J. Atherton, E. S. Brigham, T. E. Mallouk, *J. Phys. Chem.* **1993**, *97*, 11802.

[2] [2a] H. Ishida, T. Terada, K. Tanaka, T. Tanaka, *Inorg. Chem.* **1990**, *29*, 905. [2b] J. M. Lehn, R. Ziessel, *J. Organomet. Chem.* **1990**, *382*, 157. [2c] H. Ishida, K. Tanaka, T. Tanaka, *Chem. Lett.* **1988**, 339. [2d] H. Ishida, K. Tanaka, T. Tanaka, *Chem. Lett.* **1987**, 1035. [2e] J. Hawecker, J. Lehn, R. Ziessel, *J. Chem. Soc., Chem. Commun.* **1985**, 56.

[3] [3a] S. Chardon-Noblat, G. H. Cripps, A. Deronzier, J. S. Field, S. Gouws, R. J. Haines, F. Southway, *Organometallics* **2001**, *20*, 1668. [3b] S. Chardon-Noblat, A. Deronzier, R. Ziessel, D. Zsoldos, *Inorg. Chem.* **1997**, *36*, 5384. [3c] R. Ziessel, L. Toupet, S. Chardon-Noblat, A. Deronzier, D. Matt, *J. Chem. Soc., Dalton Trans.* **1997**, 3777. [3d] H. Nakajima, Y. Kushi, H. Nagao, K. Tanaka, *Organometallics* **1995**, *14*, 5093. [3e] H. Nagao, T. Mizukawa, K. Tanaka, *Inorg. Chem.* **1994**, *33*, 3415. [3f] M. N. Collomb-Dunand-Sauthier, A. Deronzier, R. Ziessel, *J. Chem. Soc., Chem. Commun.* **1994**, 189. [3g] M. N. Collomb-Dunand-Sauthier, A. Deronzier, R. Ziessel, *Inorg. Chem.* **1994**, *33*, 2961. [3h] S. Chardon-Noblat, M. N. Collomb-Dunand-Sauthier, A. Deronzier, R. Ziessel, D. Zsoldos, *Inorg. Chem.* **1994**, *33*, 4410. [3i] J. R. Pugh, M. R. M. Bruce, B. P. Sullivan, T. J. Meyer, *Inorg. Chem.* **1991**, *30*, 86. [3j] H. Ishida, K. Tanaka, T. Tanaka, *Organometallics* **1987**, *6*, 181. [3k] C. M. Bolinger, B. P. Sullivan, D. Conrad, J. A. Gilbert, N. Story, T. J. Meyer, *J. Chem. Soc., Chem. Commun.* **1985**, 796.

[4] [4a] S.-L. Zheng, J.-P. Zhang, W.-T. Wong, X.-M. Chen, *J. Am. Chem. Soc.* **2003**, *125*, 6882. [4b] X.-M. Zhang, M.-L. Tong, M.-L. Gong, H.-K. Lee, L. Luo, K.-F. Li, Y.-X. Tong, X.-M. Chen, *Chem. Eur. J.* **2002**, *8*, 3187. [4c] X.-M. Zhang, M.-L. Tong, X.-M. Chen, *Angew. Chem. Int. Ed.* **2002**, *41*, 1029. [4d] S. Mukhopadhyay, R. J. Staples, W. H. Armstrong, *Chem. Commun.* **2002**, 864. [4e] G. Y. S. K. Swamy, K. C. Mohan, K. Ravikumar, *Cryst. Res. Technol.* **2001**, *36*, 615.

[5] H. Nakajima, K. Tanaka, *Chem. Lett.* **1995**, 891.

[6] [6a] P. Nombel, N. Lugan, B. Donnadieu, G. Lavigne, *Organometallics* **1999**, *18*, 187−196. [6b] O. C. P. Beers, J. G. P. Delis, W. P. Mul, K. Vrieze, C. J. Elsevier, *Inorg. Chem.* **1993**, *32*, 3640. [6c] M. Nonoyama, *Polyhedron* **1985**, *4*, 765.

[7] [7a] A. L. Jorgenson, R. A. Nadeau, V. G. Young Jr, W. L. Gladfelter, *J. Organomet. Chem.* **1998**, *563*, 1. [7b] M. Wijnkoop, P. P. M. Lange, H.-W. Fruhauf, K. Vrieze, *Organometallics* **1995**, *14*, 4781. [7c] M. Wijnkoop, P. P. M. Lange, H.-W. Fruhauf, K. Vrieze, *Organometallics* **1992**, *11*, 3607. [7d] N. G. Connelly, M. J. Freeman, I. Manners, A. G. Orpen, *J. Chem. Soc., Dalton Trans.* **1984**, 2703.

[8] The orientation of the bpyOH group in [Ru(terpy)(bpyOH)Cl]$^+$ was determined unequivocally by the X-ray crystal structure analysis but the quality of the crystals of the complex was not enough to allow a discussion of the bond angles and lengths (R_1 = 11.8%, R_w = 20.5%).

[9] E. P. Kelson, P. P. Phengsy, *J. Chem. Soc., Dalton Trans.* **2000**, 4023.

[10] L. S. Hollis, S. J. Lippard, *Inorg. Chem.* **1983**, *22*, 2708.

[11] C. R. Hecker, P. E. Fanwick, D. R. McMillin, *Inorg. Chem.* **1991**, *30*, 659.

[12] The controlled-potential electrolysis of [**1**]$^+$ and [**2**]$^+$ at −1.80 V revealed that both complexes undergo one-electron reduction (n = 1.0) at the first cathodic wave. The potentials of the second cathodic waves of both complexes are too negative to determine the number of electrons by controlled-potential electrolysis. Based on the comparison of the peak currents of the first and the second waves of the complexes, both [**1**]^0 and [**2**]^0 are supposed to undergo one-electron reduction at the second cathodic wave.

[13] [13a] N. E. Tokel-Takvoryan, R. E. Hemingway, A. J. Bard, *J. Am. Chem. Soc.* **1973**, *95*, 6582. [13b] J. M. Calvert, T. J. Meyer, *Inorg. Chem.* **1981**, *20*, 27. [13c] B. Jing, W. Wang, M. Zhang, T. Shen, *Dyes Pigm.* **1998**, *37*, 177.

[14] The third cathodic wave of [**1**H]$^{2+}$ ($E_{p,c}$ = −1.85 V) was not assigned.

[15] A poorly resolved peak at about −1.40 V in the CV of [**2H**]$^{2+}$ (Figure 4b) results from H_2 evolution [Equation (5)]. Accordingly, addition of Et_3N to the solution converts [**2H**]$^{2+}$ to [**2**]$^+$. As a result, the pattern of the CV was sharpened and the irreversible cathodic wave of Et_4NH^+ was observed at −1.75 V.

[16] The first and second reductions of [**2**]$^+$ are associated with terpy- and bpyO-localized redox reactions, respectively. The second reduction causes metallocyclization of the complex. However, the oxidation processes of [**1**]$^-$ and [**2**]$^-$ are not clearly observed in the CV (Figure 3). The electrochemical oxidation of those two-electron-reduced complexes, therefore, was conducted at 0 V.

[17] B. P. Sullivan, J. M. Calvert, T. J. Meyer, *Inorg. Chem.* **1980**, *19*, 1404.

[18] [18a] P. Gros, Y. Fort, *Synthesis* **1999**, 754. [18b] P. M. Pojer, L. A. Summers, *J. Heterocycl. Chem.* **1974**, *11*, 303.

[19] S. Rozen, D. Hebel, *Heterocycles* **1989**, *28*, 249.

[20] *teXsan, Crystal Structure Analysis Package*, version 1.11, Molecular Structure Corporation, Rigaku Corporatiuon, **2000**.

Received June 16, 2004
Early View Article
Published Online December 2, 2004

 © 2005 Wiley-VCH Verlag GmbH & Co. KGaA, Weinheim

Towards the Design of Linear Homo-Trinuclear Metal Complexes Based on a New Phenol-Functionalised Diazamesocyclic Ligand: Structural Analysis and Magnetism

Miao Du,*[a] Xiao-Jun Zhao,[a,b] Jian-Hua Guo,[a] Xian-He Bu,*[b] and Joan Ribas*[c]

Keywords: Functionalised diazamesocyclic ligand / Copper(II) and Nickel(II) / Crystal structures / Magnetochemistry / Trinuclear complexes

The formation of two novel phenoxo-bridged linear trimetallic Cu^{II} and Ni^{II} complexes, $[Cu_3(\mu\text{-}\mathbf{L})_2](CH_3OH)_2(ClO_4)_2$ (**1**) and $[Ni_3(\mu\text{-}\mathbf{L})_2(CH_3OH)_2](ClO_4)_2$ (**2**), with a new diazamesocyclic ligand functionalised by additional phenol donor pendants ($H_2\mathbf{L}$ = *N*,*N*′- bis(2-hydroxybenzyl)-1,4-diazacycloheptane), has been achieved and both complexes have been characterised by IR spectroscopy, elemental analyses, conductivity measurements, thermal analyses and UV/Vis techniques. Single-crystal X-ray diffraction analyses revealed that both **1** and **2** have the similar phenoxo-bridged linear trinuclear cores. For **1**, two terminal and the central Cu^{II} ion are in square-planar environments with the adjacent intramolecular Cu···Cu separation of 2.9376(9) Å. For **2**, however, two terminal Ni^{II} ions are in square-planar environments and the central Ni^{II} ion assumes an octahedral geometry by axial coordination of two methanol ligands, the adjacent intramolecular Ni···Ni distance being 3.007(3) Å. In both cases, the 1,4-diazacycloheptane (DACH) ring adopts the normal boat configuration. The magnetic properties of complexes **1** and **2** have been investigated by variable-temperature magnetic susceptibility measurements in the solid state. Complex **1** displays a very strong antiferromagnetic coupling interaction between the neighbouring μ-phenoxo Cu^{II} centres with a *J* parameter of –314 cm^{-1} and the magneto-structural correlation for such complexes is discussed in detail. For complex **2**, the result indicates that both terminal Ni^{II} ions are diamagnetic and the central Ni^{II} shows typical paramagnetic behaviour. The presence of zero-field splitting for Ni^{II} with a *D* parameter of 11 cm^{-1}, being active at low temperature, is further corroborated by the magnetisation measurement at 2 K. Additionally, the interesting ESR spectra of **1** at different temperatures (from 298 K to 8 K) were investigated and interpreted.

(© Wiley-VCH Verlag GmbH & Co. KGaA, 69451 Weinheim, Germany, 2005)

Introduction

The development of routes and strategies for the design and preparation of polynuclear complexes of 3d metals in moderate oxidation states is of great importance in bioinorganic chemistry, magnetochemistry, materials chemistry and solid-state chemistry.[1] Trinuclear compounds can be classified as linear or nonlinear according to the arrangements of the metal centres and a number of linear trinuclear compounds have been structurally and magnetically characterised to date.[2] Of further importance is the fact that most of the known trinuclear complexes have two, three or four simple and/or intricate bridging ligands between the metal centres which usually contain simple anions such as chloride,[3] hydroxide,[4] acetate,[5] methoxide[6] or azide[7] and only a minority of them have the M_3 core bridged by just a single organic ligand. Thus, the rational design and preparation of such trinuclear complexes still remains a difficult challenge and attracts continuing interest.

As described in many other publications by us, we have been exploring the coordination chemistry of diazamesocyclic systems, especially the typical 1,5-diazacyclooctane (DACO) which exhibits an exceptionally strong ligand field, a unique configuration and the potential for further functionalisation.[8–11] It has been well demonstrated by us and others[12] that DACO modified by suitable functional pendants, such as heterocyclic, phenolic, thiol and carboxylic groups could be used as good building blocks for constructing polymeric systems with unique structures and properties. Based on our experimental findings, a general rule for the coordination chemistry of functionalised DACO compounds has been established according to the types and numbers of the additional pendant arms. One of

[a] College of Chemistry and Life Science,
Tianjin Normal University,
Tianjin 300074, P. R. China
Fax: (internat.) +86-22-23540315
E-mail: dumiao@public.tpt.tj.cn
[b] Department of Chemistry, Nankai University,
Tianjin 300071, P. R. China
E-mail: buxh@nankai.edu.cn
[c] Departament de Química Inorgànica, Universitat de Barcelona,
Diagonal, 647, 08028 Barcelona, Spain
E-mail: joan.ribas@qi.ub.es

 © 2005 Wiley-VCH Verlag GmbH & Co. KGaA, Weinheim **DOI: 10.1002/ejic.200400618**

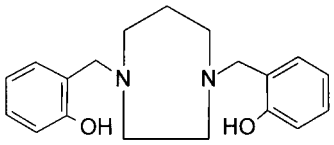

H_2L

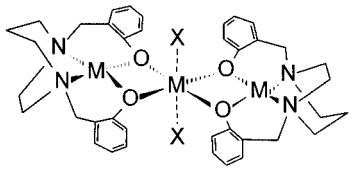

M = Cu^{II} or Ni^{II} (x = lattice/coordination methanol)

Scheme 1

the main reasons that justifies the continuous interest in such attractive system is the construction of other novel metal complexes with special frameworks and properties by modifying the backbone of the diazamesocycle, for example choosing 1,4-diazacycloheptane (DACH) as the initial material. Our preliminary results indicate that the metal complexes of the heterocycle-functionalised DACH derivatives usually exhibit similar structures to those of the corresponding DACO compounds but with a change in the coordination environments of the metal centres due to their different configurations (normally, boat-chair for DACO ring, and boat for DACH).[13] It should be noted that almost all metal centres chelated to DACO derivatives assume pentacoordinate geometries[8−12] but this is not the case for DACH.[13] For metal complexes with the DACO ligand bearing two phenol arms, phenoxo-bridged linear trimetallic Cu^{II} and Ni^{II} frameworks were obtained. The former exhibits a square pyramid/square plane/square pyramid Cu_3 core[10a] and the latter is the first square pyramid/octahedral/square pyramid Ni_3 complex.[10b] Thus, as a continuation of our work, we report herein the design and preparation of a new phenol-functionalised DACH ligand *N*,*N*′-bis(2-hydroxybenzyl)-1,4-diazacycloheptane (H_2**L**, see Scheme 1) and its Cu^{II} and Ni^{II} complexes $[Cu_3(\mu\text{-}\mathbf{L})_2](CH_3OH)_2(ClO_4)_2$ (**1**) and $[Ni_3(\mu\text{-}\mathbf{L})_2(CH_3OH)_2](ClO_4)_2$ (**2**). The magnetic properties of both complexes have been investigated and the magneto-structural correlation between **1** and related compounds has been discussed. Of further interest is the fact that relatively few trinuclear Cu^{II} compounds have been studied by ESR techniques[14] and, thus, the ESR properties of **1** at different temperatures (from 298 K to 8 K) were analysed in detail in this study.

Results and Discussion

Preparation, Characterisation and Spectra of Compounds 1 and 2

The new ligand H_2**L** was synthesised using an excess of 2-bromomethyl phenylacetate in order to largely obtain the doubly substituted product as described in detail in our previous report.[10a] The yield was moderate. All analytical and spectroscopic data are in good agreement with the theoretical requirements. The preparations of **1** and **2** were achieved directly by treatment of the ligand with the corresponding metal perchlorate and the ligand becomes doubly deprotonated when forming the metal complex.

In the IR spectra of H_2**L** and both complexes, the absorption bands resulting from the skeletal vibrations of the aromatic rings appear in the 1400−1600 cm^{-1} region. The broad band centred at ca. 3400 cm^{-1} results from the O−H stretching of the phenol groups (for H_2**L**) or the solvent methanol molecules (for **1** and **2**). The very strong bands at 1256 cm^{-1} (for H_2**L**), 1264 and 1247 cm^{-1} (for **1**) and 1261 cm^{-1} (for **2**) are the characteristic absorptions of the C−O groups of the phenol pendant arms. Additionally, in the IR spectra of both complexes, the strong bands that appear at ca. 1100 and 624 cm^{-1} suggest the presence of the perchlorate anions.[15]

The UV/Vis spectra of complexes **1** and **2** (CH_3CN and H_2O, respectively) have been investigated at room temperature. It is important to know the structures of the complexes in solution prior to spectroscopic discussions. Thus, the conductivities of both complexes were measured and the molar conductivities of **1** and **2** indicate both complexes behave as the typical 2:1 electrolytes in the corresponding solution, this being consistent with their solid structures. Evidently the phenoxo bridges are retained in solution. The visible spectrum of **1** shows a moderate shoulder band at ca. 558 nm and a more intense absorption band at 386 nm which can be assigned to the *d*−*d* component of Cu^{II} ions with a square-planar geometry and the charge-transfer (CT) transition band from the filled p_π orbital of the phenolic oxygen to the vacant *d* orbitals of Cu^{II}, respectively.[16] For complex **2**, two such types of absorptions appear at 498 nm and 362/324 nm (one is due to the terminal Ni^{II} CT and the other to the central Ni^{II} CT with different coordination geometries[2c]), respectively. In addition, the intense bands observed in the 200−300 nm region in the spectra of both complexes can be attributed to the π→π* ligand transitions.

Both **1** and **2** are air stable at room temperature but decomposition occurs at elevated temperature, however. Thermogravimetric analyses (from room temperature to 600 °C) indicate that for **1**, the first weight loss of 6.44% from 118 to 164 °C (peak: 132 °C) corresponds to the loss of two CH_3OH solvent molecules (calculated: 5.96%). The remaining substance does not lose weight upon further heating until a rapid weight loss in the 244−264 °C region (peak: 258 °C). Further heating to 600 °C induces a continuous and slow weight loss. The thermal behaviour of **2** is similar to **1**, the first weight loss of 5.84% from 85 to 160 °C (peak: 138 °C) corresponds to the release of two coordinated methanol ligands (calculated: 6.04%). The remaining coor-

 © 2005 Wiley-VCH Verlag GmbH & Co. KGaA, Weinheim

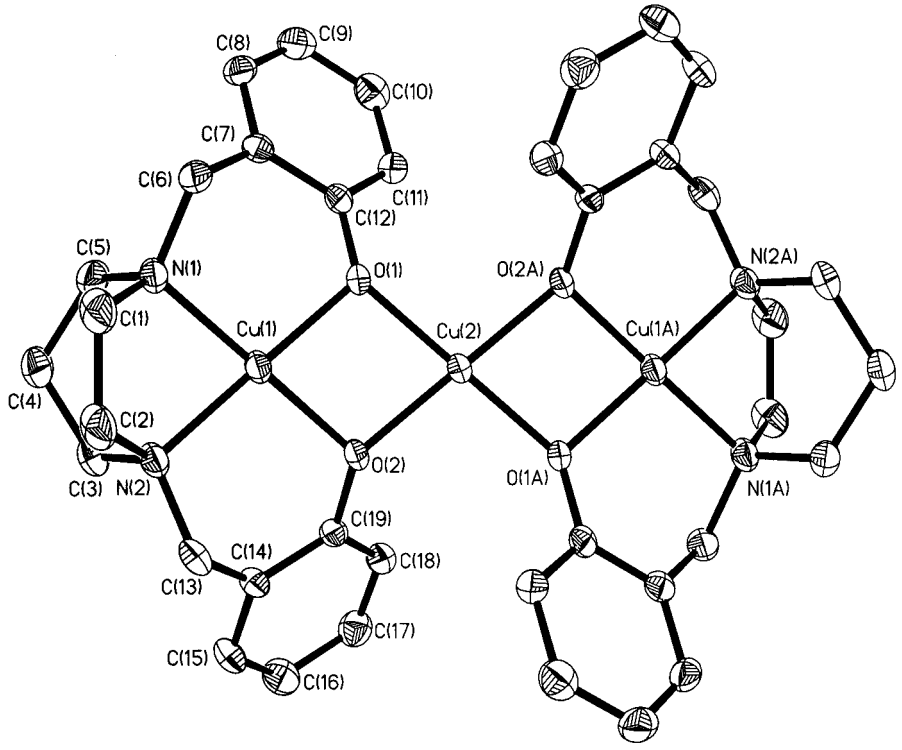

Figure 1. ORTEP view of the molecular structure of **1** including atomic labelling of the asymmetric unit (hydrogen atoms, perchlorate anions and methanol solvents are omitted for clarity) with displacement ellipsoids drawn at the 30% probability level

dinated framework does not lose weight upon further heating until two consecutive weight losses occur in the 270−325 °C region (peak: 288 and 312 °C). As for **1**, further heating to 600 °C only shows a continuous and slow weight loss.

Single-Crystal X-ray Structures of Complexes 1 and 2

Structure Description of $[Cu_3(\mu\text{-}L)_2](CH_3OH)_2(ClO_4)_2$ (1)

An ORTEP diagram of complex **1** is shown in Figure 1 and selected bond lengths and angles are listed in Table 1. The structure consists of a discrete $[Cu_3(\mu\text{-}\mathbf{L})_2]^{2+}$ cation in which the ligands are doubly deprotonated, two perchlorate counter anions and two lattice methanol solvent molecules. The asymmetric unit is formed by half a molecule which exhibits inversion in the centre of the rhombohedral which itself consists of four phenol oxygen atoms [Cu(2) is just on this inversion centre]. Two terminal Cu(1) and Cu(1A) atoms, located in general positions, are centrosymmetrically related to each other and, hence, three Cu^{II} ions linked by the phenoxo bridges lie in a straight line. Each terminal Cu^{II} ion is coordinated to two nitrogen atoms from the DACH ring (Cu−N distances: 1.973(3) and 1.981(3) Å) and two phenolate oxygen donors (Cu−O lengths: 1.927(3) and 1.928(3) Å), adopting an approximately square-planar geometry (CuN_2O_2). The central Cu(2) atom is coordinated to four bridging phenolate oxygens (Cu−O lengths: 1.956(3) and 1.953(3) Å) which further link the other two Cu^{II} ions to form the linear Cu_3 array, resulting in a CuO_4 plane. Additionally, weak interactions between the central Cu(2) and the perchlorate anions (located in the axial position of the Cu^{II} coordination sphere) can be observed with a Cu(2)−O(3) distance of 2.589(3) Å which is significantly longer than the normal Cu−O coordination bond. The terminal Cu(1) ion is only ca. 0.035 Å above the basal least-squares plane and the central Cu(2) is located exactly on its coordination plane due to the site symmetry. The folding angle between the perfect square plane O(1)−O(1A)−O(2)−O(2A) and the best calculated plane N(1)−N(2)−O(1)−O(2) is 10.8° and the dihedral angle between the two Cu(1)−O(1)−Cu(2) and Cu(1)−O(2)−Cu(2) planes is 10.9°. The intramolecular Cu···Cu separation is 2.9376(9) Å whereas the Cu(1)−O−Cu(2) bridging angles are 98.31(12) and 98.38(11)° for O(1) and O(2), respectively. For the ligand, the DACH ring takes the normal boat configuration and the dihedral angle between two phenol planes is 117.6°. A pair of nitrogen atoms from DACH and two oxygen atoms of phenolate pendant arms are in *cis* positions in the coordination plane of the chelated Cu(1) atom.

Analysis of the crystal packing of complex **1** indicates that the trimers are well isolated in the unit cell, with the intermolecular contacts between the Cu^{II} centres above 5.8 Å. There exists only an intramolecular O(7)−H(7)···O(3) hydrogen bond between the methanol molecule and the per-

 © 2005 Wiley-VCH Verlag GmbH & Co. KGaA, Weinheim

Table 1. Selective bond lengths (Å) and angles (°) for complex **1**

Bond lengths			
Cu(1)−O(1)	1.927(3)	Cu(1)−O(2)	1.928(3)
Cu(1)−N(1)	1.973(3)	Cu(1)−N(2)	1.981(3)
Cu(2)−O(1)	1.956(3)	Cu(2)−O(2)	1.953(3)
C(12)−O(1)	1.364(5)	C(19)−O(2)	1.379(4)
Cu(1)−Cu(2)	2.9376(9)		
Bond angles			
O(1)−Cu(1)−O(2)	81.89(11)	O(1)−Cu(1)−N(1)	98.73(13)
O(2)−Cu(1)−N(1)	178.79(13)	O(1)−Cu(1)−N(2)	176.92(13)
O(2)−Cu(1)−N(2)	97.83(13)	N(1)−Cu(1)−N(2)	81.49(14)
O(2)−Cu(2)−O(1)	80.52(11)	O(2)−Cu(2)−O(1)^{i}	99.48(11)
Cu(1)−O(1)−Cu(2)	98.31(12)	Cu(1)−O(2)−Cu(2)	98.38(11)

Symmetry code: (*i*) $1 - x, 1 - y, 1 - z$

chlorate anion. The O···O separation is 2.995 Å with an H···O distance of 2.242 Å and the bond angle is 152.7° which is in the normal range for such a weak interaction.[17]

Structure Description of $[Ni_3(\mu\text{-}L)_2(CH_3OH)_2](ClO_4)_2$ (2)

A single-crystal X-ray determination indicates that the structure of complex **2** consists of a $[Ni_3(\mu\text{-}\mathbf{L})_2(CH_3OH)_2]^{2+}$ cation exhibiting a similar M_3 framework to **1** and two perchlorate anions. Selected bond lengths and angles for **2** are listed in Table 2. As depicted in Figure 2, the asymmetric unit is formed by half of the complex which shows an inversion centre [Ni(2)] in the middle of the rhombohedral plane. Since Ni(2) occupies the inversion centre, the resultant Ni(1)−Ni(2)−Ni(1A) array is linear. As in **1**, a pair of nitrogen atoms from DACH (Ni−N distances: 1.903(4) and 1.897(4) Å) and two oxygen atoms of the phenolate pendant arms (Ni−O lengths: 1.872(3) and 1.873(3) Å) are in a *cis* position. These positions constitute the approximate coordination plane of the terminal Ni(1) atom with a derivation from planarity of 0.022 Å. However, the central Ni(2) is six-coordinate: four phenol oxygen atoms are in the equatorial plane with Ni−O distances of 2.040(3) and 2.050(3) Å with two methanol ligands occupying the axial positions with Ni−O lengths of 2.067(3) Å. Thus, the coordination environment of Ni(2) can be described as a slightly distorted elongated octahedron with the *cis* O−Ni−O angles being in the range of 75.33(11)−104.67(11)°. In **2**, the folding angle between the perfect square plane O(1)−O(1A)−O(2)−O(2A) and the best calculated plane N(1)−N(2)−O(1)−O(2) is 6.3° and the dihedral angle between the two Ni(1)−O(1)−Ni(2) and Ni(1)−O(2)−Ni(2) planes is 8.7°. The intramolecular Ni···Ni separation is 3.007(2) Å and the Ni(1)−O−Ni(2) bridging angles are 100.39(13) and 98.98(14)° for O(1) and O(2), respectively. For the doubly deprotonated ligand, the DACH ring assumes the normal boat configuration and the dihedral angle between two phenol planes is 56°. Similar to **1**, the trinuclear subunits are well isolated in the unit cell with the intermolecular contacts between the Ni^{II} centres above 6.0 Å. An intramolecular O(3)−H(3C)···O(4) hydrogen-bonding interaction between the coordinated methanol molecule and the perchlorate anion can be observed and this further stabilises the structure. The O···O separation is 2.861 Å with an H···O distance of 2.074 Å and the bond angle is 160.8°, which is in the normal range for such weak interactions.[17]

Table 2. Selective bond lengths (Å) and angles (°) for complex **2**

Bond lengths			
Ni(1)−O(1)	1.872(3)	Ni(1)−O(2)	1.873(3)
Ni(1)−N(1)	1.903(4)	Ni(1)−N(2)	1.897(4)
Ni(2)−O(1)	2.040(3)	Ni(2)−O(2)	2.050(3)
Ni(2)−O(3)	2.067(3)	Ni(1)−Ni(2)	3.007(2)
C(12)−O(1)	1.357(5)	C(19)−O(2)	1.361(5)
Bond angles			
O(1)−Ni(1)−O(2)	83.75(12)	O(1)−Ni(1)−N(1)	96.61(14)
O(2)−Ni(1)−N(1)	178.27(15)	O(1)−Ni(1)−N(2)	178.93(15)
O(2)−Ni(1)−N(2)	96.48(14)	N(1)−Ni(1)−N(2)	83.12(16)
O(2)−Ni(2)−O(1)	75.33(11)	O(2)−Ni(2)−O(1)^{i}	104.67(11)
O(3)−Ni(2)−O(1)	87.43(11)	O(3)−Ni(2)−O(1)^{i}	92.57(11)
O(3)−Ni(2)−O(2)	88.29(12)	O(3)−Ni(2)−O(2)^{i}	91.71(13)
Ni(1)−O(1)−Ni(2)	100.39(13)	Ni(1)−O(2)−Ni(2)	98.98(14)

Symmetry code: (*i*) $1 - x, -y, 1 - z$

ESR Spectra of Complex 1

For the interpretation of the ESR spectra of complex **1**, it is convenient to consider the relative energies of the states deduced by coupling the three $S = 1/2$ ions. A demonstration of these states and the corresponding energies can be found in the book of O. Kahn.[18] The spin diagram is given in Figure 3 in which the occurrence of *ZFS* in the state $|3/2, 1/2>$ is considered, giving two doublets corresponding to $m_s = \pm 3/2$ and $\pm 1/2$. As shown, $m_s = \pm 1/2$ is strongly anisotropic.[19]

The ESR spectra of **1**, as a function of temperature, are given in Figure 4. The easiest spectrum to interpret is that corresponding to the lowest temperature measured (8 K). The spectrum shows a very narrow almost isotropic band centred at $g = 2.05$. When the temperature is raised this signal broadens and at close to liquid nitrogen temperature it begins to appear as broad band near 1500 Gauss. The intensity of the spectrum diminishes as the temperature increases and at 298 K (final temperature we measured) the spectrum shows two clear and very broad signals, the first one centred at 3000 G ($g = 2.08$) and a new band centred at 1200−1300 G which corresponds to a *g* value of approximately 5.15. It must be pointed out that the difference in the intensities of the limiting spectra (room temperature and 8 K) is in the region of five orders of magnitudes (10^5).

At low temperature, only the $|1/2, 1>$ ground state is populated ($J = -314$ cm^{-1} according to the susceptibility measurements as described below). Thus the strong signal

 © 2005 Wiley-VCH Verlag GmbH & Co. KGaA, Weinheim

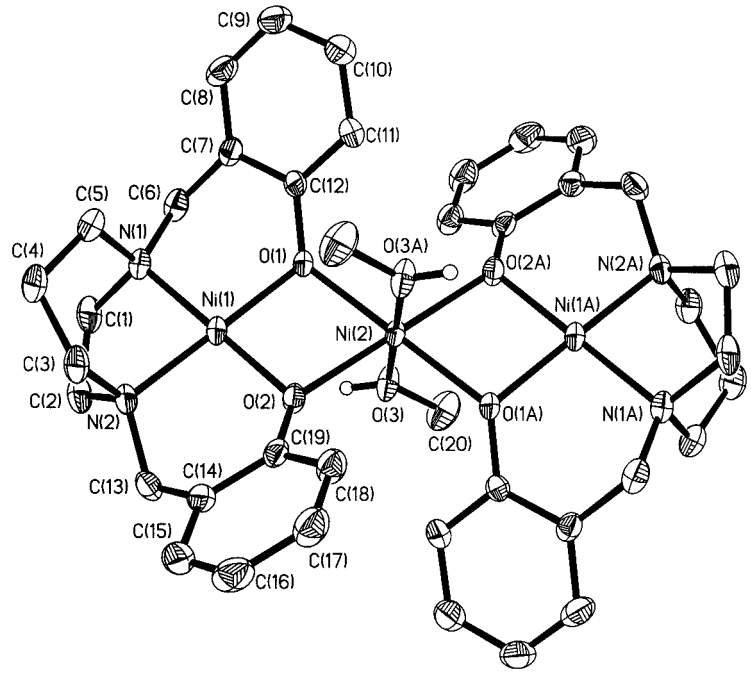

Figure 2. ORTEP structure of the molecular structure of **2** including atomic labelling of the asymmetric unit (hydrogen atoms and perchlorate anions are omitted for clarity) with displacement ellipsoids drawn at the 30% probability level

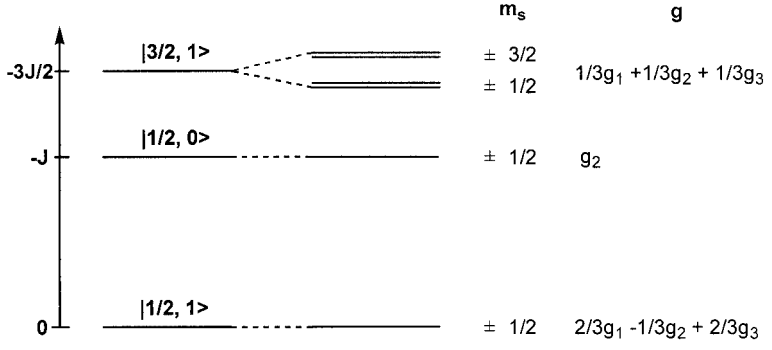

Figure 3. Spin levels, energies and g values in a trinuclear Cu_3 complex ($J < 0$)

at $g = 2.05$ is due to this ground state. This g value is an average of the g values of the three Cu^{II} ions ($g = 1/3\ [2g_{T1} - g_C + 2g_{T2}]$ where C and T are the central and terminal Cu ions).[19,20] The g values for the |1/2, 0> and |3/2, 1> states are different, provided that the individual g_i values are different.[20] If we assume that the rate of transition from the lowest to the excited multiplets is fast on the ESR time scale, the observed spectrum at a given temperature would be the thermal average of the spectra of three different multiplets. Therefore, the liquid helium temperature spectra should be those of the lowest doublet, while those at higher temperatures should also bear the contributions of the excited multiplets. For this reason, the anisotropy of the molecular g value is usually not well defined. Only in a few trinuclear Cu^{II} complexes is this anisotropy manifested.[21] In complex **1**, the observed g value is an average of two different Cu^{II} environments. On the other hand, in solid state, the trinuclear cations are not perfectly isolated from a magnetic point of view. Effectively, we have found a nonnegligible J' value (molecular-field approach, see below). As has been pointed out,[22] even an extremely weak value for the intermolecular exchange interaction leads to the exchange averaging effect which is responsible for the isotropic or quasi-isotropic spectra observed (such as in complex **1**).

Only on a few occasions for this kind of trinuclear Cu^{II} complex, has any evidence of signals attributable to a spin quadruplet been found. In contrast, this spin quadruplet is clearly visible at 4 K when the coupling is ferromagnetic because this is the ground state in this case.[5,23] A broad transition between $g = 4.25-5.5$ occurs and can be assigned to the transition between the ± 1/2 levels of the $S = 3/2$ system. Thus, this is undoubtedly the origin of the broad signal centred at $g \approx 5$ in complex **1**.

 © 2005 Wiley-VCH Verlag GmbH & Co. KGaA, Weinheim

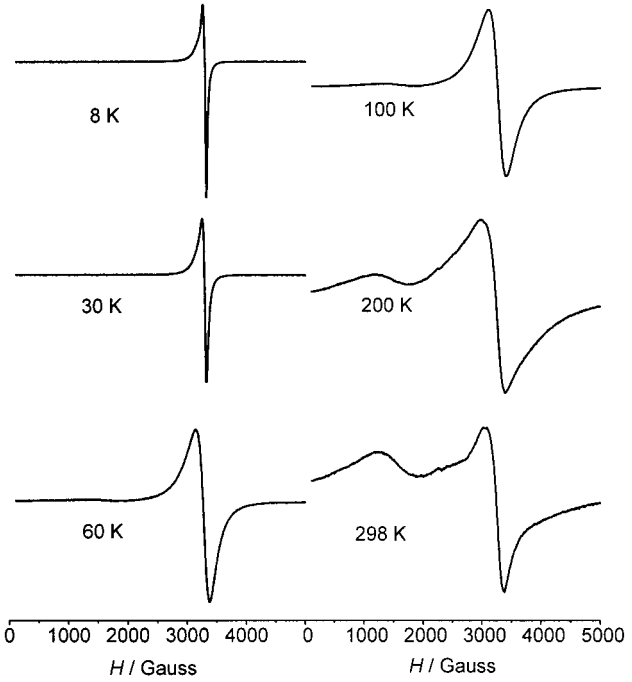

Figure 4. X-band powder ESR spectra at different temperatures for complex **1**; the ratio of the intensities at 8 K and 298 K is 10^5

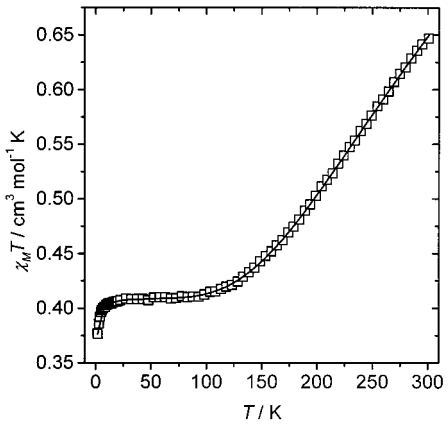

Figure 5. Plot of the temperature dependence of $\chi_M T$ for **1**; the solid line corresponds to the best fit (see text for parameters calculated)

Magnetic Properties of 1 and 2

Complex 1

The magnetic properties of complex **1** in the form of a $\chi_M T$ vs. T plot are shown in Figure 5 (magnetic susceptibility per three Cu^{II} ions). The $\chi_M T$ value is 0.65 cm^3 mol^{-1} K at 300 K which is far from the value of 1.2 cm^3 mol^{-1} K corresponding to three isolated spin doublets. The $\chi_M T$ value decreases to 0.40 cm^3 mol^{-1} K upon cooling to ca. 80 K. At this point there is a clear plateau from 80 K to 10 K and, finally, there is a slight decrease to 0.38 cm^3 mol^{-1} K at 2 K. This curve suggests strong antiferromagnetic coupling between the Cu^{II} centres with the presence of very small intermolecular antiferromagnetic interactions being active only at very low temperature. Thus, in the light of the above structural discussion of complex **1**, we can interpret its magnetic behaviour through a simple model with only one intramolecular J parameter using the following spin Hamiltonian:

$$H = -J_1 (S_1S_2 + S_2S_3)$$

From this Hamiltonian it is possible to deduce a simple equation for $\chi_M T$ vs. T:[18]

$$\chi_M T = \frac{Ng^2\beta^2[1+\exp(J/KT)+10\exp(3J/2KT)]}{4K[1+\exp(J/KT)+2\exp(3J/2KT)]}$$

This equation has been completed by introducing a J' parameter and considering the possible small interactions between the trinuclear entities using the molecular-field approach:[18]

$$\chi_M = Ng^2\beta^2F(J,T)/(kT - zJ'F(J,T))$$

The fit of the magnetic data, assuming that the g factors are identical for Cu(1) and Cu(2), leads to $J = -314.0 \pm 0.8$ cm^{-1}, $J' = -0.5 \pm 0.01$ cm^{-1}, $g = 2.09$ and $R = 1.5 \times 10^{-6}$ (R is the agreement factor defined as $\Sigma_i[(\chi_M T)_{obs} - (\chi_M T)_{calc}]^2 / \Sigma[(\chi_M T)_{obs}]^2$).

Magneto-Structural Correlations in Cu_2O_2 Cores

Magneto-structural correlations in dinuclear Cu^{II} complexes bridged equatorially by pairs of hydroxo[24] or alkoxo[25] groups show that the major factor controlling the spin coupling between the $S = 1/2$ metal centres is the Cu−O(R)−Cu angle. Hatfield and Hodgson found a linear correlation between the experimentally determined exchange coupling constant and the Cu−O−Cu bond angle (φ) (see a in Figure 6).[24] Antiferromagnetic behaviour is observed for complexes with φ larger than 97.6°, while ferromagnetism appears for those with smaller values of φ. An apparently similar linear relationship for the alkoxo cases[25] shows that at angles around 95.6°, the exchange integral approaches zero, i.e. the point of experimental "accidental orthogonality". For such dimeric Cu^{II} complexes, Nieminen[26] described correlations between the singlet-triplet splitting energy and the Cu−O−Cu angle φ, the deviation d_c of the carbon atom connected to the bridging oxygen atoms from the Cu−O−Cu plane and the sum of the angles around the bridging oxygen atoms. Walz et al.[27] reported the influence of the coordination geometry around the Cu^{II} atom on the exchange interaction in alkoxo-bridged complexes. These experimental observations are consistent with studies using the angular overlap approach by Bencini and Gatteschi[28] as well as extended Hückel MO treatments by Hoffmann[29] and Kahn.[30] More recent ab initio and DFT calculations on simple model dimers examined the effects of the bridging angles, Cu−O distances, fold (hinge) angle along the O−O axis and degree of tetrahedral (for square-planar geometry) or sp → bpt (for square-pyramidal geometry) distortions at the Cu^{II} centres.[25,31−33] These theoretical studies showed that although the major factor affecting the magnetic exchange is the Cu−O−Cu

 © 2005 Wiley-VCH Verlag GmbH & Co. KGaA, Weinheim

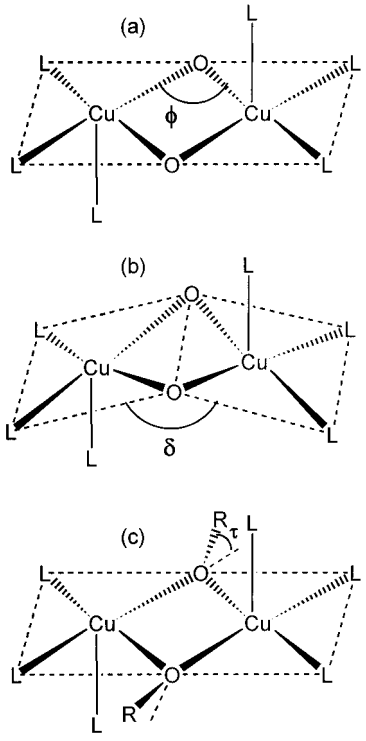

Figure 6. The three main factors in the Cu_2O_2 entities that tune the antiferromagnetic coupling in μ-phenoxo derivatives

bridge, other features can also significantly lead to the increase in the ferromagnetic contributions which effectively reduces any antiferromagnetic term associated with the hydroxo/alkoxo bridges. Among these features, we can underline the distortions of the coordination geometry of the Cu^{II} centre,[34,35] the variation in Cu−O bond lengths,[32] the hinge (roof shape) distortion of the core (δ, see b in Figure 6),[31−33,36] the torsion angle created by the H (or R) group with regard to the Cu_2O_2 plane (τ angle, see c in Figure 6)[32] and different electronic factors.[31,32,37,38] Some of these geometric factors are shown in Figure 6.

Roughly the same features discussed for the hydroxo-bridged complexes also seem apparent in alkoxo-bridged complexes. Thompson et al. found significant differences in magnetic coupling between μ-hydroxo (or μ-alkoxo) and μ-phenoxo complexes.[39] From this work, it is apparent that the slopes of the graphs ($2J$ vs. Cu−O−Cu angle) of the hydroxo and alkoxo cases are comparable but the absolute values of $-2J$ are larger for the alkoxo species. However, the slope of the graph for the phenoxo system is smaller and the absolute values of $-2J$ are inherently larger. For lower angles (95°) the J values approach zero for the alkoxo species but this is not the case for phenoxo bridging complexes. The range of the average angles for these phenoxo complexes is very small (from 99 to 105°). The couplings lie between $-700\ cm^{-1}$ (for smaller angles) and $-900\ cm^{-1}$ (for larger angles) as shown in Figure 7.[39] For $J = 0$ the Cu−O−Cu angle should be 77°, although this angle has not been experimentally observed at present. The observation of greater J values for −OR than −OH is due to the effect of replacing the hydrogen of the hydroxo with a more electronegative carbon group which reduces the electron density on the oxygen bridge.[36]

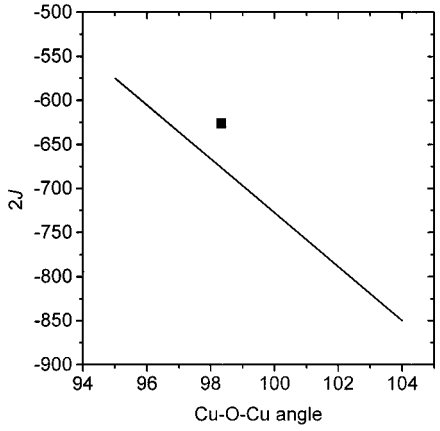

Figure 7. Schematic plot of the $2J$ values vs. Cu−O−Cu angles given by Thompson et al. in ref.[42] together with the point indicating the experimental value for **1**; in this figure the symbolism of $2J$ has been kept, although in the text we have used the Hamiltonian $-J$ instead of $-2J$

Similar correlations can be established for comparable macrocyclic dicopper(II) systems, such as "Robson" type macrocyclic complexes, formed by Cu^{II} ions acting as templates for the condensation of diformylphenols and various diamines. These systems contain phenoxo oxygen atoms bridging the two Cu^{II} centres and represent ideal systems for examining the exchange coupling via the phenoxo oxygen. The degree of distortional flexibility available to simple dimeric Cu^{II} complexes with hydroxo or alkoxo bridges can be expected to be reduced when the Cu−$(O)_2$−Cu entity is enclosed within the cavity of a macrocyclic ligand and, thus, one might expect a more straightforward relationship between the bridging angle and the exchange with respect to electronic perturbations. Only a few structural examples of this sort of complex have been reported in which the linker group between the azomethanide nitrogens is two-membered, thereby creating a five-membered chelate ring.[39] The Cu−$O_{phenoxo}$−Cu angles fall in the range 98.8−100.9°, this being at the lower end of the range of angles typical for phenoxo systems. In all cases, the molecules themselves and the dinuclear centres are almost flat. There are no unusual structural or electronic perturbations which might be expected to influence the exchange in a significant way in those complexes. Thus, the phenoxo bridging angle can be considered to be the principal factor controlling the spin coupling.

In summary, the main conclusion for phenoxo systems is that strong antiferromagnetic exchange will dominate in these complexes. For comparison with complex **1**, structural and magnetic parameters for some related [Cu_2(μ-OR)] complexes are listed in Table 3. In the present case, complex **1** belongs to the μ-phenoxo-bridged group of complexes. The Cu−O−Cu angles are 98.31(12) and 98.38(11)°, respectively, and the intramolecular Cu···Cu separation is 2.9376(9) Å. The hinge angle (δ) through the O(1)−O(2)

 © 2005 Wiley-VCH Verlag GmbH & Co. KGaA, Weinheim

Table 3. Structural and magnetic parameters for some relevant $[Cu_2(\mu\text{-}OR)_2]$ complexes (basal-basal coordination)

Compound	φ[a]	τ[a]	δ[a]	*J*	Ref.
$[Cu(L)(CH_3COO)_2]$(*O*-acetato)	95.7/102.6	–	–	≈ +1	[40]
$[Cu(AE)(CH_3COO)]_2$(*O*-acetato)	95.34	–	180	≈ −1	[41]
$[Cu(bpy)_2\{\mu\text{-}Ph(OCH_2)Npy\}_2](ClO_4)_2$ (alkoxo)	97.8	62	180	+10 (2*J*)	[42]
$[Cu(phen)_2\{\mu\text{-}Ph(OCH_2)Npy\}_2](ClO_4)_2$ (alkoxo)	98.3	48.7	180	−98 (2*J*)	[42]
$[Cu_2(b2b)_2(OR)_2](ClO_4)_2$ (alkoxo)	130.21	–	180	diamag.	[43]
$[Cu_2(b3b)_2(OR')_2](ClO_4)_2$ (alkoxo)	102.9	–	180	diamag.	[43]
$[Cu(papen)]_2\cdot 2H_2O$ (alkoxo)	98.3	–	164.1	−128 (2*J*)	[48]
$[Cu_2(HL)_2](NO_3)_2$ (phenoxo no-macro)	102.8/103.1	–	141.1	−714	[44]
$[Cu_2(L)(HL)](ClO_4)$ (phenoxo no-macro)	103.81/101.8	–	–	−277	[44]
$[Cu_2(fsa_2en)]$ (phenoxo no-macro)	100.1	–	–	−650 (2*J*)	[45]
$[Cu(etsal)NO_3]_2$ (phenoxo no-macro)	101.1	–	180	−166 (2*J*)	[46]
$[Cu(ips)Cl]_2$ (phenoxo no-macro)	103.6	–	180	−145	[34]
$[Cu_2(L1)(H_2O)_2]F_2$ (phenoxo macro)	103.65	–	180	−790	[39]
$[Cu_2(L2)Cl_2][Cu_2(L2)(H_2O)_2]Cl\cdot ClO_4$ (phenoxo macro)	105 (av)	–	–	−800	[39]
$[Cu_2(L3)(H_2O)_2]BF_4$ (phenoxo macro)	98.8	–	180	−690	[39]
$[Cu_2L1(ClO_4)_2]$ (phenoxo macro)	102.8	–	180	−740	[47]

[a] The meaning of Greek symbols is given in Figure 6.

axis is 170°, i.e. very close to 180° which corresponds to an exactly planar structure. The torsion angles (τ) created by C(19) and C(12) (phenoxo ligands) from the Cu_2O_2 plane are 140/147.2 and 138.9/145.6°, respectively. Thus, we can expect strong antiferromagnetic coupling as experimentally observed. Plotting the 2*J* values indicated by Thompson et al. in reference 42 and adding the Cu−O−Cu angles and the 2*J* parameter for complex **1**, a rather good agreement can be observed (Figure 7). The difference could be due to the hinge angle (very small in this case) and, mainly, to the τ distortion (considerable in complex **1** as stated above).

Complex 2

The magnetic properties of **2** in the form of $\chi_M T$ vs. *T* plots are shown in Figure 8, these representing the magnetic susceptibility *per* Ni^{II} ion (the terminal ones are diamagnetic). The $\chi_M T$ value is 1.32 $cm^3\ mol^{-1}$ K at 300 K which is a typical value for an isolated Ni^{II} ion with $g > 2.00$. $\chi_M T$ is practically constant to 25 K and then decreases to 0.3 $cm^3\ mol^{-1}$ K at 2 K. This feature suggests typical paramagnetic behaviour for a Ni^{II} ion in which the *D* parameter and/or intermolecular interactions (usually antiferromagnetic) are active at low temperature. In an attempt to calculate the *D* value, we have fitted the experimental $\chi_M T$ values to the formula given by Kahn for a mononuclear Ni^{II} ion taking into consideration the *ZFS* of the $S = 1$ ground state.[18] The best fit values are $|D| = 11\ cm^{-1}$ and g (average) = 2.30. The *D* value is higher than that typical for Ni^{II} ions (close to 5−8 cm^{-1}), indicating that the possible intermolecular interactions are superimposed on this *D* value. The magnetisation measurement at 2 K corroborates the effect of the *D* parameter, i.e. the reduced magnetisation ($M/N\beta$) at 5 T is only consistent with 1.4 electrons instead of two electrons which should be the theoretical value for an isolated Ni^{II} ion with $g = 2.00$ (see inset in Figure 8).

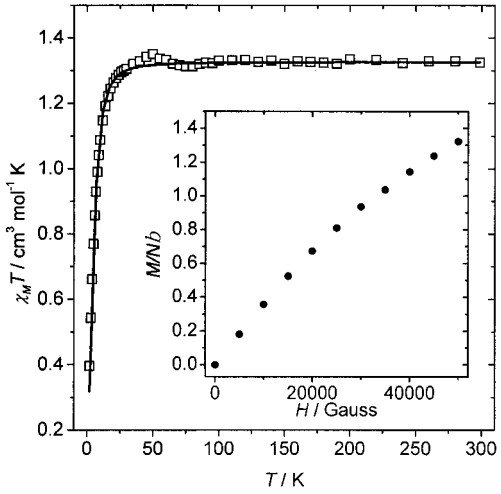

Figure 8. Plot of $\chi_M T$ vs. *T* for complex **2**; the solid line in the $\chi_M T$ curve represents the best fit for calculating the *D* value (see text); inset: plot of the reduced magnetisation ($M/N\beta$) vs. *H* at 2 K for complex **2**

Conclusions and Perspectives

Two novel linear phenoxo-bridged trinuclear Cu^{II} and Ni^{II} complexes were rationally designed and prepared based on a new diazamesocyclic ligand bearing two pendant phenol donors. From a magnetic point of view, the data for complex **1** show two features: the very strong antiferromagnetic coupling interaction between the neighbouring μ-phenoxo Cu^{II} centres and the small possible interactions between the trinuclear entities. The magneto-structural correlations for related complexes containing Cu_2O_2 cores have been analysed in detail. For **2**, both terminal Ni^{II} ions are diamagnetic and the central Ni^{II} shows typical paramagnetic behaviour. The zero-field splitting for Ni^{II} can be ob-

 © 2005 Wiley-VCH Verlag GmbH & Co. KGaA, Weinheim

served and further corroborated by the magnetisation measurements. Additionally, the interesting ESR properties of **1** at different temperatures (from 298 K to 8 K) were investigated. Further studies of the coordination chemistry of such attractive systems are under way in our laboratory.

Experimental Section

Materials and Physical Measurements: With the exception of 2-bromomethyl phenylacetate, which was synthesised according to the reported literature procedure,[49] all of the starting materials and solvents for the syntheses and the analyses were obtained commercially and used as received. ^{1}H NMR spectra were recorded on a Bruker AC-P 400 spectrometer (400 MHz) at 25 °C with tetramethylsilane as the internal reference. FT-IR spectra (KBr pellets) were recorded on an AVATAR-370 (Nicolet) spectrometer and electronic spectra were acquired with a CARY300 (Varian) spectrophotometer. C, H and N analyses were performed on a CE-440 (Leemanlabs) analyser. Conductivities of the complexes were measured at room temperature using a DDS 11A conductometer. Thermal stability (TGA) experiments were carried out on a Dupont thermal analyser from room temperature to 600 °C under a nitrogen atmosphere at a heating rate of 10 °C/min.

Synthesis of the Ligand *N*,*N*′-Bis(2-hydroxybenzyl)-1,4-diazacycloheptane (H_2L): 2-Bromomethyl phenylacetate (8.12 g, 35.5 mmol) was added to a solution of DACH (1.54 g, 15.4 mmol) in C_2H_5OH (80 mL) with vigorous stirring at room temperature. Suitable portions of solid KOH were added to the above mixture to ensure that the pH value stayed at 7−8 for ca. 3 days. After filtration of the mixture, the solvent was removed by rotary evaporation. The residue was purified by silica gel column chromatography (CH_2Cl_2/CH_3OH/NH_3·H_2O from 10:10:1 to 5:5:1). The final product was obtained as a white solid in 55% yield (2.65 g, based on DACH). ^{1}H NMR ($CDCl_3$): δ = 1.91−1.97 (m, 2 H, CH_2), 2.79−2.85 (m, 8 H, CH_2), 3.80 (s, 4 H, CH_2), 6.75−6.84 (m, 4 H, Ph), 6.94 (d, J = 1.5 Hz, 1 H, Ph), 6.96 (d, J = 1.5 Hz, 1 H, Ph), 7.14−7.26 (m, 2 H, Ph). IR [KBr pellet (cm^{-1})]: 3432 b, 3043 m, 2934 m, 2912 w, 2876 w, 2841 m, 2717 w, 2627 w, 1933 w, 1897 w, 1784 w, 1613 s, 1590 vs, 1479 vs, 1458 vs, 1421s, 1383 w, 1357 s, 1349 s, 1334 m, 1307 w, 1256 vs, 1183 m, 1151 s, 1090 s, 1057 m, 1034 s, 1016 m, 983 s, 936 m, 917 m, 871 m, 850 w, 811 s, 755 vs, 720 m, 625 m, 595 w, 547 m, 459 s. $C_{19}H_{24}N_2O_2$ (312.41): calcd. C 73.05, H 7.74, N 8.97; found C 73.19, H 7.51, N 8.84.

[Cu_3(μ-L)$_2$](CH_3OH)$_2$(ClO_4)$_2$ (1): To a solution of H_2**L** (63 mg, 0.2 mmol) in $CHCl_3$ (20 mL) was slowly added a CH_3OH solution (15 mL) of $Cu(ClO_4)_2$·$6H_2O$ (110 mg, 0.3 mmol) with stirring and a brown powder of complex **1** precipitated gradually. The powder was filtered off, washed with methanol/water and dried under vacuum. Yield: 97 mg (90%). Single crystals of **1** suitable for X-ray analysis were obtained as follows: a solution of $Cu(ClO_4)_2$·$6H_2O$ in CH_3OH was carefully layered onto a solution of H_2**L** in $CHCl_3$ in a 3:2 molar ratio in a straight glass tube and rhombic brown crystals were observed after ca. two weeks. $C_{40}H_{52}Cl_2Cu_3N_4O_{14}$ (1074.41): calcd. C 44.72, H 4.88, N 5.21; found C 44.61, H 4.74, N 5.17. IR (cm^{-1}): 3446 b, 3061 w, 2940 w, 2905 w, 2860 m, 1598 s, 1574 w, 1482 vs, 1445 s, 1395 m, 1340 w, 1327 w, 1264 s, 1247 vs, 1212 m, 1198 m, 1102 vs, 1061 vs, 970 m, 923 m, 881 m, 864 m, 785 m, 773 s, 763 vs, 761 w, 642 m, 623 s, 577m. Λ_M (CH_3CN): 266 cm^2 Ω^{-1} mol^{-1}. λ_{max}/nm (ε/dm^3 mol^{-1} cm^{-1}) (CH_3CN): 558 (220) and 386 (520).

[Ni_3(μ-L)$_2$(CH_3OH)$_2$](ClO_4)$_2$ (2): The same synthetic procedure (for both polycrystalline and single-crystal preparation) for **1** was used except that $Cu(ClO_4)_2$·$6H_2O$ was replaced by $Ni(ClO_4)_2$·$6H_2O$. This afforded a red powder in 85% yield (or block-type single crystals). $C_{40}H_{52}Cl_2Ni_3N_4O_{14}$ (1059.83): calcd. C 45.33, H 4.95, N 5.29; found C 45.61, H 4.58, N 5.04%. IR (cm^{-1}): 3357 b, 3059 w, 3020 w, 2939 w, 2911 w, 2860 m, 1599 s, 1577 m, 1485 vs, 1457 vs, 1398 m, 1342 w, 1325 w, 1261 vs, 1208 m, 1112 vs, 1045 vs, 1027 vs, 972 m, 943 w, 927 m, 883 s, 867 m, 794 s, 767 vs, 734 m, 657 m, 624 s, 605 w, 590 m. Λ_M (H_2O): 182 cm^2 Ω^{-1} mol^{-1}. λ_{max}/nm (ε/dm^3 mol^{-1} cm^{-1}) (H_2O): 498 (340), 362 (1150) and 324 (1020).

Caution! Although no problems were encountered in this study, transition metal perchlorate complexes are potentially explosive and should be handled with proper precautions.

Magnetic Studies: The variable-temperature magnetic susceptibilities were measured at the "Servei de Magnetoquímica (Universitat de Barcelona)" on polycrystalline samples (30 mg) with a Quantum Design MPMS SQUID magnetometer operating at a magnetic field of 0.1 T between 2 and 300 K. The diamagnetic corrections were evaluated from Pascal's constants for all the constituent atoms. Magnetisation measurements were carried out at 2 K in the 0−5 T range. ESR spectra were recorded on powder samples at the X-band frequency with a Bruker 300E automatic spectrometer, varying the temperature between 8 and 298 K.

X-ray Crystallographic Data Collections and Refinements: Single-crystal X-ray diffraction measurements of **1** (brown, 0.30 × 0.25 × 0.20 mm) and **2** (red, 0.30 × 0.25 × 0.20 mm) were carried out with a Bruker Smart 1000 CCD diffractometer equipped with a graphite crystal monochromator situated in the incident beam for data collection at 293(2) K. The lattice parameters were obtained by least-squares refinements of the diffraction data of 781 (for **1**) and 582 (for **2**) reflections, respectively, and data collections were performed with Mo-$K\alpha$ radiation (λ = 0.71073 Å) by the ω scan

Table 4. Crystallographic data and structural refinement parameters of complexes **1** and **2**

	1	**2**
Empirical formula	$C_{40}H_{52}Cl_2Cu_3N_4O_{14}$	$C_{40}H_{52}Cl_2Ni_3N_4O_{14}$
Mr	1074.41	1059.83
Crystal system	monoclinic	triclinic
Space group	$P2_1/n$	$P\bar{1}$
a (Å)	10.915(4)	9.682(4)
b (Å)	14.208(5)	11.182(4)
c (Å)	14.114(5)	11.278(5)
α (°)	90	76.624(7)
β (°)	98.412(6)	81.561(7)
γ (°)	90	68.404(7)
V (Å^3)	2165.3(13)	1101.9(8)
Z	2	1
D_c [g cm^{-3}]	1.648	1.597
μ [mm^{-1}]	1.655	1.460
F(000)	1106	550
Total data	10022	4702
Unique data	4392	3850
Data [$I > 2\sigma(I)$]	2860	2377
R_{int}	0.0448	0.0322
$R1$[a]	0.0470	0.0447
$wR2$[b]	0.1011	0.0842
GOF[c]	1.008	1.011
Residuals [e·Å^{-3}]	0.575, −0.393	0.340, −0.357

[a] $R1 = \Sigma F_o - F_c / \Sigma F_o$. [b] $wR2 = [\Sigma w(F_o^2 - F_c^2)^2 / \Sigma w(F_o^2)^2]^{1/2}$. [c] GOF = $\{\Sigma[w(F_o^2 - F_c^2)^2]/(n - p)\}^{1/2}$.

 © 2005 Wiley-VCH Verlag GmbH & Co. KGaA, Weinheim

mode in the range of $2.21 < \theta < 26.39°$ (for **1**) and $2.00 < \theta < 25.00°$ (for **2**). There was no evidence of crystal decay during data collection for both complexes. All the measured independent reflections were used in the structural analyses and semi-empirical absorption corrections were applied using the SADABS program. The program SAINT[50] was used for integration of the diffraction profiles. Both structures were solved by direct methods using the SHELXS program of the SHELXTL package and refined with SHELXL.[51] Metal atoms were located from the *E*-maps and other nonhydrogen atoms were located in successive difference Fourier syntheses. The final refinements were performed by full-matrix least-squares methods with anisotropic thermal parameters for all the nonhydrogen atoms on F^2. All hydrogen atoms were first found in difference electron density maps and then placed in the calculated sites and included in the final refinement in the riding model approximation with displacement parameters derived from the parent atoms to which they were bonded. In the refinement of both complexes, a disorder model of the perchlorate anion was used (two constraint components for four oxygen atoms of the perchlorate anion have occupancy factors of 0.5) to make the oxygen atoms exhibit suitable displacement ellipsoids. A summary of the crystallographic data and structure refinements are listed in Table 4.

CCDC-232051 (for **1**) and -232052 (for **2**) contains the supplementary crystallographic data for this paper. These data can be obtained free of charge via www.ccdc.cam.ac.uk/cons/ retrieving.html (or from the CCDC, 12 Union Road, Cambridge CB2 1EZ, UK; Fax: +44-1223-336-033; E-mail: deposit@ccdc.cam.ac.uk).

Acknowledgments

This work was financially supported by the National Natural Science Foundation of China (No. 20401012) and the Key Project of Tianjin Natural Science Foundation (to M. D.). X. H. B. acknowledges financial support from the Outstanding Youth Foundation of NSFC (No. 20225101) and J. R. from the Spanish Government (Grant BQU2003/00539).

[1] [1a] D. Gatteschi, *Adv. Mater.* **1994**, *6*, 635−645. [1b] R. E. P. Winpenny, *Comments Inorg. Chem.* **1999**, *20*, 233−262. [1c] S. Leininger, B. Olenyuk, P. J. Stang, *Chem. Rev.* **2000**, *100*, 853−908. [1d] E. I. Solomon, R. K. Szilagyi, S. D. George, L. Basumallick, *Chem. Rev.* **2004**, *104*, 419−458. [1e] D. Gatteschi, R. Sessoli, *Angew. Chem. Int. Ed.* **2003**, *42*, 268−297. [1f] M. A. Halcrow, G. Christou, *Chem. Rev.* **1994**, *94*, 2421−2481.

[2] For examples, see: [2a] G. A. van Albada, I. Mutikainen, U. Turpeinen, J. Reedijk, *Eur. J. Inorg. Chem.* **1998**, 547−549. [2b] L. Cronin, P. H. Walton, *Inorg. Chim. Acta* **1998**, *269*, 241−245. [2c] T. C. Higgs, K. Spartalian, C. J. O'Connor, B. F. Matzanke, C. J. Carrano, *Inorg. Chem.* **1998**, *37*, 2263−2272.

[3] For examples, see: [3a] R. Prins, M. Biagini-Cingi, M. Drillon, R. A. G. de Graaff, J. G. Haasnoot, A. M. Manotti-Lanfredi, P. Rabu, J. Reedijk, F. Uggozzoli, *Inorg. Chim. Acta* **1996**, *248*, 35−44. [3b] P. A. Angaridis, P. Baran, R. Boca, F. Cervantes-Lee, W. Haase, G. Mezei, R. G. Raptis, R. Werner, *Inorg. Chem.* **2002**, *41*, 2219−2228.

[4] For examples, see: S. Ferrer, J. G. Haasnoot, J. Reedijk, E. Muller, M. B. Cingi, M. Lanfranchi, A. M. M. Lanfredi, J. Ribas, *Inorg. Chem.* **2000**, *39*, 1859−1867.

[5] For examples, see: [5a] R. L. Beddoes, J. A. Conner, D. Dubowski, A. C. Jones, O. S. Mills, R. Price, *J. Chem. Soc., Dalton Trans.* **1981**, 2119−2126. [5b] L. Gutiérrez, G. Alzuet, J. A. Real, J. Cano, J. Borrás, A. Castiñeiras, *Inorg. Chem.* **2000**, *39*, 3608−3614.

[6] For examples, see: X. M. Liu, M. P. de Miranda, E. J. L. McInnes, C. A. Kilner, M. A. Halcrow, *Dalton Trans.* **2004**, 59−64.

[7] For examples, see: J. Ribas, A. Escuer, M. Monfort, R. Vicente, R. Cortes, L. Lezama, T. Rojo, *Coord. Chem. Rev.* **1999**, *195*, 1027−1068.

[8] [8a] M. Du, X. H. Bu, G. C. Wang, Y. M. Guo, R. H. Zhang, *Inorg. Chim. Acta* **2001**, *320*, 190−197. [8b] M. Du, Y. M. Guo, X. H. Bu, *Inorg. Chim. Acta* **2002**, *335*, 136−140.

[9] [9a] X. H. Bu, M. Du, L. Zhang, Z. L. Shang, R. H. Zhang, M. Shionoya, *J. Chem. Soc., Dalton Trans.* **2001**, 729−735. [9b] X. H. Bu, M. Du, Z. L. Shang, L. Zhang, Q. H. Zhao, R. H. Zhang, M. Shionoya, *Eur. J. Inorg. Chem.* **2001**, 1551−1558. [9c] M. Du, Z. L. Shang, X. B. Leng, X. H. Bu, *Polyhedron* **2001**, *20*, 3065−3071.

[10] [10a] X. H. Bu, M. Du, Z. L. Shang, R. H. Zhang, D. Z. Liao, M. Shionoya, T. Clifford, *Inorg. Chem.* **2000**, *39*, 4190−4199. [10b] X. H. Bu, M. Du, L. Zhang, D. Z. Liao, J. K. Tang, R. H. Zhang, M. Shionoya, *J. Chem. Soc., Dalton Trans.* **2001**, 593−598. [10c] M. Du, Y. M. Guo, X. H. Bu, J. Ribas, M. Monfort, *New J. Chem.* **2002**, *26*, 645−650.

[11] [11a] M. Du, X. H. Bu, Y. M. Guo, L. Zhang, D. Z. Liao, J. Ribas, *Chem. Commun.* **2002**, 1478−1479. [11b] M. Du, X. H. Bu, Y. M. Guo, J. Ribas, C. Diaz, *Chem. Commun.* **2002**, 2550−2551. [11c] M. Du, X. H. Bu, Y. M. Guo, J. Ribas, *Chem. Eur. J.* **2004**, *10*, 1345−1354.

[12] C. A. Grapperhaus, M. Y. Darensbourg, *Acc. Chem. Res.* **1998**, *31*, 451−459 and references cited therein.

[13] [13a] D. L. An, Y. M. Guo, M. Du, X. S. Shi, X. H. Bu, *Chin. J. Struct. Chem.* **2004**, *23*, 126−130. [13b] M. Du, Y. M. Guo, S. T. Chen, X. H. Bu, *J. Mol. Struct.* **2002**, *641*, 29. [13c] Y. M. Guo, M. Du, X. H. Bu, *J. Mol. Struct.* **2002**, *610*, 27−31. [13d] M. Du, Y. M. Guo, X. H. Bu, J. Ribas, M. Monfort, *New J. Chem.* **2002**, *26*, 939−945. [13e] Y. M. Guo, Doctor Dissertation, **2001**, Nankai University.

[14] [14a] H. Okawa, M. Koikawa, S. Kida, D. Luneau, H. Oshio, *J. Chem. Soc., Dalton Trans.* **1990**, 469−475. [14b] F. Akagi, Y. Nakao, K. Matsumoto, S. Takamizawa, W. Mori, S. Suzuki, *Chem. Lett.* **1997**, 181−182. [14c] W. L. Driessen, L. Chang, C. Finazzo, S. Gorter, D. Rehorst, J. Reedijk, M. Lutz, A. L. Spek, *Inorg. Chim. Acta* **2003**, *350*, 25−31.

[15] K. Nakamoto, *Infrared and Raman Spectra of Inorganic and Coordination Compounds*, Wiley, New York, **1986**.

[16] E. V. RybakAkimova, D. H. Busch, P. K. Kahol, N. Pinto, N. W. Alcock, H. J. Clase, *Inorg. Chem.* **1997**, *36*, 510−520.

[17] G. R. Desiraju, T. Steiner, *The Weak Hydrogen Bond in Structural Chemistry and Biology*, Oxford University Press, **1999**.

[18] O. Kahn, *Molecular Magnetism*, VCH Publishers, New York, **1993**.

[19] A. Bencini, D. Gatteschi, *EPR of Exchange Coupled Systems*, Springer-Verlag, Berlin, **1989**.

[20] L. Banci, A. Bencini, D. Gatteschi, *Inorg. Chem.* **1983**, *22*, 2681−2683.

[21] R. Veit, J. J. Girerd, O. Kahn, F. Robert, Y. Jeannin, *Inorg. Chem.* **1986**, *25*, 4175−4180.

[22] R. Costa, A. García, J. Ribas, T. Mallah, Y. Journaux, X. Solans, V. Rodríguez, *Inorg. Chem.* **1993**, *32*, 3733−3742 and references cited therein.

[23] L. Gutiérrez, G. Alzuet, J. A. Real, J. Cano, J. Borrás, A. Castiñeiras, *Eur. J. Inorg. Chem.* **2002**, 2094−2102.

[24] V. H. Crawford, H. W. Richardson, J. R. Wason, D. J. Hodgson, W. E. Hatfield, *Inorg. Chem.* **1976**, *15*, 2107−2110.

[25] [25a] L. Merz, W. Haase, *J. Chem. Soc., Dalton Trans.* **1980**, 875−879. [25b] M. Handa, N. Koga, S. Kida, *Bull. Chem. Soc., Jpn.* **1988**, *61*, 3853−3857.

[26] K. Nieminen, *Ann. Acad. Sci. Fennicae A II* **1982**, *197*, 1−60.

[27] L. Walz, H. Paulus, W. Haase, *J. Chem. Soc., Dalton Trans.* **1985**, 913−920.

[28] A. Bencini, D. Gatteschi, *Inorg. Chim. Acta* **1978**, *31*, 11−18.

[29] P. J. Hay, J. C. Thibault, R. Hoffman, *J. Am. Chem. Soc.* **1975**, *97*, 4884−4899.

[30] [30a] O. Kahn, *Inorg. Chim. Acta* **1982**, *62*, 3−14. [30b] J. Commarmond, P. Plumere, J. M. Lehn, Y. Agnus, P. Louis, R. Weiss,

 © 2005 Wiley-VCH Verlag GmbH & Co. KGaA, Weinheim

O. Kahn, I. Morgenstern-Badarau, *J. Am. Chem. Soc.* **1982**, *104*, 6330−6340.
[31] H. Astheimer, W. Haase, *J. Chem. Phys.* **1986**, *85*, 1427−1432.
[32] [32a] E. Ruiz, P. Alemany, S. Alvarez, J. Cano, *J. Am. Chem. Soc.* **1997**, *119*, 1297−1303. [32b] E. Ruiz, P. Alemany, S. Alvarez, J. Cano, *Inorg. Chem.* **1997**, *36*, 3683−3688.
[33] C. Blanchet-Boiteux, J. M. Muesca, *J. Phys. Chem. A* **2000**, *104*, 2091−2097.
[34] R. J. Butcher, E. Sinn, *Inorg. Chem.* **1976**, *15*, 1604−1608 and references cited therein.
[35] A. W. Addison, T. N. Rao, J. Reedijk, J. V. Rijn, G. C. Verschoor, *J. Chem. Soc., Dalton Trans.* **1984**, 1349−1356**.**
[36] [36a] M. F. Charlot, S. Jeannin, Y. Jeannin, O. Kahn, J. Lucrece-Abaul, J. Martin-Frere, *Inorg. Chem.* **1979**, *18*, 1675−1681. [36b] M. F. Charlot, S. Jeannin, Y. Jeannin, O. Kahn, J. Lucrece-Abaul, J. Martin-Frere, *Inorg. Chem.* **1980**, *19*, 1410−1411.
[37] [37a] S. Youngme, G. A van Albada, H. Kooijman, O. Roubeau, W. Somjitsripunya, A. L. Spek, C. Pakawatchai, J. Reedijk, *Eur. J. Inorg. Chem.* **2002**, 2367−2374. [37b] I. Castro, M. Julve, G. de Munno, G. Bruno, J. A. Real, F. Lloret, J. Faus, *J. Chem. Soc., Dalton Trans.* **1992**, 1739−1744.
[38] [38a] S. Youngme, W. Somjitsripunya, K. Chinnakali, S. Chantraproma, H. K. Fun, *Polyhedron* **1999**, *18*, 857−862. [38b] L. P. Wu, M. E. Keniry, B. J. Hathaway, *Acta Crystallogr., Sect. C* **1992**, *48*, 35−40.
[39] L. K. Thompson, S. K. Mandal, S. S. Tandon, J. N. Bridson, M. K. Park, *Inorg. Chem.* **1996**, *35*, 3117−3125.
[40] A. M. Greenaway, C. J. O'Connor, J. W. Overman, E. Sinn, *Inorg. Chem.* **1981**, *20*, 1508−1513.
[41] J. P. Costes, F. Dahan, J. P. Laurent, *Inorg. Chem.* **1985**, *24*, 1018−1022.
[42] J. M. Seco, U. Amador, M. J. González-Garmendia, *Inorg. Chim. Acta* **2000**, *303*, 256−264.
[43] G. A. van Albada, I. Mutikainen, I. Riggio, U. Turpeinen, J. Reedijk, *Polyhedron* **2002**, *21*, 141−146.
[44] H. Saimiya, Y. Sunatsuki, M. Kojima, S. Kashino, T. Kambe, M. Hirotsu, H. Akashi, K. Nakajima, T. Tokii, *Dalton Trans.* **2002**, 3737−3742.
[45] J. Galy, J. Jaud, O. Kahn, P. Tola, *Inorg. Chim. Acta* **1979**, *36*, 229−236.
[46] E. Sinn, *Inorg. Chem.* **1976**, *15*, 366−369.
[47] S. K. Mandal, L. K. Thompson, K. Nag, J. P. Charland, E. J. Gabe, *Inorg. Chem.* **1987**, *26*, 1391−1395.
[48] J. A. Bertrand, E. Fujita, P. G. Eller, *Inorg. Chem.* **1974**, *13*, 2067−2071.
[49] R. Range, *Tetrahedron* **1971**, *27*, 1499−1502.
[50] Bruker AXS, *SAINT Software Reference Manual*, Madison, WI, **1998**.
[51] G. M. Sheldrick, *SHELXTL NT Version 5.1. Program for Solution and Refinement of Crystal Structures,* University of Göttingen, Germany, **1997**.

Received July 16, 2004
Early View Article
Published Online November 24, 2004

Highly Efficient Disproportionation of Dihydrogen Peroxide: Synthesis, Structure, and Catalase Activity of Manganese Complexes of the Salicylimidate Ligand

Meenal D. Godbole,[a] Michael Kloskowski,[c] Ronald Hage,[a] Annette Rompel,[c] Allison M. Mills,[b] Anthony L. Spek,[b] and Elisabeth Bouwman*[a]

Keywords: Catalase / Michaelis−Menten kinetics / Hydrogen peroxide disproportionation / Enzyme mimics / Manganese / Kinetics

Two complexes, $[Mn_2(etsalim)_4(Hetsalim)_2](ClO_4)_2$ (**1**), and $[Mn(mesalim)_2(OAc)(MeOH)]\cdot MeOH$ (**2**), in which Hmesalim and Hetsalim are methyl and ethyl salicylimidate, respectively, have been synthesized, fully characterized by X-ray analyses, magnetic susceptibility, UV/Vis and IR spectroscopy, and their catalase activity has been studied. Complex **1** is dinuclear and shows an Mn–Mn distance of 3.37 Å while complex **2** is mononuclear. Both complexes catalyze the disproportionation of hydrogen peroxide into water and dioxygen; they show very high catalase activity exhibiting saturation kinetics in the presence of NaOH. The rate and turnover number of the catalyzed reaction increase dramatically when a few equivalents of base (NaOH) are added to the reaction mixture. The turnover numbers for hydrogen peroxide disproportionation increase from approximately 200 to more than 1500 per manganese ion in less than 2 min for both complexes after addition of a few equivalents of NaOH. Kinetic studies of the catalyzed reaction performed on the dinuclear complex **1** in the presence of 5 equiv. of NaOH, gives k_{cat} = 807 s^{-1} (± 16) and K_M = 0.091 M (± 0.003). The effective catalytic efficiency is k_{cat}/K_M = 8900 $M^{-1}s^{-1}$. The kinetic parameters of the mononuclear complex **2** in the presence of 5 equiv. of NaOH, are k_{cat} = 190 s^{-1} (± 4) and K_M = 0.022 M (± 0.001). The effective catalytic efficiency is k_{cat}/K_M = 8600 $M^{-1}s^{-1}$. The catalase activity of the mononuclear complex, $[Mn(mesalim)_2Cl]$ (**3**) has also been studied, and it shows turnover numbers that are comparable to those of complex **2**. ESI-MS analyses in deuterated solvents have been used to understand the nature of the active species formed on addition of 5 equiv. of NaOH.
(© Wiley-VCH Verlag GmbH & Co. KGaA, 69451 Weinheim, Germany, 2005)

Introduction

Manganese is present in the active sites of enzymes, such as superoxide dismutase (SOD), manganese catalase, extradiol dioxygenase, arginase and ribonucleotide reductase, the oxygen-evolving complex (OEC) of photosystem II (PSII), and lipoxygenase.[1] The mechanisms of action of these enzymes are very diverse and include oxo atom transfer (SOD, catalase, extradiol dioxygenase), the reduction of ribonucleotides to water and deoxyribonucleotides, the oxidation of thiosulfate to sulfate and the four-electron oxidation of water to dioxygen in Photosystem II.[2] The principal mechanism of defense of living cells makes use of superoxide dismutase or catalase enzymes to protect the cell structure against harmful and reactive oxygen species, such as superoxide radicals or dihydrogen peroxide. In addition to widely distributed heme-type catalases, a second class of relatively rare manganese catalases has been found in three bacteria, *Lactobacillus plantarum*,[3] *Thermus thermophilus*,[4] and *Thermoleophilium album*.[5] A dinuclear active site is present in these Mn-catalases, possessing either a $Mn^{II}-Mn^{II}$ or $Mn^{III}-Mn^{III}$ dimer bridged by a μ-(1,3)-carboxylate from glutamate and two μ-oxo bridges from solvent molecules that electronically couple the metal centers. The rate of oxygen evolution by these enzymes is very high, i.e. of the order of 10^5 to 10^6 molecules per second.[6]

There is high interest in understanding the chemistry of dinuclear manganese complexes, as much structural and mechanistic information regarding the activity of the enzyme could be obtained through studies on model complexes.[7,8] The interaction of hydrogen peroxide and dioxygen with dinuclear manganese complexes has been studied in detail by various groups using several structural as well

[a] Leiden Institute of Chemistry, Gorlaeus Laboratories, Leiden University,
P. O. Box 9502, 2300 RA Leiden, The Netherlands
Fax: (internat.) + 31-71-5274550
E-mail: bouwman@chem.leidenuniv.nl
[b] Bijvoet Center for Biomolecular Research, Crystal and Structural Chemistry, Utrecht University,
The Netherlands
[c] Institut für Anorganische und Analytische Chemie, Westfälische Wilhelms-Universität,
Wilhelm-Klemm-Str. 8, 48149 Münster, Germany
Supporting information for this article is available on the WWW under http://www.eurjic.org or from the author.

as functional model complexes.[9−11] Interaction of metal complexes of Schiff-base ligands with hydrogen peroxide has been a matter of study for a long time now, for many of these have been shown to be good oxidation catalysts[12] or enzyme mimics.[10,13,14]

In this paper, we report the synthesis, full characterization and catalase activity of two manganese complexes, $[Mn_2(etsalim)_4(Hetsalim)_2](ClO_4)_2$ (**1**), and $[Mn(mesalim)_2(OAc)(MeOH)]\cdot MeOH$ (**2**), in which Hmesalim and Hetsalim are methyl and ethyl salicylimidate, respectively (shown in Figure 1). We also report the catalase studies on the complex $[Mn(mesalim)_2Cl]$ (**3**), the crystal structure of which has been recently reported.[15] In addition, a comparison of the structural and spectroscopic characteristics of the three complexes is made. The Hmesalim ligand is commonly used in organic syntheses as a precursor for several other ligands, such as oxazolines.[16] The transition-metal coordination chemistry of this simple ligand is, however, completely unexplored.

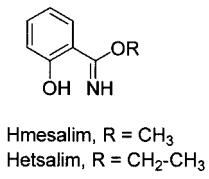

Figure 1. The ligands Hmesalim and Hetsalim

Results and Discussion

Synthetic Aspects

The ligand Hmesalim has been known for over 30 years and is commonly used as a precursor for the synthesis of heterocyclic ligands. Surprisingly, it has very rarely been used in transition metal chemistry. The coordination chemistry of this ligand, however, appears to be very rich.[17] Reaction of $Mn(ClO_4)_2$ with Hmesalim in ethanol unexpectedly results in the formation of the dinuclear, phenoxo bridged complex **1**, in which the methoxy group on the ligand is exchanged with the solvent ethoxy group. ESI-MS analyses of a solution of the ligand Hmesalim in ethanol shows two peaks, one for Hmesalim and another for Hetsalim, indicating that the presence of a Lewis acid is not necessary for solvolysis to occur. The complex **1** was synthesized by initially dissolving the Hmesalim ligand in ethanol, thus, in fact by the reaction of the manganese salt with Hetsalim formed (in situ). The mesalim-analog of **1** might also be formed in the solution but complex **1** is the sole product isolated from the reaction mixture. When the reaction is performed in methanol a green product is isolated, which has an IR spectrum similar to that of the complex **1**, but crystals good enough for structure determination could not be obtained and the product did not give good elemental analyses. The synthesis of complex **2** is more complicated. The recrystallization of a concentrated solution of the reaction mixture, by slow evaporation or ether diffusion, gave the complex **2** in pure form. Recrystallization of a dilute solution led to the formation of several polynuclear manganese clusters over time, thus making the isolation of this pure mononuclear compound difficult. In fact two novel clusters, a hexanuclear cluster with an interesting double-cubane structure, and another octanuclear cluster have been isolated and crystallographically characterized after attempts at recrystallization of the mononuclear complex **2**.[17]

Description of the Crystal Structures

The X-ray structures of the two new manganese complexes, $[Mn_2(etsalim)_4(Hetsalim)_2](ClO_4)_2$ (**1**), and $[Mn(mesalim)_2(OAc)(MeOH)]$ (**2**) have been determined. Numerical data and details of the data collection and refinement are presented in Table 1.

Table 1. Crystallographic data for complexes, $[Mn_2(etsalim)_4(Hetsalim)_2](ClO_4)_2$ (**1**), and $[Mn(mesalim)_2(OAc)(MeOH)]\cdot MeOH$ (**2**·MeOH)

	1	**2**·MeOH
Empirical formula	$C_{54}H_{62}Cl_2Mn_2N_6O_{20}$	$C_{20}H_{27}MnN_2O_8$
Formula mass	1295.88	478.38
a [Å]	10.7886(2)	30.5140(7)
b [Å]	11.7621(2)	30.5140(7)
c [Å]	11.9448(3)	12.3108(4)
α [°]	105.827(1)	90
β [°]	92.536(1)	90
γ [°]	100.032(1)	120
V [Å^3]	1429.24(5)	9926.9(5)
Z	1	18
Space group	$P\bar{1}$	$R\bar{3}$
Crystal system	triclinic	rhombohedral
$\rho_{calcd.}$ [g/cm^3]	1.506	1.440
T [K]	150	150
μ [cm^{-1}]	6.17	6.47
R, $wR2$	0.044, 0.1029	0.0408, 0.109
S	1.03	1.04

A PLUTON projection of the dinuclear complex **1** is shown in Figure 2. Selected bond lengths and angles are given in Table 2. The molecule is located on an inversion center. Each manganese(II) ion is bound by four different etsalim ligands, in a distorted octahedral N_2O_4 geometry. Two *trans*-chelating ligands, one of which participates in a μ-phenoxo bridge to the other manganese center, form the equatorial plane of the octahedron. One axial site is occupied by the phenolate oxygen atom of a terminally binding ligand and the other by bridging phenolate oxygen from the symmetry-related manganese center.

The Mn−O and Mn−N distances are comparable to other Mn^{III} complexes of this type that are known in the literature.[18] The axial Mn−O(57) an Mn−O(17a) distances are considerably longer (0.2−0.4 Å) than the Mn−O(phenolate) distances in the equatorial plane. There are two μ-phenoxo bridges in the dinuclear core, separating the two manganese ions at a distance of 3.3705(5) Å. This distance is within the normal range of phenoxo-bridged Mn^{III} complexes.[18] The Mn(1)−O(17)−Mn(1a) angle of 103.99(6)° is also similar to those in Mn^{III}-salen com-

 © 2005 Wiley-VCH Verlag GmbH & Co. KGaA, Weinheim

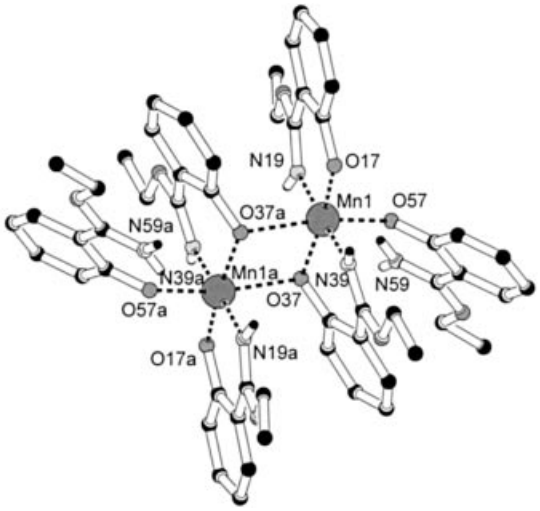

Figure 2. PLUTON projection of the complex $[Mn_2(etsalim)_4(Hetsalim)_2]^{2+}$ cation in complex (**1**); hydrogen atoms, except those attached to the nitrogen atoms, are omitted for clarity

Table 2. Selected bond lengths [Å] and angles [°] for **1**; symmetry code: a) $1 - x, -y, 2 - z$

Distance		Angle	
Mn(1)−N(19)	1.9927(17)	Mn(1)−O(17)−Mn(1a)	103.99(6)
Mn(1)−N(39)	2.0005(18)	O(17)−Mn(1)−O(37)	168.99(7)
Mn(1)−O(17)	1.9133(15)	O(17)−Mn(1)−O(57)	90.07(6)
Mn(1)−O(37)	1.8487(15)	O(17)−Mn(1)−N(19)	87.94(7)
Mn(1)−O(57)	2.1284(16)	O(17)−Mn(1)−N(39)	94.33(7)
Mn(1)−O(17a)	2.3507(15)	O(37)−Mn(1)−O(57)	100.31(7)
		O(37)−Mn(1)−N(19)	87.73(7)
		O(37)−Mn(1)−N(39)	89.97(7)
		N(19)−Mn(1)−O(57)	93.70(7)
		N(39)−Mn(1)−O(17a)	90.84(6)
		O(17a)−Mn(1)−O(37)	93.83(6)
		O(57)−Mn(1)−N(19)	93.70(7)
		O(57)−Mn(1)−N(39)	86.65(7)
		O(17a)−Mn(1)−O(57)	165.64(6)
		N(19)−Mn(1)−N(39)	177.70(8)
		O(17a)−Mn(1)−N(19)	89.37(6)

plexes.[18] Protonation of the imine nitrogen atoms on the two terminal ligands leaves two positive charges on the complex that are balanced by two perchlorate ions present in the crystal lattice. Each of the imine groups is involved in hydrogen bonding with perchlorate ions in the crystal lattice. The free imine group of the terminal ligand participates in an additional intramolecular hydrogen bond with the coordinated phenolate oxygen atom of the same ligand. (Table 4) (see Figure 1 in the Supporting Information; for Supporting Information see also the footnote on the first page of this article).

A PLUTON projection of the mononuclear complex **2** is shown in Figure 3. Selected bond lengths and angles are given in Table 3. The manganese(III) ion has a distorted octahedral N_2O_4 coordination environment. Two chelating mesalim ligand molecules are bound to the metal atom, *cis* to each other in a square plane. A methanol and a monodentate acetate molecule occupy the two remaining apical positions and complete the octahedron. The Mn−N and Mn−O distances involving the mesalim ligand are slightly longer than those in the complex $[Mn(mesalim)_2Cl]$ (**3**),[15] perhaps because the ligands are involved in extensive hydrogen bonding interactions. A PLUTON view of the hydrogen bonding in the crystal lattice is shown in Figure 4, and geometric parameters for the intermolecular hydrogen bonding interactions are listed in Table 4. The complex molecules are paired in a head-to-tail arrangement to form a dimer. Both oxygen atoms from the monodentate acetate ion of each complex molecule form bifurcated hydrogen bonds to each of the two *cis*-imine nitrogen atoms on the neighboring complex molecule and vice versa. Thus, the axially coordinated acetate molecule seems to enforce a *cis* coordination of the mesalim ligands to allow strong hydrogen bonding. The non-coordinated acetate oxygen atom of each complex molecule forms an additional hydrogen bond to the methanol molecule of a neighboring dimer and vice versa. The metal complex cocrystallizes with one independent molecule of methanol. The methanol solvent molecule undergoes intermolecular hydrogen bonding with itself, forming a six-membered ring. A view down the [001] direction of **2**·MeOH is presented in Figure 5.

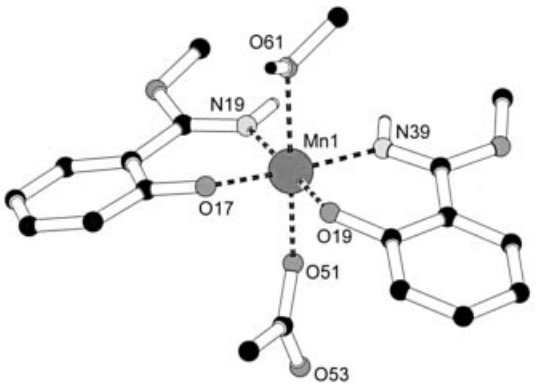

Figure 3. PLUTON projection of $[Mn(mesalim)_2(OAc)(MeOH)]$ (**2**); hydrogen atoms except those attached to nitrogen atoms and methanol are omitted for clarity

Spectroscopic Studies

Complexes **1** and **2** display ligand field bands that are very similar in position. The molar extinction coefficients of **1** are, however, approximately the double of those of absorption intensities of the mononuclear complex **2** because of the presence of two manganese centers and six ligands. In both complexes the peak at 304 nm is assigned to π-π* transitions within the ligands, because of its high intensity ($> 10^4$ $M^{-1}cm^{-1}$). The high-intensity band at 357 nm and shoulder at 418 nm can be assigned to the LMCT transition from the phenoxo oxygen to Mn^{III}.[19−21] The low-intensity peak at 567 nm ($\varepsilon = 277$ $M^{-1}cm^{-1}$ in the mononuclear complex and $\varepsilon = 400$ $M^{-1}cm^{-1}$ in the dinuclear complex) can be assigned to a d-d transition.[19] As the position of this

 © 2005 Wiley-VCH Verlag GmbH & Co. KGaA, Weinheim

Table 3. Selected bond lengths [Å] and angles [°] for **2**·MeOH

	Distance		Angle
Mn(1)−N(19)	2.007(2)	O(17)−Mn(1)−O(37)	88.70(7)
Mn(1)−N(39)	2.018(2)	O(17)−Mn(1)−O(51)	95.50(8)
Mn(1)−O(17)	1.8914(17)	O(17)−Mn(1)−O(61)	87.05(8)
Mn(1)−O(37)	1.8850(17)	O(17)−Mn(1)−N(19)	89.68(8)
Mn(1)−O(51)	2.1535(18)	O(17)−Mn(1)−N(39)	174.09(10)
Mn(1)−O(61)	2.2698(18)	O(37)−Mn(1)−O(51)	91.53(9)
		O(37)−Mn(1)−O(61)	94.71(9)
		O(37)−Mn(1)−N(19)	178.12(9)
		O(37)−Mn(1)−N(39)	88.97(8)
		O(51)−Mn(1)−O(61)	173.32(7)
		O(51)−Mn(1)−N(19)	89.56(9)
		O(51)−Mn(1)−N(39)	89.99(9)
		O(61)−Mn(1)−N(19)	84.27(9)
		O(61)−Mn(1)−N(39)	87.73(9)
		N(19)−Mn(1)−N(39)	92.56(9)

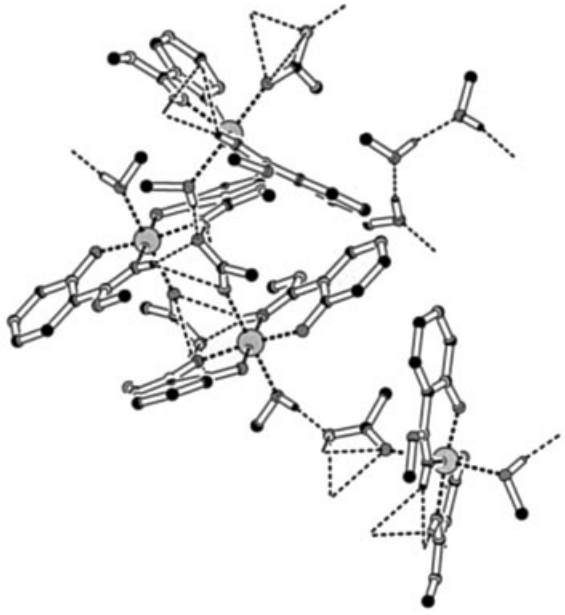

Figure 4. PLUTON projection of hydrogen bonding in [Mn(mesalim)$_2$(OAc)(MeOH)] (**2**)

band is independent of the anions,[15] it can be assigned to the $d_{xy} \rightarrow d_{x^2y^2}$ transition.[19] In addition to these bands complex **1** also shows a weak absorption at 976 nm (ε = 76 $M^{-1}cm^{-1}$). A band similar to this has also been reported for the dinuclear complex, $[Mn_2O(O_2CCH_3)_2(tacn)_2]^{2+}$, which has a band at 990 nm (ε = 28 $M^{-1}cm^{-1}$).[22] This band can be compared to that of manganese catalase from *Thermus thermophilus* also, where a broad tail is observed going into the near-IR region and a d-d transition is centered at approximately 492 nm.[23]

The IR spectrum of the free ligand displays a broad peak characteristic of the phenol O−H at 2538 cm^{-1}. The imine C=N frequency in the free ligand occurs at 1653 cm^{-1} and shifts to 1615−1605 cm^{-1} after complexation to Mn in all complexes. The presence of the perchlorate anion in the complex **1** is confirmed by a very intense band at 1088 cm^{-1}. For both complexes **1** and **2**, N−H stretching vibrations are seen at 3278 cm^{-1} and 3175 cm^{-1}, respectively. For complex **2**, the acetate vibrating modes could not be

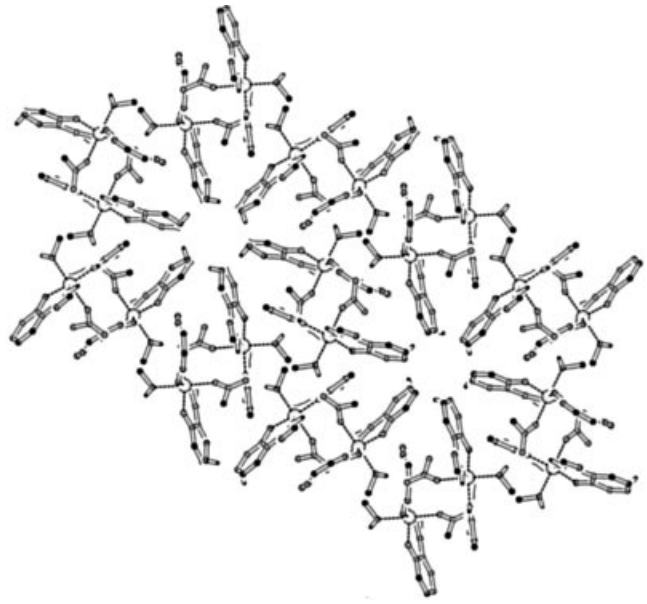

Figure 5. Projection of part of the crystal structure of **2** down the [001] axis; solvent methanol molecules joined in six-membered hydrogen-bonded rings around the threefold inversion axes

Table 4. Hydrogen bond details (distances [Å] and angles [°]) for compounds **1** and **2**·MeOH; symmetry codes: a) $-x, -y, 1-z$; b) $1-x, -y, 1-z$; c) $1/3-x, 2/3-y, 2/3-z$; d) $x-y, x, 1-z$; e) $y, -x+y, -z$

Donor (D)−H···Acceptor (A)[a]	H···A	D···A	D−H···A
1			
N19−H19···O4a	2.45	3.251(3)	152
N39−H39···O3b	2.28	3.131(3)	162
N59−H59A···O5b	2.15	2.987(3)	159
N59−H59B···O57	1.87	2.567(3)	135
2·MeOH			
N19−H19···O51c	2.57	3.210(3)	130
N19−H19···O53c	2.19	3.044(3)	164
N39−H39···O51c	2.47	3.098(3)	129
N39−H39···O53c	2.28	3.126(3)	162
O61−H61···O53d	1.77(3)	2.616(3)	174(3)
O71−H71···O71e	1.88	2.711(4)	169

[a] D−H distances are all constrained to 0.88 Å except for O61−H61···O53d and O71−H71···O71e that is 0.84 Å.

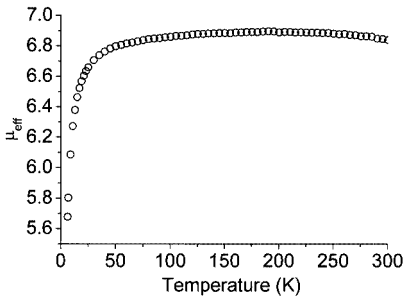

Figure 6. Variable-temperature magnetic susceptibility of complex **1**

exactly assigned because several ligand peaks were present in the region. Room temperature magnetic measurements for all complexes are consistent with the presence of Mn^{III}. Variable temperature magnetic susceptibility measurements were performed for complex **1**, and a plot of the effective magnetic moment versus temperature is shown in Figure 6. The steep decrease in magnetic moment at temperatures below 25 K is due to the zero-field splitting typical for Mn^{III} ions.

Catalase Activity and Kinetics

The catalase activity of three complexes $[Mn_2(etsalim)_4(Hetsalim)_2](ClO_4)_2$ (**1**), $[Mn(mesalim)_2(OAc)(MeOH)]\cdot MeOH$ (**2**·MeOH) and $[Mn(mesalim)_2Cl]$ (**3**)[15] has been studied, both in the presence and absence of different amounts of sodium hydroxide (NaOH), because the enhancing effect of small amounts of NaOH on catalase activity has been reported recently.[24] Addition of hydrogen peroxide to alcoholic solutions of the new manganese−mesalim and −etsalim complexes leads to vigorous evolution of dioxygen. The green solutions of the complexes turn brown when NaOH is added, and when subsequently H_2O_2 is added to these alkaline solutions, the reaction mixture turns from brown to colorless, with a brown precipitate, meanwhile showing even more vigorous evolution of dioxygen. The total conversion of hydrogen peroxide disproportionation was measured using a manometric method, while the kinetic studies were performed on the basis of fluorescence quenching using an oxygen sensor.[11,25] The total catalytic activity as well as the rate of the reaction increases significantly when a few equivalents of NaOH are added. In Table 5 the turnover numbers for the disproportionation of H_2O_2 by the manganese complexes in the presence and absence of NaOH are compared. It is interesting to note that the mononuclear complexes **2** and **3** also show very high catalase activity and reach comparable turnovers of manganese ion per minute (TON ≈ 1500) as the dinuclear complex. In fact, the mononuclear complex **2** shows even higher turnover per manganese ion (1800) than the dinuclear complex **1** (1575). The complexes **2** and **3** show very similar catalase activity, possibly indicating that a similar active species is formed. A plot of the percentage conversion of hydrogen peroxide for complex **1** followed in time as a function of the amount of NaOH that is added is shown in Figure 7. The highest initial rate is observed when 5 equiv. of NaOH are added. When 7 equiv. of NaOH are added, the initial rate is lower than for 5 equiv. of NaOH, but the catalyst is active for a longer time, which results in turnover numbers above 3000 for complex **1** and 5 equiv. of NaOH in less than 2 min. A similar observation of a breakpoint in the rate acceleration when 5 equiv. of NaOH are added has been reported previously.[24] When more hydrogen peroxide is added at the end of a reaction, only very slow evolution of dioxygen occurs, indicating that the catalyst has decomposed. The reactions reach completion within the first two minutes. No lag phase is observed for the reaction with or without addition of NaOH. The blank reaction performed with Mn^{II} perchlorate yields only 190 turnover numbers in total after 4 min even in the presence of 5−6 equiv. of NaOH, while no reaction is observed in the absence of NaOH.

The kinetics for the catalase reaction of the two complexes **1** and **2** has been studied. Figure 8 shows saturation kinetics for the two complexes **1** and **2** in combination with 5 equiv. of NaOH each. Figure 9 shows Lineweaver−Burk plots of the two systems, demonstrating a linear relationship between the rate of substrate disproportionation and substrate concentration for both systems, from which the Michaelis−Menten parameters can be extracted. For the system consisting of complex **1** and 5 equiv. of NaOH, k_{cat} = 807 s^{-1} (± 16) and K_M = 0.091 M (± 0.003), and k_{cat}/K_M = 8900 $M^{-1}s^{-1}$ (Figure 9, a), and for the system consisting of complex **2** and 5 equiv. of NaOH, k_{cat} = 190 s^{-1} (± 4), K_M = 0.022 M (± 0.001), and k_{cat}/K_M = 8600 $M^{-1}s^{-1}$ (Figure 9, b). A comparison of the kinetic parameters for the two systems, **1** and 5 equiv. of NaOH and **2** and 5 equiv. of NaOH, shows that, in fact both of them have similar catalytic efficiency. The value of k_{cat}, the turnover efficiency of the complex **2** and 5 equiv. of NaOH system, is actually lower than the complex **1** and 5 equiv. of NaOH system, but this is compensated by the very low K_M value. Thus, the ratio k_{cat}/K_M becomes similar to that of complex **1** and 5 equiv. of NaOH. Apparently, the two complexes catalyze the reactions probably by different mechanisms, but ultimately reach similar catalytic efficiency. The nature of the mechanisms however, cannot be anticipated at the present moment. The complexes themselves, without addition of NaOH, also show good catalase activity (Table 5) but their Michaelis−Menten parameters could not be determined as they did not give saturation kinetics for the range of hydrogen peroxide concentrations studied.

Spectroscopic Studies on the Catalyst Solution

Ligand field spectra of complex **1** taken during stepwise addition of NaOH show small but clear changes with three distinct isosbestic points at 310, 350 and 392 nm. On addition of 1 and 2 equiv. of NaOH, hardly any changes are observed in the spectrum of complex **1**. On addition of successive equivalents of NaOH (3−10 equiv.), the peaks at 330 nm start growing in intensity and the peaks at 357, 418 and 565 nm decrease in intensity. At 5 equiv. of NaOH added, the same trend continues, and no new clearly defined peaks are formed. On addition of more equivalents of NaOH, the peak at 330 nm is of high intensity,[19−21] and the spectrum from 400 to 700 nm appears as a broad tail going into the visible region. A brown precipitate appears concomitantly in the solution, indicating degradation of the complex.

A frozen solution EPR spectrum of a reaction mixture containing only complex **1** and hydrogen peroxide in ethanol taken 3 minutes after the addition of hydrogen peroxide (i.e after the reaction has finished) shows a six-line signal typical of Mn^{II} (g = 2.01, A = 90 G). No EPR signal can be detected, however, after the stepwise addition of NaOH to a solution of **1**, nor after the subsequent addition of hydrogen peroxide, suggesting that manganese(II) or mixed-

 © 2005 Wiley-VCH Verlag GmbH & Co. KGaA, Weinheim

Table 5. Disproportionation of hydrogen peroxide by the three Mn−mesalim complexes (TON = Turnover number; moles of substrate molecules converted per mol of the catalyst)

Complexes[a]	TON in H_2O_2 (without NaOH)	TON in H_2O_2 (5 equiv. NaOH)	Conversion (%) (5 equiv. NaOH)
$Mn(ClO_4)_2$	0[b]	190[b]	48%
$[Mn_2(etsalim)_4(Hetsalim)_2](ClO_4)_2]$ (**1**)	180	3150[c]	90%
$[Mn(mesalim)_2(OAc)(MeOH)]$ (**2**)	350	1810	91%
$[Mn(mesalim)_2Cl]$ (**3**)	270	1360	68%

[a] Reaction conditions: 1 mL of a 1 mM solution of the catalyst in methanol (**2**) or ethanol (**1**), H_2O_2 = 2 mmol, room temp., turnovers after 3 min (catalyst/H_2O_2 = 1:2000). [b] 5 mL of a 1 m M catalyst solution used (catalyst/H_2O_2 = 1:400). [c] 3.5 mmol of H_2O_2 used (catalyst/H_2O_2 = 1:3500).

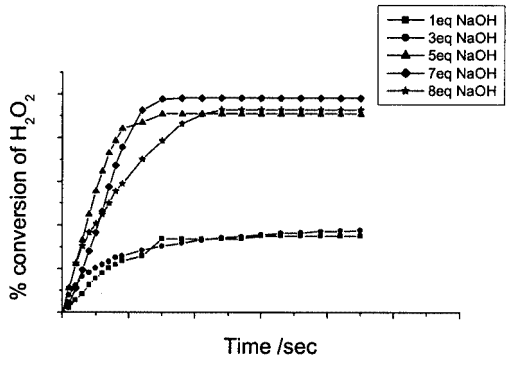

Figure 7. Conversion of H_2O_2 vs. time, with successive amounts of NaOH added; catalyst = complex **1** (1 μmol) and 3.18 mmol of H_2O_2 in 1 mL of ethanol

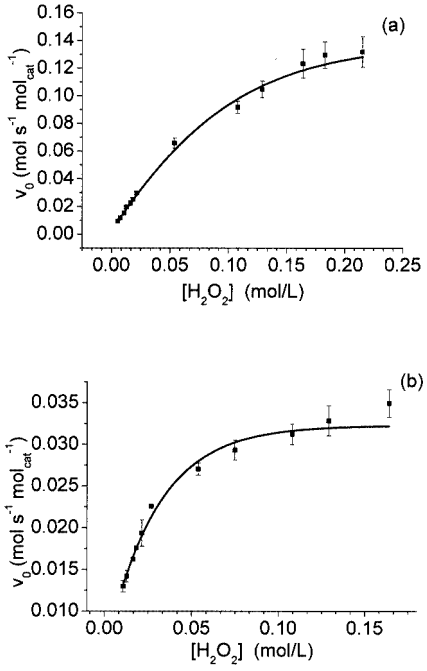

Figure 8. (a) Initial rate of substrate conversion versus substrate concentration at constant concentration of $[Mn_2(etsalim)_4(Hetsalim)_2](ClO_4)_2$ (**1**) + 5 equiv. NaOH in ethanol and (b) $[Mn(mesalim)_2(OAc)(MeOH)]$ (**2**) + 5 equiv. NaOH in methanol

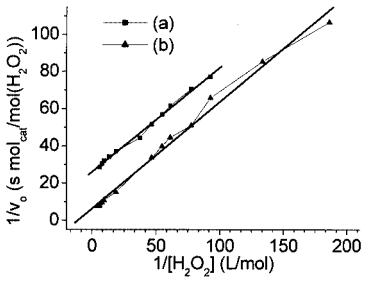

Figure 9. Lineweaver−Burk plot for (a) $[Mn_2(etsalim)_4(Hetsalim)_2](ClO_4)_2$ (**1**) + 5 equiv. NaOH in ethanol, and (b) $[Mn(mesalim)_2(MeOH)(OAc)]$ (**2**) + 5 equiv. NaOH in methanol

valent manganese(III)/(IV) species are not formed in this case.

Positive mode ESI-MS analysis was used to understand the nature of the species formed on addition of NaOH to a solution containing complex **1**. To assist the assignment of peaks, the spectra were also measured from the solution of the complex prepared in [D_6]ethanol (C_2D_5OD). Nondeuterated ethanol was used as the solvent for elution. A part of the complex ions undergo exchange with deuterated ethanol, and because of this, a pattern of lines with species ranging from nondeuterated, partly deuterated to completely deuterated complex ions can be observed. Analyzing the pattern of the peaks, it is clear that the ethoxy group on the ligand is rather labile, and in the metal complex it exchanges rapidly with the ethoxy group of the solvent ethanol, consistent with the earlier observation during complex synthesis (see above). Tables listing full details, relative intensities and assignments are available as Supporting Informations.

A solution of complex **1** in ethanol exhibits peaks at 383.15 $[Mn^{III}(etsalim)_2]^+$, 429.22 $[Mn^{III}(etsalim)_2(EtOH)]^+$, 811.35 $[Mn_2^{III}(etsalim)_4(EtOH)-H^+]^+$ and 865.30 $\{[Mn_2^{III}(etsalim)_4](ClO_4)\}^+$. The presence of the latter two peaks suggests that the dinuclear core of the complex does persist in the solution. In deuterated ethanol the complex shows clusters of peaks at 383.15 $[Mn^{III}(etsalim)_2]^+$, 388.19 $[Mn^{III}(etsalim)([D_5]etsalim)]^+$ and 393.19 $[Mn^{III}([D_5]-etsalim)_2]^+$ and at 429.23 $[Mn^{III}(etsalim)_2(EtOH)]^+$, 434.26 $[Mn^{III}(etsalim)([D_5]etsalim)(EtOH)]^+$ and 439.29 $[Mn^{III}-$

 © 2005 Wiley-VCH Verlag GmbH & Co. KGaA, Weinheim

$([D_5]etsalim)_2(EtOH)]^+$, as well as 5-line patterns for the dinuclear species in the ranges 811−831 and 865−885.

ESI-MS spectra of complex **1** and 5 equiv. of NaOH in ethanol reveal peaks at 451.26 $\{Na[Mn(etsalim)_3(EtOH) - H^+]\}^+$, 497.28 $\{Na[Mn(etsalim)_2(EtOH)_2 - H^+]\}^+$, 570.35 $\{Na[Mn(etsalim)_3]\}^+$, 787.47 $\{Na[Mn_2(etsalim)_4 - 2 H^+]\}^+$, 833.46 $\{Na[Mn_2(etsalim)_4(EtOH) - H^+]\}$, 850.57 $\{Na[Mn_2(etsalim)_4(EtOH)(O)]\}^+$, and 952.57 $\{Na[Mn_2(etsalim)_5 - H^+]\}^+$. The most interesting observation after addition of NaOH is the peak at 850.57, which is tentatively assigned to a dinuclear Mn−μ-oxo species. These assignments were all confirmed by the presence of the respective multi-line signals in the ESI-MS spectra with deuterated ethanol and NaOH in D_2O. Furthermore, in the deuterated solvent a group of peaks of low intensity at 959−974 is observed, which could possibly be assigned to a di-μ-oxo species, $\{Na^+[Mn_2^{IV}(etsalim)_4(EtOH)_3(O)_2]\}^+$. However, this species was not observed in nondeuterated ethanol which unfortunately makes unambiguous assignment of these peaks not possible. Addition of hydrogen peroxide to this reaction mixture did not give rise any other peaks in the ESI-MS spectrum, as most of it was degraded before the active species could be measured.

Discussion and Comparison to Other Systems

The k_{cat} and K_M values for the complexes **1** and **2** in combination with 5 equiv. of NaOH, can be compared to those of $[Mn(bpia)(\mu\text{-}OAc)]_2(ClO_4)_2$ [bpia = bis(pyridylmethyl)(*N*-methylimidazol-2-ylmethyl)amine] which are k_{cat} = 1100 s^{-1}, K_M = 31.5 mM and k_{cat}/K_M = 34000 $M^{-1}s^{-1}$.[11] The present complex **1** or **2** and 5 equiv. of NaOH systems show the second best activity that has been reported until now for the manganese catalase mimics with the Mn(bpia) system in the first position. For the present studies, addition of a few equivalents of base was used successfully for increasing the catalase activity as has already been reported for other systems.[24] The rate acceleration on addition of NaOH possibly correlates with the availability of an intramolecular hydroxide for substrate deprotonation and with binding of the substrate at the bridging site between Mn ions in the reductive O−O bond-cleavage step.[24] After addition of NaOH, there might be μ-oxo or μ-hydroxo bond formation between the two manganese ions as is demonstrated by the use of sodium hydroxide for the syntheses of several μ-oxo-bridged, dinuclear manganese complexes.[26] For the $[Mn(2\text{-}OH\text{-}salpn)]_2$ (k_{cat} = 4-22 s^{-1}) and $[Mn_2(salpn)O_2]$ (k_{cat} = 2500 s^{-1}) systems [salpn = *N*,*N*′-bis(salicylidene)-1,3-diaminopropane and 2-OH-salpn = *N*,*N*′-bis(salicylidene)-2-hydroxy-1,3-diaminopropane], the rate increases tremendously when the alkoxo-bridged dimer is replaced by a μ-oxo-bridged manganese dimer.[10] NaOH and *N*-methylimidazole were studied as bases in the catalase reaction with the manganese-mesalim and -etsalim complexes. Both bases increased the total conversion as well as the rate of the catalase reaction. The present system also gives higher catalytic efficiency than the recently reported $[Mn_2(L)_2Cl_2]$ system {L = 2-[bis(pyridin-2-ylmethyl)aminomethyl]-6-methoxyphenol}.[25]

The ligand field spectra recorded upon successive additions of NaOH indicate that the LMCT bands (300 nm and 360 nm) show clear changes with isosbestic points due to formation of one species from the original complex. Addition of more than 5 equiv. of NaOH results in formation of a precipitate, and the ligand field spectrum becomes broadened. ESI-MS analysis proved to be a useful tool for the interpretation of the species formed on addition of NaOH to the complex solution. The first role of NaOH may be to withdraw the proton on the imine nitrogen atom and thus make the complex more oxidizable. The removal of the proton from the imine nitrogen atom is evident from the peaks at 787.14 $\{Na^+[Mn_2(L)_4 - 2 H^+]\}^+$ and at 833.18 $\{Na^+[Mn_2(L)_4(EtOH) - 2 H^+]\}$ on addition of 5 equiv. of NaOH to the complex **1** solution, where both or at least one proton has to be withdrawn from the imine nitrogen atom on the etsalim ligand. The only species that could give a hint to the μ-oxo species formation was observed at 850.57, which could be assigned to a μ-oxo-bridged species with a relative intensity of 10%. Dinuclear Mn^{III}/Mn^{III} species have been proposed to be the active catalysts for H_2O_2 disproportionation in several manganese catalases as well as functional catalase model complexes. X-band EPR spectra recorded at 77 K did not show the formation of a Mn^{IV} species or a mixed-valent Mn^{II}/Mn^{III} or Mn^{III}/Mn^{IV} species, neither after addition of NaOH nor immediately after addition of hydrogen peroxide (i.e. during catalytic turnover). A brown precipitate that is insoluble in many solvents, characteristic of MnO_2, is formed at the end of the reaction. Thus, the catalytically inactive species formed at the end of the reaction is probably due to the decomposition of the metal complex to form insoluble Mn^{IV} oxides.

Conclusion

In this study the synthesis, crystal structures, full characterization and catalase studies of three manganese complexes have been presented. It has been shown that complexes **1**−**3** in combination with 5−6 equiv. of NaOH show very high catalase activity and are only surpassed by the Mn−bpia system reported by Krebs and co-workers.[11] However, compared to the Mn−catalase enzyme, the k_{cat} value is still 20−30 times lower than the manganese−catalase enzymes and thus the catalytic efficiency (k_{cat}/K_M) is still 200−300 times lower than that of the manganese−catalase enzymes. The turnover as well as the rate of the reaction increase remarkably with the addition of a few equivalents of NaOH to the catalyst solution. The complexes in combination with a few equivalents of sodium hydroxide (NaOH) are among the few catalase model systems that show turnover numbers up to 3000 in hydrogen peroxide disproportionation. ESI-MS analyses in deuterated solvents have been used to understand the nature of the active species formed on addition of 5 equiv. of of NaOH. The exact nature of the active species participating

 © 2005 Wiley-VCH Verlag GmbH & Co. KGaA, Weinheim

during turnover, however, could not be confirmed at the present moment.

Experimental Section

Physical Measurements: UV/Vis/NIR measurements were performed with a Perkin−Elmer Lambda 900 UV/Vis/NIR spectrometer. IR spectra were recorded with a Perkin−Elmer FT-IR Paragon 1000 spectrometer. ^{1}H NMR spectra were recorded with a Bruker 300 DPX MHz spectrometer. Elemental analyses were performed with a Perkin−Elmer series II CHNS/O analyzer 2400. EPR measurements were performed at 77 K using a Jeol Esprit RE-2X spectrometer with a Jeol Esprit 330 ESRE data system. EPR *g* values were determined relative to DPPH as an external "*g*-marker" (g = 2.0037). Electrospray mass spectra were recorded with a Thermo Finnigan AQA apparatus. All solvents were of analytical grade and used without further purification unless stated otherwise.

Catalase Activity: Two different methods were carried out to get the turnover number, k_{cat}, the Michaelis constant, K_M, and k_{cat}/K_M. In the first experiment an aqueous solution of H_2O_2 was added to a solution of the complex at room temperature. Dioxygen evolution was observed instantaneously and monitored manometrically. In a typical experiment, to find out the total conversion of dihydrogen peroxide, H_2O_2 (2 mmol, 2000 equiv., 0.17 mL of a 35% aqueous solution) was added to the complex (1 mL of a 1 mM solution in EtOH for **2** and in MeOH for **1** and **3**) at room temperature. Dioxygen evolution was observed instantaneously and monitored manometrically. Initial rate measurements were performed by plotting the volume of dioxygen evolved versus time in seconds.

Kinetic Measurements: In the second experiment, for the kinetic studies, an optical oxygen sensor was used to measure the initial rates of the H_2O_2 decomposition. The complex was added to an aqueous H_2O_2 solution of increasing concentration and the initial rate was recorded. The data were fitted into the Michaelis−Menten equation, and the turnover number, k_{cat}, the Michaelis constant, K_M, and k_{cat}/K_M were determined from the double reciprocal Lineweaver−Burk plot (Figure 9). K_M is a criterion for substrate affinity, the turnover number, k_{cat}, can be interpreted as the rate of substrate conversion into the corresponding products and k_{cat}/K_M is a criterion for catalytic efficiency.

Syntheses: ***Caution:*** *Perchlorate salts are potentially explosive and should be handled with appropriate care!* The following abbreviations are used throughout the text: Hmesalim = methyl salicylimidate, Hetsalim = ethyl salicylimidate. All reagents and solvents were used as received with no attempt to remove water or molecular oxygen. The ligand Hmesalim was synthesized according to a published procedure.[16,27,28]

$[Mn_2(etsalim)_4(Hetsalim)_2](ClO_4)_2$ (1): The ligand Hmesalim (0.2 g, 1.32 mmol) was dissolved in absolute EtOH (10 mL). Manganese(II) perchlorate (0.108 g, 0.44 mmol) was added to the solution. The solution was stirred for 15 min and filtered. Green crystals were obtained after a few days by layering the reaction mixture with diethyl ether and hexane. Yield of crude product: 55% (0.156 g). UV/Vis (CH_3CN): $\lambda_{max.}$ (ε [$M^{-1}cm^{-1}$]) = 304 (38×10^3), 357 (20×10^3), 418 (2400), 565 (400), 971 (76) nm. IR (diamond): $\tilde{\nu}$ = 3268 (m), 1606 (s), 1588 (s), 1455 (s), 1399 (s), 1214 (m), 1088 (vs), 959 (m), 868 (m), 758 (s), 618 (s), 523 (s), 427 (s) cm^{-1}. $C_{27}H_{31}ClMnN_{30}O_{10}$ (1295.88): calcd. C 50.05, H 4.82, N 6.4; found C 50.0, H 5.07, N 6.67. μ_B = 4.8 BM per manganese(III). MS (ESI): m/z = 383 $[Mn^{III}(etsalim)_2]^+$, 429.22 $[Mn(etsalim)_2(EtOH)]^+$, 811.35 $[Mn_2(etsalim)_4(EtOH) - H^+]^+$, 865.30 $[Mn_2^{III}(etsalim)_4(ClO_4)]^+$.

$[Mn(mesalim)_2(OAc)(MeOH]\cdot MeOH$ (2): The ligand Hmesalim (1.85 g, 12.25 mmol) was dissolved in absolute MeOH (10 mL). Manganese(II) acetate (1 g, 4.08 mmol) was added to the solution, and the solution was stirred for 15 min. Then diethyl ether (20 mL) was added to the solution, and again the reaction mixture was stirred for 15 min. The solution was filtered, and crystals were grown in a few days by layering the MeOH/ether solution with hexane. Yield of crude product: 61.5% (1.2 g) UV/Vis (CH_3CN): $\lambda_{max.}$ (ε [$M^{-1}cm^{-1}$]) = 304 (16×10^3), 353 (9×10^3), 411 (1860), 562 (277) nm. IR (diamond): $\tilde{\nu}$ = 3446 (m), 3167 (m), 1609 (s), 1590 (s), 1542 (vs), 1452 (s), 1412 (s), 1330 (m), 1231 (vs), 1158 (s), 1098 (s), 863 (s), 748 (s), 626 (s), 492 (s) cm^{-1}. $C_{19}H_{23}MnN_2O_7\cdot 2MeOH$ (510.42): calcd. C 49.42, H 6.12, N 5.49; found C 49.12, H 6.51, N 5.86. μ_B= 4.6 BM. MS (ESI): m/z = 354.5 $[Mn^{III}(mesalim_2)]^+$, 415 $\{[Mn(mesalim)_2(OAc)] + H^+\}^+$, 447 $\{[Mn(mesalim)_2(OAc)(MeOH)] + H^+\}^+$ and 506 $\{[Mn(mesalim)_3] + H^+\}^+$.

X-ray Crystallographic Study: Intensity data for single crystals of **1** and **2** were collected at 150 K using graphite-monochromated Mo-K_α radiation, with a Nonius Kappa CCD diffractometer on rotating anode. A correction for absorption was considered unnecessary in the case of **1**. For **2**, a multi-scan absorption correction was applied using PLATON/MULABS (0.678−0.903 transmission range).[29] The structures were solved by direct methods using SHELXS-97[30] (**1**) or SIR97[31] (**2**), and refined on F^2 using SHELXL-97.[30] All non-hydrogen atoms were refined with anisotropic displacement parameters. All hydrogen atoms, and in particular those attached to nitrogen and oxygen atoms, were positively identified in a difference Fourier map. The position of the hydroxy hydrogen atom of the coordinated methanol molecule in **2** was refined with a restraint on the O−H distance. All other hydrogen atoms were constrained to idealized geometries and allowed to ride on their carrier atoms. All hydrogen atoms were refined with an isotropic displacement parameter related to the equivalent displacement parameter of their carrier atoms. Structure validation and preparation of molecular graphics were performed with the PLATON package.[29] CCDC-244114 (**1**) and -244115 (**2**) contain the supplementary crystallographic data for this paper. These data can be obtained free of charge at www.ccdc.cam.ac.uk/conts/retrieving.html [or from the Cambridge Crystallographic Data Centre, 12 Union Road, Cambridge CB2 1EZ, UK; Fax: (internat.) + 44-1223-336-033; E-mail: deposit@ccdc.cam.ac.uk].

Acknowledgments

This work has been carried out within the framework of the Council for Chemical Sciences of the Netherlands Foundation for Scientific Research (CW-NWO), through a grant from the special program "Aspasia". Financial support by the DFG (Deutsche Forschungsgemeinschaft, SPP 1118) is gratefully acknowledged. The authors thank Prof. Dr. Jan Reedijk for stimulating discussions. We thank one of the referees for useful suggestions.

[1] J. Reedijk, E. Bouwman, *Bioinorganic catalysis*, Marcel Dekker Inc., New York, **1999**.
[2] G. C. Dismukes, in *Bioinorganic catalysis* (Ed.: J. Reedijk), Marcel Dekker, New York, **1993**, pp. 317−346.

[3] Y. Kono, I. Fridovich, *J. Biol. Chem.* **1983**, *258*, 3646−3648.
[4] I. Michaud-Soret, L. Jacquamet, N. Debaecker-Petit, L. Le Pape, V. V. Barynin, J. M. Latour, *Inorg. Chem.* **1998**, *37*, 3874−3876.
[5] G. S. Allgood, J. J. Perry, *J. Bacteriol.* **1986**, *168*, 563−567.
[6] J. Penner-Hahn, *Manganese Redox Enzymes*, VCH Publishers, New York, **1992**.
[7] L. Dubois, F. Caspar, L. Jacquamet, P. E. Petit, M. F. Charlot, C. Baffert, M. N. Collomb, A. Deronzier, J. M. Latour, *Inorg. Chem.* **2003**, *42*, 4817−4827.
[8] P. J. Pessiki, G. C. Dismukes, *J. Am. Chem. Soc.* **1994**, *116*, 898−903.
[9] L. Dubois, D. F. Xiang, X. S. Tan, J. Pecaut, P. Jones, S. Baudron, L. Le Pape, J. M. Latour, C. Baffert, S. Chardon-Noblat, M. N. Collomb, A. Deronzier, *Inorg. Chem.* **2003**, *42*, 750−760.
[10] A. Gelasco, S. Bensiek, V. L. Pecoraro, *Inorg. Chem.* **1998**, *37*, 3301−3309.
[11] M. U. Triller, W. Y. Hsieh, V. L. Pecoraro, A. Rompel, B. Krebs, *Inorg. Chem.* **2002**, *41*, 5544−5554.
[12] T. Katsuki, *Coord. Chem. Rev.* **1995**, *140*, 189−214.
[13] A. Gelasco, A. Askenas, V. L. Pecoraro, *Inorg. Chem.* **1996**, *35*, 1419−1420.
[14] A. Gelasco, V. L. Pecoraro, *J. Am. Chem. Soc.* **1993**, *115*, 7928−7929.
[15] M. D. Godbole, E. Grigiotti, P. Zanello, A. M. Mills, A. L. Spek, E. Bouwman, *Inorg. Chim. Acta*, in press.
[16] D. S. C. Black, M. J. Wade, *Aust. J. Chem.* **1972**, *25*, 1797−1810.
[17] M. D. Godbole, O. S. Roubeau, A. M. Mills, H. Kooijman, E. Bouwman, manuscript in preparation.
[18] H. L. Shyu, H. H. Wei, Y. Wang, *Inorg. Chim. Acta* **1999**, *290*, 8−13.
[19] L. J. Boucher, V. W. Day, *Inorg. Chem.* **1977**, *16*, 1360−1367.
[20] M. Marappan, V. Narayanan, M. Kandaswamy, *J. Chem. Soc., Dalton Trans.* **1998**, 3405−3409.
[21] A. Neves, S. M. D. Erthal, I. Vencato, A. S. Ceccato, Y. P. Mascarenhas, O. R. Nascimento, M. Horner, A. A. Batista, *Inorg. Chem.* **1992**, *31*, 4749−4755.
[22] K. Wieghardt, U. Bossek, D. Ventur, J. Weiss, *J. Chem. Soc., Chem. Commun.* **1985**, 347−349.
[23] M. M. Whittaker, V. V. Barynin, S. V. Antonyuk, J. Whittaker, *Biochemistry* **1999**, *38*, 9126−9136.
[24] A. E. M. Boelrijk, G. C. Dismukes, *Inorg. Chem.* **2000**, *39*, 3020−3028.
[25] N. Reddig, D. Pursche, M. Kloskowski, C. Slinn, S. M. Baldeau, A. Rompel, *Eur. J. Inorg. Chem.* **2004**, 879−887.
[26] M. Maneiro, M. R. Bermejo, R. Fondo, A. M. Gonzalez, J. Sanmartin, J. C. Garcia-Monteagudo, R. G. Pritchard, A. M. Tyryshkin, *Polyhedron* **2001**, *20*, 711−719.
[27] P. Stoss, *Chem. Ber.* **1978**, *111*, 314−319.
[28] P. Vinkler, K. Thimm, J. Vob, *Justus Liebigs Ann. Chem.* **1976**, *1976*, 2083− 2093.
[29] A. L. Spek, *J. Appl. Crystallogr.* **2003**, *36*, 7−13.
[30] G. M. Sheldrick, University of Göttingen, Göttingen, Germany, **1997**.
[31] A. Altomare, M. C. Burla, M. Camalli, G. L. Cascarano, C. Giacovazzo, A. Guagliardi, A. G. G. Moliterni, G. Polidori, R. Spagna, *J. Appl. Crystallogr.* **1999**, *32*, 115−119.

Received July 16, 2004
Early View Article
Published Online November 24, 2004

 © 2005 Wiley-VCH Verlag GmbH & Co. KGaA, Weinheim

Anionic Phosphane − A New Ligand with a Phosphane and a Weakly Coordinating Heteroborate Moiety

Benno Ronig,[a] Herbert Schulze,[a] Ingo Pantenburg,[a] and Lars Wesemann*[b]

Dedicated to Professor Ekkehard Lindner on the occasion of his 70th birthday

Keywords: Boranes / Cluster compounds / Phosphane ligands / Tin

Reaction of chloropropyl-substituted stanna-*closo*-dodecaborate $[Cl(CH_2)_3SnB_{11}H_{11}]^-$ with the nucleophile $Li[CH_2PPh_2]$ provided a straightforward synthesis of an anionic phosphane $[Ph_2PCH_2SnB_{11}H_{11}]^-$. Derivatization of the phosphane was carried out in reaction with sulfur and hydrochloric acid to give $[Bu_3MeN][Ph_2P(S)CH_2SnB_{11}H_{11}]$ and the zwitterion $[Ph_2P(H)CH_2SnB_{11}H_{11}]$. In reaction with various transition metal electrophiles, complexation reactions were accomplished resulting in the isolation of *trans*-substituted palladium and platinum complexes $[Bu_3MeN]_2[trans\text{-}(Ph_2PCH_2SnB_{11}H_{11})_2MCl_2]$ (M = Pd, Pt), a neutral silver adduct $[(acetone)Ag(Ph_2PCH_2SnB_{11}H_{11})]$, and a linearly coordinated bisphosphane of gold $[Bu_3MeN][Au(Ph_2PCH_2\text{-}SnB_{11}H_{11})_2]$. The solid state structures of the ligand salt, the palladium and gold coordination compounds were determined and discussed.
(© Wiley-VCH Verlag GmbH & Co. KGaA, 69451 Weinheim, Germany, 2005)

Introduction

In coordination chemistry phosphane ligands play a key role and are often used to control the properties of a certain transition metal complex. Phosphanes with an ionic moiety like sulfonate, carboxylate, ammonium or phosphonium are of interest for the synthesis of coordination compounds soluble in very polar solvents for two-phase catalysis purposes.[1] Recently Peters started to study systematically the coordination chemistry of monoanionic phosphane ligands provided with a tetracoordinated boron atom in the backbone of the ligand. Zwitterions with a cationic transition metal center have been isolated with chelating phosphides.[2−6] With the synthesis of the aluminate $Li[Al(CH_2PMe_2)_4]$ Karsch et al. found an anionic tetradentate phosphide.[7] Substitution reactions at the boron atom of borabenzene−trimethylphosphane with $K[PPh_2]$ resulted to give the phosphide $K[C_5H_5BPPh_2]$ in excellent yield.[8] Syntheses of monoboranephosphides $[R_2PBH_3]^-$ and examples for their coordination at Li, Al, Fe, Pd, and Pt can also be found in the literature.[9] Another class of anionic phosphanes, having a heteroborate as the anionic moiety, were presented by Teixidor.[10−11] Two diphenylphosphane groups are connected at the carbon atoms of the 7,8-dicarba-*nido*-undecaborate framework. This bis(diphenylphosphanyl)borate was shown to be a versatile ligand in transition metal chemistry.

Our group is interested in the coordination chemistry of ligands with a typical donor function and a weakly coordinating anionic moiety. Here we present a synthesis for a phosphane ligand connected at an anionic *closo*-heteroborate cluster.

Results and Discussion

Recently we found a method for the nucleophilic substitution at monoanionic alkylstanna-*closo*-dodecaborate.[12] Attack at the γ-chloropropyl-substituted cluster **1** with strong nucleophiles like RLi or RMgX resulted in the isolation of derivatives $[RSnB_{11}H_{11}]^-$ together with the formation of cyclopropane and the chloride anion as the leaving groups (Scheme 1).

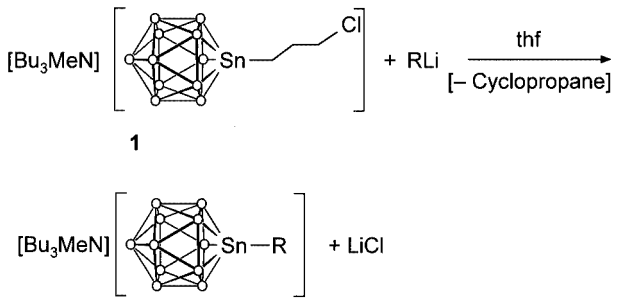

Scheme 1. Nucleophilic substitution at the tin vertex with strong nucleophiles

[a] Institut für Anorganische Chemie Universität zu Köln, Greinstrasse 6, 50939 Köln
[b] Institut für Anorganische Chemie Universität Tübingen, Auf der Morgenstelle 18, 72076 Tübingen

 © 2005 Wiley-VCH Verlag GmbH & Co. KGaA, Weinheim **DOI: 10.1002/ejic.200400636**

This method was transferred to the preparation of a new phosphane ligand by reacting the γ-chloropropyl-substituted heteroborate **1** with the anion $[Ph_2PCH_2]^-$ (Scheme 2).

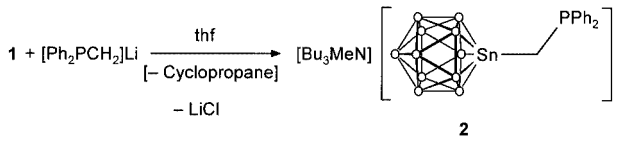

Scheme 2. Syntheses of an anionic phosphane

The new phosphane **2** was characterized by NMR spectroscopy and X-ray structure analysis. In the ^{31}P NMR spectrum the resonance at $\delta = -15.5$ ppm showing tin satellites ($^2J_{P,Sn} = 71$ Hz) gives clear evidence for the successful coupling of the phosphane moiety at the anionic stannaborate cage. Single crystals suitable for X-ray structure analysis were prepared by slow diffusion of hexane into a dichloromethane solution of the coupling product **2**. The structure of the borate salt is depicted in Figure 1, and the data of the structure solution and refinement are listed in Table 1. This ligand is of interest to us since standard phosphane coordination chemistry can be combined with well-known B−H−M three-center-twoelectron bond coordination.[13] Anionic boron clusters show mono-, di- or trihapto coordination modes at transition metal centers. These agostic interactions can be detected either in the ^1H NMR spectrum from high-field proton resonances for the B−H−M unit or in the ^{11}B NMR spectrum exhibiting reduced $^1J_{BH}$ coupling constants.

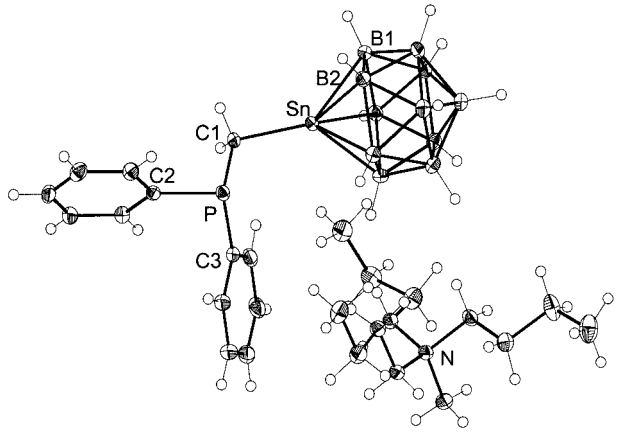

Figure 1. Molecular structure of the phosphane salt $[Bu_3MeN][Ph_2PCH_2SnB_{11}H_{11}]$ (**2**) in the solid state; interatomic distances in pm and angles in degrees (with estimated standard deviations in parentheses): Sn−C1 212.7 (2), Sn−B1 227.9(3), Sn−B2 228.1(3), Sn−B3 228.5(3), Sn−B4 228.9(3), Sn−B5 230.1(3), P−C1 182.9(2), P−C2 184.3(2), P−C3 184.7(2); P−C1−Sn 110.9, C1−Sn−B1 140.3(1), C1−Sn−B2 128.4(1), C1−Sn−B3 124.9(1), C1−Sn−B4 133.8(1), C1−Sn−B5 144.5(1)

In reaction with elemental sulfur and hydrochloric acid two derivatives of the phosphane were synthesized and characterized (Scheme 3). The sulfur compound exhibits in the ^1H NMR spectrum a doublet ($^2J_{H,P} = 4.5$ Hz) with tin satellites $^2J_{H,Sn} = 100$ Hz at $\delta = 3.08$ ppm for the PCH_2Sn moiety. A characteristic signal at $\delta = 6.85$ ppm for the proton connected at the phosphorus *H*P and a down-field shift of 1.2 ppm for the resonance of the PCH_2Sn unit [4.26 ppm ($^2J_{H,P} = 12$ Hz, $-P-CH_2-Sn$, $^2J_{H,Sn} = 98$ Hz)] was detected in the case of the zwitterionic phosphonium borate.

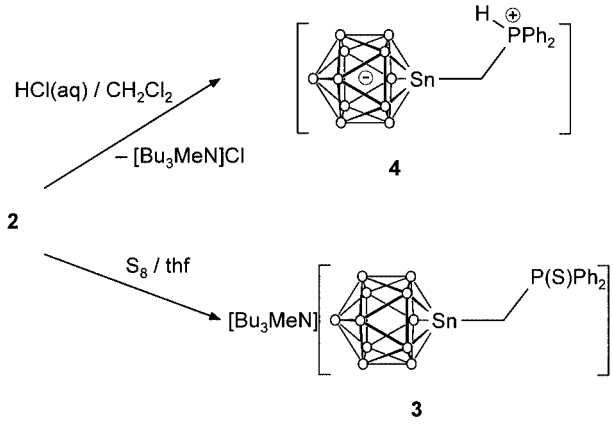

Scheme 3. Reaction with sulfur and protonation of the anionic phosphane

First complexation reactions of the new ligand **2** were carried out with the following transition metal complexes: [*cis*-$(Ph_3P)_2PdCl_2$], [$(cod)PtCl_2$], [$AgBF_4$], and [$(Ph_3P)AuCl$] (Scheme 4, Scheme 5, Scheme 6). *trans*-Substituted coordination compounds **5** and **6** have been isolated and characterized with platinum and palladium chlorides. In the case of the platinum derivative the $^1J_{Pt,P}$ coupling constant of 1850 Hz allows unambiguous assignment for *trans*-coordination.[14] Obviously the anionic part of the ligand is not of the nucleophilicity to substitute the chloride atoms and form M−H−B bonds. The products **5** and **6** are stable towards moisture, and air and crystallization from CH_2Cl_2/hexane resulted in the isolation of single crystals in the case of the palladium complex.

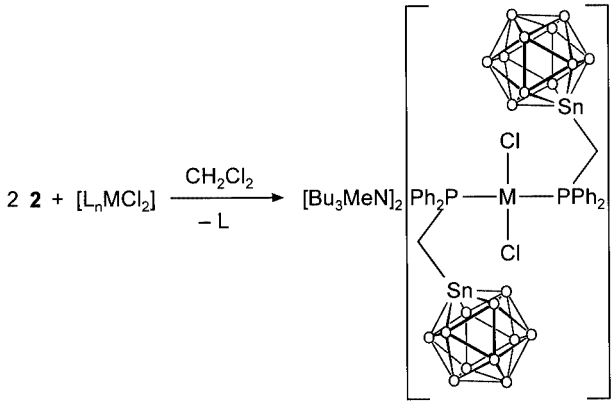

Scheme 4. Complexation reaction with palladium and platinum coordination compounds (L_nMCl_2 = [*cis*-$(Ph_3P)_2PdCl_2$], M = Pd for **5**; L_nMCl_2 = [$(cod)PtCl_2$], M = Pt for **6**)

 © 2005 Wiley-VCH Verlag GmbH & Co. KGaA, Weinheim

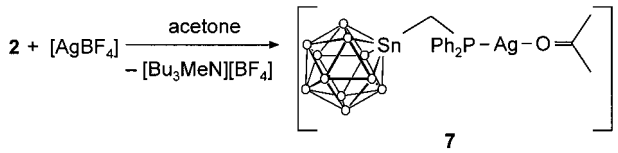

Scheme 5. Complexation with a silver electrophile, formation of a zwitterion

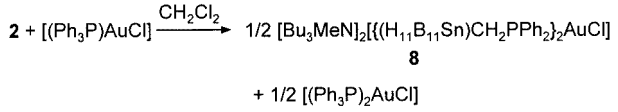

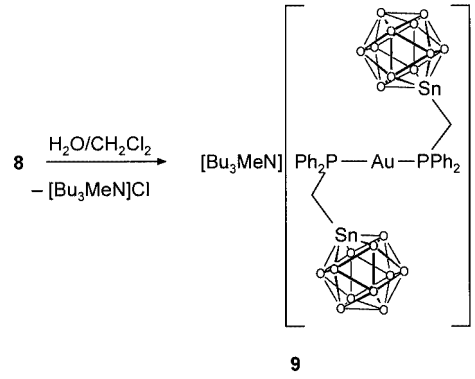

Scheme 6. Formation of a triply coordinated gold complex; loss of the chloride substituent under the contact with water

The salt **5** crystallizes under the inclusion of two equivalents of CH_2Cl_2 in the monoclinic space group $P2_1/n$, with the dianion lying on the twofold rotation axis. In Figure 2 the structure of the anion in the solid state is shown, and the data of the structure solution and refinement are listed in Table 1. The coordination at the palladium center is in close relation to the structure of [*trans*-$(Ph_2MeP)_2PdCl_2$] crystallizing in the same space group with almost identical Pd–P 233.06(12) pm and Pd–Cl 230.45(9) pm interatomic distances.[15]

A neutral silver complex was synthesized from the reaction of the phosphane **2** with $AgBF_4$ (Scheme 5). This zwitterionic molecule was characterized by NMR spectroscopy and elemental analysis and should be a versatile starting material for further complexation reactions. With respect to the phosphane ligand, the monosubstituted product was the only isolated silver complex, whereas in the case of [(Ph_3P)AuCl] two anionic phosphanes coordinate at the gold center (Scheme 6) to give a diphosphanyl chloride complex **8**.[16]

The primarily formed reaction product **8** was stirred with water to give the linearly coordinated complex **9** in high yield. The salt **9** was crystallized and the structure in the solid state was determined by X-ray diffraction. The molecular structure of the anion of **9** is shown in Figure 3, and the data of the structure solution and refinement are listed in Table 1.

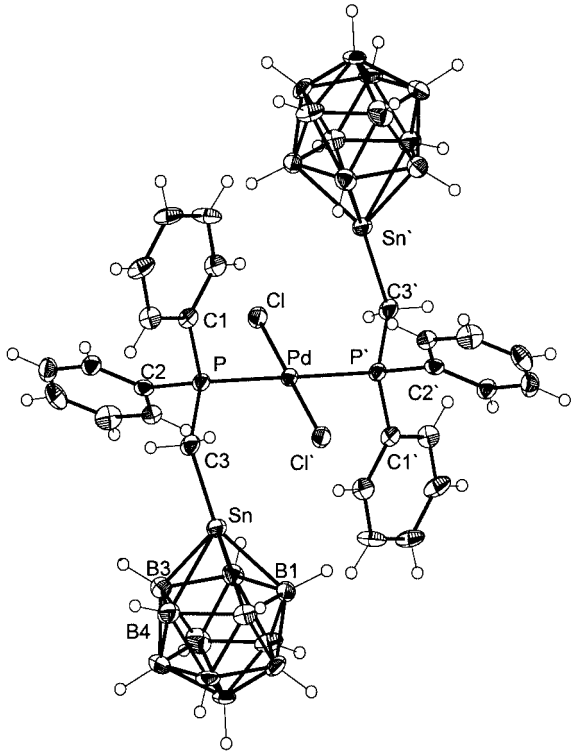

Figure 2. Molecular structure of the anion of $[Bu_3MeN]_2$-$[PdCl_2(PPh_2CH_2SnB_{11}H_{11})_2]$ (**5**) in the solid state; interatomic distances in pm and angles in degrees (with estimated standard deviations in parentheses): Pd–Cl 229.6(2), Pd–P 233.2(2), P–C3, 184.0(8), Sn–C3 211.7(7), Sn–B1 228.7(8), Sn–B2 228.9(9), Sn–B3 227.9(10), Sn–B4 228.8(10), Sn–B5 227.8(8), C3–Sn–B1 150.4(3), C3–Sn–B2 140.6(3), C3–Sn–B3 122.9(3), C3–Sn–B4 121.1(3), C3–Sn–B5 134.4(3), Cl–Pd–P 91.0(1), Cl′–Pd–P 89.0(1)

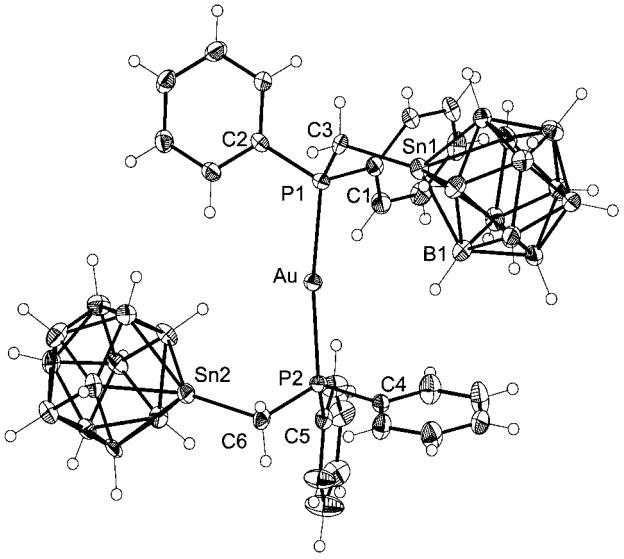

Figure 3. Molecular structure of the anion of $[Bu_3MeN]$-$[Au(PPh_2CH_2SnB_{11}H_{11})_2]$ (**9**) in the solid state. Interatomic distances in pm and angles in degrees (with estimated standard deviations in parentheses): P1–Au 231.0(2), P2–Au 231.4(2), C3–P1 181.6(7), Sn1–C3 213.7(6), C6–P2 187.8(8), Sn2–C6 214.6(7), P1–Au–P2 171.1(1), Au–P1–C3 113.5(3), P1–C3–Sn1, 113.9(3), Au–P2–C6 114.8(3), P2–C6–Sn2 109.1(4)

 © 2005 Wiley-VCH Verlag GmbH & Co. KGaA, Weinheim

Nearly linearly coordinated gold(I) cations $[Au(PR_3)_2]^+$ are well-known in the literature and the metal−ligand bonding has been studied with respect to relativistic and non relativistic structure calculations.[17,18] In the crystal structure a very weak interaction (H−Au 268.0 pm) between a BH unit and the gold center, which results in the formation of dimer, can be detected (Figure 4). Stone et al. have found much shorter BH−Au interatomic distances in the range of 190−210 pm.[19] Nevertheless, we interpret this contact as a weak electrostatic interaction of the cationic gold fragment with the anionic borate moiety.

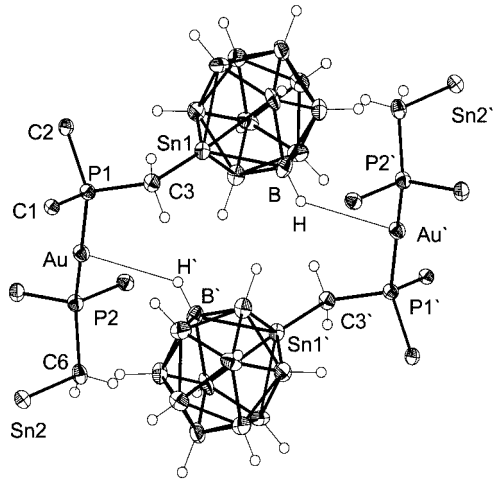

Figure 4. Weak interaction between a stannaborate cluster and gold center in compound **9**; H−Au 268.0 pm (all hydrogen atoms at calculated positions); phenyl substituents and boron cluster cages at Sn2 and Sn2′ have been omitted for the sake of clarity

To conclude, a synthesis for an anionic phosphane with two different coordination sites is presented: a diarylalkylphosphane nucleophile and an anionic borate where common B−H−M coordination can take place.

Experimental Section

General Procedures: All manipulations were carried out using Schlenk techniques under an atmosphere of dry N_2. All solvents were dried and purified by standard methods and were stored under dry N_2. $[Bu_3MeN]_2[SnB_{11}H_{11}]$ was synthesized following a modification of Todd's procedure.[25] The compounds $[Bu_3MeN][H_{11}B_{11}Sn-(CH_2)_3-Cl]$, [*cis*-$(PPh_3)_2PdCl_2$],[26] [$PPh_3$-CuCl],[27] and $Li[CH_2PPh_2]$[28] were synthesized by literature procedures. All other chemicals were purchased from Aldrich and were used without further purification. ^1H, ^{11}B, and ^{31}P NMR spectra were recorded on a Bruker AC 200 instrument and referenced to the deuterated solvent. Elemental analyses were carried out on a Hekatech EuroEA C,H,N,S,O elemental analyzer at Institut für Anorganische Chemie der Universität zu Köln.

$[Bu_3MeN][H_{11}B_{11}Sn-CH_2-P(C_6H_5)_2]$ (2): A solution of $[Bu_3MeN][H_{11}B_{11}Sn-(CH_2)_3-Cl]$ (6.17 g, 11.72 mmol) in THF (60 mL) was added to a solution of $Li[CH_2PPh_2]$ (3.14 g, 15.23 mmol) in THF (60 mL) dropwise at room temperature. After stirring overnight at room temperature all volatiles were removed. The residue was dissolved in CH_2Cl_2 (60 mL) and treated with water (3 × 30 mL). The organic phase was separated and stirred over anhydrous Na_2SO_4. After the solvent was removed, the yellow, semifluid raw product was dissolved in a little CH_2Cl_2 and washed with *n*-hexane and Et_2O. Removing the solvent resulted in isolation of the yellow, semifluid but translucent product. Yield: 77%, 5.85 g, 9.02 mmol. ^1H NMR (200 MHz, 25 °C, CD_2Cl_2): δ = 1.01 (t, 9 H, ^3J = 7.1 Hz, $-CH_2-CH_3$), 1.42 (m, 6 H, ^3J = 7.2 Hz, $-CH_2-CH_3$), 1.65 (m, 6 H, ^3J = 7.3 Hz, $-CH_2-CH_2-CH_3$), 2.98 (s, 3 H, $N-CH_3$), 3.06 (d, 2 H, $^2J_{H,P}$ = 4.5 Hz, $P-CH_2-Sn$), 3.16 (m, 6 H, ^3J = 7.3 Hz, $N-CH_2-CH_2-$), 7.39−7.54 ppm [m, 10 H, $-P-(C_6H_5)_2$]. $^{11}B\{^1H\}$ NMR (64 MHz, 25 °C, CD_2Cl_2): δ = −12.3 (s, B12), −17.0 (s, B2−6 and B7−11) ppm. $^{13}C\{^1H\}$ NMR (50 MHz, 25 °C, C_3D_6O): δ = 13.8 (d, $^1J_{C,P}$ = 35 Hz, $-P-CH_2-Sn$), 16.8 (s, $-CH_2-CH_3$), 23.2 (s, $-CH_2-CH_3$), 27.6 (s, $N-CH_2-CH_2-$), 51.8 (s, $N-CH_3$), 65.2 (s, $N-CH_2-CH_2-$), 132.4 (d, $^3J_{C,P}$ = 7 Hz, C_{meta}, $-P-(C_6H_5)_2$], 132.8 (s, C_{para}, $-P-(C_6H_5)_2$], 136.0 (d, $^2J_{C,P}$ = 20 Hz, C_{ortho}, $-P-(C_6H_5)_2$], 143.3 ppm [d, $^1J_{C,P}$ = 14 Hz, C_{ipso}, $-P-(C_6H_5)_2$]. $^{31}P\{^1H\}$ NMR (81 MHz, 25 °C, C_3D_6O): δ = −15.5 ppm (s, $^2J_{P,Sn}$ = 71 Hz, $-P-(C_6H_5)_2$]. $C_{26}H_{53}B_{11}NPSn$ (648.32): calcd. C 48.17, H 8.24, N 2.16; found C 46.77, H 8.76, N 1.50.

$[Bu_3MeN][H_{11}B_{11}Sn-CH_2-P(S)-(C_6H_5)_2]$ (3): A solution of $[Bu_3MeN][H_{11}B_{11}Sn-CH_2-P(C_6H_5)_2]$ (**1**, 0.82 g, 1.26 mmol) in CH_2Cl_2 (20 mL) was added dropwise to a suspension of sulfur (0.04 g, 1.26 mmol) in CH_2Cl_2 (20 mL). After stirring for 4 h at room temperature, the sulfur had dissolved by then, all volatiles were removed, and **2** was isolated as a yellow, hygroscopic solid. Yield: 89%, 0.76 g, 1.12 mmol. ^1H NMR (200 MHz, 25 °C, CD_2Cl_2): δ = 3.80 (d, 2 H, $^2J_{H,P}$ = 11, $^2J_{H,Sn}$ = 100 Hz, $-P-CH_2-Sn$), 7.51−7.95 ppm (m, 10 H, $-P-(C_6H_5)_2$]. $^{11}B\{^1H\}$ NMR (64 MHz, 25 °C, CD_2Cl_2): δ (ppm) = −11.8 (s, B12), −17.1 (s, B2−6 and B7−11). $^{31}P\{^1H\}$ NMR (81 MHz, 25 °C, CD_2Cl_2): δ = 40.98 ppm (s, $^2J_{P,Sn}$ = 46 Hz, $-P-(C_6H_5)_2$]. $C_{26}H_{53}B_{11}NPSSn$ (680.38): calcd. C 45.90, H 7.85, N 2.06, S 4.71; found C 44.17, H 7.88, N 2.02, S 4.65.

$[H_{11}B_{11}Sn-CH_2-P(H)-(C_6H_5)_2]$ (4): A solution of $[Bu_3MeN][H_{11}B_{11}Sn-CH_2-P(C_6H_5)_2]$ (**1**, 1.00 g, 1.54 mmol) in CH_2Cl_2 (20 mL) was stirred rapidly under a layer of diluted hydrochloric acid (25 mL) overnight. The resulting colorless solid was separated, washed with water and dried in vacuo. Yield: 94%, 0.65 g, 1.45 mmol. ^1H NMR (200 MHz, 25 °C, C_3D_6O): δ = 4.26 (d, 2 H, $^2J_{H,P}$ = 12 Hz, $-P-CH_2-Sn$, $^2J_{H,Sn}$ = 98 Hz), 6.85 (d, 1 H, $^1J_{H,P}$ = 12 Hz, $-P-H$), 7.78−7.94 (m, 10 H, $-P-(C_6H_5)_2$] ppm. $^{11}B\{^1H\}$ NMR (64 MHz, 25 °C, C_3D_6O): δ = −12.5 (s, B12), −17.3 ppm (s, B2−6 and B7−11). $^{31}P\{^1H\}$ NMR (81 MHz, 25 °C, C_3D_6O): δ = 33.27 ppm (s, $^2J_{P,Sn}$ = 59 Hz, $-P(H)-(C_6H_5)_2$]. $C_{13}H_{24}B_{11}PSn$ (448.94): calcd. C 34.78, H 5.39; found C 35.36, H 5.82.

$[Bu_3MeN]_2$[*trans*-$\{H_{11}B_{11}Sn-CH_2-P(C_6H_5)_2\}_2PdCl_2$] (5): A solution of $[Bu_3MeN][H_{11}B_{11}Sn-CH_2-P(C_6H_5)_2]$ (1.43 g, 2.20 mmol) in CH_2Cl_2 (25 mL) was added dropwise to a stirred solution of $(PPh_3)_2PdCl_2$ (0.77 g, 1.10 mmol) in CH_2Cl_2 (20 mL). After the mixture was stirred for 16 h at room temperature, the solvent was removed under reduced pressure, and the yellow residue was washed with benzene, toluene, and *n*-hexane (3 × 20 mL). The yellow product was isolated by filtration and dried in vacuo. Yield: 64%, 1.04 g, 0.70 mmol. ^1H NMR (200 MHz, 25 °C, CD_2Cl_2): δ (ppm) = 0.99 (t, 18 H, ^3J = 7.1 Hz, $-CH_2-CH_3$), 1.37 (m, 12 H, ^3J = 6.9 Hz, $-CH_2-CH_3$), 1.64 (m, 12 H, ^3J = 7.0 Hz, $-CH_2-CH_2-CH_3$), 2.99 (s, 6 H, $N-CH_3$), 3.17 (m, 12 H, ^3J = 8.3 Hz, $N-CH_2-CH_2-$), 3.43 (d, 4 H, $^2J_{H,P}$ = 7 Hz, $-P-CH_2-Sn$), 7.26−7.90 (m, 20 H, $-P-(C_6H_5)_2$]. $^{11}B\{^1H\}$ NMR (64 MHz, 25 °C, CD_2Cl_2): δ = −12.2 (s, B12), −16.8 ppm

 © 2005 Wiley-VCH Verlag GmbH & Co. KGaA, Weinheim

Table 1. Crystal data and structure refinement parameters for $[Bu_3MeN][Ph_2PCH_2SnB_{11}H_{11}]$ (**2**), $[Bu_3MeN][PdCl_2(PPh_2CH_2SnB_{11}H_{11})_2]\cdot 2CH_2Cl_2$ (**5**) and $[Bu_3MeN][Au(PPh_2CH_2SnB_{11}H_{11})_2]$ (**9**)

	2	**5**	**9**
Empirical formula	$C_{26}H_{53}B_{11}NPSn$	$C_{54}H_{110}B_{22}Cl_6N_2P_2PdSn_2$	$C_{39}H_{76}AuB_{22}NP_2Sn_2$
Formula mass	648.26	1643.68	1293.11
Data collection			
Diffractometer	STOE IPDS II		
Radiation	Mo-K_α (graphite-monochromated, λ = 71.073 pm)		
Temperature [K]	130(2)	120(2)	150(2)
Index range	$-15 \le h \le 15$	$-22 \le h \le 21$	$-16 \le h \le 14$
	$-16 \le k \le 18$	$-13 \le k \le 13$	$-20 \le k \le 20$
	$-18 \le l \le 18$	$-24 \le l \le 24$	$-20 \le l \le 20$
Rotation angle range	$0° \le \omega \le 180°$; $\psi = 0°$	$0° \le \omega \le 180°$; $\psi = 0°$	$0° \le \omega \le 180°$; $\psi = 0°$
	$0° \le \omega \le 180°$; $\psi = 90°$	$0° \le \omega \le 60°$; $\psi = 90°$	$0° \le \omega \le 150°$; $\psi = 90°$
Increment	$\Delta\omega = 2°$	$\Delta\omega = 2°$	$\Delta\omega = 2°$
No. of images	180	120	165
Exposure time [min]	3	15	12
Detector distance (mm)	100	120	120
2θ range (°)	2.2−59.5	1.9−54.8	1.9−54.8
Total data collected	34041	31861	40319
Unique data	9653	6910	12307
Observed data	7697	2840	6403
R_{merg}	0.0463	0.1879	0.1003
Absorption correction	numerical, after crystal shape optimization[20,21]		
Transmission min./max.	0.7858/0.9442	0.7470/0.9277	0.4312/0.7568
Crystallographic data[22]			
Crystal size (mm)	0.3×0.3×0.2	0.2×0.2×0.1	0.2×0.2×0.1
Color, habit	colorless, polyhedron	yellow, plate	colourless, plate
Crystal system	triclinic	monoclinic	triclinic
Space group	$P\bar{1}$ (no. 2)	$P2_1/n$ (no. 14)	$P\bar{1}$ (no. 2)
a [pm]	1138.1(1)	1885.1(3)	1282.0(2)
b [pm]	1311.5(1)	1111.1(2)	1579.1(2)
c [pm]	1304.1(1)	2072.1(2)	1612.2(2)
α (°)	76.07(1)		65.52(1)
β (°)	88.77(1)	115.23(1)	79.28(1)
γ (°)	67.04(1)		68.83(1)
Volume [nm^3]	1.7338(3)	3.9261(9)	2.7674
Z	2	2	2
$\rho_{calcd.}$ [g cm^{-3}]	1.242	1.390	1.552
μ [mm^{-1}]	0.801	1.138	3.628
F(000)	672	1672	1272
Structure analysis and refinement			
Refinement method	Full-matrix least-squares on F^2		
Structure determination	SHELXS-97[23] and SHELXL-93[24]		
No. of variables	574	407	608
R indexes [$I > 2\sigma(I)$]	R_1 = 0.0350	R_1 = 0.0495	R_1 = 0.0431
	wR_2 = 0.0809	wR_2 = 0.0682	wR_2 = 0.0764
R indexes (all data)	R_1 = 0.0488	R_1 = 0.1508	R_1 = 0.1062
	wR_2 = 0.0859	wR_2 = 0.0860	wR_2 = 0.0911
Goodness of fit (S_{obs})	1.004	0.707	0.823
Goodness of fit (S_{all})	1.004	0.707	0.823
Largest difference map hole/peak [e·10^{-6}pm^{-3}]	−1.096/0.789	−0.675/0.738	−2.881/1.151

$R_1 = \Sigma| |F_o| - |F_c| |/\Sigma|F_o|$, $wR_2 = [\Sigma w (|F_o|^2 - |F_c|^2)^2/\Sigma w (|F_o|^2)^2]^{1/2}$, $S_2 = [\Sigma w (|F_o|^2 - |F_c|^2)^2/(n-p)]^{1/2}$, with $w = 1/[\sigma^2 (F_o)^2 + (0.0533\ P)^2]$ for **2**, $w = 1/[\sigma^2 (F_o)^2 + (0.0131\ P)^2]$ for **5** and $w = 1/[\sigma^2 (F_o)^2 + (0.0307\ P)^2]$ for **9**, were $P = (F_o^2 + 2F_c^2)/3$. $F_c^* = k\ F_c\ [1 + 0.001\ |F_c|^2\ \lambda^3/\sin(2\theta)]^{-1/4}$. The H atoms for **2** were derived from the difference Fourier map. Hydrogen atoms for (**5**) and (**9**) were generated geometrically and allowed to ride on their parent carbon/boron atoms.

(s, B2−6 and B7−11). $^{31}P\{^1H\}$ NMR (81 MHz, 25 °C, CD_2Cl_2): δ = 30.3 ppm (s, $-P-(C_6H_5)_2$]. $C_{52}H_{106}B_{22}Cl_2N_2P_2PdSn_2$ (1473.96): calcd. C 42.37, H 7.25, N 1.90; found C 43.57, H 7.25, N 1.82.

$[Bu_3MeN]_2$[*trans*-{$H_{11}B_{11}Sn-CH_2-P(C_6H_5)_2$}$_2$$PtCl_2$] (6): A solution of $[Bu_3MeN][H_{11}B_{11}Sn-CH_2-P(C_6H_5)_2]$ (1.28 g, 1.98 mmol) in CH_2Cl_2 (25 mL) was added dropwise to a stirred solution of $(cod)PtCl_2$ (0.37 g, 0.99 mmol) in CH_2Cl_2 (25 mL). After the mix-

 © 2005 Wiley-VCH Verlag GmbH & Co. KGaA, Weinheim

ture was stirred at room temperature overnight, all volatiles were removed under reduced pressure and the residue was washed with *n*-hexane and diethyl ether (3 × 20 mL). The light brown product was isolated by filtration and dried in vacuo. Yield: 56%, 0.86 g, 0.55 mmol. ^{1}H NMR (200 MHz, 25 °C, CD_2Cl_2): δ = 0.99 (t, 18 H, ^3J = 6.8 Hz, $-CH_2-CH_3$), 1.41 (m, 12 H, ^3J = 6.7 Hz, $-CH_2-CH_3$), 1.65 (m, 12 H, ^3J = 7.0 Hz, $-CH_2-CH_2-CH_3$), 3.02 (s, 6 H, $N-CH_3$), 3.17 (m, 12 H, ^3J = 8.3 Hz, $N-CH_2-CH_2-$), 3.58 (d, 4 H, $^2J_{H,P}$ = 8 Hz, $-P-CH_2-Sn$), 7.23−7.62 ppm (m, 20 H, $-P-(C_6H_5)_2$]. ^{11}B{^{1}H} NMR (64 MHz, 25 °C, CD_2Cl_2): δ = −11.9 (s, B12), −17.0 ppm (s, B2−6 and B7−11). ^{31}P{^{1}H} NMR (81 MHz, 25 °C, CD_2Cl_2): δ = 8.67 ppm (s, $^1J_{P,Pt}$ = 1850 Hz, $-P-(C_6H_5)_2$]. $C_{52}H_{106}B_{22}Cl_2N_2P_2PtSn_2$ (1562.62): calcd. C 39.97, H 6.84, N 1.79; found C 40.00, H 7.54, N 1.51.

[$H_{11}B_{11}Sn-CH_2-P(C_6H_5)_2Ag(OC_3H_6)$] (7): Because of the sensitivity of the silver compounds, this synthesis was carried out in darkness. A solution of [Bu_3MeN][$H_{11}B_{11}Sn-CH_2-P(C_6H_5)_2$] (0.15 g, 0.23 mmol) in C_3H_6O (25 mL) was added dropwise to a stirred suspension of $AgBF_4$ (0.05 g, 0.23 mmol) in C_3H_6O (25 mL). After being stirred at room temperature overnight, the mixture was filtered, and the solvent of the filtrate was removed under reduced pressure. The product was isolated as light-brown powder. Yield: 65%, 0.08 g, 0.15 mmol. ^{1}H NMR (200 MHz, 25 °C, CD_3CN): δ = 2.08 (s, 6 H, Ag-OC_3H_6), δ = 3.46 (d, 2 H, $^2J_{H,P}$ = 6 Hz, $-P-CH_2-Sn$, $^2J_{H,Sn}$ = 98 Hz), 7.50−7.75 ppm (m, 10 H, $-P-(C_6H_5)_2$]. ^{11}B{^{1}H} NMR (64 MHz, 25 °C, CD_3CN): δ = −12.3 (s, B12), −17.1 ppm (s, B2−6 and B7−11). ^{31}P{^{1}H} NMR (81 MHz, 25 °C, C_3D_6O): δ = 3.69 ppm (s, $-P-(C_6H_5)_2$]. $C_{16}H_{29}AgB_{11}OPSn$ (613.88): calcd. C 31.31, H 4.76; found C 32.14, H 4.81.

[Bu_3MeN]$_2$[{$H_{11}B_{11}Sn-CH_2-P(C_6H_5)_2$}$_2$AuCl] (8): A solution of [Bu_3MeN][$H_{11}B_{11}Sn-CH_2-P(C_6H_5)_2$] (0.40 g, 0.62 mmol) in CH_2Cl_2 (25 mL) was added dropwise to a stirred solution of (PPh_3)AuCl (0.31 g, 0.62 mmol) in CH_2Cl_2 (25 mL). After the mixture was stirred for 16 h at room temperature, the solvent was removed under reduced pressure. The residue was dissolved in CH_2Cl_2 (10 mL) and reprecipitated by addition of toluene (40 mL). This procedure was repeated three times. Finally, the solid was separated by filtration and washed with toluene and diethyl ether (3 × 10 mL). The colorless product was isolated by filtration and dried in vacuo. Yield: 31%, 0.29 g, 0.19 mmol. ^{1}H NMR (200 MHz, 25 °C, CD_2Cl_2): δ = 1.00 (t, 18 H, ^3J = 7.3 Hz, $-CH_2-CH_3$), 1.41 (m, 12 H, ^3J = 7.2 Hz, $-CH_2-CH_3$), 1.66 (m, 12 H, ^3J = 7.3 Hz, $-CH_2-CH_2-CH_3$), 3.04 (s, 6 H, $N-CH_3$), 3.21 (m, 12 H, ^3J = 7.7 Hz, $N-CH_2-CH_2-$), 3.48 (d, 4 H, $^2J_{H,P}$ = 8 Hz, $-P-CH_2-Sn$), 7.54−7.86 ppm (m, 20 H, $-P-(C_6H_5)_2$]. ^{11}B{^{1}H} NMR (64 MHz, 25 °C, CD_2Cl_2): δ = −13.4 (s, B12), −17.2 ppm (s, B2−6 and B7−11). ^{31}P{^{1}H} NMR (81 MHz, 25 °C, CD_2Cl_2): δ = 34.36 ppm (s, $-P-(C_6H_5)_2$]. $C_{52}H_{106}AuB_{11}ClN_2P_2Sn_2$ (1529.06): calcd. C 40.85, H 6.99, N 1.83; found C 41.36, H 7.30, N 1.41.

[Bu_3MeN][{$H_{11}B_{11}Sn-CH_2-P(C_6H_5)_2$}$_2$Au] (9): A solution of [$Bu_3MeN$]$_2$[{$H_{11}B_{11}Sn-CH_2-P(C_6H_5)_2$}$_2$AuCl] (**9**, 0.15 g, 0.10 mmol) in CH_2Cl_2 (25 mL) was stirred rapidly under a layer of water (25 mL) overnight. The organic phase was separated and dried over Na_2SO_4. After being separated from the desiccant, the solvent was removed under reduced pressure, and **9** was isolated as a colorless solid. Yield: 89%, 0.11 g, 0.09 mmol. ^{1}H NMR (200 MHz, 25 °C, CD_2Cl_2): δ = 1.00 (t, 9 H, ^3J = 7.2 Hz, $-CH_2-CH_3$), 1.41 (m, 6 H, ^3J = 7.3 Hz, $-CH_2-CH_3$), 1.64 (m, 6 H, ^3J = 7.4 Hz, $-CH_2-CH_2-CH_3$), 3.04 (s, 3 H, $N-CH_3$), 3.14 (m, 6 H, ^3J = 7.5 Hz, $N-CH_2-CH_2-$), 3.53 (s, 4 H, $^2J_{H,Sn}$ = 93 Hz, $-P-CH_2-Sn$), 7.56−7.95 ppm (m, 20 H, $-P-(C_6H_5)_2$]. ^{11}B{^{1}H} NMR (64 MHz, 25 °C, CD_2Cl_2): δ (ppm) = −11.7 (s, B12), −17.0 (s, B2−6 and B7−11). ^{31}P{^{1}H} NMR (81 MHz, 25 °C, CD_2Cl_2, 213 K): δ = 40.79 ppm (s, $-P-(C_6H_5)_2$]. $C_{39}H_{76}AuB_{22}NP_2Sn_2$ (1293.22): calcd. C 36.22, H 5.92, N 1.08; found C 36.21, H 6.11, N 0.88.

Acknowledgments

We thank the Deutsche Forschungsgemeinschaft (Schwerpunktprogramm Polyeder) and the Fonds der Chemischen Industrie for financial support.

[1] [1a] W. A. Herrmann, C. W. Kohlpaintner, *Angew. Chem. Int. Ed. Engl.* **1993**, *32*, 1524. [1b] *Aqueous-Phase Organometallic Catalysis, Concepts and Applications* (Ed.: B. Cornils, W. A. Herrmann), Wiley-VCH, Weinheim, **2004**.
[2] C. C. Lu, J. C. Peters, *J. Am. Chem. Soc.* **2002**, *124*, 5272.
[3] D. M. Jenkins, A. J. Di Bilio, M. J. Allen, T. A. Betley, J. C. Peters, *J. Am. Chem. Soc.* **2002**, *124*, 15336.
[4] J. C. Thomas, J. C. Peters, *Inorg. Chem.* **2003**, *42*, 5055.
[5] T. A. Betley, J. C. Peters, *Angew. Chem. Int. Ed.* **2003**, *42*, 2003.
[6] C. M. Thomas, J. C. Peters, *Inorg. Chem.* **2004**, *43*, 8.
[7] H. H. Karsch, A. Appelt, F. H. Köhler, G. Müller, *Organometallics* **1985**, *4*, 231.
[8] S. Qiao, D. A. Hoic, G. Fu, *J. Am. Chem. Soc.* **1996**, *118*, 6329.
[9] [9a] G. Müller, J. Brand, *Organometallics* **2003**, *22*, 1463. [9b] H. Dorn, C. A. Jaska, R. A. Singh, A. J. Lough, I. Manners, *Chem. Commun.* **2000**, 1041. [9c] A.-C. Gaumont, M. B. Hursthouse, S. J. Coles, J. M. Brown, *Chem. Commun.* **1999**, 63. [9d] W. Angerer, W. S. Sheldrick, W. Malisch, *Chem. Ber.* **1985**, *118*, 1261.
[10] F. Teixidor, C. Viñas, M. M. Abad, M. Lopez, J. Casabó, *Organometallics* **1993**, *12*, 3766.
[11] F. Teixidor, C. Viñas, M. M. Abad, C. Whitaker, J. Rius, *Organometallics* **1996**, *15*, 3154.
[12] B. Ronig, T. Bick, I. Pantenburg, L. Wesemann, *Eur. J. Inorg. Chem.* **2004**, 689.
[13] [13a] M. Elrington, N. N. Greenwood, J. D. Kennedy, M. Thornton-Pett, *J. Chem. Soc., Dalton Trans.* **1987**, 451. [13b] C. Viñas, R. Nuñez, M. A. Flores, F. Teixidor, R. Kivekäs, R. Sillanpäa, *Organometallics* **1995**, *14*, 3952. [13c] I. T. Chizhevsky, I. A. Lobanova, P. V. Petrovskii, V. I. Bregadze, F. M. Dolgushin, A. I. Yanovsky, Y. T. Struchkov, A. L. Chistyakov, I. V. Stankevich, C. B. Knobler, M. F. Hawthorne, *Organometallics* **1999**, *18*, 726. [13d] G. G. Hlatky, H. W. Turner, R. R. Eckman, *Inorg. Chem.* **1989**, *111*, 2728. [13e] G. G. Hlatky, R. R. Eckman, H. W. Turner, *Organometallics* **1992**, *11*, 1413.
[14] W. P. Power, R. E. Wasylishen, *Inorg. Chem.* **1992**, *31*, 2176.
[15] I. Y. Guzman-Jimenez, K. H. Whitmire, *Acta Crystallogr., Sect. C* **1999**, *55*, 9900028.
[16] N. C. Baenziger, K. M. Dittemore, J. R. Doyle, *Inorg. Chem.* **1974**, *4*, 805.
[17] J. J. Guy, P. G. Jones, G. M. Sheldrick, *Acta Crystallogr., Sect. B* **1976**, *32*, 1937.
[18] [18a] G. A. Bowmaker, H. Schmidbaur, S. Krüger, N. Rösch, *Inorg. Chem.* **1997**, *36*, 1754. [18b] P. Römbke, A. Schier, H. Schmidbaur, *J. Chem. Soc., Dalton Trans.* **2001**, 2482.
[19] J. C. Jeffrey, P. A. Jelliss, F. G. A. Stone, *Organometallics* **1994**, *13*, 2651.
[20] X-RED 1.22, Stoe Data Reduction Program (C) 2001 Stoe & Cie GmbH, Darmstadt.
[21] X-Shape 1.06, Crystal Optimisation for Numerical Absorption Correction (C), **1999**, STOE & Cie GmbH, Darmstadt.
[22] CCDC-244840 (for **2**), -244841 (for **5**) and -244842 (for **9**)

 © 2005 Wiley-VCH Verlag GmbH & Co. KGaA, Weinheim

contain the supplementary crystallographic data for this paper. These data can be obtained free of charge at www.ccdc.cam.ac.uk/conts/retrieving.html [or from the Cambridge Crystallographic Data Centre, 12 Union Road, Cambridge CB2 1EZ, UK; Fax: +44-1223-336-033; E-mail: deposit@ccdc. cam. ac. uk].

[23] G. M. Sheldrick, *SHELXS-97, Program for Structure Analysis*, Göttingen, **1998**.

[24] G. M. Sheldrick, *SHELXL-93*, *Program for Crystal Structure Refinement*, Göttingen, **1993**.

[25] R. W. Chapman, J. G. Kester, K. Folting, W. E. Streib, L. J. Todd, *Inorg. Chem.* **1992**, *31*, 979.

[26] W. P. Fehlhammer, W. A. Herrmann, K. Öfele, *Handbuch der Präparativen Anorganischen Chemie*, 3rd ed., G. Brauer (Ed.), Ferdinand-Enke-Verlag, Stuttgart, **1981**.

[27] W. T. Reichle, *Inorg. Chim. Acta* **1971**, *5*, 325.

[28] N. E. Schore, B. E. LaBelle, *J. Org. Chem.* **1981**, *46*, 2306.

Received July 20, 2004
Early View Article
Published Online December 2, 2004

 © 2005 Wiley-VCH Verlag GmbH & Co. KGaA, Weinheim

Syntheses and Characterizations of Multidimensional Metal-Organic Frameworks Based on Rings and 1D Chains

Xiaoju Li,[a] Rong Cao,*[a] Yanqiong Sun,[a] Wenhua Bi,[a] Xing Li,[a] and Yanqin Wang[a]

Keywords: Bridging ligand / Polymers / Hydrothermal reaction / Hydrogen bonds

Four novel multidimensional coordination polymers, {[Cd(3-PYD)$_2$(H$_2$O)]·2H$_2$O}$_n$ (**1**), [Pb(3-PYD)$_2$]$_n$ (**2**), {[Cu$_{1.5}$(3-PYD)$_3$(H$_2$O)]·1.5H$_2$O}$_n$ (**3**) and [Zn(3-PYD)$_2$(H$_2$O)$_2$]$_n$ (**4**), have been hydrothermally synthesized from 3-(3-pyridyl)acrylic acid (3-HPYD). In **1**, 3-PYD in a head-to-head arranged fashion bridges Cd^{II}, generating a two-dimensional layer, which is further extended into a three-dimensional supramolecular network by hydrogen-bonding interactions. Compound **2** shows a two-dimensional wave-like layer that consists of {Pb(3-PYD)}$_4$ rings from head-to-tail arranged 3-PYD. Compound **3** is a twofold interpenetrating three-dimensional network consisting of {Cu(3-PYD)}$_6$ rings formed through the mixed head-to-head and head-to-tail arrangements of 3-PYD. However, **4** is a three-dimensional supramolecular framework constructed by one-dimensional zinc-3-PYD chains through hydrogen-bonding interactions.
(© Wiley-VCH Verlag GmbH & Co. KGaA, 69451 Weinheim, Germany, 2005)

Introduction

The rational design and syntheses of multidimensional coordination polymers have been of increasing interest recently in material science and chemical research.[1,2] This is justified not only by their unique application as functional materials but also by the particular structural diversity of their architectures,[3−5] which can be much greater than those of metal oxides and other simple inorganic solid materials, owing to incorporation of many organic ligands.[6] As a result, the selection of organic ligands with appropriate coordination sites linked by specific connectors is the key to forming metal-organic complexes with desirable physical and chemical properties.

Multidentate N- or O-donor ligands have been employed extensively as organic spacers in the construction of extended structures. For example, the use of 4,4′-bipyridine[7] and its analogues,[8] as neutral N-donor ligands, is a most promising approach towards the syntheses of extended metal-organic frameworks owing to their simple bridging mode and strong coordination ability to transition metal ions. However, assembly of these ligands with metal ions is heavily dependent on the presence of different counterions. Conversely, di-[9] or polycarboxylate[10] ligands, as O-donor ligands via anionic groups, are another candidate for the preparation of multidimensional coordination networks, owing to the rich coordination modes of the carboxylate groups, and can afford neutral metal-organic frameworks. Our research aim is to incorporate both neutral and anionic donor groups into a single organic ligand that can be used to construct desired coordination polymers. Different donor groups can hold great promise for incorporating accessibility, structural diversity and geometrical control of properties into the resulting coordination networks. Moreover, both neutral and anionic donor groups can coordinate to metal centers, and afford opportunities for generating neutral polymeric networks without counterions, thereby simplifying the control of final products.[11,12] In this context, extended coordination structures have been constructed using rigid pyridinecarboxylate ligands.[12−14] We employed 3-(3-pyridyl)acrylic acid (3-HPYD), which possesses an appropriate angle (120°) and a long arm between coordination sites. Assembly of 3-HPYD with metal ions not only can produce aesthetically beautiful complexes with useful properties, which can not be obtained by common pyridinecarboxylate ligands, but can also generate some predicted, controlled structural frameworks through changing the coordination nature of metal ions. However, few compounds with 3-HPYD have been reported.[14] Herein, we report the syntheses and characterizations of four coordination polymers: {[Cd(3-PYD)$_2$(H$_2$O)]·2H$_2$O}$_n$ (**1**), [Pb(3-PYD)$_2$]$_n$ (**2**), {[Cu$_{1.5}$(3-PYD)$_3$(H$_2$O)]·1.5H$_2$O}$_n$ (**3**) and [Zn(3-PYD)$_2$(H$_2$O)$_2$]$_n$ (**4**), constructed from 3-HPYD with different metal ions.

[a] State Key Laboratory of Structural Chemistry, Fujian Institute of Research on the Structure of Matter, Chinese Academy of Sciences,
Fujian, Fuzhou, 350002, China
Fax: (internat.) +86-591-3714946
E-mail: rcao@ms.fjirsm.ac.cn

Results and Discussions

Syntheses

Two distinct characteristics of 3-HPYD, an angle of 120° and a long arm between pyridyl and carboxylate donor

 DOI: 10.1002/ejic.200400648 © 2005 Wiley-VCH Verlag GmbH & Co. KGaA, Weinheim

groups, render it ideal for the assembly of molecular polygons. Two types of polygons can be obtained from head-to-head or head-to-tail arrangement of the deprotonated 3-HPYD (3-PYD) when using four ML units with 120° corners (Scheme 1, a and b). In addition, their mixed arrangement can also generate other building units, such as a $\{ML\}_6$ basal ring (Scheme 1, c). Based on these points, we carried out a series of hydrothermal reactions of 3-HPYD and transition metal ions to formulate novel coordination polymers. As expected, when Cd^{II} and Cu^{II} was used as nodes, compound **1** based on $\{ML\}_4$ rings from the head-to-head arrangement of 3-PYD, and compound **3** based on $\{ML\}_6$ rings from the head-to-head and head-to-tail mixed arrangements of 3-PYD, were successfully obtained, respectively. However, the compound containing $\{ML\}_4$ rings from head-to-tail arrangement of 3-PYD was not obtained, although other transition metal ions, such as Co^{2+}, Ni^{2+}, Mn^{2+} and Zn^{2+}, were employed. Notably, the hydrothermal reaction of Zn^{2+} and 3-HPYD produced compound **4**, which was not from the ring units but from 1D zinc-carboxylate chains extended by hydrogen-bonding interactions. Pb^{2+}, which has an ample coordination preference,[15] was used to investigate further the conformation and arranged fashion of 3-PYD. Consequently, compound **2**, a 2D network consisting of $\{Pb(3\text{-PYD})\}_4$ basal rings from head-to-tail arrangement of 3-PYD, was produced. Accordingly, the diverse geometries of different metal ions may play critical roles in the assembly of metal-organic frameworks with various structures. This has also been testified to in some other research systems.[16]

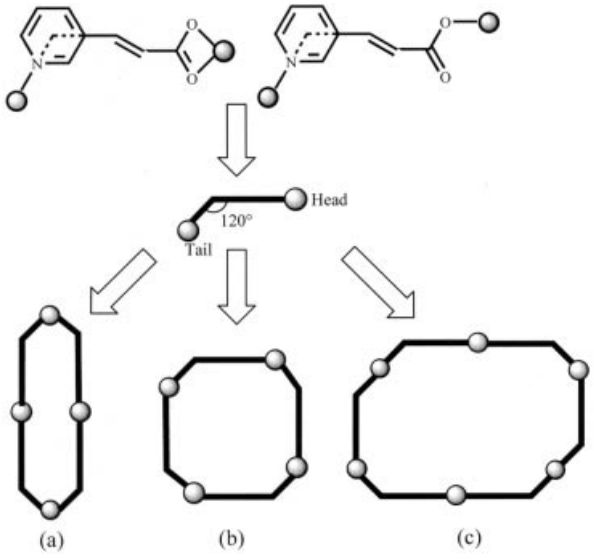

Scheme 1. (a) $\{ML\}_4$ ring from head-to-head (or tail-to-tail) arrangement of 3-PYD; (b) $\{ML\}_4$ ring from head-to-tail arrangement of 3-PYD; (c) $\{ML\}_6$ ring from head-to-head and head-to-tail mixed arrangements of 3-PYD

Structural Descriptions

$\{[Cd(3\text{-PYD})_2(H_2O)]\cdot 2H_2O\}_n$ (1): Single-crystal X-ray diffraction analysis reveals that **1** is a 3D supramolecular network consisting of $\{Cd(3\text{-PYD})\}_4$ rings derived from head-to-head arranged 3-PYD. The asymmetric unit of **1** consists of one Cd^{II}, two 3-PYD, one coordinated water molecule and two free water molecules (Figure 1). Each Cd^{II} is in a distorted pentagonal bipyramidal geometry. The equatorial basal plane is determined by two chelating carboxylate groups from different 3-PYD and one coordinated water molecule. Cd−O bond lengths are in the range 2.303(8)−2.462(10) Å. Apical positions are occupied by two pyridyl nitrogen atoms from different 3-PYD, with an average Cd−N distance and N(1)−Cd−N(2) bond angle of 2.382(8) Å and 164.0(3)°, respectively. The Cd^{II} is approximately coplanar with the mean plane of the five equatorial atoms, with a deviation of 0.1000 Å. 3-PYD acts as a bridging ligand, through its pyridyl nitrogen atom and chelating carboxylate group, linking different Cd^{II} centers. Four 3-PYD with a head-to-head aggregation link Cd^{II} into a $\{Cd(3\text{-PYD})\}_4$ ring (Scheme 1, a), in which four metal ions and four 3-PYD are all in one plane (Figure 2, a). Based on $Cd^{II}\cdots Cd^{II}$ distances, the ring is 7.449 × 15.139 $Å^2$. Interestingly, each $\{Cd(3\text{-PYD})\}_4$ ring is surrounded by four other perpendicular $\{Cd(3\text{-PYD})\}_4$ rings through shar-

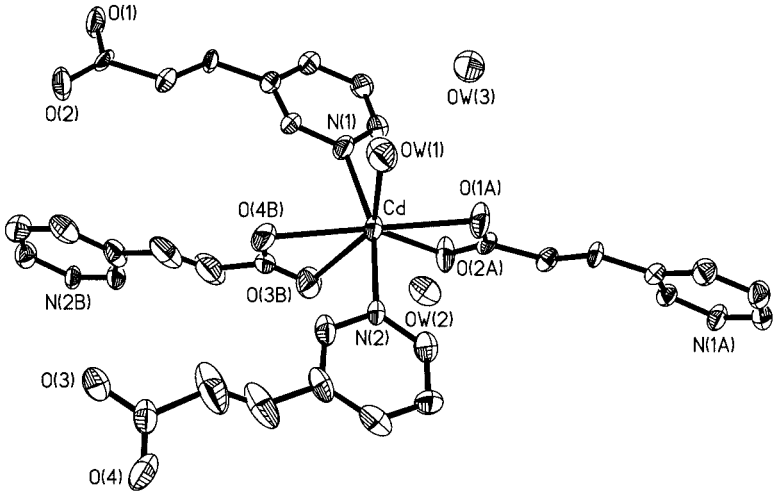

Figure 1. Coordination environment around Cd^{II} in **1** with the thermal ellipsoids at 30% probability level

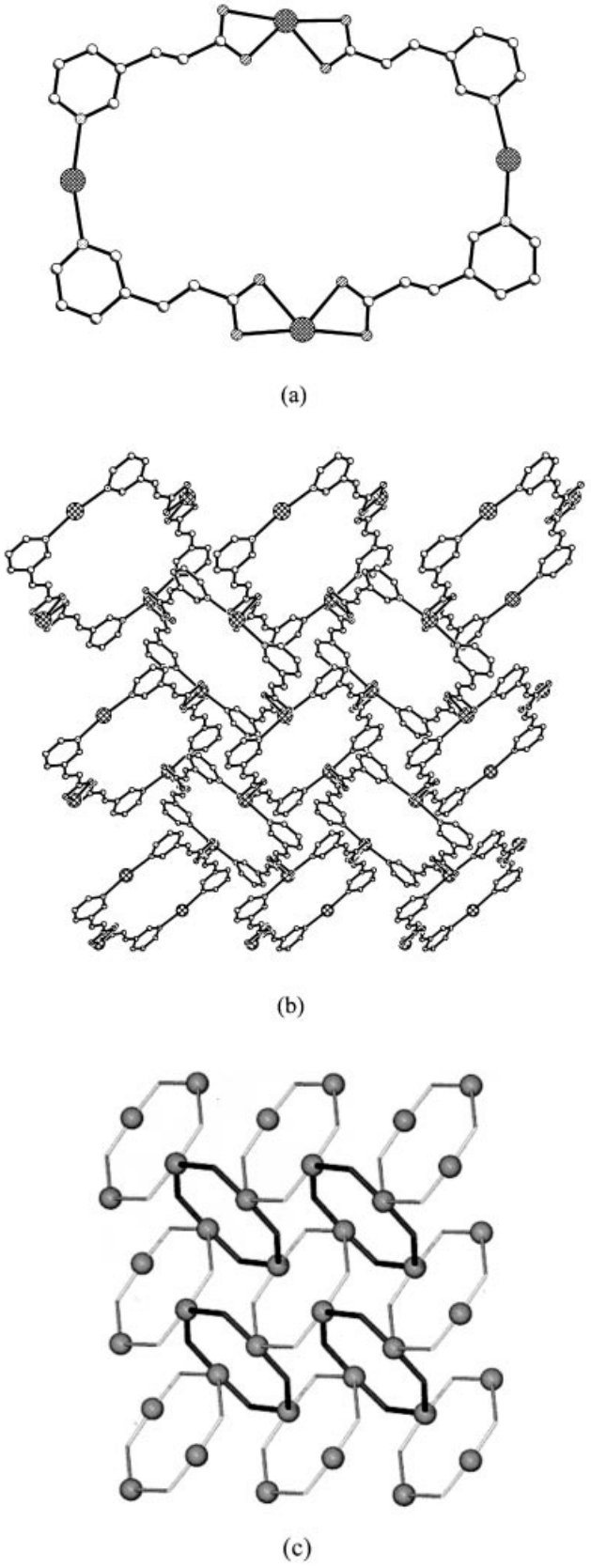

Figure 2. (a) $\{Cd(3\text{-PYD})\}_4$ ring from head-to-head arrangement of 3-PYD; (b) a 2D layer in **1** along the *c* axis; free water molecules omitted for clarity; (c) schematic showing the 2D layer derived from reciprocally vertical $\{Cd(3\text{-PYD})\}_4$ rings; only the Cd^{II} centers are shown for clarity, with the bonds representing bridging ligands

ing Cd^{II} joints, which may be due to the proper geometry of the metal ion. Thereby, a 2D layer framework is generated from the reciprocally vertical $\{Cd(3\text{-PYD})\}_4$ rings (Figure 2, b and c); the free water molecules are accommodated in the rings. Finally, neighboring layers are further extended into a 3D supramolecular architecture through hydrogen-bonding interactions between coordinated water molecules and carboxylate oxygen atoms [$OW(1)-H\cdots O(4)^i$ 2.701 Å; symmetry codes: (i) $x - 1/2, -y + 5/2, z - 1/2$] (Figure 3). Thus, hydrogen-bonding interactions play an important role in the construction and stabilization of the extended structure.

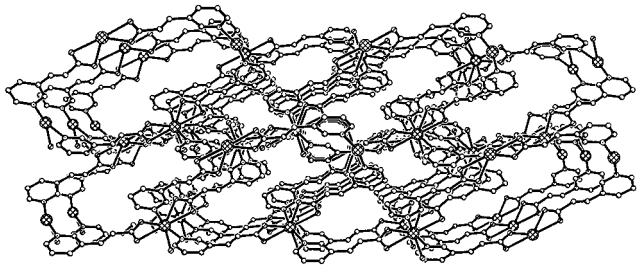

Figure 3. Packing structure of **1** along the *b* axis; free water molecules omitted for clarity

$[Pb(3\text{-PYD})_2]_n$ (2): 2 is a 2D wave-like layer based on $\{Pb(3\text{-PYD})\}_4$ rings from head-to-tail arranged 3-PYD. The four-coordinate Pb^{II} is in a highly distorted tetragonal pyramid geometry (Figure 4). The basal plane is defined by two pyridyl nitrogen atoms and two carboxylate oxygen atoms from different 3-PYD, while Pb^{II} occupies the apex. Pb^{II} deviates from the N_2O_2 basal plane by 0.9217 Å. Average Pb−N and Pb−O distances are 2.652(8) and 2.374(7) Å, respectively, and the N(1A)−Pb−N(2) and O(1)−Pb−O(3B) bond angles are 158.8(3) and 79.3(2)°, respectively. Unlike **1**, 3-PYD bridges Pb^{II} through its pyridyl nitrogen atom and monodentate carboxylate group, generating a head-to-tail aggregated $\{Pb(3\text{-PYD})\}_4$ ring (Scheme 1, b). In the $\{Pb(3\text{-PYD})\}_4$ ring, four Pb^{II} ions and four 3-PYD are *not* coplanar, which may be due to the different arrangement of 3-PYD and the coordination geometry of the metal ion. The $\{Pb(3\text{-PYD})\}_4$ rings are further extended into a 2D wave-like layer by sharing Pb^{II} joints and 3-PYD edges (Figure 5). Although there is large void space in the wave-like layer, no guest or water molecules are included. Adjoining layers are 4.348 Å apart, and there are no hydrogen bonding or other weak interactions between them (Figure 6).

$\{[Cu_{1.5}(3\text{-PYD})_3(H_2O)]\cdot 1.5H_2O\}_n$ (3): 3 is a twofold interpenetrating 3D framework based on $\{Cu(3\text{-PYD})\}_6$ rings formed through head-to-head and head-to-tail mixed arrangements of 3-PYD (Scheme 1, c). There are two crystallographically independent Cu^{II} centers (Figure 7). Cu(1) adopts a distorted square-pyramidal coordination geometry. Two *trans*-carboxylate oxygen atoms and two *trans*-pyridyl nitrogen atoms of different 3-PYD comprise the equatorial plane. Average Cu(1)−O and Cu(1)−N bond lengths are 1.960(2) and 2.024(4) Å, respectively. Cu(1) deviates from the mean plane determined by the four equatorial atoms by

 © 2005 Wiley-VCH Verlag GmbH & Co. KGaA, Weinheim

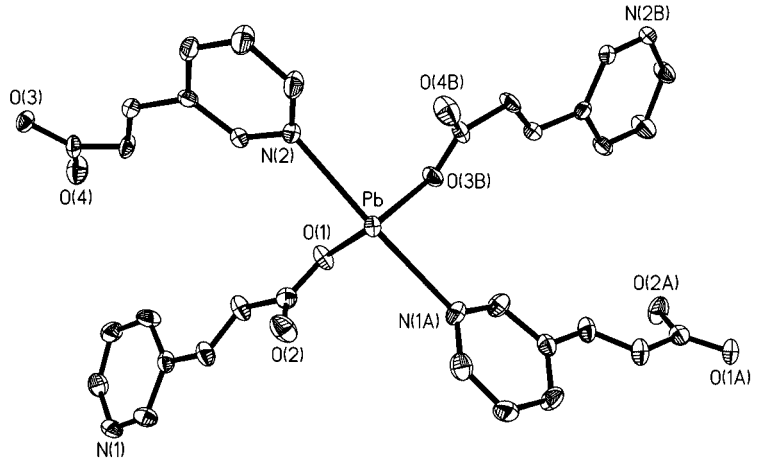

Figure 4. Coordination environment around Pb^{II} in **2** with thermal ellipsoids at 30% probability level

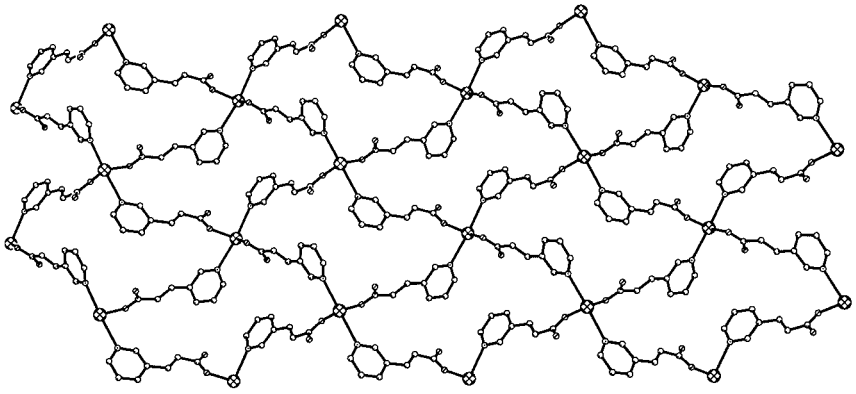

Figure 5. Two-dimensional wave-like layer in **2**

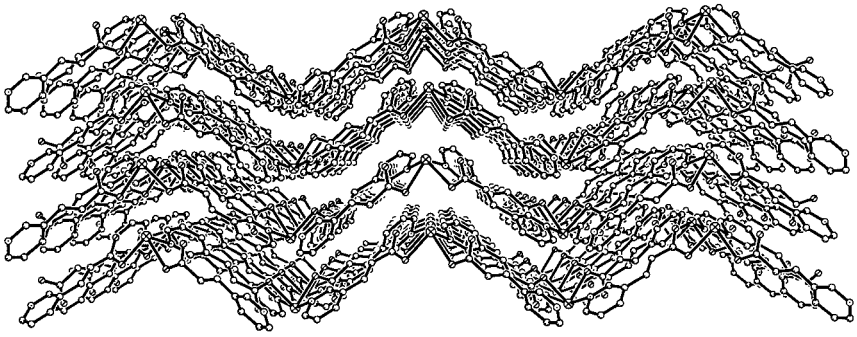

Figure 6. Packing diagram of **2** along the *a* axis

0.0827 Å. One water molecule occupies its axial position with the Cu(1)−OW(1) bond length is 2.403(3) Å. However, Cu(2) is in a square-planar geometry defined by two *trans*-carboxylate oxygen atoms [O(3) and O(3C)] and two *trans*-pyridyl nitrogen atoms [N3 and N(3C)] of different 3-PYD. The bond lengths of Cu(2)−O(3) and Cu(2)−N(3) are 1.959(3) and 2.008(3) Å, respectively. Similar to that in **2**, 3-PYD also uses its nitrogen atom and monodentate carboxylate group to bridge metal centers.

The most interesting feature of the structure is the chair-like $\{Cu(3\text{-PYD})\}_6$ ring arising from four Cu(1) atoms and two Cu(2) atoms connected by six 3-PYD through both head-to-head and head-to-tail aggregations (Figure 8, a). Each chair-like $\{Cu(3\text{-PYD})\}_6$ ring is further surrounded by six identical units through sharing the metal ions; thereby, a 3D framework is generated (Figure 8, b). However, owing to the absence of guest molecules to fill the large voids in the $\{Cu(3\text{-PYD})\}_6$ rings, the voids are filled via mutual interpenetration of independent equivalent frameworks to generate a twofold interpenetrating 3D architecture (Figure 9). Hydrogen-bonding interactions between coordinated water molecules and carboxylate oxygen atoms of 3-PYD as well as between uncoordinated water molecules and carboxylate oxygen atoms of 3-PYD, with lengths from 2.565 to 2.893 Å, further stabilize the whole framework.

 © 2005 Wiley-VCH Verlag GmbH & Co. KGaA, Weinheim

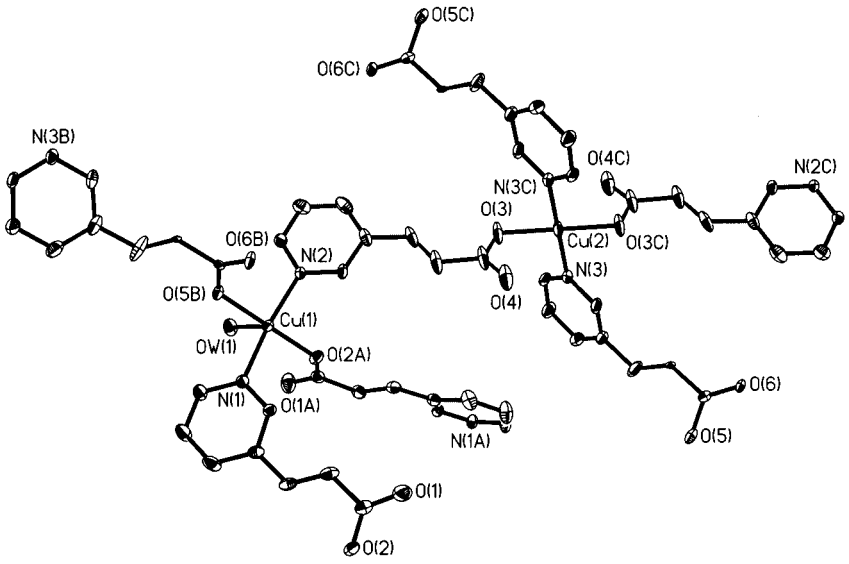

Figure 7. Coordination environment around Cu^{II} in **3** with thermal ellipsoids at 30% probability level

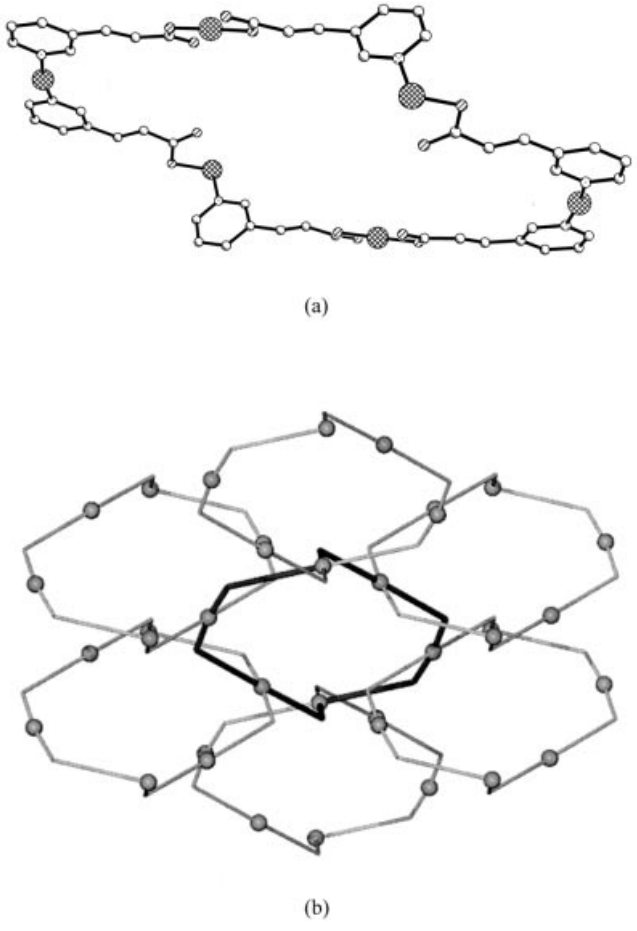

Figure 8. (a) $\{Cu(3\text{-}PYD)\}_6$ ring formed by four Cu(1), two Cu(2) atoms and six 3-PYD; (b) perspective of a chair-like $\{Cu(3\text{-}PYD)\}_6$ ring surrounded by six identical units; 3-PYD ligands omitted for clarity

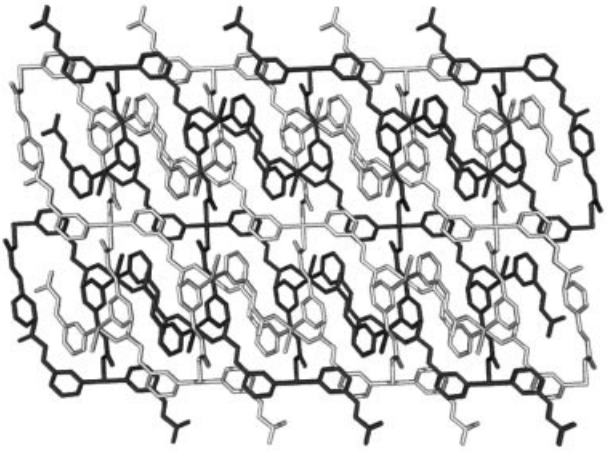

Figure 9. View of a twofold interpenetrating 3D network in **3** along the *b* axis

$[Zn(3\text{-}PYD)_2(H_2O)_2]_n$ (4): Unlike compounds **1**−**3** based on $\{ML\}_4$ or $\{ML\}_6$ rings, **4** is a 3D supramolecular framework constructed by 1D metal-3-PYD chains through hydrogen-bonding interactions. Figure 10 shows that each Zn^{II} is coordinated by four oxygen atoms from one chelating carboxylate group of 3-PYD, two water molecules, and two nitrogen atoms from different 3-PYD, in a distorted octahedral geometry. The equatorial plane is determined by N(2), O(3A), O(4A) and OW(2), while axial positions are occupied by N(1) and OW(1) with the N(1)−Zn−OW(1) bond angle being 176.31(4)°. There are two kinds of 3-PYD: one acts as a bridging ligand through its pyridyl nitrogen atom and chelating carboxylate group; the other serves as a terminal ligand through its pyridyl nitrogen atom participating in coordination, the carboxylate group is not involved in the coordination and acts as an acceptor of the hydrogen bonding. Hence, the Zn^{II} center is linked by bridging 3-PYD to generate a neutral 1D metal-3-PYD chain with the help of terminal 3-PYD (Figure 11). The 1D chains are further extended into a 3D supramolecular network through the abundant hydrogen-bonding interactions

 © 2005 Wiley-VCH Verlag GmbH & Co. KGaA, Weinheim

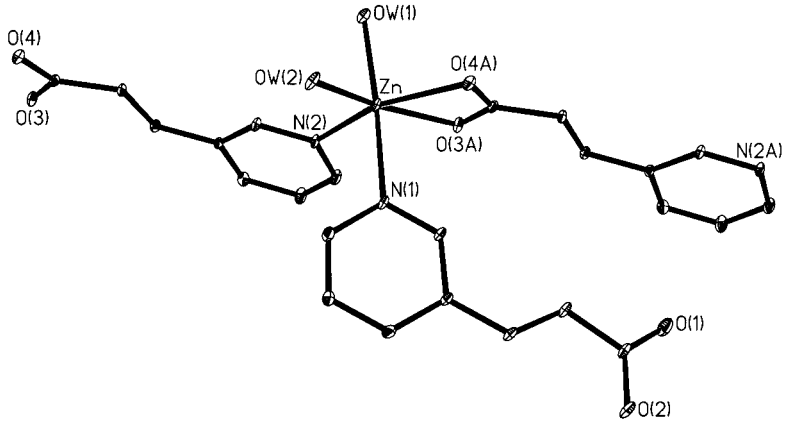

Figure 10. Coordination environment around Zn^{II} in **4** with thermal ellipsoids at 30% probability level

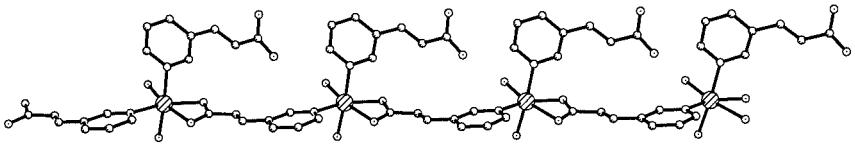

Figure 11. One-dimensional metal-3-PYD chain in **4**

between coordinated water molecules and carboxylate groups [OW(1)−H···O3^{i} 2.797 Å; OW(2)−H···O2^{ii} 2.602 Å; OW(2)−H···O2^{iii} 2.661 Å; symmetry codes: (i) $-x$, $-y$ + 4, $-z$ + 1; (ii) x −1, y + 1, z; (iii) $-x$ + 1, $-y$ + 4, $-z$] (Figure 12).

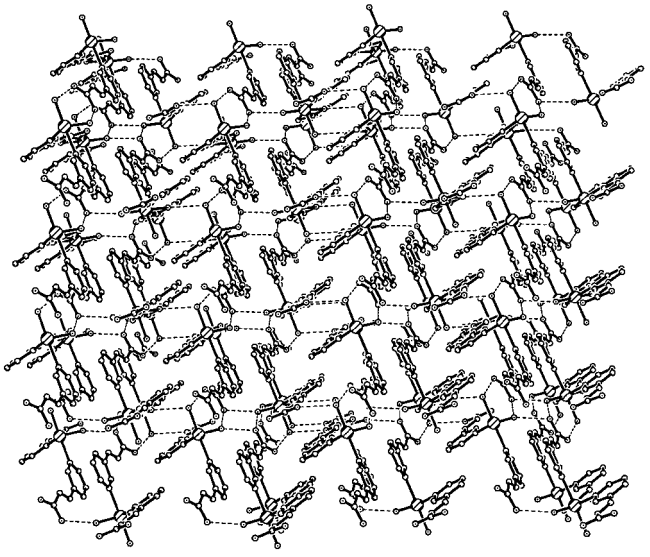

Figure 12. Three-dimensional supramolecular network formed by 1D metal-3-PYD chains through hydrogen-bonding interactions along the *b* axis in **4**

IR Spectroscopy

The IR spectrum of **1** shows a strong, broad peak at 3413 cm^{-1}, which can be ascribed to the presence of water molecules. Characteristic carboxylate group bands appear at 1552 and 1400 cm^{-1} for asymmetric and symmetric vibrations, respectively. Δ, which represents the separation between ν_{asym}(COO) and ν_{sym}(COO) and reflects the coordination modes of the carboxylate groups,[17] is 152 cm^{-1}. For **2**, bands characteristic of the carboxylate group are exhibited at 1564 cm^{-1} for asymmetric vibrations and at 1354 cm^{-1} for symmetric vibrations; Δ is 210 cm^{-1}. For **3**, similar to **1**, the strong, broad band at 3433 cm^{-1} indicates the presence of water molecules. Absorption peaks at 1562 and 1378 cm^{-1} display the asymmetric and symmetric vibrations, respectively; Δ is 184 cm^{-1}. The single Δ in the three compounds is consistent with a single coordination mode of carboxylate group in their structures.[18] For **4**, the strong, broad peak at 3109 cm^{-1} also displays the presence of water molecules. Interestingly, besides the asymmetric (1546 cm^{-1}) and symmetric (1363 cm^{-1}) vibrations (Δ of ca. 183 cm^{-1}), the strong characteristic band at 1407 cm^{-1} indicates the presence of uncoordinated carboxylate group, which is in agreement with the results of its crystal structure.

Thermogravimetric Analyses

The thermal stability of **1**−**4** has been determined on polycrystalline samples in a nitrogen atmosphere by thermogravimetric analysis (TGA). For **1**, the weight loss of 11.55% from 61 to 118 °C is equivalent to the loss of one coordinated water molecule and two free water molecules [$3H_2O$/$Cd(3\text{-}PYD)_2(H_2O)]\cdot 2H_2O$, calculated: 11.68%). The second weight loss of 60.68%, from 331 to 900 °C, corresponds to the decomposition of **1**. The residual weight of 27.77% is ascribed to CdO (calculated: 27.75%). For **2**, TGA shows that chemical decomposition starts at 338 °C and ends at 398 °C with the weight loss of 55.59%; the remaining weight (44.41%) corresponds to PbO (calculated: 44.33%). For **3**, TGA exhibits two weight losses: One (7.52%) from 49 to 120 °C is attributed to the loss of coordinated water molecule and free water molecules ($2\cdot 5H_2O$/$[Cu_{1.5}(3\text{-}PYD)_3(H_2O)]\cdot 1.5H_2O$, calculated: 7.70%), suggesting the

 © 2005 Wiley-VCH Verlag GmbH & Co. KGaA, Weinheim

weak interaction of Cu(1)−OW(1) [2.403(3) Å]. The other (64.92%), from 245 to 478 °C, corresponds to the decomposition of **3**. In **4**, a weight loss of 9.12% from 119 to 160 °C displays the loss of two coordinated water molecules [$2H_2O$/$Zn(3\text{-PYD})_2(H_2O)_2$, calculated: 9.06%]. Above 268 °C, the framework starts to decompose.

Conclusions

Hydrothermal reactions of 3-(3-pyridyl)acrylic acid (3-HPYD) with different metal ions have afforded four coordination polymers based on $\{ML\}_4$ and $\{ML\}_6$ rings or metal-carboxylate chains, respectively. It may be conceivable to design and synthesize desired metal-organic frameworks when using the selected organic ligands with special conformations.

Experimental Section

Materials and General Methods: 3-(3-Pyridyl)acrylic acid was purchased from Aldrich and used without further purification; all other reagents were commercially available and used as purchased. Thermogravimetric experiments were performed using a TGA/SDTA851 instrument (heating rate of 15 °C min^{-1}, nitrogen stream). IR spectra were recorded as KBr pellets with a Magna 750 FT-IR spectrophotometer. Elemental analyses of C, H and N were determined using a Perkin-Elmer 240C elemental analyzer.

Synthesis of $\{[Cd(3\text{-PYD})_2(H_2O)]\cdot 2H_2O\}_n$ (1): A mixture of 3-HPYD (0.037 g, 0.25 mmol), $Cd(NO_3)_2\cdot 4H_2O$ (0.077 g, 0.25 mmol), KOH (0.014 g, 0.25 mmol) and H_2O (18 mL) was placed in a Teflon-lined stainless steel vessel and heated to 170 °C for 72 hours. The reaction system was then cooled to room temperature during 24 hours, and the resulting solution was filtered and left undisturbed in the air. After a day, light yellow block crystals of **1** (0.065 g) were obtained. Yield: 56% (based on Cd). $C_{16}H_{18}CdN_2O_7$ (462.72): calcd. C 41.53, H 3.92, N, 6.05; found C 41.55, H 3.82, N 6.13. IR (KBr, cm^{-1}): $\tilde{\nu}$ = 3413 (s), 1640 (s), 1552 (vs), 1478 (s), 1437 (w), 1400 (vs), 984 (s), 749 (m), 692 (s).

Synthesis of $[Pb(3\text{-PYD})_2]_n$ (2): $Pb(NO_3)_2$ (0.066 g, 0.20 mmol) and 3-HPYD (0.019 g, 0.125 mmol) in H_2O (18 mL) were stirred for 20 min, and then the pH was adjusted to 5 with Et_3N. After stirring for another 20 min, the mixture was transferred to a 25 mL stainless steel reactor with a Teflon liner and heated to 150 °C for 96 hours. The reaction system was then cooled to room temperature during 24 hours. A large amount of yellow cube-shaped crystals of **2** (0.078 g) was obtained. Yield: 78% (based on Pb). $C_{16}H_{12}PbN_2O_4$ (503.47): calcd. C 38.17, H 2.40, N 5.56; found C 38.12, H 2.48, N 5.55. IR (KBr, cm^{-1}): $\tilde{\nu}$ = 3445 (w), 1642 (s), 1564 (vs), 1420 (s), 1354 (vs), 1294 (m), 1242 (m), 806 (s), 693 (vs), 639 (vs).

Synthesis of $\{[Cu_{1.5}(3\text{-PYD})_3(H_2O)]\cdot 1.5H_2O\}_n$ (3): $Cu(NO_3)_2\cdot 3H_2O$ (0.036 g, 0.15 mmol) and 3-HPYD (0.030 g, 0.20 mmol) in H_2O (18 mL) were stirred for 20 min; the pH was then adjusted to 4 with Et_3N. After stirring for a further 20 min, the mixture was transferred to a 25 mL stainless steel reactor with a Teflon liner and heated to 165 °C for 96 hours. The reaction system was then cooled to room temperature during 24 hours. Blue block crystals of **3** (0.022 g) were obtained (based on Cu). Yield: 38%. $C_{24}H_{23}Cu_{1.5}N_3O_{8.5}$ (584.76): calcd. C 49.30, H 3.96, N 7.19; found C 49.27, H 4.10, N 7.11. IR (KBr, cm^{-1}): $\tilde{\nu}$ = 3433 (s), 3107 (w), 1644 (s), 1602 (w), 1562 (vs), 1474 (w), 1431 (s), 1378 (vs), 1053 (m), 988 (s), 805 (s), 693 (s), 606 (m).

Table 1. Crystal data and structure determination summary for **1**−**4**

	1	**2**	**3**	**4**
Formula	$C_{16}H_{18}CdN_2O_7$	$C_{16}H_{12}N_2O_4Pb$	$C_{24}H_{23}Cu_{1.5}N_3O_{8.5}$	$C_{16}H_{16}N_2O_6Zn$
Fw	462.72	503.47	584.76	397.68
Crystal size (mm)	0.40 × 0.16 × 0.14	0.60 × 0.24 × 0.14	0.25 × 0.20 × 0.20	0.20 × 0.20 × 0.20
Crystal system	monoclinic	monoclinic	monoclinic	triclinic
Space group	$P2_1/n$	$P2_1/c$	$P2_1/c$	$P\bar{1}$
a (Å)	12.0510(9)	10.3546(7)	13.342(13)	7.552(2)
b (Å)	12.1079(9)	17.0014(11)	11.016(4)	9.627(3)
c (Å)	12.4511(10)	8.6821(6)	16.404(14)	11.897(4)
β (°)	102.948(2)	93.864(1)	91.862(12)	81.748(9)
V ($Å^3$)	1770.6(2)	1524.95(18)	2410(3)	786.2(4)
Z	4	4	4	2
$D_{calcd.}$ ($g\cdot cm^{-3}$)	1.736	2.193	1.612	1.680
μ (mm^{-1})	1.275	11.085	1.394	1.600
T (K)	293(2)	293(2)	173(2)	173(2)
λ (Mo-K_α) (°)	0.71073	0.71073	0.71073	0.71073
Reflections collected	3139	4846	18440	6308
Unique reflections	1651	2684	5532	3766
R_{int}	0.0511	0.0306	0.0245	0.0107
Parameters	235	208	392	242
S on F^2	1.299	1.118	1.041	0.913
R_1 [$I > 2\sigma(I)$][a]	0.0591	0.0417	0.0521	0.0249
wR_2 [$I > 2\sigma(I)$][b]	0.1554	0.1136	0.1394	0.0975
R_1 (all data)	0.0751	0.0506	0.0600	0.0260
wR_2 (all data)[b]	0.1706	0.1237	0.1464	0.0994
$\Delta\rho_{min.}$ and $_{max.}$ ($e/Å^3$)	0.948 and −1.312	1.253 and −2.438	0.820 and −0.678	1.492 and −0.492

[a] $R = \Sigma||F_o| - |F_c||/\Sigma|F_o|$. [b] $[\Sigma w(F_o^2 - F_c^2)^2/\Sigma w(F_o^2)^2]^{1/2}$.

 © 2005 Wiley-VCH Verlag GmbH & Co. KGaA, Weinheim

Synthesis of $[Zn(3\text{-}PYD)_2(H_2O)_2]_n$ (4): $Zn(NO_3)_2{\cdot}6H_2O$ (0.037 g, 0.125 mmol) and 3-HPYD (0.030 g, 0.20 mmol) in H_2O (18 mL) were stirred for 20 min, and the pH was then adjusted to 5 with Et_3N. After stirred for a further 20 min, the mixture was transferred to a 25 mL stainless steel reactor with a Teflon liner and heated to 165 °C for 96 hours. After cooling the reaction system to room temperature during 24 hours, yellow block crystals of **4** (0.026 g) were obtained. Yield: 52% (based on Zn). $C_{16}H_{16}ZnN_2O_6$ (397.68): calcd. C 48.32, H 6.59, N 7.04; found C 48.29, H 6.65, N 6.98. IR (KBr, cm^{-1}): $\tilde{\nu}$ = 3109 (s), 1645 (s), 1546 (vs), 1481 (s), 1407 (vs), 1363 (vs), 1268 (w), 996 (m), 975 (m), 885 (w), 808 (s), 750 (m), 689 (s), 645 (w), 602 (w).

Table 2. Selected bond lengths (Å) and angles (°) for **1**−**4**

Compound **1**			
Cd−OW(1)	2.303(8)	Cd−N(2)	2.363(8)
Cd−O(1A)	2.391(8)	Cd−O(3B)	2.439(8)
Cd−O(2A)	2.394(8)	Cd−O(4B)	2.462(10)
Cd−N(1)	2.401(9)		
OW(1)−Cd−N(2)	94.3(3)	N(2)−Cd−O(3B)	89.4(3)
OW(1)−Cd−O(1A)	77.7(3)	O(1A)−Cd−O(3B)	135.0(3)
N(2)−Cd−O(1A)	88.3(3)	O(2A)−Cd−O(3B)	83.6(3)
OW(1)−Cd−O(2A)	127.0(3)	N(1)−Cd−O(3B)	83.7(3)
N(2)−Cd−O(2A)	102.0(3)	OW(1)−Cd−O(4B)	95.0(4)
O(1A)−Cd−O(2A)	53.2(3)	N(2)−Cd−O(4B)	84.9(3)
OW(1)−Cd−N(1)	83.9(3)	O(1A)−Cd−O(4B)	169.6(4)
N(2)−Cd−N(1)	164.0(3)	O(2A)−Cd−O(4B)	136.1(4)
O(1A)−Cd−N(1)	106.7(3)	N(1)−Cd−O(4)	79.5(3)
O(2A)−Cd−N(1)	91.6(3)	O(3B)−Cd−O(4B)	52.9(3)
OW(1)−Cd−O(3B)	147.2(3)		
Compound **2**			
Pb−O(3B)	2.354(7)	Pb−O(1)	2.395(7)
Pb−N(2)	2.637(9)	Pb−N(1A)	2.668(9)
O(3B)−Pb−O(1)	79.3(2)	O(3B)−Pb−N(1A)	76.4(3)
O(3B)−Pb−N(2)	87.4(3)	O(1)−Pb−N(1A)	83.6(3)
O(1)−Pb−N(2)	80.0(3)	N(2)−Pb−N(1A)	158.8(3)
Compound **3**			
Cu(1)−OW(1)	2.403(3)	Cu(2)−O(3)	1.959(3)
Cu(1)−O(5B)	1.956(2)	Cu(2)−O(3C)	1.959(3)
Cu(1)−O(2A)	1.964(2)	Cu(2)−N(3)	2.008(3)
Cu(1)−N(1)	2.024(3)	Cu(2)−N(3C)	2.008(3)
Cu(1)−N(2)	2.025(3)		
O(5B)−Cu(1)−O(2A)	178.60(10)	N(1)−Cu(1)−N(2)	170.34(10)
O(5B)−Cu(1)−N(1)	91.66(11)	O(5B)−Cu(1)−OW(1)	83.80(12)
O(2A)−Cu(1)−N(1)	89.39(11)	O(2A)−Cu(1)−OW(1)	95.17(12)
O(5B)−Cu(1)−N(2)	92.17(11)	N(1)−Cu(1)−OW(1)	95.76(10)
O(2A)−Cu(1)−N(2)	86.95(11)	N(2)−Cu(1)−OW(1)	93.47(10)
O(3)−Cu(2)−N(3)	91.27(11)	O(3)−Cu(2)−N(3C)	88.73(11)
O(3C)−Cu(2)−N(3)	88.73(11)	O(3C)−Cu(2)−N(3C)	91.27(11)
Compound **4**			
Zn−OW(2)	1.9977(13)	Zn−OW(1)	2.1368(13)
Zn−N(2)	2.1002(13)	Zn−N(1)	2.2307(14)
Zn−O(4A)	2.1191(12)	Zn−O(3A)	2.2326(13)
OW(2)−Zn−N(2)	98.95(6)	O(4A)−Zn−N(1)	88.84(5)
OW(2)−Zn−O(4A)	105.98(5)	OW(1)−Zn−N(1)	176.31(4)
N(2)−Zn−O(4A)	154.90(5)	OW(2)−Zn−O(3A)	166.68(5)
OW(2)−Zn−OW(1)	89.56(5)	N(2)−Zn−O(3A)	94.22(5)
N(2)−Zn−OW(1)	88.95(5)	O(4A)−Zn−O(3A)	60.77(5)
O(4A)−Zn−OW(1)	93.99(5)	OW(1)−Zn−O(3A)	92.65(5)
OW(2)−Zn−N(1)	87.37(5)	N(1)−Zn−O(3A)	90.80(5)
N(2)−Zn−N(1)	89.49(5)		

Symmetry code: for 1 (A) $x + 1/2, -y + 3/2, z - 1/2$, (B) $-x + 1/2, y - 1/2, -z + 5/2$. 2 (A) $-x + 1, y + 1/2, -z - 1/2$, (B) $-x, y + 1/2, -z - 1/2$. 3 (A) $-x + 2, y - 1/2, -z + 1/2$, (B) $x - 1, -y + 1/2, z - 1/2$, (C) $-x + 3, -y, -z$. 4 (A) $x, y - 1, z$.

X-ray Crystallographic Study: Intensity data for **1** and **2** were measured with a Siemens Smart CCD diffractometer with graphite-monochromated Mo-K_α radiation (λ = 0.71073 Å) at room temperature;[19] empirical absorption corrections were applied by using the SADABS program. Measurements of **3** and **4** were conducted on a Rigaku Mercury CCD diffractometer with graphite-monochromated Mo-K_α radiation (λ = 0.71073 Å) at −100 °C.[20] Structures for **1**−**4** were solved by direct methods and refined on F^2 by full-matrix least-squares using the SHELXL-97 program package.[21] For **3**, C17, C18 and O6 were handled as disordered at two positions with occupancies of 50%. The positions of H atoms were generated geometrically (C−H bond fixed at 0.96 Å), assigned isotropic thermal parameters, and allowed to ride on their parent carbon atoms before the final cycle of refinement. Crystal data and structure determination summaries (Table 1) and selected bond lengths and angles (Table 2) for **1**−**4** are given here.

CCDC-245500 to -245503 contain the supplementary crystallographic data for this paper. These data can be obtained free of charge at www.ccdc.cam.ac.uk/conts/retrieving.html [or from the Cambridge Crystallographic Data Centre, 12 Union Road, Cambridge CB2 1EZ, UK; Fax: (internat.) +44-1223-336-033; E-mail: deposit@ccdc.cam.ac.uk].

Acknowledgments

The authors are grateful for financial support from NNSF of China (90206040, 20325106, 20333070), NSF of Fujian Province (B982003), and the key and the "One Hundred Talent" projects from CAS. We also thank Professor Guoyu Yang for the thermogravimetric analysis.

[1] [1a] J. M. Lehn, *Supramolecular Chemistry: Concepts and Perspectives*, Wiley-VCH, Weinheim, **1995**. [1b] J. W. Steed, J. L. Atwood, *Supramolecular Chemistry*; John Wiley & Sons, New York, **2000**. [1c] R. Robson, B. F. Abrahams, S. R. Batten, R. W. Gable, B. F. Hoskins, J. Liu, *Supramolecular Architecture*, ACS Publications, Washington, **1992**, ch. 19.

[2] [2a] S. A. Bourne, J. Lu, A. Mondal, B. Moulton, M. J. Zaworotko, *Angew. Chem. Int. Ed.* **2001**, *40*, 2111−2113. [2b] S. Leininger, B. Olenyuk, P. J. Stang, *Chem. Rev.* **2000**, *100*, 853−908. [2c] M. Munakata, L. P. Wu, T. Kuroda-Sowa, *Adv. Inorg. Chem.* **1999**, *46*, 173−303. [2d] P. J. Hagrman, D. Hagrman, J. Zubieta, *Angew. Chem. Int. Ed.* **1999**, *38*, 2639−2684.

[3] [3a] C. Janlak, *Dalton Trans.* **2003**, 2781−2804 and references cited therein. [3b] C. Benelli, D. Gatteschi, *Chem. Rev.* **2002**, *102*, 2369−2387 and references cited therein.

[4] [4a] J. A. Real, E. Andres, M. C. Munoz, M. Julve, T. Granier, A. Boussekou, F. Varret, *Science* **1995**, *268*, 265−267. [4b] C. R. Woods, M. Benaglia, F. Cozzi, J. S. Siegel, *Angew. Chem. Int. Ed. Engl.* **1996**, *35*, 1830−1834. [4c] E. Q. Gao, S. Q. Bai, Z. M. Wang, C. H. Yan, *J. Am. Chem. Soc.* **2003**, *125*, 4984−4985.

[5] [5a] K. Barthelet, J. Marrot, D. Riou, G. Férey, *Angew. Chem. Int. Ed.* **2002**, *41*, 281−284. [5b] J. M. Vincent, C. Philouze, I. Pianet, J. B. Verlhac, *Chem. Eur. J.* **2000**, *6*, 3595−3599. [5c] D. A. McMorran, P. J. Steel, *Chem. Commun.* **2002**, 2120−2121. [5d] F. A. A. Paz, Y. Z. Khimyak, A. D. Bond, J. Rocha, J. Klinowski, *Eur. J. Inorg. Chem.* **2002**, 2823−2828.

 © 2005 Wiley-VCH Verlag GmbH & Co. KGaA, Weinheim

[6] [6a] S. Rozen, S. Dayan, *Angew. Chem. Int. Ed.* **1999**, *38*, 3472−3473. [6b] J. M. Rueff, S. Pillet, N. Claiser, G. Bonaventure, M. Souhassou, P. Rabu, *Eur. J. Inorg. Chem.* **2002**, 895−900. [6c] D. W. Smithenry, S. R. Wilson, K. S. Suslick, *Inorg. Chem.* **2003**, *42*, 7719−7721. [6d] A. Mukherjee, M. K. Saha, M. Nethaji, A. R. Chakravarty, *Chem. Commun.* **2004**, 716−717.

[7] [7a] M. Fujita, Y. J. Kwon, S. Washizu, K. Ogura, *J. Am. Chem. Soc.* **1994**, *116*, 1151−1152. [7b] S. Kitagawa, M. Kondo, *Bull. Chem. Soc., Jpn.* **1998**, *71*, 1799−1806. [7c] A. J. Blake, N. R. Champness, P. Hubberstey, W. S. Li, M. A. Withersby, M. Schröder, *Coord. Chem. Rev.* **1999**, *183*, 117−138. [7d] H. W. Park, S. M. Sung, K. S. Min, H. Bang, M. P. Suh, *Eur. J. Inorg. Chem.* **2001**, 2857−2863.

[8] [8a] O. S. Jung, Y. J. Kim, Y. A. Lee, J. K. Park, H. K. Chae, *J. Am. Chem. Soc.* **2000**, *122*, 9921−9925. [8b] C. He, B. G. Zhang, C. Y. Duan, J. H. Li, Q. J. Meng, *Eur. J. Inorg. Chem.* **2000**, 2549−2554. [8c] M. Kondo, M. Shimamura, S. Noro, Y. Kimura, K. Uemura, S. Kitagawa, *J. Solid State Chem.* **2000**, *162*, 113−119. [8d] R. Horikoshi, T. Mochida, H. Moriyama, *Inorg. Chem.* **2001**, *40*, 2430−2435. [8e] G. D. Munno, F. Cipriani, D. Armentano, M. Julve, J. A. Real, *New J. Chem.* **2001**, *25*, 1031−1036. [8f] D. Ghoshal, T. K. Maji, G. Mostafa, T. H. Lu, N. R. Chaudhuri, *Cryst. Growth Des.* **2003**, *3*, 9−11.

[9] [9a] M. Eddaoudi, D. B. Moler, H. Li, B. Chen, T. M. Reineke, M. O'Keeffe, O. M. Yaghi, *Acc. Chem. Res.* **2001**, *34*, 319−330 and references cited therein. [9b] B. Moulton, J. Lu, A. Mondal, M. J. Zaworotko, *Chem. Commun.* **2001**, 863−864. [9c] M. Edgar, R. Mitchell, A. M. Z. Slawin, P. Lightfoot, P. A. Wright, *Chem. Eur. J.* **2001**, *7*, 5168−5175. [9d] R. H. Wang, M. C. Hong, D. Q. Yuan, Y. Q. Sun, L. J. Xu, J. H. Luo, R. Cao, A. S. C. Chan, *Eur. J. Inorg. Chem.* **2004**, 37−43.

[10] [10a] S. S. Y. Chui, S. M. F. Lo, J. P. H. Charmant, A. G. Orpen, I. D. Williams, *Science* **1999**, *283*, 1148−1150. [10b] Y. G. Li, N. Hao, E. B. Wang, Y. Lu, C. W. Hu, L. Xu, *Eur. J. Inorg. Chem.* **2003**, 2567−2571. [10c] T. J. Prior, M. J. Rosseinsky, *Inorg. Chem.* **2003**, *42*, 1564−1575. [10d] Z. Shi, G. Li, L. Wang, L. Gao, X. Chen, J. Hua, S. Feng, *Cryst. Growth Des.* **2004**, *4*, 25−27.

[11] [11a] J. S. Seo, D. Whang, H. Lee, S. I. Jun, J. Oh, Y. J. Jeon, K. Kim, *Nature* **2000**, *404*, 982−986. [11b] Z. L. Huang, M. Drillon, N. Masciocchi, A. Sironi, J. T. Zhao, P. Rabu, P. Panissod, *Chem. Mater.* **2000**, *12*, 2805−2812. [11c] X. Li, R. Cao, Y. Q. Sun, Q. Shi, D. Q. Yuan, D. F. Sun, W. H. Bi, M. C. Hong, *Cryst. Growth Des.* **2004**, *4*, 255−261.

[12] O. R. Evan, W. B. Lin, *Acc. Chem. Res.* **2002**, *35*, 511−522 and references cited therein.

[13] [13a] B. Zhao, P. Cheng, X. Chen, C. Cheng, W. Shi, D. Liao, S. Yan, Z. Jiang, *J. Am. Chem. Soc.* **2004**, *126*, 3012−3013. [13b] X. Wang, C. Qin, E. Wang, Y. Li, C. Hu, L. Xu, *Chem. Commun.* **2004**, 378−379. [13c] J. Y. Lu, V. Schauss, *Eur. J. Inorg. Chem.* **2002**, 1945−1947.

[14] [14a] M. L. Tong, X. M Chen, S. R. Batten, *J. Am. Chem. Soc.* **2003**, *125*, 16170−16171. [14b] P. Ayyappan, O. R. Evans, W. Lin, *Inorg. Chem.* **2001**, *40*, 4627−4632. [14c] J. Zhang, R. G. Xiong, J. L. Zuo, X. Z. You, *J. Chem. Soc., Dalton Trans.* **2000**, 2898−2900. [14d] J. Zhang, R. G. Xiong, X. T. Chen, C. M. Che, Z. Xue, X. Z. You, *Organometallics* **2001**, *20*, 4118−4121.

[15] G. Li, H. Hou, L. Li, X. Meng, Y. Fan, Y. Zhu, *Inorg. Chem.* **2003**, *42*, 4995−5004.

[16] [16a] J. Y. Lu, M. A. Lawandy, J. Li, *Inorg. Chem.* **1999**, *38*, 2695−2704. [16b] L. Carlucci, G. Ciani, D. M. Proserpio, S. Rizzato, *CrystEngComm* **2003**, *5*, 190−199. [16c] R. Bronisz, *Eur. J. Inorg. Chem.* **2004**, 3688−3695.

[17] K. Nakamoto, *Infrared and Raman Spectra of Inorganic and Coordination Compounds*, John Wiley & Sons, New York, **1986**.

[18] H. X. Zhang, B. S. Kang, A. W. Xu, Z. N. Chen, Z. Y. Zhou, A. S. C. Chan, K. B. Yu, C. Ren, *J. Chem. Soc., Dalton Trans.* **2001**, 2559−2566.

[19] G. M. Sheldrick, *SADABS, Program for Empirical Absorption Correction of Area Detector Data*, University of Göttingen: Göttingen, **1996**.

[20] Crystalclear, version 1.36; *Molecular Structure Corporation*; Rigaku, MSC/SSI, 491, South Orem Blvd, Orem, UT 84058, **2001**.

[21] G. M. Sheldrick, *SHELXS-97, Program for Crystal Structure Solution*; University of Göttingen: Göttingen, **1997**.

Received July 2004, 2004
Early View Article
Published Online November 24, 2004

 © 2005 Wiley-VCH Verlag GmbH & Co. KGaA, Weinheim

Synthesis, Characterization, and Hydrolysis Products of $(\eta^2$-*t*$Bu_2pz)AlH(\mu{:}\eta^1,\eta^1$-*t*$Bu_2pz)_2AlH_2$ − Structural Characterization of a Complex Containing η^1-, η^2-, and $\mu{:}\eta^1,\eta^1$-Pyrazolato Ligands and a Complex Containing a Terminal Hydroxo Ligand

Zhengkun Yu,[a][‡] John E. Knox,[a] Andrey V. Korolev,[a][‡‡] Mary Jane Heeg,[a] H. Bernhard Schlegel,[a] and Charles H. Winter*[a]

Keywords: Hydrogen bond / N ligands / Aluminum / Pyrazolato ligands / Molecular orbital calculations

Treatment of alane–ethyldimethylamine with 3,5-di-*tert*-butylpyrazole (*t*Bu_2pzH) in a 2:3 molar ratio afforded $[(\eta^2$-*t*$Bu_2pz)AlH(\mu{:}\eta^1,\eta^1$-*t*$Bu_2pz)_2AlH_2]$ in 57% yield. Hydrolysis of $[(\eta^2$-*t*$Bu_2pz)AlH(\mu{:}\eta^1,\eta^1$-*t*$Bu_2pz)_2AlH_2]$ afforded variable mixtures of Al(*t*$Bu_2pz)_3$, $[(\eta^2$-*t*$Bu_2pz)AlH(\mu{:}\eta^1,\eta^1$-*t*$Bu_2pz)_2$Al-H(OH)], and $[(\eta^2$-*t*$Bu_2pz)AlH(\mu{:}\eta^1,\eta^1$-*t*$Bu_2pz)_2AlH(\eta^1$-*t*$Bu_2pz)]$. The structures of all new complexes were assigned from spectral and analytical data. In addition, the X-ray crystal structures of $[(\eta^2$-*t*$Bu_2pz)AlH(\mu{:}\eta^1,\eta^1$-*t*$Bu_2pz)_2AlH(OH)]$ and $[(\eta^2$-*t*$Bu_2pz)AlH(\mu{:}\eta^1,\eta^1$-*t*$Bu_2pz)_2AlH(\eta^1$-*t*$Bu_2pz)]$ were determined. $[(\eta^2$-*t*$Bu_2pz)AlH(\mu{:}\eta^1,\eta^1$-*t*$Bu_2pz)_2AlH(OH)]$ crystallizes as a dimeric molecule, and contains two bridging pyrazolato ligands, one η^2-pyrazolato ligand, as well as terminal hydrido and hydroxo ligands. The hydroxo and η^2-pyrazolato ligands possess a syn-relationship within the dimer. The hydroxy group proton does not participate in dihydrogen bonding, and instead appears to be intramolecularly hydrogen-bonded to the π-cloud of the η^2-pyrazolato ligand. The overall structure of $[(\eta^2$-*t*$Bu_2pz)AlH(\mu{:}\eta^1,\eta^1$-*t*$Bu_2pz)_2AlH(\eta^1$-*t*$Bu_2pz)]$ is very similar to that of $[(\eta^2$-*t*$Bu_2pz)AlH(\mu{:}\eta^1,\eta^1$-*t*$Bu_2pz)_2AlH(OH)]$, except that the η^1- and η^2-pyrazolato ligands have an anti-disposition within the dimer. Molecular orbital calculations were carried out on $[(\eta^2$-*t*$Bu_2pz)AlH(\mu{:}\eta^1,\eta^1$-*t*$Bu_2pz)_2AlH(OH)]$ to understand the hydrogen bonding and the η^2-pyrazolato ligand coordination. The calculations predict that there is a 1.4 kcal/mol energy difference between η^1- and η^2-pyrazolato ligand coordination, which implies that the observed η^2-pyrazolato ligand occurs due to accommodation of the bulky *tert*-butyl groups. The intramolecular hydrogen bond between the hydroxo ligand proton and the π-cloud of the η^2-pyrazolato ligand is estimated to have a bond strength of 3.7 kcal/mol.
(© Wiley-VCH Verlag GmbH & Co. KGaA, 69451 Weinheim, Germany, 2005)

Introduction

The chemistry of aluminum complexes containing the bulky 3,5-di-*tert*-butylpyrazolato (*t*Bu_2pz) ligand has been an active area of research over the past several years.[1−4] Advances that have emerged from this work include the first examples of η^2-pyrazolato ligand coordination to a group 13 element,[2,3c] structural models for ligand species that occur in alumoxanes,[3b,3g] new coordination modes for acetylide groups,[3d,3f] as well as stabilization of bridging alkyl and hydride groups in pyrazolate-bridged dimers.[4] Roesky has reported the synthesis of the complex $[H_2Al(\mu{:}\eta^1,\eta^1$-*t*$Bu_2pz)_2AlH_2]$, which was obtained by treatment of equimolar amounts of alane−trimethylamine with *t*Bu_2pzH,[3f] and has also described many reactions of this complex.[3b,3d,3e,3g] As part of our work relating to the synthesis of aluminum complexes with bridging hydride ligands,[4a] we have discovered a family of dimeric pyrazolato complexes that are derived from the reaction of alane−ethyldimethylamine with *t*Bu_2pzH in a 2:3 stoichiometry. These complexes are of the general formula $[(\eta^2$-*t*$Bu_2pz)AlH(\mu{:}\eta^1,\eta^1$-*t*$Bu_2pz)_2Al(X)H]$, where X = H, OH, or η^1-*t*Bu_2pz. In addition to providing additional rare examples of structurally characterized group 13 complexes containing η^2-pyrazolato ligands, this work describes the first crystal structure of a complex containing η^1-, η^2-, and $\mu{:}\eta^1,\eta^1$-pyrazolato ligands as well as a structurally characterized aluminum complex containing a terminal hydroxo ligand. Aluminum complexes containing terminal hydroxo ligands are very rare,[5] and have been of significant recent interest as models for species that might be present in methylalumoxanes used in olefin polymerization processes.[5,6] The terminal hydroxoaluminum ligand described herein is stabilized by formation of an intramolecular hydrogen bond to the π-cloud of an adjacent pyrazolato ligand, which constitutes a novel hydrogen bonding interaction for a terminal hydroxo complex.

[a] Department of Chemistry, Wayne State University, Detroit, Michigan 48202, USA
Fax: (internat.) + 1-313-577-8289
E-mail: chw@chem.wayne.edu
[‡] Current address: Dalian Institute of Chemical Physics, Chinese Academy of Sciences, 457 Zhongshan Road, Dalian, Liaoning 116023, P. R. China
[‡‡] Current address: Sigma−Aldrich Corporation, 5485 County Rd. V, Sheboygan, Wisconsin 53085, USA

 © 2005 Wiley-VCH Verlag GmbH & Co. KGaA, Weinheim DOI: 10.1002/ejic.200400660

Results

Synthetic Chemistry

Scheme 1 outlines the synthetic approaches to the complexes that were prepared in this study. Treatment of alane−ethyldimethylamine with tBu$_2$pzH in a 2:3 stoichiometry led to the dimeric pyrazolato complex **1** in 57% crystallized yield. ^{1}H NMR spectroscopic analysis of the reaction product demonstrated that **1** was the only product formed, when extreme care was taken to exclude water from the reaction. The structure of **1** is proposed based upon spectral and analytical data and from correlation with the structurally characterized hydrolysis products **3** and **4** described below.

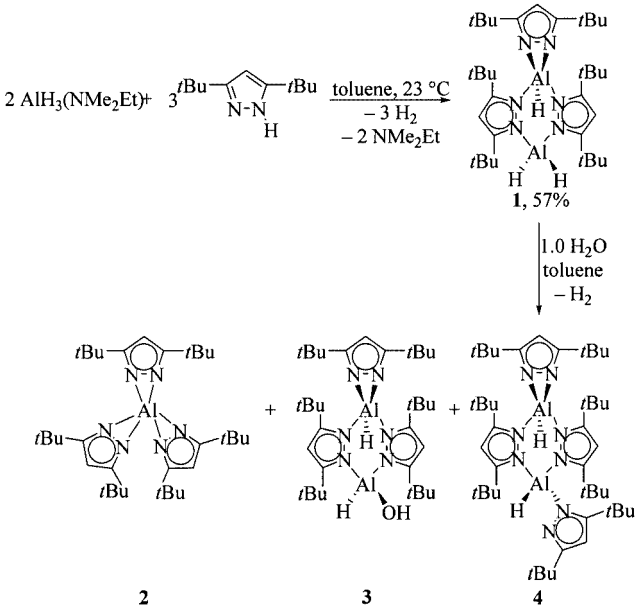

Scheme 1. Preparation and hydrolysis of **1**

In the ^{1}H NMR spectrum of **1** in [D$_8$]toluene at −90 °C, the *tert*-butyl methyl groups appear as three equal intensity singlets at δ = 1.73, 1.43, and 1.22 ppm. The hydride resonances are observed as 1:1:1 intensity broad singlets at δ = 6.1, 5.4, and 3.3 ppm, and the pyrazolato CH groups appear as singlets at δ = 6.32 and 6.20 ppm in a 1:2 ratio. The infrared spectrum shows the Al−H absorptions at 1962, 1905, and 1890 cm^{-1}. It was discovered that extended standing (> 1 week) of a hexane solution at 23 °C led to the slow decomposition of **1** to tBu$_2$pzH, **2**, and new compounds. As described below, the new compounds were obtained as pure materials and identified to be **3** and **4** from the hydrolysis of **1**.

Treatment of **1** with water (1 equiv.) at −78 °C in toluene led to immediate gas evolution and the formation of a white, insoluble precipitate. Workup of the reaction mixture, followed by fractional crystallization from hexane, afforded pure samples of **2** (8%), **3** (15%), and **4** (23%) as colorless crystalline solids. The identity of **2** was confirmed by comparison of its ^{1}H and ^{13}C{^{1}H} NMR spectra with those previously reported by Deacon.[2] The formulations of **3** and **4** were based upon their spectral and analytical data, and from their X-ray crystal structures as described below. The ^{1}H NMR spectrum of **3** in [D$_8$]toluene at ambient temperature showed resonances for one type of pyrazolato ligand, implying that exchange between the μ:η^1,η^1- and the η^2-pyrazolato ligands is faster than the NMR timescale. Upon cooling to −60 °C, three equal intensity singlets for the *tert*-butyl methyl groups are observed at δ = 1.47, 1.43, and 1.18 ppm and the pyrazolato methine resonances appear as a broad singlet at δ = 6.22 ppm. In addition, extremely broad resonances are observed at δ = 5.5 and 4.4 ppm in a 1:2 ratio, which correspond to some combination of the Al−H and Al−OH fragments. The low temperature ^{1}H NMR spectrum of **3** is very similar to that of **1** and indicates similar structures. The infrared spectrum of **3** shows a strong hydroxy stretch at 3227 cm^{-1} and aluminum−hydrogen stretches at 1961, 1908, and 1860 cm^{-1}. The low position of the hydroxy stretch is consistent with hydrogen bonding, yet there is no evidence in the crystal structure for dihydrogen bonding or intermolecular hydrogen bonding. Instead, it is likely that the hydroxy hydrogen atom is intramolecularly hydrogen-bonded to the π-cloud of the adjacent η^2-pyrazolato ligand. This possibility is explored below in more detail using molecular orbital calculations. The ^{1}H NMR spectra of **4** show little difference at room temperature and −80 °C, and reveal two equal intensity pyrazolato ligands. These data are consistent with slow exchange between the μ:η^1,η^1-pyrazolato ligands and the η^1- and η^2-pyrazolato ligand sites, but with rapid exchange between the η^1- and η^2-pyrazolato ligand sites. The infrared spectrum of **4** shows an aluminum−hydrogen stretch at 1937 cm^{-1}.

The yield of **3** could be increased to 45% in a one-pot reaction of alane−ethyldimethylamine with 3,5-di-*tert*-butylpyrazole in a 2:3 ratio, followed by addition of water (1 equiv.), stirring for 2 h, workup, and then fractional crystallization from hexane. Attempts to increase the yield of **4** did not meet with much success. Treatment of alane−ethyldimethylamine with tBu$_2$pzH in a 2:4 ratio, followed by workup, afforded a crude product consisting of **2** (68%), **3** (24%), and **4** (8%).

X-ray Crystal Structures of 3 and 4

Complexes **3** and **4** were characterized by X-ray crystallography in order to understand their three dimensional structures. The molecular structures of **3** and **4** are shown in Figures 1 and 2, respectively. The crystal data are given in Table 1.

Complex **3** consists of a dinuclear unit in a boat conformation held together by two μ:η^1,η^1-tBu$_2$pz ligands. One aluminum center is bonded to η^2-tBu$_2$pz and hydride ligands, while the other aluminum atom is bonded to hydroxo and hydride ligands. The hydroxo and η^2-pyrazolato ligands are *syn* to each other within the dimer. The aluminum−nitrogen bond lengths to five-coordinate Al(1) range between 1.936−1.968 Å, and are slightly shorter for four-coordinate Al(2) [1.914(3), 1.920(3) Å]. The

 © 2005 Wiley-VCH Verlag GmbH & Co. KGaA, Weinheim

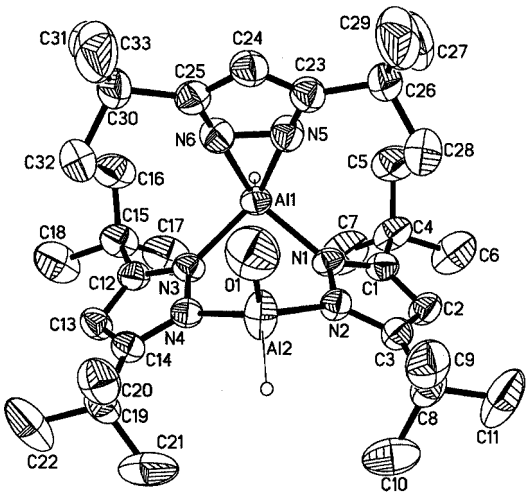

Figure 1. Perspective view of **3** with thermal ellipsoids at the 50% probability level

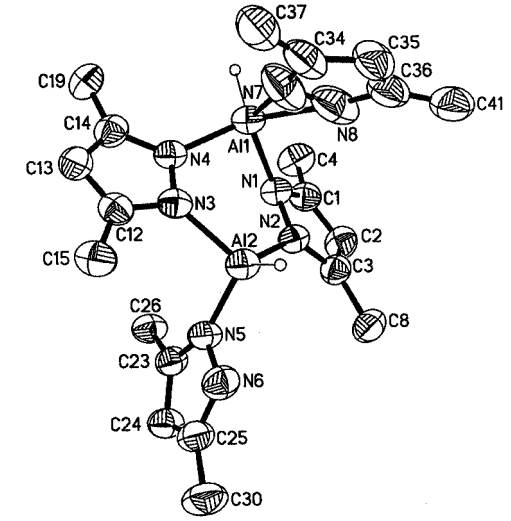

Figure 2. Perspective view of **4** with thermal ellipsoids at the 50% probability level; the *tert*-butyl methyl groups have been omitted for clarity

aluminum−oxygen bond length is 1.867(3) Å. The μ:η^1,η^1-pyrazolato ligands place the aluminum centers far enough apart [Al(1)−Al(2) 3.289(2) Å], so that hydrogen or oxygen atoms do not bridge in **3**. The N(5)−Al(1)−N(6) angle is 42.32(11)°, which is typical of η^2-pyrazolato ligands bonded to aluminum.[2,3c] All intermolecular OH···H(hydride) contacts are > 6 Å, and the closest intermolecular OH···O contact is > 4.3 Å. Thus, intermolecular dihydrogen bonding or intermolecular hydrogen bonding in **3** can be ruled out. The low hydroxy stretch noted above in the infrared spectrum of **3**, however, may be due to intramolecular hydrogen bonding between the hydroxy hydrogen atom and the π-cloud of the η^2-pyrazolato ligand (OH···centroid distance = 2.574 Å).

The molecular structure of **4** is similar to that of **3** except that it contains an η^1-*t*Bu$_2$pz ligand instead of a hydroxo ligand on the four-coordinate aluminum atom. The η^1- and η^2-pyrazolato ligands are *anti* to each other within the dinuclear unit to minimize steric interactions. The non-bridging pyrazolato ligand planes are nearly perpendicular to each other due to the steric hindrance of the *tert*-butyl groups. The five-coordinate Al(1)−N bond lengths range between 1.892−2.082 Å, and are slightly longer than those of the four-coordinate Al(2)−N bonds (1.871−1.933 Å). The Al(1)−N(7) bond length [1.892(3) Å] is much shorter than the Al(1)−N(8) bond length [2.082(4) Å], indicating unsymmetrical coordination of the η^2-pyrazolato ligand.[3c,7] The Al(2)−N(6) distance is 2.559(3) Å, which clearly demonstrates η^1-coordination. The N(7)−Al(1)−N(8) angle is 40.55(13)°, which is slightly smaller than the value in **3**. The Al(1)−Al(2) distance is 3.414(2) Å, which is slightly longer than in **3**, possibly due to increased steric crowding in **4**. Additionally, the intramolecular hydrogen bond in **3** may serve to reduce the aluminum−aluminum distance.

Molecular Orbital Calculations of 3

To gain better insight into the nature of the pyrazolato ligand bonding and the intramolecular hydrogen bond in **3**, molecular orbital calculations were performed. All calculations were carried out using the Gaussian suite of programs.[8] First we studied the model system **5**, in which the *tert*-butyl groups on the pyrazolato ligands were replaced by hydrogen atoms. Previous work from our laboratories indicated that replacement of alkyl groups by hydrogen atoms in pyrazolato ligands does not significantly affect the electronic structure of the molecule.[9] Optimization of **5** at the B3LYP/6-311++G(d,p) level of theory[10−13] led to the transformation of the η^2-pz ligand in **5** to an η^1-pz ligand. In addition, the π-cloud of the η^1-pyrazolato ligand twisted away from the hydroxy group hydrogen atom on the adjacent Al atom. Hence, **5** was not an acceptable theoretical model for **3**, which suggested that the bulky *tert*-butyl groups on the pyrazolato ligands in **3** may play an important role in determining the overall structure.

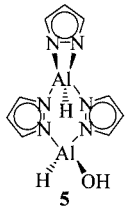

5

We next sought to carry out molecular orbital calculations on the full experimental molecule **3**. Since **3** has a large number of atoms, an ONIOM approach was employed to reduce the cost of the overall calculation.[14] The high level portion of **3** was the same as the model system and was calculated by B3LYP/6-311++G(d,p). The *tert*-butyl groups on the pyrazolato ligands were included in the low-level portion and were calculated by the AM1 semi-empirical method.[15,16] Figure 3 presents the results of this treatment. Optimization of **3** afforded a less dramatic movement of the η^2-pyrazolato ligand to the η^1-bonding mode

 © 2005 Wiley-VCH Verlag GmbH & Co. KGaA, Weinheim

Table 1. Summary of crystallographic data for **3** and **4**

	3	**4**
Empirical formula	$C_{33}H_{60}Al_2N_6O$	$C_{44}H_{78}Al_2N_8$
Formula mass	610.83	773.10
Temp. [K]	295(2)	295(2)
Crystal system	Triclinic	Triclinic
Space group	$P\bar{1}$	$P\bar{1}$
a [Å]	11.7811(11)	9.9494(14)
b [Å]	13.1426(13)	11.7026(16)
c [Å]	14.6042(14)	21.031(3)
α [°]	63.993(2)	93.582(3)
β [°]	83.503(3)	90.742(3)
γ [°]	68.072(2)	90.646(4)
V [Å^{-3}]	1881.8(3)	2442.5(6)
Z	2	2
$D_{calcd.}$ [g/cm^3]	1.078	1.051
Abs coeff [mm^{-1}]	0.109	0.096
F(000)	668	848
Cryst size [mm]	0.35 × 0.20 × 0.12	0.20 × 0.20 × 0.15
θ range [°]	1.83 to 28.32	1.94 to 28.30
Index ranges	$-14 \le h \le 15$ $-15 \le k \le 16$ $0 \le l \le 19$	$-12 \le h \le 12$ $-15 \le k \le 15$ $0 \le l \le 27$
No. of reflections collected	13657	17562
No. of independent reflections	8616 (R_{int} = 0.035)	11119 (R_{int} = 0.040)
No. of data/restraints/parameters	8616/0/406	11119/0/536
GOF/F^2	0.837	0.820
R indices [$I > 2\sigma(I)$]	R_1 = 0.0621 wR_2 = 0.1519	R_1 = 0.0605 wR_2 = 0.1448
R indices (all data)	R_1 = 0.1822 wR_2 = 0.1853	R_1 = 0.1957 wR_2 = 0.1837
Largest diff peak/hole [e·Å^{-3}]	0.264/−0.622	0.574/−0.252

$R(F) = \Sigma\|F_o| - |F_c\|/\Sigma|F_o|$; $Rw(F) = [\Sigma w(F_o^2 - F_c^2)^2/\Sigma w(F_o^2)^2]^{1/2}$

(Figure 3, a). The computed aluminum−nitrogen bond lengths were 1.89 Å and 2.43 Å, compared to 1.96 Å determined experimentally for both bonds. A constrained system was optimized in which the aluminum−nitrogen bonds were fixed at the experimentally observed distances. This treatment led to an energy increase of only 1.4 kcal/mol (Figure 3, c), and subsequent unconstrained optimization of this system afforded the structure shown in Figure 3 (a). This small energy difference indicates that the stabilization for the η^2-configuration is within the energy of crystal packing, and suggests that the η^2-*t*Bu$_2$pz ligand in **3** originates due to accommodation of the bulky *tert*-butyl groups. In both cases it is evident that there is an intramolecular hydrogen bond. In the fixed bond structure (Figure 3, c), the range of distances for the hydroxy hydrogen atom to the atoms in the pyrazolato ring core is 2.68−3.18 Å. In the case where the aluminum−nitrogen bond lengths were not frozen (Figure 3, a), these numbers have a slightly higher range of 2.61−3.56 Å. To obtain an estimate of the stabilization energy resulting from the hydrogen bond, the hydrogen atom on the hydroxy group was turned away from the pyrazolato ligand so that the hydroxy hydrogen atom was not in the proximity of the π-cloud of the η^2-pyrazolato ligand (Figure 3, b). The optimized geometry for this system had aluminum−nitrogen bond lengths of 1.88 Å and 2.32 Å. The distances from the oxygen atom of the hydroxo ligand to the atoms in the adjacent pyrazoato ligand ranged from 3.72−5.11 Å. Removing the ability to hydrogen bond from the system led to an ONIOM energy increase of 3.7 kcal/mol. This may be a slight underestimate of the true bond strength due to some steric differences in the low-level portion of the ONIOM calculation.

Discussion

The significance of this work resides principally in the unusual structures of **3** and **4**. Complex **4** is the first species that contains η^1-, η^2-, and μ:η^1,η^1-pyrazolato ligands within a single molecule. Many pyrazolato complexes have been reported that contain two of these coordination modes,[1,3b,17] but none until now has contained all three. Aluminum complexes containing η^2-pyrazolato ligands remain extremely rare,[2,3c] so **3** and **4** are additionally novel from this perspective.

Complex **3** is a rare example of an aluminum compound that contains a terminal hydroxo ligand.[18] The first structurally characterized aluminum complexes containing terminal hydroxo ligands were reported in 1987.[5d,5e] A terminal hydroxo ligand was structurally documented in $[Al_4Si_4H_8O_{20}\cdot 24H_2O]^{4-}$, and has a hydroxoaluminum−oxygen bond length of 1.783 Å.[5d] Each hydroxo ligand is extensively hydrogen-bonded to interstitial water molecules.

 © 2005 Wiley-VCH Verlag GmbH & Co. KGaA, Weinheim

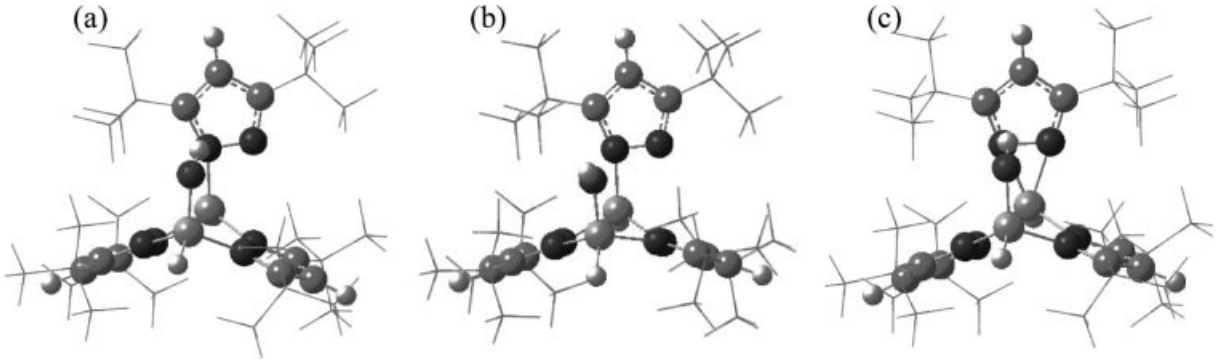

Figure 3. The three configurations of the model system with the DFT contribution as ball-and-stick and the AM1 portion as line drawing; (a) model system with intramolecular hydrogen bond; (b) model system with hydroxy group reversed so there is no intramolecular hydrogen bond; (c) model system with the aluminum−nitrogen bond lengths constrained to experimental values

The other initial report described the structure of quinuclidinium hydroxo(2,2′,2′′-nitrilotriphenoxy)aluminate, which contains an anionic aluminum center bonded to a terminal hydroxo ligand.[5e] The quinuclidinium ion is also associated with the oxygen atom through a N−H···O hydrogen bond. The aluminum−oxygen bond length is 1.765(2) Å. Recently, Roesky and co-workers have reported a series of aluminum complexes containing terminal hydroxo ligands.[5a−5c,18] The complexes are of the formula $L_{Ar}Al(OH)_2$,[5a] $\{L_{Ar}Al(OH)\}_2(\mu\text{-}O)$,[5b] and $L_{Ar}Al(OH)OAl(L_{Ar})(OCH{=}N\textit{t}Bu)$,[5c] where L_{Ar} = HC{(CMe)(2,6-iPr$_2$C$_6$H$_3$N)}$_2$. The aluminum−oxygen bond lengths in $L_{Ar}Al(OH)_2$ are 1.6947(15) and 1.7107(16) Å.[5a] In the solid state, this molecule forms dimeric units with $Al_2O_4H_2$ rings that contain intramolecular Al−O−H···O(H)(Al) hydrogen bonds. $\{L_{Ar}Al(OH)\}_2(\mu\text{-}O)$ exists as a monomer in the solid state, with aluminum−oxygen bond lengths of 1.738(2) and 1.741(3) Å.[5b] Infrared spectroscopy suggests that the hydroxy groups do not participate in hydrogen bonding. It was proposed that the hydroxo ligand hydrogen atoms reside within the shielding cone of the L_{Ar} aromatic rings, due to an unusually upfield resonance for these hydrogen atoms (δ = −0.30 ppm). $L_{Ar}Al(OH)OAl(L_{Ar})(OCH{=}N\textit{t}Bu)$ exists in the solid state with an eight-membered Al_2CHNO_3 ring that includes a strong O−H···N hydrogen bond.[5c] The aluminum−oxygen bond length is 1.727(2) Å. Parkin reported the synthesis of $[HB(Me_2pz)_3]Al(OH)_2$ in 1990, although this complex was not structurally characterized and it is therefore not clear if it contains terminal hydroxo ligands.[5f]

The metrics and stabilization of the terminal hydroxo ligand in **3** can be compared with those of the previously reported terminal hydroxo complexes noted above. The aluminum−oxygen bond length in **3** is 1.867(3) Å, which is considerably longer than the values in related terminal hydroxo complexes. However, the aluminum−oxygen bond length in **3** is similar to values observed in recently reported aluminum complexes containing bridging hydroxo ligands (1.81−2.09 Å).[19] The hydroxo ligand hydrogen atom in **3** participates in hydrogen bonding to the π-cloud of the adjacent η^2-pyrazolato ligand within the dimer, and thus constitutes a unique coordination environment for the hydroxo ligand. Apparently, the tBu$_2$pz ligands in **3** are so bulky that intermolecular hydrogen or dihydrogen bonding is not possible, and the only hydrogen-bond donor available is the π-cloud of the adjacent η^2-pyrazolato ligand. To the best of our knowledge, this is the first example of a hydrogen bond to the π-cloud of a pyrazolato ligand. Hydrogen bonding between nitrogen−hydrogen and oxygen−hydrogen bonds and the π-clouds of various neutral aromatic compounds is well precedented.[20] Since the tBu$_2$pz ligand is aromatic and possibly more electron rich than a neutral aromatic compound due to the formal negative charge, its π-system is probably a good hydrogen-bond acceptor. Molecular orbital calculations suggest that there is a preference for the formation of the O−H···pz$_\pi$ hydrogen bond, and that an estimate of the bond strength for this interaction is about 3.7 kcal/mol. This bond strength is in the range of a typical weak hydrogen bond, but is enough to orient the hydroxo ligand hydrogen atom. Molecular orbital calculations suggest that there is a very small energy difference (1.4 kcal/mol) between η^1- and η^2-pyrazolato ligands in **3**. It is possible that the hydrogen bond in **3** helps to stabilize the η^2-pyrazolato ligand, since the molecular orbital calculations suggested that there may be stronger hydrogen bonding to this ligand coordination mode compared to the η^1-pyrazolato ligand mode. The hydrogen bond in **3** requires that the hydroxo ligand hydrogen atom is pointed directly at the shielding cone of the aromatic tBu$_2$pz ligand. Thus, the ^{1}H NMR chemical shift of this hydrogen atom should be considerably upfield of where it would appear in the absence of this interaction. There is some ambiguity regarding the assignment of this resonance in **3**, since it appears in the same region as the aluminum-bound hydrido ligands. However, it resonates in the region of δ = 4.6−5.5 ppm. For comparison, the ^{1}H NMR chemical shift of the hydroxo ligand protons in $L_{Ar}Al(OH)_2$ was δ = 12.47 ppm.[5a] In $\{L_{Ar}Al(OH)\}_2(\mu\text{-}O)$, where it was proposed that the hydroxo ligand protons reside within the shielding cone of the LAr aromatic rings, the hydroxo proton resonance appeared at δ = −0.30 ppm.[5c] Roesky has argued that terminal Al−OH protons are strong Brønsted

 © 2005 Wiley-VCH Verlag GmbH & Co. KGaA, Weinheim

acids, and should resonate at low fields in the ^{1}H NMR spectra in the absence of other effects.[5a] This speculation supports the low field position of the hydroxo ligand resonance in $L_{Ar}Al(OH)_2$. The hydroxo ligand resonance in **3** is considerably upfield of that in $L_{Ar}Al(OH)_2$, and therefore may be shifted due to the interaction with the shielding cone of the pyrazolato π-cloud.

Complex **3** is relevant to alumoxane chemistry,[12] since terminal hydroxo ligands may be present in some alumoxanes and the acidic hydroxo ligand hydrogen atom may activate polymerization precatalysts through protonation of a metal−alkyl bond. The existence of **3** must be related to the presence of the extremely bulky tBu$_2$pz ligands, which block further reactions such as protonation of hydrido or pyrazolato ligands. The stabilization of terminal hydroxo ligands in the previously reported aluminum complexes[5] is generally achieved only in the presence of very bulky ancillary ligands, which can block further reactions. Thus, terminal hydroxo ligands, if they occur in methylalumoxanes, probably occupy extremely hindered sites. The high Brønsted acidity of the aluminum-bound hydroxo ligand proton leads to a strong preference for hydrogen bond formation. As noted above, most of the known terminal hydroxo complexes of aluminum are stabilized by hydrogen bonding and have unique hydrogen-bond acceptors. The only exception is $\{L_{Ar}Al(OH)\}_2(\mu$-O), for which infrared spectroscopy suggested a non-hydrogen-bonded hydroxo ligand. In **3**, we have documented the presence of unique intramolecular O−H···pz$_\pi$ hydrogen bonding.

Experimental Section

General: All reactions were performed under dry argon using standard Schlenk and dry-box techniques. Solvents were distilled from various drying agents under argon prior to use. Alane−ethyldimethylamine was purchased from commercial sources. 3,5-Di-*tert*-butylpyrazole was prepared according to a literature procedure.[21] ^{1}H and ^{13}C{^{1}H} NMR spectra were obtained in dry, degassed [D$_8$]toluene, and were referenced to the residual proton or carbon atom resonances of this solvent. Infrared spectra were obtained using Nujol as the medium. Elemental analyses were performed by Midwest Microlab, Indianapolis, IN. Melting points were obtained on a Haake-Buchler HBI digital melting point apparatus and are uncorrected.

Synthesis of 1: A 100-mL Schlenk flask was charged with a 0.5 M solution of $AlH_3(NMe_2Et)$ in toluene (6.0 mL, 3.0 mmol) and was further diluted with toluene (40 mL). tBu$_2$pzH (0.811 g, 4.5 mmol) was added to this solution at 23 °C in small portions over 0.25 h. The mixture was stirred at 23 °C for 16 h. At this point, the volatile components were removed under reduced pressure to afford a white solid. This solid was dissolved in hexane (30 mL) and the solution was filtered through a 2-cm pad of Celite on a coarse glass frit. The filtered solution was placed in a −20 °C freezer for 24 h, during which time crystallization occurred. Removal of the solvent by cannula, followed by vacuum drying, afforded **1** as colorless crystals (0.505 g, 57%); m.p. 110 °C (dec). IR (Nujol): $\tilde{\nu}_{AlH}$ = 1961 (m), 1906 (m), 1885 (m) cm^{-1}. ^{1}H NMR ([D$_8$]toluene, 23 °C): δ = 1.40 [s, 54 H, C(CH_3)$_3$], 4.5 (br. s, 3 H, Al−H), 6.16 (s, 3 H, pz C−H) ppm. ^{13}C{^{1}H} NMR ([D$_8$]toluene, 23 °C): δ = 31.00 [s, C(CH_3)$_3$], 32.44 [s, C(CH$_3$)$_3$], 103.49 (s, pz C−H), 164.37 [s, C−C(CH$_3$)$_3$] ppm. $C_{33}H_{60}Al_2N_6$ (594.84): calcd. C 66.63, H 10.17, N 14.13; found C 66.84, H 10.10, N 13.95.

Hydrolysis of 1 to Afford 2, 3, and 4: A 100-mL Schlenk flask containing a solution of **1** (0.479 g, 0.805 mmol) in toluene (20 mL) was treated with water (14.5 mg, 0.805 mmol) at −78 °C. Gas evolution was immediately noted and small amount of insoluble white material precipitated. The mixture was stirred at −78 °C for 3 h and was then warmed to ambient temperature and was further stirred for 15 h. The volatile components were then removed under reduced pressure to afford a white solid. Dissolution of this solid in hexane (20 mL), followed by filtration through a 2-cm pad of Celite on a coarse glass frit to remove a small amount of insoluble white solid, afforded a colorless solution. Fractional crystallization of this solution at −20 °C afforded colorless crystals of **2** (0.035 g, 7.7%), **3** (0.075 g, 15%), and **4** (0.145 g, 23%). The order of crystallization was **3**, **2**, and **4**. The isolated yields were diminished due to the care that was required to achieve pure samples. NMR spectroscopic analysis of the white solid removed by filtration showed it to contain tBu$_2$pzH as well as a solid that was insoluble in [D$_1$]chloroform.

Complex 2: This compound was identified by comparison of its ^{1}H and ^{13}C NMR chemical shifts with the reported values.[2]

Data for 3: M.p. 145 °C. IR (Nujol): $\tilde{\nu}$ = 3227 (s, ν_{AlOH}), 1961 (m, ν_{AlH}), 1908 (m, ν_{AlH}), 1860 (m, ν_{AlH}) cm^{-1}. ^{1}H NMR ([D$_8$]toluene, 23 °C): δ = 1.41 [s, 54 H, C(CH_3)$_3$], 5.5, 4.6 (2 br. s, 3 H, 2 Al−H, Al−OH), 6.16 (s, 3 H, pz C−H) ppm. ^{13}C{^{1}H} NMR ([D$_8$]toluene, 23 °C): δ = 31.14 [s, C(CH$_3$)$_3$], 32.58 [s, C(CH$_3$)$_3$], 103.61 (s, pz C−H), 164.55 (s, C−C(CH$_3$)$_3$] ppm. $C_{33}H_{60}Al_2N_6O$ (610.83): calcd. C 64.87, H 9.90, N 13.76; found C 64.59, H 9.76, N 13.94.

Data for 4: M.p. 135 °C (dec). IR (Nujol): $\tilde{\nu}$ = 1937 (w, ν_{AlH}) cm^{-1}. ^{1}H NMR ([D$_8$]toluene, 23 °C): δ = 1.12 (s, 36 H, 4 C(CH_3)$_3$], 1.41 (s, 36 H, 4 C(CH_3)$_3$], 4.9 (br. s, 2 H, Al−H), 6.02 (s, 2 H, pz C−H), 6.22 (s, 2 H, pz C−H) ppm. ^{13}C{^{1}H} NMR ([D$_8$]toluene, 23 °C): δ = 31.00 [s, C(CH$_3$)$_3$], 31.39 [s, C(CH$_3$)$_3$], 31.94 [s, C(CH$_3$)$_3$], 33.31 [s, C(CH$_3$)$_3$], 101.12 (s, pz C−H), 106.93 (s, pz C−H), 162.12 [s, C−C(CH$_3$)$_3$], 168.69 [s, C−C(CH$_3$)$_3$] ppm. $C_{44}H_{78}Al_2N_8$ (773.10): calcd. C 68.36, H 10.17, N 14.49; found C 68.22, H 10.10, N 14.27.

X-ray Crystallography: Crystals of **3** (M = 610.83) and **4** (M = 773.10) were grown as described above and crystallized in the triclinic crystal system in the space group P$\bar{1}$. Relevant details and data are summarized in Tables 1−3. The crystals were mounted in thin glass capillaries under nitrogen. Diffraction data were collected with a Bruker P4 four-circle diffractometer coupled to a Bruker CCD area detector at 295(2) K, with graphite-monochromated Mo-K_α radiation (λ = 0.71073 Å). The structures were solved from the Patterson maps using SHELX-97[22] and refined against F^2 on all data by full-matrix least-squares with the same program. All non-hydrogen atoms were refined anisotropically. The hydrogen atoms were included in the model at their geometrically calculated positions and held riding or observed on a difference fourier and refined. CCDC-185702 (**3**) and -185701 (**4**) contain the supplementary crystallographic data for this paper. These data can be obtained free of charge on application to CCDC, 12 Union Road, Cambridge CB21EZ, UK [Fax: (internat.) + 44-1223-336-033; E-mail: deposit@ccdc.cam.ac.uk]. Structure searches were conducted using the Cambridge Crystallographic Database, Version 5.25, November 2003.

 © 2005 Wiley-VCH Verlag GmbH & Co. KGaA, Weinheim

Table 2. Selected distances [Å] and angles [°] for **3**

Al(1)−N(1)	1.964(3)
Al(1)−N(5)	1.936(3)
Al(1)−N(6)	1.954(3)
Al(2)−N(2)	1.920(3)
Al(2)−N(4)	1.914(3)
Al(2)−O(1)	1.867(3)
Al(1)−H(1)	1.423(5)
Al(2)−H(2)	1.534(5)
H(O1)···centroid[η^2-pz]	2.574
Al(1) ··Al(2)	3.289(2)
N(1)−Al(1)−N(3)	95.11(11)
N(5)−Al(1)−N(6)	42.32(11)
N(2)−Al(2)−N(4)	102.64(11)
N(2)−Al(2)−O(1)	119.45(14)
N(4)−Al(2)−O(1)	115.19(15)
O(1)−H(O1)-centroid(η^2-pz)	152.9

Table 3. Selected distances [Å] and angles [°] for **4**

Al(1)−N(1)	1.947(3)
Al(1)−N(4)	1.952(3)
Al(1)−N(7)	1.892(3)
Al(1)−N(8)	2.082(4)
Al(2)−N(2)	1.922(3)
Al(2)−N(3)	1.933(3)
Al(2)−N(5)	1.871(3)
Al(2)−N(6)	2.559(3)
Al(1)−H	1.521(5)
Al(2)−H	1.453(5)
Al(1)···Al(2)	3.414(2)
N(1)−Al(1)−N(4)	96.45(11)
N(1)−Al(1)−N(7)	123.90(16)
N(1)−Al(1)−N(8)	91.57(14)
N(7)−Al(1)−N(8)	40.55(13)
N(2)−Al(2)−N(3)	109.12(12)
N(2)−Al(2)−N(5)	104.28(11)
N(3)−Al(2)−N(5)	105.63(11)

Acknowledgments

C. H. W. and H. B. S. thank the U.S. National Science Foundation for support of this research (C. H. W.: Grant Nos. CHE-9807269, Special Creativity Extension thereto, CHE-0314615; H. B. S.: Grant No. CHE-0131157). J. E. K. thanks the Wayne State University Institute for Scientific Computing for support provided by an NSF-IGERT Fellowship.

[1] For reviews of pyrazolato complexes, see: [1a] A. P. Sadimenko, *Adv. Heterocyclic Chem.* **2001**, *80*, 157−240. [1b] J. E. Cosgriff, G. B. Deacon, *Angew. Chem. Int. Ed.* **1998**, *37*, 286−287; *Angew. Chem.* **1998**, *110*, 298−299. [1c] G. La Monica, G. A. Ardizzoia, *Progr. Inorg. Chem.* **1997**, *46*, 151−238. [1d] A. P. Sadimenko, S. S. Basson, *Coord. Chem. Rev.* **1996**, *147*, 247−297. [1e] S. Trofimenko, *Progr. Inorg. Chem.* **1986**, *34*, 115−210. [1f] S. Trofimenko, *Chem. Rev.* **1972**, *72*, 497−508.

[2] G. B. Deacon, E. E. Delbridge, C. M. Forsyth, P. C. Junk, B. W. Skelton, A. H. White, *Aust. J. Chem.* **1999**, *52*, 733−739.

[3] [3a] W. Zheng, H. W. Roesky, N. C. Mösch-Zanetti, H.-G. Schmidt, M. Noltemeyer, *Eur. J. Inorg. Chem.* **2002**, 1056−1059. [3b] W. Zheng, H. W. Roesky, M. Noltemeyer, *Organometallics* **2001**, *20*, 1033−1035. [3c] W. Zheng, N. C. Mösch-Zanetti, T. Blunck, H. W. Roesky, M. Noltemeyer, H.-G. Schmidt, *Organometallics* **2001**, *20*, 3299−3303. [3d] W. Zheng, H. Hohmeister, N. C. Mösch-Zanetti, H. W. Roesky, M. Noltemeyer, H.-G. Schmidt, *Inorg. Chem.* **2001**, *40*, 2363−2367. [3e] W. Zheng, A. Stasch, J. Prust, H. W. Roesky, F. Cimpoesu, M. Noltemeyer, H.-G. Schmidt, *Angew. Chem. Int. Ed.* **2001**, *40*, 3461−3464; *Angew. Chem.* **2001**, *113*, 3569−3572. [3f] W. Zheng, N. C. Mösch-Zanetti, H. W. Roesky, M. Hewitt, F. Cimpoesu, T. R. Schneider, A. Stasch, J. Prust, *Angew. Chem. Int. Ed.* **2000**, *39*, 3099−3101; *Angew. Chem.* **2000**, *112*, 3229−3231. [3g] W. Zheng, N. C. Mösch-Zanetti, H. W. Roesky, M. Noltemeyer, M. Hewitt, H.-G. Schmidt, T. R. Schneider, *Angew. Chem. Int. Ed.* **2000**, *39*, 4276−4279; *Angew. Chem.* **2000**, *112*, 4446−4449.

[4] [4a] Z. K. Yu, J. M. Wittbrodt, A. Xia, M. J. Heeg, H. B. Schlegel, C. H. Winter, *Organometallics* **2001**, *20*, 4301−4303. [4b] Z. K. Yu, M. J. Heeg, C. H. Winter, *Chem. Commun.* **2001**, 353−354. [4c] Z. K. Yu, J. M. Wittbrodt, M. J. Heeg, H. B. Schlegel, C. H. Winter, *J. Am. Chem. Soc.* **2000**, *122*, 9338−9939.

[5] [5a] Y. Peng, G. Bai, H. Fan, D. Vidovic, H. W. Roesky, J. Magull, *Inorg. Chem.* **2004**, *43*, 1217−1219. [5b] G. Bai, H. W. Roesky, J. Li, M. Noltemeyer, H.-G. Schmidt, *Angew. Chem. Int. Ed.* **2003**, *42*, 5502−5506. [5c] G. Bai, Y. Peng, H. W. Roesky, J. Li, H.-G. Schmidt, M. Noltemeyer, *Angew. Chem. Int. Ed.* **2003**, *42*, 1132−1135. [5d] I. Smolin, Y. F. Shepelev, A. S. Ershov, D. Khobbel, *Dokl. Akad. Nauk SSSR* **1987**, *297*, 1377. [5e] E. Muller, H.-B. Bürgi, *Helv. Chim. Acta* **1987**, *70*, 520−533. [5f] A. Looney, G. Parkin, *Polyhedron* **1990**, *9*, 265−276.

[6] For selected leading reviews of alumoxanes, see: [6a] E. Y.-X. Chen, T. J. Marks, *Chem. Rev.* **2000**, *100*, 1391−1434. [6b] H. W. Roesky, M. G. Walawalkar, R. Murugavel, *Acc. Chem. Res.* **2001**, *34*, 201−211. [6c] S. Pasynkiewicz, *Polyhedron* **1990**, *9*, 429−453.

[7] For other examples of slipped η^2-pyrazolato ligands, see: [7a] I. A. Guzei, G. P. A. Yap, C. H. Winter, *Inorg. Chem.* **1997**, *36*, 1738−1739. [7b] G. B. Deacon, E. E. Delbridge, C. M. Forsyth, B. W. Skelton, A. H. White, *J. Chem. Soc., Dalton Trans.* **2000**, 745−754.

[8] Gaussian 01 (Development Version): M. J. Frisch, G. W. Trucks, H. B. Schlegel, G. E. Scuseria, M. A. Robb, J. R. Cheeseman, J. A. Montgomery Jr., T. Vreven, K. N. Kudin, J. C. Burant, J. M. Millam, S. S. Iyengar, J. Tomasi, V. Barone, B. Mennucci, M. Cossi, G. Scalmani, N. Rega, G. A. Petersson, H. Nakatsuji, M. Hada, M. Ehara, K. Toyota, R. Fukuda, J. Hasegawa, M. Ishida, T. Nakajima, H. Honda, O. Kitao, H. Nakai, M. Klene, X. Li, J. E. Knox, H. P. Hratchian, J. B. Cross, C. Adamo, J. Jaramillo, R. Gomperts, R. E. Stratmann, O. Yazyev, A. J. Austin, R. Cammi, C. Pomelli, J. W. Ochterski, P. Y. Ayala, K. Morokuma, G. A. Voth, P. Salvador, J. J. Dannenberg, V. G. Zakrzewski, S. Dapprich, A. D. Daniels, M. C. Strain, O. Farkas, D. K. Malick, A. D. Rabuck, K. Raghavachari, J. B. Foresman, J. V. Ortiz, Q. Cui, A. G. Baboul, S. Clifford, J. Cioslowski, B. B. Stefanov, G. Liu, A. Liashenko, P. Piskorz, I. Komaromi, R. L. Martin, D. J. Fox, T. Keith, M. A. Al-Laham, C. Y. Peng, A. Nanayakkara, M. Challacombe, P. M. W. Gill, B. Johnson, W. Chen, M. W. Wong, C. Gonzalez, J. A. Pople, Gaussian Inc., Pittsburgh, PA, **2002**.

[9] I. A. Guzei, A. G. Baboul, G. P. A. Yap, A. L. Rheingold, H. B. Schlegel, C. H. Winter, *J. Am. Chem. Soc.* **1997**, *119*, 3387−3388.

[10] A. D. Becke, *J. Chem. Phys.* **1993**, *98*, 5648−5652.

[11] A. D. Becke, *Phys. Rev. A* **1988**, *38*, 3098−3100.

[12] C. Lee, W. Yang, R. D. Parr, *Phys. Rev. B* **1988**, *37*, 785−789.

[13] A. D. McLean, G. S. Chandler, *J. Chem. Phys.* **1980**, *72*, 5639.

[14] S. Dapprich, I. Komaromi, K. S. Byun, K. Morokuma, M. J. Frisch, *Theochem − J. Mol. Struct.* **1999**, *462*, 1−21.

[15] M. J. S. Dewar, E. G. Zoebisch, E. F. Healy, J. J. P. Stewart, *J. Am. Chem. Soc.* **1985**, *107*, 3902−3909.

[16] M. J. S. Dewar, A. J. Holder, *Organometallics* **1990**, *9*, 508−511.

[17] For selected recent examples of pyrazolato complexes contain-

 © 2005 Wiley-VCH Verlag GmbH & Co. KGaA, Weinheim

ing two distinct coordination modes, see: [17a] G. B. Deacon, A. Gitlits, B. W. Skelton, A. H. White, *Chem. Commun.* **1999**, 1213−1214. [17b] G. A. Aridizzoia, G. La Monica, A. Maspero, N. Masciocchi, M. Moret, *Eur. J. Inorg. Chem.* **1999**, 1301−1307. [17c] G. B. Deacon, E. E. Delbridge, B. W. Skelton, A. H. White, *Angew. Chem. Int. Ed.* **1998**, *37*, 2251−2252; *Angew. Chem.* **1998**, *110*, 2372−2373. [17d] D. Carmona, F. J. Lahoz, L. A. Oro, M. P. Lamata, S. Buzarra, *Organometallics* **1991**, *10*, 3123−3131. [17e] M. K. Ehlert, S. J. Rettig, A. Storr, R. C. Thompson, J. Trotter, *Can. J. Chem.* **1990**, *68*, 1494−1498. [17f] H. Schumann, P. R. Lee, J. Loebel, *Angew. Chem. Int. Ed. Engl.* **1989**, *28*, 1033−1035; *Angew. Chem.* **1989**, *101*, 1073−1075. [17g] L. A. Oro, D. Carmona, M. P. Lamata, C. Foces-Foces, F. H. Cano, *Inorg. Chim. Acta* **1985**, *97*, 19−23.

[18] For a recent overview, see: H. W. Roesky, R. Murugavel, M. R. Walawalkar, *Chem. Eur. J.* **2004**, *10*, 324−331.

[19] For selected examples of structurally characterized aluminum complexes containing bridging hydroxo ligands [Al−O 1.81−2.09 Å], see: [19a] P. Wei, D.A. Atwood, *Polyhedron* **1999**, *18*, 641−646. [19b] J. Storre, A. Klemp, H. W. Roesky, H.-G. Schmidt, M. Noltemeyer, R. Fleischer, D. Stalke, *J. Am. Chem. Soc.* **1996**, *118*, 1380−1386. [19c] R. J. Wehmschulte, W. J. Grigsby, B. Schiemenz, R. A. Bartlett, P. P. Power, *Inorg. Chem.* **1996**, *35*, 6694−6702. [19d] Y. Koide, A. R. Barron, *Organometallics* **1995**, *14*, 4026−4029. [19e] C. C. Landry, C. J. Harlan, S. G. Bott, A. R. Barron, *Angew. Chem. Int. Ed. Engl.* **1995**, *34*, 1201−1202; *Angew. Chem.* **1995**, *107*, 1315−1317. [19f] C. J. Harlan, M. R. Mason, A. R. Barron, *Organometallics* **1994**, *13*, 2957−2969. [19g] M. R. Mason, J. M. Smith, S. G. Bott, A. R. Barron, *J. Am. Chem. Soc.* **1993**, *115*, 4971−4984.

[20] For leading references, see: [20a] M. A. Muñoz, O. Sama, M. Galán, P. Guardado, C. Carmona, M. Balón, *Spectrochim. Acta, Part A* **2001**, *57*, 1049−1054. [20b] V. Stefov, Lj. Pejov, B. Šoptrajanov, *J. Mol. Struct.* **2000**, *555*, 363−368. [20c] P. Ganis, A. Ceccon, T. Köhler, F. Manoli, S. Santi, A. Venzo, *Inorg. Chem. Commun.* **1998**, *1*, 15−17. [20d] A. Nikolic, A. Petrovic, D. Antonovic, L. Gobor, *J. Mol. Struct.* **1997**, *408/409*, 355−359. [20e] F. D. Lewis, J.-S. Yang, C. L. Stern, *J. Am. Chem. Soc.* **1996**, *118*, 12029−12038. [20f] M. Crisma, F. Formaggio, G. Valle, C. Toniolo, M. Saviano, R. Iacovino, L. Zaccaro, E. Bendetti, *Biopolymers* **1997**, *42*, 1−8.

[21] J. Elguéro, E. Gonzalez, R. Jacquier, *Bull. Soc. Chim. Fr.* **1968**, 707−709.

[22] G. Sheldrick, University of Göttingen, Germany, **1997**.

Received July 28, 2004
Early View Article
Published Online November 18, 2004

 © 2005 Wiley-VCH Verlag GmbH & Co. KGaA, Weinheim

Studies of the Nature of the Catalytic Species in the α-Olefin Polymerisation Processes Generated by the Reaction of Diamido(cyclopentadienyl)titanium Complexes with Aluminium Reagents as Cocatalysts

VanessaTabernero[a] and Tomás Cuenca*[a]

Keywords: Titanium / Diamido ligands / Olefin polymerisation / Trimethylaluminium / Methylaluminoxane

The reaction of the diamido(chloro)cyclopentadienyltitanium compounds $TiCp^{Rx}[1,2\text{-}C_6H_4(NR')_2]Cl$ [Cp^{Rx} = η^5-C_5H_5, η^5-$C_5(CH_3)_5$, η^5-$C_5H_4(SiMe_3)$; R′ = CH_2tBu, Pr] with the Grignard reagent MgClR (R = Me, CH_2Ph) affords the monomethyl and monobenzyl derivatives $TiCp^{Rx}[1,2\text{-}C_6H_4(NR')_2]R$. Upon addition of methylaluminoxane (MAO), the chloro- and alkyltitanium complexes show low activity towards the polymerisation of ethylene and styrene. However, no methylation was observed during the treatment of trimethylaluminium with the chloro compounds $TiCp^{Rx}[1,2\text{-}C_6H_4(NR')_2]Cl$. Instead, these reactions give the dinuclear aluminium complexes $Al_2[1,2\text{-}C_6H_4(NR')_2]Me_4$ (R′ = CH_2tBu, Pr) through transmetallation of the diamido ligand, suggesting a deactivation process of the catalysts in the olefin polymerisation reactions. In an additional effort to model the catalytic species, stoichiometric reactions between the methyl derivatives $TiCp^{Rx}[1,2\text{-}C_6H_4(NR')_2]Me$ and solid methylaluminoxane (MAO) were studied by NMR spectroscopy. Monitoring of these reactions revealed the formation of zwitterionic species depending on the nature of the solvent.
(© Wiley-VCH Verlag GmbH & Co. KGaA, 69451 Weinheim, Germany, 2005)

Introduction

In recent years, one of the achievements in transition metal organometallic chemistry has been the development of Ziegler−Natta catalysis for the polymerisation of ethylene and α-olefins and the research in this field has resulted in a good understanding of the mechanism of the olefin polymerisation process.[1−6] According to this, the minimum requirement for a catalyst precursor has been established as the existence of an unreactive ancillary ligand system (generally the cyclopentadienyl ligand) with at least two coordination sites which can be activated to provide a metal alkyl bond *cis* to a vacant coordination site for monomer binding. Descriptions of group 4 metal complexes with these features used as catalysts for olefin polymerisation have been extensive.[4,7−12] However, examples of precatalysts containing only one such group which can be active for olefin polymerisation are scarce.[13−15]

Over the past few years a growing interest in developing organometallic compound alternatives to classical group 4 cyclopentadienyl complexes has emerged. Some of the more significant recent developments have occurred with early and late transition metal systems. High-performance compounds bearing a chelate ligand such as diimino(pyridino)[16,17] (Fe and Co), imino(phenoxo)[13,18] (Ni), diamido[19,20] (Ti) and iminobis(phenoxo)[21−23] ligands(Zr) are examples which have provided excellent activity for α-olefin polymerisation and in some cases for promoting copolymerisation of an α-olefin with polar monomers[24] as well as living polymerisation.[25−27]

As part of our investigations directed at obtaining a new class of organometallic compounds combining cyclopentadienyl and diamido ligands, we recently published the synthesis of diamido(chloro)cyclopentadienyltitanium compounds $TiCp^{Rx}[1,2\text{-}C_6H_4(NR')_2]Cl$ [Cp^{Rx} = η^5-C_5H_5, η^5-$C_5(CH_3)_5$, η^5-$C_5H_4(SiMe_3)$; R′ = CH_2tBu, Pr] and as assessment of their behaviour as precatalysts for α-olefin polymerisation. As a continuation of this field, we report herein the synthesis of alkyl derivatives $TiCp^{Rx}[1,2\text{-}C_6H_4(NR')_2]R$ and their activation with solid MAO to give active species in ethylene and styrene polymerisation reactions. To identify the nature of the catalytic species in the olefin polymerisation processes arising from the interaction of this class of precursor of organometallic complexes (with only one alkyl group bonded to the metal centre) with aluminium compounds as cocatalysts, the reactions of the chloro compounds $TiCp^{Rx}[1,2\text{-}C_6H_4(NR')_2]Cl$ with trimethylaluminium (TMA) and the methyl compounds $TiCp^{Rx}[1,2\text{-}C_6H_4(NR')_2]Me$ with solid methylaluminoxane (MAO) were tested. The objective of the present work was to gain a direct insight into the role of these species in polymerisation activity.

[a] Departamento de Química Inorgánica, Universidad de Alcalá, Campus Universitario,
28871 Alcalá de Henares Spain
Fax: (internat.) + 34-91-8854683
E-mail: tomas.cuenca@uah.es

 © 2005 Wiley-VCH Verlag GmbH & Co. KGaA, Weinheim **DOI: 10.1002/ejic.200400661**

Results and Discussion

Synthesis of Dialkyl Derivatives

The reaction of 1 equiv. of MgClR (R = Me, 3 M solution in THF; R = CH_2Ph, 2 M solution in THF) with a solution of $TiCp^{Rx}[1,2\text{-}C_6H_4(NR')_2]Cl$ [Cp^{Rx} = $\eta^5\text{-}C_5H_5$, $\eta^5\text{-}C_5(CH_3)_5$, $\eta^5\text{-}C_5H_4(SiMe_3)$; R′ = CH_2tBu, Pr] in hexane at −78 °C proceeds with substitution of the chloro ligand by the alkyl group affording the methyl and benzyl derivatives $TiCp^{Rx}[1,2\text{-}C_6H_4(NR')_2]R$ (**1**−**12**) (Scheme 1, Table 1). The methyl (**1** and **2**) and the benzyl (**7** and **8**) compounds were isolated, after purification, as red and dark solids respectively, while the complexes **3**−**6** and **9**−**12** exist as red or dark oils which are difficult to handle and recrystallise due to their very high solubility in all common solvents. For compound **8**, the alkylation of the Ti−Cl bond in hexane is not totally effective due to steric hindrance at the titanium centre and a mixture of the chloro and the benzyl compounds is obtained. However, the reaction between $Ti(\eta^5\text{-}C_5Me_5)[1,2\text{-}C_6H_4(NCH_2t\text{Bu})_2]Cl$ and MgClBz in a polar solvent proceeds with the formation of the pure benzyl complex **8**.

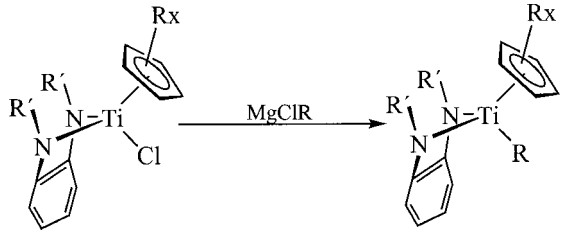

Scheme 1

Table 1. Amido- and titanium-alkyl groups in compounds **1**−**12**

Cp^{Rx}	R′	R	
$\eta^5\text{-}C_5H_5$	CH_2tBu	Me	(**1**)
		CH_2Bz	(**7**)
	Pr	Me	(**4**)
		CH_2Bz	(**10**)
$\eta^5\text{-}C_5Me_5$	CH_2tBu	Me	(**2**)
		CH_2Bz	(**8**)
	Pr	Me	(**5**)
		CH_2Bz	(**11**)
$\eta^5\text{-}C_5H_4(SiMe_3)$	CH_2tBu	Me	(**3**)
		CH_2Bz	(**9**)
	Pr	Me	(**6**)
		CH_2Bz	(**12**)

Complexes **1**−**12** are soluble in aromatic hydrocarbons, dichloromethane, chloroform, diethyl ether and alkanes (hexane and pentane). They are air- and moisture-sensitive in solution as well as in the solid state, although they can be stored unchanged for weeks under an inert gas. The complexes were characterised by the usual analytical and spectroscopic methods. In some cases, the ^1H NMR spectra of the $TiCp^{Rx}[1,2\text{-}C_6H_4(NPr)_2]R$ compounds in deuterated chlorinated solvents could not be obtained since the corresponding chloro compounds are formed in these solvents. In contrast, the $TiCp^{Rx}[1,2\text{-}C_6H_4(NCH_2t\text{Bu})_2]R$ derivatives can be dissolved in chlorinated solutions for long periods without transformation into the corresponding chloro compounds since the neopentyl substituent affords greater steric protection for the metal centre than the propyl substituent.

The NMR spectra of these compounds show patterns for the proton and carbon resonances similar to those described for the analogous chloro compounds.[28] The ^1H resonances (C_6D_6, room temperature) of the cyclopentadienyl protons appear at δ = 6.01−6.15 for the Cp and δ = 1.45−1.71 for the C_5Me_5 ligands. The $C_5H_4(SiMe_3)$ ring protons give AA′BB′ spin systems at δ = 6.13−6.53. The methyl protons of the $SiMe_3$ group exhibit one singlet located at δ = 0.17−0.31. The spectra for the propyl compounds show sets of multiplets and triplet resonances for the N-CH_2−CH_2−CH_3 fragment protons, while the expected signals for the neopentyl ligand protons can be observed in the spectra of the corresponding derivatives. The phenyl protons of the diamido ligands appear as two multiplets in the usual range. Furthermore, the ^1H NMR spectra show the expected signals assignable to the methyl and the benzyl ligands attached to titanium. Similar structural features to those described from ^1H NMR spectroscopy can be deduced from the $^{13}C\{^1H\}$ NMR spectra (C_6D_6, room temperature). These spectroscopic data are in agreement with C_s symmetry and are consistent with the presence of a mirror plane containing the Ti and C_α atoms of the alkyl groups bisecting the N−Ti−N angle of the chelate diamido ligand.

In this type of complex, the diamido ligand can adopt different coordination modes and has two possible conformation modes (*supine* or *prone*) relative to the cyclopentadienyl ring. A Nuclear Overhauser Enhancement (NOE) study of the benzyl complex **7** containing the Cp ligand enabled us to distinguish between these two possible dispositions. Irradiation of the Cp resonance resulted in a significant NOE enhancement in the methylene signals of the neopentyl group, while no NOE enhancements in the phenyl signals were observed. These observations suggest that the neopentyl group is located close to the Cp ring with the diamido ligand adopting a *supine* conformation, in accordance with the chemical shifts observed for the cyclopentadienyl ring protons in the ^1H NMR spectrum which are not influenced by phenylene magnetic anisotropy.[29] Similar results were obtained for the corresponding chloro derivatives which is consistent with the disposition found in the solid state using X-ray crystallography.[28]

Polymerisation Reactions

Given our interest in the polymerisation chemistry of group 4 diamido(cyclopentadienyl)-[15,30,31] or dialkoxometal complexes,[32] we undertook a study of α-olefin polymerisation processes of the alkyldiamido(cyclopentadienyl) compounds $TiCp^{Rx}[1,2\text{-}C_6H_4(NR')_2]R$ with methylaluminoxane (MAO) as a cocatalyst. The reaction conditions and the results are summarised in Table 2 and 3. The results

 © 2005 Wiley-VCH Verlag GmbH & Co. KGaA, Weinheim

show the averages of two or more polymerisation runs which showed good reproducibility between them.

Table 2. Polymerisation studies of ethylene with $TiCp^{Rx}[1,2\text{-}C_6H_4(NR')_2]R$ in the presence of MAO as cocatalyst

Entry	Catalyst[a]	Activity[b]	ΔH_m (J g^{-1})[c]	T_m °C)[c]
1	1	8.0	59	130
2	2	4.3	45	126
3	3	1.6	52	122
4	4	47	55	130
5	7	3.0	24	133
6	8	7.5	45	129
7	10	51	28	135

[a] Reaction conditions: temperature = 25 °C, 10 mg of precatalyst, molar ratio Al/Ti = 400, 50 mL of toluene, 5 atm of ethylene pressure, 15 min. [b] g PE/mmol Ti h atm. [c] Determined by DSC.

Table 2. Polymerisation studies of styrene with $TiCp^{Rx}[1,2\text{-}C_6H_4(NR')_2]R$ in the presence of MAO as a cocatalyst

Entry	Catalyst[a]	Activity[b]	T_m(°C)
1	**1**	25	252
2	**2**	35	250
3	**3**	15	260
4	**4**	18	248
5	**7**	15	256
6	**8**	10	246
7	**10**	13	257

[a] Reaction conditions: temperature = 50 °C, 10 mg of precatalyst, molar ratio Al/Ti = 400, 50 mL of toluene, 5 mL styrene, 15 min. [b] g PS/mmol Ti h. [c] Determined by DSC.

When activated with MAO, low activities for ethylene homopolymerisation were obtained with the neopentyl compounds **1**−**3** and **7**−**8** (Entries 1−3 and 5−6), while moderate activities with the propyl complexes **4** and **10** (Entries 4 and 7) were observed (Table 2). These activity values show a pronounced dependence on the steric requirements of the diamido ligand with the higher activity observed for the smaller substituent on the nitrogen atom of the amido ligand. Similar control of steric crowding at the metal centre has been observed in bulky amidinato complexes.[33,34] The activities exhibited for these complexes are of the same order of magnitude as those described for similar diamido(cyclopentadienyl)titanium compounds,[35−37] although they are smaller than those reported for noncyclopentadienyl diamido complexes.[17,38,39] Polymer samples show melting point values (T_m measured by DSC) typical of high-density polyethylene.

The $TiCp^{Rx}[1,2\text{-}C_6H_4(NR')_2]R$ precatalysts were tested for styrene polymerisation upon activation with MAO but poor catalytic activities were found (Table 3). The observed activity values are markedly lower than those obtained with the well-known $CpTiCl_3$ used as a reference point.[40] The PS samples obtained are in the range typical for syndiotactic polymers (NMR spectroscopy), as expected for cyclopentadienyltitanium precatalysts,[41−46] with low molecular weights (as deduced from their T_m analyses).

$B(C_6F_5)_3$ was also used as a cocatalyst in our polymerisation experiments but, unfortunately, no catalytic activity was observed even after using TIBA as scavenger in the reaction mixture. In the catalyst systems obtained by combining **1** or **2** with $B(C_6F_5)_3$, the colour of the solutions were different from those obtained in the reaction with solid MAO as a cocatalyst, suggesting that different species are formed. While **1** and solid MAO mixtures result in a green solution, a red colour was observed using $B(C_6F_5)_3$ as a cocatalyst. These results can be attributed to the ability of aluminium derivatives to abstract the diamido ligand providing the alkyl group requirement for polymerisation in a Ziegler−Natta manner, whereas this possibility is unavailable in the perfluoroborane compound.

The low activity trend observed for the $TiCp^{Rx}[1,2\text{-}C_6H_4(NR')_2]R$ precatalysts in the α-olefin polymerisation reactions might be due to a catalyst decomposition process through ligand abstraction by MAO which may cause partial or complete loss of the ligand thus resulting in one or more inactive species for α-olefin polymerisation.[47] In an effort to model the nature of the catalytic species generated in these catalyst systems, the reactions of the cyclopentadienyldiamido, monochloro and monoalkyltitanium derivatives with trimethylaluminium (TMA) and solid methylaluminoxane MAO were examined.

Reactions of $TiCp^{Rx}[1,2\text{-}C_6H_4(NR')_2]Cl$ with TMA

Attempts to obtain methyltitanium derivatives under the conditions described above from the $Ti(\eta^5\text{-}C_5H_5)[1,2\text{-}C_6H_4(NR)_2]Cl$ starting compound using alkylating aluminium reagents such as TMA were unsuccessful. The methylated products was not observed but evolution of the starting material by ligand transfer from titanium to aluminium occurred.

Treatment of a red-brown solution of the monochloro compound $Ti(\eta^5\text{-}C_5H_5)[1,2\text{-}C_6H_4(NCH_2tBu)_2]Cl$ in hexane at −78 °C with one equivalent of TMA resulted in the im-

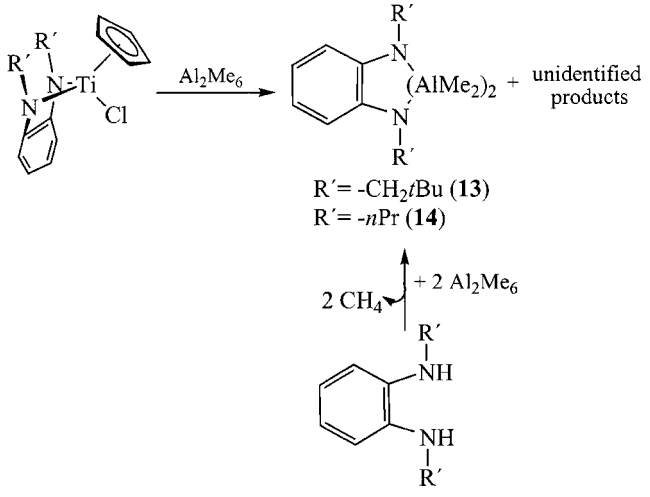

Scheme 2

mediate formation of a yellow solution but the expected monomethyl titanium complex **1** was not observed (monitoring by NMR spectroscopy). Concentration of the solution enabled isolation of the amidoalane compound $Al_2[1,2\text{-}C_6H_4(NCH_2tBu)_2]Me_4$ (**13**) and a mixture of unidentified and intractable titanium species. Similarly, when the reaction was carried out in a Ti:Al molar ratio of 1:100, formation of the amidoalane was observed along with a more complicated final mixture of products. In an analogous reaction, treatment of $Ti(\eta^5\text{-}C_5H_5)[1,2\text{-}C_6H_4(NPr)_2]Cl$ with TMA (in a Ti:Al molar ratio 1:1 and 1:100) afforded the amidoalane compound $Al_2[1,2\text{-}C_6H_4(NnPr)_2]Me_4$ (**14**) (Scheme 2).

These aluminium compounds can be synthesised as pure substances through a direct route by treating $1,2\text{-}C_6H_4(NHR')_2$ (R′ = CH_2tBu, Pr) with 2 equiv. of TMA in toluene with partial precipitation of the aluminium compounds occurring in 1 h (Scheme 2). Reactions between amines and aluminium compounds are well known[48−50] and in the first step, an adduct of the type N−Al is probably formed which then eliminates methane generating the amidoaluminium compound.

Compound **13** was characterised by elemental analysis, while the elemental analysis values found for **14** were inaccurate due to the presence of small amounts of impurities which could not be removed although both aluminium compounds were also characterised by spectroscopic methods. The ^1H NMR spectra (C_6D_6, room temperature) show two different types of methyl groups with each signal corresponding to six protons (see Exp. Sect.). The proposed structural dispositions (Figure 1) are similar to those described for analogous compounds[18,51,52] in which two "$AlMe_2$" moieties are symmetrically chelated by a diamido ligand. They exhibit two aluminium centres with tetrahedral geometry and two nitrogen atoms forming a four membered butterfly shaped metallacycle. Methyl groups are positioned in two different chemical environments with two being located towards the phenyl group and the other being orientated in the opposite direction.

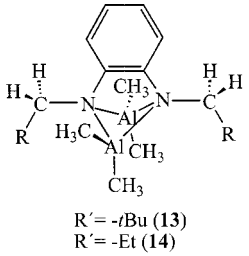

Figure 1. Proposed structural disposition for compounds **13** and **14**

Such reactions starting from monocyclopentadienyl diamido titanium compounds forming aluminium derivatives therefore indicate that transmetallation reactions offer a facile reaction pathway in early transition metal complexes. Similar transmetallation reactions have been proposed for group 4[53] and more recently for group 6[54] complexes bearing diamido ligands. We believe that the resistance of the monocyclopentadienyl diamido chloro titanium complexes to form the alkylated product in the reaction with aluminium reagents and the ligand transfer processes are associated with the low activity of the chloro complexes $TiCp^{Rx}[1,2\text{-}C_6H_4(NR')_2]Cl$ for ethylene and styrene polymerisations. These results provide an insight into the nature of the catalytic species generated during the olefin polymerisation processes through interaction of the precatalyst based on titanium complexes with the aluminium reagents as cocatalysts.

Reaction between $Ti(\eta^5\text{-}C_5H_5)[1,2\text{-}C_6H_4(NCH_2tBu)_2]Me$ (1) and Solid MAO

In order to obtain a better understanding of the nature of the active species and the chemical behaviour of the $TiCp^{Rx}[1,2\text{-}C_6H_4(NR')_2]R$ precatalyst systems in the ethylene and styrene polymerisation processes, the reaction of **1** with solid MAO was carried out using a stoichiometric 1:1 Ti/Al ratio and studied by ^1H NMR spectroscopy. Solid MAO was selected to avoid the inexorable presence of free TMA in commercial MAO[55] since this compound causes transmetallation which could be a crucial factor in the evolution of the reaction.

The ^1H NMR spectrum recorded immediately after mixing the reagents in CD_2Cl_2 at room temperature shows a broadening of Ti-Me resonance accompanied by a downfield shift with respect to the initial situation.[56] In the ^1H NMR spectrum of **1**, the methyl group protons appear at $\delta = -1.5$. After the reaction with MAO, this resonance overlaps with the corresponding MAO signals. These features are in accordance with the interaction of the methyl group of compound **1** with the aluminium atoms present in the MAO which act as Lewis acidic sites[57−61] (Structure A in Scheme 3) or, alternatively, with abstraction of this methyl group to generate an anionic aluminium centre which interacts with the cationic titanium atom through methyl group bridging (Structure B in Scheme 3). The broadness could be due to the closer position of the methyl group, initially bound to titanium, to the "diversification" centres provided by different Lewis acidic sites present in MAO.[62,63] The broadening of Ti-Me resonances of an adduct with MAO has also been reported by Talsi et al.[59,64] When the polarity of the solvent is high, as in this case, methyl group abstraction by MAO is favoured and solvent-separated ion pairs are preferentially formed.[65−67] After allowing the sample to stand for one day in solution, the ^1H NMR spectrum shows clear formation of the chlorinated compound $Ti(\eta^5\text{-}C_5H_5)[1,2\text{-}C_6H_4(NCH_2tBu)_2]Cl$ which indicates chloro abstraction from the solvent.

When the same reaction is carried out in a less polar solvent such as C_6D_6, the process proceeds in a different way. Initially, after mixing the reagents at room temperature for 5 min, the ^1H NMR spectrum features are consistent with the formation of the zwitterionic species in which the methyl ligand acts as a bridging group between the titanium and aluminium centres (Structure A in Scheme 3 favoured).

 © 2005 Wiley-VCH Verlag GmbH & Co. KGaA, Weinheim

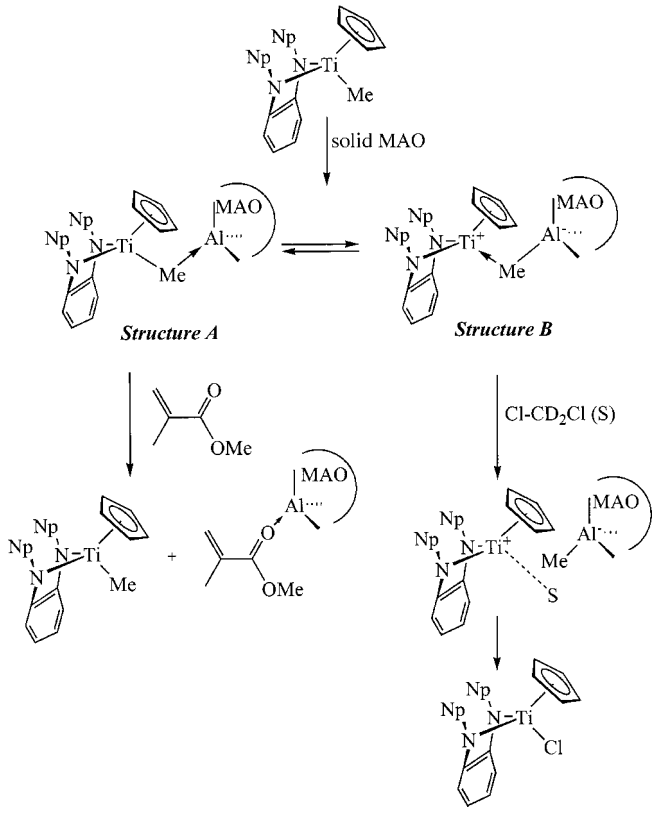

Scheme 3

It is believed that the formation of separated ions, in this case, is not favoured because there is no stabilisation conferred by solvent coordination. After 1 d in solution, no significant changes in the ^{1}H NMR spectrum were observed.

When the solution in C_6D_6 was saturated[68−70] with ethylene, polyethylene was not formed. However, the addition of a polar monomer such as methyl methacrylate (MMA) to the C_6D_6 solution caused the displacement of the MAO initially attached to the titanium centre. The ^{1}H NMR spectrum shows signals indicating the presence of the methylated compound **1** (Scheme 3) and a complicated set of resonances assignable to products exhibiting interactions between MMA and MAO.

Treatment of compound **1** with an excess of solid MAO was rather difficult to study by NMR spectroscopy because the signals of the products overlap with the MAO resonances. We suggest the excess aluminium centres provided by such a large amount of solid MAO, used generally for polymerisation runs, could cause the deactivation of the $TiCp^{Rx}[1,2\text{-}C_6H_4(NR')_2]R$ catalysts by transmetallation reactions of the diamido groups in a similar way to observations made in the reaction of $TiCp^{Rx}[1,2\text{-}C_6H_4(NR')_2]Cl$ with TMA.

Conclusion

The synthesis and characterisation of new monocyclopentadienyl diamido alkyl titanium $TiCp^{Rx}[1,2\text{-}C_6H_4(NR')_2]R$ compounds from the reaction of the corresponding chloro derivatives with Grignard reagents has been described. After activation with methylaluminoxane, the diamido complexes exhibit low activity towards α-olefin polymerisation. While the chloro derivatives $TiCp^{Rx}[1,2\text{-}C_6H_4(NR')_2]Cl$ can be easily methylated by reaction with MgClMe, reaction with trimethylaluminium results in the transmetallation of the diamido ligand to produce dinuclear aluminium compounds. This behaviour must be associated with the low activity of the chloro and alkyl derivatives in the ethylene and styrene polymerisations. The reactivity of the alkyl complexes $TiCp^{Rx}[1,2\text{-}C_6H_4(NR')_2]R$ with MAO has also been studied by NMR spectroscopy. This indicated the formation of intermediate species which can be considered to exert an important effect on the catalytic activity of these precatalysts in the α-olefin polymerisation process.

Experimental Section

General Considerations: All manipulations of air- and moisture-sensitive materials were performed under argon using Schlenk and high-vacuum line techniques or in a glove box model MO40-2. Solvents were predried with activated molecular sieves (4 Å) and were then purified by distillation under argon before use by employing the appropriate drying/deoxygenating agent. Deuterated solvents were degassed by several freeze-thaw cycles and stored in ampoules equipped with Young's Teflon valves over activated molecular sieves (4 Å). C, H and N microanalyses were performed with a Perkin−Elmer 2400 microanalyser. NMR spectra, measured at 25 °C, were recorded with a Varian Unity FT-300 (^{1}H NMR at 300 MHz, ^{13}C NMR at 75 MHz) spectrometer and chemical shifts were referenced to $SiMe_4$ via the ^{13}C resonances and the residual protons (^{1}H) of the deuterated solvent. MAO was purchased from Witco as a toluene solution (10% wt). Reagent grade styrene (Aldrich) was distilled under reduced pressure from calcium hydride and stored in a refrigerator under argon. The polymerisation solvent was dried by heating to reflux in the presence of sodium/benzophenone under argon. MgClMe (3 M solution in THF) and MgClBz (2 M solution in THF) were purchased from Aldrich and used as received. The chlorinated compounds $TiCp^{Rx}[1,2\text{-}C_6H_4(NR')_2]Cl$ [Cp^{Rx} = η^5-C_5H_5, η^5-$C_5(CH_3)_5$, η^5-$C_5H_4(SiMe_3)$; R′ = CH_2tBu, Pr] and the *N*,*N*′-dialkyl-1,2-phenylenediamines $1,2\text{-}C_6H_4(NHR')_2$ (R′ = CH_2tBu, Pr) were prepared as described in previous work.[28]

Preparation of MAO Samples: To obtain MAO with a reduced amount of TMA, a sample of commercial MAO was distilled under vacuum at 20 °C. The white powder obtained (polymeric MAO with residual TMA ca. 3 wt-%) was stored in dry box before use in the preparation of the samples. Calculated quantities of the desired compound and solid MAO were taken into the dry box to prepare the samples with the desired Ti/Al ratio. Solids were mixed and the selected solvent was added directly to the NMR tube equipped with a Young's Teflon valve. All operations were carried out at room temperature.

Polymerisation Procedure: For ethylene polymerisation, the typical procedure was as follows. Toluene (50 mL), solid MAO (Al/Ti = 400) and the desired precatalyst (10 mg) in a sealed glass vial were placed in a high-pressure glass reaction vessel (Büchi). Subsequently, the polymerisation temperature was adjusted and the

 © 2005 Wiley-VCH Verlag GmbH & Co. KGaA, Weinheim

mixture was pressurized to 5 atm for 1 h before cracking the vial. After 15 min of venting of the ethylene gas and quenching with HCl/CH_3OH (10 mL), the reaction was stopped. The solution was then poured into a large excess of this solvent mixture and the resultant polyethylene was separated by filtration, washed several times (HCl/CH_3OH) and dried under vacuum overnight. Polymerisation of styrene was performed under argon in toluene at 50 °C using solid MAO as the cocatalyst according to the following procedure. Toluene (30 mL), styrene (5 mL) and MAO were injected into the Schlenk flasks with magnetic stirring at the desired temperature. The titanium compound was dissolved in toluene (5 mL) and added to the mixture. In a manner similar to the polyethylenes, the polystyrenes were coagulated with a large excess of acidified methanol and isolated by filtration.

Characterisation of Polymers: The thermal properties of the samples were studied using a Perkin−Elmer DSC 6 instrument calibrated by measuring the melting point of indium. Thus, 5−10 mg each of the dried polymers were fused into standard aluminium pans and measured using the following temperature programme for polyethylene samples: first a heating phase (10 °C/min) from 50 to 200 °C, followed by a cooling phase (−10 °C/min) to 50 °C. The peak maximum of the second heating curve was indicated as the melting point (T_m). ΔH_m derived from the data of the second heating course of the DSC was selected. Polystyrene samples were subjected to the following steps: heating at 10 °C/min from 30 to 270 °C and then cooling at 10 °C/min from this temperature to 30 °C and finally heating at 10 °C/min from 30 to 270 °C to obtain the melting peak temperature (T_m). The NMR-PS samples were prepared by dissolving the polymer in tetrachloro-1,2-dideuterioethane. The spectra were recorded at 25 °C.

Ti(η^5-C_5H_5)[1,2-C_6H_4(NCH$_2$*t*Bu)$_2$](CH$_3$) (1): A 3 M solution of MeMgCl in THF (0.42 mL, 0.93 mmol) was added to a solution of Ti(η^5-C_5H_5)[1,2-C_6H_4(NCH$_2$*t*Bu)$_2$]Cl (0.50 g, 1.27 mmol) in hexane (50 mL) at −78 °C. The cooling bath was removed and the reaction mixture was warmed to room temperature after stirring for 12 h. The resultant residue was filtered and the solution cooled to −40 °C to afford **1** as a red solid (0.35 g, 74%). $C_{22}H_{34}N_2Ti$ (374.40): calcd. C 70.58, H 9.15, N 7.48; found C 70.50, H 9.29, N 7.51. ^{1}H NMR (300 MHz, C_6D_6, 25 °C): δ = 7.33 (s, 4 H, Ph), 6.15 (s, 5 H, C_5H_5), 3.89 (d, J = 12.6 Hz, 2 H, CH_2), 3.83 (d, J = 12.6 Hz, 2 H, CH_2), 0.71 (s, 18 H, *t*Bu), −0.90 (s, 3 H, CH_3) ppm. ^{1}H NMR (300 MHz, $CDCl_3$, 25 °C): δ = 7.36 (m, 4 H, Ph), 6.28 (s, 5 H, C_5H_5), 4.01(s, 4 H, CH_2), 0.73 (s, 18 H, *t*Bu), −1.46 (s, 3 H, CH_3) ppm. ^{13}C{^{1}H} NMR (75 MHz, C_6D_6, 25 °C): δ = 126.1, 118.9 (Ph), 124.8 (*ipso*-Ph), 113.1 (C_5H_5), 65.6 (CH_2), 33.3 (Ti-CH_3), 35.7 (*ipso*-*t*Bu), 28.6 (*t*Bu) ppm.

Ti(η^5-C_5Me_5)[1,2-C_6H_4(NCH$_2$*t*Bu)$_2$](CH$_3$) (2): Compound **2** was prepared by treating Ti(η^5-C_5Me_5)[1,2-C_6H_4(NCH$_2$*t*Bu)$_2$]Cl (1.86 g, 4.00 mmol) in hexane with a 3 M solution of MeMgCl in THF (1.33 mL) according to the procedure described for **1** and was obtained as a dark solid (1.40 g, 3.15 mmol, 78%). $C_{27}H_{44}N_2Ti$ (444.54): calcd. C 72.95, H 9.98, N 6.30; found C 72.98, H 9.87, N 6.15. ^{1}H NMR (300 MHz, C_6D_6, 25 °C): δ = 7.22 (m, 4 H, Ph), 3.86 (d, J = 13.2 Hz, 2 H, CH_2), 3.67 (d, J = 13.2 Hz, 2 H, CH_2), 1.56 (s, 15 H, C_5Me_5), 0.96 (s, 3 H, CH_3), 0.91 (s, 18 H, *t*Bu) ppm. ^{1}H NMR (300 MHz, $CDCl_3$, 25 °C): δ = 7.24 (m, 2 H, Ph), 7.18 (m, 2 H, Ph), 3.87 (d, J = 13.2 Hz, 2 H, CH_2), 3.59 (d, J = 13.2 Hz, 2 H, CH_2), 1.58 (s, 15 H, C_5Me_5), 0.78 (s, 18 H, *t*Bu), 0.57 (s, 3 H, CH_3) ppm. ^{13}C{^{1}H} NMR (75 MHz, C_6D_6, 25 °C): δ = 124.6 (*ipso*-Ph), 123.3, 116.6 (Ph), 117.9 (*ipso*-C_5Me_5), 61.2 (CH_2), 50.5 (Ti−CH_3), 36.9 (*ipso*-*t*Bu), 29.5 (*t*Bu), 10.5 (C_5Me_5) ppm.

Ti[η^5-C_5H_4(SiMe$_3$)][1,2-C_6H_4(NCH$_2$*t*Bu)$_2$](CH$_3$) (3): Compound **3** was prepared by treating Ti[η^5-C_5H_4(SiMe$_3$)][1,2-C_6H_4(NCH$_2$-*t*Bu)$_2$]Cl (0.22 g, 0.47 mmol) with a 3 M solution of MeMgCl in THF (0.16 mL) according to the procedure described for **1** and was obtained as a red-brown oil (0.11 g, 2.46 mmol, 52%). The isolated oil consisted mainly of **3** and some LiCl as an impurity which could not be removed. The correct elemental analytical data could not be obtained, although satisfactory spectroscopic data were obtained. ^{1}H NMR (300 MHz, C_6D_6, 25 °C): δ = 7.31 (s, 4 H, Ph), 6.53, 6.28 (AA′BB′ spin system, 2 H, 2 H, C_5H_4), 4.00 (d, J = 12.0 Hz, 2 H, CH_2), 3.95 (d, J = 12.0 Hz, 2 H, CH_2), 0.75 (s, 18 H, *t*Bu), 0.28 (s, 9 H, $SiMe_3$), −0.91 (s, 3 H, CH_3) ppm. ^{1}H NMR (300 MH, $CDCl_3$, 25 °C): δ = 7.33 (m, 4 H, Ph), 6.46, 6.31 (AA′BB′ spin system, 2 H, 2 H, C_5H_4), 4.00 (s, 4 H, CH_2), 0.73 (s, 18 H, *t*Bu), 0.19 (s, 9 H, $SiMe_3$), −1.49 (s, 3 H, CH_3) ppm. ^{13}C{^{1}H} NMR (75 MHz, C_6D_6, 25 °C): δ = 125.5 (*ipso*-Ph), 126.2, 119.1 (Ph), 115.2 (*ipso*-C_5H_4), 120.1, 114.9 (C_5H_4), 66.1 (CH_2), 35.8 (*ipso*-*t*Bu), 33.2 (Ti−CH_3), 28.9 (*t*Bu), 0.29 ($SiMe_3$) ppm.

Ti(η^5-C_5H_5)[1,2-C_6H_4(NCH$_2$CH$_2$CH$_3$)$_2$](CH$_3$) (4): A 3 M solution of MeMgCl in THF (0.53 mL) was added to a stirred solution of Ti(η^5-C_5H_5)[1,2-C_6H_4(NCH$_2$CH$_2$CH$_3$)$_2$]Cl (0.54 g, 1.59 mmol) in hexane (50 mL) at −78 °C. The cooling bath was removed and the reaction mixture was slowly warmed to room temperature and stirred for 12 h. The residue was filtered and the solution concentrated and cooled. Compound **4** was obtained as a dark oil (0.37 g, 1.16 mmol, 73%). $C_{18}H_{26}N_2Ti$ (318.30): calcd. C 67.92, H 8.23, N 8.80; found C 68.30; H 8.15; N 9.01. ^{1}H NMR (300 MHz, C_6D_6, 25 °C): δ = 7.33 (m, 2 H, Ph), 7.00 (m, 2 H, Ph), 6.11 (s, 5 H, C_5H_5), 3.67 (m, 4 H, CH_2), 1.35 (m, 4 H, CH_2), 0.65 (t, J = 7.5 Hz, 6 H, CH_3), −0.25 (s, 3 H, CH_3) ppm. ^{13}C{^{1}H} NMR (75 MHz, C_6D_6, 25 °C): δ = 125.0, 115.1 (Ph), 129.7 (*ipso*-Ph), 113.1 (C_5H_5), 57.5 (N−CH_2), 35.9 (Ti−CH_3), 24.9 (CH_2), 12.1 (CH_3) ppm.

Ti(η^5-C_5Me_5)[1,2-C_6H_4(NCH$_2$CH$_2$CH$_3$)$_2$](CH$_3$) (5): A 3 M solution of MeMgCl in THF (0.17 mL) was added to a solution of Ti(η^5-C_5Me_5)[1,2-C_6H_4(NCH$_2$CH$_2$CH$_3$)$_2$]Cl (0.21 g, 0.51 mmol) in hexane (50 mL) at −78 °C. The cooling bath was removed and the reaction mixture was slowly warmed to room temperature and stirred for 12 h. After filtration, the resultant solution was concentrated and cooled to −20 °C. Complex **5** was obtained as a black oil (0.12 g, 0.31 mmol, 60%). $C_{23}H_{36}N_2Ti$ (388.43): calcd. C 71.12, H 9.34, N 7.21; found C 70.83, H 9.15, N 7.01. ^{1}H NMR (300 MHz, C_6D_6, 25 °C): δ = 7.28 (m, 2 H, Ph), 6.89 (m, 2 H, Ph), 3.64 (m, 2 H, N−CH_2), 3.47 (m, 2 H, N−CH_2), 1.68 (s, 15 H, C_5Me_5), 1.60 (m, 4 H, CH_2), 0.80 (t, J = 7.5 Hz, 6 H, CH_3), 0.82 (s, 3 H, CH_3) ppm. ^{13}C{^{1}H} NMR (75 MHz, C_6D_6, 25 °C): δ = 130.0 (*ipso*-Ph), 123.0, 113.4 (Ph), 119.5 (*ipso*-C_5Me_5), 53.3 (N−CH_2), 48.1 (Ti−CH_3), 23.4 (CH_2), 12.4 (CH_3), 10.7 (C_5Me_5) ppm.

Ti[η^5-C_5H_4(SiMe$_3$)][1,2-C_6H_4(NCH$_2$CH$_2$CH$_3$)$_2$](CH$_3$) (6): Compound **6** was prepared by treating Ti[η^5-C_5H_4(SiMe$_3$)][1,2-C_6H_4(NCH$_2$CH$_2$CH$_3$)$_2$]Cl (0.17 g, 0.41 mmol) with a 3 M solution of MeMgCl in THF (0.14 mL, 0.41 mmol) according to the procedure described for **4** and was obtained as a dark oil (0.11 g, 0.28 mmol, 68%). $C_{21}H_{34}N_2SiTi$ (390.48): calcd. C 64.60, H 8.78, N 7.17; found C 65.06, H 8.92, N 7.12. ^{1}H NMR (300 MHz, C_6D_6, 25 °C): δ = 7.32 (m, 2 H, Ph), 6.99 (m, 2 H, Ph), 6.40, 6.29 (AA′BB′ spin system, 2 H, 2 H, C_5H_4), 3.78 (m, 4 H, CH_2), 1.36 (m, 4 H, CH_2), 0.67 (t, J = 7.5 Hz, 6 H, CH_3), 0.22 (s, 9 H, $SiMe_3$), −0.23 (s, 3 H, CH_3) ppm. ^{1}H NMR (300 MHz, $CDCl_3$, 25 °C): δ = 7.22 (m, 2 H, Ph), 6.94 (m, 2 H, Ph), 6.47, 6.45 (AA′BB′ spin system, 2 H, 2 H, C_5H_4), 3.86 (m, 4 H, CH_2), 1.46 (m, 4 H, CH_2), 0.79 (t, J = 7.5 Hz, 6 H, CH_3), 0.19 (s, 9 H, $SiMe_3$), −0.69 (s, 3

 © 2005 Wiley-VCH Verlag GmbH & Co. KGaA, Weinheim

H, CH_3) ppm. $^{13}C\{^1H\}$ NMR (75 MHz, C_6D_6, 25 °C): δ = 125.8 (*ipso*-C_5H_4), 125.0, 115.2 (Ph), 120.3, 115.5 (C_5H_4), 58.4 (N−CH_2), 35.0 (Ti-CH_3), 23.7 (CH_2), 12.0 (CH_3), 0.60 ($SiMe_3$) ppm, the signal for *ipso*-Ph is not observed.

Ti(η^5-C_5H_5)[1,2-C_6H_4(NCH_2tBu)$_2$](CH_2Ph) (7): A 2 M solution of BzMgCl in THF (0.63 mL, 1.27 mmol) was added dropwise to a stirred solution of Ti(η^5-C_5H_5)[1,2-C_6H_4(NCH_2tBu)$_2$]Cl (0.50 g, 1.27 mmol) in hexane (50 mL) at −78 °C. After the addition was complete, the reaction mixture was warmed to room temperature and stirred for 12 h. The white precipitate formed was filtered and the resultant solution cooled to −40 °C. A red-brown solid was collected after filtration which was characterised as **7** (0.30 g, 0.66 mmol, 53%). $C_{28}H_{38}N_2Ti$ (450.50): calcd. C 74.65, H 8.50, N 6.22; found C 74.30, H 8.40, N 6.10. ^1H NMR (300 MHz, C_6D_6, 25 °C): δ = 7.35 (s, 4 H, Ph), 7.17, 6.86, 6.57 (t, t, d, 5 H, CH_2Ph), 6.01 (s, 5 H, C_5H_5), 3.89 (d, J = 13.8 Hz, 2 H, CH_2), 3.81 (d, J = 13.5 Hz, 2 H, CH_2), 0.89 (s, 2 H, CH_2Ph), 0.68 (s, 18 H, *t*Bu) ppm. ^1H NMR (300 MHz, $CDCl_3$, 25 °C): δ = 7.50 (m, 2 H, Ph), 7.40 (m, 2 H, Ph), 6.97, 6.60, 6.32 (t, t, d, 5 H, CH_2Ph), 6.07 (s, 5 H, C_5H_5), 4.05 (d, J = 13.8 Hz, 2 H, CH_2), 3.97 (d, J = 13.5 Hz, 2 H, CH_2), 0.74 (s, 18 H, *t*Bu), 0.44 (s, 2 H, CH_2Ph) ppm. $^{13}C\{^1H\}$ NMR (75 MH, C_6D_6, 25 °C): δ = 150.0 (*ipso*-CH_2Ph), 126.4, 118.9 (Ph), 128.1, 127.8, 120.8 (CH_2Ph), 124.9 (*ipso*-Ph), 114.8 (C_5H_5), 65.8 (CH_2), 61.52 (CH$_2$Ph). 35.8 (*ipso*-*t*Bu), 29.1 (*t*Bu) ppm.

Ti(η^5-C_5Me_5)[1,2-C_6H_4(NCH_2tBu)$_2$](CH_2Ph) (8): Compound **8** was prepared by treating Ti(η^5-C_5Me_5)[1,2-C_6H_4(NCH_2tBu)$_2$]Cl (0.50 g, 1.07 mmol) in toluene (50 mL) at −78 °C with a 2 M solution of BzMgCl in THF (0.54 mL) according to the procedure described for **7**. Recrystallisation of the final product with pentane afforded **8** as a dark-red solid (0.40 g, 0.77 mmol, 72%). $C_{33}H_{48}N_2Ti$ (520.64): calcd. C 76.13, H 9.29, N 5.38; found C 76.43, H 9.37, N 5.61. ^1H NMR (300 MHz, C_6D_6, 25 °C): δ = 7.23 (s, 4 H, Ph), 7.22, 7.12, 6.95 (t, t, d, 5 H, CH_2Ph), 4.05 (d, J = 13.5 Hz, 2 H, CH_2), 3.97 (d, J = 13.5 Hz, 2 H, CH_2), 2.67 (s, 2 H, CH_2Ph), 1.45 (s, 15 H, C_5Me_5), 0.95 (s, 18 H, *t*Bu) ppm. ^1H NMR (300 MHz, $CDCl_3$, 25 °C): δ = 7.33 (m, 2 H, Ph), 7.21 (m, 2 H, Ph), 7.18, 6.95, 6.89 (t, t, d, 5 H, CH_2Ph), 3.92 (d, J = 13.5 Hz, 2 H, CH_2), 4.14 (d, J = 13.5 Hz, 2 H, CH_2), 2.39 (s, 2 H, CH_2Ph), 1.42 (s, 15 H, C_5Me_5), 0.86 (s, 18 H, *t*Bu) ppm. $^{13}C\{^1H\}$ NMR (75 MHz, C_6D_6, 25 °C): δ = 151.3 (*ipso*-CH_2Ph), 127−128 (CH_2Ph), 123.7, 117.6 (Ph), 124.7 (*ipso*-Ph), 119.0 (*ipso*-C_5Me_5), 74.5 (CH$_2$Ph), 60.9 (CH_2), 37.4 (*ipso*-*t*Bu), 30.1 (*t*Bu), 10.6 (C_5Me_5) ppm.

Ti[η^5-C_5H_4($SiMe_3$)][1,2-C_6H_4(NCH_2tBu)$_2$](CH_2Ph) (9): Compound **9** was prepared by treating Ti[η^5-C_5H_4($SiMe_3$)][1,2-C_6H_4(NCH_2tBu)$_2$]Cl (0.22 g, 0.47 mmol) with a 2 M solution of BzMgCl in THF (0.23 mL) according to the same procedure described for **8** and was obtained as a red-brown oil (0.15 g, 0.28 mmol, 61%). $C_{31}H_{46}N_2SiTi$ (522.68): calcd. C 71.24, H 8.87, N 5.36; found C 70.80, H 8.72, N 5.20. ^1H NMR (300 MHz, C_6D_6, 25 °C): δ = 7.33 (s, 4 H, Ph), 7.17, 6.86, 6.64 (t, t, d, 5 H, CH_2Ph), 6.51, 6.18 (AA′BB′ spin system, 2 H, 2 H, C_5H_4), 3.99 (d, J = 13.5 Hz, 2 H, CH_2), 3.93 (d, J = 13.8 Hz, 2 H, CH_2), 0.85 (s, 2 H, CH_2Ph), 0.71 (s, 18 H, *t*Bu), 0.31 (s, 9 H, $SiMe_3$) ppm. ^1H NMR (300 MHz, $CDCl_3$, 25 °C): δ = 7.45 (m, 2 H, Ph), 7.38 (m, 2 H, Ph), 6.96, 6.66, 6.32 (t, t, d, 5 H, CH_2Ph), 6.34, 6.15 (AA′BB′ spin system, 2 H, 2 H, C_5H_4), 3.96 (s, 4 H, CH_2), 0.73 (s, 18 H, *t*Bu), 0.45 (s, 2 H, CH_2Ph), 0.28 (s, 9 H, $SiMe_3$) ppm. $^{13}C\{^1H\}$ NMR (75 MHz, C_6D_6, 25 °C): δ = 150.8 (*ipso*-CH_2Ph), 126.5, 119.6 (Ph), 126−128 (CH_2Ph), 124.9 (*ipso*-Ph), 122.5, 115.9 (C_5H_4), 66.1 (CH_2), 60.2 (CH_2Ph), 35.9 (*ipso*-*t*Bu), 29.2 (*t*Bu), 1.6 ($SiMe_3$) ppm, the signal for *ipso*-C_5H_4 is not observed.

Ti(η^5-C_5H_5)[1,2-C_6H_4($NCH_2CH_2CH_3$)$_2$](CH_2Ph) (10): A 2 M solution of BzMgCl in THF (1.27 mL) was added dropwise to a stirred solution of Ti(η^5-C_5H_5)[1,2-C_6H_4($NCH_2CH_2CH_3$)$_2$]Cl (0.85 g, 2.51 mmol) in hexane (50 mL) at −78 °C. After the addition was complete, the reaction mixture was warmed to room temperature and stirred for 12 h. The white precipitate formed was filtered and the resultant solution cooled to −40 °C. A dark oil was collected after filtration and was characterised as **10** (0.69 g, 1.75 mmol, 70%). Due to its high solubility in all common solvents **10** could not be recrystallised and an accurate analysis was not possible. ^1H NMR (300 MHz, C_6D_6, 25 °C): δ = 7.36 (m, 2 H, Ph), 6.97 (m, 2 H, Ph), 7.12, 6.84, 6.63 (t, t, d, 5 H, CH_2Ph), 6.01 (s, 5 H, C_5H_5), 3.57 (m, 4 H, CH_2), 1.63 (s, 2 H, CH_2Ph), 1.27 (m, 4 H, CH_2), 0.59 (t, J = 7.3 Hz, 6 H, CH_3) ppm. $^{13}C\{^1H\}$ NMR (75 MHz, C_6D_6, 25 °C): δ = 149.2 (*ipso*-CH_2Ph), 126.2 (*ipso*-Ph), 125.4, 114.5 (Ph), 125−128 (CH_2Ph), 115.5 (C_5H_5), 62.9 (CH$_2$Ph), 57.2 (N−CH_2), 23.9 (CH_2), 11.8 (CH_3).

Ti(η^5-C_5Me_5)[1,2-C_6H_4($NCH_2CH_2CH_3$)$_2$](CH_2Ph) (11): Compound **11** was prepared by treating Ti(η^5-C_5Me_5)[1,2-C_6H_4($NCH_2CH_2CH_3$)$_2$]Cl (0.80 g, 1.96 mmol) with a 2 M solution of BzMgCl in THF (0.98 mL) according to the procedure described for **10** and was obtained as a black oil (0.70 g, 1.51 mmol, 77%). $C_{29}H_{40}N_2Ti$ (464.53): calcd. C 74.98, H 8.68, N 6.03; found C 74.02, H 8.32, N 5.98. ^1H NMR (300 MHz, C_6D_6, 25 °C): δ = 7.18 (m, 2 H, Ph), 6.69 (m, 2 H, Ph), 6.80−7.11 (m, 5 H, CH_2Ph), 3.50 (t, J = 8.4 Hz, 4 H, CH_2), 2.25 (s, 2 H, CH_2Ph), 1.71 (s, 15 H, C_5Me_5), 1.49 (broad, 4 H, CH_2), 0.75 (t, J = 7.5 Hz, 6 H, CH_3) ppm. $^{13}C\{^1H\}$ NMR (75 MHz, C_6D_6, 25 °C): δ = 150.9 (*ipso*-CH_2Ph), 126−128 (CH_2Ph), 123.0, 113.3 (Ph), 121.0 (*ipso*-Ph), 120.6 (*ipso*-C_5Me_5), 73.1 (CH$_2$Ph), 53.8 (N-CH_2), 22.5 (CH_2), 12.0 (CH_3), 11.0 (C_5Me_5) ppm.

Ti[η^5-C_5H_4($SiMe_3$)][1,2-C_6H_4($NCH_2CH_2CH_3$)$_2$](CH_2Ph) (12): Compound **12** was prepared by treating Ti[η^5-C_5H_4($SiMe_3$)][1,2-C_6H_4($NCH_2CH_2CH_3$)$_2$]Cl (0.34 g, 0.83 mmol) with a 2 M solution of BzMgCl in THF (0.41 mL) according to the procedure described for **10** and was obtained as a black oil (0.25 g, 0.53 mmol, 64%). $C_{27}H_{38}N_2SiTi$ (466.58): calcd. C 69.51, H 8.21, N 6.00; found C 68.92, H 8.02, N 5.94. ^1H NMR (300 MHz, C_6D_6, 25 °C): δ = 7.34 (m, 2 H, Ph), 6.92 (m, 2 H, Ph), 6.99, 6.84, 6.66 (t, t, d, 5 H, CH_2Ph), 6.40, 6.13 (AA′BB′ spin system, 2 H, 2 H, C_5H_4), 3.68 (t, J = 7.5 Hz, 4 H, CH_2), 1.68 (s, 2 H, CH_2Ph), 1.33 (m, 4 H, CH_2), 0.64 (t, J = 7.5 Hz, 6 H, CH_3), 0.19 (s, 9 H, $SiMe_3$) ppm. ^1H NMR (300 MHz, $CDCl_3$, 25 °C): δ = 7.26 (m, 2 H, Ph), 6.99 (m, 2 H, Ph), 6.94, 6.64, 6.36 (t, t, d, 5 H, CH_2Ph), 6.45, 6.22 (AA′BB′ spin system, 2 H, 2 H, C_5H_4), 3.74 (t, J = 7.5 Hz, 4 H, CH_2), 1.46 (m, 4 H, CH_2), 1.39 (s, 2 H, CH_2Ph), 0.78 (t, J = 7.5 Hz, 6 H, CH_3), 0.22 (s, 9 H, $SiMe_3$) ppm. $^{13}C\{^1H\}$ NMR (75 MHz, C_6D_6, 25 °C): δ = 149.8 (*ipso*-CH_2Ph), 125−128 (CH_2Ph), 125.4, 115.6 (Ph), 120.8, 118.1 (C_5H_4), 63.4 (CH$_2$Bz), 57.9 (N−CH_2), 24.0 (CH_2), 12.1 (CH_3), 0.78 ($SiMe_3$) ppm, the signal for *ipso*-C_5H_4 is not observed.

Al_2[1,2-C_6H_4(NCH_2tBu)$_2$]Me_4 (13): A 2 M solution of TMA (1.21 mL, 2.42 mmol) in toluene was added to a solution of 1,2-C_6H_4($NHCH_2tBu$)$_2$ (0.3 g, 1.21 mmol) in toluene (30 mL) at −78 °C. After stirring for 12 h, the solvent was completely removed and the resultant solid extracted successively with hexane/toluene mixtures. The resultant solution was concentrated and cooled to −20 °C to give a purple solid which was identified as **13** (0.32 g, 0.88 mmol, 73%). $C_{20}H_{38}Al_2N_2$ (360.50): calcd. C 66.64, H 10.62, N 7.77; found C 65.98, H 10.26, N 7.39. ^1H NMR (300 MHz, C_6D_6, 25 °C): δ = 6.81 (m, 2 H, Ph), 6.97 (m, 2 H, Ph), 2.93 (s, 4 H, CH_2), 0.89 (s, 18 H, *t*Bu), −0.07 (s, 6 H, Al−CH_3), −0.90 (s, 6

 © 2005 Wiley-VCH Verlag GmbH & Co. KGaA, Weinheim

H, Al−CH_3) ppm. ^{1}H NMR (300 MHz, $CDCl_3$, 25 °C): δ = 6.88 (s, 4 H, Ph), 3.02 (s, 4 H, CH_2), 1.03 (s, 18 H, *t*Bu), −0.45 (s, 6 H, Al-CH_3), −1.33 (s, 6 H, Al−CH_3) ^{13}C{^{1}H} NMR (75 MHz, C_6D_6, 25 °C): δ = 142.8 (*ipso*-Ph), 121.9, 114.0 (Ph), 56.7 (CH_2), 33.7 (*ipso*-*t*Bu), 29.4 (*t*Bu), −5.4, −11.1 (broad, Al−CH_3) ppm.

Al_2[1,2-C_6H_4($NCH_2CH_2CH_3$)$_2$]Me_4 (14): The same procedure described for **13** using the TMA solution in toluene (2.44 mL, 4.89 mmol) and 1,2-C_6H_4($NCH_2CH_2CH_3$)$_2$ (0.47 g, 2.44 mmol) gave **14** as a dark purple oil (0.40, 1.31 mmol, 54%). An elemental analysis could not be obtained due to the presence of small amounts of impurities which could not be removed. ^{1}H NMR (300 MHz, C_6D_6, 25 °C): δ = 6.85 (m, 2 H, Ph), 6.51 (m, 2 H, Ph), 2.72 (m, 4 H, CH_2), 1.58 (m, 4 H, CH_2), 0.68 (t, J = 7.2 Hz, 6 H, CH_3), −0.13 (s, 6 H, Al−CH_3), −1.04 (s, 6 H, Al−CH_3) ppm. ^{1}H NMR (300 MHz, $CDCl_3$, 25 °C): δ = 6.90 (m, 2 H, Ph), 6.70 (m, 2 H, Ph), 2.99 (m, 4 H, CH_2), 1.71 (m, 4 H, CH_2), 1.01 (t, J = 7.2 Hz, 6 H, CH_3), −0.47 (s, 6 H, Al−CH_3), −1.46 (s, 6 H, Al−CH_3) ppm. ^{13}C{^{1}H} NMR (75 MHz, C_6D_6, 25 °C): δ = 141.6 (*ipso*-Ph), 112.6, 122.4 (Ph), 46.5 (CH_2), 23.3 (CH_2), 12.0 (CH_3), −6.4, −13.0 (broad, Al−CH_3) ppm.

Acknowledgments

Generous financial assistance from the DGICYT (Project MAT2001-1309) is gratefully acknowledged.

[1] A. T. Rappé, W. M. Skiff, C. J. Casewit, *Chem. Rev.* **2000**, *100*, 1435−1456.
[2] G. G. Hlatky, *Coord. Chem. Rev.* **2000**, *199*, 235−329.
[3] H. G. Alt, A. Koppl, *Chem. Rev.* **2000**, *100*, 1205−1221.
[4] P. C. Möhring, N. J. Coville, *J. Organomet. Chem.* **1994**, *479*, 1−29.
[5] H. H. Brintzinger, D. Fischer, R. Mülhaupt, B. Rieger, R. M. Waymouth, *Angew. Chem. Int. Ed. Engl.* **1995**, *34*, 1143−1170.
[6] M. Bochmann, *J. Chem. Soc., Dalton Trans.* **1996**, 255−270.
[7] S. W. Ewart, M. J. Sarsfield, D. Jeremic, T. L. Tremblay, E. F. Williams, M. C. Baird, *Organometallics* **1998**, *17*, 1502−1510.
[8] W. Kaminsky, M. Arndt, in *Polymer Synthesis/Polymer Catalysis*, vol. 127 ("Advances in Polymer Science"), Springer-Verlag, Berlin, **1997**, pp. 143−187.
[9] G. Guerra, P. Longo, L. Cavallo, P. Corradini, L. Resconi, *J. Am. Chem. Soc.* **1997**, *119*, 4394−4403.
[10] A. M. Thayer, *Chem. Eng. News* **1995**, *73*, 15−20.
[11] K. B. Sinclair, R. B. Wilson, *Chem. Ind.* **1994**, 857−862.
[12] V. K. Gupta, S. Satish, I. S. Bhardwaj, *J. Macromol. Sci. Rev. Macromol. Chem. Phys.* **1994**, *C34*, 439−514.
[13] T. R. Younkin, E. F. Connor, J. I. Henderson, S. K. Friedrich, R. H. Grubbs, D. A. Bansleben, *Science* **2000**, *288*, 1750−1751.
[14] M. González-Maupoey, T. Cuenca, L. M. Frutos, O. Castaño, E. Herdtweck, *Organometallics* **2003**, *22*, 2694−2704.
[15] J. Cano, P. Royo, M. Lanfranchi, M. A. Pellinghelli, A. Tiripicchio, *Angew. Chem. Int. Ed.* **2001**, *40*, 2495−2496.
[16] G. J. P. Britovsek, M. Bruce, V. C. Gibson, B. S. Kimberley, P. J. Maddox, S. Mastroianni, S. J. McTavish, C. Redshaw, G. A. Solan, S. Stromberg, A. J. P. White, D. J. Williams, *J. Am. Chem. Soc.* **1999**, *121*, 8728−8740.
[17] G. J. P. Britovsek, V. C. Gibson, B. S. Kimberley, P. J. Maddox, S. J. McTavish, G. A. Solan, A. J. P. White, D. J. Williams, *Chem. Commun.* **1998**, 849−850.
[18] C. M. Wang, S. Friedrich, T. R. Younkin, R. T. Li, R. H. Grubbs, D. A. Bansleben, M. W. Day, *Organometallics* **1998**, *17*, 3149−3151.
[19] J. D. Scollard, D. H. McConville, *J. Am. Chem. Soc.* **1996**, *118*, 10008−10009.
[20] J. D. Scollard, D. H. McConville, N. C. Payne, J. J. Vittal, *Macromolecules* **1996**, *29*, 5241−5243.
[21] Y. Yoshida, S. Matsui, Y. Takagi, M. Mitani, M. Nitabaru, T. Nakano, H. Tanaka, T. Fujita, *Chem. Lett.* **2000**, 1270−1271.
[22] Y. Yoshida, S. Matsui, Y. Takagi, M. Mitani, T. Nakano, H. Tanaka, N. Kashiwa, T. Fujita, *Organometallics* **2001**, *20*, 4793−4799.
[23] Y. Yoshida, J. Saito, M. Mitani, Y. Takagi, S. Matsui, S. Ishii, T. Nakano, N. Kashiwa, T. Fujita, *Chem. Commun.* **2002**, 1298−1299.
[24] S. Mecking, L. K. Johnson, L. Wang, M. Brookhart, *J. Am. Chem. Soc.* **1998**, *120*, 888−899.
[25] B. J. Burger, M. E. Thompson, W. D. Cotter, J. E. Bercaw, *J. Am. Chem. Soc.* **1990**, *112*, 1566−1577.
[26] C. M. Killian, D. J. Tempel, L. K. Johnson, M. Brookhart, *J. Am. Chem. Soc.* **1996**, *118*, 11664−11665.
[27] M. Brookhart, J. M. Desimone, B. E. Grant, M. J. Tanner, *Macromolecules* **1995**, *28*, 5378−5380.
[28] V. Tabernero, T. Cuenca, E. Herdtweck, *Eur. J. Inorg. Chem.* **2004**, 3154−3162.
[29] M. L. H. Green, J. Sassmannshausen, *Chem. Commun.* **1999**, 115−116.
[30] J. C. Flores, J. C. W. Chien, M. D. Rausch, *Organometallics* **1995**, *14*, 1827−1833.
[31] R. Gómez, R. Duchateau, A. N. Chernega, J. H. Teuben, F. T. Edelmann, M. L. H. Green, *J. Organomet. Chem.* **1995**, *491*, 153−158.
[32] M. Gonzalez-Maupoey, T. Cuenca, L. M. Frutos, O. Castano, E. Herdtweck, *Organometallics* **2003**, *22*, 2694−2704.
[33] M. P. Coles, D. C. Swenson, R. F. Jordan, V. G. Young, *Organometallics* **1997**, *16*, 5183−5194.
[34] S. J. Kim, I. N. Jung, B. R. Yoo, S. H. Kim, J. J. Ko, D. J. Byun, S. O. Kang, *Organometallics* **2001**, *20*, 2136−2144.
[35] S. Danièle, C. Drost, B. Gehrhus, S. M. Hawkins, P. B. Hitchcock, M. F. Lappert, P. G. Merle, S. G. Bott, *J. Chem. Soc., Dalton Trans.* **2001**, 3179−3188.
[36] T. I. Gountchev, T. D. Tilley, *Inorg. Chim. Acta* **2003**, *345*, 81−88.
[37] S. Danièle, P. B. Hitchcock, M. F. Lappert, *Chem. Commun.* **1999**, 1909−1910.
[38] N. A. H. Male, M. ThorntonPett, M. Bochmann, *J. Chem. Soc., Dalton Trans.* **1997**, 2487−2494.
[39] Y. M. Jeon, S. J. Park, J. Heo, K. Kim, *Organometallics* **1998**, *17*, 3161−3163.
[40] S. Saccheo, G. Gioia, A. Grassi, D. E. Bowen, R. F. Jordan, *J. Mol. Catal. A: Chem.* **1998**, *128*, 111−118.
[41] A. Zambelli, L. Oliva, C. Pellecchia, *Macromolecules* **1989**, *22*, 2129−2130.
[42] N. Ishihara, M. Kuramoto, M. Uoi, *Macromolecules* **1988**, *21*, 3356−3360.
[43] N. Ishihara, T. Seimiya, M. Kuramoto, M. Uoi, *Macromolecules* **1986**, *19*, 2464−2465.
[44] A. Kucht, H. Kucht, S. Barry, J. C. W. Chien, M. D. Rausch, *Organometallics* **1993**, *12*, 3075−3078.
[45] P. Longo, A. Proto, A. Zambelli, *Macromol. Chem. Phys.* **1995**, *196*, 3015−3029.
[46] A. Grassi, M. Caprio, A. Zambelli, D. E. Bowen, *Macromolecules* **2000**, *33*, 8130−8135.
[47] I. Kim, R. F. Jordan, *Macromolecules* **1996**, *29*, 489−491.
[48] J. J. Eisch, K. Mackenzie, H. Windisch, C. Krüger, *Eur. J. Inorg. Chem.* **1999**, 153−162.
[49] M. M. Lynam, L. V. Interrante, C. H. Patterson, R. P. Messmer, *Inorg. Chem.* **1991**, *30*, 1918−1922.
[50] Z. Jiang, L. V. Interrante, D. Kwon, F. S. Tham, R. Kullnig, *Inorg. Chem.* **1991**, *30*, 995−1000.
[51] J. J. Byers, B. S. Lee, W. T. Pennington, G. H. Robinson, *Polyhedron* **1992**, *11*, 967−972.
[52] J. L. Atwood, S. M. Lawrence, C. L. Raston, *J. Chem. Soc., Chem. Commun.* **1994**, 73−74.

 © 2005 Wiley-VCH Verlag GmbH & Co. KGaA, Weinheim

[53] X. H. Bei, D. C. Swenson, R. F. Jordan, *Organometallics* **1997**, *16*, 3282−3302.
[54] E. A. Ison, K. A. Abboud, I. Ghiviriga, J. M. Boncella, *Organometallics* **2004**, *23*, 929−931.
[55] L. Resconi, S. Bossi, L. Abis, *Macromolecules* **1990**, *23*, 4489−4491.
[56] C. Sishta, R. M. Hathorn, T. J. Marks, *J. Am. Chem. Soc.* **1992**, *114*, 1112−1114.
[57] I. Tritto, S. X. Li, M. C. Sacchi, G. Zannoni, *Macromolecules* **1993**, *26*, 7111−7115.
[58] I. Tritto, R. Donetti, M. C. Sacchi, P. Locatelli, G. Zannoni, *Macromolecules* **1999**, *32*, 264−269.
[59] K. P. Bryliakov, N. V. Semikolenova, D. V. Yudaev, V. A. Zakharov, H. H. Brintzinger, M. Ystenes, E. Rytter, E. P. Talsi, *J. Organomet. Chem.* **2003**, *683*, 92−102.
[60] K. P. Bryliakov, N. V. Semikolenova, V. A. Zakharov, E. P. Talsi, *J. Organomet. Chem.* **2003**, *683*, 23−28.
[61] D. E. Babushkin, N. V. Semikolenova, V. A. Zakharov, E. P. Talsi, *Macromol. Chem. Phys.* **2000**, *201*, 558−567.
[62] S. Pasynkiewicz, *Polyhedron* **1990**, *9*, 429−453.
[63] C. J. Harlan, S. G. Bott, A. R. Barron, *J. Am. Chem. Soc.* **1995**, *117*, 6465−6474.
[64] K. P. Bryliakov, N. V. Semikolenova, D. V. Yudaev, M. Ystenes, E. Rytter, V. A. Zakharov, E. P. Talsi, *Macromol. Chem. Phys.* **2003**, *204*, 1110−1117.
[65] V. Volkis, M. Shmulinson, C. Averbuj, A. Lisovskii, F. T. Edelmann, M. S. Eisen, *Organometallics* **1998**, *17*, 3155−3157.
[66] J. Sassmannshausen, M. E. Bochmann, J. Rosch, D. Lilge, *J. Organomet. Chem.* **1997**, *548*, 23−28.
[67] E. Giannetti, G. M. Nicoletti, R. Mazzocchi, *J. Polym. Sci. Pol. Chem.* **1985**, *23*, 2117−2134.
[68] R. F. Jordan, C. S. Bajgur, R. Willett, B. Scott, *J. Am. Chem. Soc.* **1986**, *108*, 7410−7411.
[69] R. F. Jordan, R. E. Lapointe, P. K. Bradley, N. Baenziger, *Organometallics* **1989**, *8*, 2892−2903.
[70] H. Yasuda, K. Tatsumi, T. Okamoto, K. Mashima, K. Lee, A. Nakamura, Y. Kai, N. Kanehisa, N. Kasai, *J. Am. Chem. Soc.* **1985**, *107*, 2410−2422.

Received July 29, 2004
Early View Article
Published Online November 24, 2004

 © 2005 Wiley-VCH Verlag GmbH & Co. KGaA, Weinheim

N-Ferrocenyl-Substituted Planar-Chiral N-Heterocyclic Carbenes and Their Pd^{II} Complexes

Andreas Bertogg,[a] Francesco Camponovo,[a] and Antonio Togni*[a]

Keywords: Carbene ligands / Chirality / Ferrocenes / Nitrogen heterocycles / Palladium

The *N*-ferrocenyl-linked N-heterocyclic carbenes **1a** and **1b** were obtained by treatment of their imidazolium salts **12a** and **12b** with potassium *tert*-butoxide. The latter were shown to be accessible from (*R*)-1-amino-2-methylferrocene (**9**) and aminoferrocene, respectively, which were converted into the corresponding formamidines and then subjected to a novel cyclization procedure. Treating the ligand precursors **12a** and **12b** with $[Pd(OAc)_2]_3$ under different reaction conditions afforded the *trans*-pyridine-substituted Pd^{II} complexes **14a** and **14b** as well as their *trans*-triphenylphosphane-substituted counterparts **16a** and **16b** and, in the case of the chiral ligand precursor, the dinuclear Pd^{II} complex **15a**. Conformational analysis of the ligands based on the X-ray structures of **12a**, **12b** and **16a** revealed the dependence of the two torsion angles between the central imidazolium core and the adjacent ferrocenyl substituents on the steric and electronic properties of the observed systems.

(© Wiley-VCH Verlag GmbH & Co. KGaA, 69451 Weinheim, Germany, 2005)

Introduction

Phosphanes bearing planar-chiral ferrocenyl groups are established ligands in coordination chemistry and have proven to be very successful in asymmetric catalysis.[1] Although N-heterocyclic carbenes (NHCs) may often act as phosphane substitutes, leading to considerably improved performances of the resultant catalysts,[2−5] both achiral and chiral ferrocenyl-substituted NHCs are still rare.[6−16] These can be divided into two classes: either directly *N*-ferrocenyl-substituted[6,7] or linked by a methylene, ethylene[10,11,16] or an ethenyl spacer.[12−15] The latter are of particular interest as bi- or tridentate ligands,[13,15] while for monodentate ligands it seems appropriate to further restrict the conformational freedom to the rotation around the two nitrogen−ferrocenyl bonds, thus leading to directly *N*-ferrocenyl-substituted carbenes.[17] Achiral *N*,*N*′-diferrocenyl-substituted imidazolium salts[18] are known in the literature but the reported yields of their synthesis are moderate and the salts resisted controlled deprotonation.[6]

Square-planar Pd^{II} complexes serve as catalyst precursors in numerous cross-coupling and Heck-type reactions. Recently, chiral monodentate NHCs have been shown to be the ligands of choice in Pd-catalyzed asymmetric α-arylations of carbonyl compounds, of which cyclic amide α-arylations gave the best results.[19] Pd complexes bearing chiral monodentate NHCs are still rare and complexes bearing planar-chiral monodentate NHCs are as-yet unknown. We reasoned that ligands showing the steric features of **1a** and **1b** attached to Pd^{II}, in combination with two halides and one potentially labile ligand, might lead to active systems for the above-mentioned asymmetric catalytic applications. We report here a new, high-yielding synthetic strategy leading to the isolation of both achiral and chiral imidazolium iodides **12a** and **12b** that can be deprotonated to the carbenes **1a** and **1b** (Scheme 1). Complexes showing the desired constitution were synthesized from $[Pd(OAc)_2]_3$ and proved to be active catalyst precursors in amide α-arylations.

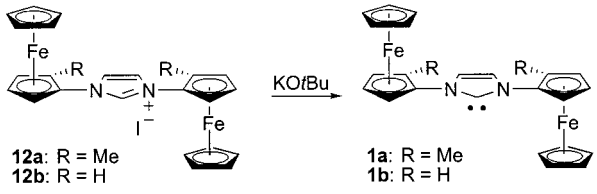

Scheme 1

Results and Discussion

Ligand Synthesis

The chiral imidazolium iodide **12a** was synthesized from the known chiral acetal **2**[20] in ten steps in an overall yield of 30% (Scheme 2). Thus, stereoselective lithiation of **2** followed by electrophilic quenching with methyl iodide led to the planar-chiral acetal **3**, which was then converted into the aldehyde **4**. The carboxylic acid **6a**, which served as starting material in the following reaction sequence, was

[a] Department of Chemistry and Applied Biosciences, Swiss Federal Institute of Technology, ETH,
Hönggerberg, 8093 Zürich, Switzerland
Fax: + 41-1632-1310
E-mail: togni@inorg.chem.ethz.ch

 DOI: 10.1002/ejic.200400691 © 2005 Wiley-VCH Verlag GmbH & Co. KGaA, Weinheim

produced by iodine-mediated oxidation of the aldehyde **4**[21] to the ester **5**, followed by saponification. Its achiral counterpart **6b** is accessible by carboxylation of monolithioferrocene generated in situ from ferrocene (Scheme 3).[22]

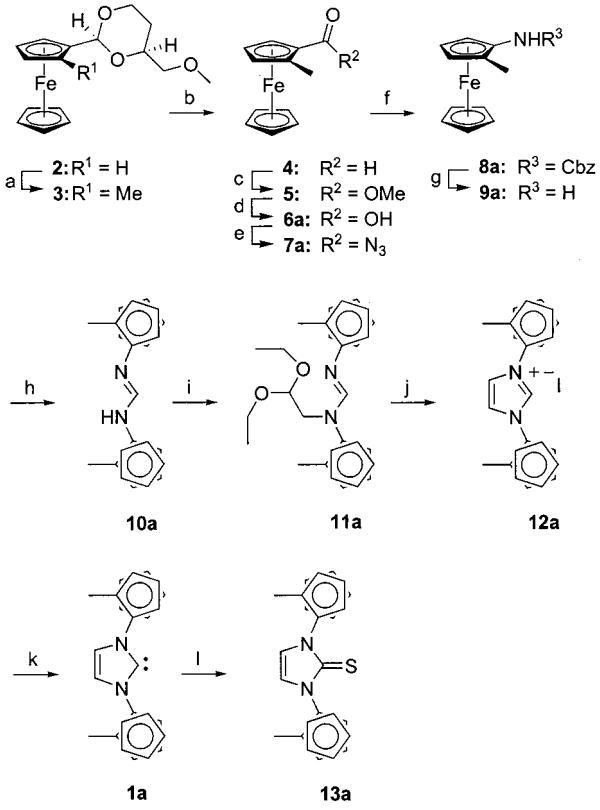

Scheme 2. Conditions: (a) *t*BuLi, Et_2O, −78 °C to room temp. then MeI, Et_2O, −78 °C, 95%; (b) PTSA monohydrate, H_2O, CH_2Cl_2, room temp., 98%; (c) I_2, KOH, MeOH, 0 °C to room temp. 77%; (d) NaOH, EtOH, H_2O, room temp., 93%; (e) i) preparation of activating reagent (in situ): DMF, thionyl chloride, benzene, room temp.; ii) reaction: activating reagent, NaN_3, py, Bu_4NBr, CH_2Cl_2, room temp., in situ; (f) benzylic alcohol, 90 °C, 81% (two steps); (g) H_2, Pd/C, Me_2CHOH, room temp., quant.; (h) *s*-triazine, dioxane, 100 °C, quant.; (i) bromoacetaldehyde diethylacetal, NaH, DMF, 75 °C, 82%; (j) $BF_3{\cdot}OEt_2$, NaI, MeCN, room temp., 71%; (k) KO*t*Bu, pentane, room temp.; (l) S_8, benzene, room temp.

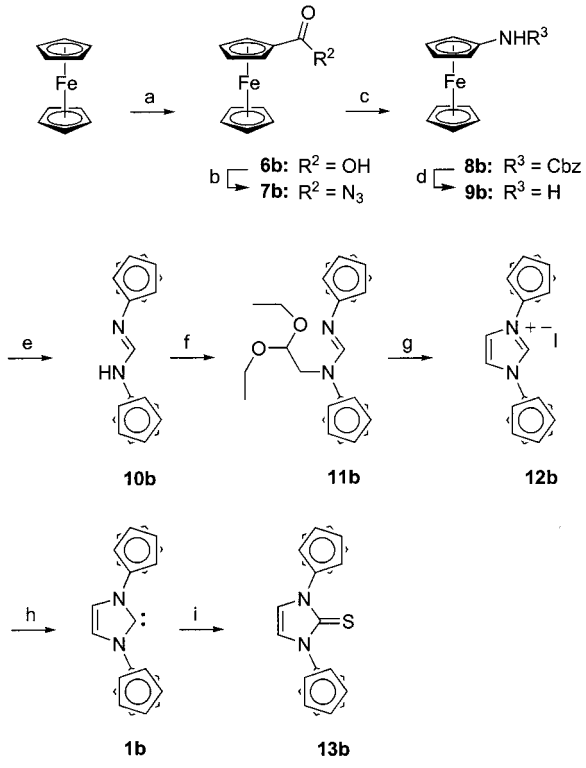

Scheme 3. Conditions: (a) *t*BuLi, THF, −78 °C to room temp. 67%; (b) i) preparation of activating reagent (in situ): DMF, thionyl chloride, benzene, room temp.; ii) reaction: activating reagent, NaN_3, py, Bu_4NBr, CH_2Cl_2, room temp., in situ; (c) benzylic alcohol, 90 °C, 55% (two steps); (d) H_2, Pd/C, Me_2CHOH, room temp., 96%; (e) *s*-triazine, dioxane, 100 °C, 96%.; (f) 2-bromo-1,1-diethoxyethane, NaH, DMF, 75 °C, 79%; (g) $BF_3{\cdot}OEt_2$, NaI, MeCN, room temp., 75%; (h) KO*t*Bu, pentane, room temp.; (i) S_8, benzene, room temp.

Apart from the cyclization procedure discussed below, another major challenge in the present ligand synthesis was the generation of the nitrogen-ferrocene bond. Since aminoferrocenes serve as intermediates in the synthesis of various ligands and optically active materials, this problem has attracted considerable interest.[23−28] One of the oldest routes[26] is based on a Curtius degradation of ferrocenecarboxylic acid chloride; other methods have used bromoferrocene[29−31] or ferroceneboronic acid[32] as starting material for copper-mediated amination reactions. Based on its simplicity and on the easy accessibility of its starting materials, we chose to use the Curtius rearrangement sequence, which, in our case, proved to be attractive both in terms of synthetic feasibility and the high isolated yields of the products. The chiral acid **6a** as well as the achiral acid **6b** were activated[33] and converted, in situ, into the ferrocenyl carbonyl azides **7a** and **7b**, which rearranged upon heating to the corresponding isocyanates. Addition of benzylic alcohol followed by heating generated the carbamic acid esters **8a**,**b** in a one-pot procedure from **6a**,**b** (Scheme 2 and 3). Reductive deprotection of the Cbz-protected amines **8a**,**b** led to the electron rich, strongly nucleophilic and air-sensitive amines **9a**,**b**.[34]

The most frequently used reaction sequence from primary amines to imidazolium salts involves condensation of the amines with a 1,2-dialdehyde to yield the corresponding diimine. Conversion of the latter with a one-carbon synthetic equivalent in the formal oxidation state of formaldehyde then leads to an imidazolium salt that is suitable for deprotonation. In contrast to a recently published procedure,[6] we decided not to construct the heterocyclic core of the target molecule by condensation of the ferrocenylamines with glyoxal, followed by cyclization with formaldehyde, due to low reported yields and demanding purifications. Instead, we chose to transform the ferrocenylamines **9a** and **9b** into *N*,*N*′-diferrocenyl-substituted amidines and to use the latter as intermediates in the cyclization sequence. The amidines **10a**,**b** were easily obtained from the amines **9a**,**b** by methinyl group transfer from *s*-triazine[35] and could be considered as being interesting potential ligands in their own right. The missing C_2 fragment was in-

 © 2005 Wiley-VCH Verlag GmbH & Co. KGaA, Weinheim

corporated into the structures by treating the amidinate anions of **10a**,**b** with 2-bromo-1,1-diethoxyethane to give the acetals **11a**,**b**.[36] Addition of an excess of $BF_3{\cdot}OEt_2$ led to the desired cyclization and to the 4-ethoxy-4,5-dihydroimidazolium cation, which, under prolonged heating, eliminated ethanol to form the aromatic target core. The imidazolium iodides **12a**,**b** were obtained after anion exchange and column chromatography. It is noteworthy that in the high yielding reaction sequence from the carbamic acid esters **8a**,**b** to the imidazolium iodides **12a**,**b** only one chromatographic purification of the products and intermediates is required. Both chiral and achiral carbenes **1a** and **1b** were prepared by adding potassium *tert*-butoxide to a slurry of the imidazolium iodides **12a** or **12b** in pentane, followed by evaporation of the solvent and selective extraction of the products with benzene. The carbenes proved to be stable in solution in C_6D_6 over a period of 24 hours without any sign of decomposition, as ascertained by ^{1}H NMR spectroscopy. In the ^{13}C NMR spectra the diagnostic chemical shifts at δ = 221.1 ppm (**1a**) and 216.1 ppm (**1b**) were detected. Adding S_8 to either of the carbenes resulted in the formation of the corresponding thiones **13a** and **13b** (Scheme 2 and 3).

Synthesis of Palladium Complexes

A series of NHC-substituted Pd^{II} complexes were obtained from the reaction of the imidazolium iodides **12a**,**b** with $[Pd(OAc)_2]_3$ under different reaction conditions (Scheme 4). We reasoned that Pd complexes substituted with one NHC, two halides and one hemilabile ligand might be potent precatalysts for both Heck-type and cross-coupling reactions since, in both cases, at least one ligand stabilizing the active Pd^0 species as well as two free coordination sites *cis* to each other are required in the catalytic cycle. While the bulky and strongly bound carbene ligand is supposed to stabilize the active Pd^0 species and prevent precipitation of Pd black, the hemilabile ligand can be split off previous to oxidative addition of the aryl halide substrate. Pyridine seemed to be an advantageous hemilabile ligand as it can also be used in large excess as a solvent in the preparation of the catalyst precursor. Further advantage can be taken of its high dielectric constant, which allows complete dissolution of the imidazolium iodides, and of its ability to act as a base, which might facilitate the in situ deprotonation of the imidazolium iodides. Thus, reaction of **12b** and $[Pd(OAc)_2]_3$ in the presence of sodium iodide in pyridine afforded the pyridine-substituted complex **14b** regardless of whether one or two equivalents of the imidazolium iodide were used. Small amounts of the known complex $PdI_2(pyridine)_2$ were separated from the main product by column chromatography. Subjecting the chiral imidazolium iodide **12a** to the same reaction conditions resulted in an isolated equimolar mixture of both the pyridine-substituted complex **14a** and the equivalent iodo-bridged dinuclear derivative **15a**. Interestingly, the ^{1}H NMR spectrum of the chromatographed mixture showed that the iodo-bridged dimer **15a** contains two non-equivalent ferrocenyl ligands, thereby indicating restricted rotation around the Pd−C bond. This phenomenon has been observed before in an analogous bridged complex bearing two ethenyl-linked, diferrocenyl-substituted chiral NHCs that have been characterized by NMR spectroscopy and X-ray diffraction studies.[37] In analogy to that case it seems very likely that the observed anisotropy of the ferrocenyl substituents results from the typical butterfly conformation of the Pd_2I_2 core.[38] Upon adding triphenylphosphane, the mixture of the two chiral complexes **14a** and **15a** was cleanly converted into the carbene phosphane complex **16a**, whose *trans* configuration was determined by X-ray analysis (vide infra). The achiral, pyridine-substituted complex **14b**, under the same reaction conditions, gave the analogous complex **16b**. The *trans* configuration of both complexes **16a** and **16b** was further supported by the large coupling constants between the phosphorus nuclei and the carbene carbon nuclei.[39] Long-range coupling to the olefinic carbons of the NHC over four bonds and long-range coupling to the olefinic hy-

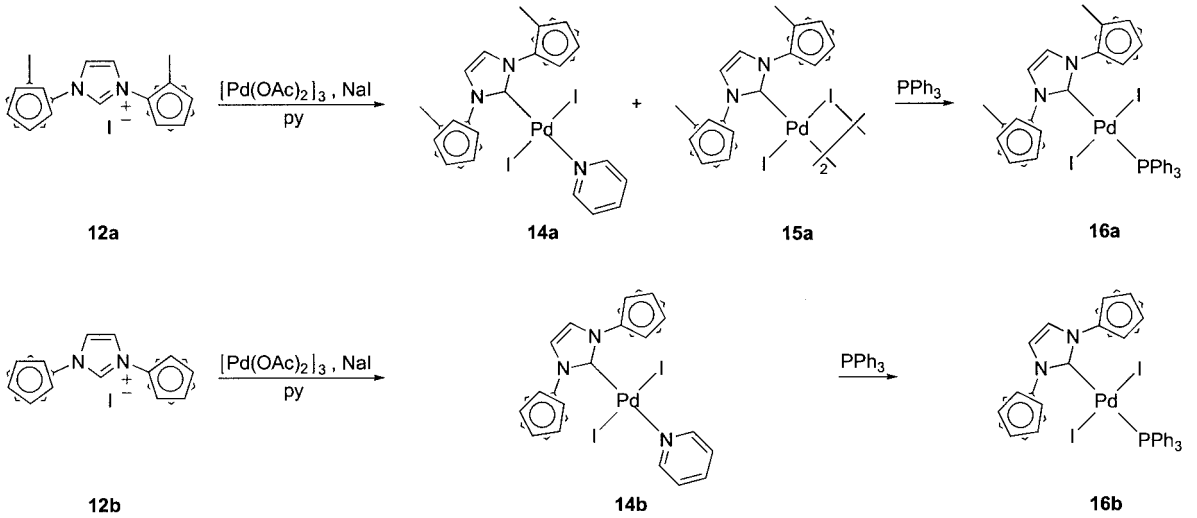

Scheme 4

 © 2005 Wiley-VCH Verlag GmbH & Co. KGaA, Weinheim

drogen atoms over five bonds were observed.[39] Selective saturation of the phosphorus hydrogen transition resulted in a decoupled ^{1}H NMR spectrum, as performed in the case of **16a**.

Crystal Structures and Conformational Analysis

Single-crystal X-ray analysis of the imidazolium iodides **12a** (Figure 1) and **12b** (Figure 2) showed the expected bond lengths and angles within the imidazolium cores, thus indicating that the steric and electronic features of the ferrocenyl subunits do not significantly alter the properties of the heterocycle. In both cations the ferrocenyl−imidazolium bond lengths lie in the range of a C−N single bond, thus excluding delocalisation of the π electrons between the cyclic moieties of the molecules. This conclusion is in agreement with the observed non-planar arrangement of the three connected cyclic subunits.[40] The ferrocenyl−methyl bond lengths in **12a** do not show any deviation from the expected value.

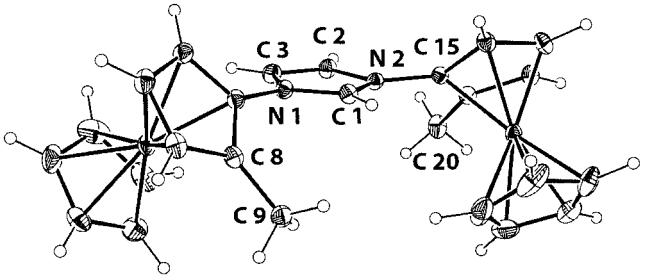

Figure 1. ORTEP view of the cation of **12a**, with 30% thermal ellipsoids; selected bond lengths [A] and angles [°]: C(1)−N(1) 1.327(3), C(1)−N(2) 1.332(3), C(2)−C(3) 1.346(4), N(1)−C(3) 1.378(3), N(2)−C(2) 1.387(3), N(1)−C(4) 1.426(3), N(2)−C(15) 1.420(3), C(8)−C(9) 1.498(4), C(19)−C(20) 1.492(3); N(1)−C(1)−N(2) 108.6(2), C(1)−N(1)−C(4)−C(8) 310.5(4), C(1)−N(2)−C(15)−C(19) 143.8(3)

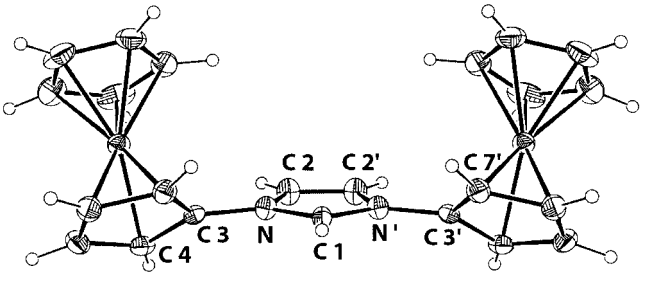

Figure 2. ORTEP view of the cation of **12b**, with 30% thermal ellipsoids; selected bond lengths [A] and angles [°]: C(1)−N(1) 1.329(8), C(2)−C(2′) 1.331(14), N−C(2) 1.380(8), N−C(3) 1.419(8); N−C(1)−N′ 108.4(8), C(1)−N−C(3)−C(4) 139.4(8), C(1)−N′−C(3′)−C(7′) 320.9(11)

X-ray analysis of the chiral Pd complex **16a** (Figure 3) reveals that the main structural features of **12a**, apart from the torsion angles, are preserved in the ligand. While the extent of delocalization in the heterocyclic fragment is slightly decreased and the N−C−N angle is reduced from 108.6(2)° to 104.9(3)°, the ferrocenyl−imidazolium bond lengths stay constant. The palladium−carbon bond of 2.004(3) Å lies in the typical range.[40]

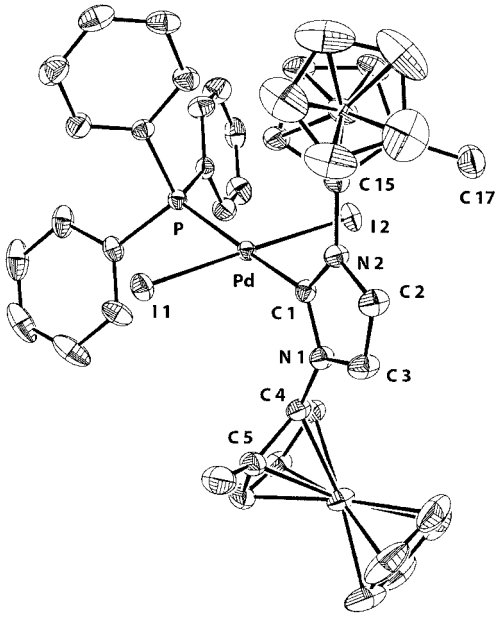

Figure 3. ORTEP view of the complex **16a**, with 30% thermal ellipsoids; hydrogen atoms are omitted for clarity; selected bond lengths [A] and angles [°]: C(1)−Pd 2.004(3), Pd−P 2.3298(9), Pd−I(1) 2.6280(5), Pd−I(2) 2.5932(5), C(1)−N(1) 1.351(4), C(1)−N(2) 1.359(4), C(2)−C(3) 1.323(5), N(1)−C(3) 1.385(4), N(2)−C(2) 1.386(5), N(1)−C(4) 1.426(4), N(2)−C(15) 1.430(4), C(5)−C(6) 1.489(6), C(16)−C(17) 1.502(6); N(1)−C(1)−N(2) 104.9(3), C(1)−N(1)−C(4)−C(5) 246.0(4), C(1)−N(2)−C(15)−C(16) 245.4(4)

Since the overall shape of the ligand and, as a consequence, its ability to efficiently transfer chirality in asymmetric catalytic reactions depends on its conformation, it is important to note that the latter is fully described by the two torsion angles between the central imidazolium core and the adjacent ferrocenyl substituents. Rotation around the two ferrocenyl−nitrogen bonds in solution at room temperature proved to be fast on the NMR timescale for **12b**, **13b**, **14b** and **16b**. No such conclusions can be drawn for their chiral counterparts due to symmetry restrictions. In the crystal structures, however, well-defined conformations could be studied. In **12a** torsion angles of 310.5(4)° and 143.8(3)° around C(1)−N(1)−C(4)−C(8) and C(1)−N(2)−C(15)−C(19), respectively, were detected. The corresponding angles in **12b** around C(1)−N−C(3)−C(4) and around C(1)−N′−C(3′)−C(7′) are 139.4(8)° and 320.9(11)°, respectively, whereas the C(1)−N(1)−C(4)−C(5) and C(1)−N(2)−C(15)−C(16) angles in **16a** are 246.0(4)° and 245.4(4)°, respectively. These at-first-sight arbitrary results can be rationalized by uncovering the forces that determine the torsion angles.

Conformational analysis of the solid-state structures of compounds **12a**, **12b**, **16a** and of two analogous achiral derivatives reported by Bildstein et al.[6] reveals that their conformations are mainly governed by two opposing forces: i) pseudo allylic repulsion[41] between the *ortho* substituents of the ferrocenyl fragments and the *ortho* substituents of the heterocycle, and ii) steric interactions between the substituents on the imidazolium core and the unsubstituted Cp

 © 2005 Wiley-VCH Verlag GmbH & Co. KGaA, Weinheim

ring. The orientation of the two ferrocenyl planes with respect to each other appears to be of minor importance, as can be seen by comparing the orientations in the crystal structures of, for example, **12a** and **12b**. Therefore, the two torsion angles in a molecule can be analyzed separately, thus simplifying the analysis: only the tilt angles ($0° \leq$ tilt angle $\leq 90°$) between the ferrocenyl planes and the heterocyclic plane need to be considered as relevant. As shown in Figure 4, all known tilt angles of the discussed imidazolium salts lie in a specific range between 36.2(3)° and 49.5(4)°, whereas the sulfur adduct **13b**[6] shows slightly larger angles of 53.7(3)°. This shows that even small atoms or substituents such as hydrogen, methyl or thiooxo attached to the position adjacent to the bond connecting the Cp and the heterocycle on either of the cyclic moieties exclude tilt angles near to 0° or 90°. The rotational potential energy changes around the energy minima seem to be small. Only in **16a**, where two substituents *ortho* to the flexible bond are present, is it not surprising to find considerably increased torsion angles of 65.4(4)° and 66.0(4)° (Figure 4).

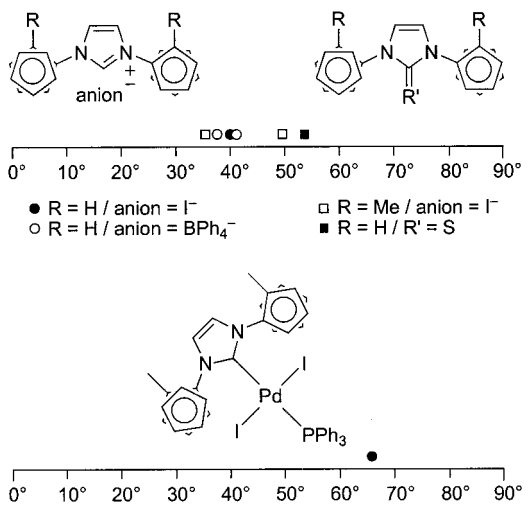

Figure 4. Tilt angles between planes of the Cp substituent and the heterocyclic core in imidazolium cations, in a thione and in a Pd-bound carbene ligand

Conclusion

The bulky, planar-chiral, *N*-ferrocenyl-substituted NHC **1a** as well as its achiral analog **1b** were synthesized by deprotonation of their imidazolium iodide precursors **12a** and **12b**. The latter were prepared by a synthetic strategy based on a Curtius degradation to form the ferrocenyl−nitrogen bond and a novel cyclization procedure to build up the heterocyclic cores of the target molecules. The reaction of **12b** with $[Pd(OAc)_2]_3$ in the presence of pyridine led to the *trans*-pyridine-substituted complex **14b**, but when **12a** was subjected to the same reaction conditions a mixture of the mononuclear complex **14a** and the dinuclear complex **15a** was isolated. Both **16a** and **16b** were obtained by addition of triphenylphosphane to **14b** and to a mixture of **14a** and **15b**, respectively.

First attempts to perform the catalytic asymmetric amide cyclizations[42] previously studied by Lee et al.[19] using the newly synthesized chiral ligand gave the expected cyclization product in 70% yield and 9% *ee*. Although this result does not compare favorably with that reported in the study mentioned above, where *ee* values of up to 70% were obtained, it shows the high activity of the observed system and marks a starting point for systematic variations in the chiral ligand. Efforts to shorten the ligand synthesis while introducing sterically more demanding groups attached to the ferrocenyl moieties are currently being undertaken.

Experimental Section

General Remarks: All experiments were conducted under argon or dinitrogen using standard Schlenk-type glassware or a glovebox. Unless otherwise stated, the reactions were carried out at room temperature. All solvents were stored over activated molecular sieves (4 Å) unless otherwise indicated. In the case of freshly distilled solvents, the following drying agents were used: CaH_2 for CH_2Cl_2, MeCN, MeOH and pyridine; Na/benzophenone for pentane; Na for benzene and C_6D_6. Chromatography was carried out with Merck silica gel 60. The NMR spectra were recorded with Bruker Avance 250 (250.1 MHz, ^{1}H; 62.5 MHz, ^{13}C; 101 MHz, ^{31}P), 300 (300.1 MHz, ^{1}H; 75.0 MHz, ^{13}C; 122 MHz, ^{31}P) and 500 (500.2 MHz, ^{1}H; 125 MHz, ^{13}C; 50.7 MHz, ^{15}N; 203 MHz, ^{31}P) spectrometers. ^{1}H and ^{13}C{^{1}H} NMR chemical shifts (δ) were referenced internally by the residual solvent signal relative to tetramethylsilane. ^{31}P NMR and ^{15}N NMR chemical shifts were referenced with respect to H_3PO_4 and $MeNO_2$, respectively. All spectra were recorded at room temperature. Optical rotations were measured in 1-dm cells with a Perkin−Elmer model 341 polarimeter at 22 °C. High-resolution MALDI mass spectra were measured by the analytical service of the Laboratorium für Organische Chemie of the ETH Zürich with an IonSpec ultima FT MALDI mass spectrometer. Elemental analyses were obtained with a Leco CHN-900 analyzer. All chemicals were purchased from Fluka, Aldrich, Acros, Lancaster or ABCR and were used without further purification. (2*S*,4*S*)-2-Ferrocenyl-4-(hydroxymethyl)-1,3-dioxane,[20] (2*S*,4*S*)-2-ferrocenyl-4-(methoxymethyl)-1,3-dioxane,[20] (2*S*,4*S*,R_{Fc})-4-(methoxymethyl)-2-(2-methylferrocenyl)-1,3-dioxane (**3**),[43] (*R*)-2-methylferrocenecarboxaldehyde (**4**),[43] and ferrocenecarboxylic acid (**6b**)[22] were prepared as reported.

Benzyl *N*-Ferrocenylcarbamate (8b): Ferrocenecarboxylic acid (1.25 g, 5.43 mmol, 1.0 equiv.), Bu_4NBr (349 mg, 1.10 μmol, 0.2 equiv.) and NaN_3 (723 mg, 11.0 mmol, 2.0 equiv.) were placed in a 100-mL Schlenk flask. Addition of 35 mL of distilled CH_2Cl_2 and pyridine (1.34 mL, 1.30 g, 16.5 mmol, 3.0 equiv.) caused the formation of an orange slurry. In a separate 10-mL Schlenk flask *N*,*N*-dimethylchlorosulfitomethaniminium chloride was prepared in situ by adding thionyl chloride (0.8 mL, 11.0 mmol) to a mixture of DMF (1.0 mL, 10.2 mmol) and 5 mL of benzene. After approximately 1 min, two phases separated, with the lower one containing the desired reagent. Addition of 730 μL of the fresh, clear and colorless *N*,*N*-dimethylchlorosulfitomethaniminium chloride to the vigorously stirred orange slurry during 3 min led to a clear wine-red solution and a white precipitate (presumably Bu_4NBr). After 1 h, water was added. Extraction of the organic layer with CH_2Cl_2, followed by drying with Na_2SO_4 and evaporation of the solvents led to an intensely red-colored oil. Benzylic alcohol (6 mL) was then added and the remaining pyridine was evaporated under vac-

 © 2005 Wiley-VCH Verlag GmbH & Co. KGaA, Weinheim

uum. The resulting solution of ferrocenecarboxylic azide (**7b**) in benzylic alcohol was stored in a 100-mL round-bottomed flask at room temperature under argon overnight. Upon heating to 90 °C during 30 min, the red color disappeared. The resulting brown yellowish mixture was concentrated to dryness under reduced pressure by using a distillation apparatus. A pure, orange, solid product was obtained by column chromatography (CC; CH_2Cl_2 + 1% Et_3N) on silica gel. Yield: 994 mg (55%). ^{1}H NMR ($CDCl_3$): δ = 3.99 (s, 2 H, 2 Cp_{subst}−C*H*), 4.15 (s, 5 H, Cp), 4.48 (br. s, 2 H, 2 Cp_{subst}−C*H*), 5.17 (s, 2 H, CH_2), 5.86 (br. s, 1 H, N*H*), 7.34−7.40 (m, 5 H, phenyl) ppm. MS (HR MALDI): *m*/*z* = 335.0609 (calcd. for $C_{18}H_{17}FeNO_2$); found 335.0606 [M^+]. $C_{18}H_{17}FeNO_2$ (335.18): calcd. C 64.50, H 5.11, N 4.18; found C 64.42, H 5.30, N 4.03. CAS 98639-14-6.

Aminoferrocene (9b): Compound **8b** (962 mg, 2.87 mmol, 1.0 equiv.) was suspended in 35 mL of isopropyl alcohol in a dry 100-mL Schlenk flask. After degassing the suspension in an ultrasonic bath by passing argon over it, the reaction vessel was heated to 60 °C until the substrate had dissolved completely, resulting in a clear orange solution. Pd on charcoal (10% Pd, 301 mg, 261 μmol, 0.09 equiv.) was added at room temperature and H_2 was placed over the reaction mixture. After 90 min, the solvent was removed under reduced pressure, and the residue was taken up in distilled CH_2Cl_2 and filtered. The resulting yellow solution was concentrated to dryness. The pure product was isolated as an orange solid and stored in a glovebox. Yield: 553 mg (96%). ^{1}H NMR ($CDCl_3$): δ = 2.59 (br. s, 2 H, NH_2), 3.84 (t, *J* = 1.8 Hz, 2 H, 2 Cp_{subst}−C*H*), 3.99 (t, *J* = 1.8 Hz, 2 H, 2 Cp_{subst}−C*H*), 4.10 (s, 5 H, Cp) ppm. CAS 1273-82-1.

***N*,*N*′-Diferrocenylformamidine (10b):** In a glovebox, compound **9b** (2.42 g, 12.0 mmol, 1.0 equiv.) and 1,3,5-triazine (2.92 g, 36.0 mmol, 3.0 equiv.) were placed in a dry, 500-mL round-bottomed Schlenk flask. After taking the flask out of the glovebox, 42 mL of dioxane was added, the resulting suspension was degassed in an ultrasonic bath by passing argon over it, and the reaction vessel was heated to 100 °C for 4.5 h, which led to a wine-red solution and an orange precipitate. The strong smell of ammonia upon careful opening of the reaction vessel (preventing the entry of air) indicated product formation. The reaction solvents were evaporated to dryness under reduced pressure using a distillation apparatus. At the same time, excess 1,3,5-triazine was completely sublimed, leading to an analytically pure amorphous orange solid that was stored in a glovebox. Yield: 2.37 g (96%). ^{1}H NMR ($CDCl_3$): δ = 4.04 (t, *J* = 1.8 Hz, 4 H, 4 Cp_{subst}−C*H*), 4.20 (s, 10 H, 2 Cp), 4.26 (t, *J* = 1.8 Hz, 4 H, 4 Cp_{subst}−C*H*), 8.03 (s, 1 H, N=C*H*−N) ppm. ^{13}C{^{1}H} NMR ($CDCl_3$): δ = 60.5 (Cp_{subst}−*C*H), 65.1 (Cp_{subst}−*C*H), 67.2 (Cp_{subst}−C_{quat}), 69.2 (Cp), 150.2 (N=*C*H−N) ppm. MS (HR MALDI): *m*/*z* = 412.033 (calcd. for $C_{21}H_{20}Fe_2N_2$); found 412.032 [M^+]. $C_{21}H_{20}Fe_2N_2$ (412.09): calcd. C 61.21, H 4.89, N 6.80; found C 61.15, H 4.97, N 6.68.

***N*-(2,2-Diethoxyethyl)-*N*,*N*′-diferrocenylformamidine (11b):** Compound **10b** (500 mg, 1.23 mmol, 1.0 equiv.) was suspended in 10 mL of DMF in a 50-mL Schlenk flask and cooled to 0 °C. After addition of NaH (55−65% in mineral oil, 100 mg, 2.25 mmol, 1.8 equiv.), the mixture was kept at 0 °C for 5 min and then slowly warmed to room temperature, leading to gas evolution (H_2). After 100 min stirring at room temperature 2-bromo-1,1-diethoxyethane (380 μL, 477 mg, 2.45 mmol, 2.0 equiv.) was added and the clear red solution was quickly heated to 76 °C. After 90 min, the darkened, hot mixture was concentrated to dryness under vacuum. The crude product was dissolved in MeCN followed by filtration under argon. The pure product was isolated as a clear, red oil. Yield: 515 mg (79%). ^{1}H NMR (C_6D_6): δ = 1.16 (t, *J* = 7.1 Hz, 3 H, CH_3), 1.16 (t, *J* = 7.1 Hz, 3 H, CH_3), 3.44−3.54 (m, 2 H, CH_2CH$_3$), 3.68−3.78 (m, 2 H, CH_2CH$_3$), 3.81 (t, *J* = 1.8 Hz, 1 H, Cp_{subst}−C*H*), 3.81 (t, *J* = 1.8 Hz, 1 H, Cp_{subst}−C*H*), 3.98 (t, *J* = 1.8 Hz, 1 H, Cp_{subst}−C*H*), 3.98 (t, *J* = 1.8 Hz, 1 H, Cp_{subst}−C*H*), 4.02 (s, 5 H, Cp), 4.12 (d, *J* = 5.3 Hz, 2 H, NCH_2CH), 4.19 (s, 5 H, Cp), 4.31−4.35 (m, 4 H, 4 Cp_{subst}−C*H*), 5.13 (t, *J* = 5.2 Hz, 1 H, NCH$_2$C*H*), 8.28 (s, 1 H, N=C*H*−N) ppm. ^{13}C{^{1}H} NMR ($CDCl_3$): δ = 15.6 (CH$_2$*C*H$_3$), 52.5 (N*C*H$_2$CH), 60.3 (Cp_{subst}−*C*H), 61.7 (Cp_{subst}−*C*H), 64.0 (*C*H$_2$CH$_3$), 65.0 (Cp_{subst}−*C*H), 65.2 (Cp_{subst}−*C*H), 69.0 (Cp), 100.5 (NCH$_2$*C*H), 105.5 (Cp_{subst}−C_{quat}), 108.4 (Cp_{subst}−C_{quat}), 150.6 (N=*C*H−N) ppm. MS (HR MALDI): *m*/*z* = 528.116 (calcd. for $C_{27}H_{32}Fe_2N_2O_2$); found 528.116 [M^+]. $C_{27}H_{32}Fe_2N_2O_2$ (528.25): calcd. C 61.39, H 6.11, N 5.30; found C 61.54, H 6.18, N 5.32.

***N*,*N*′-Diferrocenylimidazolium Iodide (12b):** Compound **11b** (2.38 g, 4.51 mmol, 1.0 equiv.) was dissolved in 50 mL of distilled MeCN in a dry 100-mL Schlenk flask. After addition of BF_3·OEt_2 (3.4 mL, 3.8 g, 27 mmol, 6.0 equiv.), which caused an immediate darkening of the clear, red solution, the reaction temperature was raised to 70 °C. After 3 h, additional BF_3·OEt_2 (1.7 mL, 1.9 g, 14 mmol, 3.0 equiv.) was added and the reaction mixture was stirred for 15 h. Evaporation of the solvent under reduced pressure gave a brown yellowish solid. NaI (3.38 g, 22.6 mmol, 5.0 equiv.) and 50 mL of distilled MeOH were added and the resulting mixture was stirred at 70 °C for 30 min. After evaporation of the solvent, the crude product was chromatographed on silica gel (CH_2Cl_2 + 5% MeOH) to give the pure product as a light-yellow foam. Yield: 1.92 g (75%). ^{1}H NMR ($CDCl_3$): δ = 4.34 (s, 10 H, 2 Cp), 4.36 (t, *J* = 2.0 Hz, 4 H, 2 Cp_{subst}C*H*), 5.33 (t, *J* = 2.0 Hz, 2 H, Cp_{subst}−C*H*), 7.64 (d, *J* = 1.5 Hz, 2 H, NC*H*C*H*N), 10.74 (t, *J* = 1.5 Hz, 1 H, N=C*H*−N) ppm. ^{13}C{^{1}H} NMR (CD_2Cl_2): δ = 63.2 (Cp_{subst}−*C*H), 67.8 (Cp_{subst}−*C*H), 70.8 (Cp), 92.0 (Cp_{subst}−C_{quat}), 122.2 (N*C*H*C*HN), 135.1 (N=*C*H−N) ppm. MS (HR MALDI): *m*/*z* = 437.0404 (calcd. for $C_{23}H_{21}Fe_2N_2^+$); found 437.0406 [M^+ − I]. $C_{23}H_{21}Fe_2IN_2$ (564.02): calcd. C 48.98, H 3.75, I 22.50, N 4.97; found C 49.12, H 4.03, I 22.55, N 4.87.

***N*,*N*′-Diferrocenylimidazol-2-ylidene (1b):** A 20-mL Schlenk vessel was charged with compound **12b** (30 mg, 53 μmol, 1.0 equiv.) and KO*t*Bu (12 mg, 106 μmol, 2.0 equiv.) in a glovebox. Addition of 1.5 mL of distilled pentane caused the formation of an orange slurry. After stirring for 14 h, all volatiles were evaporated under reduced pressure, the residue was taken up in 1 mL of distilled deuterated benzene and filtered through a 4 Å frit. A light orange, clear solution of the product was obtained; the yield was not determined. ^{1}H NMR (C_6D_6): δ = 3.86 (t, *J* = 2.0 Hz, 4 H, 2 Cp_{subst}C*H*), 4.02 (s, 10 H, 2 Cp), 4.82 (t, *J* = 2.0 Hz, 4 H, 2 Cp_{subst}C*H*), 6.86 (s, 2 H, NC*H*C*H*N) ppm. ^{13}C{^{1}H} NMR (C_6D_6): δ = 62.2 (Cp_{subst}−*C*H), 65.8 (Cp_{subst}−*C*H), 69.2 (Cp), 100.4 (Cp_{subst}−*C*N), 118.9 (N*C*H*C*HN), 216.1 (N*C*N) ppm. ^{15}N NMR (C_6D_6): δ = −186.3 ppm.

***N*,*N*′-Diferrocenylimidazole-2-thione (13b):** A 20-mL Schlenk vessel was charged with compound **1b** (45 mg, 103 μmol, 1 equiv.) and S_8 (6.2 mg, 192 μmol, 2 equiv.) in a glovebox. Addition of 1 mL of distilled THF led to a brown solution and a small amount of precipitate. After 16 h, the reaction vessel was taken out of the glovebox and water was added, leading to a color change to bright yellow. The mixture was extracted with CH_2Cl_2, washed with water and dried with Na_2SO_4. ^{1}H NMR ($CDCl_3$): δ = 4.24 (t, *J* = 2.0 Hz, 4 H, 2 Cp_{subst}C*H*), 4.28 (s, 10 H, 2 Cp), 4.90 (t, *J* = 2.0 Hz, 4 H, 2 Cp_{subst}C*H*), 7.13 (s, 2 H, NC*H*C*H*N). CAS 249644-45-9.

 © 2005 Wiley-VCH Verlag GmbH & Co. KGaA, Weinheim

Methyl (*R*)-2-Methylferrocenecarboxylate (5): (*R*)-2-Methylferrocenecarboxaldehyde (**4**) (6.74 g, 29.6 mmol, 1.0 equiv.) and 120 mL of MeOH were added to a 1-L flask and cooled to 0 °C. Addition of KOH (16.6 g, 296 mmol, 10 equiv.) was followed by addition of I_2 (37.5 g, 148 mmol, 5.0 equiv.). After 4 h, the solvents were evaporated under reduced pressure at 0 °C (to prevent overoxidation to the corresponding ferrocenium cation) and the remaining residue was chromatographed on silica gel (CH_2Cl_2) to give a red oil. Yield: 5.87 mg (77%). ^{1}H NMR ($CDCl_3$): δ = 2.28 (s, 3 H, Cp−C*H*$_3$), 3.81 [s, 3 H, C(O)OC*H*$_3$], 4.12 (s, 5 H, Cp), 4.23 (t, J = 2.6 Hz, 1 H, Cp_{subst}−C*H*), 4.31 (t, J = 1.6 Hz, 1 H, Cp_{subst}−C*H*), 4.71 (dd, J_1 = 2.6, J_2 = 1.6 Hz, 1 H, Cp_{subst}−C*H*) ppm. CAS 12242-23-8.

(*R*)-2-Methylferrocenecarboxylic Acid (6a): Compound **5** (7.33 g, 28.4 mmol) was dissolved in 140 mL of EtOH in a 500-mL round-bottomed flask. An aqueous solution of NaOH (70 mL, 1.1 M) was added, then the reaction mixture was stirred for 4 h at room temperature and for a further 12 h at 60 °C. Water was then added and the organic impurities were extracted with *tert*-butyl methyl ether. The aqueous phases were acidified with 0.7 M aqueous HCl and extracted with CH_2Cl_2. The organic layers were dried with $NaSO_4$, the solvent was evaporated and the product was isolated in the form of red crystals. Yield: 6.45 g (93%). ^{1}H NMR ($CDCl_3$): δ = 2.31 (s, 3 H, C*H*$_3$), 4.20 (s, 5 H, Cp), 4.31 (t, J = 2.5 Hz, 1 H, Cp_{subst}−C*H*), 4.39 (t, J = 1.9 Hz, 1 H, Cp_{subst}−C*H*), 4.80 (dd, J_1 = 2.5, J_2 = 1.8 Hz, 1 H, Cp_{subst}−C*H*) ppm. ^{13}C{^{1}H} NMR (CD_2Cl_2): δ = 14.8 (*C*H$_3$), 68.1 (Cp_{subst}−*C*$_{quat}$), 69.7 (Cp_{subst}−*C*H), 70.8 (Cp), 71.0 (Cp_{subst}−*C*H), 74.4 (Cp_{subst}−*C*H), 87.7 (Cp_{subst}−*C*$_{quat}$), 178.9 (*C*OOH) ppm. CAS 12241-80-4.

Benzyl *N*-[(*R*)-2-Methylferrocenyl]carbamate (8a): Compound **6a** (4.10 g, 16.82 mmol, 1.0 equiv.), Bu_4NBr (1.09 g, 3.44 mol, 0.2 equiv.) and NaN_3 (2.26 g, 34.4 mmol, 2.0 equiv.) were placed in a 500-mL Schlenk flask. Addition of 114 mL of distilled CH_2Cl_2 and pyridine (4.18 mL, 4.07 g, 515 mmol, 3.0 equiv.) gave an orange-red solution. In a separate 10-mL Schlenk flask, *N*,*N*-dimethylchlorosulfitomethaniminium chloride was prepared in situ by adding thionyl chloride (4.6 mL, 62.9 mmol) to a mixture of DMF (5.7 mL, 58.4 mmol) and 28 mL of benzene. After approximately 1 min, two phases separated, with the lower one containing the desired reagent. Addition of 2.29 mL of the fresh, clear and colorless *N*,*N*-dimethylchlorosulfitomethaniminium chloride to the vigorously stirred orange slurry during 3 min led to a clear wine-red solution and a white precipitate (presumably Bu_4NBr). After 1 h 25 min, 23 mL of benzylic alcohol was added and the remaining dichloromethane and pyridine were evaporated under high vacuum. The resulting solution of (*R*)-2-methylferrocenecarboxylic azide (**7a**) in benzylic alcohol was stirred at 90 °C during 10 min, which caused darkening of the reaction mixture. The resulting brownish-yellow solvents were evaporated to dryness under reduced pressure during 45 min at 90 °C by using a distillation apparatus. A pure, orange, solid product was obtained by CC (CH_2Cl_2 + 1% NEt_3) on silica gel. Yield: 4.72 g (81%). ^{1}H NMR ($CDCl_3$): δ = 1.95 (s, C*H*$_3$), 3.90 (t, J = 2.5 Hz, 1 H, Cp_{subst}−C*H*), 3.95−3.97 (m, 1 H, Cp_{subst}−C*H*), 4.06 (s, 5 H, Cp), 4.62 (br. s, 1 H, Cp_{subst}−C*H*), 5.18 (s, 2 H, C*H*$_2$), 5.89 (br. s, 1 H, N*H*), 7.34−7.38 (m, 5 H, phenyl) ppm. MS (HR MALDI): *m*/*z* = 349.0765 (calcd. for $C_{19}H_{19}FeNO_2$); found 349.0757 [M^+]. $C_{19}H_{19}FeNO_2$ (349.20): calcd. C 65.35, H 5.48, N 4.01; found C 65.46, H 5.44, N 3.92. CAS 32196−69−3.

(*R*)-1-Amino-2-methylferrocene (9a): Compound **8a** (2.00 g, 5.73 mmol, 1.0 equiv.) was suspended in 35 mL of isopropyl alcohol in a dry 100-mL Schlenk flask. After degassing the suspension in an ultrasonic bath by passing argon over it, the reaction vessel was heated to 70 °C until the substrate had dissolved completely, resulting in a clear orange solution. Pd on charcoal (10% Pd, 656 mg, 573 μmol, 0.1 equiv.) was added at room temperature and H_2 was placed over the reaction mixture. After 110 min, the solvent was removed under reduced pressure, the residue was taken up in distilled CH_2Cl_2 and filtered. The resulting yellow solution was concentrated to dryness. The pure product was isolated as a bright-orange solid and stored in a glovebox. Yield: 1.23 g (quant). ^{1}H NMR (C_6D_6): δ = 1.72 (s, 3 H, C*H*$_3$), 2.03 (br. s, 2 H, N*H*$_2$), 3.66 (t, J = 2.1 Hz, 1 H, Cp_{subst}−C*H*), 3.70−3.77 (m, 2 H, Cp_{subst}−C*H*), 3.91 (s, 5 H, Cp) ppm. CAS 31760-79-9.

***N*,*N*′-Bis[(*R*)-2-methylferrocen-1-yl]formamidine (10a):** Compound **9a** (1.17 g, 5.44 mmol, 1.0 equiv.) and 1,3,5-triazine (1.32 g, 16.3 mmol, 3.0 equiv.) were placed in a dried 100-mL, round-bottomed Schlenk flask in a glovebox. After taking the flask out of the glovebox, 18 mL of dioxane was added and the resulting suspension was degassed in an ultrasonic bath by passing argon over it. The reaction vessel was then heated to 100 °C for 2.25 h, which led to a clear red solution. The strong smell of ammonia upon careful opening of the reaction vessel (preventing the entry of air) indicated product formation. The reaction solvents were evaporated to dryness under reduced pressure using a distillation apparatus. At the same time, excess 1,3,5-triazine was completely sublimed, leading to an analytically pure amorphous orange solid that was stored in a glovebox. Yield: 1.48 g (quant). ^{1}H NMR (C_6D_6): δ = 1.95 (s, 6 H, 2 C*H*$_3$), 3.81 (t, J = 2.6 Hz, 2 H, 2 Cp_{subst}−C*H*), 3.89 (t, J = 1.7 Hz, 2 H, 2 Cp_{subst}−C*H*), 4.04 (s, 10 H, 2 Cp), 4.22 (br. s, 2 H, 2 Cp_{subst}−C*H*), 7.99 (s, 1 H, N=C*H*−N) ppm. ^{13}C{^{1}H} NMR ($CDCl_3$): δ = 12.2 (C*H*$_3$), 58.8 (Cp_{subst}−*C*H), 62.3 (Cp_{subst}−*C*H), 66.6 (Cp_{subst}−*C*H), 69.1 (Cp_{subst}−*C*$_{quat}$), 69.4 (Cp), 76.5 (Cp_{subst}−*C*$_{quat}$), 150.6 (N=*C*H−N) ppm. MS (HR MALDI): *m*/*z* = 440.0638 (calcd. for $C_{23}H_{24}Fe_2N_2$); found 440.0630 [M^+]. $C_{23}H_{24}Fe_2N_2$ (440.14): calcd. C 62.76, H 5.50, N 6.36; found C 62.59, H 5.38, N 6.55. $[\alpha]_{22}$ = +1229 (c = 1, $CHCl_3$).

***N*-(2,2-Diethoxyethyl)-*N*,*N*′-bis[(*R*)-2-methylferrocen-1-yl]formamidine (11a):** Compound **10a** (1.14 mg, 2.58 mmol, 1.0 equiv.) was dissolved in 20 mL of DMF in a 100-mL Schlenk flask. The mixture was degassed in an ultrasonic bath by passing argon over it and cooled to 0 °C. After addition of NaH (55−65% in mineral oil, 203 mg, 4.64 mmol, 1.8 equiv.), the mixture was kept at 0 °C for 15 min and then slowly warmed to room temperature, leading to gas evolution (H_2). After 2 h 40 min of stirring at room temperature, 2-bromo-1,1-diethoxyethane (802 μL, 1.02 g, 5.17 mmol, 2.0 equiv.) was added and the clear red solution was quickly heated to 80 °C. After 3 h 20 min, another portion of bromoacetaldehyde diethylacetal (802 μL, 254 mg, 1.29 mmol, 0.5 equiv.) was added and stirring was continued for 90 min. The reaction solvents were evaporated to dryness under vacuum. The crude product was dissolved in distilled MeCN and filtered under argon. The pure product was isolated as a clear, red oil. Yield: 1.17 g (82%). ^{1}H NMR (C_6D_6): δ = 1.13 (t, J = 6.8 Hz, 3 H, CH_2CH_3), 1.18 (t, J = 7.0 Hz, 3 H, CH_2CH_3), 1.86 (s, 3 H, Cp−C*H*$_3$), 2.24 (s, 3 H, Cp−C*H*$_3$), 3.45−3.74 (m, 4 H, 2 CH_2CH_3), 3.74−3.77 (m, 1 H, Cp_{subst}−C*H*), 3.77−3.80 (m, 1 H, Cp_{subst}−C*H*), 3.89−3.92 (m, 1 H, Cp_{subst}−C*H*), 4.04 (s, 5 H, Cp), 4.09 (d, J = 5.5 Hz, 2 H, NC*H*$_2$CH), 4.13 (s, 5 H, Cp), 4.18−4.22 (m, 1 H, Cp_{subst}−C*H*), 4.25−4.29 (m, 1 H, Cp_{subst}−C*H*), 5.30 (t, J = 5.2 Hz, 1 H, NCH$_2$C*H*), 8.57 (s, 1 H, N=C*H*−N) ppm. ^{13}C{^{1}H} NMR ($CDCl_3$): δ = 12.9 (cp−*C*H$_3$), 13.3 (cp−*C*H$_3$), 15.6 (CH_2CH_3), 15.6 (CH_2CH_3), 53.4 (N*C*H$_2$CH), 57.7 (Cp_{subst}−*C*H), 62.6 (Cp_{subst}−*C*H), 62.7 (2 Cp_{subst}−*C*H), 63.7 (CH_2CH_3), 64.0

 © 2005 Wiley-VCH Verlag GmbH & Co. KGaA, Weinheim

(CH_2CH_3), 67.0 ($Cp_{subst}-CH$), 67.2 ($Cp_{subst}-CH$), 69.8 (Cp), 70.0 (Cp), 78.8 ($Cp_{subst}-CCH_3$), 79.3 ($Cp_{subst}-CCH_3$), 99.9 (NCH_2CH), 104.7 ($Cp_{subst}-CN$), 107.2 ($Cp_{subst}-CN$), 153.3 (N=CH−N) ppm. MS (HR MALDI): m/z = 556.1476 (calcd. for $C_{29}H_{36}Fe_2N_2O_2$); found 556.1475 [M^+]. $C_{29}H_{36}Fe_2N_2O_2$ (556.30): calcd. C 62.61, H 6.52, N 5.04; found C 62.46, H 6.68, N 5.33. $[\alpha]_{22}$ = +675 (c = 1, $CHCl_3$).

***N,N′*-Bis[(*R*)-2-methylferrocen-1-yl]imidazolium Iodide (12a):** Compound **11a** (1.36 g, 2.45 mmol, 1.0 equiv.) was dissolved in 28 mL of distilled MeCN in a dry 100-mL Schlenk flask. After addition of $BF_3{\cdot}OEt_2$ (1.88 mL, 2.09 g, 14.7 mmol, 6.0 equiv.) at room temperature, which caused an immediate darkening of the reaction mixture, the reaction temperature was raised to 70 °C. After 3 h, additional $BF_3{\cdot}OEt_2$ (0.9 mL, 1.0 g, 7.0 mmol, 2.9 equiv.) was added and the reaction mixture was stirred for 15 h. Evaporation of the solvent under reduced pressure gave a brown yellowish solid. NaI (1.83 g, 12.3 mmol, 5.0 equiv.) and 28 mL of distilled MeOH were added and the resulting mixture was stirred at 70 °C for 2 h. After evaporation of the solvent, the crude product was first filtered through a silica-gel pad (CH_2Cl_2 + 5% MeOH) to remove excess NaI and borate waste, and then chromatographed on silica gel (CH_2Cl_2 + 5% MeOH) to give the product as a light-yellow foam. Yield: 1.03 g (71%). ^{1}H NMR (CD_2Cl_2): δ = 1.99 (s, 6 H, 2 CH_3), 4.28 (t, J = 2.7 Hz, 2 H, 2 Cp_{subst}−CH), 4.33 (s, 10 H, 2 Cp), 4.39−4.42 (m, 2 H, 2 Cp_{subst}−CH), 4.85 (dd, J_1 = 2.7, J_2 = 1.2 Hz, 2 H, 2 Cp_{subst}−CH), 7.85 (d, J = 1.5 Hz, 2 H, NCHCHN), 9.03 (t, J = 1.5 Hz, 1 H, N=CH−N) ppm. ^{13}C{^{1}H} NMR (CD_2Cl_2): δ = 13.0 ($Cp_{subst}-CH_3$), 65.6 ($Cp_{subst}-CH$), 65.8 ($Cp_{subst}-CH$), 69.5 ($Cp_{subst}-CH$), 71.2 (Cp), 79.2 ($Cp_{subst}-C_{quat}$), 92.6 ($Cp_{subst}-C_{quat}$), 125.4 (NCHCHN), 137.3 (N=CHCHN) ppm. MS (HR MALDI): m/z = 465.0717 (calcd. for $C_{25}H_{25}Fe_2N_2^+$); found 465.0715 [M^+ − I]. $C_{25}H_{25}Fe_2IN_2$ (592.07): calcd. C 50.71, H 4.26, N 4.73; found C 50.93, H 4.49, N 4.68. $[\alpha]_{22}$ = +104 (c = 1, $CHCl_3$).

***N,N′*-Bis[(*R*)-2-methylferrocen-1-yl]imidazol-2-ylidene (1a):** A 20-mL Schlenk vessel was charged with compound **12a** (20 mg, 34 μmol, 1.0 equiv.) and KO*t*Bu (8 mg, 71 μmol, 2.1 equiv.) in a glovebox. Addition of 2 mL of distilled pentane caused the formation of an orange slurry. After stirring for 3.5 h, all volatiles were evaporated under reduced pressure, the residue was taken up in 1 mL of distilled deuterated benzene and filtered through a 4 Å frit, which led to a clear light-yellow solution. ^{1}H NMR (C_6D_6): δ = 2.26 (s, 6 H, 2 CH_3), 3.81 (t, J = 2.5 Hz, 2 H, 2 Cp_{subst}CH), 3.90 (t, J = 2.0 Hz, 2 H, 2 Cp_{subst}CH), 4.07 (s, 10 H, 2 Cp), 4.38−4.40 (m, 2 H, 2 Cp_{subst}CH), 7.01 (s, 2 H, NCHCHN) ppm. ^{13}C{^{1}H} NMR (C_6D_6): δ = 14.5 ($Cp_{subst}-CH_3$), 63.6 ($Cp_{subst}-CH$), 64.2 ($Cp_{subst}-CH$), 68.0 ($Cp_{subst}-CH$), 70.0 (Cp), 79.6 ($Cp_{subst}-CCH_3$), 99.8 ($Cp_{subst}-CN$), 120.8 (NCHCHN), 221.2 (NCN) ppm. ^{15}N NMR (C_6D_6): δ = −188.2 ppm.

***N,N′*-Bis[(*R*)-2-methylferrocen-1-yl]imidazole-2-thione (13a):** S_8 (4.1 mg, 128 μmol, 3.5 equiv.) was added to the solution of compound **1a** in benzene prepared above. After a reaction time of 30 min, ^{1}H NMR analysis of the solution showed complete and clean conversion. ^{1}H NMR (C_6D_6): δ = 1.94 (s, 6 H, 2 CH_3), 3.79 (t, J = 2.5 Hz, 2 H, 2 Cp_{subst}CH), 3.86 (t, J = 2.1 Hz, 2 H, 2 Cp_{subst}CH), 3.98 (s, 10 H, 2 Cp), 4.49−4.51 (m, 2 H, 2 Cp_{subst}CH), 7.01 (s, 2 H, NCHCHN) ppm. ^{13}C{^{1}H} NMR (C_6D_6): δ = 13.5 ($Cp_{subst}-CH_3$), 64.6 ($Cp_{subst}-CH$), 67.6 ($Cp_{subst}-CH$), 68.0 ($Cp_{subst}-CH$), 70.1 (Cp), 81.7 ($Cp_{subst}-CCH_3$), 96.5 ($Cp_{subst}-CN$), 119.6 (NCHCHN), 170.3 (NCN) ppm. MS (HR MALDI): m/z = 496.0359 (calcd. for $C_{25}H_{24}Fe_2N_2S$); found 496.0359 [M^+].

Palladium Complex 14b: Compound **12b** (200 mg, 354 μmol, 1.0 equiv.) and $[Pd(OAc)_2]_3$ (79.6 mg, 351 μmol, 1.0 equiv.) were dissolved in 7 mL of distilled pyridine in a dry 20-mL Schlenk flask. The resulting yellow solution was stirred for 3 h, then NaI (270 mg, 1.80 mmol, 5.1 equiv.) was added, leading to a color change to brown and the formation of a precipitate (other than NaI). After 18 h of stirring, all volatiles were evaporated under reduced pressure. The pure orange product was obtained by CC (CH_2Cl_2) on silica gel. Yield: 160 mg (59%). ^{1}H NMR (C_6D_6): δ = 3.99 (t, J = 1.9 Hz, 4 H, 2 Cp_{subst}-CH), 4.10 (s, 10 H, 2 Cp), 5.50 (t, J = 1.8 Hz, 4 H, 2 Cp_{subst}−CH), 6.22−6.26 (m, 2 H, py), 6.53 (tt, J_1 = 1.8, J_2 = 7.8 Hz, 1 H, py), 7.03 (s, 2 H, NCHCHN), 8.98−9.00 (m, 2 H, py) ppm. ^{13}C{^{1}H} NMR (C_6D_6): δ = 66.3 ($Cp_{subst}-CH$), 66.6 ($Cp_{subst}-CH$), 70.1 (Cp), 97.7 ($Cp_{subst}-C_{quat}$), 123.5 (NCHCHN), 123.9 (py), 136.8 (py), 151.1 (N−CPd−N), 154.4 (py) ppm. MS (HR MALDI): m/z = 795.7450 (calcd. for $C_{23}H_{20}Fe_2N_2I_2Pd$); found 795.7470 [M − py]$^+$ with the expected isotopic pattern. $C_{28}H_{25}Fe_2I_2N_3Pd$ (769.02): calcd. C 38.37, H 2.99, N 4.79, I 28.96; found C 38.57, H 3.08, N 4.59, I 29.08.

Palldium Complexes 14a and 15a: Compound **12a** (100 mg, 169 μmol, 1.0 equiv.) and $[Pd(OAc)_2]_3$ (38.0 mg, 169 μmol, 1.0 equiv.) were dissolved in 5 mL of distilled pyridine in a dry 20-mL Schlenk flask. The resulting clear, brown solution was stirred for 3.5 h, then NaI (132 mg, 879 μmol, 5.2 equiv.) was added to the darkened mixture, which caused a slight lightening of the color and the formation of a precipitate (other than NaI). After 15 h of stirring, all volatiles were evaporated under reduced pressure. An orange mixture of the two products was obtained by CC (CH_2Cl_2) on silica gel. Yield: 106 mg (54%). The mixture consists of 53.5 mg (59.2 μmol) of the mononuclear and 52.3 mg (31.7 μmol) of the dinuclear species, as determined by ^{1}H NMR spectroscopy. ^{1}H NMR (C_6D_6; resonances that belong to **14a** are designated with M, those belonging to **15a** with D): δ = 1.69 (s, 6 H, 2 CH_3, D), 2.01 (s, 6 H, 2 CH_3; D), 2.11 (s, 6 H, 2 CH_3, M), 3.86 (s, 10 H, 2 Cp, D), 3.92 (s, 10 H, 2 Cp, D), 3.97 (s, 10 H, 2 Cp, M), 4.02 (t, J = 2.6 Hz, 2 H, 2 Cp_{subst}−CH, M), 4.27 (t, J = 2.5 Hz, 2 H, 2 Cp_{subst}−CH, D), 5.64−5.68 (m, 2 H, 2 Cp_{subst}−CH, D), 5.71−5.75 (m, 2 H, 2 Cp_{subst}−CH, D), 6.00 (dd, J_1 = 2.5, J_2 = 1.0 Hz, 2 H, 2 Cp_{subst}−CH, M), 6.10−6.17 (m, 2 H, py, M), 6.39−6.48 (m, 1 H, py, M), 7.19−7.22 (m, 2 H, NCHCHN, D), 7.34 (s, 2 H, NCHCHN, M), 8.76−8.81 (m, 2 H, py, M) ppm.

Palladium Complex 16a: Addition of 1.5 mL of CH_2Cl_2 to a dry 20-mL Schlenk flask containing a mixture of **14a** and **15a** (97 mg, 123 μmol Pd^{II}, 1.0 equiv.) and triphenylphosphane (60.2 mg, 230 μmol, 2.8 equiv.) caused the formation of a clear red to orange solution. After 1 h of stirring, all volatiles were removed under reduced pressure and the residue was rinsed five times with pentane. Drying under reduced pressure yielded a pale-yellow solid. Yield: 115 mg (86%). ^{1}H NMR (CD_2Cl_2): δ = 2.08 (s, 6 H, 2 CH_3), 4.27−4.30 (m, 14 H, 2 cp and 4 Cp_{subst}−CH), 5.34 (t, 2 H, 2 Cp_{subst}−CH, J = 2.0 Hz), 7.29−7.33 (m, 6 H, PPh_3), 7.34−7.40 (m, 3 H, PPh_3), 7.43−7.49 (m, 6 H, PPh_3), 7.72 (d, 2 H, J = 1.0 Hz, NCHCHN) ppm. ^{13}C NMR (CD_2Cl_2): δ = 13.1 ($Cp_{subst}-CH_3$), 64.0 ($Cp_{subst}-CH$), 68.1 ($Cp_{subst}-CH$), 68.7 ($Cp_{subst}-CH$), 70.0 (Cp), 79.3 ($Cp_{subst}-CN$), 97.9 ($Cp_{subst}-CCH_3$), 124.6 (d, J = 5.6 Hz, (NCHCHN), 127.5 (d, J = 10.1 Hz, PPh_3), 129.9 (d, J = 2.3 Hz, PPh_3), 133.0 (d, J = 44.3 Hz, PPh_3), 135.4 (d, J = 11.0 Hz, PPh_3), 165.2 (d, J = 193.7 Hz, N−CPd−N) ppm. ^{31}P NMR (CD_2Cl_2): δ = 17.7 ppm. MS (HR MALDI): m/z = 958.9629 (calcd. for $C_{43}H_{39}Fe_2IN_2PPd$); found 958.9654 [M − I$^+$] with the expected isotopic pattern. $C_{43}H_{39}Fe_2I_2N_2PPd$ (1086.68): calcd. C 47.53, H 3.62, I 23.36, N 2.58, P 2.85; found C 47.60, H 3.73, I 23.11, N 2.51, P 3.02. $[\alpha]_{22}$ = +79 (c = 1, $CHCl_3$).

 © 2005 Wiley-VCH Verlag GmbH & Co. KGaA, Weinheim

Table 1. X-ray crystallographic data of **12a**, **12b** and **16a**

	12a	**12b**	**16a**
Empirical formula	$C_{25}H_{25}Fe_2IN_2$	$C_{23}H_{21}Fe_2IN_2$	$C_{43}H_{39}Fe_2I_2N_2PPd$
Formula mass	592.07	564.02	1086.63
Temperature [K]	200(2)	298(2)	293(2)
Wavelength [Å]	0.71073	0.71073	0.71073
Crystal system	triclinic	orthorhombic	monoclinic
Space group	*P*1	*Pnma*	$P2_1$
Unit cell dimensions	a = 9.0692(7) Å	a = 7.1601(4) Å	a = 10.299(3) Å
	b = 25.0236(19) Å	b = 7.5642(4) Å	b = 11.827(3) Å
	c = 9.1270(7) Å	c = 10.9701(6) Å	c = 16.900(4) Å
	α = 90°	α = 84.6960(10)°	α = 90°
	β = 90°	β = 85.4760(10)°	β = 99.772(5)°
	γ = 90°	γ = 73.4130(10)°	γ = 90°
Volume [Å^3]	566.13(5)	2071.3(3)	2028.7(9)
Z	1	4	2
Calcd. density [g/cm^3]	1.737	1.809	1.779
Absorption coefficient [mm^{-1}]	2.659	2.902	2.738
Crystal size [mm]	0.39 × 0.23 × 0.14	0.21 × 0.08 × 0.05	0.60 × 0.28 × 0.23
Reflections collected, unique	5840, 5118	12775, 2172	20853, 9926
R_{int}	0.0114	0.0346	0.0253
Refinement method		full-matrix least squares on F^2	
Data, restraints, parameters	5118, 3, 273	2172, 0, 130	9926, 1, 462
GOF	1.057	1.322	1.048
R, R_w	0.0214, 0.0531	0.0822, 0.1525	0.0290, 0.0635
Min./max. residual [e·Å^{-3}]	0.695/−0.287	1.706/−1.334	0.994/−0.505

Palladium Complex 16b: A 100-mL Schlenk vessel was charged with compound **14b** (157 mg, 204 μmol, 1.0 equiv.) and triphenylphosphane (107 mg, 408 μmol, 2.0 equiv.). After addition of 3.0 mL of CH_2Cl_2, the cloudy orange mixture turned into a clear yellow solution within 5 min. After 2 h, the solvent was evaporated under reduced pressure, and the product was separated from excess PPh_3, as a yellow powder, by repeated washing with pentane. Yield: 195 mg (94%). ^{1}H NMR (CD_2Cl_2): δ = 4.26−431 (m, 14 H, 2 cp and 2 Cp_{subst}−*C*H), 5.18 (t, J = 2.0 Hz, 2 Cp_{subst}−*C*H), 7.24−7.61 (m, 15 H, PPh_3), 7.58 (d, J = 1.2 Hz, 2 H, NC*HCH*N) ppm. ^{13}C NMR (CD_2Cl_2): δ = 65.6 (Cp_{subst}−*C*H), 66.1 (Cp_{subst}−*C*H), 69.7 (Cp), 97.3 (d, J = 0.8 Hz, Cp_{subst}−*C*N), 123.6, (d, J = 5.6 Hz, (N*CHCH*N), 127.6 (d, J = 10.2 Hz, PPh_3), 130.0 (d, J = 2.3 Hz, PPh_3), 132.7 (d, J = 44.4 Hz, PPh_3), 135.2 (d, J = 10.9 Hz, PPh_3), 159.8 (d, J = 189.9 Hz, N−*C*Pd−N) ppm. ^{31}P NMR (CD_2Cl_2): δ = 16.7 ppm. MS (HRes MALDI): m/z = 930.9316 (calcd. for $C_{41}H_{35}Fe_2IN_2PPd$); found 930.9334 [M − I$^+$] with the expected isotopic pattern. $C_{41}H_{35}Fe_2I_2N_2PPd$ (1058.64): calcd. C 46.52, H 3.33, N 2.65; found C 47.30, H 3.44, N 2.63.

X-ray Crystallographic Study: X-ray structural measurements were carried out with a Bruker CCD diffractometer (Bruker SMART PLATFORM, with CCD detector, graphite monochromator, Mo-K_α radiation). The program SMART was used for data collection. Integration was performed with SAINT. The structure solution and refinement on F^2 were accomplished with SHELXTL 97. Model plots were made with ORTEP32. All structures were solved by direct methods. All non-hydrogen atoms were refined freely with anisotropic displacement parameters. Hydrogen atoms were refined at calculated positions riding on their carrier atoms. Weights were optimized in the final refinement cycles. A summary of the most important crystallographic data is given in Table 1. CCDC-239875 (**12b**), -239876 (**16a**) and -239877 (**12a**) contain the supplementary crystallographic data for this paper. These data can be obtained free of charge at www.ccdc.cam.ac.uk/conts/retrieving.html [or from the Cambridge Crystallographic Data Centre, 12 Union Road, Cambridge CB2 1EZ, UK; Fax: +44 1223-336-033; E-mail: deposit@ccdc.cam.ac.uk].

Acknowledgments

Support from the Swiss National Science Foundation is gratefully acknowledged. We thank Sebastian Gischig for performing the X-ray crystallographic studies of compounds **12a**, **12b** and **16a**.

[1] *Ferrocenes* (Eds.: A. Togni, T. Hayashi), Wiley-VCH, Weinheim, **1995**.
[2] C. W. K. Gstoettmayr, V. P. W. Bohm, E. Herdtweck, M. Grosche, W. A. Herrmann, *Angew. Chem. Int. Ed.* **2002**, *41*, 1363.
[3] C. L. Yang, H. M. Lee, S. P. Nolan, *Org. Lett.* **2001**, *3*, 1511.
[4] T. M. Trnka, R. H. Grubbs, *Acc. Chem. Res.* **2001**, *34*, 18.
[5] S. R. Stauffer, S. W. Lee, J. P. Stambuli, S. I. Hauck, J. F. Hartwig, *Org. Lett.* **2000**, *2*, 1423.
[6] B. Bildstein, M. Malaun, H. Kopacka, K. Wurst, M. Mitterbock, K. H. Ongania, G. Opromolla, P. Zanello, *Organometallics* **1999**, *18*, 4325.
[7] B. Bildstein, M. Malaun, H. Kopacka, K. H. Ongania, K. Wurst, *J. Organomet. Chem.* **1999**, *572*, 177.
[8] B. Bildstein, *J. Organomet. Chem.* **2001**, *617*, 28.
[9] R. Jackstell, A. Frisch, M. Beller, D. Rottger, M. Malaun, B. Bildstein, *J. Mol. Catal. A* **2002**, *18*, 105.
[10] B. Bildstein, M. Malaun, H. Kopacka, K. H. Ongania, K. Wurst, *J. Organomet. Chem.* **1998**, *552*, 45.
[11] C. Bolm, M. Kesselgruber, G. Raabe, *Organometallics* **2002**, *21*, 707.
[12] D. Broggini, A. Togni, *Helv. Chim. Acta* **2002**, *85*, 2518.
[13] H. Seo, H. Park, B. Y. Kim, J. H. Lee, S. U. Son, Y. K. Chung, *Organometallics* **2003**, *22*, 618.
[14] H. Seo, B. Y. Kim, J. H. Lee, H. J. Park, S. U. Son, Y. K. Chung, *Organometallics* **2003**, *22*, 4783.
[15] S. Gischig, A. Togni, *Organometallics* **2004**, *23*, 2479.
[16] F. Demirhan, O. Yildirim, B. Cetinkaya, *Trans. Met. Chem.* **2003**, *28*, 558.
[17] An *N*,*N*′-dicyclophane-substituted carbene analogous to **1a**

 © 2005 Wiley-VCH Verlag GmbH & Co. KGaA, Weinheim

and a related Rh complex have been reported recently: Y. D. Ma, C. Song, C. Q. Ma, Z. J. Sun, Q. Chai, M. B. Andrus, *Angew. Chem. Int. Ed.* **2003**, *42*, 5871. Interesting results were obtained in the asymmetric addition of arylboron reagents to enones (*ee* up to 98%).

[18] Anions: BPh_4^-, TfO^-.

[19] S. Lee, J. F. Hartwig, *J. Org. Chem.* **2001**, *66*, 3402.

[20] O. Riant, O. Samuel, T. Flessner, S. Taudien, H. B. Kagan, *J. Org. Chem.* **1997**, *62*, 6733.

[21] A. Brunner, S. Taudien, O. Riant, H. B. Kagan, *Chirality* **1997**, *9*, 478.

[22] F. Rebiere, O. Samuel, H. B. Kagan, *Tetrahedron Lett.* **1990**, *31*, 3121.

[23] Aminoferrocene was first synthesized by Nesmeyanov (ref.[25]), who treated lithiated ferrocene with the *O*-benzyl ether of hydroxylamine and isolated the product in 25% yield. In the same year Arimoto and Haven synthesized aminoferrocene (ref.[26]) from ferrocenecarboxylic acid by using the Curtius synthetic strategy, but the overall yield was lower than 20%. Other approaches including Beckmann rearrangement from the oxime proved fruitless. Lehner and Schlögl, in 1970 (ref.[27]), reported the synthesis of planar-chiral (*R*)-1-amino-2-methylferrocene in 26% yield from (*R*)-2-methylferrocenecarboxylic acid by a modified procedure and determined its absolute configuration. The approach presented here differs from Schlögl's approach in various reaction conditions such as temperatures, solvents, the activation of the carboxylic acid and the fact that the sequence was performed in two steps in 82% yield. A recent example of a high yielding (80%) Curtius degradation sequence leading to achiral aminoferrocene can be found in ref.[28]

[24] M. Herberhold, "Ferrocene Compounds Containing Heteroelements", in *Ferrocenes* (Eds.: A. Togni, T. Hayashi), Wiley-VCH, Weinheim, **1995**.

[25] A. N. Nesmeyanov, E. G. Perevalova, R. V. Golovnya, L. S. Shilovtseva, *Dokl. Akad. Nauk. SSSR* **1955**, *102*, 535; *Chem. Abstr.* **1956**, *50*, 4925g.

[26] F. S. Arimoto, A. C. Haven, *J. Am. Chem. Soc.* **1955**, *77*, 6295.

[27] H. Lehner, K. Schlögl, *Monatsh. Chem.* **1970**, *101*, 895.

[28] D. C. D. Butler, C. J. Richards, *Organometallics* **2002**, *21*, 5433.

[29] A. N. Nesmejanow, W. A. Sasonowa, V. N. Drosd, *Chem. Ber.* **1960**, *93*, 2717.

[30] M. Sato, S. Ebine, S. Akabori, *Synthesis* **1981**, 472.

[31] M. Herberhold, M. Ellinger, W. Kremnitz, *J. Organomet. Chem.* **1983**, *241*, 227.

[32] N. Montserrat, A. W. Parkins, A. R. Tomkins, *J. Chem. Res. (S)* **1995**, *8*, 336.

[33] A. Arrieta, J. M. Aizpurua, C. Palomo, *Tetrahedron Lett.* **1984**, *25*, 3365.

[34] The amines **9a** and **9b** could have been produced directly from the isocyanate by adding water instead of benzylic alcohol but the purification and storage of the air-stable carbamate **8** proved to be more convenient.

[35] C. Grundmann, A. Kreutzberger, *J. Am. Chem. Soc.* **1955**, *77*, 6559.

[36] The acetal was synthesized instead of the aldehyde in order to prevent oxazole formation in the following cyclization step.

[37] D. Broggini, PhD thesis Nr. 15041, ETH Zürich, **2003**.

[38] G. Aullon, G. Ujaque, A. Lledos, S. Alvarez, P. Alemany, *Inorg. Chem.* **1998**, *37*, 804.

[39] **16a**: $J_{P,C(carbene)} = 194$, $J_{P,C(olefinic)} = 5.6$, $J_{PH(olefinic)} = 1.0$ Hz. **16b**: $J_{P,C(carbene)} = 190$, $J_{P,C(olefinic)} = 5.6$, $J_{PH(olefinic)} = 1.2$ Hz.

[40] D. Enders, H. Gielen, G. Raabe, J. Runsink, J. H. Teles, *Chem. Ber.* **1996**, *129*, 1483.

[41] R. W. Hoffmann, *Chem. Rev.* **1989**, *89*, 1841.

[42] The asymmetric intramolecular cyclization of *N*-(2-bromophenyl)-*N*-methyl-2-(1-naphthyl)propanamide using 10% of $Pd(dba)_2$, 15% of **12a** and 1.5 equiv. of NaO*t*Bu in 1,4-dioxane at 50 °C for 26 h gave (+)-1,3-dimethyl-3-(1-naphthyl)oxindole in the mentioned yield and *ee*. When **16a** was used, the *ee* values and activity were slightly lower.

[43] G. G. A. Balavoine, J.-C. Daran, G. Iftime, P. G. Lacroix, E. Manoury, *Organometallics* **1999**, *18*, 21.

Received August 11, 2004
Early View Article
Published Online December 2, 2004

 © 2005 Wiley-VCH Verlag GmbH & Co. KGaA, Weinheim

A New Type of Supramolecular Assembly by Hydrogen Bond Templating: Identification of Rare Monodentate Acetate Coordination in $[Fe_3(\mu_3\text{-}O)(\mu_2\text{-}CH_3COO)_6(H_2O)_2(CH_3COO)]\cdot T\cdot ClO_4$ (T = 2,6-Diaminopyridinium Cation, $C_5H_8N_3$ and 2-Aminopyridinium Cation, $C_5H_7N_2$)

Sabbani Supriya,[a] K. Swarna Latha,[a] and Samar K. Das*[a]

In memory of Professor Bhaskar G. Maiya

Keywords: Iron trinuclear cluster / Hydrogen bond templating / Monodentate acetate / Supramolecular assembly

The complexes $[Fe_3(\mu_3\text{-}O)(\mu_2\text{-}CH_3COO)_6(H_2O)_2(CH_3COO)]\cdot C_5H_8N_3\cdot ClO_4$ ($C_5H_8N_3$ = 2,6-diaminopyridinium cation) (**1**) and $[Fe_3(\mu_3\text{-}O)(\mu_2\text{-}CH_3COO)_6(H_2O)_2(CH_3COO)]\cdot C_5H_7N_2\cdot ClO_4$ ($C_5H_7N_2$ = 2-aminopyridinium cation) (**2**) show novel self-assembled supramolecular structures in their crystals as elucidated by X-ray analysis. The structures contain $[Fe_3(\mu_3\text{-}O)(\mu_2\text{-}CH_3COO)_6(H_2O)_2(CH_3COO)]$ units as the building blocks. A detailed examination of the structures revealed that monodentate acetate, which is stabilised by a hydrogen-bond template T (2,6-diaminopyridinium cation in **1** and the 2-aminopyridinium cation in **2**), plays a directing role in forming these new types of hydrogen-bonded assemblies in **1** and **2**. Crystal data for **1** and **2** were determined by X-ray structure analysis.
(© Wiley-VCH Verlag GmbH & Co. KGaA, 69451 Weinheim, Germany, 2005)

Introduction

Oxo-bridged trinuclear iron clusters such as $[Fe_3(\mu_3\text{-}O)(\mu_2\text{-}RCOO)_6L_3]^{1+}$ (where L is a neutral monodentate ligand, e.g. H_2O and R is an alkyl or aryl group),[1] popularly known as "basic iron carboxylates", have been known for more than a century.[2] These trinuclear complexes are considered an important class of compounds because the $\{Fe_3(\mu_3\text{-}O)\}^{7+}$ unit has been proposed as the smallest building block for the formation of the iron core in ferritin, an iron storage protein.[3] However, examples of extended structures based on this building unit showing chain- or layer-like networks are scarce in the literature.[4,5] Recently, we reported a trinuclear iron(III) complex which aggregates to a 1D zig-zag chain-like structure through N−H···O hydrogen bonds.[5] In our continued efforts, we recently observed a new type of H-bonded supramolecular assembly in the complexes $[Fe_3(\mu_3\text{-}O)(\mu_2\text{-}CH_3COO)_6(H_2O)_2(CH_3COO)]\cdot C_5H_8N_3\cdot ClO_4$ ($C_5H_8N_3$ = 2,6-diaminopyridinium cation) (**1**) and $[Fe_3(\mu_3\text{-}O)(\mu_2\text{-}CH_3COO)_6(H_2O)_2(CH_3COO)]\cdot C_5H_7N_2\cdot ClO_4$ ($C_5H_7N_2$ = 2-aminopyridinium cation) (**2**). These species have $[Fe_3(\mu_3\text{-}O)(\mu_2\text{-}CH_3COO)_6(H_2O)_2(CH_3COO)]$ as a basic building block. The 2,6-diaminopyridinium cation (in **1**) and the 2-aminopyridinium cation (in **2**) play an important role in the templating of these H-bonded assemblies (Scheme 1) by stabilising a monodentate acetate coordinated to one of the iron centres in $[Fe_3(\mu_3\text{-}O)(\mu_2\text{-}CH_3COO)_6(H_2O)_2(CH_3COO)]$. The stabilisation achieved here is through hydrogen bonding between the template (T) and monodentate acetate (Scheme 1). To the best of our knowledge, $[Fe_3(\mu_3\text{-}O)(\mu_2\text{-}CH_3COO)_6(H_2O)_2(CH_3COO)]$ is the first structurally characterised complex among "basic metal carboxylates" that has unusual monodentate acetate coordination.

[a] School of Chemistry, University of Hyderabad, Hyderabad 500046, India
Fax: (internat.) + 91-40-2301-2460
E-Mail: skdsc@uohyd.ernet.in

Results and Discussion

Compounds **1** and **2** were isolated from aqueous solutions (pH 3.5) by dissolving ferric chloride, acetic acid, 2,6-diaminopyridine (for compound **1**) or 2-aminopyridine (for compound **2**) and sodium perchlorate. The neutral complex $[Fe_3(\mu_3\text{-}O)(\mu_2\text{-}CH_3COO)_6(H_2O)_2(CH_3COO)]$ cocrystallises with 2,6-diaminopyridinium and 2-aminopyridinium perchlorate in **1** and **2**, respectively. Protonation of 2,6-diaminopyridine or 2-aminopyridine in **1** and **2** is not surprising because the synthesis of these complexes were carried out at a low pH value. Compounds **1** and **2** were obtained in moderate yields and gave elemental analyses consistent with formulae $[Fe_3(\mu_3\text{-}O)(\mu_2\text{-}CH_3COO)_6(H_2O)_2(CH_3COO)]\cdot C_5H_8N_3\cdot ClO_4$ (**1**) and $[Fe_3(\mu_3\text{-}O)(\mu_2\text{-}CH_3COO)_6(H_2O)_2(CH_3COO)]\cdot C_5H_7N_2\cdot ClO_4$ (**2**). Interestingly, compounds **1** and **2** both always crystallise with only one molecule of the respective aminopyridine regardless of the amount of aminopyridine used in the synthesis.

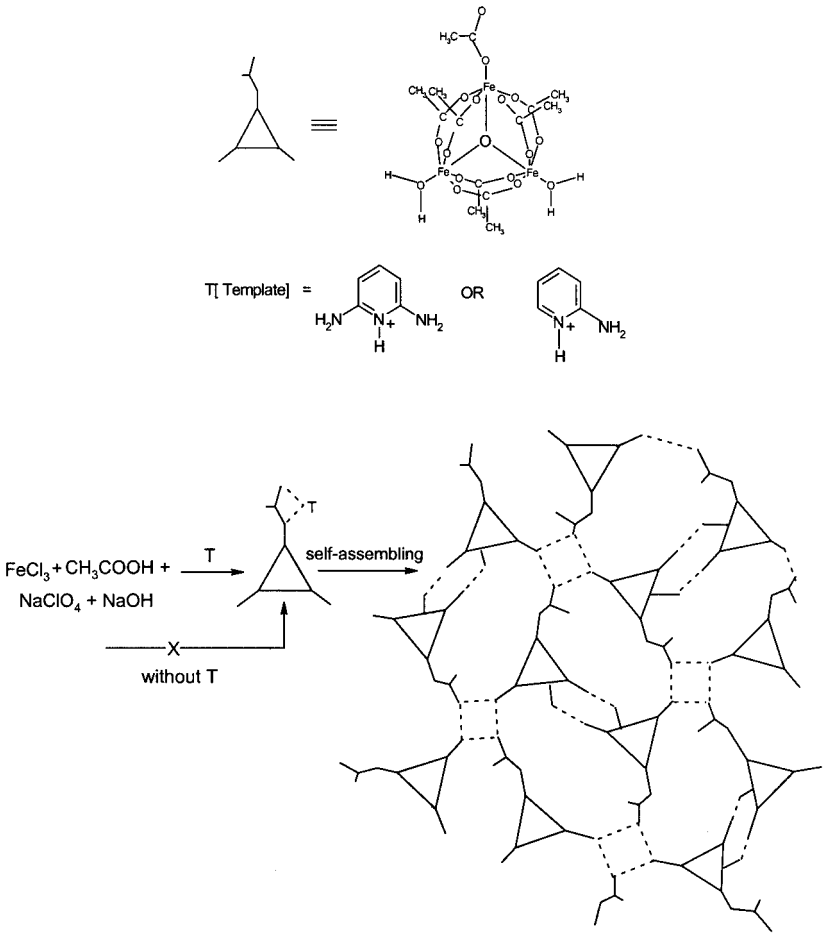

Scheme 1

Both the complexes crystallise in the monoclinic space group $P2_1/c$. The structural features of the $[Fe_3(\mu_3\text{-}O)(\mu_2\text{-}CH_3COO)_6(H_2O)_2(CH_3COO)]$ motif in **1** and **2** are comparable. The thermal ellipsoid plots of $[Fe_3(\mu_3\text{-}O)(\mu_2\text{-}CH_3COO)_6(H_2O)_2(CH_3COO)]$ in **1** and **2** are presented in Figure 1. Its overall structure is similar to that found in other trinuclear $\{M_3(\mu_3\text{-}O)\}$ compounds.[6] Unlike usual symmetric μ_3-oxotriiron(III) centres in basic metal carboxylates,[1] the unusual asymmetry in the present trinuclear structure $[Fe_3(\mu_3\text{-}O)(\mu_2\text{-}CH_3COO)_6(H_2O)_2(CH_3COO)]$ (in **1** and **2**) arises from the differences in the coordination environments of the three metal ions. Whereas one of the iron centres is coordinated to a monodentate acetate ligand, the other two are bonded to two water molecules. Monodentate acetate coordination is not unusual in transition metal chemistry although it is rare in basic iron carboxylate chemistry.[1] Among the basic carboxylate complexes in which the carboxylate is reported to act as a monodentate ligand, the formato complex $Fe_3O(OOCH)_7{\cdot}5H_2O$ is the best known example. Here, one of the formate ligands has been described as being monodentate in nature.[7] $[Fe_3(OH)(OOCCH_3)_7(NO_3)]{\cdot}nH_2O$ is another such example.[2c] However, the ambiguity of whether the extra carboxylate remain as an adduct (coordinated ligand) or a solvated carboxylic acid has not resolved in both these cases due to the lack of unambiguous characterisation data for the complexes especially single-crystal structure analyses. The crystal structure of an analogous complex, $[Cr_2Fe(\mu_3\text{-}O)(\mu_2\text{-}CH_3COO)_6(H_2O)_3]\ NO_3{\cdot}CH_3COOH$, in which the seventh carboxylate remains as a solvate of acetic acid, has been described.[8] The crystal structures of **1** and **2** thus represent the first examples of a structurally characterised $\{Fe_3(O)\}^{7+}$ complexes (Figure 1) having monodentate carboxylate coordination at one of the metal centres. Relevant crystallographic data for **1** and **2** are presented in Table 1 and selected bond lengths and angles are listed in Tables 2 and 3, respectively.

At 298 K, the values of the effective magnetic moments for **1** and **2** were found to be 5.57 μ_B and 5.65 μ_B, respectively. These values are considerably smaller than the spin only value (10.25 μ_B) for a trinuclear cluster containing three high spin Fe^{III} ions (s = 5/2). This indicates an antiferromagnetic interaction between the three Fe^{III} centres in the trinuclear cluster. Similar antiferromagnetic interactions have been reported for $[Fe_3(\mu_3\text{-}O)(O_2CR)L_3]^{1+}$ complexes (R = alkyl groups, L = monodentate ligands).[1c,5b]

Hydrogen Bond Templating and Supramolecular Structure

2,6-Diaminopyridine and 2-aminopyridine are present in monoprotonated forms in the crystal structures of **1** and **2**

 © 2005 Wiley-VCH Verlag GmbH & Co. KGaA, Weinheim

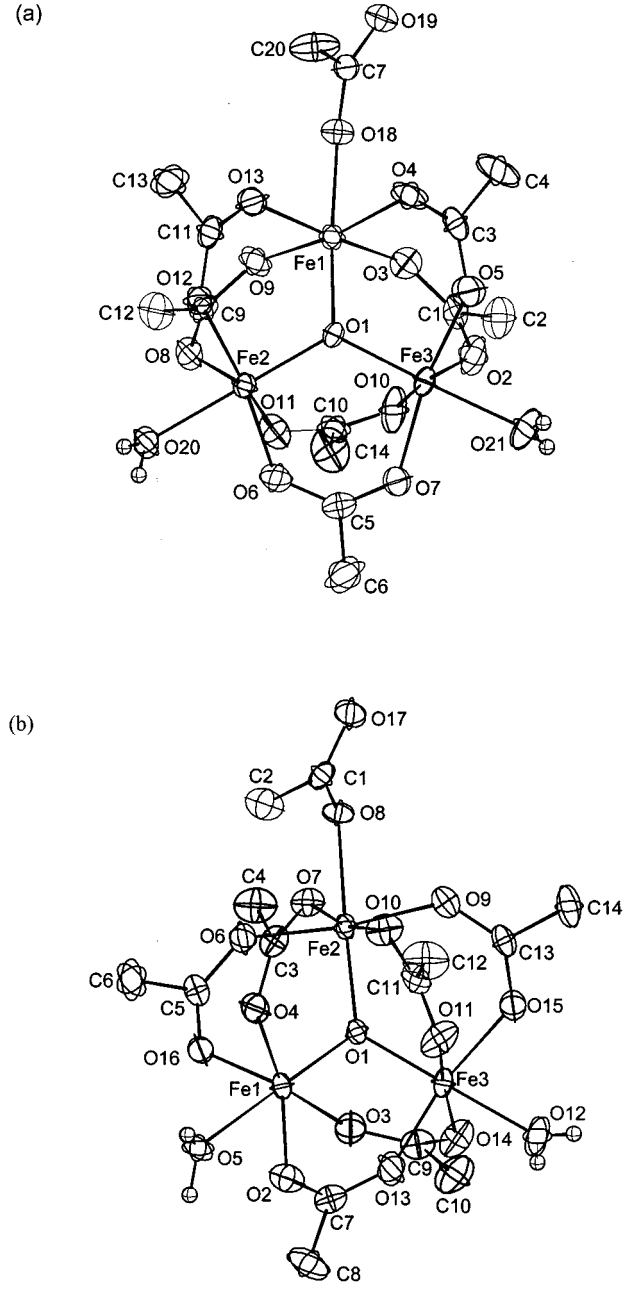

Figure 1. (a) Thermal ellipsoidal plot of $[Fe_3(\mu_3\text{-}O)(\mu_2\text{-}CH_3COO)_6(H_2O)_2(CH_3COO)]$ in **1**; (b) thermal ellipsoidal plot of $[Fe_3(\mu_3\text{-}O)(\mu_2\text{-}CH_3COO)_6(H_2O)_2(CH_3COO)]$ in **2**; acetate hydrogen atoms are omitted for clarity

Table 1. Crystallographic data for **1** and **2**

	1	**2**
Formula	$C_{19}H_{33}ClFe_3N_3O_{21}$	$C_{19}H_{32}ClFe_3N_2O_{21}$
Molecular mass	842.48	827.47
Crystal system	monoclinic	monoclinic
Space group	$P2_1/c$	$P2_1/c$
T (K)	293	293
a (Å)	10.992(10)	10.722(3)
b (Å)	18.711(13)	18.544(2)
c (Å)	16.564(11)	16.6100(15)
β (°)	106.35(7)	105.961(12)
Volume (Å^3)	3269(4)	3175.4(10)
Z	4	4
$D_{calcd.}$ (g cm^{-3})	1.712	1.731
Absorption coefficient (mm^{-1})	1.484	1.525
F(000)	1724	1692
λ (Å)	0.71073	0.71073
Crystal size (mm)	0.60 × 0.56 × 0.44	0.64 × 0.36 × 0.28
Theta range (°)	1.68/24.97	1.68/24.99
N	5736	5576
N_o [$I > 2\sigma(I)$]	3822	4548
R	0.0446	0.0394
wR	0.1027	0.1086
Largest diff. peak and hole (e Å^{-3})	0.654/ −0.539	0.934/−0.660

Table 2. Selected interatomic distances (Å) and angles (°) in $[Fe_3(\mu_3\text{-}O)(\mu_2\text{-}CH_3COO)_6(H_2O)_2(CH_3COO)]\cdot C_5H_8N_3$ in **1**

Fe1−O1	1.909(3)	Fe1−O13	1.985(4)
Fe1−O3	2.018(4)	Fe1−O18	2.072(3)
Fe2−O1	1.888(3)	Fe2−O20	2.092(4)
Fe3−O1	1.897(3)	Fe3−O21	2.063(4)
O18−C7	1.267(5)	O3−C1	1.257(6)
C7−O19	1.255(6)	C7−C20	1.497(7)
N2−C19	1.345(8)	N2−C15	1.360(7)
C15−N4	1.331(8)	N3−C19	1.322(8)
C15−C16	1.381(8)	C19−C18	1.394(9)
O13−Fe1−O4	91.87(16)	O3−Fe1−O9	85.16(15)
O1−Fe1−O18	175.99(13)	O4−Fe1−O18	83.13(13)
O3−Fe1−O18	82.87(13)	O1−Fe2−O20	178.61(15)
O8−Fe2−O20	83.78(16)	O12−Fe2−O20	85.26(16)
O1−Fe3−O21	177.66(18)	Fe2−O1−Fe3	119.47(16)
Fe2−O1−Fe1	120.53(15)	Fe3−O1−Fe1	119.99(16)
C7−O18−Fe1	132.2(3)	O19−C7 −O18	121.0(5)
O19−C7−C20	118.0(4)	O12−C11−O13	124.4(4)
C19−N2−C15	124.3(5)	N4−C15−N2	118.7(5)
N4−C15−C16	124.0(6)	N2−C15−C16	117.3(6)
N3−C19−N2	117.6(5)	N3−C19−C18	124.5(7)
N2−C19−C18	117.9(7)	C17−C18−C19	119.0(7)

and are involved in noncovalent supramolecular interactions with monodentate acetates as depicted in Figure 2. We were unable to isolate $[Fe_3(\mu_3\text{-}O)(\mu_2\text{-}CH_3COO)_6(H_2O)_2(CH_3COO)]$ without adding 2,6-diaminopyridine or 2-aminopyridine (along with $NaClO_4$). This in itself suggests that these two amines are involved in the stabilisation of both the monodentate acetates which are coordinated to the $\{Fe_3\}$ clusters and the extended structures (vide infra). Indeed, as seen in Figures 2 and 3, the unusual iron-coordinated monodentate acetate anion is hydrogen-bonded to protonated 2,6-diaminopyridine (in **1**) and 2-aminopyridine (in **2**) and is directly involved in the construction of a new type of supramolecular network. A closer look at the structures (see Figure 3) suggests that these hydrogen-bonding assemblies would not have formed without involvement of the monodentate acetates and that the monodentate acetate could not have been incorporated if it were not stabilised by the 2,6-diaminopyridinium or 2-aminopyridinium cation (Figure 2). In other words, the 2,6-diaminopyridinium or 2-aminopyridinium cation acts as a hydrogen bond template, stabilising the monodentate acet-

 © 2005 Wiley-VCH Verlag GmbH & Co. KGaA, Weinheim

Table 3. Selected interatomic distances (Å) and angles (°) in $[Fe_3(\mu_3\text{-}O)(\mu_2\text{-}CH_3COO)_6(H_2O)_2(CH_3COO)]\cdot C_5H_7N_2$ in **2**

Fe1−O1	1.889(2)	Fe1−O5	2.103(3)
Fe2−O1	1.911(3)	Fe2−O10	2.002(3)
Fe2−O7	2.013(3)	Fe2−O8	2.083(3)
Fe3−O1	1.892(3)	Fe3−O12	2.053(3)
O9−C13	1.253(5)	O8−C1	1.272(5)
O17−C1	1.249(5)	C13−C14	1.492(6)
C1−C2	1.502(6)	N1−C15	1.335(7)
N1−C19	1.356(8)	C15−N2	1.300(8)
C15−C16	1.433(7)	C19−C18	1.337(8)
O1−Fe1−O5	178.66(12)	O 4−Fe1−O5	84.23(12)
O16−Fe1−O5	85.00(12)	O1−Fe2−O9	93.72(12)
O1−Fe2−O7	96.04(11)	O1−Fe2−O8	176.56(11)
O10−Fe2 −O8	82.19(11)	O7−Fe2−O8	86.94(11)
O1−Fe3−O12	178.00(14)	O15−Fe3−O12	84.91(15)
O11−Fe3−O12	84.26(14)	Fe1−O1−Fe3	119.15(13)
Fe1−O1−Fe(2)	120.16(13)	Fe3−O1−Fe2	120.69(13)
C7−O13−Fe3	132.1(3)	C9−O3−Fe1	130.3(3)
O14−C9−O3	125.0(4)	O14−C9−C10	117.4(4)
O17−C1−O8	121.3(4)	O17−C1−C2	118.4(4)
O8−C1−C2	120.2(4)	O16−C5−C6	117.8(4)
C15−N1−C19	123.5(5)	N2−C15−N1	119.0(5)
N2−C15−C16	124.2(6)	N1−C15−C16	116.8(5)
C17−C16−C15	118.6(5)	C18−C19−N1	120.0(6)
C16−C17−C18	122.7(6)	C19−C18−C17	118.3(7)

ate anion which in turn is responsible for the formation of the novel layer-like hydrogen-bonded network of $[Fe_3(\mu_3\text{-}O)(\mu_2\text{-}CH_3COO)_6(H_2O)_2(CH_3COO)]$.

Description of the Supramolecular Networks

There are two different types of intermolecular hydrogen bonds in the layer-like, 2D assembly formed in **1** (Figure 3a and Figure 4). These can be described as follows: (i) Type I: each hydrogen atom belonging to the Fe(2)-coordinated water molecule O(20) makes a hydrogen bond with a Fe(1)-coordinated monodentate acetate oxygen O(19). This results in a tetramer consisting of two O(20) waters and two O(19) acetate oxygen atoms (Figure 3a and Figure 4). (ii) Type II: one hydrogen atom attached to O(21)water [which is coordinated to Fe(3)] undergoes bifurcated H-bonding interactions with O(5) and O(10) from two different bidentate acetate anions from an adjacent Fe_3 cluster and vice versa (Figure 3a and Figure 4). The geometrical parameters of the hydrogen bonds involved in constructing this 2D supramolecular assembly are listed in Table 4. Because of the equivalency of the all Fe_3 clusters in the whole crystal, it was possible to have these two types of hydrogen bonds to form an infinite 2D layer network. In the layer, each $\{Fe_3\}$ cluster is surrounded by six identical clusters and is interlinked by both types (I and II) of hydrogen bonding. Interestingly, in the supramolecular network, Fe(1) of an $\{Fe_3\}$ cluster faces Fe(1) of an adjacent $\{Fe_3\}$ cluster. Similarly, Fe(2) and Fe(3) of the same $\{Fe_3\}$ cluster face Fe(2) and Fe(3) from two different adjacent $\{Fe_3\}$ clusters, respectively.

In the crystal structure of **2**, a similar layer-like assembly is formed from intermolecular hydrogen bonding interactions of $[Fe_3(\mu_3\text{-}O)(\mu_2\text{-}CH_3COO)_6(H_2O)_2(CH_3COO)]$ as

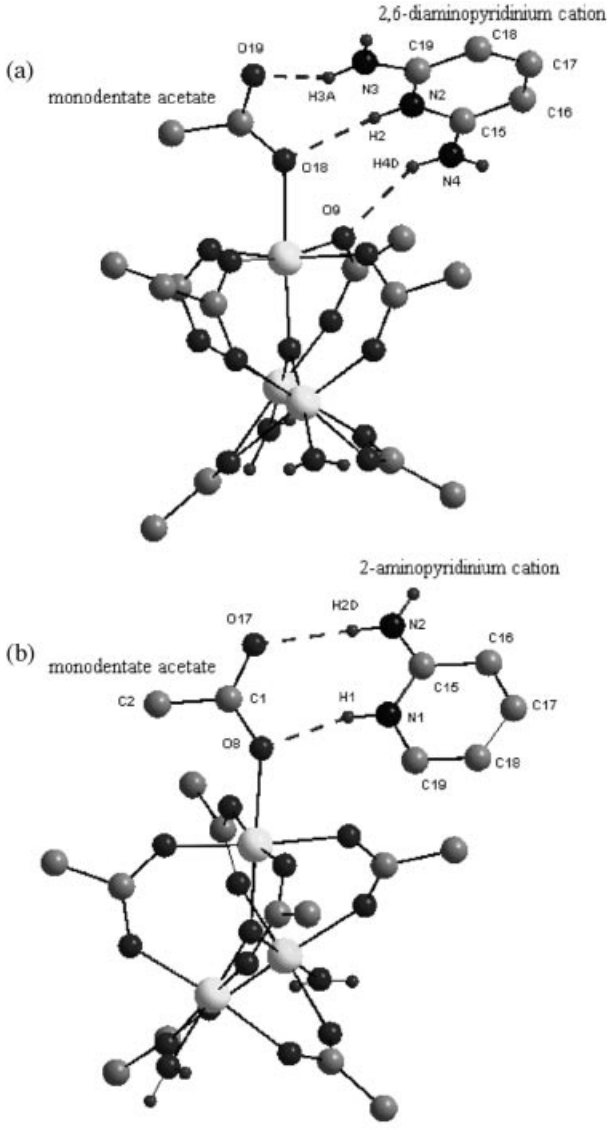

Figure 2. (a) Ball-and-stick representation of $[Fe_3(\mu_3\text{-}O)(\mu_2\text{-}CH_3COO)_6(H_2O)_2(CH_3COO)]\cdot C_5H_8N_3^+$ showing N−H···O hydrogen bonding interactions between the 2,6-diaminopyridinium cation and the coordinated monodentate acetate ligand in **1**; hydrogen bonding parameters (Å, °): N(3)−H(3A)···O(19), 0.86, 2.08, 2.849 (7), 148.4; N(2)−H(2)···O(18), 0.86, 2.19, 3.045(6), 173.2; N(4)−H(4D)···O(9), 0.86, 2.21, 2.988(7), 151.1; (b) ball-and-stick representation of $[Fe_3(\mu_3\text{-}O)(\mu_2\text{-}CH_3COO)_6(H_2O)_2(CH_3COO)]\cdot C_5H_7N_2^+$ showing N−H···O hydrogen bonding interactions between the 2-aminopyridinium cation and the coordinated monodentate acetate ligand in **2**; hydrogen bonding parameters (Å, °): N(2)−H(2D)···O(17), 0.86, 2.13, 2.932(6), 154.6; N(1)−H(1)···O(8), 0.86, 1.97, 2.804(5), 163.8

shown in (see Figure 3b). The hydrogen atoms of O(5)water [coordinated to Fe(1)] are hydrogen bonded to two O(17) acetate oxygen atoms from two different adjacent $\{Fe_3\}$ clusters resulting in a supramolecular $\{O_4\}$ cluster which consists of two O(5) waters and two O(17) acetate oxygen atoms. This is similar to the type I hydrogen bonding interaction in compound **1**. One hydrogen atom of O(12)water [coordinated to Fe(3)] undergoes a hydrogen bonding interaction with O(11) belonging to a bidentate acetate ligand from an adjacent $\{Fe_3\}$ cluster and vice versa. Unlike the

 © 2005 Wiley-VCH Verlag GmbH & Co. KGaA, Weinheim

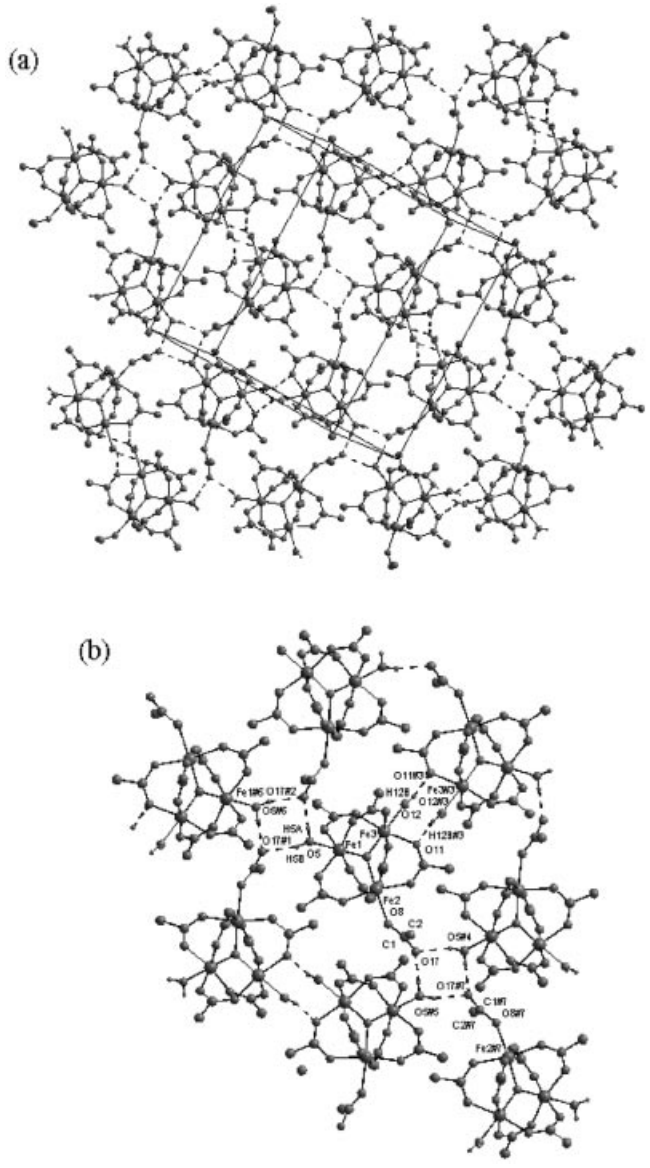

Figure 3. (a) 2D hydrogen-bonding supramolecular network present in **1** based on $Fe_3(\mu_3\text{-}O)(\mu_2\text{-}CH_3COO)_6(H_2O)_2(CH_3COO)]$ as a building block and involving coordinated water hydrogen atoms and acetate oxygen atoms; (b) intermolecular hydrogen bonds of $Fe_3(\mu_3\text{-}O)(\mu_2\text{-}CH_3COO)_6(H_2O)_2(CH_3COO)]$ in **2**; atoms with additional labels #1−#7 are related by symmetry transformations to generate equivalent atoms: #1: x, $1.5 - y$, $-0.5 + z$; #2: $1 - x$, $0.5 + y$, $1.5 - z$; #3: $1 - x$, $2 - y$, $2 - z$; #4: x, $1.5 - y$, $0.5 + z$; #5: $1 - x$, $-0.5 + y$, $1.5 - z$; #6: $1 - x$, $2 - y$, $1 - z$; #7: $1 - x$, $1 - y$, $2 - z$

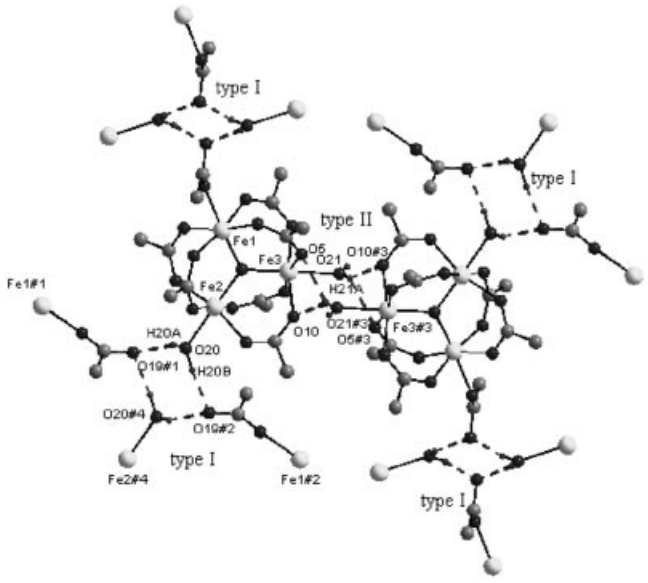

Figure 4. Drawing of two types of the intermolecular hydrogen bonds in **1** as shown in dashed lines; type I: O(20)−H(20A)···O(19); O(20)−H(20B)···O(19); type II: O(21)−H(21A)···O(5); O(21)−H(21A)···O(10); atoms with additional labels #1−#4 are related by symmetry transformations to generate equivalent atoms: #1: x, $0.5 - y$, $-0.5 + z$; #2: $1 - x$, $-0.5 + y$, $0.5 - z$; #3: $1 - x$, $-y$, $1 - z$; #4: $1 - x$, $-y$, $-z$

Table 4. Geometrical parameters of hydrogen bonds (Å, °) involved in the supramolecular construction (in **1**) as shown in Figures 3a and Figure 4; D = donor; A = acceptor; atoms with additional labels #1−#3 are related by symmetry operations specified in the caption of Figure 4

D−H···A	d(D−H)	d(H···A)	d(D···A)	∠(DHA)
O(20)−H(20A)···O(19) # 1	0.65(6)	2.17(6)	2.795(6)	161(7)
O(20)−H(20B)···O(19) #2	0.94(7)	1.83(7)	2.755(5)	168(5)
O(21)−H(21A)···O(5) #3	0.66(7)	2.47(7)	3.021(7)	143(8)
O(21)−H(21A)···O(10) #3	0.66(7)	2.47(7)	3.064(7)	150(8)

Table 5. Geometrical parameters of hydrogen bonds (Å, °) involved in the supramolecular construction (in **2**) as shown in Figure 3b; D = donor; A = acceptor; atoms with additional labels #1−#3 are related by symmetry operations specified in the caption of Figure 3b

D−H···A	d(D−H)	d(H···A)	d(D···A)	∠(DHA)
O(5)−H(5B)···O(17)# 1	0.83(5)	1.98(5)	2.785(4)	163(4)
O(5)−H(5A)···O(17) #2	0.87(4)	1.97(5)	2.832(4)	175(4)
O(12)−H(12B)···O(11) #3	0.84(7)	2.04(7)	2.858(5)	167(6)

type II hydrogen bonds in compound **1**, the hydrogen atom of O(12)water does not undergo bifurcated hydrogen bonding interactions in compound **2** (see Figure 3b). The relevant hydrogen bonding parameters in compound **2** are summarised in Table 5.

In the crystal structures of both compounds **1** and **2**, the supramolecular hydrogen bonding interactions result in the layer-like two-dimensional networks (Figure 3). In the three-dimensional structure, the packing of these two-dimensional layers gives rise to nano-sized channels when viewed down to crystallographic *a* axis (Figure 5). The layers are well-separated in this stacking (along crystallographic *a* axis) with inter-layer distance of about 11 Å.

Removal of Template

Thermogravimetric analysis (TGA) of **1** under nitrogen showed an initial weight loss of ca. 25% at 240°C due to loss of 2,6-diaminopyridinium perchlorate. The compound is unstable beyond 245°C losing iron coordinated acetates

 © 2005 Wiley-VCH Verlag GmbH & Co. KGaA, Weinheim

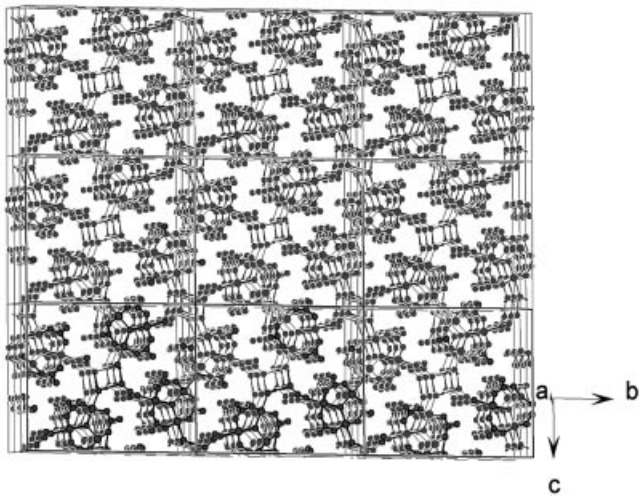

Figure 5. 3D structure of **1** (2,6-diaminopyridinium cation and perchlorate anion are not shown) showing the packing of the layers when viewed along the crystallographic *a* axis (3 × 3 × 3 cells)

including the (μ_3-O) atom with the decomposition of the trinuclear cluster (75.78% calcd, 75.44% obsd). As expected, the TGA curve of compound **2** is comparable with that of compound **1**. We wanted to check whether the template would be removed thermally but with retention of the supramolecular structure. The IR bands (700−850 cm^{-1}: γ-CH and pyridine ring bending bands, 2900−3350 cm^{-1}: N−H stretching vibrations) corresponding to the template gradually disappear on heating **1** and are completely lost when **1** is heated at 150°C for two hours. The resultant solid retains the {$Fe_3(\mu_3\text{-O})$} cluster as supported by the presence of $\nu_{as}(Fe_3O)$ vibrations at 660 cm^{-1} and 625 cm^{-1} in the IR spectrum but the solid loses its crystallinity as evidenced by X-ray powder diffraction studies. We also attempted to remove the template by washing **1** or **2** with an organic solvent in which 2,6-diaminopyridine and 2-aminopyridine are soluble but **1** and **2** are insoluble. However, we were not successful in removing the templates of **1** and **2** whilst maintaining their supramolecular structures (see Exp. Sect.). The fact that the amino bases (templates) cannot be removed from the crystal structure without resorting to heating the sample is probably due to the strong hydrogen bonding interactions of the template with the host trinuclear iron cluster.

Conclusion

A new type of layer-like network, constructed from an unusual trinuclear iron cluster [$Fe_3(\mu_3\text{-})(\mu_2\text{-}CH_3COO)_6(H_2O)_2(CH_3COO)$] using supramolecular interactions, has been presented. The building complex unit represents the first example of a structurally characterised {$M_3(\mu_3\text{-O})$} cluster in which a carboxylate anion acts as a monodentate ligand. The 2,6-diaminopyridinium cation in **1** and the 2-aminopyridinium cation in **2** act as hydrogen bonding templates and stabilise the monodentate acetates which in turn result in the formation of novel supramolecular networks in **1** and **2**. Despite the amine groups of the template being free for metal coordination, the fact that the aminopyridines are not involved in the covalent bonding interactions is very significant. These results help the understanding of the basic principles of supramolecular chemistry.

Experimental Section

Chemicals and Reagents: Doubly distilled water was used throughout. All other chemical reagents were of analytical grade purity.

Physical Methods: TGA analyses of compounds **1** and **2** were performed with a Mettler Toledo Star System thermal analyser under nitrogen at a scan rate of 10°C min^{-1}. Powder X-ray diffraction data were collected with a Phillips PW 3710 diffractometer. Microanalytical (C, H, N) data were obtained with a Perkin−Elmer model 240C elemental analyser. The infrared spectra were recorded by using KBr pellets with a Jasco-5300 FT-IR spectrophotometer. Room temperature (298 K) solid state magnetic susceptibility was measured by using a Sherwood Scientific magnetic susceptibility balance. $Hg[Co(NCS)_4]$ was used as the standard. Diamagnetic corrections {-375×10^{-6} cgsu for $[Fe_3(\mu_3\text{-O})(\mu_2\text{-}CH_3COO)_6(H_2O)_2(CH_3COO)]\cdot C_5H_8N_3\cdot ClO_4$ (**1**) and -366.5×10^{-6} cgsu for $[Fe_3(\mu_3\text{-O})(\mu_2\text{-}CH_3COO)_6(H_2O)_2(CH_3COO)]\cdot C_5H_7N_2\cdot ClO_4$ (**2**), calculated from Pascal's constants,[9] were used to obtain the molar paramagnetic susceptibilities.

Synthesis of $[Fe_3(\mu_3\text{-O})(\mu_2\text{-}CH_3COO)_6(H_2O)_2(CH_3COO)]\cdot C_5H_8N_3\cdot ClO_4$ (1): To a stirred aqueous solution (30 mL) of $FeCl_3$ (2 g, 12.33 mmol) were added CH_3COOH (10 mL), 2,6-diaminopyridine (9.16 mmol, 1 g) and $NaClO_4$ (36.75 mmol, 4.5 g), followed by drop wise addition of 1 M NaOH (until the pH of solution reached 3.5. Further addition of NaOH resulted in the formation of a precipitate). The resultant red solution was filtered into 100 mL beaker which was subsequently kept covered with perforated aluminium foil for a week at room temperature. The red crystals of **1** which formed during this time were separated by filtration, washed with cold water and dried at room temperature. Yield: 1.8 g (52% based on Fe). Selected data for **1**, IR (KBr pellet): $\tilde{\nu}$ = 3470 (w), 3350 (m), 3244 (w), 3013 (m), 2939 (m), 2471(w), 2378 (w), 1666 (s), 1601 (s), 1521 (s), 1442 (s), 1174 (m), 1101 (s), 939 (w), 817 (m), 775 (m), 717 (w), 661 (s), 619 cm^{-1} (s). $C_{19}H_{33}ClFe_3N_3O_{21}$ (842.48): calcd. C 27.09, H 3.95, N 4.99; found C 26.98, H 3.99, N 4.92.

Synthesis of $[Fe_3(\mu_3\text{-O})(\mu_2\text{-}CH_3COO)_6(H_2O)_2(CH_3COO)]\cdot C_5H_7N_2\cdot ClO_4$ (2): To a stirred aqueous solution (30 mL) of $FeCl_3$ (2 g, 12.33 mmol) were added CH_3COOH (10 mL), 2-aminopyridine (9.14 mmol, 0.861 g) and $NaClO_4$ (36.75 mmol, 4.5 g), followed by drop wise addition of 1 M NaOH (until the pH of solution reached 3.56. Further addition of NaOH resulted in formation of precipitate). The resultant red solution was filtered and was kept at room temperature for a week. The red crystals of compound **2** which formed during this time were separated by filtration, washed with cold water and dried at room temperature. Yield: 1.79 g (53% based on Fe). Selected data for **2**, IR (KBr pellet): $\tilde{\nu}$ = 3431 (w), 1670 (s), 1602 (s), 1446 (s), 1172 (m), 1103 (s), 773 (m), 659 (s), 615 (s), 522 cm^{-1} (m). $C_{19}H_{32}ClFe_3N_2O_{21}$ (827.47): calcd. C 27.58, H 3.89, N 3.38; found C 27.46, H 3.83, N 3.32.

Caution! *Although no problems were encountered in this work, care should be taken in the handling of perchlorate salts.*

 © 2005 Wiley-VCH Verlag GmbH & Co. KGaA, Weinheim

Attempted Reaction for the Removal of the Template: Complex **1** (0.418 mmol, 0.352 g) was suspended in toluene (40 mL) and stirred for 24 h. The suspension was then filtered, washed with toluene and dried at room temperature in the air. The solid was identified as **1** by elemental analysis ($C_{19}H_{33}ClFe_3N_3O_{21}$: calcd. C 27.09, H 3.95, N 4.99; found C 27.15, H 3.89, N 4.93) and IR studies. Similar attempts with **2** for the removal of its template were also unsuccessful (both 2,6-diaminopyridine and 2-aminopyridine are soluble in toluene).

X-ray Crystallography: Data for **1** and **2** were collected at 293 K on an Enraf−Nonius Mach-3 diffractometer using graphite-monochromated Mo-K_α radiation. The structures were solved (SHELXS-97)[10] and refined over F^2 using the SHELXL-97 program.[11] All nonhydrogen atoms were refined anisotropically. The hydrogen atoms of the 2,6-diaminopyridinium and 2-aminopyridinium cations and the acetate ligands were assigned their positions on the basis of geometrical considerations and were allowed to ride upon the respective carbon and nitrogen atoms. The hydrogen atoms of the coordinated water molecules were located in the differential Fourier maps and were refined using isotropic thermal parameters. CCDC-234723 and -234724 (for compounds **1** and **2** respectively) contain the supplementary crystallographic data for this paper. These data can be obtained free of charge at http://www.ccdc.cam.ac.uk/conts/retrieving.html. [or from the Cambridge Crystallographic Data Centre, 12 Union Road, Cambridge CB2 1EZ, UK; Fax: (internat.) + 44-1223-336-033; E-mail: deposit@ccdc.cam.ac.uk]

Acknowledgments

We are grateful for the financial support of the Council of Scientific and Industrial Research (CSIR), Government of India [Project No. O1(1737)/02/EMR-II]. We also thank UGC, the Government of India for the infrastructure facility at the University of Hyderabad under a UPE (University with potential for excellence) grant. The national X-ray diffractometer facility at University of Hyderabad, by the Department of Science and Technology, Government of India, is gratefully acknowledged.

[1] [1a] F. A. Cotton, *Advanced Inorganic Chemistry*, Wiley, New York, **1980**, pp. 154−155. [1b] J. Catterick, P. Thornton, *Adv. Inorg. Chem. Radiochem.* **1977**, *20*, 291−362. [1c] R. D. Cannon, R. P. White, *Prog. Inorg. Chem.* **1988**, *36*, 195−298.

[2] [2a] M. Scheurer-Kestner, *Ann. Chim. Phys. Ser 3* **1861**, *63*, 422−447. [2b] L. A. Welo, *Philos. Mag. 7S* **1928**, *6*, 481−509. [2c] R. F. Weinland, A. Hohn, *Z. Anorg. Allg. Chem.* **1926**, *152*, 1−15.

[3] [3a] E. M. Holt, S. L. Holt, W. F. Tucker, R. O. Asplund, K. J. Watson, *J. Am. Chem. Soc.* **1974**, *96*, 2621−2623. [3b] S. M. Heald, E. A. Stearn, B. Bunker, E. M. Holt, S. L. Holt, *J. Am. Chem. Soc.* **1979**, *101*, 67−73.

[4] T. Nakamoto, M. Katada, S. Kawata, S. Kitagawa, K. Kikuchi, I. Ikemoto, K. Endo, H. Sano, *Chem. Lett.* **1993**, 1463−1466.

[5] [5a] S. Supriya, S. Mani Kumari, P. Raghavaiah, S. K. Das, *New J. Chem.* **2003**, *27*, 218−220. [5b] S. Supriya, S. K. Das, *New J. Chem.* **2003**, *27*, 1568−1574.

[6] [6a] K. Anzenhofer, J. J. De Boer, *Recl. Trav. Chim. Pays-Bas.* **1969**, *88*, 286−288. [6b] S. C. Chang, G. A. Jeffrey, *Acta Crystallogr., Sect. B* **1970**, *26*, 673−683. [6c] F. A. Cotton, J. G. Norman, *Inorg. Chim. Acta* **1972**, *6*, 411−419. [6d] B. N. Figgis, G. B. Robertson, *Nature, London* **1965**, *205*, 694−696. [6e] T. Glowiak, M. Kubiak, T. Szymanska-Buzar, *Acta Crystallogr., Sect. B* **1977**, *33*, 1732−1737. [6f] L. W. Hessel, C. Romers, *Recl. Trav. Chim. Pays-Bas* **1969**, *88*, 545−552. [6g] T. Lis, B. Jezowska-Trzebiatowska, *Acta Crystallogr., Sect. B* **1977**, *33*, 2112−2116.

[7] [7a] *Gmelins Handbuch der Anorganischen Chemie, Eisen, Teil B, Lieferung 3*, 8th ed., **1930**. [7b] O. F. Tower, *J. Am. Chem. Soc.* **1910**, *32*, 953−957.

[8] T. Glowiak, M. Kubiak, T. Szymanska-Buzar, B. Jezowska-Trzebiatowska, *Acta Crystallogr., Sect. B* **1977**, *33*, 3106−3109.

[9] W. E. Hatfield in *Theory and Applications of Molecular Paramagnetism* (Eds.: E. A. Boudreaux, L. N. Mulay), Wiley, New York, **1976**, p. 491.

[10] G. M. Sheldrick, *SHELXS-97: Program for Crystal Structure Solution*, University of Göttingen, Germany, **1997**.

[11] G. M. Sheldrick, *SHELXL-97: Program for Crystal Structure Refinement*, University of Göttingen, Germany, **1997**.

Received May 5, 2004
Early View Article
Published Online November 24, 2004

 © 2005 Wiley-VCH Verlag GmbH & Co. KGaA, Weinheim

$Ni^{II}Ru^{II}$ and $Cu^{II}Ru^{II}$ Coordination Polymers Constructed from $[Ru(CN)_6]^{4-}$

Iris Pui-Yee Shek,[a] Wai-Fun Yeung,[a] Tai-Chu Lau,*[a] Jing Zhang,[b] Song Gao,*[b] Lap Szeto,[c] and Wing-Tak Wong[c]

Keywords: Coordination polymers / Cyanides / Magnetic properties / Ruthenium

The dimetallic compounds $[Ni(2,3,2\text{-tet})]_2[Ru(CN)_6]\cdot 8H_2O$ (**1**), $[Ni(pn)_2]_2[Ru(CN)_6]\cdot 5H_2O$ (**2**) $[Ni(tacd)(H_2O)]_2[Ru(CN)_6]\cdot 8H_2O$ (**3**) and $\{[Cu(dipn)]_3[Ru(CN)_6]\}(ClO_4)_2\cdot 4H_2O$ (**4**) [2,3,2-tet = *N*,*N*′-bis(2-aminoethyl)-1,3-propanediamine, pn = 1,3-diaminopropane, tacd = 1,5,9-triazacyclododecane, dipn = dipropylenetriamine] have been prepared from the reaction of $[Ru(CN)_6]^{4-}$ with $[Ni(2,3,2\text{-tet})]^{2+}$, $[Ni(pn)_2]^{2+}$, $[Ni(tacd)(H_2O)]^{2+}$ and $[Cu(dipn)]^{2+}$, respectively. Compounds **1** and **2** contain a two-dimensional square network, compound **3** has a one-dimensional, crossed-double chain structure, while compound **4** has an unusual, two-dimensional, double-edged, honeycomb network. A very weak antiferromagnetic interaction is observed in **2**.

(© Wiley-VCH Verlag GmbH & Co. KGaA, 69451 Weinheim, Germany, 2005)

Introduction

In the past decade, metal cyanides such as $[M(CN)_6]^{n-}$ (M = V^{II}, Cr^{III}, Mn^{II}, Mn^{III} or Mn^{IV}, Fe^{II} or Fe^{III}) have been used as building blocks for the construction of a variety of coordination polymers with various interesting structures and properties.[1−28] The use of 4d-metal cyanides as building blocks, however, has not received much attention until more recently. Most of the examples are limited to the heptacyanometallate $[Mo^{III}(CN)_7]^{4-}$ and the octacyanometallates $[M^{IV/V}(CN)_8]^{3/4-}$ (M = $W^{IV/V}$, $Mo^{IV/V}$ or Nb^{IV}).[29] Only a few examples of coordination polymers containing $[Ru(CN)_6]^{4-}$ have been reported.[29p,30−33] We describe here a number of heterodimetallic coordination polymers made from the reaction of $[Ru(CN)_6]^{4-}$ with Cu^{2+} or Ni^{2+} in the presence of an amine ligand such as 2,3,2-tet, pn, tacd, or dipn [2,3,2-tet = *N*,*N*′-bis(2-aminoethyl)-1,3-propanediamine, pn = 1,3-diaminopropane, tacd = 1,5,9-triazacyclododecane, dipn = dipropylenetriamine]. One of our objectives was to compare the structure and magnetic properties of these polymers with the corresponding ones made from $[Fe(CN)_6]^{4-}$. A number of polynuclear cyano-bridged complexes containing $[Fe(CN)_6]^{4-}$ are known. For example, reaction of $[Ni(L)_3]X_2$ with $K_4[Fe(CN)_6]$ in water produces a 3D network, $[Ni(L)_2]_3[Fe(CN)_6]X_2$ [L = ethylenediamine (en), trimethylenediamine (tn); X = PF_6^-, ClO_4^-], which exhibits a ferromagnetic interaction between the nearest Ni^{II} ions through the diamagnetic Fe^{II} ion.[19] On the other hand, reaction of $Cu(ClO_4)_2\cdot 6H_2O$, ept and $K_4[Fe(CN)_6]$ produces the 2D molecule $\{[Cu(ept)]_3[Fe(CN)_6]\}(ClO_4)_2\cdot 5H_2O$ [ept = *N*-(2-aminoethyl)-1,3-diaminopropane], which exhibits little or no coupling between the copper atoms via the −NC−Fe−CN− bridges.[28]

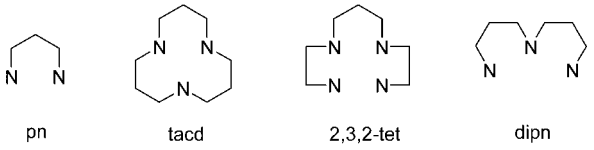

Results and Discussion

Structure of $[Ni(2,3,2\text{-tet})]_2[Ru(CN)_6]\cdot 8H_2O$ (1)

The pale-pink, dimetallic compound **1** was obtained by reacting $Ni(CH_3COO)_2\cdot 4H_2O$ with one molar equivalent of 2,3,2-tet and $K_4[Ru(CN)_6]$. The structure was determined by X-ray crystallography; selected bond lengths and angles are summarized in Table 1. The compound is isomorphous to $[Ni^{II}(diamine)_2]_2[Fe^{III}(CN)_6]X$.[7,17,18] The asymmetric unit of **1** contains a $[Ni(2,3,2\text{-tet})]^{2+}$ cation, one-half of a $[Ru(CN)_6]^{4-}$ anion, and four water molecules (Figure 1a). The four equatorial cyanides of each $[Ru(CN)_6]^{4-}$ unit are coordinated to four *trans*-$[Ni(2,3,2\text{-tet})]^{2+}$ moieties to pro-

[a] Department of Biology and Chemistry, City University of Hong Kong,
Tat Chee Avenue, Kowloon Tong, Hong Kong, P. R. China
[b] State Key Laboratory of Rare Earth Materials Chemistry and Applications, PKU-HKU Joint Laboratory on Rare Earth Materials and Bioinorganic Chemistry, College of Chemistry, Peking University, Beijing 100871, P. R. China
[c] Department of Chemistry, The University of Hong Kong, Pokfulam, Hong Kong, P. R. China
Supporting information for this article is available on the WWW under http://www.eurjic.org or from the author.

 © 2005 Wiley-VCH Verlag GmbH & Co. KGaA, Weinheim DOI: 10.1002/ejic.200400537

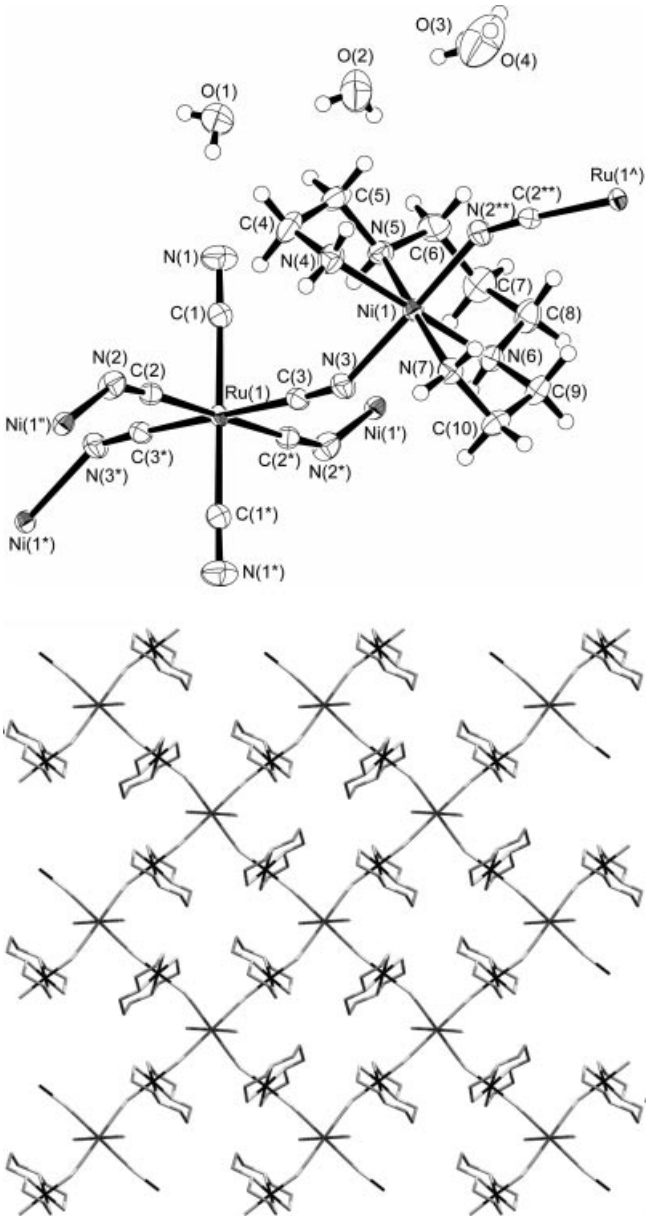

Figure 1. (a) Asymmetric unit of $[Ni(2,3,2\text{-tet})]_2[Ru(CN)_6]\cdot 8H_2O$ (**1**) showing the atom labeling scheme; (b) view of the 2D structure of $[Ni(2,3,2\text{-tet})]_2[Ru(CN)_6]\cdot 8H_2O$ (**1**); water molecules and hydrogen atoms have been omitted for clarity

duce a square 2D network which has an aaa-type sequence (Figure 1b). The average Ru−C bond length of 2.03 Å and C≡N bond length of 1.156 Å are similar to those in $Mn_2[Ru(CN)_6]\cdot 8H_2O$.[30] The bond lengths of bridging [1.156(3) Å] and terminal cyanides [1.154(3) and 1.157(3) Å] are essentially identical. The Ni−N bond lengths in *trans*-$[Ni(2,3,2\text{-tet})]^{2+}$ range from 2.102(2) to 2.109(2) Å, and are similar to those in other *trans*-$[Ni(2,3,2\text{-tet})]^{2+}$ compounds.[34] There are N−H···O, O−H···N, O−H···O hydrogen-bond interactions in the crystal structure which are mainly between the water solvates and two of the amine nitrogens. The O···O distances range from 2.794(4)−2.880(5) Å and the N···O distances are 2.873(6) and 3.064(4) Å (Table S1, Supporting Information). The Ni···Ni separation through -NC−Ru−CN- is 10.06 Å, and the shortest interlayer Ni···Ni distance is 8.91 Å.

Table 1. Selected bond lengths [Å] and angles [°] of **1**

Ru(1)−C(1)	2.041(2)	Ru(1)−C(2)	2.025(2)
Ru(1)−C(3)	2.029(2)	Ni(1)−N(2)	2.085(2)
Ni(1)−N(3)	2.101(2)	Ni(1)−N(4)	2.108(3)
Ni(1)−N(5)	2.109(2)	Ni(1)−N(6)	2.102(2)
Ni(1)−N(7)	2.103(2)	N(1)−C(1)	1.154(3)
N(2)−C(2)	1.157(3)	N(3)−C(3)	1.156(3)
C(1)−Ru(1)−C(2)	89.95(9)	C(1)−Ru(1)−C(3)	90.79(9)
C(2)−Ru(1)−C(3)	90.27(9)	Ru(1)−C(1)−N(1)	178.7(2)
Ru(1)−C(2)−N(2)	176.1(2)	Ru(1)−C(3)−N(3)	176.3(2)
Ni(1)−N(2)−C(2)	148.2(2)	Ni(1)−N(3)−C(3)	145.2(2)

Structure of $[Ni(pn)_2]_2[Ru(CN)_6]\cdot 5H_2O$ (2)

Blue crystals of compound **2** were obtained by treating $Ni(CH_3COO)_2\cdot 4H_2O$ with 2 mol-equiv. of pn and 1 mol-equiv. of $K_4[Ru(CN)_6]$ in water. The structure was determined by X-ray crystallography; selected bond lengths and angles are summarized in Table 2. The asymmetric unit of **2** consists of a $[Ni(pn)_2]^{2+}$ cation, one-half of a $[Ru(CN)_6]^{4-}$ anion, and two and a half water molecules (Figure 2a). The four equatorial cyanides of each $[Ru(CN)_6]^{4-}$ unit are coordinated to four *trans*-$[Ni(pn)_2]^{2+}$ moieties to produce a square 2D network that is similar to that of compound **1** (Figure 2b). Bridging of the cyano group leads to only a small deviation of the C(cyanide)−Ru−C(cyanide) angles [89.63(11)−90.37(11)°] from a right angle, as in compound **1**. The average Ru−C bond length of 2.03 Å and C≡N bond length of 1.15 Å are similar to those in compound **1**; the bond lengths of bridging (1.152 Å) and terminal cyanides (1.146 Å) also show little difference. The separation of neighboring nickel atoms through −NC−Ru−CN− is 10.30 Å.

Table 2. Selected bond lengths [Å] and angles [°] of **2**; symmetry transformations used to generate equivalent atoms: $-x + 1, -y, -z$

Ru−C(1)	2.029(3)	Ni(2)−N(1)	2.104(3)
Ru−C(2)	2.025(3)	Ni(2)−N(6)	2.125(3)
Ru−C(3)	2.036(3)	Ni(2)−N(7)	2.117(3)
Ni(1)−N(2)	2.070(3)	N(1)−C(1)	1.151(4)
Ni(1)−N(4)	2.103(3)	N(2)−C(2)	1.154(4)
Ni(1)−N(5)	2.118(3)	N(3)−C(3)	1.146(5)
C(2′)−Ru−C(1)	90.37(11)	N(1)−C(1)−Ru	178.1(3)
C(2)−Ru−C(1)	89.63(11)	N(2)−C(2)−Ru	177.8(2)
C(1)−Ru−C(3′)	90.17(14)	N(3)−C(3)−Ru	178.8(4)
C(1′)−Ru−C(3′)	89.83(14)	C(1)−N(1)−Ni(2)	154.6(3)
C(2′)−Ru−C(3)	88.92(12)	C(2)−N(2)−Ni(1)	158.0(2)
C(2)−Ru−C(3)	91.08(12)		

 © 2005 Wiley-VCH Verlag GmbH & Co. KGaA, Weinheim

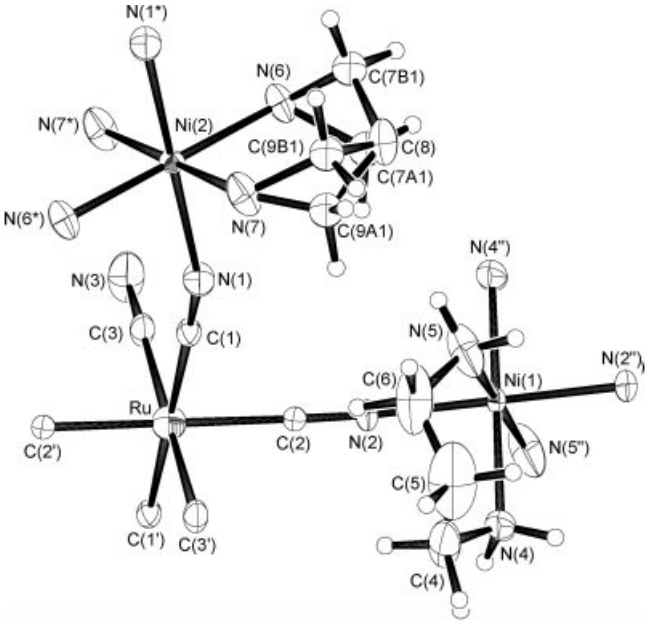

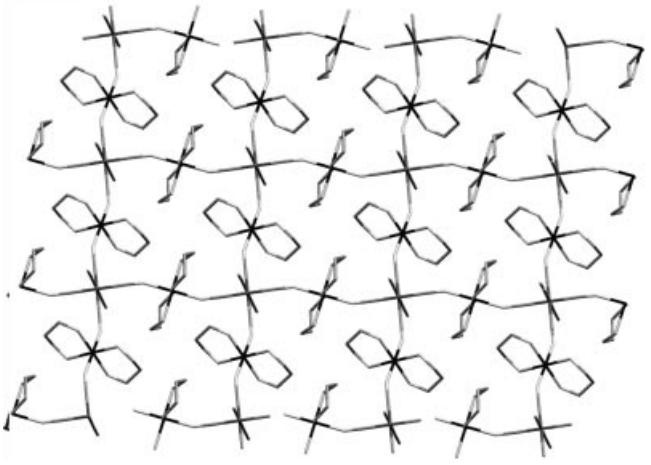

Figure 2. (a) Asymmetric unit of $[Ni(pn)_2]_2[Ru(CN)_6]\cdot 5H_2O$ (**2**) showing the atom labeling scheme; water molecules have been omitted for clarity; (b) view of the 2D structure of $[Ni(pn)_2]_2[Ru(CN)_6]\cdot 5H_2O$ (**2**); water molecules and hydrogen atoms have been omitted for clarity

Structure of $[Ni(tacd)(H_2O)]_2[Ru(CN)_6]\cdot 8H_2O$ (3)

Red crystals of **3** were obtained from the reaction of $Ni(CH_3COO)_2\cdot 4H_2O$ with tacd and $K_4[Ru(CN)_6]$. Compound **3** has a 1D crossed double-chain structure (Figure 3b), as determined by X-ray crystallography. Selected bond lengths and angles are summarized in Table 3. The asymmetric unit consists of two $[Ni(tacd)(H_2O)]^{2+}$ cations, one $[Ru(CN)_6]^{4-}$ anion, and eight water molecules (Figure 3a). Each $[Ru(CN)_6]^{4-}$ unit is connected to four $[Ni(tacd)(H_2O)]^{2+}$ units through two axial and two equatorial cyanides, and each $[Ni(tacd)(H_2O)]^{2+}$ unit is connected to two $[Ru(CN)_6]^{4-}$ units in a *cis* fashion. This produces Ru−Ni squares. Each square is perpendicular to adjacent squares and this arrangement results in a zig-zag structure. The angles C(1)−Ru(1)−C(6), C(2)−Ru(1)−C(5), N(2)−Ni(1)−N(5) and N(1)−Ni(2)−N(6) are 91.5(2)°, 89.7(2)°, 90.7(2)° and 89.7(2)°, respectively. Each nickel(II) atom is coordinated to the three nitrogen atoms of tacd, two nitrogen atoms of cyanide and one oxygen atom of a

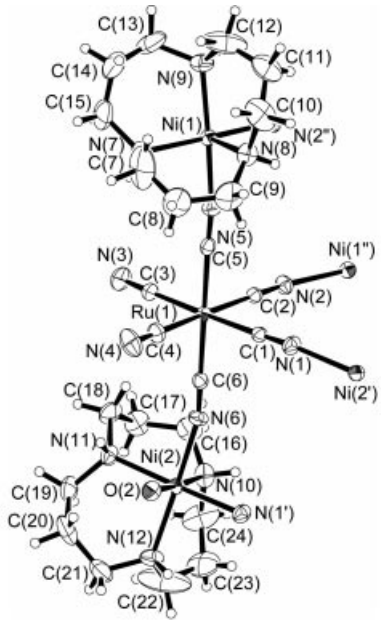

Figure 3. (a) Asymmetric unit of $[Ni(tacd)(H_2O)]_2[Ru(CN)_6]\cdot 8H_2O$ (**3**) showing the atom labeling scheme; water molecules have been omitted for clarity; (b) view of the 1D structure of $[Ni(tacd)(H_2O)]_2[Ru(CN)_6]\cdot 8H_2O$ (**3**); water molecules and hydrogen atoms have been omitted for clarity

Table 3. Selected bond lengths [Å] and angles [°] of **3**

Ru(1)−C(1)	2.025(4)	Ru(1)−C(4)	2.043(5)
Ru(1)−C(2)	2.024(5)	Ru(1)−C(5)	2.028(5)
Ru(1)−C(3)	2.038(5)	Ru(1)−C(6)	2.032(5)
Ni(1)−O(1)	2.272(3)	Ni(2)−O(2)	2.217(3)
Ni(1)−N(2)	2.063(4)	Ni(2)−N(1)	2.055(4)
Ni(1)−N(5)	2.040(4)	Ni(2)−N(6)	2.067(4)
Ni(1)−N(7)	2.101(4)	Ni(2)−N(10)	2.089(4)
Ni(1)−N(8)	2.099(4)	Ni(2)−N(11)	2.095(4)
Ni(1)−N(9)	2.106(4)	Ni(2)−N(12)	2.124(4)
N(1)−C(1)	1.144(6)	N(4)−C(4)	1.155(7)
N(2)−C(2)	1.142(6)	N(5)−C(5)	1.153(6)
N(3)−C(3)	1.147(6)	N(6)−C(6)	1.151(6)
Ru(1)−C(1)−N(1)	178.0(4)	Ru(1)−C(2)−N(2)	176.9(4)
Ru(1)−C(3)−N(3)	177.6(5)	Ru(1)−C(4)−N(4)	177.3(5)
Ru(1)−C(5)−N(5)	177.9(4)	Ru(1)−C(6)−N(6)	177.8(4)
C(1)−Ru(1)−C(6)	91.5(2)	C(2)−Ru(1)−C(5)	89.7(2)
C(1)−Ru(1)−C(3)	177.8(2)	C(2)−Ru(1)−C(4)	176.5(2)
C(5)−Ru(1)−C(6)	178.4(2)	Ni(1)−N(2)−C(2)	168.0(4)
Ni(1)−N(5)−C(5)	170.3(4)	Ni(2)−N(1)−C(1)	163.5(4)
Ni(2)−N(6)−C(6)	163.8(4)	N(1)−Ni(2)−N(6)	89.7(2)
N(2)−Ni(1)−N(5)	90.7(2)		

water molecule, forming a distorted octahedral geometry. The Ni−N(tacd) distances range from 2.099(4) to 2.106(4) Å for Ni(1) and 2.089(4) to 2.124(4) Å for Ni(2), which are within the normal range of Ni−N(amine) distances. The Ni−N(cyanide) distances range from 2.040(4) to 2.067(4) Å. The bridging C≡N distances of 1.142(6)−1.153(6) Å are similar to those in $Mn_2[Ru(CN)_6]\cdot 8H_2O$ [1.152(9)−1.165(8) Å].[30] The Ru−C bond lengths are 2.024(5)−2.043(5) Å. The Ru−C≡N bond angles are close to linear [176.9(4)−178.0(4)°] while the Ni−N≡C angles are bent [163.5(4)−170.3(4)°]. There is intramolecular hydrogen bonding between the coordinated water molecules, with an O(1)···O(2) distance of 2.847(5) Å. The uncoordinated water molecules are positioned between the chains and are hydrogen-bonded to the terminal cyanides of $[Ru(CN)_6]^{4-}$; the N···O distances range from 2.800(6) to 3.523(6) Å. The Ni···Ni separation through -NC−Ru−CN- is 10.38 Å, and the shortest interchain Ni···Ni distance is 9.56 Å.

Structure of $\{[Cu(dipn)]_3[Ru(CN)_6]\}(ClO_4)_2\cdot 4H_2O$ (4)

Green crystals of **4** were obtained from the reaction of $Cu(CH_3COO)_2\cdot H_2O$ with dipn, $K_4[Ru(CN)_6]$ and $NaClO_4$. The structure of **4** was determined by X-ray crystallography; selected bond lengths and angles are summarized in Table 4. The asymmetric unit consists of three $[Cu(dipn)]^{2+}$, one $[Ru(CN)_6]^{4-}$, two ClO_4^-, and four water molecules (Figure 4a). The Cu^{II} in each $[Cu(dipn)]^{2+}$ unit is five-coordinate and is bonded to two nitrogen atoms of two $[Ru(CN)_6]^{4-}$ and the three nitrogen atoms of a dipn. Each $[Ru(CN)_6]^{4-}$ is connected to six $[Cu(dipn)]^{2+}$ units through cyano bridges to form an unusual 2D double-edged honeycomb network (Figure 4b), which is similar to that of $\{[Cu(ept)]_3[Fe(CN)_6]\}(ClO_4)_2\cdot 5H_2O$.[28] The Ru−C bond lengths lie in the range 2.018(7)−2.044(8) Å. The bridging C≡N distances range from 1.144(10) to 1.159(9) Å, and are similar to those in $Mn_2[Ru(CN)_6]\cdot 8H_2O$.[30] The Cu−N(amine) bond lengths [2.007(7)−2.090(7) Å] are similar to those in $\{[Cu(ept)]_3[Fe(CN)_6]\}(ClO_4)_2\cdot 5H_2O$ (2.000−2.050 Å). The Cu−N≡C angles [153.7(6)−168.3(7)°] show significant deviations from 180°, and the Cu atom in each $[Cu(dipn)]^{2+}$ moiety has a distorted square-pyramidal geometry, with τ values of 0.16 for Cu(1), 0.38 for Cu(2) and 0.61 for Cu(3). There are N−H···O interactions in the crystal structure which involve mainly the water solvates and the amine nitrogen, with N···O distances ranging from 3.077(12) to 3.240(13) Å. Hydrogen bonding involving the perchlorate ion is also observed, with N···O distances ranging from 3.071(19) to 3.211(15) Å (Table S2, Supporting Information). The adjacent Cu···Cu separations are 6.590−8.270 Å, and the Cu···Cu distance through −NC−Ru−CN− is 10.093−10.318 Å.

Table 4. Selected bond lengths [Å] and angles [°] of **4**

Cu(1)−N(1)	2.155(7)	Cu(1)−N(4)	2.006(7)
Cu(1)−N(7)	2.009(7)	Cu(1)−N(8)	2.067(7)
Cu(1)−N(9)	2.018(7)	Cu(2)−N(2)	2.166(7)
Cu(2)−N(5)	2.009(7)	Cu(2)−N(10)	2.023(8)
Cu(2)−N(11)	2.060(6)	Cu(2)−N(12)	2.032(7)
Cu(3)−N(3)	2.039(7)	Cu(3)−N(6)	2.116(7)
Cu(3)−N(13)	2.007(7)	Cu(3)−N(14)	2.090(7)
Cu(3)−N(15)	2.015(7)	Ru(1)−C(1)	2.019(8)
Ru(1)−C(2)	2.030(8)	Ru(1)−C(3)	2.026(8)
Ru(1)−C(4)	2.020(8)	Ru(1)−C(5)	2.018(8)
Ru(1)−C(6)	2.044(8)	N(1)−C(1)	1.158(10)
N(2)−C(2)	1.144(10)	N(3)−C(3)	1.159(9)
N(4)−C(4)	1.147(10)	N(5)−C(5)	1.149(9)
N(6)−C(6)	1.153(10)		
C(1)−Ru(1)−C(6)	177.6(3)	C(2)−Ru(1)−C(4)	174.0(3)
C(3)−Ru(1)−C(5)	178.2(3)	Ru(1)−C(1)−N(1)	179.4(7)
Ru(1)−C(2)−N(2)	173.6(7)	Ru(1)−C(3)−N(3)	176.5(7)
Ru(1)−C(4)−N(4)	174.5(7)	Ru(1)−C(5)−N(5)	179.4(6)
Ru(1)−C(6)−N(6)	174.4(7)	Cu(1)−N(1)−C(1)	155.3(7)
Cu(1)−N(4)−C(4)	161.0(7)	Cu(2)−N(2)−C(2)	159.4(7)
Cu(2)−N(5)−C(5)	153.7(6)	Cu(3)−N(3)−C(3)	157.1(7)
Cu(3)−N(6)−C(6)	168.3(7)		

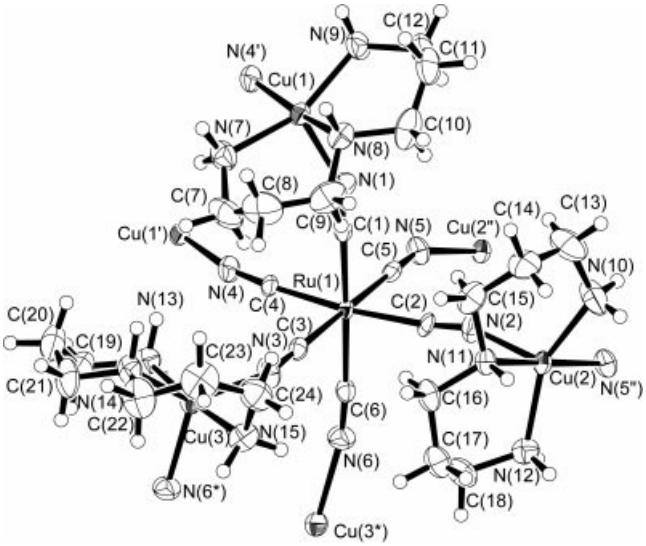

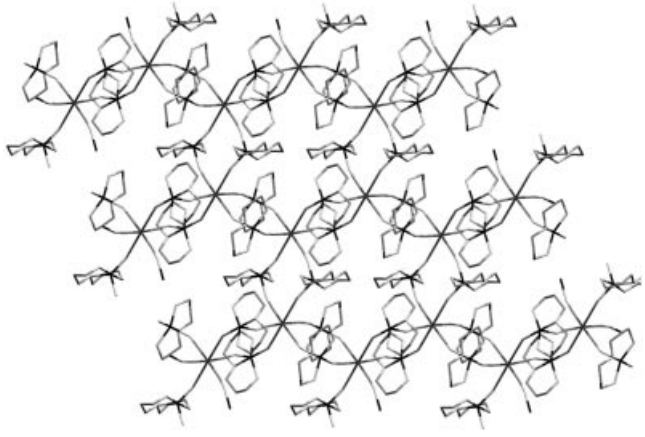

Figure 4. (a) Asymmetric unit of $[Cu(dipn)]_3[Ru(CN)_6](ClO_4)_2\cdot 4H_2O$ (**4**) showing the atom labeling scheme; water molecules and perchlorate ions have been omitted for clarity; (b) view of the 2D honeycomb structure of $[Cu(dipn)]_3[Ru(CN)_6](ClO_4)_2\cdot 4H_2O$ (**4**); water molecules and perchlorate ions have been omitted for clarity

 © 2005 Wiley-VCH Verlag GmbH & Co. KGaA, Weinheim

Magnetic Properties

Figure 5 illustrates the temperature dependence of $\chi_M T$ and $\chi_M{}^{-1}$ per Ni_2Ru unit of compound **1**. The $\chi_M T$ value remains more or less constant from 300 K to 10 K. Below 10 K the $\chi_M T$ value decreases rapidly with decreasing temperature. A plot of $\chi_M{}^{-1}$ vs. T obeys the Curie−Weiss law with a Curie constant, C, of 2.468 $cm^3 \cdot K \cdot mol^{-1}$ and a Weiss constant, θ, of 0.01 K. The C value is slightly larger than the expected value of 2.00 $cm^3 \cdot K \cdot mol^{-1}$ for non-coupled, spin-only Ni ($S = 1$) and diamagnetic Ru ions. The very small Weiss constant suggests there is negligible magnetic interaction between the Ni^{II} centers through the diamagnetic $[Ru^{II}(CN)_6]^{4-}$ bridges.

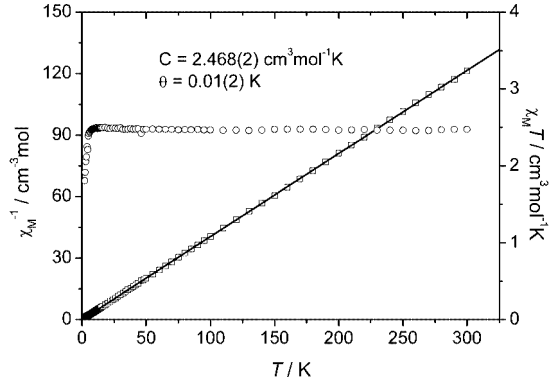

Figure 5. Temperature dependence of $\chi_M T$ (squares) and $\chi_M{}^{-1}$ (circles) for compound **1** per Ni_2Ru unit

The plot of $\chi_M{}^{-1}$ vs. T for compound **2** (Figure S1, Supporting Information) obeys the Curie−Weiss law with a Curie constant of 2.56 $cm^3 \cdot K \cdot mol^{-1}$ and a small negative Weiss constant of −2.95 K. The C value is slightly larger than the expected value (2.00 $cm^3 \cdot K \cdot mol^{-1}$) for non-coupled, spin-only Ni ($S = 1$) and diamagnetic Ru ions. The negative Weiss constant suggests that a very weak antiferromagnetic interaction between the Ni^{II} centers through the diamagnetic $[Ru^{II}(CN)_6]^{4-}$ bridges may be present.

For compound **3**, the plot of $\chi_M{}^{-1}$ vs. T in the range of 2−300 K (Figure S2; Supporting Information) obeys the Curie−Weiss law, with a small positive Weiss constant of 1.0 K and a Curie constant of 2.17 $cm^3 \cdot K \cdot mol^{-1}$. For compound **4**, the plot of $\chi_M{}^{-1}$ vs. T in the range of 2−300 K (Figure S3, Supporting Information) also obeys the Curie−Weiss law, with a small positive Weiss constant of +1.1 K and a Curie constant of 1.16 $cm^3 \cdot K \cdot mol^{-1}$. The small positive Weiss constants in compounds **3** and **4** do not necessarily imply ferromagnetic interaction between the Ni atoms through the −NC−Ru−CN− bridge, since we have no other supporting data available.

Conclusion

In this work four dimetallic assemblies made from $K_4[Ru(CN)_6]$ are reported. Although 3D NiFe assemblies have been obtained from the reaction of $[Ni(L)_3]X_2$ (L = en, tn; X = PF_6^-, ClO_4^-) with $K_4[Fe(CN)_6]$, similar reactions using $K_4[Ru(CN)_6]$ produce only either 2D (**1**, **2**) or 1D (**3**) compounds. In the case of CuM, however, both $[Cu(dipn)]_3[Ru(CN)_6]\}(ClO_4)_2 \cdot 4H_2O$ (**4**) and $\{[Cu(ept)]_3[Fe(CN)_6]\}(ClO_4)_2 \cdot 5H_2O$ have the same unusual, double-edged honeycomb structure.

In all the compounds there is little or no magnetic interaction between the paramagnetic metal centers through the diamagnetic $[Ru^{II}(CN)_6]^{4-}$ bridge. Compounds **1** and **3** involve interesting octahedral Ni^{II} coordination compounds, and it is notable that the magnetic moments of the less deformed NiN_6 octahedra in **1** and **2** reflect more spin-orbit coupling than the clearly more distorted octahedron in **3**.

Experimental Section

Reagents and Physical Measurements: *N*,*N*′-Bis(2-aminoethyl)-1,3-propanediamine (2,3,2-tet), 1,3-diaminopropane (pn), and dipropylenetriamine (dipn) were purchased from Acros. 1,5,9-Triazacyclododecane (tacd) was obtained from Aldrich. All other reagents and solvents were of reagent grade and used without further purification. Potassium hexacyanoruthenate(II) was prepared according to a literature method.[35] Infrared spectra were recorded as KBr discs in the region of 400−4000 cm^{-1} with an Avatar 360 FTIR spectrophotometer. Elemental analyses were carried out with an Elementar Vario EL Analyser. The variable-temperature magnetic susceptibilities for a collection of small single crystals of **1**−**4** were measured in the temperature range of 2−300 K using either an MPMS XL-5 SQUID (for **1**, **3**, **4**) or an Oxford MagLab 2000 system (for **2**).

Preparation of $[Ni(2,3,2\text{-tet})]_2[Ru(CN)_6] \cdot 8H_2O$ (1): An aqueous solution (10 mL) of 2,3,2-tet (38.7 μL, 0.24 mmol) and $K_4[Ru(CN)_6]$ (0.1 g, 0.24 mmol) was slowly added to a methanolic solution (10 mL) of $Ni(CH_3COO)_2 \cdot 4H_2O$ (0.06 g, 0.24 mmol). The resulting solution was filtered to remove some pale-pink precipitate and the filtrate was then allowed to stand in the dark at room temperature for a few days. The resulting pale-pink crystals were collected by filtration and washed with methanol and then diethyl ether (79 mg, 76%). $C_{20}H_{56}N_{14}Ni_2O_8Ru$ (839.22): calcd. C 28.62, H 6.73, N, 23.37; found C 28.38, H 6.81, N 23.51. IR (KBr): $\tilde{\nu}$ = 2066 s (C≡N) cm^{-1}.

Preparation of $[Ni(pn)_2]_2[Ru(CN)_6] \cdot 5H_2O$ (2): An aqueous solution (10 mL) containing pn (0.06 g, 0.8 mmol) and $K_4[Ru(CN)_6]$ (0.2 g, 0.48 mmol) was added dropwise to an aqueous solution (10 mL) of $Ni(CH_3COO)_2 \cdot 4H_2O$ (0.2 g, 0.8 mmol). The resulting blue solution was placed in the dark at room temperature for several days. The resulting blue crystals were filtered, washed with methanol and diethyl ether, and dried in air (225 mg, 74%). $C_{18}H_{50}N_{14}Ni_2O_5Ru$ (761.22): calcd. C 28.40, H 6.62, N 25.76; found C 28.49, H 6.51, N 25.52. IR (KBr): $\tilde{\nu}$ = 2062, 2094 (C≡N) cm^{-1}.

Preparation of $[Ni(tacd)(H_2O)]_2[Ru(CN)_6] \cdot 8H_2O$ (3): An aqueous solution (5 mL) of tacd (0.1 g, 0.24 mmol) and $K_4[Ru(CN)_6]$ (0.1 g, 0.24 mmol) was added dropwise to an aqueous solution (3 mL) of $Ni(CH_3COO)_2 \cdot 4H_2O$ (0.06 g, 0.24 mmol). The resulting blue solution was placed in the dark at room temperature for several days. The resulting red crystals were filtered, washed with methanol and diethyl ether, and dried in air. (178 mg, 83%). $C_{24}H_{62}N_{12}Ni_2O_{10}Ru$ (897.30): calcd. C 32.13, H 6.96, N 18.73; found C 32.14, H 6.91, N 18.75. IR (KBr): $\tilde{\nu}$ = 2066 s (C≡N) cm^{-1}.

 © 2005 Wiley-VCH Verlag GmbH & Co. KGaA, Weinheim

Table 5. Crystal data and structure refinements for compounds **1**−**4**

	1	**2**	**3**	**4**
Empirical formula	$C_{20}H_{56}N_{14}O_8Ni_2Ru$	$C_{18}H_{50}N_{14}O_5Ni_2Ru$	$C_{24}H_{62}N_{12}O_{10}RuNi_2$	$C_{24}H_{59}Cl_2N_{15}O_{12}Cu_3Ru$
Formula mass	839.22	761.22	897.30	1112.44
Crystal system	monoclinic	triclinic	triclinic	triclinic
Space group	$P2_1/c$ (no. 14)	$P\bar{1}$ (no. 2)	$P\bar{1}$ (no. 2)	$P\bar{1}$ (no.2)
a [Å]	8.907(2)	8.6964(17)	12.016(1)	13.436(7)
b [Å]	13.815(3)	9.2072(18)	12.635(2)	14.570(5)
c [Å]	14.607(3)	10.289(2)	15.111(1)	12.92(1)
α [°]	90	86.06(3)	68.60(1)	94.30(8)
β [°]	99.66(1)	84.32(3)	72.62(1)	118.24(4)
γ [°]	90	70.14(3)	83.75(2)	81.13(6)
V [Å^3]	1771.9(7)	770.5(3)	2038.5(4)	2201(2)
Z	2	1	2	2
$D_{calcd.}$ [g cm^{-3}]	1.573	1.641	1.462	1.678
T [K]	298(1)	293(2)	298(2)	298(2)
μ [cm^{-1}]	15.33	17.46	13.40	19.56
F_{000}	876.00	396	940.00	1138.00
Measured/independent reflections	21830/4085	15727/3521	12836/8856	8097/7738
R_{int}	0.027	0.0295	0.021	0.072
R,[a] R_w[b]	0.024, 0.021	0.032,0.095	0.048, 0.068	0.059, 0.067
Goodness of fit	0.994	1.053	1.97	1.97

[a] $\Sigma||F_o| - |F_c||/\Sigma|F_o|$. [b] $[(\Sigma w(|F_o| - |F_c|)^2/\Sigma(wF_o^2)]^{0.5}$.

Preparation of $\{[Cu(dipn)]_3[Ru(CN)_6]\}(ClO_4)_2\cdot 4H_2O$ (4): An aqueous solution (10 mL) of $Cu(CH_3COO)_2\cdot H_2O$ (0.1 g, 0.5 mmol) was added to an aqueous solution (5 mL) of $K_4[Ru(CN)_6]$ (0.21 g, 0.5 mmol) and dipn (65 μL, 0.5 mmol). An aqueous solution (2 mL) of $NaClO_4$ (0.06 g, 0.5 mmol) was then added dropwise to the resulting solution. After filtration, the filtrate was allowed to stand in the dark at room temperature for two weeks. The resulting green crystals were collected and washed with a small amount of methanol and then diethyl ether (79 mg, 76%). $C_{24}H_{59}Cl_2Cu_3N_{15}O_{12}Ru$ (1112.4): calcd. C 25.91, H 5.35, N 18.89; found C 25.72, H 5.30, N 18.76. IR (KBr): $\tilde{\nu}$ = 2075 s (C≡N) cm^{-1}.

Crystallographic Data Collection and Structure Determination: Diffraction data for a crystal of **1** or **3** were collected with a Bruker SMART CCD diffractometer with graphite-monochromated Mo-K_α radiation (λ = 0.71069 Å) at 298 K. Data for a crystal of **2** was collected with a Nonius Kappa CCD diffractometer with graphite-monochromated Mo-K_α radiation (λ = 0.71073 Å) at 293 K. Data for a crystal of **4** was collected with a Rigaku AFC7R diffractometer with graphite-monochromated Mo-K_α radiation (λ = 0.71069 Å) at 298 K. The structure of **1** was solved by direct methods with PATTY,[36] the structure of **2** was solved by direct methods and refined by a full-matrix least-squares technique based on F^2 using the SHELXL 97 program,[37] and the structures of **3** and **4** were solved by direct methods with SIR92[38] and refined by a full-matrix least-squares technique based on F^2 using teXsan.[39] Hydrogen atoms were included but not refined. All calculations were performed with a Silicon Graphic computer, using the teXsan crystallographic software package from Molecular Structure Corporation. All crystallographic data and other details and parameters are summarized in Table 5. CCDC-242152 (**1**), -242160 (**2**), -242151 (**3**), and -242150 (**4**) contain the supplementary crystallographic data for this paper. These data can be obtained free of charge at www.ccdc.cam.ac.uk/conts/retrieving.html or from the Cambridge Crystallographic Data Centre, 12 Union Road, Cambridge CB2 1EZ, UK [Fax: + 44-1223-336-033; E-mail: deposit@ccdc.cam.ac.uk].

Acknowledgments

The work described in this paper was supported by grants from the City University of Hong Kong (7001180) and NSFC 20318001, 20490210 (China).

[1] A. G. Sharpe, *The Chemistry of Cyano Complexes of the Transition Metals*, Academic Press, Inc., Great Britain, **1976**.
[2] R. Klenze, B. Kanellakopulos, G. Trageser, H. H. Eysel, *J. Chem. Phys.* **1980**, *72*, 5819−5828.
[3] V. Gadet, T. Mallah, I. Castro, M. Verdaguer, P. Veillet, *J. Am. Chem. Soc.* **1992**, *114*, 9213−9214.
[4] T. Mallah, S. Thiébaut, M. Verdaguer, P. Veillet, *Science* **1993**, *262*, 1554−1557.
[5] W. R. Entley, G. S. Girolami, *Inorg. Chem.* **1994**, *33*, 5165−5166.
[6] M. Ohba, N. Maruono, H. Ōkawa, T. Enoki, J.-M. Latour, *J. Am. Chem. Soc.* **1994**, *116*, 11566−11567.
[7] M. Ohba, H. Ōkawa, T. Ito, A. Ohto, *J. Chem. Soc., Chem. Commun.* **1995**, 1545−1546.
[8] W. R. Entley, C. R. Treadway, G. S. Girolami, *Mol. Cryst. Liq. Cryst.* **1995**, *273*, 591−604.
[9] S. Ferlay, T. Mallah, R. Ouahès, P. Veillet, M. Verdaguer, *Nature* **1995**, *378*, 701−703.
[10] W. R. Entley, G. S. Girolami, *Science* **1995**, *268*, 397−400.
[11] O. Sato, T. Iyoda, A. Fujishima, K. Hashimoto, *Science* **1996**, *271*, 49−51.
[12] M. Verdaguer, *Science* **1996**, *272*, 698−699.
[13] O. Sato, T. Iyoda, A. Fujishima, K. Hashimoto, *Science* **1996**, *272*, 704−705.
[14] M. Ohba, N. Fukita, H. Ōkawa, *J. Chem. Soc., Dalton Trans.* **1997**, 1733−1737.
[15] K. R. Dunbar, R. A. Heintz, *Prog. Inorg. Chem.* **1997**, *45*, 283−391.
[16] K. van Langenberg, S. R. Batten, K. J. Berry, D. C. R. Hockless, B. Moubaraki, K. S. Murray, *Inorg. Chem.* **1997**, *36*, 5006−5015.
[17] M. Ohba, H. Okawa, N. Fukita, Y. Hashimoto, *J. Am. Chem. Soc.* **1997**, *119*, 1011−1019.
[18] H.-Z. Kou, W.-M. Bu, D.-Z. Liao, Z.-H. Jiang, S.-P. Yan, Y.-

 © 2005 Wiley-VCH Verlag GmbH & Co. KGaA, Weinheim

G. Fan, G.-L. Wang, *J. Chem. Soc., Dalton Trans.* **1998**, 4161−4164.
[19] N. Fukita, M. Ohba, H. Ōkawa, K. Matsuda, H. Iwamura, *Inorg. Chem.* **1998**, *37*, 842−848.
[20] M. Ohba, N. Usuki, N. Fukita, H. Ōkawa, *Inorg. Chem.* **1998**, *37*, 3349−3354.
[21] Ø. Hatlevik, W. E. Buschmann, J. Zhang, J. L. Manson, J. S. Miller, *Adv. Mater.* **1999**, *11*, 914−918.
[22] E. Colacio, J. M. Domínguez-Vera, M. Ghazi, R. Kivekäs, F. Lloret, J. M. Moreno, H. Stoeckli-Evans, *Chem. Commun.* **1999**, 987−988.
[23] S. M. Holmes, G. S. Girolami, *J. Am. Chem. Soc.* **1999**, *121*, 5593−5594.
[24] H. Z. Kou, S. Gao, B. Q. Ma, D. Z. Liao, *Chem. Commun.* **2000**, 1309−1310.
[25] H. Z. Kou, W. M. Bu, S. Gao, D. Z. Liao, Z. H. Jiang, S. P. Yan, Y. G. Fan, G. L. Wang, *J. Chem. Soc., Dalton Trans.* **2000**, 2996−3000.
[26] S. W. Zhang, D. G. Fu, W. Y. Sun, Z. Hu, K. B. Yu, W. X. Tang, *Inorg. Chem.* **2000**, *39*, 1142−1146.
[27] T. Lu, H. Xiang, C. Su, P. Cheng, Z. Mao, L. Ji, *New J. Chem.* **2001**, *25*, 216−217.
[28] Z. Trávníček, Z. Smékal, A. Escuer, J. Marek, *New J. Chem.* **2001**, *25*, 655−658.
[29] [29a] J. Lu, W. T. A. Harrison, A. J. Jacobson, *Angew. Chem. Int. Ed. Engl.* **1995**, *34*, 2557−2559. [29b] J. Larionova, R. Clérac, J. Sanchiz, O. Kahn, S. Golhen, L. Ouahab, *J. Am. Chem. Soc.* **1998**, *120*, 13088−13095. [29c] A. K. Sra, M. Andruh, O. Kahn, S. Golhen, L. Ouahab, J. V. Yakhmi, *Angew. Chem. Int. Ed.* **1999**, *38*, 2606−2609. [29d] J. Larionova, O. Kahn, S. Golhen, L. Ouahab, R. Clérac, *Inorg. Chem.* **1999**, *38*, 3621−3627. [29e] J. Larionova, O. Kahn, S. Gohlen, L. Ouahab, R. Clérac, *J. Am. Chem. Soc.* **1999**, *121*, 3349−3356. [29f] J. Larionova, M. Gross, M. Pilkington, H. Andres, H. Stoeckli-Evans, H. U. Güdel, S. Decurtins, *Angew. Chem. Int. Ed.* **2000**, *39*, 1605−1609. [29g] Z.-J. Zhong, H. Seino, Y. Mizobe, Y. Hidai, M. Verdaguer, S.-I. Ohkoshi, K. Hashimoto, *Inorg. Chem.* **2000**, *39*, 5095−5101. [29h] A. K. Sra, G. Rombaut, F. Lahitête, S. Golhen, L. Ouahab, C. Mathonière, J. V. Yakhmi, O. Kahn, *New J. Chem.* **2000**, *24*, 871−876. [29i] G. Rombaut, M. Verelst, S. Golhen, L. Ouahab, C. Mathonière, O. Kahn, *Inorg. Chem.* **2001**, *40*, 1151−1159. [29j] R. Podgajny, T. Korzeniak, M. Balanda, T. Wasiutynski, W. Errington, T. J. Kemp, N. W. Alcock, B. Sieklucka, *Chem. Commun.* **2002**, 1138−1139. [29k] D.-F. Li, S. Gao, L.-M. Zheng, W.-X. Tang, *J. Chem. Soc., Dalton Trans.* **2002**, 2805−2806. [29l] D.-F. Li, L.-M. Zheng, X.-Y. Wang, J. Huang, S. Gao, W.-X. Tang, *Chem. Mater.* **2003**, *15*, 2094−2098. [29m] S. Willemin, J. Larionova, R. Clérac, B. Donnadieu, B. Henner, X. F. Le Goff, C. Guerin, *Eur. J. Inorg. Chem.* **2003**, 1866−1872. [29n] R. Pradhan, C. Desplanches, P. Guionneau, J.-P. Sutter, *Inorg. Chem.* **2003**, *42*, 6607−6609. [29o] S. Tanase, F. Tuna, P. Guionneau, T. Maris, G. Rombaut, C. Mathonière, M. Andruh, O. Kahn, J.-P. Sutter, *Inorg. Chem.* **2003**, *42*, 1625−1631. [29p] R. Eckhardt, H. Hanika-Heidl, R. D. Fischer, *Chem. Eur. J.* **2003**, *9*, 1795−1804.
[30] M. Rüegg, A. Ludi, K. Rieder, *Inorg. Chem.* **1971**, *10*, 1773−1777.
[31] S. Eller, M. Adam, R. D. Fischer, *Angew. Chem. Int. Ed. Engl.* **1990**, *29*, 1126−1128.
[32] A. Gómez, E. Reguera, *Int. J. Inorg. Mater.* **2001**, *3*, 1045−1051.
[33] H. Hanika-Heidl, R. D. Fischer, *Inorg. Chim. Acta* **2004**, *357*, 1748−1760.
[34] [34a] R. Vicente, A. Escuer, J. Ribas, M. Salah El Fallah, X. Solans, M. Font-Bardía, *Inorg. Chem.* **1993**, *32*, 1920−1924. [34b] A. Escuer, R. Vicente, J. Ribas, M. Salah El Fallah, X. Solans, M. Font-Bardía, *Inorg. Chem.* **1993**, *32*, 3727−3732. [34c] A. Escuer, R. Vicente, M. Salah El Fallah, J. Jaud, *Inorg. Chim. Acta* **1995**, *232*, 151−156.
[35] J. C. Curtis, T. J. Meyer, *Inorg. Chem.* **1982**, *21*, 1562−1571.
[36] P. T. Beurskens, G. Beurskens, R. de Gelder, S. Garcia Granda, R. O. Gould, R. Israel, J. M. M. Smits, *DIRDIF-99: Technical Report of the Crystallography Laboratory*, University of Nijmegen, The Netherlands.
[37] G. M. Sheldrick, *SHELXL 97, Program for crystal structure refinement*, University of Göttingen, **1997**.
[38] A. Altomare, G. Cascarano, C. Giacovazzo, A. Guagliardi, M. C. Burla, G. Polidori, M. Camalli, *J. Appl. Crystallogr.* **1994**, *27*, 435.
[39] *TeXsan: Crystal Structure Analysis Package*, Molecular Structure Corporation, The Woodlands, TX, USA, **1992**.

Received June 18, 2004
Early View Article
Published Online December 2, 2004

 © 2005 Wiley-VCH Verlag GmbH & Co. KGaA, Weinheim

Trinuclear [NiFe] Clusters as Structural Models for [NiFe] Hydrogenase Active Sites[‡]

Dieter Sellmann,[a][†] Frank Lauderbach,*[a] and Frank W. Heinemann[a]

Keywords: Nickel / Iron / Cluster compounds / Carbonyl ligands / S ligands

[Fe($CH_3COCH{=}CHPh$)$(CO)_3$] reacts with [Ni('S_4')]$_x$ (x = 1, 2) or [Ni('$S_4C_3Me_2$')] ['S_4'$^{2-}$ = 1,2-bis(2-mercaptophenylthio)-ethane(2-),'$S_4C_3Me_2$'$^{2-}$ = 1,3-bis(2-mercaptophenylthio)-2,2-dimethylpropane(2-)] to afford trinuclear [NiFe] clusters [Ni('S_4'){Fe$(CO)_3$}$_2$] (**1**) and [Ni('$S_4C_3Me_2$'){Fe$(CO)_3$}$_2$] (**2**) and the dinuclear $Fe^{II}Fe^0$ complex [Fe(CO)('$S_4C_3Me_2$')Fe$(CO)_3$] (**3**). Clusters **1** and **2** have Ni–Fe bond lengths similar to those of active or reduced states of [NiFe] hydrogenases, a sulfur-dominated coordination sphere of Ni and iron-bound CO. Therefore, **1** and **2** may serve as structural model complexes for the [NiFe] hydrogenase active site. Combination of the '$S_4C_3Me_2$' ligand with $FeCl_2{\cdot}4H_2O$ yielded [Fe('$S_4C_3Me_2$')]$_2$ (**4**), the dinuclearity of which suggests that the '$S_4C_3Me_2$' ligand is less flexible than its ethylene-bridged derivative, which affords a tetrameric [Fe('S_4')]$_4$ complex reported earlier. Compound **4** reacts with 2 equiv. of CO to give [Fe(CO)('$S_4C_3Me_2$')]$_2$ (**5**), which like **4** is only sparingly soluble in all common organic solvents. Complex **5** easily loses CO even if stored in the solid state. [Fe($CH_3COCH{=}CHPh$)$(CO)_3$] reacts with **5** to afford **3** as the only product.
(© Wiley-VCH Verlag GmbH & Co. KGaA, 69451 Weinheim, Germany, 2005)

Introduction

Hydrogenases catalyze the reversible oxidation of molecular hydrogen according to $H_2 \rightleftarrows 2\ H^+ + 2\ e^-$ and, therefore, play a central role in hydrogen and energy metabolism in nature.[1] They are essential for many microorganisms, which acquire energy by the reduction of CO_2, carbonates, sulfates or nitrates.[2] These enzymes are of great biotechnological interest[3] as they can produce molecular hydrogen.[4] [NiFe] hydrogenases are the most predominant of the four major types of hydrogenases commonly known.[3,5] Figure 1

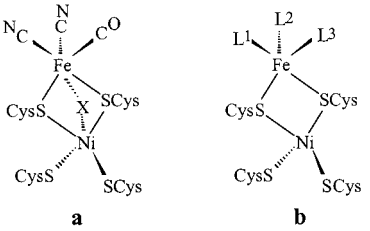

Figure 1. Schematic structure of the active center from (a) *D. gigas* in the oxidized form (X represents, probably, OH^- or O^{2-})[6a,6b] and (b) *D. vulgaris Miyazaki F* hydrogenase in the reduced form (L^1 = SO, CN or CO, L^2 = CN or CO, L^3 = CN or CO)[6c]

depicts the active centers of oxidized and reduced [NiFe] hydrogenases, consisting of Ni–S–Fe bridges.

The mechanism of the reversible H_2 oxidation is still poorly understood. [NiFe] hydrogenases exist in various redox states that can be labeled by their EPR spectra and individual ν(CO) frequencies.[3,7] The relationship between these redox states and the metal oxidation states is still unclear. Furthermore, it is not known if only one or both metal atoms are involved in the activation process. To shed light on these questions, several di- and oligonuclear compounds have been synthesized.[8] Despite intensive research, the number of compounds containing sulfur–bridged Ni *and* Fe centers remains very limited.[9] Recently, we succeeded in synthesizing such complexes as [('S_2')Ni–μ-('S_3')Fe(CO)$(PMe_3)_2$] ['S_2'$^{2-}$ = 1,2-benzenedithiolate(2–), 'S_3'$^{2-}$ = bis(2-mercaptophenyl)sulfide(2–)][10] and [('S_2'){Ni(PMe_3)}$_2$Fe(CO)('S_2')$_2$].[11] Moreover, the latter remarkably reduces protons to dihydrogen, affording the cationic species [('S_2'){Ni(PMe_3)}$_2$Fe(CO)('S_2')$_2$]$^+$.[11] This exciting result encouraged us to further synthesize such complexes without any abiological phosphane ligands and to investigate their reactivity towards protons and hydrogen. Herein, we report the synthesis of the new trinuclear [NiFe] clusters [Ni('S_4'){Fe$(CO)_3$}$_2$] (**1**) and [Ni('$S_4C_3Me_2$'){Fe$(CO)_3$}$_2$] (**2**). The reaction of these complexes with H^+ and H_2 is also investigated.

Results and Discussion

In order to obtain dinuclear [NiFe] complexes, [Fe(CH_3-$COCH{=}CHPh$)$(CO)_3$] and [Ni(L)]$_x$ (L = 'S_4', x = 1, 2;

[‡] Transition Metal Complexes with Sulfur Ligands, 170. Part 169: D. Sellmann, S. Y. Shaban, F. W. Heinemann, *Inorg. Chim. Acta*, in press.

[a] Institut für Anorganische Chemie der Universität Erlangen-Nürnberg,
Egerlandstrasse 1, 91058 Erlangen, Germany
Fax: (internat.) + 49-9131-85-27367
E-mail: lauder@anorganik.chemie.uni-erlangen.de
[†] Deceased.

'$S_4C_3Me_2$', $x = 1$) were combined in equimolar ratio. Unexpectedly, this method did not yield dinuclear complexes but afforded instead the trinuclear clusters **1** and **2** (Scheme 1).

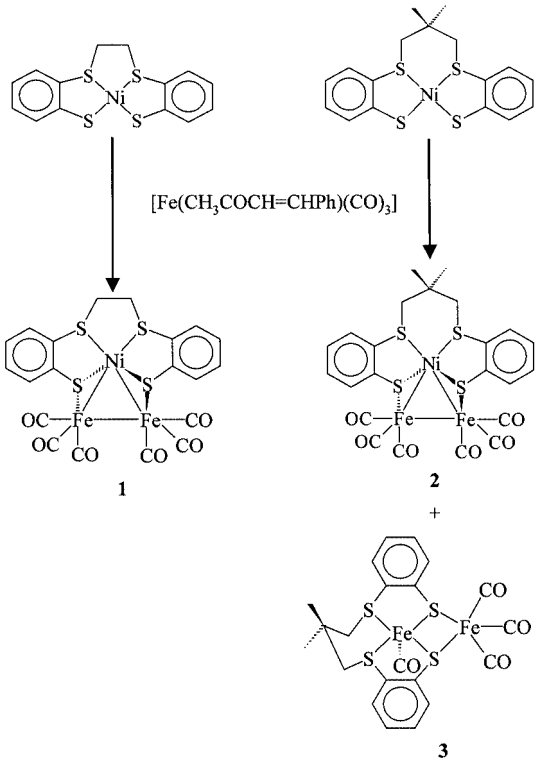

Scheme 1. Syntheses of [NiFe] clusters

During this reaction, the solution changed from bright red to dark red (L = 'S_4') or brown (L = '$S_4C_3Me_2$'). The complexes were isolated by column chromatography in 60% (**1**) and 29% (**2**) yield. During the preparation of **2**, an additional complex [Fe(CO)('$S_4C_3Me_2$')Fe(CO)$_3$] (**3**) could be isolated (vide infra). Clusters **1** and **2** have good solubility in THF and CH_2Cl_2, but are insoluble in pentane. According to their NMR spectra, both **1** and **2** are diamagnetic and possess a twofold symmetry in solution. For **2**, which in contrast to **1** does not exhibit a crystallographically imposed C_2 symmetry, this may be explained by a rapid movement of the neopentylene bridge in solution. Figures 2 and 3 depict stereo views of the molecular structures of **1** and **2**. The coordination spheres of the metal atoms in both clusters exhibit no significant differences. Selected bond lengths and angles (Table 1) illustrate the similar structural properties of these complexes.

Both complexes consist of a trinuclear arrangement of two Fe and one Ni atom that are linked by additional metal−metal interactions. The Ni−Fe distances in **1** (248.6 pm) and **2** (ca. 250 pm) closely resemble that of the active sites of reduced [NiFe] hydrogenases (ca. 255 pm).[12] The average Ni−$S_{thiolate}$ bond length, 217.7 pm (**1**) and 218.5 pm (**2**), matches perfectly the reported Ni−S bond lengths.[13] One known complex, [Ni('$S_4C_3Me_2$')], is the hypothetical residue when all [Fe(CO)$_3$] moieties of **2** are removed; it exhibits equal Ni−$S_{thioether}$ and Ni−$S_{thiolate}$ distances. The trinuclear clusters **1** and **2** show quite long Ni−$S_{thioether}$ bonds (227.8 pm in **1**, 227.4 pm in **2**) due to weaker back-bonding to the thioether ligands. This indicates a lower electron density at the Ni center, which may be caused by additional metal−metal interactions with the two iron atoms. Despite the resulting increased steric strain upon replacing an ethylene bridge in **1** with a neopentylene bridge in **2**, the structural parameters do not change significantly. Thus, only the S2−Ni−S3 angle in **2** (101.3°) is slightly larger than the corresponding S2−Ni−S2A angle in **1** (91.8°). This small variation does not decrease the $S_{thiolate}$−Ni−$S_{thiolate}$ angle in **2** as compared with **1**. Therefore, it is understandable that no dinuclear but only a trinuclear [NiFe] complex was observed. This argument agrees well with previous results on the influence of this angle on the selectivity of complex formation.[14] Very recently, two [Ni'S_4'$Fe_2(CO)_6$] ['S_4' = $(RC_6H_3S_2)_2(CH_2)_3$; R = Me, H] complexes have been reported.[15] In these complexes, which are nearly a perfect match of the structural properties of **1** and **2**, again the corresponding $S_{thioether}$−Ni−$S_{thioether}$ angles [144.88(5)°, R = Me) and 143.22(3)°, R = H] are too big to lead to dinuclear [NiFe] compounds.

Although the molecular structures of **1** and **2** and the methods of their preparation are very similar, complex **3** is formed only in the reaction with the neopentylene-bridged nickel complex [Ni('$S_4C_3Me_2$')]. IR monitoring of the synthesis carried out at 60 °C indicated an increased amount of **3** compared with **2**. Even then, we were unable to obtain exclusively one product. The two products could be separated by column chromatography and subsequent recrystallization. Dinuclear thiolate-bridged [Fe(CO)('$S_4C_3Me_2$')-Fe(CO)$_3$] (**3**) consists of one 18 and one 16 valence electron fragment, containing Fe^0 and Fe^{II}. Complex **3** is diamagnetic and soluble in THF and CH_2Cl_2, but is insoluble in

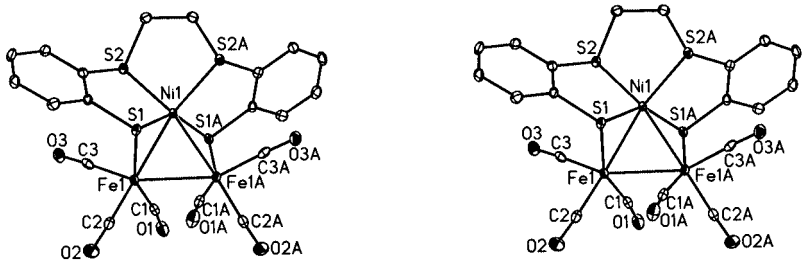

Figure 2. Stereo view of the molecular structure of **1** (50% probability ellipsoids, H atoms omitted)

 © 2005 Wiley-VCH Verlag GmbH & Co. KGaA, Weinheim

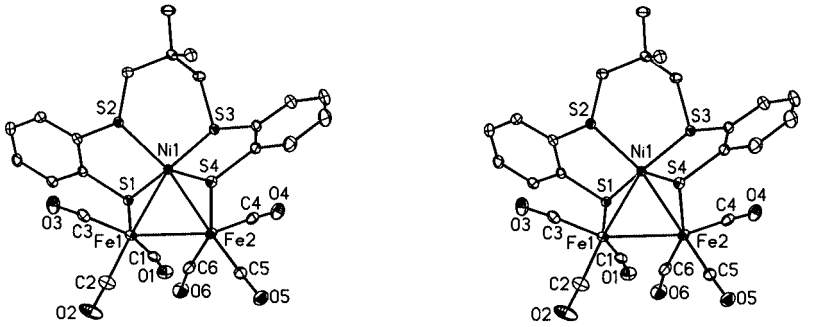

Figure 3. Stereo view of the molecular structure of **2** (50% probability ellipsoids, H atoms omitted)

Table 1. Selected bond lengths [pm] and angles [°] of clusters **1** and **2**

	1	**2**
Ni1−Fe1	248.59(6)	250.38(4)
Fe1−Fe1A[a]	260.50(7)	260.99(5)
Ni1−S1	217.67(6)	218.31(6)
Ni1−S2	227.79(7)	227.25(6)
Fe1−S1	227.32(7)	226.99(6)
Fe1−Ni1−Fe1A[a]	63.20(2)	62.94(2)
Ni1−Fe1−Fe1A[a]	58.40(1)	58.39(2)
S1−Ni1−S2	93.35(2)	93.37(2)
S2−Ni1−S2A[b]	91.76(4)	101.31(2)
S1−Ni1−S2A[b]	112.74(2)	112.10(2)
S1−Ni1−S1A[c]	142.72(4)	141.42(2)
Ni1−S1−Fe1	67.88(2)	68.39(2)
S1−Fe1−Fe1A[a]	84.29(2)	84.30(2)

[a] Fe1A in **1** = Fe2 in **2**. [b] S2A in **1** = S3 in **2**. [c] S1A in **1** = S4 in **2**.

Table 2. Selected bond lengths [pm] and angles [°] of complex **3**

Fe1−Fe2	259.16(6)	Fe1−S1	220.59(9)
Fe1−S2	222.50(9)	Fe1−S3	223.03(10)
Fe1−S4	221.02(9)	Fe2−S1	229.97(9)
Fe2−S4	230.03(10)	S1−Fe1−S2	90.35(3)
S2−Fe1−S3	91.34(3)	S3−Fe1−S4	90.47(4)
Fe1−S1−Fe2	70.19(3)	Fe1−S4−Fe2	70.11(3)
S1−Fe1−S3	162.08(4)	S2−Fe1−S4	162.34(4)
C1−Fe1−S1	98.6(2)	C1−Fe1−S2	95.2(2)
C1−Fe1−S3	99.0(2)	C1−Fe1−S4	101.8(2)
C2−Fe2−C3	100.6(2)	C2−Fe2−C4	89.3(2)
C3−Fe2−C4	97.9(2)		

pentane. NMR results reveal that this complex is of twofold symmetry. Though in its crystal structure the molecules of **3** are not situated on a crystallographic mirror plane, the molecular structure exhibits a well approximated C_s symmetry. Figure 4 depicts a stereo view of the molecular structure of **3**, and Table 2 gives selected bond lengths and angles.

A rational synthesis of **3** was finally developed using fragments this complex consists of (Scheme 2). Treatment of the ligand with iron yielded the dinuclear compound **4**. The molecular structure of the diamagnetic dimeric complex **4** is shown in Figure 5. It exhibits a twofold symmetry and is sparingly soluble in common organic solvents. Two edge-linked square pyramids are formed by sulfur donors coordinating the Fe^{II} atoms. Table 3 shows selected bond lengths and angles. Regarding its dinuclearity, **4** clearly shows that the '$S_4C_3Me_2$' ligand is less flexible than its ethylene-bridged derivative 'S_4'. Reaction of the latter ligand with iron chloride affords the tetrameric [Fe('S_4')]$_4$ compound, as already reported.[16]

Complex **4** reacts with CO (2 equiv.) to give [Fe(CO)('$S_4C_3Me_2$')]$_2$ (**5**), which also shows low solubility in common organic solvents and slowly loses its CO ligand, even in the solid state at room temperature. Complex **5** can easily be identified by its IR ν(CO) frequency. As already reported, the [Fe(CO)('S_4')]$_2$ complex is a dimer.[17] It is anticipated that **5** also consists of a dimeric structure. If complex **5** is combined with [Fe($CH_3COCH{=}CHPh$)$(CO)_3$] (2 equiv.) and stirred at 60 °C for several hours, the solution's red color increases and the only IR detectable species in the reaction solution is **3**.

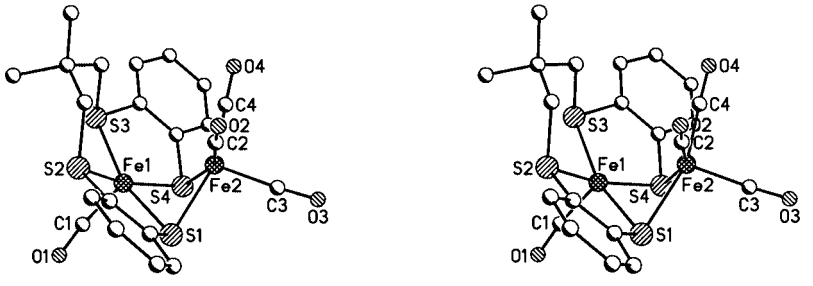

Figure 4. Stereo view of the molecular structure of **3** (H atoms omitted)

 © 2005 Wiley-VCH Verlag GmbH & Co. KGaA, Weinheim

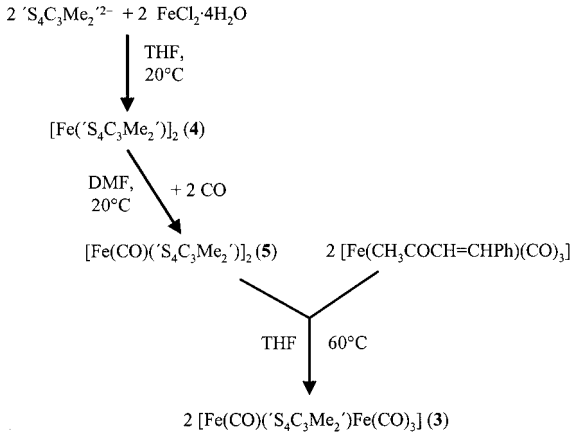

Scheme 2. Rational synthesis for the dinuclear complex **3**

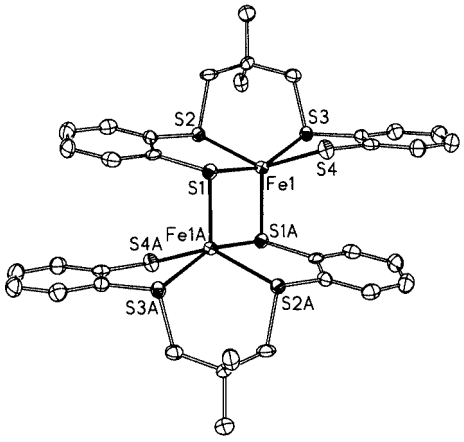

Figure 5. Molecular structure of **4** (80% probability ellipsoids, H atoms omitted)

Table 3. Selected bond lengths [pm] and angles [°] of compound **4**

Fe1−Fe1A	293.45(7)	Fe1−S1	240.72(7)
Fe1−S2	243.38(7)	Fe1−S3	250.27(8)
Fe1−S4	233.23(7)	S1−Fe1−S2	84.99(2)
S1−Fe1−S3	158.20(3)	S1−Fe1−S4	90.78(3)
S2−Fe1−S3	85.41(2)	S2−Fe1−S4	142.54(3)
S3−Fe1−S4	85.04(2)	S1−Fe1−S1A	104.28(2)
Fe1−S1−Fe1A	75.72(2)	S4−Fe1−S1A	115.22(3)
S3−Fe1−S1A	96.82(3)	S2−Fe1−S1A	101.85(2)

Reactivity of 2 and 3 towards Protons and H_2

IR monitoring indicated that compounds **2** and **3** decompose upon addition of one drop of HBF_4, with no hint of protonation or oxidation of the complexes after this treatment. The structural features of **1**−**3** encouraged us to investigate their reactivity towards hydrogen. Since **1** and **2** contain a sulfur-dominated distorted Ni coordination sphere, heterolytic splitting of the H_2 molecule might be possible, as was reported recently for related Ni−S complexes.[18] Complex **3** contains both a free coordination site and sulfur donors where hydrogen could bind and also be heterolyzed. However, even prolonged, high-pressure NMR experiments with **2** and **3** indicated no reaction between either complex and molecular hydrogen.

Summary

Although few di- and trinuclear [NiFe] complexes are known, we present here two examples of the small family of phosphane-free [NiFe] clusters that exhibit a sulfur-dominated coordination sphere of Ni, Ni−$S_{thiolate}$−Fe bridges, Ni−Fe bond lengths as in the reduced active site of [NiFe] hydrogenases, and iron-bound carbon monoxide. The clusters are stable for weeks, both in solution and in the solid state. When changing the bridging alkyl chain from an ethylene bridge in **1** to a neopentylene bridge in **2**, the structural parameters did not change. Unlike the synthesis of **1**, with **2** an additional dinuclear Fe complex (**3**) was formed. Higher yields of **3** were obtained for the synthesis at 60 °C. Even when the steric strain of the ligand in **1** was increased in **2**, their structural properties did not differ significantly. These new complexes demonstrate that *cis*-thiolate ligands can connect Ni and Fe, resulting in trinuclear [NiFe] clusters with a sulfur-dominated coordination sphere.

Experimental Section

General Remarks: All manipulations were carried out in absolute solvents under exclusion of air. '$S_4C_3Me_2$'−H_2,[13b] 'S_4'−H_2[19] ligands and the complexes [Ni('S_4')]$_x$ [20] (x = 1 or 2) and [Ni('$S_4C_3Me_2$')][13b] were prepared as described in the literature. IR: Perkin−Elmer 983, 1620 FT IR and 16PC FT-IR; NMR: Jeol FT-JNM-GX 270 and EX 270; mass spectrometry: Jeol MSTATION 700; elemental analysis: Carlo−Erba EA 1106 or 1108.

[Ni('S_4'){Fe(CO)$_3$}$_2$] (1): A solution of [Fe(CH_3COCH=CHPh)-$(CO)_3$] (460 mg, 1.609 mmol) in THF (20 mL) was added to 1/x equiv. of [Ni('S_4')]$_x$ (500 mg, 1.609 mmol). The reaction suspension was then stirred for 24 h and the obtained solid material was removed and the solution concentrated to dryness. The resultant residue was dissolved in toluene and separated by column chromatography (silica gel, 60 cm, eluent: toluene). After the first two starting material containing fractions were eluted, a large red product fraction was washed with MeOH from the silica gel and the solvents evaporated to dryness. The residue was redissolved in THF (20 mL) and pentane (120 mL) was added. The resulting brown microcrystalline material was washed with pentane (60 mL) and dried in vacuo. Yield 310 mg (60%). ^{1}H NMR (269.6 MHz, CD_2Cl_2): δ = 8.06 (m, 2 H, C_6H_4), 7.70 (m, 2 H, C_6H_4), 7.32 (m, 4 H, C_6H_4), 3.60 (m, 2 H, CH_2), 2.38 (m, 2 H, CH_2). ^{13}C{^{1}H} NMR (67.7 MHz, CD_2Cl_2): δ = 213.3 (*C*O), 157.3, 133.0, 132.4, 130.0, 128.2, (C_6H_4), 42.4 (CH_2). IR (KBr): $\tilde{\nu}$ = 2028, 1993, 1942 (CO) cm^{-1}. MS (FD, THF): m/z = 646 [Ni('S_4'){Fe(CO)$_3$}$_2$]$^+$. $C_{20}H_{12}Fe_2NiO_6S_4$ (645.76): calcd. C 37.13, H 1.87, S 19.82; found C 38.91, H 2.08, S 19.36.

[Ni('$S_4C_3Me_2$'){Fe(CO)$_3$}$_2$] (2): A solution of [Fe(CH_3COCH=CHPh)$(CO)_3$] (736 mg, 2.573 mmol) in THF (40 mL) was added to [Ni('$S_4C_3Me_2$')] (1050 mg, 2.566 mmol). The reaction suspension was then stirred for 24 h and the resultant solid material was removed and the solution concentrated to dryness. The residue was

 © 2005 Wiley-VCH Verlag GmbH & Co. KGaA, Weinheim

then dissolved in a toluene/hexane (3:1) mixture, and a column for chromatography was prepared (silica gel, 60 cm, toluene/hexane, 3:1). Red and brown fractions were collected and the solvents were evaporated to dryness. The brown fraction was redissolved in THF (6 mL) and filtered; pentane (100 mL) was then added and the mixture was stored at −20 °C for 5 d, after which the solvent was decanted carefully and the resulting crystalline material was dried in vacuo. Yield 260 mg (29%). ^{1}H NMR (269.6 MHz, CD_2Cl_2): δ = 8.13 (m, 2 H, C_6H_4), 7.61 (m, 2 H, C_6H_4), 7.30 (m, 4 H, C_6H_4), 3.18 (d, 2 H, CH_2, $^2J_{H,H}$ = 13.2 Hz), 2.64 (d, 2 H, CH_2, $^2J_{H,H}$ = 13.2 Hz), 0.84 (s, 6 H, CH_3). ^{13}C{^{1}H} NMR (67.7 MHz, CD_2Cl_2): δ = 212.5 (*C*O), 157.2, 137.0, 131.8, 131.4, 129.0, 127.9, (C_6H_4), 49.1 (CH_2), 36.3 (C_q), 28.1 (CH_3). IR (KBr): $\tilde{\nu}$ = 2033, 1992, 1957 (CO) cm^{-1}. MS (FD, THF): *m*/*z* = 688 [Ni('$S_4C_3Me_2$')$\{Fe(CO)_3\}_2$]$^+$. $C_{23}H_{18}Fe_2NiO_6S_4$ (687.80): calcd. C 40.09, H 2.63, S 18.61; found C 39.85, H 2.50, S 18.21.

[Fe(CO)('$S_4C_3Me_2$')Fe(CO)$_3$] (3). (a) The red fraction obtained from column chromatography during the synthesis of **2** (see above) was concentrated to dryness and redissolved in THF (6 mL). The solution was then treated with pentane (100 mL) and kept at −20 °C for 5 d, after which the solvent was decanted carefully and the resulting crystalline material was dried in vacuo. Yield 210 mg (14%). ^{1}H NMR (269.6 MHz, CD_2Cl_2): δ = 7.82 (m, 4 H, C_6H_4), 7.33 (m, 4 H, C_6H_4), 3.55 (d, 2 H, CH_2, $^2J_{H,H}$ = 9.7 Hz); 2.23 (d, 2 H, CH_2, $^2J_{H,H}$ = 10.0 Hz), 1.50 (s, 3 H, CH_3), 1.19 (s, 3 H, CH_3). ^{13}C{^{1}H} NMR (67.7 MHz, CD_2Cl_2): δ = 216.9, 213.9 (*C*O), 148.9, 141.2, 131.5, 131.5, 128.6, 127.4, (C_6H_4), 54.1 (CH_2), 36.8 (C_q), 32.6, 24.1 (CH_3). IR (KBr): $\tilde{\nu}$ = 2009, 1944, 1921 (CO) cm^{-1}. MS (FD, THF): *m*/*z* = 574 [Fe(CO)('$S_4C_3Me_2$')Fe(CO)$_3$}]$^+$. $C_{21}H_{18}Fe_2O_4S_4$ (573.88): calcd. C 43.92, H 3.16, S 22.33; found C 43.90, H 3.25, S 22.26. **(b)** A solution of [Fe(CH_3COCH=CHPh)(CO)$_3$] (66 mg, 0.23 mmol) in THF (10 mL) was added to a suspension of **5** (100 mg, 0.12 mmol) in THF (20 mL) and the resultant reaction mixture was stirred at 60 °C for 24 h. After filtration, the solution was then dried in vacuo, redissolved in THF (2 mL), and pentane (50 mL) was added. This mixture was then kept at −30 °C for 6 d to afford microcrystalline material that was isolated, washed with pentane (15 mL) and dried in vacuo. Yield 50 mg (38%).

[Fe('$S_4C_3Me_2$')]$_2$ (4): The ligand '$S_4C_3Me_2$'−H_2 (120 mg, 0.34 mmol) in MeOH (7 mL) was treated with LiOMe (2 equiv., 26 mg, 0.68 mmol) and added to a solution of $FeCl_2$·4H_2O (68 mg, 0.34 mmol) in MeOH (5 mL). The resultant brown microcrystalline precipitate was filtered off, washed with MeOH (20 mL) and dried in vacuo. Yield 125 mg (90%). ^{1}H NMR (269.6 MHz, [D$_7$]DMF): δ = 7.60 (m, 2 H, C_6H_4), 7.45 (m, 2 H, C_6H_4), 7.25 (m, 4 H, C_6H_4), 3.20 (s, 4 H, CH_2), 1.15 (s, 6 H, CH_3). ^{13}C{^{1}H} NMR (67.7 MHz, [D7]DMF): δ = 139.7, 134.6, 134.4, 129.1, 127.6, 125.9, (C_6H_4), 48.4 (CH_2), 38.2 (C_q), 26.2 (CH_3). MS (FD, DMF): *m*/*z*: = 406 [Fe('$S_4C_3Me_2$')]$^+$. $C_{34}H_{36}Fe_2S_8$·CH_3OH (843.95): calcd. C 49.76, H 4.77, S 30.36; found C 49.24, H 4.84, S 30.61.

[Fe(CO)('$S_4C_3Me_2$')]$_2$ (5): CO (2 equiv., 22.4 mL, 1 mmol) was added through a septum to a suspension of **4** (405 mg, 0.50 mmol) in DMF (20 mL). This mixture was then stirred for 12 h, and the resultant solid material was filtered off, washed with DMF (10 mL) and THF (20 mL), and dried in vacuo. Yield 315 mg (73%). ^{1}H NMR (269.6 MHz, [D$_7$]DMF): δ = 7.94−6.82 (m, 8 H, C_6H_4), 3.93 (d, 1 H, CH_2, $^2J_{H,H}$ = 11.3 Hz), 3.63 (d, 1 H, CH_2, $^2J_{H,H}$ = 11.6 Hz), 2.49 (d, 1 H, CH_2, $^2J_{H,H}$ = 11.6 Hz); 2.22 (d, 1 H, CH_2, $^2J_{H,H}$ = 11.3 Hz), 1.17 (s, 3 H, CH_3), 0.68 (s, 3 H, CH_3); ^{13}C{^{1}H} NMR (67.7 MHz, [D7]DMF): δ = 217.3 (*C*O), 157.1, 145.6, 145.1, 135.2, 133.7, 130.7, 129.8, 128.9, 128.7, 128.1, 126.5, 121.6 (C_6H_4), 50.7, 49.7 (CH_2), 36.1 (C_q), 31.9, 23.1 (CH_3). IR (KBr): $\tilde{\nu}$ = 1938 (CO) cm^{-1}. MS (FD, DMF): *m*/*z*: = 406 [Fe('$S_4C_3Me_2$')]$^+$. $C_{18}H_{18}FeOS_4$ (867.92): calcd. C 49.77, H 4.18, S 29.52; found C 49.77, H 4.18, S 28.60.

Table 4. Selected crystallographic data for [Ni('S_4')$\{Fe(CO)_3\}_2$] (**1**), [Ni('$S_4C_3Me_2$')$\{Fe(CO)_3\}_2$]·THF (**2**·THF), [Fe(CO)('$S_4C_3Me_2$')-Fe(CO)$_3$] (**3**), and [Fe('$S_4C_3Me_2$')]$_2$ (**4**)

	1	**2·THF**	**3**	**4**
Empirical formula	$C_{20}H_{12}Fe_2NiO_6S_4$	$C_{27}H_{26}Fe_2NiO_7S_4$	$C_{21}H_{18}Fe_2O_4S_4$	$C_{34}H_{36}Fe_2S_8$
M_r [g·mol^{-1}]	646.95	761.13	574.29	812.81
Crystal system	monoclinic	triclinic	monoclinic	orthorhombic
Space group	*P*2/*c*	$P\bar{1}$	$P2_1/n$	*Pbca*
a [pm]	1997.6(2)	1141.61(2)	1001.62(7)	1384.9(1)
b [pm]	997.58(8)	1226.32(2)	1649.20(7)	1160.2(1)
c [pm]	1176.92(7)	1296.79(2)	1411.8(2)	2152.1(2)
α [°]	90	67.808(1)	90	90
β [°]	103.772(5)	77.265(1)	91.399(6)	90
γ [°]	90	64.779(1)	90	90
V [nm^3]	2.2779(3)	1.51691(4)	2.3315(3)	3.4579(5)
Z	4	2	4	4
$\rho_{calcd.}$ [g·cm^{-3}]	1.886	1.666	1.636	1.561
μ [mm^{-1}]	2.478	1.876	1.628	1.348
Crystal size [mm]	0.21 × 0.14 × 0.03	0.38 × 0.28 × 0.12	0.25 × 0.24 × 0.17	0.13 × 0.10 × 0.05
T_{min}/T_{max}	0.648/0.926	0.662/0.874	0.741/1.000	0.898/1.000
Measured reflections	39372	40271	16767	34714
Independent reflections	5429	10461	5773	3797
Observed reflections[a]	4192	6696	3419	2716
Refined parameters	335	448	333	253
Max./min. residual density [e·nm^{-3}]	511/−651	630/−745	432/−451	383/−360
*R*1,[a] *wR*2[b] [%]	3.21, 6.59	3.88, 8.64	4.38, 8.88	3.46, 7.08

[a] [$I > 2\sigma(I)$]. [b] All data.

 © 2005 Wiley-VCH Verlag GmbH & Co. KGaA, Weinheim

Reaction of 2 and 3 with Protons: $HBF_4{\cdot}Et_2O$ (one drop) was added to a solution of **2** (5 mg, 0.007 mmol) or **3** (5 mg, 0.009 mmol) in CH_2Cl_2 (5 mL). IR monitoring showed a decrease in CO band intensity and many new small CO bands.

Reaction of 2 and 3 with Hydrogen: A solution of **2** (10 mg, 0.015 mmol) or **3** (10 mg, 0.017 mmol) in [D_8]THF (0.4 mL) in a high-pressure NMR tube (524-PV-1, Wilmad, USA) was treated with D_2O (one drop) and 15 bar of H_2. ^1H NMR spectra were then collected over the following 70 d. Between measurements, the high-pressure NMR tubes were rotated continuously.

X-ray Structure Determination of [Ni('S_4'){Fe(CO)$_3$}$_2$] (1), [Ni('$S_4C_3Me_2$'){Fe(CO)$_3$}$_2$]·THF (2·THF), [Fe(CO)('$S_4C_3Me_2$')-Fe(CO)$_3$] (3), and [Fe('$S_4C_3Me_2$')]$_2$ (4): Slow diffusion of pentane into a saturated THF solution of **1** at 10 °C yielded, after 4 weeks, black plates of **1**. Black blocks of **2·THF** were obtained by maintaining a layered saturated THF solution of **2** with pentane at −30 °C for 1 week. Slow diffusion of pentane into a saturated THF solution of **3** yielded dark brown crystals of **3**. A saturated DMF solution of **4** prepared at 120 °C was cooled to room temperature, filtered, and kept at −30 °C to give, after 8 weeks, black plates of **4**. Suitable single crystals were embedded in protective perfluoro polyether oil. Data were collected at 100 K with a Nonius KappaCCD diffractometer using Mo-K_α radiation (λ = 71.073 pm), and a graphite monochromator. For **1** and **2** a numerical absorption correction was applied.[21] For **3** and **4**, a semiempirical absorption correction on the basis of multiple scans was performed.[22] Structures were solved by direct methods; full-matrix least-squares refinement was carried out on F^2 using SHELXTL NT 6.12[23] (**1**, **3**, **4**) or SHELXTL NT 5.1 (**2**).[24] All non-hydrogen atoms were refined anisotropically. All H atom positions were derived from a difference Fourier synthesis and refined with a fixed common isotropic displacement parameter. Selected crystallographic data are summarized in Table 4.[25]

Acknowledgments

We gratefully acknowledge financial support by the Deutsche Forschungsgemeinschaft (SFB 583: "Redoxaktive Metallkomplexe") and the Fonds der Chemischen Industrie. We also thank Professor Dr. Horst Kisch for supporting assistance and fruitful discussions.

[1] [1a] R. Cammack, *Nature* **1999**, *397*, 214−215. [1b] M. W. W. Adams, E. I. Stiefel, *Science* **1998**, *282*, 1842−1843. [1c] R. K. Thauer, A. R. Klein, G. C. Hartmann, *Chem. Rev.* **1996**, *96*, 3031−3042. [1d] S. P. J. Albracht, *Biochem. Biophys. Acta* **1994**, *1188*, 167−204.

[2] A. E. Przybyla, J. Robbins, N. Menon, H. D. Peck Jr., *FEMS Microbiol. Reviews* **1992**, *88*, 109−135.

[3] M. Frey, *Struct. Bonding (Berlin)* **1998**, *90*, 97−126.

[4] [4a] M. W. W. Adams, L. E. Mortenson, J.-S. Chen, *Biochim. Biophys. Acta* **1981**, *594*, 105−176. [4b] T. Lissolo, S. Pulvin, D. Thomas, *J. Biol. Chem.* **1984**, *259*, 11725−11729.

[5] [5a] J. C. Fontecilla-Camps, *Struct. Bonding (Berlin)* **1998**, *91*, 1−29. [5b] M. J. Maroney, G. Davidson, C. B. Allan, J. Figlar, *Struct. Bonding (Berlin)* **1998**, *92*, 2−65.

[6] [6a] A. Volbeda, M. H. Charon, C. Piras, E. C. Hatchikian, M. Frey, J. C. Fontecilla-Camps, *Nature* **1995**, *373*, 580−587. [6b] A. Volbeda, E. Garcin, A. L. de Lacey, V. M. Fernandes, E. C. Hatchikian, M. Frey, J. C. Fontecilla-Camps, *J. Am. Chem. Soc.* **1996**, *118*, 12989−12996. [6c] H. Ogata, Y. Mizoguchi, N. Mizuno, K. Miki, S. Adachi, N. Yasuoka, T. Yagi, O. Yamauchi, S. Hirota, Y. Higuchi, *J. Am. Chem. Soc.* **2002**, *124*, 11628−11635.

[7] [7a] A. L. de Lacey, E. C. Hatchikian, A. Volbeda, M. Frey, J. C. Fontecilla-Camps, V. M. Fernandez, *J. Am. Chem. Soc.* **1997**, *119*, 7181−7189. [7b] F. Dole, A. Fournel, V. Magro, E. C. Hatchikian, P. Bertrand, B. Guigliarelli, *Biochemistry* **1997**, *36*, 7847−7854.

[8] [8a] M. Y. Darensbourg, E. J. Lyon, J. J. Smee, *Coord. Chem. Rev.* **2000**, 553−561 and references cited therein. [8b] F. Osterloh, W. Saak, D. Haase, S. Pohl, *Chem. Commun.* **1997**, 979−980. [8c] E. Bouwman, R. K. Henderson, A. L. Spek, J. Reedijk, *Eur. J. Inorg. Chem.* **1999**, *4*, 217−219. [8d] S. C. Davies, D. J. Evans, D. L. Hughes, S. Longhurst, J. R. Sanders, *Chem. Commun.* **1999**, 1935−1936. [8e] G. Steinfeld, B. Kersting, *Chem. Commun.* **2000**, 205−206. [8f] W.-F. Liaw, J.-H. Lee, H.-B. Gau, C.-H. Chen, G.-H. Lee, *Inorg. Chim. Acta* **2001**, *322*, 99−105. [8g] M.-C. Chalbot, A. M. Mills, A. L. Spek, G. J. Long, E. Bouwman, *Eur. J. Inorg. Chem.* **2003**, 453−457. [8h] M. C. Smith, J. E. Barclay, S. P. Cramer, S. C. Davies, W.-W. Gu, D. L. Hughes, S. Longhurst, D. J. Evans, *J. Chem. Soc., Dalton Trans.* **2002**, 2641−2647. [8i] T. Glaser, F. Kesting, T. Beissel, E. Bill, T. Weyhermüller, W. Meyer-Klaucke, K. Wieghardt, *Inorg. Chem.* **1999**, *38*, 722−732. [8j] W. Saak, S. Pohl, *Angew. Chem. Int. Ed. Engl.* **1991**, *30*, 881−883. [8k] J. Zhou, M. J. Scott, Z. Hu, G. Peng, E. Munck, R. H. Holm, *J. Am. Chem. Soc.* **1992**, *114*, 10843−10854. [8l] F. Osterloh, W. Saak, S. Pohl, *J. Am. Chem. Soc.* **1997**, *119*, 5648−5656. [8m] P. Braunstein, E. Sappa, A. Tiripicchio, M. Tiripicchio Camellini, *Inorg. Chim. Acta* **1980**, *45*, L191−L193. [8n] C. Junghans, W. Saak, S. Pohl, *J. Chem. Soc., Chem. Commun.* **1994**, 2327−2328. [8o] S. Ciurli, S.-B. Yu, R. H. Holm, K. K. P. Srivastava, E. Munck, *J. Am. Chem. Soc.* **1990**, *112*, 8169−8171. [8p] S. Ciurli, P. K. Ross, M. J. Scott, S.-B. Yu, R. H. Holm, *J. Am. Chem. Soc.* **1992**, *114*, 5415−5423. [8q] W. H. Watson, A. Nagl, M.-J. Don, M. G. Richmond, *J. Chem. Cryst.* **1999**, *29*, 871−876. [8r] R. L. Holliday, L. C. Roof, B. Hargus, D. M. Smith, P. T. Wood, W. T. Pennington, J. W. Kolis, *Inorg. Chem.* **1995**, *34*, 4392−4401. [8s] F. Osterloh, W. Saak, D. Haase, S. Pohl, *Chem. Commun.* **1996**, 777−778.

[9] A search of the Cambridge Structural Database (F. H. Allen, *Acta Crystallogr.* **2002**, *B58*, 380−388) for Ni−S−Fe resulted in only 37 hits (May **2004**).

[10] D. Sellmann, F. Geipel, F. Lauderbach, F. W. Heinemann, *Angew. Chem. Int. Ed.* **2002**, *41*, 632−634.

[11] D. Sellmann, F. Lauderbach, F. Geipel, F. W. Heinemann, M. Moll, *Angew. Chem. Int. Ed.* **2004**, *43*, 3141−3144.

[12] [12a] M. Y. Darensbourg, E. J. Lyon, J. J. Smee, *Coord. Chem. Rev.* **2000**, 553−561 and references cited therein. [12b] A. Volbeda, J. C. Fontecilla-Camps, *Dalton Trans.* **2003**, 4030−4038.

[13] [13a] D. Sellmann, S. Fünfgelder, F. Knoch, M. Moll, *Z. Naturforsch., Teil B* **1991**, *46*, 1601−1608. [13b] D. Sellmann, D. Häussinger, F. Knoch, M. Moll, *J. Am. Chem. Soc.* **1996**, *118*, 5368−5374. [13c] D. Sellmann, S. Fünfgelder, G. Pöhlmann, F. Knoch, M. Moll, *Inorg. Chem.* **1990**, *29*, 4772−4778.

[14] M.-C. Chalbot, A. M. Mills, A. L. Spek, G. J. Long, E. Bouwman, *Eur. J. Inorg. Chem.* **2003**, 453−457.

[15] Q. Wang, J. E. Barclay, A. J. Blake, E. S. Davies, D. J. Evans, A. C. Marr, E. J. L. McInnes, J. McMaster, C. Wilson, M. Schröder, *Chem. Eur. J.* **2004**, *10*, 3384−3396.

[16] D. Sellmann, H. Friedrich, F. Knoch, *Z. Naturforsch., Teil B* **1993**, *48*, 1675−1680.

[17] D. Sellmann, R. Weiss, F. Knoch, G. Ritter, J. Dengler, *Inorg. Chem.* **1990**, *29*, 4107−4114.

[18] D. Sellmann, R. Prakash, F. W. Heinemann, *Eur. J. Inorg. Chem.* **2004**, 1847−1858.

[19] D. Sellmann, E. Böhlen, *Z. Naturforsch., Teil B* **1982**, *37*, 1026−1033.

[20] D. Sellmann, H. Schillinger, F. Knoch, *Z. Naturforsch., Teil B* **1992**, *47*, 645−655.

[21] P. Coppens, *Crystallographic Computing (Copenhagen)* **1970**, 225−270.

[22] *SADABS*, Bruker AXS, Inc., Madison, WI, U.S.A., **2002**.

[23] *SHELXTL NT 6.12*,, Bruker AXS, Inc., Madison, WI, U.S.A., **2002**.

[24] *SHELXTL NT 5.1*, Bruker AXS, Inc., Madison, WI, U.S.A., **1998**.
[25] CCDC-243920 (**1**), -243921 (**2**), -243922 (**3**) and -243923 (**4**) contain the supplementary crystallographic data for this paper. These data can be obtained free of charge at www.ccdc.cam.ac.uk/conts/retrieving.html [or from the Cambridge Crystallographic Data Centre, 12 Union Road, Cambridge CB2 1EZ, UK; Fax: (internat.) + 44-1223-336-033; E-mail: deposit@ccdc.cam.ac.uk].

Received July 7, 2004
Early View Article
Published Online November 24, 2004

 © 2005 Wiley-VCH Verlag GmbH & Co. KGaA, Weinheim

Novel Binary Compounds of Group 15 Elements: Synthesis and Characterisation of $[Sb_4(PSiMe_2Thex)_4]$, $[Sb_4(AsSi\mathit{i}Pr_3)_4]$ and $[Sb_2(PSiPh_2\mathit{t}Bu)_4]$

Donna Nikolova[a] and Carsten von Hänisch*[a]

Keywords: Arsenic / Antimony / Cage compounds / Phosphorus

The low-temperature reactions of $Me_2ThexSiPLi_2$ (Thex = $CMe_2\mathit{i}Pr$) and $\mathit{i}Pr_3SiAsLi_2$ with $SbCl_3$ in a 3:2 molar ratio yields the cage compounds $[Sb_4(PSiMe_2Thex)_4]$ (**1**) and $[Sb_4(AsSi\mathit{i}Pr_3)_4]$ (**2**), respectively. The metal salt $SbBr_3$ reacts with $\mathit{t}BuPh_2SiPLi_2$ at –70 °C to give the bicyclic compound $[Sb_2(PSiPh_2\mathit{t}Bu)_4]$ (**3**). Compounds **1**–**3** were characterised by NMR and IR spectroscopy, mass spectrometry, elemental analysis and single-crystal X-ray diffraction. The structures of **1** and **2** reveal that the both compounds adopt a structure similar to those of realgar (As_4S_4). The central structural motif is an Sb_4Y_4 cage (Y = P, As), consisting of four five-membered rings with common edges. The bicyclic compound **3** is composed of five-membered and three-membered rings sharing a common Sb_2 bridgehead.
(© Wiley-VCH Verlag GmbH & Co. KGaA, 69451 Weinheim, Germany, 2005)

Introduction

The formation of homonuclear cyclic, polycyclic and cage-like compounds of group 15 elements has been the focus of intensive research efforts for a long time.[1–3] These studies have revealed a very diverse range of structure types, which extend from simple small rings like $P_3\mathit{t}Bu_3$ [2] through five- and six-membered rings, to polycycles and cages containing up to fourteen atoms.[3] Few analogous binary compounds containing a combination of heavier group 15 elements have been structurally characterised. Although not as widely studied as the organophosphorus homocycles, cyclic As/P and Sb/P compounds are known. The first P_2As heterocycle was synthesized by cyclocondensation of $\mathit{t}Bu_2P_2K_2$ with $\mathit{t}BuAsCl_2$.[4] Other reported species are the bicyclic compounds $[As_2(PAr)_2]$ and $[Sb_2(PAr)_2]$, which are obtained by the reaction of $ArP(SiMe_3)Li$ [Ar = 2,4,6-$(\mathit{t}Bu)_3C_6H_2$] with $Cp^*E'Cl_2$ (E′ = As, Sb) as well as $[(\mathit{t}BuP)_3As]_2$ and $[(\mathit{t}BuP)_3Sb]_2$.[5] The most recent extension of group 15 element chemistry is the formation of heterocyclic compounds containing Sb–As bonds. To the best of our knowledge, the only structurally characterised Sb/As heterocycle is the coordination complex $[Sb_2Cl_6\{o\text{-}C_6H_4(AsMe_2)_2\}]$.[6]

Herein we report on the synthesis and crystal structures of the cage and bicyclic compounds $[Sb_4(PSiMe_2Thex)_4]$ (**1**), $[Sb_4(AsSi\mathit{i}Pr_3)_4]$ (**2**) and $[Sb_2(PSiPh_2\mathit{t}Bu)_4]$ (**3**), obtained from the reactions of lithium phosphanides and arsanides with the antimony salts $SbCl_3$ and $SbBr_3$, respectively.[7]

Results and Discussion

The reaction of $Me_2ThexSiPLi_2$ (Thex = $CMe_2\mathit{i}Pr$) with $SbCl_3$ in a 3:2 molar ratio leads to the formation of **1**, which can be isolated as orange crystals by cooling the reaction mixture to −35 °C. Compound **1** crystallises in the orthorhombic space group $P4_2/n$. The central structural motif is an Sb_4P_4 cage (Figure 1). It consists of four Sb_3P_2 five-membered rings with common Sb–P–Sb edges. The structure can be thought of as being derived from an Sb_4 tetrahedron by placing bridging $PSiMe_2Thex$ fragments above four of the six edges. All of the phosphorus atoms are coordinated to two antimony atoms and one $ThexMe_2Si$ group, forming a trigonal-pyramidal environment; the Sb atoms possess no exocyclic ligands and also have a coordination number of three. The availability of the Sb–Sb bonds (Sb1–Sb1′′ and Sb1′–Sb1′′′) in the molecule is indicative of a reduction process that must have taken place parallel to the lithium chloride elimination reaction. The Sb–Sb bond length in **1** is 287.9 pm, which is in the usual range for single Sb–Sb bonds. Similar Sb–Sb bond lengths of 286.7 pm, for example, can be observed in $Sb_2(SiMe_3)_4$,[8] whereas in the polycycles Sb_8R_6 and Sb_8R_4 [R = $CH(SiMe_3)_2$] these bonds are slightly shorter (278.4–287.3 pm).[9] The Sb–P bond lengths in **1** are in the range 249.4–252.4 pm and therefore are similar to the spread of values observed in $[(tmeda)(Me_2NH)Na(CyP)_4Sb]_2$ (248.9–254.1 pm).[10] In the bicycle $[Sb_2(PAr)_2]$ (Ar = 2,4,6-$\mathit{t}Bu_3C_6H_2$) mentioned above these bonds are significantly longer (average value

[a] Institut für Nanotechnologie, Forschungszentrum Karlsruhe
Postfach 3640, 76021 Karlsruhe, Germany
Fax: + 49-7247-82-6368
E-mail: carsten.vonhaenisch@int.fzk.de

 © 2005 Wiley-VCH Verlag GmbH & Co. KGaA, Weinheim DOI: 10.1002/ejic.200400610

257.3 pm).[5b] It is assumed that the longer Sb−P bonds in the latter compound are due to the large steric requirements of the 2,4,6-tBu$_3$C$_6$H$_2$ substituents. The Sb_4P_4 motif in **1** can be regarded as being related to the P_8 segment in the structure of Hittorf's violet phosphorus; an analogous P_8R_4 compound, however, could not be isolated in a pure form,[11] whereas a variety of transition metal complexes with P_8 ligands have been described in the literature.[12] The closest structural relative of **1** is the antimony cage Sb_8R_4 [R = CH(SiMe$_3$)$_2$], isolated from the reduction of RSbCl$_2$with Mg.[9]

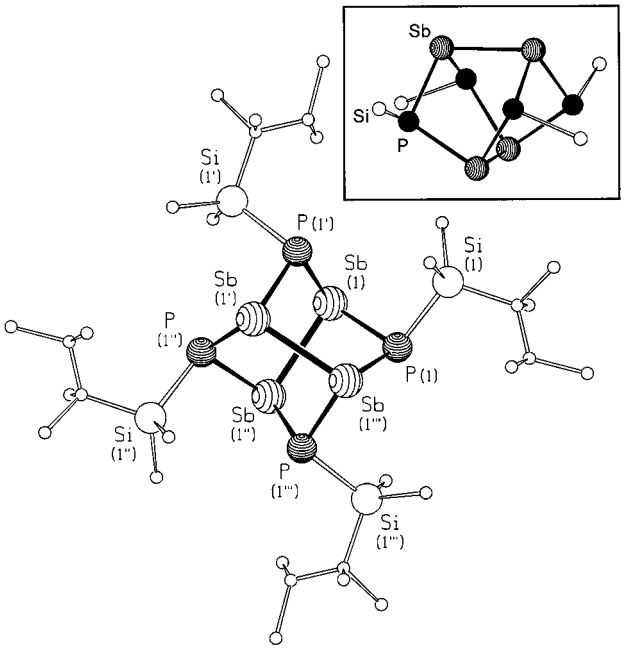

Figure 1. Molecular structure of **1** (inset: side view of the heavy atom frame); selected bond lengths [pm] and angles [°]: Sb(1)−P(1) 249.4(2), Sb(1′′′)−P(1) 252.4(2), Sb−Sb 287.9(1), P(1)−Si(1) 228.5(2); Sb(1′′)−Sb(1)−P(1) 90.42, Sb(1′′)−Sb(1)−P(1′) 104.71, P(1)−Sb(1)−P(1′) 92.97, Sb(1)−P(1)−Sb(1′′′) 102.23, Si(1)−P(1)−Sb(1) 105.10, Si(1)−P(1)−Sb(1′′′) 106.22

The $^{31}P\{^1H\}$ NMR spectrum of **1** displays, as expected, one singlet at $\delta = -104.5$ ppm. An additional singlet appears at $\delta = -65.1$ ppm in the $^{31}P\{^1H\}$ NMR spectrum of the reaction mixture, which presumably can be attributed to significant amounts of (PSiMe$_2$Thex)$_n$ (n = 4 or 6), which is obtained as a by-product from the reduction process. Unfortunately, this by-product could not be isolated.

[Sb_4(AsSiiPr$_3$)$_4$] (**2**) is obtained from the reaction of iPr$_3$SiAsLi$_2$ and SbCl$_3$. It crystallises in the monoclinic space group $C2/c$ with two independent inversion-symmetric molecules in the elementary cell. The molecular structure of **2** (Figure 2) is almost identical to the phosphorus compound **1**, but with AsSiiPr$_3$ groups as building blocks instead of the PSiMe$_2$Thex fragments. The Sb−Sb bonds in **2** are slightly longer (288.1−289.0 pm) than those in **1**. The Sb−As bonds are in the range 260.1−261.6 pm, whereas in the coordination compound [Sb_2Cl_6{o-C_6H_4(AsMe$_2$)$_2$}] these bonds are significantly longer (266.4 pm).

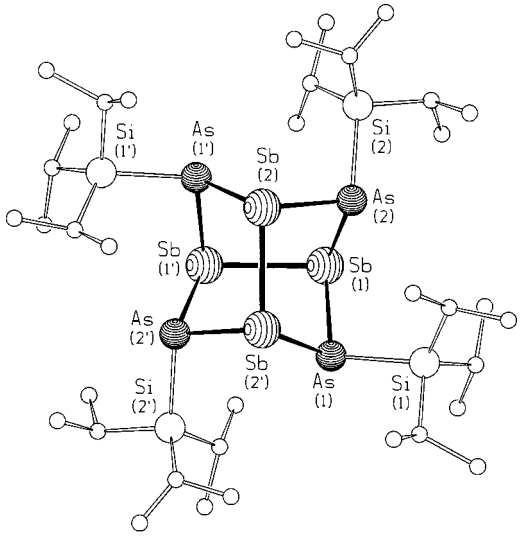

Figure 2. Molecular structure of **2**; selected bond lengths [pm] and angles [°]: Sb(1)−Sb(1′) 289.0(2), Sb(2)−Sb(2′) 288.4(2), Sb−As 260.1(2)−261.6(2), Si−As 239.3−240.2; Sb(1)−As(1)−Sb(2) 101.24(5), Sb(1′)−As(2)−Sb(2) 100.69(5), As(1)−Sb(1)−As(2) 93.72(5), As(1)−Sb(2)−As(2) 92.09(5), As(1)−Sb(1)−Sb(1′) 94.94(5), As(2′)−Sb(1)−Sb(1′) 103.96(5), As(1)−Sb(2)−Sb(2′) 103.99(5), As(2)−Sb(2)−Sb(2′) 95.46(5)

In the mass spectra of **1** and **2** the molecular ion peaks at m/z = 1184 and 1416, respectively, as well as the characteristic fragments [Sb_4P_4(SiMe$_2$Thex)$_3$]$^+$, [Sb_3P_4Me$_2$-(SiMe$_2$Thex)$_3$]$^+$ and [Sb_4As_4(SiiPr$_3$)$_3$]$^+$, [Sb_4(AsSiiPr$_3$)$_3$]$^+$, [Sb_4As_3(SiiPr$_3$)$_2$]$^+$, [Sb_2(AsSiiPr$_3$)$_2$]$^+$ can be observed.

The novel bicyclic compound **3** was isolated as yellow crystals from the LiBr elimination reaction of tBuPh$_2$SiPLi$_2$ and SbBr$_3$ in a 3:2 molar ratio. The compound crystallizes in the triclinic space group $P\bar{1}$. It is composed of five-membered P_3Sb_2 and three-membered PSb_2 rings sharing a common Sb_2 bridgehead (Figure 3). Both the P and the Sb atoms are three-coordinate, with the antimony atoms possessing no exocyclic ligands. The central Sb_2P_4 unit shows a non-planar configuration; the plane through Sb(1), Sb(2), P(4) is virtually perpendicular to the Sb_2P_3 ring. Examination of the bond lengths and angles found in the bicyclic Sb_2P_4 core of **3** indicates that there is a considerable amount of strain in this arrangement. The fold angles P(1)−Sb(1)−P(4) and P(3)−Sb(2)−P(4) are 86.11° and 104.3° respectively. The comparatively large difference between these angles results from the manner of orientation of the sterically demanding silyl groups coordinated to P(1) and P(3). The tBuPh$_2$Si substituent of P(1) is in a *trans* position to the Sb(1)−P(4) bond, whereas the silyl group bonded to P(3) is in a *cis* position to the Sb(2)−P(4) bond. The torsion angles Si(3)−P(3)−Sb(2)−P(4) and Si(1)−P(1)−Sb(1)−P(4) are 46.1° and 135.7° respectively. A similar molecular structure occurs in the homonuclear bicyclic compound tBu$_4$P$_6$ reported by Baudler and co-wor-

 © 2005 Wiley-VCH Verlag GmbH & Co. KGaA, Weinheim

kers.[13] However the arrangement of the *t*Bu groups in this structure is all-*trans*. Of particular interest in comparison of **3** with the other title compounds is the appearance of P−P bonds in the structure, resulting from oxidation of the P atoms and corresponding reduction of the Sb atoms to Sb−Sb bonds. The Sb−Sb bond in **3** is 276.8 pm, and is therefore shorter than the corresponding bonds in **1** and **2**. This bond shortening is possibly a consequence of the fact that the Sb_2 unit is bridged by the P(4) atom. The average P−P bond length is 219.6 pm, and the Sb−P bonds are 255.2 pm on average. These values lie in the usual range for single bonds between these elements.

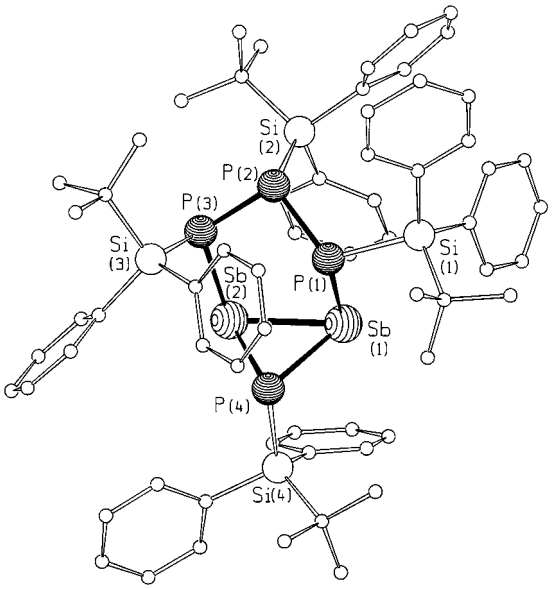

Figure 3. Molecular structure of **3**; selected bond lengths [pm] and angles [°]: Sb(1)−Sb(2) 276.8(2), Sb(1)−P(1) 255.3(2), Sb(1)−P(4) 255.3(2), Sb(2)−P(3) 255.9(2), Sb(2)−P(4) 254.4(2), P(1)−P(2) 219.9(2), P(2)−P(3) 219.9(2), P(1)−Si(1) 228.7(2), P(2)−Si(2) 229.4(2), P(3)−Si(3) 226.9(2), P(4)−Si(4) 227.8(2); Sb(1)−Sb(2)−P(4) 57.28(5), Sb(2)−Sb(1)−P(1) 92.63(4), Sb(2)−Sb(1)−P(4) 56.94(5), Sb(1)−P(4)−Sb(2) 65.77(6), Sb(1)−P(1)−P(2) 110.71(7), Sb(2)−P(3)−P(2) 112.99(6), P(1)−P(2)−P(3) 99.86(8), P(1)−Sb(1)−P(4) 86.11(6), P(3)−Sb(2)−P(4) 104.30(6)

The structure of **3** can be deduced from $^{31}P\{^1H\}$ NMR spectrum (Figure 4), which shows at room temperature two triplet signals at $\delta = -245$ and -31 ppm for the P(4) and P(2) centres, respectively. An additional broad signal appears at $\delta = -120$ ppm. At +70 °C the signal at $\delta = -120$ ppm appears as a doublet of doublets, which is consistent with chemically identical P(1) and P(3) atoms (AM_2X spin system, $^1J_{P,P} = 400$, $^2J_{P,P} = 96$ Hz). At −50 °C the $^{31}P\{^1H\}$ NMR spectrum of **3** shows four multiplets corresponding to the four different P atoms observed in the crystal structure (AEMX spin system). The mass spectrum of **3** does not show the molecular peak, although the characteristic fragment $[(PSi\textit{t}BuPh_2)_3]^+$ is observed at $m/z = 810$.

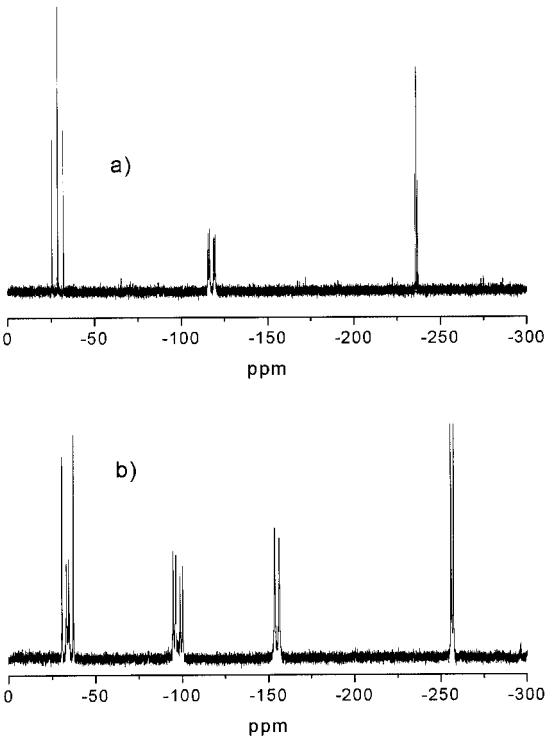

Figure 4. $^{31}P\{^1H\}$ NMR spectra of **3** in [D_8]toluene: a) at +70 °C, b) at −50 °C

Experimental Section

General: All manipulations were carried out with rigorous exclusion of oxygen and moisture, using a Schlenk line and nitrogen atmosphere. Solvents were dried and freshly distilled before use. The starting materials $i\text{Pr}_3\text{SiAsH}_2$ and $\text{ThexMe}_2\text{SiPH}_2$ were prepared according to relevant procedures found in the literature.[14] $SbCl_3$ and $SbBr_3$ were obtained from Aldrich and sublimed before use. The ^1H and ^{31}P NMR spectra were recorded on a Bruker AC 250 spectrometer. All isolated compounds gave elemental analyses consistent with their formulas.

***t*BuPh$_2$SiPH$_2$:** A solution of $t\text{BuPh}_2\text{SiCl}$ (41.2 g, 0.15 mol) in 50 mL of THF was added dropwise to a solution of $[(\text{dme})\text{LiPH}_2]$ (19.5 g, 0.15 mol) in 150 mL of THF at 0 °C. After stirring the mixture overnight at room temperature, the THF was replaced by 100 mL of pentane. The precipitated lithium chloride was subsequently removed by filtration. After removal of the solvent, a vacuum distillation yielded 20 g (50%) of $t\text{BuPh}_2\text{SiPH}_2$, B.p.: 100−103 °C ($10^{-3}$ mbar). ^1H NMR (C_6D_6): $\delta = 1.20$ [s, 9 H, $C(CH_3)_3$], 1.73 (d, $^1J_{P,H} = 187$ Hz, 2 H, PH_2), 7.26 (m, 5 H, Ph), 7.78 (m, 5 H, Ph) ppm. $^{13}C\{^1H\}$ NMR (C_6D_6): $\delta = 19.8$ [d, $^2J_{P,C} = 21.5$ Hz, $C(CH_3)_3$], 28.1 [d, $^3J_{P,C} = 6.8$ Hz, $C(CH_3)_3$], 129.9 (s, Ph), 135.7 (d, $J_{P,C} = 8.9$ Hz, Ph), 136.3 (d, $J_{P,C} = 8.9$ Hz, Ph). ^{31}P NMR (C_6D_6): $\delta = -252.2$ (t, $^1J_{P,H} = 187$ Hz) ppm.

1: *n*-Butyllithium [1.2 mL (1.92 mmol) of a 1.6 M solution] was added to a solution of $\text{ThexMe}_2\text{SiPH}_2$ (0.17 g, 0.96 mmol) in 5 mL of Et_2O at 0 °C. After stirring for 10 min, this solution was added to a solution of $SbCl_3$ (0.15 g, 0.64 mmol) in 15 mL of toluene at

 © 2005 Wiley-VCH Verlag GmbH & Co. KGaA, Weinheim

Table 1. Crystallographic data for **1**−**3**[7]

	1	**2**	**3**
Empirical formula	$C_{32}H_{76}P_4Sb_4Si_4$	$C_{36}H_{84}As_4Sb_4Si_4$	$C_{64}H_{76}P_4Sb_2Si_4$
Space group	$P4_2/n$	$C2/c$	$P\bar{1}$
Formula units	2	8	2
Temperature	220 K	200 K	200 K
Lattice constants	a = 1881.7(3) pm	a = 2691.7(5) pm	a = 1391.8(3) pm
	b = 1881.7(3) pm	b = 1620.5(3) pm	b = 1414.0(3) pm
	c = 698.8(1) pm	c = 2655.6(5) pm	c = 2133.2(4) pm
	α = 90°	α = 90°	α = 106.25(3)°
	β = 90°	β = 110.27(3)°	β = 92.17(3)°
	γ = 90°	γ = 90°	γ = 118.74(3)°
Volume	2474.3(7) Å^3	10866(4) Å^3	3459.0(12) Å^3
Density	1.589 g/cm^3	1.723 g/cm^3	1.272 g/cm^3
2Θ range	3−46°	3−48°	3.5−52°
Reflections measured	3571	15734	12686
Independent reflections	1697 (R_{int} = 0.0304)	7299 (R_{int} = 0.0476)	9753 (R_{int} = 0.0525)
Independent reflections with $F_o > 4\sigma(F_o)$	1246	5693	7520
Parameters	100	422	667
μ(Mo-K_α)	2.407 mm^{-1}	4.496 mm^{-1}	0.977 mm^{-1}
$R1$	0.0351	0.0598	0.0536
$wR2$ (all data)	0.0962	0.1796	0.1565
Residual electron density	0.664 e/Å^3	2.539 e/Å^3	1.266 e/Å^3

−70 °C. The reaction mixture was allowed to warm to −35 °C and then kept at the same temperature for an additional 12 h. The resulting orange solution was filtered to remove the precipitated LiCl and cooled to −35 °C. Orange crystals of **1** were obtained over a period of 5 d. Yield: 0.05 g (26%). $C_{32}H_{76}P_4Sb_4Si_4$ (1184.2): calcd. C 32.46, H 6.47; found C 32.89, H 6.46. ^{1}H NMR (C_6D_6): δ = 0.39 (s, 24 H, SiCH_3), 1.08 (m, 48 H, overlap of SiCCH_3 and SiCCCH_3), 2.14 [sept, $^3J_{H,H}$ = 6.9 Hz, 4 H, SiCH(CH$_3$)$_2$] ppm. ^{31}P{^{1}H} NMR (C_6D_6): δ = −104.5 (s) ppm. MS (EI, 70 eV, 200 °C): m/z (%) = 1184 (13) [M$^+$], 1041 (100) [M$^+$ − SiThexMe$_2$], 949 (9.4) [Sb$_3$P$_4$Me$_2$(SiThexMe$_2$)$_3$]$^+$. IR (KBr): $\tilde{\nu}$ = 2957 (s), 2867 (m), 1459 (m), 1389 (w), 1376 (m), 1363 (w), 1261 (m), 1241 (s), 1088 (m), 1033 (m), 915 (w), 870 (m), 835 (s), 798 (vs), 773 (w), 760 (w), 685 (w), 666 (m), 601 (m), 501 (w), 441 (s) cm^{-1}.

2: *n*-Butyllithium [1.13 mL (1.81 mmol) of a 1.6 M solution] was added to a solution of *i*Pr$_3$SiAsH$_2$ (0.21 g, 0.9 mmol) in 10 mL of Et$_2$O at 0 °C. After warming to room temperature, the solution of *i*Pr$_3$SiAsLi$_2$ was added to a solution of SbCl$_3$ (0.14 g, 0.60 mmol) in 15 mL of Et$_2$O at −70 °C. The red mixture was subsequently warmed to −35 °C while stirring and kept at the same temperature overnight. After filtration and cooling of the solution to −35 °C red crystals of **2** crystallised over a period of 5 d. Yield: 0.06 g (29%) $C_{36}H_{84}As_4Sb_4Si_4$ (1416.1): calcd. C 30.53, H 5.98; found C 31.24, H 6.09. MS (EI, 70 eV, 200 °C): m/z (%) = 1416 (11) [M$^+$], 1259 (36) [M$^+$ − Si*i*Pr$_3$], 1184 (19) [Sb$_4$(AsSi*i*Pr$_3$)$_3$]$^+$, 1027 (23) [Sb$_4$As$_3$(Si*i*Pr$_3$)$_2$]$^+$, 708 (19) [M/2]$^+$. IR (KBr): $\tilde{\nu}$ = 2937 (vs), 2861 (vs), 1457 (s), 1382 (m), 1362 (m), 1288 (w), 1261 (m), 1226 (m), 1068 (m), 1018 (s), 989 (m), 966 (w), 915 (m), 875 (s), 803 (m), 660 (s), 630 (vs), 588 (m), 555 (s) 499 (vs), 466 (m), 419 (w) cm^{-1}.

3: *n*-Butyllithium [1.15 mL (1.84 mmol) of a 1.6 M solution] was added to a solution of *t*BuPh$_2$SiPH$_2$ (0.25 g, 0.92 mmol) in 5 mL of Et$_2$O at 0 °C. The resulting yellow solution was added dropwise at −70 °C to a stirred solution of SbBr$_3$ (0.22 g, 0.61 mmol) in 15 mL of toluene. The purple-red mixture was allowed to warm to room temperature and stirred for an additional 16 h. The solvent was removed in vacuo and the residue was dissolved in 5 mL of heptane. After filtration and cooling of the solution to 0 °C yellow crystals of **3** were obtained over a period of 3 d. Yield: 0.20 g (66%). $C_{64}H_{76}P_4Sb_2Si_4$ (1325.0): calcd. C 58.01, H 5.78; found C 57.14, H 6.28. ^{1}H NMR ([D$_8$]toluene): δ = 1.16 (s, 9 H, Si*t*Bu), 1.21 (s, 9 H, Si*t*Bu), 1.33 (s, 18 H, Si*t*Bu), 6.78 (m), 7.19 (m), 7.28 (m), 7.43 (m), 7.68 (m), 7.93 (m) (all Si−Ph, 40 H) ppm. ^{31}P{^{1}H} NMR ([D$_8$]toluene, 70 °C): δ = −235.6 (t, $^2J_{P,P}$ = 96 Hz), −117.3 (dd, $^1J_{P,P}$ = 400, $^2J_{P,P}$ = 96 Hz), −28.8 (t, $^1J_{P,P}$ = 400 Hz) ppm. MS (EI, 70 eV, 210 °C): m/z (%) = 810 (100) [(PSi*t*BuPh$_2$)$_3$]$^+$, 753 (29) [P$_3$(Si*t*BuPh$_2$)$_2$SiPh$_2$]$^+$, 239 (33) [Si*t*BuPh$_2$]$^+$. IR (KBr): $\tilde{\nu}$ = 2940 (vs), 2862 (vs), 2097 (w), 1703 (vs, br), 1461 (s), 1379 (m), 1362 (m), 1293 (w), 1227 (m), 1157 (vw), 1068 (m), 1049 (m), 1014 (m), 992 (s), 881 (vs), 700 (vs), 633 (vs), 570 (s), 502 (s), 465 (s), 380 (m) cm^{-1}.

X-ray Crystallography: A summary of the crystallographic data for all three compounds can be found in Table 1 and ref.[7]

Acknowledgments

The authors thank Dr. Dale Cave for his valuable help with the manuscript and Prof. Dr. D. Fenske for helpful discussions and for providing excellent working conditions.

[1] Review articles: [1a] L. Balázs, H. J. Breunig, *Coord. Chem. Rev.* **2004**, *248*, 603−621. [1b] H. J. Breunig, R. Rösler, *Coord. Chem. Rev.* **1997**, *163*, 33−53. [1c] M. Baudler, *Angew. Chem.* **1987**, *99*, 429−451; *Angew. Chem. Int. Ed. Engl.* **1987**, *26*, 419−441. [1d] M. Baudler, *Angew. Chem.* **1982**, *94*, 520−539; *Angew. Chem. Int. Ed. Engl.* **1982**, *21*, 492−512.

[2] [2a] J. Hahn, M. Baudler, *Z. Naturforsch., Teil B* **1982**, *37*, 797−805. [2b] O. Mundt, G. Becker, H.-J. Wessely, *Z. Anorg. Allg. Chem.* **1982**, *486*, 70−89. [2c] M. Baudler, P. Bachmann, *Angew. Chem.* **1981**, *93*, 112−113; *Angew. Chem. Int. Ed. Engl.* **1981**, *20*, 123−124.

[3] [3a] M. Westerhausen, S. Weinrich, P. Mayer, *Z. Anorg. Allg. Chem.* **2003**, *629*, 1153−1156. [3b] G. Linti, W. Köstler, *Z. Anorg. Allg. Chem.* **2002**, *628*, 63−66. [3c] C. von Hänisch, D. Fenske, *Z. Anorg. Allg. Chem.* **1997**, *623*, 1040−1042. [3d] M.

 © 2005 Wiley-VCH Verlag GmbH & Co. KGaA, Weinheim

Baudler, H. Jachow, B. Lieser, K.-F. Tebbe, M. Fehér, *Angew. Chem.* **1989**, *101*, 1245−1247; *Angew. Chem. Int. Ed. Engl.* **1989**, *28*, 1231−1232. [3e] C. Mujica, D. Weber, H.-G. Schnering, *Z. Naturforsch., Teil B* **1986**, *41*, 991−999. [3f] M. Baudler, S. Wietfeldt-Haltenhoff, *Angew. Chem.* **1985**, *97*, 986−987; *Angew. Chem. Int. Ed. Engl.* **1985**, *24*, 991−992. [3g] M. Baudler, S. Wietfeldt-Haltenhoff, *Angew. Chem.* **1984**, *96*, 361−362; *Angew. Chem. Int. Ed. Engl.* **1984**, *23*, 379−380. [3h] M. Baudler, P. Bachmann, *Z. Anorg. Allg. Chem.* **1982**, *485*, 129−132. [3i] M. Baudler, J. Hellmann, P. Bachmann, K.-F. Tebbe, R. Fröhlich, M. Feher, *Angew. Chem.* **1981**, *91*, 415−417; *Angew. Chem. Int. Ed. Engl.* **1981**, *20*, 406−407. [3j] H.-G. von Schnering, D. Fenske, W. Hönle, M. Binnewies, K. Peters, *Angew. Chem.* **1979**, *91*, 755−756; *Angew. Chem. Int. Ed. Engl.* **1979**, *18*, 679. [3k] A. Tzschach, V. Kiesel, *J. Prakt. Chem.* **1971**, *313*, 259−264.

[4] [4a] M. Baudler, S. Klautke, *Z. Naturforsch., Teil B* **1981**, *36*, 527−531. [4b] M. Baudler, D. Habermann, *Angew. Chem.* **1979**, *91*, 939−940; *Angew. Chem. Int. Ed. Engl.* **1979**, *18*, 877−878.

[5] [5a] A. Bashall, F. Garcia, G. T. Lawson, M. McPartlin, A. Rothenberger, A. D. Woods, D. S. Wright, *Can. J. Chem.* **2002**, *80*, 1421−1427. [5b] P. Jutzi, U. Meyer, S. Opiela, M. Olmstead, P. P. Power, *Organometallics* **1990**, *9*, 1459−1463. [5c] M. Baudler, Y. Aktalay, T. Heinlein, K.-F. Tebbe, *Z. Naturforsch., Teil B* **1982**, *37*, 299−305.

[6] A. R. J. Genge, N. J. Hill, W. Levason, G. Reid, *J. Chem. Soc., Dalton Trans.* **2001**, 1007−1012.

[7] STOE-IPDS2 (Mo-K_α radiation, λ = 0.71073 Å). The structures were solved by direct methods and refined by full-matrix least-squares techniques against F^2 (Sb, As, P, Si, C refined anisotropically, H atoms were calculated at ideal positions). CCDC-242997 (**1**), -242995 (**2**) and -242996 (**3**) contain the supplementary crystallographic data for this paper. These data can be obtained free of charge via www.ccdc.cam.ac.uk/conts/retrieving.html (or from Cambridge Crystallographic Data Centre, 12 Union Road, Cambridge CB2 1EZ, UK; Fax: + 44-1223-336-033; E-mail: deposit@ccdc.cam.ac.uk).

[8] G. Becker, H. Freudenblum, C. Witthauer, *Z. Anorg. Allg. Chem.* **1982**, *492*, 37−51.

[9] [9a] G. Balázs, H. J. Breunig, E. Lork, S. Mason, *Organometallics* **2003**, *22*, 576−585. [9b] H. J. Breunig, R. Rösler, E. Lork, *Angew. Chem.* **1997**, *109*, 2333−2334; *Angew. Chem. Int. Ed. Engl.* **1997**, *36*, 2237−2238.

[10] M. A. Beswick, N. Choi, A. D. Hopkins, M. McPartlin, M. E. G. Mosquera, P. R. Raithby, A. Rothenberger, D. Stalke, A. J. Wheatley, D. S. Wright, *Chem. Commun.* **1998**, 2485−2486.

[11] [11a] M. Baudler, B. Koll, C. Adamek, R. Gleiter, *Angew. Chem.* **1987**, *99*, 371−373; *Angew. Chem. Int. Ed. Engl.* **1987**, *26*, 347−348. [11b] M. Baudler, V. Arndt, *Z. Naturforsch., Teil B* **1984**, *39*, 275−283.

[12] [12a] M. Scheer, U. Becker, E. Matern, *Chem. Ber.* **1996**, *129*, 721−724. [12b] M. E. Barr, B. R. Adams, R. R. Weller, L. F. Dahl, *J. Am. Chem. Soc.* **1991**, *113*, 3052−3060.

[13] M. Baudler, Y. Aktalay, K.-F. Tebbe, T. Heinlein, *Angew. Chem.* **1981**, *93*, 1020−1022; *Angew. Chem. Int. Ed. Engl.* **1981**, *20*, 967−969.

[14] [14a] M. Westerhausen, M. Wieneke, W. Schwarz, *J. Organomet. Chem.* **1999**, *572*, 249−257. [14b] H. R. G. Bender, M. Nieger, E. Niecke, *Z. Naturforsch., Teil B* **1993**, *48*, 1742−1752.

Received July 4, 2004
Early View Article
Published Online November 24, 2004

 © 2005 Wiley-VCH Verlag GmbH & Co. KGaA, Weinheim

Electronic Interactions in Ferrocene- and Ruthenocene-Functionalized Tetraazamacrcocyclic Ligand Complexes of $Fe^{II/III}$, Co^{II}, Ni^{II}, Cu^{II} and Zn^{II}

Peter Comba,*[a] Gerald Linti,[a] Kathrin Merz,[a] Hans Pritzkow,[a] and Franz Renz[b]

Keywords: Macrocyclic ligands / Transition metals / Ferrocene / Ruthenocene

The syntheses of ferrocene- and ruthenocene-functionalized tetraazamacrocyclic ligands and their corresponding transition metal complexes are described. Reaction of *N*,*N*′-bis(2-aminoethyl)-1,3-propanediamine (2,3,2-tet) with 1,1′-diformylferrocene and 1,1′-diformylruthenocene produces the ligands fcmac and rcmac in 81–85% yield. Examination of their Cu^{II}, Ni^{II}, Co^{II}, Zn^{II} and $Fe^{II/III}$ complexes by IR, UV/Vis, EPR and Mössbauer spectroscopy as well as by electrochemical studies suggests electronic communication between the two metal centers of each complex. The molecular structure of $[Cu^{II}(fcmac)(FBF_3)]BF_4$, determined by X-ray structure analysis, is reported and shows that the distance between the two metals is 4.54 Å. Stability constants, determined by potentiometric titration, indicate that the copper(II) complexes are of similar stability as those with unfunctionalized tetraazamacrocyclic ligands (e.g. cyclam = 1,4,8,11-tetraazacyclotetradecane); stability constants of cobalt(II) complexes are about 2 log units smaller, those of nickel(II) and zinc(II) complexes are reduced by more than 10 log units. This selectivity is discussed on the basis of the structural studies.
(© Wiley-VCH Verlag GmbH & Co. KGaA, 69451 Weinheim, Germany, 2005)

Introduction

A large variety of metallocene-functionalized macrocyclic ligands have been reported, including crown ethers as well as polyaza- and polythiamacrocycles, Schiff-base and mixed-donor ligand systems, with various binding motifs of the metallocene functional groups.[1−11] With metal ions coordinated to the macrocyclic ligands, tunable energy- and electron transfer processes have been suggested, observed and studied,[12] and molecular switches as well as artificial regulatory systems have been designed.[4] The majority of applications, however, have used the macrocyclic ligands or the macrocyclic ligand complexes as selective receptors for cations or anions, and the metallocene (usually ferrocene) substituents as electrochemical probes, in order to construct highly selective electrochemical sensors.[2,5,9,10] An important feature in these applications is the interaction between the metallocene site and the metal ion coordinated to the macrocyclic donor set, and this has been studied by a variety of electrochemical and spectroscopic techniques.[2,4,5,11]

We report here the synthesis and the structural, electrochemical, and spectroscopic characterization of cyclam-derived ferrocene- and ruthenocene-containing macrocycles, based on a Schiff-base condensation of 2,3,2-tet [2,3,2-tet = *N*,*N*′-bis(2-aminoethyl)-1,3-propanediamine] with 1,1′-diformylmetallocene, and their iron(II)/(III), cobalt(II), nickel(II), copper(II), and zinc(II) complexes. The structural and electrochemical data together with the stability constants, determined by pH titrations, suggest that these ligands may be used as electrochemical sensors for specific metal ions (Cu^{II}), and preliminary Mössbauer spectra of the iron complexes indicate that optical as well as thermal switching between different electronic states is possible; this latter application is currently under further investigation. Here, we report the preparative and structural data as well as stability constants, the spectroscopic and electrochemical characterization of the ligands and their complexes.

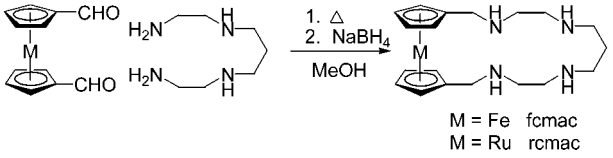

Results and Discussion

Syntheses and Structures

The synthesis of the ferrocene- and ruthenocene-substituted ligands fcmac and rcmac is a simple [1+1] Schiff-base condensation, followed by $NaBH_4$ reduction of the imines, which proceeds, as in published examples of similar ligands,[9] in high over-all yield (over 80%). Complexation

[a] Universität Heidelberg, Anorganisch-Chemisches Institut, INF 270
69120 Heidelberg, Germany
Fax: (internat.) + 49-6226-548453
E-mail: peter.comba@aci.uni-heidelberg.de
[b] Universität Mainz, Institut für Anorganische und Analytische Chemie
Duesbergweg 10−14, 55099 Mainz

to iron(II)/(III), cobalt(II), nickel(II), copper(II), and zinc(II) results in dinuclear complexes in respectable yields.

The single crystal structure of $[Cu(fcmac)(FBF_3)]BF_4$ was solved by X-ray crystallography. A plot of the molecular structure is given in Figure 1 (a), and selected structural parameters are presented in Table 1. Crystals of $[Ni(fcmac)(NCCH_3)_2](BF_4)_2$ and $[Ni(rcmac)(NCCH_3)_2](BF_4)_2$ were also isolated but were not of high enough quality for a full structural analysis and submission of the data to CCDC. However, plots of these two structures also appear in Figure 1, and the determined approximate structural parameters are tabulated for comparison. The macrocycles are in the unusual *trans*-II (*S*,*S*,*R*,S; pseudo-*R*,S,*R*,*R*) configuration. This must be due to the unusually large and rigid ferrocene-appended chelate ring. However, the fact that all Cu−N distances (and the Ni−N distances) are in the expected ranges[13] indicates that little strain is imposed by the ferrocene or ruthenocene group on the macrocyclic ligand complex. This also follows from the other structural parameters; only the N1−M−N4 angles are slightly larger than usual. Another indication for the fairly strain-free geometry of the macrocyclic ligand copper(II) complex are the spectroscopic and electrochemical parameters and stability constants, which are all as expected for cyclam-type tetraazamacrocyclic ligand copper(II) complexes (see Tables 2 and 3 below; note, however, the stability constants of the other transition metal complexes and the relevant discussion). With respect to the geometry of the substituted metallocene group, the three structures are very similar to each other. The two Cp rings are staggered, and the only significant distortion is a small tilt of the two Cp planes by 5−7°, because of the coordination of the copper(II) or nickel(II) centers to the methylamine substituents at the Cp rings. The angles between the averaged Cp and the macrocycle planes are around 35°. The fact that, in terms of spectroscopic and electrochemical properties, all other macrocyclic ligand complexes show similar trends suggests that the structures of the complexes for which no structural data are available are also similar to those reported here.

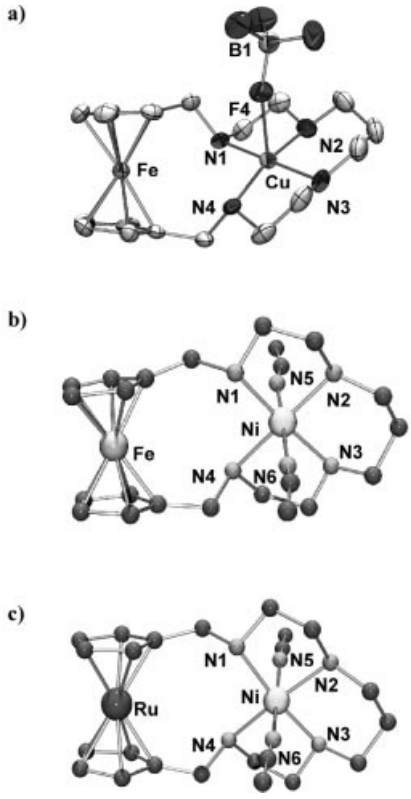

Figure 1. Structural plots of the molecular cations of $[Cu(fcmac)(FBF_3)]BF_4$, $[Ni(fcmac)(NCCH_3)_2](BF_4)_2$, and $[Ni(rcmac)(NCCH_3)_2](BF_4)_2$ (the structures of the two nickel complexes are of low quality and appear only for comparison (see text)

Complex Stabilities

Because of problems with the solubility of the ferrocene- and ruthenocene-appended macrocycles, the protonation constants and complex stabilities were determined in 1,4-dioxane/water mixtures. Similar solvent mixtures have been used for other ferrocene-functionalized macrocycles,[11] and those for cyclam (1,4,8,11-tetraazacyclotetradecane) have also been determined here under the same conditions for comparison (see Table 2). The two new ligands fcmac and rcmac have similar protonation constants, and these are also similar to those of another published ferrocene-functionalized cyclam ligand, FcCyclam, which is the 1,1′-ferrocenebis(methyl)-bridged 1,8-substituted cyclam ligand, bridged at 1,8-positions,[11] but the amine donors are significantly less basic than those of the unfunctionalized cyclam macrocycle. For the discussion of the complex stabilities we will concentrate here primarily on the complex formation constants of $[M(L)]^{2+}$, with L = fcmac, rcmac, FcCyclam and cyclam, and M = Cu^{2+}, as well as Co^{2+}, Ni^{2+}, and Zn^{2+}. The complex stabilities with fcmac and rcmac are nearly identical, and, as seen in the Cu^{2+} systems, they are significantly larger than those for the FcCyclam ligand system ($\Delta\log K \approx 10$). Note that the difference in solvent (water/dioxane, 3:7 vs. 7:3) probably does not lead to these large differences {$[Cu(cyclam)]^{2+}$ in H_2O: $\log K = 27.2$;[14] in water/dioxane, 3:7: $\log K = 23.5$} and the stability is smaller than that for cyclam ($\Delta\log K \approx 3$). The reduced stability (vs. cyclam) is due to a distortion from planarity of the CuN_4 chromophore (see below) and the interaction with the metallocene site. The difference between the fcmac/rcmac systems on one hand and FcCyclam on the other, which is also obvious from the protonation constants, must partially be due to the significantly different Fe···M (Cu) distances (4.5 Å, see Table 1, vs. 3.8 Å).[11]

More interesting is the variation of stabilities along the transition metal series. This usually follows the Irving−Williams series,[15] and for cyclam the corresponding $\log K$ values (measured in water)[16] for nickel(II), copper(II), and zinc(II) are 19.4, 27.2, and 15.5, respectively. It appears that fcmac and rcmac stabilize in particular copper(II); cobalt(II) and zinc(II) have stabilities which are a little lower than expected (see above), but nickel(II) is strongly destabilized. We attribute this behavior to the enforced *trans*-II configuration, which must be a result of the large and rather rigid ferrocene-appended chelate ring,

 © 2005 Wiley-VCH Verlag GmbH & Co. KGaA, Weinheim

Table 1. Selected structural parameters of $[Cu(fcmac)(FBF_3)]BF_4$, $[Ni(fcmac)(NCCH_3)_2](BF_4)_2$, and $[Ni(rcmac)(NCCH_3)_2](BF_4)_2$ (the data of the two nickel complexes are of low quality and appear only for comparison, see text)

	$[Cu(fcmac)(FBF_3)]BF_4$ M′ = Fe, M = Cu	$[Ni(fcmac)(NCCH_3)_2](BF_4)_2$ M′ = Fe, M = Ni	$[Ni(rcmac)(NCCH_3)_2](BF_4)_2$ M′ = Ru, M = Ni
Distances [Å]			
M−N1	2.062(3)	2.09(3)	2.140(9)
M−N2	2.016(3)	2.05(3)	2.10(1)
M−N3	2.032(3)	2.16(3)	2.083(9)
M−N4	2.039(3)	2.16(3)	2.134(9)
M−X	2.428(4)(F4)	2.14(3)(N5)	2.09 (1)(N5)
		2.01(3)(N6)	2.16(1)(N6)
M′−Cp[a]	1.63, 1.64	1.63, 1.64	1.88
N_4-plane (rms)	0.16	0.01	0.01
M-plane	0.12	0.05	0.05
M′···M	4.54	4.88	4.88
Angles [°]			
N1−M−N4	96.8(1)	98(1)	101.4(4)
N1−M−N2	86.5(1)	84(1)	84.1(4)
N4−M−N3	85.1(1)	85(1)	84.3(4)
N3−M−N2	91.2(1)	92(1)	90.0(4)
Φ [b]	37.1	10.7	10.6
θ [c]	6.9	6.6	5.4
τ [d]	34.5	33.2	30.0
α [e]	11.6°	3.9	5.1°

[a] Distance to the centroid of the Cp ring (Fe−Cp: 1.641).[27] [b] Torsional angle between the two Cp rings (amine substituents). [c] Tilt angle between the two Cp planes. [d] Angle between the average of the two Cp planes and the N_4 best plane. [e] Averaged tetrahedral twist of the MN_4 chromophores.

Table 2. Potentiometrically determined protonation and complex stability constants (log K values) of fcmac, rcmac and other tetraazamacrocyclic ligands [water/dioxane, 30:70, T = 25 °C, μ = 0.1 M (KCl)]

Protonation constants	fcmac	rcmac	FcCyclam[11] [a]	cyclam
$L + H^+ \rightleftarrows [LH]^+$	9.77	10.05	9.21	11.10
$L + 2H^+ \rightleftarrows [LH_2]^{2+}$	17.75	18.10	15.27	21.80
$L + 3H^+ \rightleftarrows [LH_3]^{3+}$	23.35	23.2	18.46	24.70
$L + 4H^+ \rightleftarrows [LH_4]^{4+}$	27.40	26.0	–	26.00

Stability constants	Cu/Fcmac	Cu/rcmac	Cu/FcCyclam	Cu/Cyclam	Co/fcmac	Co/rcmac	Ni/fcmac	Ni/rcmac	Zn/fcmac	Zn/rcmac
$M^{2+} + L + 2H^+ \rightleftarrows [MLH_2]^{4+}$	26.50	26.00	–	–	26.0	26.0	21.3	–	20.5	20.0
$M^{2+} + L + H^+ \rightleftarrows [MLH]^{3+}$	24.00	23.00	13.9	29.0	23.0	23.0	15.8	15.5	15.6	15.1
$M^{2+} + L \rightleftarrows [ML]^{2+}$	20.40	20.50	9.3	23.5	18.0	18.0	9.6	9.6	8.5	10.2
$M^{2+} + L + OH^- \rightleftarrows [ML(OH)]^+$	6.80	7.30	−3.3	9.5	12.0	12.0	0.7	1.8	0.2	2.1
$M^{2+} + L + 2OH^- \rightleftarrows [ML(OH)_2]$	–	–	–	–	4.1	6.3	–	–	–	–

[a] In water/dioxane, 30:70.

which enforces a considerable tetrahedral twist. The tetrahedral twist angles (angle between the planes N2/N3/Cu and N1/N4/Cu) for Cu(fcmac), Ni(fcmac), and Cu(cyclam) are 12°, 4°, and 0°, respectively. A deformation from planarity of the $M(N_4)$ chromophore is more destabilizing for nickel(II) than for copper(II), and the result in the present case (see structural parameters above) leads both to a substantial electronic destabilization and an increase in ligand strain for nickel(II). Probably, it is primarily ligand strain which leads to the relatively low stability of the nickel(II) complex. The result is a strong preference for copper(II), and this selectivity is an important prerequisite for efficient copper-selective sensors, based on fcmac, rcmac, and corresponding derivatives.

Spectroscopy and Electrochemistry

The guest-dependent shift of the Fc/Fc^+ couple in ferrocene-substituted host molecules has often been used to analyze the interaction between the ferrocene iron center and a guest molecule. With cationic guests (metal ions) the reduced form is generally stabilized (shifts towards more positive potentials by a few hundred millivolts).[6,17−20] Primarily, this is due to electrostatic effects, but direct electronic interactions might also contribute (see data in Table 3, see also below).[21] Similar shifts were also observed for the Rc/Rc^+ couple in complexes with rcmac ($[Cu(rcmac)](BF_4)_2$ 834 mV, $[Ni(rcmac)(NCCH_3)_2](BF_4)_2$ 716 mV, measured vs. $Ag/AgNO_3$ under the same conditions). The ligand rcmac

 © 2005 Wiley-VCH Verlag GmbH & Co. KGaA, Weinheim

Table 3. Electrochemical and spectroscopic data of fcmac and the corresponding complexes

Compound	E_p (ΔE_p)[a] [mV]	IR C−H out-of-plane[c] [cm^{-1}]	Mössbauer[b] δ_{IS} [mm/s]	Mössbauer[b] ΔE_Q [mm/s]
Ferrocene	87	815	0.416	2.370
fcmac	109 (47)	840[d]	–[e]	–
fcmac·HCl	–[f]	–	0.392	2.350
$[Cu(fcmac)(FBF_3)]BF_4$	308 (50)	820	0.423	2.410
$[Ni(fcmac)(NCCH_3)_2](BF_4)_2$	233 (87)	816	0.403; 0.384	2.390; 2.254
$[Zn(fcmac)](ClO_4)_2$	264 (82)	–	0.380; 0.407	2.231; 2.368
$[Co(fcmac)](BF_4)_2$	–[g]	812	0.387; 0.404	2.201; 2.374
$[Fe(fcmac)](SCN)_3$	–[h]	809	0.397; 0.250	2.323; 0.515
$[Fe(fcmac)]Fe(SO_4)_2$	–[h]	809	–	–
$[Cu(fcmac)(BF_4)_2]PF_6$	–[f]	834	0.394; 0.405	2.250; 0.435

[a] CH_3CN, 0.1 M Bu_4NPF_6, 298 K, Fc/Fc^+-centered process. [b] Relative to Co in Rh, 10 K. [c] KBr pellets. [d] $Fcmac^+PF_6^-$. [e] Ligand is a liquid. [f] Decomposition during measurement. [g] Irreversible oxidation. [h] Insoluble in all common solvents.

itself decomposes under the measurement conditions and therefore gives no interpretable voltammogram.

Another efficient tool to analyze metal···metal interactions in ferrocene-appended host molecules is the C−H out-of-plane bending vibration in ferrocene (815 cm^{-1}), shifted to higher energies (840 cm^{-1}) in the ferrocenium ion. The comparably small shifts[6] observed in the present examples indicate that the distance between the ferrocene (or ruthenocene) subunits and the guest metal ion is large, and that the metal···metal interaction is relatively weak. The fact that the shift with Cu^{2+} is largest correlates well with the observed reduction potentials, and this indicates that some electron transfer is involved.

Both the UV/Vis and the EPR spectra of $[Cu(fcmac)]^{2+}$ indicate that the CuN_4 plane is significantly distorted ($g_{x,y}$ = 2.06, g_z = 2.20, $A_{x,y}$ = 18 × 10^{-4} cm^{-1}, A_z = 197 × 10^{-4} cm^{-1}, λ_{max} = 557 nm; the corresponding data for a 15-membered N_4 macrocycle {$[Cu[15]ane\ N_4]^{2+}$; [15]ane N_4] = 1,4,8,12-tetraazacyclopentadecane, which is known to have a tetrahedral distortion similar to that of $[Cu(fcmac)]^{2+}$, with a twist angle of 16°},[22] are 2.05, 2.19, 24 × 10^{-4}, 194 × 10^{-4}, 582, respectively). This is as expected from the solid state structural data.

The isomer shifts δ_{IS} and quadrupole splitting values ΔE_Q in the ^{57}Fe Mössbauer spectra (10 K) of the fcmac complexes are also summarized in Table 3, where the corresponding values of ferrocene and fcmac·HCl appear for comparison. The parameters for fcmac·HCl (δ_{IS} = 0.392 mm s^{-1}, ΔE_Q = 2.350 mm s^{-1}) are typical for low-spin Fe^{II} in a metallocene coordination sphere and indicate, in comparison with ferrocene (δ_{IS} = 0.416 mm s^{-1}, ΔE_Q = 2.370 mm s^{-1}), a reduced electron density at the nucleus and an increased distortion of the iron center. The linear correlation of the reduction potentials with the isomer shifts[23] (see Figure 2) is significant and reflects primarily the electrostatic perturbation of the electronic properties of the ferrocene iron centers. For the Ni^{II}, Zn^{II}, and Co^{II} complexes of fcmac two slightly different doublets were observed, and upon irradiation (Ar laser, 514.5 nm) the relative populations were altered.[24] Preliminary results suggest that the corresponding Fe^{II} and Fe^{III} complexes, $[Fe(fcmac)]Fe(SO_4)_2$ and $[Fe(fcmac)](SCN)_3$, appear as thermally and optically induced switches. These features are currently under thorough investigation and will be published in due course.

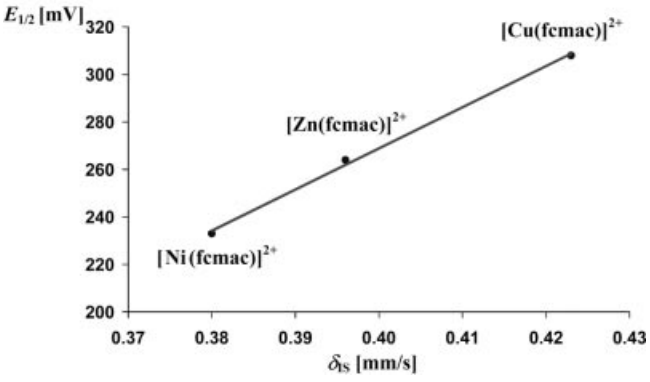

Figure 2. Correlation of the reduction potentials of $[Cu(fcmac)]^{2+}$, $[Ni(fcmac)]^{2+}$, and $[Zn(fcmac)]^{2+}$ with the corresponding Mössbauer isomer shifts

Conclusion

Two novel tetraazamacrocyclic ligands with metallocene (Fe, Ru) bridges and their heterodinuclear transition metal complexes [iron(II)/(III), cobalt(II), nickel(II), copper(II), and zinc(II)] have been prepared and fully characterized. The two main features are (i) that there is significant electronic communication between the metal centers, and this is due to a relatively short metal···metal distance {4.54 Å in the structurally characterized $[Cu(fcmac)(FBF_3)]BF_4$ complex}, and (ii) that the complex stabilities with the two macrocycles do not follow the usual Irving−Williams-type behavior; the copper(II) complexes have stabilities which are, as expected, similar to those with tetraazamacrocycles with the usual alkyl bridges; the nickel(II) complexes are unusually unstable. This is probably due to the uncommon *trans*-II configuration of the metallocene-substituted macrocycle, which induces considerable strain on and a distortion from planarity of the macrocycle.

 © 2005 Wiley-VCH Verlag GmbH & Co. KGaA, Weinheim

Experimental Section

Measurements and Materials: Commercially available solvents and reagents were used without further purification. The syntheses of the ligands were carried out under argon. 1,1′-Diformylferrocene and 1,1′-diformylruthenocene were prepared as described in the literature.[25] NMR spectra were recorded with a Bruker AS 200 (^{1}H NMR 200.13 MHz, ^{13}C NMR 50.33 MHz) spectrometer. The spectra were referenced to the solvent signals. Mass spectra were recorded with a Finnigan 8400 instrument. IR spectra were recorded with a Perkin−Elmer 16C spectrometer as KBr pellets. UV/Vis spectra were measured with a Varian Cary 1E spectrometer in MeOH or MeCN. Potentiometric titrations were carried out in 1,4-dioxane/water (30:70 v/v, 0.1 M KCl) using a reaction vessel thermostatted at 25.0 ± 0.1 °C under nitrogen. The computer program HYPERQUAD[14,26] was used to calculate the protonation and stability constants. The concentrations of the ligands were 0.05 mmol/L; 0.8 equiv. of metal salts were used. Electrochemical measurements were obtained with a BAS100 W electrochemical analysis instrument. A glassy carbon working electrode and a platinum auxiliary electrode were used; 2×10^{-3} M solutions in CH_3CN with tetrabutylammonium hexafluorophosphate (0.1 M). Potentials were measured relative to $Ag/AgNO_3$ (0.01 M $AgNO_3$). The scan rate was varied from 10 to 100 mV s^{-1}. EPR spectra were recorded with a Bruker ELEXSYS E500 spectrometer (X band) as approximately 10^{-3} mol L^{-1} frozen solutions (liquid N_2) in DMF/water, 2:1. XSophe, version 1.0.2β, on a Linux workstation was used for the simulation of the spectra. A standard transmission Mössbauer spectrometer was used. The ^{57}Co source was kept at room temperature and the isomeric shifts are relative to Co in Rh. An argon ion laser was used for the irradiation at 514.5 nm and 35 mW/cm^2. The Mössbauer spectra were fitted with the software MOSFUN and RECOIL.

Syntheses of the Ligands

fcmac: A solution of 1,1′-diformylferrocene (1.00 g, 4.13 mmol) and 2.3.2-tet (0.66 g, 4.13 mmol) in absolute methanol (40 mL) was refluxed for 4 h. After cooling to room temperature, $NaBH_4$ (0.48 g, 12.69 mmol) in degassed water (10 mL) was added, and the reaction mixture was stirred overnight. The solvent was evaporated, and the water phase was extracted with CH_2Cl_2 (3 × 20 mL). The collected organic extracts were filtered through Celite, and the solvent was evaporated, yielding 1.24 g (3.35 mmol, 81%) of a brown and highly viscous oil. ^{1}H NMR (CD_2Cl_2, 200.13 MHz): δ = 1.49−1.79 (m, 2 H, CH_2), 2.10 (br. s, 4 H, NH), 2.37−2.84 (m, 12 H, CH_2), 3.39 (s, 4 H, Cp−CH_2), 4.00−4.30 (m, 8 H, Cp−H) ppm. ^{13}C NMR (CD_2Cl_2, 50.33 MHz): δ = 28.7 (1 C, CH_2), 48.1 (2 C, CH_2), 49.1 (2 C, CH_2), 49.4 (2 C, Cp−CH_2), 67.3 (4 C, Cp), 67.8 (4 C, Cp), 88.5 (2 C, Cq, Cp) ppm. UV/Vis (MeOH): λ = 309 (ε = 733 M^{-1}cm^{-1}), 436 (ε = 251 M^{-1}cm^{-1}) nm. MS-FAB (NBA): *m/z* = 371.1 $[M + H]^+$.

rcmac: As described for fcmac, the reaction of 1,1′-diformylruthenocene (0.50 g, 1.74 mmol) with 2.3.2-tet (0.28 g, 1.74 mmol) in absolute methanol (20 mL), followed by reduction with $NaBH_4$ (0.20 g, 5.29 mmol) in degassed water (5 mL) yielded 0.61 g (1.48 mmol, 85%) of rcmac as a yellow and highly viscous oil. ^{1}H NMR (200 MHz, CD_2Cl_2): δ = 1.42−1.98 (m, 6 H, CH_2 and NH), 2.49−2.77 (m, 12 H, CH_2), 3.21 (s, 4 H, Cp−CH_2), 4.38 (m, 4 H, Cp−H), 4.54 (m, 4 H, Cp−H) ppm. ^{13}C NMR (CD_2Cl_2): 28.0 (1 C, CH_2), 49.7 (2 C, CH_2), 50.2 (4 C, CH_2), 50.3 (2 C, Cp-CH_2), 70.2 (4 C, Cp-C), 71.5 (4 C, Cp−C), 94.0 (2 C, C_q, Cp−C) ppm. MS-FAB (NBA): *m/z* = 417.2 $[M + H]^+$.

fcmac$^+$PF$_6$: A solution of fcmac (478 mg, 1.29 mmol) and ferrocenyl hexafluorophosphate (427 mg, 1.29 mmol) in abs. CH_2Cl_2 (20 mL) was stirred at room temperature for 2.5 h. It was filtered, and the solvent was evaporated. The resulting brown solid was washed with Et_2O until washings were colorless. Drying in vacuo yielded 371 mg (0.72 mmol, 56%) of a brown powder. MS-FAB (NBA): *m/z* = 514.3 $[M]^+$, 371.3 $[M - PF_6]^+$. UV/Vis (MeOH): λ = 317 (ε = 353 M^{-1}cm^{-1}), 440 (ε = 197 M^{-1}cm^{-1}) nm. IR: $\tilde{\nu}$ = 3235 (w), 3078 (w), 2932 (w), 2833 (w), 2358 (w), 1457 (m), 1106 (w), 1040 (w), 840 (s), 557 (m) cm^{-1}.

Metal Complexes of fcmac and rcmac: Complexes of fcmac and rcmac were obtained by reaction of equal amounts of ligand and metal salt in methanol (0.5 mmol in 5 mL) at room temperature and stirring overnight. The resulting precipitate was filtered off, washed with methanol, and dried in vacuo. If necessary the compounds were recrystallized from acetonitrile. Single crystals for X-ray diffraction were obtained by ether diffusion into complex solutions in acetonitrile.

[Cu(fcmac)(FBF$_3$)]BF$_4$: Yield 46% of a pink solid. $C_{19}H_{30}B_2CuF_8FeN_4$ (607.38): calcd. C 37.57, H 4.98, N 9.22; found C 37.67, H 5.19, N 8.95. MS-FAB (NBA): *m/z* = 607.1 $[Cu(fcmac)(BF_4)_2]^+$, 520.1 $[Cu(fcmac)(BF_4)]^+$, 433.1 $[Cu(fcmac)]^+$. UV/Vis (MeCN): λ = 411 (ε = 302 M^{-1}cm^{-1}), 557 (ε = 150 M^{-1}cm^{-1}) nm. IR: $\tilde{\nu}$ = 3252 (m), 2922 (w), 2870 (w), 2358 (m), 2336 (w), 1636 (w), 1456 (w), 1420 (w), 1082 (s), 880 (w), 820 (w), 522 (w), 478 (w) cm^{-1}. Single crystals were obtained by ether diffusion into an acetonitrile solution.

[Ni(fcmac)(NCCH$_3$)$_2$](BF$_4$)$_2$: Yield 23% of a brown solid. $C_{19}H_{30}B_2F_8FeN_4Ni$ (602.62): calcd. C 37.87, H 5.02, N 9.30; found C 38.72, H 5.37, N 8.92. UV/Vis (MeCN): λ = 310 (ε = 223 M^{-1}cm^{-1}), 436 (ε = 84 M^{-1}cm^{-1}) nm. IR: $\tilde{\nu}$ = 3534 (s), 3232 (s), 2942 (m), 2876 (m), 2358 (w), 1636 (m), 1462 (m), 1430 (m), 1058 (s), 816 (m), 764 (w), 520 (m), 484 (w) cm^{-1}.

[Zn(fcmac)](ClO$_4$)$_2$×MeOH: Yield 21% of a brown solid. $C_{20}H_{34}Cl_2FeN_4O_9Zn$ (666.65): calcd. C 36.03, H 5.14, N 8.40; found C 36.47, H 5.24, N 8.59.

[Fe(fcmac)](SCN)$_3$: Yield 47% of a brown solid. MS-FAB (NBA): *m/z* = 542.1 $[Fe(fcmac)(SCN)_2]^+$, 484.1 $[Fe(fcmac)(SCN)]^+$. IR: $\tilde{\nu}$ = 3391 (m), 3068 (w), 2939 (w), 2042 (s, SCN), 1647 (m), 1443 (w), 1238 (w), 1039 (w), 828 (w), 478 (w) cm^{-1}.

[Fe(fcmac)]Fe(SO$_4$)$_2$×3MeOH: Yield 51% of a brown solid. $C_{22}H_{44}Fe_3N_4O_{11}S_2$ (772.27): calcd. C 34.22, H 5.74, N 7.25; found C 34.63, H 5.51, N 6.73. IR: $\tilde{\nu}$ = 3386 (s), 3217 (m), 3080 (m), 2923 (m), 2358 (m), 2343 (w), 1635 (m), 1458 (m), 1109 (s, SO_4), 1026 (s), 966 (w), 809 (w), 602 (w), 484 (w) cm^{-1}.

[Cu(rcmac)](BF$_4$)$_2$: Yield 64% of a violet solid. $C_{19}H_{30}B_2CuF_8N_4Ru$ (652.69): calcd. C 34.96, H 4.63, N 8.58; found C 35.02, H 4.74, N 8.33. MS-FAB (NBA): *m/z* = 479.4 $[Cu(rcmac)]^+$. UV/Vis (MeCN): λ = 532 (ε = 120 M^{-1}cm^{-1}) nm. IR: $\tilde{\nu}$ = 3251 (m), 3103 (w), 2930 (w), 2886 (w), 1418 (m), 1069 (s), 812 (m), 519 (w), 429 (w) cm^{-1}.

[Ni(rcmac)(NCCH$_3$)$_2$]](BF$_4$)$_2$: Yield 52% of a yellow solid. $C_{19}H_{30}B_2F_8N_4NiRu$ (647.84): calcd. C 35.23, H 4.67, N 8.65; found C 35.29, H 4.73, N 8.55. MS-FAB (NBA): *m/z* = 561.5 $[Ni(rcmac)(BF_4)]^+$. UV/Vis (MeCN): λ = 309 (ε = 201 M^{-1}cm^{-1}), 400 (ε = 36 M^{-1}cm^{-1}) nm. IR: $\tilde{\nu}$ = 3262 (m), 3228 (m), 2949 (w), 2879 (w), 1460 (m), 1420 (m), 1034 (s), 819 (w), 518 (w) cm^{-1}. Single crystals were obtained by ether diffusion into an acetonitrile solution.

 © 2005 Wiley-VCH Verlag GmbH & Co. KGaA, Weinheim

[Cu(fcmac$^+$)](BF$_4$)$_2$PF$_6$: A solution of fcmac$^+$PF$_6^-$ (116 mg, 0.23 mmol) and Cu(BF$_4$)$_2$·6H$_2$O (78 mg, 0.23 mmol) in absolute methanol (7 mL) was stirred at room temperature overnight. The solution was filtered, and the solvent was evaporated. The resulting violet solid was dried in vacuo. Yield 98 mg (0.11 mmol, 49%). MS-ESI (MeOH): *m*/*z* = 502.6 [Cu(fcmac$_{ox}$)BF$_4$]$^+$, 434.6 [Cu(fcmac$_{ox}$)]$^+$. UV/Vis (MeOH): λ = 353 (ε = 1243 м$^{-1}$cm^{-1}), 489 (ε = 376 м$^{-1}$cm^{-1}), 609 (ε = 191 м$^{-1}$cm^{-1}) nm. IR: $\tilde{\nu}$ = 3419 (w), 3262 (w), 3114 (w), 2949 (w), 2921 (w), 1050 (s), 834 (s), 558 (m) cm^{-1}.

Crystal Structure Determinations: Crystal data and details of the structure determinations are listed in Table 4. Intensity data were collected at low temperature with a Stoe IPDS image plate (Mo-K_α radiation, λ = 0.71073 Å). The structures were solved by direct methods and refined by full-matrix least squares, based on F^2 with all reflections using the SHELXTL programs (G. M. Sheldrick, *SHELXTL NT*, v5.10, Bruker AXS, Madison, Wisconsin, USA, **1998**). CCDC-218906 contains the supplementary crystallographic data for this paper. These data can be obtained free of charge via www.ccdc.cam.ac.uk/conts/retrieving.html [or from the CCDC, 12 Union Road, Cambridge CB2 1EZ, UK; Fax: (internat.) + 44-1223-336-033; E-mail:deposit@ccdc.cam.ac.uk].

Table 4. Crystallographic data and data collection parameters for [Cu(fcmac)(FBF$_3$)]BF$_4$

Empirical formula	$C_{19}H_{30}B_2CuF_8FeN_4$
M_r	607.48
T [K]	203(2)
λ [Å]	0.71073
Crystal system, space group	orthorhombic, $P2_12_12_1$
Unit cell dimensions	a = 8.094 (2) Å
	b = 14.352 (3) Å
	c = 4.0611 (8) Å
Crystal size [mm]	0.30 × 0.30 × 0.05
Volume [nm^3]	4.717(2)
Z	8
Density (calculated) [g/cm^3]	1.711
Absorption coefficient [mm^{-1}]	1.596
F(000)	2472
Goodness-of-fit on F^2	0.961
Final R indices {$R1$ [$I > 2\sigma(I)$]; $wR2$ (all data)}	$R1$ = 0.0300; $wR2$ = 0.0713
Largest diff. peak/hole [e·Å^{-3}]	0.313/−0.391

Acknowledgments

Generous financial support by the German Science Foundation (DFG), the Fonds of the Chemical Industry (FCI), the MWFZ, and the Forschungsfonds of the University Mainz are gratefully acknowledged.

[1] P. D. Beer, *Chem. Soc., Rev.* **1989**, *18*, 409.
[2] P. D. Beer, *Acc. Chem. Res.* **1998**, *31*, 71.
[3] J. M. Lloris, R. Martinez-Manez, M. Padialla-Tasta, T. Pardo, J. Soto, M. J. L. Tendero, *J. Chem. Soc., Dalton Trans.* **1998**, 3657.
[4] H. Plenio, C. Aberle, *Angew. Chem.* **1998**, *110*, 1467; *Angew. Chem. Int. Ed.* **1998**, *37*, 1397.
[5] P. D. Beer, P. A. Gale, G. Z. Chen, *J. Chem. Soc., Dalton Trans.* **1999**, 1897.
[6] P. Comba, J. Ensling, P. Gütlich, A. Kühner, A. Peters, H. Pritzkow, *Inorg. Chem.* **1999**, *38*, 3316.
[7] P. Comba, A. Kühner, A. Peters, *J. Chem. Soc., Dalton Trans.* **1999**, 509.
[8] P. D. Beer, D. Hesek, K. C. Nam, M. G. B. Drew, *Organometallics* **1999**, *18*, 3933.
[9] P. D. Beer, J. Cadman, J. M. Lloris, R. Martinez-Manez, M. E. Padilla, T. Pardo, D. K. Smith, J. Soto, *J. Chem. Soc., Dalton Trans.* **1999**, 127.
[10] P. D. Beer, P. V. Bernhardt, *J. Chem. Soc., Dalton Trans.* **2001**, 1428.
[11] H. Plenio, C. Aberle, Y. Al Shihadd, J. M. Lloris, R. Matinez-Manez, T. Pardo, J. Soto, *Chem. Eur. J.* **2001**, *7*, 2848.
[12] D. Astruc, *New. J. Chem.* **1992**, *16*, 305.
[13] J. C. A. Boeyens, S. M. Dobson, in *Stereochemical and Stereophysical Behaviour of Macrocycles* (Ed.: I. Bernal), Elsevier, Amsterdam, New York, **1987**, p. 1.
[14] L. Alderighi, P. Gans, A. Ienco, D. Peters, A. Sabbatini, A. Vacca, *Coord. Chem. Rev.* **1999**, *148*, 311.
[15] H. Irving, R. J. P. Williams, *Nature* **1948**, *162*, 746.
[16] R. C. Luckay, R. D. Hancock, *J. Chem. Soc., Dalton Trans.* **1991**, 1491.
[17] A. Togni, T. Hayashi, in *Ferrocenes: Homogeneous Catalysis, Organic Synthesis, Materials Science* (Eds.: A. Togni, T. Hayashi), VCH, Weinheim, New York, **1995**.
[18] P. D. Beer, J. N. Nation, S. L. W. Mcwhinnie, M. E. Harman, M. B. Hursthouse, M. I. Ogden, A. H. White, *J. Chem. Soc., Dalton Trans.* **1991**, 2485.
[19] P. D. Beer, Z. Cheng, M. G. B. Drew, J. Kingston, M. Ogden, P. Spencer, *J. Chem. Soc., Chem. Commun.* **1993**, 1046.
[20] U. Siemeling, *J. Chem. Soc., Dalton Trans.* **1997**, 4705.
[21] A. J. Evans, S. E. Watkins, D. C. Craig, S. B. Colbran, *J. Chem. Soc., Dalton Trans.* **2002**, 983.
[22] P. Comba, T. W. Hambley, M. A. Hitchman, H. Stratemeier, *Inorg. Chem.* **1995**, *34*, 3903.
[23] P. Gütlich, R. Link, A. Trautwein, *Mössbauer Spectroscopy and Transition Metal Chemistry*, Springer-Verlag, Berlin, New York, **1978**.
[24] P. Comba, K. Merz, F. Renz, manuscript in preparation.
[25] G. G. A. Balavoine, G. Doisenau, T. Fillebeen-Khan, *J. Organomet. Chem.* **1991**, *412*, 381.
[26] P. Gans, A. Sabatini, A. Vacca, *Talanta* **1996**, *43*, 1739.
[27] J. D. Dunitz, L. E. Orgel, A. Rich, *Actra Crystallogr.* **1956**, *9*, 373.

Received July 16, 2004
Early View Article
Published Online December 2, 2004

 © 2005 Wiley-VCH Verlag GmbH & Co. KGaA, Weinheim

Hybrid Magnetic Materials Based on Nitroxide Free Radicals and Extended Oxalato-Bridged Bimetallic Networks

Antonio Alberola,[a] Eugenio Coronado,*[a] Carlos Giménez-Saiz,[a] Carlos J. Gómez-García,[a] Francisco M. Romero,*[a] and Ana Tarazón[a]

Keywords: Magnetic properties / Heterometallic complexes / Hybrid materials / Radicals / Layered compounds

A series of hybrid organic-inorganic magnets of formula *p*-rad[$M^{II}Cr(ox)_3$] [M = Mn (**1**), Co (**2**), Ni (**3**), Zn (**4**)] and *m*-rad[$M^{II}Cr(ox)_3$] [M = Mn (**5**), Co (**6**)], in which *N*-methylpyridinium cations bearing a nitronyl nitroxide moiety in positions 3 (*m*-rad) or 4 (*p*-rad) of the pyridine ring coexist with the 2D honeycomb-like oxalato-bridged bimetallic lattice, has been prepared and studied by AC and DC magnetic susceptibility measurements and EPR spectroscopy. In general, the physical properties of these magnets are not altered significantly by the insertion of the nitronyl nitroxide radicals although these paramagnetic molecules seem to interact weakly with the inorganic network as demonstrated by EPR spectroscopy. Some differences can also be observed between the *p*-rad and *m*-rad series, i.e. *m*-rad derivatives have smaller values for the critical temperatures and coercive fields. We also report on the X-ray crystal structures and magnetic properties of *p*-rad[$Mn(H_2O)Cr(ox)_3]\cdot 2H_2O$ (**7**) and *m*-rad[$Mn(H_2O)_2Cr(ox)_3]\cdot 2H_2O$ (**8**), two extended oxalato-bridged compounds with new topologies. Compound **7** is antiferromagnetic and its structure is a 3D achiral lattice in which zigzag ferromagnetic MnCr chains (J/k = +0.8 K) are interconnected to form hellicoidal hexagonal channels with the cationic free radicals residing in the free space. Compound **8**, however, exhibits a ladder-like structural pattern with competing magnetic interactions and paramagnetic behaviour down to low temperatures.
(© Wiley-VCH Verlag GmbH & Co. KGaA, 69451 Weinheim, Germany, 2005)

Introduction

For more than fifteen years, magnetochemists have been successfully surmounting the challenge of designing and constructing new crystalline solid-state materials from molecular building blocks.[1,2] In the rational design of these compounds, the building blocks are not merely virtual units in which the crystal structure is subdivided in order to get a better understanding but, rather, they are real entities which are stable in solution and can be assembled to form a particular crystal lattice with interesting properties. The well-known concepts of structural coordination chemistry provide useful design methods for the purpose of lattice engineering, since coordination geometries are defined by strong and highly directional bonds. Fortunately, coordination chemistry also affords the basic ingredients of molecule-based magnetic materials, i.e. spin carriers (metal ions) and ligands through which magnetic interactions can occur.

The homoleptic tris(oxalatometallate) anions $[M(ox)_3]^{3-}$ ($M = Cr^{III}$, Fe^{III}, Ru^{III}) are rather inert metal complex ions which can be assembled with metal cations to give extended heterometallic systems.[3−5] The majority of the resultant structures are composed of edge-sharing octahedra and belong to two categories, namely a) 2D bimetallic compounds of formula $A[M'M(ox)_3]$ (A = quaternary onium cation, M′ = metal) with a honeycomb-layered structure[6,7] and b) 3D homometallic compounds of formulae $A[M'_2(ox)_3]$, $A[M'M(ox)_3]$ or $A[M'M(ox)_3](ClO_4)$ ($A = [M(bpy)_3]^{2+}$) with a cubic chiral packing.[8,9] Since the formation of each structural type depends on the use of a particular A^{m+} cation, these have been considered as templating agents for the host structure.[10] It has also been recognised that chirality plays a crucial role in this molecular recognition process, i.e. chiral tris(bipyridine) metal cations induce the spontaneous resolution of 3D chiral lattices with the same configuration as the tris(oxalatometalate) sites.[11] Cross effects (magnetochiral dichroism)[12] may arise from the combination of magnetic order and chirality in 3D oxalato-based compounds.[13] In general, multiproperty hybrid materials can be synthesised from functional A^{m+} cations which introduce an additional physical property in the magnetic system. In this context, 2D compounds containing paramagnetic decamethylferricenium species,[14,15] NLO-active molecules[16] and organic π-electron donors have been studied. The latter include the first examples of the coexistence of magnetic order and metal-like conductivity in a molecular solid.[17]

Nitronyl nitroxide (NN) radicals have become commonplace in the synthesis of purely organic magnetic materi-

[a] Institut de Ciència Molecular, Universitat de València, Dr. Moliner 50, 46100 Burjassot, Spain
Fax: (internat.) +34-963544859
E-mail: fmrm@uv.es
Supporting information for this article is available on the WWW under http://www.eurjic.org or from the author.

als[18] and mixed metal-radical magnets.[19−21] Cationic NNs of the *N*-alkylpyridinium type were reported by Awaga in combination with simple anionic metal complexes.[22−26] The same nitroxide cations have also been employed as bridging units in conjunction with the well-known bimetallic chains based on the opba ligand.[27−29] These studies prompted us to investigate the use of these free radicals as functional cations in the formation of oxalato-bridged extended bimetallic compounds. In a previous communication, we reported such a hybrid magnet based on a novel 3D achiral $[MnCr(ox)_3]^-$ lattice.[30] Herein, we extend these results to other first-row divalent metal ions. The influence of the position of the NN fragment with respect to the pyridinium ring is also discussed in this paper.

Results and Discussion

Synthesis and Characterisation: The cationic free radicals employed in this study were 1-methylpyridinium derivatives bearing an NN moiety in positions 4 (*p*-rad) or 3 (*m*-rad) of the pyridine ring (Scheme 1). They were synthesised as iodide salts by a previously described procedure.[22,23] Their reaction with $Ag_3[Cr(ox)_3]$ affords *p*(*m*)-rad$_3$[Cr(ox)$_3$] which was allowed to further react with a mixture of the corresponding metal cation, M^{2+}, and $[Cr(ox)_3]^{3-}$ to yield the family of compounds *p*(*m*)-rad[MCr(ox)$_3$]. From the study of the magnetic properties of these hybrid materials (vide infra), it became clear that they belong to the 2D type of structure.

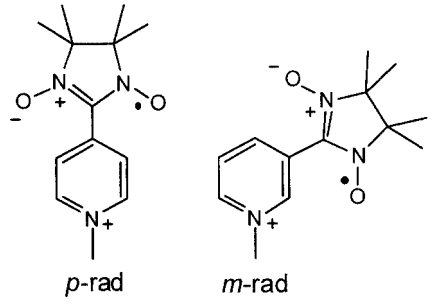

Scheme 1

$$3\,p(m)\text{-radI} + Ag_3[Cr(ox)_3] \rightarrow 3\,p(m)\text{-rad}^+ + [Cr(ox)_3]^{3-} + 3\,AgI\downarrow \quad (1)$$

$$3\,MCl_2{\cdot}nH_2O + 2\,Ag_3[Cr(ox)_3] \rightarrow 3\,M^{2+} + 2\,[Cr(ox)_3]^{3-} + 6\,AgCl\downarrow \quad (2)$$

$$3\,p(m)\text{-rad}^+ + 3\,[Cr(ox)_3]^{3-} + 3\,M^{2+} \rightarrow 3\,\text{rad}[MCr(ox)_3] \quad (3)$$

All reactions were performed in ethanol/water mixtures. The different products *p*-rad[MCr(ox)$_3$]·*n*H$_2$O [M = Mn (**1**), Co (**2**), Ni (**3**), Zn (**4**)] can be obtained in moderate yields by fast precipitation, provided that a high ethanol/water ratio and rather concentrated solutions are used in the last step. The water content was evaluated by thermogravimetric analysis for all the compounds. The same experimental conditions were applied for the synthesis of the *m*-rad series. In this case, however, the yields were lower and the radical content in the final compounds (as estimated from elemental analysis) was smaller. The deficiency of cationic radicals has to be compensated for with the absence of some $[Cr(ox)_3]^{3-}$ anions, thus increasing the M/Cr ratio. This aspect was confirmed by SEM metal analyses. Adding an excess of the free radical and/or the divalent metal resulted in compounds with the correct stoichiometry, i.e. *m*-rad[MCr(ox)$_3$]·*n*H$_2$O [M = Mn (**5**), Co (**6**)]. The corresponding Ni^{II} and Zn^{II} compounds could not be obtained, however. Clearly, the more symmetric *p*-rad cation has a stronger affinity for the 2D honeycomb lattice than *m*-rad. It seems that the formation of the hexagonal cavities around the pyridinium cation is partially hindered by the presence of the bulky NN group in the *m*-position.

The precipitation of the manganese(II)-containing products (**1** and **5**) can be avoided if reaction (3) is performed in a more aqueous and/or a more dilute solution. Under these conditions, single-crystals of the 3D *p*-rad[MnCr(ox)$_3$(H$_2$O)]·2H$_2$O (**7**) and 1D *m*-rad[MCr(ox)$_3$(H$_2$O)$_2$]·2H$_2$O (**8**) compounds could be obtained by slow evaporation. The reaction conditions are therefore critical in the synthesis of the Mn^{2+} analogues. Due to the larger size of this cation, the formation of complexes with the tris(oxalate) chromate(III) species is reduced and a competition between these anions and the solvent water molecules occurs. Under less polar and/or more concentrated conditions (kinetic control), fast precipitation occurs and the well-known 2D phases are obtained. On the other hand, increasing the water content and/or working with more dilute solutions (thermodynamic control) induces the coordination of water molecules to the Mn^{2+} ions with a complete change in the crystal structure.

Crystal Structures of 7 and 8: The hybrid salt **7** crystallises in the monoclinic space group C_c. The conformation of the *p*-rad cation (Figure 1, a) with a torsion angle of 26.6(4)° between the NN fragment and the pyridine ring is similar to that found in other salts. The packing of the free radicals (Figure 2) forms zigzag chains running along the *z*-axis. The shortest contact between proximate radicals within the chain is O2···C10 [x, 1− y, z − 1/2, 4.312(5) Å]. The N−O functions are well separated from each other with a minimum intermolecular O1···O2 (x, 1− y, z − 1/2) distance of 6.891(5) Å. This situation is special in the context of magnetic materials containing nitroxide radicals, where shorter O···O contacts of about 3.5 Å are generally observed.

The oxalato-based inorganic lattice is also shown in Figure 2 and emphasises the role of the free radicals as directing agents for the whole structure. The zigzag chain motif of the packing of NN radicals is translated to the inorganic counterpart. Indeed, the 3D bimetallic network can be viewed, in a first step, as zigzag alternating Mn−Cr chains oriented in the same direction (continuous bonds). A detailed picture of this 1D fragment is given in Figure 3 where the linkage between neighbouring metal ions by

 © 2005 Wiley-VCH Verlag GmbH & Co. KGaA, Weinheim

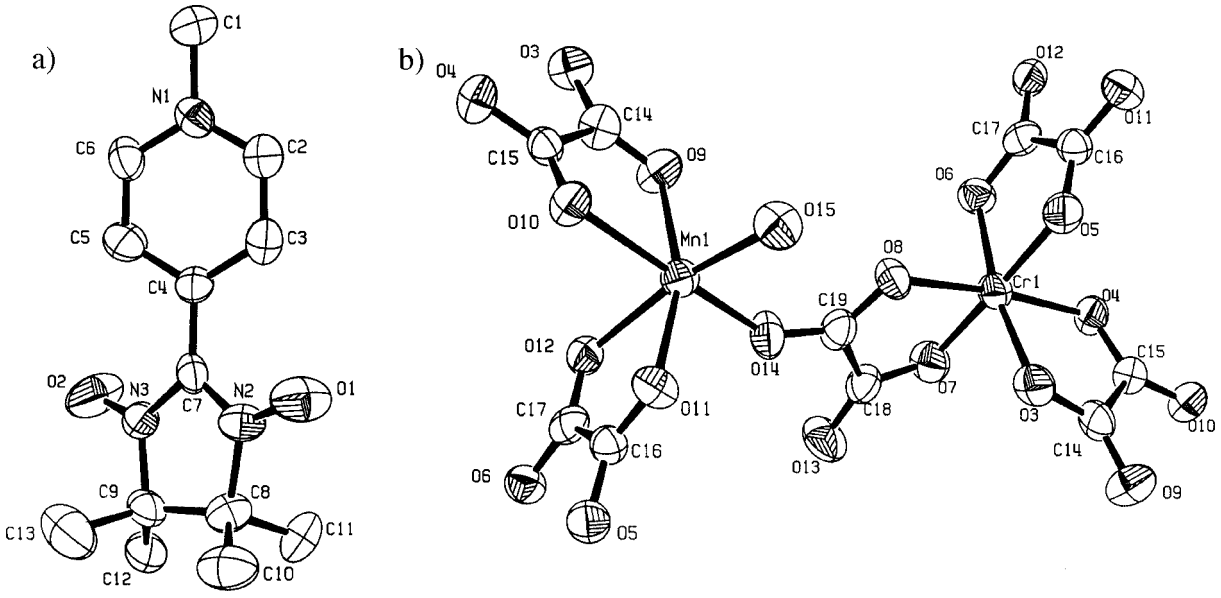

Figure 1. Molecular structure of a) *p*-rad and b) $[Mn(H_2O)Cr(ox)_3]^-$ (ellipsoids are shown at the 50% probability level; all H atoms have been omitted for clarity); selected distances (A), N2−O1 1.271(3), N3−O2 1.271(3)

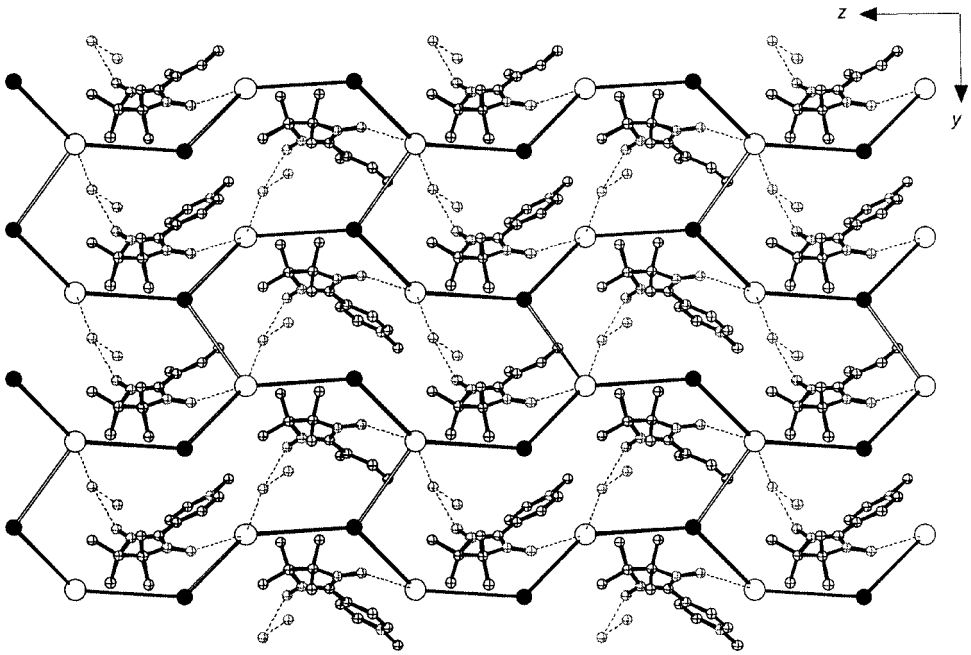

Figure 2. View of the crystal structure of **7** along the *a* axis; oxalate anions have been replaced by straight rods: black [bis(bidentate)] and white (bidentate/monodentate); dotted lines refer to hydrogen bonds, open circles = Mn, filled circles = Cr

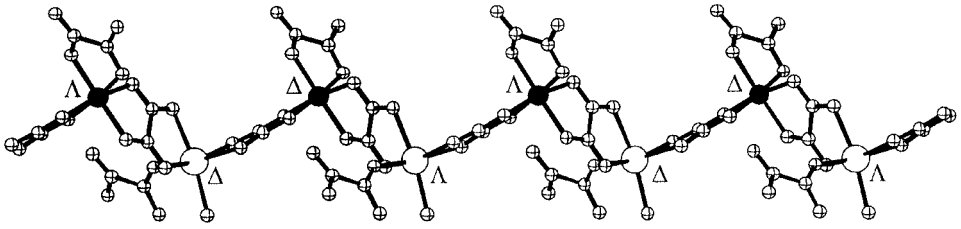

Figure 3. View along the *b* axis of the oxalato-bridged MnCr ferromagnetic chains in **7**; the absolute configuration of the metal centres is also shown, open circles = Mn, filled circles = Cr

 © 2005 Wiley-VCH Verlag GmbH & Co. KGaA, Weinheim

bis(bidentate) μ-oxalate bridges can be clearly seen. In contrast to the classical 3D network built up from homochiral building blocks which combine into helical chains, the chirality of the metal centres follows the sequence ···ΔΔΛΛΔΔ··· along the chains of **7**. Two distinct bis(bidentate) bridges are then found, i.e. one connecting metal centres of the same chirality [Mn1···Cr1: 5.421(3) Å] and a second one connecting centres of opposite chirality [Mn1···Cr1 (x, 2 − y, z + 1/2): 5.3927(16) Å].

The chains are linked by a new type of oxalate bridge (see Figure 1, b) which is simultaneously bidentate (towards chromium) and monodentate (towards manganese). As expected, the metal-metal distance [Mn1···Cr1e (x + 1/2, 3/2 − y, z + 1/2): 5.5977(14) Å] is higher when compared with the bis(bidentate) bridging mode. A water molecule occupies the vacant position in the Mn^{2+} coordination sphere at a distance Mn1−O15 = 2.138(2) Å. Previous reports concerning this unusual bridging mode are very scarce.[31−33] In complex **7**, the linkage (white rods in Figure 2) takes place between $Cr(ox)_3$ and $Mn(H_2O)(ox)_3$ units of opposite chirality. This results in the formation of an achiral 3-connected decagonal network. The decagonal units are arranged out of this plane in such a way that helical hexagonal channels are formed. Since the resultant network is achiral, both types of helices are found in the structure (Figure 4).

Interestingly, the radicals are tightly bound to the inorganic lattice through an extended hydrogen-bonded network. Short hydrogen bonds are found between the nitroxide oxygen atoms and two water molecules [Mn1−O15···O2−N3 (x + 1/2, 3/2 − y, z + 1/2): 2.733(4) Å; O17···O1−N2: 2.800(3) Å]. The water molecules of crystallisation are also linked to each other [O17···O16 (x + 1, y, z): 2.762(4) Å] and are hydrogen-bonded to the coordinated water [Mn1−O15···O17: 2.674(4) Å].

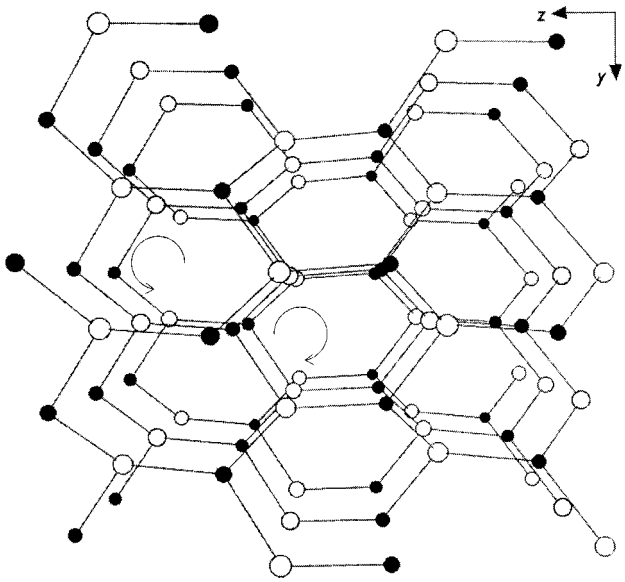

Figure 4. Perspective view along the a axis of the heterometallic lattice of **7** showing the metal connectivity and the helical channels formed; open circles = Mn, filled circles = Cr

The *m*-rad analogue **8** crystallises in the centrosymmetric $P\bar{1}$ space group. The cationic free radical (Figure 5, a) exhibits a more planar conformation with a torsion angle between the NN fragment and the pyridine ring of 15.51(10)°. The Mn^{2+} environment is markedly different with respect to **7** and only one oxalate anion now behaves in a bis(bidentate) manner with the other two (Figure 5, b) binding in the bidentate/monodentate mode occupying *trans* positions in the Mn^{2+} coordination sphere. This situation leaves two vacant *cis* positions which are occupied by water molecules. This causes the organisation of a ladder-like chain.[34−36]

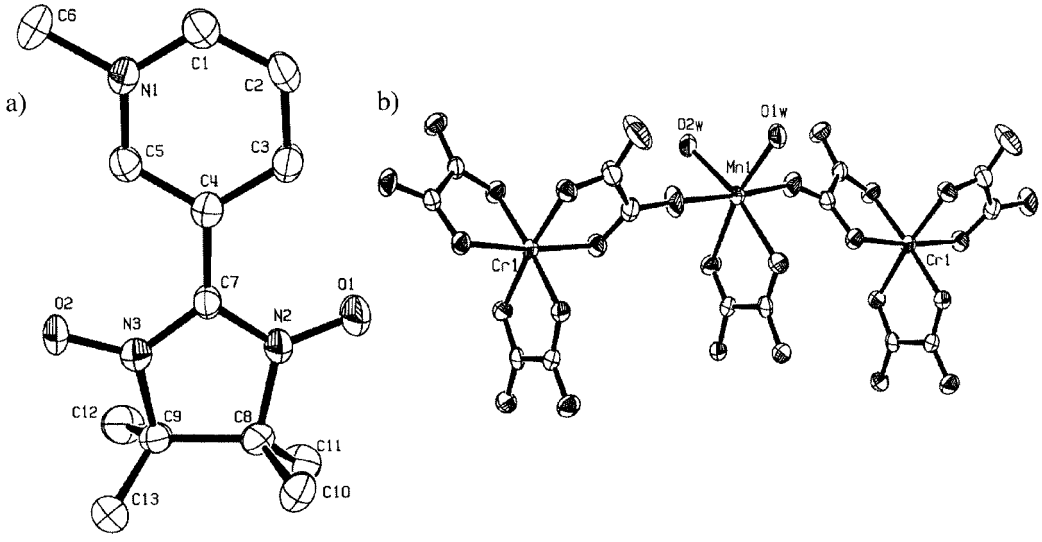

Figure 5. Molecular structure of a) *m*-rad and b) $\{Mn(H_2O)_2(ox)[Cr(ox)_3]_2\}$ fragment (ellipsoids are shown at the 50% probability level; all H atoms have been omitted for clarity); selected distances (Å): N2−O1 1.277(4), N3−O2 1.283(4)

 © 2005 Wiley-VCH Verlag GmbH & Co. KGaA, Weinheim

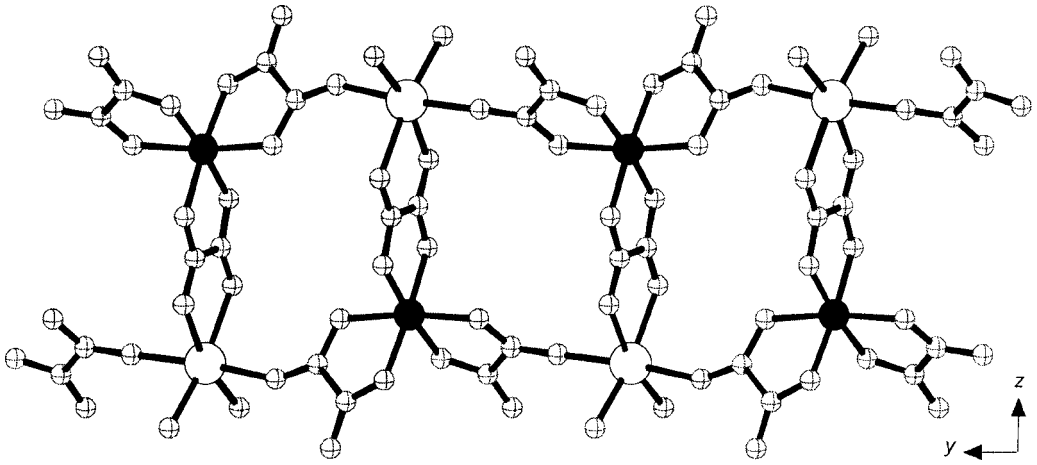

Figure 6. Projection of the crystal structure of **8** onto the *bc* plane, showing the oxalato-bridged MnCr ladder-like chains, open circles = Mn, filled circles = Cr

The steps of the ladder (Figure 6) are defined by bis(bidentate) bridges with an intermetallic distance Mn1···Cr1 = 5.4631(7) Å, while the bidentate/monodentate bridging mode propagates the lateral chains in the direction of the *b* axis. As expected, longer intermetallic distances [Cr1···Mn1($-x$ + 1, $-y$, $-z$ + 1) = 5.8370(7) Å and Mn1···Cr1($-x$ + 1, $-y$ + 1, $-z$ + 1) = 5.9902(7) Å] are found in this case. The chains are related by an inversion centre and the resultant ladder is achiral.

The free radicals (Figure 7) also form zigzag chains running along the *b*-axis. They can be viewed as chains of centrosymmetric dimers with the shortest intradimer distance of C40···C40 = 3.512(5) Å ($-x$, $-$,$-z$). The N−O moieties are even more isolated than in compound **7** and their minimum O···O distance in the crystal is 7.478(5) Å. Again, the water molecules of crystallisation are linked to each other [O3W···O4 W($-x$, 1$-$ y, 2 $-$ z) = 2.908(5) Å] and hydrogen-bonded to the coordinated water

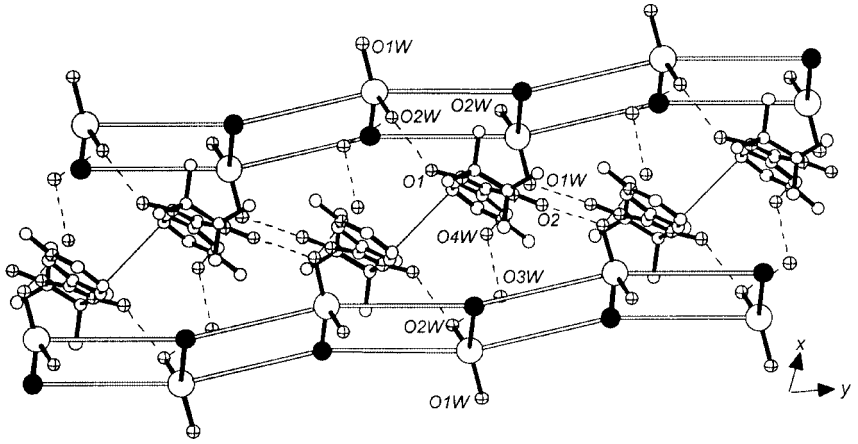

Figure 7. Projection of the crystal structure of **8** onto the *ab* plane, showing the radical zigzag chains of dimers and the oxalato-bridged ladder; oxalate anions have been replaced by straight rods: black [bis(bidentate)] and white (bidentate/monodentate); dotted lines refer to hydrogen bonds, open circles: Mn, filled circles: Cr

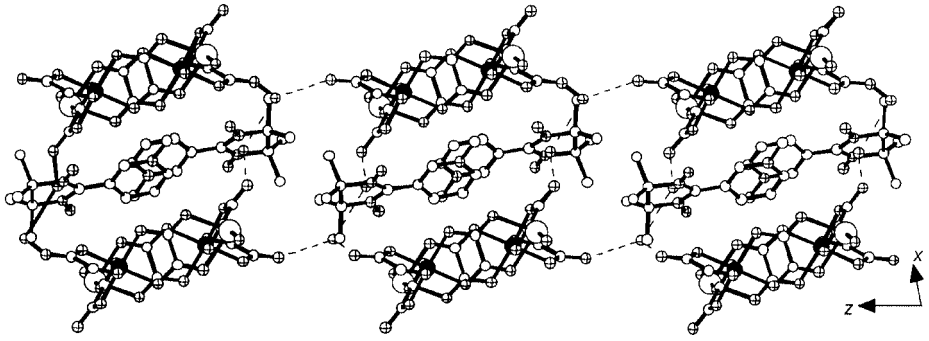

Figure 8. View along the *b* axis of the ladder-like oxalato-bridged lattice and the zigzag nitroxide chains of **8** showing the participation of the oxalate anions in hydrogen bonding; open circles: Mn, filled circles: Cr

 © 2005 Wiley-VCH Verlag GmbH & Co. KGaA, Weinheim

Table 1. Magnetic parameters for the series *p*-rad[$M^{II}M^{III}(ox)_3$] and *m*-rad[$M^{II}M^{III}(ox)_3$] (**1**−**7**): critical temperature (T_c), Weiss constant (θ), Curie constant (C), saturation magnetisation (M_{sat}) and coercive field at 2 K (H_{coer})

$M^{II}M^{III}$	*p*-rad					*m*-rad				
	T_c (K)	θ (K)	C (emu·K·mol^{-1})	M_{sat} (μ_B)	H_{coer} (G)	T_c (K)	θ (K)	C (emu·K·mol^{-1})	M_{sat} (μ_B)	H_{coer} (G)
MnCr	5.7	8.0	6.13	7.74	66	5.3	7.0	6.55	7.37	17
CoCr	13.8	10.0	5.37	6.22	4400	11.3	11.0	5.24	5.17	230
NiCr	15.5	17.2	3.14	5.57	1500	–	–	–	–	–
ZnCr	–	2.8	2.29	–	–	–	–	–	–	–

[Mn1−O2W···O3 W(x, y, z − 1) = 2.688(4) Å, Mn1−O1W···O4 W(1 − x, 1 − y, 1 − z) = 2.653(4) Å]. The nitroxide functions are bonded to coordinated and free water molecules [O1···O2 W(1 − x, 1 − y,1 − z) = 2.714(4) Å; O2···O1 W(2 − x, −y, 1 − z) = 2.719(4) Å]. The free radicals are thus held in the lattice by an intricate network of hydrogen bonds.

A view parallel to the chains (Figure 8) shows how these 1D organic and inorganic units alternate in the solid-state and also emphasises the role played by the oxalate anions in stabilising additional hydrogen bonds which link the ladders along the z direction.

Magnetic Properties of the Mn-Containing Hybrid Salts (1, 5, 7−8): It is interesting to compare these CrMn bimetallic compounds since only the noncrystalline materials obtained by fast precipitation (**1** and **5**) exhibit ferromagnetic ordering. Table 1 lists the values of χT (at 300 K), magnetisation (at 5 T), the coercive field and critical temperatures for all the compounds studied in this work. At room temperature, the four CrMn hybrid salts exhibit similar values of χT which lie close to the expected values for the sum of the isolated spins [nitroxide radical (S = 1/2), Mn^{2+} (S = 5/2) and Cr^{3+} (S = 3/2) cations]. On lowering the temperature, χT continuously increases (see Supporting Information) for all the compounds, suggesting the existence of short-range ferromagnetic interactions. Compounds **1** and **5** exhibit clear indications of ferromagnetic ordering, such as the onset of out-of-phase AC susceptibility signals below 5.7 K and 5.3 K, respectively (Figure 9). Hysteresis loops with very small coercive fields (66 G for **1**, 17 G for **5**) can also be observed. Both features clearly demonstrate that **1** and **5** belong to the 2D structural family of mixed-metal oxalates. In contrast, the magnetic behaviour of compounds **7**−**8** points to the presence of competing antiferromagnetic interactions. Both hybrid salts exhibit a rounded maximum in the χT vs. T curve and **7** even shows the presence of a sharp maximum at 6 K in the χ vs. T plot, a signature of antiferromagnetic ordering. Complex **8**, however, remains paramagnetic in the whole temperature range studied.

The magnetic properties of **7**−**8** can be understood by considering the crystal structures of these hybrid metal-radical salts. All previous studies have indicated that the Mn^{II}−Cr^{III} exchange coupling through bis(bidentate) oxalate anions is ferromagnetic. Indeed, the thermal variation (Figure 10) of the χT product for **7** (at temperatures above the Néel point) is well described in terms of a regular AB ferromagnetic chain model[37] with classical spins S_A = 5/2

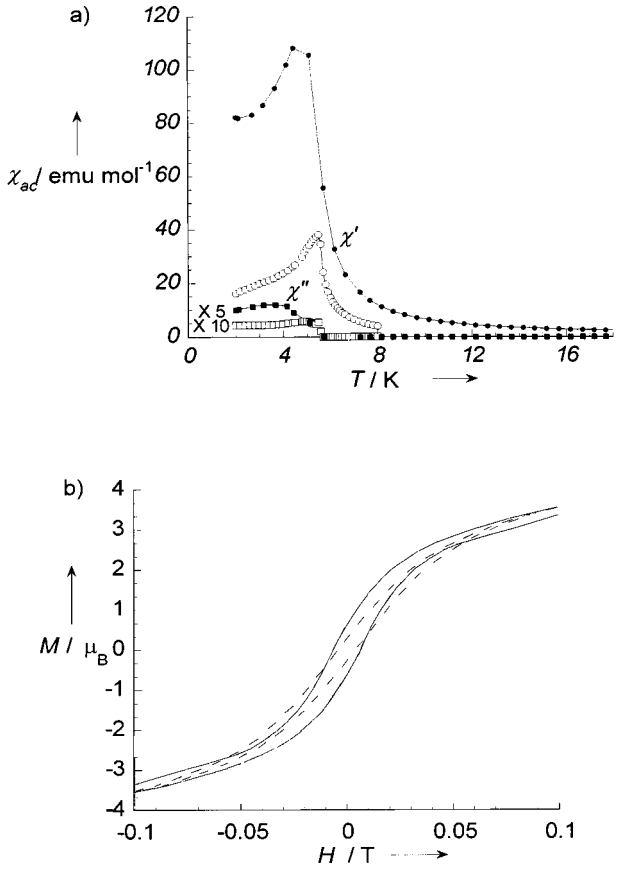

Figure 9. a) Temperature dependence of the real and imaginary components of the ac magnetic susceptibility of **1** (empty symbols, operating frequency: 1 Hz) and **5** (filled symbols, operating frequency: 110 Hz); b) low-field region of the hysteresis loops of **1** (solid line) and **5** (dashed line) measured at 2 K

and S_B = 3/2 ($H_{ex} = -J\Sigma S_{Ai}S_{Bi}$).[38] The best-fit value for the exchange coupling constant is J = +0.6 cm^{-1}, a value which is in agreement with previous observations. The antiferromagnetic order is then driven by weak antiferromagnetic interactions between the chains. These interactions are certainly transmitted through the bidentate/monodentate oxalate anion. The lower symmetry of this bridge decreases the efficiency of the ferromagnetic pathway (compared with the bis(bidentate) ligand) and the antiferromagnetic term becomes dominant, as has been shown recently in a chromium-manganese tetramer.[33] Antiferromagnetic ordering is generated in the inorganic lattice and the radicals seem to remain uncoupled to this magnetically ordered network, a hypothesis which is corroborated by the presence of a

 © 2005 Wiley-VCH Verlag GmbH & Co. KGaA, Weinheim

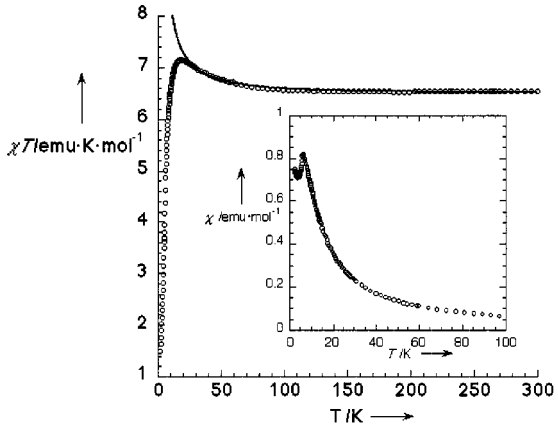

Figure 10. Thermal variation of the χT product (open circles) for **7**. The solid line represents the best-fit data for a ferromagnetic MnCr chain with $J = +0.6$ K; inset: temperature dependence of χ for the same compound

Curie tail at low temperatures. This is observed despite the fact that the nitroxide oxygen atom is hydrogen-bonded to the coordinated water molecule and, consequently, close to the manganese centre [Mn1···O2 ($x + 1/2$, $3/2 - y$, $z + 1/2$) = 3.8510(27) Å]. It seems that the magnetic interaction through this bridge is too weak to be appreciated in the temperature range of study.

The magnetostructural correlations found for complex **7** (ferromagnetic interaction transmitted through bis(bidentate) oxalate anions and antiferromagnetic coupling mediated via the asymmetric bridge) suggest the use of a spin-ladder chain model with competing interactions for the analysis of the magnetic properties of **8**.[39] Ferromagnetic interactions take place in the steps of the ladder, while the antiferromagnetic coupling propagates along the rungs, giving rise to a diamagnetic ground state. The free radicals can be considered as an independent paramagnetic contribution, as for **7**. In the absence of an exact solution for this system, the ladder chain can be approximated to a cluster-type model of isotropic spins (Figure 11).[40] The best-fit data for the two magnetic coupling parameters are $J = +0.8$ cm^{-1} and $j = -0.35$ cm^{-1}. As expected, the positive interaction is of the same order of magnitude as that estimated for the *p*-rad analogue.

Magnetic Properties of the Co-Containing Hybrid Salts (2 and 6): At room temperature, the value of χT for **2** (Figure S2a, see Supporting Information and the corresponding footnote on the first page of this article) is 5.88 emu·K·mol^{-1}. Subtraction of the radical and chromium(III) contributions leads to a reasonable value of 3.63 emu·K·mol^{-1} per cobalt(II) centre. On lowering the temperature, χ increases and eventually reaches saturation at a high value of 16.8 emu·K·mol^{-1} at 2.1 K, suggesting ferromagnetic ordering at low temperatures. Confirmation of the magnetic order (Figure 12) is provided by the observation of an out-of-phase signal in the AC susceptibility measurements below $T_C = 13.8$ K. Magnetisation hysteresis loops can be observed below this temperature with very high coercive field values ($H_{coer} = 4400$ G at 2 K) compared with those previously reported for CoCr oxalato-bridged 2D magnets. Saturation is almost reached in a 5 T field with a magnetisation value of 6.2 μ_B.

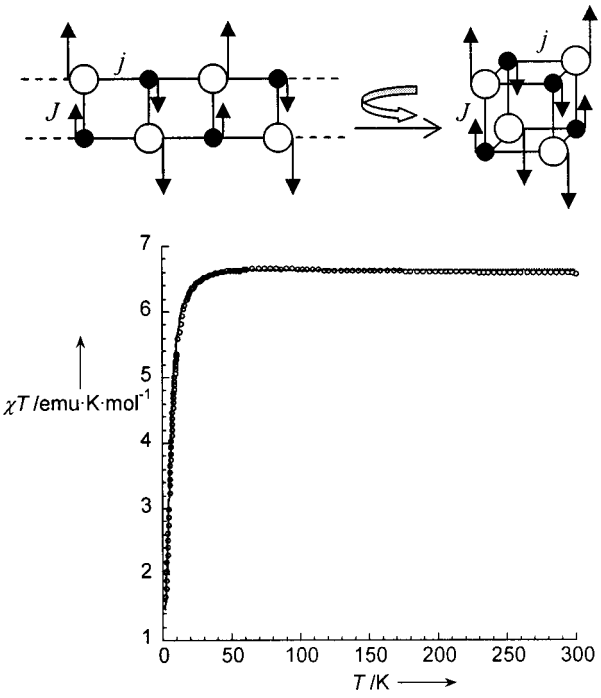

Figure 11. Top: 8-spin ring cubane model adopted for the spin-ladder chain; bottom: thermal variation of the χT product (open circles) for **8**; the solid line represents the best-fit data ($J = +0.8$ cm^{-1}; $j = -0.35$ cm^{-1})

Compound **6** exhibits (Figure S2b, Supp. Inf.) a room-temperature χT value of 5.52 emu·K·mol^{-1}. Taking into account the contributions of the radical and chromium(III) centres, a value of 3.27 emu·K·mol^{-1} per cobalt(II) centre can be calculated. This is close to the expected value for a free Co^{2+} ion showing orbital degeneracy. χ increases continuously on cooling and undergoes saturation with a value of 17.2 emu·K·mol^{-1} at 2 K. Compounds **2** and **6** show a similar thermal dependence in the DC susceptibility. The AC data, however, show clear differences between the *p*-rad and *m*-rad derivatives. The latter orders ferromagnetically at $T_C = 11.3$ K and exhibits a rounded maximum in the thermal dependence of the in-phase component. This is in contrast to the extremely sharp peak observed for the *p*-rad analogue (**6**). Also, field-dependent studies show a much smaller coercive field ($H_{coer} = 230$ G at 2 K) compared with that in **2**. The different magnetic behaviour of both compounds may be ascribed to the presence of metal defects and/or disorder in the *m*-compound which push the T_C to lower temperatures. The differences in coercive field values may also be explained in terms of a different morphology of the samples: The *p*-rad derivative (**2**) has an unusually large particle size (8 μm) compared with the other compounds (the particle size of **6** is 250 nm).

Magnetic Properties of the Ni-Containing Hybrid Salt (3): The value of χT at 300 K for **3** (3.53 emu·K·mol^{-1}) is slightly higher than the sum of the paramagnetic contri-

 © 2005 Wiley-VCH Verlag GmbH & Co. KGaA, Weinheim

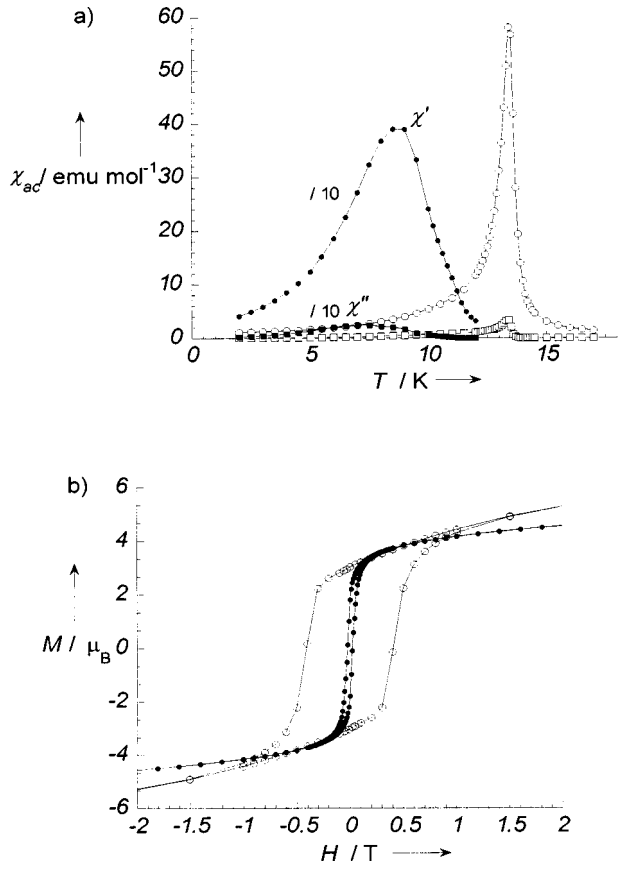

Figure 12. a) Temperature dependence of the real and imaginary components of the ac magnetic susceptibility of **2** (empty symbols) and **6** (filled symbols); operating frequency: 110 Hz; b) low-field region of the hysteresis loops of **2** (empty symbols) and **6** (filled symbols) measured at 2 K

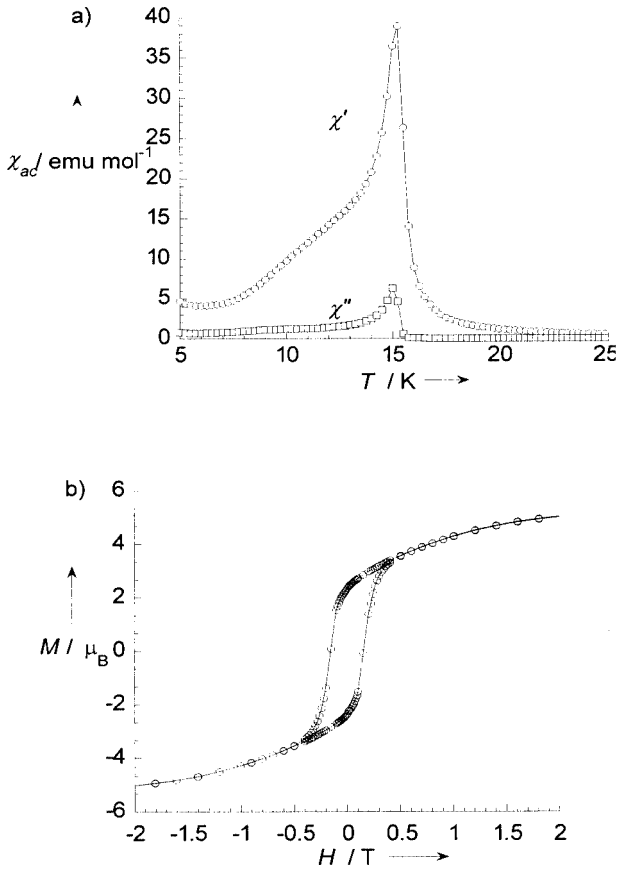

Figure 13. a) Temperature dependence of the real and imaginary components of the ac magnetic susceptibility of **3**; operating frequency: 110 Hz; b) low-field region of the hysteresis loops of **3** measured at 2 K

butions of the different spin carriers (Figure S3, Supp. Inf.). χ increases considerably upon cooling, indicating the presence of a ferromagnetically ordered phase at low temperatures. The onset of an out-of-phase signal in the AC susceptibility (Figure 13) measurements below T_C = 15.5 K provides further evidence of magnetic order. Again, magnetisation hysteresis loops were observed with very high coercive field values (H_{coer} = 1500 G at 2 K) compared with those previously reported for NiCr oxalato-bridged 2D magnets. Saturation is almost reached in a 5 T field with a magnetisation value of 5.6 μ_B.

Magnetic Properties of the Zn-Containing Hybrid Salt (4): This product exhibits room-temperature χT values that lie close to the sum of the calculated contributions for isolated Cr^{III} and free radical units. χT remains practically constant (Figure 14) upon cooling down to 10 K. Below this point, χT increases constantly upon decreasing the temperature, indicating that an intermolecular ferromagnetic interaction between radicals may also be present. In the absence of structural characterisation, it is difficult to ascribe this behaviour to particular intermolecular contacts so that an interaction between the free radical and the chromium(III) centres cannot be ruled out. The field dependence of the magnetisation shows typical Brillouin behaviour. As quoted in Table 1, saturation is not reached in a 5 T field.

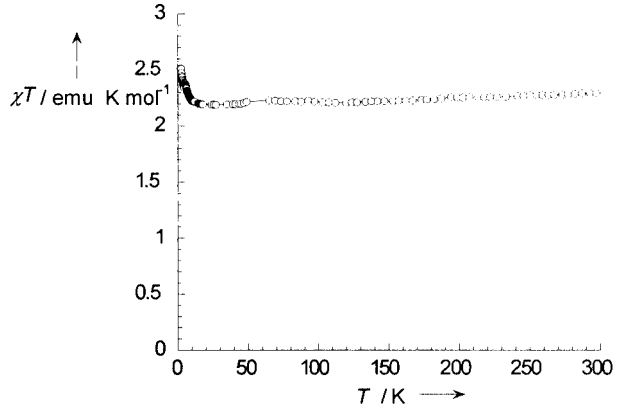

Figure 14. Thermal variation of χT for compound **4** measured in a 0.1 T field

EPR Spectroscopy: The magnetic transitions of the different compounds can be monitored by EPR spectroscopy. At room temperature, the EPR spectrum (Figure 15) of the paramagnetic derivative *p*-rad[ZnCr(ox)$_3$] (**4**) can be viewed as the sum of the contributions of the different spin carriers in the lattice. An asymmetric signal can be observed with a maximum at g = 4.1. This signal is characteristic of the $[Cr(ox)_3]^{3-}$ fragment with a zero-field splitting of the ground state.[41] In the g = 2.0 region, the expected free

 © 2005 Wiley-VCH Verlag GmbH & Co. KGaA, Weinheim

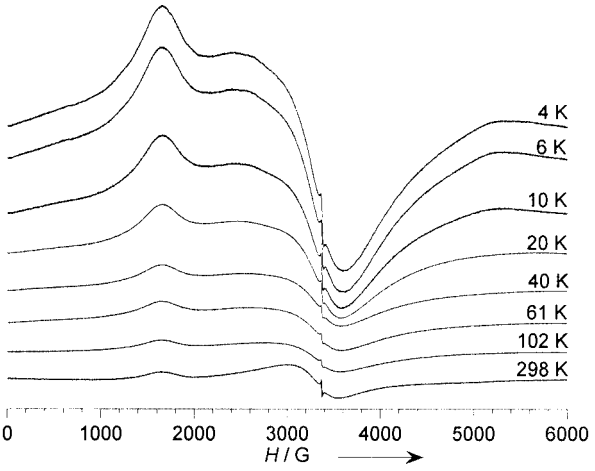

Figure 15. EPR spectra of *p*-rad[$ZnCr(ox)_3$] (**4**) at different temperatures

radical signal is superimposed with a weak contribution which originates from the chromium(III) centres. This feature is relatively broad (g = 2.057; ΔH_{pp} = 560 G) compared with previously reported salts based on *p*-rad (dipolar broadening). On lowering the temperature, the signal continuously broadens and becomes more asymmetric. At 3.2 K, the peak-to-peak width ΔH_{pp} is equal to 1130 G. A nitroxide impurity can be seen in the whole-temperature range at g = 2.005.

On the other hand, the EPR spectrum at room temperature (Figure 16) of *p*-rad[$MnCr(ox)_3$]·H_2O (**1**) shows a single line centred at g = 1.996 with a peak-to-peak width ΔH_{pp} = 350 G. The asymmetric signal of the chromium(III) moiety and the characteristic peak of the free radical are not observed. On lowering the temperature, the intensity of the signal increases and broadens to a peak-to-peak width value of 900 G at 7.6 K. Below the critical temperature, the signal splits into two components centred at g = 1.44 and g = 4.52 G. These features parallel the previously reported data for [$FeCp^*_2$][$MnCr(ox)_3$]. In this case, however, the

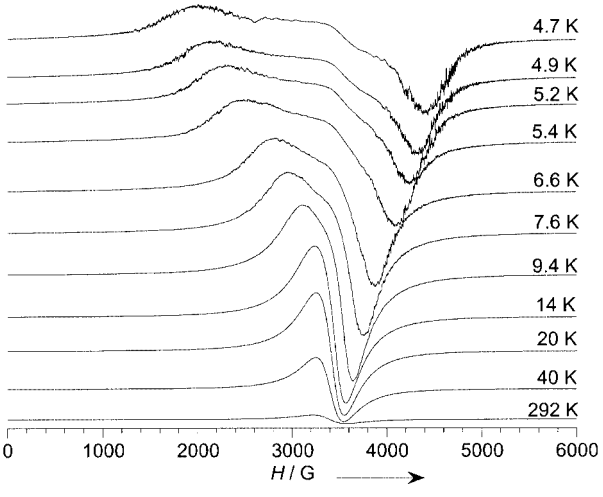

Figure 16. EPR spectra of *p*-rad[$MnCr(ox)_3$]·H_2O (**1**) at different temperatures

free radical does not show an intrinsic signal, indicating exchange interactions between the two magnetic sublattices.

The temperature dependence (Figure 17) of the EPR properties of the antiferromagnetic compound *p*-rad[$Mn(H_2O)Cr(ox)_3$]·$2H_2O$ (**7**) was investigated to allow comparison with the 2D ferromagnetic isomer *p*-rad[$MnCr(ox)_3$]·H_2O (**1**). The experiment was performed on a collection of single crystals. At room temperature, the EPR spectrum of **7** also shows a single line centred at the same g-value (1.996) with a peak-to-peak width ΔH_{pp} = 420 G. On lowering the temperature, the intensity of the signal increases, reaches a maximum around 12 K. It then decreases and broadens to a peak-to-peak width value of 560 G at 7.9 K. Below the Néel temperature the signal decreases dramatically, as expected for an antiferromagnetic ordered phase. A very weak anisotropic signal remains at low temperature which can be ascribed to the radical contribution and possible traces of chromium(III).

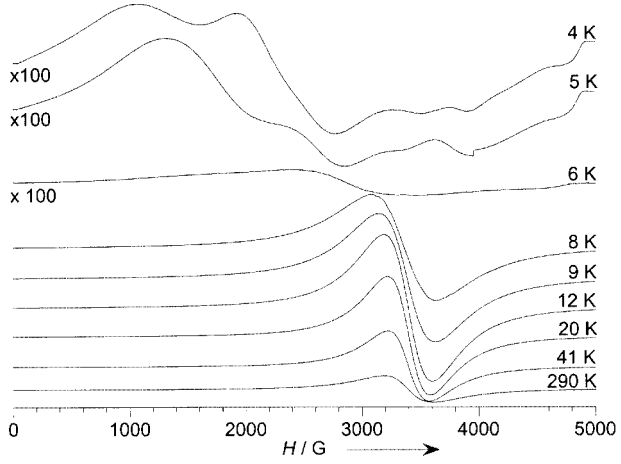

Figure 17. EPR spectra of *p*-rad[$Mn(H_2O)Cr(ox)_3$]·$2H_2O$ (**7**) at different temperatures

The EPR spectrum (Figure S4) of *p*-rad[$CoCr(ox)_3$]·$2H_2O$ (**2**) at room temperature is essentially featureless. The presence of the orbitally degenerate Co^{2+} cation induces a fast spin relaxation at high temperatures. Below 60 K, a broad and asymmetric feature appears at g = 1.54. On decreasing the temperature further, the signal becomes more intense and shifts slowly upfield. Below T_C, the main feature is accompanied by a small hump at very low fields which can be attributed to ferromagnetic resonance.

The temperature dependence of the EPR spectrum (Figure S5) for *p*-rad[$NiCr(ox)_3$]·H_2O (**3**) is similar to that observed for **1**. Only one broader signal (ΔH_{pp} = 1230 G) centred at g = 2.049 can be detected in the paramagnetic regime (the sharp line at g = 2.005 can be ascribed to a nitroxide impurity representing less than 0.01%). This is again an indication of the exchange interaction between the free radical and the magnetic network. At temperatures close to T_C, the main feature becomes anisotropic and a low-field component appears. This signal shifts downfield at a high rate (700 G/K) when decreasing the temperature, indicating the rise of the internal field in the solid.

 © 2005 Wiley-VCH Verlag GmbH & Co. KGaA, Weinheim

As expected, the systematic study of the EPR spectra reveals drastic changes which occur close to T_C for all the magnetically ordered compounds. In general, the shift of the radical resonance below the ordering temperature could be used to monitor the strength of the internal magnetic field. This has been the case in hybrid metal-radical layered systems of the brucite type[42] or in the family of compounds $[FeCp^*_2][MM'(ox)_3]$. In our case, however, the radical is not merely a spectator since it couples with the anionic lattice by exchange interactions. Compared with the decamethylferricenium derivative, where most of the spin density is located in the iron centre and hence sandwiched by Cp* molecules, the nitroxide radical is less protected from the surroundings and it can readily interact with the neighbouring spin carriers.

Conclusion

The ability of cationic nitronyl nitroxide type free radicals to act as countercations of oxalato-bridged bimetallic compounds has been studied in this work. Hybrid materials which combine nitroxide free radicals and ferromagnetic layers with similar magnetic properties as those previously observed in the quaternary onium analogues $[AR_4][MCr(ox)_3]$ (A = N, P) have been obtained. The syntheses of the latter proceed in high yield by fast precipitation in aqueous solutions due to the nonpolar character of the tetrabutylammonium or tetraphenylphosphonium cations. In our case, the presence of the radical moiety confers high polarity on the cation, solvation becomes more effective and precipitation of the extended compound is hindered. This is particularly the case for M = Mn (and also Zn) since the tris(oxalate)chromate(III) ligand has a lower affinity for this larger cation. Working in concentrated conditions and in less polar solvents (ethanol/water mixtures) invariably affords the hybrid 2D magnets as fine powders (*kinetic control*) while performing the syntheses in more dilute aqueous solutions (*thermodynamic control*) yields new heterodimetallic oxalato-based lattices which result from partial occupation, by water molecules, of the vacant positions of the divalent metal. We have shown that the size and shape of the free radical determines the geometry and dimensionality of these novel hybrid materials: *p*-rad stabilizes a 3D achiral network of hellicoidal hexagonal channels, while *m*-rad acts as countercation to a ladder-like anionic structure. The influence of the free radical in the structure of the inorganic host is made possible by the formation of hydrogen bonds which involve adventitious solvent molecules.

This family of compounds, in which ferromagnetic layers coexist with free radical species, can be considered as multifunctional hybrid magnets such as those based on the paramagnetic decamethylferricinium cation $[FeCp^*][M^{II}M^{III}(ox)_3]$. As was observed in this previously reported example, the paramagnetic cation (in this case, the nitronyl nitroxide free radical) has little influence on the ordering temperatures but has a marked effect on the coercive field values, although this effect can be correlated with other features such as the particle size. Both magnetic parameters (critical temperatures and coercive fields) are similar to those found in other families of 2D oxalate-based magnets with low T_C (around 5 K) and H_{coer} values for the Mn-containing compounds and higher ordering temperatures (11−15 K) for the Ni and Co complexes. The most important difference between the two families of hybrid magnets is that whereas the two magnetic sublattices are quasi-independent in $[FeCp^*][M^{II}M^{III}(ox)_3]$, a sizeable interaction between the free radicals and the inorganic layers has been indicated by EPR spectroscopic studies in the present case.

Further work on this topic will be directed towards the preparation of nitronyl nitroxide cationic free radicals based on tetraalkylammonium salts which can be more efficient templates of the 2D hexagonal oxalate-based network.

Experimental Section

General Procedure for the Preparation of Hybrid Magnets 1−6: $Ag_3[Cr(ox)_3]$ (0.08 mmol) was added to a solution of the cationic free radical (prepared as the iodide salts *p*-radI or *m*-radI) (0.25 mmol) in EtOH (5 mL, 96%) and H_2O (1 mL). After 30 min stirring, AgI was removed by centrifugation. In a separate beaker, a solution of $[M(H_2O)_n]Cl_2$ (M = Mn, Co, Ni, Zn) (0.25 mmol) in EtOH (5 mL, 96%) and H_2O (1 mL) was allowed to react with $Ag_3[Cr(ox)]_3$ (0.17 mmol). After stirring for 30 min, AgCl was removed by centrifugation. The two supernatant solutions were mixed and the precipitated green powder was collected by centrifugation.

***p*-rad[MnCr(ox)$_3$]·H$_2$O (1):** Yield: 121 mg (75%). IR (KBr): $\tilde{\nu}$ = 1631 (CO), 1373 (NO), 1143 cm^{-1} (NO). $C_{19}H_{21}CrMnN_3O_{15}$ (638.3): calcd. C 35.75, H 3.32, N 6.58; found C 35.23, H 3.24, N 6.02.

***p*-rad[CoCr(ox)$_3$]·2H$_2$O (2):** Yield: 107 mg (65%). IR (KBr): $\tilde{\nu}$ = 1626 (CO), 1377 (NO), 1137 cm^{-1} (NO). $C_{19}H_{23}CoCrN_3O_{16}$ (660.3): calcd. C 34.56, H 3.51, N 6.36; found C 34.36, H 3.21, N 6.16.

***p*-rad[NiCr(ox)$_3$]·H$_2$O (3):** Yield: 98 mg (61%). IR (KBr): $\tilde{\nu}$ = 1623 (CO), 1377 (NO), 1139 cm^{-1} (NO). $C_{19}H_{21}CrN_3NiO_{15}$ (642.1): calcd. C 35.54, H 3.30, N 6.54; found C 35.73, H 3.37, N 6.61.

***p*-rad[ZnCr(ox)$_3$] (4):** Yield: 102 mg (64%). IR (KBr): $\tilde{\nu}$ = 1629 (CO), 1384 (NO), 1137 cm^{-1} (NO). $C_{19}H_{19}CrN_3O_{14}Zn$ (630.7): calcd. C 36.18, H 3.04, N 6.66; found C 37.15, H 3.63, N 7.21.

***m*-rad[MnCr(ox)$_3$]·H$_2$O (5):** Yield: 96 mg (55%). IR (KBr): $\tilde{\nu}$ = 1653 (CO), 1383 (NO), 1139 cm^{-1} (NO). $C_{19}H_{21}CrMnN_3O_{15}$ (638.3): calcd. C 35.75, H 3.32, N 6.58; found C 36.14, H 3.51, N 6.76.

***m*-rad[CoCr(ox)$_3$]·H$_2$O (6):** Yield: 94 mg (69%). IR (KBr): $\tilde{\nu}$ = 1628 (CO), 1377 (NO), 1137 cm^{-1} (NO). $C_{19}H_{21}CoCrN_3O_{15}$ (642.3): calcd. C 35.53, H 3.30, N 6.54; found C 35.13, H 3.48, N 6.37.

Preparation of 7−8: The cationic free radical (*p*-radI or *m*-radI) (100 mg, 0.26 mmol) was added to a suspension of $Ag_3[Cr(ox)_3]$ in EtOH (5 mL). After 30 min stirring, AgI was filtered and a solution of $Mn(ClO_4)_2·6H_2O$ (32 mg, 0.088 mmol) in a minimum amount of water was added to the filtrate. The resultant green suspension became clear after addition of H_2O (2 mL) and the mixture was

 © 2005 Wiley-VCH Verlag GmbH & Co. KGaA, Weinheim

left undisturbed in the dark. Green single crystals suitable for X-ray structure analysis appeared within a few hours.

***p*-rad[MnCr(ox)$_3$(H$_2$O)]·2H$_2$O (7):** Yield: 94 mg (60%). IR (KBr): $\tilde{\nu}$ = 1630 (CO), 1376 (NO), 1140 cm^{-1} (NO). $C_{19}H_{25}CrMnN_3O_{17}$ (674.3): calcd. C 33.84, H 3.74, N 6.23; found C 33.73, H 3.75, N 6.14.

***m*-rad[MnCr(ox)$_3$(H$_2$O)$_2$]·2H$_2$O (8):** Yield: 96 mg (62%). IR (KBr): $\tilde{\nu}$ = 1634 (CO), 1378 (NO), 1139 cm^{-1} (NO). $C_{19}H_{27}CrMnN_3O_{18}$ (692.4): calcd. C 32.96, H 3.93, N 6.07; found C 32.78, H 3.86, N 6.19.

Physical Measurements: All magnetic measurements were carried out on powdered samples with a Quantum Design MPMS-XL-5 SQUID magnetometer. Variable temperature susceptibility measurements were carried out on polycrystalline samples in the 2−300 K temperature range at a magnetic field of 0.1 T. Diamagnetic contributions were corrected with Pascal's constants. Isothermal magnetisation measurements were collected in the H = 0−5 T field range at 2 K. The hysteresis studies were performed between 5 and −5 T, at 2 K, cooling the samples at zero field. AC measurements were performed at different frequencies with an oscillating magnetic field of 0.395 mT. The ESR spectra were recorded on powdered samples in the X-band region (ν = 9.47 GHz) with a Bruker E500 ELEXSYS spectrometer equipped with a helium cryostat in order to study the thermal dependence in the temperature range 300−3 K. IR transmission measurements of pressed KBr pellets were recorded at room temperature with a Nicolet Avatar 320 FT-IR spectrophotometer in the range 4000−400 cm^{-1}. CHN elemental analyses were carried out with a CE instruments EA 1110 CHNS analyser on samples dried under vacuum. Thermogravimetric measurements were carried out with a Mettler Toledo TGA/SDTA 851e apparatus.

X-ray Crystallographic Studies: X-ray diffraction data of **7** and **8** were collected at room temperature with a Nonius KappaCCD diffractometer using a graphite-monochromated Mo-K_α radiation source (λ = 0.71073 Å). The Denzo and Scalepack[43] programs were used for cell refinements and data reduction. The structures were solved by direct methods using the SIR97[44] program with the WinGX[45] graphical user interface. The structural refinements were carried out with SHELX-97.[46] All nonhydrogen atoms were refined anisotropically. A multiscan absorption correction, based on equivalent reflections, was applied to the data using the program SORTAV[47] ($T_{max.}/T_{min.}$ 0.8972/0.5899 for **7** and 0.995/0.898 for **8**). H atoms of water molecules were found from difference maps and were positionally refined with geometric restraints (O−H 0.82 Å and H···H 1.30 Å) and with U_{iso}(H) = 1.2U_{eq}(O). The remaining H atoms were placed in calculated positions and refined using a riding model with C−H = 0.97 Å and U_{iso}(H) = 1.2U_{eq}(C). All nonhydrogen atoms were refined anisotropically. Crystallographic data are summarised in Table 2.

CCDC-149375 and -236227 contain the supplementary crystallographic data for this paper. These data can be obtained free of charge via www.ccdc.cam.ac.uk/conts/retrieving.html (or from the Cambridge Crystallographic Data Centre, 12 Union Road, Cambridge CB2 1EZ, UK; fax: (internat.) +44-1223-336-033; E-mail: deposit@ccdc.cam.ac.uk).

Supporting Information (see also the footnote on the first page of this article): Figures S1−S3 show χT vs. T plots for compounds **1**−**3** and **5**−**6**. Figures S4 and S5 show, respectively, the EPR spectra of *p*-rad[CoCr(ox)$_3$]·2H$_2$O (**2**) and *p*-rad[NiCr(ox)$_3$]·H$_2$O (**3**) at different temperatures.

Table 2. Crystal data and structure refinement for **7**−**8**

Compound	**7**	**8**
Empirical formula	$C_{19}H_{25}CrMnN_3O_{17}$	$C_{19}H_{27}CrMnN_3O_{18}$
Molecular mass	674.36	692.38
a (Å)	11.343(2)	8.7890(2)
b (Å)	14.311(2)	11.5290(2)
c (Å)	16.928(10)	14.4980(3)
α (°)	90	89.1000(8)
β (°)	104.14(3)	82.2150(9)
γ (°)	90	70.8690(9)
Z	2	2
d (Mg·m^{-3})	1.681	1.673
Crystal system	monoclinic	triclinic
Space group	C_c	$P\bar{1}$
Crystal dimensions (mm)	0.61 × 0.19 × 0.12	0.32 × 0.12 × 0.05
T (K)	293(2)	225(2)
Θ Range	4.68 < 2Θ < 61.24	2.84 < 2Θ < 57.42
Reflections collected	11092	34160
Independent reflections	6821	7040
Data/restraints/parameters	6821/2/402	7040/14/408
Final R indices [$I > 2\sigma(I)$]	R_1 = 0.0309, wR_2 = 0.0603	R_1 = 0.0507, wR_2 = 0.1058
R indices (all data)	R_1 = 0.0463, wR_2 = 0.0642	R_1 = 0.1391, wR_2 = 0.1417

Acknowledgments

This work was supported by the Ministerio de Ciencia y Tecnología (MCyT) (Project no. MAT2001-3507-C02-01). CGS and FMR acknowledge research contracts from MCyT (Programa "Ramón y Cajal"). We also thank J. M. Martínez-Agudo for his help with the magnetic measurements and thermogravimetric analysis.

[1] O. Kahn, *Molecular Magnetism*, Wiley-VCH, Weinheim, **1993**.
[2] For an overview of the richness of structural design in molecular magnetism see the Proceedings of the 8th International Conference on Molecule-based Magnets: *Polyhedron* **2003**, *14*−*17*, 1725−2584.
[3] H. Tamaki, Z. J. Zhong, N. Matsumoto, S. Kida, M. Koikawa, N. Achiwa, Y. Hashimoto, H. Okawa, *J. Am. Chem. Soc.* **1992**, *114*, 6974−6979.
[4] S. Decurtins, H. W. Schmalle, P. Schneuwly, H. R. Oswald, *Inorg. Chem.* **1993**, *32*, 1888−1892.
[5] S. Decurtins, H. W. Schmalle, H. R. Oswald, A. Linden, J. Ensling, P. Gütlich, A. Hauser, *Inorg. Chim. Acta* **1994**, *216*, 65−73.
[6] S.G. Carling, C. Mathonière, P. Day, K. M. A. Malik, S. J. Coles, M. B. Hursthouse, *J. Chem. Soc., Dalton Trans.* **1996**, 1839−1843.
[7] R. Pellaux, H. W. Schmalle, R. Huber, P. Fischer, T. Hauss, B. Ouladdiaf, S. Decurtins, *Inorg. Chem.* **1997**, *36*, 2301−2308.
[8] S. Decurtins, H. W. Schmalle, P. Schneuwly, J. Ensling, P. Gütlich, *J. Am. Chem. Soc.* **1994**, *116*, 9521.
[9] S. Decurtins, H. W. Schmalle, R. Pellaux, R. Huber, P. Fischer, B. Ouladdiaf, *Adv. Mater.* **1996**, *8*, 647−651.
[10] S. Decurtins, H. W. Schmalle, R. Pellaux, *New J. Chem.* **1998**, *22*, 117−121.
[11] R. Andrés, M. Gruselle, B. Malézieux, M. Verdaguer, J. Vaissermann, *Inorg. Chem.* **1999**, *38*, 4637−4646.
[12] G. L. J. A. Rikken, E. Raupach, *Nature* **1997**, *390*, 493−494.
[13] E. Coronado, J. R. Galán-Mascarós, C. J. Gómez-García, J. M. Martínez-Agudo, *Inorg. Chem.* **2001**, *40*, 113−120.
[14] M. Clemente-León, E. Coronado, J. R. Galán-Mascarós, C. J. Gómez-García, *Chem. Commun.* **1997**, 1727.

 © 2005 Wiley-VCH Verlag GmbH & Co. KGaA, Weinheim

[15] E. Coronado, J. R. Galán-Mascarós, C. J. Gómez-García, J. Ensling, P. Gütlich, *Chem. Eur. J.* **2000**, *6*, 552−563.
[16] P. G. Lacroix, I. Malfant, S. Benard, P. Yu, E. Riviere, K. Nakatani, *Chem. Mater.* **2001**, *13*, 441−449.
[17] E. Coronado, J. R. Galán-Mascarós, C. J. Gómez-García, V. Laukhin, *Nature* **2000**, *408*, 447−449.
[18] M. Deumal, J. Cirujeda, J. Veciana, J. J. Novoa, *Chem. Eur. J.* **1999**, *5*, 1631−1642.
[19] A. Caneschi, D. Gatteschi, R. Sessoli, P. Rey, *Acc. Chem. Res.* **1989**, *22*, 392−398.
[20] A. Caneschi, D. Gatteschi, P. Rey, *Prog. Inorg. Chem.* **1991**, *39*, 331−429.
[21] K. Fegy, D. Luneau, T. Ohm, C. Paulsen, P. Rey, *Angew. Chem.* **1998**, *110*, 1331−1335; *Angew. Chem. Int. Ed.* **1998**, *37*, 1270−1273.
[22] K. Awaga, T. Inabe, U. Nagashima, T. Nakamura, M. Matsumoto, Y. Kawabata, Y. Maruyama, *Chem. Lett.* **1991**, 1777−1780.
[23] A. Yamaguchi, K. Awaga, T. Inabe, T. Nakamura, M. Matsumoto, Y. Maruyama, *Chem. Lett.* **1993**, 1443−1446.
[24] A. Yamaguchi, T. Okuno, K. Awaga, *Bull. Chem. Soc. Jpn.* **1996**, *69*, 875−882.
[25] C. Michaut, L. Ouahab, P. Bergerat, O. Kahn, A. Bousseksou, *J. Am. Chem. Soc.* **1996**, *118*, 3610−3616.
[26] H. Imai, T. Otsuka, T. Naito, K. Awaga, T. Inabe, *J. Am. Chem. Soc.* **1999**, *121*, 8098−8103.
[27] H. O. Stumpf, L. Ouahab, Y. Pei, D. Grandjean, O. Kahn, *Science* **1993**, *261*, 447.
[28] H. O. Stumpf, L. Ouahab, Y. Pei, P. Bergerat, O. Kahn, *J. Am. Chem. Soc.* **1994**, *116*, 3866−3874.
[29] M. G. F. Vaz, L. M. M. Pinheiro, H. O. Stumpf, A. F. C. Alcântara, S. Golhen, L. Ouahab, O. Cador, C. Mathonière, O. Kahn, *Chem. Eur. J.* **1999**, *5*, 1486−1495.
[30] G. Ballester, E. Coronado, C. Giménez-Saiz, F. M. Romero, *Angew. Chem. Int. Ed.* **2001**, *40*, 792−795.
[31] U. Geiser, B. L. Ramakrishna, R. D. Willett, F. B. Hulsbergen, J. Reedijk, *Inorg. Chem.* **1987**, *26*, 3750.
[32] H. Oshio, U. Nagashima, *Inorg. Chem.* **1992**, *31*, 3295−3301.
[33] G. Marinescu, M. Andruh, R. Lescouëzec, M. C. Muñoz, J. Cano, F. Lloret, M. Julve, *New J. Chem.* **2000**, *24*, 527−536.
[34] S. Decurtins, M. Gross, H. W. Schmalle, S. Ferlay, *Inorg. Chem.* **1998**, *37*, 2443−2449.
[35] D. J. Price, A. K. Powell, P. T. Wood, *J. Chem. Soc., Dalton Trans.* **2000**, 3566−3569.
[36] R. Lescouëzec, J. Vaissermann, L. M. Toma, R. Carrasco, F. Lloret, M. Julve, *Inorg. Chem.* **2004**, *43*, 2234−2236.
[37] M. Drillon, E. Coronado, D. Beltrán, R. Georges, *Chem. Phys.* **1983**, *79*, 449.
[38] The total spin Hamiltonian is the sum of exchange and Zeeman terms. The latter includes also the contribution of the radical: $H = H_{ex} - g\mu_B \mathbf{H}(S_A + S_B + S_{rad})$.
[39] For a review on molecular spin ladders, see: C. Rovira, *Chem. Eur. J.* **2000**, *6*, 1723−1729.
[40] The program MAGPACK was used for the calculation of the spin states and thermodynamic properties: J. J. Borrás-Almenar, J. M. Clemente-Juan, E. Coronado, B. S. Tsukerblat, *J. Comput. Chem.* **2001**, *22*, 985.
[41] R. Karthein, H. Motschi, A. Schweiger, S. Ibric, B. Sulzberger, W. Stumm, *Inorg. Chem.* **1991**, *30*, 1606−1611.
[42] V. Laget, C. Hornick, P. Rabu, M. Drillon, P. Turek, R. Ziessel, *Adv. Mater.* **1998**, *10*, 1024−1028.
[43] Z. Otwinowski, W. Minor, *Methods in Enzymology* **1997**, *276*, 307.
[44] A. Altomare, M. C. Burla, M. Camalli, G. Cascarano, C. Giacovazzo, A. Guagliardi, A. G. G. Moliterni, G. Polidori, R. Spagna, *J. Appl. Cryst.* **1999**, *32*, 115.
[45] L. J. Farrugia, *J. Appl. Cryst.* **1999**, *32*, 837.
[46] G. M. Sheldrick, SHELX-97, an integrated system for solving and refining crystal structures from diffraction data, University of Göttingen (Germany), **1997**.
[47] R. H. Blessing, *J. Appl. Cryst.* **1997**, *30*, 421.

Received August 8, 2004
Early View Article
Published Online November 24, 2004

 © 2005 Wiley-VCH Verlag GmbH & Co. KGaA, Weinheim

Novel Topotactic Conversion of an Organically Templated Vanadyl Phosphate Framework into Layered Structures

Minakshi Asnani,[a] Sanjeev Sharma,[a] Samuel E. Lofland,[b] Kandalam V. Ramanujachary,[b] Philippe A. Buffat,[c] and Arunachalam Ramanan*[a]

Keywords: Vanadyl phosphate / Topotactic / Intercalation / Ion exchange

This paper reports a novel topotactic exchange reaction of the ethylenediammonium intercalated mixed-valent vanadyl phosphate, $(H_3NCH_2CH_2NH_3)_{0.5}[V^{4+}_{0.45}V^{5+}_{0.55}O_2PO_4\{P(OH)_2\}_{0.483}]$, with monovalent cations at room temperature. Alkali metal ions and other monovalent cations (e.g. K^+, Rb^+, Tl^+, NH_4^+) behave similarly, leading to intercalated layered vanadyl phosphates (basal spacing about 6.3–6.5Å). The amount of cations incorporated between the layers is essentially dictated by the charge present on the layers (equivalent to the amount of V^{4+} present). The present approach has enabled us to obtain a new phase, $Tl_{0.45}VOPO_4{\cdot}0.33H_2O$, under ambient conditions. All the layered solids show low-temperature magnetic behaviour similar to hydrothermally synthesised products. Treatment with silver ions resulted in a new silver vanadium(V) phosphate $Ag_{3.5}VP_{1.5}O_8$ [monoclinic; a = 22.557(4), b = 7.973(3), c = 12.430(3) Å and β = 112.26(2)°] coated with silver metal nanospheres (ca. 15 nm) which, on heating above 400 °C, yielded a 2:1 mixture of two thermodynamically stable phases, $Ag_2VO_2PO_4$ and Ag_3PO_4.

(© Wiley-VCH Verlag GmbH & Co. KGaA, 69451 Weinheim, Germany, 2005)

Introduction

Inorganic layered materials have received considerable attention as hosts for the intercalation of guest molecules and ion exchange reactions.[1] Intercalation compounds of vanadyl phosphate with aliphatic and aromatic amines,[2] heterocycles,[3] alcohols and diols[4] as well as carboxylic acids[5] and their amides[6] have been extensively studied. Vanadyl phosphates are important materials owing to their potential uses as sensors, fuel cells and catalysts for the oxidation of hydrocarbons.[7,8] Intercalated vanadyl phosphates can be synthesised either through direct hydrothermal treatment or via ion-exchange reactions.[9−16] The ion-exchange behaviour of several organically intercalated oxides is well-known.[17,18] However, to the best of our knowledge, exchange reactions with organically intercalated vanadyl phosphates have not been reported. In this paper, we describe a novel room temperature topotactic reaction of ethylenediammonium intercalated vanadyl phosphate with various metal ions. Our investigations reveal that only monovalent ions viz. K^+, Rb^+, Tl^+ and NH_4^+ undergo facile exchange reactions with ethylenediammonium intercalated vanadyl phosphate. The reaction with silver ions is unusual since it leads to the formation of a hitherto unknown silver vanadium phosphate coated with silver nanoparticles.

[a] Department of Chemistry, Indian Institute of Technology, New Delhi 110016, India
Fax: (internat.) + 91-11-26582037
E-mail: aramanan@chemistry.iitd.ac.in
[b] Department of Chemistry and Biochemistry, Rowan University, Glassboro, NJ 08028, USA
[c] EPFL, 1015 Lausanne, Switzerland

Results and Discussion

A single-crystal structure analysis of the parent compound, ethylenediammonium intercalated mixed-valent vanadyl phosphate, $(H_3NCH_2CH_2NH_3)_{0.5}[V^{4+}_{0.45}V^{5+}_{0.55}O_2PO_4\{P(OH)_2\}_{0.483}]$ (hereafter referred to as enVPO) has been reported earlier.[19] The crystal structure of this phase is analogous to that of $(H_3NCH_2CH_2NH_3)$ $[(VO)_2(PO_4)_2(H_2PO_4)]$ reported by Harrison et al.[20] except that the phosphate groups linking the vanadyl phosphate layers (VPO) are partially disordered in our case. The structure contains layers consisting of VO_5 square pyramids and PO_4 tetrahedra sharing vertices in the *ab*-plane. VO_5 groups in adjacent layers are connected through a disordered tetrahedral $PO_2(OH)_2$ unit and the unprotonated oxygen atoms of these tetrahedra can also be considered as a part of the vanadium octahedra with long V−O bonds (2.2 Å) (Figure 1). The VPO configuration results in puckered $[VO_2PO_4]^{2-}$ layers oriented in the [101] direction. The layers are connected by $PO_2(OH)_2$ tetrahedral units to form a 3D network along the *c*-axis. Ethylenediammonium cations occupy the cavities formed between the $PO_2(OH)_2$ tetrahedra in the interlayer region. The open framework structure of

enVPO makes the organic cation and the bridging phosphate group accessible to metal cation guest species. In this work, we attempted to exchange the ethylenediammonium cation with various metal ions. Before every exchange reaction, care was taken to ascertain the single-phase nature of enVPO using powder X-ray diffraction, TGA, DTA, cerimetric titration and EDAX. Initial reactions indicated that enVPO was quite stable in aqueous solutions for several days in the presence of lithium, sodium, cesium and various divalent metal ions (Mg^{2+}, Ca^{2+}, Mn^{2+}, Co^{2+}, Ni^{2+} or Cu^{2+}). A reaction occurred only when the metal ion was potassium, rubidium, thallium, ammonium or silver. A preliminary analysis clearly showed the presence of both ethylenediammonium and phosphate groups in the filtrate.

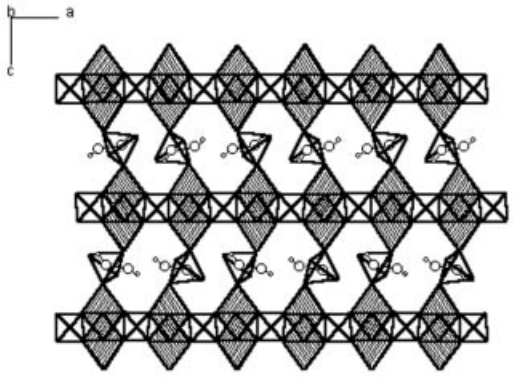

Figure 1. Crystal structure of enVPO viewed along *b* axis; during the exchange reaction, the bridging phosphate groups (coloured orange) and the ethylenediammonium cations leach out

Reactivity with Metal Ions and the Ammonium Ion

EnVPO undergoes a facile exchange reaction with K^+, Rb^+, Tl^+ and NH_4^+ under mild conditions to form metal or ammonium intercalated vanadyl phosphates, M_xVPO (M = K, Rb, Tl and NH_4). Powder X-ray diffraction patterns of the exchanged products were very different from that of parent enVPO (Figure 2) with a basal spacing of 7.9Å. The presence of dominant 00l reflections in the products indicates strong lamellar characteristics ($c \approx$ 6.3−6.5Å) similar to other metal intercalated layered vanadyl phosphates. In the cases of the potassium,[21−24] rubidium[21−26] and ammonium[26,27] incorporated solids, the observed basal spacings were similar to those reported in the literature. Furthermore, powder X-ray diffraction patterns of the exchanged products matched well with simulated patterns of metal intercalated vanadyl phosphates.[11,12] While the parent enVPO did not contain any water molecules, the exchanged products M_xVPO were hydrated as indicated by FTIR spectroscopy and thermal analyses. The amount of water and the phase changes of the solids were determined by TGA and DTA studies (Figure 3). Upon heating, all solids exhibited an initial weight loss below 100 °C. K_xVPO showed an additional weight loss of 6.3% in the temperature range 150 to 230 °C. Above this temperature there were no further weight losses. Rb_xVPO also showed similar thermal behaviour. $(NH_4)_xVPO$ exhibited two additional weight losses, namely 6.6% in the temperature range 130 to 200 °C and a broad weight loss of 8.3% in the temperature range 210 to 430 °C. Thallium intercalated vanadyl phosphate Tl_xVPO, exhibited a much lower weight loss (<2%) suggesting very little incorporation of water. It should be mentioned here that thallium intercalated vanadyl phosphate, Tl_xVPO has been synthesised for the first time by a low temperature method in this study. DTA of all the solids showed a broad endothermic peak corresponding to the loss of water molecules except in $(NH_4)_xVPO$ in which it also includes loss of ammonia. In all cases, the products were X-ray amorphous after heating above 300 °C.

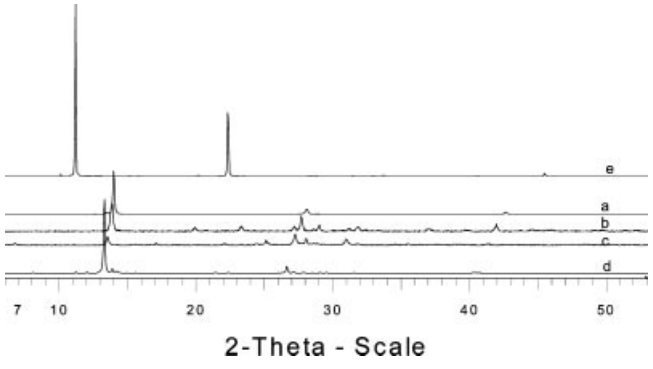

Figure 2. Powder X-ray patterns of (a) K_xVPO, (b) Rb_xVPO, (c) Tl_xVPO, (d) $(NH_4)_xVPO$ and (e) enVPO

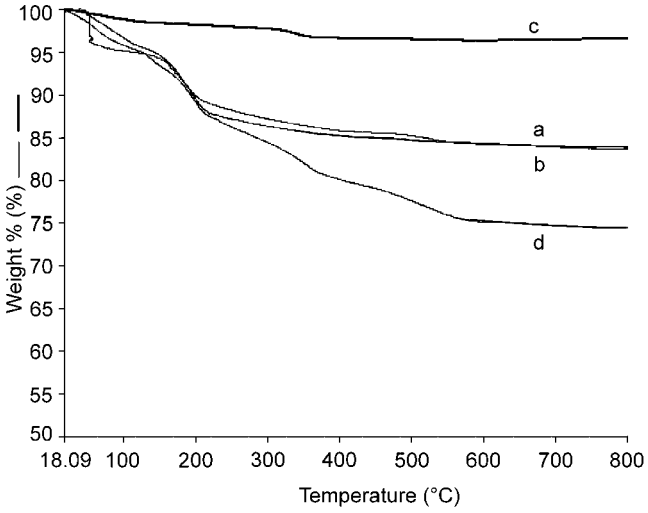

Figure 3. TGA curves of (a) K_xVPO, (b) Rb_xVPO, (c) Tl_xVPO and (d) $(NH_4)_xVPO$

The absence of the ethylenediammonium ion was further confirmed by FTIR spectroscopy. All the exchanged solids showed the presence of strong bands around 1055 and 940 cm^{-1} due to PO_4 groups, a peak around 990 cm^{-1} due to the V=O stretch and, similar to alkali metal intercalated vanadyl phosphates, a broad weak band around 680 cm^{-1} due to the V−O−P lattice.[10,11] In the case of $(NH_4)_xVPO$, additional peaks were observed around 3300 and 1350 cm^{-1} due to N−H stretching and bending vibrations. SEM

 © 2005 Wiley-VCH Verlag GmbH & Co. KGaA, Weinheim

$$(H_3NCH_2CH_2NH_3)_{0.5}[V^{4+}_{0.45}V^{5+}_{0.55}O_2PO_4\{P(OH)_2\}_{0.483}] + 0.45M^+(aq) + yH_2O \longrightarrow M^+_{0.45}V^{4+}_{0.45}V^{5+}_{0.55}OPO_4.yH_2O + 0.5[H_3NCH_2CH_2NH_3]^{2+}(aq) + 0.966[H_2PO_4]^-(aq) + 0.034(OH)^-(aq) \quad (1)$$

studies revealed a plate like morphology for all solids which is similar to metal intercalated layered vanadyl phosphates.[11] Cerimetric titrations showed that the V^{4+}/V^{5+} ratio in the parent enVPO as well as in the metal exchanged products remained almost the same within experimental error. EDAX analysis indicated that the P/V ratio in the parent enVPO was about 1.5 which is closer to the composition established by a single-crystal X-ray diffraction analysis.[19] However, in the exchanged products, the P/V ratio was about 1 with $x \approx 0.5$ for all solids. On the basis of powder X-ray diffraction, TG, EDAX and chemical analyses, we established the general composition $M_xVOPO_4{\cdot}yH_2O$ for all the exchanged products (Table 1).

As in normal ion exchange reactions, we expected that the ethylenediammonium cations would be replaced by an equivalent amount of metal ions. However, our observations suggest that in addition to the organic cations diffusing out of the structure, the phosphate groups linking VPO layers also leached out as a result of excess alkali metal cations [Equation (1)]. It seems that the amount of metal cations incorporated between the layers of the final products is essentially dictated by the charge present on the layers (equivalent to the amount of V^{4+} present). Also, the amount of water molecules entering between the layers depends on the nature of the cation. During the exchange reaction, the oxidation state of vanadium remained the same, i.e. no redox reaction occurred between the species present in the aqueous solution and the mixed-valent vanadyl phosphate. Since the product (M_xVPO) shows a strong structural resemblance to the parent phase (enVPO) along the [101] direction, the reaction can be considered as *topotactic*.[28] The structural change taking part in the exchange reaction is shown in Scheme 1. During the exchange reaction, ethylenediammonium groups are exchanged by metal ions. In addition, the phosphate groups linking the layers are leached out due to the presence of excess metal cations. The scheme also shows the reduction in the basal axis during the transformation. The exchange reaction can be written as in Equation (1).

Our results indicate that exchange reactions take place only when diameter of the monovalent cation is in the range of 2.7−3.0 Å, i.e. similar to the kinetic diameter of the ethylenediammonium cation (2.8 Å). The reaction with thallium ions led to the formation of a yet uncharacterised solid, $Tl_{0.45}VOPO_4{\cdot}0.33H_2O$. The mild conditions that we employed here imply a broad scope for investigating exchange reactions of other organically intercalated solids and, in particular, metal phosphates in order to obtain new metastable phases.

We also examined whether the ion-exchange behaviour of M_xVPO prepared by the topotactic reaction is similar to that reported in the literature for related systems. For example, K_xVPO exhibits facile and complete ion exchange with ammonium ions. A similar observation has been reported by Zima et al.[29] where the ion exchange ceased after 14 days at $x = 0.15$. However, in our case a complete

Table 1. Compositional analysis of M_xVPO

M in $M_xVOPO_4{\cdot}yH_2O$	Amount of metal intercalated,[a] x	No. of water molecules, y	Basal spacing [Å]	Ionic radius [Å][b]	Curie constant, C [emu K/mol]
K^+	0.53	1.15	6.33	1.38	0.38
Rb^+	0.57	1.22	6.40	1.52	0.39
Tl^+	0.54	0.33	6.54	1.50	0.41
$(NH_4)^+$	0.56	1.42	6.67	1.46	0.35
enVPO	–	–	7.89	–	0.40

[a] The value of x is equivalent to the amount of V^{4+} estimated from a cerimetric titration. [b] R. D. Shannon, *Acta Crystallog., Sect. A* **1976**, *32*, 751; radii based on coordination number 6.

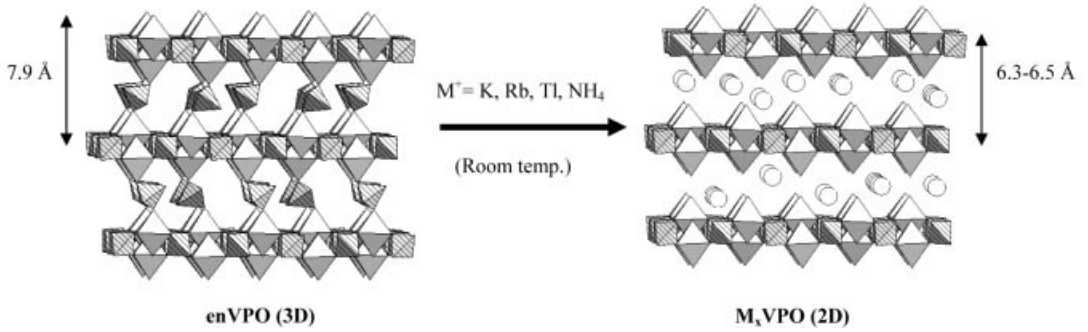

Scheme 1

 © 2005 Wiley-VCH Verlag GmbH & Co. KGaA, Weinheim

conversion into $(NH_4)_xVPO$ was achieved within 2 days. The reverse reaction, i.e. conversion of $(NH_4)_xVPO$ to K_xVPO which has not reported so far, could also be achieved. However, in this case only partial ion exchange was observed (Figure 4). It is quite possible that the arrangement of the metal atoms and the stacking of vanadyl phosphate layers in M_xVPO may be different if the method of preparation is varied since a true equilibrium is possible only when crystals are grown under hydrothermal conditions. Powder X-ray diffraction is insufficient to give deeper insight into the complete crystal structure.

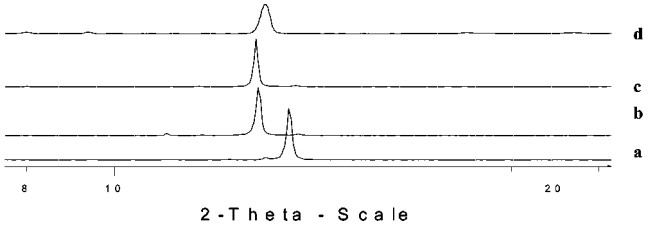

Figure 4. Powder X-ray diffraction patterns of (a) K_xVPO, (b) $(NH_4)_xVPO$ (c) ammonium exchanged K_xVPO and (d) potassium exchanged $(NH_4)_xVPO$

Magnetic Properties

Low-temperature magnetic measurements were performed on all metal exchanged products to establish the nature of their magnetic properties and spin concentrations. The magnetic behaviour of powdered samples of the mixed-valent M_xVPO is shown in Figure 5 in the form of a $1/\chi_m$ versus T plot. The susceptibility data for all samples were modelled over the temperature range 5 to 60 K according to the Curie−Weiss equation. While Rb_xVPO and K_xVPO showed ferromagnetic interactions, Tl_xVPO and $(NH_4)_xVPO$ showed antiferromagnetic interactions at low temperature. This behaviour is clear in the $\chi_m T$ versus T plots (Figure 6). The values of the Curie constants (0.38 and 0.39 emu K mol^{-1}) for the K and Rb compounds, respectively, are close to the values obtained for compounds of similar composition. Analogous behaviour was observed for the hydrothermally prepared $K_{0.5}VOPO_4{\cdot}2H_2O$ using the iodide method[30] and $NaBH_4$ as a reducing agent.[32] Our data is in accordance with that reported by Papoutsakis et al.[27] but is in contrast to the observations of Roca et al.[31] A plot of $\chi_m T$ versus T for $(NH_4)_xVPO$ and

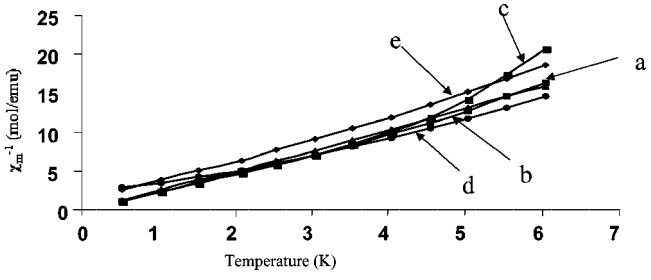

Figure 5. χ_m^{-1} versus temperature plots for (a) enVPO, (b) K_xVPO, (c) Rb_xVPO, (d) Tl_xVPO and (e) $(NH_4)_xVPO$; the susceptibilities have been corrected for the amount of reduced vanadium

Tl_xVPO shows a strong deviation below 25 K indicating antiferromagnetic nearest-neighbour exchange interactions. Similar magnetic behaviour has been observed for $(NH_4)VOPO_4$ prepared under hydrothermal conditions.[33,34] A fully reduced thallium vanadyl phosphate $Tl_3(V^{IV}O)(HV_2{}^{IV}O_3)(PO_4)_2(HPO_4)$ and fully oxidised $Tl(V^VO_2)(HPO_4)$ were reported to be paramagnetic even at low temperatures.[35] However, mixed valent $Tl_6V_6P_6O_{31}$ showed low temperature antiferromagnetic behaviour.[36]

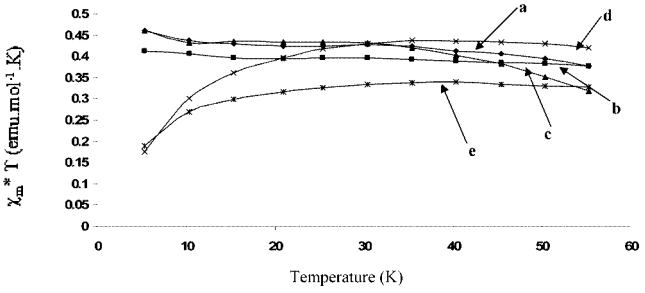

Figure 6. $\chi_m T$ versus temperature plots for (a) enVPO, (b) K_xVPO, (c) Rb_xVPO, (d) Tl_xVPO and (e) $(NH_4)_xVPO$; the susceptibilities have been corrected for the amount of reduced vanadium

Reactivity with Silver Ions

While the organic cation in enVPO could be readily exchanged with alkali metal or ammonium cations, different behaviour was observed with silver. A powder X-ray diffraction pattern of the product indicated a complete collapse of the parent layered structure. The reflections of this phase did not match with any of those reported previously. However, all peaks could be indexed to the monoclinic system with cell parameters, a = 22.557(4), b = 7.973(3) and c = 12.430(3) Å and β = 112.26(2)° using CRYSFIRE[37] (Figure 7).

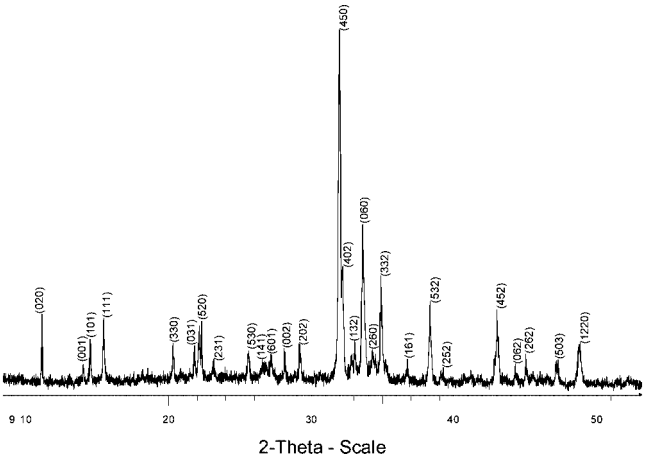

Figure 7. Powder X-ray diffraction pattern of $Ag_{3.5}VP_{1.5}O_8$

The solid did not show any appreciable weight loss as indicated by TG analysis (<3%) whereas DTA showed an endothermic peak around 620 K. TGA and DTA indicated the absence of organic groups which was further confirmed by FTIR spectroscopy and EDAX analysis. On the basis of

 © 2005 Wiley-VCH Verlag GmbH & Co. KGaA, Weinheim

$$(H_3NCH_2CH_2NH_3)_{0.5}[V^{4+}_{0.45}V^{5+}_{0.55}O_2PO_4\{P(OH)_2\}_{0.483}] + 3.5Ag^+ \text{ (excess)} + H_2O \longrightarrow Ag_{3..5}VP_{1.483}O_{7..958} (\sim Ag_{3..5}VP_{1..5}O_8) + 2.966\ H^+ (aq) + 0.5\ (H_3NCH_2CH_2NH_3)^{2+} (aq) \quad (2)$$

EDAX, we determined the approximate composition of the solid to be $Ag_{3.5}VP_{1.5}O_8$. Cerimetric titrations confirmed that the solid was a fully oxidised vanadium(V) phosphate. The reaction of silver ions with enVPO can be written as in Equation (2) and (3).

$$(H_3NCH_2CH_2NH_3)^{2+} \rightleftharpoons (H_2NCH_2CH_2NH_2) + 2H^+ \longrightarrow Ag\ (metal) \quad (3)$$

To eliminate the possibility of photoreduction, the treatment of enVPO with silver ions was also carried out in dark. The products obtained under these conditions were identical. In order to confirm the presence of metallic silver and the cell parameters derived from powder X-ray pattern, we conducted electron microscopic studies on the silver exchanged enVPO product. The phase was found to be sensitive to the electron beam, resulting in rapid amorphisation. Transmission electron microscopic studies (Figure 8) clearly revealed the presence of nanospheres of silver metal particles (≈15 nm) decorated on plate like crystals of silver vanadyl phosphate. This was further confirmed by spot emission analysis. Since the fraction of silver metal in the sample was considerably low, its presence could not be observed in the powder X-ray diffraction pattern.

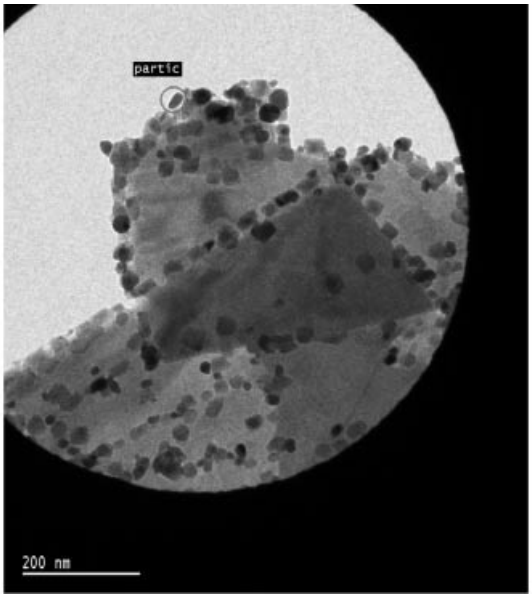

Figure 8. TEM of $Ag_{3.5}VP_{1.5}O_8$ showing nanoparticles of Ag (ca. 15 nm) on the AgVPO crystals

The exchanged products obtained in this work are all metastable. To probe the phase changes, if any, in $Ag_{3.5}VP_{1.5}O_8$, the sample was heated in air at various temperatures. A powder X-ray diffraction pattern showed (Figure 9) that the phase was stable up to 200 °C. Further heating in the temperature range 250 to 350 °C resulted in the loss of crystallinity. Interestingly, above 400 °C,

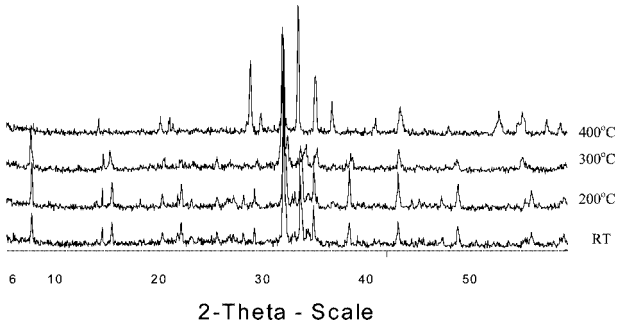

Figure 9. Powder X-ray diffraction patterns of $Ag_{3.5}VP_{1.5}O_8$ on heating: At 400 °C transformation to $Ag_2VO_2PO_4$ and Ag_3PO_4 takes place

$Ag_{3.5}VP_{1.5}O_8$ became completely transformed into a mixture of two thermodynamically stable phases, $Ag_2VO_2PO_4$ and Ag_3PO_4 [Equation (4)]. It should be remembered that TGA did not indicate any weight loss during this transformation. The presence of these two phases was further confirmed by refining the powder pattern using the Rietveld profile fitting technique (using TOPAS Version 2) on the basis of structural models reported for $Ag_2VO_2PO_4$ and Ag_3PO_4.[38,39] Using the software TOPAS 2, we also estimated the ratio of the two phases $Ag_2VO_2PO_4$ and Ag_3PO_4 to be 2:1 (Figure 10). On the basis of powder X-ray diffraction data and chemical analysis, we inferred the initial composition of the phase to be $Ag_{3.5}VP_{1.5}O_8$ according to the equation given below. EDAX analysis is also consistent with this observation.

$$Ag_{3.5}VP_{1.5}O_8 \xrightarrow{\Delta,\ 400^oC} Ag_2VO_2PO_4 + 0.5Ag_3PO_4 \quad (4)$$

The structural change taking part in the exchange reaction with silver ions is shown in Scheme 2. During the exchange reaction, ethylenediammonium groups are exchanged by metal ions. Unlike alkali metal cations, the phosphate groups linking the vanadyl phosphate layers remain intact. It appears that the initial reaction of enVPO with silver ions occurs via ion exchange to form silver intercalated vanadyl phosphate. It appears that the weakly acidic ethylenediammonium cations appearing in the aqueous phase dissociate to form ethylenediamine which reduces silver ions to metallic silver [Scheme 2, Equations (2) and (3)]. This mechanism is quite probable in view of the electron microscopic observation that nanoparticles of silver metal are deposited on the edges of the plate-like crystals.

In order to rationalise the occurrence of excess silver in the phase, we further investigated room temperature reac-

 © 2005 Wiley-VCH Verlag GmbH & Co. KGaA, Weinheim

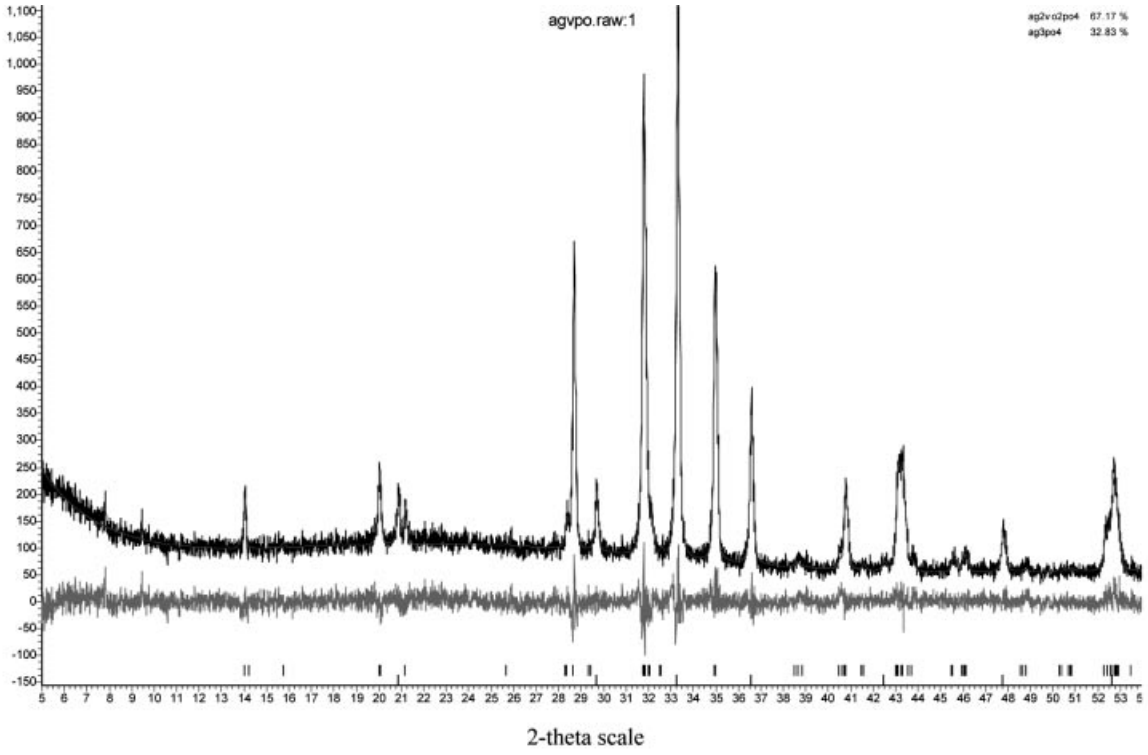

Figure 10. Quantitative phase analysis using TOPAS 2 of $Ag_{3.5}VP_{1.5}O_8$ heated at 400 °C

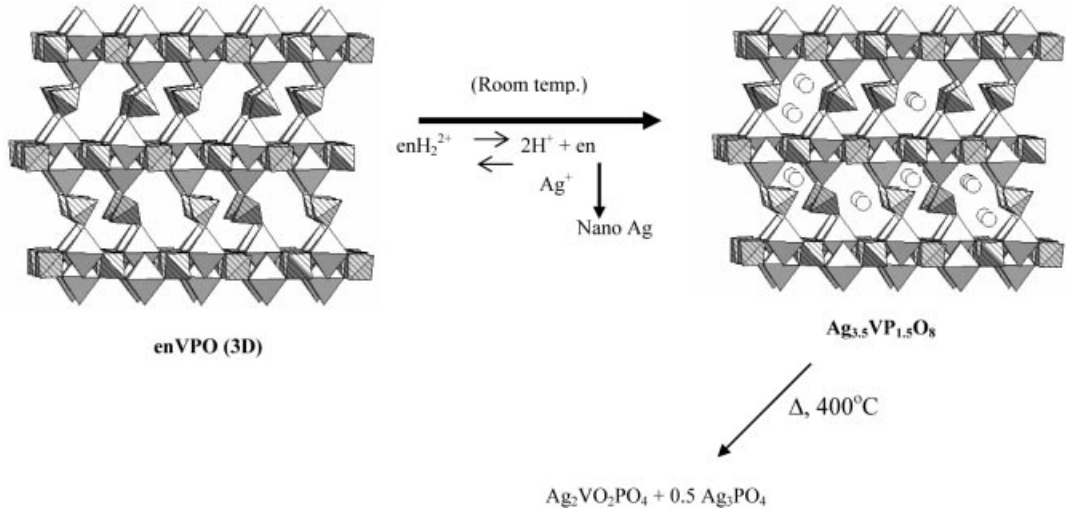

Scheme 2

tions of silver ions with other known vanadium phosphates such as $VOPO_4{\cdot}2H_2O$ and $VO(H_2PO_4)_2$. To our surprise, we obtained two possibly new phases whose powder X-ray patterns did not match with those of any other AgVPO phases reported in the literature. Also, the patterns did not show any resemblance to that of $Ag_{3.5}VP_{1.5}O_8$, suggesting that the reactions occur through different mechanisms. An EDAX analysis of the two phases indicated an Ag:V:P ratio of 2:1:1. SEM of the two solids revealed differences in morphology, i.e. a rod like morphology for the product from treatment of $VOPO_4{\cdot}2H_2O$ with silver whereas a globular morphology was observed for the phase resulting from treatment of $VO(H_2PO_4)_2$ with silver ions (Figure 11). The powder pattern of silver exchanged $VOPO_4{\cdot}2H_2O$ showed dominant 00l reflections and a basal spacing of 10.7 Å (Figure 12). However, all peaks corresponding to the solid obtained by treatment of Ag^+(aq) with $VO(H_2PO_4)_2$ could be indexed to the monoclinic system with $a = 10.904(7)$, $b = 23.196(2)$, $c = 5.680(2)$ Å and $\beta = 96.83(4)°$ using CRYSFIRE[37] (Figure 13). Since single-crystals could not be grown for these metastable products, further structural characterisations of these new silver vanadium phosphates are currently being attempted using ab initio computer modelling methods. Interestingly, both products undergo

 © 2005 Wiley-VCH Verlag GmbH & Co. KGaA, Weinheim

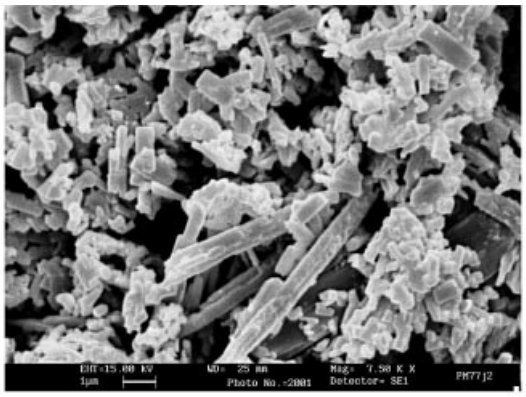

(a)

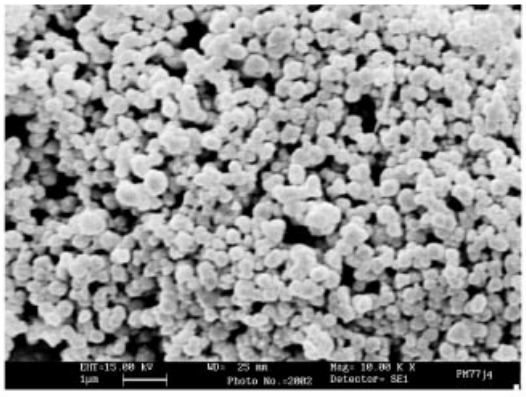

(b)

Figure 11. Scanning electron micrographs of silver exchanged (a) $VOPO_4{\cdot}2H_2O$ and (b) $VO(H_2PO_4)_2$

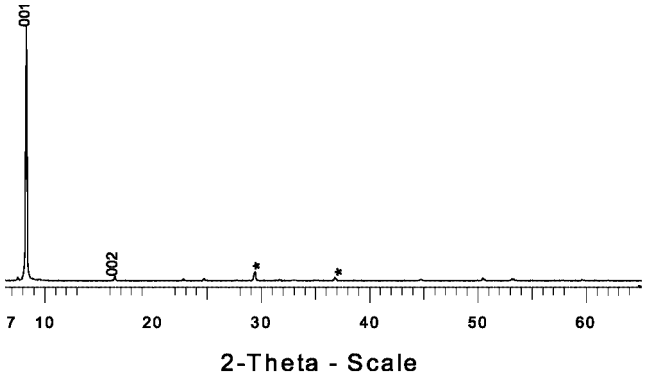

Figure 12. Powder X-ray diffraction pattern of the product obtained from the reaction of silver ions with $VOPO_4{\cdot}2H_2O$; * indicates reflections which have not been indexed

transformation to $Ag_2VO_2PO_4$ upon heating to around 100 °C in air confirming that the Ag:V:P ratio is 2:1:1. $Ag_2VO_2PO_4$ has also been prepared previously by a solid state reaction carried out at high temperatures (>500 °C).[38] However, our method appears to be a convenient low temperature route for the preparation of single phase $Ag_2VO_2PO_4$. It is significant to note that silver vanadium phosphates are mostly synthesised using solid-state reactions whereas the soft chemistry route remains somewhat unexplored. It appears from our work as well as from other

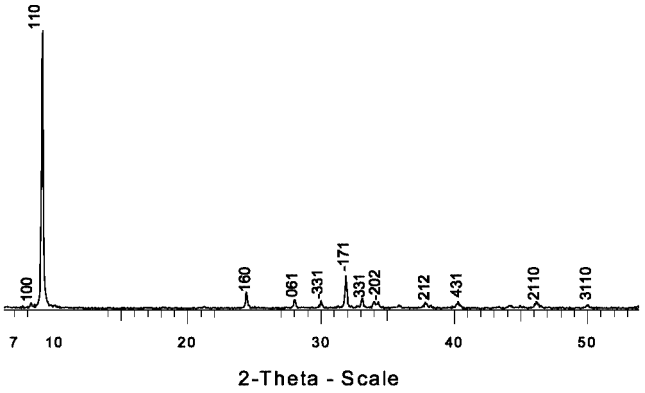

Figure 13. Powder X-ray diffraction pattern of the product obtained from the reaction of silver ions with $VO(H_2PO_4)_2$

reports available in the literature that vanadium based solids such as VO_2, V_2O_5, $NaVO_3$ etc. as well as vanadyl phosphates show unusual reactivity towards silver ions in aqueous solution at room temperature yielding fully oxidised vanadate or vanadium phosphate phases. For example, Kittaka[40] and Znaidi et al.[41] observed the formation of $AgVO_3$ by treatment of vanadium oxide xerogel with aqueous silver ions. We have also synthesised β-$AgVO_3$ nanorods coated with nanosilver through a reaction between organically intercalated vanadium oxides, $(org)_xV_2O_5$, with an excess of silver ions.[42,43] In this context, our observations and the earlier findings are quite significant for further investigations of the unusual reaction between vanadium compounds and silver ions. Further experiments are necessary to fully understand the reaction mechanism.

Conclusions

The reaction of enVPO with suitably sized aqueous cations viz. K, Rb, Tl, NH_4 at room temperature is *topotactic* and forms intercalated vanadyl phosphates, $M_{0.45}VOPO_4{\cdot}yH_2O$. Vanadyl phosphate shows unusual room temperature reactivity with silver ions under aqueous conditions. The reaction of enVPO with silver ions occurs through a different mechanism and forms a new metastable phase, $Ag_{3.5}VP_{1.5}O_8$. The current approach may be quite significant for the exploitation of using other organically intercalated phosphates in the formation of new phases particularly with alkali metal ions.

Experimental Section

Syntheses: All the reagents were obtained from Aldrich and were used without further purification. Ethylenediammonium intercalated vanadyl phosphate, $(H_3NCH_2CH_2NH_3)_{0.5}[V^{4+}{}_{0.45}V^{5+}{}_{0.55}O_2PO_4\{P(OH)_2\}_{0.483}]$ (enVPO) was synthesised by a hydrothermal reaction of ethylenediamine (en), vanadium pentoxide and phosphoric acid at 180 °C for 10 h as described earlier.[19] In a typical synthesis, V_2O_5 (0.2 g) was treated with H_3PO_4 (2 mL, 85%), en (0.17 mL) and distilled water (30 mL) in the molar ratio

 © 2005 Wiley-VCH Verlag GmbH & Co. KGaA, Weinheim

V_2O_5:H_3PO_4:en:H_2O = 1:32.4:2.4:1515. The mixture was transferred to a 45 mL Teflon lined Parr acid digestion reactor and the reaction vessel was heated at 180 °C for 10 h under autogenous pressure before cooling to room temperature at 10 °C/h. The resultant green coloured powder was washed with distilled water, acetone and allowed to dry in air. Whenever we employed nickel or cobalt powder, we obtained a phase close to enVPO but with varying degrees in the oxidation state of the vanadium. In this work, the initial precursor enVPO was prepared in the absence of metal powders. Cerimetric titrations showed that the average oxidation state of vanadium was around 4.55. On the basis of EDAX, CHN analysis and cerimetric titration, we arrived at the approximate composition for enVPO given above. Exchange reactions were carried out by suspending enVPO (0.5 g) in an aqueous solution of the appropriate metal chlorides (75 mL, 2 M; for silver, silver nitrate was used) for two days at room temperature. Complete exchange took a longer time with lower concentrations of the metal salt (e.g. 4 d with 1 M and 6 d with 0.5 M aqueous solutions). With alkali metals and ammonium salts, there was no visible colour change. However, in case of silver ions, the progress of exchange was clearly evident from the colour change (from green to yellow) during the course of reaction. All the exchanged products were filtered, washed with distilled water and dried in air. A suspension of enVPO showed no reactivity towards lithium, sodium or divalent ions as shown by powder XRD, cerimetric titration, EDAX analysis and FTIR spectroscopy. For further ion exchanges of the layered VPO species synthesised in this study, M_xVPO (0.2 g) was suspended in an appropriate metal solution (0.5 g in 30 mL of distilled water) and stirred at room temperature (30 °C) for 2 d. The product was isolated by filtration, washed with distilled water and dried in air.

Methods: FTIR spectra were recorded in KBr pellets using a Nicolet 5DX spectrophotometer. TG/DT analyses were carried out using a Perkin−Elmer TGA7 and DTA7 system on well ground samples under a flow of nitrogen with a heating rate of 10 °C/min. SEM and EDAX were recorded using a Philips XL30 microscope. Room-temperature X-ray powder diffraction data were collected on a Bruker D8 Advance diffractometer using Ni-filtered CuK_α radiation. Data were collected with a step size of 0.02° and a count time of 2 s per step over the range $4° < 2\theta < 60°$. Transmission electron microscopic studies were carried out on a Philips CM 20 instrument operating at 200 kV. The susceptibility measurements as a function of temperature were performed with a SQUID magnetometer. Diamagnetic corrections were estimated using Pascal's constants. The average oxidation state of vanadium and the total vanadium content were determined using a cerimetric titration.

Acknowledgments

M. A. acknowledges CSIR for a fellowship. A. R. acknowledges DST under IRHPA for the powder X-ray diffraction facility to Department of Chemistry, IIT, Delhi. A. R. thanks Unispec Marketing, New Delhi, India, for providing the software, TOPAS version 2. KVR and SEL acknowledge the support of the New Jersey Commission on Higher Education through the High Tech Work Force Grant.

[1] G. Centi, F. Trifiro, J. R. Ebner, V. M. Franchetti, *Chem. Rev.* **1998**, *88*, 55−80.
[2] K. Beneke, G. Lagaly, *Inorg. Chem.* **1983**, *22*, 1503−1507.
[3] J. W. Johnson, A. J. Jacobson, J. F. Brody, S. M. Rich, *Inorg. Chem.* **1982**, *21*, 3820−3825.
[4] L. Benes, K. Melanova, V. Zima, J. Kalousova, J. Votinsky, *Inorg. Chem.* **1997**, *36*, 2850−2853.
[5] L. Benes, J. Votinsky, J. Kalousova, K. Handlir, *Inorg. Chim. Acta* **1990**, *176*, 255−259.
[6] M. Martinez-Lara, L. Moreno-Real, A. Jimenez-Lopez, S. Bruque-Gamez, A. Rodriguez-Garcia, *Mat. Res. Bull.* **1986**, *21*, 13−23.
[7] C. Costentin, L. Savary, J. C. Lavelly, M. M. Borel, A. Grandin, *Chem. Mater.* **1998**, *10*, 59−64.
[8] D. Beltran-Porter, A. Beltran-Porter, P. Amoros, R. Ibanez, E. Martinez, A. Le Bail, G. Ferey, G. Villeneuve, *Eur. J. Solid State Inorg. Chem.* **1991**, *28*, 131−161.
[9] S. Boudin, A. Guesdon, A. Leclaire, M. M. Borel, *Int. J. Inorg. Mater.* **2000**, *2*, 561−579.
[10] K. K. Rangan, J. Gopalakrishnan, *J. Solid State Chem.* **1994**, *109*, 116−121.
[11] P. Ayyappan, A. Ramanan, P. A. Joy, A. Pring, *Solid State Ionics* **1998**, *107*, 53−57.
[12] P. Ayyappan, A. Ramanan, C. Torardi, *Inorg. Chem.* **1998**, *37*, 3628−3634.
[13] K. H. Lii, H. J. Tsai, *Inorg. Chem.* **1991**, *30*, 446−448.
[14] L. Benhamada, A. Grandin, M. M. Borel, A. Leclaire, M. Leblanc, B. Raveau, *J. Solid State Chem.* **1992**, *96*, 390−396.
[15] M. L. F. Phillips, W.T.A. Harrisson, T. E. Gier, G. D. Stucky, G. V. Kulkarni, J. K. Burdett, *Inorg. Chem.* **1990**, *29*, 2158−2163.
[16] R. C. Haushalter, Z. Wang, M. E. Thompson, J. Zubieta, *Inorg. Chem.* **1993**, *32*, 3700−3704.
[17] L. F. Nazar, B. E. Koene, J. F. Britten, *Chem. Mater.* **1996**, *8*, 327−329.
[18] Y.-J. Liu, J. A. Cowen, T. A. Kaplan, D. C. DeGroot, J. Schindler, C. R. Kannewurf, M. G. Kanatzidis, *Chem. Mater.* **1995**, *7*, 1616−1624.
[19] P. Ayyappan, M. Asnani, A. Ramanan, Y. Piffard, *Proc. Ind. Acad. Sci. (Chem. Sci.)* **2003**, *115*, 33−40.
[20] W. T. A. Harrison, K. Hsu, A. J. Jacobson, *Chem. Mater.* **1995**, *7*, 2004−2006.
[21] V. Zima, L. Benes, K. Melanova, M. Vlcek, *J. Solid State Chem.* **2002**, *163*, 281−285.
[22] A. J. Jacobson, J. W. Johnson, J. F. Brody, J. C. Scanlon, J. T. Lewandowski, *Inorg. Chem.* **1985**, *24*, 1782−1787.
[23] V. Zima, L. Benes, J. Votinsky, J. Kalousova, *Solid State Ionics* **1995**, *82*, 33−38.
[24] A. Chauvel, M. E. de Roy, J. P. Besse, A. Benarbia, A. Legrouri, A. Barroug, *Mater. Chem. Phys.* **1995**, *40*, 207−211.
[25] V. Zima, M. Kilian, M. Casciola, L. Massinelli, *Chem. Mater.* **1999**, *11*, 3258−3262.
[26] J. W. Johnson, A. J. Jacobson, *Angew. Chem. Int. Ed. Engl.* **1983**, *22*, 412−413.
[27] J. Do, R. P. Bontchev, A. J. Jacobson, *Inorg. Chem.* **2000**, *39*, 3230−3237.
[28] J. W. Johnson, D. C. Johnston, A. J. Jacobson, J. F. Brody, *J. Am. Chem. Soc.* **1984**, *106*, 8123−8128.
[29] V. Zima, L. Benes, K. Melanova, J. Svoboda, *J. Solid State Chem.* **2004**, *177*, 1173−1178.
[30] D. Papoutsakis, J. E. Jackson, D. G. Nocera, *Inorg. Chem.* **1996**, *35*, 800−801.
[31] M. Roca, P. Amoros, J. Cano, M. D. Marcos, J. Alamo, A. Beltran-Porter, D. Beltran-Porter, *Inorg. Chem.* **1998**, *37*, 3167−3174.
[32] P. Ayyappan, PhD Thesis, Indian Institute of Technology, Delhi, **1999**.
[33] C. J. O′Connor, V. Soghomonian, R. C. Haushalter, Z. Wang, J. Zubieta, *J. Appl. Phys.* **1994**, *75*, 5859−5861.
[34] R. C. Haushalter, Q. Chen, V. Soghomonian, J. Zubieta, C. J. O′Connor, *J. Solid State Chem.* **1994**, *108*, 128−133.
[35] G. Huan, J. W. Johnson, A. J. Jacobson, E. W. Corcoran, D. P. Goshorn, *J. Solid State Chem.* **1991**, *93*, 514−525.
[36] B. B. Das, I. L. Benhamada, A. Grandin, M. M. Borel, A. Leclaire, B. Raveau, *Mater. Chem. Phys.* **1995**, *39*, 239−242.
[37] Robin Shirley, *CRYSFIRE V3.1*, **2000**.

 © 2005 Wiley-VCH Verlag GmbH & Co. KGaA, Weinheim

[38] H. Y. Kang, S. L. Wang, P. P. Tsai, K. H. Lii, *J. Chem. Soc., Dalton Trans.* **1993**, 1525−1528.
[39] H. N. Ng, C. Calvo, R. Faggiani, *Acta Crystallogr., Sect. B* **1978**, *34*, 898−899.
[40] S. Kittaka, K. Matsuno, H. Akashi, *J. Solid State Chem.* **1999**, *142*, 360−367.
[41] L. Znaidi, N. Baffier, M. Huber, *Mater. Res. Bull.* **1989**, *24*, 1501−1514.
[42] S. Sharma, M. Jansen, A. Ramanan, *Solid State Ionics* **2004**, *170*, 93−98.
[43] S. Sharma, A. Ramanan, M. Panthöfer, M. Jansen, *Mater. Chem. Phys.*, paper accepted for publication.

Received June 5, 2004
Early View Article
Published Online November 24, 2004

 © 2005 Wiley-VCH Verlag GmbH & Co. KGaA, Weinheim

X-ray Absorption Spectra of Cu^{II} and Cu^{III} Complexes of *N*,*N*′-1,2-Phenylenebis(2-mercapto-2-methylpropionamide)

Giampaolo Barone,[a] Gianfranco La Manna,[b] and Dario Duca*[a]

Keywords: Copper / N,S ligands / X-ray absorption spectroscopy / Density functional calculations / Ab initio molecular orbital calculations

The X-ray absorption spectra of Cu^{II} and Cu^{III} complexes of *N*,*N*′-1,2-phenylenebis(2-mercapto-2-methylpropionamide) were recorded and analysed in solid phase. The EXAFS spectra of the two samples were refined with full multiple scattering path. Geometry optimisations on the Cu^{II} and Cu^{III} complexes were performed by the B3LYP density functional method, with the 6-31G(d,p) basis set, considering different spin multiplicities. The singlet state of the Cu^{III} complex was shown to be more stable than the triplet state, and a good agreement between the calculated and the corresponding experimental structure was found. Further single-point calculations on the optimised geometry were carried out at the Hartree–Fock level for obtaining molecular orbital eigenvectors and eigenvalues. The latter were employed as parameters in a new fitting approach to rationalise the shape of the K-edge of the XAS spectra.
(© Wiley-VCH Verlag GmbH & Co. KGaA, 69451 Weinheim, Germany, 2005)

Introduction

Stable mononuclear Cu^{III} complexes of chelating ligands can be obtained by electrochemical oxidation of the corresponding Cu^{II} complexes in solution.[1] The *N*,*N*′-1,2-phenylenebis(2-mercapto-2-methylpropionamide) Cu^{II} and Cu^{III} ions (Figure 1),[2] containing aliphatic thiolate groups in a square-planar coordination environment, can be considered as models of electron transfer copper proteins.[3−5]

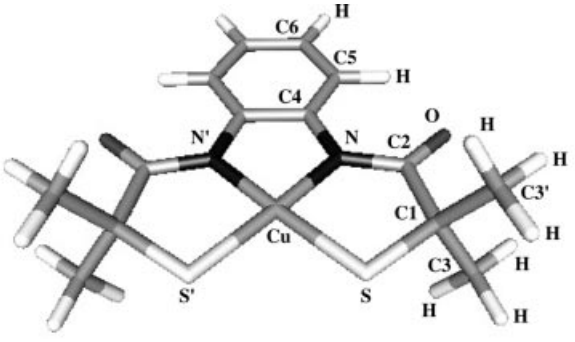

Figure 1. Structure of the square-planar Cu^{II} and Cu^{III} ionic systems considered in the B3LYP calculations

[a] Dipartimento di Chimica Inorganica e Analitica "S. Cannizzaro" dell'Università di Palermo
Viale delle Scienze, Parco d'Orleans II, 90128 Palermo, Italy
Fax: (internat.) + 39-091-427584
E-mail: dduca@unipa.it
[b] Dipartimento di Chimica Fisica "F. Accascina" dell'Università di Palermo
Viale delle Scienze, Parco d'Orleans II, 90128 Palermo, Italy

X-ray absorption spectroscopy (XAS) is used to determine electronic and geometric structures of the metal centres in metal-containing proteins and model systems.[6] Indeed, information on the local environment of the probe atom can be extracted with high accuracy, by utilising fine structure analysis. Moreover, the shape and position of the absorption edge help to distinguish different oxidation states of the metal atoms in analogous complexes.[7] In particular, in the rising edge of the XAS spectra of the copper complex, a few weak peaks and shoulders might originate from transitions from 1s to 3d or 4p orbitals, which are typically attributed to bound state forbidden transitions.[6] This information is usually employed to determine the local symmetry of the transition-metal environments.[8−12]

When discussing XAS spectra, two distinct pictures are introduced: i) the photoexcitation of core electrons to bound state energy levels, in the edge region: the X-ray absorption near edge spectrum (XANES), and ii) the backscattering of the photoejected core electrons, mainly in the high energy part of the spectrum, namely the extended X-ray absorption fine structure (EXAFS). Multiple scattering (MS) EXAFS analysis allows one to neglect the contributions of the excitation of the core electrons to the bound state energy levels. MS analysis has successfully been extended into the XANES region analysis.[13−15]

A recent study on Cu^{II} and Cu^{III} complexes[8] concluded that the shape of the corresponding K-edge region depends on the electronic properties and the coordination geometry of the chelating ligand. Moreover, a shift of about 2 eV was observed in the assigned resonances when going from Cu^{II} to Cu^{III} species.

 © 2005 Wiley-VCH Verlag GmbH & Co. KGaA, Weinheim **DOI: 10.1002/ejic.200400495**

The K-edge shape is usually very similar in complexes having the same ligands and different metal oxidation states.[7,8] The presence of three edge peaks was attributed to three electronic transitions involving the 1s, 3d and 4p orbitals of copper.[8] The positions and intensity of such transitions were evaluated by fitting the spectra and rationalised by empirical configuration interaction methods;[8] the parameters were obtained from X-ray photoelectron spectroscopy and XAS studies.

Cu^{III} complexes, characterised by chelating sulfur groups, have been recently studied by XAS, confirming that the high-spin d^8 electron configuration of Cu^{III} is stabilised by six bridged thiolate ligands.[16]

In the present work, the EXAFS spectra of the title complexes are shown, and an attempt to rationalise the XANES region by a new fitting procedure based on quantum mechanical information is carried out. For the latter, a qualitative picture of the transitions that are responsible for the XAS signals can be accomplished by the hopping of an electron from the lowest occupied molecular orbital to the lowest virtual ones,[17−19] within the frame of the orbital approximation, hence by employing a single-determinantal wave function. In the following fit procedure, the energetics determined in this way are used to reproduce the experimental XANES profile.

The necessary information from the electronic structure can be obtained by using quantum chemistry packages, such as G98W.[20] A more correct theoretical description should be given by overcoming the orbital approximation through the configuration interaction approach, for example by using recent versions of the CASSCF and CASPT2[21] methods. However, such algorithms are very time consuming, thus are not easily applicable to molecular systems of notable size, as those considered here.

Results and Discussion

1. EXAFS Spectra

The Cu^{III}-phmi (see Exp. Sect.) EXAFS spectrum, together with its Fourier transform, is shown, as an example, in Figure 2. The interatomic distances were extracted from the extended X-ray absorption fine structure, by the full multiple scattering theory,[22] and shows good agreement with previous X-ray crystallographic studies.[2]

These distances are compared with crystallographic reference data in Table 1, which also shows the calculated structural parameters and the relative energy values of the Cu^{II} and Cu^{III} complexes, at the indicated spin multiplicity.

The B3LYP[23] energy of the closed shell Cu^{III} compound was found to be 0.96 eV below the corresponding energy of the triplet spin state. The calculations for different spin states give rise to considerably different structural parameters (see Table 1). In the case of the Cu^{III} compound, the calculated structural parameters of the singlet-state species mostly match the corresponding experimental ones. This allowed us to conclude that the Cu^{III} compound is likely a singlet state, in agreement with the apparent absence of ESR signals.[2]

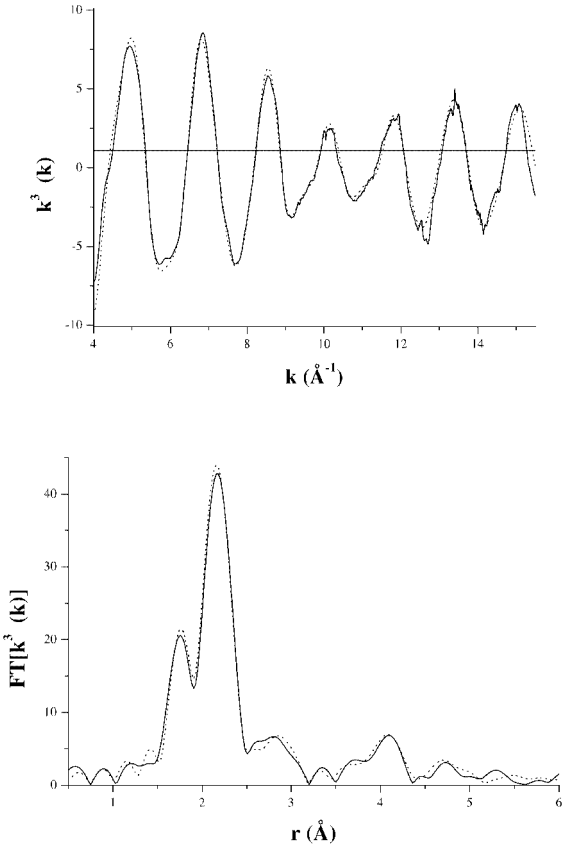

Figure 2. k^2-weighted EXAFS spectra and its fit (upper), $k^3\chi(k)$ vs. k, and the corresponding Fourier transforms (lower), FT[$k^3\chi(k)$] vs. r, of the Cu^{III}-phmi complex: the experimental and fit results are represented by the solid and dotted lines, respectively

Table 1. Distances and angles (Å and °), at given copper oxidation number (ON), obtained by geometry optimisation, at B3LYP/6-31G(d,p) level for different spin multiplicity (Spin), by X-ray crystallography[2] and by EXAFS analysis and calculated difference energy values ΔE (eV)

	B3LYP/6-31G(d,p)			X-ray[2]		EXAFS	
ON	III	III	II	III	II	III	II
Spin	1	3	2	–	–	–	–
Cu−N	1.862	1.951	1.964	1.864	1.963	1.861	1.913
Cu−S	2.177	2.256	2.287	2.147	2.241	2.143	2.220
Cu−C1	3.066	3.133	3.145	3.030	3.109	3.07	3.02
Cu−C2	2.851	2.935	2.940	2.839	2.904	2.79	2.83
Cu−C3	4.136	4.206	4.227	4.080	4.173	4.11	4.20
Cu−O	4.029	4.115	4.145	4.020	4.095	4.01	4.10
Cu−C4	2.733	2.802	2.797	2.743	2.839	2.76	2.80
Cu−C5	4.106	4.195	4.198	4.106	4.208	4.11	4.20
Cu−C6	5.110	5.186	5.191	5.107	5.220	5.25	5.24
N−Cu−N′	87.4	83.3	84.6	87.5	84.0	–	–
S−Cu−S′	92.5	100.0	98.9	92.1	100.3	–	–
S−Cu−N	90.0	88.4	88.2	90.4	87.9	–	–
S−Cu−N′	177.5	171.7	172.9	175.6	171.7	–	–
ΔE	0.00	0.96	4.77	–	–	–	–

Both theoretical and experimental data confirm that a change in the copper oxidation number from II to III de-

 © 2005 Wiley-VCH Verlag GmbH & Co. KGaA, Weinheim

creases the metal−ligand distances of the atoms of the first coordination shell;[1,2,7,8] conversely, an increase in the spin multiplicity, at a given oxidation state of the metal, increases the same metal−ligand distances (see, for example, the calculated Cu−S or Cu−N distances).

2. K-edge Analysis

The K-edge region of both copper samples, together with their second derivative, is reported in Figure 3. In the inset, a portion of the low intensity pre-edge peak regions is highlighted. Two main changes are caused by the variation of the metal oxidation state: a) the position of the Cu^{III} K-edge is, as previously reported for other complexes,[8] shifted by about 2 eV in the energy axis; b) the spectrum curve in the first peak region, at about 8979−8981 eV, is seemingly slightly lower in the Cu^{II} sample; see the inset and the second derivative of the spectrum for details.

An attempt to interpret the K-edge transitions was carried out by using a molecular orbital (MO) Hartree−Fock (HF) description of the systems at the geometries previously optimised with the density functional (DFT) approach. This was needed to obtain reliable geometrical parameters through the DFT method and a further MO description, providing a set of HF eigenvalues to be used in our monoelectronic approach. In fact, the Kohn−Sham eigenvalues cannot be used for describing electronic vertical transitions.[24]

As reported in the Introduction, the edge electronic transitions were qualitatively described here in terms of hopping from the first occupied MO, which is essentially the 1s atomic orbital of the copper atom, to some of the lowest virtual MOs. Several approximations are inherent in this qualitative approach, orbital approximation and neglect of relativistic effects, inter alia.

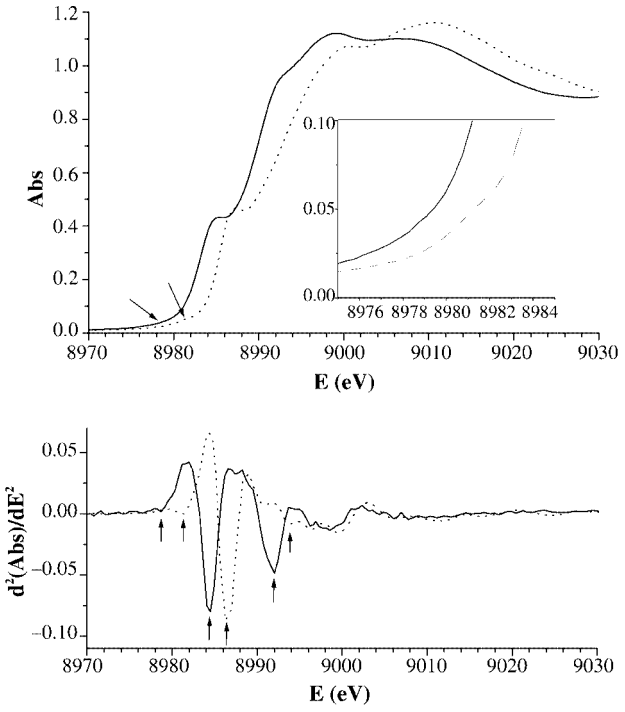

Figure 3. K-edge absorption Abs (upper) and its second derivative $d^2(Abs)/dE^2$ (lower) vs. the transition energy (E) of Cu^{II}-phmi (solid line) and Cu^{III}-phmi (dotted line); in the inset, a portion of the low intensity peak region is highlighted

Table 2. Eigenvalues differences E[MO(n)] − E[MO(1)] (eV) and dipole strengths D (a.u.) calculated for the electronic transitions involving the MO(1) and MO(n) of the Cu^{II} and Cu^{III} systems

	Cu^{II}		Cu^{III}	
n	E[MO(n)] − E[MO(1)]	D	E[MO(n)] − E[MO(1)]	D
98	8954.25	$2.0(2)\cdot10^{-12}$	8957.92	$4.1(1)\cdot10^{-7}$
99	8954.44	$3.3(7)\cdot10^{-7}$	8957.99	$2.0(5)\cdot10^{-11}$
100	8954.68	$3.8(1)\cdot10^{-4}$	8958.00	$3.3(3)\cdot10^{-4}$
101	8954.72	$3.7(4)\cdot10^{-9}$	8958.12	$1.8(2)\cdot10^{-11}$
102	8955.58	$2.7(4)\cdot10^{-8}$	8958.99	$1.2(5)\cdot10^{-7}$
103	8955.71	$4.7(9)\cdot10^{-12}$	8959.25	$2.5(8)\cdot10^{-10}$
104	8956.73	$1.5(5)\cdot10^{-5}$	8959.73	$2.5(7)\cdot10^{-6}$
105	8956.90	$4.4(6)\cdot10^{-12}$	8960.09	$7.5(9)\cdot10^{-8}$
106	8956.94	$7.4(8)\cdot10^{-8}$	8960.38	$1.3(7)\cdot10^{-11}$
107	8957.05	$1.5(8)\cdot10^{-6}$	8960.92	$1.8(9)\cdot10^{-7}$
108	8957.55	$1.2(6)\cdot10^{-4}$	8961.19	$9.9(4)\cdot10^{-5}$
109	8957.69	$4.8(8)\cdot10^{-9}$	8961.37	$1.9(9)\cdot10^{-8}$
110	8958.09	$7.2(2)\cdot10^{-8}$	8961.79	$5.7(6)\cdot10^{-8}$
111	8958.25	$6.4(6)\cdot10^{-5}$	8962.02	$7.7(6)\cdot10^{-5}$
112	8958.35	$4.6(0)\cdot10^{-8}$	8962.34	$2.8(8)\cdot10^{-5}$
113	8958.68	$4.5(3)\cdot10^{-5}$	8962.44.	$3.8(4)\cdot10^{-8}$
114	8958.71	$4.8(5)\cdot10^{-14}$	8962.52	$3.9(5)\cdot10^{-13}$
115	8958.78	$1.0(2)\cdot10^{-8}$	8962.53	$1.2(1)\cdot10^{-7}$
116	8959.02	$2.3(5)\cdot10^{-8}$	8962.65	$1.8(0)\cdot10^{-8}$
117	8959.29	$6.0(8)\cdot10^{-8}$	8962.89	$2.9(5)\cdot10^{-9}$
118	8959.54	$3.2(6)\cdot10^{-12}$	8963.15	$2.2(1)\cdot10^{-12}$
119	8959.67	$6.9(6)\cdot10^{-7}$	8963.28	$5.4(8)\cdot10^{-14}$
120	8959.91	$3.8(1)\cdot10^{-17}$	8963.55	$6.9(1)\cdot10^{-11}$

 © 2005 Wiley-VCH Verlag GmbH & Co. KGaA, Weinheim

The dipole strengths, $D = |<MO(1)|\boldsymbol{r}|MO(n)>|^2$, connecting the first occupied MO and the virtual MOs of the Cu^{II} and Cu^{III} systems, were numerically calculated by a home-made code based on the VEGAS algorithm.[25]

The transition energy values were considered as the differences between the eigenvalues of MO(1) and MO(*n*), where $n = 98-120$. In the case of the Cu^{II} complex, which is an open-shell system, only α-eigenvalues and eigenvectors were considered, but very similar values could be obtained by using the β-manifold. The values for the transition energies and *D* are reported in Table 2 for both Cu^{II} and Cu^{III} complexes.

Notably, in spite of the approximations introduced in the present treatment, the estimated frequency values for both compounds are just 0.3% lower than the experimental ones. Moreover, the transition energy values of the Cu^{III} complex are shifted towards higher values by about 3 eV, with respect to the corresponding transitions of the Cu^{II} complex, in line with the observed spectra. This is a clear indication that such a "naïve" treatment is able to account for the main features of the XAS spectrum.

Taking into account the results above, we tried to fit the experimental Cu^{II}-phmi and Cu^{III}-phmi XAS K-edge regions, considering the theoretical electronic transitions corresponding to the largest values of the *D* integrals. A single Gaussian function was assigned to each transition, having a full-width at half maximum (FWHM) equal to 1.5 eV and a height proportional to the corresponding *D* value. The resulting sets of Cu^{II} and Cu^{III} Gaussians were therefore two multifunction combs where the positions of the Gaussians were fixed by the DFT transition energies, and the relative intensities were modulated by the corresponding *D* values. Thus, the only two fit parameters, involving the core electronic transitions in both copper systems, were the position of the leading peak and its height.

One arctan function has been added in order to take into account the long-range trend of the EXAFS pattern, therefore, two more fit parameters are introduced. In fact, the arctan maximums, 1.1 (in absorption arbitrary units) both for the Cu^{II} and Cu^{III} systems, were qualitatively fixed by the analysis of the experimental spectra. The overall fitting process was finally performed within the 8950−9000 eV range, and the results are depicted in Figure 4. The good agreement between calculated and experimental spectra for both copper compounds is apparent ($R\chi^2 = 0.05$ and 0.15 for Cu^{II} and Cu^{III}, respectively).

The area under the leading peaks of the Cu^{II} and Cu^{III} systems proved to be very similar, whereas the mean of the same leading peaks, in agreement with the experimental results, were shifted by about 2.5 eV. An analogous shift can be observed between the mean values of the arctan functions employed to fit the Cu^{II} and Cu^{III} complex spectra. These findings, supported by the observation that the arctan slope parameter is very similar in both systems [5.9(7) and 6.3(4) for Cu^{II} and Cu^{III} species, respectively] point out clearly that the proposed fit procedure is quite heuristic.

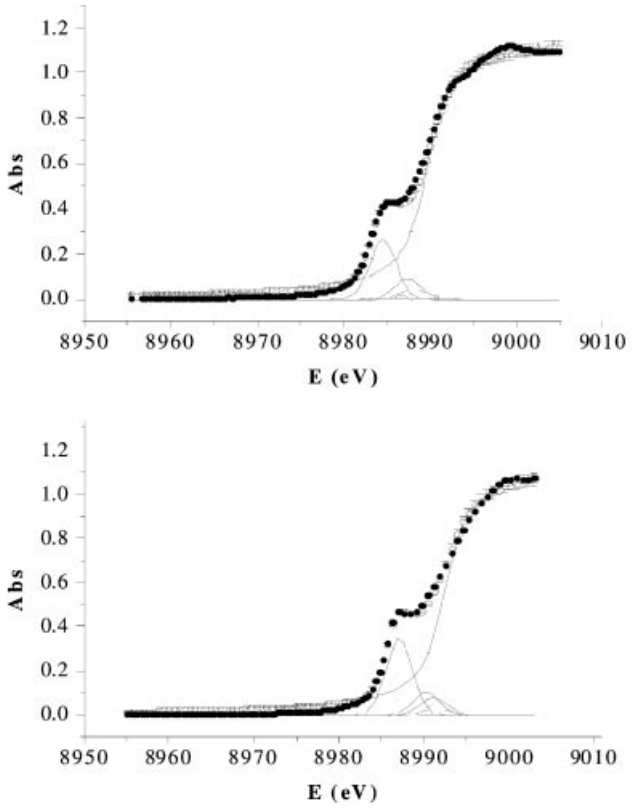

Figure 4. Fitting of the Cu^{II}-phmi (upper) and Cu^{III}-phmi (lower) XAS K-edge region: K-edge absorption Abs vs. transition energy *E*, experimental and fitting points are represented by filled and open circles, respectively; the continuous curves represent the fitting functions; the error bars (almost hidden and just visible on the points at higher energies), corresponding to the 2.5% of the fit values, visually show the agreement between experimental and fitted results

Conclusion

EXAFS spectra enable information on the interatomic distances of the considered systems to be obtained. The whole set of the obtained geometrical results confirms the values already determined by using different experimental techniques, validating the possibility of performing EXAFS spectral analysis along with quantum mechanical calculations. Moreover, this approach is able to discriminate between the atomic oxidation numbers and the molecular spin states.

The K-edge region shape has been reproduced well by a simple quantum mechanical description of the core vertical transitions in the orbital approximation combined with an accustomed fitting procedure.

Experimental Section

General Remarks: The XAS spectra on the K-edge of (PPh_4)-[Cu(*N*,*N*′-1,2-phenylenebis(2-mercapto-2-methylpropionamide)] (Cu^{III}-phmi) and $(NEt_4)_2$[Cu(*N*,*N*′-1,2-phenylenebis(2-mercapto-2-methylpropionamide)] (Cu^{II}-phmi) were recorded at the EMBL D2 bending magnet beam line of the DORIS storage ring (DESY,

 © 2005 Wiley-VCH Verlag GmbH & Co. KGaA, Weinheim

Hamburg), running at 4.5 GeV and with a 50−100 mA ring current.

The samples were prepared by homogenising the powdered crystalline compounds (40 mg Cu^{III}-phmi and 30 mg Cu^{II}-phmi) in boron nitride and pressing the mixtures in 1-mm sample cells sealed with Kapton foil. The spectra were recorded at 20 K. Standard EXAFS analysis[26] was performed by the EXPROG[27] and EXCURVE98[22] programme packages. The full multiple scattering path was included in the fitting process of the molecular system. Its starting coordinates, excluding the hydrogen atoms, were taken from a previous X-ray crystallography study.[2]

Electronic Structure Calculations and Fitting Procedure: Quantum-mechanical calculations were performed at the B3LYP level, by the GAUSSIAN98 programme package,[20] by using the extended split-valence double-zeta 6-31G(d,p) basis set with full geometry optimisation.

The Cu oxidation states +2, with spin multiplicity of 2 for the complex, and +3, with spin multiplicities of 1 and 3, were considered. The calculations were performed by imposing C_{2v} symmetry on the ionic complexes.

Further calculations at the HF level were carried out in order to obtain eigenvalues and eigenvectors of the MOs needed to evaluate vertical transition energies and dipole strengths.

The number of the considered virtual MOs, 23 for both Cu^{II} and Cu^{III} systems, corresponding to the number of the calculated transition moment integrals, was fixed to take into account the energy range of about 6 eV characterising the shoulder width in the K-edge rising region. The integral was calculated by a Fortran home-made code employing the Monte Carlo routine VEGAS along with the random number generator RAN2.[24] The reliability of the numerical integration procedure was verified by checking the *ortho*-normalisation condition of the MOs.

The fitting function, designed to mimic the XANES profile, was defined as in the following:

$$f = \arctan(h,\eta,\sigma) + g_p(h_p,\eta_p,\sigma_p) + \sum_i^n g_i(h_i,\eta_i,\sigma_i)$$

where g_p and g_i are Gaussian functions, simulating the pivot peak, i.e. the largest one, and n minor peaks under the XANES profile. To reproduce the characteristic stepping behaviour of the latter, the arctan function was introduced.

The FWHM of all the Gaussians, σ_p and σ_i, were fixed to 1.5 eV, whereas h, the arctan maximum value, was set to 1.1 (arbitrary absorption units). The values of h_i/(arbitrary absorption units) and η_i/eV were defined as $h_i = A_i h_p$ and $\eta_i = B_i + \eta_p$. The A_i values corresponded to the calculated ratios between the dipole strength square of the given ith and the pivot transitions, whereas the B_i/eV parameters concerned the energy difference between the quantum mechanical and the fitting transition energy value, corresponding to the pivot peak.

Finally, f was driven by four fitting parameters, h_p (arbitrary absorption units), η_p (eV), η (eV) and σ (eV), which are the other significant parameters fixed by the quantum mechanical calculations.

In the fitting procedure, the simplex AMOEBA[24] minimised the restricted chi-squared function:

$$R\chi^2 = \frac{1}{m < E >} \sum_k^m \frac{(C_k - E_k)^2}{E_k}$$

where m is the number of experimental points considered in the fit, E_k and C_k the experimental and calculated absorptions and $<E>$ the average experimental absorption along the energy range analysed.

Acknowledgments

This work was funded by the University of Palermo and by the Italian MIUR. The European Community supported G.B., contract HPRI-CT-1999−00017, within the frame of the Access to Research Infrastructure Action of the Improving Human Potential Programme to the EMBL Hamburg Outstation. Authors thank Prof. Björn Roos (University of Lund, Sweden) for fruitful discussions and Dr. Manuel Gnida (EMBL, Hamburg, Germany) for assistance in recording and analysing the EXAFS spectra.

[1] J. Hanss, A. Beckmann, H.-J. Krüger, *Eur. J. Inorg. Chem.* **1999**, 163−172.
[2] J. Hanss, H.-J. Krüger, *Angew. Chem. Int. Ed. Engl.* **1996**, *35*, 2827−2830.
[3] M. C. Machczynski, H. B. Gray, J. H. Richards, *J. Inorg. Biochem.* **2002**, *88*, 375−380.
[4] B. G. Malmström, P. Wittung-Stafshede, *Coord. Chem. Rev.* **1999**, *185−186*, 127−140.
[5] R. K Szilagyi, E. I Solomon, *Curr. Opin. Chem. Biol.* **2002**, *6*, 250−258.
[6] J. E. Penner-Hahn, *Coord. Chem. Rev.* **1999**, *190−192*, 1101−1123.
[7] T. Glaser, T. Beissel, E. Bill, T. Weyhermüller, V. Schünemann, W. Meyer-Klaucke, A. X. Trautwein, K. Wieghardt, *J. Am. Chem. Soc.* **1999**, *121*, 2193−2208.
[8] J. L. Du Bois, P. Mukherjee, T. D. P. Stack, B. Hedman, E. I. Solomon, K. O. Hodgson, *J. Am. Chem. Soc.* **2000**, *122*, 5775−5787.
[9] M. Gnida, R. Ferner, L. Gremer, O. Meyer, W. Meyer-Klaucke, *Biochemistry* **2003**, *42*, 222−230.
[10] L.-S. Kau, D. J. Spira-Solomon, J. E. Penner-Hahn, K. O. Hodgson, E. I. Solomon, *J. Am. Chem. Soc.* **1987**, *109*, 6433−6442.
[11] A. L. Roe, D. J. Schneider, R. J. Mayer, J. W. Pyrz, J. Widom, L. Que Jr., *J. Am. Chem. Soc.* **1984**, *106*, 1676−1681.
[12] T. E. Westre, P. Kennepohl, J. G. De Witt, B. Hedman, K. O. Hodgson, E. I. Solomon, *J. Am. Chem. Soc.* **1997**, *119*, 6297−6314.
[13] M. Benfatto, S. Della Longa, *J. Synchrotron Rad.* **2001**, *8*, 1087−1094.
[14] J. J. Rehr, R. C. Albers, *Rev. Mod. Phys.* **2000**, *72*, 621−654.
[15] A. Mijovilovich, W. Meyer-Klaucke, *J. Synchrotron Rad.* **2003**, *10*, 64−68.
[16] C. Krebs, T. Glaser, E. Bill, T. Weyhermüller, W. Meyer-Klaucke, K. Wieghardt, *Angew. Chem. Int. Ed.* **1999**, *38*, 359−361.
[17] F. A. Cotton, *Chemical Applications of Group Theory*, 3rd ed., Wiley-Interscience, New York, **1990**.
[18] M. Orchin, H. H. Jaffé, *Symmetry, Orbitals and Spectra (S. O. S)*, Wiley-Interscience, New York, **1971**.
[19] D. C. Haris, M. D. Bertolucci, *Symmetry and Spectroscopy*, Dover Publication, New York, **1989**.
[20] M. J. Frisch, G. W. Trucks, H. B. Schlegel, G. E. Scuseria, M. A. Robb, J. R. Cheeseman, V. G. Zakrzewski, J. A. Montgomery Jr., R. E. Stratmann, J. C. Burant, S. Dapprich, J. M. Millam, A. D. Daniels, K. N. Kudin, M. C. Strain, O. Farkas, J. Tomasi, V. Barone, M. Cossi, R. Cammi, B. Mennucci, C. Pomelli, C. Adamo, S. Clifford, J. Ochterski, G. A. Petersson, P. Y. Ayala, Q. Cui, K. Morokuma, D. K. Malick, A. D. Rabuck, K. Raghavachari, J. B. Foresman, J. Cioslowski, J. V. Ortiz, A.

 © 2005 Wiley-VCH Verlag GmbH & Co. KGaA, Weinheim

G. Baboul, B. B. Stefanov, G. Liu, A. Liashenko, P. Piskorz, I. Komaromi, R. Gomperts, R. L. Martin, D. J. Fox, T. Keith, M. A. Al-Laham, C. Y. Peng, A. Nanayakkara, M. Challacombe, P. M. W. Gill, B. Johnson, W. Chen, M. W. Wong, J. L. Andres, C. Gonzalez, M. Head-Gordon, E. S. Replogle, J. A. Pople, *GAUSSIAN 98*, Revision A.8, Gaussian, Inc., Pittsburgh PA, **1998**.

[21] K. Pierloot, J. O. A. De Kerpel, U. Ryde, B. O. Roos, *J. Am. Chem. Soc.* **1997**, *119*, 218−226.

[22] N. Binsted, R. W. Strange, S. S. Hasnain, *Biochemistry* **1992**, *31*, 12117−12125.

[23] A. D. Becke, *J. Chem. Phys.* **1993**, *98*, 5648−5652.

[24] I. N. Levine, *Quantum Chemistry*, 5th ed., Prentice-Hall, Upper Saddle River, NJ, **2000**, p. 580.

[25] W. H. Press, S. A. Teukolsky, W. T. Vetterling, B. P. Flammery, *Numerical Recipes*, Cambridge University Press, Cambridge, **1992**.

[26] R. A. Scott, *Methods Enzymol.* **1985**, *111*, 414−459.

[27] H. F. Nolting, C. Hermes, EMBL Hamburg, **1992**.

Received June 9, 2004
Early View Article
Published Online November 24, 2004

 © 2005 Wiley-VCH Verlag GmbH & Co. KGaA, Weinheim

Oxidative Addition of Phenylselenyl Halides to Platinum(0) Complexes: Characterisation and Reactivity of the Products [PtX(SePh)-(*N*,*N*-chelate)(olefin)] (X = Cl, Br, I)

Vincenzo G. Albano,*[a] Vincenzo De Felice,[b] Magda Monari,[a] Giuseppina Roviello,[c] and Francesco Ruffo*[c]

Keywords: Isomers / Oxidative addition / Platinum / Selenium

The oxidative addition of PhSeX (X = Cl, Br, I) to Pt^0 complexes of formula [Pt(*N*,*N*-chelate)(olefin)] is described. The reaction quantitatively affords the trigonal-bipyramidal products [PtX(SePh)(*N*,*N*-chelate)(olefin)] with the X and SePh fragments in the axial positions. NMR spectroscopic data have allowed us to gain insights into the geometrical isomerism of some of these complexes. The reactivity of the axial ligands towards electrophilic reagents is also investigated, and the molecular structures of [PtX(SePh)(dmphen)(dimethyl fumarate)] (X = Br, I) are compared.
(© Wiley-VCH Verlag GmbH & Co. KGaA, 69451 Weinheim, Germany, 2005)

Introduction

Five-coordinate [M(X)(Y)(*N*,*N*-chelate)(olefin)] (**1**; M = Pd or Pt) complexes have proved to be particularly suitable for studying the coordination properties of several ions and molecules (Figure 1).[1] Due to their stability and inertness, metal adducts of a series of ligand fragments have been isolated,[1,2] including some containing ligands with poor stability in the "free" state.[3] For example, a variety of organometallic fragments can sturdily occupy an axial position in a series of compounds containing the same {MX(*N*,*N*-chelate)(olefin)} moiety, thus offering the possibility to assess trends.[2] Alternatively, unstable vinyl alcohol can be coordinated and its fairly rich chemical behaviour at the metal centre can be compared with that of a variety of olefins in the same environment.[3]

Recently,[4] we have focused our attention on five-coordinate complexes bearing organochalcogenide ligands ER (E = O, S, Se, Te) in the axial position. This study was started because coordinatively saturated Pt^{II} compounds with chalcogenide ligands were not known[5] and very limited information on the reactivity of these coordinated fragments was available.[6]

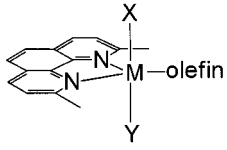

1

Figure 1. General formula for complexes **1**; M = Pd, Pt; X = Cl, Br, I, OR, SeR, TeR; Y = H, R, Ar, GeR_nCl_{3-n}, SnR_nCl_{3-n}, PbR_nCl_{3-n}, HgR, SeR, TeR

Our previous work[4a,4b] dealt with the characterisation of complexes of type **1** (M = Pt)[7] containing two organochalcogenide ligands obtained by oxidative addition of RE−ER molecules to suitable Pt^0 precursors **2** [Reaction (1) in Scheme 1]. During these studies we also found that, when E = Se, the reaction is a rare example of an equilibrium. This offered the uncommon opportunity to analyse the subtle effects of the ligand properties on the equilibrium.

In this paper we report on the addition of phenylselenyl halides to the same Pt^0 precursors [Reaction (2) in Scheme 1]. This has led to new five-coordinate compounds containing SePh and X in the apical sites. Analysis of the NMR spectroscopic and structural data of the new species revealed new information on the coordination properties of both organochalcogenides and halides. Furthermore, relevant aspects of the reactivity of the new compounds have been examined.

[a] Dipartimento di Chimica "G. Ciamician" Università di Bologna,
Via Selmi 2, 40126 Bologna, Italy
Fax: + 39-051-209-9456
E-mail: vincenzo.albano@unibo.it
[b] Dipartimento STAT,
Via Mazzini 8, 86170 Isernia, Italy
[c] Dipartimento di Chimica, Università di Napoli "Federico II", Complesso Universitario di Monte S. Angelo,
Via Cintia, 80126 Napoli, Italy
Fax: + 39-081-674-090
E-mail: ruffo@unina.it
Supporting information for this article is available on the WWW under http://www.eurjic.org or from the author.

 © 2005 Wiley-VCH Verlag GmbH & Co. KGaA, Weinheim **DOI: 10.1002/ejic.200400536**

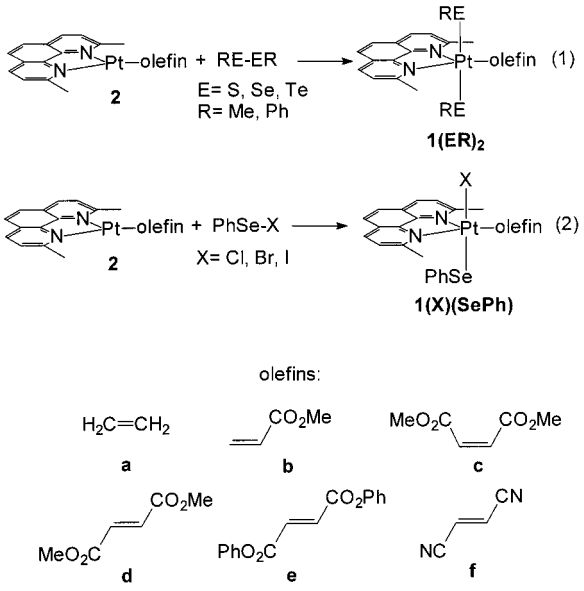

Scheme 1

Results and Discussion

Synthesis of the Complexes

Oxidative addition of the phenylselenyl halides was carried out with the three-coordinate precursors **2** shown in Scheme 1. The chelating ligand 2,9-dimethyl-1,10-phenanthroline (dmphen) was used due to its well-known ability to stabilise trigonal bipyramidal complexes of d^8 ions.[1] Olefins with increasing electron-acceptor properties were used: ethylene (**a**), methyl acrylate (**b**), dimethyl maleate (**c**), dimethyl fumarate (**d**), diphenyl fumarate (**e**) and fumarodinitrile (**f**). As a consequence the metal−olefin bond in the Pt^0 complexes containing **c**, **d**, **e** or **f** is characterised by a substantial π-backdonation contribution, thus enhancing the stability of the five-coordinate complexes by removing electronic density from the metal. These compounds are stable in solution and can be stored at room temperature for several days without appreciable decomposition. The ethylene or methylacrylate precursors are more sensitive to moisture, oxidising agents or heat, and were therefore freshly prepared before use.

All the additions were performed in chloroform, in which the complexes generally display reasonable solubility. The reactions were complete within a few seconds, as revealed by the change of the solution colour from yellow (red for ethylene derivative) to pink. The products were crystallised in high yield by dropwise addition of diethyl ether to the reaction mixture. The ethylene complex could be isolated in pure form only with Cl-SePh, while in the case of the other haloselenides it was always accompanied by significant impurities, which could not be removed even by careful crystallisation. The compounds are soluble in chloroform or dichloromethane with the exception of **[1f(Br)(SePh)]** (M = Pt), which displays a fair solubility only in tetrachloroethane.

Characterisation of the Products

The characterisation of the products was carried out by ^1H and ^{13}C NMR spectroscopy (Table 1) and elemental analysis. In two cases, namely **[1d(Br)(SePh)]** and **[1d(I)-(SePh)]**, the X-ray molecular structure was also determined.

Analysis of the ^1H NMR spectra confirmed that the additions proceed by activation of the selenium−halogen bond and unequivocally confirmed the trigonal bipyramidal geometry of the products. The most relevant features are the high-field shift of the olefin protons signals by at least 2 ppm with respect to the free alkene, as typically found in complexes of type **1**,[1] and the significant high-field shift of the PhSe- protons, which is attributable to the presence of a specific interaction between the phenyl ring of the selenide ligand and the rings of dmphen. This interaction is also present in the solid state, and has already been discussed for **[1(EPh)$_2$]** complexes.[4a]

As for the stereochemical aspects, the number of possible isomers depends on the symmetry of the alkene. Of course, ethylene (D_{2h}) affords only one isomer and the alkene protons resonate as an AB quadruplet. In the presence of dimethyl maleate (C_{2v}), two isomers[8] may exist according to the orientation of the olefin substituents. The NMR spectra of freshly dissolved **[1c(Cl)(SePh)]** and **[1c(Br)(SePh)]** suggest the presence of only one rotamer whose olefin protons resonate at $\delta = 4.31$ and $\delta = 4.28$ ppm, respectively. In both cases, on standing in solution, slow conversion (days to completion) to the thermodynamically stable isomers was observed. The chemical shifts of the olefin protons for the latter species are $\delta = 4.60$ and $\delta = 4.74$, respectively.

The correct geometry of the two isomers can be reasonably assigned by considering the NMR spectroscopic data of the known complexes [Pt(SePh)$_2$(dmphen)(dimethyl maleate)][4b] and [PtCl$_2$(dmphen)(dimethyl maleate)].[9] In the former species the olefin protons are necessarily oriented towards the SePh ligand, and resonate at $\delta = 4.34$ ppm. This value is very close to that found for the first, kinetically formed isomer of **[1c(Cl)(SePh)]**. In the dichloro species the maleate protons face the halide and their signal appears at $\delta = 4.79$ ppm, a value close to that found for the thermodynamically stable rotamer of **[1c(Cl)(SePh)]**. Hence, it is inferred that the olefin protons are likely to face the selenide ligand in the initially formed isomer, while they are oriented towards the chloride in the thermodynamically stable rotamer. This correlation can be reasonably extended to the bromo species **[1c(Br)(SePh)]**. It should be noted that an analogous relationship holds true for complexes of **1** bearing a halide and a hydrocarbyl group[7] in the axial positions. In all cases, the chemical shift of the maleate protons is higher in the isomer in which these nuclei are oriented towards the halogen.

Coordination of dimethyl fumarate or fumarodinitrile (C_{2h}) results in the formation of an enantiomeric couple, which, of course, is not distinguishable by NMR spectroscopy in the absence of a shift reagent. The olefin protons here are not equivalent, and resonate as doublets. It is interesting to note that the chemical-shift difference ($\Delta\delta$)

 © 2005 Wiley-VCH Verlag GmbH & Co. KGaA, Weinheim

Table 1. Selected $^{1}H^{a}$ and $^{13}C^{b}$ NMR spectroscopic data for complexes [Pt(X)(SePh)(dmphen)(olefin)]

Compound	Olefin[c]	Me(dmphen)	Other selected signals
X = Cl, olefin = ethylene	3.36 (app d, 2 H)	3.36 (s, 6 H)	6.68 (t, 1 H), 6.46 (d, 2 H), 6.30 (t, 2 H)
1a(Cl)(SePh)	3.16 [app d, 2 H (70)]		
	[32.8 (325)]		
X = Cl, olefin = methyl acrylate	Diast.:[d] 4.43 (dd, 1 H)	Diast.[d]: 3.49 (s, 3 H)	Diast.[d]: 6.74 (t, 1 H), 6.49 (d, 2 H)
1b(Cl)(SePh)	3.90 (d, 1 H), 3.17 (d, 1 H)	3.28 (s, 3 H)	6.35 (t, 2 H), 3.75 (s, 3 H, OMe)
	Diast.:[e] 4.60 (dd, 1 H),	Diast.[e]: 3.60 (s, 3 H)	Diast.[e]: 6.49 (t, 1 H), 6.26 (d, 2 H)
	3.65 (d, 1 H), 3.41 (d, 1 H)	3.46 (s, 3 H)	6.03 (t, 3 H), 3.82 (s, 3 H, OMe)
X = Cl, olefin = dimethyl maleate	4.31 [s, 2 H (75)][d]	3.42 (s, 6 H)[d]	Diast.[d]: 6.74 (t, 1 H), 6.49 (d, 2 H)
1c(Cl)(SePh)	4.60 [s, 2 H (79)][e]	3.50 (s, 6 H)[e]	6.33 (t, 2 H), 3.78 (s, 6 H, OMe)
	[32.6 (376)][e]		Diast.[e]: 6.58 (t, 1 H), 6.33 (d, 2 H)
			6.13 (t, 2 H), 3.83 (s, 6 H, OMe)
X = Cl, olefin = dimethyl fumarate	5.16 [d, 1 H (82)]	3.70 (s, 3 H)	6.47 (t, 1 H), 6.27 (d, 2 H), 6.03 (t, 2 H)
1d(Cl)(SePh)	4.98 [d, 1 H (76)]	3.62 (s, 3 H)	3.82 (s, 3 H, OMe), 3.72 (s, 3 H, OMe)
	[32.7 (332), 31.4 (346)]		
X = Cl, olefin = diphenyl fumarate	5.54 [d, 1 H (82)]	3.74 (s, 3 H)	7.45−7.10 (m, 10 H), 6.51 (t, 1 H)
1e(Cl)(SePh)	5.29 [d, 1 H (77)]	3.72 (s, 3 H)	6.32 (d, 2 H), 6.08 (t, 2 H)
	[33.3 (340), 32.0 (341)]		
X = Cl, olefin = fumarodinitrile	4.25 [d, 1 H (75)]	3.40 (s, 3 H)	6.82 (t,1 H), 6.49 (d,2 H), 6.35 (t, 2 H)
1f(Cl)(SePh)	4.03 [d, 1 H (63)]	3.26 (s, 3 H)	
	[14.4 (374), 13.5 (354)][f]		
X = Br, olefin = methyl acrylate	Diast.[d]: 4.52 (dd, 1 H)	Diast.[d]: 3.58 (s, 3 H)	Diast.[d]: 6.74 (t, 1 H), 6.46 (d, 2 H)
1b(Br)(SePh)	4.12 (d, 1 H), 3.28 (d, 1 H)	3.38 (s, 3 H)	6.34 (t, 2 H), 3.86 (s, 3 H, OMe)
	Diast.[e]: 4.85 (dd, 1 H),	Diast.[e]: 3.68 (s, 3 H)	Diast.[e]: 6.46 (t, 1 H), 6.23 (d, 2 H)
	3.88 (d, 1 H), 3.61 (d, 1 H)	3.54 (s, 3 H)	6.02 (t, 2 H), 3.92 (s, 3 H, OMe)
X = Br, olefin = dimethyl maleate	4.28 [s, 2 H (75)][d]	3.38 (s, 6 H)[d]	Diast.[d]: 6.73 (t, 1 H), 6.48 (d, 2 H)
1c(Br)(SePh)	4.74 [s, 2 H (83)][e]	3.48 (s, 6 H)[e]	6.33 (t, 2 H), 3.80 (s, 6 H, OMe)
	[34.2 (364)][e]		Diast.[e]: 6.62 (t, 1 H), 6.34 (d, 2 H)
			6.18 (t, 2 H), 3.83 (s, 6 H, OMe)
X = Br, olefin = dimethyl fumarate	5.24 [d, 1 H (84)]	3.68 (s, 3 H)	6.50 (t, 1 H), 6.25 (d, 2 H)
1d(Br)(SePh)	4.93 [d, 1 H (78)]	3.61 (s, 3 H)	6.06 (t, 2 H), 3.82 (s, 3 H, OMe)
	[32.6 (322), 32.0 (353)]		3.72 (s, 3 H, OMe)
X = Br, olefin = diphenyl fumarate	5.65 [d, 1 H (74)]	3.68 (s, 3 H)	7.40−7.20 (m, 10 H), 6.64 (br, 1 H)
1e(Br)(SePh)	5.33 [d, 1 H (83)]	3.63 (s, 3 H)	6.36 (br, 2 H), 6.20 (br, 2 H)
X = Br, olefin = fumarodinitrile	4.38 [d, 1 H (76)]	3.41 (s, 3 H)	6.83 (t, 1 H), 6.48 (d, 2 H), 6.40 (t, 2 H)
1f(Br)(SePh)	4.02 [d, 1 H (67)]	3.26 (s, 3 H)	
	[12.1 (388), 11.8 (362)][f]		
X = I, olefin = dimethyl fumarate	5.34 [d, 1 H (83)]	3.62 (s, 3 H)	6.55 (t, 1 H), 6.22 (d, 2 H), 6.06 (t, 2 H)
1d(I)(SePh)	4.84 [d, 1 H (76)]	3.59 (s, 3 H)	3.80 (s, 3 H, OMe), 3.75 (s, 3 H, OMe)
	[31.0 (356), 30.7 (346)]		
[PtCl(dmphen){Se(Ph)Me}(ethylene)]BF_4	3.62 (app d, 2 H)	3.46 (s, 3 H)	7.17 (t, 1 H), 6.84 (t, 2 H), 6.51 (d, 2 H)
1a(Cl)(SePhMe)	3.41 (app d, 2 H)	3.24 (s, 3 H)	2.35 (s, 3 H, SeMe, $^{3}J_{Pt,H}$ = 35, $^{2}J_{Se,H}$ = 9 Hz)
[PtCl(dmphen){Se(Ph)Me}-	Diast.[d]: 4.56 [ABq, 2 H (71)]	Diast.[d]: 3.58 (s, 3 H)	Diast.[d]: 3.78 (s, 6 H, OMe)
(dimethyl maleate)]BF_4	Diast.[e]: 4.99 [d, 1 H (77)],	3.36 (s, 3 H)	2.51 (s, 3 H, SeMe, $^{3}J_{Pt,H}$ = 33, $^{2}J_{Se,H}$ = 6 Hz)
1c(Cl)(SePhMe)	4.62 [d, 1 H (76)]	Diast.[e]: 3.42 (s, 3 H)	Diast.[e]: 3.88 (s, 3 H, OMe), 3.86 (s, 3 H, OMe)
		3.21 (s, 3 H)	1.84 (s, 3 H, SeMe, $^{3}J_{Pt,H}$ = 36, $^{2}J_{Se,H}$ = 6 Hz)
[PtCl(dmphen){Se(Ph)Me}-	5.00 [ABq, 2 H (72)][g]	3.69 (s, 3 H)	6.81 (t, 1 H), 6.49 (t, 2 H), 6.28 (d, 2 H)
(dimethyl fumarate)]BF_4		3.42 (s, 3 H)	3.98 (s, 3 H, OMe), 3.78 (s, 3 H, OMe)
1d(Cl)(SePhMe)			3.01 (s, 3 H, SeMe, $^{3}J_{Pt,H}$ = 30, $^{2}J_{Se,H}$ = 7 Hz)
[Pt(SePh)(dmphen)(MeCN)(ethylene)]BF_4	3.78 (app d, 2 H, 69)	3.18 (s, 6 H)	6.99 (m, 1 H), 6.57 (m, 4 H)
1a(SePh)(MeCN)	3.41 (app d, 2 H, 61)		

[a] At 200 or 300 MHz and 298 K. [b] At 50.2 or 75.4 MHz and 298 K; values given in square brackets. [c] $^{2}J_{Pt,H}$ and $^{1}J_{Pt,C}$ [Hz] in parentheses (when measurable). [d] Kinetically formed isomer. [e] Thermodynamically stable isomer. [f] Spectra recorded in $C_2D_2Cl_4$ ($^{13}C_2D_2Cl_4$: δ = 74.15 ppm as internal standard). [g] More abundant isomer.

between the CH= signals in the dimethyl fumarate complexes is close to that for the corresponding maleate rotamers. This is in agreement with the fact that one fumarate proton is oriented towards the halide, while the other faces the selenide ligand.

Finally, two enantiomeric couples are formed with methyl acrylate. Actually, two patterns are present in the NMR spectra of both [**1b(Cl)(SePh)**] and [**1b(Br)(SePh)**]. The spectrum of a freshly prepared solution of the latter compound shows the two isomers in a 2:1 ratio. After three

 © 2005 Wiley-VCH Verlag GmbH & Co. KGaA, Weinheim

hours the species are present in equimolar amounts, and within six days the conversion to the stable isomer is complete. In a similar fashion the isomeric ratio for the chloro derivative is initially 1:1 and after five days one isomer becomes by far the more abundant. The correlation mentioned above for the dimethyl maleate complexes (see Table 1) indicates that the carboxymethyl groups are oriented towards the halide in the thermodynamically stable isomer.

The X-ray Molecular Structures of [1d(Br)(SePh)] and [1d(I)(SePh)]

The crystals of the title species are isomorphous (see Exp. Sect.), therefore the molecules are strictly isostructural in the solid state and experience equal force fields. This situation allows close comparisons of the bond values so that even minor differences can be discussed. Figure 2 shows a perspective drawing of the molecules; an axial view is shown in Figure 3. Table 2 contains a comparison of the most significant bond parameters of the two species.

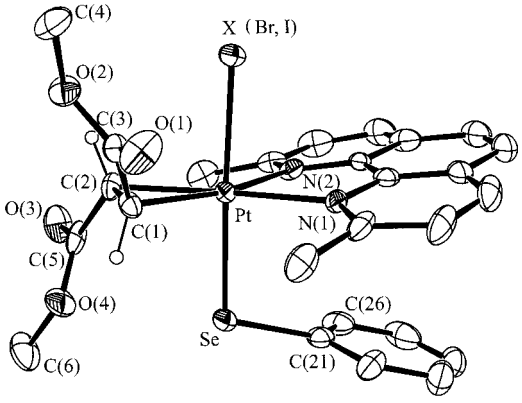

Figure 2. ORTEP drawing (30% probability thermal ellipsoids) of [PtX(SePh)(dmphen)(dimethyl fumarate)] [**1d(X)(SePh)**] (X= Br, I); only the olefinic hydrogens are shown for the sake of clarity

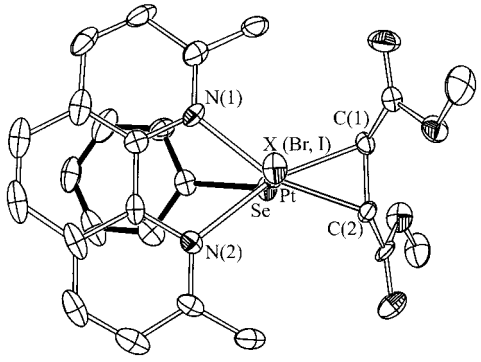

Figure 3. View down the X−Se−Pt axis (X = Br, I) of [PtX(SePh)(dmphen)(dimethyl fumarate)] [**1d(X)(SePh)**]; hydrogen atoms are omitted for clarity

The molecular geometry is as expected. The phenanthroline nitrogen atoms and fumarate double bond define the equatorial coordination plane, and the halide and selenide atoms occupy the axial positions. The molecules exhibit an asymmetric configuration because the C_2 symmetry of dimethyl fumarate does not match the idealised C_s symmetry of the remaining moiety. It should be noted that the phenyl ring of the SePh ligand is approximately placed above the central ring of the phenanthroline (Figure 2), while in the bis(phenylselenide) derivative [Pt(SePh)$_2$(dimethyl fumarate)(dmphen)] the phenyl rings match both pyridine rings from opposite sides.[4a] In that case we assumed the presence of preferential interactions between the ring dipoles. It is likely that the C_s geometry found in the present case allows an efficient crystal packing rather than a conformation that would optimise the intramolecular interactions. The non-equivalence of the axial ligands causes a tilting of the phenanthroline on the side of the less bulky halide ligand [angle between coordination and phenanthroline planes of 10.6(3)° and 10.5(4)° for bromide and iodide, respectively].

Table 2. Selected bond lengths [Å] and angles [°] for [**1d(Br)(SePh)**] and [**1d(I)(SePh)**]

	[1d(Br)(SePh)]	[1d(I)(SePh)]
Pt−Br	2.5195(9)	
Pt−I	–	2.6855(9)
Pt−Se	2.4537(9)	2.472(1)
Pt−N(1)	2.160(7)	2.190(8)
Pt−N(2)	2.201(7)	2.180(9)
Pt−C(1)	2.087(9)	2.09(1)
Pt−C(2)	2.101(8)	2.11(1)
C(1)−C(2)	1.44(1)	1.43(2)
Se−C(21)	1.930(5)	1.922(6)
N(1)−Pt−N(2)	76.2(3)	75.9(3)
Se−Pt−Br	177.12(3)	–
Se−Pt−I	–	176.81(4)
Pt−Se−C(21)	103.6(2)	104.0(2)
I−Pt−C(1)	–	91.9(3)
I−Pt−C(2)	–	91.0(3)
I−Pt−N(1)	–	87.0(2)
I−Pt−N(2)	–	86.1(2)
Br−Pt−C(1)	91.7(3)	–
Br−Pt−C(2)	90.6(3)	–
Br−Pt−N(1)	87.5(2)	–
Br−Pt−N(2)	85.7(2)	–

Significant variations are observed for the bonding interactions of the axial ligands. The difference in the Pt−halogen distances [Pt−Br 2.520(1) and Pt−I 2.685(1) Å] is consistent with the difference between their covalent radii (0.19 Å). The Pt−Se interaction is 0.02 Å shorter in the bromide derivative [2.453(1) and 2.472(1) Å, respectively]. This effect, if compared with the even longer value found in the bis(selenide) derivative [Pt(SePh)$_2$(dimethyl fumarate)(dmphen)] [average value 2.517(1) Å],[4a] suggests a correlation of the Pt−Se distance with the electronegativity difference between the apical donor atoms. In other words, as the bonds in the linear Se−Pt−X unit (X = Br, I, Se) result from interactions with the same metal-atom orbitals, the ligand-to-metal donation is balanced between the competitors according to their donor properties, and the Pt−Se bond becomes stronger in the bromide and weaker in the bis(selenide) derivative.

 © 2005 Wiley-VCH Verlag GmbH & Co. KGaA, Weinheim

The equatorial Pt−N and Pt−C interactions are affected much less by the changes in the axial ligands, and the differences are barely significant in terms of experimental errors. However, we note that, in agreement with the situation discussed for the axial ligands, the bonds in the bromide derivative are slightly, but systematically, shorter than in the iodide. The average values are as follows: Pt−N 2.180(7), 2.185(8) and Pt−C 2.086(8), 2.097(9) Å, respectively. Correspondingly, the olefin C=C distance is slightly longer in the bromide derivative [1.437(12) against 1.425(15) Å], and the C−C=C−C torsion angle is slightly higher in the bromide [46.1(9) against 44.5(9)°], indicating slightly more sp^3 rehybridisation where more donation is allowed.

Reactivity

In no case was the oxidative addition of phenylselenyl halides to the platinum(0) precursors found to be an equilibrium. The reaction was quantitative even with fumarodinitrile, which stabilises the low oxidation state of the metal through a very effective π-backdonation. These results parallel those obtained when PhSe-SePh[4b] is allowed to react with the same complexes, while with MeSe-SeMe[4a] the reactions were found to be an equilibrium. However, these findings are not surprising since the Pt−X bond strengths[10] are relatively high compared to those of the other bonds that form or break in the reaction. Thus, the addition of the selenenyl halides is enthalpically driven towards the products. Furthermore, the above-mentioned intramolecular interaction between aromatic rings helps to stabilise the five-coordinate complexes.

Some relevant aspects of the reactivity of the new complexes have been explored. The ability of the coordinated SeR ligands to undergo electrophilic attack was confirmed by reacting [**1a(Cl)(SePh)**], [**1c(Cl)(SePh)**] (kinetic isomer) and [**1d(Cl)(SePh)**] with trimethyloxonium tetrafluoroborate (reaction 1 of Scheme 2). The corresponding products are formally monopositive cationic complexes bearing Se(Me)Ph as the axial ligand. Accordingly, the compounds are fairly soluble only in nitromethane. The presence of Me on selenium was confirmed by the presence of a singlet coupled to both ^{77}Se and ^{195}Pt in the ^{1}H NMR spectrum. Of course, upon addition of the methyl group, the selenium atom becomes stereogenic. In the presence of a prochiral olefin such as dimethyl fumarate, two diastereomeric couples form, and these were observed in solution for [**1d(Cl)(SePhMe)**] in an 8:3 ratio.

In the spectrum of [**1c(Cl)(SePhMe)**], which is obtained upon addition of trimethyloxonium tetrafluoroborate to the kinetic isomer of [**1c(Cl)(SePh)**], the CH= protons resonate as two doublets, while the methoxy groups are still equivalent. The lack of sensitivity of the methoxy protons towards the transformation of the selenide ligand suggests that the coordination stereochemistry of the olefin is retained. In solution, the compound slowly isomerises into the most stable isomer, as is the case for the parent compound.

Another aspect of this study has dealt with the reactivity of the other axial ligand — the halide. This can be replaced by a neutral ligand, for example acetonitrile, upon treatment with a silver salt (reaction 2 of Scheme 2). The reaction was performed with the ethylene compound [**1a(Cl)(SePh)**] and affords the corresponding monopositive cation of [**1a(SePh)(MeCN)**], which, again, is fairly soluble only in nitromethane.

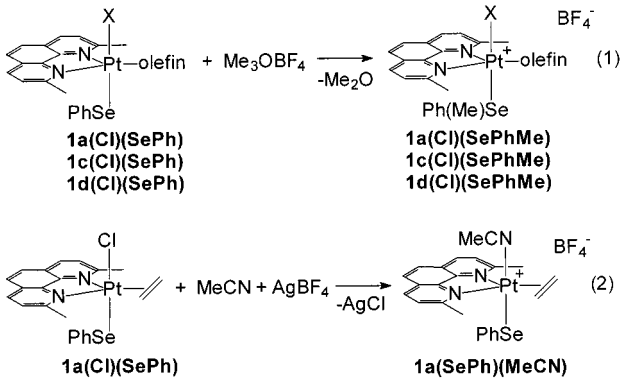

Scheme 2

Conclusions

The chemistry described in this paper confirms the peculiar aptitude of trigonal bipyramidal complexes of platinum(II), such as **1**, to function as effective models for comparing the behaviour of ligands. Thus, new five-coordinate Pt^{II} complexes with a halide and the SePh ligand in axial positions have been isolated and relevant aspects of their reactivity elucidated. The availability of the new compounds has allowed a comparison of the coordination and spectral properties of halides and organochalcogenides in identical environments. NMR spectroscopy has also been employed for this homogeneous class of compounds to analyse the geometrical isomerism displayed by some of the compounds.

Experimental Section

General: ^{1}H and ^{13}C NMR spectra were recorded with Varian XL-200 or Varian Gemini spectrometers. The NMR spectroscopic data are reported in Table 1. ^{1}H and ^{13}C NMR chemical shifts are reported in δ units (ppm) relative to the solvent ($CHCl_3$: δ = 7.26 ppm; CHD_2NO_2: δ = 4.33 ppm; $^{13}CDCl_3$: δ = 77.0 ppm; $^{13}C_2D_2Cl_4$: δ = 74.15 ppm). Phenylselenyl chloride, phenylselenyl bromide, the diphenyl diselenide compound with iodine (1:1) and the trimethyloxonium salt were commercially available. Platinum(0) precursors were obtained according to a described method.[11] Solvents and reagents were of AnalaR grade and used without further purification.

Synthesis of Complexes 1 of Formula [PtX(SePh)(dmphen)(olefin)] (X= Cl, Br): A solution of the appropriate selenyl compound PhSeX (0.15 mmol) in a minimum amount of chloroform (0.5 mL) was added to a suspension of the three-coordinate compound **2a−f** (0.15 mmol) in chloroform (0.5 mL). After stirring at room temperature for 5 min, addition of diethyl ether afforded the deep rose-

 © 2005 Wiley-VCH Verlag GmbH & Co. KGaA, Weinheim

violet product, which was washed with diethyl ether and dried. **[1a(Cl)(SePh)]:** Yield: 75 mg (80%). $C_{22}H_{21}ClN_2PtSe$ (622.8) calcd. C 42.43, H 3.40, N 4.50; found C 42.12, H 3.22, N 4.37. **[1b(Cl)(SePh)]:** Yield: 85 mg (83%). **[1c(Cl)(SePh)]:** Yield: 100 mg (90%). $C_{26}H_{25}ClN_2O_4PtSe$ (738.8) calcd. C 42.27, H 3.41, N 3.79; found C 42.03, H 3.54, N 3.63. **[1d(Cl)(SePh)]:** Yield: 98 mg (88%). **[1e(Cl)(SePh)]:** Yield: 110 mg (85%). **[1f(Cl)(SePh)]:** Yield: 91 mg (90%). **[1b(Br)(SePh)]:** Yield: 87 mg (80%). **[1c(Br)(SePh)]:** Yield: 102 mg (87%). **[1d(Br)(SePh)]:** Yield: 96 mg (82%). $C_{26}H_{25}BrN_2O_4PtSe$ (783.3) calcd. C 39.87, H 3.22, N 3.58; found C 40.02, H 3.18, N 3.69. **[1e(Br)(SePh)]:** Yield: 112 mg (82%). **[1f(Br)(SePh)]:** Yield: 92 mg (86%). $C_{24}H_{19}BrN_4PtSe$ (717.2) calcd. C 40.19, H 2.67, N 7.81; found C 40.35, H 2.81, N 7.60.

Synthesis of [PtI(SePh)(dmphen)(dimethylfumarate)] [1d(I)(SePh)]: The 1:1 diphenyl diselenide compound with iodine (0.11 mmol) was added to a magnetically stirred suspension of **2d** (0.12 g, 0.22 mmol) in chloroform (1 mL). The dark-red solution was stirred at room temperature for 5 min. Subsequent addition of diethyl ether afforded the product, which was washed with diethyl ether and dried. Yield: 100 mg (80%).

Synthesis of Complexes 1 of Formula [PtCl(dmphen){Se(Ph)Me}-(olefin)]BF_4: A solution of trimethyloxonium tetrafluoborate salt (0.019 g, 0.13 mmol) in nitromethane (0.5 mL) was added to the appropriate coordinatively saturated compound [**1a(Cl)(SePhMe)**], [**1c(Cl)(SePhMe)**] or [**1d(Cl)(SePhMe)**] (0.13 mmol). After stirring at room temperature for 5 min, slow addition of diethyl ether to the resulting solution afforded the yellow product, which was washed with diethyl ether and dried. **[1a(Cl)(SePhMe)]:** Yield: 70 mg (74%).**[1c(Cl)(SePhMe)]:** Yield: 77 mg (70%). $C_{27}H_{28}BClF_4N_2O_4PtSe$ (840.7) calcd. C 38.58, H 3.36, N 3.33; found C 39.01, H 3.35, N 3.40. **[1d(Cl)(SePhMe)]:** Yield: 74 mg (68%).

Synthesis of [Pt(SePh)(dmphen)(MeCN)(ethylene)]BF_4 [1a(SePh)-(MeCN)]: A solution of silver tetrafluoroborate in acetonitrile (0.13 mmol) was added to a solution of five-coordinate product [**1a(Cl)(SePh)**] (0.13 mmol) in nitromethane under nitrogen at 273 K. After stirring for 30 min, the residual solid was filtered through a small Celite pad. The addition of diethyl ether to the resulting solution afforded the light-yellow product, which was washed with diethyl ether and dried. Yield: 74 mg (80%).

X-ray Crystallography: Crystals of suitable quality were grown from a 1:1 mixture of chloroform and diethyl ether. The X-ray intensity data for [**1d(Br)(SePh)**] and [**1d(I)(SePh)**] were measured with a Bruker AXS SMART 2000 diffractometer, equipped with a CCD detector. Cell dimensions and the orientation matrix were initially determined from a least-squares refinement on reflections measured in three sets of 20 exposures, collected in three different ω regions, and eventually refined against all data. For all crystals, a full sphere of reciprocal space was scanned by 0.3° ω steps, with the detector kept at a distance of 5.0 cm from the sample. The software SMART[12] was used for collecting frames of data, indexing the reflections and determining the lattice parameters. The collected frames were then processed for integration by the SAINT program,[12] and an empirical absorption correction was applied using SADABS.[13] The structures were solved by direct methods (SIR 97)[14] and subsequent Fourier syntheses and refined by full-matrix least-squares on F^2 (SHELXTL),[15] using anisotropic thermal parameters for all non-hydrogen atoms. All hydrogen atoms except the olefinic hydrogen atoms, which were located in the Fourier map and refined isotropically, were added in calculated positions, included in the final stage of refinement with isotropic thermal parameters, U(H), of 1.2 U_{eq}(C) [U(H) = 1.5 U_{eq}(C-Me)], and allowed to ride on their carrier carbon atoms. Crystal data and details of the data collection for all structures are reported in Table 3. CCDC-237837 and -237838 for [**1d(Br)(SePh)**] and [**1d(I)(SePh)**], respectively, contain the supplementary crystallographic data for this paper. These data can be obtained free of charge at www.ccdc.cam.ac.uk/conts/retrieving.html [or from the Cambridge

Table 3. Crystal data and experimental details for [**1d(Br)(SePh)**] and [**1d(I)(SePh)**]

	[**1d(Br)(SePh)**]	[**1d(I)(SePh)**]
Empirical formula	$C_{26}H_{25}BrN_2O_4PtSe$	$C_{26}H_{25}IN_2O_4PtSe$
Formula mass	783.44	830.43
T [K]	298(2)	298(2)
λ [Å]	0.71073	0.71073
Crystal symmetry	monoclinic	monoclinic
Space group	$P2_1/c$	$P2_1/c$
a [Å]	11.3454(4)	11.4073(5)
b [Å]	16.1178(7)	16.1014(7)
c [Å]	14.0108(6)	14.1829(6)
β [°]	93.367(1)	93.194(1)
Cell volume [Å^3]	2557.6(2)	2601.0(2)
Z	4	4
D_c [Mg·m^{-3}]	2.035	2.121
μ(Mo-K_α) [mm^{-1}]	8.507	8.016
F(000)	1496	1568
Crystal size [mm]	0.14 × 0.16 × 0.25	0.12 × 0.15 × 0.15
θ limits [°]	2.53−24.99	2.53−29.99
Reflections collected	20312 (±h, ±k, ±l)	21966 (±h, ±k, ±l)
Unique observed reflections [$F_o > 4\sigma(F_o)$]	4355 [R(int) = 0.055]	7523 [R(int) = 0.079]
Goodness-of-fit-on F^2	1.069	0.989
R_1 (F)[a] wR_2 (F^2)[b]	0.0430, 0.0979	0.0542, 0.1375
Largest diff. peak and hole [e·Å^{-3}]	1.95 and −1.48	1.68 and −2.56

[a] $R_1 = \Sigma||F_o| - |F_c||/\Sigma|F_o|$. [b] $wR_2 = [\Sigma w(F_o^2 - F_c^2)^2/\Sigma w(F_o^2)^2]^{1/2}$ where $w = 1/[\sigma^2(F_o^2) + (aP)^2 + bP]$ and $P = (F_o^2 + 2F_c^2)/3$.

 © 2005 Wiley-VCH Verlag GmbH & Co. KGaA, Weinheim

Crystallographic Data, 12 Union Road, Cambridge, CB2 1EZ, UK; Fax: + 44-1223-336-033; E-mail: deposit@ccdc.cam.ac.uk].

Acknowledgments

The authors thank the MIUR (Programmi di Ricerca Scientifica di Rilevante Interesse Nazionale, Cofinanziamento 2001−2002) and the Universita' di Bologna and Napoli for financial support and the Centro Interdipartimentale di Metodologie Chimico-Fisiche, Università di Napoli "Federico II" for NMR facilities.

[1] V. G. Albano, G. Natile, A. Panunzi, *Coord. Chem. Rev.* **1994**, *133*, 67−114.

[2] [2a] M. E. Cucciolito, F. Giordano, A. Panunzi, F. Ruffo, V. De Felice, *J. Chem. Soc., Dalton Trans.* **1993**, 3421−3426. [2b] V. G. Albano, C. Castellari, M. Monari, V. De Felice, M. L. Ferrara, F. Ruffo, *Organometallics* **1995**, *14*, 4213−4221. [2c] V. G. Albano, M. L. Ferrara, M. Monari, A. Panunzi, F. Ruffo, *Inorg. Chim. Acta* **1999**, *285*, 70−75.

[3] F. Giordano, F. Ruffo, A. Saporito, A. Panunzi, *Inorg. Chim. Acta* **1997**, *264*, 231−237.

[4] [4a] V. G. Albano, M. Monari, I. Orabona, A. Panunzi, F. Ruffo, *J. Am. Chem. Soc.* **2001**, *123*, 4352−4353. [4b] V. G. Albano, M. Monari, I. Orabona, A. Panunzi, G. Roviello, F. Ruffo, *Organometallics* **2003**, *22*, 1223−1230. [4c] A. Panunzi, G. Roviello, F. Ruffo, *Organometallics* **2002**, *21*, 3503−3505. [4d] A. Panunzi, G. Roviello, F. Ruffo, *Inorg. Chem. Commun.* **2003**, *6*, 1282−1286.

[5] The only known species containing chalcogenide ligands σ-bonded to platinum are square-planar complexes of Pt^{II} and octahedral Pt^{IV} derivatives. For recent examples of Pt^{II} species, see: [5a] R. Oilunkaniemi, R. S. Laitinen, M. Ahlgrén, *J. Organomet. Chem.* **2001**, *623*, 168−175. [5b] S. Ford, M. R. Lewtas, C. P. Morley, M. Di Vaira, *Eur. J. Inorg. Chem.* **2000**, 933−938. [5c] A. K. Singh, S. Sharma, *Coord. Chem. Rev.* **2000**, *209*, 49−98 and references cited therein. [5d] R. Oilunkaniemi, R. S. Laitinen, M. Ahlgrén, *J. Organomet. Chem.* **1999**, *587*, 200−206. [5e] L.-B. Han, N. Choi, M. Tanaka, *J. Am. Chem. Soc.* **1997**, *119*, 1795−1796. [5f] L.-B. Han, S. Shimada, M. Tanaka, *J. Am. Chem. Soc.* **1997**, *119*, 8133−8134. For recent examples related to Pt^{IV} or Pd^{IV} species, see: [5g] A. J. Canty, M. C. Denney, J. Patel, H. Sun, B. W. Skelton, A. H. White, *J. Organomet. Chem.* **2004**, *689*, 672−677. [5h] M. C. Janzen, M. C. Jennings, R. J. Puddephatt, *Inorg. Chem.* **2003**, *42*, 4553−4558. [5i] V. V. Rostovtsev, L. M. Henling, J. A. Labinger, J. E. Bercaw, *Inorg. Chem.* **2002**, *41*, 3608−3619. [5j] M. Rashidi, M. Nabavizadeh, R. Hakimelahi, S. Jamali, *J. Chem. Soc., Dalton Trans.* **2001**, 3430−3434. [5k] R. Song, K. M. Kim, S. S. Lee, J. S. Sohn, *Inorg. Chem.* **2000**, *39*, 3567−3571. [5l] A. J. Canty, H. Jin, *J. Organomet. Chem.* **1998**, *565*, 135−140. [5m] A. J. Canty, H. Jin, B. W. Skelton, A. H. White, *Inorg. Chem.* **1998**, *37*, 3975−3981. [5n] K. M. Kim, Y. S. Sohn, *Inorg. Chem.* **1998**, *37*, 6109−6112. [5o] M. S. Davies, T. W. Hambley, *Inorg. Chem.* **1998**, *37*, 5408−5409. [5p] A. J. Canty, S. D. Fritsche, H. Jin, J. Patel, B. W. Skelton, A. H. White, *Organometallics* **1997**, *16*, 2175−2182. [5q] U. Bierbach, T. W. Hambley, J. D. Roberts, N. Farrell, *Inorg. Chem.* **1996**, *35*, 4865−4872. [5r] K. T. Aye, J. J. Vittal, R. J. Puddephatt, *J. Chem. Soc., Dalton Trans.* **1993**, 1835−1839.

[6] [6a] R. E. Barrientos-Astigarraga, P. Castellani, J. V. Comasseto, H. B. Formiga, N. C. da Silva, C. Y. Sumida, M. L. Vieira, *J. Organomet. Chem.* **2001**, *623*, 43−47. [6b] A. Ogawa, *J. Organomet. Chem.* **2000**, *611*, 463−474. [6c] S.-K. Kang, S.-W. Lee, H.-C. Ryu, *Chem. Commun.* **1999**, 2117−2118. [6d] J. C. Bayòn, C. Claver, A. M. Masdeu-Bultò, *Coord. Chem. Rev.* **1999**, *193−195*, 73−145. [6e] L.-B. Han, M. Tanaka, *J. Am. Chem. Soc.* **1998**, *120*, 8249−8250. [6f] H. Kuniyasu, K. Sugoh, M. Song Su, H. Kurosawa, *J. Am. Chem. Soc.* **1997**, *119*, 4669−4677.

[7] Throughout this paper the labels of compounds **1** and **2** contain a letter, which identifies the alkene (see Scheme 1), followed by the axial ligands (only for **1**).

[8] [8a] M. L. Ferrara, I. Orabona, F. Ruffo, V. De Felice, *J. Organomet. Chem.* **1996**, *519*, 75−82. [8b] S. Bartolucci, P. Carpinelli, V. De Felice, B. Giovannitti, A. De Renzi, *Inorg. Chim. Acta* **1992**, *197*, 51−57.

[9] V. G. Albano, C. Castellari, M. L. Ferrara, A. Panunzi, F. Ruffo, *J. Organomet. Chem.* **1994**, *469*, 237−244.

[10] F. R. Hartley, *Nature, Phys. Sci.* **1972**, *236*, 75−77.

[11] A. De Renzi, A. Panunzi, F. Ruffo, *Inorg. Synth.* **1998**, *32*, 158−162.

[12] SMART & SAINT Software Reference Manuals, version 5.051 (Windows NT Version), Bruker Analytical X-ray Instruments Inc., Madison, WI, **1998**.

[13] G. M. Sheldrick, *SADABS, program for empirical absorption correction*, University of Göttingen, Germany, **1996**.

[14] A. Altomare, G. Cascarano, C. Giacovazzo, A. Guagliardi, A. G. G. Moliterni, M. C. Burla, G. Polidori, M. Camalli, D. Siliqi, *Acta Crystallogr., Sect. A* **1996**, *52*, C79.

[15] G. M. Sheldrick, SHELXTL*plus (Windows NT Version) Structure Determination Package, Version 5.1.*, Bruker Analytical X-ray Instruments Inc., Madison, WI, USA, **1998**.

Received June 18, 2004
Early View Article
Published Online November 24, 2004

Temperature-Controlled Solvothermal Syntheses, Structures and Characterizations of a Novel Class of Zn Complexes Constructed from 1,4-Bis[2-(5-phenyloxazolyl)]benzene

Shu-Mei Chen,[a] Can-Zhong Lu,*[a] Quan-Zheng Zhang,[a] Jiu-Hui Liu,[a] and Xiao-Yuan Wu[a]

Keywords: Complexes / N ligands / Crystal engineering / Coordination modes / Properties

Three novel complexes, $ZnCl_2(H_2O)(POPOP)\cdot POPOP$ (**1**), $[ZnCl_2(POPOP)]_n$ (**2**), and $\{Zn_2(CH_3COO)(POPOP)_{1.5}Cl_3\}_n$ (**3**) {POPOP = 1,4-bis[2-(5-phenyloxazolyl)]benzene}, of zinc–POPOP coordination polymers have been obtained from an identical starting mixture using temperature as the only independent variable. Complexes **1**–**3** all crystallize in the triclinic $P\bar{1}$ space group, but their Zn^{II} centers adopt different coordinations. Complex **1** consists of POPOP-coordinated zinc units and discrete POPOP molecules, **2** features an interesting zigzag chain structure, and **3** consists of unique ladder-like double-chains bridged by POPOP units. Furthermore, **1**–**3** display some different fluorescent emissions based on their different coordination architectures.

(© Wiley-VCH Verlag GmbH & Co. KGaA, 69451 Weinheim, Germany, 2005)

Introduction

Transition metal containing organic materials have attracted considerable recent interest because of their potential applications in optical and electrooptical devices such as organic light-emitting diodes (OLEDs), electrochromic, photovoltaic and photoconductive devices, and photorefractive optical elements.[1−9] Polynuclear d^{10} metal (Cu^I, Ag^I, Au^I, Zn^{II}, or Cd^{II}) complexes have also attracted extensive interest owing to their appealing structures and photoluminescent properties. A series of d^{10} metal organic frameworks have been described.[10,11] Some organic N-donors such as bipyridine or related species are often chosen to fabricate these various species.[12,13] Interest in the chemistry of transition metal−diimine compounds with a conjugated π-system has grown rapidly because of their unique physical properties. Molecular structure-property relationships of organic π-conjugated materials have been explored.[14−16] POPOP {POPOP = 1,4-bis[2-(5-phenyloxazolyl)]benzene} is a long π-conjugated ligand and often acts as a photoluminescent chromophore.[17] However, to the best of our knowledge, no studies have been reported based on POPOP with transition metals. To understand the coordination chemistry of POPOP and to prepare new materials with interesting structural topology and excellent physical properties, we have been particularly concerned with such polymers and attempted to prepare some materials with interesting physical properties.

In addition, the design and synthesis of novel coordination architectures controlled by varying the reaction conditions (including temperature,[18,19] metal/ligand ratio,[20] pH,[21] solvents,[22] and counter anions[23,24]) are of great interest in coordination chemistry and reactions. Appropriate control of the reaction conditions makes it possible to construct new materials with useful properties. For example, Forster and co-workers have carried out systematic studies on the role of synthesis temperature as an isolated reaction variable.[19] In this paper, we report the synthesis of three novel complexes of zinc−POPOP coordination polymers, $ZnCl_2(H_2O)(POPOP)\cdot(POPOP)$ (**1**), $[ZnCl_2(POPOP)]_n$ (**2**), and $\{Zn_2(CH_3COO)(POPOP)_{1.5}Cl_3\}_n$ (**3**), from identical starting materials but at different temperatures.

Results and Discussion

Synthesis and General Characterization

To design new organic−inorganic hybrid compounds with some multifunctional ligands, hydro(solvo)thermal synthesis is a powerful method. At such a relatively low temperature and under autogenous pressure, the problems of ligand solubility and reactivity are minimized, and appropriate O- and N-donor ligands can be selected by the metal centers for efficient molecular constructions during crystallization. Complexes **1**−**3** were synthesized simply un-

[a] The State Key Laboratory of Structural Chemistry, Fujian Institute of Research on the Structure of Matter, National Center for Nanoscience and Nanotechnology, the Chinese Academy of Sciences,
Fuzhou, Fujian 350002, China
Fax: (internat.) + 81-591-371-4946
E-mail: czlu@fjirsm.ac.cn

Supporting information for this article is available on the WWW under http://www.eurjic.org or from the author.

der solvothermal reaction conditions. As mentioned above, POPOP is a long π-conjugated ligand that can offer two N atoms for coordination. The synthesis of zinc−POPOP described here demonstrates that a single starting mixture can be used to obtain different zinc−POPOP structures by varying only the reaction temperatures. The same precursors under different reaction temperatures lead to three novel complexes, **1**−**3**, exhibiting different architectures with different coordination fashions (Scheme 1). The coordination numbers of Zn^{II} ions in **1**−**3** are the same, but their differing topologies are a discrete arrangement, a 1D zigzag chain arrangement, and a 1D ladder-like double-chain arrangement, respectively.

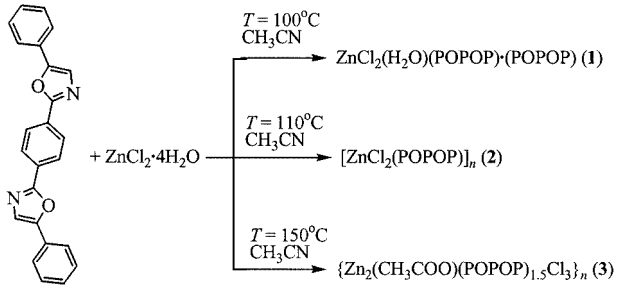

Scheme 1. Role of temperature in the synthesis of zinc−POPOP complexes

Crystal Structures of Complexes

$ZnCl_2(H_2O)(POPOP)\cdot(POPOP)$ (1)

The structure determination reveals that complex **1** is discrete, consisting of POPOP-coordinated zinc units and POPOP molecules (Figure 1). The zinc(II) atom exhibits a tetrahedral configuration coordinated by two chlorine atoms [Zn(1)−Cl(1) = 2.2238(4) Å, Zn(1)−Cl(2) = 2.2124(4) Å], one nitrogen atom of the POPOP ligand with a Zn(1)−N(1) bond length of 2.0629(11) Å, and one oxygen atom [Zn(1)−Ow1 = 2.0193(10) Å] of a water group. There are three crystallographically independent POPOP ligands with different orientations in one unit: one monodentately coordinates to one Zn center, while the other two do not participate in coordination and orient vertically to each other. Interestingly, each POPOP ligand is almost coplanar. Figure 2 shows that there is a discrete POPOP unit between two adjacent POPOP-coordinated zinc units in which Zn^{II} atoms are located on opposite direction mutually. These three units are parallel and combine to form a basic group by obvious π−π interactions, with distances of 3.518(5)−3.929(6) Å. A further POPOP molecule, which is vertical relative to the parallel layers, fills in the large cavity formed by the staggered arrangement of four groups.

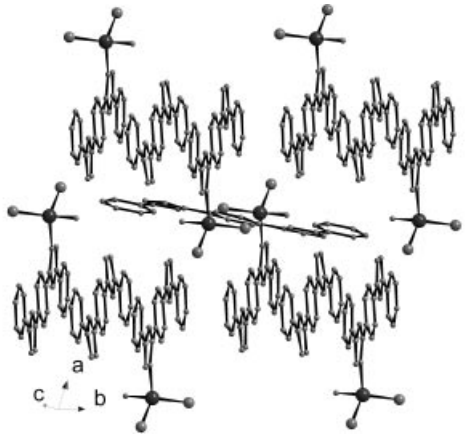

Figure 2. Ball-and-stick representation of the packing diagram of **1**

$[ZnCl_2(POPOP)]_n$ (2)

A single-crystal X-ray structural analysis shows that complex **2** has an interesting one-dimensional zigzag chain framework, which is built up by one POPOP linked to two Zn atoms. The zinc(II) atom has a tetrahedral configuration coordinated by two chlorine atoms [Zn(1)−Cl(1) = 2.2258(6) Å, Zn(1)−Cl(2) = 2.2114(7) Å] and two nitrogen atoms [Zn(1)−N(1) = 2.0596(12) Å, Zn(1)−N(2) = 2.0587(12) Å] from two different POPOP ligands (Figure 3). Cl−Zn−Cl and N−Zn−N bond angles are 115.15(3)° and 96.73(5)° respectively. N−Zn−Cl bond angles range from 105.96(3) to 109.56(3)°. The shortest Zn···Zn distance between POPOP ligands is 9.184 Å. Figure 4 shows that each Zn atom is coordinated by two POPOP ligands, i.e. each POPOP ligand is connected with two zinc atoms. Based on this coordination mode, the 1D infinite chain framework is formed. The most interesting feature of complex **2** is that such a coordination mode produces a unique zigzag chain structure. The two dihedral angles between the 5-phenyloxazolyl rings and the center benzene ring plane are 25.05°.

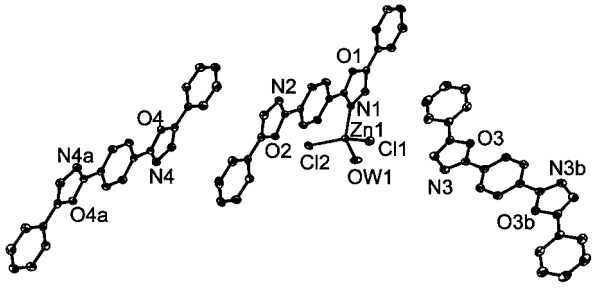

Figure 1. ORTEP drawing of $ZnCl_2(H_2O)(POPOP)\cdot(POPOP)$ (**1**), showing the local coordination of Zn^{II} and atomic numbering scheme (30% probability thermal ellipsoids)

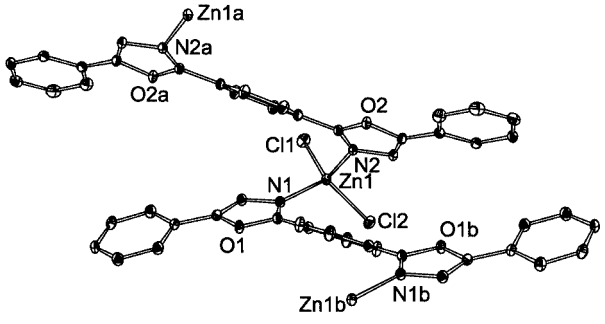

Figure 3. ORTEP drawing of $[ZnCl_2(POPOP)]_n$ (**2**)

 © 2005 Wiley-VCH Verlag GmbH & Co. KGaA, Weinheim

This is presumably a consequence of the bridging nature of the ligands, with effective coordination to the metals being of primary importance.

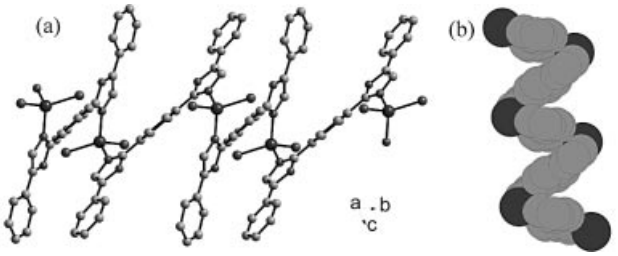

Figure 4. (a) Zig-zag chain structure in **2**; (b) space-filling plots of the zig-zag chain

{Zn$_2$(CH$_3$COO)(POPOP)$_{1.5}$Cl$_3$}$_n$ (3)

X-ray crystallographic analysis reveals that complex **3** consists of an infinite ladder-like double-chain bridged by POPOP ligands. The fundamental unit is shown in Figure 5. There are two crystallographically different Zn centers in the asymmetric unit, both displaying tetrahedral coordination geometry. The Zn(1) center is defined by two chlorine atoms [Zn(1)−Cl(1) = 2.2160(9) Å, Zn(1)−Cl(2) = 2.2166(10) Å], one nitrogen atom from a distorted POPOP ligand with a Zn(1)−N(2) bond length of 2.100(2) Å, and one oxygen atom [Zn(1)−O(4) = 2.007(2) Å] of a carboxylate group. N−Zn(1)−Cl bond angles are 109.64(7)° and 109.79(7)°, and O−Zn−Cl bond angles are 106.08(7)° and 113.99(7)°, respectively. O−Zn−N and Cl−Zn−Cl bond angles are 95.67(9)° and 119.12(4)° respectively. The Zn(2) center is coordinated by one chlorine atom [Zn(2)−Cl(3) = 2.2099(9) Å], two nitrogen atoms [Zn(2)−N(1) = 2.047(3) Å, Zn(2)−N(3) = 2.044(2) Å] from one rather distorted POPOP ligand and one slightly distorted POPOP ligand, and one oxygen atom [Zn(2)−O(5) = 1.964(2) Å] of a carboxylate group. Unlike in **1** and **2**, carboxyl groups, arising from the hydrolyzation of CH$_3$CN solvent, also coordinate with Zn atoms. There are also two crystallographically different POPOP ligands in the asymmetric unit: one is strongly distorted, with dihedral angles between the 5-phenyloxazolyl ring and the center benzene ring plane of 37.64° and 9.36° respectively,

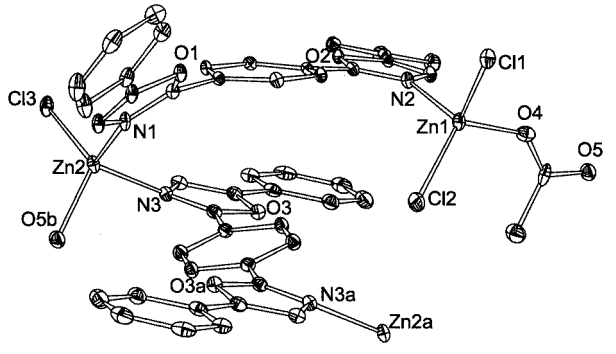

Figure 5. ORTEP drawing of {Zn$_2$(CH$_3$COO)(POPOP)$_{1.5}$Cl$_3$}$_n$ (**3**)

and coordinates to two different Zn centers. The second is slightly distorted, with dihedral angles of 25.91°, and coordinates to two symmetric relative Zn centers. In other words, each carboxyl group coordinates to two Zn atoms and each strongly distorted POPOP ligand provides two N atoms to coordinate with Zn atoms to form an interesting infinite chain. In addition, the slightly distorted POPOP ligands bridge two adjacent chains to produce the final ladder-like double-chain (Figure 6).

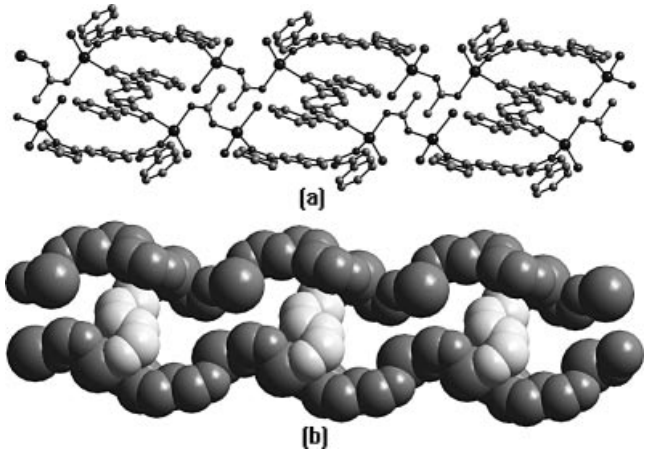

Figure 6. (a) 1D ladder-like double-chain structure in **3**; (b) space-filling plots of the 1D ladder-like double-chain (for clarity, only the backbone is shown)

The above structural descriptions show that temperature plays a crucial role in the formation of the complexes. A water molecule coordinates to Zn in complex **1**, but no water molecule exists in **2** or **3**. However, with increasing temperature some CH$_3$CN solvent was hydrolyzed to form CH$_3$COO$^-$ ligands in **3**. At the same time, the co-planar POPOP ligand also becomes distorted on going from complex **1** to **3**. Complexes **1**−**3** show increasing condensation and density at higher synthesis temperatures. Increasing temperatures also lead to changes in topological structure and favor higher overall dimensionality. The overall dimensionality of structures **1**−**3** also increases − from discrete at 100 °C, to a 1D chain at 110 °C, and a 1D double-chain at 150 °C, respectively. The successful preparation of **1**−**3** reveals a clear relationship between synthesis temperature and structure.

Thermogravimetric Analysis (TGA)

The stability of **2** and **3** was examined by thermogravimetric analysis (TGA), which revealed an onset temperature for decomposition above 330 °C. Such stabilities make the compounds potential candidates for practical applications.

Photoluminescence Properties

Emission spectra of complexes **1**−**3** in the solid state at room temperature show intense emissions at 452 nm (λ_{ex} = 396 nm) for **1**, 452 nm (λ_{ex} = 396 nm) for **2** and 460 nm (λ_{ex} = 397 nm) for **3**. To understand the nature of these

 © 2005 Wiley-VCH Verlag GmbH & Co. KGaA, Weinheim

emission bands, we analyzed the photoluminescence properties of the POPOP ligand and found that the strongest emission peak for POPOP is at 448 nm, which is near to the above values. Notably, the four values do differ slightly, which may be attributable to ligand center charge transfer. Similar enhancements of intraligand fluorescence occur in (polypyridyl)metal polymers.[25−26] Especially, the emission intensity is strongest in complex **3**, and its emission peak is also slightly larger, which may be ascribed to the presence of (CH_3COO) coordinated to Zn atoms.

Conclusion

We have successfully combined Zn metal and POPOP {1,4-bis[2-(5-phenyloxazolyl)]benzene} to obtain three novel zinc−POPOP coordination polymers, $ZnCl_2(H_2O)$·(POPOP)·(POPOP) (**1**), $[ZnCl_2(POPOP)]_n$ (**2**), and $\{Zn_2(CH_3COO)(POPOP)_{1.5}Cl_3\}_n$ (**3**), with different coordination architectures under solvothermal reactions. We have also investigated the photoluminescence properties of POPOP with a d^{10} transition metal. Incorporation of Zn^{II} complexes into the π-electron system of a conjugated molecule revealed a clear relationship between synthesis temperature and structure.

Experimental Section

General Remarks: All syntheses were performed in poly(tetrafluoroethylene)-lined stainless steel autoclaves under autogenous pressure. Reagents were purchased commercially and were used without further purification. Elemental analyses of C and H were performed with an EA1110 CHNS-0 CE elemental analyzer. IR (KBr pellets) spectra were recorded with a Nicolet Magna 750FT-IR spectrometer. Fluorescent data were collected with an Edinburgh FLS920 TCSPC system. TGA analysises were carried under nitrogen with an STA449C integration thermal analyzer.

$ZnCl_2(H_2O)$(POPOP)·(POPOP) (1): A mixture of POPOP (0.036 g, 0.10 mmol), $ZnCl_2·4H_2O$ (0.10 g, 0.48 mmol) and CH_3CN (10 mL) was heated in a stainless steel reactor with a Teflon liner at 100 °C for 72 h. After cooling, within 24 h yellow crystals of **1** were obtained in 68% yield (0.030 g based on POPOP). $C_{48}H_{34}Cl_2N_4O_5Zn$ (883.06): calcd. C 65.45, H 3.89, N 6.36; found C 65.29, H 3.76, N 6.14. IR (KBr): $\tilde{\nu}$ = 3514 (m), 3124 (w), 1617 (m), 1594 (m), 1557 (w), 1483 (s), 1449 (w), 1416 (m), 1281 (m), 1151 (m), 1130 (w), 1025 (w), 948 (s), 849 (m), 827 (w), 762 (s), 722 (s), 688 (s), 564 (w), 492 (w) cm^{-1}.

$[ZnCl_2(POPOP)]_n$ (2): A mixture of POPOP (0.036 g, 0.10 mmol), $ZnCl_2·4H_2O$ (0.10 g, 0.48 mmol) and CH_3CN (10 mL) was heated in a stainless steel reactor with a Teflon liner at 110 °C for 72 h. After cooling, within 24 h yellow crystals of **2** were obtained in 65% yield (0.033 g based on POPOP). $C_{48}H_{32}Cl_4N_4O_4Zn_2$ (500.68): calcd. C 57.83, H 3.24, N 5.62; found C 57.58, H 3.15, N 5.64. IR (KBr): $\tilde{\nu}$ = 3454 (w), 3123 (w), 1649 (m), 1617 (m), 1595 (m), 1557 (m), 1483 (s), 1449 (w), 1416 (m), 1351 (w), 1271 (w), 1150 (s), 1130 (w), 1104 (w), 1027 (w), 981 (w), 947 (s), 868 (w), 849 (m), 829 (m), 762 (s), 722 (s), 687 (s), 659 (w), 564 (w), 492 (w) cm^{-1}.

$\{Zn_2(CH_3COO)(POPOP)_{1.5}Cl_3\}_n$ (3): A mixture of POPOP (0.036 g, 0.10 mmol), $ZnCl_2·4H_2O$ (0.10 g, 0.48 mmol) and CH_3CN (10 mL) was heated in a stainless steel reactor with a Teflon liner at 150 °C for 72 h. After cooling, within 24 h yellow crystals of **3** were obtained in 65% yield (0.037 g based on POPOP). $C_{38}H_{27}Cl_3N_3O_5Zn_2$ (842.72): calcd. C 54.42, H 3.25, N 5.01; found C 54.45, H 3.20, N 5.20. IR (KBr): $\tilde{\nu}$ = 3466 (w), 3123 (w), 3090 (w), 1615 (m), 1593 (m), 1559 (s), 1480 (s), 1415 (m), 1363 (w), 1239 (w), 1149 (m), 1124 (w), 1025 (w), 947 (s), 872 (w), 850 (m), 776 (m), 765 (s), 723 (s), 689 (s), 661 (w), 610 (w), 532 (w), 495 (w) cm^{-1}.

X-ray Crystallographic Study: X-ray intensities of complexes **1**−**3** were collected with a Bruker Smart CCD diffractometer equipped with graphite-monochromated Mo-K_α radiation (λ = 0.71073 Å)

Table 1. Crystallographic data for complexes **1**−**3**

	1	**2**	**3**
Empirical formula	$C_{48}H_{34}Cl_2N_4O_5Zn$	$C_{24}H_{16}Cl_2N_2O_2Zn$	$C_{38}H_{27}Cl_3N_3O_5Zn_2$
Formula mass	883.06	500.68	842.72
Crystal size [mm]	0.65 × 0.45 × 0.25	0.40 × 0.35 × 0.25	0.25 × 0.20 × 0.15
Crystal color	yellow	yellow	yellow
Crystal system	triclinic	triclinic	triclinic
Space group	$P\bar{1}$	$P\bar{1}$	$P\bar{1}$
a [Å]	9.8858(10)	9.011(3)	12.264
b [Å]	12.8480(14)	10.790(3)	12.937
c [Å]	16.8502(13)	12.288(3)	13.399
α [°]	89.927(3)	64.604(6)	62.833(10)
β [°]	84.235(4)	89.571(9)	69.486(13)
γ [°]	69.942(5)	83.515(8)	75.666(14)
V [Å^3]	1999.0(3)	1071.3(5)	1761.6
$D_{calcd.}$ [g·cm^{-3}]	1.467	1.552	1.589
λ (Mo-K_α) [Å]	0.71073	0.71073	0.71073
Z	2	2	2
T [K]	130.15	130.15	130.15
μ (Mo-K_α) [mm^{-1}]	0.803	1.420	1.638
F (000)	908	508	854
R_1, wR_2 [$I > 2\sigma(I)$]	0.0283, 0.0752	0.0234, 0.0625	0.0410, 0.1042
R_1, wR_2 (all data)	0.0307, 0.0772	0.0250, 0.0641	0.0464, 0.1081

 © 2005 Wiley-VCH Verlag GmbH & Co. KGaA, Weinheim

at 130.15 K. Empirical absorption corrections were applied to the data using the SADABS program. Structures were solved by the direct method and refined by full-matrix least squares on F^2 using the SHELXTL-97 program. All non-hydrogen atoms were refined anisotropically. A summary of crystallographic data and other pertinent information for **1**−**3** (Table 1) and selected bond lengths and angles (Table 2) are given here. CCDC-244407 to -244409 contain the supplementary crystallographic data for this paper. These data can be obtained free of charge at www.ccdc.cam.ac.uk/conts/retrieving.html [or from the Cambridge Crystallographic Data Centre, 12 Union Road, Cambridge CB2 1EZ, UK; Fax: (internat.) + 44-1223-336-033; E-mail: deposit@ccdc.cam.ac.uk].

Table 2. Selected bond lengths [Å] and angles [°] for **1**−**3**

Complex **1**			
Zn(1)−OW1	2.0193(10)	Zn(1)−Cl(2)	2.2124(4)
Zn(1)−N(1)	2.0629(11)	Zn(1)−Cl(1)	2.2238(4)
OW1−Zn(1)−N(1)	106.57(4)	OW1−Zn(1)−Cl(1)	108.72(4)
OW1−Zn(1)−Cl(2)	107.60(3)	N(1)−Zn(1)−Cl(1)	102.54(3)
N(1)−Zn(1)−Cl(2)	112.95(3)	Cl(2)−Zn(1)−Cl(1)	117.871(15)
Complex **2**			
Zn(1)−N(2)	2.0587(12)	Zn(1)−Cl(2)	2.2114(7)
Zn(1)−N(1)	2.0596(12)	Zn(1)−Cl(1)	2.2258(6)
N(2)−Zn(1)−N(1)	96.73(5)	N(2)−Zn(1)−Cl(1)	113.08(3)
N(2)−Zn(1)−Cl(2)	105.96(3)	N(1)−Zn(1)−Cl(1)	109.56(3)
N(1)−Zn(1)−Cl(2)	114.89(3)	Cl(2)−Zn(1)−Cl(1)	115.15(2)
Complex **3**			
Zn(1)−O(4)	2.014(3)	Zn(2)−O(5)[a]	1.965(2)
Zn(1)−N(2)	2.103(3)	Zn(2)−N(1)	2.045(3)
Zn(1)−Cl(1)	2.2154(10)	Zn(2)−N(3)	2.046(3)
Zn(1)−Cl(2)	2.2162(11)	Zn(2)−Cl(3)	2.2101(10)
O(4)−Zn(1)−N(2)	95.71(10)	O(5)[a]−Zn(2)−N(1)	117.71(11)
O(4)−Zn(1)−Cl(1)	106.04(7)	O(5)[a] −Zn(2)−N(3)	97.14(10)
N(2)−Zn(1)−Cl(1)	109.83(8)	N(1)−Zn(2)−N(3)	103.10(10)
O(4)−Zn(1)−Cl(2)	113.99(7)	O(5)[a] −Zn(2)−Cl(3)	114.91(8)
N(2)−Zn(1)−Cl(2)	109.59(8)	N(1)−Zn(2)−Cl(3)	112.06(8)
Cl(1)−Zn(1)−Cl(2)	119.14(4)	N(3)−Zn(2)−Cl(3)	109.79(8)

[a] Symmetry transformations used to generate equivalent atoms: x, $y - 1$, z.

Supporting Information: The Supporting Information(see also the footnote on the first page of this article) contains TGA analyses for complexes **2** and **3**, IR and solid-state emission spectra of the three complexes, and the 3D packing structures of **2** and **3**.

Acknowledgments

This work was supported by the 973 program of the MOST (001CB108906), the National Natural Science Foundation of China (90206040, 20333070 and 20303021), the Natural Science Foundation of Fujian Province (20002F015 and 2002J006) and the Chinese Academy of Sciences.

[1] M. A. Baldo, D. F. O'Brien, Y. You, A. Shoustikov, S. Sibley, M. E. Thompson, S. R. Forrest, *Nature* **1998**, *395*, 151−154.
[2] C. Adachi, M. A. Baldo, M. E. Thompson, S. R. Forrest, *J. Appl. Phys.* **2001**, *90*, 5048−5051.
[3] S. Lamansky, P. Djurovich, D. Murphy, F. Abdel-Razzaq, H. E. Lee, C. Adachi, P. E. Burrows, S. R. Forrest, M. E. Thompson, *J. Am. Chem. Soc.* **2001**, *123*, 4304−4312.
[4] J. S. Wilson, A. S. Dhoot, A. J. A. B. Seeley, M. S. Khan, A. Köhler, R. H. Friend, *Nature* **2001**, *413*, 828−831.
[5] E. S. Handy, A. J. Pal, M. F. Rubner, *J. Am. Chem. Soc.* **1999**, *121*, 3525−3528.
[6] B. Carlson, G. D. Phelan, W. Kaminsky, L. Dalton, X. Jiang, S. Liu, A. K. Y. Jen, *J. Am. Chem. Soc.* **2002**, *124*, 14162−14172.
[7] A. M. McDonagh, S. R. Bayly, D. J. Riley, M. D. Ward, J. A. McCleverty, M. A. Cowin, C. N. Morgan, R. Varrazza, R. V. Penty, I. H. White, *Chem. Mater.* **2000**, *12*, 2523−2524.
[8] A. Hagfeldt, M. Grätzel, *Acc. Chem. Res.* **2000**, *33*, 269−277.
[9] Z. H. Peng, A. R. Gharavi, L. P. Yu, *J. Am. Chem. Soc.* **1997**, *119*, 4622−4632.
[10] P. C. Ford, E. Cariati, J. Bourassa, *J. Chem. Res.* **1999**, *99*, 3625−3648.
[11] M. L. Tong, X. M. Chen, B. H. Ye, L. N. Ji, *Angew. Chem. Int. Ed.* **1999**, *38*, 2237−2240.
[12] G. J. E. Davidson, S. J. Loeb, *Angew. Chem. Int. Ed.* **2003**, *42*, 74−77.
[13] K. Biradha, C. Seward, M. J. Zaworotko, *Angew. Chem. Int. Ed.* **1999**, *38*, 492−495.
[14] K. A. Walters, K. D. Ley, C. S. P. Cavalaheiro, S. E. Miller, D. Gosztola, M. R. Wasielewski, A. P. Bussandri, H. van Willigen, K. S. Schanze, *J. Am. Chem. Soc.* **2001**, *123*, 8329−8342.
[15] Y. Li, C. E. Whittle, K. A. Walters, K. D. Ley, K. S. Schanze, in *Electronic, Optical and Optoelectronic Polymers and Oligomers* (Eds.: G. E. Jabbour, E. W. Meijer, N. S. Sariciftci, T. M. Swager), Materials Research Society, Warrendale, PA, **2002**, vol. 665, p. 61.
[16] K. D. Glusac, S. Jiang, K. S. Schanze, *Chem. Commun.* **2002**, 2504−2505.
[17] S. Megelski, A. Lieb, M. Pauchard, A. Drechsler, S. Glaus, C. Debus, A. J. Meixner, G. Calzaferri, *J. Phys. Chem. B* **2001**, *105*, 25−35.
[18] M.-L. Tong, S. Kitagawa, H.-C. Changa, M. Ohbaa, *J. Chem. Soc., Chem. Commun.* **2004**, 418−419.
[19] P. M. Forster, A. R. Burbank, C. Livage, G. Féreyb, A. K. Cheetham, *J. Chem. Soc., Chem. Commun.* **2004**, 368−369.
[20] A. J. Blake, N. R. Brooks, N. R. Champness, P. A. Cooke, A. M. Deveson, D. Fenske, P. Hubberstey, W.-S. Li, M. Schröder, *J. Chem. Soc., Dalton Trans.* **1999**, 2103−2110.
[21] X.-X. Hu, J.-Q. Xu, P. Cheng, X.-Y. Chen, X.-B. Cui, J.-F. Song, G.-D. Yang, T.-G. Wang, *Inorg. Chem.* **2004**, *43*, 2261−2266.
[22] M. A. Withersby, A. J. Blake, N. R. Champness, P. A. Cooke, P. Hubberstey, W.-S. Li, M. Schröder, *Inorg. Chem.* **1999**, *38*, 2259−2266.
[23] J. R. Black, N. R. Champness, W. Levason, G. Reid, *J. Chem. Soc., Chem. Commun.* **1995**, 1277−1278.
[24] J. R. Black, N. R. Champness, W. Levason, G. Reid, *J. Chem. Soc., Dalton Trans.* **1995**, 3439−3445.
[25] J. Zhang, Y.-R. Xie, Q. Ye, R.-G. Xiong, Z.-L. Xue, X.-Z. You, *Eur. J. Inorg. Chem.* **2003**, 2572−2577.
[26] L. Han, M.-C. Hong, R.-H. Wang, J.-H. Luo, Zh.-Zh. Lin, D.-Q. Yuan, *Chem. Commun.* **2003**, 2580−2581.

Received July 15, 2004
Early View Article
Published Online November 24, 2004

 © 2005 Wiley-VCH Verlag GmbH & Co. KGaA, Weinheim

EurJIC
European Journal of Inorganic Chemistry

Issue 3/2005

Pages 433–616

Papers available ahead of print in Early View at www.interscience.wiley.com

Earliest available Table of Contents:
Automatically, free of charge by e-mail through
www.interscience.wiley.com/alerts

COVER PICTURE

The cover picture shows two examples of stable polynuclear ruthenium systems containing delocalized carbon-rich bridges with unusual topologies. In this work, the synthesis, the spectroscopic and voltammetric studies of a new family of bis(allenylidene) and mixed allenylidene–acetylide complexes are presented. The nature of the reduced species, which are mainly ligand-centered, is pointed out by means of ESR and IR spectroscopy. The UV/Vis and electrochemical studies show the large influence of the bridge on the electronic interaction between the redox centers and the fine tuning of this property. These new conjugated molecules appear to be promising alternatives to the classical bis(acetylide) systems for the construction of metal-containing unsaturated oligomers or polymers to mediate electron-transfer processes. Details are discussed in the article by S. Rigaut, D. Touchard et al. on p. 447 ff.

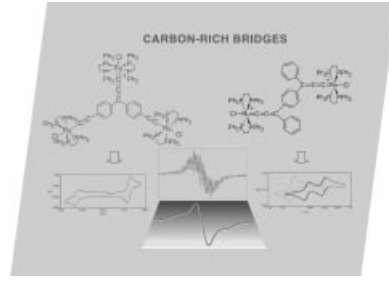

FULL PAPERS

Contents

447 **S. Rigaut,* J. Perruchon, S. Guesmi, C. Fave, D. Touchard,* P. H. Dixneuf**

Carbon-Rich Ruthenium Complexes Containing Bis(allenylidene) and Mixed Alkynyl–Allenylidene Bridges

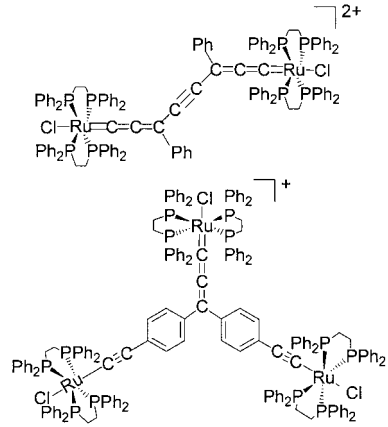

Keywords: Allenylidene / Bridging ligands / Ruthenium / Redox systems / Alkynyl ligands

 © 2005 Wiley-VCH Verlag GmbH & Co. KGaA, Weinheim

461 **K. A. Brylev, G. Pilet, N. G. Naumov,* A. Perrin, V. E. Fedorov**

Structural Diversity of Low-Dimensional Compounds in $[M(en)_2]^{2+}/[Re_6Q_8(CN)_6]^{4-}$ Systems (M = Mn, Ni, Cu)

Keywords: Amines / Cluster compounds / Cyanides / Rhenium / Solid-state structures

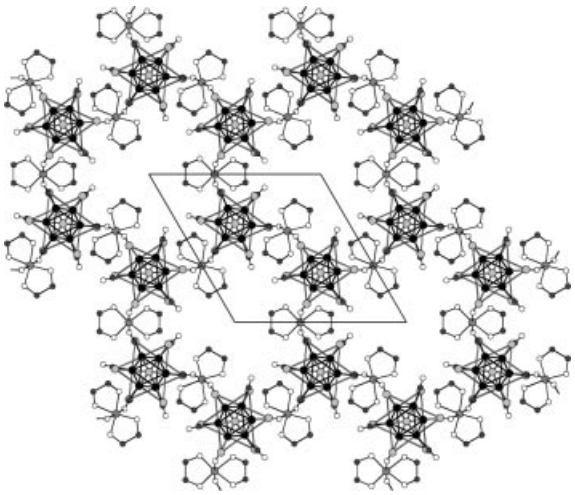

467 **F. Biaso, C. Duboc, B. Barbara, G. Seratrice, F. Thomas, D. Charapoff, C. Béguin***

High-Field EPR Study of Frozen Aqueous Solutions of Iron(III) Citrate Complexes

Keywords: High-field EPR spectroscopy / Iron / Coordination chemistry / Citrate ligand / Tripodal ligand / Spin crossover

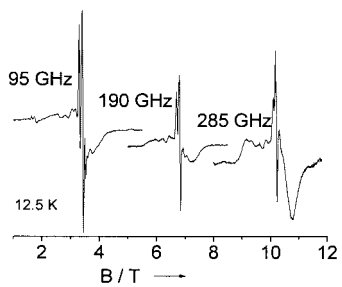

479 **G. J. Grant,* W. Chen, A. M. Goforth, C. L. Baucom, K. Patel, P. Repovic, D. G. VanDerveer, W. T. Pennington**

Anion and Solvent Effects upon the Structures of Platinum(II) Complexes with Thiacrown Ligands: The Crystal Structures of $[Pt(9S3)_2](PF_6)_2 \cdot 2\ CH_3NO_2$, $[Pt(9S3)_2](BF_4)_2 \cdot 2\ CH_3NO_2$, $[Pt(9S3)_2](OTf)_2 \cdot 2\ CH_3NO_2$, and $[Pt(18S6)](BF_4)_2$

Keywords: S ligands / Platinum

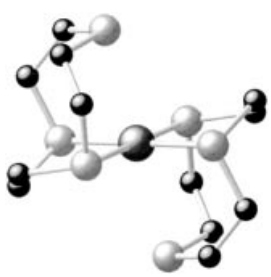

486 **C. Alonso, L. Ballester, A. Gutiérrez,* M. F. Perpiñán, A. E. Sánchez, M. T. Azcondo**

Tetracyanoquinodimethanido Derivatives of (Terpyridine)- and (Phenanthroline)metal Complexes − Structural and Magnetic Studies of Radical-Ion Salts

Keywords: Radical ions / Stacking interactions / Supramolecular chemistry / Magnetic properties

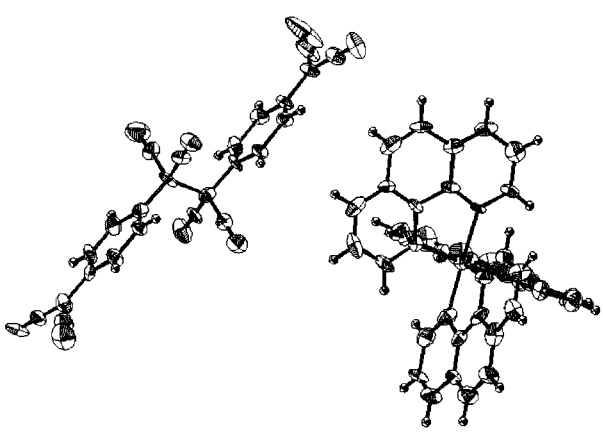

 © 2005 Wiley-VCH Verlag GmbH & Co. KGaA, Weinheim

496 **N. T. Lucas, J. M. Hook, A. M. McDonagh,* S. B. Colbran***

Titanium Dioxide Nanoparticles Functionalized with Pd and W Complexes of a Catechol-phosphane Ligand

Keywords: Palladium / Tungsten / Phosphane ligands / Titanium

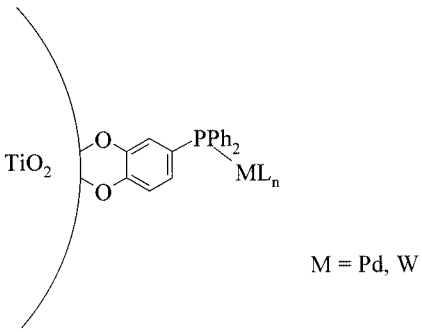

504 **V. Lozan, B. Kersting***

Preparation and Characterisation of Cd^{II}, Hg^{II} and Pb^{II} Complexes of a Macrodinucleating Hexaaza-dithiophenolate Ligand

Keywords: Macrocyclic ligands / Cadmium / Mercury / Lead / Complexes

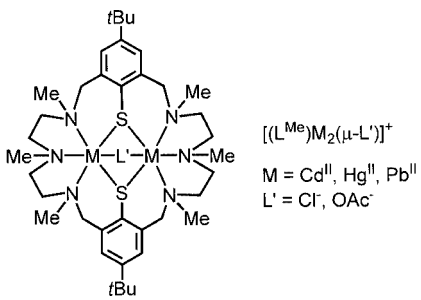

513 **W.-P. Leung,* C.-W. So, Y.-S. Wu, H.-W. Li, T. C. W. Mak**

Synthesis of Group 14 Metal Enamido, Alkenyl, Imido and Alkenyl-Amido Complexes from a Monoanionic Pyridyl-1-azaallyl Ligand

Keywords: Germanium / Group 14 elements / Lead / N ligands / Tin

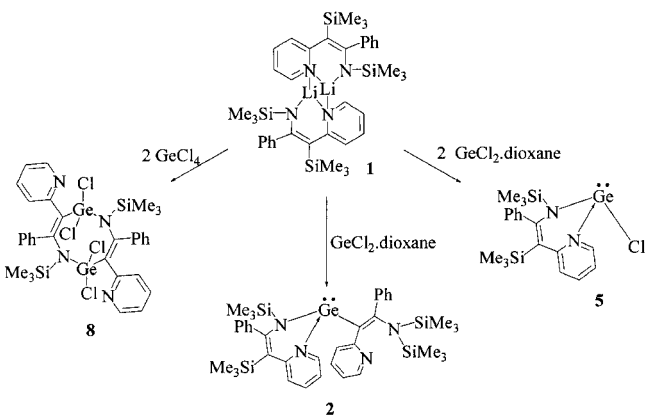

522 **D. S. Jacob, V. Kahlenberg, K. Wurst, L. A. Solovyov, I. Felner, L. Shimon, H. E. Gottlieb, A. Gedanken***

Sonochemical Reaction of $[Fe(CO)_5]$ with 1-Methylimidazole in An Ionic Liquid: Formation of $[(1\text{-Methylimidazole})_6Fe^{II}](PF_6)_2$

Keywords: Ionic liquid / Sonochemistry / Iron imidazole complex

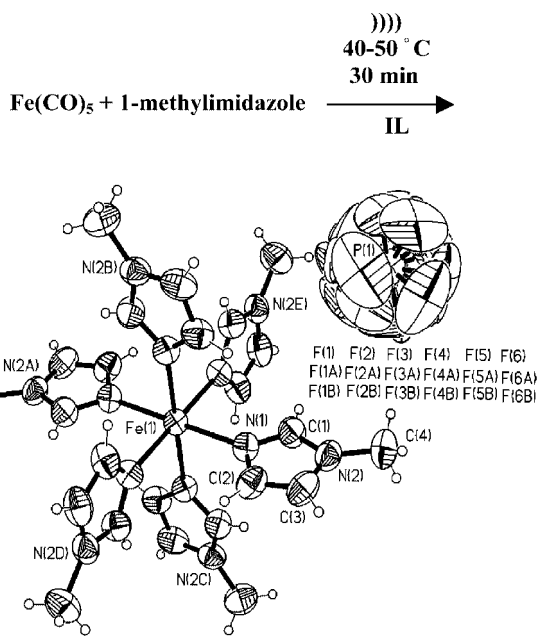

 © 2005 Wiley-VCH Verlag GmbH & Co. KGaA, Weinheim

529 **M. Pley, M. S. Wickleder***

Monomers, Chains and Layers of $[Pt_2(SO_4)_4]$ Units in the Crystal Structures of the Platinum(III) Sulfates $(NH_4)_2[Pt_2(SO_4)_4(H_2O)_2]$, $K_4[Pt_2(SO_4)_5]$ and $Cs[Pt_2(SO_4)_3(HSO_4)]$

Keywords: Solid state structures / Platinum / Sulfates / Metal−metal bonds / IR data

536 **M. A. Hasnaoui, A. Simon-Masseron,* V. Gramlich, J. Patarin, A. Bengueddach**

A New Organic-Inorganic Hybrid Gallophosphate Prepared in the Presence of Glycine

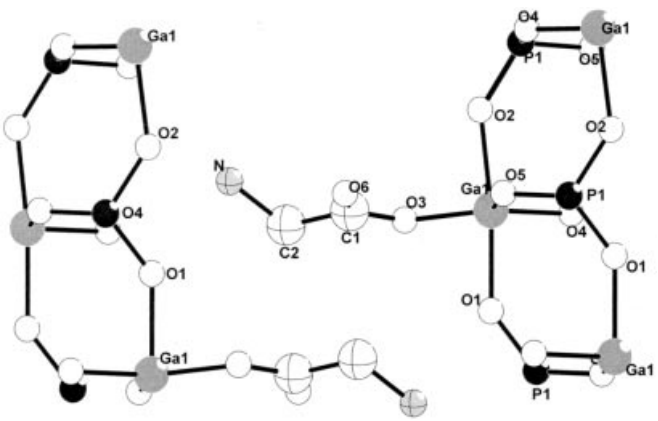

Keywords: Gallium / Gallophosphate / Glycine / Hydrothermal synthesis / Fluorides

543 **A. F. Popa, L. Courthéoux, E. Gautron, S. Rossignol,* C. Kappenstein**

Aerogel and Xerogel Catalysts Based on θ-Alumina Doped with Silicon for High Temperature Reactions

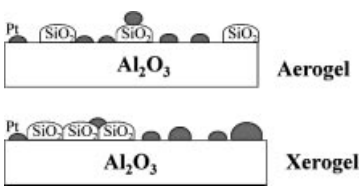

Keywords: Aerogel / Xerogel / Catalyst / Platinum / Alumina

555 **M. Czerwiński,* J. Narbutt**

Outer-Sphere Hydration and Liquid−Liquid Partition of Metal(III) Chelates − Density Functional Calculations

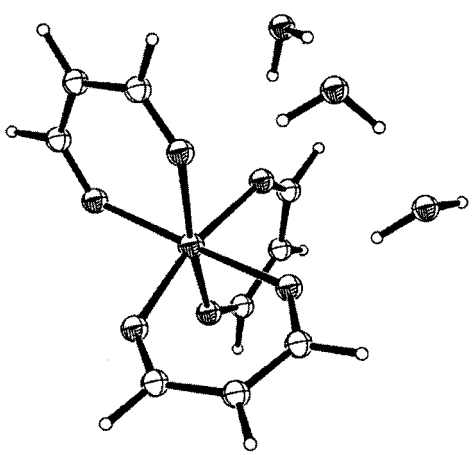

Keywords: Metal chelates / Outer-sphere hydration / Hydrogen bonding / Aqueous solution / Liquid−liquid partition / Enthalpy of transfer / Density functional calculations / Solvent effects / Implicit solvation model

 © 2005 Wiley-VCH Verlag GmbH & Co. KGaA, Weinheim

563 **R. Van Deun, J. Ramaekers, P. Nockemann, K. Van Hecke, L. Van Meervelt, K. Binnemans***

Alkali-Metal Salts of Aromatic Carboxylic Acids: Liquid Crystals without Flexible Chains

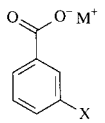

Smectic A

Keywords: Alkali metals / Layered compounds / Liquid crystals / Metallomesogens / Smectic mesophases

572 **A. R. Turner, F. Blockhuys, C. Van Alsenoy, H. E. Robertson, S. L. Hinchley, A. V. Zibarev, A. Y. Makarov, D. W. H. Rankin***

Causes of Nonplanarity in Fluorinated 1,3λ⁴δ²,2,4-Benzodithiadiazines: Gas-Phase Electron Diffraction, Ab initio and DFT Structures

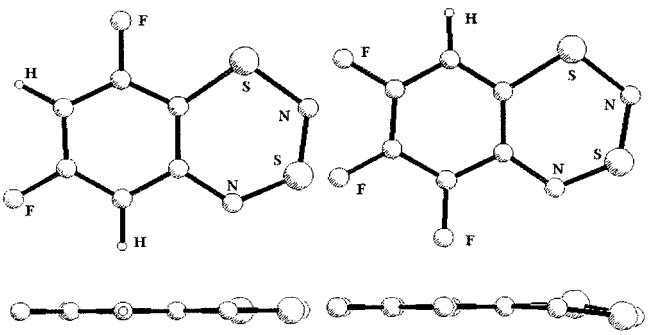

Keywords: Antiaromaticity / Fluorinated 1,3λ⁴δ²,2,4-benzodithiadiazines / Molecular structure / Ab initio calculations / Density functional calculations

582 **V. Gallo, P. Mastrorilli,* C. F. Nobile, R. Paolillo, N. Taccardi**

Ionic Liquids as Reaction Media for Palladium-Catalysed Cross-Coupling of Aryldiazonium Tetrafluoroborates with Potassium Organotrifluoroborates

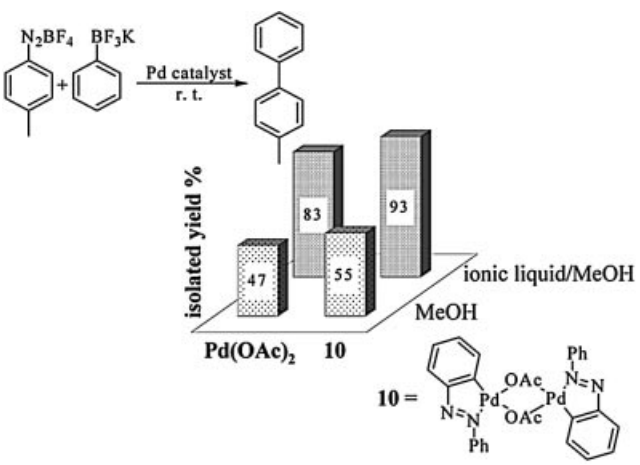

Keywords: C-C coupling / Diazonium salts / Homogeneous catalysis / Ionic liquids / Organotrifluoroborates

589 **G. L. Abbati, M. C. Aragoni, M. Arca, M. Bonaria Carrea, F. A. Devillanova, A. Garau, F. Isaia,* V. Lippolis, M. Marcelli, C. Silvestru, G. Verani**

Gold(0) and Gold(III) Reactivity towards the Tetraphenyldithioimidodiphosphinic Acid, $[Ph_2P(S)NHP(S)Ph_2]$

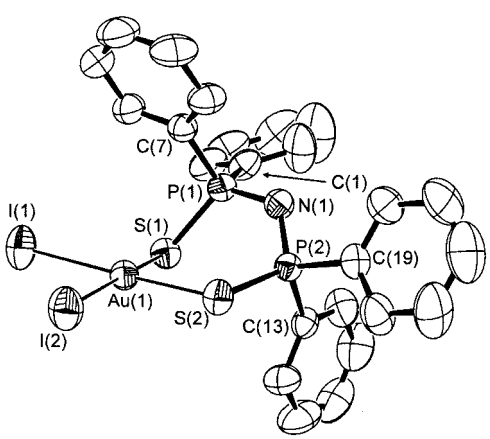

Keywords: Gold(I) complexes / S ligands / Bridging ligands / Iodine / Density functional calculations

 © 2005 Wiley-VCH Verlag GmbH & Co. KGaA, Weinheim

597 **M. A. Esteves,* A. Cachudo, S. Chaves, M. A. Santos**

Synthesis and Metal-Complexation Properties of a New Hydroxypyrimidinone-Functionalized Sepharose

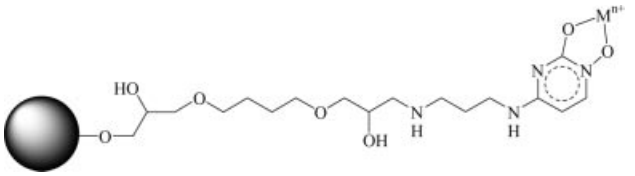

Keywords: Actinides / Chelates / Environmental chemistry / O ligands / Functionalized sepharose

606 **C. Garino, R. Gobetto,* C. Nervi, L. Salassa, G. Croce, M. Milanesio, E. Rosenberg, J. B. A. Ross**

Solid-State Structure, Quantum Calculations and Spectroscopic Characterization of the Hydrogen-Bonded Complex $[Os(bpy)_2(CO)(EtO\cdots H\text{-}DMAP)][PF_6]_2$

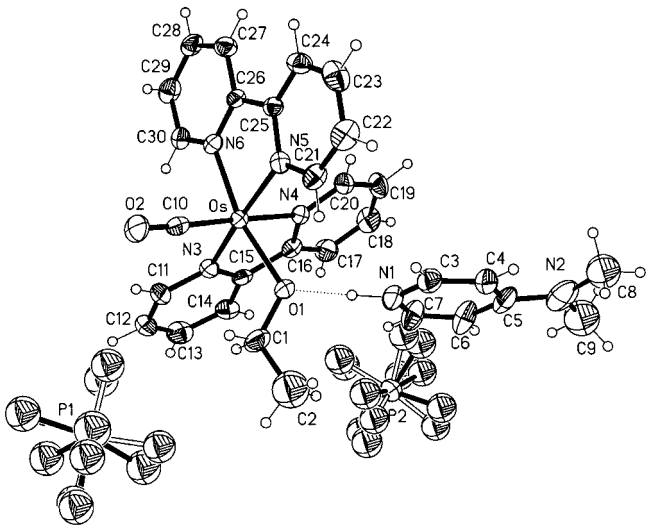

Keywords: Density functional calculations / Hydrogen bonds / N ligands / NMR spectroscopy / Osmium

 © 2005 Wiley-VCH Verlag GmbH & Co. KGaA, Weinheim

Carbon-Rich Ruthenium Complexes Containing Bis(allenylidene) and Mixed Alkynyl−Allenylidene Bridges

Stéphane Rigaut,*[a] Johann Perruchon,[a] Salaheddine Guesmi,[b] Claire Fave,[a] Daniel Touchard,*[a] and Pierre H. Dixneuf[a]

Keywords: Allenylidene / Bridging ligands / Ruthenium / Redox systems / Alkynyl ligands

Complexes *cis*-[RuCl(dppe)$_2$][X] (**2a** X = PF_6, **2b** X = CF_3SO_3) react with a variety of bis(propargylic) alcohols to selectively lead to mono-*trans*-[Cl(dppe)$_2$Ru=C=C=C(R)–T–C(R)(OH)-(C≡C–H)][X] (**4**) [R = H, Ph; T = *m*,*p*-(C_6H_4), 2,5-(thiophene), 5,5′-(2,2′-bithiophene), 5,5′′-(2,2′:5′2′′-terthiophene), –C≡C–] or bis(allenylidene) *trans*-[Cl(dppe)$_2$Ru=C=C=C(R)–T–(R)C=C=C=RuCl(dppe)$_2$][X]$_2$ (**5**) complexes. New dimetallic and trimetallic complexes containing mixed alkynyl–allenylidene bridges, *trans*-[Cl(dppe)$_2$Ru–C≡C–*p*-(C_6H_4)–(Ph)C=C=C=RuCl(dppe)$_2$][CF_3SO_3] (**12**) and *trans*-[{Cl(dppe)$_2$Ru–C≡C–*p*-(C_6H_4)}$_2$C=C=C=RuCl(dppe)$_2$][CF_3SO_3] (**17**)}, were prepared by modification of the carbon-rich ligand of acetylide precursors. UV/Vis and cyclic voltammetry studies show the influence of the unsaturated conjugated bridge on the electronic interaction between the redox centers, and the fine tuning of this property.
(© Wiley-VCH Verlag GmbH & Co. KGaA, 69451 Weinheim, Germany, 2005)

Introduction

Organometallic complexes with π-conjugated bridges are attracting interest for their electronic and structural properties in fields including liquid crystals,[1] nonlinear optical devices,[2] luminescence,[3] and electronic communication.[4−11] Electronic communication between two functionalities is a fundamental aspect related to a variety of complex systems ranging from life[12] to photoactive donor/acceptor processes[13] and electronic devices.[14] These properties are usually the result of their linear rigid structure and of their π-electron conjugation. Thus, it is crucial to understand the behavior of such systems with multiple redox components, the influence of the linkers, and to develop straightforward methods of access to them.

Dimetallic complexes have been obtained by coupling of organometallic terminal acetylides to bis(vinylidene) and bis(alkynyl) complexes.[4,5] By contrast, few dimetallic mixed alkynyl−vinylidene or alkynyl−allenylidene complexes have been selectively synthesized by activation of conjugated organic molecules.[10] For example, the activation of HC≡C−CH(OH)−C≡CH has led to a dimetallic system with a C_5 bridging ligand [$CpRu(PPh_3)_2$=C=C=CH−C≡C−$Ru(PPh_3)_2Cp$]BF_4.[10a] Highly conjugated molecules resulting from the coupling of an acetylide complex with a vinylidene[8,9] or an allenylidene[6] complex are also emerging examples.

Ruthenium systems[15] present opportunities for the synthesis of novel organometallic compounds as models for electron conduction, and with unusual and stable topologies.[16,17] The ruthenium [$RuCl_2(dppe)_2$] (dppe = $Ph_2PCH_2CH_2PPh_2$) species offers the possibility to easily link two carbon-rich chains to form reversible redox systems[16,18] with an optical transition highly dependent on the nature of the chain.[6,19] This fact gave us impetus to build polynuclear systems containing new types of delocalized carbon-rich bridges and linking reversible redox active moieties, especially allenylidenes. We now report the easy synthesis of stable dimetallic complexes containing a variety of new bis(allenylidene) bridges separated by a tunable conjugated linker and the synthesis of novel di- and triruthenium compounds containing mixed allenylidene and alkynyl groups. We further illustrate, in the light of UV/Vis and electrochemical studies, the large influence of the bridge on the electronic interaction between the redox centers.

Results and Discussion

The activation of terminal alkyne functionalities with the sixteen-electron species [$ClRu(dppe)_2$]$^+$ can be potentially employed to access polymetallic systems with carbon-rich unsaturated bridges, as previously shown with the synthesis

[a] Institut de Chimie de Rennes, UMR 6509 CNRS-Université de Rennes 1, Organométalliques et Catalyse,
Campus de Beaulieu, 35042 Rennes Cedex, France
Fax: (internat.) + 33-2-2323-6939
E-mail: Daniel.touchard@univ-rennes1.fr
stephane.rigaut@univ-rennes1.fr
[b] Laboratoire de Chimie de Coordination et Analytique, Faculté des Sciences, Université Chouaib Doukkali,
B. P. 20, El-Jadida, Morocco,

of bis(vinylidene) and bis(acetylide) derivatives.[20] Herein, we use the selective activation of a variety of functional groups with the intent of forming carbon-rich allenylidene ruthenium derivatives: (i) The simple or double activation of molecules containing two terminal propargylic alcohol functional groups, via the Selegue method,[21] offers access to mono(allenylidenes) or bis(allenylidenes).[22] (ii) New mixed terminal alkynyl−allenylidene functionalities separated by a phenyl linker were achieved by using an original step-by-step organometallic synthesis, i.e. by modification and activation of the organic carbon-rich ligand of mono- and dimetallic acetylides to introduce the conjugated allenylidene function.

It has to be noted that we described recently the protonation of a ruthenium bis(allenylidene), obtained by means of the Selegue strategy, into a bis(carbyne).[19] It is also noteworthy that Werner et al. obtained a similar bis(allenylidene) with rhodium [Cl(P*i*Pr$_3$)$_2$Rh=C=C=C(Ph)−*m*-C$_6$H$_4$−(Ph)C=C=C=Rh(P*i*Pr$_3$)$_2$Cl] by an identical approach.[23] A different kind of bis(allenylidene) not connected through the allenylidene functions such as (Ph$_2$C=C=C=Rh(P*i*Pr$_3$)$_2$−C≡C−)$_2$ was also synthesized by the same group.[24] However, no electrochemical studies were reported for these complexes.

Synthesis of Mono(allenylidene)ruthenium Complexes: The reaction of the 16-electron salts **2a** or **2b** with an excess of bis(propargylic) alcohols[25] **3a**−**h** leads to the formation of red monoallenylidene ruthenium complexes **4a**−**h** (41−81% yield) bearing a free propargylic alcohol group (Scheme 1). These allenylidenes are stable with respect to the addition of methanol to the C$_\alpha$ carbon.[26] The FTIR spectra of the allenylidenes **4a**−**h** show characteristic features for such compounds with $\nu_{C=C=C}$ = 1921−1939 cm^{-1} and $\nu_{C\equiv C}$ = 2100−2200 cm^{-1}. The ^{31}P NMR spectra display the equivalence of the four phosphorus nuclei and thus the relative *trans* disposition of the chlorine atom and of the allenylidene ligand. The characteristic allenylidene low-field ^{13}C signal for the C$_\alpha$ carbon nucleus appears as a quintuplet at δ = 288−320 ppm with $^2J_{P,C}$ = 15 Hz.

Synthesis of Bis(allenylidene)ruthenium Complexes: The free prop-2-yn-1-ol functionality of complexes **4a**−**h** can be activated with 1 equiv. of **2a** or **2b** in dichloromethane, leading to the slow formation of the bis(allenylidene) complexes **5a**−**h** (7 d). The same bridged molecules were also readily prepared by the assembly of 2 equiv. of **2a** or **2b** and 1 equiv. of the corresponding bis(propargylic) alcohol and isolated in 42−78% yield after stirring for 7 d (Scheme 1). The tertiary allenylidenes **5c**−**h** are more stable than the secondary allenylidenes **5a**−**b** (see Scheme 1). Hence, our studies have been mainly focused on these former complexes. For all complexes, the ^{31}P NMR spectrum demonstrates the high symmetry of the molecule with only one sharp singlet for the eight phosphorus nuclei. The two allenylidene groups are then equivalent, and therefore the ^{13}C NMR spectra show only one set of three different signals for the C$_\alpha$, C$_\beta$ and C$_\gamma$ carbon atoms. However, complex **5h**

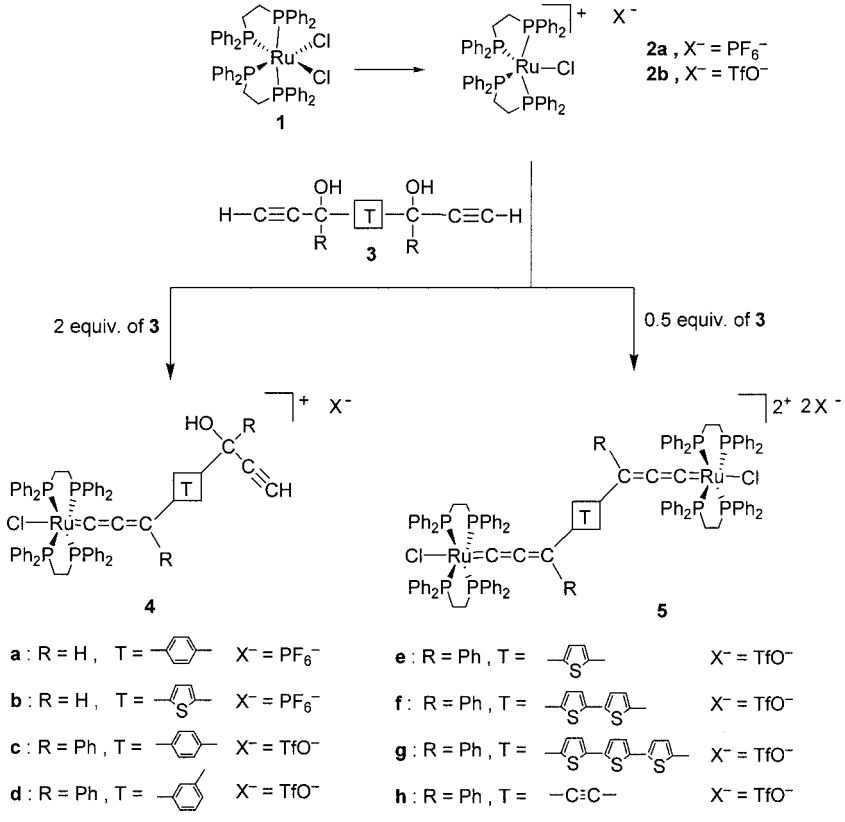

Scheme 1

 © 2005 Wiley-VCH Verlag GmbH & Co. KGaA, Weinheim

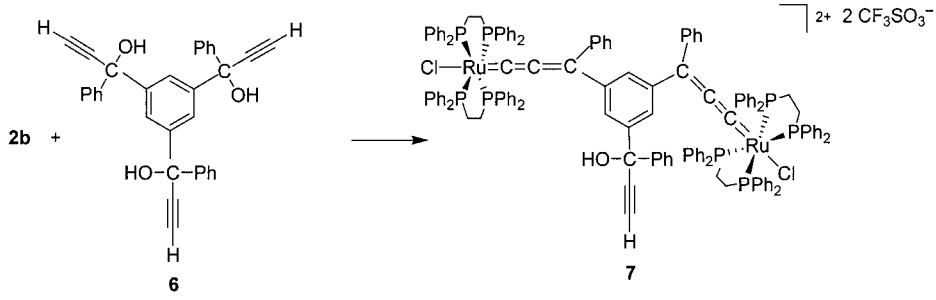

Scheme 2

with the triple bond is not stable enough in solution, and the ^{13}C NMR spectrum could not be obtained. Finally, the attempt to obtain a trisallenylidene complex by triple activation of the propargylic alcohol **6** with **2b** failed. Only the bis(allenylidene) complex **7** was recovered (Scheme 2), probably for steric reasons, as a trisallenylidene ruthenium complex was obtained when the propargylic alcohol functionalities were separated by a larger nonconjugated tripodal core.[27]

Synthesis of (Alkynyl−Allenylidene)ruthenium Complexes: The activation of terminal alkyne **8** or **13** bearing a ketone further convertible into a propargylic alcohol function with **2b**, led to the mono- (**9**) and the bis(vinylidene) (**14**) complexes in good yields (Scheme 3). The vinylidenes display characteristic FTIR vibration stretches $\nu_{C=C}$ = 1588 cm^{-1} and ν_{CO} = 1640 cm^{-1}. The ^1H NMR spectra shows a quintet for the vinylidene proton at δ = 4.82 ppm for **9** and at δ = 4.74 ppm for the two identical vinylidene protons of **14**

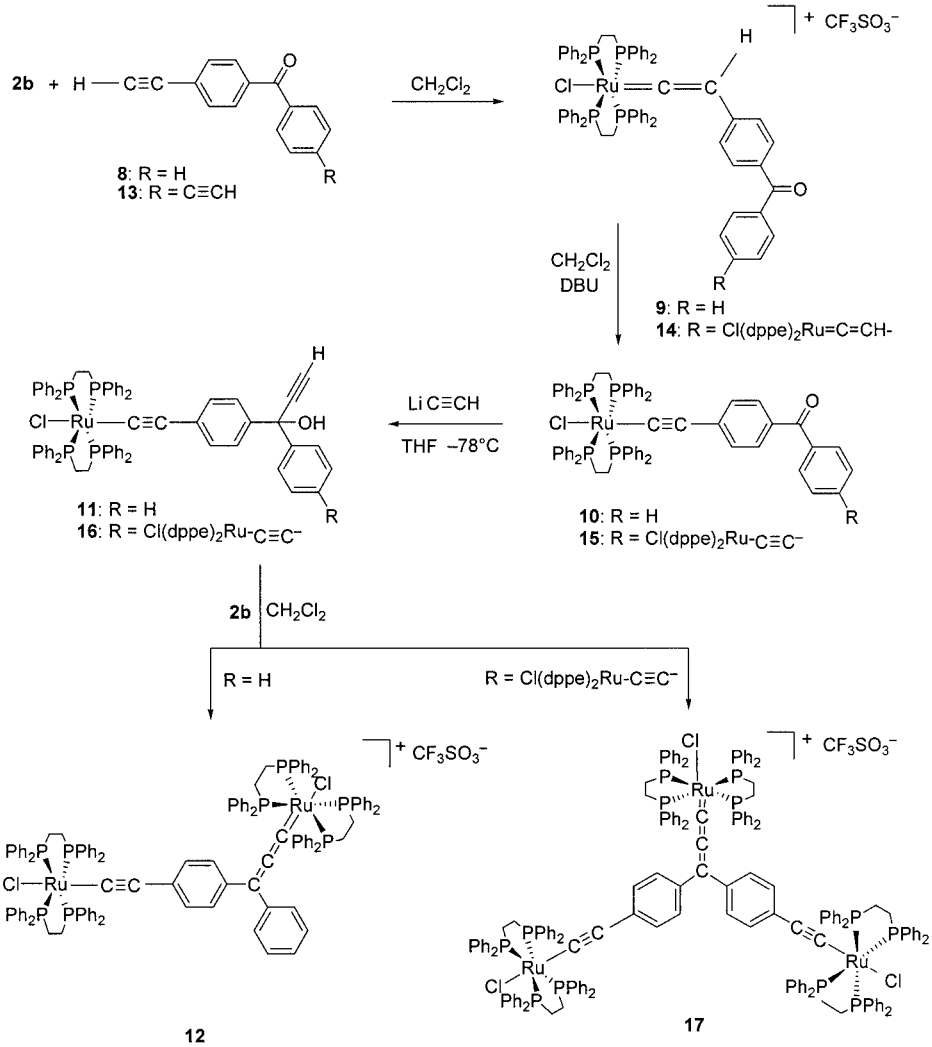

Scheme 3

 © 2005 Wiley-VCH Verlag GmbH & Co. KGaA, Weinheim

with $^4J_{PH}$ = 3 Hz. The low-field ^{13}C signal for the C_α carbon nucleus appears as a quintet at δ = 352 ppm for **9** and 354 ppm for **14**, and a singlet at δ = 195 ppm for the pendant ketone carbon nucleus is also observed. These vinylidene complexes can be easily deprotonated with a base such as DBU to form the neutral alkynyl−ruthenium derivatives **10** and **15**. The alkynyl−ruthenium complexes show characteristic vibration stretches $\nu_{C\equiv C}$ = 2057 for **10** and $\nu_{C\equiv C}$ = 2053 for **15**. The carbonyl group of these complexes is further converted into a propargylic alcohol function by action of lithium acetylide to give **11** and **16**. Characteristic FTIR vibration stretches are observed at $\nu_{\equiv C-H}$ = 3050, $\nu_{C\equiv CH}$ = 2135, $\nu_{C\equiv C}$ = 2065 cm^{-1} for **11** and $\nu_{\equiv C-H}$ = 3052, $\nu_{C\equiv CH}$ = 2136, $\nu_{C\equiv C}$ = 2068 cm^{-1} for **16**. Finally, the activation of these propargylic alcohol groups by the active 16-electron species **2b** leads to the isolation of the dimetallic mixed alkynyl−allenylidene **12** or of the trimetallic complex **17** bearing two alkynyl and one allenylidene groups. The overall yields for complexes **12** and **17** are 37 and 50% starting from **2b** after four steps, and they display two typical absorptions at 2040 and 1926 (**12**), 2008 and 1912 (**17**) cm^{-1}. The ^{13}C spectrum shows the presence of the allenylidene group with characteristic resonances for **12** and **17** at δ = 345 and 342 ppm respectively for C_α, and also of the acetylide group with δ = 135 and 134 ppm for C_α'.

Electrochemical and UV/Vis Studies: The bis(allenylidene) complexes are composed of two one-electron redox-active units and of a bridge that allows for electronic communication. To understand the nature of the redox behavior and the role of the linker, the cyclic voltammograms of **4** and **5** were recorded in CH_2Cl_2 solutions (0.1 M Bu_4NPF_6). The reduction potentials and other relevant data for all compounds are reported in Table 1. All complexes exhibite a linear dependence of the peak current on the square root of the sweep rate ($v^{1/2}$) from 60 to 600 mV·s^{-1}, as expected for a diffusion controlled process, and the ratio of the peak currents (i_{pa}/i_{pc}) is close to unity. These electrochemical studies show that the cationic monoallenylidenes **4c**−**h** can undergo a one-electron reduction, and the bis(allenylidenes) **5a**−**h**, **7**, two consecutive one-electron reductions. The cyclic voltammograms of complexes **4e** and **5e** are presented in Figure 1 for illustration. It is noteworthy that these tertiary monoallenylidenes undergo one reversible process, in contrast to secondary allenylidene complexes, which present an irreversible process.[22] The electrochemical behavior of the bis(allenylidenes) show several interesting features: (i) the two reversible processes are well separated from each other, and (ii) a significant anodic shift of both reduction potentials indicates that the reductions are thermodynamically favored with respect to the mononuclear analog when the two allenylidene moieties are conjugated in **5a**−**c**, **e**−**h**. For example the reduction of **4e** occurs at E° = −1.000 V vs. Fc, and reductions of the corresponding dimetallic complex **5e** are observed at less negative potentials, i.e. at E°_1 = −0.439 and E°_2 = −0.749 V vs. Fc. No such anodic shift is observed in the nonconjugated complexes **5d** or **7**, in which the allenylidene moieties are in a *meta* orientation on the phenyl linker. Indeed, for **5d**, the two reductions occur at E°_1 = −0.877 and E°_2 = −1.056 V vs. Fc, while **4d** shows a reduction wave at E° = −0.910 V vs. Fc. When two different redox processes exist for two otherwise identical redox systems in the same molecule, an important parameter is the comproportionation constant K_c. The large wave separation observed for each dimetallic complex (ΔE° > 180 mV) leads to large comproportionation constants [$K_c > 1.0\times10^3$; $-(RT/F)\ln(K_c) = \Delta E^\circ$] and establishes that all the monoreduced species are stable in solution with respect to disproportionation.[28]

It has already been mentioned that the reduction of allenylidene complexes mainly involves the allenylidene ligands,[29−32] in contrast to the oxidation of neutral acetyl-

Table 1. Electrochemistry and optical data for complexes **4**, **5** and **7**

	CV[a]					UV/Vis[b]	
	E°_1 [V]	ΔE [mV]	E°_2 [V]	ΔE [mV]	$E^\circ_2 - E^\circ_1$ [mV]	K_c	$\lambda_{max.}$ (MLCT) [nm]	ε [mol^{-1}·L·cm^{-1}]
5a	−0.509	66	−0.711	81	202	2.3×10^3		
5b	−0.335	71	−0.606	80	270	3.2×10^4		
4c	−0.910	60					530	28000
5c	−0.500	60	−0.680	60	180	1.0×10^3	588	54000
4d	−0.910	60					520	28000
5d	−0.877	60	−1.056	60	180	1.0×10^3	522	36000
4e	−1.000	66					560	26400
5e	−0.439	66	−0.749	90	310	1.5×10^5	714	86000
4f	−1.012	60					660	28000
5f	−0.434	66	−0.746	90	320	2.2×10^5	730	48000
4g	−1.027	60					692	25000
5g	−0.427	66	−0.760	69	330	3.2×10^5	752	65000
4h	−0.805	60					512	26000
5h	−0.285	60	−0.645	60	360	1.0×10^6	720	60000
7	−0.890	60	−1.100	60	210	3.2×10^3	520	38000

[a] Sample 1 mM; Bu_4NPF_6 (0.1 M) in CH_2Cl_2; v = 100 mV s^{-1}; potentials are reported in V vs. ferrocene as an internal standard. Reversible redox processes. [b] In CH_2Cl_2.

 © 2005 Wiley-VCH Verlag GmbH & Co. KGaA, Weinheim

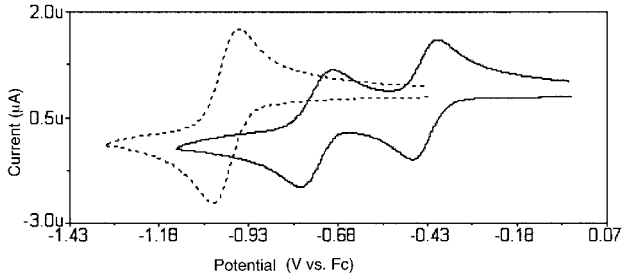

Figure 1. Cyclic voltammetry for **4c** (dashed) and **5c** (solid); Bu_4NPF_6 (0.1 M) in CH_2Cl_2; v = 100 mV·s^{-1}

ide, which occurs on the metal center.[33] Thus, the reduction processes of the mono- and the bis(allenylidene) can be attributed to the reduction of the carbon-rich chain in analogy to the mono(allenylidene) species *trans*-$[Cl(dppe)_2Ru{=}C{=}C{=}CPh_2]PF_6$ (**A1**) and *trans*-$[Cl(dppe)_2Ru{=}C{=}C{=}CMe_2]PF_6$ (**A2**). Nevertheless, this attribution was verified for **4c** and **5c** with the *p*-phenyl linker. For complex **4c**, the most appropriate reducing agent is the cobaltocene $[Cp_2Co]$ (i) as its reduction potential $E°$ is −1.33 V vs. ferrocene,[34] and (ii) it is ESR silent down to temperatures considerably below that of liquid nitrogen.[34b] We generated the reduced form in situ by dropping a crystal of cobaltocene in a THF solution of **4c** in a capped ESR tube. Reduced complex **4c** showed an intense and persistent signal (g = 2.0048) similar to that observed for **A1** (g = 2.0042), hence centered close to the free electron g value (a in Figure 2). The complex pattern could best be rationalized by the coupling of the unpaired electron with the four phosphorus nuclei and further coupling with the *ortho*, *meta* and *para* hydrogens of the phenyl groups, showing the delocalization of the single electron on the carbon-rich bridge.[35a] On the other hand, the first reduction of **5c** with decamethylferrocene ($E°$ = −0.590 V vs. ferrocene) or with a deficient amount of cobaltocene in the ESR cavity leads to the observation of a broad signal with g = 2.0244 (b in Figure 2). The observed shoulders may indicate some transition metal contribution (d-orbitals of the ruthenium atoms) resulting in the coupling of the free electron with the ^{99}Ru and ^{101}Ru isotopes (nuclear spin S = 5/2, and natural abundances of 12.7 and 17% respectively) with an estimated coupling constant of approximately 5 G.[35b] It is possible that the large number of magnetically independent nuclei on the chain together with this metal participation give rise to strongly overlapping resonance lines that cannot be resolved. However, this result suggests that the radical is highly centered on the organic bridge and is stabilized by delocalization along the carbon bridge between the ruthenium centers. Interestingly, further addition of cobaltocene leads to the two-electron reduction and to the disappearance of the signal, which suggest the formation of a diamagnetic doubly reduced species. ^{31}P NMR studies of the latter, obtained with 2 equivalents of cobaltocene, show a single signal with δ = 49.3 ppm consistent with a diacetylide species **18** (Scheme 4), that corroborates the communication through the bridge. Unfortunately, the spectra were broad, certainly because of the presence of residual paramagnetic compound (the reductant or first reduced species), and no exploitable proton or carbon spectra could be obtained.

IR studies, recorded in CH_2Cl_2, show the shift of the allenylidene band upon reduction of **4c** from 1925 cm^{-1} to a sharper but more intense band at 1948 cm^{-1}, similar to that observed for **A1** (from 1926 to 1945 cm^{-1}). This new value is somewhat different from that of true acetylide (2000 cm^{-1}) but coherent with the increase of the acetylide character of the reduced complexes, and with the presence of a delocalized electron mainly on the allenylidene carbon atoms of the chain (Scheme 4). Winter's et al. observed similar shifts for other reduced allenylidene complexes.[31] On the other hand, the first reduction of **5c** leads to a small opposite shift of the allenylidene band from 1912 to 1906 cm^{-1}. This last band is similar to that found for *trans*-$[Cl(dppe)_2Ru{-}C{\equiv}C{-}C(CH_3){=}C(H){-}C(CH_3){=}C{=}C{=}Ru(dppe)_2Cl]BF_4$ (**C**)[6] (1898 cm^{-1}) and consistent with the presence of delocalized allenylidene and acetylide moieties on the same bridge; two possible mesomeric forms are represented in Scheme 4. The second reduction leads to the vanishing of the former band, and to the concomitant formation a weak absorption at 1988 cm^{-1} (Figure 3). This corroborates the formation of a diamagnetic bis(acetylide) species such as **18**. It is noteworthy that all these observations are not related to the decomposition of the reduced species. Indeed, all reduced forms were thermally stable and reductions followed by oxidations with ferrocenium salt 30 min later led to the pure starting materials on the basis of ^{31}P NMR spectroscopy. Hence, in conclusion to these

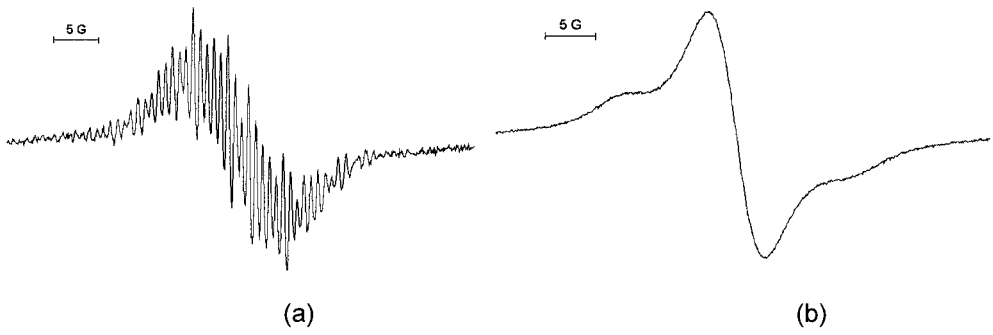

Figure 2. ESR spectra resulting from the reduction of (a) **4c** (g = 2.0048), and of (b) **5c** (g = 2.0244)

 © 2005 Wiley-VCH Verlag GmbH & Co. KGaA, Weinheim

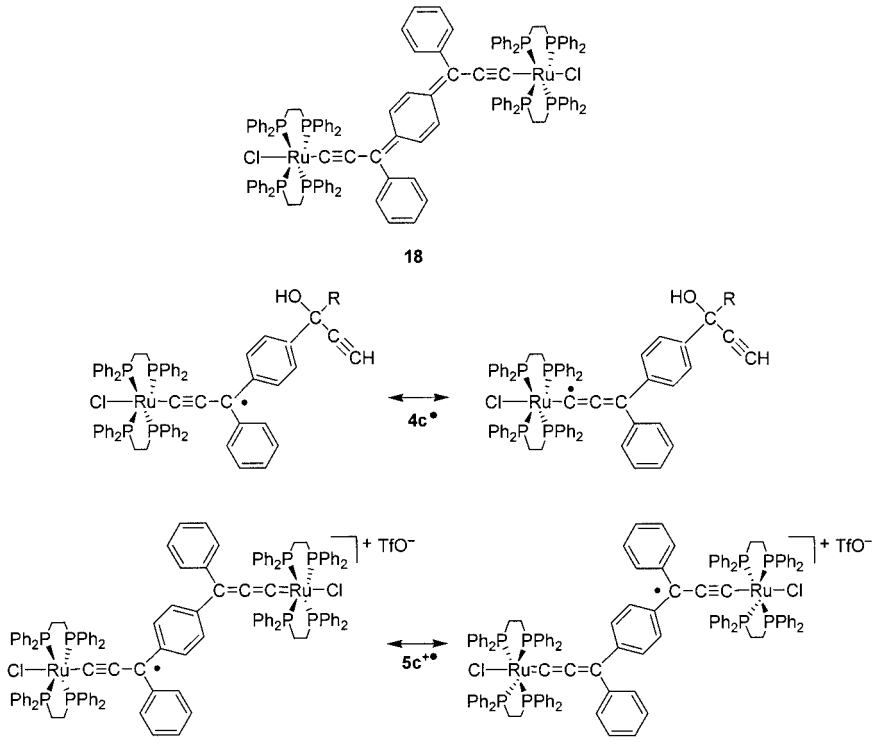

Scheme 4

spectroscopic studies, it is likely that all the electrons issued from reduction processes reside in an orbital with a significant carbon-rich ligand character but also with a non-negligible metal contribution.[32]

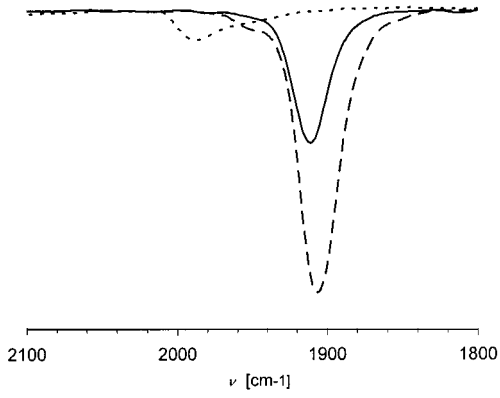

Figure 3. IR spectra of **5c** (—), its first (---), and second (···) reduced species

The dependence of redox potentials on the nature of the carbon-rich-ligand (Table 1) complexes is consistent with the ligand character of the LUMO. The reduction potential within the set of monoallenylidene species is located between 0.805 V and 1.027 V vs. ferrocene. A lower potential, that is, a higher electron stabilization along the chain is observed for **4h** with the triple bond as transmitter with $E^\circ = -0.805$ V vs. Fc. Within the series of bis(allenylidene) species, the variations of E° for both reductions are expected to be much greater. The complexes with the improved conjugation will show the stronger variation for both reduction processes in comparison to analogous monometallic species (Figure 1). According to common belief, the difference in electrochemical half-wave potential reflects the strength of interaction between the allenylidene moieties. There are, however, various additional factors that contribute to a stabilization of symmetrical mono- and bireduced complexes and especially electron delocalization. By contrast, when two redox centers are isolated from each other, E_1 and E_2 would be expected to be not only the same or similar but also very close to the potential of the comparable mononuclear analog.[36] The observed first and second reduction potentials of bis(allenylidene) species such as **5c** are less negative than those of the corresponding mononuclear species; this indicates considerable stabilization of the reduced forms by resonance and allows an analysis of the relative stabilization effects. The variation in potential is greater with less aromatic linkers (thiophene) relative to the phenyl transmitter, and the most efficient group to effect communication is the triple bond (**5h**). For example, this effect was already observed with dimetallic iron acetylides [Cp*(dppe)Fe−C≡C−R−C≡C−Fe(dppe)Cp*] (R = −2,5-C_4H_2S−, −*m*-C_6H_4−).[37] For the nonconjugated complexes **5d** or **7** (with $E^\circ_1 = -0.877$ and -0.890 V vs. Fc respectively) the first reduction potential is very close to that of the monometallic species ($E^\circ = -0.910$ V vs. Fc for **4d**) as the allenylide centers interact weakly. We also observed that the separation between the two processes (ΔE°) also depends on the nature of the transmitter. The ΔE° value of 180 mV ($K_c = 1.0 \times 10^3$) is observed with the nonconjugated systems **5d** and **7**. Surprisingly, the conjugated *p*-phenyl linker **5c** displays the same value, in contrast

 © 2005 Wiley-VCH Verlag GmbH & Co. KGaA, Weinheim

to the acetylide iron systems.[37] K_c assumes a value of 4 when the two redox sites are completely noninteracting and goes to much higher values as electronic and electrostatic interactions increase. Therefore, the present value is principally attributed to a structural rearrangement, solvation or electrostatic interactions. For the complexes **5a**, **5b**, **5e** and **5h**, this value is noticeably higher, and the greatest difference is observed with **5h** (ΔE° = 360 mV, $K_c = 1.0 \times 10^6$). We then assign this significant increase to an additional contribution from the resonance interaction between the allenylidene moieties through the linkers. Thus, in addition to the largest anodic shift, the less aromatic linkers with the shorter pathways display the greater differences in potential between the reduction processes (**5e**−**h**) in the following order: Triple bond > thiophene ≈ bithiophene ≈ terthiophene > phenyl.

UV/Vis studies were performed to compare mono- and dimetallic complexes. Figure 4 shows the absorption spectra obtained for **4c** and **5c**. The intense short-wavelength absorption band for the n−π* type transition originating from the dppe ligand at high energy remains unchanged. By contrast, the lower-energy transition is shifted from $\lambda_{max.}$ = 530 nm for **4c** to a broader band at $\lambda_{max.}$ = 588 nm for **5c**. This phenomenon is consistent with the observation made for the bis(carbyne) complex *trans*-[Cl(dppe)$_2$Ru≡C−HC=C(CH$_3$)−C$_6$H$_4$−(CH$_3$)C=CH−C≡Ru(dppe)$_2$Cl](BF$_4$)$_2$, which displays a broad band at $\lambda_{max.}$ = 559 nm, whereas the monometallic compound, *trans*-[Cl(dppe)$_2$Ru≡C−CH=C(CH$_3$)R](BF$_4$)$_2$, absorbs at $\lambda_{max.}$ = 426 nm.[19] For monoallenylidenes, the transition is attributed to the allowed transition from the metal-based HOMO-1 to the LUMO which is delocalized over the allenylidene ligand (the HOMO/LUMO symmetry is forbidden),[31] and accounts for the strong Metal-to-Ligand Charge Transfer (MLCT). Concerning the new broad band observed for the dimetallic species, an important MLCT character also seems to be present. This large bathochromic shift of the band is observed for all bis(allenylidenes) with respect to monoallenylidenes, except for compounds with nonconjugated linkers (Table 1). The $\lambda_{max.}$ value is almost the same for **4d** and **5d**, $\lambda_{max.}$ = 520 and 522 nm respectively, with the *m*-phenyl linker. By contrast, the decrease in the absorption energy in the bis(allenylidene)s **5c**, **5e**, **5f**, **5g** and **5h** is consistent with a more effective conjugated path between the two organometallic moieties, and with a decreasing energy of the LUMO, as observed in the electrochemical studies. Even though the tendency is the same in the UV/Vis studies, in electrochemistry, some differences are observed. The energy difference between the mono- and the bis(allenylidene) band ($\Delta\lambda$) follows the order: triple bond ($\Delta\lambda$ = 192 nm) > thiophene ($\Delta\lambda$ = 154 nm) > *p*-phenyl ($\Delta\lambda$ =58 nm), but with bithiophene ($\Delta\lambda$ = 70 nm) and terthiophene ($\Delta\lambda$ = 60 nm) the difference is barely larger than that for the phenyl group. This observation could be related to the well-known rotational disorder of oligothiophenes in the ground state and to the corresponding reorganization energy necessary in the excited state. In addition, an energy modification of the heavily metal-centered HOMOs arising from a lower metal d-orbital contribution in complexes with more extended π-conjugated ligands cannot be excluded.[32,38,39] It is noteworthy that the absorption bands are very broad, certainly including several transitions, and these conclusions need to be considered with care, even if similar trends were already observed in acetylide systems.[5e]

In conclusion, according to both UV/Vis and electrochemical studies, an important contribution from a less aromatic π-conjugated system undoubtedly increases the electronic communication between the allenylidene moieties and stabilizes the LUMO of the bis(allenylidene) complexes, the orbital in which the electrons are injected upon reduction. These results are consistent with the general result that the separation between energy levels continually diminishes in π-conjugated systems with decreasing aromaticity.

The cationic allenylidene complexes with one (**12**) or two (**17**) acetylide moieties were also studied (Figure 5, Table 2). They both show a one-electron reduction wave at E°_{red} = −1.170 and −1.240 V vs. Fc respectively, and **12** displays a one-electron oxidation wave at E°_{ox} = 0.140 V vs. Fc while **17** shows a two-electron oxidation wave at E°_{ox} = 0.120 V vs. Fc. In comparison to the monometallic complexes allenylidene **A1** and the acetylide *trans*-[Cl(dppe)$_2$Ru−C≡C−CHPh$_2$] (**B**),[40] we observed that for the bi- or trimetallic species the reduction and the oxidation(s) were more difficult to perform. This difficulty results from electronic communication through the bridge between one metal center and the other, and notably from the donor effect of the neutral acetylide−ruthenium group(s)

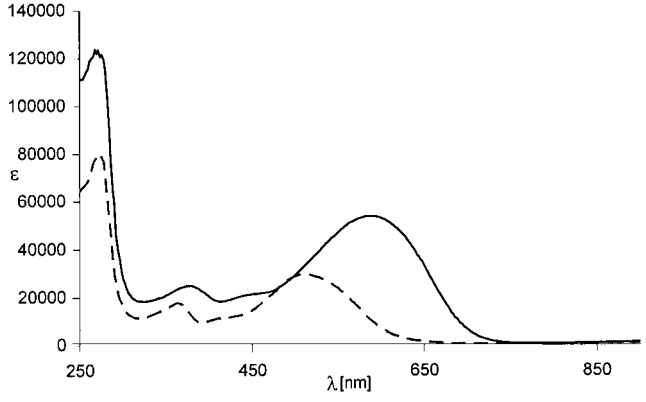

Figure 4. UV/Vis spectra of **4c** (---), and **5c** (—) in CH_2Cl_2

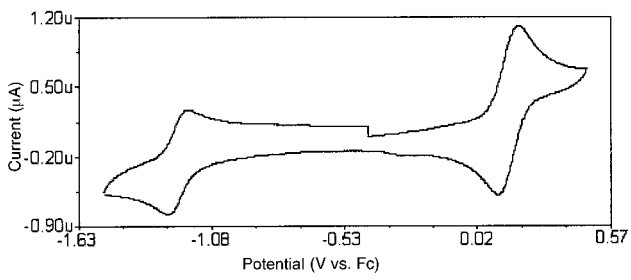

Figure 5. Cyclic voltammetry of **17**; Bu_4NPF_6 (0.1 M) in CH_2Cl_2; v = 100 mV·s^{-1}

 © 2005 Wiley-VCH Verlag GmbH & Co. KGaA, Weinheim

Table 2. Electrochemistry and optical data for complexes **12** and **17**

	CV[a]				UV/Vis[b]	
	$E°_{ox}$ [V]	ΔE [mV]	$E°_{red}$ [V]	ΔE [mV]	λ_{max} (MLCT) [nm]	ε [mol^{-1}·L·cm^{-1}]
12	+0.140	60	−1.170	60	764	63000
17	+0.120	60	−1.240	60	782	84000
A1			−1.030	60	504	18000
B	+0.020	60			360	6000
C	+0.310	60	−1.380	60	763	109000

[a] Sample 1 mM; Bu_4NPF_6 (0.1 M) in CH_2Cl_2; v = 100 mV s^{-1}; potentials are reported in V vs. ferrocene as an internal standard. Reversible redox processes. [b] In CH_2Cl_2.

and from the withdrawing power of the cationic allenylidene−ruthenium moiety. In analogy to allenylidene and acetylide complexes, the reduction processes are attributed to the reduction of the carbon-rich bridges, and the oxidations are believed to be mainly metal-centered.[33] Interestingly, in complex **17**, the two acetylide moieties are oxidized at the same potential (two-electron wave). This shows the lack of interaction between these two metal centers in an oxidation process (Figure 5), whereas the variation of the oxidation potential between **17** and **12** is consistent with the presence of an additional electron donor acetylide in **17**. The UV/Vis spectra of **12** and **17** present very high $\lambda_{max.}$ values with a large ε for the presumed MLCT at lower energy than for **A1**.[6a] This phenomenon might be attributed to the admixing of some charge-transfer character of the acetylide to the allenylidene moiety and to the longer conjugated bridge. Finally, the original complex **12** can be considered as a bis(ruthenium) species with a delocalized bridge allowing nine carbon atoms to connect the two ruthenium centers, and it can be compared with the seven-carbon-atom bridge bis(ruthenium) complexes such as *trans*-[Cl(dppe)$_2$Ru−C≡C−C(CH$_3$)=C(H)−C(CH$_3$)=C=C=Ru(dppe)$_2$Cl]BF$_4$ (**C**).[6] The reduction potential is slightly higher and the oxidation potential is slightly lower for **12** than for **C**, both potentials are getting closer to those of the monometallic species. Hence, as observed for bis(allenylidenes), the aromatic cycle in the delocalized pathway and the slightly longer bridge lead to a decrease in the electronic coupling between the redox centers in the mixed complexes.

Conclusion

This work presents the synthesis, the spectroscopic, and the voltammetric studies of a new family of carbon-rich organometallic complexes with novel topologies. First, the formation of stable bis(allenylidene) complexes was reported, and the nature of their reduced species, which are mainly ligand-centered, was studied by means of ESR and IR spectroscopy. The general trends observed with polymetallic acetylides prevail in bis(allenylidene) species: (i) the allenylidene moieties can interact substantially through a linker if the linker is conjugated, and (ii) the UV/Vis and the electrochemical properties significantly depend on the nature of the linker. This opens the door to a potential fine tuning of their properties. In addition, the original step-by-step synthesis of mixed allenylidene−acetylide di- and trimetallic complexes with nine conjugated atoms were described and the existence of electronic communication between allenylidene and acetylide moieties was demonstrated. As the formation of a nanoscale network is needed for molecular electronic devices, these new long molecules, obtained via controlled preparations, are interesting alternatives to the classical bis(acetylides). Their abilities for *trans* chlorine atom substitution with an acetylide or a cumulenic chain make them interesting building blocks for the construction of metal-containing unsaturated oligomers and polymers to mediate electron transfer processes.

Experimental Section

General Remarks: All reactions were performed under argon or nitrogen with use of Schlenk techniques. The solvents were deoxygenated and dried by standard methods. Infrared spectra were recorded with a Nicolet 205FTIR spectrometer in solution for oils, and in KBr pellets for solids. The ^{1}H (300.13 MHz), ^{31}P (121.50 MHz) and ^{13}C (75.47 MHz) NMR spectra were recorded at 25 °C with a Bruker AV300 spectrometer. Elemental analyses were performed by the "Service Central d'Analyses du CNRS", Vernaison, France and CRMPO, Rennes, France. The synthesis of *cis*-[(dppe)$_2$RuCl$_2$] (**1**),[41] **2a**, and **2b**,[42] 1-phenyl-3-trimethylsilylpropynone,[43] 1,2-dibenzoylacetylene,[44] and of propargyl alcohols **3a**−**b**[25] were performed by using literature methods. Compounds **3c**−**d**,[45] **8**,[46] and **13**[47], reported in this section, were previously described.

HC≡C−(OH)C(Ph)−*p*-(C$_6$H$_4$)−(Ph)C(OH)−C≡CH (3c): In a Schlenk tube, acetylene (40 mmol) was dissolved in THF (40 mL) at −78 °C. Then, *n*BuLi (18.75 mL, 30 mmol, 1.6 M in hexane) was slowly added. The mixture was stirred at −78 °C for 30 min. In another tube, *p*-dibenzoylbenzene (3.57 g, 12.5 mmol) was dissolved in THF (10 mL) and added to the solution. The mixture was stirred overnight at room temperature before being hydrolyzed with a saturated NH_4Cl solution (10 mL). The crude product was extracted with diethyl ether (4 × 50 mL), washed with water (3 × 20 mL), and dried. Further purification was achieved by chromatography over silica gel (10% diethyl ether in pentane) to afford **3c** (3.29 g) as a white powder in 78% yield. ^{1}H NMR ($CDCl_3$): δ = 7.64−7.15 (m, 14 H, Ph), 5.68 (s, 2 H, OH), 3.31 (s, 2 H, C≡CH) ppm. ^{13}C{^{1}H} NMR ($CDCl_3$): δ = 145.19−125.64 (Ph), 87.08 (C≡*C*H), 75.53 (C−OH), 73.30 (*C*≡CH) ppm. IR: $\tilde{\nu}$ = 2146 ($\nu_{C\equiv C}$) cm^{-1}. HRMS (EI): *m*/*z* = 338.1267; [M]$^+$; calcd. 338.1307.

 © 2005 Wiley-VCH Verlag GmbH & Co. KGaA, Weinheim

HC≡C−(OH)C(Ph)−*m*-(C_6H_4)−(Ph)C(OH)−C≡CH (3d): By the same procedure, from commercial *m*-dibenzoylbenzene (3.58 g), **3d** (3.04 g) was obtained as a white powder in 72% yield. ^{1}H NMR ($CDCl_3$): δ = 7.99−7.21 (m, 14 H, Ph), 3.34 (s, 2 H, OH), 2.83 (s, 2 H, C≡CH) ppm. $^{13}C\{^1H\}$ NMR ($CDCl_3$): δ = 144.56−123.44 (Ph), 86.25 (C≡*C*H), 75.73 (C−OH), 74.37 (*C*≡CH) ppm. IR: $\tilde{\nu}$ = 2113 ($\nu_{C\equiv C}$) cm^{-1}. HRMS (EI): *m*/*z* = 338.1270; $[M]^+$, calcd. 338.1307.

HC≡C−(OH)C(Ph)−2,5-(thiophene)−(Ph)C(OH)−C≡CH (3e): *n*BuLi (6.74 mL, 10.7 mmol, 1.6 M) was added dropwise to a solution of thiophene (378 mg) in THF (20 mL) at −78 °C. After stirring for 1 h, 1-phenyl-3-trimethylsilylpropynone (2 g, 9.88 mmol) dissolved in THF (10 mL) was also added dropwise. The resulting mixture was stirred for 15 min at −78 °C and for 12 h at room temperature. Then, water (15 mL) and tetrabutylammoniumfluoride solution (18 mL, 1 M in THF) were added slowly, and the resulting mixture was stirred at room temperature for 2 h . The solution was extracted with diethyl ether (3 × 50 mL), and the organic layer was washed with aqueous solution of NH_4Cl. After drying with $MgSO_4$, the solvents were evaporated to afford a brownish oil. Further purification was achieved by flash chromatography on silica gel with a mixture of diethyl ether/pentane as eluent to give **3e** (1.62 g) as a white solid in 52% yield. ^{1}H NMR ($CDCl_3$): δ = 7.71−7.28 (m, 10 H, Ph), 6.88 and 6.82 (2 H, thiophene), 2.92 (s, 2 H, OH), 2.84 (s, 2 H, C≡CH) ppm. $^{13}C\{^1H\}$ NMR ($CDCl_3$): δ = 150.07−149.83 (C_{quat}, thiophene), 143.3−125.8 (Ph), 124.96−124.91(CH, thiophene), 85.56 and 85.51 (C≡*C*H), 75.17 and 75.14 (C−OH), 71.78 (*C*≡CH) ppm. IR: $\tilde{\nu}$ = 2152 ($\nu_{C\equiv C}$) cm^{-1}. HRMS (EI): *m*/*z* = 344.0855 $[M]^+$; calcd. 344.0871. $C_{22}H_{16}O_2S$ (344.43): calcd. C 76.72, H 4.68; found C 76.42, H 4.58.

HC≡C−(OH)C(Ph)−5,5′-(2,2′-bithiophene)−(Ph)C(OH)−C≡CH (3f): By the same procedure, from 2,2′-bithiophene (1 g, 6.0 mmol), *n*BuLi (8.25 mL, 13.2 mmol), and 1-phenyl-3-trimethylsilylpropynone (2.67 g, 13.2 mmol), compound **3f** (1.5 g) was obtained in 74% yield as a brownish oil. ^{1}H NMR ($CDCl_3$): δ = 7.71−7.21 (m, 10 H, Ph), 6.94 (d, $^3J_{H,H}$ = 4 Hz, 2 H, thiophene), 6.87 (d, $^3J_{H,H}$ = 4 Hz, 2 H, thiophene), 3.31 (s, 2 H, OH), 2.86 (s, 2 H, C≡CH) ppm. $^{13}C\{^1H\}$ NMR ($CDCl_3$): δ = 148.63 and 143.39 (s, C_{quat}, thiophene) 137.91−125.77 (Ph), 126.01 and 123.04 (CH, thiophene), 85.45 (C≡*C*H), 75.28 (C−OH), 71.70 (*C*≡CH) ppm. IR: $\tilde{\nu}$ = 2149 ($\nu_{C\equiv C}$) cm^{-1}. HR-MS (EI): *m*/*z* = 426.0730 $[M]^+$; calcd. 426.0748. $C_{26}H_{18}O_2S_2$ (426.56): calcd. C 73.21, H 4.25; found C 73.10, H 4.21.

HC≡C−(OH)C(Ph)−5,5′′-(2,2′:5′,2′′-terthiophene)−(Ph)C-(OH)−C≡CH (3g): By the same procedure, from 2,2′,5′,2′′-terthiophene (248 mg, 1.0 mmol), *n*BuLi (1.37 mL, 2.2 mmol) and 1-phenyl-3-(trimethylsilyl)propynone (445 mg, 2.2 mmol), compound **3g** (300 mg) was obtained in 59% yield as a brownish oil. ^{1}H NMR ($CDCl_3$): δ = 7.71−7.23 (m, 10 H, Ph), 6.98 (m, 4 H, thiophene), 6.91 (d, 2 H, $^3J_{H,H}$ = 4 Hz, thiophene), 3.31 (s, 2 H, OH), 2.86 (s, 2 H, C≡CH) ppm. $^{13}C\{^1H\}$ NMR ($CDCl_3$): δ = 148.85 and 143.66 (s, C_{quat}, thiophene) 136.54−126.11 (Ph), 124.87, 123.38 and 110.10 (CH, thiophene), 85.74 (C≡*C*H), 75.72 (C−OH), 72.16 (*C*≡CH) ppm. IR: $\tilde{\nu}$ = 2146 ($\nu_{C\equiv C}$) cm^{-1}. HRMS (EI): *m*/*z* = 508.0633 $[M]^+$; calcd. 508.0625. $C_{30}H_{20}O_2S_3$ (508.68): calcd. C 70.84, H 3.96; found C 70.52, H 3.78.

HC≡C−(OH)C(Ph)−C≡C−(Ph)C(OH)−C≡CH (3h): By the same method as that for the formation of **3c** or **3d**, from 1,2-dibenzoylacetylene (2.93 g, 1.25 mmol), compound **3h** (2.90 g) was obtained as a white solid in 81% yield. ^{1}H NMR ($CDCl_3$): δ = 7.80−7.33 (m, 10 H, Ph), 3.61 (s, 2 H, OH), 2.76 (s, 2 H, C≡CH) ppm. $^{13}C\{^1H\}$ NMR ($CDCl_3$): δ = 140.82−125.97 (Ph), 84.87 (C≡*C*), 83.24 (*C*≡CH), 74.25 (*C*≡CH), 64.88 (C−OH) ppm. IR: $\tilde{\nu}$ = 2121 ($\nu_{C\equiv C}$) cm^{-1}. HRMS (EI): *m*/*z* = 286.0989; $[M]^+$; calcd. 286.0994. $C_{20}H_{14}O_2$ (286.33): calcd. C 83.90, H 4.93; found C 83.99, H 4.98.

1-[3,5-Bis(1-hydroxy-1-phenylprop-2-ynyl)phenyl]-1-phenylpropynol (6): By the same procedure as that for **3h**, from 1,3,5-tribenzoylbenzene(4.88 g, 12.5 mmol), compound **6** (4.09 g) was obtained in 70% yield as a white powder. ^{1}H NMR ($CDCl_3$): δ = 7.89−7.12 (m, 18 H, Ph), 5.67 (s, 3 H, OH), 3.24 (s, 3 H, C≡CH) ppm. $^{13}C\{^1H\}$ NMR ($CDCl_3$): δ = 145.94−122.91 (Ph), 87.11 (C≡*C*H), 75.35 (C−OH), 73.55 (*C*≡CH) ppm. IR: $\tilde{\nu}$ = 2113 ($\nu_{C\equiv C}$) cm^{-1}. HRMS (EI): *m*/*z* = 468.1744 $[M]^+$; calcd. 468.1725. $C_{33}H_{24}O_3$ (468.55): calcd. C 84.60, H 5.16; found C 84.75, H 5.28.

4-Ethynylbenzophenone (8): In a Schlenk tube, *p*-bromobenzophenone (2.6 g, 9.9 mmol), CuI (180 mg, 0.99 mmol), and $[PdCl_2(PPh_3)_2]$ (690 mg, 0.495 mmol) were dissolved in Et_3N (40 mL) and THF (20 mL). Then, trimethylacetylene (1.81 mL, 1.386 mmol) was added, and the mixture was stirred for 48 h at 50 °C. After cooling, the solvent was removed and the crude product was extracted with diethyl ether and filtered through a celite pad. After evaporation, a yellow solid was obtained. In a flask, 2.4 g of this compound was dissolved in a mixture of THF/MeOH (25 mL) and KOH (12 mL, 1.6 M) was added slowly. The resulting dark mixture was stirred for 1 h at room temperature, and then the solvents were evaporated off. Purification, first by flash chromatography (silica gel, diethyl ether) and then by recrystallization in pentane, afforded **8** (1.51 g) as a pale yellow solid in 85% yield. ^{1}H NMR ($CDCl_3$): δ = 7.85−7.38 (m, 9 H, Ph), 3.22 (s, 1 H, C≡CH) ppm. $^{13}C\{^1H\}$ NMR ($CDCl_3$): δ = 195.93 (CO) 137.46−126.30 (Ph), 82.87 (C≡*C*H), 80.21 (*C*≡CH) ppm. IR: $\tilde{\nu}$ = 2150 ($\nu_{C\equiv C}$), 1647 (ν_{CO}) cm^{-1}. HRMS (EI): *m*/*z* = 206.0730 $[M]^+$; calcd. 206.0732. $C_{15}H_{10}O$ (206.24): calcd. C 87.36, H 4.89; found C 87.15, H 4.87.

4,4′-Bis(ethynyl)benzophenone (13): Starting from 4,4′-dibromobenzophenone (1.69 g) and using the same procedure as that for the formation of **8**, we obtained **13** (0.98 g) as a pale yellow solid in 95% yield. ^{1}H NMR ($CDCl_3$): δ = 7.72−7.57 (m, 8 H, Ph), 3.23 (s, 2 H, C≡CH) ppm. $^{13}C\{^1H\}$ NMR ($CDCl_3$): δ = 195.06 (CO), 137.10−126.56 (Ph), 82.76 (C≡*C*H), 80.35 (*C*≡CH) ppm. IR: $\tilde{\nu}$ = 2158 ($\nu_{C\equiv C}$), 1645 (ν_{CO}) cm^{-1}. HRMS (EI): *m*/*z* = 230.0730 $[M]^+$; calcd. 230.0732. $C_{17}H_{10}O$ (230.27): calcd. C 88.67, H 4.38; found C 88.86, H 4.48.

Synthesis of Monoallenylidene Ruthenium Complexes (4a−b, X = PF_6; 4c−h, X = OTf): Dichloromethane (50 mL) was added to a mixture of $[Cl(dppe)_2Ru][X]$ (**2**) (0.5 mmol) and dipropargylic alcohol (**3**) (1 mmol). The resulting mixture was stirred at room temperature for 24 h, and the solvent was pumped to dryness. The resulting solid was washed with diethyl ether (4 × 25 mL) in order to eliminate the excess of organic reactant. Further purification was achieved by biphasic recrystallization in dichloromethane/pentane (1:2) to afford monoallenylidene complexes (**4a−h**) as powdery solids.

***trans*-[Cl(dppe)$_2$Ru=C=C=C(H)−*p*-(C_6H_4)−C(H)(OH)-(C≡C−H)][PF_6] (4a):** From **3a** (186 mg), complex **4a** (486 mg) was obtained as a deep red crystalline solid in 71% yield. ^{1}H NMR (CD_2Cl_2): δ = 9.20 (quint, $^5J_{PH}$ = 2.6 Hz, 1 H, Ru=C=C=CH), 7.53−6.88 (m, 44 H, Ph) 5.44 [d broad, $^4J_{H,H}$ = 2 Hz, 1 H, *H*C(OH)], 3.01 (m, 4 H, CH_2 dppe), 2.81 (m, 4 H, CH_2 dppe), 2.72 (d, $^4J_{H,H}$ = 2 Hz, 1 H, C≡CH) ppm. $^{13}C\{^1H\}$ NMR (CD_2Cl_2): δ = 320.76 (quint, $^2J_{P,C}$ = 14.4 Hz, Ru=*C*), 221.91 (quint, $^3J_{P,C}$ =

 © 2005 Wiley-VCH Verlag GmbH & Co. KGaA, Weinheim

2.2 Hz, Ru=C=*C*), 151.66 (Ru=C=C=*C*), 146.57−128.39 (Ph), 83.42 (*C*≡CH), 74.87 (C≡*C*H), 63.95 (*C*−OH), 29.42 (quint, $^1J_{P,C}$ + $^3J_{P,C}$ = 23 Hz, PCH_2CH_2P) ppm. ^{31}P NMR (CD_2Cl_2): δ = 40.0 (s, dppe), −143.9 (sept., $^1J_{PF}$ = 713 Hz, PF_6) ppm. IR: $\tilde{\nu}$ = 1939 (s, $\nu_{C=C=C}$), 841 (s, ν_{PF}) cm^{-1}. $C_{64}H_{56}ClF_6OP_5Ru{\cdot}CH_2Cl_2$ (1246.53): calcd. C 58.64, H 4.39; found C 58.76, H 4.61.

***trans*-[Cl(dppe)$_2$Ru=C=C=C(H)−2,5-(thiophene)−C(H)(OH)-(C≡C−H)][PF_6] (4b):** From compound **3b** (192 mg), complex **4b** (257 mg) was obtained as a red crystalline solid in 41% yield. ^1H NMR (CD_2Cl_2): δ = 8.78 (quint, $^5J_{PH}$ = 2.6 Hz, 1 H, Ru=C=C=CH), 7.32−6.85 (m, 42 H, Ph, C_4H_2S) 5.39 (d broad, $^4J_{H,H}$ = 2 Hz, C(OH)*H*), 2.68 (d, $^4J_{H,H}$ = 2 Hz, ≡CH), 2.99 (m, 4 H, dppe), 2.85(m, 4 H, dppe) ppm. ^{31}P NMR (CD_2Cl_2): δ = 41.8 (s, dppe), −143.5 (sept., $^1J_{PF}$ = 713 Hz, PF_6) ppm. IR: $\tilde{\nu}$ = 1927 (s, $\nu_{C=C=C}$), 841 (s, ν_{PF}) cm^{-1}. $C_{62}H_{54}ClF_6OP_5RuS$ (1252.56): calcd. C 59.45, H 4.35; found C 59.60, H 4.35.

***trans*-[Cl(dppe)$_2$Ru=C=C=C(Ph)−*p*-(C_6H_4)−C(Ph)(OH)-(C≡C−H)][CF_3SO_3] (4c):** From compound **3c** (338 mg), complex **4c** (568 mg) was obtained as a deep red crystalline solid in 81% yield. ^1H NMR (CD_2Cl_2): δ = 7.75−6.68 (m, 54 H, Ph) 4.90 (s broad, 1 H, OH), 3.08 (m, 4 H, dppe), 3.04 (s, ≡CH), 2.92 (m, 4 H, dppe) ppm. $^{13}C\{^1H\}$ NMR (CD_2Cl_2): δ = 307.06 (quint, $^2J_{P,C}$ = 14.5 Hz, Ru=*C*), 215.14 (Ru=C=*C*), 160.25 (Ru=C=C=*C*), 148.97−125.99 (Ph), 121.43 (q, $^1J_{C,F}$ = 319 Hz, CF_3SO_3), 85.17 (C≡*C*H), 76.43 (*C*−OH), 74.09 (*C*≡CH), 27.46 (quint, $^1J_{P,C}$ + $^3J_{P,C}$ = 23 Hz, PCH_2CH_2P) ppm. ^{31}P NMR (CD_2Cl_2): δ = 38.2 (s, dppe) ppm. IR: $\tilde{\nu}$ = 1921 (s, $\nu_{C=C=C}$) cm^{-1}. HRMS (FAB): *m*/*z* = 1253.2660 $[M]^+$; calcd. 1253.2640. $C_{77}H_{64}ClF_3O_4P_4RuS$ (1402.85): calcd. C 65.93, H 4.60; found C 65.51, H 4.64.

***trans*-[Cl(dppe)$_2$Ru=C=C=C(Ph)−*m*-(C_6H_4)−C(Ph)(OH)-(C≡C−H)][CF_3SO_3] (4d):** From compound **3d** (338 mg), complex **4d** (519 mg) was obtained as a deep red crystalline solid in 74% yield. ^1H NMR (CD_2Cl_2): δ = 7.78−6.58 (m, 54 H, Ph) 4.99 (s broad, 1 H, OH), 3.09 (m, 4 H, dppe), 3.05 (s, ≡CH), 2.94 (m, 4 H, dppe) ppm. $^{13}C\{^1H\}$ NMR (CD_2Cl_2): δ = 308.12 (quint, $^2J_{P,C}$ = 14.5 Hz, Ru=*C*), 216.17 (Ru=C=*C*), 161.25 (Ru=C=C=*C*), 148.98−126.90(Ph), 121.38 (q, $^1J_{C,F}$ = 320 Hz, CF_3SO_3), 85.18 (C≡*C*H), 76.48 (*C*−OH), 74.01 (*C*≡CH), 27.40 (quint, $^1J_{P,C}$ + $^3J_{P,C}$ = 23 Hz, PCH_2CH_2P) ppm. ^{31}P NMR (CD_2Cl_2): δ = 38.2 (s, dppe) ppm. IR: $\tilde{\nu}$ = 1921 (s, $\nu_{C=C=C}$) cm^{-1}. HRMS (FAB): *m*/*z* = 1253.2670 $[M]^+$; calcd. 1253.2640. $C_{77}H_{64}ClF_3O_4P_4RuS$ (1402.85): calcd. C 65.93, H 4.60; found C 65.61, H 4.69.

***trans*-[Cl(dppe)$_2$Ru=C=C=C(Ph)−2,5-(thiophene)−C(Ph)(OH)-(C≡C−H)][CF_3SO_3] (4e):** From compound **3e** (344 mg), complex **4e** (452 mg) was obtained as a deep violet crystalline solid in 64% yield. ^1H NMR (CD_2Cl_2): δ = 7.68 (quint, $^3J_{PH}$ = 4 Hz, 1 H, thiophene), 7.60−6.78 (m, 51 H, Ph+C_4H_2S) 4.85 (s broad, 1 H, OH), 2.95 (s, ≡CH), 2.94 (m, 4 H, dppe), 2.76(m, 4 H, dppe) ppm. $^{13}C\{^1H\}$ NMR (CD_2Cl_2): δ = 288.47 (quint, $^2J_{P,C}$ = 15 Hz, Ru=*C*), 202.24 (Ru=C=*C*), 164.12 (Ru=C=C=*C*), 150.86−125.84 (Ph, thiophene) 85.17 (C≡*C*H), 76.43 (*C*−OH), 74.09 (*C*≡CH), 27.46 (quint, $^1J_{P,C}$ + $^3J_{P,C}$ = 23 Hz, PCH_2CH_2P) ppm. ^{31}P NMR (CD_2Cl_2): δ = 41.0 (s, dppe) ppm. IR: $\tilde{\nu}$ = 1928 (s, $\nu_{C=C=C}$) cm^{-1}. $C_{75}H_{62}ClF_3O_4P_4RuS_2$ (1408.61): calcd. C 63.94, H 4.44; found C 63.77, H 4.39.

***trans*-[Cl(dppe)$_2$Ru=C=C=C(Ph)−5,5′-(2,2′-bithiophene)−C(Ph)-(OH)(C≡C−H)][CF_3SO_3] (4f):** From compound **3f** (426 mg), complex **4f** (477 mg) was obtained as a dark violet solid in 64% yield. ^1H NMR (CD_2Cl_2): δ = 7.69−6.78 (m, 54 H, Ph, bithiophene) 4.92 (s broad, 1 H, OH, 3.01 (s, ≡CH), 2.95 (m, 4 H, dppe), 2.79 (m, 4 H, dppe) ppm. $^{13}C\{^1H\}$ NMR (CD_2Cl_2): δ = 288.47 (quint, $^2J_{P,C}$ = 15 Hz, Ru=*C*), 202.24 (Ru=C=*C*), 164.12 (Ru=C=C=*C*), 150.86−125.84 (Ph, thiophene), 85.17 (C≡*C*H), 76.43 (*C*−OH), 74.09 (*C*≡CH), 27.46 (quint, $^1J_{P,C}$ + $^3J_{P,C}$ = 23 Hz, PCH_2CH_2P) ppm. ^{31}P NMR (CD_2Cl_2): δ = 41.0 (s, dppe) ppm. IR: $\tilde{\nu}$ = 1928 (s, $\nu_{C=C=C}$) cm^{-1}. HRMS (FAB): *m*/*z* = 1341.2076 $[M]^+$; calcd. 1341.2081. $C_{79}H_{64}ClF_3O_4P_4RuS_3$ (1458.92): calcd. C 63.67, H 4.33; found C 63.25, H 4.19.

***trans*-[Cl(dppe)$_2$Ru=C=C=C(Ph)−5,5′′-(2,2′:5′2′′-terthiophene)−C(Ph)(OH)(C≡C−H)][CF_3SO_3] (4g).** From compound **3g** (508 mg), complex **4g** (452 mg) was obtained as a deep blue crystalline solid in 58% yield. ^1H NMR (CD_2Cl_2): δ = 7.78−6.78 (m, 56 H, Ph + terthiophene) 4.95 (s broad, 1 H, OH), 3.05 (s, 1 H, ≡CH), 2.98 (m, 4 H, dppe), 2.79 (m, 4 H, dppe) ppm. $^{13}C\{^1H\}$ NMR (CD_2Cl_2): δ = 294.48 (quint, $^2J_{P,C}$ = 15 Hz, Ru=*C*), 206.55 (Ru=C=*C*), 169.52 (Ru=C=C=*C*), 151.44−126.23 (Ph, thiophene) 85.81 (C≡*C*H), 76.95 (*C*−OH), 74.25 (*C*≡CH), 27.41 (quint, $^1J_{P,C}$ + $^3J_{P,C}$ = 23 Hz, PCH_2CH_2P) ppm. ^{31}P NMR (CD_2Cl_2): δ = 41.2 (s, dppe) ppm. IR: $\tilde{\nu}$ = 1922 (s, $\nu_{C=C=C}$) cm^{-1}. HRMS (FAB): *m*/*z* = 1423.1970 $[M]^+$; calcd. 1423.1958).

***trans*-[Cl(dppe)$_2$Ru=C=C=C(Ph)−(C≡C)−C(Ph)(OH)-(C≡C−H)][CF_3SO_3] (4h):** From compound **3h** (286 mg), complex **4h** (506 mg) was obtained as a deep red solid in 75% yield. ^1H NMR (CD_2Cl_2): δ = 7.85−6.66 (m, 50 H, Ph), 3.08 (m, 8 H, dppe), 3.06 (s, ≡CH) ppm. $^{13}C\{^1H\}$ NMR (CD_2Cl_2): δ = 301.20 (quint, $^2J_{P,C}$ = 15 Hz, Ru=*C*), 229.68 (Ru=C=*C*), 142.24 and 141.05 (s, Ph), 134.77 (Ru=C=C=*C*), 133.92−125.95 (Ph), 120.89 (q, $^1J_{C,F}$ = 320 Hz, CF_3SO_3), 95.60 and 91.04 (C≡C), 82.17 (*C*≡CH), 75.07 (C≡*C*H), 65.59 (*C*−OH), 27.25 (quint, $^1J_{P,C}$ + $^3J_{P,C}$ = 23 Hz, PCH_2CH_2P) ppm. ^{31}P NMR (CD_2Cl_2): δ = 38.0 (s, dppe) ppm. IR: $\tilde{\nu}$ = 1921 (s, $\nu_{C=C=C}$) cm^{-1}. HRMS (FAB): *m*/*z* = 1201.2336 $[M]^+$; calcd. 1201.2327. $C_{73}H_{60}ClF_3O_4P_4RuS$ (1350.76): calcd. C 64.91, H 4.48; found C 64.97, H 4.47.

Synthesis of Bis(allenylidene)ruthenium Complexes (5a−b, X=PF6; 5c−h, X=OTf): To a mixture of [Cl(dppe)$_2$Ru][X] (0.5 mmol) and dipropargylic alcohol (**3**) (0.2 mmol), dichloromethane (50 mL) was added. The resulting mixture was stirred at room temperature for 7 d, and the solvent was evaporated. The resulting solid was washed with diethyl ether (4 × 25 mL) in order to eliminate the organic reactant excess, and was precipitated three times with 60 mL of pentane after dissolution in dichloromethane (20 mL). Further purification was achieved by biphasic recrystallization in dichloromethane/pentane (1:2) to afford the bis(allenylidene) complexes **5a−h** as powdery solids.

***trans*-[Cl(dppe)$_2$Ru=C=C=C(H)−*p*-(C_6H_4)−(H)C=C=C=RuCl-(dppe)$_2$][PF_6]$_2$ (5a):** From **3a** (36 mg), complex **5a** (208 mg) was obtained as a blue crystalline solid in 45% yield. ^1H NMR (CD_2Cl_2): δ = 9.64 (quint, $^5J_{PH}$ = 2.8 Hz, 2 H, Ru=C=C=CH), 7.31−6.46 (m, 84 H, Ph), 2.99 (m, 16 H, dppe) ppm. $^{13}C\{^1H\}$ NMR (CD_2Cl_2): δ = 326.28 (quint, $^2J_{P,C}$ = 15 Hz, Ru=*C*), 241.33 (Ru=C=*C*), 152.01 (Ru=C=C=*C*), 143.24−128.41 (Ph), 29.52 (quint, $^1J_{pc}$ + $^3J_{pc}$ = 23 Hz, PCH_2CH_2P) ppm. ^{31}P NMR (CD_2Cl_2): δ = 39.2 (s, dppe) ppm. IR: $\tilde{\nu}$ = 1918 (s, $\nu_{C=C=C}$) cm^{-1}. $C_{116}H_{102}Cl_2F_{12}P_{10}Ru_2$ (2306.85): calcd. C 60.44, H 4.46; found C 59.87, H 4.28.

***trans*-[Cl(dppe)$_2$Ru=C=C=C(H)−2,5-(thiophene)−(H)C=C=C=RuCl(dppe)$_2$][PF_6]$_2$ (5b):** From **3b** (39 mg), complex **5b** (224 mg) was obtained as a deep blue solid in 49% yield. ^1H NMR (CD_2Cl_2): δ = 9.36 (m, 2 H, Ru=C=C=CH), 7.31−6.90 (m, 82 H, Ph, thiophene), 3.06 (m, 16 H, dppe) ppm. $^{13}C\{^1H\}$ NMR (CD_2Cl_2): δ = 310.53 (quint, $^2J_{P,C}$ = 17 Hz, Ru=*C*), 237.55 (Ru=C=*C*), 158.33 (Ru=C=C=*C*), 134.31−128.37 (Ph, thiophene), 29.76 (quint, $^1J_{P,C}$ + $^3J_{P,C}$ = 23 Hz, PCH_2CH_2P) ppm. ^{31}P NMR (CD_2Cl_2): δ = 39.1

 © 2005 Wiley-VCH Verlag GmbH & Co. KGaA, Weinheim

(s, dppe) ppm. IR: $\tilde{\nu}$ = 1913 (s, $\nu_{C=C=C}$) cm^{-1}. $C_{114}H_{100}Cl_2F_{12}P_{10}Ru_2S$ (2312.22): calcd. C 59.20, H 4.36; found C 59.40, H 4.76.

***trans*-[Cl(dppe)$_2$Ru=C=C=C(Ph)−*p*-(C$_6$H$_4$)−(Ph)C=C=C=RuCl(dppe)$_2$][CF$_3$SO$_3$]$_2$ (5c):** From **3c** (68 mg), complex **5c** (385 mg) was obtained as a deep blue solid in 78% yield. ^{1}H NMR (CD_2Cl_2): δ = 7.33−6.56 (m, 94 H, Ph), 3.04 (m, 8 H, dppe), 2.79 (m, 8 H, dppe) ppm. $^{13}C\{^1H\}$ NMR (CD_2Cl_2): δ = 310.98 (quint, $^2J_{P,C}$ = 15 Hz, Ru=*C*), 228.87 (Ru=C=*C*), 158.17 (Ru=C=C=*C*), 145.91−128.41 (s, Ph), 121.51 (q, $^1J_{C,F}$ = 320 Hz, CF_3SO_3), 27.88 (quint, $^1J_{P,C}$ + $^3J_{P,C}$ = 23 Hz, PCH_2CH_2P) ppm. ^{31}P NMR (CD_2Cl_2): δ = 38.0 (s, dppe) ppm. IR: $\tilde{\nu}$ = 1912 (s, $\nu_{C=C=C}$) cm^{-1}. HRMS (FAB): *m*/*z* = 2317.3563 $[M]^{++}$; calcd. 2317.3493. $C_{130}H_{110}Cl_2F_6P_8O_6Ru_2S_2$ (2467.26): calcd. C 63.29, H 4.49; found C 62.49, H 4.45.

***trans*-[Cl(dppe)$_2$Ru=C=C=C(Ph)−*m*-(C$_6$H$_4$)−(Ph)C=C=C=RuCl(dppe)$_2$][CF$_3$SO$_3$]$_2$ (5d):** From **3d** (64 mg), complex **5d** (222 mg) was obtained as a deep red solid in 45% yield. ^{1}H NMR (CD_2Cl_2): δ = 7.72−6.78 (m, 94 H, Ph), 3.07 (m, 8 H, dppe), 2.97 (m, 8 H, dppe) ppm. $^{13}C\{^1H\}$ NMR (CD_2Cl_2): δ = 310.01 (quint, $^2J_{P,C}$ = 15 Hz, Ru=*C*), 224.21 (Ru=C=*C*), 157.47 (s, Ru=C=C=*C*), 145.84−128.37 (Ph), 121.55 (q, $^1J_{C,F}$ = 320 Hz, CF_3SO_3), 28.15 (quint, $^1J_{P,C}$ + $^3J_{P,C}$ = 23 Hz, PCH_2CH_2P) ppm. ^{31}P NMR (CD_2Cl_2): δ = 38.8 (s, dppe) ppm. IR: $\tilde{\nu}$ = 1913 (s, $\nu_{C=C=C}$) cm^{-1}. HRMS (FAB): *m*/*z* = 2317.3507 $[M]^{++}$; calcd. 2317.3493. $C_{130}H_{110}Cl_2F_6P_8O_6Ru_2S_2$ (2467.26): calcd. C 63.29, H 4.49; found C 63.11, H 4.51.

***trans*-[Cl(dppe)$_2$Ru=C=C=C(Ph)−2,5-(thiophene)−(Ph)C=C=C=RuCl(dppe)$_2$][CF$_3$SO$_3$]$_2$ (5e):** From **3e** (69 mg), complex **5e** (306 mg) was obtained as a deep blue solid in 62% yield. ^{1}H NMR (CD_2Cl_2): δ = 7.85−6.82 (m, 90 H, Ph), 6.30(s, 2 H, thiophene), 3.18 (m, 8 H, dppe), 2.85 (m, 8 H, dppe) ppm. $^{13}C\{^1H\}$ NMR (CD_2Cl_2): δ = 311.53 (quint, $^2J_{P,C}$ = 15 Hz, Ru=*C*), 237.85 (Ru=C=*C*), 159.33 (Ru=C=C=*C*), 134.39−128.87 (Ph, thiophene), 121.55 (q, $^1J_{C,F}$ = 320 Hz CF_3SO_3), 29.66 (quint, $^1J_{P,C}$ + $^3J_{P,C}$ = 23 Hz, PCH_2CH_2P) ppm. ^{31}P NMR (CD_2Cl_2): δ = 39.3 (s, dppe) ppm. IR: $\tilde{\nu}$ = 1904 (s, $\nu_{C=C=C}$) cm^{-1}. HRMS (FAB): *m*/*z* = 2173.3587 $[M^{++} - H^+]$; calcd. 2173.3459. $C_{128}H_{108}Cl_2F_6P_8O_6Ru_2S_3$ (2473.29): calcd. C 62.16, H 4.40; found C 61.97, H 4.37.

***trans*-[Cl(dppe)$_2$Ru=C=C=C(Ph)−5,5′-(2,2′-bithiophene)(Ph)C=C=C=RuCl(dppe)$_2$][CF$_3$SO$_3$]$_2$ (5f):** From **3f** (85 mg), complex **5f** (260 mg) was obtained as a deep blue solid in 51% yield. ^{1}H NMR (CD_2Cl_2): δ = 7.85−6.82 (m, 94 H, Ph, thiophene), 3.04 (m, 16 H, dppe) ppm. $^{13}C\{^1H\}$ NMR (CD_2Cl_2): δ = 312.24 (quint, $^2J_{P,C}$ = 17 Hz, Ru=*C*), 236.47 (Ru=C=*C*), 158.99 (Ru=C=C=*C*), 135.30−128.47 (Ph, thiophene), 121.55 (q, $^1J_{C,F}$ = 320 Hz, CF_3SO_3), 30.05 (quint, $^1J_{P,C}$ + $^3J_{P,C}$ = 23 Hz, PCH_2CH_2P) ppm. ^{31}P NMR (CD_2Cl_2): δ = 39.6 (s, dppe) ppm. IR: $\tilde{\nu}$ = 1925 (s, $\nu_{C=C=C}$) cm^{-1}. $C_{132}H_{110}Cl_2F_6P_8O_6Ru_2S_4$ (2555.41): calcd. C 62.07, H 4.30; found C 61.87, H 4.20.

***trans*-[Cl(dppe)$_2$Ru=C=C=C(Ph)−5,5′′-(2,2′:5′,2′′terthiophene)−(Ph)C=C=C=RuCl(dppe)$_2$][CF$_3$SO$_3$]$_2$(5g):** From **3g** (102 mg), complex **5g** (232 mg) were obtained as a deep blue solid in 44% yield. ^{1}H NMR (CD_2Cl_2): δ = 7.85−6.82 (m, 96 H, Ph, thiophene), 2.99 (m, 16 H, dppe) ppm. $^{13}C\{^1H\}$ NMR (CD_2Cl_2): δ = 313.83 (quint, $^2J_{P,C}$ = 17 Hz, Ru=*C*), 237.85 (Ru=C=*C*), 159.33 (Ru=C=C=*C*), 136.30−127.37 (Ph, thiophene), 121.55 (q, $^1J_{C,F}$ = 320 Hz, CF_3SO_3), 30.96 (quint, $^1J_{P,C}$ + $^3J_{P,C}$ = 23 Hz, PCH_2CH_2P) ppm. ^{31}P NMR (CD_2Cl_2): δ = 40.3 (s, dppe) ppm. IR: $\tilde{\nu}$ = 1929 (s, $\nu_{C=C=C}$) cm^{-1}. HRMS (FAB): *m*/*z* = 2254.3332 $[M]^{++}$; calcd. 2254.3336. $C_{136}H_{112}Cl_2F_6P_8O_6Ru_2S_5$ (2637.54): calcd. C 61.93, H 4.28; found C 62.07, H 4.19.

***trans*-[Cl(dppe)$_2$Ru=C=C=C(Ph)−(C≡C)−(Ph)C=C=C=RuCl(dppe)$_2$][CF$_3$SO$_3$]$_2$ (5h):** From **3h** (57 mg), complex **5h** (203 mg) was obtained as a deep blue solid in 42% yield. ^{1}H NMR (CD_2Cl_2): δ = 7.74−6.67 (m, 90 H, Ph), 2.98 (m, 16 H, dppe) ppm. ^{31}P NMR (CD_2Cl_2): δ = 37.8 (s, dppe) ppm. IR: $\tilde{\nu}$ = 1921 (s, $\nu_{C=C=C}$) cm^{-1}. HRMS (FAB): *m*/*z* = 2116.3666 $[M]^{++}$; calcd. 2116.3659.

***trans*-[3,5-Bis[Cl(dppe)$_2$Ru=C=C=C(Ph)]$_2$−(C$_6$H$_3$)−C(Ph)(OH)(C≡C−H)][CF$_3$SO$_3$]$_2$ (7):** From **6** (36 mg), complex **7** (208 mg) was obtained as a deep red solid in 63% yield. ^{1}H NMR (CD_2Cl_2): δ = 7.75−6.48 (m, 98 H, Ph), 4.91(s broad, 1 H, OH), 3.07 (m, 8 H, dppe), 3.05 (s,1 H, C≡CH), 2.93 (m, 8 H, dppe) ppm. $^{13}C\{^1H\}$ NMR (CD_2Cl_2): δ = 311.55 (quint, $^2J_{P,C}$ = 15 Hz, Ru=*C*), 225.52 (Ru=C=*C*), 156.73 (Ru=C=C=*C*), 149.38−127.47 (Ph), 121.55 (q, $^1J_{C,F}$ = 320 Hz, CF_3SO_3), 86.30(C≡*C*H), 77.62(*C*−OH), 73.09(s, C≡*C*H), 28.11 (quint, $^1J_{P,C}$ + $^3J_{P,C}$ = 23 Hz, PCH_2CH_2P) ppm. ^{31}P NMR (CD_2Cl_2): δ = 38.1 (s, dppe) ppm. IR: $\tilde{\nu}$ = 1921 (s, $\nu_{C=C=C}$) cm^{-1}. HRMS (FAB): *m*/*z* = 2448.3392 $([M]^{++},CF_3SO_3^-)^+$; calcd. 2448.3960. $C_{139}H_{116}Cl_2F_6P_8O_7Ru_2S_2$ (2581.41): calcd. C 64.28, H 4.50; found C 65.51, H 4.64.

Synthesis of (Acetylide−allenylidene)ruthenium Complexes

***trans*-[Cl(dppe)$_2$Ru=C=CH−*p*-(C$_6$H$_4$)−CO−Ph][CF$_3$SO$_3$] (9):** In a Schlenk tube, **2b** (1.67 g, 1.55 mmol) and 4-ethynylbenzophenone (**8**) (350 mg, 1.7 mmol) were dissolved in dry dichloromethane (40 mL) and stirred at room temperature for 18 h. Then, the brown solution was filtered, and the solvent was evaporated. The crude product was washed with diethyl ether. Purification was achieved by biphasic recrystallization (CH_2Cl_2/pentane) to afford complex **9** (1.42 g) as orange crystals in 71% yield. ^{1}H NMR (CD_2Cl_2): δ = 7.82−6.95 (m, 49 H, Ph), 4.82 (quint, $^4J_{PH}$ = 3 Hz, 1 H, Ru=C=CH), 2.92 (m, 8 H, dppe) ppm. $^{13}C\{^1H\}$ NMR (CD_2Cl_2): δ = 352.01 (quint, $^2J_{P,C}$ = 14 Hz, Ru=*C*), 195.41 (CO), 138.01−126.85 (Ph), 123.05 (q, $^1J_{C,F}$ = 320 Hz, CF_3SO_3), 109.64 (quint, $^2J_{P,C}$ = 3 Hz, Ru=C=*C*H), 29.16 (quint, $^1J_{P,C}$ + $^3J_{P,C}$ = 23 Hz, PCH_2CH_2P) ppm. ^{31}P NMR (CD_2Cl_2): δ = 36.3 (s, dppe) ppm. IR: $\tilde{\nu}$ = 1588 (s, $\nu_{C=C}$), 1647 (s, ν_{CO}) cm^{-1}. HRMS (FAB): *m*/*z* = 1139.2186 $[M]^+$; calcd. 1139.2170. $C_{68}H_{58}ClF_3P_4O_4RuS$ (1288.69): calcd. C 63.38, H 4.54; found C 63.40, H 4.53.

***trans*-[Cl(dppe)$_2$Ru−C≡C−*p*-(C$_6$H$_4$)−CO−Ph] (10):** In a Schlenk tube, complex **9** (625 mg, 0.485 mmol) was dissolved in dry dichloromethane (20 mL) and DBU (0.150 mL, 0.970 mmol) was added. The solution was stirred at room temperature for 2 h and filtered through neutral alumina. The solvent was evaporated to afford **10** (518 mg) as a yellow solid in 92% yield. ^{1}H NMR (CD_2Cl_2): δ = 7.83−6.64 (m, 49 H, Ph), 2.76 (m, 8 H, dppe) ppm. $^{13}C\{^1H\}$ NMR (CD_2Cl_2): δ = 195.9 (CO), 139.26−127.49 (Ph), 138.98 ($^2J_{P,C}$ = 15 Hz, Ru−*C*≡C), 115.62 (Ru−C≡*C*), 30.99 (quint, $^1J_{P,C}$ + $^3J_{P,C}$ = 23 Hz, PCH_2CH_2P) ppm. ^{31}P NMR (CD_2Cl_2): δ = 48.9 (s, dppe) ppm. IR: $\tilde{\nu}$ = 2057 (s, $\nu_{C\equiv C}$), 1584 (s, ν_{CO}) cm^{-1}. HRMS (FAB): *m*/*z* = 1138.2076 $[M]^+$; calcd. 1138.2092. $C_{67}H_{57}ClP_4ORu$ (1138.61): calcd. C 70.68, H 5.05; found C 70.08, H 4.92.

***trans*-[Cl(dppe)$_2$Ru−C≡C−*p*-(C$_6$H$_4$)−C(OH)(Ph)C≡CH] (11):** In a Schlenk tube, acetylene (5 mmol) was dissolved in dry THF (20 mL) cooled to −78 °C. *n*-Butyllithium (1.6 mL, 1 mmol, 1.6 M in hexane) was added slowly under argon and the mixture was stirred at −78 °C for 1 h. Then, **10** (445 mg 0.4 mmol) dissolved in THF (5 mL) was added dropwise. The solution was stirred for 1 h at −78 °C and 1 h at room temperature. After evaporation of the

 © 2005 Wiley-VCH Verlag GmbH & Co. KGaA, Weinheim

solvent, the crude product was dissolved in dichloromethane (50 mL), washed with water and dried with magnesium sulfate. Purification by flash chromatography (neutral alumina, dichloromethane) provided **11** (366 mg) as a pale yellow powder in 78% yield. ^{1}H NMR (CD_2Cl_2): δ = 7.79−6.58 (m, 49 H, Ph), 2.86 (s, 1 H, C≡CH), 2.75 (s, 1 H, OH), 2.64 (m, 8 H, dppe) ppm. $^{13}C\{^1H\}$ NMR (CD_2Cl_2): δ = 144.77−135.46 (Ph), 134.89 (quint, $^2J_{P,C}$ = 15 Hz, Ru−*C*≡C−), 134.39−125.35 (Ph), 113.63 (Ru−C≡*C*), 30.99 (quint, $^1J_{P,C}$ + $^3J_{P,C}$ = 23 Hz, PCH_2CH_2P) ppm. ^{31}P NMR (CD_2Cl_2): δ = 50.2 (s, dppe) ppm. IR: $\tilde{\nu}$ = 3050 (s, $\nu_{\equiv CH}$), 2135 (s, $\nu_{C\equiv CH}$), 2065 (s, $\nu_{C\equiv C}$) cm^{-1}. HRMS (FAB): *m*/*z* = 1164.2255 [M]$^+$; calcd. 1164.2249). $C_{69}H_{59}ClP_4ORu$ (1164.65): calcd. C 71.16, H 5.11; found C 71.23, H 5.14.

***trans*-[Cl(dppe)$_2$Ru−C≡C−*p*-(C$_6$H$_4$)−(Ph)C=C=C=RuCl(dppe)$_2$][CF$_3$SO$_3$] (12):** In a Schlenk tube **11** (300 mg, 0.258 mmol) and **2b** (200 mg, 0.284 mmol) were dissolved in dichloromethane (50 mL), and the resulting mixture was stirred at room temperature for 8 days. After evaporation of the solvent, the crude product was washed with ether (4 × 25 mL) and precipitated three times with 60 mL of pentane after dissolution in dichloromethane (20 mL). Purification was achieved by biphasic recrystallization (dichloromethane/pentane 1:2) to afford **12** (420 mg) as a deep purple solid in 72% yield. ^{1}H NMR (CD_2Cl_2): δ = 7.84−6.18 (m, 89 H, Ph), 3.04 (m, 8 H, dppe), 2.77 (m, 8 H, dppe) ppm. $^{13}C\{^1H\}$ NMR (CD_2Cl_2): δ = 345.62 (quint, $^2J_{P,C}$ = 15 Hz, Ru=*C*), 192.85 (Ru=C=*C*), 158.32 (Ru=C=C=*C*), 143.51−123.21 (Ph), 135.45 (quint, $^2J_{P,C}$ = 15 Hz, Ru−*C*≡C−), 113.63 (Ru−C≡*C*), 30.71 (quint, $^1J_{P,C}$ + $^3J_{P,C}$ = 23 Hz, PCH_2CH_2P), 27.82 (quint, $^1J_{P,C}$ + $^3J_{P,C}$ = 23 Hz, PCH_2CH_2P), ppm. ^{31}P NMR (CD_2Cl_2): δ = 49.2 (s, dppe), 40.7 (s, dppe) ppm. IR: $\tilde{\nu}$ = 2040 (s, $\nu_{C\equiv C}$), 1926 ($\nu_{C=C=C}$) cm^{-1}. HRMS (FAB): *m*/*z* = 2079.3555 [M]$^+$; calcd. 2079.3581. $C_{122}H_{105}F_3Cl_2O_3P_8Ru_2S$ (2229.08): calcd. C 65.74, H 4.75; found C 65.90, H 4.88.

***trans*-[Cl(dppe)$_2$Ru=C=CH−*p*-(C$_6$H$_4$)−CO−*p*-(C$_6$H$_4$)−CH=C=RuCl(dppe)$_2$][CF$_3$SO$_3$]$_2$ (14):** In a Schlenk tube **2b** (1.62 g, 1.5 mmol) and 4,4′-bis(ethynyl)benzophenone (**13**) (154 mg, 0.67 mmol) were dissolved in dry dichloromethane (30 mL), and the mixture was stirred for 18 h at room temperature. After filtration and evaporation of the solvent, the crude product was washed with ether (4 × 40 mL) and recrystallized by the biphasic method to afford **14** (1.31 g) as orange crystals in 82% yield. ^{1}H NMR (CD_2Cl_2): δ = 7.67−5.77 (m, 88 H, Ph), 4.74 (quint,2H $^4J_{PH}$ = 3 Hz, Ru=C=CH), 3.01 (m, 16 H, dppe) ppm. $^{13}C\{^1H\}$ NMR (CD_2Cl_2): δ = 354.02 (quint, $^2J_{P,C}$ = 14 Hz, Ru=*C*), 196.81 (CO), 138.48−126.95 (Ph), 123.15 (q, $^1J_{C,F}$ = 320 Hz, CF_3SO_3), 109.84 (quint, $^3J_{P,C}$ = 3 Hz, Ru=C=CH), 30.16 (quint, $^1J_{P,C}$ + $^3J_{P,C}$ = 23 Hz, PCH_2CH_2P) ppm. ^{31}P NMR (CD_2Cl_2): δ = 37.3 (s, dppe) ppm. IR: $\tilde{\nu}$ = 1592 (s, $\nu_{C=C}$), 1633 (ν_{CO}) cm^{-1}. HRMS (FAB): *m*/*z* = 2095.3564 [M]$^{++}$; calcd. 2095.3530. $C_{123}H_{106}Cl_2F_6O_7P_8Ru_2S_2$ (2295.15): calcd. C 61.68, H 4.46; found C 61.55, H 4.27.

***trans*-[Cl(dppe)$_2$Ru−C≡C−*p*-(C$_6$H$_4$)−CO−*p*-(C$_6$H$_4$)−C≡C−RuCl(dppe)$_2$] (15):** In a Schlenk tube **14** (1.31 g, 0.55 mmol) was dissolved in dry dichloromethane (30 mL) and DBU (0.175 mL, 1.10 mmol) was added slowly. The solution was stirred at room temperature for 2 h. After filtration through neutral alumina and evaporation of the solvent, **15** (1.01 g) was obtained as a yellow solid in 87% yield. ^{1}H NMR (CD_2Cl_2): δ = 7.59−6.64 (m, 88 H, Ph), 2.68 (m, 16 H, dppe) ppm. $^{13}C\{^1H\}$ NMR (CD_2Cl_2): δ = 191.16 (CO), 136.98 (quint, $^2J_{P,C}$ = 15 Hz, Ru−*C*≡C−), 135.41−127.45 (Ph), 115.84 (Ru−C≡*C*), 31.10 (quint, $^1J_{P,C}$ + $^3J_{P,C}$ = 23 Hz, PCH_2CH_2P) ppm. ^{31}P NMR (CD_2Cl_2): δ = 50.0 (s, dppe) ppm. IR: $\tilde{\nu}$ = 2053 (s, $\nu_{C\equiv C}$), 1584 (s, ν_{CO}) cm^{-1}. HRMS (FAB): *m*/*z* = 2094.3440 [M]$^{++}$; calcd. 2094.3452. $C_{121}H_{101}Cl_2P_8ORu_2$ (2091.15): calcd. C 69.37, H 5.00; found C 69.12, H 4.87.

***trans*-[Cl(dppe)$_2$Ru−C≡C−*p*-(C$_6$H$_4$)−C(OH)(C≡CH)−*p*-(C$_6$H$_4$)−C≡C−RuCl(dppe)$_2$] (16):** In a Schlenk tube, acetylene (4 mmol) was dissolved in dry THF (20 mL) cooled to −78 °C, *n*-butyllithium (0.8 mL, 0.5 mmol, 1.6 M in hexane) was added slowly, and the mixture was stirred for 1 h at −78 °C. Then, **15** (500 mg, 0.238 mmol) was dissolved in dry THF (5 mL) and added dropwise to the mixture. The solution was stirred for 30 min at −78 °C and 1 h at room temperature. The solvent was evaporated, the crude product dissolved in dichloromethane (40 mL), washed with water, and dried with $MgSO_4$. Purification by flash chromatography (aluminum oxide, dichloromethane) afforded **16** (431 mg) as a yellow solid in 85% yield. ^{1}H NMR (CD_2Cl_2): δ = 7.66−6.92 (m, 88 H, Ph), 2.95 (s, 1 H, OH), 2.63 (m, 16 H, dppe), 2.58 (s, 1 H, C≡CH) ppm. $^{13}C\{^1H\}$ NMR (CD_2Cl_2): δ = 138.64−125.42 (Ph), 134.89 (quint, $^2J_{P,C}$ = 15 Hz, Ru−*C*≡C−), 113.75 (Ru−C≡*C*), 86.28 (C≡*C*H), 74.91(*C*≡CH), 74.54 (*C*−OH), 30.77 (quint, $^1J_{P,C}$ + $^3J_{P,C}$ = 23 Hz, PCH_2CH_2P) ppm. ^{31}P NMR (CD_2Cl_2): δ = 50.1 (s, dppe) ppm. IR: $\tilde{\nu}$ = 3052 (s, $\nu_{\equiv CH}$), 2136 (s, $\nu_{C\equiv CH}$), 2068 (s, $\nu_{C\equiv C}$) cm^{-1}. HRMS (FAB): *m*/*z* = 2120.3666 [M]$^{++}$; calcd. 2120.3609. $C_{123}H_{106}Cl_2P_8ORu_2$ (2221.4): calcd. C 69.65, H 5.04; found C 69.37, H 5.12.

***trans*-[{Cl(dppe)$_2$Ru−C≡C−*p*-(C$_6$H$_4$)}$_2$C=C=C=RuCl(dppe)$_2$][CF$_3$SO$_3$] (17):** In a Schlenk tube, **16** (250 mg, 0.118 mmol) and **2b** (139 mg, 0.129 mmol) were dissolved in dichloromethane (50 mL). The mixture was stirred at room temperature for 14 d. The solvent was removed under vacuum, and the crude product was washed with diethyl ether. The product was precipitated three times with 60 mL of pentane after dissolution in dichloromethane (20 mL), and purification was achieved by biphasic recrystallization (dichloromethane/pentane, 1:2) to afford **17** (420 mg) as a deep green solid in 83% yield. ^{1}H NMR (CD_2Cl_2): δ = 7.57−6.20 (m, 128 H, Ph), 2.94 (m, 8 H, dppe), 2.74 (m, 8 H, dppe), 2.54 (m, 8 H, dppe) ppm. $^{13}C\{^1H\}$ NMR (CD_2Cl_2): δ = 342.32 (quint, $^2J_{P,C}$ = 14 Hz, Ru=*C*), 190.85 (Ru=C=*C*), 154.32 (Ru=C=C=*C*), 138.64−125.42 (Ph), 134.29 (quint, $^2J_{P,C}$ = 15 Hz, Ru−*C*≡C−), 116.75 (s, Ru−C≡*C*), 30.69 (quint, $^1J_{P,C}$ + $^3J_{P,C}$ = 23 Hz, PCH_2CH_2P), 28.77 (quint, $^1J_{P,C}$ + $^3J_{P,C}$ = 23 Hz, PCH_2CH_2P) ppm. ^{31}P NMR (CD_2Cl_2): δ = 49.3 (s, dppe), 40.6 (s, dppe) ppm. IR: $\tilde{\nu}$ = 2008 (s, $\nu_{C\equiv C}$), 1912 (s, $\nu_{C=C=C}$) cm^{-1}. HRMS (FAB): *m*/*z* = 3035.4966 [M]$^{++}$; calcd. 3035.4941. $C_{176}H_{152}Cl_3F_3O_3P_{12}Ru_3S$ (3185.46): calcd. C 66.36, H 4.81; found C 66.65, H 4.90.

Acknowledgments

We thank the French-Ministry MNESR for the award of a thesis grant to J. P., CNRS and the University of Rennes 1 for support, Dr. P. Guenot (Rennes) for helpful discussion, and Prof. P. Turek (Strasbourg) for help in structure determination.

[1] S. A. Hudson, P. M. Maitlis, *Chem. Rev.* **1993**, *93*, 861.
[2] I. R. Whittall, A. M. McDonagh, M. G. Humphrey, M. Samoc, *Adv. Organomet. Chem.* **1999**, *43*, 349. S. K. Hurst, M. G. Humphrey, T. Isoshima, K. Wostyn, I. Asselberghs, K. Clays, A. Persoons, M. Samoc, B. Luther-Davies, *Organometallics* **2002**, *21*, 2024. T. Weyland, I. Ledoux, S. Brasselet, J. Zyss, C. Lapinte, *Organometallics* **2000**, *19*, 5235. A. M. McDonagh, M. G. Humphrey, M. Samoc, B. Luther-Davies, S. Houbrechts, T. Wada, H. Sasabe, A. Persoons, *J. Am. Chem.*

Soc. **1999**, *121*, 1405. K. Senechal, O. Maury, H. Le Bozec, I. Ledoux, J. Zyss, *J. Am. Chem. Soc.* **2002**, *124*, 4560. N. J. Long, *Angew. Chem. Int. Ed.* **1995**, *34*, 21.

[3] V. W. W. Yam, *Acc. Chem. Res.* **2002**, *35*, 555.

[4] F. Paul, C. Lapinte, *Coord. Chem. Rev.* **1998**, *178–180*, 431.

[5] For selected representative examples in various fields see: [5a] F. Paul, W. E. Meyer, L. Toupet, H. Jiao, J. A. Gladysz, C. Lapinte, *J. Am. Chem. Soc.* **2000**, *122*, 9405. [5b] R. Ziessel, M. Hissler, A. El-Gayhouri, A. Harriman, *Coord. Chem. Rev.* **1998**, *178–180*, 1251. [5c] P. F. H. Schab, M. D. Levin, J. Michl, *Chem. Rev.* **1999**, *99*, 1863. [5d] J. Gil-Rubio, M. Laubender, H. Werner, *Organometallics* **2000**, *19*, 1365. [5e] R. Dembinski, T. Bartik, B. Bartik, M. Jaeger, J. A. Gladysz, *J. Am. Chem. Soc.* **2000**, *122*, 810. [5f] F. J. Fernandez, O. Blacque, M. Alfonso, H. Berke, *Chem. Commun.* **2001**, 1266. [5g] M. I. Bruce, P. J. Low, K. Costuas, J.-F. Halet, S. P. Best, G. A. Heath, *J. Am. Chem. Soc.* **2000**, *122*, 1949. [5h] M. I. Bruce, B. G. Ellis, P. J. Low, B. W. Skelton, A. H. White, *Organometallics* **2003**, *22*, 3184. [5i] P. Siemen, U. Gubler, C. Bosshard, P. Günter, F. Diederich, *Chem. Eur. J.* **2001**, *7*, 1333. [5j] D. B. Werz, R. Gleiter, F. Rominger, *Organometallics* **2003**, *22*, 843. [5k] W. Lu, H.-F. Xiang, N. Zhu, C.-M. Che, *Organometallics* **2002**, *21*, 2343. [5l] H. Qi, S. Sharma, Z. Li, S. L. Snider, A. O. Orlov, C. S. Lent, T. P. Fehlner, *J. Am. Chem. Soc.* **2003**, *125*, 15251. [5m] G.-L. Xu, G. Xu, Y.-H. Ni, M. C. DeRosa, R. J. Crutchley, T. Ren, *J. Am. Chem. Soc.* **2003**, *125*, 10057.

[6] [6a] S. Rigaut, L. Le Pichon, J.-C. Daran, D. Touchard, P. H. Dixneuf, *Chem. Commun.* **2001**, 1206. [6b] S. Rigaut, J. Massue, D. Touchard, J.-L. Fillaut, S. Golhen, P. H. Dixneuf, *Angew. Chem. Int. Ed.* **2002**, *41*, 4513.

[7] [7a] S. H. Liu, H. Xia, T. B. Wen, Z. Zhou, G. Jia, *Organometallics* **2003**, *22*, 737. [7b] M.-C. Chung, X. Gu, B. A. Etzenhouser, A. M. Spuches, P. T. Rye, S. K. Seetaraman, D. J. Rose, J. Zubieta, M. B. Sponsler, *Organometallics* **2003**, *22*, 3485.

[8] [8a] W. Weng, T. Bartik, M. T. Johnson, A. M. Arif, J. A. Gladysz, *Organometallics* **1995**, *14*, 889. [8b] H. Fischer, F. Leroux, R. Stumpf, G. Roth, *Chem. Ber.* **1996**, *129*, 1475. [8c] F. Leroux, R. Stumpf, H. Fischer, *Eur. J. Inorg. Chem.* **1998**, 1225. [8d] N. Y. Kolokova, V. V. Skripkin, G. G. Alexandrov, Y. T. Struchkov, *J. Organomet. Chem.* **1979**, *169*, 293. [8e] J. R. Berenguer, J. Fornies, E. Lalind, F. Martinez, L. Sanchez, B. Serrano, *Organometallics* **1998**, *17*, 1640. [8f] R. M. Bullock, *J. Am. Chem. Soc.* **1987**, *109*, 8087. [8g] G. Roth, D. Reindl, M. Gockel, C. Troll, H. Fischer, *Organometallics* **1998**, *17*, 1393.

[9] [9a] T. Bartik, W. J. Weng, A. Ramsden, S. Szafert, S. B. Falloon, A. M. Arif, J. A. Gladysz, *J. Am. Chem. Soc.* **1998**, *120*, 11071. [9b] R. Dembinski, S. Szafert, P. Haquette, T. Lis, J. A. Gladysz, *Organometallics* **1999**, *18*, 5438. [9c] B. Fuss, M. Dede, B. Weibert, H. Fischer, *Organometallics* **2002**, *21*, 4425.

[10] [10a] H. P. Xia, W. S. Ng, J. S. Ye, X. Y. Li, W. T. Wong, Z. Lin, C. Yang, G. Jia, *Organometallics* **1999**, *18*, 4552. [10b] J. P. Selegue, *J. Am. Chem. Soc.* **1983**, *105*, 5921.

[11] [11a] G. Xu, T. Ren, *Organometallics* **2001**, *20*, 2400. [11b] K. T Wong, J.-M. Lehn, S.-M. Peng, G.-H. Lee, *Chem. Commun.* **2000**, 2259.

[12] For example, see: [12a] S. J. Lippard, J. M. Berg, *Principles of Bioinorganic Chemistry*; University Science Books, Mill Valley, California, **1994**. [12b] G. B. Schuster, *Acc. Chem. Res.* **2000**, *33*, 253.

[13] [13a] J. F. Endicott, K. Kumar, T. Ramasami, F. P. Rotzinger, *Prog. Inorg. Chem.* **1983**, *30*, 141. [13b] F. Barigelletti, L. Flamigni, *Chem. Soc., Rev.* **2000**, *29*, 1.

[14] [14a] J. H. Wosnick, T. M. Swager, *Curr. Opin. Chem. Biol.* **2000**, *4*, 715. [14b] J. M. Tour, A. M. Rawlett, M. Kozaki, Y. Yao, R. C. Jagessar, S. M. Dirk, D. W. Price, M. A. Reed, C.-W. Zhou, J. Chen, W. Wang, I. Campbell, *Chem. Eur. J.* **2001**, *7*, 5118. [14c] J.-P. Launay, *Chem. Soc., Rev.* **2001**, *30*, 386. [14d] D. Cahen, G. Hodes, *Adv. Mater.* **2002**, *14*, 789. [14e] M. A. Ratner, *Mater. Today* **2002**, *5*, 20. [14f] K. S. Kwok, J. C. Ellenbogen, *Mater. Today* **2002**, *5*, 28.

[15] [15a] M. I. Bruce, *Chem. Rev.* **1998**, *98*, 2797. [15b] M. I. Bruce, *Chem. Rev.* **1991**, *91*, 197. [15c] V. Cardieno, M. P. Gamasa, J. Gimeno, *Eur. J. Inorg. Chem.* **2001**, 571. [15d] H. Werner, *Chem. Commun.* **1997**, 903.

[16] [16a] S. Rigaut, K. Costuas, D. Touchard, J.-Y. Saillard, S. Golhen, P. H. Dixneuf, *J. Am. Chem. Soc.* **2004**, *126*, 4072. [16b] G.-L. Xu, M. C. DeRosa, R. J. Crutchley, T. Ren, *J. Am. Chem. Soc.* **2004**, *126*, 3728. [16c] Y. Zhu, O. Clot, M. O. Wolf, G. P. A. Yap, *J. Am. Chem. Soc.* **1998**, *120*, 1812. [16d] C. Lebreton, D. Touchard, L. Le Pichon, A. Daridor, L. Toupet, P. H. Dixneuf, *Inorg. Chim. Acta* **1998**, *272*, 188.

[17] C.-Y. Wong, C.-M. Che, M. C. W. Chan, K.-H. Leung, D. L. Phillips, N. Zhu, *J. Am. Chem. Soc.* **2004**, *126*, 2501.

[18] S. Rigaut, J. Perruchon, L. Le Pichon, D. Touchard, P. H. Dixneuf, *J. Organomet. Chem.* **2003**, *670*, 37.

[19] S. Rigaut, D. Touchard, P. H. Dixneuf, *Organometallics* **2003**, *22*, 3980.

[20] O. Lavastre, J. Plass, P. Backmann, S. Guesmi, C. Moinet, P. H. Dixneuf, *Organometallics* **1997**, *16*, 184.

[21] J. P. Selegue, *Organometallics* **1982**, *1*, 217.

[22] S. Guesmi, D. Touchard, P. H. Dixneuf, *Chem. Commun.* **1996**, 2773.

[23] B. Castellas-Gaspar, M. Laubender, H. Werner, *J. Organomet. Chem.* **2003**, *684*, 144.

[24] J. Gil-Rubio, B. Weberndörfer, H. Werner, *Angew. Chem. Int. Ed.* **2000**, *39*, 786. M. Laubender, H. Werner, *Chem. Eur. J.* **1999**, *5*, 2937.

[25] K. Ulrich, E. Porhiel, V. Peron, V. Ferrand, H. Le Bozec, *J. Organomet. Chem.* **2000**, *601*, 78.

[26] D. Touchard, N. Pirio, P. H. Dixneuf, *Organometallics* **1995**, *14*, 4920.

[27] [27a] D. Weiss, P. H. Dixneuf, *Organometallics* **2003**, *22*, 2209. [27b] M. Uno, P. H. Dixneuf, *Angew. Chem. Int. Ed.* **1998**, *37*, 1714.

[28] D. Astruc, *Electron Transfer and Radical Processes in Transition Metal Chemistry*, VCH Publishers, New York, **1995**.

[29] S. Rigaut, O. Maury, D. Touchard, P. H. Dixneuf, *Chem. Commun.* **2001**, 373.

[30] [30a] N. Re, A. Sgamellotti, C. Fioriani, *Organometallics* **2000**, *19*, 1115. [30b] A. Marrone, N. Re, *Organometallics* **2002**, *21*, 3562.

[31] R. F. Winter, K. W. Klinkhammer, *Organometallics* **2001**, *20*, 1317. S. Hartmann, R. F. Winter, B. M. Brunner, B. Sarkar, A. Knödler, I. Hartenbach, *Eur. J. Inorg. Chem.* **2003**, 876.

[32] N. Auger, D. Touchard, S. Rigaut, J.-F. Halet, J.-Y. Saillard, *Organometallics* **2003**, *22*, 1638.

[33] [33a] O. F. Koentjoro, R. Rousseau, P. J. Low, *Organometallics* **2001**, *20*, 4502. [33b] J. E. McGrady, T. Lovell, R. Stranger, M. G. Humphrey, *Organometallics* **1997**, *16*, 4004. [33c] R. F. Winter, *Eur. J. Inorg. Chem.* **1999**, 2121. [33d] R. F. Winter, F. M. Hornung, *Organometallics* **1999**, *18*, 4005.

[34] [34a] N. G. Connelly, W. E. Geiger, *Chem. Rev.* **1996**, *96*, 877. [34b] J. H. Ameter, J. D. Swallen, *J. Phys. Chem.* **1972**, *57*, 678.

[35] [35a] A full investigation of our systems (ENDOR) is currently in progress to identify the different couplings, and will be reported in due course. [35b] It can be noted that similar, but very weak shoulders are sometimes observed with monometallic allenylidene complexes, and that simulated spectra are consistent with the coupling of the electron with the ruthenium atom. Thus, the presence of two ruthenium atoms in bis(allenylidenes) gives rise to a more complex system, with different isotope combinations that account here for the increased intensity of the shoulders: S. Choua, P. Turek, S. Rigaut, D. Touchard, unpublished work.

[36] M. C. Chung, K. Gu, B. A. Etzenhouser, A. M. Spuches, P. T. Rye, S. K. Seetheraman, D. J. Rose, J. Zubieta, M. B. Sponsler, *Organometallics* **2003**, *22*, 3485.

[37] S. Le Stang, F. Paul, C. Lapinte, *Organometallics* **2000**, *19*, 1035. N. Le Narvor, C. Lapinte, *Organometallics* **1995**, *14*, 634. S. Roué, C. Lapinte, T. Bataille, *Organometallics* **2004**, *23*, 2558.

 © 2005 Wiley-VCH Verlag GmbH & Co. KGaA, Weinheim

[38] O. F. Koentjoro, R. Rousseau, P. J. Low, *Organometallics* **2001**, *20*, 4502.
[39] F. Coat, F. Paul, C. Lapinte, L. Toupet, K. Costuas, J.-F. Halet, *J. Organomet. Chem.* **2003**, *683*, 368.
[40] S. Rigaut, F. Monnier, F. Mousset, D. Touchard, P. H. Dixneuf, *Organometallics* **2002**, *21*, 2657.
[41] B. Chaudret, G. Commengues, R. Poilblanc, *J. Chem. Soc., Dalton Trans.* **1984**, 1635.
[42] [42a] B. Chin, A. J. Lough, R. H. Morris, C. T. Sweitzer, C. D'Agostino, *Inorg. Chem.* **1994**, *33*, 6278. [42b] J. R. Polam, L. C. Porter, *J. Coord. Chem.* **1993**, *29*, 109.
[43] M. W. Logue, G. L. Moore, *J. Org. Chem.* **1975**, *40*, 131.
[44] J. J. Zhang, G. B. Schuster, *J. Am. Chem. Soc.* **1989**, *111*, 7149.
[45] J. Rauss-Godineau, W. Chodkiewicz, P. Cadiot, *Bull. Soc. Chim. Fr.* **1966**, 2877.
[46] J. A. Johnston, F. M. Li, F. W. Harris, T. Takekoshi, *Polymer* **1994**, *35*, 4865.
[47] A. G. Avent, P. R. Birkett, F. Paolucci, S. Roffia, R. Taylor, N. K. Wachter, *J. Chem. Soc., Perkin Trans. 2* **2000**, 1409.

Received June 2, 2004
Early View Article
Published Online November 10, 2004

 © 2005 Wiley-VCH Verlag GmbH & Co. KGaA, Weinheim

Structural Diversity of Low-Dimensional Compounds in $[M(en)_2]^{2+}/[Re_6Q_8(CN)_6]^{4-}$ Systems (M = Mn, Ni, Cu)

Konstantin A. Brylev,[a] Guillaume Pilet,[b] Nikolai G. Naumov,*[a] Andre Perrin,[b] and Vladimir E. Fedorov[a]

Keywords: Amines / Cluster compounds / Cyanides / Rhenium / Solid-state structures

Five new octahedral chalcocyanide cluster compounds $[\{Mn(H_2O)(en)_2\}\{Mn(en)_2\}Re_6Te_8(CN)_6]\cdot 3H_2O$ (**1**), $[Ni(NH_3)_2(en)_2]_2[\{Ni(NH_3)_4\}Re_6Se_8(CN)_6]Cl_2\cdot 2H_2O$ (**2**), $[Ni(NH_3)_2(en)_2]_2[\{Ni(NH_3)_4\}Re_6Te_8(CN)_6]Cl_2\cdot H_2O$ (**3**), $(NH_4)_2[\{Ni(en)_2\}_3\{Re_6Te_8(CN)_6\}_2]\cdot 6H_2O$ (**4**) and $(Et_4N)_2[Cu(NH_3)(en)_2]_2[\{Cu(en)_2\}\{Re_6Te_8(CN)_6\}_2]\cdot 2H_2O$ (**5**) (en = ethylenediamine), have been synthesised. All five compounds have been characterised by single-crystal X-ray diffraction analysis. Compounds **1**–**3** have chain-like polymeric structures, whereas compound **4** exhibits a two-dimensional polymeric structure, with negatively charged $[\{Ni(en)_2\}_3\{Re_6Te_8(CN)_6\}_2]^{2-}_{\infty\infty}$ layers, and compound **5** has an ionic structure where anionic $[\{Cu(en)_2\}\{Re_6Te_8(CN)_6\}_2]^{6-}$ dimers are packed with cationic $[Cu(NH_3)(en)_2]^{2+}$ complexes and Et_4N^+ cations.
(© Wiley-VCH Verlag GmbH & Co. KGaA, 69451 Weinheim, Germany, 2005)

Introduction

The coordination chemistry of octahedral rhenium chalcocyanide cluster complexes $[Re_6Q_8(CN)_6]^{4-/3-}$ (Q = S, Se, Te) is in a stage of a rapid development.[1−5] The interaction of these anions with aqua cations of different metals $[M(H_2O)_6]^{n+}$ results in a partial or total replacement of the coordinated water molecules by nitrogen atoms of the more nucleophilic CN ligands. As a rule such interactions lead to three-dimensional polymeric structures where four or all six CN ligands of the cluster anions coordinate to cations through Re−CN−M bridges.[6−12] The number of low-dimensional structures is limited.[13,14]

A set of chain structures and structures with isolated $[\{M(H_2O)_5\}Re_6Q_8(CN)_6]^{2-}$ fragments has been obtained by using large organic cations like Pr_4N^+ or Bu_4N^+ as "spacers" to separate low-dimensional fragments, thus preventing the formation of framework or layered arrays.[15−17] Another approach to obtain low-dimensional structures is to restrict the coordination abilities of the transition metals. This method has been widely used for mononuclear cyanides.[18−26] Recently, this approach has also been applied to octahedral rhenium chalcocyanide cluster anions such as $[Re_6Q_8(CN)_6]^{4-}$. Several types of organic chelate ligands like en (ethylenediamine),[27,28] trien (triethylenetetramine),[29] salen [*N*,*N*′-ethylenebis(salicylideneaminato)],[30,31] OEP (octaethylporphyrinato dianion) and TPP (tetraphenylporphyrinato dianion)[32] were used and it was shown that the coordination of chelating ligands to the metal effectively reduces the dimensionality of the network.

In the present work we continue the study of the interaction of $[Re_6Q_8(CN)_6]^{4-}$ anions with transition metal cations in the presence of the simplest chelating ligand — ethylenediamine. Five new compounds $[\{Mn(H_2O)(en)_2\}\{Mn(en)_2\}Re_6Te_8(CN)_6]\cdot 3H_2O$ (**1**), $[Ni(NH_3)_2(en)_2]_2[\{Ni(NH_3)_4\}Re_6Se_8(CN)_6]Cl_2\cdot 2H_2O$ (**2**), $[Ni(NH_3)_2(en)_2]_2[\{Ni(NH_3)_4\}Re_6Te_8(CN)_6]Cl_2\cdot H_2O$ (**3**), $(NH_4)_2[\{Ni(en)_2\}_3\{Re_6Te_8(CN)_6\}_2]\cdot 6H_2O$ (**4**) and $(Et_4N)_2[Cu(NH_3)(en)_2]_2[\{Cu(en)_2\}\{Re_6Te_8(CN)_6\}_2]\cdot 2H_2O$ (**5**) have been prepared and characterised by X-ray diffraction analysis. They demonstrate the structural diversity of compounds formed in the system "$[M(en)_2]^{2+}$ + $[Re_6Q_8(CN)_6]^{4-}$", where M^{2+} is Mn^{2+}, Ni^{2+} or Cu^{2+} and Q is Se or Te.

Results and Discussion

The crystals of compound **1**−**3** were obtained by diffusion of a water solution of $Cs_4[Re_6Te_8(CN)_6]\cdot 2H_2O$ (**1**) or aqueous ammonia solutions of $K_4[Re_6Se_8(CN)_6]\cdot 3.5H_2O$ (**2**) or $Cs_4[Re_6Te_8(CN)_6]\cdot 2H_2O$ (**3**) into the glycerol solutions of $Mn(OAc)_2\cdot 4H_2O$ (**1**) or $NiCl_2\cdot 6H_2O$ (**2** and **3**) in the presence of ethylenediamine. Compounds **4** and **5** were crystallised by mixing of aqueous ammonia solutions of $Cs_4[Re_6Te_8(CN)_6]\cdot 2H_2O$ and $NiCl_2\cdot 6H_2O$ or $CuCl_2\cdot 2H_2O$, respectively, in the presence of ethylenediamine [Bu_4NBr (**4**) or Et_4NBr (**5**) were added to the reacting systems].

[a] Nikolaev Institute of Inorganic Chemistry, Siberian Branch of the Russian Academy of Sciences,
3 Acad. Lavrentiev pr., Novosibirsk 630090, Russia
Fax: + 7-383-2-344489
E-mail: naumov@che.nsk.su
[b] Institut de Chimie de Rennes, Laboratoire de Chimie du Solide et Inorganique Moléculaire, UMR 6511 CNRS − Université de Rennes 1,
Avenue du Général Leclerc, 35042 Rennes Cedex, France

In compounds **1**−**5** the structure of the $[Re_6Q_8(CN)_6]^{4-}$ (Q = Se, Te) anions is similar to that in the starting compounds and related complexes.[2−11,14,16,17,27−32] The Re_6 cluster is an almost ideal octahedron, and the Re−Re bond lengths vary from 2.6714(8) to 2.6988(9) Å in **1**, from 2.6270(7) to 2.6330(3) Å in **2**, 2.6828(7) to 2.6880(6) Å in **3**, from 2.677(2) to 2.698(2) Å in **4** and from 2.6862(8) to 2.6937(8) Å in **5**. The chalcogen atoms cap each triangular face of the Re_6 octahedron. The Re−Q bonds range from 2.683(1) to 2.714(1) Å in **1**, from 2.5247(8) to 2.5275(8) Å in **2**, from 2.6927(5) to 2.6984(6) Å in **3**, from 2.688(2) to 2.701(3) Å in **4** and from 2.679(1) to 2.717(1) Å in **5**. Six cyanide ligands coordinate to rhenium atoms through carbon and stick out in pairs in a mutually perpendicular fashion. The Re−C distances range from 2.07(2) to 2.11(2) Å in **1**, from 2.08(1) to 2.104(9) Å in **2**, from 2.063(14) to 2.085(9) Å in **3**, from 2.03(3) to 2.18(3) Å in **4** and from 2.07(1) to 2.11(2) Å in **5**; the C−N distances range from 1.12(2) to 1.17(3) Å in **1**, from 1.15(1) to 1.16(2) Å in **2**, from 1.16(1) to 1.17(2) Å in **3**, from 1.10(4) to 1.22(4) Å in **4** and from 1.14(2) to 1.20(2) Å in **5**.

In the structure of **1** there are two crystallographically independent manganese cations. Each manganese atom is coordinated by two ethylenediamine molecules, which lie in the equatorial plane and occupy four coordination sites, with Mn−N distances ranging from 2.24(3) to 2.32(2) Å. The atoms coordinated in the axial positions differ for each Mn centre: Mn1 is coordinated by the nitrogen atom of a CN group of the cluster anion [Mn−N distance is 2.26(2) Å] and a water molecule, with an Mn−O length of 2.20(1) Å (Figure 1a), whereas the axial coordination sites of Mn2 (Figure 1b) are coordinated by two nitrogens of CN ligands from neighbouring cluster anions, with Mn−N(CN) distances of 2.23(1) Å and 2.25(2) Å, to form a polymeric zig-zag chain of composition $[\{Mn(H_2O)(en)_2\}\{Mn(en)_2\}Re_6Te_8(CN)_6]_\infty$ (Figure 2). The chains are neutral and are connected to each other by hydrogen bonds to solvate water molecules.

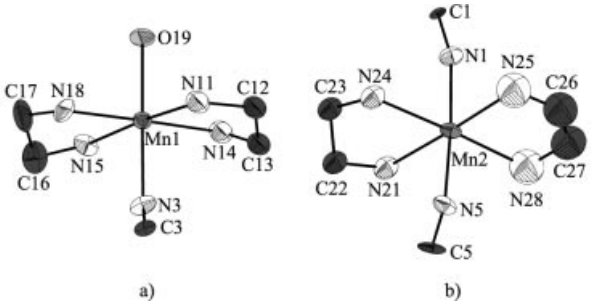

Figure 1. Ligand environment of Mn1 (a) and Mn2 (b) in **1**; displacement ellipsoids are drawn at the 30% probability level; all hydrogen atoms have been omitted for clarity

Compounds **2** and **3** are isostructural. In these compounds there are two crystallographically independent nickel cations. The Ni2 atom and the $[Re_6Q_8(CN)_6]$ clusters have crystallographically imposed *mmm* symmetry, while Ni1 and the Cl atoms have crystallographically imposed 2/*m* and 2*mm* symmetry, respectively. Ni2 is *trans*-coordinated by two nitrogen atoms of CN ligands from neighbouring cluster anions, with Ni2−N(CN) distances of 2.10(1) Å in **2** and 2.06(1) Å in **3**; the four remaining coordination sites are occupied by four molecules of ammonia, with Ni2−N(NH_3) distances of 2.12(2) Å in both compounds (Figure 3a). The Re−CN−Ni2−NC−Re interactions extend along the *a* axis to give infinite negatively charged linear $\{\cdots N{\equiv}C{-}[Re_6Q_8(CN)_4]{-}C{\equiv}N{-}Ni2{-}N{\equiv}C{-}[Re_6Q_8(CN)_4]{-}C{\equiv}N\cdots\}_\infty$ chains (Figure 4a). Ni1 forms the cationic complex *trans*-$[Ni(NH_3)_2(en)_2]^{2+}$ (Figure 3b). The Ni1−N(NH_3) distances are 2.183(8) Å in **2** and 2.187(8) Å in **3**, and the Ni1−N(en) distances are 2.109(6) Å in **2** and 2.108(6) Å in **3**. The structure also contains Cl^- anions surrounded by two $[Ni(NH_3)_2(en)_2]^{2+}$ complex cations [shortest Cl−N(en) distances are 3.41 Å in **2** and 3.47 Å in **3**]. The water molecules are situated near these Cl atoms. The shortest Cl−O distances are 3.15 Å in **2** and 3.27 Å in **3** and correspond to relatively strong Cl···H−O hydrogen bonds.

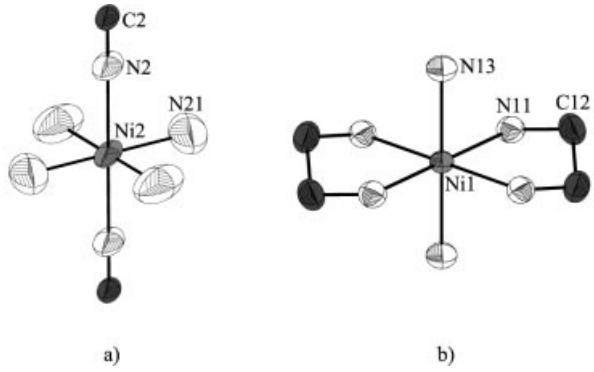

Figure 3. Ligand environment of Ni2 (a) and Ni1 (b) in **2** and **3** (only **2** is shown); displacement ellipsoids are drawn at the 50% probability level; all hydrogen atoms have been omitted for clarity

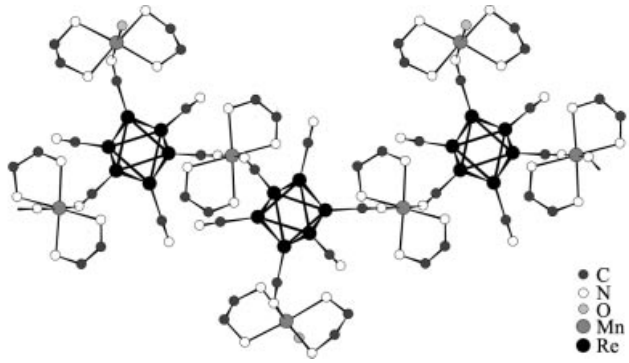

Figure 2. Fragment of the polymer chain $[\{Mn(H_2O)(en)_2\}\{Mn(en)_2\}Re_6Te_8(CN)_6]_\infty$; all hydrogen and tellurium atoms have been omitted for clarity

Infinite anionic chains are located in the same plane and are shifted relative to each other by half a unit cell translation along the *a* axis, as shown in Figure 4b. The distances between chains lying in adjacent planes are 11.822(5) Å in **2** and 12.1078(3) Å in **3**, and 8.078(3) Å in **2** and 8.2025(2) Å in **3** between chains lying in the same plane;

 © 2005 Wiley-VCH Verlag GmbH & Co. KGaA, Weinheim

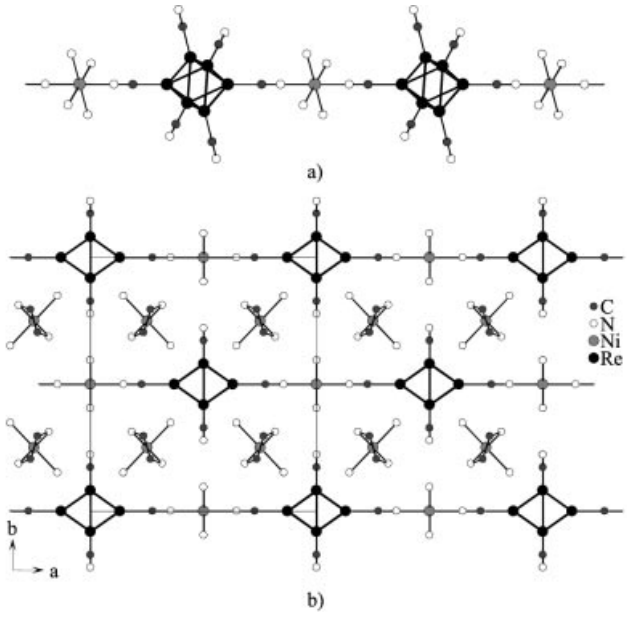

Figure 4. A fragment of the negatively charged linear $\{\cdots N{\equiv}C{-}[Re_6Q_8(CN)_4]{-}C{\equiv}N{-}Ni2{-}N{\equiv}C{-}[Re_6Q_8(CN)_4]{-}C{\equiv}N\cdots\}_\infty$ chain (a) and a view along [001] of the crystal packing in $[Ni(NH_3)_2(en)_2]_2[\{Ni(NH_3)_4\}Re_6Q_8(CN)_6]Cl_2{\cdot}nH_2O$ (Q = Se and $n = 2$ for **2;** Q = Te and $n = 1$ for **3**) (b); all hydrogen and chalcogen atoms, water molecules and Cl^- anions have been omitted for clarity

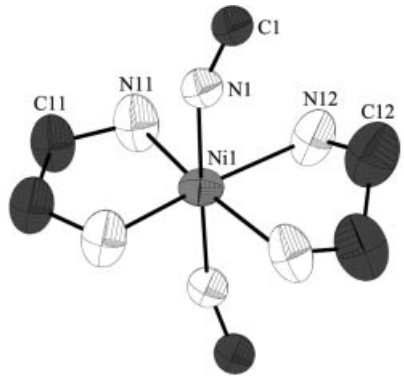

Figure 5. Ligand environment of Ni1 in **4**; displacement ellipsoids are drawn at the 50% probability level; all hydrogen atoms have been omitted for clarity

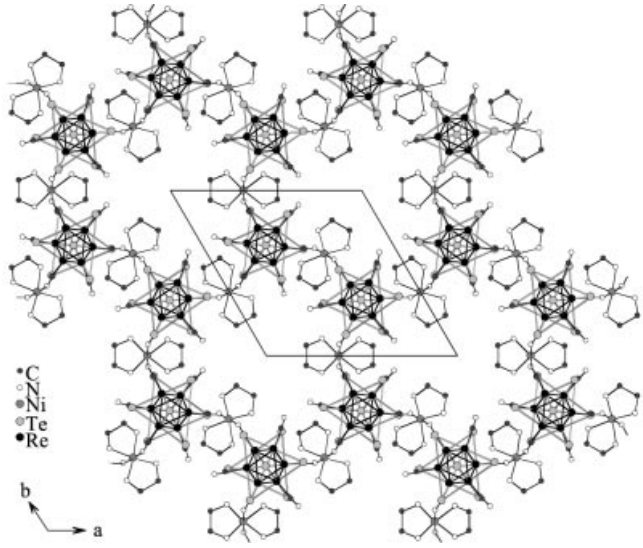

Figure 6. View along [001] of the crystal packing in $(NH_4)_2[\{Ni(en)_2\}_3\{Re_6Te_8(CN)_6\}_2]{\cdot}6H_2O$ (**4**); all hydrogen and tellurium atoms, ammonium cations and water molecules have been omitted for clarity

these values correspond to the *c* and *b*/2 cell parameters, respectively.

In the structure of compound **4** there is one crystallographically independent nickel cation that is located in a special position 3*f* (*x*, 0, 1/2; 0, *x*, 1/2; −*x*, −*x*, 1/2) and has crystallographically imposed C_2 symmetry. It is coordinated by two ethylenediamine molecules lying in the equatorial plane, with Ni−N(en) distances ranging from 2.09(3) to 2.16(3) Å. There are two independent rhenium atoms that belong to the same cluster core. The centre of the cluster anion coincides with the special crystallographic position 2*d* (1/3, 2/3, *z*; 2/3, 1/3, −*z*). Three CN groups from the same face of the Re_6 octahedron take part in the formation of negatively charged infinite wavy $[\{Ni(en)_2\}_3\{Re_6Te_8(CN)_6\}_2]^{2-}_{\infty\infty}$ layers by coordination to cationic $[Ni(en)_2]^{2+}$ units, which are coordinated by one more CN group from neighbouring clusters. The Ni−N(CN) distances are equal to 2.11(3) Å. Finally, the Ni atoms have an octahedral arrangement (Figure 5). In the structure the wavy layers lying in the *ab* plane are packed exactly above each other to form channels with approximate dimensions ranging from 4 Å to 7.2 Å (Figure 6).

Compound **5** contains one cluster anion built from six crystallographically independent rhenium atoms located in general positions and two crystallographically independent copper cations. Cu1 is located in a general position. Its coordination number is equal to five (4 + 1) resulting in the cationic complex $[Cu(NH_3)(en)_2]^{2+}$ (Figure 7a). Four coordination sites of Cu1 are occupied by two ethylenediamine molecules lying in the equatorial plane, with Cu1−N(en) distances in the range from 1.96(2) to 2.02(2) Å, and the fifth coordination site is occupied by ammonia, with a Cu1−N(NH_3) distance equal to 2.32(2) Å. Cu2 is located in the special position 2*c* (0, 1/2, 0; 1/2, 1/2, 1/2) and has imposed $\bar{1}$ symmetry. The coordination number of Cu2 is six (or 4 + 2). Four coordination sites of Cu2 are occupied by two ethylenediamine molecules lying in the equatorial plane, with Cu2−N(en) distances ranging from 2.00(2) to 2.05(2) Å, and the two axial coordination sites are occupied by nitrogen atoms of CN groups of neighbouring clusters, with Cu2−N(CN) distances equal to 2.59(2) Å (Figure 7b). Such a ligand environment of Cu2 results in anionic $[\{Cu(en)_2\}\{Re_6Te_8(CN)_6\}_2]^{6-}$ dimers (Figure 8a). The cationic complexes $[Cu(NH_3)(en)_2]^{2+}$ and cations Et_4N^+ compensate the negative charge of the $[\{Cu(en)_2\}\{Re_6Te_8(CN)_6\}_2]^{6-}$ anions. Inside the structure of $(Et_4N)_2[Cu(NH_3)(en)_2]_2[\{Cu(en)_2\}\{Re_6Te_8(CN)_6\}_2]{\cdot}2H_2O$ (Figure 8b) the anionic $[\{Cu(en)_2\}\{Re_6Te_8(CN)_6\}_2]^{6-}$ dimers adopt two orientations. One of these orientations lies nearly along the (b + c) direction, whereas the second

 © 2005 Wiley-VCH Verlag GmbH & Co. KGaA, Weinheim

orientation is symmetry related and is situated nearly along the (b − c) direction.

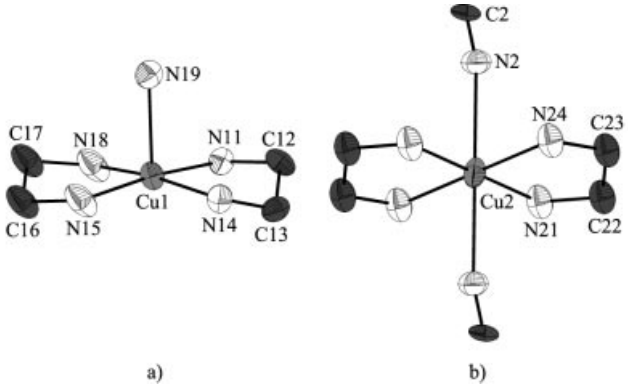

Figure 7. Ligand environment of Cu1 (a) and Cu2 (b) in **5**; displacement ellipsoids are drawn at the 30% probability level; all hydrogen atoms have been omitted for clarity

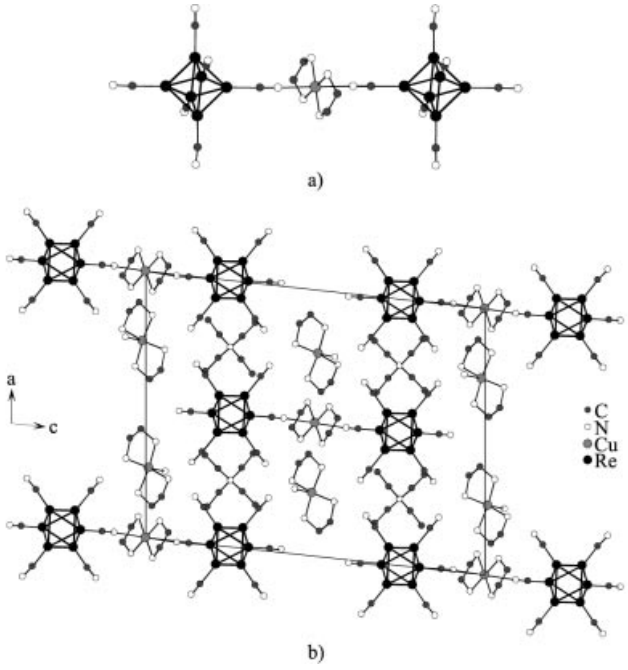

Figure 8. Structure of anionic dimer $[\{Cu(en)_2\}\{Re_6Te_8(CN)_6\}_2]^{6-}$ (a) and view along [010] of the crystal packing in $(Et_4N)_2[Cu(NH_3)(en)_2]_2[\{Cu(en)_2\}\{Re_6Te_8(CN)_6\}_2]\cdot 2H_2O$ (**5**) (b); all hydrogen and tellurium atoms and water molecules have been omitted for clarity

As was expected the use of ethylenediamine leads to a decrease in the overall number of M−NC−Re interactions and, hence, to a decrease in the dimensionality of the formed compounds compared to compounds reported earlier for $M^{2+}/[Re_6Q_8(CN)_6]^{4-}$ systems.[6−12] In general, the simultaneous presence of 3d transition metal cations and the chelating ligand ethylenediamine in solution generates different $[ML_{6-2x}(en)_x]^{2+}$ moieties, all of which can serve as building blocks.[27,28,33]

All the structures described here are based on the interaction of cationic $[M(en)_2]^{2+}$ moieties and $[Re_6Q_8(CN)_6]^{4-}$ (Q = Se, Te) anions. The different coordination of $[M(en)_2]^{2+}$ fragments by additional ligands, namely water, ammonia or nitrogen atoms from the cyano groups of the $[Re_6Q_8(CN)_6]^{4-}$ anion, leads to the structural diversity of the compounds. Compounds **1**−**3** have chain-like structures that differ in the binding modes between the cluster anions and metal centres. In **1** the cluster anion $[Re_6Te_8(CN)_6]^{4-}$ is coordinated by three $Mn(en)_2$ fragments (Figure 2), two of which in a *cis*-orientation relative to the Re_6 cluster core, form additional bonds with neighbouring cluster anions. Such binding leads to a zig-zag chain. The third coordinated $Mn(en)_2$ fragment is terminated by a water molecule.

In contrast to **1**, in isostructural **2** and **3** the nickel atoms are bound to *trans*-cyano groups of the anion, which leads to linear chains. Additionally, the nickel atoms are coordinated by four ammonia molecules. The $[Ni(NH_3)_2(en)_2]^{2+}$ cations serve as spacers and are located between the chains along with Cl^- anions, which adjust the charge balance in the structure. It is interesting that in the isomorphous compound $[Co(NH_3)_2(en)_2]_2[\{Co(en)_2\}Re_6Te_8(CN)_6]Cl_2\cdot H_2O$ the transition metal atoms in the polymeric chains are coordinated by ethylenediamine, not by ammonia.[28]

The inclusion of tetraethylammonium cations in **5** results in a change of connectivity in the structure. The structure does not contain infinite chains but only isolated anionic $[\{Cu(en)_2\}\{Re_6Te_8(CN)_6\}_2]^{6-}$ dimer complexes. The formation of such fragments can be described formally as cleavage of $\{\cdots N{\equiv}C{-}[Re_6Q_8(CN)_4]{-}C{\equiv}N{-}M{-}N{\equiv}C{-}[Re_6Q_8(CN)_4]{-}C{\equiv}N\cdots\}_\infty$ chains similar to those found in **2** and **3** due to insertion of the more voluminous Et_4N^+ cations (Figure 9). The influence of cation size on the dimensionality of cyano-bridged clusters has been reported previously.[15,34]

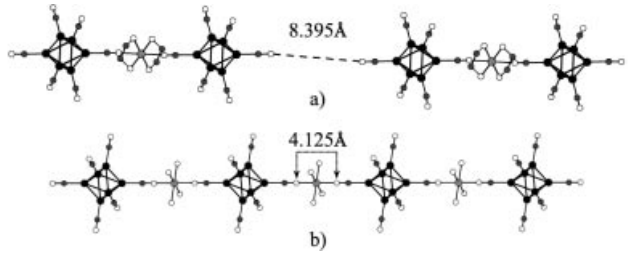

Figure 9. Arrangement of two anionic $[\{Cu(en)_2\}\{Re_6Te_8(CN)_6\}_2]^{6-}$ dimers in **5** (a) in comparison with the chain fragment $\{\cdots N{\equiv}C{-}[Re_6Te_8(CN)_4]{-}C{\equiv}N{-}Ni2{-}N{\equiv}C{-}[Re_6Te_8(CN)_4]{-}C{\equiv}N\cdots\}_\infty$ of compound **3** (b)

On the other hand, the use of Bu_4NBr during crystallisation in the Ni/en/$[Re_6Te_8(CN)_6]^{4-}$ system led to intriguing results: the formation of **4** with a two-dimensional framework. Although Bu_4N^+ was not found in the structure of **4**, the presence of Bu_4N^+ in solution is crucial for the formation of this compound, otherwise chain-like compound **3** is formed. In the structure **4** the corrugated $[\{Ni(en)_2\}_3\{Re_6Te_8(CN)_6\}_2]^{2-}_{\infty\infty}$ sheets are stacked exactly above each another. This stacking gives large accessible channels directed along the *c* axis. These channels have a variable profile with dimensions vary from about 4 Å to 7.2 Å based on the estimated van der Waals radii. The CH_2 groups of the ethylenediamine molecules coordinated to the

 © 2005 Wiley-VCH Verlag GmbH & Co. KGaA, Weinheim

nickel atoms form the narrow section of channels that separate large spherical cavities with a volume of 631 Å^3 (based on calculations performed with PLATON[35]). The cavities centered near the origin (0,0,0) are decorated by six nitrogen atoms from cyano groups of cluster anions. They are filled by solvate water molecules and ammonium cations for charge balance of the framework.

Conclusion

The use of the simplest chelating ligand — ethylenediamine — during co-crystallisation of $[Re_6Q_8(CN)_6]^{4-}$ (Q = Se, Te) with 3d transition metals has resulted in the structural diversity of the formed compounds.

Experimental Section

General: Elemental analyses for C, H, N and S (Carlo Erba 1106) were performed in the Laboratory of Microanalysis of the Institute of Organic Chemistry, Novosibirsk. IR spectra were measured on KBr disks with a Bruker IFS-85 Fourier spectrometer. The starting cluster compounds were synthesised as described previously: $K_4[Re_6Se_8(CN)_6]\cdot 3.5H_2O$ was prepared from polymeric $Re_6Se_8Br_2$;[3] $Cs_4[Re_6Te_8(CN)_6]\cdot 2H_2O$ was prepared by adding CsCl to an aqueous solution of the reaction product of polymeric Re_6Te_{15} with molten KCN.[5]

$[\{Mn(H_2O)(en)_2\}\{Mn(en)_2\}Re_6Te_8(CN)_6]\cdot 3H_2O$ (1): The reaction was carried out by layering a solution of $Cs_4[Re_6Te_8(CN)_6]\cdot 2H_2O$ (2.0 mg, 0.7 μmol) in water (1 mL) on top of a solution of $Mn(OAc)_2\cdot 4H_2O$ (7 mg, 0.03 mmol) and ethylenediamine (0.01 mL, 0.15 mmol) in glycerol (1 mL). After two weeks, dark red-brown crystals were obtained. These crystals were filtered off and dried on filter paper. The yield was quantitative based on Re. IR: ν_{CN} = 2052s, 2098s and 2112m cm^{-1}. $C_{14}H_{40}Mn_2N_{14}O_4Re_6Te_8$ (2716.5): calcd. C 6.19, H 1.48, N 7.22; found C 6.04, H 1.52, N 7.13.

$[Ni(NH_3)_2(en)_2]_2[\{Ni(NH_3)_4\}Re_6Se_8(CN)_6]Cl_2\cdot 2H_2O$ (2): In a similar manner, layering a solution of $K_4[Re_6Se_8(CN)_6]\cdot 3.5H_2O$ (2.0 mg, 0.94 μmol) in aqueous ammonia (1 mL) on top of a solution of $NiCl_2\cdot 6H_2O$ (7 mg, 0.03 mmol) and ethylenediamine (0.002 mL, 0.03 mmol) in glycerol (1 mL) afforded dark red-brown crystals. The yield was quantitative based on Re. $C_{14}H_{60}Cl_2N_{22}Ni_3O_2Re_6Se_8$ (2564.7): calcd. C 6.56, H 2.36, N 12.02; found C 6.61, H 2.24, N 11.97.

$[Ni(NH_3)_2(en)_2]_2[\{Ni(NH_3)_4\}Re_6Te_8(CN)_6]Cl_2\cdot H_2O$ (3): This compound was synthesised as for **2** by substituting $Cs_4[Re_6Te_8(CN)_6]\cdot 2H_2O$ (2.0 mg, 0.7 μmol) for $K_4[Re_6Se_8(CN)_6]\cdot 3.5H_2O$. The resultant dark red-brown crystals were filtered off and dried on filter paper. The yield was quantitative based on Re. $C_{14}H_{58}Cl_2N_{22}Ni_3ORe_6Te_8$ (2935.8): calcd. C 5.73, H 1.99, N 10.50; found C 5.73, H 1.87, N 10.44.

$(NH_4)_2[\{Ni(en)_2\}_3\{Re_6Te_8(CN)_6\}_2]\cdot 6H_2O$ (4): A solution of $NiCl_2\cdot 6H_2O$ (3.33 mg, 0.014 mmol) and ethylenediamine (1.9 μL, 0.028 mmol) in aqueous ammonia (0.5 mL) was added to a solution of $Cs_4[Re_6Te_8(CN)_6]\cdot 2H_2O$ (20 mg, 7.0 μmol) and Bu_4NBr (11.28 mg, 0.035 mmol) in aqueous ammonia (10 mL). The resultant solution was kept in a tightly closed vessel at room temperature for two weeks, during which time dark red-brown crystals formed. These crystals were filtered off and dried on filter paper. The yield was quantitative based on Re. IR: ν_{CN} = 2051s, 2091w, 2119m and 2133w cm^{-1}. $C_{12}H_{34}N_{13}Ni_{1.5}O_3Re_6Te_8$ (2634.57): calcd. C 5.47, H 1.30, N 6.91; found C 5.60, H 1.21, N 6.84.

$(Et_4N)_2[Cu(NH_3)(en)_2]_2[\{Cu(en)_2\}\{Re_6Te_8(CN)_6\}_2]\cdot 2H_2O$ (5): A solution of $CuCl_2\cdot 2H_2O$ (12 mg, 0.07 mmol) and ethylenediamine (0.047 mL, 0.7 mmol) in aqueous ammonia (1.5 mL) was added to

Table 1. Crystal data and structure refinements for **1**−**5**

	1	**2**	**3**	**4**	**5**
Empirical formula	$C_{14}H_{40}Mn_2N_{14}O_4Re_6Te_8$	$C_{14}H_{60}Cl_2N_{22}Ni_3O_2Re_6Se_8$	$C_{14}H_{58}Cl_2N_{22}Ni_3ORe_6Te_8$	$C_{12}H_{34}N_{13}Ni_{1.5}O_3Re_6Te_8$	$C_{20}H_{49}Cu_{1.5}N_{14}ORe_6Te_8$
Formula mass	2716.48	2564.68	2935.79	2634.57	2735.06
Crystal system	monoclinic	monoclinic	monoclinic	trigonal	monoclinic
Space group	$P2_1/n$	$Cmmm$	$Cmmm$	$P321$	$P2/n$
a [Å]	10.7940(1)	14.408(5)	14.3725(3)	15.794(5)	19.445(5)
b [Å]	16.8011(3)	16.155(5)	16.4050(3)		11.534(5)
c [Å]	24.6467(5)	11.822(5)	12.1078(3)	10.646(5)	24.870(5)
β [°]	92.055(1)				96.328(5)
V [Å^3]	4466.8(1)	2752(2)	2854.8(1)	2300(2)	5544(3)
Z	4	2	2	2	4
$\rho_{calcd.}$ [g·cm^{-3}]	3.957	3.095	3.347	3.755	3.298
Crystal size [mm]	0.02×0.03×0.06	0.20 × 0.28 × 0.35	0.12 × 0.13 × 0.16	0.03 × 0.04 × 0.07	0.05 × 0.05 × 0.15
θ_{max} [°]	27.495	35.005	34.945	27.079	30.040
Exp. hkl limits	$-14 \le h \le 13$ $-19 \le k \le 21$ $-31 \le l \le 30$	$-23 \le h \le 23$ $-26 \le k \le 20$ $-19 \le l \le 18$	$0 \le h \le 23$ $-26 \le k \le 26$ $-15 \le l \le 19$	$-20 \le h \le 20$ $-20 \le k \le 20$ $-12 \le l \le 13$	$-27 \le h \le 27$ $-16 \le k \le 15$ $-27 \le l \le 35$
Refl. collected/unique	49870/10235	25142/3338	26490/3451	27676/3402	67318/16189
$R_{(int)}$	0.06	0.13	0.06	0.10	0.07
μ [cm^{-1}]	218.91	195.66	177.65	213.25	177.62
Max./min. transm.	0.51/0.27	0.11/0.01	0.25/0.14	0.53/0.45	0.51/0.21
Refined parameters/ refl. with $F_o \ge 4\sigma(F)$	351/4350	88/1776	89/1723	83/1207	411/6985
$R(F)$[a]/$R_w(F^2)$[b]	0.0295/0.0624	0.0336/0.0556	0.0310/0.0481	0.0364/0.0485	0.0441/0.0718
$\Delta\rho_{max.}/\Delta\rho_{min.}$ [e·Å^{-3}]	1.50/−1.71	2.22/−2.83	3.09/−2.34	2.97/−2.83	4.72/−3.13

[a] $R(F) = \Sigma||F_o| - |F_c||/\Sigma|F_o|$ for $F_o^2 > 2\sigma(F_o^2)$. [b] $R_w(F_o^2) = \{\Sigma[w(F_o^2 - F_c^2)^2]/\Sigma wF_o^4\}^{1/2}$.

 © 2005 Wiley-VCH Verlag GmbH & Co. KGaA, Weinheim

a solution of $Cs_4[Re_6Te_8(CN)_6]\cdot 2H_2O$ (20 mg, 7.0 μmol) and Et_4NBr (7.35 mg, 0.035 mmol) in aqueous ammonia (10 mL). The resultant solution was kept in a tightly closed vessel at room temperature for two weeks, during which time dark red-brown crystals formed. These crystals were filtered off and dried on filter paper. The yield was quantitative based on Re. IR: ν_{CN} = 2074s, 2103m and 2141m cm^{-1}. $C_{20}H_{49}Cu_{1.5}N_{14}ORe_6Te_8$ (2735.1): calcd. C 8.78, H 1.81, N 7.17; found C 8.83, H 1.62, N 7.15.

X-ray Crystallographic Study: Selected single crystals were mounted, as usual, on the top of a glass fibre. Diffraction data were collected at room temperature (293 K) with a Nonius Kappa CCD diffractometer with graphite-monochromated Mo-K_α radiation (λ = 0.71073 Å). Experimental details for complexes **1**−**5** are given in Table 1. The data processing was performed by the Kappa CCD analysis software;[36] the lattice constants were refined by least-square refinement. Absorption corrections based on the crystal shapes were applied to the data sets with the ANALYTICAL program[37,38] for all structures. Structure solution and refinement: Complexes **1** and **5** crystallised in the monoclinic system. The systematic absences led to the $P2_1/n$ *and* $P2/n$ space groups, respectively. For **2** and **3**, the observed systematic absences suggested an orthorhombic crystal system with a *C* lattice. Among the possible space groups, the refinement procedure allowed us to determine unambiguously the *Cmmm* space group. Complex **4** crystallised in the trigonal system with a *P* lattice. The systematic absences led to the *P*321 space group. The structures were solved by direct methods (SIR97 program[39]) combined with Fourier-difference syntheses and refined against *F* using reflections with $I > 3\sigma(I)$ (CRYSTALS program[40]). All atoms were refined anisotropically. CCDC-234060 to -234064 (**1**−**5**) contain the supplementary crystallographic data for this paper. These data can be obtained free of charge via www.ccdc.cam.ac.uk/conts/retrieving.html (or from the Cambridge Crystallographic Data Centre (CCDC), 12 Union Road, Cambridge, CB2 1EZ, UK; Fax: + 44-1223-336-033; or deposit@ccdc.cam.ac.uk).

Acknowledgments

This work was supported by INTAS (grant no. INTAS-00-00689) and the Russian Foundation for Basic Research (grant no. 02-03-32264).

[1] A. Slougui, Y. V. Mironov, A. Perrin, V. E. Fedorov, *Croat. Chim. Acta* **1995**, *68*, 885−890.
[2] Y. V. Mironov, A. V. Virovets, V. E. Fedorov, N. V. Podberezskaya, O. V. Shishkin, Y. T. Struchkov, *Polyhedron* **1995**, *14*, 3171−3173.
[3] N. G. Naumov, A. V. Virovets, N. V. Podberezskaya, V. E. Fedorov, *J. Struct. Chem. (Engl. Trans.)* **1997**, *38*, 857−862.
[4] Y. V. Mironov, J. A. Cody, T. E. AlbrechtSchmitt, J. A. Ibers, *J. Am. Chem. Soc.* **1997**, *119*, 493−498.
[5] H. Imoto, N. G. Naumov, A. V. Virovets, T. Saito, V. E. Fedorov, *J. Struct. Chem. (Engl. Trans.)* **1998**, *39*, 720−727.
[6] N. G. Naumov, A. V. Virovets, M. N. Sokolov, S. B. Artemkina, V. E. Fedorov, *Angew. Chem. Int. Ed.* **1998**, *37*, 1943−1945.
[7] N. G. Naumov, A. V. Virovets, V. E. Fedorov, *Inorg. Chem. Commun.* **2000**, *3*, 71−72.
[8] L. G. Beauvais, M. P. Shores, J. R. Long, *J. Am. Chem. Soc.* **2000**, *122*, 2763−2772.
[9] N. G. Naumov, M. N. Sokolov, H. Imoto, T. Saito, V. E. Fedorov, *J. Struct. Chem. (Engl. Trans.)* **2001**, *42*, 326−330.
[10] N. G. Naumov, D. V. Soldatov, J. A. Ripmeester, S. B. Artemkina, V. E. Fedorov, *Chem. Commun.* **2001**, 571−572.
[11] M. V. Bennett, L. G. Beauvais, M. P. Shores, J. R. Long, *J. Am. Chem. Soc.* **2001**, *123*, 8022−8032.
[12] V. E. Fedorov, N. G. Naumov, Y. V. Mironov, A. V. Virovets, S. B. Artemkina, K. A. Brylev, S. S. Yarovoi, O. A. Efremova, U. H. Peak, *J. Struct. Chem. (Engl. Trans.)* **2002**, *43*, 669−684.
[13] N. G. Naumov, A. V. Virovets, Y. I. Mironov, S. B. Artemkina, V. E. Fedorov, *Ukr. Khim. Zh.* **1999**, *65*, 21−27; *Chem. Abstr.* **2000**, *132*, 58327.
[14] M. V. Bennett, M. P. Shores, L. G. Beauvais, J. R. Long, *J. Am. Chem. Soc.* **2000**, *122*, 6664−6668.
[15] N. G. Naumov, S. B. Artemkina, A. V. Virovets, V. E. Fedorov, *Solid State Sci.* **1999**, *1*, 473−482.
[16] N. G. Naumov, S. B. Artemkina, A. V. Virovets, V. E. Fedorov, *J. Solid State Chem.* **2000**, *153*, 195−204.
[17] S. B. Artemkina, N. G. Naumov, A. V. Virovets, O. Oeckler, A. Simon, S. B. Erenburg, N. V. Bausk, V. E. Fedorov, *Eur. J. Inorg. Chem.* **2002**, 1198−1202.
[18] H. Yuge, T. Iwamoto, *J. Chem. Soc., Dalton Trans.* **1994**, 1237−1242.
[19] H. Yuge, A. Mamada, M. Asai, S. Nishikiori, T. Iwamoto, *J. Chem. Soc., Dalton Trans.* **1995**, 3195−3205.
[20] M. S. ElFallah, E. Rentschler, A. Caneschi, R. Sessoli, D. Gatteschi, *Angew. Chem. Int. Ed. Engl.* **1996**, *35*, 1947−1949.
[21] H. Z. Kou, D. Z. Liao, P. Cheng, Z. H. Jiang, S. P. Yan, G. L. Wang, X. K. Yao, H. G. Wang, *J. Chem. Soc., Dalton Trans.* **1997**, 1503−1506.
[22] P. V. Bernhardt, M. Martinez, *Inorg. Chem.* **1999**, *38*, 424−425.
[23] H. Z. Kou, S. Gao, W. M. Bu, D. Z. Liao, B. Q. Ma, Z. H. Jiang, S. P. Yan, Y. G. Fan, G. L. Wang, *J. Chem. Soc., Dalton Trans.* **1999**, 2477−2480.
[24] H. Z. Kou, S. Gao, B. Q. Ma, D. Z. Liao, *Chem. Commun.* **2000**, 1309−1310.
[25] E. Colacio, J. M. DominguezVera, M. Ghazi, R. Kivekas, J. M. Moreno, A. Pajunen, *J. Chem. Soc., Dalton Trans.* **2000**, 505−509.
[26] M. Ohba, H. Okawa, *Coord. Chem. Rev.* **2000**, *198*, 313−328.
[27] Y. V. Mironov, V. E. Fedorov, I. Ijjaali, J. A. Ibers, *Inorg. Chem.* **2001**, *40*, 6320−6323.
[28] K. A. Brylev, Y. V. Mironov, N. G. Naumov, V. E. Fedorov, J. A. Ibers, *Inorg. Chem.* **2004**, *43*, 4833−4838.
[29] K. A. Brylev, N. G. Naumov, G. Peris, R. Llusar, V. E. Fedorov, *Polyhedron* **2003**, *22*, 3383−3387.
[30] Y. Kim, S. M. Park, W. Nam, S. J. Kim, *Chem. Commun.* **2001**, 1470−1471.
[31] Y. Kim, S. M. Park, S. J. Kim, *Inorg. Chem. Commun.* **2002**, *5*, 592−595.
[32] Y. Kim, S. K. Choi, S. M. Park, W. Nam, S. J. Kim, *Inorg. Chem. Commun.* **2002**, *5*, 612−615.
[33] K. R. Dunbar, R. A. Heintz, *Prog. Inorg. Chem.* **1997**, *45*, 283−391, and references therein.
[34] N. G. Naumov, A. V. Virovets, S. B. Artemkina, D. Y. Naumov, J. A. K. Howard, V. E. Fedorov, *J. Solid State Chem.* **2004**, *177*, 1896−1904.
[35] A. L. Spek, *Acta Crystallogr., Sect. A* **1990**, *46*, C34.
[36] Nonius, *COLLECT, DENZO, SCALEPACK, SORTAV: KappaCCD program Package*, Nonius B. V., Delft, The Netherlands, **1999**.
[37] J. de Meulenaar, H. Tompa, *Acta Crystallogr., Sect. A* **1965**, *19*, 1014−1018.
[38] C. Katayama, *Acta Crystallogr., Sect. A* **1986**, *42*, 19−23.
[39] A. Altomare, M. C. Burla, M. Camalli, G. L. Cascarano, C. Giacovazzo, A. Guagliardi, A. G. G. Moliterni, G. Polidori, R. Spagna, *J. Appl. Crystallogr.* **1999**, *32*, 115−119.
[40] D. J. Watkin, C. K. Prout, J. R. Carruthers, P. W. Betteridge, *CRYSTALS Issue 11*, Chemical Crystallography Laboratory, Oxford, UK, **1999**.

Received May 5, 2004
Early View Article
Published Online December 6, 2004

 © 2005 Wiley-VCH Verlag GmbH & Co. KGaA, Weinheim

High-Field EPR Study of Frozen Aqueous Solutions of Iron(III) Citrate Complexes

Frédéric Biaso,[a] Carole Duboc,[b] Bernard Barbara,[c] Guy Serratrice,[a] Fabrice Thomas,[a] Denis Charapoff,[a] and Claude Béguin*[a]

Keywords: High-field EPR spectroscopy / Iron / Coordination chemistry / Citrate ligand / Tripodal ligand / Spin crossover

High-field electron paramagnetic resonance spectra have been measured for frozen aqueous solutions of Fe^{III} citrate at acidic and neutral pH values. At high fields (up to 12 T) and high frequencies (95, 190 and 285 GHz), fine-structure peaks due to resonance between Kramers doublets (±1/2, ±3/2, ±5/2) of an $S = 5/2$ species can be observed when the experiments are performed at high temperatures. A full-matrix diagonalisation approach has been used to derive the spin-Hamiltonian parameters for the $S = 5/2$ spin state. In acidic media (pH = 2), the spacing of the fine structure reveals that the value of the axial zero-field splitting (ZFS) parameter D is -0.12 cm^{-1} without rhombicity. A small but significant g anisotropy can be observed which depends slightly on the frequency and the temperature ($g_x = 2.014$, $g_y = 2.014$ and $g_z = 1.983$, at 60 K and 285 GHz). In neutral media (pH = 6), complete rhombic HF-EPR spectra were observed with a fivefold lower $|D|$ value (0.024 cm^{-1}) and $E = 0.008$ cm^{-1}. A satisfactory simulation of the experimental data was obtained with a g value equal to 2.00. The different ZFS parameters obtained under neutral and acidic conditions are discussed in terms of the symmetry of the complex. At low temperatures, a spin transition from 5/2 to 1/2 occurs at all frequencies. The transition temperature is pH- and field-dependent. A model including magnetoelasticity has been suggested in order to interpret the field dependency of the spin transition observed for the two systems.
(© Wiley-VCH Verlag GmbH & Co. KGaA, 69451 Weinheim, Germany, 2005)

Introduction

Citric acid is widely known for its abundance in biological fluids and plays key roles in the biochemical processes of bacteria, plants, animals and humans. Its structure, with three carboxylate groups and one hydroxy group, bestows on it unique chemical properties which render it essential in biological media.[1] Besides participation in the Krebs cycle[2] and acting as a component in a number of metalloenzyme active sites,[3] citric acid is a target ligand of a large number of trace metal ions found in biological fluids. Its chelating ability, exemplified in a multitude of coordination modes, plays an important role in metal solubilisation, mobilisation and bioavailability in biological media.[1,4] Among these metal ions, we have a particular interest in ferric ions.[5−7] In humans, citrate is present in blood plasma at a concentration of about 0.1 mM and is believed to be one of the major components of nontransferrin-bound iron (NTBI).[8a,9] It has been proposed that NTBI in the plasma of iron-overloaded patients exists largely in the form of complexes with citrate.[10] Citrate has also been proposed as a component of the cytosolic (or intracellular) iron pool known as the "Labile Iron Pool" (LIP). Other ligands involved in the LIP (which is also called the chelatable pool, transit pool or low molecular weight iron pool) could be AMP, ATP, pyrophosphate, amino acids or nucleoside phosphates.[8b,11] In vivo approaches have been developed to obtain information about the concentration and the nature of this LIP.[8] For a correct interpretation of the biological processes related to the Fe^{III} citrate system, it is necessary to obtain more insight, using noninvasive approaches, into the nature of the chemical species of this system present in aqueous solutions. The dependence of the system on the experimental conditions (stoichiometry, solvent, pH, added ligand or bases etc.) could therefore be easily studied.

High field electron paramagnetic resonance (HF-EPR) experiments performed on aqueous solutions of Fe^{III} citrate should be a good in vitro noninvasive approach. At high frequencies (95, 190 and 285 GHz, i.e. high energy radiation of ca. 3−10 cm^{-1}) and high fields (up to 12 T), we could directly observe EPR resonances between the energy levels. The splitting of these levels depends on the Zero-Field Splitting (ZFS) parameters (Kramers doublets) and on the Zeeman effect. At high fields, the Zeeman interaction is

[a] Institut de Chimie Moléculaire de Grenoble, Laboratoire de Chimie Biomimétique, LEDSS, UMR-CNRS 5616, Université Joseph Fourier,
B. P. 53, 38041 Grenoble, Cedex 9, France
Fax: (internat.) + 33-4-76514836
E-mail: Claude.Beguin@ujf-grenoble.fr
[b] High Magnetic Field Laboratory of Grenoble, HMFL, CNRS-MPI UPR 5021,
B. P. 166, 38042 Grenoble, Cedex 9, France
[c] Laboratoire Louis Néel, CNRS-LLN UPR 5051,
B. P. 166, 38042 Grenoble, Cedex 9, France
Supporting information for this article is available on the WWW under http://www.eurjic.org or from the author.

dominant compared with the ZFS interaction. As a consequence, the ZFS parameters could be determined much more precisely than with conventional X-band EPR spectroscopy (9.4 GHz).[12] By performing measurements at high frequencies, the resonance positions of a Kramer transition may be tracked in order to determine the anisotropy of the *g* tensor even if it is weak (ranging between 1.950 and 2.040 in our case). This might lead to a considerably improved understanding of the symmetries and electronic structures of these biologically relevant Fe^{III} complexes.

The major aim of this study was to measure the ZFS parameters of mononuclear Fe^{III} citrate complexes in aqueous solutions and to find a correlation between the ZFS and the geometry around the iron. Another aim was to confirm, for these experimental conditions, the mononuclear structures of these complexes since the reported coordination chemistry of ferric citrate remains sketchy.[8] The complexes were obtained from solutions where citrate was in excess of the ferric ions (20:1 as respective molar ratio) at two different pH levels. We studied the anions **1** (at pH = 1.95) and **2** (at pH = 6.2) with Na^+ as the counterion. The protonation states of these chemical species cannot be obtained by UV/Vis spectrophotometry or by potentiometric titration. We believe, however, from comparisons with literature data (vide infra), that the structure of **1** is $[Fe(HCit)(H_2Cit)]^{2-}$. Complex **2** has been previously identified using electrospray mass spectrometry as having the structure $[Fe(HCit)(Cit)]^{4-}$ and this was confirmed by X-ray analysis (where Cit is the completely deprotonated citric acid) as shown in Figure 1.[13]

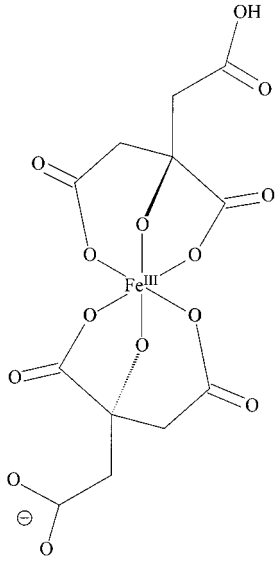

Figure 1. Schematic representation of the anion $[Fe(HCit)(Cit)]^{3-}$

Results

1. High-Field EPR Spectra of 1 and 2 at 60K

The 60 K HF-EPR spectra of **1** and **2**, at frequencies ranging between 95 and 285 GHz, are shown in Figures 2 and 3, respectively. They have been simulated using the spin-Hamiltonian parameters reported in Table 1 (see Exp. Sect. for details). Compound **1** exhibits purely axial symmetry with a *D* value of $|0.12|$ cm^{-1}. The values of the Landé factor vary slightly as a function of the frequency (small increase of $g_\perp$ and small decrease of $g_{//}$ when the frequency decreases, Table 2). All the transitions are shown in Figure 2 with their interpretations using energy level diagrams (e−f in Figure 2). $\Delta M_S = 2$ transitions centred at 1.75 T for 95 GHz can also be recalculated from the energy level diagrams (see d−f in Figure 2).

The negative sign of *D* was determined by careful examination of the intensities of the transitions as a function of temperature (from 20 to 60 K). At 285 GHz, when the temperature increases, the intensities of the [5/2,1/2> to 5/2,3/2>]$_{//}$ and [5/2,1/2> to 5/2,3/2>]$_\perp$ transitions, located at 10.52 T and 9.98 T, respectively, increase, while that of the 5/2,−3/2>$_\perp$ to 5/2,−1/2>$_\perp$ transition decreases at 10.23 T. This agrees with the energy level diagram shown on the right of Figure 2.

For compound **2**, both the high field (Figure 3 and Figure SI1 in the Supporting Information; for Supporting Informations see also the footnote on the first page of this article) and X-band EPR spectra (data not shown) are rhombic. The experimental and simulated 285 GHz EPR spectra recorded at 60 K are shown in Figure 3. At this frequency, the EPR spectrum is constrained between 10.0 and 10.5 T in agreement with a magnitude of *D* five times smaller than that for compound **1** ($|D| = 0.024$ cm^{-1}, with $|E|$ equal to 0.008 cm^{-1}; $\lambda = |E/D| = 1/3$). Since the zfs tensor is completely rhombic, the sign of D has no significance. The different transitions of the $S = 5/2$ paramagnet with their interpretations using energy level diagrams are shown in the Supporting Information (SI1).

2. Evolution of the High-Field EPR Spectra of 1 and 2 as a Function of Temperature from 60 to 5 K

The 285 GHz HF-EPR spectra were found to be temperature-dependent in the 5 to 60 K range (Figure 4) for compound **1** and between 5 and 30 K for compound **2** (Figure SI2 in the Supporting Information). At 5 K, the $S = 5/2$ spectrum was not observed. Instead, an axial $S = 1/2$ signal dominates the spectra of **1** and **2**. The $S = 1/2$ spectra are characterised by a very large line width ($w_{1/2} = 0.5$ T) suggesting a much higher relaxation rate of the $S = 1/2$ species than for the $S = 5/2$ species. However, the line widths of each spin state for compounds **1** and **2** are similar at all frequencies indicating that the frequency has no effect on the relaxation rate of the different species. The $S = 1/2$ signals for compounds **1** and **2** were simulated (see Exp. Sect.) with a small *g* anisotropy in the perpendicular region of the spectra (Table 3). The differences in relaxation rates between the $S = 5/2$ and the $S = 1/2$ spectra are so high that their relative contribution to the spectra could not be precisely obtained. Therefore, it was difficult to evaluate the critical temperature (i.e. T_c, the transition temperature where the molar fractions of the two spin states are equal). However, Figure 4 and SI2 show that the spin conversion is

 © 2005 Wiley-VCH Verlag GmbH & Co. KGaA, Weinheim

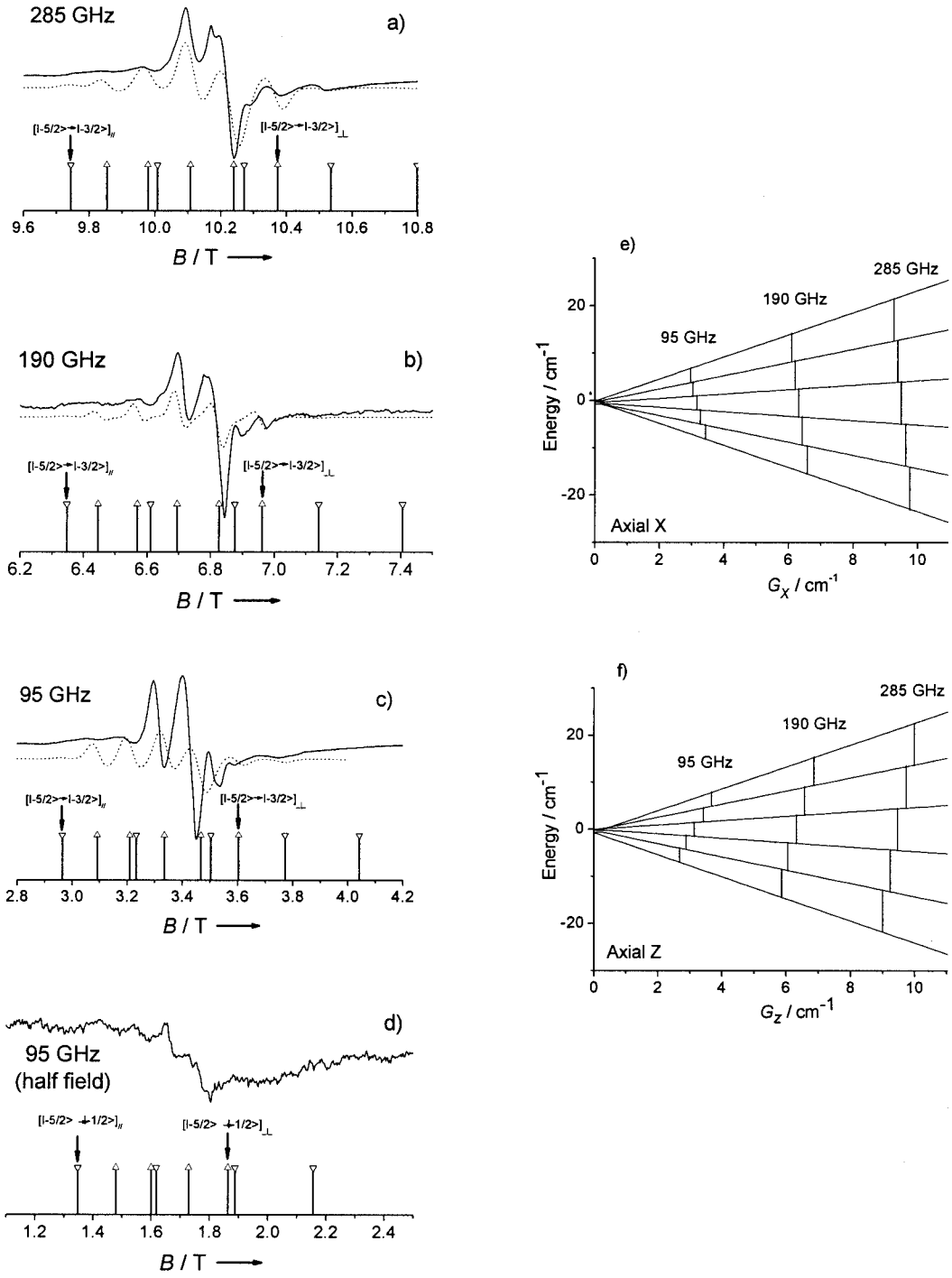

Figure 2. Experimental (bold lines) and simulated (dotted lines, with $D = -0.12$ cm^{-1} and g_x, g_y and g_z according to Table 2) HF-EPR spectra of compound **1** recorded at 60 K and at 285 (a), 190 (b) and 95 GHz (c and d); the assignments of the different transitions are represented as sticks (// parallel and ⊥ perpendicular); in the right-hand part, energy levels calculated for the axial spin-Hamiltonian (see Exp. Sect.) as a function of G_q ($g_q\beta B_o$) are shown; the expected resonances at 95, 190 and 285 GHz are indicated by vertical bars (e) for G_x and (f) for G_z

not abrupt for **1** and **2** but they do not show the presence of a hysteresis loop around T_c.

In Figure 5, the frequency dependence of the HF-EPR spectra of compound **1** is shown at 12.5 K. The $S = 5/2$ component dominates the spectrum with a minor $S = 1/2$ component at 95 GHz, whereas the reverse is true at 285 GHz with a major contribution to the spectrum from the $S = 1/2$ species. This reveals that T_c increases as the field increases. Another way to illustrate this phenomenon is to look at HF-EPR spectra recorded at different frequencies and at different temperatures which appear with similar shapes as shown in Figure 6. At the particular tem-

 © 2005 Wiley-VCH Verlag GmbH & Co. KGaA, Weinheim

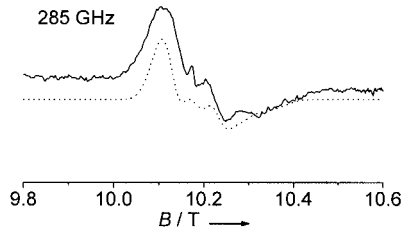

Figure 3. Experimental and simulated HF-EPR spectra for compound **2** at 60 K and at 285 GHz

peratures of 5.0, 9.0 and 12.5 K for 95, 190 and 285 GHz, respectively, the relative intensities of the signals corresponding to the two spin states appear almost equivalent. Thus, these temperatures can be an estimate of the T_c at each frequency, demonstrating that T_c increases almost linearly with the external magnetic field (Figure SI3, Supp. Inf.).

At 285 GHz, the estimate of T_c for compound **2** is much lower than for compound **1** since the $S = 5/2$ spectrum can be observed even at 5 K.

Table 1. Energy matrix of 6 × 6 elements for the $S = 5/2$ spin state characterised by a rhombic zero-field splitting with an external magnetic field B_0, oriented along the molecular axis of the complex, according to the Cartesian components B_x, B_y and B_z; the notations are $G_z = \beta g_z B_z$, $z = G_x + iG_y$ and $z^* = G_x - iG_y$ with $G_x = \beta g_x B_x$ and $G_y = \beta g_y B_y$; all parameters (D, E, G_x, G_y and G_z) have to be treated with the same energy unit (cm^{-1})

M_s	|+5/2>	|+3/2>	|+1/2>	|−1/2>	|−3/2>	|−5/2>
<+5/2|	$10/3D + 5/2G_z$	$\sqrt{5/2}\ z^*$	$\sqrt{10}\ E$	0	0	0
<+3/2|	$\sqrt{5/2}\ z$	$-2/3D + 3/2G_z$	$\sqrt{2}\ z^*$	$3\sqrt{2}\ E$	0	0
<+1/2|	$\sqrt{10}\ E$	$\sqrt{2}\ z$	$-8/3D + 1/2G_z$	$3/2\ z^*$	$3\sqrt{2}\ E$	0
<−1/2|	0	$3\sqrt{2}\ E$	$3/2\ z$	$-8/3D - {}^1/_2G_z$	$\sqrt{2}\ z^*$	$\sqrt{10}\ E$
<−3/2|	0	0	$3\sqrt{2}\ E$	$\sqrt{2}\ z$	$-2/3D - 3/2G_z$	$\sqrt{5/2}\ z^*$
<−5/2|	0	0	0	$\sqrt{10}\ E$	$\sqrt{5/2}\ z$	$10/3D - 5/2G_z$

Table 2. ZFS parameters and g factors of the high-spin Fe^{III} complexes **1** (pH = 2.0) and **2** (pH = 6.2) at 60 K

pH	Frequency [GHz]	D [cm^{-1}]	E [cm^{-1}]	λ	g_x	g_y	g_z
2.0	285	− 0.122	0	0	2.014	2.014	1.983
2.0	190	− 0.122	0	0	2.026	2.026	1.975
2.0	95	− 0.122	0	0	2.030	2.030	1.939
6.2	285	± 0.024	0.008	0.33	2.015	1.990	1.985

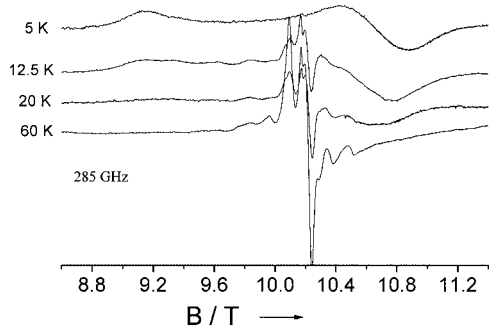

Figure 4. Experimental HF-EPR spectra of compound **1** at 285 GHz as a function of temperature (from 5 to 60 K)

Table 3. g factors of the low-spin Fe^{III} complex **1** as a function of frequency and of the low-spin Fe^{III} complex **2**

pH	Frequency [GHz]	g_x	g_y	g_z
2.0	285	1.850	1.915	2.370
2.0	190	1.875	1.915	2.225
6.2	285	1.870	1.910	2.245

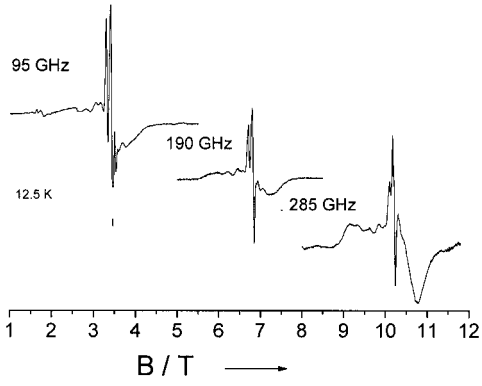

Figure 5. Experimental HF-EPR spectra of compound **1** at 12.5 K as a function of frequency (95, 190 and 285 GHz)

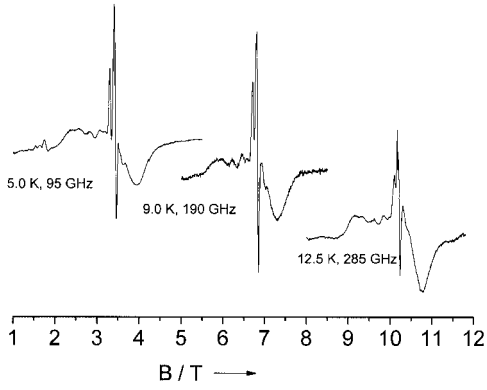

Figure 6. Experimental HF-EPR spectra of compound **1** at 95 GHz (5 K), 190 GHz (9 K) and 285 GHz (12.5 K)

 © 2005 Wiley-VCH Verlag GmbH & Co. KGaA, Weinheim

Discussion

1. Comparison of the Zero-Field Splitting Parameters with Literature Data

Values of ZFS parameters for high-spin Fe^{III} complexes have been reported in the literature only recently due to the development of high-field EPR techniques. A very early (1973!) paper by Y. Alpert et al. has indisputably been the classic in biological HF-EPR spectroscopy with measurements at various microwave frequencies in the millimetre region (called far-infra red magnetic resonance by some authors).[14] In some cases, measurements of spectra as a function of temperature give the sign of *D*. EPR measurements at X- or Q-band frequencies (with an appropriate treatment of the data), magnetic susceptibility measurements or Mössbauer experiments have also been reported as giving *D* values usually without sign determination.

In Table 4, we have gathered several *D* and λ values determined for low molecular weight mononuclear Fe^{III} complexes or metalloproteins. Absolute *D* values vary from very small up to 12 cm^{-1} while those of λ vary from 0 (complete axial symmetry) to 0.33 (complete rhombic symmetry). We discuss the data in three main groups.

(i) The first group concerns the non-heme octahedral Fe^{III} complexes. The complexes $[Fe(dpm)_3]$, $K_3[Fe(malonate)_3]$, $K_3[Fe(oxalate)_3]$, $K_3[Fe(acac)_3]$ and ferrichrome A have three bidentate ligands for which the denticity only originates from oxygen atoms.[15−18] They are characterized by small *D* values ($|D| < 0.3$ cm^{-1}). Three of these complexes exhibit a quasi-axial ZFS ($\lambda < 0.055$) while the other two show a moderate rhombicity with $\lambda \approx 0.25$. Since a discrepancy in *D* appears in the literature for ferrichrome A we retained, in Table 4, only the values extracted from HF-EPR measurements.[17,18] When nitrogen atoms are present in the coordination shell of Fe^{III}, the magnitude of *D* (0.3−1.7 cm^{-1}) increases in comparison with the values for the previous complexes. The coordination mode varies between $[N_2O_4]$,[19−22] $[N_4O_2]$[23] and $[N_5O]$.[24] EPR measure-

Table 4. ZFS parameters of compounds described in the literature with the spectroscopic method used for the measurements

Compound	*D* [cm^{-1}]	λ	Method[a]	Ref.
Octahedral iron(III)				
Molecular complex				
$Fe(citrate)_2$ pH 1.95	−0.12	0.0	HF	this work
pH 6.2	|0.024|	0.33	HF	this work
$Fe(dpm)_3$ [b]	−0.18	0.25	HF	[15]
$K_3Fe(malonate)_3$	|0.12|	0.032	X,Q	[16]
$K_3Fe(oxalate)_3$	|0.18|	0.055	X,Q	[16]
$K_3Fe(acac)_3$[c]	|0.14|	0.028	X,Q	[16]
Ferrichrome A	−0.27	0.25	HF	[17,18]
Fe^{III}-EDTA[d]	+ 0.8	0.33	HF	[19,20]
	+ 0.78	0.33	HF	[21]
	|0.83|	0.31	X	[22]
2 trispicMeen (OO)[e]	−1.7	0.0	X,Mos.	[23]
Fe bztpem[f]	|0.3|	0.15	X	[24]
Tris(dithiocarbamate)	− 2.14	0.10	HF	[17]
Protein				
Transferrin	+0.3	0.29	HF	[19,21]
	+0.27	0.31		[22]
Lipoxygenase	2	−	HF	[25]
	≈|2|	−	X,Q	[26]
Fe-SOD	−2	0.23	X	[28]
Pentacoordinated iron(III)				
Bis(dithiocarbamateFeBr)bis(dithiocarbamateFeCl)	+7	0.07	HF	[17]
	−2	0.04	HF	[17]
Schiff base (square planar)	|10| (|7.2|)	0.33 (0.33)	Magn.	[29]
Bis(substituted-thiohydroxamate)	|10|	0.3	Magn.	[30]
Heme complex				
Protoporphyrin IX-F^- (Br^-)	|5| (|11.8|)	0	FIR	[17,31]
Protohemes	|10|	0	FIR	[31]
	|7|	0	Magn.	[32]
	|6|	0	Magn.	[33]
Metmyoglobin	|10|	0	HF	[34]
	+9.5	0	HF	[17,21]
Metmyoglobin + F-	5.9, 5.0	0, 0	HF	[17,21]
Methemoglobin	|10.7|	0	FIR	[34]
Methemoglobin (F-)	+6.3	0	FIR	[17]

[a] HF: HF-EPR measurements; X,Q: EPR measurements at X or Q band frequencies; Mos: Mössbauer spectroscopy; Magn: magnetic susceptibility measurements and FIR: Far Infra-Red spectroscopy. [b] dpm: dipivaloylmethane. [c] acac: pentane-2,4-dionate. [d] EDTA: ethylenediaminetetraacetate. [e] trispicMeen: *N*-methyl-*N*,*N*′,*N*′-tris(pyridylmethyl)ethane-1,2-diamine. [f] bztpem: *N*-benzyl-*N*,*N*,*N*′,*N*′-tetrakis(pyridylmethyl)ethane-1,2-diamine.

 © 2005 Wiley-VCH Verlag GmbH & Co. KGaA, Weinheim

ments performed at several high frequencies are well documented for the Fe^{III}-EDTA complex.[21] For all these octahedral complexes, the $|D|$ values increase as a function of the nature of the coordinating atoms in the order: $[O_6] < [N_2O_4] < [N_4O_2] < [N_5O] < [S_6]$. Among the non-heme proteins, only three iron sites have been studied and the magnitude of D is < 3 cm^{-1}. In the case of transferrin, rhombic spectra have been correlated with the distorted octahedral structure found in the enzyme.[19−21] The iron is coordinated by four monodentate amino acid residues and one bidentate carbonate anion giving an $[NO_5]$ set of donor atoms.[8c] For lipoxygenase, EPR measurements both at low (X band) and high frequencies have been made and give the same magnitude of D (sign determined at high frequencies).[25−26] The corresponding structural data show an $[N_3O_3]$ coordination mode.[27] In the case of the bacterial Fe-superoxide dismutase (Fe-SOD), attention must be drawn to the detailed X-band EPR study. From a precise temperature-dependent spectroscopic analysis, the magnitude and sign of D were obtained.[28] The observed rhombicity ($\lambda = 0.23$) can be explained in relation to the X ray structure of the Fe-SOD from *E. coli* which reveals that the active site is a pentacoordinate complex. The iron atom is coordinated by three histidines, one aspartate and a hydroxide anion resulting in a distorted structure.

(ii) The second group concerns Fe^{III} complexes characterised by a C_{4v} geometry in the coordination sphere. All of these complexes possess halogen ligands. The magnitude of D varies in a large range (2 to 10 cm^{-1}) and has been correlated with the nature of the halogen ligand. For instance, D increases from -2 to $+7$ cm^{-1} when the chloride ligand is replaced by a bromide ligand in $[(R_2NCS_2)_2FeX]$ [R_2NCS_2 is a bis(dithiocarbamate)].[17] The other chloro iron complex [chlorobis(*N*-methylbenzothiohydroamato)Fe^{III}] is characterised by a larger D value (between 7 and 10 cm^{-1}).[29−30] From the X-ray structures determined for several complexes, the magnitude of D can be correlated with the distance between the iron ion and the plane formed by the four equatorial ligands along the axis formed by the fifth ligand and the metal atom. $|D|$ increases when the distances become smaller.

(iii) The third group concerns the (heme)Fe^{III} complexes such as (porphyrin)Fe^{III} and (protein)Fe^{III} complexes such as metmyoglobin and hemoglobin.[14,17,21,31−34] The systematic axial symmetry originates from the conjugated electronic structure of the haeme. When the metal atom lies in the heminic plane, the D values are in the range of 9 to 12 cm^{-1}.[14,17,31−34] On the other hand, when the iron atom lies above the heme plane, the D values become smaller, between 5 and 10 cm^{-1}.[14,17,31−34] The shift of the iron atom above the plane occurs when an additional ligand coordinates to the iron site giving a sixth coordination site. Recently, the sign of D was clearly obtained as being positive for metmyoglobin.[21]

In conclusion, compounds **1** and **2** can be compared with the non-heme octahedral complexes. The D value of 0.12 cm^1 determined for **1** is in the range found for complexes characterised by a $[O_6]$ coordination sphere ($0.12 < D <$ 0.28 cm^1). For compound **2**, the D value of 0.024 cm^{-1} is smaller but can be closely compared with the other complexes extending the previous range. However, all these D values are smaller than those of the other octahedral complexes in which the coordination spheres contain other heteroatoms as for the EDTA complex ($[N_2O_4]$) with $D = 0.8$ cm^{-1}. In our case, the pH change between compounds **1** and **2** leads to a drastic evolution of λ from a purely axial to a totally rhombic system.

2. Zero-Field Splitting Parameters and Structures of Compounds 1 and 2

It is interesting to compare the ZFS parameters with structural data. Different chemical species have been identified in aqueous solutions depending on the pH. In solutions containing 1 μM Fe^{3+} and 0.1 mM citrate at pH = 5−6, $[Fe(citH)_2]^{3-}$ and $[Fe(cit)]^-$ were observed.[35] More recently, different complexes formed from Fe^{III} and citric acid in the pH range 1−13 have been studied by magnetic susceptibility measurements.[36]

The crystal structures of several mononuclear dicitrate complexes with metal(III) ions, with different degrees of protonation, have been obtained in our laboratory. From these results, we should be able to suggest likely structures for compounds **1** and **2**.

At pH = 7, $(NH_4)_5[Fe(Cit)_2]\cdot 2H_2O$ was isolated.[13] The structure is centrosymmetric with the Fe^{III} ion located on an inversion centre. The coordinated oxygen atoms with the similar chemical functions of each citrate are in *trans* positions. This coordination mode involves the formation of a seven-, a six- and a five-membered coordination ring. The remaining terminal carboxylates are noncoordinating. These results are in agreement with those reported in the literature at almost the same pH.[37] The shortest Fe−O bond is 1.942 Å for the Fe−O (alkoxide) bond. The other distances are 1.995 Å for the Fe−O (central carboxylate) bond and 2.055 Å for the Fe−O (terminal carboxylate) bonds.[13]

At pH = 6, single crystals of $(NH_4)_4[Fe(HCit)(Cit)]\cdot 3H_2O$ were isolated.[13] Since the protonation state of each ligand is different, the Fe^{III} ion is no longer located on an inversion centre thus inducing a pseudo-centrosymmetrical complex. The proton in the (Hcit) ligand is located on the pendant terminal carboxylic acid. The Fe−O bond lengths are nevertheless in the same range as those of the previous complex $(NH_4)_5[Fe(Cit)_2]\cdot 2H_2O$. The values of the Fe−O bond lengths are: 1.932 and 1.944 Å for the Fe−O (alkoxide) bonds, 2.007 and 2.019 Å for the Fe−O (central carboxylate) bonds, and 2.035 Å and 2.064 Å for the Fe−O (terminal carboxylate) bonds, for the nonprotonated and protonated ligands in each case, respectively. No crystals could be obtained at other acidic pH values.

Crystal structures of related complexes found in the literature give an idea of the structure of compound **1**. The structure of $(NH_4)_4[Fe(HCit)(Cit)]\cdot 3H_2O$ is isostructural with $(NH_4)_4[Al(HCit)(Cit)]\cdot 3H_2O$ and $(NH_4)_4[Ga(HCit)(Cit)]\cdot 3H_2O$ which have been previously characterised.[38]

 © 2005 Wiley-VCH Verlag GmbH & Co. KGaA, Weinheim

The Ga−O bond lengths are 1.893 and 1.900 Å for the Ga−O (alkoxide) bonds, 1.976 and 1.983 Å for the Ga−O (central carboxylate) bonds, and 2.022 and 2.058 Å for the Ga−O (terminal carboxylate) bonds, for the nonprotonated and protonated ligand in each case, respectively. The $[Ga(HCit)(H_2Cit)]^{2-}$ species was recently characterised in the laboratory at pH = 1.5.[39] This complex has two pendant terminal carboxylic acid functions and the Ga^{III} centre is linked to an alkoxide oxygen atom for the monoprotonated ligand and an alcoholic oxygen atom for the diprotonated ligand. The Ga−O bond lengths are 1.878 Å for the Ga−O (alkoxide) bond and 2.038 Å for the Ga−O (alcoholic) bond, the other distances are 1.945 and 1.936 Å for the Ga−O (central carboxylate) bonds, and 2.013 and 2.003 Å for the Ga−O (terminal carboxylate) bonds. These results unambiguously demonstrate that protonation of the alkoxide oxygen increases the Ga−O bond distance.

We therefore suggest that the geometry of compound **2** is strongly related to that of $(NH_4)_4[Fe(HCit)(Cit)]\cdot 3H_2O$. The only difference comes from the difference in the counterion (Na^+ instead of NH_4^+). All of the Fe−O bonds distances are in the range of 1.932 to 2.035 Å, within an interval of 0.1 Å suggesting a rhombic octahedral geometry around the Fe^{III} ion. Although the geometry of compound **1** is still unknown, a comparison of isostructural Ga^{III} and Fe^{III} citrates with different degrees of protonation suggests that the protonation of one or two alcoholic oxygen atoms increases the Fe−O (alcoholic) bond distances leading to an axial octahedron with a long O(alcoholic)−Fe−O(alcoholic) axis. This change of structure related to the variation in the acidity of the medium can therefore be correlated with the strong evolution of the ZFS parameters, extracted from the high-field EPR spectra, when the pH of the medium shifts from 6 to 2.

3. Spin Crossover in 1 and 2

All of our results suggest that complexes **1** and **2** are mononuclear, and we will attempt to explain the different phenomena that we observed starting with the following hypothesis.

We therefore exclude to interpret our data on the basis of two different spin states originating from a trinuclear high-spin Fe^{III} complex. For instance, in the literature, the $[Fe_3S_4]^+$ sites of ferredoxins were characterised by an S = 1/2 ground state and an S = 5/2 excited state. The spin ground state S = 5/2 or S = 1/2 depends on the magnitude of the different antiferromagnetic exchange couplings between the three iron sites.[40] Nevertheless, it has been found by Girerd et al., that in a certain temperature range, an S = 3/2 species becomes stabilised for such trinuclear iron−sulfur complexes. In our case, no evidence of an S = 3/2 spectrum arising from a trinuclear Fe^{III} complex has been found in our experimental data.

Moreover, the observation of such a spin crossover for our $[O_6]$-coordinated iron(III) complexes was quite unpredictable.[41] Indeed, no critical temperature of a spin transition has been described for such compounds. Nevertheless, a spin transition has been established for an iron(III)-substituted acac complex by magnetic moment measurements.[42] From a general point of view, iron(III) spin-crossover compounds are less common than those of iron(II).[41,43] However, early studies on tris(dithiocarbamato)iron(III) complexes $[Fe(S_2CNRR')_3]$ indicated that, depending on the nature of R and R′, the iron(III) is high or low spin or spin crossover in this $[S_6]$ coordination sphere.[41,44] In the case of porphyrinic systems, including ferric haemo proteins, characterised by a $[N_4L_2]$ coordination sphere, spin crossover has been observed (L represents different types of monodentate ligands).[41,45] The origin of this phenomenon has been related to a spin state stereochemical relationship. Spin crossover has also been seen for complexes with $[N_6]$ and $[N_4O_2]$ coordination spheres.[46−47]

Spin Transition Equilibrium and Critical Temperature T_c

At 5 K, the 1/2 spin state corresponds to the major species in solution. When the temperature is increased, the S = 5/2 species appears at the expense of the 1/2 species (Figure 4). Since the relaxation properties of the two species differ strongly, it is difficult to evaluate the critical temperature T_c. Comparing the relative appearance of the two spectra it is possible, however, to characterise the variation of these T_c values as a function of the nature of the complex and the field (see below). For instance, at 285 GHz, T_c is smaller for the complex in a neutral medium ($T_c < 10$ K) than it is under acidic conditions (T_c = 12.5 K) (Figure 4 and SI2, Supp. Inf.). For the compounds **1** and **2**, their T_c values are, by far, smaller than that those already found in the literature for Fe^{III} complexes with $[S_6]$, $[N_6]$ or $[N_4O_2]$ coordination shells. For these last compounds, the T_c values are in the range from room temperature to 70 K.[41]

The experimental data are reproducible even if measurements are performed by increasing or decreasing the temperature, implying that no hysteresis phenomena occur. Thus, we have interpreted the presence of these two paramagnetic species as a thermal spin transition (or spin-crossover) of a unique chemical species changing from the 1/2 spin state to the 5/2 spin state according to the following equilibrium:

$$LS\ (^2T_2) \rightleftarrows HS\ (^6A_1)$$

The spin-state interconversion seems to be "prepared" below T_c. Indeed, the evolution of the g anisotropy of the S = 1/2 species with temperature (seen at 285 GHz in Figure 4) can be attributed to small structural modifications around the metal. These slight changes are likely related to the spin transition. Changes in metal−ligand bond lengths accompanying a spin state transition can be obtained from X-ray crystallography. As an example, for Fe^{III} complexes, differences of 0.17 Å can be found for the Fe−N distances but of only 0.04 Å for the Fe−O distances in a series of hexadentate ligands derived from triethylentetramine with a $[N_4O_2]$ donor set.[48]

 © 2005 Wiley-VCH Verlag GmbH & Co. KGaA, Weinheim

The rate of the spin-state interconversion for each compound is slower at all temperatures than the EPR time scale (ca. 10^{11} s^{-1}), but chemically fast. At first sight, it seems strange that at these temperatures the reaction rates are fast. In the literature, however, Buhks et al. suggested that dynamics in spin-crossover should be treated as a nonadiabatic process within the theory of radiationless multiphonon relaxation.[49] They predicted that the LS/HS relaxation would be a thermally activated process at elevated temperatures with a nonvanishing tunnelling rate at cryogenic temperatures. Recently, these relaxation rate constants were measured for several Fe^{III} complexes using laser flash photolysis experiments.[50] Two temperature domains were observed. Clearly, the general temperature behaviour consisting of a thermally activated process at elevated temperatures and a tunneling at low temperatures was experimentally observed. Therefore, even at low temperatures, the LS to HS relaxation rate constant remains high. Under these conditions, the equilibrium between the low-spin (LS) and the high-spin (HS) complexes can thus be instantaneously obtained.

Influence of the External Magnetic Field on Spin Crossover

It can be seen from Figure 5 that the critical temperature is also field dependent and T_c increases as the magnetic field increases. To explain this phenomenon, we have treated the spin transition as an equilibrium reaction between two chemical species, the LS and the HS complexes, with x as the molar fraction of the high-spin complex.

$$\begin{array}{lcl} \text{LS} & \leftrightarrows & \text{HS} \\ (1-x) & & x \end{array}$$

Three different situations can be considered:

(i) In the absence of a magnetic field, the molar free enthalpy (Gibbs free energy, G per mol) for this reaction can be written as the weighted sum of the standard free enthalpy ($G_H°$ and $G_L°$) of the pure HS and LS systems in the absence of any cooperative interaction terms, plus two other terms accounting for the mixing entropy (S_{mix}) and the interactions [$I(x)$]:

$$G = xG_H° + (1-x)G_L° - T\,S_{mix} + I(x) \quad (1)$$

If a regular solution of molecules is assumed for the two states, the mixing entropy S_{mix} for the mixing of the chemical species, according to Guggenheim is:[51]

$$S_{mix} = -R[x\ln x + (1-x)\ln(1-x)] \quad (2)$$

The interaction term can be treated by following a model initially introduced by Slichter, then later modified by König and revisited by Kahn, as:[52−54]

$$I(x) = \gamma_{LL}(1-x)^2 + 2\gamma_{LH}(1-x)x + \gamma_{HH}x^2 \quad (3)$$

where γ_{LL}, γ_{LH} and γ_{HH} are pair interaction terms between two LS ions, a LS and a HS pair, and two HS ions, respectively. These terms are likely related to the magnetoelastic coupling between each cell of the two types of spin (mean field approximation). For convenience, $I(x)$ can be rewritten as:

$$I(x) = \gamma_0 + \gamma_1 x + \gamma_2 x^2 \quad (4)$$

with $\gamma_0 = \gamma_{LL}$, $\gamma_1 = 2(\gamma_{LH} - \gamma_{LL})$ and $\gamma_2 = \gamma_{LL} - 2\gamma_{LH} + \gamma_{HH}$.[52−54] If we introduce equilibrium conditions, the differentiation of the free enthalpy as a function of the molar fraction of the high-spin species gives the following equation:

$$\partial G/\partial x = 0 = \Delta G° + \gamma_1 + 2\gamma_2 x + RT\ln[x/(1-x)] \quad (5)$$

where $\Delta G° = G_H° - G_L°$ is the molar standard free enthalpy of the reaction. This expression gives the equilibrium molar fraction x as a function of temperature with $\Delta G° = \Delta H° - T\Delta S°$ where $\Delta H°$ and $\Delta S°$ are the standard molar enthalpy and entropy of the equilibrium reaction, respectively. $\Delta S°$ for the reaction is positive and is much larger than the entropy variation associated with the mere change of spin state, i.e. $R[x\ln(2S_H + 1) + (1-x)\ln(2S_L + 1)] = R\ln(3) = 9.1$ $J\cdot K^{-1}\cdot mol^{-1}$, where S_H and S_L are the total spin value of the high-spin and low-spin states, respectively.

We now defined the critical temperature of the spin-transition in the absence of an external magnetic field $T_c(0)$, from this equation, for $x = 0.5$:

$$T_c(0) = (\Delta H° + \gamma_1 + \gamma_2)/\Delta S\Theta \quad (6)$$

(ii) The application of a static magnetic field, B, to this sample can be described by adding into Equation (1) a Zeeman energy term ΔG_Z ($= -MB/2$). The total magnetisation is the weighted sum of the magnetisation of the two paramagnetic species as:

$$M = x\chi_H B + (1-x)\chi_L B = [\chi_L + x\Delta\chi)]B = [C_L + x\Delta C]B/T \quad (7)$$

where χ_L and χ_H are the high-spin and low-spin susceptibilities and $\Delta\chi = \chi_H - \chi_L$ and $\Delta C = C_H - C_L$. In this last term, C_H and C_L represent the Curie constants of the two species ($\chi = C/T$).

The Zeeman energy term follows as:

$$\Delta G_Z = -[C_L + x\,\Delta C]B^2/2T \quad (8)$$

With this added term, the equilibrium Equation (5) becomes:

$$\partial G/\partial x = 0 = \Delta G° + \gamma_1 + 2\gamma_2 x + RT\ln[x/(1-x)] - (\Delta C/2T)B^2 \quad (9)$$

 © 2005 Wiley-VCH Verlag GmbH & Co. KGaA, Weinheim

For $x = 0.5$, the critical temperature of the spin-transition, T_c, is now field-dependent, according to:

$$(\partial G/\partial x)_{x=0.5} = \Delta H^\circ - T_c\Delta S^\circ + \gamma_1 + \gamma_2 - (\Delta C/2T_c)B^2 = 0 \quad (10)$$

giving two solutions (see appendix): (a) one around $T_c(0)$ $T_c = T_c(0) - a'B^2$ with

$$a' = [\Delta C/(2T_c(0)\Delta S^\circ)] \quad (11)$$

This model predicts a parabolic decrease in the critical temperature when the external magnetic field increases. This type of variation has already been observed in good agreement with the predictions for several transition metal ion compounds [$LaCo^{III}O_3$ and $[Fe^{II}(Phen)_2(NCS)_2]$ (Phen: 1,10-phenanthroline)][55−56] and particularly with very high B values from pulsed magnetic fields for $[Fe^{II}(Phen)_2(NCS)_2]$ and $[(Mn^{III}(pyrrol)_3(tren)]$ [pyrrol: pyrrole-2-carboxaldehyde; tren: 2,2′,2′′-tris(ethylamino)-amine)].[57−58] These effects are characterised by a relatively small amplitude (1.5 K from 0 to 23 T). These experiments have been recently reviewed.[59] (b) The other solution gives values at very low temperatures:

$$T_c = a'B^2 \quad (12)$$

This model predicts a parabolic increase in the critical temperature when the external magnetic field increases. However, this effect should be small since a′ is the same coefficient as in Equation (11). In our experiments, however, no such phenomena were observed. In our systems, the variation in the T_c value of the spin-transition as a function of the external magnetic field B is completely different. Instead of becoming saturated, at very low temperature, we found a relatively large and almost linear dependence and as shown in SI2 (Supporting Information; 7.5 K from 3.4 to 10.2 T). The main discrepancy is that Equation (12) is related to a transition between high-spin and low-spin states which is contrary to our observations (always a low-spin state at low temperatures for each field). This behaviour cannot be understood in terms of the framework of the model given above even through the pair interactions γ_{LL}, γ_{LH} and γ_{HH}.

In order to interpret our results we introduced another effect, namely the magnetoelastic coupling associated with low-spin and high-spin volume anomalies.

(iii) We now take into account a magnetoelastic term, according to which the local moment is coupled to the volume of each coordination sphere leading to the fact that the magnetoelastic term of a low spin is different from that of a high spin. The free energy related to this magnetoelasticity for a chemical species can be shown to be proportional to $(\delta V/V_o)$ and M^2 as:[60]

$$\Delta G_{ms} = k_{ms}(\delta V/V_o)M^2 \quad (13)$$

where $\delta V/V_o$ (noted below as ε) represents the relative variation of volume between the ordered and disordered states (also called anomaly of volume), M is the magnetisation in the external magnetic field and k_{ms} is a constant. This is a local coupling which does not imply a cooperative mechanism. In our case, we have a mixture of two species and the total free energy related to the volume anomaly is the weighted sum of the terms of the magnetisation relative to the two species (neglecting the interfacial energies).[54]

$$\Delta G_{ms} = k_{ms}[(1 - x)\varepsilon_L M_L^2 + x\varepsilon_H M_H^2] = k_{ms}[\varepsilon_L C_L^2 + x(\varepsilon_H C_H^2 - \varepsilon_L C_L^2](B/T)^2 \quad (14)$$

with M being $(C/T)B$. By adding this term, Equation (9) becomes:

$$\partial G/\partial x = \Delta G^\circ + \gamma_1 + 2\gamma_2 x + RT[\ln(x/(1 - x)] - (\Delta C/2T)B^2 + k_{ms}[\varepsilon_H C_H^2 - \varepsilon_L C_L^2](B/T)^2 = 0 \quad (15)$$

and $(\partial G/\partial x)_{x=0.5}$ has two solutions for low temperatures (see appendix):

a) field-independent:

$$T_c = 2k_{ms}[\varepsilon_H C_H^2 - \varepsilon_L C_L^2]/\Delta C \quad (16)$$

and b) second-order field-dependent:

$$T_c = \{\Delta C/[2\Delta S^\circ T_c(0)^2] - k_{ms}[\varepsilon_H C_H^2 - \varepsilon_L C_L^2]/[\Delta S^\circ T_c(0)^3]\}B^2 \quad (17)$$

The unknown values of all these parameters prevent further progress at this stage. Nevertheless, it seems that this treatment can be in agreement with the observation of the low-spin state for each field at low temperatures. A more sophisticated treatment is now in progress. The contribution of the magnetoelasticity term in our systems compared with those systems where it was not observed,[55−60] probably originates from the fact that our experiments were performed in frozen solutions as opposed to in the solid-state used in previous studies. Moreover, in our studies, complexes **1** and **2** present very flexible structures because of the nature of the ligands, allowing for the development of volume anomalies.

Conclusion

Our analysis of the HF-EPR spectroscopic data of the two studied complexes has shown that the ZFS parameters strongly depend on the symmetry of the metal ions in the complexes. Conversely, measurements of these ZFS parameters can give information on the symmetry in solution when no other methods give any data. Surprisingly, this work has revealed a spin-crossover (from spin 1/2 to spin 5/2 species) at low temperatures. Another surprise was the observation that the critical temperature of the spin transition was field-dependent but in a somewhat unconven-

 © 2005 Wiley-VCH Verlag GmbH & Co. KGaA, Weinheim

tional manner (large positive change instead of small negative one). This phenomenon is likely related to the magnetoelastic properties of the mixture of the two species with their different spin states. Further magnetic studies are in progress to interpret these observations.

Experimental Section

Preparation of the Solutions: Complex **1** was prepared from a 0.1 M aqueous solution of ferric perchlorate [$Fe(ClO_4)_3 \cdot 9H_2O$] (Aldrich) and a 2 M solution of citric acid (Aldrich). The pH was adjusted to 1.95 with sodium hydroxide solution. Complex **2** was prepared from a 0.09 M aqueous solution of ferric perchlorate and a 1.8 M solution of citric acid. The pH was adjusted to 6.25 with sodium hydroxide solution. 1 mL of the respective solution was inserted into an appropriate flask for introduction into the EPR spectrometer.

EPR Instrumentation: High-frequency and high-field EPR spectra were recorded with a laboratory-built spectrometer,[61−62] using frozen solutions. Gunn diodes operating at 95 GHz and equipped with a second and third harmonic generator were used as the radiation source. The high magnetic field was produced by a superconducting magnet (0−12 T). We used a temperature regulation apparatus to maintain the temperature between 4 K and room temperature. Measurements were performed in unsaturated conditions.

Theory for the High-Spin Ferric Ion EPR Spectra

(i) Review of the Spin Hamiltonian for High-Spin Ferric Iron (S = 5/2) in Octahedral Symmetry: This review is given as an introduction to the treatment of the data in the frozen solution state. EPR spectra of paramagnetic complexes under the effect of an external magnetic field and as a function of temperature can adequately be described in the framework of the spin-Hamiltonian parametrisation. This was originally introduced by Abragam and Pryce[63] and then systematically discussed in the book of Abragam and Bleaney.[12] For the high spin iron(III) complexes, the ion ($3d^5$) is in a $^6S_{5/2}$ state. We recall, that in this system with an odd numbers of electrons, at least a twofold degeneracy must remain in the absence of a magnetic field. Thus, the ZFS gives pairs of states (Kramers doublets) related by a time-reversal operator.[12a,64] In EPR experiments, the spin-Hamiltonian therefore has two terms, the Zeeman and the ZFS terms, expressed with the Steven's spin operator equivalents of appropriate symmetry, O_n^m, as:

$$\mathbf{H} = \beta \boldsymbol{B_0 g S} + \sum_{0<n<2S}^{n} \sum_{|m|\leq n}^{m} B_n^m \mathbf{O_n^m} \qquad (18)$$

where B_n^m are parameters to be determined, S is the total electron spin, and n and m are integers with the following constraints: $0 < n < 2S$ (terms with odd n disappear due to time-reversal symmetry)[12a] and the only nonzero terms have $m = lp$ (where l is integral or zero) when the highest rotational symmetry axis is p-fold.[12,65−66] The spin operators O_n^m and the corresponding matrix elements $<M_S|O_n^m|M_{S'}>$ (with M_S, $M_{S'}$ spanning the six values −5/2, −3/2, −1/2, 1/2, 3/2 and 5/2) have been tabulated.[12b] It should be noted that nonzero elements only occur when $|M_S - M_{S'}| = m$ for each $B_n^m O_n^m$ term. The general spin-Hamiltonian for high spin iron(III) can therefore be written as:

$$\mathbf{H} = \beta \boldsymbol{B_0 g S} + B_2^0 \boldsymbol{O_2}^0 + B_2^2 \boldsymbol{O_2}^2 + B_4^0 \boldsymbol{O_4}^0 + B_4^2 \boldsymbol{O_4}^2 + B_4^3 \boldsymbol{O_4}^3 + B_4^4 \boldsymbol{O_4}^4 \qquad (19)$$

The occurrence of the different terms of the ZFS depends on the symmetry around the Fe^{III} centre in the complex. For complexes with pure cubic symmetry, only terms related to $\boldsymbol{O_4}^0$ and $\boldsymbol{O_4}^4$ [12c] occur, as in $Fe^{III}(H_2O)_6$.[67] It will be seen, as in our Fe^{III} citrate system, that the fourth-order terms B_4^m in the spin-Hamiltonian can be neglected and that only the effects of B_2^0 and B_2^2 need to be considered (with the notations $D = B_2^0/3$ and $E = B_2^2$).[68] Under these conditions, the spin-Hamiltonian can be rewritten as:

$$H = \beta B_0 g S + D[\boldsymbol{S_z}^2 - 1/3S(S+1)] + E[\boldsymbol{S_x}^2 - \boldsymbol{S_y}^2] \qquad (20)$$

where D is the axial ZFS and E gauges the rhombic ZFS. For a complex with pure axial symmetry, $E = 0$. When the anisotropy of the Landé tensor g occurs in the same axis as the ZFS, a complete expression of the spin-Hamiltonian for this 6S5/2 state is:

$$H = (G_x/2)[\boldsymbol{S_+} + \boldsymbol{S_-}] - (iG_y/2)[\boldsymbol{S_+} - \boldsymbol{S_-}] + G_z \boldsymbol{S_z} + D[\boldsymbol{S_z}^2 - 1/3S(S+1)] + E/2[\boldsymbol{S_+}^2 + \boldsymbol{S_-}^2] \qquad (21)$$

where $Gq = \beta g_q B_{oq}$, with $q = x$, y or z. The corresponding energy matrix containing 6 × 6 elements $<M_S|H|M_{S'}>$ is shown in Table 1, with $\boldsymbol{z} = G_z + iG_y$ and $\boldsymbol{z^*} = G_z - iG_y$. The locations of $\boldsymbol{S_z}$, $\boldsymbol{S_+}$ (or $\boldsymbol{S_-}$) and $\boldsymbol{S_+^2}$ (or $\boldsymbol{S_-^2}$) are, respectively, the origin of the elements on the diagonal line, on one line above (or under) the diagonal and on two lines above (or under) the diagonal.

(ii) Principle of the Treatment of the Data: The corresponding eigenvalues ε_j and the eigenstates $|\varphi_j>$, with j from 1 to $2S + 1 = 6$, can be obtained by diagonalising the matrix. For the pure axial case, with $E = 0$, two diagonalisations have to be made, one for the orientation according to z, with $z = 0$ (written for this case as a diagonal matrix) and the other, for the orientation according to x or y, with $G_z = 0$ and $z = G_x$. For the rhombic case, where E is different from 0, three diagonalisations have to be made, the first for the orientation according to z, with $z = 0$, the second is made for the orientation according to x, with $G_z = 0$ and $z = G_x$ and the third, for the orientation according to y, with $G_z = 0$ and $z = iG_y$ (diagonalisation of a 6 × 6 matrix with imaginary number elements). In each case, five transitions related to the change of Zeeman level states from −5/2 to −3/2, −3/2 to −1/2, −1/2 to 1/2, 1/2 to 3/2 and 3/2 to 5/2 can be expected. These levels are clearly defined when the Zeeman term is large compared with the ZFS term. For the randomly orientated molecules of the frozen aqueous solutions, the intensity of absorption varies from those parallel to the magnetic field to those perpendicular to the magnetic field (which are more numerous by far). For the axial systems, the perpendicular transitions are only of one type whereas for the rhombic systems, the x and y orientations have to be distinguished. In the axial systems, a qualitative interpretation of the spectra can be made when $g\beta B_o >> D$ (high-field limit). The five ($2S$) permitted M to $M + 1$ transitions between the 6 ($2S + 1$) energy levels can be observed for the following resonance field: $B_r(M) = g_e/g[B_o + (M + 1/2)D']$, where $D' = (3\cos^2\theta - 1)D/(g_e\beta)$ and θ is the angle of the external magnetic field with respect to the main axis of symmetry of the complex.[69] Therefore, when the external magnetic field is parallel to the axis, the neighbouring lines are separated by $2|D|$ and centred at $B_{r//} = g_e B_o/g_{//}$ while they are separated by $|D|$ and centred at $B_{r\perp} = g_e B_o/g_\perp$ when it is perpendicular to the axis.

(iii) Treatment of the Spectroscopic Data for the High-Spin Ferric Ion: In Figure 2, we compare the field location of the transitions

in the experimental spectra with those of the transitions obtained in the energy level diagrams for compound **1**. In the left-hand section (Figure 2, a−d), the experimental spectra are displayed along with the simulations calculated using the program available from Weihe et al.[70] The same simulations can be obtained when the X-Sophe software from Bruker is used.[71] Marks have been added to point out the pure z transitions centred at $B_{0//} = \nu_0/\beta g_{//}$ and the pure x, y transitions centred at $B_{0\perp} = \nu_0/\beta g_{\perp}$. In the right-hand section (e−f in Figure 2), we show the energy level diagrams as a function of the product $g\beta B_0$ in cm^{-1} and the allowed $\Delta M_s = \pm 1$ transitions for the zero-field splitting parameter, D, obtained above. The same type of information is given for compound **2** in Figure SI1 (Supporting Information). These diagrams show the energy value (in cm^{-1}) as a function of $G_q = g_q\beta B_o$ with q for x, y or z (G in cm^{-1}). These energy values are eigenvalues of the energy matrix reported in Table 1. The diagonalisations of the real or imaginary, hermitian and symmetric 6×6 matrices were carried out using the Jacobi method, as described in "Numerical Recipes in Fortran"[72] and using the C programming language with a Linux System. We tried several values for the D and E parameters. The segments related to the five transitions according to the parallel or perpendicular axis for axial systems (e−f in Figure 1) or those related to the five transitions according to the x, y or z axis for rhombic systems (Figure SI 1, Supporting Information) were calculated using Mathmab for each frequency (9.507, 6.338 and 3.169 cm^{-1} related to the 285, 190 and 95 GHz measurement frequencies, respectively). The field positions of these calculated transitions are reported in Figure 2 (a−d) under each experimental spectrum taking into account the $g_{//}$ and $g_{\perp}$ values for the axial systems and in Figure SI1 (Supporting Information) with the g_x, g_y and g_z values for the rhombic systems. These g_q values were evaluated from the field positions of the centres of the set of the five transitions related to each orientation relative to the field. With a negative value of D, in the axial system, Figure 2 (e−f) show that the parallel transition from the lowest level ($M_s = -5/2$) can be observed at low field compared with the centre of the set of the five parallel transitions whereas the perpendicular one is at high field. The agreement seems to be satisfactory both for the field positions and for the evolution of the intensities of the transitions as a function of the temperature.

Appendix

(i) Equation (10) can be resolved as a second order equation with $u = T_c/T_c(0)$:

$(\partial G/\partial x)_{x=0.5} = u^2 - u + a = 0$

with $a = (\Delta C/2\Delta S^\circ)[B/T_c(0)]^2$. The general solution is $u = [1 \pm (1 - 4a)^{1/2}]/2$. The solution for T_c around $T_c(0)$ is, with sign "+" for $\pm$, $u = 1 - a$, i.e.:

$T_c = T_c(0) - a'B^2$
with $a' = (\Delta C/[2T_c(0)\Delta S^\circ)]$.

The second solution, for very low temperatures (sign "−" for $\pm$), is $u = a$, i.e. with the same coefficient a':

$T_c = a'B^2$

(ii) Equation (15) can be resolved as a third-order equation with $u = T_c/T_c(0)$:

$(\partial G/\partial x)_{x=0.5} = u^3 - u^2 + bu - c = 0$

with $b = b'B^2$, $b' = \Delta C/[2\Delta S^\circ T_c(0)^2]$ and $c = c'B^2$, $c' = k_{ms}[\varepsilon_H C_H{}^2 - \varepsilon_L C_L{}^2]/(\Delta S^\circ T_c(0)^3]$.
At low temperatures, around 0 K, i.e. and with $u = \varepsilon$, we obtain the solution for the first-order treatment:

$u = c'/b' = 2k_{ms}[\varepsilon_H C_H{}^2 - \varepsilon_L C_L{}^2]/[\Delta C T_c(0)]$

and for the second-order treatment, the only likely solution is:

$u = (c' - b')\ B^2$

Supporting Information (see also footnote on the first page of this article): Figure SI1 shows simulated and experimental 285 GHz HF-EPR spectra of compound **2** recorded at 60 K with the assignments of the different transitions presented as well as energy level diagrams. Figure SI2 shows the experimental 285 GHz-EPR spectra of compound **2** recorded between 5 and 30 K. Figure SI3 shows the plot of the observed T_c of the 1/2 to 5/2 spin transition of compound **1** as a function of the field.

Acknowledgments

The authors thank Professor Jean-Louis Pierre for his interest in this study and as the initiator of this research in iron in biology. We thank Dr. Yves Frapart (Chimie et Biochimie Pharmacologiques et Toxicologiques, University of Paris V), Dr. Geneviève Blondin (Institut de Chimie Moléculaire d'Orsay, University of Paris XI) and Dr. P. Höfer (Bruker Industry, Wissembourg) for providing X-Sophe simulations. C. B. thanks Prof. Jean-Paul Bertrandias (Institut de Mathématiqes Appliquées, UJF) and Dr. André Eberhard (Laboratoire Modélisation et Calcul, UJF) for their help with the mathematics and the use of Mathlab software, respectively. C. B. thanks Prof. I. Gautier-Luneau (Laboratoire de Cristallographie, UJF) for discussions on the X-ray data for compounds related to those studied here and for fruitful discussions about the influence of the state of protonation on the geometries of complexes of Fe^{III} and Ga^{III} with organic ligands. C. B. thanks also Prof. Andreas Hauser (Département de Chimie Physique, University of Geneva), Prof. M. Cyrot (Laboratoire Louis Néel, UJF) and Dr. M. Guillot (HMFL) for general fruitful discussions. We thank also the "Centre National de la Recherche Scientifique" for support through the GdR 1879 "Deregulation of Iron Metabolism: Chemistry, Biology and Therapeutics".

[1] J. P. Glusker, *Acc. Chem. Res.* **1980**, *13*, 345−352.
[2] D. C. Crans, in *Metals Ions in Biological Systems: Vanadium and its role in Life* (Eds.: H. Siegel, A. E. Siegel), Marcel Dekker, New York, **1995**, chapter 5, p. 147−209.
[3] S. J. Lippard, J. M. Berg, in *Principles of Bioinorganic Chemistry* University Science Books: Mill Valley, CA, **1994**, chapter 12, p. 352−354.
[4] M. J. Milewska, *Z. Chem.* **1988**, *28*, 204−211.
[5] P. Baret, C. Béguin, H. Boukhalfa, C. Caris, J. P. Laulhère, J. L. Pierre, G. Serratrice, *J. Am. Chem. Soc.* **1995**, *117*, 9760−9761.
[6] G. Serratrice, H. Boukhalfa, C. Béguin, P. Baret, C. Caris, J. L. Pierre, *Inorg. Chem.* **1997**, *36*, 3898−3910.
[7] J. L. Pierre, I. Gautier-Luneau, *Biometals* **2000**, *13*, 91−96.
[8] [8a] R. Crichton, *Inorganic Biochemistry of Iron Metabolism*, 2nd ed., J. Wiley, Chichester, **2001**, chapter 5. [8b] R. Crichton, *Inorganic Biochemistry of Iron Metabolism*, 2nd ed., J. Wiley, Chichester, **2001**, chapter 7. [8c] R. Crichton, *Inorganic Biochemistry of Iron Metabolism*, 2nd ed., J. Wiley, Chichester, **2001**, Figure 5-5.
[9] H. G. Parkes, R. E. Allen, A. Furst, D. R. Blake, M. C. Grootveld, *J. Pharm. Biomed. Anal.* **1991**, *9*, 29−32.
[10] M. Grootveld, J. D. Bell, B. Halliwell, O. I. Aruoma, A. Bomford, P. J. Sadler, *J. Biol. Chem.* **1989**, *264*, 4417−4422.
[11] D. L. Bakkeren, C. M. H. De Jeu-Jaspars, C. Van der Heud, H. G. Van Eijk, *Int. J. Biochem.* **1985**, *17*, 925−930.
[12] [12a] A. Abragam, B. Bleaney, *Electron Paramagnetic Resonance of Transition Ions*, Clarendon Press, Oxford, **1970**, p. 140, or: same authors, French translation by Y. Ayant, E. Belorizky, R. Buisson, Y. Merle d'Aubigné, J. Rosset, P. U. F., Paris, **1971**. [12b] A. Abragam, B. Bleaney, *Electron Paramagnetic Resonance*

 © 2005 Wiley-VCH Verlag GmbH & Co. KGaA, Weinheim

of Transition Ions, Clarendon Press, Oxford, **1970**, p. 863, or: same authors, French translation by Y. Ayant, E. Belorizky, R. Buisson, Y. Merle d'Aubigné, J. Rosset, P. U. F., Paris, **1971**.
[12c] A. Abragam, B. Bleaney, *Electron Paramagnetic Resonance of Transition Ions*, Clarendon Press, Oxford, **1970**, p. 142, or: same authors, French translation by Y. Ayant, E. Belorizky, R. Buisson, Y. Merle d'Aubigné, J. Rosset, P. U. F., Paris, **1971**.
[13] I. Gautier-Luneau, C. Merle, D. Phanon, C. Lebrun, F. Biaso, G. Serratrice, J.-L. Pierre, *Chem. Eur. J.*, to be submitted.
[14] Y. Alpert, Y. Couder, J. Tuchendler, H. Thome, *Biochim. Biophys. Acta* **1973**, *322*, 34−38.
[15] A.-L. Barra, A. Caneschi, A. Cornia, F. Fabrizi de Biani, D. Gatteschi, C. Sangregorio, R. Sessoli, L. Sorace, *J. Am. Chem. Soc.* **1999**, *121*, 5302−5310.
[16] D. Collison, A.K. Powell, *Inorg. Chem.* **1990**, *29*, 4735−4746.
[17] G. C. Brackett, P. L. Richards, W. S. Caughey, *J. Chem. Phys.* **1971**, *54*, 4383−4401.
[18] R. D. Dowsing, J. F. Gibson, *J. Chem. Phys.* **1969**, *50*, 294−301.
[19] P. P. Schmidt, A.-L. Barra, K. K. Andersson, *High Frequency EPR: New Frontiers in Biology, Chemistry and Physics, an European Workshop*, St Pierre de Chartreuse, June **2000**.
[20] K. K. Andersson, A.-L. Barra, *Spectrochim. Acta* **2002**, *A58*, 1101−1112.
[21] K. K. Anderson, P. P. Schmidt, B. Katterle, K. R. Strand, A. E. Palmer, S.-K. Lee, E. I. Solomon, A. Gräslund, A.-L. Barra, *J. Biol. Inorg. Chem.* **2003**, *8*, 235−247.
[22] R. Aasa, *J. Chem. Phys.* **1970**, *52*, 3919−3930.
[23] A. J. Simaan, F. Banse, J.-J. Girerd, K. Wieghardt, E. Bill, *Inorg. Chem.* **2001**, *40*, 6538−6540.
[24] L. Duelund, R. Hazell, C. J. McKenzie, L. P. Nielsen, H. Toftlund, *J. Chem. Soc., Dalton Trans.* **2001**, 152−156.
[25] K. S. Doctor, B. J. Gaffney, *Appl. Magn. Reson.* **1996**, *11*, 425−435.
[26] S. Slappendel, G. A. Veldink, J. F. G. Vliegenthart, R. Aasa, B. G. Malmstrom, *Biohim. Biophys. Acta* **1980**, *642*, 30−39.
[27] E. K. Pistorius, B. Axelrod, G. Palmer, *J. Biol. Chem.* **1976**, *251*, 7144−7148.
[28] J. P. Renault, C. Verchère-Béaur, I. Morgenstern-Badarau, F. Yamakura, M. Gerloch, *Inorg. Chem.* **2000**, *39*, 2666−2675.
[29] H.-L. Shyu, H.-H. Wei, G.-H. Lee, Y. Wang, *J. Chem. Soc., Dalton Trans.* **2000**, 915−918.
[30] K. J. Berry, P. E. Clark, K. S. Muray, C. L. Raston, A. H. White, *Inorg. Chem.* **1983**, *22*, 3928−3934.
[31] W. R. Hagen, *Coord. Chem. Rev.* **1999**, *190−192*, 209−229.
[32] G. Feher, P. L. Richards, *in Magnetic Resonance in Biological Systems* (Eds.: A. Ehrenberg, B. G. Malmstöm, T. Vännggain), Pergamon Press, **1967**, p. 141−144.
[33] T. J. Neal, S.-J. Kang, I. Turowska-Tyrk, C. E. Schulz, W. R. Scheidt, *Inorg. Chem.* **2000**, *39*, 872−880.
[34] P. J. M. van Kan, E. van der Horst, E. J. Reijerse, P. van Bentum, W. R. Hagen, *J. Chem. Soc., Faraday Trans.* **1998**, *94*, 2975−2978.
[35] M. Matzapetakis, M. Kourgiantakis, M. Dakanali, C. P. Raptopoulou, A. Terkis, A. Lalatos, T. Kiss, I. Banyai, L. Iordanidis, T. Mavromoutakos, A. Salifoglou, *Inorg. Chem.* **2001**, *40*, 1734−1744.
[36] M. Matzapetakis, C. P. Raptopoulou, A. Tsohos, V. Papaefthymiou, N. Moon, A. Salifoglou, *J. Am. Chem. Soc.* **1998**, *120*, 13266−13267.
[37] H. Yokoi, T. Mitani, Y. Mori, S. Kawata, *Chem. Letters* **1994**, 281−284.
[38] R. B. Martin, *J. Inorg. Biochem.* **1986**, *28*, 181−187.
[39] I. Gautier-Luneau, personal communication.
[40] J.-J. Girerd, G. C. Papaefthymiou, A. D. Watson, E. Gamp, K. S. Hagen, N. Edelstein, R. B. Frankel, R. H. Holm, *J. Am. Chem. Soc.* **1984**, *106*, 5941−5947.
[41] P. J. van Konningsbruggen, Y. Maeda, H. Oshio, *Top. Curr. Chem.* **2004**, *233*, 259−324.
[42] A. A. Adimado, *Polyhedron* **1983**, *2*, 1059−1063.
[43] P. Gütlich, H. A. Goodwin, *Top. Curr. Chem.* **2004**, *233*, 3−47.
[44] L. Cambi, A. Cagnasso, *Atti Accad. Naz. Lincei* **1931**, *13*, 809−813.
[45] W. R. Scheidt, C. A. Reed, *Chem. Rev.* **1981**, *81*, 543−555.
[46] M. M. Bhadbhade, D. Srinivas, *Polyhedron* **1998**, *17*, 2699−2711.
[47] C. Brewer, G. Brewer, C. Luckett, G. S. Marbury, C. Viragh, A. M. Beatty, W. R. Scheidt, *Inorg. Chem.* **2004**, *43*, 2402−2415.
[48] E. König, in *Structure and Bonding*, Springer, Berlin **1991**, vol. 76, p. 53−152.
[49] E. Buchks, G. Navoon, M. Bixon, J. Jortner, *J. Am. Chem. Soc.* **1980**, *102*, 2918−2923.
[50] S. Schenker, A. Hauser, R. M. Dyson, *Inorg. Chem.* **1996**, *35*, 4676−4682.
[51] E. A. Guggenheim, in *Mixtures*, Oxford University Press, London, **1952**.
[52] C. P. Slichter, H. G. Drickamer, *J. Chem. Phys.* **1972**, *56*, 2142−2160.
[53] R. Zimmerman, E. König, *J. Phys. Chem. Solids* **1977**, *38*, 779−788.
[54] O. Kahn, in *Molecular Magnetism*, Wiley-VCH, Weinheim **1993**, p. 53.
[55] R. A. Bari, J. Sivardière, *Phys. Rev. B.* **1972**, *5*, 4466−4471.
[56] Y. Qi, E. W. Müller, H. Spiering, P. Gütlich, *Chem. Phys. Lett.* **1983**, *101*, 503−505.
[57] A. Bousseksou, N. Negre, M. Goiran, L. Salmon, J.-P. Tuchagues, M.-L. Boillot, K. Boukheddaden, F. Varret, *Eur. Phys. J. B* **2000**, *13*, 451−456.
[58] Y. Garcia, O. Kahn, J.-P. Ader, A. Buzdin, Y. Meurdesoif, M. Guillot, *Phys. Lett. A* **2000**, *271*, 145−154.
[59] A. Bousseksou, F. Varret, M. Goiran, K. Boukheddaden, J.-P. Tuchagues, *Top. Curr. Chem.* **2004**, *235*, 65−84.
[60] A. Herpin, in *Théorie du magnétisme*, PUF, Paris **1968**, p. 264.
[61] A.-L. Barra, J.-C. Brunel, J.-B. Robert, *J. Chem. Phys. Lett.* **1990**, *165*, 107−115.
[62] F. Muller, M. A. Hopkins, N. Coron, M. Grynderg, L.-C. Brunel, G. Martinez, *Rev. Sci. Instrum.* **1989**, *60*, 3681−3984.
[63] A. Abragam, M. H. L. Pryce, *Proc. Roy. Soc. (London)* **1951**, *205A*, 135−153.
[64] J. S. Griffith, *The Theory of Transition-Metal Ions*, University Press, Cambridge, **1961**, p. 205.
[65] W. Weltner Jr., *Magnetic Atoms and Molecules*, Dover, New York, **1983**.
[66] R. Bramley, S. J. Strach, *Chem. Rev.* **1983**, *83*, 49−82.
[67] C. Béguin, unpublished results.
[68] A. X. Trautwein, E. Bill, E. L. Boominaar, H. Winkler, in *Structure and Bonding*, Springer, Berlin **1991**, vol. 78, p. 1−95.
[69] A.-L. Barra, L.-C. Brunel, D. Gatteschi, L. Pardi, R. Sessoli, *Acc. Chem. Res.* **1998**, *31*, 460−466.
[70] *SIM*, by H. Weihe, Department of Chemistry, University of Copenhagen: J. Glerup, H. Weihe, *Acta Chem. Scand.* **1991**, *45*, 444−448.
[71] M. Griffin, A. Muys, C. Noble, D. Wang, C. Eldershaw, K.E. Gates, K. Burrage, G. R. Hanson, *Molec. Phys. Reports* **1999**, *26*, 60−84.
[72] W. H. Press, S. A. Teukolsky, W. T. Vetterburg, B. P. Flanning, *Numerical Recipes in Fortran: this Art of Scientific Computing*, Cambridge University Press, Cambridge, **1992**.

Received May 19, 2004
Early View Article
Published Online December 6, 2004

 © 2005 Wiley-VCH Verlag GmbH & Co. KGaA, Weinheim

Anion and Solvent Effects upon the Structures of Platinum(II) Complexes with Thiacrown Ligands: The Crystal Structures of $[Pt(9S3)_2](PF_6)_2 \cdot 2\ CH_3NO_2$, $[Pt(9S3)_2](BF_4)_2 \cdot 2\ CH_3NO_2$, $[Pt(9S3)_2](OTf)_2 \cdot 2\ CH_3NO_2$, and $[Pt(18S6)](BF_4)_2$

Gregory J. Grant,*[a] Weinan Chen,[a] Andrea M. Goforth,[a] Clarilyn L. Baucom,[a] Ketankumar Patel,[a] Pavle Repovic,[a] Donald G. VanDerveer,[b,c] and William T. Pennington[c]

Keywords: S ligands / Platinum

The synthesis and crystal structures of four mononuclear Pt^{II} homoleptic complexes with two thiacrown ligands are presented. The binding mode for both macrocycles to the platinum center contrasts with previous structural reports involving identical complex cations but differing anions or crystallization solvents. All three bis(1,4,7-trithiacyclononane(9S3))platinum(II) complexes (with tetrafluoroborate, hexafluorophosphate, and triflate as counterions) are centrosymmetric, with *endodentate* binding of the trithioether resulting in $[S_4 + S_2]$ coordination. The Pt^{II} complex of 1,4,7,10,13,16-hexathiacyclooctadecane(18S6) shows an elongated square pyramidal structure with one *exodentate* sulfur in a $[S_4 + S_1]$ mode. Our work illustrates how changes of counterion and solvent dramatically affect the crystal structures for such complexes, suggesting that packing forces are more important than ligand conformation in determining solid-state structures. In addition, the full spectroscopic and electrochemical properties of the complex $[Pt(18S6)](BF_4)_2$ are reported. The electronic spectrum shows a d–d transition near 430 nm, and an irreversible Pt^{II}/Pt^{III} couple occurs at +564 mV vs. Fc/Fc^+ in cyclic voltammetry. Both these data are consistent with other hexakis(thioether) Pt^{II} complexes. ^{13}C NMR measurements show a non-fluxional 18S6 ligand in the complex while the platinum-195 NMR resonance at –4152 ppm indicates a mixed orientation of lone pair electrons on the sulfur donors.
(© Wiley-VCH Verlag GmbH & Co. KGaA, 69451 Weinheim, Germany, 2005)

Introduction

The complexation of both transition metal and main group metal ions by thiacrown ligands, such as 1,4,7-trithiacyclononane (9S3) and 1,4,7,10,13,16-hexathiacyclooctadecane (18S6), has been well researched over the past decade.[1–5] Complexes involving Pt^{II} and Pd^{II} with these macrocycles have been a particularly active area.[6–12] Such complexes are quite stable due to coordination of the soft metal center by the soft thioether ligand. The unique spectroscopic and electrochemical properties of crown thioether complexes containing the two divalent metal ions are a further impetus for research. Unusual d–d electronic transitions in the visible region result in atypical colors for both Pt^{II} (orange) and Pd^{II} (blue-green) complexes. Furthermore, the complexes exhibit a fully reversible M^{II}/M^{III} couple, observed in non-aqueous cyclic voltammetry; they also display fluxional trithioether ligands whose barriers of conversion are exceedingly small (near the limit of NMR detection of dynamic processes).[13] These physicochemical properties arise from the long M–S axial interactions between the metal ion and the sulfur donors of the thiacrown; long M–S interactions in solution have been correlated with the conformational preferences of individual crown thioether ligands.[14] Figure 1 shows the three distinct binding modes of thiacrowns to Pd^{II} and Pt^{II}, involving zero, one, and two long metal–sulfur interactions. These long interactions fall in the range 2.7–3.2 Å, which is longer than typical divalent palladium and platinum thioether sulfur bond lengths (2.3–2.4 Å), but less than the corresponding metal–sulfur Van der Waals distances.[15] Also, the electronic nature of these interactions is of considerable theoretical interest as they serve as intermediate cases between bonding and non-bonding situations.[16]

The initial report of the crystal structure of the complex $[Pt(9S3)_2](PF_6)_2$ revealed, surprisingly,[6] an elongated

[a] Department of Chemistry, The University of Tennessee at Chattanooga,
Chattanooga, TN 37403, USA
Fax: (internat.) +1-423-425-5234
E-mail: Greg-Grant@utc.edu
[b] School of Chemistry and Biochemistry, Georgia Institute of Technology,
Atlanta, GA 30332
[c] Department of Chemistry, Clemson University,
Clemson, SC 29638

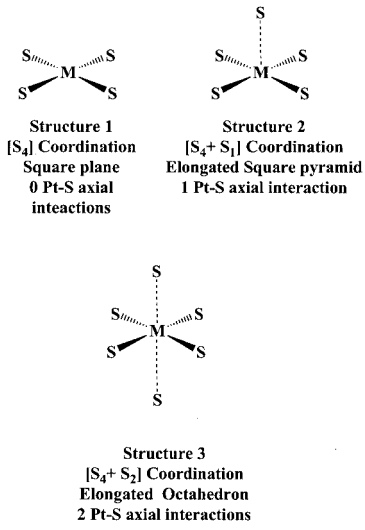

Figure 1. Three coordination modes of d^8 metal ions displayed by thiacrowns

square pyramidal structure ([S_4 + S_1], Figure 1, Structure 2) rather than the more common, and anticipated, elongated octahedral structure ([S_4 + S_2], Figure 1, Structure 3). In the reported structure, the two 9S3 ligands were not centrosymmetrically bound to the Pt^{II}. One 9S3 was positioned *endodentate* to the metal ion while the second ligand was in an uncommon *exodentate* conformation. The *exodentate* conformation of 9S3 contrasts with that of the identical bis Pd^{II} analog.[8] Indeed, to the best of our knowledge, only one other *exodentate* binding case of 9S3 in a Pt^{II} structure has been reported.[17] Therefore, we undertook the current crystallographic study of the $[Pt(9S3)_2]^{2+}$ cation with various anions to see if this atypical 9S3 complex structure might be duplicated. The length of the axial sulfur−metal interaction serves as a sensitive probe for the examination of anion and solvent effects.[18a−18e] For example, dramatic solvent effects on Pd^{II} complexes containing thiacrown ligands have been reported for the analogous thiacrown 10S3 (1,4,7-trithiacyclodecane).[19,20] Interestingly, the linkage isomer obtained for the $[Pd(10S3)_2]^{2+}$ complex, reported by McAuley, has a six-membered chelate ring between the equatorial sulfurs, while our structure contains a five-membered chelate ring between the sulfurs. The switch in linkage isomer appears to be due to packing forces associated with a particular solvent (nitromethane vs. acetonitrile); this solvent−complex interaction has been confirmed via low temperature ^{13}C NMR studies. Similarly, macrocyclic hexathioether 18S6 complexes with Pd^{II} to form two different salts with different solid-state structures. The tetraphenylborate salt of $[Pd(18S6]^{2+}$ is yellow-brown while the hexafluorophosphate salt is green.[1,9] In addition, the Pd−S bond lengths and conformations of ethylene linkages also differ, illustrating how counterion effects can alter structures. As the spectroscopic and electrochemical properties of $[Pt(18S6]^{2+}$ have not been reported, those data are included here, along with our X-ray structure of the tetrafluoroborate salt.[9] Control of complex cation structure by solvent and counterion could have important implications in crystal engineering applications. Both Pd^{II} and Pt^{II} complexes of thiacrowns have been used by the Schröder and Lippolis groups as templates for control and the self-assembly of three-dimensional structures.[21,22]

Results and Discussion

Structures of $[Pt(9S3)_2]^{2+}$ Complexes

The tetrafluoroborates and hexafluorophosphates both crystallize in the monoclinic space group, $P2_1/c$ (No. 14), while the triflate salt crystallizes in the orthorhombic space group, *Pbca* (No. 61). The asymmetric unit in all three lattices consists of the platinum(II) center, situated on an inversion center, one 9S3 ligand, one anion, and one nitromethane solvent molecule, each occupying general positions within the cell. For the hexafluorophosphate salt, both 9S3 ligands are centrosymmetrically bound to the Pt^{II} ion in the three structures (Figure 2), and the ligand shows an *endodentate* conformation with a [S_4 + S_2] coordination mode. There are four equatorial Pt−S bonds and two long distance Pt−S axial interactions forming an elongated octahedral structure. Notably, all three structures contrast with the prior structure of $[Pt(9S3)_2](PF_6)_2$, which shows one *exodentate* sulfur, non-centrosymmetrical binding of the two ligands, and no solvent molecules.[6] Our structural results, therefore, do not support the hypothesis that [S_4 + S_1] binding of 9S3 to Pt^{II} is its common and preferred coordination mode due to the conformation of the ligand.[11] Rather, packing effects, which depend upon the specific counterion and crystallization solvent, control whether [S_4 + S_2] or [S_4 + S_1] coordination is observed in structures of 9S3 and related macrocycles with d^8 metal ions such as Pt^{II} and Pd^{II}.

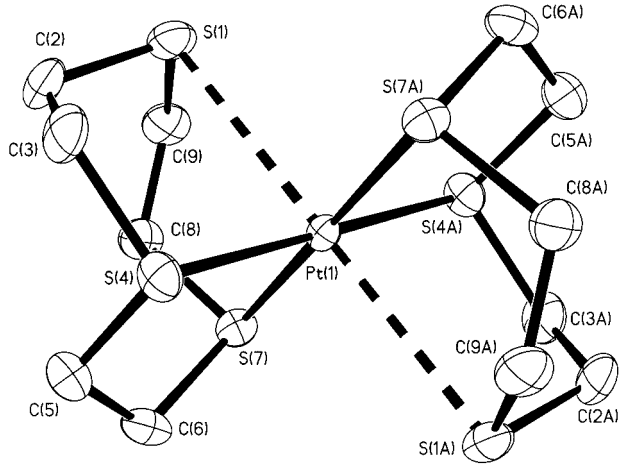

Figure 2. Thermal ellipsoid perspective (50% probability) of cation in $[Pt(9S3)_2]](PF_6)_2 \cdot 2\ CH_3NO_2$

Equatorial Pt−S bond lengths increase only very slightly, in the order $BF_4^- < PF_6^- < OTf^-$. Greater variation is seen, not unexpectedly, in the Pt−S axial distances, with the triflate showing a larger distance (over 0.1 Å) than the other two structures. However, the Pt−S distance is markedly

 © 2005 Wiley-VCH Verlag GmbH & Co. KGaA, Weinheim

greater, over 0.3 Å, than for the earlier $[Pt(9S3)_2](PF_6)_2$ structure − a dramatic effect arising from packing forces.[6] S−Pt−S chelate bite angles in the three structures are slightly less than 90°, with a commensurate expansion of the non-chelate angle to slightly above 90°. This effect is also seen in the $S_{equatorial}-Pt-S_{axial}$ angles (Table 1), which are less than 90°, showing the axial sulfur bending towards the metal center.

Table 1. Selected bond lengths (Å) and angles (°) for $[Pt(9S3)_2](PF_6)_2{\cdot}2CH_3NO_2$ (**1**), $[Pt(9S3)_2](BF_4)_2{\cdot}2CH_3NO_2$ (**2**), $[Pt(9S3)_2](OTf)_2{\cdot}2CH_3NO_2$ (**3**), and $[Pt(18S6)](BF_4)_2$ (**4**)

	1	**2**	**3**	**4**
Distances (Å)				
M−Seq				
	2.2923(8)	2.2901(1)	2.2962(16)	2.303(3)
	2.2939(9)	2.2927(1)	2.2987(15)	2.318(3)
				2.321(3)
				2.322(3)
M−Sax	3.072(8)	3.043(7)	3.185(7)	2.809(3)
M−S, exo	NA	NA	NA	4.099(3)
S−S, chelate	3.220(8)	3.214(7)	3.237(8)	3.250(3)
				3.230(3)
Angles, degrees				
S−M−S, chelate	89.20(3)	89.07(4)	89.58(6)	88.61(10)
				88.90(10)
S−M−S, non-chelate	90.80(3)	90.93(4)	90.42(6)	90.65(10)
				91.66(10)
S−M−S, axial	82.729(8)	82.906(4)	78.629(6)	84.23(10)
	84.265(8)	84.373(4)	80.458(6)	84.81(3)

Structure of $[Pt(18S6)]^{2+}$

The structure crystallizes in a triclinic cell with space group, $P\bar{1}$ (No. 2); Figure 3 shows a thermal ellipsoid perspective. The asymmetric unit consists of one $[Pt(18S6)]^{2+}$ cation and two BF_4^- anions, all occupying general positions within the cell. Note that, unlike the three 9S3 structures, there are no solvent molecules incorporated into the lattice. The 18S6 forms an elongated square pyramidal structure (Figure 1, Structure 2) with $[S_4 + S_1]$ coordination. One long Pt−S axial interaction is observed [2.809(3) Å], but the sixth sulfur donor is oriented *exodentate* to the Pt^{II} and at too great a distance [4.099(3) Å] to interact. Notably, our structure contrasts with the earlier $[Pt(18S6)]^{2+}$ structure with tetraphenylborate, which shows a symmetrical $[S_4 + S_2]$ binding of the 18S6.[9] As seen in the 9S3 structures, the coordination mode of the 18S6 can be switched between $[S_4 + S_2]$ and $[S_4 + S_1]$ depending upon crystal packing forces that arise from the counterion or crystallization solvent. Although the preferred conformation of the ligand is generally important in determining how it will bind to a metal ion, there appears to be some limited flexibility in coordination modes towards d^8 metal ions like Pt^{II} and Pd^{II}. For exclusively ethylene bridged thioether macrocycles like 9S3 and 18S6, the coordination mode can switch between $[S_4 + S_2]$ and $[S_4 + S_1]$, depending upon the solvent or anion. In that regard, our recent report of homoleptic Pt^{II} and Pd^{II} complexes of 12S3 (1,5,9-trithiacyclodecane, exclusive propylene bridges) shows examples of both $[S_4]$ and $[S_4 + S_1]$, but never $[S_4 + S_2]$ coordination.[10] The all-sulfur *exodentate* conformation of the12S3 ligand precludes its forming two Pt−S axial interactions, but it, too, has limited flexibility in its ability to coordinate these ions.

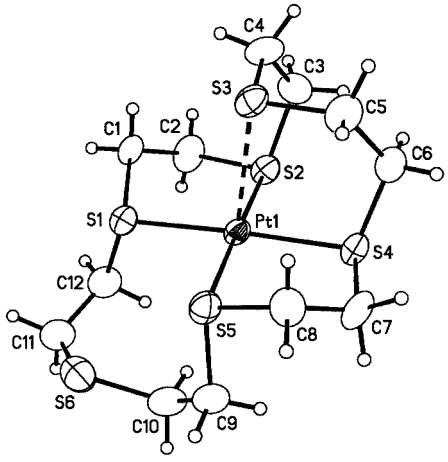

Figure 3. Thermal ellipsoid perspective (50% probability) of cation in $[Pt(18S6)](BF_4)_2$

The five-sulfur square pyramidal portion of the 18S6 ligand is in the eclipsed conformation, but strain within the macrocycle causes the remaining portion (involving the one *exodentate* sulfur atom) to adopt a staggered conformation. Previous 18S6 structures with Pd^{II} and Pt^{II} reported exclusively staggered or eclipsed conformers, so our structure represents an interesting intermediate case.[1,9] S−Pt−S chelate bite angles in the 18S6 structure are even smaller than the for the three 9S3 structures at slightly less than 89°. The four sulfur atoms in the equatorial plane (S1, S2, S4, and S5) are co-planar to within 0.126 Å. The Pt^{II} ion is displaced by 0.067(2) Å above the mean square plane and is directed towards the axial sulfur donor, S3. Equatorial distances are longer by 0.02 Å than in the earlier tetrafluoroborate structure, but the axial distance is surprisingly short. Indeed this is the shortest Pt−S axial distance observed in a homoleptic thioether complex of platinum(II). A full listing of Pt−S equatorial and axial distances for Pt^{II} thiacrown complexes that exhibit these two types of structures appears in Table 2. The two shortest Pt−S axial distances are observed, notably, for the two $[S_4 + S_1]$ structures, and both $[S_4 + S_1]$ structures show the platinum displaced towards the axial sulfur above the least-squares plane of the four sulfur donors. In general, the average Pt−S equatorial bond lengths show little variation, but there is a large difference in Pt−S axial distances.

Although there are no interionic contacts shorter than van der Waal's radii sums, there are interesting S···F contacts involving all six sulfur atoms, with distances ranging from 3.31(1) to 3.52(1) Å (average of 3.43(9) Å] − just outside the van der Waal's sum for sulfur and fluorine (S 1.80 Å; F 1.47 Å).[23] These contacts are roughly co-linear with the Pt−S bonds (range of Pt−S···F angles: 144(1)−175(1)°; average 166(11)°] and approximately along the line expected

 © 2005 Wiley-VCH Verlag GmbH & Co. KGaA, Weinheim

Table 2. Listing of Pt−S equatorial and Pt−S axial distances for Pt^{II} thiacrown complexes that display [S_4 + S_1] or [S_4 + S_2] coordination

Complex	Anion	Solid state structure	Pt−S equatorial	Pt−S axial	Reference
$[Pt(9S3)_2]^{2+}$	PF_6^-	S_4 + S_1	2.29 Å	2.89 Å	[6]
$[Pt(18S6)]^{2+}$	BF_4^-	S_4 + S_1	2.32 Å	2.81 Å	this work
$[Pt(9S3)_2]^{2+}$	PF_6^-	S_4 + S_2	2.29 Å	3.07 Å	this work
$[Pt(9S3)_2]^{2+}$	BF_4^-	S_4 + S_2	2.29 Å	3.04 Å	this work
$[Pt(9S3)_2]^{2+}$	OTf^-	S_4 + S_2	2.30 Å	3.24 Å	this work
$[Pt(10S3)_2]^{2+}$	PF_6^-	S_4 + S_2	2.30 Å	3.21 Å	[11]
$[Pt(10S3)_2]^{2+}$	PF_6^-	S_4 + S_2	2.30 Å	3.23 Å	[14]
$[Pt(18S6)]^{2+}$	BPh_4^-	S_4 + S_2	2.30 Å	3.38 Å	[9]

for a lone-pair on fluorine (range of B−F···S angles: 127(1)−149(1)°; average 136(9)°], suggesting a weak donor−acceptor character of these interactions. Indeed, we observe very similar behavior in the tetrafluoroborate salt of $[Pt(9S3)_2]^{2+}$, which also has S···F contacts in the range 3.49(3)−3.61(3) Å, which are approximately co-linear with the Pt−S bonds (Pt−S···F angles: 165°−169°). In our hexafluorophosphate structure, we observe very short S···F contacts between the fluorides of the anion and the axial sulfur. At 3.191(8) Å, these are shorter than the van der Waal's sum. There is also a short contact between the axial sulfur and one oxygen of the nitromethane solvent at 3.34 Å. The two hexafluorophosphate structures of $[Pt(9S3)_2]^{2+}$ show noticeable differences in the nature of the S···F contacts. The previous structure shows one short S···F contact (3.43 Å) between the *exodentate* sulfur and a fluorine atom in one hexafluorophosphate anion.[6] A second fluorine in the same anion, *cis* to this first fluorine, links to an equatorial sulfur in a different cation at 3.23 Å. For the triflate structure, the anions and solvent lie along the open side of the complex cation, away from the axial sulfur position. We feel that the solid-state structures obtained for this series of compounds can be influenced by weak donor−acceptor interactions between the sulfur atoms of the thioether macrocycle and anions or solvent.

Spectroscopic and Electrochemical Measurements

A d−d electronic transition at 426 nm results in the orange color of the $[Pt(18S6)]^{2+}$ complex. The relatively small extinction coefficient confirms that this absorption band is a d−d transition. The analogous Pt^{II} complexes, $[Pt(9S3)_2]^{2+}$ and $[Pt(10S3)_2]^{2+}$, also show similar transitions near 430 nm.[8,11,14] Note that these three ligands are the ones whose complexes have the shortest platinum−sulfur axial interactions. When these strong axial interactions are not present, the color of the complex is dominated by the position of charge-transfer bands, and may range from yellow to colorless.[10,14]

Carbon NMR spectroscopy was undertaken on the 18S6 complex to see if there was evidence for fluxionality in solution, as observed for trithioether complexes of Pt^{II}. The $^{13}C\{^1H\}$ NMR spectra in two different solvents both show a simple three-line carbon spectrum consistent with a centrosymmetric binding of 18S6. There is little change in the appearance of the spectrum with temperature, even up to 150 °C, and so we do not see evidence for fluxionality of the coordinated 18S6 ligand. The simple NMR spectrum is not consistent with the [S_4 + S_1] binding mode in the crystal structure, but rather the symmetrical [S_4 + S_2] structure shown by the tetraphenylborate salt.[9] Our NMR spectroscopic data suggest that the ligand, in solution, forms an S-shaped elongated octahedral structure, and that packing effects during crystallization result in the [S_4 + S_1] structure seen in our X-ray data. Another important result from the NMR study is the lack of fluxionality for the 18S6 ligand. Virtually every known 9S3 and 10S3 Pt^{II} complex shows fluxionality of the trithioether ligand. However, the 18S6 does not. The lack of fluxionality of the 18S6 may be due to the increased number of platinum−sulfur interactions (six vs. three) with the larger hexathioether macrocycle, supporting the 1,4-metallotropic shift exchange mechanism.[13]

Under the conditions of our cyclic voltammetry study, the complex $[Pt(18S6)]^{2+}$ exhibits an irreversible oxidation wave at +0.564 V and a second irreversible oxidation wave at +1.358 V. (both vs. Fc/Fc^+). Both are metal-centered oxidations and are assigned as a Pt^{II}/Pt^{III} couple and a Pt^{III}/Pt^{IV} couple, respectively. The electrochemical behavior resembles $[Pt(9S3)_2]^{2+}$ and $[Pt(10S3)_2]^{2+}$, but with two distinctions. First, the oxidation wave in the 18S6 complex appears at a higher positive potential, indicating greater difficulty in oxidizing the Pt^{II} center. Second, the +2/+3 couple for the trithioether complexes is fully reversible − not irreversible as observed for the 18S6 complex. We propose that the less flexible 18S6 cannot re-orient to facilitate oxidation of the Pt^{II}, thereby accounting for the greater difficulty of its oxidation and lack of reversibility in the electron transfer.

Lastly, the ^{195}Pt NMR spectrum of $[Pt(18S6)]^{2+}$ shows a single resonance at $\delta = -4152$ ppm, confirming the presence of a single complex in solution. The chemical shift is consistent with the hypothesis, regarding lone pair orientation on sulfur donors in macrocyclic thioether complexes,[10,12] that complexes with a mixed (half up, half down) orientation of lone pairs show values in the −4000 to −4300 ppm range, while those with all lone pairs on the sulfur donors oriented in the same direction have Pt resonances shifted upfield by ca. 500 ppm. Thus, the ^{195}Pt NMR chemical shift value agrees with the mixed lone pair orientation on the sulfur donors in the coordinated 18S6 ligand, as confirmed in our carbon-13 NMR work. We believe

 © 2005 Wiley-VCH Verlag GmbH & Co. KGaA, Weinheim

there is sufficient ^{195}Pt NMR spectroscopic data to establish a definite correlation between chemical shift and sulfur lone pair orientation in this series of complexes.

Conclusion

The crystal structures of four mononuclear Pt^{II} homoleptic complexes with two thiacrown ligands contrast with previous structural reports involving identical complex cations but differing anions or crystallization solvents. In the solid state, both [S_4 + S_1] and [S_4 + S_2] coordination of Pt^{II} by 9S3 and 18S6 are observed, depending upon packing forces. Our work illustrates how changes of counterion and solvent can have dramatic effects on the crystal structures for their complexes, suggesting that packing forces play a more dominant role than ligand conformation in determining specific solid-state structures. The spectroscopic and electrochemical properties of the complex $[Pt(18S6)](BF_4)_2$ are consistent with the presence of two Pt−S axial interactions in solution. The 18S6 ligand is non-fluxional in solution, in contrast to the trithiacrowns, and the ^{195}Pt NMR chemical shift indicates an alternating orientation of lone pair electrons on the sulfur donors.

Experimental Section

Materials: Thioether ligands 9S3 and 18S6, inorganic salts and K_2PtCl_4, and all solvents were purchased from the Aldrich Chemical Company, and used as received. The starting complex $[PtCl_2(C_2H_5CN)_2]$ was prepared according to the literature method.[24]

Measurements: Elemental analyses were performed by Atlantic Microlab, Inc. of Atlanta, Georgia. Fourier transform infrared spectra were obtained using a Galaxy FT IR 5000 spectrophotometer and ultraviolet-visible spectra were obtained on a Varian DMS 200 UV/Visible spectrophotometer. $^{13}C\{^1H\}$ and ^1H NMR spectra were recorded on a Varian Gemini 300 NMR spectrometer using CD_3NO_2 for both the deuterium lock and reference. $^{195}Pt\{^1H\}$ NMR spectra were recorded near 64.208 MHz using aqueous solutions of $[PtCl_6]^{2-}$ (δ = 0 ppm) as an external reference and a delay time of 0.01 s. Referencing was verified versus authentic samples of $[PtCl_4]^{2-}$, which had a chemical shift at δ = −1626 ppm, in agreement with its reported value of −1624 ppm.[25] A Biological Analytical Systems 50 Analyzer was used for all electrochemical measurements. The supporting electrolyte was 0.1 M $(Bu)_4NBF_4$ in CH_3CN, and sample concentrations were 1 mM. Voltammograms were recorded at a scan rate of 100 mV s^{-1}. The standard three-electrode configuration was as follows: platinum working electrode, Pt-wire auxiliary electrode, and Ag/AgCl reference electrode. All potentials were referenced against a Fc/Fc^+ couple.

Synthesis of $[Pt(9S3)_2]^{2+}$ Complex Salts

$[Pt(9S3_2](BF_4)_2$: A mixture of $K_2[PtCl_4]$ (100.8 mg, 0.243 mmol) and 1,4,7-trithiacyclononane (88.5 mg, 0.491 mmol) was boiled under reflux in a 2:1 methanol/distilled water solution (26 mL). The resultant brownish-orange reaction mixture was allowed to cool and was then partitioned into two equal volumes for the subsequent addition of counterion. $NaBF_4$ (56.3 mg, 0.513 mmol) was added to one aliquot and then cooled to 0 °C. Orange crystals thus formed were filtered off, washed with cold methanol (3 × 15 mL) and diethyl ether (3 × 15 mL) to yield bis(1,4,7-trithiacyclononane)-platinum(II) tetrafluoroborate (76.2 mg, 86.3%). FT-IR (KBr): $\tilde{\nu}$ = 2980, 2935, 2832, 1427, 1401, 1320, 1285, 1225, 1165, 1061(s, BF_4^-), 834, 646, 526 cm^{-1}. $C_{12}H_{24}B_2F_8PtS_6$ (729.38): calcd. C 19.76, H 3.32, S 26.37; found C 19.99, H 3.25, S 26.25. Slow diffusion of diethyl ether into a nitromethane solution yielded X-ray quality crystals as a nitromethane solvate.

$[Pt(9S3)_2](BPh_4)_2$: $NaBPh_4$ (167.2 mg, 0.4886 mmol) was added to the remaining aliquot of $[Pt(9S3)_2]^{2+}$ and the resultant mixture chilled to 0 °C. The so-obtained dark orange crystals were then filtered off, washed with cold methanol (3 × 15 mL) and diethyl ether (3 × 15 mL) to yield bis(1,4,7-trithiacyclononane)platinum(II) tetraphenylborate (130 mg, 89.7%) as a dark orange solid. FT-IR (KBr): 3050, 2985, 1577, 1476, 1155, 746, and 608 cm^{-1}. Poor solubility of the complex in common solvents limited additional study. $C_{60}H_{64}B_2PtS_6$ (1194.25): calcd. C 60.34, H 5.40, S 16.11; found C 60.04, H 5.55, S 15.99.

$[Pt(9S3_2](PF_6)_2$: This compound has been previously reported, and a crystal grown from acetonitrile.[6] We were interested in repeating the crystallization using nitromethane. A mixture of $K_2[PtCl_4]$ (206 mg, 0.497 mmol) and 9S3 (195 mg, 1.00 mmol) were boiled under reflux in 2:1 methanol−water (v/v, 49 mL) solution for 19 h. The resulting yellow solution was filtered off and concentrated to 2/3 of its original volume. Upon addition of NH_4PF_6 (176 mg, 0.491 mmol), yellow crystals of the complex formed. After cooling to 0 °C, the crystals were filtered off, washed with cold methanol (3 × 15 mL), anhydrous diethyl ether (3 × 15 mL), and air-dried. The reaction produced bis(1,4,7-trithiacyclodecane)platinum(II) hexafluorophosphate (334 mg, 79.3%) as an orange crystalline solid. FT-IR (KBr): 2995, 2944, 2925, 2848, 1444, 1410, 1290, 1272, 932, 837 (s, PF_6^-), 558 cm^{-1}. The electronic absorption spectrum measured in acetonitrile showed three λ_{max}s, at 430 (ε = 120), 287 (ε = 11,000) and 250 nm (ε = 15,000), matching its literature spectrum.[6] Slow diffusion of diethyl ether into a nitromethane solution yielded X-ray quality crystals as a nitromethane solvate.

$[Pt(9S3_2](OTf)_2$: Silver triflate, AgOTf, $AgSO_3CF_3$ (277 mg, 1.08 mmol) was added to a solution of $[PtCl_2(C_2H_5CN)_2]$ (193 mg, 0.513 mmol) dissolved in dichloromethane (3.5 mL) and propanenitrile (0.10 mL). This suspension was stirred vigorously for 5 h and the resultant white AgCl precipitate removed by filtration to yield a light yellow solution. The AgCl precipitate was then washed twice with additional CH_2Cl_2 (2 mL). 9S3 (200 mg, 1.11 mmol) was quickly added and stirred overnight. If too much time lapses before the addition of the 9S3 ligand, the Pt solution turns blue, evidently due to the formation of an aqua complex.[24] Diethyl ether was then added drop-wise to precipitate orange crystals of $[Pt(9S3_2](OTf)_2$ (129 mg, 29.6% yield). $C_{14}H_{24}F_6O_6PtS_8$ (853.90): calcd. C 19.69, H 2.83; found C 19.61, H 2.86. The visible electronic absorption spectrum measured in acetonitrile showed one λ_{max} at 420 nm (ε = 110). Slow diffusion of diethyl ether into a nitromethane solution yielded X-ray quality orange prismatic crystals as a nitromethane solvate. The crystals readily desolvate in air, but are quite stable when protected.

Synthesis of $[Pt(18S6]^{2+}$ Salts

A mixture of $K_2[PtCl_4]$ (315 mg, 0.759 mmol) and 18S6 (278 mg, 0.771 mmol) was boiled under reflux in a methanol−water (2:1 v/v, 84 mL) solution for 17.5 h. The resulting yellow solution was filtered and then concentrated to 40 mL. Four 10 mL portions of

 © 2005 Wiley-VCH Verlag GmbH & Co. KGaA, Weinheim

the solution were then divided and used for subsequent anion metathesis reactions.

[Pt(18S6](BF$_4$)$_2$: An aliquot of the [Pt(18S6]$^{2+}$ solution (10 mL) was mixed with $NaBF_4$ (42.2 mg, 0.384 mmol), and the resultant solution filtered. Slow evaporation of the filtrate yielded crystals (36.0 mg, 26.0% yield) of 1,4,7,10,13,16-hexathiacyclooctadecaneplatinum(II) tetrafluoroborate suitable for X-ray diffraction studies. IR (KBr): 2990, 2945, 2844, 1427, 1320, 1285, 1234, 1177, 1075−1033 (s, BF_4^-), 925, 808, 656, 574, 564 cm^{-1}. $C_{12}H_{24}B_2F_8PtS_6$ (729.38): calcd. C 19.76, H 3.32, S 26.37; found C 20.04, H 3.27, S 26.18.3

[Pt(18S6](PF$_6$)$_2$: An aliquot of the [Pt(18S6]$^{2+}$ solution (10 mL) was mixed with NH_4PF_6 (59.5 mg, 0.365 mmol), and the solution was chilled in an ice bath for 1.5 hours to afford light orange crystals that were filtered off and washed with chloroform (5 mL) to yield 1,4,7,10,13,16-hexathiacyclooctadecaneplatinum(II) hexafluorophosphate (126 mg, 78.4%) as an orange crystalline solid. IR (KBr): 2991, 2952, 2850, 1430, 1285, 1244, 1180, 1077, 1056, 841 (s, P−F), 651, 574, 558 cm^{-1}. $C_{12}H_{24}P_2F_{12}PtS_6$ (845.70): calcd. C 17.04, H 2.86, S 22.75; found C 17.15, H 2.85, S 22.66. As this salt offered the best solubility properties, most solution work was performed on it. The electronic absorption spectrum measured in acetonitrile showed two λ_{max}s, at 426 nm (ε = 84) and at 235 (ε = 28222). The electrochemistry of the complex showed one irreversible oxidation wave at +564 mV and a second irreversible oxidation wave at +1358 mV vs. Fc/Fc$^+$. ^{1}H NMR (300 MHz, CD_3CN, 25 °C): broad, poorly resolved resonances from 2.8 to 3.6 ppm. $^{13}C\{^1H\}$ NMR (75 MHz, CD_3CN, 25 °C): three peaks of approximately equal intensity at 27.54, 38.86, and 42.59 ppm. These were all confirmed to be methylene resonances by a DEPT experiment. $^{195}Pt\{^1H\}$ NMR (64.4 MHz, CD_3NO_2, 25 °C), δ ($\nu_{1/2}$): singlet at δ = −4152 ppm (91 Hz).

[Pt(18S6](BPh$_4$)$_2$: The synthesis and X-ray structure of this compound has been reported previously.[1] An aliquot of the [Pt(18S6]$^{2+}$ solution (10 mL) was mixed with $NaBPh_4$ (131 mg, 0.383 mmol), and the solution was then chilled in an ice bath for 1.5 hours to give light orange crystals that were filtered off and washed with chloroform (5 mL) to yield 1,4,7,10,13,16-hexathiacyclooctadecaneplatinum(II) tetraphenylborate (55.0 mg, 24.7%). IR (KBr): 3090, 3050, 2993, 2954, 1430, 1285, 1244, 1180, 1077, 1056, 750, 750, 670, 574 cm^{-1}. The electronic absorption spectrum measured in acetonitrile matched the reported literature spectrum.[1]

[Pt(18S6](ClO$_4$)$_2$: An aliquot of the [Pt(18S6]$^{2+}$ solution (10 mL) was mixed with $NaClO_4$ (53.9 mg, 0.440 mmol), and the solution was allowed to slowly evaporate to afford light orange crystals that were filtered off. These crystals were then washed with chloroform (5 mL) to yield 1,4,7,10,13,16-hexathiacyclooctadecaneplatinum(II) perchlorate (32.0 mg, 22.3%). IR (KBr): 2981, 2945, 2914, 1430, 1285, 1094−1074 (s, ClO_4^-), 925, 777, 623, 574 cm^{-1}. $C_{12}H_{24}Cl_2O_8PtS_6$ (754.68): calcd. C 19.10, H 3.21, Cl 9.40, S 25.44; found C 19.18, H 3.19, Cl 9.45, S 25.57. $^{13}C\{^1H\}$ NMR (75 MHz, [D$_6$]DMSO, 25 °C): three broad peaks of approximately equal intensity at δ = 25.8, 27.2, and 40.7 ppm.

Caution! Although the perchlorate salt prepared in this report did not appear to be shock-sensitive, they should always be handled with caution and used only in very small quantities.

X-Ray Data Collection and Processing

Suitable crystals of all complexes were grown by slow diffusion of diethyl ether into a nitromethane solution. Table 3 summarizes the key crystallographic details for the structures.

9S3 Complexes: For the tetrafluoroborate and hexafluorophosphate structures, intensity data were collected at low temperature

Table 3. Crystallographic data summary for [Pt(9S3)$_2$](PF$_6$)$_2$·2CH$_3$NO$_2$ (**1**), [Pt(9S3)$_2$](BF$_4$)$_2$·2CH$_3$NO$_2$ (**2**), [Pt(9S3)$_2$](OTf)$_2$·2CH$_3$NO$_2$ (**3**), and [Pt(18S6)](BF$_4$)$_2$ (**4**)

	1	**2**	**3**	**4**
Empirical formula	$C_{14}H_{30}F_{12}P_2N_2O_4S_6Pt$	$C_{14}H_{30}F_8B_2N_2O_4S_6Pt$	$C_{16}H_{30}F_6N_2O_{10}S_8Pt$	$C_{12}H_{24}B_2F_8S_6Pt$
fw, amu	967.9	851.47	975.99	729.38
Size/mm	0.44 × 0.34 × 0.17	0.34 × 0.29 × 0.10	0.48 × 0.14 × 0.12	0.36 × 0.27 × 0.11
Appearance	orange prisms	orange prisms	orange prisms	yellow, parallelepiped
Space group	monoclinic	monoclinic	orthorhombic	triclinic
Crystal system	$P2_1/c$	$P2_1/c$	$Pbca$	$P\bar{1}$
a (Å)	9.9379(15)	9.5710(12)	14.024(3)	5.463(2)
b (Å)	15.310(2)	15.227(19)	11.353(2)	10.436(2)
c (Å)	10.0017(15)	9.7031(12)	20.665(4)	10.094(7)
α (°)	90	90	90	93.22(2)
β (°)	99.587(2)	102.178(3)	90	94.34(3)
γ (°)	90	90	90	90.99(3)
V (Å)^3	1500.5(4)	1382.3(3)	3290.4(11)	1083.7(6)
Z	2	2	4	2
$\rho_{calcd.}$ (g cm^{-3})	2.142	2.046	1.970	2.235
Radiation [λ (Å)]	0.71073	0.71073	0.71073	0.71073
μ (mm^{-1})	5.203	5.609	4.854	7.118
Trans. coeff.	0.2028 and 0.4660	0.2515 and 0.5985	0.2040 and 0.5935	0.657 and 1.000
T (K)	193(2)	193(2)	173(2)	293(2)
Refls. collected	8593	7369	26774	4038
Refls. unique	3538	3119	2969	3807
R index[a] [$I > 2\sigma(I)$]	$R1$ = 0.0327	$R1$ = 0.0340	$R1$ = 0.0445	$R1$ = 0.0457
R indices[a] (all data)	R1= 0.0371	$R1$ = 0.0462	$R1$ = 0.0504	$R1$ = 0.0729
	$wR2$ = 0.0930	$wR2$ = 0.1175	$wR2$ = 0.0964	$wR2$= 0.1343

[a] $R1 = (\Sigma||F_o| - |F_c||)/\Sigma|F_o|$; with $wR2 = \{\Sigma[w(F_o^2 - F_c^2)^2]/\Sigma[w(F_o^2)^2]\}^{1/2}$.

 © 2005 Wiley-VCH Verlag GmbH & Co. KGaA, Weinheim

on a Siemens SMART 1 K CCD diffractometer[26,27] equipped with graphite-monochromated Mo-K_α radiation (λ = 0.71073 Å). Structures were solved by direct methods,[26] and refinement was done using full-matrix least-squares techniques (on F^2). Structure solution, refinement and the calculation of derived results were performed with the SHELXTL[28] package of computer programs. For the triflate structure, intensity data were measured at room temperature with graphite-monochromated Mo-K_α radiation (λ = 0.71073 Å) on a Rigaku AFC-8 diffractometer[29,30] equipped with a 1 K mercury CCD detector.

18S6 Complex: Intensity data were measured at room temperature with graphite-monochromated Mo-K_α radiation (λ = 0.71073 Å) on a Rigaku AFC7R diffractometer. Data were corrected for Lorentz and polarization effects, and for absorption, using semi-empirical methods. The structure of the 18S6 complex was solved by direct methods and refined by using full-matrix least-squares techniques (on F^2). All non-hydrogen atoms were refined anisotropically; hydrogen atoms were placed in optimized positions (d_{C-H} = 0.96 Å) with assigned thermal parameters equal to 120% of the U_{eq} value of their host atom. Structure solution, refinement and the calculation of derived results were performed with the SHELXTL[28] package of computer programs. Neutral atom scattering factors were those of Cromer and Waber,[31a] and the real and imaginary anomalous dispersion corrections were those of Cromer.[31b]

CCDC-219803 (for $[Pt(9S3)_2](PF_6)_2{\cdot}2CH_3NO_2$), -219804 (for $[Pt(9S3)_2](BF_4)_2{\cdot}2CH_3NO_2$), -238122 (for $[Pt(9S3)_2](OTf)_2{\cdot}2CH_3NO_2$) and -238123 (for $[Pt(18S6)](BF_4)_2$) contain the supplementary crystallographic data for this paper. These data can be obtained free of charge at www.ccdc.cam.ac.uk/conts/retrieving.html [or from the Cambridge Crystallographic Data Centre, 12 Union Road, Cambridge CB2 1EZ, UK; Fax: (internat.) +44-1223-336-033; E-mail: deposit@ccdc.cam.ac.uk].

Acknowledgments

This work was generously supported by the Petroleum Research Fund, administered by the American Chemical Society, the Grote Chemistry Fund, the Research Corporation, and the William L. Wheeler Center for Odor Research at the University of Tennessee at Chattanooga. We thank David Galas for his assistance with some of the NMR measurements.

[1] A. J. Blake, M. Schröder, in *Advances in Inorganic Chemistry* (Ed.: A. G. Sykes), vol. 35, Academic Press, Inc., New York, **1990**, 2.
[2] S. R. Cooper, *Acc. Chem. Res.* **1988**, *21*, 41.
[3] S. R. Cooper, S. C. Rawle, *Structure and Bonding* (*Berlin*) **1990**, *72*, 1.
[4] M. Schröder, *Pure and Appl. Chem.* **1988**, *60*, 517.
[5] W. N. Setzer, E. L. Cacioppo, Q. Guo, G. J. Grant, D. D. Kim, J. L. Hubbard, D. G. VanDerveer, *Inorg. Chem.* **1990**, *29*, 2672.
[6] A. J. Blake, R. O. Gould, A. J. Holder, T. I. Hyde, A. J. Lavery, M. O. Odulate, M. Schröder, *J. Chem. Soc., Chem. Commun.* **1987**, 118.
[7] A. J. Blake, A. J. Holder, G. Reid, M. Schröder, *J. Chem. Soc., Dalton Trans.* **1994**, 627.
[8] A. J. Blake, A. J. Holder, T. I. Hyde, Y. V. Roberts, A. J. Lavery, M. Schröder, *J. Organomet. Chem.* **1987**, *323*, 261.
[9] A. J. Blake, R. O. Gould, A. J. Lavery, M. Schröder, *Angew. Chem. Int. Ed. Engl.* **1986**, *25*, 274.
[10] G. J. Grant, A. M. Goforth, D. G. VanDerveer, W. T. Pennington, *Inorg. Chim. Acta* **2004**, *357*, 2107.
[11] A. J. Blake, R. D. Crofts, M. Schröder, *J. Chem. Soc., Dalton Trans.* **1993**, 2259.
[12] A. J. Blake, Y. V. Roberts, M. Schröder, *J. Chem. Soc., Dalton Trans.* **1996**, 1885.
[13] H. Nikol, H.-B. Bürgi, K. I. Hardcastle, H. B. Gray, *Inorg. Chem.* **1995**, *34*, 6319.
[14] G. J. Grant, N. S. Spangler, W. N. Setzer, D. G. VanDerveer, *Inorg. Chim. Acta* **1996**, *246*, 41.
[15] T. W. Hambley, *Inorg. Chem.* **1998**, *37*, 3767.
[16] The sum of the van der Waals radii is 3.50 Å for platinum(II) and sulfur and 3.40 Å for palladium(II) and sulfur. J. E. Huheey, E. A. Keiter, R. L. Keiter, *Inorganic Chemistry*, 4th edition, Harper Collins: New York, **1993**, 292.
[17] M. A. Bennett, A. J. Canty, J. K. Felixberger, L. M. Rendina, C. Sunderland, A. C. Willis, *Inorg. Chem.* **1993**, *32*, 1951.
[18] Over twenty structures of 9S3 coordinated to Pt^{II} are known. For a few examples, see: [18a] G. J. Grant, I. M. Poullaos, D. F. Galas, D. G. VanDerveer, J. D. Zubkowski, E. J. Valente, *Inorg. Chem.* **2001**, *40*, 564. [18b] G.-H. Lee, *Acta Crystallogr., Sect. C* **1998**, *54*, 906. [18c] G. J. Grant, C. G. Brandow, D. F. Galas, J. P. Davis, W. T. Pennington, J. D. Zubkowski, E. J. Valente, *Polyhedron* **2001**, *20*, 3333. [18d] G. J. Grant, I. M. Poullaos, D. F. Galas, S. C. Carter, D. G. VanDerveer, *J. Chem. Soc., Dalton Trans.* **2002**, 2973. [18e] G. J. Grant, D. F. Galas, D. G. VanDerveer, *Polyhedron* **2002**, *21*, 879. [18f] G. J. Grant, S. M. Carter, I. M. Poullaos, A. L. Russell, D. G. VanDerveer, *J. Organomet. Chem.* **2001**, *637–639*, 683. [18g] G. J. Grant, J. D. Pool, D. G. VanDerveer, *Dalton Trans.* **2003**, 3981.
[19] S. Chandrasekhar, A. McAuley, *Inorg. Chem.* **1992**, *30*, 2663.
[20] G. J. Grant, K. A. Sanders, W. N. Setzer, D. G. VanDerveer, *Inorg. Chem.* **1991**, *30*, 4053.
[21] A. J. Blake, R. O. Gould, W.-S. Li, V. Lippolis, S. Parsons, M. Schröder, *Crystal Engineering* **1999**, *2*, 153.
[22] A. J. Blake, L. M. Gilby, R. O. Gould, V. Lippolis, S. Parsons, M. Schröder, *Acta Crystallogr., Sect. C* **1998**, *54*, 295.
[23] A. Bondi, *J. Phys. Chem.* **1964**, *68*, 441.
[24] V. Y. Kukushkin, A. Oskarsson, L. I. Elding, *Inorg. Syntheses* **1997**, *31* 279.
[25] P. S. Pregosin (Ed.) in *Transition Metal Nuclear Magnetic Resonance*, Elsevier: New York, **1991**, 251, and references cited therein.
[26] Programs used for data collection, solution and refinement of this structure were: *SMART 5.054, SAINT$^+$ 6.01, SHELXTL 5.1*, **1998–1999**, Bruker AXS, Madison, WI, USA.
[27] SADABS, R. H. Blessing, *Acta Crystallogr., Sect. A* **1995**, *51*, 33.
[28] *SHELXTL 5.1*, **1998–1999**, Bruker AXS, Madison, WI, USA.
[29] *CrystalClear*; Rigaku/MSC, The Woodlands, TX, USA, **1999**.
[30] R. A. Jacobson, REQAB, subroutine of *CrystalClear*; Rigaku/MSC, The Woodlands, TX, USA, **1999**.
[31] [31a] D. T. Cromer, J. T. Waber, *International Tables for X-ray Crystallography*, vol. IV, Table 2.2B, The Kynoch Press, Birmingham, England, **1974**. [31b] D. T. Cromer, *International Tables for X-ray Crystallography*, vol. IV, Table 2.3.1, The Kynoch Press, Birmingham England, **1974**.

Received June 2, 2004
Early View Article
Published Online December 6, 2004

 © 2005 Wiley-VCH Verlag GmbH & Co. KGaA, Weinheim

Tetracyanoquinodimethanido Derivatives of (Terpyridine)- and (Phenanthroline)metal Complexes − Structural and Magnetic Studies of Radical-Ion Salts[‡]

Cristina Alonso,[a] Loreto Ballester,[a] Angel Gutiérrez,*[a] M. Felisa Perpiñán,[a] Ana E. Sánchez,[a] and M. Teresa Azcondo[b]

Keywords: Radical ions / Stacking interactions / Supramolecular chemistry / Magnetic properties

Several derivatives of formulae $[M(terpy)_2](TCNQ)_2$ or $[M(terpy)_2](TCNQ)_3$ (M = Ni, Cu, Zn; terpy = 2,2′:6′,2"-terpyridine; TCNQ= 7,7,8,8-tetracyanoquinodimethane) and $[M(phen)_3](TCNQ)_2$ or $[M(phen)_3](TCNQ)_4$ (M = Fe, Ni; phen = 1,10-phenanthroline) have been obtained. The crystal structures of $[M(terpy)_2](TCNQ)_2$ (M = Ni, Cu) show that the metal is surrounded by the terpyridine nitrogen atoms in a closed octahedral environment and the TCNQ anions are dimerised by π overlap. The cationic $[M(terpy)_2]^{2+}$ and the anionic $[TCNQ]_2^{2-}$ groups alternate in the crystal. For the derivatives with three TCNQ groups, the existence of a stack of trimeric $[TCNQ]_3^{2-}$ ions having electronic delocalisation is proposed. The compound $[Fe(phen)_3](TCNQ)_2$, which shows a strong interaction between TCNQ anions, led to the formation of a σ bond in the diamagnetic species [TCNQ–TCNQ], while the nickel analogue is expected to have a localised structure formed by alternation of cationic metal complexes and dimeric $[TCNQ]_2^{2-}$ anions similar to those observed in the analogous terpy derivatives. The derivatives having four TCNQ groups also show electronic delocalisation and a 1D stack based on the magnetic data is proposed.

(© Wiley-VCH Verlag GmbH & Co. KGaA, 69451 Weinheim, Germany, 2005)

Introduction

In the field of molecular networks containing organic radicals, macroscopic properties such as magnetic order or electric conductivity can be produced when the appropriate supramolecular arrangement is achieved.[1,2] On this basis, when paramagnetic metallic centres are integrated within organic radicals as building blocks in molecular networks, "hybrid" materials combining the properties of the organic and inorganic components can be formed.[3,4]

Special attention has been given to the assembly of organonitrile radical complexes with transition metals because of their rich interaction possibilities. One of the most extensively used radicals in these studies has been the planar organic molecule 7,7,8,8-tetracyanoquinodimethane (TCNQ) since it shows a low reduction potential which makes it a suitable acceptor in charge transfer processes and also shows, in its anion-radical form, a high σ-donor ability for coordinating to transition metals.[5−8] Another typical feature of this acceptor is the tendency to overlap its π-delocalised system with neighbouring molecules to form stacks with different degrees of electronic delocalisation.[9−12]

The compounds having vacant positions around the metal react with TCNQ salts forming new compounds where the anion-radical is coordinated via one or more of its nitrile groups.[6,8,13−15] When complexes with a fully coordinated metal environment are used, new species without direct bonding interactions between the metal and the TCNQ are formed. When TCNQ is fully reduced, dimerisation to $[TCNQ]_2^{2-}$ is usually observed[7,8,16] but when TCNQ is partially reduced, a greater electronic delocalisation along with the formation of infinite stacks is observed.[9−12]

The present work reports our studies on the interactions of TCNQ in different formal oxidation states with closed shell first row transition metal complexes aimed at looking for electronic delocalisation in our systems. We have used nitrogen donor ligands with aromatic rings such as terpy (2,2′:6′,2"-terpyridine) or phen (1,10-phenanthroline) which are susceptible to forming weak π interactions with the TCNQ rings.[17−26] These interactions are more common when neutral TCNQ is present and can modulate the TCNQ overlap responsible for the stacking.

[‡] A portion of this work was previously published in communication form: L. Ballester, A. Gutiérrez, M. F. Perpiñán, M. T. Azcondo, A. E. Sánchez, *Synth. Met.* **2001**, *120*, 965.

[a] Departamento de Química Inorgánica I, Facultad de Ciencias Químicas, Universidad Complutense,
28040 Madrid, Spain
Fax: (internat.) + 34-913944352
E-mail: alonso@quim.ucm.es
[b] Departamento de Ciencias Químicas, Facultad de Ciencias Experimentales y de la Salud, Universidad San Pablo, CEU,
28668 Boadilla del Monte, Madrid, Spain

 © 2005 Wiley-VCH Verlag GmbH & Co. KGaA, Weinheim **DOI: 10.1002/ejic.200400540**

Results and Discussion

All metallic compounds were obtained by metathesis reactions from the parent derivatives. When only anionic TCNQ was added to the reaction mixture in the form of LiTCNQ, the compounds $[M(terpy)_2](TCNQ)_2$, (M = Ni, **1**; Cu **2**; Zn, **3**) or $[M(phen)_3](TCNQ)_2$, (M = Fe, **7**, Ni **8**) were obtained. TCNQ is in the anionic form in each case since it must neutralise the two positive charges on the metal ion. The tendency for TCNQ to dimerise means that the anions appear as dimers, i.e. $[TCNQ]_2^{2-}$. The exception to this behaviour is $[Fe(phen)_3](TCNQ)_2$ where the π interaction between the radical anions is so strong that a σ-carbon−carbon bond is formed. The formation of this σ-dianion (TCNQ−TCNQ) has previously been observed only in a few cases.[27−31]

In the reaction with $(NEt_3H)(TCNQ)_2$, with both neutral and anionic TCNQ present, the derivatives obtained correspond to the formulae $[M(terpy)_2](TCNQ)_3$ (M = Ni **4**; Cu **5**; Zn **6**) or $[M(phen)_3](TCNQ)_4$ (M = Fe **9**; Ni **10**). The TCNQ species in these compounds show an average formal charge of 0.66 e^- and 0.5 e^-, respectively, suggesting some degree of electronic delocalisation, a fact that is usually reflected in the formation of 1D TCNQ chains resulting from overlap of the π clouds of adjacent units.[11,12,32−38]

The new compounds are only slightly soluble in polar solvents such as acetonitrile or dimethyl sulfoxide. These solvents break any interactions between the metal cations and the TCNQ units which could be present in the solid state. For this reason, the solutions behave as a mixture of the metallocations and TCNQ, either in anionic or in neutral form. The spectroscopic and electrochemical data of these solutions do not give any additional information to that obtained for solid state samples, as previously described.[8,11,14] The spectroscopic data from solid-state samples will be commented upon below.

Crystal Structures

$[Ni(terpy)_2](TCNQ)_2$ (1)

This compound crystallises in the $P2_1/n$ space group. Figure 1 shows an ORTEP view of the molecular unit. The crystal structure can best be described as formed from alternating $[Ni(terpy)_2]^{2+}$ cations and dimeric $[TCNQ]_2^{2-}$anions. The nickel atom is hexacoordinated by the nitrogen atoms of the two terpy ligands in a *mer* arrangement which is expected for the ligand geometry. The nickel−nitrogen distances range between 1.994(1) and 2.132(1) Å with the shortest distances corresponding to the central nitrogen of each terpy ligand due to the strain imposed by the coordination.[39−41]

There are two crystallographically independent TCNQ molecules, A and B, in the asymmetric unit. The carbon−carbon bond lengths in the TCNQ rings are characteristic of the fully reduced radical-anion.[42] This is expected since the two positive charges in the metallic cation must be neutralised. Every $TCNQ_A$ overlaps with a $TCNQ_B$ in the ring-over-ring mode, thereby forming

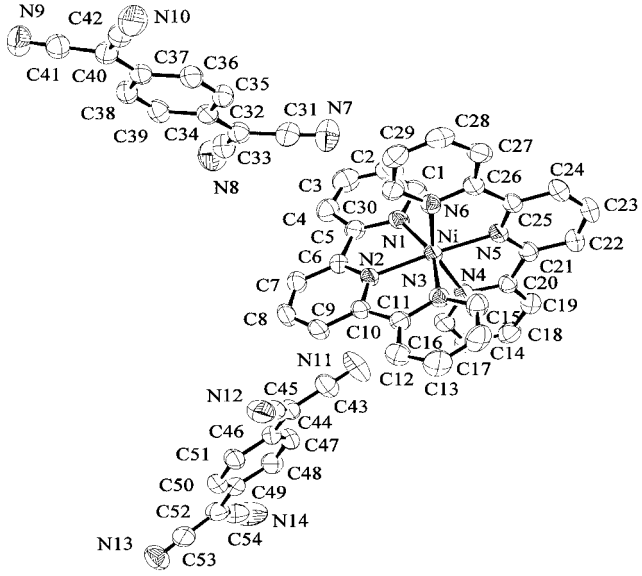

Figure 1. ORTEP view and labelling scheme of $[Ni(terpy)_2](TCNQ)_2$ (**1**); the atom labelling of the copper compound (**2**) is identical

$[TCNQ]_2^{2-}$ dianions with the shortest interplanar distance being 3.28(1) Å. The TCNQ planes are parallel to within 1.38(6)°. These planes form an angle of 31.32(6)° with one of the terpy ligands but no short contacts (less than 3.4 Å) could be found, suggesting that the cations and anions only interact by electrostatic forces in the crystal (Figure 2).

$[Cu(terpy)_2](TCNQ)_2$ (2)

This compound crystallises in the $P2_1/c$ space group. Its labelling scheme is identical to that shown in Figure 1 for the nickel derivative.

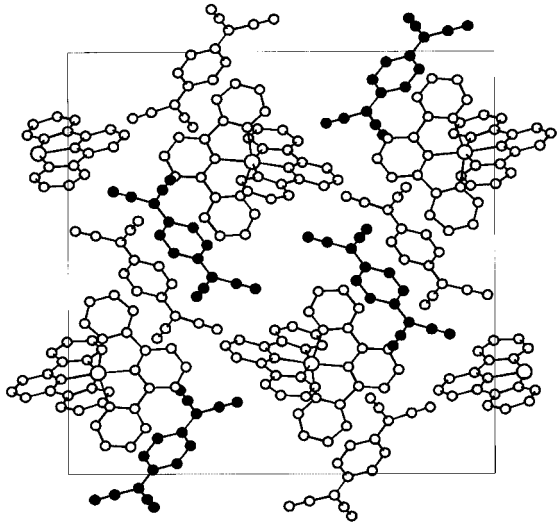

Figure 2. Unit cell contents for $[Ni(terpy)_2](TCNQ)_2$ (**1**); atoms in TCNQ A are shown as white circles and in TCNQ B as black circles

The metal environment is similar to that of the nickel derivative but the Cu−N distances vary more due to the Jahn−Teller effect which is expected for the copper centre.

 © 2005 Wiley-VCH Verlag GmbH & Co. KGaA, Weinheim

This induces a rhombic distortion with opposite distances of 1.956(6) and 2.016(7) Å for the central nitrogen atoms, 2.103(6) and 2.137(7) Å for one pair of extreme nitrogen atoms and 2.250(7) and 2.277(7) Å for the other pair. A similar distortion has been observed in the structure of the parent nitrate and in related derivatives.[43−45] In accordance with these data the EPR spectrum of this compound at room temperature shows a rhombic pattern with *g* values of 2.20, 2.12 and 2.02.

There are also two crystallographically independent TCNQ anions in the cell, namely A and B, but in contrast with the nickel derivative each TCNQ overlaps with a symmetry related anion giving rise to two different $[TCNQ_A]_2^{2-}$ dimers with a ring-over-external bond overlap and a shortest interplanar distance of 3.14(1) Å and a $[TCNQ_B]_2^{2-}$ dianion overlapping in the ring-over-ring mode with a shortest distance of 3.19(1) Å (Figure 3).

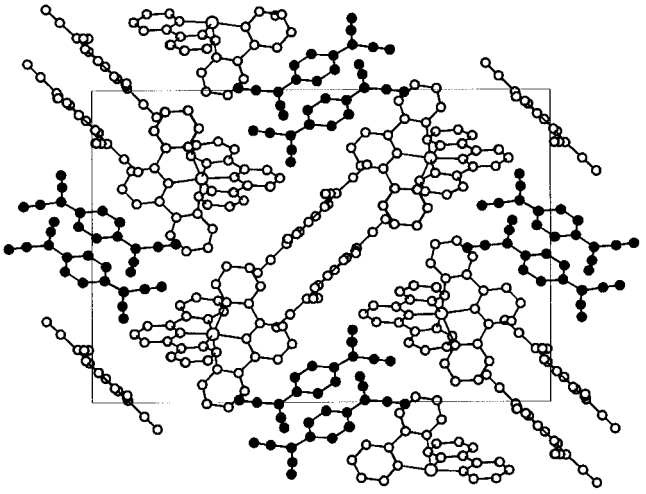

Figure 3. Unit cell contents for $[Cu(terpy)_2](TCNQ)_2$ (**2**); atoms in TCNQ A are shown as white circles and in TCNQ B as black circles

The $TCNQ_A$ dimers are isolated from the $[Cu(terpy)_2]^{2+}$ cations although the $TCNQ_B$ centres do overlap with the terpy rings of different cations through their external bonds (Figure 4) with shortest distances of 3.29(1) and 3.31(1) Å. The angle formed between the terpy and the $TCNQ_B$ is 28.0(2)°. These overlaps allow a small degree of electronic delocalisation along the tetrameric terpy·$TCNQ_B$·$TCNQ_B$·terpy stack. The stack does not continue through the solid, thus limiting possible delocalisation.

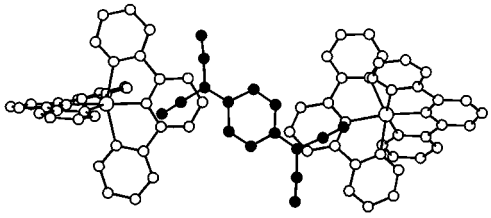

Figure 4. View of the overlap between $TCNQ_B$ and the terpy ligands of two adjacent $[Cu(terpy)_2]$ cations

[Fe(phen)$_3$](TCNQ−TCNQ) (7)

This compound crystallises in the *Cc* space group. Figure 5 shows the molecular unit with the labelling scheme. The structure can be described as formed from alternating sheets of $[Fe(phen)_3]^{2+}$ cations and σ-dimerised $[TCNQ-TCNQ]^{2-}$ anions. In the cations, the iron atom is hexacoordinated by the nitrogen atoms of three phen ligands with iron-nitrogen distances between 1.95 and 2.01 Å which is in the range usually found in other iron−phen derivatives.[46,47] The dimerised anion is obtained through the formation of a long bond between two exocyclic carbons. The carbon−carbon distance of 1.645(7) Å is similar to that found in the few cases in which this σ dimerization has been observed.[27−31] The formation of this bond is reflected in the tetrahedral conformation adopted by the linked carbon atoms, with angles between the ring plane

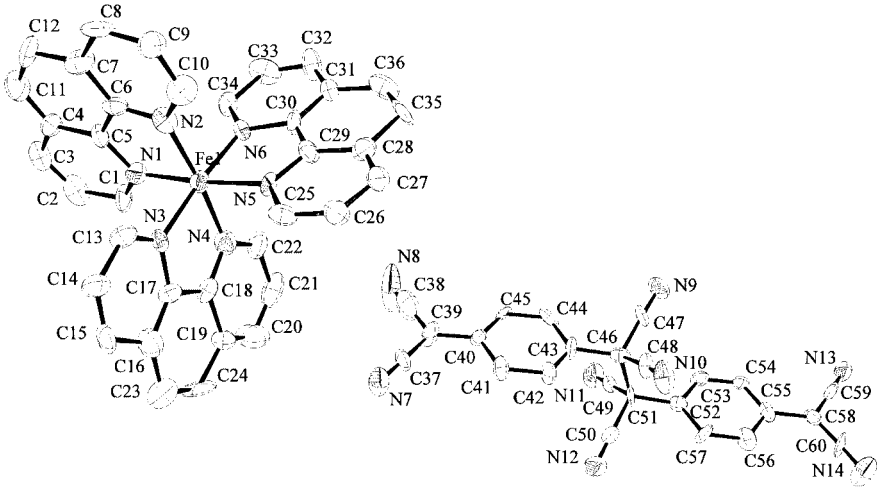

Figure 5. ORTEP view and labelling scheme of $[Fe(phen)_3](TCNQ)_2$ (**7**)

 © 2005 Wiley-VCH Verlag GmbH & Co. KGaA, Weinheim

and the $C(CN)_2$ plane of 49.4(7) and 46.4(7)°, while the rest of the molecule is essentially planar.

The anions and cations are packed (Figure 6) in alternating sheets parallel to the *ab* plane and no interactions other than the usual van der Waals contacts can be found between them. Inside the anionic sheets the [TCNQ−TCNQ] units are arranged in chains along the [−1 1 0] direction with shortest contacts of 3.37(2) Å between C45 and C56.

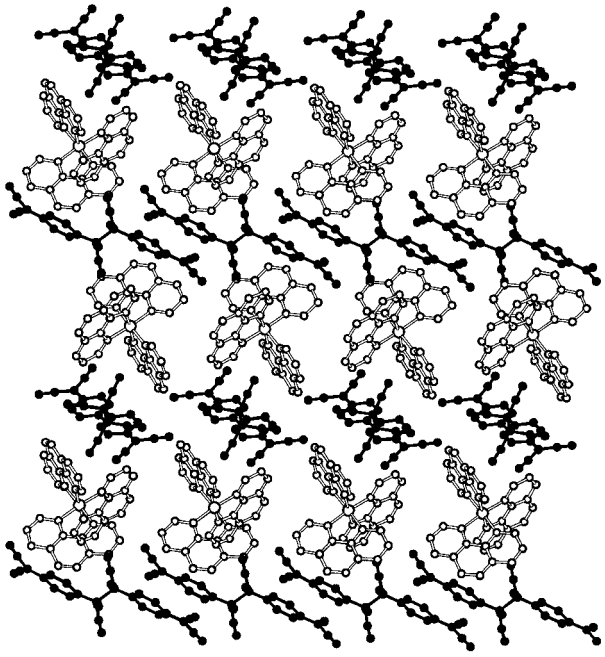

Figure 6. View of the alternating sheets of $[Fe(phen)_3]^{2+}$ cations and $[TCNQ-TCNQ]^{2-}$ anions in the structure of **7**

Spectroscopic Studies

The IR spectra of the studied derivatives show the typical features found in other uncoordinated TCNQ compounds.[48−50] The most significant bands for the neutral TCNQ are ν(CN) = 2228 cm^{-1}, $\nu_{20}(b_{1u})$ = 1530 cm^{-1} and $\nu_{50}(b_{3u})$ = 860 cm^{-1}. These bands are shifted to lower frequencies on increasing the electronic charge on the TCNQ.

The derivatives with two TCNQ units per metal atom, **1**−**3** and **8**, show these bands with typical values for the uncoordinated anion-radical, in accord with the localised picture of dimeric $[TCNQ]_2^{2-}$ anions alternating with cationic $[MN_6]^{2+}$ units in the solid structure, as the crystal structure of **1** and **2** revealed.

The spectrum of **7** shows different features attributable to the formation of a TCNQ−TCNQ σ bond. Thus, in the ν(CN) region there are two bands, the first appears at 2172 cm^{-1} and is composed of several component bands as a consequence of the lowering of the symmetry imposed by the bond formation. The second band, however, appears at 2125 cm^{-1}, a value shifted to lower frequency compared with those usually found in the anion radical. The out of plane bending mode ν_{50} also appears at 805 cm^{-1} and has been suggested as characteristic of the presence of the σ dimer,[30] since the usual value for the monoanionic species is 825 cm^{-1}.

The derivatives with three or four TCNQ units per metal atom always have the organic acceptor partially reduced, forming stacks with some degree of electronic delocalisation. This fact is reflected in the IR spectra of these species whose main feature is the presence of the tail of a low energy electronic absorption (CT_2) with broad vibrational bands superimposed on it.[51−53] The frequency values, especially the ν_{50} band, are intermediate between the usual values of the neutral and monoanionic TCNQ, suggesting that the acceptor has a formally nonintegral oxidation state. The low energy electronic transition (CT_2) appears in our compounds in the 3500−5000 cm^{-1} region and can be attributed to a charge transfer between adjacent radical anionic and neutral TCNQ groups, the lower the value the higher the electronic delocalisation.

As a consequence of this delocalisation, these compounds show semiconducting behaviour with relatively high values of electrical conductivity at room temperature and low activation energies which can be correlated with the frequency of the CT_2 electronic charge transfer as can be seen in Table 1. The activation energy was obtained by always assuming an Arrhenius dependence of the conductivity on temperature.

As expected, the derivatives with two TCNQ molecules per formula unit have localised electronic charges leading to very low conductivity values. The terpy derivatives with three TCNQ groups are much better semiconducting species. This fact can be explained if we attribute, to these compounds, a solid-state structure consisting of infinite stacks of TCNQ units separated by rows of $[M(terpy)_2]^{2+}$ cations. Every acceptor molecule in the stack would bear a negative charge of 0.66 giving rise to the formation of overlapping $[TCNQ]_3^{2-}$ trimers with partial electronic delocalisation. This structure has been previously observed in related derivatives exhibiting similar properties but with three TCNQ groups per metal atom.[11,12]

Table 1. Electronic spectra and electrical conductivity data of some representative compounds

Compound	CT_2 [cm^{-1}]	σ [S cm^{-1}] (298 K)	E_a [eV]
$[Ni(terpy)_2](TCNQ)_2$ (**1**)		$1.1\ 10^{-10}$	1.12
$[Ni(terpy)_2](TCNQ)_3$ (**4**)	3754	$1.9\ 10^{-2}$	0.25
$[Zn(terpy)_2](TCNQ)_3$ (**6**)	4378	$3.6\ 10^{-3}$	0.38
$[Ni(phen)_3](TCNQ)_4{\cdot}2CH_3CN$ (**10**)	4630	$1.8\ 10^{-4}$	0.41

 © 2005 Wiley-VCH Verlag GmbH & Co. KGaA, Weinheim

The derivatives with four TCNQ groups per metal atom also show electronic delocalisation since the formal charge on every acceptor is 0.5. The reported structures of derivatives consisting of $TCNQ^{0.5-}$ show these anions stacked in nonuniform columns either forming dimerised ($[TCNQ]_2^{-}$)[38,54] or tetramerised ($[TCNQ]_4^{2-}$)[33,34,36,55] units. Both pictures correspond to a semiconductor and could suggest, for our derivatives **9**−**10**, a similar structure in the solid state.

Magnetic Properties

The bulk magnetic susceptibilities of the new compounds have been measured in the temperature range 2−300 K.

The magnetic moments of the nickel derivatives **1** and **4** follow the Curie law above 25 K with an abrupt descent in their values below this temperature as is shown for the former in Figure 7. This fact can be attributed to an anisotropic distortion of the nickel(II) environment which results in a zero field splitting of the ground state.[56] Equation (1) for the average magnetic susceptibility takes into account this single-ion anisotropy, where g_{Ni} is the Landé g factor for the nickel ion, k_B is Boltzmann's constant, β is the Bohr magneton, $x = D/k_BT$ with the parameter D measuring the zero-field splitting and $N\alpha$ is the temperature-independent paramagnetism.

$$<\chi>=(2Ng_{Ni}^2\beta^2/3k_BT)\{[2-2\exp(-x)]/x+\exp(-x)\}/[1+2\exp(-x)]+N\alpha \qquad (1)$$

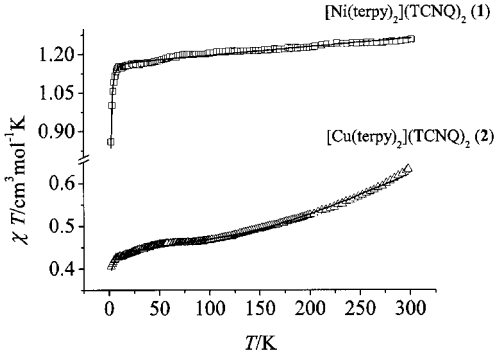

Figure 7. Temperature dependence of χT for **1** and **2**; the solid lines represent the best fit using the equations described in the text

The best fit was obtained when $g_{Ni} = 2.156$, $D = 3.34$ cm^{-1} and $N\alpha = 3.3\times10^{-4}$ cm^3mol^{-1} for **1,** and 2.07, 3.87 cm^{-1} and 9×10^{-5} cm^3mol^{-1}, respectively, for **4**. In both cases the values are typical of slightly distorted octahedral nickel(II) environments with no contribution to the magnetic moment from the organic radical anions. This is consistent with the presence of the dimerised anion-radical. The formation of dimeric $[TCNQ]_2^{2-}$ implies a strong antiferromagnetic coupling of both spins which renders the dianion diamagnetic at room temperature. The magnetic susceptibility variation can then be exclusively attributed to the contribution of the isolated metal ion. In accord with this behaviour, the zinc derivatives **3** and **6** are diamagnetic since no magnetic contribution can be expected from the metal ion.

The copper derivative **2** shows a steady increase in its χT value on increasing the temperature (Figure 7). The small decrease in the value at low temperatures can be ascribed to very weak antiferromagnetic interactions between the almost isolated copper(II) centres and can be fitted with the Curie−Weiss law. The increase in the χT value above 125 K is due to a small contribution from the TCNQ dimers which show a lower antiferromagnetic coupling than exhibited by the nickel and zinc derivatives. The lower value of the coupling implies that the triplet state is thermally accessible and populated near room temperature, giving rise to the contribution from the radicals to the magnetic susceptibility. Taking these two contributions into account, the molar magnetic susceptibility was fit, using Equation (2), to the sum of the Curie−Weiss law for the copper(II) ion and the Bleaney−Bowers equation[57] for the antiferromagnetically interacting TCNQ radicals, where g_{Cu} is the Landé g factor for the copper ion, J is the exchanging coupling constant for the TCNQ dimers, g is the Landé g factor for the TCNQ radicals and is assumed to be 2.003.

$$\chi=\frac{Ng_{Cu}^2\beta^2}{4k_B(T-\theta)}+\frac{Ng^2\beta^2}{k_BT}\left[\frac{2}{3+\exp(-J/k_BT)}\right]+N\alpha \qquad (2)$$

The rest of the parameters are the same as in Equation (1). The best fit for the experimental data, represented as a solid line in Figure 7, corresponds to $g_{Cu} = 2.161$, $\theta = -0.21$ K, $J = -278$ cm^{-1} and $N\alpha = 3.2\times10^{-4}$ cm^3mol^{-1}.

In contrast, compound **5** does not show any contribution from the organic radicals to the magnetic susceptibility which can be fit to the sum of the Curie−Weiss contribution from the copper ion, the first term in Equation (2) and the temperature-independent paramagnetism. The values obtained are $g_{Cu} = 2.26$, $\theta = -0.9$ K and $N\alpha = 8.4\times10^{-4}$ cm^3mol^{-1}. The high value of the TIP compared with those of the other compounds can probably be attributed to an incomplete diamagnetic correction although it is also plausible that it is due to a Pauli contribution originating from the delocalised electron of the anion radicals since the value is in the range of the paramagnetism observed in other conducting radical salts.[12,58] On the other hand, the low θ value for both copper derivatives indicates that the exchange between neighbouring copper spins can be considered negligible.

The phen derivatives show different behaviour, especially those showing electronic delocalisation. The iron derivative **7** is diamagnetic and corresponds to the presence of a low spin iron(II) and coupling between the two electrons with the formation of a TCNQ−TCNQ σ-bond. The magnetic susceptibility of the nickel derivative **8** is characteristic of isolated S = 1 spins and can be fitted to Equation (1) with values of $g_{Ni} = 1.94$, $D = 1.28$ cm^{-1} and $N_\alpha = 10^{-4}$ cm^3mol^{-1}.

 © 2005 Wiley-VCH Verlag GmbH & Co. KGaA, Weinheim

The magnetic susceptibilities of the derivatives **9** and **10**, with four TCNQ units per metal atom, show the contribution of the organic radicals which only partially couple in an antiferromagnetic manner.

The iron derivative **9** is weakly paramagnetic and this paramagnetism can only be attributed to the organic radicals since the low spin iron(II) has no unpaired electrons. The susceptibility dependence with temperature (Figure 8) can be interpreted as the sum of three contributions: (i) the contribution of the spins located on the TCNQ which can be adjusted to a 1D antiferromagnetic chain of S = 1/2 spins and which is responsible for the maximum around 65 K, (ii) a Curie contribution from a paramagnetic impurity which may arise from isolated radicals in the structure which gives the increase in susceptibility at lower temperatures and (iii) temperature-independent paramagnetism. The first contribution has been fit with a Heisenberg linear chain model using the expression derived by Hatfield et al.[59] and constitutes the first term of Equation (3) where $x = |J|/k_BT$ and A, B, C, D, E and F are functions of α, a parameter that takes into account the distortion in the chain and can vary from $\alpha = 0$ (corresponding to isolated $TCNQ^-$ dimers) to $\alpha = 1$ (corresponding to a uniform chain of S = 1/2 spins). The second term of Equation (3) is the Curie contribution from the impurities with C being the Curie constant, while the final term is the TIP. The other parameters have the same meaning as in Equations (1) and (2).

$$\chi = \frac{Ng^2\beta^2}{k_BT}\left[\frac{A+Bx+Cx^2}{1+Dx+Ex^2+Fx^3}\right]+\frac{C}{T}+N\alpha \quad (3)$$

The best fit has been obtained assuming $g = 2.003$ for the TCNQ group and affords $J = -44$ cm^{-1}, $\alpha = 0.67$, $C = 0.007$ cm^{3}mol^{-1}K and $N\alpha = 1.5\times10^{-4}$ cm^{3}mol^{-1}. These parameters indicate the presence of a 2% of paramagnetic impurity and that the TCNQ units are probably stacked into infinite chains. The low values of the exchange constant and the α parameter suggest that these molecules can form dimeric $[TCNQ]_2^-$ units with poorer π overlap between adjacent dimers than can be found inside the dimer. Similar behaviour was found in [Fe(cyclam)(NCS)$_2$](TCNQ)$_2$ [38] with a similar J value (-43 cm^{-1}) but with a more uniform stack reflected in a higher α value (0.85) and also in [Zn(phen)$_3$](TCNQ)$_2$[5] which shows only half of the TCNQ anions stacked in an alternating chain ($J = -41$ cm^{-1}, $\alpha = 0.8$).

The nickel derivative **10** shows different magnetic behaviour. The general variation of χT (Figure 9) shows typical values for a nickel(II) ion in the 15−50 K range with a pronounced decrease at low temperatures which can be interpreted in terms of the zero-field splitting induced by the anisotropy in the nickel environment and an increase in χT values at higher temperatures, attributable to the contribution of the stacked TCNQ units. The data below 50 K were then fit to Equation (1) affording the values $g_{Ni} = 2.139$, $D = 1.54$ cm^{-1} and $N\alpha = 2.1\times10^{-4}$ cm^{3}mol^{-1}, while the data above 50 K were treated as consisting of three contributions: that of the nickel ion, the contribution from the antiferromagnetically interacting TCNQ radicals and the temperature-independent paramagnetism [Equation (4)]. In this temperature range we have ignored the contribution from the nickel zero field splitting since the low value previously found can be considered negligible. For this reason the nickel contribution is simply that obtained by the Curie law. The TCNQ groups have been assumed to be showing behaviour similar to that found in the iron derivative and their contribution has therefore been fit to a Heisenberg linear chain model where χ_{TCNQ} corresponds to the first term of Equation (3).

$$\chi = \frac{2Ng_{Ni}^2\beta^2}{3k_BT}+\chi_{TCNQ}+N\alpha \quad (4)$$

The best fit, shown in Figure 9 as a solid line, affords the following values $g_{Ni} = 2.14$, $J = -103$ cm^{-1}, $\alpha = 0.36$ and $N\alpha = 5\times10^{-4}$ cm^{3}mol^{-1}. The picture given by these data suggests an even less uniform chain in this compound which shows pairs of S = 1/2 spins coupling strongly in an antiferromagnetic way with weaker coupling between adjacent pairs. However, the lack of crystal structures precludes closer conclusions being drawn between the nonuniform 1D TCNQ stack deduced from magnetic observations and the actual structure in the solid state.

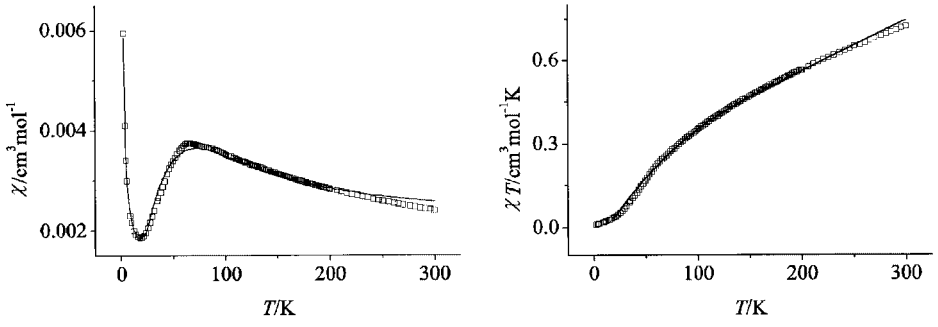

Figure 8. Plots of the magnetic susceptibility (left) and χT (right) of **9** as a function of the temperature; the solid line corresponds to the fit of the experimental data

 © 2005 Wiley-VCH Verlag GmbH & Co. KGaA, Weinheim

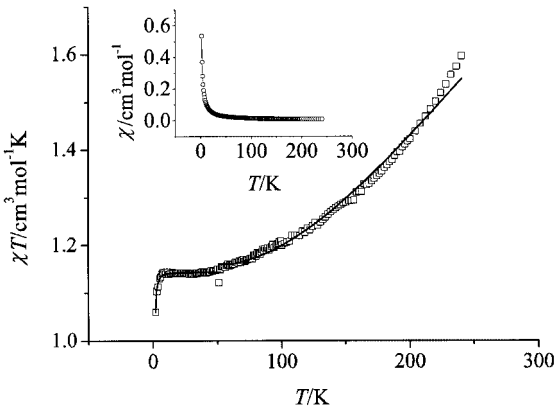

Figure 9. Plot of χT for **10** as a function of the temperature; the solid line corresponds to the fit of the experimental data; the inset shows the magnetic susceptibility plot of this compound

Concluding Remarks

The formation TCNQ derivatives with different stoichiometries can be seen as the result of the combination of two factors, namely the electrostatic interaction resulting from the neutralisation of the positive charges in the metallic fragment by the $TCNQ^-$ anion-radicals and the steric requirements that the cationic fragment imposes.[36] In derivatives having only monoanionic TCNQ, namely $[M(terpy)_2](TCNQ)_2$ and $[M(phen)_3](TCNQ)_2$, the tendency of the anion-radical to dimerise gives rise to the formation of S = 0 dianions $[TCNQ]_2^{2-}$. Since the metal coordination environment is saturated, no direct interaction with the TCNQ can be observed and the packing of metal cations surrounded by dimeric dianions is the structural motif which describes the solid state arrangement. This is also true when the strong interaction between adjacent TCNQ gives rise to the formation of a σ-bonded dimer in $[Fe(phen)_3](TCNQ)_2$. The strong coupling inside the $[TCNQ]_2^{2-}$ dimer leads to a diamagnetic state for the organic acceptors which do not contribute to the magnetic susceptibility. The exception is $[Cu(terpy)_2](TCNQ)_2$, for which the dimer excited triplet state becomes thermally accessible. This fact can be attributed to a weakening in the antiferromagnetic intradimer coupling as a consequence of the π interactions between $TCNQ^-$ and the aromatic ring of one terpy ligand found in the crystal structure of this compound. This is not observed in the analogous nickel derivative. In previous reports, the isolated $[TCNQ]_2^{2-}$ never contributes to the magnetic susceptibility[8,12,13,50] but when the dimers overlap with adjacent π systems, a weaker coupling can be observed.[11,50,55,60] In the previous cases, the dimeric dianion overlapped with a more or less neutral TCNQ but the unprecedented situation in this complex is that this role is assumed by one of the aromatic rings of the ligand.

In the derivatives with TCNQ in nonintegral oxidation states two compositions have been found, namely $[M(terpy)_2](TCNQ)_3$ and $[M(phen)_3](TCNQ)_4$. The magnetic properties of these derivatives are in accordance with the presence of 1D stacks of either trimeric $[TCNQ]_3^{2-}$ or tetrameric $[TCNQ]_4^{2-}$ units. Thus, in derivatives with $TCNQ^{0.66-}$, no contribution from the organic acceptor is usually observed,[12] whereas with stacked $TCNQ^{0.5-}$ units, linear chain magnetic behaviour from the organic part has been proposed.[38,61] The different stoichiometry for these derivatives can be explained in terms of the size of the metal cation and on the basis that only electrostatic interactions can occur between the cationic units and the negative TCNQ stacks. Assuming that the cations behave as rigid spheres which do not interpenetrate, we can estimate the diameter of the $[M(terpy)_2]^{2+}$ unit as ca. 11.3 Å, i.e. as measured in **1** (in fact the measured nickel-nickel distance of 11.8 Å matches well with this assumption), while a diameter for the $[M(phen)_3]^{2+}$ unit of ca. 13.4 Å has been estimated from the crystal structure of **7**. The TCNQ stack must then accommodate the three or four TCNQ units, bearing the two negative charges, in the same space occupied by the counterion. Since the stacking distances between adjacent TCNQ units appear in the 3.10−3.25 Å range, three TCNQ units will occupy 9.3−9.75 Å, while four TCNQ units need 12.4−13.0 Å in the stack. According to this picture, three TCNQ derivatives will form next to a dipositive cation of less than ca. 12 Å in diameter whereas the four TCNQ unit derivative must be obtained with bigger cations.

Experimental Section

General Remarks: All reactions were carried out under oxygen-free nitrogen. The parent reagents $[M(terpy)_2](NO_3)_2$,[43,62] $[M(phen)_3](NO_3)_2$,[63] LiTCNQ[64] and $(NEt_3H)(TCNQ)_2$ [64] were obtained by the published methods and their purities were checked by elemental analysis. Elemental analyses were carried out by the Servicio de Microanálisis of the Universidad Complutense de Madrid. Infrared spectra were recorded as KBr pellets with a Nicolet Magna-550 FT-IR spectrophotometer. Electronic spectra were recorded using a Cary-5 spectrophotometer. The spectra were recorded either in solution or in the solid state. The solid samples were prepared by rubbing the sample on optical glass. Magnetic experiments were carried out on polycrystalline samples using a SQUID magnetometer MPMS-XL-5 manufactured by Quantum Design. The temperature dependence of the magnetisation in the range between 2 and 300 K was recorded using a constant magnetic field of 0.5 T. The experimental data were corrected for the magnetisation of the sample holder and for atomic diamagnetism as calculated from Pascal's constants. Electrical conductivity data were measured by the two points method on single crystals using an APD cryogenics INC HC2 helium cryostat.

Preparation of the $[M(terpy)_2](TCNQ)_2$ Derivatives: All compounds of this type were obtained by the same procedure. A solution containing LiTCNQ (0.15 mmol) in methanol (15 mL) was added dropwise to a solution of the starting nitrate (0.075 mmol) in a mixture of methanol (15 mL)/water (5 mL). After complete mixing a blue solid appeared which was filtered, washed with methanol and dried under vacuum.

$[Ni(terpy)_2](TCNQ)_2$ (1): Yield 45 mg, 64%. $C_{54}H_{30}N_{14}Ni$ (933.6): calcd. C 69.5, H 3.2, N 21.0; found C 69.6, H 3.2, N 20.9. IR

 © 2005 Wiley-VCH Verlag GmbH & Co. KGaA, Weinheim

(KBr): $\tilde{\nu}$ = 2183 s, 2176 s, 2155 s, 1584 m, 1504 m, 1473 m, 1450 w, 1350 m, 1177 m, 987 w, 830 w, 820 w, 772 m cm^{-1}.

[Cu(terpy)$_2$](TCNQ)$_2$ (2): Yield 50 mg, 71%. $C_{54}H_{30}CuN_{14}$ (938.5): calcd. C 69.1, H 3.2, N 20.9; found C 68.8, H 3.4, N 21.1. IR (KBr): $\tilde{\nu}$ = 2183 s, 2174 s, 2157 s, 1583 m, 1505 m, 1474 m, 1450 w, 1363 m, 1175 m, 987 w, 824 w, 770 m cm^{-1}.

[Zn(terpy)$_2$](TCNQ)$_2$ (3): Yield 47 mg, 67%. $C_{54}H_{30}N_{14}Zn$ (940.3): calcd. C 69.0, H 3.2, N 20.8; found C 68.4, H 3.3, N 20.5. IR (KBr): $\tilde{\nu}$ = 2184 s, 2174 s, 2151 s, 1583 m, 1506 m, 1475 m, 1452 w, 1358 m, 1182 m, 988 w, 828 w, 772 m cm^{-1}.

Preparation of the [M(terpy)$_2$](TCNQ)$_3$ Derivatives: A solution containing $(NEt_3H)(TCNQ)_2$ (0.13 mmol) in acetonitrile (20 mL) was added dropwise to a solution of the starting nitrate (0.065 mmol) in a mixture of methanol (15 mL)/water (5 mL). After complete mixing a dark blue solid appeared which was filtered, washed with methanol and dried under vacuum.

[Ni(terpy)$_2$](TCNQ)$_3$ (4): Yield 46 mg, 62%. $C_{66}H_{34}N_{18}Ni$ (1137.8): calcd. C 69.7, H 3.0, N 22.2; found C 69.6, H 3.1, N 22.3. IR (KBr): $\tilde{\nu}$ = 2200 m, 2186 s, 2175 s, 2155 s, 1572 m, 1505 m, 1472 m, 1449 w, 1357 m, 1159 m, 983 w, 833 w, 826 w, 773 m cm^{-1}.

[Cu(terpy)$_2$](TCNQ)$_3$ (5): Yield 49 mg, 66%. $C_{66}H_{34}CuN_{18}$ (1142.7): calcd. C 69.4, H 3.0, N 22.1; found C 69.5, H 3.0, N 21.9. IR (KBr): $\tilde{\nu}$ = 2196 s, 2168 s, 2155 s, 1570 m, 1508 m, 1476 m, 1451 w, 1352 m, 1330 m, 1182 m, 990 w, 837 w, 826 w, 773 m cm^{-1}.

[Zn(terpy)$_2$](TCNQ)$_3$ (6): Yield 43 mg, 58%. $C_{66}H_{34}N_{18}Zn$ (1144.5): calcd. C 69.3, H 3.0, N 22.0; found C 68.7, H 3.1, N 21.7. IR (KBr): $\tilde{\nu}$ = 2194 s, 2168 s, 2155 s, 1564 m, 1506 m, 1476 m, 1454 w, 1361 m, 1323 m, 1134 m, 985 w, 832 w, 773 m cm^{-1}.

Preparation of the [M(phen)$_3$](TCNQ)$_2$ Derivatives: A solution containing LiTCNQ (0.2 mmol) in methanol (15 mL) was added dropwise to a solution of the starting nitrate (0.1 mmol) in a methanol/water (15 mL + 5 mL) mixture. After complete mixing, a blue solid appeared which was filtered, washed with methanol and dried under vacuum.

[Fe(phen)$_3$](TCNQ)$_2$ 2CH$_3$OH (7): Yield 68 mg, 64%. $C_{62}H_{40}FeN_{14}O_2$ (1068.9): calcd. C 69.7, H 3.8, N 18.3; found C 69.3, H 3.7, N 18.1. IR (KBr): $\tilde{\nu}$ = 2179 s, 2125 s, 1600 s, 1580 m, 1503 s, 1330 m, 1179 m, 846 m, 804 w, 723 m cm^{-1}.

[Ni(phen)$_3$](TCNQ)$_2$ (8): Yield 69 mg, 69%. $C_{60}H_{32}N_{14}Ni$ (1007.7): calcd. C 71.5, H 3.2, N 19.4; found C 70.8, H 3.3, N 19.2. IR (KBr): $\tilde{\nu}$ = 2177 s, 2152 s, 1585 m, 1505 w, 1426 m, 1357 s, 1180 m, 987 w, 844 w, 838 w, 827 w, 726 m cm^{-1}.

Preparation of the [M(phen)$_3$](TCNQ)$_4$ Derivatives: A solution containing $(NEt_3H)(TCNQ)_2$ (1 mmol) in acetonitrile (15 mL) was added dropwise to a solution of the starting nitrate (0.5 mmol) in methanol (15 mL). After complete mixing, a dark blue solid appeared which was filtered, washed with methanol and diethyl ether and dried under vacuum.

[Fe(phen)$_3$](TCNQ)$_4$·2CH$_3$CN (9): Yield 46 mg, 61%. $C_{88}H_{46}FeN_{24}$ (1495.4): calcd. C 70.7, H 3.1, N 22.5; found C 71.3, H 3.2, N 22.0. IR (KBr): $\tilde{\nu}$ = 2200 s, 2158 s, 1558 m, 1520 w, 1506 w, 1425 m, 1320 s, 1304 s, 1096 s, 952 w, 850 w, 841 w, 721 w, 688 m cm^{-1}.

[Ni(phen)$_3$](TCNQ)$_4$·2CH$_3$CN (10): Yield 43 mg, 57%. $C_{88}H_{46}N_{24}Ni$ (1498.2): calcd. C 70.5, H 3.1, N 22.4; found C 70.3, H 3.2, N 22.3. IR (KBr): $\tilde{\nu}$ = 2196 w, 2169 s, 2156 s, 1558 m, 1520 m, 1505 m, 1426 m, 1328 m, 1131 m, 953 w, 845 w, 728 m, 697 m cm^{-1}.

X-ray Crystallographic Studies: Good quality crystals of **1**, **2** and **7** were obtained by slow diffusion of dilute solutions of the reactants. A summary of the fundamental crystal data is given in Table 2. The crystal data were collected at the "CAI de Difracción de Rayos X, UCM". In each of the three cases, a deep blue crystal was co-

Table 2. Crystal and refinement data for [Ni(terpy)$_2$](TCNQ)$_2$ (**1**), [Cu(terpy)$_2$](TCNQ)$_2$ (**2**) and [Fe(phen)$_3$](TCNQ)$_2$·2CH$_3$OH (**7**)

	1	**2**	**7**
Empirical formula	$C_{54}H_{30}N_{14}Ni$	$C_{54}H_{30}CuN_{14}$	$C_{62}H_{40}FeN_{14}O_2$
Formula mass	933.63	938.46	1068.93
Crystal system	monoclinic	monoclinic	monoclinic
Space group	$P2_1/n$ (No. 14)	$P2_1/c$ (No. 14)	Cc (No. 9)
a [Å]	8.653(2)	8.858(1)	12.856(1)
b [Å]	22.828(5)	18.569(1)	14.955(1)
c [Å]	23.779(5)	27.463(1)	25.999(3)
α [°]	90	90	90
β [°]	93.16(3)	94.51(1)	91.718(2)
γ [°]	90	90	90
Z	4	4	4
V [Å^3]	4690(1)	4503.4(6)	4996.3(8)
$D_{calcd.}$ [Mg·m^{-3}]	1.322	1.384	1.422
μ [mm^{-1}]	0.468	0.541	0.366
θ range [°]	1.72−30.55	1.49−22.97	1.57−28.74
Reflections collected	53215	5096	9448
Independent reflections	13777	4975	5591
Refined parameters	622	622	716
Goodness of fit	0.893	0.920	0.604
Absolute structure parameter	−	−	0.05(5)
$R1$[a] [$I > 2\sigma(I)$]	0.0416	0.0496	0.0423
$wR2$[b] [$I > 2\sigma(I)$]	0.0892	0.0863	0.1084

[a] $R1 = \Sigma(|F_o| - |F_c|)^2/\Sigma F_o^2$. [b] $wR2 = \{\Sigma[w(F_o^2 - F_c^2)^2]/\Sigma[w(F_o^2)^2]\}^{1/2}$.

 © 2005 Wiley-VCH Verlag GmbH & Co. KGaA, Weinheim

ated with resin epoxy and mounted on a Bruker Smart CCD diffractometer using graphite-monochromated Mo-K_α radiation (λ = 0.71073 Å) operating at 50 kV and 25A. Data were collected over a reciprocal space hemisphere by combination of three exposure sets. Each frame exposure time was 20 s covering 0.3° in ω. The cell parameters were determined and refined by least-squares fits of all reflections collected. The first 50 frames were recollected at the end of the data collection to monitor crystal decay but no appreciable decay was observed. The structures were solved by direct and Fourier methods and refined by applying full-matrix least squares on F^2 with anisotropic thermal parameters for the non-hydrogen atoms. The hydrogen atoms were included with fixed isotropic contributions in their calculated positions determined by molecular geometry. The calculations were carried out with the SHELX97 software package.[65] CCDC-238898 (**1**), -238899 (**2**) and -238900 (**7**) contain the supplementary crystallographic data for this paper. These data can be obtained free of charge at www.ccdc.cam.ac.uk/conts/retrieving.html (or from the Cambridge Crystallographic Data Centre, 12 Union Road, Cambridge CB2 1EZ, UK; Fax: (internat.) + 44-1223-336-033; E-mail: deposit@ccdc.cam.ac.uk).

Acknowledgments

We gratefully acknowledge the Spanish Ministerio de Ciencia y Tecnología, project BQU2002-01409, for financial support.

[1] M. Kurmoo, A. W. Graham, P. Day, S. J. Coles, M. B. Hursthouse, J. L. Caulfield, J. Singleton, F. L. Pratt, W. Hayes, L. Ducasse, P. Guionneau, *J. Am. Chem. Soc.* **1995**, *117*, 12209.
[2] C. Chen, K. S. Suslick, *Coord. Chem. Rev.* **1993**, *128*, 293.
[3] W. Kaim, M. Moscherosch, *Coord. Chem. Rev.* **1994**, *129*, 157.
[4] H. Zhao, R. A. Heintz, K. R. Dunbar, R. D. Rogers, *J. Am. Chem. Soc.* **1996**, *118*, 12844.
[5] A. Bencini, S. Mindolini, C. Zanchini, *Inorg. Chem.* **1989**, *28*, 1963.
[6] J. P. Cornelissen, J. H. Diemen, L. R. Groenveld, J. G. Hasnoot, A. L. Speck, R. J. Reedijk, *Inorg. Chem.* **1992**, *31*, 198.
[7] M. C. Muñoz, J. Cano, R. Ruiz, F. Lloret, J. Faus, *Acta Crystallogr., Sect. C* **1995**, *51*, 873.
[8] L. Ballester, A. Gutiérrez, M. F. Perpiñán, U. Amador, M. T. Azcondo, A. E. Sánchez-Peláez, C. Bellitto, *Inorg. Chem.* **1997**, *36*, 6390.
[9] H. Endress, *Angew. Chem. Int. Ed. Engl.* **1982**, *21*, 524.
[10] H. Endress, *Angew. Chem. Int. Ed. Engl.* **1984**, *23*, 999.
[11] M. T. Azcondo, L. Ballester, S. Golhen, A. Gutiérrez, L. Ouahab, S. Yartsev, P. Delhaes, *J. Mater. Chem.* **1999**, *9*, 1237.
[12] L. Ballester, A. M. Gil, A. Gutiérrez, M. F. Perpiñán, M. T. Azcondo, A. E. Sánchez-Peláez, E. Coronado, C. J. Gómez-García, *Inorg. Chem.* **2000**, *39*, 2837.
[13] P. J. Kunkeler, P. J. van Koningsbruggen, J. P. Cornelissen, A. N. van der Horst, A. M. van der Kraan, A. L. Spek, J. G. Haasnoot, J. Reedijk, *J. Am. Chem. Soc.* **1996**, *118*, 2190.
[14] L. Ballester, M. C. Barral, A. Gutiérrez, A. Monge, M. F. Perpiñán, C. Ruiz-Valero, A. Sánchez-Peláez, *Inorg. Chem.* **1994**, *33*, 2142.
[15] M. T. Azcondo, L. Ballester, A. Gutiérrez, M. F. Perpiñán, U. Amador, C. Ruiz-Valero, C. Bellitto, *J. Chem. Soc., Dalton Trans.* **1996**, 3015.
[16] L. Ballester, A. Gutiérrez, M. F. Perpiñán, M. T. Azcondo, A. E. Sánchez-Peláez, U. Amador, *Anal. Quim. Int. Ed.* **1996**, *92*, 275.
[17] H. J. Keller, I. Leichert, M. Megnamisi-Belombre, D. Nothe, J. Weiss, *Z. Anorg. Allg. Chem.* **1977**, *429*, 231.
[18] N. Matsumoto, Y. Nonaka, S. Kida, S. Kawano, I. Ueda, *Inorg. Chim. Acta* **1979**, *37*, 27.
[19] P. Cassoux, A. Gleizes, *Inorg. Chem.* **1980**, *19*, 665.
[20] L. J. Pace, A. Ulman, J. A. Ibers, *Inorg. Chem.* **1982**, *21*, 199.
[21] N. Matsumoto, T. Miyazaki, Y. Sagara, A. Ohyoshi, *Inorg. Chim. Acta* **1982**, *63*, 249.
[22] M. Soriano-Garcia, R. A. Toscano, J. Gomez-Lara, M. E. Lopez-Morales, *Acta Crystallogr., Sect. C* **1985**, *41*, 1024.
[23] P. Bergamini, V. Bertolasi, V. Ferretti, S. Sostero, *Inorg. Chim. Acta* **1987**, *126*, 151.
[24] P. J. Spellane, L. V. Interrante, R. K. Kullnig, F. S. Tham, *Inorg. Chem.* **1989**, *28*, 1587.
[25] M. Shiotsuka, Y. Okaue, N. Matsumoto, H. Okawa, T. Isobe, *J. Chem. Soc., Dalton Trans.* **1994**, 2065.
[26] A. Togni, M. Hobi, G. Rihs, G. Rist, A. Albinati, P. Zanello, D. Zech, H. Keller, *Organometallics* **1994**, *13*, 1224.
[27] V. Dong, H. Endres, H. J. Keller, W. Moroni, D. Nöthe, *Acta Crystallogr., Sect. B* **1977**, *33*, 2428.
[28] B. Morosin, H. J. Plastas, L. B. Coleman, J. M. Stewart, *Acta Crystallogr., Sect. B* **1978**, *54*, 540.
[29] S. K. Hoffmann, P. J. Corvan, P. Singh, C. N. Sethulekshmi, W. E. Hatfield, *J. Am. Chem. Soc.* **1983**, *105*, 4608.
[30] H. Zhao, R. A. Heintz, X. Ouyang, K. R. Dunbar, C. F. Campana, R. D. Rogers, *Chem. Mater.* **1999**, *11*, 736.
[31] S. Mikami, K. Sugiura, J. S. Miller, Y. Sakata, *Chem. Lett.* **1999**, 413.
[32] H. Kobayashi, Y. Ohashi, F. Marumo, Y. Saito, *Acta Crystallogr., Sect. B* **1970**, *26*, 459.
[33] S. Z. Goldberg, R. Eisenberg, J. S. Millar, A. J. Epstein, *J. Am. Chem. Soc.* **1976**, *98*, 5173.
[34] A. Bosch, B. van Bodegom, *Acta Crystallogr., Sect. B* **1977**, *33*, 3013.
[35] C. P. Lau, P. Singh, S. J. Cline, R. Seiders, M. Brookhart, W. E. Marsh, D. J. Hodgson, W. E. Hatfield, *Inorg. Chem.* **1982**, *21*, 208.
[36] M. D. Ward, P. J. Fagan, J. C. Calabrese, D. C. Johnson, *J. Am. Chem. Soc.* **1989**, *111*, 1719.
[37] F. Conan, J. S. Pala, M. T. Garland, R. Baggio, *Inorg. Chim. Acta* **1998**, *278*, 108.
[38] L. Ballester, A. Gutiérrez, M. F. Perpiñán, S. Rico, M. T. Azcondo, C. Bellitto, *Inorg. Chem.* **1999**, *38*, 4430.
[39] E. N. Maslen, C. L. Raston, A. H. White, *J. Chem. Soc., Dalton Trans.* **1974**, 1803.
[40] C. L. Raston, A. H. White, *J. Chem. Soc., Dalton Trans.* **1976**, 7.
[41] A. T. Baker, D. C. Craig, A. D. Rae, *Aust. J. Chem.* **1995**, *48*, 1373.
[42] S. Flandrois, D. Chasseau, *Acta Crystallogr., Sect. B* **1977**, *33*, 2744.
[43] R. Allmann, W. Henke, D. Reinen, *Inorg. Chem.* **1978**, *17*, 378.
[44] M. I. Arriortua, T. Rojo, J. M. Amigo, G. Germain, J. P. Declercq, *Acta Crystallogr., Sect. B* **1982**, *38*, 1323.
[45] J. Valdes-Martinez, R. A. Toscazo, D. Salazar-Mendoza, *Acta Crystallogr., Sect. E* **2001**, *57*, 331.
[46] A. Zalkin, D. H. Templeton, T. Ueki, *Inorg. Chem.* **1973**, *12*, 1641.
[47] J. Baker, L. M. Engelhardt, B. N. Figgis, A. H. White, *J. Chem. Soc., Dalton Trans.* **1975**, 530.
[48] R. Bozio, A. Girlando, C. Pecile, *J. Chem. Soc., Faraday Trans.* **1975**, *71*, 1237.
[49] R. Bozio, I. Zanon, A. Girlando, C. Pecile, *J. Chem. Soc., Faraday Trans. 2* **1978**, *74*, 235.
[50] L. Ballester, A. Gutiérrez, M. F. Perpiñán, M. T. Azcondo, *Coord. Chem. Rev.* **1999**, *190−192*, 447.
[51] M. Inoue, M. B. Inoue, *J. Chem. Soc., Faraday Trans.* **1985**, *81*, 539.
[52] E. Ghezzal, A. Brau, J. P. Farges, P. Dupuis, *Mol. Cryst. Liq. Cryst.* **1992**, *211*, 327.
[53] J. B. Torrance, *Acc. Chem. Res.* **1979**, *12*, 79.
[54] C. Willi, A. H. Reis Jr., E. Gebert, J. S. Miller, *Inorg. Chem.* **1981**, *20*, 313.
[55] M. Fourmigué, V. Perrocheau, R. Clérac, C. Coulon, *J. Mater. Chem.* **1997**, *7*, 2235.

 © 2005 Wiley-VCH Verlag GmbH & Co. KGaA, Weinheim

[56] R. L. Carlin, *Magnetochemistry*, Springer-Verlag, Berlin, **1986**, p. 24.
[57] B. Bleaney, K. D. Bowers, *Proc. R. Soc. London, Ser. A* **1952**, *214*, 451.
[58] J. M. Williams, J. R. Ferraro, R. J. Thorn, K. D. Carlson, U. Geiser, H. H. Wang, A. M. Kini, M. H. Whangbo in *Organic Superconductors. Synthesis, Structure, Properties and Theory* (Ed.: R. N. Grimes), Prentice Hall, Englewood Cliffs, New Jersey, USA, **1992**.
[59] J. W. Hall, W. E. Marsh, R. R. Weller, W. E. Hatfield, *Inorg. Chem.* **1981**, *20*, 1033.
[60] L. Ballester, A. Gutiérrez, M. F. Perpiñán, A. E. Sánchez, M. T. Azcondo, M. J. González, *Inorg. Chim. Acta* **2004**, *357*, 1054.
[61] S. Huizinga, G. Kommandeur, G. A. Sawatzky, B. T. Thole, L. Kopinga, W. J. M. de Jonge, J. Ros, *Phys. Rev. B* **1979**, *19*, 4723.
[62] S. Kremer, W. Henke, D. Reinen, *Inorg. Chem.* **1982**, *21*, 3013.
[63] R. G. Inskeep, *J. Inorg. Nucl. Chem.* **1962**, *24*, 763.
[64] L. R. Melby, R. J. Herder, W. Mahler, R. E. Benson, W. E. Mochel, *J. Am. Chem. Soc.* **1962**, *84*, 3374.
[65] G. M. Sheldrick, *SHELX-97*, University of Göttingen, Germany, **1997**.

Received June 18, 2004
Early View Article
Published Online December 13, 2004

 © 2005 Wiley-VCH Verlag GmbH & Co. KGaA, Weinheim

Titanium Dioxide Nanoparticles Functionalized with Pd and W Complexes of a Catecholphosphane Ligand

Nigel T. Lucas,[a] James M. Hook,[a] Andrew M. McDonagh,*[a,b] and Stephen B. Colbran*[a]

Keywords: Palladium / Tungsten / Phosphane ligands / Titanium

Palladium and tungsten complexes containing the bifunctional ligand 4-diphenylphosphanylcatechol (L^1) have been synthesized. The catecholate functionality strongly binds to titanium dioxide nanoparticles, effectively anchoring the complexes to the TiO_2 surface. Solid-state ^{31}P NMR spectroscopy was used to probe the surface-bound compounds. Diffuse reflectance infrared spectroscopy also provided data on surface-bound tungsten carbonyl complexes. Preliminary experiments show that the palladium phosphane complex $[PdBr_2(L^1)_2]$ supported on TiO_2 catalyzes the Sonogashira coupling of phenylacetylene with 4-iodonitrobenzene.

(© Wiley-VCH Verlag GmbH & Co. KGaA, 69451 Weinheim, Germany, 2005)

Introduction

Immobilizing materials on metal oxide supports is attracting sustained interest with applications in areas such as catalysis, electrocatalysis, electrochromic display, photodegradation of organic compounds, and photovoltaic power generation.[1−4] Titanium dioxide is a useful support because it is inexpensive, inert, and nontoxic, as well as having an electronic band structure suitable for the aforementioned applications.

Our aim was to use a bifunctional catechol (1,2-dihydroxybenzene)−phosphane compound to anchor transition metal complexes ligated via the P atom to TiO_2 bound by the catecholate group. We envisaged that the soft phosphane donor should preferentially coordinate to soft metal centers,[5−8] and the catechol group, which is a source of the hard catecholate dianion, should preferentially bind to hard Ti^{IV} metal centers.[9−18] Anchoring groups such as carboxylate and phosphonate are regularly used to immobilize molecules on TiO_2 and other metal oxide surfaces. Although it is known that catechol forms a strongly immobilized complex with TiO_2 surfaces,[13,14] the use of catechol as an anchoring substituent for metal complexes has been scarcely documented.[15] The catecholate binding group is "non-innocent" in the sense that it is redox active, able to bind metal centers as catecholate, semiquinone and quinonoid forms.[16−18] Attractively, use of a catechol anchor could potentially increase communication between a surface-immobilized transition metal species and the titania surface.[19] We chose phosphanes as the metal-binding groups because phosphanes are amongst the most common ligands in transition metal chemistry and phosphane complexes of transition metals exhibit a diverse range of desirable photophysical and redox properties in addition to being the largest class of molecular catalysts.[5,6]

Scheme 1 outlines two approaches toward our goal of phosphane-substituted metal complexes on titania. We anticipated that either TiO_2 particles could be functionalized with a phosphanyl-catechol and then treated with transition metal sources or that metal phosphane complexes bearing the free catechol group could be prepared which would directly attach to the TiO_2 surface. Phosphanes bearing phosphonite or alkoxysilane-substituted tethers have been previously employed to immobilize metal complexes on SiO_2,[20−32] but to the best of our knowledge not to titania, and never before has the "non-innocent" catecholate group been employed to anchor a transition metal phosphane complex to a metal oxide surface. Raymond et al.[12] recently reported a catecholphosphane (L^1, see below) that suited our purposes. In this paper, we present the results of investigations on L^1 and transition metal complexes of L^1 immobilized on nanocrystalline TiO_2 particles.

Results and Discussion

Syntheses

The precursor 4-(diphenylphosphanyl)veratrole (L^2) was prepared using an adaptation of the method of Schmid et

[a] School of Chemical Sciences, The University of New South Wales,
Sydney, NSW 2052, Australia
Fax: (internat.) + 61-2-9385-6141
E-mail: s.colbran@unsw.edu.au
[b] Current address: Department of Chemistry, Materials and Forensics, University of Technology Sydney,
Sydney, NSW 2007, Australia
E-mail: andrew.mcdonagh@uts.edu.au

 © 2005 Wiley-VCH Verlag GmbH & Co. KGaA, Weinheim DOI: 10.1002/ejic.200400584

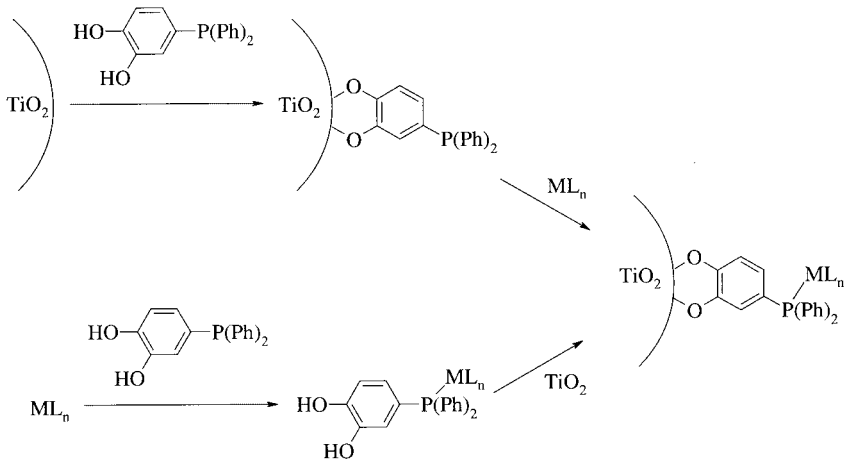

Scheme 1. Approaches to using a bifunctional catecholphosphane compound to anchor transition metals complexes to TiO_2 surfaces

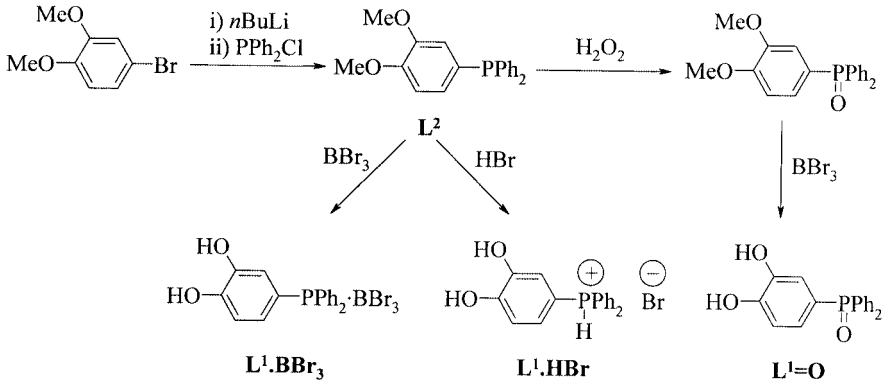

Scheme 2. Preparation of derivatives of catecholphosphane L^1

al.[33] Lithiation of 4-bromoveratrole in tetrahydrofuran using *n*-butyllithium and subsequent reaction with chlorodiphenylphosphane gave L^2 in 95% yield (Scheme 2). Attempted demethylation of L^2 to afford L^1 using boron tribromide yielded instead the boron tribromide adduct $L^1{\cdot}BBr_3$. The ^{31}P NMR spectrum of $L^1{\cdot}BBr_3$ has four peaks of equal intensity because of ^{31}P-^{11}B scalar coupling (^{11}B: $I = {}^3/_2$, 80.4% abundance). The chemical shift, $\delta = -2.4$ ppm, is consistent with other $P(Ar)_3BBr_3$ adducts.[34] The P−B bond was found to be quite stable and we were unable to cleanly displace the boron tribromide by reaction with strong Lewis bases such as di- and triethylamine, or by hydrolysis with aqueous hydroxide. Demethylation of L^2 was achieved by the procedure of Raymond et al.[12] to yield the catecholphosphane hydrobromide, $L^1{\cdot}HBr$. Oxidation of L^2 with hydrogen peroxide followed by demethylation with boron tribromide afforded the catecholphosphane oxide $L^1{=}O$ in 81% overall yield.

The reaction of $[PdCl_2(PhCN)_2]$ with L^2 gave $[PdCl_2(L^2)_2]$ in 80% yield (Scheme 3). Treatment of this complex with boron tribromide did not yield the desired catecholphosphane complex, $[PdBr_2(L^1)_2]$ (**1**), but the bromide-bridged bi-metallic complex $[Pd_2Br_4(L^1)_2]$, which was isolated in 70% yield. The ^1H and ^{31}P NMR spectra, ESI-MS, and elemental microanalysis are all consistent with the dimeric structure for $[Pd_2Br_4(L^1)_2]$. The presence of the adduct $L^1{\cdot}BBr_3$ in the crude reaction mixture (about 1:1 by ^1H NMR spectroscopy) suggests that one of the phosphane groups is captured by boron tribromide resulting in a coordinatively unsaturated palladium species. Combination of two such species would give the stable bromide-bridged dimer. A similar reaction has been previously reported by Sembiring et al.[35] Complex **1** was eventually and conveniently obtained in 70% yield from the reaction of $[PdCl_2(PhCN)_2]$ with $L^1{\cdot}HBr$ followed by treatment with excess KBr. During this reaction, bromide for chloride li-

 © 2005 Wiley-VCH Verlag GmbH & Co. KGaA, Weinheim

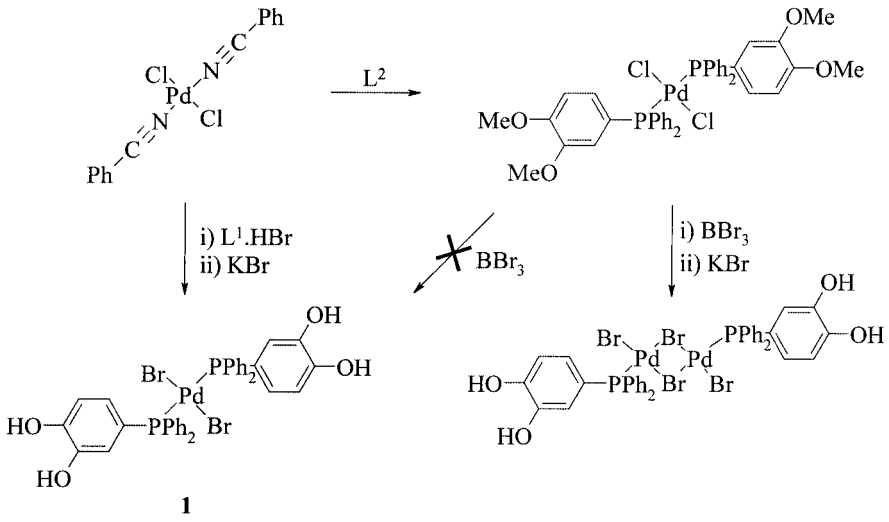

Scheme 3. Preparation of catecholphosphane palladium(II) complexes

gand metathesis occurs and stirring the crude reaction mixture with excess potassium bromide ensures that the amount of chloride-containing complex in the product is negligibly small.

The tungsten(0) carbonyl complex $[W(CO)_5(L^2)]$ was prepared by the in situ reaction of L^2 with freshly prepared $[W(CO)_5(THF)]$ (THF = tetrahydrofuran) (Scheme 4). Boron tribromide effected cleavage of the methyl groups in $[W(CO)_5(L^2)]$, without significant decomplexation of the phosphane from the tungsten, to afford the tungsten(0) carbonyl derivative $[W(CO)_5(L^1)]$ (**2**) in 72% yield.

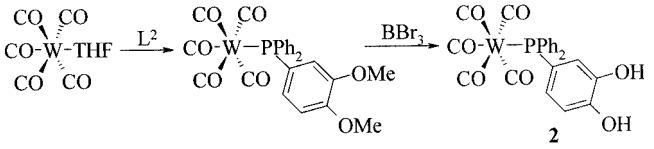

Scheme 4. Preparation of catecholphosphane tungsten(0) complexes

Preparation of TiO_2-Bound Catecholphosphane Compounds

The TiO_2-bound compounds were prepared by stirring a solution of the compound with TiO_2 nanoparticles (Degussa P-25). The particles were then filtered and rinsed successively with a number of solvents to ensure that no free compound remained before drying in vacuo at room temperature.

Solid-State ^{31}P NMR Studies of TiO_2-Bound Catecholphosphane Compounds

Solid state $^{31}P\{^1H\}$ NMR spectra have been acquired of the catecholphosphane L^1, its oxide $L^1{=}O$, and its metal complexes, **1** and **2**, adsorbed onto titanium dioxide nanoparticles as well as in their pure form. Spectra were obtained using cross-polarization to enhance the NMR sensitivity of the dilute species bound to titania.

The CP/MAS ^{31}P NMR spectrum of $L^1{\cdot}HBr$ (Figure 1, a) shows an isotropic signal at $\delta_P = -3.6$ ppm, (linewidth, $\nu_{1/2} = 450$ Hz, chemical shift anisotropy, $\Delta\sigma = 100$ ppm) little shifted from the solution value, $\delta_P = -6.73$ ppm ([D_7]dimethylformamide).[12] In contrast, the CP/MAS ^{31}P NMR spectrum of the phosphane oxide $L^1{=}O$ (Figure 1, e) yields two values for the isotropic chemical shift, δ_P =

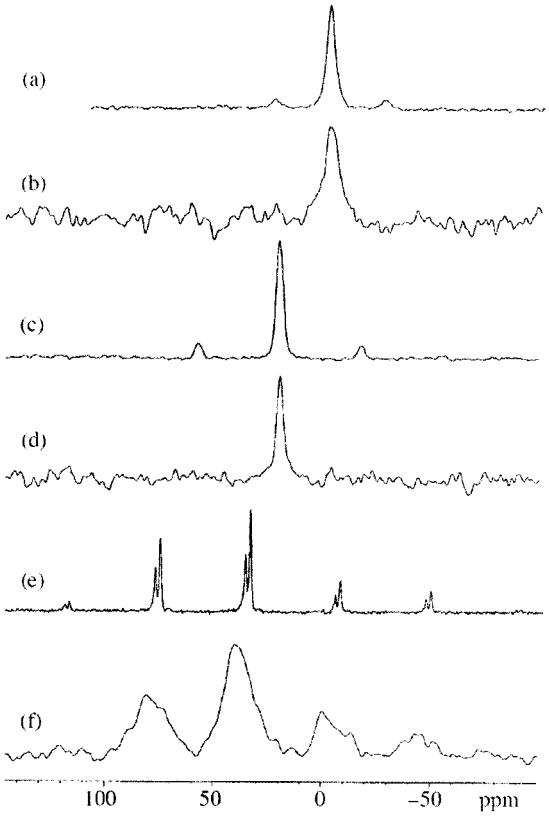

Figure 1. ^{31}P CP/MAS solid-state NMR spectra of (a) pure $L^1{\cdot}HBr$; (b) TiO_2-bound L^1; (c) pure **2**; (d) TiO_2-bound **2**; (e) pure $L^1{=}O$; (f) TiO_2-bound $L^1{=}O$; for all spectra, the temperature was 303 K and the spin rate was 5 kHz, except for (e): 3 kHz

 © 2005 Wiley-VCH Verlag GmbH & Co. KGaA, Weinheim

36.0 and 33.9 ppm, suggestive of two chemically distinct phosphorus environments either within the crystal lattice or in two crystal polymorphs. The chemical shift anisotropy, $\Delta\sigma$ = 200 ppm, is indicative of a less isotropic electronic distribution about the phosphorus(v) atom in L^1=O than about the phosphorus(iii) atom in L^1·HBr. The magnitude of the chemical shift anisotropy for L^1=O is identical to the literature value for $OPPh_3$.[20] Interestingly, the linewidths for L^1=O, $\nu_{1/2}$ = 145 Hz, are appreciably narrower than those for L^1·HBr, perhaps reflecting increased crystallinity for the L^1=O sample.

It was anticipated that immobilization of L^1 on the TiO_2 surface would provide titania particles functionalized with phosphane groups. The spectra of L^1·HBr adsorbed to TiO_2 (Figure 1, b) yielded an isotropic chemical shift, δ_P = −2.8 ppm, similar to that for unbound L^1·HBr. The spectra show no peaks for the phosphane oxide L^1=O (see below). Clearly, the catechol group effectively immobilizes L^1 on the TiO_2 surface without significant oxidation of the phosphane functionality. The linewidth of L^1 on TiO_2, $\nu_{1/2}$ = 750 Hz, is of a comparable order of magnitude to that for pure L^1·HBr, $\nu_{1/2}$ = 400 Hz. Likewise, the CP/MAS ^{31}P NMR spectrum of pure **2** shows an isotropic signal at δ_P = 20.1 ppm (Figure 1, c), while that of TiO_2-bound **2** (Figure 1, d) is at δ_P = 19.9 ppm. Again the linewidths of **2**, $\nu_{1/2}$ = 370 Hz, and TiO_2-bound **2**, $\nu_{1/2}$ = 260 Hz, are comparable. The relatively invariant chemical shift dispersion upon immobilization of ligand L^1 or complex **2** is indicative of the surface-bound species, in each case, occupying near identical environments on the TiO_2 surface. In each case, the surface sites occupied by the immobilized species appear remarkably the same.

The CP/MAS ^{31}P NMR spectrum of phosphane oxide L^1=O adsorbed to TiO_2 (Figure 1, f) yields an isotropic chemical shift, δ_P = 39.7 ppm, and chemical shift anisotropy, $\Delta\sigma$ = 200 ppm, suggesting the local environment of the phosphorus atom does not appreciably change upon binding to TiO_2. The linewidth for TiO_2-bound L^1=O, $\nu_{1/2}$ = 1.5 kHz, however, is substantially broader than anticipated. Phosphane oxides are known to bind to TiO_2 surfaces,[36−38] and it is possible that, for TiO_2-bound L^1=O, the phosphane oxide oxygen atom also binds to the surface, which leads to disordered surface environments and consequently to substantial chemical shift dispersion. This is in agreement with the trend observed for solid PPh_3 and $OPPh_3$ bound to silica surfaces.[20−23,25−30,32,36−38]

Infrared Experiments on TiO_2-Bound Tungsten Complexes

The strong infrared-active carbonyl absorption bands of the tungsten(0) carbonyl **2** make it an appropriate probe for the binding of the catechol group of L^1 to titania. Figure 2 shows solution and diffuse reflectance infrared spectra of **2**. The solution spectrum of **2** (Figure 2, a) is characteristic of complexes of the type $[W(CO)_5(PAr_3)]$. The bands at approximately 2070 and 1935 cm^{-1} are assigned to the A_1^{eq} and E vibrational modes,[39] respectively, and are associated with the four equivalent carbonyl ligands.

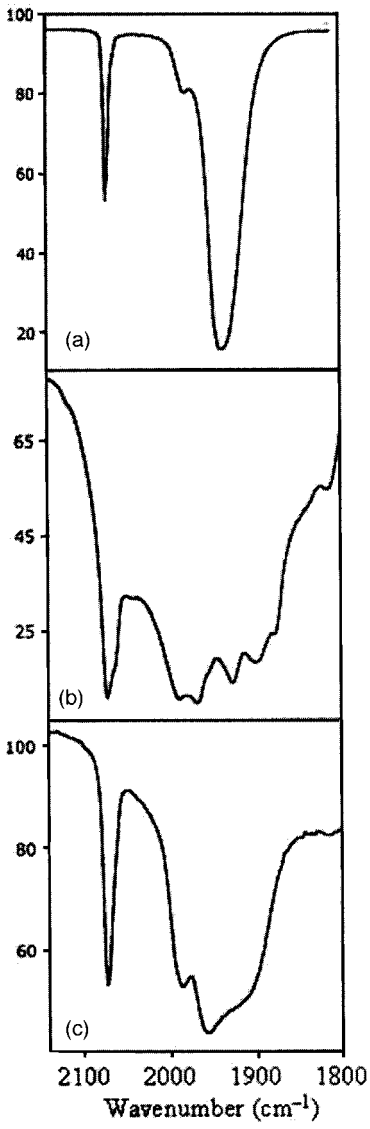

Figure 2. (a) FTIR spectrum of **2** in dichloromethane solution; (b) diffuse reflectance FTIR spectrum of solid **2**; (c) diffuse reflectance FTIR spectrum of TiO_2-supported **2**

The diffuse reflectance infrared spectrum of a solid sample of **2** is shown in Figure 2, b. The A_1^{eq} band appears at 2071 cm^{-1}, a value similar to that observed in the solution spectrum. Most noticeable is the splitting of the E infrared modes, with peaks at 1967, 1926, and 1900 cm^{-1}, due to different carbonyl environments created by packing in the solid state.

The diffuse reflectance infrared spectrum of TiO_2-bound **2** is shown in Figure 2, c. The A_1^{eq} band is seen at 2073 cm^{-1}, almost unchanged from the previous two spectra. A broad E band with a transmittance minimum at approximately 1956 cm^{-1} is observed with a much less symmetrical shape than that in the solution spectrum. This may also be attributed to packing-induced anisotropy and indicates the TiO_2-bound **2** also experiences different carbonyl environments, created by packing and orientation on the surface.

 © 2005 Wiley-VCH Verlag GmbH & Co. KGaA, Weinheim

To explore if TiO_2 particles treated with L^1·HBr react with a metal center, we treated $[W(CO)_5(THF)]$ with TiO_2 particles bearing surface-bound ligands. The diffuse reflectance infrared spectrum was recorded. Bands at 2072, 1984 and a broad strong band at approximately 1955 cm^{-1} may be attributed to successful reaction between $[W(CO)_5(THF)]$ and L^1-derivatized TiO_2 to afford TiO_2-bound **2**. We also found that stirring $[W(CO)_5(THF)]$ with untreated TiO_2 particles followed by washing resulted in a surface-bound tungsten carbonyl species. The diffuse reflectance infrared spectrum of this species exhibits characteristic carbonyl stretching bands. Comparison with solution infrared spectra of $[W(CO)_5OH]^-$ [40,41] gives some indication of the nature of the bound tungsten carbonyl species.

These spectra are similar to the surface-bound tungsten carbonyl species formed upon reaction of $[W(CO)_5(THF)]$ with TiO_2. It appears that the species formed involves a Ti−O−W bond such as that illustrated in Figure 3.

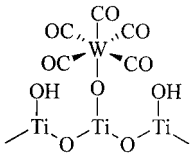

Figure 3. A possible surface-bound tungsten carbonyl species resulting from the reaction of $[W(CO)_5(THF)]$ and TiO_2

Coupling of Phenylacetylene with 4-Iodonitrobenzene Catalyzed by $[PdBr_2(L^1)_2]$ Supported on TiO_2

Palladium complexes are effective catalysts in the coupling reaction between aryl halides and terminal alkynes (Sonogashira coupling).[42−43,44,45] In order to establish the potential of surface-immobilized catecholphosphane metal complexes in catalysis, a preliminary study of the coupling between 4-iodonitrobenzene and phenylacetylene in the presence of the palladium complex **1** supported on TiO_2 (Scheme 5) was undertaken.

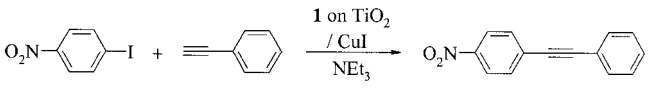

Scheme 5. Coupling reaction between 4-iodonitrobenzene and phenylacetylene catalyzed by CuI and TiO_2-supported **1**

The supported catalyst was prepared by stirring a dichloromethane solution of **1** with TiO_2 at room temperature for 24 h (no special treatment was undertaken to remove any TiO_2 surface-bound water). The suspension was filtered and rinsed successively with dichloromethane, acetone, methanol and diethyl ether to ensure that no unbound material remained. The estimated loading of **4** on titania was 1−2% w/w. The TiO_2-supported **1** was added to a triethylamine solution of 4-iodonitrobenzene and phenylacetylene, together with a cocatalyst, copper(I) iodide. The reaction proceeded to completion after stirring at room temperature for 24 h (^1H NMR spectroscopy showed quantitative conversion of 4-iodonitrobenzene to (4-nitrophenyl)phenylethyne). The reaction mixture was decanted from the settled catalyst, and fresh solvent, reactants, and copper(I) iodide were added. After the same reaction time and conditions as the first batch, the reaction had again proceeded to completion (as evidenced by ^1H NMR spectroscopy). The process was repeated a third time whereupon the reaction reached about 75% completion after the same reaction time, because of the deactivation of the palladium catalyst. A control reaction was also performed where unmodified TiO_2 was added to a triethylamine solution of 4-iodonitrobenzene and phenylacetylene, together with a cocatalyst, copper(I) iodide. After 24 h, no coupling was detected using ^1H NMR spectroscopy.

These preliminary results suggest that palladium complexes anchored to TiO_2 by catecholphosphane ligands do function as catalysts, although with limited turnover cycles. A full study is required to establish the cause of deactivation of the palladium catalyst as well as comparative studies with existing catalysts. Overall, the amount of palladium employed is no larger than that used in conventional homogeneous catalysis (typically 1−5 mol %). Because of the ease of catalyst separation (simple filtering from the reaction mixture) this TiO_2-confined catalyst may be useful in situations where product and catalyst are difficult to separate such as where the reagents and products have highly polar groups and are difficult to purify by the usual chromatographic procedures.

Conclusion

Our results reveal that TiO_2-immobilized transition metal−phosphane complexes are readily accessible starting from catecholphosphanes. Infrared experiments indicate binding of a pre-formed catecholphosphane complex to TiO_2 to give a more precisely defined material than does sequential surface derivatization with the catecholphosphane ligand and subsequent reaction with a metal precursor. Further investigations of applications, such as those summarized in the Introduction, are clearly warranted.

Experimental Section

General Remarks: Reactions were carried out under nitrogen by using Schlenk techniques. All solvents were analytical grade (AR). The following reaction solvents were dried and distilled under nitrogen using standard methods: dichloromethane over calcium hydride; tetrahydrofuran over sodium or potassium benzophenone ketyl. Acetone, diethyl ether, absolute ethanol and triethylamine were used without drying but were purged with nitrogen prior to use. Column chromatography was performed using Merck silica gel 60 of particle size 0.040−0.063 mm (230−400 mesh ASTM). Analytical TLC was carried out on Merck aluminum sheets coated with 0.25 mm silica gel 50 PF_{254}.

The reagents 4-bromoveratrole, *n*-butyllithium, boron tribromide, tungsten hexacarbonyl, phenylacetylene (Aldrich), hydrogen peroxide (20%), MnO_2, KBr, 4-nitroiodobenzene and CuI were purchased commercially and used as received. Chlorodiphenylphos-

 © 2005 Wiley-VCH Verlag GmbH & Co. KGaA, Weinheim

phane (Aldrich) was distilled before use. The titanium dioxide (TiO_2) was Degussa P25 (ca. 25-nm particles). Literature procedures were used to prepare 4-(diphenylphosphanyl)catechol hydrobromide (L^1·HBr),[12] and $[PdCl_2(NCPh)_2]$.[46]

^1H and ^{31}P NMR solution spectra were recorded in $CDCl_3$ (Cambridge Isotope Laboratories or Aldrich) or [D_6]acetone (Aldrich) using a Bruker Avance 300 spectrometer (at 300 MHz for ^1H, 121 MHz for ^{31}P). The ^1H NMR spectra were referenced internally to residual protic solvent, and ^{31}P to external 85% H_3PO_4.

Solid state ^{31}P NMR spectra were obtained using a Varian Inova 300 NMR spectrometer at 121.395 MHz using Chemagnetics cross-polarization magic-angle spinning (CP/MAS) probes. The samples were packed into 4 mm or 7.5 mm o.d. zirconia rotors and spun at between 3 and 5 kHz. Spectra were recorded at 303 K and referenced to the CP/MAS spectrum of external solid ammonium dihydrogen phosphate, $\delta_P = 1.0$ ppm.[47] Cross-polarized spectra were obtained after optimizing by using the following parameters: recycle time, 20−120 s; contact time, 4−5 ms; ^1H 90° pulse width, 5−6 μs.

Infrared spectra were recorded on a Nicolet Avatar 320 FT-IR spectrometer in a solution cell or using a diffuse reflectance infrared FT (DRIFTS) attachment. The background for DRIFTS samples was air (for neat samples) or oven-dried TiO_2 (for supported samples). Electrospray ionization mass spectra (ESI-MS) were acquired on a VG Quattro mass spectrometer with a capillary voltage of 4 kV and a cone voltage of 30 V. Elemental microanalyses were carried out by the Microanalytical Service Unit at the Research School of Chemistry, Australian National University.

Synthesis of 4-(Diphenylphosphanyl)veratrole (L^2): A solution of 4-bromoveratrole (4.00 mL, 27.8 mmol) in freshly distilled tetrahydrofuran (110 mL) was cooled to −78 °C and *n*-butyllithium solution (1.55 M) was added dropwise over 3 min. After stirring for 15 min, chlorodiphenylphosphane was added dropwise to the cooled solution. The stirred solution was allowed to warm to room temperature over 17 h after which all volatile materials were removed in vacuo. The white residue was extracted several times with dichloromethane and the washings taken to dryness in a rotary evaporator. The crude material was loaded onto a 15 × 3 cm silica column and eluted with petroleum spirit/dichloromethane (up to 1:1) with the collection of fractions. Fractions containing the product (as identified by analytical TLC, $R_f = 0.55$, petroleum ether/dichloromethane, 1:1) were combined and taken to dryness using a rotary evaporator to afford white−pale green crystals identified as 4-(diphenylphosphanyl)veratrole (L^2) (8.50 g, 26.4 mmol, 95%).[5,11] ^1H NMR ($CDCl_3$): δ = 3.76 (s, 3 H, Me), 3.92 (s, 3 H, Me), 6.92−6.86 (m, 3 H, C_6H_3), 7.37−7.28 (m, 10 H, Ph) ppm. ^{31}P NMR ($CDCl_3$): δ = −3.2 ppm.

Attempted Synthesis of 4-(Diphenylphosphanyl)catechol (L^1): A solution of 4-(diphenylphosphanyl)veratrole (982 mg, 3.0 mmol) in dichloromethane (20 mL) was cooled to −78 °C and BBr_3 (1.05 mL, 11.1 mmol) was added dropwise with stirring. The mixture was stirred for a further 10 min before the cooling bath was removed and the mixture allowed to warm to room temperature over 3 h. Methanol (1 mL) was carefully added to quench the excess BBr_3, followed by water (5 mL), and the mixture was transferred to a separating funnel. The aqueous phase was neutralized and the dichloromethane phase collected, dried with $MgSO_4$, filtered, and taken to dryness on a rotary evaporator. A fluffy white solid was isolated and identified as the adduct, 4-(diphenylphosphanyl)catechol−boron tribromide (L^1·BBr_3) (1.38 g, 83%). ^1H NMR ([D_6]acetone): δ = 7.04 (dd, $^1J_{H,H}$ = 8, $^2J_{PH}$ = 3 Hz, 1 H, 6-C_6H_3), 7.14 (ddd, $^1J_{PH}$ = 11, $^1J_{H,H}$ = 8, $^2J_{H,H}$ = 2 Hz, 1 H, 5-C_6H_3), 7.38 (dd, $^1J_{PH}$ = 12, $^2J_{H,H}$ = 2 Hz, 1 H, 3-C_6H_3), 8.70 (br. s, 1 H, OH), 7.95−7.57 (m, 10 H, Ph), 8.92 (br. s, 1 H, OH) ppm. ^{31}P NMR ($CDCl_3$): δ = −2.4 (1:1:1:1 q, J_{BP} = 149 Hz).

Synthesis of L^2=O: A solution of L^2 (1.02 g, 3.2 mmol) in acetone (50 mL) was cooled to 0 °C and hydrogen peroxide solution (3.5 mL) was added dropwise with stirring. The mixture was stirred at 0 °C for 2 h at which point TLC indicated that the reaction was complete. MnO_2 was added in batches until no effervescence was observed, then the suspension was stirred for a further 1 h. The brown residue was removed by paper filtration, the filtrate tested for peroxides before being taken to dryness in a rotary evaporator to yield a cream colored solid identified as L^2=O (0.90 g, 84%).[10,11] ^1H NMR ($CDCl_3$): δ = 3.83 (s, 3 H, Me), 3.90 (s, 3 H, Me), 6.87 (dd, $^1J_{H,H}$ = 8, $^2J_{PH}$ = 3 Hz, 1 H, 6-C_6H_3), 7.01 (ddd, $^1J_{PH}$ = 12, $^1J_{H,H}$ = 8, $^2J_{H,H}$ = 2 Hz, 1 H, 5-C_6H_3), 7.28 (dd, $^1J_{PH}$ = 12, $^2J_{H,H}$ = 2 Hz, 1 H, 3-C_6H_3), 7.39−7.54 (m, 6 H, Ph), 7.59−7.67 (m, 4 H, Ph) ppm. ^{31}P NMR ($CDCl_3$): δ = 32.0 ppm.

Synthesis of L^1=O: A solution of L^2=O (900 mg, 2.7 mmol) in dichloromethane (80 mL) was cooled to −78 °C and BBr_3 (0.80 mL, 8.4 mmol) was added dropwise with stirring. The mixture was allowed to warm to room temperature over 18 h. Dilute NaOH solution was carefully added to destroy excess BBr_3, then the reaction mixture was transferred to a separating funnel, acidified with HCl (5 M), and the dichloromethane layer was collected. The aqueous phase was extracted again with dichloromethane (2 × 25 mL). The dichloromethane washings were combined and washed with dilute acid (ca. 0.1 M HCl, 20 mL), dried with $MgSO_4$, filtered, and taken to dryness in a rotary evaporator. A cream-colored powder was isolated and identified as the hydrate of the product, L^1=O·H_2O (800 mg, 96%). ^1H NMR ($CDCl_3$): δ = 6.61 (ddd, $^1J_{PH}$ = 12, $^1J_{H,H}$ = 8, $^2J_{H,H}$ = 2 Hz, 1 H, 5-C_6H_3), 6.85 (dd, $^1J_{H,H}$ = 8, $^2J_{PH}$ = 4 Hz, 1 H, 6-C_6H_3), 7.40−7.65 (m, 10 H, Ph), 8.00 (br. m, 2 H, OH), 7.81 (dd, $^1J_{PH}$ = 13, $^2J_{H,H}$ = 2 Hz, 1 H, 3-C_6H_3) ppm. ^{31}P NMR ($CDCl_3$): δ = 35.3 ppm. ^{31}P CP/MAS NMR: δ = 33.9, 36.1 (about 3:1). $C_{18}H_{15}O_3P$·H_2O (328.30): calcd. C 65.85, H 5.22; found C 66.82, H 4.87.

Synthesis of $[PdCl_2(L^2)_2]$: A solution of $[PdCl_2(NCPh)_2]$ (500 mg, 1.30 mmol) in dichloromethane (15 mL) was added to a solution of L^2 (890 mg, 2.76 mmol) in dichloromethane (15 mL) at room temperature. The resulting clear yellow solution was stirred for 30 min, the volume was reduced to about 10 mL, and methanol was added dropwise to give a yellow precipitate. The mixture was cooled in ice, and the precipitate was collected on a sintered glass funnel, washed with methanol and dried at the pump. Slow diffusion of diethyl ether into an acetone solution of the crude material yielded yellow-orange prisms of $[PdCl_2(L^2)_2]$ (862 mg, 80%). ^1H NMR ($CDCl_3$): δ = 6.86 (br. d, 2 H, C_6H_3), 3.89 (s, 6 H, Me), 3.75 (s, 6 H, Me), 7.11−7.18 (m, 2 H, C_6H_3), 7.33−7.45 (m, 12 H, Ph), 7.54−7.59 (m, 2 H, C_6H_3), 7.71−7.63 (m, 8 H, Ph) ppm. ^{31}P NMR ($CDCl_3$): δ = 25.3 ppm. $C_{40}H_{38}Cl_2O_4P_2Pd$ (822.01): calcd. C 58.45, H 4.66; found C 57.55, H 4.72.

Synthesis of $[PdBr_2(L^1)_2]$ (1): A solution of $[PdCl_2(NCPh)_2]$ (240 mg, 0.63 mmol) in acetone (20 mL) was added to a stirred suspension of L^1·HBr (496 mg, 1.32 mmol) in acetone (30 mL) at room temperature. The resulting clear orange solution was stirred for a further 1 h, then KBr (6.30 g, 53 mmol) was added and the suspension stirred vigorously for 16 h. The mixture was filtered and taken to dryness to yield $[PdBr_2(L^1)_2]$ (**1**) (375 mg, 70%) as a yellow solid. ^1H NMR ([D_6]acetone): δ = 6.92 (br. d, 2 H, C_6H_3), 7.16−7.28 (m, 4 H, C_6H_3), 7.37−7.45 (m, 12 H, Ph), 7.64−7.72

 © 2005 Wiley-VCH Verlag GmbH & Co. KGaA, Weinheim

(m, 8 H, Ph) ppm. ^{31}P NMR ([D$_6$]acetone): δ = 23.7 ppm. Negative ion ESI-MS (methanol): 935 ([M + Br]$^-$, 100), 854 ([M − H]$^-$, 55). Positive ion ESI-MS (methanol): 775 ([M − Br]$^+$, 100). $C_{36}H_{30}Br_2O_4P_2Pd$ (854.81): calcd. C 50.59, H 3.54; found C 49.64, H 4.07.

Reaction of [PdCl$_2$(L^2)$_2$] with BBr$_3$: A solution of [PdCl$_2$(L^2)$_2$] (1.00 g, 1.2 mmol) in dichloromethane (30 mL) was cooled to −80 °C, and BBr_3 (0.56 mL, 5.9 mmol) was added dropwise. The reaction mixture was allowed to warm to room temperature overnight, the excess BBr_3 quenched with water, and the mixture was transferred to a separating funnel. Diethyl ether was added, and the organic phase was washed with brine (acidified with HCl), dried, filtered and taken to dryness. The crude material was dissolved in acetone (30 mL), KBr (5.8 g, 4.9 mmol) was added, and the suspension was stirred vigorously for 16 h. The mixture was transferred to a separating funnel, diethyl ether (30 mL) was added, and the resulting organic layer was washed twice and then dried over $MgSO_4$. The mixture was filtered and taken to dryness to give an orange solid identified as [Pd$_2$Br$_4$(L^1)$_2$] (375 mg, 70%). ^{1}H NMR ([D$_6$]acetone): δ = 6.95 (dd, $^1J_{H,H}$ = 8, $^2J_{PH}$ = 3 Hz, 2 H, 5-C$_6$H$_3$), 7.08−7.17 (m, 2 H, 6-C$_6$H$_3$), 7.28 (dd, $^1J_{PH}$ = 13, $^2J_{H,H}$ = 2 Hz, 2 H, 3-C$_6$H$_3$), 7.43−7.59 (m, 12 H, Ph), 7.67−7.77 (m, 8 H, Ph), 8.67 (s, 4 H, OH) ppm. ^{31}P NMR ($CDCl_3$): δ = 36.8 ppm. Negative ion ESI-MS (methanol): 1121 ([M]$^-$, 100). Positive ion ESI-MS (methanol): 775 ([M/2]$^+$, 45). $C_{36}H_{30}Br_4O_4P_2Pd_2$ (1121.04): calcd. C 38.57, H 2.70; found C 38.39, H 2.68.

Synthesis of [W(CO)$_5$(L^2)]: L^2 (1.38 g, 4.3 mmol) was added to a rapidly stirred yellow solution of [W(CO)$_5$(THF)], obtained by irradiating [W(CO)$_6$] (1.50 g, 4.3 mmol) in tetrahydrofuran (60 mL) with a mercury lamp for 3 h (with N_2 purge). The mixture was stirred at room temperature for 2 h after which all the volatile materials were removed in vacuo. The pale yellow residue was purified on a silica column by eluting with petroleum spirit/dichloromethane mixtures (up to 1:1). Fractions were collected and compared by using analytical thin-layer chromatography; the major band (pale yellow) was evaporated to dryness to give a pale yellow solid, identified as [W(CO)$_5$(L^2)] (1.69 mg, 61%). ^{1}H NMR ($CDCl_3$): δ = 3.79 (s, 3 H, Me), 3.91 (s, 3 H, Me), 6.87−6.98 (m, 2 H, 5,6-C$_6$H$_3$), 7.07 (br. d, $^1J_{PH}$ = 13 Hz, 1 H, 3-C$_6$H$_3$), 7.41−7.47 (m, 10 H, Ph); ([D$_6$]acetone): δ = 3.74 (s, 3 H, Me), 3.88 (s, 3 H, Me), 6.98−7.15 (m, 3 H, C$_6$H$_3$), 7.48−7.57 (m, 10 H, Ph) ppm. ^{31}P NMR ($CDCl_3$): δ = 23.0 (J_{WP} = 242 Hz) ppm; ([D$_6$]acetone): δ = 21.9 (J_{WP} = 242 Hz) ppm. $C_{25}H_{19}O_7PW$ (646.25): calcd. C 46.46, H 2.96; found C 46.82, H 2.93.

Synthesis of [W(CO)$_5$(L^1)]: A solution of [W(CO)$_5$(L^2)] (615 mg, 0.95 mmol) in dichloromethane (10 mL) was cooled to −80 °C, and BBr_3 (0.30 mL, 3.2 mmol) was added dropwise. The mixture was allowed to warm to about −10 °C over 1.5 h, before it was cooled again to −80 °C, and NEt_3 (1 mL) and methanol (1 mL) were added to quench the excess BBr_3. After warming to room temperature, water (1 mL) was carefully added, and the mixture was transferred to a separating funnel and washed with dilute HCl solution (3 × 20 mL). The organic phase was dried over $MgSO_4$, filtered and taken to dryness to yield [W(CO)$_5$(L^1)] (**2**) (425 mg, 72%) as a cream-colored powder. ^{1}H NMR ([D$_6$]acetone): δ = 6.91−7.03 (m, 3 H, C$_6$H$_3$), 7.47−7.55 (m, 10 H, Ph), 8.41 (s, 1 H, OH), 8.53 (s, 1 H, OH) ppm. ^{31}P NMR ([D$_6$]acetone): δ = 20.8 (J_{WP} = 241 Hz). ^{31}P CP/MAS NMR: δ = 20.1 ppm. Negative ion ESI-MS (methanol): 1236 ([2M]$^-$ dimer, 100). $C_{23}H_{15}O_7PW$ (618.19): calcd. C 44.69, H 2.45; found C 44.98, H 2.45.

Adsorption of Phosphanylcatechol-Containing Compounds onto TiO$_2$

L^1 on TiO$_2$: L^1·HBr (320 mg, 0.85 mmol) was added to a rapidly stirred suspension of TiO_2 (3.4 g) in methanol (150 mL). The color of the particles changed rapidly from white to pale orange. After stirring at room temperature for 1 h, triethylamine (0.5 mL, 3.6 mmol) was added, and the stirring was continued for a further 3 h. The suspension was then allowed to settle, and the colorless solution was removed using a cannula. The material was washed with methanol (150 mL), then filtered and rinsed successively with methanol (150 mL), acetone (2 × 50 mL), tetrahydrofuran (2 × 50 mL), dichloromethane (2 × 50 mL), and diethyl ether (2 × 15 mL), and then dried in vacuo at room temperature for 8 h. ^{31}P CP/MAS NMR: δ = −2.8 ppm.

L^1=O on TiO$_2$: TiO_2 (1.50 g) was added to a colorless solution of L^1=O (203 mg, 0.65 mmol) in methanol (30 mL), and the suspension was stirred at room temperature for 18 h. The pale orange suspension was filtered and rinsed successively with methanol (3 × 15 mL) and diethyl ether (10 mL), and then dried in vacuo at room temperature for 6 h. ^{31}P CP/MAS NMR: δ = 40.1 ppm.

[W(CO)$_5$(L^1)] on TiO$_2$: TiO_2 (1.0 g) was added to a solution of [W(CO)$_5$(L^1)] (100 mg, 0.16 mmol) in dichloromethane (100 mL), and the suspension was stirred at room temperature for 24 h. The pale orange suspension was then filtered and rinsed successively with dichloromethane (5 × 20 mL), acetone (2 × 20 mL), and diethyl ether (2 × 20 mL), then dried in vacuo at room temperature for 3 h. ^{31}P CP/MAS NMR: δ = 19.91 ppm.

[W(CO)$_5$(THF)] on TiO$_2$: Photolytically generated [W(CO)$_5$(THF)] (10 mL, 28.4 mM in tetrahydrofuran, 0.284 mmol) was added to TiO_2 (1.0 g) and the suspension was stirred at room temperature for 24 h. The white-gray suspension was then filtered and rinsed successively with tetrahydrofuran (3 × 40 mL), acetone (2 × 40 mL), and diethyl ether (2 × 40 mL), then dried in vacuo at room temperature for 3 h.

[PdBr$_2$(L^1)$_2$] on TiO$_2$: TiO_2 (1.50 g) was added to an orange-yellow solution of [PdBr$_2$(L^1)$_2$] (150 mg, 0.18 mmol) in dichloromethane (100 mL), and the suspension was stirred at room temperature for 24 h. The suspension was then filtered and rinsed successively with dichloromethane (2 × 20 mL), acetone (2 × 15 mL), methanol (2 × 15 mL), and diethyl ether (2 × 15 mL), then dried in vacuo at room temperature for 8 h.

Catalytic Studies

Coupling of Phenylacetylene with 4-Iodonitrobenzene Catalyzed by [PdBr$_2$(L^1)$_2$] Supported on TiO$_2$: Phenylacetylene (0.15 mL, 1.3 mmol), CuI (10 mg, 0.05 mmol) and [PdBr$_2$(L^1)$_2$]-TiO_2 (800 mg, ca. 1% w/w) was added to a solution of 4-iodonitrobenzene (80 mg, 0.32 mmol) in triethylamine (30 mL, N_2-purged), and the suspension was stirred at room temperature for 24 h. The particles were allowed to settle, and the solution was transferred to a second flask using a cannula. The solid residue was washed with triethylamine (20 mL). The combined reaction solution and washing was taken to dryness, and the crude residue was passed through a short silica plug by using CH_2Cl_2/hexane (3:7) eluent. The ^{1}H NMR spectrum of the resulting pale yellow solid indicated quantitative conversion of 4-iodonitrobenzene to the product (4-nitrophenyl)phenylethyne[48] (<1% of the homo-coupled tolane product was also observed). A second batch of reactants and CuI catalyst (same scale) was added to a triethylamine (30 mL) suspension of the same Pd catalyst from above. Again, quantitative conversion into (4-nitrophenyl)phenylethyne was observed. The cycle was repeated a third time using the same Pd catalyst with a reduction of conversion to 75%.

 © 2005 Wiley-VCH Verlag GmbH & Co. KGaA, Weinheim

Acknowledgments

The authors thank Chris Blake at the University NMR Centre, Australian National University, for preliminary solid-state NMR measurements.

[1] D. W. Goodman, *J. Catal.* **2003**, *216*, 213−222.
[2] A. Fujishima, T. N. Rao, D. A. Tryk, *J. Photochem. Photobiol. C: Photochem. Rev.* **2000**, *1*, 1−21.
[3] M. Grätzel, *Prog. Photovoltaics: Res. Appl.* **2000**, *8*, 171−185.
[4] D. J. Cole-Hamilton, *Science* **2003**, *299*, 1702−1706.
[5] E. W. Abel, F. G. A. Stone, G. Wilkinson, J. A. Labinger, M. J. Winter (Eds.), *Comprehensive Organometallic Chemistry II*, Pergamon Press, Oxford, **1995**.
[6] B. Cornils, W. A. Herrman, *Applied Homogeneous Catalysis with Organometallic Compounds*, VCH, Weinheim (Germany), **1996**.
[7] S. E. Watkins, D. C. Craig, S. B. Colbran, *J. Chem. Soc., Dalton Trans.* **2002**, 2423−2436.
[8] S. E. Watkins, D. C. Craig, X.-H. Yang, S. B. Colbran, *J. Chem. Soc., Dalton Trans.* **1999**, 1539−1540.
[9] M. Albrecht, R. J. Frohlich, *J. Am. Chem. Soc.* **1997**, *119*, 1656−1661.
[10] M. Albrecht, *Chem. Eur. J.* **1997**, *3*, 1466−1471.
[11] M. Albrecht, M. Napp, M. Schneider, P. Weis, R. Fröhlich, *Chem. Eur. J.* **2001**, *7*, 3966−3975.
[12] X. Sun, D. W. Johnson, D. L. Caulder, K. N. Raymond, E. H. Wong, *J. Am. Chem. Soc.* **2001**, *123*, 2752−2763.
[13] R. Rodríguez, M. A. Blesa, A. E. Regazzoni, *J. Colloid Interface Sci.* **1996**, *177*, 122−131.
[14] P. A. Connor, K. D. Dobson, A. J. McQuillan, *Langmuir* **1995**, *11*, 4193−4195.
[15] C. R. Rice, M. D. Ward, M. K. Nazeeruddin, M. Grätzel, *New J. Chem.* **2000**, *24*, 651−652.
[16] C. G. Pierpont, *Coord. Chem. Rev.* **2001**, *216-217*, 99−125.
[17] C. G. Pierpont, C. W. Lange, *Prog. Inorg. Chem.* **1994**, *41*, 331−442.
[18] C. G. Pierpont, R. M. Buchanan, *Coord. Chem. Rev.* **1981**, *38*, 45−87.
[19] M. Grätzel, *Pure Appl. Chem.* **2001**, *73*, 459−467.
[20] L. Bemi, H. C. Clark, J. A. Davies, C. A. Fyfe, R. E. Wasylishen, *J. Am. Chem. Soc.* **1982**, *104*, 438−445.
[21] R. A. Komoroski, A. J. Magistro, P. P. Nicholas, *Inorg. Chem.* **1986**, *25*, 3917−3925.
[22] L. Reven, *J. Mol. Catal.* **1994**, *86*, 447−477.
[23] J. Blumel, *Inorg. Chem.* **1994**, *33*, 5050−5056.
[24] K. D. Behringer, J. Blumel, *Chem. Commun.* **1996**, 653−654.
[25] O. Krocher, R. A. Koppel, M. Froba, A. Baiker, *J. Catal.* **1998**, *178*, 284−298.
[26] P. Braunstein, H. P. Kormann, W. Meyer-Zaika, R. Pugin, G. Schmid, *Chem. Eur. J.* **2000**, *6*, 4637−4646.
[27] C. M. Crudden, D. Allen, M. D. Mikoluk, J. Sun, *Chem. Commun.* **2001**, 1154.
[28] A. J. Sandee, J. N. H. Reek, P. C. J. Kamer, P. W. N. M. van Leeuwen, *J. Am. Chem. Soc.* **2001**, *123*, 8468−8476.
[29] H. H. Wagner, H. Hausmann, W. F. Holderich, *J. Catal.* **2001**, *203*, 150−156.
[30] C. Merckle, J. Blumel, *Chem. Mater.* **2001**, *13*, 3617−3623.
[31] P. W. N. M. van Leeuwen, A. J. Sandee, J. N. H. Reek, P. C. J. Kamer, *J. Mol. Catal. A-Chem.* **2002**, *182*, 107−123.
[32] Z. L. Lu, E. Lindner, H. A. Mayer, *Chem. Rev.* **2002**, *102*, 3543−3578.
[33] R. Schmid, J. Foricher, M. Cereghetti, P. Schönholzer, *Helv. Chim. Acta* **1991**, *74*, 370−389.
[34] E. Muylle, G. P. Van Der Kelen, *Spectrochim. Acta A: Mol. Biomol. Spectr.* **1976**, *32*, 599−603.
[35] S. B. Sembiring, S. B. Colbran, D. C. Craig, M. L. Scudder, *J. Chem. Soc., Dalton Trans.* **1995**, *22*, 3731−3741.
[36] G. Guerrero, P. H. Mutin, A. Vioux, *Chem. Mater.* **2001**, *13*, 4367−4373.
[37] B. Hu, I. D. Gay, *Langmuir* **1995**, *11*, 3845−3847.
[38] L. Baltusis, J. S. Frye, G. E. Maciel, *J. Am. Chem. Soc.* **1986**, *108*, 7119−7120.
[39] R. J. Angelici, M. D. Malone, *Inorg. Chem.* **1967**, *9*, 1731−1736.
[40] D. J. Darensbourg, M. L. Meckfessel Jones, J. H. Reibenspies, *Inorg. Chem.* **1993**, *32*, 4675−4676.
[41] J. L. Cihonski, R. A. Levenson, *Inorg. Chem.* **1975**, *14*, 1717−1720.
[42] S. Takahashi, Y. Kuroyama, K. Sonogashira, N. Hagihara, *Synthesis* **1980**, 627−630.
[43] F. Quignard, S. Larbot, S. Goutodier, A. Choplin, *J. Chem. Soc., Dalton Trans.* **2002**, 1147−1152.
[44] C. C. Tzschucke, C. Markert, H. Glatz, W. Bannwarth, *Angew. Chem. Int. Ed.* **2002**, *41*, 4500−4503.
[45] E. Gonthier, R. Breinbauer, *Synlett* **2003**, 1049−1051.
[46] P. Braunstein, R. Bender, J. Jud, *Inorg. Synth.* **1989**, *26*, 341−350.
[47] S. Hayashi, K. Hayamizu, *Bull. Chem. Soc., Jpn.* **1989**, *62*, 2429−2430.
[48] K. Okuro, M. Furuune, M. Enna, M. Miura, M. Nomura, *J. Org. Chem.* **1993**, *58*, 4716−4721.

Received July 6, 2004
Early View Article
Published Online December 2, 2004

 © 2005 Wiley-VCH Verlag GmbH & Co. KGaA, Weinheim

Preparation and Characterisation of Cd^{II}, Hg^{II} and Pb^{II} Complexes of a Macrodinucleating Hexaaza-dithiophenolate Ligand

Vasile Lozan[a] and Berthold Kersting*[a]

Keywords: Macrocyclic ligands / Cadmium / Mercury / Lead / Complexes

The ligating properties of a Robson-type 24-membered macrodinucleating hexaaza-dithiophenolate ligand towards the heavy metal ions Cd^{II}, Hg^{II} and Pb^{II} have been examined. The complexation of H_2L^{Me} with $CdCl_2$ or $Cd(OAc)_2$ in the presence of triethylamine leads to monocationic $[(L^{Me})Cd_2(\mu\text{-}L')]^+$ complexes bearing additional coligands [L′ = Cl^- (**2**) or OAc^- (**3**)]. With $Hg(OAc)_2$ and $Pb(OAc)_2$, the respective dicationic complexes $[(L^{Me})Hg_2]^{2+}$ (**4**) and $[(L^{Me})Pb_2]^{2+}$ (**5**) were obtained. The latter show no tendency to bind to further coligands. The crystal structure determinations of **2**·BPh_4 and **3**·BPh_4 revealed the presence of bowl-shaped, calixarene-like $[(L^{Me})Cd_2(\mu\text{-}L')]^+$ cations featuring six-coordinate Cd^{II} ions with N_3S_2Cl (**2**) or N_3S_2O (**3**) environments. The metal ions in the dications **4** and **5** display highly irregular N_3S coordination environments, presumably as a consequence of the steric constraints imposed by the rigid macrocyclic nature of $(L^{Me})^{2-}$. All complexes could also be fully characterised by ^1H and ^{13}C NMR spectroscopy. These results have thus established the ability of the macrodinucleating polyaza-dithiophenolate ligand to support the formation of stable dinuclear complexes of toxic heavy metals.

(© Wiley-VCH Verlag GmbH & Co. KGaA, 69451 Weinheim, Germany, 2005)

Introduction

It is well established that macrodinucleating ligands of the Robson type[1] are ideally suited to the formation of kinetically and thermodynamically stable complexes of the 3d elements.[2] Since these ligands also bind strongly to a range of toxic and precious heavy metal ions,[3−5] they may serve as complexing or extracting agents for biological, environmental or recycling purposes.[6−8] With regards to the soft characteristics of the heavy metal ions,[9] it could be advantageous to use macrocyclic ligands with mixed nitrogen-sulfur donor sets to improve their metal-ion selectivity. Consequently, a large number of N,S-based macrocycles have been reported and their binding properties towards environmentally important elements have been investigated.[10,11] To the best of our knowledge, the thiophenolate derivatives[12−14] of Robson-type macrocycles have not yet been tested in this respect. This led us to investigate the ligating properties of the dinucleating hexaaza-thiophenolate ligand $(L^{Me})^{2-}$ (see Scheme 1)[15,16] towards the metal ions Cd^{II}, Hg^{II} and Pb^{II}.

Herein we demonstrate that such metal ions can be readily accommodated in the two binding pockets of H_2L^{Me}. In each case we have obtained single crystals suitable for X-ray structure determinations. It has therefore been possible to study, in detail, the binding of the metal ions to the octadentate N_6S_2 macrocycle H_2L^{Me}. The results of IR and NMR spectroscopic investigations are also reported.

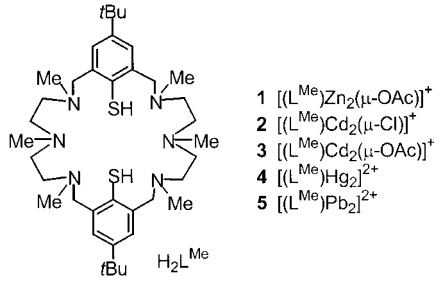

Scheme 1. Structure of the ligand H_2L^{Me}

Results and Discussion

Preparation

The synthesised compounds and their labels are collected in Scheme 1 with Scheme 2 depicting the synthetic procedures. The complexation reactions of the free macrocycle H_2L^{Me}·6HCl with $CdCl_2$, $Cd(OAc)_2$, $Hg(OAc)_2$ and $Pb(OAc)_2$ were all carried out in methanol in the presence of triethylamine. All reactions proceeded smoothly and produced clear solutions from which, upon addition of an excess of $LiClO_4$, the highly crystalline salts $[(L^{Me})Cd_2(\mu\text{-}Cl)]ClO_4$ (**2**·ClO_4), $[(L^{Me})Cd_2(\mu\text{-}OAc)]ClO_4$ (**3**·ClO_4), $[(L^{Me})Hg_2](ClO_4)_2$ (**4**·ClO_4) and $[(L^{Me})Pb_2](ClO_4)_2$ (**5**·ClO_4) precipitated in good to excellent yields. Complex **3** was also

[a] Institut für Anorganische Chemie, Universität Leipzig
Johannisallee 29, 04103 Leipzig
Fax: (internat.) + 49-341-9736143
E-mail: b.kersting@uni-leipzig.de

 © 2005 Wiley-VCH Verlag GmbH & Co. KGaA, Weinheim DOI: 10.1002/ejic.200400603

accessible from $[(L^{Me})Cd_2(\mu\text{-}Cl)]ClO_4$ (**2**·ClO_4) and sodium acetate.

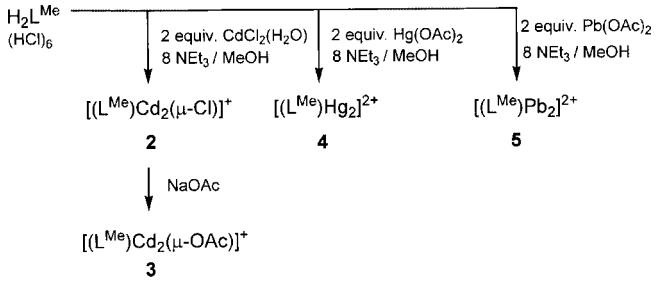

Scheme 2. Synthesis of complexes and their labels; the complexes were either isolated as ClO_4^- or BPh_4^- salts

The new compounds are colourless to pale-yellow solids and dissolve readily in polar protic solvents such as methanol or ethanol. With the exception of complex **2**, which fixes carbon dioxide from air to give the methyl carbonate complex $[(L^{Me})Cd_2(\mu\text{-}O_2COMe)]^+$, all compounds are stable in air both in solution and in the solid state. All compounds gave satisfactory elemental analyses and were characterised by spectroscopic methods (IR, ^1H and ^{13}C NMR spectroscopy) and X-ray crystallography.

Spectroscopic Characterisation

Infrared Spectroscopy

The infrared spectra of all compounds are dominated by the absorptions of the $[(L^{Me})M_2]^{2+}$ fragments and the counterions (ClO_4^- or BPh_4^-).[17] The IR spectrum of **3**·ClO_4 shows two bands at 1577 and 1422 cm^{-1} which can be assigned to the asymmetric $[\nu_{asym}(OAc^-)]$ and symmetric stretching modes $[\nu_{sym}(OAc^-)]$ of the acetate group, respectively.[18] These values are very similar to those of the zinc complex $[(L^{Me})Zn_2(\mu\text{-}OAc)]^+$ (**1**),[16] indicating that the acetate group in the cadmium complex **3** is also in the $\mu_{1,3}$-bridging mode. The IR spectra of complexes **4** and **5** lack these two bands which is in good agreement with the presence of unligated $[(L^{Me})M_2]^{2+}$ dications. The IR spectra of **4** and **5** were otherwise not very informative with regards to the compositions and structures of the complexes.

NMR Spectroscopy

All of the new complexes were further characterised by ^1H and ^{13}C NMR spectroscopy. Table 1 lists selected NMR spectroscopic data for complexes **2**−**5**. The data for complex **1** have been reported previously and are included for comparative purposes. As can be seen, the ^1H NMR spectroscopic data of the acetato-bridged complexes **1** and **3** are very similar. Both complexes display only one set of signals, indicating that both exist as single isomers in solution. Furthermore, the four aromatic protons (ArH), the methyl protons on the benzylic nitrogens ($N^{Bz}CH_3$), the methyl protons on the central amine nitrogen of the linking diethylene triamine units (NCH_3) and the *tert*-butyl protons $[C(CH_3)_3]$ appear as singlets, indicative of C_{2v} symmetry for the $[(L^{Me})M_2(\mu\text{-}OAc)]^+$ cations in solution. This is further supported by the fact that the $[(L^{Me})M_2]^{2+}$ fragments give rise to only eleven ^{13}C signals (7 for the aliphatic and 4 for the aromatic carbon atoms). Of note is the appearance of the ^1H NMR signals for the methyl protons of the acetato coligands in **1** and **3** at $\delta = 0.85$ and $\delta = 0.98$ ppm, respectively. The signals are shifted considerably to high-field compared with the value recorded for free sodium acetate in the same solvent ($\delta = 1.83$ ppm). This provides strong

Table 1. Selected ^1H and ^{13}C NMR spectroscopic data for complexes **1**−**5**

	1[a][b]	**2**[a]	**3**[a]	**4**[a]	**5**[a]
ArH	7.13 s	7.20 s	7.12 s	7.36 d, 7.31 d	7.69 d
				7.27 d, 7.26 d	7.45 d
NCH_3	2.92 s	2.84 s	2.84 s	2.80 s, 2.57 s	3.33 s
				2.42 s, 2.33 s	
$N^{Bz}CH_3$	2.48 s	2.33 s	2.36 s	2.31 s, 2.24 s	2.40 s, 2.27 s
*t*Bu	1.28 s	1.26 s	1.23 s	1.23 s, 1.19 s	1.36 s
OAc	0.85 s	–	0.98 s	–	–
$C^{arom.}$	145.7	147.1	146.4	151.3, 149.9	151.2
	142.5	141.8	141.5	137.5, 137.4	139.9
	136.8	135.8	136.1	136.9, 136.7	139.1
	134.3	131.0	130.5	135.3, 134.1	138.7
				133.9, 133.7	131.4
				133.6, 132.6	130.8
CH_2	64.2	63.8	63.0	66.8, 64.5, 63.3	64.3, 63.2
	59.2	60.8	60.4	62.9, 62.0, 60.0	60.5, 59.7
	57.9	58.0	57.9	58.6, 57.3, 55.6	57.1, 56.7
				54.9, 52.0, 51.3	
NCH_3	49.8	50.1	50.3	49.7, 49.3, 46.4	48.1, 43.8, 39.9
	46.7	46.0	46.7	46.3, 46.2, 44.9	
$C(CH_3)_3$	34.4	34.7	34.7	35.2, 35.1	35.1
$C(CH_3)_3$	31.8	31.6	31.6	31.4, 31.3	31.8

[a] All spectra were recorded in CD_3CN at ambient temperature. [b] ^{13}C NMR spectroscopic data recorded for the BPh_4^- salt in $CDCl_3$.

 © 2005 Wiley-VCH Verlag GmbH & Co. KGaA, Weinheim

evidence that the coordinated acetate groups sense the ring-currents of the two flanking phenyl rings of $(L^{Me})^{2-}$. As can be seen from Figure 2 (see below), the methyl protons of the acetate groups are positioned in the binding cavity of the $[(L^{Me})M_2]^{2+}$ fragment slightly above the centre of the two phenyl rings in the shielded region. Since the angle between the phenyl rings in the zinc complex **1** (80.0°)[16] is much smaller than in the cadmium complex **3** (94.4°), the distance of the methyl protons to the centre of the phenyl rings is smaller in the former and hence the shielding effect is more pronounced in this compound. These spectroscopic findings thus clearly show that the coligands in **1** and **3** remain attached to the metal ions in solution with retention of their solid-state structures.

The ^{1}H NMR spectroscopic data of the dicadmium complex **2** are very similar to those of **3**. Again, the ArH, $N^{Bz}CH_3$, NCH_3 and $C(CH_3)_3$ protons all appear as well-resolved singlets. Likewise, there are only eleven signals in the ^{13}C spectrum. On the basis of these data, one can also conclude the existence of C_{2v} symmetry in the $[(L^{Me})Cd_2(\mu\text{-}Cl)]^+$ cation. The most striking feature in the ^{1}H NMR spectrum of **2**·ClO_4 is the rare observation of satellites for the $ArCH_2N$ and the $N^{Bz}CH_3$ protons that presumably arise from three-bond $^1H-^{111,113}Cd$ couplings [$^3J(^{111,113}Cd-^1H)$ = 4.6 Hz and 4.0 Hz, respectively].[19] This reflects kinetic inertness of the complex cation in solution as well as a degree of covalency in the Cd−ligand bonds. Similar findings have been observed for other cadmium complexes of macrocyclic ligands.[10,20]

The ^{13}C NMR spectroscopic data of the mercury complex **4** differ significantly from those of the compounds above and, as we will show below, this complex exhibits C_1 symmetry in the solid state. This symmetry arises because of different configurations for the two chiral amine donors in the two opposing diethylene triamine units [e.g. (*R*)-N(1), (*R*)-N(3) vs. (*S*)-N(4), (*R*)-N(6), see Figure 3 below]. This in turn renders all carbon atoms of the present complex chemically inequivalent and, given that its solid-state structure is maintained in solution, a total of 34[21] resonances (12 aromatic C atoms, 4 benzylic C atoms, 8 ethylene C atoms, 4 *tert*-butyl C atoms and 6 *N*-methyl C atoms) are, in principle, observable. The experiment clearly shows that this is indeed the case (see Table 1). At 75 MHz, the differences in the ^{13}C chemical shift values are sufficiently large for all the expected 34 resonances to be resolved. The 12 aromatic carbon atoms resonate in the region δ = 150−120 and the 22 aliphatic carbon atoms can be observed between 70 and 30 ppm. The fact that **4** is a C_1-symmetric species is also supported by ^{1}H NMR spectroscopy. In the case of the benzylic CH_2 and the ethylenic CH_2 protons the chemical shift differences are too small for full resolution of all expected 16 resonances. However, the expected 14 signals for the four aromatic protons, the four CH_3 groups on the benzylic nitrogen atoms, the two CH_3 groups on the central amine N atoms of the diethylene triamine units and the two *tert*-butyl groups are all observable with the correct intensity ratios. It can therefore be concluded that **4** maintains its solid-state structure in solution.

The lead complex **5** displays only half as many ^{13}C NMR signals as **4** but the total number of 17 resonances is still larger than the 11 resonances observed for **3**, indicating symmetry higher than C_1 but lower than C_{2v}. The ^{1}H NMR spectroscopic data suggest that it is C_2 symmetry which was observed in the solid state. The higher symmetry of **5** (relative to **4**) is easily detectable in the identical configurations for the four benzylic amine nitrogen donors in the two opposing diethylene triamine units [e.g. (*S*)-N(1), (*S*)-N(3), (*S*)-N(4), and (*S*)-N(6), see Figure 4, below]. In summary, the NMR spectroscopic investigations have clearly established that all complexes exist as discrete and stable species in solution.

X-ray Crystallography

Further confirmation regarding the composition and structures of the complexes was provided by X-ray diffraction studies. Single crystals of X-ray quality were obtained for the tetraphenylborate salts of **2**−**4** and for the diperchlorate salt of **5**. The molecular structures of the complexes are displayed in Figures 1−4 and selected bond lengths and angles are given in Tables 2 and 3.

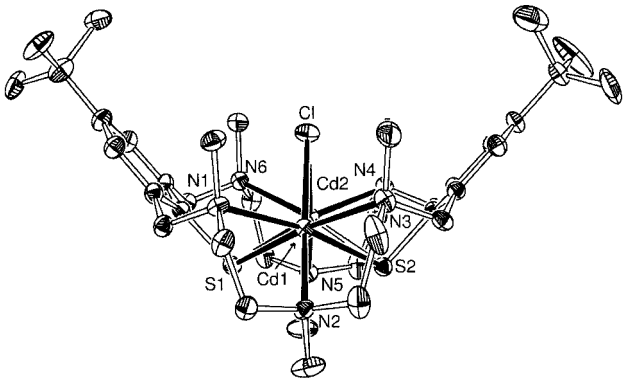

Figure 1. Molecular structure of the cation **2**; thermal ellipsoids are drawn at the 50% probability level; hydrogen atoms are omitted for clarity

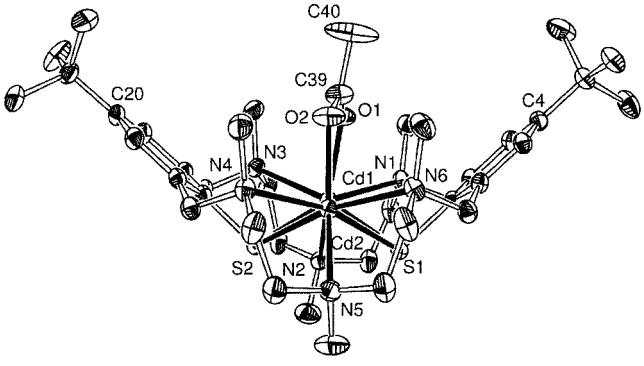

Figure 2. Molecular structure of the cation **3**; thermal ellipsoids are drawn at the 30% probability level; hydrogen atoms are omitted for clarity

 © 2005 Wiley-VCH Verlag GmbH & Co. KGaA, Weinheim

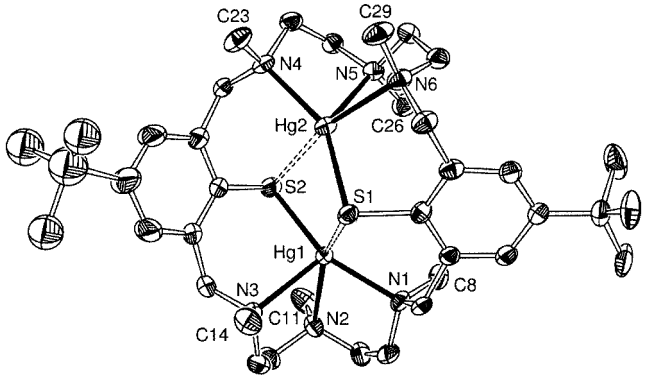

Figure 3. Molecular structure of the dication **4**; thermal ellipsoids are drawn at the 30% probability level; hydrogen atoms are omitted for clarity

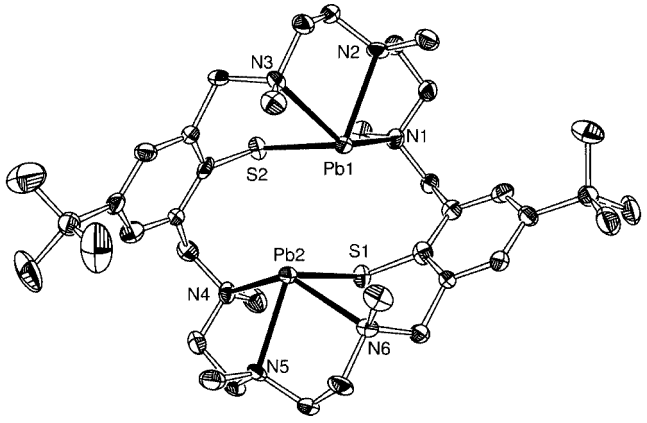

Figure 4. Molecular structure of the dication **5**; thermal ellipsoids are drawn at the 50% probability level; hydrogen atoms are omitted for clarity

Description of the Crystal Structures

*[(L^{Me})Cd_2(μ-Cl)]BPh_4·1.5MeOH (**2**·BPh_4·1.5MeOH)*

This salt crystallises in the triclinic space group $P\bar{1}$. The structure revealed the presence of discrete dinuclear $[(L^{Me})Cd_2(\mu\text{-}Cl)]^+$ cations, tetraphenylborate anions and methanol solvate molecules. The dicadmium complex exhibits idealized C_{2v} symmetry as was established by NMR spectroscopy. As can be seen in Figure 1, the cadmium(II) ions are coordinated in a distorted octahedral fashion by three *facially* oriented nitrogen atoms, two bridging thiophenolate sulfur atoms and a bridging halide ion. The minimum and maximum deviations from the ideal 90° and 180° bond angles of a perfect octahedron are −14.8° for N(1)−Cd(1)−N(2) and −10.4° for Cl−Cd(2)−N(5), respectively. The mean cadmium−ligand bond lengths (Cd−N 2.421 Å, Cd−S 2.677 Å, Cd−Cl 2.703 Å) show no unusual features and compare well with those in **3** (see below) and related complexes with mixed N and S ligation.[20,22] It is also worth mentioning that the macrocycle in **2** adopts the "conical" calixarene-like conformation which differs from the alternative "partial cone" conformation seen in the related complexes $[(L^{Me})M_2(\mu\text{-}Cl)]^+$ of the lighter 3d elements Co^{II}, Ni^{II} and Zn^{II}.[15,24] The preference of the latter for adopting the "partial cone" conformation is presumably due to the smaller ionic radii of these metal ions (Co^{II}: 0.885 Å, Ni^{II}: 0.83 Å, Zn^{II}: 0.88 Å vs. 1.06 Å for Cd^{II})[23] and presumably also due to the rigid nature of the 24-membered macrocycle.

*[(L^{Me})Cd_2(μ-OAc)]BPh_4·2MeCN·MeOH (**3**·BPh_4·2MeCN·MeOH)*

The crystal structure determination of the title compound showed the structure of the dinuclear $[(L^{Me})Cd_2(\mu\text{-}OAc)]^+$ complex to be isostructural with the zinc complex $[(L^{Me})Zn_2(\mu\text{-}OAc)]^+$ (**1**).[16] The hexaaza-dithiophenolate ligand assumes a bowl-shaped "calixarene-like" conformation which is typical for carboxylato-bridged complexes of this ligand.[24] The acetate ion bridges the two cadmium ions in a symmetrical fashion [O(1)−C(39) 1.222(4) Å, O(2)−C(39) 1.232(4) Å] with a Cd···Cd distance of 3.402(2) Å. It is deeply buried in the binding cavity of the $[(L^{Me})Cd_2]^{2+}$ fragment. As a consequence, its methyl protons are positioned above the centre of the two phenyl rings in the shielding region. The angle between the planes through the two phenyl rings of 94.4° is larger than in **1** (80.0°). This explains why the acetate protons in **1** experience a larger high-field shift compared with those in **3** (vide supra). The average Cd−N bond length of 2.439 Å is normal for six-coordinate cadmium complexes with amine donor ligands.[25,26] The same holds for the average Cd−S distance of 2.669 Å and the average Cd−O distance of 2.238 Å.[27,28] As expected, the metal-ligand bond lengths in **3** are larger than those in **1**. The mean difference of 0.13 Å is close to the difference between the ionic radii of the two elements.

*[(L^{Me})Hg_2](BPh_4)$_2$·MeCN [**4**·(BPh_4)$_2$·MeCN]*

The crystal structure determination of **4**·$(BPh_4)_2$·MeCN unambiguously confirmed the identity of the dimercury(II) complex **4**. Its molecular structure is illustrated in Figure 3. The $[(L^{Me})Hg_2]^{2+}$ dication bears no additional coligands and has an intramolecular Hg···Hg separation of 3.725(1) Å. The Hg^{II} ions are surrounded by three nitrogen and two sulfur donor atoms from $(L^{Me})^{2-}$ in highly irregular N_3S_2 coordination environments (coordination number of Hg^{II}: 4 + 1). The intramolecular separations Hg(1)···S(1) of 2.897(2) Å and Hg(2)···S(2) of 3.313(2) Å are much longer than the other two Hg−S distances of 2.383 and 2.395 Å, indicating that the latter exhibit more covalent character while the former are more electrostatic in nature. The diethylene triamine units are *facially* coordinated with one large and two smaller N−Hg−N bond angles, this being the most commonly observed situation in complexes with this tridentate unit.[29] The Hg−N bond lengths (mean value: 2.413 Å) are somewhat longer in comparison with the more covalent Hg−S bonds but are similar to those in related mercury complexes.[30,31] In $[Hg(en)_2](ClO_4)_2$ for example (en = ethylene diamine), an average Hg−N distance of 2.32 Å has been reported.[32]

 © 2005 Wiley-VCH Verlag GmbH & Co. KGaA, Weinheim

Table 2. Selected bond lengths [Å] and angles [°] in the cations $[(L^{Me})Zn_2(OAc)]^+$ (**1**), $[(L^{Me})Cd_2(Cl)]^+$ (**2**), $[(L^{Me})Cd_2(OAc)]^+$ (**3**)

	1 M = Zn, X = Y = O	**2** M = Cd, X = Y = Cl	**3** M = Cd, X = Y = O
M(1)−X	2.026(2)	2.682(1)	2.245(2)
M(1)−N(1)	2.379(2)	2.453(3)	2.474(3)
M(1)−N(2)	2.202(2)	2.424(3)	2.436(3)
M(1)−N(3)	2.316(2)	2.410(4)	2.408(3)
M(1)−S(1)	2.551(1)	2.653(1)	2.654(1)
M(1)−S(2)	2.515(1)	2.699(2)	2.677(1)
M(2)−Y	2.027(2)	2.723(1)	2.230(2)
M(2)−N(4)	2.314(2)	2.441(3)	2.467(3)
M(2)−N(5)	2.219(2)	2.388(3)	2.411(3)
M(2)−N(6)	2.388(2)	2.409(3)	2.442(3)
M(2)−S(1)	2.572(1)	2.696(1)	2.698(1)
M(2)−S(2)	2.508(1)	2.659(1)	2.645(1)
M−N[a]	2.303	2.421	2.439
M−X[a]	2.027	2.703	2.238
M−S[a]	2.536	2.677	2.669
M(1)−S(1)−M(2)	84.00(4)	77.78(4)	78.92(4)
M(1)−S(2)−M(2)	86.05(3)	77.63(4)	79.46(4)
M(1)−μCl−M(2)	–	76.83(4)	–
N(1)−M(1)−N(2)	78.92(8)	75.17(11)	75.22(9)
N(1)−M(1)−N(3)	98.84(7)	99.40(12)	101.87(9)
N(2)−M(1)−N(3)	80.98(9)	76.48(12)	75.99(9)
N(4)−M(2)−N(5)	80.23(7)	75.97(12)	75.84(10)
N(4)−M(2)−N(6)	99.00(7)	99.77(12)	103.53(10)
N(5)−M(2)−N(6)	79.05(7)	76.83(12)	76.31(9)
C(4)···C(20)	9.404	9.824	10.247
Ph/Ph[b]	80.0	83.7	94.4
M···M	3.427(1)	3.358(1)	3.402(2)

[a] Average values. [b] Angle between the normals of the planes of the two aryl rings.

Table 3. Selected bond lengths [Å] and angles [°] in $[(L^{Me})Hg_2]^{2+}$ (**4**) and $[(L^{Me})Pb_2]^{2+}$ (**5**)

4		**5**	
Hg(1)···S(1)	2.897(2)	Pb(1)···S(1)	3.465(3)
Hg(1)−S(2)	2.383(2)	Pb(1)−S(2)	2.640(3)
Hg(1)−N(1)	2.276(5)	Pb(1)−N(1)	2.584(10)
Hg(1)−N(2)	2.566(5)	Pb(1)−N(2)	2.427(9)
Hg(1)−N(3)	2.449(5)	Pb(1)−N(3)	2.552(10)
Hg(2)−S(1)	2.395(2)	Pb(2)−S(1)	2.554(3)
Hg(2)···S(2)	3.313(2)	Pb(2)···S(2)	3.824(3)
Hg(2)−N(4)	2.269(5)	Pb(2)−N(4)	2.591(10)
Hg(2)−N(5)	2.401(5)	Pb(2)−N(5)	2.403(8)
Hg(2)−N(6)	2.517(5)	Pb(2)−N(6)	2.600(9)
Hg(1)···Hg(2)	3.725(1)	Pb(1)···Pb(2)	3.4192(8)
Hg−N[a]	2.413	Pb−N[a]	2.526
Hg−S[a]	2.389	Pb−S[a]	2.597
N(1)−Hg(1)−N(2)	76.17(18)	N(1)−Pb(1)−N(2)	71.0(3)
N(1)−Hg(1)−N(3)	108.91(19)	N(1)−Pb(1)−N(3)	137.0(3)
N(2)−Hg(1)−N(3)	73.24(17)	N(2)−Pb(1)−N(3)	74.1(3)
N(4)−Hg(2)−N(5)	78.36(18)	N(4)−Pb(2)−N(5)	73.8(3)
N(4)−Hg(2)−N(6)	108.81(18)	N(4)−Pb(2)−N(6)	139.3(3)
N(5)−Hg(2)−N(6)	73.83(18)	N(5)−Pb(2)−N(6)	74.5(3)

[a] Average values.

It should be noted that the configurations of the benzylic nitrogen atoms in the opposing diethylene triamine are different. Thus, the configurations are (*R*)-N(1) and (*R*)-N(3) for one diethylene linker, whereas they are (*S*)-N(4) and (*R*)-N(6) for the other. The differences in the secondary Hg···S interactions [i.e. Hg(2)···S(2), Hg(2)···S(1)] are, at least in part, a consequence of these different N configurations. They are also responsible for the C_1 symmetry of the $[(L^{Me})Hg_2]^{2+}$ dication.

[(L^Me)Pb2](ClO4)2·MeCN [5·(ClO4)2·MeCN]

This structure contains discrete $[(L^{Me})Pb_2]^{2+}$ cations, perchlorate anions and acetonitrile solvate molecules. Figure 4 shows the structure of the cation **5** together with the atomic numbering scheme. Similar to **4**, the dication is not bound to any further coligands. Complex **5** exhibits no crystallographically imposed symmetry but has idealized C_2 symmetry. The coordination environment of each lead(II) ion consists of three tertiary amine donors and one thiophenolate sulfur atom. The coordination geometry is best considered as distorted square pyramidal, with the lead ion sitting ca 1.3 Å above the plane formed from the four donor atoms [mean deviation from the planes N(1)N(2)N(3)S(2): 0.32 Å, N(4)N(5)N(6)S(1): 0.31 Å]. The empty space above the lead(II) ion on the apex of the pyramid is indicative of a stereochemically active lone pair as in PbO (yellow modification).[33] In contrast to the dimercury complex **4**, the diethylene triamine units bind in a meridional fashion which results in larger N(1)−Pb(1)−N(3) [137.0(3)°] and N(4)−Pb(2)−N(6) [139.3(3)°] angles. This has also been observed in lead complexes of macrodinucleating polyazaphenolate ligands.[34] The average Pb−N bond length of

 © 2005 Wiley-VCH Verlag GmbH & Co. KGaA, Weinheim

2.526 Å is normal for lead(II) complexes.[35,36] The same is true for the Pb−S distances.

Conclusion

The main findings of the present work can be summarised as follows: a) The 24-membered hexaaza-dithiophenolate macrocycle H_2L^{Me} supports the formation of dinuclear complexes of Cd^{II}, Hg^{II} and Pb^{II}. b) The complexes dissolve in organic solvents without decomposition. c) The dicadmium complexes $[(L^{Me})M_2(\mu\text{-}L')]$ differ from the Hg and Pb complexes in that they bind additional coligands. This offers the opportunity to selectively recognise or separate Cd from a mixture of the three elements. d) The structures of $[(L^{Me})Hg_2]^{2+}$ and $[(L^{Me})Pb_2]^{2+}$ have clarified the binding preferences of the two toxic heavy metal ions towards the donors of H_2L^{Me}. This can now be used as a guide for fine-tuning the ligand to achieve high metal-ion selectivity. Current studies in this laboratory are focusing on the determination of the complex stability constants and on methods of metal-ion extraction.

Experimental Section

General: Unless otherwise noted, the preparations of the metal complexes were carried out under argon using standard Schlenk techniques. The compound $H_2L^{Me}\cdot 6HCl$ was prepared as described in the literature.[15,37] All other compounds and reagents were purchased. Melting points were determined in capillaries and are uncorrected. ^1H and ^{13}C NMR spectra were recorded with a Bruker AVANCE DPX-200 or a Varian 300 unity spectrometer. Elemental analyses were performed with a Vario EL analyser (Elementaranalysensysteme GmbH). IR spectra were recorded with a Bruker VECTOR 22 FT-IR spectrometer as KBr pellets.

Safety Note: *Caution; perchlorate salts of transition metal complexes are hazardous and may explode; only small quantities should be prepared and great care should be taken!*

$[(L^{Me})Cd_2(\mu\text{-}Cl)]ClO_4$ (2·ClO_4): To a suspension of $H_2L^{Me}\cdot 6HCl$ (890 mg, 1.00 mmol) in methanol (40 mL) was added solid $CdCl_2\cdot H_2O$ (403 mg, 2.00 mmol). A solution of triethylamine (808 mg, 8.00 mmol) in methanol (2 mL) was then added to give a colourless solution. After stirring at room temperature for 3 h, solid $LiClO_4\cdot 3H_2O$ (2.50 g, 15.6 mmol) was added to give the perchlorate salt **2**·ClO_4 as a white microcrystalline solid. This material was filtered, washed with cold ethanol (5 mL) and diethyl ether (5 mL), and dried in vacuo. Yield 876 mg (85%). M.p. 302−303 °C (decomposes without melting). IR (KBr pellet): $\tilde{\nu}$ = 3446 s br, 2958 s, 2865 s, 1630 m, 1457 s, 1394 w, 1365 m, 1314 m, 1291 m, 1267 m, 1234 m, 1203 w, 1168 w, 1158 w, 1100 vs. [$\nu(ClO_4)$], 1046 s, 1012 w, 1000 w, 978 m, 928 m, 910 m, 887 m, 815 s, 802 m, 746 m, 686 w, 664 w, 624 s, 593 w, 555 w, 484 w cm^{-1}. ^1H NMR (300 MHz, CD_3CN, 25 °C, TMS): δ = 7.20 (s, 4 H, ArH), 4.70 [d, ^2J = 11.5, $^3J(^{111,113}Cd\text{-}^1H)$ = 4.6 Hz, 4 H, $ArCH_2$], 3.42 (m, 4 H, NCH_2), 3.24 (m, 4 H, NCH_2), 2.88−2.78 (m, 4 H +4 H, NCH_2+$ArCH_2$), 2.84 (s, 6 H, NCH_3), 2.50 (m, 4 H, NCH_2), 2.33 [s, $^3J(^{111,113}Cd\text{-}^1H)$ = 4.6 Hz, 12 H, *Bz*NCH_3], 1.26 [s, 18 H, $C(CH_3)_3$] ppm. $^{13}C\{^1H\}$ NMR (75.42 MHz, $[D_3]CH_3CN$, 25 °C, TMS): δ = 147.1, 141.8, 135.8 (CH), 131.0 (CH) (aromatic carbon atoms), 63.8, 60.8, 58.0 (all CH_2), 50.1, 46.0 (all NCH_3), 34.7 [$C(CH_3)_3$], 31.6 [$C(CH_3)_3$] ppm. $C_{38}H_{64}Cd_2Cl_2N_6O_4S_2$ (1028.81): calcd. C 44.36, H 6.27, N 8.17, S 6.23; found C 43.92, H 6.12, N 8.00, S 5.77. The tetraphenylborate salt, $[(L^{Me})Cd_2(\mu\text{-}Cl)]BPh_4$ (**2**·BPh_4), was prepared by adding a solution of $NaBPh_4$ (198 mg, 0.580 mmol) in methanol (3 mL) to an argon-purged solution of **1**·ClO_4 (103 mg, 0.100 mmol) in methanol (50 mL). The resultant colourless precipitate was isolated by filtration, washed with 5 mL of cold methanol and dried in air. Yield 112 mg (90%). M.p. 293−294 °C (decomp.). IR (KBr pellet): $\tilde{\nu}$ = 3053 m, 3032 w, 2996 w, 2964 s, 2925 w, 2900 w, 2862 m, 2835 w, 2807 w, 1477 m, 1457 s, 1425 m, 1394 m, 1365 m, 1352 w, 1313 m, 1290 m, 1267 m, 1232 m, 1203 w, 1181 w, 1170 w, 1157 m, 1131 w, 1114 w, 1083 s, 1044 s, 1011 w, 1000 w, 981 w, 927 w, 910 m, 887 m, 844 m, 815 m, 802 m, 734 s, 705 s [$\nu(BPh_4^-)$], 625 m, 612 m, 555 w, 475 w cm^{-1}. The tetraphenylborate salt was additionally characterised by X-ray crystallography.

$[(L^{Me})Cd_2(\mu\text{-}OAc)]ClO_4$ (3·ClO_4): To a solution of **2**·ClO_4 (103 mg, 0.100 mmol) in methanol (50 mL) was added a solution of sodium acetate (12.3 mg, 0.150 mmol) in methanol (5 mL). After the reaction mixture had been stirred for 3 h, a solution of $LiClO_4\cdot 3H_2O$ (802 mg, 5.00 mmol) in methanol (2 mL) was added. The resultant colourless microcrystalline solid was isolated by filtration, washed with methanol and dried in air. Yield 91 mg (86%). M.p. 352−353 °C (decomp.). IR (KBr, pellet): $\tilde{\nu}$ = 2960 s, 2900 m, 2865 s, 2837 sh, 2806 m, 1577 s [$\nu_{as}(OAc^-)$], 1456 s, 1422 s [$\nu_s(OAc^-)$], 1396 w, 1365 m, 1314 w, 1293 m, 1267 m, 1230 m, 1203 m, 1170 w, 1155 w, 1093 vs. [$\nu(ClO_4^-)$], 1044 s, 1012 w, 1000 w, 981 w, 925 w, 911 m, 884 m, 816 s, 802 m, 744 m, 684 w, 654 m, 624 s, 596 w, 555 w, 535 w cm^{-1}. ^1H NMR (200 MHz, $[D_3]CH_3CN$, 25 °C, TMS): δ = 7.12 (s, 4 H, ArH), 4.54 (d, ^2J = 11.5 Hz, 4 H, $ArCH_2$), 3.40 (m, 4 H, CH_2), 3.18 (m, 4 H, CH_2), 2.84 (s, 6 H, NCH_3), 2.82 (m, 4 H, CH_2), 2.74 (d, 4 H, $ArCH_2$), 2.48 (m, 4 H, CH_2), 2.36 (s, 12 H, NCH_3), 1.23 (s, 18 H, CH_3), 0.98 (s, 3 H, O_2CCH_3) ppm. ^{13}C NMR (75.42 MHz, $[D_3]CH_3CN$, 25 °C, TMS): δ = 176.3 (OAc), 146.4, 141.5, 136.1, 130.5, 63.0 (CH_2), 60.4 (CH_2), 57.9 (CH_2), 50.3 (NCH_3), 46.7 (NCH_3), 34.7 (*C*), 31.6 [$C(CH_3)_3$], 23.2 (OAc) ppm. The tetraphenylborate salt, $[(L^{Me})Cd_2(\mu\text{-}OAc)]BPh_4$ (**3**·BPh_4), was prepared by adding $NaBPh_4$ (342 mg, 1.00 mmol) to a solution of **3**·ClO_4 (103 mg, 0.100 mmol) in methanol (50 mL). The resultant colourless solid was recrystallised from a mixed acetonitrile/methanol (1:1) solvent system. Yield 116 mg (91%). M.p. 304−305 °C (decomp.). IR (KBr pellet): $\tilde{\nu}$ = 3055 m, 3034 m, 2908 sh, 2963 s, 2924 m, 2899 m, 2866 m, 2836 m, 2804 w, 1576 s [$\nu_{asym}(OAc^-)$], 1476 w, 1455 s, 1425 s [$\nu_{sym}(OAc^-)$], 1395 w, 1364 w, 1353 w, 1313 w, 1291 w, 1267 w, 1230 w, 1203 w, 1181 w, 1170 w, 1155 m, 1133 w, 1116 w, 1082 s, 1045 s, 1012 w, 996 w, 981 w, 924 m, 911 m, 886 m, 842w, 815 s, 800 m, 744 m, 734 s, 704 s [$\nu(BPh_4^-)$], 653 w, 625 m, 612 m, 594 w, 556 w cm^{-1}. $C_{64}H_{87}BCd_2N_6O_2S_2$ (1272.18): calcd. C 60.42, H 6.89, N 6.61, S 5.04; found C 60.24, H 6.72, N 6.47, S 4.94. This salt was additionally characterised by X-ray crystallography.

$[(L^{Me})Hg_2](ClO_4)_2$ [4·$(ClO_4)_2$]: To a suspension of $H_2L^{Me}\cdot 6HCl$ (890 mg, 1.00 mmol) in methanol (40 mL) was added a solution of $Hg(CH_3COO)_2$ (637 mg, 2.00 mmol) in methanol (10 mL). A solution of triethylamine (808 mg, 8.00 mmol) in methanol (5 mL) was then added to give a colourless solution. The reaction mixture was stirred for 12 h after which time a solution of $LiClO_4\cdot 3H_2O$ (802 mg, 5.00 mmol) in methanol (2 mL) was added. The resultant colourless microcrystalline solid was isolated by filtration, washed with methanol and dried in air. Yield 901 mg (71%). M.p. 246−247 °C (decomp). IR (KBr pellet): $\tilde{\nu}$ = 2958 s, 2902 w, 2864 s, 1463 m, 1394 w, 1366 m, 1307 w, 1290 w, 1266 w, 1231 m, 1202 w, 1183 w,

 © 2005 Wiley-VCH Verlag GmbH & Co. KGaA, Weinheim

1143 m, 1119 s, 1107 s, 1088 s [ν(ClO_4^-)], 1045 w, 1022 w, 1010 w, 991 w, 960 w, 948 w, 927 w, 910 m, 901 m, 889 m, 810 m, 796 m, 782 w, 753 w, 742 w, 685 w, 630 m, 624 s. ^{1}H NMR (300 MHz, [D$_3$]CH_3CN, 25 °C, TMS): δ = 7.36 (d, ^4J = 2.3 Hz, 1 H, ArH), 7.31 (d, ^4J = 2.3 Hz, 1 H, ArH), 7.27 (d, ^4J = 2.3 Hz, 1 H, ArH), 7.26 (d, ^4J = 2.3 Hz, 1 H, ArH), 4.91 (d, ^2J = 12.0 Hz, 1 H, $ArCH_2$), 4.74 (d, ^2J = 12.0 Hz, 1 H, $ArCH_2$), 4.26 (d, ^2J = 12.0 Hz, 1 H, $ArCH_2$), 4.20 (d, ^2J = 12.0 Hz, 1 H, $ArCH_2$), 3.71 (d, ^2J = 12.0 Hz, 1 H, $ArCH_2$), 3.44 (d, ^2J = 12.0 Hz, 1 H, $ArCH_2$), 3.38 (d, ^2J = 12.0 Hz, 1 H, $ArCH_2$), 3.25−2.50 (m, 1 H +16 H, $ArCH_2$ + NCH_2CH_2N), 2.80 (s, 3 H, NCH_3), 2.57 (s, 3 H, NCH_3), 2.42 (s, 3 H, NCH_3) 2.33 (s, 3 H, NCH_3) 2.31 (s, 3 H, NCH_3) 2.24 (s, 3 H, NCH_3), 1.23 (s, 9 H, CH_3), 1.19 (s, 9 H, CH_3) ppm. ^{13}C{^{1}H} NMR (75.42 MHz, [D$_3$]CH_3CN, 25 °C, TMS): δ = 151.3, 149.9, 137.5, 137.4, 136.9, 136.7, 135.3, 134.1, 133.9, 133.7, 133.6, 132.6 (aromatic carbon atoms), 66.8, 64.5, 63.3, 62.9, 62.0, 60.0, 58.6, 57.3, 55.6, 54.9, 52.0, 51.3 (all CH_2), 49.7, 49.3, 46.4, 46.3, 46.2, 44.9 (all NCH_3), 35.2, 35.1 [$C(CH_3)_3$], 31.4, 31.3 [C(CH_3)$_3$] ppm. The tetraphenylborate salt, [(L^{Me})Hg_2](BPh_4)$_2$ [**4**·(BPh_4)$_2$], was prepared by adding a solution of $NaBPh_4$ (342 mg, 1.00 mmol) in methanol (3 mL) to a solution of [(L^{Me})Hg_2](ClO_4)$_2$ (127 mg, 0.100 mmol) in methanol (50 mL). The resultant colourless solid was isolated by filtration, washed with 5 mL of cold methanol, and dried in air. Yield 150 mg (88%). M.p. 170−171 °C (decomp.). IR (KBr pellet): $\tilde{\nu}$ = 3054 s, 3034 s, 2997 m, 2982 m, 2961 s, 2927 w, 2903 w, 2864 m, 2808 w, 1579 w, 1559 w, 1476 m, 1460 s, 1439 sh, 1425 m, 1396 m, 1375 w, 1364 m, 1351 w, 1307 w, 1285 w, 1265 m, 1229 m, 1202 w, 1183 w, 1157 m, 1133 m, 1111 w, 1087 m, 1063 m, 1042 m, 1032 m, 1009 vw, 992 w, 961 vw, 951 vw, 911 m, 890 m, 845 m, 810 m, 797 w, 784 w, 749 sh, 735 s, 706 s [ν(BPh_4)], 625 m, 613 s cm^{-1}.

[(L^{Me})Pb_2](ClO_4)$_2$ [5·(ClO_4)$_2$]: To a suspension of H_2L^{Me} 6HCl (890 mg, 1.00 mmol) in methanol (40 mL) was added a solution of $Pb(CH_3COO)_2$·3H_2O (759 mg, 2.00 mmol) in methanol (20 mL). A solution of triethylamine (808 mg, 8.00 mmol) in methanol (5 mL) was then added to give a pale yellow solution. After stirring for 12 h, a solution of $LiClO_4$·3H_2O (802 mg, 5.00 mmol) in methanol (5 mL) was added. The resultant pale-yellow precipitate was isolated by filtration, washed with methanol and dried in air. Yield 1.03 g (80%). M.p. 346−347 °C (decomp.). IR (KBr pellet): $\tilde{\nu}$ = 2955 s, 2901 m, 2862 s, 2810 m, 1459 m, 1396 w, 1364 m, 1304 w, 1296 w, 1259 w, 1228 w, 1203 w, 1175 w, 1144 m, 1107 sh, 1091 vs [ν(ClO_4^-)], 1045 w, 1000 w, 958 w, 927 w, 918 w, 888 w, 811 m, 797 m, 759 m, 625 s, 460 w cm^{-1}. ^{1}H NMR (300 MHz, [D$_3$]CH_3CN, 25 °C, TMS): δ = 7.69 (d, ^4J = 2.2 Hz, 2 H, ArH), 7.45 (d, ^4J = 2.2 Hz, 2 H, ArH), 4.92 (d, ^2J = 13.2 Hz, 2 H, $ArCH_2$), 4.59 (d, ^2J = 11.7 Hz, 2 H, $ArCH_2$), 4.29 (d, ^2J = 13.2 Hz, 2 H, $ArCH_2$), 3.88 (d, ^2J = 11.6 Hz, 2 H, $ArCH_2$), 3.86−2.92 (m, 16 H, NCH_2), 3.33 (s, 6 H, NCH_3), 2.40 (s, 6 H, NCH_3), 2.27 (s, 6 H, NCH_3), 1.36 [s, 18 H, C(CH_3)$_3$] ppm. ^{13}C{^{1}H} NMR (75.42 MHz, [D$_3$]CH_3CN, 25 °C, TMS): δ = 151.2, 139.9, 139.1, 138.7, 131.4, 130.8 (aromatic carbon atoms), 64.3, 63.2, 60.5, 59.7, 57.1, 56.7 (all CH_2), 48.1, 43.8, 39.9 (all NCH_3), 35.1 [$C(CH_3)_3$], 31.8 [$C(CH_3)_3$] ppm. $C_{38}H_{64}Cl_2N_6O_8Pb_2S_2$ (1282.39): calcd. C 35.59, H 5.03, N 6.55, S 5.00; found C 35.49, H 5.21, N 6.33, S 4.69.

Crystal Structure Determinations: Single-crystals suitable for X-ray structural analyses were grown by recrystallisation from methanol (**2**·BPh_4·1.5MeOH), acetonitrile [**4**·(BPh_4)$_2$·MeCN, **5**(ClO_4)$_2$·MeCN] or a mixed acetonitrile/methanol solvent system (**3**·BPh_4·2MeCN·MeOH). The crystals were mounted on glass fibres using perfluoropolyether oil. Intensity data were collected at 210(2) K using a Bruker SMART CCD diffractometer. Graphite-monochromated Mo-K_α radiation (λ = 0.71073 Å) was used throughout. The data were processed with SAINT and corrected for absorption using SADABS[38] (transmission factors: 1.00−0.95 for **2**·BPh_4, 1.00−0.85 for **3**·BPh_4, 1.00−0.64 for **4**·(BPh_4)$_2$ and 1.00−0.70 for **5**·(ClO_4)$_2$]. The structures were solved by direct methods using the program SHELXS-86[39] and refined by full-matrix least-squares techniques against F^2 using SHELXL-97.[40] The SHELXTL version 5.10 program package was used for the structure solutions and

Table 4. Crystallographic data for **2**·BPh_4·1.5MeOH, **3**·BPh_4·2MeCN·MeOH, **4**(BPh_4)$_2$MeCN, **5**(ClO_4)$_2$MeCN

	2	**3**	**4**	**5**
Empirical formula	$C_{63.50}H_{90}BCd_2ClN_6O_{1.50}S_2$	$C_{69}H_{97}BCd_2N_8O_3S_2$	$C_{88}H_{107}B_2Hg_2N_7S_2$	$C_{40}H_{67}Cl_2N_7O_8Pb_2S_2$
M_r (gmol^{-1})	1296.60	1386.28	1749.73	1323.41
Space group	$P\bar{1}$	$P\bar{1}$	$P2_1/n$	$P2_1/n$
a [Å]	13.717(3)	14.661(3)	15.857(2)	16.333(3)
b [Å]	16.016(3)	16.726(3)	27.246(4)	14.428(3)
c [Å]	16.650(3)	17.348(3)	19.388(3)	22.556(5)
α [°]	110.49(3)	112.80(3)	90	90
β [°]	91.15(3)	110.47(3)	97.944(3)	94.32(3)
γ [°9	108.21(3)	95.46(3)	90	90
V [Å^3]	3220.2(11)	3540.6(11)	8296(2)	5300(2)
Z	2	2	4	4
$d_{calcd.}$ [gcm^{-3}]	1.337	1.300	1.401	1.658
Crystal size [mm]	0.25 × 0.25 × 0.25	0.30 × 0.20 × 0.20	0.20 × 0.20 × 0.20	0.20 × 0.20 × 0.20
μ(Mo-K_α) [mm^{-1}]	0.811	0.708	3.794	6.575
2θ limits [°]	2.64−56.64	2.74−57.68	2.60−57.84	2.89−59.66
Measured refl.	29690	32216	51765	48229
Independent refl.	15205	16591	19837	13351
Observed refl.[a]	7769	11397	11519	6018
No. of parameters	721	754	920	549
$R1$[b] ($R1$ all data)	0.0400 (0.1021)	0.0364 (0.0645)	0.0460 (0.0916)	0.0537 (0.1628)
$wR2$[c]($wR2$ all data)	0.0760 (0.0913)	0.0915 (0.1039)	0.1126 (0.1251)	0.1263 (0.1628)
Max, min peaks (eÅ^{-3})	0.703, −0.611	0.776, −0.670	5.333; −1.498	1.623; −1.951

[a] Observation criterion: $I > 2\sigma(I)$. [b] $R1 = \Sigma||F_o| - |F_c||/\Sigma|F_o|$. [c] $wR2 = \{\Sigma[w(F_o^2-F_c^2)^2]/\Sigma[w(F_o^2)^2]\}^{1/2}$.

refinements.[41] PLATON was used to search for higher symmetry.[42] ORTEP3 was used for generating the ORTEP diagrams.[43] Unless otherwise noted, the anisotropic thermal parameters of all nonhydrogen atoms were refined. Hydrogen atoms were included in calculated positions with their bond lengths and thermal parameters 1.2 times (1.5 times for CH_3 groups) the thermal parameter of the atoms to which they are attached. Selected details of the data collection and refinements are given in Table 4. In the crystal structure of **2**·BPh_4·1.5MeOH one *tert*-butyl group was found to be disordered over two positions. A split atom model was applied for the disordered *t*Bu groups. The site occupancies of the two orientations were refined as 0.67(1)/0.33(1) [for C(36a/c), C(37a/c), C(38a/c)]. In the crystal structure of **3**·BPh_4·2MeCN·MeOH the methanol solvent molecule of crystallisation was found to be disordered over two positions. The site occupancies of the two orientations were fixed at half occupancy. The C and O atoms of this molecule were refined isotropically. In the crystal structure of **4**·$(BPh_4)_2$·MeCN, the *tert*-butyl groups were found to be disordered over two positions. A split atom model was applied for these alkyl groups. The site occupancies of the two orientations were refined as 0.66(3)/0.34(3) [for C(32a/c), C(33a/c), C(34a/c)] and 0.56(2)/0.44(2) [for C(36a/c), C(37a/c), C(38a/c)]. The non-hydrogen atoms of the disordered *t*Bu groups and the acetonitrile solvate molecule were refined isotropically. No hydrogen atoms were calculated for these two residues. In the crystal structure of **5**·$(ClO_4)_2$, the acetonitrile molecule of solvation and one of the two perchlorate anions were found to be disordered over two positions. The site occupancy factors of the two orientations of the acetonitrile molecule were fixed at 0.50 and its C and N atoms were refined isotropically. No hydrogen atoms were calculated for the MeCN molecule. The site occupancy factors of the two orientations of the perchlorate anion were refined as 0.68(2) and 0.32(2) for O(5)O(6a)O(7a)O(8a) and O(5)O(6b)O(7b)O(8b). These atoms could not be refined anisotropically and, for this reason, were treated as isotropic scatterers. CCDC-243454 (**2**), -243455 (**3**), -243456 (**4**) and -243457 (**5**) contain the supplementary crystallographic data for this paper. These data can be obtained free of charge at www.ccdc.cam.ac.uk/conts/retrieving.html [or from the Cambridge Crystallographic Data Centre, 12 Union Road, Cambridge CB2 1EZ, UK; Fax: (internat.) + 44-1223-336-033; E-mail: deposit@ccdc.cam.ac.uk].

Acknowledgments

We are particularly grateful to Prof. Dr. H. Vahrenkamp for providing facilities for NMR spectroscopic and X-ray crystallographic measurements. Financial support of this work from the Deutsche Forschungsgemeinschaft (Priority programme "Sekundäre Wechselwirkungen", KE 585/3-1,2) and the Wissenschaftliche Gesellschaft in Freiburg is gratefully acknowledged.

[1] N. H. Pilkington, R. Robson, *Aust. J. Chem.* **1970**, *23*, 2225−2236.
[2] [2a] P. A. Vigato, S. Tamburini, D. Fenton, *Coord. Chem. Rev.* **1990**, *106*, 25−170. [2b] D. Fenton, *Chem. Soc., Rev.* **1999**, *28*, 159−168.
[3] M. Yamami, H. Furutachi, T. Yokoyama, H. Okawa, *Inorg. Chem.* **1998**, *37*, 6832−6838.
[4] [4a] H. Okawa, H. Furutachi, D. E. Fenton, *Coord. Chem. Rev.* **1998**, *174*, 51−75. [4b] M. Shinoura, S. Kita, M. Ohba, H. Okawa, H. Furutachi, M. Suzuki, *Inorg. Chem.* **2000**, *39*, 4520−4526.
[5] Q. Zeng, M. Qian, S. Gou, H.-K. Fun, C. Duan, X. You, *Inorg. Chim. Acta* **1999**, *294*, 1−7.
[6] C. G. Rampley, K. L. Ogden, *Environ. Sci. Technol.* **1998**, *32*, 987−993.
[7] K. Abu-Dari, F. E. Hahn, K. N. Raymond, *J. Am. Chem. Soc.* **1990**, *112*, 1519−1524.
[8] M. Di Vaira, F. Mani, P. Stoppioni, *Eur. J. Inorg. Chem.* **1999**, 833−837.
[9] G. Henkel, B. Krebs, *Chem. Rev.* **2004**, *104*, 801−824.
[10] A. Bashall, M. McPartlin, B. P. Murphy, H. R. Powell, S. Waikar, *J. Chem. Soc., Dalton Trans.* **1994**, 1383−1390.
[11] E. C. Constable, C. Sacht, G. Palo, D. A. Tocher, M. Truter, *J. Chem. Soc., Dalton Trans.* **1993**, 1307−1312.
[12] [12a] S. Brooker, *Coord. Chem. Rev.* **2001**, *222*, 33−56. [12b] S. Brooker, P. D. Croucher, T. C. Davidson, G. S. Dunbar, C. U. Beck, S. Subramanian, *Eur. J. Inorg. Chem.* **2000**, 169−179.
[13] A. J. Atkins, D. Black, A. J. Blake, A. Marin-Becerra, S. Parsons, L. Ruiz-Ramirez, M. Schröder, *Chem. Commun.* **1996**, 457−464.
[14] B. Kersting, *Z. Anorg. Allg. Chem.* **2004**, *630*, 765−780.
[15] B. Kersting, G. Steinfeld, *Chem. Commun.* **2001**, 1376−1377.
[16] B. Kersting, *Angew. Chem.* **2001**, *113*, 4109−4112; *Angew. Chem. Int. Ed.* **2001**, *40*, 3987−3990.
[17] For a complete list of the IR absorptions, see Exp. Sect.
[18] K. Nakamoto, *Infrared and Raman Spectra of Inorganic and Coordination Compounds*, 5th ed., VCH-Wiley, New York, **1997**.
[19] Similar cadmium satellites are intimated for the $ArCH_2$, $N^{Bz}CH_3$ and NCH_3 signals in **3**·ClO_4, but are not resolved presumably due to smaller $^3J(^{111,113}Cd\text{-}^1H)$ couplings. The zinc complex **1** shows neither satellites nor broadening of these signals.
[20] M. G. B. Drew, O. W. Howarth, G. G. Morgan, J. Nelson, *J. Chem. Soc., Dalton Trans.* **1994**, 3149−3158.
[21] The six *tert*-butyl methyl carbon atoms give only two signals.
[22] S. S. Tandon, S. Chander, L. K. Thompson, J. N. Bridson, V. McKee, *Inorg. Chim. Acta* **1994**, *219*, 55−65.
[23] J. E. Huheey, E. A. Keiter, R. L. Keiter, *Anorganische Chemie*, 2. Aufl., de Gruyter, Berlin, **1995**, p. 134.
[24] [24a] J. Hausmann, M. H. Klingele, V. Lozan, G. Steinfeld, D. Siebert, Y. Journaux, J. J. Girerd, B. Kersting, *Chem. Eur. J.* **2004**, *10*, 1716−1728. [24b] B. Kersting, G. Steinfeld, *Inorg. Chem.* **2002**, *41*, 1140−1150.
[25] O. Schlager, K. Wieghardt, H. Grondey, A. Rufinska, B. Nuber, *Inorg. Chem.* **1995**, *34*, 6440−6448.
[26] P. V. Bernhardt, P. Comba, T. W. Hambley, G. A. Lawrance, K. Varnagy, *J. Chem. Soc., Dalton Trans.* **1992**, 355−359.
[27] H. Strasdeit, A. K. Duhme, M. Weber, S. Pohl, *Acta Crystallogr., Sect. B* **1992**, *48*, 437−440.
[28] B. Krebs, G. Henkel, *Angew. Chem.* **1991**, *103*, 785−804, *Angew. Chem. Int. Ed. Engl.* **1991**, *30*, 769−788.
[29] D. A. House, *Comprehensive Coordination Chemistry* (Eds.: G. Wilkinson, R. D. Gillard, J. A. McCleverty), Pergamon Press, Oxford, **1996**, vol. 2, p. 23−72.
[30] T. C. W. Mak, Y.-K. Wu, *Inorg. Chim. Acta* **1985**, *104*, 149−153.
[31] A. J. Carty, N. J. Taylor, *Inorg. Chem.* **1977**, *16*, 177−181.
[32] T. J. Duplanicic, D. Grdenic, B. Kamenar, P. Matkovic, M. Sikirica, *J. Chem. Soc., Dalton Trans.* **1976**, 887−890.
[33] N. N. Greenwood, A. Earnshaw, *Chemistry of the Elements*, VCH, Weinheim, **1988**.
[34] [34a] J. Nishio, H. Okawa, S. Ohtsuka, M. Tomono, *Inorg. Chim. Acta* **1994**, *218*, 27−32. [34b] J. Shimoda, H. Furutachi, M. Yonemura, M. Ohba, N. Matsumoto, H. Okawa, *Chem. Lett.* **1996**, 979−980. [34c] H. Furutachi, H. Okawa, *Inorg. Chem.* **1997**, *36*, 3911−3918.
[35] [35a] M. Di Vaira, F. Mani, P. Stoppioni, *J. Chem. Soc., Dalton Trans.* **1998**, 3209−3213. [35b] M. Di Vaira, M. Guerra, F. Mani, P. Stoppioni, *J. Chem. Soc., Dalton Trans.* **1996**, 1173−1179.

 © 2005 Wiley-VCH Verlag GmbH & Co. KGaA, Weinheim

[36] K. Wieghardt, M. Kleine-Boymann, B. Nuber, J. Weiss, L. Zsolnai, G. Huttner, *Inorg. Chem.* **1986**, *25*, 1647−1650.

[37] [37a] M. H. Klingele, G. Steinfeld, B. Kersting, *Z. Naturforsch., Teil B* **2001**, *56*, 901−907. [37b] G. Siedle, B. Kersting, *Z. Anorg. Allg. Chem.* **2003**, *629*, 2083−2090.

[38] *SADABS, An empirical absorption correction program*, part of the SAINTPlus NT version 5.10 package, BRUKER AXS, Madison, WI, **1998**.

[39] G. M. Sheldrick, *Acta Crystallogr., Sect. A* **1990**, *46*, 467−473.

[40] G. M. Sheldrick, *SHELXL-97, Computer program for crystal structure refinement*, University of Göttingen, Göttingen, Germany, **1997**.

[41] *SHELXTL*, version 5.10, Bruker AXS, Madison, WI, **1998**.

[42] A. L. Spek, *PLATON − A Multipurpose Crystallographic Tool*, Utrecht University, Utrecht, The Netherlands, **2000**.

[43] L. J. Farrugia, *J. Appl. Crystallogr.* **1997**, *30*, 565−568.

Received July 13, 2004
Early View Article
Published Online December 2, 2004

 © 2005 Wiley-VCH Verlag GmbH & Co. KGaA, Weinheim

Synthesis of Group 14 Metal Enamido, Alkenyl, Imido and Alkenyl-Amido Complexes from a Monoanionic Pyridyl-1-azaallyl Ligand

Wing-Por Leung,*[a] Cheuk-Wai So,[a] Yuen-Sze Wu,[a] Hung-Wing Li,[a] and Thomas C. W. Mak[a]

Keywords: Germanium / Group 14 elements / Lead / N ligands / Tin

The reactivity of the lithium pyridyl-1-azaallyl complex [Li{N(SiMe$_3$)C(Ph)C(R)(C$_5$H$_4$N-2)}]$_2$ [R = SiMe$_3$ (**1**) or H (**10**)] with group 14 metal halides has been studied under various conditions. It undergoes a salt-elimination reaction with MCl$_2$ (M = Ge, Sn or Pb) to form [Ge{C(C$_5$H$_4$N-2)C(Ph)N(SiMe$_3$)$_2$}{N(SiMe$_3$)C(Ph)C(SiMe$_3$)(C$_5$H$_4$N-2)}] (**2**), [M{N(SiMe$_3$)C(Ph)C(SiMe$_3$)(C$_5$H$_4$N-2)}$_2$] [M = Sn (**3**), Pb (**4**)], and [M{N(SiMe$_3$)C(Ph)C(SiMe$_3$)(C$_5$H$_4$N-2)}Cl] [M = Ge (**5**), Sn (**6**), Pb (**7**)], where the azaaalyl moiety acts as a monodentate ligand. However, the reaction of **1** with GeCl$_4$ or HSiCl$_3$ forms [Ge{C(C$_5$H$_4$N-2)C(Ph)N(SiMe$_3$)}Cl$_2$]$_2$ (**8**) or [{(C$_5$H$_4$N-2)C(SiMe$_3$)C(Ph)N}(μ-SiHCl)]$_2$ (**9**), respectively, by elimination of both the lithium salt and Me$_3$SiCl; the reaction of **10** with GeCl$_4$ gives [{(C$_5$H$_4$N-2)C(H)C(Ph)N}(μ-GeCl$_2$)]$_2$ (**11**) in a similar manner. X-ray structural analysis of compounds **2**–**5**, **7**–**9** and **11** showed that the pyridyl-1-azaallyl ligand bonds to the metal center in enamido, alkenyl, alkenyl-amido, and imido bonding modes. A mechanism for the formation of these compounds is proposed and discussed.

(© Wiley-VCH Verlag GmbH & Co. KGaA, 69451 Weinheim, Germany, 2005)

Introduction

Alkali metal 1-azaallyl complexes are commonly used as monoanionic ligand-transfer reagents in the synthesis of main-group, transition-metal, and lanthanide complexes.[1] For example, [Ni{N(R)C(Ph)C(H)(R)}$_2$],[2] [Mg{N(R)C(*t*Bu)C(H)(R)}$_2$],[3] [Cu{μ-N(R)C(*t*Bu)C(H)(R)}]$_2$,[4] [Al{N(R)C(Ph)C(R)$_2$}Cl$_2$],[5] and [Yb{N(R)C(*t*Bu)C(H)(R)}$_2$][6] (R = SiMe$_3$) have been prepared. 1-Azaallyllithium complexes can be prepared by insertion of Li(CH$_{3-n}$R$_n$) (n = 1, 2 or 3; R = SiMe$_3$) into an α-H-free nitrile R′CN (R′ = *t*Bu, Ph or 2,6-Me$_2$C$_6$H$_3$). Other alkali metal 1-azaallyl complexes can be derived from the metathesis reaction of lithium complexes with MO*t*Bu (M = Na or K).[7]

We have reported the synthesis of [MCl$_2${N(SiMe$_3$)C(Ph)C(H)(C$_9$H$_6$N-2)}] (M = Hf and Zr) from the reaction of MCl$_4$ with the quinolyl-1-azaallyllithium complex [Li{N(SiMe$_3$)C(Ph)C(H)(C$_9$H$_6$N-2)}]$_2$ previously.[8] In this paper we report different reactivities of the pyridyl-1-azaallyllithium compound [Li{N(SiMe$_3$)C(Ph)C(R)(C$_5$H$_4$N-2)}]$_2$ [R = SiMe$_3$ (**1**) or H (**10**)][9] with a variety of Group 14 metal halides. It acts as both a monoanionic and dianionic ligand by using the SiMe$_3$ group as the leaving group during the metathesis reaction. The pyridyl-1-azaallyl ligand can bind to a metal in bonding modes **A**−**D** (Scheme 1).

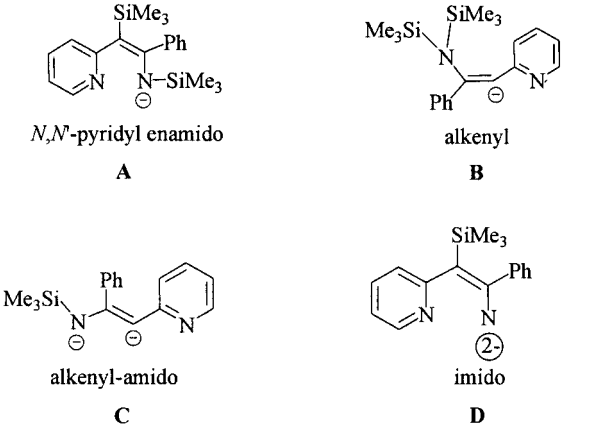

Scheme 1

Results and Discussion

Synthesis of Group 14 Metal Pyridyl-1-azaallyl Complexes

Treatment of [Li{N(SiMe$_3$)C(Ph)C(SiMe$_3$)(C$_5$H$_4$N-2)}]$_2$ (**1**) with an equimolar amount of GeCl$_2$·dioxane in Et$_2$O afforded [Ge{C(C$_5$H$_4$N-2)C(Ph)N(SiMe$_3$)$_2$}{N(SiMe$_3$)C(Ph)C(SiMe$_3$)(C$_5$H$_4$N-2)}] (**2**) (Scheme 2). The X-ray structure shows that the germanium(II) center in **2** is bonded to an *N*,*N*′-pyridyl-enamido ligand and an η^1-alkenyl ligand, which suggests that the smaller size of the germanium

[a] Department of Chemistry,
The Chinese University of Hong Kong,
Shatin, New Territories, Hong Kong, China
E-mail: kevinleung@cuhk.edu.hk

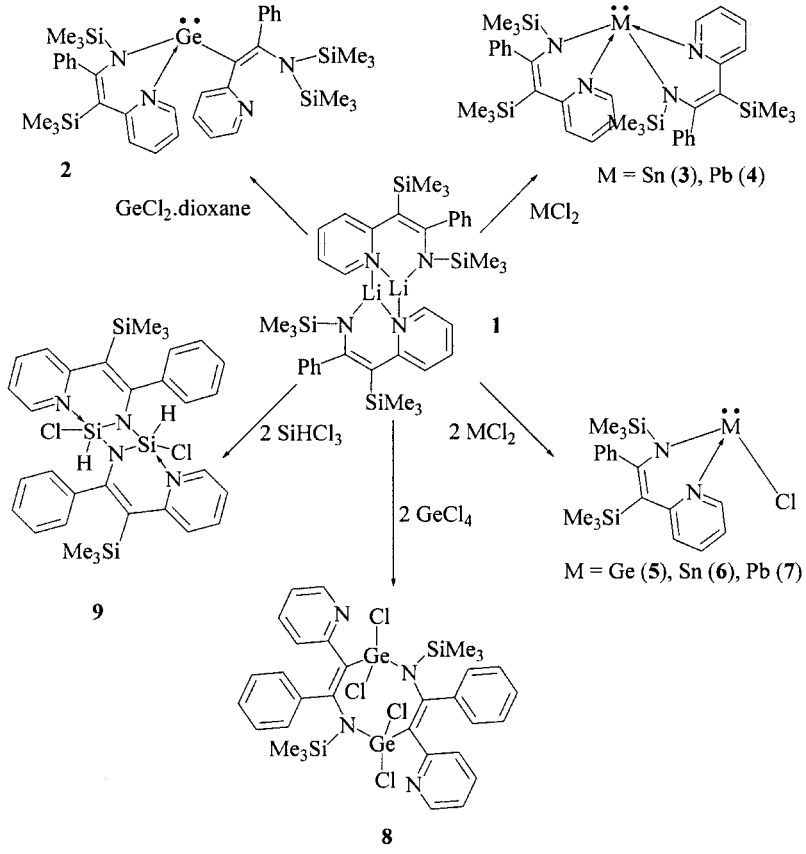

Scheme 2

center prevents both pyridyl-1-azaallyl ligands from bonding in an *N*,*N*′-chelate fashion. One of the ligands has undergone a 1,3-silyl migration in order to release the steric crowding at the germanium(II) center (Scheme 3). A similar silyl migration has been reported in the thermal isomerization of the ketimine $[Me_3SiN{=}C(CMe_3)CH(SiMe_3)_2]$ to the enamine $[(Me_3Si)_2NC(CMe_3){=}CH(SiMe_3)]$.[10] In another example, a 1,2-silyl migration on the 1-azaallyl ligand backbone results in the formation of the asymmetric distannene [{1-[N(*t*Bu)C(SiMe$_3$)C(H)]-2-[N(*t*Bu)CC(H)]C$_6$H$_4$}-Sn→Sn{1,2-[N(*t*Bu)(SiMe$_3$)CC(H)]$_2$C$_6$H$_4$}].[11]

A similar reaction of **1** with MCl_2 (M = Ge, Sn or Pb) in a 1:1 or 1:2 ratio gave the metal enamides [M{N(SiMe$_3$)-C(Ph)C(SiMe$_3$)(C$_5$H$_4$N-2)}$_2$] [M = Sn (**3**) and Pb (**4**)] or [M{N(SiMe$_3$)C(Ph)C(SiMe$_3$)(C$_5$H$_4$N-2)}Cl] [M = Ge (**5**), Sn (**6**) and Pb (**7**)], respectively (Scheme 2).

The reaction of **1** with two equivalents of $GeCl_4$ in THF, however, afforded [Ge{C(C$_5$H$_4$N-2)C(Ph)N(SiMe$_3$)}Cl$_2$]$_2$ (**8**). The X-ray structure of **8** shows that the germanium center is bonded to two alkenyl-amido ligands to form an eight-membered heterocyclic ring. The pyridyl-1-azaallyl ligand acts here as a *C*-centered nucleophile, and undergoes 1,3-silyl migration and elimination of Me_3SiCl to form **8** (Scheme 4).

Treatment of **1** with two equivalents of $HSiCl_3$ in THF afforded [{(C$_5$H$_4$N-2)C(SiMe$_3$)C(Ph)N}(μ-SiHCl)]$_2$ (**9**).

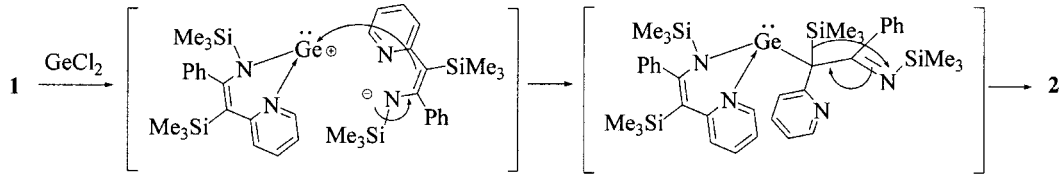

Scheme 3

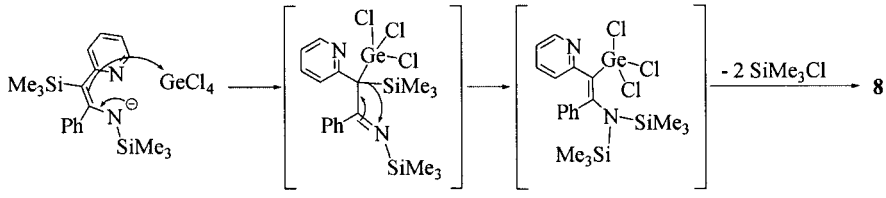

Scheme 4

 © 2005 Wiley-VCH Verlag GmbH & Co. KGaA, Weinheim

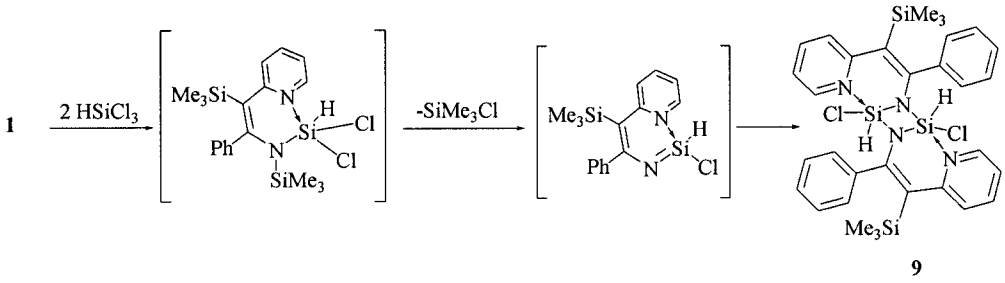

Scheme 5

The X-ray structure of **9** shows that the pyridyl-1-azaallyl ligand acts as an *N*-centered nucleophile rather than a *C*-centered towards $HSiCl_3$. The intermediate $[HSi\{N(SiMe_3)C(Ph)C(SiMe_3)(C_5H_4N\text{-}2)\}Cl_2]$ eliminates Me_3SiCl and dimerizes to form compound **9** (Scheme 5). Each silicon center is bonded to two imido ligand to form a four-membered ring. A similar result has been reported in the synthesis of $ClPN(R)P(Cl)NR$ [R = C(*t*Bu)=C(H)$SiMe_3$] from the reaction of $[Li\{N(SiMe_3)C(tBu)C(H)(SiMe_3)\}]_2$ and PCl_3.[10]

In contrast, the reaction of $[Li\{N(SiMe_3)C(Ph)C(H)(C_5H_4N\text{-}2)\}]_2$ (**10**) with two equivalents of $GeCl_4$ in THF gave $[\{(C_5H_4N\text{-}2)C(H)C(Ph)N\}(\mu\text{-}GeCl_2)]_2$ (**11**), with a structure similar to that of **9** (Scheme 6). The $C_{alkenyl}-H$ bond is much stronger than the $C_{alkenyl}-SiMe_3$ bond, therefore a 1,3-H shift is less feasible than a 1,3-silyl migration. The pyridyl-1-azaallyl ligand preferably acts as an *N*-centered nucleophile; the formation of **11** is similar to that of **9**.

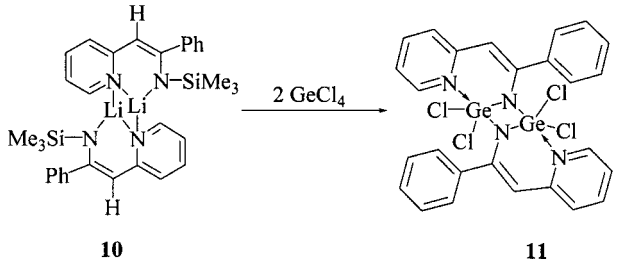

Scheme 6

Spectroscopic Properties

Compounds **2**−**9** and **11** are yellow crystalline solids that are soluble in Et_2O, toluene, and THF, and sparingly soluble in hydrocarbon solvents. The ^1H and ^{13}C NMR spectra of **2** display three sharp singlets in ratio of 1:1:2 assignable to the three types of $SiMe_3$ groups, this is consistent with the solid-state structure.

The ^1H and ^{13}C NMR spectra of **3**−**7** show a similar pattern and display one set of signals due to the pyridyl-1-azaallyl ligand. The chemical shifts of the ^{119}Sn NMR signals of **3** (δ = −140.0 ppm) and **6** (δ = −197.95 ppm) are similar to those of four-coordinate $[Sn\{N(SiMe_3)C(Ph)NC(Ph)=C(SiMe_3)_2\}_2]$ (δ = −141.4 ppm)[12] and three-coordinate $[\{HC(CMeNAr)_2\}SnCl]$ (δ = −224.0 ppm),[13] respectively.

The ^1H NMR spectra of **8**, **9** and **11** show one set of signals due to the pyridyl and phenyl rings. In the ^1H NMR spectrum of **9**, the Si−H chemical shift (δ = 5.46 ppm) is similar to that in $[SiH\{(C_{10}H_6\text{-}2)(NMe_2)\}_3]$ (δ = 6.61 ppm)[14] and $[SiH_2\{(C_6H_3\text{-}2,6)(NMe_2)_2\}]$ (δ = 4.87 ppm).[15] In the ^1H NMR spectrum of **11** the *H*-C=C signal (δ = 5.09 ppm) is shifted upfield relative to the value of δ = 6.24 ppm in $[Li\{N(SiMe_3)C(Ph)C(H)(C_5H_4N\text{-}2)\}]_2$ (**10**).

X-ray Crystal Structures

Compound **2** (Figure 1, Table 1) is a monomeric, heteroleptic germylene complex. The germanium center is bonded to an *N*,*N*′-pyridyl-enamido chelate and a monohapto η^1-alkenyl ligand. The Ge−C(26) bond length of 2.039(2) Å is similar to the Ge−C single bond lengths of 2.067 Å and 2.012 Å in $[Ge\{CH(SiMe_3)_2\}\{C(SiMe_3)_3\}]$[16] and 2.116 Å in $[Ge\{CPh(SiMe_3)C_5H_4N\text{-}2\}_2]$.[17] The Ge−N(2) bond length of 1.940(2) Å in **2** is comparable to those of 2.096(1) Å and 2.088(6) Å in $[Ge\{N(SiMe_3)_2\}_2]$[18] and 1.90(1) Å and 1.87(1) Å in $[Ge\{NCMe_2(CH_2)_3CMe_2\}_2]$.[19]

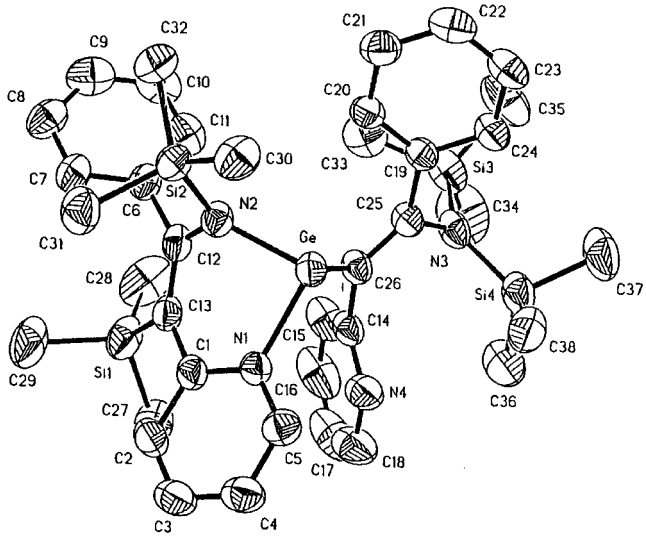

Figure 1. Molecular structure of **2**

Compounds **3** and **4** (Figure 2, Table 2) are isostructural. The $Sn-N_{amide}$ bond lengths of 2.162(2) Å and 2.174(2) Å in **3** are similar to that of 2.130 Å in the κ^1-enamidotin(II)

 © 2005 Wiley-VCH Verlag GmbH & Co. KGaA, Weinheim

Table 1. Selected bond lengths (Å) and angles (°) for compound **2**

Ge−N(1)	2.065(15)	Ge−C(26)	2.039(2)
Ge−N(2)	1.942(17)	C(14)−C(26)	1.488(3)
N(2)−C(12)	1.405(2)	C(25)−C(26)	1.356(3)
C(12)−C(13)	1.357(3)	C(19)−C(25)	1.491(3)
C(13)−C(1)	1.471(3)	N(3)−C(25)	1.453(3)
Si(2)−N(2)	1.746(18)	Si(3)−N(3)	1.750(19)
Si(1)−C(13)	1.897(2)	Si(4)−N(3)	1.751(2)
N(2)−Ge−C(26)	105.16(18)	C(25)−C(26)−Ge	118.52(14)
N(2)−Ge−N(1)	86.3(7)	C(25)−C(26)−C(14)	119.6(2)
C(26)−Ge−N(1)	98.5(7)	C(14)−C(26)−Ge	118.96(13)
C(1)−N(1)−Ge	124.04(12)	N(3)−C(25)−C(19)	114.23(16)
N(1)−C(1)−C(13)	120.68(16)	C(26)−C(25)−C(19)	120.5(2)
C(12)−N(2)−Ge	118.59(13)	C(13)−C(12)−C(6)	121.87(17)
C(12)−C(13)−C(1)	119.11(17)	C(13)−C(12)−N(2)	124.23(17)

complex [Sn{N(SiMe$_3$)C(*t*Bu)C(H)C$_6$H$_3$Me$_2$-2,5}$_2$], but significantly shorter than that of 2.510(2) Å in the η^3-(1-azaallyl)tin(II) complex [Sn{N(SiMe$_3$)C(*t*Bu)C(H)(SiMe$_3$)}$_2$].[20] The Pb−N$_{amide}$ bond lengths of 2.277(7) Å and 2.275(7) Å in **4** are shorter than that of 2.381(7) Å in the η^3-(1-azaallyl)lead(II) complex [Pb{N(SiMe$_3$)C(Ph)C(SiMe$_3$)$_2$}Cl].[21] The short C(6)−C(10) and C(25)−C(29) and long N(2)−C(10) and N(4)−C(29) bond lengths correspond to double and single bonds, respectively. Thus, the bonding within the NCCCN ligand backbone is localized, and the pyridyl-1-azaallyl ligand bonds to the metal center in an enamido bonding mode.

Compounds **5** and **7** (Figure 3, Table 3) are isostructural. The metal−amide bond lengths of 1.920(2) Å and 2.279(7) Å in **5** and **7** are similar to those in **2** and **4**, respectively. The Ge−Cl bond length of 2.283(9) Å in **5** is similar to that of 2.203(10) Å in [Ge(C$_6$H$_3$-2,6-Trip$_2$)Cl][22] (Trip = C$_6$H$_2$-2,4,6-*i*Pr$_3$) and 2.295(12) Å in [{HC(CMeNAr)$_2$}GeCl].[13]

Table 2. Selected bond lengths (Å) and angles (°) for compounds **3** and **4**

[M{N(SiMe$_3$)C(Ph)C(SiMe$_3$)(C$_5$H$_4$N-2)}$_2$]	M = Sn (**3**)	M = Pb (**4**)
M−N(1)	2.441(2)	2.626(8)
M−N(2)	2.162(2)	2.277(7)
M−N(3)	2.503(2)	2.570(8)
M−N(4)	2.174(2)	2.274(7)
N(1)−C(5)	1.364(3)	1.336(12)
C(5)−C(6)	1.449(3)	1.483(13)
C(6)−C(10)	1.366(4)	1.361(13)
C(10)−N(2)	1.403(3)	1.391(12)
N(3)−C(24)	1.335(3)	1.356(12)
C(24)−C(25)	1.457(4)	1.462(12)
C(25)−C(29)	1.402(3)	1.384(13)
C(29)−N(4)	1.384(3)	1.387(11)
N(1)−M−N(2)	78.1(7)	76.5(3)
N(1)−M−N(4)	91.3(7)	94.0(3)
N(4)−M−N(3)	76.7(7)	74.3(2)
N(2)−M−N(3)	91.6(7)	97.3(3)
M−N(1)−C(5)	123.8(2)	118.6(6)
N(1)−C(5)−C(6)	121.8(2)	121.5(8)
C(5)−C(6)−C(10)	120.5(2)	119.5(8)
C(6)−C(10)−N(2)	126.6(2)	126.1(8)
C(10)−N(2)−M	124.0(2)	123.1(6)
M−N(3)−C(24)	123.8(2)	123.3(6)
N(3)−C(24)−C(25)	121.7(2)	122.4(8)
C(25)−C(29)−N(4)	126.0(2)	126.6(8)
C(29)−N(4)−M	123.9(2)	122.1(5)

The Pb−Cl bond length of 2.599(3) Å in **7** is similar to that of 2.6096(3) Å in [Pb{N(SiMe$_3$)C(Ph)C(SiMe$_3$)$_2$}Cl].[21]

Compound **8** (Figure 4, Table 4) is centrosymmetric: each germanium(IV) center is bonded to amido nitrogen and alkenyl carbon atoms with an angle of 116.7(3)°, which is

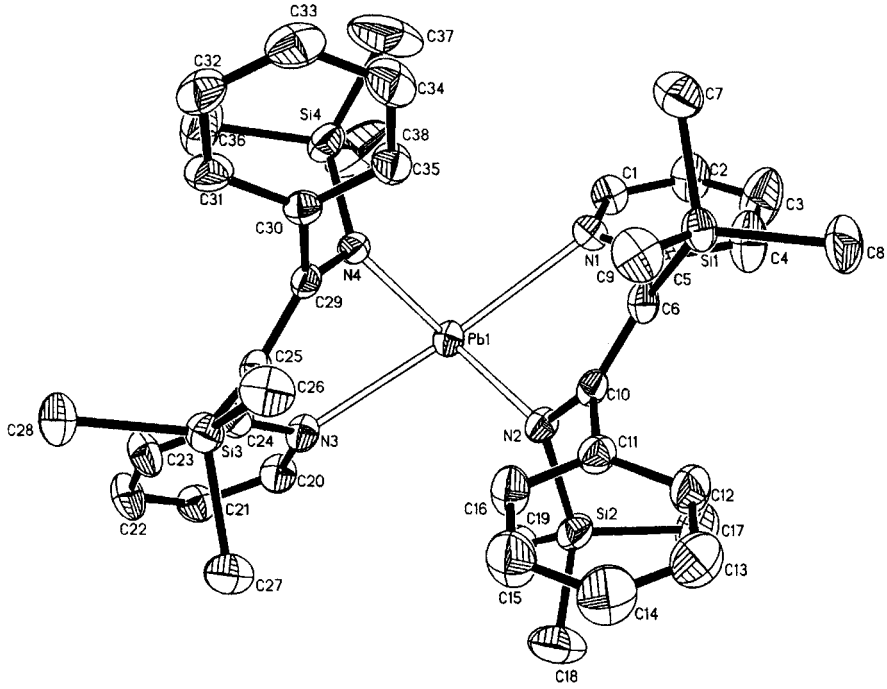

Figure 2. Molecular structure of **4**

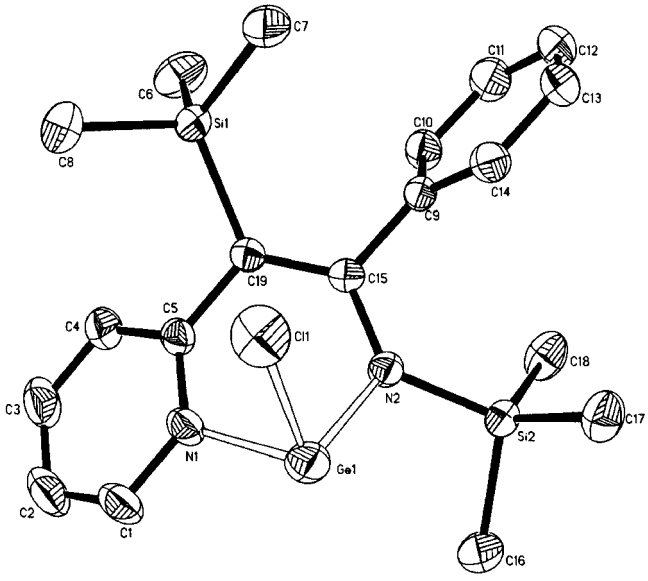

Figure 3. Molecular structure of **5**

Table 3. Selected bond lengths (Å) and angles (°) for compounds **5** and **7**

$[M\{N(SiMe_3)C(Ph)C(SiMe_3)(C_5H_4N\text{-}2)\}Cl]$	M = Ge (**5**)	M = Pb (**7**)
M−Cl	2.283(9)	2.599(3)
M−N(1)	2.021(2)	2.320(6)
M−N(2)	1.920(2)	2.279(7)
N(1)−C(5)	1.354(3)	1.365(11)
C(5)−C(19)	1.462(3)	1.467(11)
C(19)−C(15)	1.375(3)	1.411(11)
C(15)−N(2)	1.384(3)	1.352(10)
N(1)−M−N(2)	88.8(8)	78.9(2)
N(1)−M−Cl	93.6(6)	92.7(2)
N(2)−M−Cl	97.7(6)	98.9(2)
M−N(1)−C(5)	122.4(2)	111.7(5)
N(1)−C(5)−C(19)	121.6(2)	117.7(7)
C(5)−C(19)−C(15)	119.8(2)	117.4(7)
C(15)−N(2)−M	118.3(1)	99.2(5)
C(19)−C(15)−N(2)	125.2(2)	124.8(7)

Table 4. Selected bond lengths (Å) and angles (°) for compounds **8**, **9** and **11**

$[Ge\{C(C_5H_4N\text{-}2)C(Ph)N(SiMe_3)\}Cl_2]_2$ (**8**)			
Ge(1)−Cl(1)	2.143(2)	Ge(1)−N(2)	1.813(6)
Ge(1)−Cl(2)	2.157(2)	N(2)−C(7)	1.443(9)
Ge(1)−C(1)	1.924(7)	C(7)−C(1A)	1.353(10)
N(2)−Ge(1)−C(1)	116.7(3)	C(1)−Ge(1)−Cl(2)	107.1(2)
N(2)−Ge(1)−Cl(1)	107.6(2)	Cl(1)−Ge(1)−Cl(2)	102.4(1)
C(1)−Ge(1)−Cl(1)	115.6(2)	Ge(1)−N(2)−C(7)	121.3(5)
N(2)−Ge(1)−Cl(2)	106.0(2)	N(2)−C(7)−C(1A)	119.7(7)
		C(7A)−C(1)−Ge(1)	117.3(6)
$[\{(C_5H_4N\text{-}2)C(SiMe_3)C(Ph)N\}(\mu\text{-}SiHCl)]_2$ (**9**)			
Si(1)−Cl(1)	2.108(1)	N(1)−C(5)	1.361(3)
Si(1)−N(2)	1.864(2)	C(5)−C(13A)	1.465(3)
Si(1)−N(2A)	1.741(2)	C(6)−N(2)	1.371(3)
Si(1)−N(1)	2.003(2)		
N(2)−Si(1)−N(2A)	81.4(1)	Si(1)−N(1)−C(5)	126.7(2)
Si(1)−N(2A)−Si(1A)	98.6(1)	N(1)−C(5)−C(13A)	121.3(2)
N(1)−Si(1)−N(2)	170.8(8)	C(5)−C(13A)−C(6A)	119.7(2)
N(2)−Si(1)−Cl(1)	98.1(7)	C(6)−N(2)−Si(1)	130.0(1)
N(2A)−Si(1)−Cl(1)	116.6(8)	C(6)−N(2)−Si(1A)	130.6(2)
N(1)−Si(1)−Cl(1)	90.4(7)		
$[\{(C_5H_4N\text{-}2)C(H)C(Ph)N\}(\mu\text{-}GeCl_2)]_2$ (**11**)			
Ge(1)−N(2)	1.834(2)	N(2)−C(7)	1.369(3)
Ge(1)−N(2A)	1.944(2)	C(6)−C(7)	1.357(4)
Ge(1)−Cl(1)	2.172(8)	C(5)−C(6)	1.422(4)
Ge(2)−Cl(2)	2.187(9)	N(1)−C(5)	1.350(3)
Ge(1)−N(1)	2.080(2)		
N(2)−Ge(1)−N(2A)	80.7(1)	N(1)−Ge(1)−Cl(1)	86.1(7)
Ge(1A)−N(2)−Ge(1)	99.3(1)	N(1)−Ge(1)−Cl(2)	87.9(7)
N(1)−Ge(1)−N(2A)	173.7(9)	Ge(1)−N(1)−C(5)	124.1(2)
Cl(1)−Ge(1)−Cl(2)	115.7(3)	N(1)−C(5)−C(6)	121.3(3)
N(2A)−Ge(1)−Cl(1)	96.6(7)	C(5)−C(6)−C(7)	128.2(3)
N(2A)−Ge(1)−Cl(2)	96.0(7)	C(6)−C(7)−N(2)	125.3(3)
N(2)−Ge(1)−Cl(1)	122.4(8)	C(7)−N(2)−Ge(1)	127.6(2)
N(2)−Ge(1)−Cl(2)	121.9(8)	C(7)−N(2)−Ge(1A)	132.7(2)

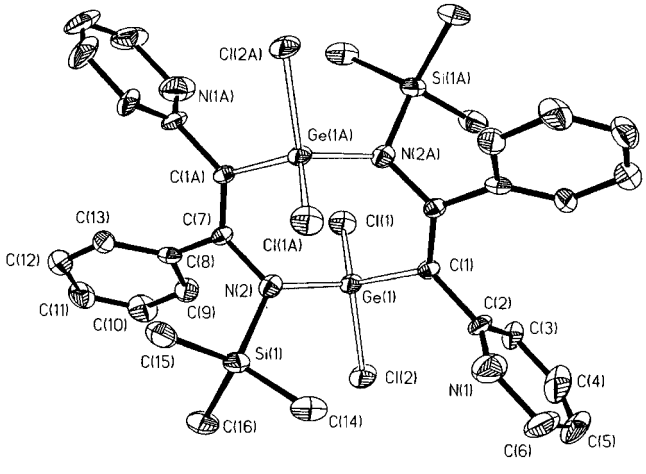

Figure 4. Molecular structure of **8**

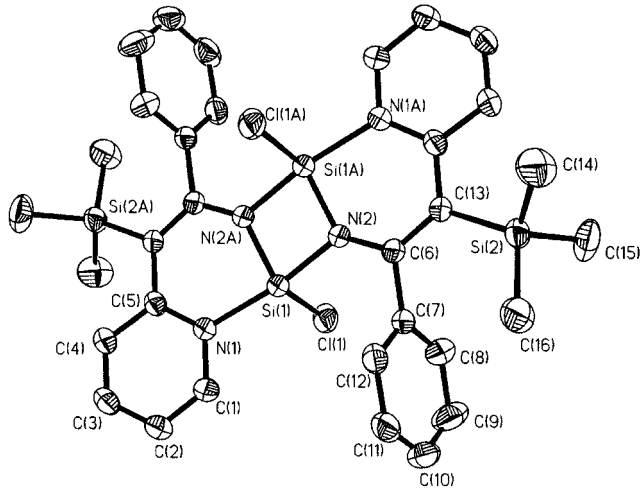

Figure 5. Molecular structure of **9**

 © 2005 Wiley-VCH Verlag GmbH & Co. KGaA, Weinheim

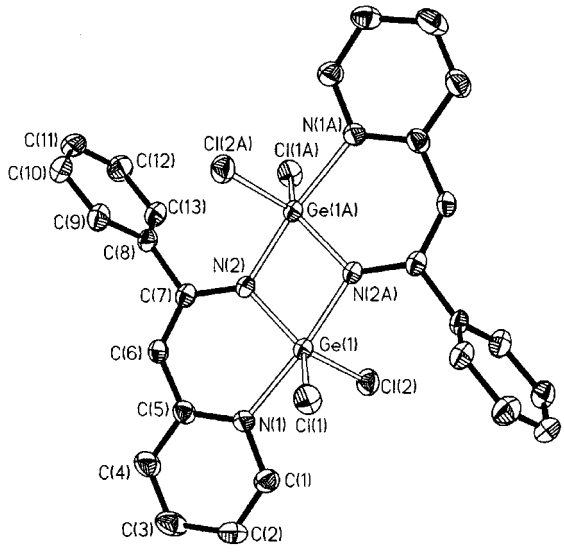

Figure 6. Molecular structure of **11**

larger than the N−Ge−C angle of 105.2(2)° in **2**. The Ge(1)−C(1) [1.924(7) Å] and Ge(1)−N(2) [1.813(6) Å] bond lengths in **8** are shorter than the Ge−C and Ge−N distances of 2.039(2) Å and 1.942(17) Å, respectively, in **2**.

The molecular structures of **9** (Figure 5, Table 4) and **11** (Figure 6, Table 4) are similar. They are centrosymmetric with the metal centers bonded to two imino nitrogen atoms to form a planar N_2M_2 ring [M = Si (**9**), Ge (**11**)]. The geometry around the metal center is trigonal bipyramidal with the N-donor at the axial position. The average bond length of 1.802 Å within the Si_2N_2 ring in **9** is longer than that of 1.750 Å in [{μ-MesN}Si(H)(*t*Bu)]$_2$ [23] and 1.770 Å in [Me_2Si(μ-*N*-C_9H_6N)(μ-*N*-C_9H_6N)SiMe_2].[24] The Ge−N_{imino} bond lengths of 1.843(2) Å and 1.944(2) Å in **11** are longer than those reported in similar Ge_2N_2 ring systems, such as [{N(CH_3)CH_2CH_2N(CH_3)}Ge{μ-NSi(O*t*C_4H_9)}]$_2$ (1.836 Å and 1.843 Å).[25]

Conclusion

A series of Group 14 metal pyridyl-1-azaallyl complexes has been synthesized: [Ge{C(C_5H_4N-2)C(Ph)N($SiMe_3$)$_2$}-{N($SiMe_3$)C(Ph)C($SiMe_3$)(C_5H_4N-2)}] (**2**), [M{N($SiMe_3$)C-(Ph)C($SiMe_3$)-(C_5H_4N-2)}$_2$] [M = Sn (**3**), Pb (**4**)], [M{N($SiMe_3$)C(Ph)C($SiMe_3$)(C_5H_4N-2)}Cl] [M = Ge (**5**), Sn (**6**), Pb (**7**)], [Ge{C(C_5H_4N-2)C(Ph)N($SiMe_3$)}Cl_2]$_2$ (**8**), [{(C_5H_4N-2)C($SiMe_3$)C(Ph)N}(μ-SiHCl)]$_2$ (**9**) and [{(C_5H_4N-2)C(H)C(Ph)N}(μ-$GeCl_2$)]$_2$ (**11**). The results show that the pyridyl-1-azaallyl ligand bonds to the metal center in enamido and alkenyl bonding modes in compound **2**, an enamido mode in compounds **3**−**7**, an alkenyl-amido mode in compound **8**, and an imido mode in compounds **9** and **11**.

Experimental Section

General Remarks: All manipulations were performed under an inert atmosphere of dinitrogen gas by standard Schlenk techniques. Solvents were dried over and distilled from CaH_2 (hexane) and/or Na (Et_2O, toluene and THF). Anhydrous $SnCl_2$, $PbCl_2$, $GeCl_4$, and $HSiCl_3$ were purchased from Aldrich Chemicals and used without further purification. $GeCl_2$·dioxane[26] and [Li{N($SiMe_3$)C-(Ph)C(R)(C_5H_4N-2)}]$_2$ (R = Ph, H)[9] were prepared by literature procedures. The ^{1}H, ^{13}C and ^{119}Sn NMR spectra were recorded on Bruker WM-300 or Varian 400 instruments. All spectra were recorded in [D_6]benzene or [D_8]THF, and the chemical shifts are quoted relative to $SiMe_4$ and $SnMe_4$ for ^{1}H/^{13}C and ^{119}Sn, respectively.

[Ge{C(C_5H_4N-2)C(Ph)N($SiMe_3$)$_2$}{N($SiMe_3$)C(Ph)C($SiMe_3$)-(C_5H_4N-2)}] (2): A solution of **1** (3.75 g, 5.41 mmol) in Et_2O (30 mL) was added slowly to a suspension of $GeCl_2$·dioxane (1.25 g, 5.41 mmol) in Et_2O (25 mL) at 0 °C. The orange mixture was warmed to ambient temperature and stirred for 16 h. The solvent was then removed under reduced pressure and the residue was extracted with toluene (50 mL). The precipitate was filtered and the orange filtrate was concentrated. *n*-Hexane (5 mL) was added and the solution was kept at 4 °C for 1 day to yield orange crystals of **2**. Yield: 2.55 g (62%); m.p.: 206−208 °C (dec.). $C_{38}H_{54}GeN_4Si_4$: calcd. C 60.75, H 7.19, N 7.46; found C 60.69, H 7.19, N 7.70. ^{1}H NMR (300 MHz, C_6D_6, 25 °C): δ = −0.04 (s, 9 H, $SiMe_3$), 0.06 (s, 18 H, $SiMe_3$), 0.21 (s, 9 H, $SiMe_3$), 6.52 (t, J = 6.3 Hz, 1 H, py), 6.67 (br, 1 H, py), 7.05 (m, 5 H, Ph), 7.12 (br, 3 H, py), 7.50 (m, 5 H, Ph), 7.77 (d, J = 6.9 Hz, 2 H, py), 8.59 (d, J = 4.8 Hz, 1 H, py) ppm. ^{13}C{^{1}H} NMR (300 MHz, C_6D_6, 25 °C): δ = 2.94, 3.02, 3.11 ($SiMe_3$), 114.21 (*C*$SiMe_3$), 117.93, 118.98, 119.13, 123.73, 124.20, 124.96, 125.59, 127.39, 127.79, 128.33, 128.79, 129.00, 130.69, 131.13, 135.05, 136.66, 144.09, 145.31, 147.22, 147.99, 150.80, 153.57 (Ph and Py), 155.88 (py*C*Ge), 166.79, 171.46 (N*C*Ph) ppm.

[Sn{N($SiMe_3$)C(Ph)C($SiMe_3$)(C_5H_4N-2)}$_2$] (3): A solution of **1** (0.71 g, 1.02 mmol) in Et_2O (30 mL) was added slowly to a suspension of $SnCl_2$ (0.19 g, 1.02 mmol) in Et_2O (25 mL) at 0 °C. The yellow mixture was then warmed to ambient temperature and stirred for 16 h. The solvent was removed under reduced pressure and the residue was extracted with toluene (50 mL). The precipitate was filtered and the yellow filtrate was concentrated. *n*-Hexane (5 mL) was added and kept at 4 °C for 1 day to yield yellow crystals of **3**. Yield: 0.42 g (52%); m.p.: 149−151 °C (dec.). $C_{38}H_{54}N_4Si_4Sn$: calcd. C 57.20, H 6.82, N 7.02; found C 56.82, H 6.83, N 6.94. ^{1}H NMR (300 MHz, C_6D_6, 25 °C): δ = −0.16 (s, 9 H, $SiMe_3$), −0.03 (s, 9 H, $SiMe_3$), −0.01 (s, 9 H, $SiMe_3$), 0.22 (s, 9 H, $SiMe_3$), 6.49 (br, 1 H, py), 6.57 (m, 2 H, py), 7.08 (m, 5 H, Ph), 7.49 (m, 3 H, py), 7.75 (d, J = 6.90 Hz, 5 H, Ph), 8.83 (br, 1 H, py), 9.09 (br, 1 H, py) ppm. ^{13}C{^{1}H} NMR (300 MHz, C_6D_6, 25 °C): δ = 1.38, 2.41, 3.65, 4.59 ($SiMe_3$), 118.08, 118.77 (*C*$SiMe_3$), 118.87, 123.91, 124.10, 124.80, 125.64, 127.23, 127.68, 128.56, 129.28, 130.47, 131.12, 135.20, 135.58, 137.07, 141.95, 144.29, 146.06, 147.51, 147.68, 147.98, 151.68, 158.76, 159.24 (Ph and Py), 168.17, 173.09 (N*C*Ph) ppm. ^{119}Sn{^{1}H} NMR (149 MHz, C_6D_6, 25 °C): δ = −140.00 ppm.

[Pb{N($SiMe_3$)C(Ph)C($SiMe_3$)(C_5H_4N-2)}$_2$] (4): A solution of **1** (0.96 g, 1.38 mmol) in Et_2O (20 mL) was added slowly to a solution of $PbCl_2$ (0.38 g, 1.38 mmol) in Et_2O (20 mL) at −90 °C in the absence of light. The yellow suspension was warmed to ambient temperature and stirred for 18 h. The precipitate was then filtered. *n*-Hexane was added to the filtrate, concentrated under reduced

 © 2005 Wiley-VCH Verlag GmbH & Co. KGaA, Weinheim

pressure and stored at −30 °C. Compound **4** was obtained as yellow crystals. Yield: 0.45 g (37%); m.p.: 201−203 °C. $C_{38}H_{54}N_4PbSi_4$: calcd. C 51.49, H 6.14, N 6.32; found C 51.12, H 6.06, N 6.27. ^{1}H NMR (300 MHz, [D$_8$]THF, 25 °C): δ = −0.28 (s, 9 H, $SiMe_3$), −0.21 (s, 9 H, $SiMe_3$), 6.95−7.01 (m, 1 H, 5-py), 7.18−7.24 (d, J = 8.0 Hz, 1 H, 3-py), 7.35−7.41 (m, 3 H, Ph), 7.42−7.48 (m, 2 H, Ph), 7.55−7.64 (m, 1 H, 4-py), 8.45 (d, J = 4.1 Hz, 1 H, 6-py) ppm. ^{13}C{^{1}H} NMR (300 MHz, [D$_8$]THF, 25 °C): δ = 1.17, 2.34 ($SiMe_3$), 119.48 (*C*$SiMe_3$), 121.80, 123.43, 125.29, 128.52, 129.64, 131.79, 135.90, 142.62, 148.02, 150.03, 159.77 (Ph and Py), 164.63 (N*C*Ph).

[Ge{N(SiMe$_3$)C(Ph)C(SiMe$_3$)(C$_5$H$_4$N-2)}Cl] (5): A solution of **1** (0.94 g, 1.36 mmol) in Et_2O (30 mL) was added slowly to a solution of $GeCl_2$·dioxane (0.66 g, 2.85 mmol) in Et_2O (30 mL) at 0 °C. The yellow suspension was warmed to ambient temperature and stirred for 18 h. The precipitate was then filtered. Hexane was added to the filtrate and concentrated, yielding pale-yellow crystals of **5**. Yield: 0.76 g (62%); m.p.: 124−125 °C. $C_{19}H_{27}ClGeN_2Si_2$: calcd. C 50.98, H 6.08, N 6.25; found C 50.77, H 5.91, N 6.13. ^{1}H NMR (300 MHz, [D$_8$]THF, 25 °C): δ = −0.22 (s, 9 H, $SiMe_3$), −0.18 (s, 9 H, $SiMe_3$), 7.33−7.40 (m, 4 H, Ph), 7.41−7.49 (d, 1 H, 5-py), 7.49−7.63 (m, 1 H, Ph), 7.63−7.66 (d, J = 7.4 Hz, 1 H, 3-py), 7.95 (t, J = 7.1 Hz, 1 H, 4-py), 8.70 (d, J = 5.5 Hz, 1 H, 6-py) ppm. ^{13}C{^{1}H} NMR (300 MHz, [D$_8$]THF, 25 °C): δ = 1.62, 3.08 ($SiMe_3$), 95.62 (*C*$SiMe_3$), 120.69, 126.33, 127.97, 129.28, 130.06, 131.11, 133.53, 140.47, 144.38, 145.61, 155.57 (Ph and Py), 164.94 (N*C*Ph) ppm.

[Sn{N(SiMe$_3$)C(Ph)C(SiMe$_3$)(C$_5$H$_4$N-2)}Cl] (6): A solution of **1** (0.86 g, 1.23 mmol) in Et_2O (30 mL) was added slowly to a solution of $SnCl_2$ (0.47 g, 2.47 mmol) in Et_2O (30 mL) at 0 °C. The yellow suspension was warmed to ambient temperature and stirred for 18 h. The precipitate was then filtered. The filtrate was removed under reduced pressure and the residue was extracted with THF/*n*-hexane (1:10) and concentrated to yield **6** as a yellow solid. Yield: 0.51 g (42%); m.p.: 210−213 °C. $C_{19}H_{27}ClN_2Si_2Sn$: calcd. C 46.22, H 5.51, N 5.67; found C 46.29, H 5.58, N 5.88. ^{1}H NMR (300 MHz, [D$_8$]THF, 25 °C): δ = −0.28 (s, 9 H, $SiMe_3$), −0.27 (s, 9 H, $SiMe_3$), 7.13−7.26 (m, 1 H, 5-py), 7.30−7.35 (m, 3 H, Ph), 7.35−7.40 (m, 2 H, Ph), 7.44−7.47 (m, 1 H, 4-py), 7.56−7.59 (d, J = 8.7 Hz, 1 H, 3-py), 8.48 (d, J = 6.0 Hz, 1 H, 6-py) ppm. ^{13}C{^{1}H} NMR (300 MHz, [D$_8$]THF, 25 °C): δ = 0.96, 1.96 ($SiMe_3$), 100.12 (*C*$SiMe_3$), 118.72, 127.56, 128.69, 130.89, 135.14, 140.72, 147.36, 160.03 (Ph and Py), 162.93 (N*C*Ph) ppm. ^{119}Sn{^{1}H} NMR (149 MHz, [D$_8$]THF, 25 °C): δ = −197.95 ppm.

[Pb{N(SiMe$_3$)C(Ph)C(SiMe$_3$)(C$_5$H$_4$N-2)}Cl] (7): A solution of **1** (1.25 g, 1.80 mmol) in THF (20 mL) was added slowly to a solution of $PbCl_2$ (1.10 g, 3.96 mmol) in THF (20 mL) at −90 °C. The yellow suspension was warmed to ambient temperature and stirred for 18 h. The volatiles were then removed under reduced pressure and the residue was extracted with toluene. The yellow mixture was filtered and concentrated to give yellow crystals of the title compound. Yield: 0.73 g (69%); m.p.: 190−192 °C. $C_{19}H_{27}ClN_2PbSi_2$: calcd. C 39.19, H 4.67, N 4.81; found C 38.94, H 4.53, N 4.73. ^{1}H NMR (300 MHz, C_6D_6, 25 °C): δ = −0.07 (s, 9 H, $SiMe_3$), −0.08 (s, 9 H, $SiMe_3$), 6.40 (m, 1 H, 5-py), 6.90 (m, 1 H, 3-py), 7.07 (m, 1 H, 4-py), 7.23−7.27 (m, 2 H, Ph), 7.47−7.50 (m, 3 H, Ph), 8.24 (d, J = 4.1 Hz, 1 H, 6-py) ppm. ^{13}C{^{1}H} NMR (300 MHz, C_6D_6, 25 °C): δ = 2.07, 2.94 ($SiMe_3$), 89.40 (*C*$SiMe_3$), 120.50, 123.30, 128.63, 129.00, 130.67, 130.79, 138.33, 145.26, 159.49 (Ph and Py), 166.23 (N*C*Ph) ppm.

[Ge{C(C$_5$H$_4$N-2)C(Ph)N(SiMe$_3$)}Cl$_2$]$_2$ (8): A solution of **1** (1.48 g, 2.13 mmol) in THF (30 mL) was added slowly to a solution of $GeCl_4$ (0.54 mL, 4.69 mmol) in THF (20 mL) at −90 °C. The yellow solution was warmed to ambient temperature and stirred for two days. The volatiles were removed under reduced pressure and the residue was extracted with toluene. The yellow mixture was filtered and concentrated to give yellow crystals of the title compound. Yield: 0.84 g (48%); m.p.: 226−227 °C. $C_{32}H_{36}Cl_4Ge_2N_4Si_2$: calcd. C 46.88, H 4.43, N 4.83; found C 46.51, H 4.31, N 4.63. ^{1}H NMR (300 MHz, C_6D_6, 25 °C): δ = 0.03 (s, 4 H, $SiMe_3$), 0.31 (s, 5 H, $SiMe_3$), 6.86 (t, J = 7.1 Hz, 1 H, 5-py), 6.98 (d, J = 7.1 Hz, 1 H, 3-py), 7.08−7.15 (m, 3 H, Ph), 7.17−7.22 (m, 2 H, Ph), 7.41 (t, J = 7.7 Hz, 1 H, 4-py), 7.73 (d, J = 5.5 Hz, 1 H, 6-py) ppm. ^{13}C{^{1}H} NMR (300 MHz, C_6D_6, 25 °C): δ = 2.60 ($SiMe_3$), 119.13 (*C*$SiMe_3$), 122.97, 126.04, 127.80, 128.91, 129.67, 132.07, 133.09, 139.98, 145.62 (Ph and Py), 167.73 (N*C*Ph) ppm.

[{(C$_5$H$_4$N-2)C(SiMe$_3$)C(Ph)N}(μ-SiHCl)]$_2$ (9): A solution of **1** (1.28 g, 1.84 mmol) in THF (30 mL) was added slowly to a solution of $HSiCl_3$ (0.41 mL, 4.05 mmol) in THF (20 mL) at −90 °C. The yellow solution was warmed to ambient temperature and stirred for two days. The volatiles were removed under reduced pressure and the residue was extracted with toluene. The yellow mixture was filtered and concentrated to give yellow crystals of the title compound. Yield: 0.97 g (79%); m.p.: 232−233 °C. $C_{32}H_{38}Cl_2Si_4N_4$: calcd. C 58.07, H 5.79, N 8.46; found C 58.55, H 5.62, N 7.64. ^{1}H NMR (300 MHz, [D$_8$]THF, 25 °C): δ = −0.16 (s, 6 H, $SiMe_3$), 0.41 (s, 3 H, $SiMe_3$), 5.46 (s, 1 H, SiH), 6.92−6.96 (t, J = 6.0 Hz, 1 H, 5-py), 6.99−7.02 (d, J = 7.4 Hz, 1 H, 3-py), 7.11−7.19 (m, 2 H, Ph), 7.36−7.37 (m, 3 H, Ph), 7.41−7.44 (m, 1 H, 4-py), 7.80−7.82 (d, J = 5.8 Hz, 1 H, 6-py) ppm. ^{13}C{^{1}H} NMR (300 MHz, [D$_8$]THF, 25 °C): δ = 2.90, 3.13 ($SiMe_3$), 101.36 (*C*$SiMe_3$), 118.44, 123.80, 126.05, 127.92, 128.35, 128.91, 129.59, 139.36, 141.80, 155.89 (Ph and Py) 162.51 (N*C*Ph) ppm.

[{(C$_5$H$_4$N-2)C(H)C(Ph)N}(μ-GeCl$_2$)]$_2$ (11): A solution of **10** (0.84 g, 1.53 mmol) in THF (30 mL) was added slowly to a solution of $GeCl_4$ (0.38 mL, 3.36 mmol) in THF (20 mL) at −90 °C. The yellow suspension was warmed to ambient temperature and stirred for two days. The volatiles were removed under reduced pressure and the residue was extracted with toluene. The yellow mixture was filtered and concentrated to give yellow crystals of the title compound. Yield: 0.39 g (37%); m.p.: 210−211 °C. $C_{26}H_{36}Cl_4Ge_2N_4$: calcd. C 46.23, H 2.90, N 8.29; found C 46.03, H 3.08, N 8.23. ^{1}H NMR [300 MHz, C_6D_6/[D$_8$]THF (2:1), 25 °C]: δ = 5.09 (s, 1 H, *H*CC), 6.57 (t, J = 6.6 Hz, 1 H, 5-py), 6.68 (d, J = 8.5 Hz, 1 H, 3-py), 6.91 (t, J = 8.0 Hz, 1 H, 4-py), 7.10−7.14 (m, 5 H, Ph), 8.65 (d, J = 6.3 Hz, 1 H, 6-py) ppm. ^{13}C{^{1}H} NMR (300 MHz, C_6D_6/[D$_8$]THF 2:1, 25 °C): δ = 96.51 (H*C*C), 116.70, 119.56, 121.62, 124.71, 125.92, 126.85, 129.69, 130.36, 139.85, 142.27, 145.48 (Ph and Py), 155.79 (N*C*Ph) ppm.

X-ray Crystallographic Study: Single crystals were sealed in Lindemann glass capillaries under nitrogen. The X-ray data of **2**−**5**, **7**−**9**, and **11** were collected on a Rigaku R-AXIS II imaging plate using graphite-monochromated Mo-K_α radiation (λ = 0.71073 Å) from a rotating-anode generator operating at 50 kV and 90 mA. Crystal data for **2**−**5**, **7**−**9**, and **11** are summarized in Table 5 and 6. The structures were solved by direct phase determination using the computer program SHELXTL-PC[27] on a PC 486 and refined by full-matrix least-squares with anisotropic thermal parameters for the non-hydrogen atoms. Hydrogen atoms were introduced in their idealized positions and included in structure factor calculations with assigned isotropic temperature factor calculations.

CCDC-250383 to -250390 (**2**−**5**, **7**−**9** and **11**, respectively) contain the supplementary crystallographic data for this paper. These data can be obtained free of charge at www.ccdc.cam.ac.uk/conts/

 © 2005 Wiley-VCH Verlag GmbH & Co. KGaA, Weinheim

Table 5. Crystallographic data for compounds **2**−**5**

	2	**3**	**4**	**5**
Formula	$C_{38}H_{54}GeN_4Si_4$	$C_{38}H_{54}N_4Si_4Sn$	$C_{38}H_{54}N_4PbSi_4$	$C_{19}H_{27}ClGeN_2Si_2$
Mol. mass	751.80	797.90	886.40	447.65
Color	orange	yellow	yellow	yellow
Cryst. syst.	monoclinic	triclinic	triclinic	monoclinic
Space group	$P2_1/c$	$P\bar{1}$	$P\bar{1}$	$C2/c$
a (Å)	15.233(3)	11.986(2)	10.3383(14)	33.0609(15)
b (Å)	17.245(3)	12.005(2)	12.1593(16)	6.4912(3)
c (Å)	17.625(4)	17.091(3)	19.033(3)	21.3079(10)
α (°)	90	73.89(3)	99.863(2)	90
β (°)	111.76(3)	85.94(3)	96.010(3)	91.5900(10)
γ (°)	90	63.27(3)	113.164(2)	90
V (Å^3)	4300.1(15)	2106.2(7)	2127.7(5)	4571.0
Z	4	2	2	8
$D_{calcd.}$ (g cm^{-3})	1.161	1.258	1.384	1.301
μ (mm^{-1})	0.853	0.750	4.107	1.567
F(000)	1592	832	896	1856
Cryst. size (mm)	0.30 × 0.25 × 0.24	0.24 × 0.22 × 0.18	1.21 × 0.82 × 0.46	0.80 × 0.34 × 0.29
2θ range (°)	1.44−25.58	2.02−26.00	1.87−25.00	1.91−28.02
Index range	$0 \le h \le 18$, $-20 \le k \le 20$, $-21 \le l \le 19$	$-14 \le h \le 13$, $-13 \le k \le 0$, $-21 \le l \le 20$	$-12 \le h \le 11$, $-14 \le k \le 14$, $-22 \le l \le 18$	$-37 \le h \le 43$, $-8 \le k \le 8$, $-27 \le l \le 28$
No. of rflns. collected	11403	7173	11333	14869
No. of indep. rflns.	6811	6770	7400	5516
$R1$, $wR2$ [$I > 2(\sigma)I$]	0.0567, 0.1420	0.0616, 0.1688	0.0613, 0.1613	0.0403, 0.0998
$R1$, $wR2$ (all data)	0.0763, 0.1530	0.1162, 0.1966	0.0669, 0.1646	0.0679, 0.1082
Goodness of fit, F^2	1.091	1.175	1.048	0.933
No. of data/restraints/params.	6811/0/433	6770/0/425	7400/0/424	5516/0/226
Largest diff peaks (e·Å^{-3})	0.316 to −0.372	0.957 to −0.926	3.551 to −1.759	0.709 to −0.453

Table 6. Crystallographic data for compounds **7**−**9** and **11**

	7	**8**	**9**	**11**
Formula	$C_{19}H_{27}ClN_2PbSi_2$	$C_{32}H_{36}Cl_4Ge_2N_4Si_2$	$C_{33}H_{38}Cl_4N_4Si_4$	$C_{26}H_{36}Cl_4Ge_2N_4$
Mol. mass	582.25	819.81	744.83	675.44
Color	yellow	yellow	yellow	yellow
Cryst. syst.	monoclinic	monoclinic	monoclinic	monoclinic
Space group	$P2_1/n$	$P2_1/n$	$P2_1/n$	$P2_1/n$
a (Å)	10.0657(9)	10.541(3)	9.2060(18)	10.891(2)
b (Å)	37.042(3)	14.276(4)	13.528(3)	10.0333(19)
c (Å)	18.7631(15)	12.879(4)	17.123(3)	12.227(2)
α (°)	90	90	90	90
β (°)	98.403(2)	110.786(6)	94.69(3)	92.150(4)
γ (°)	90	90	90	90
V (Å^3)	6920.8(10)	1181.9(9)	2125.3(7)	1335.2(4)
Z	12	2	2	2
$D_{calcd.}$ (g cm^{-3})	1.676	1.503	1.164	1.680
μ (mm^{-1})	7.538	2.049	0.417	2.676
F(000)	3384	832	776	672
Cryst. size (mm)	0.54 × 0.26 × 0.21	0.16 × 0.13 × 0.11	0.60 × 0.40 × 0.40	0.32 × 0.31 × 0.20
2θ range (°)	1.55-22.50	2.21-25.00	1.92-24.00	2.46-28.09
Index range	$-10 \le h \le 10$, $-38 \le k \le 39$, $-18 \le l \le 20$	$-11 \le h \le 12$, $-16 \le k \le 14$, $-15 \le l \le 14$	$0 \le h \le 10$, $-15 \le k \le 15$, $-19 \le l \le 19$	$-14 \le h \le 13$, $-13 \le k \le 13$, $-10 \le l \le 16$
No. of rflns. collected	30866	9917	5303	9182
No. of indep. rflns.	8988	3177	3056	3222
$R1$, $wR2$ [$I > 2(\sigma)I$]	0.0604, 0.1252	0.0682, 0.1514	0.0902, 0.2415	0.0319, 0.0617
$R1$, $wR2$ (all data)	0.1691, 0.1564	0.1241, 0.1736	0.0960, 0.2494	0.0588, 0.0683
Goodness of fit, F^2	0.849	0.826	1.022	0.908
No. of data/restraints/params.	8988/28/667	3177/0/200	3056/0/218	3222/0/164
Largest diff peaks (e·Å^{-3})	2.646 to −1.438	1.376 to −1.549	0.578 to −0.751	0.364 to −0.319

 © 2005 Wiley-VCH Verlag GmbH & Co. KGaA, Weinheim

retrieving.html [or from the Cambridge Crystallographic Data Centre, 12, Union Road, Cambridge CB2 1EZ, UK; Fax: +44 1223-336-033; E-mail: deposit@ccdc.cam.ac.uk].

Acknowledgments

This work was supported by the Hong Kong Research Grants Council (Project No. CUHK 4265-00P).

[1] Selected reviews and examples of metal 1-azaallyl complexes: [1a] C. F. Caro, M. F. Lappert, P. G. Merle, *Coord. Chem. Rev.* **2001**, *219*, 605. [1b] M. F. Lappert, D.-S. Liu, *J. Organomet. Chem.* **1995**, *500*, 203. [1c] P. B. Hitchcock, M. F. Lappert, D.-S. Liu, *J. Chem. Soc., Chem. Commun.* **1994**, 1699. [1d] W.-P. Leung, H. Cheng, D.-S. Liu, Q.-G. Wang, T. C. W. Mak, *Organometallics* **2000**, *19*, 3001. [1e] P. B. Hitchcock, M. F. Lappert, M. Layh, D.-S. Liu, R. Sablong, T. Shum, *J. Chem. Soc., Dalton Trans.* **2000**, 2301. [1f] P. B. Hitchcock, M. F. Lappert, M. Layh, *J. Chem. Soc., Dalton Trans.* **2001**, 2416. [1g] D. R. Armstrong, W. Clegg, L. Dunbar, S. T. Liddle, M. MacGregor, R. E. Mulvey, D. Reed, S. A. Quinn, *J. Chem. Soc., Dalton Trans.* **1998**, 3431. [1h] P. C. Andrews, S. M. Calleja, M. Maguire, P. J. Nichols, *Eur. J. Inorg. Chem.* **2002**, 1583. [1i] X. Chen, C. Du, J.-P. Guo, X.-H. Wei, D.-S. Liu, *J. Organomet. Chem.* **2002**, *655*, 889. [1j] L. Bourget, P. B. Hitchcock, M. F. Lappert, *J. Chem. Soc., Dalton Trans.* **1999**, 2645. [1k] K. S. Klimek, C. Cui, H. W. Roesky, M. Noltemeyer, H.-G. Schmidt, *Organometallics* **2000**, *19*, 3085. [1l] P. B. Hitchcock, M. F. Lappert, M. Layh, A. Klein, *J. Chem. Soc., Dalton Trans.* **1999**, 1455. [1m] P. J. Daff, A. Monge, P. Palma, M. L. Poveda, C. Ruiz, P. Valerga, E. Carmona, *Organometallics* **1997**, *16*, 2263. [1n] J. de With, A. D. Horton, A. G. Orpen, *Organometallics* **1993**, *12*, 1493.

[2] P. B. Hitchcock, M. F. Lappert, M. Layh, *Z. Anorg. Allg. Chem.* **2000**, *626*, 1081.

[3] C. F. Caro, P. B. Hitchcock, M. F. Lappert, *Chem. Commun.* **1999**, 1433.

[4] P. B. Hitchcock, M. F. Lappert, M. Layh, *J. Chem. Soc., Dalton Trans.* **1998**, 1619.

[5] C. Cui, H. W. Roesky, M. Noltemeyer, M. F. Lappert, H.-G. Schmidt, H. Huo, *Organometallics* **1999**, *18*, 2256.

[6] P. B. Hitchcock, M. F. Lappert, S. Tian, *J. Organomet. Chem.* **1997**, *549*, 1.

[7] [7a] L. Lochmann, J. Pospísíl, D. Lim, *Tetrahedron Lett.* **1996**, 257. [7b] W.-P. Leung, H. Cheng, H. L. Hou, Q.-C. Yang, Q.-G. Wang, T. C. W. Mak, *Organometallics* **2000**, *19*, 5431.

[8] B. J. Deelman, P. B. Hitchcock, M. F. Lappert, W.-P. Leung, H.-K. Lee, T. C. W. Mak, *Organometallics* **1999**, *18*, 1444.

[9] B. J. Deelman, M. F. Lappert, H.-K. Lee, T. C. W. Mak, W.-P. Leung, P.-R. Wei, *Organometallics* **1997**, *16*, 1247.

[10] P. B. Hitchcock, M. F. Lappert, M. Layh, *J. Organomet. Chem.* **1997**, *529*, 243.

[11] W.-P. Leung, H. Cheng, R. B. Huang, Q.-C. Yang, T. C. W. Mak, *Chem. Commun.* **2000**, 451.

[12] P. B. Hitchcock, M. F. Lappert, M. Layh, *J. Chem. Soc., Dalton Trans.* **1998**, 3113.

[13] Y. Ding, H. W. Roesky, M. Noltemeyer, H.-G. Schmidt, *Organometallics* **2001**, *20*, 1190.

[14] C. Brelière, F. Carré, R. J. P. Corriu, G. Royo, M. W. C. Man, J. Lapasset, *Organometallics* **1994**, *13*, 307.

[15] F. Carré, C. Chuit, R. J. P. Corriu, A. Mehdi, C. Reyé, *Angew. Chem. Int. Ed. Engl.* **1994**, *33*, 1097.

[16] P. Jutzi, A. Becker, H. G. Stammler, B. Neumann, *Organometallics* **1991**, *10*, 1647.

[17] W.-P. Leung, W.-H. Kwok, L.-H. Weng, L. T. C. Law, Z.-Y. Zhou, T. C. W. Mak, *J. Chem. Soc., Dalton Trans.* **1997**, *22*, 4301.

[18] T. Fjeldberg, H. Hope, M. F. Lappert, P. P. Power, A. J. Thorne, *J. Chem. Soc., Chem. Commun.* **1983**, 639.

[19] M. F. Lappert, M. J. Slade, J. L. Atwood, M. J. Zaworotko, *J. Chem. Soc., Chem. Commun.* **1980**, 621.

[20] P. B. Hitchcock, J. Hu, M. F. Lappert, M. Layh, J. Severn, *Chem. Commun.* **1997**, 1189.

[21] P. B. Hitchcock, M. F. Lappert, M. Layh, *Inorg. Chim. Acta* **1998**, *269*, 181.

[22] L. Pu, M. M. Olmstead, P. P. Power, S. Berthold, *Organometallics* **1998**, *17*, 5602.

[23] J. L. Shibley, R. West, J. Belz, R. K. Hayashi, *Organometallics* **1994**, *13*, 2305.

[24] L. M. Englehardt, P. C. Junk, W. C. Patalimghug, R. E. Sue, C. L. Raston, B. W. Skelton, A. H. White, *J. Chem. Soc., Chem. Commun.* **1991**, 930.

[25] J. Pfeiffer, W. Maringgele, M. Noltemeyer, A. Meller, *Chem. Ber.* **1989**, 245.

[26] T. Fjeldberg, A. Haaland, B. E. R. Schilling, M. F. Lappert, A. J. Thorne, *J. Chem. Soc., Dalton Trans.* **1986**, 1551.

[27] G. M. Sheldrick, in *Crystallographic Computing 3: Data Collection, Structure Determination, Proteins, and Databases* (Eds.: G. M. Sheldrick, C. Krüger, R. Goddard), Oxford University Press, New York, **1985**; p. 175.

Received July 22, 2004
Early View Article
Published Online December 17, 2004

 © 2005 Wiley-VCH Verlag GmbH & Co. KGaA, Weinheim

Sonochemical Reaction of $[Fe(CO)_5]$ with 1-Methylimidazole in An Ionic Liquid: Formation of $[(1\text{-Methylimidazole})_6Fe^{II}](PF_6)_2$

David S. Jacob,[a] Volker Kahlenberg,[b] Klaus Wurst,[c] Leonid A. Solovyov,[d] Israel Felner,[e] Linda Shimon,[f] Hugo E. Gottlieb,[a] and Aharon Gedanken*[a]

Keywords: Ionic liquid / Sonochemistry / Iron imidazole complex

The ionic liquid 1-butyl-3-methylimidazolium hexafluorophosphate, $(BMI^+)(PF_6^-)$, has been used as a solvent in the sonochemical reaction of 1-methylimidazole and $[Fe(CO)_5]$ at 40–50 °C under air. The reaction afforded $[(1\text{-methylimidazole})_6Fe^{II}](PF_6)_2$, the structure of which was determined at 293 K by single-crystal X-ray diffraction methods. The salt crystallizes in the trigonal space group $P\bar{3}$ with unit-cell parameters of a = 11.4603(16) Å, c = 8.0172(11) Å, and Z = 1. The crystals showed twinning by merohedry, which was accounted for in the structure determination and refinement calculations. All the 1-methylimidazole ligands are equivalent, with a Fe–N bond length of 2.204(3) Å. Mössbauer spectroscopy confirmed the presence of Fe^{2+}.

(© Wiley-VCH Verlag GmbH & Co. KGaA, 69451 Weinheim, Germany, 2005)

Introduction

Ionic liquids are generally considered to be noncoordinating green solvents in organic synthesis and catalysis.[1] However, there are few examples where ionic liquids behave as templates or charge-compensating groups in the reactions. Xiao et al.[2] were the first to report the in situ formation of 1-butyl-3-methylimidazole-2-ylidene (bmiy) complexes of palladium $[Br(\mu\text{-}Br)(bmiy)Pd]_2$ and $[Br_2(bmiy)_2Pd]$ in 1-butyl-3-methylimidazolium bromide ionic liquid. Welton et al.[3] have studied the in situ formation of the mixed phosphane imidazolylidene palladium complexes $[(PPh_3)_2Pd(bmimy)X](BF_4^-)$ at room temperature in 1-butyl-3-methylimidazolium tetrafluoroborate ionic liquid (where X = Cl, Br). These references show the solvent incorporation behavior of the ionic liquid in the final product. Aggarwal et al.[4] have reported unexpected side reaction of imidazole-based ionic liquids in the base-catalysed Baylis–Hillman reaction. Zaworotko et al.[5] synthesized *trans*-$[(1\text{-Meim})_4F_2Fe]BF_4$ in 1-methylimidazolium tetrafluoroborate ionic liquid as a reactant. In the solvothermal synthesis of the coordination polymer $[Cu^I(bpp)]BF_4$, using 1-butyl-3-methylimidazolium tetrafluoroborate ionic liquid as solvent, Li et al.[6] found that BF_4^- anions entered the final structure as a charge-compensating species.

Although ionic liquids have several important properties that could make them useful in various chemical processes,[1,7–16] experimental evidence is lacking in the field of coordination chemistry, wherein ionic liquids act as clean, effective solvents for the crystallization of complexes. To explore the reactions in ionic liquids, we report here the inorganic synthesis of (1-methylimidazole)iron complex in ionic liquid (as solvents) under sonochemical conditions.

Transition metals and imidazole play an important role as an active centre of metalloproteins, as well as in many other biological systems such as hemoglobin, vitamin B_{12},[17] and F_{430}. The interaction between imidazole ligand and transition metal ions[17–20] forms well-defined complexes whose stoichiometry is $M(Im)_6X_2$, M = Fe^{II}, Co^{II}, Ni^{II}, and Cu^{II} ions.[18,19] The structures of known *N*-substituted imidazole complexes of transition metal ions have been studied extensively.[21] An $[(1\text{-methylimidazole})_6Fe^{II}]^{2+}$ complex has been prepared using iron(II) salts as precursors for iron.[21b,21c]

A further literature survey revealed a reaction of ferrocene and cyclopentadienyl irondicarbonyl with imidazole

[a] Department of Chemistry and Kanbar Laboratory for Nanomaterials at the Bar-Ilan University Center for Advanced Materials and Nanotechnology, Bar-Ilan University, Ramat-Gan 52900, Israel
E-mail: gedanken@mail.biu.ac.il
[b] Institut für Mineralogie und Petrographie, Leopold-Franzens-Universität Innsbruck, Innrain 52, 6020 Innsbruck, Austria
[c] Institut für Allgemeine, Anorganische und Theoretische Chemie, Leopold-Franzens-Universität Innsbruck, Innrain 52a, 6020 Innsbruck, Austria
[d] Institute of Chemistry and Chemical Technology, Siberian Branch, Russian Academy of Sciences, Akademgorodok, 660049 Krasnoyarsk, Russia
[e] The Racah Institute of Physics, The Hebrew University of Jerusalem, 91904, Jerusalem, Israel
[f] Chemical Services, Weizmann Institute of Science, Rehovot 76100, Israel

(unsubstituted), yielding $Fe(N_2C_3H_3)\cdot 0.71N_2C_3H_4$ with fourfold, as well as sixfold, coordinated metal ions.[22] For substituted imidazole, only a fourfold coordinated iron is detected.[22]

In 1980 a paper reported on the reaction of 1-methyl-, 1-ethyl-, 1,2-dimethyl- and 1,2,3,4-tetramethylimidazole with $[Fe(CO)_5]$, yielding $(FeIm_6)[Fe(CO)_8]$, $(FeIm6)[Fe(CO)_4]_2$, $(FeIm_4)[Fe(CO)_4]$ and $Fe(Im)(CO)_2$, respectively, (Im = substituted imidazole).[23] The reaction product of $[Fe(CO)_5]$ with 2-ethylimidazole shows that the anion is $[HFe(CO)_5]^-$ rather than $[Fe(CO)_4]^-$, as proposed by Seel et al.[23,24]

The ionic liquid used in our system is composed of an asymmetric 1-butyl-3-methylimidazolium cation (BMI^+) with a bulky hexafluorophosphate (PF_6^-) anion. Ionic liquids exhibit unique properties, including high thermal stability, a large liquid range, and negligible vapour pressure.[25] The latter property could change the characteristics of acoustic cavitation and make ionic liquids potentially attractive for use in sonochemical reactions. Acoustic cavitation, i.e., the formation, growth and implosive collapse of bubbles in a liquid medium, is principally responsible for sonochemistry.[26] The collapse of such bubbles creates hot spots ($\approx$ 5000 °C), high pressures (1000 atm), and very high cooling rates (10^{10} K·s^{-1}),[27] leading to the extreme conditions responsible for various chemical and physical effects.

Upon cavitational collapse, vapours inside the bubble undergo a gas-phase reaction. It is of great importance that only vapours of the volatile solutes, and not of the solvent, are inside the collapsing bubble, and so low vapour pressure solvents such as decalin, hexadecane, and isodurene are common in sonochemistry.[28] Suslick et al. have shown that sonication of $[Fe(CO)_5]$ in decane (for 3 h in a dry-ice acetone bath) affords amorphous iron that contains 3% carbon, 2% hydrogen, and 1% oxygen, by weight.[29] The amount of contaminants was reduced sharply upon a shorter sonication time.[30] Such contaminants originate from the small amount of decane vapour found inside the collapsing bubble. The search for low vapour solvents has led recently to the use of diphenylmethane.[31] Ionic liquids are good candidates for this purpose due to their low vapour pressure.

Recently, Suslick et al. have studied the effect of acoustic cavitation on pure ionic liquids sonicated at 20 kHz, and at ca. 60 W·cm^{-2} for 3 h at 85−135 °C. The reaction led to the decomposition of the ionic liquid and the products in the headgas were analyzed by gas-chromatography.[32] The ionic liquid decomposed at 1.9−3.8 μmol·min^{-1}, so that after 180 min less than 1% of the ionic liquid had decomposed. $[Fe(CO)_5]$ yields amorphous iron nanoparticles upon sonication under argon, wheras sonication under air affords nanosized amorphous Fe_2O_3.[33,28] Decalin was used as solvent for both sonications.

The current paper reports an *inorganic* sonochemical reaction carried out in an ionic solvent. $[Fe(CO)_5]$ (reactant I), and 1-methylimidazole (reactant II) were reactants, while the ionic solvent was 1-butyl-3-methylimidazole hexafluorophosphate (BMI^+)(PF_6^-). The product was composed of iron originating from reactant I, 1-methylimidazole from reactant II, and the PF_6^- anion from the ionic liquid. This product differs from the sonochemical product obtained in the dissociation of $[Fe(CO)_5]$ in organic solvents such as decalin or hexadecane.[28,29a] Products of all the reactions conducted using transition metal carbonyls were amorphous. This due to the fast cooling rates obtained when the bubble collapses, which prevent crystallization of the product. Here, our focus is on the crystalline product obtained after the sonication reaction. The possibility of producing crystalline products under sonochemical reaction makes our research especially interesting. The structure of the complex was characterized by single crystal and powder X-ray diffraction (XRD) analysis.

Results and Discussion

The single-crystal structure analysis shows that the Fe^{2+} atoms are coordinated by six 1-methylimidazolium groups with an equivalent Fe−N (2.204(3) Å) bond length. This distance is within the range observed for other reported Fe−N distances.[5,21a,21c] Two PF_6^- ions balance the positive charge. The coordination polyhedron around the P atom is slightly disordered and the fluorine atoms were refined with an occupancy factor of 0.333. Figure 1 shows an ORTEP perspective of the [(1-methylimidazole)$_6$Fe^{II}](PF$_6$)$_2$. Table 1 presents crystal and structure refinement data.

Table 1. Crystal and structure refinement data for [(1-methylimidazole)$_6$Fe^{II}](PF$_6$)$_2$

Empirical formula	$C_{24}H_{36}F_{12}FeN_{12}P_2$
Molecular mass	838.44
Temperature	293(2) K
Wavelength	0.71073 Å (Mo-K_α)
Crystal system	trigonal
Space group	$P\bar{3}$ (No.147)
Unit cell dimensions	a = 11.4603(16) Å; α = 90 deg.
b = 11.4603(16) Å; β = 90 deg.	
c = 8.0172(11) Å; γ = 120 deg.	
Volume	911.9(2) Å^3
Z, calculated density	1, 1.527 Mg/m^3
Absorption coefficient	0.599 mm^{-1}
F(000)	428
Color, habit	colorless, needle
Crystal size	0.02 × 0.02 × 0.4 mm
Theta range for data collection	2.05−25.17 deg.
Limiting indices	$-13 \le h \le 12$, $-13 \le k \le 13$, $-9 \le l \le 9$
Reflection collected/unique	5824/1078 [$R_{(int)}$ = 0.0806]
Reflections with $I > 2\sigma(I)$	890
Absorption correction	none
Refinement method	full-matrix least-squares on F^2
Data/restraints/parameters	1078/0/116
Goodness-of-fit on F^2	1.116
Final R indices [$I > 2\sigma(I)$]	$R1$ = 0.0440, $wR2$ = 0.0718
R indices (all data)	$R1$ = 0.0597, $wR2$ = 0.0764
Largest diff. Peak and hole	0.159 and −0.198 Å^{-3}

 © 2005 Wiley-VCH Verlag GmbH & Co. KGaA, Weinheim

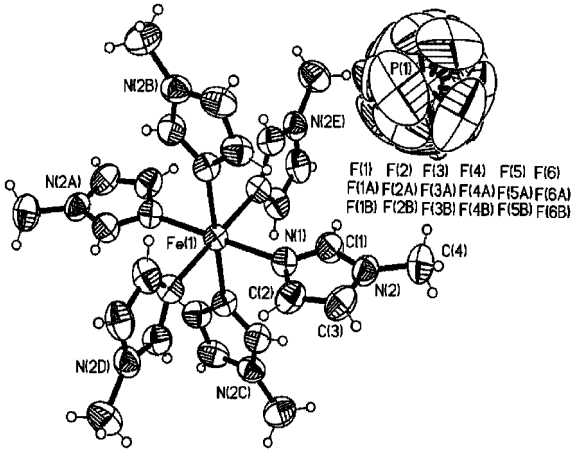

Figure 1. Perspective ORTEP view of [(1-methylimidazole)$_6$Fe^{II}]-(PF_6)$_2$ (50% probability displacement ellipsoids); hydrogen atoms omitted for clarity

In parallel, powder XRD (PXRD) structural investigations of the bulk sample reproduced the single crystal results, and confirmed the single-phase purity of the product. Figure 2 illustrates the final agreement between the experimental and calculated PXRD profiles. All observed PXRD peaks are explained fairly well by the refined structure model.

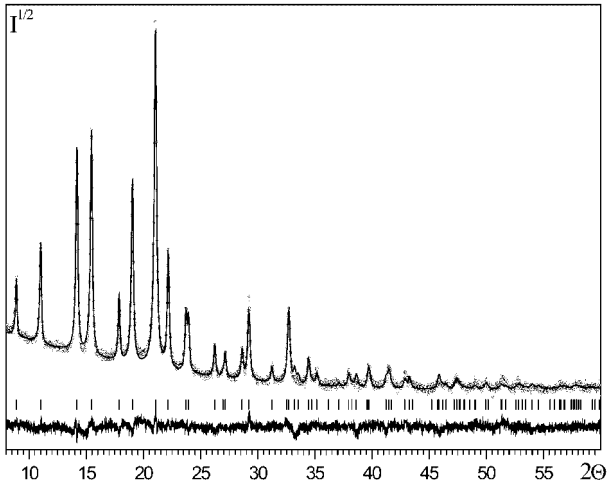

Figure 2. Weighted experimental (circles), calculated (solid line) and difference (bottom curve) PXRD profiles for [(1-methylimidazole)$_6$Fe^{II}](PF_6)$_2$. Reflection positions are marked by ticks

Vibrational bands in the Raman and IR absorption spectra of the complex (Figure 3) are assigned in Table 2. The vibrational bands of the ligands are shifted, as reported previously by Reedijk,[34] Perchard and Novak.[35] M−N vibrations in the Raman spectrum below 300 cm^{-1} are in accordance with the literature values.[34] The intense Raman line at 739 cm^{-1} is assigned to the symmetric ν_1 mode of the PF_6^- ion.[36]

NMR studies of ^{31}P and ^{19}F confirm the presence of PF_6^- anions (Figure 4). The ^{31}P NMR spectrum shows septet with respect to fluorine and the ^{19}F NMR spectrum

Table 2. Raman and IR vibration bands (cm^{-1}) for Fe^{II}(1-methylimidazole)$_6$(PF_6)$_2$ (w = weak, m = medium, s = strong and br. = broad)

Assignments	Vibration frequency [$(C_4H_6N_2)_6$Fe](PF_6)$_2$	
	IR (cm^{-1})	Raman (cm^{-1})
C−H stretching	3139 m	3153 m
CH_3 stretchings	2971 m	2970 m
Combination bands	1614 w	−
Ring stretching (R^1)	1533 s	1531 m
Ring stretching (R^2)	−	1513 m
CH_3 bending	1465 w	−
CH_3 bending	1425 m	1425 m
Ring stretching (R^3)	−	1346 s, br.
Ring stretching (R^4)	1335 w	−
In plane C−H bending	1287 s	1281 m
Ring stretching (R^5) + CN stretch	1233 s	1229 m
In plane C−H bending	1092 s	1087 m, br.
CH_3 deformation	1029 m	1024 s
Ring stretching (R^6)	939 s	933 m
Out-of-plane C−H bending	845 s, br.	−
Out-of-plane C−H bending	760 m	−
Ring stretching and CN stretching	661 m	666 s
Ring deformation	618 m	−
C−N deformation	−	368 m
C−N deformation	−	237 m

shows the doublet with respect to phosphorus (where I_P = 1/2 and I_F = 1/2).

Mössbauer spectroscopic data confirm the +2 oxidation state of iron with an isomeric shift (IS) = 1.041 mm s^{-1} and a quadrupole splitting (QS) = 0.769 mm s^{-1}, which agree with the literature values.[19,23] The Mössbauer spectrum does not show Fe^{III} impurities. The mass spectrum of the complex, obtained by desorption chemical ionization (DCI) using methane, shows the 1-methylimidazole peak at m/z = 82. The PF_6^-anion of the complex appears at m/z = 145 under fast atom bombardment (FAB)-glycerol in methanol. Elemental analysis for [(1-methylimidazole)$_6$Fe^{II}](PF_6)$_2$ also matches the calculated theoretical values.

Following previous sonochemical experiments,[29] we assume that the first stage of the current reaction involves the decomposition of [Fe(CO)$_5$] to Fe and CO. The CO is then released from the sonication cell, while the Fe(0) is oxidized by air to Fe^{2+} ions in the (BMI^+)(PF_6^-) ionic liquid. Sonication of [Fe(CO)$_5$] under the same conditions in decalin gave amorphous Fe_2O_3.[28] Unlike the reaction in decalin, here the surrounding environment of the 1-methylimidazole and the ionic liquid (BMI^+)(PF_6^-) prevented complete oxidation of the iron. Our first assumption is, following earlier reports,[2−6] that the ionic liquid is the source of the imidazole ring and the counterion (PF_6^-) in the product, while losing a 1-butyl group during the reaction. This assumption might also agree with the decomposition product of the sonication of (BMI^+)(PF_6^-) under argon[32] where the cation of the ionic liquid (BMI^+)(PF_6^-) loses a butyl/methyl group. ^{1}H and ^{13}C NMR analysis of the product of the ionic liquid reaction indicates the presence of a 1-methylimidazole, but no butyl group. This means that the 1-meth-

 © 2005 Wiley-VCH Verlag GmbH & Co. KGaA, Weinheim

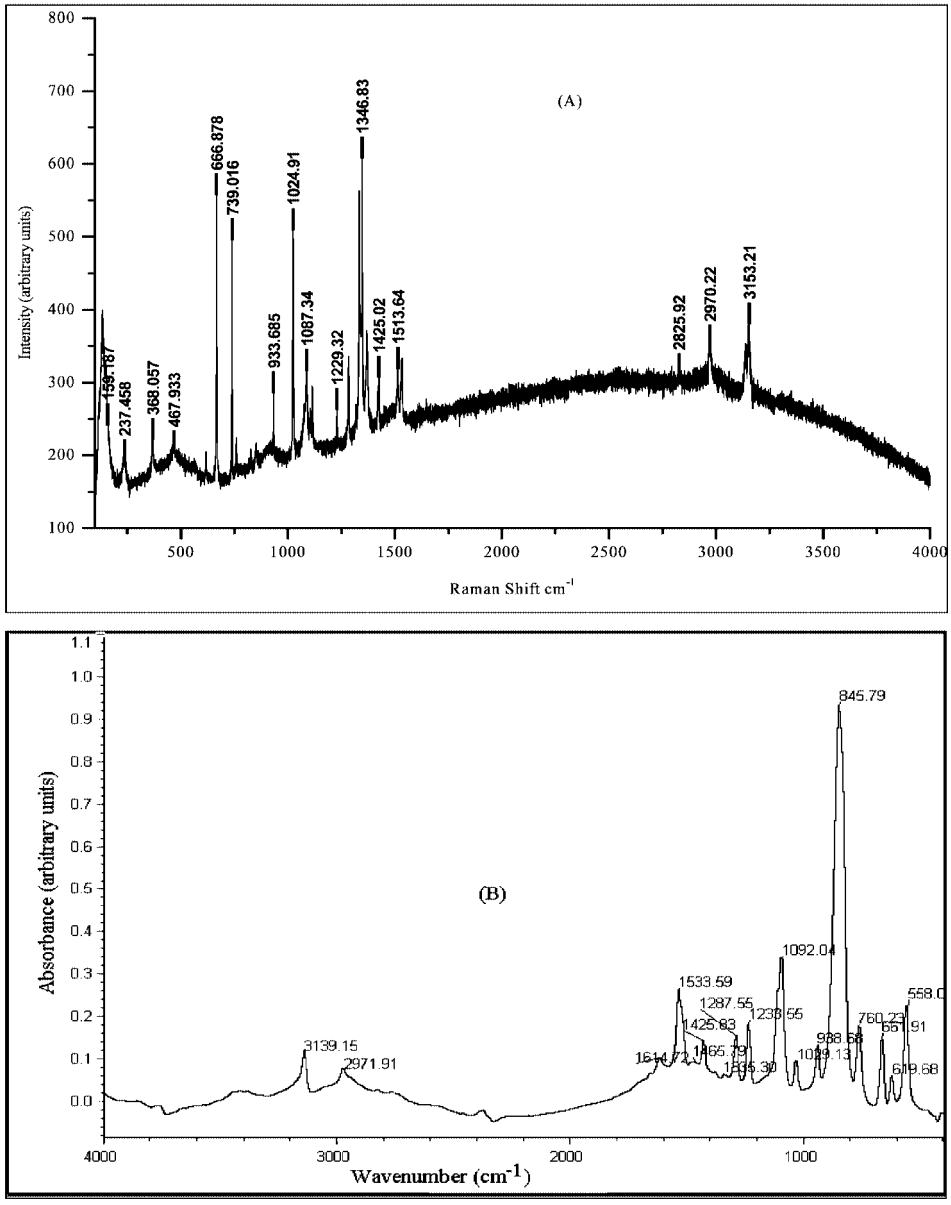

Figure 3. Raman (A) and IR (B) absorption spectrum of [(1-methylimidazole)$_6$Fe^{II}](PF$_6$)$_2$

ylimidazole source is not the ionic liquid, but the reactant II. Conversely, the anions in the product originate from the ionic liquid.

To investigate the purity of the ionic liquid, (BMI$^+$)(PF$_6^-$), its thermal decomposition[37] was studied by TGA (Thermo Gravimetric Analysis) between 25 and 1000 °C at 3 °C min^{-1} in a N_2 flow. Water, as an impurity, causes the partial decomposition of the ionic liquid, with the formation of phosphate, HF and transition metal fluorides.[38] The (BMI$^+$)(PF$_6^-$) was thermally stable at 330 °C and decomposed completely at 516 °C, confirming that it is stable at the reaction temperature, without forming metal fluorides, and that it undergoes a chemical reaction only due to the temperature developed as a result of the bubble collapse.

A control reaction sonicating the same concentration of [Fe(CO)$_5$] in the ionic liquid (BMI$^+$)(PF$_6^-$) (without 1-methylimidazole) under an air atmosphere at 40−50 °C yielded a very small amount of an amorphous product (6 mg). A second control reaction, conducted by sonicating [Fe(CO)$_5$] in 1-methylimidazole (no ionic liquid), gave an amorphous product. After crystallization Fe_2O_3 was identified (PXRD) as the product. This is a main difference between the sonochemical reaction and that in ref.[23], which produces a crystalline product. The time and temperature of the reaction (30 min, 40−50 °C here) also differ (3−6 h, 60−80 °C[23]). The difference between a regular reaction[23] and that of [Fe(CO)$_5$] and imidazole in an ionic liquid is that sonication leads to the loss of CO while the products of a regular reaction contain the carbonyl. Moreover, the

 © 2005 Wiley-VCH Verlag GmbH & Co. KGaA, Weinheim

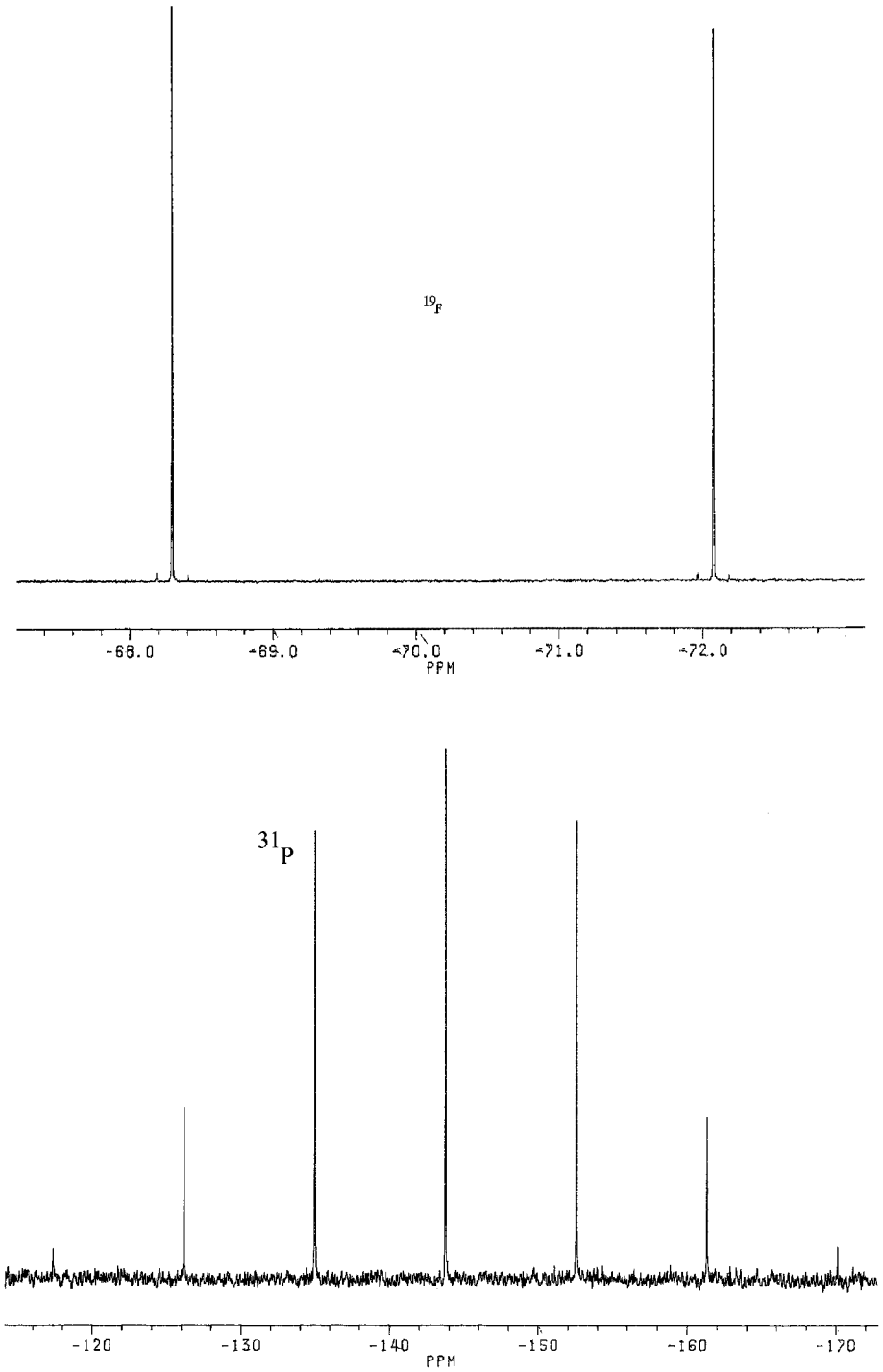

Figure 4. ^{19}F and ^{31}P NMR spectrum of [(1-methylimidazole)$_6$Fe^{II}](PF$_6$)$_2$

negative ions originate from the ionic liquid in our reaction, while [Fe(CO)$_5$] is their source in a regular reaction.[23]

Conclusions

The sonication product of 1-methylimidazole and [Fe(CO)$_5$] in (BMI$^+$)(PF$_6^-$) (which acts as a solvent) gives a complex of [(1-methylimidazole)$_6$Fe^{II}](PF$_6$)$_2$ under air. Unlike ref.[2,3,5], where the cation and the anion contribute to the structure of the final product, here only the anion is part of the product, which is similar to ref.[6]. In this sonochemical reaction, Fe^{2+} ion is coordinated octahedrally by six 1-methylimidazole. PF_6^- acts as a charge-stabilizing agent in the formation of the crystal salt, which is characterized by a trigonal crystal lattice with a $P\bar{3}$ space

 © 2005 Wiley-VCH Verlag GmbH & Co. KGaA, Weinheim

group. To probe the effect of the ionic liquid as a solvent on sonochemical reactions, studies on similar systems using different ionic liquids and transition metal carbonyls are in progress and will be reported soon.

Experimental Section

General Remarks: Ionic liquid 1-butyl-3-methylimidazolium hexafluorophosphate [(BMI$^+$)(PF$_6^-$)] (Aldrich, 96%), 1-methylimidazole (Aldrich, 99%), and pentacarbonyliron (Strem chemicals, USA, 99.5%, refer to MSDS for safety precaution) were purchased from the Aldrich Chemical Co. and used without further purification.

Synthesis of Complex: Pentacarbonyliron [Fe(CO)$_5$] (1.49 g, 6.08 mmol) and 1-methylimidazole (2 g, 24.3 mmol) were dispersed in the ionic liquid (BMI$^+$)(PF$_6^-$) (5 g, 17.6 mmol) under ultrasonic conditions. Sonication was carried out with a high intensity ultrasonic horn (Sonics and Materials Model VC-600, Ti-horn, 20 kHz, 40 W·cm^{-2}) for 30 min under an air atmosphere. The reaction cell was placed in the exhaust hood so that CO was not released into the laboratory (please refer to MSDS for correct handling of these chemicals). The temperature was maintained at around 40−50 °C using a (Julabo FT 901) acetone cooler bath, as the reaction temperature in ionic liquids rises to about 200 °C without cooling. After completion of the reaction, the ionic liquid changed from clear brown to black. Ethanol was used to precipitate a grey powder and to develop the transparent crystals. The amount of product collected after 30 min of sonication was 1.414 g (1.68 mmol). The yield with respect to iron was 28%.

X-ray Crystallographic Study

Single Crystal XRD: A needle-shaped crystal (0.02 × 0.02 × 0.40 mm^3) was mounted on the tip of a glass fiber. Diffraction data were recorded on a Stoe imaging plate detector system (IPDS-II). The diffraction symmetry was consistent with Laue group $\bar{3}$. Since no systematically extinct reflections were observed, space groups $P3$ and $P\bar{3}$ were taken into consideration. Subsequent structure determination confirmed the adequacy of the centrosymmetric space group. Due to the low linear absorption coefficient of the material (μ = 0.6 mm^{-1}) for Mo-K_α radiation, no absorption correction has been applied. Data reduction included Lorentz and polarization corrections. The structure was solved by direct methods using the SHELXS-86 program system.[39] Subsequent refinement calculations were also performed with SHELXL-97,[40] using neutral atomic scattering factors. In the initial stages of the structure determination, several models were obtained that were less satisfactory from a crystal chemical point of view. Finally, a possible twinning of the crystal was considered to explain these difficulties. Since the differences between the internal residuals for merging the data in the two Laue groups $\bar{3}$ and 6/m were not very pronounced (0.078 and 0.109, respectively), a twinning according to m$_{[001]}$ was assumed. This type of twinning results in an exact superposition of the reciprocal lattices of the two twin domains. The twinning model was introduced into the refinements and resulted in a significant improvement. The volume fraction of the twin component I was refined to 0.438(3). For the final, least-squares cycles, anisotropic displacement parameters were used for the non-hydrogen atoms. Hydrogen atoms were added geometrically, and refined using a riding model with isotropic displacement parameters 1.2 or 1.5 times higher than U_{eq} of the aromatic or methyl carbon atoms.

Powder-XRD: PXRD data were collected in Bragg−Brentano geometry using a DRON-4 diffractometer with graphite secondary monochromator (Cu-K_α radiation) and scintillation counter. Measurements were taken at room temperature in air. The unit cell parameters of the crystalline powder product were determined from the PXRD peak positions. A preliminary structure model was estimated by searching the Cambridge Structure Database.[41] Several structures were found with similar crystal lattice dimensions and cognate structure units to those expected for the studied compound: hexakis(*N*-methylimidazole)ruthenium(II) bis(trifluoromethanesulfonate), hexakis(2-methyltetrazole)nickel(II) bis(tetrafluoroborate), and hexakis(5-methylpyrazole)nickel diperchlorate.[42] Considering the synthesis mixture composition and the analogous structures, the formula of the studied compound was assumed to be hexakis(*N*-methylimidazole)iron(II) bis(hexafluorophosphate). A trial structure model was built based on the atomic coordinates of the analogues. Further full-profile PXRD structure refinement utilizing the Rietveld[43] method confirmed the structure model, which was identical to that obtained from the single-crystal study.

Instrumentation: A Raman absorption spectrum of the title compound was recorded with a Jobin Yvon Horiba Raman spectrometer using a 514.532 nm laser in the range 100−4000 cm^{-1}. An IR absorption spectrum was recorded with a Nicolet (Impact 410) spectrometer in the range 400−4000 cm^{-1}. For IR measurements, a pellet containing 200 mg of KBr and 1 mg of the product was prepared. NMR spectra were recorded with an AC Bruker 200 instrument. Mass spectra were recorded with a VG-autospec instrument.

[(1-Methylimidazole)$_6$Fe^{II}](PF$_6$)$_2$: ^{1}H NMR ([200.1 MHz, [D$_6$]DMSO, ppm): δ = 3.59 [s, 3 H, N−CH$_3$], 6.86 [s, 1 H, H(5)], 7.06 [s, 1 H, H(4)], 7.55 [s, 1 H, H(2)].^{13}C NMR (50.3 MHz, [D$_6$]DMSO, ppm): δ = 33.66 [N−CH$_3$)], 121.61 [C(5)], 128.55 [C(4)], 138.57 [C(2)]. ^{31}P NMR (81.0 MHz, [D$_6$]DMSO, ppm): δ = −143.85 (septet, J_{PF} = 709 Hz). ^{19}F NMR (188.3 MHz, [D$_6$]DMSO, ppm): δ = −70.21 (d, J_{PF} = 709 Hz). $C_{24}H_{36}F_{12}FeN_{12}P_2$ (838.44): calcd. C 34.34, N 20.03, H 4.29; found C 34.61, N 19.98, H 4.33.

CCDC-228751 contains the supplementary crystallographic data for this paper. These data can be obtained free of charge from The Cambridge Crystallographic Data Centre via www.ccdc.cam.ac.uk/data_request/cif.

Acknowledgments

A. G. thanks Professors M. Sprecher and S. Hoz for helpful discussions during the course of this research. A. G. also thanks the DIP (Deutsch-Israelische Projekte) organization for their financial support.

[1] [1a] T. Welton, *Chem. Rev.* **1999**, *99*, 2071−2083. [1b] J. Dupont, R. Souza, P. Suarez, *Chem. Rev.* **2002**, *102*, 3667−3692. [1c] D. Zhao, M. Wu, Y. Kon, E. Min, *Catal. Today* **2002**, *74*, 157−189. [1d] K. Marsh, A. Deev, A. Wu, E. Tran, A. Klamt, *Korean J. Chem. Eng.* **2002**, *19(3)*, 357−362.
[2] L. Xu, W. Chen, J. Xiao, *Organometallics* **2000**, *19*, 1123−1127.
[3] [3a] C. Mathews, P. Smith, T. Welton, A. White, D. Williams, *Organometallics* **2001**, *20*, 3848−3850. [3b] F. McLachlan, C. J. Mathews, P. J. Smith, T. Welton, *Organometallics* **2003**, *22*, 5350−5357. [3c] J. E. L. Dullius, P. A. Z. Suarez, S. Einloft, R. F. De Souza, J. Dupont, J. Fischer, A. De Cian, *Organometallics* **1998**, *17*, 815−819.
[4] V. Aggrawal, I. Emme, A. Mereu, *Chem. Commun.* **2002**, *15*, 1612−1613.
[5] S. Christie, S. Subramanian, L. Wang, M. J. Zaworotko, *Inorg. Chem.* **1993**, *32*, 5415−5417.

 © 2005 Wiley-VCH Verlag GmbH & Co. KGaA, Weinheim

[6] K. Jin, X. Huang, L. Pang, J. Li, A. Appel, S. Wherland, *Chem. Commun.* **2002**, 2872−2873.
[7] J. Dupont, G. S. Fonseca, A. P. Umpierre, P. F. P. Fichtner, S. Teixeira, *J. Am. Chem. Soc.* **2002**, *124*, 4228−4229.
[8] C. Baudequin, J. Baudoux, J. Levillain, D. Cahard, A. Gaumont, J. Plaquevent, *Tetrahedron: Asymmetry* **2003**, *14*, 3081−3093.
[9] [9a] F. Endres, M. Bukowski, H. Hempelmann, H. Natter, *Angew. Chem. Int. Ed.* **2003**, *42*, 3428−3430. [9b] S. Z. El Abedin, N. Borissenko, F. Endres, *Electrochem. Commun.* **2004**, *6*, 510−514.
[10] [10a] P. Wasserscheid, W. Keim, *Angew. Chem. Int. Ed.* **2000**, *39*, 3772−3789. [10b] J. S. Wilkes, *J. Mol. Catal. A: Chem.* **2004**, *214*, 11−17.
[11] M. C. Law, K. Y. Wong, T. H. Chan, *Green Chem.* **2004**, *6*, 241−244.
[12] [12a] C. Hardacre, D. J. Holbreg, S. P. Katdare, K. R. Seddon, *Green Chem.* **2002**, *4*, 143−146. [12b] A. J. Carmichael, D. M. Haddleton, S. A. F. Bon, K. R. Seddon, *Chem. Commun.* **2000**, *14*, 1237−1238. [12c] H. X. Gao, T. Jiang, B. X. Han, Y. Wang, J. M. Du, Z. M. Liu, J. L. Zhang, *Polymer* **2004**, *45*, 3017−3019.
[13] R. A. Sheldon, R. Maderia Lau, M. J. Sorgedrager, F. Rantwijk, K. R. Seddon, *Green Chem.* **2002**, *4*, 147−151.
[14] R. P. Swatloski, A. E. Visser, W. M. Reichert, G. A. Broker, L. M. Farina, J. D. Holbrey, R. D. Rogers, *Green Chem.* **2002**, *4*, 81−87.
[15] L. A. Blanchard, D. Hancu, E. J. Beckmann, J. F. Brennecke, *Nature* **1999**, *399*, 28−29.
[16] R. P. Swatloski, S. K. Spear, J. D. Holbrey, R. D. Rogers, *J. Am. Chem. Soc.* **2002**, *124*, 4974−4975.
[17] M. Goodgame, F. A. Cotton, *J. Am. Chem. Soc.* **1962**, *84*, 1543−1548.
[18] W. J. Eilbeck, F. Holmes, A. E. Underhill, *J. Chem. Soc. (A)* **1967**, 757.
[19] C. D. Burbridge, D. M. L. Goodgame, *Inorg. Chem. Acta* **1970**, *4*, 231−234.
[20] D. M. L. Goodgame, M. Goodgame, G. W. Rayner-Canham, *Inorg. Chem. Acta* **1969**, *3*, 406−410.
[21] [21a] G. Carver, P. L. W. Tregenna-Piggott, A. Barra, A. Neels, J. A. Stride, *Inorg. Chem.* **2003**, *42*, 5771−5777. [21b] J. Reedijk, *Inorg. Chem. Acta* **1969**, *3*, 517−522. [21c] L. L. Miller, R. A. Jacobson, Y. Chen, D. M. Kurtz Jr, *Acta Crystallogr., Sect. B* **1989**, 45−3), 527−529. [21d] J. A. Garcia-Vazquez, J. Romero, A. Sousa-Pedrares, A. Sousa, A. D. Garnovskii, D. A. Garnovskii, *J. Chem. Crystallogr.* **2000**, *30*, 23−26. [21e] A. Marzotto, A. Bianchi, G. Valle, D. A. Clemente, *Acta Crystallogr., Sect. B* **1989**, *45*, 582−585. [21f] A. A. Latif, C. Woods, *Inorg. Chem.* **2002**, *5*, 269−273. [21g] K. Tebbe, S. Nafepour, *Acta Crystallogr., Sect. C* **1994**, *50*, 1566−1569.
[22] F. Seel, P. Wende, H. E. Macrolin, A. T. Trautwein, Y. Maeda, *Z. Anorg. Allg. Chem.* **1976**, *426(2)*, 198−204.
[23] F. Seel, R. Lehnert, E. Bill, A. Trautwein, *Z. Naturforsch.* **1980**, 35b, 631−638.
[24] E. Bill, N. Blaes, K. F. Fischer, U. Gonser, K. H. Pauly, R. Preston, F. Seel, R. Staab, A. X. Trautwein, *Z. Naturforsch., Teil B* **1984**, *39*, 333−340.
[25] H. L. Ngo, K. LeCompte, L. Hargens, A. B. McEwen, *Thermochim. Acta* **2000**, *357*, 97.
[26] K. S. Suslick, in *Handbook of Heterogeneous Catalysis* (Eds.: G. Ertl, H. Knozinger, J. Witkamp), Wiley-VCH, Weinheim, Germany, **1997**, vol. 3, pp. 1350−1357.
[27] K. S. Suslick, G. J. Price, *J. Annu. Rev. Mater. Sci.* **1999**, *29*, 295−326.
[28] [28a] X. Cao, Yu. Koltypin, R. Prozorov, G. Kataby, A. Gedanken, *J. Mater. Chem.* **1997**, *7(12)*, 2447−2451. [28b] K. V. P. M. Shafi, S. Wizel, T. Prozorov, A. Gedanken, *Thin Solid Films* **1998**, *318(1−2)*, 38−41. [28c] N. A. Dhas, A. Ekhtiarzadeb, K. S. Suslick, *J. Am. Chem. Soc.* **2001**, *123*, 8310−8316.
[29] [29a] K. S. Suslick, S. Choe, A. A. Cichowlas, A. W. Grinstaff, *Nature* **1991**, *353*, 414−416. [29b] R. Bellissent, G. Galli, A. W. Grinstaff, P. Migliardo, K. S. Suslick, *Phys. Rev.* **1993**, *B48*, 15797−15800.
[30] G. J. Long, D. Hautot, Q. A. Pankhurst, D. Vandormael, F. Grandjean, J. P. Gaspard, V. Briois, T. Hyeon, K. S. Suslick, *Phys. Rev.* **1998**, *B57*, 10716−10722.
[31] S. I. Nikitento, Y. Koltyoin, O. Palchik, I. Felner, N. X. Xiao, A. Gedanken, *Angew. Chem. Int. Ed.* **2001**, *40(23)*, 4447−4449.
[32] J. D. Oxley, T. Prozorov, K. S. Suslick, *J. Am. Chem. Soc.* **2003**, *125*, 11138−11139.
[33] K. V. P. M. Shafi, A. Gedanken, R. Prozorov, A. Revesz, J. Lendvai, *J. Mater. Res.* **2000**, *15(2)*, 332−337.
[34] [34a] J. Reedijk, *Inorg. Chem.* Acta **1969**, *3*, 517−522. [34b]J. Reedijk, *J. Inorg. Nucl. Chem.* **1971**, *33*, 179−188.
[35] C. Perchard, A. Novak, *Spectrochim. Acta* **1967**, *23A*, 1953.
[36] L. Woodward, L. Anderson, *J. Inorg. Nucl. Chem.* **1956**, *3*, 326−327.
[37] [37a] K. J. Baranyai, G. B. Deacon, D. R. MacFarlane, J. M. Pringle, J. L. Scott, *Aust. J. Chem.* **2004**, *57(2)*, 145−147. [37b] M. Kosmulski, J. Gustafsson, J. B. Rosenholm, *Thermochim. Acta* **2004**, *412*, 47−53.
[38] G. S. Fonseca, A. P. Umpierre, P. F. P. Fichtner, S. R. Teixeira, J. Dupont, *Chem. Eu. J.* **2003**, *9*, 3263−3269.
[39] G. M. Sheldrick, *SHELXS-86: Program for Crystal Structure Solution*, University of Göttingen, **1986**.
[40] G. M. Sheldrick, *SHELXL-97: Program for Crystal Structure Refinement*, University of Göttingen, **1997**.
[41] F. H. Allen, O. Kennard, *Chem. Design Autom. News* **1993**, *8*, 31.
[42] [42a] I. R. Baird, S. J. Rettig, B. R. James, K. A. Skov, *Can. J. Chem.* **1998**, *76*, 1379−1388. [42b] E. J. Heuvel, P. L. Franke, G. C. Verschoor, A. P. Zuur, *Acta Crystallogr., Sect. C: Cryst. Struct. Commun.* **1983**, *39*, 337−339. [42c] D. Collison, M. Helliwell, V. M. Jones, F. E. Mabbs, E. J. L. McInnes, P. C. Riedi, G. M. Smith, R. G. Pritchard, W. I. Cross, *J. Chem. Soc., Faraday Trans.* **1998**, *94*, 3019−3025.
[43] H. M. J. Rietveld, *J. Appl. Crystallogr.* **1969**, *2*, 65−71.

Received August 22, 2004
Early View Article
Published Online December 17, 2004

Monomers, Chains and Layers of $[Pt_2(SO_4)_4]$ Units in the Crystal Structures of the Platinum(III) Sulfates $(NH_4)_2[Pt_2(SO_4)_4(H_2O)_2]$, $K_4[Pt_2(SO_4)_5]$ and $Cs[Pt_2(SO_4)_3(HSO_4)]$

Martin Pley[a] and Mathias S. Wickleder*[a][‡]

Keywords: Solid state structures / Platinum / Sulfates / Metal−metal bonds / IR data

The reaction of $Pt(NO_3)_2$ with concentrated sulfuric acid in sealed glass ampoules at 400 °C causes reduction of the nitrate ion to NH_4^+ and leads to single crystals of $(NH_4)_2[Pt_2(SO_4)_4(H_2O)_2]$ [triclinic, $P\bar{1}$, $Z = 1$, $a = 749.96(9)$, $b = 754.2(1)$, $c = 765.4(1)$ pm, $\alpha = 102.15\ (1)°$, $\beta = 110.23(1)°$, $\gamma = 100.87(1)°$, $R_{all} = 0.0677$]. In the crystal structure, Pt_2 dumbbells are coordinated by four bidentate-bridging sulfate ions and two axial H_2O molecules. The replacement of the axial H_2O molecules with SO_4^{2-}, which can be observed in the crystal structure of $K_4[Pt_2(SO_4)_5]$ [triclinic, $P\bar{1}$, $Z = 2$, $a = 975.6(1)$, $b = 1331.8(1)$, $c = 1491.0(1)$ pm, $\alpha = 101.156(8)°$, $\beta = 96.278(8)°$, $\gamma = 102.849(8)°$, $R_{all} = 0.0459$], causes a connection of the dumbbells into chains of the composition $^1_\infty[Pt_2(SO_4)_{4/1}(SO_4)_{2/2}]^{4-}$. $K_4[Pt_2(SO_4)_5]$ has been obtained from the reaction of $K_2[PtCl_4]$ and concentrated H_2SO_4 at 400 °C in sealed glass tubes. The same reaction with $Cs_2[PtCl_4]$ instead of $K_2[PtCl_4]$ leads to $Cs[Pt_2(SO_4)_3(HSO_4)]$ [monoclinic, $P2_1/c$, $Z = 4$, $a = 1724.8(2)$, $b = 881.28(9)$, $c = 935.1(1)$ pm, $\beta = 100.397(8)°$, $R_{all} = 0.0458$]. In the crystal structure, part of the bidentate-bridging sulfate ions of the $[Pt_2(SO_4)_4]$ core act as monodentate ligands to further Pt_2 dumbbells leading to anionic layers of the composition $^2_\infty[Pt_2(SO_4)_{4/2}(SO_4)_{2/1}]^{2-}$ and neutral units with the formula $^2_\infty[Pt_2(SO_4)_{4/2}(HSO_4)_{2/1}]$. The two types of layers are stacked alternatingly with the ten coordinate Cs^+ ions.

(© Wiley-VCH Verlag GmbH & Co. KGaA, 69451 Weinheim, Germany, 2005)

Introduction

The dumbbell shaped Pt_2^{6+} ion was reported for the first time by Muraveiskaya et al. in the complex salt $K_2[Pt_2(SO_4)_4(H_2O)_2]$.[1,2] In the crystal structure of the latter, Pt_2^{6+} is coordinated by four bidentate-bridging sulfate groups and two monodentate water molecules which are located in the axial positions of the dumbbell. This motif has been extensively varied by Cotton and co-workers and other groups[3−10] by introducing other bridging ligands, for example HPO_4^{2-}. Furthermore the H_2O molecules in the axial positions can be replaced by other ligands, for example DMSO or pyridine but also by anions such as Cl^- and OH^-.[11] In all of the compounds which have been structurally characterised so far, the complexes remain monomeric, i.e. they are binuclear anions such as $[Pt_2(SO_4)_4(H_2O)_2]^{2-}$ or $[Pt_2(SO_4)_4Cl_2]^{4-}$. Recently we have shown that a linkage of the $[Pt_2(SO_4)_4]$ entities is possible if the axial positions of the Pt_2 dumbbell are occupied by further sulfate ions. For example, in $Pt_2(HSO_4)_2(SO_4)_2$, the SO_4^{2-} ions act as bidentate-bridging ligands to one platinum dumbbell and as monodentate ligands to the next Pt_2^{6+} ion so that layers of formula $^2_\infty[Pt_2(SO_4)_{4/2}(HSO_4)_{2/1}]$ are formed.[12] Another linkage may be found in the unique structure of $(NH_4)_4[Pt_{12}O_8(SO_4)_{12}]$ which shows six Pt_2^{6+} ions linked by sulfate groups and oxide ions into the cluster anions $[Pt_{12}O_8(SO_4)_{12}]^{4-}$ with a distorted icosahedral Pt_{12} core.[13] As an extension of our work we present, in this paper, the first example of the linkage of $[Pt_2(SO_4)_4]$ units into chains as observed in the crystal structure of $K_4[Pt_2(SO_4)_5]$. Furthermore, we were able to characterise a second example with $[Pt_2(SO_4)_4]$ groups connected into sheets, namely the new sulfate $Cs[Pt_2(SO_4)_3(HSO_4)]$. Finally we report the crystallographic data for $(NH_4)_2[Pt_2(SO_4)_4(H_2O)_2]$ as a representative of the monomeric species.

Results and Discussion

As described recently, the reaction of $Pt(NO_3)_2$ with concentrated sulfuric acid in sealed glass ampoules at 400 °C leads to deep red single crystals of $(NH_4)_4[Pt_{12}O_8(SO_4)_{12}]$.[13] As a side product of this reaction, yellow single crystals were also observed. According to an X-ray investigation, this side product is $(NH_4)_2[Pt_2(SO_4)_4(H_2O)_2]$. This compound has been reported previously, however, but without accompanying crystallographic data.[2,5] It is worth-

[a] Universität zu Köln, Institut für Anorganische Chemie, Greinstraße 6, 50939 Köln
Fax: (internat.) + 49-(0)221-470-5083
E-mail: mathias.wickleder@uni-koeln.de
[‡] New address: Carl von Ossietzky Universität Oldenburg, Institut für Reine und Angewandte Chemie, 26111 Oldenburg
Fax: +49-(0)441-798-3352
E-mail: mathias.wickleder@uni-oldenburg.de

while mentioning that the NH_4^+ ion originates from the reduction of the initial nitrate, clearly by Pt^{2+}.

$(NH_4)_2[Pt_2(SO_4)_4(H_2O)_2]$ crystallizes in the form of yellow plates and can be easily separated from the deep red single crystals of $(NH_4)_4[Pt_{12}O_8(SO_4)_{12}]$. $(NH_4)_2[Pt_2(SO_4)_4(H_2O)_2]$ is isotypic with $K_2[Pt_2(SO_4)_4(H_2O)_2]$ as can be expected from the comparable radii of K^+ and NH_4^+. The compound contains the typical lantern shaped $[Pt_2(SO_4)_4(H_2O)_2]^{2-}$ anion as can be seen in Figure 1. The Pt−Pt distance within the ion was found to be 246.3(1) pm which is not significantly different from the values reported previously for similar compounds.[1−11] The four sulfate groups act as bidentate-bridging ligands with the Pt-O distances being uniformly around 200 pm (Table 2). The S−O distances within the SO_4^{2-} ions differ remarkably. Those to the oxygen atoms which are attached to platinum atoms lie between 151.2(11) and 154.7(13) pm, the noncoordinated oxygen atoms can be found at distances from 142.1(15) up to 144.3(12) pm. The significant differences in the bond lengths also affect the energies of the IR bands (Table 5). For an ideal SO_4^{2-} tetrahedron (T_d symmetry), four vibrations can be theoretically predicted but only the two of symmetry species F_2 can be observed in the IR spectrum at around 1100 [ν_{as}(S−O)] and 610 cm^{-1} [$\delta_{as}(SO_4)$], respectively. In the present case, the SO_4^{2-} ions exhibits only C_1 symmetry and a factor group splitting must also be assumed. Thus, many more bands may be found covering quite a wide range from 1284 down to 850 cm^{-1} [ν(S−O)] and from 651 to 453 cm^{-1} [$\delta(SO_4)$]. In particular, the symmetric stretching vibrations are shifted remarkably to lower wavenumbers compared with the values usually found for sulfates. This can be expected owing to the very long S−O distances of up to almost 155 pm. Such distances are more typical of hydrogensulfates (S−OH) and, for the latter, stretching vibrations around 870 cm^{-1} are not unusual.[14,15]

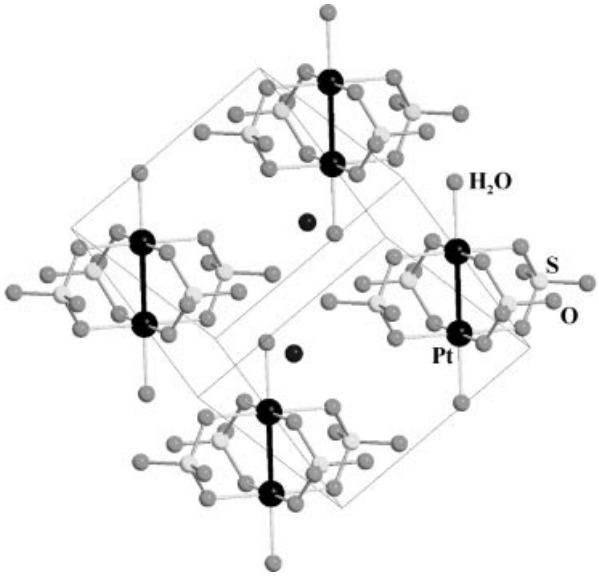

Figure 1. Crystal structure of $(NH_4)_2[Pt_2(SO_4)_4(H_2O)_2]$. The Pt−Pt distance within the lantern shaped complex anion is 246.3(1) pm.

The oxygen stoms of the water molecules (O1) in the axial positions of the Pt_2 dumbbell are at a distance of 209.9(11) pm from the platinum centres and the angle Pt−Pt′−O(1) is 179.3(4)°. According to the space group symmetry of the compound, the $[Pt_2(SO_4)_4(H_2O)_2]^{2-}$ anion should belong to the point group C_i with the inversion centre in the mid-point of the Pt−Pt bond but in fact it has nearly C_{4h} symmetry. The NH_4^+ ions which act as charge compensators are in ninefold coordination environments of oxygen atoms with the NH_4−O distances ranging from 282(2) up to 333(4) pm (Table 2). Besides the findings from the X-ray investigation, the presence of NH_4^+ is also clear from the IR spectra which display typical bands at 3245 cm^{-1} [ν(N−H)] and 1431 cm^{-1} [$\delta(NH_4)$].

The replacement of the axial water molecules in the $[Pt_2(SO_4)_4(H_2O)_2]^{2-}$ anion by monodentate SO_4^{2-} ions can be observed in the crystal structure of $K_4[Pt_2(SO_4)_5]$. This species can be obtained as orange prismatic single crystals from the reaction of $K_2[PtCl_4]$ with concentrated H_2SO_4. Like $(NH_4)_2[Pt_2(SO_4)_4(H_2O)_2]$, $K_4[Pt_2(SO_4)_5]$ is quite stable towards moisture but in contrast to the former, only slightly soluble in water. The four crystallographically different $[Pt_2(SO_4)_4]$ cores of the compound remain nearly unchanged compared with those in $(NH_4)_2[Pt_2(SO_4)_4(H_2O)_2]$. The respective Pt−O distances lie in the same range from 200.6(6) up to 202.6(5) pm and the sulfate groups also show the same significant bond length differences for coordinating ($d_{av.}$ = 143.3 pm) and noncoordinating oxygen atoms ($d_{av.}$ = 152.9 pm), respectively. Accordingly, the findings of the IR spectroscopic measurements (Table 5) are almost the same as those discussed for $(NH_4)_2[Pt_2(SO_4)_4(H_2O)_2]$.

The Pt−O distances to the axial oxygen atoms range from 211.0(5) up to 213.2(5) pm. These distances are slightly longer than observed in $(NH_4)_2[Pt_2(SO_4)_4(H_2O)_2]$. Furthermore, in contrast to the related angles mentioned previously, the Pt−Pt′−O angles in this species involving the axial oxygen atoms show slight but significant deviations from linearity with values between 171.9(1) and 173.7(1)°. The axial oxygen atoms belong to the sulfate groups $S(8)O_4^{2-}$ and $S(10)O_4^{2-}$. These anions link the $[Pt_2(SO_4)_4]$ units into two crystallographically different infinite chains according to the formula $^1_\infty[Pt_2(SO_4)_{4/1}(SO_4)_{2/2}]^{4-}$ (Figure 2) which are oriented in the [110] direction (Figure 3). The linking sulfate groups show the same characteristics as observed for the bidentate-bridging sulfate groups. Thus, the S−O distances to the oxygen atoms which are coordinated to the platinum atoms are about 10 pm longer than the respective values for the noncoordinating oxygen atoms. The charge compensation for the $^1_\infty[Pt_2(SO_4)_{4/1}(SO_4)_{2/2}]^{4-}$ chains is achieved by eight crystallographically different K^+ ions which show coordination numbers between 7 and 11 if distances up to 339.5(6) pm from these centres are taken into account (Table 3).

The linkage of $[Pt_2(SO_4)_4]$ units into layers can be seen in the crystal structure of $Cs[Pt_2(SO_4)_3(HSO_4)]$ which is formed from the reaction of $Cs_2[PtCl_4]$ and concentrated H_2SO_4. The plate-shaped red single crystals of

 © 2005 Wiley-VCH Verlag GmbH & Co. KGaA, Weinheim

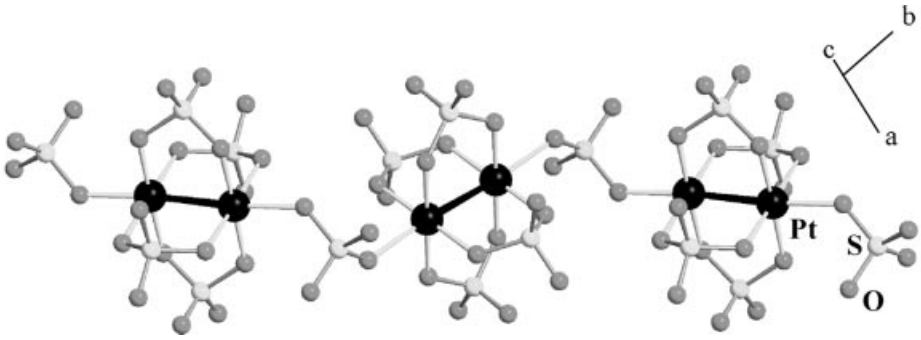

Figure 2. Connection of $[Pt_2(SO_4)_4]$ units via sulfate ions to anionic chains with the formula $^1_\infty[Pt_2(SO_4)_{4/1}(SO_4)_{2/2}]^{4-}$ in the crystal structure of $K_4[Pt_2(SO_4)_5]$. There are two crystallographically different chains which, however, do not differ significantly. The linking SO_4^{2-} ions act as bidentate bridging ligands and the O−S−O angles between their coordinated oxygen atoms and the sulfur atoms are 104.2(3)° and 108.4(3)°, respectively.

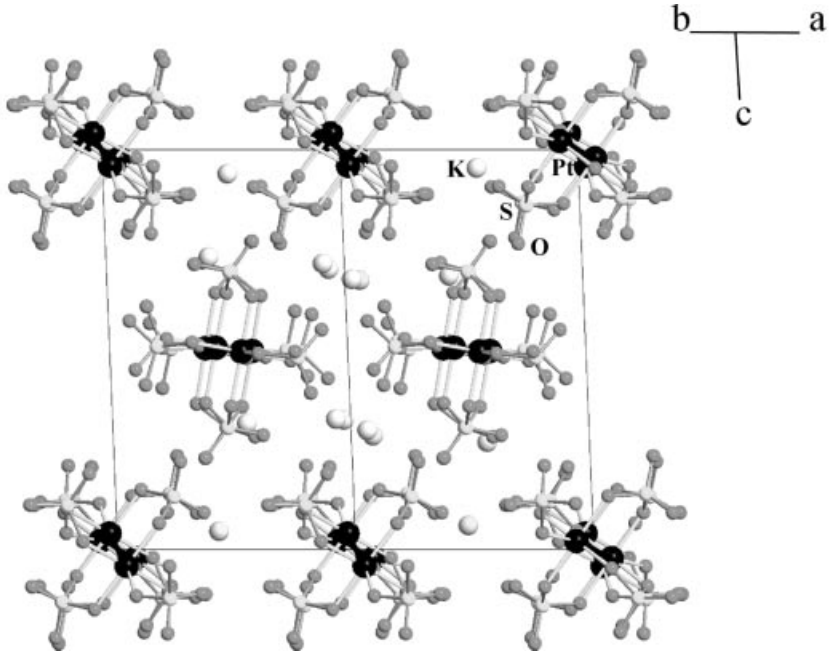

Figure 3. Arrangement of the $^1_\infty[Pt_2(SO_4)_{4/1}(SO_4)_{2/2}]^{4-}$ chains shown in Figure 2 along the [110] direction in the triclinic unit cell of $K_4[Pt_2(SO_4)_5]$. The K^+ ions take act as charge compensators and exhibit coordination numbers between 7 and 11.

$Cs[Pt_2(SO_4)_3(HSO_4)]$ are extremely moisture sensitive and turn immediately cloudy when exposed to air. As described for $K_4[Pt_2(SO_4)_5]$, the Pt_2^{6+} dumbbells in this compound are also coordinated by four bidentate-bridging and two monodentate tetrahedra. The Pt−O distances are comparable to those observed in $K_4[Pt_2(SO_4)_5]$ and lie between 199.2(4) and 202.0(4) pm for the bidentate-bridging ligands and at 212.2(4) and 215.6(4) pm for the monodentate ones (Table 4). In contrast to $K_4[Pt_2(SO_4)_5]$, the axial sulfate groups do not act as *monodentate* but as *bidentate-bridging* ligands towards further Pt_2^{6+} ions and, vice versa, two of the bidentate-bridging tetrahedra are monodentate towards neighbouring Pt_2 dumbbells. The remaining two bidentate-bridging tetrahedra are not bonded to further platinum atoms. The connection leads to layers as depicted in Figure 4. Two different layers can be distinguished crystallographically. One can be formulated as $^2_\infty[Pt_2(SO_4)_{4/2}(SO_4)_{2/1}]^{2-}$ while for the second, half of the tetrahedra can be clearly viewed as hydrogensulfate ions leading to neutral sheets with the composition $^2_\infty[Pt_2(SO_4)_{4/2}(HSO_4)_{2/1}]$. The identification of HSO_4^- ions can be carried out unambiguously with respect to the S−O distances which range from 140.7(4) up to 147.8(4) pm for the oxygen atoms which are not attached to platinum atoms and from 150.1(4) up to 152.7(4) pm for the Pt coordinated oxygen atoms. The only exception is O42 which shows a distance of 150.9(4) pm to the sulfur atom *without* being attached to a platinum atom itself. Furthermore, the hydrogen atom of the HSO_4^- ion can be found in the difference Fourier map. It is involved in a short hydrogen bond with O21 as the acceptor atom

 © 2005 Wiley-VCH Verlag GmbH & Co. KGaA, Weinheim

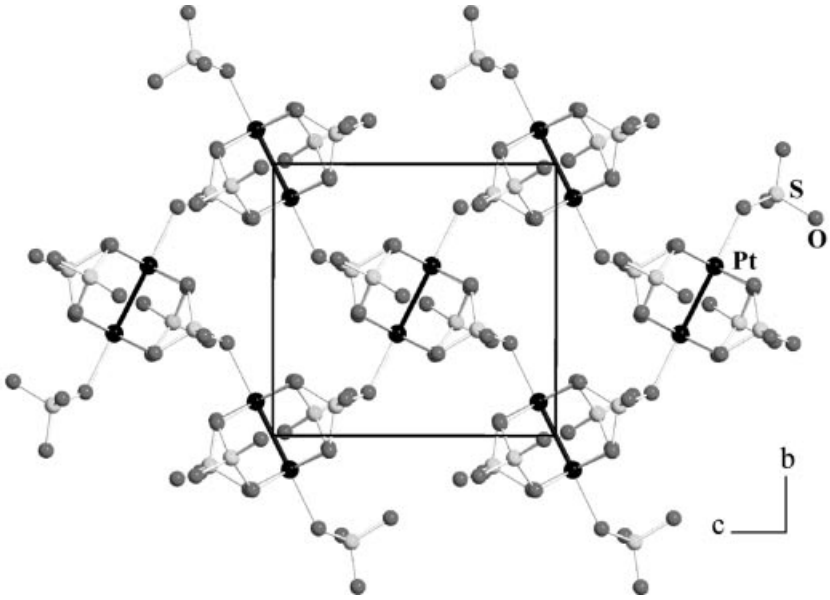

Figure 4. Connection of $[Pt_2(SO_4)_4]$ units by sulfate ions to anionic layers of forumla to $^2_\infty[Pt_2(SO_4)_{4/2}(SO_4)_{2/1}]^{2-}$ in the crystal structure of $Cs[Pt_2(SO_4)_3(HSO_4)]$. One half of the sulfate ions acts as bidentate-bridging ligands, the other half of them are bidentate-bridging to one Pt_2 dumbbell and monodentate to the next. In a second very similar layer, the two uniquely bidentate-bridging sulfate groups are replaced by HSO_4^- ions leading to neutral sheets with the composition $^2_\infty[Pt_2(SO_4)_{4/2}(HSO_4)_{2/1}]$.

with a short distance of 246.7(6) pm from O42 and an angle O42−H−O21 of 167(2)°. With respect to the donor−acceptor distance, the hydrogen bond can be classified as strong.[16,17] It is worthwhile pointing out that the observed O−H−O angle is relatively small for a strong hydrogen bond which usually show values around 180°. However, similar observations of other compounds have been made and a fairly recent neutron diffraction study on NaH_2PO_4 (donor−acceptor distance: 248.5 pm, angle O−H−O: 167.7°) may serve as an example.[17,18] Interestingly, the structural characteristics of the neutral $^2_\infty[Pt_2(SO_4)_{4/2}(HSO_4)_{2/1}]$ sheets are identical to those recently reported for $Pt_2(SO_4)_2(HSO_4)_2$.[12] Thus, the structure of $Cs[Pt_2(SO_4)_3(HSO_4)]$ might be described as a composite of $Pt_2(SO_4)_2(HSO_4)_2$ and the hitherto unknown sulfate $Cs_2[Pt_2(SO_4)_4]$. The neutral and anionic layers are stacked in the [100] direction and alternate with the Cs^+ ions (Figure 5). The latter are in tenfold coordination environments of oxygen atoms with the Cs−O distances ranging from 295.2(4) up to 366.9(5) (Table 4).

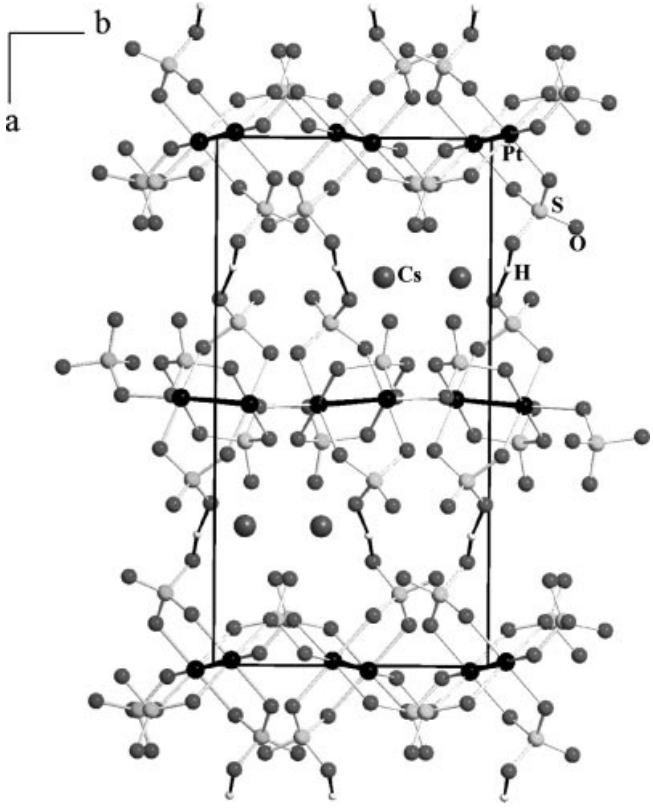

Figure 5. Stacking of the two different layers in the crystal structure of $Cs[Pt_2(SO_4)_3(HSO_4)]$ along the [100] direction. The layers are connected by Cs^+ ions in tenfold coordination environments of oxygen atoms and short hydrogen bonds with a donor (O42) acceptor (O21) distance of 246.7(6) pm.

Experimental Section

Synthesis: All reactions were carried out in sealed thick-walled (2 mm) glass ampoules (ϕ = 10 mm, l = 100 mm) which were placed in a resistance furnace at a temperature of 400 °C. In all cases 2 mL (37.31 mmol) of concentrated sulfuric acid were used. For the synthesis of $(NH_4)_2[Pt_2(SO_4)_4(H_2O)_2]$ the platinum source was $Pt(NO_3)_2$ (0.7 g, 5.59 mmol, ABCR, 99.99%) which was used as purchased. For the preparation of $K_4[Pt_2(SO_4)_5]$ and $Cs[Pt_2(SO_4)_3(HSO_4)]$ $K_2[PtCl_4]$ (0.5 g, 1.20 mmol) and $Cs_2[PtCl_4]$ (0.5 g, 0.83 mmol), respectively, were used in the reactions. $K_2[PtCl_4]$ was synthesised from elemental platinum according to literature procedures.[19] $Cs_2[PtCl_4]$ cannot be obtained in the same way due to the very low solubility of $Cs_2[PtCl_6]$. Instead, it was precipitated from a solution of $H_2[PtCl_4]$ which was obtained by reducing $H_2[PtCl_6]$ with $(N_2H_6)Cl_2$. The preparation of $H_2[PtCl_6]$

 © 2005 Wiley-VCH Verlag GmbH & Co. KGaA, Weinheim

Table 1. Crystal data and structure refinements

Compound	$(NH_4)_2[Pt_2(SO_4)_4(H_2O)_2]$	$K_4[Pt_2(SO_4)_5]$	$Cs[Pt_2(SO_4)_3(HSO_4)]$
Lattice constants	a = 749.96 (9) pm	a = 975.6 (1) pm	a = 1724.8 (2) pm
	b = 754.2 (1) pm	b = 1331.8 (1) pm	b = 881.28 (9) pm
	c = 765.4 (1) pm	c = 1491.0 (1) pm	c = 935.1 (1) pm
	α = 102.15 (1)°	α = 101.156 (8)°	
	β = 110.23 (1)°	β = 96.278 (8)°	β = 100.397 (8)°
	γ = 100.87 (1)°	γ = 102.849 (8)°	
Cell volume	380.67(8) Å^3	1829.3(3) Å^3	1398.1(2) Å^3
No. of formula units	1	2	4
Crystal system	triclinic	triclinic	monoclinic
Space group	$P\bar{1}$ (no.1)	$P\bar{1}$ (no.1)	$P2_1/c$ (no. 14)
Diffractometer	Stoe IPDS II	Stoe IPDS II	Stoe IPDS II
Radiation	Mo-K_α (graphite-monochromated, λ = 71.07 pm)		
Temperature	293K		
Theta range	5° < 2θ <56°	5° < 2θ < 56°	5° < 2θ <56°
Rotation range; ~ increment	0° < ω < 180°; 2°	0° < ω < 180°	0° < ω < 180°
φ-Positions	0°, 90°	0°, 90°, 135°	0°, 90°
Index range	$-9 \le h \le 9$	$-12 \le h \le 12$	$-22 \le h \le 22$
	$-8 \le k \le 8$	$-17 \le k \le 17$	$-11 \le k \le 11$
	$-9 \le l \le 10$	$-19 \le l \le 19$	$-12 \le l \le 12$
No. of images	180	270	180
Exposure time	5 min	1 min	3 min
Detector distance	80 mm	80 mm	80 mm
Absorption correction	numerical after crystal shape optimisation[9]		
μ	19.01 mm^{-1}	16.86 mm^{-1}	23.24 mm^{-1}
Measured reflections	3497	24347	13324
Unique reflections	1667	8830	3383
With $I_o > 2\sigma$ (I)	1302	6882	2971
No. of parameters	119	560	213
$R_{int.}/R_\sigma$	0.0794/0.1084	0.0623/0.0544	0.0507/0.0327
Structure determinations	SHELXS-97 and SHELXL-97[10][11]		
Scattering factors	Intern. Tables, Vol. C		
Goodness of fit	0.962	0.933	1.039
Extinction coefficient	0.007(2)	0.00066(4)	0.00104(5)
$R1$; $wR2$ [$I_o > 2\sigma(I_o)$]	0.0481; 0.1095	0.0311; 0.0678	0.0232; 0.0299
$R1$; $wR2$ (all data)	0.0677; 0.1196	0.0459; 0.0719	0.0458; 0.0473
ICSD	414037	414039	414038

is well-known.[19] $(NH_4)_2[Pt_2(SO_4)_4(H_2O)_2]$ crystallises in the form of yellow plates which can be easily separated from the deep red single crystals of $(NH_4)_4[Pt_{12}O_8(SO_4)_{12}]$ which are formed in the same reaction.[13] $(NH_4)_2[Pt_2(SO_4)_4(H_2O)_2]$ is the minor product of the reaction and the yield is about 20% with respect to the initial nitrate. With respect to the X-ray powder patterns of the products, the other two compounds are the only phases to be formed in the reactions. They were obtained in a 50% yield with respect to the initial chlorides. The single crystals of $K_4[Pt_2(SO_4)_5]$ and $(NH_4)_2[Pt_2(SO_4)_4(H_2O)_2]$ can be handled under ambient conditions while $Cs[Pt_2(SO_4)_3(HSO_4)]$ is extremely moisture sensitive.

X-ray Diffraction: Several single crystals of each compound were selected under sodium dried paraffin and mounted in glass capillaries. Their quality was checked with the help of a precession camera equipped with an image plate system. For the best specimens, intensity data were collected with an image plate diffractometer (STOE IPDS II). A numerical absorption correction was applied to the data using the programs X-SHAPE and X-RED in each case.[20,21] The solutions of the crystal structures were successful using direct methods provided by the program SHELXS-97.[22] For the refinements of the structures the program SHELXL-97[23] was used, introducing anisotropic thermal parameters for all nonhydrogen atoms. The position of the H atom in $Cs[Pt_2(SO_4)_3(HSO_4)]$ was observed in the final difference Fourier map. It was refined isotropically without restrains. Further details of the data collection and relevant crystallographic data are summarised in Table 1−4. Furthermore, the data have been deposited with the Fach-

Table 2. Selected distances (pm) and angles (°) in $(NH_4)_2[Pt_2(SO_4)_4(H_2O)_2]$ (# symmetry transformation for equivalent atoms: $-x$, $-y$, $-z$)

Pt−O11	199.4(12)	S1−O13	142.5(11)
−O24	200.6(9)	−O14	143.7(13)
−O12	200.9(13)	−O12	151.5(15)
−O23	200.9(10)	−O11	154.7(11)
−O1	209.9(11)		
		S2−O22	142.1(15)
Pt−Pt#	246.3(1)	−O21	144.3(12)
		−O24	151.2(11)
N−O22	282(2)	−O23	154.7(13)
−O13	286(2)		
−O14	287(2)	Pt−Pt#−O1	179.3(4)
−O13	292(2)		
−O21	295(2)		
−O11	297(2)		
−O14	306(3)		
−O23	309(3)		
−O21	333(4)		

 © 2005 Wiley-VCH Verlag GmbH & Co. KGaA, Weinheim

Table 3. Selected distances (pm) and angles (°) in $K_4[Pt_2(SO_4)_5]$ ($^{\#}$symmetry transformation for equivalent atoms: $-x, -y, -z$)

Pt1−O62	200.8(5)	Pt2−O21	200.6(6)
−O34	201.8(5)	−O91	201.4(6)
−O31	201.9(5)	−O22	201.4(5)
−O61	202.6(5)	−O92	202.2(6)
−O83	211.0(5)	−O102	213.2(5)
Pt1−Pt1$^{\#}$	247.60(6)	Pt2−Pt2$^{\#}$	248.02(6)
Pt1−Pt1$^{\#}$−O83	172.6(2)	Pt2−Pt2$^{\#}$−O102	171.9(1)
Pt3−O72	201.0(5)	Pt4−O42	201.5(5)
−O71	201.3(5)	−O13	201.7(5)
−O52	201.3(5)	−O41	202.0(5)
−O51	201.4(5)	−O11	202.0(5)
−O82	211.0(5)	−O101	212.7(4)
Pt3−Pt3$^{\#}$	247.62(6)	Pt4−Pt4$^{\#}$	248.96(6)
Pt3−Pt3$^{\#}$−O82	173.6(2)	Pt4−Pt4$^{\#}$−O101	173.7(1)
S1−O12	143.8(6)	S2−O24	142.5(7)
−O14	144.1(6)	−O23	144.1(7)
−O13	152.3(5)	−O21	151.9(6)
−O11	153.1(5)	−O22	152.4(6)
S3−O32	142.8(6)	S4−O44	142.9(6)
−O33	143.1(5)	−O43	143.3(6)
−O31	152.3(6)	−O41	153.0(5)
−O34	154.2(5)	−O42	153.2(5)
S5−O53	142.8(6)	S6−O64	142.9(7)
−O54	143.4(6)	−O63	143.7(6)
−O51	151.8(6)	−O61	152.2(6)
−O52	153.4(5)	−O62	154.3(6)
S7−O73	143.1(6)	S8−O81	139.6(8)
−O74	144.2(7)	−O84	143.7(6)
−O72	151.8(6)	−O82	149.4(6)
−O71	153.5(5)	−O83	150.4(5)
S9−O94	142.1(7)	S10−O103	144.0(6)
−O93	143.3(6)	−O104	144.8(5)
−O91	153.0(6)	−O102	150.5(5)
−O92	153.4(6)	−O101	151.2(5)
K1−O73	261.8(6)	K2−O24	260.1(7)
−O44	275.5(6)	−O53	271.4(6)
−O102	275.8(6)	−O32	274.6(6)
−O103	278.9(6)	−O33	286.7(6)
−O103	282.2(6)	−O34	291.5(6)
−O13	288.9(6)	−O93	292.9(8)
−O14	290.1(7)	−O62	304.1(6)
		−O83	329.7(6)
		−O92	333.3(7)
K3−O104	267.1(7)	K4−O93	283.3(8)
−O43	278.6(7)	−O23	294.3(7)
−O33	280.1(6)	−O72	301.3(5)
−O61	283.6(5)	−O14	305.2(6)
−O63	289.5(7)	−O31	309.1(6)
−O71	291.2(6)	−O94	315.6(8)
−O51	294.1(6)	−O62	322.1(6)
−O74	303.5(6)	−O83	325.2(7)
−O82	323.2(7)	−O82	327.2(8)
−O103	335.2(6)	−O84	329.3(10)
		−O64	332.2(7)
K5−O14	282.0(6)	K6−O73	276.4(7)
−O23	282.1(7)	−O12	277.4(7)
−O94	289.2(7)	−O53	279.1(7)
−O11	293.9(6)	−O84	282.0(7)
−O63	295.2(7)	−O24	283.5(7)
−O23	308.3(7)	−O43	297.2(7)
−O22	311.5(7)	−O71	300.9(6)
−O64	326.7(7)		
−O44	326.9(7)		
−O94	328.3(7)		
K7−O104	266.6(7)	K8−O81	256.0(8)
−O54	266.9(6)	−O12	268.6(6)
−O64	272.0(7)	−O84	275.5(7)
−O32	278.6(6)	−O54	282.2(6)
−O101	297.7(5)	−O74	286.6(7)
−O34	305.7(5)	−O13	327.5(6)
−O33	330.8(6)	−O43	336.1(7)
−O92	339.5(6)		

Table 4. Selected distances (pm) and angles (°) in $Cs[Pt_2(SO_4)_3(HSO_4)]$ ($^{\#}$symmetry transformation for equivalent atoms: $-x, -y, -z$)

Pt1−O12	199.2(4)	Pt2−O44	200.0(4)
−O23	200.6(4)	−O43	200.7(4)
−O11	201.1(4)	−O34	201.1(4)
−O22	202.0(4)	−O33	201.4(4)
−O14	212.2(4)	−O31	215.6(4)
Pt1−Pt1$^{\#}$	246.84(4)	Pt2−Pt2$^{\#}$	247.66(4)
Pt1−Pt1$^{\#}$−O14	177.7(1)	Pt2−Pt2$^{\#}$−O31	176.6(1)
S1−O13	143.5(4)	S2−O24	143.0(4)
−O14	147.8(4)	−O21	146.8(5)
−O12	150.1(4)	−O22	152.3(4)
−O11	152.7(4)	−O23	152.4(4)
S3−O32	143.2(4)	S4−O41	140.7(4)
−O31	147.6(4)	−O43	150.9(4)
−O34	151.7(4)	−O42	150.9(4)
−O33	152.2(4)	−O44	151.8(4)
Cs−O13	295.2(4)	Hydrogen bonds	
−O24	309.9(4)	O42−H	101(15)
−O32	311.3(4)	O21−H	146(15)
−O41	313.6(4)	O42−O21	246.7(6)
−O32	318.2(4)	O42−H−O21	167(2)
−O11	327.7(4)		
−O22	335.5(3)		
−O13	338.7(4)		
−O33	345.9(4)		
−O21	366.9(5)		

Table 5. IR bands (cm^{-1}) and their assignments for $(NH_4)_2[Pt_2(SO_4)_4(H_2O)_2]$ and $K_4[Pt_2(SO_4)_5]$

Assignment	$(NH_4)_2[Pt_2(SO_4)_4(H_2O)_2]$	$K_4[Pt_2(SO_4)_5]$
ν(O−H)	3405 (s)	
ν(N−H)	3245 (s)	
δ(H_2O)	1656 (ms)	
δ(NH_4)	1431 (ms)	
ν_{as}(S−O)	1284 (s), 1232 (ms), 1170 (vs)	1291 (s), 1249 (ms), 1169 (vs)
ν_s(S−O)	1070 (s), 1006 (s), 855 (s), 850 (s)	1069 (s), 1005 (vs), 961 (w), 891 (s), 851 (ms)
δ_{as}(SO_4)	651 (w), 613 (w) 576 (vs)	675 (w), 649 (w), 582 (s)
δ_s(SO_4)	503 (w), 453 (ms)	499 (w), 454 (ms)

informationzentrum Karlsruhe, 76344 Eggenstein-Leopoldshafen (crysdata@FIZ-Karlsruhe.de) and are available on quoting the deposition numbers given in Table 1.

IR Spectroscopy: For the collection of IR data several single crystals of $(NH_4)_2[Pt_2(SO_4)_4(H_2O)_2]$ and $K_4[Pt_2(SO_4)_5]$ were selected and prepared in KBr pellets. No IR data for $Cs[Pt_2(SO_4)_3(HSO_4)]$ could be gained due its extreme moisture sensitivity. Data collection was performed with a Bruker IFS66v/s IR spectrometer in the range from 400 to 4000 cm^{-1}. Data are summarised in Table 5.

Acknowledgments

The support of Prof. Dr. G. Meyer, Universität zu Köln and the Deutsche Forschungsgemeinschaft (Graduiertenkolleg 549) is gratefully acknowledged.

[1] G. S. Muraveiskaya, V. S. Orlova, O.N. Evstaf'eva, *Russ. J. Inorg. Chem.* **1974**, *19*, 1030.
[2] G. S. Muraveiskaya, G. A. Kukina, V. S. Orlova, O. N. Ev-

 © 2005 Wiley-VCH Verlag GmbH & Co. KGaA, Weinheim

staf′eva, M. A. Porai-Koshits, *Dokl. Akad. Nauk SSSR* **1976**, *226*, 596.
[3] D. P. Bancroft, F. A. Cotton, L. R. Falvello, S. Han, W. Schwotzer, *Inorg. Chim. Acta* **1984**, *87*, 147.
[4] F. A. Cotton, L. R. Falvello, S. Han, *Inorg. Chem.* **1982**, *21*, 2889.
[5] H. L. Conder, F. A. Cotton, L. R. Falvello, S. Han, R. A. Walton, *Inorg. Chem.* **1983**, *22*, 1887.
[6] A. Zipp, *Coord. Chem. Rev.* **1988**, *84*, 47.
[7] J. D. Woollins, P. F. Kelly, *Coord. Chem. Rev.* **1985**, *65*, 115.
[8] D. M. Roundhill, H. B. Gray, C.-M. Che, *Acc. Chem. Res.* **1989**, *22*, 55.
[9] R. El-Mehdawi, F. R. Fronczek, D. M. Roundhill, *Inorg. Chem.* **1986**, *25*, 1155.
[10] R. J. H. Clark, *Chem. Soc., Rev.* **1990**, *19*, 107.
[11] V. S. Orlova, G. S. Muraveiskaya, O.N. Evstaf′eva, *Russ. J. Inorg. Chem.* **1975**, *20*, 753.
[12] M. Pley, M. S. Wickleder, *Z. Anorg. Allg. Chem.* **2004**, *630*, 1036.
[13] M. Pley, M. S. Wickleder, *Angew. Chem.* **2004**, *116*, 4262; *Angew. Chem. Int. Ed.* **2004**, *43*, 4168.
[14] J. Weidlein, U. Müller, K. Dehnicke, *Schwingungsspektroskopie*, Georg Thieme Verlag, Stuttgart, New York **1988**.
[15] J. Weidlein, U. Müller, K. Dehnicke, *Schwingungsfrequenzen I, Hauptgruppenelemente*, Georg Thieme Verlag Stuttgart, New York **1981**.
[16] Th. Steiner, *Angew. Chem.* **2002**, *114*, 50; *Angew. Chem. Int. Ed.* **2002**, *41*, 48.
[17] G. A. Jeffrey, *An Introduction to Hydrogen Bonding*, Oxford University Press, Oxford, **1997**.
[18] R.N.P. Choudhary, R.J. Nelmes, K.D. Rouse, *Chem. Phys. Lett.* **1981**, *78*, 102.
[19] G. Brauer, *Handbuch der Präparativen Anorganischen Chemie*, F. Enke Verlag, Stuttgart **1975**.
[20] Fa. STOE & Cie, X-RED 1.07, Data Reduction for STADI4 and IPDS, Darmstadt **1996**.
[21] Fa. STOE & Cie, X-SHAPE 1.01, Crystal Optimisation for Numerical Absorption Correction, Darmstadt **1996**.
[22] G. M. Sheldrick, SHELXS-97, *Program for the Solution of Crystal Structures*, Göttingen **1997**.
[23] G. M. Sheldrick, SHELXL-97, *Program for Crystal Structure Refinement*, Göttingen **1997**.

Received September 13, 2004
Early View Article
Published Online December 13, 2004

 © 2005 Wiley-VCH Verlag GmbH & Co. KGaA, Weinheim

A New Organic-Inorganic Hybrid Gallophosphate Prepared in the Presence of Glycine

Mohammed Abdelkrim Hasnaoui,[a,c] Angélique Simon-Masseron,*[a] Volker Gramlich,[b] Joël Patarin,[a] and Abdelkader Bengueddach[c]

Keywords: Gallium / Gallophosphate / Glycine / Hydrothermal synthesis / Fluorides

A new layered gallophosphate, $Ga_4P_4O_{16}(C_2H_5NO_2)_4$, known as Mu-32 has been synthesised hydrothermally using the amino acid glycine ($H_2NCH_2CO_2H$) as an original template. Such a template has never been used before for the synthesis of microporous and phosphate-based materials such as gallophosphates. The structure was determined by a single-crystal X-ray diffraction study and further characterised by scanning electron microscopy, elemental and thermal analyses and by ^{13}C and ^{31}P solid-state NMR spectroscopy. The compound crystallises in the monoclinic space group $P2_1/c$ with a = 9.177(2), b = 5.1540(10), c = 12.513(3) Å and β = 90.67(3)°. The inorganic layer is built up from four-membered rings sharing T–O–T bonds. In addition to the nature of the template, the original properties of this new gallophosphate come from the coordination environment of the Ga which is only pentacoordinated with oxygen atoms and has strong bonds (Ga–O–C) between the organic template and the inorganic sheet.
(© Wiley-VCH Verlag GmbH & Co. KGaA, 69451 Weinheim, Germany, 2005)

Introduction

During the last decade, extensive investigations by numerous researchers have given rise to many new open-framework materials.[1] Among these, the aluminophosphates,[2−6] gallophosphates[7−13] and zincophosphates[14−18] appear to be the most studied. These materials are typically synthesised under hydrothermal or solvothermal conditions in the presence of various organic amines as structure-directing agents. In several cases, the introduction of fluoride ions is crucial for the formation of the phosphate-based material.[19] F^- can act as a mineraliser, it can become trapped in the cages of the framework playing a templating role as shown in the fluorogallophosphate cloverite[20] or it may form a bridge between the atoms of the framework.[21] The amine molecules occupy the cavities or the channels of the framework and are usually removed by calcination of the synthesised sample. Most of the time, the organic molecules are hydrogen-bonded to the inorganic framework. They can also be directly linked to the inorganic structure via T−N or T−O−C bonds (T = Al, Zn,Ga, ...).[22,23] Such connections can be found, for instance, in the oxalate-phosphate[24,25] and -phosphonate systems where a P atom is directly linked to the carbon atom in PO_3R.[26−28] Aluminophosphates and gallophosphates showing such organic-inorganic bonds are rarely encountered. However, the use of the cyclam molecule (1,4,8,11-tetraazacyclotetradecane) as a structure-directing agent in these systems induces the crystallisation of such compounds (STA-6,[29] Cyclam-Co-$AlPO_4$,[30] Mu-5[31] and Mu-6[32]). It was shown, in the $AlPO_4$-SOD material synthesised in the presence of dimethylformamide, that the organic template is bonded to the inorganic framework via Al−O−C bonds.[33] More recently, bipyridine-gallophosphate hybrid materials have also been obtained.[34,35] In these compounds, Ga−N, F−N or Ga−O−Co−cyclam bonds have been revealed. The majority of the open-framework metal phosphates were synthesised in the presence of amines. To the best of our knowledge, there are no open-framework metal phosphates which have been prepared with bifunctional molecules such as amino acids (NH_2−R−COOH) as structure-directing agents.

In this paper, we describe the structure of a new layered gallophosphate, Mu-32, prepared with the amino acid glycine as an organic template. Its characterisation by thermal analysis, scanning electron microscopy and solid-state NMR spectroscopy is also reported.

[a] Laboratoire de Matériaux Minéraux CNRS UMR 7016, ENSCMu, Université de Haute Alsace,
3 rue Alfred Werner, 68093 Mulhouse Cedex, France
Fax: (internat.) + 33-3-89336885
E-mail: Angelique.Simon-Masseron@uha.fr
[b] Laboratory of Crystallography, ETH-Zentrum
8092 Zürich, Switzerland
[c] Laboratoire de Chimie des Matériaux, Université d'Oran,
B. P. 1524, El M'Nouar Es Senia, Oran, Algeria

 © 2005 Wiley-VCH Verlag GmbH & Co. KGaA, Weinheim **DOI: 10.1002/ejic.200400392**

Results and Discussion

Synthesis and Crystal Morphology

The most characteristic synthetic results are summarised in Table 1. It has been shown that strongly acidic media are unfavourable for the formation of the gallophosphate Mu-32. Indeed a starting mixture with a pH of 1 induces the formation of a material called the "S phase" which is related to the mineral strengite (sample A, Table 1). Therefore TriPA was added in order to increase the initial pH to ca. 4−5.

With a TriPA/Ga_2O_3 molar ratio of 1.5 at 130 °C, the strengite phase crystallises (sample B, Table 1). It was necessary to increase the temperature to 170 °C in order to obtain large crystals of pure Mu-32 (sample C, Table 1). The influence of the gallium source was also studied. Instead of β-Ga_2O_3, the use of GaOOH (prepared by heating a gallium nitrate solution at 250 °C for 24 h) induces formation of larger crystals of Mu-32 but in this case, traces of an impurity can also be detected by XRD (sample D, Table 1). It should be noted that the presence of fluoride ions is of prime importance for the formation of Mu-32. They act as catalysts since their presence cannot be detected in the finally prepared material. On the other hand, β-Ga_2O_3 (sample E, Table 1) or a quartz-type gallophosphate is obtained (sample F, Table 1) in the absence of fluoride anions under similar reaction conditions and pH. Large crystals of Mu-32 display a hexagonal prismatic morphology as shown in Figure 1. Their average sizes are 150 × 830 × 980 μm.

The experimental XRD pattern of Mu-32 is reported in Figure 2 (a). For comparison, the simulated pattern calculated from the structural data is given in Figure 2 (b).

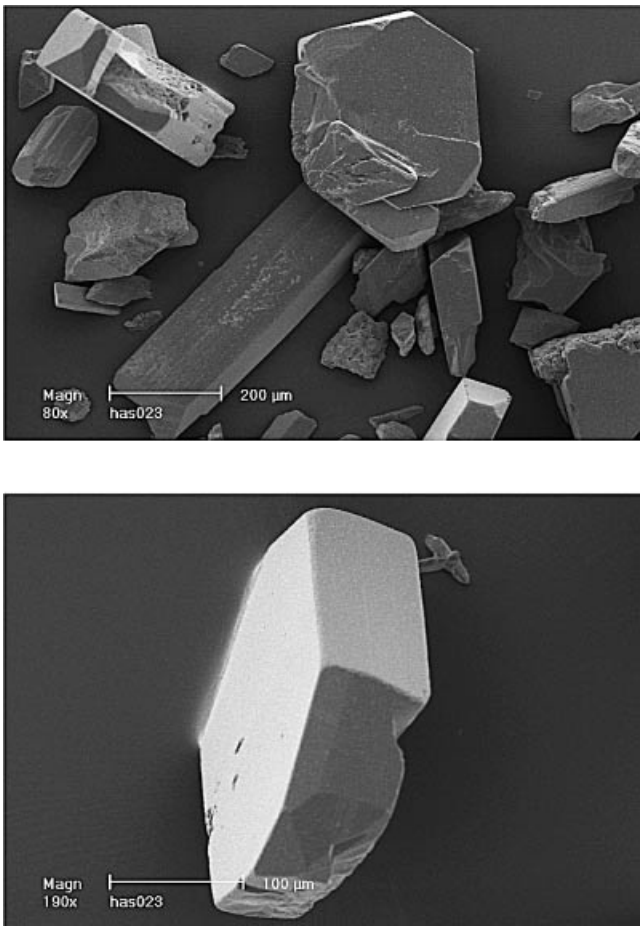

Figure 1. Scanning electron micrographs of some crystals of the gallophosphate Mu-32

Chemical Formula Determination

According to the microprobe and chemical analyses, the synthesised Mu-32 sample has Ga/P and C/N molar ratios close to 1 (Ga/P exp = 1.06) and 2 (C/N exp = 2.08), respectively. No fluoride was detected by scanning electron microprobe analysis.

The thermal behaviour of Mu-32 was investigated by TG/DTA thermal analyses. The TG and DTA curves of the material are given in Figure 3. The total weight loss occurs in two steps. The first occurs between 380 and 480 °C (23.8 wt%) and the second between ca. 480 °C and 1100 °C (3.8 wt%). The first weight loss is associated with the oxidation of the template (exothermic component on the DTA curve), consistent with the structure determination (weight loss expected: 27 wt%) and with a collapsing of the structure. The latter was confirmed by XRD analyses (not reported) recorded on an Mu-32 sample previously heated to 450 °C and by the presence in the DTA curve (reproducible) of an endotherm at about 450 °C. The second weight loss may correspond to dehydroxylation reactions including hydroxyl groups probably formed during the oxidation of the template by cleavage of the C(1)−O(3)−Ga(1) bonds (see struc-

Table 1. Synthesis performed using the system $Ga_2O_3/P_2O_5/x$HF/yTriPA/160H_2O

Sample	Composition of the starting gel		Crystallisation time [d]	Temp. [°C]	XRD results
	xHF	yTriPA [a]			
A	1	0	7	170	S phase[b]
B	1	1.5	7	130	S phase[b]
C	1	1.5	3	170	Mu-32
D[c]	1	1.5	7	170	Mu-32 + impurity[d]
E	0	0	7	170	β-Ga_2O_3
F	0	1.5	6	170	$GaPO_4$ quartz

[a] TriPA= tripropylamine (pH modifier). [b] Isostructural to the mineral strengite [(Fe,Al)PO_4·2H_2O, ICDD 15-0391]. [c] Gallium source: gallium oxyhydroxide, GaOOH. [d] Not identified, traces.

 © 2005 Wiley-VCH Verlag GmbH & Co. KGaA, Weinheim

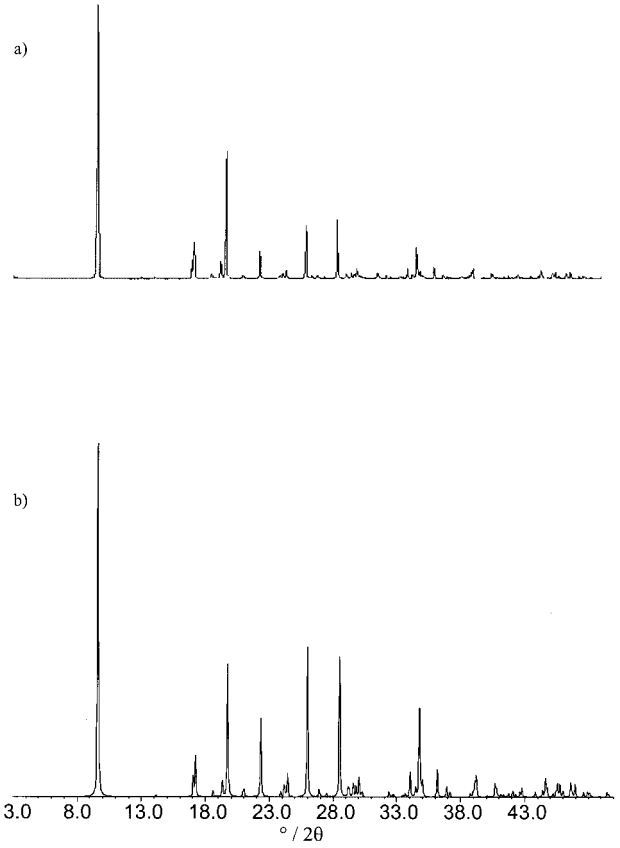

Figure 2. Experimental (a) and calculated (from crystal data) (b) XRD patterns of the gallophosphate Mu-32

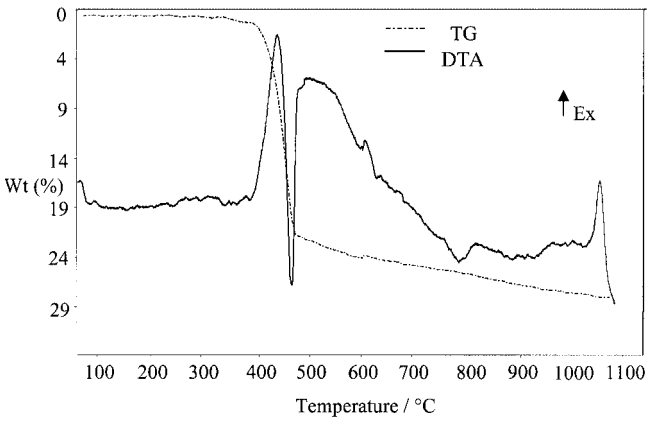

Figure 3. Thermal analyses (TG and DTA) of the gallophosphate Mu-32 under air

ture determination). After heating to 1000 °C, the XRD pattern of the sample showed that a cristobalite-type gallophosphate was formed (ICDD 89-3606). Its formation might also be the cause of the exothermic signal on the DTA curve at about 1050 °C. Taking into account the results of these analyses, the following unit cell formula can be proposed for the gallophosphate Mu-32: $Ga_4P_4O_{16}$-$(C_2H_5NO_2)_4$.

Structure Description

The framework of Mu-32 exhibits only four-membered rings formed by the alternation of Ga-centred trigonal pyramids (GaO_5) with P-centred tetrahedra (PO_4). This alternating pattern leads to the formation of an inorganic sheet parallel to the *bc* plane [Figure 4 (a)].

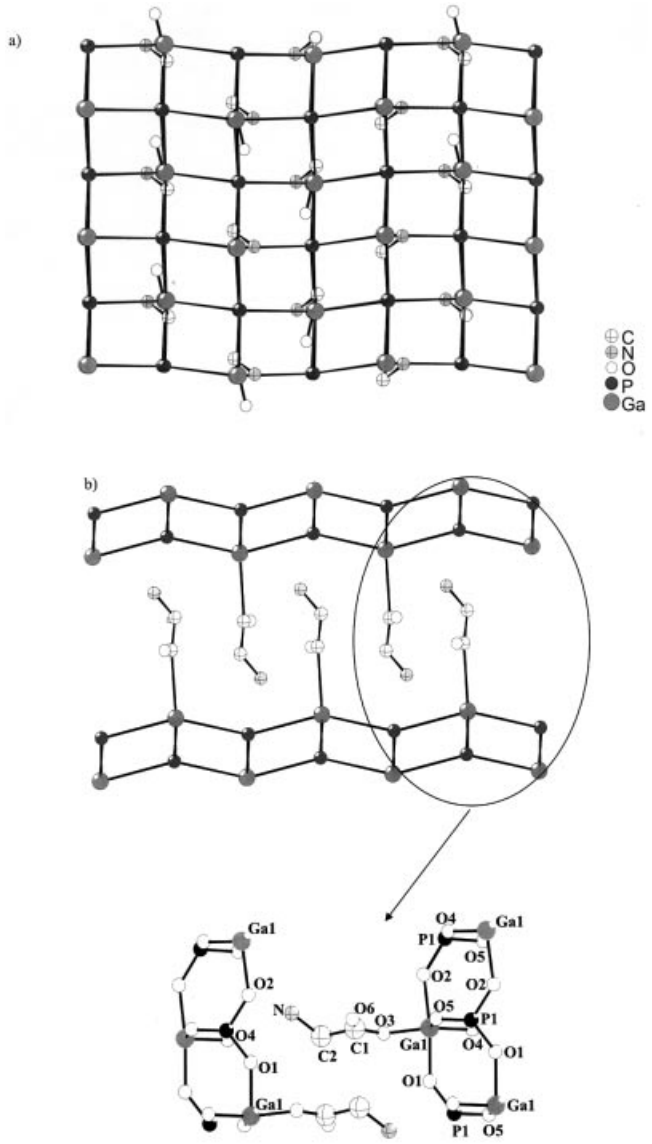

Figure 4. View along the [100] (a) and the [010] directions (b) of the framework of the gallophosphate Mu-32; oxygen atoms of the inorganic sheet are omitted for clarity

The most striking feature of this structure is the coordination sphere of each gallium atom. They are in pentacoordinate environments of oxygen atoms. Four oxygen atoms are shared with P-centred tetrahedra and the remaining one comes from the glycine template. The inorganic sheet interacts with the template via a hydrogen bond between its nitrogen atom and the O2 framework oxygen (bond length N···O2 = 2.821 Å) but also via a strong bond between its O3 oxygen (from OH group in the free glycine molecule) and the gallium atom of the inorganic layer (bond length

 © 2005 Wiley-VCH Verlag GmbH & Co. KGaA, Weinheim

O3···Ga1 = 1.913 Å) [Figure 4 (b)]. A bond valence calculation[36] performed on this O3 oxygen atom shows clearly that it corresponds to an oxygen atom and not to an OH group (Σs = 2.02, Table 2). The trigonal-pyramidal GaO_5 is quite regular since its angles, shown in Table 3, are close to the expected values of 90°, 120° and 180°. Nevertheless, it should be noted that the axial bonds of the pyramids, i.e. Ga1−O1 and Ga1−O2, are relatively longer than the equatorial ones, Ga1−O3, Ga1−O4 and Ga1−O5. In addition, the equatorial bond length Ga1−O3 is slightly longer than Ga−O4 and Ga−O5 since O3 bridges the gallium to the carbon atom C1. The phosphorus tetrahedra are quite regular with O−P−O angles in the range of 105.3(3)−111.9(3)°.

Table 2. Bond valence analysis of the gallophosphate Mu-32, according to Brown;[36] the results refer to the equation: $s = \exp[(R_0 - d)/B]$ with d = experimental distance, R_0 = 1.62, B = 0.36 for P−O and R_0 = 1.73, B = 0.38 for Ga−O; for C−O, $s = (d/R_0)^{-N}$ with R_0 = 1.37 and N = 4.4

Atoms	Ga1	P1	C1	Σs	Expected valence
O5	0.68	1.27		1.95	2
O4	0.67	1.22		1.89	2
O3	0.61		1.40	2.02	2
O2	0.55	1.29		1.84	2
O1	0.59	1.27		1.86	2
Σs	3.1	5.05			
Expected valence	3	5			

Table 3. Selected angles [°] in the gallophosphate Mu-32 (symmetry transformation used to generate equivalent atoms; #1: x, 0.5 − y, 0.5 + z; #2: $-x$, $-y$, 1 − z; #3: − x, 1 − y, 1 − z; #4: x, 0.5 − y, −0.5 + z

O5−Ga1−O4	114.46(9)	O1−P1−O4#3	110.81(12)
O5−Ga1−O3	123.88(10)	O2#1−P1−O4#3	108.51(12)
O4−Ga1−O3	121.63(10)	O5#2−P1−O4#3	108.49(13)
O5−Ga1−O1	93.09(10)	P1−O1−Ga1	134.87(16)
O4−Ga1−O1	91.81(11)	P1#4−O2−Ga1	137.77(16)
O3−Ga1−O1	87.18(11)	C1−O3−Ga1	121.73(25)
O5−Ga1−O2	91.06(10)	P1#3−O4−Ga1	134.98(13)
O4−Ga1−O2	91.86(11)	P1#2−O5−Ga1	128.31(14)
O3−Ga1−O2	85.59(11)	N−C2−C1	109.75(29)
O1−Ga1−O2	172.77(11)	O6−C1−O3	126.31(31)
O1−P1−O2#1	105.34(14)	O6−C1−C2	119.3(3)
O1−P1−O5#2	111.72(14)	O3−C1−C2	114.37(32)
O2#1−P1−O5#2	111.92(14)		

The structure of Mu-32 can be compared with that of the fluorogallophosphate ULM-9.[37] Although these 2D structures have different crystallographic data, they do have similar frameworks. Besides the conditions for their synthesis (structure-directing agent, ...), a difference can be observed in one of the equatorial bonds of the pentacoordinate gallium atom: the Ga−O−C bonds in Mu-32 are replaced by $Ga-F_{terminal}$ bonds in ULM-9.

NMR Spectroscopy

The ^{13}C CP MAS NMR spectra of the gallophosphate Mu-32 recorded at 4 kHz and 744 Hz display two isotropic chemical shifts at 45 (CH_2) and 160 ppm (C=O, oxygen O6) [Figure 5 (a and b)]. The resultant tensor associated with the carbonyl group cannot be decomposed into only one tensor. At least two tensors are necessary to reconstruct this part of the spectrum. Thus, the ^{13}C NMR spectrum enables the distinguishing of at least two kinds of carbonyl groups associated with the same isotropic chemical shift. It could reveal two different delocalisations of the electronic charge in the O6−C1−O3 bonds. Such a distinction cannot be observed by single-crystal XRD analysis.

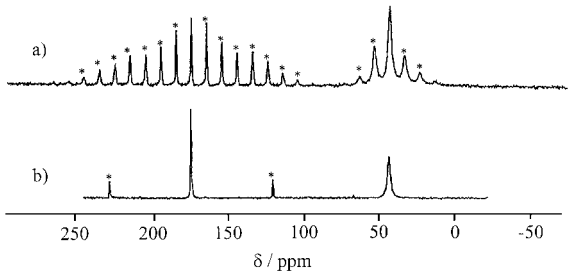

Figure 5. ^{13}C CP MAS NMR spectra of the gallophosphate Mu-32 recorded at 744 Hz (a), 4 kHz (b); * spinning side bands

The ^1H MAS NMR spectrum exhibits two signals at δ = 7.6 and 3.9 ppm (Figure 6). A decomposition allows the determination of the proportion of the different populations as 58 and 42%, respectively. These can be attributed to NH_3^+ and CH_2 groups, respectively, in agreement with the structure determination. The ^1H MAS NMR spectrum does not display a signal corresponding to an OH group (between δ = 9 and 12 ppm) which confirms that the glycine template is strongly bonded to the inorganic layer

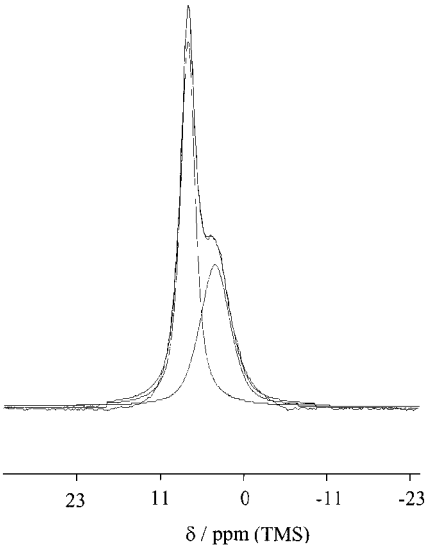

Figure 6. ^1H MAS NMR spectrum of the gallophosphate Mu-32; the two inner curves represent the decomposition of the spectrum

 © 2005 Wiley-VCH Verlag GmbH & Co. KGaA, Weinheim

through its oxygen atom O3 (OH group in the free glycine molecule).

The ^{31}P MAS NMR spectrum of Mu-32 displays only one signal located at $\delta = -9.2$ ppm (Figure 7) in agreement with the structural data in which only one crystallographic phosphorus site is present. Such a chemical shift value is similar to those traditionally observed for PO_4 groups in gallophosphates.[9,10]

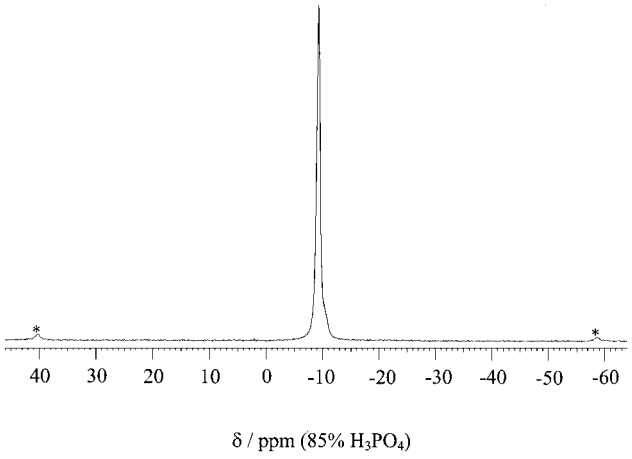

Figure 7. ^{31}P MAS NMR spectrum of the gallophosphate Mu-32; * spinning side bands

Conclusion

The gallophosphate Mu-32 shows several original features. The first is the nature of the template, i.e. the amino acid glycine, which has never been used before as a structure-directing agent in the synthesis of microporous and phosphate based materials such as gallophosphates. This work shows that under certain particular synthetic conditions, such an organic molecule can have a templating effect. The second feature comes from the coordination sphere of the gallium atoms. They are in pentacoordinate environments of oxygen atoms. Four oxygens are shared with P-centred tetrahedra and the last oxygen comes from the glycine template. The latter is, therefore, part of the framework.

Experimental Section

Synthesis: The reactants were glycine (Gly) (Fluka, 99%), phosphoric acid (Labosi, 85%) and hydrofluoric acid (Prolabo, 40%). The gallium source was the oxide β-Ga_2O_3 (ICDD 41-1103) obtained by heating a gallium nitrate solution to 250 °C for 24 h followed by calcination at 1000 °C for 6 h. Tripropylamine (TriPA) (Fluka, purum >98%) was used as a pH modifier. Previous experiments indicated that this amine does not play a templating role in the synthesis of gallophosphates in fluoride media.[31] Mu-32 was obtained by hydrothermal synthesis at 170 °C in a fluoride medium. The starting molar composition of the gel was: 1 Ga_2O_3/1 P_2O_5/1 HF/1 Gly/1.5 TriPA/160 H_2O. The gel was prepared by adding H_3PO_4 to the mixture of the gallium source and water with stirring. After a homogenisation time of 10 min, the amino acid glycine was introduced. Finally, the pH was adjusted to 4−5 with tripropylamine. The resultant gel was mixed at room temperature for 2 h and transferred to a 20-mL PTFE-lined stainless steel autoclave. The crystallisation was carried out at 170 °C under static conditions. After 3 d of heating, the product was recovered, washed with distilled water and dried at 60 °C overnight.

Structure Determination: On the basis of Weissenberg photographs, the powder XRD pattern of Mu-32 reported in Figure 2 (a) was indexed to the monoclinic crystal system, space group $P2_1/c$, with the following unit cell parameters: $a = 9.1766(3)$ Å, $b = 5.1520(16)$ Å, $c = 12.5093(4) =$ Å and $\beta = 90.6685(16)$. The structure was then determined by a single-crystal X-ray diffraction study using direct methods. A crystal with dimensions 200 × 90 × 50 μm was selected from the batch and mounted on a Picker 4-circle STOE diffractometer. 1036 reflections were recorded from 3.26° up to 24.95° in θ in the ω-scan mode, of which 1004 fulfilled the condition $I > 2\sigma(I)$. A summary of the experimental and crystallographic data is reported in Table 4. The structure was solved by direct methods using SHELXS-86[38] and refined using SHELXL-93.[39] The refinement converged to $R_1 = 0.0293$ $\{R_1 = \Sigma(F_o - F_c)/\Sigma F_o]$ and $wR_2 = 0.1041$ $\{R_2 = [\Sigma w(F_o^2 - F_c^2)^2/\Sigma w(F_o^2)^2]^{1/2}\}$ for 1004 reflections $[I > 2\sigma(I)]$. Using direct methods, the positions of the Ga and P atoms were revealed and all the remaining atoms, except the hydrogen atoms, were located from successive Fourier maps. Hydrogen atoms were placed with geometrical constraints. None of the hydrogen atoms were refined with anisotropic displacement parameters. CCDC-236894 contains the supplementary crystallographic data for this paper. These data can be obtained free of charge at www.ccdc.cam.ac.uk/conts/retrieving.html [or from the Cambridge Crystallographic Data Centre, 12 Union Road, Cambridge CB2 1EZ, UK; Fax: (internat.) + 44-1223-336-033; E-mail:

Table 4. Experimental and crystallographic data for the gallophosphate Mu-32

Chemical formula	$GaPO_4(C_2H_5NO_2)$
Crystal system	monoclinic
Crystal space group	$P2_1/c$
a [Å]	9.177(2)
b [Å]	5.1540(10)
c [Å]	12.513(3)
β [°]	90.67(3)
M [g.mol^{-1}]	894.8
Density (calcd.) [g ml^{-3}]	1.875
Cell volume [Å^3]	591.8(2)
Z (formula units/cell)	4
Crystal size [μm]	200 × 90 × 50
Diffractometer	PICKER 4-circle Stoe
Mo-K_α [Å]	0.71073
Absorption coefficient [mm^{-1}]	3.843
Absorption correction	not applied
$F(000)$	321
Data collection temperature [K]	293(2)
θ range [°]	3.26 to 24.95
(hkl)min., (hkl)max.	(−10,−6,−14), (10,0,0)
Independent reflections	1036
Observed reflections	1004
Data/restraints/parameters	1036/0/102
Residuals (observed data) $[I > 2\sigma(I)]$	$R1 = 0.0293$, $wR2 = 0.1041$
Residuals (all data)	$R1 = 0.0300$, $wR2 = 0.1062$
Goodness-of-fit (all data)	1.023
Largest diff. peak/hole [e·Å^{-3}]	1.395/−0.775

 © 2005 Wiley-VCH Verlag GmbH & Co. KGaA, Weinheim

deposit@ccdc.cam.ac.uk]. Selected bond angles and lengths are reported in Tables 3 and Table 5, respectively.

Table 5. Selected bond lengths [Å] in the gallophosphate Mu-32; symmetry transformation used to generate equivalent atoms: #1: x, 0.5 − y, 0.5 + z; #2: −x, −y, 1 − z; #3: − x, 1 − y, 1 − z; #4: x, 0.5 − y, −0.5 + z

Ga1−O5	1.873(3)	C2−N	1.476(18)
Ga1−O4	1.879(3)	C2−C1	1.519(7)
Ga1−O3	1.913(4)	C1−O6	1.223(4)
Ga1−O1	1.930(4)	O3−C1	1.270(6)
Ga1−O2	1.955(5)		
P1−O1	1.525(19)		
P1−O2#1	1.532(22)		
P1−O5#2	1.533(4)		
P1−O4#3	1.549(2)		

Characterisation: The powder XRD patterns were recorded with a STOE STADI-P diffractometer equipped with a curved germanium (111) primary monochromator and a linear position-sensitive detector using Cu-$K_{\alpha 1}$ radiation (λ = 1.5406Å). The morphology and size of the crystals were determined by scanning electron microscopy using a Philips XL30 microscope. Thermogravimetric (TGA) and differential thermal analyses (DTA) were performed under air with a Setaram Labsys thermoanalyser with a heating rate of 5 °C/min up to 1100 °C. At this final temperature, a white product was obtained indicating that the total amount of the organic template had been eliminated. The amounts of Ga, F and P in the gallophosphate Mu-32 were determined by scanning electron microprobe analysis with a Castaing type (CAMEBAX) electron microscope. Carbon and nitrogen quantities were determined by coulometric and catharometric methods, respectively. The ^{13}C CP MAS NMR spectrum was recorded with a Bruker MSL 300 spectrometer and the ^{1}H and ^{31}P MAS NMR spectra with a Bruker DSX 400 spectrometer. The recording conditions of the CP MAS and MAS spectra are given in Table 6.

Table 6. Recording conditions for the MAS and CP MAS NMR spectra

	^{13}C CP MAS	^{31}P MAS	^{1}H MAS
Chemical shift standard	TMS	85% H_3PO_4	TMS
Frequency [MHz]	75.47	161.98	400.14
Pulse width [μs]	3.7	3.5	5.8
Flip angle	π/2	π/2	π/2
Contact time [ms]	1	−	−
Recycle time [s]	8	30	8
Spinning rate [Hz]	5000	8000	20000
Number of scans	624	8	700

Acknowledgments

The authors thank Dr. Luc Delmotte for fruitful discussions and the IFP (Institut Français du Pétrole) which kindly provided the gallium nitrate.

[1] J. Patarin, J. L. Paillaud, H. Kessler in *Handbook of Porous Solids*, vol. 2 (Eds.: F. Schüth, K. S. W. Sing, J. Weitkamp), Wiley-VCH Verlag GmbH, Germany, **2002**, pp. 815−876.
[2] L. Vidal, C. Marichal, L. Delmotte, V. Gramlich, J. Patarin, *Phosphorus Res. Bull.* **1999**, *10*, 177−182.
[3] S. T. Wilson, B. M. Lok, C. A. Messian, T. R. Cannan, E. M. Flanigen, *J. Am. Chem. Soc.* **1982**, *104*, 1146−1147.
[4] M. E. Davis, C. Saldarriage, C. Montes, J. Garces, C. Crowder, *Nature* **1988**, *331*, 698−369.
[5] L. Sierra, C. Deroche, H. Gies, J. L. Guth, *Microporous Mater.* **1994**, *3*, 29−38.
[6] J. L. Paillaud, P. Caullet, L. Schreyeck, B. Marler, *Microporous Mesoporous Mater.* **2001**, *42*, 177−189.
[7] J. B. Parise, *J. Chem. Soc., Chem. Commun.* **1985**, 606−607.
[8] M. Estermann, L. B. McCusker, C. Baerlocher, A. Merrouche, H. Kessler, *Nature* **1991**, *352*, 320−322.
[9] L. Josien, A. Simon-Masseron, V. Gramlich, J. Patarin, *Chem. Eur. J.* **2002**, *8*, 1614−1620.
[10] L. Josien, A. Simon, V. Gramlich, J. Patarin, *Chem. Mater.* **2001**, *13*, 1305−1311.
[11] F. Millange, R. I. Walton, N. Guillou, T. Loiseau, D. O'Hare, G. Férey, *Chem. Mater.* **2002**, *14*, 4448−4459.
[12] F. Bonhomme, S. G. Thoma, T. M. Nenoff, *J. Mater. Chem.* **2001**, *11*, 2559−2563.
[13] D. S. Wragg, A. M. Z. Slawin, R. E. Morris, *J. Mater. Chem.* **2001**, *11*, 1850−1857.
[14] T. E. Gier, G. D. Stucky, *Nature* **1991**, *349*, 508−510.
[15] S. Fleith, L. Josien, A. Simon-Masseron, V. Gramlich, J. Patarin, *Solid State Sci.* **2002**, *4*, 135−141.
[16] A. Simon-Masseron, J. L. Paillaud, J. Patarin, *Chem. Mater.* **2003**, *15*, 1000−1005.
[17] A. Simon, L. Josien, V. Gramlich, J. Patarin, *Microporous. Mesoporous Mater.* **2001**, *47*, 135−146.
[18] C. N. R. Rao, S. Natarajan, S. Neeraj, *J. Am. Chem. Soc.* **2000**, *122*, 2810−2817.
[19] H. Kessler, J. Patarin, C. Schott-Darie in *Advanced Zeolite Science and Applications, Studies in Surface Science and Catalysis*, vol. 85 (Eds.: J. C. Jansen, M. Stöker, H. G. Karge, J. W. Weitkamp), Elsevier, Amsterdam, **1994**, pp. 75−110.
[20] A. Merrouche, J. Patarin, H. Kessler, M. Soulard, L. Delmotte, J. L Guth, *Zeolites* **1992**, *12*, 226−232.
[21] L. Josien, A. Simon, V. Gramlich, J. Patarin, *Chem. Eur. J.* **2002**, *8*, 1614−1620.
[22] A. K. Cheetham, G. Férey, T. Loiseau, *Angew. Chem. Int. Ed.* **1999**, *38*, 3268−3292.
[23] W. T. A. Harrison, T. M. Nenoff, M. M. Eddy, T. E. Martin, G. D. Stucky, *J. Mater. Chem.* **1992**, *2*, 1127−1134.
[24] P. Lightfoot, Z. A. D. Letherbridge, P. E. Morris, *J. Solid State Chem.* **1999**, *143*, 74−76.
[25] C. Chen, P. P. Chen, K. H. Lii, *Chem. Commun.* **1999**, 1473−1474.
[26] K. Maeda, J. Akimoto, Y. Kiyozumi, F. Mizukami, *Angew. Chem. Int. Ed. Engl.* **1995**, *34*, 1199−1201.
[27] M. R. Mason, A. M. Perkins, P. M. Matthews, J. D. Fisher, M. S. Mashuta, A. Vij, *Inorg. Chem.* **1998**, *37*, 3734−3746.
[28] T. Loiseau, S. Neeraj, A. K. Cheetham, *Acta Crystallogr., Sect. C* **2002**, *58*, 379−381.
[29] V. Patinec, P. A. Wright, P. Lightfoot, R. A. Aitken, P. A. Cox, *J. Chem. Soc., Dalton Trans.* **1999**, 3909−3911.
[30] M. J. Maple, E. F. Philip, A. M. Z. Salwin, P. Lightfoot, P. A. Cox, P. A. Wright, *J. Mater. Chem.* **2001**, *11*, 98−104.
[31] T. Wessels, L. B. McCusker, C. Baerlocher, P. Reinert, J. Patarin, *Microporous Mesoporous Mater.* **1998**, *23*, 67−77.
[32] P. Reinert, J. Patarin, B. Marler, *Eur. J. Solid State, Inorg. Chem.* **1998**, *35*, 389−403.
[33] L. Vidal, J. L. Paillaud, Z. Gabelica, *Microporous Mesoporous Mater.* **1998**, *24*, 189−197.
[34] W.-J. Chang, C.-Y. Chen, K.-H. Lii, *J. Solid State Chem.* **2003**, *172*, 6−11.

 © 2005 Wiley-VCH Verlag GmbH & Co. KGaA, Weinheim

[35] C. Y. Chen, K.-H. Lii, A. J. Jacobson, *J. Solid State Chem.* **2003**, *172*, 252−256.
[36] I. D. Brown in *Structure and Bonding in Crystals*, vol. 2 (Eds.: M. O'Keeffe, A. Navrotsky), Academic Press, New York, **1981**, chapter 14, pp. 1−30.
[37] D. Riou, G. Férey, *Eur. J. Solid State, Inorg. Chem.* **1994**, *31*, 605−613.
[38] G. M. Sheldrick, *SHELXS-86, Program for the Solution of Crystal Structures*, University of Göttingen, Germany, **1986**.
[39] G. M. Sheldrick, *SHELXL-93, Program for Crystal Structure Determination*, University of Göttingen, Germany, **1993**.
Received May 13, 2004
Early View Article
Published Online December 6, 2004

 © 2005 Wiley-VCH Verlag GmbH & Co. KGaA, Weinheim

Aerogel and Xerogel Catalysts Based on θ-Alumina Doped with Silicon for High Temperature Reactions

Aurelien Florin Popa,[a] Laurence Courthéoux,[b] Eric Gautron,[b] Sylvie Rossignol,*[b] and Charles Kappenstein[b]

Keywords: Aerogel / Xerogel / Catalyst / Platinum / Alumina

Numerous materials (supports and catalysts) based on alumina have been prepared using the sol-gel process and carbon dioxide supercritical drying. In this work two types of solids, i.e. xerogels and aerogels, were systematically compared and a way of introducing platinum metal with a content of 5% percent by weight was examined. The structural data, the surface area, Pt dispersion and catalytic activity for the decomposition of the propellant were measured for the various samples. The $(Al_2O_3)_{0.88}(SiO_2)_{0.12}$ samples prepared show very interesting porosity values, especially for the aerogel. For this reason, they were chosen as supports for the synthesis of 5 wt% platinum on alumina catalysts. The results presented in this work allowed us to obtain an overall view of the influence of the preparation mode on the properties of platinum on alumina supported catalysts. The dispersion of the metal phase is directly dependent on the specific surface of the support. A significant value for the surface area implies a large amount of centers for interaction with the metal precursor and, consequently, the appearance of more centres of simultaneous germination. Although aerogels obtained by carbon dioxide supercritical drying always show superior properties compared with xerogels, for catalytic decompositions the xerogels still remain superior.

(© Wiley-VCH Verlag GmbH & Co. KGaA, 69451 Weinheim, Germany, 2005)

Introduction

The sol-gel method represents a way of synthesising materials which display excellent properties suitable for many applications such as catalysis, ceramics and glasses, and nano-materials.[1] Therefore, numerous catalyst supports or catalysts have been prepared by this procedure which leads to high purity, homogeneous materials with large surface areas. These properties are key factors for the application of these materials.[2,3] Their properties are comparable and, in some cases, superior to some catalysts prepared using conventional procedures such as co-precipitation or conventional ceramic methods. In particular, we have focussed our interest in recent years on the preparation and evaluation of alumina-based catalysts for applications concerning the decomposition of monopropellants.[4] For this specific purpose, it is important to obtain catalytic materials or supports displaying high thermal stability (i.e. at 1200 °C or even higher). The selected supports for achieving this purpose are aerogel aluminas[5] or doped aluminas. In the latter case, the doping element (lanthanum, praseodymium, barium or silicon) can be introduced during the sol-gel process.[6−10] Moreover, for catalytic applications, it is generally necessary to add an active phase (a metal phase such as platinum, palladium etc.) to improve the properties.

Numerous authors have used alumina-supported platinum catalysts, prepared generally by the impregnation of commercially available supports. The literature concerning the sol-gel method was less important until the 1990′s during which time more papers appeared. Samples have been generally prepared by conventional drying processes (293 to 393 K) leading to xerogels. The use of supercritical drying, generally in carbon dioxide, leads to aerogels but the corresponding reports are much less numerous and focus mainly on pure alumina supports. The first paper concerning a Pt catalyst supported on alumina (aerogel and xerogel) and prepared by the sol-gel method was published in 1993 by Balakhrishnan et al.[11] The alumina precursor used was aluminium tri-*sec*-butoxide Al(O-*sec*-$C_4H_9)_3$ (ATB) following the work of Yoldas[12] and the platinum was introduced during the sol-gel transformation using H_2PtCl_6 as a precursor. The supercritical conditions for obtaining the aerogels were T = 295 °C and P = 85 bar with methanol. The samples were then treated at 773 K under helium. The main conclusions from this work were: (i) during the treatment, a reduction of the surface area can be observed and (ii) aerogels display a lower Pt metal dispersion in comparison with xerogels of similar loading. In 1998, Cho et al.[13] prepared the same materials using aluminium tripropoxide Al-

[a] Alexandru Ioan Cuza University, Faculty of Chemistry, Department of Inorganic Chemistry, 6600 Iasi, Romania
[b] University of Poitiers, LACCO UMR 6503, Laboratoire de Catalyse par les Métaux, 40 Avenue du Recteur Pineau, 86022 Poitiers Cedex, France
Fax: (internat.) +33-5-49454157
E-mail: sylvie.rossignol@univ-poitiers.fr

$(OC_3H_7)_3$ (ATP) and H_2PtCl_6, with a final treatment at 773 K. They demonstrated that the sol-gel (xerogel) catalyst displays a higher thermal stability of the metal particles than the conventionally impregnated catalyst. For the sol-gel sample, the exposed Pt metal particles are anchored to the alumina surface by metal−oxygen bonding. Other xerogel Pt/Al_2O_3 catalysts prepared by Castillo et al.[14] and Manasilp et al.[15] using the same precursors (ATB-ATP, H_2PtCl_6) and treated at 823 K and 773 K, respectively, demonstrate that the co-gelation of alkoxides and noble metals induces the stabilisation of the metallic phase and its incorporation into the alumina network producing better metal-support interactions. Recently, using ATB with acetylacetonate and $LiBH_4$ as precursors, Sault et al.[16] demonstrated that after calcination at 873 K, the metal particles are not encapsulated or occluded into the support. All these observations confirm that the metal-support interactions strongly depend on the precursors used, on the thermal treatment and on the method of drying. In order to extend the use of such samples to high temperature applications, it seemed important to study the influence of the drying conditions and to then compare xerogels and aerogels.

In this paper, we present our results on the sol-gel preparation of alumina or alumina doped with silica as a support. A systematic comparison has been made between support samples dried under conventional conditions (xerogels) and under supercritical conditions using CO_2 (aerogels) including the behaviour after the thermal treatment. The introduction of platinum was carried out using the conventional impregnation of dried or calcined sol-gel supports or during the sol-gel process. Powder X-ray diffraction (XRD), transmission electron microscopy (TEM) and thermal analyses (TDA-TGA) were used to determine the structural properties. To determine the effects of the synthesis on the catalytic activity, an evaluation of the properties of the catalyst towards the propellant decomposition has been performed with aqueous solutions of hydroxylammonium nitrate $NH_3OH^+ NO_3^-$ (HAN). The preliminary results are presented here.

Results and Discussion

A. Supports

The diffraction patterns of the four different types of supports, after drying, are presented in Figure 1. They are all composed of nanocrystalline hydrated boehmite γ-$AlO(OH)\cdot nH_2O$, see PDF file 21−1307 mentioned in ref.[17] The peak positions are essentially identical for all samples which also show the same cell parameters. The shift of the first diffraction peak has been discussed previously.[18]

The thermal analyses curves (Figure 2) indicate two major weight losses accompanied by endothermic effects which correspond firstly to the dehydration of the hydrated boehmite and then to the transformation of boehmite into gamma alumina. Assuming that at the end of the analyses the final product is the anhydrous α-alumina, the TG curves enable the determination of evolved water and thus the formula of the initially dried solids. At the beginning of the measurements, the dried samples always contain an excess of water and are known as hydrated boehmites. For both samples presented in Figure 2, the complete formulas are $AlOOH\cdot 0.94H_2O$ and $(AlOOH)_{0.94}\text{-}(SiO_2)_{0.06}\cdot 1.0H_2O$. Therefore, in the low temperature range (20−800 °C), the behaviour of the doped samples is similar to that of pure boehmites. On the other hand, the TDA curves reveal an important difference at high temperature: the exothermic peak at about 1200 °C which characterises the transformation into alpha alumina is clearly visible in the case of the pure boehmites but is shifted to a higher temperature for the doped samples. In this case, the boehmite is transformed into transition alumina but its structure is more stable and leads to alpha alumina at much higher temperatures (>1350 °C). This thermal behaviour is the same for the aerogel and xerogel samples. Consequently, we expected that the doped samples would not be transformed into alpha alumina, even after a hard thermal treatment (5 h calcination at 1200 °C).

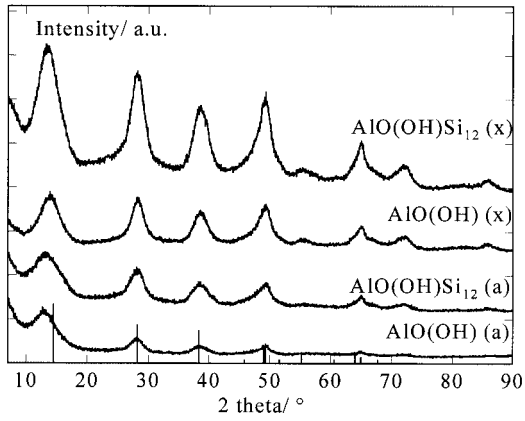

Figure 1. X-ray diffraction patterns of pure and doped boehmites, xerogels and aerogels (lines: PDF file 21−1307).

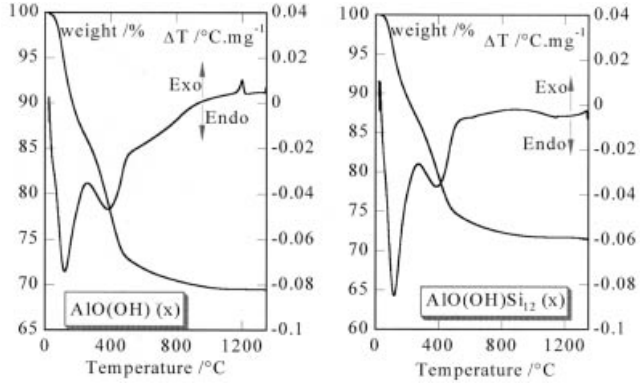

Figure 2. Thermal analyses of dried samples of AlO(OH) (x) and $AlO(OH)\text{-}Si_{12}$ (x)

The diffraction patterns of the calcined supports (Figure 3) confirm this fact, revealing that the transformation into alpha alumina is delayed by doping. After the thermal treatment, the structure of the Al_2O_3Si12 xerogel or aerogel corresponds to θ alumina (monoclinic, PDF file 23−1009) with a well ordered structure. By comparison, the nondoped aerogel (Al_2O_3) is entirely transformed into alpha alumina after the same treatment (Figure 7).

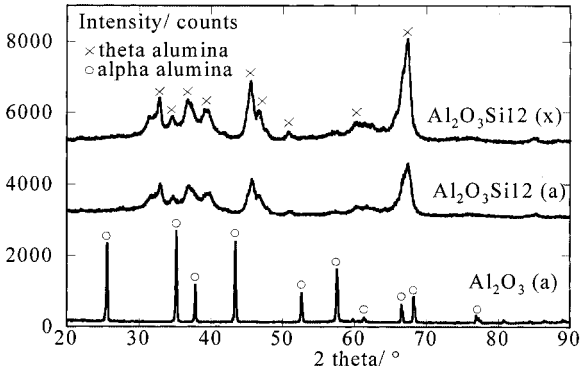

Figure 3. X-ray diffraction patterns of doped samples of Al_2O_3-Si12 (a) and (x) and nondoped Al_2O_3 (a), calcined at 1200 °C for 5 h (θ Al_2O_3, PDF: 23−1009; α Al_2O_3, PDF: 46−1212)

The values found for the BET surface area of the samples (Table 1) confirm that the doping retards the transformation into alpha alumina. The doped xerogel retains a good specific surface area (65 $m^2 \cdot g^{-1}$) whereas the aerogel has a much better value of 120 $m^2 \cdot g^{-1}$ (compared with 1−3 $m^2 \cdot g^{-1}$ for the nondoped alumina). This value is similar to that published by Mizushima,[8,9] (114 $m^2 \cdot g^{-1}$) for a 10% doped sample prepared in an alcoholic medium. The porous volume is slightly larger for the ASi12 (a) sample (0.24 $cm^3 \cdot g^{-1}$) than for the ASi12 (x) sample (0.16 $cm^3 \cdot g^{-1}$). The mean pore sizes of the two doped aluminas are comparable at 9.5 and 9.7 nm, respectively.

The transmission electron microscopy images enabled us to analyse the morphology of these calcined supports. Furthermore, the X-ray mapping revealed the atomic distribution of Al and Si across the samples. For the sake of clarity, we present a previously published diagram (Figure 4).[17] For ASi12 (a) (aerogel sample) we can see that the distribution of both aluminium and silicon atoms is homogeneous over the entire zone of the sample which was analysed. Other explored zones show that this homogeneity is a characteristic of the aerogel samples (see 2 in Figure 4). Xerogel sample ASi12 (x) contains some zones showing obvious microscale heterogeneity (see 1 Figure 4). This latter sample contains domains where the silicon concentration is enhanced. From EDX analyses, the Si and Al atomic compositions were quantified. For the aerogel, the atomic Si:Al ratio of 6:94 is in excellent agreement with the expected value (6.3:93.7). For the xerogel, this ratio strongly depends on the analysed zone (200 nm). In Figure 4 (1), the analysed zone exhibits a very important excess of silicon: Si:Al = 33:67. In fact, the large (200 nm) dark particle clearly visible on the image of the xerogel (see 2 in Figure 4) contains only silicon and oxygen atoms which correspond to pure amorphous silica. The aluminium content is smaller in the zones where this silicon agglomeration appears. In compensation, other zones are reduced in their silicon content leading to a higher content of aluminium in comparison with the calculated value. In these zones, the aluminium content can reach values as high as 95.7%.

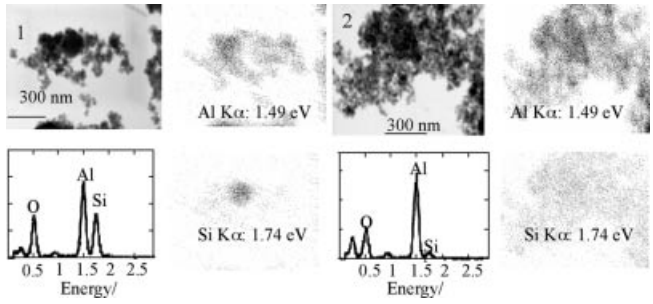

Figure 4. Electron microscopy (X-ray mapping and EDX analyses for the: (1) Al_2O_3-Si_{12} (x) and (2) $Al_2O_3Si_{12}$ (a) samples

Table 1. Samples prepared, mode of platinum introduction, thermal treatment, nomenclature, specific surface area (BET) and experimental platinum load (expected value 5 wt.-%)

Sample aerogel (a); xerogel (x)	Pt introduction impregnation sol-gel	Nomenclature	BET [m^2/g]	Pt [%]	Pt size [nm]
Al_2O_3 (a)	1	A (a)	3		
Al_2O_3 (x)	1	A (x)	1		
$(Al_2O_3)_{0.88}(SiO)_{0.12}$ (a)	1	ASi12 (a)	120		
$(Al_2O_3)_{0.88}(SiO)_{0.12}$ (x)	1	ASi12 (x)	65		
5% Pt/Al_2O_3 (a)	SG-1	SG-Pt-B-c (a)	41	3.0	7.0
5% Pt/Al_2O_3 (x)	SG-1	SG-Pt-B-c (x)	44	3.0[a]	11.0
5% Pt/$(Al_2O_3)_{0.88}(SiO)_{0.12}$ (a)	SG-1	SG-Pt-BSi12-c (a)	130	3.5	5.6
5% Pt/$(Al_2O_3)_{0.88}(SiO)_{0.12}$ (x)	SG-1	SG-Pt-BSi12-c (x)	41	2.6	4.3
5% Pt/Al_2O_3 (a)	Imp-2	Pt-A-r (a)	3	2.2[a]	2.6
5% Pt/Al_2O_3 (x)	Imp-2	Pt-A-r (x)	1	2.6	3.0
5% Pt/$(Al_2O_3)_{0.88}(SiO)_{0.12}$ (a)	Imp-2	Pt-ASi12-r (a)	120	2.4	
5% Pt/$(Al_2O_3)_{0.88}(SiO)_{0.12}$ (x)	Imp-2	Pt-ASi12-r (x)	68	3.5	3.8

[a] Values obtained by XRD quantification. 1. calcination at 1200 ° (5 h); 2. reduction at 400 ° (3 h).

 © 2005 Wiley-VCH Verlag GmbH & Co. KGaA, Weinheim

The silica segregation can explain the lower specific surface area (Table 1) of the xerogel sample 1-Asi12(x) after the thermal treatment at high temperature. During the transformation of alumina into the alpha form, small sites are first formed by a nucleation process. The corundum formation then continues by a growing and sintering process which requires contact between the former crystallites and migration of cations or cationic vacancies from the alumina particles of the previous transition.[25]

The stabilising effect of silicon occurs at the surfaces of the crystallites. When the silicon distribution is homogeneous, the silicon atoms are bonded tetrahedrally through μ-oxo bridges Al−O−Si−O−Al− and cannot take part at the sintering process because the α-Al_2O_3 structure contains the cations in octahedral sites. It is much more difficult for these sites to be occupied by silicon. The surface silicon layer behaves as a barrier between the growing areas and limits the transformation. Another explanation for the delay of the transformation into alpha alumina is related to the crystalline structure of the transition alumina. Beyond 600−700 °C, the quantity of surface OH groups contained in alumina is no longer sufficient to maintain the stability of the structure. The removal of these hydroxyl groups leads to the formation of tetrahedral vacancies which destabilise the structure. In the presence of well distributed silicon atoms, the influence of these tetrahedral vacancies is lowered and the transformation is delayed.[19−22]

The diffraction peaks of the two samples after the high temperature treatment have been enlarged to focus on the peak displacement (Figure 5). We observed a systematic and slight but visible displacement of the aerogel peaks to higher 2θ values. This displacement varies between 0.09 and 0.29° and can be explained by the cell parameters shrinking due to the replacement of aluminium by silicon atoms in the structure. Silicon atoms are slightly smaller than Al atoms (bond length Si−O = 1.91 Å compared with Al−O = 2.03 Å).[23] If the structure of θ−Al_2O_3 can be viewed as a distorted spinel structure,[24] we can approximate the peak displacement on the basis of a cubic structure. Assuming that all the silicon atoms are located in the tetrahedral sites of the θ−Al_2O_3 structure, we can estimate the 2θ displacement from the bond length difference to be of the order of 0.2 to 0.5°. The experimental shifts between the aerogel and the xerogel peak positions range from 0.1 to 0.3°, indicating that the silicon content incorporated into the structure is far superior in the case of the aerogel (of the order of 50%).

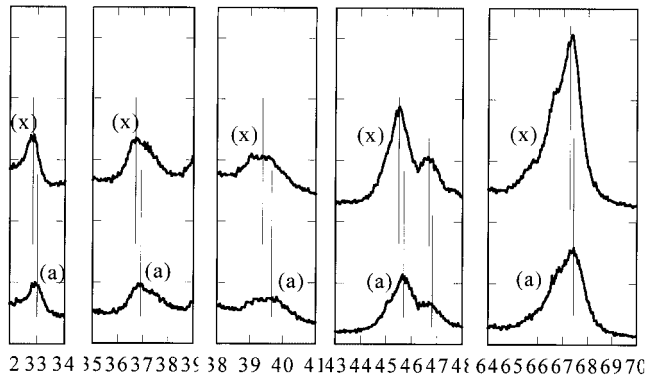

Figure 5. Enlargement of the diffraction patterns of the Al_2O_3Si12 samples X: (a) = aerogel, (x) = xerogel

This cell parameter difference does not exist for the non-calcined samples displaying the boehmite pattern (Figure 1). No displacements can be seen, in agreement with the boehmite structure which displays only octahedral aluminium sites. These sites are able to host aluminium atoms but not silicon atoms. During the sol synthesis, boehmite nanocrystallites are formed first by hydrolysis of the aluminium precursor. After addition of the silicon precursor, hydrolysis occurs later and produces silicon species which may be bonded to the surface aluminium atoms of the boehmite particles by a μ_2-oxo bridge, this being a consequence of an oxolation reaction: $-Si-OH + HO-Al- \rightarrow -Si-O-Al- + H_2O$

Thus, before calcination, silicon atoms are located mainly at the surface of the crystallites and only during the transformation of boehmite into γ alumina can they participate in the transition γ-alumina structure by substituting tetrahedral aluminium atoms. In Figure 6, which shows a possible structural rearrangement during the transformation of boehmite, the surface Si atom is linked to a surface HO group of boehmite and to an external hydroxyl group. The transformation of the hydroxyl group and a slight silicon displacement leads to the position of silica in a tetrahedral site of the transition alumina. The presence of these silicon atoms stabilises the alumina defect structure and can explain the delay in the transformation into corundum.

The results presented in this section show that the drying technique has an important influence on the features of doped alumina. The morphology, thermal stability, homogeneity, fine structure and the textural properties are depen-

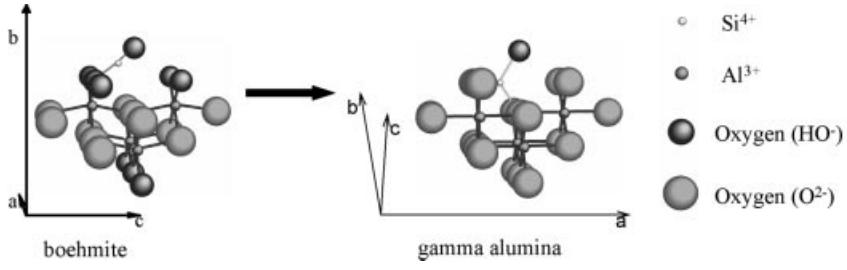

Figure 6. Model of silicon insertion into the gamma alumina structure during the boehmite transformation

 © 2005 Wiley-VCH Verlag GmbH & Co. KGaA, Weinheim

dent on this. The ASi12 samples prepared show very interesting porosity values, especially for the aerogel. For this reason, they were chosen as supports for the synthesis of 5 wt.-% platinum on alumina catalysts.

B. Catalysts

1. Effective Catalyst Metal Load

For a selection of catalysts (6 samples), the platinum content was analysed in order to establish precisely the effective metal load after the thermal treatment. For two other samples, SG-Pt-B-c (x) and Pt-A-r (a), the metal load was estimated from a quantitative analysis of the X-ray diffraction patterns with respect to their homologues SG-Pt-B-c (a) and Pt-A-r (x).[25] The results are presented in Table 1. The metal content is between 47 and 71% of the calculated value, so that a quantity of platinum is lost during the preparation of the catalysts. This loss probably takes place during the thermal treatment processes (calcination and reduction).[26] During the introduction of the platinum precursor, the anions present in solution ($[PtCl_6]^{2-}$, $[Pt(H_2O)Cl_5]^-$ or others) are adsorbed into the surfaces of the crystallites and this fixation is mainly due to electrostatic interactions between negative complexes and surface OH_2^+ groups of the support present in acidic solutions or to ligand substitution around the platinum atoms (Cl^- by surface OH groups). The fraction of platinum atoms which is not firmly anchored on the surface can become detached and leave during the thermal treatments, probably in the form of more volatile oxychloride species. Nevertheless, hexachloroplatinic acid remains the best precursor because it allows the preparation of catalysts with high metal dispersions.[11,27] We expect also a lower metal percentage for the materials displaying the α-Al_2O_3 structure due to the strong decrease of the BET surface area (Table 1).

For the samples supported on doped alumina, this platinum content decrease could be related to the surface Si−OH groups which can prevent the metal from bonding firmly to the surface.[28]

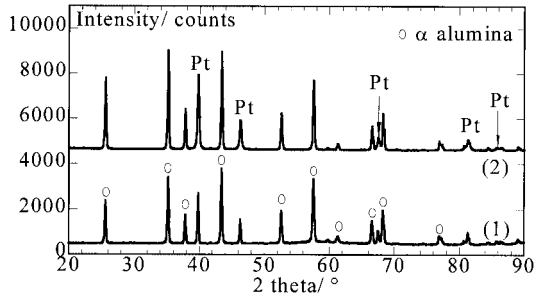

Figure 7. Diffraction patterns of catalysts on nondoped supports: (1) SG Pt-B-c (a) sample; (2) Pt-A-r (a) sample. (PDF: Pt: 04−0802; αAl_2O_3: 46−1212)

2. Physico-Chemical Characterisation

a) Catalysts on Nondoped Supports

The diffraction patterns of both aerogel catalysts (sol-gel and impregnated) are presented in Figure 7. As expected, the structure of the support is α-Al_2O_3 and the metal phase appears as large sized crystallites. The average size values calculated from peak breadths are around 70 nm for the sol-gel catalyst and 26 nm for the impregnated one. For the xerogel sample, the respective values are of the same order (Table 1). The sintering is slightly more pronounced for the sol-gel samples compared with the samples prepared by impregnation.

For the Pt-A-r (a) sample, transmission electron microscopy agrees well with this average size. The image reveals a rather large distribution of the crystallite sizes, ranging from a few tenths to several hundred angstroms. We present two different characteristic zones of the sample in Figure 8.

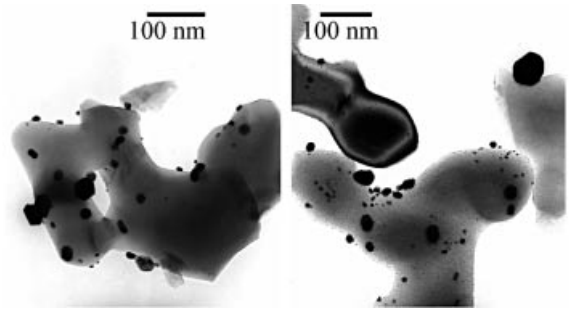

Figure 8. Two transmission electron microscopy images of the Pt-A-r (a) sample

b) Catalysts on Doped Supports

Catalysts Prepared by Sol-Gel Synthesis: The diffraction patterns indicate the presence of θ alumina for the support and the same large metal crystallites (Figure 9) of average size 43 nm for the xerogel and 56 nm for the aerogel. This is the only case when the aerogel crystallites are larger than the xerogel ones. This fact is probably related to the particular texture of the sample of SG Pt−BSi12-c (a). In fact, the precursor anions can be adsorbed onto the boehmite sites concurrently with the silicon species. As a consequent, the

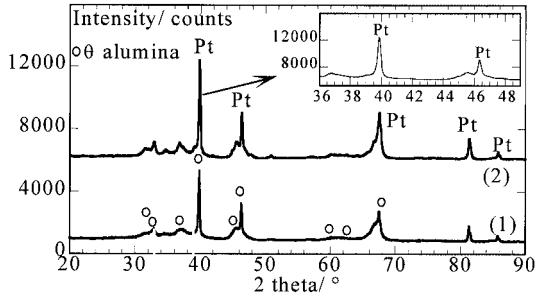

Figure 9. Diffraction patterns of (1) SG Pt-BSi12-c (a) and (2) SG Pt-BSi12-c (x) samples (θ Al_2O_3, PDF: 23−1009)

 © 2005 Wiley-VCH Verlag GmbH & Co. KGaA, Weinheim

surface nature and the interactions between crystallites may be different from the case of a pure boehmite sol.

After the thermal treatment at 1200 °C, the sample SG Pt-BSi12-c (a) exhibits the largest specific surface area (130 $m^2 \cdot g^{-1}$), compared with only 41 $m^2 \cdot g^{-1}$ for its xerogel homologue SG Pt-BSi12-c (x). The porous volume is 0.45 $cm^3 \cdot g^{-1}$, five times larger than for the xerogel (0.09 $cm^3 \cdot g^{-1}$) and the mean pore sizes are 14 and 7 nm, respectively. Consequently, the platinum crystallites located inside the aerogel pores can develop and reach larger sizes.

The TEM pictures (Figure 10) show, for the xerogel sample, some zones with a normal aspect of the porous support and metal crystallites with sizes ranging from 7 to 100 nm and some other singular zones particles with different textures can be observed. In order to identify the nature of the particles visible on the B image, we recorded three EDX spectra, shown in Figure 11. The first (a) corresponds to a homogeneous zone. We could establish the presence of aluminium and silicon but not platinum. The second reveals platinum crystallites and, finally, the third (c) indicates a large particle containing only aluminium atoms. The appearance of such particles can be explained by the presence of the metal precursor in the boehmite sol in the earlier stages of the synthesis. The competition of adsorption on boehmite crystallites between the platinum and silicon species leads to crystallites covered by more platinum and less silicon. The X-ray analysis reveals that a small fraction of platinum atoms is rather well dispersed over the sample but the other fraction exists as isolated crystallites. In the same way as observed for the supports, some zones with a silicon agglomeration can be identified.

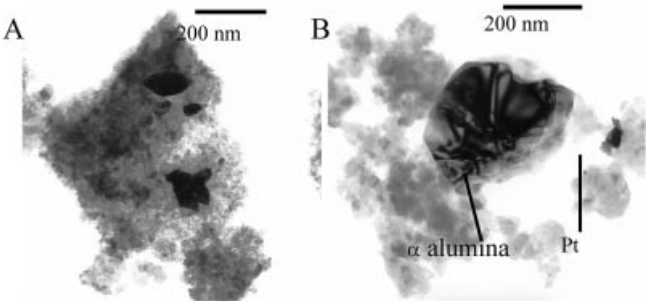

Figure 10. Two transmission electron microscopy images for the sample SG Pt-BSi12-c (x)

For the aerogel, we observed similar behaviour with platinum isolated crystallites and α-Al_2O_3 particles. The X-ray mapping, performed on a zone around the α alumina particle, revealed a better silicon repartition compared with the xerogel. Instead, the signal due to the platinum atoms is practically invisible over the zone showing that the metal is present only as isolated crystallites.

Catalysts Prepared by Impregnation on Doped Alumina: The diffraction patterns of the catalysts impregnated on doped alumina are presented in Figure 12. In the case of the aerogel, the peaks corresponding to platinum are practically indiscernible from the background indicating a very small crystallite size. For the xerogel, the platinum peaks are weak but visible. By comparing the intensity of the isolated (311) peak (36 counts degree) with the SG-Pt-BSi12 c (x) sample (which has practically the same metal load, 304 counts degree) we can estimate that only about 10 wt% of the platinum contributes to the diffraction peaks in the Pt-ASi12-r (x) sample. By using the width of the (311) peak, which appears well isolated at $2\theta = 81.3°$, we can estimate a size of 40 nm. In fact, for a large size distribution, the mean value calculated on the basis of peak's width is largely overestimated since the small crystallites make very little contribution and the peak profile is mainly influenced by the large crystallites.[27,29] We can therefore assume that a large part of the crystallites are small in size and only a small other part of the better developed crystallites will be responsible for the diffraction signal.

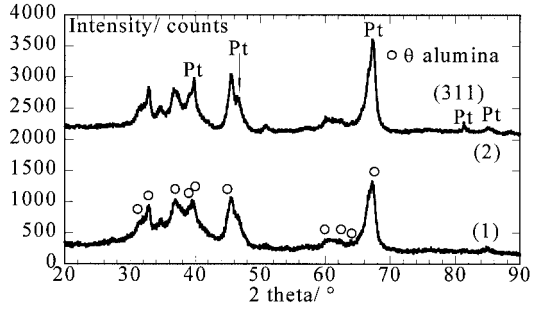

Figure 12. Diffraction patterns of the (1) Pt-ASi12-r (a) and (2) Pt-ASi12-r (x) samples (the circles correspond to θ Al_2O_3, PDF: 23−1009)

The specific surface areas of these catalysts are 68 $m^2 \cdot g^{-1}$ for the xerogel and 120 $m^2 \cdot g^{-1}$ for the aerogel. This is practically the same as in the supports and indicates no pore blocking which is in agreement with the small sizes of most of the crystallites.

Transmission electron microscopy confirmed these results. For the aerogel, almost all the platinum particles are smaller than 4 nm (Figure 13, left). The xerogel exhibits a

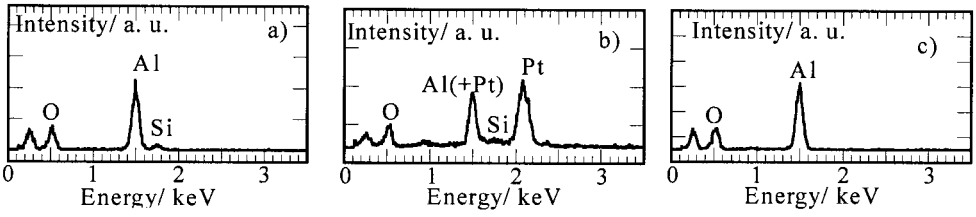

Figure 11. EDX spectra corresponding to different zones of the sample SG Pt-BSi12-c (x)

 © 2005 Wiley-VCH Verlag GmbH & Co. KGaA, Weinheim

larger size distribution with crystallites smaller than 4 nm but with larger particles (Figure 13, right). Both histograms are shown in Figure 14 as well as the average crystallite sizes. From the metal dispersion measurements, an average surface crystallite size can be determined (Table 2). Two models may be used used, a cubic model with one face in contact with the support and a hemispherical model. The average sizes refer to the cube parameter or the diameter. The results for the aerogel are in good agreement with the average sizes determined from the electron microscopy histogram. For the xerogel, this agreement is poorer because of the larger size distribution revealed by electron microscopy and X-ray diffraction (90% of the platinum appears as crystallites with average sizes of about 4 nm, i.e. 10% larger and visible by XRD). It is also possible that a part of the metal crystallites, located in closed pores, is not accessible for the hydrogen adsorption.[30,16]

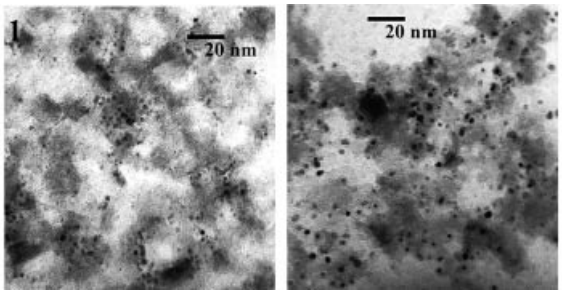

Figure 13. Transmission electron microscopy photos of the (left) Pt-ASi12-r (a) and (right) Pt-ASi12-r (x) samples

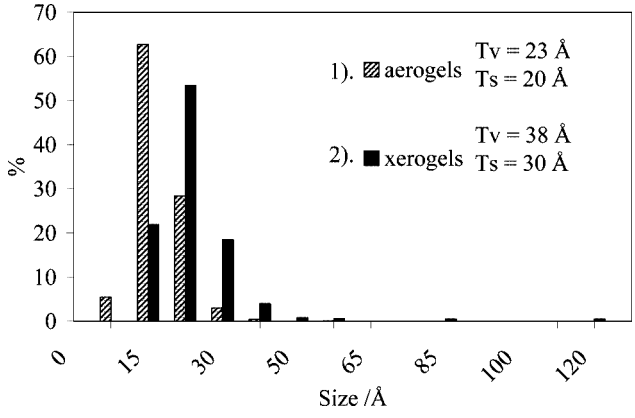

Figure 14. Histogram of the size repartition of the platinum crystallites for the (1) Pt-ASi12-r (a) and (2) Pt-ASi12-r (x) samples (Tv, Ts: see Table 2)

$$T(\text{Å}) = \frac{K}{D\,(\%)} \qquad (1)$$

T (Å) = mean crystallite size (Å) cube: length, hemisphere: diameter

K = constant (Å) (cube: 946, hemisphere: 568)

Table 2. Comparison between average crystallite sizes determined by transmission electron microscopy or by metal dispersion measurements

Sample	Mean size, microscopy (nm)		Mean size, dispersion (nm)		Dispersion (%)
	T_V	T_S	Cube	Hemisphere	
Pt-ASi$_{12}$-r (x)	3.8	3.0	6.7	8.2	13
Pt-ASi$_{12}$-r (a)	2.3	2.0	1.8	2.2	51

$$\overline{T_S} = \frac{\sum_{i=0}^{n} T_i \cdot S_i}{\sum_{i=0}^{n} S_i} = \frac{\sum_{i=0}^{n} T_i^3}{\sum_{i=0}^{n} T_i^2}$$

$\overline{T_S}$ = surface weighted mean crystallite size (Å)
T_i = size of a i particle (Å)
S_i = surface of a particle T_i (Å^2)
n = number of particles

$$\overline{T_V} = \frac{\sum_{i=0}^{n} T_i \cdot V_i}{\sum_{i=0}^{n} V_i} = \frac{\sum_{i=0}^{n} T_i^4}{\sum_{i=0}^{n} T_i^3}$$

$\overline{T_V}$ = volume weighted mean crystallite size (Å)
T_i = size of a particle i (Å)
V_i = volume of a particle T_i (Å^3)
n = number of particles

C. Discussion

1. Influence of the Preparation Mode by Impregnation versus the One-Step Method (Sol-Gel)

For the samples prepared by the sol-gel method, the calcination at 1200 °C induces an important sintering of the metal phase, whatever the nature of the support (xerogel or aerogel). The SG Pt-BSi12-c (a) sample is of particular note, displaying a very large specific surface area of 130 $m^2 \cdot g^{-1}$. This important difference is due to the specific synthetic conditions (simultaneous presence of silicon and platinum species in the sol) as well as to the supercritical drying which allows the retention of the gel morphology. The metal dispersion is not related to the porosity of the support because the mean size of the platinum crystallites for the SG Pt-BSi12-c (a) sample is still greater than 50 nm. Therefore, the metal dispersion is mainly determined by the growth and sintering of the particles.

In contrast, the catalysts prepared by impregnation on calcined alumina contain smaller metal particles because sintering cannot occur during the reduction process. In this case, the dispersion of the metal phase is directly dependent on the specific surface of the support. A large value of the surface area implies a large amount of adsorption centers within the metal precursor (i.e. H_2PtCl_6) and, consequently, the formation of numerous centers for germination of platinum particles during the reduction. The catalysts supported on doped alumina also exhibit special characteristics, especially for the aerogel sample Pt-ASi12-r (a), namely a specific surface area higher than 120 $m^2 \cdot g^{-1}$ after thermal treatment, good metal dispersion (> 50%) and a homogeneous distribution of silicon and platinum atoms over the sample. As a consequence, this sample could be tested as an interesting catalytic material for applications requiring high temperatures.

Nevertheless, it must be stated that the great difference in dispersion between sol-gel and impregnated catalysts is related to the temperature difference applied to the plati-

 © 2005 Wiley-VCH Verlag GmbH & Co. KGaA, Weinheim

num precursor. For the sol-gel samples, the platinum precursor is decomposed to platinum crystallites during the high temperature treatment (1200 °C, 5 h) in an oxidising atmosphere leading to a strong sintering effect. In the other case, the impregnated sample is reduced at low temperatures (see Exp. Sect.) and the maximum temperature experienced by the platinum particles is only 400 °C. To confirm the critical role of the temperature, the xerogel sample (Pt-ASi12-r (x)) was treated with the same high temperature conditions after reduction at 400 °C. A small decrease in the surface area could be observed from 68 $m^2 \cdot g^{-1}$ to 43 $m^2 \cdot g^{-1}$, accompanied by a strong sintering of the platinum particles. The average size was between 4 nm and 30 nm before treatment and 40 nm after treatment. It must be said that the real catalytic conditions used will not be so drastic, the high temperatures being reached over very short time ranges.

2. *Influence of the Drying Mode: Xerogel versus Aerogel*

The main advantage of the supercritical drying is the possibility of maintaining the microporosity of the wet gel and obtaining materials with high specific surfaces and porosities. Indeed, the specific surface area of the aerogel supports and catalysts is about 120 $m^2 \cdot g^{-1}$even after a thermal treatment at 1200 °C (5 h). By comparison, the xerogel catalysts reveal a specific surface area respectively for the sol-gel, 41 $m^2 \cdot g^{-1}$ and for the impregnated, 68 $m^2 \cdot g^{-1}$. Those values are related to the high porosity of the aerogel materials (0.24 $cm^3 \cdot g^{-1}$ for the doped alumina and only 0.16 $cm^3 \cdot g^{-1}$ for the corresponding xerogel). An other important aspect is the platinum size distribution which is shorter for the catalyst prepared by impregnation on doped aerogel than for the xerogel catalyst. Furthermore, the platinum particles are more homogeneously distributed on the aerogel support. All these remarks display the importance of the drying mode for the final properties of the materials.

D. *Catalytic Tests*

The decomposition temperatures of the HAN/water mixtures, with and without the presence of supports or catalysts are reported in Figure 15. For the catalysts, the effective platinum content is also reported. The decomposition of the $HAN_{79\%}$/water mixture alone appears at a temperature of 165 °C.

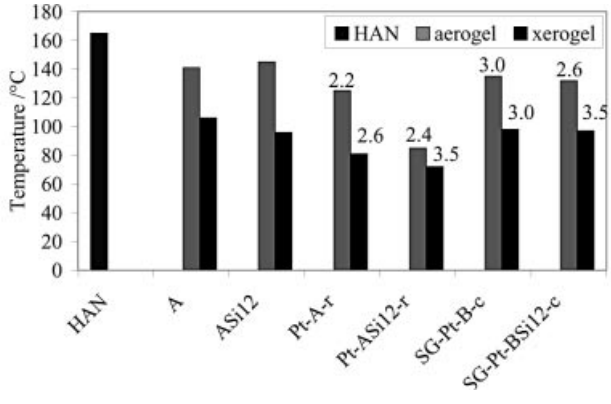

Figure 15. Decomposition temperatures of HAN/water mixtures with and without supports or catalysts and metal content for aerogels and xerogels materials

All the supports (without the active phase) display a catalytic effect. This effect is more pronounced in the case of the xerogel samples (106 °C for A (x) and 96 °C for ASi12 (x)). For the aerogels, the decomposition temperatures are higher and similar for each sample (140 °C). The very strong difference in the surface area between nondoped and Si-doped alumina seems to have a limited influence on this reaction. The introduction of platinum leads to a further catalytic effect in the case of the impregnated catalysts. A further decrease in the decomposition temperature, in comparison with the support, is of the order of 25 °C except for the Si-doped aerogel which display a decrease of 60 °C. For the sol-gel catalysts, the effect of platinum is much more limited.

With regard to the supports, the effect of the surface area remains very limited for the catalysts except for the impregnated aerogel samples Pt-ASi12-r (x) which display an important decomposition temperature decrease (from 125 °C to 85 °C) related to the surface area increase (1 $m^2 \cdot g^{-1}$ to 68 $m^2 \cdot g^{-1}$). For both samples the platinum is of the same order. The higher decomposition temperatures of the sol-gel catalysts compared with the impregnated catalysts are mainly due to the platinum particles sintering during the calcinations leading to a very low platinum accessibility. This effect is clearly observed for the samples Pt-ASi12-r (x) and SG-Pt-BSi12-c (x) which have the same effective metal content (3.5%) but exhibit a decomposition temperature difference of 20 °C. This indicates the importance of the preparation mode.

The comparison between aerogel and xerogel supports and catalysts shows that the xerogel samples are always more efficient (Figure 15). A possible explanation for this difference can be related to the higher insulation properties of the aerogels.[31] Due to its lower thermal conductivity and higher porosity, the temperature within the aerogel is lower than the measured crucible temperature, leading to a temperature difference higher than for xerogels and thus to a higher measured decomposition temperature. Moreover, when the exothermic decomposition starts on the external surface of the catalyst powder, the release energy propagates more slowly to the centre of the aerogel powder resulting in a delay in the decomposition reaction of the monopropellant.

Catalysts supported on silicon-doped alumina are promising for high temperature applications. Moreover, xerogel catalysts have been revealed to be better than aerogel catalysts despite the heterogeneous dispersion of silicon. To confirm this hypothesis, studies must be carried out on the decomposition characteristics, i.e. the temperature increase, pressure increase and ignition delay.

Conclusion

We have synthesised sol-gel materials based on pure or doped alumina using classical and supercritical drying con-

 © 2005 Wiley-VCH Verlag GmbH & Co. KGaA, Weinheim

ditions. For the supports, the morphology, thermal stability, homogeneity and the structure depend strongly on the drying technique used. The ASi12 sample displays a high parosity and it was selected as support of catalyst.

A general characteristic of all catalysts is that a fraction of the platinum is lost during the preparation of the catalysts and the real metal content is between 47 and 71% of the calculated value (5 wt.-%).

The comparison between the aerogel and xerogel samples displays, respectively, a fine distribution on the surface and a heterogeneous distribution of the metallic phase. This feature can be linked to the larger specific surface area of the aerogels.

The introduction mode of platinum by impregnation leads to smaller particles which are well dispersed. On the other hand, the sol-gel method results in the formation of large particles.

Finely, from our evaluation experiments on HAN solutions, the best catalytic activity is displayed by platinum catalysts prepared by impregnation on Si-doped xerogel alumina.

Experimental Section

A. Preparations

a) Support: Pure Alumina and Doped Alumina

The preparation procedure for pure alumina and Si-doped alumina $[(Al_2O_3)_{0.88}(SiO_2)_{0.12}]$ by the sol gel method has been described in previous work and is shown in Figure 16.[6] The ASi12 label for this material (Table 1) indicates the final molar composition (after drying and firing) as $SiO_2/(SiO_2+Al_2O_3) = 0.12$. The silica weight percent in the dried sample is 7.4%, corresponding to an atomic ratio Si:Al = 6.3:93.7.

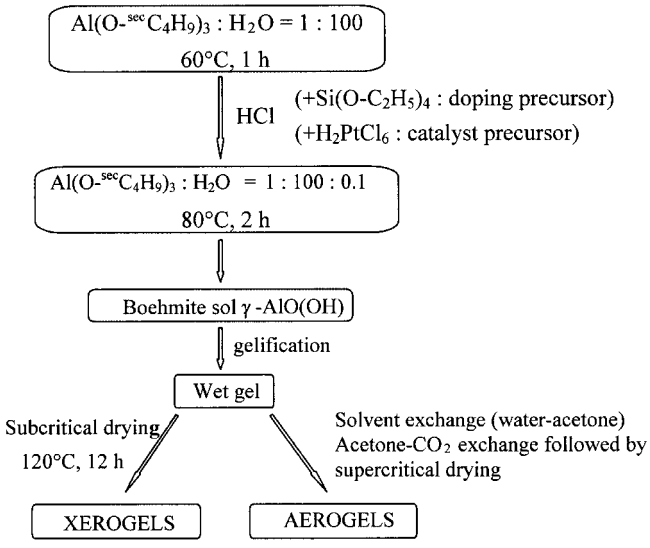

Figure 16. Scheme of the sol-gel preparation procedure

To prepare 2 g of support, aluminium tri-*sec*-butoxide (8.48 g, 0.0334 mol, 97%, Aldrich) and pure water (60.1 g, 3.34 mol) were stirred at 60 °C for 1 h. Concentrated hydrochloric acid (0.28 mL, 3.3 10^{-3} mol, 12 mol·L^{-1}) and, if necessary, tetraethoxysilane (0.51 mL, 2.24 10^{-3} mol, 98%, Aldrich) as a doping precursor were then added and the temperature was raised and maintained at 80 °C for 2 h.

The xerogel samples were obtained after drying overnight at 120 °C in a ventilated oven. For the aerogel samples, about 75% of the water content evaporated at 80 °C over 3 h affording a viscous sol which was poured in the drying mould (stainless steel, $d = 3.6$ cm, $h = 3.5$ cm). A 5-mm hole in the bottom of the mould enables the solvent exchange. After 15 h, the solvent exchange started: water was replaced first by acetone (complete miscibility) and then acetone was replaced by CO_2 just before the supercritical drying. The solvent exchange procedure was as follows: the wet gel was covered with acetone (about 25 mL) and the solvent was evacuated through the bottom hole before the addition of acetone (25 mL, three times a day over 5 days). The mould was then introduced into the autoclave (300 mL, Parr Instruments) and acetone (100 mL) was added. The autoclave was equipped with two entries (liquid CO_2 and argon) and two outflows (gas and liquid) and the temperature and the pressure can be controlled as shown in Figure 17.

The reactor was filled with liquid carbon dioxide using several filling and purging steps in order to quantitatively evacuate the acetone and the air contained in the autoclave. Upon completely filling the autoclave with liquid CO_2, a temperature difference was obtained between the bottle (room temperature) and the autoclave (water cooling system). The temperature difference (about 4−5 °C) was sufficient to push liquid CO_2 into the reactor because the pressure in the bottle (55 bar at 20 °C) exceeded the equilibrium pressure in the reactor (49 bar at 14 °C). After complete filling, the pressure was about 55 bar (Figure 18, point 1). The reactor was isolated and the temperature increased from 15 °C to 40 °C which led to an important pressure increase (step 1−2) up to 140−150 bar (inside the supercritical domain). After 1 h, the supercritical fluid was evacuated over 1 h at the same temperature and the pressure was decreased to 1 bar (step 2−3). The heating was then turned off and argon was flushed through the reactor (step 3−4). The aerogel was then taken out of the reactor.

Pure boehmites and Si-doped boehmites (aerogels and xerogels) were calcined at 1200 °C under air for 5 h (ramp of 5 °C·min^{-1}) to obtain pure or doped aluminas.

$$2\ AlOOH\ (s) \xrightarrow{1200°C} Al_2O_3\ (s) + H_2O\ (g) \quad (2)$$

b) Supported Platinum Catalysts (5 wt.-%)

The catalysts were prepared by two procedures: (i) a one step procedure using the sol-gel method or (ii) an impregnation procedure on a calcined support (pure or doped alumina).

Sol-Gel Procedure: The platinum precursor solution (H_2PtCl_6) was introduced during the preparation of the support in the sol with the hydrochloric acid (see Figure 16). The preparation procedure follows the same steps used for the support (drying, calcination at 1200 °C). The high temperature calcination induces the formation of metal by a redox reaction:[1]

$$H_2PtCl_6 \xrightarrow{1200°C} Pt^0\ (s) + 2\ Cl_2\ (g) + 2\ HCl\ (g) \quad (3)$$

Impregnation Procedure: A volume of the metallic solution (H_2PtCl_6) corresponding to the porous volume of the support

 © 2005 Wiley-VCH Verlag GmbH & Co. KGaA, Weinheim

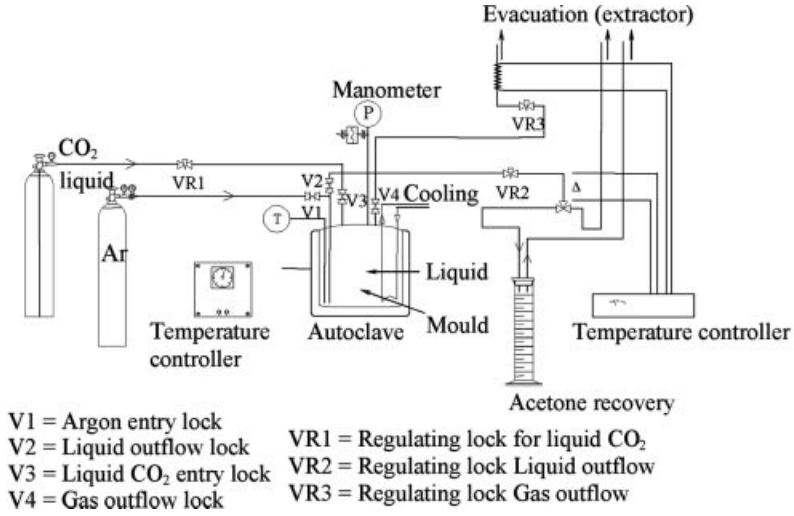

Figure 17. Diagram of the supercritical drying apparatus

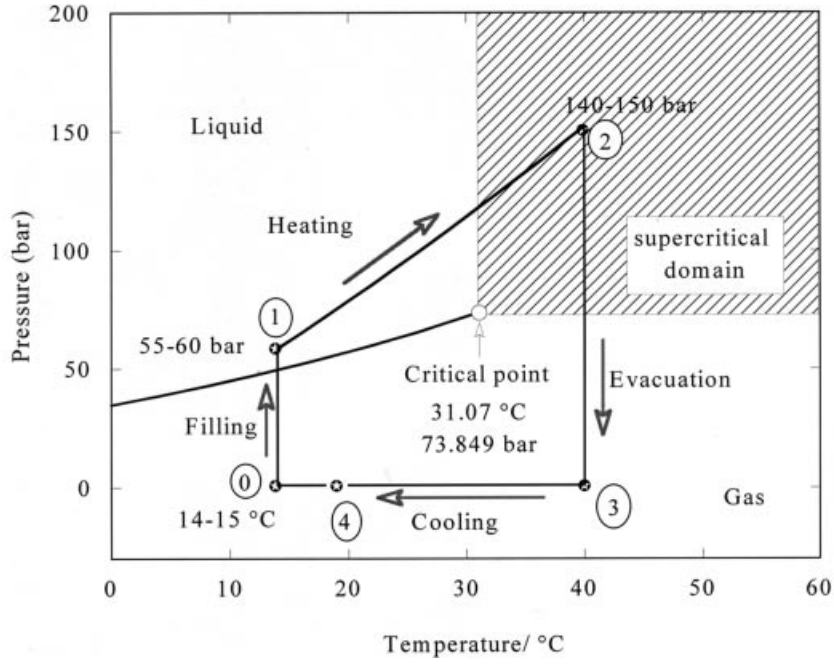

Figure 18. Diagram of the pressure and temperature for supercritical drying

(1.5 mL·g^{-1}) was added to the alumina (wetness impregnation). The concentration of the solution was then calculated giving a metal content of 5 wt.-%. The catalysts were dried overnight at 120 °C, calcined at 400 °C for 3 h under air (20 mL·min^{-1}) and reduced under H_2 (20 mL·min^{-1}) for 1 h at 200 °C and 2 h at 400 °C to obtain platinum supported alumina.

$$H_2PtCl_6\,(l) + 2\,H_2\,(g) \xrightarrow{400°C} Pt\,(s) + 6\,HCl\,(g) \quad (4)$$

Whatever the procedure, the introduction of the metallic precursor did not affect the acidity (pH near 1).

B. Characterisations

The effective metal load was determined from the CNRS analyses. The specific surface areas of the samples were determined by the BET method from the nitrogen adsorption isotherms at −196 °C in an automated Micromeritics ASAP 2000 apparatus after evacuation for 1 h 30 min at 350 °C. The method used is a simple BET 7 points procedure with P/P_0 values between 0.05 and 0.25. The complete adsorption and desorption isotherm was obtained for a few samples leading to the porous volume values.

Differential thermal analyses (DTA) and thermogravimetric analyses (TGA) were recorded in order to characterise the supports after

 © 2005 Wiley-VCH Verlag GmbH & Co. KGaA, Weinheim

drying. TDA-TGA experiments were carried out between 25 and 1350 °C using a thermal analyst 2100 TA instrument with platinum crucibles. The samples were heated in a nitrogen flow (100 mL·min^{-1}) with a ramp of 10 °C·min^{-1}.

Diffraction patterns and particles sizes were determined by X-ray diffraction (XRD) experiments performed on a Siemens D 5005 powder θ-θ diffractometer using the Cu-*Kα* radiation ($\lambda_{K\alpha}$ = 0.15186 nm) and a graphite monochromator. The diffraction patterns were obtained under the following conditions: dwell time: 2 s, step: 0.04°, constant divergence slit: 1°.

Crystalline phases were identified by comparison with PDF standards (Powder Diffraction Files) from ICDD. (AlOOH: 21−1307, α-Al_2O_3: 46-1212, θ-Al_2O_3: 23−1009, Pt: 04−0802)

The average crystallite sizes (D) were determined from the Scherrer equation: $D = (0.9\cdot\lambda)/(B\cdot\cos\theta)$, $\lambda = 0.15186$ nm, B is the width at half maximum and θ the Bragg angle for the peak in question (rad). For boehmite, the peak (020) was used without any correction due to the very small size of the particles. For platinum, the peaks (311) and (222) were used and a width correction was introduced, i.e. $B_{cor} = (B_{exp}^2 - B_{inst}^2)^{1/2}$. To determine B_{inst}, the analysis of standard LaB_6 powder was performed under the same conditions. The widths of the peaks were obtained by profile analyses using a pseudovoigt function from the diffract AT software (socabim, France).

The structural pictures were obtained using the software CaRine Crystallography.[32]

The platinum dispersion was obtained by hydrogen chemisorption at room temperature with a lab-build apparatus using pressure measurements. The samples (300 to 500 mg) were reduced at 400 °C over 1 h under a static pressure of hydrogen, degassed at this temperature over 1 h and cooled to ambient temperature. The adsorption isotherms enabled the determination of reversibly and irreversibly adsorbed hydrogen. The dispersion was calculated using the stoichiometric ratio H/Pt = 1.[4]

Platinum particle sizes and size distributions were obtained from transmission electron microscopy using a Philips CM 120 microscope with a linear resolution of 3.5 Å. Analyses by EDX enabled us to determine the distribution and quantification of atomic species (Al, Si and Pt). The lines used were *Lα* at 9.441 keV (Pt), *Kα* at 1.486 keV (Al) and *Kα* at 1.739 keV (Si), respectively.

C. Catalytic Tests

All samples were tested by the decomposition of an aqueous solution of HAN (hydroxylammonium nitrate, 79 wt.-%) prepared by water evaporation of a 20 wt.-% HAN solution [from SME (SME: French society of explosive materials)] in a rotating evaporator apparatus at 50 °C under vacuum conditions (water pump), the concentration was controlled by density measurements. The experiments were carried out in a TDA-TGA apparatus which gives a good estimation of the decomposition temperature.[4] The procedure was as follows. After placing the sample (15 mg) in an aluminium pan with a cover, the propellant was added with a micropipette (10 μL). The system was heated (10 °C·min^{-1}) to 250 °C under an argon flow (100 cm^3·min^{-1}). An example of the catalytic decomposition is given in Figure 19. The inflexion point of the temperature curve indicates the decomposition temperature. The analyses by TDA-TGA allowed us to obtain the following information: (i) the onset temperature of the decomposition, (ii) the concentration of the HAN solution at decomposition and (iii) the efficiency of the catalyst, i.e. the exothermic peak. The weight loss after a completed reaction is often different from the expected value due to the high exothermicity of the decomposition which destroys a small amount of catalyst.

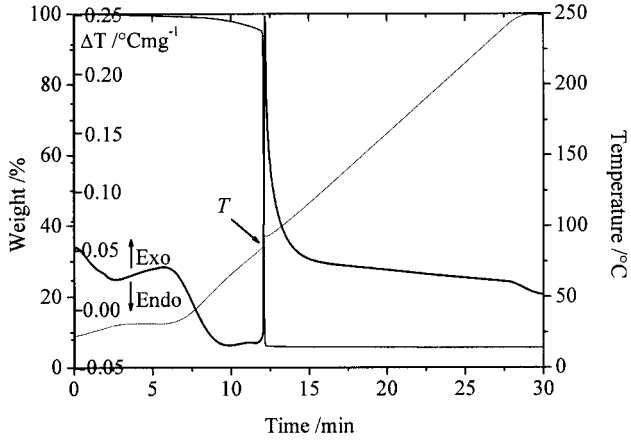

Figure 19. Example of the catalytic decomposition temperature of a HAN/water mixture on Pt-ASi-r (x)

Acknowledgments

The authors thank all the people working in the "service de Mesure Physique" of the LACCO.

[1] C. Wang, C. Yeh, *Appl. Catal.* **2001**, *209*, 1−9.
[2] E. Seker, N. Yasyerli, E. Gulari, C. Lambert, R. H. Hammerle, *Appl. Catal. B* **2002**, *37*, 27−35.
[3] R. D. Gonzalez, T. Lopez, R. Gomez, *Catalyis Today* **1997**, *35*, 293−317.
[4] R Eloidi, S. Rossignol, C. Kappenstein, D. Duprez, N. Pillet, *J. Prop. Power* **2003**, *19*, 213−219.
[5] G. M. Pajonj, *Catal. Today* **1999**, *52*, 3−13.
[6] S. Rossignol, C. Kappenstein, *Intern. J. Inorg. Mat.* **2001**, *3*, 51−58.
[7] J. S. Church, N. W. Cant, D. L. Trimm, *Appl. Catal. A.* **1993**, *101*, 105−116.
[8] Y. Mizushima, M. Hori, *J. Mater. Res.* **1993**, *8*, 2993−3014.
[9] Y. Mizushima, M. Hori, *J. Non-Cryst. Solids* **1994**, *167*, 1−8.
[10] C. K. Long, J. W. Richardson, M. Ozawa, *J. Alloys and Compounds* **1997**, *250*, 356−359.
[11] K. Balakrishnan, R. D. Gonzales, *J. Catal.* **1993**, *144*, 395−413.
[12] B. E. Yoldas, *J. Am. Ceram. Soc.* **1982**, *65*, 387−393.
[13] I. H. Cho, S. B. Park, S. J. Cho, R. Ryoo, *J. Catal.* **1998**, *173*, 295−303.
[14] S. Casillo, M. Moran-Pineda, V. Molina, R. Gomez, T. Lopez, *Appl. Catal. B* **1998**, *15*, 203−209.
[15] A. Manasilp, E. Gulari, *Appl. Catal.* **2002**, *37*, 17−25.
[16] A. G. Sault, A. Martino, *J. Catal.* **2000**, *191*, 474−479.
[17] A. F. Popa, S. Rossignol, C. Kappenstein, *J. Mater. Chem.* **2002**, *12*, 2866−2868.
[18] M Nguefack, A. F. Popa, S. Rossignol, C. Kappenstein, *Phys. Chem. Chem. Phys.* **2003**, *5*, 4279−4289.
[19] M. Trombetta, G. Busca, R. J. Wiley, *J. Colloid & Interf. Sci.* **1997**, *190*, 416−426.
[20] J. B. Miller, E. I. Ko, *Catal. Today* **1998**, *43*, 51−67.
[21] T. Horiuchi, T. Osaki, T. Sugiyama, *J. Non-Cryst. Solis* **2001**, *291*, 187−198.
[22] T. Horiuchi, L. Chen, T. Osaki, *Catal. Letters* **1999**, *58*, 89−92.

 © 2005 Wiley-VCH Verlag GmbH & Co. KGaA, Weinheim

[23] L. E. Sutton, *Tables of Interatomic Distances and Configuration in Molecules and Ions*, The Chemical Society, London, **1965**, 11 and 18.
[24] R. S. Zhou, R. L. Snyder, *Acta Crystallogr., Sect. B* **1991**, *47*, 617−630.
[25] A. F. Popa, PhD Dissertation, University of Poitiers, France, **2002**.
[26] C. K. Lambert, R. D. Gonzales, *Appl. Catal.* **1998**, *172*, 233−239.
[27] L. Khelifi, A. Ghorbel, E. Garbowski, *J. Chim. Phys.* **1997**, *94*, 2016−2026.
[28] A. Douidah, P. Marécot, S. Szabo, J. Barbier, *Appl. Catal.* **2002**, *225*, 21−31.
[29] W. L. Smith, *J. Appl. Cryst.* **1972**, *5*, 127−130.
[30] A. Martino, A. G. Sault, J. S. Kawola, *J. Catal.* **1999**, *187*, 30−38.
[31] L. W. Hrubesh, *J. Non-Cryst. Solids* **1998**, *2225*, 335−342.
[32] CaRine Crystallography 3.1 software, Boudias and Monceau, France.

Received July 28, 2004
Early View Article
Published Online December 6, 2004

 © 2005 Wiley-VCH Verlag GmbH & Co. KGaA, Weinheim

Outer-Sphere Hydration and Liquid−Liquid Partition of Metal(III) Chelates − Density Functional Calculations

Marian Czerwiński*[a] and Jerzy Narbutt[b]

Keywords: Metal chelates / Outer-sphere hydration / Hydrogen bonding / Aqueous solution / Liquid−liquid partition / Enthalpy of transfer / Density functional calculations / Solvent effects / Implicit solvation model

Hydration of two coordinatively saturated metal chelates, tris(propane-1,3-dionato)scandium(III) and tris(propane-1,3-dionato)cobalt(III), was studied theoretically using the density functional method with a three-parameter B3LYP implementation at different variants for calculating the hydration energy, including corrections for ZPVE, BSSE, polarisation functions, temperature and the number of hydrating water molecules in the system. Formation of hydrates was demonstrated, with water hydrogen-bonded to ligands (outer-sphere hydration). After corrections for side effects, good correlations were found between the energy and the length of these hydrogen bonds in the hydrates of both chelates. Also, the calculated changes in charge distribution on the atoms of hydrogen-bonded water in these model chelates qualitatively agree with the experimental ^{1}H NMR spectroscopic data for the analogous tris(pentane-2,4-dionato)cobalt(III) species. An implicit solvation model (SCI-PCM) was used to take into account solvent effects of water and heptane on the energies of the model chelates studied and to calculate their enthalpies of transfer from heptane to water. In spite of simplifications in the model, satisfactory agreement was found between the calculated values and the experimental standard enthalpies of transfer of the analogous chelates, namely the tris(pentane-2,4-dionates) of scandium and cobalt(III).
(© Wiley-VCH Verlag GmbH & Co. KGaA, 69451 Weinheim, Germany, 2005)

Introduction

Interactions between amphiphilic molecules and water play an important role in numerous chemical and biochemical processes. References cited in ref.[1] are devoted to theoretical studies on hydrogen bonding in systems consisting of relatively simple molecules. Theoretical chemistry well describes simple hydrogen bonded systems composed of two small molecules.[2] On the other hand, large hydrogen-bonded structures are of greater interest not only because of their chemical complexity but also due to their practical importance. Theoretical calculations make it possible to quantify hydrogen-bonding interactions in large supermolecular systems with light atoms (organic species), not only in vacuo but also in solvent-modelling environments.[3] Less common are theoretical studies on hydrogen bonding in metal complexes. Because of computational problems, investigations on such systems develop rather slowly, although fast and efficient methods based on density functional theory (DFT), supplemented by using polarisation functions, have been successfully applied to solve various chemical problems dealing with *d*- and *f*-electron metal ions.[4−8] DFT calculations were used to study the effect of hydrogen bonding between solvent molecules and ligands on the stability of copper(I) thiocyanate complexes. However, scarce information is available on the calculation details.[9] More informative in this context are extensive theoretical studies on the hydrogen bonding of various proton donors to metal hydrides.[10]

With only moderate success gained from theory, experimental methods still predominate in studying large hydrogen-bonded, metal containing structures. From the numerous problems intensively studied in this field, we have focussed on the interactions of amphiphilic metal chelates with solvent water. Hydrogen bonding is responsible for two effects observed in aqueous solutions of the chelates: (1) Hydrophobic hydration which makes the thermodynamic activity of the solute (chelate molecule) higher because of promotion of the local structure of water around the hydrocarbon fragments of ligands, resulting from hydrogen bonding between neighbouring water molecules and (2) outer-sphere hydration of metal chelates, i.e. hydrogen bonding of water molecules to hydrophilic fragments of coordinated ligands, in particular to electron-donor oxygen atoms that coordinate to the central metal ion. The latter process, resulting in a decrease in the thermodynamic activity of the

[a] Jan Dlugosz University, Institute of Chemistry and Environmental Protection,
Al. Armii Krajowej 13/15, 42200 Czestochowa, Poland
E-mail: mar_czerw@wp.pl
[b] Department of Radiochemistry, Institute of Nuclear Chemistry and Technology,
Dorodna 16, 03-195 Warsaw, Poland
Fax: (internat.) + 48-22-8111-532
E-mail: jnarbut@ichtj.waw.pl
Supporting information for this article is available on the WWW under http://www.eurjic.org or from the author.

solute, has been observed and comprehensively studied in a series of experimental studies by our group.[11]

All these aqueous-phase interactions influence liquid−liquid partition of metal chelates and play an important role in solvent extraction of metal ions. Unfortunately, as shown in our recent review,[12] many researchers who studied solvent extraction processes by computational modelling, focused their attention on the complex formation step and neglected hydration phenomena. The aims of the present work were: (1) To point out importance of the outer-sphere hydration, by supplying theoretical evidence for hydrogen bonding between molecules of water and coordinatively saturated metal chelates, (2) to reproduce properties of these hydrogen-bonded systems in terms of energy and (3) to evaluate the effects of various calculation approaches, including models, basis sets, polarisation functions and temperature, etc on the reliability of the calculation results.

A supermolecular approach[13] was used in this work which assumes formation of molecular adducts, i.e. the outer-sphere hydrates of metal chelates. Model molecules were studied with a fewer number of ligand CH_2 groups than in real chelates. Apart from the energies of adduct formation in the gas phase, standard enthalpies of transfer (heptane → water) of the model molecules were calculated and compared with experimental data for two coordinatively saturated metal acetylacetonates. Therefore, solvent effects were included in the calculations by modelling both liquid phases (heptane and water) with continuous electrostatic fields which surrounded the molecules studied. In the next section, various approaches used for the calculation of total energies of all the species studied after optimisation of their structures in the gas phase are presented.

Calculation Method

Let us assume that two molecules, X and HY, form a hydrogen-bonded adduct (hydrate) X···HY, accompanied by some deformation of the original molecules. The relative positions of X and HY in the hydrate can be described by the system of intermolecular coordinates, R. The internal coordinates of X and HY in the hydrate, r_X and r_{HY}, differ from the respective equilibrium values in the free molecules, r_Xf and r_{HY}f. According to the supermolecular approach, a fundamental formula for the energy of interaction (at 0 K) between X and HY is:

$$E_{int} = E_{XHY}(R,r_X, r_{HY}) - E_X(r_X f) - E_{HY}(r_{HY} f) + \Delta ZPVE \quad (1)$$

where $E_{XHY}(R,r_X,r_{HY})$ is the total energy of the hydrate and $E_X(r_X f)$ and $E_{HY}(r_{HY} f)$ are the total energies of the chelate and water molecules (fully optimised). The E_{int} value must be corrected for the difference between the zero-point vibrational energies (ZPVE − energy of molecular vibrations at 0 K) of the hydrate and its free components, ΔZPVE. If polarisation functions are included in the basis sets used, we denote the energies with *, e.g. E^*_{int}.

Because Equation (1) overestimates the intermolecular attraction, the interaction energy in weakly bound supermolecules should be corrected for the basis set superposition error (BSSE). We applied the counterpoise procedure described by Boys and Bernardi[14] and calculated total energies of the X and HY molecules in the hydrate geometry and in the hydrate basis set: $E_{X(HY)}(R,r_X,r_{HY})$ and $E_{HY(X)}(R,r_X,r_{HY})$:

$$E^0_{int.} = E_{XHY}(R,r_X,r_{HY}) - E_{X(HY)}(R,r_X,r_{HY}) - E_{HY(X)}(R,r_X,r_{HY}) + \Delta ZPVE \quad (2)$$

In many systems this correction, BSSE = $E^0_{int} - E_{int}$, is larger than the energy difference which results from the Born-Oppenheimer approximation and from neglecting anharmonicity.

The calculations [Equations (1)−(2)] refer to 0 K. In order to predict the energy of the system at a nonzero temperature T, terms for a thermal energy correction must be added to the total energies, i.e. E_A (A = XHY, HY, or X) which includes the effects of molecular vibration $E_{A,vib}$, rotation $E_{A,rot}$ and translation $E_{A,transl}$:

$$E^T_A = E_A + E_{A,vib} + E_{A,rot} + E_{A,transl} \quad (3)$$

The energy of interaction can then be calculated without the zero-point correction:

$$E^T_{int.} = E^T_{XHY} - E^T_X - E^T_{HY} \quad (4)$$

All the energies calculated for the gas phase are not directly comparable with the experimental data which refer to the process of the chelate transfer from heptane to water. To make such a comparison plausible, solvent effects of the liquid environment on the solute energy must be taken into account in the calculations, e.g. by use of a Self-Consistent Isodensity Polarised Continuum Model (SCI-PCM).[15] This procedure locates the solute molecule within a cavity formed in the field with the dielectric constant of a given liquid, either water (ε_w = 78.3) or heptane (ε_h = 1.92), and then the electron density is determined which minimises the energy of the whole system. The optimised gas-phase structures of all the species (hydrate, chelate and water molecules) were used.

From the thermodynamic point of view, the process of aqueous-phase hydration of a solute molecule (e.g. metal chelate) originally present in another phase (e.g. heptane) can be divided into two steps: (1) Transfer of the chelate molecule to the aqueous solution, followed by (2) addition of water molecule(s) present in bulk water to the chelate by, for example, hydrogen bonding, i.e. formation of a supermolecule (hydrate) in the aqueous phase. The energy change (at 0 K) corresponding to formation of the 1:1 adduct is

 © 2005 Wiley-VCH Verlag GmbH & Co. KGaA, Weinheim

$$E_{h-w} = E_{XHY}(w) - E_X(h) - E_{HY}(w) + \Delta ZPVE \quad (5)$$

where the total energies of the molecules (defined by the indexes) are calculated in the field of either water (w) or heptane (h). Assuming that the small temperature correction, $\Delta E^T = E^T_{int.} - E_{int}$, does not depend on the environment, the energy change at temperature T is equal to $E^T_{h-w} = E_{h-w} + \Delta E^T$ and (with the definition $H^T_A = E^T_A + RT$) the enthalpy change for the 1:1 adduct formation is $\Delta H^T_{h-w} = E^T_{h-w} - RT$. The same also holds for the 1:3 adduct, assuming that one of its components is a single molecule of a water trimer.

The calculations were first carried out in the model systems consisting of a molecule of water and a molecule of the metal chelate, i.e. M(mala)$_3$ = tris(propane-1,3-dionato)scandium(III) or tris(propane-1,3-dionato)cobalt(III). The ligand was a deprotonated enol form of malonaldehyde, [O=CH−CH=CH−O]$^-$, abbreviated as mala$^-$, which we assumed to be a suitable model for the pentane-2,4-dionate (acetylacetonate) anion. The metal ions scandium and cobalt(III) were selected for this study because their tris(acetylacetonates), M(acac)$_3$, have been experimentally[11d,11c] characterised as having the highest and the lowest standard enthalpies of transfer (see Table 5) within the whole series of 3d metal(III) ions. In other calculation systems, more water molecules were then used (see below). In all cases, the addition of water molecule(s) to the chelates resulted in the formation of the water adducts, either M(mala)$_3$·H$_2$O or M(mala)$_3$·3H$_2$O, further referred to as hydrates.

The present calculations were based on the Density Functional Theory (DFT),[16] using the Lanl2dz double-ζ basis set[17] and the three-parameter Becke functionals of the B3LYP[18] type. The Berny geometry-optimisation algorithm[19] was applied to calculate the geometries of the neutral metal chelates, water and its multimers, as well as the 1:1 and 1:3 hydrates. The system Hessian with $(3n-6)$ eigenvalues confirms that the minimum energies were found for all the compounds. The calculations have also been performed with the use of the Huzinaga polarisation functions on each atom.[20] All the calculations were carried out by means of the Gaussian 94 package[21] using Cray J90 and Cray Y-MP supercomputers.

Results and Discussion

Geometry and Charge Distribution

Table 1 shows some selected B3LYP geometrical parameters of the model chelate molecules [distorted octahedral Sc(mala)$_3$ and Co(mala)$_3$] in the gas phase and the charge distributions on some of their atoms. The geometries mirror the experimental data for their crystalline analogues, Sc(acac)$_3$ and Co(acac)$_3$, within an acceptable error. The calculated M−O distances are somewhat shorter (by 0.02 - 0.03 Å). This is in accordance with the temperature difference (room temp. vs. 0 K for the calculations) and with the difference in the structure of the ligands, i.e. lack of two electron-releasing methyl groups in each mala$^-$ ligand in comparison with acac$^-$. The much larger span of the calculated atomic charges on Sc−O compared with Co-O (Table 1) can be interpreted in terms of a stronger covalent nature of the Co−O bond. The full set of calculation data for all components studied, including the hydrates (see below), is given in the Supporting Information (Table 8; for Supporting Information see also the footnote on the first page of this article).

The interaction between water and the metal chelates leads to formation of the adducts (hydrates) which can be considered to be supermolecules. Theoretical calculations of the structures of these adducts were carried out by minimising the energy of systems consisting of one molecule of a given chelate and one (or more) water molecule(s) in the gas phase (vacuum). The initial position(s) of the water molecule(s), i.e. the initial distance between the central metal ion M and the oxygen atom of water (or of a water molecule in a cyclic multimer), O$_w$, was varied. For the 1:1 adducts, three different cases were considered: (1) d(M−O$_w$) < 2.5 Å, the water molecule would be expected to coordinate directly to the M^{3+} ion by means of a lone electron pair on the O$_w$ atom, thus increasing the coordination number (CN) of M^{3+}. This model corresponds to the inner-sphere hydration of the chelate. Optimisation of such a structure led to strong deformations and eventually "decomposition" of the water molecule which is inconsistent with the experiments on tris(acetylacetonates) of scandium[11d] and cobalt(III).[11c] This result confirms our basic assumption that the chelates studied are coordinatively saturated. (2) d(M−O$_w$) > 4.5 Å, the water molecule approached the CH groups or π-electrons of the ligand,

Table 1. Selected geometrical parameters of M(mala)$_3$ chelates in the gas phase and charge distributions on some of their atoms after DFT-B3LYP optimisation, and experimental structural parameters for crystalline M(acac)$_3$ chelates

Chelate	State	d(M−O) (Å)	Bite angle (°)[a]	q(M)	q(O) av.	Reference
Sc(mala)$_3$	gas	2.093	80.6	1.320	−0.445	this work
Co(mala)$_3$	gas	1.913	96.8	0.328	−0.289	this work
Sc(acac)$_3$	cryst.	2.070(9)	81.5(2) −82.3(2)	–	–	[22]
Co(acac)$_3$	cryst.	1.888(4)	96.2(2) −96.7(2)	–	–	[23]

[a] The angle O−M−O, both O atoms belonging to the same ligand.

 © 2005 Wiley-VCH Verlag GmbH & Co. KGaA, Weinheim

weakly interacting with them. However, the total energy of such systems was rather high, therefore this was not the case of interest. (3) 4.0 Å < d(M−O_w) < 4.5 Å, the system attained the lowest energy. The water molecule formed a hydrogen bond with one of the oxygen atoms of a ligand in the M(mala)$_3$ molecule. The reliability of our model of the outer-sphere hydration of the chelates has been confirmed this way. Additional calculations of the second derivatives of the energies for Sc(mala)$_3$ − H_2O and Co(mala)$_3$ − H_2O systems confirmed that the true energy minimum was attained. The optimised structure of the Co(mala)$_3$·H_2O adduct in the gas phase is given in Figure 1.

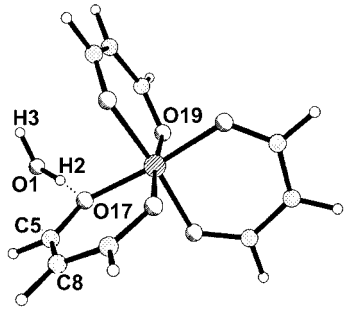

Figure 1. The optimised gas-phase structure of monohydrate Co(mala)$_3$·H_2O. The metal ion occupies the central position. The other atoms mentioned in the text are numbered. Full numbering is given in the Supporting Information (Figure 8.2). The hydrogen bond between the water molecule and a ligand oxygen atom is shown by a dotted line.

Table 2 shows some selected geometrical parameters of the 1:1 hydrates and the changes in the charge distribution on selected atoms due to the hydrate formation. In both hydrates the oxygen atom of the water molecule is located at a short distance (ca. 2.8 Å typical for hydrogen bonding) from one of the oxygen atoms (O17 − For numbering of atoms in the hydrates see Figure 1 and Figure 2 and also Supporting Information, Figures 8.2 and 8.3) of a mala$^-$ ligand. The angles α (O1−H2−O17), β (O1−O17−C5) and γ (C8−C5−O17−O1) deviate slightly (by less than 10°-20°) from the expected values (sp^2 hybridisation of the ligand oxygen atoms was assumed): 180°, 120° and 180°, respectively. This shows that the hydrogen bond O1−O17 is nearly linear and only slightly deviates from the direction of the lone electron pair on the O17 atom. The small difference between O1−O17 distances in Co(mala)$_3$·H_2O and in Sc(mala)$_3$·H_2O points to a stronger hydrogen bond in the former hydrate, in spite of much less negative charge on the oxygen atoms in Co(mala)$_3$ than that in Sc(mala)$_3$ (Table 1). The electrostatic model of hydrogen bonding is, therefore, inapplicable for the hydrates studied.

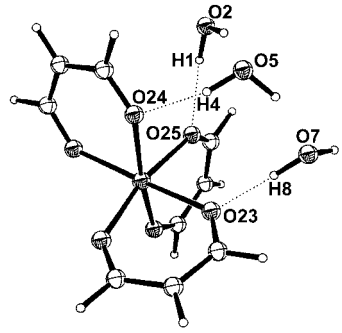

Figure 2. The optimised gas-phase structure of the trihydrate Sc(mala)$_3$·3H_2O. The metal ion occupies the central position. The other atoms mentioned in the text are numbered. Full numbering is given in the Supporting Information (Figure 8.3). The hydrogen bonds between water molecules and ligand oxygen atoms are shown by dotted lines.

Table 2. DFT-B3LYP optimisation of monohydrates M(mala)$_3$·H_2O in the gas phase: Selected geometrical parameters, changes of charge distribution on selected atoms in the chelates upon hydrate formation (the numbering of indicated atoms is given in Figure 1)

M	Distances (Å)		Bond angles[a] (°)			Charge distribution changes on some atoms[b]					
	O1−O17	O1−O19	α	β	γ	M	O17	O19	H2	O1	H3
Sc	2. 806	3.244	171.1	111.5	175.2	−0.012	−0.060	−0.014	+0.074	−0.050	−0.008
Co	2.799	3.501	160.1	110.5	170.1	+0.009	−0.086	−0.003	+0.068	−0.042	−0.015

[a] The angles are: α = O1−H2−O17; β = O1−O17−C5; γ = C8−C5−O17−O1. [b] The charge change, Δq, is the difference between the atom charge in a given hydrate and in the respective chelate or water, calculated using Mulliken population analysis.

Table 3. DFT-B3LYP optimisation of trihydrates M(mala)$_3$·3H_2O in the gas phase: selected geometrical parameters and changes in charge distribution on selected atoms upon hydrate formation (the numbering of indicated atoms is given in Figure 2).

M	Hydrogen bond lengths (Å)					Water bond angles[a]	Charge distribution changes, Δq			
	O2−O25	O5−O24	O7-23	O2−O7	O5−O7		M	O_{ch}[b]	H_w [b]	O_w [b]
Sc	3.003	2.918	2.693	2.748	2.711	158	−0.030	−0.059	+0.023	+0.010
Co	2.949	2.874	2.759	2.847	2.829	160	+0.022	−0.087	+0.023	+0.018

[a] Average angles between the O−H bonds in the three hydrating water molecules (°). [b] Average changes in charge distribution on selected atoms: oxygens in the water molecules (O_w = O2, O5 and O7); the hydrogens in the water molecules participating in hydrogen bonding (H_w = H1, H4 and H8) and the oxygens in the chelate molecules participating in hydrogen bonding (O_{ch} = O25, O24 and O23). Δq is defined in Table 2.

 © 2005 Wiley-VCH Verlag GmbH & Co. KGaA, Weinheim

Formation of the $M(mala)_3 \cdot nH_2O$ adducts is accompanied by small changes in the geometries of the original molecules and in the charge distributions on their atoms (Table 2 and Table 3, as well as Table 8 in Supporting Information). For example, in the 1:1 adducts, the Sc−O17 distance increases by about 0.03 Å, while the Co-O17 distance increases only by 0.004 Å. This difference may be explained in terms of a stronger covalency and greater strength of the Co−O bond compared with the Sc−O distance. The other M−O distances remain practically unchanged. In both systems the O1−H2 distances increase by about 0.01 Å and the angles H3−O1−H2 slightly decrease. The electron densities increase on the hydrogen-bonded oxygen atoms (O17, O1) and decrease on the hydrogen (H2). The summed-up decrease in the electron density on all hydrogen atoms of water in the hydrates is consistent with the significant downfield shift of the water proton resonance observed in the ^1H NMR spectrum of the $Co(acac)_3$ solution.[11b] All the results give us a picture of the hydrogen bonded systems which is in accordance with the hypothesis of outer-sphere hydration of metal chelates, based on the earlier experiments.[11]

Quite surprisingly, the analysis of the geometries of the hydrates has shown that apart from the expected hydrogen bond between the water molecule and a donor oxygen atom in the ligand of each chelate, an additional hydrogen bond has been detected in the scandium (but not the cobalt) hydrate. The relatively short O1−O19 distance in $Sc(mala)_3 \cdot H_2O$, equal to 3.24 Å, can be considered as evidence for a very weak hydrogen bond between the water molecule and another ligand in the chelate. The corresponding distance of 3.50 Å in $Co(mala)_3 \cdot H_2O$ is too long for hydrogen bonding. This additional interaction may explain why the total decrease in the electron density on the whole hydrogen bonded water molecule is larger in $Sc(mala)_3 \cdot H_2O$ ($\Delta q = +0.016$) than in $Co(mala)_3 \cdot H_2O$ ($\Delta q = +0.011$).

Since each chelate molecule in question has more than one hydrophilic site, we also studied its hydration taking into account more than one water molecule. Earlier semiempirical and ab initio calculations have shown that the lowest energy of a system consisting of a number of H_2O molecules in the gas phase is attained when the water molecules form cyclic multimers.[24,25] We have optimised the structures of the cyclic multimers consisting of three, six and nine H_2O molecules. After placing each multimer close to the chelate molecule [4.0 Å $< d(M\text{-}O_w) <$ 4.5 Å, where O_w denotes one of the oxygen atoms in the multimer], the systems were optimised again until the global minimum for each system (hydrate) was attained. Full optimisation of the 1:3 hydrates resulted in strong structural changes in the cyclic water trimer, i.e. breaking one of its hydrogen bonds, stretching the resultant chain and attaching it by means of hydrogen bonding to three oxygen atoms in the three mala ligands (Figure 2).

These structural changes may be considered to be a template effect. Optimisation of the systems with the water hexamer and nonamer led to formation of the 1:3 hydrate as well. The remaining water molecules were separated from the hydrate and moved away.

Table 3 shows some selected geometrical parameters (B3LYP) of the 1:3 hydrates and changes in the charge distributions on chosen atoms due to the hydrogen bonding. The average length of hydrogen bonds formed between the water molecules and the three mala ligands is somewhat shorter in $Co(mala)_3 \cdot 3H_2O$ (2.86 Å) than in $Sc(mala)_3 \cdot 3H_2O$ (2.87 Å) although the difference is small. In contrast, the deformation of the original water trimer is much stronger in the former hydrate. This is evidenced by longer distances between the neighbouring oxygens in the trimer chain in $Co(mala)_3 \cdot 3H_2O$ than in $Sc(mala)_3 \cdot 3H_2O$, 2.84 Å versus 2.73 Å on average. Both distances have significantly increased from the original 2.58 Å calculated for the cyclic water trimer (see Supporting Information, Table 8.5).

The summed-up decrease in the electron density on the three hydrogen bonded water molecules is greater in $Sc(mala)_3 \cdot 3H_2O$ ($\Delta q = +0.051$) than in $Co(mala)_3 \cdot 3H_2O$ ($\Delta q = +0.030$). This agrees very well with the respective changes on the single water molecules in the corresponding monohydrates, which are three times less (see above).

Energy of Hydrogen Bonding

The next challenge was to explain, at least at a model level, a possible reason for the stronger hydration (in aqueous solution) of $Co(acac)_3$ compared with $Sc(acac)_3$,[11d] something which was unexpected from the viewpoint of the electrostatic model of hydrogen bonding (see above). Therefore, the energy of hydrogen bonding between $M(mala)_3$ and water molecule(s) was calculated. It was assumed to be

Table 4. Energies of hydrogen bonding in the $M(mala)_3 \cdot nH_2O$ hydrates in the gas phase, X [kJ·mol^{-1}], calculated (DFT-B3LYP) in various variants

n	*T*, K	X	X_{Sc}/X_{Sc}^{cor} [a]	X_{Co}	$\Delta X_{Sc/Co}$[b]	X^*_{Sc}/X^{cor}_{Sc} [a,c]	X^*_{Co}[c]	$\Delta X^*_{Sc/Co}$[b,c]
1	0	E_{int}	−27.4/−18.7	−23.8	−3.6/+5.1	−18.3/−12.4	−16.9	−1.4/+4.5
1	0	E^0_{int}	−18.1/−9.4	−13.3	−4.8/+3.9	−11.6/−4.7	−8.1	−3.5/+3.4
1	298	E^T_{int}[d]	−26.5/−17.8	−22.5	−4.0/+4.7	−17.4/−11.5	−15.6	−1.8/+4.1
1	0	E_{int} − ZPVE[d]	−35.4	−31.2	−4.2	−26.3	−24.3	−2.0
3	0	E_{int} − ZPVE[d]	−26.1	−23.7	−2.4	−28.7	−26.7	−2.0

[a] $X_{Sc}{}^{cor} = E_{HB} = E_{int} - E_{HB}'$. $E_{HB}' = -8.7$ kJ·mol^{-1} (for X_{Sc}) or -5.9 kJ·mol^{-1} (for X^*_{Sc}). [b] $X_{Sc} - X_{Co}$ or $X_{Sc} - X_{Co}/X_{Sc}{}^{cor} - X_{Co}$. [c] X^* values calculated with the use of polarisation functions. [d] For the values of ΔZPVE and temperature corrections see Supporting information, Table 6b.

 © 2005 Wiley-VCH Verlag GmbH & Co. KGaA, Weinheim

the energy of interaction between the given molecules in the gas phase at 0 K (Table 4).

Since the DFT method takes into consideration a significant part of the electron correlation energy,[26] we could expect high accuracy and reliability from the calculations. Furthermore, the method was verified based on the comparison of the results obtained by the density functional calculations (using BLYP and BP functionals) with the exact solution of the Schrödinger equation for the helium atom in a model of harmonic interactions (Hooke model). Within the BLYP functional, the error in the total energy amounted to 0.87%, which was a half the error resulting from the Hartree−Fock method, while the BP functional energy error was only 0.08%.[27] This means that the DFT method with various correlation potentials is quite effective.

For the 1:1 hydrates the calculations were carried out in different variants, including (or not) corrections for the BSSE, ZPVE and temperature using (or not) the polarisation functions on each atom. Corrections for BSSE made the results even worse. An improvement was obtained using calculations with the polarisation functions. The temperature corrections gave negligible effects. On the other hand, a correction for the energy of the additional H-bond in $Sc(mala)_3{\cdot}H_2O$ (see above) appeared to be very important. This was calculated as the difference between the total energy of the optimised $Sc(mala)_3{\cdot}H_2O$ molecule, E_{XHY}, and the total energy of the same molecule with a somewhat distorted geometry, E_{XHY}', i.e. where the water molecule was twisted around the O1−O17 axis enough to break this additional bond but keeping unchanged all other important interactions, in particular the length of the main (O1−O17) hydrogen bond. The magnitude of this correction, E_{HB}', depended on the calculation variant (see Table 4−5 and Supporting Information, Table 6). The energy of formation of the main H-bond, E_{HB}, in $Sc(mala)_3{\cdot}H_2O$ was calculated by subtracting the E_{HB}' value from the interaction energy, e.g. E_{int}, while in $Co(mala)_3{\cdot}H_2O$ the E_{HB} value was equal to E_{int}. This led to a significant improvement in the results. The differences between the E_{HB} values in $Sc(mala)_3{\cdot}H_2O$ and $Co(mala)_3{\cdot}H_2O$ became positive, independently of the calculation variant (in particular, corrections for polarisation functions appeared negligible). In this way, the expected relationship between the calculated energies and lengths of the hydrogen bonds was achieved.

For the 1:3 hydrates, the calculations were carried out only in the simplest variant with no corrections for BSSE, ZPVE and temperature. In contrast to the expectation that three water molecules would bind to the chelate much more strongly than one, the calculated energies of gas-phase interactions of the chelates with the water trimer appeared comparable with those calculated in the same variant for the single H_2O molecule (Table 4, two last Entries). Moreover, the negative $\Delta E_{Sc/Co}$ values observed for the formation of the trihydrates, $Sc(mala)_3{\cdot}3H_2O$ and $Co(mala)_3{\cdot}3H_2O$, again led to incorrect correlation between the formation energy and the average length of the three hydrogen bonds in the trihydrates considered. This inconsistency is probably due to the significant energy required to break one hydrogen bond in the original cyclic water trimer and to stretch out the remaining two. Geometrical considerations (see above) showed that the energy must be larger in $Co(mala)_3{\cdot}3H_2O$ than in $Sc(mala)_3{\cdot}3H_2O$ because of stronger distortions of the water trimer in the former hydrate. Subtracting these contributions from the formation energies of the trihydrates would make the energies of hydrogen bonding much more negative (as expected) and restore the correct length-energy correlation. These conclusions were corroborated by the energies calculated in the SCI-PCM field.

Chelate Hydration in an Aqueous Medium. Enthalpy of Chelate Transfer

The final goal of the present work was to verify the calculated energies by comparison with the experimental data. The energies calculated for the gas phase can hardly be used for this purpose because the interaction energy significantly depends on the environment of the interacting species. The experimental values we can use for the comparison are standard enthalpies of transfer (heptane → water) of the tris(acetylacetonates) $Sc(acac)_3$ [11d] and $Co(acac)_3$ [11c] at 298 K which include the energy changes due to chelate hydration in the aqueous phase.

In order to compare these values, the enthalpy of transfer of $M(mala)_3$ chelates was calculated, taking into account solvent effects of the aqueous and heptane environments as was discussed above. The reasons why only the enthalpies and not the Gibbs free energies were used for the comparison of hydrogen bonding of water molecule(s) with the

Table 5. Enthalpies of transfer (heptane → water) of $M(mala)_3$ chelates [$kJ{\cdot}mol^{-1}$]. The energies of the species were calculated (DFT-B3LYP) in the SCI-PCM field corresponding to either water (H_2O and hydrates) or heptane (chelates); no BSSE correction

Model[a]	T, K	ΔH_{Sc}	ΔH_{Co}	$\Delta(\Delta H)_{Sc/Co}$
Field only, no hydrate formation	0 K	−36.8	−41.7	+4.9
1:1 hydrate[b]	0 K	−46.0	−50.6	+4.6
1:1 hydrate[b]	298 K	−45.1	−49.3	+4.2
1:1 hydrate, no ZPVE[b]	0 K	−54.1	−58.0	+3.9
1:3 hydrate, no ZPVE	0 K	−64.2	−67.3	+3.1
Experimental enthalpies of transfer of $Sc(acac)_3$ and $Co(acac)_3$	298 K	−41.4 ± 1.8	−52.7 ± 0.6	+11.3 ± 1.9

[a] For the energies of transfer for the formation of monohydrates, in all the calculation variants available, see Supporting information, Table 7. [b] For $Sc(mala)_3{\cdot}H_2O$, $E_{HB}' = -2.3\ kJ{\cdot}mol^{-1}$ was subtracted (see Table 4) from ΔH_{Sc}.

 © 2005 Wiley-VCH Verlag GmbH & Co. KGaA, Weinheim

model and real chelates differing in the number of CH_2 groups in the ligands were as follows: (1) It was experimentally shown that for similar, coordinatively saturated beryllium β-diketonates with ligands belonging to the homologous series of acetylacetone, the enthalpies of transfer did not practically differ,[11a,28] while the free energies regularly increased with each CH_2 group added. (2) The implicit solvation model, SCI-PCM, used in the calculations does not take into account the interactions of the solute with solvent molecules which leads to formation of a solvation shell around the solute.[12] This is particularly important for aqueous solutions where the entropy term, related to this specific hydration, strongly contributes to the Gibbs energy. Therefore, to calculate the free energy of hydration of neutral molecules a special approach[29] must be used.

The electrostatic fields, used in modelling the liquid phases, modified the energies of interaction of the chelates with water to a different extent which made the energy in the cobalt system distinctly more negative than that in the scandium case, in line with the experimental observations.

Table 5 shows the enthalpies of transfer (heptane → water) of the model chelates, calculated for three different cases which refer to the species in the field of water, the species being the chelate molecule alone (no hydrate formation), the 1:1 hydrate and the 1:3 hydrate. The results shown relate to some selected variants, while the energies of transfer for the case of formation of monohydrates, calculated in all variants including BSSE corrections, the use of polarisation functions etc. are shown in Supporting Information, Table 7. The numerical values calculated with polarisation functions are somewhat less negative than the corresponding values given in Table 5, but the respective differences are very close to those in Table 5. The calculated enthalpies of transfer became more negative when more water molecules were involved in hydrogen bonding with the chelates, according to expectations. A comparison of the calculated enthalpies with the experimental standard enthalpies of transfer of the analogous tris(acetylacetonates) shows that all the values are similar, even those calculated for the case which assumed only the effect of the environment (field) with no hydrate formation. The latter result, which was rather unexpected, shows that the implicit solvation model used estimates the energy of the solute-solvent interactions in aqueous solutions very well. The calculated energy of transfer of the chelate ("solute") molecules to the field modelling water is only by about 10−20 kJ·mol^{-1} higher than the values which include the energy of hydrogen bonding of the chelate with individual (explicit) water molecule(s) which form a solvation shell around the "solute". Simply, the interactions of the "water field" with the hydrophilic sites of all "solutes" produce negative contributions to the total energies of the solutes. If these hydrophilic sites are already hydrated, the contributions are smaller. That is why the energies of chelate hydration calculated in the water field are higher than those calculated in the gas phase. (This is also in line with the observation that the E_{HB}' corrections calculated in the SCI-PCM field are distinctly smaller than those calculated in the gas phase.) Most probably, the water field interacts with the hydrated hydrophilic sites via the attached water molecule(s). The more "open" the structure of the site, the stronger the interactions. This is the case with both hydrates of $Co(mala)_3$: the lack of additional hydrogen bonding in the monohydrate and a more distorted structure of the water trimer in the trihydrate. Stronger interactions with the water field of these structures, more "open" that those in the hydrates of $Sc(mala)_3$, restore the correct relationship between the calculated energies of hydration (enthalpies of transfer) of both chelates. This consistency confirms that the model used in this work may be considered not only qualitatively but also quantitatively reliable.

In all cases, the differences between the calculated enthalpies of transfer, $\Delta(\Delta H)_{Sc/Co}$, are significantly smaller than the experimental value (Table 5) but because of simplifications in the model, they seem to be acceptable. It has been shown, therefore, that theoretical calculations can be used to evaluate the thermodynamic functions (at least the enthalpy) of the partition of neutral molecules of coordinatively saturated metal chelates between water and organic solvents. This possibility is particularly important when studying solvent extraction of metal ions.[12]

Conclusions

The calculations by means of the DFT B3LYP method on large hydrogen bonded systems, i.e. hydrates of two neutral, coordinatively saturated chelates of scandium and cobalt(III), confirm our earlier assumption that hydration of the chelates takes place in their outer coordination spheres by ligand hydration through hydrogen bonding. Simple calculations for the gas phase at 0 K result, however, in incorrect correlations between the length and the energy of the hydrogen bonds for the two hydrates. More careful examinations of the systems studied, allowed us to find interactions other than the expected hydrogen bonding which contributed to the energy of hydrate formation and disturbed the correlation. These were (1) an additional hydrogen bond in the 1:1 hydrate of the scandium (but not cobalt) chelate and (2) different distortions of the original water trimer in the 1:3 hydrates. Subtracting these contributions from the energy of hydrate formation restored the correct length vs. energy relationship for the hydrogen bonds considered.

However, the calculations of the interaction energy in the gas phase do not correctly reflect the interactions in aqueous solution because solvent effects to a different degree contribute to the total energy of the solutes (hydrates). The use of an implicit solvation model, SCI-PCM, allowed us to compare the energies calculated for this model system with the experimental standard enthalpies of transfer (heptane → water) of two analogous chelates, namely tris(acetylacetonates) of scandium and cobalt(III). In spite of simplifications in the models used and discussed in the paper, a good agreement was observed. Therefore, a correct understanding of phenomena related to the outer-sphere hydration and their quantitative description became possible.

 © 2005 Wiley-VCH Verlag GmbH & Co. KGaA, Weinheim

In particular, standard enthalpies of partition of simple, coordinatively saturated metal chelates in solvent extraction systems (water/organic solvent) can be evaluated. Moreover, even the use of the most simplified solvation model, consisting of the electrostatic field alone without assuming hydrate formation, resulted in a quite satisfactory agreement with solvent extraction experiments, as far as the enthalpy of transfer was concerned.

General conclusions can also be drawn, namely (1) the present-day state of computational chemistry makes possible reliable calculations of hydrogen bonding energies in large metal-containing systems, (2) the supermolecular model well describes hydrogen bonding interactions between metal chelates and water molecules and (3) the implicit solvation model (SCI-PCM) is an adequate tool for calculating the energy of solute-solvent interactions of coordinatively saturated metal chelates and water and, in particular, standard enthalpies of transferring the chelates from an organic solvent to water.

Acknowledgments

The numerical calculations were carried out at the Interdisciplinary Centre for Mathematical and Computational Modelling, Warsaw, the Poznań Supercomputing & Networking Centre and the WCSS of the Technical University of Wrocław, Poland. We acknowledge access to the computer resources and the kind cooperation of the staff.

[1] *Theoretical Treatment of Hydrogen Bonding* (Ed.: D. Hadzi), John Wiley & Sons, New York, **1997**.
[2] H. Guo, S. Sirois, E. I. Proynov, D. R. Salahub, in ref. [1], pp. 49−74.
[3] T. K. Ghanty, S. K. Ghosh, *J. Phys. Chem. A* **2003**, *107*, 7062−7067, and references cited therein.
[4] T. Ziegler, *Chem. Rev.* **1991**, *91*, 651−667.
[5] A. Berces, T. Ziegler, *Top. Curr. Chem.* **1996**, *182*, 41−85.
[6] M. Czerwiński, *Int. J. Quantum Chem.* **1999**, *72*, 39−51.
[7] J. Narbutt, M. Czerwiński, J. Krejzler, *Eur. J. Inorg. Chem.* **2001**, 3187−3197.
[8] V. R. Polyakov, M. Czerwiński, *Inorg. Chem.* **2001**, *40*, 4798−4802.
[9] [9a] J. A. Dobado, R. Uggla, M. R. Sundberg, J. Molina, *Proc. 7th Intern. Conf. on the Applications of the Density Functional Theory in Chemistry and Physics*, Vienna, Sept. 2−6, **1997**, p. 54. [9b] J. A. Dobado, R. Uggla, M. R. Sundberg, J. Molina, *J. Chem. Soc., Dalton Trans.* **1999**, 489−496.
[10] [10a] I. Alkorta, I. Rozas, J. Elguero, *Chem. Soc., Rev.* **1998**, *27*, 155−162. [10b] N. V. Belkova, M. Besora, L. M. Epstein, A. Lledos, F. Maseras, E. S. Shubina, *J. Am. Chem. Soc.* **2003**, *125*, 7715−7725, and references cited therein.
[11] [11a] J. Narbutt, *J. Inorg. Nucl. Chem.* **1981**, *43*, 3343−3349. [11b] P. Moore, J. Narbutt, *J. Solut. Chem.* **1991**, *20*, 1227−1235. [11c] J. Narbutt, *J. Phys. Chem.* **1991**, *95*, 3432−3435. [11d] J. Narbutt, B. Bartoś, S. Siekierski, *Solv. Extr. Ion Exch.* **1994**, *12*, 1001−1011. [11e] J. Narbutt, L. Fuks, *Radiochim. Acta* **1997**, *78*, 27−31.
[12] J. Narbutt, M. Czerwiński, in *Solvent Extraction, Principles and Practices*, 2nd Ed. (Eds.: J. Rydberg, C. Musikas, G. R. Choppin, M. Cox), Marcel Dekker, New York, **2004**, p. 679−714.
[13] J. G. C. M. Van Duijneveldt van de Rijdt, F. B. van Duijneveldt, in ref.[1], p. 13−47.
[14] [14a] S. F. Boys, F. Bernardi, *Mol. Phys.* **1970**, *19*, 553−566. [14b] I. Mayer, *Int. J. Quantum Chem.* **1998**, *70*, 41.
[15] J. B. Foresman, T. A. Keith, K. B. Wiberg, J. Snoonian, M. J. Frisch, *J. Phys. Chem.* **1996**, *100*, 16098.
[16] R. G. Parr, W. Yang, *Density Functional Theory of Atoms and Molecules*, Oxford University Press, Oxford, **1989**.
[17] [17a] P. J. Hay, W. R. Wadt, *J. Chem. Phys.* **1985**, *82*, 270−283. [17b] W. R. Wadt, P. J. Hay, *J. Chem. Phys.* **1985**, *82*, 284−298. [17c] P. J. Hay, W. R. Wadt, *J. Chem. Phys.* **1985**, *82*, 299−310.
[18] [18a] A. D. Becke, *J. Chem. Phys.* **1988**, *88*, 52. [18b] C. Lee, W. Yang, R. G. Parr, *Phys. Rev. B* **1988**, *37*, 785−789. [18c] A. D. Becke, *J. Chem. Phys.* **1993**, *98*, 5648−5652.
[19] H. B. Schlegel, *J. Comp. Chem.* **1982**, *3*, 214−218.
[20] *Gaussian Basis Sets for Molecular Calculations* (Ed.: S. Huzinaga), Elsevier, New York, **1984**.
[21] M. J. Frisch, G. W. Trucks, H. B. Schlegel, P. M. W. Gill, B. G. Johnson, M. A. Robb, J. R. Cheeseman, T. Keith, G. A. Petersson, J. A. Montgomery, K. Raghavachari, M. A. Al-Laham, V. G. Zakrzewski, J. V. Ortiz, J. B. Foresman, J. Cioslowski, B. B. Stefanov, A. Nanayakkara, M. Challacombe, C. Y. Peng, P. Y. Ayala, W. Chen, M. W. Wong, J. L. Andres, E. S. Replogle, R. Gomperts, R. L. Martin, D. J. Fox, J. S. Binkley, D. J. Defrees, J. Baker, J. P. Stewart, M. Head-Gordon, C. Gonzalez, J. A. Pople, *GAUSSIAN 94, Revision D.3*, Gaussian, Inc., Pittsburgh PA, **1995**.
[22] T. J. Anderson, M. A. Neuman, G. A. Melson, *Inorg. Chem.* **1973**, *12*, 927−930.
[23] [23a] G. J. Kruger, E. C. Reynhardt, *Acta Crystallogr., Sect. B* **1974**, *30*, 822−824. [23b] P. K. Hon, C. E. Pfluger, *J. Coord. Chem.* **1973**, *3*, 67−76.
[24] P. A. Kollman, L. C. Allen, *J. Chem. Phys.* **1969**, *51*, 3286−3293.
[25] J. Del Bene, J. A. Pople, *J. Chem. Phys.* **1970**, *52*, 4858−4866.
[26] J. Andzelm, E. Wimmer, *J. Chem. Phys.* **1992**, *96*, 1280.
[27] S. Kais, D. R. Herschbach, N. C. Handy, C. W. Murray, G. J Laming, *J. Chem. Phys.* **1993**, *99*, 417.
[28] J. Narbutt, *Report INCT-2119/V*, Warszawa, **1991**, p. 25.
[29] G. Hummer, S. Garde, A. E. Garcia, L. R. Pratt, *Chem. Phys.* **2000**, *258*, 349−370.

Received April 2, 2004
Early View Article
Published Online December 17, 2004

 © 2005 Wiley-VCH Verlag GmbH & Co. KGaA, Weinheim

Alkali-Metal Salts of Aromatic Carboxylic Acids: Liquid Crystals without Flexible Chains

Rik Van Deun,[a] Jan Ramaekers,[a] Peter Nockemann,[a] Kristof Van Hecke,[a] Luc Van Meervelt,[a] and Koen Binnemans*[a]

Keywords: Alkali metals / Layered compounds / Liquid crystals / Metallomesogens / Smectic mesophases

The alkali-metal salts of *meta*-substituted benzoic acids exhibit a smectic A mesophase at high temperatures. These compounds are examples of liquid crystals without terminal alkyl chains. The influence of the metal ion and of the type of substituents on the transition temperatures is discussed. Compounds with the substituent in the *ortho*- and *para*-positions are non-mesomorphic. The crystal structures of the compounds $Rb(C_7H_4ClO_2)(C_7H_4ClO_2H)$, $Na(C_7H_4IO_2)(H_2O)$, $K(C_7H_4ClO_2)(C_7H_4ClO_2H)$ and $Rb(C_7H_4BrO_2)(C_7H_4BrO_2H)$ have been determined by X-ray crystallography. These compounds possess a layerlike structure in the solid state.

(© Wiley-VCH Verlag GmbH & Co. KGaA, 69451 Weinheim, Germany, 2005)

1 Introduction

In the classic picture, liquid crystals are either calamitic (rodlike) or discotic (disklike) molecules. However, many types of liquid crystals cannot be classified as rodlike or disklike, and several intermediate forms are possible.[1,2] In general, the rodlike mesogenic molecules have one or two terminal alkyl chains. The function of these flexible chains is not only to stabilize the mesophase, but also to reduce the melting point. This may give the wrong impression that such flexible chains are necessary to obtain liquid crystals, as some compounds without a flexible chain are able to form a mesophase as well. Typical examples are the *para*-oligophenyls, such as *para*-quinquephenyl and *para*-sexiphenyl.[3−6] Tschierske and co-workers[7] have investigated semi-rigid substituted benzyloxybiphenyl compounds with diol head groups. The indenes and pseudo-azulenes with peripheral chloro groups reported by Barbera et al.[8] were the first examples of mesomorphic discotic molecules without a flexible chain. The rodlike or disklike shape of all these molecules is very distinct. We can therefore ask ourselves what happens if the length of the rodlike molecules is reduced. Do simple aromatic compounds consisting of one phenyl ring exhibit a mesophase? The answer is no; compounds such as benzoic acid, phenol, aniline, chlorobenzene are not liquid crystals. However, the situation changes when alkali-metal salts of aromatic carboxylic acids (for example sodium benzoate) are considered. The liquid-crystalline behaviour of these compounds was discovered in 1910 by the great pioneer in liquid-crystal research, Daniel Vorländer,[9,10] Vorländer investigated the lithium, sodium, potassium and rubidium salts of benzoic acid. In addition, he investigated the alkali-metal salts of the *ortho*-, *meta*- and *para*-isomers of chlorobenzoic acid, bromobenzoic acid, iodobenzoic acid, methylbenzoic acid and nitrobenzoic acids. The sodium and potassium salts were prepared for all these compounds and a few lithium, rubidium and cesium salts as well. Vorländer mentions only the presence and absence of a mesophase, but gives no mesophase identification. These mesophases often have a low viscosity, and approximate transition temperatures were given for a limited number of compounds only. Demus and co-workers[11] re-examined some of the compounds described by Vörlander — the lithium, sodium, potassium, rubidium and cesium salts of 3-bromobenzoic acid, and the potassium salt of 3-iodobenzoic acid — in 1970. In some instances they used the original samples prepared by Vorländer sixty years before, and they found no signs of deterioration. These authors determined the transition temperatures by optical microscopy and identified the mesophase as a "neat" phase (smectic A). In addition, they constructed binary phase-diagrams by mixing the compounds with other aliphatic and aromatic carboxylate salts. Unfortunately, there is not complete agreement between the results of Vorländer and Demus: transition temperatures for the same compound reported by the two authors differ by up to 35 °C in some cases, and for cesium 3-bromobenzoate Vorländer found a mesophase, whereas Demus and co-workers didn't.

Given the intrinsic scientific interest of these low-molecular-weight liquid crystals, we reinvestigated the compounds described by Vorländer in order to obtain more detailed quantitative thermodynamic and structural data. The com-

[a] Katholieke Universiteit Leuven, Department of Chemistry
Celestijnenlaan 200F, 3001 Leuven, Belgium
Fax: + 32-16-327-992
E-mail: Koen.Binnemans@chem.kuleuven.ac.be

pounds were investigated by polarizing optical microscopy (POM) and by differential scanning calorimetry (DSC), and some compounds by high-temperature X-ray diffraction. This work extends Vorländer's work by including some alkali-metal salts of substituted benzoic acids not studied by Vorländer, for instance salts of the *ortho*-, *meta*- and *para*-isomers of fluorobenzoic acid and methoxybenzoic acid. In addition, we have determined the crystal structures of four alkali-metal salts.

Results and Discussion

The first series of compounds we prepared were the alkali-metal salts of benzoic acid. These compounds have much higher transition temperatures than benzoic acid, which melts at 122 °C. The melting points of the corresponding alkali-metal salts range from 369 °C (lithium benzoate) to 444 °C (rubidium benzoate). While benzoic acid does not exhibit liquid-crystalline behaviour, sodium benzoate is an enantiotropic liquid crystal. The other salts (the lithium, potassium, rubidium and cesium benzoates) do not exhibit mesomorphism. The optical texture of the sodium benzoate shows the typical features of a smectic A phase (SmA): bâtonnets appear from the isotropic liquid and coalesce to a fan-shaped texture with homeotropic regions. If the sample is quickly cooled after isotropisation, thermal decomposition can be limited and formation of a mesophase can be observed upon cooling, thus illustrating the enantiotropic nature of the SmA mesophase. The DSC thermogram (first heating run) of sodium benzoate is shown in Figure 1. The thermal behaviour of the alkali-metal benzoates is summarised in Table 1.

Table 1. Thermal behaviour of benzoic acid and its alkali-metal salts

Compound	Transition temperatures (°C)[a]
Benzoic acid	Cr·122·I
Lithium benzoate	Cr·369·I
Sodium benzoate	Cr·431·SmA·451·I
Potassium benzoate	Cr·439·I
Rubidium benzoate	Cr·444·I
Cesium benzoate	Cr_I·383·Cr_{II}·398·I

[a] Cr, Cr_I, Cr_{II}: solid crystalline phases; SmA: smectic A phase; I: isotropic phase.

These findings are in partial disagreement with the data of Vorländer, who reported that the lithium, sodium, potassium and rubidium salts of benzoic acid are all enantiotropic liquid crystals, while benzoic acid is not liquid-crystalline. He described the texture as small rods which flow together to form drops. The transition temperatures of sodium benzoate were given (melting point: 410 °C, clearing point: 430 °C), but not for the other unsubstituted alkali-metal benzoates. Vorländer had problems to record the transition temperatures of these high-melting solids accurately due to their thermal decomposition at high temperatures. For rubidium benzoate, Vorländer wrote that this

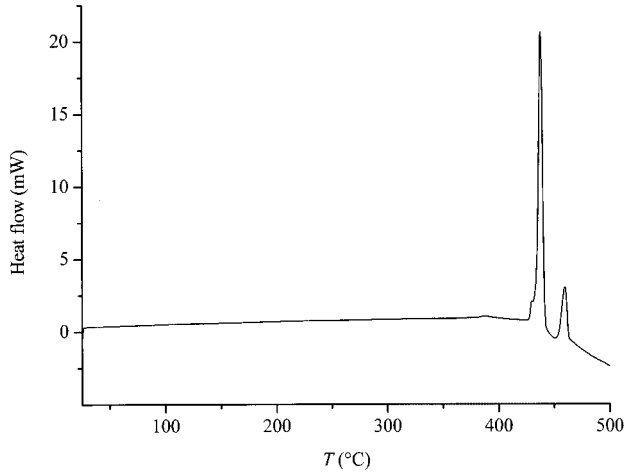

Figure 1. DSC thermogram (first heating) of sodium benzoate; endothermic peaks are pointing upwards

compound decomposed before the clearing point had been reached. Modern techniques indicate that only the sodium salt is a liquid crystal, and the other salts of benzoic acid melt to an isotropic liquid without showing a mesophase, just like benzoic acid itself. No evidence for monotropic mesophases was found.

A second group of compounds we investigated are the sodium salts of different *meta* (or 3)-substituted benzoic acids: sodium 3-fluorobenzoate, sodium 3-chlorobenzoate, sodium 3-bromobenzoate, sodium 3-iodobenzoate, sodium 3-methylbenzoate and sodium 3-methoxybenzoate (Figure 2). Their thermal behaviour was compared to that of unsubstituted sodium benzoate; the data are summarised in Table 2. As can be seen, all *meta*-substituted sodium benzoates are

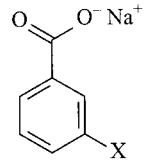

X = H, F, Cl, Br, I, CH_3, OCH_3

Figure 2. Structures of sodium salts of *meta*-substituted benzoic acids

Table 2. Thermal behaviour of *meta*-substituted sodium benzoates

Compound	Transition temperatures (°C)[a]
Sodium benzoate	Cr·431·SmA·451·I
Sodium 3-fluorobenzoate	Cr·406·SmA·415·I
Sodium 3-chlorobenzoate	Cr·337·SmA·408·I
Sodium 3-bromobenzoate	Cr·306·SmA·389·I
Sodium 3-iodobenzoate	Cr·278·SmA·372·I
Sodium 3-methylbenzoate	Cr·333·SmA·384·I
Sodium 3-methoxybenzoate	Cr·275·SmA·291·I

[a] Cr: solid crystalline phase; SmA: smectic A phase; I: isotropic phase.

 © 2005 Wiley-VCH Verlag GmbH & Co. KGaA, Weinheim

enantiotropic liquid crystals. For the *meta*-halogen-substituted compounds, the melting points decrease with increasing size of the halogen substituent in the *meta*-position, as is also the case for the clearing points (Figure 3). However, the melting points decrease in a more pronounced way than the clearing points, which results in an increase of the mesophase range.

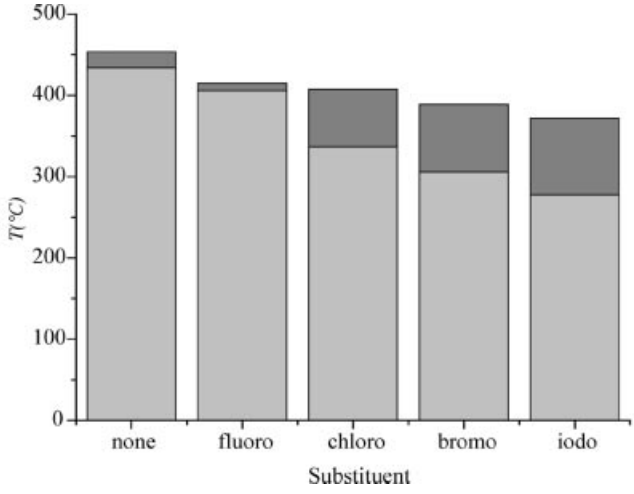

Figure 3. Influence of the size of the halogen atom on the transition temperatures of the sodium salts of *meta*-halogen-substituted benzoic acids; the light-grey shading represents the solid state and the dark-grey shading the smectic A phase

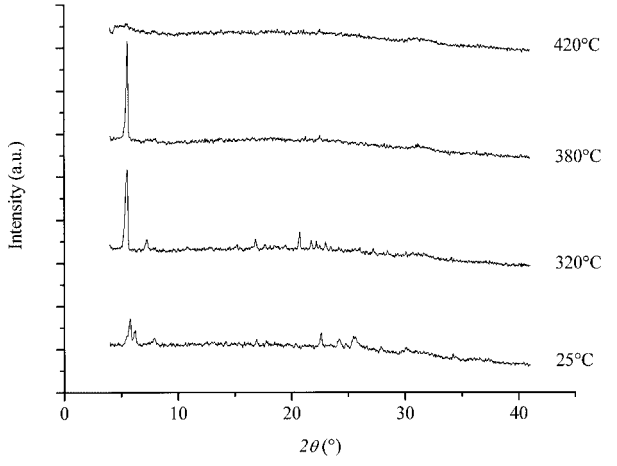

Figure 4. X-ray diffractograms of sodium 3-chlorobenzoate recorded at different temperatures

Figure 4 shows the X-ray diffractograms of sodium 3-chlorobenzoate. The bottom trace is that of a powder diffractogram at room temperature. At small diffraction angles, the diffraction peaks indicate a rather long-distance ordering, while the peaks at wider diffraction angles (around $2\theta = 25°$) result from an ordering at low dimensions. The observation of a number of diffraction peaks in the X-ray diffractogram confirms the crystallinity of the compound at room temperature. The second-from-bottom trace shows the compound after heating to 320 °C. The compound is still in the solid state, but evidence of a layered structure is already given by the first-order diffraction peak at around $2\theta = 6°$, which is of a rather high intensity. The third trace shows the situation at 380 °C, where the compound is in the SmA mesophase. Only the long-range order of the layered smectic phase remains, as witnessed by the absence of all but the first-order peak in the diffractogram. This is a typical diffractogram of a disordered smectic phase. The upper trace is of the sample in the isotropic liquid. No order remains, as can be seen from the absence of sharp diffraction peaks. The identification of the mesophase was supported by the observation of the texture given in Figure 5, which shows the formation of bâtonnets, which is typical for a smectic A phase. The thermal stability of the compounds at high temperatures is limited, as can be seen from the DSC curve of sodium 3-chlorobenzoate shown in Figure 6. Although the melting and clearing peaks are

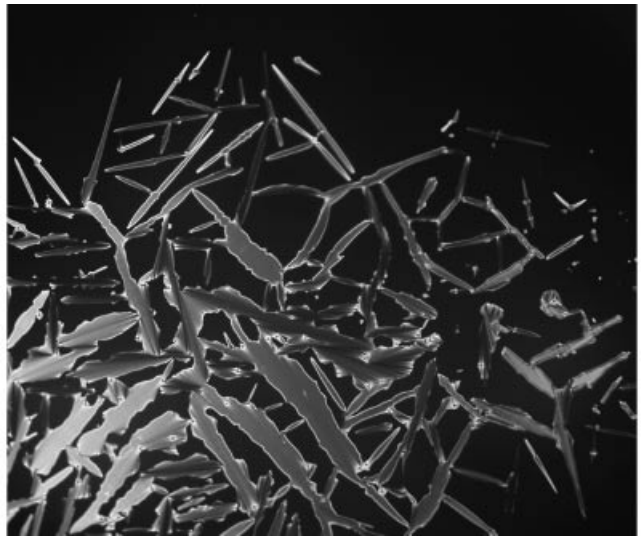

Figure 5. Texture of sodium 3-bromobenzoate at the clearing point at 389 °C, after cooling down from the isotropic liquid

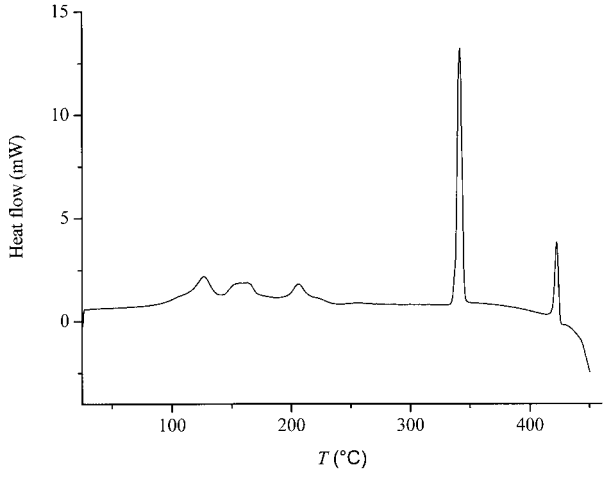

Figure 6. DSC thermogram of sodium 3-chlorobenzoate (first heating); endothermic peaks are pointing upward; the transitions between 100 and 250 °C are crystal−crystal transitions

 © 2005 Wiley-VCH Verlag GmbH & Co. KGaA, Weinheim

sharp, which indicates a high purity, decomposition of the sample occurs already at temperatures below 400 °C.

The potassium salts of *meta*-substituted benzoic acids form a third group of compounds. The general trends observed for the sodium salts remain the same for the potassium salts: the melting and clearing temperatures decrease with increasing size of the *meta*-halogen substituent, whereas the mesophase range increases in the same way. However, unsubstituted potassium benzoate does not show a mesophase (see discussion of unsubstituted alkali-metal benzoates and Table 1), and neither does potassium 3-fluorobenzoate. Generally speaking, the transition temperatures of the potassium salts are lower than those of the corresponding sodium salts, and the mesophase range for an analogous potassium salt is narrower than that of the comparable sodium salt. The thermal behaviour of the potassium *meta*-substituted benzoates is summarised in Table 3.

Table 3. Thermal behaviour of *meta*-substituted potassium benzoates

Compound	Transition temperatures (°C)[a]
Potassium benzoate	Cr·439·I
Potassium 3-fluorobenzoate	Cr·407·I
Potassium 3-chlorobenzoate	Cr·316·SmA·377·I
Potassium 3-bromobenzoate	Cr·292·SmA·367·I
Potassium 3-iodobenzoate	Cr·265·SmA·357·I
Potassium 3-methylbenzoate	Cr·295·SmA·406·I
Potassium 3-methoxybenzoate	Cr·261·SmA·301·I

[a] Cr: solid crystalline phase; SmA: smectic A phase; I: isotropic phase.

The fourth and fifth group, consisting of the rubidium and cesium salts of *meta*-substituted benzoates, respectively, follow the same trend as the second and third group: the melting and clearing points decrease with increasing size of the halogen substituent. However, the mesophase range decreases with increasing size for the rubidium salts, whereas the opposite was true for the sodium and potassium salts. Neither unsubstituted rubidium benzoate nor rubidium 3-fluorobenzoate show mesomorphism. Neither do any of the cesium salts. The thermal data of the rubidium and cesium salts of *meta*-substituted benzoates are given in Table 4 and 5, respectively.

Table 4. Thermal behaviour of *meta*-substituted rubidium benzoates

Compound	Transition temperatures (°C)[a]
Rubidium benzoate	Cr·444·I
Rubidium 3-fluorobenzoate	Cr_I·268·Cr_{II}·369·I
Rubidium 3-chlorobenzoate	Cr·308·SmA·334·I
Rubidium 3-bromobenzoate	Cr·260·SmA·279·I
Rubidium 3-iodobenzoate	Cr·232·SmA·244·I
Rubidium 3-methylbenzoate	Cr_I·248·Cr_{II}·299·SmA·375 ·I
Rubidium 3-methoxybenzoate	Cr_I·150·Cr_{II}·232·SmA·251·I

[a] Cr, Cr_I, Cr_{II}: solid crystalline phases; SmA: smectic A phase; I: isotropic phase.

Table 5. Thermal behaviour of *meta*-substituted cesium benzoates

Compound	Transition temperatures (°C)[a]
Cesium benzoate	Cr_I·383·Cr_{II}·398·I
Cesium 3-fluorobenzoate	Cr_I·256·Cr_{II}·303·I
Cesium 3-chlorobenzoate	Cr_I·218·Cr_{II}·288·I
Cesium 3-bromobenzoate	Cr_I·240·Cr_{II}·268·I
Cesium 3-iodobenzoate	Cr_I·221·Cr_{II}·235·I
Cesium 3-methylbenzoate	Cr_I·200·Cr_{II}·331·I
Cesium 3-methoxybenzoate	Cr_I·170·Cr_{II}·239·I

[a] Cr, Cr_I, Cr_{II}: solid crystalline phases; I: isotropic phase.

A sixth group of compounds comprises the lithium salts of the *meta*-substituted benzoates. The reason why they have not been discussed first is the aberrant behaviour of lithium in the alkali-metal series. The lithium−oxygen bonds are less ionic than the metal−oxygen bonds of the other alkali-metal ions. As a result, the thermal data of the lithium series are not in line with the results of the other *meta*-substituted benzoate salts. The mesophase range of the corresponding *meta*-chlorobenzoate increases in the same way, from 0 °C for the cesium salt (which is non-mesopmorphic) through 26 °C for the rubidium salt and 61 °C for the potassium salt to 71 °C for the sodium salt. Looking only at the ionic radius of the alkali-metal ion, one would expect an even wider mesophase range for the lithium salt. This is not the case: lithium 3-chlorobenzoate has a mesophase range of 64 °C. The mesophase of lithium 3-iodobenzoate could not be identified (although it is very likely a highly ordered smectic phase). No nice texture could be observed under the microscope for any of the synthesised compounds. A very viscous mesophase is formed upon cooling the isotropic liquid, with no easily recognisable features present. This viscous phase does not crystallise when cooling further. This behaviour was observed in the DSC thermogram by the absence of a crystallisation peak in the first cooling run and a ''cold'' recrystallisation peak in the second heating run. The thermal behaviour of the lithium *meta*-substituted benzoates is summarised in Table 6.

Table 6. Thermal behaviour of *meta*-substituted lithium benzoates

Compound	Transition temperatures (°C)[a]
Lithium benzoate	Cr·369·I
Lithium 3-fluorobenzoate	Cr·310·SmA·340·I
Lithium 3-chlorobenzoate	Cr_I·186·Cr_{II}·284·SmA·348·I
Lithium 3-bromobenzoate	Cr·284·SmA·338·I
Lithium 3-iodobenzoate	Cr_I·197·Cr_{II}·265·M·333·I
Lithium 3-methylbenzoate	Cr·271·I

[a] Cr, Cr_I, Cr_{II}: solid crystalline phases; SmA: smectic A phase; M: unidentified smectic mesophase; I: isotropic phase.

The *ortho*- and *para*-substituted benzoates have also been studied. None of the *ortho*- (or 2-) or *para*- (or 4-)substituted benzoates shows mesomorphism. They all melt directly from the solid crystalline state to the isotropic liquid state. The melting points of the *para*-substituted salts are

 © 2005 Wiley-VCH Verlag GmbH & Co. KGaA, Weinheim

higher than those of the *ortho*-substituted salts. Within the series of the *ortho*-substituted salts, the melting points decrease with increasing size of the halogen substituent. The same is true for the *para*-substituted series, although here the melting points of the 4-chloro-, 4-bromo- and 4-iodobenzoates are virtually the same. The thermal data for these compounds are collected in Table 7.

Table 7. Thermal behaviour of *ortho*- and *para*-substituted sodium benzoates

Compound	Transition temperatures (°C)[a]
Sodium benzoate	Cr·431·SmA·451·I
Sodium 2-fluorobenzoate	Cr·350·I
Sodium 2-chlorobenzoate	Cr·270·I
Sodium 2-bromobenzoate	Cr·260·I
Sodium 2-iodobenzoate	Cr·250·I
Sodium 4-fluorobenzoate	Cr·451·I
Sodium 4-chlorobenzoate	Cr·419·I
Sodium 4-bromobenzoate	Cr·420·I
Sodium 4-iodobenzoate	Cr·424·I

[a] Cr: solid crystalline phases; SmA: smectic A phase; I: isotropic phase.

The layer-like structure of the compounds in the smectic A phase indicates that a layer structure is also present in the solid state, as it is very unlikely that a layered structure is formed upon melting of these compounds. In the absence of a layered structure in the solid phase, the compound will directly melt to an isotropic liquid. Surprisingly few crystal-structure data of alkali-metal benzoates are available, and most of the structures described in the literature are those of acid salts (obtained by partial neutralisation of 1 mol of the benzoic acid with 0.5 mol of alkali-metal hydroxide).[12,13] To the best of our knowledge, only one crystal structure of an anhydrous alkali-metal benzoate is known: anhydrous lithium benzoate.[14] The lithium benzoate molecules form a two-dimensional structure consisting of a grid of lithium and carboxylate oxygen atoms, with the phenyl groups forming a covering layer on each side. The polymeric layers are stacked, with the CH groups in the *para*-position pointing towards each other, so that a bilayer structure is formed. The layers are held together by weak van der Waals forces. The authors relate the presence of the weak van der Waals forces to the easy cleavability of the sheetlike crystals.

The thermal behaviour of the alkali-metal benzoates can be described as follows: at the melting point the van der Waals bonds between the phenyl rings are broken, so that the layers can move relative to one another. Hence, we observe a smectic A mesophase. Most probably, the ionic layer containing the alkali-metal ions is partially destroyed too, otherwise the viscosity of the mesophase would be much higher than what we observe. At the clearing point, the polymeric ionic layer is totally broken into pieces, so that an ionic melt is formed. The substituents in the *ortho*-, *meta*- or *para*-position will have an influence on the stacking of the molecules. This effect will be most pronounced for compounds with substituents in the *ortho*-position, and less so for compounds with substituents in the *meta*-position and in the *para*-position.

Although we tried out different routes, we were not able to obtain the anhydrous alkali-metal benzoates as single crystals of a quality high enough for X-ray diffraction. When an organic solvent was chosen as the crystallisation solvent only a fine polycrystalline precipitate was formed. Crystallisation from an aqueous solution resulted either in the formation of hydrated salts or of acid salts. The fact that those acids salts are formed in water, even though we started from pure alkali-metal benzoates, can be rationalised from the fact that, in water, partial hydrolysis occurs and the carboxylate groups get protonated. Nevertheless, these hydrated salts and acid salts do show the presence of a layered structure in the solid phase.

Single crystal data were obtained for four compounds: $Rb(C_7H_4ClO_2)(C_7H_4ClO_2H)$ (**1**), $Na(C_7H_4IO_2)(H_2O)$ (**2**), $K(C_7H_4ClO_2)(C_7H_4ClO_2H)$ (**3**) and $Rb(C_7H_4BrO_2)(C_7H_4BrO_2H)$ (**4**). All these compounds are salts of *meta*-substituted benzoic acids. The crystal data of compounds **1**−**4** are summarised in Table 8. Compounds **1**, **3** and **4** crystallised in the space group $C2/c$, whereas compound **2** crystallised in $P\bar{1}$ with two extra water molecules in the asymmetric unit. Consequently, the crystal packing of compounds **1**, **3** and **4** is isotypic, whereas compound **2** is differently packed. For compounds **1**, **3** and **4** the *meta*-chloro/bromobenzoic acid residues are linked together by a short, strong hydrogen bond across a centre of symmetry. The atom H7 lies on a centre of symmetry and bridges O2 and O2′ of two centrosymmetrical equivalent residues (see Figure 7). The distances for this hydrogen bond (O···H···O distance) are 2.448(2), 2.438(3) and 2.434(9) Å for compounds **1**, **3** and **4** respectively. A search of the CSD[15] for benzoic acid compounds that exhibit a strong hydrogen bond with the hydrogen atom on a centre of symmetry gave an average distance of 2.451 Å, with a range of 2.432−2.480 Å, for 12 structures. No such hydrogen bonds were found for compound **2** (see Figure 8). The dihedral angles between the plane formed by the atoms of the planar phenyl ring and the plane through the carboxylic group are 8.4(1), 7.9(2) and 8.4(4)° for compounds **1**, **3** and **4** respectively. For compound **2** the carboxylic groups lie nearly perfectly in the plane of their respective phenyl rings. The angles are 0.56(17) and 0.73(17)° respectively.

For compounds **1**, **3** and **4** the coordination sphere of the alkali-metal ions (potassium or rubidium) can be described by a distorted octahedron. Each alkali-metal ion is surrounded by six carboxylate oxygen atoms from different benzoic acid residues. These six oxygen atoms actually consist of four O1 and two O2 atoms. Thus, every carboxylic O1 atom coordinates to two alkali-metal ions and every O2 atom to only one alkali-metal ion. The alkali metal−oxygen distances vary for the rubidium compounds in the range of 2.838(2)−3.043(2) and 2.845(7)−3.068(7) Å for compounds **1** and **4**, respectively, and for the potassium compound **3** from 2.724(4)−2.885(3) Å. Notice that the distances of the latter are a little shorter than for the rubidium compounds due to the smaller ionic radius. For compound **2** the asym-

 © 2005 Wiley-VCH Verlag GmbH & Co. KGaA, Weinheim

Table 8. Summary of crystal data, intensity measurements, and structure refinement for compounds **1**−**4**

	1	**2**	**3**	**4**
Empirical formula	$Rb(C_7H_4ClO_2)$-$(C_7H_4ClO_2H)$	$Na(C_7H_4IO_2)$-(H_2O)	$K(C_7H_4ClO_2)$-$(C_7H_5ClO_2H)$	$Rb(C_7H_4BrO_2)$-$(C_7H_4BrO_2H)$
Formula mass	397.58	571.98	351.21	486.48
Dimensions (mm)	0.15 × 0.15 × 0.1	0.2 × 0.1 × 0.05	0.5 × 0.2 × 0.1	0.2 × 0.1 × 0.1
Crystal system	monoclinic	triclinic	monoclinic	monoclinic
Space group	*C*2/*c*	$P\bar{1}$	*C*2/*c*	*C*2/*c*
a (Å)	32.1084(12)	6.8673(3)	32.448(2)	32.889(2)
b (Å)	3.8104(10)	7.0112(3)	3.7577(3)	3.8563(3)
c (Å)	11.6212(4)	18.4121(7)	11.4010(8)	11.6525(8)
α (°)	90	84.104(3)	90	90
β (°)	96.446(2)	82.745(3)	94.631(4)	95.976(4)
γ (°)	90	89.622(6)	90	90
V (Å^3)	1413.82(8)	874.74(6)	1385.58(17)	1469.85(18)
Z	4	2	4	4
$D_{calcd.}$ (g cm^{-3})	1.869	2.172	1.684	2.198
$2\theta_{max}$ (°)	142.78	142.56	141.84	142.98
$\mu_{Cu\text{-}K\alpha}$ (mm^{-1})	8.426	28.984	7.033	11.125
F(000)	784	536	712	928
Measured reflections	2388	7854	4618	4171
Unique reflections	1354	3211	1313	1359
Observed reflections [$F_o > 4\sigma(F_o)$]	1293	2853	1073	942
Parameters refined	108	217	96	96
R_1	0.0351	0.0424	0.0464	0.0536
wR_2 [a]	0.0854	0.1070	0.1094	0.1161
R_1 (all data)	0.0364	0.0457	0.0586	0.0795
wR_2 (all data)	0.0871	0.1096	0.1164	0.1258

[a] Weighting scheme as defined for compound **1**: $w = 1/[\rho^2(F_o^2) + (0.0422P)^2 + 0.8172P]$, where $P = [(F_o^2 + 2F_c^2)/3]$; compound **2**: $w = 1/[\rho^2(F_o^2) + (0.0711P)^2]$, where $P = [(F_o^2 + 2F_c^2)/3]$; compound **3**: $w = 1/[\rho^2(F_o^2) + (0.0596P)^2]$, where $P = [(F_o^2 + 2F_c^2)/3]$; compound **4**: $w = 1/[\rho^2(F_o^2) + (0.0353P)^2]$ where $P = [(F_o^2 + 2F_c^2)/3]$.

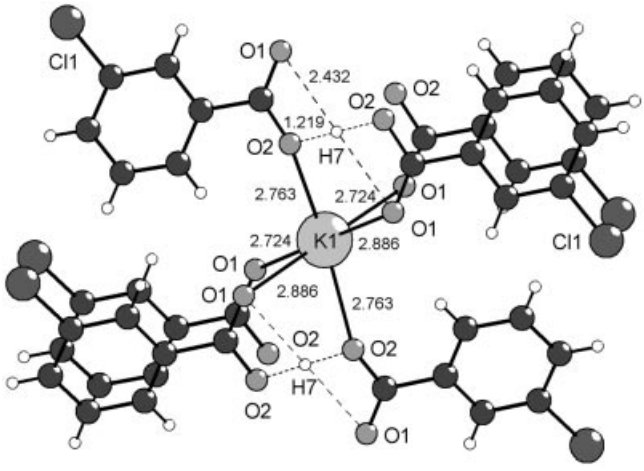

Figure 7. Crystal structure of compound **3** showing the coordination environment of the potassium ion; compounds **1** and **4** are isostructural

metric unit contains two alkali-metal (sodium) atoms. The coordination sphere of Na1 can be described by a distorted octahedron, which consists of six oxygen atoms, three from coordinated water molecules (O6 and two O5 atoms) and three from carboxylate oxygen atoms (O3, O2 and O4). The alkali metal−oxygen distances vary in the range 2.290(5)−2.609(5) Å. However, two additional longer contacts with O1 [2.903(6) Å] and O4′ of another equivalent residue [2.995(5) Å] could be noticed. Na2 also exhibits an octahedral coordination sphere, although it is less distorted than for Na1. The alkali metal−oxygen distances vary in the range 2.308(5)−2.831(5) Å with no additional contacts appearing. For compounds **1**, **3** and **4** the overall structure is built up by strands along the (010) direction, which are formed by the carboxyl O1 atom bridging the alkali-metal ions (see Figure 9). These strands are linked together in the (001) direction with the carboxylic groups acting as bridges (via O1) and with strong hydrogen-bonding between the O2 and O2′ atoms of equivalent residues. As a result, a two-dimensional coordination polymer is formed. In the (100) direction only van der Waals forces are observed between these coordination polymer units: the shortest distance is between two Cl/Br atoms [3.503(3), 3.532(5) and 3.597(6) Å for compounds **1**, **3** and **4** respectively]. For compound **2**, however, a strand of sodium atoms is formed by the carboxylic O2 and O4 atoms, which bridge Na1 and Na2 along the (010) direction (see Figure 10). The carboxylic O1 and O3 atoms form additional contacts with Na1. Thus, in the (010) direction two different carboxylic groups bridge two strands of sodium ions. These double strands of sodium ions are linked together in the (100) direction by water molecules (O5 and O6), each contacting Na1 and Na2, which results in a two-dimensional coordination polymer. In the (001) direction no contacts other than van der Waals contacts could be observed; the shortest distance between two iodine atoms is 4.158(5) Å. The position of the benzoic acid substituent does not influence the overall crystal packing.

 © 2005 Wiley-VCH Verlag GmbH & Co. KGaA, Weinheim

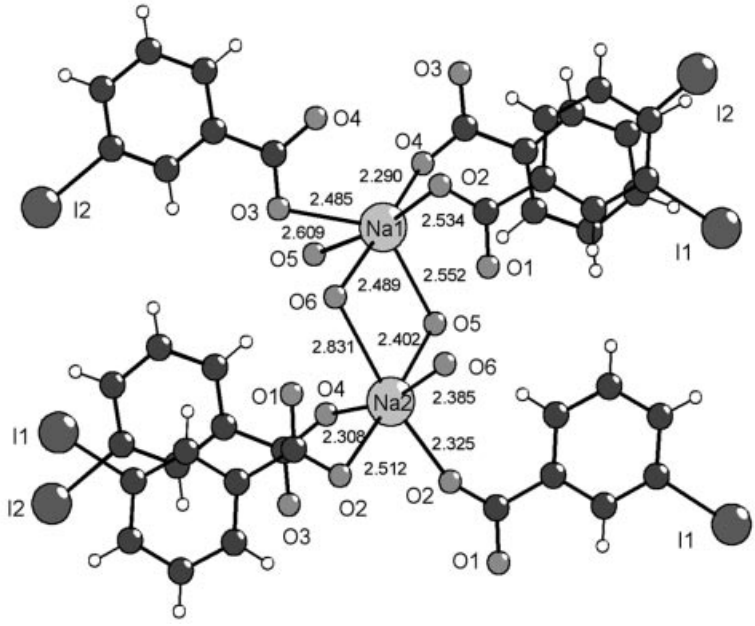

Figure 8. Crystal structure of compound **2** showing the coordination environment of the sodium ions

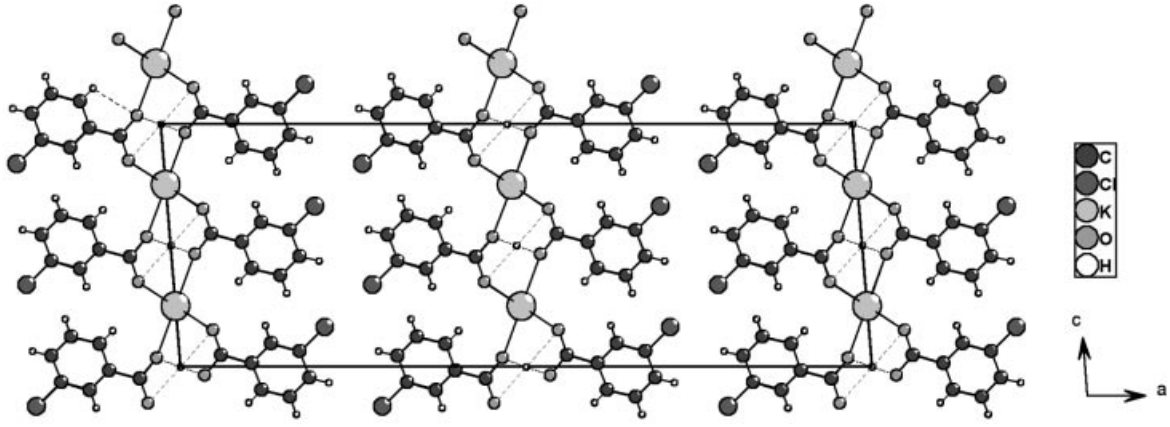

Figure 9. Crystal packing of compounds **1**, **3** and **4**

Indeed, for CSD[15] entry BINZAZ,[16] with a fluorine atom in the *para*-position, and for KHPHBZ10,[17] with a hydroxyl group in the *para*-position, a similar packing is observed. The latter crystallises in *P*2/*c* instead of *C*2/*c* (the *a*-axis is reduced to half length resulting in a similar packing) and contains one water molecule not in contact with the alkali-metal ion. Water molecules in contact with the alkali-metal ion influence the packing, as in compound **3**. The layered structures found for compounds **1**−**4** give an indication that it is likely that the anhydrous alkali-metal salts also have a layerlike structure in their solid phase. This idea is also supported by the fact that a layerlike structure is observed for lithium benzoate.[14] On the other hand, no layer structure is observed for benzoic acid. This compound forms dimers by intramolecular hydrogen bonding.[18] These dimers are not packed into layers, but are stacked on each other. The structure as a whole is built up by such stackings which alternate perpendicularly to one another. When the crystal melts, each dimer behaves as a separate entity, but its length-to-width ratio is too small to form a mesophase. Therefore, benzoic acid and the substituted benzoic acids melt directly to the isotropic liquid without passing through a mesophase.

Due to the absence of alkyl chains, the transition temperatures of the compounds are very high. At these high temperatures, the thermal energy of the molecules is high as well and only compounds with a strong interaction between the metal and carboxylate groups will exhibit a mesophase. Based on the concept of the hardness of Lewis acids and Lewis bases,[19] the strength of the metal−carboxylate bond decreases in the order $Na^+ > K^+ > Rb^+ > Cs^+$. Therefore, sodium compounds have the highest tendency to form a mesophase. This is indeed observed experimentally. The high transition temperatures result in several compounds starting to decompose in the mesophase (or even before the mesophase is reached). Lithium compounds are an exception, because the lithium−oxygen bond has a higher covalent contribution than the same bond in the

 © 2005 Wiley-VCH Verlag GmbH & Co. KGaA, Weinheim

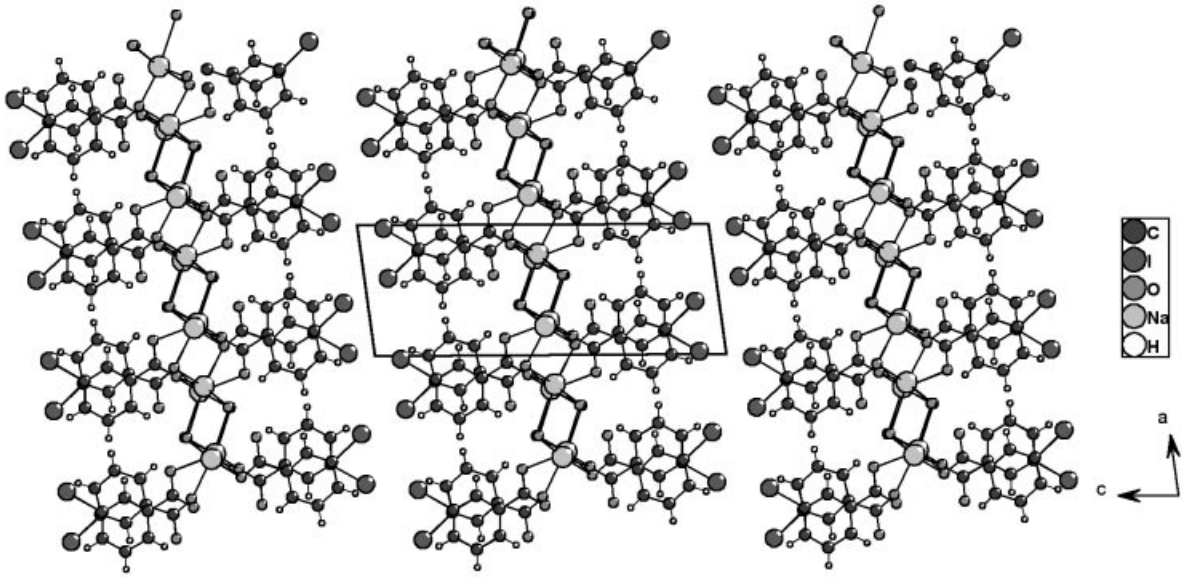

Figure 10. Crystal packing of compound **2**

other alkali metals. The higher the transition temperatures, the higher the chance that the compounds will melt from the solid state directly to the isotropic liquid. This is especially true when the strength of the ionic layer is weakened by (bulky) substituents in the *ortho*-position of the benzene ring. Bulky groups in the *para*-position prevent the formation of a mesophase, because the molecules will experience larger van der Waals forces or even dipole−dipole interactions, and because the bulky groups make it more difficult for the layers to glide along one another (and thus also give a higher viscosity). From this viewpoint, it is understandable that the most stable mesophases are formed for the alkali-metal salts of the *meta*-substituted benzoic acids. No mesophase is expected for the alkali-metal salts of terephthalic acid, because in this case no layer structure with an alternation of layers with ionic and van der Waals forces will be formed, but a succession of ionic layers.

Conclusion

Although the alkali-metal salts of aromatic carboxylic acids don't have the rodlike or disklike shape of conventional liquid crystals, they can form a mesophase at high temperatures. This has been illustrated for the salts of different substituted benzoic acids. The position of the substituent is of prime importance, since only the salts of *meta*-substituted benzoic acids exhibit mesomorphism. No liquid-crystalline behaviour was observed for *ortho*- and *para*-substituted compounds. The mesomorphism not only depends on the type of substituent and its position, but also on the type of alkali metal. The most stable mesophases were observed for the sodium salts, and of the salts of unsubstituted benzoic acid, only sodium benzoate is mesomorphic. Investigation by polarizing optical microscopy and by high-temperature X-ray diffraction shows that the structure of the mesophase is similar to that of the smectic A phase of conventional organic liquid crystals. Crystal structures of similar, but hydrated or solvated compounds show that a layer-like structure is already present in the solid state.

Experimental Section

The alkali-metal salts were prepared by a neutralisation titration of an ethanolic solution of the carboxylic acid with an aqueous standard solution (0.5 M) of the corresponding alkali-metal hydroxide (LiOH, NaOH, KOH, CsOH or RbOH), with phenolphthalein as the indicator. After reaching the equivalence point, the carboxylate salts were recovered by evaporation of the solvent under reduced pressure. The compounds were redissolved in a small amount of ethanol at room temperature and were reprecitated by addition of acetone or a mixture of acetone and diethyl ether. An acetone/diethyl ether mixture was used for the precipitation of the rubidium and the cesium salts of sodium 2-chlorobenzoate and sodium 2-bromobenzoate. The precipitate was filtered off on a Buchner funnel, washed with acetone and dried in vacuo at 120 °C. The purity of the samples could not be checked by CHN elemental analysis, because the carbon dioxide, resulting from the combustion of the benzoic acids in the CHN apparatus, reacts with the alkali metals to form alkali-metal carbonates, which are very stable at high temperatures, resulting in a too low measured carbon content. All samples were prepared in triplicate to check the reproducibility of the transition temperatures. Infrared measurements were performed to check the absence of free carboxylic acid.

Differential scanning calorimetry (DSC) measurements were performed on a Mettler-Toledo DSC821e module (scan rate 10 °C min^{-1} under a helium flow of 35 mL min^{-1}). The reported transition temperatures are onset temperatures. The optical textures of the mesophases were observed with an Olympus BX60 polarizing optical microscope equipped with a Linkam THMS600 hot stage and a Linkam TMS93 programmable temperature controller. In order to avoid or reduce the oxidative degradation of the compounds, the hot stage was flushed with a stream of nitrogen gas. High-temperature X-ray diffraction was measured on a STOE Transmission Powder Diffractometer System STADI P, with a high temperature attachment version 0.65.1 (temperature range from

 © 2005 Wiley-VCH Verlag GmbH & Co. KGaA, Weinheim

room temperature to 1000 °C). Monochromatic Cu-$K_{\alpha 1}$ radiation (λ = 1.5406 Å) was obtained with the aid of a curved germanium primary monochromator. The diffracted X-rays were measured by a linear Position Sensitive Detector (PSD). The sample was placed in a quartz glass capillary (outer diameter 0.3 mm, wall thickness 0.01 mm) and spun during the measurement.

Crystals of salts of the *meta*-substituted benzoates of a quality suitable for X-ray diffraction were obtained for $Rb(C_7H_4ClO_2)(C_7H_4ClO_2H)$ (**1**), $Na(C_7H_4IO_2)(H_2O)$ (**2**), $K(C_7H_4ClO_2)(C_7H_4ClO_2H)$ (**3**) and $Rb(C_7H_4BrO_2)(C_7H_4BrO_2H)$ (**4**) by slow evaporation of the solvent from an H_2O/EtOH (1:1) mixture at room temperature, and mounted in a nylon loop for data collection at 100 K on a SMART 6000 diffractometer equipped with a CCD detector using Cu-K_α radiation (λ = 1.54178 Å). The images were interpreted and integrated with the program SAINT from Bruker.[20] The four structures were solved by direct methods and refined by full-matrix least-squares on F^2 using the SHELXTL program package.[21] Non-hydrogen atoms were refined anisotropically and the hydrogen atoms were refined in the riding mode with isotropic temperature factors fixed at 1.2-times *U*(eq) of the parent atoms, except for compound **1**, where the positions of all hydrogen atoms could be localised from the difference Fourier maps without applying any further restraints. For compounds **1**, **3** and **4** the H atoms occur on special positions — the H7 atom bridges O2 and O2′ of a symmetry-equivalent molecule. Only for compound **4** could this H atom not be localised from the difference Fourier maps; it was modelled by assigning the coordinates of the special position. Compound **3** is essentially the same as the one found in the CSD[15] with code KHCBZO10,[12] but in the latter one aromatic hydrogen atom and the one at the special position are not included in the structure.

CCDC-256797 (**1**), -256798 (**2**), -256799 (**3**) and -256800 (**4**) contain the supplementary crystallographic data for this paper. These data can be obtained free of charge at www.ccdc.cam.ac.uk/conts/retrieving.html [or from the Cambridge Crystallographic Data Centre, 12 Union Road, Cambridge CB2 1EZ, UK; Fax: + 44-1223-336-033; E-mail: deposit@ccdc.co.uk].

Acknowledgments

K. B. and R. V. D. thank the F.W.O.-Flanders (Belgium) for a Postdoctoral Fellowship. Financial support by the F.W.O.-Flanders (G.0117.03) and by the K. U. Leuven (GOA 03/03) is gratefully acknowledged. The authors thank Prof. Gerd Meyer and Dr. Dirk Hinz-Hübner (University of Cologne, Germany) for access to XRD facilities and for measurements of X-ray diffractograms, respectively.

[1] C. Tschierske, *J. Mater. Chem.* **1998**, *8*, 1485−1508.
[2] *Handbook of Liquid Crystals*, vols. I and IIB (Eds.: D. Demus, J. Goodby, G. W. Gray, H.-W. Spiess, V. Vill, Wiley-VCH, Weinheim, **1998**.
[3] D. Vorländer, *Z. Physik. Chem.* **1927**, *126*, 449−472.
[4] P. A. Irvine, D. C. Wu, P. J. Flory, *J. Chem. Soc., Faraday Trans. 1* **1984**, *80*, 1795−1807.
[5] I. C. Lewis, C. A. Kovac, *Mol. Cryst. Liq. Cryst.* **1979**, *51*, 173−178.
[6] T. J. Dingemans, N. S. Murthy, E. T. Samulski, *J. Phys. Chem. B* **2001**, *105*, 8845−8860.
[7] M. Kölbel, T. Beyersdorff, C. Tschierske, S. Diele, J. Kain, *Chem. Eur. J.* **2000**, *6*, 3821−3837.
[8] J. Barbera, O. A. Rakitin, M. B. Ros, T. Torroba, *Angew. Chem. Int. Ed.* **1998**, *37*, 296−299.
[9] D. Vorländer, *Ber. Dtsch. Chem. Ges.* **1910**, *43*, 3120−3135.
[10] D. W. Bruce, K. Heyns, V. Vill, *Liq. Cryst.* **1997**, *23*, 813−819.
[11] D. Demus, H. Sackmann, K. Seibert, *Wiss. Z. Univ. Halle* **1970**, *19*, 47−62; *Chem. Abstr.* **1971**, *75*, 123351w.
[12] A. L. Macdonald, J. C. Speakman, *J. Chem. Soc., Perkin Trans. 2* **1972**, 1564−1566.
[13] H. N. Shrivastava, J. C. Speakman, *J. Chem. Soc.* **1961**, 1151−1163.
[14] D. A. Plattner, W. Petter, D. Seebach, *Chimia* **1994**, *48*, 138−141.
[15] F. H. Allen, *Acta Crystallogr., Sect. B* **2002**, *58*, 380−388.
[16] J. Longo, M. F. Richardson, *Acta Crystallogr., Sect. B* **1982**, *38*, 2482−2483.
[17] L. Manojlovic, *Acta Crystallogr., Sect. B* **1968**, *24*, 326−330.
[18] R. Feld, M. S. Lehmann, *Z. Kristallogr.* **1981**, *157*, 215−231.
[19] R. G. Pearson, *J. Am. Chem. Soc.* **1963**, *85*, 3533−3539.
[20] *SAINT*, Manual Version 5/6.0, Bruker Analytical X-ray Systems Inc., Madison, Wisconsin, **1997**.
[21] *SHELXTL-NT*, Manual Version 5.1, Bruker Analytical X-ray Systems Inc., Madison, Wisconsin, **1997**.

Received May 13, 2004
Early View Article
Published Online December 13, 2004

 © 2005 Wiley-VCH Verlag GmbH & Co. KGaA, Weinheim

Causes of Nonplanarity in Fluorinated 1,3λ⁴δ²,2,4-Benzodithiadiazines: Gas-Phase Electron Diffraction, Ab initio and DFT Structures

Andrew R. Turner,[a] Frank Blockhuys,[b] Christian Van Alsenoy,[b] Heather E. Robertson,[a] Sarah L. Hinchley,[a] Andrey V. Zibarev,[c] Alexander Yu. Makarov,[c] and David W. H. Rankin*[a]

Keywords: Antiaromaticity / Fluorinated 1,3λ⁴δ²,2,4-benzodithiadiazines / Molecular structure / Ab initio calculations / Density functional calculations

The gas-phase molecular structures of 6,8-difluoro-1,3λ⁴δ²,2,4-benzodithiadiazine and 5,6,7-trifluoro-1,3λ⁴δ²,2,4-benzodithiadiazine have been determined using quantum chemical calculations and electron diffraction via the SARACEN method of structural analysis. Of particular interest was the planarity or nonplanarity of the heterocyclic fragments of the molecules. It was shown that the difluoro compound is planar with respect to the heterocyclic fragment [folding angle: 0.0(5)° (figures in parenthesis indicate e.s.d.s in the final digits)] and that the trifluoro compound probably deviates from planarity to a small extent [folding angle: 4.0(–30;+3)°; the large uncertainty in the value of this angle is due to the low-frequency, large-amplitude vibrational motion associated with the folding of the heterocyclic fragment]. Pertinent structural parameters from the electron diffraction data (r_{h1} structure) of the difluoro compound are *av*[*r*(S=N)] = 155.7(7) pm, *r*(S–N) = 175.8(5) pm, *r*(C–S) = 176.6(8) pm and *r*(C–N) = 141.6(2) pm. For the trifluoro compound the equivalent structural parameters are *av*[*r*(S=N)] = 155.5(7) pm, *r*(S–N) = 170.7(6) pm, *r*(C–S) = 180.6(8) pm and *r*(C–N) = 140.6(2) pm. The gas-phase electron diffraction structures have been compared with results from ab initio and DFT calculations and also with experimental solid-state structures.

(© Wiley-VCH Verlag GmbH & Co. KGaA, 69451 Weinheim, Germany, 2005)

Introduction

Antiaromatic structures (i.e. those with 4*n* π-electrons) containing a benzenoid ring fused to a heterocyclic ring have been the subject of recent scrutiny due to their unusual structural properties.[1−4] Of particular interest have been 1,3λ⁴δ²,2,4-benzodithiadiazine and its fluorinated derivatives. The basic structural unit of these compounds consists of a benzene ring fused to a S_2N_2 fragment to give a 12 π-electron system. A gas-phase electron diffraction (GED) study of the parent compound 1,3λ⁴δ²,2,4-benzodithiadiazine (**1**)[3] showed that the heterocyclic fragment adopts a nonplanar conformation in the gas phase. In the same study it was shown that the tetrafluoro derivative (5,6,7,8-tetrafluoro-1,3λ⁴δ²,2,4-benzodithiadiazine, compound **2**) has a planar heterocyclic fragment in the gas phase. The nonplanar conformation of compound **1** was rationalised as a pseudo-Jahn−Teller distortion[5] which minimises the destabilisation caused by the antiaromaticity. For the tetrafluoro derivative it was postulated that a π-fluoro effect, due to the fluorine substituted in the 8-position, would counteract the pseudo-Jahn−Teller distortion leading to a planar conformation.

The study also revealed an unexpected conflict in the conformation predicted for compound **2** by ab initio molecular orbital (MO) methods and DFT calculations. The DFT calculations predicted the planar conformation as seen in the refined GED structure, whilst the MO calculations predicted the nonplanar conformation. This work extends the study by employing both GED and theoretical structural studies to deduce the gas-phase structures of the 6,8-difluoro derivative **3** and the 5,6,7-trifluoro derivative **4**. From the π-fluoro hypothesis we would expect compound **3** to show a planar conformation with respect to the heterocyclic fragment and compound **4** to show a nonplanar conformation. Along with **1** and **2**, these are the simplest accessible compounds that can be used to investigate the influence of fluorine substitution at position 8.

Preparation and Characterisation

Compounds **3** and **4** were prepared, purified and structurally characterised by single-crystal X-ray diffraction

[a] School of Chemistry, University of Edinburgh, West Mains Road, Edinburgh, EH9 3JJ, UK
Fax: (internat.) + 44-131-650-6452
E-mail: d.w.h.rankin@ed.ac.uk
[b] Department of Chemistry, University of Antwerp, Universiteitsplein 1, 2610 Wilrijk, Belgium
[c] Institute of Organic Chemistry, Russian Academy of Sciences, 630090 Novosibirsk, Russia
Supporting information for this article is available on the WWW under http://www.eurjic.org or from the author.

 © 2005 Wiley-VCH Verlag GmbH & Co. KGaA, Weinheim DOI: 10.1002/ejic.200400601

studies as described in reference 4. IR spectra of the compounds in KBr were recorded on an FT Bruker Vector 22 spectrometer. Raman spectra were recorded with an FT Bruker IFS 66 spectrometer equipped with a Nd/YAG laser with an excitation line at 1064 nm.

GED Measurements

Electron diffraction data were captured with Kodak Electron Image photographic films using the Edinburgh gas-phase electron diffraction apparatus.[6] For compound **3**, at the short camera distance, the sample was maintained at a temperature of 423 K whilst the nozzle temperature was held at the higher temperature of 443 K to prevent sample condensation in the nozzle. At the long camera distance, the sample temperature was 381 K whilst the nozzle temperature was 413 K. The four corresponding temperatures for compound **4** were 431, 450, 386 and 413 K, respectively. The vapours were injected into the diffraction chamber through a metal nozzle with camera distances of approximately 98 mm and 250 mm. The electron accelerating voltage was approximately 40 kV, giving an electron wavelength close to 6 pm. The precise camera distances (d) and electron wavelengths (λ) were determined from scattering patterns for benzene vapour recorded immediately before or after the sample patterns. Details are given in Table 1, together with the weighting functions used to set up the diagonal elements of the weight matrix used in the least-squares refinement process (sw_1, sw_2), the s-ranges ($s_{min.}$, $s_{max.}$), the scale factors (k) and the correlation parameters (ratio of the off-diagonal terms to the diagonal terms of the weight matrix, q) which were used to define the immediate off-diagonal elements of the weight matrix.[7] The remaining elements of the weight matrix were set to zero.

Table 1. GED experimental details; figures in parentheses are the estimated standard deviations of the last digits

	d [mm]	Weighting functions [nm^{-1}]					q	k	λ [pm]
		Δs	$s_{min.}$	sw_1	sw_2	$s_{max.}$			
3	97.69	4	100	120	264	308	0.4406	0.673(15)	6.020
	256.19	2	20	40	128	150	0.3511	0.872(7)	6.020
4	97.85	4	100	120	264	308	0.4692	0.691(11)	6.020
	251.21	2	20	40	136	158	0.4009	0.861(7)	6.020

Details of the electron scattering patterns were converted into digital form using a PDS densitometer at the Institute of Astronomy in Cambridge. For compound **3**, the results spanning the ranges 20 nm^{-1} ≤ s ≤ 150 nm^{-1} and 100 nm^{-1} ≤ s ≤ 308 nm^{-1} and for compound **4**, the results spanning the ranges 20 nm^{-1} ≤ s ≤ 158 nm^{-1} and 100 nm^{-1} ≤ s ≤ 308 nm^{-1} were reduced and analysed using the ed@ed program[8] employing the scattering factors tabulated by Ross et al.[9]

Results and Discussion

Theoretical Studies

Calculations were performed at various levels, using the Gaussian98 suite of quantum chemistry programs,[10] to gauge the effects of different methodologies and basis sets on the structures. They also provide guidelines for the uncertainties of the SARACEN restraints[11] in the GED structure refinements (see GED Structure Refinements). The results are listed in Table 2 for compound **3** and in Table 3 for compound **4**.

The most obvious feature of the calculations is the disagreement between the ab initio results (MP2, 2nd order Møller-Plesset perturbation theory[12]) and the DFT results (B3LYP hybrid functional[13]) in the conformation predicted for compound **3**. The DFT calculations all agree on the planar conformation for the heterocyclic fragment while the ab initio calculations predict a nonplanar conformation. Although the two methods agree on the nonplanar conformation for compound **4**, the largest differences between the DFT and ab initio calculations are in the geometry of the heterocyclic fragment. The same patterns were noted and explained in a previous study of compounds of this type.[3] In short, the DFT results seem to agree consistently and more closely with previous GED experiments than the ab initio results.

GED Structure Refinements

6,8-Difluoro-1,3λ⁴δ²,2,4-benzodithiadiazine (3)

The refined structure and associated atom numbering scheme for compound **3** are shown in Figure 1. The molecular model was constructed in C_1 symmetry, thus allowing for the out-of-plane movement of the heterocyclic fragment. The $C_6H_2F_2$ fragment was assumed to be planar since all of the ab initio and DFT calculations show negligible deviations from planarity. Twenty-eight independent geometrical parameters were used to describe the molecular structure and these are defined in Table 4. Eleven of the parameters correspond to bond angles and four to torsional angles. The remaining thirteen describe the various bond lengths in the molecule. The two C−H distances are described by a single parameter (p_8) as are the two C−F distances (p_9). In both of these cases the calculations indicated insignificant differences between the two different occurrences of the bonds. The parameter p_1 corresponds to the mean of all the C−C and C−N bond lengths, with p_2 to p_7 corresponding to various combinations of differences between these distances. The mean and the difference between the S(12)−N(13) and S(12)−N(11) bond lengths are given by p_{12} and p_{13},respectively, since these distances are similar according to the ab initio and DFT calculations.

A force field in Cartesian coordinates, calculated using the DFT method with a B3LYP functional and a 6-311+G* basis set,[14] was used (after scaling, see below) to compute values for the root-mean-square (RMS) amplitudes of vibration (u_{h1}) and perpendicular distance corrections (k_{h1}) using the methods of Sipachev.[15] This takes account of the curvilinear motions of the atoms in the molecular vibrations and yields the r_{h1} structure from the refinement process.

IR and Raman spectra were recorded and used to scale the calculated force field to obtain the most realistic esti-

 © 2005 Wiley-VCH Verlag GmbH & Co. KGaA, Weinheim

Table 2. Results of theoretical calculations for compound **3**; all distances in pm and all angles in degrees

Parameter	MP2 6-311+G*[a]	DFT-B3LYP 6-311+G*[a]	aug-cc-pVTZ[b]
r[C(1)−C(2)]	141.0	141.4	141.9
r[C(2)−C(3)]	139.5	138.2	137.4
r[C(3)−C(4)]	139.4	139.7	139.5
r[C(4)−C(5)]	139.0	137.7	137.4
r[C(5)−C(6)]	139.1	139.3	139.1
r[C(6)−C(1)]	140.2	139.3	138.9
r[C(1)−N(11)]	141.2	140.9	140.7
r[C(2)−S(14)]	177.6	182.6	181.6
r[N(13)−S(14)]	173.4	169.7	168.9
r[S(12)−N(13)]	160.3	156.5	155.7
r[N(11)−S(12)]	158.9	156.7	155.8
r[C(3)−F(7)]	134.4	135.3	135.9
r[C(4)−H(8)]	108.5	108.2	107.9
r[C(5)−F(9)]	134.6	134.8	134.5
r[C(6)−H(10)]	108.6	108.3	108.0
a[C(6)−C(1)−C(2)]	120.7	119.4	119.4
a[C(5)−C(6)−C(1)]	118.6	119.8	119.8
a[C(4)−C(5)−C(6)]	122.6	122.5	122.5
a[F(7)−C(3)−C(4)]	118.0	117.9	118.0
a[H(8)−C(4)−C(5)]	121.7	122.5	122.4
a[F(9)−C(5)−C(6)]	118.9	118.4	118.4
a[H(10)−C(6)−C(2)]	120.0	119.4	119.6
a[N(11)−C(1)−C(2)]	123.3	124.7	124.4
a[S(14)−N(13)−S(12)]	116.4	124.9	124.3
a[N(13)−S(14)−C(2)]	100.5	103.9	104.5
a[S(14)−C(2)−C(1)]	121.2	125.1	124.9
d[N(11)−C(1)−C(2)−S(14)]	12.8	0.0	0.0
d[S(12)−N(13)−S(14)−C(2)]	42.6	0.0	0.0
d[N(13)−S(14)−C(2)−C(1)]	−44.5	0.0	0.0
d[S(14)−C(2)−C(1)−C(6)]	−176.1	180.0	180.0

[a] Ref.[14] [b] Dunning correlation-consistent triple-ζ with diffuse functions.[16]

mates for the u_{h1} values. Table 5 lists the experimental frequencies as well as the scaled theoretical frequencies. The scaling factors for the theoretical frequencies were 0.92 for CH stretching modes, 0.98 for CH out-of-plane bending modes and 0.97 for the CC stretching modes. The RMS difference between the experimental and theoretical frequencies is 9 cm^{-1} and the largest difference is 17 cm^{-1}.

The refinement was carried out using the ed@ed program.[8] SARACEN restraints were applied to a large number of the independent parameters in order to allow all similar distances to be refined simultaneously. All the restraints are listed in Table 4. Reasonably tight restraints were applied to all the parameters describing the carbocyclic fragment since the consistency of the calculations gave us a large amount of confidence in the computed values for these parameters. Restraints were also placed on the C−H distance and C−F distance parameters (p_8 and p_9, respectively). The only restraints applied to the heterocyclic fragment were to the S−N distance average and difference parameters (p_{12} and p_{13}, respectively). The starting values for the refinement and the values for the restraints were taken from a DFT calculation using the B3LYP functional with a Dunning correlation-consistent basis set of triple-ζ quality, augmented by one diffuse function on each atom.[16]

It is immediately obvious that the positions of the hydrogen atoms are determined almost entirely by the restraints, with the exception of the C−H bond length. All of the difference parameters pertaining to the structure of the carbocycle (p_2−p_7) are also determined by the restraints (indicated by the equivalence of the parameter estimated standard deviation, e.s.d., and the restraint uncertainty). The unrestrained parameter p_1 (the average of the C−C and C−N distances) differs by just 0.5 pm from the computed value (DFT/B3LYP/aug-cc-pVTZ). The remaining restrained parameter values fall within the restraint uncertainties apart from p_{20}, the value of which lies just outside the uncertainty range of the restraint.

Restraints were also applied to the RMS amplitudes of vibration which could not be refined independently. Values for these restraints were calculated directly from the DFT force field, with uncertainties of 10% in the absolute computed values. With these restraints in place, all the significant RMS amplitudes of vibration were refined. The full set of refined RMS amplitudes of vibration is presented as Supporting Information (Table S1; for Supporting Informations see also the footnote on the first page of this article) along with their associated interatomic distances. The final R_G factor for the refinement was 0.049 (for the individual datasets: $R_G^{(long)} = 0.155$; $R_G^{(long)} = 0.032$). The molecu-

 © 2005 Wiley-VCH Verlag GmbH & Co. KGaA, Weinheim

Table 3. Results of theoretical calculations for compound **4**; all distances in pm and all angles in degrees

Parameter	MP2 6-311+G*[a]	DFT-B3LYP 6-311+G*[a]	aug-cc-pVTZ[b]
r[C(1)−C(2)]	141.0	141.0	140.5
r[C(2)−C(3)]	139.6	138.3	137.9
r[C(3)−C(4)]	139.3	139.5	139.3
r[C(4)−C(5)]	139.4	138.2	137.8
r[C(5)−C(6)]	139.6	139.8	139.7
r[C(6)−C(1)]	140.5	139.7	139.4
r[C(1)−N(11)]	140.4	140.2	140.2
r[C(2)−S(14)]	177.7	181.4	180.9
r[N(13)−S(14)]	173.6	171.3	170.0
r[S(12)−N(13)]	160.0	156.8	156.0
r[N(11)−S(12)]	159.4	156.6	155.6
r[C(3)−H(7)]	108.7	108.5	108.1
r[C(4)−F(8)]	133.7	134.0	133.8
r[C(5)−F(9)]	133.2	133.5	133.3
r[C(6)−F(10)]	132.9	133.2	133.0
a[C(6)−C(1)−C(2)]	117.8	117.4	117.4
a[C(5)−C(6)−C(1)]	121.3	121.9	121.9
a[C(4)−C(5)−C(6)]	119.3	119.1	119.0
a[H(7)−C(3)−C(4)]	119.5	118.7	118.7
a[F(8)−C(4)−C(5)]	118.6	119.4	119.4
a[F(9)−C(5)−C(6)]	120.1	119.9	119.8
a[F(10)−C(6)−C(2)]	120.5	120.2	120.2
a[N(11)−C(1)−C(2)]	125.3	125.6	125.5
a[S(14)−N(13)−S(12)]	116.2	121.7	122.2
a[N(13)−S(14)−C(2)]	100.6	103.8	105.0
a[S(14)−C(2)−C(1)]	118.9	121.6	122.2
d[N(11)−C(1)−C(2)−S(14)]	15.4	8.2	6.0
d[S(12)−N(13)−S(14)−C(2)]	43.9	25.2	18.8
d[N(13)−S(14)−C(2)−C(1)]	−46.6	−26.1	−19.3
d[S(14)−C(2)−C(1)−C(6)]	−174.6	−176.0	−176.9

[a] Ref.[14] [b] Dunning correlation-consistent triple-ζ with diffuse functions.[16]

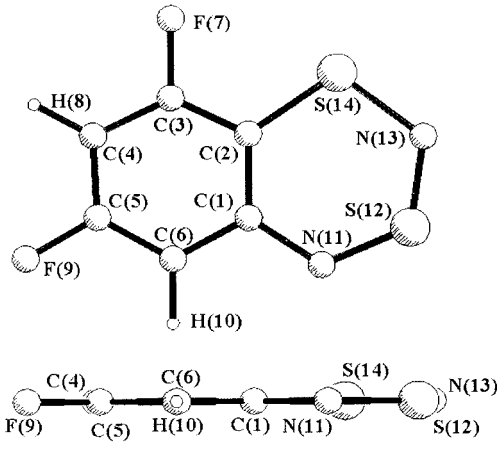

Figure 1. Refined molecular structure and atom numbering scheme for 6,8-difluoro-1,3λ⁴δ²,2,4-benzodithiadiazine (**3**)

lar scattering intensities are available in the Supporting Information (Figure S1) and the final RDCs are shown in Figure 2.

The parameters describing the folding of the heterocyclic ring ($p_{25}-p_{28}$), a key aspect of this study, were initially held fixed in the computed geometry (i.e. a planar conformation). Once this constrained refinement had been completed, the four folding parameters were combined into one parameter describing the folding motion (p_{25}), the other three parameters being determined from it by fixed ratios (as in Blockhuys et al.[3]). The ratios were determined from the displacements of the atoms of the heterocycle for the lowest-frequency folding mode calculated from the DFT force field [$p_{26} = 3.05 \times p_{25}$; $p_{27} = -3.46 \times p_{25}$; $p_{28} = (0.39 \times p_{25}) - 180$]. This folding parameter was then fixed at various nonzero values and the refinement repeated. The variation of the R_G factor with folding angle was monitored and is plotted in Figure 3. It is immediately obvious that the molecule adopts the planar conformation in the gas phase. The tables of Hamilton[17] were used to compute the 99.5% confidence limit (ca. 3σ) in order to determine the estimated standard deviation for the folding angle, leading to a value of 0.0(5)° (where the figure in parentheses indicates the e.s.d. in the last digit). The refined values of the structural parameters (r_{h1} structure) of this conformation are shown in Table 4. The planar conformation is in agreement with both the predictions of the π-fluoro hypothesis and those of the DFT calculations.

The Supporting Information (see also footnote on the first page of article) contains numerical data corresponding to the molecular scattering intensity curves (Table S2) and

 © 2005 Wiley-VCH Verlag GmbH & Co. KGaA, Weinheim

Table 4. Independent and dependent geometrical parameters (r_{h1}) from the SARACEN GED structural refinement of compound **3**; figures in parentheses are the estimated standard deviations of the last digits; all distances in pm and all angles in degrees

	Parameter	GED	Restraint/constraint
Independent parameters			
p_1	av{*r*[C−C], *r*[C−N]}	140.0(2)	
p_2	av{*r*[C(1)−C(2)], *r*[C(3)−C(4)], *r*[C(1)−C(6)], *r*[C(1)−N(11)]} − av{*r*[C(2)−C(3)], *r*[C(4)−C(5)], *r*[C(5)−C(6)]}	2.0(1)	2.0(1)
p_3	*r*[C(5)−C(6)] − av{*r*[C(2)−C(3)], *r*[C(4)−C(5)]}	1.7(1)	1.7(1)
p_4	*r*[C(2)−C(3)] − *r*[C(4)−C(5)]	0.1(1)	0.1(1)
p_5	*r*[C(1)−C(2)] − av{*r*[C(3)−C(4)], *r*[C(1)−C(6)], *r*[C(1)−N(11)]}	1.2(1)	1.2(1)
p_6	*r*[C(1)−N(11)] − av{*r*[C(3)−C(4)], *r*[C(1)−C(6)]}	1.5(1)	1.5(1)
p_7	*r*[C(3)−C(4)] − *r*[C(1)−C(6)]	0.6(1)	0.6(1)
p_8	av{*r*[C−H]}	108.6(10)	107.9(10)
p_9	av{*r*[C−F]}	134.5(5)	134.6(10)
p_{10}	*r*[C(2)−S(14)]	176.6(8)	
p_{11}	*r*[S(14)−N(13)]	175.8(5)	
p_{12}	av{*r*[S(12)−N(13)], *r*[S(12)−N(11)]}	155.7(7)	155.8(10)
p_{13}	*r*[S(12)−N(13)] − *r*[S(12)−N(11)]	−0.1(1)	−0.1(1)
p_{14}	*a*[C(6)−C(1)−C(2)]	119.6(4)	119.4(5)
p_{15}	*a*[C(5)−C(6)−C(1)]	120.2(3)	119.8(5)
p_{16}	*a*[C(4)−C(5)−C(6)]	123.0(5)	122.5(5)
p_{17}	*a*[H(10)−C(6)−C(1)]	119.7(5)	119.6(5)
p_{18}	*a*[F(9)−C(5)−C(6)]	118.8(5)	118.4(5)
p_{19}	*a*[H(8)−C(4)−C(5)]	122.3(5)	122.4(5)
p_{20}	*a*[F(7)−C(3)−C(4)]	117.3(5)	118.0(5)
p_{21}	*a*[N(11)−C(1)−C(2)]	124.4(5)	
p_{22}	*a*[S(14)−N(13)−S(12)]	119.9(4)	
p_{23}	*a*[N(13)−S(14)−C(2)]	106.3(3)	
p_{24}	*a*[S(14)−C(1)−C(2)]	125.6(4)	
p_{25}	*d*[N(11)−C(1)−C(2)−S(14)]	0.0(5)	
p_{26}	*d*[S(12)−N(13)−S(14)−C(2)]	0.0	tied to p_{25}
p_{27}	*d*[N(13)−S(14)−C(2)−C(1)]	0.0	tied to p_{25}
p_{28}	*d*[S(14)−C(2)−C(1)−C(6)]	180.0	tied to p_{25}
Dependent parameters			
d_1	*r*[C(1)−C(2)]	141.8(2)	
d_2	*r*[C(2)−C(3)]	138.4(2)	
d_3	*r*[C(3)−C(4)]	140.4(2)	
d_4	*r*[C(4)−C(5)]	138.3(2)	
d_5	*r*[C(5)−C(6)]	140.0(2)	
d_6	*r*[C(1)−C(6)]	139.8(2)	
d_7	*r*[C(1)−N(11)]	141.6(2)	
d_8	*r*[N(11)−S(12)]	155.8(7)	
d_9	*r*[N(13)−S(12)]	155.7(7)	

the R_G factor plot (Table S3) along with the Cartesian coordinates of the final refined structure (Table S4) and the least-squares correlation matrix (Table S5).

5,6,7-Trifluoro-1,3λ⁴δ²,2,4-benzodithiadiazine (4)

The model for compound **4** was constructed in an analogous way to that for compound **3**. Figure 4 shows the refined structure and atom numbering scheme for compound **4**. The differences between the models are listed below:

p_8 now describes only one C−H bond length.

p_9 now describes three C−F distances.

p_{19} now describes an F−C−C angle.

IR and Raman spectra were recorded and used to scale the calculated force-field (computed in an analogous way to that for compound **3**) to obtain the most realistic estimates of the u_{h1} values. Table 6 lists the experimental frequencies as well as the scaled theoretical frequencies. The scaling factors for the theoretical frequencies were 0.92 for CH stretching modes, 0.98 for CH out-of-plane bending modes and 0.97 for the CC stretching modes. The RMS difference between the experimental and theoretical frequencies is 9 cm^{-1} and the largest difference is 17 cm^{-1}.

Once again, SARACEN restraints were applied to many of the independent parameters in order to allow all similar distances to be refined simultaneously. All the restraints are listed in Table 7. Restraints were also placed on the C−H distance and C−F distance parameters (p_8 and p_9, respectively). The only restraints applied to the heterocyclic fragment were on the S−N average distance parameter and the S−N distance difference parameter (p_{12} and p_{13}). The starting values for the refinement and the values for the restraints were taken from a DFT calculation using the B3LYP functional with a Dunning correlation-consistent basis set of triple-ζ quality augmented with one diffuse function on each atom.

 © 2005 Wiley-VCH Verlag GmbH & Co. KGaA, Weinheim

Table 5. Experimental and scaled theoretical vibrational data for compound **3**; see text for scaling factors; frequencies ($\tilde{\nu}$) in cm^{-1}, IR intensities (I) in $km \cdot mol^{-1}$

$\tilde{\nu}_{calcd.}$	($I_{calcd.}$)	$\tilde{\nu}_{exp}$ [a]		$\tilde{\nu}_{calcd.}$	($I_{calcd.}$)	$\tilde{\nu}_{exp}$ [a]	
3102	(3)	3099	r	713	(7)		
3092	(1)	3081	r	617	(46)	629	m
1615	(102)	1632	w	609	(8)	615	m
1606	(116)	1595	m	603	(4)	602	m
1467	(114)	1460	m	592	(2)	581	vw
1422	(63)	1415	r	559	(3)	566	r
1353	(21)	1338	m	514	(11)	519	w
1280	(13)	1295	r	478	(13)	476	w
1195	(41)	1187	r	372	(0)	371	r
1139	(211)	1136	r	361	(1)		
1105	(21)	1106	w	359	(6)		
1044	(17)	1052	r	321	(5)		
1012	(56)	1017	m	293	(2)	299	r
1000	(13)	1000	m	241	(2)		
890	(19)	896	r	212	(1)		
873	(29)	860	m	201	(0)		
832	(21)	836	m	95	(0)		
724	(3)			21	(1)		

[a] vw: very weak; w: weak; m: medium; r: Raman band not observed in IR.

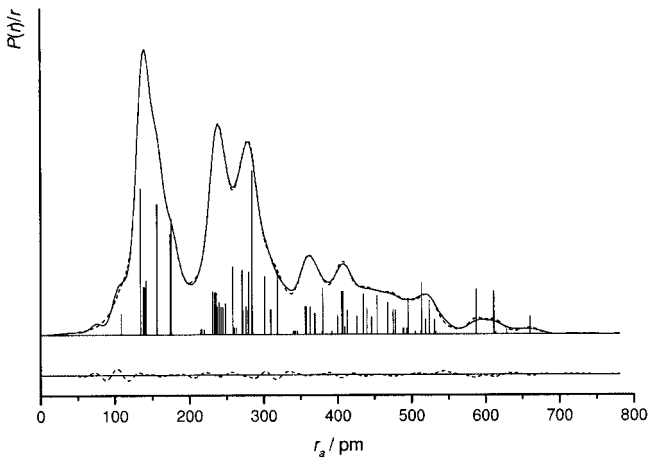

Figure 2. Radial distribution and difference curves for compound **3**; solid curve: observed radial distribution curve; dashed curve: calculated radial distribution curve at refined geometry; lower dashed curve: difference between observed and calculated radial distribution curves; before Fourier inversion all data were multiplied by $s[\exp(-0.00002s^2)/(Z_S - f_S)(Z_F - f_F)]$

Restraints were also applied to the RMS amplitudes of vibration which could not be refined independently. Values for these restraints were calculated directly from the DFT force field, with uncertainties of 10% in the absolute computed values. With these restraints in place, all the significant RMS amplitudes of vibration were refined. The full set of refined RMS amplitudes of vibration is available in the Supporting Information (Table S6) along with their associated interatomic distances. The final R_G factor for the refinement was 0.039 (for the individual data sets: $R_G^{(short)} = 0.112$; $R_G^{(long)} = 0.025$). The molecular scattering intensities are available in the Supporting Information (Figure S2) and the final RDCs are shown in Figure 5. Once again, all of

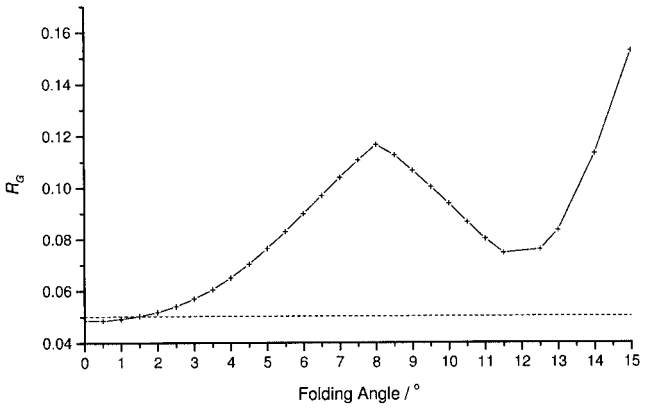

Figure 3. Variation of R_G with folding angle of the heterocyclic fragment for compound **3**; a 0° folding angle corresponds to the planar conformation; the dashed line marks the 99.5% confidence limit

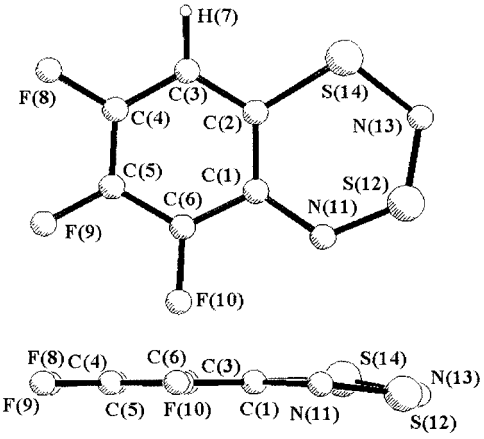

Figure 4. Refined molecular structure and atom numbering scheme for 5,6,7-trifluoro-1,3λ⁴δ²,2,4-benzodithiadiazine (**4**)

Table 6. Experimental and scaled theoretical vibrational data for compound **4**; see text for scaling factors; frequencies ($\tilde{\nu}$) in cm^{-1}, IR intensities (I) in $km \cdot mol^{-1}$

$\tilde{\nu}_{calcd.}$	($I_{calcd.}$)	$\tilde{\nu}_{exp}$ [a]		$\tilde{\nu}_{calcd.}$	($I_{calcd.}$)	$\tilde{\nu}_{exp}$ [a]	
3054	(2)	3048	w	655	(1)		
1625	(66)	1614	m	616	(33)	631	m
1604	(20)	1595	m	569	(4)	561	w
1501	(342)	1505	s	535	(3)	541	w
1443	(147)	1439	s	511	(5)	519	w
1352	(35)	1340	m	458	(7)	449	w
1276	(46)	1274	w	414	(1)	421	w
1257	(6)	1244	m	359	(7)		
1218	(66)	1215	m	340	(1)		
1119	(140)	1136	s	327	(6)		
1059	(82)	1068	s	294	(5)		
995	(27)	1007	m	281	(2)		
924	(4)	930	w	275	(1)		
860	(18)	858	m	220	(0)		
811	(35)	821	m	178	(1)		
757	(6)	743	m	148	(0)		
742	(10)			100	(0)		
677	(21)	678	m	51	(0)		

[a] w: weak; m: medium; s: strong.

 © 2005 Wiley-VCH Verlag GmbH & Co. KGaA, Weinheim

Table 7. Independent and dependent geometrical parameters (r_{h1}) from the SARACEN GED structural refinement of compound **4**; figures in parentheses are the estimated standard deviations of the last digits; all distances in pm and all angles in degrees

	Parameter	GED	Restraint/constraint
Independent parameters			
p_1	av{*r*[C−C], *r*[C−N]}	139.9(2)	
p_2	av{*r*[C(1)−C(2)], *r*[C(3)−C(4)], *r*[C(1)−C(6)], *r*[C(1)−N(11)]} − av{*r*[C(2)−C(3)], *r*[C(4)−C(5)], *r*[C(5)−C(6)]}	1.3(5)	1.4(5)
p_3	*r*[C(5)−C(6)] − av{*r*[C(2)−C(3)], *r*[C(4)−C(5)]}	1.6(5)	1.6(5)
p_4	*r*[C(2)−C(3)] − *r*[C(4)−C(5)]	0.1(1)	0.1(1)
p_5	*r*[C(1)−C(2)] − av{*r*[C(3)−C(4)], *r*[C(1)−C(6)], *r*[C(1)−N(11)]}	1.1(5)	1.2(5)
p_6	*r*[C(1)−N(11)] − av{*r*[C(3)−C(4)], *r*[C(1)−C(6)]}	0.6(1)	0.6(1)
p_7	*r*[C(3)−C(4)] − *r*[C(1)−C(6)]	−0.2(1)	−0.2(1)
p_8	*r*[C−H]	108.2(10)	108.94(10)
p_9	av{*r*[C−F]}	133.5(4)	133.6(5)
p_{10}	*r*[C(2)−S(14)]	180.6(8)	
p_{11}	*r*[S(14)−N(13)]	170.7(6)	
p_{12}	av{*r*[S(12)−N(13)], *r*[S(12)−N(11)]}	155.5(7)	155.6(10)
p_{13}	*r*[S(12)−N(13)] − *r*[S(12)−N(11)]	0.2(1)	0.3(1)
p_{14}	*a*[C(6)−C(1)−C(2)]	116.9(6)	
p_{15}	*a*[C(5)−C(6)−C(1)]	121.8(7)	
p_{16}	*a*[C(4)−C(5)−C(6)]	118.7(6)	
p_{17}	*a*[H(7)−C(6)−C(1)]	119.9(5)	120.2(10)
p_{18}	*a*[F(8)−C(5)−C(6)]	119.4(7)	119.8(10)
p_{19}	*a*[F(9)−C(4)−C(5)]	119.7(7)	119.4(10)
p_{20}	*a*[F(10)−C(3)−C(4)]	118.6(10)	118.7(10)
p_{21}	*a*[N(11)−C(1)−C(2)]	125.7(8)	
p_{22}	*a*[S(14)−N(13)−S(12)]	119.9(8)	
p_{23}	*a*[N(13)−S(14)−C(2)]	106.9(6)	
p_{24}	*a*[S(14)−C(1)−C(2)]	122.6(6)	
p_{25}	*d*[N(11)−C(1)−C(2)−S(14)]	4.0(−30;+3)	
p_{26}	*d*[S(12)−N(13)−S(14)−C(2)]	12.2	tied to p_{25}
p_{27}	*d*[N(13)−S(14)−C(2)−C(1)]	−12.6	tied to p_{25}
p_{28}	*d*[S(14)−C(2)−C(1)−C(6)]	−178.0	tied to p_{25}
Dependent parameters			
d_1	*r*[C(1)−C(2)]	141.3(5)	
d_2	*r*[C(2)−C(3)]	138.6(4)	
d_3	*r*[C(3)−C(4)]	139.9(3)	
d_4	*r*[C(4)−C(5)]	138.5(4)	
d_5	*r*[C(5)−C(6)]	140.2(4)	
d_6	*r*[C(1)−C(6)]	140.1(3)	
d_7	*r*[C(1)−N(11)]	140.6(2)	
d_8	*r*[N(11)−S(12)]	154.6(7)	
d_9	*r*[N(13)−S(12)]	155.6(7)	

the difference parameters defining the structure of the carbocycle (p_2−p_7) are determined entirely by the restraints. The unrestrained parameter describing the average of the C−C and C−N distances (p_1) differs by just 0.3 pm from the computed value (DFT/B3LYP/aug-cc-pVTZ).

As for compound **3**, we were particularly interested in the planarity or nonplanarity of the heterocyclic fragment. In order to investigate this, the four parameters describing the folding of the heterocyclic fragment were combined into just one folding parameter (p_{25}). The ratios were determined from the displacements of the atoms of the heterocycle for the lowest-frequency folding mode calculated from the DFT force field [$p_{26} = 3.05 \times p_{25}$; $p_{27} = -3.16 \times p_{25}$; $p_{28} = (0.49 \times p_{25}) - 180$]. This parameter was fixed at various values and the refinement repeated. The variation of the R_G factor with folding angle is presented in Figure 6 along with the 99.5% confidence limit, calculated as described above. The graph indicates that the folding angle parameter can take effectively any value between 0° (planar) and about 6°. The variation of the R_G factor from its minimum value of 0.038 (4.0°) up to its value of 0.042 at 6° is just 0.004. Nevertheless, the R_G factor analysis suggests a folding angle of 4.0(−30;+3)°. More evidence for the slightly nonplanar geometry of the heterocyclic fragment comes from the fact that in the refinement at the planar geometry, some of the parameter values lie outside their SARACEN restraint uncertainties. In the nonplanar geometry refinement the parameter values lie within the restraint uncertainties.

The Supporting Information contains numerical data corresponding to the molecular scattering intensity curves (Table S7) and the R_G factor plot (Table S8) along with the Cartesian coordinates of the final refined structure (Table S9) and the least-squares correlation matrix (Table S10).

 © 2005 Wiley-VCH Verlag GmbH & Co. KGaA, Weinheim

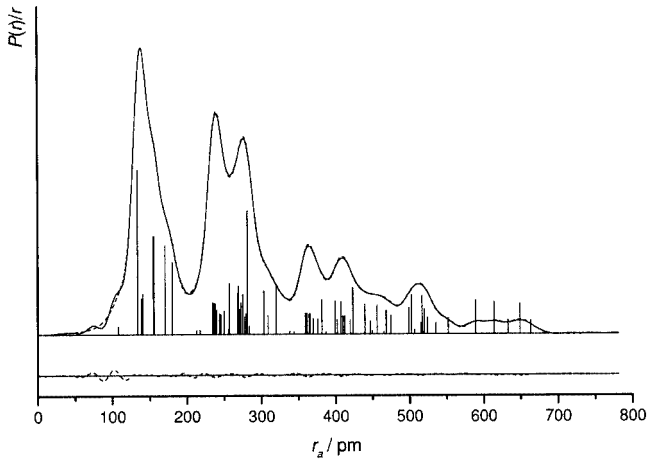

Figure 5. Radial distribution and difference curves for compound **4**; solid curve: observed radial distribution curve; dashed curve: calculated radial distribution curve at refined geometry; lower dashed curve: difference between observed and calculated radial distribution curves; before Fourier inversion all data were multiplied by $s[\exp(-0.00002s^2)/(Z_S - f_S)(Z_F - f_F)]$

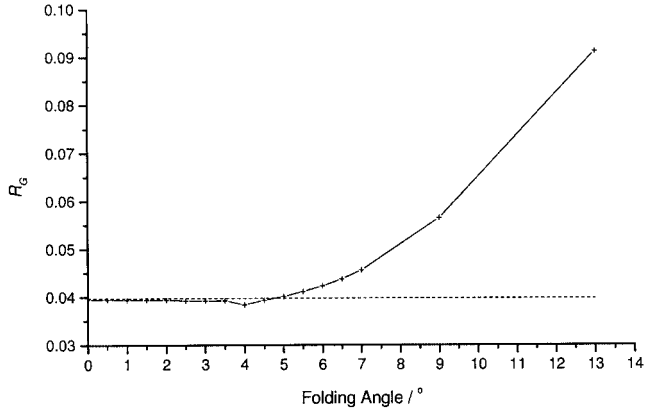

Figure 6. Variation of R_G with folding angle of the heterocyclic fragment for compound **4**; a 0° folding angle corresponds to the planar conformation; the dashed line marks the 99.5% confidence limit

Structural Comparisons

Table 8 enables a comparison of the available experimental and theoretical structural data (DFT/B3LYP/aug-cc-pVTZ) for compound **3** and Table 9 shows the same comparison for compound **4**.

For compound **3**, both GED and theory agree on a planar conformation with respect to the heterocyclic ring in the gas phase, while the XRD study shows that the compound is bent in the crystal. The major differences between the GED structure and the theoretical structure are in the S(14)−N(13) and C(1)−S(14) bond lengths. In the GED structure, the S(14)−N(13) bond is 6.9 pm longer than the theoretical value and the C(2)−S(14) bond length is 5 pm shorter than the theoretical value. Refinements with the bond lengths restrained to the theoretical distances show significantly larger R_G factors than for the final refined structure. 1st row to 2nd row *p*-block bond lengths have been found to be particularly difficult to determine using ab initio techniques.[18]

Table 8. Comparison of pertinent structural parameters from different techniques for compound **3**; all distances in pm and all angles in degrees

Parameter	GED (r_{h1})[a]	XRD[b]	Theory (r_e)[a]
r[S(14)−N(13)]	175.8(5)	166.8(5)	168.9
r[N(13)−S(12)]	155.7(7)	155.1(5)	155.7
r[S(12)−N(11)]	155.8(7)	153.6(5)	155.8
r[N(11)−C(1)]	141.6(2)	142.5(6)	140.7
r[C(1)−C(2)]	141.8(2)	139.8(7)	140.9
r[C(2)−S(14)]	176.6(8)	177.9(5)	181.6
a[S(14)−N(13)−S(12)]	119.9(4)	123.9(3)	124.3
a[N(13)−S(12)−N(11)]	121.6(4)	118.3(2)	118.8
a[S(12)−N(11)−C(1)]	122.2(4)	123.2(4)	123.1
a[N(11)−C(1)−C(2)]	124.4(5)	123.6(4)	124.4
a[C(1)−C(2)−S(14)]	125.6(4)	124.6(4)	124.9
a[C(2)−S(14)−N(13)]	106.3(3)	105.0(2)	104.5
d[N(11)−C(1)−C(2)−S14)]	0.0(5)	8.2(8)	0.0

[a] This work (DFT/B3LYP/aug-cc-pVTZ). [b] Makarov et al.[4]

Table 9. Comparison of pertinent structural parameters from different techniques for compound **4**; all distances in pm and all angles in degrees

Parameter	GED (r_{h1})[a]	XRD[b]	Theory (r_e)[a]
r[S(14)−N(13)]	170.7(6)	168.3(5)	170.0
r[N(13)−S(12)]	155.6(7)	153.9(5)	156.0
r[S(12)−N(11)]	154.6(7)	153.2(4)	155.6
r[N(11)−C(1)]	140.6(3)	143.0(6)	140.2
r[C(1)−C(2)]	141.3(5)	138.9(7)	140.5
r[C(2)−S(14)]	180.6(8)	178.6(5)	180.9
a[S(14)−N(13)−S(12)]	119.9(8)	123.9(3)	122.2
a[N(13)−S(12)−N(11)]	121.8(6)	119.7(2)	118.5
a[S(12)−N(11)−C(1)]	121.6(6)	121.4(4)	122.5
a[N(11)−C(1)−C(2)]	125.8(8)	125.7(4)	125.5
a[C(1)−C(2)−S(14)]	122.6(6)	123.9(4)	122.2
a[C(2)−S(14)−N(13)]	106.9(6)	105.3(2)	105.0
d[N(11)−C(1)−C(2)−S(14)]	4.0(−30;+3)	1.7(7)	6.0

[a] This work (DFT/B3LYP/aug-cc-pVTZ). [b] Makarov et al.[4]

For compound **4**, the theoretical structure shows a bent conformation for the heterocyclic ring and the XRD study shows that the heterocycle is almost flat in the crystal. In the gas phase, the indications are that the heterocyclic ring is slightly bent. This is supported by the fact that generally, the GED structural parameters agree more closely with the theoretical (bent) structure than with the XRD (almost planar) structure. All the S−N bond lengths and the C−S bond length agree to within 1 pm. The magnitude of the folding angle is also very similar in the GED and theoretical structures.

Table 10 shows a comparison of the relevant structural parameters for compounds **1**, **2**, **3** and **4** as determined by GED. The major differences between the compounds are in the S(14)−N(13) and C(2)−S(14) bond lengths. For the S(14)−N(13) bond, the largest difference is 6.1 pm (between compound **1** and compound **3**) and for the C(2)−S(14) bond length, the largest difference is 4.6 pm (between compound **2** and compound **3**). It is worth noting that although the S=N bond lengths [N(11)−S(12), S(12)−N(13)] stay

 © 2005 Wiley-VCH Verlag GmbH & Co. KGaA, Weinheim

Table 10. Comparison of pertinent structural parameters (r_{h1}) from GED structural refinements of benzodithiadiazine derivatives; all distances in pm and all angles in degrees

Parameter	Compound 1[a]	2[a]	3[b]	4[b]
r[S(14)−N(13)]	169.7(5)	172.3(8)	175.8(5)	170.7(6)
r[N(13)−S(12)]	154.8(3)	155.3(3)	155.7(7)	155.6(7)
r[S(12)−N(11)]	154.3(3)	155.2(3)	155.8(7)	154.6(7)
r[N(11)−C(1)]	139.3(6)	139.6(7)	141.6(2)	140.6(3)
r[C(1)−C(2)]	139.1(6)	140.5(8)	141.8(2)	141.3(5)
r[C(2)−S(14)]	178.4(5)	181.2(9)	176.6(8)	180.6(8)
a[S(14)−N(13)−S(12)]	119.9(5)	122.8(5)	119.9(4)	119.9(8)
a[N(13)−S(12)−N(11)]	−	−	121.6(4)	121.8(6)
a[S(12)−N(11)−C(1)]	−	−	122.2(4)	121.6(6)
a[N(11)−C(1)−C(2)]	123.3(7)	125.4(7)	124.4(5)	125.8(8)
a[C(1)−C(2)−S(14)]	122.7(6)	124.6(6)	125.6(4)	122.6(6)
a[C(2)−S(14)−N(13)]	101.5(7)	104.5(3)	106.3(3)	106.9(6)
d[N(11)−C(1)−C(2)−S(14)]	−17.0(30)	0.0(5)	0.0(5)	4.0(−30;+3)

[a] Blockhuys et al.[3] [b] This work.

reasonably consistent over all the compounds, the S−N bond length [S(14)−N(13)] is slightly greater in the two planar compounds. The lack of other obvious trends in the structures is indicative of the complex effects that different fluorine substitution patterns have on the structures of the compounds. Although the calculations predict that both the S(14)−N(13) and C(2)−S(14) bond lengths should be similar in both compounds **3** and **4**, the GED results do not replicate this trend. To assess whether or not this is a real effect we restrained the values in the GED refinement to the theoretical values. In both compounds this resulted in the values lying well outside the restraint uncertainties and a large increase in the R_G factors showing that the experimentally determined values are indeed correct.

Our studies show that compound **3** is planar and that compound **4** is slightly nonplanar, in line with the π-fluoro hypothesis. The energy difference between the planar and nonplanar conformations of compound **4** has been calculated using a number of different methods and the results are shown in Table 11. These values have been corrected by adding the calculated zero-point vibrational energies (scaled according to the constants of Wong et al.). All of the energy differences between the bent and flat conformers are effectively zero, reflecting the low-frequency, large-amplitude nature of the out-of-plane bending mode. At the temperature of the GED experiment we would expect the vibrational mode corresponding to the folding of the heterocyclic ring to have a large amplitude, leading to the very large uncertainties we see in the value of the folding angle.

Table 11. Calculated energy differences between bent and flat conformations of compound **4**; all energy differences include scaled zero-point vibrational energy corrections

Method	Energy difference [kJ·mol^{-1}]
RHF/aug-cc-pVDZ	1.3
MP2/aug-cc-pVDZ	0.3
DFT/B3LYP/aug-cc-pVDZ	0.9
DFT/B3LYP/aug-cc-pVTZ	0.07

Conclusion

We have successfully used the new graphical structural refinement program ed@ed to obtain the SARACEN gas-phase structures of 6,8-difluoro-1,3λ^{4}δ^2,2,4-benzodithiadiazine (**3**) and 5,6,7-trifluoro-1,3λ^{4}δ^2,2,4-benzodithiadiazine (**4**) from GED data.

These GED structures have been compared with both the theoretical and crystal structures and the differences, in particular the conformations of the heterocyclic fragments, have been noted and discussed. Compound **3** is planar in the gas phase with respect to the heterocyclic fragment and compound **4** is slightly nonplanar, as predicted by the π-fluoro hypothesis postulated by Blockhuys et al.[3] The large uncertainties in the folding of the heterocyclic fragment for compound **4** are due to the low-frequency bending mode of the heterocyclic fragment. On the whole, this work and Blockhuys et al.[3] describe and explain interesting stereoelectronic effects in benzo-fused sulfur-nitrogen antiaromatic heterocycles. In particular, it has been shown that for free molecules, the conformation of the heterocyclic ring can be affected by substitutions on the carbocyclic fragment.

Acknowledgments

F. B. and C. V. A. gratefully acknowledge support from the University of Antwerp under Grant GOA-BOF-UA No. 23. We thank the UK Engineering and Physical Sciences Research Council for support for gas-phase electron diffraction (grant GR/R17768).

[1] A. V. Zibarev, Y. V. Gatilov, A. O. Miller, *Polyhedron* **1992**, *11*, 1137.
[2] A. W. Cordes, M. Hojo, H. Koenig, M. C. Noble, R. T. Oakley, W. T. Pennington, *Inorg. Chem.* **1986**, *25*, 1137.
[3] F. Blockhuys, S. L. Hinchley, A. Yu. Makarov, Y. V. Gatilov,

 © 2005 Wiley-VCH Verlag GmbH & Co. KGaA, Weinheim

A. V. Zibarev, J. D. Woollins, D. W. H. Rankin, *Chem. Eur. J.* **2001**, *7*, 3592.

[4] A. Yu. Makarov, I. Yu. Bagryanskaya, F. Blockhuys, C. Van Alsenoy, Y. V. Gatilov, V. V. Knyazev, A. M. Maksimov, T. V. Mikhalina, V. E. Platonov, M. M. Shakirov, A. V. Zibarev, *Eur. J. Inorg. Chem.* **2003**, 77.

[5] P. V. Schastnev, L. N. Schegoleva, *Molecular Distortion in Ionic and Excited States*, CRC, Boca Raton, **1995**.

[6] C. M. Huntley, G. S. Laurenson, D. W. H. Rankin, *J. Chem. Soc., Dalton Trans.* **1980**, 954.

[7] Y. Murata, Y. Morino, *Acta Crystallogr.* **1966**, *20*, 605.

[8] S. L. Hinchley, H. E. Robertson, K. B. Borisenko, A. R. Turner, B. F. Johnston, D. W. H. Rankin, M. Ahmadian, J. N. Jones, A. H. Cowley, *Dalton Trans.*, in press.

[9] A. W. Ross, M. Fink, R. Hilderbrandt, in *International Tables for Crystallography* (Ed.: A. J. C. Wilson) Kluwer, Dordrecht, **1992**, vol. C, p. 245.

[10] M. J. Frisch, G. W. Trucks, H. B. Schlegel, G. E. Scuseria, M. A. Robb, J. R. Cheeseman, V. G. Zakrzewski, J. A. Montgomery, R. E. Stratmann, J. C. Burant, S. Dapprich, J. M. Millam, A. D. Daniels, K. N. Kudin, M. C. Strain, O. Farkas, J. Tomasi, V. Barone, M. Cossi, R. Cammi, B. Mennucci, C. Pomelli, C. Adamo, S. Clifford, J. Ochterski, G. A. Petersson, P. Y. Ayala, Q. Cui, K. Morokuma, D. K. Malick, A. D. Rabuck, K. Raghavachari, J. B. Foresman, J. Cioslowski, J. V. Ortiz, B. B. Stefanov, G. Liu, A. Liashenko, P. Piskorz, I. Komaromi, R. Gomperts, R. L. Martin, D. J. Fox, T. Keith, M. A. Al-Laham, C. Y. Peng, A. Nanayakkara, C. Gonzalez, M. Challacombe, P. M. W. Gill, B. G. Johnson, W. Chen, M. W. Wong, J. L. Andres, M. Head-Gordon, E. S. Replogle, J. A. Pople, *Gaussian98*, revision A.7, Gaussian Inc., Pittsburgh PA, **1998**.

[11] [11a] N. W. Mitzel, D. W. H. Rankin, *Dalton Trans.* **2003**, *19*, 3650. [11b] N. W. Mitzel, B. A. Smart, A. J. Blake, H. E. Robertson, D. W. H. Rankin, *J. Phys. Chem.* **1996**, *100*, 9339. [11c] A. J. Blake, P. T. Brain, H. McNab, J. Millar, C. A. Morrison, S. Parsons, D. W. H. Rankin, H. E. Robertson, B. A. Smart, *J. Phys. Chem.* **1996**, *100*, 12280.

[12] [12a] C. Møller, M. S. Plesset, *Phys. Rev.* **1934**, *46*, 618. [12b] M. Head-Gordon, J. A. Pople, M. J. Frisch, *Chem. Phys. Lett.* **1988**, *153*, 503. [12c] M. J. Frisch, M. Head-Gordon, J. A. Pople, *Chem. Phys. Lett.* **1990**, *166*, 275. [12d] M. J. Frisch, M. Head-Gordon, J. A. Pople, *Chem. Phys. Lett.* **1990**, *166*, 281. [12e] M. Head-Gordon, T. Head-Gordon, *Chem. Phys. Lett.* **1994**, *220*, 122. [12f] S. Saebo, J. Almlöf, *Chem. Phys. Lett.* **1989**, *154*, 83.

[13] [13a] A. D. Becke, *J. Chem. Phys.* **1993**, *98*, 5648; C. Lee, W. Yang, R. G. Parr, *Phys. Rev. B.* **1988**, *37*, 785. [13b] B. Miehlich, A. Savin, H. Still, H. Preuss, *Chem. Phys. Lett.* **1989**, *157*, 200.

[14] [14a] A. D. McLean, G. S. Chandler, *J. Chem. Phys.* **1980**, *72*, 5639. [14b] R. Krishnan, J. S. Binkley, R. Seeger, J. A. Pople, *J. Chem. Phys.* **1980**, *72*, 650. [14c] T. Clark, J. Chandrasekhar, G. W. Spitznagel, P. v. R. Schleyer, *J. Comp. Chem.* **1983**, *4*, 294.

[15] V. A. Sipachev, *J. Mol. Struct.* **1985**, *121*, 143; V. A. Sipachev, in *Advances in Molecular Structure Research* (Eds.: I. Hargittai, M. Hargittai), JAI, Greenwich, **1999**, vol. 5, p. 263.

[16] R. A. Kendall, T. H. Dunning Jr., R. J. Harrison, *J. Chem. Phys.* **1992**, *96*, 6796.

[17] W. C. Hamilton, *Acta Crystallogr.* **1965**, *18*, 502.

[18] S. L. Hinchley, P. Trickey, H. E. Robertson, B. A. Smart, D. W. H. Rankin, D. Leusser, B. Walfort, D. Stalke, M. Bühl, S. J. Obrey, *Dalton Trans.* **2002**, 4607.

Received July 12, 2004
Early View Article
Published Online December 6, 2004

 © 2005 Wiley-VCH Verlag GmbH & Co. KGaA, Weinheim

Ionic Liquids as Reaction Media for Palladium-Catalysed Cross-Coupling of Aryldiazonium Tetrafluoroborates with Potassium Organotrifluoroborates

Vito Gallo,[a] Piero Mastrorilli,*[a] Cosimo F. Nobile,[a] Rossella Paolillo,[a] and Nicola Taccardi[a]

Keywords: C-C coupling / Diazonium salts / Homogeneous catalysis / Ionic liquids / Organotrifluoroborates

The system comprising a palladium complex in a 1-butyl-3-methylimidazolium tetrafluoroborate/methanol mixture efficiently catalyses the cross-coupling reaction between *p*-tolyldiazonium tetrafluoroborate and potassium phenyltrifluoroborate at room temperature. The presence of methanol (or water) in the reaction mixture is necessary in order to achieve quantitative conversions, due to its scavenging behaviour towards the BF_3 formed during the reaction. Yields higher than 90% were obtained using $Pd_2(dba)_3$ or the azapalladacycle **10** as the palladium source. With the latter complex a turnover frequency of about 6000 h^{-1} was attained in the coupling of aryldiazonium tetrafluoroborates with potassium vinyltrifluoroborate. Recycling of the catalytic solution could be performed provided that a slight excess of diazonium salt was used in the first run.

(© Wiley-VCH Verlag GmbH & Co. KGaA, 69451 Weinheim, Germany, 2005)

Introduction

Palladium-catalysed cross-coupling utilizing organoboron compounds (the Suzuki reaction) is a powerful tool for the formation of carbon−carbon bonds.[1,2] The practical advantages of this reaction are mainly related to the wide range of functionalized substrates that can be used under mild conditions. Typical reaction protocols exploit aryl iodides, bromides and triflates, which are not as cheap and readily available as aryl chlorides, although the latter are less reactive. It has been demonstrated[3−8] that aryldiazonium tetrafluoroborates derived from inexpensive and easily accessible anilines can be efficiently used in the cross-coupling with organoboronic acids or esters. Moreover, the cross-coupling has also been performed at room temperature and without added base using potassium organotrifluoroborates, which are more stable and reactive than the corresponding boronic acid derivatives.[9]

Ionic liquids (ILs) have emerged as potentially useful reaction media in catalysis because of their peculiar physical and chemical properties.[10] The latest efforts of the scientific community have been addressed towards finding new, possibly recyclable catalytic systems that exhibit higher activity than with classical solvents.

The palladium-catalyzed Suzuki reaction between boronic acids and aryl halides has been successfully carried out in ILs. Welton et al.[11−13] have demonstrated that, under suitable conditions, the use of imidazolium-based IL/H_2O mixtures leads to increased reactivity and selectivity compared to conventional reaction media and permits the recycling of the catalytic solutions. Other catalytic systems employed for the same reaction include $PdCl_2$ in alkylammonium tetrafluoroborate/H_2O mixtures,[14] $Pd_2(dba)_3$ in a ternary system made up of tetradecyltrihexylphosphonium chloride, water and toluene[15] and phosphane-free $Pd(OAc)_2$ or bisimidazolin-2-ylidene palladium complex in IL/MeOH mixtures under ultrasonic irradiation.[16]

In the framework of our studies on metal-catalysed carbon−carbon bond forming reactions in ILs[17−20] we decided to investigate the palladium-catalysed cross-coupling of aryldiazonium salts with organotrifluoroborates. Figure 1 shows the ILs used in this work.

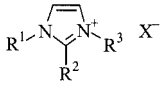

[bmim]$^+$: R^1 = methyl, R^2 = H, R^3 = *n*-butyl
[bmmim]$^+$: R^1, R^2 = methyl, R^3 = *n*-butyl
[bbim]$^+$: R^1, R^3 = *n*-butyl, R^2 = H
X^-: BF_4^-, PF_6^-, $N(SO_2CF_3)_2^-$

Figure 1. Ionic liquids employed: [bmim]BF_4, [bmim]PF_6, [bmim]$N(SO_2CF_3)_2$, [bmmim]BF_4, [bbim]BF_4

Results and Discussion

Optimisation of the Solvent

The cross-coupling reaction between *p*-tolyldiazonium tetrafluoroborate (**1a**) and potassium phenyltrifluoroborate (**2**) was chosen as the model system (Reaction 1).

[a] Dipartimento di Ingegneria delle Acque e di Chimica del Politecnico di Bari,
Via Orabona 4, 70125 Bari, Italy
Fax: + 39-080-596-3611
E-mail: p.mastrorilli@poliba.it

 © 2005 Wiley-VCH Verlag GmbH & Co. KGaA, Weinheim DOI: 10.1002/ejic.200400637

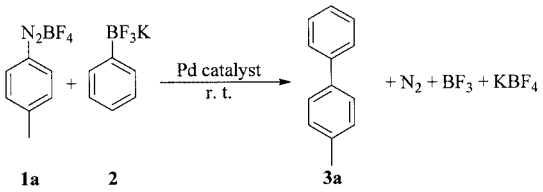

Reaction 1. Cross-coupling between *p*-tolyldiazonium tetrafluoroborate and potassium phenyltrifluoroborate

Table 1 summarises the results obtained when carrying out reaction 1 in several ILs with 2.0 mol % $Pd(OAc)_2$ as catalyst, which is a palladium loading less than half of that used in previous works.[9]

Table 1. Solvent screening; reaction conditions: IL: 10 mmol; $Pd(OAc)_2$: 0.02 mmol; **1a**: 1.0 mmol; **2**: 1.2 mmol

Entry	Solvent	Time [h]	Conv.[a] (%)	Isolated yield (%)
1-1	[bmim]BF_4	6	51	49
2-1	[bmim]$N(SO_2CF_3)_2$	6	60	38
3-1	[bmim]PF_6	14	50	41
4-1	[bmmim]BF_4	12	53	45
5-1	[bbim]BF_4	12	45	34

[a] Calculated at the time at which a plateau was reached in the consumption of the diazonium salt.

The results show that there is an effect of the IL used on the course of the reaction. Using [bmim]BF_4 (bmim = 1-*n*-butyl-3-methylimidazolium) gave 51% conversion after 6 h with 96% selectivity towards **3a** (Entry 1-1). Catalysis in [bmim]$N(SO_2CF_3)_2$ was more efficient (60% conv. after 6 h) but significantly less selective (63%, Entry 2-1), whereas when [bmim]PF_6 was used as solvent a drop in both activity (50% conv. after 14 h) and selectivity (82%) was observed (Entry 3-1 vs. Entry 1-1). The effect of the cation of the IL is shown in Entries 1-1, 4-1 and 5-1, from which it is apparent that comparable yields of **3a** were obtained after significantly different times. Among all the ILs tested [bmim]BF_4 gave the best results in terms of both activity and selectivity and was chosen as solvent for further investigations.

A common point which emerges from Table 1 is that, after variable times, the reactions did not reach completion but stopped when the conversion was about 50−60%. Figure 2 shows the reaction course in the case of Entry 1-1.

Such a behavior could, in theory, be ascribed to two causes: a) catalyst deactivation, or b) formation of a product that inhibits the reaction.

The first hypothesis was ruled out by the observation that the conversion did not improve significantly when performing the reaction with a higher amount of palladium: carrying out the catalysis with 5 or 10 mol % Pd resulted in 65% or 70% conversion, respectively.

In search of the reaction product that could act as inhibitor for the reaction we focused our attention on BF_3. It is known[21,22] that BF_3 reacts with **2** in halogenated solvents to afford potassium tetrafluoroborate and phenyldifluoroborane (Reaction 2).

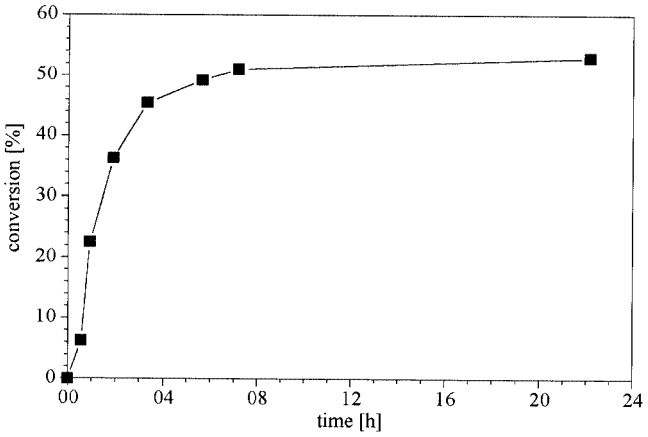

Figure 2. Reaction course of Entry 1-1

$$BF_3 + KPhBF_3 \rightarrow PhBF_2 + KBF_4$$

Reaction 2

This reaction could therefore be responsible for unsatisfactory conversions as the formed $PhBF_2$ is inactive in Suzuki cross-coupling.

The detrimental effect of BF_3 on the reaction course was circumvented by using MeOH as a BF_3 scavenger. In fact, reactions performed in [bmim]BF_4/MeOH mixtures gave quantitative conversions. Figure 3 shows the effect of the molar fraction (x_{MeOH}) of added methanol on the catalysis performed in [bmim]BF_4. Isolated yields of **3a** and reaction times are dependent on the molar fraction of MeOH. At x_{MeOH} = 0.25 the reaction reaches completion in 120 min with a 68% yield of **3a**. The discrepancy between yield and conversion is due to decomposition of the diazonium salt, since only traces of homo-coupling products (biphenyl and 4,4′-dimethylbiphenyl) were formed. At x_{MeOH} = 0.75 a 67% yield of **3a** was achieved along with the formation of biphenyl (25%) and 4,4′-dimethylbiphenyl (6%) by-products. The reaction carried out in pure MeOH was very fast and exothermic but poorly selective, giving only 47% yield of **3a**, 30% of biphenyl and 16% of 4,4′-dimethylbiphenyl. Hence, MeOH has the side effect of accelerating the decomposition of the diazonium salt over long reaction times when used at low molar fractions; at high x_{MeOH} the selectivity of the reaction is strongly reduced, mainly owing to formation of homocoupling by-products. Carrying out the reaction with a x_{MeOH} of 0.50 gave the best result (83% yield of **3a** after 30 min). In this case the formation of

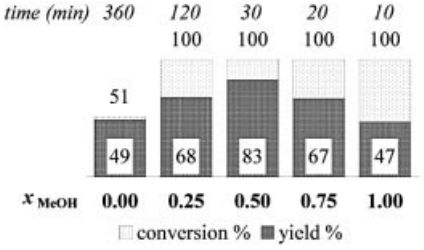

Figure 3. Effect of the MeOH molar fraction

 © 2005 Wiley-VCH Verlag GmbH & Co. KGaA, Weinheim

homo-coupling products was negligible and the decomposition of diazonium salt minimised.

Palladium Source

Results obtained using several Pd sources in [bmim]BF_4/MeOH (x_{MeOH} = 0.50) as catalysts for reaction 1 are summarized in Table 2. A comparison of Entry 1-2 with Entry 2-2 clearly shows the strong influence exerted by the anion of the Pd^{II} salt on the catalysis: $PdCl_2$ gave only 40% conversion and 15% yield of **3a** after 28 h. The reactions involving Pd^0 complexes gave nearly quantitative conversions. In particular, $Pd_2(dba)_3$ gave a higher yield (90%) than that (63%) obtained with $Pd(PPh_3)_4$, but needed a longer reaction time (Entries 3-2 and 4-2).

Table 2. Screening of palladium source; reaction conditions: degassed solvent mixture IL/MeOH (x_{MeOH} = 0.50): 2.0 mL; Pd: 0.02 mmol; **1a**: 1.0 mmol; **2**: 1.2 mmol

Entry	Catalyst	Time [min]	Conv. (%)	Isolated yield (%)
1-2	$Pd(OAc)_2$	30	100	83
2-2	$PdCl_2$	1680	40	15
3-2	$Pd_2(dba)_3{\cdot}CHCl_3$	330	95	90
4-2	$Pd(PPh_3)_4$	150	100	63
5-2	**4**	1800	80	44
6-2	**5**	1260	23	traces
7-2	**6**	1320	64	54
8-2	**7**	900	98	86
9-2	**8**	30	100	65
10-2	**9**	10	100	84
11-2	**10**	30	100	93
12-2	**10**[a]	15	100	55
13-2	**10**[b]	120	96	87
14-2	**10**[c]	720	83	67

[a] Pure methanol (4 mL) as solvent. [b] Solvent mixture: 4 mL; Pd: 5.0×10^{-3} mmol; **1a**: 2.0 mmol; **2**: 2.4 mmol. [c] Pd: 1.0×10^{-3} mmol.

Several palladium(II) acetate derivatives (Figure 4) were tested. Mononuclear complexes bearing chelating ligands gave unsatisfactory results: 2,2′-bipyridyl complex **4** gave a 44% yield of **3a** while the 1,2-bis(diphenylphosphanyl)-ethane complex **5** was almost inactive (Entries 5-2 and 6-2). Conversely, dinuclear phosphapalladacycles were found to be active catalysts for reaction 1: complex **6** gave 64% conversion together with 54% yield after 22 h (Entry 7-2), while **7** gave a quantitative conversion and 86% yield in a shorter reaction time (Entry 8-2). The dinuclear azapalladacycles **8**−**10** were found to be the most active catalysts. In all cases quantitative conversions were obtained in 30 min or less, with selectivities towards the desired product **3a** ranging from 65% obtained with the 8-methylquinoline derivative **8** (Entry 9-2) to 93% obtained with the azobenzene derivative **10** (Entry 11-2). A remarkably short reaction time was observed with the iminopalladacycle **9**, which afforded an 84% yield in less than 10 min (Entry 10-2). Complex **10** was also used for comparison in pure methanol, giving only 55% yield after 15 min (Entry 12-2).

$Pd(OAc)_2$ and complexes **6**−**10** were also used in an equimolar mixture of [bmim]BF_4 and H_2O. In all cases quantitative conversions were achieved owing to the ability of water to act as a BF_3 scavenger. $Pd(OAc)_2$ gave 65% yield of **3a** after 2 h whereas the yields obtained with complexes **6** and **7** were 85% and 87%, respectively, after 20 h. Complexes **8**−**10** gave 64%, 60% and 70% isolated yields, respectively, in less than 30 min. Figure 5 shows a comparison of the results obtained with $Pd(OAc)_2$ and complexes **6**−**10** in IL/MeOH with those in IL/H_2O. All the catalysts shown in Figure 5, except phosphapalladacycles **6** and **7**, were more selective when the cosolvent was MeOH.

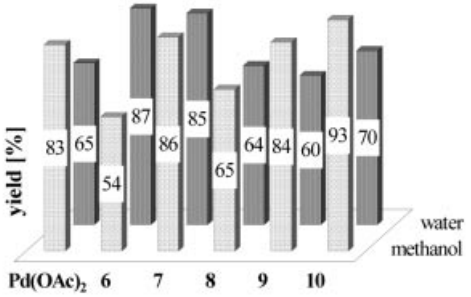

Figure 5. Performance of catalysts **4**−**10** in equimolar [bmim]BF_4/cosolvent mixtures

Palladium Loading and Recycling

The effect of palladium loading was investigated using complex **10** in an equimolar [bmim]BF_4/MeOH mixture. At 0.5% Pd loading (0.25 mol % of the dinuclear complex) the catalyst was still active and selective, reaching nearly quantitative conversion with an 87% yield after 2 h (Entry 13-2); at 0.1% loading the reaction afforded 67% of **3a** with an 83% conversion after 12 h (Entry 14-2).

Optimization tests aimed at recycling the catalytic solution, performed with complex **10** in IL, showed that an excess of the aryldiazonium **1a** was necessary in order to obtain a recyclable catalytic solution. When a 20% excess of phenyltrifluoroborate **2** was employed the second cycle did

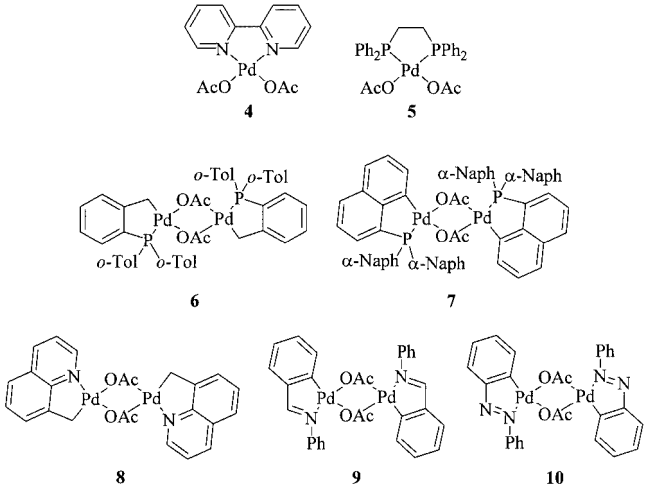

Figure 4. Palladium acetate derived catalysts; Naph = naphthyl

 © 2005 Wiley-VCH Verlag GmbH & Co. KGaA, Weinheim

not reach completion (60% conv. after 3 d), giving only 37% of **3a**; the catalyst decomposed into Pd black (formation of Pd black during the reaction was observed in almost all the reactions described so far). On the other hand, when a 20% excess of **1a** was used no Pd black formed after the first run and the catalytic solution was recyclable (Figure 6). The excess of **1a** renders the catalytic system less efficient as, with an excess of **2**, a 93% yield was achieved after 30 min (Entry 11-2), whereas with **1a** in excess a 72% yield was achieved after 2 h.

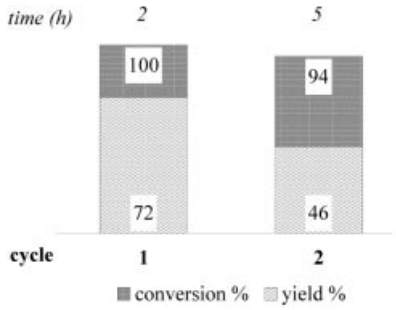

Figure 6. Recyclability of the catalytic solution (initial **1a**/**2** molar ratio = 1.2)

Possible Active Species: Preliminary Investigations

Mechanistic investigations on Suzuki coupling involving aryldiazonium salts have not been performed so far. However, different active species have been suggested for "classical" Suzuki reactions in ILs. Zou et al. have proposed that the catalytic activity observed in alkylammonium tetrafluoroborate/H_2O mixtures is due to palladium metal stabilised by the reaction medium.[14] On the other hand, Srinivasan's group has ruled out colloidal Pd nanoparticles as the active species in the Suzuki reaction performed in imidazolium-based IL/MeOH mixtures.[16] Welton et al.[12] have suggested the intermediacy of mixed (carbene)(phosphane)Pd^{II} complexes formed by reaction of $Pd(PPh_3)_4$ with [bmim]BF_4 in the presence of aryl halide and a halide salt under basic conditions.

Although palladium nanocolloids are known to catalyze the strictly related Heck reaction in ILs,[23] in our case the progressive formation of palladium black observed nearly invariably during catalysis is more probably the consequence of catalyst decomposition, since no Pd black formed in the catalytic solutions that could be successfully recycled. That palladium metal is not involved in the catalytic act is further demonstrated by poisoning experiments with Hg metal.[24] When performing reaction 1 catalyzed by complex **10** in the presence of added Hg (Hg/Pd = 150 mol/mol) no inhibition was observed (Entry 1-3, Table 3). This result suggests that palladium nanocolloids are not involved in the catalytic cycle and that a homogeneous mechanism should be operating.

Table 3. Reaction conditions: degassed solvent mixture LI/MeOH (x_{MeOH} = 0.50): 2.0 mL; Pd: 0.02 mmol; **1a**: 1.0 mmol; **2**: 1.2 mmol

Entry	Catalyst	Time [min]	Isolated yield (%)[a]
1-3[b]	**10**	30	85
2-3	**11**	260	65
3-3	**12**	1600	45
4-3	**13**	480	55
5-3[c]	**10**	40	90

[a] Quantitative conversions. [b] Hg added; Hg/Pd = 150 mol/mol. [c] Reaction performed in [bmmim]BF_4/MeOH.

Among the possible candidates for the active species in the present reaction we focused our attention on (carbene)Pd^{II} species. According to Wasserscheid,[10] three simple experiments should be carried out to verify the intermediacy of carbene complexes as catalytically active species in ILs, namely variation of the ligands, tests with independently prepared, well-defined (carbene)Pd^{II} complexes, and reactions in ILs that are not capable of carbene formation. Replacing the bridging acetates with bridging bromides (Figure 7) in complex **10** resulted in a drop of activity (Entry 11-2 vs 2-3); this might be rationalised by invoking the inability of bromide to generate carbene species by abstraction of the acidic proton in the 2-position of the imidazolium ring. However, reactions performed with the preformed carbene complexes **12** and **13** (Entries 3-3 and 4-3) were much slower than that performed with complex **10** (Entry 11-2). This seems to indicate that, even if they form in the reaction mixture, carbene species are not mainly responsible for the catalytic activity observed with azapalladacycles. Accordingly, replacing [bmim]BF_4 with [bmmim]BF_4, an imidazolium-based IL that is not capable of carbene formation due to the presence of the methyl group in the 2-position, gave essentially equal activity and selectivity (see Entries 11-2 and 5-3).

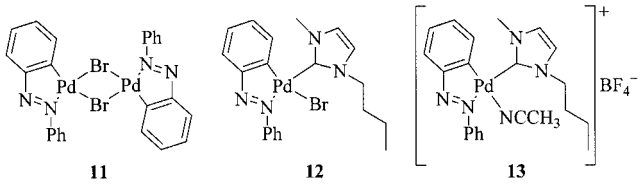

Figure 7. (Azobenzene)Pd^{II} complexes

The above-mentioned detrimental effect of bromides on catalysis could, therefore, be due to the strong coordinating ability of halide species towards palladium. This strong tendency to bind palladium could also be held responsible for the difference in activity between bromo complex **12** and acetonitrile complex **13**, and can also rationalize the sluggishness of the reaction catalyzed by $PdCl_2$ (Entry 2-2).

At this stage, the following points seem to emerge: (i) catalysis is molecular and influenced by the ligands on the palladium atom; (ii) the presence of easily dissociable li-

 © 2005 Wiley-VCH Verlag GmbH & Co. KGaA, Weinheim

gands in palladium(II) precatalysts has a beneficial effect on catalysis (compare activities of acetate complex **10** vs. bromide complex **11** or of acetonitrile complex **13** vs. bromide complex **12**). Although no definitive conclusion can be drawn about the active species that triggers the catalysis starting from azapalladacycle **10**, these observations lead us to suggest, on the basis of the commonly accepted Pd^0/Pd^{II} cycle, the anionic Pd^0 complex depicted in Figure 8 as the possible active species. Such a species, which could be generated by reduction of **10** by **2**, might start the catalytic cycle by forming an arylpalladium complex by reaction with the diazonium salt.

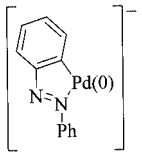

Figure 8. Possible active species in reactions catalysed by complex **10**

Anionic Pd^0 complexes have been suggested as active species in related cross-coupling reactions. Amatore et al.,[25] for example, have demonstrated that $[Pd(PPh_3)_2(OAc)]^-$, formed from $Pd(OAc)_2$ and PPh_3, is an active species for the catalytic cycle of Heck reactions between aryl halides and olefins, and Hermann et al.[26] have proposed the palladacycle [(di-*o*-tolylphosphanyl)benzyl]-palladate(0) as the active species in Heck couplings catalyzed by complex **6**.

Screening of Substrates

The reactivity of several substrates was explored (Table 4). Substituted aryldiazonium salts (Reaction 3) gave fair to good yields: 4-methoxybiphenyl was obtained with a 78% yield after 3 h (Entry 1-4) while aryldiazonium salt **1c**, containing an electron-withdrawing group (Entry 2-4), reacted faster to give the relevant biphenyl in 82% yield. Halogen-substituted substrates **1d** and **1e** were less reactive and required 4% palladium to give quantitative conversions and 79% and 95% yields, respectively (Entries 3-4 and 4-4). Vinyltrifluoroborates were far more reactive than the aromatic ones (Reaction 4): quantitative conversions and yields of up to 83% were obtained after 10 min using as little as 0.1% palladium (turnover frequency $\approx$ 6000 h^{-1}; Entries 5-4 and 6-4).

Table 4. Screening of substrates; reaction conditions: degassed solvent mixture LI/MeOH (x_{MeOH} = 0.50): 2 mL; ArN_2BF_4: 1.0 mmol; $KRBF_3$: 1.2 mmol; quantitative yields were obtained

Entry	ArN_2BF_4	$K(RBF_3)$	Pd loading [mmol]	Time [min]	Product	Isolated yield (%)
1-4	**1b**	**2**	0.02	180	**3b**	78
2-4	**1c**	**2**	0.02	5	**3c**	82
3-4	**1d**	**2**	0.04	180	**3d**	79
4-4	**1e**	**2**	0.04	3	**3e**	95
5-4	**1a**	**14**	0.001	10	**15a**	83
6-4	**1f**	**14**	0.001	10	**15f**	80

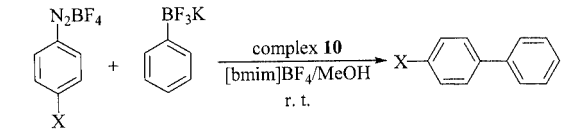

1b, X = OMe
1c, X = COOEt
1d, X = Br
1e, X = Cl

2

3b
3c
3d
3e

Reaction 3

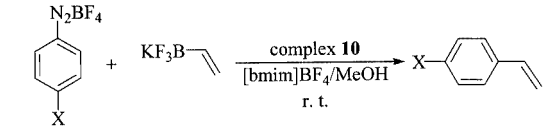

1a
1f, X = H

14

15a
15f

Reaction 4

Conclusion

This study demonstrates that ILs are suitable solvents for the title reaction. Used neat, ILs give high selectivities for the cross-coupling product. High activity and selectivity were shown by catalytic systems comprised of azapalladacycles in $[bmim]BF_4$/MeOH mixtures. Using a slight excess of diazonium salt with respect to aryltrifluoroborate allowed the recycling of the catalytic solution. Preliminary mechanistic studies carried out with the precatalyst **10** indicate that a homogeneous process takes place and that carbene species are not the main active species. Further studies on this subject are in progress.

Experimental Section

General: Unless otherwise specified all the manipulations were conducted under an inert gas (nitrogen) using standard Schlenk techniques. Flash-chromatography was performed on SiO_2 Kieselgel 230−400 mesh. The NMR spectra were recorded with a Bruker AX400 spectrometer (400 MHz for ^1H) at 295.0 K; chemical shifts are reported in ppm referenced to $SiMe_4$ for ^1H and ^{13}C, and $CFCl_3$ for ^{19}F. LC-MS analyses of complexes **11**, **12** and **13** were performed with an Agilent HPLC system equipped with DAD, autosampler and MS systems (Agilent 1100 LC-MS SL series). All samples were dissolved in the same HPLC-grade solvent that was used as eluent. The used interfaces were APCI for neutral complexes **11** and **12**, and ESI for cationic complex **13**. APCI conditions: positive-ion mode, flow rate 0.5 mL/min, nitrogen as nebulizing and drying gas, nebulizer pressure 4 atm, vaporizer temperature 350 °C, corona current 4.0 μA, drying-gas flow 5 L/min, drying-gas temperature 350 °C, capillary voltage 4000 V. ESI conditions: positive-ion mode, flow rate 0.3 mL/min, nitrogen as nebulizing and drying gas, nebulizer pressure 2 atm, capillary voltage 4000 V. Mass spectrometry data were acquired in the scan mode (mass range m/z = 50−3000). C, H, N elemental analyses were carried out with a Eurovector CHNS-O Elemental Analyser. Pd analyses were performed with a Perkin−Elmer SIMAA6000 Atomic Absorption spectrometer. The IR spectra were recorded with a Bruker Vector 22 FT-IR spectrometer. GC analyses were

 © 2005 Wiley-VCH Verlag GmbH & Co. KGaA, Weinheim

performed with an HP5890 instrument equipped with a Supelco SPB-1 capillary column (30 m × 320 μm × 0.25 μm). GC-MS analyses were performed with an HP6890-HP5973MSD instrument equipped with an HP-5MS capillary column (30 m × 250 μm × 0.25 μm). The halide content of the ionic liquids was determined in aqueous solution by a potentiometric automatic titration using a Metrohm 716 DMS Titrino (300 mg sample, ca. 30 mL deionized water, three runs) while the water content was determined by the Karl−Fischer method using a Metrohm 716 DMS Titrino equipped with a 703 titration stand using sodium tartrate-2-hydrate as standard and dry methanol as solvent (1 g sample, ca. 30 mL MeOH, three runs). All commercial reagents were used as received without further purification. Solvents were dried and distilled under nitrogen according to standard procedures; water (resistivity $> 17.5 \cdot M\Omega\ cm^{-1}$) was deionized with a Millipore Simplicity unit. [bmim]Cl,[27] [bmmim]Cl,[27] [bbim]Br[28] and [bmim]Br[29] were synthesised from 1-chlorobutane or 1-bromobutane and the relevant imidazole salt according to literature procedures. [bmim]Cl, [bmmim]Cl and [bmim]Br were purified by crystallisation from acetonitrile/ethyl acetate (1:4) until a colourless mother liquor was obtained, and then filtered and dried under vacuum; all compounds were obtained as white solids. [bbim]Br was obtained as a viscous brown liquid, washed with CH_2Cl_2/diethyl ether (1:4) and dried under vacuum. All compounds were stored under nitrogen. [bmim]BF_4, [bmim]PF_6, [bmim]$N(SO_2CF_3)_2$, [bmmim]BF_4, [bbim]BF_4 were synthesised by metathesis from the corresponding alkali metal salts in dichloromethane; the resulting suspension was filtered through Celite and washed with the minimal amount of water until the $AgNO_3$ test on the aqueous layer was negative. The solvent was then evaporated and the resulting IL was dried at 40−50 °C under vacuum for 48 h and stored under nitrogen. The ionic liquids were obtained as pale-yellow or colourless liquids and fully characterised by multinuclear NMR spectroscopy. Their water content was less than 460 ppm whereas their halide content was below the detection limit of 0.38 mg/L. Complexes **4**,[30] **5**,[31] **6**,[26] **7**,[32] **8**,[33] **9**[34] and **10**[35] were synthesised according to literature procedures.

Di-μ-bromo-bis[*o*-(phenylazo)phenyl]dipalladium(II) (11): Complex **10** (0.173 g, 0.25 mmol) and tetrabutylammonium bromide (0.167 g, 0.52 mmol) were dissolved in dry dichloromethane (10 mL). After stirring for 3 h, the volume was reduced in vacuo to a half and dry methanol (50 mL) was added. The resulting red solid was filtered off, washed with methanol (3 × 5 mL) and hexane (15 mL) and dried in vacuo to afford **11** as a red powder (0.151 g, 82%); m.p. > 250 °C. IR (KBr): $\tilde{\nu}_{max}$ = 1575 (m), 1553 (w), 1482 (w), 1458 (w), 1444 (w), 1393 (m), 1318 (w), 1306 (w), 1263 (w), 1242 (w), 762 (m), 753 (m), 706 (w), 691 (m), 595 (w), 550 (w), 525 (w) cm^{-1}. ^1H NMR ([D]$_6$DMSO): δ = 7.07 (t, J = 7.31 Hz, 1 H), 7.17 (t, J = 7.31 Hz, 1 H), 7.44 (m, 3 H), 7.65 (m, 2 H), 7.86 (d, J = 7.31 Hz, 1 H), 7.89 (d, J = 7.92 Hz, 1 H) ppm. ^{13}C NMR ([D]$_6$DMSO): δ = 124.36, 126.06, 128.84, 130.24, 131.38, 132.22, 139.12, 150.88, 153.88, 164.13 ppm. LC-MS (CH_3CN/CH_2Cl_2, 9:1): exact mass calcd. for $C_{24}H_{18}Br_2N_4Pd_2$: 731.80; found 732 $[M]^+$, 773 $[M + CH_3CN]^+$. $C_{24}H_{18}Br_2N_4Pd_2$: calcd. C 39.21, H 2.47, N 7.62, Pd 28.95; found C 39.65, H 2.70, N 7.41, Pd 28.79.

Bromo(1-butyl-3-methylimidazolin-2-ylidene)[*o*-(phenylazo)phenyl]-palladium(II) (12): Complex **10** (0.39 g, 0.56 mmol) and [bmim]Br (0.25 g, 1.13 mmol) were dissolved in dry THF (50 mL) in a round-bottomed flask. After refluxing under nitrogen for 3 h and cooling to ambient temperature, the solvent was evaporated in vacuo to give an orange solid. Crystallization from acetone/hexane afforded **12** as a dark-orange, microcrystalline solid (0.470 g, 82%); m.p. 202−205°. IR (KBr): $\tilde{\nu}_{max}$ = 3156 (w), 3124 (m), 3042 (w), 2954 (m), 2929 (m), 2870 (m), 1574 (m), 1551 (m), 1460 (m), 1445 (m), 1388 (m), 1254 (m), 1233 (m), 1204 (w), 1107 (w), 774 (s), 731 (m), 716 (m), 691 (s), 584 (w), 547 (w), 522 (w) cm^{-1}. ^1H NMR (CD_2Cl_2): δ = 0.80 (t, J = 7.31 Hz, 3 H, CH_2CH_3), 1.25 (m, 2 H, $CH_2CH_2CH_3$), 1.77 (m, 2 H, $CH_2CH_2CH_2$), 3.78 (s, 3 H, NCH_3), 4.18 (m, 2 H, NCH_2), 6.12 (d, J = 7.92 Hz, 1 H), 7.00 (m, 3 H), 7.16 (t, J = 7.31 Hz, 1 H), 7.41 (m, 3 H), 7.94 (d, J = 6.7 Hz, 1 H), 7.99 (m, 2 H, NC*H*) ppm. ^{13}C NMR (CD_2Cl_2): δ = 13.40 (CH_3), 19.78 ($CH_2CH_2CH_3$), 32.20 ($CH_2CH_2CH_2$), 38.40 (NCH_2CH_2), 51.12 (NCH_3), 121.44, 122.54, 124.66, 125.14, 127.86, 130.35 (NC*H*), 130.48 (NC*H*), 132.57, 135.45, 151.93, 155.82, 164.54, 169.35 (N*C*N) ppm. LC-MS (CH_3CN/CH_3OH 99:1): exact mass calcd. for $C_{20}H_{23}BrN_4Pd$: 504.00; found 505 $[M + H]^+$, 465 $[M - Br + CH_3CN]^+$, 424 $[M - Br]$. $C_{20}H_{23}BrN_4Pd$: calcd. C 47.50, H 4.58, N 11.08, Pd 21.04; found C 47.78, H 4.75, N 10.86, Pd 20.96.

Acetonitrile(1-butyl-3-methylimidazolin-2-ylidene)[*o*-(phenylazo)-phenyl]palladium(II) Tetrafluoroborate (13): $AgBF_4$ (0.110 g, 0.57 mmol) dissolved in dry acetonitrile (5 mL) was added to a THF (30 mL) solution of complex **12** (0.286 g, 0.57 mmol). After stirring for 45 min, the solvent was evaporated in vacuo. The pale-orange residue was extracted with dry dichloromethane (30 mL) and the resulting suspension filtered through Celite. Crystallization from THF/hexane gave **13** as a pale-orange powder (0.276 g, 88%) m.p. 168° (dec.). IR (nujol mull): $\tilde{\nu}_{max}$ = 3167 (w), 3136 (w), 2318 (w) [ν(C≡N)], 2290 (w) [ν(C≡N)], 1575 (w), 1555 (w), 1463 (s), 1401 (w), 1377 (m), 1257 (w), 1236 (m), 1056 (vs) [ν(B−F)], 773 (m), 713 (m), 696 (m), 588 (w), 548 (w), 523 (w) cm^{-1}. ^1H NMR (CD_2Cl_2): δ = 0.81 (br. t, J = 7.31 Hz, 3 H, CH_2CH_3), 1.25 (br. sext, J = 7.31, 2 H, $CH_2CH_2CH_3$), 1.76 (br. quint, J = 7.31 Hz, 2 H, $CH_2CH_2CH_2$), 2.13 (s, 3 H, $NCCH_3$), 3.83 (s, 3 H, NCH_3), 4.15 (br. t, J = 7.31 Hz, 2 H, NCH_2), 6.03 (d, J = 7.31 Hz, 1 H), 7.00 (t, J = 7.31 Hz, 1 H), 7.14 (s, 1 H, NC*H*), 7.18 (s, 1 H, NC*H*), 7.22 (t, J = 7.31 Hz, 1 H), 7.51 (br. s, 3 H), 7.72 (m, 2 H), 7.97 (d, J = 7.31 Hz, 1 H) ppm. ^{13}C NMR (CD_2Cl_2): δ = 2.78 ($NCCH_3$), 13.35 (CH_2CH_3), 19.62 ($CH_2CH_2CH_3$), 32.64 ($CH_2CH_2CH_2$), 38.45 (NCH_2CH_2), 51.18 (NCH_3), 122.48, 122.75, 123.98, 129.03, 131.51 (NC*H*), 131.62 (NC*H*), 133.25, 136.17, 151.22, 151.56, 164.92, 165.04 ppm. LC-MS (CH_3CN): exact mass calcd. for the cation $C_{22}H_{26}N_5Pd$: 466.12; found 466 $[M]^+$, 425 $[M - CH_3CN]^+$. $C_{22}H_{26}BF_4N_5Pd$: calcd. C 47.72, H 4.73, N 12.65, Pd 19.22; found C 47.61, H 4.85, N 12.74, Pd 19.12.

Substrates: The aryldiazonium tetrafluoroborates **1a**−**1f** were synthesised as reported in the literature[36] and characterised by ^1H and ^{13}C NMR (CD_3CN) and IR (nujol mull) spectroscopy. Potassium aryltrifluoroborate **2** and vinyltrifluoroborate **14** were also synthesised according to a literature procedure.[9]

General Procedure for the Catalytic Reactions: All catalytic runs were repeated at least three times and yields and conversions were reproducible within ±3%. The course of the reactions was monitored by measuring the evolution of N_2 vs. time by means of a mercury gas-burette. Reactions were stopped when no further gas evolution was observed. In neat ILs, the decomposition of diazonium salt was negligible (4−5% per day) as demonstrated by blank tests.

Typical Reaction in Neat IL: Compounds **2** (221 mg, 1.2 mmol) and **1a** (206 mg, 1.0 mmol) were added, with vigorous stirring, to a suspension of $Pd(OAc)_2$ (4.48 mg, 0.02 mmol) in [bmim]BF_4 (2.260 g, 10 mmol) in a 10-mL Schlenk tube. At the end of reaction, the mixture was diluted with water (100 mL) and the products were

 © 2005 Wiley-VCH Verlag GmbH & Co. KGaA, Weinheim

extracted with diethyl ether (3 × 25 mL); the organic phases were collected and dried with Na_2SO_4. The products were purified by flash chromatography and characterised by GC-MS and the selectivity assessed by GC using naphthalene as internal standard.

Reactions in [bmim]BF_4/Cosolvent: 2 mL of the degassed solvent mixture was poured into a 10-mL Schlenk tube containing Pd catalyst (0.02 mmol of Pd), $KRBF_3$ (1.2 mmol) and ArN_2BF_4 (1.0 mmol) and stirred vigorously.

Recycle: Compounds **2** (184 mg, 1.0 mmol) and **1a** (247 mg, 1.2 mmol) were added, with vigorous stirring, to a suspension of **10** (6.93 mg, 0.01 mmol) in [bmim]BF_4 (2.260 g, 10 mmol) and MeOH (405 μL 10 mmol) in a 10-mL Schlenk tube. At the end of reaction, the MeOH was evaporated off in vacuo and the products were extracted with dry *n*-hexane (6 × 3 mL); after evaporation of the solvent, fresh MeOH (405 μL, 10 mmol), **2** (184 mg, 1.0 mmol) and **1a** (206 mg, 1.0 mmol) were added to the resulting catalytic solution.

Acknowledgments

Dr. G. Ciccarella is gratefully acknowledged for performing the LC/MS experiments. We also thank Mr. G. Di Gregorio for experimental assistance and Engelhard for a generous loan of palladium acetate. The Polytechnic of Bari is acknowledged for financial support (F.R.A. ex 60%).

[1] A. Suzuki, N. Miyaura, *Chem. Rev.* **1995**, *95*, 2457−2483.
[2] A. Suzuki, *J. Organomet. Chem.* **1999**, *576*, 147−168.
[3] S. Darses, T. Jeffery, J. L. Brayer, J. P. Demoute, J. P. Genet, *Bull. Soc. Chim. Fr.* **1996**, *133*, 1095−1102.
[4] S. Darses, T. Jeffery, J. P. Genet, J. L. Brayer, J. P. Demoute, *Tetrahedron Lett.* **1996**, *37*, 3857−3860.
[5] S. Sengupta, S. Bhattacharyya, *J. Org. Chem.* **1997**, *62*, 3405−3406.
[6] D. M. Willis, R. M. Strongin, *Tetrahedron Lett.* **2000**, *41*, 6271−6274.
[7] M. B. Andrus, C. Song, *Org. Lett.* **2001**, *3*, 3761−3764.
[8] K. Selvakumar, A. Zapf, A. Spannenberg, M. Beller, *Chem. Eur. J.* **2002**, *8*, 3901−3906.
[9] S. Darses, G. Michaud, J. P. Genet, *Eur. J. Org. Chem.* **1999**, 1875−1883.
[10] *Ionic Liquids in Synthesis* (Eds.: P. Wasserscheid, T. Welton), Wiley-VCH, Weinheim, **2003**.
[11] C. J. Mathews, P. J. Smith, T. Welton, *Chem. Commun.* **2000**, 1249−1250.
[12] F. McLachlan, C. J. Mathews, P. J. Smith, T. Welton, *Organometallics* **2003**, *22*, 5350−5357.
[13] C. J. Mathews, P. J. Smith, T. Welton, *J. Mol. Catal. A* **2004**, *214*, 27−32.
[14] G. Zou, Z. Wang, J. Zhu, J. Tang, M. Y. He, *J. Mol. Catal. A* **2003**, *206*, 193−198.
[15] J. McNulty, A. Capretta, J. Wilson, J. Dyck, G. Adjabeng, A. Robertson, *Chem. Commun.* **2002**, 1986−1987.
[16] R. Rajagopal, D. V. Jarikote, K. V. Srinivasan, *Chem. Commun.* **2002**, 616−617.
[17] M. M. Dell'Anna, V. Gallo, P. Mastrorilli, C. F. Nobile, G. Romanazzi, G. P. Suranna, *Chem. Commun.* **2002**, 434−435.
[18] P. Mastrorilli, C. F. Nobile, V. Gallo, G. P. Suranna, G. Farinola, *J. Mol. Catal. A* **2002**, *184*, 73−78.
[19] V. Gallo, P. Mastrorilli, C. F. Nobile, G. Romanazzi, G. P. Suranna, *J. Chem. Soc., Dalton Trans.* **2002**, 4339−4342.
[20] P. Mastrorilli, C. F. Nobile, R. Paolillo, G. P. Suranna, *J. Mol. Catal. A* **2004**, *214*, 103−106.
[21] H. J. Frohn, F. Bailly, V. V. Bardin, *Z. Anorg. Allg. Chem.* **2002**, *628*, 723−724.
[22] H. J. Frohn, H. Franke, P. Fritzen, V. V. Bardin, *J. Organomet. Chem.* **2000**, *598*, 127−135.
[23] N. A. Hamill, C. Hardacre, S. E. J. McMath, *Green Chem.* **2002**, *4*, 139−142.
[24] The suppression of catalysis by Hg^0 is often used distinguish heterogeneous from homogeneous catalysis since Hg^0 is known to poison metal(0) catalysts by formation of amalgams: Y. Na, S. P. S. B. Han, H. Han, S. Ko, S. Chang, *J. Am. Chem. Soc.* **2004**, *126*, 250−258 and references cited therein.
[25] C. Amatore, A. Jutand, *J. Organomet. Chem.* **1999**, *576*, 254−278.
[26] V. P. W. Böhm, W. A. Herrmann, *Chem. Eur. J.* **2001**, *7*, 4191−4197.
[27] L. Cammarata, S. G. Kazarian, P. A. Salter, T. Welton, *Phys. Chem. Chem. Phys.* **2001**, *3*, 5192−5200.
[28] R. R. Deshmukh, R. Rajagopal, K. V. Srinivasan, *Chem. Commun.* **2001**, 1544−1545.
[29] P. Bonhôte, A. P. Dias, N. Papageorgiou, K. Kalyanasundaram, M. Grätzel, *Inorg. Chem.* **1996**, *35*, 1168−1178.
[30] T. A. Stephenson, S. M. Morehouse, A. R. Powell, J. P. Heffer, G. Wilkinson, *J. Chem. Soc.* **1965**, 3632−3640.
[31] C. Bianchini, H. M. Lee, A. Meli, W. Oberhauser, M. Peruzzini, F. Vizzi, *Organometallics* **2002**, *21*, 16−33.
[32] B. L. Shaw, S. D. Perera, E. A. Staley, *Chem. Commun.* **1998**, 1361−1362.
[33] A. J. Deeming, I. P. Rothwell, *J. Organomet. Chem.* **1981**, *205*, 117−131.
[34] J. Granell, D. Sainz, J. Sales, X. Solans, M. Font-Altaba, *J. Chem. Soc., Dalton Trans.* **1986**, 1785−1790.
[35] I. Aiello, A. Crispini, M. Ghedini, M. LaDeda, F. Barigelletti, *Inorg. Chim. Acta* **2000**, *308*, 121−128.
[36] A. Roe, *Organic Reactions, Coll. Vol.* **1949**, *5*, 193−228.

Received July 20, 2004
Early View Article
Published Online December 6, 2004

 © 2005 Wiley-VCH Verlag GmbH & Co. KGaA, Weinheim

Gold(0) and Gold(III) Reactivity towards the Tetraphenyldithioimidodiphosphinic Acid, $[Ph_2P(S)NHP(S)Ph_2]$

G. Luca Abbati,[a] M. Carla Aragoni,[b] Massimiliano Arca,[b] M. Bonaria Carrea,[b] Francesco A. Devillanova,[b] Alessandra Garau,[b] Francesco Isaia,*[b] Vito Lippolis,[b] Marco Marcelli,[b] Cristian Silvestru,[c] and Gaetano Verani[b]

Keywords: Gold(I) complexes / S ligands / Bridging ligands / Iodine / Density functional calculations

The reaction of gold powder with the iodine adduct of $Ph_2P(S)NHP(S)Ph_2$ (H**L**) in Et_2O gave the complex $[Au(\mathbf{L})I_2]$ under mild reaction conditions. Its crystal structure is comprised of discrete, monomeric molecules with a central Au^{III} ion bonded to two sulfur atoms by an anionic ligand **L** and two iodide anions in a slightly distorted square-planar coordination geometry. From the reaction of $[AuCl_3(tht)]$ with H**L** in CH_2Cl_2 it is possible, besides the main complex $[Au(\mathbf{L})]_2$, to separate the neutral Au^{I} complex $[Au(\mathbf{L}'_2H)]$, **L**′ = $[Ph_2P(S)NP(O)Ph_2]^-$, the crystal structure of which features a Au^{I} ion linearly coordinated to two sulfur atoms and a proton bridging two oxygen atoms of the PO groups. ^{31}P NMR CP MAS spectroscopy is in accordance with the nature of the ligands in the complex. The reaction chemistry of $[Au(\mathbf{L}'_2H)]$ in CH_2Cl_2 towards the acid CF_3COOH and the organic base 1,8-bis(dimethylamino)naphthalene is reported.
(© Wiley-VCH Verlag GmbH & Co. KGaA, 69451 Weinheim, Germany, 2005)

Introduction

The transition metal chemistry of tetraphenyldithioimidodiphosphinic acid, $Ph_2P(S)NHP(S)Ph_2$ (H**L**), has received great attention during the past years[1] and continues to remain an area of interest since the ligand H**L** has found applications as a selective extraction agent for metals,[2] as a lanthanide NMR shift reagent[3] and more recently in catalysis.[4] The reaction of H**L** with metal ions usually leads to deprotonation of the NH group and concomitant formation of the anionic tetraphenyldithioimidodiphosphinate ligand $[Ph_2P(S)NP(S)Ph_2]^-$ (**L**) which features the negative charge delocalised throughout the SPNPS skeleton.[1] A vast body of results show that **L** commonly coordinates to the metal atom through both sulfur atoms, either symmetrically or asymmetrically,[1] resulting in chelate structures (see **a** and **b** in Scheme 1). Alternatively, supramolecular polymeric structures and bridging modes such as **c** (Scheme 1) with formation of homobimetallic compounds are possible.[1]

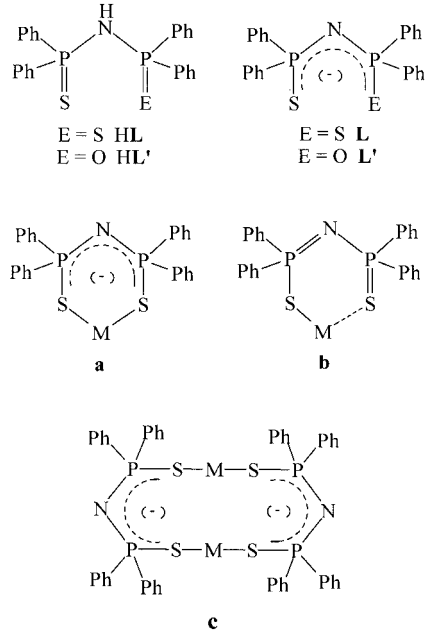

Scheme 1

The chemistry of H**L** with gold(I) and gold(III) ions has yielded only two X-ray characterised complexes, i.e. $[Au(\mathbf{L})Cl_2]$ (**1**), in which the Au^{III} centre is tetracoordinated in a square-planar fashion[5] and $[(Ph_3P)Au(\mathbf{L})]$ which con-

[a] Dipartimento di Chimica, Università di Modena e Reggio Emilia & INSTM, UdR di Modena,
Via G. Campi 183, 41100 Modena, Italy
[b] Dipartimento di Chimica Inorganica ed Analitica, Università di Cagliari,
S.S. 554 Bivio per Sestu, 09042 Cagliari, Italy
E-mail: isaia@unica.it
[c] Facultatea de Chimie si Inginerie Chimica, Universitatea Babes-Bolyai,
3400 Cluj-Napoca, Romania
Supporting information for this article is available on the WWW under http://www.eurjic.org or from the author.

tains a three-coordinate Au^{I} atom.[6] A few other complexes obtained from the reaction of H**L** with [RAu(tht)], [AuCl(tht)] or $[R_2AuCl]_2$ (R = C_6F_5; tht = tetrahydrothiophene) and containing the ligand in its deprotonated form were only partially characterised.[7,8] As part of an ongoing study on the coordination ability of H**L**,[9–12] we have further explored its reactivity towards the complex $[Au^{III}Cl_3(tht)]$ in CH_2Cl_2 and tested the oxidation in diethyl ether at room temperature of Au^0 metal powder with I_2 in the presence of H**L**. In addition, the structures of the neutral complexes $[Au^{III}(\mathbf{L})I_2]$ (**2**) and $[Au^{I}(\mathbf{L}'_2H)]$ (**3**) {$\mathbf{L}'$ = $[Ph_2P(S)NP(O)Ph_2]^-$}, the latter being obtained as a by-product from the reaction of H**L** with $[AuCl_3(tht)]$, have been determined by single-crystal X-ray diffraction studies.

Results and Discussion

Oxidation of Gold Powder by the Adduct HL·I_2

The oxidation/complexation reaction of metal powders by the iodine adducts of phosphane,[13] thiophosphane[9–12] and polyfunctional thione donors[14–17] has been well documented in recent years. The numerous papers on the subject have shown this synthetic route to be a useful tool in obtaining coordination compounds with unusual geometries, stoichiometries and oxidation numbers at the metal centre. In particular, the I_2 and IBr adducts of *N*,*N*′-dimethyl-perhydro-diazepine-2,3-dithione[15–17] have been applied successfully to noble metals such as gold and platinum for the recovery of these precious metals from waste materials.

The reaction between the adduct H**L**·I_2, generated in situ, and Au metal powder (1:1 molar ratio; H**L** = 2.22×10^{-3} mol·dm^{-3}, 25 °C) in anhydrous Et_2O yielded a dark-red solution from which air-stable dark-red crystals of formula $[Au(\mathbf{L})I_2]$ (**2**) could be separated (yield 20% based upon Au). Concentration of the filtrate solution to dryness yielded a sticky red oil, the FT-Raman spectrum of which showed intense peaks in the low frequency region at 169, 144 and 112 cm^{-1}. The peaks at 112 and 144 cm^{-1} indicate the presence of asymmetric I_3^-, while the peak at 169 cm^{-1} is due to weakly perturbed I_2 molecules.[18] The course of the reaction was also monitored by ^{31}P NMR spectroscopy over a three-week period. As the adduct H**L**·I_2 in Et_2O (δ = 57.4 ppm) reacts with the gold powder, a new species appears which shows a signal at δ = 37.4 ppm. The assignment of this signal to complex **2** is straightforward and supported by a comparison with the spectrum of the neat compound recorded in $CDCl_3$, δ = 36.4 ppm. During the course of the reaction the signal related to H**L**·I_2 decreases in intensity and, since complex **2** has a low solubility in Et_2O, the separation of a dark-red fine powder can be observed during this time. Though the synthesis of complex **2** occurs in low yield (Equation 1), the mixture of H**L** with I_2 can oxidise Au^0 to Au^{III} (Equation 1). The influence of this mixture on the process of oxidation is not yet fully understood, though there is no doubt that the reaction of gold powder with either H**L** or I_2 alone leaves the gold unchanged.

$$\mathbf{HL} + 1.5I_2 + Au \xrightarrow[\text{r.t.}]{Et_2O} Au(\mathbf{L})I_2 + HI + \text{other products} \quad (1)$$

On the basis of cyclic voltammetry (CV) measurements, presented in a previous paper,[10] we have shown that neither iodine ($I_2/2I^-$, E_{pc} = −0.05 V) nor the adduct H**L**·I_2 (H**L**·$I_2/2I^-$, E_{pc} = −0.19 V) have reduction potentials capable of matching those of noble metals such as Pd, Pt, or Au. Presumably, however, the simultaneous presence of H**L** and I_2 lowers the oxidation potentials of the metals allowing their oxidation, dissolution and complexation. Similar conclusions have also been reached by other researchers employing iodine adducts of sulfur-containing ligands on metal(0) powders or thin sheets.[17] Although complex **2** is known in the literature,[5] its crystal structure has not yet been reported. The results of our single-crystal X-ray structural analysis are reported in Figure 1 as an ORTEP plot, while crystal data and selected geometric parameters of the compound are listed in Table 1 and Table 2, respectively.[19–24] Complex **2** shows a molecular structure similar to that of **1** reported by Laguna et al.,[5] despite showing marked differences in unit cell parameters. It consists of a central Au^{III} ion bonded to two sulfur atoms from an anionic ligand **L** and two iodide anions in a slightly distorted square-planar coordination geometry, showing a maximum deviation from the Au(1)S(1)S(2)I(1)I(2) mean plane of 0.0769(4) Å and a dihedral angle between the I(1)Au(1)I(2) and S(1)Au(1)S(2) planes of 4.70(5)°. A comparison of the structures of **1** and **2** shows some differences, mainly due to the arrangement of the bulky iodide ions around the central Au^{III} ion (Table 3). As already observed in **1**, as well as in various other metal-dichalcogenoimidodiphosphinate complexes,[1] the anionic ligand **L** adopts a pseudo-boat conformation where S(1) and P(2) act as "bow" and "stern", with deviations of 1.1839(12) and 0.6131(3) Å, respectively, from the mean Au(1)P(1)N(1)S(2)

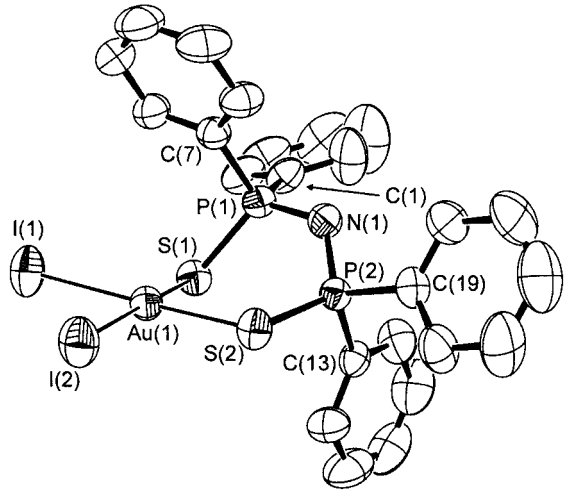

Figure 1. ORTEP plot of **2** showing the atom labelling scheme and 50% probability thermal ellipsoids; hydrogen atoms have been omitted for clarity

 © 2005 Wiley-VCH Verlag GmbH & Co. KGaA, Weinheim

Table 1. Crystal data and experimental parameters for **2** and **3**

	2	**3**
Chemical formula	$C_{24}H_{20}AuI_2NP_2S_2$	$C_{48}H_{41}AuN_2O_2P_4S_2$
M	899.24	1062.79
Crystal system	monoclinic	monoclinic
a (Å)	10.5624(3)	9.557(4)
b (Å)	16.1600(5)	26.007(3)
c (Å)	16.4393(5)	19.453(4)
β (°)	99.9250(10)	91.54(2)
U (Å^3)	2764.00(14)	4833(2)
Space group (no.)[24]	$P2_1/n$ (14)	$P2_1/n$ (14)
Z	4	4
μ (mm^{-1})	7.837	3.301
Collected reflections	39937	10515
Unique reflections	9953[a]	8424[b]
R indices [$I > 2\sigma(I)$]	$R_1 = 0.0327$ $wR_2 = 0.0735$	$R_1 = 0.0820$ $wR_2 = 0.2034$
R indices (all data)	$R_1 = 0.0591$ $wR_2 = 0.0820$	$R_1 = 0.1553$ $wR_2 = 0.2506$

[a] R(int.) = 0.0537. [b] R(int.) = 0.0662.

Table 2. Selected interatomic distances (Å) and angles (°) for complex **2**

Au(1)−S(2)	2.3509(10)	Au(1)−S(1)	2.3575(10)
Au(1)−I(1)	2.6104(3)	Au(1)−I(2)	2.6207(3)
S(1)−P(1)	2.0456(14)	S(2)−P(2)	2.0603(13)
P(1)−N(1)	1.593(3)	N(1)−P(2)	1.584(3)
S(1)···S(2)	3.5677(13)	I(1)···I(2)	3.7109(5)
I(1)···S(1)	3.4194(11)	I(2)···S(2)	3.3480(10)
S(2)−Au(1)−S(1)	98.53(3)	I(1)−Au(1)−I(2)	90.368(11)
S(2)−Au(1)−I(2)	84.48(2)	S(1)−Au(1)−I(1)	86.83(3)
S(1)−Au(1)−I(2)	175.51(2)	S(2)−Au(1)−I(1)	173.70(3)
P(1)−S(1)−Au(1)	100.35(5)	P(2)−S(2)−Au(1)	108.46(5)
N(1)−P(1)−S(1)	115.48(13)	N(1)−P(2)−S(2)	116.88(14)
P(2)−N(1)−P(1)	123.9(2)		
C(1)−P(1)−S(1)	104.81(17)	C(7)−P(1)−S(1)	109.33(13)
N(1)−P(1)−C(1)	109.1(2)	N(1)−P(1)−C(7)	108.68(18)
C(1)−P(1)−C(7)	109.27(19)		
C(13)−P(2)−S(2)	110.47(14)	C(19)−P(2)−S(2)	102.37(13)
N(1)−P(2)−C(13)	111.99(19)	N(1)−P(2)−C(19)	107.45(19)
C(19)−P(2)−C(13)	106.71(18)		

plane and dihedral angles between the Au(1)P(1)N(1)S(2) and Au(1)S(1)P(1) [S(2)P(2)N(1)] planes of 57.46(3) [41.33(10)]°. Some extent of π-electron delocalisation can be observed over the whole nonplanar [Au(SP)$_2$N] ring, as indicated by the shorter P−N and longer P−S bond lengths observed in **2** [1.593(3)−1.584(3) and 2.0456(14)−2.0603(13) Å, respectively] with respect to those in the free ligand H**L** [1.672(2)−1.683(2) and 1.937(1)−1.950(1) Å, respectively].[25] The presence of a metal-bonded iodide acting as a terminal ligand is not very common among gold(III) compounds containing a sulfur-bonded metal ion, as observed in **2**. To the best of our knowledge, a similar feature has been observed only in the square-planar cation [Au(**D**)I$_2$]$^+$ (**D** = *N*,*N*′-dimethylperhydrodiazepine-2,3-dithione), obtained by oxidation of gold powder employing a **D**·2I$_2$ adduct[15,17] and in [Au$_2^{I,III}$I$_2$(C$_6$H$_3$-2-PPh$_2$-5-Me)(S$_2$CN*n*Bu$_2$)] which is a mixed-valence complex featuring a square-planar, iodide-bound Au^{III} ion bridged by the C$_6$H$_3$-2-PPh$_2$-5-Me group to a linear [Au^I−I] moiety.[26]

Table 3. Selected structural data [inter-atomic distances (Å) and angles (°)] for **1**[5] and **2**

	2	**1**[5]
Au−S(1)	2.3575(10)	2.314(2)
Au−S(2)	2.3509(10)	2.303(2)
Au−X(1)[a]	2.6104(3)	2.307(2)
Au−X(2)[a]	2.6207(3)	2.314(2)
S(1)−P(1)	2.0456(14)	2.052(2)
S(2)−P(2)	2.0603(13)	2.055(2)
X(1)−Au−X(2)	90.368(11)	91.0(1)
S(1)−Au−S(2)	98.53(3)	99.9(1)
S(1)−Au−X(1)	86.83(3)	85.6(1)
S(2)−Au−X(2)	84.48(2)	83.5(1)
S(1)−P(1)−N(1)	115.48(5)	116.1(1)
S(2)−P(2)−N(1)	116.88(5)	109.9(1)
P(1)−N(1)−P(2)	123.9(2)	122.6(3)

[a] X = I and Cl for **1** and **2**, respectively.

Gold(III) Reactivity towards HL, Crystal Structure of [Au(L′$_2$H)]

The reaction between [Au^{III}Cl$_3$(tht)] and H**L** in CH$_2$Cl$_2$ has been partly studied by Laguna et al.[5] who were able to separate the complexes [Au^{III}(**L**)Cl$_2$] (**1**) and [Au^I(**L**)]$_2$ (**4**) using reagent molar ratios of 1:1 and 1:2, respectively. In order to further investigate the reduction reaction of Au^{III} during the formation of complex **4**, we have reconsidered the reaction between [Au^{III}Cl$_3$(tht)] and H**L** in CH$_2$Cl$_2$ using a 1:2 molar ratio. The red colour of the reaction mixture disappeared after a few hours with concomitant formation of buff-coloured fine powder which proved to be elemental sulfur. The subsequently formed insoluble white powder proved to be the expected gold(I) complex **4**. The ^{31}P NMR spectrum of the filtered solution revealed the presence of further phosphorus-containing species besides very small amounts of **4**. In fact, the solvent was slowly evaporated to firstly give a white powder which, on the basis of elemental analysis and ^{31}P NMR spectroscopy [δ = 57.5 and 21.6 ppm; d, $^2J_{P,P}$ = 16.5 Hz, CH$_2$Cl$_2$], was identified as the unsymmetrical oxygen/sulfur containing ligand Ph$_2$P(S)NHP(O)Ph$_2$, (H**L**′).[27,28] Secondly, white stable crystals of a new compound (**3**) were formed which, on the basis of elemental analysis, were tentatively assigned as the neutral Au^I complex [Au(**L**′)(H**L**′)] containing the ligand H**L**′ (Scheme 1) in both the protonated and deprotonated forms. In the Au^{III} to Au^I redox reaction the ligand H**L** has, therefore, a double role acting firstly as a reducing agent with production of the oxidised species H**L**′ and elemental sulfur and consequently as a complexing agent towards the Au^I ion. However, the solid state ^{31}P CP MAS spectrum of **3** which shows peaks at δ = 33.6 ($\Delta\nu_{1/2}$ = 143 Hz), 25.6

 © 2005 Wiley-VCH Verlag GmbH & Co. KGaA, Weinheim

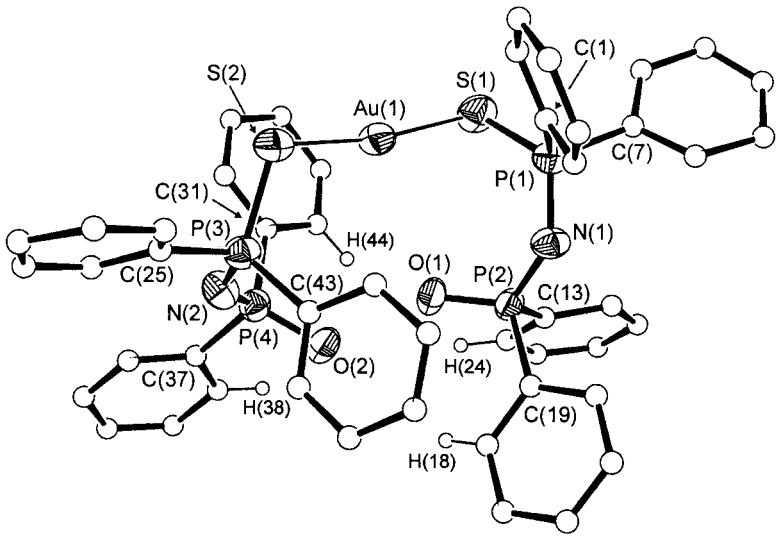

Figure 2. ORTEP plot of **3** showing the atom labelling scheme and 40% probability thermal ellipsoids for the Au, S, O, P and N atoms; C atoms are represented as spheres with arbitrary radii; hydrogen atoms have partly been omitted for clarity

($\Delta\nu_{1/2}$ = 180 Hz) and 18.4 ppm ($\Delta\nu_{1/2}$ = 212 Hz) with a relative intensity ratio of 1:1:2 does not support the presence of **HL′** in its neutral form in the complex since no signal in the 50−60 ppm range was detected (**HL′**, ^{31}P CP MAS: δ = 57.9 and 20.0). Fortunately, we have obtained good quality crystals of **3** for a single-crystal X-ray diffraction study. The molecular structure of **3** is shown in Figure 2, while selected structural parameters are listed in Table 4. The crystal lattice is made up of an Au^{I} complex featuring a quite distorted linear coordination geometry with the sulfur atoms of two ligand molecules [S−Au−S angle 170.24(12)°; average Au−S bond length 2.286(7) Å; nonbonding Au···O distances of 3.212(10) and 4.321(11) Å, for O(1) and O(2), respectively]. Both ligand molecules show a *syn* conformation of the sulfur and oxygen atoms with respect to the PNP fragment, with dihedral angles S(1)P(1)N(1)[O(1)P(2)N(1)]−P(1)N(1)P(2) and S(2)P(3)-N(2)[O(2)P(4)N(2)]−P(3)N(2)P(4) of 9(2) [49.8(12)] and 59.7(11) [55.4(15)]°, respectively, and deviations from the corresponding PNP basal planes in the ranges 0.27(4)−1.52(3) Å for sulfur [S(1) and S(2), respectively] and 1.02(3)−1.12(2) Å for the oxygen atoms [O(1) and O(2), respectively]. This arrangement of ligand moieties gives rise to a nonplanar Au[SO(P$_2$N)]$_2$ ring [deviations from the average atom plane ±1.479(5) Å] which can also be regarded as the connection of two almost planar fragments, namely S(1)Au(1)S(2)P(3) and P(4)O(2)O(1)P(2)N(1) (deviations from the mean plane of ±0.023(2) and ±0.062(7) Å, respectively) by the N(2) and P(1) ′bridging′ atoms. The absence of any counterion in the lattice is the most intriguing feature of the structure since it requires the simultaneous presence, in the molecule, of the ligand both in its neutral (**HL′**) and anionic (**L′**) forms to achieve electroneutrality. In the chemistry of metal tetraorganodichalcogenoimidodiphosphinate complexes, the presence of differentially protonated ligands in the same molecule is quite uncommon and, to the best of our knowledge, only two examples have been reported so far, namely the cationic complex [Pd{*i*Pr$_2$P(S)NHP(S)*i*Pr$_2$}{*i*Pr$_2$P(S)NP-(S)*i*Pr$_2$}]$^+$ [29] and [Au{Ph$_2$P(S)NP(O)Ph$_2$-*S*}{Ph$_2$PNHP-(O)Ph$_2$-*P*}] (**5**)[30] which shows a phosphorus-coordinated Au^{I} ion. Interestingly, in both complexes, the neutral ligands feature an N−H group and effectively retain the hy-

Table 4. Selected interatomic distances (Å) and angles (°) for complex **3**

Au(1)−S(1)	2.297(5)	Au(1)−S(2)	2.274(5)
S(1)−P(1)	2.025(6)	S(2)−P(3)	2.023(6)
O(1)−P(2)	1.496(10)	O(2)−P(4)	1.542(11)
P(1)−N(1)	1.581(12)	P(3)−N(2)	1.579(13)
P(2)−N(1)	1.579(12)	P(4)−N(2)	1.553(14)
Au(1)···O(1)	3.212(10)	Au(1)···O(2)	4.321(11)
S(1)···S(2)	4.554(7)	O(1)···O(2)	2.399(15)
O(1)···H(18)[a]	2.7123	O(1)···H(24)[a]	2.7596
O(2)···H(38)[a]	2.6907	O(2)···H(44)[a]	2.6347
S(2)−Au(1)−S(1)	170.24(16)		
P(1)−S(1)−Au(1)	97.6(2)	P(3)−S(2)−Au(1)	108.2(2)
N(1)−P(1)−S(1)	118.6(5)	N(2)−P(3)−S(2)	119.4(5)
P(2)−N(1)−P(1)	134.0(8)	P(4)−N(2)−P(3)	138.1(9)
O(1)−P(2)−N(1)	116.5(7)	O(2)−P(4)−N(2)	117.8(7)
C(7)−P(1)−S(1)	104.6(7)	C(1)−P(1)−S(1)	110.8(6)
N(1)−P(1)−C(1)	106.3(7)	N(1)−P(1)−C(7)	111.6(8)
C(7)−P(1)−C(1)	104.2(8)		
O(1)−P(2)−C(13)	109.0(7)	O(1)−P(2)−C(19)	110.0(7)
N(1)−P(2)−C(13)	111.9(7)	N(1)−P(2)−C(19)	105.0(6)
C(13)−P(2)−C(19)	103.6(6)		
C(25)−P(3)−S(2)	101.4(6)	C(31)−P(3)−S(2)	112.5(6)
N(2)−P(3)−C(25)	108.3(8)	N(2)−P(3)−C(31)	108.2(7)
C(31)−P(3)−C(25)	105.9(7)		
O(2)−P(4)−C(37)	105.0(7)	O(2)−P(4)−C(43)	108.1(8)
N(2)−P(4)−C(37)	107.8(7)	N(2)−P(4)−C(43)	111.4(8)
C(43)−P(4)−C(37)	105.9(7)		

[a] Hydrogen atoms in calculated positions.

drogen atom topology shown by the corresponding free molecules.[27,31] This seems not to be true in the case of **3**. Although the metric parameters of the two ligands are substantially equivalent and do not allow the identification of a protonated molecule, they do indeed reveal a surprisingly short O(1)···O(2) distance of 2.399(15) Å which strongly suggests the presence of an *intramolecular* hydrogen bond between the two oxygen atoms. Though experimental detection of a bridging hydrogen atom is not possible due to the quality of the solid-state structural determination, such a feature would be reasonable. The presence of a strong negative-Charge Assisted Hydrogen Bond[32] would in fact involve a negative charge-sharing between the two oxygen atoms and explain the equivalence, to within 3σ, of the P−O and N−P bond lengths in the ligands as well as the presence of P−O bonds significantly longer [1.496(10)−1.542(11) Å] than the usual P=O distances [1.47−1.50 Å][25,33,34] observed in *both* ligand fragments of the molecule of **3**. The latter bond length, in particular, could not be ascribed to other intramolecular interactions since the oxygen atoms show only weak nonbonding C−H···O interactions at distances of about 2.7 Å. On the basis of these structural data it is therefore possible to explain the solid state ^{31}P NMR spectroscopic data. The values at δ 33.6 and 25.6 reflect the different phosphorus environments of the *P*S groups in the complex, whereas the broad band at δ = 18.4 ppm reflects the similarity of the two *P*O groups.

It is worthy of note that the presence of strong *intramolecular* hydrogen bonds is not unusual in phosphane-derived compounds. Some examples reported in the literature include complex **5**[30] which features a (N−H···O$^-$) bridge, the chloro-bridged platinum(III) dimer $[PtCl(Ph_2PO)_2H]_2$ [35] and $[(Ph_2PO)_2H(Ph_3PO)]^+I_3^-$ in which an *intramolecular* hydrogen bond drives the cation conformation[36a] and the salts $[(Ph_3PO)H(Ph_3PO)]^+[AuCl_4]^-$[36b] and $[(Ph_3PO)H(Ph_3PO)]^+[ICl_4]^-$.[36c]

Further support of the structural data of **3** and of the stabilisation exerted by the *intramolecular* hydrogen bond between O(1)···O(2) comes from DFT calculations. Starting from the structural data of **3**, the geometry of the model complex $[Au(\mathbf{L}'')_2]^-$ was optimised, {[H**L**′′ = $H_2P(S)NHP(O)H_2$; **L**′′ = $H_2P(S)NP(O)H_2]^-$}. Subsequently, a hydrogen atom was positioned on the nitrogen or on the oxygen atom of an **L**′′ unit so as to form the model complexes [Au(H**L**′′)(**L**′′)] and [Au(**L**′′$_2$H)], respectively, and these complexes were then optimised. While the calculated structure of [Au(H**L**′′)(**L**′′)] is markedly different from that of **3**, the one related to [Au(**L**′′$_2$H)] features a P−O···H···O−P bridge with a calculated O−O bond length of 2.401 Å which agrees well with the experimental value of 2.399(15) Å found in **3**. Moreover, the energy of the model complex [Au(**L**′′$_2$H)] was found to be 20 kcal/mol more stable than that of [Au(H**L**′′)(**L**′′)]. An NBO analysis of [Au(**L**′′$_2$H)] showed that the two ligand units **L**′′ feature a similar charge distribution (differing by 0.09 e) and that the bridging hydrogen has a strong positive charge (0.539 e); see also Supplementary Information.

Acid/Base Behaviour of Complex 3

The protonation and deprotonation reactions of complex **3** were investigated by ^{31}P NMR spectroscopy. The solution ^{31}P NMR spectrum of **3** (CH_2Cl_2)[37] features a pair of doublets with the same integrated intensity at δ(*P*S) 32.8 ppm and δ(*P*O) 18.4 ppm (Table 5). The similarity of these values to those reported for the solid-state sample indicates that the structure of **3** is retained in solution with the proton bridging the two oxygen atoms. Treatment of complex **3** dissolved in CH_2Cl_2 with increasing amounts of a very strong base, 1,8-bis(dimethylamino)naphthalene (DMAN), produced the broadening and lowering of peaks related to **3** and the concomitant formation of two new peaks at δ = 29.0 ppm and 12.7 ppm. Notably, these values are similar to those previously observed for the **L**′ moiety in [Au{$Ph_2P(O)NP(S)Ph_2-S$}{$Ph_2P(O)NHPPh_2-P$}] [δ(*P*S) 28.5 ppm, δ(*P*O) 14.0 ppm, $CDCl_3$] in which **L**′ coordinates to the gold ion *via* the sulfur atom only, leaving the PO group pendant. This indicates that DMAN is able to deprotonate complex **3** with formation of the anionic complex $[Au(\mathbf{L}')_2]^-$ in which the metal ion is coordinated only by the sulfur atoms of two **L**′ ligands leaving, in this case also, the PO groups as pendants. This also agrees very well with the fact that the variation of the chemical shifts of (*P*O) is more pronounced with respect to that observed for (*P*S).

Table 5. ^{31}P NMR spectroscopic data for complex **3**, H**L**′ and related reactions

Compound/reaction[a]	δ(*P*S) / ppm	δ(*P*O) / ppm	$^2J(P_SP_O)$ / Hz
3 (solid state)	33.6 25.6	18.4	
3 (CH_2Cl_2)	32.8	18.4	2.5
3 + DMAN[b][c] (CH_2Cl_2)	29.0	12.7	
3 + CF_3COOH[b][d] (CH_2Cl_2)	56.4	26.8	14
H**L**′ (CH_2Cl_2)	57.5	21.6	16.5
H**L**′ + CF_3COOH[b][e] (CH_2Cl_2)	57.4	28.8	15.9

[a] All measurements carried out at 25 °C. [b] In situ reaction. [c] **3**/DMAN 1:2 molar ratio; **3** = 5×10^{-2} mol·dm^{-3}. [d] **3**/CF_3COOH 1:1 molar ratio; **3** = 5×10^{-2} mol·dm^{-3}. [e] H**L**′/CF_3COOH 1:1 molar ratio; H**L**′ = 5×10^{-2} mol·dm^{-3}.

The addition of an equivalent of CF_3COOH to a solution of **3** in CH_2Cl_2 resulted in a considerable change in the ^{31}P NMR spectrum of the complex with both the (*P*S) and (*P*O) resonance signals shifted to higher values of δ = 56.4 ppm and 26.8 ppm, respectively. The value of δ(*P*S) at 56.4 ppm, which is strongly indicative of *N*-protonation of the ligands in the complex, agrees well with the signal observed for the neutral complexes $[Pd(HL)I_2]$[10] [δ(*P*S) 56.5 ppm, $CHCl_3/CH_3CN$, v:v, 1:1] and $[Hg(HL)I_2]$[38] [δ(*P*S) 57.8 ppm, CH_2Cl_2] and for *cis*-[Pd{$Ph_2P(O)NHP(S)Ph_2-O,S$}$_2$][BF_4]$_2$ [δ(*P*S) 57.6 ppm, δ(*P*O) 45.9 ppm, d,

 © 2005 Wiley-VCH Verlag GmbH & Co. KGaA, Weinheim

$^2J_{P,P}$ = 7.0 Hz), $CDCl_3$] in which the ligand acts in an *O*,*S*-bidentate manner thus forming a six-membered Pd−O−P−N−P−S ring. It is interesting to note that the (*P*O) signal for the protonated complex **3** is very different from that observed for the palladium complex *cis*-$[Pd\{Ph_2P(O)NHP(S)Ph_2\text{-}O,S\}_2][BF_4]_2$, while it is comparable with that measured for an acidic solution of H**L**′′ [δ(*P*O) 28.8 ppm, CH_2Cl_2] (Table 5). Hence it is reasonable to hypothesise that in acidic media the PO groups in **3** remain uncoordinated to the metal and protonated, and that the variation observed at the δ(*P*O) depends on the *N*-protonation of the ligands.

Conclusion

It has been demonstrated that the adduct H**L**·I_2 in Et_2O can oxidise Au^0 powder to produce the complex $[Au^{III}(\mathbf{L})I_2]$ under mild conditions in a single step. This reaction indicates that the oxidation of Au^0 by charge transfer adducts of iodine can be accomplished using very different donor molecules and, consequently, it may be of some importance in the gold-based technology of semiconductor devices since it avoids the use of unattractive reagents in the etching process. As a result of an interest in the reactions between $[Au^{III}Cl_3(tht)]$ with H**L**, it has been shown that the reducing agent is the ligand HL and the products are the complex $[Au^{I}(\mathbf{L})]_2$, sulfur, the free ligand $Ph_2P(S)NHP(O)Ph_2$ (H**L**′) and a very small amount of its Au^I complex. The nature of this unusual complex has been investigated by X-ray crystallography and ^{31}P CP MAS spectroscopy. Interestingly, this complex shows a structure similar to that depicted in Scheme 1 (see **c**), with an Au^I ion bridging two sulfur atoms of two anionic ligands **L**′ and a proton bridging two oxygen atoms of the PO groups. The nature of this complex is also supported by DFT calculations. The protonation and deprotonation reactions of $[Au(\mathbf{L}'_2H)]$ leave the coordination environment of the Au^I centre unaffected. ^{31}P NMR spectroscopic data suggest that in the case of protonation, both ligands are protonated at the nitrogen atoms.

Experimental Section

Materials and Instrumentation: Reagents were used as purchased from Aldrich. Diethyl ether was distilled form $LiAlH_4$ shortly before use.

$^{31}P\{^1H\}$ NMR spectra were recorded on a Varian Unity 400 MHz spectrometer. Chemical shift values were referenced to an external standard of 85% H_3PO_4 (δ_{31P} = 0.0) inserted in a sealed co-axial tube. All solution NMR experiments were carried out in NMR tubes with PTFE valves (Aldrich). ^{31}P NMR CP MAS spectra were calibrated indirectly through the 85% H_3PO_4 peak (δ_{31P} = 0.0). IR spectra were measured as KBr (4000−400 cm^{-1}) and polyethylene pellets (400−50 cm^{-1}) on a Bruker Equinox 55 FT-IR spectrometer. FT-Raman spectra were recorded on a Bruker FRS 100/S Fourier transform Raman spectrometer operating with a diode-pumped Nd:YAG exciting laser emitting at 1064 nm.

Syntheses: Compounds $[Ph_2P(S)NHP(S)Ph_2]$ (H**L**) and $Cs[Ph_2P(S)NP(S)Ph_2]$ (Cs**L**) were prepared according to ref.[39] and ref.[11], respectively. Complexes [AuCl(tht)] and $[AuCl_3(tht)]$ were prepared according to ref.[7]; complex $[Au(\mathbf{L})Cl_2]$ was prepared according to ref.[5]

[Au(L)I_2] (2): A mixture of H**L** (0.100 g, 0.222 mmol) and I_2 (0.084 g, 0.333 mmol) in diethyl ether (200 mL) was stirred at 25 °C under N_2 until the reagents were completely dissolved. Gold metal powder (100 mesh) (0.044 g, 0.222 mmol) was added with stirring. Stirring was continued at room temperature for ca. 3 weeks. The resultant red-black solid and crystals were collected by suction filtration, washed with a mixture of CH_2Cl_2 and *n*-hexane (1:5, v:v) and dried in vacuo. Yield 0.040 g, 20%. m.p. 230−232 °C. Elemental analysis for $C_{24}H_{20}AuI_2NP_2S_2$ (899.24): calcd. C 32.06, H 2.24, N 1.56, S 7.13; found C 32.5, H 2.4, N 1.8, S 7.6. ^{31}P NMR ($CDCl_3$): δ = 36.4 ppm. IR (KBr): $\tilde{\nu}$ = 3051 w, 1476 w, 1436 s, 1308 w, 1187 s, 1172 vs, 1108 vs, 1026 w, 997 w, 923 w, 827 m, 746 s, 721 s, 700 vs, 690 vs, 567 vs, 554 vs, 523 m, 511 s, 491 m cm^{-1}.

[Au(L′$_2$H)] (3): $Ph_2P(S)NHP(S)Ph_2$ (0.233 g, 0.520 mmol) was added to a solution of $AuCl_3(tht)$ (0.100 g, 0.260 mmol) in dichloromethane (50 mL) and the mixture was stirred for 2 h at room temperature. The cloudy mixture was then filtered to separate a fine buff-coloured powder (sulfur) and, after 48 hours, filtration was again carried out to separate complex **4**. The filtrate was reduced by two-thirds to give the white compound $Ph_2P(S)NHP(O)Ph_2$. Further evaporation of the solvent to almost dryness yielded white crystals of **3**, yield 5%, m.p. 208−210 °C. Elemental analysis for $C_{48}H_{41}AuN_2O_2P_4S_2$ (1062.79): calcd. C 54.24, H 3.89, N 2.64, S 6.03; found C 54.6, H 4.0, N 2.8, S 6.5. ^{31}P NMR (CH_2Cl_2): δ(*P*S) 32.8, δ(*P*O) 18.4 ppm, $^2J_{PSPO}$ = 2.5 Hz. IR (KBr): $\tilde{\nu}$ = 3055 m, 1591 w, 1481 m, 1436 s, 1253 br, 1179 m 1124 s, 1110 s, 1067 m, 1027 m, 1000 m, 889 br, 746 ms, 722 s, 691 vs, 618 w, 579 s, 565 s, 546 s, 509 s cm^{-1}.

X-ray Crystallography: X-ray quality crystals of **2** and **3** were obtained directly as described above. The structures were solved by direct methods (SIR-97[20] and SHELXS-97[21] for **2** and **3**, respectively) and refined using the SHELXL-97 program[21] implemented in the WINGX suite.[22] Details of the crystal data and structural refinements are reported in Table 1. All non-hydrogen atoms were refined with anisotropic thermal parameters. Hydrogen atoms were treated as idealised contributors in calculated positions and refined isotropically. Selected interatomic distances and angles can be found in Table 2 and Table 4. CCDC-233084 (for **2**) and -233085 (for **3**) contain the supplementary crystallographic data for this paper. These data can be obtained free of charge at www.ccdc.cam.ac.uk/conts/retrieving.html [or from the Cambridge Crystallographic Data Centre, 12 Union Road, Cambridge CB2 1EZ, UK; Fax: +44-1223-336-033; E-mail: deposit@ccdc.cam.ac.uk].

Complex 2: Diffraction data were collected at room temperature on an Bruker SMART-CCD system automatic diffractometer equipped with a graphite-monochromated Mo-K_α radiation (λ = 0.71073 Å) in the range $3.6 < 2\theta < 66.6°$. Refinement of 290 parameters on 9953 independent reflections gave *R1* [*wR2*] = 0.0327 [0.0819] on $I > 2\sigma(I)$ [all data]. The maximum and minimum residual electron densities on the final ΔF map were 0.95 and −1.06 e·Å^{-3}.

Complex 3: A 0.58 × 0.22 × 0.10 mm crystal was mounted at room temperature on a Siemens P4-RA automatic diffractometer equipped with graphite-monochromated Mo-K_α radiation (a = 0.71073 Å). A total of 10515 reflections (8424 unique) were col-

 © 2005 Wiley-VCH Verlag GmbH & Co. KGaA, Weinheim

lected in the range $3.8 < 2\theta < 50.1°$. Intensities were corrected for Lorentz-polarisation effects and an empirical absorption correction was applied (ψ-scan).[23] Refinement of 532 parameters gave *R1* [*wR2*] = 0.0820 [0.2506] on $I > 2\sigma(I)$ [all data]. The maximum and minimum residual electron densities on the final ΔF map were 1.59 and −0.83 e·Å^{-3}.

Computations: Density Functional Calculations (DFT) were carried out on the model complexes [Au(**L**′′)$_2$]$^-$, [Au(H**L**′′)(**L**′′)] and [Au(**L**′′$_2$H)] using the Gaussian 98 suite of programs (Rev. A11)[40] with the hybrid Becke3LYP functional[41−43] and the LanL2DZ basis set for C, H, N, O, P, S and Au. The NBO charge distribution[44] was calculated for all the examined compounds. The results were examined with the Molden 3.9 program.[45]

Supporting Information Available (see also footnote on the first page of this article): Table S1, Optimised geometry calculated for the complex [Au(**L**′′$_2$H)] in the orthogonal Cartesian coordinate format; Table S2, Mulliken atomic charges at the optimised geometry calculated for the complex [Au(**L**′′$_2$H)]; Table S3, Summary of natural population analysis at the optimised geometry calculated for the complex [Au(**L**′′$_2$H)].

Acknowledgments

This research was financially supported by the "Regione Autonoma della Sardegna". We are grateful to Dr. M. Monari and Prof. V. Albano (Dipartimento di Chimica "G. Ciamician", Università di Bologna, Italy) for assistance with the X-ray data collection of compound **2**. We are grateful to CINECA for providing computational facilities.

[1] [1a] I. Haiduc, *Comprehensive Coordination Chemistry II* (Ed.: A. B. P. Lever), Elsevier Pergamon, Amsterdam, Oxford, **2004**, vol. 1, p. 323−347. [1b]C. Silvestru, J. E. Drake, *Coord. Chem. Rev.* **2001**, *223*, 117−216. [1c] T. Q. Ly, J. D. Woollins, *Coord. Chem. Rev.* **1998**, *176*, 451−481; and references cited therein.
[2] O. Navratil, E. Herrmann, G. Grossmann, J. Teply, *J. Coll. Czech. Chem. Commun.* **1990**, *55*, 364−371.
[3] L. Barkaoui, M. Charrouf, M. N. Rager, B. Denise, N. Platzer, H. Rudler, *Bull. Soc. Chim. France* **1997**, *134*, 167−175.
[4] H. Rudler, B. Denise, J. R. Gregorio, J. Vaissermann, *Chem. Commun.* **1997**, 2299−2300.
[5] A. Laguna, M. Laguna, A. Rojo, M. N. Fraile, E. Fernandez, P. G. Jones, *Inorg. Chim. Acta* **1988**, *150*, 233−236.
[6] W. C. Herndon, I. Haiduc, *J. Mol. Struct.* **2001**, *598*, 127−131.
[7] A. Laguna, M. Laguna, A. Rojo, M. N. Fraile, *J. Organomet. Chem.* **1986**, *315*, 269−276.
[8] R. Uson, A. Laguna, M. Laguna, M. Conception Gimeno, *J. Chem. Soc., Dalton Trans.* **1989**, 1883−1886.
[9] G. L. Abbati, M. C. Aragoni, M. Arca, A. C. Fabretti, F. A. Devillanova, A. Garau, F. Isaia, V. Lippolis, G. Verani, *Dalton Trans.* **2003**, 1515−1519.
[10] G. L. Abbati, M. C. Aragoni, M. Arca, A. C. Fabretti, F. A. Devillanova, A. Garau, F. Isaia, V. Lippolis, G. Verani, *J. Chem. Soc., Dalton Trans.* **2001**, 1105−1110.
[11] M. C. Aragoni, M. Arca, A. Garau, F. Isaia, V. Lippolis, G. L. Abbati, A. C. Fabretti, *Z. Anorg. Allg. Chem.* **2000**, *626*, 1454−1459.
[12] M. Arca, A. Garau, F. A. Devillanova, F. Isaia, V. Lippolis, G. Verani, G. L. Abbati, A. Cornia, *Z. Anorg. Allg. Chem.* **1999**, *625*, 517−520.
[13] S. M. Godfrey, N. Ho, C. A. McAuliffe, R. G. Pritchard, *Angew. Chem. Int. Ed. Engl.* **1996**, *35*, 2344−2345; and references cited therein.
[14] F. Bigoli, P. Deplano, F. A. Devillanova, V. Lippolis, M. L. Mercuri, M. A. Pellinghelli, E. F. Trogu, *Inorg. Chim. Acta* **1998**, *267*, 115−121.
[15] F. Bigoli, P. Deplano, M. L Mercuri, M. A. Pellinghelli, G. Pintus, M. A. Serpe, E. F. Trogu, *Chem. Commun.* **1998**, 2351−2352.
[16] F. Bigoli, P. Deplano, M. L. Mercuri, M. A. Pellinghelli, G. Pintus, M. A. Serpe, E. F. Trogu, *J. Am. Chem. Soc.* **2001**, *123*, 1788−1789.
[17] L. Cau, P. Deplano, L. Marchiò, M. L. Mercuri, L. Pilia, A. Serpe, E. F. Trogu, *Dalton Trans.* **2003**, 1969−1974.
[18] A. J. Blake, F. A. Devillanova, R. O. Gould, W.-S. Lee, V. Lippolis, C. Radek, M. Schröder, *Chem. Soc. Rev.* **1998**, *27*, 195−206.
[19] L. J. Farrugia, *J. Appl. Cryst.* **1997**, *30*, 565−566.
[20] A. Altomare, M. C. Burla, M. Camalli, G. L. Cascarano, C. Giacovazzo, A. Guagliardi, A. G. G. Moliterni, G. Polidori, R. Spagna, *J. Appl. Cryst.* **1999**, *32*, 115−119.
[21] G. M. Sheldrick, *SHELX97 − Programs for Crystal Structure Analysis (Release 97−2)*; University of Göttingen, Germany, **1998**.
[22] L. J. Farrugia, *J. Appl. Cryst.* **1999**, *32*, 837−838.
[23] A. C. T. North, D. C. Phillips, F. S. Mathews, *Acta Crystallogr., Sect. A* **1968**, *24*, 351−359.
[24] *International Tables for X-ray Crystallography* (Eds.: T. Hanh, D. Riedel), Dordrecht, The Netherlands, **1983**.
[25] S. Husebye, K. Maartmann-Moe, *Acta Chem. Scand.* **1983**, *37*, 439−441.
[26] S. K. Bhargava, F. Mohr, M. A. Bennett, L. L. Welling, A. C. Willis, *Inorg. Chem.* **2001**, *40*, 4271−4275.
[27] A. M. Z. Slawin, M. B. Smith, J. D. Woollins, *J. Chem. Soc., Dalton Trans.* **1996**, 3659−3665.
[28] M. B. Smith, A. M. Z. Slawin, *Polyhedron* **2000**, *19*, 695−704.
[29] D. Cupertino, R. Keyte, A. M. Z. Slawin, J. D. Woollins, D. J. Williams, *Polyhedron* **1996**, *15*, 4441−4445.
[30] A. M. Z. Slawin, M. B. Smith, J. D. Woollins, *J. Chem. Soc., Dalton Trans.* **1998**, 1537−1539.
[31] A. M. Z. Slawin, M. B. Smith, J. D. Woollins, *J. Chem. Soc., Dalton Trans.* **1996**, 1283−1293.
[32] P. Gilli, V. Bortolasi, V. Ferretti, G. Gilli, *J. Am. Chem. Soc.* **1994**, *116*, 909−915.
[33] G. Annibale, P. Bergamini, V. Bertolasi, E. Besco, M. Cattabriga, R. Rossi, *Inorg. Chim. Acta* **2002**, *333*, 116−123.
[34] N. J. Goodwin, W. Henderson, B. K. Nicholson, *Inorg. Chim. Acta* **2002**, *335*, 113−118.
[35] P. Bergamini, V. Bertolasi, M. Cattabriga, V. Ferretti, U. Loprieno, N. Mantovani, L. Martelli, *Eur. J. Inorg. Chem.* **2003**, *5*, 918−925.
[36] [36a] F. Bigoli, P. Deplano, M. L. Mercuri, M. A. Pellinghelli, E. F. Trogu, *Phosphorus, Sulfur Silicon Relat. Elem.* **1992**, *70*, 145−152. [36b] P. G. Jones, G. M. Sheldrick, *Acta Crystallogr., Sect. B* **1978**, *34*, 1353−1355. [36c] C. J. Carmalt, N. C. Norman, L. J. Farrugia, *Polyhedron* **1993**, *12*, 2081−2090.
[37] Variable-temperature measurements in the range +30 to −75 °C, the lowest temperature for which NMR spectroscopic data were recordable, showed no significant changes in the spectra.
[38] F. Demartin, M. C. Aragoni, M. Arca, M. B. Carrea, F. A. Devillanova, A. Garau, F. Isaia, V. Lippolis, G. Verani, *Eur. J. Inorg. Chem.* **2004**, 4660−4668.
[39] A. Schmidpeter, R. H. Bohm, H. Groenger, *Angew. Chem.* **1964**, *76*, 860−861.
[40] M. J. Frisch, G. W. Trucks, H. B. Schlegel, G. E. Scuseria, M. A. Robb, J. R. Cheeseman, V. G. Zakrzewski, J. A. Montgomery, R. E. Stratmann, J. C. Burant, S. Dapprich, J. M. Millam, A. D. Daniels, K. N. Kudin, M. C. Strain, O. Farkas, J. Tomasi, V. Barone, M. Cossi, R. Cammi, B. Mennucci, C. Pomelli, C. Adamo, S. Clifford, J. Ochterski, G. A. Petersson, P. Y. Ayala, Q. Cui, K. Morokuma, D. K. Malick, A. D. Rabuck, K. Raghavachari, J. B. Foresman, J. Cioslowski, J. V. Ortiz, B. B. Stefanov, G. Liu, A. Liashenko, P. Piskorz, I. Komaromi, R.

 © 2005 Wiley-VCH Verlag GmbH & Co. KGaA, Weinheim

Gomperts, R. L. Martin, D. J. Fox, T. Keith, M. A. Al-Laham, C. Y. Peng, A. Nanayakkara, C. Gonzalez, M. Challacombe, P. M. W. Gill, B. G. Johnson, W. Chen, M. W. Wong, J. L. Andres, M. Head-Gordon, E. S. Replogle, J. A. Pople, GAUSSIAN 98 (Revision A 11), Gaussian, Inc., Pittsburgh, PA, **1998**.
[41] A. D. Becke, *J. Chem. Phys.* **1993**, *98*, 1372−1377.
[42] A. D. Becke, *J. Chem. Phys.* **1993**, *98*, 5648−5652.
[43] C. Lee, W. Yang, R. G. Parr, *Phys. Rev.* **1988**, *37*, 785−789.
[44] A. E. Reed, L. A. Curtiss, F. Weinholt, *Chem. Rev.* **1988**, *88*, 899−926.
[45] Schaftenaar, J. H. Noordik, MOLDEN 3.9: a pre-and post-processing program for molecular and electronic structures, *J. Comp.-Aided Mol. Design* **2000**, *14*, 123−124.

Received July 26, 2004
Early View Article
Published Online December 17, 2004

 © 2005 Wiley-VCH Verlag GmbH & Co. KGaA, Weinheim

Synthesis and Metal-Complexation Properties of a New Hydroxypyrimidinone-Functionalized Sepharose

M. Alexandra Esteves,*[a] Anabela Cachudo,[a] Sílvia Chaves,[b] and M. Amélia Santos[b]

Keywords: Actinides / Chelates / Environmental chemistry / O ligands / Functionalized sepharose

The 1-hydroxy-2-(1*H*)-pyrimidinone derivative 4-(3-aminopropylamino)-1-hydroxy-2-(1*H*)-pyrimidinone (HOPY-PrN) was synthesized and its acid-base and complexation properties towards a set of metal ions (Fe^{III}, Al^{III}, and Th^{IV}) were studied by potentiometry and spectrophotometry. The ligand was further immobilized in an epoxy-activated sepharose by chemical coupling through the aminoalkyl pendent group with the aim of improving its sequestering capacity for residual amounts of metals. The new hydroxypyrimidinone-functionalized sepharose shows a high chelating capacity for metal ions in the pH range 3–8, thus suggesting good perspectives for potential environmental applications.
(© Wiley-VCH Verlag GmbH & Co. KGaA, 69451 Weinheim, Germany, 2005)

Introduction

The need to manage, safely store, and limit the potential environmental or injurious effects of toxic metal ions, such as the actinides (e.g.: plutonium) produced from nuclear reactors, is becoming increasingly urgent.[1] Accordingly, the requirement for effective metal-sequestering agents, namely solid supports functionalized with specific chelators, has increased.[2,3] Those materials can find practical applications as extraction agents for the removal of residual amounts of actinides and other hazardous metal ions from waste waters. Immobilized chelators have also been used in biological and pharmacological applications, such as the removal of metal contaminants from biological systems, and as supports for affinity chromatography.[4]

For all these purposes the functionalized solid matrix should have an adequate hydrophilicity and stability, in order to guarantee a good interaction with water, and a low bleeding potential to prevent the introduction of further contaminants into the environment. On the other hand, immobilized metal-chelators should also have important properties such as a high affinity for a specific metal ion (or group of metal ions) and adequate spacer groups to avoid steric hindrance. A variety of supports are known for chelator immobilization, such as silicas, organic polymers, agaroses, and celluloses.[5] The search for specific chelators for hard metal ions has been quite active, and has been especially aimed at finding substitutes for Desferrioxamine B (a hydroxamate-based medicinal chelating drug with limitations due to oral inactivity)[6] and also substitutes of hydroxamate-immobilized matrices for potential environmental applications without their inherent problems of instability and re-usability.[7] *N*-Hydroxyamide-containing heterocycles, such as 1-hydroxy-2-pyridinones (1,2-HOPO),[8] hydroxypyrimidinones (HOPY),[9,10] and hydroxypyrazones (HOPR)[11] (see Scheme 1), have been

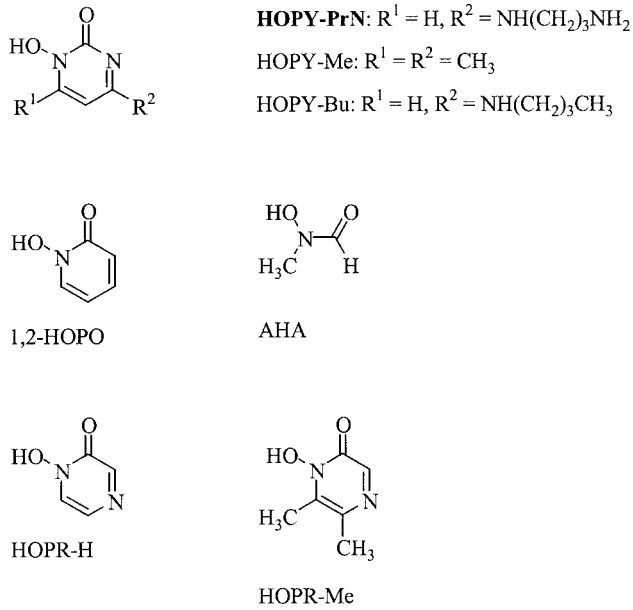

Scheme 1. Structural formulae for 4-(3-aminopropylamino)-1-hydroxy-2-(1*H*)-pyrimidinone (HOPY-PrN), 1-hydroxy-4,6-dimethyl-2(1*H*)-pyrimidinone (HOPY-Me), 1-hydroxy-4-(*N*-butylamino)-2(1*H*)-pyrimidinone (HOPY-Bu), 1-hydroxy-2(1*H*)-pyridinone (1,2-HOPO), acetohydroxamic acid (AHA), 1-hydroxy-2(1*H*)-pyrazinone (HOPR-H), and 1-hydroxy-5,6-dimethyl-2(1*H*)-pyrazinone (HOPR-Me)

[a] INETI, Departamento de Tecnologia de Indústrias Químicas, Estrada do Paço do Lumiar, 22, 1649−038 Lisboa, Portugal
Fax: (internat.) + 351-217-168-100
E-mail: alexandra.esteves@ineti.pt
[b] Centro de Química Estrutural, Complexo 1, Instituto Superior Técnico
Av. Rovisco Pais, 1049-001 Lisboa, Portugal

considered of great interest owing to their effectiveness in the selective sequestration of hard metal ions, particularly Fe^{III}, those of group IIIA, and some actinides (e.g. Pu^{IV} and Th^{IV}).[1] These *N*-hydroxyamide-containing mono- and diazines can be regarded as hydroxamic acids (HAs), but with endocyclic structures, which makes them much more stable in aqueous medium than linear or exocyclic HAs. On the other hand, their π-electron-deficient ring system allows a considerable amount of electron delocalization, which contributes to the high stability of the metal complexes.

Although some 1-hydroxy-2-pyridinone derivatives have already been studied in terms of chelating properties and immobilization onto polystyrene supports for the removal of hard metal-ions (e.g. Pu^{IV}) from water streams,[2,12,13] only a few published data are available on the coordination chemistry of hydroxypirimidinone derivatives.[11,14] Also, to the best of our knowledge, there are no reports of the immobilization of this kind of ligand on solid supports. Hydroxypyrimidinones have an extra nitrogen atom in the heterocyclic ring, which makes them less toxic and more promising compounds for environmental and biomedical applications[9,15−17] by increasing their acidity and water solubility.

As part of an ongoing project on hydroxypyrimidinone-based chelating resins, we present herein the synthesis and study of a water-soluble hydroxypyrimidinone and its sepharose-supported derivative. Thus, 4-(3-aminopropylamino)-1-hydroxy-2-(1*H*)-pyrimidinone (HOPY-PrN) was synthesized and studied in terms of its acid-base and chelating properties towards Fe^{III}, Al^{III}, and Th^{IV}, in aqueous solution, by potentiometric and spectrophotometric techniques. This ligand was further immobilized in an epoxy-activated sepharose and then the new functionalized support was studied with regards to its ligand density, stability, and capacity for the removal of some hard metal ions from aqueous medium. In these studies, Th^{IV} was chosen as a model of Pu^{IV}. In fact, isotopes of thorium are formed as daughter products of the most important isotopes of uranium, and although thorium is also a potential contaminant in the reprocessing of nuclear fuels, it has a very low specific radioactivity and so it is a quite safe actinide ion for model studies.

Results and Discussion

Synthesis of HOPY-PrN

The general procedure for the synthesis of HOPY-PrN is outlined in Scheme 2.

1-(Benzyloxy)uracil (**1**), which was synthesized by a previously reported procedure,[11] was condensed with 1,2,4-triazole in the presence of 4-chlorophenyldichlorophosphate in dry pyridine[18] to give 1-(benzyloxy)-4-(1′,2′,4′-triazol-1′-yl)-2(1*H*)-pyrimidinone (**2**) in 50% yield. To enable the posterior coupling of the ligand to the solid support, an *N*-protected alkylamine segment was introduced as a heterocyclic substituent group by reacting **2** with 3-[(benzyloxycarbonyl)amino]propylamine[19] in refluxing THF to give 4-{3-[(benzyloxycarbonyl)amino]propylamino}-1-(benzyloxy)-2(1*H*)-pyrimidinone (**3**) in 80% yield. Finally, HOPY-PrN was obtained by removing the protecting benzyl groups from both benzyloxycarbonyl/amino and hydroxyl groups of **3** by standard catalytic hydrogenolysis in methanol.[11]

Immobilization of HOPY-PrN

The coupling reaction of the ligand to the commercially available 6B epoxy-sepharose (SEPH, Scheme 3) was carried out under slightly basic conditions according to a published procedure.[20] Care was taken in the selection of the pH for the coupling reaction because it should be just high enough to ensure the deprotonation of the amino group but not so high to promote coupling of the hydroxyl group or even the degradation of the ligand. Therefore, the epoxy sepharose gel was added to a solution of HOPY-PrN in a buffer solution at pH 9 and the mixture was shaken in a water bath at 40 °C for 48 h.

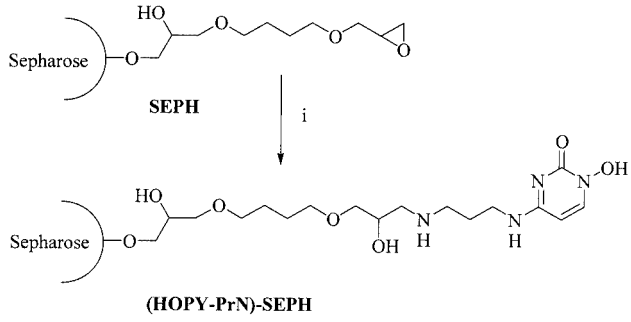

Scheme 3. Immobilization of HOPY-PrN in epoxy-activated 6B sepharose (SEPH): (i) universal buffer, pH 9, $T = 40$ °C (48 h)

A series of preliminary coupling reactions were performed to find the dependence of the ligand concentration on the extent of the HOPY-PrN immobilization. As is shown in Figure 1, a 60-fold ligand excess, relative to the expected amount of active sites in the epoxy-sepharose (ca. 103 μmol active sites per gram dry gel with additives),[20]

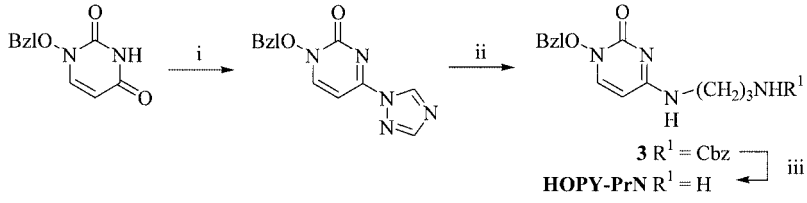

Scheme 2. Synthesis of HOPY-PrN: (i) 1,2,4-triazole, 4-chlorophenyldichlorophosphate, pyridine; (ii) $NH_2(CH_2)_3NHCbz$, THF, Δ; (iii) 10% Pd/C, H_2, MeOH

 © 2005 Wiley-VCH Verlag GmbH & Co. KGaA, Weinheim

gave the highest (HOPY-PrN)-SEPH density [263 μmol ligand per gram (dry weight)], which corresponds to 54% conversion of the active sites. The ligand density in the functionalized sepharose was easily calculated from the nitrogen amount determined by elemental analysis, since the ligand is the only source of this element in the matrix.

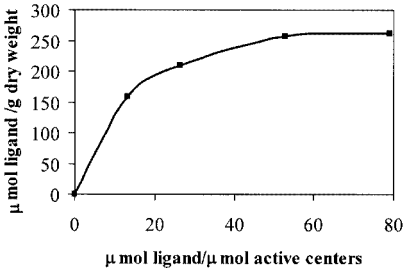

Figure 1. Plot of ligand density in (HOPY-PrN)-SEPH vs. ligand concentration in the coupling reaction

Stability of the Functionalized Support (HOPY-PrN)-SEPH

The stability of the functionalized support in aqueous solution was tested under different pH conditions (pH 3, 7, and 9) at room temperature. The support was added to buffered aqueous solutions at the selected pH and the suspensions were left shaking at room temperature for 24 h. To calculate the amount of ligand released into solution the suspensions were periodically centrifuged during the experiment and the absorbance of the supernatants was measured at the maximum absorption wavelength (λ_{max} = 318 nm) for HOPY-PrN. Plots of percentage of ligand released vs. time (Figure 2) showed that, after 24 h, less than 0.5% of the ligand had been released from the solid matrix for all the experimental pH values, thus indicating that the functionalized sepharose is quite stable.

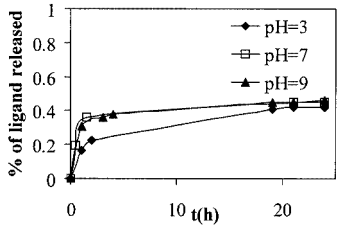

Figure 2. Plot of the percentage of ligand released from the functionalized sepharose vs. time in aqueous solution at pH 3, 7, and 9

Equilibrium Solution Studies

Acid-Base Properties

The ligand was obtained as a neutral species even though, in the fully protonated form, it has three dissociable protons. The corresponding protonation constants were determined from the fitting analysis of the potentiometric titration curve, and its protonation sequence was deduced from the ^{1}H NMR titration curves (Figure 3). The protonation sequence of the ligand is in agreement with the chemical evidence, namely the downfield shifts of the labile protons, which follow the order terminal *N*-amine group (at pD ≈ 10.1−12.5 peaks *c*, *d*, *e*), hydroxy group (at pD ≈ 6−8.8 peaks *a* and *b*), and 4-imine group (at pD ≈ 1.5−4.1 all the peaks, but mostly on *a* and *b*, probably due to the enamine-imine equilibrium). This ^{1}H NMR titration was checked for reversibility and the ligand proved to be stable under both acidic and basic pH conditions.

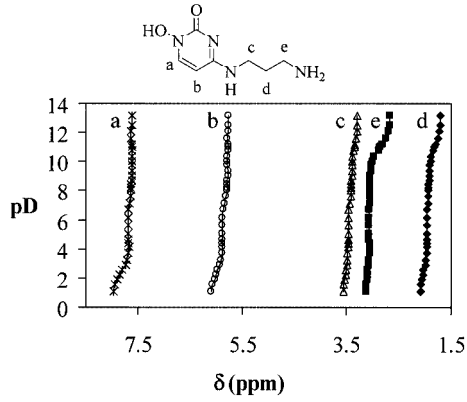

Figure 3. ^{1}H NMR titration curves for HOPY-PrN

The calculated protonation constants (log K_i,) for the ligand are reported in Table 1, which also includes the corresponding values for some analogous compounds, namely 1-hydroxy-4,6-dimethyl-2(1*H*)-pyrimidinone (HOPY-Me),[14] 1-hydroxy-2(1*H*)-pyridinone (1,2-HOPO),[8,21] 1-hydroxy-2(1*H*)-pyrazinone (HOPR-H),[9] 1-hydroxy-5,6-dimethyl-2(1*H*)-pyrazinone (HOPR-Me),[9] and acetohydroxamic acid (AHA).[22]

Table 1. Stepwise protonation constants (log K_i) of HOPY-PrN and other ligands, for comparison, as well as global formation constants (log $\beta_{M_mH_hL_l}$) of the corresponding Fe^{3+}, Al^{3+}, and Th^{4+} complexes (I = 0.1 M KNO_3, T = 25.0 ± 0.1 °C)

Ligand	H^+ log K_i	Fe^{3+}	Al^{3+} (m,h,l) log $\beta_{M_mH_hL_l}$	Th^{4+}
HOPY-PrN	10.11(2)	(111) 19.88(1)	(111) 16.84(2)	(111) 18.74(6)
	6.84(4)	(122) 38.12(6)	(122) 34.04(4)	(122) 37.14(4)
	2.21(5)	(123) 48.04(3)	–	(123) 47.70(6)
		(133) 55.26(5)	(133) 49.67(2)	(133) 53.91(5)
		–	–	(144) 69.54(6)
HOPY-Me[14]	6.1	(103) 22.1	–	–
1,2-HOPO	5.78[8]	(101) 9.0[8]	(101) 8.16[21]	–
	5.86[21]	10.6[21]	(102) 5.54[21]	–
		(102) 16.6[8]	(103) 21.59[21]	
		20.1[21]		
		(103) 26.9[8]		
		27.2[21]		
HOPR-H[9]	4.4	(103) 18.2	–	–
HOPR-Me[9]	4.7	(103) 20.2	–	–
AHA[22][a]	9.36	(101) 11.42	(101) 7.95	
		(102) 21.10	(102) 15.29	–
		(103) 28.33	(103) 21.47	

[a] At 20 °C.

 © 2005 Wiley-VCH Verlag GmbH & Co. KGaA, Weinheim

The terminal *N*-amine group of HOPY-PrN is slightly more acidic (log K = 10.11) than that of propylamine (10.57)[23] or 1,3-diaminopropane (10.49)[24] due to the electron-withdrawing effect of the pyrimidinone ring. The log K_2 value (6.84), which corresponds to the protonation of the hydroxy group, is lower than that of an aliphatic hydroxamic acid, such as acetohydroxamic acid (log K = 9.36),[22] due to the stabilization of the negative charge of the conjugated base by the electron-withdrawing and resonance effects of the aromatic ring. It is also lower than that of HOPY-Bu (7.5)[11] due to the electron-donating effect of the butyl group. However, log K_2 is higher than the reported values for the corresponding hydroxy groups of HOPY-Me (6.1), 1,2-HOPO (5.78,[8] 5.86[21]), HOPR-Me (4.7), and HOPR-H (4.4) due to the interplay of different effects such as the inductive/electron-donating effect of the substituting groups at the C-4 position, the electron-withdrawing effect of the additional ring-nitrogen atom and its different positioning relative to N-OH group (e.g. *meta*- or *para*-positioned for HOPY and HOPR derivatives, respectively, with a concomitant difference in the resonance stabilization). From the ^{1}H NMR titration curves there is also evidence of a third labile proton (log K_3 = 2.21), which was determined after addition of excess of mineral acid. It is attributed to the 4-amino group, and its high acidity should be due to the enamine/imine equilibrium and the electron-withdrawing resonance effect of the aromatic ring.

Complexation Studies

The stability constants of the M^{3+} (M = Fe, Al) and Th^{4+} complexes with HOPY-PrN were determined by potentiometric and spectrophotometric techniques; they are collected in Table 1, together with reported values for some structural analogs (HOPY-Me, 1,2-HOPO, HOPR-H, HOPR-Me, AHA), all of which form five-membered chelate rings through the adjacent *N*-hydroxy- and keto-oxygen atoms. For all M/(HOPY-PrN) systems studied herein, the potentiometric titration curves show that the complex formation is already underway at the beginning of the titration. They also indicate the existence of a break at a = 0 (a = mol of base per mol of ligand), which suggests the non-involvement of the appended amine groups in the metal coordination, and also the apparent formation of mixed hydroxo-ligand complexes before the complete deprotonation of the fully coordinated complex species. At the beginning of the titration of the Fe^{3+}/HOPY-PrN or Th^{4+}/HOPY-PrN systems the extent of complexation was too high to allow the use of a direct potentiometric method. Therefore, spectrophotometric titrations at 1:1 metal-to-ligand molar ratios were performed in order to determine the formation constants of the corresponding MHL (L being the fully deprotonated form of a ligand) species. On the other hand, since precipitation started at around pH 4 during the potentiometric titration of the Fe^{3+}/ligand system with a 1:3 metal-to-ligand molar ratio, the formation constants of the bis- and tris-chelated species were obtained from the fitting analysis of the spectrophotometric titration data for a 10-fold ligand excess, but keeping the previously determined log β_{FeHL} value constant. Figure 4 shows the pH dependence of the spectrum during this titration. There is a blue shift of the absorption band with increasing pH, thus indicating a concomitant increase of the coordination number. Along the range of pH 2.5−5, there is one isosbestic point at around $\lambda \approx 510$ nm, which is associated with the interconversion from bis- to tris-chelated complexes. Over the range of pH 5.3−7.7 there is no apparent change in the λ_{max} value, thus indicating the presence of the same chromophoric species. The observed spectral parameters (λ_{max} = 465 nm, ε = 5624 $M^{-1}\cdot cm^{-1}$) are comparable to the reported values for the charge-transfer (CT) bands of ferric tris-chelated complexes with hydroxypyrimidinone analogs (HOPY, HOPR),[9,11] which indicates the existence of a tris-chelated species, although with different protonation extents. Above a pH of about 8 the formation of Fe^{3+} ligand-hydroxide mixed complex species and their precipitation is indicated by the intensity decay and hypsochromic shift of the absorption bands.

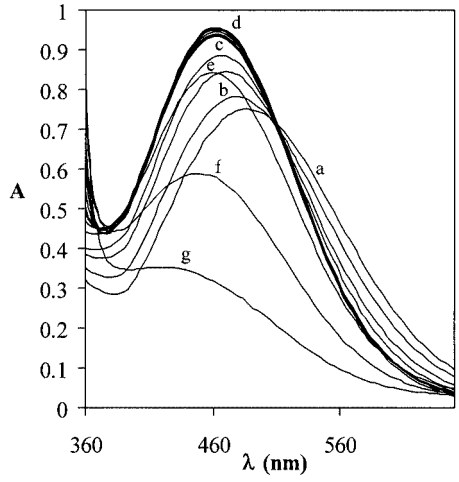

Figure 4. Spectrophotometric absorbance curves at various pH values (a = 2.53, b = 2.78, c = 3.42, d = 5.31−7.72, e = 8.56, f = 9.04, g = 9.31) for the Fe^{3+}/HOPY-PrN system (C_L/C_{Fe} = 10, $C_L = 1.7 \times 10^{-3}$ M)

For the Th^{4+}/HOPY-PrN system the stability constants of the complexes with 1:2, 1:3, and 1:4 metal-to-ligand stoichiometries were evaluated from the potentiometric titration curves for 1:4 and 1:8 metal-to-ligand molar ratios while holding constant the β_{ThHL} value previously determined by spectrophotometry.

The stability constants for the Al^{3+}/HOPY-PrN system were determined by a fitting analysis of the potentiometric data obtained for the 1:1, 1:3, and 1:6 stoichiometries.

A rough comparison between the stability constants of the ligand-metal complexes and the corresponding values for the analogous systems (see Table 1) can be made, assuming that the terminal amine group in the ligand is not

 © 2005 Wiley-VCH Verlag GmbH & Co. KGaA, Weinheim

involved in the coordination and so $\log \beta_{MHL} = \log \beta_{ML} + \log K_1$. Analysis of Table 1 indicates that the stability constants for the ligand-metal complexes follow the order Fe > Th > Al, in accordance with the corresponding log K_{MOH} values reported for the same metal ions (11.8, 10.8, and 9.0 respectively).[25] This feature reflects the ionic nature of this type of complex, with no preponderance of the crystal-field stabilization effect. The speciation at different pH values for the ligand (HOPY-PrN) and the corresponding ligand/metal-ion systems are illustrated in Figure 5. For all the metal/ligand systems studied herein, Figure 5 clearly evidences the strong chelating capacity of HOPY-PrN, with the complexation starting in quite acidic conditions (even at pH ≈ 2, for M = Fe^{3+} and Th^{4+}). The speciation curves for the iron and thorium systems confirm that, at pH 2, MHL is already formed, thus rendering impossible the determination of log β_{MHL} by potentiometry, as stated above.

Analysis of the speciation curves further shows the existence of a stepwise formation of $M(HL)_i$ species whose metal-ligand binding mode can be derived from chemical evidence, namely a protonated ligand molecule with the hydroxypyrimidinone moiety coordinated to the metal ion but the terminal amino groups protonated. For the thorium system there is a minor species present above pH 5 which can be ascribed either to a partially amino-deprotonated tris-chelated species or to a hydroxo-ligand mixed complex such as $[Th(HL)_3(OH)]$. However, those species are indistinguishable by potentiometry and they are just assigned as ThH_2L_3.

Since comparison between the metal-binding affinity of different ligands must take into account their distinct proton concentration dependency, pM values (pM = −log [M] for $C_L/C_M = 10$ and $C_L = 10^{-5}$ M) have been calculated at different pH conditions for HOPY-PrN and its analogs. Plots of pM (M = Fe, Al) versus pH have been calculated and are shown in Figure 6 and 7. It must be mentioned that these pM values were calculated based on the complex stability and ligand-protonation constants calculated herein or reported in the literature (Table 1), as well as the corresponding hydrolytic species used above for the equilibrium models, but neglecting effects of different ionic strengths and temperatures (as in the case of AHA) on the complexation models and assuming that no precipitation takes place.

Analysis of Figure 6 shows that all these *N*-hydroxamide compounds present a steady variation of pFe with pH. Furthermore, among these compounds (excluding 1,2-HOPO which clearly presents the highest pFe value), HOPY-PrN seems to be the most promising chelating agent in the pH range 2−3.9 and above 5. For pH values between 3.9 and 5 HOPR-Me has slightly higher pFe values, probably due to the electron-donation effect of the ring methyl groups. Therefore the inclusion of methyl groups as substituents in the HOPY-PrN ring should also be expected to improve the chelating capacity of the ligand; this will be a challenge for future work.

Figure 7 indicates that although 1,2-HOPO presents higher pAl values than HOPY-PrN in the acid region, under neutral and basic pH conditions both these ligands and AHA possess the same aluminum-complexation strength.

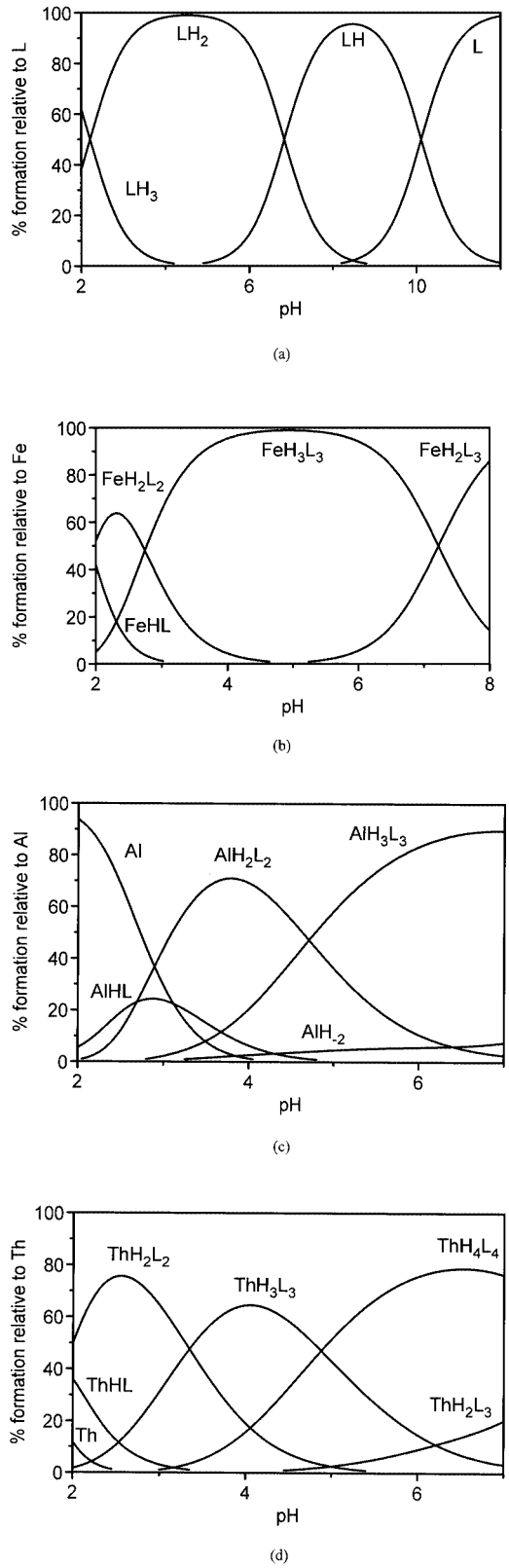

Figure 5. Species-distribution diagrams for HOPY-PrN (a) and M/HOPY-PrN systems with M = Fe^{3+} ($C_L/C_{Fe} = 10$; b); M = Al^{3+} ($C_L/C_{Al} = 3$; c); M = Th^{4+} ($C_L/C_{Th} = 4$; d); $C_L = 2 \times 10^{-3}$ M

 © 2005 Wiley-VCH Verlag GmbH & Co. KGaA, Weinheim

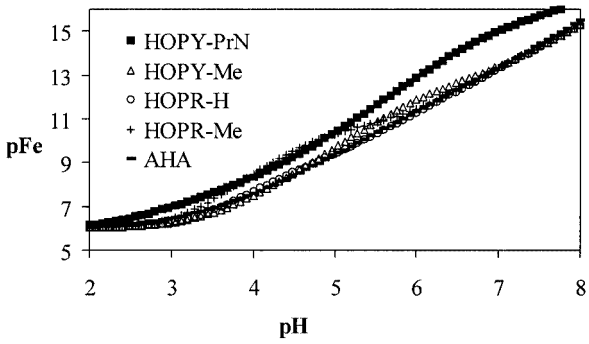

Figure 6. Metal-complexation strength, reported as pFe, versus pH, for HOPY-PrN and some of the hydroxypyrimidinone analogs presented in Table 1; $C_L/C_M = 10$ and $C_L = 10^{-5}$ M

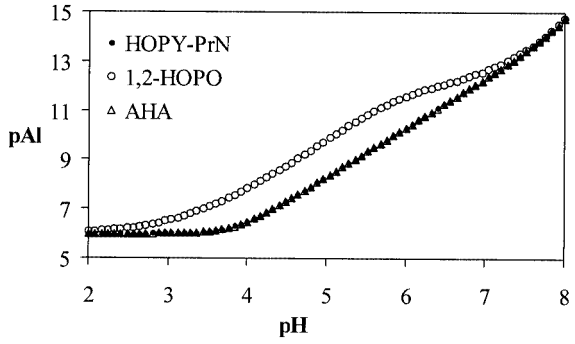

Figure 7. Metal-complexation strength, reported as pAl, versus pH, for HOPY-PrN, 1,2-HOPO, and AHA; $C_L/C_M = 10$ and $C_L = 10^{-5}$ M

Chelating Capacity of (HOPY-PrN)-SEPH

To evaluate the chelating capabilities of (HOPY-PrN)-SEPH towards Fe^{III}, Al^{III}, and Th^{IV}, batch experiments were used. Typically, for Fe^{III}, the functionalized support was added to a universal buffer solution at pH 7 containing Fe^{III}-citrate in fourfold excess relative to the amount of ligand immobilized in the solid matrix, and the mixture was shaken at room temperature for 4 h. During the experiment it could be observed that the solid support gained the characteristic red color of the iron complex almost immediately upon addition of the iron solution. After filtration and careful washing of the functionalized support to remove the excess of metal ions, the Fe^{III} retained on (HOPY-PrN)-SEPH was released by treatment with an acidic solution. The Fe-chelating capacity of the support was calculated from the iron content of the collected filtrates, which was determined by atomic absorption spectrophotometry (AAS). The obtained values (Table 2) indicate that the metal complexes possess an approximate 1:1 ligand-Fe^{III} stoichiometry. Comparison of the ligand density in the modified sepharose with the corresponding chelating capacity indicates that, at neutral pH, (HOPY-PrN)-SEPH is 100% efficient in iron removal, but at pH 3 its chelating efficiency is slightly lower, as expected from the pH dependence of the pM (Figure 6). However, it should be emphasized that the presence of the citrate buffer at pH 3 could be responsible for some underevaluation of the chelating efficacy of these functionalized supports because citrate can also compete with the ligand for the metal ions.

Table 2. Chelating capacity of (HOPY-PrN)-SEPH towards Fe^{III}, Al^{III}, and Th^{IV} at pH 3 and 7

Ligand density (μmol/g dry weight)	pH	Chelating capacity (μmol/g dry weight)		
		Fe^{III}	Al^{III}	Th^{IV}
263 ± 8	3	(16 ± 1) × 10	<70	90 ± 8
263 ± 8	7	(26 ± 1) × 10	(24 ± 2) × 10	(25 ± 2) × 10

The chelating capacities of the functionalized sepharose for Al^{III} and Th^{IV} were also calculated by following the same procedure; the results show that the complexation behavior of the supported hydroxypyrimidinone towards these metal ions is similar to that found for Fe^{III}. Interestingly, the metal chelating capacities at pH 7 follow the same order ($Fe^{III} > Th^{IV} > Al^{III}$) found for the stability constants of the corresponding metal-ligand complexes in aqueous solution (Table 1). So, although comparisons between the solution and the two-phase conditions have to be made with care, the eventual formation of ligand-hydroxo mixed species in the solid phase is only expected at pH values above 8, but without the precipitation problems found in the solution studies, which means that this functionalized resin can be used in the pH range 3−8. The fact that both the ligand and the functionalized resin proved to be very stable under acid conditions is noteworthy. Furthermore, an extra experiment showed that, upon removal of the iron under very acidic conditions, the iron-chelating capacity was kept constant (within the experimental error range) and so there are good perspectives for its reutilization. This feature is very important and it represents an advantage of this chelating support over other ones, such as the linear hydroxamate-based supports, because these groups are easily hydrolysable under such acidic conditions.

Conclusion

Solution studies of a 1-hydroxy-2-(1*H*)-pyrimidinone substituted with an alkylamino group at the C-4 position, HOPY-PrN, by potentiometry and spectrophotometry have shown a strong metal-binding affinity for hard metal-ions, particularly Fe^{III}, Al^{III}, and Th^{IV}, and its ability to compete with other analogous *N*-hydroxamide ligands. This compound was then immobilized in an epoxy-activated sepharose by chemical coupling through the aminoalkyl pendent group. This new hydroxypyrimidinone-functionalized sepharose shows high stability in water over a wide pH range (3−9), a high sequestering capacity for this type of hard metal-ions at mildly basic or even acidic pH conditions, and an ability for reutilization. Therefore, there are good perspectives for its potential use for the removal of traces of toxic hard metal-ions from aqueous media, and thus for environmental purposes.

 © 2005 Wiley-VCH Verlag GmbH & Co. KGaA, Weinheim

Experimental Section

Materials: 6B Epoxy-sepharose was purchased from Amersham Pharmacia Biotech. All reagents were analytically pure. Thin Layer Chromatography (TLC) was performed on silica gel 60 F254 plates with 0.2 mm layer thickness from Macherey−Nagel and the compounds visualized by illumination under UV light at 254 nm. Column chromatography (CC) was carried out with Macherey−Nagel Si gel 60 (230−400 mesh). Whenever necessary, solvents were dried according to standard methods.[26] 1-(Benzyloxy)uracil (**1**) was prepared according to the literature.[11]

The 0.050 M Al^{3+} and Th^{4+} solutions were prepared from the corresponding nitrate salts and were standardized by atomic absorption and inductively coupled plasma emission, respectively. The 1000 ppm $Fe(NO_3)_3$ standard solution was purchased from Merck. The solutions of trivalent metal ions were prepared with an excess of nitric acid to prevent hydrolysis. The exact concentration of HNO_3 in each solution was determined by titration with 0.1 M HNO_3 (Titrisol, 0.1 M HNO_3 ampoules) for values of pH ≥ 2. The titrant was prepared from carbonate-free commercial concentrate (Titrisol, KOH 0.1 M ampoules) and was standardized by titration with a solution of potassium hydrogenphthalate. KOH solutions were discarded whenever the percentage of carbonate, determined by Gran's method,[27] was superior to 0.5% of the total amount of base.

Instrumentation and General Information: FTIR spectra were recorded on a Perkin−Elmer 1725 spectrometer and UV/Vis spectra on a Hitachi 150−20 spectrophotometer. Melting points were determined on a Reichert Thermovar melting-point apparatus and are uncorrected. Fourier transform (FT) NMR spectra were run at ambient temperature on a General Electric QE-300 spectrometer with a resonance frequency of 300.65 for ^1H and 75.6 MHz for ^{13}C, using an appropriate solvent. The chemical shifts are reported in δ (ppm) relative to internal references (TMS for organic solvents or sodium 3-trimethylsilyl-D_4-propionate for aqueous solutions). Coupling constants (J) are expressed in hertz. Electrospray ionization mass spectra (ESI-MS) were determined on a Bruker Esquire 3000 mass spectrometer.

1-(Benzyloxy)-4-(1′,2′,4′-triazol-1′-yl)-2(1*H*)-pyrimidinone (2): 1,3,4 Triazole (0.509 g, 7.28 mmol) was added to a solution of 1-(benzyloxy)uracil (**1**; 0.500 g, 2.46 mmol) in dry pyridine (32 mL) at room temperature. Then, 4-chlorophenyldichlorophosphate (0.50 mL, 3.69 mmol) was added and the reaction mixture stirred for 3 d at room temperature. Water was added to the mixture and the solvents evaporated. A saturated $NaHCO_3$ solution was added to the residue and this aqueous suspension extracted with $CHCl_3$ (5 × 50 mL). The combined organic extracts were dried over anhydrous Na_2SO_4. After evaporation of the solvent, the resulting residue was purified by CC on silica gel using a mixture of ethyl acetate/*n*-hexane (2:1) as eluent to give pure **2** as a yellowish solid (0.443 g; yield 67%), m.p. 202−205 °C (206−209 °C).[11] ESI-MS: m/z = 270 $[M^+ + 1]^+$. FT-IR (KBr): $\tilde{\nu}$ = 1453, 1541, 1616, 1692, 2930, 3099 cm^{-1}. ^1H NMR ($CDCl_3$): δ = 5.38 (s, 2 H, $PhCH_2O$), 6.73 (d, J = 8.5 Hz, 1 H, 5-H), 7.39 (s, 5 H, ArH), 7.50 (d, J = 8.5 Hz, 1 H, 6-H), 8.09 (s, 1 H, 3′-H or 5′-H), 9.22 (s, 1 H, 5′-H or 3′-H) ppm.

4-{3-[(Benzyloxycarbonyl)amino]propylamino}-1-(benzyloxy)-2(1*H*)-pyrimidinone (3): A solution of **2** (0.50 g, 1.86 mmol) and 3-[(benzyloxycarbonyl)amino]propylamine[19] (0.50 g, 2.4 mmol) in dry THF (15 mL) was stirred overnight at reflux temperature, under N_2. The solvent was then evaporated and H_2O added to the residue. The aqueous layer was extracted with $CHCl_3$ (5 × 20 mL) and the combined organic extracts were washed successively with 5% citric acid solution, H_2O, and brine, and dried over anhydrous Na_2SO_4. The solvent was evaporated and the crude product recrystallized from MeOH to afford **3** as a pale-yellow solid (0.60 g; yield 80%), m.p. 154−156 °C. ESI-MS: m/z = 408 $[M + H]^+$, 301 $[M - 107]^+$. ^1H NMR ($CDCl_3$): δ = 1.74 (quin, J = 6.15 Hz, 2 H, $CH_2CH_2CH_2$), 3.28 (q, J = 6.30 Hz, 2 H, $NHCH_2$), 3.53 (q, J = 6.30 Hz, 2 H, CH_2NH), 5.11 (s, 2 H, $PhCH_2O$), 5.22 [s, 2 H, $NHC(O)OCH_2$], 5.91 (m, 1 H, 5-H), 6.89−6.92 (m, 1 H, 6-H), 7.36−7.39 (m, 10 H, 2 ArH) ppm. ^{13}C NMR ($CDCl_3$): δ = 29.2 ($CH_2CH_2CH_2$), 38.0 ($NHCH_2$), 38.1 (CH_2NH), 66.8 [$C(O)OCH_2$], 78.5 (OCH_2), 94.4 (C-5), 128.0, 128.2, 128.6, 128.9, 129.5, 130.3 (ArCH),142.6 (C-6), 154.6 (C-2), 157.7 [C(O)O], 162.8 (C-4) ppm. $C_{22}H_{24}N_4O_4$ (408.45): calcd. C 64.69, H 5.92, N 13.72; found C 64.66, H 5.89, N 13.52.

4-(3-Aminopropylamino)-1-hydroxy-2-(1*H*)-pyrimidinone (HOPY-PrN): A suspension of 10% Pd/C (0.23 g) in dry MeOH (50 mL) was prehydrogenated with H_2 (1 atm) for 30 min. A solution of **3** (0.40 g; 1.06 mmol) in dry MeOH (200 mL) was added to this suspension and the mixture stirred under H_2 (1 atm) for 3 h at room temperature. The catalyst was removed by filtration and the solvent evaporated under reduced pressure. The residue obtained was recrystallized from H_2O/MeOH to afford pure HOPY-PrN (0.185 g; yield 95%), m.p. 216−218 °C. ESI-MS: m/z = 185 $[M + H]^+$, 168 $[M - 16]^+$. FT-IR (KBr): $\tilde{\nu}$ = 2926−3401, 1626, 1524 cm^{-1}. ^1H NMR (D_2O): δ = 1.82 (quin, J = 5.30 Hz, 2 H, $CH_2CH_2CH_2$), 2.93 (t, J = 5.30 Hz, 2 H, CH_2NH_2), 3.31 (t, J = 4.80 Hz, 2 H, $NHCH_2$), 5.64 (dd, J = 7.2, 1.9 Hz, 1 H, 5-H), 7.48 (dd, J = 7.2, 1.9 Hz, 1 H, 6-H) ppm. ^{13}C NMR (D_2O): δ = 29.6 ($CH_2CH_2CH_2$), 39.2 (CH_2NH_2), 39.4 ($NHCH_2$), 95.1 (C-5), 147.2 (C-6), 160.1 (C-2), 163.4 (C-4) ppm. $C_7H_{12}N_4O_2$ (184.20): calcd. C 45.64, H 6.57, N 30.42; found C 45.52, H 6.66, N 30.20.

General Procedure for the Preparation of (HOPY-PrN)-SEPH: Epoxy-activated sepharose 6B freeze-dried powder (500 mg) was washed with distilled H_2O (100 mL) in a sintered glass filter and then suspended in coupling buffer (10 mL of universal buffer, pH 9).[28] HOPY-PrN (500 mg) was dissolved in coupling buffer and added to the matrix suspension. The coupling mixture was adjusted to pH 9 and then shaken in a shaker water bath at 40 °C for 48 h. After that time, the mixture was filtered and the excess ligand was washed away with coupling buffer, distilled H_2O, or, alternatively, with 0.1 M $NaHCO_3$ containing 0.5 M NaCl (pH 8) and 0.1 M acetate buffer containing 0.1 M NaCl, (pH 4) at least three times. The functionalized gel obtained was freeze-dried and stored at 0−4 °C.

Stability Studies of (HOPY-PrN)-SEPH: Freeze-dried (HOPY-PrN)-SEPH (15 mg) was placed in distilled water at pH 3, 7, and 9 and the suspensions shaken at room temperature for 24 h. Aliquots (3 mL) were taken several times, diluted with water, and the absorbance of the resulting solutions measured at λ = 318 nm. Plots of percentage of ligand released from the solid support vs. time were obtained from the values of ligand concentration in solution for each aliquot calculated from a calibration curve.

^1H NMR Titration of HOPY-PrN: ^1H NMR spectra were recorded with a Varian Unity 300 spectrometer at probe temperature. Solutions of HOPY-PrN (approx. 0.02 M) were prepared in D_2O using DSS as internal reference. The pD was adjusted by addition of DCl or CO_2-free KOD, using a Crison 2001 instrument fitted with a combined Mettler Toledo U402-M3 S7/200 microelectrode. This microelectrode was previously calibrated with standard buffered aqueous solutions; $-\log[D^+]$ was measured in the NMR tubes. The final values of pD were determined from the equation pD = pD*

 © 2005 Wiley-VCH Verlag GmbH & Co. KGaA, Weinheim

+ 0.40,[29] in which pD* corresponds to the reading of the pH meter previously calibrated with aqueous buffers at pH 4 and 7.

Potentiometric Measurements: The equipment used has been described before.[30] All the potentiometric measurements were carried out under thermostatted conditions ($T = 25.0 \pm 0.1$ °C) at an ionic strength, I, of 0.10 M (KNO_3); the experiments were monitored by computer. Atmospheric CO_2 was excluded from the cell during the titration by passing purified N_2 across the top of the experimental solution in the reaction cell. The potentiometric measurements were performed at ligand concentrations of 2.0×10^{-3} M, first in the absence of metal ions and then in the presence of each metal ion with corresponding C_M/C_L ratios (1:3 for Fe^{3+}; 1:3 and 1:6 for Al^{3+}; 1:4 and 1:8 for Th^{4+}). The $[H^+]$ of the solutions was determined by measuring the electromotive force of the cell, as described previously;[31] the determined value of K_w used in the computations was $10^{-13.80}$.
At the beginning of the titrations of the ligand with Fe^{3+} and Th^{4+}, the extent of formation of the metal complexes was too high to allow the use of the direct potentiometric method, therefore spectrophotometric titrations were performed.

UV Spectrophotometric Measurements: Electronic spectra were recorded with a Perkin−Elmer model Lambda 9 spectrophotometer, using aqueous solutions of the complexes, in 1 cm path-length cells. The temperature of the solutions was kept at 25.0 ± 0.1 °C, using a Grant W6 thermostat, and $I = 0.10$ M (KNO_3). The spectra were recorded in the range 250−350 or 350−650 nm for the Th^{4+} and the Fe^{3+} systems, respectively. The solution of the Fe^{3+} complex (1:10 stoichiometry) was prepared as indicated for potentiometric measurements. For the 1:1 Fe^{3+}/ligand and Th^{4+}/ligand systems, the measurements were made for $0.8 \leq pH \leq 2$ and the amount of acid to be added (from standard solutions of 0.097 or 1 M HNO_3) was calculated for the total volume solution under study.

Calculation of Equilibrium Constants: Ligand protonation constants, $K_i = [H_iL]/[H_{i-1}L][H]$, were calculated by fitting the potentiometric data obtained for the free ligand using the program HYPERQUAD version 2.1.[32] Stability constants of the metal-ion complexes formed in solution were determined from the experimental data corresponding to the titration of solutions with different ligand and metal-ion ratios, also with the aid of the same program. Whenever a high extent of formation of the metal complexes at the beginning of the titration was present, the PSEQUAD program[33] was used to treat the spectrophotometric data. The results were obtained in the form of overall stability constants or $\beta_{M_mH_hL_l} = [M_mH_hL_l]/[M]^m[H]^h[L]^l$. In the analysis of the potentiometric as well as the spectrophotometric data, the hydrolytic species[31,34−36] of the respective metal ions were considered. Species-distribution curves were plotted with the HYSS program.[32] The errors quoted are the standard deviations of the overall stability constants given directly by the program. In the case of K_i, the standard deviations were determined by the normal propagation rules and do not represent the total experimental errors.

Determination of the Chelating Capacity of (HOPY-PrN)-SEPH: To evaluate the Fe^{III} chelation, (HOPY-PrN)-SEPH freeze-dried gel (50 mg) was placed in a buffer solution at pH 7 containing 90 ppm Fe^{III} citrate, and the suspension was shaken at room temperature for 4 h. The gel was filtered, washed with deionized water, and HNO_3 was added to the filtrate solution. Then, the gel was washed with an acidic solution of HNO_3 to release the complexed Fe^{III}. The Fe^{III} chelating capacity of the gel was calculated from the difference in the iron content of the filtrate solutions determined by AAS. To determine the Al^{III} chelation, a procedure identical to that described above was followed but with Al^{III} citrate[37] instead of Fe^{III} citrate. As for the evaluation of the Th^{IV} chelation, the same technique used for the Fe^{III} system was applied, but the Th^{IV} citrate was generated by preparing an aqueous solution containing equimolar amounts of Th^{IV} nitrate and citric acid (1.72×10^{-3} M).

Acknowledgments

The authors thank the Portuguese Foundation for Science and Technology (FCT) and FEDER for financial support (POCTI/38094/QUI/2001). We also thank Eng. Ascensão Trancoso and Eng. Alexandra Viana for running the AAS measurements, Eng. Fátima Pedrosa for the ICP analysis, and Dr. Mafalda Costa (INETI) for measuring the mass spectra.

[1] A. E. V. Gorden, J. Xu, K. N. Raymond, *Chem. Rev.* **2003**, *103*, 4207−4282.
[2] M. Feng, L. Van der Does, A. Bantjes, *J. Biomater. Sci., Polymer Ed.* **1992**, *4*, 145−154.
[3] H. Kumagai, Y. Inoue, T. Yokohama, T. Suzuki, *Anal. Chem.* **1998**, *70*, 4070−4073.
[4] *Affinity Chromatography: a Practical Approach* (Eds.: P. D. G. Dean, W. S. Johnson, F. A. Middle), IRL Press, London, **1985**.
[5] S. Bourg, J.-C. Broudic, O. Conocar, J. J. E. Moreau, D. Meyer, M. W. C. Man, *Chem. Mater.* **2001**, *13*, 491−499.
[6] C. Hershko, A. M. Konijn, G. Link, *Br. J. Haematol.* **1998**, *101*, 399−406.
[7] N. Ramadan, J. Porath, *J. Chromatograph.* **1985**, *321*, 81−91.
[8] R. C. Scarrow, P. E. Riley, K. Abu-Dari, D. L. White, K. N. Raymond, *Inorg. Chem.* **1985**, *24*, 954−967.
[9] J. Okhanda, T. Tokumitsu, K. Mitsuhashi, A. Katoh, *Bull. Chem. Soc. Jpn.* **1993**, *66*, 841−847.
[10] T. Masuda, J. Hayashi, S. Tamagaki, *J. Chem. Soc., Perkin Trans. 2* **2000**, 161−167.
[11] J. Ohkanda, J. Kamitani, T. Tokumitsu, Y. Hida, T. Konakahara, A. Katoh, *J. Org. Chem.* **1997**, *62*, 3618−3624.
[12] J. Xu, E. Radkov, M. Ziegler, K. N. Raymond, *Inorg. Chem.* **2000**, *39*, 4156−4164.
[13] *Sequestering Agents for the Removal of Actinides from Waste Streams.* K. N. Raymond, http://www.ornl.gov/divisions/ctd/ESP.
[14] G. Zvilichovsky, *Tetrahedron* **1967**, *23*, 353−357.
[15] A. Katoh, Y. Hida, J. Kamitani, J. Okhanda, *J. Chem. Soc., Dalton Trans.* **1998**, 3859−3864.
[16] M. A. Santos, R. Grazina, A. Q. Neto, G. Cantinho, L. Gano, L. Patrício, *J. Inorg. Biochem.* **2000**, *78*, 303−311.
[17] S. M. Cohen, B. O'Sullivan, K. N. Raymond, *Inorg. Chem.* **2000**, *39*, 4339−4346.
[18] W. L. Sung, *J. Chem. Soc., Chem. Commun.* **1981**, 1089.
[19] S. A. Boyd, A. K. L. Fung, W. R. Baker, R. A. Mantei, H. H. Stein, J. Cohen, J. L. Barlow, V. Klinghofer, J. L. Wessale, K. M. Verburg, J. S. Polakowski, A. L. Adler, S. V. Calzadilla, P. Kovar, Z. Yao, C. W. Hutchins, J. F. Denissen, B. A. Grabowski, S. Cepa, D. J. Hoffman, K. W. Garren, H. D. Kleinert, *J. Med. Chem.* **1994**, *37*, 2991−3007.
[20] A*ffinity Chromatography, Principles and Methods*, Amersham Pharmacia Biotech, **2001**.
[21] Y. Y. Lin, A. E. Martell, *Inorg. Chim. Acta* **1993**, *214*, 103−111.
[22] R. M. Smith, A. E. Martell, *Critical Stability Constants, Vol. 3*, Plenum Press, New York, **1977**, pp. 301.
[23] R. M. Smith, A. E. Martell, *Critical Stability Constants, Vol. 2*, Plenum Press, New York, **1976**, pp. 3.
[24] R. M. Smith, A. E. Martell, *Critical Stability Constants, Vol. 2*, Plenum Press, New York, **1976**, pp. 51.
[25] R. M. Smith, A. E. Martell, *Critical Stability Constants, Vol. 4*, Plenum Press, New York, **1976**, pp. 4−11.
[26] D. D. Perrin, W. L. F. Almarrego, *Purification of Laboratory Chemicals*, 3rd ed., Pergamon, Oxford, **1988**.

 © 2005 Wiley-VCH Verlag GmbH & Co. KGaA, Weinheim

[27] F. J. C. Rossotti, H. Rossotti, *J. Chem. Educ.* **1965**, *42*, 375−378.
[28] J. Lurie, *Handbook of Analytical Chemistry*, MIR Publishers, Moscow, **1975**, 263.
[29] A. K. Covington, M. Paabo, R. A. Robinson, R. G. Bates, *Anal. Chem.* **1968**, *40*, 700−706.
[30] S. Chaves, M. Gil, S. Marques, L. Gano, M. A. Santos, *J. Inorg. Biochem.* **2003**, *97*, 161−172.
[31] M. A. Santos, M. Gil, S. Marques, L. Gano, G. Cantinho, S. Chaves, *J. Inorg. Biochem.* **2002**, *92*, 43−54.
[32] P. Gans, A. Sabatini, A. Vacca, *Talanta* **1996**, *43*, 1739−1753.
[33] L. Zékány, I. Nagypál, G. Peintler, PSEQUAD 501, **2001**.
[34] L. O. Öhman, W. Forschling, *Acta Chem. Scand., Ser. A* **1981**, *35*, 795−802.
[35] C. F. Baes, R. E. Mesmer, *The Hydrolysis of Cations*, John Wiley & Sons, New York, **1976**.
[36] R. M. Smith, A. E. Martell, *Critical Stability Constants, Vol. 4*, Plenum Press, New York, **1976**, pp. 4.
[37] T. L. Feng, P. L. Gurian, M. D. Healy, A. R. Barron, *Inorg. Chem.* **1990**, *29*, 408−411.

Received April 30, 2004
Early View Article
Published Online December 6, 2004

 © 2005 Wiley-VCH Verlag GmbH & Co. KGaA, Weinheim

Solid-State Structure, Quantum Calculations and Spectroscopic Characterization of the Hydrogen-Bonded Complex $[Os(bpy)_2(CO)(EtO\cdots H\text{-}DMAP)][PF_6]_2$

Claudio Garino,[a] Roberto Gobetto,*[a] Carlo Nervi,[a] Luca Salassa,[a] Gianluca Croce,[b] Marco Milanesio,[b] Edward Rosenberg,[c] and J. B. Alexander Ross[c]

Keywords: Density functional calculations / Hydrogen bonds / N ligands / NMR spectroscopy / Osmium

The new H-bonded complex $[Os(bpy)_2(CO)(EtO\cdots H\text{-}DMAP)][PF_6]_2$, where DMAP = 4-(dimethylamino)pyridine and bpy = 2,2′-bipyridine, has been synthesized and characterized by X-ray diffraction, IR, solution and solid-state NMR spectroscopy. The complex shows a strong hydrogen bond between the protonated DMAP moiety and the deprotonated ethanolic group directly bonded to the Os atom. High-speed (28 KHz) solid-state ^1H MAS NMR spectroscopy and quantum-mechanical calculations were used to assess the location of the hydrogen atom involved in the H-bond. Both confirmed a proton characteristic of an N–H···O–Y hydrogen bond. A molecular orbital analysis was performed to elucidate the IR CO stretching frequency red shift of the H-bonded complex with respect to $[Os(bpy)_2(CO)O(H)Et][OTf]_2$. Absorption spectra indicate that the H-bond is present both in water and dichloromethane solutions. However, no direct evidence of the H-bond interaction in solution is observed from the ^1H NMR spectrum (CD_2Cl_2) between 298 and 193 K.

(© Wiley-VCH Verlag GmbH & Co. KGaA, 69451 Weinheim, Germany, 2005)

Introduction

The complex $[Os(bpy)_2(CO)(OTf)][OTf]$, where OTf = $CF_3SO_3^-$, was first synthesized in the 1980s as a potential reactive intermediate for the chemically mild synthesis of a new series of metal-ligand complexes with strong ligand-field donor ligands. Many nitrile and isocyanide derivatives were produced and their excited-state properties explored.[1,2]

Following our earlier studies devoted to the synthesis of new $[Os(bpy)_2(CO)L]^{n+}$ complexes with interesting and potentially useful fluorescence properties,[3] we investigated the substitution of OTf[4−7] with alcohols. Many structures of $Ru(bpy)_2$ derivatives (bpy = 2,2′-bipyridine) have been reported in the literature, but few $Os(bpy)_2$ structures can be found in the Cambridge Structural Database (CSD),[8] as summarized in our recent paper.[9]

In an attempt to extend the reactivity of the $[Os(bpy)_2(CO)(OTf)][OTf]$ complex, we found that DMAP[10−14] [4-(dimethylamino)pyridine] has an active role in its reaction with alcohols. We have characterized the resulting $[Os(bpy)_2(CO)(EtO\cdots H\text{-}DMAP)][PF_6]_2$ (**1[PF$_6$]$_2$**) complex by X-ray crystallography and solid-state ^1H NMR and solution spectroscopic techniques. We have also examined the solution properties of the triflate analog **1[OTf]$_2$**. The main feature of these complexes is the presence of a strong N−H···O hydrogen bond between a protonated dimethylaminopyridine moiety ($H\text{-}DMAP^+$) and an alkoxide group directly bonded to the Os atom.

It is significant that the heteronuclear N−H···O bond plays a central role not only in protein folding and DNA base-pairing, but also in the ever-growing areas of molecular recognition and crystal-engineering research.[15−20] Important reviews in recent decades have highlighted the field of strong H-bonds,[21−24] and the electrostatic versus covalent nature of the H-bond has been extensively debated and investigated.[22,25−30] A new model, the Electrostatic-Covalent H-Bond Model (ECHBM),[31−33] has been developed to rationalize the electrostatic nature of weak homonuclear O−H···O H-bonds and the covalent nature of strong ones. The ECHBM has been applied to heteronuclear cases with good results, although additional aspects require further investigation.[34]

Recent studies of *intramolecular* X−N−H···O−Y hydrogen bonds[35,36] in ketohydrazone-azoenol systems demonstrated the presence of very strong H-bonds. The H-bond is stronger if the two resonance forms X−N−H···O−Y and

[a] Dipartimento di Chimica I. F. M.,
Via P. Giuria 7, 10125 Torino, Italy
Fax: + 39-011-670-7855
E-mail: roberto.gobetto@unito.it
[b] Dipartimento di Scienze e Tecnologie Avanzate, Università del Piemonte Orientale "A. Avogadro",
Corso T. Borsalino 54, 15100 Alessandria, Italy
[c] Department of Chemistry, University of Montana,
Missoula, Montana 59812, USA

 © 2005 Wiley-VCH Verlag GmbH & Co. KGaA, Weinheim DOI: 10.1002/ejic.200400631

X−N···H−O−Y have similar energy, a condition that occurs when the intrinsic proton affinity (PA) of the N atom is reduced.[34] Thus, a weak hydrogen bond can be strengthened by introducing chemical substituents that reduce the PA difference between the H-bond donor and acceptor atoms and cause the resonance forms to become isoenergetic. This observation helps to explain the behavior of the homonuclear H-bond.

There are three classes of strong intramolecular H-bonds: (i) (−)CAHB, a negative-charge-assisted H-bond; (ii) (+)CAHB, a positive-charge-assisted H-bond; and (iii) RAHB, a resonance-assisted H-bond. These classifications can be extended to *intermolecular* interactions as well, as demonstrated by an extensive analysis of *intermolecular* N−H···O/N···H−O bonds[34] using the Cambridge Crystallographic Database (CSD).[8] In most examples of intermolecular H-bonds, the H-bond results from an acid-base equilibrium, usually referred to as "a salt bridge" in the biochemical literature.[24] For example, Jerzykiewicz et al. have reported an intriguing case of a strong *intermolecular* N−H···O/N···H−O bond in the complex between 3,5-dimethylpyridine and 3,5-dinitrobenzoic acid (DMP-DNB) that is characterized by an almost linear N−H···O angle (177°) and a nitrogen−oxygen distance of about 2.550 Å.[37]

In this paper we report the study of the heteronuclear H-bond of $[Os(bpy)_2(CO)(EtO\cdots H\text{-}DMAP)]^{2+}$ using several complementary physical techniques in combination with quantum-mechanical calculations. Furthermore, we describe how theoretical computation can play a critical role in developing an understanding of the structural properties of the complex and in rationalization of the spectroscopy data.

The goal is to identify where the observed strong hydrogen bond fits into the currently available hydrogen bonding models and to understand how the d-orbital energies and electron distributions are impacted by this bond relative to previously reported $Os(bpy)_2(CO)(L)$ systems.

Results and Discussion

Crystal Structure of $[Os(bpy)_2(CO)(EtO\cdots H\text{-}DMAP)][PF_6]_2$

The dissolution of $[Os(bpy)_2(CO)(OTf)][OTf]$[38] in ethanol in the presence of a tenfold excess of DMAP gave a dark-red solution that slowly changed to violet. The crystalline product **1[PF$_6$]$_2$**, which was obtained after purification and careful recrystallization, was analyzed by single-crystal X-ray diffraction (see Exp. Sect.).

The structure determined for the complex is illustrated in Figure 1 and the crystallographic data are given in the Exp. Sect. The most interesting feature of **1[PF$_6$]$_2$** is the strong N−H···O hydrogen bond (dotted line in Figure 1) between the H-DMAP$^+$ moiety and a deprotonated ethanol molecule directly bonded to the Os atom.

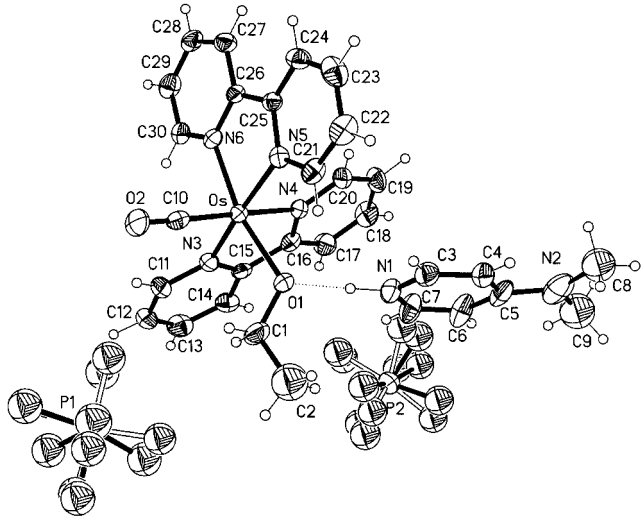

Figure 1. Molecular structure of $[Os(bpy)_2(CO)(EtO\cdots H\text{-}DMAP)][PF_6]_2$ showing the adopted labeling scheme, with displacement ellipsoids drawn at the 25% probability; the PF_6^- moiety is disordered with black and white bonds indicating the two possible positions

The strength of the N−H···O interaction is implied by the geometric features of the hydrogen bond, as summarized in Table 1. The H-bond is close to linear [N−H···O angle is approximately 175(1)° both from X-ray data and theoretical calculations, see below] and the donor−acceptor distance is short [2.614(9) Å] and close to the values observed in two-center hydrogen bonds[35,37] in which the hydrogen is approximately midway between the two electronegative atoms (O1 and N1 in Figure 1). It is worth noting that the O atom of the ethanol ligand is tightly bonded to the Os atom while the methyl group is rather mobile, as indicated by their anisotropic displacement parameters

Table 1. Geometric features of the strong N−H···O hydrogen bond in the crystal structure of $[Os(bpy)_2(CO)(EtO\cdots H\text{-}DMAP)][PF_6]_2$ and from theoretical calculations at the B3LYP/BS3//B3LYP/BS3 level of theory, with LACVP ECP on the Os atom

	X-ray data	Theoretical calculations			
		H-OPT[a]	**1a** (alkoxide form)	**1b** (alcohol form)	EtOH−DMAP
N···O [Å]	2.614(9)	2.614	2.635	2.599	2.890
N−H [Å]	0.99(2)[b]	1.102	1.085	1.539	1.911
H−O [Å]	1.62(2)[b]	1.514	1.550	1.060	0.979
Os···O [Å]	2.083(6)	2.083	2.128	2.178	−
N···H···O [°]	174.7(9)[b]	177.1	176.9	177.1	177.6

[a] Geometry optimization with non-H atoms fixed to the X-ray structure. [b] Hydrogen position refined as discussed in the text.

 © 2005 Wiley-VCH Verlag GmbH & Co. KGaA, Weinheim

(ADP) (depicted at 25% of probability in Figure 1). Atom O1 shows a small averaged ADP [0.058(2) Å^2], while the very mobile C2 atom has a significantly larger ADP value [0.152(7) Å^2] and C1 has intermediate mobility, its ADP value being 0.087(4) Å^2. Similarly, in the case of the H-DMAP$^+$ moiety the atoms of the molecule showing smaller ADPs are those closest to the N−H bond and those directly bound to the Os complex through the N−H···O hydrogen bond. This is illustrated by the monotonic increase in the ADPs going from N1 to C8 [ADP = 0.066(2), 0.070(3), 0.077(3), 0.085(4), 0.114(4), 0.130(6) for atoms N1, C3, C4, C5, N2, and C8, respectively].

The crystal packing of the osmium complex is driven by various intermolecular interactions. First, the positively charged Os complex and the H-DMAP$^+$ moiety are bound together by the previously described strong N−H···O hydrogen bond. Next, the negative PF_6^- anions are bound to the positive Os-containing moiety and to the H-DMAP$^+$ by ionic forces. Finally, weak interactions are present between the C−H groups belonging to the bpy groups and to the H-DMAP$^+$ moiety and those of the hydrogen-bond acceptors [CO bonded to Os and F belonging to PF_6^- anions; H···F and H···O contacts ranging from 2.42(1) to 2.91(1) Å]. As already observed in other PF_6^--containing crystal structures,[9] each PF_6^- moiety is disordered over two positions (black and white bonds in Figure 1 for the major and the minor components, respectively).

Defining the location of the H1 position was not straightforward and different strategies for the X-ray data refinement were carefully checked. As discussed below, an Os−O distance of 2.083(6) Å is consistent with both the alcohol and the alkoxide form. Nevertheless, in the Fourier difference map, after location of all the non-hydrogen atoms and of all the H-atoms (whose locations were calculated using the program XP as implemented in SHELX-TL)[39] except H1, a well-defined peak was observed at about 1.0 Å from N1. With unconstrained refinement, the H1-atom coordinates retain a position consistent with the alkoxide form. Moreover, if in the initial model an H-atom is bonded to O1 to obtain an N···H−O alcohol form, refinement moves the H atom towards N1, into the position expected for formation of an N−H···O alkoxide. We are aware, however, that it is difficult to determine the precise location of an H-atom only on the basis of X-ray data, particularly considering that $wR2 = 0.12$ for the refined structure of **1[PF$_6$]$_2$**. Therefore, to compare the stability of the two different forms (**1a** and **1b**) depicted in Scheme 1, and to give a more general overview of the literature on such inorganic systems, we carried out theoretical calculations and also performed an extensive search in the Cambridge Structural Database (CSD).[8] This search of the two alkoxide-containing fragments **3** and **4** depicted in Scheme 2, where the oxygen atom can be protonated or deprotonated, returned 51 structures. The alcohol-alkoxide geometric features were indirectly analyzed by monitoring the Os−O distance in these structures, thus avoiding a comprehensive study of distances and angles involving H-atoms whose exact location cannot be defined from X-ray analysis. The Os−O bond lengths are obviously dependent on the presence of the ancillary ligands. Nevertheless, distances shorter than 2.00 Å are generally consistent with the alkoxide form, as reported, for example, by Richter-Addo et al.,[40] where the Os−O distance is 1.89(2) Å in (octaethylporphyrinato)Os(NO)(OEt). Conversely, Os−O distances larger than 2.20 Å are always attributed to the alcohol form as, for example, in the [*N*,*N*′-bis(salicylidene)-*o*-phenylenediamine](methanol)(nitrido)-osmium(VI) perchlorate complex reported by Tsz-Wing et al.,[41] where the Os−O distance is 2.265 Å. Os−O distances in the range 2.00−2.20 Å have been attributed to either form. For example, in the tetraphenylarsonium pentachloroosmium ethanol solvate, [AsPh$_4$][OsCl$_5$EtOH]·EtOH, reported by Lang et al.,[42] the acceptor is a second ethanol molecule where the located hydrogen is clearly much closer to the EtOH in the first coordination sphere. Thus, the alkoxide form can be excluded, even if the Os−O distance (2.078 Å) is short. Also, several alkoxide-like complexes that have the alkoxy group in a bridged coordination show Os−O distances around 2.10 Å, as reported, for example, in the nonacarbonyl(μ-σ-η-dimethylamino-1-methoxy-1-

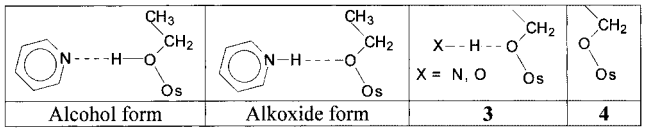

Scheme 2

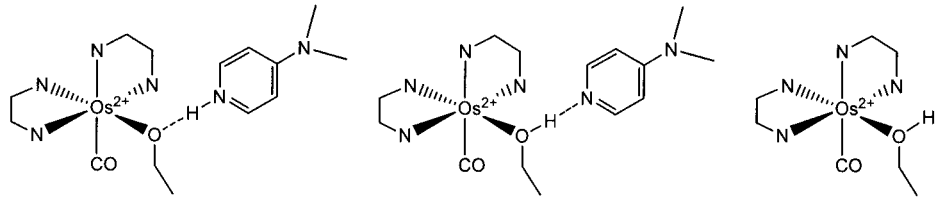

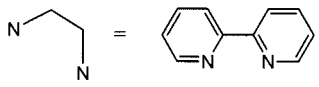

Scheme 1

oxobut-2-ene-2,4-diyl)(μ-methoxo)triosmium dichloromethane solvate complex by Adams et al.[43] Finally, the Os−O distance can be substantially larger {up to 2.40 Å as in the [diethylsilylene(tetrahydrofuran-*O*)](tetrahydrofuran)[*meso*-(tetra-*p*-tolyl)porphyrin]osmium tetrahydrofuran solvate complex reported by Woo et al.}[44] when the ligand is bound to the Os atom in the alcoholic form.

Theoretical Calculations of the Hydrogen-Bond Geometry

Because the observed Os−O distance in our crystal structure (2.078 Å) is consistent with the two possible forms (alcohol and alkoxide) depicted in Scheme 2, theoretical calculations were carried out to better understand this situation in **1[PF$_6$]$_2$**. However, the quantum treatment of a charged H-bonded complex containing a third-row transition metal is not straightforward. Consequently, several different strategies were adopted for evaluation of the electron correlation effects and the basis-set superposition error (BSSE).[45] The geometric optimization was carried out first at the Hartree−Fock (HF) level of theory, employing the BS1 basis set and then employing the density functional method, with the B3LYP and B3PW91 schemes and different basis sets (see Table 2). Finally, a single-point calculation was carried out employing the post-SCF local MP2 correction (L-MP2 in Table 2), as implemented in the Jaguar software, using the BS3 basis set, on the geometry optimized at the HF/BS1 level. At this level of calculation, the electron-correlation effects can be treated correctly at a fraction of the computational time of a "normal" MP2 calculation, and the BSSE should be of limited importance. The energy values reported in Table 2 indicate that the Hartree−Fock method is inadequate for estimating the energy difference between the alcohol and the alkoxide forms (unique negative ΔE in Table 2). On the other hand, the DFT methods give results in keeping with the L-MP2 value, which suggests a slight energetic preference for the alkoxide form.

In compound **1**, the geometric features and the small energy difference between the two forms indicate that the N−H···O interaction is a rather strong, almost linear, resonance-assisted hydrogen bond. Nevertheless, it cannot be considered a three-center hydrogen bond because the O···N distance is too long [2.614(9) Å, which is longer compared, for example, to the 2.550(2) Å of the DMP-DNB complex reported by Jerzykiewicz et al.].[37] Indeed, the N−H···O hydrogen bond is sufficiently strong to be stable in solution, as indicated by spectroscopic measurements (see below).

Table 2. Energy (ΔE) of the alcohol form (N···H−O hydrogen bond present), with respect to the alkoxide one (N−H···O hydrogen bond present); the LACVP ECP was employed for the Os atom in all calculations, while different basis sets (see computational details) were adopted; ΔE is calculated taking the energy of the alkoxide form as reference

Level of the calculation	ΔE [kJ/mol]
HF/BS1//HF/BS1	−21.2
HF/BS1//L-MP2/BS3	3.8
B3LYP/BS1	4.7
B3LYP/BS3	2.9
B3PW91/BS1	4.7
B3PW91/BS2	6.3
B3PW91/BS3	10.0

The case of the EtO−H···DMAP couple was also considered at the B3LYP/BS3 level of calculation. We attempted to optimize the geometry of the complex $EtO^-\cdots H\text{-}DMAP^+$, but the proton moved toward the alcoholic oxygen. The uncomplexed DMAP−EtOH complex has a nitrogen−oxygen distance that is longer than in models **1a** and **1b** (Scheme 1) due to withdrawal of electron density from the oxygen by the metal center. The acid-base equilibrium between a nitrogen base and an organic or inorganic acid can be described in terms of a positive/negative-charge-assisted H-bond, (±)CAHB; the approximate proton position can be estimated from the pK_a values (or the PA). The pK_a values for ethanol and $H\text{-}DMAP^+$ in water are about 16 and 9.2, respectively. This difference accounts for the large d(N−O) in the EtO−H···DMAP couple and for the failure of all attempts to optimize the geometry of the hypothetical $EtO^-\cdots H\text{-}DMAP^+$ complex, thus confirming that when the ethanol is not bonded to an organometallic moiety, a stable alkoxide structure is not formed. The ethanol bonded to the osmium should possess a lower pK_a value, and consequently the ΔPA moves toward zero, shortening the N−O distance.

Spectroscopic Measurements

In order to corroborate the conclusions drawn from the solid-state structure determination and the theoretical calculations we made a detailed investigation of the spectroscopic properties of **1[OTf]$_2$** and $[Os(bpy)_2(CO)(EtOH)(OTf)_2]$ (**2[OTf]$_2$**). Solid-state ^{1}H NMR spectroscopy offers an alternative method for detecting the presence of an H-bond when dynamic behavior or the presence of trace moisture can mask its presence in solution. The main constraint of this approach with organic solids, however, is the presence of strong dipole-dipole interactions that cause line broadening of up to some tens of kilohertz. This homonuclear dipolar interaction is only partly averaged by the rotation of the solid sample at the spinning speeds routinely used in magic angle spinning (MAS) experiments. Nevertheless, relatively high resolution can be achieved in many cases at high magnetic fields by rotating the sample at very high spinning speeds (28−30 KHz). The solid-state ^{1}H NMR spectrum of **1[OTf]$_2$**, recorded under these experimental conditions, is shown in Figure 2.[46−48] The peaks at δ = 0.6 and 2.8 ppm are readily assigned to the CH_3 and CH_2 groups of the ethanol ligand, respectively, whereas the resonance at δ = 2.3 ppm is assigned to the methyl groups of DMAP (small differences between solution and solid-state proton chemical shifts are accepted due to the bulk magnetic susceptivity and crystal-packing effects).[46−48] The spectrum is dominated by the strong signal centered at δ = 7.4 ppm, which is attributed to the large array of aromatic protons. At chemical shifts greater than δ =

 © 2005 Wiley-VCH Verlag GmbH & Co. KGaA, Weinheim

11.0 ppm, a broad resonance is evident as a shoulder of the aromatic peaks. This resonance does not have any counterparts in the solution spectrum, and it is in the region expected for an N−H···O proton involved in an alkoxide hydrogen bond. Indeed, the proportion of aromatic, aliphatic, and hydrogen-bond protons, as determined by integration of the peaks, well agrees with the proposed assignment. A magnetic shielding calculation using the GIAO method gave a value of δ = 13.17 ppm, which also confirms the proposed assignment.

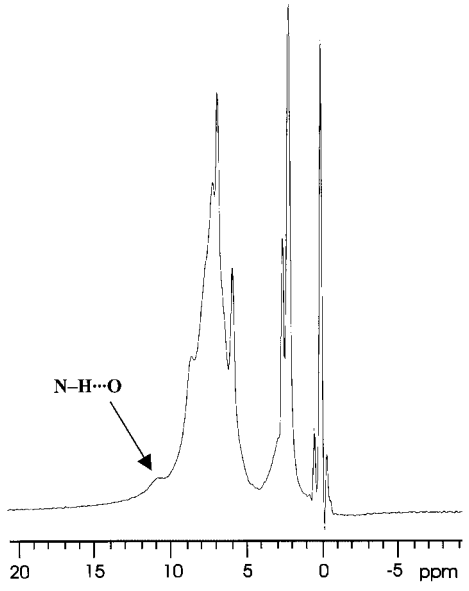

Figure 2. ^{1}H MAS NMR spectrum of **1** measured at 499.7 MHz, 64 transients, pulse delay 10 s, rotational speed 28 kHz

Evidence of formation of the H-bonded complex in solution is inferred from the initial rapid change in the color of the solutions of **2[OTf]$_2$** during the addition of DMAP. A comparison of the color of **1[OTf]$_2$** and **2[OTf]$_2$**, either in the reaction solvent (ethanol) or in CH_2Cl_2, confirms that an interaction between the osmium moiety and DMAP persists in solution. Prior to addition of DMAP to carefully dried dichloromethane solutions of **2[OTf]$_2$** a broad peak is detected at δ = 2.17 ppm in the ^{1}H NMR spectrum; this indicates the presence of coordinated ethanol as opposed to an alkoxide complex for this species. On addition of DMAP this resonance disappears and the characteristic color change to violet is observed. Although direct observation of the H-bond was not possible using solution NMR techniques in the range of temperature we investigated (298−193 K), these spectra contain the following features that suggest the interaction is maintained in CD_2Cl_2: (i) the two diastereotopic CH_2 protons of the coordinated ethanol are well separated both in **1[OTf]$_2$** and in **2[OTf]$_2$** (Figure 3); (ii) although the signal pattern is practically equivalent, the coupling constants are different (**1[OTf]$_2$**, ^2J = 10.55, ^3J = 6.42, ^3J = 6.86 Hz; **2[OTf]$_2$** ^2J = 10.88, ^3J = 7.10, ^3J = 7.09 Hz); (iii) for **1[OTf]$_2$** and **2[OTf]$_2$** the methyl protons and aromatic protons have different chemical shifts, and (iv) the coordinated DMAP signals are clearly different

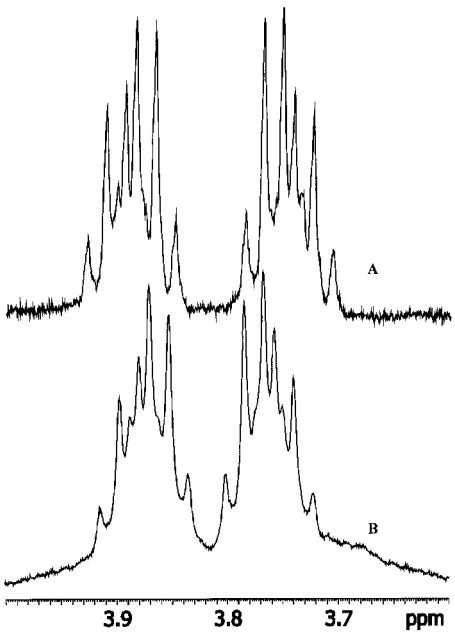

Figure 3. Expansion of the ^{1}H NMR spectra for the diastereotopic CH_2 protons of the coordinated ethanol group in **1** (**A**) and **2** (**B**); the spectra were recorded in CD_2Cl_2 solution at 399.78 MHz and 298 K

from those of free DMAP. In the former case, the signals occur at δ = 3.09 ppm (methyl group, 6 H), 6.61 ppm (*meta*, 2 H), and 7.67 ppm (*ortho*, 2 H), whereas in the latter case they fall at δ = 2.95, 6.46, and 8.15 ppm, respectively. From the literature,[34] we would expect a value of $\delta_{NH\cdots O}$ in the range 9.28−14.18 ppm. A broad signal can be observed in the solution ^{1}H NMR spectrum in the range δ = 5.90−6.75 ppm, and its chemical shift changes markedly with temperature. A possible explanation for this behavior could be rapid equilibria involving traces of water. This is also consistent with the lack of the O−D signal in the ^{2}H NMR spectrum of [Os(bpy)$_2$(CO)(CD_3CD_2O···D−DMAP)][OTf]$_2$. According to the previously reported studies of Limbach and co-workers, the inability to detect the H-bond resonance could be related to fast exchange of the hydrogen-bonded ligand with water.[49] Lowering the temperature could be a way to overcome the fast exchange.[50,51] We measured spectra at 193 K, but it still did not resolve the anticipated resonance due to the strong hydrogen bond. Apparently, the hypothesized equilibria are not sufficiently slow at this temperature, either for the protonated or deuterated complex. Attempts to rigorously dry solid samples prior to dissolution in carefully dried NMR solvents did not eliminate all traces of water.

The IR spectrum of **1[OTf]$_2$** in KBr, prepared under anhydrous conditions, shows two sets of adsorptions in the region around 3000 cm^{-1}, which are typical for C−H stretching modes. It also shows a broad band at 3273 cm^{-1} that can be attributed to the hydrogen-bond interaction; this broad band is not present in the IR spectrum of the deuterated analog [Os(bpy)$_2$(CO)(CD_3CD_2O···D−DMAP)][OTf]$_2$. The presence of the H-bond between the osmium moiety and DMAP can also be indirectly deter-

 © 2005 Wiley-VCH Verlag GmbH & Co. KGaA, Weinheim

mined by the shift of the CO frequency. The CO stretching in **1[OTf]$_2$** falls at 1929 cm^{-1} whereas in **2[OTf]$_2$** it appears at 1939 cm^{-1}, showing a red shift due to the presence of the hydrogen bond, in agreement with the theoretical calculations (see discussion below). The electronic absorption spectra of **1[OTf]$_2$** and **2[OTf]$_2$** are quite different (λ_{max} = 280, 340, and 455 nm for **1** and 266, 302, 352, and 444 nm for **2**). Solutions of **1[OTf]$_2$** give a barely detectable emission at 549 nm when excited at 450 nm while solutions of **2[OTf]$_2$** give a more-pronounced emission at 557 nm. This difference in behavior could result from the quenching of the MLCT excited of the complex by the electron-donating DMAP group.[2,52]

Electron Distribution on the Os-Containing Moiety

The electron distribution on the Os−CO and Os−OEt moieties was investigated by employing the calculated and experimental vibrational data and the NBO[53] orbital analysis, using the three models proposed above (**1a, 1b** and **2** in Scheme 1). As described above, the calculations were carried out at the B3LYP/BS3//B3LYP/BS3 (with LACVP ECP for Os atom) level of theory with the Jaguar software.

The CO stretching frequency (ν_{CO}) is a traditional diagnostic tool that has been used to estimate electron availability in a metal complex.[54,55] As shown in Table 3, comparing model **2**, which lacks the hydrogen bond, to model **1a**, which has the hydrogen bond, we observe that the strength of the Os−O interaction is increased and the strength of the CO bond decreased, as a consequence of the H-bond formation. This is indicated by a shortening of the Os−O bond, a lengthening of the CO bond, and a red shift of the calculated and experimental ν(CO) frequencies (even if the calculated frequencies show the expected systematic over-estimation error). In **1a**, the proton is further removed from the ethanolic oxygen and the ν(CO) is further red-shifted. Also, the trend in the Os−C and C−O bond lengths is in keeping with the proposed explanation in which the electron density on the metal center increases on passing from model **1b** to model **1a**.

Additional details can be observed by employing the NBO approach. The Os−O interaction is described in the same way for the three models depicted in Scheme 1, with the electron density confined to the two lone-pairs localized on the oxygen atom, which have about 30% s and about 70% p character. It is worth noting that no NBOs can be found that give rise to two-center bonds (referred to as BD in NBO nomenclature).[53] In fact, the Os−O interaction is described by electron donation from the oxygen lone-pairs to two empty osmium d-orbital NBOs. The lowest-energy osmium NBO has 99% d character whereas the next-highest-energy d-orbital has about an 80% s and a 20% d character. The energy stabilization arising from this delocalization can be estimated using Perturbation Theory Analysis as provided in the NBO package. The decrease in the Os−O distance is reflected in the stabilization energies, which are 293.80, 357.27, and 537.76 kJ/mol for models **2**, **1b** and **1a**, respectively. A similar trend can be observed for the Os−C and C−O bonds (see Table 3). In the latter case the C−O bond is described by a single BD NBO. Again, application of Perturbation Theory Analysis results in donation of electrons from two oxygen lone-pairs to two vacant carbon NBOs, which again gives stabilization energies following the trend **2** > **1b** > **1a** (see Table 3). This trend is also in agreement with the H-bond-induced red shift of the CO stretching measured experimentally and confirmed by the theoretical calculations.

The slight increase in electron density at the metal with the introduction of the H-bond is entirely consistent with the expected increase in the lone pair π-donor ability of the O-atom resulting from partial deprotonation. This, in turn, increases back-donation by the metal to the CO ligand and results in the observed slight red-shift of the CO stretching frequency.

Table 3. Selected distances [Å], calculated C≡O frequency [cm^{-1}], and stabilization energy [kJ/mol] for the three models of Scheme 1 at the B3LYP/BS3//B3LYP/BS3 level of theory, with LACVP ECP on the Os atom

	d(Os−O)	*d*(Os−C)	*d*(C≡O)	ν(C≡O)	*E*(Os−O)	*E*(C≡O)
1a	2.125	1.8791	1.161	2043	537	1895
1b	2.169	1.883	1.160	2065	357	1919
2	2.213	1.887	1.158	2065	293	1946

Conclusion

The strong N−H···O hydrogen bond formed between the protonated DMAP moiety and the deprotonated ethanolic group in the complex $[Os(bpy)_2(CO)(EtO\cdots H\text{-}DMAP][PF_6]_2$ has been investigated by a combination of single-crystal X-ray diffraction analysis, spectroscopic techniques, and theoretical quantum calculations. The dominance of the alkoxide form over the alcoholic one in the solid state has been supported by the results from different, complementary experimental and theoretical approaches. The ^1H MAS NMR spectrum, recorded at very high spinning speeds, is characterized by the presence of a broad proton signal in the expected N−H region. Although discrimination between the two possible forms **1a** and **1b** was not possible from the solution data alone, IR and ^1H NMR spectra also support the persistence of the H-bonded complex in solution.

The theoretical and experimental studies clearly show that the hydrogen atom is closer to N than to O, but the closeness in energy of the alcohol and alkoxide forms realized from the calculations suggest that the hydrogen bond in **1** is a resonance-assisted hydrogen bond. However, the resonance contribution of the nitrogen moiety to this strong hydrogen bond must await a survey of the PAs of the nitrogen bases employed. The experimental and theoretical data also support a significant perturbation of the electronic environment at the Os atom of **1** relative to **2** and that the alcohol ligand is in a predominantly alkoxide form. The

 © 2005 Wiley-VCH Verlag GmbH & Co. KGaA, Weinheim

latter is exactly the opposite of the case for the free alcohol H-bonding to DMAP and points to the importance of the metal complex in establishing the observed hydrogen bond.

Preliminary results prompt us to believe that the reactivity generated by formation of this strong hydrogen bond could be widely extended by using different alcohols (or amines), different bases, and different metal triflate complexes. For example, the principles underlying the chemistry of the strong hydrogen bond could be adapted to different reactants with relevant biological roles, such as purinic and pyrimidinic bases in DNA or RNA, or nucleophilic amino acids in proteins or polypeptides. Such investigations could assume relevance in the anti-tumour drug field. For example, different ruthenium-based metal complexes have been studied for their anti-tumour properties,[56−59] but only one complex with covalently coordinated DNA bases at the metal center has been reported in the literature.[60]

Experimental Section

General Remarks: $(NH_4)_2OsCl_6$ was purchased from Novachimica. 2,2′-Bipyridine, obtained from Aldrich, was purified by crystallization from hexane and dried under vacuum over P_2O_5.[61] Neutral alumina for chromatography was obtained from Aldrich. All other reagents were reagent grade and used as received without further purification.

Spectroscopic Methods: The NMR spectra were recorded with a JEOL EX 400 spectrometer (operating at 399.78 MHz for ^1H) with chemical shifts referenced to residual protons of the solvent (CD_2Cl_2). VT NMR experiments were performed according to standard procedures. ^1H MAS measurements were performed with a Varian InfinityPlus 500 spectrometer operating at 499.7 MHz for ^1H. Powdered samples were spun at 28 KHz in a Varian 2.5 mm HX probe (courtesy of Department of Chemistry, University of Durham, UK). Spectra were acquired using a π/2 pulse of 2.8 μs in duration and a pulse delay of 10 s over a spectral width of 150 KHz. A total of 64 transients were collected for each spectrum. Proton chemical shifts were referenced to the resonance of PDMSO [poly(dimethylsiloxane)] at $\delta = 0.14$ ppm relative to tetramethylsilane (TMS). UV/Vis absorption spectra were measured at room temperature in deionized water, using a Hitachi U-3210 double-beam spectrophotometer, and emission spectra were measured using a SLM 4800 spectrofluorimeter. The IR spectra were measured as either KBr pellets or in CH_2Cl_2 or CD_2Cl_2 solution using a Bruker Equinox 55 FT-IR spectrophotometer with a resolution of 1 cm^{-1} and an accumulation of 64 scans.

$[Os(bpy)_2(CO)(EtO\cdots H-DMAP)][OTf]_2$ (1[OTf]$_2$): $[Os(bpy)_2(CO)(OTf)][OTf]$[38] (OTf = $CF_3SO_3^-$; 25 mg) was dissolved in ethanol and a tenfold excess of DMAP was added. The solution rapidly changed color from yellow to dark red. The solution was stirred for approximately 48 h and finally became violet. The solvent was then evaporated and the compound was suspended in a toluene solution to dissolve the free DMAP. Finally, the solid was separated and washed several times with diethyl ether. Conversion of the starting complex to the H-bonded product was essentially quantitative; yield 91% (27.4 mg). ^1H NMR (CD_2Cl_2): $\delta = 1.01$ (t, 3 H, CH_3CH$_2$OH), 3.10 (s, 6 H, DMAP), 3.75 (m, 1 H, CH$_3$CH$_2$OH), 3.89 (m, 1 H, CH$_3$CH$_2$OH), 6.60 (d, 2 H, DMAP), 7.20 (d, 1 H), 7.26 (m, 2 H), 7.67 (d, 2 H, DMAP), 7.85 (m, 2 H), 7.97 (t, 1 H), 8.04 (m, 3 H), 8.37 (t, 1 H), 8.41 (d, 1 H), 8.47 (d, 1 H), 8.58 (d, 1 H), 8.65 (d, 1 H), 9.34 (d, 1 H), 9.49 (d, 1 H) ppm. Selected ^{13}C NMR spectroscopic data (CD_2Cl_2): $\delta = 19.82$ (*C*H$_3$CH$_2$OH), 39.70 (CH$_3$, DMAP), 69.46 (CH$_3$*C*H$_2$OH), 106.84 (*meta*, DMAP), 140.97 (*ortho*, DMAP), 177.99 (CO) ppm. Selected IR data (KBr): $\tilde{\nu} = 1929$ (CO); (CH_2Cl_2): $\tilde{\nu} = 1945$ (CO); (CD_2Cl_2): $\tilde{\nu} = 1951$ cm^{-1} (CO). Absorption spectrum (H_2O): $\lambda_{max} = 280, 340, 455$ nm. Emission spectrum (H_2O, $\lambda_{exc} = 450$ nm): weak emission with $\lambda_{max} = 549$ nm.

$[Os(bpy)_2(CO)(EtO\cdots H-DMAP)][PF_6]_2$ (1[PF$_6$]$_2$): Crystals of the complex were obtained by precipitating the ethanol solution of **1[OTf]$_2$** with a saturated solution of $(NH_4)PF_6$. ^1H NMR (CD_2Cl_2): $\delta = 1.03$ (t, 3 H, CH_3CH$_2$OH), 3.13 (s, 6 H, DMAP), 3.83 (m, 1 H, CH$_3$CH$_2$OH), 3.93 (m, 1 H, CH$_3$CH$_2$OH), 6.61 (d, 2 H, DMAP), 7.16 (d, 1 H), 7.52 (d, 2 H, DMAP), 7.27 (m, 2 H), 7.71 (t, 1 H), 7.83 (d, 1 H), 7.96 (t, 1 H), 8.03 (m, 2 H), 8.29 (m, 3 H), 8.38 (t, 1 H), 8.47 (d, 1 H), 8.52 (d, 1 H), 9.31 (d, 1 H), 9.50 (d, 1 H) ppm. Selected IR data (CH_2Cl_2): $\tilde{\nu} = 1945 cm^{-1}$ (CO).

$[Os(bpy)_2(CO)O(H)Et][OTf]_2$ (2[OTf]$_2$): This complex was prepared by dissolving 25 mg of $[Os(bpy)_2(CO)(OTf)][OTf]$ in ethanol and stirring the solution for 5 d. After evaporation of the solvent, the orange solid was characterized spectroscopically; yield 82% (21.6 mg). ^1H NMR (CD_2Cl_2): $\delta = 1.15$ (t, 3 H, CH_3CH$_2$OH), 2.17 (br, CH$_3$CH$_2$O*H*), 3.77 (m, 1 H, CH$_3$CH$_2$OH), 3.87 (m, 1 H, CH$_3$CH$_2$OH), 7.27 (d, 1 H), 7.33 (t, 1 H), 7.49 (t, 1 H), 7.80 (m, 2 H), 7.94 (t, 1 H), 8.00 (t, 1 H), 8.13 (t, 1 H), 8.14 (t, 1 H), 8.38 (t, 1 H), 8.48 (t, 2 H), 8.57 (d, 1 H), 8.65 (d, 1 H), 9.10 (d, 1 H), 9.45 (d, 1 H) ppm. Selected IR data (KBr): $\tilde{\nu} = 1939$ (CO); (CH_2Cl_2): $\tilde{\nu} = 1956$ (CO); (CD_2Cl_2): $\tilde{\nu} = 1963$ cm^{-1} (CO). Absorption spectrum (H_2O): $\lambda_{max} = 266, 302, 352, 444$ nm.

X-ray Crystallographic Study: The crystal structure of **1[PF$_6$]$_2$** was solved by single-crystal X-ray diffraction analysis. Suitable crystals were obtained by slow evaporation of the solvent from a water/ethanol solution. Diffraction data were collected at room temp. with a Bruker SMART-APEX CCD[62] area detector diffractometer, using graphite-monochromated Mo-K_α ($\lambda = 0.71073$ Å) radiation. Absorption correction was performed using SADABS.[63] The structure was solved by direct methods (SIR97)[64] and refined by full-matrix least squares (SHELX97).[39] All hydrogen atoms except H1 were generated in their calculated positions with the XP[65] software. Because the location of atom H1, which is involved in the strong hydrogen bond, is not straightforward, different refining techniques were adopted. These results were compared to those from theoretical quantum calculations, as described in the crystal structure section. Crystallographic data and details of data collections and refinements are given in Table 4. CCDC-244832 contains the supplementary crystallographic data for this paper. These data can be obtained free of charge at www.ccdc.cam.ac.uk/conts/retrieving.html [or from the Cambridge Crystallographic Data Centre, 12 Union Road, Cambridge CB2 1EZ, UK; Fax: + 44-1223-336-033; E-mail: deposit@ccdc.cam.ac.uk].

Computational Details: All the calculations on the osmium complex were performed on the cationic complexes (**1a**, **1b**, **2**; see Scheme 1) using the Jaguar software,[66] except for the magnetic shielding tensor calculations, which were calculated with the Gaussian 98 (G98)[67] program. The Hartree−Fock (HF)[68] and density-functional theory (DFT) methods were adopted for geometry optimization. DFT calculations were carried out using Becke's[69] three-parameter hybrid functional and either the Lee−Yang−Parr[70] or Perdew−Wang[71] gradient-corrected correlation functional. The

 © 2005 Wiley-VCH Verlag GmbH & Co. KGaA, Weinheim

Table 4. Crystal data for $[Os(bpy)_2(CO)(EtO\cdots H\text{-}DMAP)][PF_6]_2$

	$[Os(bpy)_2(CO)(EtO\cdots H\text{-}DMAP)][PF_6]_2$
Empirical formula	$C_{30}H_{32}F_{12}N_6O_2OsP_2$
Formula mass	988.76
Temperature	293(2) K
Wavelength	0.71069 Å
Crystal system	triclinic
Space group	$P\bar{1}$
Unit cell dimensions	a = 8.626(1) Å b = 10.227(2) Å c = 21.354(4) Å α = 103.399(4)° β = 97.066(6)° γ = 94.283(5)°
Volume	1808.2(5) Å^3
Z	2
Density (calculated)	1.816 Mg/m^3
Absorption coefficient	3.715 mm^{-1}
F(000)	968
Crystal size	0.20 × 0.15 × 0.02 mm
θ range for data collection	4.08−23.25°
Index ranges	$-9 \le h \le 9$, $-11 \le k \le 11$, $-23 \le l \le 23$
Reflections collected	16348
Independent reflections	4935 [R(int) = 0.0357]
Completeness to θ = 23.25°	94.9%
Refinement method	Full-matrix least-squares on F^2
Data/restraints/parameters	4935/60/454
Goodness-of-fit on F^2	1.001
Final R indices [$I > 2\sigma(I)$]	$R1$ = 0.0466; $wR2$ = 0.1155
R indices (all data)	$R1$ = 0.0558; $wR2$ = 0.1202
Largest diff. peak/hole	0.980/−0.646 e·Å^{-3}

importance of the electron correlation effects was then taken into account by performing calculations that use the local MP2 (L-MP2) method[72−75] as implemented in the Jaguar software. The Los Alamos Effective Core Potential (ECP) Double-ζ (LanL2Dz) was used for the Os atom in the Gaussian 98 calculations, while the LANL ECP named LACVP[76] was employed for all calculations carried out with the Jaguar program. Different basis sets were employed for the geometry optimizations (main results summarized in Tables 1 and 3) and for the calculations of the energetic features (Table 2), i.e. 6-31G(d,p), 6-31+G(d,p), 6-31++G(d,p), and 6-311++G(2d,p),[68] hereafter named BS1, BS2, BS3, and BS4, respectively. For the NMR calculations on model **1a**, a B3LYP/BS3//B3LYP/BS4 (geometry optimization//NMR calculation) level of theory was used, employing the GIAO[77] method as implemented in Gaussian 98. The σ values were converted into proton chemical shifts, δ, relative to the magnetic shielding of TMS computed with the corresponding basis set. The vibrational frequencies were then calculated (without applying any scaling factor) for the CO groups at the B3LYP/BS3//B3LYP/BS3 levels (with the LACVP ECP for Os atom), using numerical algorithms implemented in the Jaguar software. The Natural Bonding Orbital (NBO)[53] analysis was carried out with the Jaguar software to rationalize, by means of geometric features and orbital analysis, the IR spectral characteristics of **1a**, **1b** and **2**. Finally, a geometry optimization calculation on the two possible forms of the non-metal-containing organic couple formed by ethanol and DMAP ($EtOH\cdots DMAP$ and $EtO^-\cdots H-DMAP^+$) was performed at the B3LYP/BS3 level of theory. All attempts to optimize the geometry of the hypothetical $EtO^-\cdots H-DMAP^+$ complex failed.

Acknowledgments

This work was supported by Italian MURST (FIRB RBAU015MJ9 004). J. B. A. R. gratefully acknowledges support by NIH grants R01-CA63317 and P20-RR15583, and by NSF grant EPS-0091995. E. R. and J. B. A. R. both thank the BRIN faculty Travel Program, and E. R. thanks the DOE for support. The authors acknowledge Prof. D. Viterbo (Università del Piemonte Orientale, Italy) and Prof. P. Ugliengo (Università di Torino, Italy) for useful discussions. Finally, we are indebted to Prof. R. K. Harris and Dr. D. Apperley (Durham University, UK) for performing the high-speed ^{1}H MAS NMR measurements.

[1] L. Sacksteder, J. N. Demas, B. A. DeGraff, *Inorg. Chem.* **1989**, *28*, 1787−1792.
[2] T. A. Perkins, D. B. Porreau, T. L. Netzel, K. S. Schanze, *J. Phys. Chem.* **1989**, *93*, 4511−4522.
[3] J. R. Lakowicz, *Principles of Fluorescence Spectroscopy*, Kluwer Academic/Plenum Publishers, New York, **1999**.
[4] A. Scott, H. Taube, *Inorg. Chem.* **1971**, *10*, 62−66.
[5] N. E. Dixon, W. G. Jackson, M. J. Lancaster, G. A. Lawrance, A. M. Sargeson, *Inorg. Chem.* **1981**, *20*, 470−476.
[6] J. M. Harrowfield, A. M. Sargeson, B. Singh, J. C. Sullivan, *Inorg. Chem.* **1975**, *14*, 2864−2865.
[7] W. G. Jackson, C. M. Begbie, *Inorg. Chem.* **1981**, *20*, 1654−1659.
[8] F. H. Allen, *Acta Crystallogr., Sect. B* **2002**, *58*, 380−388.
[9] R. Gobetto, C. Nervi, B. Romanin, L. Salassa, M. Milanesio, G. Croce, *Organometallics* **2003**, *22*, 4012−4019.
[10] G. Höfle, W. Steglich, H. Vorbrüggen, *Angew. Chem. Int. Ed. Engl.* **1978**, *17*, 569−583.
[11] A. C. Spivey, A. Maddaford, T. Fekner, A. J. Redgrave, S. F. Christopher, *J. Chem. Soc., Perkin Trans. 1* **2000**, 3460−3468.
[12] A. C. Spivey, A. Maddaford, D. P. Leese, A. J. Redgrave, *J. Chem. Soc., Perkin Trans. 1* **2001**, 1785−1794.
[13] P. Somfai, *Angew. Chem. Int. Ed. Engl.* **1997**, *36*, 2731−2733.
[14] A. M. P. Koskinen, A. M. Klibanov, *Enzymatic Asymmetric Acylation*, Kluwer Academic Publishers, London, **1995**.
[15] D. S. Chemla, J. Zyss, *Nonlinear Optical Properties of Organic Molecules and Crystals*, Academic Press, Orlando, FL, **1987**.
[16] S. M. Roberts, *Molecular Recognition: Chemical and Biochemical Problems II*, The Royal Society of Chemistry, Cambridge, U.K., **1992**.
[17] G. R. Desiraju, *Crystal Engineering: The Design of Organic Solids*, Elsevier, Amsterdam, **1989**.
[18] J. Bernstein, R. E. Davis, L. Shimoni, N. L. Chang, *Angew. Chem. Int. Ed. Engl.* **1995**, *34*, 1555−1573.
[19] G. R. Desiraju, *Acc. Chem. Res.* **2002**, *35*, 565−573.
[20] T. Steiner, *Angew. Chem. Int. Ed.* **2002**, *41*, 48−76.
[21] J. C. Speakman, *Struct. Bond.* **1972**, *12*, 141−199.
[22] M. L. Huggins, *Angew. Chem. Int. Ed. Engl.* **1971**, *10*, 147−151.
[23] J. Emsley, *Chem. Soc. Rev.* **1980**, *9*, 91−124.
[24] G. A. Jeffrey, *An Introduction to Hydrogen Bonding*, Oxford University Press, New York, **1997**.
[25] C. A. Coulson, *Valence*, Oxford University Press, Oxford, **1952**.
[26] C. A. Coulson, U. Danielsson, *Ark. Fysik* **1954**, *8*, 239; *Chem. Abstr.* **1955**, *49*, 2134d.
[27] C. A. Coulson, U. Danielsson, *Ark. Fysik* **1954**, *8*, 245; *Chem. Abstr.* **1955**, *49*, 2134d.
[28] H. Umeyama, K. Morokuma, *J. Am. Chem. Soc.* **1977**, *99*, 1316−1336.
[29] K. Morokuma, *Acc. Chem. Res.* **1977**, *10*, 294−300.
[30] R. F. W. Bader, *Atoms in Molecules: A Quantum Theory*, Oxford University Press, New York, **1990**.
[31] P. Gilli, V. Bertolasi, V. Ferretti, G. Gilli, *J. Am. Chem. Soc.* **1994**, *116*, 909−915.

 © 2005 Wiley-VCH Verlag GmbH & Co. KGaA, Weinheim

[32] G. Gilli, F. Bellucci, V. Ferretti, V. Bertolasi, *J. Am. Chem. Soc.* **1989**, *111*, 1023−1028.
[33] V. Bertolasi, P. Gilli, V. Ferretti, G. Gilli, *J. Am. Chem. Soc.* **1991**, *113*, 4917−4925.
[34] G. Gilli, P. Gilli, *J. Mol. Struct.* **2000**, *552*, 1−15.
[35] P. Gilli, V. Bertolasi, L. Pretto, A. Lycka, G. Gilli, *J. Am. Chem. Soc.* **2002**, *124*, 13554−13567.
[36] P. Gilli, V. Bertolasi, V. Ferretti, G. Gilli, *J. Am. Chem. Soc.* **2002**, *122*, 10405−10417.
[37] L. B. Jerzykiewicz, Z. Malarski, L. Sobczyk, T. Lis, E. Grech, *J. Mol. Struct.* **1998**, *440*, 175−185.
[38] B. P. Sullivan, V. J. Caspar, R. S. Johnson, J. T. Meyer, *Organometallics* **1984**, *3*, 1241−1251.
[39] G. M. Sheldrick, *SHELXL-97*, University of Göttingen, Germany, **1997.**
[40] L. Cheng, D. R. Powell, M. A. Khan, G. B. Richter-Addo, *Inorg. Chem.* **2001**, *40*, 125−133.
[41] W. Tsz-Wing, L. Tai-Chu, W. Wing-Tak, *Inorg. Chem.* **1999**, *38*, 6181−6186.
[42] I. Maiboroda, G. Rheinwald, H. Lang, *Inorg. Chem.* **2000**, *39*, 5725−5730.
[43] R. D. Adams, J. E. Babin, *Organometallics* **1988**, *7*, 2300−2306.
[44] L. K. Woo, D. A. Smith, V. G. J. Young, *Organometallics* **1991**, *10*, 3977−3982.
[45] A. R. Leach, *Molecular Modelling: Principles and Applications*, Prentice Hall, Harlow, England, **2001**.
[46] W. L. Earl, D. L. VanderHart, *J. Magn. Reson.* **1982**, *48*, 35−54.
[47] D. Doskocilová, D. D. Tao, B. Schneider, *Czech. J. Phys.* **1975**, *B25*, 202.
[48] D. Doskocilová, B. Schneider, *Macromolecules* **1972**, *5*, 125−127.
[49] M. Rospenk, L. Sobczyk, P. Schah-Mohammedi, H. H. Limbach, N. S. Golubev, S. M. Melikova, *Magnetic Resonance in Chemistry* **2001**, *39*, S81−S90.
[50] N. S. Golubev, S. N. Smirnov, V. A. Gindin, G. S. Denisov, H. Benedict, H. H. Limbach, *J. Am. Chem. Soc.* **1994**, *116*, 12055−12056.
[51] N. S. Golubev, G. S. Denisov, *J. Mol. Struct.* **1992**, *270*, 263−267.
[52] J. T. Meyer, *Acc. Chem. Res.* **1978**, *11*, 94−100.
[53] E. D. Glendening, J. K. Badenhoop, A. E. Reed, J. E. Carpenter, J. A. Bohmann, C. M. Morales, F. Weinhold, *NBO 5.0*, University of Wisconsin, Madison, WI, **2001**.
[54] J. T. Poulton, M. P. Sigalas, K. Folting, W. E. Streib, O. Eisenstein, K. G. Caulton, *Inorg. Chem.* **1994**, *33*, 1476−1485.
[55] S. A. Macgregor, D. MacQueen, *Inorg. Chem.* **1999**, *38*, 4868−4876.
[56] J. K. Barton, E. Lolis, *J. Am. Chem. Soc.* **1981**, *107*, 708−709.
[57] N. Grover, N. Gupta, H. H. Thorp, *J. Am. Chem. Soc.* **1992**, *114*, 3390−3393.
[58] O. Novakova, J. Kasparkova, O. Vrana, P. M. van Vliet, J. Reedijk, V. Brabec, *Biochemistry* **1995**, 12369−12378.
[59] S. Cauci, P. Viglino, G. Esposito, F. Quadrifoglio, *J. Inorg. Biochem.* **1991**, *43*, 739−751.
[60] F. Zobi, M. Hohl, I. Zimmermann, R. Alberto, *Inorg. Chem.* **2004**, *43*, 2771−2772.
[61] L. F. Amarengo, D. D. Perrin, *Purification of Laboratory Chemicals*, Butterworth-Heinemann, Oxford, **1998**.
[62] *SMART*, Bruker AXS, Inc., Madison, WI 53719, USA, **1998**.
[63] G. M. Sheldrick, *SADABS*, University of Göttingen, Germany, **1996**.
[64] A. Altomare, M. C. Burla, M. Camalli, G. L. Cascarano, C. Giacovazzo, A. Guagliardi, A. G. Moliterni, G. Polidori, R. Spagna, *J. Appl. Crystallogr.* **1999**, *32*, 115−119.
[65] *SHELXTL*, Bruker AXS, Inc., Madison, WI 53719, USA, **1998**.
[66] *Jaguar*, version 5.5, Schrödinger Inc., Portland, OR, **2003**.
[67] M. J. Frisch, G. W. Trucks, H. B. Schlegel, G. E. Scuseria, M. A. Robb, J. R. Cheeseman, V. G. Zakrzewski, J. A. Jr. Montgomery, R. E. Stratmann, J. C. Burant, S. Dapprich, J. M. Millam, A. D. Daniels, K. N. Kudin, M. C. Strain, O. Farkas, J. Tomasi, V. Barone, M. Cossi, R. Cammi, B. Mennucci, C. Pomelli, C. Adamo, S. Clifford, J. Ochterski, G. A. Petersson, P. Y. Ayala, Q. Cui, K. Morokuma, D. K. Malick, A. D. Rabuck, K. Raghavachari, J. B. Forestman, J. Cioslowski, J. V. Ortiz, A. G. Baboul, B. B. Stefanov, G. Liu, A. Liashenko, P. Piskorz, I. Komaromi, R. Gomperts, R. L. Martin, D. J. Fox, T. Keith, M. A. Al-Laham, C. Y. Peng, A. Nanayakkara, M. Challacombe, P. M. W. Gill, B. Johnson, W. Chen, M. W. Wong, J. L. Andres, C. Gonzales, M. Head-Gordon, E. S. Replogle, J. A. Pople, *Gaussian 98*, version revision A.9, Gaussian Inc., Pittsburgh, PA, **1998**.
[68] W. J. Hehre, L. Radom, P. v. R. Schleyer, J. A. Pople, *Ab Initio Molecular Orbital Theory*, John Wiley & Sons, New York, **1986**.
[69] A. D. Becke, *J. Chem. Phys.* **1993**, *98*, 5648−5652.
[70] C. Lee, W. Yang, R. G. Parr, *Phys. Rev. B: Condens. Matter* **1988**, *37*, 785−789.
[71] J. P. Perdew, J. A. Chevary, S. H. Vosko, K. A. Jackson, M. R. Pederson, C. Fiolhais, *Phys. Rev. B: Condens. Matter* **1992**, *46*, 6671−6687.
[72] C. Møller, M. S. Plesset, *Phys. Rev.* **1934**, *46*, 618−622.
[73] S. Sæbø, P. Pulay, *Theor. Chim. Acta* **1986**, *69*, 357.
[74] S. Sæbø, P. Pulay, *Ann. Rev. Phys. Chem.* **1993**, *44*, 213−236.
[75] S. Sæbø, W. Tong, P. Pulay, *J. Phys. Chem.* **1993**, *98*, 2170−2175.
[76] P. J. Hay, W. R. Wadt, *J. Chem. Phys.* **1985**, *82*, 299−310.
[77] T. Helgaker, M. Jaszunski, K. Ruud, *Chem. Rev.* **1999**, *99*, 293−352.

Received July 19, 2004
Early View Article
Published Online December 13, 2004

 © 2005 Wiley-VCH Verlag GmbH & Co. KGaA, Weinheim

EurJIC
European Journal of Inorganic Chemistry

Issue 4/2005

Pages 617–800

Papers available ahead of print in Early View at www.interscience.wiley.com

Earliest available Table of Contents:
Automatically, free of charge by e-mail through
www.interscience.wiley.com/alerts

COVER PICTURE

The cover picture shows the X-ray crystal structure of bis(1,3-di-*tert*-butylcyclopentadienyl)thulium(tetrahydrofuran), a new organothulium(II) complex and the first one with all-carbon π-ligands. Two new and particularly stable phospholylthulium(II) complexes are also described. The very existence and relative ease of formation of the so far described thulium(II) molecular compounds strongly suggest that many more such compounds can be prepared, provided that adequate steric and/or electronic protection of the thulium(II) ion can be archieved, thus paving the way to new and hopefully exciting studies in the field of thulium(II) chemistry. Details are discussed in the article by F. Nief et al. on p. 637 ff. The cover picture was rendered in POVRAY 3.5, and the initial input file was obtained with Louis J. Farrugia's ORTEP-III for Windows programme.

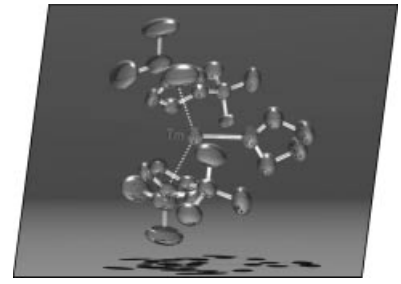

SHORT COMMUNICATION

Contents

631 **A. Jutand,* S. Négri, A. Principaud**

Formation of ArPdXL(amine) Complexes by Substitution of One Phosphane Ligand by an Amine in *trans*-$ArPdX(PPh_3)_2$ Complexes

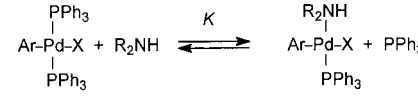

trans-**1** **2**

Ar = Ph, 4-CN–C_6H_4, 4-MeOC–C_6H_4, 2-Th
X = I, Br, Cl
R_2NH = piperidine, morpholine, diisopropylamine

Keywords: Amines / Phosphanes / Palladium / Ligand substitution

 © 2005 Wiley-VCH Verlag GmbH & Co. KGaA, Weinheim

FULL PAPERS

637 **F. Nief,* B. Tayart de Borms, L. Ricard, D. Carmichael**

New Complexes of Divalent Thulium with Substituted Phospholyl and Cyclopentadienyl Ligands

Keywords: Phosphorus heterocycles / Lanthanides / Subvalent compounds / Thulium / Cyclopentadienyl ligands

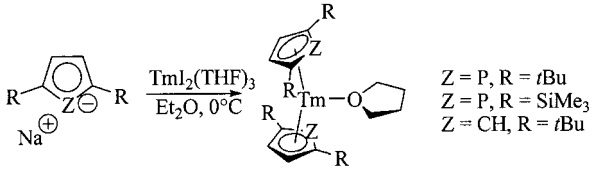

644 **T. Sakano, M. Horie, K. Osakada,* H. Nakao**

Azaferrocenophanes with Azobenzene-Containing Ligands − Protonation and Electrochemical Oxidation of the Molecule Influences the Absorption Spectra and *cis*−*trans* Isomerization of the Azobenzene Group

Keywords: Azobenzene / Chromophores / Ferrocene / Photochemistry / Redox chemistry

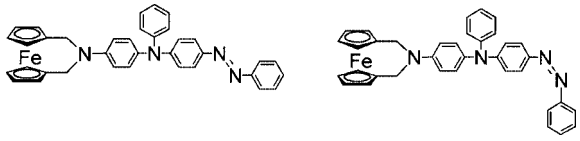

653 **W. Zhang, L. Xu, K. Tang, F. Li, Y. Qian***

Solvothermal Synthesis of NiS 3D Nanostructures

Keywords: Nickel sulfide / Nanostructures / Complexes / Crystal growth

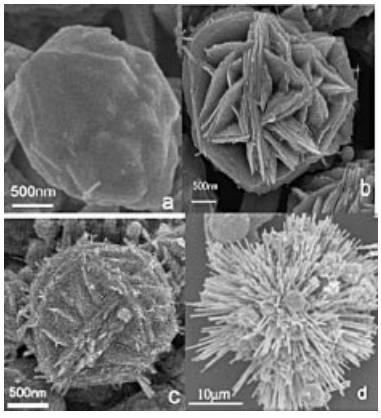

657 **Y. V. Mironov,* M. A. Shestopalov, K. A. Brylev, S. S. Yarovoi, G. V. Romanenko, V. E. Fedorov, H. Spies, H.-J. Pietzsch, H. Stephan, G. Geipel, G. Bernhard, W. Kraus**

$[Re_6Q_7O(3,5\text{-}Me_2PzH)_6]Br_2\cdot 3,5\text{-}Me_2PzH$ (Q = S, Se) − New Octahedral Rhenium Cluster Complexes with Organic Ligands: Original Synthetic Approach and Unexpected Ligand Exchange in the Cluster Core

Keywords: Rhenium / Cluster compounds / Ligand exchange / Organic ligands / Structure elucidation / Laser fluorescence spectroscopy

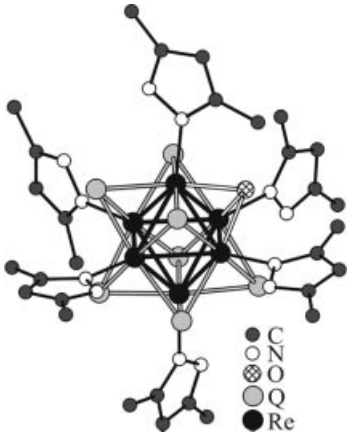

 © 2005 Wiley-VCH Verlag GmbH & Co. KGaA, Weinheim

662 **A. Beghidja, S. Hallynck, R. Welter,* P. Rabu***

Syntheses, Structures and Magnetic Properties of Layered Metal(II) Mandelates

Keywords: Carboxylate ligands / Layered compounds / Magnetic properties / Transition metals / X-ray powder diffraction

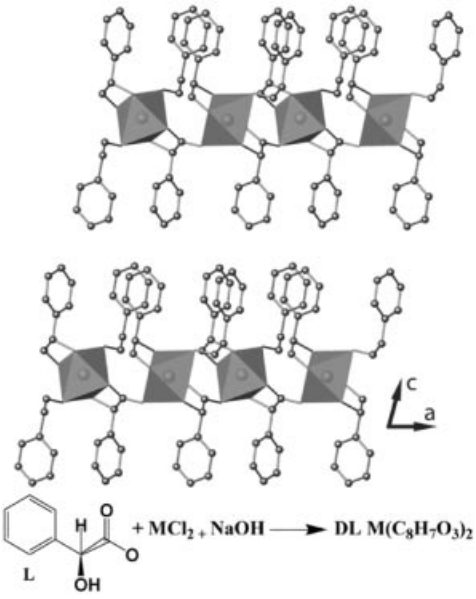

670 **M. Lindsjö, A. Fischer, L. Kloo***

Improvements of and Insights into the Isolation of Bismuth Polycations from Benzene Solution − Single-Crystal Structure Determinations of $Bi_8[GaCl_4]_2$ and $Bi_5[GaCl_4]_3$

Keywords: Bismuth / Cluster compounds / Polycations / Subvalent compounds

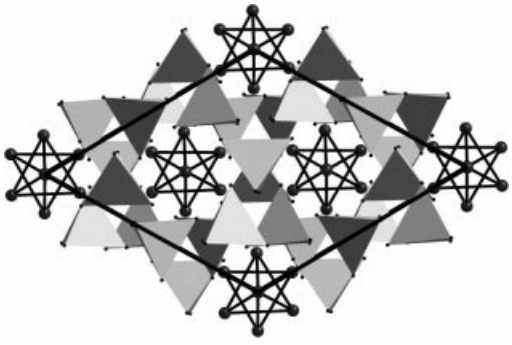

676 **X. Xu, M. Ma, Y. Yao,* Y. Zhang, Q. Shen***

Synthesis, Characterisation of Carbon-Bridged (Diphenolato)lanthanide Complexes and Their Catalytic Activity for Diels−Alder Reactions

Keywords: Lanthanides / O ligands / Structure elucidation / Catalysis / Diels−Alder reaction / Cyclopentadiene

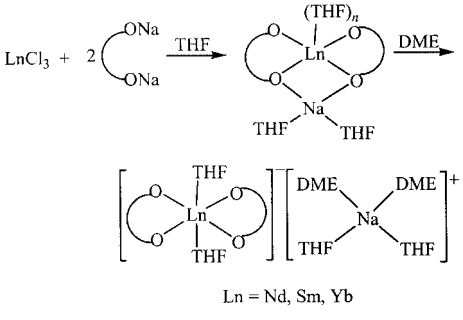

685 **A. Muñoz,* J. A. Alonso, M. T. Casais, M. J. Martínez-Lope, J. L. Martínez, M. T. Fernández-Díaz**

A Study of the Magnetic Structure of $LaMn_2O_5$ from Neutron Powder Diffraction Data

Keywords: Lanthanides / Magnetic properties / Neutron diffraction / Spin glass / Superexchange interaction

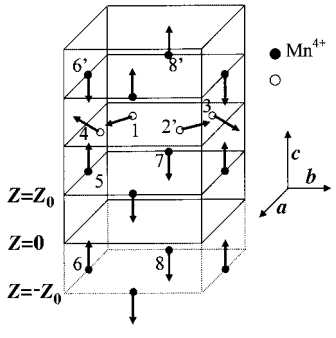

 © 2005 Wiley-VCH Verlag GmbH & Co. KGaA, Weinheim

692 **M. Viertelhaus, P. Adler, R. Clérac, C. E. Anson, A. K. Powell***

Iron(II) Formate $[Fe(O_2CH)_2]\cdot 1/3HCO_2H$: A Mesoporous Magnet − Solvothermal Syntheses and Crystal Structures of the Isomorphous Framework Metal(II) Formates $[M(O_2CH)_2]\cdot n$(Solvent) (M = Fe, Co, Ni, Zn, Mg)

Keywords: Iron / Solvothermal synthesis / Framework material / Magnetic properties / Mössbauer spectroscopy

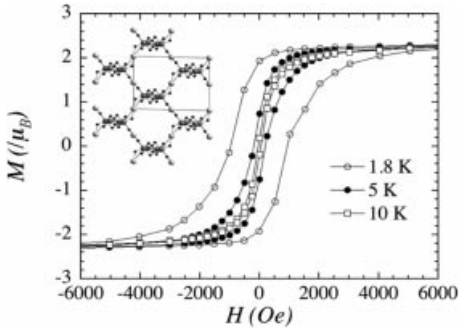

704 **M. Calligaris, E. Zangrando,* B. Milani, A. Marson**

Stereochemical Investigation of Palladium(II) Complexes with Phenanthroline Ligands: A Molecular Mechanics Approach

Keywords: Stereochemistry / Molecular mechanics / Copolymerisation / Phenanthroline / Palladium

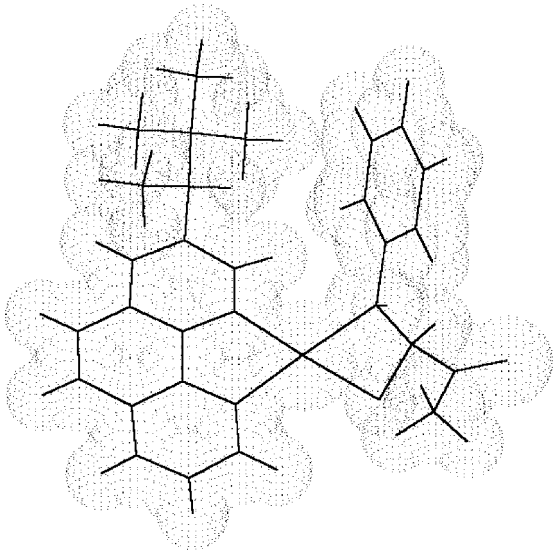

713 **A. M. Z. Slawin, J. Wheatley, J. D. Woollins***

Preparation and Coordination Chemistry of *n*-Allylaminophosphane

Keywords: Phosphanes / Alkenes / Hemilabile complexes / X-ray structures

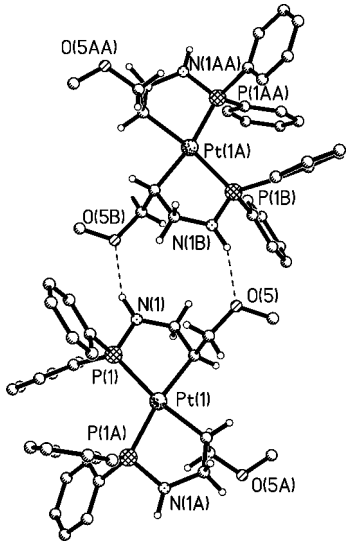

 © 2005 Wiley-VCH Verlag GmbH & Co. KGaA, Weinheim

721 **S. L. Jain, A. M. Z. Slawin, J. D. Woollins,* P. Bhattacharyya**

The Reactions of Elemental Iron with Dipicolinic Acid (H_2dipic) and Quinaldic Acid (Hquin) − X-ray Crystal Structures of $[C_5H_5NH][Fe(Dipic)(Hdipic)(C_5H_5N)_2]\cdot 3C_5H_5N$, $[Fe_2(\mu\text{-}O)(Dipic)_2(C_5H_5N)_4]\cdot 2C_5H_5N\cdot 2H_2O$ and *trans*-$[Fe(Quin)_2(MeOH)_2]$

Keywords: Iron / Dipicolinic acid / Carboxylates / Quinaldic acid / Gif chemistry

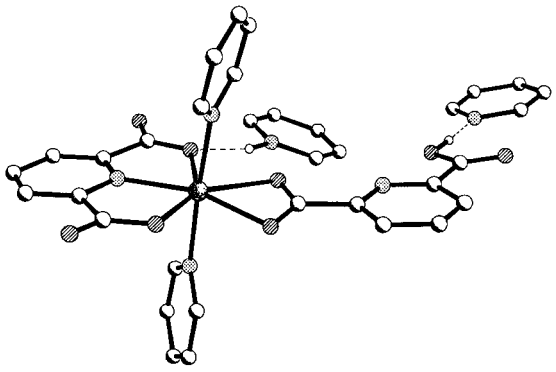

727 **Y.-d. Wang,* S. Zhang, X.-h. Wu**

Green Light Luminescence from ZnO/Dodecylamine Mesolamellar Nanocomposites Synthesized by Self-Assembly

Keywords: Mesoporous materials / Nanocomposites / Luminescence / Interfacial interactions

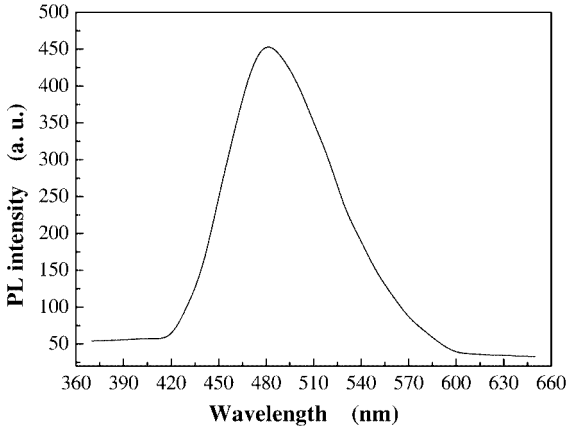

732 **I. Correia, J. Costa Pessoa,* M. T. Duarte, M. F. M. da Piedade, T. Jackush, T. Kiss,* M. M. C. A. Castro, C. F. G. C. Geraldes, F. Avecilla**

Vanadium(IV and V) Complexes of Schiff Bases and Reduced Schiff Bases Derived from the Reaction of Aromatic *o*-Hydroxyaldehydes and Diamines: Synthesis, Characterisation and Solution Studies

Keywords: Vanadium complexes / Schiff bases / Reduced Schiff bases / Crystal structures / Speciation

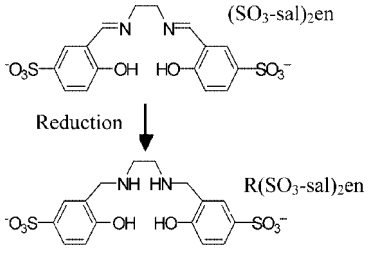

745 **L. Jekki, C. Pala, B. Calmuschi, C. Ganter***

Synthesis of Chiral, Half-Sandwich Ruthenium Complexes from Weakly Coordinated Solvent Species

Keywords: Chirality / P ligands / Ruthenium / Sandwich complexes

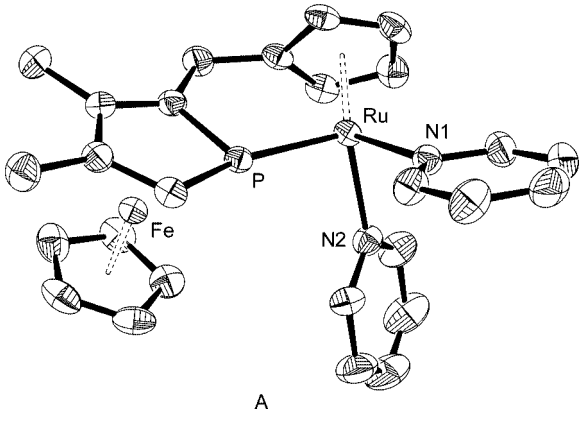

A

 © 2005 Wiley-VCH Verlag GmbH & Co. KGaA, Weinheim

751 **R. Wang, L. Xu, J. Ji, Q. Shi, Y. Li, Z. Zhou, M. Hong,* A. S. C. Chan***

Metal-Directed Stereoselective Syntheses of Homochiral Complexes of *exo*-Bidentate Binaphthol Derivatives

Keywords: Cadmium / N ligands / Palladium / Silver / Zinc

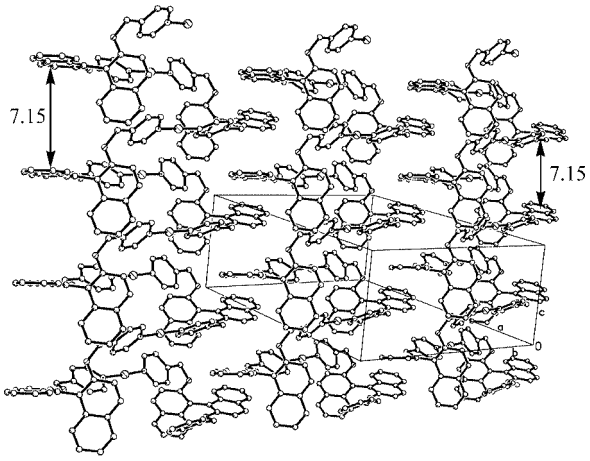

759 **S. Wörl, I. O. Fritsky, D. Hellwinkel, H. Pritzkow, R. Krämer***

Mono-, Di- and Polymeric Calcium and Gadolinium Complexes of the Tripodal Ligand 2,2′,2′′-Nitrilotribenzoic Acid

Keywords: Calcium / Gadolinium / N,O ligands / Tripodal ligands / X-ray crystallography

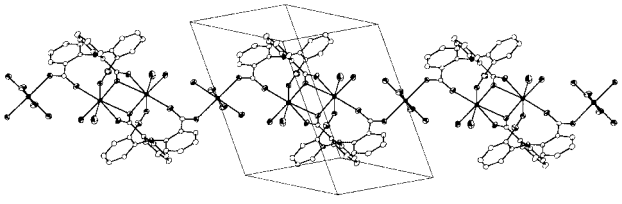

766 **H.-T. Zhang, Y. Song, Y.-X. Li, J.-L. Zuo, S. Gao, X.-Z. You***

Three-Dimensional Lanthanoid-Containing Coordination Frameworks: Structure, Magnetic and Fluorescent Properties

Keywords: Lanthanides / Coordination polymers / Magnetic properties / Fluorescence / Solid-state structures

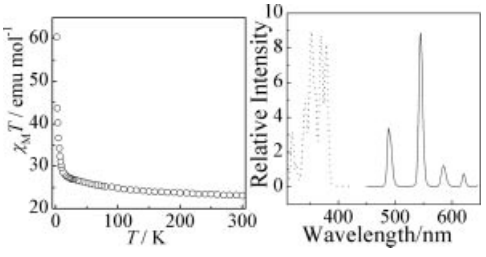

773 **C.-F. Leung, T.-W. Wong, T.-C. Lau,* W.-T. Wong**

Addition of Carbenes to an Osmium(IV) Nitride Complex

Keywords: Carbenes / N,O ligands / Nitrides / Osmium / Vinylidene ligands

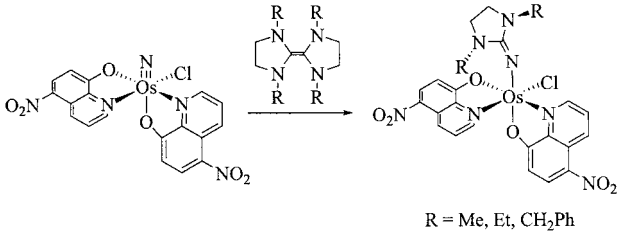

 © 2005 Wiley-VCH Verlag GmbH & Co. KGaA, Weinheim

779 **P. C. A. Bruijnincx, M. Lutz, A. L. Spek, E. E. van Faassen, B. M. Weckhuysen, G. van Koten, R. J. M. Klein Gebbink***

Bis(1-methylimidazol-2-yl)propionates and Bis-(1-methylbenzimidazol-2-yl)propionates: A New Family of Biomimetic *N,N,O* Ligands − Synthesis, Structures and Cu^{II} Coordination Complexes

Keywords: N,N,O ligands / Ligand design / Facial capping / Copper / Carboxylate ligands

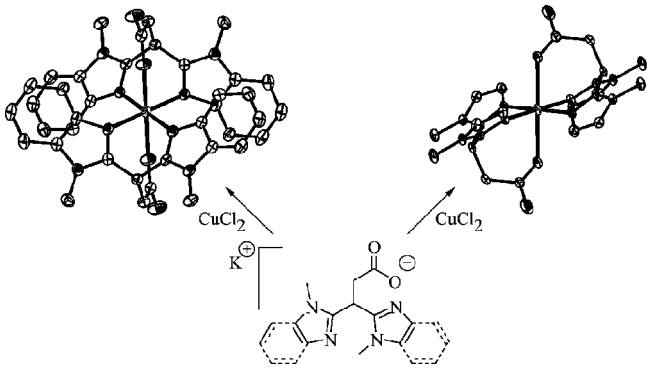

788 **S. A. De Pascali, P. Papadia, A. Ciccarese, C. Pacifico, F. P. Fanizzi***

First Examples of β-Diketonate Platinum(II) Complexes with Sulfoxide Ligands

Keywords: Platinum / β-Diketonate / S ligands

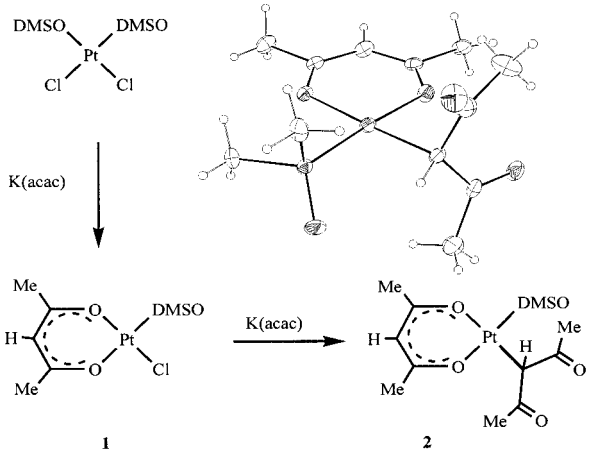

 © 2005 Wiley-VCH Verlag GmbH & Co. KGaA, Weinheim

Formation of ArPdXL(amine) Complexes by Substitution of One Phosphane Ligand by an Amine in *trans*-ArPdX(PPh_3)$_2$ Complexes

Anny Jutand,*[a] Serge Négri,[a] and Anna Principaud[a]

Keywords: Amines / Phosphanes / Palladium / Ligand substitution

Amines (piperidine, morpholine, diisopropylamine, terbutylamine), which may be used as bases in copper-free palladium-catalyzed Sonogashira reactions, substitute one phosphane PPh_3 in *trans*-ArPdX(PPh_3)$_2$ complexes (Ar = Ph, 4-NC–C_6H_4, 4-MeOC–C_6H_4, 2-thienyl; X = I, Br, Cl) to generate ArPdX(PPh_3)(amine) complexes in a reversible reaction whose equilibrium constant is determined in chloroform, THF, and DMF. The equilibrium constant depends on Ar, X, the basicity, and the steric hindrance of the amine.

(© Wiley-VCH Verlag GmbH & Co. KGaA, 69451 Weinheim, Germany, 2005)

Palladium-catalyzed Sonogashira reactions (Scheme 1) require the presence of a base, which is very often an amine.[1,2]

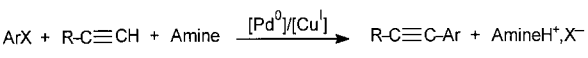

Scheme 1.

In copper-free Sonogashira reactions (Scheme 2), the role of the base is crucial, and specific amines are required.[3–10] Among them, secondary amines such as piperidine,[3,6,8–10] morpholine,[10] and diisopropylamine[8,10] proved to be very efficient. The amines are usually used in excess,[5,6,8,9] even as the solvent.[3,6,7] PPh_3 is often a ligand of the palladium catalyst when aryl iodides, bromides or triflates are used.[3,4,7–9]

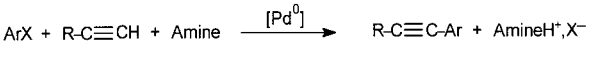

Scheme 2.

The mechanism of the copper-free reaction is not well known. The first step of the reaction is an oxidative addition of ArX to a Pd^0 complex, which generates $ArPdXL_2$ complexes (e.g. L = PPh_3). However, the second step of the reaction is under debate. The amines employed in such reactions (e.g. piperidine, morpholine, etc.) are usually not able to deprotonate the alkyne to generate the anionic nucleophile RC≡C$^-$ that is able to react with $ArPdXL_2$ in a transmetallation step. It is for this reason that complexation of the alkyne to the *trans*-$ArPdXL_2$ complexes is supposed to proceed first with displacement of one ligand to give intermediate complexes: ArPdXL(η^2-HC≡CR).[10] The ligated alkyne would then be more easily deprotonated by the amine, and a new complex would be formed ArPd(–C≡CR)L_n (n = 1 or 2), which gives the coupling product ArC≡CR by reductive elimination. In the absence of any amine, a carbopalladation step[11,12] takes place, which leads to R–C($PdXL_2$)=CH–Ar complexes,[12] presumably by formation of ArPdXL(η^2-HC≡CR) complexes.[11]

Herein we report that amines react with *trans*-ArPdX(PPh_3)$_2$ (**1**) complexes by substitution of one PPh_3 to generate ArPdX(PPh_3)(amine) (**2**) complexes (Scheme 3). In other words, competition between the amine and the alkyne for the substitution of one phosphane group in ArPdX(PPh_3)$_2$ complexes may occur in palladium-catalyzed copper-free Sonogashira reactions.

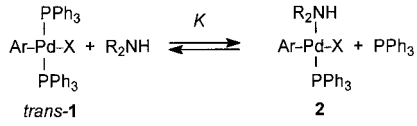

Scheme 3.

The reactions of the secondary (piperidine, morpholine, and diisopropylamine) and primary amines (terbutylamine) with **1** were monitored by ^1H and ^{31}P NMR spectroscopy in DMF, THF, acetone, and chloroform, after successive additions of known amounts of amine. Besides the set of the ^1H NMR signals for the protons of the Ar group in **1**, a new set of signals appears at lower field, suggesting that a new complex **2** is formed. The magnitude of the ^1H NMR signals of **2** increases at the expense of those of complexes **1** as the amine concentration is increased. Concomitant ^{31}P NMR spectroscopy performed on the same solutions shows that signals for free PPh_3[13] are detected in the ^{31}P NMR spectra, together with a new singlet (δ_2 in Table 1) located

[a] Ecole Normale Supérieure, Département de Chimie, UMR CNRS-ENS-UPMC 8640,
24 Rue Lhomond, 75231 Paris Cedex 5, France
Fax: +33-1-4432-3325
E-mail: Anny.Jutand@ens.fr

Supporting information for this article is available on the WWW under http://www.eurjic.org or from the author.

Table 1. Equilibrium constants K and ^{31}P NMR shifts (101 MHz, H_3PO_4) of *trans*-ArPdX(PPh_3)$_2$ (δ_1)and ArPdX(PPh_3)(amine) (δ_2) generated by the reversible substitution of one PPh_3 group by the amine group (Scheme 3)

Entry	*trans*-ArPdX(PPh_3)$_2$	δ_1 [ppm]	ArPdX(PPh_3)(amine)	δ_2 [ppm][a]	K
Solvent		[D_7]DMF		[D_7]DMF	[D_7]DMF
1	PhPdI(PPh_3)$_2$	23.14	PhPdI(PPh_3)(piperidine)	32.56[b]	0.095
Solvent		[D_8]THF		[D_8]THF	[D_8]THF
2	PhPdI(PPh_3)$_2$	23.22	PhPdI(PPh_3)(piperidine)	33.18 [c]	0.14
Solvent		[D_6]acetone		[D_6]acetone	[D_6]acetone
3	PhPdI(PPh_3)$_2$	23.04	PhPdI(PPh_3)(piperidine)	32.83	n.d.[j]
Solvent		$CDCl_3$		$CDCl_3$	$CDCl_3$
4	PhPdI(PPh_3)$_2$	23.03	PhPdI(PPh_3)(piperidine)	32.45	0.11
5			PhPdI(PPh_3)(morpholine)	32.73	0.026
6			PhPdI(PPh_3)(tBuNH$_2$)	32.09[d]	0.002
7			PhPdI(PPh_3)(iPr$_2$NH)	31.72[e]	7×10^{-5}
8	PhPdBr(PPh_3)$_2$	23.72	PhPdBr(PPh_3)(piperidine)	32.08	0.28
9			PhPdBr(PPh_3)(morpholine)	32.37	0.014
10	PhPdCl(PPh_3)$_2$	23.73	PhPdCl(PPh_3)(piperidine)	31.76[f]	0.21
11			PhPdCl(PPh_3)(morpholine)	31.98	0.013
12	(4-NC–C_6H_4)PdI(PPh_3)$_2$	22.97	(4-NC–C_6H_4)PdI(PPh_3)(piperidine)	31.83[g]	0.023
13			(4-NC–C_6H_4)PdI(PPh_3)(morpholine)	32.25[h]	0.0038
14	(4-NC–C_6H_4)PdBr(PPh_3)$_2$	23.75	(4-NC–C_6H_4)PdBr(PPh_3)(piperidine)	31.48	0.038
15			(4-NC–C_6H_4)PdBr(PPh_3)(morpholine)	31.97	0.0033
16	(4-MeOC–C_6H_4) PdBr(PPh_3)$_2$	23.69	(4-MeOC–C_6H_4)PdBr(PPh_3)-(piperidine)	31.71[i]	n.d.[k]
17	(2-Th)PdI(PPh_3)$_2$[l]	21.97	(2-Th)PdI(PPh_3)(piperidine)	30.72	0.1

[a] δ_2 is the shift of the major isomer. [b] A minor isomer (16%) was observed at δ = 30.52 ppm. [c] A minor isomer (6%) was observed at δ = 32.22 ppm. [d] A minor isomer (11%) was observed at δ = 27.62 ppm. [e] Two other isomers (11%) were observed at δ = 28.20 and 30.10 ppm. [f] A minor isomer (13%) was observed at δ = 33.82 ppm.[g] A minor isomer (27%) was observed at δ = 31.31 ppm. [h] A minor isomer (40%) was observed at δ = 31.62 ppm. [i] A minor isomer (39%) was observed at δ = 31.42 ppm. [j] None determined because of the very low solubility of *trans*-PhPdI(PPh_3)$_2$ in acetone. [k] None determined because of the presence of some triphenylphosphane oxide. [l] Th means thienyl.

at lower field than those of the initial complexes **1** (δ_1 in Table 1). The magnitude of the singlet for free PPh_3 is similar to those of the new complexes **2** and both increase concomitantly at the expense of those of **1** as the amine concentration is increased. These experiments establish that one PPh_3 group is substituted by one amine group (Scheme 3).[14–18] The coordinated amine was characterized by its ^1H and ^{13}C NMR signals in isolated complexes **2**.

The reversibility of the substitution is proved by the fact that the amount of **2** increases at the expense of **1** when the amine concentration is increased, and addition of PPh_3 to solutions containing both complexes **1** and **2** results in an increase in the amount of **1** to the detriment of **2**. Addition of PPh_3 to the isolated complex 2-ThPdI(PPh_3)(piperidine) (Th = thienyl) results in the formation of *trans*-2-ThPdI(PPh_3)$_2$, and the release of the free piperidine is clearly detected by the ^1H NMR spectroscopy – further evidence of the equilibrium in Scheme 3. Complexes **1** and **2** are involved in equilibria that are slow relative to the time scale of NMR spectroscopy.

The substitution of the two PPh_3 was never observed,[19] even in the presence of a large amount of amine. Indeed, the integration of the ^{31}P NMR signal for the free phosphane never exceeded that of the monosubstituted complex ArPdX(PPh_3)(amine).

The substitution of PPh_3 in *trans*-ArPdX(PPh_3)$_2$ (**1**) by the amine occurs irrespective of the identity of X (= I, Br, Cl) and the aryl groups (Ar = Ph, 2-thienyl, 4-NC–C_6H_4, 4-MeOC–C_6H_4) investigated here (Table 1). One major complex of type **2** is generally generated (Table 1). Its structure, given in Scheme 3, was deduced from its ^{13}C NMR spectrum, in agreement with the value of the J_{CP} coupling, characteristic of a phosphane *cis* to the aryl group. In some cases, a second minor singlet near that observed at δ_2 is detected (Table 1), which suggests isomerisation of the ligands of **2** around the Pd^{II} centre, as observed for the P(*o*-Tol)$_3$ (*o*-Tol: *ortho*-tolyl) ligand.[20] Indeed, related complexes ArPdBr(amine)(P[*o*-Tol]$_3$) have been synthesized by a quite different reaction, not by ligand substitution but by cleavage of the bromide bridges by the amine in dimeric [ArPdBr(P[*o*-Tol]$_3$)]$_2$ complexes (Scheme 4).[20,21] The major isomer ArPd(amine)(P[*o*-Tol]$_3$) has the same structure as complexes **2** with the phosphane *trans* to the amine group.[20] Two other minor isomers only characterized by ^{31}P NMR singlets are also observed.[20]

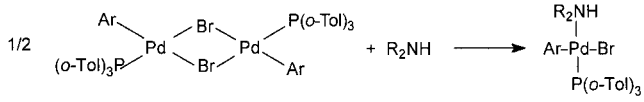

Scheme 4.

The complexes ArPdX(PPh_3)(amine) **2** generated in situ were rather stable with time in chloroform. After some days, phosphane oxide was detected as a by-product, with the effect that the amount of complexes **2** had increased relative to that of complexes **1**, by the shift of the equilibrium in Scheme 3 to the right as a result of the oxidation of PPh_3. As an isolated complex, PhPdI(PPh_3)(piperidine) was stable for at least four days in chloroform.

 © 2005 Wiley-VCH Verlag GmbH & Co. KGaA, Weinheim

The value of the equilibrium constant in Scheme 3, K = [**2**][PPh_3]/[**1**][amine] was determined by ^{31}P NMR spectroscopy by using the respective integration of the singlets of complexes **1** and **2**;[22] $K = x^2/(1-x)(n-x)$, where x is the molar fraction of **2** in the equilibrium: $x = 2S_2/(S_1 + 2S_2)$ [S_1 and S_2: magnitude of the singlet of **1** and **2**, respectively], n is the equiv. of amine added to **1**. The plot of x^2 versus $(1-x)(n-x)$ is linear, and K is determined from the slope of the straight line (Figure 1,Table 1).

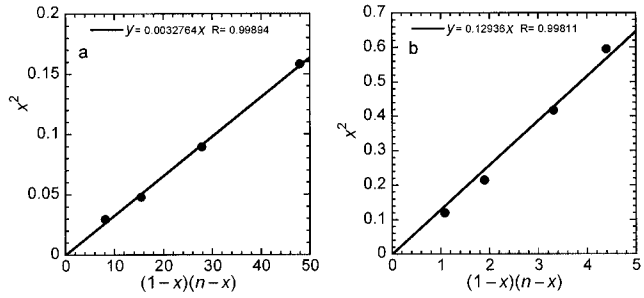

Figure 1.Determination of the equilibrium constant K between *trans*-ArPdX(PPh_3)$_2$**1** and ArPdX(PPh_3)(amine) **2** (Scheme 3) as monitored by ^{31}P NMR spectroscopy; plot of x^2 versus $(1-x)(n-x)$ [x is the molar fraction of **2** in the equilibrium; n is the equiv. of amine added to **1**]; K is determined from the slope; a) equilibrium between *trans*-(4-NC–C_6H_4)PdBr(PPh_3)$_2$ (initially 30 mM) and (4-NC–C_6H_4)PdBr(PPh_3)(morpholine) in $CDCl_3$ (n = 10, 20, 40, 80); b) equilibrium between *trans*-PhPdI(PPh_3)$_2$ (initially 20 mM) and PhPdI(PPh_3)(piperidine) in [D_8]THF (n = 2, 4, 10, 20)

The value of K is less than 1 (Table 1), which means that, under identical concentrations of ArPdX(PPh_3)$_2$ and amine, the equilibrium lies in favor of ArPdX(PPh_3)$_2$. However, in catalytic reactions where the concentration of the amine is always considerably higher than that of the catalytic palladium species, the equilibrium will be shifted toward the formation of ArPdX(PPh_3)(amine). As an example, if the concentration of the piperidine is 50 times higher than that of *trans*-PhPdI(PPh_3)$_2$ in DMF (corresponding to a catalytic reaction run with 2% of catalyst), then, with K = 0.095 (Table 1), one calculates that the concentration of PhPdI(PPh_3)(piperidine) will be 5.5 times higher than that of *trans*-PhPdI(PPh_3)$_2$.

The ligand substitution was studied under reversible conditions. We only have the thermodynamic data for the formation of complexes **2**. From the values of the equilibrium constant K collected in Table 1, it can be seen that for a given Ar group and X, K increases, and consequently the substitution is favored as the amine basicity[23] increases within the cyclic series (piperidine and morpholine: compare entries 4 and 5, 8 and 9, 10 and 11, 12 and 13, and 14 and 15). However, the magnitude of K follows the order (compare entries 4–7): piperidine > morpholine > $tBuNH_2$ >> iPr_2NH.

This does not reflect the amine basicity order since on one hand morpholine is less basic than tBuNH$_2$ and iPr$_2$NH, and on the other hand iPr$_2$NH is slightly more basic than tBuNH$_2$.[23] The steric hindrance of the amine may also affect the substitution. Indeed, *N*-methylmorpholine, even when used at high concentrations, could not displace the phosphane. The equilibrium constant is not significantly affected by the solvent (entries 1,2,4).

For a given X, amine and solvent, K decreases when the *para* substituent on the aryl group is an electron acceptor (entries 4 and 12, 5 and 13, 8 and 14, and 9 and 15).[24,25] The reaction was not tested with an electron-donor substituent because of the instability of the related *trans*-ArPdX(PPh_3)$_2$ due to scrambling between the Ph group of the ligand and the Ar group.[26,27]

The influence of X (X = I, Br, Cl) on the substitution was tested for a given Ar group, amine and solvent. Whereas for the substitution of PPh_3 by the piperidine K follows the order: Br > Cl > I (entries 4, 8,10; entries 12, 14), a reverse order: I > Br ≈ Cl (entries 5, 9, 11; entries 13,15) is found for the substitution by morpholine. The effect of the halides is hard to rationalize, since they cannot have a *trans* influence on the substitution of the phosphane due to the structure of the initial complexes **1**.[24,25]

In conclusion, ArPdX(PPh_3)(amine) complexes were generated by the reaction of amines with *trans*-ArPdX(PPh_3)$_2$ complexes. The reversible substitution of one PPh_3 group by one amine was characterized by the determination of the equilibrium constant between the two complexes. These results establish that in copper-free Sonogashira reactions, the formation of ArPdX(PPh_3)(amine) complexes has to be taken into account. There will be an evident competition between the alkyne and the amine for the substitution of one PPh_3 group in ArPdX(PPh_3)$_2$ complexes. The fact that the amine is often used in large excess[5,6,8,9] or as the solvent[3,6,7] encourages the substitution of the phosphane by the amine group. Work is in progress to better define the contribution of such new amine complexes in the mechanism of palladium-catalyzed reactions involving amines in copper-free Sonogashira reactions.

Experimental Section

General: All experiments were conducted under argon. The deuterated solvents DMF, THF, acetone and chloroform were obtained commercially and degassed just before use. The amines (piperidine; morpholine, diisopropylamine, terbutylamine), phenyl halides (X = I, Br, Cl), 4-NC–C_6H_4–X (X = Br, Cl), 4-MeOC–C_6H_4–Br, 2-iodothiophene were obtained commercially. The complexes *trans*-ArPdX(PPh_3)$_2$ were synthesized by reacting aryl halides with $Pd^0(PPh_3)_4$.[28–30]

General Procedure for the Ligand Exchange as Monitored by ^1H and ^{31}P NMR Spectroscopy: *trans*-PhPdI(PPh_3)$_2$ (8.3 mg, 0.01 mmol) was introduced in $CDCl_3$ (0.5 mL). The ^1H and ^{31}P NMR spectra were recorded at room temperature. Piperidine (2 μL, 0.02 mmol) was first added, followed by further additions of piperidine (0.02, 0.06 and 0.10 mmol, respectively). ^1H and ^{31}P NMR spectra were recorded after each addition of piperidine.

General Procedure for the Synthesis of ArPdX(PPh_3)(amine): Piperidine (500 μL, 5 mmol) was added to *trans*-PhPdI(PPh_3)$_2$ (83 mg, 0.1 mmol) in chloroform (5 mL). After 30 min, the solution was concentrated under vacuum. Precipitation in pentane gave 48 mg of PhPdI(PPh_3)(piperidine), as a gray-white solid (72 % yield). The isolated complex exhibits the same ^1H and ^{31}P NMR spectra as those recorded during ligand exchange in the NMR tube, but the

 © 2005 Wiley-VCH Verlag GmbH & Co. KGaA, Weinheim

protons of the ligated piperidine are more clearly detected because of the absence of excess piperidine. A ^{13}C NMR spectrum was also recorded on the isolated complex to elucidate its structure.

The complexes with morpholine, $ArPdX(PPh_3)$(morpholine), could not be isolated as pure compounds because the equilibrium lies less in favor of their formation than for the formation of $ArPdX(PPh_3)$(piperidine). The reversibility explains the difficulty in their isolation. Consequently, most of them were characterized in situ in solution.

***trans*-PhPdI(PPh$_3$)$_2$:**[28] ^1H NMR (250 MHz, $CDCl_3$, TMS): δ = 6.21 (t, J = 7 Hz, 2 H, *m*-H of Ph), 6.33 (t, J = 7 Hz, 1 H, *p*-H of Ph), 6.60 (d, J = 7 Hz, 2 H, *o*-H of Ph), 7.23 (t, J = 7 Hz, 12 H, *m*-H in PPh_3), 7.32 (t, J = 7 Hz, 6 H, *p*-H in PPh_3), 7.50 (dd, J = 7, J = 6 Hz, 12 H, *o*-H in PPh_3) ppm. ^{13}C NMR (62.89 MHz, $CDCl_3$, TMS): δ = 127.76 (t, J_{C3P} = 5 Hz, C_3 of Ph in PPh_3), 127.90 (t, J_{C3P} = 4 Hz, C_3 of Ph–Pd), 129.69 (s, C_4 of Ph in PPh_3), 131.31 (s, C_4 of Ph–Pd), 132.21 (t, J_{C1P} = 23 Hz, C_1 of Ph in PPh_3), 134.65 (t, J_{C2P} = 6 Hz, C_2 of Ph–Pd), 134.89 (t, J_{C2P} = 6 Hz, C_2 of Ph in PPh_3), 136.03 (t, J_{C1P} = 5 Hz, C_1 of Ph–Pd) ppm. ^{31}P NMR (101 MHz, $CDCl_3$, H_3PO_4): δ = 23.03 (s) ppm.

***trans*-(4-NC–C$_6$H$_4$)PdBr(PPh$_3$)$_2$:**[30] ^1H NMR ($CDCl_3$, TMS): δ = 6.41 (d, J = 8 Hz, 2 H, *m*-H), 6.80 (d, J = 8 Hz, 2 H, *o*-H), 7.30 (m, 18 H, *m*-H and *p*-H in PPh_3), 7.52 (dd, J = 7, J = 6 Hz, 12 H, *o*-H in PPh_3) ppm. ^{31}P NMR ($CDCl_3$, H_3PO_4): δ = 23.75 (s) ppm.

***trans*-(2-Th)PdI(PPh$_3$)$_2$:** ^1H NMR ($CDCl_3$, TMS): δ = 5.89 (d, J = 3.3 Hz, 1 H, 5-H in Th), 6.34 (dd, J = 5, J = 3.3 Hz, 1 H, 4-H in Th), 6.82 (d, J = 5 Hz, 1 H, 3-H in Th), 7.29 (m, 18 H, *m*-H and *p*-H in PPh_3), 7.53 (dd, J = 6, J = 5.5 Hz, 12 H, *o*-H in PPh_3) ppm. ^{31}P NMR ($CDCl_3$, H_3PO_4): δ = 30.72 (s) ppm.

PhPdI(PPh$_3$)(piperidine): Isolated complex, yield 72%. ^1H NMR (250 MHz, $CDCl_3$, TMS): δ = 1.25 (m, 2 H, γCH_2), 1.38 (m, 2 H, βCH_2), 1.55 (m, 2 H, βCH_2), 2.39 (ddd, J = 13 Hz, 2 H, HC–N–CH), 3.29 (d, J = 13 Hz, 2 H, HC–N–CH), 3.43 (br. s, 1H, NH), 6.67 (m, 3 H, *m*-H and *p*-H of Ph), 6.95 (br. d, J = 4.5 Hz, 2 H, *o*-H of Ph), 7.22 (t, J = 6 Hz, 6 H, *m*-H in PPh_3), 7.25 (m, 3 H, *p*-H in PPh_3), 7.46 (t, 6 H, *o*-H in PPh_3) ppm. ^{13}C NMR (62.89 MHz, $CDCl_3$, TMS): δ = 23.83 (CH_2–*C*H_2–CH_2 of piperidine), 24.75 (N–CH_2–*C*H_2 of piperidine), 49.34 (N*C*H_2 of piperidine), 127.53 (d, J_{C3P} = 1.5 Hz, C_3 of Ph–Pd), 127.76 (d, J_{C3P} = 10.5 Hz, C_3 of Ph in PPh_3), 127.99 (s, C_4 of Ph–Pd), 129.99 (s, C_4 of Ph in PPh_3), 132.1 (d, J_{C1P} = 50 Hz, C_1 of Ph in PPh_3), 134.28 (d, J_{C2P} = 4.6 Hz, C_2 of Ph–Pd), 134.78 (d, J_{C2P} = 11 Hz, C_2 of Ph in PPh_3), 160.58 (d, J_{C1P} = 2.3 Hz, C_1 of Ph–Pd) ppm. ^{31}P NMR (101 MHz, $CDCl_3$, H_3PO_4): δ = 32.45 (s) ppm. $C_{29}H_{31}INPPd$ (657.8): calcd. C 52.9, H 4.7, N 2.1; found C 51.9, H 4.2, N 1.8.

(4-NC–C$_6$H$_4$)PdBr(PPh$_3$)(morpholine): Isolated complex. ^1H NMR (250 MHz, $CDCl_3$, TMS): δ = 2.57 (ddd, J = 12 Hz, 2 H, HCNCH), 3.10 (d, J = 12 Hz, 2 H, HCNCH), 3.49 (dd, J = 12 Hz, 2 H, HCOCH), 3.73 (m, 2 H, HCOCH), 6.92 (d, J = 8 Hz, 2 H, *m*-H), 7.17 (d, J = 8 Hz, 2 H, *o*-H), 7.30 (m, 9 H, *m*-H and *p*-H in PPh_3), 7.52 (m, 6 H, *o*-H in PPh_3) ppm. ^{31}P NMR (101 MHz, $CDCl_3$, H_3PO_4): δ = 32.38 (s) ppm.

(2-Th)PdI(PPh$_3$)(piperidine): Isolated complex. ^1H NMR (250 MHz, $CDCl_3$, TMS): δ = 1.32 (m, 2 H, γCH_2), 1.65 (br. t, 4 H, βCH_2), 2.70 (ddd, J = 12 Hz, 2 H, HCNCH), 3.09 (s, 1 H, NH), 3.25 (d, J = 13.5 Hz, 2 H, HCNCH), 6.35 (d, J = 3.3 Hz, 1 H, 5-H in Th), 6.72 (dd, J = 5, J = 3.3 Hz, 1 H, 4-H in Th), 7.10 (d, J = 5 Hz, 1 H, 3-H in Th), 7.32 (m, 9 H, *m*-H and *p*-H in PPh_3), 7.52 (m, 6 H, *o*-H in PPh_3) ppm. ^{31}P NMR (101 MHz, $CDCl_3$, H_3PO_4): δ = 30.72 (s) ppm.

Acknowledgments

This work has been supported in part by the Centre National de la Recherche Scientifique (UMR CNRS-ENS-UPMC 8640) and the Ministère de la Recherche (Ecole Normale Supérieure). We thank Johnson Matthey for the loan of sodium tetrachloropalladate.

[1] K. Sonogashira, N. Hagihara, *Tetrahadron Lett.* **1975**, 4467–4470.
[2] K. Sonogashira, "Sonogashira Alkynes Synthesis", in *The Handbook of Organopalladium Chemistry for Organic Synthesis* (Ed.: E. Negishi), Wiley-Interscience, New York, **2002**, vol. 1, pp. 493–529.
[3] M. Alami, F. Ferri, G. Linstrumelle, *Tetrahedron Lett.* **1993**, *34*, 6403–6406.
[4] J. F. Nguefack, V. Bolitt, D. Sinou, *Tetrahedron Lett.* **1996**, *37*, 5527–5530.
[5] V. P. W. Böhm, W. A. Herrmann, *Eur. J. Org. Chem.* **2000**, 3679–3681.
[6] R. G. Heidenreich, K. Kölher, J. G. E. Krauter, J. Pietsch, *Synlett* **2002**, 1118–1122.
[7] M. Pal, K. Parasuraman, S. Gupta, K. R. Yeleswarapu, *Synlett* **2002**, 1976–1982.
[8] T. Fukuyama, M. Shinmen, S. Nishitani, M. Sato, I. Ryu, *Org. Lett.* **2002**, *4*, 1691–1694.
[9] N. E. Leadbeater, B. J. Tominack, *Tetrahedron Lett.* **2003**, *44*, 8653–8656.
[10] A. Soheili, J. Albaneze-Walker, J. A. Murry, P. G. Dormer, D. L. Hughes, *Org. Lett.* **2003**, *5*, 4191–4194.
[11] S. Cacchi, G. Fabrizi, "Carbopalladation of Alkynes Followed by Trapping with Nucleophilic Reagents", in *The Handbook of Organopalladium Chemistry for Organic Synthesis* (Ed.: E. Negishi), Wiley-Interscience, New York, **2002**, vol. 1, pp. 1335–1367.
[12] C. Amatore, S. Bensalem, S. Ghalem, A. Jutand, *J. Organomet. Chem.* **2004**, 689, 4642–4646.
[13] The ^{31}P NMR singlet of the free PPh_3 was located at –5.24 in [D$_8$]THF, –5.62 in [D$_9$]DMF, –5.46 in [D$_6$]acetone and –5.18 ppm in $CDCl_3$.
[14] The substitution of one phosphane group by one amine group in square-planar d^8 complexes *trans*-$RMXL_2$ (M = Pt, Pd; R = organic group; X = halide andL = PR'_3) is quite unusual.[15,16] What is often observed is the substitution of one halide ligand in *trans*-$RMXL_2$ (M = Pt, Pd; X = Br, Cl) complexes by an amine to generate cationic complexes [RM(amine)L_2]$^+X^-$, as in the reaction of pyridine (py) with *trans*-$ArPtCl(PEt_3)_2$ complexes that forms *trans*-[$ArPt(PEt_3)_2$(py)]$^+Cl^-$.[17,18]
[15] For substitutions reactions in square-planar d^8 complexes *trans*-$RMXL_2$ see: M. L. Tobe, "Reactions Mechanisms", in *Comprehensive Coordination Chemistry* (Eds.: G. Wilkinson, R. D. Gillard, J. A. McCleverty), Pergamon Press, **1987**, vol. 1., pp. 281–329.
[16] See also: R. B. Jordan, "Ligand Substitution Reactions," in *Reaction Mechanisms of Inorganic and Organometallic system*, 2nd ed., Oxford University Press, **1998**, pp. 35–101.
[17] F. Basolo, J. Chatt, H. B. Gray, R. G. Pearson, B. L. Shaw, *J. Chem. Soc.* **1961**, 2207–2215.
[18] G. Faraone, V. Ricevuto, R. Romeo, M. Trozzi, *J. Chem. Soc. Dalton Trans.* **1974**, 1377–1380.
[19] This is in contrast to monobenzylamines [e.g. Me($PhCH_2$)NH] which, when used in large excess, can displace the P(*o*-Tol)$_3$ ligand in the dimers [$ArPdX(P[o\text{-Tol}]_3)]_2$ (X = I, Br, Cl) to generate bis(amine) $ArPdX(Me[PhCH_2]NH)_2$ complexes via the intermediate mono(amine) complex $ArPdX(Me[PhCH_2]$-NH)(P[*o*-Tol]$_3$). See: R. A. Widenhoefer, S. L. Buchwald, *Organometallics* **1996**, *15*, 3534–3542.

 © 2005 Wiley-VCH Verlag GmbH & Co. KGaA, Weinheim

[20] F. Paul, J. Patt, J. F. Hartwig, *Organometallics* **1995**, *14*, 3030–3039.
[21] The reaction in Scheme 4 is reversible for benzylamines. The geometry of the resulting complexes is not established. The amine is supposed to be *trans* to the phosphane. R. A. Widenhoefer, A. H. Zhong, S. L. Buchwald, *Organometallics* **1996**, *15*, 2745–2754.
[22] When a second isomer was formed and detected by its singlet (Table 1), its integration was taken into account to determine the equilibrium constant.
[23] The basicity scale is given in aqueous solution (pK_a): piperidine (11.12), iPr$_2$NH (10.96), tBuNH$_2$ (10.83), morpholine (8.21); R. C. Weast (Ed.), *Handbook of Chemistry and Physics*, 52nd ed., The Chemical Rubber Co., Ohio, USA, **1971/1972**, p. D-117.
[24] It has been established that the ligand in a *trans* position to the leaving group has a significant effect on the rate of the substitution reactions (*trans* effect). Here we are discussing thermodynamic factors (*trans* influence),[25] i.e. how the ligand *trans* to the leaving group can weaken the bond of the leaving group in the ground state of the reactant. In complexes **1**, the aryl group and the halide are in a *cis* position to the leaving group and would have a *cis* influence on the substitution. In general, the *cis* influence is less effective than the *trans* influence.[25]
[25] T. G. Appleton, H. C. Clark, L. E. Manzer, *Coord. Chem. Rev.* **1973**, *10*, 335–422.
[26] For scrambling reactions, see: F. E. Goodson, T. I. Wallow, B. M. Novak, *J. Am. Chem. Soc.* **1997**, *119*, 12441–12453.
[27] A scrambling reaction was also observed with *trans*-(4-NC–C$_6$H$_4$)PdCl(PPh$_3$)$_2$, which suggests that the scrambling also depends on the halide ligated to the Pd^{II} centre.
[28] P. Fitton, M. P. Johnson, J. E. McKeon, *Chem. Commun.* **1968**, 6–7.
[29] D. R. Coulson, *Chem. Commun.* **1968**, 1530–1532.
[30] P. Fitton, E. A. Rick, *J. Organomet. Chem.***1971**, *28*, 287–791.

Received May 19, 2004

 © 2005 Wiley-VCH Verlag GmbH & Co. KGaA, Weinheim

New Complexes of Divalent Thulium with Substituted Phospholyl and Cyclopentadienyl Ligands

François Nief,*[a] Brice Tayart de Borms,[a] Louis Ricard,[a] and Duncan Carmichael[a]

Keywords: Phosphorus heterocycles / Lanthanides / Subvalent compounds / Thulium / Cyclopentadienyl ligands

In order to try to stabilise the Tm^{II} ion with phospholyl ligands lacking methyl groups at the 3 and 4 positions, the following ligand precursors were prepared: sodium 2,5-di-*tert*-butylphospholyl [Na(Htp)] (**3**) and sodium 2,5-bis(trimethylsilyl)phospholyl [Na(Hsp)] (**8**). Because of its similar steric bulk, we also decided to use sodium di-*tert*-butylcyclopentadienyl [$NaCp^{tt}$] (**9**) as a ligand precursor. Compound **3** was obtained by sodium cleavage of the P–P bond of 2,5,2′,5′-tetra-*tert*-butyl-1,1′-diphosphole (**2**). Halogen-lithium exchange in 1,4-diiodo-1,4-bis(trimethylsilyl)buta-1,3-diene (**4**) followed by reaction with $PhPCl_2$ afforded 1-phenyl-2,5-bis(trimethylsilyl)phosphole (**5**). Treatment of **5** with lithium metal followed by oxidative treatment with iodine gave 2,5,2′,5′-tetrakis(trimethylsilyl)-1,1′-diphosphole (**7**) which could be transformed into **8** by treatment with sodium. Treatment of **3**, **8** and **9** with $[TmI_2(THF)_3]$ in diethylether yielded three new organothulium(II) complexes $[Tm(Htp)_2(THF)]$ (**10**), $[Tm(Hsp)_2(THF)]$ (**11**) and $[Tm(Cp^{tt})_2(THF)]$ (**12**), respectively, which could be isolated pure as crystalline solids in low to moderate yields. Complexes **10**, **11** and **12** were studied by X-ray crystallography and their structures compared with those of two previously described complexes, $[Tm(Cp'')_2(THF)]$ **1** [Cp′′ = 1,3-bis(trimethylsilyl)cyclopentadienyl] and $[Tm(Dtp)_2(THF)]$ (**13**) (Dtp = 3,4-dimethyl-2,5-di-*tert*-butylphospholyl). Although the phospholyl ligands may be slightly more bulky than their cyclopentadienyl counterparts, the structures of **1**, **10**, **11** and **12** are remarkably similar and are substantially different from that of the more bulky **13**.

(© Wiley-VCH Verlag GmbH & Co. KGaA, 69451 Weinheim, Germany, 2005)

Introduction

For a long time, the coordination chemistry of divalent lanthanide (Ln) ions has been limited to the classical Eu^{II}, Yb^{II} and Sm^{II}.[1] Although other Ln^{II} species can exit in the solid state, these ions were until recently considered too reactive to be isolated as molecular compounds.[2]

However, this statement has been challenged very recently by the isolation of molecular solvates of the type $[MI_2(solv.)_n]$ where M = Nd, Dy or Tm and solv. is a donor solvent such as THF or dimethoxyethane (DME).[3–7] As expected, these species are highly reducing. While solvated TmI_2[3,4] is reasonably stable, solvated DyI_2[6] and NdI_2[7] are highly reactive complexes which are only stable below room temperature.

In coordination chemistry, no other complexes of Nd^{II} and Dy^{II} have been isolated up to now although their transient nature has been postulated in trapping reactions. Likewise, some transient Tm^{II} complexes have also been observed this way. For instance the M^{II} cations can be trapped with nitrogen, forming [μ-(N_2^{2-})] complexes[8–10] or by oxidative splitting of the coordinated solvent[8,11] or the ligand[12] thus yielding M^{III} complexes. They are also able to reduce aromatic hydrocarbons[6,13] or acetonitrile.[14] Interestingly, reduction of Ho^{III} or Y^{III} amides in the presence of nitrogen also yields products in which N_2 has been activated.[15]

In the case of Tm^{II}, however, after some unsuccessful attempts, Evans et al. isolated the first structurally characterised organometallic complex of thulium(II), $[TmCp''_2(THF)]$ (**1**) [Cp′′ = $C_5H_3(SiMe_3)_2$].[8] Since then, by using very bulky phospholyl or arsolyl ligands, we have been able to isolate several other Tm^{II} compounds[16,17] including a homoleptic complex.[17] The chemistry of the "new" divalent lanthanides has been very recently reviewed.[18]

The phospholyl and arsolyl ligands appear particularly suitable for the stabilisation of low-valent complexes because of their reduced π-donating ability. So far, we have used the following ligands around Tm^{II}: Dsp = $PC_4Me_2(Tms)_2$, Dsas = $AsC_4Me_2(Tms)_2$ and Dtp = $PC_4Me_2tBu_2$. These ligands differ from the Cp′′ ligand by the presence of the heteroatom in the ring but also by their higher bulkiness due to the presence of two extra methyl groups as substituents.

At this point, we wanted to expand the scope of Tm^{II} chemistry by synthesising new complexes which would be sterically more similar to that of Evans (**1**).[8] Thus, we decided to attempt to stabilise the Tm^{II} ion with phospholyl

[a] Laboratoire Hétéroéléments et Coordination, CNRS UMR 7653, DCPH, Ecole Polytechnique,
91128 Palaiseau, France
Fax: +33-1-69333990
E-mail: nief@poly.polytechnique.fr

ligands lacking the two methyl groups on the rings which are present in Dsp and Dtp. These ligands are Hsp = $PC_4H_2(Tms)_2$ and Htp = $PC_4H_2tBu_2$. In order to have a complete picture, we also decided to use the well known Cp^{tt} ligand [Cp^{tt} = $C_5H_3tBu_2$] (Scheme 1). Interestingly, Lappert has recently characterised an unusual La^{II} anionic complex with this ligand, namely [K(18-crown-6)(η-$C_6H_6)_2$][$(LaCp^{tt}_2)_2$(μ-C_6H_6)] by reduction of the trivalent precursor [$(LaCp^{tt}_2)_3$].[19]

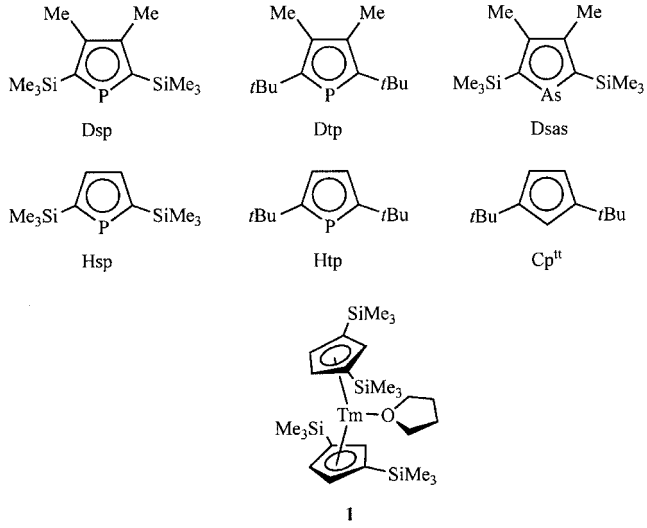

Scheme 1. Ligands and complexes in Tm^{II} chemistry

In this paper we report the synthesis of the new ligand Hsp, the synthesis of three new Tm^{II} complexes with the Hsp, Htp and Cp^{tt} ligands, and a structural study of these complexes by comparison with that of **1**.

Results and Discussion

Ligands

The synthesis of 2,5,2′,5′-tetra-*tert*-butyl-1,1′-diphosphole $(Htp)_2$ (**2**) has been described in the literature.[20] The new ligand precursor [Na(Htp)] (**3**) was simply obtained in good yield by sodium cleavage of the P–P bond in **2** (Scheme 2).

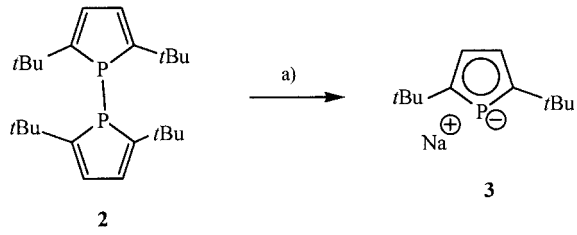

Scheme 2. Synthesis of Na(Htp) (**3**); reagents and conditions: a) excess Na, THF, room temp., 85%

The Hsp ring has not been described in the literature although Sato et al. have recently described a silole (silacyclopentadiene) possessing the same substituents on the heterocyclic ring. These authors, using trimethylsilylacetylene as a starting material, employed Ti^{II}-based chemistry in order to prepare 1,4-diiodo-1,4-bis(trimethylsilyl)buta-1,3-diene (**4**) as a key intermediate. Further iodine-lithium exchange followed by treatment with $Si(OEt)_4$ allowed them to isolate 1,1-dimethoxy-2,5-bis(trimethylsilyl)silole.[21]

Compound **4** was prepared with slight modifications to the original procedure due to scale-up. Iodine-lithium exchange in **4** with *n*BuLi in Et_2O followed by treatment with $PhPCl_2$ gave 1-phenyl-2,5-bis(trimethylsilyl)phosphole (**5**) in fair yield. Further treatment of **5** with potassium metal under the conditions previously used for the synthesis of [K(Dsp)][16] was less satisfactory and although [K(Hsp)] (**6**) was obtained as the major product, it was invariably contaminated with up to 20% of a product resulting from desilylation, i.e. [K{$PC_4H_3(SiMe_3)$}] (^{31}P NMR: δ = 116 ppm). Although repeated extraction of the crude solid with Et_2O could reduce the side product content of **6** to less than 10%, we nevertheless sought a better synthesis of the Hsp anion. We found that no concomitant desilylation took place when **4** was treated with lithium instead of potassium and the

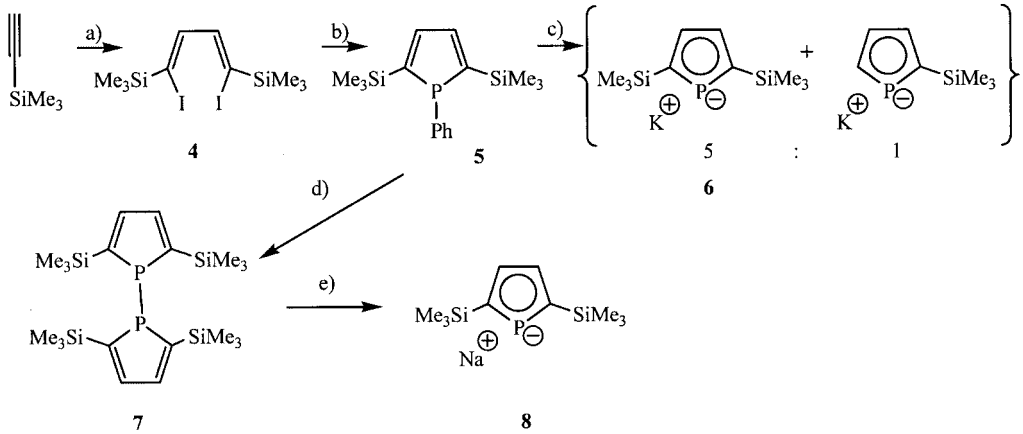

Scheme 3. Synthesis of Na(Hsp) (**8**); reagents and conditions: a) $Ti(OiPr)_4$ + *i*PrMgCl, Et_2O, –78 °C to –50 °C, 2 h, then I_2, –50 °C to room temp., 2 h, 67%; b) 2 *n*BuLi, Et_2O, –78° to room temp., 1h, then $PhPCl_2$, –78° to room temp., 30 min, 42%; c) excess K, DME, 70 °C, 2h; d) excess Li, THF, room temp., 3 h, then $AlCl_3$, 0 °C, 30 min, then I_2, room temp., 15min, 66%; e) excess Na, THF, room temp., 79%

 © 2005 Wiley-VCH Verlag GmbH & Co. KGaA, Weinheim

resultant [Li(Hsp)] could be transformed, in situ, into $(Hsp)_2$ (**7**) by treatment with iodine. Pure [Na(Hsp)] (**8**) was then obtained by treatment of **7** with sodium in THF (Scheme 3).

Finally, 1,3-di-*tert*-butylcyclopentadiene (HCp^{tt}) was prepared by literature methods[22] and transformed into [$NaCp^{tt}$] (**9**) by treatment with $NaNH_2$ in THF.[23]

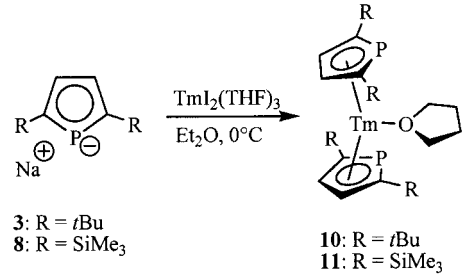

Scheme 4. Synthesis of Tm^{II} phospholyl complexes

New Complexes of Thulium(II)

We then tried to synthesise Tm^{II} complexes of the Htp, Hsp and Cp^{tt} ligands by utilising their sodium salts (**3**, **8**, and **9**, respectively) in reactions with [$TmI_2(THF)_3$], in a 2:1 mole ratio, at 0 °C and with diethylether as a solvent. With the phospholyl anions **3** and **8**, the reaction mixtures quickly turned dark green. After 1 hour, the solutions were checked by ^{31}P NMR spectroscopy and the spectra showed complete disappearance of the starting anions and the presence of two new, broad peaks at δ = –290 and –235 ppm, respectively, with Htp and Hsp as the ligands. These signals provided good evidence for the presence of Tm^{II} phospholyl complexes, their chemical shifts being similar to those of the already described [$Tm(Dtp)_2(THF)$] and [$Tm(Dsp)_2$-(THF)].[16] Complexes formulated as [$Tm(Htp)_2(THF)$] (**10**) and [$Tm(Hsp)_2(THF)$] (**11**) could be subsequently isolated as dark green crystalline powders from pentane at –30 °C (Scheme 4).

Complexes **10** and **11** exhibit reasonably well-resolved (and quite similar) proton NMR spectra in C_6D_6. Whilst the methyl groups could be clearly identified at low field (δ = 57 ppm for **10** and 43 ppm for **11**), the remaining signals (corresponding to the coordinated THF and the β-protons on the ring) were present as three sets of broad humps at high field which were difficult to integrate accurately due to their large width and baseline roll. In order to simplify this situation, we decided to prepare an analogue of **10** in which the THF was replaced by perdeuterated THF. This was accomplished by allowing **3** to react with unsolvated TmI_2 in diethylether in the presence ofca. 0.1 mL of [D_8]THF. Afterstandard workup, [$Tm(Htp)_2$([D_8]THF)] (**10-d**) could be isolated and its proton spectrum is presented below together with that of **10** (Figure 1).

A comparison of these spectra suggests that the signals around –30 ppm and –45 ppm in **10** belong to the THF solvent and that the peak at highest field around –70 ppm corresponds to the β-protons on the phospholyl ring. The assignment of the high-field signals in the spectrum of **11** was inferred accordingly (see experimental section). Finally, magnetic susceptibility measurements confirmed the +II oxidation state of thulium in **10** and **11**.

The reaction of **9** with [$TmI_2(THF)_3$] proceeded similarly to those described above but the solution colour was purplish-red. Evaporation to dryness of the filtered solution induced some apparent decomposition of the product since further extraction with pentane invariably resulted in the

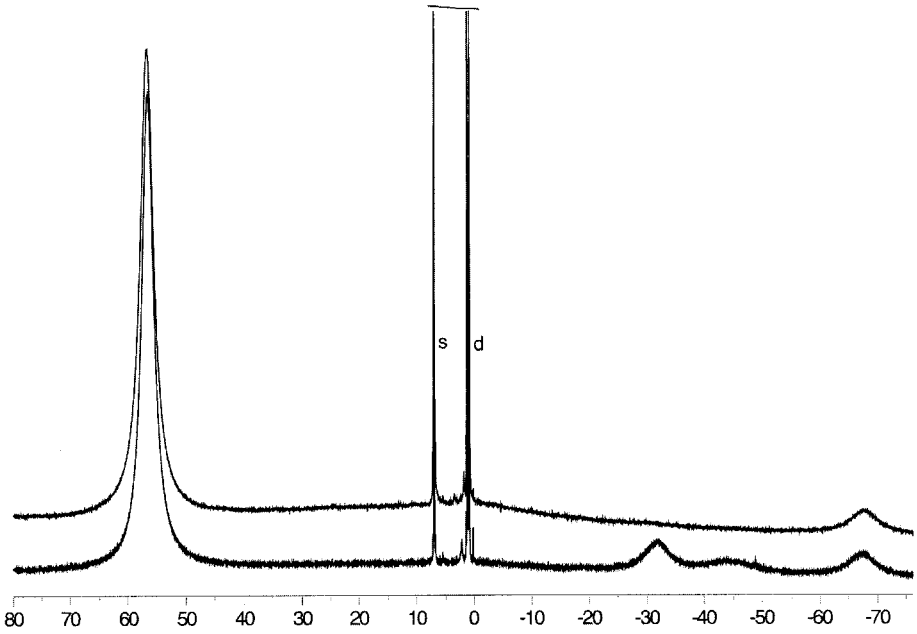

Figure 1. Proton NMR spectra (C_6D_6 solutions, ppm values) of **10**–**d** (upper trace) and **10** (lower trace) (s = C_6D_5H, d = diamagnetic impurities)

 © 2005 Wiley-VCH Verlag GmbH & Co. KGaA, Weinheim

precipitation of large amounts of white, insoluble material (this was not the case with the phospholyl compounds). We found that a red crystalline solid, formulated as [Tm(Cp^{tt})$_2$(THF)] (**12**) could be obtained in low yield by concentrating the filtered reaction mixture by evaporation of diethylether and allowing the solution to stand at –30 °C for two days. The proton NMR spectra of a solution of these crystals in [D_6]benzene or [D_{12}]cyclohexanedisplayed a peak at δ = 63 ppm which can reasonably be attributed to the methyl groups but the other parts of the spectra were less clear. We found that for **12** μ_{eff}= 4.6 μ_B, a value which is compatible with Tm^{II} (Scheme 5).

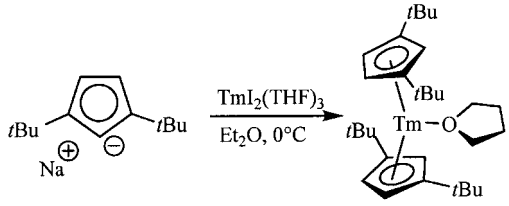

9 **12**

Scheme 5. Synthesis of a Tm^{II} cyclopentadienyl complex

Diethyl ether solutions of **10**, **11** and **12** were then exposed to 1atm. of nitrogen. In the case of **10** and **11**, no reaction had taken place after 24h at room temperature. In contrast, in the case of **12**, a colour change to light brown occurred within a few minutes. Unfortunately, however, despite several attempts, we could not isolate any crystalline product from this reaction mixture. Thus, no definite compounds could be isolated from the reaction of our new Tm^{II} complexes with N_2. Nevertheless, we can confirm that coordination of the phospholyl ligand considerably lessens the reactivity of thulium(II).

X-ray Crystal Structures

Suitable crystals of **10**, **11** and **12** were obtained by low-temperature crystallisation. A summary of the X-ray data is presented in Table 1 and Figure 2 shows ORTEP plots of one molecule each of **10**, **11** and **12**, respectively.

In the structures of **11** and **12**, the Tm–O bond coincides with a crystallographic symmetry axis. In addition, in **12**, the coordinated THF molecule is disordered over two positions and only one is presented in Figure 2. Table 2 displays relevant distances and angles for **10**, **11** and **12** together with relevant data for **1**[8] (the trimethylsilyl analogue of **12**) and [Tm(Dtp)$_2$(THF)] **13**[16] (analogue of **10** with two methyl substituents on the phospholyl ring).

The structures of **1**, **10**, **11** and **12** are strikingly similar. The Tm–O bond lengths and the ligand bending, as indicated by both the centroid-Tm-centroid angles and the dihedral angles between the mean planes of the π-ligands (referred to as ligand plane angles in Table 2), are almost identical in these four complexes. The main difference between the phospholyl complexes **10** and **11** and their cyclopentadienyl analogues (**12** and **1**, respectively) is that in **10** and **11** the C–Tm bonds are longer. This is probably due to the fact that the phospholyl complexes have to accommodate a long P–Tm bond in the Tm^{II} coordination sphere. Incidentally, this bond length in **10** and **11** falls in the range of the tabulated values for Yb^{II}–P bonds[24] (the ionic radii of Yb^{II} and Tm^{II} are similar). On these grounds, the steric bulk of the Hsp and Htp ligands should be larger than their all-carbon counterparts (Cp'' and Cp^{tt}, respectively). However, this is not reflected by the Tm–O distances and ligand bending in **1**, **10**, **11** and **12**. On the contrary, in **13**, all parameters relevant to steric crowding (Tm–O and Tm–C bond lengths, cnt–Tm–cnt and ligand plane angles) are higher than in **1**, **10**, **11** and **12**. This is most likely due to inter-

Table 1. Crystallographic data and data collection parameters

Compound	**10**	**11**	**12**
Mol. formula	$C_{28}H_{48}OP_2Tm$	$C_{24}H_{48}OP_2Si_4Tm$	$C_{30}H_{50}OTm$
Mol. mass	631.53	695.85	595.63
Crystal habit	green block	green block	deep red block
Crystal size [mm]	0.20 × 0.18 × 0.18	0.20 × 0.20 × 0.20	0.18 × 0.16 × 0.16
Crystal system	monoclinic	monoclinic	orthorhombic
Space group	$P2_1/n$ (No.14)	$C2/c$ (No.15)	$Pbcn$ (No.60)
a [Å]	11.2140(10)	20.2000(10)	10.9610(10)
b [Å]	17.0150(10)	11.1120(10)	15.2930(10)
c [Å]	15.4690(10)	14.9950(10)	17.1860(10)
β [°]	91.0540(10)	98.7800(10)	90
V [Å^3]	2951.1(4)	3326.4(4)	2880.8(4)
Z	4	4	4
d [g cm^{-3}]	1.421	1.389	1.373
F(000)	1292	1420	1228
μ [cm^{-1}]	3.132	2.922	3.098
Maximum θ [°]	30.00	30.03	30.03
Reflections measured	14403	13656	7936
Unique data	8577	4849	4221
R_{int}	0.0176	0.0663	0.0279
Reflections used	7111	3826	2778
wR_2 (all data)	0.0714	0.0912	0.1549
R_1	0.0275	0.0374	0.0544
GoF	1.034	0.965	1.102

 © 2005 Wiley-VCH Verlag GmbH & Co. KGaA, Weinheim

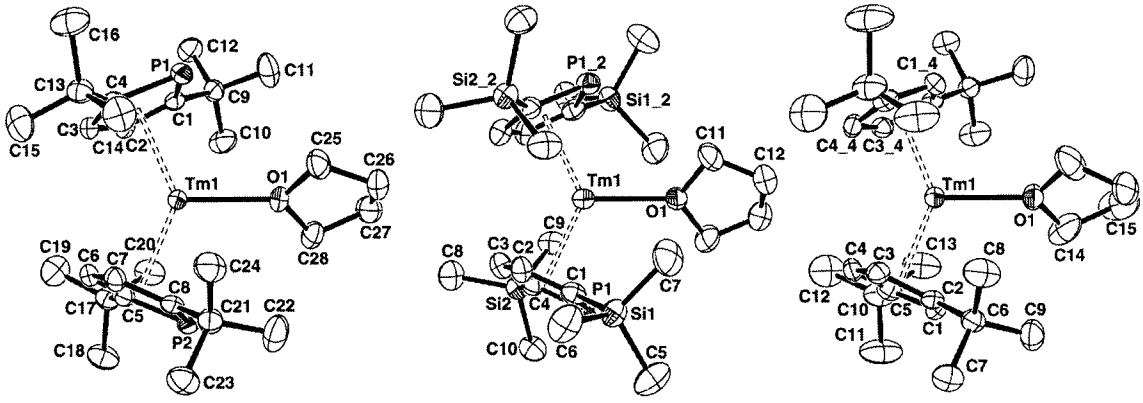

Figure 2. ORTEP plots of **10**, **11** and **12** together with the numbering schemes used (50% probability ellipsoids, H atoms omitted)

Table 2. Selected distances [Å] and angles [°] for complexes **1**, **10**, **11**, **12** and **13**

Distances [Å]	**1**[8]	**10**	**11**	**12**	**13**[16]
Tm–O	2.365(5)	2.393(2)	2.398(3)	2.388(7)	2.455(2)
Tm–C (min./av./max.)	2.65/2.68/2.71	2.72/2.76/2.80	2.72/2.75/2.79	2.65/2.68/2.74	2.77/2.83/2.90
Tm–P	–	2.941(2) (av.)	2.921(1)	–	2.95(1) (av.)
Tm–centroid (cnt)	2.39	2.45 (av.)	2.46	2.40	2.53 (av.)
Angles [°]					
Cnt–Tm–cnt	135	135	130	136	145
Ligand planes	133	131	128	131	146

ring steric repulsion of the methyl groups in **13**. Thus, adding methyl groups to the ring induces more structural changes than a CH ↔ P substitution.

Conclusions

In this report, we have described access to the new 2,5-bis(trimethylsilyl)phospholyl (Hsp) ring system and the successful isolation of two new Tm^{II} phospholyl complexes, [$Tm(Htp)_2(THF)$] (**10**) and [$Tm(Hsp)_2(THF)$] (**11**) as well as the second Tm^{II} cyclopentadienyl complex, [$Tm(Cp^{tt})_2$-(THF)] (**12**). Preliminary studies seem to indicate that the reactivity of **12** is higher than that of **10** and **11**.

We feel that organothulium(II) π complexes can no longer be considered as rarities. They are not especially difficult to isolate as long as the ligands provide adequate steric protection of the Tm^{II} environment and oxygen, nitrogen and water are excluded during their synthesis. We are convinced that many more Tm^{II} compounds can be made, thus opening the way to more studies of the chemistry of divalent thulium.

Experimental Section

General Remarks: All manipulations involving lanthanide complexes were performed on a vacuum line or in a drybox under argon using dry, oxygen-free solvents. All other reactions were performed in Schlenk glassware under nitrogen. Diphosphole (**2**)[20] and TmI_2[17] were prepared as described previously. [$TmI_2(THF)_3$] was obtained by extraction of TmI_2 with THF. All other reagents were commercial and used as received from the suppliers. Magnetic susceptibility data were obtained by the Evans NMR method. Elemental analyses were performed at the Service de microanalyse du CNRS, Gif-sur-Yvette, France, and at the Service de microanalyse de l′université de Dijon, Dijon, France.

Phospholyl 3: To a solution of diphosphole **2**[20] (1.5 g, 3.84 mmol) in THF (30 mL) at room temperature was added excess sodium in small pieces (0.35 g). After 3 h, the remaining sodium was removed from the reaction mixture which was then evaporated to dryness under vacuum. The residue was rinsed with hexane and sodium 2,5-di-*tert*-butylphospholyl (**3**) was obtained as an air-sensitive white powder which was dried in vacuo (1.43 g, 6.55 mmol, 85%). ^{1}H NMR (300 MHz, [D_8]THF): δ = 1.32 (s, 18 H, CH_3), 6.47 ppm (d, J_{HP} = 4 Hz, 2 H, CH). ^{13}C NMR (75.5 MHz, [D_8]THF): δ = 35.2 (d, J_{CP} = 18 Hz, C), 35.3 (d, J_{CP} = 8 Hz, CH_3), 113.1 (d, J_{CP} = 2 Hz, C3), 160.3 ppm (d, J_{CP} = 47 Hz, C2). ^{31}P NMR (122 MHz, [D_8]THF): δ = 56 ppm.

Diiodide 4:[21] This was prepared by a modification of the literature procedure. To a diethylether (300 mL) solution of $Ti(OiPr)_4$ (18 mL, 17.28 g, 60.7 mmol) and TmsCCH (14 mL, 9.94 g, 103 mmol) at –70 °C was added an ether solution of *i*PrMgCl (60 mL of 2 M soln., 120 mmol) The mixture was warmed to –50 °C over 1 h. After stirring for an additional 1 h, I_2 (31.75g, 125 mmol) was added as a solid to the mixture at –50 °C. The mixture was warmed to room temperature and stirred for 2 h. A saturated aqueous solution of $Na_2S_2O_3$ was then added and the mixture was extracted with hexane. The extract was dried with $MgSO_4$, filtered and evaporated whereupon the resultant oil partially crystallised. The residue was recrystallised from methanol at 0 °C and 1,4-diiodo-1,4-bis(trimethylsilyl)buta-1,3-diene (**4**) (15.15g, 33.6 mmol, 67%) was obtained as tan crystals. ^{1}H NMR (300 MHz, C_6D_6): δ = 0.14 (s, 18 H, CH_3), 7.31 ppm (s, 2 H, CH).

Phosphole 5: A solution of diiodide **4** (9 g, 20 mmol) in diethylether (80 mL) was cooled to –78 °C and a solution of *n*BuLi in hexane (30 mL of 1.33 M soln., 40 mmol) was added dropwise. After 1 h stirring at this temperature, a solution of $PhPCl_2$ (4.5 g, 25 mmol)

 © 2005 Wiley-VCH Verlag GmbH & Co. KGaA, Weinheim

in hexane (20 mL) was added dropwise and the reaction mixture was allowed to warm to room temperature. The solution was then evaporated to dryness and taken up in a 1:1 hexane/satd. aq. $NaHCO_3$ mixture (200 mL). This mixture was decanted, the aqueous phase extracted with hexane, the combined organic phases dried with $MgSO_4$ and the solvents evaporated to dryness. The residue was chromatographed on silica gel using hexane as the eluent. The compound 1-phenyl-2,5-bis(trimethylsilyl)phosphole (**5**) was obtained as a colourless oil (2.55 g, 8.37 mmol, 42%). ^{1}H NMR (300 MHz, C_6D_6): δ = 0.11 (s, 18 H, CH_3) 6.95 (m, 3 H, Ph), 7.21 (d, J_{HP} = 19.5 Hz, 2 H, CH), 7.25 ppm (m, 2 H, Ph). ^{13}C NMR (75.5 MHz, C_6D_6): δ = 0.18 (d, J_{CP} = 2.5 Hz, CH_3), 128.4 (d, J_{CP} = 9.0 Hz, C *meta*-Ph), 129.8 (d, J_{CP} = 1.5 Hz, C *para*-Ph), 131.0 (d, J_{CP} = 8.5 Hz, C *ipso*-Ph), 135.0 (d, J_{CP} = 20.5 Hz, C *ortho*-Ph), 144.9 (d, J_{CP} = 10.5 Hz, C3), 158.4 ppm (d, J_{CP} = 31.5 Hz, C2). ^{31}P NMR (122 MHz, C_6D_6): δ = 38.5 ppm. MS (70 eV, CI/NH_3): *m*/*z* (%) 305 $[M + H]^+$ (100). $C_{16}H_{25}PSi$ (304.5): calcd. C 63.1, H 8.3; found C 63.0, H 8.3.

Diphosphole 7: A solution of phosphole **5** (1 g, 3.28 mmol) in THF (30 mL) was treated with lithium metal (0.18 g, excess). After 3 h at room temperature, the excess lithium was removed and the solution was treated with $AlCl_3$ (0.15 g, 1.1 mmol). After 30min at room temperature, solid iodine (0.42 g, 1.64 mmol) was added to the reaction mixture which was then evaporated to dryness under vacuum. The crystalline residue was dissolved in hexane, the solution was evaporated and the resultant solid recrystallised from methanol. The product 2,5,2′,5′-tetrakis(trimethylsilyl)-1,1′-diphosphole (**7**) was obtained as pale yellow crystals (0.49 g, 2.16 mmol, 66%). ^{1}H NMR (300 MHz, C_6D_6): δ = 0.27 (s, 36 H, CH_3), 7.22 ppm (pseudo-t, $J_{HP(app.)}$ = 22 Hz, 4 H, CH). ^{13}C NMR (75.5 MHz, C_6D_6): δ = 0.63 (s, CH_3) 144.6 (pseudo-t, $J_{CP(app.)}$ = 16 Hz, C3), 152.1 ppm (pseudo-t, $J_{CP(app.)}$ = 37 Hz, C2). ^{31}P NMR (122 MHz, C_6D_6): δ = –3 ppm. MS (70 eV, CI/NH_3) *m*/*z* (%) 455 $[M + H]^+$ (100). $C_{20}H_{40}P_2Si_4$ (454.8): calcd. C 52.8, H 8.9; found C 52.7, H 9.0.

Phospholyl 8: This was prepared similarly to **3** by cleavage of diphosphole **7** (0.3 g, 0.66 mmol) with sodium (0.15 g, excess) in THF solution (10 mL). Yield: 0.26 g (1.04 mmol, 79%) of sodium 2,5-bis(trimethylsilyl)phospholyl (**8**) as an air-sensitive white powder. ^{1}H NMR (300 MHz, [D$_8$]THF): δ = 0.19 (s, 18 H, CH_3), 7.14 ppm (d, J_{HP} = 8.5 Hz, 2 H, CH). ^{13}C NMR (75.5 MHz, [D$_8$]THF): δ = 2.50 (d, J_{CP} = 2 Hz, CH_3) 127.5 (d, J_{CP} = 2 Hz, C3), 144.4 ppm (d., J_{CP} = 67.5 Hz, C2). ^{31}P NMR (122 MHz, [D$_8$]THF): δ = 145 ppm. $C_{10}H_{20}NaPSi_2$ (250.4): calcd. C 48.0, H 8.0; found C 48.0, H 7.6.

General Method for the Synthesis of the Tm^{II} Complexes: Dry diethylether was condensed at –78 °C onto a mixture of $TmI_2(THF)_3$ (1 equiv.) and the anions **3**, **8** or **9** (2 equiv.). The reaction mixture was stirred at 0 °C for 2 h then worked up as described below.

Complex 10: This was prepared from $TmI_2(THF)_3$ (0.150 g, 0.23 mmol) and **3** (0.102 g, 0.47 mmol). The dark green solution was evaporated to dryness and the residue extracted with pentane. The pentane solution was evaporated to dryness and the residue rinsed with cold pentane. Yield 0.056 g of **6** as dark green crystals (0.089 mmol, 38%). ^{1}H NMR (300 MHz, C_6D_6): δ = –68 (br., 4 H, CH), –44 (br., 4 H, THF), –32 (br., 4 H, THF), 57 ppm (br., 36 H, CH_3). ^{31}P NMR (122 MHz, C_6D_6): δ = –290 ppm (br). μ_{eff} = 4.7 μ_B.

Complex 11: This was prepared from $TmI_2(THF)_3$ (0.128 g, 0.200 mmol) and **8** (0.100 g, 0.40 mmol). The dark green solution was filtered, evaporated to dryness and the residue dissolved in pentane. The pentane solution was filtered, concentrated to a small volume and cooled to –30 °C whereupon the product crystallised. Complex **11** was obtained as dark green crystals (0.067 g, 0.096 mmol, 48%). ^{1}H NMR (300 MHz, C_6D_6): δ = –63 (br., 4 H, CH), –52 (br., 4 H, THF), –34 (br., 4 H, THF), 43 ppm (br., 36 H, CH_3). ^{31}P NMR (122 MHz, C_6D_6): δ = –240 ppm (br. s). μ_{eff} = 4.7 μ_B.

Complex 12: This was prepared from $TmI_2(THF)_3$ (0.200 g, 0.31 mmol) and **9** (0.26 g, 0.62 mmol). The purplish-red solution was filtered and concentrated to a small volume and this solution was kept for 2 days at –30 °C whereupon the product crystallised. Complex **11** was obtained as a dark reddish-purple powder (0.036 g, 0.06 mmol, 19%). ^{1}H NMR (300 MHz, C_6D_6): δ = 63 ppm (br. s, CH_3). Other small peaks were present at 89, 83 and –77 ppm. μ_{eff}= 4.6 μ_B.

X-ray Crystallographic Study: Suitable single-crystals of **10** and **11** were obtained from saturated pentane solutions at –30 °C and those of **12** were obtained from a saturated diethylether solution at –30 °C. X-ray intensities were measured with a Nonius KappaCCD diffractometer at 150(1) K using graphite monochromated Mo-K_α radiation (λ = 0.71073 Å). A summary of the crystal structure determinations is presented in Table 1. CCDC-250697–250699 contain the supplementary crystallographic data for this paper. These data can be obtained free of charge from The Cambridge Crystallographic Data Centre via www.ccdc.cam.ac.uk/data_request/cif.

Acknowledgments

Financial support from CNRS and Ecole Polytechnique is gratefully acknowledged.

[1] F. T. Edelmann, in *Comprehensive Organometallic Chemistry II*, vol. 4 (Eds.: E. W. Abel, F. G. A. Stone, G. Wilkinson), Pergamon Press, Oxford (UK), **1995**, pp. 12–130.
[2] S. A. Cotton, in *Encyclopaedia of Inorganic Chemistry, vol. 7* (Editor in chief: R. B. King), John Wiley & Sons, Chichester (UK), **1994**, pp. 3595–3619.
[3] M. N. Bochkarev, I. L. Fedushkin, A. A. Fagin, T. V. Petrovskaia, J. W. Ziller, R. N. R. Broomhall-Dillard, W. J. Evans, *Angew. Chem.* **1997**, *109*, 123–124; *Angew. Chem. Int. Ed. Engl.* **1997**, *36*, 133–135.
[4] W. J. Evans, N. T. Allen, *J. Am. Chem. Soc.* **2000**, *122*, 2118–2119.
[5] M. N. Bochkarev, A. A. Fagin, *Chem. Eur. J.* **1999**, *5*, 2990–2992.
[6] W. J. Evans, N. T. Allen, J. W. Ziller, *J. Am. Chem. Soc.* **2000**, *122*, 11749–11750.
[7] M. N. Bochkarev, I. L. Fedushkin, S. Dechert, A. A. Fagin, H. Schumann, *Angew. Chem.* **2001**, *113*, 3268–3270; *Angew. Chem. Int. Ed.* **2001**, *40*, 3176–3178.
[8] W. J. Evans, N. T. Allen, J. W. Ziller, *Angew. Chem.* **2002**, *114*, 369–371; *Angew. Chem. Int. Ed.* **2002**, *41*, 359–361.
[9] W. J. Evans, N. T. Allen, J. W. Ziller, *J. Am. Chem. Soc.* **2001**, *123*, 7927–7928.
[10] W. J. Evans, G. Zucchi, J. W. Ziller, *J. Am. Chem. Soc.* **2003**, *125*, 10–11.
[11] I. L. Fedushkin, F. Girgsdies, H. Schumann, M. N. Bochkarev, *Eur. J. Inorg. Chem.* **2001**, 2405–2410.
[12] I. Korobkov, G. Aharonian, S. Gambarotta, G. P. A. Yap, *Organometallics* **2002**, *21*, 4899–4901.
[13] I. L. Fedushkin, M. N. Bochkarev, S. Dechert, H. Schumann, *Chem. Eur. J.* **2001**, *7*, 3558–3563.
[14] M. N. Bochkarev, G. V. Khoroshenkov, H. Schumann, S. Dechert, *J. Am. Chem. Soc.* **2003**, *125*, 2894–2895.

 © 2005 Wiley-VCH Verlag GmbH & Co. KGaA, Weinheim

[15] W. J. Evans, D. S. Lee, J. W. Ziller, *J. Am. Chem. Soc.* **2004**, *126*, 454–455.
[16] F. Nief, D. Turcitu, L. Ricard, *Chem. Commun.* **2002**, 1646–1647.
[17] D. Turcitu, F. Nief, L. Ricard, *Chem. Eur. J.* **2003**, *9*, 4916–4923.
[18] M. N. Bochkarev, *Coord. Chem. Rev.* **2004**, *248*, 835–851.
[19] M. C. Cassani, D. J. Duncalf, M. F. Lappert, *J. Am. Chem. Soc.* **1998**, *120*, 12958–12959.
[20] D. Carmichael, L. Ricard, F. Mathey, *J. Chem. Soc., Chem. Commun.* **1994**, 1167–1168.
[21] S. Yamaguchi, R.-Z. Jin, K. Tamao, F. Sato, *J. Org. Chem.* **1998**, *63*, 10060–10062.
[22] R. Riemschneider, *Z. Naturforsch., Teil B* **1963**, *18*, 641–645.
[23] M. Schultz, C. J. Burns, D. J. Schwartz, R. A. Andersen, *Organometallics* **2000**, *19*, 781–789.
[24] F. Nief, *Coord. Chem. Rev.* **1998**, *178–180*, 13–81.

Received: September 22, 2004

 © 2005 Wiley-VCH Verlag GmbH & Co. KGaA, Weinheim

Azaferrocenophanes with Azobenzene-Containing Ligands − Protonation and Electrochemical Oxidation of the Molecule Influences the Absorption Spectra and *cis*−*trans* Isomerization of the Azobenzene Group

Tatsuaki Sakano,[a] Masaki Horie,[a] Kohtaro Osakada,*[a] and Hidenobu Nakao[b]

Keywords: Azobenzene / Chromophores / Ferrocene / Photochemistry / Redox chemistry

N-{4-(Phenylazo)phenyl}aminophenyl-2-aza-[3]-ferrocenophane (**4**) and *N*-{3-(phenylazo)phenyl}aminophenyl-2-aza-[3]-ferrocenophane (**5**) have been prepared by C–N bond-forming reactions catalyzed by Ru and Pd complexes. The absorption peaks due to the π–π^* transition of the *trans*-azobenzene group of **4** and **5** appear at 442 and 426 nm, respectively, in toluene. Photoirradiation of solutions of **4** and **5** at 420 nm causes partial isomerization of the *trans*-azobenzene group to *cis*-azobenzene and reaches a photostationary state. The compounds at the photostationary state undergo thermal isomerization of the *cis*-azobenzene group to the *trans* isomer. The isomerization after one-electron oxidation of the compounds takes place more rapidly than that without electrochemical oxidation.
(© Wiley-VCH Verlag GmbH & Co. KGaA, 69451 Weinheim, Germany, 2005)

Introduction

Several organometallic compounds have potential utility as materials for opto-electronic devices which exhibit electroluminescence, liquid-crystalline properties, and perform as biosensors.[1] The introduction of functional groups to the cyclopentadienyl ligands of ferrocene forms ferrocene derivatives, which can be utilized as a mediator and electron donor in electrochemical reactions and electron-transfer systems.[2] Since azobenzene changes its molecular shape and the absorption peak positions upon photoirradiation or heating,[3] binding the ferrocene and azobenzene with a suitable linker would provide compounds where the electrochemical properties of the Fe center and the optical response of the organic group are linked to each other.[4] Nishihara has reported the unique properties of *m*-ferrocenylazobenzene, in which azobenzene is directly bonded to a cyclopentadienyl ligand.[5] One-electron oxidation of the compound led to the formation of a *trans*-rich mixture in the Fe^{III} state upon irradiation with a single green light, while it was converted to a *cis*-rich mixture upon electrochemical reduction to Fe^{II}.

Recently we have prepared ferrocene derivatives with an aminomethyl substituent at the cyclopentadienyl ligand and found electrochemical communication between the ferrocene and the organic group of the ligand by electron transfer between the Fe center and the N atom.[6] N-Substituted 2-aza-[3]-ferrocenophanes also undergo similar electron transfer between the metal center and the organic group of the ligand.[7,8] These compounds may show cooperative responses to a photo- or electrochemical stimulus. In this paper we report the preparation of new 2-aza-[3]-ferrocenophanes containing azobenzene in the ligand, as well as their molecular structures and their absorption spectra, which change upon protonation and electrochemical oxidation. Part of this work has been reported in a preliminary form.[9]

[a] Chemical Resources Laboratory, Tokyo Institute of Technology, 4259 Nagatsuta, Midori-ku, Yokohama, 226-8503 Japan
Fax: (internat.) + 81-45-924-5224
E-mail: kosakada@res.titech.ac.jp
[b] Instrumentational Engineering Laboratory, National Food Research Institute, 2-1-12 Kannodai, Tsukuba, 305-8642 Japan

Results and Discussions

Preparation and Characterization

The synthesis of the new ferrocenophanes with an azobenzene group is summarized in Scheme 1. Dehydrative condensation of 1,1′-ferrocenedimethanol with 4-aminoazobenzene catalyzed by $[RuCl_2(PPh_3)_3]$[10] produces *N*-{4-(phenylazo)phenyl}-2-aza-[3]-ferrocenophane (**1**). Similar reactions with 4-bromoaniline and with 3-bromoaniline form *N*-(4-bromophenyl)-2-aza-[3]-ferrocenophane (**2**) and *N*-(3-bromophenyl)-2-aza-[3]-ferrocenophane (**3**), respectively. The ferrocenophanes react with 4-(phenylamino)azobenzene in the presence of $Pd_2(dba)_3$/P*t*Bu$_3$ [dba = di-(benzylidene)acetone] catalyst and NaO*t*Bu to afford *N*-{4-(phenylazo)phenyl}-2-aza-[3]-ferrocenophane (**4**) and *N*-{3-(phenylazo)phenyl}-2-aza-[3]-ferrocenophane (**5**), respectively. Analogous Pd-catalyzed cross-coupling reactions of bromoarene with secondary amines have been reported to form a new C−N bond.[11−13]

 © 2005 Wiley-VCH Verlag GmbH & Co. KGaA, Weinheim DOI: 10.1002/ejic.200400592

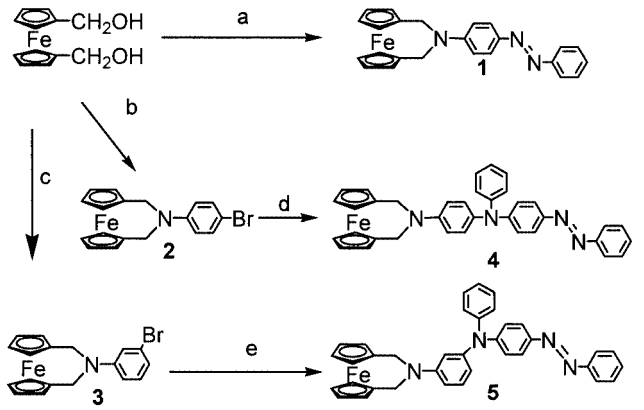

Scheme 1. (a) 4-phenylazoaniline (1 equiv.), $[RuCl_2(PPh_3)_3]$ (5 mol %), 180 °C, NMP; (b) 4-bromoaniline (1 equiv.), $[RuCl_2(PPh_3)_3]$ (5 mol %), 180 °C, NMP; (c) 3-bromoaniline (1 equiv.), $[RuCl_2(PPh_3)_3]$ (5 mol %), 180 °C, NMP; (d) 4-phenylazodiphenylamine (1 equiv.), $[Pd_2(dba)_3]$ (1.3 mol %), NaO*t*Bu (1.5 equiv.), P(*t*Bu)$_3$ (7.5 mol %), 100 °C, toluene

The ferrocenophanes with azobenzene-containing ligands (**1**, **4**, and **5**) were characterized by NMR spectroscopy and X-ray crystallography. Figure 1 depicts the molecular structures of **1**, **4**, and **5**, as determined by X-ray crystallography. The two cyclopentadienyl ligands have a staggered conformation, similar to other structurally characterized [3]-ferrocenophanes.[8,9] The diazene moiety (N=N bond) in the compounds has a *trans* conformation [N=N bond lengths: **1**: 1.276(7) Å; **4**: 1.232(7) and 1.197(7) Å; **5**: 1.227(5) Å; C−N=N bond angles: **1**: 113.3(6) and 116.2(6)°; **4**: 113.0(6), 110.4(6), 109.7(6), and 109.1(6)°; **5**: 112.1(5) and 113.2(5)°]. The N−C(phenyl) bond in the ferrocenophane ring [**1**: 1.355(8) Å; **4**: 1.393(8) and 1.398(8) Å; **5**: 1.384(4) Å] is shorter than the N−CH_2 bond (1.45−1.48 Å), which suggests a partial double-bond character of the former.[14]

Absorption Spectra and trans−cis Isomerization

Figure 2 shows the absorption spectra of **1**, **4**, and **5**. These complexes have peaks due to the π−π* transition of the *trans*-azobenzene group at 413 nm (**1**; ε = 19900 $M^{-1}\cdot cm^{-1}$), 442 nm (**4**; ε = 28000 $M^{-1}\cdot cm^{-1}$), and 426 nm (**5**; ε = 31500 $M^{-1}\cdot cm^{-1}$). The order of wavelengths of the π−π* transition, **4** > **5** > **1**, can be attributed to different degrees of π-conjugation of the azobenzene-containing ligands. Compound **4**, with a *p*-diaminophenylene group bonded to the phenylaminoazobenzene group, has the absorption peak at longer wavelength than **1**, without a diaminophenylene group, and **5**, with a *m*-diaminophenylene group.

The *trans*-azobenzene group of **4** undergoes partial isomerization to the *cis* form upon irradiation at 420 nm (Xenon lamp). Figure 3a shows change of the absorption spectra during the reaction at 25 °C in toluene. The peak intensity of the π−π* band of the *trans*-azobenzene group of **4** decreases in intensity and is accompanied by a shift of the peak to 457 nm. The new minor absorption is assigned to the n−π* transition of the *cis*-azobenzene group formed by photo-induced isomerization. The intensity of the ab-

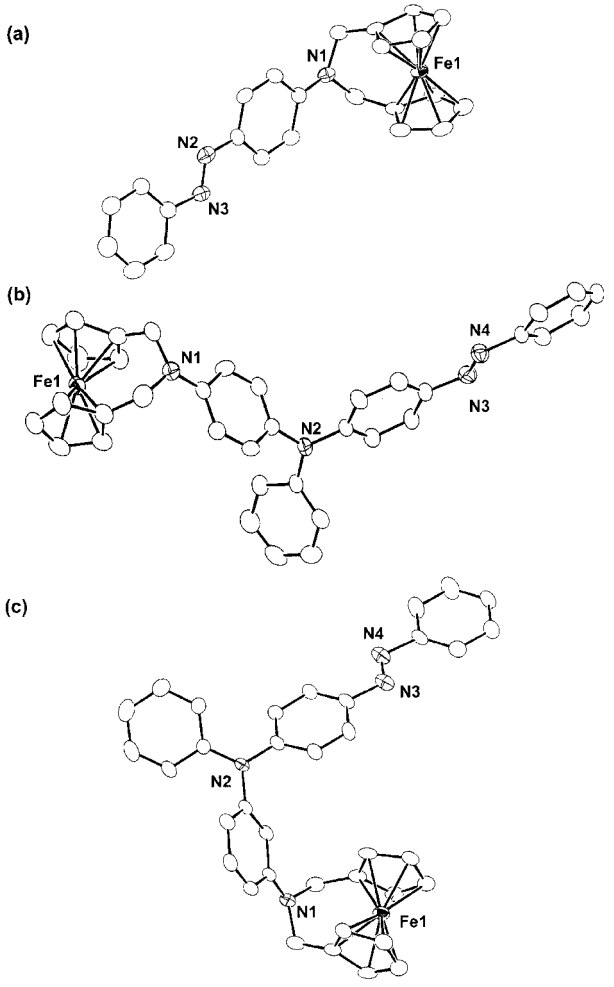

Figure 1. (a) An ORTEP drawing of **1**; selected bond lengths (Å) and angles (°): C1−C11 1.497(9), C6−C12 1.500(9) N1−C11 1.467(7), N1−C12 1.484(8), N1−C13 1.355(8), N2−C16 1.402(8), N2−C19 1.436(8), N2−N3 1.276(7); C11−N1−C12 112.9(5), C11−N1−C13 122.9(5), C12−N1−C13 121.8(6), N1−C11−C1 114.5(5), N1−C12−C6 114.4(5), N2−C16−C15 116.9(6), N2−C16−C17 125.0(6), N2−N3−C19 113.3(6), N3−N2−C16 116.2(6), N3−C19−C20 123.8(7), N3−C19−C24 115.6(7); (b) An ORTEP drawing of **4**; only one of the crystallographically independent molecules is shown; selected bond lengths (Å) and angles (°): C1−C11 1.52(1), C6−C12 1.51(1) N1−C11 1.44(1), N1−C12 1.46(1), N1−C13 1.393(8), N2−C16 1.433(8), N2−C19 1.410(8), N2−C25 1.429(8), N3−C28 1.456(8), N4−C31 1.470(8), N3−N4 1.232(7); C11−N1−C12 113.1(6), C11−N1−C13 121.3(7), C12−N1−C13 120.6 (6), C16−N2−C19 118.5(6), C16−N2−C25 121.7(6), C19−N2−C25 119.6(6), N1−C11−C1 114.6(6), N1−C12−C6 116.1(6), N1−C13−C14 121.3(8), N1−C13−C18 122.8(5), N2−C16−C15 120.4(7), N2−C16−C17 120.4(7), N2−C19−C20 119.3(7), N2−C19−C24 122.3(7), N2−C25−C26 119.2(6), N2−C25−C30 121.0(6), N3−C28−C27 124.1(6), N3−C28−C29 116.0(6), N3−N4−C28 113.0(6), N3−N4−C31 110.4(6), N4−N3−C28 113.0(6), N4−N3−C31 110.4(6), N4−C31−C32 114.1(6), N4−C31−C36 125.5(6); (c) An ORTEP drawing of **5**; selected bond lengths (Å) and angles (°): C1−C11 1.512(7), C6−C12 1.497(7) N1−C11 1.458(6), N1−C12 1.467(6), N1−C13 1.384(6), N2−C15 1.441(6), N2−C19 1.401(6), N2−C25 1.424(6), N3−C28 1.441(6), N4−C31 1.463(7), N3−N4 1.227(5); C11−N1−C12 113.4(5), C11−N1−C13 120.2(4), C12−N1−C13 120.5 (4), C15−N2−C19 119.1(4), C15−N2−C25 119.1(4), C19−N2−C25 121.7(4), N1−C11−C1 113.8(4), N1−C12−C6 115.0(4), N1−C13−C14 121.3(8), N1−C13−C18 122.8(5), N2−C15−C14 118.8(5), N2−C15−C16 119.3(5), N2−C19−C20 120.4(5), N2−C19−C24 121.2(5), N2−C25−C26 120.5(6), N2−C25−C30 120.7(5), N3−C28−C27 114.5(6), N3−C28−C29 125.6(5), N3−N4−C31 113.2(5), N4−N3−C28 112.1(5), N4−C31−C32 125.1(6), N4−C31−C36 114.0(6)

 © 2005 Wiley-VCH Verlag GmbH & Co. KGaA, Weinheim

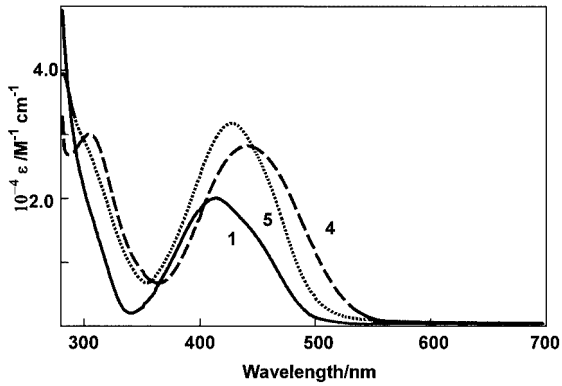

Figure 2. Absorption spectra of **1** (2.5×10^{-5} M in $CHCl_3$, solid line), **4** (2.5×10^{-5} M in toluene, dashed line), and **5** (2.5×10^{-5} M in toluene, dotted line) at 25 °C; wavelength at maximum absorbance and absorption coefficients are determined as: λ_{max} = 413 nm and ε = 19900 $M^{-1}\cdot cm^{-1}$ (**1**); λ_{max} = 442 nm and ε = 28000 $M^{-1}\cdot cm^{-1}$ (**4**); λ_{max} = 426 nm and ε = 31500 $M^{-1}\cdot cm^{-1}$ (**5**)

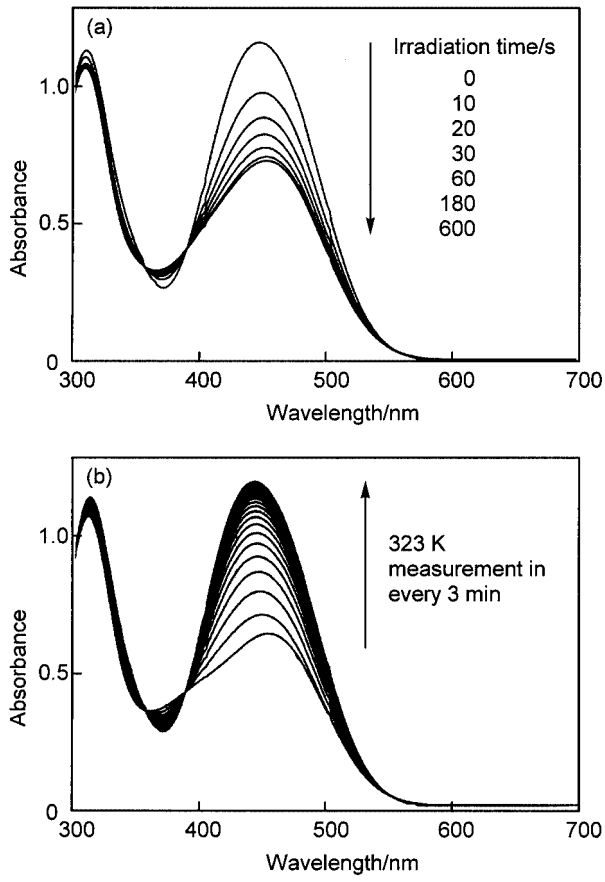

Figure 3. Change of the absorption spectrum of **4** caused by (a) photoisomerization with irradiation at 420 nm at 25 °C in toluene, and (b) thermal isomerization of the photostationary state at 50 °C in toluene

sorbance at 442 nm decreases to 41% of the original spectrum of **4**.

Heating the solution of **4** at the photostationary state in the dark at 50 °C causes growth of the π−π* band of *trans*-azobenzene group (Figure 3b). Recovery of the absorbance of **4** with all the azobenzene groups *trans* takes 30 min at this temperature. The spectra taken during the photo-induced isomerization of the *trans*-azobenzene group to *cis* the structure and thermal isomerization in the reverse direction contain isosbestic points at 335 nm and 387 nm, respectively. Table 1 summarizes the kinetic data of the thermal isomerization of **4** monitored by the increase of the absorbance at 430 nm at 30−70 °C. The reaction obeys first-order kinetics with respect to the concentration of the *cis*-azobenzene group. The reaction enthalpies are estimated to be 9.5 kcal·mol^{-1} in toluene and 7.9 kcal mol^{-1} in MeCN. Compound **5** also undergoes photochemical isomerization of the *trans*-azobenzene group to the *cis* form and thermally induced isomerization of the *cis*-azobenzene group to the *trans* form. The reaction enthalpies of the latter reaction were determined to be 13.5 kcal mol^{-1} and 7.0 kcal mol^{-1} in toluene and in MeCN, respectively. The rate constants of the reaction in toluene are larger than those in MeCN.

Table 1. Kinetic data of the thermally induced *cis*-to-*trans* isomerization

	Solvent	10^3 k_{obs} (s^{-1})			$\Delta H^{\ddagger}$ (kcal mol^{-1})
		323 K	333 K	343 K	
4	toluene	1.02	2.63	5.99	9.5
4	MeCN	0.83	1.93	3.81	7.9
5	toluene	4.01	5.30	10.3	13.5
5	MeCN	0.48	0.92	1.88	7.0

Protonation of 1 and 4

Addition of CF_3COOH to $CHCl_3$ solutions of **1** and **4** with *trans*-azobenzene groups causes a significant change of the spectra, as shown in Figure 4. Addition of CF_3COOH to the solution of **1** causes a decrease in the intensity of the π−π* transition peak at 398 nm and the growth of a new peak at 550 nm (Figure 4a). An isosbestic point at 460 nm is observed throughout the reaction. The new peak can be assigned to a diazaquinoid structure by comparison of the peak position with those of oxidized species of polyaniline and *p*-bis(dimethylamino)benzene.[15] Protonation of 4-(phenylamino)azobenzene with CF_3COOH also results in a decrease of the intensity of the initial peak at 400 nm and the growth of a new peak at 541 nm. Scheme 2 shows a plausible pathway to account for the change of the spectra. Initial protonation takes place either at the nitrogen of the ferrocenophane or the nitrogen of azobenzene. The two species formed can be transformed reversibly into each other by proton transfer. The species protonated at the azobenzene nitrogen is stabilized by a contribution from structure **A**, with a diazaquinoid group. The absorption of the protonated compound at 550 nm is attributed to structure **A**.

Protonation of compound **4** occurs in a stepwise manner, as shown in Figure 4b. Initial addition of CF_3COOH causes a shift of the peak at 450 nm to 405 nm, which is a similar position to **1**. Further addition of CF_3COOH causes a decrease of the intensity of the peak at 405 nm with concomi-

 © 2005 Wiley-VCH Verlag GmbH & Co. KGaA, Weinheim

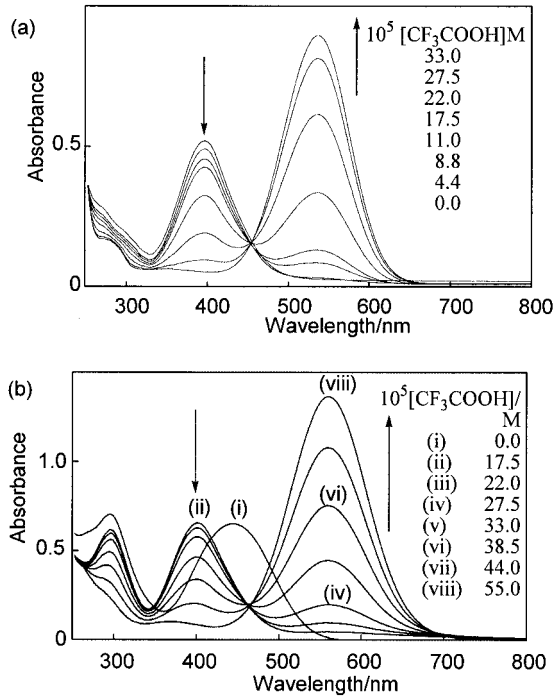

Figure 4. Change in the absorption spectra of (a) **1** (2.5×10^{-5} M in $CHCl_3$) and (b) **4** (2.5×10^{-5} M in $CHCl_3$) upon addition of CF_3COOH

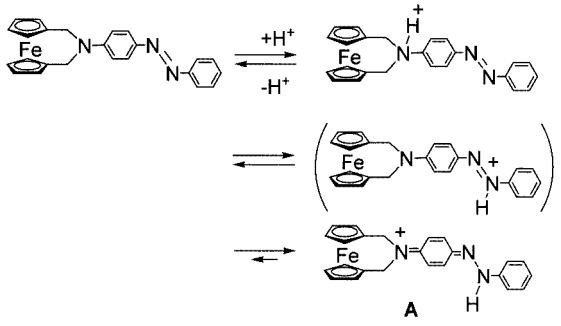

Scheme 2

tant growth of a peak at 570 nm with an isosbestic point at 472 nm. A plausible mechanism for the stepwise protonation of **4** is summarized in Scheme 3.

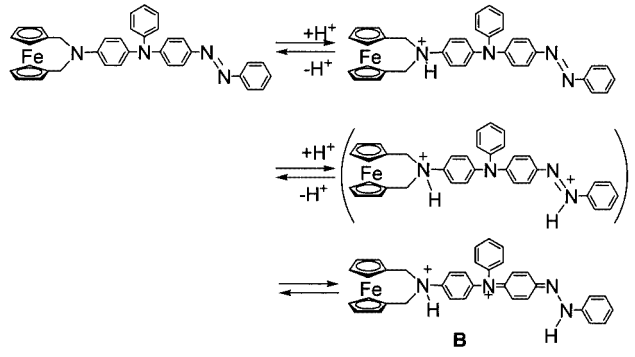

Scheme 3

Initial protonation occurs at the nitrogen atom in the ferrocenophane ring, which restricts π-conjugation of the *p*-diaminophenyelene group and causes a shift of the π−π* transition peak to a higher energy level. Further protonation of the azobenzene nitrogen causes formation of a tautomeric dication **B**. A resonance structure with a diazaquinoid group in the ligand serves to generate a π-conjugated system which shows an intense π−π* absorption at 570 nm.

Electrochemical Oxidation

Previously we have reported the electrochemical oxidation of various 2-aza-[3]-ferrocenophane derivatives.[7,8] The compounds with 4-hydroxyphenyl and with 4-aminophenyl substituents at the nitrogen atoms exhibit three reversible cycles of oxidation and reduction in the cyclic voltammograms, while those with phenyl or alkyl substituents undergo one reversible and one irreversible oxidation reaction. These results suggest a different structure for the product of the second oxidation, as shown in Scheme 4. The ferrocenium species formed upon initial oxidation of the Fe center is in equilibrium with the Fe^{II} species having a cation radical at the nitrogen within the ferrocenophane ring. The cation radical formed in Scheme 4(i) undergoes further electrochemical oxidation to produce the stable quinodiimine. The formed cation radical would release both a proton and an electron under the oxidation conditions to form an iminium-containing product. Similar electron transfer between an Fe center and an amino group, followed by irreversible reaction has been discussed previously for the electrochemical oxidation of ferrocenophanes containing pendant amino groups.[7]

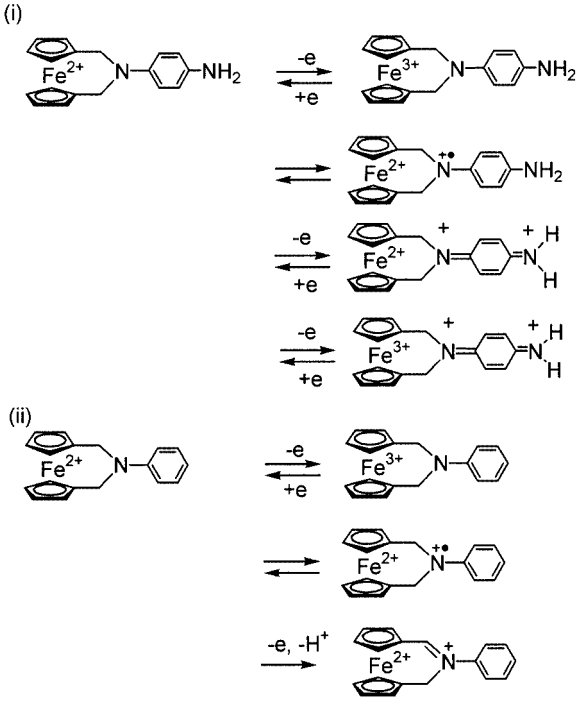

Scheme 4

 © 2005 Wiley-VCH Verlag GmbH & Co. KGaA, Weinheim

The cyclic voltammograms of **1**, **4**, and **5** in CH_2Cl_2 are shown in Figure 5. Compound **1** undergoes a reversible reduction at $E_{1/2}$ = +0.05 V and an irreversible oxidation at E_{pa} = +0.75 V. The former was assigned to the redox potential of the ferrocenophane group, based on a comparison of the reduction potential of ferrocene ($E_{1/2}$ = +0.08 V). The CV peak at +0.75 V is due to further electrochemical oxidation of the organic group in the molecule.[6,16] The cyclic voltammogram of **4** in CH_2Cl_2 solution (see b in Figure 5) exhibits three redox peaks at $E_{1/2}$ = +0.17, +0.41, and +0.92 V. The second electrochemical oxidation occurs more easily than the second oxidation of **1**. Scheme 5 summarizes a plausible mechanism for the total electrochemical reaction. The oxidation of the ferrocene group ($E_{1/2}$ = +0.17 V) leads to formation of the ferrocenium cation, which is in equilibrium with the species with Fe^{II} and a cation radical at the nitrogen atom. The second oxidation occurs easily at the nitrogen bonded to three benzene rings (+0.41 V) to afford the stable dicationic quinodiimine structure. Further reversible oxidation (+0.92 V) occurs at the Fe^{II} center of the product of the second oxidation to afford the dicationic Fe^{III} product.

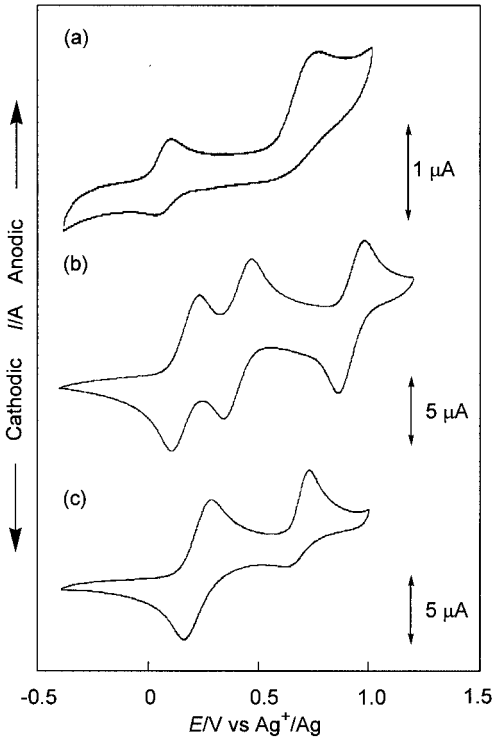

Figure 5. Cyclic voltammograms of (a) **1** (1.0 mM) in CH_2Cl_2 containing 0.10 M Et_4NBF_4 ($E_{1/2}$ = 0.05 V and E_{pa} = 0.75 V), (b) **4** (1.0 mM) in CH_2Cl_2 containing 0.10 M Et_4NBF_4 ($E_{1/2}$ = 0.17 V, 0.41 V, and 0.92 V), and (c) **5** (1.0 mM) in CH_2Cl_2 containing 0.10 M nBu_4NPF_6 ($E_{1/2}$ = 0.22 V and E_{pa} = 0.73 V); sweep rate: 0.10 V s^{-1}; measurement was carried out at 25 °C

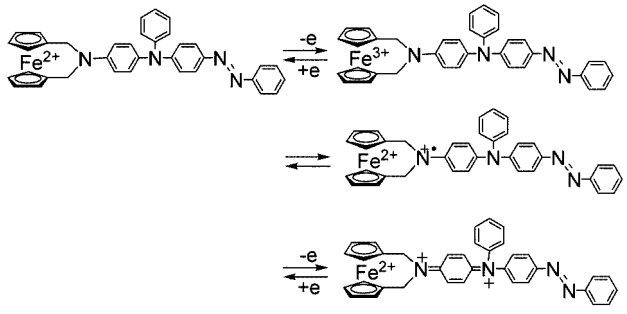

Scheme 5

The cyclic voltammogram of **5** contains a reversible redox peak at $E_{1/2}$ = +0.22 and a quasi-reversible oxidation peak at E_{pa} = +0.73 V. The second oxidation accompanies loss of a proton from the CH_2CN group to form a *meta*-azaquinoid structure.

Figure 6 (a) depicts the change of the absorption spectra during the electrochemical oxidation of **4** in a flow electrolysis cell. Spectrum (i) shows the absorption peak due to **4** (440 nm) exclusively. Spectra (ii) (obtained at −0.1 V) and (iii) (0.3 V) contain peaks at 440 nm and 770 nm, respectively. The latter peak is assigned to the radical cation in Scheme 5. The peak position suggest delocalization of the radical within the π-conjugated ligand. Spectrum (iv) (at 1.0 V) exhibits a new absorption band at 550 nm, which is ascribed to the species with a quinodiimine structure. The change of the absorbance at 440 nm, 550 nm, and 770 nm is shown in part b of Figure 6. It is consistent with the re-

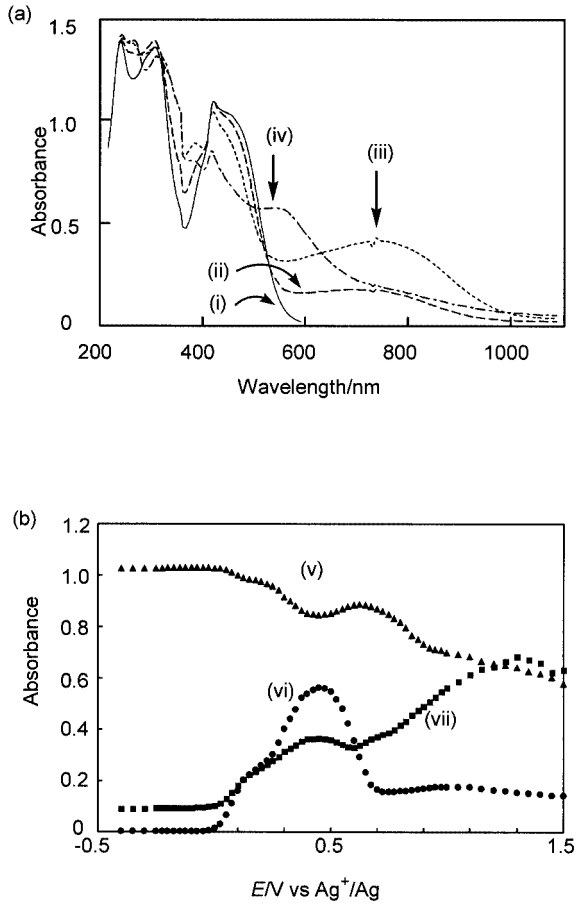

Figure 6. (a) Changes of absorption spectra of **4** (0.05 mM) in acetonitrile solution of 0.1 M Et_4NBF_4 at (i) −0.4 V, (ii) −0.1 V, (iii) 0.3 V, and (iv) 1.0 V (vs Ag^+/Ag); (b) relative intensity changes of absorption spectra of **4** induced by oxidation potentials (v) at 440 nm, (vi) at 550 nm, and (vii) at 770 nm

 © 2005 Wiley-VCH Verlag GmbH & Co. KGaA, Weinheim

sults of CV (see b in Figure 5) and the proposed mechanism of the reaction shown in Scheme 5: the peaks at 770 nm and at 550 nm grow upon oxidation at −0.05−0.3 V and that at 0.3−0.4 V, respectively. Attempts to obtain clear ^{1}H NMR spectra of the oxidized species did not succeed due to significant broadening of the signals.

Electrochemical oxidation of **4** and **5**, both with the azobenzene group *trans*, at 0.30 and 0.40 V (vs Ag^+/Ag), causes little change in the positions of the π−π* transition peaks compared to those before electrolysis. Irradiation of the solutions at 420 nm after electrolysis causes a slight decrease of the peak intensity [approximately 5% (**4**) and 8% (**5**) of the original absorbance], as shown in Figure 7, which suggests that the photostationary states of the oxidized compounds contain *cis*-azobenzene as the minor components. The spectra returned rapidly to the original spectra containing the *trans*-azobenzene group. This can be ascribed to the higher stability of the *trans*-azobenzene group than the *cis*-azobenzene group even during photoirradiation, or faster, thermally induced isomerization of the *cis*-azobenzene group to the *trans* than the photo-assisted isomerization in the reverse direction. In order to obtain further insights, thermal isomerization of the *cis*-azobenzene obtained in the photostationary state of **4** and **5** was conducted after electrochemical oxidation.

Figure 8 compares the kinetic data of the thermal isomerization of the *cis*-azobenzene group to the *trans* form before and after electrolysis, which was monitored by the change in the absorbance at 430 nm. The rate of thermal isomerization actually increases with the electrochemical oxidation. The thermal isomerization was monitored by the spectroscopic change at 10 °C; it is complete within 5 min at this temperature.

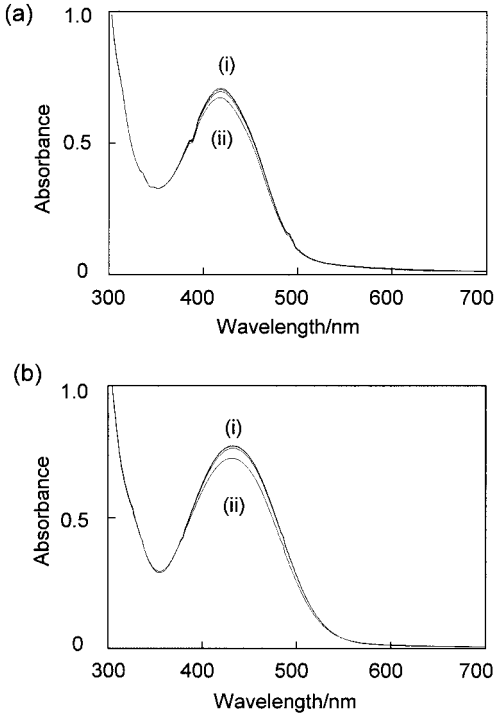

Figure 7. (a) Absorption spectra of **4** (i) before and (ii) after irradiation at 420 nm from a cut-off filtered Xenon lamp for 1 h at 20 °C in toluene; (b) absorption spectra of **5** (i) before and (ii) after irradiation; the data were obtained by flow-electrolysis at 0.3 V (a) and at 0.4 V (b)

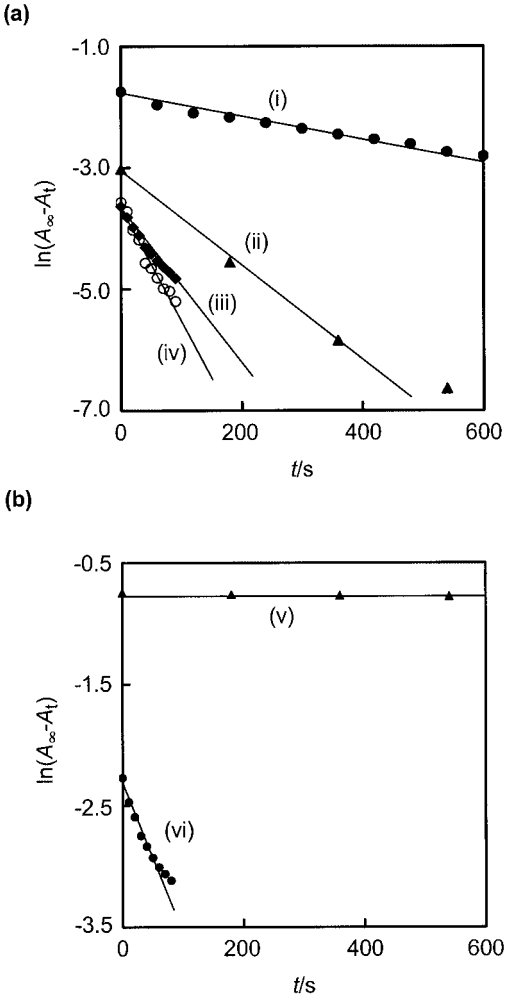

Figure 8. First-order plots of thermal isomerization (283 K) of (a) **4** in the photostationary state (i) without oxidation, (ii) after oxidation at 0.3 V, (iii) 0.6 V and (iv) 1.0 V, and (b) **5** in the photostationary state (iv) without oxidation and (v) after oxidation at 0.4 V; A_t denotes the absorption at 440 nm

Scheme 6 summarizes a mechanism that accounts for the rapid isomerization of the oxidized species. One-electron oxidation of **4** and **5**, with the azobenzene group *cis*, forms the Fe^{III} center, which is in equilibrium with the species having an Fe^{II} center and a cation radical at the N atom[16] due to electron transfer between the Fe and two N atoms.[7] This intermediate is responsible for the rapid isomerization of the *cis*-azobenzene to the *trans* form.[17] The positive charge at the N atom attached to the azobenzene unit enhances the isomerization of the N=N bond significantly due to rapid N−N bond rotation of the oxidized form. A canonical structure containing a diazaquionid moiety and a radical at an azobenzene nitrogen is involved in the oxidized species. Although the amount of the intermediate is small, rapid rotation of the N−N bond due to the single-bond

 © 2005 Wiley-VCH Verlag GmbH & Co. KGaA, Weinheim

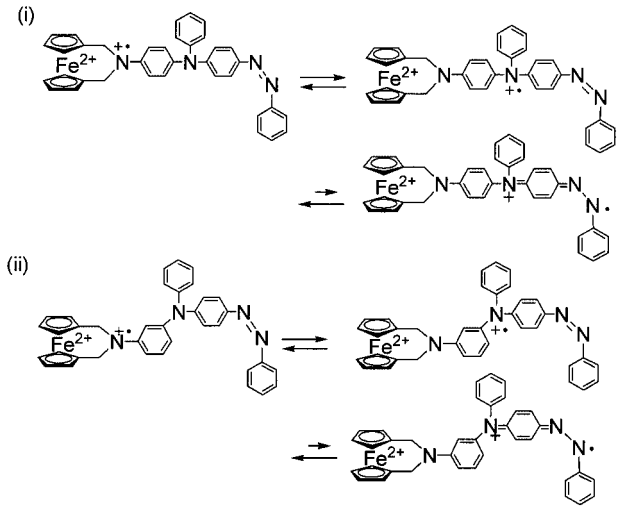

Scheme 6

character of the azobenzene group and intermolecular transfer of the positive charge at the organic ligand renders thermally induced isomerization facile.

In summary, the synthesis of new ferrocenophanes containing an azobenzene group has been achieved by using two types of bond-forming reactions catalyzed by transition metal complexes. The introduced azobenzene group performs as a redox-active site and as a chromophore that varies its absorption upon treatment with protic acid. The presence of ferrocenophane does not influence the optical properties of the azobenzene group significantly. Reversible multi-step redox reactions of **1** and **4** and the color change caused by addition of H^+ suggest a potential use of these compounds as electron- or acid-responsive organic materials.

Experimental Section

General Methods: $RuCl_2(PPh_3)_3$,[18] 1,1′-ferrocenedimethanol,[19] and $Pd_2(dba)_3$ [20] were prepared according to the literature. Preparation of the complexes and ferrocenophanes was carried out under nitrogen or argon using standard Schlenk techniques. Solvents were distilled from CaH_2 and stored under argon. The IR spectra were obtained with a JASCO-IR810 spectrophotometer. The ^1H and ^{13}C NMR spectra were recorded with a JEOL EX-400 spectrometer at 25 °C unless otherwise stated. A YANACO MT-5 CHN Autocorder was used for the elemental analyses. Cyclic voltammetry was recorded with a MeCN solution of 0.10 M Et_4NBF_4 with an ALS Electrochemical Analyzer Model-600A. The potentials were referenced to Ag^+/Ag. Spectroscopic measurements of the electrochemically oxidized species were carried out by using a combination of a flow-through electrolysis cell, ALS Electrochemical Analyzer Model-600A and EYELA peristaltic pump SMP-11, and JASCO V-530 UV/Vis spectrometer. Details of apparatus have been reported previously.[8,21]

Preparation of 1: 4-Phenylazoaniline (429 mg, 2.2 mmol) and then 1,1′-ferrocenedimethanol (536 mg, 2.2 mmol) were added at room temperature to a solution of $[RuCl_2(PPh_3)_3]$ (139 mg, 0.15 mmol) in 1-methyl-2-pyrrolidone (NMP) (3 mL) under nitrogen. The mixture was heated for 48 h at 180 °C. After removal of the solvent under vacuum, the product was extracted with ethyl acetate and purified by column chromatography (silica gel; hexane/ethyl acetate, 3:1). The yellow solid thus obtained was recrystallized from a dichloromethane/methanol mixture to afford **1** as orange crystals (253.0 mg, 38%). $C_{24}H_{21}FeN_3 \cdot 0.5C_6H_{14}$ (450.38): calcd. C 71.95, H 6.22, N 9.33; found C 72.11, H 6.07, N 9.33. ^1H NMR (400 MHz, $CDCl_3$, 25 °C): δ = 3.95 (s, 4 H, Cp-CH_2-N), 4.00, 4.15 (t, J = 2 Hz, 8 H, Cp), 6.95 (d, J = 10 Hz, 2 H, *meta*-N=NC$_6$H$_4$-), 7.37 (t, J = 7 Hz, 1 H, *para*-C$_6$H$_5$N=N-), 7.41 (t, J = 8 Hz, 2 H, *meta*-C$_6$H$_5$N=N-), 7.78 (d, J = 9 Hz, 2 H, *ortho*-N=NC$_6$H$_4$), 7.83 (d, J = 9 Hz, 2 H, *ortho*-C$_6$H$_5$N=N) ppm. $^{13}C\{^1H\}$ NMR (100 MHz, $CDCl_3$, 25 °C): δ = 45.8 (Cp-*C*H$_2$-N), 69.4 (Cp), 70.0, 83.4 (*Cp*-CH$_2$-), 112.0 (*para*-C$_6$H$_5$N=N-), 122.2 (*ortho*-C$_6$H$_5$N=N), 125.4 (*ortho*-C$_6$H$_4$N=N), 129.0 (*meta*-C$_6$H$_5$N=N-), 129.5 (*para*-C$_6$H$_5$N=N-), 144.2 (*ipso*-C$_6$H$_4$N=N), 151.1 (*para*-N=N C$_6$H$_4$-), 153.2 (*ipso*-C$_6$H$_5$N=N) ppm.

Preparation of 2: 4-Bromoaniline (571 mg, 3.3 mmol) and then 1,1′-ferrocenedimethanol (817 mg, 3.3 mmol) were added at room temperature to a solution of $[RuCl_2(PPh_3)_3]$ (139 mg, 0.15 mmol) in NMP (5 mL) under nitrogen. The mixture was heated for 24 h at 180 °C. After removal of the solvent under vacuum, the product was extracted with acetone. Column chromatography (silica gel; hexane/ethyl acetate, 1:1) of the extract gave a yellow solid which was recrystallized from a dichloromethane/methanol mixture to afford **2** as yellow crystals (883 mg, 70%). $C_{18}H_{16}BrFeN$ (382.08): calcd. C 56.58, H 4.22, Br 20.91, N 3.67; found C 56.85, H 4.06, Br 21.21, N 3.69. ^1H NMR (400 MHz, $CDCl_3$, 25 °C): δ = 3.84 (s, 4 H, Cp-CH_2-N), 4.06, (t, J = 2 Hz, 8 H, Cp), 6.83 (t, J = 9 Hz, 2 H, *meta*-BrC$_6$H$_4$), 7.32 (d, J = 9 Hz, 2 H, *ortho*-BrC$_6$H$_4$) ppm. $^{13}C\{^1H\}$ NMR (100 MHz, $CDCl_3$, 25 °C): δ = 46.1 (Cp-*C*H$_2$-N), 69.3, 70.0 (Cp), 84.0 (*Cp*-CH$_2$-), 113.1 (*ipso*-BrC$_6$H$_4$), 115.0 (*meta*-BrC$_6$H$_4$), 132.1 (*ortho*-BrC$_6$H$_4$), 148.3 (*para*-BrC$_6$H$_4$) ppm.

Preparation of 3: 3-Bromoaniline (571 mg, 3.3 mmol) and then 1,1′-ferrocenedimethanol (817 mg, 3.3 mmol) were added at room temperature to a solution of $[RuCl_2(PPh_3)_3]$ (139 mg, 0.15 mmol) in NMP (5 mL) under nitrogen. The mixture was heated for 24 h at 180 °C. After removal of the solvent under vacuum, the product was extracted with acetone. Column chromatography (silica gel; hexane/ethyl acetate, 1:1) of the extract gave a yellow solid which was recrystallized from a dichloromethane/methanol mixture to afford **3** as yellow crystals (857 mg, 68%). ^1H NMR (400 MHz, $CDCl_3$, 25 °C): δ = 3.84 (s, 4 H, Cp-CH_2-N), 4.06, 4.18 (t, J = 2 Hz, 8 H, Cp), 6.84 (d, J = 7 Hz, 1 H, *para*-BrC$_6$H$_4$), 6.85 (s, 1 H, *ortho*-BrC$_6$H$_4$), 7.08 (dd, J = 7 Hz, 1 H, *meta*-BrC$_6$H$_4$), 7.09 (d, J = 7 Hz, 1 H, *ortho*, BrC$_6$H$_4$) ppm. $^{13}C\{^1H\}$ NMR (100 MHz, $CDCl_3$, 25 °C): δ = 46.0 (Cp-*C*H$_2$-N), 69.3, 69.9 (Cp), 83.8 (*Cp*-CH$_2$-), 111.7 (*para*-BrC$_6$H$_4$), 115.9 (*ortho*-BrC$_6$H$_4$-N), 119.8 (*ortho*-BrC$_6$H$_4$), 123.7 (*ipso*-BrC$_6$H$_4$), 130.6 (*meta*-BrC$_6$H$_4$), 150.4 (*meta*-BrC$_6$H$_4$-N) ppm.

Preparation of 4: A mixture of **2** (382 mg, 1.0 mmol) and 4-phenylazodiphenylamine (273 mg, 1.0 mmol) was dissolved in toluene (20 mL). NaO*t*Bu (145 mg, 1.5 mmol), $Pd_2(dba)_3$ (12 mg, 0.013 mmol), and P(*t*Bu)$_3$ (15 mg, 0.075 mmol) were then added to the solution, which was stirred at 100 °C for 40 h under argon. After cooling, the reaction mixture was quenched by adding NH_4OH. The product was extracted with $CHCl_3$ and purified by column chromatography (silica gel; hexane/$CHCl_3$, 1:1) to give a red-orange solid. Recrystallization from a $CHCl_3$/hexane mixture gave **4** as red crystals (471 mg, 82%). $C_{36}H_{30}FeN_4$ (574.50): calcd. C 75.26, H 5.26, N 9.75; found C 74.99, H 5.17, N 9.71. ^1H NMR (400 MHz, $CDCl_3$, 25 °C): δ = 3.86 (s, 4 H, Cp-CH_2-N), 4.11, 4.22 (d, J = 2 Hz, 8 H, Cp), 6.95 (d, J = 9 Hz, 2 H, *meta*-CH$_2$NC$_6$H$_4$),

 © 2005 Wiley-VCH Verlag GmbH & Co. KGaA, Weinheim

Table 2. Crystal data and details of structure refinement of **1**, **4**, and **5**

Compound	**1**	**4**	**5**
Formula	$C_{24}H_{21}FeN_3$	$C_{36}H_{30}FeN_4$	$C_{36}H_{30}FeN_4$
Molecular mass	407.30	574.50	574.50
Crystal system	monoclinic	monoclinic	triclinic
Space group	$P2_1/n$ (no. 14)	$P2_1$ (no. 4)	$P\bar{1}$ (no. 2)
a (Å)	13.186(2)	12.174(4)	10.362(2)
b (Å)	10.485(2)	10.819(3)	18.639(4)
c (Å)	15.008(3)	22.819(5)	7.399(2)
α (°)			97.97(2)
β (°)	113.59(1)	92.20(3)	102.67(2)
γ (°)			86.58(2)
V (Å^3)	1901.4(7)	2806(1)	1380.1(5)
Z	4	4	2
μ(Mo-K_α) (cm^{-1})	8.07	5.70	5.79
F(000)	848.00	1200.00	600.00
D_{calcd} (g cm^{-1})	1.423	1.360	1.382
Crystal size (mm)	0.2 × 0.4 × 0.4	0.8 × 0.8 × 1.0	0.4 × 0.5 × 0.7
Unique reflections	4613	6822	5105
Obsvd. reflections [$I \geq 3.0\sigma(I)$]	1438	2938	2381
No. of variables	253	738	370
R	0.043	0.046	0.047
R_w	0.038	0.054	0.033

7.09 (d, J = 7 or 9 Hz, 5 H, *ortho*-$CH_2NC_6H_4$, *ortho*- and *para*-NC_6H_5), 7.21 (d, J = 7 Hz, 2 H, *meta*-$C_6H_4N{=}N$), 7.31 (t, J = 7 Hz, 2 H, *meta*-C_6H_5N-), 7.41 (t, J = 7 Hz, 1 H, *para*-$C_6H_5N{=}N$-), 7.49 (t, J = 7 Hz, 2 H, *meta*-$C_6H_5N{=}N$-), 7.80 (d, J = 9 Hz, 2 H, *ortho*-$C_6H_4N{=}N$), 7.85 (d, J = 9 Hz, 2 H, *ortho*- $C_6H_5N{=}N$) ppm. $^{13}C\{^1H\}$ NMR (100 MHz, $CDCl_3$, 25 °C): δ = 45.8 (Cp-*C*H_2-N), 69.4 (Cp), 70.0, 83.4 (*Cp*-CH_2-), 115.1, 119.9, 122.4, 123.5, 124.2, 124.8, 128.1, 128.9, 129.3, 129.9, 136.7, 146.5, 147.0, 147.3, 151.1, 153.1 ppm.

Preparation of 5: A mixture of **3** (382 mg, 1.0 mmol) and 4-phenylazodiphenylamine (273 mg, 1.0 mmol) was dissolved in toluene (20 mL). NaO*t*Bu (145 mg, 1.5 mmol), $Pd_2(dba)_3$ (12 mg, 0.013 mmol), and P(*t*Bu)$_3$ (15 mg, 0.075 mmol) were then added to the solution, which was stirred at 100 °C for 40 h under argon. After cooling, the reaction mixture was quenched by adding NH_4OH. The product was extracted with $CHCl_3$ and purified by column chromatography (silica gel; hexane/$CHCl_3$, 1:1) to give a red-orange solid. Recrystallization from a $CHCl_3$/hexane mixture gave **5** as red crystals (448 mg, 78%). $C_{36}H_{30}FeN_4$ (574.50): calcd. C 75.26, H 5.26, N 9.75; found C 75.14, H 5.13, N 9.65. ^1H NMR (400 MHz, $CDCl_3$, 25 °C): δ = 3.81 (s, 4 H, Cp-C*H*$_2$-N), 4.07, 4.17 (d, J = 2 Hz, 8 H, Cp), 7.87−6.55 (aromatic protons) ppm. $^{13}C\{^1H\}$ NMR (100 MHz, $CDCl_3$, 25 °C): δ = 45.9 (Cp-*C*H_2-N), 69.2, 69.9 (Cp), 84.3 (*Cp*-CH_2-), 109.7, 111.1, 115.5, 121.3, 122.5, 123.9, 124.2, 125.4, 129.0, 129.4, 130.1, 130.4, 147.0, 148.2, 150.4, 150.7, 153.0 ppm.

X-ray Structure Analyses: Crystals of **1**, **4**, and **5** suitable for an X-ray diffraction study were obtained by recrystallization from CH_2Cl_2/MeOH and mounted in glass capillaries under argon. Data were collected at 23 °C on a Rigaku AFC-5R automated four-circle diffractometer equipped with monochromated Mo-K_α radiation (λ = 0.71073 Å). Calculations were carried out with the program package teXsan for Windows.[22] The structures were solved by direct methods and subsequent Fourier techniques. All non-hydrogen atoms were refined anisotropically. The hydrogen atoms were located by assuming an ideal geometry, and are included in the structure calculation without further refinement of the parameters. Crystallographic data and details of refinement are summarized in Table 2.

CCDC-242244 (for **1**), -213721 (for **4**), and -213722 (for **5**) contain the supplementary crystallographic data for this paper. These data can be obtained free of charge from The Cambridge Crystallographic Data Centre via www.ccdc.cam.ac.uk/data_request/cif.

Acknowledgments

This work was financially supported by the Shourai Foundation and a Grant-in-aid for Scientific Research for Priority Area (no. 15036223 "Dynamic Complexes") from the Ministry of Education, Culture, Sports, Science, and Technology Japan. M. H. acknowledges a Fellowship for Young Researchers from the Kitasato University Alumni Association.

[1] J. Chen, M. A. Reed, A. M. Rawlett, J. M. Tour, *Science* **1999**, *286*, 1550−1552.

[2] H. D. Sikes, J. F. Smalley, S. P. Dudek, A. R. Cook, M. D. Newton, C. E. Chidsey, S. W. Feldberg, *Science* **2001**, *291*, 1519−1523.

[3] [3a] D. M. Junge, D. V. McGrath, *J. Am. Chem. Soc.* **1999**, *121*, 4912−4913. [3b] A. M. Sanchez, M. Barra, R. H. de Rossi, *J. Org. Chem.* **1999**, *64*, 1604−1609. [3c] M. A. Lockwood, P. E. Fanwick, O. Einsenstein, I. P. Rothwell, *J. Am. Chem. Soc.* **1996**, *118*, 2762−2763. [3d] M. Ghedini, D. Pucci, A. Crispini, G. Barberio, *Organometallics* **1999**, *18*, 2116−2124.

[4] [4a] B. J. Coe, C. J. Jones, J. A. McCleverty, D. Bloon, P. V. Kolinsky, R. J. Jones, *J. Chem. Soc., Chem. Commun.* **1989**, 1485−1487. [4b] S.-M. Lee, M. Marcaccio, J. A. McCleverty, M. D. Ward, *Chem. Mater.* **1998**, *10*, 3272−3274. [4c] S. Barlow, H. E. Bunting, C. Ringham, J. C. Green, G. U. Bublitz, S. G. Boxer, J. W. Perry, S. R. Marder, *J. Am. Chem. Soc.* **1999**, *121*, 3715−3723. [4d] D. G. Walter, D. J. Compbell, C. A. Mirkin, *J. Phys. Chem. B* **1999**, *103*, 402−405. [4e] Y. Miyaki, T. Onishi, H. Kurosawa, *Chem. Lett.* **2000**, 1334−1335. [4f] M. Murata, M. Yamada, T. Fujita, K. Kojima, M. Kurihara, K. Kubo, Y. Kobayashi, H. Nishihara, *J. Am. Chem. Soc.* **2001**, *123*,

 © 2005 Wiley-VCH Verlag GmbH & Co. KGaA, Weinheim

12903−12904. [4g] T. Muraoka, K. Kinbara, Y. Kobayashi, T. Aida, *J. Am. Chem. Soc.* **2003**, *125*, 5612−5613.
[5] [5a] M. Kurihara, K. Matsuda, A. Hirooka, T. Yutaka, H. Nishihara, *J. Am. Chem. Soc.* **2000**, *122*, 12373−12374. [5b] M. Kurihara, A. Hirooka, S. Kume, M. Sugimoto, H. Nishihara, *J. Am. Chem. Soc.* **2002**, *124*, 8800−8801.
[6] [6a] M. Horie, Y. Suzaki, K. Osakada, *J. Am. Chem. Soc.* **2004**, *126*, 3684−3685. [6b] H. Plenio, J. Yang, R. Diodone, J. Heinze, *Inorg. Chem.* **1994**, *33*, 4098−4104.
[7] [7a] I. Yamaguchi, T. Sakano, H. Ishii, K. Osakada, T. Yamamoto, *J. Organomet. Chem.* **1999**, *584*, 213−216. [7b] T. Sakano, H. Ishii, I. Yamaguchi, K. Osakada, T. Yamamoto, *Inorg. Chim. Acta* **1999**, *296*, 176−182. [7c] T. Sakano, K. Osakada, *Macromol. Chem. Phys.* **2001**, *202*, 1829−1836.
[8] T. Sakano, M. Horie, K. Osakada, H. Nakao, *Bull. Chem. Soc. Jpn.* **2001**, *74*, 2059−2065.
[9] M. Horie, T. Sakano, K. Osakada, H. Nakao, *Organometallics* **2004**, *23*, 18−20.
[10] [10a] S.-I. Murahashi, K. Kondo, T. Hakata, *Tetrahedron Lett.* **1982**, *23*, 229−232. [10b] Y. Watanabe, Y. Tsuji, H. Ige, Y. Ohsugi, T. Ohta, *J. Org. Chem.* **1984**, *49*, 3359−3363. [10c] Y. Tsuji, K.-T. Huh, Y. Ohsugi, Y. Watanabe, *J. Org. Chem.* **1985**, *50*, 1365−1370. [10d] Y. Tsuji, K.-T. Huh, Y. Yokoyama, Y. Watanabe, *J. Chem. Soc., Chem. Commun.* **1986**, 1575−1576. [10e] Y. Tsuji, Y. Yokoyama, K.-T. Huh, Y. Watanabe, *Bull. Chem. Soc. Jpn.* **1987**, *60*, 3456−3458.
[11] [11a] J. F. Hartwig, S. Richards, D. Barañano, F. Paul, *J. Am. Chem. Soc.* **1996**, *118*, 3626−3633. [11b] J. F. Hartwig, *Synlett* **1997**, 329−340. [11c] M. S. Driver, J. F. Hartwig, *J. Am. Chem. Soc.* **1997**, *119*, 8232−8245. [11d] L. M. Alcazar-Roman, J. F. Hartwig, A. L. Rheingold, L. M. Liable-Sands; I. A. Guzei, *J. Am. Chem. Soc.* **2000**, *122*, 4618−4630.
[12] [12a] A. S. Guram, R. A. Rennels, S. L. Buchwald, *Angew. Chem. Int. Ed. Engl.* **1995**, *34*, 1348−1350. [12b] J. P. Wolfe, S. Wagaw, S. L. Buchwald, *J. Am. Chem. Soc.* **1996**, *118*, 7215−7216. [12c] S. Wagaw, R. A. Rennels, S. L. Buchwald, *J. Am. Chem. Soc.* **1997**, *119*, 8451−8458. [12d] J.-F. Marcoux, S. Wagaw, S. L. Buchwald, *J. Org. Chem.* **1997**, *62*, 1568−1569. [12e] R. A. Singer, J. P. Sadighi, S. L. Buchwald, *J. Am. Chem. Soc.* **1998**, *120*, 213−214. [12f] D. W. Old, M. C. Harris, S. L. Buchwald, *Org. Lett.* **2000**, *2*, 1403−1406.
[13] [13a] N. P. Reddy, M. Tanaka, *Tetrahedron Lett.* **1997**, *38*, 4807−4810. [13b] M. Nishiyama, T. Yamamoto, Y. Koie, *Tetrahedron Lett.* **1998**, *39*, 617−620. [13c] M. Nishiyama, T. Yamamoto, Y. Koie, *Tetrahedron Lett.* **1998**, *39*, 2367−2370.
[14] [14a] J. D. Dunitz, L. E. Orgel, *Nature* **1953**, *171*, 121−122. [14b] N. D. Jones, R. E. Marsh, J. H. Richards, *Acta Crystallogr.* **1965**, *19*, 330−336. [14c] S.-J. Jong, J.-M. Fang, *Org. Lett.* **2000**, *2*, 1947−1949.
[15] [15a] R. Somoano, V. Hadek, S. P. S. Yen, A. Rembaum, *J. Chem. Phys.* **1975**, *62*, 1061−1067. [15b] J. Yamaguchi, H. Fujita, *Bull. Chem. Soc., Jpn.* **1990**, *63*, 2928−2932. [15c] A. G. MacDiarmid, J. C. Chiang, M. Halpern, W.-S. Huang, S.-B. Mu, N. L. D. Somasiri, W. Wu, S. Yaniger, *Mol. Cryst. Liq. Cryst.* **1985**, *125*, 173−176. [15d] H. Owano, H. Murakami, T. Yamashita, H. Ohigashi, *Synth. Met.* **1991**, *39*, 327−341. [15e] E. T. Kang, K. G. Neoh, K. L. Tan, *Prog. Polym. Sci.* **1988**, *23*, 277−324.
[16] [16a] M. R. Buchmeiser, N. Schuler, G. Kaltenhauser, K.-H. Ongania, I. Lagoja, K. Wurst, H. Schottenberger, *Macromolecules* **1998**, *31*, 3175−3183. [16b] M. R. Buchmeiser, *Macromolecules* **1998**, *31*, 3175−3183.
[17] [17a] A. Sanchez, R. H. de Rossi, *J. Org. Chem.* **1993**, *58*, 2094−2096. [17b] T. Enomoto, H. Hagiwara, D. A. Tryk, Z.-F. Liu, K. Hashimoto, A. Fujishima, *J. Phys. Chem. B* **1997**, *101*, 7422−7427.
[18] P. S. Hallman, T. A. Stephenson, G. Wilkinson, *Inorg. Synth.* **1970**, *12*, 237−240.
[19] A. S. Carlström, T. Frejd, *J. Org. Chem.* **1990**, *55*, 4175−4180.
[20] T. Ukai, H. Kawazura, Y. Ishii, J. J. Bonnet, J. A. Ibers, *J. Organomet. Chem.* **1974**, *65*, 253−266.
[21] [21a] T. Sakano, M. Horie, K. Osakada, H. Nakao, *Bull. Chem. Soc. Jpn.* **2001**, *74*, 2059−2065. [21b] H. Nakao, H. Hayashi, K. Okita, *Anal. Sci.* **2001**, *17*, 545−549.
[22] *CrystalStructure 3.6.0, Crystal analysis package*, Rigaku and Rigaku/MSC, **2000**−**2004**.

Received July 9, 2004
Published Online January 7, 2005

 © 2005 Wiley-VCH Verlag GmbH & Co. KGaA, Weinheim

Solvothermal Synthesis of NiS 3D Nanostructures

Wanqun Zhang,[a] Liqiang Xu,[a] Kaibin Tang,[a] Fanqing Li,[a] and Yitai Qian*[a,b]

Keywords: Nickel sulfide / Nanostructures / Complexes / Crystal growth

Highly uniform urchin-like nanostructures (in the structures, nanoneedles or nanobelts grow radially from the core particles) of NiS (millerite) were successfully prepared by a solvothermal synthetic route using $Ni(Ac)_2{\cdot}6H_2O$ and dithizone as reagents and ethylenediamine as solvent in the temperature range of 220–240 °C. The prepared nickel sulfides with urchin-like 3D architectures were characterized by X-ray diffraction (XRD), field emission scanning electron microscopy (FE-SEM) and high-resolution transmission electron microscopy (HRTEM). The reaction temperature, sulfur sources, and solvent are of great importance on the final urchin-like structures. On the basis of the experimental results, a possible growth mechanism of the urchin-like NiS crystals is proposed, which is supported by the technical characterizations.

(© Wiley-VCH Verlag GmbH & Co. KGaA, 69451 Weinheim, Germany, 2005)

Introduction

Many properties of crystalline materials depend on the crystallographic direction, for example, the spontaneous polarization in ferroelectrics and the magnetic coercivity and remanence in ferromagnets.[1] Over the past few years, there has been growing interest in low dimensional nanostructure semiconductors because of their novel electrical and optical properties, and potential applications in nanodevices.[2] Recently, research is expanding into the assembly of nanoparticles in two-dimensional and three-dimensional ordered superstructures.[3] Much effort has been made to construct patterns of well-arranged nanocrystallites, especially arrangements of nanotubes and nanorods due to their interesting physical properties and potential applications in many areas.[4] To obtain highly oriented growth of nanorods, solid templates are usually required, such as porous alumina, polymer nanotubes, and patterned catalysts, to control the directional growth.[5] However, the introduction of templates and substrates introduces heterogeneous impurities, increases the production cost, and thus leads to the difficulty for scale-up production. The development of facile, mild, easily controlled, and template-free methods to create novel patterns on self-generated homogeneous substrates therefore is of great significance.

Nickel monosulfide (NiS) has been the subject of considerable interest because of its properties as a metal insulator, paramagnetic–antiferromagnetic phase-changing material, and its use in hydrosulfurization catalysts and solar storage.[6] In this paper, we present the synthesis of highly uniform urchin-like 3D nickel sulfide nanostructures by the reaction between nickel acetate and dithizone (H_2DZ, $C_{13}H_{12}N_4S$) in ethylenediamine without the use of any template, polymer, and surfactant. Although Xie's group synthesized 3D NiS with flowerlike architectures via a polymer assistant, recently NiS (millerite) nanorods and triangular nanoprisms were synthesized, and other several geometrical urchin-like patterns have also been presented.[7] Up to now, there has not been a report on these kind of urchin-like 3D nickel sulfides nanostructures (in the structures, nanoneedles or nanobelts grow radially from the core particles) synthesized by a simple, efficient method under mild conditions. As a catalyst, the urchin-like nanostructures, which have highly specific area on the surface of the particles, may provide directional catalyst ability and realize region-dependent surface reactivity.

Results and Discussion

Figure 1 shows the XRD patterns of NiS obtained at 220 °C for 5 h. All the peaks in Figure 1 can be indexed as pure millerite NiS (space group: *R*3*m*) with cell parameters a = 9.63 Å, c = 3.15 Å, which are close to the literature data (JCPDS file number: 12–0041). Similar XRD patterns were obtained from other products of the comparison experiment, all of which exhibited millerite NiS.

The morphology of the product was determined by FR-SEM and TEM. Figure 2 shows the obtained urchin-like nanostructures synthesized at 220 °C for 5 h. After careful observation (Figure 2, b, c), it has been found that the ur-

[a] Department of Chemistry, University Science and Technology of China,
Hefei, Anhui, 230026, People's Republic of China
Fax: (internat.) +86-5513607402
E-mail: ytqian@ustc.edu.cn
[b] Structure Research Laboratory, University Science and Technology of China,
Hefei, Anhui, 230026, People's Republic of China

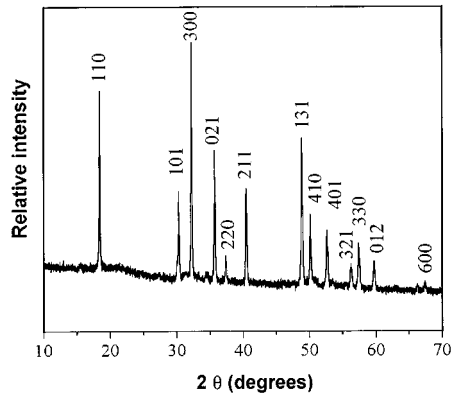

Figure 1. XRD pattern of the synthetic millerite NiS at 220 °C for 5 h

chin-like pattern usually has a diameter of about 30 μm with acicular crystallites radiating from the center in a uniform size distribution. The nanoneedles grown from the center have almost uniform diameters: the bottom of the nanoneedles is about 150 nm; the tip of the nanoneedles is about 50 nm. The nanoneedles were investigated in more detail by high-resolution transmission electron microscopy (HRTEM) (Figure 2, d) and by the SAED pattern (inset in Figure 2, d). The HRTEM image of an individual nanoneedle in Figure 2 (d) shows that lattice spacing of about 0.48 nm and 0.29 nm correspond to the (110) and (011) planes, respectively, of rhombohedral phase NiS. The obtained ED spots projected along the [1 $\bar{1}$ 1] zone axis could be indexed as millerite NiS (110) and (011) planes. The HRTEM and SAED images indicate that the nanoneedles are single crystals grown in the direction parallel to the (110) lattice planes. With a raised temperature of 240 °C, we obtained nanobelts with high aspect ratios, grown radially from the core particles. As shown in Figure 3 (a), these nanobelts have widths ranging from 20 nm to 70 nm and lengths of up to 12 μm. We have characterized these NiS nanobelts by HRTEM and SAED (Figure 3, b). The nanobelts exhibit lattice planes with a spacing of 0.48 nm parallel to the long axis of the nanobelt, which corresponds to the *d* spacing of the (110) planes of NiS (millerite). HRTEM images reveal that the nanobelts grow along the direction parallel to the (110) planes of NiS, which is similar to the nanoneedles. The inset image in Figure 3 (b) shows a typical SAED of the millerite NiS nanobelt, which was obtained by focusing the electron beam along the [0 $\bar{2}$ 1] zone axis of this nanobelt. The SAED pattern further confirms that this nanobelt is a single crystal of millerite NiS.

It is well known that H_2DZ is a good linker ligand, which can form $Ni(HDz)_2$ with Ni^{2+} under alkaline conditions.[8] The reaction in the present system is based on the formation of Ni-dithizone complexes followed by thermal decomposition of these complexes to obtain the final product. The whole reaction process may be expressed as follows:

$$Ni^{2+} + C_{13}H_{12}N_4S \rightarrow Ni(C_{13}H_{11}N_4S)_2 \rightarrow NiS$$

Different sulfur reagents were tested to reveal the dithizone effect, and the results showed that the dithizone was the optimum. When Na_2S was used, the product is a mixture of bulky particles of NiS and Ni_3S_2. When using thio-

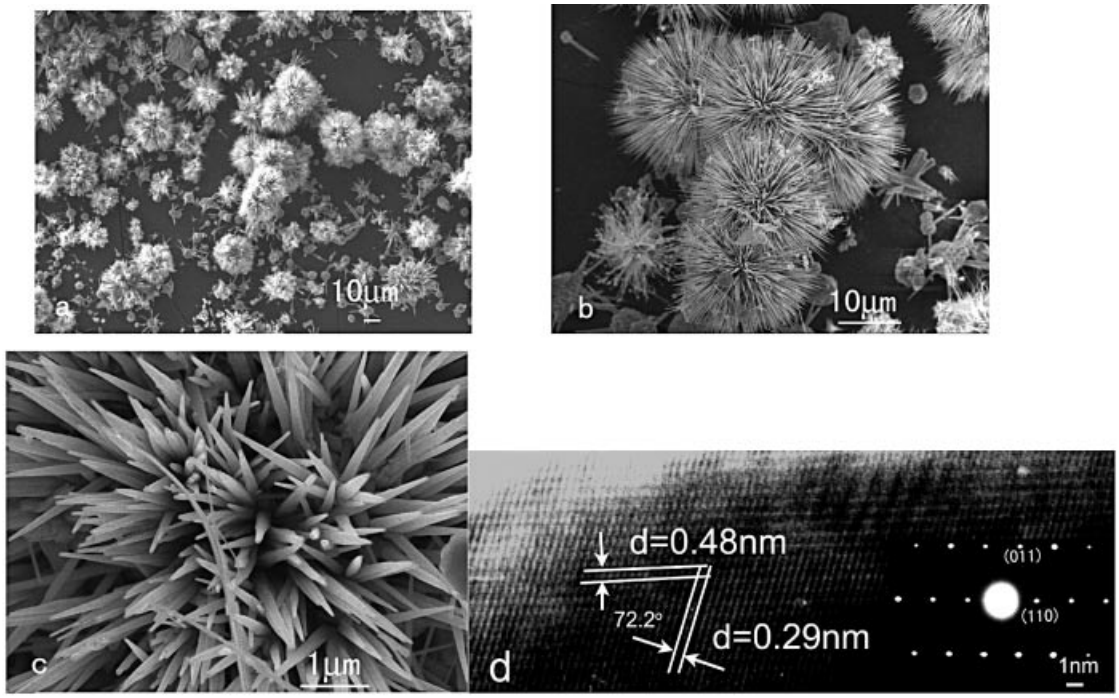

Figure 2. FE-SEM images of the synthesized urchin-like nanostructure at 220 °C for 5 h: (a) the panoramic morphologies; (b) low magnification image; (c) high magnification image; (d) HRTEM image of the NiS nanoneedles covered on urchin-like nanostructures (inset shows its corresponding ED pattern)

 © 2005 Wiley-VCH Verlag GmbH & Co. KGaA, Weinheim

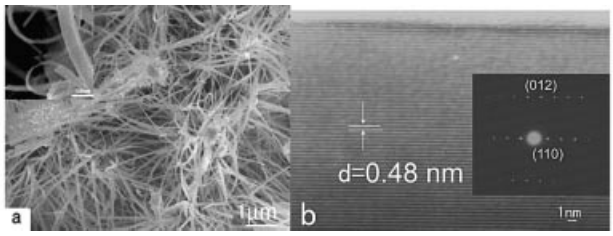

Figure 3. (a) FE-SEM image of the urchin-like nanostructure radiated with high aspect ratio nanobelts at 240 °C for 5 h, (inset shows a high-magnification FE-SEM image); (b) HRTEM image of the NiS nanobelts covered on urchin-like nanostructures (inset shows its corresponding ED pattern)

urea, podgy rods of NiS (millerite) were obtained. It is ordinarily accepted that dithizone metal complexes prevent the production of large free metal ions and sulfur ions, and thus are favorable for the oriented growth of the final product.

Generally, the growth process of crystals can be separated into two steps: an initial nucleating stage and a subsequent crystal growth process. At the initial nucleating stage, the crystalline phase of the seeds is critical for directing the intrinsic shapes of the crystals due to its characteristic symmetry and structure. In the subsequent step, the crystal growth stage is a kinetically and thermodynamically controlled process that can yield 1D and other more complicated shapes with some degree of shape tenability through changes in the reaction parameters such as temperature, reaction time, concentration, and so on.[9] In the present system, we find that the reaction temperature is undoubtedly vital in the formation of the unique urchin-like patterns of NiS nanoneedles and nanobelts. To investigate the influence of reaction temperature, the reactions were carried out at different temperatures, and the results are listed in Table 1. It is generally believed that temperature can affect crystal growth in several ways, all of them resulting in a smaller crystal size at lower temperatures. From our experiments, it can be clearly seen that a higher temperature is preferable for the anisotropic growth of crystal and results in the product with high aspect ratios (Figure 3, a). Meanwhile, at lower temperatures of 160 °C and 180 °C, only podgy rods and nail-like crystals with lower aspect ratios are obtained. Based on FE-SEM studies, by changing the reaction time a possible formation mechanism of 3D urchin-like NiS nanostructure can be obtained and is described as follows: at the beginning of the reaction, some nuclei are formed. These nuclei rapidly develope into aggregated particles (Figure 4, a). ED patterns of the aggregated particles confirm that the aggregated particles are polycrystal. All the diffraction rings in the ED patterns can be indexed to millerite NiS (inset in Figure 4, a). Because the initial growth may be too rapid to be separated from the nucleation,[10] sheets are formed on the surface of the aggregated particles (Figure 4, b), and then at elevated temperature and pressure, the layer structures directly collapse into nanorods (Figure 4, c).[11] During the following solvothermal process, the shorter nanorods may redissolve into the solution phase, and the longer nanorods grow much longer (Figure 4, d), which is similar to the formation process of silver nanowires.[12] With the rapid growth of nanorods, the concentration of the reactants decreases, which does not completely satisfy the growth of nanorods and finally results in the formation of needlelike nanocrystals (Figure 2, a). Further studies are necessary to understand the exact formation mechanism of 3D NiS nanocrystals.

Ethylenediamine also played an important role in the formation of urchin-like NiS. When Ethylenediamine was substituted by ammonia, ethylamine (65−70%), or 1,6-hexanediamine, the results, shown in Table 2, indicated that neither NiS (millerite) nor urchin-like morphology was obtained. Therefore, it is believed that the solvent affected the phase formation in the reaction system. The exact influence of the solvent undoubtedly needs further investigation.

Table 1. The relationship between temperature and different morphology products

Temperature	Time	Phase	Morphology	Figures	Aspect ratio
160 °C	5 h	–	–	–	–
160 °C	96 h	NiS	podgy rod	–	low
180 °C	5 h	NiS	nail-like	–	lower
220 °C	5 h	NiS	urchin-like (nanoneedles)	2, a	high
240 °C	5 h	NiS	urchin-like (nanobelts)	3, a	higher

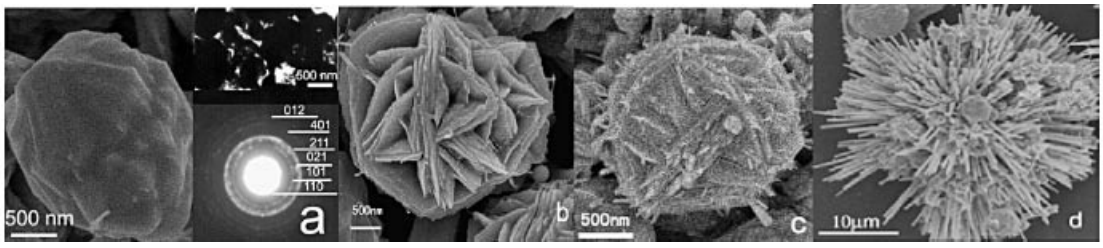

Figure 4. FE-SEM images of the products obtained by the solvothermal treatment at 220 °C for various times: (a) 30 min, the insets show the corresponding TEM and ED patterns; (b) 60 min; (c) 90 min; (d) 120 min

 © 2005 Wiley-VCH Verlag GmbH & Co. KGaA, Weinheim

Table 2. Results of the reaction of $Ni(AC)_2 \cdot 6H_2O$ and dithizone at 220 °C for 5h

Solvent	Product	Morphology
ammonia/water	Ni_3S_2	irregular
ethylamine (65−70%)	Ni_3S_2, Ni_7S_6	−
1,6-hexanediamine	Ni_3S_2	spherical

Conclusion

In summary, in this paper we have developed a facile solvothermal method for the preparation of highly uniform urchin-like 3D nickel sulfide nanostructures by altering the reaction temperature. A possible mechanism was proposed to explain their formation. This low-temperature synthetic route, free of templates, polymer and surfactant, can be easily adjusted to prepare urchin-like 3D nickel sulfides and might be expanded to the preparation of other low-dimension nanomaterials.

Experimental Section

Preparation of Uniform Urchinlike Nanostructures: All the reagents were analytical grade and purchased from Shanghai Chemical. In a typical synthesis, equivalent molar amounts of $Ni(Ac)_2 \cdot 6H_2O$ and H_2DZ (1.2 mmol) were placed in ethylenediamine (50 mL), and the mixture was stirred strongly for about 1 hour to form a homogeneous solution. The resulting solution was transferred into a 60 mL Teflon-lined autoclave, which was sealed and maintained between 220−240 °C for 5 h, before being left to cool to room temperature naturally. The precipitate was filtered off, and washed with distilled water and absolute ethanol several times, and dried in vacuo at 60 °C for 4 h.

Sample Characterization: SEM images were obtained on a Hitachi (X-650) scanning electron microanalyzer and a JSM-6700F field emission scanning electron microscope (FE-SEM). XRD patterns of the products were recorded by employing a Philips X'pert X-ray diffractometer with Cu-K_α radiation (λ = 1.54187 Å). The electron diffraction (ED) patterns and high-resolution transmission electron microscopy (HRTEM) images were carried out on a JEOL-2010 TEM at an acceleration voltage of 200 kV.

Acknowledgments

Financial support from the National Science Foundation of China is gratefully acknowledged.

[1] [1a] S. J. Park, S. Kim, S. Lee, Z. G. Khim, K. Char, T. Hyeon, *J. Am. Chem. Soc.* **2000**, *122*, 8581−8582. [1b] T. Sasaki, A. Katxuragi, O. Mochizuki, Y. Nakazawa, *J. Phys. Chem. B* **2003**, *107*, 7659−7665. [1c] D. L. Leslie-Pelecky, R. D. Rieke, *Chem. Mater.* **1996**, *8*, 1770−1783. [1d] Y. W. Jun, Y. Y. Jung, J. Cheon, *J. Am. Chem. Soc.* **2002**, *124*, 615−619. [1e] N. Cordente, M. Respaud, F. Senocq, M. J. Casanove, C. Amiens, B. Chaudret, *Nano Lett.* **2001**, *1*, 565−568.

[2] [2a] Y. Cui, Q. Wei, H. Park, C. M. Lieber, *Science* **2001**, *293*, 1289−1292. [2b] G. Schmid, *Chem. Rew* **1992**, *92*, 1709−1727.

[3] [3a] R. Maoz, E. Frydman, S. R. Cohen, J. Sagiv, *Adv. Mater.* **2000**, *12*, 424−429. [3b] T. Yonezawa, S. Onous, N. Kimizuka, *Adv. Mater.* **2001**, *13*, 140−142. [3c] Z. Y. Pan, X. J. Liu, S. Y. Zhang, G. J. Shen, L. G. Zhang, Z. H. Lu, J. Z. Liu, *J. Phys. Chem. B* **1997**, *101*, 9703−9709.

[4] [4a] H Yu, P. C. Gibbons, K. F. Kelton, W. E. Bubro, *J. Am. Chem. Soc.* **2001**, *123*, 9198−9199. [4b] A. P. Alivisatos, *Science* **1996**, *271*, 933−937. [4c] A. M. Morales, C. M. Lieber, *Science* **1998**, *279*, 208−211. [4d] S. Saito, *Science* **1997**, *278*, 77−78.

[5] [5a] D. Routkevitch, T. Bigioni, M. Moskovits, J. M. Xu, *J. Phys. Chem.* **1996**, *100*, 14037−14047. [5b] H. Cao, Z. Xu, H. Sang, D. Sheng, C. Tie, *Adv. Mater.* **2001**, *13*, 121−123. [5c] M. H. Huang, S. Mao, H. Feich, H. Yan, Y. Wu, H. Kind, E. Weber, R. Russo, P. Yang, *Science* **2001**, *292*, 1897−1899.

[6] [6a] E. Wong, C. W. Sheeleigh, S. B. Rananvare, *Proceedings of the Sixth Annual Conference on Fossil Energy Materials* **1992**, 143−144. [6b] A. M Fernandez, M. T. S. Nair, P. K. Nair, *Mater. Manuf. Processes* **1993**, *8*, 535−537.

[7] [7a] F. Xu, Y. Xie, X. Zhang, C. Z. Wu, X. Wang, H. Jie, X. B. Tian, *New J. Chem.* **2003**, *27*, 1331−1335. [7b] S. Sharma, M. K. Sunkara, *J. Am. Chem. Soc.* **2002**, *124*, 12288−12293. [7c] P. Boudjouk, M. P. Remington, J. D. G. Grier, B. R. Jarabek, G. J. Mecarthy, *Inorg. Chem.* **1998**, *37*, 3538−3541. [7d] G. Z. Shen, D. Chen, K. B. Tang, F. Q. Li, Y. T. Qian, *Chem. Phys. Lett.* **2003**, *370*, 334−337. [7e] A. Ghezelbash, M. B. Sigman, Jr., B. A. Korgel, *Nano Lett.* **2004**, *4*, 537−542.

[8] [8a] G. Iwantscheff, *Das Dithizon und seine Anwendung in der Mikro-und Spurenanalyse*, 2nd ed., Verlag Chemie, Weinheim, **1972**. [8b] E. B. Sandell, *Colorimetric Determination of Trances of Metals*, Science Publishers, Inc., New York, **1959**. [8c]Freiser, *Chemist-Analyst* **1961**, *50*, 62−65. [8d] L. S. Merlwether, E. C. Breitner, C. L. Sloan, *J. Am. Chem. Soc.* **1965**, *20*, 4448−4454.

[9] [9a] Y. W. Jun, S. M. Lee, N. J. Kang, J. Cheon, *J. Am. Chem. Soc.* **2001**, *123*, 5150−5151. [9b] Y. H. Kim, Y. W. Jun, B. H. Jun, S. M. Lee, J. Cheon, *J. Am. Chem. Soc.* **2002**, *124*, 13656−13657. [9c] V. F. Puntes, D. Zanchet, C. K. Erdonmez, A. P. Alivisatos, *J. Am. Chem. Soc.* **2002**, *124*, 12874−12880. [9d] V. F. Puntes, K. M. Krishnan, A. P. Alivisatos, *Science* **2002**, *291*, 2115−2117.

[10] R. He, X. F. Qian, J. Yin, Z. K. Zhu, *J. Crystal Growth* **2003**, *252*, 505−510.

[11] X. Wang, Y. Li, *Chem. Eur. J.* **2003**, *9*, 300−306.

[12] [12a] Y. Sun, Y. Xia, *Adv. Mater.* **2002**, *14*, 833−837. [12b] Y. Sun, B. Gates, B. Mayers, Y. Xia, *Nano. Lett.* **2002**, *2*, 165−168.

Received July 19, 2004
Published Online January 7, 2005

 © 2005 Wiley-VCH Verlag GmbH & Co. KGaA, Weinheim

$[Re_6Q_7O(3,5\text{-}Me_2PzH)_6]Br_2 \cdot 3,5\text{-}Me_2PzH$ (Q = S, Se) − New Octahedral Rhenium Cluster Complexes with Organic Ligands: Original Synthetic Approach and Unexpected Ligand Exchange in the Cluster Core

Yuri V. Mironov,*[a] Michael A. Shestopalov,[a] Konstantin A. Brylev,[a] Spartak S. Yarovoi,[a] Galina V. Romanenko,[a] Vladimir E. Fedorov,[a] Hartmut Spies,[b] Hans-Juergen Pietzsch,[b] Holger Stephan,[b] Gerhard Geipel,[c] Gert Bernhard,[c] and Werner Kraus[d]

Dedicated to Prof. Dr. Heinrich Oppermann on the occasion of his 70th birthday

Keywords: Rhenium / Cluster compounds / Ligand exchange / Organic ligands / Structure elucidation / Laser fluorescence spectroscopy

Two new octahedral rhenium cluster complexes, $[Re_6S_7O(3,5\text{-}Me_2PzH)_6]Br_2 \cdot 3,5\text{-}Me_2PzH$ (**1**) and $[Re_6Se_7O(3,5\text{-}Me_2PzH)_6]Br_2 \cdot 3,5\text{-}Me_2PzH$ (**2**), with the organic ligand 3,5-dimethylpyrazole (3,5-Me_2PzH), have been synthesised by reaction of rhenium chalcobromides $Cs_3[Re_6(\mu_3\text{-}Q_7Br)Br_6]$ (Q = S, Se) with molten dimethylpyrazole. During the reaction, all six apical bromine ligands of the cluster complexes are substituted by the organic ligand, which is coordinated through the aromatic nitrogen atom N2. Additionally, the inner ligand μ_3-Br in the cluster core $[Re_6(\mu_3\text{-}Q_7Br)]^{3+}$ is substituted by oxygen, giving cluster cores $[Re_6(\mu_3\text{-}Q_7O)]^{2+}$ with mixed chalcogen/oxygen ligands. Compounds **1** and **2** have been characterised by single-crystal X-ray diffraction analysis. They are isostructural and crystallise with four formula units in the unit cell. Absorption spectra and luminescence characteristics of these two cluster compounds have been investigated in methanol. Absorption starts below 400 nm. For both compounds, broad emissions were found. The fluorescence decays of the two compounds follow a diexponential decay behaviour. The main fluorescence intensity decays have longer fluorescence lifetimes of 3.07 ± 0.03 (**1**) and 3.96 ± 0.02 μs (**2**). Studying the thermal stability of both compounds in vacuo showed that the release of 3,5-dimethylpyrazole ligands begins near 200 °C, and decomposition, with the removal of 7 molecules of 3,5-Me_2PzH, is complete at 330 °C.
(© Wiley-VCH Verlag GmbH & Co. KGaA, 69451 Weinheim, Germany, 2005)

Introduction

The chemistry of the rhenium octahedral cluster compounds with the cluster core $\{Re_6Q_8\}^{2+}$ (Q = S, Se) coordinated by organic N- and P-donor ligands is in a stage of rapid development.[1−14] Such organic−inorganic hybrids show interesting electronic, optical and structural properties. Synthetic strategies span both simple cluster modification and more demanding programmed supramolecular arrays. The latter includes hydrogen-bonded and metal-assisted supramolecular networks based on rhenium clusters possessing nicotinamide, isonicotinamide, 3,5-pyridinedicarboxylic acid and 4,4′-dipyridine as apical organic ligands. Furthermore, the dendritic encapsulation of rhenium clusters by polyetheraryl dendrons having pyridine and pyridone units at the focal point has been realised. In all, there is an almost infinite variability regarding the structural modification of such rhenium clusters. This provides the opportunity to achieve properties useful for possible in vivo applications. Thus, it is very appealing to develop metallic drugs based on rhenium clusters. In this context, particularly porphyrin and modified dendritic rhenium clusters show promising luminescence properties for the development of photosensitizers that could be applied to photodynamic therapy.[15,16] Furthermore, rhenium clusters may play an important role as agents in photon activation therapy (PAT).[17] This relatively new treatment paradigm in cancer therapy requires a sufficiently high density of metals in target regions. This could be achieved by organic-inorganic rhenium cluster complexes.

Because of this background, we are especially interested in an efficient synthetic procedure to introduce organic ligands into the rhenium cluster core. Thus, a new synthetic

[a] Nikolaev Institute of Inorganic Chemistry SB RAS,
3 Acad. Lavrentiev Ave., 630090 Novosibirsk, Russia
Fax: (internat.) + 7-3832-344-489
E-mail: yuri@che.nsk.su
[b] Institut für Bioanorganische und Radiopharmazeutische Chemie, Forschungszentrum Rossendorf,
P. O. Box 510119, 01314 Dresden, Germany
[c] Institut für Radiochemie, Forschungszentrum Rossendorf,
P. O. Box 510119, 01314 Dresden, Germany
[d] Bundesanstalt für Materialforschung und Prüfung,
Richard-Willstätter-Straße 11, 12489 Berlin, Germany

approach for grafting N-donor ligands to octahedral rhenium cluster compounds has been developed. Here we report the preparation and crystal structures of two new rhenium octahedral cluster complexes, $[Re_6S_7O(3,5\text{-}Me_2PzH)_6]Br_2\cdot 3,5\text{-}Me_2PzH$ (**1**) and $[Re_6Se_7O(3,5\text{-}Me_2PzH)_6]Br_2\cdot 3,5\text{-}Me_2PzH$ (**2**), which were synthesised by the reaction of rhenium chalcobromides $Cs_3[Re_6(\mu_3\text{-}Q_7Br)Br_6]$ (Q = S, Se) with molten 3,5-dimethylpyrazole (3,5-Me_2PzH). The spectroscopic, photophysical and thermal properties of these cluster compounds are also discussed.

Results and Discussion

Syntheses

As a general rule, rhenium cluster compounds containing cluster cores $\{Re_6Q_8\}^{2+}$ (Q = S, Se) and apical organic ligands have been prepared by solution chemistry. A disadvantage of solution chemistry in such syntheses is the rather low rate of interaction and possible hydrolysis (in the case of aqueous solutions or non-anhydrous organic solvents), which limit synthetic resources for preparation of desirable compositions. To overcome these difficulties, we employed a new approach using molten ligands as reaction media for the synthesis of cluster complexes with organic ligands. We applied this method to the reaction of the rhenium cluster compounds $Cs_3[Re_6(\mu_3\text{-}Q_7Br)Br_6]$ (Q = S, Se) with 3,5-dimethylpyrazole as the organic ligand. In the anionic rhenium complexes $[Re_6(\mu_3\text{-}Q_7Br)Br_6]^{3-}$ (Q = S, Se) used, the octahedron Re_6 is surrounded by a cube of eight (μ_3-Q_7Br) atoms (so-called "inner" ligands). Such an "octahedron into cube" forms the cluster core $\{Re_6(\mu_3\text{-}Q_7Br)\}^{3+}$. The six apical positions in the cluster complexes $[Re_6(\mu_3\text{-}Q_7Br)Br_6]^{3-}$ are fully occupied by Br atoms, which are called "outer" ligands. The outer bromide ligands in similar complexes possess anticipated substitutional lability, whereas inner ligands are bonded more strongly. So we expected that in reactions of these clusters with dimethylpyrazole, the apical ligands could be substituted by organic ligands without any change in the cluster core $\{Re_6(\mu_3\text{-}Q_7Br)\}$ as the fundamental building block.

Experimental results show that indeed all apical Br atoms are substituted by organic ligands. On the other hand, an interesting feature of these reactions is an unexpected ligand exchange in the octahedral cluster core, namely the replacement of the inner μ_3-Br ligand by an oxygen atom. Such a substitution is rather unusual in the chemistry of octahedral clusters. The possible source of oxygen for such a substitution is the solvated molecules of H_2O in the starting complexes.

Few examples are known of the substitution of one or two μ_3-Cl ligands by oxygen in the cluster core of octahedral rhenium chalcohalide complexes, and examples of μ_3-Br substitution with oxygen were not found in the literature. The complexes containing two O atoms in the cluster cores $\{Re_6Se_4O_2Cl_2\}^{4+}$ [18] and $\{Re_6S_6O_2\}^{2+}$ [3] were obtained starting from $Re_6Se_4Cl_{10}$ and $[Re_6S_6Cl_8]^{2-}$, respectively. Complexes with the cluster core $\{Re_6S_5OCl_2\}^{2+}$ containing one O atom were obtained from the cluster anion $[Re_6S_5Cl_9]^-$.[19–21] There are two typical sources of oxygen in these reactions: $OSiMe_3$[3,19] or water. Water either came from wet solvent[18] or was added directly to the reaction mixture.[18,20] Here we succeeded in the preparation of oxochalcogenide complexes with a cluster core having the composition $\{Re_6Q_7O\}^{2+}$.

Structures

Compounds **1** and **2** have been characterised by single-crystal X-ray diffraction. The compounds are isostructural. The cluster cations $[Re_6Q_7O(3,5\text{-}Me_2PzH)_6]^{2+}$ (Q = S, Se) contain the Re_6 octahedron residing in a Q_7O pseudocube. There is no disorder in the present structures: seven corner positions of the Q_7O cube are occupied exclusively by S (**1**) or Se (**2**) atoms and one by an O atom. Due to the presence of the O atom in the cluster core $\{Re_6Q_8\}$, the Re_6 octahedrons in both compounds are slightly irregular. Re–Re distances between Re atoms coordinated by the μ_3-O atom are shorter than those for other Re atoms. Each Re atom is coordinated by a 3,5-Me_2PzH. The structure of a complete molecule is shown in Figure 1. The Re–Re distances range from 2.5210(7) to 2.5995(7) Å in **1** and from 2.5465(13) to 2.6386(14) Å in **2**; the Re–Q distances range from 2.392(3) to 2.417(3) Å in **1** and from 2.509(2) to 2.544(2) Å in **2**; the Re–O distances range from 2.114(8) to 2.129(8) Å in **1** and from 2.022(8) to 2.036(8) Å in **2**; the Re–N distances are 2.13(1)–2.16(1) (**1**) and 2.16(2)–2.21(2) Å (**2**). The Re–O distances in **1** are slightly longer than those found in $(Bu_4N)_2[Re_6S_5OCl_8]$ [2.08(1)–2.09(1) Å][19] or $(Bu_4N)_4[(Re_6S_5OCl_7)_2O]$ (average Re–O: 2.087(6) Å)[20] and shorter than in $[Re_6S_6O_2(PPr_3)_6][Re_6S_6Cl_8]$, where Re–O distances are in

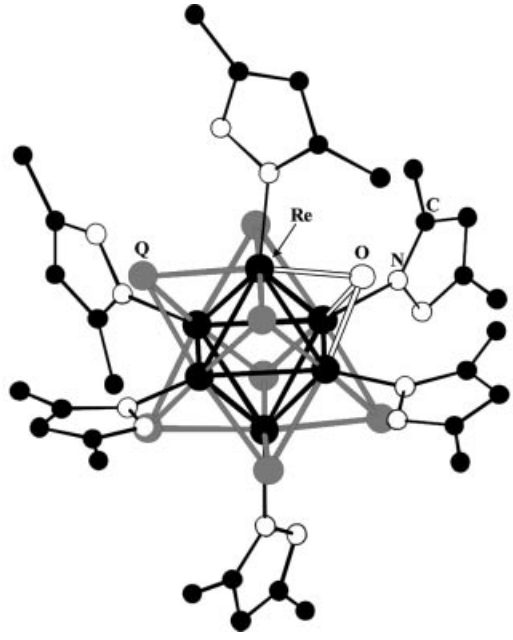

Figure 1. Structure of the cluster cation $[Re_6Q_7O(3,5\text{-}Me_2PzH)_6]^{2+}$ [Q = S (**1**), Se (**2**)]; all hydrogen atoms are omitted for clarity

 © 2005 Wiley-VCH Verlag GmbH & Co. KGaA, Weinheim

the range 2.192(11)−2.226(11) Å.[3] The Re−O distances in **2** are the shortest among all known compounds of this type. Average Re−O distances in α- and β-$(Pr_4N)_2[Re_6Se_4O_2Cl_8]$ are equal to 2.083(14) and 2.094(19) Å, respectively.[18] There are two types of Br atoms in the structure: one bromine atom, Br1, is connected by hydrogen bonds to one cluster (Br···H−N distances are 3.25 and 3.31 Å in **1** and 3.24 and 3.28 Å in **2**) (Figure 2, a), whereas the other one, Br2, is bridged between two cluster cations with Br···H−N distances ranging from 3.41 to 3.68 Å in **1** and from 3.43 to 3.66 Å in **2** to form extended chains along the *a*-axes (Figure 2, b). Both compounds have additional noncoordinated molecules of $3,5\text{-}Me_2PzH$.

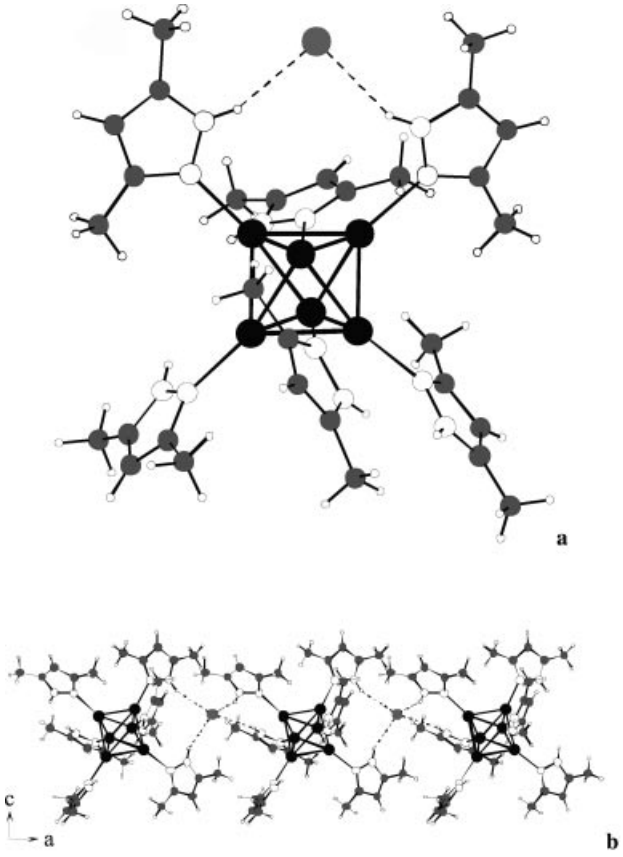

Figure 2. Connection of cluster cations with Br^- anions in compounds **1** and **2**: a) location of Br1; b) location of Br2 bridging cluster units; hydrogen bonds are denoted by dotted lines; all sulfur and oxygen atoms of the cluster core are omitted for clarity

Absorption Spectra and Luminescence Characteristics

Solutions (1.0×10^{-5} M) of the two compounds were prepared in methanol. Absorption spectra were recorded in the wavelength range from 190 to 500 nm. The absorption of light starts at around 400 nm. For compound **1**, absorption maxima were located at 221, 247, 272, 294 and 321 nm. Compound **2** had absorption maxima at 211, 241, 260, 277, 294 and 338 nm (Figure 3).

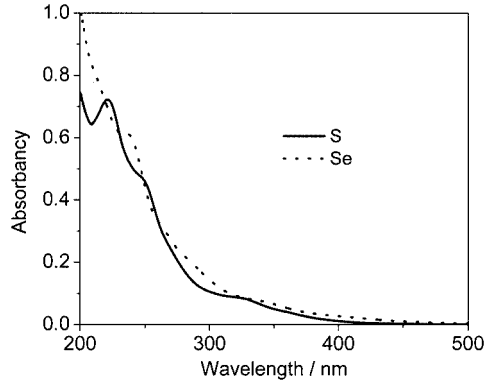

Figure 3. Absorption spectra of $[Re_6S_7O(3,5\text{-}Me_2PzH)_6]Br_2\cdot 3,5\text{-}Me_2PzH$ (**1**) and $[Re_6Se_7O(3,5\text{-}Me_2PzH)_6]Br_2\cdot 3,5\text{-}Me_2PzH$ (**2**)

For excitation of the luminescence, a Nd:YAG laser with fourth harmonic generation (266 nm) was used. To avoid destruction of the compound, the applied laser energy was set to be less than 300 μJ per pulse. The emission spectra were recorded in the wavelength range 560−785 nm. For both compounds broad emission spectra were found. The light emission of **2** was shifted about 30 nm to the red, relative to **1**. Figure 4 shows the emission spectra of the two compounds in methanol solution. Both emission spectra were fitted with two Gaussian peaks (Table 1). For the determination of the fluorescence decay constants, the fluorescence intensity was integrated in the wavelength range from 560 to 785 nm. The resulting fluorescence decay as a function of the increasing time between the laser pulse and the detection of the fluorescence is shown in Figure 5. The derived fluorescence decay times are summarised in Table 1. For compound **1**, the longer fluorescence decay time corresponds to 84.0% of the fluorescence intensity at time $t = 0$, and for compound **2** to 72.5%. Compound **2** shows a somewhat longer fluorescence decay time than **1**. However, the two Gaussian emission distributions found for each compound do not show any remarkable difference in their fluorescence decay behaviour.

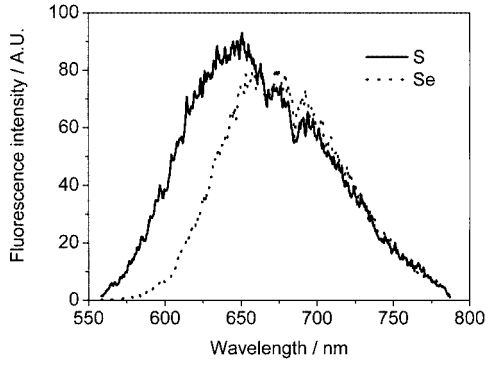

Figure 4. Emission spectra of $[Re_6S_7O(3,5\text{-}Me_2PzH)_6]Br_2\cdot 3,5\text{-}Me_2PzH$ (**1**) and $[Re_6Se_7O(3,5\text{-}Me_2PzH)_6]Br_2\cdot 3,5\text{-}Me_2PzH$ (**2**) in methanol

 © 2005 Wiley-VCH Verlag GmbH & Co. KGaA, Weinheim

Table 1. Fluorescence spectroscopic data

Compound	Fluorescence decay time [μs]/ Fluorescence emission maxima [nm]	
1	0.61±0.06/632.4 (49%)	3.07±0.03/692.8 (51%)
2	0.49±0.02/650.0 (24%)	3.96±0.02/688.3 (76%)

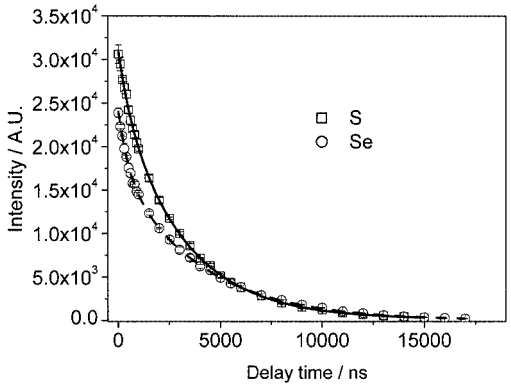

Figure 5. Fluorescence decay of $[Re_6S_7O(3,5\text{-}Me_2PzH)_6]Br_2\cdot 3,5\text{-}Me_2PzH$ (**1**) and $[Re_6Se_7O(3,5\text{-}Me_2PzH)_6]Br_2\cdot 3,5\text{-}Me_2PzH$ (**2**) in methanol

The emissive properties of these clusters could be used in photodynamic therapy. This phenomenon will be the subject of our future investigations.

Thermal Properties

Studying the thermal stability of both compounds in vacuo showed that the release of 3,5-dimethylpyrazole ligands begins near 200 °C; decomposition with complete removal of 7 mol-equiv. of 3,5-Me_2PzH is finished at 330 °C; however, it is not possible to mark out separate steps of mass loss on the TG curve.

Conclusion

An original method for the synthesis of organic−inorganic rhenium cluster compounds has been demonstrated using the molten organic ligand 3,5-dimethylpyrazole as the reaction medium for the replacement of the apical bromide atoms in the cluster core. Two new octahedral rhenium cluster complexes, having the composition $[Re_6S_7O(3,5\text{-}Me_2PzH)_6]Br_2\cdot 3,5\text{-}Me_2PzH$ and $[Re_6Se_7O(3,5\text{-}Me_2PzH)_6]Br_2\cdot 3,5\text{-}Me_2PzH$, were synthesised in a high yield and their structures have been solved and refined. An interesting feature of the chemistry of these compounds is the unexpected ligand exchange in the octahedral cluster core $\{Re_6(\mu_3\text{-}Q_7Br)\}^{3+}$, namely the replacement of the inner μ_3-Br^- ligand by an oxygen ion O^{2-}, which results in the formation of the cluster core $\{Re_6(\mu_3\text{-}Q_7O)\}^{2+}$. Such a substitution is rather unusual in the chemistry of octahedral clusters. The cluster compounds investigated show promising spectroscopic and photophysical properties. The great variety of organic ligands grafting on the cluster core offers abundant opportunities to modify the spectroscopic and photophysical properties, and the organic shell can make the cluster molecule bioavailable. In this nexus, coupling of target-seeking biomolecules to the cluster moiety seems to be an interesting line of future research. Such organic−inorganic hybrids have great inherent potential as diagnostically and therapeutically relevant compounds.

Experimental Section

Materials and Syntheses: All reagents were used as purchased. $Cs_3[Re_6(\mu_3\text{-}Se_7Br)Br_6]\cdot H_2O$ was prepared as described.[22] $Cs_3[Re_6(\mu_3\text{-}S_7Br)Br_6]\cdot H_2O$ was synthesised similarly. Microanalyses for C, H, N, S were performed at the Laboratory of Microanalysis of Vorozhtsov Institute of Organic Chemistry, Siberian Branch RAS with a Vario EL from Elementar Analysensysteme GmbH. FTIR: Bruker IFS-85, Perkin−Elmer 1760X. UV/Vis spectra were recorded in methanol solution with a Cary 5G spectrophotometer (Varian). Emission spectra of these solutions were obtained by use of time-resolved laser-induced fluorescence spectroscopy (TRLFS). The setup is described elsewhere.[25] For excitation, a diode-pumped Nd:YAG laser with fourth harmonic generation (266 nm) was used (DIVA II; Soliton). The repetition rate was 20 Hz and the energy of the laser was set to be 300 μJ per pulse. Thermal properties were studied using Thermoanalyser TA-7000 in vacuo in the temperature interval 25−500 °C with a rate of about 10 K/min.

$[Re_6S_7O(3,5\text{-}Me_2PzH)_6]Br_2\cdot 3,5\text{-}Me_2PzH$ (1) and $[Re_6Se_7O(3,5\text{-}Me_2PzH)_6]Br_2\cdot 3,5\text{-}Me_2PzH$ (2): Synthetic procedures for both compounds were analogous. Crystals, suitable for X-ray structure determination, were separated manually from the reaction mixture. For preparation of **1**, $Cs_3Re_6S_7Br_7\cdot H_2O$ (0.2 g, 0.0863 mmol) and 3,5-dimethylpyrazole (0.2 g, 2.08 mmol) were heated in a sealed glass ampoule at 200 °C for 2 d. The ampoule was cooled at a rate of about 20 °C/h, then the excess of dimethylpyrazole was removed by washing with diethyl ether. CsBr, formed during the reaction, was removed by washing with water. Yield 95% (180 mg, 0.0819 mmol). Compound **2** was prepared in the same way: $Cs_3Re_6Se_7Br_7\cdot H_2O$ (0.2 g, 0.0756 mmol) was heated with 3,5-dimethylpyrazole (0.2 g, 2.08 mmol). Yield: 93% (177 mg, 0.0703 mmol). $C_{35}H_{56}Br_2N_{14}ORe_6S_7$ (**1**) (2190.44): calcd. C 19.2, H 2.6, N 9.0 S, 10.2; found C 19.0, H 2.6, N 8.9, S 10.1. $C_{35}H_{56}Br_2N_{14}ORe_6Se_7$ (**2**) (2518.68): calcd. C 16.7, H 2.2, N 7.8; found C 16.8, H 2.1, N 7.7. The IR spectra (400−4000 cm^{-1}) of **1** and **2** show all the peaks expected for 3,5-Me_2PzH. In the spectrum of **1** the peak at 415 cm^{-1} was assigned to Re−(μ_3-S) vibration.

Structure Determination: Single-crystal X-ray diffraction data were collected with the use of graphite-monochromatised Mo-K_α radiation (λ = 0.71073 Å) at 293 K with a Bruker SMART diffractometer, equipped with a CCD area detector. The structures were solved by direct methods using SHELXS-90[23] and refined with SHELXL-97.[24] An empirical absorption correction (Ψ-scan) was applied. All non-hydrogen atoms were refined anisotropically. In both structures there are 65 crystallographically independent non-hydrogen atoms which reside at general positions. The positions of hydrogen atoms were calculated corresponding to their geometrical conditions and refined using the riding model. CCDC-231769 (**1**) and -231770 (**2**) contain the supplementary crystallographic data for this paper. These data can be obtained free of charge from The Cambridge Crystallographic Data Centre via www.ccdc.cam.uk/data_request/cif.

 © 2005 Wiley-VCH Verlag GmbH & Co. KGaA, Weinheim

1: Orange block, crystal dimensions 0.03 × 0.04 × 0.04 mm, orthorhombic, space group $P2_12_12_1$, $Z = 4$, $a = 11.4967(7)$ Å, $b = 14.7903(9)$ Å, $c = 32.109(2)$ Å, $V = 5459.8(6)$ Å^3 ($T = 293(2)$ K), $\rho_{calcd.} = 2.664$ g cm^{-1}, $\mu = 15.02$ mm^{-1}, 23730 measured reflections, 7849 independent ($R_{int} = 0.0561$), $R(F) = 0.0332$ for 7166 reflections with $F_{hkl} \geq 4\sigma(F_{hkl})$ and $R_w(F^2) = 0.0742$ for all independent reflections. The absolute structure was established by use of the Flack parameter, which is close to 0.

2: Orange block, crystal dimensions 0.03 × 0.045 × 0.055 mm, orthorhombic, space group $P2_12_12_1$, $Z = 4$, $a = 11.473(4)$ Å, $b = 14.885(5)$ Å, $c = 32.902(12)$ Å, and $V = 5619(3)$ Å^3 [$T = 293(2)$ K], $\rho_{calcd.} = 2.977$ g cm^{-1}, $\mu = 18.872$ mm^{-1}, 33397 measured reflections, 12747 independent ($R_{int} = 0.1355$), $R(F) = 0.0669$ for 9338 reflections with $F_{hkl} \geq 4\sigma(F_{hkl})$ and $R_w(F^2) = 0.1693$ for all independent reflections. The absolute structure was established by use of the Flack parameter, which is close to 0.

Acknowledgments

This research was supported by INTAS (grant 00-00689) and by the Sächsisches Staatsministerium für Wissenschaft und Kunst, Aktenzeichen: 4-7531.50-04-844-03/7. The authors thank also the DLR Internationales Büro des BMBF (WTZ Project RUS 01/241) for support.

[1] J. C. P. Gabriel, K. Boubekeur, S. Uriel, P. Batail, *Chem. Rev.* **2001**, *101*, 2037−2066.
[2] H. D. Selby, B. K. Roland, Z. P. Zheng, *Acc. Chem. Res.* **2003**, *36*, 933−944.
[3] A. Decker, F. Simon, K. Boubekeur, D. Fenske, P. Batail, *Z. Anorg. Allg. Chem.* **2000**, *626*, 309−313.
[4] H. D. Selby, Z. P. Zheng, T. G. Gray, R. H. Holm, *Inorg. Chim. Acta* **2001**, *312*, 205−209.
[5] T. Yoshimura, K. Umakoshi, Y. Sasaki, S. Ishizaka, H. B. Kim, N. Kitamura, *Inorg. Chem.* **2000**, *39*, 1765−1772.
[6] Z. N. Chen, T. Yoshimura, M. Abe, K. Tsuge, Y. Sasaki, S. Ishizaka, H. B. Kim, N. Kitamura, *Chem. Eur. J.* **2001**, *7*, 4447−4455.
[7] A. Itasaka, M. Abe, T. Yoshimura, K. Tsuge, M. Suzuki, T. Imamura, Y. Sasaki, *Angew. Chem. Int. Ed.* **2002**, *41*, 463−466.
[8] B. K. Roland, C. Carter, Z. P. Zheng, *J. Am. Chem. Soc.* **2002**, *124*, 6234−6235.
[9] H. D. Selby, P. Orto, Z. P. Zheng, *Polyhedron* **2003**, *22*, 2999−3008.
[10] R. Wang, Z. Zheng, *J. Am. Chem. Soc.* **1999**, *121*, 3549−3550.
[11] B. K. Roland, H. D. Selby, J. R. Cole, Z. Zheng, *Dalton Trans.* **2003**, 4307−4312.
[12] H. D. Selby, B. K. Roland, M. D. Carducci, Z. Zheng, *Inorg. Chem.* **2003**, *42*, 1656−1662.
[13] H. D. Selby, P. Orto, M. D. Carducci, Z. Zheng, *Inorg. Chem.* **2002**, *41*, 6175−6177.
[14] B. K. Roland, H. D. Selby, M. D. Carducci, Z. Zheng, *J. Am. Chem. Soc.* **2002**, *124*, 3222−3223.
[15] K. M. Kadish, K. M. Smith, R. Guilard in *Handbook of Porphyrins and Related Macrocycles*, vol. 6 ("Applications: Past, Present and Future"), Academic Press, Burlington, MA, **2000**, p. 346.
[16] M. B. Vrouenraets, G. W. M. Visser, G. B. Snow, G. A. M. S. van Dongen, *Anticancer Res.* **2003**, *23*, 505−522.
[17] B. Larsson, *in Hadrontherapy in Oncology* (Eds.: U. Amaldi, B. Larsson), Elsevier, Amsterdam, Lausanne, New York, Shannon, Tokyo, **1994**.
[18] O. M. Yaghi, M. J. Scott, R. H. Holm, *Inorg. Chem.* **1992**, *31*, 4778−4784.
[19] S. Uriel, K. Boubekeur, P. Batail, J. Orduna, E. Canadell, *Inorg. Chem.* **1995**, *34*, 5307−5313.
[20] F. Simon, K. Boubekeur, J. C. P. Gabriel, P. Batail, *Chem. Commun.* **1998**, 845−846.
[21] A. Deluzet, R. Rousseau, C. Guilbaud, I. Granger, K. Boubekeur, P. Batail, E. Canadell, P. Auban-Senzier, D. Jerome, *Chem. Eur. J.* **2002**, *8*, 3884−3900.
[22] S. S. Yarovoi, Y. V. Mironov, S. F. Solodovnikov, A. V. Virovets, V. E. Fedorov, *Mater. Res. Bull.* **1999**, *34*, 1345−1351.
[23] G. M. Sheldrick, *SHELXS-97, Program for the Refinement of Crystal Structures*, University of Göttingen, Germany, **1997**.
[24] G. M. Sheldrick, *SHELXL-97*, University of Göttingen, Germany **1997**.
[25] G. Geipel, A. Brachmann, V. Brendler, G. Bernhard, H. Nitsche, *Radiochim. Acta* **1996**, *75*, 199−204.

Received June 3, 2004
Published Online January 7, 2005

 © 2005 Wiley-VCH Verlag GmbH & Co. KGaA, Weinheim

Syntheses, Structures and Magnetic Properties of Layered Metal(II) Mandelates

Adel Beghidja,[a,b] Sylvain Hallynck,[a] Richard Welter,*[b] and Pierre Rabu*[a]

Keywords: Carboxylate ligands / Layered compounds / Magnetic properties / Transition metals / X-ray powder diffraction

A series of Mn^{II}, Fe^{II}, Co^{II}, Ni^{II} and Cu^{II} layered mandelates has been synthesised in the form of crystalline powders by a hydrothermal route. The five compounds are isostructural with the copper analogue, also obtained in a single crystal form, except that the latter shows a strong Jahn–Teller distortion of the coordination spheres around the Cu^{II} centres. The complexes crystallise in the monoclinic centrosymmetric space group $P2_1/a$ and their structures consist of layers of six-coordinate metal(II) ions interconnected through carboxylato bridges in a diamond-like network. The magnetic data indicate very small antiferromagnetic in-plane couplings for **1**, **2**, **3** and **5**, with $J/k_B = -0.122$ K for **1**. The Ni^{II} compound **4** exhibits ferromagnetic coupling within the layers ($J/k_B = +1.213$ K) and ferromagnetic 3D ordering can be observed at $T_C = 2.7$ K.

(© Wiley-VCH Verlag GmbH & Co. KGaA, 69451 Weinheim, Germany, 2005)

Introduction

Correlations between the magnetic properties of molecule-based solids and their structures together with the nature of the chemical bond are useful in the design of new magnetic materials.[1,2] In this respect, low dimensional systems in which the magnetic centres interact within chains (1D) or planes (2D) are of particular interest since their physics may be approximated and analysed to a high degree. This has been possible thanks to the development of a substantial amount of experimental and theoretical work in the area over several decades[3–6] and to the efforts of synthetic chemists in providing model compounds, particularly through the molecular approach, i.e. by using molecular building blocks for the design of new interconnected networks,[7,8] involving several kinds of metallic ions or radicals, which exhibit predictable magnetic properties.[9–11] Focusing on 2D systems, as found in layered transition metal compounds, it has been shown that the occurrence of 3D magnetic ordering is mainly driven by the divergence of the correlation length within the layers which depends on the in-plane magnetic exchange coupling and on the topology of the magnetic centres.[4,6,12,13] Recent results on organic-inorganic layered magnets have shown that it is possible to tune the coupling between spin layers by using suitable organic ligands separating or connecting transition metal based layers.[14] Striking results have been obtained in the field of low dimensional magnetic materials exhibiting unusual behaviour, by carrying out solvothermal reactions.[15–19] In particular, recent reports have been concerned with the use of carboxylate moieties as bridging ligands between paramagnetic transition metal ions with the versatility of the carboxylate coordination group leading to magnetic networks with various topologies.[20–23]

Our recent investigation of Co^{II} alkanoates $[Co(O_2C(CH_2)_nCH_3)_2(H_2O)_2]_n$ has shown that for long alkane chains, layered structures are obtained when the magnetic layers consist of chains of Co^{II} ions interconnected through carboxylate bridges in a *syn-anti* configuration. This leads to weak antiferromagnetic coupling.[24] On the other hand, results on transition metal phenoxyalkanoate hydrates $[M(O_2C(CH_2)OC_6H_4R)_2(H_2O)_2]_n$ (M = Mn, Co; R = H, Cl, F, ...), the structures of which consist of stacked metal(II) carboxylate layers separated by an organic subnetwork of phenyl rings, provided suitable examples of square planar arrays of magnetic centres.[25,26] The diaquabis(phenoxyacetato)manganese(II) derivative exhibits typical behaviour for an antiferromagnetic 2D square-planar $S = 5/2$ system down to $T_C = 1.633$ K where a 3D ordered spin state leads to weak ferromagnetism. Magnetic data for the Co^{II} analogue suggest the presence of ferromagnetic interactions.[27]

As a continuation of our investigations of layered systems, the present work is concerned with the synthesis, through a hydrothermal route, of a series of layered transition metal (M) carboxylates obtained using the chiral mandelate ion $C_6H_5CH(OH)CO_2^-$ (M = Mn, Fe, Co, Ni, Cu) and an analysis of their crystal structures and magnetic

[a] Institut de Physique et Chimie des Matériaux de Strasbourg, UMR 7504 du CNRS,
23 rue du Loess, 67034 Strasbourg, France
Fax: (internat.) + 33-3-88107247
E-mail: pierre.rabu@ipcms.u-strasbg.fr
[b] Laboratoire DECMET, ILB, Université Louis Pasteur,
4 rue Blaise Pascal, 67000 Strasbourg, France

 © 2005 Wiley-VCH Verlag GmbH & Co. KGaA, Weinheim **DOI: 10.1002/ejic.200400623**

behaviour. Some molecular complexes of transition metals (Cu, Co, V) have been reported in the literature in which the mandelate anion acts as a co-ligand with lactic acid derivatives such as phenanthroline or bipyridine, resulting in peculiar coordination geometries.[28−31] Noble metal complexes were also prepared.[32] It is worth noticing, however, that very few results have been reported in the literature on compounds involving only the mandelate ion and most of these studies have concerned the solubility, vibrational spectroscopic properties and optical activities of the isolated metal complexes.[33] Only one very recent work reports the crystal structure and magnetic susceptibility measurements of a Co^{II} derivative.[34]

Results and Discussion

Synthesis and Structural Analysis

A series of five transition metal mandelates has been synthesised through a hydrothermal method by treating metal chlorides with mandelic acid and NaOH in water (see Experimental Section). The complexes of manganese (**1**), iron (**2**), cobalt (**3**) and nickel (**4**) were obtained as crystalline powders consisting of very thin platelets. The Fe^{II} solid **2** contains a small amount of a magnetic impurity, namely iron oxide, which was revealed by the magnetic measurements. The copper(II) analogue **5** crystallises from the mother solution (resulting from hydrothermal treatment) as thick single crystals suitable for X-ray analysis. It is worth noticing also that reactions under standard conditions at room temperature led, for the five metal ions, to the same products but only as fine and less crystalline powders. This highlights the importance of an interest in the hydrothermal method. The structure of **5** has been solved by a single-crystal X-ray diffraction analysis (see crystallographic section) and is similar to that reported in the literature for the Co^{II} analogue[34] except that an accurate Fourier analysis ascertained the presence of the hydrogen of the α-hydroxide coordinated to the copper(II) centres, whereas this was not considered for the cobalt species. The compound can be described as a (diaqua)copper(II)−μ-mandelate polymer, the asymmetric unit of which is displayed in Figure 1. Each Cu^{II} atom is coordinated to six oxygen atoms forming elongated octahedra. In the equatorial plane, they are surrounded by two mandelate ligands each chelating the metal through one oxygen atom of the carboxylate group [Cu−O1 1.924(2) Å] and the α-OH [Cu−O2 1.987(2) Å]. Two other mandelate groups complete the octahedral site with monodentate oxygen atoms from their carboxylate functions in apical positions [Cu−O3#1 2.418(2) Å] resulting in a distorted environment (Figure 1) similar to the Co^{II} case but with strong additional distortion of the octahedral sites around metal ions due to the Jahn−Teller effect (see Table 1).

Within the *a*,*b* planes, the copper atoms are connected to four neighbours by carboxylato bridges in a *syn-anti* conformation (Figure 1), thus forming square-planar magnetic arrays separated by a double layer of mandelate anions

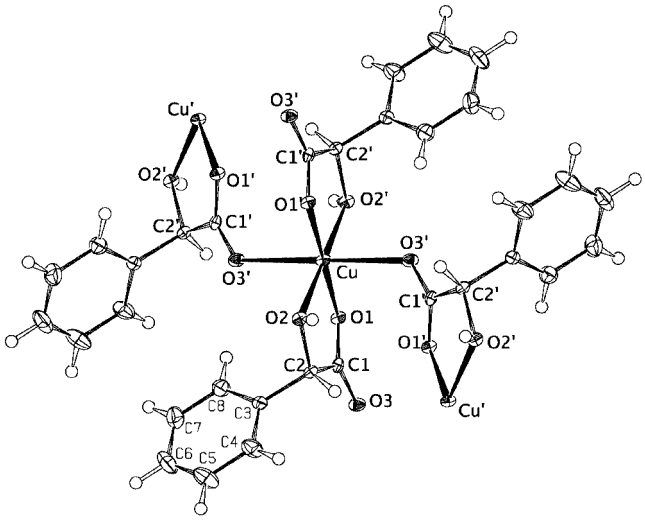

Figure 1. ORTEP plot of the structure of **5** showing coordination of the Cu^{II} atoms by the mandelate ligands and interconnection through carboxylato bridges

Table 1. Bond lengths [Å] and angles [°] in the copper dimandelate compound

Atoms	Distances	Atoms	Angles
Cu−O1	1.924(2)	O1−Cu−O2	83.41(10)
Cu−O2	1.987(2)	O1−Cu−O2#2	96.59(10)
Cu−O3#1	2.418(2)	O1−Cu−O3#1	95.18(9)
O1−C1	1.299(4)	O1#2−Cu−O3#1	84.82(9)
C1−C2	1.530(5)	O2−Cu−O3#1	95.18(9)
O2−C2	1.466(3)	O2#2−Cu−O3#1	89.63(9)
C2−C3	1.506(4)	C1−O1−Cu	115.72(19)
		C2−O2−Cu	113.32(18)
O1#3−O2#2	2.752(4)	O3−C1−O1	123.5(3)
(intermolecular)		O3−C1−C2	119.1(3)

#1: $-x + 1/2, y + 1/2, -z + 1$; #2: $-x + 1, -y, -z + 1$; #3: $-x + 1, -y + 1, -z + 1$

(Figure 2). The Cu−Cu distances across the carboxylato bridges are 5.325(5) Å which correspond to the exchange pathways schematised in Figure 3. Moreover, intermolecular hydrogen bonds can be identified [O1#3−O2#2 2.752 (4) Å, O1−H1−O2 171°], the CuO_6 octahedra thus being connected by two O1−O2 hydrogen bonds along the *b* axis. All the mandelates are positioned quasi-perpendicular to the copper layers which are 15.12(1) Å apart. In addition, a detailed examination of the structural stacking prompts a consideration of the existence of σ−π interactions between the phenyl rings related symmetrically by the crystallographic *a* mirror plane. (Figure 2).[35] These cycles form an angle of 87° and the centroid−centroid distance is 5.21 Å. The shortest distances for σ-π interactions are: C4−C8 3.70 Å, C4−C7 3.74 Å, C5−C7 3.93 Å and C5−C6 4.19 Å.

It is apparent that the structure is centrosymmetric. Accordingly, the present compounds exhibit no circular dichroism and involve both (*R*) and (*S*) enantiomers of the mandelate ligand although the pure (*R*) enantiomer was used as a starting ligand. This was also observed in the

 © 2005 Wiley-VCH Verlag GmbH & Co. KGaA, Weinheim

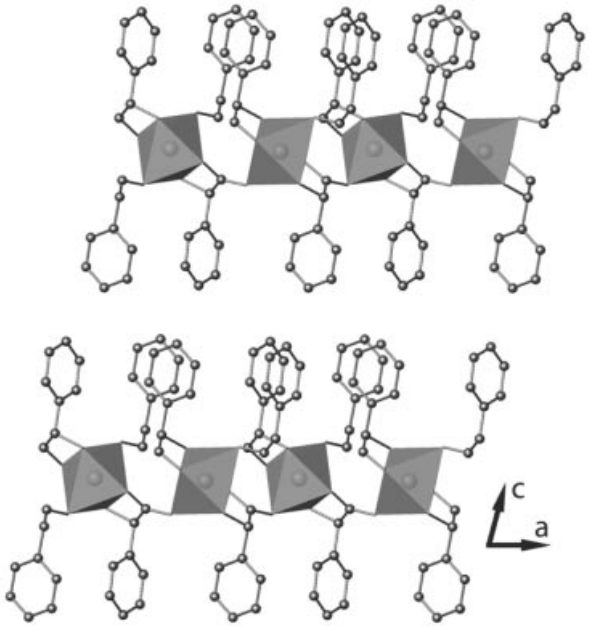

Figure 2. Partial view along the *b* axis of the layered structure of **5**

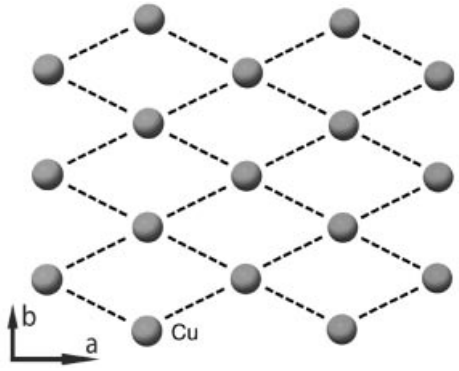

Figure 3. Drawing of the diamond-like M^{II} network in the (*a*,*b*) planes; each metal ion interacts with its four nearest neighbours as in a square planar system

cobalt(II) analogue.[34] For the latter, it was pointed out that this racemisation, on the basis of previous studies on α-hydroxycarboxylic acids, is favoured by the use of an alkaline medium.[36] It is worth noticing here that the present copper(II) analogue, contrary to all the other metal derivatives, can be obtained without addition of an alkaline base. Similarly, the same compound can be obtained as a powder from the reaction under ambient rather than hydrothermal conditions. It thus appears that significant racemisation may also occur in an acidic or neutral medium, perhaps with different kinetics however.[37]

The other M^{II} compounds were obtained as powders or very thin crystals which somewhat frustrated characterisation by single-crystal diffraction methods. However, the corresponding spectroscopic characterisations (Figure 4) and elemental analyses confirm that all complexes are isostructural with the copper(II) and cobalt(II) dimandelates described above. This was further confirmed by a comparison between their powder X-ray patterns shown in Figure 5. The powder diffraction patterns were fully indexed and the crystallographic cell parameters for the series of compounds

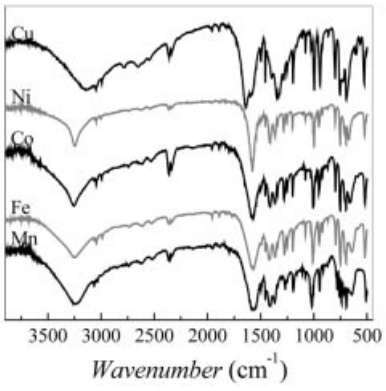

Figure 4. Infrared spectra of the transition metal mandelates; for clarity, the spectra are shifted in intensity

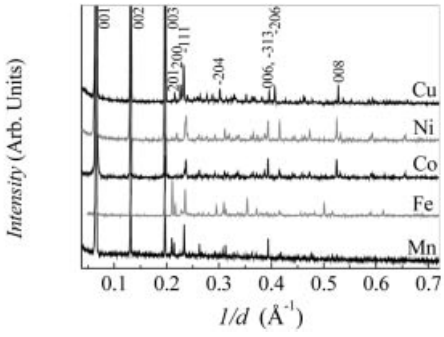

Figure 5. Comparison between the powder X-ray diffraction patterns of the five layered transition metal mandelates, shifted in intensity for clarity; some characteristic diffraction lines are labelled

Table 2. Crystallographic parameters of the first row transition metal dimandelates refined from X-ray powder patterns; all compounds crystallise in the monoclinic space group $P2_1/a$

$M(C_6H_5CH(OH)CO_2]_2$	Mn	Fe	Co	Ni	Cu[a]
a [Å]	8.925(5)	9.511(1)	9.3532(7)	9.239(2)	9.489(1)
b [Å]	4.933(1)	4.8370(8)	4.8737(3)	4.851(1)	4.9156(6)
c [Å]	15.605(4)	15.569(2)	15.495(1)	15.510(1)	15.551(1)
β [°]	101.31(5)	101.37(1)	99.95(1)	100.04(1)	102.749(9)
V [Å^3]	673.70(8)	702.19(6)	695.71(5)	684.49(6)	707.48(2)

[a] Single crystal parameters are: $a = 9.454$ Å; $b = 4.905$ Å; $c = 15.495$ Å; $\beta = 102.56°$; $V = 701.3$ Å^3.

 © 2005 Wiley-VCH Verlag GmbH & Co. KGaA, Weinheim

have been refined (Table 2) by means of a full pattern matching procedure using the Fullprof software package.[38]

Spectroscopic Properties

The IR and UV data collected for the five compounds were easy to analyse on the basis of the crystal data (see Exp. Sect.). The IR spectra exhibit characteristic bands of the mandelate ligand. The frequency difference between the symmetric and asymmetric carboxylate vibrations, $\Delta\nu$ = 150−165 cm^{-1}, is much smaller than that observed in the corresponding acid ($\Delta\nu_i \approx 270$ cm^{-1}) in agreement with the bidentate coordination mode of the carboxylate groups.[39] The presence of broad νO−H bands in the range 3200−3400 cm^{-1} is related to the mandelate OH moieties bonded to the metal ions. Interestingly, whereas the IR spectra of the Mn^{II}, Fe^{II}, Co^{II}, Ni^{II} compounds are almost identical, thus confirming very similar local structures, significant shifts of the νO−H and carboxylate bands can be observed for Cu^{II} species. The latter is merely related to the distortion of the coordination sphere around the copper atoms due to the Jahn−Teller effect, as found from the single-crystal structure analysis (Table 1). The UV spectra are also consistent with the presence of octahedral geometries for the M^{II} ions.[40,41] The values of Dq and the Racah parameter B have been calculated for the d^7 and d^8 ions giving Dq = 985 cm^{-1}, B = 710 cm^{-1} and Dq/B = 1.4 for the Co^{II} and Dq = 811 cm^{-1}, B = 977 cm^{-1} and Dq/B = 0.83 for the Ni^{II} compound in accordance with weak crystal field and high-spin configurations.[42] For Co^{II}, admixture of forbidden d-d transitions at 480 nm (20833 cm^{-1}) and 505 nm (19801 cm^{-1}) results in a multiple structured band. A value of Dq = 939 cm^{-1} can be deduced for the iron(II) ions and a shoulder at λ = 1260 nm (7936 cm^{-1}) can be attributed to splitting of the ^5E_g state. The UV spectrum of the Cu^{II} derivative exhibits the usual broad band (λ = 745 nm/13422 cm^{-1}) due to transitions from the t_{2g} components to the x^2-y^2 level.

Magnetic Properties

The magnetic properties of **1**, **2**, **3**, **4** and **5** were investigated in the temperature range 2−300 K. The temperature dependence of the magnetic susceptibilities χ above 2 K is shown in Figure 6 as χT vs. T plots for **1**, **2**, **3** and **4**, after correction for diamagnetic contributions. The iron(II) compound **2** contains small amounts of an impurity which is ferromagnetic at ambient temperature. Consequently, the susceptibility displayed in Figure 6 for this compound corresponds to the data corrected using the constant ferromagnetic moment deduced from variations in room temperature magnetisation as a function of the field.

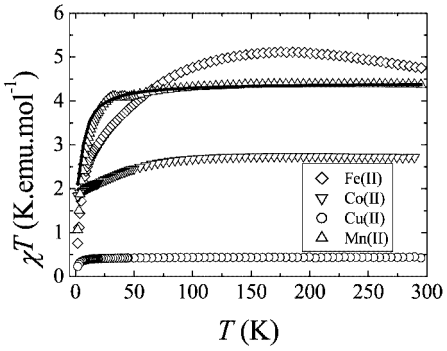

Figure 6. Temperature variation of the magnetic susceptibilities of the compounds **1**, **2**, **3** and **5** as χT vs. T plots; the full line corresponds to the fit of the data for the Mn^{II} compound **1**, as detailed in the text

The four compounds exhibit paramagnetic behaviour corresponding to quasi-isolated metal centres. The inverse-susceptibility versus T curves are linear above 200 K and were fitted using the Curie−Weiss law. The corresponding values of the Curie constants and Weiss temperatures are given in Table 3 and the corresponding values of the effective moments $\mu_{eff} = (8C)^{1/2}$ agree well with those expected for M^{II} ions in an octahedral crystal field.

Upon cooling, the χT product of the Co^{II} compound **3** exhibits a regular decrease from 2.85 $cm^3 \cdot K \cdot mol^{-1}$ at 300 K to 1.8 $cm^3 \cdot K \cdot mol^{-1}$ at 10 K. The decrease of the χT product is well understood as being due to the spin-orbit coupling effects for octahedral Co^{II} ions.[43] Indeed, high-spin octahedral Co^{II} has a $^4T_{1g}$ ground state and, as a consequence, exhibits unquenched spin-orbit coupling in addition to a zero-field splitting which dominates at low temperature and stabilises a doublet ground state. It should be pointed out that for isolated octahedral Co^{II} ions, a minimum value of $\chi T \approx 1.8$ $cm^3 \cdot K \cdot mol^{-1}$ can be expected corresponding to a pseudo spin S = 1/2 and $g \approx 4.4$. Moreover, the magnetisation vs. field variation at 2 K (not shown) is consistent with paramagnetic-like behaviour, indicating that no significant coupling takes place. The saturation moment, Ms = 2.25 $\mu_B \cdot mol^{-1}$, is in agreement with the expected value for octahedral high spin Co^{II} ions (2−3 μ_B per cobalt atom).[9]

Table 3. Main magnetic data of the first row transition metal dimandelates

$M[C_6H_5CH(OH)CO_2]_2$	Mn^{II}	Fe^{II}	Co^{II}	Ni^{II}	Cu^{II}
C [K·emu·mol^{-1}]	4.4	ca. 3.9	2.85	1.16	0.44
μ_{eff} [μ_B.mol^{-1}]	5.9	ca. 5.6	4.8	3.0	1.9
Θ [K]	−0.8	−	−5	+11.36	−3
In-plane interactions[a]	AF/J = −0.122 K	isolated	isolated	F/J = +1.213 K	isolated
3D ordering[a]	−	−	−	F/T_C = 2.7 K	−

[a] AF: antiferromagnetic; F: ferromagnetic.

 © 2005 Wiley-VCH Verlag GmbH & Co. KGaA, Weinheim

Although the corrected data for compound **2** are approximate owing to the presence of the magnetic impurity, the general behaviour of the susceptibility is in agreement with that expected for quasi-isolated Fe^{II} ions exhibiting spin-orbit coupling effects similar to the Co^{II} analogue above.

The copper(II) derivative show a quasi-constant χT product in the whole temperature range and is paramagnetic, whereas the Mn^{II} compound **3** exhibits a significant decrease below 30 K indicating short-range antiferromagnetic in-plane coupling. No long-range order is evident from either susceptibility or magnetisation measurements for this compound. The magnetic behaviour of **3** was modelled with the 2D Heisenberg approach in an effort to evaluate the magnitude of the nearest-neighbour exchange interaction. The susceptibility data were fit between 2 and 300 K with the high-temperature series expansion reported by Rushbrooke and Wood[44,45,46] for an antiferromagnetic 2D Heisenberg square planar system [Equation (1)],[47] giving g = 2.01(1) and $J/k_B = -0.122(4)$ K, Figure 6. The coupling is characteristic of very weak antiferromagnetic interactions across the three-atom dicarboxylate bridge.

$$\chi_{sp}(T) = \frac{S(S+1)Ng^2\mu_B^2}{3k_BT} \times \sum_n a_n x^n \quad (1)$$

The Ni^{II} compound **4** exhibits very different behaviour. Ferromagnetic interactions are implied by the inverse susceptibility $1/\chi$ vs. T variation (not shown) with a positive Curie−Weiss temperature (Table 3). As shown in Figure 7, the temperature variation of the dc magnetic susceptibility implies the existence of a significant ferromagnetic coupling between neighbouring nickel(II) ions within the plane, with an increase in χT from 1.21 K·emu·mol^{-1} at 295 K to 47.5 K·emu·mol^{-1} at 2 K. Ferromagnetic long range order between the layers is demonstrated by the occurrence of a peak in the out-of-phase signal χ'' of the ac susceptibility shown in the inset of Figure 7. The Curie temperature value $T_C \approx 2.5$ K can be deduced from the maximum of χ' where an onset of the imaginary part of the susceptibility χ'' occurs.

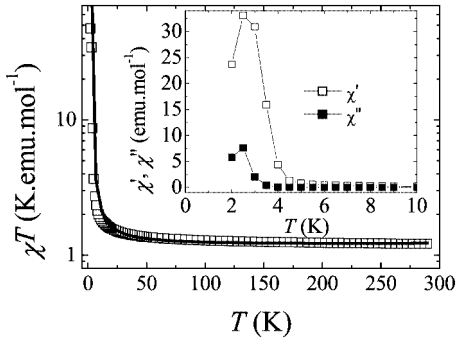

Figure 7. Temperature variation of the magnetic susceptibility of the Ni^{II} mandelate **4** as a χT vs. T plot; the full line corresponds to the fit of the data, as detailed in the text; the inset shows the variation of the real and imaginary parts of the ac susceptibility recorded in a 3.5 Oe/30 Hz magnetic field

Figure 8 shows a magnetisation loop measured at 2 K exhibiting a sharp increase in the magnetisation at low field, up to ca. the half of the saturation value. No hysteresis (at least within a few Gauss) was observed, in accordance with the isotropic character of the Heisenberg Ni^{II} ions and the magnitude of T_C. The saturation moment tends to $2\mu_B$ per Ni^{II} at 5 T which is expected at full saturation for $S = 1$ spin moments. It is important to notice, however, that M vs. H shows a smooth and quasi-linear variation in the high-field region which suggests that small canting between moments might occur, thereby explaining such particular features and leading to rather small residual moments.

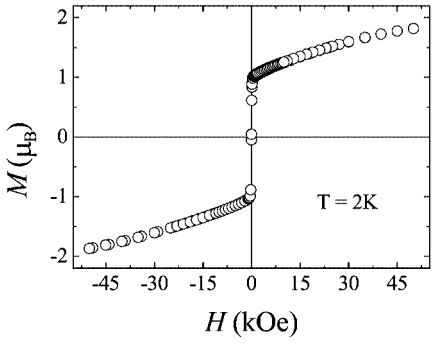

Figure 8. Magnetisation vs. field hysteresis loop for the Ni^{II} mandelate **4**, recorded at 2 K

A fit of the magnetic susceptibility above T_C was carried out using the high temperature series expansion for a ferromagnetic square planar array of $S = 1$ spins, the expression of which is similar to Equation (1) above.[48] In this expression, the zero-field splitting (D) for Ni^{II} ions is neglected although it is known to be effective in the low temperature range, typically below 10 K.[9] Within this approximation, the data are very well fit in the full temperature range with $g = 2.15(1)$ and $J/k_B = +1.213(4)$ K, Figure 7. Finally, the occurrence of 3D magnetic ordering can be undoubtedly established by the temperature variation of the specific heat recorded at low temperature, Figure 9. The curve shows a typical lambda anomaly, the maximum of which enables a

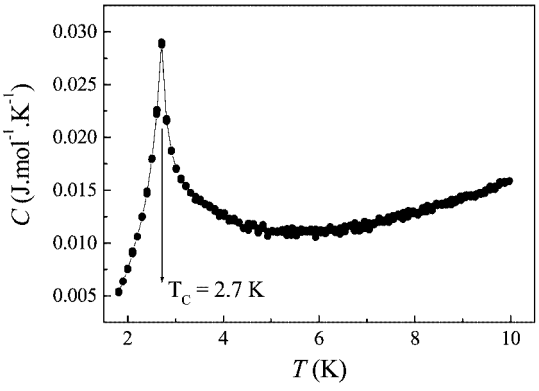

Figure 9. Low-temperature variation of the specific heat of the Ni^{II} mandelate **4**

 © 2005 Wiley-VCH Verlag GmbH & Co. KGaA, Weinheim

precise determination of the Curie temperature T_C = 2.7(1) K.

Conclusion

A series of Mn^{II}, Fe^{II}, Co^{II}, Ni^{II} and Cu^{II} mandelates has been crystallised and structurally and magnetically characterised. Although the starting mandelate was enantiomerically pure, the ligand was found to racemise during the synthetic process. The five compounds are isostructural with the copper analogue, the latter having been obtained as single crystals and showing a strong Jahn−Teller distortion of the coordination spheres around the Cu^{II} centres. Their solid-state structures consist of layers of six-coordinate metal(II) ions, thus forming planar arrays of octahedra interconnected through carboxylato bridges in a diamond-like network. The planes are separated by double layers of phenyl groups from the mandelate ligands resulting in a 2D system. From a magnetic point of view, it has been shown that the in-plane exchange pathways between neighbouring magnetic centres form a square-like planar array. The exchange coupling involving bridging carboxylate ligands in a *syn-anti* conformation is known to promote antiferromagnetic interactions between neighbouring M^{II} ions[49] and to be more favourable than the *anti-anti* conformation.[24] This agrees with the observed behaviour of the χT product for the series of transition metal mandelates except for the nickel derivative for which ferromagnetic behaviour is observed with ferromagnetic 3D ordering at $T_C = 2.7$ K.

Experimental Section

General Remarks: Thermogravimetric experiments were performed using a Setaram TG92 instrument (heating rate of 3 °C/min, air stream). FT-IR studies were performed with an ATI Mattson Genesis computer-driven instrument (0.1 mm thick powder samples in KBr). UV/Vis/NIR studies were performed with a Perkin−Elmer Lambda 19 instrument (spectra recorded by reflection with a resolution of 4 nm and a sampling rate of 480 nm/min). Elemental analyses were performed using a Thermo-Finnigan EA 1112 setup (Service d'analyses, ICS, Strasbourg, France). Magnetic studies were carried out using a Quantum Design SQUID MPMS-XL magnetometer (±5 T, 2−300 K) on several sets of crystalline or powdered samples. Low temperature specific heat measurements were carried out using a MagLab HC Oxford Instrument. Powder X-ray diffraction patterns for the whole series where obtained using Bragg−Brentano Siemens D500 (Co-$K_{\alpha 1}$, λ = 1.78897 Å) and D5000 (Cu-$K_{\alpha 1}$, λ = 1.5406 Å) diffractometers equipped with primary beam monochromators. All the powder X-ray patterns exhibit large preferential orientations of the crystallites parallel to the stacking axis *c*.

X-ray Crystallographic Study: A single crystal of the copper mandelate **5** was mounted on a Nonius Kappa-CCD area detector diffractometer (Mo-K_α, λ = 0.71073 Å). The complete conditions of data collection (Denzo software) and structure refinements are given below. The cell parameters were determined from reflections taken from one set of 10 frames (1.0° steps in φ angle), each with an exposure time of 20 s. The structure was solved by direct methods (SHELXS-97) and refined against F^2 using the SHELXL-97 software.[50] The absorption was corrected empirically with Sortav.[51] All non-hydrogen atoms were refined anisotropically. Hydrogen atoms were generated according to stereochemistry and refined using a riding model in SHELXL-97. CCDC-236368 contains the supplementary crystallographic data for this paper. These data can be obtained free of charge at www.ccdc.cam.ac.uk/conts/retrieving.html [or from the Cambridge Crystallographic Data Centre, 12 Union Road, Cambridge CB2 1EZ, UK; Fax: (internat.) + 44-1223-336-033; E-mail: deposit@ccdc.cam.ac.uk]. Green-blue crystal, crystal dimension: 0.13 × 0.10 × 0.02 mm, $C_{16}H_{14}CuO_6$, M = 365.81 g·mol^{-1}, monoclinic space group $P2_1/a$, a = 9.454(5) Å, b = 4.905(5) Å, c = 15.495(5) Å, β = 102.564(5)°, Z = 2, $D_{calcd.}$ = 1.732 g·cm^{-3}, μ (Mo-K_α) = 1.588 mm^{-1}, $T_{min.}$ = 0.890, $T_{max.}$ = 0.970 mm, a total of 2406 reflections, 2.69° < θ < 31.96°, 2406 independent reflections with 1833 having $I > 2\sigma(I)$, 106 parameters, Final results: R_1 = 0.0817, wR_2 = 0.1349, *Gof* = 1.16, maximum residual electronic density = 1.152 e·Å^{-3}.

Manganese(II) Dimandelate, $C_{16}H_{14}O_6Mn$ (1): $C_{16}H_{14}O_6Mn$ (**1**) was synthesised by a hydrothermal method from $MnCl_2{\cdot}4H_2O$ (99% Aldrich), (*R*)-mandelic acid (98% Acros) and NaOH (Merck). The starting mixture, which consisted of [$MnCl_2{\cdot}4H_2O$], $C_8H_8O_3$, NaOH and H_2O in a ratio of 2:4:4:20, was homogenised and transferred to a sealed Teflon lined hydrothermal bomb (120-mL bomb volume). After heating at 170 °C for 120 h under autogenous pressure, a white, slightly pink crystalline powder was obtained which was washed and rinsed with distilled water and absolute ethyl alcohol (yield: 0.43 g, 60% on the basis of $MnCl_2{\cdot}6H_2O$). The purity was confirmed by elemental analysis [$C_{16}H_{14}O_6Mn$ (361.21): calcd. C 53.80, H 3.95; found C 53.21, H 3.85] and oxidising pyrolysis [heating in air from 20 to 700 °C at 3 °C/min, at 700 °C for 30 min to transform manganese into Mn_2O_3 and cooling to 20 °C at 10 °C/min: calcd. Mn 15.38%; found 17.16%]. IR (KBr pellet): $\tilde{\nu}$ = 3237 cm^{-1} (νOH), 1560 cm^{-1} (ν_{asym}CO) and 1413 cm^{-1} (ν_{sym}CO).

Iron(II) Dimandelate $C_{16}H_{14}O_6Fe$ (2): $C_{16}H_{14}O_6Fe$ (**2**) was synthesised by a hydrothermal method according to the same process as for the manganese analogue **1** but using $FeCl_2{\cdot}6H_2O$ instead of Mn^{II} dichloride. A very pale green crystalline powder was obtained, washed and rinsed with distilled water and absolute ethyl alcohol (yield: 0.36 g, 50% on the basis of $FeCl_2{\cdot}6H_2O$). The purity was checked by elemental analysis [$C_{16}H_{14}O_6Fe$ (358.12): calcd. C 53.66, H 3.94; found C 53.63, H 3.91] and oxidising pyrolysis [heating in air from 20 to 700 °C at 2 °C/min, at 700 °C for 30 min to transform into Fe_3O_4 and cooling to 20 °C at 10 °C/min: calcd. Fe 15.59%; found 18.85%]. IR (KBr pellet): $\tilde{\nu}$ = 3247 cm^{-1} (νOH), 1565 cm^{-1} (ν_{asym}CO) and 1417 cm^{-1} (ν_{sym}CO). UV/Vis (reflectance for octahedral coordination of Fe^{II}): λ = 1065 nm ($^5E_g \rightarrow {}^5T_{2g}$).

Cobalt(II) Dimandelate $C_{16}H_{14}O_6Co$ (3): $C_{16}H_{14}O_6Co$ (**3**) was synthesised similarly to the above procedure but starting from $CoCl_2{\cdot}6H_2O$ (98% Acros). Very thin pink platelet-like crystals were obtained, washed and rinsed with distilled water and absolute ethyl alcohol (yield: 0.47 g, 65% on the basis of $CoCl_2{\cdot}6H_2O$). The purity was confirmed by elemental analysis [$C_{16}H_{14}CoO_6$ (361.21): calcd. C 53.20, H 3.91; found C 52.84, H 3.85] and oxidising pyrolysis [heating in air from 20 to 700 °C at 3 °C/min, at 700 °C for 30 min to transform into Co_3O_4 and cooling to 20 °C at 10 °C/min: calcd. Co 16.32%; found 16.78%]. IR (KBr pellet): $\tilde{\nu}$ = 3255 cm^{-1} (νOH), 1573 cm^{-1} (ν_{asym}CO) and 1408 cm^{-1} (ν_{sym}CO). UV/Vis (reflectance for octahedral coordination of Co^{II}): λ = 1140 nm ($^4T_{1g} \rightarrow {}^4T_{2g}$), 645 nm ($^4T_{1g} \rightarrow {}^4A_{2g}$), 545 nm [$^4T_{1g} \rightarrow {}^4T_{1g}$ (P)].

 © 2005 Wiley-VCH Verlag GmbH & Co. KGaA, Weinheim

Nickel(II) Dimandelate $C_{16}H_{14}O_6Ni$ (4): $C_{16}H_{14}O_6Ni$ (**4**) was synthesised in the same manner as above from $NiCl_2{\cdot}6H_2O$ (99.99% Sigma). A green powder was obtained, washed and rinsed with distilled water and absolute ethyl alcohol (yield: 0.5 g, 70% on the basis of $NiCl_2{\cdot}6H_2O$). The purity was confirmed by elemental analysis [$C_{16}H_{14}NiO_6$ (360.97): calcd. C 53.24, H 3.91; found C 53.15, H 3.87] and oxidising pyrolysis [heating in air from 20 to 700 °C at 3 °C/min, at 700 °C for 30 min to transform into NiO, and cooling to 20 °C at 10 °C/min: calcd. Ni 16.26%; found 17.48%]. IR (KBr pellet): $\tilde{\nu}$ = 3245 cm^{-1} (νOH), 1577 cm^{-1} ($\nu_{asym}CO$) and 1411 cm^{-1} ($\nu_{sym}CO$). UV/Vis (reflectance for octahedral coordination of Ni^{II}): λ = 410 nm ($^3A_{2g}\rightarrow{}^3T_{2g}$), 685 nm ($^3A_{2g}\rightarrow{}^3T_{1g}$), 745 nm ($^3A_{2g}\rightarrow{}^1E_g$), 1235 nm [$^3A_{2g}\rightarrow{}^3T_{1g}$(P)].

Copper(II) Dimandelate $C_{16}H_{14}O_6Cu$ (5): $C_{16}H_{14}O_6Cu$ (**5**) was synthesised from $CuCl_2{\cdot}2H_2O$ (99% Aldrich) and (*R*)-mandelic acid (98% Acros). The starting mixture, corresponding to $CuCl_2{\cdot}2H_2O$, $C_8H_8O_3$ and H_2O in a molar ratio of 2:4:20, was homogenised and transferred to a sealed, Teflon-lined hydrothermal bomb (120-mL bomb volume). Hydrothermal treatment (170 °C, 72 h, autogenous pressure) led to white-yellow crystals and a blue-green solution. These crystals were left to dissolve in the mother liquor. After 6 d, large green-blue crystals of **5** suitable for single-crystal X-ray diffraction analysis were obtained. The crystals were washed with distilled water and absolute ethyl alcohol. (yield: 0.38 g, 52% on the basis of $CuCl_2{\cdot}2H_2O$). The purity was confirmed by elemental analysis [$C_{16}H_{14}O_6Cu$ (365.82): calcd. C 53.66, H 3.94; found C 53.63, H 3.91] and oxidising pyrolysis [heating in air from 20 to 700 °C at 3 °C/min, at 700 °C for 30 min to transform into CuO and cooling to 20 °C at 10 °C/min: calcd. Cu 17.37%; found 16.99%]. IR (KBr pellet): $\tilde{\nu}$ = 3133 cm^{-1} (νOH), 1635 cm^{-1} ($\nu_{asym}CO$) and 1456 cm^{-1} ($\nu_{sym}CO$). UV/Vis (reflectance for octahedral coordination of Cu^{II}): λ = 745 nm (transition from t_{2g} components to x^2-y^2).

[1] *Research Frontiers in Magnetochemistry* (Ed.: C. O'Connor), World Scientific Publishers, Singapore, **1993**.
[2] *Magnetic Molecular Materials* (Eds.: D. Gatteschi, O. Kahn, J. S. Miller, F. Palacio), Kluwer, Dordrecht, **1991**.
[3] L. P. Kadanoff, W. Götze, D. Hamblen, R. Hecht, E. A. S. Lewis, V. V. Palciauskas, M. Rayl, J. Swift, *Rev. Mod. Phys.* **1967**, *39*, 395−431.
[4] L. J. de Jongh, A. R. Miedema, *Adv. Phys.* **1974**, *23*, 1−260.
[5] See for instance the articles in *Magnetism: Molecules to Materials-Models and Experiments* (Eds.: J. S. Miller, M. Drillon), Wiley-VCH, Weinheim, **2001**.
[6] J.-P. Renard, in *Organic and inorganic Low-dimensional crystalline materials* (Eds.: P. Delhaes, M. Drillon), *NATO-ASI Series*, Plenum Press New York and London, **1987**, p. 125−140.
[7] C. Janiak, *Dalton Trans.* **2003**, 2781.
[8] S. L. James, *Chem. Soc. Rev.* **2003**, *32*, 276.
[9] R. L. Carlin, *Magnetochemistry*, Springer-Verlag, Berlin, Heidelberg, **1986**; O. Kahn, *Molecular Magnetism*, Wiley-VCH, Weinheim, **1993**.
[10] Book review: *Molecular Magnets − Recent Highlights* (Eds.: W. Linert, M. Verdaguer), Springer, Wien, New York, **2003**.
[11] *Molecular Magnetism* (Eds.: K. Itoh, M. Kinoshita), Kodansha Ltd. and Gordon and Breach Science Publishers, Amsterdam, London, **2000**.
[12] M. Drillon, P. Panissod, *J. Magn. Magn. Mater.* **1998**, *188*, 93−99.
[13] *Magnetic Properties of Layered Transition Metal Compounds* (Ed.: L. J. de Jongh), vol. 9A ("Physics and Chemistry of Materials with Low-dimensional Structures"), Kluwer Academic Publishers, Dordrecht, **1990**.
[14] P. Rabu, S. Rouba, V. Laget, C. Hornick, M. Drillon, *Chem. Commun.* **1996**, *10*, 1107−1108; W. Fujita, K. Awaga, *Inorg. Chem.* **1996**, *35*, 1915−1917; P. Rabu, J. M. Rueff, Z. L. Huang, S. Angelov, J. Souletie, M. Drillon, *Polyhedron* **2001**, *20*, 1677−1685; P. Rabu, M. Drillon, K. Awaga, W. Fujita, T. Sekine, in *Magnetism: Molecules to Materials* (Eds.: J. S. Miller, M. Drillon), Wiley-VCH, Weinheim, Germany, **2001**, p. 357−395.
[15] P. Rabu, P. Janvier, B. Bujoli, *J. Mater. Chem.* **1999**, *9*, 1323−1326.
[16] Z.-L. Huang, M. Drillon, N. Masciocchi, A. Sironi, J.-T. Zhao, P. Rabu, P. Panissod, *Chem. Mater* **2000**, *12*, 2805−2812.
[17] S. O. H. Gutschke, D. J. Price, A. K. Powell, P. T. Wood, *Angew. Chem. Int. Ed.* **2001**, *40*, 1920−1923.
[18] D. J. Price, S. Tripp, A. K. Powell, P. T. Wood, *Chem. Eur. J.* **2001**, *7*, 200−208.
[19] R. Feyerherm, A. Loose, P. Rabu, M. Drillon, *Solid State Science* **2003**, *5*, 321−326.
[20] Y. Rodriguez-Martin, C. Ruiz-Perez, J. Sanchiz, F. Lloret, M. Julve, *Inorg. Chim. Acta* **2001**, *318*, 159165; C. Ruiz-Pérez, J. Sanchiz, M. Hernàdez-Molina, F. Lloret, M. Julve, *Inorg. Chim. Acta* **2000**, *298*, 202−208.
[21] M. Riou-Cavellec, C. Albinet, C. Livage, N. Guillou, M. Noguès, J. M. Grenèche, G. Férey, *Solid State Sciences* **2002**, *4*, 267−270.
[22] M. J. Plater, M. R. S. J. Foremen, R. A. Howie, J. M. S. Skakle, A. M. Z. Slawin, *Inorg. Chim. Acta* **2001**, *315*, 126−132.
[23] N. Snejko, E. Guttierez-Puebla, J. L. G. Smith, D. E. Lynch, T. C. W. Mak, W.-H. Yip, C. H. L. Kennard Martinez, M. A. Monge, C. Ruiz-Valero, *Chem. Mater* **2002**, *14*, 1879−1883.
[24] J. M. Rueff, N. Masciocchi, P. Rabu, A. Sironi, A. Skoulios, *Chem. Eur. J.* **2002**, 2813−2820; J. M. Rueff, N. Masciocchi, P. Rabu, A. Sironi, A. Skoulios, *Eur. J. Inorg. Chem.* **2001**, 2843−2848.
[25] G. Smith, D. E. Lynch, T. C. W. Mak, W.-H. Yip, C. H. L. Kennard, *Polyhedron* **1993**, *12*, 203−208.
[26] G. Smith, O. J. O'Reilly, C. H. L. Kennard, *J. Chem. Soc., Dalton Trans.* **1980**, 2462−2466.
[27] T. Asaji, K. Aoki, D. Nakamura, *Z. Naturforsch., Teil A* **1984**, *39*, 371−375.
[28] R. Carballo, A. Castinieras, S. Balboa, B. Covelo, J. Niclos, *Polyhedron* **2002**, *21*, 2811.
[29] R. Carballo, B. Covelo, S. Balboa, A. Castinieras, J. Niclos, *Z. Anorg. Allg. Chem.* **2001**, *627*, 948.
[30] D. A. House, J. Browning, J. R. Ripal, W. T. Robinson, *Inorg. Chim. Acta* **1999**, *292*, 73.
[31] I. K. Smatanova, J. Marek, P. Svancarek, P. Schwendt, *Acta Crystallogr., Sect. C* **2000**, *56*, 154.
[32] G. Meister, G. Rheinwald, H. Stoeckli-Evans, G. Suss-Fink, *J. Organomet. Chem.* **1995**, *496*, 197.
[33] [33a] K. N. Kovalenko, D. V. Kazachenko, V. P. Kurbatov, L. G. Kovaleva, *Zh. Neorg. Khim.* **1971**, *16*, 2444. [33b] A. Ranade, *Z. Anorg. Allg. Chem.* **1972**, *388*, 105. [33c] P. V. Khadikar, R. L. America, *Ind. J. Chem.* **1975**, *13*, 525. [33d] A. B. Sen, S. N. Kapoor, *J. Prakt. Chem.* **1963**, *20*, 237. [33e] R. Larsson, B. Folkesson, *Acta Chem. Scand.* **1968**, *22*, 1970−1980. [33f] A. J. Fischinger, A. Sarapu, A. Companion, *Can. J. Chem.* **1969**, *47*, 2629−2637. [33g] P. Spacu, S. Plostinaru, L. Patron, A. Contescuand, N. Stanica, *Rev. Roum. Chim.* **1985**, *30*, 837−842. [33h] R. P. Rajguru, C. Panda, *J. Inst. Chem. (India)* **1991**, *63*, 37−39.
[34] H. Kumagai, Y. Oka, K. Inoue, M. Kurmoo, *J. Phys. Chem. Sol.* **2004**, *65*, 55−60.
[35] C. Janiak, *J. Chem. Soc., Dalton Trans.* **2000**, 3885−3896.
[36] I. L. Finar, *Organic Chemistry*, 4th ed., Longmans, London, **1968**, vol. 2, p. 69.
[37] Winther, *Z. Physik Chem.* **1906**, *56*, 465−511; A. N. Campbell, A. J. R. Campbell *J. Am. Chem. Soc.* **1932**, *54*, 3834−3841; A. N. Campbell, A. J. R. Campbell *Nature* **1932**, *129*, 281.
[38] Fullprof: J. Rodriguez-Carvajal, *Physica* **1993**, *B192*, 55.
[39] K. Nakamoto, *Infrared and Raman Spectra of Organic and Co-*

ordination Compounds, 4th ed., Wiley − Interscience Publication, New York, **1986**, 231.

[40] A. B. P. Lever, *Inorganic Electronic Spectroscopy*, 2nd ed., Elsevier, Amsterdam, **1984**.

[41] L. Banci, A. Bencini, C. Benelli, D. Gatteschi, C. Zanchini, *Struct. Bonding* **1982**, *52*, 37−86.

[42] Y.-S. Dou, *J. Chem. Educ.* **1990**, *67*, 134.

[43] F. E. Mabbs, D. J. Machin, *Magnetism and transition metal complexes*, Chapman and Hall Ltd., London, **1973**.

[44] G. S. Rushbrooke, G. A. Baker, P. J. Wood, in *Phase Transitions and Critical Phenomena* (Eds.: C. Domb, M. S. Green), Academic Press, London, New York, **1974**, vol. III, chapter 5.

[45] K. Yamaji, J. J. Kondo, *Phys. Soc. Jpn.* **1973**, *35*, 25−32.

[46] R. Navarro, in *Magnetic Properties of Layered Transition Metal Compounds* (Ed.: L. J. de Jongh), Kluwer Academic Publishers, Dordrecht, Boston, London, **1990**, p. 105−190.

[47] $x = -J/(k_BT)$ for antiferromagnetic coupling, N = Avogadro's number, μ_B = Bohr magneton, g = Lande g value, a_1 = 23.33333, a_2 = 396.66666, a_3 = 6212.888888, a_4 = 87638.8119558377, a_5 = 1161923.54664125, a_6 = 14796191.6938613, a_7 = 180849416.031247, and a_8 = 2142650986.87194.

[48] $x = J/(k_BT)$ for ferromagnetic coupling, a_1 = 5.333333333, a_2 = 18.66666667, a_3 = 56.88888889, a_4 = 152.3950631, a_5 = 376.9415553, a_6 = 918.8538407, a_7 = 2134.805724, and a_8 = 4572.414518.

[49] E. Coronado, M. Drillon, D. Beltran, J. C. Bernier, *Inorg. Chem.* **1984**, *23*, 4000−4004.

[50] G. M. Sheldrick, *SHELXL-97*, University of Göttingen, Germany, **1997**.

[51] Sortav: R. H. Blessing, *J. Appl. Crystallogr.* **1989**, *22*, 396−397.

Received July 17, 2004
Published Online January 3, 2005

 © 2005 Wiley-VCH Verlag GmbH & Co. KGaA, Weinheim

Improvements of and Insights into the Isolation of Bismuth Polycations from Benzene Solution – Single-Crystal Structure Determinations of $Bi_8[GaCl_4]_2$ and $Bi_5[GaCl_4]_3$

Martin Lindsjö, Andreas Fischer[a] and Lars Kloo*[a]

Keywords: Bismuth / Cluster compounds / Polycations / Subvalent compounds

The synthesis, crystal growth and structure are reported for the two salts $Bi_5[GaCl_4]_3$ and $Bi_8[GaCl_4]_2$. The compounds are prepared from a solution of $BiCl_3$ and $GaCl_3$ in benzene, using gallium metal as reducing agent. $Bi_8[GaCl_4]_2$ contains a Bi_8^{2+} polycation that, essentially, adopts an ideal square antiprismatic geometry. The compound crystallizes in the $P6_3$ space group; a = 17.760(2) Å and c = 12.979(3) Å. $Bi_5[GaCl_4]_3$ crystallizes in the $R3c$ space group, a = 11.814(2) Å, c = 29.974(3) Å, and contains a Bi_5^{3+} cation adopting a trigonal-bipyramidal geometry. The cation is slightly distorted from the ideal D_{3h} symmetry.

(© Wiley-VCH Verlag GmbH & Co. KGaA, 69451 Weinheim, Germany, 2005)

Introduction

Main group clusters constitute an odd group of molecular and ionic species that have long intrigued chemists. Within this group, bismuth polycations have been one of the most studied families of species, primarily because several subvalent cations have been observed, e.g. Bi^+, Bi_5^{3+}, Bi_8^{2+} and Bi_9^{5+}.[1,2]

There are several synthetic schemes practicable for producing bismuth polycations. In early studies, syntheses were performed at high temperature by dissolving bismuth metal in liquid BiX_3 and/or AlX_3 (X = Cl, Br, I).[3–9] In these systems, several polycations were identified in solid state or in solution, mainly using X-ray diffraction and spectroscopy. In particular, both Bi_5^{3+} and Bi_8^{2+} are observed when Bi metal is dissolved in liquid $BiCl_3$–$3AlCl_3$. The major product is controlled by the acidity of the system, which, in turn, is controlled by an excess of $AlCl_3$. Due to slow equilibration, supercooling phenomena and problems with twinning, no single crystals were obtained containing either Bi_5^{3+} or Bi_8^{2+} in these early investigations. Therefore, this route was later reconsidered and refined with the purpose of obtaining single crystals of high quality, which allowed better characterization of the two salts $Bi_5[AlCl_4]_3$ and $Bi_8[AlCl_4]_2$.[10–12] Recently, this type of route has again been utilized in the synthesis of $Bi_8[InBr_4]_2$ [13] and $Bi_8[Ta_2O_2Br_7]_2$.[14]

A second synthetic route to subvalent bismuth cations was later proposed, when evidence for the formation of Bi_5^{3+} and Bi_8^{2+} in superacidic media was found.[15] For such media, the products contain, predominantly, Bi_5^{3+}, while Bi_8^{2+} could be observed as an intermediate.

A decade ago, a third method suitable for the production of bismuth polycations was presented; on adding bismuth metal to a $GaCl_3$–benzene solution, spectroscopic evidence of a dissolved subvalent bismuth species, Bi_5^{3+}, was obtained.[16] This was later supplemented by the isolation of a cubic modification of $Bi_5[GaCl_4]_3$, as a powder, by mixing the Bi–$GaCl_3$–benzene solution with *n*-heptane.[17] The advantage of this route is that it is conducted at room temperature using standard chemicals, while still being reasonably quick. However, only one bismuth polycation has been isolated, and it has been possible to crystallize the solid compound only as powder and not as single crystals. To improve the applicability of this synthetic route, methods for obtaining large single crystals have to be devised. Furthermore, as different bismuth polycations have been isolated from very similar conditions using solid-state techniques, small modifications in the conditions could also generate polycations other than Bi_5^{3+} when using arene reaction media. This hypothesis is additionally supported by quantum chemistry calculations that show several small bismuth clusters, so far not isolated experimentally, to be electronically stable.[18]

We report here a successful method for obtaining high-quality single crystals of subvalent bismuth species in benzene solution. This procedure has been used to isolate a new compound, $Bi_8[GaCl_4]_2$, for which the structure is reported. A re-determination of the structure of trigonal $Bi_5[GaCl_4]_3$ is also reported, together with a discussion on the existence and nature of the cubic modification of $Bi_5[GaCl_4]_3$.

[a] Royal Institute of Technology, Division of Inorganic Chemistry, Teknikringen 30, 10044 Stockholm, Sweden
Fax: +46-87-909-349
E-mail: larsa@kth.se

Results and Discussion

Synthesis and Crystal Growth

The original procedure for the synthesis of Bi_5^{3+} in $GaCl_3$–benzene solution used bismuth metal as starting material, which was to be oxidized by $GaCl_3$ to subvalent bismuth species. However, an alternative route is feasible using $GaCl_3$–benzene solution; instead of oxidizing bismuth metal, $BiCl_3$ can be reduced to subvalent species by Ga[$GaCl_4$], mimicking the reaction of Ga–$GaCl_3$–$BiCl_3$ in melts.[19] In this work, the primary procedure has been the reductive route, i.e. the reduction of $BiCl_3$ using Ga[$GaCl_4$]. This alternative is faster and also allows control of bismuth concentration.

As mentioned above, $Bi_5[GaCl_4]_3$ can be precipitated from the prepared benzene solution by shaking this solution with an alkane (e.g. *n*-heptane), producing a red powder.

If larger crystals are desired, a lower rate of mixing with the alkane, e.g. by applying diffusion techniques, could be effective. However, with a Bi–$GaCl_3$–benzene solution, the use of slow diffusion with an alkane normally ends in the solidification of a deeply red, glass-like phase at the bottom of the reaction vessel, together with some red powder. Nevertheless, in rare cases, brown, crystal-like cubes have been obtained using this method. The unit cell has been found to be *F*-centered cubic with a cell parameter of 17.1 Å. This corresponds well to the parameters of the cubic modification of $Bi_5[GaCl_4]_3$, which has previously been reported as the product of this reaction.[17] However, as with the powder data, only low-angle reflections are detected in X-ray diffraction experiments on the single crystals, indicating a disordered structure. The nature of this phase, and its relation to trigonal $Bi_5[GaCl_4]_3$, which has been more satisfactorily characterized, will be further discussed below.

Thus, the use of solely aliphatic hydrocarbons to obtain large single crystals from a Bi_n^{x+}–$GaCl_3$–benzene solution has clearly proved to be at best very unreliable. This is due to the extremely small solubility of the subvalent bismuth species in non-aromatic solvents. For quicker and more reproducible results, other ways have to be explored.

In this case, the obvious choice is to try aromatic hydrocarbons similar to benzene but exhibiting a lower solubility of $GaCl_3$ and Bi_n^{x+}, thus creating a less dramatic decrease in solubility using diffusion techniques. In this particular work, mesitylene has been used for this purpose.

If mesitylene is added on top of a *saturated* Bi_n^{x+}–$GaCl_3$–benzene solution, single crystals are formed, within a couple of days, in the upper part of the benzene phase. Saturation of the benzene solution is important because of the moderately high solubility of the polycations in mesitylene; otherwise only dilution, and no crystallization, will occur. The benzene phase is saturated by an initial extraction (referring mainly to excess $GaCl_3$) using *n*-heptane, but carefully avoiding the precipitation of cubic $Bi_5[GaCl_4]_3$.

Using this procedure, two different types of crystals can be isolated, i.e. black cylinders and red square plates. The black cylinder-shaped crystals consist of $Bi_8[GaCl_4]_2$, a previously uncharacterized compound. The crystals are of varying sizes, the largest being around 0.5 mm.

The red crystals, however, are often very small, <0.1 mm, and tend to form aggregates, making it difficult to select a suitable single crystal for crystallographic investigation. Even so, it has been possible to establish these crystals as trigonal $Bi_5[GaCl_4]_3$, which has previously been synthesized by a solid state route. This structure has so far only been characterized using powder data.[20]

Hence, as for the solid-state and superacid-based methods mentioned above, it can be observed that there is a special relationship between the two cations Bi_5^{3+} and Bi_8^{2+}, and different cations may appear in systems having only slightly different conditions. This is not very controversial, merely reinforcing the proposition that the $GaCl_3$–benzene system can be regarded as a "pseudo-melt".[21]

Of the two cations, Bi_5^{3+} is obviously the most stable in solution; no traceable amounts of Bi_8^{2+} were discovered using UV/Vis spectroscopy in earlier studies on this system. Likewise, only $Bi_5[GaCl_4]_3$ is formed when precipitating using an alkane. However, in contrast, the more abundant product from the approach reported above is $Bi_8[GaCl_4]_2$, while synthetic efforts aimed to generate $Bi_5[GaCl_4]_3$ exclusively in most cases have failed. Instead, red crystals of this compound are most frequently found when the two crystal types are formed in the same experiment. Again, this indicates the very subtle shifts in concentration, of one or more of the reactants, needed to render different solid products. In particular, $Bi_5[GaCl_4]_3$ displays a very narrow window of concentration in which single crystals will be formed. Exactly how this equilibrium is controlled and the mechanism for the formation and crystal growth of $Bi_8[GaCl_4]_2$ from a solution dominated by Bi_5^{3+} are questions for future research. Furthermore, it is puzzling that only these two polycations are formed as calculations have shown that several other bismuth polycations should be isolable.[18]

The route described in this work offers a very easy and good alternative way of producing high-quality crystals containing the Bi_8^{2+} polycation. The crystals can be obtained at room temperature after only a couple days of treatment. However, findings of $Bi_5[GaCl_4]_3$ crystals are far sparser, demonstrating that the optimal conditions for their isolation have very narrow borders, which need to be clarified in order for the described route to this compound to be reliable. The general usefulness of the above method has already been proven with the successful synthesis and crystal growth of $Sb_8[GaCl_4]_2$ – the first structural characterization of an antimony polycation.[22]

Crystal Structure of $Bi_8[GaCl_4]_2$

Table 1 gives the atomic parameters for this compound. The structure consists of Bi_8^{2+} polycations and tetrahedral $GaCl_4^-$ anions (Figure 1). The Bi_8^{2+} polycation geometry is very close to an ideal square antiprism (D_{4d} symmetry), although its crystallographic symmetry is only C_1. The

 © 2005 Wiley-VCH Verlag GmbH & Co. KGaA, Weinheim

structure is very similar to that reported earlier for $Bi_8[AlCl_4]_2$.[10,12] However, the space group chosen for the current chlorogallate structure is $P6_3$ while the aluminate structure was refined in space group $P6_3/m$. In the current structure the anions are all aligned and ordered, in contrast to $Bi_8[AlCl_4]_2$ in which they are reported to be disordered. Notably, all $GaCl_4$ tetrahedra on the *c* axis possess one corner pointing into the positive *c* direction (Figure 2). Adding a mirror plane perpendicular to *c* to this structure would necessarily cause disorder of the anions, leaving the cations essentially unchanged because the latter need only a minor distortion to accommodate such a mirror plane. The choice of space group $P6_3$ therefore appears unambiguous, leaving open the question of whether the chloroaluminate and chlorogallate really adopt slightly different structures or if a redetermination of the chloroaluminate in space group $P6_3$ might lead to an improved structure model without anion disorder.

Table 1. Final coordinates and isotropic thermal parameters for $Bi_8[GaCl_4]_2$

Atom	*x*/*a*	*y*/*b*	*z*/*c*	*B* [Å^2]
Bi(1)	0.8561(1)	0.6287(2)	1.1523(1)	3.7(1)
Bi(2)	0.9608(2)	0.5324(1)	1.1440(1)	4.4(1)
Bi(3)	0.9597(2)	0.5390(1)	0.9036(1)	3.9(1)
Bi(4)	0.8545(1)	0.6332(2)	0.9158(1)	4.4(1)
Bi(5)	1.1278(1)	0.6627(1)	1.0256(2)	4.6(1)
Bi(6)	1.0530(2)	0.7358(2)	0.8655(2)	3.9(1)
Bi(7)	0.9781(1)	0.8001(1)	1.0387(2)	4.9(1)
Bi(8)	1.0545(2)	0.7282(2)	1.1971(2)	4.1(1)
Ga(1)	2/3	1/3	0.7336(5)	2.5(1)
Ga(2)	1/3	2/3	0.6983(6)	3.3(2)
Ga(3)	1	1	0.7915(8)	2.9(1)
Ga(4)	0.6388(3)	0.6944(2)	1.0079(3)	3.4(1)
Cl(1)	2/3	1/3	0.567(1)	4.6(4)
Cl(2)	0.7848(9)	0.340(1)	0.789(1)	4.3(4)
Cl(3)	1/3	2/3	0.538(3)	14.5(8)
Cl(4)	0.4455(9)	0.784(1)	0.756(1)	5.2(4)
Cl(5)	1.1021(8)	0.9793(9)	1.236(1)	6.5(4)
Cl(6)	1	1	0.959(1)	3.9(4)
Cl(7)	0.883(1)	0.594(1)	0.653(1)	9.2(6)
Cl(8)	0.7632(8)	0.8013(8)	0.967(1)	6.8(4)
Cl(9)	0.6544(6)	0.5802(6)	1.015(2)	5.3(4)
Cl(10)	0.8668(8)	0.5436(7)	1.3995(9)	4.0(3)

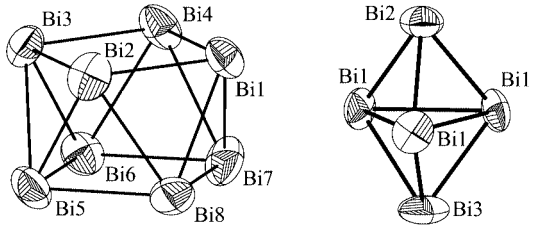

Figure 1. Polycations Bi_8^{2+} in $Bi_8[GaCl_4]_2$ (left) and Bi_5^{3+} in $Bi_5[GaCl_4]_3$ (right); thermal ellipsoids drawn at a 70% probability level

As expected, the Bi–Bi distances of the polycation are very similar to those of the previously reported structure; the bond lengths vary in the range 3.07–3.12 Å (Table 2). The average bond length within the square faces is 3.09 Å and the average bond length between the two squares is 3.10 Å (3.09 and 3.11 Å, respectively, in $Bi_8[AlCl_4]_2$). Quantum chemical calculations have previously suggested that the bonding within the square faces are more localized relative to the bonding between the squares.[18] However, in the optimized theoretical structure, the difference between the inter- and intra-square distances is larger than in the experimentally found polycations; the inter/intra distance ratio is 1.025 theoretically and 1.004 in the structure presented here. This deviation in bond length ratio may indicate that the bonding of the polycation is more extensively delocalized than the calculations predict. The Ga–Cl distances in the anions show a small variation, 2.08–2.18 Å, with the exception of one distance of 2.01 Å. The shortest Bi–Cl distance is 3.44 Å, indicating that the cation–anion interactions are weak.

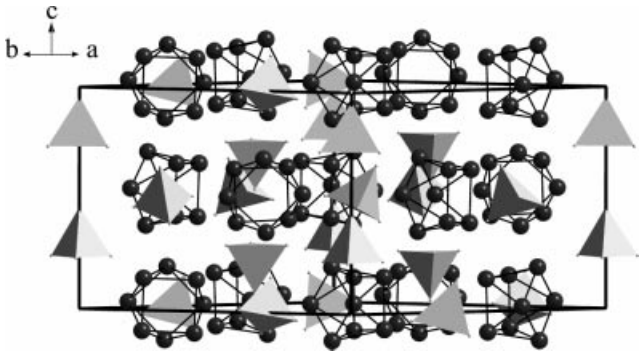

Figure 2. Unit cell of $Bi_8[GaCl_4]_2$ in a view along [110]; $GaCl_4^-$ entities on the *c* axis are aligned, thus excluding the possibility of a mirror plane perpendicular to this axis

Crystal Structure of $Bi_5[GaCl_4]_3$

The structure consists of the well-known Bi_5^{3+} polycation and $GaCl_4^-$ anions. Atomic parameters are presented in

Table 2. Comparison of unit cell parameters [Å] and distances [Å] in $Bi_8[GaCl_4]_2$ and $Bi_8[AlCl_4]_2$; atom labels given in Figure 1

Parameter	$Bi_8[GaCl_4]_2$	$Bi_8[AlCl_4]_2$[12]
Space group	$P6_3$	$P6_3/m$
a [Å]	17.760(2)	17.854(4)
c [Å]	12.979(3)	12.953(3)
Bi(1)–Bi(2)	3.095(3)	3.086(6)
Bi(2)–Bi(3)	3.123(2)	3.098(6)
Bi(3)–Bi(4)	3.072(3)	3.086(6)
Bi(1)–Bi(4)	3.071(2)	3.078(6)
Bi(5)–Bi(6)	3.079(3)	3.086(7)
Bi(6)–Bi(7)	3.107(3)	3.085(6)
Bi(7)–Bi(8)	3.072(3)	3.085(6)
Bi(5)–Bi(8)	3.084(3)	3.086(7)
Bi(1)–Bi(7)	3.089(3)	3.122(5)
Bi(1)–Bi(8)	3.107(3)	3.123(4)
Bi(2)–Bi(5)	3.106(3)	3.104(5)
Bi(2)–Bi(8)	3.091(3)	3.092(5)
Bi(3)–Bi(5)	3.112(3)	3.104(5)
Bi(3)–Bi(6)	3.067(3)	3.092(5)
Bi(4)–Bi(6)	3.124(3)	3.123(5)
Bi(4)–Bi(7)	3.105(3)	3.122(5)

 © 2005 Wiley-VCH Verlag GmbH & Co. KGaA, Weinheim

Table 3 and the unit cell is displayed in Figure 3. Bi_5^{3+} is almost a perfect trigonal bipyramid (Figure 1). This compound has previously been characterized from powder data[20] and, furthermore, it exists in an analogous aluminate structure, $Bi_5[AlCl_4]_3$.[6,11] However, the space group of the structure in the present work was found to be $R3c$, while the earlier studies found it to be $R\bar{3}c$. Even in this study on $Bi_5[GaCl_4]_3$, a structural model could be obtained in space group $R\bar{3}c$. The final result of the structure refinement yielded a much poorer result, though, with significantly larger R factors and difference-Fourier peaks in the range –5 to 5 e Å^{-3} in the proximity of the Bi cation. Additionally, the geometry of the cation changed significantly when the structure was refined in $R3c$. The apical bismuth atoms, which were crystallographically equivalent in $R\bar{3}c$, were refined to rather different final positions in space group $R3c$. This yields a cluster cation with two significantly different bond lengths between the equatorial atoms and the two apical ones, i.e. 2.97 and 3.02 Å, respectively.

Table 3. Final coordinates and isotropic thermal parameters for trigonal $Bi_5[GaCl_4]_3$

Atom	*x*/*a*	*y*/*b*	*z*/*c*	*B* [Å^2]
Bi(1)	0.0038(3)	0.1635(2)	0.24988(18)	4.6(1)
Bi(2)	0	0	0.17179(5)	4.7(1)
Bi(3)	0	0	0.32572(5)	6.3(2)
Ga(1)	0.4782(4)	0.4795(4)	0.2506(3)	2.4(1)
Cl(1)	0.592(1)	0.581(1)	0.3078(4)	2.8(3)
Cl(2)	0.581(1)	0.585(1)	0.1908(4)	4.1(3)
Cl(3)	0.455(1)	0.283(1)	0.2430(5)	3.9(3)
Cl(4)	0.286(1)	0.451(1)	0.2603(5)	4.9(4)

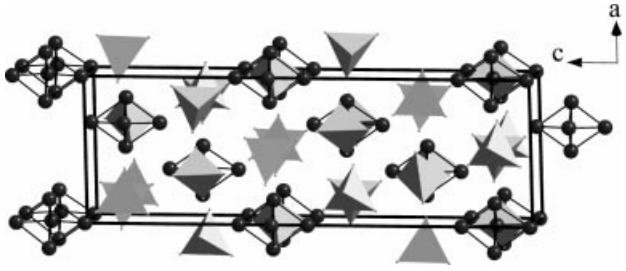

Figure 3. Unit cell of $Bi_5[GaCl_4]_3$ in a view along the *b* axis

To resolve unambiguously the choice of space group in this case, an experimental proof of noncentrosymmetry would be welcome. Unfortunately, so far, such an experiment has proved impossible due to the difficulties in controlling the production of $Bi_5[GaCl_4]_3$ single crystals, as described above. The ultimate choice of the non-centrosymmetric space group is mainly based on the fact that a removal of the centre of symmetry allows a refinement of a structural model that fits the diffraction data considerably better. Table 4 summarizes the bond lengths in $Bi_5[GaCl_4]_3$ and $Bi_5[AlCl_4]_3$.

Table 4. Comparison of unit cell parameters [Å] and distances [Å] in trigonal $Bi_5[GaCl_4]_3$ and $Bi_5[AlCl_4]_3$; atom labels are given in Figure 1

Parameter	$Bi_5[GaCl_4]_3$	$Bi_5[AlCl_4]_3$[11]
Space group	$R3c$	$R\bar{3}c$
a [Å]	11.814(2)	11.860(3)
c [Å]	29.974(3)	30.100(8)
Bi(1)–Bi(1)	3.3062(14)	3.319(2)
Bi(1)–Bi(2)	3.020(4)	3.007(2)
Bi(1)–Bi(3)	2.968(4)	3.007(2)

In the $R3c$ space group the symmetry of the cluster cation is lowered from the theoretically predicted D_{3h}, which is predestined with the centric space group, to C_{3v}, as described above. A similar small deviation from the ideal geometry has previously been reported for the isoelectronic Sn_5^{2-}, while Pb_5^{2-} retained the D_{3h} symmetry.[23]

Cubic Modification of $Bi_5[GaCl_4]_3$

As mentioned above, brown, cube-shaped crystallites have on rare occasions been obtained from benzene solution using a slow diffusion technique with *n*-heptane. These crystallites have an F-centered cubic unit cell with a cell parameter of 17.1 Å, corresponding well to the previously reported cubic modification of $Bi_5[GaCl_4]_3$.

This biphasic nature of $Bi_5[GaCl_4]_3$ is puzzling – is the cubic form really a separate phase or is it simply a twinned form of the hexagonal modification? Powder diffraction clearly indicates that the two phases are distinct,[17] but if the trigonal form is cast in a rhombohedral setting it yields cell parameters that differ from the cubic form only by 0.1 Å and 1°. Considering the quality of the data from the cubic modification, such a deviation is not unreasonable; the reflection profiles are very broad. Moreover, the atomic positions in the trigonal form nearly match onto those of the solution of the cubic structure, showing that the two are clearly locally very similar. Hence, in some aspects, the cubic form can reasonably be assumed to represent a microtwinned variety of the trigonal form. The slight mismatch of cell parameters is then explained by the strain caused by the clamping of slightly dissimilar dimensions onto each other.

Does this mean that the two forms are really different phases? Probably yes. The extensive broadening of the reflections in the cubic phase and the lack of high-angle reflections imply that the average domain size is very small, i.e. twinning occurs close to the unit cell level. The two forms are expected to have different heats of formation because of this (they clearly have different diffraction patterns) and they will form at slightly different temperatures and/or solvent conditions. However, no transition between the two phases could be found by thermal analysis (differential scanning calometry) before the compounds decomposed (disproportionation at ca. 170–190 °C).

 © 2005 Wiley-VCH Verlag GmbH & Co. KGaA, Weinheim

Conclusions

We have presented an easy route to high-quality single crystals containing bismuth polycations that were previously very difficult to obtain, demanding high temperature and long annealing times. By the stratification of mesitylene on top of a polycation-containing benzene solution, single crystals are formed. Two different crystal structures have been isolated; the previously uncharacterized compound $Bi_8[GaCl_4]_2$ and $Bi_5[GaCl_4]_3$, which has previously been characterized using powder diffraction. It is suggested that the space group of both current chlorogallate structures differs somewhat from that of known aluminate compounds.

The formation of large single crystals of $Bi_5[GaCl_4]_3$ appears to demand very special conditions; the abundant product of the approach described here is, therefore, $Bi_8[GaCl_4]_2$. This is somewhat surprising considering that the dominant polycation in benzene solution is clearly Bi_5^{3+}.

As to whether a cubic $Bi_5[GaCl_4]_3$ phase really exists, it is suggested that this phase is a likely consequence of microtwinning of the trigonal modification.

Experimental Section

General: $GaCl_3$ (Aldrich, anhydrous, 99.99%), $BiCl_3$ (Alfa, anhydrous, 99.999%) and gallium metal (Alfa, 99.999%) were used as received. Benzene (Fluka, 99.5%), heptane (Merck, 99%) and mesitylene (Janssen, 99%) were dried using molecular sieves. Due to the air and moisture sensitivity of the reactants and products, all synthetic work was performed in a glove-box under nitrogen (<1 pm H_2O and O_2).

Preparation of Bismuth Polycation Solutions: A standard reductive-route experiment was performed as follows: $BiCl_3$ (0.22 g, 0.70 mmol) was added to $GaCl_3$ (0.66 g, 3.7 mmol) dissolved in benzene (1.0 mL) in a standard NMR tube. A second solution was produced by adding gallium metal (0.080 g, 1.1 mmol) to a solution of $GaCl_3$ (0.66 g, 3.7 mmol) in benzene (1.0 mL). After 24 h, undissolved gallium metal was removed from the latter solution, and the two solutions were mixed and left overnight. The final solution was deep red.

Isolation of Single Crystals: The solution was first concentrated by gentle extraction using *n*-heptane (2 mL), carefully avoiding precipitation. The heptane phase was then removed and mesitylene (2 mL) was stratified on top of the red solution. After 24–48 h, after one exchange of the mesitylene phase, crystals had formed on the glass wall of the NMR tube, near the phase border. Most of the crystals were black cylinders, but smaller, plate-shaped, red crystals could also be obtained above the black ones, i.e. closer to the mesitylene phase.

Thermal Analysis: Differential scanning calorimetry (DSC) was performed using a Perkin-Elmer DSC 7 instrument. Samples were sealed in aluminium capsules inside the glove box prior to the measurements.

X-ray Crystallographic Data and Refinement of the Structures: Table 5 summarizes the crystallographic data for $Bi_8[GaCl_4]_2$ and $Bi_5[GaCl_4]_3$. The crystals were sealed in 0.5 mm Lindemann capillaries under dry nitrogen. Diffraction data were collected with a Bruker-Nonius KappaCCD diffractometer.

Table 5. Unit cell parameters and experimental crystal data of $Bi_8[GaCl_4]_2$ and $Bi_5[GaCl_4]_3$

Compound	$Bi_8[GaCl_4]_2$	$Bi_5[GaCl_4]_3$
Molecular mass [g mol^{-1}]	2094.88	1679.46
Crystal system	hexagonal	trigonal
Space group	$P6_3$ (no. 173)	R3*c* (no. 161)
a [Å]	17.760(2)	11.814(2)
c [Å]	12.979(3)	29.974(3)
V [Å^3]	3545(1)	3623.2(9)
Z	6	6
$D_{calcd.}$ [g cm^{-3}]	5.89	4.62
Crystal size [mm]	0.15 × 0.15 × 0.10	0.10 × 0.10 × 0.05
Temperature [K]	293	293
Radiation, λ [Å]	Mo-K_α, 0.71073	Mo-K_α, 0.71073
Monochromator	graphite	graphite
Scan range, 2θ [°]	9.18–55.02	9.64–55.00
No. measured reflections	21249	11286
No. unique reflections	4679	1837
No. reflections [$I > 2\sigma(I)$]	3396	1303
No. parameters refined	173	62
Max/min Fourier peak [e Å^{-3}]	1.98/–1.90	1.77/–2.25
$R(\|F\|)$, all	0.112	0.099
$R(\|F\|)$, $I > 2\sigma(I)$	0.070	0.060
$wR(F^2)$, all	0.116	0.121
GOF	1.283	1.215

$Bi_8[GaCl_4]_2$: The compound crystallizes in the hexagonal system, Laue group 6/*m*. The systematic absences (00*l*, *l* = 2*n*) led to the possible space groups $P6_3$ and $P6_3/m$ of which the former, noncentrosymmetric one was confirmed during structure determination. The structure was refined assuming an inversion twin (ratio of the twin components: 0.8:0.2).

$Bi_5[GaCl_4]_3$: The compound crystallizes in the rhombohedral system, Laue group –3*m*. Systematic absences led to the possible space groups *R*3*c* and $R\bar{3}c$. A structure model could be obtained in space group $R\bar{3}c$. After the refinement, rather large peaks (+5/–5 e Å^{-3}) were still present in the difference-Fourier map close to the Bi atoms and on opposite sides of them. The symmetry was therefore lowered to *R*3*c*. Upon re-refinement of the structure, the geometry of the cation changed slightly, but significantly: Bond lengths in the equatorial plane decreased from 3.284(5) to 3.269(5) Å. The structural change along the *c* axis is even more significant: The two apical Bi atoms, which were crystallographically related by a two-fold rotation axis in space group $R\bar{3}c$, become independent and the bond lengths between them and the equatorial Bi atoms change [Bi(1)–Bi(3) is 2.977(4) Å and Bi(1)–Bi(2) is 3.037(4) Å]. The difference between these interatomic distances is thus 15σ. Additionally, the maximum and minimum difference-Fourier peaks shrunk to more reasonable levels (1.77/–2.25 e Å^{-3}), which makes the description of the structure in space group *R*3*c* appear more appropriate.

All atoms were refined using anisotropic temperature parameters. Numerical absorption corrections were applied.[24] All structures were solved and refined using direct methods and difference Fourier techniques using SHELXS97/SHELXL97.[25,26] Further details of the crystal structure investigation can be obtained from the Fachinformationszentrum Karlsruhe, 76344 Eggenstein-Leopoldshafen, Germany, Fax: +49-7247-808-666; E-mail: crysdata@fiz-karlsruhe.de) on quoting the depository number CSD-414089 ($Bi_5[GaCl_4]_3$) and CSD-414090 ($Bi_8[GaCl_4]_2$).

 © 2005 Wiley-VCH Verlag GmbH & Co. KGaA, Weinheim

Acknowledgments

We thank Prof. Sven Lidin, Stockholm University, for valuable discussions regarding the micro-twinning of cubic $Bi_5[GaCl_4]_3$. This work has been supported by the Swedish Research Council and the Göran Gustafsson Foundation.

[1] I. Krossing, in *Molecular Clusters of the Main Group Elements* (Eds.: M. Driess, H. Nöth), Wiley-VCH, Weinheim, **2004**, pp. 209–229.
[2] S. Ulvenlund, L. Bengtsson-Kloo, in *Metal Clusters in Chemistry* (Eds.: P. Braunstein, L. A. Oro, P. R. Raithby), Wiley-VCH, Weinheim, **1999**, vol. 1, pp. 561–602.
[3] A. Hershaft, J. D. Corbett, *J. Chem. Phys.* **1962**, *36*, 551–552.
[4] A. Hershaft, J. D. Corbett, *Inorg. Chem.* **1963**, *2*, 979–985.
[5] J. D. Corbett, *Inorg. Nucl. Chem. Lett.* **1967**, *3*, 173–176.
[6] J. D. Corbett, *Inorg. Chem.* **1968**, *7*, 198–208.
[7] N. J. Bjerrum, C. R. Boston, G. P. Smith, H. L. Lewis, *Inorg. Nucl. Chem. Lett.* **1965**, *1*, 141–143.
[8] N. J. Bjerrum, C. R. Boston, G. P. Smith, *Inorg. Chem.* **1967**, *6*, 1162–1172.
[9] N. J. Bjerrum, G. P. Smith, *Inorg. Chem.* **1967**, *6*, 1968–1972.
[10] B. Krebs, M. Hucke, C. Brendel, *Angew. Chem.* **1982**, *94*, 453–454; *Angew. Chem. Int. Ed. Engl.* **1982**, *21*, 445–446.
[11] B. Krebs, M. Mummert, C. Brendel, *J. Less-Common Met.* **1986**, *116*, 159–168.
[12] J. Beck, C. J. Brendel, L. Bengtsson-Kloo, B. Krebs, M. Mummert, A. Stankowski, S. Ulvenlund, *Chem. Ber.* **1996**, *129*, 1219–1226.
[13] A. N. Kuznetsov, B. A. Popovkin, *Z. Anorg. Allg. Chem.* **2002**, *628*, 2179.
[14] J. Beck, T. Hillbert, *Eur. J. Inorg. Chem.* **2004**, 2019–2026.
[15] R. C. Burns, R. J. Gillespie, W.-C. Luk, *Inorg. Chem.* **1978**, *17*, 3596–3604.
[16] S. Ulvenlund, A. Wheatley, L. A. Bengtsson, *J. Chem. Soc., Chem. Commun.* **1995**, 59–60.
[17] S. Ulvenlund, L. Bengtsson-Kloo, K. Ståhl, *J. Chem. Soc., Faraday Trans.* **1995**, *91*, 4223–4234.
[18] A. N. Kuznetsov, L. Kloo, M. Lindsjö, J. Rosdahl, H. Stoll, *Chem. Eur. J.* **2001**, *7*, 2821–2828.
[19] S. Ulvenlund, PhD Thesis, Lund University, Lund, Sweden, **1995**.
[20] S. Ulvenlund, K. Ståhl, L. A. Bengtsson, *Inorg Chem.* **1996**, *35,* 223–230.
[21] S. Ulvenlund, A. Wheatley, L. A. Bengtsson, *J. Chem. Soc., Dalton Trans.* **1995**, 245–254.
[22] M. Lindsjö, A. Fischer, L. Kloo, *Angew. Chem.* **2004**, *116*, 2594–2597; *Angew. Chem. Int. Ed.* **2004** *, 43*, 2540–2543.
[23] P. A. Edwards, J. D. Corbett, *Inorg. Chem.* **1977**, *16*, 903–907.
[24] W. Herrendorf, H. Bärnighausen, *HABITUS*, a program for numerical absorption correction, Universities of Karlsruhe and Giessen, **1997**.
[25] G. Sheldrick, *SHELXS97*, a program for crystal structure solution, University of Göttingen, **1997**.
[26] G. Sheldrick, *SHELXL97*, a program for crystal structure refinement, University of Göttingen, **1997**.

Received June 3, 2004
Published Online January 26, 2005

 © 2005 Wiley-VCH Verlag GmbH & Co. KGaA, Weinheim

Synthesis, Characterisation of Carbon-Bridged (Diphenolato)lanthanide Complexes and Their Catalytic Activity for Diels–Alder Reactions

Xiaoping Xu,[a] Mengtao Ma,[a] Yingming Yao,*[a] Yong Zhang,[a] and Qi Shen*[a]

Keywords: Lanthanides / O ligands / Structure elucidation / Catalysis / Diels–Alder reaction / Cyclopentadiene

The synthesis and structures of new lanthanide complexes supported by the carbon-bridged diphenolato ligand 2,2′-methylenebis(6-*tert*-butyl-4-methylphenolato) ($MBMP^{2-}$) are described. Reactions of anhydrous lanthanide trichlorides with Na_2MBMP in a 1:2 molar ratio in THF at room temperature afforded the corresponding "ate" (diphenolato)lanthanide complexes $[(THF)_nLn(MBMP)_2Na(THF)_2]$ [Ln = Nd (**1**), Sm (**2**), n = 2; Ln = Yb, n = 1 (**3**)]. Recrystallisation of complexes **1**–**3** from toluene in the presence of DME gave the discrete ion-pair complexes $[(MBMP)_2Ln(THF)_2][Na(DME)_2(THF)_2]$ [Ln = Nd (**4**), Sm (**5**), Yb (**6**)]. These complexes have been fully characterised. The single-crystal structural analyses of **1**, **3** and **6** revealed that the coordination geometries of the lanthanide ions can be best described as distorted octahedral in complexes **1** and **6** and distorted trigonal-bipyramidal in complex **3**. It was found that these lanthanide complexes are able to act as Lewis acids to catalyse the Diels–Alder reactions of cyclopentadiene with substituted dienophiles with good activity and stereoselectivity.

(© Wiley-VCH Verlag GmbH & Co. KGaA, 69451 Weinheim, Germany, 2005)

Introduction

Of the possible alternatives to the traditional ancillary bis(cyclopentadienyl) ligand set in lanthanide chemistry, alkoxides (aryloxides) have received much attention and become increasingly popular since they are easily available, tuneable and even potentially recyclable ancillary ligand sets for mediating the reactivity of electropositive cations.[1] The synthesis and structural characterisation of a variety of di-[2] and trivalent[3] lanthanide complexes supported by monodentate aryloxides have been published and some of them have shown good catalytic activities for the polymerisation of polar and nonpolar monomers.[4] To date, the chelate diphenolates have been seldom used as ancillary ligands in lanthanide chemistry.[5]

Chelate ligands have played a remarkable role in the development of coordination chemistry. They may stabilise complexes either by thermodynamic or kinetic means and they may serve in the exploration of reaction mechanisms.[6] Carbon-bridged diphenols such as 2,2′-methylenebis(6-*tert*-butyl-4-methylphenol) ($MBMPH_2$) and 2,2′-ethylidenebis(4,6-di-*tert*-butylphenol) ($EDBPH_2$) have been found to be able to act as dianionic ligands which have the advantage of avoiding ligand redistribution reactions and providing a stereochemically rigid framework for the metal centre which could affect stereospecific transformations. The use of these carbon-bridged diphenolato ligands in transition and main-group metal complexes has attracted considerable attention in recent years and some of these complexes have shown interesting catalytic activity.[7] For example, the corresponding titanium complexes are able to catalyse not only the polymerisation of α-olefins in the presence of MAO[7a,7c,7d] but also the living anionic polymerisation of ε-caprolactone.[7b] The aluminium complexes can effectively catalyse the controllable polymerisation of propylene oxide[7f] and ε-caprolactone[7g,7h,7k] as well as MPV hydrogen transfer reactions.[7i] In view of this, it can be anticipated that organolanthanide complexes supported by carbon-bridged diphenolato ligands could lead to the activation of a range of small molecules and act as new types of Lewis acid catalysts for organic synthesis. However, these kinds of ligands have not been used in lanthanide coordination chemistry except for our recent report of the synthesis of divalent lanthanide complexes.[5i] Here we report the synthesis and characterisation of trivalent lanthanide complexes supported by the $MBMP^{2-}$ group and their catalytic activity for Diels–Alder reactions.

[a] Key Laboratory of Organic Synthesis of Jiangsu Province, Department of Chemistry and Chemical Engineering, Suzhou University,
Suzhou 215006, P. R. China
Fax: +86-512-65112371
E-mail:yaoym@suda.edu.cn

Results and Discussion

Synthesis and Characterisation of Carbon-Bridged (Diphenolato)lanthanide Complexes

Since the organolanthanide or organolanthanoid chlorides are important precursors for lanthanide derivatives, we tried to synthesise the mono(diphenolato)neodymium complex $[(MBMP)NdCl(THF)_x]$ by the general salt metath-

 DOI: 10.1002/ejic.200400519

esis reaction of anhydrous $NdCl_3$ with $MBMPNa_2$ in a 1:1 molar ratio in THF at ambient temperature but this attempt was unsuccessful. The resultant complex, isolated in moderate yield, was characterised as a ligand-redistributed product $[(THF)_2Nd(MBMP)_2Na(THF)_2]$ (**1**). The reaction was repeated with the stoichiometry appropriate for complex **1** and a yield of >78% was obtained. Thus, the isostructural complexes $[(THF)_nLn(MBMP)_2Na(THF)_2]$ [Ln = Sm (**2**), n = 2; Yb (**3**), n = 1] were synthesised by the reaction of $LnCl_3$ with $MBMPNa_2$ in 1:2 molar ratio in THF as shown in Scheme 1.

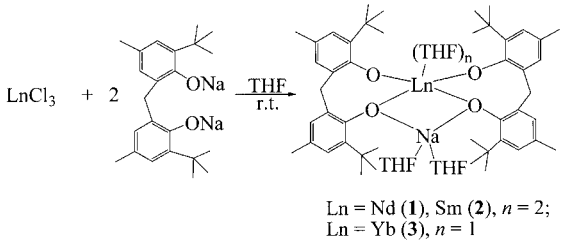

Ln = Nd (**1**), Sm (**2**), n = 2;
Ln = Yb (**3**), n = 1

Scheme 1.

These complexes gave satisfactory elemental analyses and the lanthanide and sodium analyses indicated a molar ratio of 1:1 for Ln and Na in these complexes. The definitive structures of complexes **1** and **3** were determined by X-ray diffraction studies which revealed them to be "ate" complexes in which a sodium atom is connected to one oxygen atom from each of the diphenolato ligands.

It is interesting that recrystallisation of complexes **1**–**3** from toluene in the presence of DME gave the discrete ion-pair complexes $[(MBMP)_2Ln(THF)_2][Na(DME)_2(THF)_2]$ [Ln = Nd (**4**), Sm (**5**), Yb (**6**)] which were confirmed by elemental analysis and ^1H NMR spectroscopy as well as by a structural determination in the case of **6**.[8] In the anionic (aryloxo)lanthanide complexes, most of the anions are connected to the cations by bridging ligands and the ion-pair complexes are rare. Previously reported ion-pair (aryloxo) lanthanide complexes are limited to $[Na(DME)_3][Ln(OC_6H_3\text{-}Ph_2\text{-}2,6)_4]$, $[Na(diglyme)_2][Ln(OC_6H_3\text{-}Ph_2\text{-}2,6)_4$ [diglyme = bis(2-methoxyethyl) ether, Ln = Nd, Er],[3e] $[Nd(OC_6H_3\text{-}tBu_2\text{-}2,6\text{-}Me\text{-}4)_4][Na(THF)_6]$[3d] and $[(C_5Me_5)Y(OC_6H_3\text{-}Me_2\text{-}2,6)_3][Na(THF)_6]$.[9] Due to the competition between coordinating solvents and oxygen atoms in the $MBMP^{2-}$ groups for complexation of the sodium atom, addition of DME broke the bridges between the sodium atom and the diphenolato ligands and formed a sodium cation coordinated by two DME groups and two THF groups as shown in Scheme 2. This can be attributed to the fact that the bidentate DME has a relatively stronger coordinating ability than the bridging phenolate.[3e]

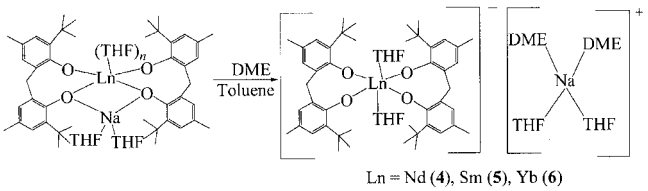

Ln = Nd (**4**), Sm (**5**), Yb (**6**)

Scheme 2.

Complexes **1**–**3** are moderately air- and moisture-sensitive. The crystals can be exposed to air for a few hours without apparent decomposition but the colours of the solutions changed gradually in a few minutes. However, complexes **4**–**6** are air- and moisture-sensitive and the crystals decompose in a few minutes when exposed to air. These complexes are freely soluble in donor solvents such as THF and DME, slightly soluble in toluene and benzene but insoluble in hexane. The neodymium complexes (**1** and **4**) did not provide any resolvable ^1H NMR spectra due to the strong paramagnetism of the neodymium ion.

Crystal Structure Analyses

Although there are many structurally characterised (dinaphtholato)lanthanide complexes in the literature,[5c,10] there are only a few examples of structurally characterised lanthanide complexes supported by diphenolato ligands. The diphenolato ligand $[1,1'\text{-}(2\text{-}OC_6H_2\text{-}tBu_2\text{-}3,5)]_2$, in which two phenols are linked directly, was first used as an ancillary ligand in organolanthanide chemistry.[5a] Recently, other (diphenolato)lanthanide complexes containing donor-functionalised linkers have been reported.[5c–5h] The crystal structures of trivalent lanthanide complexes supported by carbon-bridged diphenolate have not been reported until now.[5i] To elucidate the influence of the carbon-bridged diphenolates on the lanthanide coordination spheres, the X-ray crystal structures of complexes **1**, **3** and **6** were determined.

Crystals of complex **1** suitable for an X-ray diffraction study were grown by cooling a concentrated toluene solution to –10 °C. An ORTEP diagram with the atom-numbering scheme of **1** is shown in Figure 1, selected bond lengths and angles are given in Table 1. Complex **1** has a C_2-symmetric dinuclear structure. The overall molecular geometry consists of a six-coordinate neodymium metal centre which is coordinated by the four oxygen atoms of the two $MBMP^{2-}$ groups and two oxygen atoms from the THF molecules in a distorted octahedron as well as a four-coordinate sodium cation which is coordinated by two oxygen atoms from the $MBMP^{2-}$ groups and two THF ligands in a distorted tetrahedron. The coordination geometry around the neodymium atom is similar to that of the yttrium atom in $[(2,6\text{-}Me_2\text{-}C_6H_3O)_2Y(THF)_2(\mu\text{-}OC_6H_3\text{-}Me_2\text{-}2,6)_2(THF)_3]$.[9] The terminal phenolate [O(2), O(2_2)], one bridging phenolate [O(1)] and one THF molecule [O(3)] can be viewed as occupying equatorial positions within the octahedron about the neodymium centre with Σ(O–Nd–O) = 360.53°. The oxygen atom from another bridging phenolate ligand [O(1_2)] and one oxygen atom from the THF [O(3_2)] occupy axial positions and the O(1_2)–Nd–O(3–2) angle is slightly distorted away from the idealised 180° to 172.466(4)°.

The terminal Nd–O(Ar) bond lengths are 2.278(2) Å which compare well with the previously reported terminal

 © 2005 Wiley-VCH Verlag GmbH & Co. KGaA, Weinheim

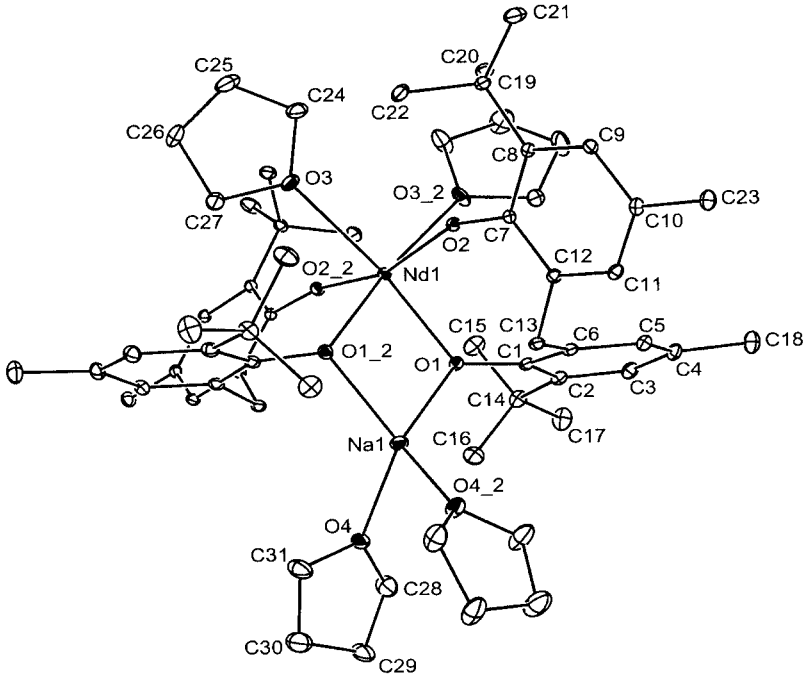

Figure 1. ORTEP diagram of **1** showing atom-numbering scheme. Thermal ellipsoids are drawn at the 10% probability level and hydrogen atoms are omitted for clarity.

Table 1. Selected bond lengths [Å] and angles [°] for complex **1**.

Nd(1)–O(1)	2.315(2)	Nd(1)–O(2)	2.278(2)
Nd(1)–O(3)	2.559(3)	Nd(1)–Na(1)	3.543(2)
C(1)–O(1)	1.352(4)	C(7)–O(2)	1.339(4)
Na(1)–O(1)	2.305(2)	Na(1)–O(4)	2.287(3)
O(1)–Nd(1)–O(2)	95.51(8)	O(2)–Nd(1)–O(3)	90.09(8)
O(3)–Nd(1)–O(2_2)	77.92(6)	O(1)–Nd(1)–O(2_2)	97.61(6)
O(1_2)–Nd(1)–O(3_2)	172.466(4)	Nd(1)–O(1)–C(1)	127.3(2)
Nd(1)–O(2)–C(7)	158.5(2)		

Nd–O(Ar) distances when the difference in coordination number is considered.[3d] The bridging Nd–O(Ar) bond length is only 0.04 Å longer than the terminal Nd–O(Ar) bond length which is comparable with that in [Na{Nd(OC_6H_3-Ph_2-2,6)$_4$}][3e] but apparently shorter than that in [(THF)La(OC_6H_3-*i*Pr_2-2,6)$_2$(μ-OC_6H_3-*i*Pr_2-2,6)$_2$Na-$(THF)_2$].[3] The O(2)–Nd–O(2_2) bond angle between the two terminal phenolato ligands is 162.90(6)° whereas the O(1)–Nd–O(1_2) angle between the two bridging phenolato ligands is dramatically smaller at 79.62(5)°. The Nd(1)–O(1)–C(1) bond angle for the bridging phenolato ligand is rather acute at 127.3(2)° reflecting its interaction with the sodium cation while the Nd(1)–O(2)–C(7) bond angle for the terminal phenolato ligand is more obtuse [158.5(2)°] and is comparable with the corresponding bond angles in K[Nd(OC_6H_3-*i*Pr_2-2,6)$_4$].[3i] The bite angle O(1)–Nd–O(2) of 95.51(8)° for the diphenolato ligand is apparently larger than those found in [{Ln[P1,1′-(2-OC_6H-*t*Bu-3-Me_2-5,6)$_2$][N($SiHMe_2$)$_2$](THF)}$_2$] [Ln = Y 88.79(6)°; La 88.83(7)°][5b] and [La{1,1′-(2-OC_6H_2-*t*Bu_2-3,5)$_2$}{CH-($SiMe_3$)$_2$}($THF)_3$] [88.1(3)°][5a] reflecting the fact that addition of a methylene linker between two phenolates increases the flexibility of the diphenolato ligand. Nd(1), Na(1), O(1) and O(1_2) are exactly coplanar (plane 1) as required by the crystallographic symmetry. The dihedral angles between plane 1 and plane 2 [C(1) to C(6)], and between plane 1 and plane 3 [C(7) to C(12)] are 90.64(8) and 81.79(9)°, respectively, indicating that the orientations of plane 1 and the arene rings of the diphenolato ligands are approximately perpendicular. The dihedral angle between two arene rings of the $MBMP^{2-}$ group is 68.9(1)°.

The sodium cation is coordinated to two THF oxygen atoms and an oxygen atom from each of the two $MBMP^{2-}$ groups. This coordination geometry is different from that in [(THF)La(OC_6H_3-*i*Pr_2-2,6)$_2$(μ-OC_6H_3-*i*Pr_2-2,6)$_2$Na-$(THF)_2$], in which one carbon atom from one of the bridging aryloxide ligands is directed to the fifth coordination site of the sodium cation,[3] as well as in [Na{Nd(OC_6H_3-Ph_2-2,6)$_4$}], in which the sodium atom is surrounded by three bridging aryloxide oxygen atoms and three phenyl groups.[3e] The Na–O(Ar) bond length of 2.305(2) Å lies within the range previously reported for Na–O(Ar) bond lengths.[3] The O(1)–Na–O(1_2) bond angle between the bridging phenolato ligands is 80.02(7)° while the O(4)–Na–O(4_2) bond angle between two THF molecules is 88.40(9)°.

Crystals of complex **3** suitable for an X-ray diffraction study were obtained from a concentrated toluene solution at room temperature. The molecular structure of complex **3** is shown in Figure 2 with selected bond lengths and bond angles listed in Table 2. The difference in the molecular

 © 2005 Wiley-VCH Verlag GmbH & Co. KGaA, Weinheim

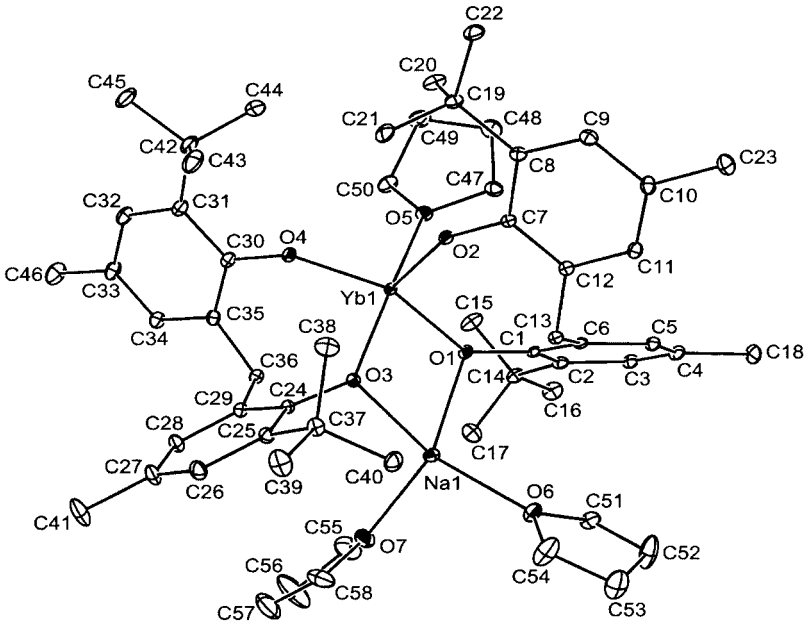

Figure 2. ORTEP diagram of **3** showing atom-numbering scheme. Thermal ellipsoids are drawn at the 10% probability level and hydrogen atoms are omitted for clarity.

Table 2. Selected bond lengths [Å] and angles [°] for complexes **3** and **6**.

	3	**6a**	**6b**
Yb(1)–O(1)	2.160(3)	2.157(5)	2.148(5)
Yb(1)–O(2)	2.059(3)	2.130(5)	2.107(4)
Yb(1)–O(3)	2.134(3)	2.156(5)	2.161(5)
Yb(1)–O(4)	2.088(3)	2.119(5)	2.118(4)
Yb(1)–O(5)	2.333(3)	2.419(5)	2.421(5)
Yb(1)–O(6)	–	2.427(5)	2.399(5)
C(1)–O(1)	1.350(5)	1.330(8)	1.328(8)
C(7)–O(2)	1.340(5)	1.317(8)	1.325(8)
C(24)–O(3)	1.349(5)	1.331(9)	1.333(8)
C(30)–O(4)	1.351(5)	1.331(8)	1.324(8)
Yb(1)–O(1)–C(1)	135.8(3)	152.1(5)	149.9(5)
Yb(1)–O(2)–C(7)	151.6(2)	154.2(5)	156.0(5)
Yb(1)–O(3)–C(24)	134.4(3)	147.1(5)	151.7(4)
Yb(1)–O(4)–C(30)	149.6(3)	156.7(5)	155.7(5)

structures of complexes **3** and **1** is that only one THF molecule is coordinated to the central metal atom in the former. Thus, the ytterbium centre is five-coordinate by four oxygen atoms from the two $MBMP^{2-}$ groups and one oxygen atom from a THF molecule in a somewhat distorted trigonal-bipyramidal geometry. The oxygen atoms O(5) and O(3) occupy axial positions and the oxygen atoms O(2), O(4) and O(1) can be considered to occupy equatorial positions. The overall molecular structure is similar to that of the previously reported $[(THF)La(OC_6H_3\text{-}i\text{Pr}_2\text{-}2,6)_2(\mu\text{-}OC_6H_3\text{-}i\text{Pr}_2\text{-}2,6)_2Na(THF)_2]$.[3] The coordination geometry of the sodium cation is identical to that observed in complex **1**.

The terminal Yb–O(Ar) bond lengths are 2.059(3) and 2.088(3) Å, respectively, giving an average of 2.073(8) Å which is comparable with those previously reported terminal Yb–O(Ar) bond lengths.[3b] Yb–O(Ar) distances to the bridging ligands are, as expected, somewhat longer at 2.147(3) Å (av.). The Na–O(Ar) and Na–O(THF) bond lengths are comparable with those found in complex **1**. As previously observed in the structure of complex **1**, the O–Yb–O angle between the bridging phenolato ligands [O(1)–Yb(1)–O(3) = 82.2(1)°] is apparently smaller than that between the two terminal phenolato ligands [O(2)–Yb(1)–O(4) = 112.6(1)°]. The average Yb–O–C bond angle for the bridging phenolato ligands is 135.1(3)° while the Yb–O–C angles for the terminal phenolato ligands average 150.6(2)° which is comparable with the corresponding bond angles in complex **1**. The dihedral angles between two arene rings in the $MBMP^{2-}$ groups are quite different, i.e. 57.4(1)° for the ligand containing O(1) and O(2) but 94.8(2)° for that containing O(3) and O(4).

Crystals of complex **6** suitable for an X-ray diffraction study were obtained from a toluene/DME solution at –5 °C. This complex is composed of a discrete six-coordinate $[(MBMP)_2Yb(THF)_2]^-$ anion and an $[Na(DME)_2(THF)_2]^+$ cation. Complex **6** crystallises with two crystallographically independent but chemically similar molecules (**6a** and **6b**) in the unit cell. The selected bond lengths and angles are provided in Table 2 for both molecules. The structure of the anion of complex **6a** with the atom-numbering scheme is shown in Figure 3.

In the cation, the sodium atom is coordinated to four oxygen atoms from two DME molecules and two oxygen atoms from two THF molecules to form a slightly distorted octahedral geometry. In the anion, the coordination geometry around the ytterbium atom is different from that in complex **3**. The ytterbium atom is located in the centre of an octahedron comprised of two $MBMP^{2-}$ groups and two THF molecules in which the oxygen atoms from the $MBMP^{2-}$ groups [O(1), O(3), O(4)] and one THF molecule

 © 2005 Wiley-VCH Verlag GmbH & Co. KGaA, Weinheim

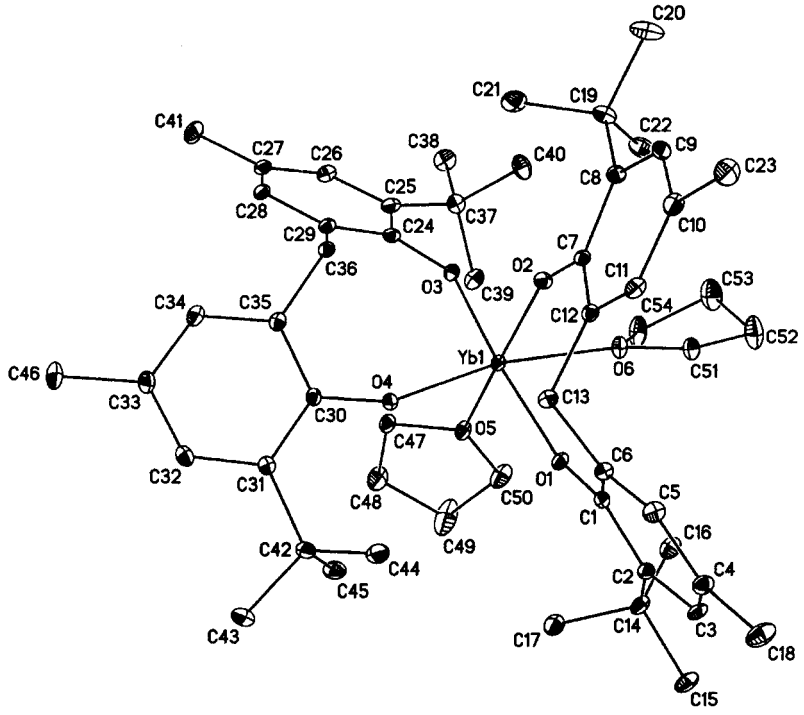

Figure 3. ORTEP diagram of the anion of **6a** showing atom-numbering scheme. Thermal ellipsoids are drawn at the 10% probability level and hydrogen atoms are omitted for clarity.

[O(6)] can be considered as occupying equatorial positions with Σ(O–Yb–O) = 359.0°. Two oxygen atoms from one $MBMP^{2-}$ group [O(2)] and the THF molecule [O(5)] occupy axial positions.

The Yb–O(Ar) bond lengths range from 2.119(5) to 2.157(5) Å, giving an average of 2.140(6) Å which is comparable with the terminal Yb–O(Ar) bond lengths in complex **3** when the difference in coordination number is considered but it is slightly longer than that in $[Na(THF)_6][(C_5Me_5)Y(OC_6H_3\text{-}Me_2\text{-}2,6)_3]$ (2.094 Å).[9] The bite angles of O–Yb–O in complex **6a** are 90.45(19)° and 95.72(19)°, respectively, which are comparable with that in complex **1**. The average Yb–O–C bond angle is 152.5(5)° which is similar to the corresponding bond angles in complexes **1** and **3**. The dihedral angles between the arene rings in the two $MBMP^{2-}$ groups are 53.9(3)° and 56.5(2)°, respectively.

A comparison of the structural geometry of the (diphenolato)lanthanide complexes with those of the structurally characterised monodentate aryloxide examples enables an evaluation of the $MBMP^{2-}$ ligand set compared with two ArO^- ligands. The yttrium centre is six-coordinate in $[(2,6\text{-}Me_2\text{-}C_6H_3O)_2Y(THF)_2(\mu\text{-}OC_6H_3\text{-}Me_2\text{-}2,6)_2(THF)_3]$ and $[Na(THF)_6][(C_5Me_5)Y(OC_6H_3\text{-}Me_2\text{-}2,6)_3]$[9] whereas the lanthanum centre is only five-coordinate in $[(THF)La(OC_6H_3\text{-}i\text{Pr}_2\text{-}2,6)_2(\mu\text{-}OC_6H_3\text{-}i\text{Pr}_2\text{-}2,6)_2Na(THF)_2]$[3] and the neodymium centre is four-coordinate in $[Na(THF)_6][Nd(OC_6H_3\text{-}t\text{Bu}_2\text{-}2,6\text{-Me-}4)_4]$,[3d] [Na(diglyme)][$Nd(OC_6H_3\text{-}Ph_2\text{-}2,6)_4$], $Na[Nd(OC_6H_3\text{-}Ph_2\text{-}2,6)_4]$[3e] and $K[Nd(OC_6H_3\text{-}i\text{Pr}_2\text{-}2,6)_4]$.[3i] However, in these (diphenolato)lanthanide complexes, the central metal atom is five- or six-coordinate. Thus, the diphenolato ligand $MBMP^{2-}$ is sterically less demanding than the two monodentate aryloxide groups $[OC_6H_3\text{-}t\text{Bu}_2\text{-}2,6\text{-Me-}4]^-$, $[OC_6H_3\text{-}Ph_2\text{-}2,6]^-$ and $[OC_6H_3\text{-}i\text{Pr}_2\text{-}2,6]^-$ but is comparable with two less bulky aryloxide groups $[OC_6H_3\text{-}Me_2\text{-}2,6]^-$. It is because of the sterically less demanding nature of $MBMP^{2-}$ that the desired (diphenolato)lanthanide chloride $[(MBMP)LnCl(THF)_x]$ could not be achieved by the general salt metathesis reaction.

Diels–Alder Reactions Catalysed by the (Diphenolato) lanthanide Complexes

In recent years, as a result of the importance of Diels–Alder reactions in the synthesis of natural products and physiologically active molecules, increased interest has been directed towards the development of efficient methods for

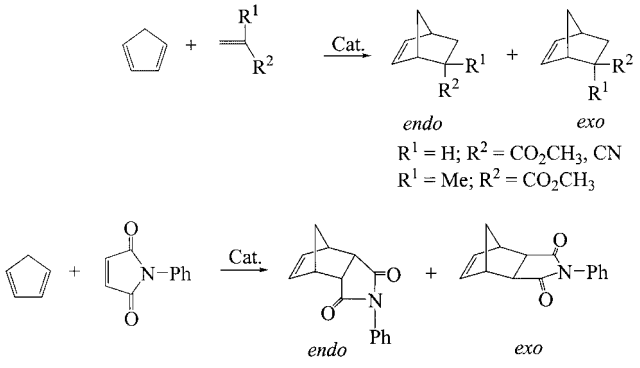

Scheme 3.

Table 3. Diels–Alder reactions of cyclopentadiene with dienophiles catalysed by carbon-bridged (diphenolato)lanthanide complexes.

Run	Cat.	Dienophile	[Cat.]/[Dienophile]	*t* [h]	Yield [%]	*endo*/*exo*
1	–	methyl acrylate	–	24	67	2.7
2	**1**	methyl acrylate	1:10	4	59	4.6
3	**1**	methyl acrylate	1:10	8	78	4.3
4	**1**	methyl acrylate	1:10	24	93	4.6
5	**2**	methyl acrylate	1:10	4	54	4.3
6	**2**	methyl acrylate	1:10	8	69	4.3
7	**3**	methyl acrylate	1:10	2	14	4.0
8	**3**	methyl acrylate	1:10	4	35	3.9
9	**3**	methyl acrylate	1:10	24	94	4.0
10	–	methyl methacrylate	–	10	25	0.45
11	**1**	methyl methacrylate	1:10	4	22	2.2
12	**1**	methyl methacrylate	1:10	10	58	2.2
13	–	acrylonitrile	–	10	36	1.2
14	**1**	acrylonitrile	1:10	4	31	1.6
15	**1**	acrylonitrile	1:10	8	54	1.6
16	–	*N*-phenyl maleimide	–	10	46	–
17	**1**	*N*-phenyl maleimide	1:10	4	35	35
18	**1**	*N*-phenyl maleimide	1:10	8	65	35

the purpose of improving the reaction rates and/or stereoselectivities of cycloaddition reactions.[11] As Lewis-acidic catalysts, lanthanide complexes are well established and have been found to be effective catalysts in numerous Diels–Alder reactions.[12] We found that these carbon-bridged (diphenonato)lanthanide complexes can also catalyse the Diels–Alder reactions of cyclopentadiene with methyl acrylate, methyl methacrylate, acrylonitrile and *N*-phenylmaleimide with relatively good activities and stereoselectivities as shown in Scheme 3 with preliminary results listed in Table 3.

As shown in Table 3, these (diphenolato)lanthanide complexes accelerate the Diels–Alder reactions of cyclopentadiene with these dienophiles and the product yields increased as a function of time whereas the stereoselectivities remained essentially the same at all reaction times. Reactions with substituted dienophiles produced a mixture of *endo* and *exo* isomers although the stereoselectivity (*endo*/*exo* ratio) is apparently dependent on the dienophile. For reactions with asymmetrically substituted dienophiles, the reaction with methyl acrylate afforded the best stereoselectivity. The *endo*/*exo* ratio of 4.6 can be achieved for this reaction at 40 °C in the presence of 10 mol-% of complex **1** as the catalyst (the *endo*/*exo* ratio is 2.7 for the blank reaction, runs 1 and 2). In comparison with other lanthanide catalysts, the activities and stereoselectivities exhibited by the (diphenolato)lanthanide complexes for the reaction of cyclopentadiene with methyl acrylate are higher than that of anhydrous lanthanide chlorides[13a] and are comparable with those of SmI_2[13b] and $Sc(OTf)_3$ if toluene is used as solvent (using $scCO_2$ as solvent, the *endo*/*exo* ratio is up to 10)[13c] but are lower than those of other Lewis acid catalysts such as aluminium,[14a–14c] copper[14d] and ruthenium[14e] complexes. It is worthy to note that the reaction of cyclopentadiene with methyl methacrylate catalysed by complex **1** is *endo*-selective and gave products with an *endo*/*exo* ratio of 2.2. The Diels–Alder reaction of cyclopentadiene with methyl methacrylate normally gave a higher amount of the *exo* stereoisomer[15a] and some organic and inorganic reagents can increase the yield of the *endo* stereoisomer.[15b,15c] Recently, there has been one example reported in which this *exo*-selective reaction can be converted to an *endo*-selective process in chloroaluminate ionic liquids.[15d] Complex **1** showed poor activity and stereoselectivity for the reaction of cyclopentadiene with acrylonitrile, although the result was similar to those reported in the literature.[16] For the symmetrically substituted dienophile *N*-phenylmaleimide, excellent stereoselectivity was obtained. The reaction with *N*-phenylmaleimide using complex **1** as catalyst gave the *endo* stereoisomer as the major product but the selectivity was lower than those of montmorillonite and alumina.[17]

Conclusions

In summary, we have successfully synthesised a series of new soluble carbon-bridged (diphenolato)lanthanide complexes and characterised some of their structural features by X-ray crystallography. Moreover, it was found that coordinated solvents dramatically affect the solid-state structures of the (diphenolato)lanthanide complexes. Crystallisation from toluene in the presence of THF afforded the "ate" complexes while in presence of DME discrete ion-pair complexes were formed. Preliminary results revealed that these "ate" (diphenolato)lanthanide complexes have good activities and stereoselectivities for the Diels–Alder reactions of cyclopentadiene with some substituted dienophiles. Further studies of these reactions are in progress in our laboratory.

Experimental Section

General Procedures: All manipulations were performed under argon using standard Schlenk techniques. THF, DME and toluene were distilled from sodium benzophenone ketyl before use. Anhydrous lanthanide trichlorides were prepared according to the literature procedures[18] and $Na_2(MBMP)$ was prepared from the reac-

 © 2005 Wiley-VCH Verlag GmbH & Co. KGaA, Weinheim

tion of $MBMPH_2$ with Na in THF [$MBMPH_2$ = 2,2′-methylenebis(6-*tert*-butyl-4-methylphenol)]. Lanthanide analyses were performed by EDTA titration with xylenol orange indicator and hexamine buffer[19] and chloride analyses were carried out using the Volhard method. The sodium content was determined with a Hitachi 180-80 polarised Zeeman atomic absorption spectrophotometer. Carbon and hydrogen analyses were performed by direct combustion with a Carlo–Erba EA-1110 instrument. IR spectra were recorded with a Nicolet-550 FTIR spectrometer as KBr pellets. Uncorrected melting points of crystalline samples in sealed capillaries (under argon) are reported as ranges. Methyl acrylate, methyl methacrylate and acrylonitrile were washed with diluted NaOH solution three times, dried with anhydrous $NaSO_4$ for 24 h and distilled before use. *N*-Phenylmaleimide was prepared according to the literature.[20] Cyclopentadiene was freshly prepared by thermally cracking dicyclopentadiene. Other reagents were commercially available.

Synthesis of [(THF)$_2$Nd(MBMP)$_2$Na(THF)$_2$] (1). Method A: To a suspension of $NdCl_3$ (1.63 g, 6.50 mmol) in THF (50 mL) was slowly added a THF solution of Na_2(MBMP) (27.6 mL, 6.50 mmol) at room temperature. After being stirred for 24 h, the precipitate was separated from the reaction mixture using a centrifuge, the solvent was completely removed in vacuo and toluene was added to extract the product. The dissolved portion was removed with a centrifuge. Light-blue microcrystals were obtained from the concentrated toluene solution. Yield: 2.41 g, 32%. M.p. 165–166 °C (dec.). IR (KBr): $\tilde{\nu}$ = 2955 (s), 2871 (m), 1632 (m), 1474 (s), 1389 (m), 1055 (w), 861 (m) cm^{-1}. $C_{62}H_{92}NaO_8Nd$ (1132.64): calcd. C 65.75, H 8.19, Nd 12.73, Na 2.03; found C 65.43, H 8.01, Nd 12.55, Na 1.91. **Method B:** To a suspension of $NdCl_3$ (1.28 g, 5.10 mmol) in THF (40 mL) was slowly added a THF solution of Na_2(MBMP) (43.3 mL, 10.2 mmol) at room temperature. After the reaction solution had been stirred for 24 h, complex **1** was isolated as described above (4.53 g, 78%).

Synthesis of [(THF)$_2$Sm(MBMP)$_2$Na(THF)$_2$] (2): The synthesis of complex **2** was carried out as described above for complex **1** (Method B) but anhydrous $SmCl_3$ (1.3 g, 5.06 mmol) was used instead of $NdCl_3$. Colourless microcrystals were obtained from toluene. Yield: 4.21 g, 73%. M.p. 144–145 °C (dec.). IR (KBr): $\tilde{\nu}$ = 2955 (s), 2920 (s), 2870 (m), 1604 (w), 1435 (s), 1385 (m), 1250 (s), 1087 (w), 860 (m) cm^{-1}. ^{1}H NMR (C_6D_6): δ = 1.47 [36 H, C(CH_3)$_3$], 2.01–2.58 (br., 28 H, THF and ArCH_3), 3.66 (16 H, THF), 3.78 (4 H, ArCH_2), 6.93–7.08 (4 H, C_6H_2) ppm. $C_{62}H_{92}NaO_8Sm$ (1138.76): calcd. C 65.39, H 8.14, Sm 13.18, Na 2.02; found C 65.27, H 7.93, Sm 13.47, Na 1.98.

Synthesis of [(THF)Yb(MBMP)$_2$Na(THF)$_2$] (3): The synthesis of complex **3** was carried out as described for complex **1** but anhydrous $YbCl_3$ (1.31 g, 4.69 mmol) was used instead of $NdCl_3$. Yellow microcrystals were obtained from toluene. Yield: 4.07 g, 75%. M.p. 142–143 °C (dec.). IR (KBr): $\tilde{\nu}$ = 2954 (s), 2909 (s), 2869 (m), 1605 (m), 1526 (m), 1434 (s), 1240 (s), 1156 (s), 1050 (m), 862 (m) cm^{-1}. ^{1}H NMR (C_6D_6): δ = 1.45 (48 H, C(CH_3)$_3$ and THF), 2.17 (12 H, ArCH_3), 3.42–3.81 (br., 16 H, THF and ArCH_2), 6.93–7.08 (8 H, C_6H_2) ppm. $C_{58}H_{84}NaO_7Yb$ (1089.33): calcd. C 63.95, H 7.77, Yb 15.88, Na 2.11; found C 63.56, H 7.74, Yb 15.60, Na 1.93.

Synthesis of [(THF)$_2$Nd(MBMP)$_2$][Na(DME)$_2$(THF)$_2$] (4): To a solution of complex **1** (3.27 g, 2.8 mmol) in toluene (50 mL) was added DME (1 mL). After stirring the solution for about 30 min, blue-purple microcrystals were obtained upon concentration and subsequent cooling of the solution to –5 °C for 3 d. Yield: 3.11 g, 85%. M.p. 109–110 °C (dec.). IR (KBr): $\tilde{\nu}$ = 2951 (s), 2912 (s), 1608 (w), 1466 (s), 1435 (s), 1385 (m), 1084 (s), 860 (m) cm^{-1}. $C_{70}H_{112}NaO_{12}Nd$ (1312.88): calcd. C 64.04, H 8.60, Nd 10.99, Na 1.75; found C 63.74, H 8.39, Nd 10.72, Na 1.68.

Synthesis of [(THF)$_2$Sm(MBMP)$_2$][Na(DME)$_2$(THF)$_2$] (5): To a solution of complex **2** (2.84 g, 2.5 mmol) in toluene (50 mL) was added DME (1 mL). After stirring the solution for about 30 min, pale-yellow microcrystals were obtained upon concentration and subsequent cooling of the solution to –5 °C for 2 d. Yield: 2.83 g, 86%. M.p. 98–99 °C (dec.). IR (KBr): $\tilde{\nu}$ = 2951 (s), 2921 (s), 2870 (m), 1605 (w), 1466 (s), 1431 (s), 1385 (m), 1292 (s), 1084 (s), 860 (m) cm^{-1}. ^{1}H NMR (C_6D_6): δ = 1.47 [36 H, C(CH_3)$_3$], 1.97 (16 H, THF), 2.17 (12 H, ArCH_3), 2.78–3.61 (br., 40 H, DME, THF and ArCH_2), 6.93 (4 H, C_6H_2), 7.08 (4 H, C_6H_2) ppm. $C_{70}H_{112}NaO_{12}Sm$ (1319.01): calcd. C 63.76, H 8.56, Sm 11.41, Na 1.74; found C 63.83, H 8.63, Sm 11.02, Na 1.62.

Synthesis of [(THF)$_2$Yb(MBMP)$_2$][Na(DME)$_2$(THF)$_2$] (6): To a solution of complex **3** (3.21 g, 2.95 mmol) in toluene (50 mL) was added DME (1 mL). After stirring the solution for about 30 min, light-yellow microcrystals were obtained upon concentration and subsequent cooling of the solution to –5 °C for 2 d. Yield: 2.28 g, 61%. M.p. 62–63 °C (dec.). IR (KBr): $\tilde{\nu}$ = 2955 (s), 2920 (m), 2870 (m), 1635 (w), 1466 (m), 1442 (s), 1234 (m), 1157 (m), 1049 (w), 864 (m) cm^{-1}. ^{1}H NMR (C_6D_6): δ = 1.45 [36 H, C(CH_3)$_3$], 1.87 (16 H, THF), 2.16 (12 H, ArCH_3), 3.12–3.85 (br., 40 H, THF DME and ArCH_2), 6.92 (4 H, C_6H_2), 7.07 (4 H, C_6H_2) ppm. $C_{70}H_{112}NaO_{12}Yb$ (1341.68): calcd. C 62.66, H 8.41, Yb 12.91, Na 1.71; found C 63.03, H 8.81, Yb 12.98, Na 1.68.

Diels–Alder Reactions Catalysed by the (Diphenolato)lanthanide Complexes: In a typical run, methyl acrylate (0.25 mL, 2.7 mmol) was added to a toluene solution of the catalyst (3.7 mL, 0.27 mmol). After stirring the solution at 40 °C for 5 min, freshly cracked cyclopentadiene (0.30 mL, 3.3 mmol) was added with a syringe and stirring was continued for the desired time. Methanol was added to the mixture to terminate the reaction and acetylbenzene was immediately added as an internal standard for quantitative analysis. The product yields and *endo*/*exo* ratios were determined using GC or NMR spectroscopy as described in the literature for different dienophiles.[13a,15c,16a,17]

X-ray Crystallography: Crystals of complexes **1**, **3** and **6** suitable for X-ray diffraction were sealed in thin-walled glass capillaries under argon. Diffraction data were collected with a Rigaku Mercury CCD area detector. The structures were solved by direct methods and refined by full-matrix least-squares procedures based on $|F|^2$. All non-hydrogen atoms were refined with anisotropic displacement coefficients. Hydrogen atoms were treated as idealised contributions. The structures were solved and refined using the CRYSTALS (for **1** and **3**) and SHELXS-97 (for **6**) programs. Crystal and refinement data are listed in Table 4. CCDC-239852 to -239854 for **1**, **3** and **6**, respectively, contain the supplementary crystallographic data for this paper. These data can be obtained free of charge from The Cambridge Crystallographic Data Centre via www.ccdc.cam.ac.uk/data_request/cif.

Acknowledgments

The authors are grateful to the Chinese National Natural Science Foundation (20272040 and 20472063) and the Key Laboratory of Organic Synthesis of Jiangsu Province for financial support.

[1] For reviews see: a) V. C. Gibson, S. K. Spitzmesser, *Chem. Rev.* **2003**, *103*, 283–315; b) G. J. P. Britovsek, V. C. Gibson, D. F. Wass, *Angew. Chem.* **1999**, *111*, 448–468; *Angew. Chem. Int.*

Table 4.Details of the crystallographic data and refinements for **1**, **3** and **6**.

	1	**3**·3C_7H_8	**6**·C_4H_8O
Empirical formula	$C_{62}H_{92}NaNdO_8$	$C_{79}H_{108}NaO_7Yb$	$C_{74}H_{120}NaO_{13}Yb$
Formula mass	1132.63	1365.75	1413.73
T [K]	193(2)	193(2)	193(2)
λ [Å]	0.7107	0.7107	0.7107
Crystal system	monoclinic	triclinic	triclinic
Space group	$C2/c$	$P\bar{1}$	$P\bar{1}$
Unit-cell dimensions:			
a [Å]	18.421(2)	12.9822(4)	13.7108(7)
b [Å]	17.955(1)	15.3241(5)	17.1666(12)
c [Å]	18.099(2)	19.3690(5)	36.308(3)
α [°]	90	79.089(7)	89.862(11)
β [°]	96.269(5)	80.662(7)	80.019(9)
γ [°]	90	78.608(6)	79.611(9)
V [Å^3]	5950.6(8)	3677.7(2)	8276.2(9)
Z	4	2	4
Density [Mg m^3]	1.264	1.233	1.135
Absorption coefficient [mm^{-1}]	0.930	1.328	1.187
F(000)	2396	1438	2996
θ_{max} [°]	27.48	27.48	27.49
Reflections collected	58952	36994	87226
Independent reflections	6953	16575	35903
Observed reflections	6046	14039	33673
Parameters refined	372	796	1366
Final R [$I > 3\sigma(I)$]	0.0390	0.0450	0.0862
wR	0.1110	0.1330	0.2066
GoF on F^2	1.004	1.034	1.189

Ed. **1999**, *38*, 428–447; c) F. T. Edelmann, *Angew. Chem.***1995**, *107*, 2647–2669; *Angew. Chem. Int. Ed. Engl.* **1995**, *34*, 2466–2488; d) L. G. Hubert-Pfalzgraf, *New J. Chem.* **1995**, *19*, 727–750; e) W. J. Evans, *New J. Chem.* **1995**, *19*, 525–533; f) R. C. Mehrotra, A. Singh, U. M. Tripathi, *Chem. Rev.* **1991**, *91*, 1287–1303.

[2] a) G. B. Deacon, C. M. Forsyth, P. C. Junk, B. W. Skelton, A. H. White, *Chem. Eur. J.* **1999**, *5*, 1452–1459; b) W. J. Evans, M. A. Greci, J. W. Ziller, *Chem. Commun.* **1998**, 2367–2368; c) G. B. Deacon, T. Feng, P. C. Junk, B. W. Skelton, A. H. White, *Chem. Ber./Recueil* **1997**, *130*, 851–857; d) W. J. Evans, M. A.Greci, J. W. Ziller, *J. Chem. Soc., Dalton Trans.* **1997**, 3035–3039; e) J. R. van den Hende, P. B. Hitchcock, S. A. Holmes, M. F. Lappert, W. Leung, T. C. W. Mak, S. Prashar, *J. Chem. Soc., Dalton Trans.* **1995**, 1427–1433; f) G. Z. Qi, Q. Shen, Y. H. Lin, *Acta Crystallogr., Sect. C* **1994**, *50*, 1456–1458; g) G. B. Deacon, T. Feng, P. MacKinnon, R. H. Newnham, S. Nickel, B. W. Skelton, A. H. White, *Aust. J. Chem.* **1993**, *46*, 387–399; h) Z. Hou, H. Yamazaki, K. Kobayashi, Y. Fujiwara, H. Taniguchi, *J. Chem. Soc., Chem. Commun.* **1992**, 722–724.

[3] a) G. B. Deacon, P. E. Fanwick, A. Gitlits, I. P. Rothwell, B. W. Skelton, A. H. White, *Eur. J. Inorg. Chem.* **2001**, 1505–1514; b) Y. M. Yao, Q. Shen, Y. Zhang, M. Q. Xue, J. Sun, *Polyhedron* **2001**, *20*, 3201–3208; c) G. B. Deacon, T. Feng, C. M. Forsyth, A. Gitlits, D. C. R. Hockless, Q. Shen, B. W. Skelton, A. H. White, *J. Chem. Soc., Dalton Trans.* **2000**, 961–966; d) L. L. Zhang, Y. M. Yao, Y. J. Luo, Q. Shen, J. Sun, *Polyhedron* **2000**, *19*, 2243–2247; e) G. B. Deacon, T. Feng, P. C. Junk, B. W. Skelton, A. H. White, *J. Chem. Soc., Dalton Trans.* **1997**, 1181–1186; f) H. C. Aspinall, M. Williams, *Inorg. Chem.* **1996**, *35*, 255–257; g) D. L. Clark, R. V. Hollis, B. L. Scott, J. G. Watkin, *Inorg. Chem.* **1996**, *35*, 667–674; h) D. L. Clark, G. B. Deacon, T. Feng, R. V. Hollis, B. L. Scott, B. W. Skelton, J. G. Watkin, A. H. White, *Chem. Commun.* **1996**, 1729–1730; i) D. L. Clark, J. C. Gordon, J. C. Huffman, R. L. Vincent-Hollis, J. G. Watkin, B. D. Zwick, *Inorg. Chem.* **1994**, *33*, 5903–5911; j) D. M. Barnhart, D. L. Clark, J. C. Gordon, J. C. Huffman, R. L. Vincent, J. G. Watkin, B. D. Zwick, *Inorg. Chem.* **1994**, *33*, 3487–3497.

[4] a) G. Qi, Q. Shen, *Chin. J. Appl. Chem.* **1995**, *12*, 94–96; b) M. Nishiura, Z. Hou, T. Koizumi, T. Imamoto, Y. Wakatsuki, *Macromolecules* **1999**, *32*, 8245–8251; c) Y. Yao, Q. Shen, J. Hu, *Gaofenzixuebao* **1997**, *6*, 672–676; d) Y. Yao, Q. Shen, L. Zhang, *Chin. Sci. Bull.* **2001**, *46*, 1443–1445; e) Y. G. Zhang, Z. M. Hou, Y. Wakatsuki, *Macromolecules* **1999**, *32*, 939; f) J. Ling, Z. Q. Shen, Q. H. Huang, *Macromolecules* **2001**, *34*, 7613–7616.

[5] a) C. J. Schaverien, N. Meijboom, A. G. Orpen, *J. Chem. Soc., Chem. Commun.* **1992**, 124–126; b) D. V. Gribkov, K. C. Hultzsch, F. Hampel, *Chem. Eur. J.* **2003**, *9*, 4796–4810; c) P. L. Arnold, L. S. Natrajan, J. J. Hall, S. J. Bird, C. Wilson, *J. Organomet. Chem.* **2002**, *647*, 205–215; d) M. E. G. Skinner, B. R. Tyrell, B. D. Ward, P. Mountford, *J. Organomet. Chem.* **2002**, *647*, 145–150; e) L. S. Natrajan, J. J. Hall, A. J. Blake, C. Wilson, P. L. Arnold, *J. Solid State Chem.* **2003**, *171*, 90–100; f) H. Y. Ma, T. P. Spaniol, J. Okuda, *Dalton Trans.* **2003**, 4770–4780; g) C. X. Cai, L. Toupet, C. W. Lehmann, J. F. Carpentier, *J. Organomet. Chem.* **2003**, *683*, 131–136; h) C. X. Cai, A. Amgoune, C. W. Lehmann, J. F. Carpentier, *Chem. Commun.* **2004**, 330–331; i) M. Y. Deng, Y. M. Yao, Q. Shen, Y. Zhang, J. Sun, *Dalton Trans.* **2004**, 944–950.

[6] F. Basolo, R. G. Pearson, "Inorganic Reaction Mechanism, A Study of Metal Complexes", in: *Solution*, 2nd ed., Wiley, New York, **1968**.

[7] For recent examples see: a) M. Gonzalez-Maupoey, T. Cuenca, *Organometallics* **2003**, *22*, 2694–2704; b) D. Takeuchi, T. Nakamura, T. Aida, *Macromolecules* **2000**, *33*, 725–729; c) F. G. Sernetz, R. Mulhaupt, S. Fokken, J. Okuda, *Macromolecules* **1997**, *30*, 1562–1569; d) A. van der Linden, C. J. Schaverien, N. Meijboom, C. Granter, A. G. Orpen, *J. Am. Chem. Soc.* **1995**, *117*, 3008–3021; e) J. Okuda, S. Fokken, H. C. Kang, W. Massa, *Chem. Ber.* **1995**, *128*, 221–227 and references herein. f) W. Braune, J. Okuda, *Angew. Chem. Int. Ed.* **2003**, *42*, 64–68; g) H. L. Chen, B. T. Ko, B. H. Huang, C. C. Lin, *Organometallics* **2001**, *20*, 5076–5083; h) Y. C. Liu, B. T. Ko, C. C. Lin, *Macromolecules* **2001**, *34*, 6196–6201; i) B. T. Ko, C. C. Wu, C. C. Lin, *Organometallics* **2000**, *19*, 1864–1869; j) B. T. Ko, Y. C. Chao, C. C. Lin, *Inorg. Chem.* **2000**, *39*, 1463–1469; k) B. T.

 © 2005 Wiley-VCH Verlag GmbH & Co. KGaA, Weinheim

Ko, C. C. Lin, *Macromolecules* **1999**, *32*, 8296–8300; l) H. C. Lin, L. F. Yan, F. C. Wang, Y. L. Sun, C. C. Lin, *J. Organomet. Chem.* **1999**, *587*, 151–159.

[8] Single-crystals of complex **4** suitable for structural analysis were also obtained and an adequate data set was collected. However, the definitive structure was not obtained due to the serious thermal motion of the coordinated solvent molecules and only the molecular skeleton could be obtained. Crystal data for complex **4**: monoclinic, space group $P2_1/n$, a = 13.175(2), b = 37.603(4), c = 15.405(2) Å, β = 108.342(6)°, V = 7244(1) Å^3, Z = 4.

[9] W. J. Evans, M. A. Ansari, J. W. Ziller, S. I. Khan, *J. Organomet. Chem.* **1998**, *553*, 141–148.

[10] M. Shibasaki, N. Yoshikawa, *Chem. Rev.* **2002**, *102*, 2187–2209.

[11] U. Pinduv, G. Lutz, C. Otto, *Chem. Rev.* **1993**, *93*, 741–761.

[12] S. Kobayashi, M. Sugiura, H. Kitagawa, W. W.-L. Lam, *Chem. Rev.* **2002**, *102*, 2227–2302.

[13] a) S. J. Liao, S. W. Yu, Z. Y. Chen, D. R. Yu, L. Shi, R. Y. Yang, Q. Shen, *J. Mol. Catal.* **1992**, *72*, 209–219; b) P. V. D. Weghe, J. Collin, *Tetrahedron Lett.* **1994**, *35*, 2545–2548; c) R. S. Oakes, T. J. Heppenstall, N. Shezad, A. A. Clifford, C. M. Rayner, *Chem. Commun.* **1999**, 1459–1460.

[14] For recent examples see: a) P. Mayo, G. Orlova, J. D. Goddard, W. Tam, *J. Org. Chem.* **2001**, *66*, 5182–5191; b) K. Ishihara, J. Kobayashi, K. Inanaga, H. Yamamoto, *Synlett* **2001**, 394–397; c) D. P. Heller, D. R. Goldberg, W. D. Wulff, *J. Am. Chem. Soc.* **1997**, *119*, 10551–10552; d) D. A. Evans, D. M. Barnes, J. S. Johnson, T. Lectka, P. von Mott, S. J. Miller, J. A. Murry, R. D. Norcross, E. A. Shaughnessy, K. R. Campos, *J. Am. Chem. Soc.* **1999**, *121*, 7582–7594; e) K. Mori, T. Hara, T. Mizugaki, K. Ebitani, K. Kaneda, *J. Am. Chem. Soc.* **2003**, *125*, 11460–11461.

[15] a) A. Gonzalez, S. L. Holt, *J. Org. Chem.* **1982**, *47*, 3186-3188; b) B. Mathieu, L. Ghosez, *Tetrahedron* **2002**, *58*, 8219–8226; c) S. S. Deshpande, U. D. Phalgune, A. Kumar, *Tetrahedron* **2002**, *58*, 8759–8762; d) A. Kumar, S. S. Pawar, *J. Org. Chem.* **2004**, *69*, 1419–1420.

[16] a) J. S. Fossey, C. J. Richards, *Organometallics* **2002**, *21*, 5259–5264; b) J. S. Fossey, C. J. Richards, *Organometallics* **2004**, *23*, 367–373.

[17] M. Avalos, R. Babiano, J. L. Bravo, P. Cintas, J. L. Jimenez, J. C. Palacios, B. C. Ranu, *Tetrahedron Lett.* **1998**, *39*, 2013–2016.

[18] M. D. Taylor, C. P. Carter, *J. Inorg. Nucl. Chem.* **1962**, *24*, 387–394.

[19] J. L. Atwood, W. E. Hunter, A. L. Wayda, W. J. Evans, *Inorg. Chem.* **1981**, *20*, 4115–4119.

[20] S. Thamizharasi, B. S. R. Reddy, *J. Appl. Polym. Sci.* **2001**, *80*, 1870–1878.

Received: June 15, 2004

 © 2005 Wiley-VCH Verlag GmbH & Co. KGaA, Weinheim

A Study of the Magnetic Structure of $LaMn_2O_5$ from Neutron Powder Diffraction Data

Angel Muñoz,*[a] Jose A. Alonso,[b] María T. Casais,[b] María J. Martínez-Lope,[b] Jose L. Martínez,[b] and María T. Fernández-Díaz[c]

Keywords: Lanthanides / Magnetic properties / Neutron diffraction / Spin glass / Superexchange interaction

Polycrystalline $LaMn_2O_5$ has been studied by neutron powder diffraction in conjunction with magnetization data. The crystal structure of this oxide contains infinite chains of edge-sharing $Mn^{4+}O_6$ octahedra, interconnected by $Mn^{3+}O_5$ pyramids and LaO_8 units. Susceptibility measurements show that $LaMn_2O_5$ presents an antiferromagnetic order below a T_N value of about 31 K. Neutron diffraction experiments confirm the long-range ordering below this temperature in a magnetic structure characterized by the propagation vector **k** = (0,0,1/2). The magnetic arrangement is defined by the basis vectors (G_x,A_y,0) and (0,0,C'_z) for the Mn^{4+} and Mn^{3+} ions, respectively. At 3.5 K, the magnetic moments are 2.59(4) and 1.61(7) μ_B for the Mn^{3+} (4h site) and Mn^{4+} ions (4f site), respectively. Superexchange interactions between the Mn^{4+} ions through Mn^{4+}–O–Mn^{4+} paths are considered in order to explain the commensurate character of the magnetic structure in comparison with the incommensurate structures observed for most of the RMn_2O_5 (R = rare earth metal) compounds. A spin-glass-type behaviour, which probably involves the short-range order in the Mn^{3+} sublattice, is observed above T_N.
(© Wiley-VCH Verlag GmbH & Co. KGaA, 69451 Weinheim, Germany, 2005)

Introduction

The discovery of a colossal magnetoresistance effect in the hole-doped rare-earth manganites $R_{1-x}A_xMnO_3$ (A = alkaline-earth metal)[1,2] has triggered the investigation of related oxides which could also present similar phenomena, in particular complex oxides containing manganese ions in a mixed-valence state. The RMn_2O_5 (R = rare-earth metal, Y or Bi) family of oxides is appealing since it contains two different oxidation states for Mn, which are located at crystallographically distinct oxygen environments. According to the first crystallographic studies devoted to the RMn_2O_5 series in the 1960s, they present an orthorhombic crystallographic structure (*Pbam*),[3,4] which was confirmed by a recent high-resolution neutron powder diffraction study[5,6] for most of the compounds of the family. The two different sites for Mn − 4f and 4h − correspond to the Mn^{4+} and Mn^{3+} oxidation states, respectively. The Mn^{4+} ions are octahedrally coordinated by oxygen atoms, and the Mn^{3+} ions are bonded to five oxygen atoms in a distorted tetragonal pyramid. Along the *c* axis the crystallographic structure contains infinite chains of edge-sharing $Mn^{4+}O_6$ octahedra. The different chains are interconnected by dimer units of the $Mn^{3+}O_5$ pyramids. The R^{3+} cations form RO_8 units, which can be considered as bicapped trigonal prisms.

As regards the magnetic properties of the RMn_2O_5 oxides, initial reports[7,8] indicated an antiferromagnetic (AFM) behaviour below 40 K. In particular, for R = Nd, Tb, Ho, Er and Y the magnetic structure is characterized by the propagation vector **k** = (1/2,0,τ) and the Mn spins are ordered according to a helicoidal structure, with the magnetic moments lying in the *ab* plane. In some of these compounds a magnetic ordering is also observed for the rare-earth moments, but at a significantly lower temperature. It seems that the R^{3+} magnetic moments present a sinusoidal magnetic structure. A further study for the compounds with R = Er and Tb[9] indicated that the magnetic structure for the Mn ions is also sinusoidally modulated. Some compounds of the family, such as $DyMn_2O_5$, present a more complicated ordering;[10] its magnetic structure is defined by two propagation vectors, $\mathbf{k_1}$ = (1/2,0,0) and $\mathbf{k_2}$ = (1/2,0,τ). The magnetic structure of $EuMn_2O_5$ has also been analysed to a certain degree. Its magnetic structure is characterised by **k** = (1/2,0,τ); τ varies with the temperature and remains constant for $T < 6$ K on achieving the commensurable value τ = 1/3.[11] Unlike most of the RMn_2O_5 compounds, $BiMn_2O_5$ presents a commensurate magnetic structure,[12,13] defined by **k** = (1/2,0,1/2).

Dielectric and magnetoelectric studies[14,15] carried out on the RMn_2O_5 oxides indicate the presence of ferroelecticity in these compounds. Many studies have been performed

[a] Dpto. Física Aplicada, EPS, Universidad Carlos III
Avda. Universidad 30, 28911 Leganés-Madrid, Spain
Fax: +34-91-624-8749
E-mail: amunoz@fis.uc3m.es
[b] Instituto de Ciencia de Materiales de Madrid, CSIC
Cantoblanco, 28049 Madrid, Spain
[c] Institut Laue Langevin
B. P. 156X, 38042 Grenoble, France

in order to characterize the coexistence of ferroelectricity and magnetism, in particular the effect on the ferroelectric properties when a magnetic field is applied. Very recently,[16] in the multiferroic $TbMn_2O_5$ compound, a strong interplay between electrical polarization and the applied magnetic field has been reported, even for small fields. This striking behaviour implies a new possible device application consisting of magnetically recorded ferroelectric memory.

The preparation and crystal structure of $LaMn_2O_5$ has not been described until recently,[6] since its synthesis requires the use of high oxygen pressure. The aim of this paper is to report on the magnetic ordering and its thermal evolution from neutron diffraction measurements for this material, in conjunction with magnetic susceptibility measurements. A comparison with the magnetic structure of other compounds of the series is also established.

Results

Magnetic Measurements

The dc magnetic susceptibility curves recorded under zero-field-cooling (ZFC) and under field-cooling (FC) conditions are shown in Figure 1. Both curves present a similar behaviour above a T_N value of about 31 K; they diverge below this temperature [see inset (a) of Figure 1]. As will be shown for the neutron diffraction results, this temperature coincides with the establishment of the long-range magnetic ordering in $LaMn_2O_5$. The evolution of the FC susceptibility below T_N corresponds to the onset of an AFM ordering. Another important feature of the dc susceptibility curve is the presence of a very broad maximum at low temperature, which is centred at around 45 K (T_{SG}). A broad maximum is also observed in the real part of the ac susceptibility (see Figure 2). As is shown in inset (a) of Figure 2, the thermal evolution of the ac curve strongly depends on the frequency, which suggests a spin-glass-like behaviour at low temperature. It is well known that irreversibility in the spin-glass behaviour leads to a non-zero out-of-phase component, χ'' (imaginary part of the ac susceptibility). This can clearly be seen in inset (b) of Figure 2, which shows χ''. This confirms the spin-glass behaviour, and the presence of two peaks indicates that the freezing of the spin-glass state takes place in a complicated way.

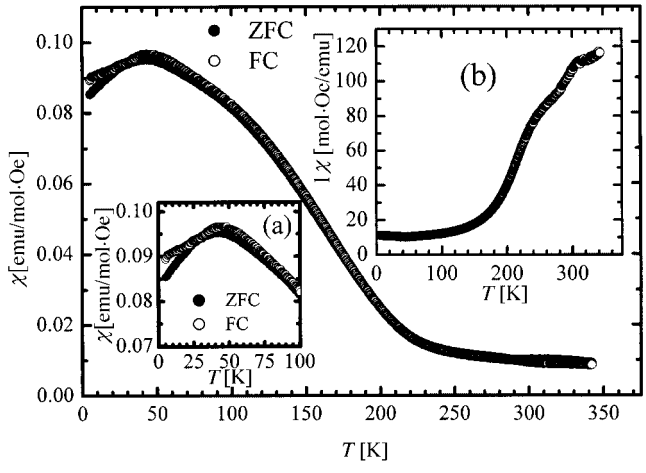

Figure 1. Thermal variation of the dc susceptibility under zero-field cooling (ZFC) and field-cooling (FC) conditions (H = 1 kOe); inset: (a) close-up of the low-temperature region; (b) plot of the reciprocal susceptibility (FC) versus temperature

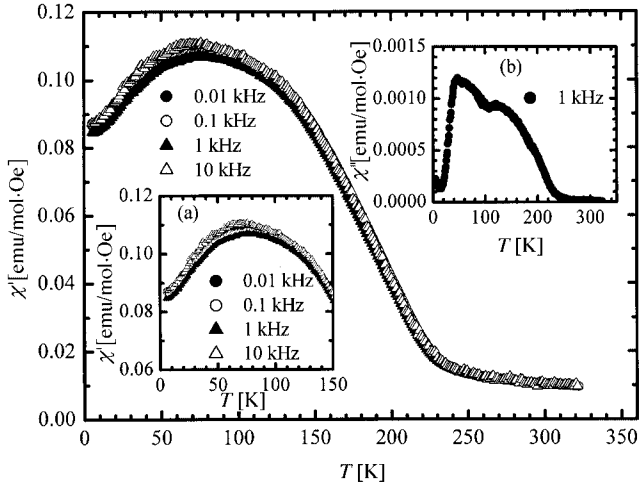

Figure 2. Real ac susceptibility curve; inset: (a) close-up of the low-temperature region; (b) imaginary component of the ac susceptibility

As regards the thermal variation of the dc susceptibility at high temperature, a linear behaviour in the reciprocal susceptibility is not observed below 300 K [inset (b) of Figure 1]. Applying the Curie–Weiss law in the temperature range 317–342 K gives a paramagnetic temperature, Θ_P, of –225 K and an effective magnetic moment of 6.25 μ_B. The effective magnetic moment is in good agreement with the theoretical value, determined as $\mu = [\mu^2(Mn^{3+}) + \mu^2(Mn^{4+})]^{1/2}$, of 6.24 μ_B, where the spin-only values of 4.90 and 3.87 μ_B are considered for the Mn^{3+} and Mn^{4+} ions, respectively. The magnetization curves displayed in Figure 3 show a negligible magnetization at low temperatures, discarding the presence of a weak ferromagnetism effect. We suggest that the change in the slope observed in the inverse of the susceptibility at around 275 K is due to crystal-field effects.

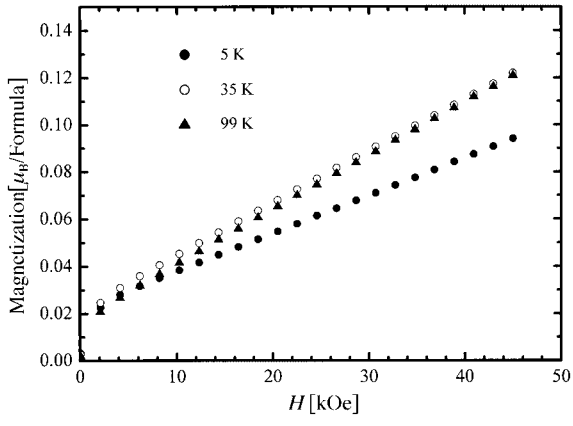

Figure 3. Isothermal magnetization curves at 5, 35 and 99 K

 © 2005 Wiley-VCH Verlag GmbH & Co. KGaA, Weinheim

Magnetic Structure from Neutron Diffraction Measurements

A set of neutron powder diffraction (NPD) patterns acquired in the temperature range 3.5–98.8 K, with λ = 2.40 Å, has been used to determine the magnetic structure and study its thermal evolution. For the high-temperature NPD patterns, all the Bragg reflections can be indexed in the orthorhombic *Pbam* space group. The lattice parameters at 98.8 K refined to a = 7.6121(8) Å, b = 8.6372(8) Å and c = 5.6691(6) Å. On decreasing the temperature to below 31 K new peaks appeared in the patterns, thus confirming the onset of a magnetic ordering with a T_N value of 31 K (see Figure 4). The new peaks can be indexed with the propagation vector **k** = (0,0,1/2), which implies a commensurable magnetic structure with a magnetic unit-cell that doubles the chemical one along the c direction. As can be seen in Figure 5, the intensity of the magnetic reflections increases monotonically below T_N and reaches saturation at low temperature, with no anomalies that could indicate a modification of the long-range spin arrangement. Therefore, the magnetic structure seems to remain stable down to 3.5 K.

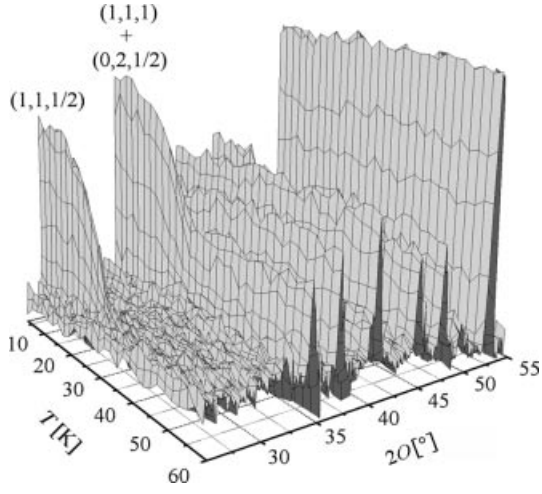

Figure 4. Thermal evolution of the NPD patterns for 3.5 < T < 60 K and 25° < 2θ < 55°

For the resolution of the magnetic structure, the solutions compatible with the symmetry of $LaMn_2O_5$ have been taken into consideration. The possible solutions were determined by a representation analysis of group theory technique described by Bertaut.[17] For **k** = (0,0,1/2), the irreducible representations of the G_k group are those given in Table 1, which have been taken from Kovalev's tables.[18] The basis vectors associated with each irreducible representation are reported in Table 2. The basis vectors define the different possible magnetic structures and were obtained by the projection operator technique. The notation for the Mn1 atoms located at the 4h site is 1(x,y,1/2), 2(–x,–y,1/2), 3(–x + 1/2,y + 1/2,1/2) and 4(x + 1/2,–y + 1/2,1/2). The Mn2 atoms of the 4f site are labelled as 5(1/2,0,z), 6(1/2,0,–z), 7(0,1/2,z) and 8(0,1/2,–z).

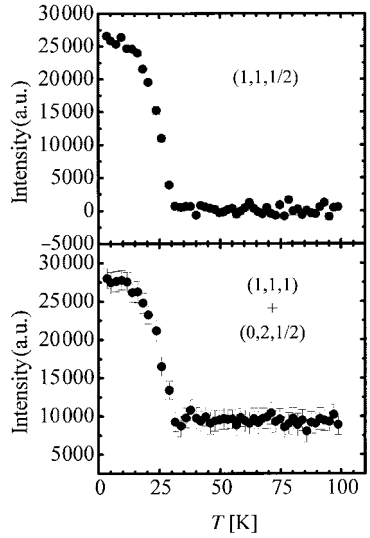

Figure 5. Thermal evolution of the magnetic reflections (1,1,1/2) and (0,2,1/2)

Table 1. Irreducible representations of the small group G_k for **k** = (0,0,1/2) following Kovalev's notation

	h_1	h_2/(**t**)	h_3/(**t**)	h_4	h_{25}	h_{26}/(**t**)	h_{27}/(**t**)	h_{28}
Γ_1	1	1	1	1	1	1	1	1
Γ_2	1	1	1	1	–1	–1	–1	–1
Γ_3	1	1	–1	–1	1	1	–1	–1
Γ_4	1	1	–1	–1	–1	–1	1	1
Γ_5	1	–1	1	–1	1	–1	1	–1
Γ_6	1	–1	1	–1	–1	1	–1	1
Γ_7	1	–1	–1	1	1	–1	–1	1
Γ_8	1	–1	–1	1	–1	1	1	–1

Table 2. Basis vectors for $LaMn_2O_5$

	Mn1 (4h)[a]	Mn2 (4f)[b]
Γ_1	(G_x,A_y,0)	(0,0,C'_z)
Γ_2	(0,0,F_z)	(0,0,G'_z)
Γ_3	(0,0,A_z)	(F'_x,C'_y,0)
Γ_4	(C_x,F_y,0)	(A'_x,G'_y,0)
Γ_5	(0,0,G_z)	(C'_x,F'_y,0)
Γ_6	(F_x,C_y,0)	(G'_x,A'_y,0)
Γ_7	(A_x,G_y,0)	(0,0,F'_z)
Γ_8	(0,0,C_z)	(0,0,A'_z)

[a] F = m1 + m2 + m3 + m4; C = m1 + m2 – m3 – m4; A = m1 – m2 – m3 + m4; G = m1 – m2 + m3 – m4. [b] F' = m5 + m6 + m7 + m8; C' = m5 + m6 – m7 – m8; A' = m5 – m6 – m7 + m8; G' = m5 – m6 + m7 – m8.

After checking the different solutions, the magnetic structure that shows the best agreement with the experimental data is defined by the basis vectors (G_x,A_y,0) for Mn1 atoms (site 4h) and (0,0,C'_z) for Mn2 atoms (site 4f). The calculated and observed NPD patterns for this solution at 3.5 K are compared in Figure 6. In the fitting, the atomic positions of $LaMn_2O_5$ are fixed to those given in Table 4 in the Exp. Sect. At 3.5 K, the magnetic moments are 2.59(4) and 1.61(7) μ_B for the Mn1 and Mn2 atoms, respectively (see Table 3). These values are significantly lower than those expected for the oxidation states Mn^{3+} at 4h sites (electronic

 © 2005 Wiley-VCH Verlag GmbH & Co. KGaA, Weinheim

configuration $t_{2g}^3e_g^1$, expected moment of 4 μ_B) and Mn^{4+} at 4f sites (electronic configuration t_{2g}^3, with 3 μ_B). This reduction could be due to covalency effects.

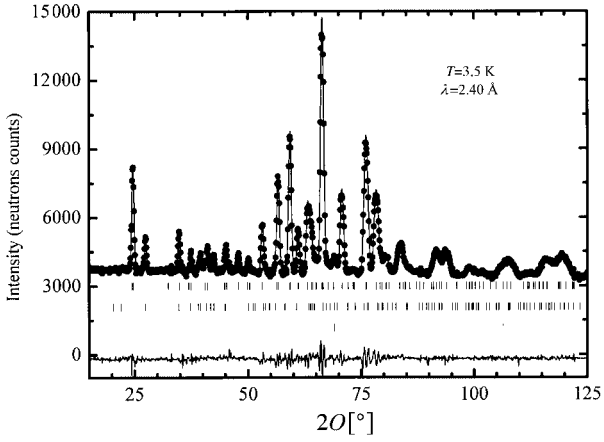

Figure 6. Observed (solid circles) and calculated (solid line) NPD patterns at 3.5 K; the first series of tick marks corresponds to the nuclear Bragg reflections of $LaMn_2O_5$, the second one to the magnetic reflections and the third one to the vanadium sample holder; the solid line at the bottom is the difference between the observed and calculated NPD patterns

The thermal evolution of the magnetic moments below T_N is displayed in Figure 7. On cooling, both the Mn1 and Mn2 ordered moments increase monotonically and reach saturation at low temperature. A view of the magnetic structure is presented in Figure 8. The magnetic moments of the Mn^{4+} ions are arranged along the *c* direction, whereas for the Mn^{3+} ions the moments are oriented in the *ab* plane. On the other hand, as displayed in Figure 8, the magnetic moments of the $z = z_0$ [$z_0 = 0.2610(8)$] and $z = -z_0$ layers, which are separated by a layer of La atoms, are ferromagnetically coupled. In contrast, the $z = z_0$ and $z = 1 - z_0$ layers, which are separated by a layer of Mn^{3+} ions, are antiferromagnetically coupled.

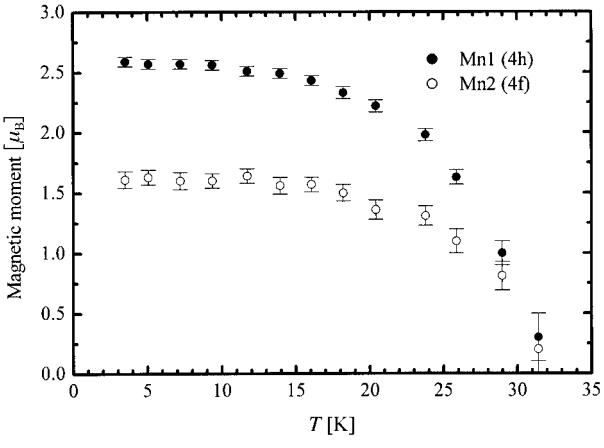

Figure 7. Thermal evolution of the magnetic moments for the Mn^{3+} (4h site) and Mn^{4+} (4f site) ions

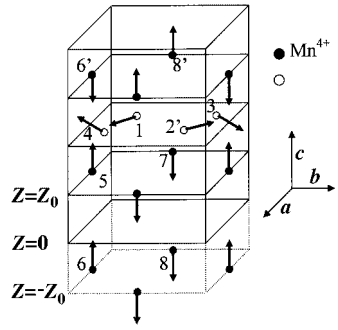

Figure 8. Schematic view of the magnetic structure; only the Mn atoms are represented; the primed atoms are related to the corresponding non-primed atoms by a lattice translation

Table 3. Results of the fitting of the NPD pattern at 3.5 K for the magnetic structure resolution

	Mn_1(4h)	Mn_2 (4f)
Solution	$(G_x,A_y,0)$	$(0,0,C'_z)$
Values (μ_B)	[2.28(4), –1.23(8),0]	[0,0,1.61(7)]
$\|m\|$ (μ_B)	2.59(4)	1.61(7)
Discrep. factors	R_B(Nuc.) = 2.4%; R_B(Magnet.) = 9.2%; χ^2 = 2.4	

The sequential refinement of the NPD patterns allowed us to determine the thermal evolution of the unit-cell parameters. The thermal variation of the *a* and *c* lattice parameters below 100 K is represented in Figure 9a. On decreasing the temperature below 100 K, the *c* lattice parameter decreases almost linearly and, below T_N, it remains virtually constant. Surprisingly, the *a* parameter increases with a sigmoidal shape when the temperature de-

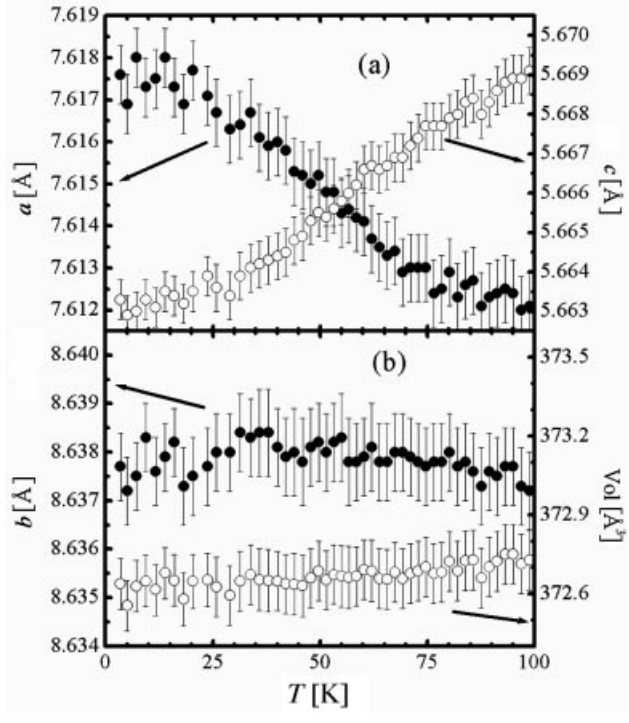

Figure 9. Thermal variation of the *a*, *b* and *c* lattice parameters and unit-cell volume

 © 2005 Wiley-VCH Verlag GmbH & Co. KGaA, Weinheim

creases. The *b* lattice parameter variation (Figure 9b) also shows a slight anomaly around T_N, which suggests a subtle magnetostrictive effect. The unit-cell volume, averaging the trends of *a* and *c* parameters, remains constant over the whole temperature range.

Discussion

The neutron diffraction measurements have shown that $LaMn_2O_5$ orders below 31 K with a magnetic structure characterized by the propagation vector **k** = (0,0,1/2) and defined by the basis vectors $(G_x,A_y,0)$ and $(0,0,C'_z)$ for the Mn^{4+} and Mn^{3+} ions, respectively. For a better understanding of the spin arrangement it is very useful to bear in mind a description of the crystallographic structure. It consists of chains of edge-sharing $Mn^{4+}O_6$ octahedra arranged along the *c* axis. Along the chain direction, the $Mn^{4+}O_6$ octahedra (Mn2) are interleaved either by a layer of La^{3+} ions or by a layer of Mn^{3+} ions (Mn1). This implies that, for a given $Mn^{4+}O_6$ octahedron, there are two closer $Mn^{4+}O_6$ octahedra, one at $d_1 = 2z_0$ (separated by La^{3+} ions) and one at $d_2 = 1 - 2z_0$ (separated by Mn^{3+} ions). For $LaMn_2O_5$ the Mn2–Mn2 distances are d_1 = 2.987 Å and d_2 = 2.735 Å (Table 4). The different chains are interconnected by $La^{3+}O_8$ and $Mn^{3+}O_5$ units; these latter polyhedra mediate the magnetic coupling between neighbouring $Mn^{4+}O_6$ chains. In fact, the $Mn^{3+}O_5$ units form dimers of two pyramids related by an inversion centre. For $LaMn_2O_5$, the distance between the two Mn^{3+} ions within the dimer is 2.894 Å. The chains of $Mn^{4+}O_6$ octahedra, separated by a lattice parameter along *a* or *b*, are connected by a dimer. On the other hand, every chain has four closer chains interconnected by a single $Mn^{3+}O_5$ pyramid. This arrangement is displayed in Figure 10.

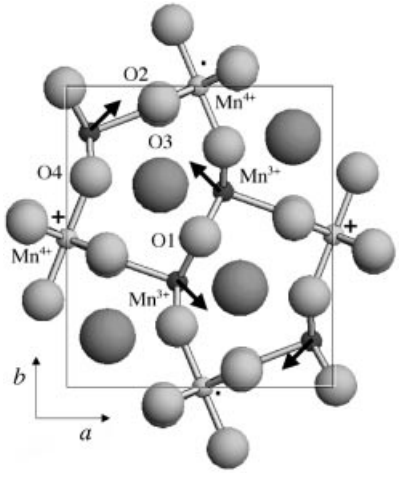

Figure 10. Projection of the crystallographic structure in the *ab* plane; the Mn^{3+} and Mn^{4+} ions are in the $z = 1/2$ and $z = 1 - z_0$ planes, respectively; the arrows indicate the direction of the Mn^{3+} magnetic moments in the *ab* plane; the + and – symbols indicate Mn^{4+} magnetic moments oriented parallel or antiparallel, respectively, to the direction of the *c* axis

In the magnetic structure, the magnetic moments of the Mn^{4+} ions are directed along *c* in the chains of $Mn^{4+}O_6$ octahedra (Figure 8). Within a single chain, the coupling between the Mn^{4+} ions of two adjacent octahedra separated by a La^{3+} layer is ferromagnetic, whereas those separated by a Mn^{3+} layer are antiferromagnetically coupled. Therefore, we have alternating FM and AFM couplings along the chains. To understand the observed magnetic arrangement, we must consider the following interactions: i) the superexchange interaction between the Mn^{4+} ions separated by an La^{3+} layer (with an Mn2–Mn2 distance, d_1, of 2.986 Å), across an Mn^{4+}–O2–Mn^{4+} path (with a bonding angle of 100.1°), assigned to the J_1 superexchange parameter; ii) the superexchange interaction between the Mn^{4+} ions separated by an Mn^{3+} layer, characterized by an Mn2–Mn2 distance, d_2, of 2.735 Å, across the superexchange path Mn^{4+}–O3–Mn^{4+} (bonding angle 93.3°), labelled J_2; and iii) the indirect superexchange interaction involving the $Mn^{3+}O_5$ units, across Mn^{4+}–O2–Mn^{3+}–O4–Mn^{4+} paths, characterized by J_3. If the indirect superexchange interaction is isotropic, J_3 would tend to couple the two Mn^{4+} ions placed at both sides of the Mn^{3+} layer ferromagnetically, as both these Mn^{4+} ions are symmetrically arranged with respect to the Mn^{3+} layer. The experimental results indicate that the coupling is AFM, which implies that J_2 must be negative and much greater than J_3. In the same way, J_1 must be positive, as the coupling between the Mn^{4+} ions separated by a La^{3+} layer is ferromagnetic. The presence of two superexchange interactions of different sign along *c* accounts for the propagation vector **k** = (0,0,1/2). Furthermore, it seems that a short Mn2–Mn2 distance along the chains favours an AFM interaction, whereas a long distance implies a ferromagnetic interaction. The J_1 and J_2 values depend on the distances d_1 and d_2, respectively. These distances are determined by the z_o position parameter for the Mn2 atoms (4f site). In the RMn_2O_5 series, on decreasing the R^{3+} ionic radius, d_1 tends to decrease; this changes makes possible the fulfilment of the condition $|J_1| < 4|J_2|$, which can give place to the incommensurate magnetic structure found in most of the RMn_2O_5 compounds ($k_z = \tau$).

On the other hand, every chain is antiferromagnetically coupled to four closer ones. In the dimers, the two Mn^{3+} ions are antiferromagnetically coupled and the magnetic moments are oriented in the *ab* plane in such a way that the moment direction is nearly perpendicular to the base of the pyramid. The path for the superexchange interaction between the Mn^{3+} ions of the dimer is Mn^{3+}–O1–Mn^{3+}, with a bonding angle of 97.5°. Taking into account the expected electronic configuration for Mn^{4+} and Mn^{3+} ions – t_{2g}^3 and $t_{2g}^3e_g^1$, respectively – the superexchange interaction across Mn^{4+}–O2–Mn^{4+} paths (along the chains) takes place via t_{2g}–t_{2g} orbitals, whereas for Mn^{3+}–O3–Mn^{3+} (within the dimers) it takes place via e_{2g}–e_{2g} orbitals. Given the directionality of the d orbitals, the latter superexchange interaction (via e_{2g}–e_{2g} orbitals) is, in general, stronger than that observed via t_{2g}–t_{2g} orbitals; this fact suggests that the coupling between Mn^{3+} moments within the dimers would take place at higher temperatures. We can consider a sce-

 © 2005 Wiley-VCH Verlag GmbH & Co. KGaA, Weinheim

nario consisting of the appearance of an AFM coupling in each dimer at temperatures well above T_N. This short-range ordering, with no coherence across the crystal, would be responsible for the spin-glass-type behaviour described above. On decreasing the temperature, the strengthening of the superexchange interactions between the Mn^{4+} ions (along the chains) and between Mn^{3+} and Mn^{4+} moments would give rise to the establishment of a long-range order below T_N.

It is worthwhile to compare the magnetic structure of $LaMn_2O_5$ with those of other members of the RMn_2O_5 family. For most RMn_2O_5 oxides the magnetic structure is defined by the propagation vector $\mathbf{k} = (1/2,0,\tau)$, except for $BiMn_2O_5$, where $\mathbf{k} = (1/2,0,1/2)$, and $DyMn_2O_5$, where $\mathbf{k_1} = (1/2,0,0)$ and $\mathbf{k_2} = (1/2,0,\tau)$. Thus, for all of them the magnetic structure propagates antiferromagnetically along the *a* direction, whereas for $LaMn_2O_5$, with $\mathbf{k} = (0,0,1/2)$, the propagation is ferromagnetic. As regards the orientation of the magnetic moments, in $LaMn_2O_5$ the moments of the Mn^{4+} ions are parallel to the *c* direction and for the rest of the compounds of the series the moments are in the *ab* plane. The magnetic anisotropy is mainly given by the symmetry of the ion environment, in this case by the symmetry of the $Mn^{4+}O_6$ octahedra. The Mn–O distances in the octahedra become more different as the R^{3+} ionic radius increases, so that the higher symmetry of the octahedra is found for $LaMn_2O_5$. The coupling of the magnetic moments of the Mn^{4+} ions along the *c* direction is also worth discussing. For RMn_2O_5 compounds with $\mathbf{k} = (1/2,0,\tau)$ two models[8] for the magnetic structure can be considered. In one of them, the coupling of the magnetic moments for the Mn^{4+} ions separated by an Mn^{3+} plane is ferromagnetic, and for those Mn^{4+} ions separated by an R^{3+} plane the magnetic moments form a certain angle, φ. In the second model, the coupling is simply the inverse. In fact, both $BiMn_2O_5$ and $LaMn_2O_5$ follow both models, but with $\varphi = 180°$ for $BiMn_2O_5$ (first model) the coupling of the magnetic moments for the Mn^{4+} ions separated by a R^{3+} plane is perfectly antiferromagnetic, whereas for $LaMn_2O_5$ the coupling is the opposite and follows the second model.

Conclusions

Both dc and ac magnetic susceptibility measurements show that $LaMn_2O_5$ undergoes an AFM ordering below 31 K (T_N), and also suggest a spin-glass-like behaviour above T_N. Neutron diffraction experiments allowed us to characterize the low-temperature magnetic arrangement: the magnetic structure is defined by the propagation vector $\mathbf{k} = (0,0,1/2)$, and the spin coupling is given by the basis vectors $(G_x,A_y,0)$ and $(0,0,C'_z)$ for the Mn^{4+} and Mn^{3+} spins, respectively. Within the chains of $Mn^{4+}O_6$ octahedra, the magnetic moments of the Mn^{4+} ions are directed along *c*; each Mn^{4+} moment displays an FM and an AFM coupling with neighbouring Mn^{4+} spins to account for the observed propagation vector. Adjacent chains are antiferromagnetically coupled. Within the dimer units of $Mn^{3+}O_5$ pyramids, the two Mn^{3+} spins also show an AFM coupling, with the magnetic moments lying in the *ab* plane. The magnitude of the two superexchange parameters defined along the chains, J_1 and J_2, is related to the two different distances between Mn2 atoms; the different sign and magnitude of J_1 and J_2 accounts for the commensurate character of the magnetic structure. We suggest that the two Mn^{3+} ions of each dimer unit are antiferromagnetically coupled above T_N, given the superior strength of the superexchange interactions through the e_{2g}–e_{2g} orbitals, which would cause a short-range magnetic order within the Mn^{3+} dimers, with no long-range coherence across the crystal. This effect would be responsible for the spin-glass-type behaviour observed in the magnetization measurements.

Experimental Section

$LaMn_2O_5$ was obtained as a dark-brown, polycrystalline powder starting from precursors previously synthesized by a wet-chemistry technique, followed by oxygenation at 1000 °C under 200 bar of oxygen pressure, as described elsewhere.[6] It is important to underline that the final treatment under high oxygen pressure is essential for the stabilization of monophase $LaMn_2O_5$. This material could not be obtained at ambient pressure starting either from citrate precursors or ceramic mixtures since the competitive, very stable $LaMnO_{3+\delta}$ perovskite was always present in the final product.

The magnetic measurements were performed in a PPMS (Quantum Design) system. The dc susceptibility curves were obtained under a 1 kOe magnetic field, under both zero-field cooling (ZFC) and field cooling (FC) conditions, for temperatures between 5.2 and 342.1 K. The ac susceptibility was measured in the temperature range 5–322 K under a small oscillating magnetic field of frequencies 0.01, 0.1, 1 and 10 kHz. Different isothermal magnetization curves were obtained at 5, 35 and 99 K in a magnetic field of between 0.05 and 45 kOe.

The study of the magnetic structure of $LaMn_2O_5$ was carried out from a set of neutron powder diffraction (NPD) patterns, collected at the high flux D20 diffractometer of the Institut Laue-Langevin in Grenoble (France). The patterns were dynamically acquired in the temperature range 3.5–98.8 K with a wavelength, λ, of 2.40 Å. The NPD data were analysed by the Rietveld method,[19] using the FULLPROF[20] program. The line-shape of the diffraction peaks was simulated by a Gaussian function and the background was fitted to a fifth-degree polynomial function. In the magnetic refinements, the atomic parameters were fixed to the values given in ref.[5], previously refined from high resolution NPD data, measured in the D2B diffractometer at the ILL-Grenoble on the same sample used in the present experiments. The atomic coordinates and main interatomic distances of $LaMn_2O_5$ taken from this reference are listed in Table 4.

Acknowledgments

We thank for financial support from the CICyT for the projects MAT2004-0479 and MAT2002-1329, and we are grateful to ILL for making all facilities available.

[1] R. M. Kusters, J. Singleton, D. A. Keen, R. McGreevy, W. Hayes, *Physica B* **1989**, *155*, 362.
[2] R. Von Helmolt, J. Wecker, B. Holzapfet, L. Schultz, K. Samwer, *Phys. Rev. Lett.* **1993**, *71*, 2331.

 © 2005 Wiley-VCH Verlag GmbH & Co. KGaA, Weinheim

Table 4. Structural parameters for $LaMn_2O_5$ at room temperature and some selected interatomic distances[a]

Atoms	Atomic coordinates			Interatomic distances [Å]			
	x	y	z	$Mn^{3+}O_5$		$Mn^{4+}O_6$	
R (4g)	0.1451	0.1736	0.0000	Mn1–O1	(×2) 1.925	Mn2–O2	(×2) 1.948
Mn1(4h)	0.4114	0.3533	0.5000	Mn1–O3	2.120	Mn2–O3	(×2) 1.881
Mn2 (4f)	0.0000	0.5000	0.2610	Mn1–O4	(×2) 1.904	Mn2–O4	(×2) 1.932
O1 (4e)	0.0000	0.0000	0.2781	<Mn1–O>	1.956	<Mn2–O>	1.921
O2 (4)	0.1525	0.4497	0.0000	Mn1–Mn1	2.894		
O3 (4h)	0.1525	0.4374	0.5000	Mn2–Mn2	2.735		
O4 (8i)	0.4068	0.2061	0.2540	Mn2–Mn2	2.986		

[a] a = 7.6823 Å; b = 8.7056 Å; c = 5.7214 Å.

[3] S. Quezel-Ambrunaz, E. F. Bertaut, G. Buisson, *C. R. Acad. Sci.* **1964**, *258*, 3025.
[4] E. F. Bertaut, G. Buisson, A. Durif, A. Mareschal, M. C. Montmory, S. Quezel-Ambrunaz, *Bull. Soc. Chim. Fr.* **1965**, 1132.
[5] J. A. Alonso, M. T. Casais, M. J. Martínez-Lope, J. L. Martínez, M. T. Fernández-Díaz, *J. Phys.: Condens. Matter* **1997**, *9*, 8515–8526.
[6] J. A. Alonso, M. T. Casais, M. J. Martínez-Lope, I. Rasines, *J. Solid State Chem.* **1997**, *129*, 105–112.
[7] G. Buisson, *Phys. Status Solidi A* **1973**, *16*, 533.
[8] G. Buisson, *Phys. Status Solidi A* **1973**, *17*, 191.
[9] P. P. Gardner, C. Wilkinson, J. B. Forsyth, B. M. Wanklyn, *J. Phys. C: Solid State Phys.* **1988**, *21*, 5653.
[10] C. Wilkinson, F. Sinclair, P. P. Gardner, J. B. Forsyth, B. M. Wanklyn, *J. Phys. C: Solid State Phys.* **1981**, *14*, 1671.
[11] V. Polyakov, V. Plakhty, M. Bonnet, P. Burlet, L. P. Regnault, S. Gavrilov, I. Zobkalo, O. Smirnov, *Physica B* **2001**, *297*, 208.
[12] E. F. Bertaut, G. Buisson, S. Quezel-Ambrunaz, G. Quezel, *Solid State Commun.* **1967**, *5*, 25.
[13] A. Muñoz, J. A. Alonso, M. T. Casais, M. J. Martínez-Lope, J. L. Martínez, M. T. Fernández-Díaz, *Phys. Rev. B* **2002**, 65, 144 423.
[14] H. Tsujino, H. Komada, H. Tanaka, K. Kohn, in *Proceedings of the 6th International Conference on Ferrites* (Tokyo and Kyoto, 1992) (Eds.: M. Abe, T. Yamaguchi), Japan Society of Powder and Powder Metallurgy, Tokyo, **1992**, p. 714.
[15] K. Saito, K. Kohn, *J. Phys.: Condens. Matter* **1995**, *7*, 2855–2863.
[16] N. Hur, S. Park, P. A. Sharma, J. S. Ahn, S. Guha, S.-W. Cheong, *Nature* **2004**, *429*, 392.
[17] E. F. Bertaut, in *Magnetism* (Eds.: G. T. Rado, H. Shul), Academic Press, New York, **1963**, vol. III, chapter 4.
[18] O. K. Kovalev, in *Representation of the Crystallographic Space Group* (Eds.: H. T. Stokes, D. M. Hatch), Gordon and Breach Publishers, New York, **1993**.
[19] H. M. Rietveld, *J. Appl. Crystallogr.* **1969**, *2*, 65.
[20] J. Rodríguez-Carvajal, *Physica B* **1993**, *192*, 55.

Received June 23, 2004

 © 2005 Wiley-VCH Verlag GmbH & Co. KGaA, Weinheim

Iron(II) Formate $[Fe(O_2CH)_2]\cdot 1/3HCO_2H$: A Mesoporous Magnet − Solvothermal Syntheses and Crystal Structures of the Isomorphous Framework Metal(II) Formates $[M(O_2CH)_2]\cdot n$(Solvent) (M = Fe, Co, Ni, Zn, Mg)

Martin Viertelhaus,[a] Peter Adler,[a] Rodolphe Clérac,[b] Christopher E. Anson,[a] and Annie K. Powell*[a]

Keywords: Iron / Solvothermal synthesis / Framework material / Magnetic properties / Mössbauer spectroscopy

Recrystallisation of iron(II) formate dihydrate from formic acid under solvothermal conditions results in single-crystals of the iron(II) formate, α-$Fe(O_2CH)_2\cdot 1/3HCO_2H$. The crystal structure of this phase has been determined by X-ray diffraction and reveals an open framework structure with formic acid molecules occupying channels in the lattice which is stable even after removal of the solvent molecules. Magnetic susceptibility and Mössbauer measurements show that the compound undergoes 3D magnetic ordering below $T_C = 16$ K. α-$Fe(O_2CH)_2\cdot 1/3HCO_2H$ and the corresponding magnesium, cobalt, nickel and zinc formates form an isomorphous series. In contrast to the iron compound, the magnetic behaviour of the cobalt analogue is dominated by antiferromagnetic interactions.

(© Wiley-VCH Verlag GmbH & Co. KGaA, 69451 Weinheim, Germany, 2005)

Introduction

The versatility of carboxylate anions as units for ligating and connecting metal centres has led to extensive research on the structures and properties of carboxylato complexes. Among the many fascinating examples in the literature are molecular entities such as the well-known oxo-centred trinuclear complexes,[1] the "Single Molecule Magnet" $[Mn_{12}O_{12}(O_2CCH_3)_{16}(OH_2)_4]\cdot 4H_2O\cdot 2CH_3CO_2H$ and related clusters[2,3] as well as extended systems, often produced using solvothermal synthesis, where the presence or absence of template molecules leads to open framework structures such as $Mn_4(PO_4)_2(C_2O_4)(H_2O)_2$[4] or very densely packed materials such as β-$Mn(O_2CMe)_2$.[5] Of particular current interest is the possibility of synthesising dual functionality materials where, for example, a mesoporous structure could also display a second useful physical property, such as cooperative magnetic behaviour.[6] These could be used to isolate and store paramagnetic molecules including gases such as dioxygen. Of the compounds which have so far been shown to display magnetic ordering and a microporous structure,[6b−6g] only $Co_3[Co(CN)_5]_2$,[6a] has displayed hysteresis and can be described as a ferrimagnet with $T_N = 38$ K. It has a defect Prussian Blue structure on the basis of its X-ray powder pattern.

We have been exploring the crystal structures and properties of compounds with the formate anion as a carboxylate linking unit, produced using solvothermal conditions.[7] Although the formate anion is the simplest carboxylate, most compounds described in the literature which have been structurally characterised using single-crystal X-ray diffraction have been synthesised using acetates and higher homologues. For most transition metal(II) formates, only single-crystal structure determinations for the dihydrates have been reported. The divalent 3*d*-transition metals, together with magnesium and cadmium, form an isomorphous series of metal(II) formate dihydrates.[8] Single-crystal structures of anhydrous diformates of these metals have only been determined for copper,[9] cadmium[10] and manganese.[11] This lack of knowledge concerning the structures of anhydrous transition metal(II) formates is comparable with that for the corresponding anhydrous nitrates or acetates[11] and is in contrast to the extensive research on the properties of such materials characterised only by X-ray powder diffraction (Mg,[12] Mn,[13] Fe,[14] Co,[15] Ni,[16] Zn[17]) and IR spectroscopy.[18] The kinetics and thermodynamics of the dehydration reactions of the dihydrates and the rehydration of the anhydrous products of dehydration[19] have been studied as well as the use of the dihydrates as precursors for dehydrogenation catalysts.[20] As far as the anhydrous metal(II) formates, $M(O_2CH)_2$, are concerned the Cu^{II} and Cd^{II} examples were synthesised at temperatures around 60−80 °C by slow evaporation of the solvent consisting of a mixture of water and formic acid. Single-crystals of other anhydrous

[a] Institut für Anorganische Chemie, Universität Karlsruhe, Engesser Str. 15, Geb. 30.45, 76128 Karlsruhe, Germany
Fax: (internat.) + 49-721-608-8142
E-mail: powell@chemie.uni-karlsruhe.de
[b] Centre de Recherche Paul Pascal, CNRS UPR-8641, 115 Avenue Dr. A. Schweitzer, 33600 Pessac, France
Supporting information for this article is available on the WWW under http://www.eurjic.org or from the author.

 © 2005 Wiley-VCH Verlag GmbH & Co. KGaA, Weinheim DOI: 10.1002/ejic.200400395

formates are not available using this synthetic route, although Vassileva and Karapetkova were able to isolate anhydrous formates of manganese, iron and zinc under ambient conditions as microcrystalline solids.[21]

We recently described the single-crystal X-ray structure of the new anhydrous formate $[Mn(O_2CH)_2]$ which can be prepared either using modified solvothermal conditions or by an unusual topotactic solid-state dehydration of the corresponding dihydrate.[11] As part of our survey of metal(II) formates we also found an isomorphous series of mesoporous framework compounds of general formula $M(O_2CH)_2\cdot 1/3HCO_2H$ for M = Fe, Co, Ni, Zn and Mg,[7] the synthesis, structures and properties of which we report here with particular reference to the Fe^{II} compound and its magnetic behaviour. Whilst we were investigating these magnetic properties, the structures of $Mn(O_2CH)_2\cdot 1/3C_4H_8O_2$ and $Mn(O_2CH)_2\cdot 1/3CH_3OH\cdot 1/3H_2O$ were reported both of which are isomorphous compounds with the same metal-formate framework we have observed.[22]

Results and Discussion

Syntheses

Recrystallisation of iron(II) formate dihydrate, $Fe(O_2CH)_2\cdot 2H_2O$, from formic acid under solvothermal conditions yields transparent green crystals of α-$Fe(O_2CH)_2\cdot 1/3HCO_2H$, suitable for X-ray diffraction (Scheme 1). The crystal structure was determined at 200 K and crystallographic details are summarised in Table 1. The same product, with a higher degree of purity but in a microcrystalline form, can be obtained in quantitative yield using milder conditions. Vassileva and Karapetkova had already observed this anhydrous iron(II) formate phase in the ternary system $Fe(O_2CH)_2-H_2O-HCO_2H$ at 25 °C with concentrations of formic acid higher than 83%.[21] The powder diffraction pattern of this product was different from the powder pattern of the product from direct dehydration of $Fe(O_2CH)_2\cdot 2H_2O$.[23] Vassileva and Karapetkova called their product anhydrous iron formate. As will be shown below, they had not prepared a pure formate free of solvent but, rather, an open framework structure with formic acid molecules occupying channels in the lattice. Since it is possible to desolvate the crystals, we refer to the synthesised or primary product $Fe(O_2CH)_2\cdot 1/3HCO_2H$ as α-FeFA·$1/3HCO_2H$. The stable crystalline network structure with-

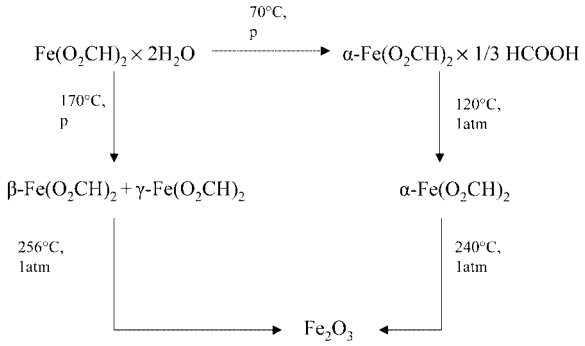

Scheme 1. Products and derivatives of mild solvothermal recrystallisation of iron(II) formate dihydrate; p = autogenous pressure of formic acid under solvothermal conditions; further heating of the amorphous Fe_2O_3 leads to haematite (α-Fe_2O_3)

Table 1. Crystal data and details of structural refinements

	α-FeFA·$1/3HCO_2H$	α-CoFA·$1/3HCO_2H\cdot 1/3(H_2O)$	α-ZnFA·$1/3HCO_2H$
Formula	$C_{2.33}H_{2.67}FeO_{4.67}$	$C_{2.33}H_{3.33}CoO_5$	$C_{2.33}H_{2.67}O_{4.67}Zn$
Molecular mass	161.23	170.31	170.75
Crystal system	monoclinic	monoclinic	monoclinic
Space group	$P2_1/n$ (no. 14)	$P2_1/n$ (no. 14)	$P2_1/n$ (no. 14)
Temperature [K]	200(2)	200(2)	200(2)
a (Å)	11.4446(10)	11.2727(9)	11.3407(9)
b (Å)	9.9304(9)	9.8335(6)	9.7856(8)
c (Å)	14.6192(15)	14.4249(12)	14.4334(13)
β (°)	91.423(11)	91.242(7)	91.449(10)
Volume (Å^3)	1661.0(3)	1598.6(2)	1601.2(2)
Z	12	12	12
D_c [g cm^{-3}]	1.934	2.106	2.125
μ [Mo-K_α] [mm^{-1}]	2.652	3.154	4.527
Crystal dimensions (mm)	0.20 × 0.20 × 0.05	0.10 × 0.10 × 0.05	0.50 × 0.40 × 0.20
Crystal shape	green plate	pink plate	colourless block
$2\theta_{max}$	52.3°	54.2°	52.4°
Reflections measured	8198	10340	10183
Independent reflections	3179	3367	3151
R_{int}	0.0889	0.0315	0.0340
Reflections with [$I > 2\sigma(I)$]	2428	3137	2899
wR_2 (all data)	0.1692	0.1412	0.1168
Goodness of fit S	0.984	1.053	1.001
R_1 [$I > 2\sigma(I)$]	0.0602	0.0497	0.0411
Parameters/restraints	235/10	245/9	257/7
Max. diff. peak/hole [e·Å^{-3}]	+1.23/−0.89	+1.12/−1.27	+0.82/−1.05

 © 2005 Wiley-VCH Verlag GmbH & Co. KGaA, Weinheim

Table 2. Unit cell parameters for the isomorphous series of formates (the compounds crystallise in space group $P2_1/n$, no.14)

Compound	ref.	a (Å)	b (Å)	c (Å)	β (°)	V (Å^3)	T (K)
α-MgFA·1/3(HCO_2H)	[a]	11.350(8)	9.876(4)	14.541(12)	91.51(5)	1629(2)	300
α-MnFA·1/3dioxane	[22a]	11.715(2)	10.248(2)	15.159(3)	91.81(2)	1819.0(7)	223
α-MnFA	[22a]	11.720(1)	10.207(1)	14.956(2)	91.44(1)	1788.6(3)	223
α-MnFA·1/3CH_3OH·1/3H_2O[b]	[22b]	11.650(1)	10.128(1)	14.861(2)	91.670(3)	1752.6(3)	180
α-FeFA·1/3HCO_2H	[a]	11.4446(10)	9.9304(9)	14.6192(15)	91.423(11)	1661.0(3)	200
α-CoFA·1/3HCO_2H·1/3H_2O	[a]	11.2727(9)	9.8335(6)	14.4249(12)	91.242(7)	1598.6(2)	200
α-NiFA·$x$$HCO_2H$·$y$$H_2O$	[a]	11.1586(6)	9.7789(4)	14.3333(8)	91.447(4)	1563.53(10)	300
α-ZnFA·1/3HCO_2H·1/3H_2O	[a]	11.3407(9)	9.7856(8)	14.4334(13)	91.449(10)	1601.2(2)	200

[a] This work. [b] This structure was published in the alternative space group setting $P2_1/c$. The appropriately transformed cell is given in the above table for consistency with the other structures.

out solvate molecules is thus α-FeFA. In the course of our work, we have also characterised two further anhydrous and solvent-free iron(II) formates, namely β- and γ-FeFA (see Scheme 1) which will be published separately.[24] The three different compounds thus necessitate use of the prefixes α, β and γ.

Similar synthetic methods were used to obtain α-MFA·1/3HCO_2H (M = Zn, Mg) and α-CoFA·1/3HCO_2H·1/3H_2O. Although the magnesium compound could only be obtained as a microcrystalline material, the solvent molecules could be identified from the IR spectrum. The nickel analogue could also be prepared but was highly unstable when removed from the mother liquor. The unit cell could be determined from a sample prepared in situ in a glass capillary, demonstrating that the nickel complex is indeed isomorphous with the other compounds but the precise solvent content of the crystals of the nickel formate remains uncertain. For convenience, the unit cell parameters for all the compounds reported here, as well as the recently reported Mn^{II} complexes,[22] are listed in Table 2.

Framework Structure

α-Fe(O_2CH)$_2$·1/3HCO_2H crystallises in the monoclinic space group $P2_1/n$ with $Z = 12$. Selected geometrical parameters are listed in Table 3. The structure of the isomorphous Mn^{II} analogue has been discussed[22] with reference to its open framework structure, where it was described as a diamondoid network of metal centres, although the channels only run through the network in one direction, rather than in the four directions implied by this description. Since we were particularly interested in investigating the magnetic behaviour of the system, which turned out to be fairly complicated, our structural description concentrates on the metal ion coordination spheres and the chemical links between the metal centres which could mediate possible magnetic interactions.

The asymmetric unit of α-FeFA·1/3HCO_2H contains four independent iron centres with Fe(1) and Fe(2) on general positions, and Fe(3) and Fe(4) representing inversion centres. All four have distorted octahedral coordination spheres of oxygen atoms from formate ions with angles in the ranges 78.00−97.34° and 164.19−180° (Table 3). Each of the six independent formate ligands forms a μ_3-(*syn,syn-anti*) carboxylate bridge between three Fe centres and for convenience the numbering is such that the odd-numbered oxygen forms the (μ_2-η^1) bridge, while the even-numbered oxygen is monodentate. The Fe−O bond lengths (Table 3) are, on average, slightly longer for the bridging oxygen atoms being in the range 2.080(4)−2.174(4) Å (mean value 2.142 Å), whereas those involving a monodentate oxygen lie in the range 2.072(4)−2.154(4) Å (mean 2.098 Å).

The framework structure is generated firstly from chains of Fe(1) and Fe(2) running along the 2_1-screw axes {Fe(1)−Fe(2)−Fe(1a)−Fe(2a)...} (Figure 1). Within the chains, pairs of iron atoms are linked by one *syn*,*syn*-for-

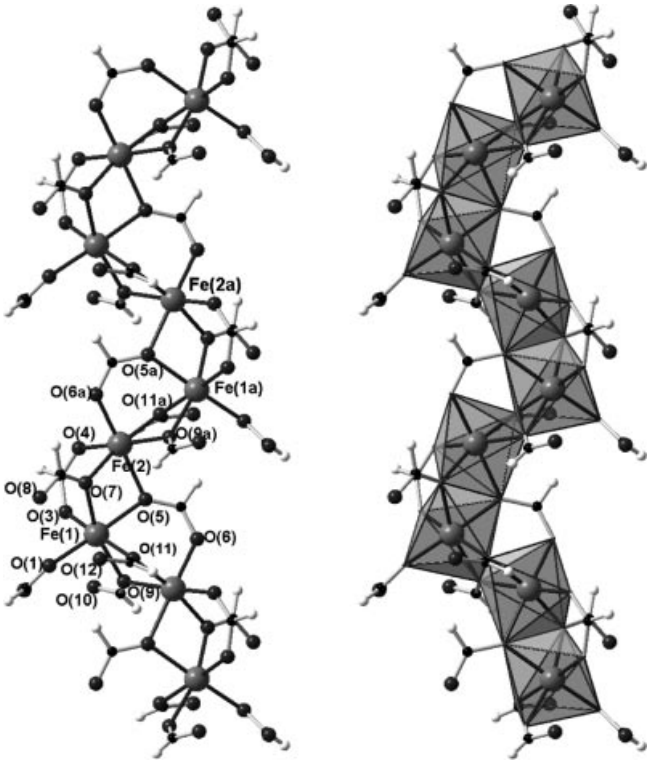

Figure 1. The serpentine chain made up of Fe(1) and Fe(2) running along the 2_1-screw axis parallel to the crystal b-axis and projected onto the {1 0 0} plane showing the formate bridges between adjacent iron centres and the edge-sharing octahedral coordination polyhedra of the iron centres; symmetry code: $a = -x + 1/2$, $y - 1/2$, $-z + 1/2$; Fe − large mid-grey circles, O − dark grey circles; C − small black circles; H − very small white circles

 © 2005 Wiley-VCH Verlag GmbH & Co. KGaA, Weinheim

Table 3. M−O distances, M−O−M angles and M···M separations

Distances (Å) and angles (°)	α-FeFA·1/3HCO_2H	α-CoFA·1/3HCO_2H·1/3H_2O	α-ZnFA·1/3HCO_2H
M(1)−O(1)	2.080(4)	2.048(3)	2.040(2)
M(1)−O(3)	2.108(4)	2.071(3)	2.070(2)
M(1)−O(5)	2.134(4)	2.091(3)	2.109(2)
M(1)−O(7)	2.155(4)	2.116(3)	2.116(2)
M(1)−O(9)	2.159(4)	2.116(3)	2.115(2)
M(1)−O(11)	2.124(4)	2.086(3)	2.111(2)
M(2)−O(4)	2.069(4)	2.042(3)	2.033(2)
M(2)−O(5)	2.145(4)	2.108(3)	2.138(2)
M(2)−O(6^{i})	2.072(4)	2.051(3)	2.023(3)
M(2)−O(7)	2.145(4)	2.106(3)	2.092(2)
M(2)−O(9^{i})	2.154(4)	2.122(3)	2.164(2)
M(2)−O(11^{i})	2.120(4)	2.051(3)	2.083(2)
M(3)−O(1)	2.175(4)	2.123(3)	2.127(2)
M(3)−O(8)	2.082(4)	2.058(3)	2.066(3)
M(3)−O(12)	2.120(5)	2.098(3)	2.090(3)
M(4)−O(2)	2.104(5)	2.078(3)	2.072(3)
M(4)−O(3)	2.160(4)	2.114(3)	2.118(2)
M(4)−O(10)	2.115(5)	2.078(3)	2.077(3)
Mean M−O(μ_1)	2.098	2.072	2.067
Mean M−O(μ_2)	2.142	2.099	2.108
M(1)−O(1)−M(3)	113.53(17)	114.79(12)	115.50(11)
M(1)−O(3)−M(4)	111.84(17)	112.72(13)	112.27(11)
M(1)−O(5)−M(2)	96.71(16)	97.37(10)	96.49(9)
M(1)−O(7)−M(2)	96.09(16)	96.69(10)	97.65(10)
M(1)−O(9)−M(2^{ii})	97.28(16)	97.32(11)	97.52(9)
M(1)−O(11)−M(2^{ii})	99.42(17)	99.70(11)	100.19(10)
M(1)···M(2)	3.1973(10)	3.1539(7)	3.1680(6)
M(1)···M(2^{ii})	3.2367(11)	3.1874(7)	3.2172(5)
M(1)···M(4)	3.5346(9)	3.4840(5)	3.4772(5)
M(1)···M(3)	3.5592(9)	3.5137(5)	3.5244(5)
M(2)···M(2^{ii})	5.2958(7)	5.2311(4)	5.2362(5)
M(3)···M(2^{ii})	5.3758(10)	5.3008(6)	5.3269(7)
M(2)···M(4)	5.5364(8)	5.4598(6)	5.4700(5)
M(2)···M(3)	5.5847(9)	5.5159(6)	5.5161(5)
M(4)···M(2^{ii})	5.6136(10)	5.5205(7)	5.5638(7)
M(3)···M(4)	5.7223(5)	5.6363(5)	5.6704(5)
Symmetry equivalents:	i: $-x + 1/2, y + 1/2, -z + 1/2$ ii: $-x + 1/2, y - 1/2, -z + 1/2$		

mate bridge with O(5) and O(7) joining Fe(1) and Fe(2), and two μ-bridging oxygen atoms with O(9) and O(11) joining Fe(1) and Fe(2a). The coordination polyhedra of Fe(1) and Fe(2) can thus be described as edge-sharing octahedra, with the shared edges defined by these four oxygens (Figure 1). This leads to two alternating crystallographically distinct, although geometrically rather similar Fe···Fe linkages. Of particular interest in terms of the magnetic behaviour is that the Fe−O−Fe angles at O(5), O(7), O(9) and O(11) all lie in the range 96.08−99.42° (Table 3) and might therefore be expected to mediate rather similar magnetic interactions (vide infra).

The chains are cross-linked via further Fe^{II} centres, namely Fe(3) and Fe(4) in the *ac*-plane (Figure 2 and Figure 3). The linkages from Fe(1) to either Fe(3) or Fe(4) both involve a single μ-oxygen bridge [O(1) and O(3), respectively] and two *syn*,*syn*-formate bridges. In contrast, Fe(2) is only linked to Fe(3) and Fe(4) through single *syn*,*anti*-formate bridges. The Fe−O−Fe angles at the bridging oxygens O(1) and O(3) are similar and significantly larger than those forming the bridges within the chains at 111.84° and 113.54°, respectively, and could thus mediate magnetic interactions similar to each other but significantly different from the intrachain linkages.

 © 2005 Wiley-VCH Verlag GmbH & Co. KGaA, Weinheim

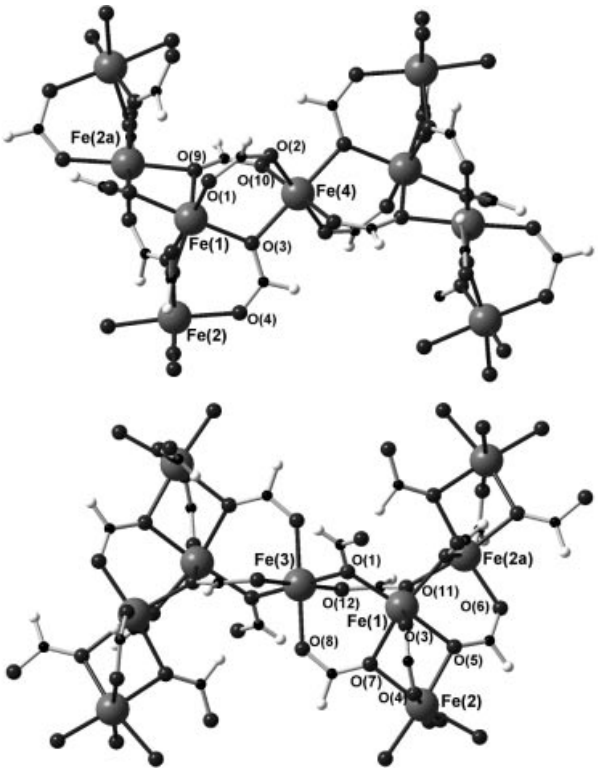

Figure 2. The interchain linkages through Fe(4) (upper) and through Fe(3) (lower); atom key and symmetry code as in Figure 1

Of further interest in terms of the magnetic behaviour is the presence of any distortion in the coordination spheres of the Fe^{II} centres which can affect the zero-field splitting and ground state term. Fe(3) and Fe(4) each show slight tetragonal elongations along one axis, with Fe−O distances of 2.175(4) and 2.159(4) Å, respectively, compared with the shorter distances in the range 2.082(4) −2.120(4) Å. However, Fe(1) and Fe(2) show no such pattern and indeed for Fe(2) the longest Fe−O distance is *trans* to the shortest.

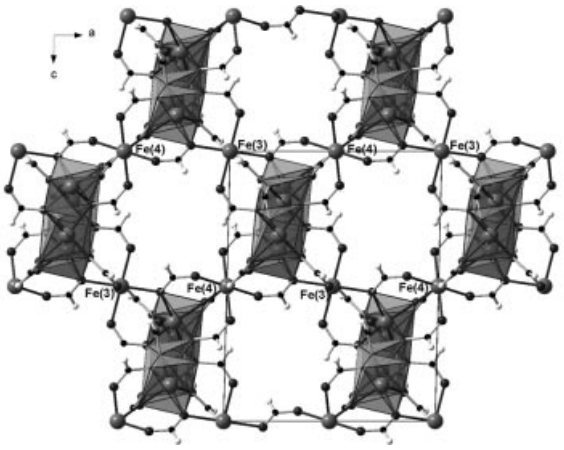

Figure 3. The structure of α-FeFA·1/3HCO_2H viewed along the *b*-direction showing its channel structure; Fe(1) and Fe(2), which form the chains bridged by pairs of μ-oxygen bridges, are shown as coordination polyhedra; Fe(3) and Fe(4) and their symmetry-equivalents, which form linkages between the chains, are shown as conventional atoms; formic acid molecules inside the channels are omitted for clarity

Mesoporous Behaviour

An examination of the stabilised open framework structure of α-FeFA·1/3HCO_2H using PLATON[25] showed that the accessible volume of the channels amounts to 505 $Å^3$ per unit cell, or 30.5% of the unit cell volume which is in good agreement with the values for the manganese compounds.[22] It has been shown that the manganese-based-framework can accommodate a wide variety of guest molecules. The channels in the synthesised iron compound contain formic acid molecules. In the structure, these solvent molecules are twofold disordered with the overlapping half-molecules occupying one general position. This results in one third of a formic acid molecule per iron atom in the formula, i.e. α-FeFA·1/3HCO_2H. The presence of formic acid in the lattice was confirmed by the IR spectrum (Table 4). In addition to the expected bands from the for-

Table 4. IR absorptions (KBr, cm^{-1}) for the complexes presented in this work (s strong, w weak, sh shoulder, vw very weak, br broad, m medium, n.o. not observed)

Vibration[42]	α-FeFA·1/3HCO_2H	α-CoFA·1/3HCO_2H·1/3H_2O	α-ZnFA·1/3HCO_2H	α-MgFA·1/3HCO_2H
ν(OH), HCO_2H	3432 mw, br	3347 m	3434 m, br	3466 mw, br
ν(OH), H_2O	−	3300 s, 3221 m	−	−
νCH	2925 m, 2888 m	2929 m, 2902 m	2926 m	2932 m
ν(C=O), HCO_2H	1742 mw,	1724 mw, 1665 sh	1728 mw	1731 m
νCO, asym.	1646 s, 1610 vs, 1586 vs	1644 sh, 1582 vs	1650 sh, 1600 sh, 1581 vs	1670 ms, 1642 vs, 1607 vs
δ(OCO)	1400 m, 1389 m	1397 s, 1378 s	1397 m, 1369 sh	1416 m, 1407 mw
νCO, sym.	1331 s	1357 s, 1328 m	1352 s, 1325 s	1340 s
ν(C−O), HCO_2H	1163 vw, 1144 w	1191 vw	1188 w	1188 w
γ(CH)	1066 vw	n.o.	n.o.	1076 vw
δ(OCO), sym.	781 m	788 m, 766 m	787 m	791 m

 © 2005 Wiley-VCH Verlag GmbH & Co. KGaA, Weinheim

mate ligands, a single band at 3430 cm^{-1}, a stronger band at 1742 cm^{-1} and a pair of bands at 1163 and 1144 cm^{-1} can be assigned to free formic acid molecules.[26] There was no evidence in the spectrum for the presence of water molecules. The stoichiometry of the formic acid can be verified by STA-experiments on a briefly-dried sample from the solvothermal synthesis. The sample loses mass in several unresolved processes between room temperature and 160 °C. The overall mass loss for these steps is 9.2% which is in good agreement with the theoretical mass loss of 9.5% for $1/3HCO_2H$ per iron atom to give α-FeFA. Between 160 and 270 °C, α-FeFA decomposes exothermally to amorphous Fe_2O_3 with a further mass loss of 39.7% (calcd. 40.9%).

Pure desolvated α-FeFA can be obtained by heating the powder α-FeFA·$1/3HCO_2H$ to 120 °C for several hours. The desolvation can be monitored by X-ray powder diffraction. For example, on heating the sample, the 002 reflection increases in intensity, whereas the $\bar{1}11$, 200 and 112 reflections decrease (Figure 4). To further verify this, the powder pattern calculated from the crystal structure of α-FeFA·$1/3HCO_2H$ was compared with the pattern calculated from the same structure with the atoms of the formic acid molecule removed. As can be seen in Figure 4, these patterns show the same trends as the experimentally measured patterns and that calculated from the structure with the formic acid atoms deleted is essentially identical to the final experimental powder pattern in which all peaks could be indexed. The structural framework is thus not merely stable to removal of the solvent but also maintains its structure with minimal changes in geometry. In contrast, if a sample of α-FeFA·$1/3HCO_2H$ is kept in vacuo for several days, no significant change in the powder diffraction pattern can be observed, indicating that heating is necessary to remove the formic acid solvent molecules.

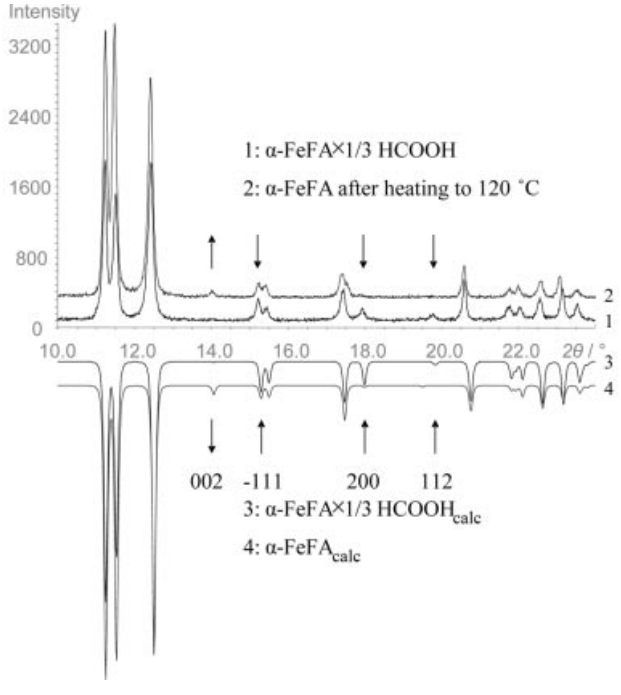

Figure 4. X-ray powder diffraction with Co-$K\alpha_1$ radiation shows the stability of the channel structure of α-FeFA on removal of the solvent molecules; significant changes in intensities on heating are marked with arrows; for comparison the calculated patterns are shown

The IR spectra of the magnesium and zinc formates show no evidence for the presence of water molecules in the lattices. STA results for the zinc and magnesium compounds indicate mass losses of 9.1 and 9.7%, respectively, in agreement with the theoretical value for loss of $1/3HCO_2H$ per metal atom (9.0 and 10.7%, respectively). We have therefore formulated both these compounds analogously to the iron formate, i.e. as α-MFA·$1/3HCO_2H$ (M = Zn, Mg). In contrast, the IR spectra of the cobalt analogue show, in addition to bands from the bridging formate ligands and formic acid solvent molecules as found for the other three complexes, two additional bands in the 3300−3200 cm^{-1} region which indicate that water molecules are present in the channels in addition to formic acid. The expected band at ca. 1630 cm^{-1} for the deformation mode of water is obscured by the very strong formate bands. The additional presence of water in the solvent lattice was confirmed by the STA results. The mass loss on heating to 140 °C is significantly higher than for the iron complex with a mean value of 13.2% which can be compared with the calculated mass losses per Co atom of 9.1% for $1/3HCO_2H$ and 12.5% for $1/3HCO_2H + 1/3H_2O$. In the crystal structure, the solvent could readily be refined as a slightly disordered formic acid molecule and a water molecule disordered between two adjacent sites. We have thus formulated the cobalt formate as α-CoFA·$1/3HCO_2H\cdot 1/3H_2O$ and note the similar formulation of MnFA·$1/3CH_3OH\cdot 1/3H_2O$ found for the compound described in ref.[22b]

Magnetic Properties

The χT product of α-FeFA·$1/3HCO_2H$ shown in Figure 5 continuously increases from 4.72 emu K mol^{-1} at 300 K up to a value of 28 emu K mol^{-1} at 20 K. Above this temperature the paramagnetic behaviour can be satisfactorily reproduced by a Curie−Weiss law with a Curie constant of 4.5 emu K mol^{-1}, corresponding to an average g value of 2.45, in agreement with typical values for high spin Fe^{II} metal ions in a distorted octahedral geometry.[27] The positive

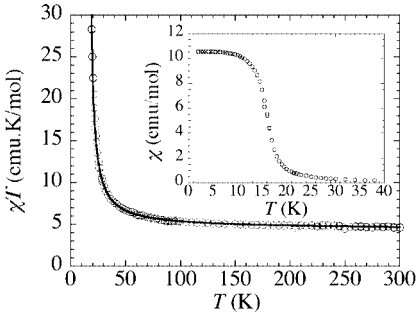

Figure 5. Temperature dependence of the χT product ($\chi = M/H$ per Fe^{II}) at 1000 Oe for α-FeFA·$1/3HCO_2H$; the solid line corresponds to the best fit obtained with the Curie−Weiss law with C = 4.5 emu K/mol, θ = +16 K and χ_{dia} = −3.5 10^{-4} emu/mol

 © 2005 Wiley-VCH Verlag GmbH & Co. KGaA, Weinheim

Weiss constant of +16 K is indicative of dominant ferromagnetic interactions within the framework. Below 20 K, the susceptibility, χ, increases dramatically and reaches a saturation value of 10.6 emu mol^{-1} at around 5 K. This behaviour is typically associated with the onset of spontaneous magnetisation and therefore with the stabilisation of magnetic 3D order. Heat capacity measurements made on a pressed pellet of α-FeFA·1/3HCO_2H confirmed the magnetic transition observed (Figure S1). A lambda peak indicative of a second order phase transition was obtained at 16 K.

In order to obtain more insight into the low temperature magnetic phase, the field dependence of the magnetisation was investigated. As shown in Figure 6, the magnetic moment (M) increases very rapidly in small magnetic fields below 15 K. This increase slows at around 2000 Oe, when the moment reaches about 2.2 μ_B/per Fe^{II} at 1.8 or 5 K. As the field increases, M increases in a quasi-linear fashion without saturation even at 50 kOe. Hysteresis loops are obtained at 15 K and below, with coercive fields up to 1000 Oe at 1.8 K.

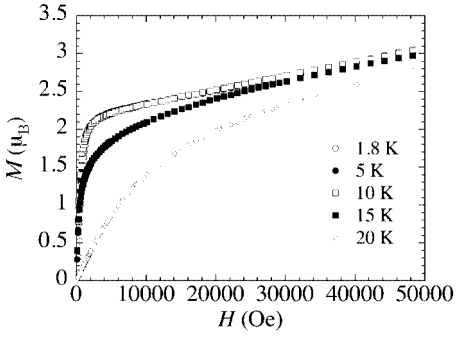

Figure 6. First magnetisation of the magnetic moment per Fe^{II} for α-FeFA·1/3HCO_2H

Fe(3) and Fe(4) each link to two Fe(1) chain centres via a single oxygen bridge (with Fe−O−Fe angles 111.84 or 113.54°) and two *syn*,*syn*-carboxylate bridges. Geometries corresponding to the interchain pathways have been previously observed in a small number of Fe^{II} complexes: $Ba_4(C_2O_4)Cl_2[\{Fe(C_2O_4)(\mu\text{-}OH)\}_4]$[28] which has an Fe−O−Fe angle of 122° and J/k_B = −9 K, $[Fe_2(\mu\text{-}OH)(\mu\text{-}OAc)_2(Me_3TACN)_2](ClO_4)$[29] (where Me_3TACN is 1,4,7-trimethyl-1,4,7-triazacyclononane) with an Fe−O−Fe angle of 113.2° and J/k_B = −18.7 K, $[Fe_2(\mu\text{-}OH)(\mu\text{-}Ph_3CCO_2)_2(Me_3TACN)_2](OTf)$[30] which displays an Fe−O−Fe angle of 119.1° and J/k_B = −17.4 K, and finally deoxyhemerythrin for which the Fe−O−Fe angle is not precisely known but for which J/k_B has been variously reported to be in the range −17 to −55 K[31] or as −21 K.[32] In all these compounds, the magnetic interactions are mediated by a single oxygen and two *syn, syn*-carboxylate bridges and have been found to be always antiferromagnetic. Due to the similarity of the geometries of these bridges to the interchain pathways in α-FeFA·1/3HCO_2H and in particular for the acetate-bridged dinuclear complex, these results enable us to conclude that our interchain linkages Fe(1)−Fe(3,4) are antiferromagnetic. Since the Weiss constant indicates that the dominant interactions in α-FeFA·1/3HCO_2H are ferromagnetic, the intrachain interaction must therefore be ferromagnetic and larger in magnitude than the antiferromagnetic interchain interaction. Unfortunately, to the best of our knowledge, no complex in which two Fe^{II} ions are linked via two oxygen bridges and one *syn, syn*-carboxylate bridge, which could confirm this conclusion, has been reported to date. However, based on this analysis, the magnetic structures of α-FeFA·1/3HCO_2H and MnFA[22b] are similar and composed of ferromagnetically-coupled Fe^{II} chains in which the magnetic moments are parallel and the linking Fe(3) and Fe(4) centres have antiparallel spins. Since the different metal centres occur in the ratio Fe(1):Fe(2):Fe(3):Fe(4) = 2:2:1:1 in the structure, this gives rise to the net magnetic moment. The saturation moment in the magnetic phase should thus be 1.6 μ_B per Fe^{II} or 9.8 μ_B per 6 Fe^{II}, based on g = 2.45 deduced from the high temperature susceptibility.

As shown in Figure 7, a rapid increase in the magnetisation with applied field is observed for low fields, as expected for a magnet. However, the magnetisation reaches 2.2 μ_B per Fe^{II} which is greater than the expected value of 1.6 μ_B. There are two possible causes for this behaviour which are not necessarily mutually exclusive: either the spins on Fe(3) and Fe(4) are not completely antiparallel to those on Fe(1) and Fe(2) or the g values for Fe(3) and Fe(4) might be smaller than for Fe(1) and Fe(2). In either or both cases, the magnetic moment of the magnetic phase is increased by an incomplete compensation of two of the four Fe(1,2) spins by the two Fe(3,4) spins. At higher fields (Figure 7) the magnetisation increases linearly with the applied magnetic field to reach ca. 3 μ_B per Fe^{II} at 5 T. This behaviour is consistent with the progressive alignment of the antiparallel magnetic spins on Fe(3,4) within the field. From the magnetic data discussed so far α-FeFA·1/3(HCO_2H), as for MnFA,[22b] can be understood in terms of ferromagnetic interactions within the chains and antiferromagnetic interchain interactions resulting in what can be described here, as in ref.[22b], as ferrimagnetic behaviour even though there is only one type of spin in the structure. This is in accordance with the definition of Néel that in a ferrimag-

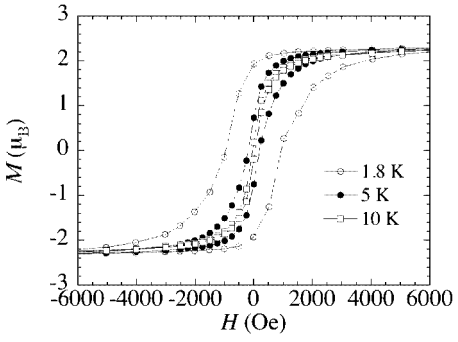

Figure 7. Hysteresis loops of the magnetic moment per Fe^{II} for α-FeFA·1/3HCO_2H obtained at a field sweep rate of 12 Oe/s

 © 2005 Wiley-VCH Verlag GmbH & Co. KGaA, Weinheim

netic material, the magnetic moments of different sublattices do not compensate and a spontaneous magnetisation remains. For the iron complex, the ordering temperature T_c is 16 K and this is considerably higher than the maximum value of 8 K reported for the series of Mn^{II} compounds in ref.[22b]

To confirm this magnetic ordering, the temperature dependence of the in-phase (χ') and out-of-phase (χ'') magnetic susceptibilities have been measured (Figure 8). Both components exhibit a peak at 1 Hz at temperatures of 15 and 12 K for χ' and χ'', respectively. Independent of the frequency, χ'' becomes nonzero around 16 K in agreement with the ordering temperature already estimated by the heat capacity and *d.c.* measurements (vide supra). Closer analysis of the *a.c.* data reveals a slight frequency dependence for both the maximum and the breadth of the peaks. The positions of the χ' and χ'' peaks increase by less than 0.5 K and ca. 1.3 K, respectively, when the frequency is increased from 1 to 1500 Hz. Mydosh established that the frequency dependence of the *a.c.* measurements can quantify the degree of glassiness in a material by the parameter γ.[33] Such analysis of the data presented here leads to a γ value of 0.015, indicating that the magnetic order observed below 16 K involves a slight degree of glassiness.

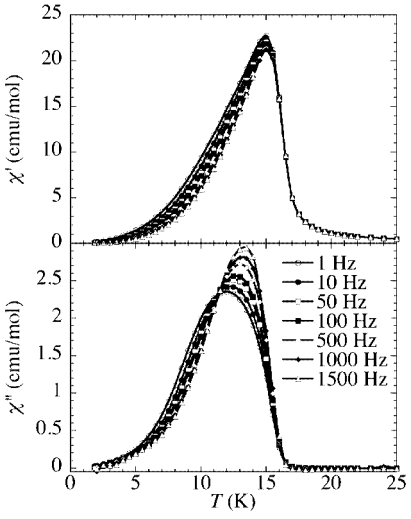

Figure 8. Temperature-dependence of the in-phase, χ', and out-of-phase, χ'', ac susceptibilities per Fe^{II} in α-$FeFA\cdot 1/3HCO_2H$ for a range of ac frequencies: dc field zero; ac field of amplitude 3 Oe

In contrast to the iron compound, the magnetic behaviour of the cobalt analogue is dominated by antiferromagnetic interactions and no magnetic order has been observed down to 1.8 K. The plot of χ^{-1} against T can be fitted (using data above 70 K) to the Curie−Weiss law with a Curie constant of 3.30 emu K mol^{-1} and a negative Weiss constant of −14.8 K. The Curie constant is in good agreement with typical values for high spin octahedral Co^{II} (S = 3/2).[27a] As indicated by the Weiss constant, dominant antiferromagnetic interactions are present between Co^{II} centres in α-$CoFA\cdot 1/3HCO_2H\cdot 1/3H_2O$. Nevertheless, a contribution from spin-orbit coupling of Co^{II} is also expected and probably enhances the Weiss constant extrinsically. In an octahedral ligand field the $^4T_{1g}$ ground state of the S = 3/2 Co^{II} metal ions is split by spin-orbit coupling into a set of three levels with an effective S = 1/2 ground state and leads to the possibility of large g values.[34]

Mössbauer Spectra

In order to investigate the relationship between electronic structure and magnetism in more detail, Mössbauer spectra of α-$FeFA\cdot 1/3HCO_2H$ were collected between 4 and 295 K (Figure 9). The spectra reflect the different iron sites in the crystal structure and are in agreement with the development of 3D magnetic order, as indicated by the pronounced changes in the shape of the spectra around 16 K (Figure 9).

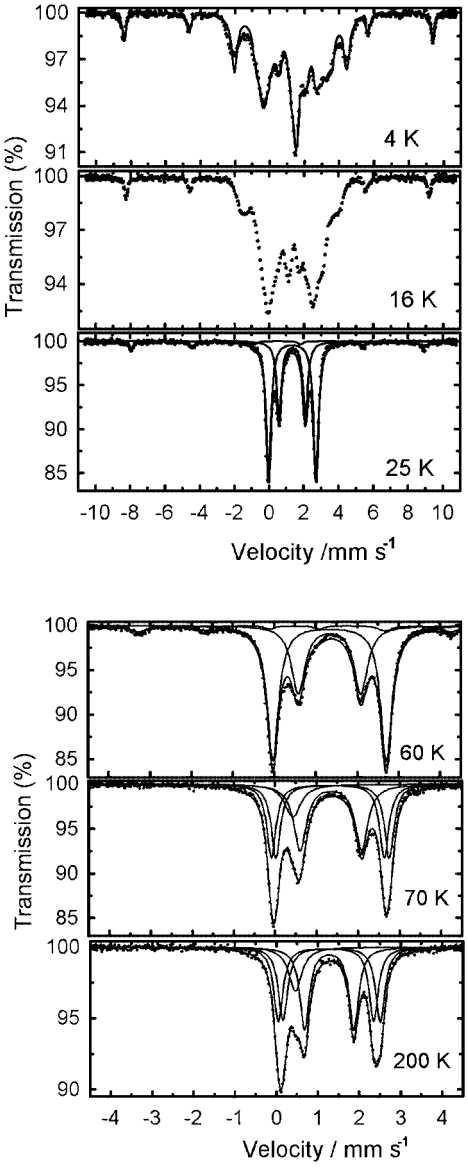

Figure 9. Mössbauer spectra of α-$FeFA\cdot 1/3HCO_2H$ in the temperature range of the magnetic phase transition (top) and in the paramagnetic phase (bottom); solid lines correspond to the best fits and the constituent subspectra

 © 2005 Wiley-VCH Verlag GmbH & Co. KGaA, Weinheim

The spectra of the paramagnetic phase above 16 K (e.g. the 25 K spectrum) essentially consist of two quadrupole doublets with an intensity ratio of roughly 2:1. Their isomer shifts *IS* (see Table 5) are nearly identical and typical for high spin Fe^{2+} sites. From the relative intensities, the outer doublet with the larger quadrupole splitting ΔE_Q can be assigned to the chain Fe(1) and Fe(2) sites with the second doublet showing the smaller ΔE_Q corresponding to the bridging Fe(3) and Fe(4) atoms. In the spectrum at 25 K, in addition to the major component arising from the Fe^{2+} paramagnetic signals, a hyperfine sextet with an isomer shift and a hyperfine field B_{hf} typical of Fe^{3+} can be observed (Table 5). The six-line pattern indicative of a magnetically-ordered phase persists up to about 60 K above which it collapses into a broad single line. This subspectrum can be attributed to the presence of about 8% of the cubic Fe^{III} formate $Fe(O_2CH)_3{\cdot}HCO_2H$ (subsequently identified by X-ray powder diffraction) which becomes antiferromagnetically ordered near 60 K and will be described elsewhere.[28] Below 60 K only two of the six lines fall within the region of the spectrum of α-FeFA·1/3HCO_2H and their shapes can be determined accurately from the four falling outside this region so that fitting the α-FeFA·1/3HCO_2H spectrum was essentially unaffected by the presence of this impurity.

Table 5. Mössbauer parameters of α-FeFA·1/3HCO_2H in the paramagnetic region at selected temperatures; the Fe(1,2) sites are described by one quadrupole doublet at 25 K and two doublets [Fe(1,2) a and b] for $T \geq 70$ K, whereas the Fe(3,4) sites were always modelled by a single somewhat broadened quadrupole doublet; errors are less than 1 in the last digit if not given explicitly in parentheses

T (K)	site	IS (mm·s^{-1})	ΔE_Q (mm·s^{-1})	Rel. area (%)
25	Fe(1,2)	1.35	2.73	60
	Fe(3,4)	1.35	1.52	32
	Fe^{3+}	0.50	–	8
70	Fe(1,2)a	1.33	2.84	56[a]
	Fe(1,2)b	1.33	2.61	
	Fe(3,4)	1.35	1.48	33
	Fe^{3+}	0.43	–	11
295	Fe(1,2)	1.22	2.14	25(2)
	Fe(1,2)b	1.20	1.85	29(2)
	Fe (3,4)	1.21	1.00	34
	Fe^{3+}	0.40	–	12

[a] Total Fe(1,2) area. The areas of Fe(1,2)a and Fe(1,2)b were assumed to be equal.

A more detailed inspection of the spectra recorded in the paramagnetic region (Figure 9) revealed that the Fe(1) and Fe(2) sites in the crystal structure of α-FeFA·1/3HCO_2H can be distinguished since their quadrupole splittings are somewhat different. This is particularly apparent from the shape of the spectrum recorded at 200 K (the temperature of the crystal structure determination). Thus, the Fe^{2+} part of the spectrum was modelled by three doublets. Although the Fe(3,4) sites cannot be similarly resolved, a certain line broadening at low temperatures indicates slightly different quadrupole splittings. As expected for $3d^6$ high spin Fe^{2+} ions, ΔE_Q is temperature dependent (Figure 10) for the Fe(1,2) as well as for the Fe(3,4) sites reflecting the aspherical electron distribution arising from the splitting of the octahedral t_{2g} orbitals in the lower symmetry ligand field. The rather small value for ΔE_Q of ca. 1.5 mm·s^{-1} for the Fe(3,4) sites even at 25 K suggests that their electronic structures result from the orbital splitting of an elongated octahedron, in agreement with the structural data (vide supra) where the d_{xz} and d_{yz} orbitals are below the d_{xy} orbital.[35] In addition, the degeneracy of the d_{xz} and d_{yz} orbitals is likely to be lifted because the equatorial bond lengths are different. The much larger ΔE_Q for the Fe(1,2) sites suggests a different sequence of orbitals for these more distorted sites but a more detailed analysis would need to take the effects of spin-orbit coupling into account.

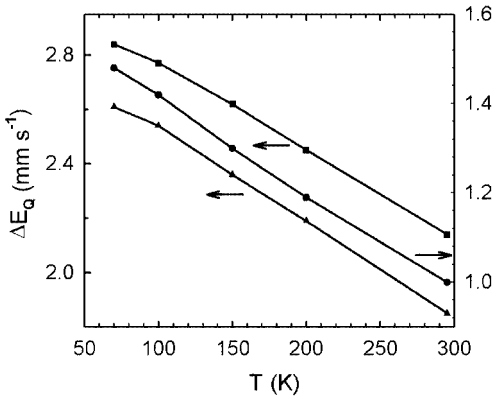

Figure 10. Temperature dependence of the quadrupole splitting for the Fe(1,2) sites (left scale) and the Fe(3,4) sites (right scale); solid lines are guides for the eye

The shape of the 4 K spectrum is completely different from that of the high temperature spectra and indicates that all the Fe^{2+} sites are magnetically ordered. Modelling of the spectrum is complicated by the fact that for Fe^{2+} compounds, electric quadrupole and magnetic hyperfine interactions are generally of comparable size and it is not possible to analyse the spectra in terms of six line patterns with an intensity ratio 3:2:1:1:2:3. Accordingly, the 4 K spectrum was modelled with the software package Recoil[36] employing the full static Hamiltonian for mixed hyperfine interactions with four Fe^{2+} sites and one Fe^{3+} site (to account for the impurity) included in the calculations. This data treatment resulted in a large number of parameters which cannot all be deduced unambiguously from powder spectra since each iron site is characterised by (i) its isomer shift *IS* (ii) the hyperfine field B_{hf} (iii) the quadrupole interaction parameter $\varepsilon = eQV_{ZZ}/2$ (where V_{ZZ} is the Z component of the diagonalised electric field gradient (efg) tensor, Q = quadrupolar moment of the iron nucleus) (iv) the asymmetry parameter η of the efg tensor ($0 \leq \eta \leq 1$) and (v) the polar and azimuthal angles Θ and Φ describing the orientation of $\mathbf{B_{hf}}$ in the efg principal axes coordinate system. For this reason it was assumed that the values for the *IS* and quadrupole splittings $\Delta E_Q = (V_{ZZ}Q/2)(1 + \eta^2/3)^{1/2}$

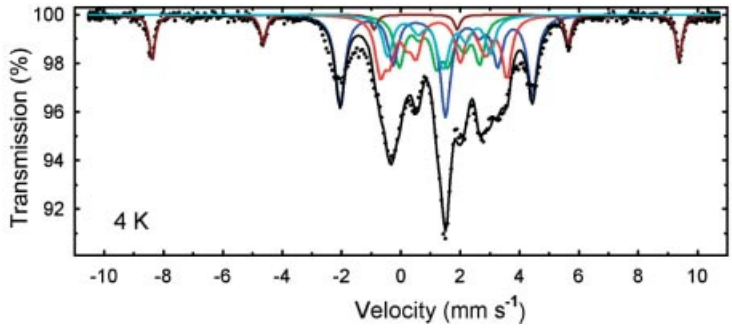

Figure 11. Analysis of the 4 K Mössbauer spectrum using the full Hamiltonian for combined quadrupole and magnetic hyperfine interactions; the black solid line corresponds to a theoretical spectrum obtained with the parameters given in Table 6; blue and red lines correspond to the Fe(1,2) subspectra, green and cyan lines to the Fe(3,4) subspectra; see text for more details

in the paramagnetic phase at 25 K and in the magnetically ordered phase at 4 K are identical. A reasonable description of the overall shape of the spectrum (Figure 11) was obtained with the parameters summarised in Table 6. In this model, the efg of the Fe(3,4) sites was assumed to be axially symmetric so that the spectra do not depend on the azimuthal angles Φ which were set to zero for these as well as for the Fe(1,2) sites. The negative value of V_{ZZ} for the Fe(3,4) sites is in agreement with an orbital doublet ground state. The best simulation of the overall shape of the spectrum was obtained also by using a negative value of V_{ZZ} for the Fe(1,2) sites, although a positive value cannot be ruled out. The experimental spectrum reveals considerable line broadening at higher velocities indicating a distribution of hyperfine fields. This was not taken into account in the data analysis and points to disorder effects which are also believed to be the origin of the frequency dependence of the *a.c.* susceptibility data (vide supra).

Table 6. Mössbauer parameters of α-$FeFA\cdot 1/3HCO_2H$ obtained from the analysis of the 4 K spectrum with the full hyperfine Hamiltonian; the full width at half maximum was set to 0.4 $mm\cdot s^{-1}$ for all Fe^{2+} sites and to 0.24 $mm\cdot s^{-1}$ for the Fe^{3+} site; the azimuthal angle Φ was kept at zero for all sites; Fe(1,2) and Fe(3,4) are split into two sites a and b, respectively

Site	IS ($mm\cdot s^{-1}$)	ε ($mm\cdot s^{-1}$)	η	B_{hf} (Tesla)	Θ (°)	rel. Area (%)
Fe(1,2)a	1.35[a]	−2.55[a]	0.6[b]	15.1	51	33
Fe(1,2)b	1.35[a]	−2.55[a]	0.6[b]	7.5	90	25
Fe(3,4)a	1.35[a]	−1.5[a]	0[b]	4.7	44	19
Fe(3,4)b	1.35[a]	−1.5[a]	0[b]	7.5	45	15
Fe^{3+}	0.50[a]	–	–	55.1	–	9

[a] Parameters taken from the 25 K spectrum. Note that $\Delta E_Q = (eQV_{ZZ}/2)(1 + \eta^2/3)^{1/2} = \varepsilon(1 + \eta^2/3)^{1/2}$. A negative sign for V_{ZZ} was assumed for both sites. [b] Parameter was not varied during fitting but analysis was performed for different η values.

The range of B_{hf} values found from this analysis for the various Fe sites in α-$FeFA\cdot 1/3HCO_2H$ (Table 6) is similar to those of other Fe^{2+} compounds.[37] The observed hyperfine field is a sum of three contributions:

$$B_{hf} = B_C + B_L + B_D$$

where B_C is the isotropic Fermi contact contribution and B_L and B_D correspond to the anisotropic dipolar interactions between the nuclear momentum and the electronic angular and spin momentum, respectively. According to a common rule of thumb,[38] the $S = 2$ state of Fe^{2+} can be expected to lead to a B_C value of roughly −44 T which is compensated by positive B_L and B_D contributions with B_L being dominant and proportional to the expectation value $<L>$ of the angular momentum. The value of $<L>$ and therefore B_L is expected to be larger for the more symmetric Fe(3,4) than for the more distorted Fe(1,2) sites implying that the sign of B_{hf} is negative for the Fe(1,2) and positive for the Fe(3,4) sites. The small hyperfine field values are evidence for the importance of the angular contribution to the magnetic moment for both kinds of Fe sites in the crystal structure of α-$FeFA\cdot 1/3HCO_2H$ and the resultant magnetic anisotropy will also influence the detailed spin structure in the magnetically ordered phase.

Finally, we note that the 16 K spectrum (Figure 9) corresponds to a superposition of magnetically ordered and paramagnetic phases in good agreement with a T_C value of 16 K derived from the magnetic susceptibility measurements. Mössbauer spectra in an external magnetic field could shed more light on the electronic structure and magnetic exchange interactions of the various Fe sites in the present compound and elastic neutron scattering studies would be a further means of probing the magnetic structures. However, based on what is already in the literature[22,29−33] and the complementary susceptibility and Mössbauer studies we have presented here, we feel that our proposed model for the spin structure is probably justified.

Conclusion

We have described the synthesis, structure and the magnetic properties of the mesoporous compound $Fe(HCO_2)_2\cdot 1/3HCO_2H$ which is a magnet below 16 K. As the member with the highest T_C of a newly-discovered family of M^{II} formate framework structures with high stabilities

 © 2005 Wiley-VCH Verlag GmbH & Co. KGaA, Weinheim

and the ability to take up specific gas molecules, it points to a promising way forward in combining magnetic and porous properties which could find applications in separation techniques.

Experimental Section

FeFD, CoFD, NiFD, ZnFD and MgFD were synthesised as reported previously.[39]

Synthesis of α-$Fe(O_2CH)_2$·1/3HCO_2H: In a typical experiment $Fe(O_2CH)_2$·2H_2O (0.1 g, 0.5 mmol) was heated in formic acid (7 mL) to 70 °C in a steel autoclave with a Teflon-insert of internal volume 10 mL for a period of 8 hours. After slow cooling, α-FeFA·1/3HCO_2H was obtained in quantitative yield. The polycrystalline product was washed with formic acid, dried and stored under an inert atmosphere. The product was shown to be a single-phase by powder diffraction except in the case of the sample used for the Mössbauer measurements which contained about 8% of the Fe^{III} impurity $Fe(O_2CH)_3$·HCO_2H as described in the text.
Single-crystals of α-FeFA·1/3HCO_2H could obtained when formic acid was allowed to evaporate slowly under solvothermal conditions. $Fe(O_2CH)_2$·2H_2O (60 mg, 0.3 mmol) was heated in formic acid (8 mL) for 12 hours at 170 °C. The mixture was then cooled to 110 °C over 2 hours, maintained at this temperature for a further 28 hours then slowly cooled to room temperature. In this preparation, the autoclave lid was not closed tightly, allowing very slow loss of solvent from the autoclave.

Synthesis of α-$Co(O_2CH)_2$·1/3HCO_2H·1/3H_2O: The synthesis of polycrystalline material was as for α-FeFA·1/3HCO_2H. Single-crystals of α-CoFA·1/3HCO_2H·1/3H_2O could be obtained under solvothermal conditions by the modification described for α-FeFA·1/3HCO_2H. $Co(O_2CH)_2$·2H_2O (200 mg, 1 mmol) was heated in formic acid (4 mL) for 100 hours at 160 °C.

Synthesis of α-$Zn(O_2CH)_2$·1/3(HCO_2H): A quantitative yield of α-$Zn(O_2CH)_2$·1/3HCO_2H was obtained by recrystallisation of $Zn(O_2CH)_2$·2H_2O (4.88 g, 25.5 mmol) with formic acid (6 mL) at 120 °C for 120 hours. The autoclave lid was not closed tightly, allowing very slow loss of solvent from the autoclave.

Synthesis of α-$Ni(O_2CH)_2$·*x*HCO_2H·*y*H_2O: A 0.5 mm i.d. glass capillary tube was filled to a depth of 1 cm with $Ni(O_2CH)_2$·2H_2O and formic acid and was placed together with formic acid (2.5 mL) in the Teflon insert of the autoclave and heated at 170 °C for 17 hours. After cooling, the capillary tube was sealed and the X-ray powder pattern was measured.

Synthesis of α-$Mg(O_2CH)_2$·1/3HCO_2H: $Mg(O_2CH)_2$·2H_2O (1.22 g, 16.2 mmol) and formic acid (2 mL) were heated for 105 hours to 120 °C. The resultant polycrystalline powder was separated from the solvent by filtration and dried in air.

Single-Crystal X-ray Diffraction Studies: Data were measured on Stoe IPDS or Stoe IPDS II image plate area detector diffractometers using graphite-monochromated Mo-*Kα* radiation (λ = 0.71073 Å). Structures were solved by direct methods and refined by full-matrix least-squares against F^2 (all data) using the SHELXTL software package.[40] Nonhydrogen atoms were assigned anisotropic thermal parameters. Hydrogen atoms were fully refined with isotropic temperature factors (Co and Zn) or positionally refined with U set at 1.2U_{eq} for the carbon atom (Fe). Crystal data and experimental details are summarised in Table 1. CCDC-238105 to -238107 contain the supplementary crystallographic data for this paper. These data can be obtained free of charge from The Cambridge Crystallographic Data Centre via www.ccdc.cam.ac.uk/data_request/cif.

X-ray Powder Diffraction: X-ray powder patterns were measured at ambient temperature on a Stoe STADI-P diffractometer using Co-$K\alpha_1$ radiation (Ge monochromator) and Debye−Scherrer geometry. The sample was held between sheets of amorphous polyacetate foil. Data analysis was carried out with the WinXPow 1.07 software suite.
The unit cell for α-$Ni(O_2CH)_2$·*x*HCO_2H·*y*H_2O was determined from powder diffraction measurements made on the ANKA-DIFF beamline at the ANKA synchrotron source at the Forschungszentrum Karlsruhe at ambient temperature and using radiation of wavelength 1.58845(3) Å.

Thermal Analyses: The differential thermal analyses (DTA) and the thermogravimetric (TG) experiments were carried out using a Netzsch STA 409C system. Samples were heated in Al_2O_3 crucibles with a heating rate of 1 K min^{-1} up to 600 °C under a nitrogen atmosphere with a flow rate of 30 L h^{-1}.

Susceptibility Measurements: The magnetic susceptibility measurements were obtained with the use of a Quantum Design SQUID magnetometer MPMS-XL. Measurements were performed on finely ground polycrystalline samples of α-FeFA·1/3HCO_2H (13.13 mg) and α-CoFA·1/3HCO_2H·1/3H_2O (5.1 mg) in the temperature range 1.8−300 K with fields up to 7 T. The magnetic data were corrected for the sample holder and the diamagnetic contribution calculated from Pascal's constants.[41]

^{57}Fe Mössbauer Spectroscopy: Temperature dependent Mössbauer spectra of powdered samples of α-FeFA·1/3HCO_2H (about 10 mg natural iron per cm^2 with the samples diluted with polyethylene to ensure homogeneous distribution of the sample in the plexiglass container) were measured in an Oxford flow cryostat with a conventional Mössbauer spectrometer operating with a sine-type drive signal. All spectra were referenced to α-Fe.

Heat Capacity Measurements: The heat capacity measurements were performed on a Quantum Design PPMS system. A pressed pellet of the sample was mounted using grease on the heat capacity sample holder.

IR Spectroscopy: FTIR spectra were measured using KBr pellets of the sample in the range from 4000 to 400 cm^{-1} with a Perkin−Elmer Spectrum One instrument.

Acknowledgments

We acknowledge the ESF "Molecular Magnets" program for funding the short scientific stays of Rodolphe Clérac. R.C. thanks the CNRS, the University of Bordeaux 1 and the Conseil Regional d'Aquitaine for financial support. M. V., P. A., C. E. A. and A. K. P. thank the DFG Centre for Functional Nanostructures (CFN) for financial support. We thank W. Hölle for technical assistance with the measurement of the Mössbauer spectra performed at the Max-Planck-Institut für Festkörperforschung, Stuttgart. We thank Stephen Doyle for the measurement of the high resolution X-ray powder data at the ANKA-DIFF beamline, Forschungszentrum Karlsruhe.

[1] R. D. Cannon, R. P. White, *Prog. Inorg. Chem.* **1988**, *36*, 195−298.

[2] T. Lis, *Acta Crystallogr., Sect. B* **1980**, *36*, 2042−2046.
[3] [3a] H. J. Eppley, H.-L. Tsai, N. de Vires, K. Folting, G. Christou, D. N. Hendrikson, *J. Am. Chem. Soc.* **1995**, *117*, 301−317. [3b] S. M. J. Aubin, Z. Sun, I. A. Guzei, A. L. Rheingold, G. Christou, D. N. Hendrikson, *Chem. Commun.* **1997**, 2239−2240.
[4] [4a] Z. A. D. Lethbridge, A. D. Hiller, R. Cywinski, P. Lightfoot, *J. Chem. Soc., Dalton Trans.* **2000**, 1595−1599. [4b] P. A. Prasad, S. Neeraj, S. Natarajan, C. N. R. Rao, *Chem. Commun.* **2000**, 1251−1252. [4c] Z. A. D. Lethbridge, S. K. Tiwary, A. Harrison, P. Lightfoot, *J. Chem. Soc., Dalton Trans.* **2001**, 1904−1910.
[5] J. D. Martin, R. F. Hess, *Chem. Commun.* **1996**, 2419−2420.
[6] [6a] L. G. Beauvais, J. R. Long, *J. Am. Chem. Soc.* **2002**, *124*, 12096−12097. [6b] M. Cavellec, D. Riou, C. Ninlaus, J.-M. Grèneche, G. Férey, *Zeolites* **1996**, *17*, 250−260. [6c] M. Cavellec, D. Riou, C. Ninlaus, J.-M. Grèneche, G. Férey, *Magn. Magn. Mater.* **1996**, *163*, 173−183. [6d] X. X. Zhang, S. S.-Y. Chui, I. D. Williams, *J. Appl. Phys.* **2000**, *87*, 6007−6009. [6e] N. Guillou, Q. Gao, P. M. Forster, J.-S. Chang, M. Noguès, S.-E. Park, G. Férey, A. K. Cheetham, *Angew. Chem. Int. Ed.* **2001**, *40*, 2831−2834. [6f] A. Rujiwatra, C. J. Kepert, J. B. Claridge, M. J. Rosseinsky, H. Kumagai, M. Kurmoo, *J. Am. Chem. Soc.* **2001**, *123*, 10584−10594. [6g] K. Barthelet, J. Marrot, D. Riou, G. Férey, *Angew. Chem. Int. Ed.* **2002**, *41*, 281−284.
[7] M. Viertelhaus, *Darstellung und Charakterisierung wasserfreier Metall(II)- und Metall(III)formiate*, Mensch und Buch Verlag, Berlin, **2003**.
[8] K. Osaki, Y. Nakai, T. Watanabe, *J. Phys. Soc. Jap.* **1963**, *18*, 919.
[9] F. Sapina, M. Burgos, E. Escrivá, J.-V. Folgado, D. Marcos, A. Beltrán, D. Beltrán, *Inorg. Chem.* **1993**, *32*, 4337−4344.
[10] G. Weber, *Acta Crystallogr., Sect. B* **1980**, *36*, 1947−1949.
[11] M. Viertelhaus, H. Henke, C. E. Anson, A. K. Powell, *Eur. J. Inorg. Chem.* **2003**, 2283−2289.
[12] D. Dollimore, J. P. Gupta, D. V. Nowell, *Thermochim. Acta* **1979**, *30*, 339−350.
[13] R. C. Eckhardt, T. B. Flanagan, *Trans. Faraday Soc.* **1964**, *60*, 1289−1298.
[14] C. Malard, *C. R. Acad. Sc. Paris Ser. C* **1966**, *263*, 480−483.
[15] T. Arii, A. Kishi, *Thermochim. Acta* **1999**, *325*, 157−165.
[16] G. Périnet, *Bull. Soc. Franc. Minér. Crist.* **1966**, *89*, 325−328.
[17] T. Arii, A. Kishi, Y. Kobayashi, *Thermochim. Acta* **1999**, *325*, 151−156.
[18] P. Baraldi, *Spectrochim. Acta A* **1979**, *35*, 1003−1007.
[19] [19a] R. C. Eckhardt, P. M. Fichte, T. B. Flanagan, *Trans. Faraday. Soc.* **1971**, *67*, 1143−1154. [19b] Y. Masuda, M. Hatakeyama, *Talanta* **1996**, *43*, 1705−1709. [19c] Y. Masuda, M. Hatakeyama, *Thermochim. Acta* **1998**, *308*, 165−170.
[20] E. Kalalova, V. Ruzicka, *Coll. Czech. Chem. Commun.* **1962**, *27*, 424−429.
[21] V. Z. Vassileva, A. L. Karapetkova, *Bulg. Chem. Commun.* **1995**, *28*, 151−159.
[22] [22a] D. N. Dybtsev, H. Chun, S. H. Yoon, D. Kim, K. Kim, *J. Am. Chem. Soc.* **2004**, *126*, 32−33. [22b] Z. Wang, B. Zhang, H. Fujiwara, H. Kobayashi, M. Kurmoo, *Chem. Commun.* **2004**, 416−417.
[23] C. Malard, *C. R. Acad. Sc. Paris Ser. C* **1966**, *263*, 480−483.
[24] Unpublished results.
[25] A. L. Spek, *PLATON − A Multipurpose Crystallographic Tool*, Utrecht University, Utrecht, The Netherlands, **2002**.
[26] K. Nakamoto, *Infrared and Raman Spectra of Inorganic and Coordination Compounds. Part B: Applications in Coordination, Organometallic and Bioinorganic Chemistry*, John Wiley & Sons, New York, **1997**.
[27] [27a] F. E. Mabbs, D. J. Machin, *Magnetism and Transition Metals Complexes*, Chapman and Hall Ltd., London, **1973**. [27b] R. L. Carlin, *Magnetochemistry*, Springer-Verlag, Berlin, Heidelberg, **1986**.
[28] D. J. Price, S. Tripp, A. K. Powell, P. T. Wood, *Chem. Eur. J.* **2001**, *7*, 200−208.
[29] J. R. Hartman, R. L. Rardin, P. Chaudhuri, K. Pohl, K. Wieghardt, B. Nuber, J. Weiss, G. C. Papefthymiou, R. B. Frankel, S. J. Lippard, *J. Am. Chem. Soc.* **1987**, *109*, 7387−7396.
[30] S. C. Payne, K. S. Hagen, *J. Am. Chem. Soc.* **2000**, *122*, 6399−6410.
[31] R. C. Reem, E. I. Solomon, *J. Am. Chem. Soc.* **1987**, *109*, 1216−1226.
[32] M. J. Maroney, D. M. Kurtz, J. N. Nocek, L. L. Pearce, L. Que Jr., *J. Am. Chem. Soc.* **1986**, *108*, 6871−6879.
[33] J. A. Mydosh, *Spin Glasses: An Experimental Introduction*, Taylor and Francis, London, **1993**, p. 64.
[34] R. L. Carlin, *Magnetochemistry*, Springer-Verlag, **1986**.
[35] H. T. Le Fever, R. C. Thiel, W. J. Huiskamp, W. J. M de Jonge, *Physica B* **1981**, *111*, 190−208.
[36] K. Lagarec, D. G. Rancourt, Mössbauer Analysis Software Recoil (1.05).
[37] [37a] K. Ono, A. Ito, *J. Phys. Soc., Jpn.* **1964**, *19*, 899−907. [37b] S. G. Carling, D. Visser, D. Hautot, I. D. Watts, P. Day, J. Ensling, P. Gütlich, G. J. Long, F. Grandjean, *Phys. Rev. B* **2002**, *66*, 104407/1−104407/12.
[38] N. N. Greenwood, T. C. Gibb, *Mössbauer Spectroscopy*, Chapman and Hall, London, **1971**; p. 103.
[39] [39a] K. Nargorny, J. F. March, *Z. Phys. Chem.* **1972**, *78*, 311−316. [39b] V. Zapletal, J. Jedlick, V. Ruzicka, *Coll. Czech. Chem. Commun.* **1957**, *22*, 171−174.
[40] G. M. Sheldrick, *SHELXTL 5.1*, Bruker AXS Inc., 6300 Enterprise Lane, Madison, WI 53719−1173, USA, **1997**.
[41] *Theory and Applications of Molecular Paramagnetism* (Eds.: E. A. Boudreaux, L. N. Mulay), John Wiley & Sons, New York, **1976**.
[42] J. D. Donaldson, J. F. Knifton, S. D. Ross, *Spectrochim. Acta* **1964**, *20*, 847−851.

Received May 13, 2004

 © 2005 Wiley-VCH Verlag GmbH & Co. KGaA, Weinheim

Stereochemical Investigation of Palladium(II) Complexes with Phenanthroline Ligands: A Molecular Mechanics Approach

Mario Calligaris,[a] Ennio Zangrando,*[a] and Barbara Milani,[a] Angelica Marson[a,‡]

Keywords: Stereochemistry / Molecular mechanics / Copolymerisation / Phenanthroline / Palladium

Specific force field parameters have been derived through an optimisation procedure based on crystal structure data to describe the geometry of Pd^{II}-phenanthroline complexes. The X-ray structure of $[Pd(CH_3)(3\text{-}s\text{Bu-phen})_2][OTf]$ is also reported. Molecular mechanics calculations show that intramolecular steric interactions yield severe distortions from a square-planar geometry of the metal atom, both in bischelated $[Pd(3\text{-R-phen})_2]^{2+}$ and monochelated $[Pd(CH_3)(3\text{-R-phen})_2]^+$ complexes. A complete stereochemical analysis of the possible diastereoisomers of this last complex (R = *s*Bu) allows the rationalisation of its fluxional behaviour observed in solution. Complexes like $[Pd(H)(3\text{-tmp-phen})_2]^+$ and $[Pd\{CH(C_6H_5)CH_2C(O)OCH_3\}(3\text{-tmp-phen})(CH_3OH)]^+$ (tmp = 1,2,2-trimethylpropyl) have also been investigated as species reasonably involved in the copolymerisation reactions. It is suggested that the remarkable increase of the copolymer molecular weight obtained with the 3-tmp-phen ligand derives from the steric destabilisation of an intermediate species postulated for the termination reaction.

(© Wiley-VCH Verlag GmbH & Co. KGaA, 69451 Weinheim, Germany, 2005)

Introduction

Bischelated palladium(II) compounds with bidentate nitrogen-donor ligands, such as 1,10-phenanthroline (phen) and its derivatives, have been shown to act as efficient precatalysts in the CO/styrene copolymerisation reaction.[1–3] Some stereochemical aspects of these complexes have been investigated both in solution and in the solid state, providing some information about the conformational flexibility of the bischelated $[Pd(phen)_2]^{2+}$ complex,[1,4] and the fluxional behaviour of the monocationic derivatives, $[Pd(R)(phen)_2]^+$ (R = CH_3,[5] and CH_2NO_2[6]), where one phen ligand is monocoordinated.

In order to rationalise the observed structural properties of this kind of complexes, a thorough molecular mechanics (MM) investigation has been undertaken, on the basis of a specific force field. The force field parameters have been derived from the available crystal data for $[Pd(phen)_2][OTf]_2$ (**1**),[7] $[Pd(3\text{-}i\text{Pr-phen})_2][PF_6]_2$ (**2**),[8] $[Pd(3\text{-}n\text{Bu-phen})_2][PF_6]_2$ (**3**),[8] and $[Pd(CH_3)(phen)_2][PF_6]$ (**4**),[5] besides those presented in this paper for $[Pd(CH_3)(3\text{-}s\text{Bu-phen})_2][PF_6]$ (**5**) (OTf = triflate, 3-*i*Pr-phen = 3-isopropyl-phenanthroline, 3-*n*Bu-phen = 3-normal-butyl-phenanthroline, 3-*s*Bu-phen = 3-secondary-butyl-phenanthroline). The crystal structure of the latter has been determined in order to examine the influence of a bulky group in position 3 of phen on the overall geometry of the organometallic cation.

The MM study has been extended to the diastereoisomers of the hydride complex, $[Pd(H)(phen)_2]^+$, and of its 3-(1,2,2-trimethylpropyl) derivative, $[Pd(H)(3\text{-tmp-phen})_2]^+$, in order to get some insight into the structure of species proposed to be present in the catalytic copolymerisation process.[1,2] The 3-tmp group has been considered in view of the significant increase of both productivity and polymer molecular weight obtained after introduction of this side group in the phen ligand.[3] Furthermore, models of the copolymer chain-initiating species, like $[Pd\{CH(C_6H_5)CH_2C(O)OCH_3\}(N\text{–}N)(CH_3OH)]^+$, have also been investigated with N–N = phen and 3-tmp-phen with the aim of elucidating the role of the side group in the chain growth process.

Results and Discussion

Force Field

The molecular strain energy, *E*, has been calculated according to the AMBER force field,[9] as the sum of the harmonic deformation functions for bond lengths (d), bond angles (θ), torsion angles (including improper-torsion angles, which model out-of-plane displacements) (ψ), and the van der Waals and electrostatic energy contributions [Equation (1)].

[a] Department of Chemical Sciences, University of Trieste, Via L. Giorgieri 1, 34127 Trieste, Italy
Fax: +39-040-558-3903
E-mail: zangrando@univ.trieste.it
[‡] Current address: Institute of Molecular Chemistry, Homogeneous Catalysis, University of Amsterdam, Nieuwe Achtergracht 166, 1018 WV Amsterdam, The Netherlands

Supporting information for this article is available on the WWW under http://www.eurjic.org or from the author.

$$E = \Sigma_b[k_b(d - d°)^2] + \Sigma_a[k^\theta(\theta - \theta°)^2] + \Sigma_t\{\tfrac{1}{2}V_n[1 + \cos(n \cdot \psi - \psi°)]\} + \Sigma_{ij}[(a_{ij}/r_{ij}^{12}) - (b_{ij}/r_{ij}^{6}) + (q_i \cdot q_j/D \cdot r_{ij})] \quad (1)$$

Summations in (1) are extended over all bonds, angles, torsions and pairs of non-bonded atoms *i*–*j*, separated by the distance r_{ij} . In the last summation, $a_{ij} = (\varepsilon_i\varepsilon_j)^{1/2}(r_i* + r_j*)^{12}$, $b_{ij} = 2(\varepsilon_i\varepsilon_j)^{1/2}(r_i* + r_j*)^6$, where r_i* is the van der Waals radius of atom type *i*, and ε_i is the well depth for two atoms of type *i*; q_i and q_j are the atomic charges and *D* is the dielectric constant, here treated as a distance-dependent variable ($D = r_{ij}$). Electrostatic and nonbonded atom interactions have both been reduced by a scale factor of 0.5 when atoms are only separated by three bonds. In all calculations, the trigonal carbon and nitrogen atoms have been treated using the improper torsion parameters of aromatic carbon atoms given in AMBER.[9] As in previous computations,[10,11] torsion barriers around the coordination bonds have been fixed to zero.

Energy calculations have been performed with a Pentium III PC, using the HyperChem. 6.01 molecular modelling system.[12] The Polak–Ribiere version of the conjugate gradient method has been used in all energy minimisation calculations with a convergence criterion of 0.001 kcal mol^{-1} Å^{-1} (1 kcal = 4.184 kJ). Atomic charges have been calculated by the semi-empirical ZINDO/1 method, suitable for the molecular orbital calculations of second-row transition metal complexes.[12] A local program has been used for all the geometrical calculations.[13]

Because phenanthroline and palladium atom types were not available in AMBER, the force field has been implemented with the addition of the new atom types (Figure SA in the Supporting Information) and the relative force field constants (Tables SA and SB in the Supporting Information). The "stretching" potential constants (k^d) for the *i*–*j* bonds have been calculated according to the Badger's rule,[14] $k^d_{ij} = 71.94 \cdot [(A_{ij} - D_{ij})/(d°_{ij} - D_{ij})]^3$ kcal mol^{-1} Å^{-2}, using the A_{ij} and D_{ij} parameters proposed by Herschbach and Laurie.[15] The $d°$ values for the phenanthroline C–N and C–C bonds have been derived from the mean values, calculated from the accurate crystal structure data of complexes **1–3**, while the $d°$ values for the Pd–N and Pd–C bonds (Table SA), together with the ε_{Pd} (0.693 kcal mol^{-1}) and $r*_{Pd}$ (1.928 Å) van der Waals parameters, have been optimised according to the Simplex-method procedure, already used for the derivation of force field constants in ruthenium(II)[10] and cobalt(III) [11] metal complexes. The minimised function is GOF = $[\Sigma_i w_i\Delta_i^2/(n_{obs} - n_p)]^{1/2}$, where the summation is extended to all the differences, Δ_i , between each observed and calculated value of the n_{obs} data (522 in the present case); w_i is the weight ($1/\sigma_i^2$) of each observation, and n_p is the total number of variable parameters (7, in the present case). The "bending" constants (k^θ) for the *i*–*j*–*k* bond angles have been calculated according to the Halgren's equation:[16] $k^\theta_{ijk} = 125.9 \cdot \{Z_iC_jZ_k(d°_{ij} + d°_{ik})^{-1}(\theta°_{ijk})^{-2}\exp[-2(d°_{ij} - d°_{jk})^2/(d°_{ij} + d°_{ik})^2]\}$ kcal mol^{-1} rad^{-2}.

The values of the *C* and *Z* parameters for palladium (1.3267 and 3.2039, respectively) have been obtained by the optimisation procedure described above, whereas for the carbon, nitrogen and hydrogen atoms, the Halgren's values have been used. No restraint has been included in the energy minimisation during the force field parameter optimisation procedure.

Because of the lack of suitable experimental structural data, the stretching (Table SA) and bending (Table SB) force constants of the Pd–H and Pd–O bonds have been simply calculated by the Badger's and Halgren's equations, assuming $d°$(Pd–H) = 1.6 Å, and $d°$(Pd–O) = 2.01 Å.

Minimum energy structures have been found by the Conformational Search routine of HyperChem[12] and the conformational analysis has been carried out with local Excel© Macro functions that allow the minimisation of the strain energy as the conformation of the cation is varied through rotation around the Pd–N bond of the monocoordinated phen ligand.

As shown in Table 1, the agreement between observed and calculated bond lengths and angles for the five complexes, **1–5**, used for the optimisation of the force field parameters, is quite satisfactory, specially after imposing a restraint on the Pd···N(apical) distance in the methyl derivatives **4** and **5** (see below). In fact, the average differences, $<\Delta>$, between observed and calculated values, are low enough to show the absence of large systematic errors, and the weighted root-mean-square deviations (wrms = $[(\Sigma_i w_i\Delta_i^2)/\Sigma_i w_i]^{1/2}$) are lower than the mean ranges of chemically equivalent structural parameters, observable in the crystal structures of **1–3** (e.g. 0.022, 0.018, and 0.023 Å for the Pd–N, N–C, and C–C bond lengths).

Table 1. Average differences $<\Delta>$ between observed and calculated bond lengths and angles, weighted root-mean-square values (wrms), and number of observations (*n*) used in the force field parameter optimisation procedure for structures **1–5**. X, Y and Z represent carbon and nitrogen atoms.

Distances [Å]	$<\Delta>$[a]	$<\Delta>$[b]	wrms[a]	wrms[b]	*n*
Pd–X	–0.010	–0.008	0.016	0.015	20
X–Y	0.001	0.001	0.016	0.016	182
Angles [°]	$<\Delta>$[a]	$<\Delta>$[b]	wrms[a]	wrms[b]	*n*
X–Pd–Y	–0.4	–0.3	2.0	1.9	30
Pd–X–Y	0.6	0.6	1.0	0.9	36
X–Y–Z	0.3	0.3	1.4	1.3	252

[a] No restraint. [b] Pd···N distance restrained to 2.730 Å with a force constant of 1000 kcal mol^{-1}.

Moreover, the overall shape of the minimised structures of the cations, $[Pd(phen)_2]^{2+}$ (**1**) and $[Pd(3\text{-R-phen})_2]^{2+}$ (R = *i*Pr for **2** and *n*Bu for **3**), is reasonably close to that found in the crystal structures (Table 2), the differences being attributable to the different packing environments.

The consistency of the force field is further illustrated by its ability to reproduce, in the methyl derivatives **4** and **5**, the increase of the Pd–N bond lengths on going from the chelate to the monocoordinated ligand, and the increase of the Pd–N bond length *trans* to the methyl group (Table 3). The deformation of the Pd–N–C bond angles in the monocoordinated phenanthroline ligand is also well reproduced, as well as the orientation of the ligands, shown by the tor-

 © 2005 Wiley-VCH Verlag GmbH & Co. KGaA, Weinheim

Table 2. Experimental and calculated (*italic*) conformational parameters for $[Pd(phen)_2]^{2+}$ and $[Pd(3\text{-R-phen})_2]^{2+}$ (R = *i*Pr, *n*Bu) complexes.

Complex	α[a]	β[a,b]	γ[a,b]
twist conformation:			
$[Pd(phen)_2][ClO_4]_2$[c]	18.7	2.9	3.0
$[Pd(phen)_2][OTf]_2$[d]	21.4	2.0, 5.6	5.2, 3.1
$[Pd(phen)_2][BF_4]_2$[e,f]	24.7	0.4	1
	20.1	0.0, 0.6	1, 3
$[Pd(phen)_2]^{2+}$[g]	*17.7*	*0.2, 0.2*	*0.7, 0.8*
$[Pd(3\text{-}i\text{Pr-phen})_2][PF_6]_2$[h]	18.8	7.4	5.0
$[Pd(3\text{-}i\text{Pr-phen})_2]^{2+}$[g]	*16.9*	*0.3*	*0.7*
$[Pd(3\text{-}n\text{Bu-phen})_2][PF_6]_2$[h]	23.2	3.6	3.4
$[Pd(3\text{-}n\text{Bu-phen})_2]^{2+}$[g]	*17.0*	*0.2*	*0.7*
bow-step conformation:			
$[Pd(phen)_2][PF_6]_2$[i]	0.0	16.2	13.4
$[Pd(phen)_2]^{2+}$[g]	*0.0*	*9.2, 9.3*	*13.4*

[a] See caption of Figure 1 for angle definitions. [b] One value for symmetry related phen moieties. [c] Ref.[17] [d] Ref.[7] [e] Ref.[1] [f] Two crystallographically independent molecules. [g] Minimum strain energy structure. [h] Ref.[8] [i] Ref.[4]

sion angle ψ and the dihedral angle τ (see footnotes h and i in Table 3). Data in Table 3 show the remarkable improvement in the structural data after inclusion of the restraint in the Pd···N distance, introduced to account for a possible weak covalent bonding interaction between Pd and the apical N atom (see below).

Table 3. Selected observed and calculated parameters in the $[Pd(CH_3)(phen)_2]^+$ (**4**), and $[Pd(CH_3)(3\text{-}s\text{Bu-phen})_2]^+$ (**5**) complexes; labels from Figure 2 apply to both complexes.

	Obs.[a]	Calcd.[a,b]	Calcd.[a,c]
Pd–C(13) [Å]	2.018(9), 2.010(10)	2.006, 2.006	2.007, 2.006
Pd–N(1) [Å][d]	2.036(8), 2.030(8)	2.053, 2.053	2.052, 2.052
Pd–N(2) [Å][f]	2.115(8), 2.122(8)	2.121, 2.121	2.119, 2.120
Pd–N(3) [Å][e]	2.040(8), 2.065(7)	2.097, 2.097	2.086, 2.086
Pd···N(4) [Å]	2.737(8), 2.716(7)	2.983, 2.987	2.752, 2.752
Pd–N(1)–C(1) [°][d]	129.1(6), 128.2(6)	127.3, 127.4	127.4, 127.6
Pd–N(3)–C(14) [°][e]	116.2(6), 116.6(7)	113.6, 113.7	116.5, 116.7
d [Å][g]	0.075, 0.062	–0.006, –0.004	0.047, 0.055
ψ [°][h]	90.5, 103.1	106.9, 110.2	99.2, 105.3
τ [°][i]	89.4, 75.5	73.7, 69.4	80.9, 73.6

[a] The first value refers to phen, the second one to 3-*s*Bu-phen. [b] Calculated values without restraints. [c] Calculated values with the Pd···N(4) distance restrained to 2.730 Å. [d] Chelate ligand. [e] Monocoordinated ligand. [f] *trans* to CH_3. [g] Metal atom displacement from the basal CN_3 plane towards the apical N atom. [h] Torsion angle N(2)–Pd–N(3)–C(14). [i] Dihedral angle between the phen (N_2C_{14}) mean planes.

Molecular and Crystal Structures

$[Pd(phen)_2]^{2+}$ and $[Pd(3\text{-R-phen})_2]^{2+}$ Complexes

Previous structural investigations of $[Pd(phen)_2]^{2+}$ complexes showed that the cations are characterised by significant ligand distortions due to the steric repulsion between the α-hydrogen atoms.[1,4,7,17] In most cases, the steric crowding is relieved by a tetrahedral distortion of the PdN_4 core yielding a *twist* conformation, in which the dihedral angle, α, between the PdN_2 planes (π_1 and π_1' in Figure 1) ranges from 18° to 25°, depending upon the nature of the anion (Table 2).[1,7,17] A similar conformation has also been found in the phenanthroline-substituted cations $[Pd(3\text{-R-phen})_2]^{2+}$ (α = 18.8 and 23.2°, for R = *i*Pr and *n*Bu, respectively),[8] and in the platinum(II) complex $[Pt(phen)_2][Cl]_2\cdot 3H_2O$ (α = 20.9°).[18] On the other hand, in the case of $[Pd(phen)_2][PF_6]_2$, the repulsive interactions are partly alleviated by a bending on opposite sides of the π_1, π_2 and π_1', π_2' planes (dihedral angles β, β') giving rise to a *step* geometry (α = 0°, $\beta = \beta'$ = 16.2°), with the five-membered rings in an *envelope* conformation.[4] This deformation is accompanied by a tilting, towards the same side, of the π_3, π_4 planes (dihedral angle γ = 13.4°) so that each phen ligand exhibits a *bow* conformation, and the cation acquires an overall *bow-step* shape.[4] However, inspection of Table 2 shows that also in the *twist* conformations there can be some "s*tepping*" and "*bowing*", like in $[Pd(3\text{-}i\text{Pr-phen})_2][PF_6]_2$ (β = 7.4° and γ = 5.0°) and in $[Pd(phen)_2][OTf]_2$, where, for one ligand, β = 5.6° and γ = 5.2°. Interestingly, in $[Pd(phen)_2][BF_4]_2$,[1] β and γ are much smaller, probably because of weaker intermolecular interactions, due to the lack of any Pd···O or Pd···F coordinating interaction, present in the other compounds.[7,17] This is in agreement with the observation that the β and γ values found in the BF_4 compound are close to those calculated for the three isolated cations, $[Pd(phen)_2]^{2+}$, $[Pd(3\text{-}i\text{Pr-phen})_2]^{2+}$ and $[Pd(3\text{-}n\text{Bu-phen})_2]^{2+}$ (Table 2), in the absence of any packing effect.

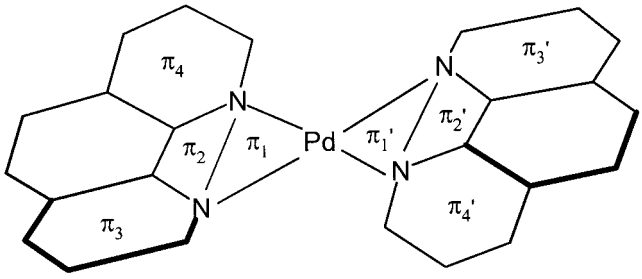

Figure 1. Planes (π_i) used to describe the conformation of the $[Pd(phen)_2]^{2+}$ complex; the dihedral angle α, between π_1 and π_1', defines the "twisting" of the two ligands, β (β'), between π_1, π_2 (π_1', π_2'), defines the "step", and γ (γ'), between π_3, π_4 (π_3', π_4'), defines the "bow".

The present MM calculations show that the $[Pd(phen)_2]^{2+}$ cation in the *twist* conformation exhibits a total strain energy about 3.7 kcal mol^{-1} lower than that in the *bow-step* conformation, mainly because of a lower torsional energy contribution. This indicates that the *bow-step* conformation is only slightly less stable, confirming the hypothesis that, in the solid state, it can be stabilised by van der Waals and electrostatic forces, without the need for particular stacking interactions.[1]

 © 2005 Wiley-VCH Verlag GmbH & Co. KGaA, Weinheim

It is interesting to observe that the *twist* distortion gives a two-bladed propeller shape to the $[Pd(phen)_2]^{2+}$ cation (C_2 point group symmetry), whose chirality can be assigned using the Δ, Λ descriptors.[19] On the contrary, the *bow-step* conformation is achiral being characterised by a C_{2v} symmetry.

Finally, it is worth noting that, in the solid state, the $[Pd(3\text{-}i\text{Pr-phen})_2]^{2+}$ and $[Pd(3\text{-}n\text{Bu-phen})_2]^{2+}$ complexes, have the side groups placed on the same side, in a *syn* geometry. In fact, MM calculations show that this isomer, for both of the isolated cations, exhibits a strain energy slightly lower than that of the *anti* isomer (*i*Pr, 0.8 kcal mol^{-1}; *n*Bu, 1.1 kcal mol^{-1}). This is qualitatively in agreement with the results of a DFT study performed on the same derivatives.[8] However, the energy differences are rather low, suggesting that the stabilisation of the *syn* isomers in the solid state is probably due to packing effects.

$[Pd(CH_3)(phen)_2]^+$ and $([Pd(CH_3)(3\text{-R-phen})_2]^+$ Complexes

The most interesting structural feature in the crystals of the $[Pd(CH_3)(phen)_2]^+$,[5] and $[Pd(CH_3)(3\text{-}s\text{Bu-phen})_2]^+$ (Figure 2) cations is the distorted square-planar geometry of the Pd atoms with one phenanthroline molecule acting as a monocoordinated ligand. The orientation of this phen group is such that the uncoordinated nitrogen atom, through rotation around the Pd–N bond, occupies a pseudo-apical position at 2.73(1) Å from the metal atom. The rotation around the Pd–N bond is measured by the torsion angle ψ (N[2]–Pd–N(3)–C(14) in Figure 2), which is 90.5° and 103.0° in $[Pd(CH_3)(phen)_2]^+$[5] and $[Pd(CH_3)(3\text{-}s\text{Bu-phen})_2]^+$, respectively (Table 3). The two phenanthroline ligands are nearly perpendicular to each other in the phen complex (dihedral angle τ = 89.4°);they form a narrower angle in the 3-*s*Bu-phen derivative (τ = 75.5°). A similar structure has been found in the related complex $[Pd(CH_2NO_2)(phen)_2][PF_6]$, where the Pd···N distance is 2.674(3) Å and τ = 88.9°.[6]

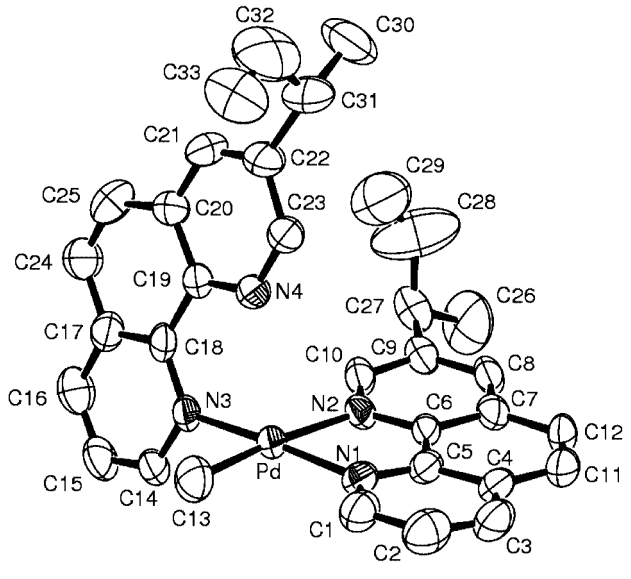

Figure 2. ORTEP drawing of the $[Pd(CH_3)(3\text{-}s\text{Bu-phen})_2]^+$ cation (thermal ellipsoids at 40% probability level).

The strain energy minimisation (without any restraint), starting from the crystal structure coordinates of $[Pd(CH_3)(phen)_2]^+$, yields for the calculated structures ψ = 106.9° and τ = 73.7°, and, in the case of $[Pd(CH_3)(3\text{-}s\text{Bu-phen})_2]^+$, ψ = 110.2° and τ = 69.4°, not too far from the solid-state values. This indicates that the orientation of the monocoordinated ligand is essentially determined by intramolecular van der Waals and electrostatic interactions. On the other hand, in the minimum-strain-energy structures, the average Pd···N distance is 2.985(1) Å. Interestingly, this distance is significantly shorter than the sum of the assumed van der Waals radii (1.93+1.82 = 3.75 Å), but much longer than the experimental distances, which suggests the presence of some Pd–N valence-bonding interaction not modelled in the present force field (no specific d^o and k^b values). In this respect, we must observe that the van der Waals radius of 1.93 Å, derived for Pd^{II} in the present force field, in correspondence with ε_{Pd} = 0.69 kcal mol^{-1}, is somewhat intermediate between the previously proposed values of 1.65 Å[20] and 2.60 Å,[21] and not far from 1.7 Å (ε_{Pd} = 0.2 kcal mol^{-1}) reported by Hambley, from MM modelling of nonbonded Pd···H and Pd···S interactions.[22] In fact, this last value might be an underestimate in the case of weakly attractive (agostic) interactions with the metal atom.[22]

The presence of a bonding contribution is further indicated by the displacement of the palladium atom from the coordination mean plane (Table 3). In fact, by restraining the Pd···N distance to 2.730 Å a remarkable improvement of the Pd out-of-plane distance is obtained, as well as of ψ and τ (Table 3). On the basis of these results, we can assume that the palladium coordination polyhedron is intermediate between a square-planar and a square-pyramidal geometry, even though, in this last case, a Pd–N distance of about 2.347 Å should be expected for an apical bond.[23] However, a constraint on such a value for the Pd···N distance causes a dramatic increase of the strain energy (≈ 75 kcal mol^{-1}), essentially because of the increase of the van der Waals energy term. Thus, the attractive bonding interaction between the Pd and N atoms seems to be in balance with significant intraligand repulsive forces.

^{1}H NMR spectroscopy has shown the equivalence, in solution, of the two phen ligands, indicating the presence of a dynamic process, which involves either the exchange between the unbound nitrogen atom of the monocoordinated ligand and that of the chelate ligand *trans* to the methyl group (*opening-closure*), or the exchange of the two nitrogen atoms at the same coordinating site (*flipping*).[5]

In order to investigate the steric aspects of this process, we have undertaken an analysis of the strain energies of the species possibly involved. From a structural point of view, we have only one stereoisomer in the case of the phen ligand ($[Pd(CH_3)(phen)_2]^+$) and four distinct diastereoisomers in the case of the 3-alkyl-phen ligands ($[Pd(CH_3)(3\text{-R-phen})_2]^+$, with R = *i*Pr and *s*Bu), depending on the relative position of the substituents (Figure 3).

 © 2005 Wiley-VCH Verlag GmbH & Co. KGaA, Weinheim

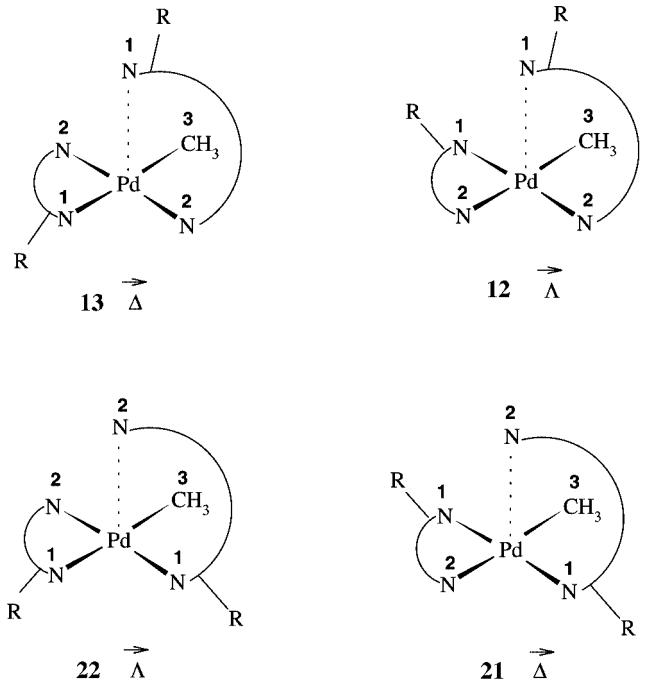

Figure 3. Sketch of the stereoisomers of the $[Pd(CH_3)(3\text{-R-phen})_2]^+$ cations, with their stereochemical descriptors; ranking numbers are also reported.

The different diastereoisomers are identified by a two-digit configuration index formally assuming a bischelated complex with a square pyramidal geometry.[19] For the 3-R-phen complexes, the priority of the ligating atoms decreases in the order N(–R) > N > C, with ranking numbers 1, 2 and 3, respectively (Figure 3). The chirality of these complexes (C_1 symmetry) can be conveniently described by the "oriented-skew-lines" reference system, considering the N···N lines of the 3-R-phen ligands oriented from N(–R) to N.[24]

It is to be noted that the change of the apical position implies an inversion of the complex configuration, with inversion of the sign of ψ. Furthermore, because of the approximate coplanarity of the atoms in the phenanthroline ligands and in the coordination basal plane, the variation of ψ implies a variation of the dihedral angle τ such that $|\psi| + \tau \approx 180°$ (Table 4). Therefore, the rotation of the phen ligand around the Pd···N axis corresponds to the swinging of the ligand plane around the Pd···N "hinge".

In order to investigate the isomer stability, we have calculated the strain energy for the four diastereoisomers of $[Pd(CH_3)(3\text{-}s\text{Bu-phen})_2]^+$, with different combinations of the *R*/*S* chirality of the *s*Bu groups (Table 4). ΔE and ψ (configuration $\vec{\Delta}$) values have been calculated with and without the restraint on the Pd···N distance. However, inspection of Table 4 shows that there are small energy differences between the two cases. It is worthy of note that after introduction of the restraint, the lowest energy is exhibited by isomer **13**, in which the asymmetric carbon atoms of the *sec*-butyl group in the chelated and that in the monocoordinated phen ligands have opposite configurations, as in the diastereoisomers **13** (*R*–*S*) and **13** (*S*–*R*). In fact, the former isomer has been found in the crystal. This shows once again that the introduction of the Pd···N restraint is necessary for the best description of the structural properties of these complexes. As shown in Table 4, in each diastereoisomer, ΔE is nearly unaffected by the chirality of the *s*Bu groups, while it increases slightly, in the order **13** < **22** < **21** < **12**, with a maximum energy difference of about 1.3 kcal mol^{-1}. Finally, calculations show that changes in the conformation of the *s*Bu groups (φ angles) cause small changes in ΔE.

Table 4. Scaled strain energies [kcal mol^{-1}] for the four diastereoisomers of $[Pd(CH_3)(3\text{-}s\text{Bu-phen})_2]^+$, all in configuration $\vec{\Delta}$ considering the possible combinations of the ligand chirality; ΔE represents the strain energy differences with respect to the lowest-energy isomer; some conformational parameters (see Figure 2 for labels) are also reported for the "restrained" structures.

Isomer	Chirality[a]	ΔE[b]	ΔE[c]	Ψ [°][d]	τ [°][e]	φ_1 [°][f]	φ_2 [°][g]	φ_1' [°][h]	φ_2' [°][i]
13	*R*–*S*	0.6	0.0	101.7	79.0	117.7	–53.6	60.8	54.8
	S–*R*	0.2	0.0	101.7	79.0	60.6	54.5	117.9	–54.3
	S–*S*	0.0	0.1	107.5	71.7	57.5	52.1	118.2	54.9
	R–*R*	0.3	0.3	106.1	73.8	–60.4	–54.2	117.1	–53.9
22	*S*–*S*	0.4	0.4	–103.3	77.5	58.8	52.5	59.0	52.4
	S–*R*	0.5	0.6	–78.7	101.6	58.1	53.2	–59.8	–53.5
	R–*S*	0.6	0.6	–103.6	76.7	–59.1	–53.5	59.7	53.1
	R–*R*	0.8	0.8	–103.3	77.0	–59.1	–53.6	116.5	–53.5
21	*S*–*S*	1.1	1.1	103.7	76.8	60.1	54.4	59.4	53.9
	S–*R*	1.2	1.1	103.4	77.2	60.1	54.4	–60.3	–54.3
	R–*S*	1.1	1.1	103.6	76.9	–60.0	–54.3	59.5	54.0
	R–*R*	1.2	1.1	103.4	77.2	–60.0	–54.3	–54.3	–54.3
12	*S*–*S*	1.4	1.3	–80.2	100.5	59.2	53.7	59.6	54.3
	S–*R*	1.4	1.3	–102.7	77.6	59.7	54.0	–60.3	–54.7
	R–*S*	1.4	1.3	–102.7	77.9	–60.1	–54.4	60.3	54.8
	R–*R*	1.4	1.3	–81.6	98.8	–60.2	–54.5	–60.4	–54.8

[a] The configuration of the asymmetric carbon atoms refers to the *s*Bu group in the chelate and in the monocoordinated ligand, respectively. [b] No restraint on the Pd···N distance, which averages 2.987(3) Å. [c] Pd···N distance restrained to 2.752 Å. d N(2)–Pd–N(3)–C(14). [e] Footnote i in Table 3. [f] C(10)–C(9)–C(27)–C(28). [g] C(9)–C(27)–C(28)–C(29). [h] C(23)–C(22)–C(31)–C(32). [i] C(22)–C(31)–C(32)–C(33).

 © 2005 Wiley-VCH Verlag GmbH & Co. KGaA, Weinheim

As shown in Table 4, the minimum energy structures are provided by *gauche*-like conformations ($\varphi \approx \pm 60°, \pm 120°$).

The possibility of rotation of the monocoordinated phen ligand around its Pd–N bond (torsion angle ψ) has been investigated through a conformational analysis of the $[Pd(CH_3)(phen)_2]^+$ and $[Pd(CH_3)(3\text{-}s\text{Bu-phen})_2]^+$ cations, imposing the Pd···N restraint, and considering the enantiomeric species with $\psi > 0$, in the range between 50° and 130°.

As shown in Figure 4, in the case of the phen complex, "free" rotation is limited to a ψ range between 65° and 115°, in correspondence of the broad low-energy region ($\Delta E < 1$ kcal mol^{-1}), with two minima around $\psi = 80°$ and $\psi = 100°$, the second one with an energy only 0.2 kcal mol^{-1} higher. A similar behaviour is found for the **22** $\vec{\Delta}$ (*R*–*S*) isomer of the 3-*s*Bu-phen derivative ($\Delta E = 0.3$ kcal mol^{-1}), whereas its other *R*–*S* diastereoisomers, as well as all those of the **12** and **21** isomers, exhibit the opposite trend, having the deepest minimum at $\psi \approx 100°$–$105°$, with ΔE values varying from 0.1 to 0.3 kcal mol^{-1}. Calculations show that in the case of isomer **13** $\vec{\Delta}$, the energy at $\psi \approx 80°$ slightly increases in the order (*R*–*R*) < (*S*–*S*) < (*S*–*R*) < (*R*–*S*), with ΔE in the range 0.4–0.6 kcal mol^{-1}.

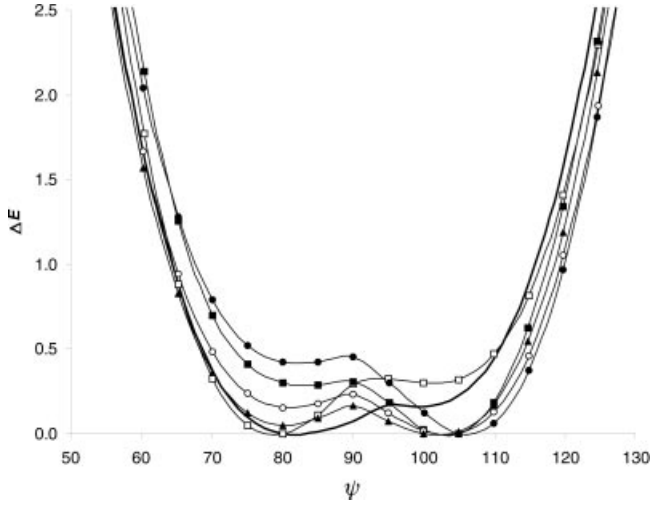

Figure 4. Plot of ΔE [kcal mol^{-1}] vs. the rotation angle ψ [°] (Pd···N restraint) for $[Pd(CH_3)(phen)_2]^+$ (thick line), and for some isomers of $[Pd(CH_3)(3\text{-}s\text{Bu-phen})_2]^+$: **22** $\vec{\Lambda}$ (*R*–*S*) (□), **22** $\vec{\Lambda}$ (*R*–*R*) (■), **12** $\vec{\Lambda}$ (*R*–*R*) (#9650;), **21** $\vec{\Delta}$ (*R*–*R*) (○), and **13** $\vec{\Delta}$ (*R*–*R*) (●).

The small differences calculated for the strain energies (Table 4) account for the fluxional behaviour in solution of this kind of complexes, and the proposed ligand exchange mechanism.[5] In fact, the *flipping* process yields the equilibration between isomers **13** and **22** ($E_{22} - E_{13} \approx 0.4$ kcal mol^{-1}), the last one also being in equilibrium with **12**, through an *opening-closure* process ($E_{12} - E_{22} \approx 0.9$ kcal mol^{-1}). Finally, a *flipping* process converts **12** into **21** ($E_{12} - E_{21} \approx 0.2$ kcal mol^{-1}). Furthermore, the *opening-closure* process converts isomer **21** into its enantiomeric form. NMR spectra show the complete equivalence of the phenanthroline ligands, indicating the presence in solution of all the isomers, but say nothing about their relative populations. On the basis of such energy differences it may be expected that the isomers are present in solution, at room temperature, in approximately equimolar ratios.

[Pd(H)(phen)$_2$]$^+$ and [Pd(H)(3-tmp-phen)$_2$]$^+$ Complexes

A palladium hydride intermediate, such as [Pd(H)(N–N)(S)]$^+$, where S represents a coordinating solvent molecule, has been proposed to be present in the termination step of the copolymerisation reaction mechanism.[2] Depending upon the reaction conditions, the Pd-hydride can be reoxidised to the catalytically active species, or can insert the olefin starting a new polymeric chain. Eventually, it can evolve to palladium metal. The stability of the active species increases with an excess of the phenanthroline ligand, probably because of the formation of species like [Pd(H)-(phen)$_2$]$^+$, which should prevent the Pd-hydride intermediate from decomposing to palladium metal.[2]

Assuming for this last complex the pseudo-square-pyramidal structure found in the methyl derivatives, MM calculations have been performed for both the phen and the 3-tmp-phen complexes, in order to get some information about their structural behaviour. Inspection of Table 5 shows that, like in the 3-*s*Bu-phen methyl complex, the strain energy slightly increases from isomer **13** to isomer **22**, while **12** and **21** exhibit slightly higher energies. However, the energy trends, as a function of the ligand chirality, are different, and the energy changes are larger.

Table 5. Scaled strain energies [kcal mol^{-1}] for the four diastereoisomers of $[Pd(H)(3\text{-tmp-phen})_2]^+$, all in configuration $\vec{\Delta}$, considering the possible combinations of the ligand chiralities; the torsion angle ψ [°] and the dihedral angle τ [°] are also reported (see footnotes h, i in Table 3).

Isomer	Chirality[a]	ΔE[b]	ψ[b]	τ[b]
13	*S*–*R*	0.0	104.6	74.7
	S–*S*	0.1	105.6	76.4
	R–*S*	1.7	69.8	110.9
	R–*R*	2.0	67.5	111.9
22	*R*–*S*	0.8	–82.3	99.7
	S–*S*	0.9	–71.0	110.2
	R–*R*	1.4	–101.1	79.4
	S–*R*	1.5	–108.2	72.6
12	*S*–*S*	0.9	–69.0	113.5
	S–*R*	1.3	–67.5	113.7
	R–*S*	1.4	–68.6	113.1
	R–*R*	1.8	–68.2	112.6
21	*R*–*S*	1.4	68.7	111.5
	S–*S*	1.4	69.1	110.4
	S–*R*	1.5	74.5	106.9
	R–*R*	1.5	74.0	108.1

[a] The configuration of the asymmetric carbon atoms refers to the tmp-phen group in the chelate and in the monocoordinated phen, respectively. [b] After energy minimisation with a restraint on the Pd···N distance, which results in 2.752 Å.

[Pd{CH(C$_6$H$_5$)CH$_2$C(O)OCH$_3$}(N–N)(L)]$^+$ Complexes

Monocations like [Pd{CH(C$_6$H$_5$)CH$_2$C(O)OCH$_3$}(N–N)(L)]$^+$, where N–N represents chelated phen and 3-tmp-

 © 2005 Wiley-VCH Verlag GmbH & Co. KGaA, Weinheim

phen ligands, and L = CH_3OH or a monocoordinated N–N molecule, are models of possible species involved in the initiation steps of the reaction mechanism for the CO/styrene copolymer chain growth.

In the case of the $[Pd\{CH(C_6H_5)CH_2C(O)OCH_3\}(3\text{-tmp-phen})(CH_3OH)]^+$ derivative, two isomers (*cis* and *trans*) are possible, depending on the relative positions of the growing polymer chain and the nitrogen atom close to the tmp group (Figure 5); while in the case of L = N–N, we have the same isomers of the methyl complexes mentioned above.

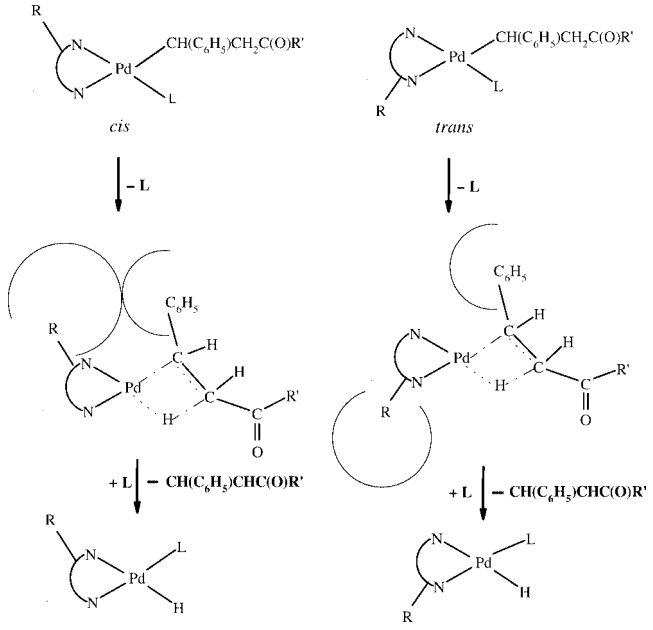

Figure 5. Sketch showing the formation of the transition states for the β-hydrogen elimination process, yielding the termination of the CO/styrene copolymer chain growth; L represents a coordinating solvent or a monocoordinated phen ligand; R′ = OCH_3 or the growing polymer chain; bonds under cleavage or formation are drawn as dotted lines; the arcs depict the steric encumbrance of the R and phenyl groups during their rotation around the C–C bonds.

Examination of molecular models shows that there is no particular difference between the phen and the 3-tmp-phen complexes, as to their steric hindrance to the attack of a further styrene molecule, both in the case of the square-planar (L = CH_3OH) and of the pseudo-square-pyramidal (L = N–N) complexes. Therefore, there is no apparent reason for the observed differences in the copolymerisation reaction, attributable to steric effects in the chain initiation steps.

As a matter of fact, the observation that increasing the bulkiness of the 3-alkyl group remarkably increases the molecular weight of the polymer chains[3] suggests that the bulkiness of the group could play an important role in the chain termination step, which proceeds through a β-hydrogen elimination reaction.[2] As depicted in Figure 5, the reaction intermediate obtained from the *cis* isomer (*cis*-β-H) is destabilised with respect to that obtained from the *trans* isomer (*trans*-β-H) by the steric interactions between the phenyl and the tmp groups, which, at the reaction temperature (≈ 50 °C), can be considered to be freely rotating around their respective single C–C bonds. Because this intermediate leads to the detachment of the copolymer chain, it seems likely that the molecular weight of the copolymer will increase to the extent the β-hydrogen elimination reaction is retarded.

Anyhow, inspection of molecular models (Figure 6, top) indicates that in the *cis*-β-H complex, the repulsive effects are efficient only when the chiral carbon atom of the tmp group and that of the Pd-bound chain exhibit opposite configurations (*R* and *S*, respectively, in Figure 6), displaying the two groups on the same side of the coordination plane. On the contrary, in the case of the *trans*-β-H intermediate (Figure 6, bottom), the two groups are sufficiently distant, even in the case of homochiral groups.

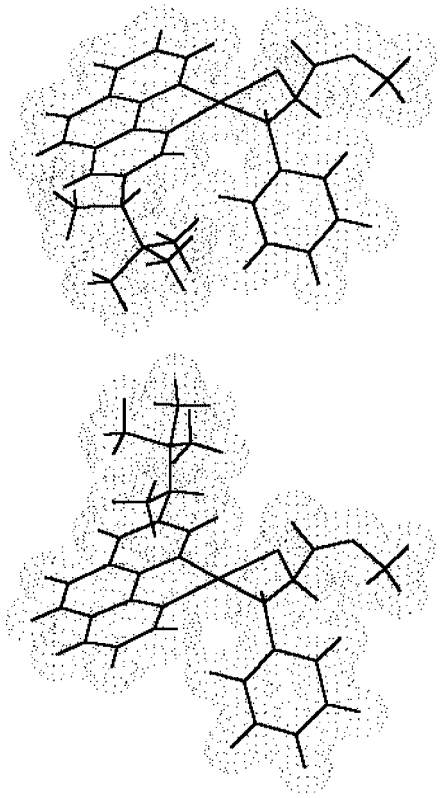

Figure 6. Sketch of the (*R*–*S*)-β-hydrogen elimination intermediate, from the *cis* (top) and *trans* (bottom) isomer of $[Pd\{CH(C_6H_5)CH_2C(O)OCH_3\}(3\text{-tmp-phen})(L)]^+$.

On this basis, it is expected that the termination reaction can occur more easily with the phen complexes rather than with the 3-tmp-phen complexes. In this last case, in fact, the *R*–*S* and *S*–*R* diastereoisomers of the *cis* complex are destabilised by steric interactions, reducing the concentration in solution of the palladium species prone to forming the β-H reaction intermediate.

Conclusions

The stereochemistry of Pd-phenanthroline complexes $[Pd(3\text{-R-phen})_2]^{2+}$ (R = H, alkyl group) has been investi-

 © 2005 Wiley-VCH Verlag GmbH & Co. KGaA, Weinheim

gated in relation with their action as precatalysts in the CO/styrene copolymerisation process.

The results of the MM investigation have shown that the specific force field, derived here, is suitable for a description of the molecular structure of the above dications and of organometallic complexes like $[Pd(CH_3)(3\text{-R-phen})_2]^+$. In the first case, steric effects are shown to determine severe distortions from a square-planar coordination geometry of the metal atom. This can explain the instability of the dications, which in solution of coordinating solvents, undergo dissociation of one chelate ligand and substitution with solvent and/or monocoordinated phen molecules, giving rise to the catalytically active species. In the methyl monocations, the coordination polyhedron results to be intermediate between square planar and square pyramidal, one phenanthroline ligand having one nitrogen atom loosely bound to Pd, in a pseudo apical position. The comparison of the strain energies of all the possible diastereoisomers, together with the results of conformational analyses, account for the possible exchange between the various isomers, in agreement with the fluxional behaviour detected in solution by NMR spectroscopy.

Molecular modelling suggests that peculiar steric effects can be displayed by bulky alkyl groups in 3-R-phen complexes during the termination step of the CO/styrene copolymerisation reaction. In fact, the β-hydrogen elimination reaction appears to be hindered in the presence of a bulky group, such as 1,2,2-trimethylpropyl, allowing the formation of longer copolymer chains.

In order to get a deeper insight into the Pd–N bonding in the square pyramidal methyl derivatives, a quantum chemical investigation appears of interest. Of great importance would also be the quantum chemical investigation of the structure of the intermediate species involved in the β-hydrogen elimination reaction, checking the influence of the phenanthroline side groups. These, in fact, cannot be properly treated by MM methods.

Experimental Section

Materials and Instrumentation: The analytical grade solvents and chemicals (Carlo Erba and Aldrich) were used without further purification for synthetic purposes. The dichloromethane used for the synthesis was purified through distillation over $CaCl_2$ and stored under an inert atmosphere. $[Pd(CH_3COO)_2]$ was a loan from Engelhard Italiana SpA. The 3-*s*Bu-phen, in the racemic form, was prepared by Serafino Gladiali from the University of Sassari. ^1H NMR spectra were recorded at 400 MHz with a JEOL EX 400 spectrometer; the resonances were referenced to the solvent peak versus TMS: $CDCl_3$ at δ = 7.26 ppm.

Synthesis of Complexes: All manipulations were carried out under argon and at room temperature by using Schlenk techniques. Elemental analyses (C, H, N), performed at Dipartimento di Scienze Chimiche (Università di Trieste), were in perfect agreement with the proposed stoichiometry. The compound $[Pd(CH_3)(CH_3CN)(3\text{-}s\text{Bu-phen})][OTf]$ was synthesised as previously reported.[5]

Synthesis of $[Pd(CH_3)(3\text{-}s\text{Bu-phen})_2][OTf]$: *rac*-3-*s*Bu-phen (0.26 mmol) was added to a suspension of $[Pd(CH_3)(CH_3CN)(3\text{-}s\text{Bu-phen})][OTf]$ (0.20 mmol) in chloroform (20 mL) (Pd/3-*s*Bu-phen = 1:1.3) yielding an orange solution. After 10 min, the solution was filtered through fine paper and concentrated under vacuum to induce precipitation of the product as an orange solid. The solid was removed by filtration, washed with diethyl ether and vacuum dried. Yield: 80 %. $C_{34}H_{35}F_3N_4O_3PdS$: calcd. C 54.95, H 4.75, N 7.54; found C 54.6, H 4.71, N 7.60. ^1H NMR ($CDCl_3$): δ = 8.73 (br., 2 H, H^9), 8.69 (br., 2 H, H^2), 8.51 (d, 2 H, H^7), 8.30 (s, 2 H, H^4), 8.02 (s, 4 H, $H^{5,6}$), 7.70 (dd, 2 H, H^8), 0.96 (s, 3 H, CH_3), 0.98 (s, 3 H, CH_3) ppm.

Crystallography: Diffraction data for $[Pd(CH_3)(3\text{-}s\text{Bu-phen})_2][PF_6]\cdot CH_2Cl_2$ were collected at room temperature with the $\omega/2\theta$ scan technique on a CAD4 Enraf–Nonius diffractometer, equipped with graphite-monochromator and Mo-K_α radiation (l = 0.71073 Å). Intensity data were corrected for Lorentz polarisation effects and also for absorption, based on an empirical ψ-scan method. The structure was solved by conventional Patterson and Fourier techniques,[25] and refined by the full-matrix least-squares method based on F^2.[25] The fluorine atoms of the PF_6^- anion were found to be disordered over two positions [refined occupancies of 0.75(2) and 0.25(2)]. A difference Fourier map allowed to detect a disordered molecule of CH_2Cl_2. All the calculations were performed with the WinGX System, Ver 1.64.05.[26] Crystal data: $C_{34}H_{37}Cl_2F_6N_4PPd$, M = 823.95, triclinic, space group $P\bar{1}$ (No. 2), a = 11.002(4), b = 12.508(4), c = 14.502(4) Å, α = 80.67(3), β = 82.37(2), γ = 65.37(3)°, V = 1785.4(10) Å^3, Z = 2, $\rho_{calcd.}$ = 1.533 g cm^{-3}, μ(Mo-K_α) = 0.776 mm^{-1}, F(000) = 836; 7670 reflections collected ($2\theta_{max}$ = 53°), 7367 unique [R(int) = 0.0363], 3332 observed reflections $I > 2\sigma(I)$, 458 parameters, $R1$ = 0.0658, $wR2$ = 0.1658, GoF = 1.017; hydrogen atoms in idealised geometry; max positive and negative peaks in ΔF map 0.561 and –0.637 e Å^{-3}, respectively. CCDC-232498 contains the supplementary crystallographic data for this paper. These data can be obtained free of charge from The Cambridge Crystallographic Data Centre via www.ccdc.cam.ac.uk/data_request/cif.

Acknowledgments

This work was supported by Ministero dell'Istruzione, dell'Università e della Ricerca (MIUR – Rome; PRIN No. 2003033857). Engelhard Italiana is gratefully acknowledged for a generous loan of $[Pd(CH_3COO)_2]$. The authors wish to thank Prof. Serafino Gladiali (University of Sassari) for providing a sample of *rac*-3-*s*Bu-phen.

[1] B. Milani, A. Anzilutti, L. Vicentini, A. Sessanta o Santi, E. Zangrando, S. Geremia, G. Mestroni, *Organometallics* **1997**, *16*, 5064–5075.
[2] B. Milani, G. Corso, G. Mestroni, C. Carfagna, M. Formica, R. Seraglia, *Organometallics* **2000**, *19*, 3435–3441.
[3] B. Milani, A. Scarel, G. Mestroni, S. Gladiali, R. Taras, C. Carfagna, L. Mosca, *Organometallics* **2002**, *21*, 1323–1325.
[4] S. Geremia, L. Randaccio, G. Mestroni, B. Milani, *J. Chem. Soc. Dalton Trans.* **1992**, 2117–2118.
[5] B. Milani, A. Marson, E. Zangrando, G. Mestroni, J. M. Ernsting, C. J. Elsevier, *Inorg. Chim. Acta* **2002**, *327*, 188–201.
[6] B. Milani, G. Corso, E. Zangrando, L. Randaccio, G. Mestroni, *Eur. J. Inorg. Chem.* **1999**, 2085–2093.
[7] P. Wehman, V. E. Kaasjager, W. G. J. De Lange, F. Hartl, P. C. J. Kamer, P. W. N. M. van Leeuwen, J. Fraanje, K. Goubitz, *Organometallics* **1995**, *14*, 3751–3761.
[8] A. Scarel, B. Milani, E. Zangrando, M. Stener, S. Furlan, G. Fronzoni, G. Mestroni, S. Gladiali, C. Carfagna, L. Mosca, *Organometallics* **2004**, *23*, 5593–5606..
[9] W. D. Cornell, P. Cieplak, I. R. Bayly, I. R. Gould, K. M. J. Merz Jr., D. M. Ferguson, D. C. Spellmeyer, T. Fox, J. W. Cald-

 © 2005 Wiley-VCH Verlag GmbH & Co. KGaA, Weinheim

well, P. A. Kollman, *J. Am. Chem. Soc.* **1995**, *117*, 5179–5197.
[10] a) S. Geremia, M. Calligaris, *J. Chem. Soc. Dalton Trans.* **1997**, 1541–1547; b) S. Geremia, L. Vicentini, M. Calligaris, *Inorg. Chem.* **1998** , *37*, 4094–4103.
[11] a) S. Geremia, M. Calligaris, L. Randaccio, *Eur. J. Inorg. Chem.* **1999**, 981–992; b) M. Calligaris, L. Randaccio, *Eur. J. Inorg. Chem.* **2002**, 2920–2927.
[12] *HyperChem*, Hypercube Inc., Waterloo, Ontario, **2000**.
[13] M. Calligaris, GEOM, **2001**, University of Trieste, Trieste, Italy.
[14] R. M. Badger, *J. Chem. Phys.* **1934**, *2*, 128–131.
[15] D. R. Herschbach, V. W. Laurie, *J. Chem. Phys.* **1961**, *35*, 458–463.
[16] T. A. Halgren, *J. Am. Chem. Soc.* **1990**, *112*, 4710–4723.
[17] J. V. Rund, A. C. Hazell, *Acta Crystallogr. Sect. B* **1980**, *36*, 3103–3105.
[18] A. Hazell, A. Mukhopadhyay, *Acta Crystallogr. Sect. B* **1980**, *36*, 1647–1649.
[19] a) G. L. Leigh (Ed.), *Nomenclature of Inorganic Chemistry*, Blackwell, Oxford, **1990**; b) A. von Zelewsky, *Stereochemistry of Coordination Compounds*, Wiley, Chichester, **1995**.
[20] A. Bondi, *J. Phys. Chem.* **1964**, *68*, 441–451.
[21] A. Vedani, D. W. Hutha, *J. Am. Chem. Soc.* **1990**, *112*, 6061–6077.
[22] T. W. Hambley, *Inorg. Chem.* **1998**, *37*, 3767–3774.
[23] J. H. Groen, B. J. de Jong, J.-M. Ernsting, P. W. N. M. van Leeuwen, K. Vrieze, W. J. J. Smeets, A. L. Spek, *J. Organomet. Chem.* **1999**, *573*, 3–13.
[24] T. Damhus, C. E. Schäffer, *Inorg. Chem.* **1983**, *22*, 2406–2412.
[25] G. M. Sheldrick, *SHELX97 Programs for Crystal Structure Analysis (Release 97–2)*, University of Göttingen, Germany, **1998**.
[26] L. J. Farrugia, *J. Appl. Crystallogr.* **1999**, *32*, 837–838.
Received May 27, 2004

 © 2005 Wiley-VCH Verlag GmbH & Co. KGaA, Weinheim

Preparation and Coordination Chemistry of *n*-Allylaminophosphane

Alexandra M. Z. Slawin,[a] Joanne Wheatley,[a] and J. Derek Woollins*[a]

Keywords: Phosphanes / Alkenes / Hemilabile complexes / X-ray structures

Reaction of allylamine with 1 equiv. of Ph_2PCl in the presence of NEt_3, proceeds in THF to give (allylamino)phosphane **1**. **1** has been coordinated as a monodentate *P* ligand with Au, Pd, Pt, Ru, Rh, Ir and as a bidentate *P,allyl* ligand to Pt. Reaction of KO*t*Bu with $[PtCl_2\{Ph_2PNH(C_3H_5)\}_2]$ in methanol gives $[Pt\{Ph_2PNH(C_3H_8O)\}_2]$. The X-ray structures of **1**.Se and four demonstrative monodentate complexes all reveal intramolecular N–H···Cl hydrogen bonding. The structure of $[Pt\{Ph_2PNH(C_3H_8O)\}_2]$ consists of an N–H···O hydrogen-bonded dimer in the solid state.
(© Wiley-VCH Verlag GmbH & Co. KGaA, 69451 Weinheim, Germany, 2005)

Introduction

Phosphane–alkenes have the potential to coordinate with the phosphorus atom or through the olefin moiety. For example, Coutinho et al.[1] treated a variety of phosphido-bridged complexes, $[(OC)_4M(\mu\text{-}PPh_2)_2RhH(CO)(PPh_3)]$, with the phosphanylalkenes $Ph_2P(CH_2)_nCH{=}CH_2$ (M = Cr, Mo or W; n = 1–3); in these reactions the olefin undergoes hydroformylation, which is of great interest today in commercial processes including the Rhone-Poulenc/Ruhr Chemie aqueous-based system.[2] Furthermore, work continues to prepare ligands that lead to greater regioselectivity and/or enantioselectivity.[3] It is of interest to investigate other potentially hemilabile ligands to increase the success and efficiency of current processes and in early work the olefinic fragment was used as a stabilising group with strongly bonding phosphane ligands.[4] More recently the study of phosphane–alkene ligands has focused on the weakly ligating nature of the alkene, for example, Brookes[4] displaced the olefinic groups of a rhodium complex with a tetraphenylborate anion to yield a piano stool metal complex. Lindner et al.[5] showed that the furan ring in (phopshanylalkyl)furan ligands could ligate to metal centres in an η^1-fashion through the oxygen atom or by an η^2-fashion through the C=C double bonds. The most favoured coordination mode of these types of phosphane–alkene ligands was shown to be the η^2-fashion as the partial donation of the lone pair from the oxygen atom makes the η^1-fashion coordination less favourable due to the oxygen atom being a poorer σ-donor than the olefinic groups. Diphenyl(vinyl) phosphane (DPVP) was shown by the Barthel-Rosa research group to be a hemilabile ligand when coordiniated to ruthenium(II) centres.[5] They showed that the (η^3-DPVP) ruthenium(II) complex could react both reversibly and irreversible depending on the small molecule that was used in the reaction. A reversible reaction was observed when acetonitrile was used; however, in the presence of CO the reaction was found to be irreversible but in both instances the DPVP ligand underwent an η^3- to η^1-shift that opened up a coordination site on the metal centre. It is clear that there is a potentially rich and diverse coordination chemistry available for phosphane–alkenes.

Here, we report the preparation of an aminophosphane which contains an olefinic side chain and thus the potential to act as a hemilabile ligand. Illustrative coordination complexes have been prepared.

Results and Discussion

Reaction of allylamine with 1 equiv. of Ph_2PCl in the presence of NEt_3, proceeds in THF to give **1** which was isolated (41 % yield) by filtration from $Et_3NH^+Cl^-$ as a colourless oil that was purified by distillation (132 °C/0.2 Torr). After storing under nitrogen at –18 °C a colourless waxy solid formed (41 % yield). The $^{31}P\{^1H\}$ NMR spectrum of **1** consists of a singlet at δ_P = 42.5 ppm. The EI^+ mass spectrum gave the expected fragmentation pattern and parent ion observed at *m*/*z* 242. The microanalysis gave satisfactory results for the suggested structure. The chalcogenides of $Ph_2PNH(C_3H_5)$ were prepared easily [Equation (1)].

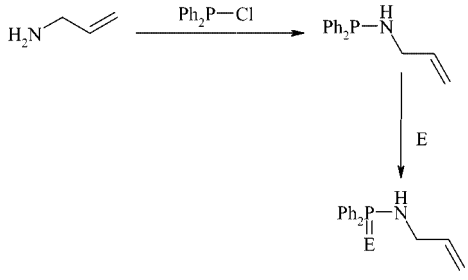

(1)

[a] School of Chemistry, University of St Andrews, St Andrews, Fife KY16 9ST
E-mail: jdw3@st-and.ac.uk

 DOI: 10.1002/ejic.200400447 © 2005 Wiley-VCH Verlag GmbH & Co. KGaA, Weinheim

The oxide $Ph_2P(O)NH(C_3H_5)$ (**2**) was prepared by addition of urea/hydrogen peroxide to a dichloromethane solution of **1** whilst the sulfur and selenium analogues **3** and **4** were prepared by the addition of elemental S or Se to the ligand in toluene. Microanalysis and EI^+ mass spectroscopic data for all the chalcogenides prepared were satisfactory and the $^{31}P\{^1H\}$ NMR showed single resonances ($CDCl_3$) at δ_P = 24.4 and 60.5 ppm for the oxide and sulfide, respectively. The selenium analogue exhibited a single $^{31}P\{^1H\}$ NMR resonance ($CDCl_3$) at δ_P = 58.1 ppm with selenium satellites [$^1J(^{31}P\text{-}^{77}Se)$ = 756 Hz] which is typical for a P=Se group.[6]

The crystal structure of **4** (Figure 1, Table 1). shows that in the solid state the molecule forms hydrogen-bonded dimers. The NH proton of one molecule is hydrogen-bonded to the selenium atom of a second and the selenium atom of the second interacts with the NH proton of the first, leading to a head to tail type arrangement of the molecules [H(2)···Se(1A) 2.63, N(2)···Se(1A) 3.61 Å, N(2)–H(2)···Se(1A) angle of 174°].

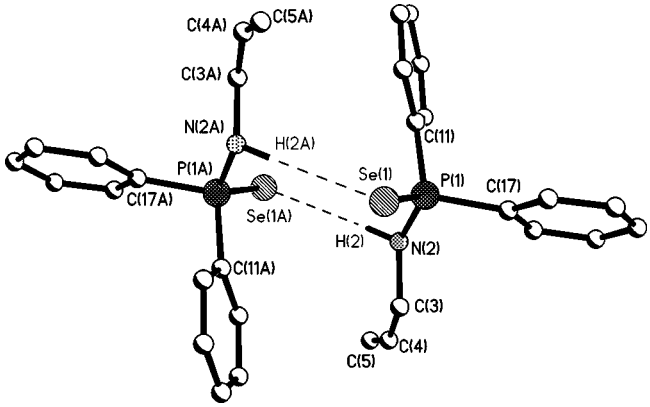

Figure 1. The X-ray structure of $Ph_2P(Se)NH(C_3H_5)$ (**4**) showing hydrogen bonding

Table 1. Selected bond lengths [Å] and angles [°] for $Ph_2P(Se)NH(C_3H_5)$ (**4**)

	4
P(1)–N(2)	1.657(4)
Se(1)–P(1)	2.1082(12)
P(1)–C(11)	1.806(4)
P(1)–C(17)	1.814(4)
N(2)–P(1)–C(11)	103.30(19)
N(2)–P(1)–C(17)	103.49(18)
C(11)–P(1)–C(17)	105.86(18)
C(11)–P(1)–Se(1)	113.32(13)
C(17)–P(1)–Se(1)	112.20(14)
N(2)–P(1)–Se(1)	117.48(15)
P(1)–N(2)–H(2)	116(3)

Coordination of **1** as a monodentate ligand was established in a number of cases. Thus, reaction of [AuCl(tht)] with **1** gave the expected product [$AuCl\{Ph_2PNH(C_3H_5)\}$] (**5**) [Table 2 summarises spectroscopic data], and reaction of [$PtCl_2$(cod)] with **1** in a 1:2 molar ratio gave [$PtCl_2\{Ph_2PNH(C_3H_5)\}_2$] (**6**) in very good yield (90 %). The FAB mass spectrum of **6** showed the expected parent ion and fragmentation pattern and the complex displays a single resonance with platinum satellites in the $^{31}P\{^1H\}$ NMR spectrum [δ_P = 34.8 ppm, $^1J(^{31}P\text{-}^{195}Pt)$ = 3949 Hz, Table 2] which indicates the presence of Cl^- *trans* to P. The IR spectrum has ν_{NH} at 3054 cm^{-1}, $\nu_{C=C}$ and ν_{PN} at 1642 and 1000 cm^{-1}, respectively, and two ν_{PtCl} bands at 305 and 288 cm^{-1} which support the *cis* geometry.

The crystal structure of **6** (Table 3, Figure 2) shows that the molecule is square-planar at Pt. The P(21)–Pt(1)–P(1) [98.81(4)°] and Cl(1)–Pt(1)–Cl(2) [84.53(4)°] angles are significantly distorted from the ideal 90° due to the bulky phosphane groups. The Pt–P bond lengths are in the normal range. In the solid state the X-ray structure displays two intramolecular N–H···Cl hydrogen bonds that result in two five-membered rings [N(13)–H(13)···Cl(1) 2.34(4) Å N(13)–H(13)···Cl(1) 127(4)°, N(33)–H(33)···Cl(2) 2.34(4) Å, N(33)–H(33)···Cl(2) angle of 128(4)°].

[$PdCl_2\{Ph_2PNH(C_3H_5)\}_2$] (**7**) was prepared in a similar way to **6**. The expected fragmentation pattern and parent ion was observed in the FAB mass spectrum whilst the $^{31}P\{^1H\}$ NMR spectrum showed two peaks at δ = 58.8 and 46.2 ppm which is indicative of a mixture of *cis* and *trans* isomers. The IR bands observed at 3054, 1643 and 997 cm^{-1} represent ν_{NH}, $\nu_{C=C}$ and ν_{PN}, respectively [Equation (2)].

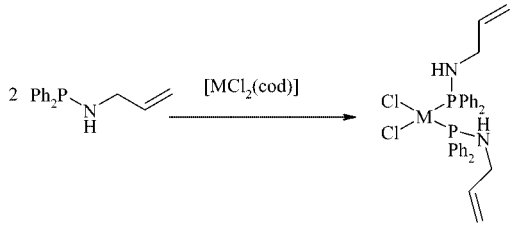

M = Pt **6**, Pd **7**
cod = 1,5-cyclooctadiene (2)

Reaction of of [{PtCl(μ-Cl)(PEt_3)}$_2$] with **1** gave [$Pt(PEt_3)Cl_2\{Ph_2PNH(C_3H_5)\}$] (**8**) in a yield of 59 %; δ_{PA} = 34.2 ppm, δ_{PX} = 7.3 ppm, $^1J(^{31}P_A\text{-}^{195}Pt)$ = 3979, $^1J(^{31}P_X\text{-}^{195}Pt)$ = 3479, $^2J(^{31}P_A\text{-}^{31}P_X)$ = 19 Hz, which is typical for complexes of this type. The PMe_2Ph analogue **9** was obtained in a similar fashion. The molecular structures of **8** and **9** (Table 4, Figure 3) confirm that the complexes contain one ligand bound to the platinum atom through the phosphorus atom; the hydrogen bonding motif is observed [in **8**: N(2)–H(2)···Cl(2) 2.74(4) Å, N(2)–H(2)···Cl(2) angle of 110(3)°].

[$PdCl(C_{10}H_8N)\{Ph_2PNH(C_3H_5)\}$] (**10**) was prepared from **1** and [{$PdCl(C_{10}H_8N)\}_2$] ($C_{10}H_8N$ = metallated naphthylamine ligand) whilst [RuCl(μ-Cl)(η^6-*p*-MeC_6H_4-*i*Pr)$\{Ph_2PNH(C_3H_5)\}$] (**11**) was prepared from [{RuCl(μ-Cl)(η^6-*p*-MeC_6H_4 *i*Pr)}$_2$] and **1** (85 % yield). The X-ray structure of **11** (Table 5, Figure 4) confirms that the complex contains one ligand and is bound to the ruthenium

 © 2005 Wiley-VCH Verlag GmbH & Co. KGaA, Weinheim

Table 2. Characterisation data for $Ph_2PNH(C_3H_5)$ and its derivatives

Compound	$^{31}P\{^1H\}$ NMR	IR [cm^{-1}]					Microanalysis: found (calcd.)		
	δ_P [ppm]	ν_{PN}	ν_{NH}	$\nu_{C=C}$	$\nu_{P=E}$	ν_{MCl}	C	H	N
$Ph_2PNH(C_3H_5)$ (**1**)	42.5				–	–	72.27 (74.67)	7.37 (6.68)	5.58 (5.81)
$Ph_2P(O)NH(C_3H_5)$ (**2**)	24.4	993	3189	1641	1181	–	69.74 (70.03)	6.22 (6.27)	5.15 (5.44)
$Ph_2P(S)NH(C_3H_5)$ (**3**)	60.5	997	3170	1642	689	–	66.01 (65.91)	6.09 (5.90)	5.11 (5.12)
$Ph_2P(Se)NH(C_3H_5)$ (**4**)	58.1[a]	991	3177	1644	573	–	55.97 (56.07)	5.25 (5.02)	4.43 (4.36)
$[AuCl\{Ph_2PNH(C_3H_5)\}]$ (**5**)	64.9	996	3069	1643	–	323	37.98 (38.03)	2.76 (3.40)	3.07 (2.96)
$[PtCl_2\{Ph_2PNH(C_3H_5)\}_2]$ (**6**)	34.8[b]	1000	3054	1642	–	305, 288	48.23 (48.14)	4.10 (4.31)	3.65 (3.74)
$[PdCl_2\{Ph_2PNH(C_3H_5)\}_2]$ (**7**)	58.8, 46.2	997	3054	1643	–	297, 277	54.80 (54.61)	4.67 (4.89)	4.06 (4.25)
$[Pt(PEt_3Cl_2\{Ph_2PNH(C_3H_5)\}]$ (**8**)	34.2, 7.3[f]	1002	3072	1641	–	309, 283	40.61 (40.38)	4.38 (5.01)	2.49 (2.24)
$[Pt(PMe_2Ph)Cl_2\{Ph_2PNH(C_3H_5)\}]$ (**9**)	35.3, –14.2[g]	1000	3053	1642	–	313, 283	42.99 (42.85)	2.26 (4.22)	2.08 (2.17)
$[PdCl(C_{10}H_8N)\{Ph_2PNH(C_3H_5)\}]$ (**10**)	65.0	993	3049	1639	–	289	56.93 (57.16)	3.93 (4.60)	5.24 (5.33)
[Ru Cl(μ-Cl)(η^6-p-MeC_6H_4 *i*Pr) $\{(Ph_2PNH(C_3H_5)\}]$ (**11**)	61.3	996	3051	1642	–	290, 283	55.71 (54.85)	5.62 (5.52)	2.71 (2.56)
$[RhCl(\mu\text{-}Cl)(\eta^5\text{-}C_5Me_5)\{(Ph_2PNH(C_3H_5)\}]$ (**12**)	66.4[e]	995	3063	1642	–	279, 267	54.32 (54.56)	5.78 (5.68)	2.44 (2.55)
$[IrCl(\mu\text{-}Cl)(\eta^5\text{-}C_5Me_5)\{(Ph_2PNH(C_3H_5)\}]$ (**13**)	34.5	994	3058	1640	–	291, 280	47.07 (46.95)	4.85 (4.89)	2.13 (2.19)
$[PdCl_2\{Ph_2PNH(C_3H_5)\}]$ (**14**)	93.6	996	3054	–	–	318, 281	43.95 (43.04)	4.26 (3.85)	2.70 (3.35)
$[PtCl_2\{Ph_2PNH(C_3H_5)\}]$ (**15**)	63.5[c]	998	3055	3051	–	328, 289	36.53 (35.52)	2.99 (3.18)	2.60 (2.76)
$[Pt\{Ph_2PNH(C_4H_8O)\}_2]$ (**16**)	91.4[d]	997	3069	–	–	–	52.06 (51.96)	4.60 (5.18)	3.70 (3.79)

[a] $^1J\{^{31}P\text{-}^{77}Se\} = 756$ Hz. [b] $^1J\{^{31}P\text{-}^{195}Pt\} = 3949$ Hz. [c] $^1J\{^{31}P\text{-}^{195}Pt\} = 3481$ Hz. [d] $^1J\{^{31}P\text{-}^{195}Pt\} = 2294$ Hz. [e] $^1J\{^{31}P\text{-}^{103}Rh\} = 148$ Hz. [f] $^1J\{^{31}P_A\text{-}^{195}Pt\} = 3979$, $^1J\{^{31}P_X\text{-}^{195}Pt\} = 3479$, $^2J(^{31}P_A\text{-}^{31}P_X) = 19$ Hz. [g] $^1J\{^{31}P_A\text{-}^{195}Pt\} = 3878$, $^1J\{^{31}P_X\text{-}^{195}Pt\} = 3625$, $^2J(^{31}P_A\text{-}^{31}P_X)$ 19 Hz.

Table 3. Selected bond lengths [Å] and angles [°] for $[PtCl_2\{Ph_2PNH(C_3H_5)\}_2]$ (**6**)

	6
Pt(1)–Cl(1)	2.3644(10)
Pt(1)–Cl(2)	2.3649(12)
Pt(1)–P(1)	2.2625(10)
Pt(1)–P(21)	2.251(9)
P(1)–N(13)	1.663(3)
P(21)–N(33)	1.660(4)
N(13)–C(14)	1.457(5)
N(33)–C(34)	1.463(6)
N(13)···Cl(1)	3.039(3)
N(33)···Cl(2)	3.050(4)
P(1)–Pt(1)–Cl(1)	88.22(4)
Cl(1)–Pt(1)–Cl(2)	84.53(4)
N(13)–P(1)–M(1)	108.03(12)
P(21)–Pt(1)–P(1)	98.81(4)
P(21)–Pt(1)–Cl(1)	172.97(3)
P(21)–Pt(1)–Cl(2)	88.45(4)
P(1)–Pt(1)–Cl(2)	172.59(4)
C(14)–N(13)–P(1)	125.3(3)
N(33)–P(21)–Pt(1)	109.64(13)
C(34)–N(33)–P(21)	123.0(3)

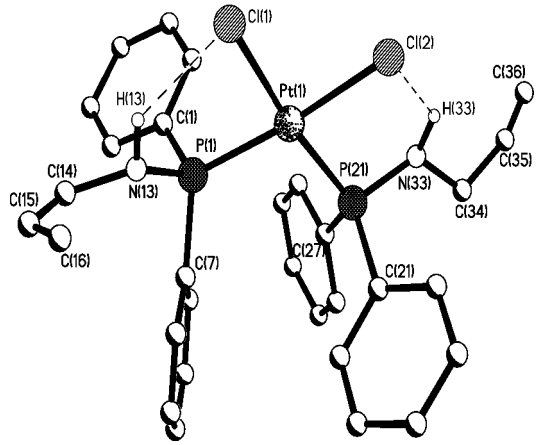

Figure 2. The X-ray structure of $[PtCl_2\{Ph_2PNH(C_3H_5)\}_2]$ (**6**)

atom through the phosphorus atom with a P(1)–Ru(1) bond length of 2.3404(11) Å and similar intramolecular hydrogen bonding to **8**.

 © 2005 Wiley-VCH Verlag GmbH & Co. KGaA, Weinheim

Table 4. Selected bond lengths [Å] and angles [°] for [Pt(PEt)$_3$-Cl$_2${Ph$_2$PNH(C$_3$H$_5$)}] (**8**) and [Pt(PPhMe$_2$)Cl$_2${Ph$_2$PNH(C$_3$H$_5$)}] (**9**)

	8	**9**
Pt(1)–Cl(1)	2.3496(19)	2.3481(17)
Pt(1)–Cl(2)	2.3716(17)	2.3741(16)
Pt(1)–P(1)	2.2587(18)	2.2505(17)
Pt(1)–P(2)	2.2520(18)	2.2487(16)
P(1)–N(2)	1.658(6)	1.677(5)
P(1)–C(11)	1.822(6)	1.824(6)
P(1)–C(17)	1.820(7)	1.820(6)
P(1)–Pt(1)–P(2)	96.82(6)	96.14(6)
Cl(2)–Pt(1)–Cl(1)	85.09(6)	86.45(6)
N(2)–P(1)–C(11)	110.6(3)	109.1(3)
N(2)–P(1)–C(17)	100.9(3)	100.3(3)
C(11)–P(1)–C(17)	105.8(3)	105.8(3)
N(2)–P(1)–Pt(1)	106.4(2)	108.4(2)
C(11)–P(1)–Pt(1)	111.9(2)	110.9(2)
C(17)–P(1)–Pt(1)	120.5(2)	121.5(2)

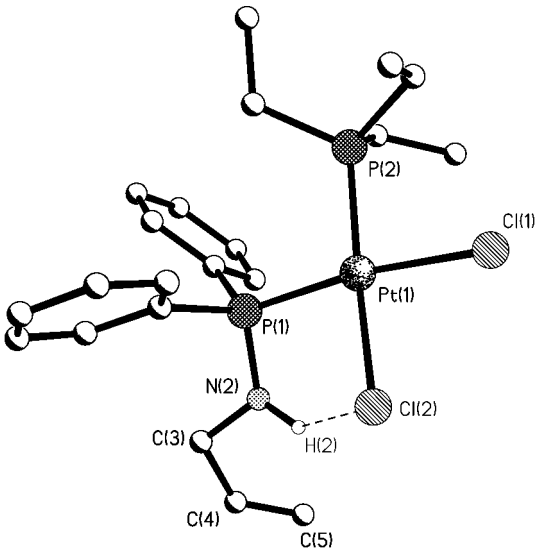

Figure 3. The X-ray structure of [Pt(PEt)$_3$Cl$_2${Ph$_2$PNH(C$_3$H$_5$)}] (**8**), the structure of [Pt(PPhMe$_2$)Cl$_2${Ph$_2$PNH(C$_3$H$_5$)}] (**9**) is very similar and is not illustrated

The reaction of Ph$_2$PNH(C$_3$H$_5$) with [{RhCl(μ-Cl)(η^5-C$_5$Me$_5$)}$_2$] and [{IrCl(μ-Cl)(η^5-C$_5$Me$_5$)}$_2$] proceeded in similar fashion to give [RhCl(μ-Cl)(η^5-C$_5$Me$_5$){Ph$_2$PNH-(C$_3$H$_5$)}] (**12**) and [IrCl(μ-Cl)(η^5-C$_5$Me$_5$){Ph$_2$PNH(C$_3$H$_5$)}] (**13**) in good yields [67 % and 65 % respectively, Equation (3), Table 2].

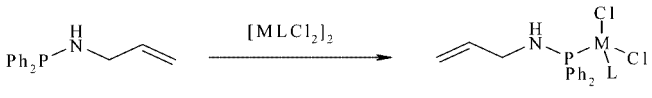

M = Rh **12**, Ir **13**
L = Cp*

(3)

In order to obtain a bidentate complex we treated **1** with 1 equiv. of [MCl$_2$(cod)] to give **14** and **15** [Equation (4),

Table 5. Selected bond lengths [Å] and angles [°] for [RuCl(μ-Cl)(η^6-*p*-MeC$_6$H$_4$ *i*Pr){Ph$_2$PNH(C$_3$H$_5$)}] (**11**)

	11
Ru(1)–Cl(1)	2.4314(11)
Ru(1)–Cl(2)	2.4037(12)
Ru(1)–P(1)	2.3404(11)
P(1)–N(2)	1.657(3)
P(1)–C(11)	1.823(4)
P(1)–C(17)	1.827(4)
N(2)···Cl(2)	3.202(3)
P(1)–Ru(1)–Cl(1)	88.54(4)
P(1)–Ru(1)–Cl(2)	85.35(4)
Cl(2)–Ru(1)–Cl(1)	87.06(4)
N(2)–P(1)–C(11)	105.94(18)
N(2)–P(1)–C(17)	106.69(17)
C(11)–P(1)–C(17)	104.36(18)
N(2)–P(1)–Ru(1)	112.64(12)
C(11)–P(1)–Ru(1)	111.88(12)
C(17)–P(1)–Ru(1)	114.61(13)

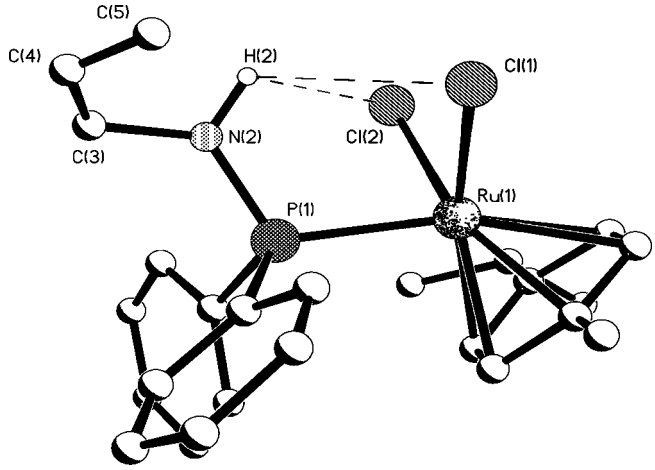

Figure 4. The X-ray structure of [RuCl(μ-Cl)(η^6-*p*-MeC$_6$H$_4$ *i*Pr){Ph$_2$PNH(C$_3$H$_5$)}] (**11**) showing hydrogen bonding

Table 2]. The magnitude of the Pt-P coupling constants strongly indicates the coordination of both phosphane and alkene group.

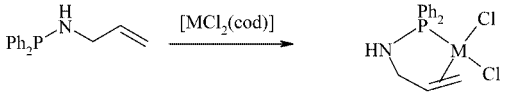

M = Pt **14**, Pd **15**
cod = 1,5-cyclooctadiene

(4)

In an interesting transformation, [Pt{Ph$_2$PNH(C$_3$H$_8$O)}$_2$] (**16**), was obtained by reaction of KO*t*Bu in methanol with **6** (51 % yield). The reaction probably proceeds by nucleophillic attack of methoxide though we have not observed this reaction for other complexes. The ^{31}P{^{1}H} NMR spectrum showed a single peak at δ_P = 91.4 ppm with platinum satellites at $^1J(^{31}P\text{-}^{195}Pt)$ = 2294 Hz. The IR spectrum shows absorptions at 2873–2809 cm^{-1}, which corre-

 © 2005 Wiley-VCH Verlag GmbH & Co. KGaA, Weinheim

spond to ν_{OMe} vibrations along with vibrations at 3069 and 997, which are assigned to ν_{NH} and ν_{PN}, respectively. The FAB mass spectral analysis gave the appropriate parent ion and fragmentation pattern and the microanalysis shows good results for the suggested structure. The crystal structure of **16** (Table 6, Figure 5) shows that in the solid state the molecule occurs as hydrogen-bonded dimers. [H(1N)···O(5) 2.241(19) Å, N(1)···O(5) 3.164(4) Å, N(1)–H(1N)···O(5) angle of 157(4)°].

Table 6. Selected bond lengths [Å] and angles [°] for [Pt{$Ph_2PNH(C_3H_5OMe)_2$}] (**16**)

	16
Pt(1)–C(3)	2.113(4)
Pt(1)–P(1)	2.2743(9)
P(1)–N(1)	1.664(3)
P(1)–C(7)	1.832(4)
P(1)–C(13)	1.827(4)
N(1)–C(2)	1.451(5)
C(3)–Pt(1)–P(1)	81.56(11)
N(1)–P(1)–C(13)	105.68(18)
N(1)–P(1)–C(7)	106.47(18)
C(13)–P(1)–C(7)	102.15(17)
N(1)–P(1)–Pt(1)	104.19(12)
C(13)–P(1)–Pt(1)	119.72(11)
C(7)–P(1)–Pt(1)	117.51(12)
C(2)–N(1)–P(1)	117.6(3)

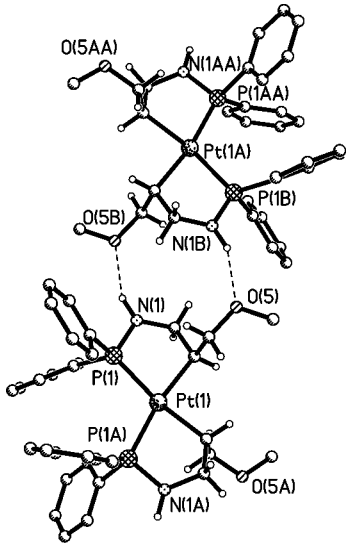

Figure 5. The X-ray structure of [Pt{$Ph_2PNH(C_3H_5OMe)_2$}] (**16**) showing hydrogen bonding

This paper clearly demonstrates the ability of (allylamino)phosphane to behave as a monodenate and bidentate ligand and illustrates a potentially useful nucleophilic addition at the allyl group.

Experimental Section

General: General conditions were as described previously.[7] Unless otherwise stated, all reactions were carried out under oxygen-free nitrogen using standard Schlenk techniques. Diethyl ether and THF were purified by reflux in the presence of sodium/benzophenone and distillation under nitrogen. Dichloromethane was heated to reflux in the presence of calcium hydride and distilled under nitrogen. Toluene and hexane were heated to reflux in the presence of sodium and distilled under nitrogen. The complexes [PtMeX(cod)] (X = Cl or Me),[8] [{Pd(μ-Cl)(η^3-C_3H_5)}$_2$],[9] [Cu(MeCN)$_4$][PF_6],[10] [AuCl(tht)] (tht = tetrahydrothiophene),[11] [MCl_2(cod)] (M = Pt or Pd),[12,13] [{RuCl(μ-Cl)(η^6-p-MeC_6H_4-*i*Pr)$_2$}],[14] [{Rh(μ-Cl)(cod)}$_2$],[15] [{MCl(μ-Cl)(η^5-C_5Me_5)}$_2$] (M = Rh or Ir),[16] [{PtCl(μ-Cl)(PMe_2Ph)}$_2$],[17] [{PtCl(μ-Cl)(PMe_2-Ph)}$_2$][18] and [{Pd(μ-Cl)($C_{10}H_8N$)}$_2$][19] were prepared according to literature procedures. Chlorodiphenylphosphane and allylamine were distilled prior to use. Et_3N (99 % purity), *t*BuOK (95 % purity), H_2O_2 (30 wt.% in H_2O) and reagent grade KBr were used without further purification. IR spectra were recorded as KBr discs in the range 4000–200 cm^{-1} with a Perkin–Elmer 2000 FTIR/RAMAN spectrometer. NMR spectra were recorded with a Gemini 2000 spectrometer (operating at 121.4 MHz for ^{31}P and 300 MHz for ^1H). Microanalyses were performed by the St. Andrews University service and mass spectra by the Swansea Mass Spectrometer Service.

$Ph_2PNH(C_3H_5)$ (1): Allylamine (3.671 g, 64.3 mmol) and triethylamine (6.831 g, 67.5 mmol) were added together in dry THF (50 mL). Chlorodiphenylphosphane (14.894 g, 67.5 mmol) in dry THF (50 mL) was added dropwise with stirring overnight. Triethylamine hydrochloride was removed by filtration under nitrogen and the solvent removed in vacuo to yield a colourless oil which was purified by distillation (132 °C/0.2 Torr) and storing under nitrogen in the freezer which yielded a colourless waxy solid. Yield 6.283 g, 41 %. $C_{15}H_{16}NP$ (241.3): calcd. C 74.67, H 6.68, N 5.81; found C 74.27, H 7.37, N 5.58. $^{31}P\{^1H\}$ NMR ($CDCl_3$): δ = 42.5 ppm. ^1H NMR ($CDCl_3$): δ = 7.3 (m, 10 H, aromatic), 5.8 (m, 1 H, CH), 5.2 (m, 1 H, CH_2), 5.1 (m, 1 H, CH_2), 3.5 (m, 2 H, NCH_2) and 1.9 (s, 1 H, NH) ppm. EI^+ MS: *m*/*z* = 242 $[M + 1]^+$.

$Ph_2P(O)NH(C_3H_5)$ (2): $Ph_2PNH(C_3H_5)$ (461 mg, 1.9 mmol) was dissolved in dichloromethane (10 mL). Urea/hydrogen peroxide (180 mg, 1.9 mmol) was added and the reaction mixture was stirred overnight. The product was extracted from the CH_2Cl_2 by addition of distilled water, washed with CH_2Cl_2 (3 × 5 mL), dried with magnesium sulfate and the solvents were evaporated to dryness to yield a colourless solid. Yield 338 mg, 67 %. $C_{15}H_{16}NOP$ (257.3): calcd. C 70.03, H 6.27, N 5.44; found C 69. 74, H 6.22, N 5.15. $^{31}P\{^1H\}$ NMR ($CDCl_3$): δ = 24.4 ppm. ^1H ($CDCl_3$): δ = 7.3 (m, 10 H, aromatic), 5.9 (m, 1 H, CH), 5.3 (m, 1 H, CH_2), 5.1 (m, 1 H, CH_2), 3.5 (m, 2 H, NCH_2) and 2.9 (br.s, 1 H, NH) ppm. EI^+ MS: *m*/*z* = 257 [M]. IR (KBr disc): $\tilde{\nu}$ = 3189, 1641, 1181, 993 cm^{-1}.

$Ph_2P(S)NH(C_3H_5)$ (3): $Ph_2PNH(C_3H_5)$ (420 mg, 1.7 mmol) and elemental sulfur (56 mg, 1.7 mmol) were dissolved in dry toluene (10 mL) to yield a yellow solution which was stirred overnight. The solvent was reduced to 1 mL before addition of hexane (10 mL) to precipitate a colourless solid that was isolated by filtration. Yield 246 mg, 52 %. $C_{15}H_{16}NPS$ (273.3): calcd. C 65.91, H 5.90, N 5.12; found C 66.01, H 6.09, N 5.11. $^{31}P\{^1H\}$ NMR ($CDCl_3$): δ = 60.5 ppm. ^1H NMR ($CDCl_3$): δ = 7.3 (m, 10 H, aromatic), 5.9 (m, 1 H, CH), 5.2 (m, 1 H, CH_2), 5.1 (m, 1 H, CH_2), 3.5 (m, 2 H, NCH_2) and 2.4 (br. s, 1 H, NH) ppm. EI^+ MS: *m*/*z* = 273 [M]. IR (KBr disc): $\tilde{\nu}$ = 3170, 1642, 997, 689 cm^{-1}.

$Ph_2P(Se)NH(C_3H_5)$ (4): $Ph_2PNH(C_3H_5)$ (235 mg, 1.0 mmol) and grey selenium (77 mg, 1.0 mmol) were refluxed in dry toluene (10 mL) for 1 h before cooling to room temperature and filtering through a Celite plug to remove any insoluble material. The solvent was reduced to 1 mL to yield a colourless solid that was isolated by suction filtration and dried in vacuo. Yield 269 mg, 86 %.

 © 2005 Wiley-VCH Verlag GmbH & Co. KGaA, Weinheim

$C_{15}H_{16}NPSe$ (320.2): calcd. C 56.07, H 5.02, N 4.36; found C 55.97, H 5.25, N 4.43. $^{31}P\{^1H\}$ NMR ($CDCl_3$): δ = 58.1 ppm [$^1J(^{31}P\text{-}^{77}Se)$ = 756 Hz]. ^1H NMR ($CDCl_3$): δ = 7.3 (m, 10 H, aromatic), 5.9 (m, 1 H, CH), 5.3 (q, 1 H, CH_2), 5.1 (m, 1 H, CH_2), 3.5 (m, 2 H, NCH_2) and 2.3 (br. s, 1 H, NH) ppm. EI^+ MS: *m*/*z* = 322 [M]. IR (KBr disc): $\tilde{\nu}$ = 3177, 1644, 991, 573 cm^{-1}.

[AuCl{Ph$_2$PNH(C$_3$H$_5$)}] (5): $Ph_2PNH(C_3H_5)$ (78 mg, 0.3 mmol) and [AuCl(tht)] (103 mg, 0.3 mmol) were dissolved in CH_2Cl_2 (5 mL) and the mixture stirred overnight in the dark. Hexane (20 mL) was added to precipitate a colourless solid that was isolated by suction filtration. Yield 44 mg, 29 %. $C_{15}H_{16}AuClPN$ (473.7): calcd. C 38.03, H 3.40, N 2.96; found C 37.98, H 2.76, N 3.07. $^{31}P\{^1H\}$ NMR ($CDCl_3$): δ = 64.9 ppm. ^1H NMR ($CDCl_3$): δ = 7.4 (m, 10 H, aromatic), 5.9 (m, 1 H, CH), 5.2 (m, 1 H, CH_2), 5.1 (m, 1 H, CH_2), 3.6 (m, 2 H, NCH_2), 2.5 (br.s, 1 H, NH) ppm. FAB^+ MS: *m*/*z* = 496 [M + Na]$^+$, 473 [M]$^+$, 438 [M – Cl]$^+$. IR (KBr disc): $\tilde{\nu}$= 3069, 1643, 996, 323 cm^{-1}.

[PtCl$_2${Ph$_2$PNH(C$_3$H$_5$)}$_2$] (6): $Ph_2PNH(C_3H_5)$ (161 mg, 0.7 mmol) and [$PtCl_2$(cod)] (125 mg, 0.3 mmol) were dissolved in dry CH_2Cl_2 (10 mL) to yield a colourless solution which was stirred overnight before reducing the solvent volume to 0.5 mL and addition of diethyl ether (20 mL) to precipitate a colourless solid which was isolated by suction filtration and dried in vacuo. Yield 226 mg, 90 %. $C_{30}H_{32}P_2N_2PtCl_2$ (748.5): calcd. C 48.14, H 4.31, N 3.74; found C 48.23, H 4.10, N 3.65. $^{31}P\{^1H\}$ NMR ($CDCl_3$): δ = 34.8 ppm [$^1J(^{31}P\text{-}^{195}Pt)$ 3949 Hz]. ^1H NMR ($CDCl_3$): δ = 7.4 (m, 20 H, aromatic), 5.5 (m, 2 H, CH), 5.0 (m, 2 H, CH_2), 4.9 (m, 2 H, CH_2), 4.1 (br.s, 2 H, NH) and 3.5 (m, 4 H, NCH_2) ppm. FAB^+ MS: *m*/*z* = 713 [M – Cl]$^+$, 677 [M – 2 Cl]$^{2+}$. IR (KBr disc): $\tilde{\nu}$= 3054, 1642, 1000, 305, 288 cm^{-1}.

[PdCl$_2${Ph$_2$PNH(C$_3$H$_5$)}$_2$] (7): $Ph_2PNH(C_3H_5)$ (179 mg, 0.7 mmol) and [$PdCl_2$(cod)] (106 mg, 0.4 mmol) were dissolved in CH_2Cl_2 (10 mL) and stirred overnight. The solvent volume was reduced to 0.5 mL before addition of hexane (20 mL) to precipitate a yellow solid that was isolated by filtration and dried in vacuo. Yield 224 mg, 91 %. $C_{30}H_{32}Cl_2N_2P_2Pd$ (659.9): calcd. C 54.61, H 4.89, N 4.25; found C 54.80, H 4.67, N 4.06. $^{31}P\{^1H\}$ NMR ($CDCl_3$): δ = 58.8 and 46.2 ppm, *cis* and *trans* isomers. ^1H NMR ($CDCl_3$): δ = 7.5–7.2 (m, 20 H, aromatic), 5.6 (m, 2 H, CH), 5.2 (m, 2 H, CH_2), 5.1 (m, 2 H, CH_2), 3.5 (m, 4 H, NCH_2) and 4.1 (br.s, 2 H, NH) ppm. FAB^+ MS: *m*/*z* = 624 [M – Cl]$^+$, 588 [M – 2 Cl]$^{2+}$. IR (KBr disc): $\tilde{\nu}$= 3054, 1643, 997, 297, 277 cm^{-1}.

[Pt(PEt$_3$)Cl$_2${Ph$_2$PNH(C$_3$H$_5$)}] (8): To a CH_2Cl_2 (10 mL) solution of [{PtCl(μ-Cl)(PEt_3)}$_2$] (56 mg, 0.07 mmol) was added dropwise a CH_2Cl_2 (10 mL) solution of $Ph_2PNH(C_3H_5)$ (35 mg, 0.1 mmol) with stirring to yield a pale yellow solution. After 30 minutes the solvent was reduced to 1 mL before addition of diethyl ether (20 mL) to precipitate a colourless solid that was isolated by suction filtration. Yield 54 mg, 59 %. $C_{21}H_{31}Cl_2NP_2Pt$ (625.4): calcd. C 40.38, H 5.01, N 2.24; found C 40.61, H 4.38, N 2.49. $^{31}P\{^1H\}$ NMR ($CDCl_3$): $\delta(P_A)$ = 34.2 (d) ppm [$^1J(^{31}P_A\text{-}^{195}Pt)$ = 3979 Hz]; $\delta(P_X)$ = 7.3 (d) ppm [$^1J(^{31}P_X\text{-}^{195}Pt)$ = 3479 Hz, $^2J(^{31}P_A\text{-}^{31}P_X)$ =19 Hz]. ^1H NMR ($CDCl_3$): δ = 7.3 (m, 10 H, aromatic), 5.7 (m, 1 H, CH), 5.2 (m, 1 H, CH_2), 5.0 (m, 1 H, CH_2), 3.5 (m, 2 H, NCH_2), 3.2 (br.s, 1 H, NH), 1.5 (m, 6 H, PCH_2) and 0.9 (m, 9 H, Me) ppm. ES^+ MS: *m*/*z* = 590 [M – Cl]$^+$. IR (KBr disc): $\tilde{\nu}$= 3072, 1641, 1002, 309, 283 cm^{-1}.

[Pt(PMe$_2$Ph)Cl$_2${Ph$_2$PNH(C$_3$H$_5$)}] (9): $Ph_2PNH(C_3H_5)$ (33 mg, 0.1 mmol) in CH_2Cl_2 (10 mL) was added dropwise to a CH_2Cl_2 (10 mL) solution of [{PtCl(μ-Cl)(PMe_2Ph)}$_2$] 56 mg, 0.07 mmol) over 10 minutes with stirring. The solution was stirred for a further 30 minutes before reduction of the solvent to 1 mL and addition of diethyl ether (20 mL) to precipitate a colourless solid that was isolated by suction filtration and dried in vacuo. Yield 55 mg, 62 %. $C_{23}H_{27}Cl_2NP_2Pt$ (645.4): calcd. C 42.85, H 4.22, N 2.17; found C 42., H 2.26, N 2.08. $^{31}P\{^1H\}$ NMR ($CDCl_3$): $\delta(P_A)$ = 35.3 (d) ppm [$^1J(^{31}P_A\text{-}^{195}Pt)$ = 3878 Hz]; $\delta(P_X)$ = –14.2 (d) ppm [$^1J(^{31}P_X\text{-}^{195}Pt)$ = 3625 Hz. $^2J(^{31}P_A\text{-}^{31}P_X)$ 19 Hz]. ^1H NMR ($CDCl_3$): δ = 7.4 (m, 15 H, aromatic), 5.6 (m, 1 H, CH), 5.1 (m, 1 H, CH_2), 4.9 (m, 1 H, CH_2), 4.5 (br.s, 1 H, NH), 3.1 (m, 2 H, NCH_2) and 1.7 [d, 6 H, $^3J(^{195}Pt\text{-}^1H)$ = 32 Hz, $^2J(^{31}P\text{-}^1H)$ = 11 Hz, PMe] ppm. ES^+ MS: *m*/*z* 645 = [M + H]$^+$, 610 [M – Cl]$^+$, 575 [M – 2 Cl]$^{2+}$. IR (KBr disc): $\tilde{\nu}$= 3053, 1642, 1000, 313, 283 cm^{-1}.

[PdCl(C$_{10}$H$_8$N){Ph$_2$PNH(C$_3$H$_5$)}] (10): To a CH_2Cl_2 (10 mL) suspension of [{PdCl($C_{10}H_8N$)}$_2$] (61 mg, 0.1 mmol) was added dropwise a CH_2Cl_2 solution of $Ph_2PNH(C_3H_5)$ (52 mg, 0.2 mmol) over 10 minutes to yield a colourless solution. After stirring for a further 30 minutes the solution was filtered through a Celite plug to remove any insoluble material remaining before reducing the solvent volume to 1 mL and addition of diethyl ether (20 mL) to precipitate a tan coloured microcrystalline solid that was isolated by filtration. Yield 78 mg, 69 %. $C_{25}H_{24}ClN_2PPd$ (525.3): calcd. C 57.16, H 4.60, N 5.33; found C 56.93, H 3.93, N 5.24. $^{31}P\{^1H\}$ NMR ($CDCl_3$): δ = 65.0 ppm. ^1H NMR ($CDCl_3$): δ = 9.6–7.8 (m, 6 H, naphthalene aromatic), 7.3 (m, 10 H, aromatic), 5.7 (m, 1 H, CH), 5.2 (m, 1 H, CH_2), 5.0 (m, 1 H, CH_2), 4.5 (br.s, 1 H, NH), 3.4 (m, 2 H, NCH_2), 2.8 [d, $^2J(^{31}P\text{-}^1H)$ 5 Hz, 2 H, CH_2] ppm. ES^+ MS: *m*/*z* = 489 [M – Cl]$^+$. IR (KBr disc): $\tilde{\nu}$= 3049, 1639, 993, 28 cm^{-1}.

[RuCl(μ-Cl)(η^6-*p*-MeC$_6$H$_4$ *i*Pr){Ph$_2$PNH(C$_3$H$_5$)}] (11): $Ph_2PNH(C_3H_5)$ (170 mg, 0.7 mmol) and [{RuCl(μ-Cl)(η^6-*p*-MeC_6H_4 *i*Pr)}$_2$] (54 mg, 0.1 mmol) were dissolved in CH_2Cl_2 (5 mL) to yield a dark red solution that was stirred for 30 min. The solvent was reduced to 0.5 mL before addition of hexane (10 mL to precipitate an orange microcrystalline solid that was isolated by suction filtration and dried in vacuo. Yield 82 mg, 85 %. $C_{25}H_{30}Cl_2NPRu$ (547.5): calcd. C 54.85, H 5.52, N 2.56; found C 55.71 54.85, H 5.62, N 2.71. $^{31}P\{^1H\}$ NMR ($CDCl_3$): δ = 61.3 ppm. ^1H NMR: δ = 7.3 (m, 14 H, aromatic), 5.5 (m, 1 H, CH), 5.2 (m, 1 H, CH_2), 5.1 (m, 1 H, CH_2), 3.5 (m, 2 H, NCH_2), 2.9 (br. s, 1 H, NH), 2.6 (m, 1 H, CH), 1.2 (m, 3 H, CH_3), 0.8 (m, 6 H, CH_3) ppm. FAB^+ MS: *m*/*z* = 570 [M + Na]$^+$, 547 [M]$^+$, 512 [M – Cl]$^+$, 476 [M – 2 Cl]$^{2+}$. IR (KBr disc): $\tilde{\nu}$ = 3051, 1642, 996, 290, 283 cm^{-1}.

[RhCl(μ-Cl)(η^5-C$_5$Me$_5$){Ph$_2$PNH(C$_3$H$_5$)}] (12): $Ph_2PNH(C_3H_5)$ (45 mg, 0.2 mmol) and [{RhCl(μ-Cl)(η^5-C_5Me_5)}$_2$] (58 mg, 0.1 mmol) were dissolved in CH_2Cl_2 (10 mL) to yield a blood red solution that stirred for 30 min before reducing the solvent to 1 mL and addition of diethyl ether (20 mL) to precipitate a red microcrystalline solid that was isolated by suction filtration and dried in vacuo. Yield 69 mg, 67 %. $C_{25}H_{31}Cl_2NPRh$ (550.3): calcd. C 54.56, H 5.68, N 2.55; found C 54.32 , H 5.78, N 2.44. $^{31}P\{^1H\}$ NMR ($CDCl_3$): δ = 66.4 ppm [$^1J(^{31}P\text{-}^{103}Rh)$ = 148 Hz]. ^1H NMR ($CDCl_3$): δ = 7.3 (m, 10 H, aromatic), 5.6 (m, 1 H, CH), 5.2 (m, 1 H, CH_2), 5.1 (m, 1 H, CH_2), 3.3 (m, 2 H, NCH_2), 3.2 (br. s, 1 H, NH), 1.3 (s, 15 H, CH_3) ppm. FAB^+ MS: *m*/*z* = 572 [M + Na]$^+$, 514 [M – Cl]$^+$, 474 [M – 2 Cl]$^{2+}$. IR (KBr disc): $\tilde{\nu}$ = 3063, 1642, 995, 279, 267 cm^{-1}.

[IrCl(μ-Cl)(η^5-C$_5$Me$_5$){Ph$_2$PNH(C$_3$H$_5$)}] (13): $Ph_2PNH(C_3H_5)$ (42 mg, 0.2 mmol) and [{IrCl(μ-Cl)(η^5-C_5Me_5)}$_2$] (69 mg, 0.1 mmol) were dissolved in CH_2Cl_2 (10 mL) to yield an orange solution. The solvent was reduced to 1 mL before diethyl ether was added to precipitate a yellow microcrystalline solid that was isolated by filtration and dried in vacuo. Yield 72 mg, 65 %. $C_{25}H_{31}Cl_2IrNP$ (639.6): calcd. C 46.95, H 4.89, N 2.19; found C 47.07, H 4.85, N 2.13. $^{31}P\{^1H\}$ NMR ($CDCl_3$): δ = 34.5 ppm. ^1H

 © 2005 Wiley-VCH Verlag GmbH & Co. KGaA, Weinheim

Table 7. Crystal data for $Ph_2PNH(C_3H_5)$ and derivatives

Compound	**4**	**6**	**8**	**9**	**11**	**16**
Empirical formula	$C_{17}H_{16}N_3PSe$	$C_{30}H_{32}Cl_2N_2P_2Pt$	$C_{21}H_{31}Cl_2NP_2Pt$	$C_{23}H_{27}Cl_2NP_2Pt$	$C_{25}H_{30}Cl_2NPRu$	$C_{32}H_{38}N_2O_2P_2Pt$
M	320.22	748.51	625.40	649.39	547.44	739.67
Crystal system	monoclinic	monoclinic	triclinic	triclinic	monoclinic	monoclinic
Space group	$P2_1/n$	$P2_1/n$	$P\bar{1}$	$P\bar{1}$	$P2_1/n$	$C2/c$
a [Å]	12.246(3)	10.012(3)	8.835(2)	9.2943(12)	9.918(3)	20229(3)
b [Å]	9.317(2)	15.065(4)	9.741(2)	9.7402(13)	13.782(4)	10.8193(17)
c [Å]	12.711(3)	19.717(6)	14.634(3)	14.1561(19)	17.566(5)	16.926(3)
α [°]	90	90	87.302(4)	90.661(2)	90	90
β [°]	92.261(5)	91.56(10)	87.343(4)	94.862(2)	94.880(5)	123.002(2)
γ [°]	90	90	71.362(3)	112.151(2)	90	90
Z	4	4	2	2	4	4
μ [mm^{-1}]	2.684	5.029	6.254	6.311	0.958	4.650
Reflections measured	5982	12495	5879	5970	10269	8848
Independent reflections	2066	4181	3327	3353	3421	2765
Final R_1, wR_2 [$I > 2\sigma(I)$]	0.0381, 0.0917	0.0214, 0.0515	0.0361, 0.0967	0.0317, 0.0788	0.0343, 0.0783	0.0229, 0.0473

NMR ($CDCl_3$): δ = 7.3 (m, 10 H, aromatic), 5.6 (m, 1 H, CH), 5.2 (m, 1 H, CH_2), 5.1 (m, 1 H, CH_2), 3.5 (m, 2 H, NCH_2), 3.2 (br. s, 1 H, NH), 1.3 (s, 15 H, CH_3) ppm. FAB$^+$ MS: m/z = 604 [M – Cl]$^+$, 568 [M – 2 Cl]$^{2+}$. IR (KBr disc): $\tilde{\nu}$ = 3058, 1640, 994, 291, 280 cm^{-1}.

[$PdCl_2${$Ph_2PNH(C_3H_5)$}] (14): $Ph_2PNH(C_3H_5)$ (52 mg, 0.2 mmol) in CH_2Cl_2 (5 mL) was added dropwise to CH_2Cl_2 (5 mL) solution of [$PdCl_2$(cod)] (53 mg, 0.2 mmol). After stirring for 30 min, the solvent was reduced in vacuo to 0.5 mL before precipitating a yellow microcrystalline solid upon addition of hexane (10 mL) and isolation by suction filtration. Yield 65 mg, 83 %. $C_{15}H_{16}PNPdCl_2$ (418.6): calcd. C 43.04, H 3.85, N 3.35; found C 43.95, H 4.26, N 2.70. $^{31}P\{^1H\}$ NMR (CD_2Cl_2): δ = 93.6 ppm. ^1H NMR (CD_2Cl_2): δ = 7.35 (m, 10 H, aromatic), 5.6 (m, 1 H, CH), 5.2 (m, 1 H, CH_2), 5.1 (m, 1 H, CH_2), 3.5 (m, 2 H, NCH_2) and 4.1 (br. s, 1 H, NH) ppm. FAB$^+$ MS: m/z = 382 [M – Cl]$^+$, 347 [M – 2 Cl]$^{2+}$. IR (KBr disc): $\tilde{\nu}$ = 3054, 996, 318, 281 cm^{-1}.

[$PtCl_2${$Ph_2PNH(C_3H_5)$}] (15): $Ph_2PNH(C_3H_5)$ (43 mg, 0.2 mmol) in CH_2Cl_2 (5 mL) was added dropwise to a CH_2Cl_2 (5 mL) solution of [$PtCl_2$(cod)] (58 mg, 0.2 mmol) over 2.5 h. The solvent was reduced to 1 mL before addition of hexane (10 mL) to yield an off-white sticky solid on reduction of solvent. The sticky solid was subsequently dissolved in CH_2Cl_2 (0.5 mL) before addition of petroleum ether (40–60°C) (10 mL) to yield a colourless solid that was isolated by suction filtration. Yield 51 mg, 65 %. $C_{15}H_{16}Cl_2NPPt$ (507.2): calcd. C 35.52, H 3.18, N 2.76; found C 36.53, H 2.99, N 2.60. $^{31}P\{^1H\}$ NMR (CD_2Cl_2): δ = 63.5 ppm [$^1J(^{31}P\text{-}^{195}Pt)$ = 3481 Hz]. ^1H NMR (CD_2Cl_2): δ = 7.35 (m, 10 H, aromatic), 5.5 (m, 1 H, CH), 5.2 (m, 1 H, CH_2), 5.1 (m, 1 H, CH_2), 3.5 (m, 2 H, NCH_2) and 4.1 (br. d, J = 8 Hz, 1 H, NH) ppm. FAB$^+$ MS: m/z = 472 [M – Cl]$^+$, 436 [M – 2 Cl]$^{2+}$. IR (KBr disc): $\tilde{\nu}$ = 3055, 998, 328, 289 cm^{-1}.

[Pt{$Ph_2PNH(C_4H_8O)$}$_2$] (16): To a CH_3OH (10 mL suspension of [$PtCl_2${$Ph_2PNH(C_3H_5)$}$_2$] (100 mg, 0.1 mmol) was added potassium *tert*-butoxide (30 mg, 0.2 mmol) with stirring to yield a colourless precipitate after 1 h. This microcrystalline solid was subsequently isolated by suction filtration and dried in vacuo. Yield 46 mg, 51 %. $C_{32}H_{38}N_2O_2P_2Pt$ (739.7): calcd. C 51.96, H 5.18, N 3.79; found C 52.06, H 4.60, N 3.70. $^{31}P\{^1H\}$ NMR ($CDCl_3$): δ = 91.4 ppm [$^1J(^{31}P\text{-}^{195}Pt)$ = 2294 Hz]. ^1H NMR ($CDCl_3$): δ = 7.4 (m, 20 H, aromatic), 5.9 (m, 2 H, CH), 5.2 (m, 2 H, CH_2), 5.1 (m, 2 H, CH_2), 3.6 (m, 4 H, NCH_2), 2.5 (br. s, 2 H, NH), 1.5 (s, 6 H, MeO) ppm. FAB$^+$ MS: m/z = 740 [M]$^+$. IR (KBr disc): $\tilde{\nu}$ = 3069, 3045, 2873–2809 (m), 997 cm^{-1}.

X-ray Crystallography: X-ray diffraction studies were performed using a Bruker SMART diffractometer with graphite-monochromated Mo-K_α radiation. The structures were solved by direct methods, non-hydrogen atoms were refined with anisotropic displacement parameters; hydrogen atoms bound to carbon atoms were idealised, the NH protons were located by a ΔF map. Structural refinements were made by the full-matrix least-squares method on F^2 using SHELXTL.[20] Details are given in Table 7. Full lists of structure refinement data, atomic coordinates, bond lengths and angles, anisotropic displacement parameters and hydrogen atom parameters have been deposited as supplementary material, CCDC-239884 to –239889 contain the supplementary crystallographic data for this paper. These data can be obtained free of charge from The Cambridge Crystallographic Data Centre via www.ccdc.cam.ac.uk/data_request/cif.

[1] K. J. Coutinho; R. S. Dickson, G. D. Fallon; W. R. Jackson, T. De Simone, B. W. Skelton, A. H. White, *J. Chem. Soc., Dalton Trans.* **1997**, 3193.

[2] B. Cornils, E. Wilbus, *Chem. Tech.* **1995**, *33*; B. Cornils, *Angew. Chem. Int. Ed. Engl.* **1995**, *34*, 1575.

[3] E. Billig, A. G. Abatjoghe, D. R. Bryant, *US Pat.* 4668651, **1987**; 4769498, **1988**; G. D. Cuny, S. L. Buchwald, *J. Am. Chem. Soc.* **1993**, *115*, 2066; T. Higashizima, N. Sakai, K. Nozaki, H. Takaya, *Tetrahedron Lett.* **1994**, *35*, 2023; M. E. Davis, *Chem. Tech.* **1992**, 498; W. A. Herrmann, C. W. Kohlpaintner, *Angew. Chem. Int. Ed. Engl.* **1993**, *32*, 1524; S. M. Aucott, M. L. Clarke, A. M. Z. Slawin, J. D. Woollins, *JCS Dalton* **2001**, 972; S. M. Aucott, A. M. Z. Slawin, J. D. Woollins, *J. Organomet. Chem.* **1999**, *582*, 83; M. L. Clarke, A. M. Z. Slawin, M. V. Wheatley, J. D. Woollins, *J. Chem. Soc., Dalton Trans.* **2001**, 3421; A. M. Z. Slawin, M. Wainwright, J. D. Woollins, *New J. Chem.* **2000**, *24*, 69; A. M. Z. Slawin, M. Wainwright, J. D Woollins, *J. Chem. Soc., Dalton Trans.* **2002**, 513.

[4] L. V. Interrante, M. A. Bennet, R. S. Nyholm, *Inorg. Chem.* **1966**, *5*, 2212; M. A. Bennett, L. V. Interrante, R. S. Nyholm, *Z. Naturforsch. B: Anorg. Chem. Org. Chem.* **1965**, *20*, 633; P. R. Brookes, *J. Organomet. Chem.* **1972**, *42*, 415.

[5] E. Lindner, C. Scheytt, P. Wegner, *J. Organomet. Chem.* **1986**, *308*, 311; L. P. Barthel-Rosa, K. Maitra, J. Fischer, J. H. Nelson, *Organometallics* **1997**, *16*, 1714; H.-L. Ji, J. H. Nelson, A. DeCian, J. Fischer, L. Solujic, E. B. Milosavljevic, *Organometallics* **1992**, *11*, 401.

 © 2005 Wiley-VCH Verlag GmbH & Co. KGaA, Weinheim

[6] A. M. Z. Slawin, J. Wheatley, M. V. Wheatley, J. D. Woollins, *Polyhedron* **2003**, *22*, 1397.
[7] S. M. Aucott, A. M. Z. Slawin, J. D. Woollins, *J. Chem. Soc., Dalton Trans.* **2000**, 2559.
[8] H. C. Clark, L. E. Manzer, *J. Organomet. Chem.* **1973**, *59*, 411.
[9] Y. Tatsuno, T. Yoshida, S. Otsuka, *Inorg. Synth.* **1979**, *19*, 220.
[10] G. J. Kubas, *Inorg. Synth.* **1979**, *19*, 90.
[11] R. Uson, A. Laguna, M. Laguna, *Inorg. Synth.* **1989**, *26*, 85.
[12] D. Drew, J. R. Doyle, *Inorg. Synth.* **1991**, *28*, 346.
[13] J. X. McDermott, J. F. White, G. M. Whiteside, *J. Am. Chem. Soc.* **1976**, *98*, 6521.
[14] M. A. Bennett, T. N. Huang, T. W. Matheson, A. R. Smith, *Inorg. Synth.* **1982**, *21*, 74.
[15] G. Giordano, R. H. Crabtree, *Inorg. Synth.* **1979**, *19*, 218.
[16] C. White, A. Yates, P. M. Maitlis, *Inorg. Synth.* **1992**, *29*, 228.
[17] W. Baratta, P. S. Pregosin, *Inorg. Chim. Acta* **1993**, *209*, 85.
[18] J. Chatt, R. G. Wilkins, *J. Chem. Soc.* **1952**, 273.
[19] J. W. Suggs, K. S. Lee, *J. Organomet. Chem.* **1986**, *299*, 297.
[20] *SHELXTL*, Bruker AXS, Madison, **2001**.

Received May 27, 2004
Published Online January 27, 2005

 © 2005 Wiley-VCH Verlag GmbH & Co. KGaA, Weinheim

The Reactions of Elemental Iron with Dipicolinic Acid (H_2dipic) and Quinaldic Acid (Hquin) – X-ray Crystal Structures of $[C_5H_5NH][Fe(Dipic)(Hdipic)(C_5H_5N)_2]\cdot 3C_5H_5N$, $[Fe_2(\mu\text{-}O)(Dipic)_2(C_5H_5N)_4]\cdot 2C_5H_5N\cdot 2H_2O$ and *trans*-$[Fe(Quin)_2(MeOH)_2]$

Sneh L. Jain,[a] Alexandra M. Z. Slawin,[a] J. Derek Woollins,*[a] and Pravat Bhattacharyya[a]

Keywords: Iron / Dipicolinic acid / Carboxylates / Quinaldic acid / Gif chemistry

Iron powder reacts with dipicolinic acid (H_2dipic) in pyridine at 110 °C to give the heptacoordinate iron(II) complex $[C_5H_5NH][Fe(dipic)(Hdipic)(C_5H_5N)_2]$; the $(Hdipic)^-$ ligand binds to the metal centre *solely* through the oxygen atoms of one carboxylate group, the first example of this coordination mode at iron. Upon dissolution in pyridine under aerobic conditions this complex transforms into the oxo-bridged di-iron(III) species $[Fe_2(\mu\text{-}O)(dipic)_2(C_5H_5N)_4]$, which possesses a linear Fe–O–Fe axis. Quinaldic acid (Hquin) reacts with iron powder in pyridine at 110 °C to give $[Fe(quin)_2(C_5H_5N)_2]$, analogous to the corresponding reactivity of picolinic acid. This complex is converted into *trans*-$[Fe(quin)_2(MeOH)_2]$ or $[Fe_2(\mu\text{-}O)(quin)_4(dmf)_2]$ in methanol or DMF respectively. The formation of an iron(II) complex in the reaction with methanol differs markedly from the picolinate system.

(© Wiley-VCH Verlag GmbH & Co. KGaA, 69451 Weinheim, Germany, 2005)

Introduction

Picolinic acid (Hpic) is a highly efficient promoter of Gif-type catalytic oxygenation of methylene groups in cycloalkane substrates using iron complexes ($GoAgg^{III}$ conditions).[1] The active catalyst in $GoAgg^{III}$ is proposed to be an iron-hydroperoxy complex, although the processes involved in the construction of this species are poorly understood. Stavropoulos[2] has reported that iron powder reacted with Hpic at room temperature to give polymeric $[Fe(pic)_2]_n$ (in dichloromethane) or $[Fe(pic)_2(C_5H_5N)_2]$ (in pyridine), from which an array of mono- and bimetallic systems was readily generated by treatment with coordinating solvents (DMF, methanol, water) and/or aerobic oxidation. The catalytic oxygenation profiles of adamantane using these picolinate complexes lend valuable support to the radical-based mechanism believed to operate in Gif chemistry. Also, Shova et al. have reported that the reaction of iron powder with Hpic in water leads to $[Fe(pic)_2(H_2O)_2]$.[3]

The richness of the iron(0)-Hpic system prompted us to investigate the behaviour of dipicolinic and quinaldic acids (H_2dipic and Hquin respectively) with elemental iron. Ferrous and ferric complexes with dipicolinate[4–14] and quinaldinate[15–21] ligands have hitherto been prepared from iron salts, however the use of iron in elemental form as a substrate with the parent acids has not been explored. There is precedent for the use of iron-dipicolinate complexes as $GoAgg^{III}$ oxygenation catalysts,[12] although doubts were later cast on the validity of these results,[10] since these complexes have a tendency to interconvert in solution. Access to a range of structurally and spectroscopically characterised iron derivatives containing dipicolinate and quinaldinate ligands is thus eminently desirable in order to evaluate their catalytic potential.

[a] School of Chemistry, University of St Andrews, St Andrews, Fife, Scotland KY16 9ST
Tel: (internat.) +44-1334-463861
Fax: (internat.) +44-1334-463808
E-mail: jdw3@st-and.ac.uk

Results and Discussion

Dipicolinate Complexes

Initial attempts at the iron(0)-H_2dipic reaction in dichloromethane, both at room temperature and under reflux, showed no visual evidence for any reaction, as the supernatant solution remained colourless throughout, with insoluble H_2dipic and iron powder present c.f. Hpic reacts at room temperature with Fe^0 to give $[Fe(pic)_2]_n$ in 63 % yield after four days.[2] The use of pyridine as the reaction solvent proved to be more profitable.

Refluxing a mixture of H_2dipic and iron powder (molar ratio 2:1) in pyridine for 5 h under argon produces a deep red solution from which unreacted iron is removed by anaerobic filtration whilst hot. Upon cooling the filtrate to –20 °C for 24 h a red crystalline solid is deposited. The molecular structure of the complex was determined crystallographically to be $[C_5H_5NH][Fe(dipic)(Hdipic)(C_5H_5N)_2]\cdot$

$3C_5H_5N$ (**1**·$3C_5H_5N$, Figure 1) in which dipic^{2-} is coordinated in tridentate fashion to Fe(1) via the N(1), O(7) and O(8) atoms, while (Hdipic)$^-$ is bound via O(16) and O(17) of one carboxylate group to give a four-membered metallacycle with the N(11), O(18) and O(19) atoms oriented away from Fe(1). **1** is the first iron complex in which the 2,6 isomer of (Hdipic)$^-$ is solely *O*,*O*′-bidentate through one carboxylate group. Fe(1) has a pentagonal bipyramidal geometry, with equatorial [NO_4] donor atoms being supplied by dipicolinate ligands and axial pyridines completing the coordination sphere. By analogy with Stavropoulos' iron(0)-Hpic system[2] and our own rigorous exclusion of dioxygen and moisture during the reaction, we assign a +2 oxidation state to the iron centre. Magnetic susceptibility measurements of powdered samples reveal $\mu_{eff} \approx 4.7$ B.M at room temperature, confirming a high-spin iron(II) species. The ^{1}H NMR spectrum of **1** in [D_5]pyridine at room temperature comprises broad singlets at $\delta_H = 75.5$, 52.7 and 4.7 ppm. The bond lengths and angles in **1** concur with other (dipicolinato)iron complexes,[8–11,13] with O(16)–Fe(1)–O(17) 58.11(7)°, the Fe(1)–O lengths span the range 2.1614(19)–2.2905(19) Å. The pyridinium counterion and one of the solvate pyridine molecules hydrogen-bond to the iron complex [H(51)···O(8) 1.81(2) Å, N(51)···O(8) 2.737(3) Å, N(51)–H(51)···O(8) 156(4)°; H(19)···N(41) 1.62(1) Å, O(19)···N(41) 2.598(4) Å, O(19)–H(19)···N(41) 177(4)°]. This interaction between O(8) and the pyridinium cation lengthens Fe(1)–O(8) by ca. 0.04 Å compared to Fe(1)–O(7).

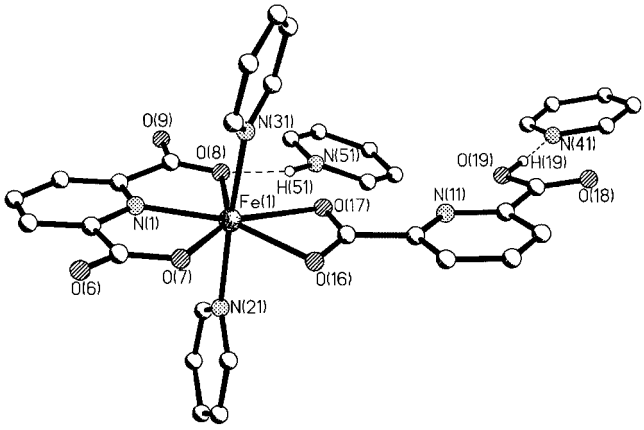

Figure 1. Molecular structure of **1**·$3C_5H_5N$ (hydrogen atoms and non-H bonded solvate molecules omitted for clarity); selected bond lengths (Å) and angles (°): Fe(1)–N(1) 2.133(2), Fe(1)–O(7) 2.1614(19), Fe(1)–O(8) 2.2095(18), Fe(1)–N(31) 2.218(2), Fe(1)–N(21) 2.234(2), Fe(1)–O(17) 2.246(2), Fe(1)–O(16) 2.2905(19), N(1)–Fe(1)–O(7) 73.49(8), N(1)–Fe(1)–O(8) 72.36(8), O(7)–Fe(1)–O(8) 145.71(7), N(1)–Fe(1)–N(31) 95.14(8), O(7)–Fe(1)–N(31) 90.12(8), O(8)–Fe(1)–N(31) 90.00(8), N(1)–Fe(1)–N(21) 88.21(8), O(7)–Fe(1)–N(21) 90.04(8), O(8)–Fe(1)–N(21) 91.80(8), N(31)–Fe(1)–N(21) 176.55(9), N(1)–Fe(1)–O(17) 147.06(8), O(7)–Fe(1)–O(17) 139.39(7), O(8)–Fe(1)–O(17) 74.71(7), N(31)–Fe(1)–O(17) 84.92(8), N(21)–Fe(1)–O(17) 92.72(8), N(1)–Fe(1)–O(16) 154.74(8), O(7)–Fe(1)–O(16) 81.54(7), O(8)–Fe(1)–O(16) 132.74(7), N(31)–Fe(1)–O(16) 88.50(8), N(21)–Fe(1)–O(16) 88.12(8), O(17)–Fe(1)–O(16) 58.11(7)

Compound **1** is stable for prolonged periods in the solid state under an inert atmosphere. The pyridine solvate molecules are lost upon removal of crystals from the mother liquor, thermogravimetric analysis shows that at 118 °C a sample of the freshly crystallised complex loses 27.8 % of its mass, c.f. for **1**·$3C_5H_5N$ the solvent of crystallisation constitutes 27.5 % by mass. The FAB$^+$ mass spectrum contains a peak at *m*/*z* = 388 corresponding to [Fe(dipic)]$^+$, peaks at higher *m*/*z* ratios could not be assigned.

Following dissolution of **1** in wet pyridine under aerobic conditions, [$C_5H_5NH]_2$[dipic] (^{1}H NMR and infra-red spectroscopic evidence) is precipitated. Upon filtration and standing in air overnight, deep red crystals deposit from the filtrate. X-ray crystallography reveals the product to be the diiron(III) complex [Fe_2(μ-O)(dipic)$_2$($C_5H_5N)_4$] (**2**) (Figure 2) in which dipic^{2-} is tridentate at Fe(1) via the N(7), O(11) and O(11B) atoms with N(7) *trans* to the μ-oxo atom O(1); the complex co-crystallises with molecules of pyridine and water. The octahedral coordination at Fe(1) is completed by pyridine ligands bound axially through N(1) and N(1B). The oxo atom O(1) lies on an crystallographic inversion centre, hence the Fe(1)–O(1)–Fe(1A) axis is 180°. The acute bite angle of dipic^{2-} distorts the geometry at Fe(1), thus O(11)–Fe(1)–O(11B) and O(1)–Fe(1)–O(11) are 150.67(18)° and 104.67(9)°, respectively. The shortness of Fe(1)–O(1) [1.7808(8) Å] compared to Fe(1)–O(11) [2.048(3) Å] suggests significant π-bonding within the Fe(1)–O(1) linkage. The *trans* influence of O(1) lengthens Fe(1)–N(7) [2.106(6) Å] compared with [Fe(dipic)$_2$]$^-$ species [2.037(3)–2.076(3) Å],[8,9,22] Fe(1)–O(11) [2.048(3) Å] being marginally longer than in the homoleptic complexes [2.001(2)–2.035(2) Å]. The Fe(1)–N(1) bonds [2.218(5) Å] are identical in length to **1** [2.218(2), 2.234(2) Å]. The solv-

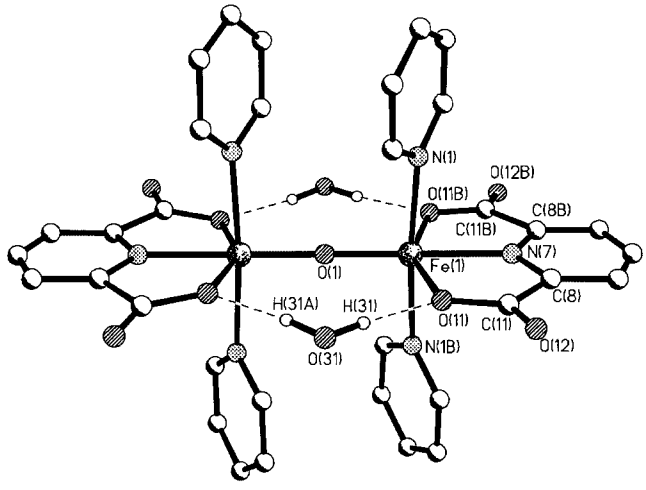

Figure 2. Molecular structure of **2**·$2C_5H_5N$·$2H_2O$ (C–H bonds and pyridine solvate molecules omitted for clarity); selected bond lengths (Å) and angles (°): Fe(1)–O(1) 1.7808(8), Fe(1)–O(11) 2.048(3), Fe(1)–N(7) 2.106(6), Fe(1)–N(1) 2.218(5), O(10)–Fe(1)–O(11) 104.67(9), O(11)–Fe(1)–O(11B) 150.67(18), O(1)–Fe(1)–N(7) 180.0, O(11)–Fe(1)–N(7) 75.33(9), O(11)–Fe(1)–N(1) 87.72(12), N(7)–Fe(1)–N(1) 87.45(10), O(1)–Fe(1)–N(1) 92.55(10), O(11B)–Fe(1)–N(1) 90.99(12), N(7)–Fe(1)–N(1) 87.45(10), N(1B)–Fe(1)–N(1) 174.9(2), Fe(1)–O(1)–Fe(1A) 180.0

 © 2005 Wiley-VCH Verlag GmbH & Co. KGaA, Weinheim

ate water molecule hydrogen bonds to the dipicolinate [H(31)···O(11) 1.895(11) Å, O(31)···O(11) 2.868(5) Å, O(31)–H(31)···O(11) 172(5)°], O(31) being essentially coplanar with this ligand. There are no other significant intermolecular contacts. In its infra-red spectrum, the band for the asymmetric ν_{FeOFe} stretch appears at 862 cm^{-1}.

Upon storage in a sample vial for several days the deep red crystals of **2** transform into a pale brown solid with the release of pyridine vapour (olfactory evidence). Microanalysis suggested the stoichiometry $[Fe_2O(dipic)_2(H_2O)_4]$ i. e. the pyridine ligands and solvate molecules are lost upon removal from contact with the mother liquor. We propose that the μ-oxo bridge is retained during this process and that the new aqua complex is isostructural with $[Fe_2(\mu\text{-}O)(4\text{-}Cl\text{-}dipic)_2(H_2O)_4]$ (4-Cl-dipic = 4-chlorodipicolinate, Figure 3), which is accessible from iron(III) chloride hexahydrate, the diethyl ester of 4-Cl-dipicH_2 and urea.[5] Pyridine loss is suppressed when **2** is stored in a sample vial housed within a larger one containing a small volume of this solvent. The lability of the pyridine ligands in **2** suggests that this compound may be a useful synthon for new complexes with the $Fe_2(\mu\text{-}O)(dipic)_2$ subunit.

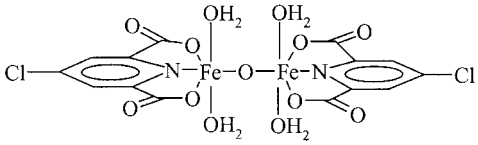

Figure 3. The structure of $[Fe_2(\mu\text{-}O)(4\text{-}Cl\text{-}dipic)_2(H_2O)_4]$;[5] complex $[Fe_2(\mu\text{-}O)(dipic)_2(H_2O)_4]$ is proposed to be isostructural

Quinaldinate Complexes

The reaction of Hquin with elemental iron has not been reported elsewhere. We have found that Hquin reacts with iron powder (molar ratio 2:1) under identical conditions to those used to synthesise **1** to give $[Fe(quin)_2(C_5H_5N)_2]$ (**3**). The ν_{COO} bands in **3** (1652, 1361 cm^{-1}) are comparable to $[Fe(pic)_2(C_5H_5N)_2]$ (1645, 1348 cm^{-1}),[2] microanalytical data confirms the proposed stoichiometry although the FAB^+ mass spectrum contains no peaks which are assignable to a molecular ion or daughter fragments. Compound **3** is air- and moisture-stable in the solid state under ambient conditions. We have been unable to obtain crystals suitable for X-ray crystallographic analysis in order to establish its geometry. As with **1**, there is paramagnetic shifting of the signals in the ^1H NMR spectrum.

Complex **3** is more stable towards methanol under aerobic conditions than its picolinate counterpart. Whereas $[Fe(pic)_2(C_5H_5N)_2]$ reacts with methanol at room temperature to give a diiron(III) complex $[Fe_2(\mu\text{-}OMe)_2(pic)_4]$,[23] refluxing a methanolic suspension of **3** for four days is sufficient only to displace the coordinated pyridine ligands and generate the iron(II) species $[Fe(quin)_2(MeOH)_2]$ (**4**). The sluggishness of this reaction reflects the greater steric bulk of quinaldinate compared with picolinate and, possibly, that **3** is polymeric. The directing influence of the pyridine ligands on the course of the picolinate reactions is crucial, as under anaerobic conditions $[Fe(pic)_2]_n$ reacts at room temperature with methanol to give $[Fe(pic)_2(MeOH)_2]$.[2]

Crystals of **4** suitable for X-ray analysis were deposited from the reaction mixture. The molecular structure (Figure 4) reveals a centrosymmetric geometry at the iron centre, with an FeN_2O_4 core comprising methanol ligands in axial positions and *N,O*-chelating quinaldinate anions with a *trans*-arrangement in the equatorial plane. The geometric parameters of **4** and the formation of one-dimensional hydrogen-bonded chains between carbonyl oxygen atoms and methanol ligands in adjacent molecules [H(21O)···O(11′) 1.650(6) Å, O(21)···O(11′) 2.621(1) Å, O(21)-H(21O)··· O(11′) 170(3)°] correspond with the diaqua, diethanol and di(*n*-propanol) analogues, as well as $[Fe(pic)_2(MeOH)_2]$.[2,17,18,21] Additionally, there are only very modest dimensional differences between **1, 2** and **4**. In the infra-red spectrum ν_{OH} appears at 3180 cm^{-1} and ν_{COO} at 1635 and 1387 cm^{-1}. Complex **4** is stable towards moisture and oxidation over several months in the solid state.

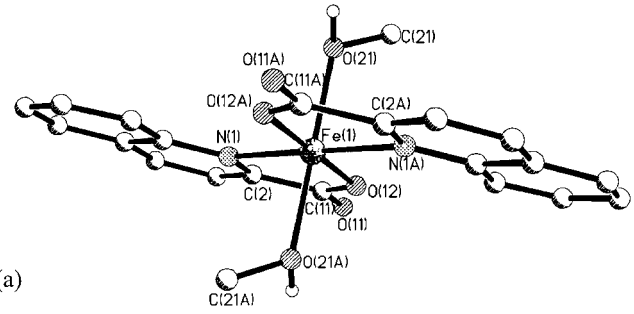

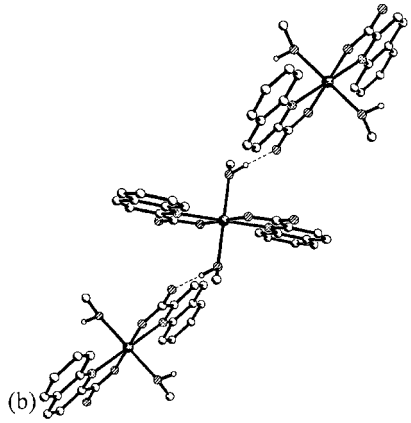

Figure 4. (a) Molecular structure of **4** (C–H bonds omitted for clarity); selected bond lengths (Å) and angles (°): Fe(1)–O(12) 2.0534(14), Fe(1)–O(21) 2.1624(14), Fe(1)–N(1) 2.2571(17), O(21)–C(21) 1.439(2), O(12)–Fe(1)–N(1) 76.39(6), N(1A)–Fe(1)–N(1) 180.0, O(21A)–Fe(1)–N(1) 88.98(6), O(21)–Fe(1)–N(1) 91.02(6), O(21A)–Fe(1)–O(21) 180.0, O(12A)–Fe(1)–O(12) 180.00(3), O(12)–Fe(1)–O(21) 91.48(5), O(12)–Fe(1)–N(1A) 103.61(6), O(12)–Fe(1)–O(21A) 88.52(5); (b) hydrogen-bonding networks in **4**

Following dissolution of **3** in DMF, vapour diffusion with diethyl ether gives golden-brown needles of $[Fe_2(\mu$-

 © 2005 Wiley-VCH Verlag GmbH & Co. KGaA, Weinheim

O)(quin)$_4$(dmf)$_2$] (**5**). This conversion mirrors the behaviour of [Fe(pic)$_2$(C$_5$H$_5$N)$_2$] towards dmf, which affords [Fe$_2$(μ-O)(pic)$_4$(dmf)$_2$].[2] The asymmetric ν_{FeOFe} and ν_{COO} vibrations in **5** (882, 1676, 1315 cm^{-1}) differ by 15–30 cm^{-1} from the picolinate complex (867, 1653, 1344 cm^{-1}). The insolubility of this complex in organic solvents prevented acquisition of ^{1}H NMR and mass spectra.

Although Hquin and Hpic behave in a similar fashion towards iron powder, there is a significant difference towards iron(III) salts. Whereas Hpic gives [Fe(pic)$_3$],[2] the corresponding reaction with Hquin in methanol at room temperature gives the binuclear complex [Fe$_2$(μ-OH)$_2$(quin)$_4$] (**6**).[15,20] Presumably steric constraints preclude tris(chelation) of quin$^-$ at an iron(III) centre, since [M(quin)$_3$] complexes exist for bismuth(III) and lanthanide(III) ions.[24,25]

Summary

The reaction of H$_2$dipic with iron powder in pyridine affords [C$_5$H$_5$NH][Fe(dipic)(Hdipic)(C$_5$H$_5$N)$_2$], in which the deprotonated acid exhibits two different coordination modes. In wet pyridine this complex converts into the oxo-bridged diiron(III) species [Fe$_2$(μ-O)(dipic)$_2$(C$_5$H$_5$N)$_4$] whose coordinated solvent molecules are susceptible to displacement by atmospheric water in the solid state. Hquin reacts with iron powder to give [Fe(quin)$_2$(C$_5$H$_5$N)$_2$], whose pyridine ligands are displaced under forcing conditions by methanol or at room temperature by dmf, affording *trans*-[Fe(quin)$_2$(MeOH)$_2$] and [Fe$_2$(μ-O)(quin)$_4$(dmf)$_2$] respectively.

The detailed investigation of (dipicolinato)iron complexes in aqueous media by Gourdon et al. demonstrates that several structural motifs can be readily derived.[4,7,10,11] The chemistry of (Hdipic)$^-$ and dipic^{2-} is enriched by the capacity of the carbonyl oxygens of the carboxylate groups to bind to adjacent metal centres, generating polynuclear structures.[27–30] A recent example illustrates that the carboxylate oxygen atom can also engage in hydrogen-bonding interactions with coordinated water molecules to form supramolecular networks.[31] That (Hdipic)$^-$ binds to iron(II) in **1** without the formation of a polymeric structure via the pendant carboxylate group is unusual, instances of this *O*,*O*′ mode at europium(III) and silver(I) generate infinite chains wherein both of the acid groups link metal ions.[32,33] 2,6-H$_2$dipic is the sole positional isomer of this ligand for whom geometric constraints do not preclude *N*,*O*,*O*′ chelation to a single metal centre. Studies using other isomers where such tridentate chelation is prohibited by the disposition of the acid groups lead to coordination polymers.[34–37] Investigations into how these other diacids react with elemental iron are currently underway in our laboratory.

The lability of the coordinated solvent molecules in **1**–**3** suggests that these complexes could be valuable precursors to new mono- and polyiron dipic/quin species, which will benefit investigations into Gif chemistry. The facility of the reactions of H$_2$dipic and Hquin with elemental iron also indicates that reactions of these acids with other electropositive metals will undoubtedly deliver complexes with new structural motifs.

Experimental Section

Materials and Instrumentation: Syntheses and work-up procedures were conducted under argon or oxygen-free dinitrogen using Schlenk line techniques, unless stated otherwise. Pyridine was distilled from calcium hydride, all other solvents and reagents were used as supplied. Infra-red spectra were recorded as pressed KBr discs with Perkin–Elmer System 2000 and Nicolet Nexus FTIR/Raman spectrometers, microanalyses were carried out by the University of St. Andrews and UMIST Microanalytical Services. FAB mass spectra (positive ionisation mode, 3-nitrobenzyl alcohol matrix) were recorded by the EPSRC National Mass Spectrometry Service (Swansea), ^{1}H NMR spectra (200.0 MHz) were recorded with a Bruker DPX 200 spectrometer.

Synthesis of Complexes 1–6

[C$_5$H$_5$NH][Fe(dipic)(Hdipic)(C$_5$H$_5$N)$_2$] (1): Iron powder (320 mg, 5.7 mmol) and H$_2$dipic (1.80 g, 10.8 mmol) were heated in pyridine (50 cm^3) at 110 °C under argon for 5 h. The red solution was filtered anaerobically while hot to remove unreacted iron, and the filtrate was cooled to –20 °C overnight. Red crystals of **1**·3C$_5$H$_5$N suitable for X-ray analysis were collected by filtration under argon, concentration of the filtrate in vacuo gave a second crop of complex. Yield 2.29 g (74 %). C$_{24}$H$_{17}$FeN$_4$O$_8$ (545.2): calcd. C 52.87, H 3.14, N 10.28; found C 52.24, H 3.19, N 9.85. Selected IR bands (cm^{-1}): $\tilde{\nu}$ = 3435 s (ν_{OH}), 1673 s, 1648 s, 1368 s, 1350 s (ν_{COO}). MS: *m*/*z* = 388 [Fe(dipic)]$^+$. ^{1}H NMR ([D$_5$]pyridine): δ = 75.5 (br), 52.7 (br), 4.7 (br) ppm.

[Fe$_2$(μ-O)(dipic)$_2$(C$_5$H$_5$N)$_4$] (2): Under aerobic conditions **1** (200 mg) was dissolved in pyridine (10 cm^3) with sonication, giving a red solution with a colourless precipitate of [C$_5$H$_5$NH]$_2$[dipic]. The solution was filtered and the filtrate left open to air for 12 h, after which time deep red crystals of **2**.2C$_5$H$_5$N·2H$_2$O (118 mg) suitable for X-ray analysis had deposited. C$_{34}$H$_{26}$Fe$_2$N$_6$O$_9$ (774.2): calcd. C 52.7, H 3.4, N 10.9; found C 52.1, H 2.9, N 10.4. Selected IR bands (cm^{-1}): $\tilde{\nu}$ = 1674 s, 1367 m (ν_{COO}), 862 m ($\nu_{FeOFe(asym)}$). Crystalline **2** changed colour from dark red to beige with the release of pyridine over four days at room temperature upon storage in a sample vial. Microanalysis suggested conversion to [Fe$_2$(μ-O)(dipic)$_2$(H$_2$O)$_4$]. C$_{14}$H$_{14}$Fe$_2$N$_2$O$_{13}$ (529.9): calcd. C 31.73, H 2.66, N 5.28; found C 31.91, H 2.43, N 5.24. Selected IR bands (cm^{-1}): $\tilde{\nu}$ = 3462 s, 2923 s (ν_{OH}), 1656 s, 1626 s, 1379 s, 1366 s (ν_{COO}), 924 m ($\nu_{FeOFe(asym)}$).

[Fe(quin)$_2$(C$_5$H$_5$N)$_2$] (3): Iron powder (75 mg, 1.35 mmol) and Hquin (352 mg, 2.03 mmol) were heated in pyridine (40 cm^3) at 110 °C for 3.5 h under argon. Unreacted iron powder was filtered off anaerobically whilst hot, **3** precipitated as a purple solid from the filtrate upon cooling to room temperature and was collected by filtration under argon. Yield 370 mg (49 %). C$_{30}$H$_{22}$FeN$_4$O$_4$ (558.3): calcd. C 64.53, H 3.97, N 10.03; found C 63.92, H 3.99, N 9.80. Selected IR bands (cm^{-1}): $\tilde{\nu}$ = 1652 s, 1361 m (ν_{COO}). ^{1}H NMR (CDCl$_3$): δ = 42.0 (br), 37.9 (br), 32.6 (br), 30.8 (br), 29.5 (br), 28.6 (br), 26.3 (br), 25.4 (br), 13.0 (br), 10.4 (br) ppm.

***trans*-[Fe(quin)$_2$(MeOH)$_2$] (4):** Under aerobic conditions a suspension of **3** (140 mg, 0.25 mmol) in methanol (20 cm^3) was heated at reflux for four days. The resulting brown microcrystalline solid was filtered off and washed with diethyl ether. Yield 89 mg (76 %).

 © 2005 Wiley-VCH Verlag GmbH & Co. KGaA, Weinheim

Crystals amenable to X-ray crystallographic analysis were obtained directly from the reaction. $C_{22}H_{20}FeN_2O_6$ (464.2): calcd. C 56.9, H 4.0, N 6.0; found C 56.0, H 4.4, N 6.1. Selected IR bands (cm^{-1}): $\tilde{\nu}$ = 3180 s (ν_{OH}), 1635 s, 1387 s (ν_{COO}). ^1H NMR ([D_7]DMF): δ = 34.1 (br), 32.1 (br), 12.0 (br), 4.4 (br), 2.3 (br) ppm.

[Fe_2(μ -O)(quin)$_4$(dmf)$_2$] (5): Under aerobic conditions a solution of **3** (84 mg, 0.15 mmol) in DMF (5 cm^3) was vapour-diffused with diethyl ether. After three days golden-brown needles of **5** were deposited. Yield 51 mg (67 %). $C_{50}H_{38}Fe_2N_6O_{11}$ (1010.5): calcd. C 59.4, H 3.8, N 8.3; found C 59.2, H 3.6, N 8.4. Selected IR bands (cm^{-1}): $\tilde{\nu}$ = 1676 s, 1315 m (ν_{COO}), 882 m ($\nu_{FeOFe(asym)}$).

[Fe_2(μ -OH)$_2$(quin)$_4$] (6): Under aerobic conditions, Hquin (256 mg, 1.45 mmol) was added to iron(III) nitrate nonahydrate (194 mg, 0.48 mmol) in methanol (10 cm^3), giving a yellow solution. Addition of diethyl ether precipitated **6** as a yellow solid. Yield 295 mg (80 %). $C_{40}H_{26}Fe_2N_4O_{10}\cdot 2H_2O$ (870.3): calcd. C 55.20, H 3.47, N 6.44; found C 55.71, H 3.03, N 6.37. Selected IR bands (cm^{-1}): $\tilde{\nu}$ = 3456 m (ν_{OH}), 1663 s, 1372 s (ν_{COO}). MS: m/z = 802 $[Fe_2(quin)_4]^+$.

X-ray Crystallography: Diffraction studies on **1**·3C_5H_5N and **2**·2C_5H_5N·2H_2O were performed using a Bruker SMART-CCD diffractometer, for **4** a Rigaku MM007/Saturn was used, with graphite-monochromated Mo-K_α radiation (λ = 0.71073 Å) in each case. All data were corrected for Lorentz polarisation and long-term intensity fluctuations. The structures were solved by direct methods, non-hydrogen atoms were refined with anisotropic displacement parameters, all hydrogen atom positions were idealised. In **2** ·2C_5H_5N·2H_2O the disordered pyridine solvate molecules were refined with all of the ring atoms as carbons and the hydrogen atoms distributed over all of the possible sites. Structural refinements were by the full-matrix least-squares method on F^2 using the program SHELXTL-PC.[26] CCDC-225950 (for **2**), -225951 (for **1**) and -248948 (for **4**) contain the supplementary crystallographic data for this paper. These data can be obtained free of charge from The Cambridge Crystallographic Data Centre via www.ccdc.cam.ac.uk/data_request/cif.

1·3C_5H_5N: $C_{44}H_{38}FeN_8O_8$, T = 125(2) K, M = 862.67, monoclinic, space group $P2_1/n$, a = 9.5494(11) Å, b = 20.107(2) Å, c = 21.744(3) Å, β = 98.873(2)°, V = 4124.0 $Å^3$, Z = 4, D_c = 1.389 Mg·m^{-3}, μ = 0.430 mm^{-1}, F_{000} = 1792. Of 17970 measured data, 5899 were unique (R_{int} = 0.0508) to give $R1[I > 2\sigma(I)]$ = 0.0387, $wR2$ = 0.0777.

2·2C_5H_5N·2H_2O: $C_{44}H_{40}Fe_2N_8O_{11}$, T = 293(2)K, M = 968.54, orthorhombic, space group $Ccca$, a = 14.0035(5) Å, b = 25.4518(10) Å, c = 12.2416(5) Å, V = 4363.1(3) $Å^3$, Z = 4, D_c = 1.474 Mg·m^{-3}, μ = 0.736 mm^{-1}, F_{000} = 2000. Of 10044 measured data, 1473 were unique (R_{int} = 0.0280) to give $R1[I > 2\sigma(I)]$ = 0.0573, $wR2$ = 0.1589.

4: $C_{22}H_{20}FeN_2O_6$, T = 93(2)K, M = 464.25, monoclinic, space group $P2_1/n$, a = 10.493(4) Å, b = 7.227(2) Å, c = 13.506(5) Å, β = 107.095(7)°, V = 978.9(6) $Å^3$, Z = 2, D_c = 1.575 Mg·m^{-3}, μ = 0.815 mm^{-1}, F_{000} = 480. Of 7718 measured data, 1731 were unique (R_{int} = 0.0379) to give $R1[I > 2\sigma(I)]$ = 0.0347, $wR2$ = 0.0768.

Acknowledgments

We are grateful to the EPSRC (P. B.) and BBSRC (S. L. J.) for financial support.

[1] a) P. Stavropoulos, R. Çelenligil-Çetin, A. E. Tapper, *Acc. Chem. Res.* **2001**, *34*, 745–752; b) F. Gozzo, *J. Mol. Catal. (A)* **2001**, *171*, 1–22.
[2] S. Kiani, A. Tapper, R. J. Staples, P. Stavropoulos, *J. Am. Chem. Soc.* **2000**, *122*, 7503–7517.
[3] S. G. Shova, N. V. Brashovyanu, K. I. Turte, M. D. Mazus, *Russ. J. Coord. Chem.* **1996**, *22*, 438–443.
[4] P. Laine, A. Gourdon, J. P. Launay, J. P. Tuchagues, *Inorg. Chem.* **1995**, *34*, 5150–5155.
[5] J. Thich, C. C. Ou, D. Powers, B. Vasiliou, D. Mastropaolo, J. A. Potenza, H. J. Schugar, *J. Am. Chem. Soc.* **1976**, *98*, 1425–1433.
[6] C. C. Ou, R. G. Wollmann, D. N. Hendrickson, J. A. Potenza, H. J. Schugar, *J. Am. Chem. Soc.* **1978**, *100*, 4717–4724.
[7] P. Laine, A. Gourdon, J. P. Launay, *Inorg. Chem.* **1995**, *34*, 5129–5137.
[8] G. S. Sanyal, R. Ganguly, P. K. Nath, R. J. Butcher, *J. Indian Chem. Soc.* **2002**, *79*, 489–491.
[9] J. F. Hseu, J. J. Chen, C. C. Chuang, H. H. Wei, M. C. Cheng, Y. Wang, Y. D. Yau, *Inorg. Chim. Acta* **1991**, *184*, 1–5.
[10] P. Laine, A. Gourdon, J. P. Launay, *Inorg. Chem.* **1995**, *34*, 5138–5149.
[11] P. Laine, A. Gourdon, J. P. Launay, *Inorg. Chem.* **1995**, *34*, 5156–5165.
[12] C. Sheu, S. A. Richert, P. Cofré, B. Ross, A. Sobkowiak, D. T. Sawyer, J. R. Kanofsky, *J. Am. Chem. Soc.* **1990**, *112*, 1936–1942.
[13] K. Abboud, C. Xu, R. S. Drago, *Acta Crystallogr. Sect. C* **1998**, *54*, 1270–1272.
[14] R. D. Hancock, A. E. Martell, D. Chen, R. J. Motekaitis, D. McManus, *Can. J. Chem.* **1997**, *75*, 591–600.
[15] K. Hashimoto, S. Nagatomo, S. Fujinami, H. Furutachi, S. Ogo, M. Suzuki, A. Uehara, Y. Maeda, Y. Watanabe, T. Kitagawa, *Angew. Chem. Int. Ed.* **2002**, *41*, 1202–1205.
[16] S. A. G. Högberg, K. Madan, C. Moberg, B. Sjöberg, M. Weber, M. Muhammed, *Polyhedron* **1985**, *4*, 971–977.
[17] K. Osawa, H. Furutachi, S. Fujinami, M. Suzuki, *Acta Crystallogr. Sect. E* **2003**, *59*, 315–316.
[18] N. Okabe, T. Makino, *Acta Crystallogr. Sect. C* **1998**, *54*, 1279–1280.
[19] N. Okabe, Y. Muranishi, *Acta Crystallogr. Sect. E* **2003**, *59*, m220–m222.
[20] W. Li, M. M. Olmstead, D. Miggins, R. H. Fish, *Inorg. Chem.* **1996**, *35*, 51–55.
[21] D. Dobrzyńska, M. Duczmal, L. B. Jerzykiewicz, J. Warchulska, K. Drabent, *Eur. J. Inorg. Chem.* **2004**, 110–117.
[22] A. Cousson, F. Nectoux, F. Robert, E. N. Rizkalla, *Acta Crystallogr. Sect C* **1995**, *51*, 838–840.
[23] S. L. Jain, P. Bhattacharyya, H. L. Milton, A. M. Z. Slawin, J. D. Woollins, *Inorg. Chem. Commun.* **2004**, *7*, 423–425.
[24] C. Coin, T. Zevaco, E. Dunach, M. Rostel, *Bull. Soc. Chim. Fr.* **1996**, *133*, 913–918.
[25] A. Seminara, A. Musumeci, *J. Inorg. Nucl. Chem.* **1977**, *39*, 599–605.
[26] G. M. Sheldrick, *SHELXTL, structure solution, determination package*, Bruker AXS, Madison, WI, **1999**.
[27] M. Ranjbar, H. Aghabozorg, A. Moghimi, *Acta Crystallogr. Sect. E* **2002**, *58*, m304–m306.
[28] N. Okabe, H. Kyoyama, A. Fujimoto, *Acta Crystallogr. Sect. E* **2002**, *58*, m354–m356.
[29] S. K. Ghosh, J. Ribas, P. K. Bharadwaj, *Cryst. Eng. Commun.* **2004**, *6*, 250–256.
[30] W. Starosta, H. Ptasiewicz-Bak, J. Leciejewicz, *J. Coord. Chem.* **2002**, *55*, 1147–1153.
[31] L. Mao, Y. Wang, Y. Qi, M. Cao, C. Hu, *J. Mol. Struct. J. Mol. Struc.* **2004**, *688*, 197–201.
[32] Z. Liu, D. Zhang, C. Liu, D. Zhu, *Chem. Lett.* **2004**, *33*, 180–181.

 © 2005 Wiley-VCH Verlag GmbH & Co. KGaA, Weinheim

[33] G. Smith, A. N. Reddy, K. A. Byriel, C. H. L. Kennard, *Polyhedron* **1994**, *13*, 2425–2430.
[34] S. Noro, S. Kitagawa, M. Yamashita, T. Wada, *Cryst. Eng. Commun.* **2002**, *4*, 162–164.
[35] E. E. Sileo, A. S. de Araujo, G. Rigotti, O. E. Piro, E. E. Castellano, *J. Mol. Struc.* **2003**, *644*, 67–76.
[36] S.-Q. Xia, S.-M. Hu, J.-C. Dai, X.-T.Wu, J.-J. Zhang, Z.-Y. Fu, W.-X. Du, *Inorg. Chem. Commun.* **2004**, *7*, 51–53.
[37] D. Min, S. S. Yoon, J. H. Lee, M. Suh, S. W. Lee, *Inorg. Chem. Commun.* **2001**, *4*, 297–300.

Received August 27, 2004
Published Online January 27, 2005

 © 2005 Wiley-VCH Verlag GmbH & Co. KGaA, Weinheim

Green Light Luminescence from ZnO/Dodecylamine Mesolamellar Nanocomposites Synthesized by Self-Assembly

Yu-de Wang,*[a] Shuo Zhang,[a] and Xing-hui Wu[a]

Keywords: Mesoporous materials / Nanocomposites / Luminescence / Interfacial interactions

The synthesis, structural characterization and optical properties of a semiconducting zinc oxide based dodecylamine surfactant, mesolamellar zinc oxide/surfactant nanocomposite (Zn-L) are described. XRD and TEM results showed the formation of a lamellar mesostructure with two layer spacings ca. 28 Å. A red-shift in the absorption band edge of absorption spectrum and the green light photoluminescence of the resulted nanocomposite were observed at room temperature. The red-shift of the absorption band edge and the room temperature photoluminescence (RTPL) of the Zn-L nanocomposite might be induced by the dielectric confinement effect and the interfacial interaction between the ZnO and the surfactant, respectively.

(© Wiley-VCH Verlag GmbH & Co. KGaA, 69451 Weinheim, Germany, 2005)

Introduction

Recent developments in the synthesis of self-assembled inorganic/organic surfactant composites have opened up a new field in the study of composite materials.[1] Lamellar inorganic species/surfactant composite consist of surfactant layers, alternating with inorganic layers. When the inorganic layers are semiconducting materials, a novel nanostructured semiconductor–surfactant superlattice may result with, possibly,novel properties.[2] A novel chemical synthetic approach based on self-assembly between inorganic species and surfactant has been presented for inorganic species and organic surfactant into two- and three-dimensional superlattice structures,[3,4] and has been successfully extended to numerous ordered inorganic–organic composites with nanometer scale periodicities.[2,5] To date, a series of semiconductor lamellar mesophase in which a semiconductor oxide is sandwiched between organic components has been successfully synthesized.[6–8] Zinc oxide is a promising luminescent material with a wide bandgap (3.37 eV), large exciton binding energy (60 meV) and is used for various applications such as vacuum fluorescent displays due to its nonlinear optical properties and room temperature ultraviolet emission.[9] As a large-bandgap semiconductor and luminescence material, nanostructured ZnO (nanoparticles, nanowires, nanobelts, and nanotuble) has been widely studied.[10–12] However, to the best of our knowledge, ZnO lamellar mesophase, relative to its room temperature photoluminescence, has rarely been mentioned. In this letter, we report the synthesis and room temperature photoluminescence of a mesolamellar zinc oxide/surfactant nanocomposite, the morphology of which appears to be distinctively different from those previously reported.

[a] Department of Materials Science & Engineering, Yunnan University,
Kunming 650091, China
Fax: (internat.) +86-871-515-3832
E-mail: wangyude@tsinghua.org.cn

Results and Discussion

Powder XRD data clearly demonstrate the ordered lamellar mesostructure of the zinc oxide/surfactant composite (Figure 1): a series of equally spaced peaks appear in the low-angle region. Similar to lamellar silicate, aluminophosphate, and TiO_2 mesophase,[1,2] the peaks are attributed to the 00*l* rational reflections, characteristic of a lamellar structure. The first diffraction peak, assumed to be (001), corresponds to a *d*-spacing of about 28.5 Å. Reflections up to the 5th order of the (001) diffraction are observed. Besides the (00*l*) series, other diffraction peaks in the low-angle diffraction region are best assigned to positional ordering of the dodecylamine molecules within the bilayer. The fully extended dodecylamine bilayer can be estimated to be about 39 Å long. Crystalline dodecylamine displays a very similar XRD patter in this range.

The powder XRD pattern of the Zn-L composite clearly displays the characteristics of a well-ordered layered structure with evidence of registry between the sheets. The flaky morphology of Zn-L the composite, displayed in the SEM image, Figure 2(a), supports this proposal. The lamellar composite is further confirmed by a TEM study. Well-defined parallel lines [Figure 2(b)] confirm that the Zn-L composite is a lamellar structure[3] – consistent with the results of XRD. The inter-lamellar distance is 28 Å, in accordance with the *d*-spacing calculated from the first diffraction peak in the XRD pattern.

The FT-IR spectrum of the Zn-L composite shows a zinc–oxygen stretching band in the region 500–1000 cm^{-1}

 DOI: 10.1002/ejic.200400450 © 2005 Wiley-VCH Verlag GmbH & Co. KGaA, Weinheim

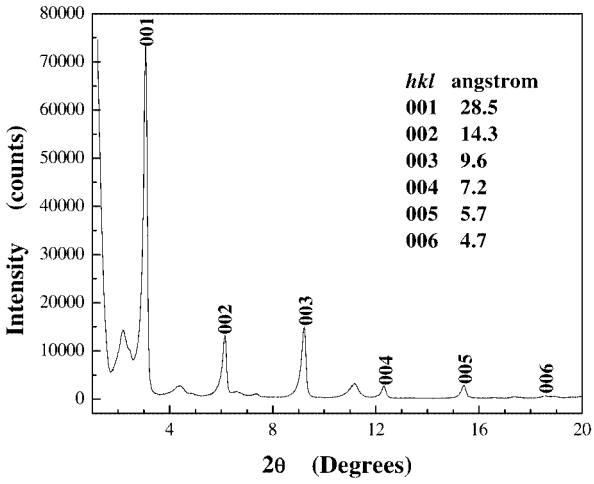

Figure 1. XRD pattern of as-synthesized Zn-L composite.

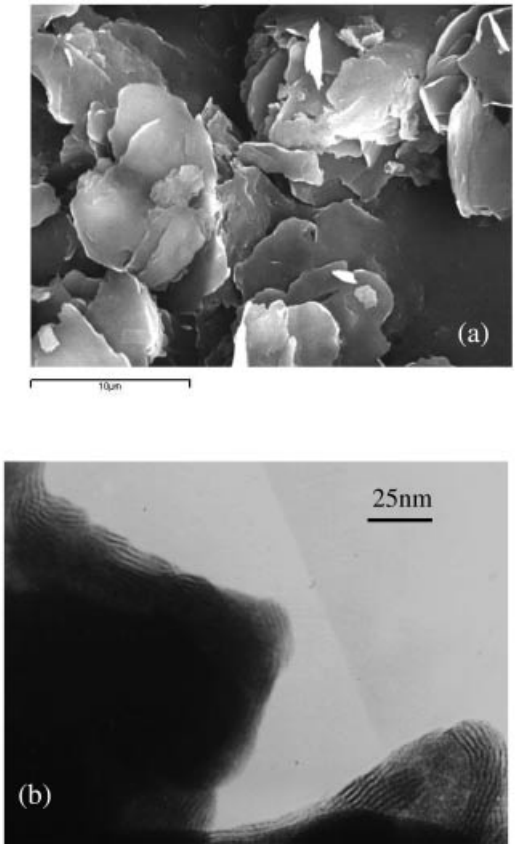

Figure 2. (a) Representative SEM image of Zn-L composite. (b) TEM image to the Zn-L composite showing the lamellar.

(Figure 3). Some bands in the region 3300–3500 cm^{-1} are due to N–H stretches of DDA, and sharp bands at 2853 and 2913 cm^{-1} are due to C–H stretches of the hydrocarbon chain of DDA. Sharp bands in the region 1370–1600 cm^{-1} are attributed to the deformation of $–CH_2–$ and $–CH_3$ of the incorporated DDA. The CH_2 stretching vibrations are considered to be related with the physical state (monomer, micelle or solid) of dodecylamine. These band vibrations indicate that the dodecylamine is present in the as-synthesized nickel oxide mesostructure. They provide evidence for the incorporation of dodecylamine into the hydrous oxide.[13] Figure 3 also reveals a C–N band at 1333 cm^{-1}, which is blue-shifted by 33 cm^{-1} compared with the spectrum of DDA (C–N at 1300 cm^{-1}). The affinity of Zn^{2+} ions to amine and imine ligands is well known. This allows us to assume chemical interaction between NHgroups of the DDA chains and surface Zn^{2+} ions of the Zn-L nanocomposites. It can be inferred that the formation of new surface states may results from chemical binding between the components of the neighbouring layers.

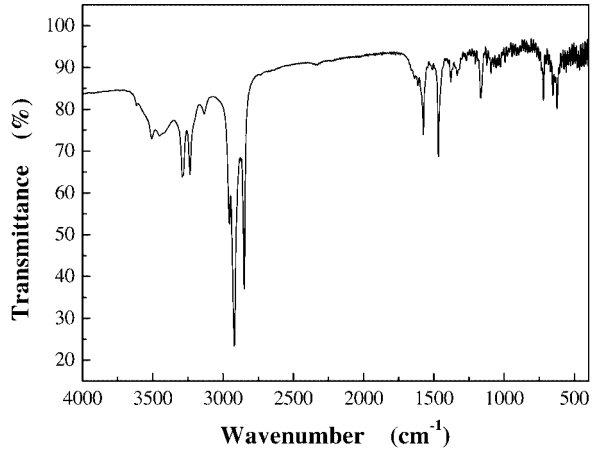

Figure 3. FTIR spectrum of Zn-L nanocomposite.

The two XPS spectrum peaks [Figure 4(a)], of $2p_{\frac{3}{2}}$ and $2p_{\frac{1}{2}}$ at 1022.9 eV and 1045.9 eV, with a better symmetry, are assigned to lattice zinc in zinc oxide. The peaks are 23.0 eV apart. The values correspond to a 2p3 binding energy of Zn^{II} ion (indexed Standard ESCA Spectra of the Elements and Line Energy Information, Φ Co., USA). The small shift in the $2p_{\frac{3}{2}}$ peak position from the crystalline ZnO to the mesolamellar structure ZnO, from 1021.7 eV (indexed Hand of X-ray photoelectron spectroscopy) to 1022.9 eV, indicates a change of microenvironments for zinc. This shift (1.2 eV) confirms that most Zn atoms remain in Zn-L nanocomposites, in the same formal valence state of Zn^{2+} within an oxygen deficient ZnO_{1-x} matrix.[14,15] This Zn enrichment or oxygen defects is due to the strong interaction between the dodecylamine and ZnO and to the weakly crystalline nature of the hydrous zinc oxide composite. Figure 4(b) shows that the O_{1s} XPS is asymmetric (the left-hand side is wider), indicating that there at least two kinds of oxygen species in the near surface region. The peak at about 531.6 eV is due to the ZnO crystal lattice oxygen, while that at about 533 eV is due to chemisorded oxygen.[16]

The lamellar mesostructured zinc oxide/surfactant composite displays interesting optical properties. UV/Vis spectroscopy was used to characterize the optical absorbance of the Zn-L nanocomposite. The absorption spectrum of Zn-L was carried out to resolve the excitonic or interband (valence-conduction band) transition of Zn-L, which allows us to calculate the bandgap. The absorption and corresponding bandgap energy of bulk ZnO is λ = 367 nm and E_g = 3.36 eV. The UV/Vis absorption spectrum of the as-synthe-

 © 2005 Wiley-VCH Verlag GmbH & Co. KGaA, Weinheim

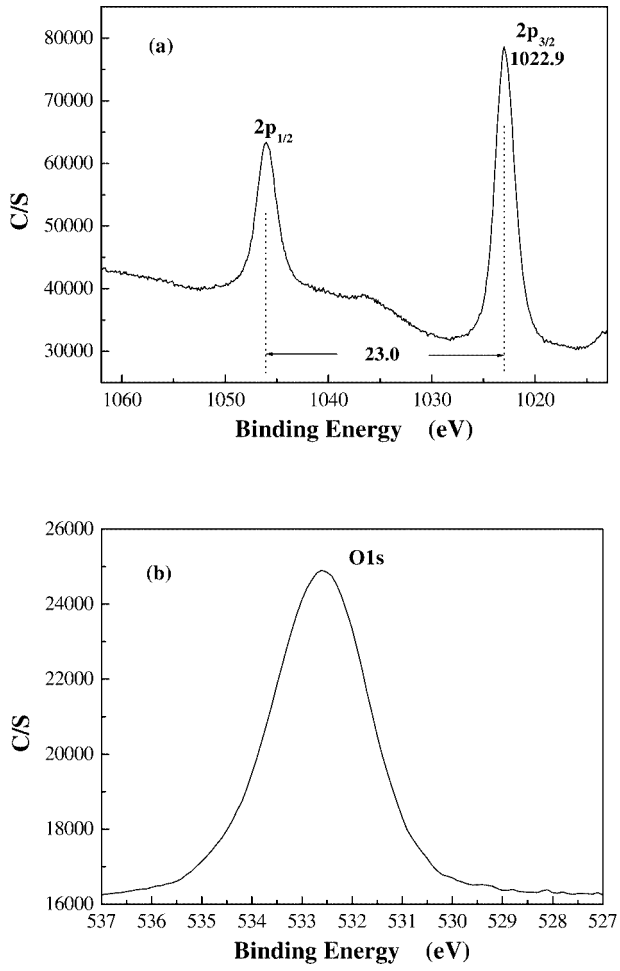

Figure 4. XPS spectra of ZnO/surfactant nanocomposites: (a) Zn2p and (b) O1s.

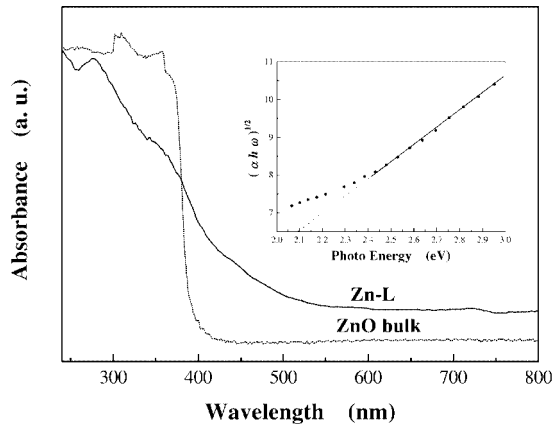

Figure 5. Absorption spectra of Zn-L composite and ZnO bulk. Inset: apparent energy gap of the Zn-L composite.

sized compositeshows a strong band edge absorption in the region above 370 nm (Figure 5). The absorption edge of Zn-L composite is red-shifted from the absorption edges of wurtzite ZnO dendrites (377 nm)[17] and bulk ZnO (367 nm). Absorption at longer wavelengths, the absorption red-shift, was also observed by Wang et al.[18] with sodium dodecylbenzenesulfonate (DBS) capped ZnO nanoparticles. The authors attributed this red-shift to intraband surface states formed by surfactant molecules chemically bound on the ZnO surface.

The absorption coefficient of an amorphous semiconductor has a characteristic relation:[19]

$$[d\hbar\omega]^{1/2} = A[\hbar\omega - E_g]$$

in which $\hbar\omega$ is the photon energy, E_g is the apparent optical bandgap, A is a constant characteristic of the amorphous semiconductor, and a is the absorption coefficient. Therefore, the E_g of zinc oxide/surfactant composite can be obtained by extrapolating the above relation to 2.09 eV (Figure 5 inset). A red-shift of ca. 1.27 eV relative to bulk ZnO is evident for the zinc oxide/surfactant inorganic–organic composite. This is contrary to the quantum size effect, which leads to a blue-shift of E_g with decreasing particle size, and has been observed in many nanometer-sized semiconductor materials.[20] Notably, however, the red-shift of absorption spectrum or apparant optical bandgap here would arise from the interface between zinc oxide and surfactant. As for the band edge shift of optical absorption of semiconductor nanoparticals in different surrounding mediums with a smaller dielectric constant than that of the semiconductors, Takagahara[21] attributes it to the dielectric confinement effect. He expressed, approximately,the bandgap of the semiconductor nanoparticles in the different surrounding mediums as

$$E_g = E_0 + \frac{\pi^2}{\bar{R}^2} - \frac{3.572}{\bar{R}} - \frac{0.248\varepsilon_1}{\varepsilon_2}$$

where E_0 is the bandgap of bulk semiconductor, $\bar{R} = R/a_B$ (R is semiconductor nanoparticles radius, a_B is exciton Bohr radius),and ε_1 and ε_2 are the dielectric constants of the semiconductor and surrounding medium, respectively. The second term is the quantum confinement energy, leading to the absorption band edge blue-shift as the size of particle radius reduces; the third term is the direct Coulomb interaction between an electron and a hole, leading to red-shift. The last term is usually called the surface polarization energy, which arises from the difference in dielectric constant between the semiconductor nanoparticles and the surrounding medium, leading to a red-shift. The dielectric confinement has a significant effect on the excition energy and can not be treated as a minor perturbation.[21] Therefore, the smallerthe semiconductor nanoparticles and the greater the difference between ε_1 and ε_2 , the greater the dielectric confinement effect becomes. For the Zn-L nanocomposites, the surfactant DDA has a smaller dielectric constant ($\varepsilon_1 \approx 1.5$) than ZnO ($\varepsilon_2 \approx 12$). The dielectric-constant ration $\varepsilon_2/\varepsilon_1$ is 8 and the dielectric confinement effect would be significant. When the dielectric confinement effect emerges, the screening effect is reduced and the Coulomb interaction between charged particles becomes enhanced, resulting in enhancement of the exciton binding energy and the exciton

 © 2005 Wiley-VCH Verlag GmbH & Co. KGaA, Weinheim

oscillation strength; thus the surface polarization energy becomes the key factor influencing the absorption band edge.[21,22] Meanwhile, the quantum confinement energy would become the subordinate factor.

The room temperature emission spectrum of the Zn-L lamellar mesophase (Figure 6) shows that the RTPL of as-synthesized Zn-L exhibits a broad, strong emission band between 440 and 560 nm, centered at 480 nm (2.58 eV), i.e. in the green region of visible range. Compared with ZnO nanowires previously reported[23] and nanosheets,[17] the Zn-L lamellar mesophase shows a peak small shift about 20 nm and 6 nm, respectively. The maximum Stokes shift $\frac{1}{2}\Delta_{max}$ ($\hbar\omega_{ex} - \hbar\omega_{em}$) is 0.327 eV. Figure 6 shows that the board emission band is asymmetric (the right-hand side is wider), indicating that the emission band is made up of at least two overlapping emission bands, and the position of the overall maximum will depend on their intensity ratios. Inner interfacial defects between the ZnO and surfactant contribute to the relatively shorter wavelength of luminescence (<480 nm), while the outmost surfactant can additionally luminescence at long wavelengths (>480 nm).[18] Similar results and discussion have been reported by Lin[2] et al. for mesolamellar TiO_2. The luminescence of the Zn-L nanocomposite is similar to that from ZnO-capped sodium dodecylbenzenesulfonate.[18] The luminescence mechanisms of ZnO have been studied for several decades.[17,23] The ultraviolet peaks can be assigned to the direct recombination of a conduction electron and a hole in the valence band, and the green peaks can be attributed to the deep-trap-mediated emission. The origin of the deep trap in ZnO is not yet clearly understood but is generally attributed to structural defects, single ionized vacancies, and impurities.[23–26]

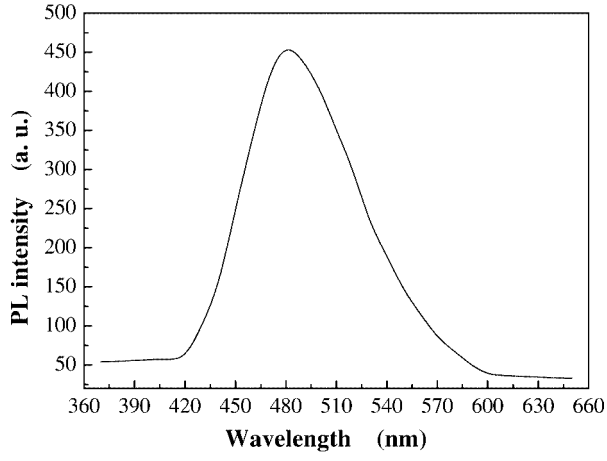

Figure 6. Emission (λ_{ex} = 383 nm) spectra of Zn-L nanocomposites.

In our investigation, the RTPL mechanism of Zn-L composite differs from that of bulk and other nanostructured ZnO. The mesolamellar zinc oxide/surfactant nanocomposites show the ordered structure to form zinc oxide/surfactant superlattices. This peculiar structure might have a profound effect on the chemical and physical properties of zinc oxide. The interfacial effect of zinc oxide/surfactants composites between zinc oxide and organic surfactants might be similar to the ZnO nanoparticles coated with sodium dodecylbenzenesulfonate reported by Wang.[18] X-ray photoelectron spectroscopic analysis indicates that the oxygen vacancies are formed in Zn-L nanocomposites. Many oxygen vacancies mainly located on the interface of the inorganic framework have interactions with interfacial capping surfactants, and surfactants might stabilize F-center-like oxygen vacancies. These interactions will lead to the formation of the trapped state that might form a series of metastable energy levels within the bandgap. Metastable energy levels are relatively long-lived and their optical transitions are dipole allowed. Thus, room temperature photoluminescence can be observed. Therefore, it could be inferred that the RTPL of the zinc oxide/surfactant mesophase might be induced by interfacial effects between the inorganic framework and the surfactants.

Conclusions

An ordered lamellar zinc oxide mesostructure was prepared in the presence of a neutral surfactant by self-assembly. Such Zn-L nanocomposites display new optical properties, such as a red-shift of absorption edge and room temperature photoluminescence. The absorption edge shifts to a low energy region (red-shift) because of the dielectric confinement effect. The interface effect between zinc oxide and surfactant is the main cause of the room temperature photoluminescence. These new optical properties of mesolamellar zinc oxide/surfactant nanocomposites also enhance their applications in optics.

Experimental Section

General: The structure was analyzed and characterized by X-ray diffraction (XRD, Rigaku D/max-RB diffractometer with Cu-K_α radiation, λ = 1.5418 Å). The sample was scanned from 1.2° to 20° (2θ) in steps of 0.02°. The scanning electron microscopy (SEM) photograph was obtained by JSM-6301F. Transmission electron micrographs (TEM) were made on a 200CX transmission electron microscope operated at 200 kV. Fourier transformed infrared (FTIR) spectra (4000–400 cm^{-1}) were recorded on a Perkin-Elmer Spectrum GX infrared spectrophotometer. Samples for FTIR were prepared using the KBr technology, which were calibrated by polystyrene. The composition of the Zn-L nanocomposite was determined by the X-ray photoemission spectra (XPS) recorded on a Perkin–Elmer PHI 5300 ESCA system with an Al-K_α X-ray beam and 250 W power. UV/Vis measurements were made with a UV2100 spectrophotometer. Photoluminescence (PL) measurements were carried out at room temperature using λ = 383 nm as the excitation wavelength with a HITACHI 850 type visible-ultraviolet spectrometer with a Xe laser as the excitation source.

Synthesis of ZnO/Dodecylamine Mesolamellar Nanocomposite: All chemical reagents used in the experiments were obtained from commercial sources as guaranteed-grade reagents and used without further purification or treatment. $ZnCl_2$ and DDA had purities of 98%. The composite was synthesized using a neutral dodecylamine ($C_{12}H_{27}N$, DDA) surfactant and zinc chloride ($ZnCl_2$). $ZnCl_2$ (1.36 g) was dissolved in distilled deionized water (DDW) (28 mL). DDA (0.74 g) dissolved in DDW (28 mL) was then added to the

 © 2005 Wiley-VCH Verlag GmbH & Co. KGaA, Weinheim

$ZnCl_2$ solution under vigorous stirring. The synthesis mixture, possessing a molar ratio $ZnCl_2$:DDA:H_2O of 1.0:0.4:156, was stirred for 4 h before being aged at room temperature for 48 h. The solid product was then recovered by filtration and washed with water. Dry composite could be exposed to air without oxidation.

Acknowledgments

We thank Y. Fu for assistance with photoluminescence spectra measurements, X. Y. Ye for her help in the XPS, S.-Q. Sun for her help in the FTIR experiments, and Q. Cai for many helpful discussions. Funding from the Natural Science Foundation of Yunnan Province, China (2002Z0004Q) and the Project for Science and Technology of Yunnan University (2003Z003A) is gratefully acknowledged.

[1] S. H. Tolbert, P. Sieger, G. D. Stucky, S. M. J. Aubin, C. C. Wu, D. N. Hendrickson, *J. Am. Chem. Soc.* **1997**, *119*, 8652–8661.
[2] W. Y. Lin, W. Q. Peng, J. Z. Sun, J. C. Shen, *J. Mater. Chem.* **1999**, *9*, 641–642.
[3] Q. S. Huo, D. I. Margolese, U. Ciesla, D. G. Demuth, P. Y. Feng, T. E. Gier, P. Sieger, A. Firouzi, B. F. Chmelka, F. Chuth, G. D. Stucky, *Chem. Mater.* **1994**, *6*, 1176–1191.
[4] G. D. Stucky, Q. S. Huo, A. Firouzi, B. F. Chmelka, S. Schacht, I. G. Voigt-Martin, F. Schuth, *Stud. Surf. Sci. Catal.* **1996**, *105*, 3–28.
[5] A. Sayari, P. Liu, *Microporous Mater.* **1997**, *12*, 149–177.
[6] P. V. Braun, P. Osenar, S. I. Stupp, *Nature* **1996**, *380*, 325–328.
[7] Z. R. Tian, W. Tong, J. Y. Wang, N. G. Duan, V. V. Krishnan, S. L. Suib, *Science* **1997**, *276*, 926–930.
[8] K. G. Severin, T. M. Abdel-Fattah, T. J. Pinnavaia, *Chem. Commun.* **1998**, 1471–1472.
[9] Y. C. Kong, D. P. Yu, B. Zhang, W. Fang, S. Q. Feng, *Appl. Phys. Lett.* **2001**, *78*, 407–409.
[10] A.vav Dijken, E. A. Meulenkamp, D. Vanmaekelbergh, A. Meijerink, *J. Lumin.* **2000**, *87 – 89*, 454–456.
[11] Y. W. Wang, L. D. Zhang, G. Z. Wang, X. S. Peng, Z. Q. Chu, C. H. Liang, *J. Cryst. Growth* **2002**, *234*, 171–175.
[12] J. Zhang, L. D. Sun, C. S. Liao, C. H. Yan, *Chem. Commun.* **2002**, 262–263.
[13] Y. Q. Wang, S. G. Chen, X. H. Tang, O. Palchik, A. Zaban, *J. Mater. Chem.* **2001**, *11*, 521–526.
[14] S. Major, S. Kumar, M. Bhatnagar, K. L. Chopra, *Appl. Phys. Lett.* **1986**, *40*, 394–396.
[15] M. Chen, X. Wang, Y. H. Yu, Z. L. Pei, X. D. Bai, C. Sun, R. F. Huang, L. S. Wen, *Appl. Surf. Sci.* **2000**, *158*, 134–140.
[16] M. Koudelka, A. Monnier, J. Sanchez, *J. Mol. Catal.* **1984**, *25*, 295–2305.
[17] S. H. Yu, J. Yang, Y. T. Qian, M. Yoshimura, *Chem. Phys. Lett.* **2002**, *361*, 362–366.
[18] R. Y. Wang, X. C. Wu, P. F. Wu, B. S. Zou, L. Wang, J. Z. Xu, J. R. Xu, X. F. Wang, Z. J. Wang, J. X. Chen, *Acta Phys. Sin.* **1998**, *7*, 203–208.
[19] G. Mills, Z. G. Li, D. Mersel, *J. Phys. Chem.* **1988**, *92*, 822–828.
[20] X. C. Wu, B. S. Zou, J. R. Xu, B. L. Yu, G. Q. Tang, G. L. Zhang, W. J. Chen, *Nanostruct. Mater.* **1997**, *8*, 179–189.
[21] T. Takagahara, *Phys. Rev. B* **1993**, *47*, 4569–4585.
[22] B. L. Yu, C. S. Zhu, F. X. Gan, *Opt. Mater.* **1997**, *7*, 15–20.
[23] M. H. Huang, Y. Y. Wu, H. Feick, N. Tran, E. Weber, P. D. Yang, *Adv. Mater.* **2001**, *13*, 113–116.
[24] M. H. Huang, S. Mao, H. Feick, H. Yan, Y. Wu, H. Kind, E. Weber, R. Russo, P. D. Yang, *Science* **2001**, *292*, 1897–1899.
[25] J. J. Wu, S. C. Liu, *Adv. Mater.* **2002**, *14*, 215–218.
[26] K. Vanheusden, W. L. Warren, C. H. Seager, D. K. Tallant, J. A. Voigt, B. E. Gnade, *J. Appl. Phys.* **1996**, *79*, 7983–7990.

Received May 28, 2004

 © 2005 Wiley-VCH Verlag GmbH & Co. KGaA, Weinheim

Vanadium(IV and V) Complexes of Schiff Bases and Reduced Schiff Bases Derived from the Reaction of Aromatic *o*-Hydroxyaldehydes and Diamines: Synthesis, Characterisation and Solution Studies

Isabel Correia,[a] João Costa Pessoa,*[a] M. Teresa Duarte,[a] M. Fátima Minas da Piedade,[a] Tamás Jackush,[b] Tamás Kiss,*[b] M. Margarida C. A. Castro,[c] Carlos F. G. C. Geraldes,[c] and Fernando Avecilla[d]

Keywords: Vanadium complexes / Schiff bases / Reduced Schiff bases / Crystal structures / Speciation

Several sal_2en-type reduced Schiff bases have been prepared from the reaction of 2 equiv. of salicylaldehyde (or derivatives) with ethylenediamine followed by reduction with $NaBH_4$ and subsequently characterised. The water-soluble ligands $(SO_3\text{-sal})_2en$ and $R(SO_3\text{-sal})_2en$ (SO_3-sal = salicylaldehyde-5-sulphonate) have been studied by pH potentiometry and ^1H NMR spectroscopy and the protonation constants of $R(SO_3\text{-sal})_2en$ have been determined. The Schiff bases are more susceptible to hydrolysis than the corresponding reduced Schiff bases. The crystal structures of $H_2(o\text{-van})_2en$ and $KH(o\text{-van})_2en$ (*o*-van = *o*-vanillin) have been determined by X-ray diffraction. The vanadium(IV) complexes have been prepared and characterised by magnetic measurements and IR, UV/Vis and EPR spectroscopy. The colours, magnetic susceptibilities and IR spectra of the new vanadium(IV) complexes of the reduced Schiff bases now obtained suggest oligomeric/polymeric structures for the compounds while the corresponding $V^{IV}O$–Schiff-base complexes are monomeric. The complexation of $[V^{IV}O]^{2+}$ and $[V^{V}O_2]^{+}$ with $R(SO_3\text{-sal})_2en$ in aqueous solution has been studied by pH potentiometry, UV/Vis as well as by EPR spectroscopy for the $V^{IV}O$ system and ^1H and ^{51}V NMR spectroscopy for the $V^{V}O_2$ system. Complex formation constants have been determined and binding modes have been proposed. *N*,*N*′-ethylenebis(pyridoxylaminato) ($Rpyr_2en$) has also been obtained and the structure of $Na[V^{V}O_2(Rpyr_2en)]\cdot CH_3OH\cdot 3H_2O$ determined by X-ray diffraction. The $Rpyr_2en^{2-}$ ligand coordinates through both the *N*-amine and *O*-phenolate moieties in a symmetrical α-*cis* type coordination mode, i.e. with both *O*-phenolato donors *cis* to the *O*-oxo atoms and *trans* to each other.

(© Wiley-VCH Verlag GmbH & Co. KGaA, 69451 Weinheim, Germany, 2005)

Introduction

The presence of vanadium in biological systems, its insulin-enhancing action[1–4] and anticancer activity[5–7] has driven a considerable amount of research. Particular interest has been given to the study of the potential benefits of vanadium compounds as oral insulin substitutes for the treatment of diabetes.[8–12] Coordinated ligands should be able to improve the absorption and intracellular mobility of vanadium, reducing the dose necessary for producing equivalent effects. Several vanadium complexes of the dianionic tetradentate Schiff base sal_2en (*N*,*N*′-disalicylideneethylenediamine) type ligands have been proposed for use as insulin-enhancing agents and for treatment of obesity and hypertension.[13–15] Saminathan and Durai[13] reported the ability of $V^{IV}O(sal_2en)$ to reverse the hyperglycaemic condition of alloxan-induced diabetic rats, thereby exerting insulin-like action. However, the rats tended to become hypoglycaemic and withdrawal of treatment brought an immediate return of hyperglycaemia.

The sal_2en-type ligands present versatile steric, electronic and lipophilic properties. They may be easily prepared by the condensation of two compounds, namely an aromatic *o*-hydroxyaldehyde and a diamine, the hydrophilic-lipophilic balance being easily fine-tuned by choosing the appropriate amine precursors and ring substituents of the aldehyde.

In solution, Schiff base (SB) ligands have the disadvantage of their potential for hydrolysis. This instability can be overcome by reduction of the SB to give an amine. This presents interesting possibilities since the reduced SB will be more flexible and not forced to remain planar when coordinated to a metal centre. In this paper, we report the preparation of the SB and reduced SB ligands of salicylaldehyde, *o*-vanillin (*o*-van) and salicylaldehyde-5-sulphonate

[a] Centro Química Estrutural, Instituto Superior Técnico, Av. Rovísco Pais, 1049-001 Lisboa, Portugal
[b] Biocoordination Chemistry Research Group of the Hungarian Academy of Sciences, University of Szeged, P. O. Box 440, 6701 Szeged, Hungary
[c] Departamento de Bioquímica, Centro de RMN e Centro de Neurociências e Biologia Celular, Universidade de Coimbra, 3001-401 Coimbra, Portugal
[d] Departamento de Química Fundamental, Universidade da Coruña, Campus de A Zapateira, 15071 A Coruña, Spain
Supporting information for this article is available on the WWW under http://www.eurjic.org or from the author.

 © 2005 Wiley-VCH Verlag GmbH & Co. KGaA, Weinheim **DOI: 10.1002/ejic.200400481**

(SO_3-sal) with ethylenediamine and the preparation of their $[V^{IV}O]^{2+}$ complexes which were characterised in the solid state and in solution.

Most of vanadium's biologically important reactions occur in water-based environments such as blood plasma and intracellular fluids. A knowledge of the distribution and chemical speciation of the vanadium compounds in aqueous solution is, therefore, of the utmost importance. Most of the sal_2en-type ligands and vanadium complexes prepared so far are not water-soluble. The compounds prepared using SO_3-sal are, however, soluble in water and may, therefore, be particularly useful for therapeutic use.

The study of the moderately water-soluble Schiff base of pyridoxal and ethylenediamine (pyr_2en) and its hydrolytically more stable reduced derivative $Rpyr_2en$ was reported in a previous paper.[15] Both proved to be efficient binders of vanadium in the +IV and +V oxidation states. Several $V^{IV}O$– and $V^{V}O_2$–$Rpyr_2en$ complexes were prepared and their properties studied. One of these, $[V^{V}O_2(HRpyr_2en)]$, was isolated in a crystalline form and structurally characterised by X-ray diffraction. Both ligands pyr_2en and $Rpyr_2en$ were found to form basically similar complexes coordinating through two $O_{phenolate}$ centres and two $N_{amine/imine}$ centres. The solution speciation revealed that the reduced SB formed more stable complexes with both $[V^{IV}O]^{2+}$ and $[V^{V}O_2]^{+}$ than the SB itself. EPR ($V^{IV}O$–$Rpyr_2en$ system), ^1H and ^{51}V NMR ($V^{V}O_2$–$Rpyr_2en$ system) spectroscopic studies indicated the presence of various isomeric species in solution.

Some of the vanadium(IV) complexes synthesised and characterised in the present and in the previous study[15] have been tested in vitro for their toxicity and insulin-mimetic behaviour, these are[16] $Cs_2[V^{IV}O(SO_3\text{-sal})_2en]$ (**8**), $[V^{IV}O(Rsal_2en)]$ (**9**), $[V^{IV}O(pyr_2en)]$ and $[V^{IV}O(Rpyr_2en)]$. At vanadium concentrations below 10 μM none of the compounds were toxic and they all proved to be effective with respect to the insulin-mimetic activity which was tested as the ability of vanadium compounds to trigger glucose uptake by cells. In that study, compound **8** was considered one of the most promising compounds with respect to its insulin-mimetic behaviour and low toxicity in the physiological concentration range.[16]

Results and Discussion

Synthesis and Characterisation

The Schiff bases **1**–**3** (see Scheme 1) were prepared in high yields (>75%) by the condensation of 2 equiv. of the appropriate aldehyde derivative with 1 equiv. of ethylenediamine. Treatment of these condensation products with sodium borohydride resulted in the reduction of the two imine bonds, yielding the reduced Schiff bases **4**–**7** (Scheme 1). All compounds gave satisfactory elemental analyses and were

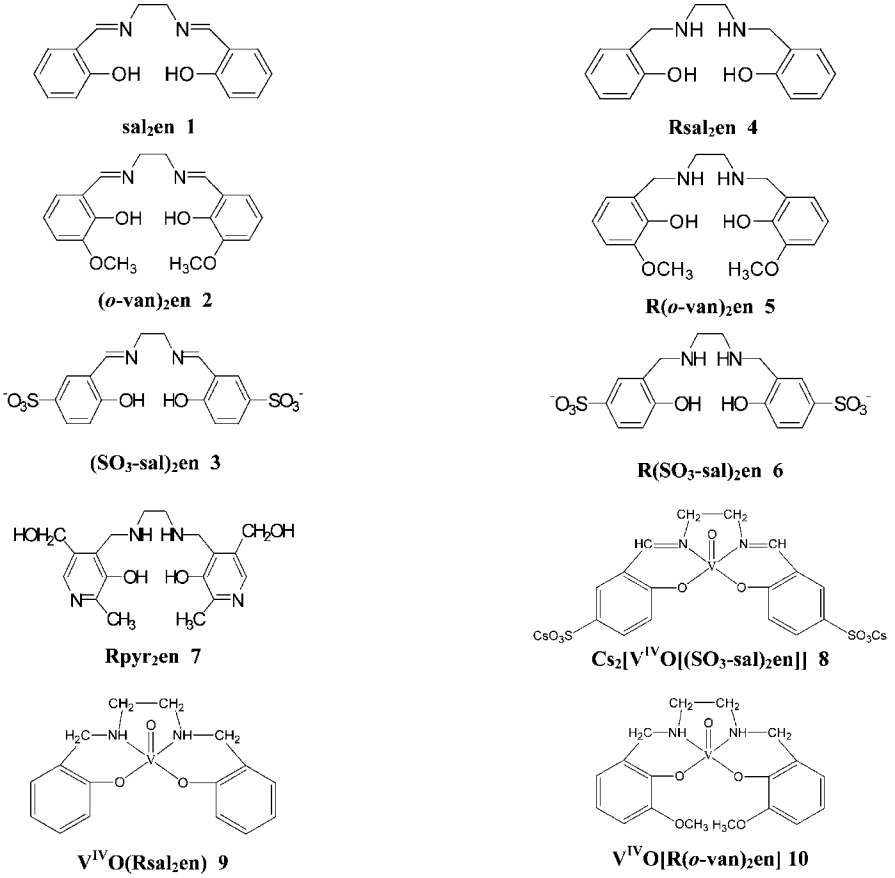

Scheme 1. Ligands and $[V^{IV}O]^{2+}$ complexes prepared and characterised in this work

 © 2005 Wiley-VCH Verlag GmbH & Co. KGaA, Weinheim

characterised by ^{1}H NMR spectroscopy and mass spectrometry. Two types of crystals suitable for X-ray diffraction studies were obtained for **2**.

By treatment of **3**–**5** with oxovanadium(IV) salts, [$V^{IV}O$] complexes with an N_2O_2 binding mode were obtained in good yields, namely [$V^{IV}O\{(SO_3\text{-sal})_2en\}$] (**8**),[17] [$V^{IV}O$-(Rsal$_2$en)] (**9**) and [$V^{IV}O\{R(o\text{-van})_2en\}$] (**10**). The complexes were characterised by elemental analysis, IR and UV/Vis spectroscopy. All our efforts to characterise the compounds obtained from the reaction of **6** with $[V^{IV}O]^{2+}$ were unsuccessful. Solids were obtained but no satisfactory formulation could be deduced. Compound **11** was obtained after slow concentration of a methanolic solution which contained a V^V salt and compound **7**.

X-ray Diffraction Studies

H_2(o-van)$_2$en (2A) and KH(o-van)$_2$en·2H_2O (2B)

ORTEP diagrams of **2A** and **2B** are presented in Figure 1 and selected bond lengths and angles are given in Table 1. A similar crystal structure for **2A** has already been reported[18] but we have included our data since it is of a better resolution (taking into account the *R* and e.s.d. values; we also included the hydrogen atoms in the refinement). The molecular structure of **2A** agrees with the published data[18] and both exhibit two geometry-determined intramolecular H-bonds between the N_{imine} and the $O_{phenolic}$ centres in both sides of the molecule [O–H···N 2.576(3), 2.608(3) Å with angles of 147.4(2)° and 146.8(2)° which dictate the molecular configuration and an N–C–C–N torsion angle of –163.0(2)° (–160.91° in ref.[18])]. The bond lengths and angles do not show any significant deviation from the expected values in similar compounds.[15,19,20] Another structure for H_2(o-van)$_2$en has recently been reported.[21] However, it is impossible to access this report to make adequate comparisons.[22]

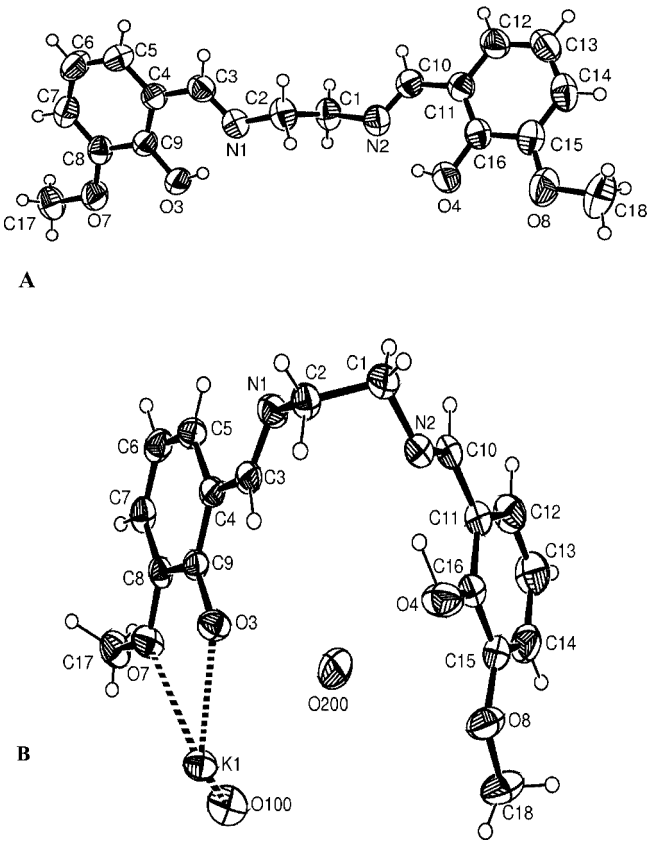

Figure 1. ORTEP diagrams of H_2(*o*-van)$_2$en (**2A**) and KH(*o*-van)$_2$en·2H_2O (**2B**), showing the atom labelling scheme; thermal ellipsoids of the non-hydrogen atoms have been drawn at the 40% probability level

The molecular structure of **2A** is comparable with that of **2B**, the latter being the same organic moiety but crystallised as an ionic pair with K^+ and two water molecules of crystallisation. In **2B**, the presence of K^+ changes the type of intramolecular H-bonds formed, thus promoting a totally different conformation of the organic moiety. One of

Table 1. Selected bond lengths [Å] and angles [°] for H_2(*o*-van)$_2$en (**2A**) and KH(*o*-van)$_2$en·2H_2O (**2B**); # symmetry operation: *–x*, *–y*, –z

H_2(*o*-van)$_2$en		KH(*o*-van)$_2$en·2H_2O		H_2(*o*-van)$_2$en		KH(*o*-van)$_2$en·2H_2O	
Bond lengths				Angles			
N(1)–C(2)	1.461(3)	N(2)–C(1)	1.509 (6)	C(2)–N(1)–C(3)	119.0(2)	C(1)–N(2)–C(10)	135.2(4)
N(1)–C(3)	1.275(4)	N(2)–C(10)	1.282(6)	C(3)–C(4)–C(5)	120.4(2)	C(10)–C(11)–C(16)	117.0(5)
O(3)–C(8)	1.347(3)	O(4)–C(16)	1.305(6)	N(1)–C(3)–C(4)	121.4(2)	N(2)–C(10)–C(11)	135.0(4)
N(2)–C(10)	1.265(4)	O(3)–C(8)	1.260(5)	O(3)–C(5)–C(4)	122.0(2)	O(4)–C(16)–C(11)	111.3(4)
O(4)–C(16)	1.355(3)	N(1)–C(3)	1.156(6)	N(1)–C(2)–C(1)	107(2)	N(2)–C(1)–C(2)	123.4(3)
		O(3)–K(1)	2.403(4)	C(4)–C(9)–O(3)	122.3	C(9)–C(8)–O(3)	111.3(4)
		O(4)$^{\#}$-K(1)	2.497(3)			C(11)–C(16)–O(4)	110.8(4)
C(3)–C(4)	1.458(4)	C(10)–C(11)	1.488(7)				
C(4)–C(5)	1.402(4)	C(11)–C(12)	1.413(7)				
C(4)–C(8)	1.399(3)	C(11)–C(16)	1.182(5)				
C(5)–C(8)	1.411(3)	C(16)–C(15)	1.422(7)				
O(7)–C(17)	1.422(3)	O(8)–C(18)	1.425(7)				
C(7)–C(6)	1.388(5)	C(14)–C(13)	1.156(7)				
C(6)–C(5)	1.364(5)	C(13)–C(12)	1.405(8)				
C(2)–C(1)	1.527(4)	C(1)–C(2)	1.768(7)				
O(3),N(1)	2.600(3)	O(4),N(2)	4.126(5)				
O(4),N(2)	2.567(3)	O(3),N(1)	2.554(5)				

 © 2005 Wiley-VCH Verlag GmbH & Co. KGaA, Weinheim

the intramolecular interactions is retained [O(4)-H···N(2) 2.556(5) Å] but the other is lost due to the direct interaction of the phenolic oxygen atom with the K^+ cation. A completely different conformation is thus obtained with an N–C–C–N torsion angle of –71.8(5)°. In the crystal structure of **2B**, the molecules pack as pseudo dimers due to the interactions with the K^+ cations and an extensive H-bonding system is promoted by the water molecules (see section ESI-A of the Supporting information for details).Figure ESI-1 (Supporting information) shows the cubic-like cage formed by the hydroxyl-oxygen, the K^+ ion and the O atoms of the water molecules. The coordination number of K^+ is six and it adopts a twisted trigonal-prismatic geometry (where the O_x···K^+ interactions, with x = hydroxy or water, range from 2.699 to 3.054 Å).

Na[V^VO_2(Rpyr$_2$en)]·CH_3OH·$3H_2O$ (11)

Rpyr$_2$en is stable to hydrolysis and ^{1}H and ^{51}V NMR spectroscopic studies for the V^VO_2–Rpyr$_2$en system indicated the presence of various complexes in solution, namely α-*cis*- and β-*cis*-type isomers[15] (Scheme 2). The pyridinium N atoms of the pyridoxal rings do not take part in the coordination but are involved in acid-base reactions which affect the number, type and relative amount of the isomers of the V^VO_2–Rpyr$_2$en complexes present in solution.[15] DFT calculations provided sensible molecular structures and the energy values for the various α-*cis*- and β-*cis*-type isomeric complexes differ by less than 4 kcal mol^{-1}, confirming that both types may coexist in solution. The α-*cis* isomer is symmetric and corresponds to the structure presently determined by X-ray diffraction.

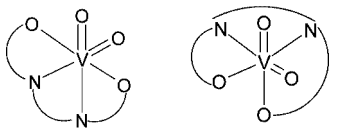

α-*cis* β-*cis*

Scheme 2. Schematic representation of the binding mode of the α- and β-*cis* isomers in the present VO_2^+ complexes

The structure of [V^VO_2(HRpyr$_2$en)] (**12**) obtained from aqueous solutions at pH ≈ 7 was reported previously.[15] The ligand coordinates to the V^V centre through the two N_{amine} and two $O_{phenolate}$ atoms. The molecule is neutral and only one of the pyridine N atoms is protonated. From methanolic solutions containing the ligand and a different metal precursor (Bu_4NVO_3), a new compound was obtained, namely Na[V^VO_2(Rpyr$_2$en)]·CH_3OH·$3H_2O$ (**11**), its molecular structure is shown in Figure 2 and some selected bond lengths and angles are included in Table 2.Both **11** and **12** correspond to the symmetrical α-*cis*-type complex.[15] The molecular structures are similar and the difference that must be emphasised is that in the present compound **11**, both pyridinic N atoms are deprotonated. Thus, both halves of the ligand become equivalent whereas they are different in **12**. The complex molecule in **11** is anionic and there is an Na^+ counterion in the crystal structure as well as one methanol and three water molecules.

The V–O_{oxo}, V–$O_{phenolate}$ and V–N_{amine} bond lengths are similar in **11** and **12** but (i) the difference between the two V–O_{oxo} internuclear distances is 0.019 Å in **11** (not significant within a 3σ criterion) while it is 0.056 Å in **12** (this is probably due to different H-bonding interactions of the O_{oxo} atoms in **11** and **12**) and (ii) in the two halves of [V^VO_2(Rpyr$_2$en)]$^-$, the two V–$O_{phenolate}$ and V–N_{amine} bond lengths differ by 0.003 (not significant) and 0.02 Å, respectively, while they differ by 0.07 and 0.06 Å, respectively, in [V^VO_2(HRpyr$_2$en)]. This is due to the deprotonation of both pyridine N atoms in **11**. The similarity of both halves of the ligand can also be observed in the mean deviation from the plane of the atoms of the chelating rings which in **11** is the same in both V–O–C–C–C–N chelating rings (0.292 Å) while they are different in **12** (0.282 and 0.300 Å).

The H-bonding network is quite complex. Several atoms are involved in H-bonding with the neighbouring solvent molecules and this is described in section ESI-A (Supporting information). The Na^+ cation interacts strongly with O(4) [Na–O(4) 2.424(6) Å] and the water molecules (see Table 2).

Infrared Spectra

A set of selected IR bands for compounds **1–12** are summarised in section ESI-B (Supporting information). The assignments were made based on refs.[15,23,24] and by comparison of the spectra. While the spectrum of **2** in the powder and crystalline forms shows only one ν(C=N) strong band at 1633 cm^{-1}, the IR spectrum of KH(*o*-van)$_2$en shows two

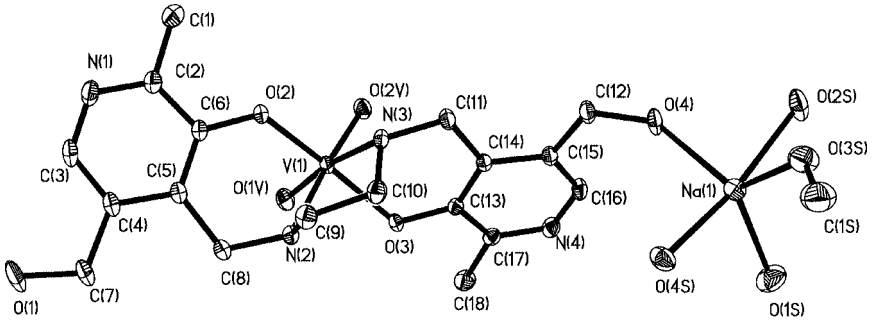

Figure 2. ORTEP diagram of Na[VO_2(Rpyr$_2$en)]·CH_3OH·$3H_2O$ (**11**) showing the atom labelling scheme; thermal ellipsoids have been drawn at the 30% probability level

 © 2005 Wiley-VCH Verlag GmbH & Co. KGaA, Weinheim

Table 2. Selected bond lengths [Å] and angles [°] for $Na[V^{V}O_2(Rpyr_2en)]\cdot CH_3OH\cdot 3H_2O$ (**11**)

Bond lengths		Angles	
V(1)–O(1V)	1.643(5)	O(1V)–V(1)–O(2V)	107.4(3)
V(1)–O(2V)	1.662(5)	O(1V)–V(1)–O(3)	96.5(2)
V(1)–O(3)	1.957(4)	O(2V)–V(1)–O(3)	96.0(2)
V(1)–O(2)	1.960(5)	O(1V)–V(1)–O(2)	98.4(2)
V(1)–N(2)	2.284(6)	O(2V)–V(1)–O(2)	97.4(2)
V(1)–N(3)	2.305(6)	O(3)–V(1)–O(2)	155.9(2)
O(3)–C(13)	1.347(7)	O(1V)–V(1)–N(2)	88.9(2)
O(2)–C(6)	1.354(7)	O(2V)–V(1)–N(2)	163.8(2)
N(2)–C(8)	1.472(8)	O(3)–V(1)–N(2)	82.0(2)
N(3)–C(11)	1.468(8)	O(2)–V(1)–N(2)	79.6(2)
N(2)–C(9)	1.464(9)	O(1V)–V(1)–N(3)	162.8(2)
N(3)–C(10)	1.479(9)	O(2V)–V(1)–N(3)	89.6(2)
		O(3)–V(1)–N(3)	78.34(19)
		O(2)–V(1)–N(3)	81.87(19)
		N(2)–V(1)–N(3)	74.2(29)

Bond lengths and angles involving the water molecules

X1–H–X2	*d*(X1–H)	*d*(H–X2)	*d*(X1–X2)	angle(X1–H–X2)
O1–H10–O2S	0.90	2.33	2.802(8)	112.3
N2–H2N–O4S	1.000(2)	2.196(16)	3.188(8)	171(7)
O2S–H2SB–O2V	0.900(2)	1.96(2)	2.843(8)	166(9)
O2S–H2SA–O1	0.900(2)	2.02(6)	2.802(8)	145(9)
N3–H3N–O2S	1.000(2)	2.39(4)	3.288(9)	149(6)
O4S–H4SA–N4	0.900(2)	1.918(14)	2.812(8)	172(9)
O4S–H4SB–O3	0.900(2)	2.93(4)	2.868(7)	154(9)

strong bands at 1638 and 1617 cm^{-1}. This may be explained by the different H-bonding networks.

The characteristic ν(V=O) of oxovanadium(IV) complexes appears as a medium-strong band at 960 cm^{-1} in the IR spectrum of **8**, in agreement with the literature.[17] For the $V^{IV}O$ complexes of the reduced SB, the ν(V=O) is shifted to lower wavenumbers by ca. 100 cm^{-1}. These low ν(V=O) values indicate V=O···V=O interactions and this is in agreement with the magnetic susceptibility measurements (see below). The binding of an O_{oxo} atom to an adjacent vanadium atom *trans* to its vanadyl O atom lengthens and weakens the bond, thereby lowering the V=O stretching frequency.

Electronic Absorption Spectra

The electronic absorption spectra of bis(salicylaldimines) and their transition metal complexes have been extensively studied.[25–28] All free Schiff bases **1**–**3** show a broad band centred at ca. 320 nm due to an n→π* transition associated with the azomethine group and another band at around 260 nm which may arise from a transition involving mainly the π molecular orbitals localised on the C=N group and/or the aromatic ring.[26] In the spectra of the reduced SB compounds, the n→π* transition is absent as expected and the 260 nm transition is red-shifted and less intense. Section ESI-C (Supporting information) summarises the UV/Vis data.

Although three (or four) d-d bands can be expected to appear in the spectra of the $V^{IV}O$ complexes in the visible region, they are often overlapping or obscured by strong LMCT bands. The spectra of **8**–**10** show broad bands in the range 500–600 nm (band II: $d_{xy}\rightarrow d_{x^2-y^2}$) and a shoulder at 600–710 nm (band I: $d_{xy}\rightarrow d_{xz}$, d_{yz}).[29] Band III ($d_{xy}\rightarrow d_{z^2}$) occurs below 500 nm and is under much stronger LMCT bands (probably $O_{phenolate}\rightarrow$d orbital).

EPR Spectra

The X-band EPR spectra of frozen solutions (77 K) of the vanadium complexes, dissolved in DMSO (except for **8** which was in water), were measured and simulated with a computer program by Rockenbauer.[30] The EPR parameters obtained are listed in Table 3. All spectra show a small rhombic distortion which can be observed in the perpendicular lines corresponding to M_I = 7/2, 5/2 and 3/2, indicating a distorted geometry around the metal centre. Although the additivity rule[31] was developed to allow the determination of the identity of the equatorial donor groups in complexes of square-pyramidal geometry (or octahedral with a weak sixth ligand), it has been successfully applied to structurally distorted molecules.[32,33] In the present $[V^{IV}O]$ complexes, the EPR parameters fit well with a binding mode involving either two equatorial N_{amine} and two $O_{phenolate}$ centres or two equatorial N_{imine} and two $O_{phenolate}$ centres. However, since the contribution of equatorial DMSO ligands to A_z is ca. 42×10^{-4} cm^{-1}, i.e. close to that of N_{amine},[15] other binding modes cannot be ruled out.

Magnetic Properties

The magnetic susceptibilities of the vanadium complexes **8** and **9** were measured by the Faraday method in the tem-

 © 2005 Wiley-VCH Verlag GmbH & Co. KGaA, Weinheim

Table 3. Spin-Hamiltonian parameters obtained by computer simulation[42]

	8	**9**	**10**
g_x, A_x ($\times 10^4$ cm^{-1})	1.983, 45.6	1.982, 45.4	1.980, 48.5
g_y, A_y ($\times 10^4$ cm^{-1})	1.980, 50.5	1.977, 50.2	1.977, 50.4
g_z, A_z ($\times 10^4$ cm^{-1})	1.960, 157.7	1.957, 158.2	1.958, 158.0

perature range of 3 to 287 K. Data were corrected for diamagnetic contributions using the Pascal's constants.[34] For both complexes the plot of $1/\chi_P$ vs. T shows deviations from linearity which can be accounted for by assuming a Curie–Weiss law and a temperature-independent paramagnetism (TIP) term. The magnetic susceptibility of compound **8** fits well the Curie–Weiss law. A μ_{eff} of 1.76 μ_B was obtained at room temperature which is typical for compounds with a spin ½, indicating that **8** is monomeric. This is in agreement with the ν(V=O) obtained. Evans[17] also reported a room-temperature magnetic moment of 1.76 μ_B for **8** in aqueous solution at pH = 8.4.

Complex **9** shows temperature dependence for the μ_{eff} values. A smaller μ_{eff} value than the theoretical for S = ½ was obtained (see section ESI-D of the Supporting information). This low magnetic moment indicates that there are V=O···V=O interactions which is in agreement with the low ν(V=O) measured for this complex (see above). Low μ_{eff} and ν(V=O) values were also found for several sal$_2$entype SB vanadium complexes[35–37] including [V^{IV}O-(Rpyr$_2$en)].[15]

Speciation Studies

(SO$_3$-sal)$_2$en (3) and R(SO$_3$-sal)$_2$en (6)

Compounds **3** and **6** are water-soluble and their acid-base behaviour was studied by pH potentiometry and ^{1}H NMR spectroscopy. The protonation constants of **6** are listed in Table 4. For the SB **3**, both the evaluation of the titration curves and the ^{1}H NMR studies indicate the occurrence of hydrolytic processes. For the reduced SB **6**, no hydrolysis could be detected in the whole pH range. The SB sal$_2$en also undergoes hydrolysis in strongly acidic DMSO/water [80:20 (w/w)] solutions.[38] In contrast, the SB *N*,*N*′-*o*-phenylenebis(salicylideneimine) is stable under the same conditions at pH > 2.5.[39]

In order to study the hydrolytic processes of compound **3**, several samples were prepared by dissolving the SB (SO$_3$-sal)$_2$en and either ^{1}H NMR or pH-potentiometric data were collected and evaluated with the computer programs PSEQUAD[40] and SUPERQUAD,[41] respectively. Our objective was to obtain a reasonably quantitative approach for the species which form as the pH is varied, but not very

Table 4. A) Protonation and formation constants of species M$_p$L$_q$H$_r$ formed in the V^{IV}O and V^{V}O$_2$– H$_2$R(SO$_3$-sal)$_2$en systems calculated from the pH-potentiometric data with the PSEQUAD program;[40] B) protonation and formation constants of species (en)$_p$(SO$_3$-sal)$_q$(H$^+$)$_r$ [the main products formed upon dissolving (SO$_3$-sal)$_2$en in water] obtained from the potentiometric and ^{1}H NMR spectroscopic data (see Figure 3 and Scheme ESI-1 in section ESI-E of Supporting information)

	A) R(SO$_3$-sal)$_2$en		B) (SO$_3$-sal)$_2$en		
	log β[a]	pK_a	Composition[c] (p,q,r)	log β (^{1}H NMR)[d]	log β (potentiometry)[e]
HL	10.70(9)	10.70			
H$_2$L	19.50(9)	8.80	(101)	9.90(7)	9.99[42]
H$_3$L	27.03(9)	7.53	(102)	16.67(10)	17.18[42]
H$_4$L	33.11(18)	6.08			
	log β (V^{IV}O^{2+})[a]	log β (V^{V}O$_2^+$)[a]	(011)	6.72(1)	6.78(2)
MLH$_2$	26.88(21)	45.2(3)	(111)	12.21(3)	12.02(4)
MLH	–	39.3(3)	(112)	20.30(2)	20.45(2)
ML	18.97(3)	32.45(12)	(121)	12.80(15)	
MLH$_{-1}$	9.50(12)	–	(122)	22.40(3)	22.42(8)
Fitting	5.19×10^{-3}[b]	1.07×10^{-2}[b]	Fitting	7.83×10^{-4}[f]	9.57×10^{-3}[g]
No. of points	290	304	No. of points	80 (4×20)	373

[a] In order to account for the range of the log β_{pqr} values obtained by pH-potentiometry in the several equilibrium models tested, the standard deviation S.D. is multiplied by 3 and the values are included in brackets. [b] Average of the difference between the experimental and calculated titration curves, expressed as the volume (mL) of titrant. [c] Other stoichiometries (110, 113, 120, 123 and 124) were not possible to fit. [d] Ambient temperature (ca. 25 °C), ionic strength not fixed. The S.D. values presented are those obtained in the particular model shown. [e] T = 25 °C, I = 0.20 M KCl. [f] Average of the difference between the experimentally determined and the calculated concentrations of en, SO$_3$-sal, HSB and SB. Some figures showing the fitting between the calculated and experimental chemical shifts are given in section ESI-E (Supporting information). [g] Average difference between the experimental and calculated titration curves, expressed in pH. Some figures showing the fitting between the calculated and experimental pH-potentiometric curves are given in section ESI-E (Supporting information).

 © 2005 Wiley-VCH Verlag GmbH & Co. KGaA, Weinheim

accurate pK values. From the ^{1}H NMR spectra, all chemical shift values were assigned and then set as constants which were used to determine all the other protonation and formation constants from the pH concentration dependence for each species. The pH dependence of the chemical shifts assigned to the peaks of the free ethylenediamine and aldehyde protons were also used to determine their pK values with PSEQUAD[40] (see ESI-E). The potentiometric data were treated separately.

The species were expressed as $(en)_p(SO_3\text{-sal})_q(H^+)_r$ and the protonation and formation constants of the main products formed were determined. Table 4B contains the protonation and formation constants, section ESI-E (Supporting information) contains information on the calculations and Figure 3 shows a concentration distribution diagram showing the total concentrations of each main compound.

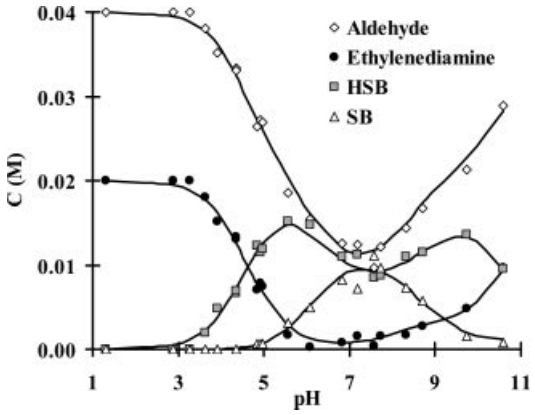

Figure 3. Concentration distribution curves of hydrolytic species formed in solutions containing compound **3** (see Scheme ESI-1 of Supporting information); only the total concentrations of each compound [aldehyde = (SO_3-sal); HSB = (SO_3-sal)en, SB = [SO_3-sal]$_2$en] are represented

We can conclude that for SB **3**, the hydrolysis is very extensive, much more than for pyr$_2$en and occurs in the whole measurable pH range. With pyr$_2$en, hydrolysis was only detected to a small extent at pH $>$ 7.[15]

Vanadium(IV) Complexes

Although potentiometric and spectroscopic studies were carried out with SB **3**, its extensive hydrolysis did not allow a consistent evaluation of the system. For the corresponding reduced SB **6**, the interaction with $[V^{IV}O]^{2+}$ and $[V^{V}O_2]^{+}$ was studied and the corresponding stability constants are also listed in Table 4. With $[V^{IV}O]^{2+}$ the pH-metric data were evaluated only up to pH $\approx$ 9.5 since slow processes occur at higher pH values (oxidation and/or hydrolysis). The species distribution diagram is presented in Figure 4a. The complex formation starts at pH $\approx$ 4 with the formation of the neutral complex $[VOLH_2]$. The ligand forms quite stable 1:1 complexes with $[V^{IV}O]^{2+}$ and the stoichiometry $[VOL]^{2-}$ predominates in the pH range 4.5–9.0. In the basic pH range, the process $[VOL]^{2-} \rightleftarrows [VOLH_{-1}]^{3-} + H^+$ has a pK of ca. 9.5.

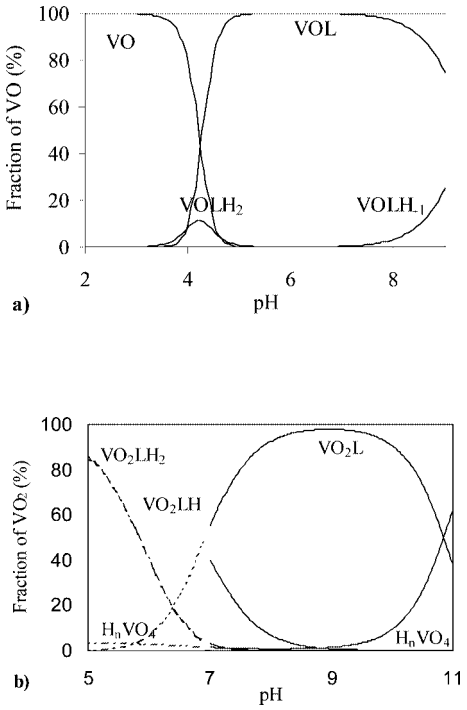

Figure 4. Concentration distribution curves of complexes formed in solutions containing: a) $[V^{IV}O]^{2+}$ and R(SO_3-sal)$_2$en with C_{VO} = 1.0 mM and L/M = 2; b) $[V^{V}O_2]^{+}$ and R(SO_3-sal)$_2$en with C_V = 3.0 mM and L/M = 2, calculated using the stability constants listed in Table 4; the dashed lines indicate that the curves only represent an approximate estimation of the relative concentrations (see text)

Figure 5 shows the high-field region of the X-band EPR spectra of "frozen" solutions containing $[V^{IV}O]^{2+}$ and **6** at several different pH values. The EPR parameters were obtained by computer simulation[30] of the EPR spectra. At pH $<$ 4 the only species present is the (aqua)vanadyl ion. At pH $>$ 4 two new species form. $[VOLH_2]$ only forms in

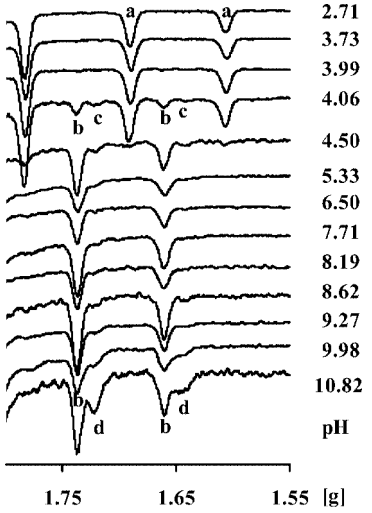

Figure 5. High-field region of the EPR spectra (77K) of frozen solutions containing $[V^{IV}O]^{2+}$ and R(SO_3-sal)$_2$en at several pH values with L/M = 1 and $C_{VO} \approx 0.004$ M; four main components can be detected a: $[VO(H_2O)_5]$, b: VOL, c: $VOLH_2$ and d: $VOLH_{-1}$ (charges omitted)

 © 2005 Wiley-VCH Verlag GmbH & Co. KGaA, Weinheim

low concentration (ca. 10%) and its EPR parameters are $g_z \approx 1.945$ and $A_z \approx 168 \times 10^{-4}$ cm^{-1}. The additivity rule[31] applied to bidentate coordination of the ligand, i.e. through equatorial binding of $O_{phenolate}$, N_{amine} and two H_2O groups yields $A_z^{estim} = 170 \times 10^{-4}$ cm^{-1}, so this is probably the binding mode of $VOLH_2$.

For VOL, the EPR parameters[30] g_x, g_y and g_z are 1.982, 1.976 and 1.957, respectively, and A_x, A_y and A_z are 52, 50 and 159×10^{-4} cm^{-1}. This indicates an equatorial binding mode involving two $O_{phenolate}$ and two N_{amine} centres, $A_z^{estim} = 157 \times 10^{-4}$ cm^{-1}. In all the EPR spectra above pH $\approx$ 4 a second minor component is present which probably corresponds to a binding mode of two equatorial $O_{phenolate}$ centres, one equatorial N_{amine} and one equatorial O_{water} centre as well as one axial N_{amine} centre, $A_z^{estim} = 164 \times 10^{-4}$ cm^{-1}. Therefore, equilibrium between *cis*/*trans* isomers apparently occurs as observed in the $V^{IV}O$–Rpyr$_2$en system.[15] However, in the present system the position of this equilibrium is shifted to the *trans* isomer (which presumably contains the H_2O ligand *trans* to the O_{oxo} atom) and the EPR spectra could be satisfactorily simulated assuming some rhombic distortion from a square-pyramidal structure.

Above pH $\approx$ 9 a new signal could be observed in the EPR spectra corresponding to the hydroxo complex [$VOLH_{-1}$]. The corresponding g_z and A_z parameters are ca. 1.948 and ca. 162×10^{-4} cm^{-1}, respectively. Possible equatorial binding modes are by two N_{amine}, an $O_{phenolate}$ and an OH^- with $A_z^{estim} = 158 \times 10^{-4}$ cm^{-1} and by two $O_{phenolate}$ centres, an N_{amine} and an OH^- with $A_z^{estim} = 156 \times 10^{-4}$ cm^{-1}. The binding mode for [$VOLH_{-1}$] probably corresponds to the first case.

The visible absorption spectra for this system confirm the speciation model obtained by pH potentiometry. At pH = 3.1 the spectrum corresponds to the spectrum of $[V^{I-V}O(H_2O)_5]^{2+}$. In the pH range 5–7 the spectra do not change and the d-d bands at λ_{max} = 535 nm (ε = 112 M^{-1} m^{-1}) and 840 nm ($\varepsilon \approx 50$ M^{-1} m^{-1}) correspond to VOL. Below 400 nm there is a charge-transfer band probably due to transitions between $O_{phenolate}$ and empty d orbitals on the V atom.

Vanadium(V) Complexes

The interaction between R(SO$_3$-sal)$_2$en and V^V was studied by pH potentiometry and ^{1}H and ^{51}V NMR spectroscopy. The species distribution diagram is shown in Figure 4B and Table 4 contains the complex formation constants. The pH-potentiometric titrations were carried out between pH = 11.5 and 2 but due to the slow formation of a small percentage of decavanadate species below pH $\approx$ 5,

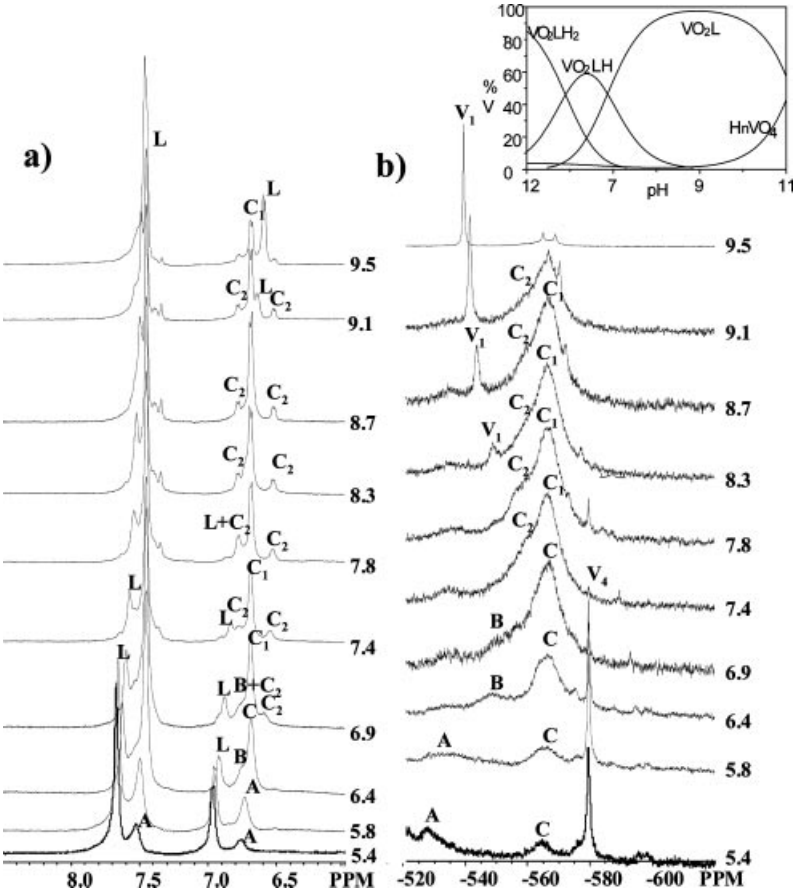

Figure 6. NMR spectra at different pH values of D_2O of solutions containing V^V and R(SO$_3$-sal)$_2$en with C_V = 20 mM and L:M $\approx$ 1.1; a) aromatic region (8.5 < δ < 6.0 ppm) of the ^{1}H NMR spectra and b) ^{51}V NMR spectra; **C** = **C$_1$** + **C$_2$**; inset: concentration distribution curves for the conditions used in the NMR experiments

 © 2005 Wiley-VCH Verlag GmbH & Co. KGaA, Weinheim

the model that showed the best fitting was obtained by considering only data at pH > 5.7. The complexes formed between V^V and **6** are quite stable and correspond to a 1:1 stoichiometry in several protonation states. For an L/M ratio of 2 (and C_V = 3 mM), some hydrolysis occurs only above pH ≈ 10 with the formation of $[HVO_4]^{2-}$ and $[VO_4]^{3-}$ (see Figure 4B).

The ^{51}V NMR spectra (Figure 6B) are quite complex, showing signals corresponding to a variety of V^V species including monovanadate (V_1), its oligomers (V_2 and V_4) and V^V–ligand complexes. Although in the potentiometric studies, decavanadate is formed only below pH ≈ 5, in these ^{51}V NMR studies weak decavanadate signals were detected even at pH ≈ 9 (data not shown). Nevertheless, the spectra clearly show complex formation between ligand **6** and $[VO_2]^+$, e.g. species **A**, **B**, $\mathbf{C_1}$and $\mathbf{C_2}$in Figure 6B. These resonances are broad due to quadrupolar relaxation and the asymmetric coordination environment of the V^V.[43]

The assignment of these ^{51}V NMR signals was done taking into account the respective chemical shift values and peak areas (the peak areas were determined with program NUTS[44] after deconvolution of the signals) and by comparison with the speciation diagram of Figure 4b. The resonance $\mathbf{C_1}$ ($\delta \approx -565$ ppm), observed above pH ≈ 5, corresponds to the α-*cis*-VO_2L complex (see Scheme 2) which predominates between pH ≈ 7 and 9, and the $\mathbf{C_2}$ signal ($\delta \approx -562$ ppm) of lower intensity appears clearly as a shoulder on signal $\mathbf{C_1}$ above pH ≈ 7. This can be assigned to the β-*cis*-VO_2L isomer. The ^{51}V NMR shifts of these resonances are in agreement with a binding mode involving N_2O_2[43] and with previous data obtained with the V^VO_2–Rpyr$_2$en system.[15] A low-intensity, broad resonance **B** ($\delta \approx -550$ ppm) appears at pH ≈ 6.4–6.9 and can be assigned to a VO_2LH species where the monoprotonated ligand coordination is probably tridentate. Several isomers may coexist since the ligand can coordinate through one or two of the N_{amine} and $O_{phenolate}$ atoms, this being a plausible explanation for the broadness of the peak. Resonance **A** ($\delta \approx -530$ ppm), with a maximum intensity at pH ≈ 5.4, is practically absent at pH = 6.4. It should correspond to a VO_2LH_2 complex, in which the coordination of the diprotonated ligand is probably bidentate. Again several isomers may coexist. Between pH = 6.9 and 8.2 a weak broad signal can be observed at $\delta \approx -535$ ppm but its assignment is not straightforward. It is probably an isomer of complex **B** since it appears in the same pH range (see Figure 6b). The ^{51}V shift trend observed as the complex is protonated is in agreement with a decreasing ligand coordination number.[45,46]

^{51}V and ^1H NMR studies for the V^VO_2–Rpyr$_2$en system have shown the existence of equilibria in solution between structural isomers of the α- and β-*cis*-type (see Scheme 2).[15] While the α-*cis* isomer is symmetric, in the β-*cis* isomer the protons of the two half-molecules are not equivalent, with peaks appearing at different chemical shifts for each half-molecule. Complex **11**, with the molecular structure depicted in Figure 2, corresponds to an α-*cis* isomer with V^VO_2L stoichiometry. In aqueous solution its ^{51}V NMR chemical shift is at $\delta \approx -563$ ppm which is close to the value for species $\mathbf{C_1}$ (Figure 6b). Although the ^{51}V NMR spectra for the present system are not as clear as for the V^VO_2–Rpyr$_2$en system, they also display an α-/β-*cis* isomeric equilibrium: the ^{51}V NMR signal for species $\mathbf{C_1}$ shows a shoulder at higher frequency (assigned to $\mathbf{C_2}$ in Figure 6b) but the signal overlap due to the proximity of the chemical shifts makes quantification of the equilibrium difficult. However, in the ^1H NMR spectra (Figure 6a), the presence of the equilibrium is particularly clear for the aromatic proton signals, e.g.at pH = 7.4–9.5, where VO_2L ($\mathbf{C_1}$ and $\mathbf{C_2}$) is the only stoichiometry present, three separate ^1H NMR resonances can be observed (besides the one corresponding to the excess of free ligand in solution, **L**). One corresponds to $\mathbf{C_1}$, the α-*cis* isomer, and the other two to $\mathbf{C_2}$, the β-*cis* isomer. Thus, as in the V^VO_2–Rpyr$_2$en system,[15] while in the α-*cis* complex the protons of each half-molecule are equivalent, in the β-*cis* complex they give rise to two separate signals. Deconvolution of the ^1H NMR peaks gave a rough estimate of the ratio between the α-*cis* and β-*cis* isomers of ca. 80:20 at pH = 7.8 which increases at lower pH. The very low percentage of the $\mathbf{C_2}$ isomer precludes observation of its ^{51}V NMR resonance at pH < 7.4 (upon formation of complexes with other stoichiometries) but at higher pH it is detectable. The small percentage of the β-*cis* species might be due to repulsion between the negative SO_3^- groups which in the β-*cis* complex are closer in space. At pH = 6.9 and lower, the broad ^1H resonances of the protonated **B** and **A** forms can be observed. Thus, in the present case, slow exchange conditions on the NMR time scale prevail, not only between the two isomers of $[VO_2L]$ and L but also with $[VO_2LH]$ and $[VO_2LH_2]$ because, in this case, ligand protonation causes a change of V^V coordination which was not the case for V^VO_2–Rpyr$_2$en in which ligand protonation only resulted in ^1H and ^{51}V chemical shift changes.[15]

Conclusions

The SB ligands sal$_2$en, (*o*-van)$_2$en, (SO$_3$-sal)$_2$en and their reduced derivatives H_2Rsal$_2$en, H_2R(*o*-van)$_2$en and H_2R(SO$_3$-sal)$_2$en were synthesised in good yields and the structures of H_2(*o*-van)$_2$en and KH(*o*-van)$_2$en·2H_2O were determined by X-ray diffraction. As expected, the Schiff bases are more susceptible to hydrolysis than the corresponding reduced SB and ^1H NMR studies in aqueous solutions of (SO$_3$-sal)$_2$en indicated the presence of several hydrolysis products, namely the "half SB", the free ethylenediamine and the free SO$_3$-salicylaldehyde.

For the present set of ligands, there is strong IR and magnetic susceptibility evidence that the Schiff base $V^{IV}O$ complexes form monomeric structures in the solid state and that the corresponding reduced Schiff-base complexes form structures with V=O···V=O-type interactions. The potentiometric and spectroscopic studies demonstrate the high affinity of the reduced SB R(SO$_3$-sal)$_2$en for $[V^{IV}O]^{2+}$ and $[V^VO_2]^+$. The ligand forms stable 1:1 complexes with vanadium in both oxidation states and for the predominant stoi-

 © 2005 Wiley-VCH Verlag GmbH & Co. KGaA, Weinheim

chiometries in solution, ML (M = $[V^{IV}O]^{2+}$ and $[V^{V}O_2]^{+}$), there is considerable evidence that there are two types of isomers.

The X-ray diffraction characterisation of both $[V^{V}O_2(HRpyr_2en)]$[15] and $Na^{+}[V^{V}O_2(Rpyr_2en)]^{-}$ (**11**) confirmed the formation of $V^{V}O_2$–$Rpyr_2en$ complexes with different degrees of protonation at the *N*-pyridine sites, thus confirming some data from the earlier report for this system.[15]

Complexes **8**, **9** and $[V^{IV}O(Rpyr_2en)]$ were tested for toxicity and insulin-mimetic effects in vitro through studies involving mice fibroblasts.[16] When compared with other compounds tested, $[V^{IV}O(Rpyr_2en)]$ showed relatively low toxicity and complex **8** showed high efficiency in promoting glucose uptake into cells as well as high aqueous solubility. All these characteristics might be important factors for the therapeutic action of the vanadium complexes.

Experimental Section

Preparation of Ligands and Complexes

Synthesis of the Schiff Bases and Reduced Schiff Bases: The Schiff-base ligands were prepared according to literature procedures[47] by reaction of the *o*-hydroxyaldehyde with ethylenediamine (2:1) in methanol, except for **3** in which the solvent was water. All compounds were characterised by elemental analysis, mass spectrometry and ^{1}H NMR spectroscopy.

sal_2en (1): Yield: 0.77g, 95%. $C_{16}H_{16}N_2O_2$ (268.32): calcd. C 71.62, H 6.01, N 10.44; found C 71.6, H 6.0, N 10.5. MS: *m*/*z* = 268 $[M]^+$. ^{1}H NMR (500 MHz, $CDCl_3$ 25 °C): δ = 3.95 (s, 4 H, –CH_2CH_2–), 7.2 (m, 8 H, $CH_{aromatic}$), 8.36 (s, 2 H, C*H* = N) ppm.

(*o*-van)$_2$en (2): Yield: 0.89g, 76%. $C_{18}H_{20}N_2O_4$ (328.37): calcd. C 65.84, H 6.14, N 8.53; found C 65.8, H 6.1, N 8.5. MS: *m*/*z* = 228 $[M]^+$. ^{1}H NMR (500 MHz, $CDCl_3$ 25 °C): δ = 3.89 (s, 6 H, CH_3–O), 3.97 (s, 4 H, –CH_2CH_2–), 6.8 (m, 6 H, $CH_{aromatic}$), 8.33 (s, 2 H, C*H* = N) ppm.

Both the filtrate and the washings were kept at room temperature for several weeks and yellow crystals of two different types were collected and characterised by X-ray diffraction. Crystals of **2A** and **2B** were obtained from the washings and filtrates from the synthesis of the Schiff base, respectively. The source of the K^+ ion was the KOH solution used to increase the pH from 4 to ca. 7.

(SO$_3$-sal)$_2$en (3): The Schiff base was prepared according to a literature procedure.[48] Yield: 1.2 g, 87%.$C_{16}H_{14}N_2Na_2O_8S_2$ (472.40): calcd. C 40.68, H 2.99, N 5.93, S 13.57; found C 40.7, H 3.0, N 5.9, S 13.4.

Rsal_2en (4): To a solution of the SB **1** (0.61 g, 2.27mmol) in dichloromethane (10 mL) at ca. 0 °C was added a methanolic solution of $NaBH_4$ (0.076g, 2.0 mmol, 5 mL containing some drops of concd. KOH solution. The pH was set to 6 and the solution stirred for several hours until the yellow colour had disappeared. The solvent was evaporated to dryness and water (10 mL) was added to the residue. The pH was set to 4–5 by addition of 3 M HCl. The white solid was filtered, washed with cold water, ethanol and diethyl ether and dried under vacuum. Yield: 0.38g, 61%. $C_{16}H_{20}N_2O_2$ (272.35): calcd. C 70.56, H 7.40, N 10.29; found C 70.8, H 7.0, N 10.4. MS: *m*/*z* = 273 $[M]^+$. ^{1}H NMR (500 MHz, $CDCl_3$ 25 °C): δ = 2.85 (s, 4 H,–CH_2CH_2–), 4.00 (s, 4 H, CH_2NH), 7.0 (m, 8 H, $CH_{aromatic}$) ppm.

R(*o*-van)$_2$en (5): The procedure was similar to the one used for **4**. Yield: 0.57g, 75%. $C_{18}H_{24}N_2O_4$·0.2MeOH (459.49): calcd. C 64.52, H 7.38, N 8.27; found C 64.6, H 7.5, N 8.1. MS: *m*/*z* = 333 $[M]^+$. ^{1}H NMR (500 MHz, $CDCl_3$ 25 °C): δ = 2.82 (s, 4 H,–CH_2CH_2–), 3.87 (s, 6 H, CH_3–O), 3.99 (s, 4 H, CH_2NH), 6.7 (m, 6 H, $CH_{aromatic}$) ppm.

R(SO$_3$-sal)$_2$en (6): The procedure was similar to the one for **4** but the solvent used was water. Yield: 0.77g, 88.0%. $C_{16}H_{20}N_2O_8S_2$·1.5H_2O (459.49): calcd. C 41.82, H 5.05, N 6.10, S 13.95; found C 41.7, H 5.1, N 6.0, S 14.3. ^{1}H NMR (500 MHz, D_2O, pH ≈ 5.7, 25 °C): δ = 3.35 (s, 4 H, –CH_2CH_2–), 4.23 (s, 4 H, CH_2NH), 6.97 (d, 2 H, $CH_{aromatic}$), 7.67 (s, 4 H, $CH_{aromatic}$) ppm.

$Rpyr_2en$ (7): The compound was prepared according to a literature procedure.[15] Yield: 0.83g, 60%. $C_{18}H_{26}N_4O_4$ (362.43): calcd. C 59.65, H 7.23, N 15.35; found C 59.5, H 7.3, N 15.4. ^{1}H NMR (500 MHz, D_2O, pH ≈ 4.8, 25 °C): δ = 2.41 (s, 6 H, CH_3), 3.35 (s, 4 H, –CH_2CH_2–), 4.35 (s, 4 H, CH_2NH), 4.63 (s, 4 H, CH_2O), 7.62 (s, 2 H, $CH_{aromatic}$) ppm.

Synthesis of the Vanadium Complexes: All reactions with the $V^{IV}O$ complexes were carried out under nitrogen.

$Cs_2[V^{IV}O\{(SO_3\text{-}sal)_2en\}]$ (8): The synthesis followed a literature procedure.[17] A pink complex was obtained. Yield: 93%. $C_{16}H_{12}N_2O_9S_2VCs_2$·0.5$H_2O$ {formulation: $Cs_2[V^{IV}O\{(SO_3\text{-}sal)_2en\}](H_2O)_{0.5}$} (766.16): calcd. C 25.08, H 1.71, N 3.66, S 8.37; found C 25.2, H 2.0, N 3.6, S 8.4.

$[V^{IV}O(Rsal_2en)]$ (9): Compound **4** (0.27g, 1.0 mmol) was dissolved in methanol/chloroform (10:1, 20 mL) containing sodium acetate (0.30g, 2.2 mmol). An aqueous solution of $VOSO_4$·5H_2O (0.25g, 1.0 mmol) was slowly added and a brownish-orange precipitate immediately formed. This was collected by filtration and washed with methanol:water (8:2), methanol and diethyl ether and then dried under vacuum. Yield: 0.30g, 90%. $C_{16}H_{18}N_2O_3V$ (337.27): calcd. C 56.98, H 5.38, N 8.31; found C 56.8, H 5.3, N 8.4.

$[V^{IV}O\{R(o\text{-}van)_2en\}]$ (10): The procedure was similar to the one used for **9**. Yield: 0.36g, 94%. $C_{18}H_{22}N_2O_5V$·2.1H_2O (435.17) {formulation: $[V^{IV}O\{R(o\text{-}van)_2en\}](H_2O)_{2.1}$}: calcd. C 49.68, H 6.07, N 6.44; found C 49.5, H 6.0, N 6.4.

$Na[V^{V}O_2(Rpyr_2en)]\cdot CH_3OH\cdot 3H_2O$ (11): A mixture of NH_4VO_3 (0.03g, 0.27mmol) and Bu_4NBr (0.09g, 0.27mmol) in methanol (10mL) was heated to reflux for 1 h. The solution turned pale yellow and was filtered to remove the solid materials. After cooling, $Rpyr_2en$ (0.10g, 0.28mmol) was added and the solution became red. As there was no precipitation after 1 h of stirring, the solution was maintained at room temperature for 2 weeks. Yellow crystals were collected and characterised by X-ray diffraction.

Physical and Spectroscopic Studies: ^{51}V and ^{1}H NMR spectra were obtained with a Varian Unity-500 Spectrometer operating at 131.404 MHz and 499.824 MHz, respectively, using a 5-mm broadband probe at 25.0 ± 0.5 °C. The ^{1}H and ^{51}V NMR chemical shifts were referenced relative to TSS [sodium 3-(trimethylsilyl)propane sulphonate] at δ = 0 ppm, and to an external $[VOCl_3]$ solution at δ = 0 ppm, respectively. The ^{51}V NMR acquisition parameters were as follows: 33 kHz spectral width, 30 μs pulse width, 1 s acquisition time and 10 Hz line broadening. A presaturation pulse sequence was used for ^{1}H NMR spectra to eliminate the residual water signal. IR spectra were recorded with a BioRad FTS 3000 MX FTIR spectrometer. Vis spectra were recorded either with a Hitachi U-2000 or with a Perkin–Elmer Lambda 9 UV/Vis/NIR spectrophotometer. The EPR spectra were recorded at 77 K (on glasses prepared by freezing solutions in liquid nitrogen) with a Bruker ESP

 © 2005 Wiley-VCH Verlag GmbH & Co. KGaA, Weinheim

Table 5. Crystal and structure refinement data

	H_2(*o*-van)$_2$en (**2A**)	KH(*o*-van)$_2$en·2H_2O (**2B**)	$Na^+[VO_2(Rpyr_2en)]^-$·CH_3OH·3H_2O (**11**)
Empirical formula	$C_{18}H_{20}N_2O_4$	$C_{18}H_{19}N_2O_6K$[a]	$C_{19}H_{34}N_4NaO_{10}V$
Formula mass	328.36	398.45	552.43
Temperature [K]	293(2)	293(2)	293(2)
Wavelength [Å]	1.5418	1.5418	0.71073
Crystal system	monoclinic	orthorhombic	monoclinic
Space group	*Pc*	*Pbca*	$P2_1/c$
a [Å]	9.409(2)	6.498(3)	19.141(2)
b [Å]	6.257(2)	27.155(3)	7.3419(8)
c [Å]	14.436(3)	22.158(3)	19.070(2)
β [°]	93.19(2)	90	114.109(2)
V[Å^3]	848.6(3)	3910(2)	2446.1(4)
Z	4	8	4
$\rho_{calcd.}$ [M gm^{-3}]	1.285	1.354	1.500
μ [mm^{-1}]	0.753	2.701	0.484
F(000)	348	1664	1160
θ [°]	4.71 to 59.98	3.25 to 64.91	2.15 to 28.26
Limiting indices	$-10 \le h \le 10$; $-1 \le k \le 7$; $-1 \le l \le 16$	$-1 \le h \le 7$; $-31 \le k \le 0$; $0 \le l \le 26$	$-25 \le h \le 23$; $-6 \le k \le 9$; $-25 \le l \le 25$
Measured/unique reflections	1687/1399 [*R*(int) = 0.0179]	3495/3322 [*R*(int) = 0.0516]	15098/3823 [*R*(int) = 0.0395]
Refinement method	Full-matrix least-squares on F^2	Full-matrix least-squares on F^2	Full-matrix least-squares on F^2
Data/restraints/parameters	1399/2/242	3322/2/332	5859/8/348
Goodness-of-fit on F^2	1.054	1.118	1.029
Final *R* indices [$I > 2\sigma(I)$]	R_1 = 0.0304; wR_2 = 0.0839	R_1 = 0.0735; wR_2 = 0.1743	R_1 = 0.0488; wR_2 = 0.1223
R indices (all data)	R_1 = 0.0306; wR_2 = 0.0844	R_1 = 0.1049; wR_2 = 0.2085	R_1 = 0.0904; wR_2 = 0.1447
Absolute structure parameter	0.1(2)	–	–
Largest difference peak/hole [e Å^{-3}]	0.099 and –0.112	0.626 and –0.813	0.742 and –0.663

[a] The formula of **2B** includes only the hydrogen atoms actually used in the refinement, i.e. H19. Hydrogen atoms of the water molecules were not found or inserted in calculated positions. Taking into account all H atoms, the correct formula for the compound is $C_{18}H_{23}KN_2O_6$.

300E X-band spectrometer. The magnetic susceptibilities were measured in the range 5–296 K using a 7 T F Oxford Instruments system coupled to a Sartorius S3D-V microbalance.

X-ray Crystal Structure Determinations: For compounds **2A** and **2B** data were collected with a TURBOCAD4 Enraf–Nonius diffractometer using Cu-K_α graphite-monochromated radiation. Data were corrected for Lorentz and polarisation effects. No absorption correction was performed. The crystal structures were solved by direct methods (program SIR97[49]) and refined with SHELXL97[50] using the WinGX package Version 1.64.03b.[51] All non-hydrogen atoms were refined anisotropically. In compound **2B**, hydrogen atoms located in the Fourier maps were refined isotropically. In compound **2A**, the hydrogen atoms were included in calculated positions and allowed to refine while riding on the parent C atom except for the hydrogen atoms on C(1), C(2), C(3) and C(4) which were located and refined isotropically. The poor quality of the crystals of compound **2B** precluded better refinement results. Further details of the crystal structure determinations are given in Table 5. Graphical representations were prepared using ORTEP[49] and Mercury 1.1.2.[52] The X-ray data for compound **11** were collected with a Siemens Smart 1000 CCD operating at 25 °C. Data were corrected for Lorentz and polarisation effects and for absorption by semiempirical methods. Structures were refined by full-matrix least squares on F^2. Complex scattering factors were taken from the program package SHELXTL. Of the 15098 reflections measured, 3823 independent reflections exceeded the significance level $|F|/\sigma(|F|) > 4.0$. Hydrogen atoms were included in calculated positions and were refined in the riding mode except the hydrogen atoms H(2N), H(3N), H(2SA), H(2SB), H(4O), H(4SA) and H(4SB) which were located from a difference electron density map and then fixed to 0.9 Å from the corresponding heteroatom [except H(4O) which was left to refine freely]. Refinement converged with allowance for thermal anisotropy of all non-hydrogen atoms. Crystal data and details of the data collection and refinement are also summarised in Table 5. CCDC-235821, -235822 and -236365 contain the supplementary crystallographic data for this paper for **2A**, **2B**, and **11**, respectively. These data can be obtained free of charge from The Cambridge Crystallographic Data Centre via www.ccdc.cam.ac.uk/data_request/cif.

Speciation Studies

Spectroscopic Measurements: For preparation of the solutions and pH calibrations we used a special glass vessel with a double wall with entries for the combined electrode (Radiometer "Red Rod" pHC2015-8), thermometer, nitrogen and reagents (e.g. base). A computerised system developed locally was used to control the titration conditions for pH calibrations. The emf measurements were made with a Denver Model 15 pH meter.

pH-Potentiometric Titrations: The purity of the ligands was checked pH-potentiometrically and the exact concentrations of the solutions were determined by the Gran method.[53] A stock solution of [$V^{IV}O$] was prepared and standardised as reported earlier[54,55] and its H^+ concentration was determined by pH potentiometry. The vanadate stock solution was prepared by dissolving KVO_3 in a KOH solution of known molarity. The vanadium content in the commercial KVO_3 was determined as reported earlier[15] and the H^+ concentration in the stock V^V solution was calculated. All solutions were manipulated under high-purity nitrogen or puri-

 © 2005 Wiley-VCH Verlag GmbH & Co. KGaA, Weinheim

fied argon. The ionic strength was adjusted to 0.20 M KCl and the temperature was 25.0 ± 0.1 °C. The pH was measured with an Orion 710A precision digital pH meter equipped with an Orion Ross 8103BN type combined glass electrode, calibrated for H^+ concentration as described earlier.[56] The ionic product of water is pK_w = 13.76. Stability constants were determined by pH-metric titration of 10.0-mL samples. The ligand concentrations were in the range 0.002–0.004 M and the metal ion/ligand molar ratio varied from 1:1 to 1:4. Titrations of solutions containing $[V^{IV}O]^{2+}$ were normally carried out with KOH solution of known concentration (ca. 0.2 M) under purified argon from pH = 2.0 up to 11.5 unless very extensive hydrolysis, precipitation or slow equilibration was detected. Titrations of solutions containing V^V were carried out by back-titrations i.e., by titrating samples from basic pH with HCl solutions of known concentration (ca. 0.2 M). The reproducibility of titration points included in the evaluation was within 0.005 pH units in the whole pH range. The protonation constants and the ligand purity were determined with the program SUPERQUAD.[41] The concentration stability constants $\beta_{pqr} = [M_pL_qH_r]/[M]^p[L]^q[H]^r$ were calculated using the PSEQUAD computer program.[40] The formation of the hydroxo complexes of $[V^{IV}O]$ was taken into account. The following species were assumed: $[V^{IV}O(OH)]^+$ ($\log\beta_{10-1}$ = –5.94), $[(V^{IV}O)_2(OH)_2]^{2+}$ ($\log\beta_{20-2}$ = –6.95), with stability constants calculated from the data of Henry et al.[57] and corrected for the different ionic strength using the Davis equation; $[(V^{IV}O)_2(OH)_5]^-$ ($\log\beta_{20-5}$ = –22.5) and $[V^{IV}O(OH)_3]^-$ ($\log\beta_{10-3}$ =–18.0).[29] For the V^V systems the stability constants were defined as $\beta_{pqr} = [M_pL_qH_r]/[M]^p[L]^q[H]^r$, where M refers to $[VO_2]^+$ (not to $[HVO_4]^-$ as is usual in the literature). The speciation of vanadate into monomeric, dimeric, tetrameric, pentameric and decameric species was taken into account and the values used for the stability constants were those of Petterson[59] (after correction for the different ionic strength using the Davis equation, and recalculation using $[VO_2]^+$ as M): $[HVO_4]^{2-}$ ($\log\beta_{1,0,-3}$ = –14.93), $[H_2VO_4]^-$($\log\beta_{1,0,-2}$ = –6.76), $[V_2O_7]^{4-}$ ($\log\beta_{2,0,-6}$ = –29.71), $[HV_2O_7]^{3-}$($\log\beta_{2,0,-5}$ = –19.37), $[H_2V_2O_7]^{2-}$ ($\log\beta_{2,0,-4}$ = –10.87), $[V_4O_{13}]^{6-}$ ($\log\beta_{4,0,-10}$ = –37.02), $[HV_4O_{13}]^{5-}$ ($\log\beta_{4,0,-9}$ = –27.67), $[V_4O_{12}]^{4-}$ ($\log\beta_{4,0,-8}$ = –17.80), $[V_5O_{15}]^{5-}$ ($\log\beta_{5,0,-10}$ = –22.63), $[V_{10}O_{28}]^{6-}$ ($\log\beta_{10,0,-16}$ = –17.32), $[HV_{10}O_{28}]^{5-}$ ($\log\beta_{10,0,-15}$ = –10.70), $[H_2V_{10}O_{28}]^{4-}$ ($\log\beta_{10,0,-14}$ = –6.53) and $[H_3V_{10}O_{28}]^{3-}$ ($\log\beta_{10,0,-13}$ = –4.67).

Spectroscopic Measurements

UV/Vis Spectroscopy: For compounds **1–10** the spectra were recorded by dissolving the ligands or complexes in the appropriate solvent (see text). For the $V^{IV}O$–R(SO_3-sal)$_2$en system, the spectra were recorded upon changing the pH, with approximately fixed total vanadium and ligand concentrations. Two sets of measurements were made with an L/M ratio of 1 and with $C_{VO} \approx 4$ and 12 mM (C_{VO} = total metal ion concentration). The temperature was kept at 25.0 ± 0.3 °C with circulating water. In the figures we represent ε_m values vs. λ, [where ε_m = absorption/($b \cdot C_{VO}$), b = optical path (either 0.1- or 1-cm cells were used)]. The spectral range covered was normally 350–900 nm.

EPR Spectroscopy: For the frozen (77 K) aqueous solution spectra in the absence of ethylene glycol, a relatively broad background was obtained. Most spectra were therefore run with solutions containing 5% ethylene glycol. The $V^{IV}O$ EPR spectra were simulated using a program from Rockenbauer.[30] The EPR spectra may help to elucidate which groups coordinate in solution.[31] For the $V^{IV}O$ systems, we used the additivity rule to estimate the hyperfine coupling constant A_z^{estim} (and g_z^{estim}) based on the contributions $A_{z,i}$ (and $g_{\|,i}$) of each of the four equatorial donor groups [e.g. $A_z^{estim} = \sum_{i=1}^{4} A_{z,i}$]. The estimated accuracy of A_z^{estim} is $\pm 3 \times 10^{-4}$ cm^{-1}.[31] These data can be used to establish the most probable binding mode of the ligand in the complexes formed, but care must be taken since the contributions of the donor groups to the hyperfine coupling may depend on their orientation[60] or the charge of the ligand.[61] The influence of the axial donor groups (if any) was not taken into account.

^{1}H and ^{51}V NMR Spectroscopy: All NMR samples were prepared at room temperature immediately before NMR spectroscopic determinations. Ligand solutions for the NMR pH titrations were prepared in D_2O (99.995% D) by weighing the appropriate amount of the ligand in order to have the desired concentration. The pD values of these solutions were adjusted with DCl and CO_2-free NaOD solutions and measured with a Crison MicropH 2002 pH-meter with an Ingold 405-M5 combined electrode calibrated at 20 ± 1 °C with standard buffers at pH = 4.0 and 7.0. The final pH values were corrected for the deuterium isotope effect using pH = pD – 0.4.[62] Solutions containing the V^V complexes were prepared by weighing the appropriate amount of ligand and dissolving it in a H_2O solution of the vanadate salt of known concentration (with 10% D_2O) to obtain ^{51}V NMR spectra, or in a D_2O solution of the V^V salt when the samples were analysed by ^{1}H NMR spectroscopy, in order to have the desired L/M ratios. Several sets of experiments as a function of pH with different L/M ratios and total concentrations were carried out. The signal intensities of the NMR resonances were obtained using the program NUTS.[44] After baseline flattening, an iterative deconvolution subroutine (LF) was used to fit the peaks of the spectrum. This subroutine adjusts several parameters, namely the frequency, height, width at half height and area of the selected peaks. The areas obtained may then be used to calculate, for example, the concentrations of the different species.

Supporting Information (see also footnote on the first page of this article): Hydrogen bonding in H_2(*o*-van)$_2$en (**2A**), KH(*o*-van)$_2$en·2H_2O (**2B**) and Na[V^VO_2(Rpyr$_2$en)]·CH_3OH·3H_2O (**11**) (ESI-A), Some IR data for compounds **1**–**12** (ESI-B), UV/Vis data for the ligands and $V^{IV}O$ complexes prepared (ESI-C), Magnetic susceptibility data for complexes **8** and **9** (ESI-D), Study of the hydrolytic processes for SB **3** in aqueous solution (ESI-E)

Acknowledgments

The authors are grateful for the financial support of the Fundo Europeu para o Desenvolvimento Regional, Fundação para a Ciência e Tecnologia, the POCTI Programme (project POCTI/35368/QUI/2000), the Hungarian National Research Fund (OTKA T31896/2000), the Hungarian Academy of Sciences and the Hungarian-Portuguese Intergovernmental S & T Co-operation Programme. F. A. thanks the Universidade da Coruña for the financial support. This work was carried out within the frame of a COST D21 project. We also thank Rui T. Henriques for the measurement of the magnetic susceptibilities.

[1] K. H. Thompson, J. H. McNeill, C. Orvig, *Chem. Rev.* **1999**, *99*, 2561–2571.
[2] K. H. Thompson, C. Orvig, *J. Chem. Soc., Dalton Trans.* **2000**, 2885–2892.
[3] C. Orvig, K. H. Thompson, *Coord. Chem. Rev.* **2001**, *219–221*, 1033–1053.
[4] H. Sakurai, Y. Kojima, Y. Yoshikawa, K. Kawabe, H. Yasui, *Coord. Chem. Rev.* **2002**, *226*, 187–198.
[5] A. E. Evangelou, *Crit. Rev. Oncol. Hematol.* **2002**, *42*, 249–265.
[6] P. Köpf-Maier, *Eur. J. Clin. Pharmacol.* **1994**, *47*, 1–16.
[7] C. Djorgevitz, in: *Metal ions in biological systems* (Eds.: H. Sigel, A. Sigel), Marcel Dekker, New York, **1995**, p. 596.

 © 2005 Wiley-VCH Verlag GmbH & Co. KGaA, Weinheim

[8] S. J. D. Karlish, Y. Shechter, *Nature* **1980**, *284*, 556–558.
[9] G. R. Dubyak, A. Kleinzeller, *J. Biol. Chem.* **1980**, *255*, 5306–5312.
[10] C. E. Heyliger, A. G. Tahiliani, J. H. McNeill, *Science* **1985**, *227*, 1474–1477.
[11] J. Meyerovitch, Z. Farfel, J. Sack, Y. Schechter, *J. Biol. Chem.* **1987**, *262*, 6658–6662.
[12] K. H. Thompson, C. Orvig, *J. Chem. Soc., Dalton Trans.* **2000**, 2885–2892.
[13] N. Durai, G. Saminathan, *J. Clin. Biochem. Nutr.* **1997**, *22*, 31–39.
[14] J. M. Lacoste, J. Duhault, D. Ravel, EUR Pat. Appl., **1993**, EP 521,787.
[15] I. Correia, J. Costa Pessoa, M. T. Duarte, R. T. Henriques, M. F. M. Piedade, L. F. Veiros, T. Jackush, A. Dornyei, T. Kiss, M. M. C. A. Castro, C. F. G. C. Geraldes, F. Avecilla, *Chem. Eur. J.* **2004**, *10*, 2301–2317.
[16] D. Rehder, J. Costa Pessoa, C. F. G. C. Geraldes, M. M. C. A. Castro, T. A. Kabanos, T. Kiss, B. Meier, G. Micera, L. Pettersson, M. Rangel, A. Salifoglou, I. Turel, D. Wang, *J. Biol. Inorg. Chem.* **2002**, *7*, 384–396.
[17] D. F. Evans, P. H. Missen, *J. Chem. Soc., Dalton Trans.* **1987**, 1279–1281.
[18] Y. Mo, G. Yang, G. Zhao, B. Li, *Jinlin Daxue Ziran Kex. Xue.* **1990**, 93–1; this is the journal where the structure was published but it was impossible to obtain so we refer to this structure with the reference code of the Cambridge Structural Database: VOJSUI.
[19] N. P. Pahor, M. Calligaris, D. Nardin, L. Randaccio, *Acta Crystallogr. Sect. B* **1978**, *34*, 1360–1363.
[20] A. Palmer, F. Brisse, *Acta Crystallogr., Sect. B* **1980**, *36*, 1447–1452.
[21] D. Cunningham, K. Gilligan, M. Hannon, C. Kelly, P. McArdle, A. O'Malley, *Organometallics* **2004**, *23*, 984–994.
[22] Since no cif file is presently available for this crystal structure, neither from CCDC nor from the supplementary data, it was not possible to access these data to make adequate comparisons. We may deduce that the structure is different since only one half of the molecule is found in the asymmetric unit. The molecule itself seems more planar and so the conformation as well as the packing are different.
[23] K. Nakamoto, *Infrared and Raman Spectra of Inorganic Compounds*, Part B, 5th ed., John Wiley & Sons, New York, **1997**, pp. 73–271.
[24] G. Socrates, *Infrared and Raman Characteristic Group Frequencies. Tables and Charts*, John Wiley & Sons, Chichester, **2001**, pp. 108–113.
[25] B. Bosnich, *J. Am. Chem. Soc.* **1968**, *90*, 627–632.
[26] M. Gullotti, A. Pasini, P. Fantucci, R. Ugo, R. D. Gillard, *Gazz. Chim. Ital.* **1972**, *102*, 853–892.
[27] H. E. Smith, J. R. Neergaard, E. P. Burrows, F. M. Chen, *J. Am. Chem. Soc.* **1974**, *96*, 2908–2916.
[28] K. S. Patel, G. A. Kolawolen, A. Earnshaw, *J. Inorg. Nucl. Chem.* **1981**, *43*, 3107–3112.
[29] L. F. Vilas Boas, J. Costa Pessoa, *Vanadium*, in *Comprehensive Coordination Chemistry* (Eds.: G. Wilkinson, R. D. Gillard, J. A. McCleverty), Pergamon Press, Oxford, **1987**, pp. 453–583.
[30] A. Rockenbauer, L. Korecz, *Appl. Magn. Reson.* **1996**, *10*, 29–43.
[31] N. D. Chasteen, in *Biological Magnetic Resonance* (Eds.: J. Lawrence, L. J. Berliner, J. Reuben), Plenum, New York, **1981**, vol. 3, pp. 53–119.
[32] C. R. Cornman, K. M. Geiser-Bush, S. P. Rowley, P. D. Boyle, *Inorg. Chem.* **1997**, *36*, 6401–6408.
[33] B. J. Hamstra, L. P. Houseman, G. J. Colpas, J. W. Kampf, R. Lobrutto, W. D. Frasch, V. L. Pecoraro, *Inorg. Chem.* **1997**, *36*, 4866–4874.
[34] P. W. Selwood, *Magnetochemistry*, Interscience, New York, **1956**.
[35] K. S. Patel, G. A. Kolawole, *J. Coord. Chem.* **1982**, *11*, 231–237.
[36] C. J. Carrano, C. M. Nunn, R. Quan, J. A. Bonadies, V. L. Pecoraro, *Inorg. Chem.* **1990**, *29*, 944–951.
[37] Y. Kuge, S. Yamada, *Inorg. Chim. Acta* **1977**, *21*, 85–88.
[38] H. Kumagai, M. Arishima, K. Susumu, K. Ymada, S. Kawata, S. Kaizaki, *Inorg. Chem.* **2002**, *41*, 1989–1992.
[39] A. Mederos, *Polyhedron* **1997**, *16*, 4191–4196.
[40] L. Zekany, I. Nagypál, in *Computational Methods for the Determination of Stability Constants* (Ed.: D.Leggett), Plenum, New York, **1985**, pp. 291–353.
[41] P. Gans, *J. Chem. Soc., Dalton Trans.* **1985**, 1195–1200.
[42] A. Gergely, I. Sóvágó, *Inorg. Chim. Acta* **1976**, *20*, 27–32.
[43] D. Rehder, *Inorg. Chem.* **1988**, *27*, 584–587.
[44] *NUTS, NMR spectroscopic data processing software*, Acorn NMR spectroscopy, **1999**.
[45] D. C. Crans, P. K. Shin, *J. Am. Chem. Soc.* **1994**, *116*, 1305–1315.
[46] A. S. Tracey, H. Li, M. J. Gresser, *Inorg. Chem.* **1990**, *29*, 2267–2271.
[47] S. N. Poddar, K. Day, S. C. N. Sarkar, *J. Indian Chem. Soc.* **1963**, *40*, 489–490.
[48] D. F. Evans, P. H. Missen, *J. Chem. Soc., Dalton Trans.* **1987**, 1279–1281.
[49] L. J. Farrugia, *J. Appl. Crystallogr.* **1997**, *30*, 565.
[50] G. M. Sheldrick, *SHELXL-97, Programs for Crystal Structure Analysis*, release 97-2, University of Göttingen, Germany, **1997**.
[51] L. J. Farrugia, *J. Appl. Crystallogr.* **2002**, *32*, 837–838.
[52] I. J. Bruno, J. C. Cole, P. R. Edgington, M. Kessler, C. F. Macrae, P. McCabe, J. Pearson, R. Taylor, *Acta Crystallogr., Sect. B* **2002**, *58*, 389–397.
[53] G. Gran, *Acta Chem. Scand.* **1950**, *4*, 559–575.
[54] J. Costa Pessoa, L. F. Vilas Boas, R. D. Gillard, R. Lancashire, *Polyhedron* **1988**, *7*, 1245–1262.
[55] I. Nagypál, I. Fábián, *Inorg. Chim. Acta* **1982**, *61*, 109–113.
[56] J. Costa Pessoa, T. Gajda, R. D. Gillard, T. Kiss, S. M. Luz, J. J. G. Moura, I. Tomaz, J. P. Telo, I. Torok, *J. Chem. Soc., Dalton Trans.* **1998**, 3587–3600.
[57] R. P. Henry, P. C. H. Mitchell, J. E. Prue, *J. Chem. Soc., Dalton Trans.* **1973**, 1156–1159.
[58] A. Komura, M. Hayashi, H. Imanaga, *Bull. Chem. Soc. Jpn.* **1977**, *50*, 2927–2931.
[59] L. Pettersson, B. Hedman, L. Andersson, N. Ingri, *Chem. Scr.* **1983**, *22*, 254–264.
[60] T. S. Smith, C. A. Root, J. W. Kampf, P. G. Rasmussen, V. L. Pecoraro, *J. Am. Chem. Soc.* **2000**, *122*, 767–775.
[61] A. J. Tasiopoulos, A. N. Troganis, A. E. Evangelou, C. P. Raptopoulou, A. Terzis, Y. Deligiannakis, T. A. Kabanos, *Chem. Eur. J.* **1999**, *5*, 910–921.
[62] P. K. Glasoe, F. A. Long, *J. Phys. Chem.* **1960**, *64*, 188–190.

Received: June 7, 2004

 © 2005 Wiley-VCH Verlag GmbH & Co. KGaA, Weinheim

Synthesis of Chiral, Half-Sandwich Ruthenium Complexes from Weakly Coordinated Solvent Species

Laetitia Jekki,[a] Corinne Pala,[a] Beatrice Calmuschi,[a] and Christian Ganter*[b]

Keywords: Chirality / P ligands / Ruthenium / Sandwich complexes

The bis(acetonitrile) species **7** has been synthesized in a multistep protocol. This chiral phosphaferrocene-containing, half-sandwich ruthenium complex easily provides two coordination sites due to the high lability of the coordinated solvent molecules. Although complex **7** could not be isolated in pure form, it serves as a valuable starting material for the preparation of other half-sandwich complexes with, for example, pyridine (**8**), tmeda (**9**), *N*-(2-dimethylaminoethyl)-morpholine (**10**), or tricyclohexylphosphine (**11**) as ligands. Whereas the morpholine complex **10** was obtained as almost a 1:1 mixture of diastereomers, the mixed MeCN/PCy_3 complex **11** was formed with a high level of diastereoselectivity (90% *de*). The molecular structures of complexes **8**, **10**, and the cyclopentadiene derivative **3a** were determined by X-ray diffraction.

(© Wiley-VCH Verlag GmbH & Co. KGaA, 69451 Weinheim, Germany, 2005)

Introduction

In a series of previous papers we have outlined the chemistry of a new type of bidentate ligands that contain a substituted phosphaferrocene moiety as a chiral building block.[1–3] The coordination chemistry employing these new ligands, as well as their applicability in asymmetric catalysis, has been studied by us[1,4] and independently by other groups.[5–11] In a more recent project we have tethered the chiral phosphaferrocene unit to a cyclopentadienyl ring and explored the properties of this anionic ligand system **1** (Scheme 1).[12] For example, the half-sandwich complexes **2** were formed in the reaction of the Na salt of the Cp anion **1** with $[RuCl_2(PPh_3)_3]$.[13] A high diastereoselectivity of 90–99% *de* was observed for the formation of the stereogenic Ru atom in complexes **2**.

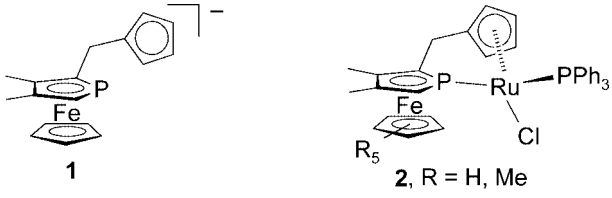

Scheme 1.

Furthermore, substitution of chloride in complex **2** for other ligands like I, H or H_2 was easily accomplished and proceeded in a stereospecific manner. However, all attempts to replace the tightly bound PPh_3 ligand by other donor ligands were unsuccessful. In order to have access to a larger array of half-sandwich complexes we set out to develop a new synthetic route based on a weakly coordinated bis(solvent) species that allows the weakly bonded ligands to be easily exchanged. Such bis(solvent) complexes might also be of interest for catalytic asymmetric transformations. Indeed, there is an increasing number of recent literature reports on the application of chiral half-sandwich complexes in catalytic asymmetric reactions.[14–19]

Results and Discussion

Our synthetic strategy had to avoid the presence of strongly binding phosphane ligands throughout the synthesis. Therefore, we chose the half-open ruthenocene **5** as a target, which should be easily converted into the cationic pentadiene complex **6** upon protonation. We hoped to exchange the diene ligand in **6** with two molecules of a donor solvent in the final step to yield the desired species with two potential coordination sites available.

A large number of attempts to prepare the half-open ruthenocene from the sodium salt of **1** were unsatisfactory, the product being obtained in low yields. However, exchange of Na for Tl as the cation gave a straightforward access to excellent yields of complex **5**. For this purpose, the Na derivative was hydrolysed in wet THF and the neutral cyclopentadiene derivative **3** was isolated as a pale-orange solid in 91% yield after chromatography. The NMR spectra indicated that **3** was formed as a 2.5:1 mixture of two isomers that differ in the distribution of the double bonds in the cyclopentadiene ring (Scheme 2).

[a] Institut für Anorganische Chemie, RWTH Aachen, Professor-Pirlet-Str. 1, 52056 Aachen, Germany
[b] Institut für Anorganische Chemie, Heinrich-Heine-Universität Düsseldorf, Universitätsstr. 1, 40225 Düsseldorf, Germany
E-mail: christian.ganter@uni-duesseldorf.de

 DOI: 10.1002/ejic.200400590 © 2005 Wiley-VCH Verlag GmbH & Co. KGaA, Weinheim

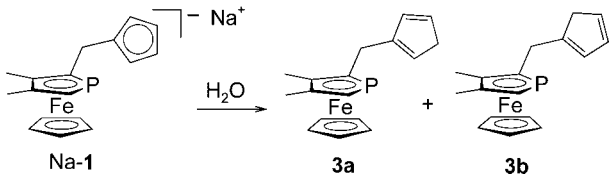

Scheme 2.

Both isomers have the phosphaferrocenylmethyl group attached to an olefinic carbon atom, as indicated by the signals for the CH_2 groups in the DEPT spectra in both cases. The isomers could not be separated by chromatography, but cooling a hexane solution of the mixture afforded crystals of one isomer suitable for X-ray diffraction. The molecular structure of **3a** is depicted in Figure 1 and relevant geometrical data are summarized in Table 1.

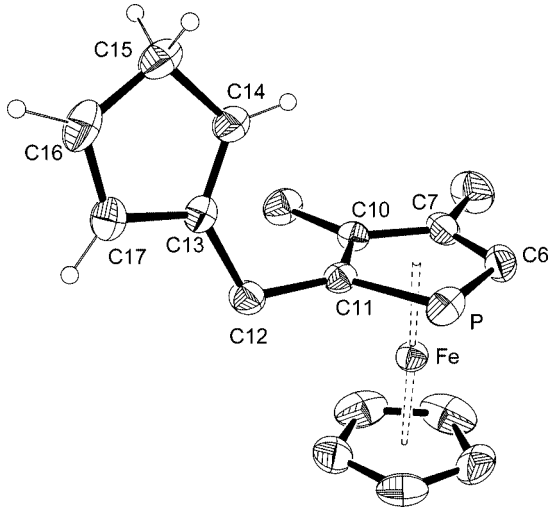

Figure 1. Molecular structure of complex **3a**.

Table 1. Selected bond lengths [Å] and angles [°] for complex **3a**.

Fe–P	2.2799(6)	P–C(6)	1.767(2)
P–C(11)	1.7794(15)	C(6)–C(7)	1.417(3)
C(7)–C(10)	1.437(2)	C(10)–C(11)	1.421(2)
C(13)–C(14)	1.345(2)	C(13)–C(17)	1.450(2)
C(14)–C(15)	1.481(2)	C(15)–C(16)	1.454(3)
C(16)–C(17)	1.368(3)		
C(6)–P–C(11)	88.93(8)	C(7)–C(6)–P	114.30(12)
C(6)–C(7)–C(10)	111.37(14)	C(11)–C(10)–C(7)	111.95(13)
C(10)–C(11)–P	113.37(11)	C(10)–C(11)–C(12)	124.10(14)
C(12)–C(11)–P	122.51(12)		

Treatment of a solution of cyclopentadiene **3** in diethyl ether with TlOEt precipitated the thallium cyclopentadienide Tl-**1**, which was isolated as a pale-yellow powder in almost quantitative yield after filtration and drying. The Tl salt was then allowed to react with the ruthenium butadiene iodide **4** [20] to give the half-open ruthenocene **5** (Scheme 3).

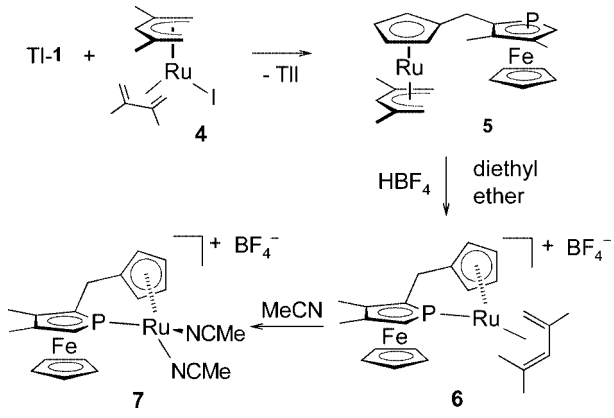

Scheme 3.

The best yield (76%) was obtained when an equimolar mixture of starting materials was heated as a slurry in toluene overnight. Complex **5** was isolated as a pale-yellow solid after removal of TlI by filtration and chromatography on alumina. The analytical data are in agreement with a half-sandwich structure, with the phosphorus not coordinated to the ruthenium atom. When an ethereal solution of complex **5** was treated dropwise with HBF_4 in diethyl ether, protonation of the pentadienyl ligand occurred at the terminal position to give an η^4-coordinated pentadiene ligand. This transformation is accompanied by the intramolecular coordination of the P atom of the phosphaferrocene moiety to the ruthenium atom, which thereby maintains an 18-electron count in the cationic product **6**. Due to the presence of the chiral phosphaferrocene group, the terminal carbons of the pentadienyl ligand are diastereotopic and the protonation leads to a 1:1 mixture of diastereomeric pentadiene complexes which could not be separated. Accordingly, the ^{31}P NMR spectrum shows two resonances at δ = 50.5 and 43.7 ppm, respectively, which are strongly downfield from the signal at δ = –76.0 ppm for the precursor complex **5** with a non-coordinated phosphorus.

The diene ligand in cationic complex **6** could easily be replaced by acetonitrile by stirring the complex in acetonitrile at room temperature for a couple of hours. Monitoring the reaction progress by ^{31}P NMR spectroscopy revealed that this is not a clean transformation. First, a new signal appears in the spectrum which is attributed to the bis(acetonitrile) species **7**; the intensity of this signal increases with time at the expense of the signals for the two isomeric diene complexes **6**. However, the bis(acetonitrile) complex has a limited stability under the reaction conditions and eventually starts to decompose to uncharacterized products before all the diene complex has been consumed. The reproducibility of the reaction is not very good: repeated experiments under identical conditions led, in some cases, to almost pure solutions of the bis(acetonitrile) species **7**, while in other runs considerable degradation occurred. Variation of the reaction parameters (concentration, temperature, irradiation) did not improve the reaction performance. Attempts to isolate complex **7** in pure form failed and the characteri-

 © 2005 Wiley-VCH Verlag GmbH & Co. KGaA, Weinheim

zation had therefore to be carried out from the reaction solution.

However, the high reactivity of the bis(solvent) complex **7** could be exploited in subsequent substitution reactions (Scheme 4). For example, when the cation **6** was stirred in acetonitrile in the presence of an excess of pyridine for five hours, the respective bis(pyridine) complex **8** could be isolated in 91% yield after precipitation from the solution with diethyl ether. During the reaction, the characteristic signals of **7** are first detected in the ^{31}P NMR spectrum, followed by the appearance of the signal of complex **8**. The use of acetonitrile as solvent is essential for a fast reaction. Indeed, when acetone was used instead of acetonitrile, the reaction proceeded much slower and the conversion was incomplete even after two days. Crystals suitable for X-ray diffraction were obtained by slow diffusion of diethyl ether into an acetone solution of bis(pyridine) complex **8**. An ORTEP view of the molecular structure is depicted in Figure 2; relevant geometrical data are summarized in Table 2.

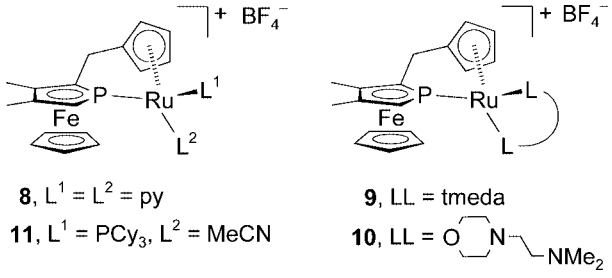

Scheme 4.

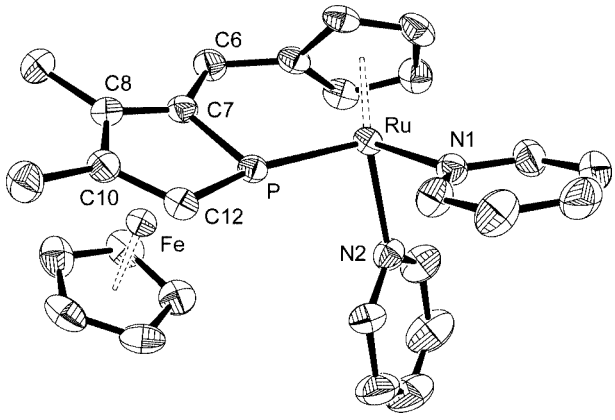

Figure 2. Molecular structure of the cation of complex **8**.

Similarly to the preparation of **8**, the tmeda complex **9** was prepared in 98% isolated yield by treatment of an acetonitrile solution of diene complex **6** with one equivalent of tmeda. When a solution of diene cation **6** in acetonitrile was treated with one equivalent of *N*-(2-dimethylaminoethyl)morpholine complex **10** was formed, with the morpholine derivative coordinated as an *N*,*N* ′-chelate ligand.

In the course of this reaction the ruthenium center becomes stereogenic and complex **10** is formed as two diastereomers in a ratio of approximately 3:2. This poor diastereoselectivity reflects the similar steric demands of the two

Table 2. Selected bond lengths [Å] and angles [°] for complex **8**.

Ru–N(1)	2.139(2)	Ru–N(2)	2.153(2)
Ru–P	2.2797(6)	P–C(7)	1.753(2)
P–C(12)	1.766(2)	C(7)–C(6)	1.521(3)
C(8)–C(7)	1.416(4)	C(8)–C(10)	1.445(4)
C(10)–C(12)	1.422(4)		
N(1)–Ru–N(2)	84.26(8)	N(1)–Ru–P	99.96(6)
N(2)–Ru–P	95.72(6)	C(7)–P–C(12)	90.88(12)
C(7)–P–Ru	108.36(8)	C(12)–P–Ru	159.05(9)
C(8)–C(7)–C(6)	130.5(2)	C(8)–C(7)–P	113.21(18)
C(6)–C(7)–P	116.26(18)		

different nitrogen donor groups of the morpholine derivative. As the two groups on nitrogen are incorporated into the heterocyclic system of the morpholine the flexibility of this donor is fairly low, and it should therefore be sterically less demanding than the open-chain NEt_2 analogue. Thus, the difference in steric bulk of the morpholine and the dimethylamino donor groups is less pronounced than one would expect at first glance. While a chromatographic separation of the two diastereomeric morpholine complexes **10** was not successful, one diastereomer could be obtained in pure form by crystallization. The molecular structure of this complex was determined by X-ray diffraction and is depicted in Figure 3; relevant geometrical data are summarized in Table 3.

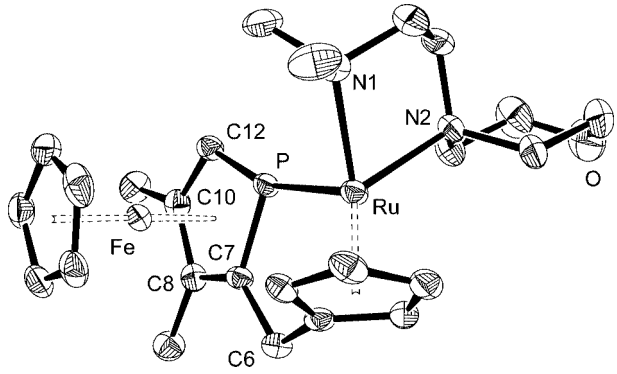

Figure 3. Molecular structure of the cation of complex **10**.

Table 3. Selected bond lengths [Å] and angles [°] for complex **10**.

Ru–N(1)	2.214(4)	Ru–N(2)	2.210(4)
Ru–P	2.2912(13)	P–C(7)	1.750(4)
P–C(12)	1.749(5)	C(7)–C(6)	1.517(6)
C(7)–C(8)	1.409(6)	C(8)–C(10)	1.444(6)
C(12)–C(10)	1.427(6)		
N(2)–Ru–N(1)	80.99(16)	N(1)–Ru–P	97.83(12)
N(2)–Ru–P	97.66(11)	C(12)–P–C(7)	90.6(2)
C(7)–P–Ru	108.69(16)	C(12)–P–Ru	160.74(16)
C(6)–C(7)–P	116.1(3)	C(8)–C(7)–P	113.5(3)
C(8)–C(7)–C(6)	130.1(4)	C(10)–C(12)–P	112.7(3)

The Ru–P distances in the two cationic complexes **8** (228 pm) and **10** (229 pm) are almost identical and slightly longer than in neutral Ru-phosphaferrocene half-sandwich complexes (224–225 pm).[2,13] As expected, the Ru–N bonds are significantly shorter in the pyridine complex **8** (214 pm) than in the morpholine derivative **10** (221 pm) with its terti-

 © 2005 Wiley-VCH Verlag GmbH & Co. KGaA, Weinheim

ary amine donor functions. As is usually observed, on going from an uncoordinated phosphaferrocene derivative (**3a**) to the metal complexes **8** and **10** the C–P–C angle in the phospholyl ring increases slightly from 88.9° (**3**) to 90.9° (**8**) and 90.6° (**10**). Furthermore, the P–C bonds in the phospholyl ring contract slightly on coordination from ca. 178 pm to 175–176 pm.

It was also possible to prepare a mono(acetonitrile) derivative starting from the cationic complex **6**. Thus, when an acetonitrile solution of **6** was treated with one equivalent of tricyclohexylphosphane (PCy_3), the mixed P,N complex **11** was formed in 96% yield. In contrast to the morpholine derivative **10**, a high level of stereodiscrimination (90% *de*) was observed for the formation of complex **11**. This reflects the different steric properties of the acetonitrile and PCy_3 ligands.

Conclusions

A high-yield route to half-sandwich ruthenium complexes with a tethered phosphaferrocene donor and two loosely coordinated acetonitrile molecules has been devised. The bis(acetonitrile) complex is very reactive and easily provides two available coordination sites at the ruthenium. The synthetic value of this approach has been corroborated by the subsequent preparation of some derivatives with mono- and bidentate nitrogen ligands. We are currently trying to extend and improve the results with respect to the stereodiscrimination in the complexation of difunctional ligands and the use of the solvent complex for catalytic applications.

Experimental Section

All experiments were performed under nitrogen using Schlenk and vacuum-line techniques. Hexane and toluene were distilled from sodium; $CHCl_3$ and CH_2Cl_2 from CaH_2. THF and diethyl ether were distilled from sodium/benzophenone. Acetonitrile was dried with P_4O_{10} and distilled from CaH_2. Methanol and acetone were dried with magnesium. The solvents were kept in Schlenk flasks under nitrogen. Silica gel or alumina were heated to 200 °C, cooled to room temperature under vacuum, and stored under nitrogen. Alumina (Riedel-de Haën) was deactivated by addition of 5% water. NMR spectra were measured with Varian Mercury 200, VXR 300 and Unity 500 spectrometers. EI and FAB mass spectra were measured on a Finnigan MAT 95 spectrometer. Elemental analyses were performed by the microanalytical laboratory of the Universität Düsseldorf. Na-**1** [12] and ruthenium iodide **4** [20] were prepared as described in the literature.

Cyclopentadiene 3: Na-**1** was obtained by addition of $NaBEt_3H$ (0.62 mmol, 0.4 mL of a 1.5 M solution in THF) to a solution of 6-(3,4-dimethylphosphaferrocen-2-yl)fulvene (127.7 mg, 0.41 mmol) in diethyl ether/THF (1:1, 30 mL) at room temperature. After stirring for 45 min water (5 mL) was added to the orange solution and the phases were separated. The organic phase was washed with water, dried with Na_2SO_4, and the solvent was removed in vacuum. The crude product was filtered through a short plug of alumina with hexane as eluent. After evaporation of the solvent, **3** (115.7 mg, 0.37 mmol, 91%) was isolated as an orange crystalline powder as a mixture of two isomers in a ratio of ca. 1:2.5. Crystals suitable for X-ray diffraction were obtained by slowly cooling a hexane solution to –18 °C. ^{1}H NMR (500 MHz, $CDCl_3$): δ = 2.21, 2.14 (s, 3 H, CH_3), 2.93 (m, 4 H, CH_2 in C_5H_5R), 3.26 (m, 4 H, PCC*H*$_2$, major + minor), 3.71 (d, $J_{C,P}$ = 35.7 Hz, 2 H, PCH, major + minor), 4.13 (s, 2 × 5 H, Cp, major + minor), 5.9 (s, 1 H, C_5H_5R, major), 6.24, 6.06 (s, 1 H, C_5H_5R, minor), 6.39 (s, 2 H, C_5H_5R, major + minor), 6.47 (s, 1 H, C_5H_5R, major) ppm. ^{13}C{^{1}H} (125.6 MHz, $CDCl_3$): major isomer: δ = 17.1, 13.7 (s, CH_3), 31.1 (d, $J_{C,P}$ = 20.2 Hz, PC*C*H$_2$), 41.0 (s, *C*H$_2$ in C_5H_5R), 72.0 (s, Cp), 75.6 (d, $J_{C,P}$ = 58.5 Hz, PCH), 93.3 (d, $J_{C,P}$ = 5.7 Hz, *C*CH$_3$), 95.6 (d, $J_{C,P}$ = 6.7 Hz, *C*CH$_3$), 97.4 (d, $J_{C,P}$ = 57.6 Hz, P*C*CH$_2$), 134.4, 133.5, 126.5 (s, CH in C_5H_5R), 146.6 (s, CR in C_5H_5R) ppm; minor isomer: δ = 17.1, 13.7 (s, CH_3), 32.0 (d, $J_{C,P}$ = 22 Hz, PC*C*H$_2$), 43.2 (s, *C*H$_2$ in C_5H_5R), 72.0 (s, Cp), 75.5 (d, $J_{C,P}$ = 57.5 Hz, PCH), 93.3 (d, $J_{C,P}$ = 5.7 Hz, *C*CH$_3$), 95.6 (d, $J_{C,P}$ = 6.7 Hz, *C*CH$_3$), 98.3 (d, $J_{C,P}$ = 57.5 Hz, P*C*CH$_2$), 132.2, 130.7, 127.0 (s, CH in C_5H_5), 149.2 (s, CR in C_5H_5R) ppm. ^{31}P NMR (80.95 MHz, $CDCl_3$): δ = –79.7 (s, minor), –80.1 (s, major) ppm. MS (70 eV): *m*/*z* (%) = 310 (42) [M$^+$], 244.9 (47) [M$^+$ – Cp]. $C_{17}H_{19}FeP$ (310.2): calcd. C 65.83, H 6.17; found C 65.61, H 6.08.

Thallium Salt Tl-1: TlOEt (0.22 mL, 3.06 mmol) was added dropwise to a solution of cyclopentadiene **3** (947 mg, 3.06 mmol) in diethyl ether (10 mL) at room temperature. After stirring for 30 min the precipitate was isolated by filtration, washed with diethyl ether, and dried in vacuo to give 1.74 g (3.03 mmol, 99%) of Tl-**1** as a pale-orange powder. ^{1}H NMR (500 MHz, $CDCl_3$): δ = 2.23 (s, CH_3), 2.26 (s, CH_3), 3.28 (dd, $J_{H,P}$ = 15.3, $J_{H,H}$ = 7.0 Hz, 1 H, CH_2), 3.49 (m, 1 H, CH_2), 3.66 (d, $J_{H,P}$ = 35.7 Hz, 1 H, PCH), 4.12 (s, 5 H, Cp), 5.84 (m, 2 H, C_5H_4), 5.99 (m, 2 H, C_5H_4) ppm. ^{13}C{^{1}H} (125.6 MHz, $CDCl_3$): δ = 14.2 (s, CH_3), 17.2 (s, CH_3), 29.9 (d, $J_{C,P}$ = 20.9 Hz, CH_2), 72.1 (s, Cp), 75.3 (d, $J_{C,P}$ = 58.1 Hz, PCH), 92.9 (d, $J_{C,P}$ = 4.4 Hz, *C*CH$_3$), 95.8 (d, $J_{C,P}$ = 6.5 Hz, *C*CH$_3$), 105.5 (s, C_5H_4), 106.1 (d, $J_{C,P}$ = 54.9 Hz, P*C*CH$_2$), 108.0 (s, C_5H_4), 132.6 (s, *C*CH$_2$) ppm. ^{31}P NMR (80.95 MHz, $CDCl_3$): δ = –77.7 (s) ppm. SIMS (70 eV): *m*/*z* = 514 [M$^+$], 310.2 [M$^+$ – Tl], 205.1 [Tl$^+$]. $C_{17}H_{18}FePTl$ (513.53): calcd. C 39.76, H 3.53, found C 39.01, H 3.39.

(Dimethylpentadienyl)ruthenium Complex 5: Tl-**1** (1.13 g, 2.21 mmol) was added to a suspension of ruthenium iodide **4** (894 mg, 2.21 mmol) in 35 mL of toluene and the mixture was refluxed overnight. TlI was removed by filtration through Kieselguhr and the filtrate was evaporated to dryness. The residue was extracted with hexane, the solution filtered through alumina, and the solvent was removed in vacuo to yield **5** (849 mg, 1.68 mmol, 76%) as an orange solid. ^{1}H NMR (500 MHz, $CDCl_3$): δ = 0.29 (d, $J_{H,H}$ = 2.4 Hz, 1 H, H$_{endo}$), 0.31 (d, $J_{H,H}$ = 2.4 Hz, 1 H, H$_{endo}$), 1.87 (s, CH_3), 1.89 (s, CH_3), 1.90 (s, CH_3), 1.92 (s, CH_3), 2.86 (d, $J_{H,H}$ = 2.4 Hz, 1 H, H$_{exo}$), 2.87 (d, $J_{H,H}$ = 2.4 Hz, 1 H, H$_{exo}$), 3.07 (m, 2 H, CH_2), 3.60 (d, $J_{H,P}$ = 36.0 Hz, 1 H, PCH), 3.90 (s, 5 H, Cp), 4.31 (m, 2 H, C_5H_4), 4.56 (m, 2 H, C_5H_4), 5.34 (s, CH) ppm. ^{13}C{^{1}H} (125.6 MHz, $CDCl_3$): δ = 13.9 (s, CH_3), 16.9 (s, CH_3), 27.9 (s, 2 × CH_3), 30.5 (d, $J_{C,P}$ = 20.9 Hz, CH_2), 42.2 (s, =CH_2), 42.3 (s, =CH_2) 72.2 (s, Cp), 76.2 (d, $J_{C,P}$ = 58.8 Hz, PCH), 77.4 (s, RC_5H_4), 78.0 (s, RC_5H_4), 78.5 (s, RC_5H_4), 79.1 (s, RC_5H_4), 92.3 (s, CH_2=*C*), 92.7 (s, CH), 95.7 (d, $J_{C,P}$ = 6.1 Hz, *C*CH$_3$), 98.8 (d, $J_{C,P}$ = 2.8 Hz, *C*CH$_3$), 100.2 (d, $J_{C,P}$ = 58.2 Hz, P*C*CH$_2$) ppm. ^{31}P NMR (80.95 MHz, $CDCl_3$): δ = –76.0 (s) ppm. MS (70 eV): *m*/*z* = 505.8 [M$^+$], 309.9 [M$^+$ – Ru – C_7H_{11}], 244.9 [M$^+$ – Ru – C_7H_{11} – Cp]. HRMS for $C_{24}H_{29}FePRu$: calcd. 506.039346; found 506.039321.

(η^4-2,4-Dimethylpentadiene)ruthenium Complex 6: HBF_4 (0.38 mL, 54% solution in diethyl ether, 2.76 mmol) was added dropwise to a

 © 2005 Wiley-VCH Verlag GmbH & Co. KGaA, Weinheim

solution of complex **5** (943 mg, 1.87 mmol) in diethyl ether (50 mL) at –78 °C. After stirring for 30 min at room temperature the precipitate was isolated by filtration, washed twice with diethyl ether, and dried in vacuo to give 1.05 g (1.78 mmol, 95%) of complex **6** as a 1:1 mixture of isomers as an orange powder. ^{1}H NMR (500 MHz, [D$_6$]acetone): isomer 1: δ = 1.46 (d, $J_{H,H}$ = 8.9 Hz, 3 H, CH_3), 2.22 (s, CH_3), 2.28 (s, CH_3), 2.34 (s, CH_3), 2.35 (m, 2 H, =CH_2), 2.40 (s, CH_3), 2.93 (m, 2 H, CH_2), 3.70 (d, $J_{H,P}$ = 32.0 Hz, 1 H, PCH), 3.81 (m, 1 H, =CH-C), 4.63 (m, 1 H, C_5H_4), 4.65 (s, 5 H, Cp), 5.38 (m, 1 H, C_5H_4), 5.61 (m, 1 H, C_5H_4), 5.83 (m, 1 H, C_5H_4) ppm; isomer 2: δ = 1.24 (d, $J_{H,H}$ = 8.4 Hz, 3 H, CH_3), 1.83 (s, CH_3), 1.91 (m, 2 H, = CH_2), 2.30 (s, CH_3), 2.31 (s, CH_3), 2.47 (s, CH_3), 3.01 (m, 2 H, CH_2), 3.38 (m, 1 H, =CH-C), 4.10 (d, $J_{H,P}$ = 32.4 Hz, 1 H, PCH), 4.51 (s, 5 H, Cp), 4.83 (m, 1 H, C_5H_4), 5.25 (m, 1 H, C_5H_4), 5.63 (m, 1 H, C_5H_4), 5.73 (m, 1 H, C_5H_4) ppm. ^{13}C{^{1}H} (125.6 MHz, [D$_6$]acetone): isomer 1: δ = 15.9 (d, $J_{C,P}$ = 6.0 Hz, CH_3), 16.1 (d, $J_{C,P}$ = 5.6 Hz, CH_3), 23.6 (d, $J_{C,P}$ = 15.9 Hz, CH_2), 24.6 (s, CH_3), 26.4 (s, CH_3), 34.3 (s, CH_3), 43.2 (s, =CH_2), 43.3 (s, =*C*H-C), 57.5 (s, PCH), 76.1 (s, Cp), 82.8 (s, RC_5H_4), 85.4 (s, RC_5H_4), 86.9 (s, RC_5H_4), 88.9 (s, RC_5H_4) ppm; isomer 2: δ = 13.9 (s, CH_3), 14.0 (d, $J_{C,P}$ = 5.0 Hz, CH_3), 23.9 (d, $J_{C,P}$ = 16.5 Hz, CH_2), 24.7 (s, CH_3), 26.0 (s, CH_3), 34.0 (s, CH_3), 43.8 (s, =CH_2), 43.9 (s, =*C*H-C), 60.4 (s, PCH), 76.5 (s, Cp), 83.3 (s, RC_5H_4), 83.6 (s, RC_5H_4), 85.8 (s, RC_5H_4), 90.2 (d, $J_{C,P}$ = 4.9 Hz, RC_5H_4) ppm. ^{31}P NMR (80.95 MHz, $CDCl_3$): δ = 50.5 (s, isomer 1), 43.7 (s, isomer 2) ppm. SIMS (70 eV): *m*/*z* = 507 [M$^+$], 411 [M$^+$ – C_7H_{11}]. $C_{24}H_{30}BF_4FePRu$ (593.2): calcd. C 48.59, H 5.10; found C 47.85, H 5.18.

Bis(acetonitrile) Complex 7: A solution of cationic complex **6** (118 mg, 0.20 mmol) in 15 mL of acetonitrile was stirred at room temperature. The reaction progress was monitored by ^{31}P NMR spectroscopy. After 4 h all volatiles were evaporated off under high vacuum to give an orange oil of **7** which was immediately characterized by NMR spectroscopy in CD_3CN. ^{1}H NMR (200 MHz, CD_3CN): δ = 2.20 (s, 6 H, CH_3CN), 2.44, 2.42 (2 × s, 3 H, CH_3), 2.72 (m, 2 H, CH_2), 3.89 (d, $J_{H,P}$ = 34.2 Hz, 1 H, PCH), 4.28 (br. s, 1 H, C_5H_4), 4.52 (s, 5 H, Cp), 5.37, 5.27, 4.71 (3 × br. s, 1 H, C_5H_4) ppm. ^{31}P NMR (202.25 MHz, CD_3CN): δ = 4.2 (s) ppm.

Bis(pyridine) Complex 8: An excess of pyridine (260 µL, 3.21 mmol) was added to a solution of cationic complex **6** (336 mg, 0.57 mmol) in 15 mL of acetonitrile at room temperature. The reaction mixture was stirred for 4 h. The solvents were removed under high vacuum to give an orange oil, which was redissolved in acetone. Complex **8** (338 mg, 0.52mmol, 91%) was isolated as an orange powder upon precipitation with diethyl ether. Red crystals were obtained by diffusion of diethyl ether into an acetone solution. ^{1}H NMR (500 MHz, $[CD_3]_2CO$): δ = 2.27, 2.26 (2 × s, 3 H, CH_3), 2.65 (m, 2 H, CH_2-Phosp.), 3.88 (d, $J_{H,P}$ = 33.3 Hz, 1 H, PCH), 4.11 (s, 5 H, Cp), 5.38, 5.10, 4.73, 4.12 (4 × s, 1 H, C_5H_4R), 7.51, 7.36 (br. t, *J* = 7.0 Hz, 2 H, C_5H_5N-H$_{meta}$), 8.00, 7.88 (2 × br. t, *J* = 7.6 Hz, 1 H, C_5H_5N-H$_{para}$), 8.94 (br. d, *J* = 5.2 Hz, 2 H, C_5H_5N-H$_{ortho}$), 9.19 (br. d, *J* = 4.9 Hz, 2 H, C_5H_5N-H$_{ortho}$) ppm. ^{13}C{^{1}H} (125.6 MHz, $[CD_3]_2CO$): δ = 16.4, 14.3 (2 × s, CH_3), 24.1 (d, $J_{C,P}$ = 16.3 Hz, CH_2), 62.2 (s, C_5H_4), 62.5 (d, $J_{C,P}$ = 36.5 Hz, PCH), 69.9 (s, C_5H_4), 74.8 (s, Cp), 83.2 (d, $J_{C,P}$ = 10.5 Hz, C_5H_4), 85.1 (d, *J* = 5.8 Hz, C_5H_4), 89.2 (s, CR in RC_5H_4), 91.2 (d, *J* = 2 Hz, P*C*CH_2), 111.4 (d, *J* = 7.66 Hz, *C*CH_3), 111.7 (d, *J* = 12.5 Hz, *C*CH_3), 126.6, 126.4 (2 × s, C$_{meta}$-C_5H_5N), 138.3, 138.2 (2 × s, C$_{para}$-C_5H_5N), 158.4, 157.9 (2 × d, $J_{C,P}$ = 7.7 Hz, C$_{ortho}$-C_5H_5N) ppm. ^{31}P NMR (202.25 MHz, $[CD_3]_2CO$): δ = 10.5 (s) ppm. $C_{27}H_{28}BF_4FePN_2Ru$ (655.2): calcd. C 49.49, H 4.31, N 4.28; found C 48.82, H 4.38, N 4.19. FAB MS: *m*/*z* = 490 [cation – py], 411 [cation – 2 py].

Tetramethylethylenediamine Complex 9: tmeda (85 µL, 0.56 mmol) was added to a solution of complex **6** (331.6 mg, 0.56 mmol) in 15 mL of acetonitrile at room temperature. The reaction mixture was stirred for 7 h and the solvent was then evaporated under high vacuum to give **9** as an orange powder (329.4 mg, 96%). ^{1}H NMR (500 MHz, CD_3CN): δ = 2.20, 2.18 (2 × s, 3 H, CCH_3), 2.33 (m, 2 H, C_5H_4-C*H* $_2$), 2.52 (m, 2 H, NCH_2), 2.72 (d, $J_{H,P}$ = 3 Hz, 3 H, NCH_3), 2.72 (m, 1 H, NCH_2), 2.87 (m, 1 H, NCH_2), 3.13 (s, 3 H, NCH_3), 3.15 (d, $J_{H,P}$ = 4 Hz, 3 H, NCH_3), 3.28 (s, 3 H, NCH_3), 3.53 (d, $J_{H,P}$ = 32 Hz, 1 H, PCH), 4.11, 4.09 (2 × m, 1 H, C_5H_4), 4.25 (s, 5 H, Cp), 5.06, 4.64 (2 × m, 1 H, C_5H_4) ppm. ^{13}C{^{1}H} (125.6 MHz, CD_3CN): δ = 14.3 (d, $J_{C,P}$ = 4.8 Hz, CH_3), 16.5 (s, CH_3), 23.8 (d, $J_{C,P}$ = 16.3 Hz, $CpCH_2$), 60.0, 59.4 (2 × s, NCH_3), 61.7 (s, C_5H_4), 61.7 (d, $J_{C,P}$ = 36.5 Hz, PCH), 62.3 (d, *J* = 15.3 Hz, NCH_3), 62.9 (d, *J* = 16.3 Hz, NCH_3), 64.5, 63.8 (2 × s, NCH_2), 66.8 (s, C_5H_4), 75.3 (s, Cp), 77.5 (d, $J_{C,P}$ = 10.5 Hz, C_5H_4), 89.5 (s, C$_{quat.}$), 90.5 (s, C_5H_4), 107.8, 110.6, 117.5 (3 × s, C$_{quat.}$) ppm. ^{31}P NMR (80.95 MHz, CD_3CN): δ = 16.5 (s) ppm. FAB MS (NBA matrix): *m*/*z* = 527 [cation], 87 [BF_4^-]. $C_{23}H_{34}BF_4FeN_2PRu$: calcd C 45.05, H 5.59, N 4.57; found C 45.90, H 5.78, N 3.84.

Morpholine Complex 10: *N*-(2-Dimethylaminoethyl)morpholine (1.3 equiv., 82 µL, 0.48 mmol) was added to a solution of cationic complex **6** (220 mg, 0.37 mmol) in 10 mL of acetonitrile and stirred for 1 d at room temperature. The solvent was evaporated under high vacuum to give **10** as a red powder (223.5 mg, 97%) as a mixture of isomers in a ratio of about 3:2. Crystals suitable for X-ray diffraction were obtained by layering a CH_2Cl_2 solution with hexane. ^{1}H NMR (500 MHz, CD_3CN, mixture of isomers): δ = 2.21, 2.20, 2.20, 2.19 (4 × s, 3 H, CH_3), 3.27, 3.25, 3.24, 3.12 (4 × s, 3 H, NCH_3), 4.24 (s, 5 H, Cp), 4.28 (s, 5 H, Cp) ppm. ^{31}P NMR (202 MHz, CD_3CN): δ = 13.9 (s, major), 12.9 (s, minor) ppm. FAB MS (NBA matrix): *m*/*z* = 569 [cation], 411 [cation – morpholine]. $C_{25}H_{36}BF_4FeN_2OPRu$ (655.3): calcd. C 45.82, H 5.54, N 4.28; found C 45.01, H 5.67, N 4.51.

Tricyclohexylphosphane Complex 11: One equivalent of tricyclohexylphosphane (97 mg, 0.37 mmol) was added to a solution of complex **6** (222 mg, 0.37 mmol) in 10 mL of acetonitrile and stirred for 1 d at room temperature. The solvent was evaporated under high vacuum to give Ru-**9** as an orange foam (291mg, 96%) as a mixture of two isomers in a ratio of about 19:1 (90% *de*). ^{1}H NMR (300 MHz, C_6D_6): major isomer: δ = 1.9–1.1 (m, 36 H, PCy_3 and CH_3CN), 1.94, 1.88 (2 × s, 3 H, CH_3), 2.38 (m, 1 H, $PCCH_2$), 2.59 (m, 1 H, $PCCH_2$), 3.33 (d, $J_{H,P}$ = 32.6 Hz, 1 H, PCH), 3.36 (s, 1 H, C_5H_4), 4.33 (s, 5 H, Cp), 5.01, 5.20, 5.86 (3 × s, 1 H, C_5H_4) ppm. ^{31}P NMR (121.45 MHz, C_6D_6): major isomer: δ = 59.6 (d, $J_{P,P}$ = 55 Hz, PFc), 18.1 (d, $J_{P,P}$ = 55 Hz, PCy_3) ppm; minor isomer: δ = 59.4 (d, $J_{P,P}$ = 48 Hz, PFc), 18.1 (d, $J_{P,P}$ = 48 Hz, PCy_3) ppm.

X-ray Crystallographic Study: Crystal data and details of the structure determination are listed in Table 4. Data collection was performed with a Bruker Smart APEX CCD (Mo-K_α radiation, λ = 0.71073 Å, graphite monochromator) area detector. The unit-cell parameters were obtained by the least-squares refinement of 8096 reflections. All the structures were solved by direct methods (SHELXS-97)[21] and refined by full-matrix least-squares procedures based on F^2 with all measured reflections (SHELXL-97).[22] The SADABS[23] program was used for absorption correction of the structures. All non-hydrogen atoms were refined anisotropically. H atoms were in part located from difference Fourier maps; the remaining hydrogens were introduced at their idealized positions [*d*(CH) = 0.98 Å] and were refined using a riding model. The absolute configuration for complex **3a** was confirmed by evaluation of the Flack parameter.[24] CCDC-237071 (for **3a**), -237069

 © 2005 Wiley-VCH Verlag GmbH & Co. KGaA, Weinheim

Table 4. Crystallographic data for compounds **3a**, **8**, and **10**.

Compound	**3a**	**8**	**10**
Formula	$C_{17}H_{19}FeP$	$C_{30}H_{34}BF_4FeN_2OPRu$	$C_{25}H_{36}BF_4FeN_2OPRu$
M	310.14	713.29	655.27
Crystal system	orthorhombic	triclinic	monoclinic
Space group	$P2_12_12_1$	$P\bar{1}$	$P2_1/c$
a/Å	9.2086(19)	9.6510(9)	8.311(3)
b/Å	11.208(2)	13.1340(13)	21.113(7)
c/Å	14.540(3)	13.3840(13)	14.944(5)
α/°	90	75.710(2)	90
β/°	90	68.860(2)	97.390(9)
γ/°	90	79.530(2)	90
V/Å^3	1500.7(5)	1525.3(3)	2600.3(15)
Z	4	2	4
T/K	293	293	293
D_c/g cm^{-3}	1.373	1.553	1.674
F_{000}	648	724	1336
μ(Mo-K_α)/cm^{-1}	1.095	1.074	1.251
$2\theta_{max}$/°	54.88	56.64	56.74
Total reflections	19492	21164	35782
Independent reflections	3423	7569	6470
Observed reflections [$I > 2\sigma(I)$]	3306	6867	4726
Parameters refined	244	411	329
$R1$/$wR2$ [$I > 2\sigma(I)$]	0.0250, 0.0627	0.0368, 0.0923	0.0577, 0.1201
$R1$/$wR2$ (all data)	0.0259, 0.0631	0.0410, 0.0951	0.0862, 0.1318
Flack's param.	0.039(12)	–	–

(for **8**) and -237070 (for **10**) contain the supplementary crystallographic data for this paper. These data can be obtained free of charge from The Cambridge Crystallographic Data Centre via www.ccdc.cam.ac.uk/data_request/cif.

Acknowledgments

Financial support of this work by the Deutsche Forschungsgemeinschaft (DFG, Graduiertenkolleg 440) is gratefully acknowledged.

[1] For a review see: C. Ganter, *J. Chem. Soc. Dalton Trans.* **2001**, 3541.
[2] C. Ganter, L. Brassat, C. Glinsböckel, B. Ganter, *Organometallics* **1997**, *16*, 2862.
[3] C. Ganter, L. Brassat, B. Ganter, *Tetrahedron: Asymmetry* **1997**, *8*, 2607.
[4] C. Ganter, C. Glinsböckel, B. Ganter, *Eur. J. Inorg. Chem.* **1998**, 1163.
[5] S. Qiao, G. C. Fu, *J. Org. Chem.* **1998**, *63*, 4168.
[6] R. Shintani, M. M.-C. Lo, G. C. Fu, *Org. Lett.* **2000**, *2*, 3695.
[7] K. Tanaka, S. Qiao, M. Tobisu, M. M.-C. Lo, G. C. Fu, *J. Am. Chem. Soc.* **2000**, *122*, 9870.
[8] M. Ogasawara, K. Yoshida, T. Hayashi, *Organometallics* **2001**, *20*, 3913.
[9] R. Shintani, G. C. Fu, *J. Am. Chem. Soc.* **2003**, *125*, 10 778.
[10] R. Shintani, G. C. Fu, *Angew. Chem.* **2003**, *115*, 4216; *Angew. Chem. Int. Ed.* **2003**, *42*, 4082.
[11] R. Shintani, G. C. Fu, *Org. Lett.* **2002**, *4*, 3699.
[12] C. Ganter, C. Kaulen, U. Englert, *Organometallics* **1999**, *18*, 5444.
[13] C. Kaulen, C. Pala, C. Hu, C. Ganter, *Organometallics* **2001**, *20*, 1614.
[14] M. Ito, M. Hirakawa, K. Murata, T. Ikariya, *Organometallics* **2001**, *20*, 379.
[15] Y. Morisaki, T. Kondo, T. Mitsudo, *Organometallics* **1999**, *18*, 4742.
[16] B. M. Trost, P. L. Fraisse, Z. T. Ball, *Angew. Chem.* **2002**, *114*, 1101; *Angew. Chem. Int. Ed.* **2002**, *41*, 1059.
[17] Y. Matsushima, K. Onitsuka, T. Kondo, T. Mitsudo, S. Takahashi, *J. Am. Chem. Soc.* **2001**, *123*, 10 405.
[18] B. M. Trost, B. Vidal, M. Thommen, *Chem. Eur. J.* **1999**, *5*, 1055.
[19] C. Standfest-Hauser, C. Slugovc, K. Mereiter, R. Schmid, K. Kirchner, L. Xiao, W. Weissensteiner, *J. Chem. Soc. Dalton Trans.* **2001**, 2989.
[20] A. Bauer, U. Englert, S. Geyser, F. Podewils, A. Salzer, *Organometallics* **2000**, *19*, 5471.
[21] G. M. Sheldrick, *SHELXS-97*, Program for solution of crystal structures, University of Göttingen, Germany, **1997**.
[22] G. M. Sheldrick, *SHELXL-97*, Program for refinement of crystal structures, University of Göttingen, Germany, **1997**.
[23] G. M. Sheldrick, *SADABS*, University of Göttingen, Germany, **1996**.
[24] H. D. Flack, *Acta Crystallogr. Sect. A* **1983**, *39*, 876.

Received July 8, 2004
Published Online January 27, 2005

 © 2005 Wiley-VCH Verlag GmbH & Co. KGaA, Weinheim

Metal-Directed Stereoselective Syntheses of Homochiral Complexes of *exo*-Bidentate Binaphthol Derivatives

Ruihu Wang,[a,b] Lijin Xu,[a] Jianxin Ji,[a] Qian Shi,[a,b] Yueming Li,[a] Zhongyuan Zhou,[a] Maochun Hong,*[b] and Albert S. C. Chan*[a]

Keywords: Cadmium / N ligands / Palladium / Silver / Zinc

The homochiral *exo*-bidentate ligands (*S*)-2,2′-bis(pyridylmethyleneoxy)-1,1′-binaphthyl [(*S*)-L] and (*R*)-2,2′-bis(pyridylmethyleneoxy)-1,1′-binaphthyl [(*R*)-L] were synthesized and employed for the preparation of coordination complexes with the aim of investigating the effect of an axially chiral 1,1′-binaphthyl connector on self-assembly process. Five homochiral complexes, $[Ag\{(S)\text{-}L\}(ClO_4)]_n$ (**1**), $[Ag\{(R)\text{-}L\}(ClO_4)]_n$ (**2**), $[\{Cd\{(S)\text{-}L\}(H_2O)Cl_2\}(H_2O)_{0.5}]_n$ (**3**), $[(Zn\{(S)\text{-}L\}Cl_2)(DMF)_{0.5}(H_2O)_{0.5}]_n$ (**4**), and $[(Pd_2\{(S)\text{-}L\}_2Cl_4)(H_2O)_{1.5}]_n$ (**5**), have been prepared and characterized by single-crystal X-ray diffraction analyses. The enantiomeric complexes **1** and **2** are isomorphous and are formed through interconnection of ligands and two-coordinate Ag^I centers. Complex **3** possesses a similar structural framework to **1** and is formed with two nitrogen atoms from (*S*)-L coordinating to six-coordinate Cd^{II} in a *trans* mode. The interlocking in part of the adjacent, one-dimensional helix-like chains stabilizes its structure. Complex **4** is a one-dimensional zigzag chain and is formed through interconnection of (*S*)-L and $ZnCl_2$ units. The *exo*-bidentate (*S*)-L ligand in **5** links square-planar Pd^{II} into a homochiral dinuclear metallomacrocycle.

(© Wiley-VCH Verlag GmbH & Co. KGaA, 69451 Weinheim, Germany, 2005)

Introduction

The design and construction of well-defined supramolecular architectures through metal-directed self-assembly of metal ions and organic ligands or organometallic substances are important for developing rational approaches to prepare novel metallosupramoleclues with intriguing structural and functional features.[1–4] In this context, the selection of multifunctional organic ligands containing appropriate coordination sites linked by a connector with specific positional orientation and/or functionality is especially crucial.[3,4] Various ligands have been tailored to recognize the intrinsic geometric preferences of specific metal ions or to encode structural constraints upon their coordination to metal ions. Metal–pyridine coordination has proved to be an excellent tool in self-assembly as it is strongly affected by the structural characteristics of the connector groups between the organic bridging ligands and the metal ions. Many pyridine-donor bis-monodentate ligands interconnected by rigid or flexible connectors, such as alkyl[5] or aryl groups,[6] or even organometallic complexes,[7] have been employed to construct metal-organic frameworks. Thus, it is of high interest to establish the rules that control the self-assembly process through chemical programming of suitable components and assembly algorithms.

In our previous study, we prepared a series of pyridine-donor ligands by connecting methylsulfanylpyridyl to aromatic ring connectors; the assembly of such ligands and metal ions resulted in several unique structural motifs, such as a metallosupramolecular cube,[8a] a one-dimensional nanotube,[8b] a dimetallomacrocycle,[8c] square rings with guest molecules,[8d] and a two-dimensional crown-like structure.[8d,8e] From the viewpoint of constructing functional complexes, it may be more valuable to introduce functionalized chiral groups directly into *exo*-bidentate pyridyl ligands as connectors instead of using nonfunctional connectors. Optically active 1,1′-bi-2-naphthol (BINOL) derivatives have been extensively applied to asymmetric synthesis and molecular recognition owing to their conformational stability and molecular flexibility.[9] Moreover, BINOL is also a good chiral connector for the design of new pyridine-donor ligands and the construction of novel, chiral, conjugated materials and fluorescent sensors.[10] We have recently investigated the effect of an axially chiral BINOL backbone on the self-assembly process through the introduction of an optically active BINOL backbone into *exo*-bidentate pyridyl ligands. The preliminary results indicated that the rigidity of the binaphthyl backbone facilitates the transfer of chiral information.[9d] In an effort to elucidate the effect of the coordination geometry of the metal ions on the self-

[a] Open Laboratory of Chirotechnology, Department of Applied Biology and Chemical Technology, The Hong Kong Polytechnic University,
Hong Hum, Hong Kong
Fax: +852-2364-9932
E-mail: bcachan@polyu.edu.hk
[b] State Key Laboratory of Structural Chemistry, Fujian Institute of the Research on the Structure of Matter, Chinese Academy of Sciences,
Fuzhou, Fujian, 350002, China

assembly process, we report herein the syntheses and characterizations of a series of homochiral complexes {[Ag{(*S*)-L}(ClO_4)]$_n$ (**1**), [Ag{(*R*)-L}(ClO_4)]$_n$ (**2**), [{Cd{(*S*)-L}(H_2O)Cl_2}(H_2O)$_{0.5}$]$_n$ (**3**), [(Zn{(*S*)-L}Cl_2)(DMF)$_{0.5}$(H_2O)$_{0.5}$]$_n$ (**4**), and [(Pd_2){(*S*)-L}$_2Cl_4$)(H_2O)$_{1.5}$]$_n$ (**5**) [(*S*)-L = (*S*)-2,2′-bis(pyridylmethyleneoxy)-1,1′-binaphthalene; (*R*)-L = (*R*)-2,2′-bis(pyridylmethyleneoxy)-1,1′-binaphthalene], in which Ag^I, Cd^{II}, Zn^{II}, and Pd^{II} adopt distorted linear, octahedral, tetrahedral, and square-planar geometries, respectively.

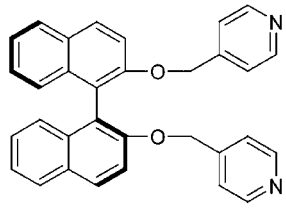

(*S*)-L

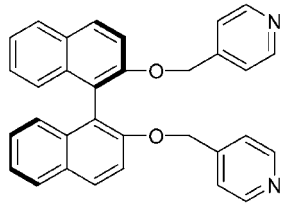

(*R*)-L

Results and Discussion

Syntheses

The reaction of (*S*)-1,1′-bi-2-naphthol or (*R*)-1,1′-bi-2-naphthol with 4-picolyl chloride hydrochloride was first carried out in the presence of K_2CO_3 in refluxing acetone under nitrogen for three days to afford *exo*-bidentate (*S*)-L or (*R*)-L in low yields (ca. 15%). The main product of the reaction was a mono-substituted compound (ca. 72%). However, when NaOH was used as the base under the same reaction conditions, (*S*)-L or (*R*)-L was obtained in high yield (88%). These results indicate that the base has a great effect on the yield of (*S*)-L or (*R*)-L. The specific optical rotations of (*S*)-L and (*R*)-L are –54.44° and 54.51° ($[\alpha]_D^{20}$, *c* = 1, THF), respectively. In comparison, the specific optical rotations of (*S*)- and (*R*)-1,1′-bi-2-naphthol are –35.50° and 35.50° ($[\alpha]_D^{20}$, *c* = 1, THF), respectively, thus indicating that the methylpyridine-donor groups in the ligands affect the chiral twist of BINOL. The ligands (*S*)-L and (*R*)-L are soluble in most organic solvents. The reaction of (*S*)-L or (*R*)-L with $AgClO_4$ in a 1:1 molar ratio in MeCN/H_2O (2:1) led to the formation of the corresponding enantiomeric complex **1** or **2**, respectively. As anticipated for (*S*) and (*R*) enantiomers, **1** and **2** possess the same structural framework and equal but opposite optical rotation. It is well known that the coordination geometry of metal ions plays an important role in the construction of supramolecular architectures. Hence, the successful syntheses of **1** and **2** prompted us to go beyond the two-coordinate Ag^I to metal ions of high coordination numbers. The reaction of (*S*)-L with $CdCl_2$ or $ZnCl_2$ in MeCN/H_2O afforded precipitates that were not soluble in any solvent. When a MeOH solution of (*S*)-L was layered on top of an aqueous solution of $CdCl_2$, suitable single crystals were formed. However, crystals of lower quality were produced using $ZnCl_2$ instead of $CdCl_2$ under the same conditions. In contrast, the diffusion of diethyl ether into a DMF/MeCN solution of (*S*)-L and $ZnCl_2$ resulted in crystals suitable for an X-ray single-crystal diffraction study.

Structural Description

[Ag{(S)-L}(ClO_4)]$_n$ (1) and [Ag{(R)-L}(ClO_4)]$_n$ (2)

As anticipated, the enantiomeric complexes **1** and **2** are isomorphous. The single-crystal X-ray structural analyses reveal that they consist of one-dimensional, helix-like chains formed through interconnection of two-coordinate Ag^I centers and homochiral ligands. As shown in Figure 1, Ag^I is in a distorted linear geometry and is coordinated by two nitrogen atoms from different ligands. The Ag–N bond distances (Table 1) are in the range of 2.157(4)–2.162(4) Å, which are typical values for Ag^I–N_{py} coordination distances.[8b,8c] The N(1)–Ag–N(2A) bond angle of 172.65(1)° in **2** is slightly smaller than that of 175.34(15)° in **1**. (*S*)-L in **1** and (*R*)-L in **2** bind in an *exo*-bidentate mode to bridge a pair of adjacent Ag^I centers. As shown in Table 2, the dihedral angles between two naphthyl rings of (*S*)-L and (*R*)-L are 69.3° and 69.8°, respectively, which are approximately equal, thus indicating that the BINOL backbone has hardly been affected. The dihedral angles between the naphthyl rings and their corresponding pyridyl rings are 41.9° and 87.7°, respectively, in **1**. The corresponding angles are 45.1° and 85.6°, respectively, in **2**. The distance between two Ag^I centers bridged by (*S*)-L and (*R*)-L are 4.74 and 4.69 Å, respectively, while the closest distances between two Ag^I centers unsupported by (*S*)-L, (*R*)-L, or the other molecular interactions are 7.28 and 7.32 Å in **1** and **2**, respectively. These slight differences are probably due to packing effects. It is noteworthy that two adjacent homochiral ligands on the same side produce a cleft with the same mean distance of 7.15 Å for **1** and **2**. This dimension is sufficient to recognize suitable aromatic guest molecules. The moiety of ligands in the adjacent helical chains is interlocked into the cleft of each other (Figure 1). The ClO_4^- counteranion, which lies inside the cleft in part through a weak interaction with Ag^I, further fills the void around the metal ions.

[(Cd{(S)-L}(H_2O)Cl_2)(H_2O)$_{0.5}$]$_n$ (3)

Complex **3** is a one-dimensional, left-handed, helix-like chain formed through the interconnection of (*S*)-L and six-coordinate Cd^{II}. As shown in Figure 2, each Cd^{II} center is coordinated by two nitrogen atoms from different (*S*)-L ligands in the apical positions [N(1)–Cd–N(2A) bond angle of 174.6(3)°; Table 1], with two bridging Cl^- ligands in a *cis* mode, a terminal Cl^-, and a water molecule occupying the

 © 2005 Wiley-VCH Verlag GmbH & Co. KGaA, Weinheim

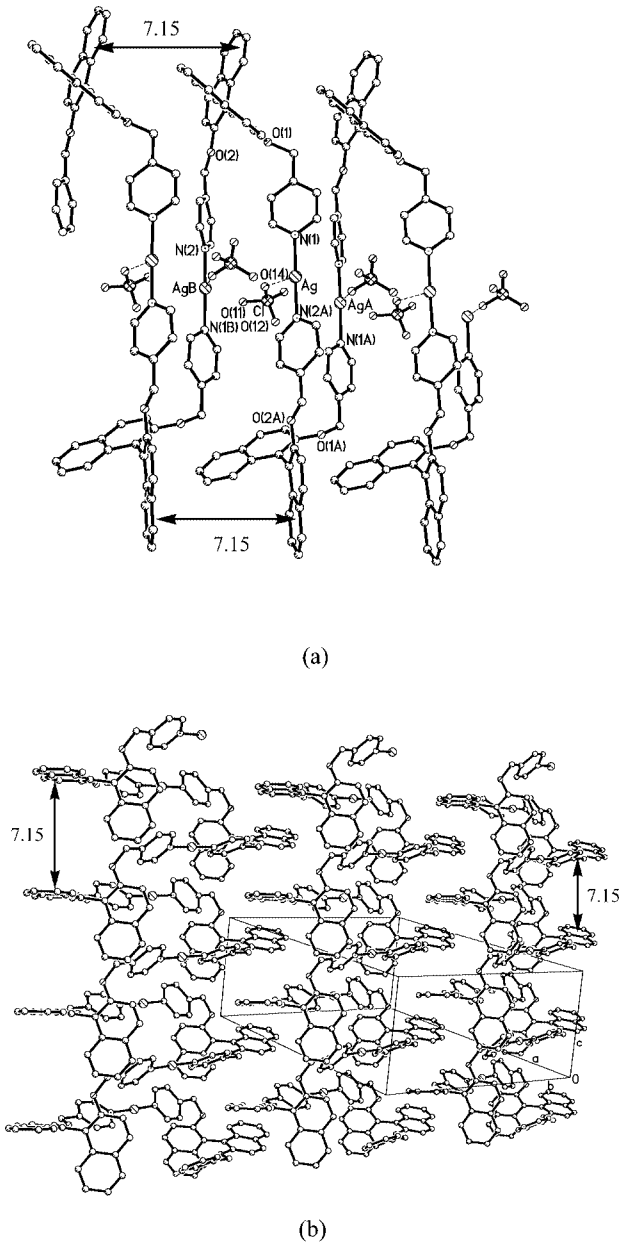

Figure 1. (a) View of the left-handed, helix-like chain in **1**; (b) packing diagram showing inter-immersion of adjacent chains in the clefts in **1** along the (210) direction

Table 1. Selected bond lengths [Å] and angles [°] for complexes **1**–**5**

Complex **1**[a]			
Ag–N(1)	2.162(4)	Ag–O(14)	2.891(12)
Ag–N(2A)	2.157(4)		
N(2A)–Ag–N(1)	175.34(15)	N(1)–Ag–O(14)	85.1(5)
N(2A)–Ag–O(14)	99.5(5)		
Complex **2**[b]			
Ag–N(1)	2.162(4)	Ag–O(12)	2.812(12)
Ag–N(2A)	2.175(4)	Ag–O(12B)	2.813(11)
N(1)–Ag–N(2A)	172.65(17)	N(1)–Ag–O(12B)	90.8(3)
N(1)–Ag–O(12)	93.5(4)	N(2A)–Ag–O(12B)	96.4(4)
N(2A)–Ag–O(12)	86.5(4)	O(12)–Ag–O(12B)	102.6(3)
Complex **3**[c]			
Cd–N(2A)	2.319(4)	Cd–Cl(2)	2.540(2)
Cd–N(1)	2.333(4)	Cd–Cl(1)	2.650(2)
Cd–O(1W)	2.401(5)	Cd–Cl(1B)	2.732(2)
N(2A)–Cd–N(1)	174.6(3)	O(1W)–Cd–Cl(1)	171.03(12)
N(2A)–Cd–O(1W)	92.1(2)	Cl(2)–Cd–Cl(1)	100.80(7)
N(1)–Cd–O(1W)	85.9(2)	N(2A)–Cd–Cl(1B)	85.53(14)
N(2A)–Cd–Cl(2)	92.20(13)	N(1)–Cd–Cl(1B)	89.17(13)
N(1)–Cd–Cl(2)	92.77(12)	O(1W)–Cd–Cl(1B)	82.36(13)
O(1W)–Cd–Cl(2)	86.88(14)	Cl(2)–Cd–Cl(1B)	168.91(7)
N(2A)–Cd–Cl(1)	92.2(2)	Cl(1)–Cd–Cl(1B)	90.14(3)
N(1)–Cd–Cl(1)	89.0(2)	Cd–Cl(1)–Cd(A)	142.52(7)
Complex **4**[d]			
Zn–N(1)	2.006(8)	Zn–Cl(1)	2.217(3)
Zn–N(2A)	2.026(8)	Zn–Cl(2)	2.223(3)
N(1)–Zn–N(2A)	104.1(3)	N(1)–Zn–Cl(2)	107.0(3)
N(1)–Zn–Cl(1)	105.3(3)	N(2A)–Zn–Cl(2)	110.6(2)
N(2A)–Zn–Cl(1)	103.9(3)	Cl(1)–Zn–Cl(2)	124.2(1)
Complex **5**			
Pd(1)–N(1)	2.021(3)	Pd(1)–N(4)	2.032(3)
Pd(2)–N(2)	1.998(3)	Pd(2)–N(3)	2.000(3)
Pd(1)–Cl(1)	2.2914(19)	Pd(1)–Cl(2)	2.315(2)
Pd(2)–Cl(3)	2.302(2)	Pd(2)–Cl(4)	2.292(2)
N(4)–Pd(1)–N(1)	172.88(11)	Cl(1)–Pd(1)–Cl(2)	174.32(9)
N(4)–Pd(1)–Cl(1)	87.15(11)	N(1)–Pd(1)–Cl(1)	88.54(8)
N(4)–Pd(1)–Cl(2)	89.84(11)	N(1)–Pd(1)–Cl(2)	94.92(9)
N(2)–Pd(2)–N(3)	173.29(13)	Cl(3)–Pd(2)–Cl(4)	174.47(10)
N(2)–Pd(2)–Cl(3)	91.65(11)	N(3)–Pd(2)–Cl(3)	91.79(12)
N(2)–Pd(2)–Cl(4)	89.06(11)	N(3)–Pd(2)–Cl(4)	88.07(11)

[a] Symmetry codes: (A) $-x + 1/2$, $y - 1/2$, $-z + 1$. [b] Symmetry codes: (A) $-x + 3/2$, $y + 1/2$, $-z + 2$; (B) $-x + 3/2$, $y - 1/2$, $-z + 2$. [c] Symmetry codes: (A) $-x + 1/2$, $y + 1/2$, $-z + 1$; (B) $-x + 1/2$, $y - 1/2$, $-z + 1$. [d] Symmetry codes: (A) $x + 1$, y, z.

equatorial plane. Thus, the coordination environment around Cd^{II} can best be described as a distorted Cl_3N_2O octahedron, which is rare in Cd^{II} complexes. Cd^{II} is approximately coplanar with the atoms in the equatorial plane, with a slight deviation of 0.027 Å. (*S*)-L serves as an *exo*-bidentate ligand, and the dihedral angles between the two naphthyl rings is 110.1°, which is close to those in **1** and **2**. However, the dihedral angle between the naphthyl rings and their corresponding pyridyl rings are 37.4° and 94.9°, respectively (Table 2). Thus, the interconnections of (*S*)-L and the six-coordinate Cd^{II} centers form a one-dimensional, helix-like chain similar to complex **1**. The Cd···Cd distance bridged by (*S*)-L and Cl^- is 5.10 Å. The uncoordinated water molecules stabilize the helix-like chain through hydrogen-bonding interactions between the uncoordinated water molecule and the coordinated water molecule [O(2W)···O(1W)^i = 2.797(12) Å; symmetry code: (i) x, $y + 1$, z,] as well as between the uncoordinated water molecule and terminal Cl^- [Cl(2)···H–O(2) = 3.129(11) Å]. It is noteworthy that the uncoordinated water molecule, coordinated water molecule, terminal Cl^-, and Cd^{II} form a trimetallocentered ten-membered hydrogen bonding ring. The Cd···Cd separation formed by uncoordinated water molecules through hydrogen-bonding interaction is 7.18 Å. The clefts from two adjacent (*S*)-L ligands are 7.04 Å, which is smaller than that in **1**. The complementary interlocking in part of the adjacent chains further stabilizes the chain by efficiently filling the void of the clefts (see b in Figure 2).

 © 2005 Wiley-VCH Verlag GmbH & Co. KGaA, Weinheim

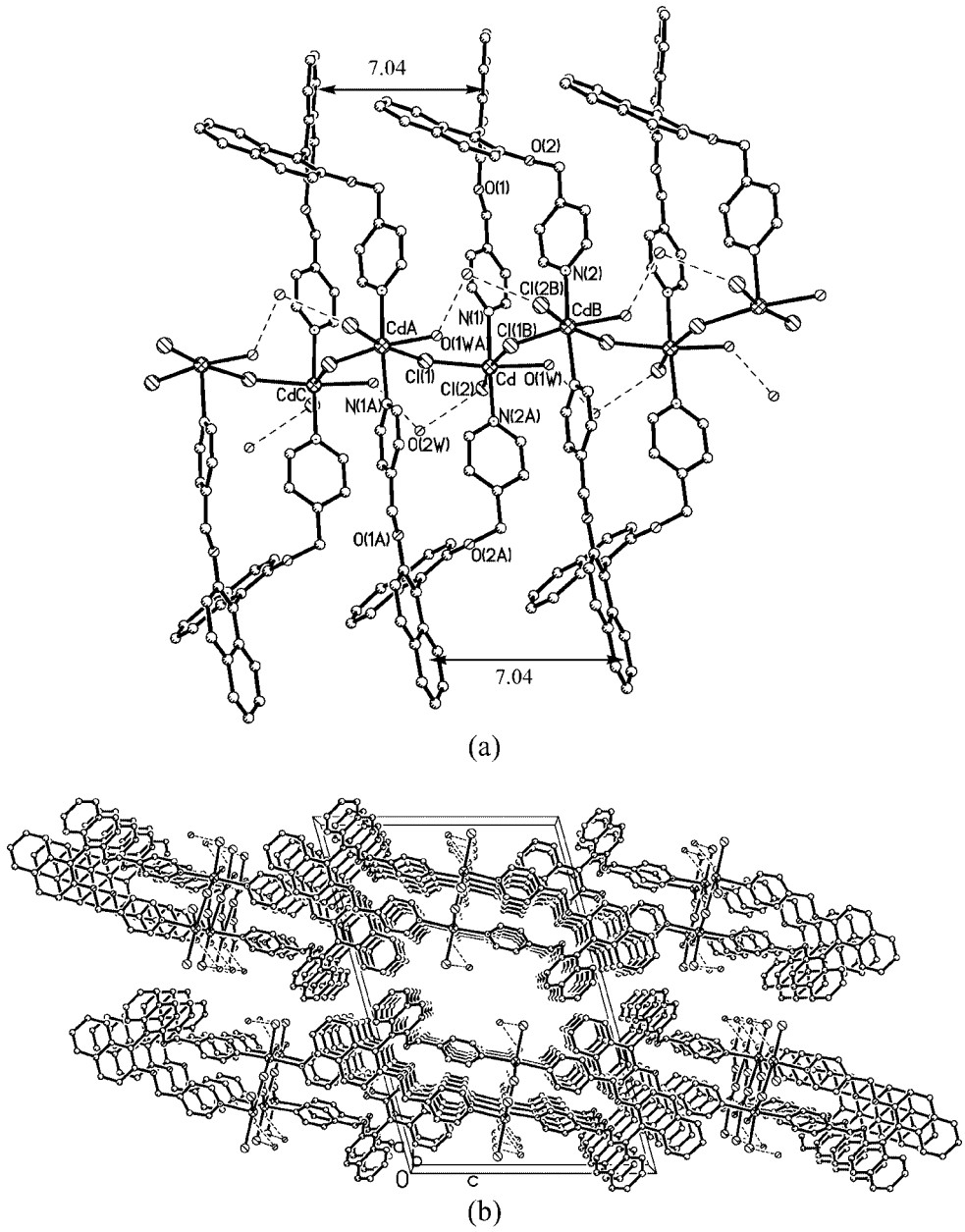

Figure 2. (a) View of the right-handed, helix-like chain in **3**; (b) view of the packing diagram of inter-immersed adjacent chains along the *b* axis

Table 2. A comparison of the structural data of the homochiral ligands in complexes **1**–**5**

Compound	Dihedral angles [°]				Distance between metal centers bridged by ligand [Å]	Structure
	Binaphthyl rings	Naphthyl ring and its pyridyl ring	Two pyridyl rings in the ligand	Two pyridyl rings at metal center		
1	69.3	41.9 and 87.7	85.4	21.6	4.74	1D helix-like chain
2	69.8	45.1 and 85.6	88.2	24.1	4.69	1D helix-like chain
3	69.9	37.3 and 85.1	83.8	27.1	5.10	1D helix-like chain
4	85.1	29.3 and 13.3	84.5	84.5	11.30	1D polymeric chain
5	81.7	30.1 and 64.8	82.4	45.5	4.644	dimetallomacrocycle

 © 2005 Wiley-VCH Verlag GmbH & Co. KGaA, Weinheim

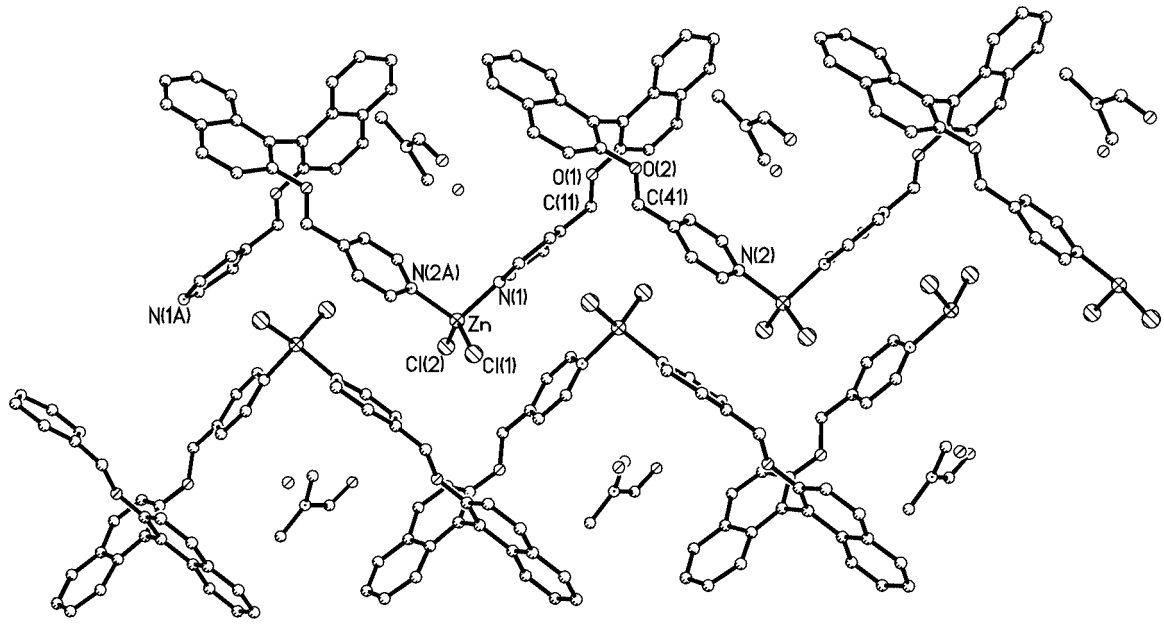

Figure 3. View of the double zigzag chains with guest DMF and water molecules in **4** along the *c* axis

[(Zn{(S)-L}Cl$_2$)(DMF)$_{0.5}$(H$_2$O)$_{0.5}$]$_n$ (4)

The single-crystal X-ray structural analysis reveals that **4** consists of a one-dimensional zigzag chain formed through the interconnection of $ZnCl_2$ units and (*S*)-L. As shown in Figure 3, each Zn^{II} ion is in a distorted tetrahedral geometry and is coordinated by two terminal Cl^- and two nitrogen atoms from different (*S*)-L ligands [Zn–N = 2.006(8) and 2.026(8) Å; N(1)–Zn–N(2A) = 104.1(3)°; Table 1]. The dihedral angle between two pyridyl rings attached to Zn^{II} is 84.5°, thus confirming the approximately perpendicular arrangement of the two coordinated pyridyl rings. All (*S*)-L ligands bind in an *exo*-bidentate mode and lie on the same side of the polymer chain, which is very different from the situation in **1**–**3**. The pyridyl rings are twisted around their naphthyl rings, with the dihedral angles between them being 13.3° and 29.3°, respectively (Table 2). A dramatic twisting between the two naphthyl rings is also observed, with the dihedral angle between them being 76.2°, which is larger than those in **1**–**3**. The combination of these twistings makes the (*S*)-L-connected $ZnCl_2$ units form a one-dimensional polymeric chain. The adjacent Zn···Zn separation bridged by (*S*)-L is 11.30 Å. The other chain with the same chirality fills the chain void between $ZnCl_2$ units in a complementary fashion to stabilize the chain structure. The DMF and water molecules, which lie outside the open cavity formed by the adjacent (*S*)-L ligands, do not generate significant weak interactions.

[(Pd$_2${(S)-L}$_2$Cl$_4$)(H$_2$O)$_{1.5}$]$_n$ 5

Complex **5** has a homochiral, binuclear metallocyclic structure. As shown in Figure 4, both Pd(1) and Pd(2) are in a distorted square-planar geometry and are coordinated by two *trans*-pyridine nitrogen atoms of different (*S*)-L and two *trans* Cl^- ligands, with *cis* angles ranging from 87.7(3)° to 94.9(3)° (Table 1). The average bond distances of Pd–N_{py} and Pd–Cl are 2.008(12) Å and 2.305(4) Å, respectively, which are typical values for Pd–N_{py} and Pd–Cl bond lengths. (*S*)-L acts as an *exo*-bidentate ligand, with its pyridyl rings slightly twisted with respect to their naphthyl rings, with the dihedral angles between them being 30.1° and 64.8° and 29.3° and 87.9°, respectively. The two naphthyl rings are also drastically twisted, with the dihedral angle between them being 81.7° and 82.7°, respectively. The combination of these twistings allows the (*S*)-L ligands to link the $PdCl_2$ units into a thirty-four-membered bimetallic macrocycle. The Pd···Pd separation in the cycle is 4.644 Å. Owing to the high distortion and flexibility of (*S*)-L, no enclathration of guest molecules is observed in **5**; the uncoordinated water molecules lie outside of the macrocycle. There are no other significant weak interactions or short contacts between the adjacent macrocycles.

It is of interest to compare the related structural data of (*S*)-L or (*R*)-L in **1**–**5**. (*S*)-L and (*R*)-L act as *exo*-bidentate ligands, and the difference of the coordinating geometry of the metal ions in **1**–**5** results in different structural topologies. In complexes **1** and **2**, owing to the configurational difference, (*S*)-L and (*R*)-L bridge two-coordinate Ag^I generating left-handed and right-handed helix-like chains, respectively. The frameworks of (*S*)-L and (*R*)-L are not crucially affected by the coordination to metal centers, as shown by the data in Table 2. In complex **3**, two nitrogen atoms from different (*S*)-L ligands occupy the axial positions of a six-coordinate Cd^{II} center, which results in a structural framework similar to **1**. Thus, the dihedral angles between the two naphthyl rings are very close and are the smallest in **1**–**5**. The slight difference between the one-dimensional, helix-like chains is due to free rotation of methylpyridine. However, the distortion angle of the BINOL connector in **4**

 © 2005 Wiley-VCH Verlag GmbH & Co. KGaA, Weinheim

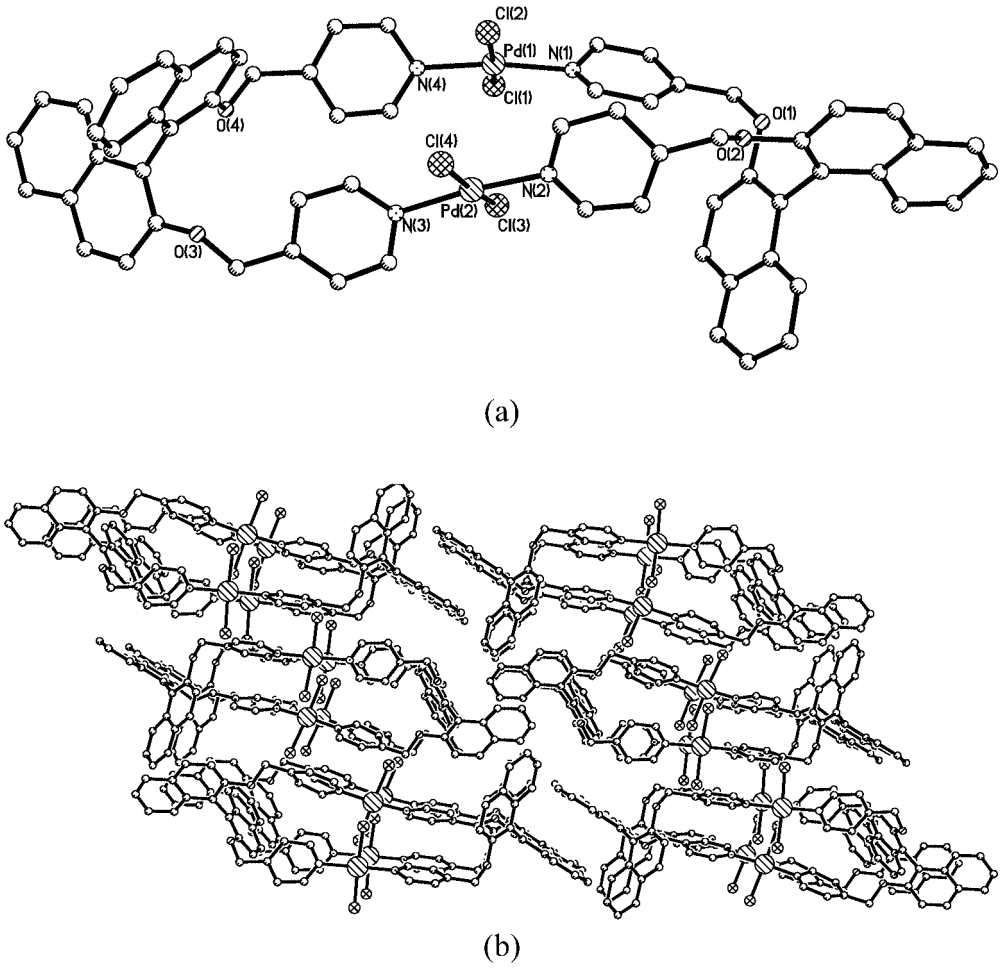

Figure 4. (a) View of the molecular structure of **5**, with uncoordinated water molecules omitted for clarity; (b) view of the packing structure along the *b* axis in **5** showing that there are no other interactions between adjacent macrocycles

(85.1°) is larger than those in **1** and **3**, which results in the formation of a one-dimensional zigzag chain with the (*S*)-L ligands on the same side, with the largest distance between metal centers bridged by (*S*)-L (11.30 Å). The shortest distance is found in dinuclear metallomacrocyclic complex **5** (4.644 Å), in which two Pd^{II} centers are bridged by two (*S*)-L ligands. Therefore, the combination of both the structural characteristics of the BINOL connector and the coordination propensity of the metal ions leads to the formation of the final frameworks of complexes **1**–**5**.

Conclusions

We have successfully synthesized the BINOL-based, homochiral, pyridyl-containing ligands (*S*)-2,2′-bis(pyridylmethyleneoxy)-1,1′-binaphthalene [(*S*)-L] and (*R*)-2,2′-bis(pyridylmethyleneoxy)-1,1′-binaphthalene [(*R*)-L]. Each ligand binds in an *exo*-bidentate mode to bridge two adjacent metal centers. In complexes **1**–**3**, the ligands on different sides link two-coordinate Ag^{I} centers (**1** and **2**) and six-coordinate Cd^{II} centers (**3**) into homochiral helix-like chains, which are stabilized through complementary interlocking in parts of the adjacent chains. In the four-coordinate Zn^{II} complex **4**, the (*S*)-L ligands on the same side link $ZnCl_2$ units into a zigzag chain and the zigzag is stabilized by interlocking with the other chain. However, in the square-planar Pd^{II} complex **5**, the (*S*)-L ligands link *trans*-coordinated $PdCl_2$ units into a homochiral dinuclear metallomacrocycle. The dihedral angle between the two naphthyl rings of the BINOL connector is different in the different structural topologies, thus suggesting that the coordination geometry of the metal ions has an important effect on the framework twisting of the BINOL moiety. It should be noted that the metal ions themselves cannot be considered to be the center of chirality in **1**–**5** as the chirality of these complexes originates from the inherently chiral twisting in the BINOL connector. Thus, assembly of (*S*)-L with Ag^{I} and Cd^{II} results in the formation of left-handed, helix-like complexes **1** and **3**, respectively Correspondingly, the assembly of (*R*)-L with Ag^{I} leads to the formation of the right-handed, helix-like complex **2**. In summary, this research shows that the assembly of dipyridyl ligands with an optically active BINOL connector and metal ions offers an attractive and promising route to generate unique structural motifs that cannot be obtained with other types of normal,

 © 2005 Wiley-VCH Verlag GmbH & Co. KGaA, Weinheim

rigid or flexible *exo*-bidentate organic ligands, such as 4,4′-bipy and related organic ligands.

Experimental Section

General: All chemicals were commercially available and were used as received without further purification. (*S*)-L and (*R*)-L were synthesized according to a literature method.[9d] The measurement of the optical rotation was performed with a Polarimeter 341. ESI mass spectra were recorded with a Fisons VG platform. The IR spectra (KBr disk) were recorded with a Magna 750 FTIR spectrophotometer. Elemental analyses were determined with an Elementar Vario ELIII elemental analyzer.

Preparation of [Ag{(*S*)-L}(ClO_4)]$_n$ (1): A solution of $AgClO_4 \cdot H_2O$ (0.021 g, 0.1 mmol) in H_2O (5 mL) was added slowly to a stirred solution of (*S*)-L (0.047 g, 0.1 mmol) in MeCN (10 mL). The reaction mixture was stirred at 60 °C for 3 h and then filtered. Colorless crystals of complex **1** were obtained by allowing the filtrate to evaporate slowly in air for two weeks. Yield (0.062 g, 92%). $C_{32}H_{24}AgClN_2O_6$ (675.9): calcd. C 56.81, H 3.55, N 4.14; found C 56.84, H 3.52, N 4.17. IR (KBr pellet): $\tilde{\nu}$ = 3583 (m, br), 3062 (m), 2922 (m), 1943 (vw), 1672 (vw), 1618 (s), 1592 (s), 1563 (m), 1505 (s), 1466 (w), 1446 (m), 1429 (s), 1357 (vw), 1324 (s), 1287 (s), 1269 (s), 1215 (s), 1151 (vw), 1073 (s, br), 1021 (m), 960 (w), 914 (w), 860 (vw), 804 (m), 746 (m), 669 (vw), 619 (m), 573 (vw), 497 (w), 458 (w), 422 cm^{-1} (w).

Preparation of [Ag{(*R*)-L}(ClO_4)]$_n$ (2): The procedure was similar to the synthesis of complex **1**, except that (*R*)-L was used instead of (*S*)-L. Yield (0.057 g, 84%). $C_{32}H_{24}AgClN_2O_6$ (675.9): calcd. C 56.81, H 3.55, N 4.14; found C 56.89, H 3.63, N 4.16. IR (KBr pellet): $\tilde{\nu}$ = 3585 (m, br), 3060 (m), 2922 (m), 1942 (vw), 1670 (w), 1617 (s), 1592 (s), 1563 (w), 1505 (s), 1468 (w), 1446 (m), 1428 (s), 1356 (w), 1321 (s), 1287 (s), 1269 (s), 1216 (s), 1151 (vw), 1091 (s, br), 1020 (s), 959 (w), 912 (w), 861 (vw), 804 (m), 747 (m), 670 (w), 619 (m), 573 (vw), 497 (w), 459 (w), 422 cm^{-1} (w).

Preparation of [(Cd{(*S*)-L}(H_2O)Cl_2)(H_2O)$_{0.5}$]$_n$ (3): A solution of (*S*)-L (0.047 g, 0.1 mmol) in MeOH (5 mL) was carefully layered on a solution of $CdCl_2 \cdot 2.5H_2O$ (0.023 g, 0.1 mmol) in H_2O (5 mL). Diffusion between the two phases over a period of two weeks produced colorless crystals of **3**. Yield (0.047 g, 69%). $C_{32}H_{27}CdCl_2N_2O_{3.5}$ (678.9): calcd. C 56.56, H 4.00, N 4.12; found C 56.58, H 4.03, N 4.13. IR (KBr pellet): $\tilde{\nu}$ = 3402(m, br), 3053 (m), 2923 (m), 1952 (vw), 1747 (vw), 1619 (s), 1593 (s), 1562(m), 1504 (s), 1467 (w), 1446 (m), 1426 (s), 1356 (w), 1321 (s), 1287 (s), 1268 (s), 1214 (s), 1151 (w), 1089 (s), 1065 (s), 1017 (s), 959 (w), 913 (w), 860 (vw), 803 (s), 746 (m), 669 (vw), 619 (m), 573 (w), 497 (w), 458 (w), 422 cm^{-1} (m).

Preparation of [(Zn{(*S*)-L}Cl_2)(DMF)$_{0.5}$(H_2O)$_{0.5}$]$_n$ (4): A solution of $ZnCl_2$ (0.07 g, 0.1 mmol) in DMF (10 mL) was added slowly to a stirred solution of (*S*)-L (0.047 g, 0.1 mmol) in MeCN (10 mL). The reaction mixture was stirred at 60 °C for 6 h and then filtered. Colorless crystalline complex **4** was obtained in high yield by slow diffusion of diethyl ether into the filtrate over several days. Yield (0.058 g, 89%). $C_{33.5}H_{28.5}Cl_2N_{2.5}O_3Zn$ (650.4): calcd. C 61.86, H 4.38, N 5.38; found C 61.75, H 3.30, N 5.33. IR (KBr pellet): $\tilde{\nu}$ = 3048 (w), 2925 (w), 2858 (w), 1665 (s), 1624 (s), 1594 (m), 1567 (w), 1511 (m), 1384 (w), 1358 (vw), 1322 (m), 1276 (s), 1240 (m), 1219 (m), 1153 (m), 1091 (s), 1066 (s), 1030 (m), 963 (w), 917 (w), 871 (vw), 815 (s), 754 (m), 666 (vw), 636 (w), 605 (vw), 492 (w), 456 (vw), 430 cm^{-1} (vw).

[(Pd_2{(*S*)-L}$_2Cl_4$)(H_2O)$_{1.5}$]$_n$ (5): A solution of [$PdCl_2$(cod)] (0.12 g, 0.1 mmol) in CH_2Cl_2 (5 mL) was added slowly to a stirred solution of (*S*)-L (0.047 g, 0.1 mmol) in CH_2Cl_2 (5 mL). The reaction mixture was stirred at reflux temperature under nitrogen for 3 h and was then evaporated under reduced pressure. Yellow crystals of complex **5** were obtained by slow diffusion of hexane into the resultant solution over several days. Yield (0.055 g, 83%). $C_{64}H_{51}Cl_4N_4O_6Pd_2$ (1326.7): calcd. C 57.94, H 3.84, N 4.21; found C 57.98, H 3.91, N 4.25. IR (KBr pellet): $\tilde{\nu}$ = 3412 (m, br), 3055 (m), 2921 (m), 1925 (vw), 1743 (vw), 1617 (s), 1592 (s), 1563 (m), 1506 (s), 1462 (w), 1445 (m), 1428 (m), 1363 (vw), 1324 (s), 1281

Table 3. Crystallographic data for complexes **1**–**5**

Compound	**1**	**2**	**3**	**4**	**5**
Formula	$C_{32}H_{24}AgClN_2O_6$	$C_{32}H_{24}AgClN_2O_6$	$C_{32}H_{27}CdCl_2N_2O_{3.5}$	$C_{33.5}H_{28.5}Cl_2N_{2.5}O_3Zn$	$C_{64}H_{51}Cl_4N_4O_6Pd_2$
Mol. mass	675.85	675.85	678.86	650.36	1326.69
Crystal size [mm]	0.48 × 0.35 × 0.20	0.40 × 0.20 × 0.20	0.58 × 0.25 × 0.15	0.40 × 0.36 × 0.34	0.38 × 0.14 × 0.12
Crystal system	monoclinic	monoclinic	monoclinic	orthorhombic	monoclinic
Space group	C_2	C_2	C_2	$P2_12_12_1$	$P2_1$
a [Å]	24.984(4)	25.135(4)	25.704(5)	11.2955(13)	16.177(5)
b [Å]	7.2818(12)	7.3173(13)	7.1752(13)	16.5633(19)	9.248(3)
c [Å]	17.170(3)	17.101(3)	17.089(3)	19.966(2)	20.061(6)
β [°]	104.245(5)	104.390(4)	105.375(4)		96.901(6)
V [Å^3]	3027.7(9)	3046.5(9)	3038.9(9)	3735.4(7)	2979.6(15)
Z	4	4	4	4	2
D_c [g cm^{-3}]	1.483	1.474	1.484	1.156	1.470
μ [mm^{-1}]	0.800	0.795	0.931	0.832	0.836
F(000)	1368	1368	1372	1340	1334
T [K]	293(2)	294(2)	294(2)	293(2)	294(2)
λ(Mo-K_α) [Å]	0.71073	0.71073	0.71073	0.71073	0.71073
Flack parameters (x)	0.01(4)	0.01(4)	0.27(18)	0.03(3)	0.19(8)
Reflns. collected	10262	10312	10340	25626	19783
Unique reflns.	6430	6454	6421	8586	13048
Obsd. reflns. [F>4.0σ(F)]	4289	4000	4289	2297	5955
Parameters	379	379	370	401	717
S on F^2	0.979	0.921	0.959	0.945	1.030
R_1	0.0546	0.0554	0.0479	0.0799	0.0717
wR	0.1622	0.1654	0.1160	0.2405	0.281
$\Delta\rho_{min}$ and $\Delta\rho_{max}$ [e·Å^{-3}]	0.879 and –0.608	0.866 and –0.567	0.866 and –0.428	0.823 and –0.380	0.996 and –0.982

 © 2005 Wiley-VCH Verlag GmbH & Co. KGaA, Weinheim

(s), 1274 (m), 1216 (m), 1154 (vw), 1092 (s), 1066 (m), 1023 (m), 914 (w), 862 (vw), 806 (s), 748 (m), 676 (vw), 610 (m), 573 (w), 523 (w), 456 (w), 421 cm^{-1} (m).

X-ray Crystallography: Intensity data for the five complexes were recorded on a Siemens Smart CCD diffractometer with graphite-monochromated Mo-K_α radiation (λ = 0.71073 Å) at room temperature. Empirical absorption corrections were applied with the SADABS program.[12] The structures were solved by direct methods and all calculations were performed using the SHELXL-97 program.[13] The positions of the H atoms in complexes **1**–**5** were generated geometrically (C–H bond fixed at 0.96 Å) and assigned isotropic thermal parameters, and allowed to ride on their parent carbon atoms before the final cycle of refinement. The structures were refined by full-matrix least-squares minimization of $\Sigma(F_o - F_c)^2$ with anisotropic thermal parameters for all atoms except the H atoms. The crystallographic data for complexes **1**–**5** are listed in Table 3.

CCDC-240015 to -240019 (for **1**–**5**, respectively) contain the supplementary crystallographic data for this paper. These data can be obtained free of charge from The Cambridge Crystallographic Data Centre via www.ccdc.cam.ac.uk/data_request/cif.

Acknowledgments

We thank the Hong Kong Research Grants Council (project no. PolyU5306/01P), The University Grants Committee Area of Excellence Scheme in Hong Kong (AoE P/10-0), and the Hong Kong Polytechnic University Area of Strategic Development Fund for financial support of this study.

[1] a) J. M. Lehn, *Supramolecular Chemistry: Concepts and Perspectives*; VCH, Weinheim, **1995**; b) J. W. Steed, J. L. Atwood, *Supramolecular Chemistry*, J. Wiley and Sons, New York, **2000**.

[2] a) B. J. Holliday, C. A. Mirkin, *Angew. Chem. Int. Ed.* **2001**, *40*, 2022–2043; b) S. Leininger, B. Olenyuk, P. J. Stang, *Chem. Rev.* **2000**, *100*, 853–907; c) M. Eddaoudi, D. B. Moler, H. Li, B. Chen, T. M. Reineke, M. O'Keeffe, O. M. Yaghi, *Acc. Chem. Res.* **2001**, *34*, 319–330; d) N. R. Champness, D. A. Lemenovskii, A. G. Majouga, N. V. Zyk, M. Schröder, *Coord. Chem. Rev.* **2001**, *222*, 155–192.

[3] a) M. A. Masood, E. J. Enemark, T. D. P. Stack, *Angew. Chem. Int. Ed.* **1998**, *37*, 928–932; b) C. M. Hartshorn, P. J. Steel, *Chem. Commun.* **1997**, 541–542; c) J. Schneider, M. Köckerling, R. Kopitzky, G. Henkel, *Eur. J. Inorg. Chem.* **2003**, 1727–1734.

[4] a) U. Knof, A. von Zelewsky, *Angew. Chem. Int. Ed.* **1999**, *38*, 302–322; b) M. Albrecht, *Chem. Rev.* **2001**, *101*, 3457–3497; c) F. A. A. Paz, Y. Z. Khimyak, A. D. Bond, J. Rocha, J. Klinowski, *Eur. J. Inorg. Chem.* **2002**, 2823–2828.

[5] See for example: a) M. Munakata, L. P. Wu, T. Kuroda-Sowa, *Adv. Inorg. Chem.* **1999**, *46*, 173–303; b) A. J. Blake, N. R. Champness, S. S. M. Chung, W. S. Li, R. P. Schröder, *Chem. Commun.* **1997**, 1005–1006; c) T. L. Hennigar, D. C. MacQuarrie, P. Losier, R. D. Rogers, M. J. Zaworotko, *Angew. Chem. Int. Ed. Engl.* **1997**, *36*, 972–973; d) E. Bermejo, R. Carballo, A. Castineiras, R. Dominguez, A. E. Liberta, C. Maichle-Moessmer, M. M. Salberg, D. X. West, *Eur. J. Inorg. Chem.* **1999**, 965–973; e) Y. B. Dong, R. C. Layland, M. D. Smith, N. G. Pschirer, U. H. F. Bunz, H. C. zur Loye, *Inorg. Chem.* **1999**, *38*, 3056–3060; f) G. D. Munno, F. Cipriani, D. Armentano, M. Julve, J. A. Real, *New J. Chem.* **2001**, *25*, 1031–1036; g) M. Maekawa, H. Konaka, Y. Suenaga, T. Kuroda-Sowa, M. Munakata, *J. Chem. Soc. Dalton Trans.* **2000**, 4160–4166; h) K. Uemura, S. Kitagawa, M. Kondo, K. Fukui, R. Kitaura, H. C. Chang, T. Mizutani, *Chem. Eur. J.* **2002**, *8*, 3586–3600.

[6] See for example: a) K. Biradha, Y. Hongo, M. Fujita, *Angew. Chem. Int. Ed.* **2000**, *39*, 3843–3845; b) D. K. Chand, K. Biradha, M. Fujita, *Chem. Commun.* **2001**, 1652–1653; c) K. Biradha, M. Fujita, *Chem. Commun.* **2002**, 1877–1878; d) S. Banfi, L. Carlucci, E. Caruso, G. Ciani, D. M. Proserpio, *J. Chem. Soc. Dalton Trans.* **2002**, 2714–2721.

[7] a) R. Horikoshi, T. Mochida, H. Moriyama, *Inorg. Chem.* **2002**, *41*, 3017–3024; b) D. Braga, M. Polito, M. Bracaccini, D. D'Addario, E. Tagliavini, D. M. Proserpio, F. Grepioni, *Chem. Commun.* **2002**, 1080–1081.

[8] a) M. C. Hong, Y. J. Zhao, W. P. Su, R. Cao, M. Fujita, Z. Y. Zhou, A. S. C. Chan, *J. Am. Chem. Soc.* **2000**, *122*, 4819–4820; b) M. C. Hong, Y. J. Zhao, W. P. Su, R. Cao, M. Fujita, Z. Y. Zhou, A. S. C. Chan, *Angew. Chem. Int. Ed.* **2000**, *39*, 2468–2470; c) Y. J. Zhao, M. C. Hong, W. P. Su, R. Cao, Z. Y. Zhou, A. S. C. Chan, *Chem. Lett.* **2000**, 28–29; d) R. H. Wang, M. C. Hong, W. P. Su, Y. C. Liang, R. Cao, Y. Z. Zhao, J. B. Weng, *Bull. Chem. Soc. Jpn.* **2002**, *75*, 725–730; e) M. C. Hong, W. P. Su, R. Cao, M. Fujita, J. X. Lu, *Chem. Eur. J.* **2000**, *6*, 427–432.

[9] a) R. Noyori, *Angew. Chem. Int. Ed.* **2002**, *41*, 2008–2022; b) L. Pu, *Chem. Rev.* **1998**, *98*, 2405–2494; c) J. K. Whitesell, *Chem. Rev.* **1989**, *89*, 1581–1590; d) R. H. Wang, L. J. Xu, X. S. Li, Y. M. Li, Q. Shi, Z. Y. Zhou, M. C. Hong, A. S. C. Chan, *Eur. J. Inorg. Chem.* **2004**, 1595–1599.

[10] a) S. J. Lee, W. Lin, *J. Am. Chem. Soc.* **2002**, *124*, 4554–4555; b) Y. Cui, S. J. Lee, W. Lin, Y. *J. Am. Chem. Soc.* **2003**, *125*, 6014–6015; c) Y. Cui, H. L. Ngo, P. S. White, W. Lin, *Chem. Commun.* **2003**, 994–995; d) Y. Cui, O. R. Evans, H. L. Ngo, P. S. White, W. Lin, *Angew. Chem. Int. Ed.* **2002**, *41*, 1159–1162; e) A. Lützen, M. Hapke, J. Griep-Raming, D. Haase, W. Saak, *Angew. Chem. Int. Ed.* **2002**, *41*, 2086–2089; f) M. Kimura, M. Sano, T. Muto, K. Hanabusa, H. Shirai, *Marcromolecules* **1999**, *32*, 7951–7953.

[11] E. P. Kyba, G. W. Gokel, F. de Jong, K. Koga, L. R. Sousa, M. G. Siegel, L. Kaplan, G. D. Y. Sogah, D. J. Cram, *J. Org. Chem.* **1977**, *42*, 4173–4184.

[12] G. M. Sheldrick, *SADABS*, Program for Empirical Absorption Correction of Area Detector Data, University of Göttingen, Germany, **1996**.

[13] G. M. Sheldrick, *SHELXS 97*, Program for Crystal Structure Solution, University of Göttingen, Germany, **1997**.

Received: July 28, 2004

Mono-, Di- and Polymeric Calcium and Gadolinium Complexes of the Tripodal Ligand 2,2′,2′′-Nitrilotribenzoic Acid

Stefan Wörl,[a] Igor O. Fritsky,[b] Dieter Hellwinkel,[c] Hans Pritzkow,[a] and Roland Krämer*[a]

Keywords: Calcium / Gadolinium / N,O ligands / Tripodal ligands / X-ray crystallography

Three novel carboxylate-bridged complexes incorporating the tripodal N,O ligand 2,2′,2′′-nitrilotribenzoic acid H_3L of formula $[Ca^{II}(H_2L)(OH_2)_4][(H_2L)]\cdot 4H_2O$ (**1**), $[Ca^{II}(OH_2)_4][Ca^{II}(L)(OH_2)_2]_2\cdot 7H_2O$ (**2**) and $[Gd^{III}(L)(OH_2)_3]_2[Gd^{III}(L)(OH_2)_4]_2\cdot 13H_2O$ (**3**) were synthesized and characterized by X-ray crystallography. In all three complexes, the ligand H_3L binds to the metal centre only by its three carboxylate donors, leaving the bridgehead nitrogen atom nonbonding. The calcium(II) ion in the monomeric complex **1** is distorted pentagonal-bipyramidal coordinated, the +1 charge of the complex cation $[Ca^{II}(H_2L)(OH_2)_4]^+$ is balanced by an H_2L^- anion and both units are connected by hydrogen bonds. The polymeric compound **2** displays a one-dimensional chain structure, in which two $[Ca^{II}(L)]^{2-}$ units form a dimeric structure and are connected by hydrated Ca^{II} ions. **3** contains two different $[Gd^{III}(L)(OH_2)_n]$ dimers. In one of them the two Gd^{III} ions are linked by two monoatomic carboxylate O-bridges showing a short Gd···Gd distance of 3.99 Å. In the second, a *syn-anti* carboxylate 1,3-bridge with a longer Gd···Gd distance of 4.96 Å is observed. Magnetic measurements of **3** show paramagnetic behaviour with weak antiferromagnetic coupling.
(© Wiley-VCH Verlag GmbH & Co. KGaA, 69451 Weinheim, Germany, 2005)

Introduction

The self-assembly of supramolecular architectures by use of metal ion-ligand interactions is one of the most powerful methods to obtain new molecular structures. The carboxylate group is a versatile ligand and favours the formation of oligomeric and polymeric complexes, it can adopt different binding modes, such as terminal monodentate, chelating to one metal center and various modes of bridging coordination of two, three four or even five metal centres.[1] Metal carboxylates have therefore emerged as an important family of supramolecular coordination compounds and inorganic open framework materials.[2] Organic di- and tricarboxylates broaden the availability of such architectures and provide an effective means to design such structures. While dicarboxylates have been extensively studied in this respect, the supramolecular coordination chemistry of ligands carrying three highly preorganized carboxylate groups has been less well explored.

Here we report mono-, oligo and polymeric complexes of the tricarboxylate ligand 2,2′,2′′-nitrilotribenzoic acid H_3L. We have recently described five-coordinate transition metal complexes of H_3L in which the triphenyl nitrogen atom is involved in metal coordination with exception of an octahedral complex $[Fe^{III}(L)(OH_2)_3]$ in which the "hard" Fe^{III} ion is complexed only by the carboxylate groups of L.[3]

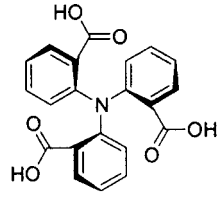

H_3L

This study focuses on Ca^{II} and Gd^{III} complexes, which display higher coordination numbers (> 6) of the metal ion and which tend to form polynuclear structures with various bridging modes of the carboxylate donor of H_3L. Studies of Ca^{II} binding to small molecules have led to generalizations about their corresponding binding preferences. Calcium may coordinate to between five and nine atoms, it exhibits irregular geometries and prefers oxygen donor ligands. The distances of Ca–O bonds show a wide variation of 2.20 to 2.80 Å.

Gadolinium coordination compounds are the subject of intense research efforts due to their applications as MRI contrast agents or as precursors for novel magnetic materials.[4] The number of di- and polynuclear Gd^{III} compounds for which structural and magnetic data are available is restricted. In Gd^{III} dimers usually weak antiferromagnetic interactions are reported.[5]

[a] Anorganisch-Chemisches Institut, Universität Heidelberg, Im Neuenheimer Feld 270, 69120 Heidelberg, Germany
Fax: (internat.) +49-6221-548439;
E-mail: Roland.Kraemer@urz.uni-heidelberg.de
[b] Department of Chemistry, National Taras Shevchenko University, 01033 Kiev, Ukraine
[c] Organisch-Chemisches Institut, Universität Heidelberg, Im Neuenheimer Feld 270, 69120 Heidelberg, Germany

 DOI: 10.1002/ejic.200400698 © 2005 Wiley-VCH Verlag GmbH & Co. KGaA, Weinheim

Results and Discussion

Synthesis and Characterization

We were able to characterize two new calcium(II) and one gadolinium(III) coordination compound containing the tripodal N,O-ligand H_3L. The synthesis of H_3L was achieved by a copper-catalyzed Ullman-nitrogen-arylation, followed by a standard base hydrolysis as described previously.[6] Compounds **1**–**3** were synthesized by mixing equimolar amounts of the ligand H_3L and the appropriate metal salt in water. $Ca(OH)_2$ was used as a base to deprotonate H_3L. Crystals suitable for X-ray crystallography were obtained by slow evaporation of the solvent after several days at room temperature. A description of the structures **1**–**3**, together with figures of the complexes is given below. Selected bond lengths and angles are given in Table 1 and Table 2. Crystal data and data collection details are presented in Table 3.

$[Ca^{II}(H_2L)(OH_2)_4][(H_2L)]\cdot 4H_2O$ (1)

Complex **1** contains a $[Ca^{II}(H_2L)(OH_2)_4]^+$ cation, a $[H_2L]^-$ anion and four water molecules (Figure 1). The distorted pentagonal-bipyramidal coordination sphere of the calcium(II) core is composed of the $[H_2L]^-$ ligand that coordinates by two COOH and one COO^- to two equatorial and one axial site, and the four remaining sites are occupied by water molecules. The presence of coordinating COOH groups is supported by the unsymmetric bond distances C14–O3 1.222(1) Å, C1–O4 1.315(1) Å and C21–O5 1.221(1) Å, C21–O6 1.317(1) Å, compared with the nearly

Table 1. Selected distances (Å) and angles (°) of **1** and **2**.

1		**2**	
Ca(1)–O(1)	2.347(1)	Ca(1)–O(1)	2.352(1)
Ca(1)–O(3)	2.421(1)	Ca(1)–O(3)	2.292(1)
Ca(1)–O(5)	2.424(1)	Ca(1)–O(5)	2.313(1)
Ca(1)–O(13)	2.336(1)	Ca(1)–O(5a)	2.572(1)
Ca(1)–O(14)	2.468(1)	Ca(1)–O(6a)	2.520(1)
Ca(1)–O(15)	2.388(1)	Ca(1)–O(7)	2.357(1)
Ca(1)–O(16)	2.396(1)	Ca(1)–O(8)	2.404(1)
Ca(1)···N(1)	3.780(1)	Ca(1)···N(1)	3.574(1)
		Ca(1)···Ca(1a)	4.008(1)
O(1)–Ca(1)–O(3)	93.16(3)	O(1)–Ca(1)–O(3)	92.49(4)
O(3)–Ca(1)–O(5)	71.69(3)	O(1)–Ca(1)–O(5)	85.86(4)
O(1)–Ca(1)–O(5)	90.75(3)	O(1)–Ca(1)–O(8)	90.42(5)
O(1)–Ca(1)–O(13)	170.98(4)	O(3)–Ca(1)–O(7)	168.09(5)
O(1)–Ca(1)–O(14)	106.49(3)	O(1)–Ca(1)–O(5a)	143.75(4)
O(1)–Ca(1)–O(15)	80.56(4)	O(1)–Ca(1)–O(7)	81.96(6)

Table 2. Selected distances (Å) and angles (°) of **3**.

Gd(1)···Gd(1′)	4.959(1)	Gd(2)···Gd(2′)	3.996(1)
Gd(1)···N(1)	3.756(2)	Gd(2)···N(2)	3.739(2)
Gd(1)–O(1)	2.293(2)	Gd(2)–O(11)	2.395(2)
Gd(1)–O(2′)	2.422(2)	Gd(2)–O(11′)	2.484(2)
Gd(1)–O(3)	2.368(2)	Gd(2)–O(12′)	2.490(2)
Gd(1)–O(5)	2.385(2)	Gd(2)–O(13)	2.279(2)
Gd(1)–O(7)	2.334(2)	Gd(2)–O(15)	2.303(2)
Gd(1)–O(8)	2.549(2)	Gd(2)–O(17)	2.355(2)
Gd(1)–O(9)	2.499(2)	Gd(2)–O(18)	2.466(2)
Gd(1)–O(10)	2.388(2)	Gd(2)–O(19)	2.409(2)
O(1)–Gd(1)–O(3)	78.79(7)	O(11)–Gd(2)–O(15)	75.78(8)
O(1)–Gd(1)–O(5)	97.04(7)	O(11)–Gd(2)–O(13)	84.32(8)
O(3)–Gd(1)–O(5)	77.79(7)	O(13)–Gd(2)–O(15)	95.35(9)
O(1)–Gd(1)–O(7)	146.92(8)	O(11)–Gd(2)–O(17)	141.98(9)
O(1)–Gd(1)–O(9)	143.24(8)	O(11)–Gd(2)–O(19)	140.11(8)

Table 3. Crystallographic data of $[Ca^{II}(H_2L)(OH_2)_4][(H_2L)]\cdot 4H_2O$ (**1**); $[Ca^{II}(OH_2)_4][Ca^{II}(L)(OH_2)_2]_2\cdot 7H_2O$ (**2**) and $[Gd^{III}(L)(OH_2)_3]_2$-$[Gd^{III}(L)(OH_2)_4]_2\cdot 13H_2O$ (**3**).

Compound	**1**	**2**	**3**
Empirical formula	$C_{42}H_{44}CaN_2O_{20}$	$C_{44}H_{60}Ca_3N_2O_{28}$	$C_{84}H_{128}Gd_4N_4O_{64}$
M_r	936.87	1185.18	2846.90
Crystal system	monoclinic	triclinic	triclinic
Space group	*Cc*	$P\bar{1}$	$P\bar{1}$
a (Å)	29.790(1)	9.7539(5)	10.8541(4)
b (Å)	9.8802(4)	10.7435(5)	13.0603(5)
c (Å)	15.3957(7)	12.8194(6)	19.9940(8)
α (°)	90	76.799(1)	100.343(1)
β (°)	106.185(1)	76.225(1)	96.564(1)
γ (°)	90	88.223(1)	107.174(1)
V (Å^3)	4351.9(3)	1269.86(11)	2621.4(2)
Z	4	1	1
$\rho_{calcd.}$ (mg/m^{-3})	1.430	1.550	1.803
μ (mm^{-1})	0.229	0.422	2.609
F_{000}	1960	622	1428
T (K)	103(2)	103(2)	103(2)
Crystal size (mm)	0.30 × 0.30 × 0.15	0.40 × 0.18 × 0.17	0.16 × 0.16 × 0.04
$\theta_{max.}$ (°)	32.03	32.00	32.01
Measured reflns.	39387	23496	52091
Unique reflns. (R_{int})	14114 [0.0272]	8612 [0.0244]	17742 [0.0435]
Parameters	763	463	942
Goodness of fit	1.057	1.081	1.044
*R*1 ($I > 2\ \sigma_I$)	0.0328	0.0441	0.0333
*wR*2 (all reflections)	0.0849	0.1277	0.0803
Residuals (e·Å^{-3})	0.492/–0.343	0.617/–1.025	2.244/–1.540

 © 2005 Wiley-VCH Verlag GmbH & Co. KGaA, Weinheim

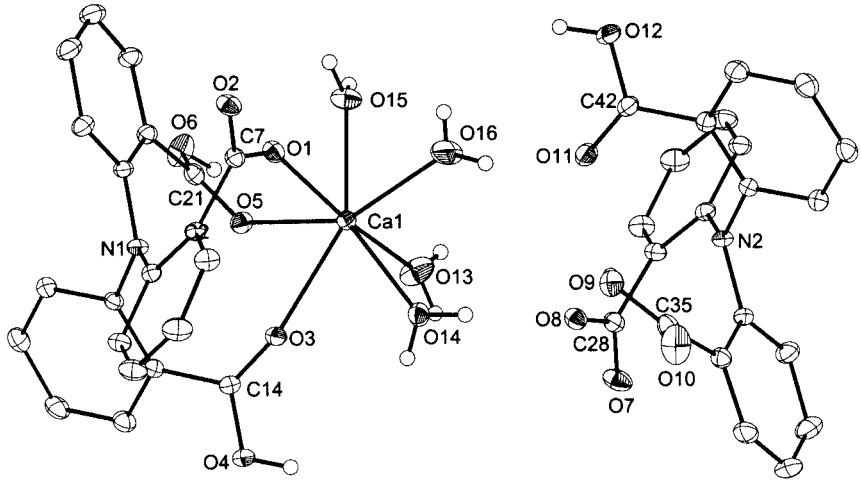

Figure 1. Ellipsoid plot of $[Ca^{II}(H_2L)(OH_2)_4][(H_2L)]$ (**1**). Aryl-H atoms and the H_2O solvent molecules have been omitted for clarity.

symmetric coordinating COO^- group: C7–O1 1.253(1) Å and C7–O2 1.273(1) Å. Also in the nonbonding $[H_2L]^-$ anion two unsymmetric bond distances are found for the COOH group: C35–O9 1.325(1) Å, C35–O10 1.217(1) Å and C42–O11 1.214(1) Å, C42–O12 1.316(1) Å, compared to the nearly symmetric bond distances of the COO^- group: C28–O7 1.265(1) Å and C28–O8 1.260(1) Å. The central nitrogen atom of $[H_2L]^-$ does not coordinate to the calcium ion [Ca1···N1 3.78 Å], resulting in a O3 coordination mode of the ligand. The two equatorial Ca–O bonds are almost identical [2.421(5) and 2.424(1) Å] and the axial Ca–O bond is, as expected, significantly shorter [2.347(1) Å]. The other Ca–O distances lie within the range of 2.336(1) and 2.468(1) Å. Planarization of the triarylamine unit is evident by an average C–N(1)–C angle of 119.0°, underlining the nonbonding property of the nitrogen atom to the calcium ion [average C–N(2)–C angle 118.4 °]. Hydrogen bonds linking $[Ca^{II}(H_2L)(OH_2)_4]^+$ and $[(H_2L)]^-$ are found between H(O16)–O11 [2.023(1) Å] and H(O14)–O8 [1.958(1) Å]. Furthermore, there are other O–H···O interactions between coordinated water and free water molecules.

$[Ca^{II}(OH_2)_4][Ca^{II}(L)(OH_2)_2]_2\ 7H_2O$ (2)

A second calcium complex $[Ca^{II}(OH_2)_4][Ca^{II}(L)(OH_2)_2]_2 \cdot 7H_2O$ (**2**) was isolated out of the reaction mixture yielding complex **1**. In contrast to **1**, the complex is a linear polymer and contains dimeric $[Ca^{II}(L)(OH_2)_2]_2^{2-}$ units, which are bridged by hydrated Ca^{II} ions (Figure 2). In the centrosymmetric $[Ca^{II}(L)(OH_2)_2]_2^{2-}$ unit, each Ca^{II} ion is hepta-coordinated and has a distorted pentagonal-bipyramidal coordination sphere, interacting with L^{3-} by three carboxylate donors. The four remaining sites are occupied by two water molecules and a bidentate bridging carboxylate group of the second $[Ca^{II}(L)]^-$ unit. The resulting –2 charge per $[Ca^{II}(L)(OH_2)_2]_2^{2-}$ unit is balanced by a hexacoordinate Ca^{II} cation. The Ca^{II} ion links the dinuclear units by axial coordination of bridging carboxylates, while its octahedral coordination sphere is completed by four equatorial water molecules. The Ca1–O distances lie in the range of 2.292(1) and 2.572(1) Å. The Ca2–O bond distances are similar to the reported ones for six-coordinate calcium complexes: Ca2–O2 2.335(2) Å, Ca2–O9 2.321(1) Å and Ca2–O10

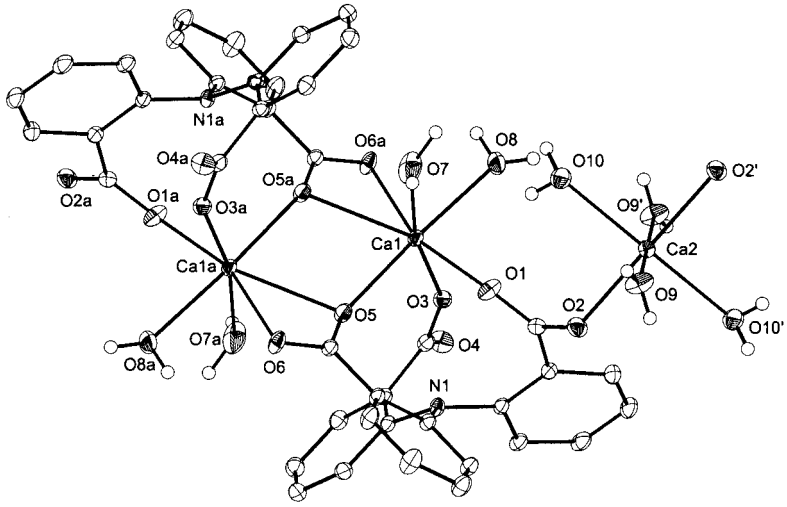

Figure 2. Ellipsoid plot of $[Ca^{II}(OH_2)_4][Ca^{II}(L)(OH_2)_2]_2$ (**2**). Aryl-H atoms and the H_2O solvent molecules have been omitted for clarity.

 © 2005 Wiley-VCH Verlag GmbH & Co. KGaA, Weinheim

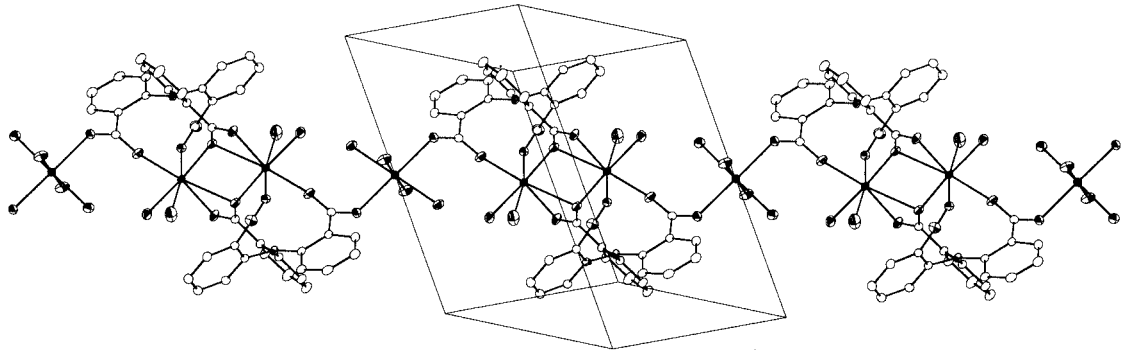

Figure 3. View of the self-assembled one-dimensional supramolecular architecture of **2** emphasizing the catenarian order of the calcium ions; hydrogen atoms and solvate molecules have been omitted for clarity.

2.369(1) Å. The Ca1···Ca1a distance of 4.008(1) Å is relatively long compared to other structurally characterized carboxylate-bridged calcium-dimers with average Ca···Ca distances around 3.8 Å.

$[Gd^{III}(L)(OH_2)_3]_2[Gd^{III}(L)(OH_2)_4]_2 \cdot 13H_2O$ (3)

H_3L reacts with gadolinium(III) to the complex $[Gd^{III}(L)(OH_2)_3]_2[Gd^{III}(L)(OH_2)_4]_2 \cdot 13H_2O$ (**3**), incorporating two dimers $[Gd^{III}(L)(OH_2)_3]_2$ and $[Gd^{III}(L)(OH_2)_4]_2$ with different Gd^{III} coordination spheres. The structure of **3** is shown in Figure 4. Two $[Gd^{III}(L)]$ moieties are joined via the carboxylate groups of L^{3-}. The gadolinium ions are eight-coordinate in both structures. The coordination geometry of the metal ion can be described as distorted square-antiprismatic. The remarkable structural feature of **3** is that the flexible ligand H_3L adopts two different coordination modes at the gadolinium(III) ions: In $[Gd^{III}(L)(OH_2)_4]_2$ (Figure 4, left) the two metal ions are bridged by two bidentate carboxylate groups in a *syn-anti* fashion, resulting in a large Gd···Gd distance of 4.959(1) Å. In the second dimer (Figure 4, right), in analogy to the Ca^{II} complex **2**, the bridging carboxylate groups are tridentate with formation of a four-membered chelate ring with one gadolinium ion, resulting in a smaller Gd···Gd distance of 3.996(2) Å; this Gd···Gd′ distance is comparable to that found in other complexes containing Gd_2O_2 rings.[7] The Gd–O distances range from 2.293(1) Å to 2.499(1) Å. The average Gd–O distance at Gd1 is 2.407(1) Å and 2.397(1) Å for Gd2, which is close to other reported Gd^{III} dimers.[8] The angles Gd2–O11–Gd2′ and O11–Gd2–O11′ are 109.96° and 70.04°, respectively. Many lanthanide(III) carboxylate complexes reported in the literature have polymeric structures [9] and only a few are dimeric.[10]

Magnetic Properties of 3

The magnetic susceptibility (χ_M) of **3** was measured in the temperature range 2–300 K. The variations of the inverse of the magnetic susceptibility, χ_M^{-1} and $\chi_M T$ of **3** are shown in Figure 6. The μ_{eff} value of 7.83 μ_B at room temperature is close to the calculated spin-only value (7.94 μ_B). The $\chi_M T$ product at 300 K (30.7 $cm^3 \cdot K \cdot mol^{-1}$) is expected for four isolated Gd^{3+} ions ($^8S_{7/2}$) and remains almost constant to 20 K. Below 10 K the $\chi_M T$ product decreases steeply down to 19.7 $cm^3 \cdot K \cdot mol^{-1}$ at 2 K. Such behaviour indicates paramagnetic behaviour of the Gd centres in **3** with weak antiferromagnetic coupling, as observed before in several binuclear Gd complexes.[11] The experimental points (7–300 K) obey the Curie–Weiss law with a Weiss constant θ = –0.18 K and Curie constant C = 30.731 which corresponds to four Gd^{3+} ions with the average g value

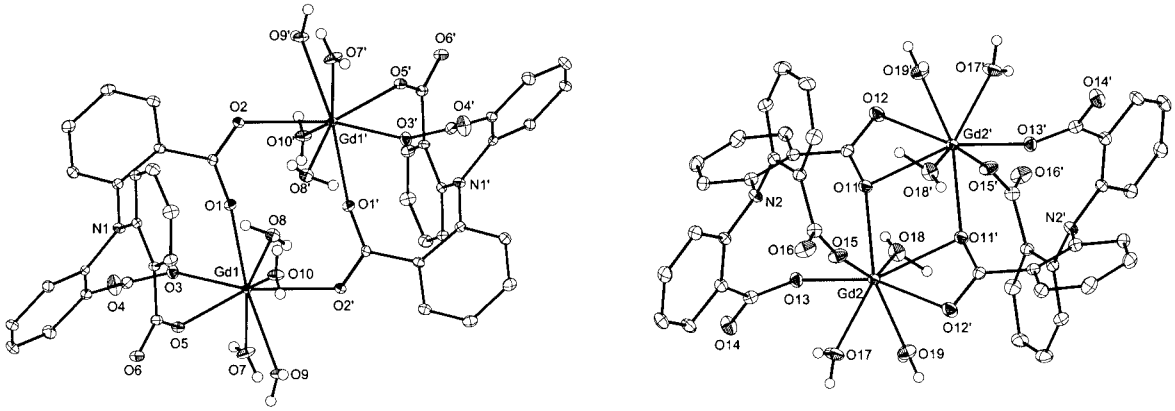

Figure 4. Ellipsoid plot of $[Gd^{III}(L)(OH_2)_3]_2[Gd^{III}(L)(OH_2)_4]_2 \cdot 13H_2O$ (**3**); aryl-H atoms and the H_2O solvent molecules have been omitted for clarity.

 © 2005 Wiley-VCH Verlag GmbH & Co. KGaA, Weinheim

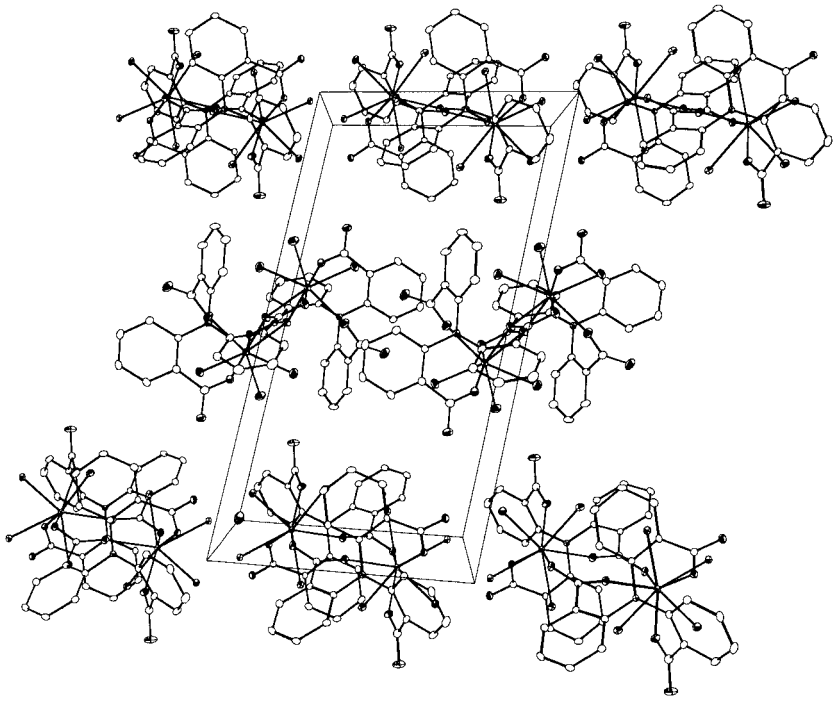

Figure 5. View of $[Gd^{III}(L)(OH_2)_3]_2[Gd^{III}(L)(OH_2)_4]_2{\cdot}13H_2O$ (**3**) showing the discrete arrangement of the $[Gd(L)]_2$ units.

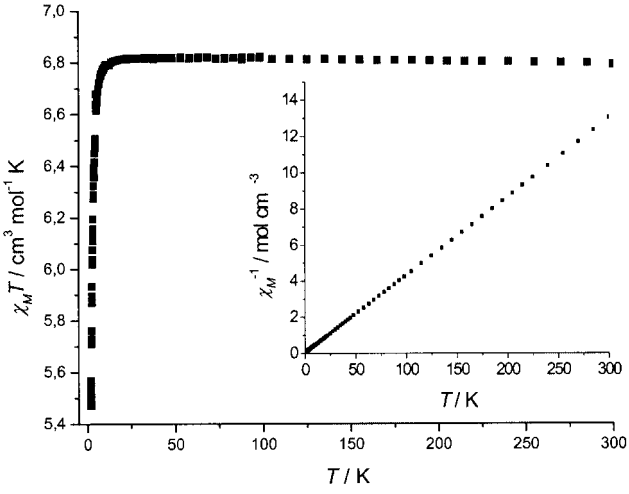

Figure 6. Plot of $\chi_M T$ and χ_M^{-1} vs. T for **3**.

equal to 1.975. Since two inequivalent exchange Gd dimeric units are present and the sample exhibits very weak antiferromagnetic interaction, it is not possible to distinguish the contribution to the observable behaviour from each coupling pattern using an analytical expression. Thus, the susceptibility data were fitted on the basis of the equation deduced from the isotropic Heisenberg model[12] envisaged the presence of an average isotropic coupling parameter $J = (J1 + J2)/2$ ($\boldsymbol{H} = -J \times \boldsymbol{S_1} \times \boldsymbol{S_{1'}} = -J \times \boldsymbol{S_2} \times \boldsymbol{S_{2'}}$, $\boldsymbol{S_1} = \boldsymbol{S_{1'}} = \boldsymbol{S_2} = \boldsymbol{S_{2'}} = 7/2$). A quantitative analysis of the data gave J to be equal to –0.084(2) cm^{-1}, the isotropic g factor to be equal to 1.975. Note, that J values in the range between –0.04 and –0.11 cm^{-1} were reported for other gadolinium dimers.[11,12]

UV/Vis-Spectrophotometric Titrations

Smooth formation of 1:1 complexes is indicated by isosbestic points, when H_3L in water/methanol at pH 7 is titrated with the appropriate metal salts (Figure 7). The UV-band at $\lambda_{max.}$ = 300 nm, that served as a probe for the M···N interaction, is nearly unchanged, in accordance to the crystal structures showing no M···N interactions. Metal coordination of this nitrogen atom is accompanied by a significant decrease of the 300 nm absorbance.[3]

Conclusions

In summary we have characterised new binding modes of lewis-hard metals to the versatile ligand H_3L. With calcium(II) a monomeric species $[Ca^{II}(H_2L)(OH_2)_4][(H_2L)]{\cdot}4H_2O$ (**1**) and a polymeric species $[Ca^{II}(OH_2)_4][Ca^{II}(L)(OH_2)_2]_2{\cdot}7H_2O$ (**2**) is formed, revealing rare examples of calcium(II) complexes with tridentate carboxylate only donor sets in mononuclear complex **1** and in one-dimensional chain-like structure **2**. With gadolinium(III) the complex $[Gd^{III}(L)(OH_2)_3]_2[Gd^{III}(L)(OH_2)_4]_2{\cdot}13H_2O$ (**3**), incorporating two different dimers with Gd···Gd distances of 4.0 and 5.0 Å, respectively, is formed. The magnetic properties of compound **3** have been studied, revealing paramagnetic behaviour of the gadolinium(III) ions with weak antiferromagnetic coupling. In all three compounds there is no interaction between the bridgehead nitrogen and the metal ions, this is in accordance with UV/Vis spectrophotometric titrations in solution. As observed previously for the iron(II) complex of L,[3] two [ML] units tend to dimerize via two carboxylate bridges in the solid state. The nonbridging car-

 © 2005 Wiley-VCH Verlag GmbH & Co. KGaA, Weinheim

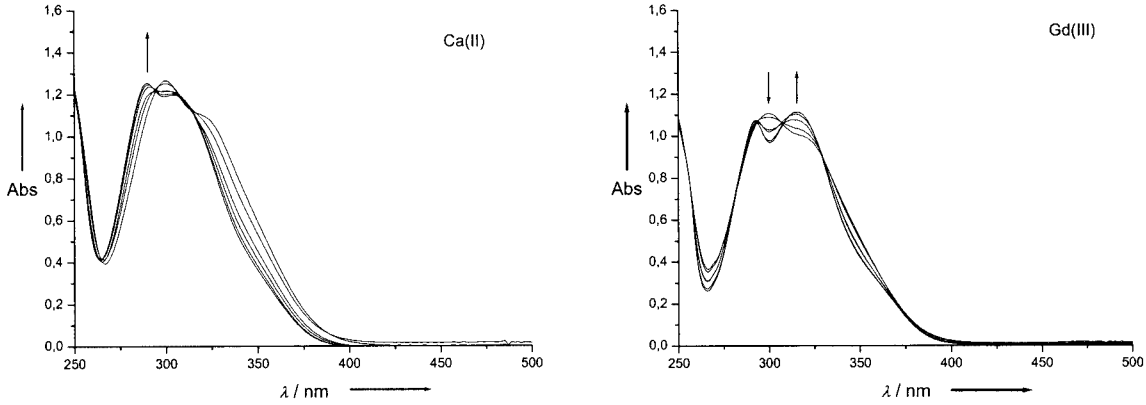

Figure 7. Spectrophotometric titration of H_3L (0.1 mM in MeOH/H_2O, pH 7, 20 mM buffer 3-(*N*-morpholino)propanesulfonic acid, T = 25 °C) with solutions of $Ca(NO_3)_2$ and $Gd(NO_3)_3$, in 0.2 equiv. steps. No further absorbance changes are observed on addition of >1 equiv. metal salt.

boxylate groups in each [ML] unit are available for interaction with "free" metal ions which link the dimers to extended structures, as exemplified by the linear-chain polymer **2**.

Experimental Section

General Remarks: All reactions were carried out in open flasks without exclusion of O_2 or H_2O. Chemicals were purchased from commercial sources (Aldrich and Acros) and were used as received without any further purifications. Electrospray ionization (ESI) mass spectra were recorded with a Q-TOF Micromass/Waters spectrometer. Absorbance UV/Vis spectra were recorded with a Specord S100 spectrophotometer (Carl Zeiss Jena). Magnetic susceptibility data were collected on ground crystals with use of a SQUID-based sample magnetometer (QUANTUM-Design, MPMS-XL-5) in the temperature range 2–300 K with an applied field of 1 T.

Preparation of the Complexes: The ligand 2,2′,2′′-nitrilotribenzoic acid H_3L was synthesised according to published methods.[6]

Synthesis of $[Ca^{II}(H_2L)(OH_2)_4][(H_2L)]\cdot 4H_2O$ (1) and $[Ca^{II}(OH_2)_4]$-$[Ca^{II}(L)(OH_2)_2]_2\cdot 7H_2O$ (2): H_3L (15.0 mg, 0.04 mmol) was dissolved in water (3 mL) and reacted with $Ca(OH)_2$ (4.4 mg, 0.06 mmol). After several days colourless crystals of **1** (monoclinic) and some of **2** (triclinic) were obtained. Yield: 13 mg (72 %). HR-ESI: *m/z*: for **1**: calcd. for $C_{21}H_{14}CaNO_6$ $[Ca(H_2L)]^+$: 416.0447; found: 416.0462; and $C_{42}H_{29}CaN_2O_{12}$ $[\{Ca(H_2L)\}\{H_2L\} + H]^+$: 793.1346; found: 793.1336; and in case of **2**: calcd. for $C_{42}H_{25}Ca_2N_2O_{12}$ $[\{CaL\}_2 + H]^-$: 829.0659; found 829.0655.

Synthesis of $[Gd^{III}(L)(OH_2)_3]_2[Gd^{III}(L)(OH_2)_4]_2\cdot 13H_2O$ (3): H_3L (15.0 mg, 0.04 mmol) was dissolved in water (3 mL) and deprotonated with $Ca(OH)_2$ (4.4 mg, 0.06 mmol). $Gd(NO_3)_3\cdot 6H_2O$ (17.9 mg, 0.04 mmol) in water (3 mL) was added to the solution and after several days colourless crystals were obtained. Yield: 18 mg (65 %). HR-ESI: *m/z*: calcd. for $C_{42}H_{26}GdN_2O_{12}$ $[(GdL)(H_2L)]^-$: 908.0727; found: 908.0725.

X-ray Crystallographic Study: Crystal data and refinement results of complexes **1**–**3** are listed in Table 3. Intensity data were collected with a BRUKER AXS Smart 1000 CCD area detector (Mo-K_α radiation, λ = 0.71073 Å, ω-scan). An empirical absorption correction was applied (SADABS). The structures were solved by direct methods and refined by full-matrix least-squares based on F^2 with all measured reflections.[13] Non-hydrogen atoms were refined anisotropically. Hydrogen atoms were located in difference Fourier maps and refined isotropically. Some of the solvent molecules in **2** and **3** were disordered. CCDC-243383 (for **1**), -243384 (for **2**) and -243385 (for **3**) contain the supplementary crystallographic data for this paper. These data can be obtained free of charge from The Cambridge Crystallographic Data Centre via www.ccdc.cam.ac.uk/data_request/cif.

Acknowledgments

This work was supported by the Fonds der Chemischen Industrie.

[1] a) *Comprehensive Coordination Chemistry I* (Ed. G. Wilkinson), Pergamon Press, New York, **1989**; b) C. Policar, F. Lambert, M. Cesario, I. Morgenstern-Badarau, *Eur. J. Inorg. Chem.* **1999**, *12*, 2201–2207; c) J.-M. Rueff, N. Masciocchi, P. Rabu, A. Sironi, A. Skoulios, *Eur. J. Inorg. Chem.* **2001**, 2843–2848.
[2] C. N. R. Rao, S. Natarajan, R. Vaidhyanathan, *Angew. Chem. Int. Ed.* **2004**, *43*, 466–1496.
[3] a) S. Wörl, D. Hellwinkel, H. Pritzkow, R. Krämer, *Chem. Commun.* **2003**, *19*, 2506–2507; b) S. Wörl, D. Hellwinkel, H. Pritzkow, M. Hofmann, R. Krämer, *Dalton Trans.* **2004**, *17*, 2750–2757.
[4] a) R. B. Lauffer, *Chem. Rev.* **1987**, *87*, 901–927; b) S. Aime, M. Botta, M. Fasano, E. Torreno, *Chem. Soc. Rev.* **1998**, *27*, 19–29; c) V. Comblin, D. Gilsoul, M. Herrmann, V. Humblet, J. Vincent, M. Mesbashi, C. Sauvage, J. F. Desreux, *Coord. Chem. Rev.* **1999**, *185–186*, 451–470; d) P. Caravan, J. J. Ellison, T. J. McMurry, R. B. Lauffer, *Chem. Rev.* **1999**, *99*, 2293–2352.
[5] a) I. Baxter, S. R. Drake, H. B. Hursthouse, K. M. Abdul Malik, J. McAleese, D. J. Otway, J. Plakatouras, *Inorg. Chem.* **1995**, *34*, 1384–1394; b) S. Nishihara, T. Akutagawa, T. Hasegawa, T. Nakamura, *Inorg. Chem.* **2003**, *42*, 2480–2482; c) J. P. Costes, F. Dahan, F. Nicodeme, *Inorg. Chem.* **2001**, *40*, 5285–5287.
[6] D. Hellwinkel, M. Melan, *Chem. Ber.* **1971**, *104*, 1001–1016.
[7] W. Moore, M. D. Glick, W. A. Baker, Jr., *J. Am. Chem. Soc.* **1972**, *94*, 1858–1865.
[8] H. Hou, G. Li, L. Li, Y. Zhu, X. Men, Y. Fan, *Inorg. Chem.* **2003**, *42*, 428–435.
[9] a) A. Ouchi, Y. Suzuki, Y. Ohki, Y. Koizumi, *Coord. Chem. Rev.* **1988**, *92*, 29–43; b) T. Imai, M. Shimoi, A. Ouchi, *Bull. Chem. Soc. Jpn.* **1987**, *60*, 159–167; c) D.-F. Sun, R. Cao, Y.-C. Liang, Q. Shi, M.-C. Hong, *J. Chem. Soc. Dalton Trans.* **2002**, 1847–1851; d) R. Vaidhyanathan, S. Natarajan, C. N. R. Rao, *Chem. Mater.* **2001**, *13*, 185–191.

 © 2005 Wiley-VCH Verlag GmbH & Co. KGaA, Weinheim

[10] a) F. Ribot, P. Toledano, C. Sanchez, *Inorg. Chim. Acta* **1991**, *185*, 239–245; b) I. A. Kahwa, S. Folkes, D. J. Williams, S. V. Ley, C. A. O'Mahoney, G. L. McPherson, *J. Chem. Soc., Chem. Commun.* **1989**, 1532–1533; c) Y. Bretonniere, M. Mazzanti, J. Pecaut, F. A. Dunand, A. E. Merbach, *Inorg. Chem.* **2001**, *40*, 6737–6745. d) P. H. Smith, R. R. Ryan, *Acta Cryst., Sect. C* **1992**, *48*, 2127–2130.

[11] a) J.-P. Costes, F. Dahan, A. Dupuis, S. Lagrave, J.-P Laurent, *Inorg. Chem.* **1998**, *37*, 153–155; b) J.-P. Costes, A. Dupuis, J.-P. Laurent, *Inorg. Chim. Acta* **1998**, *268*, 125–130; c) S. Liu, L. Gelmini, S. J. Rettig, R. C. Thompson, C. Orvig, *J. Am. Chem. Soc.* **1992**, *114*, 6081–6087; d) H. Hou, G. Li, L. Li, Y. Zhu, X. Meng, Y. Fan, *Inorg. Chem.* **2003**, *42*, 428–435.

[12] A. Panagiotopoulos, T. F. Zafiropoulos, S. P Perlepes, E. Bakalbassis, I. Masson-Ramade, O. Kahn, A Terzis, C. P. Raptopoulou, *Inorg. Chem*. **1995**, *34*, 4918–4920.

[13] G. M. Sheldrick, *SHELXTL*, V5.1, Bruker AXS, Madison, Wisconsin, **1998**.

Received August 13, 2004
Published Online January 27, 2005

 © 2005 Wiley-VCH Verlag GmbH & Co. KGaA, Weinheim

Three-Dimensional Lanthanoid-Containing Coordination Frameworks: Structure, Magnetic and Fluorescent Properties

Hong-Tao Zhang,[a] You Song,[a] Yong-Xiu Li,[a] Jing-Lin Zuo,[a] Song Gao,[b] and Xiao-Zeng You*[a]

Keywords: Lanthanides / Coordination polymers / Magnetic properties / Fluorescence / Solid-state structures

Two lanthanoid-containing 3D coordination polymers, $[Gd_2L_3(H_2O)_2]_n$ (**1**) and $\{[TbL_{1.5}(H_2O)]\cdot 0.5H_2O\}_n$ (**2**) (L = succinate), have been prepared by hydrothermal reaction. The difference in structure between the two 3D coordination polymers is a result of the flexibility of the ligand conformation. The magnetic properties of **1** and **2** have been investigated in the 1.8–300 K range. Both complexes exhibit ferromagnetic interaction between lanthanoid ions. AC magnetic measurements revealed long-range magnetic order in complex **2**. Especially **2** integrates the ferromagnetic, fluorescent and porous properties into a single entity. This motif may be developed to achieve new multifunctional molecular-based materials.

(© Wiley-VCH Verlag GmbH & Co. KGaA, 69451 Weinheim, Germany, 2005)

Introduction

Solid-state assembly of coordination polymers has attracted increasing attention due to their fascinating structure as well as their potential applications in materials science, such as zeolite-like porous structures and optoelectronic properties.[1,2] To construct coordination polymers, polydentate organic ligands are usually employed as space linkers to connect the metal ions.[3,4] The resultant functionality might not only rise from the organic ligand molecules but also from the inorganic metal ions. Accordingly, the wide-ranging functionality of the metal moiety, such as magnetic and optoelectronic properties, can be associated with the ability of the organic ligands to modulate special structural arrangements, to develop new molecular-based materials. Moreover, this supramolecular entity could lead to a multifunctional materials.[5] For this purpose, more new unique 3d- and 4f-metal containing coordination polymers have been investigated.[6–11] Most work involving lanthanoids has focused on the structures and luminescent properties of the complexes rather than on magnetic properties. In these lanthanoid-containing coordination polymers, many organic ligands containing oxygen atoms are employed as a bridge to connect the lanthanoid ions because of the high affinity of the lanthanoid ions for oxygen-containing ligands, such as the terephthalate anion[11d] and 4,4′-bipyridine *N*,*N*′-dioxide.[11a,b] Among them, aromatic polycarboxylate anions are widely used because of their rigid structure.[8,11] However, the structural variation of coordination polymers is ascribed to both the metal–ligand coordination modes and the conformational isomerism of ligands that arises from their flexibility. Generally, for aliphatic carboxylate ligands, the conformational variation of flexibility plays a more remarkable role than that in aromatic carboxylate ligands. As a simple aliphatic dicarboxylate ligand with multi-conformation isomerism, the succinate anions is the better choice to investigate the effect of conformational variation in coordination polymers because of the uncomplicated results. To date, in (succinato)metal coordination polymers, the inorganic species are mostly d-block metals such as Fe^{II} succinate[12d] and several (succinato)cobalt(II) coordination polymers with different structures.[12a–c] Recently, a few (succinato)nickel(II) coordination polymers as porous materials and one example of a (succinato)Sc^{III} 3D coordination polymer as a heterogeneous Lewis acid catalyst have been reported.[13,14] There are only two examples of lanthanoid coordination polymers involving succinate, praseodymium succinate [15a] and lutetium succinate.[15b] In this paper, we present two 3D lanthanoids coordination frameworks, $[Gd_2L_3(H_2O)_2]_n$ (**1**) (L = succinate) and $\{[TbL_{1.5}(H_2O)]\cdot 0.5H_2O\}_n$ (**2**), both of which exhibit ferromagnetic interaction between lanthanoid ions. Moreover, **2** emits an intense green fluorescence in the solid state at room temperature.

[a] State Key Laboratory of Coordination Chemistry, Nanjing University,
Nanjing 210093, China
E-mail: xyz@netra.nju.edu.cn
[b] State Key Laboratory of Rare Earth Materials Chemistry and Applications, Peking University,
Beijing 100871, China

 © 2005 Wiley-VCH Verlag GmbH & Co. KGaA, Weinheim **DOI: 10.1002/ejic.200400376**

Results and Discussion

Crystal Structures

[$Gd_2L_3(H_2O)_2$]$_n$ (1)

A single-crystal X-ray analysis revealed that the solid-state structure of gadolinium(III) succinate differs from that of previously reported praseodymium(III) succinate and lutetium succinate. There are two crystallographically independent gadolinium ions in the asymmetric unit (Figure 1a). Each gadolinium ion is ninefold coordinated by eight oxygen atoms from carboxylate groups of six succinate ions and one oxygen atom from the water molecule. Gd–O bond lengths vary in the range 2.357(8)–2.562(9) Å – in agreement with those of previously reported carboxylate-containing gadolinium complexes (2.308–2.597 Å).[9c] Table 1 gives selected bond lengths and angles. Two Gd^{III} ions are connected by three carboxylate groups, in which one acts as a carboxylate bridge in the usual $\eta^1:\eta^1:\mu_2$ mode while the other two serve as oxo-carboxylate bridges in the less common $\eta^2:\eta^1:\mu_2$ fashion.[9a] Along the *a* axis, the edge-sharing GdO_9 polyhedra extend to a 1D metal oxide like zigzag chain. In the chain, the metal–metal separation for the two symmetrically independent gadolinium ions Gd1–Gd2 is 4.0583(12) Å. The distance between two adjacent symmetrically related Gd^{III} ions is slightly elongated to 4.0595(13) Å [Gd1–Gd2^{I} (I: 1 + *x*, *y*, *z*) or Gd2–Gd1^{II} (II: *x* – 1, *y*, *z*)]. In the lattice, all metal oxide like chains are connected through the carbon–hydrogen chains of the succinate ions to produce 3D lanthanoid coordination frameworks. Notably, there are three conformations in the carbon–hydrogen chains of succinates, which can be observed along the *a* axis (Figure 2). Two of them adopt *gauche*-staggered conformations and extend along the *c* axis, approximately. One such conformation has a torsion angle of 89.5(12)° (C9–C10–C11^{III}–C12^{III}, III: 1 – *x*, 2 – *y*, 1 – *z*) and the other of 70.7(13)° (C5–C6–C7^{IV}–C8^{IV}, IV: 1 – *x*, 2 – *y*, 2 – *z*). The third succinato ligand possesses an *anti*-staggered conformation and extends along the *b* axis, approximately. Here, both carboxylate groups serve as $\eta^2:\eta^1:\mu_2$ mode bridges. In the *gauche*-staggered conformations, however, one carboxylate ion acts as a carboxylate bridge in $\eta^1:\eta^1:\mu_2$ fashion and another as a $\eta^2:\eta^1:\mu_2$ mode bridge.

Table 1. Selected bond lengths [Å], angles [°] and torsion angles [°] for **1**

Gd(1)–O(12)	2.358(9)	Gd(1)–O(7)	2.378(8)
Gd(1)–O(10)	2.454(9)	Gd(1)–O(1W)	2.457(11)
Gd(1)–O(3)[a]	2.461(9)	Gd(1)–O(2)	2.462(10)
Gd(1)–O(5)[a]	2.467(9)	Gd(1)–O(1)	2.474(8)
Gd(1)–O(9)	2.514(8)	Gd(2)–O(6)	2.357(8)
Gd(2)–O(2W)	2.402(9)	Gd(2)–O(11)	2.412(9)
Gd(2)–O(9)	2.419(8)	Gd(2)–O(1)[b]	2.427(9)
Gd(2)–O(8)	2.458(8)	Gd(2)–O(4)	2.483(10)
Gd(2)–O(3)	2.537(9)	Gd(2)–O(7)	2.562(9)
O(12)–Gd(1)–O(7)	75.8(3)	O(12)–Gd(1)–O(10)	75.2(4)
O(7)–Gd(1)–O(10)	119.3(3)	O(12)–Gd(1)–O(1W)	78.1(4)
O(12)–Gd(1)–O(3)[a]	139.7(3)	O(7)–Gd(1)–O(3)[a]	142.8(3)
O(12)–Gd(1)–O(2)	75.7(3)	O(12)–Gd(1)–O(5)[a]	142.2(3)
O(12)–Gd(1)–O(1)	125.4(3)	O(7)–Gd(1)–O(1)	101.3(3)
O(2W)–Gd(2)–O(1)[b]	142.7(3)	O(6)–Gd(2)–O(8)	79.0(3)
O(11)–Gd(2)–O(4)	113.7(4)	O(9)–Gd(2)–O(4)	75.2(3)
O(9)–Gd(2)–O(3)	99.7(3)	O(8)–Gd(2)–O(3)	140.6(3)
O(6)–Gd(2)–O(7)	124.6(3)	O(2W)–Gd(2)–O(7)	72.2(3)
O(3)–Gd(2)–O(7)	155.9(3)	C(9)–C(10)–C(11)[d]–C(12)[d]	89.4(12)
C(5)–C(6)–C(7)[c]–C(8)[c]	–70.7(14)	C(1)–C(2)–C(3)[e]–C(4)[e]	178.8(11)

Symmetry transformations used to generate equivalent atoms: [a] (I): *x* + 1, *y*, *z*. [b] (II): *x* – 1, *y*, *z*. [c] (III): –*x* + 1, –*y* + 2, –*z* + 2. [d] (IV): –*x* + 1, –*y* + 2, –*z* + 1. [e] (V): *x* + 2, *y* – 1, *z*.

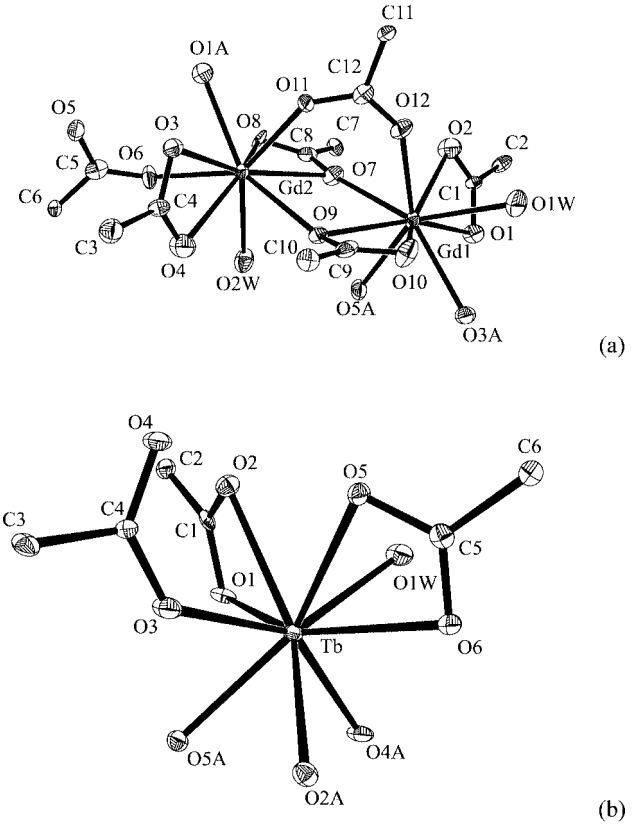

Figure 1. (a) Coordination environment of the complex [$Gd_2L_3(H_2O)_2$]$_n$ (**1**) with ellipsoids drawn at 50% probability level; for clarity, all hydrogen atoms are omitted and only the asymmetric half of the succinato ligand is shown; symmetry code: (A) = *x* + 1, *y*, *z*; (b) coordination environment of **2**; lattice water molecule and all hydrogen atoms omitted for clarity, and thermal ellipsoids shown at 50% probability; symmetry code: (A) = –*x* + ½, *y* – ½, –*z* + ½

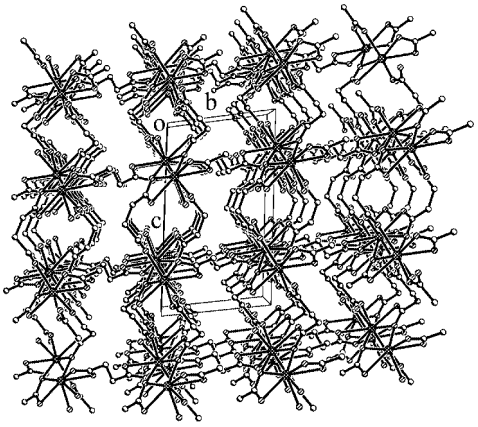

Figure 2. 3D framework of **1** projected down the 1D chain; hydrogen atoms omitted for clarity

 © 2005 Wiley-VCH Verlag GmbH & Co. KGaA, Weinheim

{[TbL$_{1.5}$(H$_2$O)]·0.5H$_2$O}$_n$ (2)

Complex **2** also has a 3D framework, but differs from complex **1**, containing a mononuclear asymmetric unit that consists of a terbium(III) ion, a coordinating water molecule, 1½ succinate ions as well as ½ a guest water molecule. The terbium(III) ion is also ninefold coordinated by eight oxygen atoms from six carboxylate groups and one water oxygen atom. All oxygen atoms around the Tb^{III} ion form a TbO_9 unit that can be viewed as a tricapped trigonal prism. Tb–O bond lengths are in the range 2.294(4)–2.507(4) Å, which are consistent with that of a previously reported carboxylate-containing terbium complex [2.264(6)–2.533(6) Å].[7b] Table 2 gives selected bond lengths and angles. Along the *b* axis, the TbO_9 polyhedra extend to a 1D zigzag chain by sharing the polyhedron edge. The 1D metal oxide like chains are linked by carbon chains of the ligands to form a 3D metal-organic framework (3D MOF). Although the succinato ligands function in the same modes as in **1**, there are 1D channels that include guest water molecules in the 3D MOF and only one Tb···Tb separation [4.0211(5) Å] in the metal oxide like chains. Guest water molecules are bound to the framework through weak hydrogen bonds, O(2W)–H(2WB)···O(1W) (Table 3). However, the conformations of the carbon–hydrogen chains of the succinato ligands differ slightly from that of **1**. There are just two conformations of the carbon chains in **2** (Figure 3), a *gauche*-staggered with a torsion angle of 72.8(7)° (C1–C2–$C3^V$–$C4^V$, V: x, $y - 1$, $z - 0.5$) and an *anti*-staggered (Table 2). Therefore, the host structural difference between the two complexes is probably caused by the flexibility of the ligand.

Table 2. Selected bond lengths [Å], angles [°] and torsion angles [°] for **2**

Tb(1)–O(4)[a]	2.294(4)	Tb(1)–O(2)[a]	2.395(4)
Tb(1)–O(5)[a]	2.398(4)	Tb(1)–O(3)	2.416(4)
Tb(1)–O(5)	2.441(4)	Tb(1)–O(1W)	2.456(4)
Tb(1)–O(6)	2.462(5)	Tb(1)–O(1)	2.465(4)
Tb(1)–O(2)	2.507(4)	O(4)[a]–Tb(1)–O(2)[a]	77.13(14)
O(4)[a]–Tb(1)–O(5)[a]	75.80(14)	O(2)[a]–Tb(1)–O(5)[a]	68.55(14)
O(4)[a]–Tb(1)–O(6)	85.74(15)	O(2)[a]–Tb(1)–O(6)	71.48(14)
O(4)[a]–Tb(1)–O(1)	82.66(15)	O(2)[a]–Tb(1)–O(1)	137.65(13)
O(2)[a]–Tb(1)–O(2)	152.63(4)	O(5)[a]–Tb(1)–O(2)	104.77(14)
O(3)–Tb(1)–O(2)	78.11(13)	O(5)–Tb(1)–O(2)	66.13(14)
O(1W)–Tb(1)–O(2)	71.45(13)	O(6)–Tb(1)–O(2)	115.54(13)
O(1)–Tb(1)–O(2)	51.65(13)	C(1)–C(2)–C(3)[b]–C(4)[b]	72.8(7)
C(4)–C(3)–C(2)[c]–C(1)[c]	–72.8(7)	C(5)–C(6)–C(6)[d]–C(5)[d]	180.000(1)

Symmetry transformations used to generate equivalent atoms: [a] (I): $-x + 1/2$, $y - 1/2$, $-z + 1/2$. [b] (III): x, $-y + 1$, $z - 1/2$. [c] (IV): x, $-y + 1$, $z + 1/2$. [d] (V): $-x + 1$, $-y + 1$, $-z + 1$.

Table 3. Hydrogen bonds for **2**

D–H···A	*d*(D–H) [Å]	*d*(H···A) [Å]	*d*(D···A) [Å]	<(DHA) [°]
O(1W)–H(1WB)···O(3)[a]	0.85	2.14	2.853(6)	141.4
O(1W)–H(1WA)···O(1)[b]	0.85	1.86	2.707(6)	173.4
O(2W)–H(2WB)···O(1W)	0.85	2.22	2.927(5)	140.5

Symmetry transformations used to generate equivalent atoms: [a] (II): $-x + 1/2$, $y + 1/2$, $-z + 1/2$. [b] (VI): $-x + 1/2$, $-y + 1/2$, $-z$.

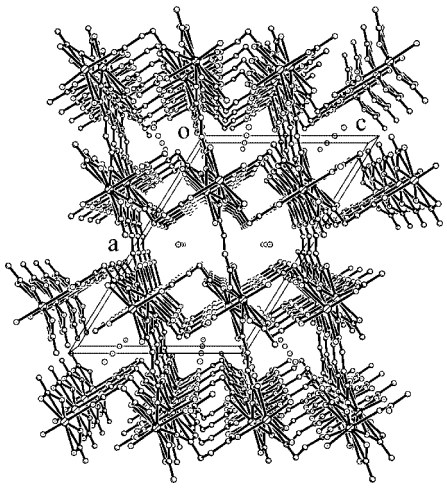

Figure 3. 1D channels including guest water molecules in the 3D frameworks of **2**; all hydrogen atoms omitted for clarity

Thermal Properties

Thermal gravimetric analysis (TGA) is consistent with the X-ray structural results of both coordination polymers. For complex **1**, the gradual weight loss from 115 to 197 °C (5.35%) corresponds to the loss of coordination water molecules (calcd. 5.16%). The complex then decomposes above 404 °C. In contrast, complex **2** shows a sharp weight loss in the range 86–94 °C (3.26%) due to the loss of the guest water (calcd. 2.50%). The thermal analysis curve confirms the presence of guest molecules in the channels of the 3D MOF containing terbium. The second weight-loss (156–202 °C, 5.52%) can be attributed to the loss of coordination water molecules (calcd. 5.13%). Complex **2** decomposes above 400 °C.

Magnetic Properties

The magnetic behavior of complex **1** is represented in Figure 4 as $\chi_M T$ vs. T. At room temperature, $\chi_M T$ is 15.55 $cm^3\,mol^{-1}\,K$, which is close to the value, 15.75 $cm^3\,mol^{-1}\,K$, of two non-interacting Gd^{3+} ions in the $^8S_{7/2}$ ground state. With decreasing temperature, $\chi_M T$ decreases smoothly and reaches a minimum of 15.17 $cm^3\,mol^{-1}$ at 50 K. Below this temperature, $\chi_M T$ increases rapidly, indicating that the ferromagnetic interaction between the Gd^{3+} ions dominates the magnetic properties of complex **1**. This overall feature indicates two conflicting effects. Ferromagnetic interaction between two Gd^{3+} ions increases the molecular magnetism, while some other factors induce the decrease of $\chi_M T$. Similar behavior observed in other lanthanoid-containing complexes[8b,9e] is suggested to arise from the Stark effect caused by the crystal-field perturbation and splitting f orbits. This effect tends to lower the local contributions of the lanthanoid ions.[16] However, the Gd^{3+} ion has a half-filled 4f shell and, to a first approximation, its ground state must not split in ligand fields. Actually, the crystal field distorts the ion symmetry and the degeneracy is broken partly, and a slight splitting always

 © 2005 Wiley-VCH Verlag GmbH & Co. KGaA, Weinheim

occurs. Generally, the Stark effect for Gd^{III} is of the order of 0.05 cm^{-1}, which is not enough to decrease $\chi_M T$ in the range 50–300 K. In both $GdCl_3$ and $Gd(OH)_3$, both ferromagnetic and antiferromagnetic interactions are present. They arise from the usual Heisenberg form of the exchange plus magnetic-dipole interaction and they do not change appreciably below 77 K.[17–19] The nearest-neighbor (J_{nn}) interactions (*nn* pairs) are antiferromagnetic while those of the next-nearest neighbor (J_{nnn}) interactions (*nnn* pairs) are ferromagnetic. The observed magnetic behavior depends on the dominant interaction. The description of this system closely follows the spin-wave theory used successfully for 3d ions.[19] In complex **1**, the two Gd–Gd separations mentioned above probably make the *nn* and *nnn* pairs, such as Gd1–Gd2 and Gd2–Gd1′. The *nnn* pairs could not, seemingly, be Gd1–Gd1′ or Gd2–Gd2′, because the shortest distance between them is ca. 7.707 Å. Interaction at this distance should be very weak and could be neglected. However, it could not be confirmed as intrinsic source. The nature of the Gd···Gd interaction in **1** is supported by magnetization measurements in the 0–7 T range at 1.83 K. The magnetization plot per Gd^{3+} ion closely follows the Brillouin function with a theoretical *g* factor (g = 2.0) (Figure 5).[20]

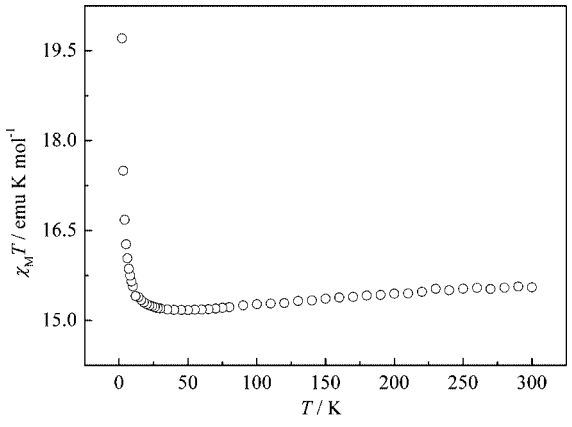

Figure 4. Temperature dependence of $\chi_M T$ for **1**

For complex **2**, $\chi_M T$ increases with decreasing temperature over the whole temperature range (Figure 6), implying that ferromagnetic coupling between Tb^{3+} ions dominates the magnetic properties. At room temperature, $\chi_M T$ is 23.10 $cm^3\ mol^{-1}$ K, which is close to the value of two non-interacting Tb^{3+} ions in the $^7F_6$ ground state (11.82 $cm^3\ mol^{-1}$ per Tb^{3+} ion).[20] $\chi_M T$ increases steadily from 300 to 20 K, and then increases rapidly on further cooling to 1.8 K. All these data indicate a ferromagnetic interaction between two terbium ions in **2**. AC magnetic measurements show a strong temperature dependence of both in-phase magnetization, χ', and out-of-phase magnetization, χ''. Both χ' and χ'' sharply increase below 4 K, suggesting long-range ordering in **1**. The ordering temperature is <1.8 K because no peaks are observed in χ' and χ'' vs. T plots (Figure 7). This appears to be the first observation of long-range ordering in fully structurally characterized lanthanoid-containing coordination compounds that display a ferromagnetic interaction.

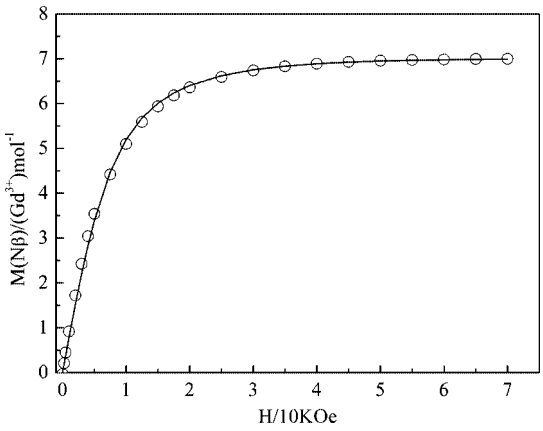

Figure 5. Field dependence of the magnetization for **1** at 1.83 K (circles); the solid line represents the Brillouin function for two magnetically isolated Gd^{III} ions with g = 2.0

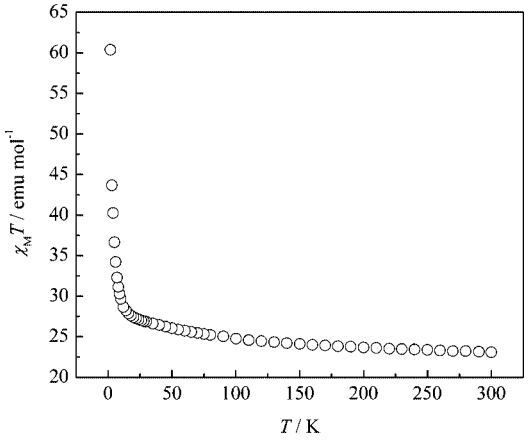

Figure 6.Temperature dependence of $\chi_M T$ for **2**

The magnetic properties of most lanthanoid ions are strongly influenced by their rather large unquenched orbital angular momentum associated with the internal nature of the valence f orbits.[20] This is one reason why lanthanoid compounds are widely applied in magnet technology, but also accounts for the difficulty in studying their magnetic properties. Recent interest has focused on the magnetic behavior of the f-block coordination compounds.[8–10,21] Only two examples of well-characterized lanthanoid complexes containing gadolinium display ferromagnetic interaction between lanthanoid ions;[9c,d] others have observed ferromagnetism in dinuclear triple-decker complexes that include Tb, Dy and Ho, but without structural characterization.[21] The ferromagnetic interaction observed here in the gadolinium carboxylate compound probably arises from the accidental orthogonality between the magnetic orbitals of the two interacting Gd^{III} ions, the angle at the oxo bridge, and the Gd···Gd separation through it.[9c]

 © 2005 Wiley-VCH Verlag GmbH & Co. KGaA, Weinheim

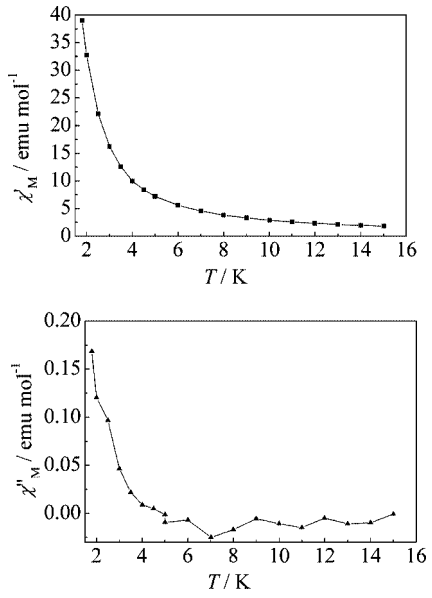

Figure 7. χ'_M(top) and χ''_M (bottom) vs. T, where χ'_M and χ''_M are in-phase-AC and out-of-phase-AC molar magnetic susceptibilities, respectively

Fluorescent Properties

Complex **2** emits an intense green light in the solid state at room temperature. Excitation and emission spectra (Figure 8) show typical Tb^{III} excitation peaks at 319 ($^7F_6 \rightarrow {}^5D_0$), 342 ($^7F_6 \rightarrow {}^5L_7$), 352 ($^7F_6 \rightarrow {}^5L_9$), 370 ($^7F_6 \rightarrow {}^5G_5$) and 379 nm ($^7F_6 \rightarrow {}^5G_6$), indicating that direct excitation of the terbium ion operates in complex **2** when emission at 544 nm is observed. The emission spectra are almost identical when excited at 352 and 370 nm. Emission peaks at 489, 544, 585 and 621 nm can be assigned to $^5D_4 \rightarrow {}^7F_n$ (n = 6, 5, 4, 3) transitions, respectively. The most intense emission, at 544 nm ($^5D_4 \rightarrow {}^7F_5$), is a magnetic dipole transition (ΔJ = ±1). Both excitation and emission spectra agree well with the spectra of a terbium-ion-doped inorganic ceramic.[22]

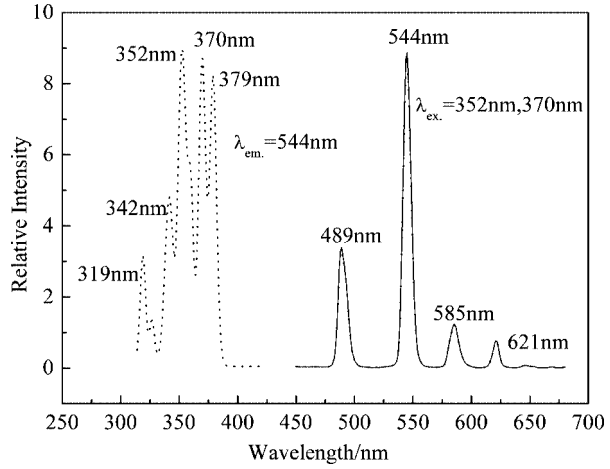

Figure 8. Excitation (dotted line) and emission (solid line) spectra of 2 in the solid state

Conclusions

Magnetic properties of the coordination frameworks in **1** and **2**, along with the fluorescence of **2**, support their structural motif. Functional carriers, such as Gd^{III} or Tb^{III} ions as the spin carriers and Tb^{III} ions as the luminescent centers, can be arranged into a special solid-state structure by the support or connection of the ligands, e.g. a 3D array of 1D chains. Such solids can display properties induced by the metals ions. Especially, the 3D framework consisting of terbium ions integrates ferromagnetic, fluorescent and porous properties into a single entity. This approach probably makes some coordination polymers promising candidates for new multifunctional molecular-based materials.

Experimental Section

Materials and Methods: All starting materials were purchased from China Medicine (Group) Shanghai Chemical Reagent Corporation and used without further purification. Elemental analyses were carried out with a Perkin–Elmer 240C elemental analyzer. IR spectra were recorded with a Bruker VECTOR22 FT-IR spectrometer using the KBr pellet technique. Thermogravimetric analyses (TGA) were performed with a TA-SDT 2960 thermal analyzer at a heating rate of 10 °Cmin^{-1} from room temperature to 600 °C under nitrogen. The solid-state excitation-emission spectrum was acquired with an AMINCO•Bowman Series AB2 Luminescence Spectrometer at room temperature. Magnetic susceptibilities were measured with a Mag Lab2000 system and a SQUID MPMS XL magnetometer. Diamagnetic corrections were made using Pascal's constants.

Syntheses and Characterization

$[Gd_2L_3(H_2O)_2]_n$ (1): A mixture of $Gd(NO_3)_3$•$6H_2O$ (45.3 mg, 0.1 mmol), succinic acid (18 mg, 0.15 mmol), NaOH (12 mg, 0.3 mmol), and H_2O (10 mL) was sealed in a 25-mL stainless-steel reactor with a Teflon liner and heated to 170 °C. After 3 d at 170 °C, the mixture was then cooled to room temperature. Colorless block-like crystals of **1** were obtained in 77.0% yield (53.8 mg) after filtration and washing with water. $C_{12}H_{16}Gd_2O_{14}$ (698.75): calcd. C 20.63, H 2.31; found C 20.62, H 2.37. IR (KBr, cm^{-1}): $\tilde{\nu}$ = 3300 (m, br.), 2983 (w), 2947 (w), 2925 (w), 2913(w), 1572 (vs, sh), 1427 (vs, sh), 1304 (s), 1215 (s), 1176 (s), 1002 (m), 909 (m), 691 (s), 652 (s), 572 (m).

$\{[TbL_{1.5}(H_2O)]\cdot 0.5H_2O\}_n$ (2): A mixture of $Tb(NO_3)_3$•$6H_2O$ (45.5 mg, 0.1 mmol), succinic acid (18 mg, 0.15 mmol), NaOH (12 mg, 0.3 mmol), and H_2O (10 mL) was sealed in a 25-mL stainless-steel reactor with Teflon liner and heated to 170 °C, kept at 170 °C for 3 d, then cooled to room temperature. Colorless block-like crystals of **2** were obtained in 69.0% yield (49.7 mg) after filtration and washed with water. $C_{12}H_{18}O_{15}Tb_2$ (720.10): calcd. C 20.02, H 2.52; found C 20.08, H 2.44. IR (KBr, cm^{-1}): $\tilde{\nu}$ = 3302 (m, br), 2983 (w), 2948 (w), 2925 (w), 2914 (w), 1576 (vs, sh), 1429 (vs, sh), 1304 (s), 1215 (s), 1176 (s), 1002 (m), 909 (m), 691 (s), 653 (s), 572 (m).

Crystallography

$[Gd_2L_3(H_2O)_2]_n$ (1): A single crystal (0.21×0.16×0.12 mm) was used for structural determination with an Enraf-Nonius CAD-4 diffractometer with graphite-monochromatized Mo-K_α radiation (λ = 0.71073) using an ω-2θ scan mode at 293 K. Intensity data were collected in the θ range 2.75–25.00°, data reduction was made with the MolEN package.[23] Absorption corrections from ψ scans were

 © 2005 Wiley-VCH Verlag GmbH & Co. KGaA, Weinheim

applied. The structure was solved by direct methods using SHELXS-97 [24] and refined on F^2 by full-matrix least squares using SHELXL-97 with anisotropic displacement parameters for all non-hydrogen atoms.[25] Hydrogen atom positions were fixed geometrically at calculated distances and allowed to ride on the parent atoms. Relevant crystallographic data are presented in Table 4.

Table 4. Crystallographic data for complexes **1** and **2**

	1	**2**
Empirical formula	$C_{12}H_{16}Gd_2O_{14}$	$C_{12}H_{18}O_{15}Tb_2$
Formula mass	698.75	720.10
Crystal system	triclinic	monoclinic
Space group	$P\bar{1}$	$C2/c$
T [K]	293(2)	293(2)
a [Å]	7.7070(15)	19.919(3)
b [Å]	8.0490(16)	7.7119(11)
c [Å]	14.128(3)	13.807(2)
α [°]	96.90(3)	90
β [°]	97.03(3)	121.605(2)
γ [°]	103.25(3)	90
V [Å^3]	836.6(3)	1806.4(4)
$D_{calcd.}$ [g cm^{-3}]	2.774	2.648
Z	2	4
μ [mm^{-1}]	7.937	7.847
R_{int}	0.0204	0.0296
Reflections measured	3165	4345
Unique reflections	2928	1592
N(parameters)$_{refined}$	257	132
Goodness-of-fit on F^2	1.004	1.006
R_1 [$I > 2\sigma(I)$][a]	0.0640	0.0253
wR_2 [$I > 2\sigma(I)$][b]	0.1850	0.0581
R_1 (all data)[a]	0.0685	0.0313
wR_2 (all data)[b]	0.1914	0.0592

[a] $R_1 = \Sigma||F_o| - |F_c||/\Sigma|F_o|$. [b] $wR_2 = [\Sigma w(|F_o^2| - |F_c^2|)^2/\Sigma w(|F_o^2|)^2]^{1/2}$.

{[TbL$_{1.5}$(H$_2$O)]·0.5H$_2$O}$_n$ (2): A single crystal (0.20×0.14×0.10 mm) was used for structural determination with a Bruker SMART CCD diffractometer with graphite-monochromatized Mo-K_α radiation (λ = 0.71073) using both Φ- and ω-scan modes at 293 K. Intensity data were collected in the θ range 2.40–25.00°, data reduction was made with the Bruker SAINT package.[26] Absorption corrections were performed using the SADABS program.[27] The structure was solved by direct methods using SHELXS-97 and was refined on F^2 by full-matrix least squares using SHELXL-97 with anisotropic displacement parameters for all non-hydrogen atoms. Hydrogen atoms were introduced in calculations using the riding model. Table 4 gives the relevant crystallographic data.

CCDC-228741 (**2**) and -28742 (**1**) contain the supplementary crystallographic data for this paper. These data can be obtained free of charge at www.ccdc.cam.ac.uk/conts/retrieving.html (or from the Cambridge Crystallographic Data Centre, 12 Union Road, Cambridge CB2 1EZ, UK; Fax: +44-1223-336-033; E-mail: deposit@ccdc.cam.ac.uk).

Acknowledgments

Financial support from the National Natural Science Foundation of China and the Major State Basic Research Development Program (G200077500)the Natrual Science Foundation of China and the Natrual Science Foundation of Jangsu Province (No. BK2004414) are gratefully acknowledged. We thank Drs. Dong-Feng Li and. Tian-Wei Wang for their kind help.

[1] a) C. Janiak, *Angew. Chem. Int. Ed. Engl.* **1997**, *36*, 1431–1434; b) S. L. James, *Chem. Soc. Rev.* **2003**, *32*, 276–288.
[2] O. R. Evans, W. Lin, *Acc. Chem. Res.* **2002**, *35*, 511–522.
[3] M. Eddaoudi, D. B. Moler, H. L. Li, B. L. Chen, T. M. Reineke, M. O'Keeffe, O. M. Yaghi, *Acc. Chem. Res.* **2001**, *34*, 319–330.
[4] B. Moulton, M. J. Zaworotko, *Chem. Rev.* **2001**, *101*, 1629–1658.
[5] S. Decurtins, R. Pellaux, G. Antorrena, F. Palacio, *Coord. Chem. Rev.* **1999**, *190–192*, 841–854.
[6] C. Janiak, *J. Chem. Soc., Dalton Trans.* **2003**, 2781–2804.
[7] a) J.-C. G. Bünzli, C. Piguet, *Chem. Rev.* **2002**, *102*, 1897–1928; b) T. M. Reineke, M. Eddaoudi, M. Fehr, D. Kelley, O. M. Yaghi, *J. Am. Chem.Soc.* **1999**, *121*, 1651–1657; c) L. Ma, O. Evans, B. M. Foxman, W. Lin, *Inorg. Chem.* **1999**, *38*, 5837–5840; d) Y. J. Kim, M. Suh, D.-Y. Jung, *Inorg. Chem.* **2004**, *43*, 245–250; e) J.-M. Shi, W. Xu, Q.-Y. Liu, F.-L. Liu, Z.-L. Huang, H. Lei, W.-T. Yu, Q. Fang, *Chem. Commun.* **2002**, 756–757.
[8] a) B.-Q. Ma, D.-S. Zhang, S. Gao, T.-Z. Jin, C-.H. Yan, G.-X. Xu, *Angew. Chem. Int. Ed.* **2000**, *39*, 3644–3646; b) J.-P. Costes, F. Dahan, A. Dupuis, F. Nicodème, *Inorg. Chem.* **2001**, *40*, 5285–5287; c) R. Hedinger, M. Ghisletta, K. Hegetschweiler, E. Toth, A. E. Merbach, R. Sessoli, D. Gatteschi, V. Gramlich, *Inorg. Chem.* **1998**, *37*, 6698–6705; d) X. Zheng, C. Sun, S. Lu, F. Liao, S. Gao, L. Jin, *Eur. J. Inorg. Chem.* **2004**, 3262–3268.
[9] a) J. P. Costes, J. M. Clemente-Juan, F. Dahan, F. Nicodème, *Angew. Chem. Int. Ed.* **2002**, *41*, 323–325; b) J.-P. Costes, F. Nicodème, *Chem. Eur. J.* **2002**, *8*, 3442–3447; c) M. Hernández-Molina, C. Ruiz-Pérez, T. López, F. Lloret, M. Julve, *Inorg. Chem.* **2003**, *42*, 5456–5458; d) J.-P. Costes, J.-M. C. Juan, F. Dahan, F. Nicodème, *J. Chem. Soc.*, *Dalton Trans.* **2003**, 1272–1275; e) X.-J. Zheng, Z.-M. Wang, S. Gao, F.-H. Liao, C.-H. Yan, L.-P. Jin, *Eur. J. Inorg. Chem.* **2004**, 2968–2973.
[10] a) F. Avecilla, C. Platas-Iglesias, R. Rodríguez-Cortiñas, G. Guillemot, J.-C. G. Bünzli, C. D. Brondino, C. F. G. C. Geraldes, A. de Blas, T. Rodríguez-Blas, *J. Chem. Soc., Dalton Trans.* **2002**, 4658–4665; b) A. Dei, D. Gatteschi, C. A. Massa, L. A. Pardi, S. Poussereau, L. Sorace, *Chem. Eur. J.* **2000**, *6*, 4580–4586; c) A. W.-H. Lam, W.-T. Wong, G. Wen, X.-X. Zhang, S. Gao, *New J. Chem.* **2001**, *25*, 531–533.
[11] a) D.-L. Long, A. J. Blake, N. R. Champness, C. Wilson, M. Schröder, *Angew. Chem. Int. Ed.* **2001**, *40*, 2444–2447; b) D.-L. Long, A. J. Blake, N. R. Champness, C. Wilson, M. Schröder, *J. Am. Chem. Soc.* **2001**, *123*, 3401–3402; c) F. A. A. Paz, J. Klinowski, *Chem. Commun.* **2003**, 1484–1485; d) T. M. Reineke, M. Eddaoudi, D. Moler, M. O'Keeffe, O. M.Yaghi, *J. Am. Chem. Soc.* **2000**, *122*, 4843–4844; e) L. Pan, E. B. Woodlock, X. Wang, *Inorg. Chem.* **2000**, *39*, 4174–4178; f) V. Kiritsis, D. Michaelides, S. Skoulika, S. Golhen, L. Ouahab, *Inorg. Chem.* **1998**, *37*, 3407–3410; g) L. Pan, X. Huang, J. Li, Y. Wu, N. Zheng, *Angew. Chem. Int. Ed.* **2000**, *39*, 527–530; h) C. Serre, F. Millange, J. Marrot, G. Férey, *Chem. Mater.* **2002**, *14*, 2409–2415; i) L. Pan, N. Zheng, Y. Wu, S. Han, R. Yang, X. Huang, J. Li, *Inorg. Chem.* **2001**, *40*, 828–830; j) A. Dimos, D. Tsaousis, A. Michaelides, S. Skoulika, S. Golhen, L. Ouahab, C. Didierjean, A. Aubry, *Chem. Mater.* **2002**, *14*, 2616–2622; k) D.-L. Long, A. J. Blake, N. R. Champness, M. Schröder, *Chem. Commun.* **2000**, 1369–1370.
[12] a) C. Livage, C. Egger, G. Férey, *Chem. Mater.* **2001**, *13*, 410–414; b) C. Livage, C. Egger, G. Férey, *Chem. Mater.* **1999**, *11*, 1546–1550; c) P. M. Forster, A. R. Burbank, C. Livage, G. Férey, A. K. Cheetham, *Chem. Commun.* **2004**, 368–369; d) Y. J. Kim, D. Y. Jung, *Bull. Korean Chem. Soc.* **1999**, *20*, 827–830.
[13] a) P. M. Forster, A. K. Cheetham, *Angew. Chem. Int. Ed.* **2002**, *41*, 457–459; b) N. Guillou, C. Livage, W. van Beek, M. Nogues, G. Férey, *Angew. Chem. Int. Ed.* **2003**, *42*, 643–647.

 © 2005 Wiley-VCH Verlag GmbH & Co. KGaA, Weinheim

[14] J. Perles, M. Iglesias, C. Ruiz-Valero, N. Snejko, *Chem. Commun.* **2003**, 346–347.
[15] a) F. Serpaggi, G. Férey, *Microporous Mesoporous Mater.* **1999**, *32*, 311–318; b) M. Fleck, *Z. Kristallogr. NCS* **2002**, *217*, 569–570.
[16] J.-C. G. Bünzli, G. R. Chopin, *Lanthanide Probes in Life, Chemical and Earth Sciences: Theory and Practice*, Elsevier, Amsterdam, **1989**.
[17] M. T. Hutchings, R. J. Birgeneau, W. P. Wolf, *Phys. Rev.* **1968**, *168*, 1026–1044.
[18] R. S. Meltzer, H. W. Moos, *Phys. Rev. B* **1972**, *6*, 264–277.
[19] S. Hüfner, *Optical Spectra of Transparent Rare Earth Compounds*, Academic Press, NewYork, **1978**.
[20] C. Benelli, D. Gatteschi, *Chem. Rev.* **2002**, *102*, 2369–2387.
[21] a) N. Ishikawa, T. Iino, Y. Kaizu, *J. Am. Chem. Soc.* **2002**, *124*, 11440–11447; b) N. Ishikawa, M. Sugita, T. Ishikawa, S. Koshihara, Y. Kaizu, *J. Am. Chem. Soc.* **2003**, *125*, 8694–8695.
[22] C. H. Kam, S. Buddhudu, *Mater. Lett.* **2002**, *54*, 337–342.
[23] C. K. Fair, *MolEN, Structure solution procedures*, Enraf–Nonius, Delft, **1990**.
[24] G. M. Sheldrick, *SHELXS-97, Program for crystal structure solution*, University of Göttingen, **1990**.
[25] G. M. Sheldrick, *SHELXL-97, Program for the refinement of crystal structure from diffraction data*, University of Göttingen, **1997**.
[26] G. M. Sheldrick, *SAINT+, Data integration software*, ver. 6.02a, Bruker AXS Inc., Madison, WI, **1997**.
[27] G. M. Sheldrick, *SADABS, Empirical absorption correction program*, ver. 2.01, University of Göttingen, **1996**.

Received May 7, 2004

 © 2005 Wiley-VCH Verlag GmbH & Co. KGaA, Weinheim

Addition of Carbenes to an Osmium(VI) Nitride Complex

Chi-Fai Leung,[a] Tsz-Wing Wong,[a] Tai-Chu Lau,*[a] and Wing-Tak Wong[b]

Keywords: Carbenes / N,O ligands / Nitrides / Osmium / Vinylidene ligands

A series of osmium(VI) nitride complexes containing 8-quinolinolato ligands, $[Os^{VI}(N)(X\text{-}Q)_2Cl]$ (X = H, 5-Cl, 5-NO_2, 2-Me; **1a**–**d**), have been synthesized by reaction of HX-Q with $[nBu_4N][Os^{VI}(N)Cl_4]$ in the presence of 2,6-dimethylpyridine. The ν(Os≡N) stretches of these compounds occur at 1056–1075 cm^{-1}, and are within the range (1050–1120 cm^{-1}) found for most osmium nitride species. The structure of **1d** has been determined by X-ray crystallography. The osmium center adopts a distorted octahedral geometry, and the two quinolinolato ligands are *cis* to each other. The three N atoms are in a facial arrangement, and the Os≡N bond distance is 1.644(6) Å. Complex **1c** readily reacts with the carbene precursors bis(1,3-dialkylimidazolidin-2-ylidene) ($L^R{}_2$; R = Me, Et, or CH_2Ph) to produce the osmium(IV) azavinylidene species, $[Os^{IV}(N{=}L^R)(NO_2\text{-}Q)_2Cl]$, which are derived from the formal addition of the carbenes L^R to $Os^{VI}{\equiv}N$. The structure of $[Os^{IV}(N{=}L^{Et})(NO_2\text{-}Q)_2Cl]$ (**2b**) has been determined by X-ray crystallography. The osmium center has a distorted octahedral geometry in which the facial arrangement of the three N atoms is retained. The Os(1)–N(5) distance of 1.875(6) Å is rather long and, together with the rather acute Os(1)–N(5)–C(19) angle of 133.8(5)°, indicates that there is no significant multiple-bond character in the Os(1)–N(5) bond.

(© Wiley-VCH Verlag GmbH & Co. KGaA, 69451 Weinheim, Germany, 2005)

Introduction

Osmium(VI) nitride species containing nitrogen-based ligands, such as *cis*- and *trans*-$[Os^{VI}(N)(tpy)Cl_2]^+$ (tpy = 2,2′:6′,2′′-terpyridine), $[Os^{VI}(N)(tpm)Cl_2]^+$ [tpm = tris(1-pyrazolyl)methane], $[Os^{VI}(N)(Tp)Cl_2]$ [Tp^- = hydrotris(1-pyrazolyl)borate], and $[Os^{VI}(N)(bpy)Cl_3]$ (bpy = 2,2′-bipyridine), have been shown to exhibit novel electrophilic properties.[1–14] A variety of reagents such as phosphanes, amines, cyanide, azide, Grignard reagents, arylboranes, amine *N*-oxides, alkenes, and disubstituted benzenethiols have been reported to add to the nitride ligand.[1–14] These reactions are summarised in Scheme 1.

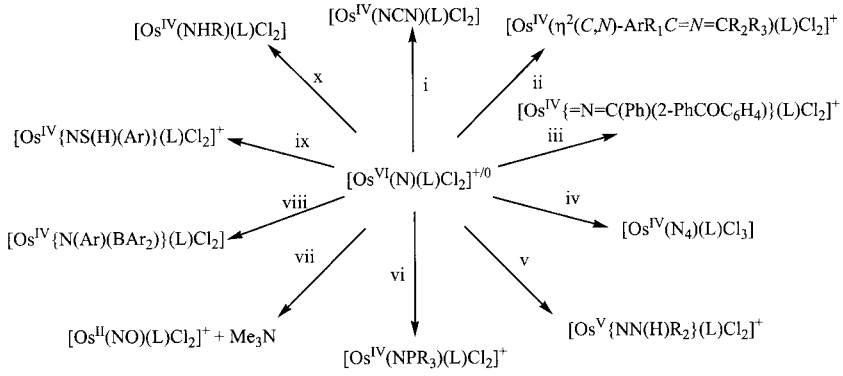

Scheme 1.Electrophilic reactions of osmium(VI) nitrido complexes: i) L = tpy, CN^-; ii) L = tpy, alkenes; iii) L = tpy, 1,3-diphenylisobenzofuran; iv) L = bpy, N_3^-; v) L = tpy/tpm, HNR_2 [R = Et, 1/2$(CH_2)_4O$, 1/2$(CH_2)_4CH_2$]; vi) L = tpy, PR_3; vii) L = tpy, Me_3NO; viii) L = Tp, arylboranes; ix) L = tpy, ArSH (Ar = 3,5-$Me_2C_6H_3$); x) L = Tp, RMgCl

We are interested in tuning the reactivities of these osmium(VI) nitride complexes by replacing tpy or Tp^- with other chelating ligands. We report here the synthesis of a series of new electrophilic osmium(VI) nitride complexes containing 8-quinolinolato ligands. These are the first examples of high-valent osmium complexes containing 8-qui-

[a] Department of Biology and Chemistry, City University of Hong Kong,
Tat Chee Avenue, Hong Kong, China
Fax: +852-2788-7406
E-mail: bhtclau@cityu.edu.hk
[b] Department of Chemistry, The University of Hong Kong, Pokfulam Rd., Hong Kong, China

nolinolato ligands. We also report the reaction of the 5-nitro-8-quinolinolato complex with the carbene precursors bis(1,3-dialkylimidazolidin-2-ylidene) (L^R_2; R = Me, Et, or CH_2Ph) to produce (azavinylidene)osmium(IV) species that are derived from the formal addition of the carbenes L^R to $Os^{VI}{\equiv}N$. This is the first example of the addition of a carbene fragment to a nitride ligand, an important "missing" reaction for electrophilic metal nitride species.

Results and Discussion

Complexes **1a**–**d** were prepared in 55–65% yields from the reaction of $[nBu_4N][Os^{VI}(N)Cl_4]$ with the appropriate 8-hydroxyquinoline at room temperature in methanol in the presence of 2,6-dimethylpyridine, which functions as a mild base (Scheme 2).

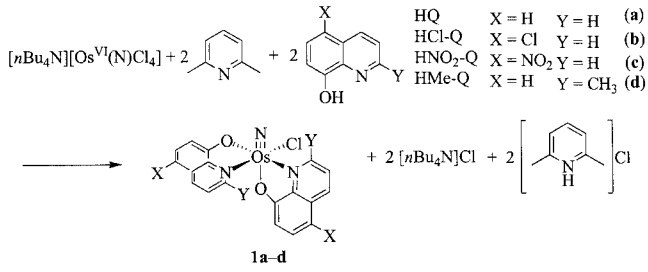

Scheme 2. Preparation of osmium nitride complexes

These complexes are air-stable, diamagnetic, orange crystalline solids. They were characterized by ^1H NMR and IR spectroscopy, and elemental analysis (see Exp. Sect.). The ν(Os≡N) stretches of these complexes occur at 1056–1075 cm^{-1}, and are within the range (1050–1120 cm^{-1}) found for most osmium nitride species.[15–17] The assignment of the ν(Os≡N) stretches was supported by ^{15}N labeling. The structure of **1d** was determined by X-ray crystallography (Figure 1). The osmium center adopts a distorted octahedral geometry, and the two quinolinolato ligands are *cis* to each other. The three N atoms are in a facial arrangement. The Os≡N bond length of 1.644(6) Å is within the range (1.52–1.70 Å) found for other osmium nitride complexes.[3,17,18] The Os(1)–O(2) and Os(1)–O(1) bond lengths are 2.111(4) and 1.974(4) Å, respectively. The long Os(1)–O(2) distance reflects the rather large *trans* influence of the nitride ligand; it is assumed that **1a**–**c** also have the same configuration as **1d**. This is supported by their ^1H NMR spectra, which show that all four complexes have similar patterns.

The reaction of **1c** with bis(1,3-dialkylimidazolidin-2-ylidene) (L^R_2; R = Me, Et, or CH_2Ph) in CH_2Cl_2 under argon produces the (azavinylidene)osmium(IV) complexes **2a**–**c** as air-stable, dark-red, rod-shaped crystals in 40–46% yield (Scheme 3). However, no reaction occurs between L^R_2 and **1a**, **1b**, or **1d**.Complex **1c** is expected to be the most electrophilic among the four nitride species due to the presence of the electron-withdrawing nitro group in the 8-quinolinolato ligand.

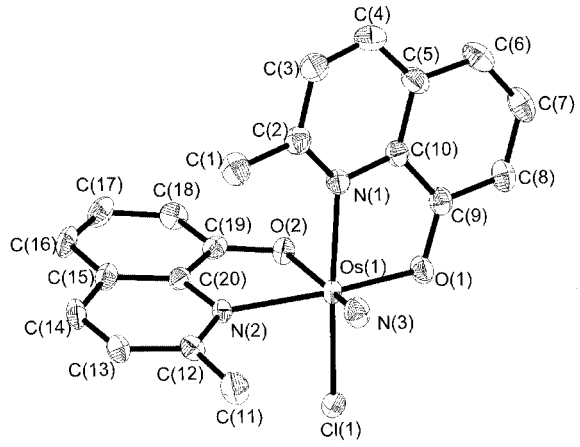

Figure 1.Molecular structure of **1d**

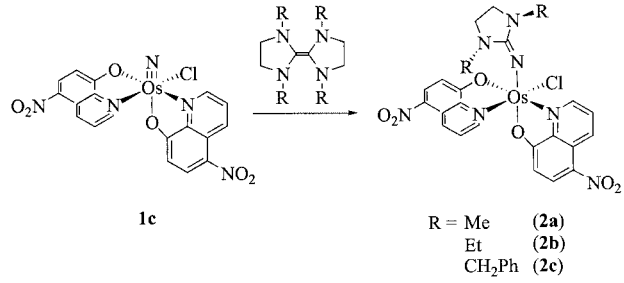

Scheme 3. Reaction of osmium nitride complex **1c** with L^R_2

The IR spectra (KBr) of the osmium(IV) complexes **2a**–**c** exhibit bands at around 2900 cm^{-1}, which correspond to the aliphatic C–H stretches of the alkyl groups on the imidazolin-2-ylidene ring. Complex **2b** has a room-temperature magnetic moment of 2.07 μ_B, which is consistent with its formulation as a d^4 Os^{IV} complex with a $d\pi_1^2$ $d\pi_2^1$ $d\pi_3^1$ electronic configuration. (Phosphoraniminato)osmium(IV) complexes have slightly lower magnetic moments of around 1.8 μ_B.[18,19] These magnetic moments are much lower than the spin-only value of 2.8 μ_B due to spin-orbit coupling.

The structure of **2b** was determined by X-ray crystallography (Figure 2). The osmium center has a distorted octahedral geometry in which the facial arrangement of the three N atoms is retained. The Os(1)–N(5) distance of 1.875(6) Å is within the range found for other (azavinylidene)osmium complexes (1.78–1.88 Å).[13,20] The Os(1)–N(5)–C(19) angle of 133.8(5)° is, however, the smallest among (azavinylidene)osmium complexes (152–176°).[13,20] The similar Os(1)–O(4) and Os(1)–O(1) distances [2.019(3) and 2.048(4) Å respectively] indicate that the *trans* influence of the azavinylidene ligand is negligible.

Complexes **2a**–**c** have extensive redox chemistry. Figure 3 displays the cyclic voltammogram of **2b** in CH_3CN (0.1 M $[nBu_4N][PF_6]$) recorded at a glassy-carbon working electrode. Three reversible waves appear at $E_{1/2}$ = +1.06 V (ΔE_p = 66 mV), +0.05 V (ΔE_p = 56 mV), and –0.95 V (ΔE_p = 64 mV) vs. ferrocenium/ferrocene (Fc^+/Fc), which are assigned to metal-centered $Os^{VI/V}$, $Os^{V/IV}$, and $Os^{IV/III}$ couples, respectively (Figure 3). There is also a quasi-reversible wave

 © 2005 Wiley-VCH Verlag GmbH & Co. KGaA, Weinheim

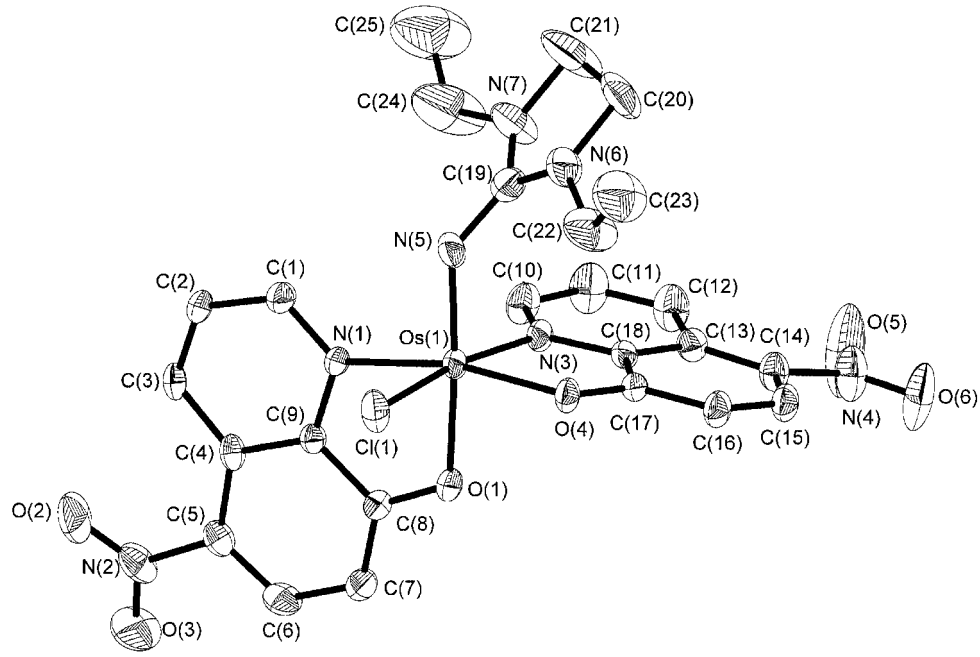

Figure 2. Molecular structure of **2b**

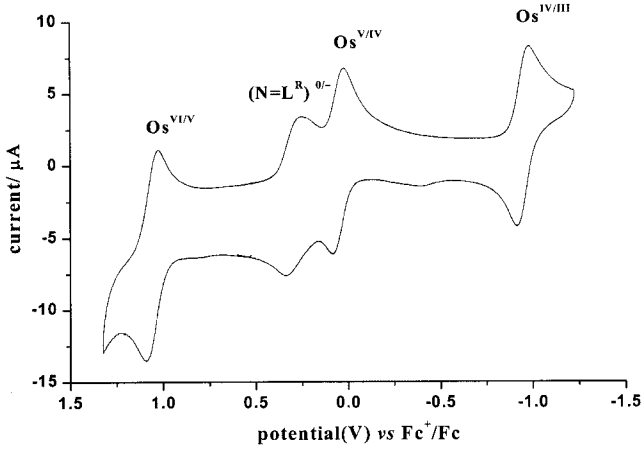

Figure 3. Cyclic voltammogram of $[Os^{IV}(N=L^{Et})(NO_2\text{-}Q)_2Cl]$ (**2b**) in CH_3CN (0.1 M $[nBu_4N][PF_6]$), scan rate = 100 mV s^{-1}

at $E_{1/2}$ = +0.29 V (ΔE_p = 86 mV), which is assigned to oxidation of the azavinylidene ligand, $(N=L^{Et})^- \rightarrow (N=L^{Et})$. The electrochemistry of **2b** is represented by Equation (1).

$$[Os^{VI}\{(N=L^{Et})^0\}(NO_2\text{-}Q)_2Cl]^{3+} \underset{-e}{\overset{+e}{\rightleftharpoons}} [Os^{V}\{(N=L^{Et})^0\}(NO_2\text{-}Q)_2Cl]^{2+} \underset{-e}{\overset{+e}{\rightleftharpoons}}$$
$$[Os^{IV}\{(N=L^{Et})\}(NO_2\text{-}Q)_2Cl] \underset{-e}{\overset{+e}{\rightleftharpoons}} [Os^{III}\{(N=L^{Et})\}(NO_2\text{-}Q)_2Cl] \quad (1)$$

Similar electrochemical behavior is found for **2a** and **2c**; the electrochemical data for **2a**–**c** are collected in Table 1. The $E_{1/2}$ of the quasi-reversible wave shifts from 0.29 V to 0.24 V on going from CH_3 or C_2H_5 to the more electron-rich CH_2Ph substituent, in accordance with its assignment as a ligand-centered redox couple.

Table 1. Electrochemical data for $[Os^{IV}(N=L^R)(NO_2\text{-}Q)_2Cl]$ (**2a**–**c**) in 0.1 M $[nBu_4N][PF_6]/CH_3CN$; scan rate = 100 mV s^{-1}; the errors in the potentials are typically 10 mV

	$E_{1/2}$ [V vs. Fc/Fc^+]			
	$Os^{VI/V}$	$(N=L^R)^{0/-}$	$Os^{V/IV}$	$Os^{IV/III}$
2a (R = Me)	1.06	0.29	0.06	–0.96
2b (R = Et)	1.06	0.29	0.05	–0.95
2c (R = CH_2Ph)	1.05	0.24	0.03	–1.01

The electron-rich alkenes $L^R{}_2$ are well-known carbene precursors; they react with a variety of transition-metal complexes to produce carbene complexes of the type $M=L^R$.[21,22] The work reported here, however, is the first example of the reaction of $L^R{}_2$ with a nitride complex that results in the formal addition of the carbene L^R to the nitride ligand. A similar, but much faster, reaction occurs between **1c** and the stable, commercially available carbene L^R (R = *tert*-butyl, 1,3-di-*tert*-butylimidazol-2-lylidene); however, in this case, attempts to purify the product have so far been unsuccessful. A proposed mechanism for the reaction of Os≡N with $L^R{}_2$, which is similar to that proposed for the formation of (carbene)metal compounds between metal complexes and $L^R{}_2$,[21] is shown in Scheme 4. It is generally believed that $L^R{}_2$ does not dissociate into the free carbene L^R prior to reaction with metal complexes. Hence, we suggest that $L^R{}_2$ reacts directly with Os≡N to produce the (azavinylidene)Os^{IV} compound.

 © 2005 Wiley-VCH Verlag GmbH & Co. KGaA, Weinheim

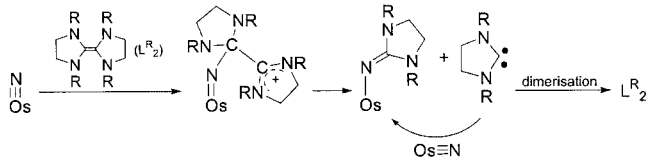

Scheme 4. Proposed mechanism for the reaction of Os≡N with L^R_2

Conclusions

A series of osmium(VI) nitride complexes containing 8-quinolinolato ligands, $[Os^{VI}(N)(X\text{-}Q)_2Cl]$ (X = H, 5-Cl, 5-NO_2, 2-Me; **1a**–**d**), have been synthesized by reaction of HX-Q with $[nBu_4N][Os^{VI}(N)Cl_4]$ in the presence of 2,6-dimethylpyridine. Among these complexes **1c** is the most electrophilic, and it reacts readily with the carbene precursors bis(1,3-dialkylimidazolidin-2-ylidene) (L^R_2; R = Me, Et, or CH_2Ph) to produce a series of (azavinylidene)osmium(IV) species, $[Os^{IV}(N{=}L^R)(NO_2\text{-}Q)_2Cl]$, that are derived from the formal addition of the carbenes L^R to $Os^{VI}{\equiv}N$.

Experimental Section

Reagents and Physical Measurements: The complexes $[nBu_4N][Os^{VI}(N)Cl_4]$ and $[nBu_4N][Os^{VI}(^{15}N)Cl_4]$[23,24] and the electron-rich olefins bis(1,3-dialkylimidazolidin-2-ylidene)[25] were prepared by literature procedures. Acetonitrile was first heated to reflux in the presence of calcium hydride and then distilled under argon. Tetrabutylammonium hexafluorophosphate (Aldrich) was recrystallized three times from boiling ethanol and dried in vacuo at 120 °C for 1 d before use. The 8-hydroxyquinoline ligands were purchased from Aldrich and were used as received. All other chemicals were of reagent grade and used without further purification. IR spectra were obtained from KBr discs with a Bomen MB-120 FTIR spectrophotometer. UV/Vis spectra were recorded with either a Perkin–Elmer Lamda 19 or a Shimadzu UV3100 spectrophotometer. ^{1}H NMR spectra were recorded with a Varian (300MHz) FT NMR spectrometer. The chemical shifts (δ, ppm) are reported relative to tetramethylsilane (TMS). Elemental analyses were performed with an Elementar Vario EL Analyzer. Cyclic voltammograms were obtained with a PAR model 273 potentiostat. A glassy-carbon disk working electrode and an $Ag/AgNO_3$ reference electrode were used. The supporting electrolyte was 0.1 M $[nBu_4N]PF_6$ in CH_3CN.

$[Os^{VI}(N)(Q)_2Cl]$ (1a): 8-Hydroxyquinoline (HQ; 50 mg, 0.34 mmol) was added to a solution of $[nBu_4N][Os^{VI}(N)Cl_4]$ (100 mg, 0.17 mmol) in 10 mL of methanol. After stirring for 15 min, 2,6-lutidine (0.5 mL) was added and the resulting orange solution was stirred for another 30 min. The orange solid was collected by filtration, washed with methanol, and dried in vacuo. Yield 47 mg (53%). $C_{18}H_{12}ClN_3O_2Os$ (528.01): calcd. C 40.95, H 2.27, N 7.96; found C 41.07, H 2.52, N 7.82. UV/Vis (DMF): λ_{max} = 266 nm (ε = 38700 dm^3 mol^{-1} cm^{-1}), 340 (3790), 407 (6710). IR (KBr): $\tilde{\nu}$ = 1573 cm^{-1} (s), 1500 (s), 1464 (s), 1381 (s), 1319 (s), 1056 (w, OsN) [1025 (w, $Os^{15}N$)]. ^{1}H NMR (300 MHz, [D$_6$]DMSO): δ = 6.57 (d, 1 H), 7.27 (d, 1 H), 7.46 (t, 1 H), 7.61 (m, 3 H), 7.80 (t, 1 H), 7.94 (m, 1 H), 8.32 (d, 1 H), 8.73 (d, 1 H), 8.82 (d, 1 H), 9.25 (d, 1 H) ppm.

$[Os^{VI}(N)(Cl\text{-}Q)_2Cl]$ (1b): This complex was prepared by a procedure similar to that for **1a** using 5-chloro-8-hydroxyquinoline (61 mg, 0.34 mmol). Yield 58 mg (57%). $C_{18}H_{10}Cl_3N_3O_2Os$ (596.92): calcd. C 36.22, H 1.69, N 7.04; found: C, 35.89, H 1.86, N 6.83. UV/Vis (DMF): λ_{max} = 269 nm (ε = 13800 dm^3 mol^{-1} cm^{-1}), 419 (3030). IR (KBr): $\tilde{\nu}$ = 1570 cm^{-1} (w), 1498 (s), 1457 (s), 1368 (s), 1302 (w), 1058 (w, OsN) [1027 (w, OsN^{15})]. ^{1}H NMR (300 MHz, [D$_6$]DMSO): δ = 6.58 (d, 1 H), 7.61 (d, 1 H), 7.63 (d, 1 H), 7.78 (m, 1 H), 8.54 (d, 1 H), 8.87 (m, 2 H), 8.37 (d, 1 H) ppm.

$[Os^{VI}(N)(NO_2\text{-}Q)_2Cl]$ (1c): This complex was prepared by a procedure similar to that for **1a** using 8-hydroxy-5-nitroquinoline (65 mg, 0.34 mmol). Yield 66 mg (63%). $C_{18}H_{10}ClN_5O_6Os$ (618.01): calcd. C 34.99, H 1.62, N 11.33; found: C, 35.17, H 1.86, N 10.97. UV/Vis (DMF): λ_{max} = 268 nm (ε = 9760 dm^3 mol^{-1} cm^{-1}), 419 (8410). IR (KBr): $\tilde{\nu}$ = 1601 cm^{-1} (w), 1503 (s), 1462 (s), 1298 (vs), 1075 (w, OsN) [1040 (w, $Os^{15}N$)]. ^{1}H NMR (300 MHz, [D$_6$]DMSO): δ = 6.67 (d, 1 H), 7.75 (d, 1 H), 7.86 (m, 1 H), 8.27 (m, 1 H), 8.60 (d, 1 H), 8.82 (d, 1 H), 8.88 (d, 1 H), 9.48 (d, 1 H), 9.58 (m, 2 H) ppm.

$[Os^{VI}(N)(Me\text{-}Q)_2Cl]$ (1d): This orange complex was prepared by a procedure similar to that for **1a** using 8-hydroxy-5-methylquinoline (54 mg, 0.34 mmol). Yield 57 mg (60%). $C_{20}H_{16}ClN_3O_2Os$ (556.07): calcd. C 43.2, H 2.88, N 7.55; found: C, 43.43, H 3.24, N 7.34. UV/Vis (DMF): λ_{max} = 269 nm (ε = 14100 dm^3 mol^{-1} cm^{-1}), 394 (2110). IR (KBr): $\tilde{\nu}$ = 1563 cm^{-1} (s), 1458 (s), 1324 (w), 1268 (w), 1056 (w, OsN) [1024 (w, $Os^{15}N$)]. ^{1}H NMR (300 MHz, [D$_6$]DMSO): δ = 2.15 (s, 3 H), 6.40 (d, 1 H), 7.15 (d, 1 H), 7.27 (t, 1 H), 7.50 (m, 3 H), 7.68 (t, 1 H), 8.00 (d, 1 H), 8.55 (m, 2 H) ppm.

$[Os^{IV}(N{=}L^{Me})(NO_2\text{-}Q)_2Cl]$ (2a): Complex **1c** (100 mg, 0.16 mmol) was added under argon to bis(1,3-dimethylimidazolidin-2-ylidene) L^{Me}_2 (31 mg, 0.16 mmol), in 15 mL of CH_2Cl_2, and the mixture was stirred for 24 h to give a red solution. After filtration, the solution was loaded onto a silica-gel column and eluted with acetone/CH_2Cl_2 (1:5). The red solid was recrystallized from CH_3CN/CH_3OH. Yield 49 mg (43%). $C_{23}H_{20}ClN_7O_6Os$ (716.16): calcd. C 38.57, H 2.82, N 13.69; found: C, 38.74, H 2.87, N 13.51. UV/Vis (CH_2Cl_2): λ_{max} = 254 nm (ε = 40300 dm^3 mol^{-1} cm^{-1}), 301 (17400), 393 (16700), 449 (19800), 480 (19600). IR (KBr): $\tilde{\nu}$ = 3105 cm^{-1} (w, CH), 2878 (w, CH), 1593 (w), 1577 (w), 1559 (s), 1503 (s), 1450 (w), 1409 (w), 1286 (vs), 1186 (w), 1145 (w), 1102 (w), 1010 (w).

$[Os^{IV}(N{=}L^{Et})(NO_2\text{-}Q)_2Cl]$ (2b): This complex was prepared by a procedure similar to that for **2a**, using bis(1,3-diethylimidazolidin-2-ylidene) L^{Et}_2 (41 mg, 0.16 mmol). Crystals suitable for X-ray crystallography were obtained from acetonitrile/methanol. Yield 55 mg (46%). $C_{25}H_{24}ClN_7O_6Os$ (744.21): calcd. C 40.35, H 3.26, N 13.18; found C 40.27, H 3.18, N 12.95. UV/Vis (CH_2Cl_2): λ_{max} = 491 nm (ε = 38800 dm^3 mol^{-1} cm^{-1}), 299 (30800), 393 (31000), 254 (72800). IR (KBr): $\tilde{\nu}$ = 2966 cm^{-1} (w), 2925 (w), 2869 (w, CH), 1596 (w), 1562 (w), 1503 (s), 1453 (w), 1288 (vs, NO), 1186 (w), 1145 (w), 1100 (w), 1009 (w).

$[Os^{IV}(N{=}L^{CH_2Ph})(NO_2\text{-}Q)_2Cl]$ (2c): The complex was prepared by a procedure similar to that for **2a**, using bis(1,3-dibenzylimidazolidin-2-ylidene), $L^{CH_2Ph}_2$ (81 mg, 0.16 mmol). Yield 49 mg (39%). $C_{35}H_{28}ClN_7O_6Os$ (868.32): calcd. C 48.41, H 3.26, N 11.29; found C 48.58, H 3.24, N 11.35. UV/Vis (CH_2Cl_2): λ_{max} = 253 nm (ε = 41800 dm^3 mol^{-1} cm^{-1}), 296 (16900), 378 (17800), 496 (22800). IR (KBr): $\tilde{\nu}$ = 3105 cm^{-1} (w), 3060 (w, CH), 1601 (w), 1505 (s), 1299 (vs, NO), 1193 (w), 1148 (w), 1100 (w), 1071 (w).

X-ray Crystallographic Study: Intensity data were collected at ambient temperature using a Rigaku AFC7R diffractometer with graphite-monochromated Mo-K_α radiation (λ = 0.71069 Å) in the ω-scan mode. Details of the intensity data collection and crystal data are given in Table 2. Selected bond lengths and angles for **1d** and **2b**

are given in Table 3 and Table 4, respectively. The data were corrected for Lorentz and polarization effects. Absorption corrections by the ψ-scan method or an approximation by inter-image scaling were applied. The structures were resolved by direct methods (SIR92[26] or SHELXS-86[27]), and expanded using Fourier techniques (DIRDIF94[28]). Hydrogen atoms are included but not refined. All calculations were performed using the TeXsan[29] crystallographic software package from Molecular Structure Corporation. CCDC-226391 (**1d**) and -226392 (**2b**) contain the supplementary crystallographic data for this paper. These data can be obtained free of charge at www.ccdc.cam.ac.uk/conts/retrieving.html or from the Cambridge Crystallographic Data Centre, 12 Union Road, Cambridge CB2 1EZ, UK (Fax: +44-1223-336-033; E-mail: deposit@ccdc.cam.ac.uk).

Table 2. Summary of crystal data, details of data collection and solution and refinement parameters for **1d** and **2b**

	1d	**2b**
Empirical formula	$C_{20}H_{16}ClN_3O_2Os$	$C_{25}H_{24}ClN_7O_6Os$
M	556.02	744.1
Crystal color, habit	brown, plate	red, plate
Crystal size [mm]	0.25 × 0.22 × 0.04	0.48 × 0.10 × 0.03
Crystal system	triclinic	monoclinic
Space group	$P\bar{1}$ (no. 2)	$P2_1/c$ (no. 14)
a [Å]	9.282(4)	14.154(2)
b [Å]	12.738(5)	13.267(2)
c [Å]	7.686(3)	15.1412(2)
α [°]	94.64(4)	–
β [°]	94.97(4)	110.46(1)
γ [°]	86.22(3)	–
Z	2	4
D_c [g cm^{-3}]	2.050	1.823
F(000)	532.00	1456.00
μ(Mo-K_α) [cm^{-1}]	72.43	48.52
Reflections collected	3381	17117
Unique reflections	3165	6415
R[a]	0.025	0.035
R_w[b]	0.034	0.029
Goodness of fit	1.27	1.09
Max. Δ/σ	0.00	0.00
No. of parameters	244	361
Max., min. residual density [e Å^{-3}]	0.72, –0.55	1.28, –0.56

[a] $R = \Sigma||F_o| - |F_c||/\Sigma|F_o|$. [b] $R_w = [\Sigma w(|F_o| - |F_c|)^2/\Sigma w|F_o|)]^{1/2}$.

Table 3.Selected bond lengths [Å] and angles [°] for [Os^{VI}(N)(Me-Q)$_2$Cl] (**1d**)

Os(1)–N(1)	2.129(5)
Os(1)–N(2)	2.155(4)
Os(1)–N(3)	1.644(6)
Os(1)–O(1)	1.974(4)
Os(1)–O(2)	2.111(4)
Os(1)–Cl(1)	2.347(2)
N(3)–Os(1)–O(1)	103.7(2)
N(3)–Os(1)–O(2)	167.0(2)
N(3)–Os(1)–N(1)	91.1(2)
N(3)–Os(1)–N(2)	94.9(2)
N(3)–Os(1)–Cl(1)	100.7(2)
N(1)–Os(1)–O(1)	81.4(2)
N(2)–Os(1)–O(2)	76.8(2)

Table 4. Selected bond lengths [Å] and angles [°] for [Os(N=L^{Et})(NO$_2$-Q)$_2$Cl] (**2b**)

Os(1)–N(5)	1.875(6)
Os(1)–N(1)	2.083(4)
Os(1)–N(3)	2.059(5)
Os(1)–O(1)	2.048(4)
Os(1)–O(4)	2.019(3)
Os(1)–Cl(1)	2.365(2)
N(5)–C(19)	1.330(8)
N(5)–Os(1)–N(1)	96.0(2)
N(5)–Os(1)–N(3)	92.7(2)
N(5)–Os(1)–O(1)	173.2(2)
N(5)–Os(1)–O(4)	96.5(2)
N(5)–Os(1)–Cl(1)	91.5(2)
N(1)–Os(1)–O(1)	78.1(2)
N(3)–Os(1)–O(4)	79.7(2)
Os(1)–N(5)–C(19)	133.8(5)
N(7)–C(19)–N(6)	110.8(7)

Acknowledgments

This work was supported by the Research Grants Council of Hong Kong (CityU 1117/00P), the City University of Hong Kong (SRG, 7001180) and the University of Hong Kong.

[1] M. H. V. Huynh, P. S. White, C. A. Carter, T. J. Meyer, *Angew. Chem. Int. Ed.* **2001**, *40*, 3037.
[2] M. H. V. Huynh, D. E. Morris, P. S. White, T. J. Meyer, *Angew. Chem. Int. Ed.* **2002**, *41*, 2330.
[3] M. H. V. Huynh, P. S. White, T. J. Meyer, *J. Am. Chem. Soc.* **2001**, *123*, 9170.
[4] M. H. V. Huynh, E.-S. El-Samanody, K. D. Demadis, P. S. White, T. J. Meyer, *J. Am. Chem. Soc.* **1999**, *121*, 1403.
[5] M. Bakir, P. S. White, A. Dovletoglou, T. J. Meyer, *Inorg. Chem.* **1991**, *30*, 2835.
[6] M. H. V. Huynh, P. S. White, T. J. Meyer, *Inorg. Chem.* **2000**, *39*, 2825.
[7] T. J. Crevier, J. M. Mayer, *Angew. Chem. Int. Ed.* **1998**, *37*, 1891.
[8] T. J. Crevier, B. K. Bennett, J. D. Soper, J. A. Bowman, A. Dehestani, D. A. Hrovat, S. Lovell, W. Kaminsky, J. M. Mayer, *J. Am. Chem. Soc.* **2001**, *123*, 1059.
[9] T. J. Crevier, J. M. Mayer, *J. Am. Chem. Soc.* **1998**, *120*, 5595.
[10] M. R. McCarthy, T. J. Crevier, B. K. Bennett, A. Dehestani, J. M. Mayer, *J. Am. Chem. Soc.* **2000**, *122*, 12391.
[11] T. J. Crevier, S. Lovell, J. M. Mayer, *J. Am. Chem. Soc.* **1998**, *120*, 6607.
[12] A. G. Maestri, K. S. Cherry, J. T. Toboni, S. N. Brown, *J. Am. Chem. Soc.* **2001**, *123*, 7459.
[13] S. N. Brown, *Inorg. Chem.* **2000**, *39*, 378.
[14] S. N. Brown, *J. Am. Chem. Soc.* **1999**, *121*, 9752.
[15] E.-S. El-Samanody, K. D. Demandis, T. J. Meyer, P. S. White, *Inorg. Chem.* **2001**, *40*, 3677.
[16] K. Dehnicke, J. Strahle, *Angew. Chem. Int. Ed. Engl.* **1992**, *31*, 955.
[17] P. M. Chan, W. Y. Yu, C. M. Che, K. K. Cheung, *J. Chem. Soc. Dalton Trans.* **1998**, 3183.
[18] T. W. Wong, T. C. Lau, W. T. Wong, *Inorg. Chem.* **1999**, *38*, 6181.
[19] K. D. Demadis, M. Bakir, B. G. Klesczewski, D. S. Williams, P. S. White, T. J. Meyer, *Inorg. Chim. Acta* **1998**, *270*, 511.
[20] a) H. Werner, W. Knaup, M. Dziallas, *Angew. Chem. Int. Ed. Engl.* **1987**, *26*, 248; b) H. Werner, T. Daniel, T. Braun, O. Nürnberg, *J. Organomet. Chem.* **1994**, *480*, 145; c) H. Werner, T. Daniel, M. Müller, N. Mahr, *J. Organomet. Chem.* **1996**, *512*, 197; d) R. Castarleñas, M. A. Esteruelas, E. Gutiérrez-Puebla,

 © 2005 Wiley-VCH Verlag GmbH & Co. KGaA, Weinheim

Y. Jean, A. Lledós, M. Martín, E. Oñate, J. Tomàs. *Organometallics* **2000**, *19*, 3100; e) R. Castarleñas, M. A. Esteruelas, E. Oñate, *Organometallics* **2000**, *19*, 5454; f) R. Castarleñas, M. A. Esteruelas, E. Gutiérrez-Puebla, E. Oñate, *Organometallics* **2001**, *20*, 1545; g) R. Castarleñas, M. A. Esteruelas, E. Oñate, *Organometallics* **2001**, *20*, 3283.
[21] M. F. Lappert, *J. Organomet. Chem.* **1988**, *358*, 185.
[22] D. Bourissou, O. Gurret, F. P. Gabbaï, G. Bertrand, *Chem. Rev.* **2000**, *100*, 39.
[23] C. D. Cowman, W. C. Trogler, K. R. Mann, H. B. Gray, *Inorg. Chem.* **1976**, *15*, 1749.
[24] D. Pawson, W. Griffith, *J. Chem. Soc. Dalton Trans.* **1974**, 417–423.
[25] H. E. Winberg, *Chem. Abstr.* **1966**, *64*, 15854h.
[26] *SIR92*: A. Altomare, G. Cascarano, C. Giacovazzo, A. Guagliardi, *J. Appl. Crystallogr.* **1993**, *26*, 343.
[27] *SHELXS 86, Program for Crystal Structure Solution*: G. M. Sheldrick, *Acta Crystallogr. Sect. A* **1990**, *46*, 467.
[28] *DIRDIF 94*: P. T. Beurskens, G. Admiraal, G. Beurskens, W. P. Bosman, R. de Gelder, R. Israel, J. M. M. Smits, *The DIRDIF 94 program system*, Technical Report of the Crystallography Laboratory, University of Nijmegen, The Netherlands, **1994**.
[29] *TeXsan: Crystal Structure Analysis Package*, Molecular Structure Corporation, The Woodlands, TX, USA, **1985** and **1992**.
Received June 18, 2004

 © 2005 Wiley-VCH Verlag GmbH & Co. KGaA, Weinheim

Bis(1-methylimidazol-2-yl)propionates and Bis(1-methylbenzimidazol-2-yl)-propionates: A New Family of Biomimetic *N,N,O* Ligands – Synthesis, Structures and Cu^{II} Coordination Complexes

Pieter C. A. Bruijnincx,[a] Martin Lutz,[b] Anthony L. Spek,[b][‡] Ernst E. van Faassen,[c] Bert M. Weckhuysen,[d] Gerard van Koten,[a] and Robertus J. M. Klein Gebbink*[a]

Keywords: N,N,O ligands / Ligand design / Facial capping / Copper / Carboxylate ligands

A general synthetic route towards new tridentate, tripodal *N,N,O* ligands, bearing one carboxylate group and two of the biologically relevant imidazole moieties, is presented. The parent compounds of this new family of ligands, A[MIm_2Pr] (**1**) and A[$BenzMIm_2Pr$] (**2**) (A = H, K, Bu_4N) were synthesized in two steps and high overall yield. The structures of $HMIm_2Pr$ (**1a**) and $HBenzMIm_2Pr$ (**2a**) were confirmed by X-ray crystal structure determination, both molecules forming infinite one-dimensional hydrogen bonded chains. The synthetic route allows for the fine-tuning of the physical properties of both ligand systems, e.g., solubility and ease of crystallization. The capability of the two ligands to coordinate facially through all donor atoms was investigated and two isostructural mononuclear copper(II) complexes of the type [CuL_2] were obtained. Both [$Cu(MIm_2Pr)_2$]·$2H_2O$ (**3**) and [$Cu(BenzMIm_2Pr)_2$]·$3.12(H_2O)$·$1.74(C_2H_5OH)$ (**4**) have been characterized by X-ray crystallography, ESI-MS, elemental analysis, UV/Vis, IR, and EPR spectroscopy. In both structures the copper atoms are on an inversion center, which results in a tetragonally distorted octahedral coordination geometry. The CuN_4O_2 chromophores consist of four equatorially coordinated imidazole nitrogen atoms and two axially coordinated carboxylate groups. The non-coordinated water molecules of both crystal structures are involved in a one-dimensional hydrogen-bonded network. Two neighboring octahedrons are connected by two water molecules, each water molecule forming two hydrogen bonds with the non-coordinated oxygen atoms of the carboxylate group. This results in the formation of infinite one-dimensional chains. EPR spectroscopy and ESI-MS measurements provide evidence for the integrity of the complexes in solution.

(© Wiley-VCH Verlag GmbH & Co. KGaA, 69451 Weinheim, Germany, 2005)

Introduction

The study of synthetic active site analogues has made a vast contribution to the understanding of the structure-function relationship of many metalloenzymes, as has been recently highlighted in a thematic review issue.[1] In particular, the use of tripodal ligand systems has received much attention, the most well-known example probably being the tris(pyrazolyl)borates.[2] Despite their remarkable versatility and the impressive results that have been obtained, these "scorpionates" also illustrate two of the drawbacks associated with many of the reported tripodal ligands. First, most ligand systems are fully symmetrical and provide, for instance, an all-*N* donor set. Second, the *N* donor groups are often found to be non-biologically relevant heterocycles (such as pyrazole or pyridine), which differ both in size, and chemical and electronic properties from the histidyl imidazole-side chain found in biological systems. Since the coordination environment of many metalloenzyme active sites is made up of different donor groups, the interest of synthetic chemists has shifted towards the design of *mixed* ligand systems incorporating different functionalities, i.e. "heteroscorpionates".[3]

We are particularly interested in a group of enzymes exhibiting the so-called 2-His-1-carboxylate motif at their active site.[4,5] This structural motif is found in several crystallographically characterized mononuclear non-heme iron enzymes,[5] like deacetoxycephalosporin C synthase (DAOCS)[6] and naphthalene 1,2-dioxygenase (NDO),[7] in which two histidines and one carboxylate occupy one face of the iron(II) coordination environment. The same facial

[a] Debye Institute, Department of Metal-Mediated Synthesis, Utrecht University,
Padualaan 8, 3584 CH Utrecht, The Netherlands
Fax: +31-302523615
E-mail: r.j.m.kleingebbink@chem.uu.nl
[b] Bijvoet Center for Biomolecular Research, Department of Crystal and Structural Chemistry, Utrecht University,
Padualaan 8, 3584 CH Utrecht, The Netherlands
E-mail: a.l.spek@chem.uu.nl
[c] Debye Institute, Department of Surfaces, Interfaces and Devices, Utrecht University,
Princetonlaan 4, 3584 CC Utrecht, The Netherlands
[d] Debye Institute, Department of Inorganic Chemistry and Catalysis, Utrecht University,
Sorbonnelaan 16, 3584 CA Utrecht, The Netherlands
[‡] Correspondence pertaining to crystallographic studies should be addressed to this author.
Supporting information for this article is available on the WWW under http://www.eurjic.org or from the author.

 DOI: 10.1002/ejic.200400830 © 2005 Wiley-VCH Verlag GmbH & Co. KGaA, Weinheim

capping by two histidines and one carboxylate is found in several zinc containing enzymes, e.g. carboxypeptidase and thermolysin.[8] This triad is therefore an interesting target for structural modeling.

Most modeling efforts at mimicking this facial triad used either the tridentate tris(pyrazolyl)borato-*N*,*N*,*N* or the tetradentate tris(2-pyridylmethyl)amine-*N*,*N*,*N*,*N*′ ligands.[5,8] However, suitable structural mimics of this triad should preferably be tridentate, tripodal, monoanionic ligands systems with a potentially facially coordinating *N*,*N*,*O* donor set. *N*,*N*,*O* ligands are relatively rare and, to the best of our knowledge, only three tridentate examples have been reported of these mixed ligands bearing a carboxylate group. The bis(pyrazol-1-yl)acetates were introduced by Otero et al.[9] and have been studied by Burzlaff et al. as mimics of the 2-His-1-carboxylate motif.[10] A drawback of this system is the use of the non-biologically relevant pyrazole groups as the two *N* donor groups. The second example is the bis(imidazolyl)propionato ligand (HBIP) already reported in the late 1970s by Joseph et al.[11] This ligand system, however, suffers from a difficult synthetic route, complicating acid-base chemistry, and limited solubility in non-aqueous media. Parkin indirectly constructed an *N*,*N*,*O* donor set by the insertion of carbon dioxide or formaldehyde into the B–H bond of a [bis(pyrazolyl)hydroborato]zinc complex.[12]

Recently, we became interested in biomimetic ligand systems which in principle could accommodate the desired facial coordination geometry and would incorporate the biologically relevant *N*,*N*,*O* donor atom set. A further requirement would be access to a straightforward synthetic route, which would allow for facile modification of the *N*,*N*,*O* ligands and therefore tuneability of their physical properties.

With this in mind, we have developed a new *N*,*N*,*O* ligand family, i.e. the 3,3-bis(1-methylimidazol-2-yl)- and 3,3-bis(1-methylbenzimidazol-2-yl)propionates **1** and **2**, incorporating the biomimetic 1-methylimidazole and carboxylate groups in a tripodal, monoanionic, tridentate ligand framework (Figure 1).

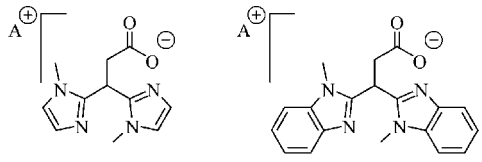

A[MIm$_2$Pr] (1) **A[BenzMIm$_2$Pr] (2)**

Figure 1. *N*,*N*,*O* ligands A[MIm$_2$Pr] (**1**) and A[BenzMIm$_2$Pr] (**2**)

These *N*,*N*,*O* ligands are also of interest in connection with the biomimetic study of copper proteins. Various (polynuclear) copper enzymes are known in which the metal centers are found in an imidazole-rich coordination environment.[13] Furthermore, copper(II) can be used as a probe metal to test the ability of the ligands to facially cap a metal center.[14]

Herein we report the synthesis and structural characterization of two new *N*,*N*,*O* ligands, A[MIm$_2$Pr] (**1**) and A[BenzMIm$_2$Pr] (**2**) (A represents different possible cations), and their copper(II) coordination complexes.

Results

Synthesis and Structural Characterization of the *N*,*N*,*O* Ligands

A general synthetic route for the 3,3-bis(1-methylimidazol-2-yl)- and 3,3-bis(1-methylbenzimidazol-2-yl)propionates was developed (Scheme 1). This route is based on the readily available bis(1-methylimidazol-2-yl)methane framework. Both bis(1-methylimidazol-2-yl)methane (**5**)[15] and bis(1-methylbenzimidazol-2-yl)methane (**6**)[16] can be easily synthesized on a multigram scale.

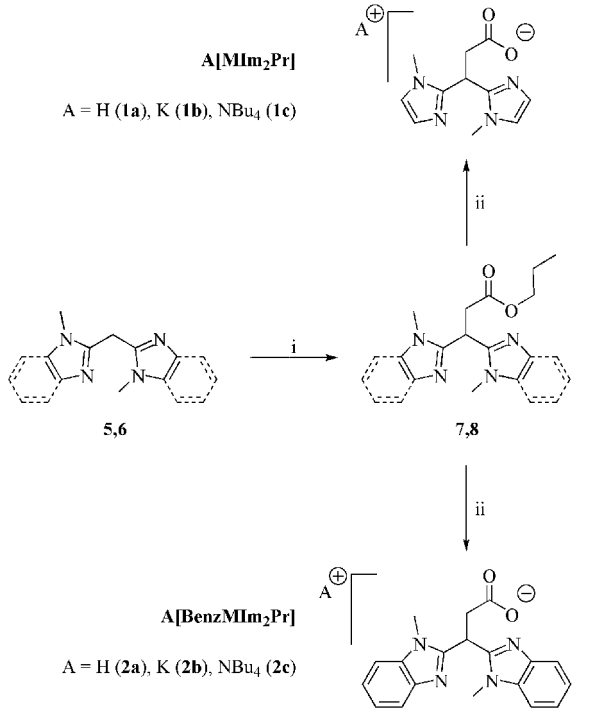

Scheme 1. i) a. *n*-butyllithium, –78 °C, 1 h, b. propyl bromoacetate, –78 °C → room temp., overnight; ii) a. 1 equiv. KOH, room temp., 3 h, b. 1 equiv. HCl (**1a/2a**); 1 equiv. KOH, room temp., 3 h (**1b/2b**); 1 equiv. [Bu$_4$N]OH, room temp., 3 h (**1c/2c**)

Lithiation of **5** and **6** at the bridging methylene group with *n*-butyllithium at –78 °C in THF and subsequent dropwise addition of propyl bromoacetate resulted in the clean formation of the propyl esters MIm$_2$PrPr (**7**) and BenzMIm$_2$PrPr (**8**). Basic hydrolysis of these ligand precursors in THF with 1 equiv. of a potassium hydroxide solution in water gave the potassium salts of 3,3-bis(1-methylimidazol-2-yl)propionic acid, K[MIm$_2$Pr] (**1b**), and 3,3-bis(1-methylbenzimidazol-2-yl)propionic acid, K[BenzMIm$_2$Pr] (**2b**), in quantitative yields. Likewise, treatment of the esters with [Bu$_4$N]OH resulted in the quantita-

 © 2005 Wiley-VCH Verlag GmbH & Co. KGaA, Weinheim

tive formation of the tetrabutylammonium salts [Bu_4N][MIm_2Pr] (**1c**) and [Bu_4N][$BenzMIm_2Pr$] (**2c**). Subsequent addition of 1 equiv. of hydrochloric acid to a solution of the hydrolyzed esters and purification by recrystallization gave 3,3-bis(1-methylimidazol-2-yl)propionic acid, $HMIm_2Pr$ (**1a**), and 3,3-bis(1-methylbenzimidazol-2-yl)propionic acid, $HBenzMIm_2Pr$ (**2a**), in good yields. The propionate salts **1b/1c** and **2b/2c** are very hygroscopic and can only be obtained as fine powders if they are completely solvent-free. This is also reflected in the IR spectra of the compounds. The exact position of the bands depends on the amount of water present in the sample or accumulated during measurement. The carboxylate group asymmetric stretching vibrations $\nu_{as}(COO^-)$ can be found at 1702 (**1a**) and 1716 cm^{-1} (**2a**) for the acids and at 1581 (**1b/1c**) and 1597 (**2c**) for the K and Bu_4N salts. The $\nu_{as}(COO^-)$ of **2b** is split into two bands of equal intensity at 1582 and 1598 cm^{-1}. The symmetric stretch vibration $\nu_s(COO^-)$ is less intense and could only be unambiguously identified for the potassium salts **1b** and **2b** (1393 and 1386 cm^{-1}, respectively).

The molecular structures of acids **1a** and **2a** were studied by single-crystal X-ray diffraction (Figure 2). Suitable single crystals of $HMIm_2Pr$ (**1a**) were obtained by slow vapor diffusion of diethyl ether into a methanolic solution. Recrystallization of the crude product from ethanol/water (95:5) resulted in the formation of a different crystalline phase.[17] Single crystals of $HBenzMIm_2Pr$ (**2a**) were obtained by slow cooling of a hot, saturated solution of **2a** in methanol.

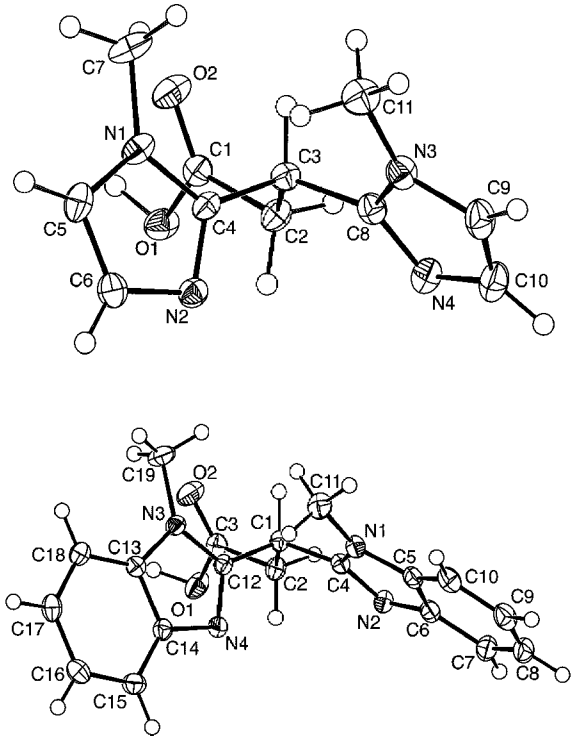

Figure 2. Molecular structure of $HMIm_2Pr{\cdot}MeOH$ (**1a**, top) and $HBenzMIm_2Pr$ (**2a**, bottom) in the crystals; the co-crystallized molecule of methanol (**1a**) has been omitted for clarity; displacement ellipsoids are drawn at the 50 % probability level

The molecular structures of the acids **1a** and **2a** are very similar and their solid-state structures clearly show the general predisposition of tripodal ligands towards facial capping of a metal center.[8b] Rotation around a single C–C bond, i.e. C2–C3 in **1a**, will orient the *N,N,O* lone pairs to a virtual metal center in a facial manner. Interestingly, **1a** and **2a** do not crystallize as zwitterions; the carboxylate oxygen atom O1 is protonated, the imidazole nitrogen atoms are non-protonated. Thus, atom O1 can act as hydrogen-bond donor and the imidazole nitrogen atoms as hydrogen-bond acceptors. In the solid state, molecules of $HMIm_2Pr$ (**1a**) thus form an infinite hydrogen-bonded chain along the crystallographic *c*-axis (Figure 3, Table 1). The co-crystallized methanol solvent molecule is also participating as a hydrogen-bond donor with imidazole nitrogen atom N4 as acceptor. Consequently, both imidazole nitrogen atoms are used for hydrogen bonding. In the crystal structure of **2a**, there are no co-crystallized solvent molecules and therefore only imidazole nitrogen atom N4 accepts hydrogen bonds to form a one-dimensional hydrogen bonded chain along the crystallographic *c*-axis (see Table 1 and Supporting Information). In both crystal structures the non-protonated oxygen atom O2 is not involved in strong hydrogen bonds. Weak C–H···O and C–H···N interactions involve O2 in both structures and nitrogen atom N2 of compound **2a**; π-π stacking interactions between the aromatic systems of the (N1,N2,C4–C10)-benzimidazole rings with average interplanar distances of 3.40 and 3.49 Å are also observed for **2a** (see Supporting Information).

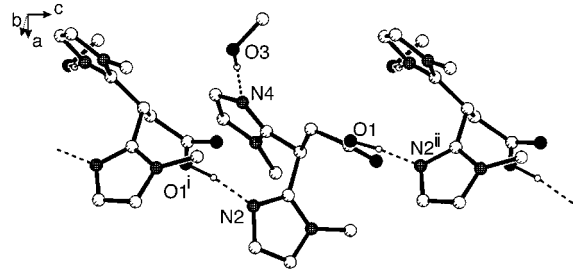

Figure 3. Hydrogen bonding pattern in $HMIm_2Pr$ (**1a**); C–H hydrogen atoms have been omitted for clarity; symmetry operations: i: *x*, 0.5 – *y*, *z* – 0.5; ii: *x*, 0.5 – *y*, *z* + 0.5

Table 1. Selected hydrogen bond lengths [Å] and angles [°] for $HMIm_2Pr{\cdot}CH_3OH$ (**1a**) and $HBenzMIm_2Pr$ (**2a**); symmetry operations: i: *x*, 0.5 – *y*, *z* + 0.5; ii: *x*, 1.5 – *y*, *z* + 0.5

	Donor–H···Acceptor	D–H	H···A	D···A	D–H···A
1a	O1–H1O···N2^{i}	1.02(2)	1.65(2)	2.6649(13)	171(2)
	O3–H3O···N4	0.86(2)	2.01(2)	2.8589(16)	171.8(17)
2a	O1–H1O···N4^{ii}	1.02(2)	1.65(2)	2.6659(13)	171(2)

Synthesis of Cu^{II} Complexes

To investigate the facial capping potential of the new *N,N,O* ligands, their coordination chemistry towards copper(II) cations was investigated. Two new, neutral copper complexes of the type [CuL_2] were synthesized and charac-

 © 2005 Wiley-VCH Verlag GmbH & Co. KGaA, Weinheim

terized by X-ray crystallography, IR, UV/Vis and EPR spectroscopy, and ESI-MS. The mononuclear copper complex $[Cu(MIm_2Pr)_2]\cdot 2H_2O$ (**3**) was obtained by reaction of 1 equiv. of $CuCl_2\cdot 2H_2O$ with 2 equiv. of $K[MIm_2Pr]$ (**1b**) in hot ethanol. Complex **4**, identified as $[Cu(BenzMIm_2Pr)_2]\cdot 3.12(H_2O)\cdot 1.74(C_2H_5OH)$, with a comparable coordination environment was isolated when $CuCl_2\cdot 2H_2O$ was treated with 2 equiv. of $K[BenzMIm_2Pr]$ (**2b**) in hot ethanol. In both cases, blue single crystals suitable for X-ray diffraction analysis crystallized after several weeks. The complexes can also be obtained directly as powders, nicely illustrating how the judicious choice of solvent and ligand cation can simplify isolation and purification (see Discussion section). In this way, reaction of $CuCl_2$ with 2 equiv. of $[Bu_4N][BenzMIm_2Pr]$ (**2c**) in dry methanol resulted in the formation of the pale blue precipitate $[Cu(BenzMIm_2Pr)_2]$. Separation by centrifugation and purification by simple washings with dichloromethane allowed for the facile isolation of the copper complex.

Description of the Crystal Structures

[Cu(MIm$_2$Pr)$_2$]·2H$_2$O (3)

Two monoanionic MIm_2Pr ligands were found to be arranged centrosymmetrically around the copper ion, coordinating through all three donor groups, i.e. two 1-methylimidazole nitrogen atoms and one carboxylate oxygen atom each, resulting in an elongated octahedral geometry (Figure 4). The four 1-methylimidazole imine nitrogen atoms occupy the equatorial plane [Cu–N 2.0109(18) and 1.9929(18) Å] and the two carboxylate oxygen atoms are located in the axial positions [Cu–O 2.4004(17) Å]. Crystallographic data and selected bond lengths and angles are given in Tables 2 and 3. The Cu–N bond lengths are similar to those found in other CuN_4O_2 chromophores with imidazole nitrogen donors.[18,19] The Cu–O bonds are shorter than those found in, for instance, bis(acetato)tetrakis(imidazole)copper(II),[20] due to ligand constraints.

The non-coordinated water molecules are involved in a one-dimensional hydrogen-bonded network. Two neighboring octahedrons are connected by two water molecules, each water molecule forming two hydrogen bonds to the non-coordinated oxygen atoms of the carboxylate group. This results in the formation of infinite linear chains in the direction of the crystallographic *a*,*b*,*c*-diagonal as shown in Figure 5. The OH stretching vibrations characteristic for hydrogen-bonded water molecules are present in the IR spectrum of **3** at 3347 cm^{-1}. A related $[CuL_2]$ structure was recently reported for $[Cu(bdmpza)_2]\cdot 2H_2O$ [bdmpza = bis(3,5-dimethylpyrazol-1-yl)acetate] by Reedijk et al. in which the two co-crystallized water molecules play an identical role.[20] Copper(II) complexes of the related HBIP ligand have also been reported, but no facial capping of the ligand through all donor atoms was observed.[21]

[Cu(BenzMIm$_2$Pr)$_2$]·3.12(H$_2$O)·1.74(C$_2$H$_5$OH) (4)

Complex **4** was found to have a comparable copper geometry as in complex **3** (Figure 6). Crystallographic data

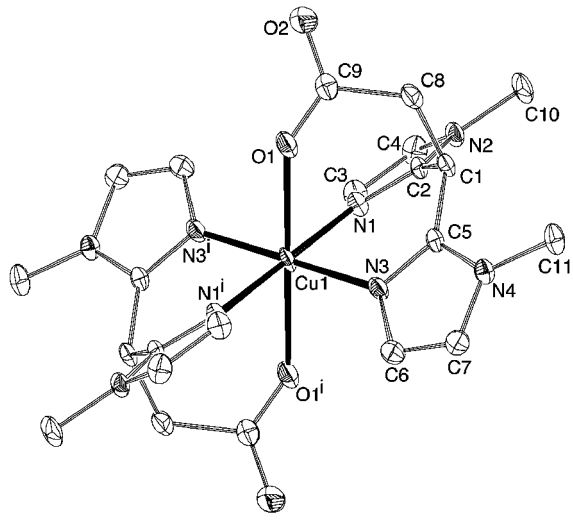

Figure 4. Molecular structure of $[Cu(MIm_2Pr)_2]\cdot 2H_2O$ (**3**) in the crystal; hydrogen atoms and non-coordinated water molecules have been omitted for clarity; displacement ellipsoids are drawn at the 50 % probability level

Table 2. Selected bond lengths [Å] and angles [°] for $[Cu(MIm_2Pr)_2]\cdot 2H_2O$ (**3**) and $[Cu(BenzMIm_2Pr)_2]\cdot 3.12(H_2O)\cdot 1.74(C_2H_5OH)$ (**4**)

$[Cu(MIm_2Pr)_2]\cdot 2H_2O$ (**3**)		$[Cu(BenzMIm_2Pr)_2]\cdot 3.12(H_2O)\cdot 1.74(C_2H_5OH)$ (**4**)	
Cu1–N1	2.0109(18)	Cu1–N1	2.0086(15)
Cu1–N3	1.9929(18)	Cu1–N11	2.0151(15)
Cu1–O1	2.4004(17)	Cu1–O24	2.3475(14)
N1–Cu1–N3	86.45(8)	N1–Cu1–N11	85.58(6)
N3–Cu1–N1^i	93.55(8)	N11–Cu1–N1^i	94.42(6)
N1–Cu1–O1	85.68(7)	N1–Cu1–O24	89.23(6)
N3–Cu1–O1	86.23(7)	N11–Cu1–O24	87.80(6)
N1^i–Cu1–O1	94.32(7)	N1^i–Cu1–O24	90.77(6)
N3^i–Cu1–O1	93.77(7)	N11^i–Cu1–O24	92.20(6)

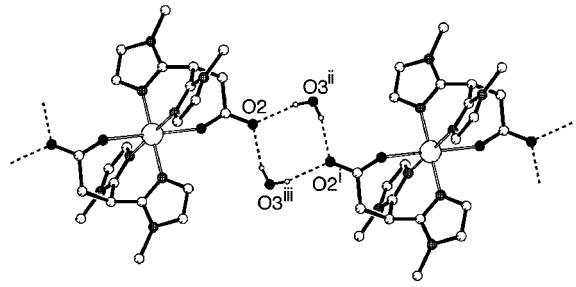

Figure 5. Hydrogen bonding network of **3** resulting in infinite linear chains; C–H hydrogen atoms have been omitted for clarity; symmetry operations: i: –*x*, –*y*, –*z*; ii: –*x*, 1 – *y*, –*z*; iii: *x*, *y* – 1, *z*

and selected bond lengths and angles are given in Tables 2 and 3. The replacement of imidazole for benzimidazole hardly affects the *N*,*N*,*O* tridentate coordination to the copper center. However, the Cu–O bond in **4** [2.3476(14) Å] is significantly shorter than the one found in **3** [2.4005(18) Å]. The Cu–N bond lengths compare well to the only other crystallographically characterized CuN_4O_2 chromophore with four benzimidazole donor groups.[22]

 © 2005 Wiley-VCH Verlag GmbH & Co. KGaA, Weinheim

Table 3. Crystallographic data for compounds **1a**, **2a**, **3**, and **4**

	1a	**2a**	**3**	**4**
Empirical formula	$C_{11}H_{14}N_4O_2 \cdot CH_3OH$	$C_{19}H_{18}N_4O_2$	$C_{22}H_{26}CuN_8O_4 \cdot 2H_2O$	$C_{38}H_{34}CuN_8O_4 \cdot 1.74(C_2H_5OH) \cdot 3.12(H_2O)$
Formula mass	266.30	334.37	566.08	866.64
Crystal size [mm]	0.06 × 0.30 × 0.43	0.18 × 0.42 × 0.42	0.12 × 0.12 × 0.18	0.09 × 0.15 × 0.33
Cryst system	monoclinic	monoclinic	triclinic	monoclinic
Space group	$P2_1/c$ (no. 14)	$P2_1/c$ (no. 14)	$P\bar{1}$ (no. 2)	$P2_1/c$ (no. 14)
a [Å]	14.8340(10)	8.5910(1)	8.3128(9)	8.5293(1)
b [Å]	8.2221(6)	22.8189(2)	8.3514(9)	18.8885(2)
c [Å]	10.6605(7)	8.2417(1)	9.9368(17)	12.6452(2)
α [°]	90	90	96.457(13)	90
β [°]	91.652(6)	102.7895(6)	94.540(10)	100.3961(4)
γ [°]	90	90	118.353(8)	90
V [Å^3]	1299.69(15)	1575.59(3)	596.27(14)	2003.77(4)
Z	4	4	1	2
$D_{calcd.}$ [g/cm^3]	1.361	1.410	1.576	1.436
μ [mm^{-1}]	0.100	0.095	0.973	0.612
Absorption correction range	0.90–1.00	-	0.69–0.89	0.88–0.94
Collected reflections	26945	29513	8358	31917
Unique reflections	2975	3623	2708	4591
Parameter/restraints	183/0	232/0	179/0	280/0
$R1/wR2$ [$I > 2\sigma(I)$]	0.0358/0.0869	0.0370/0.0957	0.0410/0.1018	0.0379/0.1033
$R1/wR2$ (all reflections)	0.0485/0.0928	0.0429/0.1000	0.0500/0.1072	0.0494/0.1106
S	1.046	1.032	1.085	1.065
Min/max residual density [e/Å^3]	–0.21/0.23	–0.28/0.29	–0.90/0.73	–0.49/0.51

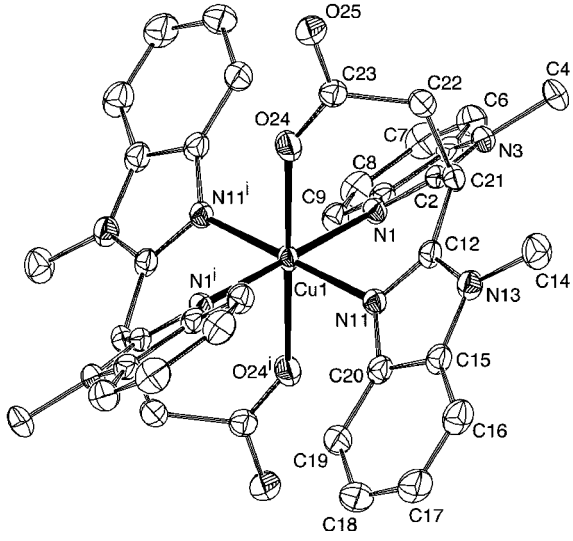

Figure 6. Molecular structure of $[Cu(BenzMIm_2Pr)_2] \cdot 3.12(H_2O) \cdot 1.74(C_2H_5OH)$ (**4**) in the crystal; hydrogen atoms and solvent molecules have been omitted for clarity; displacement ellipsoids are drawn at the 50 % probability level

Also, the hydrogen bonding pattern is similar to the one found in complex **3**. Again two water molecules connect the octahedrons through four hydrogen bonds to form an infinite chain in the direction of the crystallographic *c*-axis. Yet, the water molecules here act also as hydrogen-bond acceptors for co-crystallized ethanol molecules (Figure 7). Additionally, there are water molecules present in the crystal structure which do not participate in the hydrogen bonding. The latter water and ethanol molecule positions in the crystal lattice are not fully occupied (probably due to evaporation), hence the non-integer coefficients in the structural formulation of compound **4**.

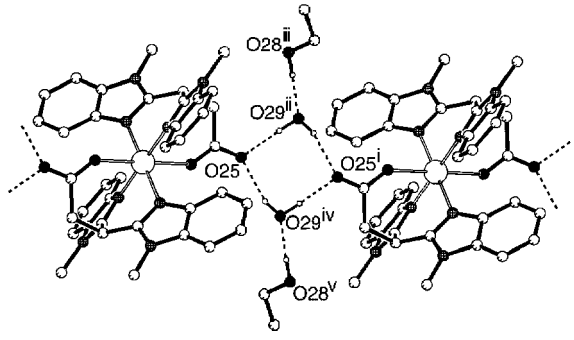

Figure 7. Hydrogen bonding network of **4** resulting in infinite linear chains; C–H hydrogen atoms and water molecules, which do not participate in the hydrogen bonding, have been omitted for clarity; symmetry operations: i: 1 – *x*, 1 – *y*, –*z*; ii: *x*, 0.5 – *y*, *z* – 0.5; iii: *x* – 1, 0.5 – *y*, *z* – 0.5; iv: 1 – *x*, *y* + 0.5, 0.5 – *z*; v: 2 – *x*, *y* + 0.5, 0.5 – *z*

ESI-MS

The ESI mass spectra of **3** and **4** dissolved in a methanol/acetonitrile mixture were recorded and very clean spectra were obtained for both complexes. Also, reference spectra of $K[MIm_2Pr]$ (**1b**) and $K[BenzMIm_2Pr]$ (**2b**) were recorded for comparison. For complex $[Cu(MIm_2Pr)_2] \cdot 2H_2O$ (**3**) only two, equally intense peaks were detected. The peak at *m*/*z* 551.78 corresponds to the $\{[Cu(MIm_2Pr)_2] + Na\}^+$ adduct ion, while the peak at *m*/*z* 529.96 is assigned to $\{[Cu(MIm_2Pr)_2] + H\}^+$. The same adduct ions were found for compound **4**, giving an *m*/*z* of 752.14 for

 © 2005 Wiley-VCH Verlag GmbH & Co. KGaA, Weinheim

{[Cu(BenzMIm$_2$Pr)$_2$] + Na}$^+$ and 730.25 for {[Cu(BenzMIm$_2$Pr)$_2$] + H}$^+$. The observed copper isotope patterns were in good agreement with the calculated ones and furthermore, no free ligand was found in the spectra of both complexes. These data strongly suggest the prevalence of the [CuL$_2$] motif and shows the complexes [Cu(MIm$_2$Pr)$_2$] and [Cu(BenzMIm$_2$Pr)$_2$] as predominant species in solution.

UV/Vis, EPR

The UV/Vis spectrum of **3** in methanol shows three absorption bands at 215, 293 (sh), and 587 nm. The first two bands are also present in reference spectra of the ligand and are therefore assigned to intraligand transitions. The broad absorption centered at 587 nm is assigned to d–d transitions of the copper(II) center. The d–d band for **4** in methanol was found around 666 nm and four intraligand transitions could be detected (228, 252, 271, and 284 nm). Changing the nitrogen donor groups from imidazole to benzimidazole affects the ligand field splitting parameter and results in a red-shift of about 80 nm for complex **4** with respect to complex **3**. This red shift reflects the smaller axial Jahn–Teller distortion and corresponds to the shorter Cu–O bond as found in the crystal structure of complex **4**. The spectral parameters are in the range expected for d–d transitions of tetragonally distorted monomeric CuN_4O_2 chromophores.[18]

The complexes **3** and **4** were studied by EPR as powders at room temperature and as frozen solutions at 77 K (Figure 8). The solid-state EPR spectra of both complexes at room temperature display broad features due to dipolar coupling of the Cu^{II} centers, but are typically axial with $g_\perp$ = 2.06 and $g_\parallel$ = 2.22 for complex **3** and $g_\perp$ = 2.06 and $g_\parallel$ = 2.25 for complex **4**. The hyperfine splitting of the spectrum with the Cu^{II} ion was observed in the parallel region in both cases with $A_\parallel$ = 200 G (**3**) and $A_\parallel$ = 177 G (**4**), the latter being better resolved. This smaller hyperfine coupling $A_\parallel$ of complex **4** is in line with the red shift observed in the UV/Vis spectra. An EPR spectrum of a frozen solution of **3** in methanol/water (1:5, v/v) was also recorded and again an EPR envelope typical for an axially elongated mononuclear Cu^{II} species was observed ($g_\perp$ = 2.04, $g_\parallel$ = 2.24, $A_\parallel$ = 193 G). Additional superhyperfine splitting due to interaction with the ^{14}N nuclei of the ligands is resolved, consistent with four equivalent nitrogens in the equatorial plane ($A_\perp$ = 15.5 G). A frozen methanolic solution of **4** gave a similar EPR spectrum. Again, both the hyperfine and superhyperfine couplings were resolved and the relevant parameters in this case are $g_\perp$ = 2.05, $g_\parallel$ = 2.25, $A_\parallel$ = 187 G, and $A_\perp$ = 14.5 G. The EPR data of the powders and the frozen solutions are consistent with the structure description derived from the X-ray analyses and the ESI-MS measurements, respectively. The spectral parameters for **3** and **4** are characteristic of tetragonally elongated monomeric copper(II) complexes[23] and are comparable to the EPR parameters obtained for other CuN_4O_2 chromophores with four imidazole nitrogen donors.[18,19]

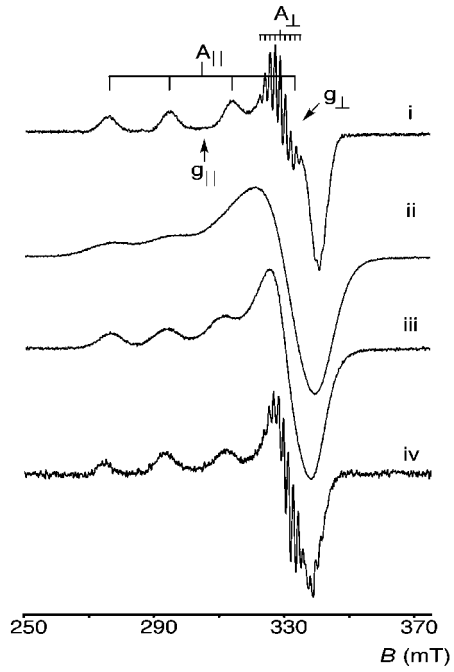

Figure 8. EPR spectra of compounds **3** and **4**; i) frozen methanol/water solution of **3** at 77K, ii) solid **3** at room temp., iii) solid **4** at room temp., iv) frozen methanol solution of **4** at 77K

Discussion and Conclusion

A relatively straightforward, high yielding, two-step route for the synthesis of two new *N*,*N*,*O* ligands on a multigram scale has been developed. Compounds **1** (A[MIm$_2$Pr]) and **2** (A[BenzMIm$_2$Pr]) can be regarded as parent compounds, as the synthetic route offers the possibility of further expansion of this series of ligands. For instance, the bis(heteroaryl)methane synthesis (**5** and **6**) [15,16] allows for the incorporation of (poly)substituted (benz)imidazoles; thus, introduction of other functionalities and further modification of this *N*,*N* backbone is feasible. Both physical properties like solubility, ease of crystallization, and steric requirements as well as the electronic properties of the ligand can therefore be controlled by design. Alterations in the fourth substituent of the central carbon atom [C3 (**1a**) and C1 (**2a**) in Figure 2] and the type of introduced electrophile offer further possibilities for structural variation.

The two cation series of ligands, A[MIm$_2$Pr] and A[BenzMIm$_2$Pr] (A = H, K, and Bu$_4$N), were developed to vary the solubility of one single member of a ligand family and simplify the syntheses and purification of different metal complexes. The reaction of a monoanionic ligand with a metal salt generally results in the formation of two new salts, i.e. the desired complex and an (inorganic) byproduct. The solubility properties of both the desired complex and the byproduct are often comparable and this then hampers purification. Choosing the right cation allows control over the solubility properties of the formed byproduct and therefore purification of the desired metal complexes can in principle be achieved by a simple washing procedure. An example of this approach is described here for the synthesis of

 © 2005 Wiley-VCH Verlag GmbH & Co. KGaA, Weinheim

[Cu(BenzMIm$_2$Pr)$_2$] (**4**). The solubility properties of the Bu$_4$N ligands (**1c**, **2c**) also allow the use of relatively apolar solvents, solvents in which the potassium salts (**1b**, **2b**) and acids (**1a**, **2a**) are insoluble.

The ligands **1** and **2** were designed to provide a transition metal with a facial donor array of one carboxylate and two imidazole groups, as found in the enzymes exhibiting the 2-His-1-carboxylate motif.[4,5,8] Using copper(II) as a probe, the neutral [CuL$_2$] complexes **3** and **4** nicely illustrate the facial *N,N,O* capping potential of both new ligands.

This facial capping of the *N,N,O* ligands A[MIm$_2$Pr] (**1**) and A[BenzMIm$_2$Pr] (**2**) renders this new family of ligands suitable candidates for mimicking the 2-His-1-carboxylate motif and we are therefore currently studying the iron and zinc coordination chemistries of these ligands.

Experimental Section

General Remarks: Air-sensitive reactions were carried out under dry, oxygen-free N$_2$ using standard Schlenk techniques. THF was dried with sodium/benzophenone ketyl and distilled under N$_2$ prior to use. Methanol was dried with magnesium methoxide and distilled under N$_2$ prior to use. ^{1}H and ^{13}C{^{1}H} NMR spectra were recorded with a Varian Inova 300 spectrometer at 300 and 75 MHz, respectively, operating at 25 °C. Elemental microanalyses were carried out by the Microanalytisches Laboratorium Dornis and Kolbe, Mülheim a. d. Ruhr, Germany. Infrared spectra were recorded with a Perkin–Elmer Spectrum One FT-IR instrument. ESI-MS spectra were recorded with a Micromass LC-TOF mass spectrometer by the department of Biomolecular Mass Spectrometry, Utrecht University. UV/Vis spectra were recorded with a Cary 50 Varian spectrometer. EPR spectra were measured with a modified Bruker ESP300 spectrometer equipped with an ER4103TM cavity (TM$_{110}$ mode with unloaded Q = 12000). The microwave frequency was near 9.52 GHz and the spectrometer settings involved 4 Gauss field modulation. Bis(1-methylimidazol-2-yl)methane and bis(1-methylbenzimidazol-2-yl)methane were prepared according to literature procedures.[15,16] All other chemicals were commercially obtained and used as received.

Propyl 3,3-Bis(1-methylimidazol-2-yl)propionate, MIm$_2$PrPr (7): A solution of *n*-butyllithium in hexanes (18 mL, 28.8 mmol, 1.6 M in hexanes) was added dropwise to a stirred solution of bis(1-methylimidazol-2-yl)methane (**5**) (5.02 g, 28.5 mmol) in THF (150 mL) at –78 °C. The solution was stirred at –78 °C for 1 h, followed by the dropwise addition of propyl bromoacetate (3.8 mL, 29 mmol). The temperature was allowed to rise to room temperature overnight, resulting in a yellow-white suspension. The reaction mixture was quenched with H$_2$O (25 mL) and all volatiles were evaporated in vacuo. The water layer was extracted with ethyl acetate (4 × 30 mL) and the combined organic layers were dried with magnesium sulfate, filtered, and the solvents evaporated to dryness. The product was obtained as a yellow oil, which solidified upon standing (6.51 g, 83 %). This product can be purified using column chromatography (silica; eluent ethyl acetate/methanol, 9:1), but the crude product is pure enough for further use. ^{1}H NMR (300 MHz, CDCl$_3$, 25 °C): δ = 0.82 (t, $^3J_{H,H}$ = 7.8 Hz, 3 H, OCH$_2$CH$_2$C*H*$_3$), 1.54 (sext, $^3J_{H,H}$ = 7.5 Hz, 2 H, OCH$_2$C*H*$_2$CH$_3$), 3.28 (d, $^3J_{H,H}$ = 7.8 Hz, 2 H, CHC*H*$_2$), 3.46 (s, 6 H, NC*H*$_3$), 3.96 (t, $^3J_{H,H}$ = 6.9 Hz, 2 H, OC*H*$_2$CH$_2$CH$_3$), 4.94 (t, $^3J_{H,H}$ = 7.8 Hz, 1 H, C*H*CH$_2$), 6.72 (s, 2 H, H_{imid}), 6.88 (s, 2 H, H_{imid}) ppm. ^{13}C{^{1}H} NMR (75 MHz, CDCl$_3$, 25 °C): δ = 10.19, 21.82, 32.81, 34.42, 36.34, 66.32, 121.95, 127.15, 145.29, 171.21 ppm. IR (solid): $\tilde{\nu}$ = 3099.1, 2967.2, 1727.1, 1492.3, 1282.9, 1189.7, 1174.9, 1129.8, 744.0 cm^{-1}. C$_{14}$H$_{20}$N$_4$O$_2$ (276.33) calcd. C 60.85, H 7.30, N 20.28; found C 60.74, H 7.22, N 20.18.

Propyl 3,3-Bis(1-methylbenzimidazol-2-yl)propionate, BenzMIm$_2$PrPr (8): Compound **8** was synthesized using the procedure described above for compound **7**. The product was obtained as an off-white solid (2.89 g, 92 %). This product can be purified using column chromatography (silica; eluent ethyl acetate/methanol, 7:1), but the crude product is pure enough for further use. ^{1}H NMR (300 MHz, CDCl$_3$, 25 °C): δ = 0.86 (t, $^3J_{H,H}$ = 7.5 Hz, 3 H, OCH$_2$CH$_2$C*H*$_3$), 1.58 (sext, $^3J_{H,H}$ = 7.2 Hz, 2 H, OCH$_2$C*H*$_2$CH$_3$), 3.61 (d, $^3J_{H,H}$ = 7.5 Hz, 2 H, CHC*H*$_2$), 3.76 (s, 6 H, NC*H*$_3$), 4.02 (t, $^3J_{H,H}$ = 6.3 Hz, 2 H, OC*H*$_2$CH$_2$CH$_3$), 5.45 (t, $^3J_{H,H}$ = 7.5 Hz, 1 H, C*H*CH$_2$), 7.26 (m, 6 H, $H_{benzimid}$), 7.76 (m, 2 H, $H_{benzimid}$) ppm. ^{13}C{^{1}H} NMR (75 MHz, CDCl$_3$, 25 °C): δ = 10.20, 21.84, 30.25, 35.94, 36.19, 66.64, 109.23, 119.74, 122.18, 122.84, 136.44, 142.07, 151.19, 170.89 ppm. IR (solid): $\tilde{\nu}$ = 2973.2, 1733.9, 1467.1, 1439.7, 1389.1, 1179.2, 733.7 cm^{-1}. C$_{22}$H$_{24}$N$_4$O$_2$ (376.45) calcd. C 70.19, H 6.43, N 14.88; found C 69.98, H 6.41, N 14.69.

3,3-Bis(1-methylimidazol-2-yl)propionic Acid, HMIm$_2$Pr (1a): To a solution of ester **7** (2.24 g, 8.1 mmol) in THF (20 mL) was added 1 equiv. of potassium hydroxide in water (8.20 mL, 0.989 M, 8.1 mmol) and the solution was stirred at room temperature for 3 h. Subsequently, 1 equiv. of a hydrochloric acid solution in water (8.11 mL, 1 M, 8.1 mmol) was added to the hydrolysed reaction mixture. Evaporation of the solvents resulted in a white mixture of product and potassium chloride. Most of the KCl was removed after extraction of the powder with dry methanol (3 × 15 mL). Evaporation of the solvent and recrystallization from EtOH/H$_2$O (95:5) gave the product as colorless crystals of composition HMIm$_2$Pr·4H$_2$O (1.6 g, 65 %). Single crystals of the composition HMIm$_2$Pr·CH$_3$OH were obtained by slow diffusion of diethyl ether in a concentrated solution of **1a** in methanol. ^{1}H NMR (300 MHz, CD$_3$OD, 25 °C): δ = 3.16 (d, $^3J_{H,H}$ = 7.8 Hz, 2 H, CHC*H*$_2$), 3.62 (s, 6 H, NC*H*$_3$), 5.00 (t, $^3J_{H,H}$ = 7.2 Hz, 1 H, C*H*CH$_2$), 6.99 (s, 2 H, H_{imid}), 7.11 (s, 2 H, H_{imid}) ppm. ^{13}C{^{1}H} NMR (75 MHz, CD$_3$OD, 25 °C): δ = 33.63, 33.86, 38.87, 123.88, 125.92, 146.76, 175.17 ppm. IR (solid): $\tilde{\nu}$ = 3130.0, 1701.5, 1491.2, 1348.4, 1285.6, 1266.7, 1220.9, 1135.5, 772.3 cm^{-1}. C$_{11}$H$_{14}$N$_4$O$_2$·4H$_2$O (306.32) calcd. C 43.13, H 7.24, N 18.29; found C 43.31, H 7.16, N 18.34.

3,3-Bis(1-methylbenzimidazol-2-yl)propionic Acid, HBenzMIm$_2$Pr (2a): The acid **2a** was synthesized using the procedure as described above for the acid **1a**. KCl could in this case be removed by washing the product with water (3 × 20 mL). Recrystallization from methanol gave the product as colorless crystals (0.59 g, 64 %). Slow cooling of a hot saturated solution of **2a** in methanol resulted in crystals suitable for X-ray analysis. ^{1}H NMR (300 MHz, CD$_3$OD, 25 °C): δ = 3.53 (d, $^3J_{H,H}$ = 7.2 Hz, 2 H, CHC*H*$_2$), 3.78 (s, 6 H, NC*H*$_3$), 5.40 (t, $^3J_{H,H}$ = 7.2 Hz, 1 H, C*H*CH$_2$), 7.28 (m, 4 H, $H_{benzimid}$), 7.48 (d, $^3J_{H,H}$ = 7.2 Hz, 2 H, $H_{benzimid}$) 7.63 (d, $^3J_{H,H}$ = 7.2 Hz, 2 H, $H_{benzimid}$) ppm. ^{13}C{^{1}H} NMR (75 MHz, CD$_3$OD, 25 °C): δ = 30.52 35.27, 37.60 111.01, 119.60, 123.59, 124.25, 137.32, 142.69, 153.46, 174.41 ppm. IR (solid): $\tilde{\nu}$ = 2934.4, 1716.3, 1467.8, 1392.8, 1332.3, 1282.8, 762.1, 739.6 cm^{-1}. C$_{19}$H$_{18}$N$_4$O$_2$ (334.37) calcd. C 68.25, H 5.43, N 16.76; found C 68.15, H 5.49, N 16.83.

General Procedure for the Synthesis of the Potassium and Tetrabutylammonium Salts 1b/c and 2b/c: To a solution of the appropriate ester **7** or **8** in THF (20 mL) was added 1 mol-equiv. of a KOH or [Bu$_4$N]OH solution in water (volumetric standard) and the reaction mixture was stirred at room temperature for 3 h. Evaporation of

 © 2005 Wiley-VCH Verlag GmbH & Co. KGaA, Weinheim

the solvents resulted in an oil. Repeated azeotropic drying of the oil with toluene, gave the desired product as a powder in quantitative yield.

Potassium 3,3-Bis(1-methylimidazol-2-yl)propionate, K[MIm$_2$Pr] (1b): Yellowish powder (1.97 g). ^{1}H NMR (300 MHz, CD_3OD, 25 °C): δ = 3.08 (d, $^3J_{H,H}$ = 7.2 Hz, 2 H, CHCH_2), 3.52 (s, 6 H, NCH_3), 4.92 (t, $^3J_{H,H}$ = 7.2 Hz, 1 H, CHCH$_2$), 6.83 (s, 2 H, H_{imid}), 6.95 (s, 2 H, H_{imid}) ppm. ^{13}C{^{1}H} NMR (75 MHz, CD_3OD, 25 °C): δ = 35.22, 35.59, 41.09, 123.16, 127.11, 148.34, 178.60 ppm. IR (solid): $\tilde{\nu}$ = 1580.2, 1393.0, 665.2 cm^{-1}. $C_{11}H_{13}KN_4O_2$ (272.34) calcd. C 48.51, H 4.81, N 20.57; found C 48.36, H 4.92, N 20.47. ESI-MS: *m*/*z* = 311.08 {(K[MIm$_2$Pr] +K)$^+$, calcd. 311.03}, 583.04 {(2K[MIm$_2$Pr] + K)$^+$, calcd. 583.10}.

Tetrabutylammonium 3,3-Bis(1-methylimidazol-2-yl)propionate, [Bu$_4$N][MIm$_2$Pr] (1c): White powder (1.97 g). ^{1}H NMR (300 MHz, $CDCl_3$, 25 °C): δ = 0.92 (m, 12 H, $CH_2CH_2CH_2CH_3$), 1.35 (m, 8 H, $CH_2CH_2CH_2CH_3$), 1.57 (m, 8 H, $CH_2CH_2CH_2CH_3$), 3.06 (d, $^3J_{H,H}$ = 6.5 Hz, 2 H, CHCH_2), 3.26 (m, 8 H, $CH_2CH_2CH_2CH_3$), 3.58 (s, 6 H, NCH_3), 5.08 (t, $^3J_{H,H}$ = 6.5 Hz, 1 H, CHCH$_2$), 6.65 (s, 2 H, H_{imid}), 6.77 (s, 2 H, H_{imid}) ppm. ^{13}C{^{1}H} NMR (75 MHz, $CDCl_3$, 25 °C): δ = 13.69, 19.68, 24.04, 33.00, 35.16, 40.80, 58.56, 120.79, 126.53, 148.87, 174.66 ppm. IR (solid) $\tilde{\nu}$ = 2962.5, 2936.7, 1581.6, 1489.7, 1363.2, 1280.6, 1128.0, 770.5 cm^{-1}. $C_{27}H_{49}N_5O_2$ (475.71) calcd. C 68.17, H 10.38, N 14.72; found C 67.89, H 10.31, N 14.63.

Potassium 3,3-Bis(1-methylbenzimidazol-2-yl)propionate, K[BenzMIm$_2$Pr] (2b): Yellowish powder (2.27 g). ^{1}H NMR (300 MHz, CD_3OD, 25 °C): δ = 3.35 (d, $^3J_{H,H}$ = 7.2 Hz, 2 H, CHCH_2), 3.78 (s, 6 H, NCH_3), 5.40 (t, $^3J_{H,H}$ = 7.2 Hz, 1 H, CHCH$_2$), 7.23 (m, 4 H, $H_{benzimid}$), 7.44 (d, $^3J_{H,H}$ = 7.8 Hz, 2 H, $H_{benzimid}$), 7.61 (d, $^3J_{H,H}$ = 7.8 Hz, 2 H, $H_{benzimid}$) ppm. ^{13}C{^{1}H} NMR (75 MHz, CD_3OD, 25 °C): δ = 29.31, 35.47, 39.84, 09.61, 118.42, 122.01, 122.66, 136.21, 141.80, 153.61, 176.78 ppm. IR (solid) $\tilde{\nu}$ = 1598.0, 1581.9, 1385.7, 1282.7, 737.8 cm^{-1}. $C_{19}H_{17}KN_4O_2$ (372.46) calcd. C 61.27, H 4.60, N 15.04; found C 61.05, H 4.68, N 14.86. ESI-MS: *m*/*z* = 327.18 {([BenzMIm$_2$C$_2$H$_2$] + K)$^+$, calcd. 327.10}, 411.12 {(K[BenzMIm$_2$Pr] + K)$^+$, calcd. 411.06}, 783.19 {(2K[BenzMim$_2$Pr] + K)$^+$, calcd. 783.16}.

Tetrabutylammonium 3,3-Bis(1-methylbenzimidazol-2-yl)propionate, [Bu$_4$N][BenzMIm$_2$Pr] (2c): Yellow powder (1.52 g). ^{1}H NMR (300 MHz, $CDCl_3$, 25 °C): δ = 0.92 (t, $^3J_{H,H}$ = 7.2 Hz, 12 H, $CH_2CH_2CH_2CH_3$), 1.33 (m, 8 H, $CH_2CH_2CH_2CH_3$), 1.53 (m, 8 H, $CH_2CH_2CH_2CH_3$), 3.19 (m, 8 H, $CH_2CH_2CH_2CH_3$), 3.37 (d, $^3J_{H,H}$ = 6.6 Hz, 2 H, CHCH_2), 3.82 (s, 6 H, NCH_3), 5.58 (t, $^3J_{H,H}$ = 6.3 Hz, 1 H, CHCH$_2$), 7.20 (m, 6 H, $H_{benzimid}$), 7.65 (m, 2 H, $H_{benzimid}$) ppm. ^{13}C{^{1}H} NMR (75 MHz, $CDCl_3$, 25 °C): δ = 13.56, 19.58, 23.91, 30.21, 36.17, 39.52, 58.65, 109.06, 119.29, 121.29, 121.89, 136.38, 142.41, 154.25, 174.12 ppm. IR (solid) $\tilde{\nu}$ = 2960.0, 2874.0, 1596.5, 1465.8, 1380.2, 1275.5, 736.1 cm^{-1}. $C_{35}H_{53}N_5O_2$ (575.83) calcd. C 73.00, H 9.28, N 12.16; found C 72.89, H 9.38, N 12.22.

[Cu(MIm$_2$Pr)$_2$]·2H$_2$O (3): To a colorless solution of K[MIm$_2$Pr] (**1b**) (414 mg, 1.52 mmol) in hot ethanol (20 mL) was added a solution of $CuCl_2$·$2H_2O$ (129 mg, 0.76 mmol) in hot ethanol (10 mL). The solution immediately turned dark blue and the reaction mixture was heated to reflux for 1 h. Upon cooling of the solution to room temperature, a white precipitate formed (KCl). The solution was filtered and concentrated in vacuo. The resulting dark blue powder was recrystallized from a minimal amount of refluxing ethanol and cooled to 4 °C to give the title compound as blue crystals (201 mg, 47 %). Single crystals formed after three weeks from a concentrated solution of **3** in ethanol upon standing. $C_{22}H_{26}CuN_8O_4$·$2H_2O$ (566.06) calcd. C 46.86, H 5.34, N 19.80; found C 46.60, H 5.44, N 19.72. IR (solid) $\tilde{\nu}$ = 3347.5, 3275.9, 3126.5, 1582.1, 1506.9, 1383.9, 1289.8, 1153.1, 745.9 cm^{-1}. UV/Vis (methanol): λ_{max} = 215, 219, 587 nm. ESI-MS: *m*/*z* = 529.96 {[{Cu(MIm$_2$Pr)$_2$} + H]$^+$, calcd. 530.14}, 551.78 {[{Cu(MIm$_2$Pr)$_2$} + Na]$^+$, calcd. 552.13}.

[Cu(BenzMIm$_2$Pr)$_2$] (4): To a colorless solution of [Bu$_4$N][BenzMIm$_2$Pr] (**2c**) (470 mg, 0.82 mmol) in hot, dry methanol (20mL) was added a solution of $CuCl_2$ (55 mg, 0.41 mmol) in hot, dry methanol (10 mL). Immediately the solution turned green-blue and the reaction mixture was refluxed for 1 h, during which a pale blue precipitate formed. The reaction mixture was allowed to cool to room temperature and the precipitate was collected by centrifugation. The crude product was washed with methanol (1 × 10 mL) and dichloromethane (3 × 10 mL) and dried in vacuo. The title compound was isolated as a light blue powder (162 mg, 54 %). Slow evaporation of the solvent of a concentrated solution of **4** in ethanol resulted in the formation of single crystals of the composition [Cu(BenzMIm$_2$Pr)$_2$]·3.12(H_2O)·1.74(C_2H_5OH) formed after six weeks. $C_{38}H_{34}CuN_8O_4$ (730.27) calcd. C 62.50, H 4.69, N 15.34; found C 62.36, H 4.62, N 15.23. IR (solid) $\tilde{\nu}$ = 3349.8, 1583.1, 1458.0, 1385.5, 1304.1, 1284.8, 742.8 cm^{-1}. UV/Vis (methanol): λ_{max} = 228, 252, 271, 666 nm. ESI-MS: *m*/*z* = 730.25 {[{Cu(BenzMIm$_2$Pr)$_2$} + H]$^+$, calcd. 730.21}, 752.14 {[{Cu(BenzMIm$_2$Pr)$_2$} + Na]$^+$, calcd. 752.19}.

X-ray Crystallographic Study: X-ray intensities were measured with a Nonius KappaCCD diffractometer with rotating anode (graphite monochromator, λ = 0.71073 Å) at a temperature of 150 K. The structures were solved with Direct Methods (compounds **1a**,[24] **2a**,[25] and **4**[24]) or automated Patterson methods (compound **3**[26]). The structures were refined with SHELXL-97[27] against F^2 of all reflections up to $(\sin\theta/\lambda)_{max}$ = 0.65 Å^{-1}. Structure calculations, drawings, and checking for higher symmetry was performed with the PLATON[28] package. Further details are given in Table 3. In crystal structures **1a**, **2a**, and **3** all hydrogen atoms were located in the difference Fourier map. C–H hydrogen atoms were refined as rigid groups. O–H hydrogen atoms were refined freely with isotropic displacement parameters. In crystal structure **4**, the position of water molecule O29 is fully occupied. Water molecule O30 was refined with an occupancy of 56 % and the ethanol molecule with an occupancy of 87 %. All hydrogen atoms were located in the difference Fourier map. C–H hydrogen atoms were refined as rigid groups. O–H hydrogen atoms were kept fixed in the located position. CCDC-249589 (**1a**), -249590 (**2a**), -249591 (**3**) and -249592 (**4**) contain the supplementary crystallographic data for this paper. These data can be obtained free from The Cambridge Crystallographic Data Centre via www.ccdc.cam.ac.uk/data_request/cif [or from the Cambridge Crystallographic Data Centre, 12 Union Road, Cambridge CB2 1EZ, UK; Fax: +44-1223/336-033; E-mail: deposit@ccdc.cam.ac.uk].

Supporting Information (see also footnote on the first page of this article): Two figures are included depicting the hydrogen bonding pattern and π-π stacking the crystal structure of HBenzMIm$_2$Pr (**2a**).

Acknowledgments

The work described here was financially supported by the National Research School Combination-Catalysis (P. C. A. B.) and the Council for Chemical Sciences of the Netherlands Organization for Scientific Research (CW-NWO) (M. L., A. L. S.).

[1] R. H. Holm, E. I. Solomon (Eds.), "Biomimetic Inorganic Chemistry", *Chem. Rev.* **2004**, *104*, 347–1200.
[2] a) S. Trofimenko, *Chem. Rev.* **1993**, *93*, 943–980; b) F. T. Edelmann, *Angew. Chem. Int. Ed.* **2001**, *40*, 1656–1660.
[3] a) A. Otero, J. Fernández-Baeza, A. Antiñolo, J. Tejeda, A Lara-Sánchez, *J. Chem. Soc., Dalton Trans.* **2004**, 1499–1510; b) B. S. Hammes, C. J. Carrano, *Inorg. Chem.* **1999**, *38*, 4593–4600; c) V. V. Karambelkar, D. Krishnamurthy, C. L. Stern, L. N. Zakharov, A. L. Rheingold, D. P. Goldberg, *Chem. Commun.* **2002**, 2772–2773; d) A. Trösch, H. Vahrenkamp, *Eur. J. Inorg. Chem.* **1998**, 827–832.
[4] a) E. L. Hegg, L. Que, Jr., *Eur. J. Biochem.* **1997**, *250*, 625–629; b) S. J. Lange, L. Que, Jr., *Curr. Op. Chem. Biol.* **1998**, *2*, 159–172; c) L. Que, Jr., *Nature Struct. Biol.* **2000**, *7*, 182–184.
[5] M. Costas, M. P. Mehn, M. P. Jensen, L. Que, Jr., *Chem. Rev.* **2004**, *104*, 939–986 and references cited therein.
[6] K. Valegård, A. C. Terwisscha van Scheltinga, M. D. Lloyd, T. Hara, S. Ramaswamy, A. Perrakis, A. Thomspon, H.-J. Lee, J. E. Baldwin, C. J. Schofield, J. Hadju, I. Andersson, *Nature* **1998**, *394*, 805–809.
[7] B. Kauppi, K. Lee, E. Carredano, R. E. Parales, D. T. Gibson, H. Eklund, S. Ramaswamy, *Structure* **1998**, *6*, 571–586.
[8] a) G. Parkin, *Chem. Rev.* **2004**, *104*, 699–768 and references cited therein. b) G. Parkin, *Chem. Commun.* **2000**, 1971–1985.
[9] A. Otero, J. Fernández-Baeza, J. Tejeda, A. Antiñolo, F. Carrillo-Hermosilla, E. Diez-Barra, A. Lara-Sánchez, M. Fernández-López, M. Lanfranchi, M. A. Pellinghelli, *J. Chem. Soc., Dalton Trans.* **1999**, 3537–3539.
[10] a) A. Beck, B. Weibert, N. Burzlaff, *Eur. J. Inorg. Chem.* **2001**, 521–527; b) A. Beck, A. Barth, E. Hubner, N. Burzlaff, *Inorg. Chem.* **2003**, *42*, 7182–7188; c) I. Hegelmann, A. Beck, C. Eichhorn, B. Weibert, N. Burzlaff, *Eur. J. Inorg. Chem.* **2003**, 339–347; d) R. Müller, E. Hübner, N. Burzlaff, *Eur. J. Inorg. Chem.* **2004**, 2151–2159.
[11] M. Joseph, T. Leigh, M. L. Swain, *Synthesis* **1977**, 459–461.
[12] a) C. Dowling, G. Parkin, *Polyhedron* **1996**, *15*, 2463–2465; b) P. Ghosh, G. Parkin, *J. Chem. Soc., Dalton Trans.* **1998**, 2281–2283.
[13] J. S. Valentine (Ed.), *Copper-containing proteins*, Academic Press, Amsterdam, **2002**.
[14] J. Gazo, I. B. Bersuker, J. Garaj, M. Kabesová, J. Kohout, H. Langfelderová, M. Melník, M. Serátor, F. Valach, *Coord. Chem. Rev.* **1976**, *19*, 253–297.
[15] a) N. Braussaud, T. Rüther, K. J. Cavell, B. W. Skelton, A. H. White, *Synthesis* **2001**, *4*, 626–632; b) P. Lucas, N. El Mehdi, H. Ang Ho, D. Bélanger, L. Breau, *Synthesis* **2000**, *9*, 1253–1258.
[16] S. Elgafi, L. D. Field, B. A. Messerle, P. Turner, T. W. Hambley, *J. Organomet. Chem.* **1999**, *558*, 69–77.
[17] P. C. A. Bruijnincx, M. Lutz, R. J. M. Klein Gebbink, unpublished results.
[18] A. L. Abuhijleh, C. Woods, *Inorg. Chim. Acta* **1992**, *194*, 9–14.
[19] a) C. Place, J.-L. Zimmermann, E. Mulliez, G. Guillot, C. Bois, J.-C. Chottard, *Inorg. Chem.* **1998**, *37*, 4030–4039; b) B. Barszcz, T. Glowiak, J. Jezierska, *Polyhedron* **1999**, *18*, 3713–3721; c) P. J. Baesjou, W. L. Driessen, G. Challa, J. Reedijk, *J. Mol. Catal. A: Chem.* **1996**, *110*, 195–210.
[20] B. Kozlevcar, P. Gamez, R. de Gelder, W. L. Driessen, J. Reedijk, *Eur. J. Inorg. Chem.* **2003**, 47–50.
[21] a) A. Sancho, B. Gimeno, J.-M. Amigó, L.-E. Ochando, T. Debaerdemaeker, J. V. Folgado, L. Soto, *Inorg. Chim. Acta* **1996**, 248, 153–158; b) Y. Akriff, J. Server-Carrió, A. Sancho, J. García-Lozano, E. Escrivá, J. V. Folgado, L. Soto, *Inorg. Chem.* **1999**, *38*, 1174–1185; c) Y. Akriff, J. Server-Carrió, A. Sancho, J. García-Lozano, E. Escrivá, L. Soto, *Inorg. Chem.* **2001**, *40*, 6832–6840.
[22] K. Isele, V. Broughton, C. J. Matthews, A. F. Williams, G. Bernardinelli, P. Franz, S. Decurtins, *J. Chem. Soc., Dalton Trans.* **2002**, 3899–3905.
[23] B. J. Hathaway, D. E. Billing, *Coord. Chem. Rev.* **1970**, *5*, 143–207.
[24] A. Altomare, M. C. Burla, M. Camalli, G. L. Cascarano, C. Giacovazzo, A. Guagliardi, A. G. G. Moliterni, G. Polidori, R. Spagna, *J. Appl. Crystallogr.* **1999**, *32*, 115–119.
[25] G. M. Sheldrick, *SHELXS-97*, Universität Göttingen, Göttingen, Germany, **1997**.
[26] P. T. Beurskens, G. Admiraal, G. Beurskens, W. P. Bosman, S. Garcia-Granda,R. O. Gould, J. M. M. Smits, C. Smykalla, *The DIRDIF99 program system*, Technical Report of the Crystallography Laboratory, University of Nijmegen, The Netherlands, **1999**.
[27] G. M. Sheldrick, *SHELXL-97*, Universität Göttingen, Göttingen, Germany, **1997**.
[28] A. L. Spek, *J. Appl. Crystallogr.* **2003**, *36*, 7–13.

Received October 5, 2004
Published Online January 27, 2005

 © 2005 Wiley-VCH Verlag GmbH & Co. KGaA, Weinheim

First Examples of β-Diketonate Platinum(II) Complexes with Sulfoxide Ligands

Sandra A. De Pascali,[a] Paride Papadia,[a] Antonella Ciccarese,[a] Concetta Pacifico,[b] and Francesco P. Fanizzi*[a]

Keywords: Platinum / β-Diketonate / S ligands

New platinum(II) complexes have been prepared as models for explaining the coordination of multiple β-diketonate ligands to give [Pt(*O,O′*-acac)(γ-acac)L] species. The new compounds containing both an *O,O′*-chelated acetylacetonate ligand and a sulfoxide in the platinum coordination sphere, [PtCl(*O,O′*-acac)(DMSO)] (**1**) and [Pt(*O,O′*-acac)(γ-acac)(DMSO)] (**2**), have been synthesised and characterised by ^{1}H, ^{13}C, ^{195}Pt 1-D and 2-D NMR heteronuclear correlation spectroscopy and, in the case of **2**, by X-ray crystal structure analysis also. Moreover, a new synthetic pathway to obtain the previously reported complex K[Pt(*O,O′*-acac)(γ-acac)$_2$] (**3**) has been developed. The data presented herein are consistent with a reaction mechanism which explains the subsequent steps of the coordination of multiple β-diketonate ligands to platinum(II) complexes, where the first species formed contains one *O,O′*-chelated acac group.
(© Wiley-VCH Verlag GmbH & Co. KGaA, 69451 Weinheim, Germany, 2004)

Introduction

Despite the fact that sulfoxides[1,2] and acetylacetone[3] have been widely used in the coordination and organometallic chemistry of platinum, to the best of our knowledge, no platinum(II) complexes containing both ligands have been described so far. In particular, platinum(II) shows a high affinity for sulfur ligands, a large number of complexes with sulfoxides are known and several studies of DMSO complexes dealing with a wide variety of different aspects of these complexes have been carried out.[4] On the other hand, the versatility of acetylacetone as a ligand was first demonstrated by Werner who employed it as a chelating agent.[5] Almost every metal has been found to give acetylacetone complexes which, in many cases, have exhibited interesting stereochemical arrangements. Several reports on acetylacetonatoplatinum(II) complexes have established the presence of two main modes of metal-ligand bonding: oxygen-bonded (chelated) acetylacetonate and carbon-bonded acetylacetonate.[6–9] In many cases, two acetylacetonate (acac) ligands, one of them oxygen-bonded (*O,O′*-chelated) and the other one carbon-bonded (σ-bonded), are coordinated to the same metal centre. Very extensive studies have been performed on the reactions of bis(β-diketonato)palladium(II) and platinum(II) complexes of the type [M(*O,O′*-acac)$_2$] (M = Pd or Pt, *O,O′*-acac = *O,O′*-acetylacetonate) with nitrogen ligands (py and Et_2NH), tertiary phosphanes (PPh_3, PCy_3 and PEt_3) and arsines which resulted in the bonding mode conversion for at least one *O,O′*-chelated β-diketonate anion to other type of coordination modes.[10,11] It was found that the addition of a series of ligands (L) to [Pt(*O,O′*-acac)$_2$] caused the rearrangement of one of the *O,O′*-chelated acac ligands to a σ-bonded form, affording complexes of the type [Pt(*O,O′*-acac)(γ-acac)L] (γ-acac = Cγ-bonded acetylacetonate).[12] The reaction of [Pt(*O,O′*-acac)$_2$] with an excess of pyridine, on the other hand, yielded a complex in which both acetylacetonate ligands are coordinated to platinum through the central carbon atoms, [Pt(γ-acac)$_2$(py)$_2$], in equilibrium with a mono-γ-acac complex, [Pt(*O,O′*-acac)(γ-acac)(py)].[13] Interestingly, reactions giving [Pt(*O,O′*-acac)(γ-acac)L] complexes starting from platinum species other than [Pt(*O,O′*-acac)$_2$] and, in general, lacking an acac ligand previously bound to the metal, appear to be much less common. Representative examples for this latter kind of reaction are the syntheses of K[Pt(*O,O′*-acac)(γ-acac)Cl][6] and [Pt(*O,O′*-acac)(γ-acac)-(Et_2S)][14] starting from $K_2[PtCl_4]$ and [$PtCl_2(Et_2S)_2$], respectively. Furthermore, the subsequent coordination of two acac ligands in the reactions of [$PtCl_2L_2$]-type complexes [L = Et_2S, 1,2-bis(ethylthio)ethane, PEt_3, PPh_3] with thallium(I) β-diketonates has been examined (Scheme 1). The factors favouring each of the two coordination modes, *O,O′*-chelated or Cγ-bonded, when the first acac binds the metal were investigated but no definitive conclusions were drawn about the pathway leading to [Pt(*O,O′*-acac)(γ-acac)-L] complexes.[14]

[a] Dipartimento di Scienze e Tecnologie Biologiche ed Ambientali, Università di Lecce,
Prov.le Monteroni/Lecce, 73100 Lecce, Italy
[b] Dipartimento Farmaco-Chimico, Università di Bari,
Via E. Orabona 4, 70125 Bari, Italy
Fax: (internat.) +39-(0)832-298626
E-mail: fp.fanizzi@unile.it
Supporting information for this article is available on the WWW under http://www.eurjic.org or from the author.

 © 2005 Wiley-VCH Verlag GmbH & Co. KGaA, Weinheim **DOI: 10.1002/ejic.200400665**

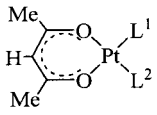

$L^1 = L^2 = \gamma$-acac, Cl, Et_2NH, PPh_3, PEt_3, piperidine
L^1 = Cl; $L^2 = PEt_3$

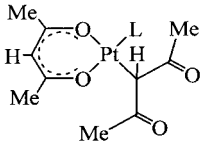

L = Cl, Et_2NH, Et_2S, PCy_3, PPh_3, Py

Scheme 1

In this context, we have synthesised two novel complexes of platinum(II), namely [PtCl(*O,O′*-acac)(DMSO)] (**1**) and [Pt(*O,O′*-acac)(γ-acac)(DMSO)] (**2**), as models for explaining the coordination of multiple β-diketonate ligands to give [Pt(*O,O′*-acac)(γ-acac)L] species. Together with the synthesis and characterisation of the new complexes **1** and **2**, we also report herein a new synthetic pathway for the homoleptic complex K[Pt(*O,O′*-acac)(γ-acac)$_2$] (**3**), previously obtained by Lewis et al.[6] Compounds **1**–**3** (Scheme 2) have been characterised by microanalysis, IR spectroscopy, multinuclear multidimensional NMR spectroscopy and, in the case of **2**, by X-ray diffraction.

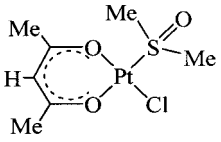

1

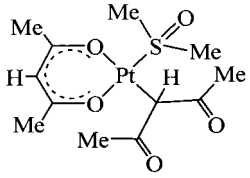

2

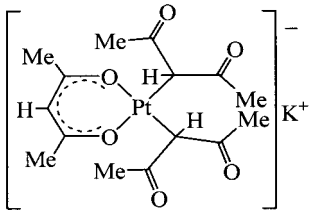

3

Scheme 2

Results and Discussion

Synthesis of the Compounds

The synthesis of [PtCl(*O,O′*-acac)(DMSO)] (**1**), containing a single chelate acac, was straightforward since, due to its low solubility in the reaction medium, it precipitates as a pale yellow powder from the reaction mixture of K[$PtCl_3$(DMSO)] with acetylacetone and KOH in water. Complexes **2** and **3** were obtained by treating [$PtCl_2(DMSO)_2$] with acetylacetone and KOH in MeOH and were isolated from their respective reaction mixtures by an appropriate workup procedure reported in the experimental section. In all cases, in order to prevent metal reduction, a slight excess of acetylacetone was used with respect to the calculated stoichiometric amount of KOH based on starting platinum complex. It should be noted that the use of the scarcely soluble [$PtCl_2(DMSO)_2$] as a starting platinum complex for the preparation of **1** in MeOH or water gave unsatisfactory results. Due to the low solubility of [$PtCl_2(DMSO)_2$], the reaction with acetylacetone and KOH in MeOH resulted in an excess of acac in solution, even when using a stoichiometric or substoichiometric amount of acac and always gave a mixture of **1**, **2** and unreacted starting material. On the other hand, the reaction of [$PtCl_2(DMSO)_2$] with acetylacetone and KOH in water, in which both the starting platinum complex and [PtCl(*O,O′*-acac)(DMSO)] are sparingly soluble, gave analytically pure **1** although a longer reaction time was required and a lower yield was obtained. Quadrangular, pale-yellow X-ray quality crystals of [Pt(*O,O′*-acac)(γ-acac)(DMSO)] (**2**) were obtained from a $CHCl_3$/pentane solution.

Characterisation of the Complexes

All complexes were characterised by microanalysis, IR spectroscopy and multinuclear, multidimensional NMR spectroscopy. In the case of compound **2**, the structure assigned on the basis of spectroscopic and microanalytical data was also confirmed by a single-crystal X-ray diffraction analysis. ^{1}H, ^{13}C NMR and ^{195}Pt NMR spectroscopic data are reported in Table 1, Table 2 and Table 3, respectively. Crystal data, data collection and refinement parameters for compound **2** are summarised in Table 4 and Table 5.

In the IR spectrum of complex **1**, the observed stretching frequencies for Cγ-H (above 3000 cm^{-1}), C=C (1570 cm^{-1}) and C=O (1520 cm^{-1}) were indicative of acetylacetonate bonded through oxygen. For chelate acetylacetonate complexes, the highest reported stretching frequencies for C=O are below 1600 cm^{-1}, in agreement with the "aromatic" nature of the system resulting from delocalization of the π elec-

Table 1. ^{1}H NMR spectroscopic data (δ) for acac ligands and complexes; * values of $J_{H\text{-}Pt}$ [in brackets] are given when assignable; # indicates the acac methyl group *cis* to DMSO

	Solvent	H/Cγ	Me/acac	Me/DMSO
acac	$CDCl_3$	5.46, 3.55	2.01, 2.20	
	CD_3OD	5.60	2.01, 2.18	
1	$CDCl_3$	5.56	2.02#, 2.06	3.44[40]*
2	$CDCl_3$	5.53(O-bonded)	1.95#, 2.01 (O-bonded)	3.31[40]
		4.80[120] (Cγ-bonded)	2.29[5] (Cγ-bonded)	
3	CD_3OD	5.39 (O-bonded)	1.77 (O-bonded)	
		4.75[120] (Cγ-bonded)	2.18 (Cγ-bonded)	
	D_2O	5.45 (O-bonded)	1.71 (O-bonded)	
		4.70[110] (Cγ-bonded)	2.07 (Cγ-bonded)	

 © 2005 Wiley-VCH Verlag GmbH & Co. KGaA, Weinheim

Table 2. ^{13}C NMR spectroscopic data (δ) of complexes; * values of $J_{H\text{-}Pt}$ [in brackets] are given when assignable; # indicates the acac methyl group *cis* to DMSO

	Solvent	C/Cγ	C/Me(acac)	C/Me(DMSO)	C/C=O
1	$CDCl_3$	102.27[73]*	26.31	44.26[56]	185.87[16] 185.06#[28]
2	$CDCl_3$	102.19[64] (O-bonded) 42.04[652] (Cγ-bonded)	27.54, 27.28# (O-bonded) 30.94[125] (Cγ-bonded)	42.95[56]	185.79#, 184.93 (O-bonded) 208.53[60] (Cγ-bonded)
3	CD_3OD	101.97 (O-bonded) 44.00 (Cγ-bonded)	27.95 (O-bonded) 30.16 (Cγ-bonded)		184.58 (O-bonded) 211.55 (Cγ-bonded)
	D_2O	101.66 (O-bonded) 43.08 (Cγ-bonded)	27.52 (O-bonded) 29.75 (Cγ-bonded)		185.76 (O-bonded) 212.69 (Cγ-bonded)

Table 3. ^{195}Pt NMR spectroscopic data (δ) of complexes

	Solvent	
1	$CDCl_3$	–2399
	CD_3OD	–2430
2	$CDCl_3$	–3198
	CD_3OD	–3168
3	CD_3OD	–2539
	D_2O	–2555

Table 4. Crystallographic data and structure refinement of complex **2**

Empirical formula	$C_{12}H_{20}O_5PtS$
Formula mass	1414.29
Temperature	293(2) K
Wavelength	0.71069 Å
Crystal system, space group	triclinic, $P\bar{1}$
Unit cell dimensions	a = 9.439(5) Å, α = 74.488(5)° b = 13.237(5) Å, β = 91.336(5)° c = 21.026(5) Å, γ = 107.607(5)°
Volume	2408.0(17) Å^3
Z, Calculated density	6, 1.951 gcm^{-3}
Absorption coefficient	8.881 mm^{-1}
F(000)	1356
θ range for data collection	1.01 to 23.25°
Limiting indices	$-10 \le h \le 10$, $-13 \le k \le 14$, $0 \le l \le 23$
Reflections collected/unique	6726/6726 [R(int) = 0.0170]
Completeness to θ = 23.25°	97.1%
Refinement method	Full-matrix least-squares on F^2
Data/restraints/parameters	6726/0/533
Goodness-of-fit on F^2	1.060
Final R indices [$I > 2\sigma(I)$]	R_1 = 0.0393, wR_2 = 0.1163
R indices (all data)	R_1 = 0.0401, wR_2 = 0.1171
Largest diff. peak/hole	1.376/–0.855 e·Å^{-3}

Table 5. Selected bond lengths [Å] and angles [°] in complex **2** (three independent molecules *2*, *2a*, and *2b*)

	2	*2a*	*2b*
Pt(1)–O(2)	2.009(6)	2.000(5)	2.003(6)
Pt(1)–O(1)	2.045(5)	2.061(5)	2.062(6)
Pt(1)–C(8)	2.095(8)	2.096(8)	2.077(9)
Pt(1)–S(1)	2.188(2)	2.186(2)	2.177(2)
S(1)–O(5)	1.47(1)	1.46(1)	1.44(1)
S(1)–C(12)	1.75(1)	1.77(1)	1.75(1)
S(1)–C(11)	1.79(1)	1.77(1)	1.76(1)
O(1)–C(2)	1.28(1)	1.29(1)	1.29(1)
O(3)–C(7)	1.21(1)	1.23(1)	1.26(1)
O(2)–C(4)	1.27(1)	1.29(1)	1.23(1)
O(4)–C(9)	1.23(1)	1.20(1)	1.20(1)
C(2)–C(3)	1.39(1)	1.37(1)	1.37(2)
C(3)–C(4)	1.34(1)	1.37(1)	1.36(2)
O(2)–Pt(1)–O(1)	91.7(2)	91.6(2)	91.1(3)
O(2)–Pt(1)–C(8)	88.0(3)	88.0(3)	88.1(3)
O(1)–Pt(1)–C(8)	178.2(3)	177.5(3)	179.0(3)
O(2)–Pt(1)–S(1)	176.5(2)	175.8(2)	178.6(2)
O(1)–Pt(1)–S(1)	90.9(2)	92.3(2)	90.4(2)
C(8)–Pt(1)–S(1)	89.4(2)	88.1(2)	90.5(3)
O(5)–S(1)–C(12)	108.4(5)	108.5(5)	107.4(6)
O(5)–S(1)–C(11)	108.4(5)	109.1(5)	107.5(7)
C(12)–S(1)–C(11)	101.3(5)	100.6(5)	100.8(6)
O(5)–S(1)–Pt(1)	115.2(3)	115.7(3)	119.4(4)
C(12)–S(1)–Pt(1)	111.2(4)	112.1(4)	111.2(4)
C(11)–S(1)–Pt(1)	111.4(3)	109.7(3)	108.8(4)

trons in the chelate ring.[7] The IR spectra of **2** and **3**, containing both oxygen-bonded and carbon-bonded acetylacetonate show two sets of absorptions in the C–H stretching region. The IR band above 3000 cm^{-1} was assigned to the Cγ-H vibration of the oxygen-bonded ligand whereas below 3000 cm^{-1}, both CH_3 and Cγ-H absorptions for the σ-bonded acac could be clearly identified. The high frequencies (1680–1630 cm^{-1}) of the C=O stretching modes observed in complexes **2** and **3** are further evidence that the carbonyl groups do not interact with platinum and strongly suggest that the complexes also contain a σ-bonded acac.

The absorption band at 1030 cm^{-1} in the IR spectra of **1** and **2** was assigned to the S=O stretching mode of the DMSO moiety whereas the band at 340 cm^{-1}, unique to the only new chloride complex here reported, was unambiguously attributed to the Pt–Cl stretching mode.

The ^1H NMR spectrum of **1** in $CDCl_3$ shows two singlets at δ = 2.02 and 2.06 ppm for the two methyl groups of the oxygen-bonded acetylacetonate, one singlet at δ = 5.56 ppm relative to the Cγ-H of acac and one singlet at δ = 3.44 ppm with a characteristic $^3J_{H-Pt}$ of 40 Hz for the methyl protons of the DMSO ligand. The resonance pattern is in agreement with an asymmetric *O,O′*-chelated complex which also shows the expected remarkable deshielding of the methyne proton (Cγ-H) due to the aromatic character of the metallacycle. The ^1H NMR spectrum of complex **2** in $CDCl_3$ shows a signal pattern very similar to that observed for compound **1** with only two extra resonances, i.e. one singlet at δ = 2.29 ppm ($^4J_{H-Pt}$ = 5 Hz) and one strongly ^{195}Pt-coupled singlet at δ = 4.80 ppm ($^2J_{H-Pt}$ = 120 Hz) account-

 © 2005 Wiley-VCH Verlag GmbH & Co. KGaA, Weinheim

ing for six protons and one proton, respectively. The occurrence of the same signal pattern observed for complex **1** also suggests, for complex **2**, the presence of one asymmetric *O,O′*-chelated acac in the platinum coordination sphere (two methyl groups, δ = 2.01 and 1.95 ppm, one Cγ-H proton, δ = 5.53 ppm) and one coordinated DMSO (δ = 3.31 ppm, $^3J_{H-Pt}$ = 40 Hz). The observed two extra signals could be easily assigned to an extra σ-bonded acac, which occupies the fourth square-planar coordination site, on the basis of both the large platinum coupling for the Cγ-H proton at δ = 4.80 ppm and the equivalence of the methyl groups (one singlet at δ = 2.29 ppm). In both **1** and **2**, the two methyl resonances of the asymmetric *O,O′*-chelated acac were assigned to the appropriate halves of the diketonate on the basis of the NOESY cross peaks originating from the interaction of one of them with the *cis*-DMSO ligand observed in the NOESY spectra.

The ^{1}H NMR spectrum of **3** in CD_3OD consists of only four resonances at 1.77, 2.18, 4.75 and 5.39 ppm accounting for six protons, twelve protons, two protons and one proton, respectively. None of the observed signals show ^{195}Pt satellites assignable to coordinated DMSO. On the other hand, the strong ^{195}Pt coupling exhibited by the resonance at δ = 4.75 ppm ($^2J_{H-Pt}$ = 120 Hz) together with proton integration data indicate the presence of two equivalent Cγ-H protons characterised by a $^2J_{H-Pt}$ of 120 Hz and, therefore, two equivalent Cγ-bonded acac groups in the platinum coordination sphere. Two equivalent Cγ-coordinated acac moieties also account for the twelve protons resonating at δ = 2.18 ppm. The other two resonances at δ = 1.77 and 5.39 ppm in the spectrum of **3** were assigned to one symmetric *O,O′*-chelate acac ligand coordinated to the metal. Consistently, the $^2J_{H-Pt}$ values observed for the single and the two equivalent Cγ-bonded acac groups of complexes **2** and **3**, respectively, are very similar due to the presence, in both cases, of an *O,O′*-chelated acac group in the *trans* position.

The ^{13}C NMR spectra of complexes **1**–**3** confirmed the structures assigned on the basis of ^{1}H NMR spectroscopic data. One bond and long range 2-D ^{1}H-^{13}C HETCOR experiments (spectra of **2** in Figure 1) allowed correct assignments for all the ^{13}C resonances. In particular, *O,O′*-chelated and Cγ-bonded acac groups show, for the Cγ atom, very different chemical shifts and ^{195}Pt couplings. The pseudo aromatic Cγ carbons of the acac chelates resonate downfield and with much smaller ^{195}Pt coupling constants (δ = 102.27 ppm, $^3J_{C-Pt}$ = 73 Hz; δ = 102.19 ppm, $^3J_{C-Pt}$ = 64 Hz; δ = 101.97 ppm, for **1**, **2** and **3**, respectively) with respect to the corresponding carbon in the σ-bonded acac (δ = 42.04 ppm, $^1J_{C-Pt}$ = 652; δ = 44.00 ppm, for **2** and **3**, respectively). Carbonyls of the acac chelate involved in the pseudo aromatic metallacycle resonate upfield with respect to those of σ-bonded acac. The long range 2-D ^{1}H-^{13}C HETCOR spectra of **1** and **2**, together with the above mentioned NOESY data, were used to correlate the carbonyls and the methyl groups belonging to the same half of the asymmetric chelate acac. In the case of complex **1**, the two carbonyl resonances observed at δ = 185.06 and 185.87 ppm show $^2J_{C-Pt}$ values of 28 and 16 Hz, respectively, in agreement with the higher *trans* effect exhibited by DMSO compared with that of the chloro ligand.

Interestingly, in the ^{1}H-^{13}C HETCOR spectrum of **2** (in which the Cγ-bonded acac and DMSO are both coordinated to platinum), the positions of the observed cross peaks due to the coupling with the magnetically active spectator nucleus (^{195}Pt) correlate with the number of bonds

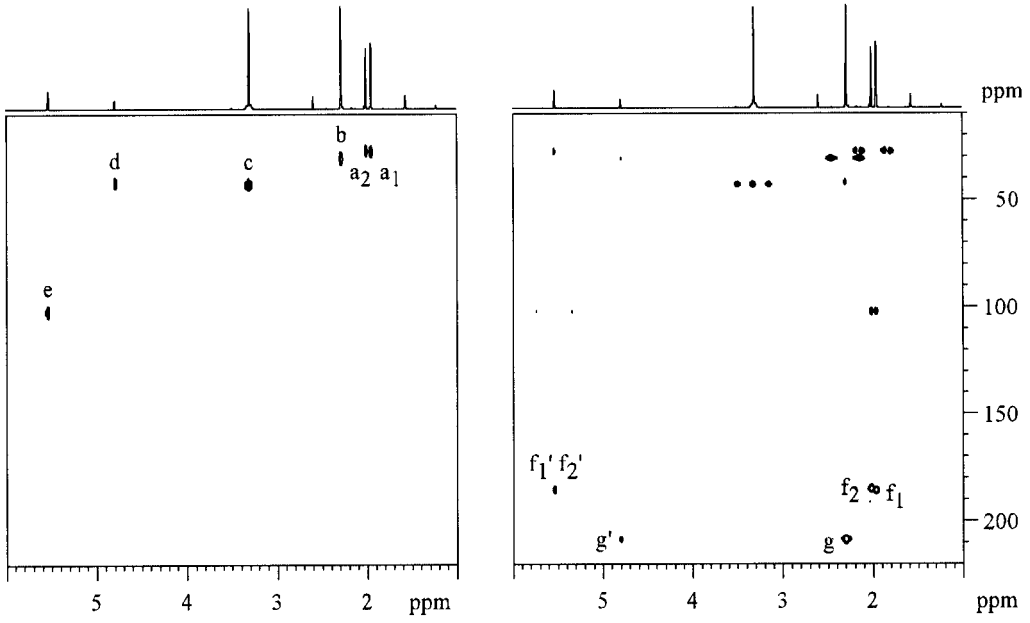

Figure 1. ^{1}H-^{13}C HETCOR (left) and ^{1}H-^{13}C long range HETCOR (right) spectra of **2**. Hydrogen bearing carbon atoms of *O,O′*-chelated acac (a_1, a_2, and e), Cγ-bonded acac (b and d) and DMSO (c) were detected by ^{1}H-^{13}C HETCOR while the carbonyls of the *O,O′*-chelated acac and the Cγ-bonded acac could be assigned according to cross peaks with methyls (f_1, f_2, and g, respectively) or according to cross peaks with Cγ-H (f_1', f_2', and g′, respectively) in the ^{1}H-^{13}C long range HETCOR spectrum

 © 2005 Wiley-VCH Verlag GmbH & Co. KGaA, Weinheim

between this latter nuclues and the observed nucleus (^{1}H). The straight line joining the ^{195}Pt cross peaks shows, in the case of the platinum bound Cγ-H acac ($^2J_{H–Pt}$ = 652 Hz) and the DMSO ligand ($^3J_{H–Pt}$ = 56 Hz), a negative and positive gradient, respectively (Figure 2).[15] Another interesting feature of the ^{195}Pt coupling exhibited by [Pt(*O,O′*-acac)(γ-acac)(DMSO)] can be shown by a 2-D ^{1}H-^{195}Pt HETCOR experiment, in which all ^{195}Pt coupled protons result in cross peaks at a single platinum chemical shift (δ = –3198 ppm in $CDCl_3$). Among all the CH_3 resonances for **2**, only the methyl groups of the σ-bonded acac exhibit small cross peaks showing a very small $J_{H–Pt}$ coupling in the ^{1}H-^{195}Pt HETCOR spectrum. This may be due to a through space interaction (Figure 3). The ^{195}Pt NMR spectroscopic data of complexes **1**–**3** are reported in Table 3. The observed ^{195}Pt chemical shifts show that in [Pt(*O,O′*-acac)(DMSO)L] complexes, the shielding effect when L = Cγ-acac is considerably higher than when L = Cl^- ($\Delta\delta$, ^{195}Pt = 738 ppm in CD_3OD), while in [Pt(*O,O′*-acac)(γ-acac)L] the shielding effect is higher when L = DMSO than when L = Cγ-acac ($\Delta\delta$, ^{195}Pt = 629 ppm in CD_3OD).

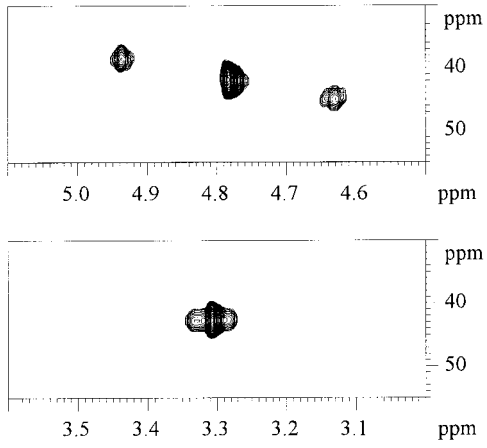

Figure 2. Expansions of ^{1}H-^{13}C HETCOR spectrum of **2** showing ^{195}Pt satellites relative to the Cγ-bonded acac (above) and the DMSO methyl groups (below)

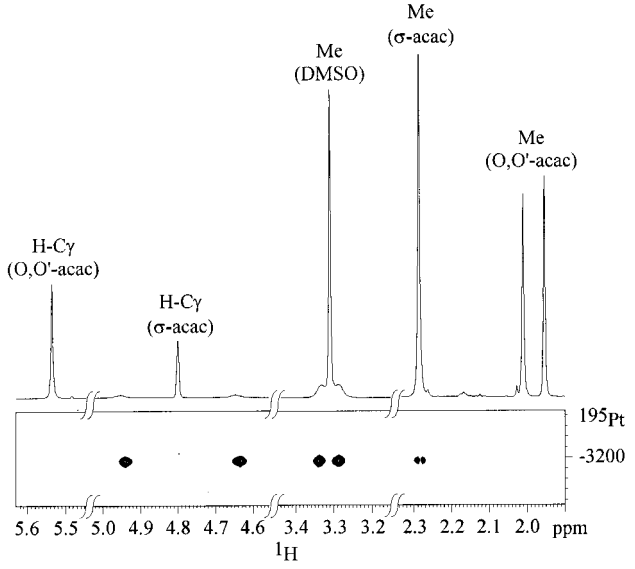

Figure 3. ^{1}H-^{195}Pt-HETCOR spectrum of **2** acquired without ^{195}Pt decoupling during acquisition. For clarity, ^{1}H projections are not on the same vertical scale

Crystal Structure of 2

The crystals obtained for complex [Pt(*O,O′*-acac)(γ-acac)(DMSO)] (Figure 4) contain three molecules in the asymmetric unit (*2*, *2a* and *2b*). The cell dimensions along with other crystallographic details are given in Table 4. In both the neutral [Pt(*O,O′*-acac)(γ-acac)(DMSO)] (**2**) and ionic [Pt(*O,O′*-acac)(γ-acac)Cl]$^-$ (**4**)[16] complexes, the oxygen-bonded acetylacetonate ligand is asymmetrically coordinated. The different Pt–O bond lengths follow the trend expected on the basis of *trans* substituents. The Pt–O lengths for the oxygen atom *trans* to the Cγ-carbon are 2.06[1] and 2.07(1) Å (square brackets indicate average values; parentheses refer to unique values) while those for the oxygen atom *trans* to the sulfur (DMSO) and chlorine atoms (complexes **2** and **4**, respectively) are 2.00[1] and 1.97(1) Å. In the σ-bonded acetylacetonate, the Pt–Cγ bond length for compound **2** is in agreement with the value for the analogous bond previously reported for **4** (2.09[2] and 2.11(2) Å, respectively). Both distances are greater than Pt–C(sp^3) σ-bonds *trans* to oxygen reported for C alkyls.[16,17] The Cγ of the σ-bonded acetylacetonate could be a weak donor, probably due to the cumulative electronegative effects of two carbonyl groups. All three *O,O′*-chelate acac moieties are planar. In all three molecules, the oxygen atoms of DMSO are oriented towards the σ-bonded acetylacetonate ligands. The modulus of the lowest torsional angles X–Pt–S–O (Ψ) (Scheme 3), according to the statistical study by Calligaris and Carugo,[2] indicates that the torsional angles Ψ lie in the low probability range [51.5(4)°, 52.4(5)° and 34.0(5)°]. This orientation of DMSO favours

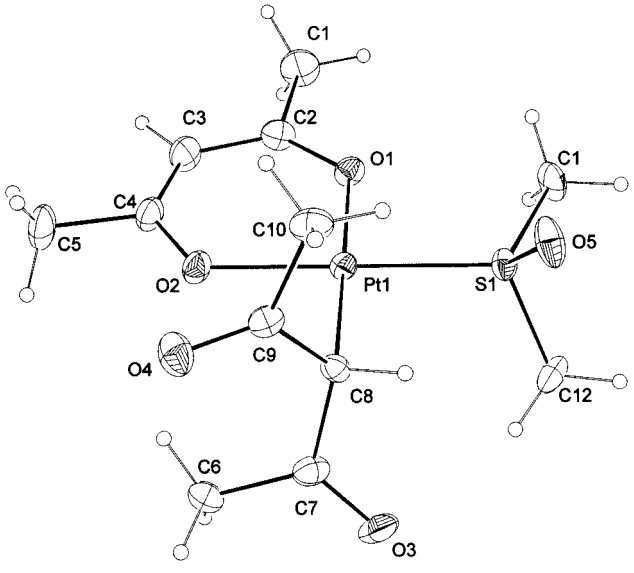

Figure 4. Molecular structure of one out of three independent molecules (molecule *2*) in the asymmetric unit of compound **2**

 © 2005 Wiley-VCH Verlag GmbH & Co. KGaA, Weinheim

interactions between the oxygen atom of the DMSO and the Cγ hydrogen atom of the σ-bonded acetylacetonate [C(8)···O(5) 3.20(5), H(8)···O(5) 2.55(5) Å, C(8)···H(8)···O(5) 124(1)°].

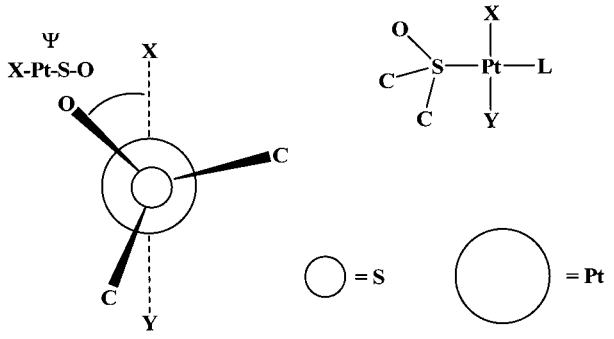

Scheme 3

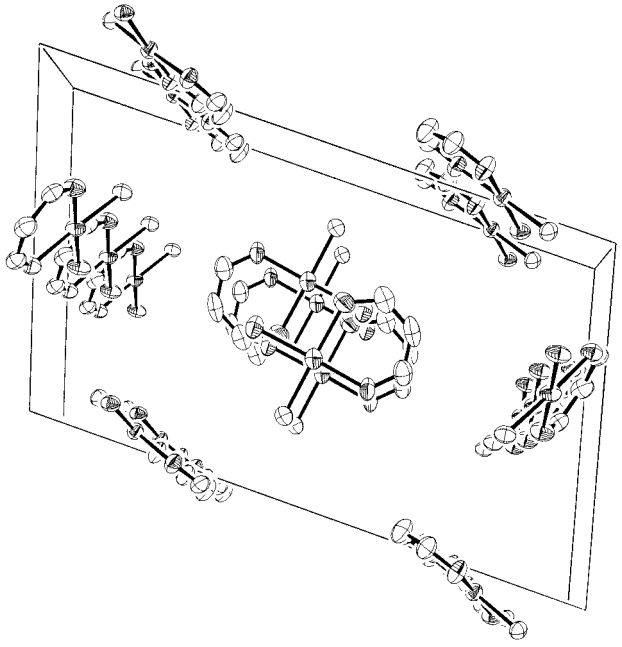

Figure 5. Unit cell projection along the *a*-axis showing alternating *2b* molecules staggered by ca. 180° and stacked inside the channel resulting from the propagation of molecules of *2* (top and bottom) and *2a* (sides). Only ligand atoms in the coordination plane are shown (see Supporting Information, S4 for the same projection with all atoms except hydrogen)

The crystal packing arrangement is shown in Figure 5. The three independent molecules of the unit cell are almost perpendicular and describe a box shape. Interestingly, the crystal structure shows subsequent boxes generating a channel by superimposition along the *a* axis. Alternating *2b* molecules are staggered by ca. 180° and stacked inside the channel created by the propagation of molecules *2* and *2a*. Selected bond distances and angles are listed in Table 5.

Reaction Mechanism

Platinum and palladium complexes of the type [M(*O,O′*-acac)(γ-acac)L] which contain one *O,O′*-chelated and one Cγ-bonded β-diketonate on the same metal together with one of a variety of nitrogen, phosphorus, arsenic and sulfur ligands (L) are well known in coordination chemistry. Usually, such complexes are produced by the addition of the ligand L to [M(*O,O′*-acac)$_2$] which causes the rearrangement of one of the two acac groups from the *O,O′*-chelate mode to the σ-bonded mode to give [M(*O,O′*-acac)(γ-acac)L] species.[12] However, in the course of our study, we have verified that treatment of the bis(β-diketonate)platinum(II) complex [Pt(*O,O′*-acac)$_2$] with excess DMSO or Et_2S[14] does not give [Pt(*O,O′*-acac)(γ-acac)L] even after two weeks. On the other hand, treatment of the starting complexes used in this work, i.e. [$PtCl_2(DMSO)_2$] and K[$PtCl_3$(DMSO)], with an excess of acetylacetone does not give [Pt(*O,O′*-acac)$_2$] in addition to [Pt(*O,O′*-acac)(γ-acac)L] and [Pt(*O,O′*-acac)(γ-acac)$_2$]$^-$. In a few cases, as for complex **2** described in this paper, [M(*O,O′*-acac)(γ-acac)L] complexes could be obtained starting from species lacking acac ligand(s) previously bound to the metal. In the case of platinum chemistry, the syntheses of K[Pt(*O,O′*-acac)(γ-acac)Cl][6] and [Pt(*O,O′*-acac)(γ-acac)(Et_2S)][14] have been reported starting from $K_2[PtCl_4]$ and [$PtCl_2$-(Et_2S)$_2$], respectively. The subsequent coordination of two acac ligands in the reactions of the [$PtCl_2L_2$]-type complexes (L = Et_2S, 1,2-bis(ethylthio)ethane, PEt_3, PPh_3) with thallium(I) β-diketonates has been studied in order to clarify the factors which could favour each of the two coordination modes, i.e. *O,O′*-chelated or Cγ-bonded, when the first acac binds to the metal. The reaction of *cis*-[$PtCl_2(PPh_3)_2$] with acac requires previous removal of the chloro ligands to give [Pt(*O,O′*-acac)(PPh_3)$_2$] while treatment of *trans*-[$PtCl_2(PEt_3)_2$] with an excess of Tl(acac) gave [Pt(*O,O′*-acac)Cl(PEt_3)]. No acetylacetonato complexes were detected in a similar reaction of *cis*-[$PtCl_2(PEt_3)_2$]. On the other hand, the reaction of *cis*- or *trans*-[$PtCl_2(Et_2S)_2$] with Tl(acac) was reported to give[Pt(*O,O′*-acac)(γ-acac)(Et_2S)] in both cases (although with different reaction rates). Interestingly, in both cases it was not possible to isolate intermediate products either by lowering the reaction temperature or by decreasing the acac/platinum complex ratio.[14] Attempts to obtain [Pt(*O,O′*-acac)$_2$] by treatment of [$PtCl_2(Et_2S)_2$] with K(acac) once again gave, after removal of the chloro ligands with silver perchlorate, [Pt(*O,O′*-acac)(γ-acac)(Et_2S)]. When [$PtCl_2$(S-S)] [S-S = 1,2-bis(ethylthio)ethane] was treated with Tl(acac), [PtCl(γ-acac)(S-S)] was exclusively formed and no other products were obtained even when a large excess of the β-diketonate was used. This latter result clearly indicates that the [PtCl(S-S)]$^+$ moiety prefers to bind to the Cγ-carbon rather than the oxygens of acac. Nevertheless, in the reaction of [$PtCl_2(Et_2S)_2$] with Tl(acac), the isolation of [Pt(*O,O′*-acac)(γ-acac)(Et_2S)] as the only product, without evidence of intermediates, does not explain which of the two coordination modes (*O,O′*-chelated or Cγ-bonded) is preferred when the first acac binds to the metal. It has been suggested that in the reaction of [$PtCl_2(Et_2S)_2$] with acac, the first β-diketonate substitutes one chloro ligand by Cγ-binding to the metal. The second β-diketonate then replaces the other

 © 2005 Wiley-VCH Verlag GmbH & Co. KGaA, Weinheim

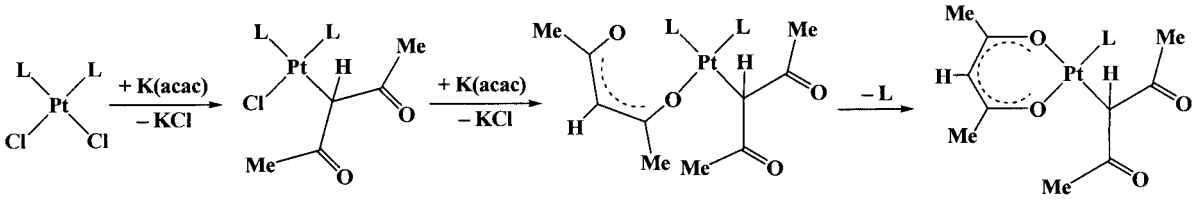

Scheme 4

chloride in a *O*-unidentate mode which finally converts to the *O,O′*-acac chelating mode by sulphide elimination (Scheme 4).

Nevertheless, there is another possible mechanism which cannot be ruled out. According to this mechanism, a cationic β-diketonate chelate first forms, i.e. [Pt(*O,O′*-acac)-$(Et_2S)]^+$, which then bonds to the carbon of the second β-diketonate to give [Pt(*O,O′*-acac)(γ-acac)(Et_2S)] (Scheme 5).[14]

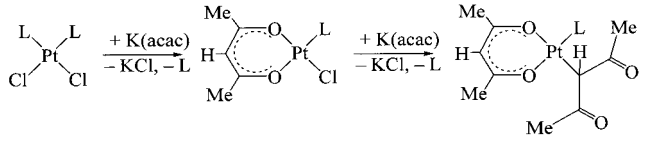

Scheme 5

In this context the synthesis reported here for the **1**, with only the *O,O′*-chelated acac ligand, may be considered important evidence for explaining whether the *O,O′*-chelated or the Cγ σ-bonded acac is the first ligand to coordinate to the metal in the reaction of multiple β-diketonates with platinum. In our investigations, we found that the use of stoichiometric or even substoichiometric amounts of acac with respect to platinum in the reactions with $[PtCl_2(DMSO)_2]$, performed in MeOH, always gave mixtures of **1** and **2**. When we used $K[PtCl_3(DMSO)]$ as a starting complex and water as the solvent, it was possible to exclusively obtain complex **1** which could be isolated in good yield. In principle, the reactivity of $[PtCl_2(DMSO)_2]$ and $K[PtCl_3(DMSO)]$ with chelates can be expected to be very similar.[18] It is well known that both $[PtCl_2(DMSO)_2]$ and $K[PtCl_3(DMSO)]$ react with chelating nitrogen ligands to give the cationic species $[PtCl(DMSO)(N\text{-}N)]^+$ via substitution of one chloride *trans* to DMSO as the first reaction step.[19] In the present case, the formation of a mixture of **1** and **2**, when a suspension of $[PtCl_2(DMSO)_2]$ in MeOH was used in the reaction with acac, can be explained in terms of the low solubility of the starting complex in the reaction medium. In the first step of the reaction, one molecule of acac reacts with the platinum complex to give **1** which is soluble in MeOH and therefore accumulates in the reaction medium. It should be noted that in the formation of compound **1**, as in the formation $[PtCl(DMSO)\text{-}(N\text{-}N)]^+$,[19] the higher *trans* effect of DMSO compared with that of chloride is responsible for both the first attack on platinum by one end of the bidentate ligand and further chelation leading to the thermodynamic product. As the reaction proceeds, complex **2** forms since the second molecule of acac reacts with [PtCl(*O,O′*-acac)(DMSO)] (**1**) rather than with $[PtCl_2(DMSO)_2]$ because of the higher availability of compound **1** in the reaction medium. When we used $K[PtCl_3(DMSO)]$ as the starting complex, [PtCl(*O,O′*-acac)(DMSO)] could be obtained in high yield. In fact **1** is scarcely soluble in water and precipitates from the reaction medium immediately after its formation. It should be noted that **1** could also be obtained by carrying out the reaction of $[PtCl_2(DMSO)_2]$ with a stoichiometric amount of acac in water. In this case, however, a longer reaction time was required due to the much lower solubility of $[PtCl_2\text{-}(DMSO)_2]$ in water compared with that of $K[PtCl_3(DMSO)]$. Finally, further treatment of [Pt(*O,O′*-acac)(γ-acac)(DMSO)] with an extra acac led to the formation of [Pt(*O,O′*-acac)(γ-acac)$_2$]. These results confirm the mechanism depicted in Scheme 5 in which the β-diketonate chelate is the first product formed and the *O,O′*-chelation of the first acac then favours Cγ-carbon bonding of the second (and eventually third) β-diketonate.

Conclusions

In this paper we have described the first two examples of platinum(II) complexes containing both acetylacetonate and sulfoxide ligands coordinated to the metal, namely [PtCl(*O,O′*-acac)(DMSO)] (**1**) and [Pt(*O,O′*-acac)(γ-acac)(DMSO)] (**2**). We have also reported a new synthesis of the homoleptic complex K[Pt(*O,O′*-acac)(γ-acac)$_2$] (**3**).[20] The formation of **2** represents a rare example of a reaction giving [Pt(*O,O′*-acac)(γ-acac)L] complexes starting from platinum species other than [Pt(*O,O′*-acac)$_2$] which also, in general, lack an acac ligand initially bound to the metal. Moreover, the isolation of **1** as an intermediate supports a mechanism in which the β-diketonate chelate is the first product formed from the reaction of multiple β-diketonate ligands with platinum. According to the results reported here, the *O,O′*-chelation of the first acac is followed by the Cγ-carbon bonding of the second (and eventually the third) β-diketonate in the platinum coordination sphere.

Experimental Section

Physical Measurements: Elemental analyses were performed using a Carlo–Erba elemental analyser, model 1106. IR Spectra were recorded with a Perkin–Elmer Spectrum 598 spectrometer using KBr as a solid support for pellets. ^1H and ^{13}C NMR spectra as well as ^1H-^1H NOESY, ^1H-^{13}C HETCOR and ^1H-^{195}Pt HETCOR 2-D experiments were performed with a DPX 400 MHz Avance Bruker instrument using $CDCl_3$, CD_3OD or D_2O as the solvent. Chemical shift are referenced to TMS using the residual protic solvent peaks

 © 2005 Wiley-VCH Verlag GmbH & Co. KGaA, Weinheim

as internal references (δ = 7.24 for $CDCl_3$, δ = 3.30 for CD_3OD and δ = 4.65 for D_2O).

Starting Materials: Commercial reagent grade chemicals, acetylacetone and solvents were used without further purification. [Pt(*O,O′*-acac)$_2$],[7] [$PtCl_2(DMSO)_2$][21] and K[$PtCl_3$(DMSO)][22] were prepared by previously reported procedures.

[PtCl(*O,O′*-acac)(DMSO)] (1): A solution of acetylacetone (97.5 mg, 0.973 mmol) and KOH (19.5 mg, 0.487 mmol) in methanol (5 mL) was added dropwise to a solution of K[$PtCl_3$(DMSO)] (204 mg, 0.487 mmol) in water (10 mL) at room temperature with stirring. After few minutes a yellow precipitate separated from the solution. The reaction mixture was left stirring overnight and the pale-yellow precipitate of [PtCl(*O,O′*-acac)(DMSO)] (**1**) was then isolated by filtration and dried under vacuum (yield 149 mg, 75%). $C_7H_{13}ClO_3SPt$ (407.79): calcd. C 20.62, H 3.21; found C 20.73, H 3.28.

Alternatively, a solution containing acetylacetone (97 mg, 0.966 mmol) and KOH (27 mg, 0.483 mmol) in water (5 mL) was added dropwise to a suspension of [$PtCl_2(DMSO)_2$] (204 mg, 0.483 mmol) in water (10 mL) at room temperature with stirring. The reaction mixture slowly became a yellow solution. After 3 h, a pale-yellow solid started to precipitate. The suspension was left stirring for one day and the solid was then filtered and dried under vacuum (yield 27 mg, 26%). $C_7H_{13}ClO_3SPt$ (407.79): calcd. C 20.62, H 3.21; found C 20.51, H 3.18.

[Pt(*O,O′*-acac)(γ-acac)(DMSO)] (2): A solution of acetylacetone (358 mg, 3.576 mmol) and KOH (114 mg, 2.860 mmol) in methanol (5 mL) was added dropwise to a suspension of [$PtCl_2(DMSO)_2$] (302 mg, 0.715 mmol) in methanol (20 mL) at room temperature with stirring. The reaction mixture slowly became a pale yellow solution. After one day, the solvent was evaporated under vacuum and the yellow residue was extracted with $CHCl_3$ (10 mL). The chloroform solution was then filtered to remove KCl and K(acac), pentane (30 mL) was added and the resultant solution kept overnight at 5 °C. Quadrangular pale-yellow crystals of [Pt(*O,O′*-acac)(γ-acac)(DMSO)] (**2**) which separated out from the solution were filtered, washed with pentane and dried under vacuum (yield 168 mg, 50%). $C_{12}H_{20}O_5SPt$ (471.441): calcd. C 30.57, H 4.28; found C 30.73, H 4.34.

K[Pt(*O,O′*-acac)(γ-acac)$_2$] (3): A solution of acetylacetone (332 mg, 3.318 mmol) and KOH (94.8 mg, 2.370 mmol) in methanol (5 mL) was added dropwise to a suspension of [$PtCl_2(DMSO)_2$] (200 mg, 0.474 mmol) in methanol (20 mL) at room temperature with stirring. After 1 h, the suspension became a pale-yellow solution which was left stirring for three days. The solvent was then removed under vacuum and the residual yellow oil was extracted with $CHCl_3$ (10 mL). The chloroform solution was then filtered to separate KCl and K(acac), and pentane (30 mL) was added causing the precipitation of K[Pt(*O,O′*-acac)(γ-acac)$_2$] (**3**) as a yellow solid. The product was separated by filtration, washed with pentane and dried under vacuum (yield 68 mg, 27%). $C_{15}H_{24}KO_6Pt$ (534.524): calcd. C 33.70, H 4.53; found C 33.46, H 4.21.

Alternatively, a solution of acetylacetone (129 mg, 1.284 mmol) and KOH (48 mg, 0.856 mmol) in methanol (10 mL) was added dropwise to a suspension of [Pt(*O,O′*-acac)(γ-acac)(DMSO)] (202 mg, 0.428 mmol) in diethylether (30 mL) at room temperature with stirring. The colour of the solid in the reaction mixture slowly turned from white to pale-yellow. After one day, the solvent was removed under vacuum and the residue was washed with diethyl ether (10 mL) then extracted with chloroform (10 mL). K[Pt(*O,O′*-acac)(γ-acac)$_2$] was obtained as a pale-yellow solid by addition of diethylether (20 mL) to the filtered chloroform solution (yield 65 mg, 28%).

Reaction of [Pt(*O,O′*-acac)$_2$] with DMSO: [Pt(*O,O′*-acac)$_2$] (2 mg, 0.005 mmol), synthesised by a previously reported procedure, was dissolved in $CDCl_3$ (0.5 mL) and the resultant solution placed in an NMR tube. DMSO (1 μL, 1.17 mg, 0.015 mmol) was added and the solution was monitored by recording ^{1}H NMR spectra periodically over a period of two weeks. The spectra did not show any significant change over that period of time.

Single-Crystal X-ray Diffraction Study: Pale-yellow crystals of [Pt(*O,O′*-acac)(γ-acac)(DMSO)] were obtained by crystallisation from $CHCl_3$/pentane. X-ray data were collected using an Enraf–Nonius CAD4 diffractometer. A least-squares algorithm using 25 automatically centred reflections was used to refine the unit cell dimensions. A total of 6726 independent reflections were collected in the range $-10 \le h \le 10$, $-13 \le k \le 14$ and $0 \le l \le 23$. Four reflections were monitored during data collection but no decay was observed. Crystallographic data are summarised in Table 4. The full data set was corrected for Lorentz and polarisation effects and an absorption correction was applied using the DIFABS package[23] at the isotropic stage of refinement. The structure was solved by direct-methods in the $P\bar{1}$ space group. The model was refined by full-matrix least-squares methods. Anisotropic thermal parameters were applied for all non-hydrogen atoms. All hydrogen atoms were placed in their geometrically calculated positions and were included in the full-matrix least-square cycles with isotropic thermal parameters (U) fixed at 1.2 and 1.5 (for methyl group) times the values of *U* of the corresponding carbon atoms. Crystallographic calculations were carried out and molecular graphics designed using the SIR97,[24] SHELXL97,[25] WinGX,[26] ORTEP for Windows[27] and PARST97[28] packages. CCDC-172448 contains the supplementary crystallographic data for this paper. These data can be obtained free of charge from The Cambridge Crystallographic Data Centre via www.ccdc.cam.ac.uk/data_request/cif.

Supporting Information (see footnote on the first page of this article): Figure S1, ^{1}H-^{13}C HETCOR and long range HETCOR NMR spectra of **1**. Figures S2, molecular structure of *2a*. Figure S3, molecular structure of *2b*. Figure S4, unit cell projection of **2** along *a*-axis with all atoms except hydrogens. Table S5, anisotropic displacement parameters for *2* and *2a*. Table S6, anisotropic displacement parameters for *2b*.

Acknowledgments

The authors gratefully acknowledge Mr. Alessandro Laurita (University of Potenza) for the X-ray diffraction data collection. This work was supported by the University of Lecce and the Ministero dell'Istruzione, dell'Università e della Ricerca (M.I.U.R.), Cofin. 2003 (No. 2003039774_005).

[1] F. P. Fanizzi, G. Natile, M. Lanfranchi, A. Tiripicchio, *Inorg. Chim. Acta* **1997**, *264*, 11–18.
[2] M. Calligaris, O. Carugo, *Coord. Chem. Rev.* **1996**, *153*, 83–154.
[3] D. A. Thomton, *Coord. Chem. Rev.* **1990**, *104*, 173–249.
[4] S. Gama de Almeida, J. L. Hubbard, N. Farrell, *Inorg. Chim. Acta* **1992**, *193*, 149–157.
[5] A. Werner, *Ber. Dtsch. Chem. Ges.* **1901**, *34*, 2584.
[6] Lewis, Long, Oldham, *J. Chem. Soc.* **1965**, 6740–6747.
[7] G. T. Behnke, K. Nakamoto, *Inorg. Chem.* **1967**, *6*, 433–440.
[8] G. T. Behnke, K. Nakamoto, *Inorg. Chem.* **1967**, *6*, 440–445.
[9] G. T. Behnke, K. Nakamoto, *Inorg. Chem.* **1968**, *7*, 330–338.

 © 2005 Wiley-VCH Verlag GmbH & Co. KGaA, Weinheim

[10] S.Okeya, Y. Nakamura, S. Kawaguchi, *Bull. Chem. Soc. Jpn.* **1982**, *55*, 1460–1466.
[11] S. Baba, T. Ogura, S. Kawaguchi, *Bull. Chem. Soc. Jpn.* **1974**, *47*, 665–668.
[12] T. Ito, T. Kiriyama, A. Yamamoto, *Bull. Chem. Soc. Jpn.* **1976**, *49*, 3250–3256.
[13] T. Ito, T. Kiriyama, Y. Nakamura, A. Yamamoto, *Bull. Chem. Soc. Jpn.* **1976**, *49*, 3257–3264.
[14] F. Sasakura, K. Isobe, S. Kawaguchi, *Bull. Chem. Soc. Jpn.* **1985**, *58*, 657–663.
[15] L. Carlton, *Relative Sign of J Couplings from Two-Dimensional NMR Spectra*, *Bruker Report* **2000**, no. 148, p. 28–29.
[16] R. Mason, G. B. Robertson, *J. Chem. Soc. A* **1969**, 485–492.
[17] K. J. Cavell, H. Jin, B. W. Skelton, A. H. White, *J. Chem. Soc. Dalton Trans.* **1993**, 1973–1978.
[18] P. Kong, D. Iyamuremye, F. D. Rochon, *Bioinorganic Chemistry* **1976**, *6*, 83–89.
[19] N. Farrell, S. Gama de Almeida, Y. Qu, *Inorg. Chim. Acta* **1990**, *178*, 209–211.
[20] T. Ito, T. Kiriyama, Y. Nakamura, A. Yamamoto, *Bull. Chem. Soc. Jpn.* **1976**, *49*, 3257–3264.
[21] Yu. N. Kukushkin, Yu. E. Vyaz'menskii, L. I. Zorina, Yu. L. Pazukhina, *Russian J. Inorg. Chem. (Engl. Transl.)* **1968**, *13*, 835–838.
[22] Yu. N. Kukushkin, Yu. E. Vyaz'menskii, L. I. Zorina, *Russian J. Inorg. Chem. (Engl. Transl.)* **1968**, *13*, 1573–1576.
[23] N. Walker, D. Stuart, *Acta Crystallogr., Sect. A* **1983**, *39*, 158–166.
[24] A. Altomare, M. C. Burla, M. Camalli, G. L. Cascarano, C. Giacovazzo, A. Guagliardi, A. G. G. Moliterno, G. Polidoro, R. Spagna, *SIR97*, *A program for automatic solution and refinement of crystal structures*, **1996**.
[25] G. M. Sheldrick, *SHELXL97*, *Program for the refinement of crystal structures*, University of Göttingen, Germany, **1997**.
[26] *An Integrated System of Windows Programs for the Solution, Refinement and Analysis of Single Crystal X-ray Diffraction Data*, L. J. Farrugia *J. Appl. Cryst.* **1999**, *32*, 837–838.
[27] *ORTEP-3 for Windows – A Version of ORTEP-III with a Graphical User Interface (GUI)*, L. J. Farrugia, *J. Appl. Cryst.* **1997**, *30*, 565.
[28] M. Nardelli, *PARST 97, A System of Computer Routines for Calculating Molecular Parameters from the Results of Crystal Structure Analysis*, University of Parma, Italy, **1996**.

Received: July 29, 2004
Published Online January 27, 2005

 © 2005 Wiley-VCH Verlag GmbH & Co. KGaA, Weinheim

EurJIC
European Journal of Inorganic Chemistry

Issue 5/2005

Pages 801–984

Papers available ahead of print in Early View at www.interscience.wiley.com

Earliest available Table of Contents:
Automatically, free of charge by e-mail through
www.interscience.wiley.com/alerts

COVER PICTURE

The cover picture shows the richness of 1,2-ethanediylbis-(iminomethylene)bis(phosphonic acid) (H_4L) used as a ligand. The left compound is cadmium phosphonate, $Cd_2Cl_2(H_2O)_4(H_2L)$, in which the Cd atoms form dimers through bridging chloride ions. These dimers are, in turn, formed into rows by the phosphonate groups, and the rows are crosslinked by the organic chain of the ligand into layers. The second picture shows $Zn_3Cl_2(H_2L)_2{\cdot}2H_2O$, in which Zn atoms are tetrahedrally coordinated. One of the Zn atoms lies in rows parallel to the *b*-axis, which are sandwiched between rows formed by the two other Zn atoms. The carbon–nitrogen chains crisscross each other forming a three-dimensional structure. The structure of this latest compound is presented in the article by A. Clearfield et al. on p. 829 ff.

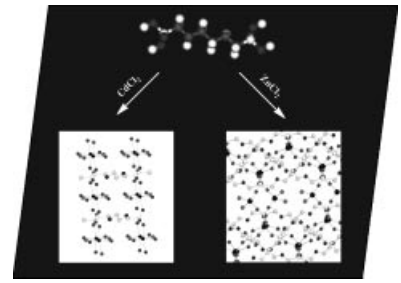

SHORT COMMUNICATIONS

Contents

817 **G. B. Deacon,* C. M. Forsyth, P. C. Junk**

η^6:η^6 Coordination of Tetraphenylborate to Ytterbium(II): A New Class of Lanthanoid *ansa*-Metallocenes

Keywords: Metallocenes / Ytterbium / Tetraphenylborate / Bis(trimethylsilyl)amide / Pyrazolate

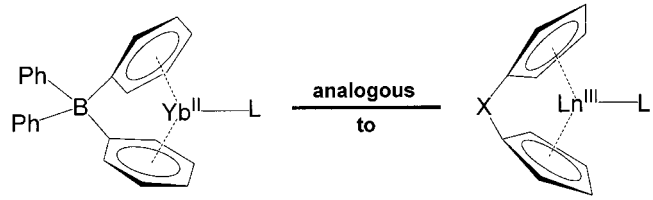

 © 2005 Wiley-VCH Verlag GmbH & Co. KGaA, Weinheim

822 **M. M. Makowska-Grzyska, K. Doyle, R. A. Allred, A. M. Arif, D. C. Bebout,* L. M. Berreau***

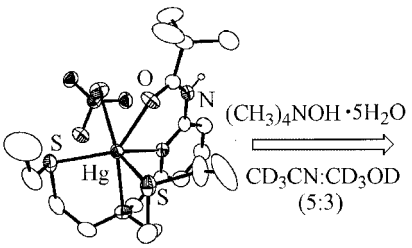

Structural, Spectroscopic, and Reactivity Properties of N_2S_2(thioether)O(amide)-Ligated Hg^{II} Complexes: The First Examples of Hg^{II}-Mediated Amide Cleavage

Keywords: Mercury / Amides / NMR Spectroscopy / Zinc / Cadmium

FULL PAPERS

829 **N. Bestaoui, E. V. Bakhmutova-Albert, A. V. Rodriguez, R. Llavona, A. Clearfield***

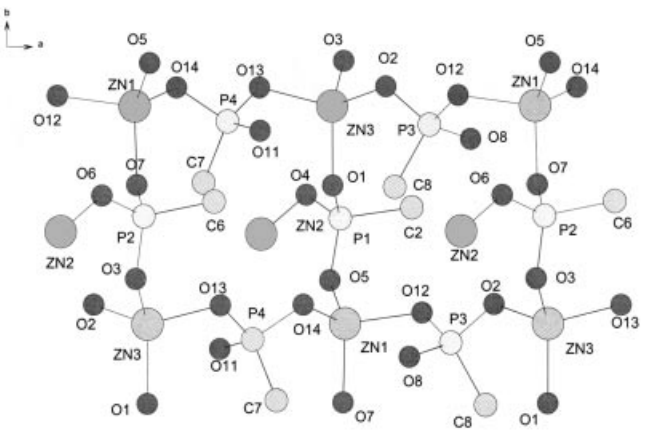

Ab-initio Powder Structure Determination of Dichloro[1,2-ethanediylbis(iminomethylene)bis-(phosphonato)]trizinc Dihydrate

Keywords: Metal phoshonates / Zinc

837 **B. Cardoso, J. Pires,* A. P. Carvalho, M. B. Carvalho, I. Kuźniarska-Biernacka, A. R. Silva, C. Freire,* and B. de Castro**

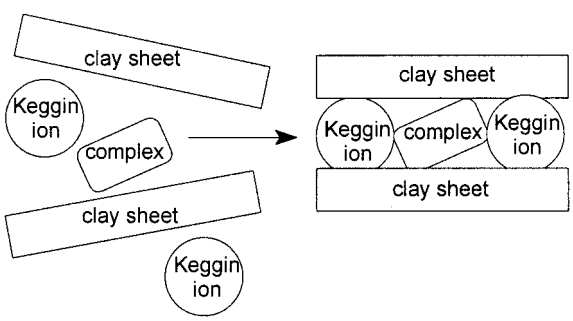

Catalytic Properties of a Mn^{III}-Salen Complex Immobilised in a Pillared Clay by Simultaneous Pillaring/Encapsulation Procedures

Keywords: Clays / Microporous materials / Heterogeneous catalysis / Manganese

845 **N. A. Bokach, V. Y. Kukushkin,* M. Haukka, A. J. L. Pombeiro***

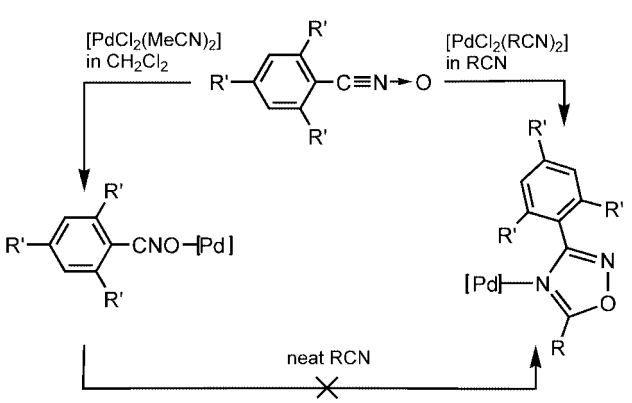

Synthesis of (1,2,4-Oxadiazole)palladium(II) Complexes by [2+3] Cycloaddition of Nitrile Oxides to Organonitriles in the Presence of $PdCl_2$

Keywords: Palladium / 1,2,4-oxadiazole complexes / Nitrile complexes / Nitrile oxide complexes / Cycloaddition

 © 2005 Wiley-VCH Verlag GmbH & Co. KGaA, Weinheim

854 **H. An, D. Xiao, E. Wang,* Y. Li, X. Wang, L. Xu**

Open-Framework Polar Compounds: Synthesis and Characterization of Rare-Earth Polyoxometalates $(C_6NO_2H_5)_2[Ln(H_2O)_5(CrMo_6H_6O_{24})]\cdot 0.5H_2O$ (Ln = Ce and La)

Keywords: Rare earth / Polyoxometalates / Open framework / Polar compounds / Magnetic properties

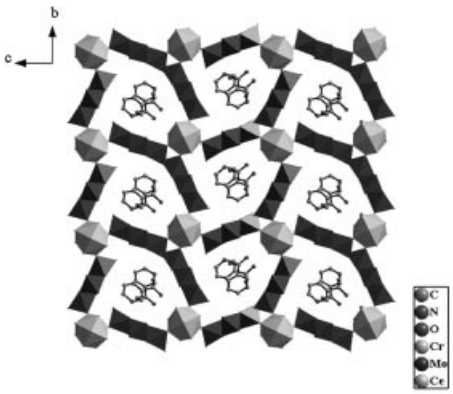

860 **Z. Fei, D. Zhao, T. J. Geldbach, R. Scopelliti, P. J. Dyson***

Structure of Nitrile-Functionalized Alkyltrifluoroborate Salts

Keywords: Anions / Borates / Boron / X-ray structure / Crystal engineering

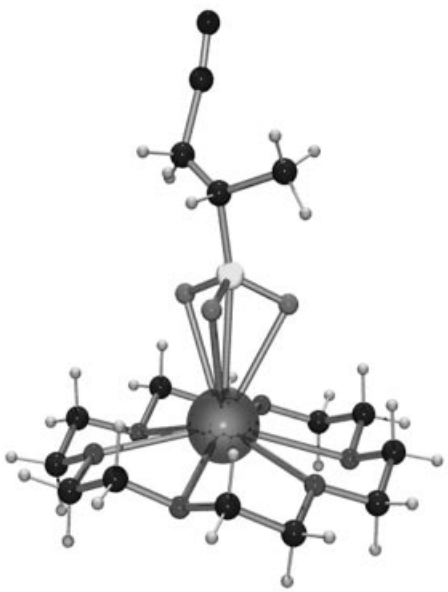

866 **M. Driess,* J. Aust, K. Merz**

From Dinuclear Zirconium(+3)-Phosphido Complexes $\{[Cp_2ZrP(H)R]_2\}$ to the First Neutral Zirconocene–Phosphinidene Dimers $[(Cp_2ZrPR)_2]$ by P–H Dehydrogenation

Keywords: Antiferromagnetic coupling / Phosphido complexes / Silylphosphanes / Zirconium / Phosphorus / P–H bonding activation

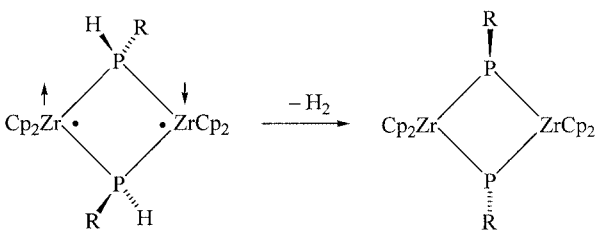

1 **2**

872 **A. N. Boa,* J. D. Crane,* R. M. Kowalczyk, N. H. Sultana**

Addition of (Pyrazol-1-yl)acetyl and (Pyridin-2-yl)acetyl Groups to the Terminal Amino Group of a Phe–Gly Dipeptide Affords ATCUN-Like Copper(II) Binding Sites

Keywords: Bioinorganic chemistry / Copper / Peptides / Tetradentate ligands

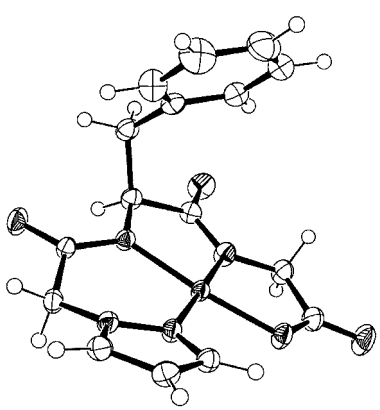

 © 2005 Wiley-VCH Verlag GmbH & Co. KGaA, Weinheim

879 **G. S. Papaefstathiou, A. Escuer, F. A. Mautner, C. Raptopoulou, A. Terzis, S. P. Perlepes,* R. Vicente***

Use of the Di-2-pyridyl Ketone/Acetate/Dicyanamide "Blend" in Manganese(II), Cobalt(II) and Nickel(II) Chemistry: Neutral Cubane Complexes

Keywords: Cobalt(II) cubanes / Dicyanamide complexes / Di-2-pyridyl ketone / Magnetic properties / Manganese(II) cubanes / Nickel(II) cubanes

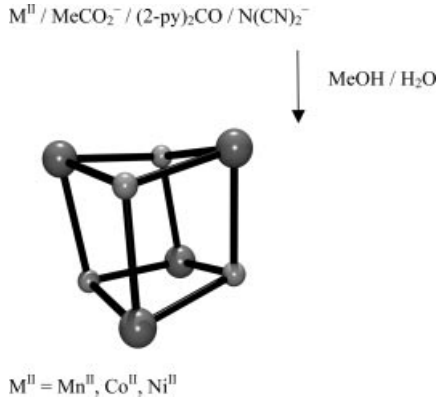

894 **L. Kovbasyuk, H. Pritzkow, R. Krämer***

Coordination Chemistry of the Ditopic Ligand 4-[6-(2-Pyridyl)-2-pyridyl]-6-(2-pyridyl)pyrimidine: Encapsulation of Nitrate by [2 × 2] Grid Complexes

Keywords: Ligand design / Self-assembly / Nitrate recognition / Grids / Nickel(II) / Cobalt(II)

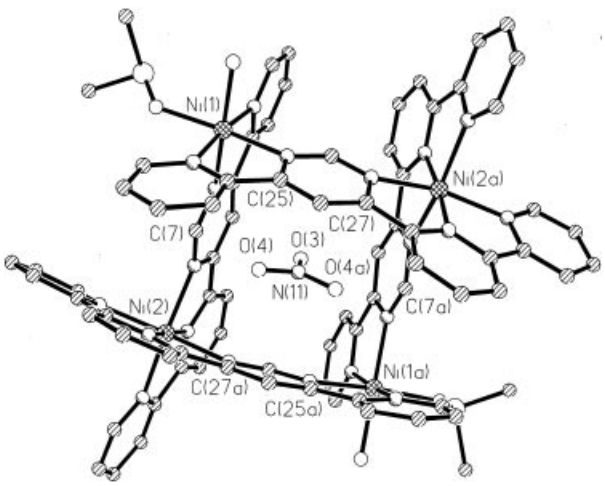

901 **K. Venkatesan, T. Fox, H. W. Schmalle, H. Berke***

New Access to Homodinuclear Half-Sandwich Vinylidenemanganese Complexes

Keywords: Cyclopentadienyl ligands / Half-sandwich complexes / Phosphanes / Molecular devices / Vinylidene ligands

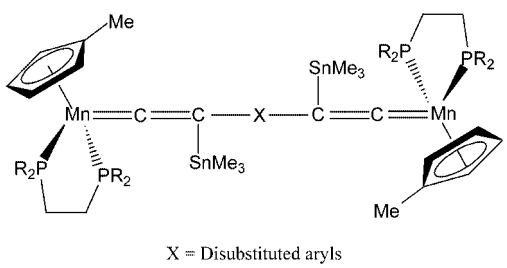

910 **M. H. Klingele, P. D. W. Boyd, B. Moubaraki, K. S. Murray, S. Brooker***

First Complexes of a 4-Alkyl-3,5-di(2-pyridyl)-4*H*-1,2,4-triazole: Synthesis, X-ray Crystal Structures and Magnetic Properties of Dinuclear Cobalt(II), Nickel(II) and Copper(II) Complexes of 4-Isobutyl-3,5-di(2-pyridyl)-4*H*-1,2,4-triazole

Keywords: 1,2,4-Triazole / Bridging ligands / N ligands / Magnetic properties / X-ray diffraction

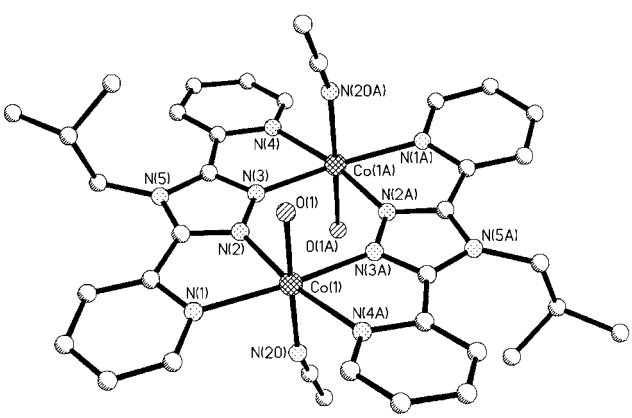

 © 2005 Wiley-VCH Verlag GmbH & Co. KGaA, Weinheim

919 **G. Pilet,* K. Kirakci, F. de Montigny, S. Cordier, C. Lapinte, C. Perrin, A. Perrin**

Assisted Crystallization of Organometallic Cations by Interplay with Inorganic Anionic Clusters Units: Synthesis and Characterizations of the $[Cp^*(dppe)Fe-NCMe]_2-M_6L_{14}$ Series (M_6L_6 = Cluster Unit: $[Re_6S_6Br_8]^{2-}$, $[Mo_6Br_{14}]^{2-}$ and $[Mo_6I_{14}]^{2-}$)

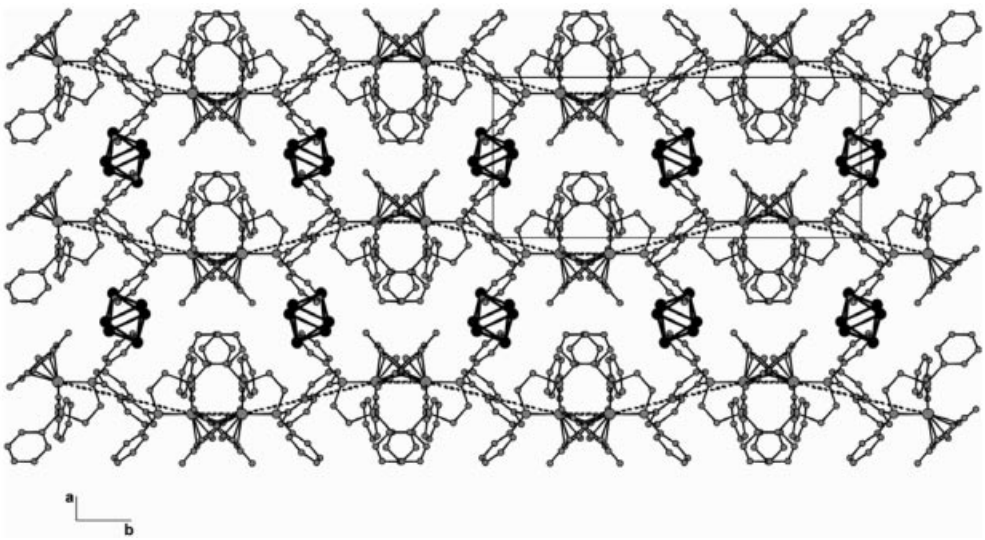

Keywords: Iron / Rhenium / Molybdenum octahedral clusters / M_6L_{14} units / Hybrid compounds / Inorganic organometallic chemistry / Single-crystal structures

929 **G. Novitchi,* J. Costes, V. Ciornea, S. Shova, I. Filippova, Y. A. Simonov, A. Gulea**

Evolution of the Structural Parameters and Magnetic Properties in a Series of Di(μ-hydroxy)-bis(nitrilotriacetato)dichromium(III) Complexes

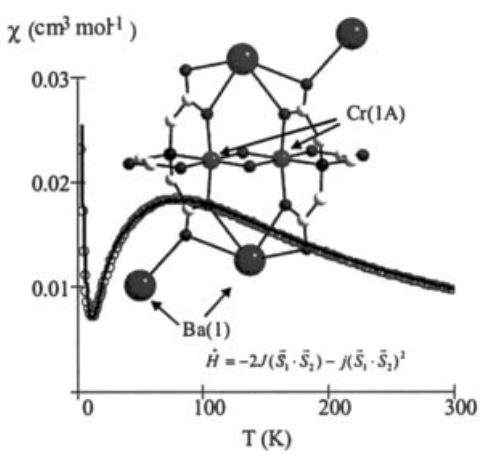

Keywords: Chromium / Alkaline earth metals / N,O ligands / Magnetic properties

 © 2005 Wiley-VCH Verlag GmbH & Co. KGaA, Weinheim

938 **I. M. Piglosiewicz, S. Kraft, R. Beckhaus,* D. Haase, W. Saak**

Selective C−H and C−F Bond Activation Reactions of Pyridine and Fluoropyridines − Formation of Binuclear μ-X Titanocene Complexes (X = H, F) with α-Functionalized N-Heterocycles

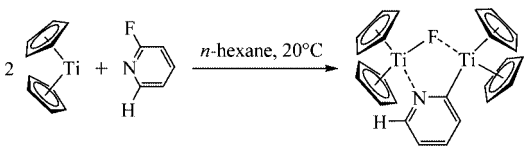

Keywords: Titanium / Bridging ligand / Fluorinated ligands / Nitrogen heterocycles / C−H activation / C−F activation

946 **W. Liu, H.-H. Chen, X.-X. Yang, J.-T. Zhao***

Two Novel Transition-Metal Phosphite Compounds with 4-, 6- and 12-Membered Rings: Hydrothermal Syntheses, Crystal Structures and Magnetic Properties of $Na_2[M(HPO_3)_2]$ (M = Fe, Co)

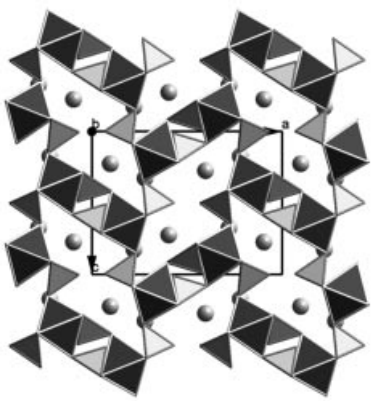

Keywords: Synthesis / Structure / Cobalt / Iron / Phosphites / Magnetic properties

952 **E. Herdtweck, F. H. Köhler,* R. Mölle**

(Cyanocyclopentadienyl)potassium and -cesium

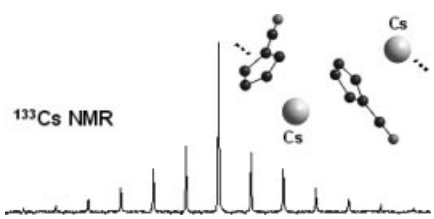

Keywords: Cyanocyclopentadienide / Crystal structure / ^{133}Cs NMR spectroscopy

959 **S. Beşli, S. J. Coles, D. B. Davies, R. J. Eaton, M. B. Hursthouse, A. Kılıç,* R. A. Shaw**

Crystallographic Proof of Double Walden Inversion in Nucleophilic Substitution Reactions of Macrocyclic Cyclotriphosphazene Derivatives

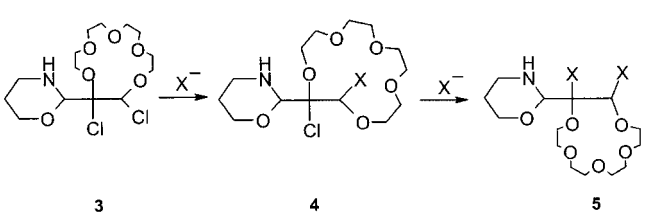

3 4 5

Keywords: Nucleophilic substitution / Inversion of configuration / Cyclotriphosphazenes / Crystal structures / Configuration determination

 © 2005 Wiley-VCH Verlag GmbH & Co. KGaA, Weinheim

967 **K. Boulahya, M. Parras, J. M. Gonzàlez-Calbet***

Synthesis, Structural and Magnetic Characterization of a New Scheelite Related Compound: $Eu_2Mo_3O_{12}$

Keywords: Molybdate / X-ray diffraction / High resolution electron microscopy / Magnetic properties

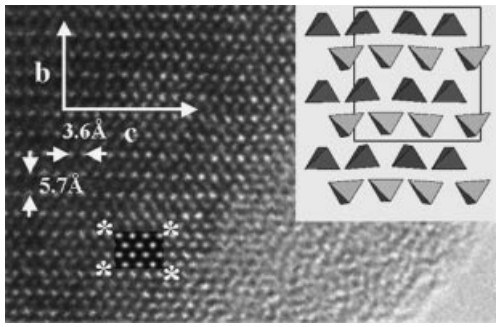

971 **M. V. Butovskii, U. Englert, G. E. Herberich,* U. Koelle**

Reaction Chemistry of the Carbenoid Butadienyl Complex Ion $[CpCo(\sigma,\eta^4\text{-}C_4HMe_4)]^+$ Formed by Protonation of the Cyclobutadiene Complex $[CpCo(C_4Me_4)]$

Keywords: Cobalt / Cyclobutadiene / Butadienyl / Carbene

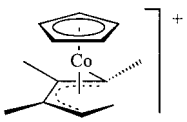

CORRECTION

981 **M. R. Maurya,* S. Agarwal, C. Bader, D. Rehder***

Dioxovanadium(V) Complexes of ONO Donor Ligands Derived from Pyridoxal and Hydrazides: Models of Vanadate-Dependent Haloperoxidases

Keywords: Vanadium / Hydrazones / Catalytic bromination / Pyridoxal

 © 2005 Wiley-VCH Verlag GmbH & Co. KGaA, Weinheim

η^6:η^6 Coordination of Tetraphenylborate to Ytterbium(II): A New Class of Lanthanoid *ansa*-Metallocenes

Glen B. Deacon,*[a] Craig M. Forsyth,[a] and Peter C. Junk[a]

Keywords: Metallocenes / Ytterbium / Tetraphenylborate / Bis(trimethylsilyl)amide / Pyrazolate

The ytterbium(II) complexes [Yb(*t*Bu$_2$pz)(THF)BPh$_4$] (**2**) (*t*Bu$_2$pzH = 3,5-di-*tert*-butylpyrazole) and [Yb{N(SiMe$_3$)$_2$}BPh$_4$] (**3**) were synthesised by reaction of [Yb{N(SiMe$_3$)$_2$}(THF)BPh$_4$] (**1**) with *t*Bu$_2$pzH or by in situ desolvation of the THF complex **1**. X-ray analysis of **2** and **3** reveals η^6:η^6 binding of chelating BPh$_4^-$ to ytterbium in both cases, generating true metallocene structures. Complex **3** is distinguished by a very short Yb–N bond and an agostic Yb–Me interaction, both indicative of a highly Lewis acidic metal centre.

(© Wiley-VCH Verlag GmbH & Co. KGaA, 69451 Weinheim, Germany, 2005)

Introduction

The recent rapid growth in the chemistry of lanthanoid-π-arene complexes has been fuelled both by an interest in their structures and bonding and by their ability to stabilise unusual oxidation states.[1–3] Readily available tetraphenylborate (BPh$_4^-$) can act as a chelating 12 e$^-$ donor through π bonding of two of the phenyl rings to a metal as in [Nb(RC≡CR)(η^6-Ph)$_2$BPh$_2$],[4,5] but not in lanthanoid tetraphenylborates, which almost exclusively have the BPh$_4^-$ simply in its classical counterion role (recent examples[6–13]). Two exceptions of note are [La(C$_5$Me$_5$){CH(SiMe$_3$)$_2$}BPh$_4$], for which the solid-state NMR spectra shows evidence of La–Ph interactions,[14] and structurally characterised [Sm(C$_5$Me$_5$)$_2$(Ph)$_2$BPh$_2$], which shows two of the Ph groups bound (η^2:η^2) to Sm^{3+}.[15] Both of these lanthanoid(III) complexes have two bulky coligands, which prevent a closer approach of BPh$_4^-$ to the metal centre. We have recently reported the isolation of the lanthanoid(II) tetraphenylborate, [Yb{N(SiMe$_3$)$_2$}(THF)(Ph)$_2$BPh$_2$] (**1**), which also has a bonded BPh$_4^-$ ligand.[16] However, the Yb–BPh$_4$ coordination is labile as indicated by the existence of two solid-state linkage isomers, one that has η^6-Ph:η^4-Ph binding to Yb (**1a**), whilst in the other isomer **1b**, an agostic Yb–Me(Si) bond and an η^1-Yb–Ph interaction replace the η^4-Ph donor.[16] Potentially, higher hapticity binding of the BPh$_4^-$ anion to Yb^{2+} may be induced by reducing either the steric bulk or the number of coligands. Following this design, we now report the synthesis and structures of two new ytterbium(II) tetraphenylborate complexes that show unequivocal η^6:η^6-Yb–Ph$_2$BPh$_2$ coordination.

[a] School of Chemistry, Monash University,
P. O. Box 23, Clayton, VIC, 3800, Australia
Fax: +61-3-9905-4597
E-mail: glen.deacon@sci.monash.edu.au

Results and Discussion

At low temperature, **1** reacts with one equivalent of *t*Bu$_2$pzH (3,5-di-*tert*-butylpyrazole) to give poorly soluble, red-purple [Yb(*t*Bu$_2$pz)(THF)BPh$_4$].2PhMe (**2**). A THF-free derivative of **1** was also prepared by in situ desolvation in PhMe to give purple [Yb{N(SiMe$_3$)$_2$}BPh$_4$] (**3**) (Scheme 1). Both compounds were obtained in moderate to good yields, and were characterised by analytical and spectroscopic data and by single-crystal X-ray structure determinations (see below). Solid-state IR spectra of **2** and **3** exhibit two ν(C=C$_{Ar}$) absorptions near 1580 cm^{-1} as well as three or more δ(C–H$_{Ar}$) bands between 700–800 cm^{-1}, consistent with the presence of both free and Yb-bound B–Ph moieties. However, in C$_6$D$_6$ solution at room temperature, only single Ph environments are observed in the ^{1}H NMR spectra of **2** and **3**. The *o*-H(Ph) resonances [δ: 8.14 (**2**), 7.84 (**3**) ppm] are shifted to higher frequency relative to free BPh$_4^-$, e.g. [Yb(MeCN)$_8$][BPh$_4$]$_2$ δ(CD$_3$CN) = 7.25 ppm[10] {compare also [Na([18]-cr-6)][BPh$_4$]·1.5H$_2$O δ(CD$_2$Cl$_2$) = 7.33 ppm[5]}, as has been observed for coordi-

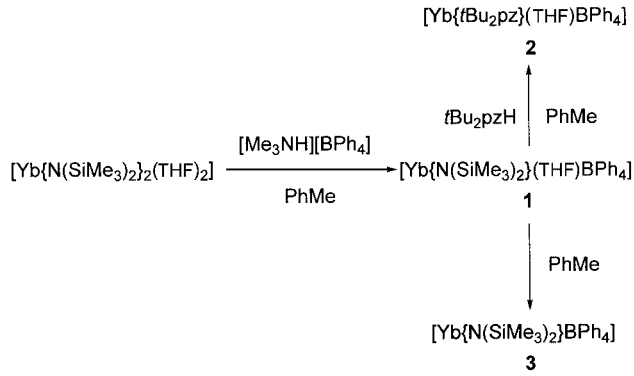

Scheme 1.

 DOI: 10.1002/ejic.200400953 © 2005 Wiley-VCH Verlag GmbH & Co. KGaA, Weinheim

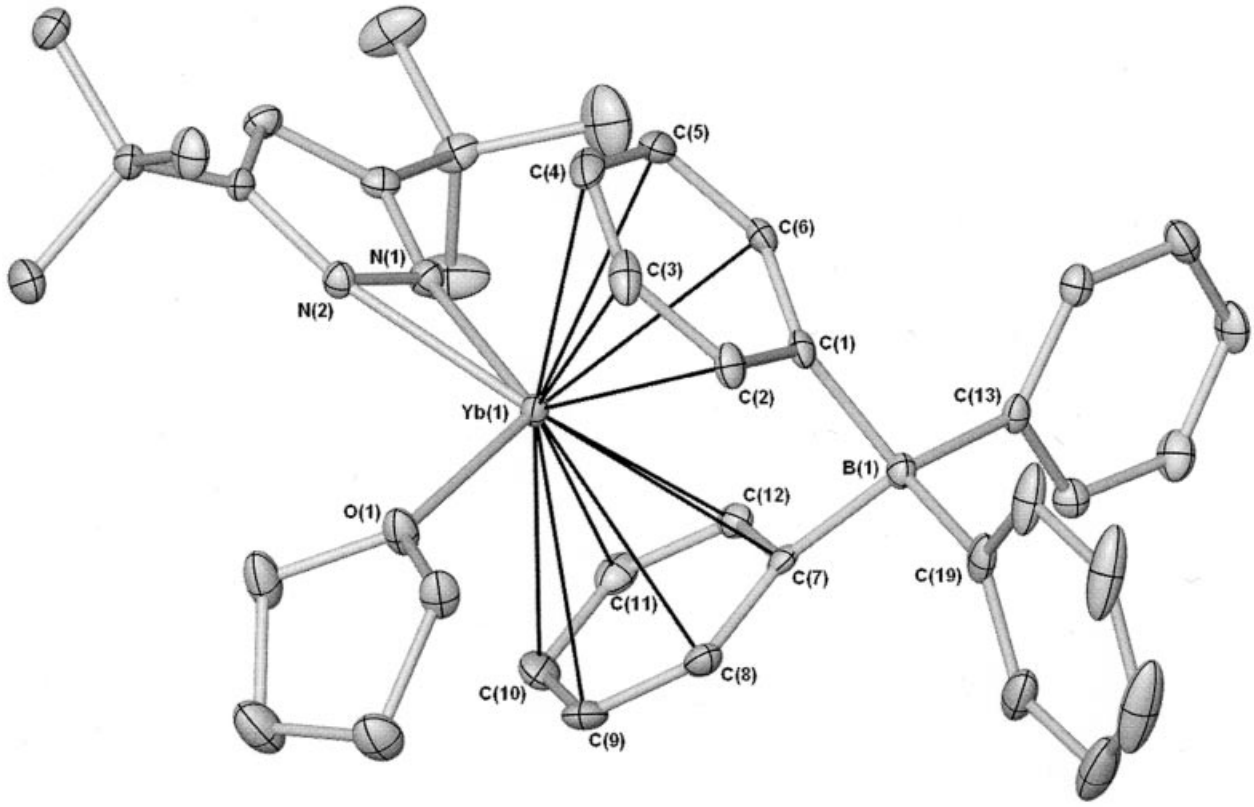

Figure 1. Molecular representation of the X-ray structure of [Yb(*t*Bu$_2$pz)(THF)BPh$_4$]·2C$_6$D$_6$ (**2a**) showing 50% thermal ellipsoids, and with lattice C$_6$D$_6$ molecules and hydrogen atoms omitted for clarity.

nation of BPh_4^- to other d^0 metals {e.g. [Zr(CH_2Ph)$_3$(η^6-Ph)BPh_3] δ_H = 8.25 ppm[17]}. Thus, the data for **2** and **3** suggest that some degree of Yb–Ph coordination occurs in C_6D_6 solution, rather than formation of ion pairs such as [Yb(L)(THF)$_n$(C_6D_6)$_2$][BPh_4] (L = *t*Bu$_2$pz, *n* = 1; L = N($SiMe_3$)$_2$, *n* = 0), but that the system is fluxional. Variable-temperature ^{13}C NMR studies of **3** in C_6D_6/PhMe (1:10) show some line broadening at –40 °C for the aromatic carbon atoms but this is insufficient to resolve the two Ph environments. Further cooling results in significant precipitation of solid **3**, and **2** was insoluble in this medium below room temperature. A ^{171}Yb or ^{29}Si NMR signal for **3** could not be located between –40 and +30 °C.

To clarify the exact bonding mode(s) for BPh_4^- in **2** and **3**, X-ray crystal structures of both complexes were determined. Difficulty was experienced in obtaining single crystals, since at room temperature or with heating, solutions of **2** or **3** slowly decompose, and deposit yellow, insoluble [Yb(BPh_4)$_2$].[18] However, suitable crystals of [Yb(*t*Bu$_2$pz)(THF)BPh_4]·2C$_6$D$_6$ (**2a**) were deposited from a warm C_6D_6 solution, along with the yellow solid, whilst **3** was crystallised by slow evaporation of a cold PhMe solution. The molecular diagrams are shown in Figure 1 and Figure 2, and selected bond distances and angles are listed in Table 1. A key feature of both structures is the unequivocal η^6-binding of *two* phenyl rings from a chelating BPh_4^- anion to each of the central ytterbium atoms. In addition, **2a** has an η^2-*t*Bu$_2$pz$^-$ anion and a coordinated THF molecule, giving a formal coordination number of nine. In contrast, the remaining coordination sphere of **3** is occupied solely by an *N*-bound N($SiMe_3$)$_2^-$ ligand supported for coordination saturation by a short Yb–Me interaction to one of the $SiMe_3$ groups. Thus, the coordination number is eight. Both complexes exhibit distorted pseudotetrahedral coordination geometries, as defined by the centroids of the bound Ph groups, and the THF oxygen atom, and the centre of the N–N bond for **2a** and the amido nitrogen atom and bound $SiMe_3$ carbon atom for **3**.

The Yb–C distance ranges for each interacting Ph ring in **2a** and **3** are narrow (0.12–0.19 Å), and the average Yb–C distances (Table 1) are comparable to those (2.85–2.99 Å) of the single η^6-Ph–Yb moieties of **1a** or **1b**,[16] despite the higher coordination number in the current complexes. The average Yb–C distances in **3** are shorter than those to a substituted neutral arene, e.g. <Yb–C> 2.94 Å in [(Yb(η^6-$C_6Me_3H_3$)($AlCl_4$)$_2$]$_n$·*n*(C_6H_6)[19] or <Yb–C> 2.96, 2.98 Å in [Yb{SC_6H_3-2-(η^6-$C_6H_2Pr^i_3$)-6-($C_6H_2Pr^i_3$)}$_2$].[20] With allowance for differences in coordination number, the upper limit for Yb–C bonding in **2a** and **3** [3.050(2) Å] is comparable with or well below the upper value for the preceding two complexes,[19,20] whilst the current Yb–C distance range (Table 1) is comparable or smaller. In the metallocene complex [Yb{N($SiMe_3$)$_2$}(C_5Me_5)$_2$Na(THF)$_3$],[21] which has an analogous ytterbium coordination environment to that of

 © 2005 Wiley-VCH Verlag GmbH & Co. KGaA, Weinheim

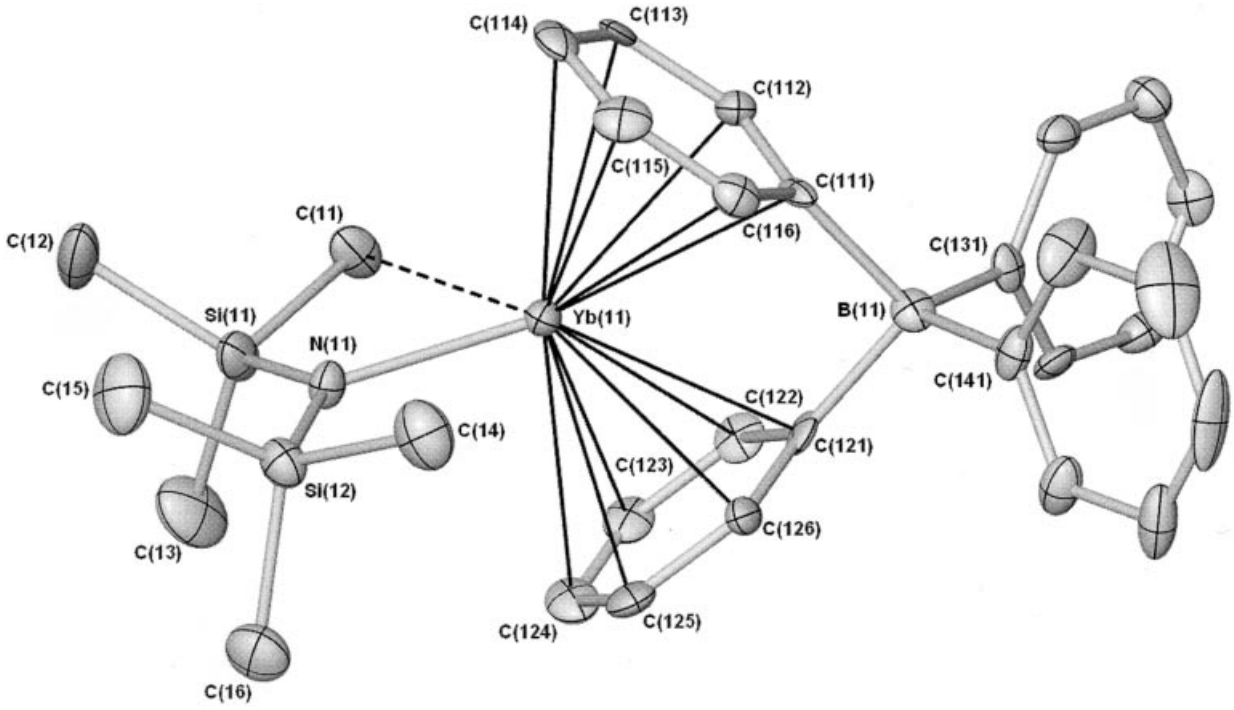

Figure 2. Molecular representation of the X-ray structure of [Yb{N(SiMe$_3$)$_2$}BPh$_4$] (**3**) showing 50% thermal ellipsoids, and with hydrogen atoms omitted for clarity. The agostic Yb–Me interaction is represented by a dotted bond. Only one of the virtually identical but crystallographically independent molecules is shown.

Table 1. Selected bond distances [Å] and angles [°] for **2a** and **3**. Entries Yb–C(Ph) refer to ranges for individual Ph rings with the average value in italics; Ph* refers to the centroid of a bonded η^6-Ph ring, N* refers to the centre of the N–N bond of the η^2-*t*Bu$_2$pz in **2a**. Complex **3** has two virtually identical independent molecules in the asymmetric unit, only values for one are listed.

	2a	**3**
Yb–C(Ph)	2.799(2)–2.945(2), *2.88* 2.860(2)–3.050(2), *2.95*	2.784(11)–2.899(11), *2.85* 2.810(7)–2.956(12), *2.87*
Yb–C(Me)		2.845(8)
Yb–N	2.351(2), 2.364(2)	2.262(6)
Yb–O	2.360(2)	
Si–C		1.854(9)–1.874(10), 1.915(8)[a]
Ph*–Yb–Ph*	112.8	114.0
Ph*–Yb–N/N*	123.5, 108.4	131.8, 110.8
Ph*–Yb–O/C	107.4, 104.4	111.5, 109.4
N/N*–Yb–O/C	98.4	67.9

[a] Si–C distance for the Me group bound to Yb.

3, the average Yb–C(C$_5$Me$_5$) bond length (2.83 Å) of the bridging (η^5:η^5) C$_5$Me$_5$ ligand is close to the average Yb–C distance in **3** (Table 1).

The amido ligands in both **2a** and **3** are characterised by short Yb–N distances, emphasising the high Lewis acidity of Yb^{2+} in the Yb(Ph)$_2$BPh$_2$ fragment. The two Yb–N distances in **2a** (Table 1) are approximately equivalent, indicating symmetrical binding of the *t*Bu$_2$pz$^-$ ligand, but the values are shorter than those of eight coordinate [Yb(Ph$_2$pz)$_2$(DME)$_2$] [2.414(7)–2.430(7) Å].[22] Similarly, the Yb–N distance in **3** [2.262(6) Å] is remarkably short relative to 2.41(2) Å in the closely related compound [Yb{N(SiMe$_3$)$_2$}(C$_5$Me$_5$)$_2$Na(THF)$_3$].[21] This difference is also likely to be influenced by the decreased steric bulk of **3** (two Ph groups compared with two C$_5$Me$_5$ groups) and the boron linkage in the chelating BPh$_4^-$ ligand, and this results in a more open residual coordination sphere. The centroid–Yb–centroid angle (Ph*–Yb–Ph* 114.0°) is significantly smaller for **3** than for [Yb{N(SiMe$_3$)$_2$}(C$_5$Me$_5$)$_2$Na(THF)$_3$] (Cp*–Yb–Cp* 134°).[21] The Ph*–Yb–Ph* angles are also considerably more acute than for BPh$_4^-$ in [Nb(RC≡CR)(η^6-Ph)$_2$BPh$_2$] (131.6°).[4] Complex **3** has a Yb–C(Me) distance [2.845(8) Å] that is much shorter than a similar interaction in **1b** [3.123(4) Å[16]) but comparable to those of [Yb{N(SiMe$_3$)$_2$}$_2$]$_2$ [2.785(4)–2.823(4) Å], which has several agostic Yb–Me$_3$Si interactions to support the YbN$_3$ coordination.[23] The Yb–Me contact is accompanied by a narrowing of the Yb–N–Si angle from 111.0(1)° in **1a** to 104.6(3)° in **3** and an apparent lengthening of the associated Si–C distance (Table 1).

Conclusions

Through the use of steric engineering that provides an appropriate coligand environment in heteroleptic Yb(L)BPh$_4$ complexes, stronger binding of BPh$_4^-$ to Yb^{2+} has been achieved with the first observation of η^6:η^6-Ph$_2$BPh$_2$ coordination to a lanthanoid. These complexes represent true *ansa*-metallocenes of ytterbium(II) and, in particular, the solvent-free complex **3** parallels the highly catalytically active *ansa*-bis(cyclopentadienyl)lanthanoid(III) species, and we are currently pursuing this aspect.

 © 2005 Wiley-VCH Verlag GmbH & Co. KGaA, Weinheim

Experimental Section

General Remarks: All reactions were carried out under dry nitrogen or argon by using dry box and standard Schlenk techniques. Solvents were dried by distillation from sodium wire/benzophenone. Elemental analyses (C,H,N) were performed by the Campbell Microanalytical Service, University of Otago, New Zealand. IR data (4000–650 cm^{-1}) were recorded for Nujol mulls sandwiched between NaCl plates with a Perkin–Elmer 1600 Fourier transform infrared spectrometer. NMR spectra were obtained with a Bruker AC300 MHz spectrometer; [D_6]benzene was degassed and distilled from Na/K alloy prior to use. **1**,[16] [Yb{N($SiMe_3$)$_2$}$_2$(THF)$_2$],[24] Me_3NHBPh_4,[25] and 3,5-tBu$_2$pzH[26] were prepared according to literature procedures.

[Yb(tBu$_2$pz)(THF)BPh$_4$].2PhMe (2): A Schlenk flask was charged with tBu$_2$pzH (0.05 g, 0.25 mmol), **1** (0.18 g, 0.25 mmol), and PhMe (20 mL), and cooled to –40 °C. The reaction mixture was stirred and allowed to warm to 0 °C over approximately 1 h. The resulting purple solution was concentrated to 10 mL and cooled to –73 °C to yield **2** as a red-purple solid, which was collected and dried under vacuum (yield 0.14 g, 67%). IR (Nujol): $\tilde{\nu}$ = 1584 (w), 1570 (w), 1496 (m), 1310 (w), 1272 (w), 1248 (m), 1220 (w), 1184 (m), 1156 (m), 1066 (w), 1030 (m), 1014 (m), 993 (w), 934 (s), 869 (m), 857 (m), 777 (m), 750 (vs), 729 (vs), 714 (vs), 695 (m) cm^{-1}. ^{1}H NMR ([D_6]benzene): δ = 8.14 [br. s, 8 H, *o*-H(BPh)], 7.22 [br. s, 8 H, *m*-H(BPh)], 7.16–7.00 (m, 10 H, *Ph*Me), 6.90 [br. t, J = 7.5 Hz, 4 H, *p*-*H*(BPh)], 6.11 [br. s, 1 H, *H*4(pz)], 2.11 (s, 6 H, Ph*Me*), 1.24 (br. s, 18 H, tBu) ppm. Resonances due to THF at $\delta \approx$ 3.5 and 1.3 ppm (underlying the tBu resonance at δ = 1.24 ppm) were extremely broad with unreliable integration. Analytical data were consistent with loss of lattice toluene molecules: [Yb(t-Bu$_2$pz)(THF)BPh$_4$], $C_{39}H_{47}BN_2OYb$ (744.32): calcd. C 62.9, H 6.4, N 3.8%; found C 62.8, H 6.7, N 3.6% {compare with [Yb(t-Bu$_2$pz)(THF)BPh$_4$]·2PhMe, $C_{53}H_{63}BN_2Yb$ (928.44): calcd. C 68.5, H 6.8, N 3.0%}. Single crystals of [Yb(tBu$_2$pz)(THF)BPh$_4$]·2C_6D_6 (**2a**) were grown from a [D_6]benzene solution of **2**.

[Yb{N(SiMe$_3$)$_2$}BPh$_4$] (3): A Schlenk flask was charged with [Yb{N($SiMe_3$)$_2$}$_2$(THF)$_2$] (0.64 g, 1.0 mmol), Me_3NHBPh_4 (0.38 g, 1.0 mmol), and PhMe (60 mL), and the reaction mixture was stirred for 2 h at –10 °C. The solvent was then removed under vacuum whilst maintaining the solution at –10 °C. PhMe (60 mL) was added to the residue, and the mixture was stirred for a further 1 h at –10 °C before the solvent was again removed, and the cycle was repeated. After the final removal of solvent, PhMe (60 mL) was added, and the resulting purple solution was filtered, concentrated to 5 mL, and hexanes (10 mL) were added. Cooling to –73 °C gave **3** as a purple solid, which was collected and dried under vacuum (yield 0.36 g, 55%). IR (Nujol): $\tilde{\nu}$ = 1583 (w), 1560 (w), 1307 (w), 1249 (m), 1240 (m), 1178 (w), 1156 (m), 1066 (vs), 976 (w), 833 (m), 816 (m), 783 (w), 748 (s), 736 (s), 712 (s) cm^{-1}. ^{1}H NMR (300 MHz, 303 K, [D_6]benzene): δ = 7.84 [br. d, J = 5.8 Hz, 8 H, *o*-*H*(BPh)], 7.06 [br. s, 8 H, *m*-*H*(BPh)], 6.90 [br. s, 4 H, *p*-*H*(BPh)], –0.19 (s, 18 H, SiMe_3) ppm. ^{13}C NMR (75.5 MHz, [D_6] benzene): δ = 135.0 [*o*-*C*H(BPh)], 129.3 [*m*-*C*H(BPh)], 124.6 [*p*-*C*H(BPh)], 4.5 (SiMe_3) ppm. The resonance for the *ipso*-C (bound to B) was not detected. ^{11}B NMR (128.4 MHz, [D_6]benzene): δ = –3.85 ppm. $C_{30}H_{38}BNSi_2Yb$ (652.65): calcd. C 55.2, H 5.9, N 2.1; found C 54.9, H 5.9, N 2.1%.

X-ray Crystallographic Study: Crystals were mounted in an inert atmosphere under viscous oil onto a glass fibre. Low-temperature (123 K) data were collected on an Enraf–Nonius KAPPA CCD area-detector diffractometer (Mo-K_α radiation, λ 0.71073 Å, frames comprised 1.0° or 0.5° increments in φ and ω yielding a sphere of data) with proprietary software (Nonius B.V., 1998). Each data set was corrected for absorption (empirical-SORTAV[27]) then merged (R_{int} as quoted) to N unique reflections. The structures were solved by conventional methods and refined with anisotropic thermal parameter forms for the non-hydrogen atoms by full-matrix least-squares on all F^2 data by using SHELX 97.[28] Hydrogen atoms were included in calculated positions and allowed to ride on the parent carbon atom.

2a: $C_{51}H_{47}D_{12}B_1N_2O_1Yb_1$ (911.92) monoclinic $P2_1/n$, a = 15.0562(1), b = 16.2227(1), c = 18.1395(3) Å, β = 97.296(1) °, V = 4394.7(1) Å^3, $D_{calcd.}$ (Z = 4) 1.378 g cm^{-3}, μ_{Mo} = 2.166 mm^{-1}, F(000) 1848, $T_{min,max}$ = 0.561, 0.653, N_{total} = 50926, N = 10752 (R_{int} = 0.053), R = 0.026, wR_2 = 0.061 (R = 0.038, wR_2 = 0.064 all data). One of the lattice C_6D_6 molecules was disordered over two positions, and the geometries of both components were modelled as rigid hexagons.

3: $C_{30}H_{38}B_1N_1Si_2Yb_1$ (652.64) orthorhombic $Pca2_1$, a = 31.2276(4), b = 9.5779(1), c = 19.6904(3) Å, V = 5889(2) Å^3, $D_{calcd.}$ (Z = 8) 1.472 g cm^{-3}, μ_{Mo} = 3.28 mm^{-1}, F(000) 2624, $T_{min,max}$ 0.549, 0.778, x_{abs} 0.066 (12), N_{total} = 59936, N = 13425 (R_{int} = 0.096), R = 0.047, wR_2 = 0.082 (R = 0.086, wR_2 = 0.094 all data). As modelled in $Pca2_1$, the asymmetric unit comprised a pair of molecules apparently related by a centre of symmetry. However, no further crystallographic symmetry was detected by using the program PLATON,[29] and no sensible solution could be found in the centrosymmetric space group *Pbcm*. The high correlation matrix elements present in the noncentrosymmetric solution as a result of the pseudosymmetry presumably contribute to the relatively large ESDs.

CCDC-255023 and CCDC-255024 contain the supplementary crystallographic data for this paper. These data can be obtained free of charge from The Cambridge Crystallographic Data Centre via www.ccdc.cam.ac.uk/data_request/cif.

Acknowledgments

We thank the Australian Research Council for support.

[1] M. N. Bochkarev, *Chem. Rev.* **2002**, *102*, 2089–2117.
[2] G. B. Deacon, Q. Shen, *J. Organomet. Chem.* **1996**, *511*, 1–17.
[3] F. G. N. Cloke, *Chem. Soc. Rev.* **1993**, *22*, 17–24.
[4] F. Calderazzo, G. Pampaloni, L. Rocchi, U. Englert, *Organometallics* **1994**, *13*, 2592–2601.
[5] M. Aresta, E. Quaranta, I. Tommasi, *New. J. Chem.* **1997**, *21*, 595–613.
[6] S. Bambirra, M. W. Bouwkamp, A. Meetsma, B. Hessen, *J. Am. Chem. Soc.* **2004**, *126*, 9182–9183.
[7] G. B. Deacon, C. M. Forsyth, *Chem. Eur. J.* **2004**, *10*, 1798–1804.
[8] S. Arndt, T. P. Spaniol, J. Okuda, *Angew. Chem. Int. Ed.* **2003**, *42*, 5075–5079; *Angew. Chem.* **2003**, *115*, 5229–5233.
[9] W. J. Evans, J. M. Perotti, J. C. Brady, J. W. Ziller, *J. Am. Chem. Soc.* **2003**, *125*, 5204–5212.
[10] W. J. Evans, M. A. Johnston, M. A. Greci, T. S. Gummersheimer, J. W. Ziller, *Polyhedron* **2003**, *22*, 119–126.
[11] S. M. Cendrowski-Guillaume, G. Le Gland, M. Lance, M. Nierlich, M. Ephritikhine, *Compt. Rend. Chim.* **2002**, *5*, 73–80.
[12] R. Taube, S. Maiwald, J. Sieler, *J. Organomet. Chem.* **2001**, *621*, 327–336.
[13] G. A. Molander, R. M. Rzasa, *J. Org. Chem.* **2000**, *65*, 1215–1217.
[14] C. J. Schaverien, *Organometallics* **1992**, *11*, 3476–3478.
[15] W. J. Evans, C. A. Siebel, J. W. Ziller, *J. Am. Chem. Soc.* **1998**, *120*, 6745–6752.

 © 2005 Wiley-VCH Verlag GmbH & Co. KGaA, Weinheim

[16] G. B. Deacon, C. M. Forsyth, *Chem. Commun.* **2002**, 2522–2523.
[17] M. Bochmann, G. Karger, A. J. Jager, *J. Chem. Soc. Chem. Commun.* **1990**, 1038–1039.
[18] [$Yb(BPh_4)_2$] was identified by IR spectroscopy and conversion to $[Yb(MeCN)_8][BPh_4]_2$.[10]
[19] S. I. Troyanov, *Russ. J. Coord. Chem.* **1998**, *24*, 351–358.
[20] M. Niemeyer, *Eur. J. Inorg. Chem.* **2001**, 1969–1981.
[21] Z. Hou, Y. Zhang, H. Tezuka, P. Xie, O. Tardif, T. Koizumi, H. Yamazkai, Y. Wakatsuki, *J. Am. Chem. Soc.* **2000**, *122*, 10533–10543.
[22] G. B. Deacon, E. E. Delbridge, B. W. Skelton, A. H. White, *Eur. J. Inorg. Chem.* **1999**, 751–761.
[23] R. Anwander, *Top. Curr. Chem.* **1996**, *179*, 32–112.
[24] G. B. Deacon, C. M. Forsyth, G. D. Fallon, H. Schumann, R. Weimann, *Chem. Ber./Recueil* **1997**, *130*, 409–415.
[25] P. K. Bakshi, A. Linden, B. R. Vincent, S. P. Roe, D. Adhikesavalu, T. S. Cameron, O. Knop, *Can. J. Chem.* **1994**, *72*, 1273–1293.
[26] J. Elguero, E. Gonzalez, J. Jacquier, *Bull. Soc. Chim. Fr.* **1968**, 707–713.
[27] R. H. Blessing, *Acta Crystallogr. Sect. A* **1995**, *51*, 33–37.
[28] G. M. Sheldrick, *SHELXL-97*, Universität Göttingen, **1997**.
[29] A. L. Spek, *PLATON*, Utrecht University, **2004**.

Received November 15, 2004

 © 2005 Wiley-VCH Verlag GmbH & Co. KGaA, Weinheim

Structural, Spectroscopic, and Reactivity Properties of N_2S_2(thioether)-O(amide)-Ligated Hg^{II} Complexes: The First Examples of Hg^{II}-Mediated Amide Cleavage

Magdalena M. Makowska-Grzyska,[a] Kelly Doyle,[a] Russell A. Allred,[a] Atta M. Arif,[b] Deborah C. Bebout,*[c] and Lisa M. Berreau*[a]

Keywords: Mercury / Amides / NMR Spectroscopy / Zinc / Cadmium

Two mercury(II) complexes [(bmppa)Hg(ClO_4)]ClO_4 {**1**, bmppa = *N,N*-bis(2-methylthio)ethyl-*N*-[(6-pivaloylamido-2-pyridyl)methyl]amine} and [(beppa)Hg(ClO_4)]ClO_4 {**2**, beppa = *N,N*-bis(2-ethylthio)ethyl-*N*-[(6-pivaloylamido-2-pyridyl)-methyl]amine} of N_2S_2(thioether)O(amide)-donor chelate ligands have been prepared and characterized by X-ray crystallography and/or spectroscopic methods. In the solid state, the Hg^{II} ion of **2** exhibits an overall coordination number of six and strong amide oxygen coordination. Comprehensive multinuclear NMR studies of **1** and **2** have yielded the first $J_{^{199}Hg^{1}H}$ and $J_{^{199}Hg^{13}C}$ coupling constants associated with a Hg–$RSCH_3$ methyl group. In the presence of one equivalent of $Me_4NOH{\cdot}5H_2O$ in methanol/acetonitrile solution, the amide appendages of **1** and **2** undergo alcoholysis.
(© Wiley-VCH Verlag GmbH & Co. KGaA, 69451 Weinheim, Germany, 2005)

Introduction

The coordination chemistry of the Hg^{II} ion in biologically-relevant ligand environments is an area of current interest. For example, recent biochemical studies have focused on the use of ^{199}Hg NMR techniques in evaluating the active site coordination environments of Hg^{II}-substituted proteins.[1–2]^1H NMR studies of Hg^{II} complexes of tripodal ligands have contributed to our understanding of the interplay of Hg^{II} coordination and spectroscopic properties by providing information regarding the magnitude of $J_{^{199}Hg^{1}H}$ and $J_{^{199}Hg^{13}C}$ coupling constants as a function of the nature of the Hg^{II} ligand environment.[3–7] Herein we outline the synthesis, structural and spectroscopic characterization, and amide cleavage properties of two Hg^{II} complexes of N_2S_2(thioether)O(amide)-donor chelate ligands. This work initiates advancement in two important areas of Hg^{II} coordination chemistry of relevance to biological systems. First, in seeking to expand the breadth of known spectroscopic features associated with Hg^{II} coordination, we have elucidated the first $J_{^{199}Hg^{1}H}$ and $J_{^{199}Hg^{13}C}$ coupling constants for Hg^{II}-$RSCH_3$ interactions. Second, we have commenced investigations into biologically-relevant reactions as a function of the group 12 metal ion present. In this context, we report herein that a Hg^{II} complex will mediate an amide cleavage reaction akin to that observed for zinc and cadmium analogs.[8] To the best of our knowledge, this work represents the first report in the chemical literature of Hg^{II}-mediated amide cleavage.

[a] Department of Chemistry and Biochemistry, Utah State University,
0300 Old Main Hill, Logan, UT, 84322-0300, USA
Fax: +1-435-797-3390
E-mail: berreau@cc.usu.edu
[b] Department of Chemistry, University of Utah,
315 S. 1400 E., Salt Lake City, UT, 84112-0850, USA
Fax: +1-801-581-8433
E-mail: arif@chemistry.utah.edu
[c] Department of Chemistry, College of William and Mary,
P. O. Box 8795,Williamsburg, VA, 23187-8795, USA
Fax: +1-757-221-2715
E-mail: dcbebo@wm.edu
Supporting information for this article is available on the WWW under http://www.eurjic.org or from the author.

Results and Discussion

Preparation and Characterization of Hg^{II} Complexes

Mercury(II) complexes of the bmppa {*N,N*-bis(2-methylathio)ethyl-*N*-[(6-pivaloylamido-2-pyridyl)methyl] amine}and beppa {*N,N*-bis(2-ethylthio)ethyl-*N*-[(6-pivaloylamido-2-pyridyl)methyl]amine} ligands were prepared with $Hg(ClO_4)_2{\cdot}3H_2O$ in methanol (Scheme 1). Following crystallization from *i*PrOH/CH_3OH/Et_2O, [(bmppa)Hg(ClO_4)]ClO_4 (**1**) and [(beppa)Hg(ClO_4)]ClO_4 (**2**) were isolated in yields of 73% and 63%, respectively. Formulation of these complexes as having the amide oxygen coordinated to the Hg^{II} ion and one inner sphere perchlorate anion in the solid state is based on the X-ray crystal structure of **2** (vida infra) and the similarity of the solid state infrared spectral features for the amide moiety and perchlorate anions in **1** and **2**.

 © 2005 Wiley-VCH Verlag GmbH & Co. KGaA, Weinheim **DOI: 10.1002/ejic.200400771**

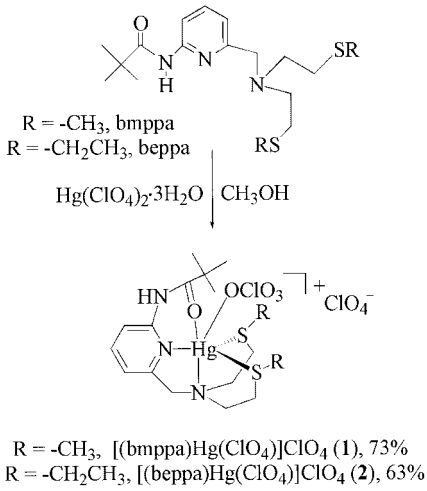

Scheme 1.

X-ray Crystallography

A summary of the X-ray data collection and refinement parameters for **2** is given in Table 1. An ORTEP representation of the cationic portion of **2** is shown in Figure 1. The Hg^{II} ion is well-known in two-coordinate linear or four-coordinate tetrahedral geometries.[9–13] However, the Hg^{II} center in **2** has an overall coordination number of six, with two short interactions involving the amide oxygen [Hg(1)–O(1) 2.271(5) Å; sum of Hg–O covalent radii 2.21 Å] and a thioether sulfur donor [Hg(1)–S(2) 2.4462(17) Å; sum of Hg–S covalent radii 2.50 Å][10] in a bent arrangement [O(1)–Hg(1)–S(2) 132.21(16)°]. As the Hg–O distance in **2** is only slightly longer than the sum of the covalent radii of the atoms, a strong interaction is present in the solid state for this complex. A search of the Cambridge Crystallographic Database revealed a complex of a 2-(pivaloylamido)-appended benzenethiolato ligand having a Hg–O (secondary amide) interaction akin to that in **2**.[14] However, the Hg–O distance in **2** is more than 0.5 Å shorter than the analogous bond length in bis[2,6-bis(pivaloylamido)benzenethiolato]mercury(II) [2.722(6) Å].[14] Typically, Hg^{II}–S(thioether) bond lengths are found in the range of 2.47–2.73 Å.[10–11,15–16] Thus, the Hg(1)–S(2) interaction is consistent with strong coordination to the Hg^{II} center, whereas the Hg(1)–S(1) bond length [2.6674(18) Å] indicates a weaker interaction. The remaining ligands to the Hg^{II} center of **2** are a pyridyl nitrogen [Hg(1)–N(2) 2.343(5) Å], a tertiary amine nitrogen [Hg(1)–N(3) 2.412(6) Å], and a weak Hg–O(perchlorate) interaction (3.01 Å). The Hg–N_{py} and Hg–N_{Am} distances in **2** are similar to the average corresponding distances found in $[(TMPA)HgCl]_2(HgCl_4)_2$ {Hg–N_{py}: 2.40 Å; Hg–N_{am}: 2.43 Å; TMPA = tris[(2-pyridyl)methyl]amine}.[3] Perchlorate coordination to Hg^{II} has been observed in several previously reported complexes.[4,17–21] In these, the Hg^{II}–O(perchlorate) bond lengths generally range from 2.66–2.95 Å. Notably, one of these reported structures has Hg^{II}–S(thioether) bonding as well as a weakly coordinated perchlorate (Hg–O, 3.08 Å) in a sixth coordination position.[18] Finally, key structural features of **2** are reminiscent of those found for the cadmium analog [(bmppa)$Cd(ClO_4)$]ClO_4.[8] Specifically, **2** and the Cd^{II} derivative both exhibit an overall six-coordinate distorted trigonal prismatic structure for the cation, with similar O(1)–M–N(2)–C(Ar) torsion angles {**2**: –13.8°; [(bmppa)$Cd(ClO_4)$]ClO_4: –22.5°} associated with coordination of the amide oxygen.

Table 1. Crystal data for **2**.[a]

	2
Empirical formula	$C_{19}H_{33}Cl_2HgN_3O_9S_2$
Formula mass	783.09
Crystal system	tetragonal
Space group	*I*-4*c*2
a [Å]	19.2193(2)
b [Å]	19.2193(2)
c [Å]	32.0617(5)
V [Å]	11843.0(3)
Z	16
Density (calcd.) [g cm^{-3}]	1.757
Temp. [K]	200(1)
Crystal size [mm]	0.27 × 0.18 × 0.12
Diffractometer	Nonius-Kappa CCD
Abs. coeff. [mm^{-1}]	5.568
$2\theta_{max}$ [°]	65.12
Reflection collected	16249
Independent reflections	9052[b]
Variable parameters	357
*R*1 [$I > 2\sigma I$]/w*R*2[c]	0.0419/0.0894
Goodness-of-fit (F^2)	1.013
Largest diff. peak [e·$Å^{-3}$]	0.746/–0.508

[a] Radiation used: Mo-*K*α (λ = 0.71073 Å). [b] All independent reflections were used in final refinement. [c] $R1 = \Sigma(||F_o| - |F_c||)/\Sigma|F_o|$; $wR2 = [\Sigma[w(F_o^2 - F_c^2)]/\Sigma[(F_o^2)^2]]^{1/2}$ where $w = 1/[\sigma^2(F_o^2) + (aP)^2 + bP]$.

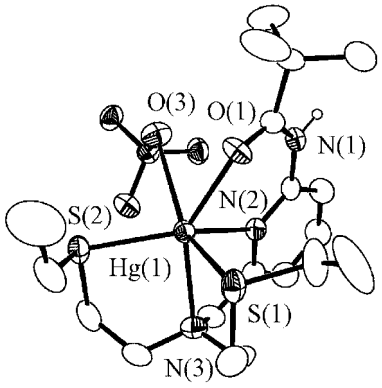

Figure 1. ORTEP representation of the cationic portion of **2**. Ellipsoids are plotted at the 30% probability level. Hydrogen atoms other than the amide N–H omitted for clarity; selected bond lengths [Å] and angles [°]: Hg(1)–O(1) 2.271(5), Hg(1)–S(1) 2.6674(18), Hg(1)–S(2) 2.4462(17), Hg(1)–N(2) 2.343(5), Hg(1)–N(3) 2.412(6), O(1)–Hg(1)–N(2) 79.02(17), N(2)–Hg(1)–S(1) 107.12(14), S(1)–Hg(1)–S(2) 112.27(6), N(2)–Hg(1)–S(2) 129.93(14).

Spectroscopic Properties of 1 and 2

Infrared Spectroscopy

In the solid state, **1** and **2** have amide carbonyl stretching vibrations at 1652 and 1647 cm^{-1}, respectively, a position

 © 2005 Wiley-VCH Verlag GmbH & Co. KGaA, Weinheim

that is ca. 36–41 cm^{-1} shifted from that observed for the free ligands (bmppa and beppa, $\nu_{C=O} \approx 1687$ and 1688 cm^{-1}, respectively, neat between NaCl plates).[8,22] The reduced energy of the carbonyl vibrations in **1** and **2** is consistent with coordination to the Hg^{II} center. No significant difference is found in the solid state carbonyl stretching vibration as a function of metal ion, as zinc {[(beppa)Zn]$(ClO_4)_2$, 1643 cm^{-1}} and cadmium analogs {[(bmppa)Cd(ClO_4)]ClO_4, 1654 cm^{-1}} have a $\nu_{C=O}$ vibration of similar energy.[8] The acetonitrile solution infrared spectrum of **1**, obtained in a new BaF_2 cell, exhibits a single $\nu_{C=O}$ vibration at 1647 cm^{-1}, indicating that amide oxygen coordination is maintained in solution. Notably, collection of a CH_3CN solution infrared spectrum of **1** in an older KBr cell yields a $\nu_{C=O}$ vibration at 1698 cm^{-1}. This higher energy $\nu_{C=O}$ vibration suggests that the amide oxygen is not coordinated to the Hg^{II} ion under these conditions. Since the solution infrared properties of **1** depend on the nature of the cell used for the infrared measurement, we currently hypothesize that the noncoordinated amide species formed in the KBr cell results from formation of a bromide derivative via anion exchange involving the cell salt.

NMR Spectroscopy

A wide array of 1D (^1H, ^{13}C, ^{199}Hg) and 2D ({^1H,^1H}COSY, {^{13}C,^1H}HMQC) NMR experiments have been used to characterize **1** (Figures S1–S3, Supporting Information) and **2** (Figures S4–S7) in acetonitrile solution. The cations of **1**, **2**, [(beppa)Zn]$(ClO_4)_2$, [(bmppa)Zn]$(ClO_4)_2$, and [(bmppa)Cd(ClO_4)]ClO_4 in acetonitrile solution, all exhibit *tert*-butyl methyl ^1H NMR resonances at a similar chemical shift (1.39–1.41 ppm).[8] Despite differences in the chemical environments of the sulfur alkyl substituents, and the differing Hg–S distances observed in the solid-state structure of **2**, a single sharp set of ^1H NMR resonances is observed for the S-CH_3 and -SCH_2CH_3 protons in CD_3CN solutions of **1** and **2** at ambient temperature. In this regard, we have previously noted a similar spectral appearance for the sulfur methyl protons in [(bmppa)Zn]$(ClO_4)_2$.[8] In this complex, the thioether appendages undergo a rapid inversion process at room temperature (in CD_3OD solution) wherein the two possible directions of -SCH_3 canting (clockwise or counterclockwise) are rapidly interconverted via an intramolecular exchange process (coalescence temperature ca. –65 °C).[23]

A large heteronuclear coupling is evident in the -SCH_3 resonance of **1** [see Figure S1(b) in the Supporting Information, Table 2]. The intensities of the satellites ($\approx$ 17%) in this resonance are consistent with the natural abundance of ^{199}Hg (I = 1/2, 16.85%). To the best of our knowledge, this is the first reported $^3J_{^{199}Hg^1H}$ coupling involving a Hg-$RSCH_3$ methyl group.[10] Coupling between ^{199}Hg and methionine methyl protons has been previously detected indirectly for Hg^{II}-substituted plastocyanin.[1] The only other reported $J_{^{199}Hg^1H}$ values for Hg^{II} thioether complexes range from 36 to 90 Hz and involve methylene protons.[24,25] In nitrogen-only ligated Hg^{II} coordination complexes, a coupling constant of a similar magnitude (Table 2) has been previously reported for the benzylic -CH_2- resonance in the $[Hg(TLA)]^{2+}$ cation {TLA = tris[(6-methylpyrid-2-yl)-methyl]amine}.[6] For the Cd^{II} analog [(bmppa)Cd(ClO_4)]-ClO_4, the $J_{^{111/113}Cd^1H}$ coupling constant in the Cd^{II}-$RSCH_3$ thioether methyl resonance is much smaller.[8,26]

Table 2. Heavy atom/proton coupling constants ($J_{^{199}Hg^1H}$ or $J_{^{111/113}Cd^1H}$) identified in the ^1H NMR spectra of **1**, **2**, and structurally related complexes.

Complex	*H*	*J* [Hz]	Ref.
[(bmppa)Hg(ClO_4)]ClO_4 (**1**)[a]	-SCH_3	91	this work
	benzylic -CH_2-	27	
[(beppa)Hg(ClO_4)]ClO_4 (**2**)[a]	benzylic -CH_2-	26	this work
[Hg(TLA)]$(ClO_4)_2$	benzylic -CH_2-	72	[6]
[(TMPA)Hg]$(ClO_4)_2$	benzylic -CH_2-	36	[3]
[(TMPA)HgCl]Cl	benzylic -CH_2-	45	[3]
[(bmppa)Cd(ClO_4)]ClO_4[b]	-SCH_3	15	[8]
	benzylic -CH_2-	9.6	

[a] Spectra recorded in dry CD_3CN at 25(1) °C on a Bruker ARX-400. [b] JEOL 270 MHz spectrometer.

For both **1** and **2**, benzylic -CH_2- resonances having ^{199}Hg coupling satellites are identifiable in the ^1H NMR spectra of the complexes [Table 2; Figures S1(a) and S4(a)]. These $^{3/4}J_{^{199}Hg^1H}$coupling constants are slightly smaller than those observed in the benzylic proton resonances of [(TMPA)Hg]$(ClO_4)_2$ {TMPA = tris[(2-pyridyl)methyl]-amine} and [(TMPA)HgCl]Cl, but are significantly larger than the $^{3/4}J_{^{111/113}Cd^1H}$ coupling constant found in benzylic -CH_2- resonance of [(bmppa)Cd(ClO_4)]ClO_4.[3,8]

The -SCH_3 resonance in the ^{13}C{^1H} NMR spectrum of **1** exhibits two-bond $^{199}Hg^{13}C$ coupling [Table 3, Figure S2(f)] as does the -SCH_2CH_3 methylene carbon resonance of **2** [Figure S5(e2)]. This methylene carbon resonance was assigned via {^{13}C,^1H}HMQC (Figure S7). For each complex the methylene linker carbons of the thioether arms exhibit $^{2/3}J_{^{199}Hg^{13}C}$ coupling [Figures S2(d) and (e); Figures S5(d) and (e1)]. Notably, the methylene C signal found at ca. 48.4–48.6 ppm in **1** and **2** exhibits a much larger $^{2/3}J_{^{199}Hg^{13}C}$coupling constant than that found for the other methylene linker C atom at about 32–35 ppm (Table 3). Conclusive identification of which of these resonances represents the carbon adjacent to the sulfur donor in the linker arms of each complex has not yet been accomplished.

Finally, ^{199}Hg heteronuclear coupling is found in two pyridyl ring carbon resonances in **1** and **2**. Specifically, an *ortho*-carbon resonance at δ = 153.7 ppm for each complex (Table 3) has a larger coupling constant than a *meta* ring carbon resonance at ~124 ppm. The assignment of these resonances as *ortho*- and *meta*-carbons was achieved via {^{13}C,^1H}HMQC experiments for both complexes.

As **1** and **2** exhibit generally similar solution NMR properties, we examined only **2** via ^{199}Hg NMR spectroscopy. For this complex, a single resonance is found at –1124 ppm, as referenced to an external standard of phenylmercuric acetate in DMSO (–1439.5 ppm). Whereas thiolate-ligated Hg^{II} centers tend to have ^{199}Hg NMR resonances in the region of –100 to –400 ppm, the ^{199}Hg chemical shift found

 © 2005 Wiley-VCH Verlag GmbH & Co. KGaA, Weinheim

Table 3. Heteroatom coupling constants ($J_{^{199}Hg^{13}C}$) observed in the $^{13}C\{^1H\}$ NMR spectra of **1** and **2**.

Complex	*C*	*J* [Hz]
[(bmppa)Hg(ClO_4)]ClO_4 (**1**)	-S*C*H_3	36
	-N*C*H_2*C*H_2S-[b]	75, 14
	benzylic -*C*H_2-	20
	o-*C*$_6H_4$N	35
	m-*C*$_6H_4$N	17
[(beppa)Hg(ClO_4)]ClO_4 (**2**)	-SCH_2*C*H_3	46
	-S*C*H_2CH$_3$	32
	-N*C*H_2*C*H_2S-[b]	73, 15
	benzylic -*C*H_2-	19
	o-*C*$_6H_4$N	33
	m-*C*$_6H_4$N	16

[a] Spectra recorded in dry CD_3CN at 25(1) °C on a Bruker ARX-400. [b] Methylene carbon resonances were not individually assigned.

for **2** is similar to that found for all nitrogen-ligated Hg^{II} complexes (–1200 to –1400 ppm).[1] A comparable result was recently identified for N_2S_2(thioether)-ligated Cd^{II} complexes.[27]

These combined infrared and NMR studies indicate that the nitrogen and sulfur donors of the bmppa and beppa chelate ligands, as well as the amide oxygen, are coordinated to the Hg^{II} centers of **1** and **2** in acetonitrile solution.

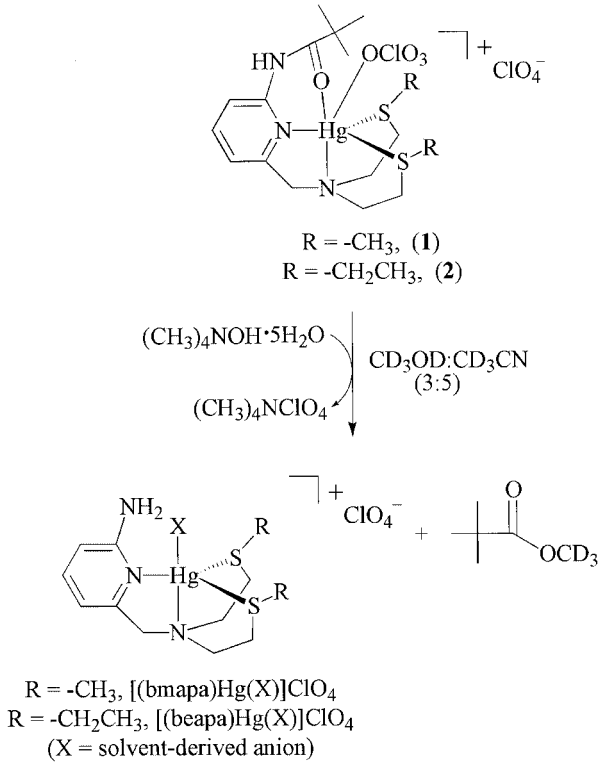

Scheme 2.

Amide Cleavage Reactivity

Reaction of **1** with an equimolar amount of $Me_4NOH{\cdot}5H_2O$ in CD_3OD/CD_3CN solution (3:5) at 55(1) °C results in amide alcoholysis of the *tert*-butyl amide moiety to quantitatively yield [D_3]methyl trimethylacetate and a Hg^{II} complex of a primary amine-appended chelate ligand (Scheme 2).

The ester product was identified by ^1H NMR [δ = 1.18 ppm (s, 9 H)] via spectral comparison to an authentic sample of methyl trimethylacetate (Aldrich).[8] One equivalent of Me_4NClO_4 is produced in the amide cleavage reaction of **1** and has been isolated from the reaction mixture in 81% yield as described for the similar amide methanolysis reaction of [(bmppa)Zn]$(ClO_4)_2$.[8] The Hg^{II} product of the amide cleavage reaction of **1** could not be isolated cleanly. This is probably due to the fact that the complex will have one solvent derived anion (OH^- or OCD_3^- or a mixture of both). However, the formation of bmapa-ligand Hg^{II} products is apparent from the ^1H NMR features of the final reaction mixture. Specifically, the signals associated with the *meta*-protons of the primary amine-appended pyridyl donor in the bmapa-ligated product resonate significantly upfield (6.63 and 6.85 ppm) of the same protons in **1**. This is consistent with the chemical transformation from an electron-withdrawing amide group to the electron-donating primary amine substituent on the pyridyl ring. A similar final reaction mixture is obtained following treatment of **2** with $Me_4NOH{\cdot}5H_2O$ in CD_3OD/CD_3CN solution (3:5) at 55(1) °C. Notably, exposure of the free bmppa or beppa ligand to $Me_4NOH{\cdot}5H_2O$ in CD_3OD/CD_3CN solution (3:5) at 55(1) °C does not result in signficant amide cleavage (< 1%) in the time required for complete amide cleavage in **1**, **2**, or the zinc and cadmium analogs that have been previously reported.[8] Further investigations are directed at elucidation of the mechanism of amide cleavage in these systems.

Conclusions

The synthesis and structural characterization of two new Hg^{II} complexes of N_2S_2(thioether)O(amide) donor chelate ligands has been accomplished. Comprehensive solution infrared and NMR studies of these complexes has revealed that strong N_2S_2 and amide oxygen coordination are maintained in CH_3CN solution. Using these complexes, heteronuclear coupling constants ($J_{^{199}Hg^1H}$and $J_{^{199}Hg^{13}C}$) for Hg^{II}–S(thioether) interactions have been determined. Particularly notable is the identification of a large $^3J_{^{199}Hg^1H}$ coupling constant (91 Hz) observed in the methyl proton resonance of a Hg^{II}-$RSCH_3$ interaction. Treatment of these amide-appended Hg^{II} derivatives with $Me_4NOH{\cdot}5H_2O$ in methanol/acetonitrile solution has provided the first examples of Hg^{II}-mediated amide cleavage.

Experimental Section

General Remarks: Reagents and solvents were purchased from commercial sources and were used as received unless otherwise noted. FTIR spectra were recorded on a Shimadzu FTIR-8400 spectrometer as KBr pellets or CH_3CN solutions between BaF_2

 © 2005 Wiley-VCH Verlag GmbH & Co. KGaA, Weinheim

or KBr plates. ^{1}H, ^{13}C{^{1}H}, {^{1}H,^{1}H}COSY, and {^{13}C,^{1}H}HMQC NMR spectra were recorded in dry CD_3CN at 25(1) °C on a Bruker ARX-400 spectrometer. Chemical shifts (in ppm) are referenced to the residual solvent peaks in CD_3CN (^{1}H: 1.94 (quintet); ^{13}C{^{1}H}: 1.39 (heptet) ppm). ^{199}Hg NMR spectra were recorded at 71.6 MHz on a Varian Mercury VX NMR spectrometer with CH_3CN as the solvent, at concentrations of about 112 mM and about 30 mM. These spectra were referenced to an external standard of 0.5 M phenylmercuric acetate in DMSO (–1439.5 ppm). Fast atom bombardment (FAB) mass spectra were collected at the University of California, Riverside using a VG ZAB2SE high resolution mass spectrometer in a matrix of *m*-nitrobenzylalcohol (NBA). The chelate ligands bmppa and beppa were prepared as previously reported.[8,22]

Caution! Perchlorate salts of metal complexes with organic ligands are potentially explosive. These compounds should be handled in small amounts and should be treated with extreme caution, especially in the solid state.[28]

[(bmppa)Hg(ClO$_4$)]ClO$_4$ (1): Prepared in an identical manner to [(bmppa)Zn](ClO$_4$)$_2$.[8] Recrystallization of a white powder by diethyl ether diffusion into a *i*PrOH/CH_3OH, 1:1 solution yielded colorless blocks (94 mg, 73%). ^{1}H NMR [CD_3CN, 400 MHz, 25(1) °C]: δ = 1.39 (s, 9 H), 2.34 (t, $^3J_{^{199}Hg^1H}$ = 91 Hz, 6 H), 2.95–3.50 (m, 8 H), 4.01 (t, $^{3/4}J_{^{199}Hg^1H}$ = 27 Hz, 2 H), 7.36 (d, $^3J_{H,H}$ = 7.5 Hz, 1 H), 7.42 (d, $^3J_{H,H}$ = 8.1 Hz, 1 H), 8.04 (t, $^3J_{H,H}$ = 7.9 Hz, 1 H), 9.04 (br. s, 1 H, N-*H*) ppm; ^{13}C{^{1}H} NMR [CD_3CN, 100 MHz, 25(1) °C]: δ = 18.0 (t, $^2J_{^{199}Hg^{13}C}$ = 36 Hz), 27.4, 34.2 (t, $^{2/3}J_{^{199}Hg^{13}C}$ = 14 Hz), 42.7, 48.4 (t, $^{2/3}J_{^{199}Hg^{13}C}$ = 75 Hz), 56.8 (t, $^{2/3}J_{^{199}Hg^{13}C}$ = 20 Hz), 118.6, 123.9 (t, $^3J_{^{199}Hg^{13}C}$ = 17 Hz), 143.6, 153.7 (t, $^{2/3}J_{^{199}Hg^{13}C}$ = 35 Hz), 154.6, 186.4 (12 signals expected and observed). FTIR (KBr, cm^{-1}): 3337 (br., ν_{N-H}), 1652 ($\nu_{C=O}$), 1613, 1529, 1092 (ν_{ClO4}), 623 (ν_{ClO4}). FTIR (CH_3CN, BaF_2 cell, cm^{-1}): 1647 ($\nu_{C=O}$). LRFAB-MS (CH_3CN/NBA), *m*/*z* (%): 656 [M – ClO$_4$]$^+$ (60%). $C_{17}H_{29}Cl_2HgN_3O_9S_2$ (755.05): calcd. C 27.02, H 3.87, N 5.56; found: C 27.07, H 3.88, N 5.57.

[(beppa)Hg(ClO$_4$)]ClO$_4$ (2): Prepared in an identical manner to [(beppa)Zn](ClO$_4$)$_2$.[8] Recrystallization of a white powder by diethyl ether diffusion into a *i*PrOH/CH_3OH, 1:1 solution yielded colorless prisms suitable for X-ray diffraction analysis (81 mg, 63%). ^{1}H NMR [CD_3CN, 400 MHz, 25(1) °C]: δ = 1.33 (t, $^3J_{H,H}$ = 7.3 Hz, 6 H), 1.39 (s, 9 H), 2.50–2.90 (m, 4 H), 2.97–3.45 (m, 8 H), 4.02 (t, $^{3/4}J_{^{199}Hg^1H}$ = 26 Hz, 2 H), 7.37 (d, $^3J_{H,H}$ = 7.5 Hz, 1 H), 7.44 (d, $^3J_{H,H}$ = 8.2 Hz, 1 H), 8.04 (t, $^3J_{H,H}$ = 7.9 Hz, 1 H), 9.09 (br., 1 H, N-*H*) ppm; ^{13}C{^{1}H} NMR [CD_3CN, 100 MHz, 25(1) °C]: δ = 14.1 (t, $^3J_{^{199}Hg^{13}C}$ = 46 Hz), 27.4, 30.2 (t, $^2J_{^{199}Hg^{13}C}$ = 32 Hz), 32.0 (t, $^{2/3}J_{^{199}Hg^{13}C}$ = 15 Hz), 42.7, 49.2 (t, $^{2/3}J_{^{199}Hg^{13}C}$ = 73 Hz), 56.9 (t, $^{2/3}J_{^{199}Hg^{13}C}$ = 19 Hz), 118.5, 124.0 (t, $^3J_{^{199}Hg^{13}C}$ = 16 Hz), 143.6, 153.7 (t, $^{2/3}J_{^{199}Hg^{13}C}$ = 33 Hz), 154.7, 186.5 ppm (13 signals expected and observed). ^{199}Hg NMR (CH_3CN, 71.6 MHz) –1124 ppm. FTIR (KBr, cm^{-1}): 3347 (br., ν_{N-H}), 1647 ($\nu_{C=O}$), 1616, 1580, 1533, 1098 (ν_{ClO4}), 625 (ν_{ClO4}); LRFAB-MS (CH_3CN/NBA), *m*/*z* (%): 684 [M – ClO$_4$]$^+$ (60%), 584 [M – 2ClO$_4$–CH_3CN+H]$^+$ (100%). $C_{19}H_{33}Cl_2HgN_3O_9S_2$ (783.10): calcd. C 29.12, H 4.25, N, 5.36; found: C 29.31, H 4.30, N 5.30.

^{1}H-NMR Analysis of Amide Cleavage Reactions of Amide-Appended Hg^{II} Complexes: To a solution of **1** (14.0 mg, 0.019 mmol) in CD_3CN/CD_3OD (500 μL:300 μL) solution was added $(CH_3)_4NOH{\cdot}5H_2O$ (3.4 mg, 0.019 mmol) and an internal standard ($CHPh_3$, 4.5 mg, 0.019 mmol). The resulting mixture was monitored by ^{1}H NMR at 55(1) °C at two-minute intervals for 50 minutes at which point the reaction had reached completion, as indicated by the formation of one equivalent of $(CH_3)_3C(O)OCD_3$. The formation of a bmapa-ligated {bmapa = *N,N*-bis(2-methylthio)-ethyl-*N*-[(6-amino-2-pyridyl)methyl]amine} Hg^{II} product is indicated by the appearance of two upfield-shifted pyridyl ring doublets at δ = 6.63 and 6.85 ppm, respectively {[(bmapa)HgX]ClO$_4$ (X = -OH or -OCD$_3$): ^{1}H NMR [CD_3CN, 270 MHz, 22(1) °C]: δ = 1.98 (s, 6 H), 2.82–3.25 (m, 8 H), 3.81 (s, 2 H), 6.63 (d, $^3J_{H,H}$ = 6.9 Hz, 1 H), 6.85 (d, $^3J_{H,H}$ = 8.6 Hz, 1 H), 7.50–7.55 (m, 1 H) ppm}. This result is very similar to that observed for the amide cleavage reaction of [(bmppa)Zn](ClO$_4$)$_2$, wherein the bmapa ligand has been removed and comprehensively characterized.[8] The reaction of **2** with $(CH_3)_4NOH{\cdot}5H_2O$ under identical conditions proceeds in a similar fashion to give a beapa-ligated {beapa = *N,N*-bis(2-ethylthio)ethyl-*N*-[(6-amino-2-pyridyl)methyl]amine[8]} Hg^{II} complex {[(beapa)HgX]ClO$_4$ (X = -OH or -OCD$_3$): ^{1}H NMR [CD_3CN, 400 MHz, 25(1) °C]: δ = 1.11 (t, $^3J_{H,H}$ = 7.4 Hz, 6 H), 2.32–2.40 (m, 4 H), 2.80–2.95 (m, 6 H), 3.15–3.22 (m, 2 H), 3.70 (t, $^3J_{^{199}Hg^1H}$ = 22 Hz, 2 H), 6.62 (d, $^3J_{H,H}$ = 6.8 Hz, 1 H), 6.84 (d, $^3J_{H,H}$ = 8.5 Hz, 1 H), 7.50–7.55 (m, 1 H) ppm} and $(CH_3)_3C(O)OCD_3$.

Identification and Quantification of [D$_3$]Methyl Trimethylacetate Produced in Amide Alcoholysis Reactions of 1 and 2: Methyl trimethylacetate formation was identified and quantified by ^{1}H NMR as described previously.[8]

Identification and Quantification of $(CH_3)_4NClO_4$ in a Hg^{II}-Mediated Amide Cleavage Reaction: To a solution of **2** (33.4 mg, 4.26×10^{-2} mmol) in methanol (or methanol/acetonitrile) solution (≈ 3 mL) was added $(CH_3)_4NOH{\cdot}5H_2O$ (7.7 mg, 4.25×10^{-2} mmol). The resulting mixture was stirred for ca. 1 minute during which time a white precipitate appeared. The solution was then carefully decanted from the white solid, which was subsequently dried (6.0 mg, 81%) and identified as $(CH_3)_4NClO_4$ by infrared spectroscopy.

X-ray Structure Determination of 2: A colorless prism shaped crystal of **2** was mounted on a glass fiber with traces of viscous oil and then transferred to a Nonius-KappaCCD diffractometer equipped with Mo-*Kα* radiation for data collection. Ten frames of data were collected at 200(1) K with an oscillation range of 1 deg/frame and an exposure time of 20 sec/frame. Indexing and unit cell refinement based on all observed reflections from those ten frames indicated a tetragonal *I* lattice. A total of 16249 reflections were indexed, integrated, and corrected for Lorentz, polarization, and absorption effects using DENZO-SMN and SCALEPACK.[29] The structure was solved by a combination of direct and heavy atom methods using SIR 97.[30] All of the non-hydrogen atoms were refined with anisotropic displacement coefficients. Hydrogen atoms were assigned isotropic displacement coefficients *U*(H) = 1.2 *U*(C) or 1.5 *U*(Cmethyl), and their coordinates were allowed to ride on their respective carbons using SHELXL97.[31] Oxygen atoms of one perchlorate anion were found to exhibit disorder. These oxygen atoms were each split into two fragments [O(6)/O(6′), O(7)/O(7′), O(8)/O(8′), and O(9)/O(9′)] and refined. This refinement led to a 0.51:0.49 ratio in occupancy over two positions for each oxygen atom. Further details of the X-ray data collection and refinement of [(beppa)Hg(ClO$_4$)]ClO$_4$ (**2**) are given in Table 1. CCDC-249460 contains the supplementary crystallographic data for this paper. These data can be obtained free of charge from The Cambridge Crystallographic Data Centre via www.ccdc.cam.ac.uk/data_request/cif.

Supporting Information (see also footnote on the first page of this article): Contains figures developed from the 1D and 2D NMR spectra of **1** and **2**.

 © 2005 Wiley-VCH Verlag GmbH & Co. KGaA, Weinheim

Acknowledgments

We thank the National Science Foundation (CAREER Award CHE-0094066 to LMB; CHE-0315934 to DCB), National Institutes of Health (1 R15 GM59043-01 to DCB), and the Petroleum Research Fund (40151-B3 to DCB) for funding of this research. We also thank Ewa Szajna and Dr. Piotr Dobrowolski for assistance with 2D NMR experiments.

[1] L. M. Utschig, J. W. Bryson, T. V. O'Halloran, *Science***1995**, *268*, 380.
[2] L. M. Utschig, T. Baynard, C. Strong. T. V. O'Halloran, *Inorg. Chem.***1997**, *36*, 2926.
[3] D. C. Bebout, D. E. Ehmann, J. C. Trinidad, K. K. Crahan, M. E. Kastner, D. A. Parrish, *Inorg. Chem.***1997**, *36*, 4257.
[4] D. C. Bebout, A. E. DeLanoy, D. E. Ehmann, M. E. Kastner, D. A. Parrish, R. J. Butcher, *Inorg. Chem.***1998**, *37*, 2952.
[5] D. C. Bebout, J. F. Bush II, K. K. Crahan, M. E. Kastner, D. A. Parrish, *Inorg. Chem.***1998**, *37*, 4641.
[6] D. C. Bebout, J. F. Bush II, K. K. Crahan, E. V. Bowers, R. J. Butcher, *Inorg. Chem.***2002**, *41*, 2529.
[7] D. C. Bebout, M. M. Garland, G. S. Murphy, E. V. Bowers, C. J. Abelt, R. J. Butcher, *Dalton Trans.***2003**, 2578.
[8] L. M. Berreau, M. M. Makowska-Grzyska, A. M. Arif, *Inorg. Chem.***2000**, *39*, 4390.
[9] B. J. Aylett, *The Chemistry of Zinc, Cadmium, and Mercury*, Pergamon, New York, **1973**.
[10] J. G. Wright, M. J. Natan, F. M. MacDonnell, D. M. Ralston, T. V. O'Halloran, *Prog. Inorg. Chem.***1990**, *38*, 323 and references cited therein.
[11] F. Cecconi, C. A. Ghilardi, S. Midollini, A. Orlandini, *Inorg. Chim. Acta***1998**, *269*, 274.
[12] M. Kaupp, H. G. von Schnering, *Inorg. Chem.***1994**, *33*, 2555 and references cited therein.
[13] D. Grdenic, *Quart. Rev.***1965**, *19*, 303.
[14] N. Ueyama, K. Taniuchi, T. Okamura, A. Nakamura, H. Maeda, S. Emura, *Inorg. Chem.***1996**, *35*, 1945.
[15] A. J. Blake, E. C. Pasteur, G. Reid, M. Schröder, *Polyhedron***1991**, *10*, 1545.
[16] M. E. Sobhia, K. Panneerselvam, K. K. Chacko, I. H. Suh, E. Weber, C. Reutel, *Inorg. Chim. Acta***1992**, *194*, 93.
[17] S.-L. Li, T. C. W. Mak, Z.-Z. Zhang, *J. Chem. Soc. Dalton Trans.***1996**, 3475.
[18] E. C. Alyea, S. Dias, G. Ferguson, M. Khan, *Can. J. Chem.***1979**, *57*, 2217.
[19] T. E. Jones, L. S. W. L. Sokol, D. B. Rorabacher, M. D. Glick, *Chem. Commun.***1979**, 140.
[20] B. F. Abrahams, D. Dakternieks, B. F. Hoskins, G. Winter, *Inorg. Chim. Acta***1992**, *201*, 95.
[21] C. M. V. Stålhandske, C. I. Stålhandske, M. Sandström, I. Persson, *Inorg. Chem.***1997**, *36*, 3167.
[22] L. M. Berreau, R. A. Allred, M. M. Makowska-Grzyska, A. M. Arif, *Chem. Commun.***2000**, 1423.
[23] P. C. Turley, P. Haake, *J. Am. Chem. Soc.***1967**, *89*, 4617.
[24] R. McCrindle, G. Ferguson, A. J. McAlees, M. Parvez, B. L. Ruhl, D. K. Stephenson, T. Wieckowski, *J. Chem. Soc. Dalton Trans.***1986**, 2351.
[25] S. M. Berry, D. C. Bebout, R. J. Butcher, *Inorg. Chem.***2005**, *44*, 27.
[26] D. C. Bebout, S. W. Stokes, R. J. Butcher, *Inorg. Chem.***1999**, *38*, 1126.
[27] R. A. Allred, L. H. McAlexander, A. M. Arif, L. M. Berreau, *Inorg. Chem.***2002**, *41*, 6790.
[28] W. C. Wolsey, *J. Chem. Educ.***1973**, *50*, A335.
[29] Z. Otwinowski, W. Minor, *Methods Enzymol.***1997**, *276*, 307.
[30] A. Altormare, M. C. Burla, M. Camalli, G. Cascarano, C. Giacovazzo, A. Guagliardi, A. G. G. Moliterni, G. Polidori, R. Spagna, *J. Appl. Crystallogr.***1999**, *32*, 115.
[31] G. M. Sheldrick, *SHELXL-97*, *Program for Crystal Structure Refinement*, University of Göttingen, Germany, **1997**.

Received September 18, 2004

 © 2005 Wiley-VCH Verlag GmbH & Co. KGaA, Weinheim

Ab-initio Powder Structure Determination of Dichloro[1,2-ethanediylbis(iminomethylene)bis(phosphonato)]trizinc Dihydrate

Naima Bestaoui,[a] Ekaterina V. Bakhmutova-Albert,[a] Ana Vega Rodriguez,[b] Ricardo Llavona,[b] and Abraham Clearfield*[a]

Keywords: Metal phoshonates / Zinc

The reaction of zinc chloride with 1,2-ethanediylbis(iminomethylene)bis(phosphonic acid) in acidic conditions yielded dichloro[1,2-ethanediylbis(iminomethylene)bis(phosphonato)]trizinc dihydrate, $Zn_3Cl_2(HO_3PCH_2NHCH_2CH_2NHCH_2PO_3H)_2{\cdot}2H_2O$ which crystallizes in the monoclinic system and space group $P2_1/n$, with the unit cell parameters a = 9.94316(4), b = 10.44577(5), c = 24.3240(1) Å, β = 90.003(1)°, and Z = 4. The crystal structure was determined ab initio from its powder pattern using the programs EXPO and GSAS. The zinc atoms are in tetrahedral environment and form 16-membered rings with the phosphonate groups. The structure is clearly different from that of the corresponding Cd complex in that the Cd is sixfold coordinated and of different ligand to metal ratio.
(© Wiley-VCH Verlag GmbH & Co. KGaA, 69451 Weinheim, Germany, 2005)

Introduction

A major effort has been devoted in our laboratory towards the synthesis and characterization of metal phosphonates.[1] Notable studies in this area of research have also been carried out by Alberti et al.,[2] Bujoli and coworkers[3] and in Ferey's laboratory.[4] One general ligand type that we utilized is the α,ω-alkyldiphosphonic acid. These acids formed semi-crystalline products of the general formula $Zr[O_3P(CH_2)_nPO_3]$ with group 4 metals whose morphology and X-ray powder patterns indicate layered structures in which the layers are cross-linked by the alkyl groups.[5] Similar compounds were prepared using Zn and Cu as the metals.[6,7] These latter compounds were sufficiently crystalline that their structures could be determined from X-ray powder data. Indeed the copper structures confirmed the layered nature of the compounds and in these compounds the alkyl chains are perpendicular to the layers.

Interlayer spacings of the zirconium alkylene derivatives indicated that the chains are inclined at about 60° to the mean plane of the layers and that the layer structures differ from those of the transition metal compounds. Subsequently, zirconium diphosphonic acid derivatives in which the alkyl chains contained amino groups were prepared. Although the compounds were amorphous, they exhibited anion exchange and complexing behavior.[8]

Divalent metals often form crystalline phosphonates; it was of interest to prepare cross-linked layered derivatives containing the amino functionality. Determination of such structures would provide a model for understanding the ion exchange and complexation reactions via structural data. In this paper we report the structure of a chloro(ethylenediaminediphosphonato)zinc. The ligand employed was $H_2O_3PCH_2NHCH_2CH_2NHCH_2PO_3H_2$ (H_4L) which exists in solution as a di-zwitterion. In a previous paper[9] we described the synthesis and characterization of chloro(amino)-(phosphonato) cadmium which crystallizes in a monoclinic system and has a layered type structure, the layers being held together by hydrogen bonding. In the cadmium compound the Cd atoms form dimers through bridging chlorides. These dimers are in turn formed into rows by the phosphonate groups and the rows are crosslinked by the organic chain of the ligand into layers.

In this paper, we are presenting the interaction of the same ligand with zinc chloride in an acidic medium. This led to the formation of $Zn_3Cl_2(H_2L)_2{\cdot}2H_2O$, whose structure, quite different from the previous cadmium structure,[9] is presented here as characterized by its X-ray structure derived from powder data and FTIR.

Results and Discussion

Thermogravimetric Studies: The TGA diagram of $Zn_3Cl_2(H_2O)_2(H_2L)_2$, presented in Figure 1, shows three weight losses. The first step begins at 100 °C and indicates the release of two water molecules by 195 °C. The observed weight loss (4.15%) is in agreement with the calculated value (4.53%). The temperature of dehydration indicates that molecules of water are either coordinated with the zinc atom or strongly hydrogen-bonded. The next process is the

[a] Department of Chemistry, Texas A&M University, College Station, Texas 77843-3255, USA
[b] Departamento de Quimica Organica e Inorganica, Universidad de Oviedo, 33071 Oviedo, Spain

 DOI: 10.1002/ejic.200400878 © 2005 Wiley-VCH Verlag GmbH & Co. KGaA, Weinheim

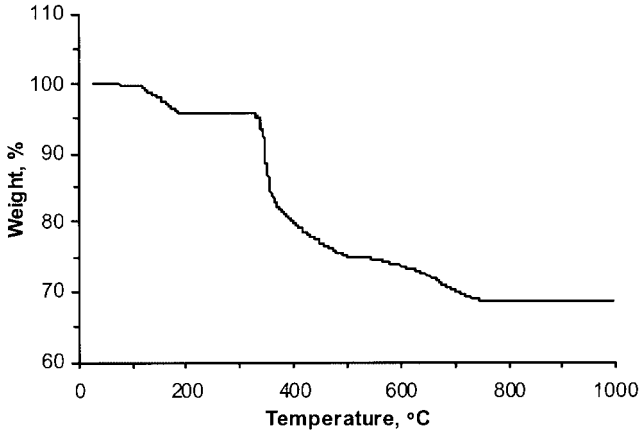

Figure 1. TGA curve for $Zn_3Cl_2L_2{\cdot}2H_2O$.

decomposition of the organic moieties and phosphonic groups accompanied by the formation of oxychloro derivatives, which begins at 350 °C. The process is completed at 758 °C with the formation of a final residue of 68.93%. The product can be formulated as a 1:1 mixture of $Zn(PO_3)_2$/$Zn_2P_2O_7$ (calcd. residue 66.40%). The total weight loss is 31.07% as compared to the calculated value of 33.43% based on the ideal formula.

Description of the Structure

The structure contains three crystallographic independent Zn atoms; they are all in a tetrahedral environment. Zn1 and Zn3 are both bonded to four oxygen atoms from the phosphonate groups. The Zn–O distances vary between 1.957(8) Å and 2.003(8) Å, and are in the order of a normal Zn–O bond. Zn2 is different as it is connected to two oxygen atoms from the phosphonate groups at distances of 1.967(9) and 2.020(9) Å and two chlorine atoms [2.254(8) Å and 2.379(8) Å].

The four phosphorus atoms are in tetrahedral environments consisting of three oxygen atoms and one carbon atom, divided into two distinct groups. In group P1 and P2, the three oxygen atoms bond to each of the three Zn atoms; in this case the order of the P–O bond is between 1.508(8) and 1.531(9) Å. In the P3 and P4 group, only two of their oxygen atoms each bond to Zn1 and Zn3. In this case the non-bonded oxygen atoms O8 and O11 are located at respective distances of 1.542(9) and 1.533(9) Å. These distances are slightly longer than the bonded P–O distance but similar considering the large e.s.d. values.

Zn1 and Zn3 are connected to each other through O–P–O bridging in both the *a*- and *b*-axis directions. Along the *a*-axis the bridging is by alternating P3 and P4 phosphonate groups and in the *b*-axis direction by P1 and P2 groups (Figure 2). This connectivity results in 16-membered rings (counting all the ring atoms). The Zn2 atoms lie in rows parallel to the *b*-axis sandwiched between the Zn1, Zn3 rows as seen in Figure 3. In the *c*-axis direction, the *z* parameter of the Zn2 atoms is very nearly 0,1/2 (Figure 3). This siting places them at intervals of every two rows of Zn1 and Zn3. The coordination of Zn2 is also tetrahedral but from both chloride ions and O4 from P1 and O6 from P2. The linkage in the *c*-axis direction is to form two sets of 16-membered rings, one involving Zn1 and Zn3 and the other with Zn3 and Zn2 alternating with Zn1, Zn2. The carbon−nitrogen chains criss-cross each other connecting P1 bonded to three Zn atoms to P4 bonded to Zn1 and Zn3 (Figure 4). Similarly, P2 bonds to three Zn atoms and P3 to two forming a three dimensional structure.

The localization of the hydrogen atoms allowed us to characterize the hydrogen bonding in the structure and led us to a better understanding of the structure. The structure show an extensive hydrogen bond network going from the chlorine atoms to the two water molecules, to the nitrogen atoms and to the non-metal-bonded oxygen atoms in phosphonate groups P3–O8 and P4–O11. There are four different nitrogen atoms. The C1–N1–C2 angle is 107.7(6)°

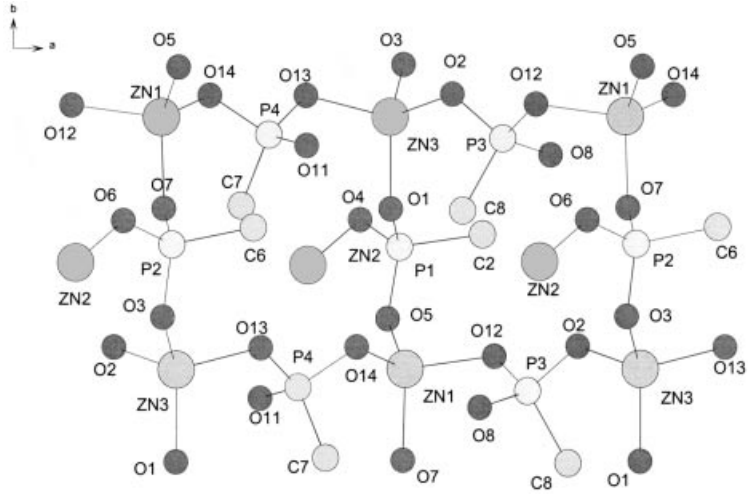

Figure 2. Connectivity of the zinc atoms in the *a*,*b* plane. Zn1 and Zn3 are four coordinates and connected to phosphonate oxygen atoms forming a 16-membered rings.

 © 2005 Wiley-VCH Verlag GmbH & Co. KGaA, Weinheim

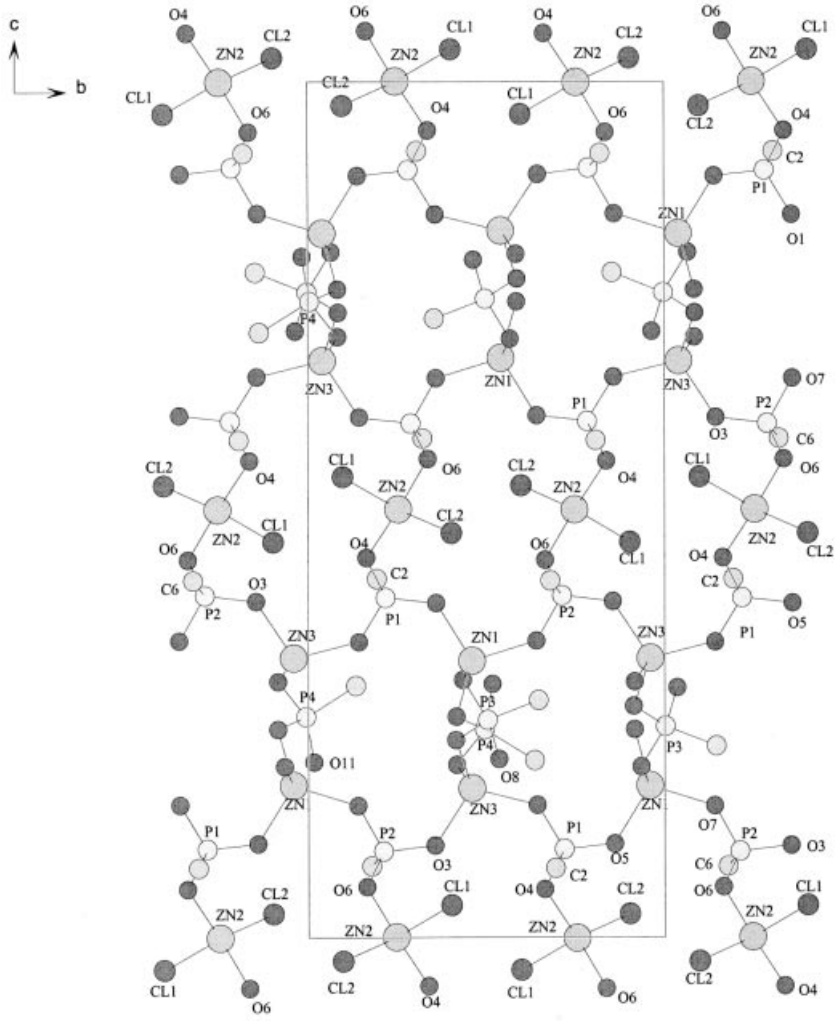

Figure 3. Connectivity of the zinc atoms in the *b*,*c* plane. Zn1, Zn2 and Zn3 are four coordinates and connected to phosphonate oxygen atoms forming a 16-membered rings.

close to the tetrahedral angle of 109°; two hydrogen atoms are located on this nitrogen atom. This shows its tetrahedral symmetry and protonated nature. This atom is hydrogen-bonded to O8 (the free oxygen from P3) through H21. The distance N1···O8 is 2.81 Å on the order of a hydrogen bond length, the bond angle N1–H21···O8 is 130.9° and the distance H21···O8 is 2.04 Å. We could not find any hydrogen atom bonded to O8, therefore O8 is negatively charged. However O8 is also hydrogen-bonded to N2 again as the acceptor. In this case the distance is shorter (2.59 Å), and the interaction between N2 and O8 is much stronger. The angle C3–N2–C7 is 118.2(6)°, close to 120°. However, two hydrogen atoms were localized on this nitrogen atom; this shows the protonated nature of this nitrogen atom and the tetrahedral symmetry. This nitrogen is also hydrogen-bonded to one of the two water molecules (O9w) at a distance of 2.91 Å through H27 with an angle of 152.8°.

The third nitrogen atom is bonded to only one hydrogen atom, the C5–N3–C6 angle is 117.72(7)°; close to 120°. This atom is non-protonated. However it is hydrogen-bonded to O11 through H18. O11 (oxygen from phosphonate group P4), is also protonated (H24), however this proton does not participate into the hydrogen bonding network, O11 is acting as an acceptor in this case and is also hydrogen-bonded with N4 (donor), which is protonated. Two hydrogen atoms (H20 and H28) were localized on this atom and the angle C4–N4–C8 is 108.2(6)° very close to the tetrahedral angle. H28 points towards O10w with an angle of 125.7° and the distance N4···O10w is 2.84 Å. H20 points towards O11 with an angle of 110.8° and the distance N4···O11 is 3.09 Å.

The two water molecules are also hydrogen-bonded to the two chlorine atoms. These two molecules are then stabilized by their multiple hydrogen bonding, which explains why they are thermally removed between 100 °C and 200 °C (thermogravimetric analyses, Figure 1). This loss of water is accompanied by structure collapse.

The distribution of protons from the phosphonate groups to three of the four nitrogen atoms (N1, N2, N4) requires that the two phosphonic acids have different negative charges. The P1, P4 ligand has both nitrogen atoms

 © 2005 Wiley-VCH Verlag GmbH & Co. KGaA, Weinheim

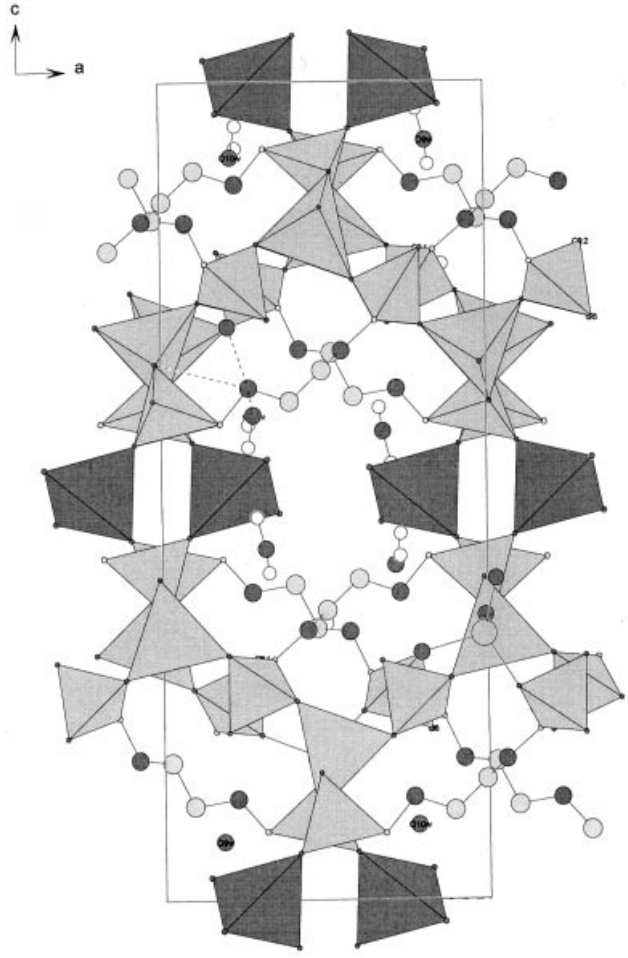

Figure 4. Tetrahedral representation of the structure in the *a,c* plane. The large gray tetraedra represent $[Zn1O_4]^{6-}$ and $[Zn3O_4]^{6-}$; darker gray tetraedra $[Zn2Cl_2O_2]^{4-}$ and small gray tetraedra the phosphonate groups.

protonated as well as O11; therefore it has a charge of minus one. The P2, P3 ligand has only N4 protonated and a charge of minus three.

Spectroscopic Studies

FTIR: The crystal structure of H_4L[13] shows both nitrogen atoms to be protonated. The IR spectrum of this zwitterion is shown in Figure 5a, together with that of the zinc compound. The range of PO vibrations in the IR spectrum of H_4L supports the betaine structure. The spectrum exhibits three strong bands at 1156, 1029 and 939 cm^{-1}, assigned respectively to $\nu_{as}(PO_2)$, $\nu_s(PO_2)$and ν(POH), indicating clearly the presence of PO_3H groups. [10] Furthermore, all the PO bands are low-frequency shifted due to the strong intra- and intermolecular hydrogen bonds with lattice water molecules and NH_2^+ groups. The NH_2^+ bands are expected to give two bands between 3000 and 2700 cm^{-1}, which are usually broad, unresolved and extended to 2273 cm^{-1}. Indeed, the IR spectrum of H_4L shows a broad and shallow band at 2800–2400 cm^{-1} revealing the presence of the protonated NH groups.

The IR spectrum of zinc phosphonate is complicated (see b in Figure 5). Phosphonic groups are coordinated with metal and the ν(P–OH) band observed in H_4L disappears upon coordination. The other vibrations associated with the POH group [ν(PO–H), 2δ(POH)] can still be detected with a decrease of their intensity. Two new sharp bands at 1130 and 1107 cm^{-1} can principally be assigned to both $\nu(PO_2)$ and $\nu(PO_3)$ vibrations. The zwitterionic structure of the compound could also be observed, in the region 3400–2500 cm^{-1} of the spectrum. In fact the NH stretching vibrations band is high-frequency shifted with much higher $\Delta\nu$ (91 cm^{-1}) value than the CdL_2H_2O[9] compound. At the same time, the $\nu(NH_2^+)$ band belonging to acid H_4L is still present in the spectrum. Only a slight decrease in the intensity of this band was observed. The NH_2^+ bending band does not appear in the spectrum. This spectrum can be interpreted in terms of partial protonation of nitrogen atoms and presence of both POH and PO groups, which is in accordance with the structure data.

Conclusions

It is interesting to note that while both the zinc and the cadmium complexes with the ligand H_4L were prepared in a very similar fashion, the stoichiometry and hence the structures are completely different. The Cd complex is octahedrally coordinated[9] by two Cl, two phosphonate oxygen atoms and two water molecules. The chloride ions bridge across two cadmiums while the phosphonate groups connect these dimers into double-stranded chains. In the process the double-stranded chains are crosslinked into layers that are hydrogen-bonded to each other. Both IR and NMR showed that the nitrogen atoms are protonated. In the zinc structure the differences are striking. The Zn atoms are four coordinate in which the chloride ions reside on a single zinc atom and do not bridge across metal atoms. The distribution of the ligand protons is also different, three of the nitrogen atoms are protonated but N3 is not and water molecules are not bonded to zinc. Therefore a moreaccurate formula is $Zn_3Cl_2(O_3PCH_2NH_2^+CH_2CH_2\text{-}NH_2^+CH_2PO_3)(HO_3PCH_2NHCH_2CH_2NH_2^+CH_2PO_3)\cdot 2H_2O$. These studies show that the H_4L ligand can adjust its coordination and behavior in several different as not yet totally explored ways.

Experimental Section

Materials and Methods: All chemicals were obtained from commercial sources and used without further purification. The ethylenediamine-*N,N'*-bis(methylenephosphonic acid) (H_4L) was synthesized as described previously.[9]

Synthesis of $Zn_3Cl_2(H_2L)_2\cdot 2H_2O$: A solution of zinc chloride (EM Science, 10.6 mmol, 15 mL) in water was added to a suspension of H_4L (5.3 mmol, 15 mL) with brisk stirring. The pH was adjusted to 2 with hydrochloric acid (5 M) and the mixture was transferred to a Teflon-lined pressure vessel and kept at 150 °C for 5 days. The lower pH aided the formation of the crystalline powder. The

 © 2005 Wiley-VCH Verlag GmbH & Co. KGaA, Weinheim

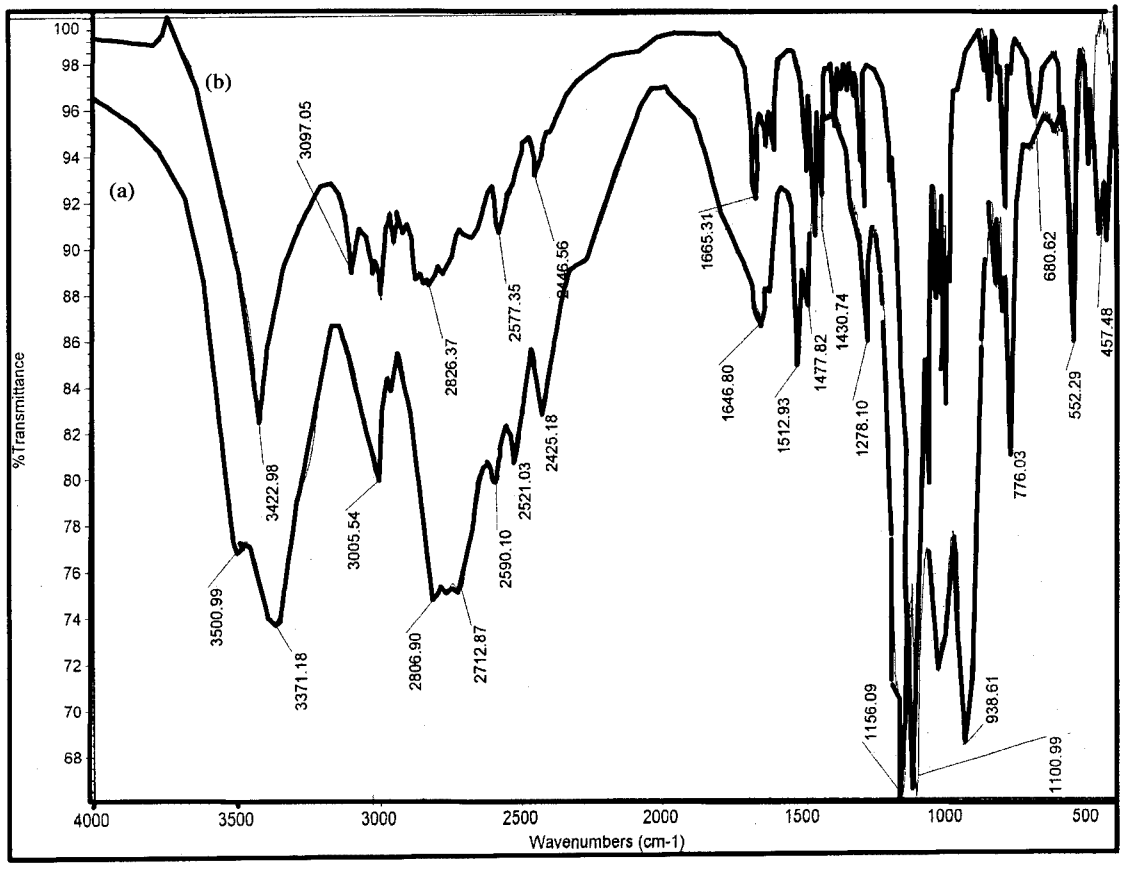

Figure 5. IR spectra of $Zn_3Cl_2L_2{\cdot}2H_2O$ (b) compared to aminophosphonic acid H_4L (a).

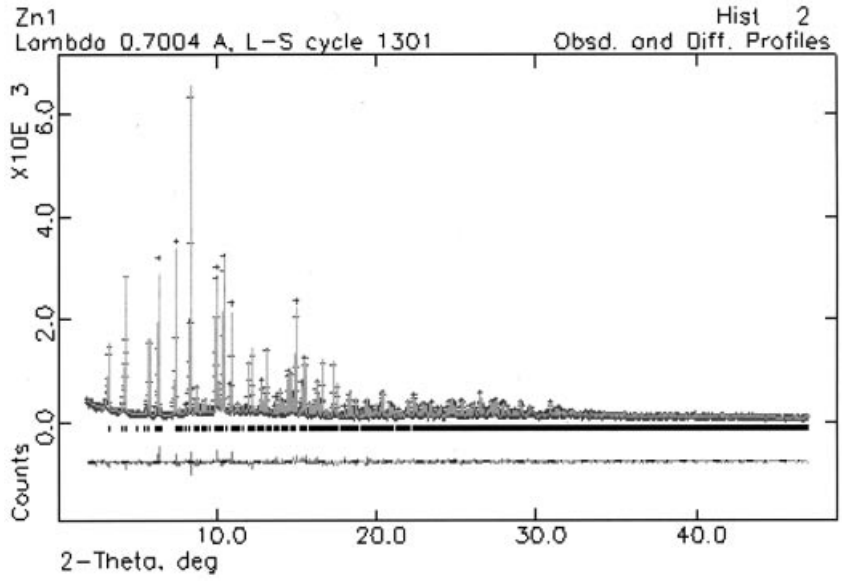

Figure 6. Observed (+), calculated (–) and difference profiles for the Rietveld refinement of $Zn_3Cl_2L_2{\cdot}2H_2O$.

resulting solid compound was filtered, washed with water and dried at 60 °C (0.96 g, 56%). $C_8H_{28}Cl_2N_4O_{14}P_4Zn_3$ (793.28): calcd. C 12.08, H 3.55, N 7.04, P 15.58, Cl 8.92, Zn 24.67; found C 12.27, H 3.72, N 7.12, P 15.13, Cl 8.67, Zn 24.16. IR: $\tilde{\nu}$ = ν(OH) 3423 cm^{-1} (ms) and $\nu(NH_2^+)$; ν(NH) 3097 cm^{-1} (mw), 3020, (mw), 2996, (mw), $\nu(CH_2)$, around 2826 cm^{-1} (bw); ν(PO–H), 2δ(POH) 2800–2400 cm^{-1} (mw); δ(HOH) 1665, 1623 cm^{-1} (w); δ NH_2^+) 1595 cm^{-1}; $\delta(CH_2)$ 1481–1384 cm^{-1} (w); $\omega(CH_2)$ 1288 cm^{-1} (mw); ν(PO) 1130 cm^{-1} (s), 1107 cm^{-1} (s).

The IR spectra were recorded with a Nicolet Nexus 470 FTIR spectrometer with spectral resolution of 2 cm^{-1} in KBr pellets. Thermo-

 © 2005 Wiley-VCH Verlag GmbH & Co. KGaA, Weinheim

gravimetric analysis was carried out with a DuPont TGA 951 instrument at a heating rate of 10 °C/min under compressed air. The obtained compounds were characterized by their X-ray powder data collected with either a Rigaku 5000 computer-automated diffractometer with rotating anode or a Bruker advance diffractometer by the step scan method with Cu-K_α radiation (λ = 1.5418 Å).

Analytical Results: Zinc and phosphorus analysis was carried out in-house with a Direct Current Plasma (DCP) spectrometer. A weighed portion of the sample was dissolved in 1 mL of 48% HF and then diluted to 200 mL. Aliquots were then removed and diluted to a composition falling well within the standard curves for Zn and P, respectively. Alternatively these elements were also determined using a Cameca 5 × 50 electron microprobe at an accelerating voltage of 15 kV and operating with a beam current of 20 mA using a wavelength-dispersive spectrometer (WDS). C,H,N analyses were performed by Galbraith laboratories.

In-house X-ray Diffraction

Parameters Determination (high-resolution data): An X-ray powder diffraction pattern was recorded using a Bruker D8 advance, high resolution X-ray diffractometer with Bragg–Brentano θ−2θ geometry (40 kV and 50 mA), using a Ge monochromator with Cu-$K_{\alpha 1}$ radiation (λ = 1.54056 Å). The data were recorded between 5 and 95° in 2θ, with a step size of 0.01° and a count time of 30 s per step. The sample was packed in a flat plastic holder, and was allowed to rotate at 15.00 RPM during the data collection.

Structure Solving and Refinement (intensity data): X-ray powder diffraction patterns were recorded using a Bruker D8 diffractometer with Bragg–Brentano θ–2θ geometry (40 kV and 50 mA), using a graphite monochromator. The data were recorded between 5 and 60° in 2θ, with a step size of 0.01° and a count time of 20 s per step, and 50 to 100° in 2θ, with a step size of 0.01° and a count time of 25 s per step. The sample was packed in a flat plastic holder.

Table 1. Crystal data.

Empirical formula	$C_8H_{26}Cl_2N_4O_{14}P_4Zn_3$
Formula mass	793.28
Crystal system	monoclinic
Space group	$P2_1/n$ (no. 14)
Unit cell dimensions	a = 9.94316(4) Å
	b = 10.44577(5) Å
	c = 24.3240(1) Å
	β = 90.003(1) °
Cell volume	2526.39(2) Å^3
Z	4
Density, calculated	2.017 g/cm^3
Rwp[a], Rp[b], R_f	0.0574, 0.07454, 0.0455

[a] $Rwp = (\Sigma\, w(I_o - I_c)^2/\Sigma w I_o^2)^{0.5}$ (w = weighting factor). [b] $Rp = \Sigma \mid I_o - I_c \mid/\Sigma\, I_o$. [c] $R_f = \Sigma\, |F_o - SF_c|/\Sigma\, |F_o|$ (S = scale factor)

Table 2. Atomic coordinates and isotropic displacement parameters (in Å^2) for non-hydrogen atoms.

Atom	Wyck.	x	y	z	U_{iso}
ZN1	4e	0.4880(3)	0.0411(3)	0.8230(1)	0.0106(2)
ZN2	4e	0.6967(2)	0.2469(8)	0.0004(3)	0.0106(2)
ZN3	4e	0.9811(3)	0.0406(3)	0.6738(1)	0.0106(2)
Cl1	4e	0.8248(5)	0.4023(5)	0.03790(3)	0.032(1)
Cl2	4e	0.1399(5)	0.9024(5)	0.0278(3)	0.032(1)
P1	4e	0.4986(5)	0.2823(5)	0.8969(2)	0.0228(6)
P2	4e	0.4894(5)	0.2119(5)	0.1004(2)	0.0228(6)
P3	4e	0.7762(5)	0.0028(5)	0.2464(2)	0.0228(6)
P4	4e	0.2193(6)	0.4946(5)	0.2428(2)	0.0228(6)
O1	4e	0.5181(10)	0.3575(6)	0.8452(3)	0.0174(8)
O2	4e	0.1153(7)	0.0859(8)	0.701(3)	0.0174(8)
O3	4e	0.5100(13)	0.3552(6)	0.1075(3)	0.0174(8)
O4	4e	0.5842(7)	0.3367(8)	0.9434(3)	0.0174(8)
O5	4e	0.5256(13)	0.1407(6)	0.8904(3)	0.0174(8)
O6	4e	0.5942(8)	0.1646(8)	0.0590(3)	0.0174(8)
O7	4e	0.4932(13)	–0.1402(6)	0.8465 (3)	0.0174(8)
O8	4e	0.8269(8)	0.5354(10)	0.2084(3)	0.0174(8)
O9w	4e	0.1814(11)	0.5132(13)	0.0714(4)	0.0174(8)
O10w	4e	0.7824(12)	–0.0106(9)	0.0913(4)	0.0174(8)
O11	4e	0.1991(9)	0.0162(11)	0.2046(3)	0.0174(8)
O12	4e	0.7045(7)	0.9338(10)	0.1994(3)	0.0174(8)
O13	4e	0.2992(7)	0.4161(9)	0.2015(3)	0.0174(8)
O14	4e	0.4078(7)	0.9155(10)	0.2428(3)	0.0174(8)
N1	4e	0.2312(5)	0.2871(7)	0.8750(3)	0.032(2)
N2	4e	0.0550(7)	0.6144(6)	0.1702(3)	0.032(2)
N3	4e	0.2247(5)	0.2188(10)	0.1236(3)	0.032(2)
N4	4e	0.9241(6)	0.1320(6)	0.1722(3)	0.032(2)
C1	4e	0.3942(6)	–0.1736(7)	0.6084(3)	0.053(3)
C2	4e	0.3202(6)	0.3068(8)	0.9189(3)	0.053(3)
C3	4e	0.4938(7)	–0.2204(6)	0.6463(3)	0.053(3)
C4	4e	−0.0239(6)	–0.2210(6)	0.8320(3)	0.053(3)
C5	4e	0.0922(6)	0.1976(8)	0.1147(3)	0.053(3)
C6	4e	0.3147(7)	0.1787(8)	0.0833(3)	0.053(3)
C7	4e	0.1595(8)	0.6351(7)	0.2066(3)	0.053(3)
C8	4e	0.8629(9)	0.1461(7)	0.2231(3)	0.053(3)

[a] $U_{iso} = B_{iso}/8\Pi^2$

 © 2005 Wiley-VCH Verlag GmbH & Co. KGaA, Weinheim

Synchrotron Powder X-ray Diffraction: Powder X-ray diffraction data were collected at ambient temperature on beamline X3B1 of the National Synchrotron Light Source at Brookhaven National Laboratory. X-rays of wavelength 0.70045(1) Å was selected by a double crystal Si(111) monochromator. The sample was sealed in a capillary, which was continuously rotated during data collection. The data collection time increased from 1 s per point at 2 degrees 2θ to 5.7 s at 46.997°, with a step size of 0.003°. The diffracted X-rays are selected by a Ge (111) analyzer crystal on a detector arm, and detected using a commercial NaI scintillation counter; the measured X-ray counts are normalized to the signal from an ionization chamber between the monochromator and the sample in order to correct for decay and fluctuations of the incident beam intensity.

Structure Determination: A first determination of cell parameters was made using Treor90 program[11] on the in-house data. The indexing yielded the cell dimensions: a = 9.942(1), b = 10.445(1), c = 23.317(4) Å, β = 90.001(1)° and V = 2526.46(2) Å^3 as the best solution [M (20) = 51]. The β angle is very close to 90°, the cell parameters are then reflective of an orthorhombic symmetry. The analyses of the systematic absences are consistent with the space group $Pna2_1$. However, we were not able to solve the structure in this space group or in any orthorhombic space group which could reproduce the powder pattern. We considered then a small distortion of the β angle to reflect a monoclinic distortion. The analyses of the systematic absences were consistent with the space group $P2_1/n$. The first attempt to solve this structure in the in-house data, using EXPO,[12] allowed us to localize a few of the atoms. Respectively, three zinc atoms, three of the four phosphorus atoms, and the two chlorine atoms. The calculation of successive Fourier difference maps followed by Rietveld refinement (using the program GSAS[13]) allowed us to locate most of the oxygen atoms and one ligand, but we were not able to go further. For this reason, we recorded a synchrotron data set, which allowed us to localize most of the atoms by direct methods and the rest of them by Fourier difference maps.

The refinement strategy consisted in a first step of a Lebail method refinement for the background (using 12 terms of a Chebychev function), zero shift, cell parameters and peak profile function, considering a dummy hydrogen atom and maintaining a scale factor constant and equal to 1. Once these parameters were satisfactory (Rp = 0.07), they were fixed, the known atoms were entered into the program and the scale factor refined. By successive refinement and Fourier difference maps, all the atoms were located. The following bond constraints were applied: Zn–O (2.0 Å), Zn–Cl (2.6 Å), P–O (1.52Å), P–C (1.80 Å), C–N (1.34 Å), C–C (1.54 Å) and C–H (1 Å) prior to position refinement of the atoms. The bond angles around the phosphorus atom were constrained to idealized tetrahedral angles by applying constraints to the non-bonded O···O (2.5 Å) and O···C (2.7 Å) distances, and tetrahedral angles around the carbon atom. The position for the hydrogen atoms were calculated for the carbon atoms and a final Fourier difference allowed us to localize the remaining hydrogen atoms. The carbon hydrogen atom position were refined but not the nitrogen hydrogen atoms or the water hydrogen. The constraint parameter was first fixed to 500 and then lowered to 100 in the last cycle of the refinement. The atomic positions were refined first, then the temperature factors, and finally all the parameters were refined simultaneously. The last set of refinement yielded a value of R_p = 0.0567, R_{wp} = 0.0733 and R_F = 0.0424.

Figure 6 shows the observed powder pattern, the calculated and the difference curve after the last refinement, from the synchrotron

Table 3. Selected geometric parameters, distances and angles [Å, °]

ZN1–O5	1.978(8)	O5–ZN1–O7	104.9(3)
ZN1–O7	1.980(7)	O5–ZN1–O12	109.7(4)
ZN1–O12	2.006(8)	O5–ZN1–O14	117.1(4)
ZN1–O14	1.958(8)	O7–ZN1–O12	103.2(5)
		O7–ZN1–O14	116.4(4)
		O12–ZN1–O14	104.7(3)
ZN2–Cl1	2.256(9)	Cl1–ZN2–O4	104.9(5)
ZN2–O4	2.012(9)	Cl1–ZN2–O6	108.4(4)
ZN2–O6	1.953(9)	Cl1–ZN2–Cl2	101.8(2)
ZN2–Cl2	2.353(8)	O4–ZN2–O6	114.7(3)
		O4–ZN2–Cl2	119.5(4)
		O6–ZN2–Cl2	106.3(5)
ZN3–O1	1.968(7)	O1–ZN3–O2	113.3(4)
ZN3–O2	1.970(8)	O1–ZN3–O3	110.1(3)
ZN3–O3	1.968(8)	O1–ZN3–O13	107.8(4)
ZN3–O13	1.982(8)	O2–ZN3–O3	109.8(4)
		O2–ZN3–O13	109.1(3)
		O3–ZN3–O13	106.6(4)
P1–O1	1.494(8)	O1–P1–C2	106.7(5)
P1–C2	1.876(8)	O1–P1–O4	110.2(5)
P1–O4	1.521(8)	O1–P1–O5	113.8(5)
P1–O5	1.512(8)	C2–P1–O4	105.3(4)
		C2–P1–O5	109.1(6)
		O4–P1–O5	110.3(6)
P2–O3	1.522(8)	O3–P2–O6	107.5(6)
P2–O6	1.530(9)	O3–P2–O7	112.2(5)
P2–O7	1.502(8)	O3–P2–C6	110.0(6)
P2–C6	1.819(8)	O6–P2–O7	109.0(6)
		O6–P2–C6	116.0(5)
		O7–P2–C6	102.2(6)
P3–O2	1.533(9)	O2–P3–O8	109.5(5)
P3–O8	1.542(9)	O2–P3–O12	108.8(5)
P3–O12	1.528(9)	O2–P3–C8	106.3(5)
P3–C8	1.817(9)	O8–P3–O12	109.2(5)
		O8–P3–C8	110.8(5)
		O12–P3–C8	112.2(5)
P4–O11	1.533(9)	O11–P4–C7	117.4(6)
P4–O13	1.521(9)	O11–P4–O13	110.8(6)
P4–O14	1.550(9)	O11–P4–O14	108.7(6)
P4–C7	1.812(9)	C7–P4–O13	106.7(5)
		C7–P4–O14	105.9(5)
		O13–P4–O14	106.8(5)
C1–C3	1.440(9)	C3–C1–N1	109.5(6)
C1–N1	1.373(8)		
C2–N1	1.403(9)	P1–C2–N1	111.2(5)
C3–N2	1.391(9)	C1–C3–N2	107.4(6)
C4–C5	1.484(9)	C5–C4–N4	106.6(6)
C4–N4	1.364(9)		
C5–N3	1.353(8)	C4–C5–N3	106.2(6)
C6–P2	1.819(8)	P2–C6–N3	113.3(6)
C6–N3	1.393(10)		
C7–N2	1.381(10)	N2–C7–P4	115.6(6)
C8–N4	1.388(9)	P3–C8–N4	113.5(5)
N1–C1	1.373(8)	C1–N1–C2	107.7(6)
N1–C2	1.403(9)	C1–N1–H21	113.4(9)
N1–H21	1.015(11)	C1–N1–H22	112.2(10
N1–H22	1.018(11)	C2–N1–H21	111.2(9)
		C2–N1–H22	110.0(10)
		H2–N1–H21	102.3(11)
N2–C3	1.391(9)	C3–N2–C7	118.2(6)
N2–C7	1.381(10)	C3–N2–H17	109.3(8)
N2–H17	1.041(12)	C3–N2–H27	108.7(8)
N2–H27	1.036(11)	C7–N2–H17	109.6(9)
		C7–N2–H27	110.0(9)
		H17–N2–H27	99.4(10)
N3–C5	1.353(8)	C5–N3–C6	117.7(7)
N3–C6	1.393(10)	C5–N3–H18	115.7(12)
N3–H18	1.000(13)	C6–N3–H18	114.3(15)
N4–C4	1.364(9)	C4–N4–C8	108.2(6)
N4–C8	1.388(9)	C4–N4–H20	112.9(9)
N4–H20	1.021(10)	C4–N4–H28	111.5(9)
N4–H28	1.021(11)	C8–N4–H20	110.7(10)
		C8–N4–H28	111.2(8)
		H20–N4–H28	102.3(12)
O9w–H14	0.96(11)	H14–O9w–H19	123.(7)
O9w–H19	1.004(21)		
O10w–H15	1.014(21)	H15–O10w–H16	93.0(32)
O10w–H16	1.005(20)		
O11–P4	1.533(9)	P4–O11–H24	93.(7)
O11–H24	1.05(10)		

 © 2005 Wiley-VCH Verlag GmbH & Co. KGaA, Weinheim

data set. Table 1 presents the crystallographic data. The atomic positions, the bond lengths and angles are represented in Table 2 and Table 3, respectively. CCDC-249450 contains the supplementary crystallographic data for this paper. This data can be obtained free of charge via www.ccdc.cam.ac.uk/data_request/cif.

Acknowledgments

This study was supported with funds provided by NSF Grant No. DMR 0332453, for which grateful acknowledgement is made. We thank Nicholas A. Spurr for the DCP analysis, Dr. Guillemette (Geology department, Texas A&M University) for the microprobe analysis and Dr. P. Stephens (Physics and Astronomy Department, SUNY Stony Brook) for his assistance with synchrotron X-ray data collection. Research carried out in part at the National Synchrotron Light Source at Brookhaven National Laboratory, which is supported by the US Department of Energy, Division of Materials Sciences and Division of Chemical Sciences. The SUNY X3 beamline at NSLS is supported by the Division of Basic Energy Sciences of the US Department of Energy under Grant No. DE-FG02-86ER45231.

[1] a) A. Clearfield, *Curr. Opin. Solid State Mater. Sci.* **1996**, *1*, 268; b) A. Clearfield, *Curr. Opin. Solid State Mater. Sci.* **2002**, *6*, 495; c) A. Clearfield, in *Progress in Inorganic Chemistry* (Ed.: K. D. Karlin), John Wiley & Sons, New York, **1998**, 371; d) C. V. K. Sharma, A. Clearfield, *J. Am. Chem. Soc.* **2000**, *122*, 4394–4402; e) C. V. K. Sharma, C. V. Hesseheimer, J. Amelia, A. Clearfield, *Polyhedron* **2001**, *20*, 2095–2104; f) A. Clearfield, C. V. K. Sharma, B. Zhang, *Chem. Mater.* **2001**, *13*, 3099–3112; g) A. Clearfield, Z. J. Wang, *J. Chem. Soc. Dalton Trans.* **2002**, *23*, 4457–4463.

[2] a) G. Alberti, in *Comprehensive Supramolecular Chemistry* (Eds.: G. Alberti, T. Bein), Elsevier Sci. Ltd., Oxford, **1996**, vol. 7, p. 151; b) G. Alberti, E. Brunet, C. Dionigi, O. Juanes, M. J. De la Mata, J. C. Rodriguez-Ubis, R. Vivani, *Angew. Chem. Int. Ed.* **1999**, *38*, 3351–3353; c) G. Alberti, E. Giontella, S. Murcia-Mascaros, *Inorg. Chem.* **1997**, *36*, 2844–2849.

[3] a) B. Bujoli, P. Palvadeau, J. Rouxel, *Chem. Mater.* **1990**, *2*, 582–489 .; b) J. Le Bideau, C. Payen, P. Palvadeau, B. Bujoli, *Inorg. Chem.* **1994**, *33*, 4885–4890; c) F. Fredoueil, D. Massiot, D. M. Poojary, M. Bujoli-Doeuff, A. Clearfield, B. Bujoli, *Chem. Commun.* **1998**, *2*, 175–176; d) F. Odobel, B. Bujoli, D. Massiot, *Chem. Mater.* **2001**, *13*, 163–173.

[4] a) D. Riou, C. Serre, G. Ferey, *J. Solid State Chem.* **1998**, *141*, 89–93; b) D. Riou, G. Ferey, *J. Mater. Chem.* **1998**, *8*, 2773–2735; c) D. Riou, C. Serre, J. Provost, G. Ferey, *J. Solid State Chem.* **2000**, *155*, 238–242; d) F. Serpaggi, G. Ferey, *J. Mater. Chem.* **1998**, *8*, 2749–2755; e) B. A. Adair, N. Guillou, A. Marisol, G. Ferey, A. K. Cheetam, *J. Solid State Chem* .**2001**, *162*, 347–353.

[5] a) A. Clearfield, Z. J. Wang, *J. Chem. Soc. Dalton Trans. Chem. Soc. Dalton Trans.* **2002**, 4457–4463; b) C. Y. Yang, Ph. D. Dissertation, Texas A&M University, Dec. **1986**; c) A. Clearfield, *Chem. Mater.* **1998**, *10*, 2801–2810.

[6] D. M. Poojary, B. Zhang, A. Clearfield, *J. Am. Chem. Soc.* **1997**, *119*, 12550–12559.

[7] D. I. Arnold, X. Ouyang, A. Clearfield, *Chem. Mater.* **2002**, *14*, 2020–2027.

[8] C. Y Ortiz-Avila, C. Bhardwaj, A. Clearfield, *Inorg. Chem.* **1994**, *33*, 2499–2500.

[9] E. V. Bakhmoutova-Albert, N. Bestaoui, V. Bakhmutov, A. Clearfield, A. V. Rodriguez, R. Llavona, *Inorg. Chem.* **2004**, *43*, 1264–1272.

[10] L. M. Shkol'nikova, G. V. Polyanchuck, V. E. Zadovnik, M. V. Rudomino, S. A. Pisareva, N. M. Dyatlova, B. V. Zdanov, I. Polyakova, *J. Struct. Chem.* **1987**, *28*, 104.

[11] P. E Werner, L. Eriksson, M. J. Westdahl, *Appl. Crystallogr.* **1985**, *18*, 367–370.

[12] "EXTRA: A program for extracting Structure-Factor Amplitudes from Powder Diffraction Data" A. Altamore, M. C. Burla., G. Cascarano, C. Giacovazzo, A. Guagliardi, A. G.G moliterni, G. Polidori, *J. Appl. Crystallogr.* **1995**, *28*, 842–846.

[13] a) A. Larson, R. B. von Dreele, GSAS: Generalized Structure Analysis System; Los Alamos National Laboratory, NM, **1986**; b) A. Z. March, *Kristallogr.* **1986**, *81*, 285; c) W. A. Dollase, *J. Appl. Crystallogr.* **1986**, *19*, 267–272..

Received: October 18, 2004

 © 2005 Wiley-VCH Verlag GmbH & Co. KGaA, Weinheim

Catalytic Properties of a Mn^{III}-Salen Complex Immobilised in a Pillared Clay by Simultaneous Pillaring/Encapsulation Procedures

Beatriz Cardoso,[a] João Pires,*[a] Ana P. Carvalho,[a] Manuela B. Carvalho,[a] Iwona Kuźniarska-Biernacka,[b,c] Ana R. Silva,[b] Cristina Freire,*[b] and Baltazar de Castro[b]

Keywords: Clays / Microporous materials / Heterogeneous catalysis / Manganese

The simultaneous encapsulation of a manganese(III)-salen complex, [Mn(salhd)Cl], and pillaring of a montmorillonite clay with aluminium polyoxycations was performed using two methods: method A – the [Mn(salhd)Cl] complex was dissolved in ethanol and added to the oligomer solution at a stage when the oligomeric species had already formed; method B – the complex, also dissolved in ethanol, was added to the clay dispersion. After calcination, both materials were Soxhlet extracted to remove the excess complex, and characterised by XRD, nitrogen adsorption at –196 °C, XPS, atomic absorption and FTIR spectroscopy. In both cases, the manganese(III)-salen complex is mainly physically entrapped within the matrix, although some host–guest interactions with the matrix may be present. Both new materials [Mn(salhd)Cl]@Al-WYO_A and [Mn(salhd)Cl]@Al-WYO_B show catalytic activity in the epoxidation of styrene at room temperature with PhIO as oxygen source in acetonitrile. The solids present high styrene epoxide selectivity, and may be reused at least four times. FTIR spectra of the catalysts after the catalytic reactions suggest that during the reaction no structural changes of the pillared clay (PILC) took place, but low extent complex leaching occurred.
(© Wiley-VCH Verlag GmbH & Co. KGaA, 69451 Weinheim, Germany, 2005)

Introduction

Pillared clays (PILCs) are a relatively well-known class of materials, whose preparation methods and catalytic properties were reviewed by different authors.[1–3] Since PILCs were initially developed because of their potential as solids with larger pores than traditional zeolites, namely those used in cracking catalysis, a large number of studies were directed to the study of catalytic reactions that use the acid–base properties of PILCs. In general, this type of reaction occurs under thermal and hydrothermal conditions that partially damage the structure of the pillared clay. These aspects are closely related to the relative unsuccessful use of PILCs as catalysts.

More recently, the use of PILCs as catalyst supports for reactions that occur at mild conditions was considered, particularly those involving transition–metal complexes as homogeneous catalysts.[4–6] The heterogenisation of metal complexes with catalytic activity, within inorganic matrices, is a field that has progressed in recent years[7–13] due to the combination of high chemical selectivity and stability, with relatively easier separation of the catalyst from the reaction media. A relevant reaction in organic chemistry that can be catalysed by transition–metal complexes is the alkene epoxidation reaction − the epoxides formed can be transformed into several different products, sometimes under regio- and stereoselective conditions − which is the most recurrent method for direct transfer of oxygen to the alkene; [14,15] manganese(III) complexes with N_2O_2 Schiff base ligands (usually denoted as salen ligands) efficiently catalyse the epoxidation of unfunctionalised alkenes.[16]

When the synthesis of pillared clays is compared, for instance, with the synthesis of large pore zeolites, the former occurs under much milder conditions of temperature and pH than the latter and thus, the integrity of the metal complexes is expected to be preserved under the conditions of PILCs synthesis. This presents the possibility to encapsulate transition metal complexes simultaneously with the pillaring process, a fact that was already shown by us in a previous study using Cu^{II} acetylacetonate based complexes.[4] In this work, we have studied the simultaneous encapsulation of a manganese(III)-salen complex, [Mn(salhd)Cl], (Scheme 1) and the pillaring of a montmorillonite clay with aluminium polyoxycations. The resulting materials were characterised by several techniques, and the catalytic activity assessed in the epoxidation of styrene. To our best knowledge, this is the first work in which the catalytic activity of a complex encapsulated simultaneously with the pillaring process of a clay was studied.

[a] Departamento de Química e Bioquímica and CQB, Faculdade de Ciências, Universidade de Lisboa,
Ed. C8, Campo Grande, 1749-016 Lisboa, Portugal
E-mail adress: jpsilva@fc.ul.pt
[b] REQUIMTE, Departamento de Química, Faculdade de Ciências, Universidade do Porto,
Rua do Campo Alegre, 4169-007 Porto, Portugal
[c] Department of Chemistry, University of Podlasie,
08-110 Siedlce, Poland

 DOI: 10.1002/ejic.200400521 © 2005 Wiley-VCH Verlag GmbH & Co. KGaA, Weinheim

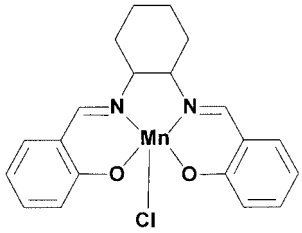

Scheme 1.

Results and Discussion

Material Characterisation

After pillaring (for Al-WYO) or after the pillaring/encapsulation procedure (methods A and B), the solids were calcined at 200 °C; this temperature is lower than that normally used when the main objective is to produce solids with thermally stable pillars (T = 350–500 °C). In this study, the calcination temperature was limited by the decomposition temperature of the complexes, which was verified to be above 200 °C. As a consequence, the stability of the pillared materials obtained at this calcination temperature was assessed by X-ray diffraction before and after the Soxhlet extraction step, since it was not clear if such a treatment could induce some changes in the pillars.

In Figure 1 the X-ray diffractograms of the nonencapsulated sample (Al-WYO) and the samples prepared by methods A and B, before and after Soxhlet extraction, are presented; Table 1 summarises the corresponding d_{001} values. Analysis of the diffractograms clearly shows that all the materials are pillared, and this can be confirmed by the increase in the d_{001} value on going from the parent nonpillared clay (d_{001} = 1.27 nm)[17] to the pillared materials (1.78 $< d_{001} <$ 1.92 nm). Furthermore, from Table 1, it can be seen that: (i) the d_{001} value of Al-WYO is slightly higher than those of the PILCs with encapsulated complexes and, (ii) the d_{001} values of materials subjected to solvent extraction are lower than those of nonextracted materials. The first observation is in contrast with what has been observed in our previous study[4] on the simultaneous pillaring/encapsulation of copper(II) acetylacetonate based complexes, where the larger pentacoordinate complexes have induced an increase in the interlayer distances (acting as templates to the PILC porous structure); the second observation results from some complex exclusion by the purification process. The diffractograms also show, although not in a very pronounced way, that Al-WYO presents a narrower diffraction peak than the samples with metal complexes, which suggest that in the former material the clay particles are better organised.

The isotherms of nitrogen adsorbed at –196 °C in the different samples are presented in Figure 2, and the corresponding values of equivalent surface areas (A_{BET}) and micropore volumes (from t-method[18]) are given in Table 1. The curves show characteristics of isotherm types I and IV, according to the IUPAC classification:[19] they have a steep initial part, typical of microporous solids, but they also present hysteresis. As expected, the A_{BET} and micropore volumes (V_μ) of the PILCs with complexes are lower than those found for Al-WYO. Moreover, the solids submitted to solvent extraction show the lowest A_{BET} and V_μ values of the series. This result is unexpected, although a similar situation was detected in a previous work.[4] In fact, since the Soxhlet extraction is used to remove the complexes that are physically adsorbed at the external surface, it would be expected that the overall surface area would increase. These results lead us to conclude that during Soxhlet extraction some diffusion of the complexes within the cavities of the pillared clay may occur towards the outer surface (probably as a consequence of concentration gradient), leading to a more obstructed structure.

As mentioned above, the presence of the metal complex within the PILC does not impart major differences in the gallery heights (estimated through XRD data) when Al-WYO is used as a reference. In contrast, the distances between the pillars are very difficult to assess, and in order to obtain additional information on the characterisation of the porosity of the materials, a DFT approach [20,21] was applied to the data from the low-temperature nitrogen adsorp-

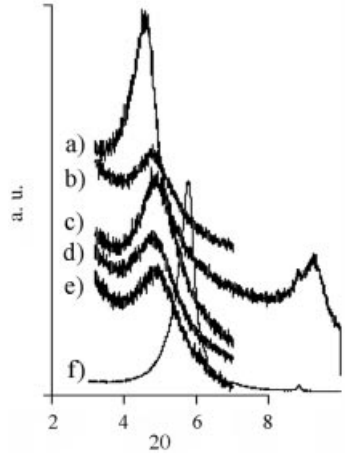

Figure 1. X-ray diffractograms for the Al-WYO sample, a), and for the solids with the [Mn(salhd)Cl] complex encapsulated by method A (b and c) and by method B (d and e). The diffractograms b) and d) refer to samples not subjected to solvent extraction. The curve f) stands for the starting clay.

Table 1. Basal spacing (d_{001}), equivalent surface areas (A_{BET}) and micropore volumes (V_μ) by the t-method, from low-temperature nitrogen adsorption. Mn content obtained by atomic absorption spectroscopy (AA) and X-ray photoelectron spectroscopy (XPS).

	d_{001} [nm]	A_{BET} [m²/g]	V_μ [cm³/g]	Mn content [μmol/g]	
				AA	XPS
Al-WYO	1.93	158	0.055		
Method A (not extracted)	1.84	114	0.027		
Method A (extracted)	1.78	85	0.026	73	68
Method B (not extracted)	1.86	119	0.036		
Method B (extracted)	1.79	61	0.016	71	62
Starting clay	1.27	32	---		

 © 2005 Wiley-VCH Verlag GmbH & Co. KGaA, Weinheim

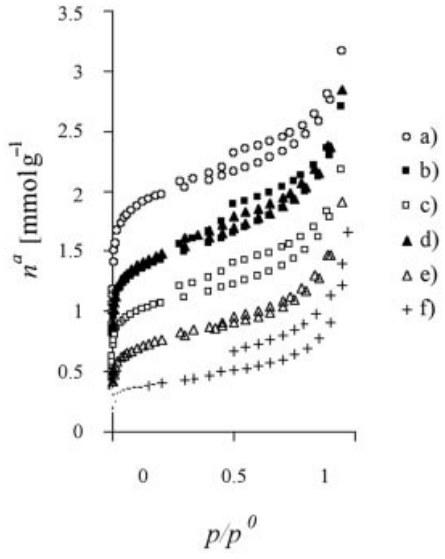

Figure 2. Nitrogen adsorption isotherms at –196 °C for the Al-WYO sample, a), and for the solids with the [Mn(salhd)Cl] complex encapsulated by method A (b and c) and by method B (d and e). The isotherms b) and d) refer to samples not subjected to solvent extraction and the curve f) to the starting clay.

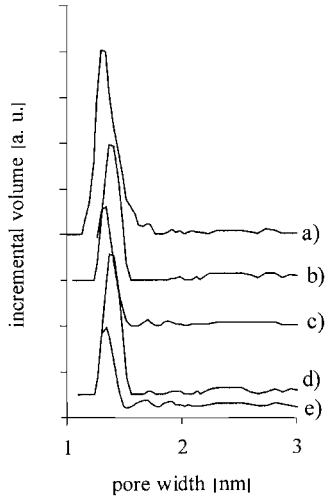

Figure 3. Pore size distributions obtained by DFT for the Al-WYO sample, a), and for the solids with the [Mn(salhd)Cl] complex encapsulated by method A (b and c) and by method B (d and e). The curves b) and d) refer to samples not subjected to solvent extraction.

tion experiments; the results of the pore size distributions obtained in this manner are given in Figure 3. The curves in the micropore region (pore widths <2 nm[19]) cannot be entirely superimposed, and some differences, albeit very small, are expected in the matrix microporosity: the values of the pore widths corresponding to the maximum of the distributions are quite similar for Al-WYO and materials with encapsulated complexes after Soxhlet extraction (1.35 nm), but the distributions obtained for the nonextracted materials are, in fact, slightly shifted to high values. This result has some parallelism with XRD data, and indicates that Soxhlet extraction (removal of adsorbed metal complexes) is essential to the final stabilisation of PILC porosity. We will not pursue the precise significance of the pore widths obtained, since the DFT approach was still not yet widely applied to PILCs; nevertheless, we believe that the results in Figure 3 suggest that the micropore size distribution of materials are, essentially, quite similar, thus confirming that the pillaring process was not significantly perturbed by the presence of the [Mn(salhd)Cl] complex.

Low-resolution XPS spectra of Al-WYO and [Mn(salhd)Cl]@WYO (methods A and B) show the presence of oxygen, silicon, aluminium and magnesium from the aluminium pillared clay lattice at similar values to those published on aluminium pillared clays based on natural Portuguese smectites.[4] The latter materials also show the typical broad Mn $2p_{3/2}$ bands with maxima at about 642 eV, in agreement with the values reported for manganese(III) complexes with salen[22] and porphyrinic[23] ligands. The most relevant surface contents (Al, Si and Mn) are summarised in Table 2. As can be verified, the Al/Si ratio decreases on going from Al-WYO to those materials with metal complexes: the decrease is slightly larger for the material prepared by method B (19%) than that prepared by method A (9%).

Table 2. XPS results for Al-WYO and metal-complex-based PILCs.

	Atomic-%				
Sample	Al	Si	Mn	Al/Si	Mn/Si
Al-WYO	18.84	15.86		1.19	
[Mn(salhd)Cl]@Al-WYO_A	15.95	14.76	0.13	1.08	0.009
[Mn(salhd)Cl]@Al-WYO_B	15.11	15.81	0.11	0.96	0.007

The bulk Mn content of the samples (obtained by AA, Table 1) indicates that almost 25% of the complex initially added was effectively immobilised in the solid matrix; we emphasise the similarity of the values obtained by both methods (A and B). The surface manganese contents obtained by XPS (Table 2) are similar to those obtained by AA, although slightly lower, suggesting that the complex was encapsulated almost homogeneously, throughout the clay during both simultaneous pillaring/encapsulation methods A and B.

It is worth mentioning that simultaneous pillaring/encapsulation methods (A and B) lead to lower Mn loadings than the in situ synthesis of the metal complex within the aluminium pillared clay.[5] This result may be a consequence of the lower pillaring efficiency of the former methods when compared to the latter as both materials present lower surface aluminium contents than Al-WYO (Table 2). However, this result is in contrast with those obtained for the simultaneous aluminium oxide pillaring and encapsulation of copper(II) Schiff base complexes in a Portuguese montmorillonite, in which encapsulation of these complexes induced not only an increase in the surface aluminium content but also higher PILC basal distances than the corresponding aluminium pillared clay prepared without the presence of complex.[4]

 © 2005 Wiley-VCH Verlag GmbH & Co. KGaA, Weinheim

FTIR and UV/Vis Spectroscopy

The FTIR spectra of Al-WYO, the free complex and those of the samples obtained by simultaneous pillaring/encapsulation are shown in Figure 4.Similar to [Mn(salhd)CH_3COO]@Al-WYO prepared by an in situ method[5] and to the aluminium pillared clays based on natural Portuguese smectites (Al-BEN) reported by us,[4] the spectrum of Al-WYO shows intense and large bands due to the clay structure: in the region 3700–3300 cm^{-1} (not shown), which are assigned to the surface hydroxyl groups from the acidic Al–OH group,[24–26] at 1626 cm^{-1} and in the range 1300–400 cm^{-1}, assigned to lattice vibrations[5,23] (asymmetric stretching vibrations of SiO_2 tetrahedra).[25] In addition to these strong bands caused by the parent material, the spectra for [Mn(salhd)Cl]@WYO_A and [Mn(salhd)Cl]-@WYO_B also show bands in the 1600–1200 cm^{-1} region, where the Al-WYO matrix does not absorb (Figure 4), and they may be attributed to the presence of the manganese(III)-salen complex. For clarity, only bands for the samples submitted to solvent extraction (which correspond to materials that have been used in the catalytic experiments described below) are seen in the region 1200–1700 cm^{-1}. Due to the low concentration of metal complex inside the PILC, the bands for the encapsulated complex are difficult to detect, but they can be seen in the range 1400–1500 cm^{-1}. These bands are broader and their frequencies are slightly different from those of the free complex, suggesting that the manganese(III)-salen complex might be distorted as a consequence of the physical constraints imposed by the matrix and/or due to host–guest interactions with the PILC framework within the pores, as observed for copper(II) complexes entrapped in aluminium pillared clays.[4]

The diffuse reflectance UV/Vis spectra of [Mn(salhd)Cl]-@WYO obtained by method A and B (not shown) are very similar to the spectra for the parent Al-WYO in the visible range, where the d-d bands due to the complexes are expected to be seen; however, for $\lambda < 350$ nm, new high-intensity bands are observed that can unambiguously be assigned to the metal complex CT bands. The lack of the d-d bands can be due to two combined factors: (i) the small extinction coefficients associated with these electronic transitions in the manganese(III) complex, and (ii) the dilution effect of the manganese(III)-salen complex within the aluminium pillared clay. Thus, no geometrical information about the entrapped manganese(III)-salen complex can be obtained by its electronic spectra.

Catalytic Experiments

The results of the epoxidation of styrene, at room temperature with the use of the manganese(III)-salen heterogeneous catalysts and PhIO as oxygen source in acetonitrile, are summarised in Table 3 and Figure 5; data from homogeneous-phase and blank experiments run under comparable conditions are also included. These results clearly show that these new catalysts are active in the epoxidation reaction and can be reused for up to four cycles, without significant decrease in the catalytic activity.

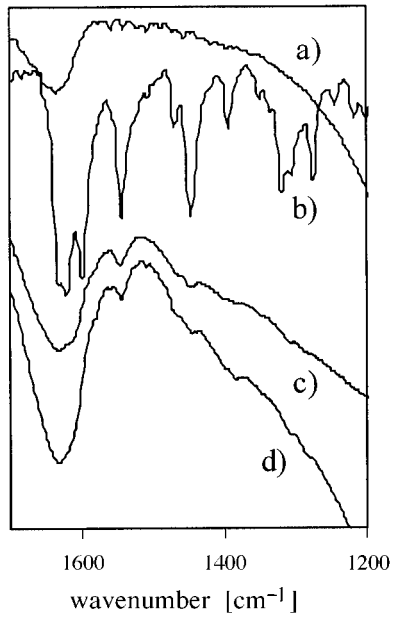

Figure 4. FTIR spectra in the range 1200–1700 cm^{-1} for: a) the Al-WYO pillared clay; b) [Mn(salhd)Cl]; c) and d) are for [Mn(salhd)Cl] encapsulated by methods A and B, respectively.

Both heterogeneous catalysts show high chemoselectivities towards styrene epoxide, which increases slightly with the number of cycles. Nevertheless, these values are lower than that obtained in an experiment run in a homogeneous phase under comparable experimental conditions (Table 3); this may be attributed to some low-extent epoxide-ring opening, owing to support surface acidity and to the higher benzaldehyde selectivity; this occurs by a different catalytic pathway involving the PILC matrix.

The [Mn(salhd)Cl]@Al-WYO_A catalyst shows a styrene conversion quite similar to that of its homogeneous counterpart, whereas for [Mn(salhd)Cl]@Al-WYO_B, styrene conversion is approximately 24% lower. The styrene conversion decreases by 35% and 23% for catalysts prepared by the method A and B, respectively, during further cycles; at the end of the fourth cycle both catalysts show almost the same value. The same trend is observed for the styrene epoxide yield.

Low catalytic activity in the epoxidation of styrene was observed in the filtrate after catalyst removal, indicating that the reaction was not fully catalysed heterogeneously, and that low-extent leaching of the active phase to solution took place; this effect is more perceptible for catalysts obtained by method B. FTIR spectra for both heterogeneous catalysts measured before catalytic reaction and after the fourth cycle show some band intensity decrease in the 1620–1200 cm^{-1} region, which corresponds to the frequency range in which vibration bands for the complex occur; conversely, the bands typical of the Al-WYO matrix do not

 © 2005 Wiley-VCH Verlag GmbH & Co. KGaA, Weinheim

Table 3. Epoxidation of styrene catalysed by homogeneous and heterogeneous [Mn(salhd)Cl] complex.[a]

Catalyst	Run	Time[b]	Conversion[c,d]	Selectivity (Yield) [%][d]		
		[h]	[%]	Styrene epoxide	Benzaldehyde	Others[e]
Al-WYO[f]		48	1	16 (0)	84 (1)	0 (0)
[Mn(salhd)Cl]@Al-WYO (method A)	1	48	57	71 (41)	19 (11)	10 (5)
	2	48	41	74 (30)	19 (8)	6 (3)
	3	48	38	75 (28)	20 (8)	5 (2)
	4	48	37	75 (28)	21 (8)	4 (1)
[Mn(salhd)Cl]@Al-WYO (method B)	1	48	47	71 (34)	19 (9)	10 (5)
	2	48	43	72 (31)	20 (9)	8 (3)
	3	48	39	73 (29)	21 (8)	7 (3)
	4	72	36	72 (26)	23 (8)	6 (2)
[Mn(salhd)Cl]		2	62	95 (60)	5 (3)	0 (0)

[a] In acetonitrile, room temperature, molar ratio styrene/PhIO = 2:1. [b] Time needed for total consumption of oxidant, measured by stabilization of the PhI area against PhCl area. [c] Styrene conversion corrected for the limiting reagent, PhIO. [d] Determined by GC-FID against internal standard. [e] Others = other reaction products. [f] Carried out under comparable conditions but with 0.1 g of Al-WYO.

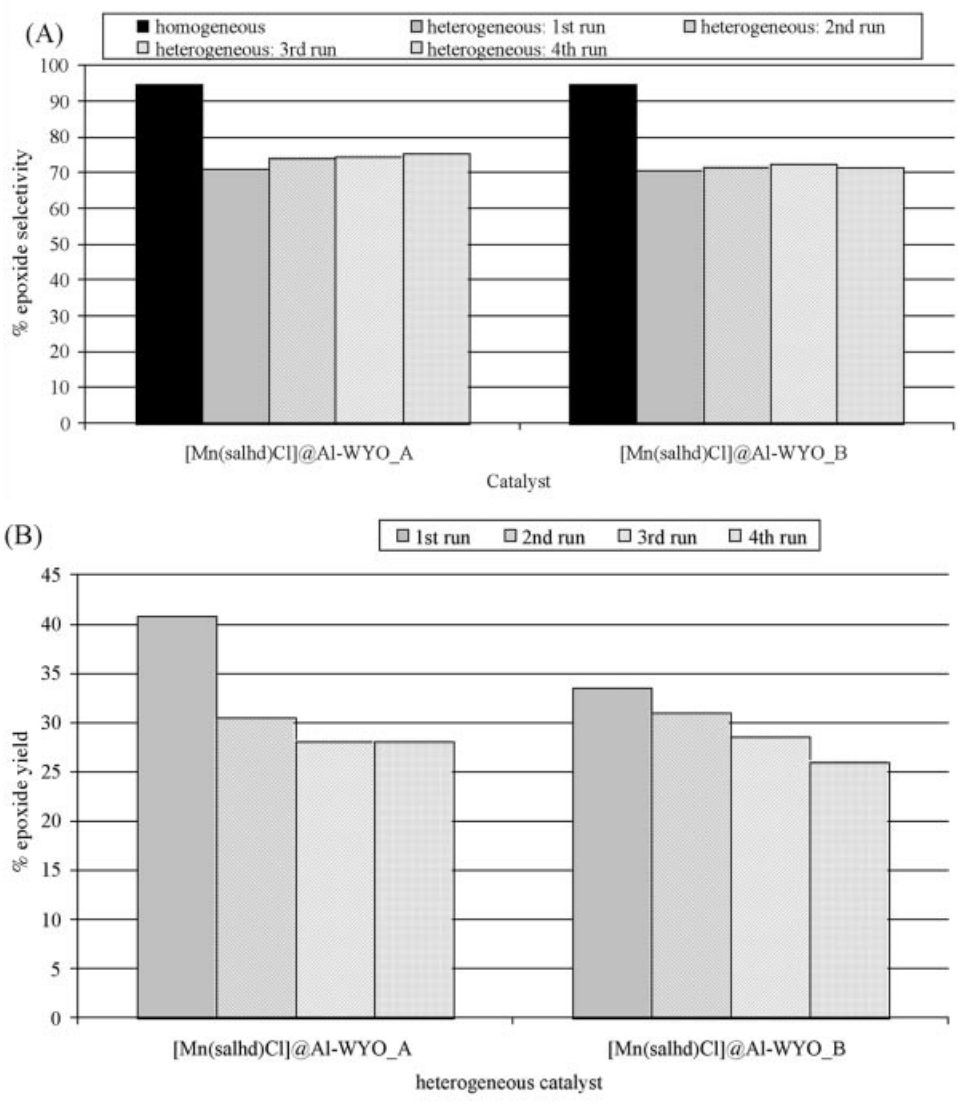

Figure 5. Epoxidation of styrene catalysed by [Mn(salhd)Cl] complex in a homogeneous phase and heterogenised onto the pillared clay: (A) styrene epoxide selectivity [%] and (B) styrene epoxide yield [%].

 © 2005 Wiley-VCH Verlag GmbH & Co. KGaA, Weinheim

show significant changes after the catalytic reaction. These observations suggest that no structural changes of the Al-WYO matrix took place during the consecutive catalytic cycles, but some metal-complex leaching must occur in the catalytic experimental conditions. Thus, the styrene epoxide yield decrease with reuse of the heterogeneous catalysts reported herein, might be correlated with some active phase leaching.

In a previous study,[5] we encapsulated, with the use of the in situ method, the same complex within a previously prepared Al-WYO. This catalyst led to comparable styrene conversions, styrene epoxide selectivity and styrene epoxide yields to those with the catalysts described in this work, under the same experimental conditions; however, no metal-complex leaching was detected. The different behaviour exhibited by the materials in which the complexes were immobilised by different procedures can be explained by considering that the pillars are less rigid (these materials are calcined at 200 °C) in the catalysts prepared by using the simultaneous pillaring/encapsulation process, and thus, a higher degree of swelling will occur during catalytic reaction; this will cause the physically entrapped metal complex to leach more easily. In contrast, the material in which the complex was immobilised by in situ synthesis starts from the pre-prepared aluminium pillared clay (calcined at 350 °C), where the higher temperature of calcination confers higher rigidity to the pillars (very low swelling) preventing metal-complex leaching during the catalytic reaction.

Garcia et al. encapsulated the same chiral manganese(III)-salen complex within the zeolite Y, and observed lower styrene epoxide selectivity (61%) than for the homogeneous counterpart (80%), with NaOCl in dichloromethane at 5 °C. This complex encapsulated within Al-WYO, reported herein, gives rise to higher styrene epoxide selectivity (71%) than within the zeolite Y, notwithstanding the different experimental condition used.[27]

It is noteworthy that when the heterogeneous catalysts were used, the reaction time increased and styrene conversion decreased relative to when homogeneous counterparts were used. The first is a general effect that arises upon immobilisation of metal-complex catalyst in porous matrices and has been attributed to diffusion constraints imposed on substrates and reactants by the porous network of the matrix. The diffusion of the reactants to the metal centre can be particularly hindered for PhIO, a solid with low solubility in acetonitrile, and that solubilisation is controlled by its rate of consumption.[28] The latter effect, lower styrene conversion, must be due to consumption of PhIO in competing reactions involving the matrix.[29]

Conclusions

New heterogeneous catalysts have been prepared by two different methods based on the simultaneous encapsulation of [Mn(salhd)Cl] and the pillaring process. In both cases, the manganese(III)-salen complex is mainly physically entrapped within the matrix, although some host–guest interactions between the complex and PILC can not be ruled out.

The new materials [Mn(salhd)Cl]@Al-WYO_A and [Mn(salhd)Cl]@Al-WYO_B have been tested in the catalytic epoxidation of styrene at room temperature with PhIO as oxygen source in acetonitrile. The heterogeneous catalysts showed similar styrene conversion to their homogeneous counterparts, high styrene epoxide selectivity and can be reused for at least four times, with a small decrease in their catalytic activity. FTIR spectra of the catalysts after the consecutive catalytic reactions suggest that no structural changes of the PILC occur, but some metal-complex leaching must take place, which is responsible for the small decrease in styrene conversion and styrene epoxide yield in further cycles.

Comparison with results from the literature, obtained with other matrices such as zeolites or MCM type materials, [10–13] is not straightforward. However, we believe that the methodology described in this work can be of interest for the immobilization of large complexes. Moreover, this is a cheap methodology, since by using natural clays as the main host there is no need for expensive silica sources or organic templates. In this way, the results obtained in this work show that the simultaneous encapsulation/pillaring procedure is a useful alternative method for the encapsulation of metal complexes within PILCs, since it produces materials that are stable within the oxidative catalytic media, although some solvent swelling is seen, which is typical of nonpillared clays. To overcome complex leaching induced by the swelling of the material during catalytic reaction, metal complexes must be anchored to the PILC matrix. Research work on complex anchoring to the PILC matrix is in progress and will be published elsewhere.

Experimental Section

Synthesis of the [Mn(salhd)Cl] Complex

The Schiff base ligand *N,N′-bis*(salicylaldehyde)cyclohexanediamine (H_2salhd) and the corresponding complex chloro-[*N,N′-bis*(salicylaldehyde)cyclohexanediaminate] manganese(III) ([Mn(salhd)Cl]) were synthesised and characterised as reported elsewhere.[5]

Preparation of the Pillared/Encapsulated Materials

A clay from Wyoming (USA) was used as the starting material. This solid presented a cation exchange capacity of 115 meq/100 g and a structural formula of $(Si_{3.91}Al_{0.09})^{IV}(Al_{1.51}Fe_{0.18}Mg_{0.26})^{VI}(Ca_{/2}, K, Na)_{0.49}$ as described elsewhere.[17,30] The pillaring process was performed using a procedure that was optimised in previous works;[17,30] two solutions were prepared: *solution 1* (which, in fact, is a dispersion) made from clay (1 g) in water (100 mL); and *solution 2*, the oligomer solution. The latter was prepared from aqueous solutions of $AlCl_3$ and NaOH, with an OH/Al ratio of 2, aged for 2 h at 60 °C, after which the pH was increased to 6. The parent pillared clay, denoted as Al-WYO, was prepared by addition of solution 2 dropwise to solution 1 whilst stirring, heated to reflux at 80 °C for 3 h, and kept at 25 °C overnight. The solid was recovered by centrifugation, washed in a dialysis tube until conductivity was lower than 1 $mS\,m^{-1}$, freeze-dried and calcined at 200 °C over

 © 2005 Wiley-VCH Verlag GmbH & Co. KGaA, Weinheim

2 h after a ramp of 1 °C/min. Several methodologies were tried to encapsulate the complexes, but only the two more successful methods are described. In the procedure, hereafter denoted as *method A*, the [Mn(salhd)Cl] complex (0.5 mmol) was dissolved in ethanol and added to the oligomer solution (solution 2) at a stage at which the oligomeric species had already formed, that is, after the aging and pH adjustment to 6. In the case of *method B*, the complex, also dissolved in ethanol, was added to the clay dispersion (solution 1). In both methods, the amount of ethanol used was in the range 50–70 mL, to ensure that the complex would not precipitate after addition to the aqueous solutions. The remaining experimental steps were the same as described above for the preparation of Al-WYO. After calcination at 200 °C, the samples were Soxhlet extracted to remove the excess complex, first with ethanol and then with dichloromethane until a colourless washing was obtained.

Characterisation Methods

X-ray diffractograms were obtained with oriented mounts,[31] with a Philips PX 1820 instrument using Cu-K_α radiation. Nitrogen adsorption isotherms at –196 °C were measured with an automatic apparatus (Asap 2010; Micromeritics). Before the adsorption experiments the samples were outgassed under vacuum over 2.5 h at 150 °C. FTIR spectra were obtained as KBr pellets (Merck, spectroscopic grade) using a Mattson spectrometer, in the range 1800–1300 cm^{-1}; all spectra were collected at room temperature, with a resolution of 4 cm^{-1} and 32 scans. Metal contents were determined by atomic absorption spectroscopy with a Pye Unicam SP9 spectrometer after solubilisation of the samples in an autoclave with a mixture of HF and aqua regia.

X-ray photoelectron spectroscopy was performed at "Centro de Materiais da Universidade do Porto" (Portugal), with a VG Scientific ESCALAB 200A spectrometer using a non-monochromatised Mg-K_α radiation (1253.6 eV). All the materials were compressed into pellets prior to the XPS studies. In order to correct possible deviations caused by electric change of the samples, the C 1s line at 285.0 eV was taken as internal standard.

GC-FID chromatograms were obtained with a Varian CP-3380 gas chromatograph using helium as carrier gas and a fused silica Varian Chrompack capillary column CP-Sil 8 CB Low Bleed/MS (30 m × 0.25 mm i.d.; 0.25 μm film thickness). Conditions used: 60 °C (3 min), 5 °C/min, 170 °C (2 min), 20 °C/min, 200 °C (10 min); injector temperature, 200 °C; detector temperature, 300 °C.

Catalysis Experiments

The catalytic activity of the new materials in the epoxidation of styrene was assessed at room temperature using styrene (substrate, 0.500 mmol), chlorobenzene (GC internal standard, 0.500 mmol), catalyst (0.100 g) and iodosylbenzene (PhIO, 0.250 mmol) as oxidant in of acetonitrile (5.00 cm^3), whilst stirring. During the experiment, aliquots (0.1 cm^3) were taken from solution with a hypodermic syringe, filtered through 0.2 μm syringe filters and directly analysed by GC-FID. After the time needed for total consumption of PhIO (the ratio of areas of iodobenzene and chlorobenzene in chromatogram was constant), the catalyst was centrifuged. To ensure that the epoxidation was only catalysed heterogeneously, a new portion of PhIO (0.25 mmol) was added to the decanted solution, and the composition of reaction media was remonitored. After use, the catalyst was washed/centrifuged with methanol (five times) and with acetonitrile (two times) to remove occluded reactants and products, and then reused using the same experimental conditions described above. The cycle catalysis/washing was performed three times. The acetonitrile solution (after washing) was checked to verify the existence of styrene. To assess the eventual catalytic activity of the support itself in the epoxidation of styrene, reactions using the same experimental conditions (vide supra) were also carried out in the presence of the support (0.1 g); only negligible catalytic activity was found using PhIO as oxidant.

Identification and quantification of products were made by GC-FID analysis (internal standard method). The assignation was made by comparison with authentic samples; the retention times, under the experimental conditions used, are: chlorobenzene 6.4, styrene 7.5, benzaldehyde 9.7, iodobenzene 12.3 and styrene epoxide 13.1 min.

Acknowledgments

This work was funded by Fundação para a Ciência e a Tecnologia (FCT) and FEDER, through the project ref. POCTI/QUI/42931/2001. ARS and IKB thank FCT for a post-doctoral fellowship.

[1] A. Gil, L. M. Gandía, M. A. Vicente, *Catal. Rev. Sci. Eng.* **2000**, *42*, 145–212.
[2] R. Burch (Ed.), *Catal. Today* **1988**, *2*, 185–186.
[3] T. J. Pinnavaia, *Science* **1983**, *220*, 365–371.
[4] A. P. Carvalho, C. Castanheira, B. Cardoso, J. Pires, A. R. Silva, C. Freire, B. de Castro, M. B. Carvalho, *J. Mater. Chem.* **2004**, *14*, 374–379.
[5] I. Kuźniarska-Biernacka, A. R. Silva, R. Ferreira, A. P. Carvalho, J. Pires, M. B. Carvalho, C. Freire, B. de Castro, *New J. Chem.* **2004**, *28*, 853–858.
[6] V. Ramaswamy, M. S. Krishnan, A. V. Ramaswamy, *J. Mol. Catal. A: Chem.* **2002**, *181*, 81–89.
[7] D. E. De Vos, M. Dams, B. F. Sels, P. A. Jacobs, *Chem. Rev.* **2002**, *102*, 3615–3640.
[8] C. E. Song, S. Lee, *Chem. Rev.* **2002**, *102*, 3495–3524.
[9] R. I. Kureshy, N. H. Khan, S. H. R. Abdi, I. Ahmad, S. Singh, R. V. Jasra, *J. Catal.* **2004**, *221*, 234–240.
[10] R. I. Kureshy, N. H. Khan, S. H. R. Abdi, I. Ahmad, S. Singh, R. V. Jasra, *Catal. Lett.* **2003**, *91*, 207–210.
[11] S. Bhattacharjee, J. A. Anderson, *Chem. Commun.* **2004**, 554–555.
[12] S. Bhattacharjee, J. A. Anderson, *Catal. Lett.* **2004**, *95*, 119–125.
[13] S. Bhattacharjee, T. J. Dines, J. A. Anderson, *J. Catal.* **2004**, *225*, 398–407.
[14] C. T. Dalton, K. M. Ryan, V. M. Wall, C. Bousquet, D. G. Gilheany, *Top. Catal.* **1998**, *5*, 75–91.
[15] W. Adam, K. J. Roschmann, C. R. Saha-Möller, D. Seebach, *J. Am. Chem. Soc.* **2002**, *124*, 5068–5073.
[16] K. Srinivasan, P. Michaud, J. K. Kochi, *J. Am. Chem. Soc.* **1986**, *108*, 2309–2320.
[17] M. B. Carvalho, J. Pires, A. P. Carvalho, *Microporous Mater.* **1996**, *6*, 65–77.
[18] S. J. Gregg, K. S. W. Sing, *Adsorption, Surface Area and Porosity*, Academic Press, London, **1982**.
[19] K. S. W.Sing, D. H. Everett, R. A. W. Haul, L. Moscou, R. A. Pierotti, J. Rouquérol, T. Siemieniewska, *Pure Appl. Chem.* **1985**, *57*, 603–619.
[20] J. P. Olivier, *J. Porous Mater.* **1995**, *2*, 9–17.
[21] J. P. Olivier, M. L. Occeli, *J. Phys. Chem. B* **2001**, *105*, 623–629.
[22] A. Doménech, P. Formentin, H. Garcia, M. J. Sabater, *Eur. J. Inorg. Chem.* **2000**, 1339–1344.
[23] Z. Li, C.-G. Xia, X-M. Zhang, *J. Mol. Catal. A: Chem.* **2002**, *185*, 47–56.
[24] G. Coudurier, F. Lefebvre, *Catalyst Characterisation. Physical Techniques for solid materials* (Eds.: B. Imelik, J. C. Vendrine), Plenum Press, New York, **1994**, p. 11.

 © 2005 Wiley-VCH Verlag GmbH & Co. KGaA, Weinheim

[25] C. Flego, L. Galasso, R. Millini, I. Kiricsi, *Appl. Catal. A* **1998**, *168*, 323–331.
[26] P. Salerno, M. B. Asenjo, S. Mendiroz, *Thermochim. Acta* **2001**, *379*, 101–109.
[27] M. J. Sabater, A. Corma, A. Domenech, V. Fornés, H. Garcia, *Chem. Commun.* **1997**, 1285–1286.
[28] B. B. De, B. B. Lohray, S. Sivaram, P. K. Dhal, *Macromolecules* **1994**, *27*, 1291–1296.
[29] A. R. Silva, J. Vital, J. L. Figueiredo, C. Freire, B. Castro, *New J. Chem.* **2003**, *27*, 1511–1517.
[30] J. Pires, M. B. Carvalho, A. P. Carvalho, *Zeolites* **1997**, *19*, 107–113.
[31] B. Velde, *Introduction to Clay Minerals*, Chapman & Hall, London, **1992**, p. 13.

Received June 15, 2004

 © 2005 Wiley-VCH Verlag GmbH & Co. KGaA, Weinheim

Synthesis of (1,2,4-Oxadiazole)palladium(II) Complexes by [2 + 3] Cycloaddition of Nitrile Oxides to Organonitriles in the Presence of $PdCl_2$

Nadezhda A. Bokach,[a,b] Vadim Yu. Kukushkin,*[b] Matti Haukka,[c] and Armando J. L. Pombeiro*[a]

Keywords: Palladium / 1,2,4-oxadiazole complexes / Nitrile complexes / Nitrile oxide complexes / Cycloaddition

The reaction between the nitrile oxides 2,4,6-$R'_3C_6H_2CNO$ (R′ = Me, OMe) and *trans*-$[PdCl_2(RCN)_2]$, or RCN (R = Me, Et, CH_2CN, NMe_2, Ph) in the presence of $PdCl_2$, proceeded smoothly under mild conditions and allowed the isolation of the 1,2,4-oxadiazole complexes *trans*-$[PdCl_2\{N^a{=}C(R){-}ON{=}C^b(C_6H_2R'_3)(N^a{-}C^b)\}_2]$ (**1**–**8**) in 40–85 % yields. In CH_2Cl_2, the reaction between 2,4,6-$R'_3C_6H_2CNO$ and $[PdCl_2(MeCN)_2]$ furnishes $[PdCl_2(ONCC_6H_2R'_3)_2]$ (**9** and **10**), which are the first representatives of metal compounds where nitrile oxides act as ligands. The 1,2,4-oxadiazole complexes **1**–**8** were characterized by elemental analysis, FAB mass spectrometry, and IR, ^1H and $^{13}C\{^1H\}$ NMR spectroscopy, while **2**, **3**, **7**, and **8** were additionally characterized by X-ray crystallography. The liberation of the heterocyclic species from **1**–**8** was successfully performed by substitution reaction either with 1,2-bis(diphenylphosphanyl)ethane or with an excess amount of $Na_2S{\cdot}7H_2O$ in MeOH; the liberated 1,2,4-oxadiazoles (**11**–**18**) were characterized by positive-ion FAB mass spectrometry and ^1H and $^{13}C\{^1H\}$ NMR spectroscopy.
(© Wiley-VCH Verlag GmbH & Co. KGaA, 69451 Weinheim, Germany, 2005)

Introduction

1,2,4-Oxadiazoles are an important class of ring systems containing one O and two N atoms.[1] These compounds have widespread applications in biology and medicine insofar as some of them exhibit intrinsic analgesic,[2] anti-inflammatory,[3] and anti-picornaviral[4] effects and show high efficacy as agonists[5] and antagonists[6] for different receptors. Other areas of research in the chemistry of 1,2,4-oxadiazoles include plant protection,[7] their use as liquid-crystalline mesophases,[8] dyeing or printing with 1,2,4-oxadiazole azo dyes,[9] and they are also constituents of fluorescent whiteners.[10] Despite the wealth of chemistry associated with 1,2,4-oxadiazoles in general, the coordination chemistry of these heterocycles has so far been little explored,[11] although the opposite holds true for the *isomeric* 1,3,4-oxadiazoles. Complexes of the latter have been intensively investigated as angular bridging ligands that give unusual coordination polymers[12] and binuclear complexes.[13] In addition, metal complexes with 1,3,4-oxadiazole-derived ligands exhibit important luminescent,[14] electroluminescent,[15] liquid crystal,[16] and magnetic properties.[17]

As a continuation of our project on [2 + 3] cycloadditions[18,19] of dipoles to metal-activated nitriles[20,21] to give heterocyclic systems, we have studied a [2 + 3] cycloaddition of nitrile oxides to nitriles in the presence of a Pd^{II} center and isolated a family of previously unknown (1,2,4-oxadiazole)palladium(II) species. We also observed that the reaction between the nitrile oxides and $[PdCl_2(MeCN)_2]$ in CH_2Cl_2 (instead of MeCN) led to the first representatives of nitrile oxide metal compounds. All these results are reported in this work.

Results and Discussion

Preparation of (1,2,4-Oxadiazole)palladium(II) Complexes

Recently we have studied the reaction of $[PtCl_4(RCN)_2]$ with the nitrile oxides 2,4,6-$R'_3C_6H_2CNO$ which, after [2 + 3] cycloaddition, gives the (1,2,4-oxadiazole)platinum(IV) complexes $[PtCl_4\{N^a{=}C(R)ON{=}C^bC_6H_2R'_3(N^a{-}C^b)\}_2]$.[19] This reaction opens up an easy route to 1,2,4-oxadiazole metal complexes and also allows the preparation of the heterocycles, after liberation of the ligands, under mild conditions. This method to achieve 1,2,4-oxadiazole complexes has been applied here to Pd^{II} systems to obtain a family of previously unknown 1,2,4-oxadiazole complexes.

As dipolarophiles for this study we used the nitrile and dialkylcyanamide palladium(II) complexes *trans*-$[PdCl_2(RCN)_2]$ because it has been shown[20,21] that the Pd^{II}

[a] Centro de Química Estrutural, Complexo I, Instituto Superior Técnico,
Av. Rovisco Pais, 1049–001 Lisboa, Portugal
Fax: +351-21-8464-455/7
E-mail: pombeiro@ist.utl.pt
[b] Department of Chemistry, St.Petersburg State University, 198504, Stary Petergof, Russian Federation
Fax: +7-812-428-6939
E-mail: kukushkin@VK2100.spb.edu
[c] Department of Chemistry, University of Joensuu, P. O. Box 111, 80101, Joensuu, Finland
Fax: +358-13-2513390
E-mail: matti.haukka@joensuu.fi

 DOI: 10.1002/ejic.200400580 © 2005 Wiley-VCH Verlag GmbH & Co. KGaA, Weinheim

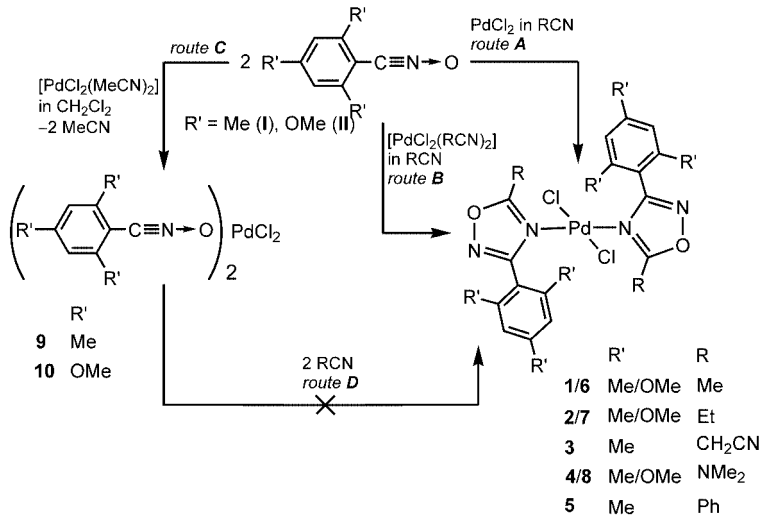

Scheme 1

center strongly activates the ligated nitriles toward the addition of various *nucleophiles* and this type of reactivity can model,[22] to some extent, the [2 + 3] cycloaddition of *dipoles*. Two relatively stable aryl nitrile oxides, i.e. 2,4,6-$Me_3C_6H_2CNO$ (**I**) and 2,4,6-$(MeO)_3C_6H_2CNO$ (**II**),[23] were chosen as dipoles.

In agreement with our expectations, the cycloaddition of **I** or **II** to nitriles in *trans*-$[PdCl_2(RCN)_2]$ to achieve 1,2,4-oxadiazole metal species proceeded smoothly and gave the complexes *trans*-$[PdCl_2\{N^a{=}C(R)ON{=}C^b(C_6H_2R'_3)(N^a–C^b)\}_2]$ (**1**–**8**) in 40–85% yields. The reaction was performed by two rather similar, albeit technically distinct, routes (Scheme 1). In the first route (**A**), both $PdCl_2$ and the nitrile oxide **I** or **II** (3–4 equiv.) were reacted in a suspension of neat nitrile RCN (R = Me, Et, NMe_2, Ph) or, in the case of the solid malonodinitrile (R = CH_2CN) (sixfold molar excess vs. $PdCl_2$), in a CH_2Cl_2 solution. In the second route (**B**), the nitrile complexes *trans*-$[PdCl_2(RCN)_2]$ (R = Me, Et, Ph), dissolved in the corresponding nitrile, were treated with the nitrile oxides **I** or **II** (3–4 equiv.). In both routes the reaction was performed at 40 °C for 12–18 h and the isolated yields for every particular compound, prepared by the two methods, are almost the same. The isolation of the (1,2,4-oxadiazole)palladium(II) products failed only in the case of treatment of the less-reactive (towards the cycloaddition, but more reactive towards the substitution; see below) nitrile oxide **II** with the reactive (but weak ligand) nitriles PhCN and $NCCH_2CN$ at the Pd^{II} center; this reaction gives a mixture of products.

Reaction of $PdCl_2$ with neat RCN is well known and is commonly applied for the preparation of the complexes *trans*-$[PdCl_2(RCN)_2]$.[24] Hence, it is not surprising that the reaction rate and the isolated yields are similar for both routes, because route **A** conceivably includes the formation of $[PdCl_2(RCN)_2]$, upon dissolution of $PdCl_2$ in RCN, followed by the cycloaddition of a nitrile oxide. Despite the similarity of routes **A** and **B**, the obvious advantage of the first method is that it allows the synthesis of complexes **1**–**8** starting directly from $PdCl_2$ and omitting the unnecessary step of the isolation of *trans*-$[PdCl_2(RCN)_2]$.

In order to get a rough estimate of the effect of the Pd^{II} center on the cycloaddition rate, the reaction between $PdCl_2$ (1 equiv.) in EtCN (3 mL) and **I** or **II** (2 equiv.) at 40 °C was compared with the reaction of **I** or **II** and EtCN under the same experimental conditions; only an approximate 1.5-fold acceleration in the metal-mediated vs. metal-free synthesis was observed. It appears that Pd^{II} acts mostly as a trapping center, thus allowing a facile isolation and characterization of 1,2,4-oxadiazoles as metal-bound species.

Binding of the Nitrile Oxides by a Pd^{II} Center

The interaction between $[PdCl_2(MeCN)_2]$ and the nitrile oxides **I** and **II** proceeds in another direction when dichloromethane is used as solvent instead of MeCN: the reaction gives (nitrile oxide)palladium(II) complexes **9** and **10** (Scheme 1, route **C**). In the electrospray mass spectra of both complexes, we observed the $[M + H]^+$ ion with the expected isotopic pattern. Complex **10** gave satisfactory C, H, and N microanalyses, whereas we failed to get reproducible data for the rather unstable **9**. In the IR spectra of both complexes, strong (**9**) or medium (**10**) bands of ν(C≡N) are shifted toward lower frequencies (15 cm^{-1} for **9** and 56 cm^{-1} for **10**) upon coordination. The ^1H NMR spectra display all required resonances with their expected integration. In $CDCl_3$, the complexes exist as a number of conformers probably because of the hindered rotation of the bulky ligands.

Although, to the best of our knowledge, metal complexes with nitrile oxides as ligands are unknown, there are a few reports of 1,3-dipolar cycloadditions where the formation of complexes between Lewis acids and nitrile oxides was assumed, from indirect evidence, to occur.[25,26] The major argument supporting the idea of the formation of (nitrile oxide)[M] complexes is based on the inhibition of the 1,3-

 © 2005 Wiley-VCH Verlag GmbH & Co. KGaA, Weinheim

dipolar cycloaddition (sometimes with an increase of selectivity of the reaction[25–29]) in the presence of metal centers, which, in agreement with the authors,[25,26,30] blocks the oxygen atom of the nitrile oxide by coordination. The latter hypothesis was supported in the framework of this study by the lack of formation of (oxadiazole)palladium(II) complexes when **9** or **10** were treated with the corresponding nitriles (route **D**, Scheme 1).

Characterization of the (1,2,4-Oxadiazole)palladium(II) Complexes

Complexes **1**–**8** were characterized by C, H, and N analyses. In their FAB spectra they display the quasi-ion $[M + Na]^+$ (**1**, **2**) and/or the fragmentation $[M - H]^+$ and/or $[M - Cl]^+$ ions (**1**, **2**, **5**, **7**, and **8**); for **3**, **4**, and **6** only deep fragmentation was observed. In their IR spectra, the oxadiazole complexes **1**–**8** exhibit two relatively strong bands in the range of 1537–1658 cm^{-1}. The first one lies in a relatively narrow interval, i.e. 1607–1614 cm^{-1}, for all these complexes, and can be attributed to a ν(C=N) stretching vibration in the oxadiazole ligand. The position of the second band varies and depends on the type of the complex. Thus, medium-to-strong and strong bands at 1537–1585 cm^{-1} (**1**, **2**, **4** derived from **I**) and 1598 cm^{-1} (**6** and **7** derived from **II**) can be attributed to the other ν(C=N) stretching vibration of the heterocycle and/or ν(C=C) stretch of the aromatic ring. In contrast to the alkyl and aryl derivatives of oxadiazoles, the dialkylcyanamide ones (**4** and **8**) do not display strong peaks in the area 1537–1585 cm^{-1} but exhibit a strong band in the range 1657–1658 cm^{-1}. This shift is probably the consequence of a different electron distribution in the dialkylcyanamide-substituted oxadiazole ligands (see below).

In the ^1H and $^{13}C\{^1H\}$ NMR spectra of $[PdCl_2(1,2,4\text{-oxadiazole})_2]$, two (**1**–**4** and **6**–**8**) or five (**5**) sets of each signal (or a group of signals) were detected; this is probably due to the hindered rotation of the bulky oxadiazole ligands around the Pd–N bond, which leads to inequivalence of the protons and carbon atoms. In the $^{13}C\{^1H\}$ NMR spectra, two carbons from the N=C–N and N=C–O moieties were detected at δ = 164–171 and 178–190 ppm, respectively. These assignments are based upon the data for similar platinum(IV) and platinum(II) oxadiazole complexes, i.e. $[PtCl_4\{N^a{=}C(R)ON{=}C^bC_6H_2R'_3)(N^a\text{–}C^b)\}_2]$ and $[PtCl_2\{N^a{=}C(R)ON{=}C^bC_6H_2R'_3)(N^a\text{–}C^b)\}_2]$, where the signals of C from the N*C*N and N*C*O groups can be distinguished by using the long-range selective INEPT technique. In the ^1H NMR spectra of both **4** and **8**, the signal from Me in NMe_2 is broad, apparently because of the hindered rotation of the NMe_2 group (see later).

Crystal Structure Determinations of (1,2,4-Oxadiazole) palladium(II) Complexes

Crystals of **2** (Figure 1), **3** (Figure 2), **7** (Figure 3), and **8** (Figure 4) were obtained directly from the reaction mixtures and their structures were determined by X-ray crystallography.

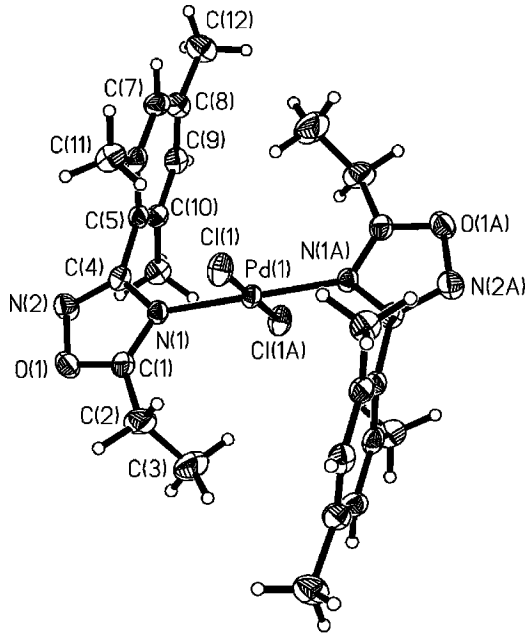

Figure 1. Thermal ellipsoid view of $[PdCl_2\{N^a{=}C(Et)ONC^b(C_6H_2Me_3)(N^a\text{–}C^b)\}_2]$ (**2**)with atomic numbering scheme; thermal ellipsoids are drawn with 50% probability

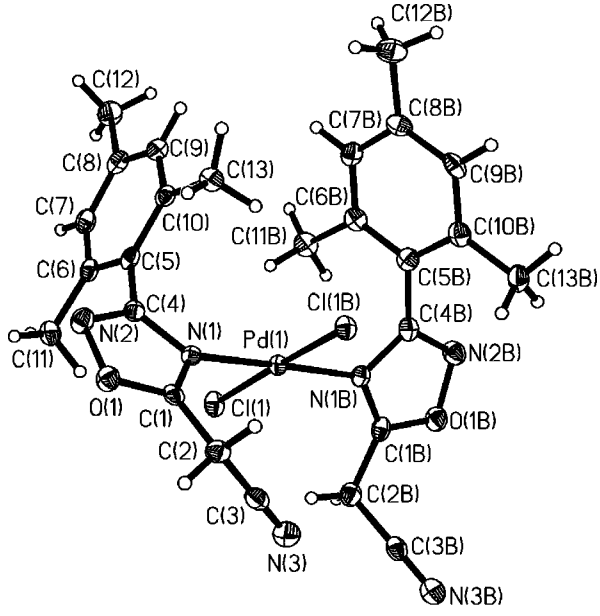

Figure 2. Thermal ellipsoid view of $[PdCl_2\{N^a{=}C(CH_2CN)ONC^b(C_6H_2Me_3)(N^a\text{–}C^b)\}_2]$ (**3**)with atomic numbering scheme; thermal ellipsoids are drawn with 50% probability

The 1,2,4-oxadiazole ligands in all these complexes are coordinated in mutual *trans* positions. In **2**, **7**, and **8** the heterocycles have an antiparallel orientation [angles between N(1)–C(1)–O(1)–N(2)–C(4) planes are 0°, 57.63(9)°, 10.16(14)°, and 0° for **2**, **3**, **7**, and **8**, respectively], while in **3**, they are turned in one direction and the torsion angle is approximately 60°. The geometrical parameters of the heterocycles in **2**, **3**, and **7** are the same within 3σ and are

 © 2005 Wiley-VCH Verlag GmbH & Co. KGaA, Weinheim

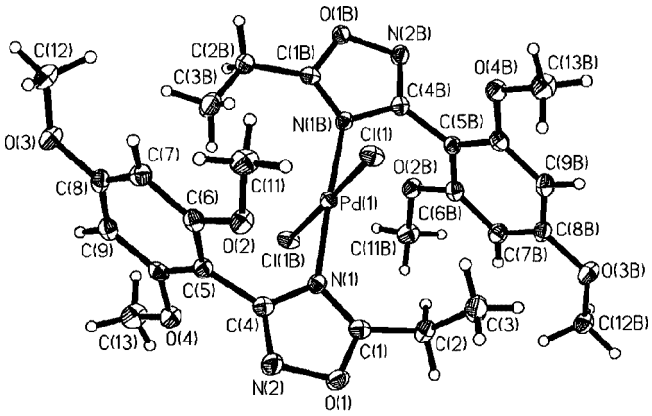

Figure 3. Thermal ellipsoid view of $[PdCl_2\{N^a{=}C(Et)ONC^b(C_6H_2(OMe)_3(N^a{-}C^b)\}_2]$ (**7**) with atomic numbering scheme; thermal ellipsoids are drawn with 50% probability

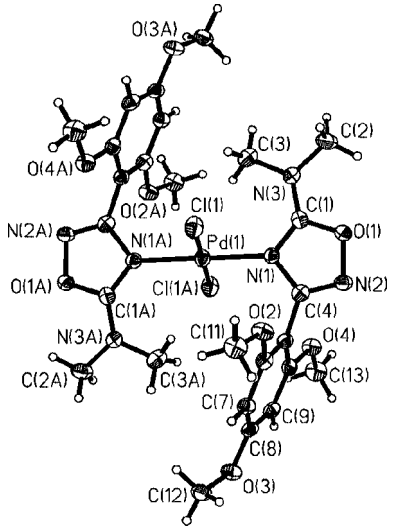

Figure 4. Thermal ellipsoid view of $[PdCl_2\{N^a{=}C(NMe_2)ONC^b(C_6H_2(OMe)_3(N^a{-}C^b)\}_2]$ (**8**)with atomic numbering scheme; thermal ellipsoids are drawn with 50% probability

similar to those in the previously described (1,2,4-oxadiazole)platinum(IV) and -platinum(II) complexes,[19] in 1,2,4-oxadiazole complexes of other metals,[31] and even in the uncomplexed heterocycles.[32–34] The Pd–N and Pd–Cl bond lengths and angles around the Pd center are similar to those given in the literature for $[PdCl_2$(N-coordinated heterocycle)$_2]$-type complexes.[35]

The C=N bond length in the Pd–N=C–N fragment of **8** [1.377(5) Å] is larger than that for the corresponding bond in **2**, **3**, and **7** [1.306(3)–1.314(3) Å] and also larger than those in the free oxadiazoles bearing NRR′ substituents.[36] In addition, the C(1)–N(3) bond length in the *CN*Me$_2$ fragment [1.315(5) Å] is shorter than a normal C–N single bond and even shorter than the C=N bond in the oxadiazole ring; all these facts favor a significant double-bond character in the *CN*Me$_2$ moiety. A possible rationale for the latter observation is the dominance of the right-hand structure (Figure 5) in the mesomeric hybrid of the heterocycle.

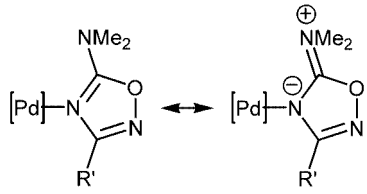

Figure 5. Possible mesomeric forms of the heterocycle in complex **8**

This observation is coherent with the unusual IR data (strong band at 1658 cm^{-1}, see above) and NMR spectroscopic data in solution, where the NMe$_2$ signal is broad probably due to hindered rotation around the partially double CN bond of the CNMe$_2$ functionality.

Liberation of the 1,2,4-Oxadiazoles

Although the activation of nitriles by Pd^{II} toward the cycloaddition is not advantageous from synthetic viewpoint, we still developed a method for liberation of 1,2,4-oxadiazoles from their complexes with the hope of further progress in this area which can be associated with either the application of cationic Pd^{II} complexes or the use of supporting ligands with pronounced π-acceptor properties.[20]

Complexes **1**–**8** are stable and remain intact in an excess of nitrile even at 40 °C for 24 h, thus preventing the reaction from being catalytic. However, the liberation of the oxadiazoles from **1**–**8** was successfully performed by substitution following two routes. In the first one, a solution of **1**–**8** in $CDCl_3$ was treated with two equivalents of 1,2-bis(diphenylphosphanyl)ethane (dppe) and, after 3 h, when the precipitation of the colorless complex $[Pd(dppe)_2]Cl_2$ [$^{31}P\{^1H\}$ ($CDCl_3$): δ = 53.15 ppm (ref.[37] δ = 56.7 ppm)] was complete, the quantitative formation of the free oxadiazoles **11**–**18** was confirmed by ^1H NMR spectroscopy. In the preparative experiment, the precipitate of $[Pd(dppe)_2]Cl_2$ can easily be separated by filtration, and subsequent evaporation of the filtrate gives the 1,2,4,-oxadiazoles in the almost quantitative yield.

In the second route, a solution of **1**–**8** in CH_2Cl_2 was treated with an excess of $Na_2S{\cdot}7H_2O$ in MeOH to immediately give a precipitate of PdS; the free oxadiazoles **11**–**18** remain in solution. After separation of PdS by filtration, the solvent was evaporated from the filtrate and the 1,2,4-oxadiazoles were extracted almost quantitatively from the residue with CH_2Cl_2. The second method is preferable because Na_2S is much cheaper than dppe and the formation of PdS proceeds substantially faster than that of $[Pd(dppe)_2]Cl_2$.

The liberated 1,2,4-oxadiazoles (**11**–**18**) were characterized by positive-ion FAB mass spectrometry − typically the $[M + H]^+$ ion is observed − and ^1H and $^{13}C\{^1H\}$ NMR spectroscopy. The chemical shifts in the ^1H and $^{13}C\{^1H\}$ NMR spectra of **11**–**18** are similar to those for the corresponding (1,2,4-oxadiazole)palladium(II) complexes. However, for **11**–**14** and **16**–**18** each proton or carbon has one set of signals, in contrast to the situation described pre-

 © 2005 Wiley-VCH Verlag GmbH & Co. KGaA, Weinheim

viously for the Pd complexes, i.e. the NMR inequivalence of the oxadiazoles **11**–**14** and **16**–**18** disappears when they are liberated from the corresponding palladium(II) complexes. However, in the case of **15**, five sets of signals are still displayed in the spectra for each proton and carbon atom (in the temperature range from 20 to 50 °C) and we believe that this is due to different conformations of the oxadiazole **15** bearing the two bulky substituents in the ring (Ph and $C_6H_2Me_3$). For all free oxadiazoles **11**–**18**, the N=C–N and N=C–O carbons lie in the ranges δ = 164–168 and 168–180 ppm, respectively.

Final Remarks

The results from this work can be considered from at least two perspectives. From the first one, the developed method, which is based on [2 + 3] cycloaddition of nitriles and nitrile oxides in the presence of a trapping metal center, is an excellent entry to 1,2,4-oxadiazole–metal complexes, whose chemistry is almost unknown, although the opposite holds true for metal compounds of the isomeric 1,3,4-oxadiazole; the latter complexes exhibit a good number of useful properties. From the second perspective, we have found the first example of nitrile oxide–metal complexes and further development of chemistry of this species may shed light on the mechanisms of the still poorly understood metal-mediated 1,3-dipolar cycloaddition of propargyl/allenyl anion type dipoles to nitriles.[19,38] We observed that the more labile Pd^{II} center (as compared to a kinetically inert Pt^{IV} center) reacts to a similar degree with both the dipolarophile and the dipole, and the latter interaction, i.e. ligation of nitrile oxide observed in this work for the first time, inhibits the 1,3-dipolar cycloaddition by blocking the oxygen center of the dipole. The latter points to the need for the selective complexation of metal centers with nitrile dipolarophiles (rather than with nitrile oxide dipoles) to promote the cycloaddition.

Experimental Section

Materials and Instrumentation: Solvents were obtained from commercial sources and used as received. The complexes $[PdCl_2(RCN)_2]$ (R = Me, Et, Ph[24]) and the nitrile oxides 2,4,6-$Me_3C_6H_2CNO$ and 2,4,6-$(MeO)_3C_6H_2CNO$[23] were prepared as described previously. C,H,N elemental analyses were carried out by the Microanalytical Service of the Instituto Superior Técnico. Positive-ion FAB mass spectra were obtained on a Trio 2000 instrument by bombarding 3-nitrobenzyl alcohol (NBA) matrices of the samples with 8 keV (ca. 1.28×10^{15} J) Xe atoms. Mass calibration for data system acquisition was achieved using CsI. Infrared spectra (4000–400 cm^{-1}) were recorded with a JASCO FT/IR-430 instrument in KBr pellets. ^1H, $^{13}C\{^1H\}$, and $^{31}P\{^1H\}$ spectra in $CDCl_3$ were measured with a Varian UNITY 300 spectrometer at ambient temperature.

Cycloaddition of Nitrile Oxides to Pd-Bound Nitriles. Method A: $PdCl_2$ (12 mg, 0.068 mmol, 1 equiv.) and 3–4 equiv. of **I** (32–44 mg, 0.200–0.271 mmol) or **II** (42–56 mg, 0.200–0.271 mmol) were suspended in RCN (R = Me, Et, Ph, NMe_2; 0.3 mL) or in a solution of $NCCH_2CN$ (27 mg, 0.408 mmol) in CH_2Cl_2 (3 mL) and the mixture was heated to 40 °C for 12–18 h. During this period the $PdCl_2$ dissolved to give orange (for **I**) or dark-brown (for **II**) solutions. In the case of complexes **1**–**3** and **6**–**8**, orange crystals were formed at the top of the vial and were removed by filtration (yields are 20–40%). The orange solution (reaction with **I**,complexes **4** and **5**) was evaporated to dryness under vacuum and the orange oil formed was crystallized under a layer of Et_2O to furnish an additional amount (yields are 30–50%) of the cycloaddition product (for **1**–**3**). All oxadiazole complexes (**6**–**8**) derived from **II** were crystallized from the reaction mixture and separated by filtration. The dark reaction mixture formed in the case of nitrile oxide **II** and PhCN and $PhCH_2CN$ contains a number of products and was not further investigated.

Method B: $[PdCl_2(RCN)_2]$ (R = Me, Et, Ph; 15 mg) was suspended with 3–4 equiv. of the nitrile oxides in the corresponding nitrile RCN (R = Me, Et, Ph; 0.3 mL), and the reaction mixture was heated to 40 °C for 12–18 h, whereupon an orange product formed. The isolation procedures are similar to those described above. This method was applied for the preparation of **1**, **2**, and **5**–**7**.

$[PdCl_2\{N^a{=}C(Me)ONC^b(C_6H_2Me_3)(N^a{-}C^b)\}_2]$ (1): Yield: 32 mg (80–85%). $C_{24}H_{28}Cl_2N_4O_2Pd$ (581.8): calcd. C 49.54, H 4.85, N 9.63; found C 49.95, H 5.15, N 9.68. FAB$^+$-MS: *m*/*z* = 605 [M + Na]$^+$, 581 [M – H]$^+$, 547 [M – Cl]$^+$, 508 [M – 2HCl]$^+$. IR (KBr, selected bands): 2976 (w) and 2925 cm^{-1} (w) ν(C–H), 1610 (mw) and 1585 (m) ν(C=N) and ν(C=C). ^1H NMR (300 MHz, $CDCl_3$; two sets of signals in the approximate ratio3:2): δ = 2.00 (major) and 2.29 (minor) (s, 6 H, *o*-$CH_3C_6H_2$), 2.40 (minor) and 2.51 (major) (s, 3 H, *p*-$CH_3C_6H_2$), 2.90 (minor) and 3.26 (major) (s, 3 H, N=CCH_3), 6.93 (major) and 7.04 (minor) (s, 2 H, *m*-Ar) ppm. $^{13}C\{^1H\}$ NMR (75.4 MHz, $CDCl_3$; two sets of signals): δ = 14.00 (minor) and 14.6 (major) (N=CCH_3), 20.4 (major) and 20.8 (minor) (*o*-$CH_3C_6H_2$), 21.4 (minor) and 21.5 (major) (*p*-$CH_3C_6H_2$), 120.3 (major) (C_{ipso}), 128.4 (minor) and 128.5 (major) (*m*-Ar), 138.8 (major) and 139.0 (minor) (*o*-Ar), 140.4 (major) and 141.2 (minor) (*p*-Ar), 166.6 (two N=C–N), 178.0 (Pd–N=C–O) ppm.

$[PdCl_2\{N^a{=}C(Et)ONC^bC_6H_2Me_3)(N^a{-}C^b)\}_2]$ (2): Yield: 32 mg (70–80%). $C_{26}H_{32}Cl_2N_4O_2Pd$ (609.9): calcd. C 51.20, H 5.29, N 9.19; found C 51.42, H 5.50, N 9.11. FAB$^+$-MS: *m*/*z* = 633 [M + Na]$^+$, 575 [M – Cl]$^+$, 537 [M–Cl–HCl]$^+$. IR (KBr, selected bands): 2982 (w) and 2921 cm^{-1} (w) ν(C–H), 1611 (mw) and 1573 (m) ν(C=N) and ν(C=C). ^1H NMR (300 MHz, $CDCl_3$; two sets of signals in the approximate ratio 1:1): δ = 1.46 and 1.72 (t, *J* = 7.5 Hz, 3 H, CH_2CH_3), 1.99 and 2.28 (s, 6 H, *o*-$CH_3C_6H_2$), 2.40 and 2.51 (s, 3 H, *p*-$CH_3C_6H_2$), 3.25 and 3.71 (q, *J* = 7.5 Hz, 2 H, CH_2CH_3), 6.93 and 7.04 (s, 2 H, *m*-Ar) ppm. $^{13}C\{^1H\}$ NMR (75.4 MHz, $CDCl_3$; two sets of signals): δ = 10.25 and 10.30 (CH_2CH_3), 20.5 and 20.9 (*o*-$CH_3C_6H_2$), 21.4 and 21.5 (*p*-$CH_3C_6H_2$), 21.7 and 22.4 (CH_2CH_3), 120.6 and 121.2 (C_{ipso}), 128.4 and 128.6 (*m*-Ar), 138.9 and 139.2 (*o*-Ar), 141.1 and 140.4 (*p*-Ar), 166.4 and 166.6 (N=C–N), 181.4 (Pd–N=C–O) ppm.

$[PdCl_2\{N^a{=}C(CH_2CN)ONC^bC_6H_2Me_3)(N^a{-}C^b)\}_2]$ (3): Yield: 17 mg (40%). $C_{26}H_{26}Cl_2N_6O_2Pd{\cdot}0.25CH_2Cl_2$ (631.9): calcd. C 48.28, H 4.10, N 12.87; found C 48.68, H 4.26, N 12.82. In our FAB experimental conditions, we were able to observe only deep fragmentation and no [M]$^+$ was found. IR (KBr, selected bands): 2966 (mw) and 2909 cm^{-1} (mw) ν(C–H), 2266 (vw)ν(C≡N), 1610 (mw) and 1585 (m) ν(C=N) and ν(C=C). ^1H NMR (300 MHz, $CDCl_3$; two sets of signals in the approximate ratio 1:6): δ = 1.98 (major) and 2.20 (minor) (s, 6 H, *o*-$CH_3C_6H_2$), 2.34 (minor) and 2.52 (major) (s, 3 H, *p*-$CH_3C_6H_2$), 3.61 (minor) and 4.89 (major) (s, 2 H, CH_2CN), 6.96 (minor) and 6.99 (major) (s, 2 H, *m*-Ar) ppm. $^{13}C\{^1H\}$ NMR (75.4 MHz, $CDCl_3$): δ = 19.3 (CH_2), 20.4 (*o*-

 © 2005 Wiley-VCH Verlag GmbH & Co. KGaA, Weinheim

$CH_3C_6H_2$), 21.5 (*p*-$CH_3C_6H_2$), 111.4 (C≡N), 128.8 (*m*-Ar), 139.0 (*o*-Ar), 141.3 (*p*-Ar), 171.4 (N=C–N), 190.5 (Pd–N=C–O) ppm; C_{ipso} was not detected.

[$PdCl_2${N^a=C(NMe$_2$)ONC^{b}C$_6$H$_2$Me$_3$)(N^a–C^b)}$_2$] (4): Yield: 17 mg (40%). $C_{26}H_{34}Cl_2N_6O_2Pd$ (639.9): calcd. C 48.89, H 5.37, N 13.17; found C 48.84, H 5.44, N 12.94. In our FAB experimental conditions, we were able to observe only deep fragmentation and no[M]$^+$ was found. IR (KBr, selected bands): 2923 cm^{-1}) (mw) ν(C–H), 1658 (ms) and 1609 (m) ν(C=N) and ν(C=C). ^{1}H NMR (300 MHz, $CDCl_3$; two sets of signals in the approximate ratio 1:2): δ = 2.29 (s, 3 H, *p*-CH_3C$_6$H$_2$, minor), 2.33 (s, 6 H, *o*-CH_3C$_6$H$_2$, major), 2.39 (s, 3 H, *p*-CH_3C$_6$H$_2$, major), 3.39 (br. s, 6 H, NMe$_2$), 6.88 (s, 2 H, *m*-Ar, minor), 6.98 (s, 2 H, *m*-Ar, major) ppm. ^{13}C{^{1}H} NMR (75.4 MHz, $CDCl_3$): δ = 20.8 (*o*-$CH_3C_6H_2$), 21.3 (*p*-$CH_3C_6H_2$), 40.1 (NMe$_2$), 128.2 (*m*-Ar), 139.6 (*o*-Ar), 140.4 (*p*-Ar), 166.9 (N=C–N) ppm; signals of other groups were not detected.

[$PdCl_2${N^a=C(Ph)ONC^{b}C$_6$H$_2$Me$_3$)(N^a–C^b)}$_2$] (5): Yield: 19 mg (40%). $C_{34}H_{32}Cl_2N_4O_2Pd$ (706.0): calcd. C 57.84, H 4.57, N 7.94; found C 57.37, H 4.38, N 7.68. FAB$^+$-MS: *m*/*z* = 668 [M – HCl]$^+$, 633 [M – 2Cl]$^+$. IR (KBr, selected bands): 2918 cm^{-1} (mw) ν(C–H), 1607 (m) and 1557 (ms) ν(C=N) and ν(C=C). ^{1}H NMR (300 MHz, $CDCl_3$; five sets for each signal in the spectrum): δ = 2.05–2.55 (several s, 9 H, *o*- and *p*-CH_3C$_6$H$_2$), 6.92–7.09 (several s, 2 H, *m*-Ar), 7.48–7.72 (several m, 3 *H*, *m*- and *p*-Ph from PhC=N), 8.20–9.28 (several d, 2 H, *o*-Ph from PhC=N) ppm. ^{13}C{^{1}H} NMR (75.4 MHz, $CDCl_3$): δ = 20.4, 20.6, 20.8, 20.9, 21.5 and 21.6 (*o*- and *p*-$CH_3C_6H_2$), 128.5–129.3, 129.9–130.6, 132.1–134.5 and 138.3–140.9 (Ph and C_6H_2), 167.5 (C=N) ppm.

[$PdCl_2${N^a=C(Me)ONC^b(C_6H_2(OMe)$_3$)(N^a–C^b)}$_2$] (6): Yield: 23 mg (50%). $C_{24}H_{28}Cl_2N_4O_8Pd$ (677.8): calcd. C 42.53, H 4.16, N 8.27; found C 42.00, H 4.27, N 8.10. In our FAB experimental conditions, we were able to observe only deep fragmentation and no $[M]^+$ was found. IR (KBr, selected bands): 2942 cm^{-1} (mw) and 2842 (w) ν(C–H), 1614 (s) and 1598 (s) ν(C=N) and ν(C=C). ^{1}H NMR (300 MHz, $CDCl_3$; two sets of signals in the approximate ratio 2:1): δ = 2.90 (major) and 3.27 (minor) (s, 3 H, Me), 3.57 (minor) and 3.83 (major) (s, 6 H, *o*-$CH_3C_6H_2$), 3.91 (major) and 3.98 (minor) (s, 3 H, *p*-$CH_3OC_6H_2$), 6.14 (minor) and 6.25 (major) (s, 2 H, *m*-Ar) ppm. ^{13}C{^{1}H} NMR (75.4 MHz, $CDCl_3$): δ = 13.9 (Me), 55.8 (*o*-$CH_3OC_6H_2$), 56.0 (*p*-$CH_3OC_6H_2$), 90.3 (*m*-Ar), 160.7 (*o*-Ar) ppm.

[$PdCl_2${N^a=C(Et)ONC^b(C_6H_2(OMe)$_3$)(N^a–C^b)}$_2$] (7): Yield: 24 mg (50%). $C_{26}H_{32}Cl_2N_4O_8Pd$ (705.9): calcd. C 44.24, H 4.57, N 7.94; found C 43.77, H 4.78, N 7.72. FAB$^+$-MS: *m*/*z* = 671 [M – Cl]$^+$. IR (KBr, selected bands): 2941 cm^{-1} (mw) and 2845 (w) ν(C–H), 1614 (s) and 1589 (ms) ν(C=N) and ν(C=C). ^{1}H NMR (300 MHz, $CDCl_3$; two sets of signals in the approximate ratio 3:1): δ = 1.50 (major) and 1.68 (minor) (t, *J* = 7.5 Hz, 3 H, Et), 3.29 (major) and 3.80 (minor) (q, *J* = 7.5 Hz, 2 H, Et), 3.57 (minor) and 3.81 (major) (s, 6 H, *o*-CH_3C$_6$H$_2$), 3.91 (major) and 3.99 (minor) (s, 3 H, *p*-CH_3OC$_6$H$_2$), 6.14 (minor) and 6.25 (major) (s, 2 H, *m*-Ar) ppm. ^{13}C{^{1}H} NMR (75.4 MHz, $CDCl_3$): δ = 10.2 (CH_3 from Et), 21.7 (CH_2 from Et), 55.7 (*o*-$CH_3OC_6H_2$), 55.9 (*p*-$CH_3OC_6H_2$), 90.2 (*m*-Ar), 160.7 (*o*-Ar), 162.7 (*p*-Ar), 164.5 (N=C–N), 180.3 (Pd–N=C–O) ppm.

[$PdCl_2${N^a=C(NMe$_2$)ONC^b(C_6H_2(OMe)$_3$)(N^a–C^b)}$_2$] (8): Yield: 20 mg (40%). $C_{24}H_{28}Cl_2N_4O_8Pd$ (735.9): calcd. C 42.43, H 4.66, N 11.42; found C 42.90, H 4.93, N 11.34. FAB$^+$-MS: *m*/*z* = 700 [M – Cl –H]$^+$. IR (KBr, selected bands): 2935 cm^{-1} (mw) and 2845 (w) ν(C–H), 1657 (s) and 1614 (s) ν(C=N) and ν(C=C). ^{1}H NMR (300 MHz, $CDCl_3$; two sets of signals in the approximate ratio 11:1; signal sets for minor isomer are not given because of its low abundance): δ = 3.45 (br. s, 3 H, Me), 3.78 (s, 6 H, *o*-$CH_3C_6H_2$), 3.92 (s, 3 H, *p*-$CH_3OC_6H_2$), 6.19 (s, 2 H, *m*-Ar) ppm. ^{13}C{^{1}H} NMR (75.4 MHz, $CDCl_3$): δ = 39.4 (NMe$_2$), 55.7 (*o*-$CH_3OC_6H_2$), 56.1 (*p*-$CH_3OC_6H_2$), 90.1 (*m*-Ar) ppm; signals for other groups were not detected due to poor solubility of compound.

(Nitrile oxide)palladium(II) Complexes: [$PdCl_2$(MeCN)$_2$] (20 mg, 0.08 mmol) and the nitrile oxides R′CNO [0.20 mmol; R′ = Me$_3$-C_6H_2**I**, (MeO)$_3$$C_6H_2$**II**] were suspended in CH_2Cl_2 (3 mL) and the mixture left to stand at room temperature for 2–4 h. During this period the [$PdCl_2$(MeCN)$_2$] dissolved to give dark-brown solutions. In case of **II** the brown solution remained unchanged after several hours, therefore the solvent was evaporated and the dark oily residue formed was crystallized under a layer of Et_2O. In the case of **I**, after several hours an orange precipitate begin to form and solution become more pale and turned to orange-yellow. The precipitate was removed by decantation and the solution was evaporated under vacuum until dryness and crystallized under a layer of Et_2O. Yield: ca. 60% (**9**) and ca. 30% (**10**).

[$PdCl_2$(ONCC_6H_2Me$_3$)$_2$] (9): ES-MS$^+$: *m*/*z* = 501 [M + H]$^+$. IR (KBr, selected bands): 2967 cm^{-1} (w) and 2922 (mw) ν(C–H), 2278 (s) ν(C≡N) 1792 (ms), 1735 (m), 1608 (s), 1456 (br. ms) [in the free nitrile oxide: 2949 (w) and 2919 (mw) ν(C–H), 2293 (s) ν(C≡N), 1608 (m)]. ^{1}H NMR (300 MHz, $CDCl_3$): δ = 2.30–2.49 (set of s, 9 H, *o*- and *p*-CH_3C$_6$H$_2$), 6.89–6.94 (set of s, 2 H, C$_6$*H*$_2$) ppm.

[$PdCl_2${ONCC_6H_2(OMe)$_3$}$_2$] (10): $C_{20}H_{22}Cl_2N_2O_8Pd$ (595.9): calcd. C 40.32, H 3.72, N 4.70; found C 40.90, H 4.64, N 4.63. ES-MS$^+$: *m*/*z* = 597 [M + H]$^+$. IR (KBr, selected bands): 2940 cm^{-1} (mw) ν(C–H), 2249 (m) ν(C≡N) 1606 (br. s), 1456 (br. m) [in the free nitrile oxide: 2985 (w) and 2949 (mw) ν(C–H), 2305 (ms) ν(C≡N), 1608 (s), 1582 (s), 1469 (ms)]. ^{1}H NMR (300 MHz, $CDCl_3$): δ = 3.76–3.94 (set of s, 9 H, *o*- and *p*-CH_3OC$_6$H$_2$), 6.02–6.14 (set of s, 2 H, C$_6$*H*$_2$) ppm.

Liberation of the Oxadiazoles from Complexes 1–8: (*i*) dppe (2 equiv.) was added to a solution of **1**–**8** (15 mg) in $CDCl_3$ (0.5 mL) and the mixture was allowed to stand at 40 °C for 30 min, whereupon colorless [Pd(dppe)$_2$]Cl_2 precipitated. The free oxadiazole was characterized in solution by ^{1}H NMR spectroscopy. Evaporation of the solvent gave **11**–**18** (see later) in almost quantitative yield.(*ii*) A solution of $Na_2S·7H_2O$ (50 mg) in MeOH (1 mL) was added dropwise to a solution of **1**–**8** (10 mg) in CH_2Cl_2 (0.5 mL). The dark-brown PdS precipitated immediately after the addition of ca. 0.15 mL of the sulfide solution (until the yellow color disappeared), whereupon the reaction mixture was evaporated to dryness and the oxadiazole was extracted from the residue with CH_2Cl_2 (1 mL). Yields are almost quantitative.

The oxadiazoles N^a=C(Et)ONC^b(C_6H_2Me$_3$)(N^a–C^b) (**12**), and N^a=C(Et)ONC^b(C_6H_2(OMe)$_3$)(N^a–C^b) (**17**) have been characterized previously.[10]

N^a=C(Me)ONC^b(C_6H_2Me$_3$)(N^a–C^b) (11): FAB$^+$-MS: *m*/*z* = 203 [M + H]$^+$. ^{1}H NMR (300 MHz, $CDCl_3$): δ = 2.18 (s, 6 H, *o*-CH_3C$_6$H$_2$), 2.33 (s, 3 H, *p*-CH_3C$_6$H$_2$), 2.68 (s, 3 H, Me), 6.94 (s, 2 H, *m*-Ar) ppm. ^{13}C{^{1}H} NMR (75.4 MHz, $CDCl_3$): δ = 12.4 (N=C*Me*), 20.0 (*o*-$CH_3C_6H_2$), 21.2 (*p*-$CH_3C_6H_2$), 128.5 (*m*-Ar), 137.7 (*o*-Ar), 139.6 (*p*-Ar) ppm.

N^a=C(CH_2CN)ONC^b(C_6H_2Me$_3$)(N^a–C^b) (13): FAB$^+$-MS: *m*/*z* = 228 [M + H]$^+$. ^{1}H NMR (300 MHz, $CDCl_3$): δ = 2.20 (s, 6 H, *o*-CH_3C$_6$H$_2$), 2.34 (s, 3 H, *p*-CH_3C$_6$H$_2$), 4.19 (s, 2 H, CH_2), 6.96 (s, 2 H, *m*-Ar) ppm. ^{13}C{^{1}H} NMR (75.4 MHz, $CDCl_3$): δ = 17.3 (Me), 20.2 (*o*-CH_3C$_6$H$_2$), 21.2 (*p*-CH_3C$_6$H$_2$), 112.0 (C≡N), 122.6 (C_{ipso}), 128.7 (*m*-Ar), 137.8 (*o*-Ar), 140.3 (*p*-Ar), 168.1 (N=C–O), 169.1 (N=C–N) ppm.

 © 2005 Wiley-VCH Verlag GmbH & Co. KGaA, Weinheim

Table 1. Crystal data for compounds **2**, **3**, **7**, and **8**

	2	**3**	**7**	**8**
Empirical formula	$C_{26}H_{32}Cl_2N_4O_2Pd$	$C_{26}H_{22}Cl_2N_6O_2Pd$	$C_{26}H_{32}Cl_2N_4O_8Pd$	$C_{26}H_{34}Cl_2N_6O_8Pd$
Mol. mass	609.86	627.80	705.86	735.89
Temp [K]	110(2)	100(2)	110(2)	100(2)
λ [Å]	0.71073	0.71073	0.71073	0.71073
Cryst. syst.	monoclinic	monoclinic	monoclinic	monoclinic
Space group	$P2_1/c$	$P2_1/c$	$P2_1/n$	$P2_1/c$
a [Å]	8.03300(10)	13.5346(2)	16.3357(2)	11.1938(5)
b [Å]	6.7074(2)	16.0527(3)	7.62820(10)	8.1204(3)
c [Å]	24.7117(6)	13.7351(3)	22.8554(3)	16.5640(7)
β [°]	92.7290(10)	117.1703(8)	91.8986(4)	94.045(2)
V [Å^3]	1329.97(5)	2654.89(9)	2846.49(6)	1501.89(11)
Z	2	4	4	2
ρ_{calc} [Mg m^{-3}]	1.523	1.571	1.647	1.627
μ(Mo-K_α) [mm^{-1}]	0.929	0.936	0.896	0.854
$R1$[a] [$I \geq 2\sigma(I)$]	0.0320	0.0310	0.0282	0.0456
$wR2$[b] [$I \geq 2\sigma(I)$]	0.0733	0.0665	0.0653	0.1128

[a] $R1 = \Sigma||F_o| - |F_c||/\Sigma|F_o|$. [b] $wR2 = \{\Sigma[w(F_o^2 - F_c^2)^2]/\Sigma[w(F_o^2)^2]\}^{1/2}$.

Table 2. Selected bond lengths [Å] and angles [°] for **2**, **3**, **7**, and **8**

	2	**3**	**3b**	**7**	**7b**	**8**
Ru(1)–Cl(1)	2.2899(8)	2.2947(6)	2.2927(6)	2.2940(6)	2.3082(6)	2.2952(10)
Ru(1)–N(1)	2.018(2)	2.018(2)	2.030(2)	2.024(2)	2.031(2)	2.045(3)
N(1)–C(1)	1.307(4)	1.307(3)	1.305(3)	1.314(3)	1.306(3)	1.337(5)
N(1)–C(4)		1.390(3)	1.394(3)	1.388(3)	1.396(3)	1.394(5)
C(1)–C(2)	1.476(4)	1.483(4)	1.484(4)	1.474(3)	1.481(3)	
C(1)–N(3)						1.315(5)
C(1)–O(1)	1.330(4)	1.319(3)	1.329(3)	1.328(3)	1.341(3)	1.341(5)
O(1)–N(2)	1.425(3)	1.433(3)	1.429(3)	1.430(3)	1.425(2)	1.441(4)
N(2)–C(4)	1.295(4)	1.304(3)	1.305(3)	1.297(3)	1.294(3)	1.287(5)
Cl(1)–Pd(1)–N(1)	91.83(7)	89.61(6)	90.23(6)	88.95(5)	90.58(5)	88.30(9)
Pd(1)–N(1)–C(1)	124.3(2)	125.3(2)	128.0(2)	126.8(2)	132.7(2)	129.9(3)
N(1)–C(1)–C(2)	128.3(3)	129.5(2)	130.2(2)	129.4(2)	132.4(2)	
N(1)–C(1)–N(3)						131.3(4)
N(1)–C(1)–O(1)	111.0(2)	112.3(2)	112.0(2)	111.0(2)	111.1(2)	110.9(3)
C(1)–O(1)–N(2)	107.6(2)	106.9(2)	107.1(2)	107.8(2)	107.6(2)	107.6(3)
O(1)–N(2)–C(4)	104.0(2)	104.0(2)	103.8(2)	103.5(2)	103.7(2)	103.3(3)
N(2)–C(4)–N(1)	112.5(2)	112.3(2)	112.5(2)	113.1(2)	113.2(2)	114.7(3)

N^a=C(NMe$_2$)ONC^b(C$_6$H$_2$Me$_3$)(N^a–C^b) (14): FAB$^+$-MS: m/z = 232 [M + H]$^+$. ^{1}H NMR (300 MHz, $CDCl_3$): δ = 2.23 (s, 6 H, *o*-CH_3C$_6$H$_2$), 2.28 (s, 3 H, *p*-CH_3C$_6$H$_2$), 3.20 (br. s, 6 H, NMe$_2$), 6.89 (s, 2 H, *m*-Ar) ppm. ^{13}C{^{1}H} NMR (75.4 MHz, $CDCl_3$): δ = 19.9 (*o*-*C*H$_3$C$_6$H$_2$), 21.1 (*p*-*C*H$_3$C$_6$H$_2$), 40.2 (NMe$_2$), 128.2 (*m*-Ar), 137.5 (*o*-Ar), 139.1 (*p*-Ar) ppm; signals for other groups were not detected.

N^a=C(Ph)ONC^b(C$_6$H$_2$Me$_3$)(N^a–C^b) (15): FAB$^+$-MS: m/z = 278 [M + Na]$^+$, 265 [M + H]$^+$. ^{1}H NMR (300 MHz, $CDCl_3$; three sets of each signal in the approximate ratio 2:2:3): δ = 2.25, 2.30, and 2.34 (three s, 6 H, *o*-CH_3C$_6$H$_2$), 2.05, 2.49, and 2.55 (three s, 3 H, *p*-CH_3C$_6$H$_2$), 6.92, 6.98, and 7.09 (three s, 2 H, *m*-Ar), 7.4–7,6 (m, 3 H, *m*- and *p*-Ph), 8.22, 8.71, and 8.98 (three d, 2 H, *o*-Ph) ppm. ^{13}C{^{1}H} NMR (75.4 MHz, $CDCl_3$): δ = 20.1, 20.9 and 21.2 (*o*-*C*H$_3$C$_6$H$_2$), 20.6, 21.5 and 21.6 (*p*-*C*H$_3$C$_6$H$_2$), 128.2, 128.6, 128.7, 128.9, 129.1, 129.9, 130.6, 132.7, 133.7, 134.0, 137.8, 139.8 and 140.9 (all Ar) ppm; signals from other groups were not detected.

N^a=C(Me)ONC^b(C$_6$H$_2$(OMe)$_3$)(N^a–C^b) (16): FAB$^+$-MS: m/z = 251 [M + H]$^+$. ^{1}H NMR (300 MHz, $CDCl_3$): δ = 2.18 (s, 6 H, *o*-CH_3OC$_6$H$_2$), 2.33 (s, 3 H, *p*-CH_3OC$_6$H$_2$), 2.68 (s, 3 H, Me), 6.94 (s, 2 *H*, *m*-Ar) ppm. ^{13}C{^{1}H} NMR (75.4 MHz, $CDCl_3$): δ = 12.5 (Me), 55.4 (*p*-*C*H$_3$OC$_6$H$_2$), 56.0 (*o*-*C*H$_3$OC$_6$H$_2$), 90.7 (*m*-Ar), 97.6 (*C$_{ipso}$*), 160.1 (*o*-Ar), 163.2 (*p*-Ar), 164.1 (N=C–N), 175.9 (N=C–O) ppm.

N^a=C(NMe$_2$)ONC^b(C$_6$H$_2$(OMe)$_3$)(N^a–C^b) (18): FAB$^+$-MS: m/z = 280 [M + H]$^+$. ^{1}H NMR (300 MHz, $CDCl_3$): δ = 3.18 (s, 3 H, Me), 3.77 (s, 6 H, *o*-CH_3OC$_6$H$_2$), 3.83 (s, 3 H, *p*-CH_3OC$_6$H$_2$), 6.15 (s, 2 H, *m*-Ar) ppm. ^{13}C{^{1}H} NMR (75.4 MHz, $CDCl_3$): δ = 40.4 (NMe$_2$), 56.0 (*o*-*C*H$_3$OC$_6$H$_2$), 55.4 (*p*-*C*H$_3$OC$_6$H$_2$), 90.7 (*m*-Ar), 160.1 (*o*-Ar), 162.9 (*p*-Ar), 164.0 (N=C–N), 171.6 (N=C–O) ppm; signals for other groups were not detected.

X-ray Crystal Structure Determinations: The crystals were immersed in perfluoropolyether, mounted in a cryo-loop and measured at 100 or 110 K. The X-ray diffraction data were collected with a Nonius KappaCCD diffractometer using Mo-K_α radiation (λ = 0.71073 Å). The Denzo-Scalepack program package[39] was used for cell refinements and data reductions. Structures were solved by direct methods using the SHELXS-97 or SIR-97 programs or by Patterson method using DIRDIF-99 with the WinGX graphical user interface.[40–43] An empirical absorption correction was applied to all data using XPREP in SHELXTL v.6.12[44] (T_{min}/T_{max}: 0.12334/0.15440, 0.31972/0.35415, 0.12648/0.15208, and 0.13741/0.17395 for **2**, **3**, **7**, and **8**, respectively). Structural refinements were carried out with SHELXL-97.[41] The asymmetric unit

 © 2005 Wiley-VCH Verlag GmbH & Co. KGaA, Weinheim

contained only half a molecule in **2** and **8**, whereas in **3** and **7** the asymmetric unit contained a whole molecule. All hydrogens were placed in idealized positions and constrained to ride on their parent atom. The crystallographic data are summarized in Table 1. Selected bond lengths and angles are shown in Table 2.

CCDC-243489 to -243492 (for **2**, **3**, **7**, and **8**, respectively) contain the supplementary crystallographic data for this paper. These data can be obtained free of charge from The Cambridge Crystallographic Data Centre via www.ccdc.cam.ac.uk/data_request/cif.

Acknowledgments

This work has been partially supported by the FCT (Foundation for Science and Technology, Portugal) and its POCTI program (POCTI/QUI/43415/2001 project; FEDER funded). N.A.B. expresses gratitude to the POCTI program, Portugal (grant SFRH/BPD/11448/2002) and the Center for Natural Sciences (Konkursnii Tsentr Fundamentalnogo Estestvoznaniya), Russia (grant PD03-1.3-28) and the Russian Fund for Basic Research (grant 05-03-32140a) for financial support. M.H. would like to thank the Academy of Finland for financial support. V.Y.K. is very much obliged to the Russian Fund for Basic Research for a grant (03-03-32363), POCTI program (FEDER funded; Cientista Convidado/Professor at the Instituto Superior Técnico, Portugal), the Royal Society of Chemistry for a Grant for International Authors, and the Academy of Finland for support of the cooperation with the University of Joensuu. The authors thank NATO for the Collaborative Linkage Grant PST.CLG.979289.

[1] a) J. C. Jochims, in *Comprehensive Heterocyclic Chemistry II* (Ed.: R. C. Storr), Elsevier, Oxford, UK **1996**, *4*, pp. 179 and 906; *Chem. Abstr*. **1997**, *126*, 157409; b) K. Hemming, *J. Chem. Res. S* **2001**, 209; c) K. Hemming, *J. Chem. Res. S* **2001**, 601; d) A. G. Tyrkov, *Izv. Vyssh. Uchebn. Zaved., Khim. Khim. Tekhnol*. **2000**, *43*, 73–77; *Chem. Abstr*. **2001**, *134*, 353264; e) I. Shibuya, *Busshitsu Kogaku Kogyo Gijutsu Kenkyusho Hokoku* **1999**, *7*, 283; *Chem. Abstr*. **2000**, *133*, 30676; f) L. B. Clapp, *Adv. Heterocycl. Chem*. **1976**, *20*, 65–116; g) F. Eloy, R. Lenaers, *Chim. Ther*. **1966**, 347–350; *Chem. Abstr*. **1967**, *66*, 37 793.

[2] a) Z.-I. Terashita, K.-I. Naruo, S. Morimoto, *PCT Int. Appl*. WO 02 604 39, **2002**; *Chem. Abstr*. **2002**, *137*, 145599; b) Yu. S. Andreichikov, S. G. Pitirimova, I. V. Krylova, V. E. Kolla, E. V. Popov, *USSR Pat*. SU 1 332 767, **1990**; *Chem. Abstr*. **1990**, *113*, 165416.

[3] a) D. N. Nicolaides, K. C. Fylaktakidou, K. E. Litinas, D. Hadjipavlou-Litina, *Eur. J. Med. Chem*. **1998**, *33*, 715–724; b) C. H. Mitch, H. E. Shannon, *PCT Int. Appl*. WO 97 20 561, **1997**; *Chem. Abstr*. **1997**, *127*, 104351; c) M. Yamamoto, Y. Ori, *Jpn. Kokai Tokkyo Koho JP* 62 96 480 [87 96 480], **1987**;*Chem. Abstr*. **1987**, *107*, 115596; d) Sumitomo Chemical Co., Ltd., *Jpn. Kokai Tokkyo Koho JP* 60 51 188 [85 51 188], **1985**;*Chem. Abstr*. **1985**, *103*, 71323; e) Sumitomo Chemical Co., Ltd., *Jpn. Kokai Tokkyo Koho JP* 81 65 881, **1981**;*Chem. Abstr*. **1981**, *95*, 150674; f) N. V. Gist-Brocades, *Neth. Appl. NL* 78 07 076, **1978**;*Chem. Abstr*. **1978**, *90*, 121611; g) F. M. Pallos, J. R. DeBaun, A. D. Gutman, *US Pat*., 3 968 224, **1976**;*Chem. Abstr*. **1976**, *85*, 104204; h) H. Breuer, U. D. Treuner, *US Pat*., 3 887 573, **1975**;*Chem. Abstr*. **1975**, *83*, 97312; i) U. D. Treuner, *Ger. Offen*., DE 2 248 940, **1973**;*Chem. Abstr*. **1973**, *79*, 18719.

[4] J. R. Romero, *Expert Opin. Inv. Drug* **2001**, *10*, 369; *Chem. Abstr.***2001**, *134*, 246803.

[5] a) J. E. Macor, T. Ordway, R. L. Smith, P. R. Verhoest, R. A. Mack, *J. Org. Chem.* **1996**, *61*, 3228–3229; b) D. A. Quagliato, P. M. Andrae, *PCT Int. Appl*. WO 02 06 250, **2002**; *Chem. Abstr*. **2002**, *136*, 118440; c) E. Gur, E. Dremencov, B. Lerer, M. E. Newman, *Eur. J. Pharmacol.* **2001**, *411*, 115–122; d) J. Watson, J. V. Selkirk, A. M. Brown, *J. Biomol. Screen.* **1998**, *3*, 101–105; e) P. J. Pauwels, T. Wurch, C. Palmier, F. C. Colpaert, *Br. J. Pharmacol*. **1998**, *123*, 51–62.

[6] a) T. Naka, K. Kubo, *Curr. Pharm. Design* **1999**, *5*, 453–472; b) H. Juraszyk, J. Gante, H. Wurziger, S. Bernotat-Danielowski, G. Melzer, *PCT Int. Appl*., 97 44 333, **1997**;*Chem. Abstr*. **1997**, *128*, 23138.

[7] a) H. Hagen, F. Becke, *Ger. Offen*., DE 2 060 082, **1972**;*Chem. Abstr*. **1972**, *77*, 88511; b) H. Hagen, F. Becke, J. Niemeyer, *Ger. Offen*., DE 2 016 692, **1971**;*Chem. Abstr.***1972**, *76*, 25299.

[8] S. I. Torgova, L. A. Karamysheva, T. A. Geivandova, A. Strigazzi, *Mol. Cryst. Liq. Cryst. A* **2001**, *365*, 99–106.

[9] a) A. Zamponi, M. Patsch, H. Hagen, B.-P. Walther, *Ger. Offen*., DE 19 640 189, **1998**; *Chem. Abstr*. **1998**, *128*, 271684; b) G. Lamm, H. Reichelt, M. Wiesenfeldt, *Ger. Offen*., DE 19 548 785, **1997**; *Chem. Abstr*. **1997**, *127*, 110290; c) H. Fuerstenwerth, *Ger. Offen*., DE 3 344 294, **1985**; *Chem. Abstr*. **1985**, *103*:215 152.

[10] a) G. Prossel, R. Erckel, E. Schinzel, D. Guenther, G. Roesch, *Ger. Offen*., DE 2 748 660, **1978**; *Chem. Abstr*. **1978**, *89*, 112427; b) H. Schlaepfer, *Ger. Offen*., DE 2 712 409, **1977**; *Chem. Abstr*. **1978**, *88*, 51973; c) A. E. Siegrist, G. Kormany, G. Kabas, *Helv. Chim. Acta* **1976**, *59*, 2469–2491; d) A. Domerque, *Ger. Offen*., DE 2 503 439, **1975**; *Chem. Abstr*. **1975**, *83*, 165 830.

[11] a) A. S. Da Silva, M. A. A. De Silva, C. E. M. Carvalho, O. A. C. Antunes, J. O. M. Herrera, I. M. Brinn, A. S. Mangrich, *Inorg. Chim. Acta* **1999**, *292*, 1–6; b) G. Orellana, C. Alvarez-Ibarra, M. Luz.Quiroga, *Bull. Soc. Chim. Belg*. **1988**, *97*, 731–741; c) Yu. I. Ryabukhin, N. V. Shibaeva, A. S. Kuzharov, V. G. Korobkova, A. V. Khokhlov, A. D. Garnovskii, *Koord. Khim*. **1987**, *13*, 869–874; d) H. A. Goodwin, F. E. Smith, *Inorg. Nucl. Chem. Lett.* **1974**, *10*, 99–103.

[12] For recent references see: a) M. Du, Y.-M. Guo, S.-T. Chen, X.-H. Bu, S. R. Batten, J. Ribas, S. Kitagawa, *Inorg. Chem.* **2004**, *43*, 1287–93; b) D. Huang, H.-B. Song, M. Du, S.-T. Chen, X.-H. Bu, J. Ribas, *Inorg. Chem.* **2004**, *43*, 931–944; c) H. Hou, L. Xie, G. Li, T. Ge, Y. Fan, Y. Zhu, *New J. Chem.* **2004**, *28*, 191–199; d) Y.-B. Dong, J.-P. Ma, R.-Q. Huang, F.-Z. Liang, M. D. Smith, *Dalton Trans.* **2003**, 1472–1479; e) Y.-B. Dong, J.-Y. Cheng, R.-Q. Huang, M. D. Smith, H.-C. Zur Loye, *Inorg. Chem.* **2003**, *42*, 5699–5706; f) M. Du, X.-H. Bu, Z. Huang, S.-T. Chen, Y.-M. Guo, C. Diaz, J. Ribas, *Inorg. Chem.* **2003**, *42*, 552–559; g) Y.-B. Dong, J.-P. Ma, R.-Q. Huang, M. D. Smith, H.-C. Zur Loye, *Inorg. Chem.* **2003**, *42*, 294–300; h) M. Du, X.-H. Bu, Y.-M. Guo, H. Liu, S. R. Batten, J. Ribas, T. C. W. Mak, *Inorg. Chem.* **2002**, *41*, 4904–4908.

[13] C. Incarvito, A. L. Rheingold, C. J. Qin, A. L. Gavrilova, B. Bosnich, *Inorg. Chem.* **2001**, *40*, 1386–1390.

[14] A. Vlcek, Jr., *Chemtracts* **2002**, *15*, 49.

[15] a) N.-X. Hu, M. Esteghamatian, S. Xie, Z. Popovich, A.-M. Hor, B. Ong, S. Wang, *Adv. Mater.* **1999**, *11*, 1460–1463; b) J. F. Wang, G. E. Jabbour, E. A. Mash, J. Anderson, Y. Zhang, P. A. Lee, N. R. Armstrong, N. Peyghambarian, B. Kippelen, *Adv. Mater.* **1999**, *11*, 1266–1269.

[16] a) P. Gomez-Saiz, J. Garcia-Tojal, M. A. Maestro, J. Mahia, F. J. Arnaiz, L. Lezama, T. Rojo, *Eur. J. Inorg. Chem.* **2003**, 2639–2650; b) P. Gomez-Saiz, J. Garcia-Tojal, F. J. Arnaiz, M. A. Maestro, L. Lezama, T. Rojo, *Inorg. Chem. Commun.* **2003**, *6*, 558–560; c) P. Gomez-Saiz, J. Garcia-Tojal, M. A. Maestro, F. J. Arnaiz, T. Rojo, *Inorg. Chem.* **2002**, *41*, 1345–1347.

[17] C. K. Lai, C.-R. Wen, J.-H. Sung, *224th ACS National Meeting*, Boston, MA, United States, August 18–22, **2002**, INOR-413, Am. Chem. Soc.: Washington, D.C.

[18] a) G. Wagner, A. J. L. Pombeiro, V. Yu. Kukushkin, *J. Am. Chem. Soc.* **2000**, *122*, 3106–3111; b) G. Wagner, M. Haukka, J. J. R. Fraústo da Silva, A. J. L. Pombeiro, V. Yu. Kukushkin, *Inorg. Chem.* **2001**, *40*, 264–271; c) M. A. J. Charmier, V. Yu. Kukushkin, A. J. L. Pombeiro, *Dalton Trans.* **2003**, 2540–2543; d) M. L. Kuznetsov, V. Yu. Kukushkin, M. Haukka, A. J. L.

Pombeiro, *Inorg. Chim. Acta* **2003**, *356*, 85–94 (special volume dedicated to J. J. R. Fraústo da Silva).
[19] N. A. Bokach, A. V. Khripoun, V. Yu. Kukushkin, M. Haukka, A. J. L. Pombeiro, *Inorg. Chem.* **2003**, *42*, 896–903.
[20] V. Yu. Kukushkin, A. J. L. Pombeiro, *Chem. Rev.* **2002**, *102*, 1771–1802 and references cited therein.
[21] A. J. L. Pombeiro, V. Yu. Kukushkin, in *Comprehensive Coordination Chemistry*, 2nd Edition, Elsevier, **2003**, vol. 1, pp. 639–660.
[22] M. L. Kuznetsov, V. Yu. Kukushkin, A. I. Dement'ev, A. J. L. Pombeiro, *J. Phys. Chem. A* **2003**, *107*, 6108–6120.
[23] Ch. Grundmann, J. M. Dean, *J. Org. Chem.* **1965**, *30*, 2809–2812.
[24] a) G. K. Anderson, M. Lin, *Inorg. Synth*. **1990**, *28*, 60–63; b) F. L. Wimmer, S. Wimmer, P. Castan, R. J. Puddephatt, *Inorg. Synth*. **1992**, *29*, 185–187; c) I. E. Bekk, E. V. Gusevskaya, V. A. Likholobov, Yu. I. Ermakov, *React. Kinet. Catal. Lett.***1987**, *33*, 209–214; d) M. A. Andrews, T. C. T. Chang, C. W. F. Cheng, T. J. Emge, K. P. Kelly, T. F. Koetzle, *J. Am. Chem. Soc.* **1984**, *106*, 5913–5920; e) B. B. Wayland, R. F. Schramm, *Inorg. Chem.* **1969**, *8*, 971–976; f) M. E. S. Doria, E. M. P. R. Branco, M. F. C. Guedes da Silva, A. J. L. Pombeiro, R. A. Michelin, R. Bertani, M. Mozzon, *Portugal. Electrochim. Acta* **1995**, *13*, 325–328.
[25] S. Kanemasa, S. Kobayashi, *Bull. Chem. Soc. Jpn*. **1993**, *66*, 2685–2693.
[26] S. Kanemasa, S. Kobayashi, M. Nishiuchi, H. Yamamoto, E. Wada, *Tetrahedron Lett.* **1991**, *32*, 6367–6370.
[27] S. Kanemasa, M. Nishiuchi, E. Wada, *Tetrahedron Lett.* **1992**, *33*, 1357–1360.
[28] H. R. Kim, J. H. Song, S. Y. Rhie, E. K. Ryu, *Synth. Commun.* **1995**, *25*, 1801–1807.
[29] A. Kamimura, Y. Kaneko, A. Ohta, K. Matsuura, Y. Fujimoto, A. Kakehi, S. Kanemasa, *Tetrahedron* **2002**, *58*, 9613–9620.
[30] P. Perez, L. R. Domingo, M. J. Aurel, R. Contreras, *Tetrahedron* **2003**, *59*, 3117–3125.
[31] a) L. Prasad, Y. Le Page, F. E. Smith, *Acta Crystallogr., Sect. B* **1982**, *38*, 2890–2893; b) B. J. Childs, D. C. Craig, M. L. Scudder, H. A. Goodwin, *Aust. J. Chem*. **1999**, *52*, 673–680.
[32] a) L. Golic, I. Leban, B. Stanovnik, M. Tisler, *Acta Crystallogr., Sect B* **1979**, *35*, 2256–2258; b) A. Albinati, S. Bruckner, *Acta Crystallogr., Sect B* **1978**, *34*, 3390–3392; c) J. B. Press, N. H. Eudy, F. M. Lovell, G. O. Morton, M. M. Siegel, *J. Am. Chem. Soc.* **1982**, *104*, 4013–4014.
[33] a) K. Horvath, D. Korbonits, G. Naray-Szabo, K. Simon, *J. Mol. Struct.* **1986**, *136*, 215–227; b) L. Eberson, J. L. Calvert, M. P. Harishom, W. T. Robinson, *Acta Chem. Scand.* **1994**, *48*, 347–355; c) R. Baker, G. A. Showell, L. J. Street, J. Saunders, K. Hoogsteen, S. B. Freedman, R. Hargreaves, *J.Chem. Soc., Chem. Commun.* **1992**, 817–819.
[34] a) H. Batista, G. B.Carpenter, R. M. Srivastava, *J. Chem. Cryst*. **2000**, *30*, 131–134; b) S. A. Hewlins, J. A. Murphy, J. Lin, D. E. Hibbs, M. B. Hursthouse, *J. Chem. Soc., Perkin Trans. 1* **1997**, 1559–1570.
[35] a) I. P. Smoliakova, K. J. Keuseman, D. C. Haagenson, D. M. Wellmann, P. B. Colligan, N. A. Kataeva, A. V. Churakov, L. G. Kuz'mina, V. V. Dunina, *J. Organomet. Chem.* **2000**, *603*, 86–97; b) M. Mitewa, T. Todorov, G. Gencheva, O. Angelova, T. N. Bakalova *J. Coord. Chem.* **2002**, *55*, 1367–1372; c) K. Kurdziel, T. Glowiak, *J. Coord. Chem.* **2002**, *55*, 327–334; d) N. Bharti, Shailendra; S. J. Coles, M. B. Hursthouse, T. A. Mayer, M. T. G. Garza, D. E. Cruz-Vega, B. D. Mata-Cardenas, F. Naqvi, M. R. Maurya, A. Azam, *Helv. Chim. Acta* **2002**, *85*, 2704–2712; e) H. Oshio, A. Ohto, T. Ito, *Chem. Commun.* **1996**,1541–1542.
[36] S. Zen, T. Nishino, K. Harada, H. Nakamura, Y. Iitaka, *Chem. Pharm. Bull.* **1983**, *31*, 4181–4184.
[37] P. S. Jarrett, O. M. Ni Dhubhghaill, P. J. Sadler, *J. Chem. Soc., Dalton Trans.* **1993**, 1863–1870.
[38] a) F. Himo, Z. P. Demko, L. Noodleman, K. B. Sharpless, *J. Am. Chem. Soc.* **2003**, *125*, 9983–9987; b) F. Himo, Z. P. Demko, L. Noodleman, K. B. Sharpless, *J. Am. Chem. Soc.* **2002**, *124*, 12 210–12 216; c) Z. P. Demko, K. B. Sharpless, *Angew. Chem. Int. Ed.* **2002**, *41*, 2113–2116; d) Z. P. Demko, K. B. Sharpless, *Org. Lett.* **2001**, *3*, 4091–4094; e) Z. P. Demko, K. B. Sharpless, *J. Org. Chem.* **2001**, *66*, 7945–7950; f) K. V. Gothelf, K. A. Jørgensen, *Chem. Commun.* **2000**, 1449–1458; g) K. V. Gothelf, K. B. Jensen, K. A. Jørgensen, *Sci. Prog.* **1999**, *82*, 327–350; h) K. V. Gothelf, K. A. Jørgensen, *Chem. Rev.* **1998**, *98*, 863–909; i) S. Kobayashi, K. A. Jørgensen, *Cycloaddition Reactions in Organic Synthesis*, Wiley-VCH, Weinheim, Germany, **2002**.
[39] Z. Otwinowski, W. Minor, *Processing of X-ray Diffraction Data Collected in Oscillation Mode*, in *Methods in Enzymology*, vol. 276, Macromolecular Crystallography, part A (Eds.: C. W. Carter, Jr., R. M. Sweet), Academic Press, New York, **1997**, pp. 307–326.
[40] A. Altomare, M. C. Burla, M. Camalli, G. L. Cascarano, C. Giacovazzo, A. Guagliardi, A. G. G. Moliterni, G. Polidori, R. Spagna, *J. Appl. Crystallogr.* **1999**, *32*, 115–119.
[41] G. M. Sheldrick, *SHELXS-97*; University of Göttingen, Germany, **1997**.
[42] P. T. Beurskens, G. Beurskens, R. de Gelder, S. Garcia-Granda, R. O. Gould, R. Israel, J. M. M. Smits, *The DIRDIF-99 program system*, Crystallography Laboratory, University of Nijmegen, The Netherlands, **1999**.
[43] L. J. Farrugia, *J. Appl. Crystallogr.* **1999**, *32*, 837–838.
[44] G. M. Sheldrick, *SHELXTL v. 6.12*, Bruker Analytical X-ray Systems, Bruker AXS, Inc. Madison, Wisconsin, USA, **2002**.

Received July 3, 2004

 © 2005 Wiley-VCH Verlag GmbH & Co. KGaA, Weinheim

Open-Framework Polar Compounds: Synthesis and Characterization of Rare-Earth Polyoxometalates $(C_6NO_2H_5)_2[Ln(H_2O)_5(CrMo_6H_6O_{24})]\cdot 0.5H_2O$ (Ln = Ce and La)

Haiyan An,[a] Dongrong Xiao,[a] Enbo Wang,*[a] Yangguang Li,[a] Xinlong Wang,[a] and Lin Xu[a]

Keywords: Rare earth / Polyoxometalates / Open framework / Polar compounds / Magnetic properties

Two unprecedented open-framework polar compounds $(C_6NO_2H_5)_2[Ln(H_2O)_5(CrMo_6H_6O_{24})]\cdot 0.5H_2O$ [Ln = Ce (**1**), La (**2**); $C_6NO_2H_5$ = pyridine-3-carboxylic acid], constructed from Anderson-type polyoxo anions and rare-earth cations, have been synthesized for the first time and characterized by elemental analysis, IR and Raman spectroscopy, TG analysis, and single-crystal X-ray diffraction. Both compounds crystallize in the polar space group $Pmn2_1$ and are made up of $[CrMo_6H_6O_{24}]^{3-}$ polyoxo anions linked by rare-earth cations to form a fascinating 3D open framework with "guest" pyridine-3-carboxylic acid molecules and free water molecules residing in the channels. To the best of our knowledge, this represents the first example of an open-framework polar compound constructed from rare-earth polyoxometalates. The magnetic properties of compound **1** have been studied by measuring its magnetic susceptibility in the temperature range 2.0–300.0 K, indicating the existence of antiferromagnetic interactions.
(© Wiley-VCH Verlag GmbH & Co. KGaA, 69451 Weinheim, Germany, 2005)

Introduction

Interest in porous polar inorganicmaterials has increased in recent times, because the potential applications of these materials range from telecommunication, optical storage, and information processing to selective separation and catalysis.[1] Although many covalent three-dimensional inorganic frameworks have been reported, few of them possess polarity.[2] Thus, the designed construction of porous polar inorganic frameworks is one of the most challenging issues in current synthetic chemistry. While the literature abounds in reports of the synthesis and characterization of aluminosilicates and aluminophosphates with polar and porous architectures,[3,4] recently porous polar compounds were extended to systems containing transition-metal oxides because of their particular properties inaccessible in main group systems.[3]

Polyoxometalates (POMs),[7,8] as anionic early transition metal oxide clusters, have been employed as inorganic building blocks for the construction of larger clusters, or one-, two-, and even three-dimensional (3D) extended solid frameworks, owing to their fascinating properties and potential applications in different areas such as catalysis, material science, and biological chemistry. In recent years, several large nanostructured polyoxometalate clusters have been reported by Müller et al.,[9] Pope et al.,[10] and Yamase et al.;[11] a number of 1D and 2D POM-based polymers have also been successfully synthesized by Zubieta et al.[12] and Pope et al.[13] In contrast, the method of assembling POMs into three-dimensional frameworks, especially open frameworks, is still in its infancy, and has been limited to using the 3d-block elements or their coordination complexes as linkers.[14,15] Although rare-earth elements are highly oxophilic and polyoxometalates have oxygen-rich compositions,[16] 3D covalent open frameworks containing both of them remain largely unexplored. In addition, special spectroscopic and magnetic properties of lanthanide ions and their compounds have inspired our research interest.[11,13,17,18]

Hence, our synthetic strategy starts by finding an appropriate POM building block, and then utilizes rare-earth cations as the linker and organic molecules as the template in an attempt to assemble them into a 3D polar network. More recently, we and others, have prepared a few extended structures based on Anderson-type polyoxo anions, ranging from 1D chains to 2D networks.[19,20] The activity of the terminal oxygen atoms on the surface of this kind of POM makes it possible to form 3D covalent structures under an appropriate reaction condition. Furthermore, the employment of low-symmetry organic molecules or complexes as structure-directing agents is promising for the synthesis of new open-framework polar compounds.[4] In this experi-

[a] Institute of Polyoxometalate Chemistry, Department of Chemistry, Northeast Normal University,
Changchun, 130024, P. R. China
Fax: +86-431-568-4009
E-mail: wangenbo@public.cc.jl.cn
Supporting information for this article is available on the WWW under http://www.eurjic.org or from the author.

 © 2005 Wiley-VCH Verlag GmbH & Co. KGaA, Weinheim **DOI: 10.1002/ejic.200400696**

ment, we chose the acentric pyridine-3-carboxylic acid molecule as the structure-directing agent instead of the widely utilized organic amines, owing to the requirement for acid reaction conditions. With the pyridine-3-carboxylic acid molecule, we have successfully obtained two unprecedented POM-based compounds possessing polarity and open framework characteristics. Herein, the rational synthesis of the two complexes $(C_6NO_2H_5)_2[Ln(H_2O)_5(CrMo_6H_6O_{24})]\cdot 0.5H_2O$ [Ln = Ce (**1**), La (**2**)] by this route and magnetic properties of compound **1** are described. It is notable that the 3D polar framework consists of two intersecting channels, within which pyridine-3-carboxylic acid molecules and free water molecules are situated.

Results and Discussion

The single-crystal X-ray diffraction analyses reveal that both compounds **1** and **2** (Tables 1 and 2) are isostructural and crystallize in the polar space group $Pmn2_1$, therefore we only discussed the structure of **1** herein. The structure of **1** is a unique 3D open framework constructed from $[Cr(OH)_6Mo_6O_{18}]^{3-}$ building blocks and Ce^{3+} cations, with pyridine-3-carboxylic acid molecules and lattice water molecules residing in the channels. The $[Cr(OH)_6Mo_6O_{18}]^{3-}$ cluster is a B-type Anderson structure made up of seven edge-sharing octahedra, six of which are $\{MoO_6\}$ octahedra, arranged hexagonally around the central $\{Cr(OH)_6\}$ octahedron. Four kinds of oxygen atoms exist in the cluster according to the manner of oxygen coordination: the terminal oxygen atom Ot, the terminal oxygen atom Ot′ linked to Ce^{3+}, the double-bridging oxygen atom Ob, and the central oxygen atom Oc. Thus, the Mo–O distances can be grouped into four sets: Mo–Ot 1.683(11)–1.732(11) Å, Mo–Ot′ 1.727(10)–1.732(9) Å, Mo–Ob 1.909(6)–1.958(9) Å, and Mo–Oc 2.254(7)–2.312(8) Å. The central Cr–Oc distances vary from 1.951(11) to 1.980(11) Å. The bond angles of O–Cr–O range from 83.5(3) to 98.1(3)°.

The asymmetric unit (Figure 1) in the structure of **1** consists of two crystallographically independent one-half Anderson anions, in which both chromium ions [Cr(1) and Cr(2)] occupy special positions, linked by the cerium cation. Crystallographically unique cerium(III), residing in a distorted bicapped square-antiprismatic coordination environment, is defined by four terminal oxygen atoms from four $[Cr(OH)_6Mo_6O_{18}]^{3-}$ units [average Ce–O 2.491(9) Å] and six water molecules [average Ce–OH_2 2.626(13) Å]. The average Ce–O bond length is 2.572(11) Å.

In the structure each Anderson anion acts as a quadridentate ligand coordinating to four cerium cations through the terminal oxygen atoms of four $\{MoO_6\}$ octahedra. As shown in Figure 2, firstly these $[Cr(OH)_6Mo_6O_{18}]^{3-}$ clusters are linked by some Ce^{3+} cations to form 1D linear chains, then each chain is connected to two other parallel chains through other Ce^{3+} cations to yield a window-like 2D layer in the *ac* plane. The 2D layer structure built up of polyoxo anions and rare-earth ions is rare. These 2D sheets are further pillared by the $[Cr(OH)_6Mo_6O_{18}]^{3-}$ subunits to form a 3D open framework. It is notable that this kind of connection mode results in the formation of two intersecting channels, which are occupied by the dissociated pyridine-3-carboxylic acid molecules (see Figure 3) and lattice water molecules. The dimensions of the two channels are about 10.0×8.5 Å along the *a* axis (shown in Figure 4) and 10.7×6.2 Å along the *b* axis, respectively (see Figure 5). It is also striking that the structure of compound **1** exhibits extensive hydrogen-bonding interactions among water molecules, pyridine-3-carboxylic acid molecules, and polyoxo anions. The typical hydrogen bonds are O37···O2 2.784, O36···O16 2.641, O37···OW3 2.922, O9···C5 3.119, and O6···C23 2.682 Å (shown in Table S1). It is believed that the extensive hydrogen-bonding interactions between guest molecules and the framework play an important role in stabilizing the 3D structure. Worth mentioning here is that the observed polarity of **1**, indicated by its polar space group $Pmn2_1$, can be partially understood in terms of the molecular recognition between the host framework and guest molecule template through hydrogen bonds.[21,22]

The bond valence sum calculations indicate that the Cr site is in the +3 oxidation state, Ce and La sites are in the +3 oxidation state, and all Mo sites are in the +6 oxidation state.[23]

Table 1. Selected bond lengths [Å] and angles [°] for **1**; symmetry transformations used to generate equivalent atoms: #1: *–x* + 1, *–y*, *–z* + 2; #2: *–x* + 2, *–y*, *–z* + 1

Ce(1)–OW4	2.468(19)	Mo(2)–O(11)	1.705(9)
Ce(1)–O(10)#1	2.471(9)	Mo(2)–O(12)	1.732(11)
Ce(1)–O(14)	2.476(9)	Mo(2)–O(6)	1.912(8)
Ce(1)–O(23)	2.502(9)	Mo(2)–O(7)	1.958(9)
Ce(1)–O(28)#2	2.515(9)	Mo(2)–O(2)	2.291(9)
Ce(1)–OW1	2.520(12)	Mo(2)–O(3)	2.301(8)
Ce(1)–OW3	2.523(12)	Mo(3)–O(13)	1.694(10)
Ce(1)–OW2	2.527(13)	Mo(3)–O(14)	1.729(10)
Ce(1)–OW5	2.83(2)	Mo(3)–O(8)	1.909(6)
Ce(1)–OW6	2.888(19)	Mo(3)–O(7)	1.919(8)
Mo(1)–O(9)	1.700(10)	Mo(3)–O(4)	2.254(7)
Mo(1)–O(10)	1.732(9)	Mo(3)–O(3)	2.286(9)
Mo(1)–O(6)	1.916(8)	Cr(1)–O(4)	1.951(11)
Mo(1)–O(5)	1.943(6)	Cr(1)–O(2)	1.960(9)
Mo(1)–O(1)	2.262(7)	Cr(1)–O(1)	1.959(11)
Mo(1)–O(2)	2.301(8)	Cr(1)–O(3)	1.966(8)
O(14)–Ce(1)–O(23)	77.0(3)	OW1–Ce(1)–OW3	75.4(5)
O(14)–Ce(1)–OW3	136.8(4)	OW2–Ce(1)–OW6	58.9(5)
O(14)–Ce(1)–OW5	65.8(5)	OW4–Ce(1)–OW2	139.2(5)
O(14)–Ce(1)–O(28)#2	75.7(3)	OW5–Ce(1)–OW6	175.9(7)
O(14)–Ce(1)–OW1	68.9(4)	O(4)–Cr(1)–O(2)	94.4(3)
O(14)–Ce(1)–OW2	76.7(4)	O(1)–Cr(1)–O(3)	98.1(3)
O(14)–Ce(1)–OW6	118.3(5)	O(9)–Mo(1)–O(10)	106.6(5)
O(23)–Ce(1)–OW3	145.7(4)	O(6)–Mo(1)–O(1)	82.9(3)
O(23)–Ce(1)–OW2	69.3(3)	O(5)–Mo(1)–O(2)	84.0(4)
O(23)–Ce(1)–OW6	117.4(4)	O(11)–Mo(2)–O(12)	106.2(5)
O(10)#1–Ce(1)–OW6	65.8(5)	O(6)–Mo(2)–O(7)	148.1(3)
O(10)#1–Ce(1)–O(23)	71.3(3)	O(2)–Mo(2)–O(3)	70.1(3)
OW1–Ce(1)–OW6	60.3(5)	O(13)–Mo(3)–O(14)	104.9(5)
OW1–Ce(1)–OW2	75.0(4)	O(8)–Mo(3)–O(7)	149.6(4)
OW1–Ce(1)–OW5	122.5(5)	O(4)–Mo(3)–O(3)	70.1(3)

 © 2005 Wiley-VCH Verlag GmbH & Co. KGaA, Weinheim

Table 2. Selected bond lengths [Å] and angles [°] for **2**; symmetry transformations used to generate equivalent atoms: #1: $-x + 1/2$, $-y + 3$, $z - 1/2$; #2: x, $y + 1$, z

La(1)–O(23)#1	2.470(12)	Mo(1)–O(10)	1.715(12)
La(1)–OW4	2.47(2)	Mo(1)–O(5)	1.919(8)
La(1)–O(28)	2.488(12)	Mo(1)–O(6)	1.932(10)
La(1)–OW1	2.531(15)	Mo(1)–O(1)	2.281(9)
La(1)–O(14)	2.530(11)	Mo(1)–O(2)	2.335(11)
La(1)–O(10)#2	2.535(11)	Mo(2)–O(12)	1.667(12)
La(1)–OW3	2.581(14)	Mo(2)–O(11)	1.705(12)
La(1)–OW2	2.622(15)	Mo(2)–O(7)	1.936(12)
La(1)–OW5	2.85(2)	Mo(2)–O(6)	1.945(12)
La(1)–OW6	2.90(3)	Mo(2)–O(2)	2.256(11)
Mo(1)–O(9)	1.689(15)	Mo(2)–O(3)	2.309(11)
Mo(3)–O(13)	1.701(13)	Cr(1)–O(3)	1.961(10)
Mo(3)–O(3)	2.277(12)	Cr(1)–O(1)	1.978(15)
Mo(3)–O(7)	1.906(10)	Cr(1)–O(4)	1.979(15)
Mo(3)–O(8)	1.932(7)	Cr(1)–O(2)	1.978(10)

O(23)#1–La(1)–O(28)	143.8(4)	OW2–La(1)–OW6	57.2(7)
O(23)#1–La(1)–O(10)#2	76.8(4)	OW1–La(1)–OW3	74.5(5)
O(23)#1–La(1)–OW3	76.3(5)	O(9)–Mo(1)–O(10)	105.8(7)
O(23)#1–La(1)–OW2	137.8(5)	O(5)–Mo(1)–O(6)	150.9(6)
O(23)#1–La(1)–OW6	119.0(8)	O(1)–Mo(1)–O(2)	71.4(4)
O(23)#1–La(1)–OW4	119.6(7)	O(11)–Mo(2)–O(6)	99.4(6)
O(23)#1–La(1)–OW5	64.0(7)	O(7)–Mo(2)–O(2)	83.2(4)
O(14)–La(1)–OW3	142.5(5)	O(12)–Mo(2)–O(3)	93.4(5)
O(14)–La(1)–O(10)#2	125.7(4)	O(13)–Mo(3)–O(7)	98.9(6)
O(14)–La(1)–OW5	62.1(5)	O(14)–Mo(3)–O(7)	102.5(5)
O(14)–La(1)–OW6	116.6(6)	O(14)–Mo(3)–O(4)	158.3(6)
OW3–La(1)–OW6	59.4(6)	O(3)–Cr(1)–O(1)	95.8(5)
O(28)–La(1)–OW5	112.7(7)	O(4)–Cr(1)–O(2)	94.8(4)

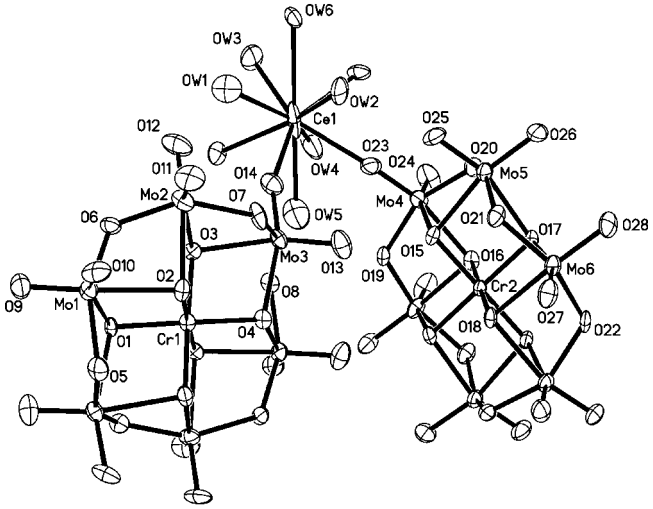

Figure 1. ORTEP drawing of compound **1** with thermal ellipsoids at 50% probability; organic molecules and partial water molecules are omitted for clarity

In the IR spectrum of compound **1**, the features at 3368, 2094, 1635, 1558, 1401, 1374, 1357, and 1304 cm^{-1} can be regarded as characteristic of the pyridine-3-carboxylic acid molecule. The peaks at 946, 909, 879, 759, 649, 578, and 412 cm^{-1} are attributed to ν(Mo–Ot), ν(Mo–Ob), and ν(Mo–Oc) of the $[Cr(OH)_6Mo_6O_{18}]^{3-}$ polyoxo anion. The IR spectrum of compound **2** is similar to that of **1** (see Figures S3a and S3b in the Supporting information). In the

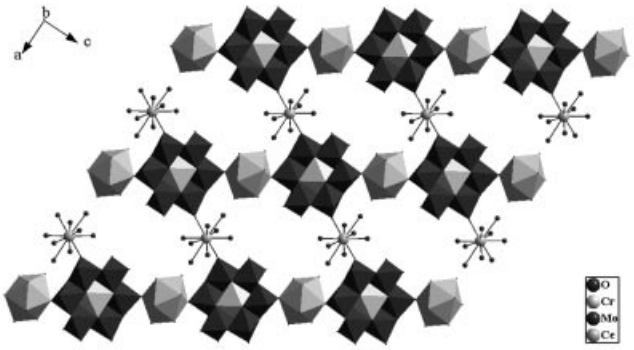

Figure 2. Polyhedral view of the 2D network in **1**

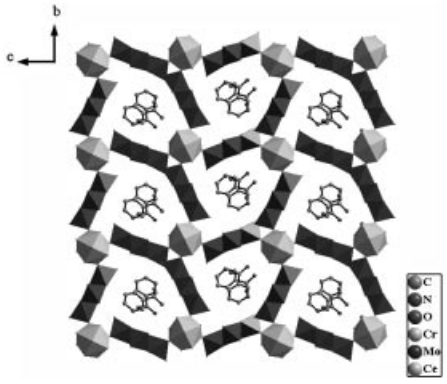

Figure 3. Polyhedral view of the 3D open framework of **1** viewing along the *a* axis, containing pyridine-3-carboxylic acid molecules in the channels

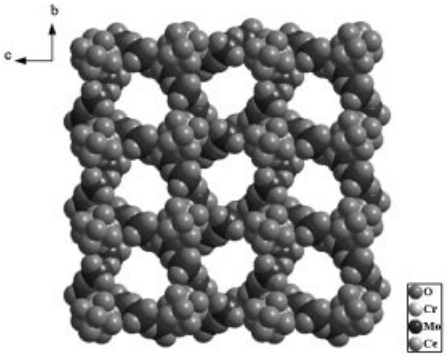

Figure 4. Space-filling diagram of the 3D open framework of **1** along the *a* axis, showing the 1D channels

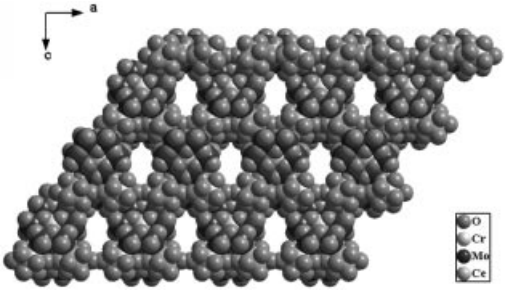

Figure 5. Space-filling diagram of the 3D porous structure of **1** along the *b* axis, representing the 1D channels

 © 2005 Wiley-VCH Verlag GmbH & Co. KGaA, Weinheim

Raman spectrum of compound **1**, the bands at 993, 942, 821, 713, 449, 337, and 286 cm^{-1} are ascribed to the $[Cr(OH)_6Mo_6O_{18}]^{3-}$ polyoxo anion. In the Raman spectrum of compound **2**, the features at 993, 929, 908, 850, 823, 550, 333, and 250 cm^{-1} are also attributed to the $[Cr(OH)_6Mo_6O_{18}]^{3-}$ polyoxo anion (shown in Figure S4).

The thermal gravimetric (TG) curve of **1** is shown in Figure S5a. The TG curve gives a total weight loss of 27.24% in the range of 45–750 °C, which agrees with the calculated value of 26.55%. The weight loss of 10.60% at 45–300 °C corresponds to the loss of all noncoordinated and coordinated water molecules (calcd. 10.18%). The weight loss of 16.64% at 340–575 °C arises from the decomposition of organic molecules (calcd. 16.37%). The TG curve of compound **2** exhibits similar weight loss stages to those of compound **1** (see Figure S5b). The whole weight loss (27.16%) is in agreement with the calculated value (26.57%).

Magnetic Properties of Compound 1

The structure of $[Cr(OH)_6Mo_6O_{18}]^{3-}$ clusters bridged by Ce^{3+} cations in compound **1** allows us to predict the existence of magnetic exchange coupling. The thermal variations of $\chi_m T$ and $1/\chi$ of **1** are displayed in Figure 6. The value of $\chi_m T$ continuously decreases as the temperature is lowered from 300.0 to 2.0 K, indicating the presence of an antiferromagnetic interaction. At 300 K, the $\chi_m T$ value is ca. 2.87 emu K mol^{-1} (4.79 μ_B), slightly higher than the total value (2.25 emu K mol^{-1}, 4.24 μ_B) of one uncoupled S = 3/2 spin of the Cr^{3+} atom and one uncoupled S = 1/2 spin of the Ce^{3+} atom. The magnetic susceptibility obeys the Curie–Weiss law in the whole range of 2.0–300.0 K with C = 2.81 emu K mol^{-1}, and θ = –5.79 K, characteristic of an overall antiferromagnetic interaction. It is too difficult to fit the experimental magnetic data of this complex system using a suitable theoretical model, and further studies on magnetic properties of similar systems are ongoing in our laboratory.

Conclusions

In conclusion, we have synthesized the only structurally characterized rare-earth POM complexes featuring an open framework and polarity reported until now, by choosing a suitable POM building block, organic template, and suitable reaction conditions. The success in synthesizing both compounds provides not only innovative examples of open-framework polar compounds, but also a new strategy for the design of polar inorganic materials with channels based on POMs. In contrast to the famous aluminosilicates and metal phosphates with porous polar frameworks, this new type of POM-based polar compound represents another important branch in the field of polarity and open-framework perspectives in the study of these materials. The magnetic properties of **1** have been studied and its antiferromagnetic behavior results from the transformation of O–Mo–O units.

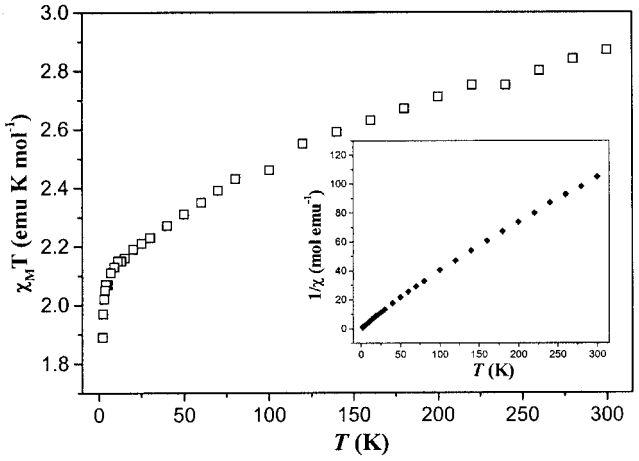

Figure 6. The temperature dependence of reciprocal magnetic susceptibility χ_M^{-1} (diamonds; inset) and the product $\chi_M T$ (squares) for compound **1**

Experimental Section

Materials and General Methods: All chemicals were commercially purchased and used without further purification. $Na_3[CrMo_6H_6O_{24}]\cdot 8H_2O$ was synthesized according to the literature,[24] and characterized by IR spectra and TG analyses. Elemental analyses (C, H, and N) were performed with a Perkin–Elmer 2400 CHN elemental analyzer; Cr, Mo, Ce, and La were analyzed with a PLASMA-SPEC(I) ICP atomic emission spectrometer. IR spectra were recorded in the range 400–4000 cm^{-1} with an Alpha Centaurt FT/IR spectrophotometer using KBr pellets. TG analyses were performed with a Perkin–Elmer TGA7 instrument in flowing N_2 with a heating rate of 10 °C min^{-1}. The Raman spectrum was recorded at ambient temperature with a Spex 1403 Raman spectrometer with an argon ion laser at an excitation wavelength of 514.5 nm. Variable-temperature magnetic susceptibility data were obtained with a SQUID magnetometer (Quantum Design, MPMS-7) in the temperature range of 2.0–300.0 K with an applied field of 10 kG.

Synthesis of 1: In a typical synthesis procedure for **1**, first pyridine-3-carboxylic acid (0.0616 g, 0.5 mmol) and then $Ce(NO_3)_3\cdot 6H_2O$ (0.2171 g, 0.5 mmol) were dissolved in hot water (10 mL). Then an aqueous solution (10 mL) of $Na_3[CrMo_6H_6O_{24}]\cdot 8H_2O$ (0.6155 g, 0.5 mmol) was added to the above solution. The initial pH value of this mixture was 3.00. The mixture was then refluxed at 80 °C for 1 h. The filtrate was kept under ambient conditions for 2 weeks, then yellow block crystals of compound **1** were isolated in about 45% yield (0.338 g, based on Ce). $C_{12}H_{27}CeCrMo_6N_2O_{33.50}$: calcd. C 9.58, Ce 9.32, Cr 3.46, Mo 38.30, N 1.86; found C 9.33, Ce 9.50, Cr 3.23, Mo 36.61, N 1.95. FT IR: $\tilde{\nu}$ = 3368 (s), 2094 (w), 1635 (m), 1558 (m), 1461 (w), 1401 (m), 1374 (m), 1357 (m), 1304 (w), 1109 (w), 946 (s), 909 (vs), 879 (s), 838 (w), 759 (m), 690 (w), 649 (vs), 618 (w), 578 (w), 541 (w), 412 (m) cm^{-1}.

Synthesis of 2: The preparation of **2** was similar to that of **1** except that $La(NO_3)_3\cdot 6H_2O$ was used instead of $Ce(NO_3)_3\cdot 6H_2O$ (0.375 g, yield 50%). $C_{12}H_{27}CrLaMo_6N_2O_{33.50}$: calcd. C 9.59, Cr 3.46, La 9.25, Mo 38.33, N 1.86; found C 9.71, Cr 3.20, La 9.62, Mo 36.55, N 1.68. FT IR: $\tilde{\nu}$ = 3367 (s), 1633 (m), 1563 (m), 1464 (w), 1393 (m), 1303 (w), 1182 (w), 1108 (w), 946 (s), 909 (vs), 887 (s), 838 (w), 760 (m), 649 (vs), 581 (w), 411 (m) cm^{-1}.

 © 2005 Wiley-VCH Verlag GmbH & Co. KGaA, Weinheim

Table 3. Crystal data and structure refinement for **1** and **2**

Complex	**1**	**2**
Empirical formula	$C_{12}H_{27}CeCrMo_6N_2O_{33.50}$	$C_{12}H_{27}LaCrMo_6N_2O_{33.50}$
Formula mass	1503.12	1501.91
T [K]	293(2)	293(2)
λ [Å]	0.71073	0.71073
Space group	$Pmn2_1$	$Pmn2_1$
a [Å]	15.0314(9)	15.080(3)
b [Å]	11.6090(7)	11.630(2)
c [Å]	23.0481(14)	23.096(5)
V [Å^3]	4021.9(4)	4050.6(14)
Z	4	4
$D_{calcd.}$ [g cm^3]	2.482	2.463
μ [mm^{-1}]	3.278	3.186
R_1[a] [$I > 2\sigma(I)$]	0.0511	0.0637
wR_2[b] [$I > 2\sigma(I)$]	0.1360	0.1535

[a] $R_1 = \Sigma||F_o| - |F_c||/\Sigma|F_o|$. [b] $wR_2 = \Sigma[w(F_o^2 - F_c^2)^2]/\Sigma[w(F_o^2)^2]^{1/2}$.

X-ray Crystallography: Suitable single crystals with dimensions of $0.26 \times 0.13 \times 0.05$ mm for **1** and $0.32 \times 0.28 \times 0.03$ mm for **2** were selected for single-crystal X-ray diffraction analysis. Data were collected with a Bruker Smart Apex CCD diffractometer with Mo-K_α (λ = 0.71073 Å) at 293 K using the ω-scan technique. Empirical absorption correction was applied. Systematic absences and the statistics of intensity distribution resulted in the space group $Pmn2_1$. The structures of **1** and **2** were solved by the direct method and refined by the full-matrix least squares on F^2 using the SHELXTL-97 software.[25] All of the non-hydrogen atoms were refined anisotropically except for C22 and O37 in **1** and O4, O18, O19, and O36 in **2**. In **1**, positions of the hydrogen atoms attached to polyanions and to coordinated water molecules except for OW4 were located from difference maps, and those attached to carbon atoms were fixed in ideal positions; the hydrogen atoms attached to OW4, free OW7, and to oxygen atoms of carboxyl groups were not located. In **2**, positions of the hydrogen atoms attached to carbon atoms were fixed in ideal positions and other hydrogen atoms are not located. A summary of the crystallographic data and structural determination for **1** and **2** is provided in Table 3. Selected bond lengths and angles of **1** and **2** are listed in Tables 1 and 2, respectively. CCDC-245443 and -245641 contain the supplementary crystallographic data for this paper. These data can be obtained free of charge from The Cambridge Crystallographic Data Centre via www.ccdc.cam.ac.uk/data_request/cif.

Acknowledgments

The authors thank the National Natural Science Foundation of China (20371011) for financial support.

[1] M. E. Davis, *Nature* **2002**, *417*, 813–821.
[2] a) M. L. Tong, S. L. Zheng, X. M. Chen, *Chem. Commun.* **1999**, 561–562; b) J. Tao, M. L. Tong, X. M. Chen, *J. Chem. Soc., Dalton Trans.* **2000**, *20*, 3669–3674; c) X. L. Wang, C. Qin, E. B. Wang, Y. G. Li, C. W. Hu, L. Xu, *Chem. Commun.* **2004**, 378–379.
[3] a) M. E. Davis, *Acc. Chem. Res.* **1993**, *26*, 111–115; b) M. M. J. Treacy, J. M. Newsam, *Nature* **1988**, *332*, 249–251.
[4] a) K. Morgan, G. Gainsford, N. Milestone, *Chem. Commun.* **1995**, 425–426; b) W. T. A. Harrison, T. E. Gier, G. D. Stucky, R. W. Broach, R. A. Bedard, *Chem. Mater.* **1996**, *8*, 145–151; c) D. A. Bruce, A. P. Wilkinson, M. G. White, J. A. Bertrand, *Chem. Commun.* **1995**, 2059–2060.
[5] a) N. Ding, D. Y. Chung, M. G. Kanatzidis, *Chem. Commun.* **2004**, 1170–1171; b) T. A. Sullens, R. A. Jensen, T. Y. Shvareva, T. E. Albrecht-Schmitt, *J. Am. Chem. Soc.* **2004**, *126*, 2676–2677; c) Y. Wang, J. H. Yu, M. Guo, R. R. Xu, *Angew. Chem. Int. Ed.* **2003**, *42*, 4089–4092.
[6] H. S. Ra, K. M. Ok, P. S. Halasyamani, *J. Am. Chem. Soc.* **2003**, *125*, 7764–7765.
[7] a) M. T. Pope, *Heteropoly and Isopoly Oxometalates*, Springer, Berlin, **1983**; b) C. L. Hill, *Chem. Rev.* **1998**, *98*, 1–2.
[8] a) U. Kortz, S. S. Hamzeh, N. A. Nasser, *Chem. Eur. J.* **2003**, *9*, 2945–2952; b) U. Kortz, M. G. Savelieff, B. S. Bassil, B. Keita, L. Nadjo, *Inorg. Chem.* **2002**, *41*, 783–789; c) E. Coronado, J. R. Galán-Mascarós, C. Giménez-Saiz, C. J. Gómez-García, S. Triki, *J. Am. Chem. Soc.* **1998**, *120*, 4671–4681.
[9] a) A. Müller, S. Q. N. Shah, H. Bögge, M. Schmidtmann, *Nature* **1999**, *397*, 48–50; b) L. Cronin, C. Beugholt, E. Krickemeyer, M. Schmidtmann, H. Bögge, P. Kögerler, T. K. K. Luong, A. Müller, *Angew. Chem. Int. Ed.* **2002**, *41*, 2805–2808.
[10] K. Wassermann, M. H. Dickman, M. T. Pope, *Angew. Chem. Int. Ed. Engl.* **1997**, *36*, 1445–1448.
[11] K. Fukaya, T. Yamase, *Angew. Chem. Int. Ed.* **2003**, *42*, 654–658.
[12] P. J. Hagrman, D. Hagrman, J. Zubieta, *Angew. Chem. Int. Ed.* **1999**, *38*, 3165–3168.
[13] a) M. Sadakane, M. H. Dickman, M. T. Pope, *Angew. Chem. Int. Ed.* **2000**, *39*, 2914–2916; b) K. C. Kin, M. T. Pope, *J. Am. Chem. Soc.* **1999**, *121*, 8512–8517.
[14] a) M. I. Khan, E. Yohannes, D. Powell, *Chem. Commun.* **1999**, 23–24; b) M. I. Khan, E. Yohannes, R. J. Doedens, *Angew. Chem. Int. Ed.* **1999**, *38*, 1292–1294.
[15] a) B. Z. Lin, S. X. Liu, *Chem. Commun.* **2002**, 2126–2127; b) Y. G. Li, N. Hao, E. B. Wang, M. Yuan, C. W. Hu, N. H. Hu, H. Q. Jia, *Inorg. Chem.* **2003**, *42*, 2729–2735; c) M. Yuan, Y. G. Li, E. B. Wang, Y. Lu, C. W. Hu, N. H. Hu, H. Q. Jia, *J. Chem. Soc., Dalton Trans.* **2002**, 2916–2920.
[16] a) R. C. Howell, F. G. Perez, S. Jain, W. D. Horrocks, A. L. Rheingold, L. C. Francesconi, *Angew. Chem. Int. Ed.* **2001**, *40*, 4031–4033; b) C. D. Wu, C. Z. Lu, H. H. Zhuang, J. S. Huang, *J. Am. Chem. Soc.* **2002**, *124*, 3836–3837; c) M. R. Antonio, L. Soderholm, C. W. Williams, N. Ullah, L. C. Francesconi, *J. Chem. Soc., Dalton Trans.* **1999**, 3825–3830.
[17] X. L. Wang, Y. Q. Guo, Y. G. Li, E. B. Wang, C. W. Hu, N. H. Hu, *Inorg. Chem.* **2003**, *42*, 4135–4140.
[18] a) A. Dolbecq, P. Mialane, L. Lisnard, J. Marrot, F. Sécheresse, *Chem. Eur. J.* **2003**, *9*, 2914–2920; b) J. Y. Niu, M. L. Wei, J. P. Wang, D. B. Dang, *Eur. J. Inorg. Chem.* **2004**, 160–170.
[19] a) H. Y. An, Y. Lan, Y. G. Li, E. B. Wang, N. Hao, D. R. Xiao, L. Y. Duan, L. Xu, *Inorg. Chem. Commun.* **2004**, *7*, 356–358;

b) H. Y. An, Y. Q. Guo, Y. G. Li, E. B. Wang, J. Lü, L. Xu, C. W. Hu, *Inorg. Chem. Commun.* **2004**, *7*, 521–523.
[20] a) V. Shivaiah, P. V. N. Reddy, L. Cronin, S. K. Das, *J. Chem. Soc., Dalton Trans.* **2002**, 3781–3783; b) D. Drewes, E. M. Limanski, B. Krebs, *J. Chem. Soc., Dalton Trans.* **2004**, 2087–2091.
[21] S. P. D. Huang, R. G. Xiong, *Polyhedron* **1997**, *16*, 3929–3939.
[22] S. P. Anthony, T. P. Radhakrishnan, *Chem. Commun.* **2001**, 931–932.
[23] I. D. Brown, D. Altermatt, *Acta Crystallogr., Sect. B* **1985**, *41*, 244.
[24] A. Perloff, *Inorg Chem.* **1970**, *9*, 2228–2239.
[25] a) G. M. Sheldrick, *SHELXL-97*, *Program for Crystal Structure Refinement*, University of Göttingen, Germany, **1997**; b) G. M. Sheldrick, *SHELXL-97*, *Program for Crystal Structure Solution*, University of Göttingen, Germany, **1997**.

Received: August 13, 2004

 © 2005 Wiley-VCH Verlag GmbH & Co. KGaA, Weinheim

Structure of Nitrile-Functionalized Alkyltrifluoroborate Salts

Zhaofu Fei,[a] Dongbin Zhao,[a] Tilmann J. Geldbach,[a] Rosario Scopelliti,[a] and Paul J. Dyson*[a]

Keywords: Anions / Borates / Boron / X-ray structure / Crystal engineering

Two nitrile-functionalized alkyltriflouroborate anion based complexes $[(Ph_3P)_2N][CH_3CH(BF_3)CH_2CN]$ and $[K(18\text{-crown-6})][CH_3CH(BF_3)CH_2CN]$ were synthesized and characterized by spectroscopic methods and single X-ray diffraction analysis. In the former complex no direct cation-anion (F→N or F→P) interactions are observed although F···H–C hydrogen bonds are present. In the later complex all three fluorine atoms interact with the potassium cation and C–H···F hydrogen bonds are also present. The ESI-MS spectra in methanol solution of the potassium complex show similar anion-cation aggregation to that observed for ionic liquids, and comparisons between the two complexes and ionic liquid systems are made.

(© Wiley-VCH Verlag GmbH & Co. KGaA, 69451 Weinheim, Germany, 2005)

Introduction

Alkyltrifluoroborates are valuable substrates for Suzuki–Miyaura coupling reactions.[1,2] The relatively mild reaction conditions under which they react with arylhalides have made this synthetic approach a highly popular route for the generation of new C–C bonds in organic synthesis, see Scheme 1. Alkyltrifluoroborates are easily prepared on a moderate scale by the addition of KHF_2 to a variety of organoboron intermediates such as boronic acids and esters, organodihaloboranes and organodiaminoboranes, which makes them particularly attractive reagents.[1,2]

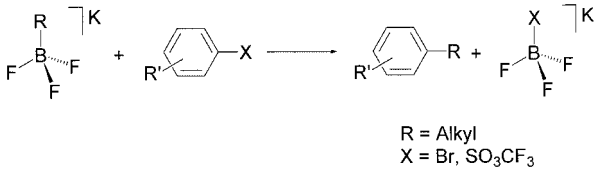

Scheme 1

Being structurally and electronically closely related to the BF_4^- anion they can be regarded as potential precursors for the formation of low-melting ionic liquids. The design and synthesis of functionalized ionic liquids is currently attracting a great deal of interest.[3,4,5] In these ionic liquid systems the emphasis lies in the modification of the cationic component, whereas the nature of the anion remains usually unchanged; typically BF_4^- and PF_6^- and to a lesser extent $SO_3CF_3^-$ and $N(SO_2CF_3)^-$ are employed. Recently, we reported on the synthesis of the first imidazolium-based ionic liquids with nitrile-functionalized alkylfluoroborate anions, see Scheme 2.[6] Even in the presence of functional groups on the imidazolium cation, these salts exhibit significantly lower melting points and viscosities relative to the well-established BF_4^- ionic liquids, an effect that has also been noted with the $CF_3BF_3^-$ anion.[7]

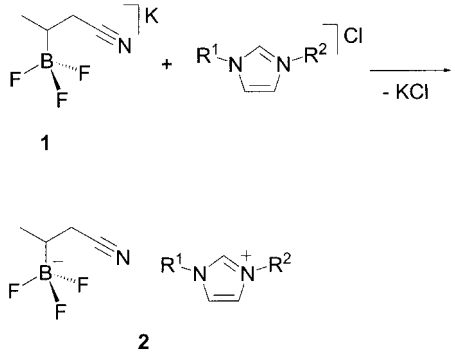

Scheme 2

Despite the fact that numerous alkyltrifluoroborate salts have been prepared over the years solid state structural studies of such compounds are extremely sparse. As far as we are aware, only three structures with a sp^3-carbon bound to a BF_3-fragment exist.[8] Apart from these, structures of BF_3-olefin,[9] -aryl,[10] -carbene[11] and -cyclopentadienyl[12] anions are also known.

Structural information of such alkylated trifluoroborates may help to estimate the physical properties of ionic liquids based on such anions. Thus far, efforts to gain insight into

[a] Ecole Polytechnique Fédérale de Lausanne, Institut des Sciences et Ingénierie Chimiques (EPFL),
1015 Lausanne, Switzerland
Fax: +41-21-693-98-85
E-mail: paul.dyson@epfl.ch

their structural characteristics have been made using IR and NMR techniques on imidazolium tetrafluoroborate systems,[13] partly because the imidazolium salts with the BF_4^- anion of most interest are liquid at room temperature, which has made it difficult to obtain crystals for X-ray studies. In this paper we present structural investigations on two novel compounds based on the alkylfluoroborate anion $CH_3CH(BF_3)CH_2CN^-$, which provide clues as to how it may interact with imidazolium cations in the liquid phase. This study also illustrates the utility of crown ethers as reagents to facilitate crystallization of anions with small metal counterions which are usually difficult to crystallize.

Results and Discussion

The potassium salt $K[CH_3CH(BF_3)CH_2CN]$, **1**, prepared as a racemic mixture using the literature protocol, crystallized as thin needles which proved unsuitable for single-crystal X-ray diffraction analysis (several attempts to give useful data failed).[6] However, exchange of the potassium cation for $[(Ph_3P)_2N]^+$ or complexation with 18-crown-6 affords compounds **3** and **4**, respectively, as crystalline products that are amenable to X-ray analysis, see Scheme 3.

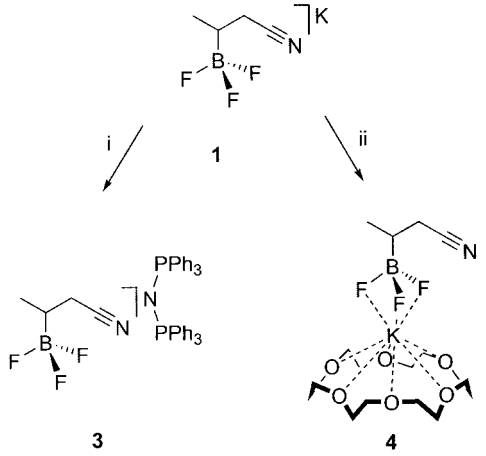

Scheme 3. Synthesis of compounds **3** and **4**; (i): $[N(PPh_3)_2]Cl$, CH_2Cl_2; (ii): 18-crown-6, THF

Both salts are obtained in essentially quantitative yield. In the case of **3**, the potassium chloride formed from the reaction was separated by filtration and the product obtained after removal of the solvent. This approach, viz. metathesis of a small cation for a large cation is a widely used method to facilitate crystallization of large anions and in some cases is referred to as crystal engineering.[14] For compound **4**, the product was easily obtained by mixing the potassium salt with stoichiometric amounts of 18-crown-6. This strategy essentially converts the small potassium cation into a larger entity by combining it with the crown moiety (rather than replacing it for another anion altogether), and it could prove to be an important way of generating good quality crystals as an alternative to the metathesis approach.

In this manner, the alkyltrifluoroborate anion is obtained either as the "free" anion or in the form of an ion-pair: In **3**, the charge on the cation $[(Ph_3P)_2N]^+$ is delocalized along the P–N–P unit while at the same time beingprotected by six phenyl groups, excluding direct cation-anion charge transfer, F→N or F→P. In contrast, in **4**, complexation by the 18-crown-6 macrocycle leaves the potassium cation accessible enough to interact with the fluorine atoms to form a tight ion-pair. Such potassium 18-crown-6 borate complexes are very rare, the synthesis of the BH_4-analog has been published[15] and the BF_4-salt appears in the patent literature as flame retardant for polycarbonates.[16]

The nitrile stretching frequency, υ_{CN}, is observed at 2233 cm^{-1} in **3** and at 2237 cm^{-1} in **4** [cf. **1** υ_{CN} = 2247 cm^{-1}. The ^1H NMR spectra of both **3** and **4** is of routine nature in that there are no noteworthy differences for protons belonging to the anion relative to the potassium salt **1** and the ionic liquid **2**. In [D_6]acetone, the ^{19}F chemical shift stemming from the BF_3-moiety in **3** and **4** is identical, with $^1J_{FB}$ coupling constants being also very similar, indicating that in this solvent, the cation and anion are solvolysed and do not interact significantly with each other. The electrospray ionisation (ESI) mass spectrum of **3** in methanol shows a parent peak at *m/z* 538 in positive ion mode for the $[(PPh_3)_2N]^+$ cation and *m/z* 136 in the negative ion mode for the $[CH_3CH(BF_3)CH_2CN]^-$ anion. Anion-cation aggregations were observed in neither the positive nor negative spectra in the concentration range of 5–50 ppm. In contrast, the ESI mass spectrum of **4** exhibits some concentration dependence, see Figure 1. At low concentration, ca. 5 ppm, a peak at *m/z* = 303 corresponding to the monomeric cation $[K(18\text{-crown-6})]^+$ dominates, whereas at higher concentration, ca. 50 ppm, the aggregate $[K(18\text{-crown-6})]_2$-$[CH_3CH(BF_3)CH_2CN]$ gives rise to the base peak at *m/z* 742.

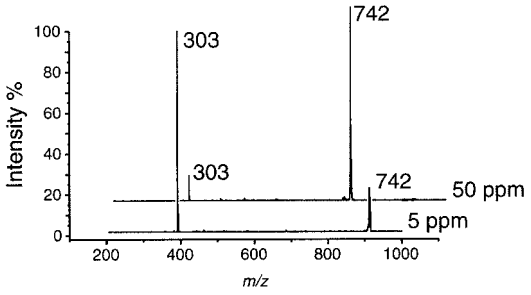

Figure 1. ESI-MS spectrum of **4** in methanol at concentrations of 5 and 50 ppm

Structural Characterization of 3 and 4

The few known structures for alkyltrifluoroborates comprise the potassium salts $K[CF_3BF_3]$[8a] and $K[CH_3BF_3]$[8b] which exhibit extensive potassium-fluorine interactions with K–F distances as short as 2.678(1) Å. The structure of the zwitterionic compound $BF_3CH_2S(O)(CH_3)_2$ has also been reported.[8c]

 © 2005 Wiley-VCH Verlag GmbH & Co. KGaA, Weinheim

Single crystals of **3** and **4** suitable for X-ray diffraction studies were grown at –21 °C from dichloromethane-diethyl ether and THF-diethyl ether solution, respectively. The structures of **3** and **4** are illustrated in Figure 2 and Figure 3, respectively, with key bond parameters in the captions. Details of the data collection and the structure determination are provided in the Experimental. There is negligible disorder in the anion of **3**, involving carbon atoms C2 and C3, whereas in **4** there is considerable disorder in the anion, where carbon atoms C2 and C4 are split over two positions with almost identical occupation factors.

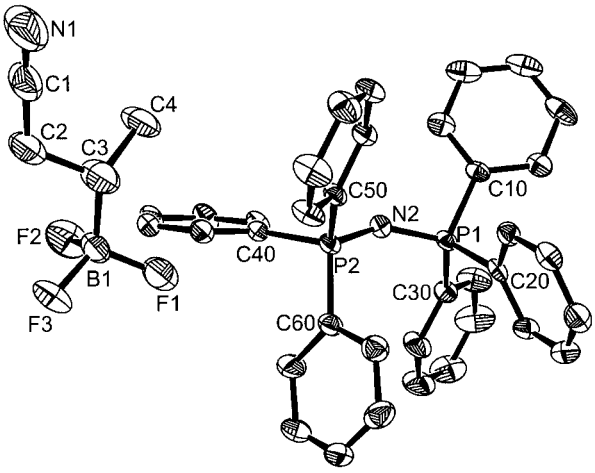

Figure 2. ORTEP-plot of **3** with ellipsoids drawn at the 50% probability level. Selected bond lengths [Å] and angles [°]: F1–B1 1.385(5), F2–B1 1.427(5), F3–B1 1.412(5), B1–C3 1.585(6), P1–N2 1.574(3), P2–N2 1.570(3), C1–N1 1.112(6); F1–B1–C3 110.7(3), F2–B1–C3 112.0(3), F3–B1–C3 110.9(4), C2–C3–C4 109.9(4), P1–N2–P2 142.8(2)

In compound **3** the anion adopts a staggered conformation about the B1–C3 bond with an alignment of F1 *anti* to the C3–C2 bond and F3 *anti* to the C3–C4 bond. This conformation influences the B–F distances, which are shorter for F1 and F3 [1.385(5) and 1.412(5) Å, respectively], than for F2 [1.427(5) Å]. In addition, the F2–B1–C3 angle is slightly larger, 112.0(3)°, but all bonding angles around B1 are within 5° of the ideal tetrahedral angle. All fluorine atoms are engaged in intra- and intermolecular hydrogen bonding with H–F distances as short as 2.386 Å (to F1). The B1–C3 distance of 1.585(6) Å is of the same order as in $K[CH_3BF_3]$, viz. 1.575(3) Å,[8b] and markedly shorter than in $BF_3CH_2S(O)(CH_3)_2$, 1.650(2) Å,[8c] reflecting the presence of a localized negative charge on the boron atom. The nitrile moiety, which exhibits a somewhat short C≡N distance of 1.112(6) Å, points away from the fluorine atoms, being almost parallel to the B1–C3 bond. This alignment is probably due to both electrostatic repulsion from the electronegative fluorine atoms and to interactions with phenyl-hydrogen atoms, which come as close as 2.567 Å to N1. The structure of the $[PPN]^+$ cation agrees well with the data reported elsewhere.[17,18] The P–N distances, 1.574(3) Å and 1.570(3) Å, are as expected; the P–N–P angle, 142.8(2)°, is slightly larger than frequently observed but still within the normal range. No close intermolecular contacts to N2 are present.

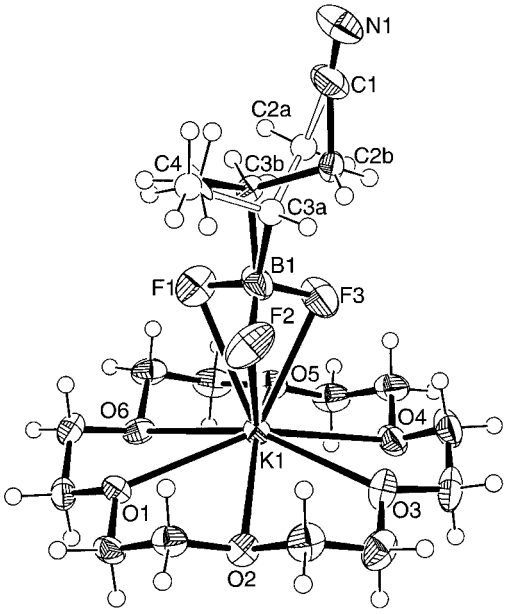

Figure 3. ORTEP-plot of **4** showing the disorder in the alkane moiety; ellipsoids drawn at the 50% probability level. Selected bond lengths [Å]: F1–B1 1.401(3), F2–B1 1.407(3), F3–B1 1.422(3), K1–F1 2.782(1), K1–F2 2.929(1), K1–F3 2.766(1), K1–O1 2.843(1), K1–O2 2.939(1), K1–O3 2.792(2), K1–O4 2.929(2), K1–O5 2.802(2), K1–O6 2.912(1)

Only few structures exist in which a potassium cation is complexed to both a crown ether and fluorine atoms. Most of these salts contain perfluorated silicates as anions,[19] but structures with, for example, hexafluorophosphate[20] and pentafluoroalkyne tungstenate[21] are also known. In addition, a KF adduct of a 21-membered crown ether containing six oxygen atoms and a tethered boronic acid moiety has also been reported.[22] Yet, complex **4** represents the first example of a structure in which a perfluorated boron moiety interacts with a potassium crown ether complex.

Due to the above mentioned disorder, which affects carbon atoms C2 and C4 in the anion in **4**,no quantitative comparison of the anionic structure with **3** is possible. As in **3**, F3 is *anti* to the C3–C4 bond, but the orientation of the C3–C2 bond relative to the fluorine atoms in not unambiguously clear. Despite interaction of the fluorine atoms with the potassium ion, no significant elongation of the B–F bond distances are observed, which range from 1.401(3) to 1.422(3) Å.

The potassium ion lies 0.450 Å above the mean plane defined by the three oxygen atoms O1, O3 and O5 and 0.844 Å above the mean plane defined by the three oxygen atoms O2, O4 and O6. The K–O bonds can accordingly be divided into two groups of three with shorter distances to O1, O3 and O5 [range 2.792(2) to 2.843(2) Å], and longer distances to O2, O4 and O6 [range 2.912(1) to 2.939(1) Å], which is in good agreement with a comparable structure.[23]

The fluorine atoms interact with both intra- and intermolecular hydrogen atoms. Yet, as a result of the bulky

 © 2005 Wiley-VCH Verlag GmbH & Co. KGaA, Weinheim

crown ether moiety only five intermolecular hydrogen bonds below 3 Å to the fluorine atoms are present, see Figure 4. Such F→H–C hydrogen bonding is very common in imidazolium based systems, where it has been probed by IR and NMR spectroscopic methods, but seldom by single-crystal X-ray analysis.[13] The cation and anion in **4** are held in place by potassium-fluorine interactions with two shorter bonds [2.766(1) and 2.782(1) Å], and one longer bond [2.929(1) Å]. These distances are of the same order as in crystals of potassium tetrafluoroborate[24] and the asymmetry of the bonding is comparable to a related fluorosilicate complex.[19a]

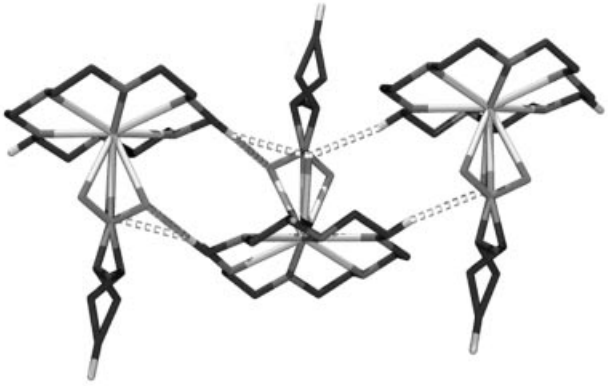

Figure 4. Crystal packing in compound **4**, showing intramolecular hydrogen bonding interactions below 3 Å to the fluorine atoms. For clarity, only those hydrogen atoms involved in the H-bonding are shown

In the context of ionic liquid chemistry it is not unreasonable to propose a similar interaction e.g. with the fluoroborate straddling the face of the imidazolium ring as shown in Scheme 4. This kind of interaction might provide additional rational for the low melting points observed in such compounds in that the intermolecular van-der-Waals forces and C–H···F hydrogen bonding interactions would be reduced.[25]

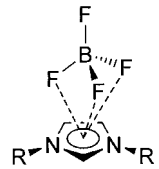

Scheme 4

In conclusion, the structural studies reported herein provide insight into the bonding characters and substitution effect of one of the F atoms in the BF_4^- anion by a functional group. The information gained is relevant to the Suzuki–Miyaura reaction and to the functionalization of ionic liquid anions. Crown ethers have been used as competitors for ion immobilization in ionic liquids[26] and to increase the solubility of amino acids in ionic liquid,[27]but their function herein was as a crystallization aid, an approach that has been used for some time in crystal engineering.[28]

Experimental Section

The potassium salt **1** was prepared following a published method.[6] Bis(triphenylphosphanyl)iminium chloride and 18-crown-6 were purchased from Aldrich and were used as received. The synthesis of compound **3** was carried out in an inert atmosphere of dry nitrogen and the synthesis of **4** was performed without precautions to exclude air or moisture. IR spectra were recorded on a Perkin–Elmer FT-IR 2000 system. NMR spectra were measured on a Bruker DMX 400 spectrometer. Chemical shifts, δ, are given in ppm and coupling constants, *J*, in Hz. Electrospray ionization mass spectra (ESI-MS) were recorded on a ThermoFinnigan LCQ™ Deca XP Plus quadrupole ion trap instrument on samples diluted in methanol. Samples were infused directly into the source at 5 μL min^{-1} using a syringe pump, the spray voltage was set at 5 kV and the capillary temperature at 50 °C.[29] Elemental analysis were carried out at the Institute of Molecular and Biological Chemistry at the EPFL.

Synthesis of $[(PPh_3)_2N][CH_3CH(BF_3)CH_2CN]$ (3): A mixture of the potassium salt **1** (175 mg, 1.0 mmol) and bis(triphenylphosphanyl)-iminium chloride (574 mg, 1.0 mmol) in dichloromethane (10.0 mL) was stirred at room temperature for 24 hours. The reaction mixture was filtered and the solid washed with dichloromethane (2 × 5.0 mL). The filtrates were combined and the solvent removed under reduced pressure to give the pure product. Yield: 654 mg, 97%, m.p. 140 °C. ESI-MS (MeOH) positive ion *m*/*z*, 538, $[(PPh_3)_2N]^+$; negative ion, 136, $[CH_3CH(BF_3)CH_2CN]^-$. IR (cm^{-1}) 3060 (m), 2938 (m), 2864 (m), 2233 (m), 1588 (m), 1482 (m), 1438 (str.), 1281 (m), 1243 (str.), 1209 (m), 1110 (str.), 1050 (m), 995 (str.), 933 (m),, 910 (m), 802 (m), 721 (str.). ^{1}H NMR (400 MHz, [D$_6$]acetone): δ = 7.85–7.68 (m, 18 H), 7.64 –7.55 (m, 12 H); 2.38 (dd, 1 H, ^2J(H,H) = 17.2, $^3J_{H,H}$ = 3.0), 1.85 (dd, 1 H, $^2J_{H,H}$ = 17.0, $^3J_{H,H}$ = 12.0), 0.92 (d, 3 H, $^3J_{H,H}$ = 6.8), 0.59 (m, 1 H).[31] P NMR (161 MHz, [D$_6$]acetone): δ = 21.1 (s). ^{19}F NMR (282 MHz, [D$_6$]acetone): δ = –151.5 (q, $^1J_{FB}$ = 60). $C_{40}H_{36}BF_3N_2P_2$ (674.48): C 71.23, H 5.38, N 4.15; found: C 71.31, H 5.41, N 4.13.

Synthesis of $[K(18\text{-crown-}6)][CH_3CH(BF_3)CH_2CN]$ (4): A mixture of potassium salt **1** (175 mg, 1.0 mmol) and 18-crown-6 (264 mg, 1.0 mmol) in THF (10.0 mL) was stirred at room temperature for 24 hours. The solvent was removed under reduced pressure to give the product in pure form. Yield: 435 mg, 99%, m.p. 145 °C. ESI-MS (MeOH) positive ion, *m*/*z* 303 $[C_{12}H_{24}O_6K]^+$; negative ion, 136, $[CH_3CH(BF_3)CH_2CN]^-$. IR (cm^{-1}) 2899 (str.), 2826 (w), 2237 (m), 1589 (w), 1479 (str.), 1458 (m), 1438 (m), 1351 (str.), 1286 (m), 1249 (str.), 1100 (str.), 1008 (str.), 962 (str.). 931 (m), 838 (m), 720 (m). ^{1}H NMR (400 MHz, [D$_6$]acetone): δ = 3.62 (s, 24 H, OCH_2), 2.38 (dd, 1 H, $^2J_{H,H}$ = 17.1, $^3J_{H,H}$ = 3.3), 1.93 (dd, 1 H, $^2J_{H,H}$ = 17.0, $^3J_{H,H}$ = 12.1), 0.93 (d, 3 H, $^3J_{H,H}$ = 6.9), 0.59 (m, 1 H). ^{19}F NMR ([D$_6$]acetone, 282 MHz): δ = –151.5 (q, $^1J_{FB}$ = 59). $C_{16}H_{30}BF_3KNO_6$ (439.32) (%): C 43.74, H 6.88, N 3.19; found: C 43.80, H 6.91, N 3.18.

Structural Characterisation of 3 and 4: Crystals of **3** suitable for X-ray diffraction studies were obtained at –21 °C from in dichloromethane/diethyl ether (1:1) solution, those of **4** (Table 1) under similar conditions from THF/diethyl ether (1:5). Single crystals were mounted on a KUMA KM4/Sapphire CCD diffractometer. Data reduction was performed using CrysAlis RED.[30] Structure solution and refinement was performed using the SHELX97 software package,[31] graphical representations of the structures were made with ORTEP32.[32] Structures were solved by direct methods and successive interpretation of the difference Fourier maps, followed by full-matrix least-squares refinement (against F^2). All non-hydrogen atoms were refined anisotropically. Hydrogen atoms were

 © 2005 Wiley-VCH Verlag GmbH & Co. KGaA, Weinheim

Table 1. Crystal data and details of the structure determination for **3** and **4**

	3	**4**
Formula	$C_{40}H_{36}BF_3N_2P_2$	$C_{16}H_{30}BF_3KNO_6$
M	674.46	439.32
Crystal system	triclinic	monoclinic
Space group	$P\bar{1}$	$P21/n$
a [Å]	9.8205(13)	13.0764(12)
b [Å]	11.0284(15)	8.5112(8)
c [Å]	17.220(2)	19.7499(18)
α [°]	107.184(11)	90
β [°]	94.231(10)	95.013(7)
γ [°]	99.666(11)	90
V [Å^3]	1741.3(4)	2189.7(4)
Z	2	4
Density [Mg/m^3]	1.286	1.333
T [K]	140	140
Θ range [°]	$3.02 \leq \Theta \leq 25.02$	$2.86 \leq \Theta \leq 25.03$
μ/mm^{-1}	0.173	0.297
Reflections measured	10233	12166
Unique reflections [$I > 2\sigma(I)$]	5378 (R_{int} = 0.0465)	3687 (R_{int} = 0.0398)
Final $R1$, $wR2$ [$I > 2\sigma(I)$]	0.0711, 0.2066	0.0375, 0.0809

placed in their geometrically generated positions and refined using a riding model. In **4**, carbon atoms C2 and C3 were split over two positions with almost identical occupancy factors and the structure refined without restraints. CCDC-250726 and CCDC-250727 contain the supplementary crystallographic data for this paper. These data can be obtained free of charge from The Cambridge Crystallographic Data Centre via www.ccdc.cam.ac.uk/data_request/cif.

Acknowledgments

We thank Swiss National Science Foundation and the EPFL for financial support. We thank Frank Breher at ETH for help with the crystal refinement.

[1] a) G. A. Molander, T. Ito, *Org. Lett.* **2001**, *3*, 393; b) G. A. Molander, M. Rodriguez Rivero, *Org. Lett.* **2002**, *4*, 107; c) G. A. Molander, C. R. Bernardi, *J. Org. Chem.* **2002**, *67*, 8424; d) G. A. Molander, B. W. Katona, F. Machrouhi, *J. Org. Chem.* **2002**, *67*, 8416; e) G. A. Molander, C.-S. Yun, M. Ribagorda, B. Biolatto, *J. Org. Chem.* **2003**, *68*, 5534.

[2] a) H.-J. Frohn, N. Y. Adonin, V. V. Bardin, V. F. Starichenko, *Tetrahedron Lett.* **2002**, *43*, 8111; b) J.-P. Tremblay-Morin, S. Raeppel, F. Gaudette, *Tetrahedron Lett.* **2004**, *45*, 3471; c) N. Y. Adonin, V. V. Bardin, U. Flörke, H.-J. Frohn, *Organometallics* **2004**, *23*, 172; d) N. Y. Adonin, V. V. Bardin, H.-J. Frohn, *Organometallics* **2004**, *23*, 535.

[3] a) L. C. Branco, J. N. Rosa, J. J. Moura Ramos, C. A. M. Alfonso, *Chem. Eur. J.* **2002**, *8*, 3671; b) Z. Fei, D. Zhao, T. J. Geldbach, R. Scopelliti, P. J. Dyson, *Chem. Eur. J.* **2004**, *10*, 4886.

[4] a) H. Schottenberger, K. Wurst, U. E. I. Horvath, S. Cronje, J. Lukasser, J. Polin, J. M. McKenzie, H. G. Raubenheimer, *J. Chem. Soc., Dalton Trans.* **2003**, 4275; b) Z. Fei, D. Zhao, R. Scopelliti, P. J. Dyson, *Organometallics* **2004**, *23*, 1622.

[5] a) C. Ye, J. M. Shreeve, *J. Org. Chem.* **2004**, *69*, 6511; b) Y. Gao, J. M. Shreeve, *Synthesis* **2004**, *7*, 1072; c) J. Kim, R. P. Singh, J. M. Shreeve, *Inorg. Chem.* **2004**, *43*, 2960; d) O. D. Gupta, B. Twamley, J. M. Shreeve, *Tetrahedron Lett.* **2004**, *45*, 1733; e) H. Xue, B. Twamley, J. M. Shreeve, *J. Org. Chem.* **2004**, *69*, 1397; f) Y. R. Mirzaei, H. Xue, J. M. Shreeve, *Inorg. Chem.* **2004**, *43*, 361.

[6] D. Zhao, Z. Fei, C. A. Ohlin, G. Laurenczy, P. J. Dyson, *Chem. Commun.* **2004**, 2500.

[7] a) Z.-B. Zhou, H. Matsumoto, K. Tatsumi, *Chem. Lett.* **2004**, *33*, 680; b) Z.-B. Zhou, M. Takeda, M. Ue, *J. Fluorine Chem.* **2004**, *125*, 471.

[8] a) D. J. Brauer, H. Bürger, G. Pawelke, *Inorg. Chem.* **1977**, *16*, 2305; b) D. J. Brauer, H. Bürger, G. Pawelke, *J. Organomet. Chem.***1982**, *238*, 267; c) J. M. Stoddard, K. J. Shea, *Organometallics* **2003**, *22*, 1124.

[9] A. N. Thadani, R. A. Batey, D. V. Smil, A. J. Lough, *Acta Crystallogr. Sect. E* **2001**, *57*, m333.

[10] a) T. D. Quach, R. A. Batey, A. J. Lough, *Acta Crystallogr. Sect. E* **2001**, *57*, o688; b) E. Vedejs, R. W. Chapman, S. Lin, M. Müller, D. R. Powell, *J. Am. Chem. Soc.* **2000**, *122*, 3047; c) G. Conole, A. Clough, A. Whiting, *Acta Crystallogr. Sect. C* **1995**, *51*, 1056.

[11] a) X. Cattoën, H. Gornitzka, D. Bourissou, G. Bertrand, *J. Am. Chem. Soc.* **2004**, *126*, 1342; b) D. J. Nielsen, K. J. Cavell, B. W. Skelton, A. H. White, *Inorg. Chim. Acta* **2003**, *352*, 143; c) A. J. Arduengo III, F. Davidson, R. Krafczyk, W. J. Marshall, R. Schmutzler, *Monatsh. Chem.* **2000**, *131*, 251; d) N. Kuhn, R. Fawzi, H. Kotowski, M. Steimann, *Z. Kristallogr.* **1997**, *212*, 259.

[12] a) J. W. Bats, M. Scheibitz, M. Wagner, *Acta Crystallogr. Sect. C* **2003**, *59*, m355; b) T. Quach, R. A. Baley, A. J. Lough, *Acta Crystallogr. Sect. E* **2001**, *57*, 320.

[13] a) P. Bonhote, A.-P. Dias, N. Papageorgiou, K. Kalyanasundaram, M. Grätzel, *Inorg. Chem.* **1996**, *35*, 1168; b) A. Noda, K. Hayamizu, M. Watanabe, *J. Phys. Chem. B* **2001**, *105*, 4603; c) J.-F. Huang, P.-Y. Chen, I-W. Sun, S. P. Wang, *Inorg. Chim. Acta* **2001**, *32*, 7.

[14] D. Braga, *Chem. Commun.* **2003**, 2751.

[15] Y. N. Shevchenko, K. B. Yatsimirskii, S. A. Minkov, *Z. Neorg. Khim.* **1985**, *30*, 1705.

[16] L. S. Thomas, US-Patent US 4439566 A 19840327.

[17] R.-Y. Liau, H. Ehlich, A. Schier, H. Schmidbaur, *Z. Naturforsch., Teil B* **2002**, *57*, 1085.

[18] a) T. S. Cameron, M. E. Peach, *J. Chem. Crystallogr.* **1998**, *28*, 919; b) S. H. Lawrence, S. G. Shore, T. F. Koetzle, J. C. Huffman, C.-Y. Wei, R. Bau, *Inorg. Chem.* **1985**, *24*, 3171.

[19] a) N. Kano, F. Komatsu, T. Kawashima, *J. Am. Chem. Soc.* **2001**, *123*, 10778; b) S. E. Johnson, J. S. Payne, R. O. Day, J. M. Holmes, R. R. Holmes, *Inorg. Chem.* **1989**, *28*, 3190.

[20] A. Zaeni, F. T. Edelmann, F. Olbrich, private communication in 2004; see also CCDC-231012 (Cambridge Crystallographic Data Centre, www.ccdc.cam.ac.uk/data_request/cif).

 © 2005 Wiley-VCH Verlag GmbH & Co. KGaA, Weinheim

[21] P. Neumann, K. Dehnicke, D. Fenske, G. Baum, *Z. Naturforsch. Teil B* **1991**, *46*, 999.
[22] M. T. Reetz, C. M. Niemeyer, K. Harms, *Angew. Chem. Int. Ed. Engl.* **1991**, *30*, 1472.
[23] D. G. Gusev, A. J. Lough, R. H. Morris, *J. Am. Chem. Soc.* **1998**, *120*, 13138.
[24] G. Brunton, *Acta Crystallogr. Sect. B* **1969**, *B25*, 2161.
[25] A. R. Katritzky, R. Jain, A. Lomaka, R. Petrukhin, U. Maran, M. Karelson, *Cryst. Growth Des.* **2001**, *1*, 261.
[26] S. Chun, S. V. Dzyuba, R. A. Bartsch, *Anal. Chem.* **2001**, *73*, 3737.
[27] S. V. Smirnova, I. I. Torocheshnikova, A. A. Formanovsky, I. V. Pletnev, *Anal. Bioanal. Chem.* **2004**, *378*, 1369.
[28] a) H. Zhang, X. Wang, B. K. Teo, *J. Am. Chem. Soc.* **1996**, *118*, 11813; b) J. A. Manskaya, K. V. Domasevitch, V. Konstantin, V. V. Ponomareva, J. Sieler, V. N. Kokozay, *Z. Naturforsch. Teil B* **1998**, *53*, 683.
[29] P. J. Dyson, J. S. McIndoe, D. Zhao, *Chem. Commun.* **2003**, 508.
[30] Oxford Diffraction Ltd., 68 Milton Park, Abingdon, OX14 4 RX, UK, **2003**.
[31] G. M. Sheldrick, *SHELX-97. Structure Solution and Refinement Package*, University of Göttingen, **1997**.
[32] L. J. Farrugia, *J. Appl. Crystallogr.* **1997**, *30*, 565.

Received: September 27, 2004

 © 2005 Wiley-VCH Verlag GmbH & Co. KGaA, Weinheim

From Dinuclear Zirconium(+3)-Phosphido Complexes {[$Cp_2ZrP(H)R]_2$} to the First Neutral Zirconocene–Phosphinidene Dimers [$(Cp_2ZrPR)_2$] by P–H Dehydrogenation

Matthias Driess,*[a] Joachim Aust,[b] and Klaus Merz[b]

Dedicated to Professor Michael Veith on the occasion of his 60th birthday

Keywords: Antiferromagnetic coupling / Phosphido complexes / Silylphosphanes / Zirconium / Phosphorus / P–H bonding activation

The syntheses and structures of the new zirconium(+3) silylphosphanido complexes {[$Cp_2ZrP(H)R]_2$} **1a** {Cp = η^5-C_5H_5; R = $SiMe_2C(i\text{Pr})Me_2$}, **1b** (R = $Si i\text{Pr}_3$), and **1c** (R = SiF(*t*Bu)(2,4,6-$i\text{Pr}_3C_6H_2$) are reported. The latter are easily accessible by the reaction of the lithium salts of the corresponding primary silylphosphanes with the Schwartz reagent [$Cp_2Zr(H)Cl$] in THF at –70 °C. They can be isolated in the form of diamagnetic red-black crystals in 68–85 % yield. The central structural motif of the complexes consists of planar (**1a**, **1b**) and slightly puckered Zr_2P_2 rings (**1c**), and contains two d^1-Zr(+3) centers, which are antiferromagnetically coupled (super exchange, through-bond interaction) although the transannular Zr–Zr separation is around 360 pm. Thus, the compounds have a biradicaloid electronic structure. Heating of solutions of **1a–c** in toluene in the presence of Pd/C or [$(Ph_3P)_2Pt(C_2H_4)$] results in catalytic dehydrogenation of the P–H bonds, affording the first neutral zirconocene–phosphinidene dimers [$Cp_2ZrPR]_2$ **3a–c** in the form of deep red crystals in 72–88 % yield. The composition of the products is proven by multinuclear NMR spectroscopy, mass spectrometry and correct C,H-combustion analyses. The molecular structures of **3a** and **3c** were additionally confirmed by X-ray crystal structure analyses, showing that they consist of Zr_2P_2 rings with significantly shorter Zr–P distances than those observed in **1a** and **1c**. Interestingly, the dehydrogenation of the mostly sterically crowded derivative **1c** occurs also in boiling toluene solutions without using a catalyst, but the process is prevented in a H_2 atmosphere. This suggests that the Zr(+3) centers in **1c** can serve as active sites for the P–H bonding activation, which, however, are deactivated in the presence of H_2.

(© Wiley-VCH Verlag GmbH & Co. KGaA, 69451 Weinheim, Germany, 2005)

Introduction

Metallocene dihalides of the group 4 transition metals (Ti, Zr, Hf) tend to undergo halogen-reductive substitution by reaction with lithium phosphanides. This has been impressively shown by the reaction of zirconocene dihalides with lithium salts of primary and secondary phosphanes which leads solely to the corresponding dinuclear μ_2-phosphanido-bridged zirconium complexes **A** having two Zr(+3) centers (Scheme 1).[1–4] Although the complexes **A** bear two Zr(+3) atoms with a d^1 electronic configuration and possess relatively large Zr–Zr distances ranging between 381 and 355 pm, they are diamagnetic because of strong "through-space" interactions ($d_{z^2-dz^2}$ bond) and "super exchange" (through ligand coupling) as confirmed by ab initio calculations.[5–7] Alternatively, derivatives of **A** with small organic groups at phosphorus are also formed by oxidative addition of tetraorgano-substituted diphosphanes onto the Zr(+2) centers of two zirconocene molecules, generated in situ by reduction of [Cp_2ZrCl_2] with elemental Mg (Scheme 1).[8]

The preference of other zirconocene derivatives to undergo redox processes [Zr(+4) → Zr(+3)] toward primary and secondary phosphanes is also distinctive for related zirconocene hydrido complexes. Thus, reaction of [$Cp_2Zr(H)Cl$] (Schwartz reagent) with primary phosphanes RPH_2 affords in several ligand-exchange and redox processes **A′**, zirconocene dichloride and the respective diphosphane $R_2P_2H_2$ (Scheme 1).[9] To our surprise, and in contrast to the well-established class of dinuclear Zr(+3) phosphido complexes **A**, related complexes of type **B**, bearing two Cp_2Zr moieties and two μ_2-PR (phosphinidene) bridging ligands, are elusive. They represent dimers of zirconocene–phosphinidene complexes [Cp_2Zr = PR] which are also difficult to detect. Stephan et al. reported in 1991 the first

[a] Institute of Chemistry: Metalorganics and Inorganic Materials, Technical University of Berlin,
Straße des 17. Juni 136, 10623 Berlin, Germany
Fax: +49-30-314-22168
E-mail: matthias.driess@tu-berlin.de
[b] Fakultät für Chemie, Universität Bochum,
Universitätsstrasse 150, 44801 Bochum, Germany

 © 2005 Wiley-VCH Verlag GmbH & Co. KGaA, Weinheim **DOI: 10.1002/ejic.200400820**

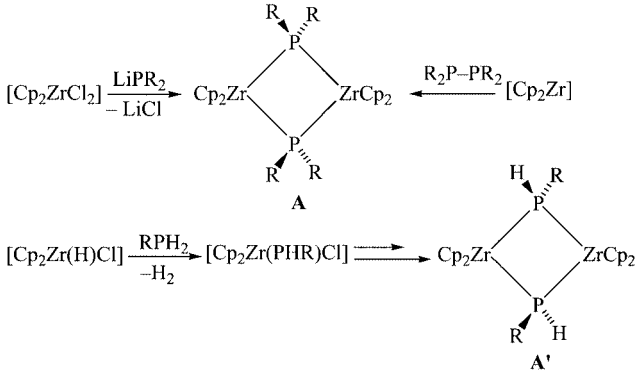

Scheme 1. Synthetic access to dinuclear zirconium(+3) phosphanido complexes **A** and **A′**.

phosphinidene-bridged zirconocene complex **C**[4] and in 1993 the first isolation of the donor-stabilized zirconocene–phosphinidene complex $Cp_2Zr(PMe_3)$=PR (R = 2,4,6-$C_6H_2tBu_3$) **D**[10] and of the dinuclear complex anion **E** with mixed-valent Zr(+3) atoms (Figure 1).[9,11,12]

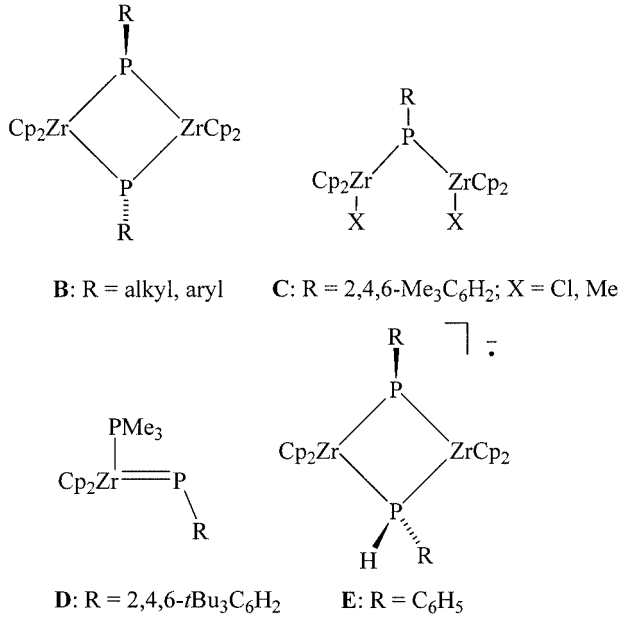

Figure 1. Structural types of zirconocene–phosphinidene complexes.

One possibility to synthesize dimeric zirconocene–phosphinidene complexes **B** can be envisioned as the catalytic dehydrogenation of complexes **A** [Equation (1)]. Since the P–H bonds in silylphosphanes are more reactive than those in organophosphanes, we set out to prepare a series of new dinuclear P–H functionalized silylphosphido Zr(+3) complexes **A**, which appeared to be suitable for P–H dehydrogenation experiments according to Equation (1). We report here the synthesis and structural characterization of the latter and their successful conversion into the corresponding dimeric zirconocene–phosphinidene complexes **B**.

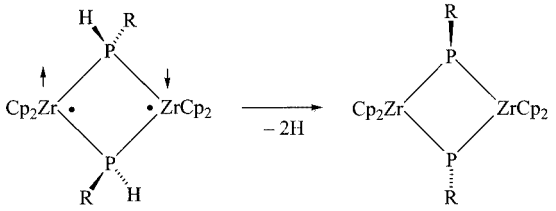

Results and Discussion

Synthesis and Structures of 1a–1c

The new bulkily substituted dinuclear Zr(+3) silylphosphanido complexes **1a**–**1c** are easily accessible in 78 (**1a**), 68 (**1b**), and 85% yield (**1c**), by conversion of $[Cp_2Zr(H)Cl]$ with the corresponding lithium silylphosphanides **2a**–**2c** in THF at –70 °C. The complexes were isolated in the form of black-red crystals, which are well soluble in aprotic aromatic solvents. Although the mechanism of the reaction is unknown and no intermediate could be detected by means of NMR spectroscopy, we assume that the initial product is the respective zirconocene-hydrido-phosphanide, which subsequently undergoes dehydrogenative dimerization to the final products **1a**–**1c** [Equation (2)]. The diamagnetic complexes have been characterized by multinuclear NMR spectroscopy and correct elemental analyses. The ^{31}P NMR spectra exhibit doublets relatively upfield with respect to *P*-alkyl-substituted derivatives **A**,[4,9,13] because of the σ-donor effect of the silyl group. However, the magnitudes of $^1J(^{31}P\text{-}^1H)$ coupling constants [236 Hz (**1a**), 228 Hz (**1b**), and 255 Hz (**1c**)] reflect identical electronic features for the P–Zr donor-acceptor bonds. The ^1H NMR spectra of **1a**–**1c** show only one type of C_5H_5 "Cp" protons, which suggests *trans* configuration or fast configurational inversion of the coordinated P atoms. The presence of dynamic

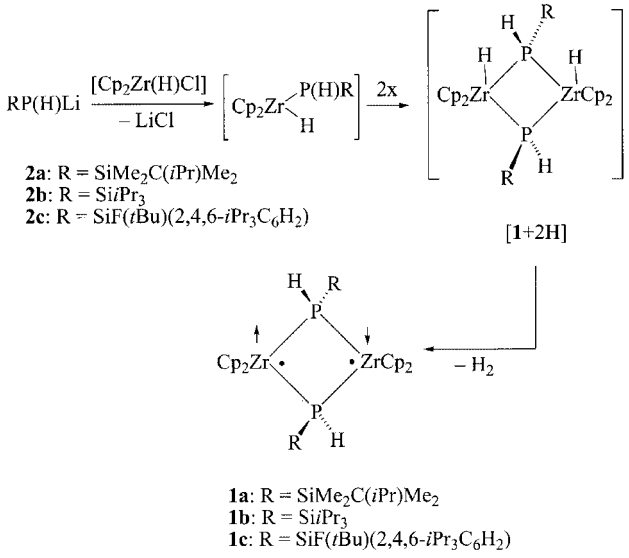

 © 2005 Wiley-VCH Verlag GmbH & Co. KGaA, Weinheim

exchange processes seems unlikely because the VT ^{1}H and ^{31}P NMR spectra are invariant from –75 to +80 °C. In fact, the preference for the *trans* configuration of the silyl groups at phosphorus is confirmed by single-crystal X-ray diffraction analyses (Figure 2, Table 1). The P atoms in **1a**–**1c** have distorted tetrahedral coordinates, and the position of the P–H hydrogen atoms could be localized from the difference Fourier map and refined. The four-membered Zr_2P_2 ring is planar in **1a** and **1b**, but slightly puckered in the case of **1c** (Zr_2P/Zr_2P' angle 3.8°) because of the larger steric demand of the silyl group.

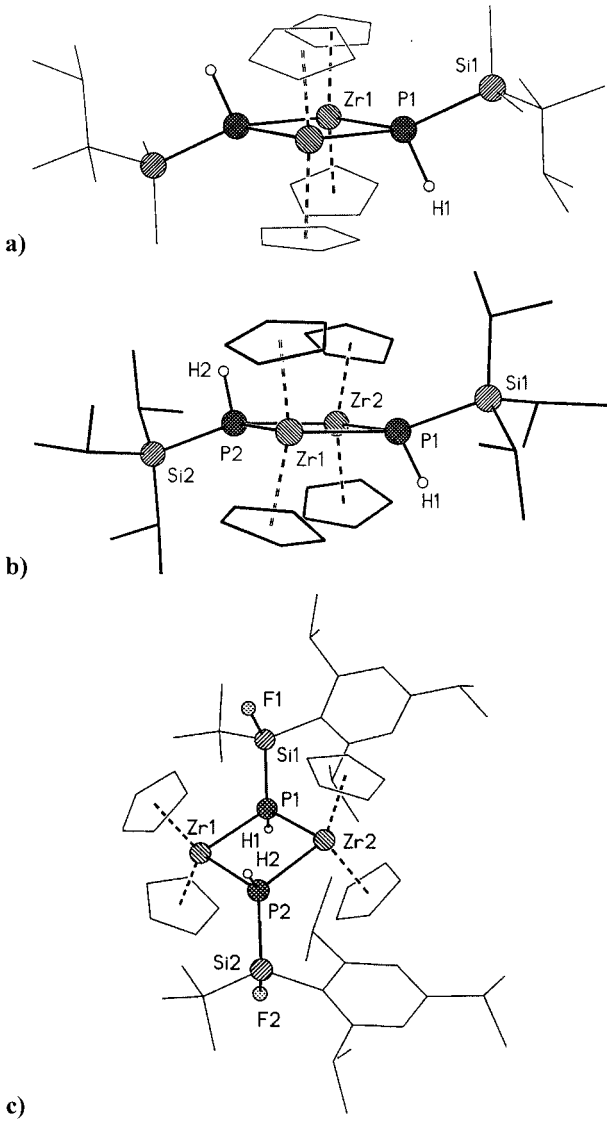

Figure 2. Molecular structures of **1a** (a), **1b** (b), and **1c** (c); the H atoms of the organic groups are omitted for clarity.

This is in contrast to other derivatives with *cis* configuration of the substituents at phosphorus, with folding-angles up to 30.6°.[13] The Zr–P distances as well as the endocyclic Zr–P–Zr and P–Zr–P angles are inconspicuous and practically identical with those in *P*-alkyl-substituted derivatives and related phosphanido-bridged Zr(+3) complexes.[4,5,9,13] The most remarkable geometrical feature is the relatively large Zr–Zr′ separation of 3.64 (**1a**), 3.57 (**1b**), and 3.61 (**1c**), which shows that there is no common transannular bonding between the d^1-Zr centers although the compounds are diamagnetic (singlet ground-state) due to antiferromagnetic coupling by ligand-mediated superexchange. Similar distances were observed in related *P*-alkyl-substituted derivatives.[9,13] According to results of ab initio calculations,[6] the extension of the transannular Zr–Zr distance results from two opposite effects: attractive Zr–Zr through-bond versus repulsive ligand-ligand interactions at the Zr and P atoms. In other words, the hypothetical form **1′** with a "short" Zr–Zr distance and a butterfly-like structure possesses much higher ring strain than the "bond-stretch" isomer **1** (Scheme 2).

Table 1. Selected distances [pm] and angles [°] for **1a**, **1b**, and **1c**.

1a	1b	1c
Zr1–P1 265.7(1)	Zr1–P1 268.0(1)	Zr1–P1 270.0(1)
		Zr1–P2 268.9(1)
P1–Si1 225.4(2)	P1–Si1 228.5(1)	P1–Si1 225.3(2)
Zr1–Zr1A 364.2(3)	Zr1–Zr1A 357.3(3)	Zr1–Zr2 360.8(2)
		Si1–F1 161.9(2)
P1–Zr1–P1A 93.53(3)	P1–Zr1–P1A 96.73(4)	P1–Zr1–P2 95.55(4)
Zr1–P1–Zr1A 86.47(3)	Zr1–P1–Zr1A 83.27(3)	P1–Zr2–P2 96.06(4)
		Zr1–P1–Zr2 84.10(4)
		Zr1–P2–Zr2 84.15(3)

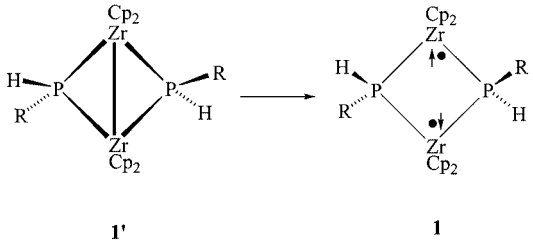

Scheme 2. Bond-stretch isomerization of **1′** to the biradicaloid **1**.

While this situation is widespread in multinuclear transition-metal complexes with unpaired electrons, similar structural and electronic features are scarce in main-group chemistry. The first iso(valence)electronic main-group metal analog, the Sn_2N_2-heterocyclobutane $[ClSn–N(SiMe_3)]_2$, which also has a biradicaloid structure and a singlet ground state, has been discovered only recently.[14]

Formation of the Dimeric Zirconocene–Phosphinidene 3a–3c by P–H Dehydrogenation of 1a–1c

Since the P–H bond in silylphosphanes is more reactive with regard to homolytic and heterolytic fission than that in organophosphanes, we expect that the P–H bonds in **1a**–**1c** can be dehydrogenated by typical dehydrogenation catalysts, leading to the first zirconocene–phosphinidene dimers. In fact, heating of solutions of **1a**–**1c** in toluene at 70 °C in the presence of Pd/C as a dehydrogenation catalystfurnishes the first neutral zirconocene–phosphinidene dimers **3a**–**3c** in good yields [Equation (3)]. Instead of Pd/C, the Pt complex $[(Ph_3P)_2Pt(C_2H_4)]$ can also be used as a catalyst (10^{-2} mol-%).

 © 2005 Wiley-VCH Verlag GmbH & Co. KGaA, Weinheim

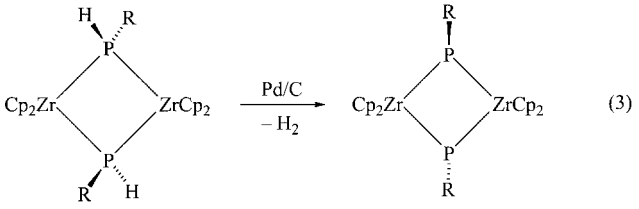

(3)

The dehydrogenation is completed after about 8 h and its progress can be monitored by ^{31}P NMR spectroscopy. Surprisingly, the dehydrogenation of the mostly sterically crowded derivative **1c** occurs also in boiling toluene solutions without using a catalyst. This irreversible process is complete after 24 h. In line with that, **3c** is inert toward H_2 in boiling toluene in a sealed tube. However, the conversion of **1c** into **3c** is hampered in a sealed tube or in H_2/D_2 gas at 1 atm without P–H/P–D exchange. Although the mechanism is still unknown we assume the dehydrogenation process involves the Zr(+3) centers as active sites. Apparently, the latter are deactivated in the presence of H_2, affording [**1c** + 2 H] as transient species in a reversible reaction [Equation (4)]. It should be mentioned here that compounds of the type [**1** + 2 H] are also possible transient species for the synthesis of **1a**–**c** [see Equation (2)] but they could not yet be detected.

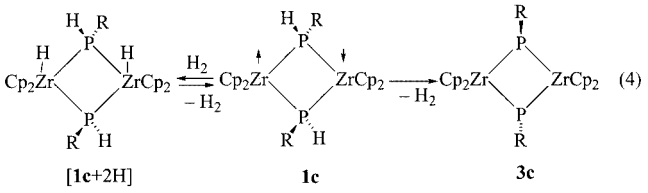

(4)

The ^{31}P nucleus in **3a** (δ = 238.9 ppm) **3b** (δ = 229.8 ppm) and **3c** (δ = 260.3 ppm) undergoes a drastic downfield shift of $\Delta\delta$ = 337.5 (**3a**), 362.3 (**3b**) and 346.6 ppm (**3c**), respectively. The strong deshielding of the ^{31}P nucleus is characteristic for μ_2-bridging phosphinidene ligands and reflects a higher contribution of the paramagnetic term to the chemical shift.[15] The ^{31}P chemical shifts of **3a**–**3c** are similar to the values of the hitherto only known neutral zirconium phosphinidene complexes **C** (δ = 325.5, 303.0 ppm; see Figure 1).[4,16] The ^{1}H, ^{31}P, and ^{13}C NMR spectra of the products clearly indicate that there is only one configurational isomer present in solution even at low (–75 °C) and high temperatures (+85 °C). The composition of the novel complexes were confirmed by mass spectrometry and correct elemental analyses. In the cases of **3a** and **3c**, the molecular structures were established by X-ray diffraction analyses (Figure 3, Table 2). Compounds **3a** and **3c** crystallize in the monoclinic space group $P2_1/c$ and in the orthorhombic space group *Pbca*, respectively.

Table 2. Selected bond lengths [pm] and angles [°] for **3a** and **3c**.

3a	**3c**
Zr1–P1 259.8 (3)	Zr1–P1 265.2 (4)
Zr1–P1A 261.7 (4)	Zr1–P2 263.0 (4)
P1–Si1 223.4 (5)	P1–Si1 220.8 (4)
Zr1–Zr1A 372.5 (1)	Zr1–Zr2 372.8 (2)
	Si1–F1 162.3 (8)
P1–Zr1–P1A 88.8 (1)	P1–Zr1–P2 89.7 (1)
Zr1–P1–Zr1A 91.2 (1)	P1–Zr2–P2 89.7 (1)
Zr1–P1–Si1 130.6 (2)	Zr1–P1–Zr2 89.6 (1)
Zr1A–P1–Si1 124.4 (2)	Zr1–P2–Zr2 90.0 (1)
	Zr1–P1–Si1 123.0 (2)
	Zr2–P2–Si2 124.3 (2)

Similar to the geometrical features of **1a** and **1c**, the Zr_2P_2 ring is planar in **3a** but is slightly puckered in **3c** because of steric repulsion (folding angle Zr_2P/Zr_2P' 10.6°). The P atoms have distorted pyramidal coordinates, with the sum of bonding angles amounting to 346.3 (**3a**), and 335.1 and 337.4° (**3c**). As expected, the Zr–P separations in **3a** [259.8(3), 261.7(4) pm] and **3c** [263.0(4), 265.2(4) pm] are significantly shorter than those for the Zr–P single bonds in **1a** [265.7(1) pm] and **1c** [268.9(1), 270.0(1) pm]. The values are between those of the Zr–P single bonds in **C** [264.8(3), 264.3(2) pm] and the Zr=P double bond in D [250.5(4) pm] but similar to the values observed for the re-

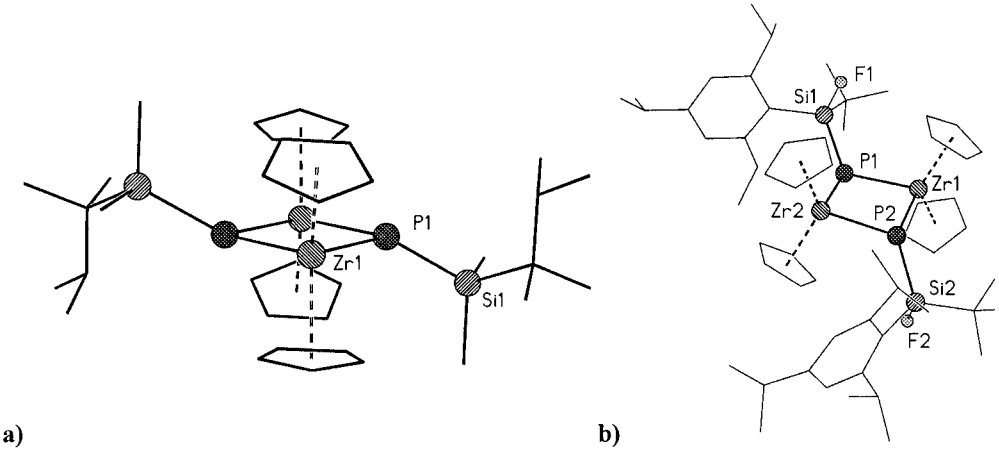

Figure 3. Solid-state structure of **3a** (a) and **3c** (b); H atoms are omitted for clarity.

 © 2005 Wiley-VCH Verlag GmbH & Co. KGaA, Weinheim

lated anionic zirconocene–phosphinidene dimer **E** [259.1(5), 256.8(5) pm] (see Figure 1). The transannular Zr–Zr separations in **3a**, and **3c** are approximately 10 pm longer than in the precursors **1a**, and **1c**, but practically identical with the values in **E**.

Conclusions

The dinuclear zirconium(+3) silylphosphanido complexes **1a**–**c** are suitable precursors for the synthesis of the first neutral zirconocene–phosphinidene dimers **3a**–**c**. The latter do not tend to dissociate in hot toluene solutions because of strong Zr–P σ bonds and partial P–Zr π-donor interactions. The desired dehydrogenation of the P–H bonds in **1a**–**c** is an irreversible process which succeeds in the presence of the well-known dehydrogenation catalysts Pd/C and $[(Ph_3P)_2Pt(C_2H_4)]$, and is certainly relieved by the sterically crowded organosilyl groups. Particularly noteworthy is the fact that **1c** undergoes voluntary dehydrogenation even without a catalyst; but the conversion is prevented in the presence of relatively high concentrations of H_2. The results suggest that the Zr(+3) centers in **1c** serve as active sites in the P–H bonding activation process. However, further (kinetic) studies are necessary in order to establish the mechanism. The results led also to the challenging questionywhether or not other Zr(+3) compounds could also be employed as efficient dehydrogenation reagents or catalysts for primary and secondary phosphanes. Respective investigations are currently in progress.

Experimental Section

General Remarks: All manipulations were carried out at anaerobic conditions under dry argon using standard Schlenk techniques. Solvents were refluxed over an appropriate drying agent, distilled and degassed prior to use. NMR spectra were recorded in C_6D_6 at ambient temperature with a Bruker Avance250 spectrometer operating at 250.1 MHz (^{1}H), 101.3 MHz (^{31}P), and 235.4 MHz (^{19}F). Chemical shifts were reported relative to TMS (^{1}H), 85% aqueous H_3PO_4 (^{31}P), and $CFCl_3$ (^{19}F) at δ = 0 ppm. EI-MS measurements were recorded with a Varian MAT CH7 spectrometer at 70eV. Combustion analyses were performed at the Analytical Service Laboratory of the Faculty of Chemistry in Bochum with a CHNO Rapid instrument (Heraeus).

Preparation of $\{(\eta^5\text{-}C_5H_5)_2ZrP(H)SiMe_2C(i\text{Pr})Me_2\}_2$ (1a): A solution of $LiP(H)SiMe_2C(i\text{Pr})Me_2$ (8.79 mmol, freshly prepared from the corresponding silylphosphane with BuLi in THF at –78 °C) in THF (30 mL) was slowly added to a suspension of $[(\eta^5\text{-}C_5H_5)_2Zr(H)Cl]$ (2.26 g, 8.79 mmol) in THF (50 mL) at –70 °C. The reaction mixture was allowed to warm up to room temperature within 8 h and subsequently all volatile components were evaporated off in vacuo (10^{-3} Torr). The solid residue was redissolved in toluene (70 mL), filtered, and the clear red solution was concentrated to about 30 mL to give, after 1d at –20 °C, deep red crystals of **1a**. Yield: 2.7 g (3.43 mmol, 78%). ^{1}H NMR: δ = 4.92 (s, 20 H, C_5H_5), 2.18 [sept, 2 H, $^3J_{H,H}$ = 6.9 Hz, C*H*(CH$_3$)$_2$], 1.26 [s, 12 H, C(C*H*$_3$)$_2$], 1.09 [d, 12 H, $^3J_{H,H}$ = 7.0 Hz, CH(C*H*$_3$)$_2$], 0.51 [s, 12 H, Si(C*H*$_3$)$_2$] ppm. ^{31}P NMR: δ = –106.6 (d, $^1J_{P\text{-}H}$ = 236.8 Hz) ppm. MS: *m*/*z* (%) = 791 [M-H$_2$]$^+$ (1), 708 [M-C(*i*Pr)Me$_2$]$^+$ (1), 621 [791 – 2{C(*i*Pr)Me$_2$}]$^+$ (0.8), 563 [621 – SiMe$_2$]$^+$ (0.8), 85 [C(*i*Pr)Me$_2$]$^+$ (58), 73 [SiMe$_3$]$^+$ (85), 43 [*i*Pr]$^+$ (100). $C_{36}H_{60}P_2Si_2Zr_2$ (793.4): calcd. C 54.50, H 7.60; found C 54.40, H 7.70.

Preparation of $\{(\eta^5\text{-}C_5H_5)_2ZrP(H)Si i\text{Pr}_3\}_2$ (1b): The compound was prepared by a procedure similar to that for **1a**, using the corresponding silylphosphane (2.15 mmol) as starting material. Crystallization in toluene afforded red crystals of **1b**. Yield: 0.6 g (0.73 mmol, 68%). ^{1}H NMR: δ = 4.92 (s, 20 H, C_5H_5), 1.28 [d, 36 H, $^3J_{H,H}$ = 6.8 Hz, CH(C*H*$_3$)$_2$], 1.06 [sept, 6 H, $^3J_{P\text{-}H}$ = 6.9 Hz, C*H*(CH$_3$)$_2$] ppm. ^{31}P NMR: δ = –132.6 (d, $^1J_{P\text{-}H}$ = 228 Hz) ppm. MS: *m*/*z* (%) = 819 [(M-H$_2$)$^+$, 1], 157 [(Si(*i*Pr)$_3$)$^+$, 100], 115 [Si(*i*Pr)$_2$)$^+$, 78], 43 [(*i*Pr)$^+$, 40]. $C_{38}H_{64}P_2Si_2Zr_2$ (821.5): calcd. C 55.55, H 7.85; found C 55.43, H 7.80.

Preparation of $\{(\eta^5\text{-}C_5H_5)_2ZrP(H)SiF(t\text{Bu})(2,4,6\text{-}i\text{Pr}_3C_6H_2)\}_2$ (1c): The compound was prepared by a procedure similar to that for **1a**, using the corresponding fluorosilylphosphane (2.3 mmol) as starting material. Crystallization in toluene afforded prismatic-shaped black crystals of **1b**. Yield: 1.1 g (0.98 mmol, 85%). ^{1}H NMR: δ = 7.33 (s, 4 H, *m*-*H*), 5.08 (s, 20 H, C_5H_5), 3.97 [sept, 4 H, $^3J_{H,H}$ = 6.9 Hz, *o*-C*H*(CH$_3$)$_2$], 2.94 [sept, 2 H, $^3J_{H,H}$ = 6.9 Hz, *p*-C*H*(CH$_3$)$_2$], 1.57 [s, 18 H, C(C*H*$_3$)$_3$], 1.43 [d, 12 H, $^3J_{H,H}$ = 6.9 Hz, *p*-CH(C*H*$_3$)$_2$], 1.36 [d, 24 H, $^3J_{H,H}$ = 6.9 Hz, *o*-CH(C*H*$_3$)$_2$] ppm. ^{31}P NMR: δ = –86.3 (dd, $^1J_{P\text{-}H}$ = 255.2, $^2J_{P\text{-}F}$ = 63.8 Hz) ppm. ^{19}F NMR: δ = –149.8 (d, $^2J_{P\text{-}F}$ = 63.6 Hz) ppm. MS: *m*/*z* (%) = 1119 [(M-H$_2$)$^+$, 1], 307 {[FSi(*t*Bu)(2,4,6-*i*Pr$_3$C$_6$H$_2$)]$^+$, 31}, 203 [(*i*Pr$_3$C$_6$H$_2$)$^+$, 48], 43 [(*i*Pr)$^+$, 100]. $C_{58}H_{86}F_2P_2Si_2Zr_2$ (1121.9): calcd. C 62.09, H 7.72; found C 61.89, H 7.61.

Preparation of $\{(\eta^5\text{-}C_5H_5)_2ZrPSiMe_2C(i\text{Pr})Me_2\}_2$ (3a): A solution of **1a** (0.83 g, 1.05 mmol) in toluene (40 mL) was heated in the presence of Pd/C (0.1 g) at 70 °C for 8 h. After filtration and concentration of the solution to about 20 mL in vacuo, the reaction solution was stored at 6 °C to afford red-black crystals. Yield: 0.6 g (0.76 mmol, 72%). ^{1}H NMR: δ = 6.29 (s, 20 H, C_5H_5), 1.61 [sept, 2 H, $^3J_{H,H}$ = 6.9 Hz, C*H*(CH$_3$)$_2$], 0.91 [d, 12 H, $^3J_{H,H}$ = 7.0 H, CH(C*H*$_3$)$_2$], 0.77 [s, 12 H, C(C*H*$_3$)$_2$], 0.64 [s, 12 H, Si(C*H*$_3$)$_2$] ppm. ^{31}P NMR: δ = 238.9 ppm (s). MS: *m*/*z* (%) = 791 [(M)$^+$, 4], 706 [(M-Thex)$^+$, 3.5], 563 [(M-2(Thex)-SiMe$_2$)$^+$, 2.5], 505 [(M-2(C(*i*Pr)Me$_2$)-2(SiMe$_2$))$^+$, 3.5], 438 [(504-(C$_5$H$_5$))$^+$, 3], 85 [(C(*i*Pr)Me$_2$)$^+$, 25], 73 [(SiMe$_3$)$^+$, 100], 43 [(*i*Pr)$^+$, 35]. $C_{36}H_{58}P_2Si_2Zr_2$ (791.4): calcd. C 54.63, H 7.38; found C 54.46, H 7.30.

Preparation of $\{(\eta^5\text{-}C_5H_5)_2ZrPSi i\text{Pr}_3\}_2$ (3b): The compound was synthesized by a procedure similar to that for **3a**, starting from **1b** (1.50 g, 1.82 mmol). Yield: 1.31 g (1.59 mmol, 87.4%). ^{1}H NMR: δ = 4.98 (s, 20 H, C_5H_5), 1.34 [d, 36 H, $^3J_{H,H}$ = 6.7 Hz, CH(C*H*$_3$)$_2$], 1.11 [sept, 6 H, $^3J_{P\text{-}H}$ = 6.9 Hz, C*H*(CH$_3$)$_2$] ppm. ^{31}P NMR: δ = 229.8 (s) ppm. MS: *m*/*z* (%) = 819 [M]$^+$ (1), 157 [Si(*i*Pr)$_3$]$^+$ (100), 115 [Si(*i*Pr)$_2$]$^+$ (78), 43 [*i*Pr]$^+$ (40). $C_{38}H_{62}P_2Si_2Zr_2$ (819.5): calcd. C 55.69, H 7.62; found C 55.45, H 7.60.

Preparation of $\{(\eta^5\text{-}C_5H_5)_2ZrPSiF(t\text{Bu})(2,4,6\text{-}i\text{Pr}_3C_6H_2)\}_2$ (3c): A solution of **1c** (1.23 g, 1.09 mmol) in toluene (50 mL) was refluxed for 12 h. Concentrating the solution to about 20 mL and cooling at 4 °C afforded brown-red crystals. Alternatively, the desired product was also accessible upon heating the solution for 8 h at 50 °C in the presence of Pd/C (0.1 g). Yield: 0.87 g (0.77 mmol, 71%). ^{1}H NMR: δ = 7.31 (s, 4 H, *m*-*H*), 6.40 (s, 20 H, C_5H_5), 4.59 [sept, 4 H, $^3J_{H,H}$ = 6.9 Hz, *o*-C*H*(CH$_3$)$_2$], 2.79 [sept, 2 H, $^3J_{H,H}$ = 6.9 Hz, *p*-C*H*(CH$_3$)$_2$], 1.02 [s, 18 H, C(C*H*$_3$)$_3$], 1.23 [d, 12 H, $^3J_{H,H}$ = 6.9 Hz, *p*-CH(C*H*$_3$)$_2$], 1.15 [d, 24 H, $^3J_{H,H}$ = 6.9 Hz, *o*-CH(C*H*$_3$)$_2$] ppm. ^{31}P NMR: δ = 260.3 (s) ppm. ^{19}F NMR: δ = –133.6 (s) ppm. MS: *m*/*z* (%) = 1119 [M]$^+$ (1), 307 [FSi(*t*Bu)(2,4,6-*i*Pr$_3$C$_6$H$_2$)]$^+$ (38), 203 [*i*Pr$_3$C$_6$H$_2$]$^+$ (51), 43 [*i*Pr]$^+$ (100). $C_{58}H_{84}F_2P_2Si_2Zr_2$ (1119.9): calcd. C 62.20, H 7.56; found C 62.02, H 7.51.

 © 2005 Wiley-VCH Verlag GmbH & Co. KGaA, Weinheim

Table 3.Crystallographic data for **1a**, **1b**, **1c**, **3a,** and **3c**.

	1a	**1b**	**1c**	**3a**	**3c**
Empirical formula	$C_{36}H_{60}P_2Si_2Zr_2$	$C_{38}H_{64}P_2Si_2Zr_2$	$C_{58}H_{86}F_2P_2Si_2Zr_2$	$C_{36}H_{58}P_2Si_2Zr_2$	$C_{58}H_{84}F_2P_2Si_2Zr_2$
Formula mass	793.40	821.45	1121.83	791.38	1119.81
Temperature [K]	203(2)	213(2)	203(2)	203(2)	203(2)
Crystal system	monoclinic	triclinic	monoclinic	monoclinic	orthorhombic
Space group	$P2_1/c$	$P\bar{1}$	$P2_1/c$	$P2_1/c$	$Pcab$
a	11.452(1)	8.474(1)	14.793(5)	11.247(5)	18.96(1)
b	16.495(2)	10.797(1)	20.032(6)	16.522(8)	20.25(1)
c	10.247(1)	11.568(1)	20.064(7)	10.335(6)	30.59(1)
α	90	77.47(1)	90	90	90
β	94.18(1)	87.28(1)	101.36(4)	95.44(2)	90
γ	90	71.24(1)	90	90	90
V [Å^3]	1930.5(3)	978.0(2)	5829(3)	1911(2)	11743(10)
Z	2	1	4	2	8
$D_{calcd.}$ [g cm^{-3}]	1.365	1.395	1.278	1.375	1.267
$F(000)$	828	430	2360	824	4704
Crystal size [mm]	0.3 × 0.2 × 0.2	0.3 × 0.1 × 0.2	0.4 × 0.35 × 0.35	0.2 × 0.2 × 0.1	0.6 × 0.4 × 0.05
$\Theta_{max.}$[degr.]	2.34 to 24.99	2.04 to 22.50	1.73 to 25.02	2.20 to 22.50	1.61 to 23.02
Measured reflections	3334	2733	10295	2610	7690
Unique reflections	3331	2526	7531	2443	3649
Abs. coeff. [cm^{-1}]	0.708	0.701	0.494	0.715	0.491
Parameters	194	203	626	191	619
Goodness-of-fit on F^2	0.970	0.960	1.012	0.925	0.963
R_1 [$I > 2\sigma(I)$]	0.0545	0.0305	0.0383	0.0890	0.0765
wR_2 (all data)	0.1487	0.0746	0.0875	0.2669	0.2309

X-ray Crystallographic Study: Crystals of **1a**, **1b,1c**, **3a**, and **3b** were mounted on top of a thin glass fiber. Data were collected with a Siemens-Stoe AED2 (**1c** and **3b**) and a Bruker-AXS SMART 1000 (**1a**, **1b**, and **3a**) diffractometer with graphite monochromated Mo-$K\alpha$ radiation (λ = 0.71073 Å). The crystal data are summarized in Table 3. Structures were solved by direct methods (SHELX-97) and refined (SHELXL-97) by full-matrix least-squares methods. The positions of the P–H hydrogen atoms were localized in the difference Fourier map and refined. All other hydrogen atoms were introduced at calculated positions (riding model), included in structure factor calculations, and not refined.

CCDC-250811 to -250815 contain the supplementary crystallographic data for this paper. These data can be obtained free of charge from The Cambridge Crystallographic Data Centre via www.ccdc.cam.ac.uk/data_request/cif.

Acknowledgments

We thank the Deutsche Forschungsgemeinschaft and the Fonds der Chemischen Industrie for support.

[1] K. Issleib, H. Häckert, *Z. Naturforsch., Teil B* **1966**, *21b*, 519.
[2] S. R. Wade, G. H. Wallbridge, G. R. Willey, *J. Chem. Soc., Dalton Trans.* **1983**, 2555.
[3] a) E. Hey-Hawkins, S. Kurz, J. Baum, *Z. Naturforsch., Teil B* **1995**, *50b*, 239; b) E. Hey-Hawkins, F. Lindenberg, *Organometallics* **1994**, *13*, 4643; c) E. Hey-Hawkins, *Chem. Rev.* **1994**, *94*, 1661 .and references cited therein.
[4] J. Ho, D. W. Stephan, *Organometallics* **1991**, *10*, 3001.
[5] D. G. Dick, D. W. Stephan, *Can. J. Chem.* **1991**, *69*, 1146.
[6] a) W. D. Stohrer, R. Hoffmann, *J. Am. Chem. Soc.* **1972**, *94*, 779; b) M. M. Rohmer, M. Bénard, *Organometallics* **1991**, *10*, 157; c) M. M. Rohmer, M. Bénard, *J. Am. Chem. Soc.* **1992**, *114*, 4785.
[7] J. H. Wengrovius, R. R. Schrock, S. C. Day, *Inorg. Chem.* **1981**, *20*, 1844.
[8] M. Y. Chiang, S. Gambarotta, F. van Bolhuis, *Organometallics* **1988**, *7*, 1864.
[9] J. Ho, Z. Hou, R. J. Drake, D. W. Stephan, *Organometallics* **1993**, *12*, 3145.
[10] Z. Hou, T. L. Breen, E. W. Stephan, *Organometallics* **1993**, *12*, 3158.
[11] J. Ho, R. J Drake, D. W. Stephan, *J. Am. Chem. Soc.* **1993**, *115*, 3792.
[12] T. A. Bazhenova, A. V. Kulikov, A. F.Shestakov, A. E. Shilov, M. Y. Antipin, K. A. Lyssenko, Y. T Struchkov, V. D. Makhaev, *J. Am. Chem. Soc.* **1995**, *117*, 12176.
[13] a) J. Ho, D. W. Stephan, *Organometallics* **1992**, *11*, 1014; b) E. Hey-Hawkins, S. Kurz, J. Sieler, G. Baum, *J. Organomet. Chem.* **1995**, *486*, 229.
[14] H. Cox, P. B. Hitchcock, M. F. Lappert, *Angew. Chem.* **2004**, *116*, 4600; *Angew. Chem. Int. Ed.***2004**, *43*, 4500.
[15] a) G. Huttner, J. Borm, L. Zsolnai, *J. Organomet. Chem.* **1984**, *263*, C33; b) H. Lang, G. Mohr, O. Scheidsteger, G. Huttner, *Chem. Ber.* **1985**, *118*, 574; c) G. Huttner, *Pure Appl. Chem.* **1986**, *58*, 585 .and references cited therein.
[16] T. L. Breen, D. W. Stephan, *Organometallics* **1996**, *15*, 4509.

Received: September 30, 2004

 © 2005 Wiley-VCH Verlag GmbH & Co. KGaA, Weinheim

Addition of (Pyrazol-1-yl)acetyl and (Pyridin-2-yl)acetyl Groups to the Terminal Amino Group of a Phe−Gly Dipeptide Affords ATCUN-Like Copper(II) Binding Sites

Andrew N. Boa,*[a] Jonathan D. Crane,*[a] Radoslaw M. Kowalczyk,[b] and Nayer H. Sultana[a]

Keywords: Bioinorganic chemistry / Copper / Peptides / Tetradentate ligands

(Pyrazol-1-yl)acetic acid (HL^1, **1**) and (pyridin-2-yl)acetic acid have been successfully condensed with the terminal amino group of a Phe−Gly dipeptide to generate the derivatives $PzCH_2$–Phe−Gly (H_3L^2, **7**) and $PyCH_2$–Phe−Gly (H_3L^3, **8**) respectively, which contain ATCUN-like metal ion binding sites. The crystal structures of **1** and the copper(II) complexes $Cu(L^1)_2(H_2O)_2$ (**2**) and $[nBu_4N][Cu(L^2)]$ (**9**) are described. Complex **2** has a tetragonally-elongated, Jahn–Teller distorted octahedral geometry and complex **9** is square-planar. The structural similarity of the copper(II) complexes of **7** and **8** is demonstrated by their almost identical electronic absorption and EPR spectra.
(© Wiley-VCH Verlag GmbH & Co. KGaA, 69451 Weinheim, Germany, 2005)

Introduction

The amino terminal copper(II) and nickel(II)-binding protein motif (H_2N)–Xaa–Xaa–His (ATCUN), where Xaa is an α-amino acid other than Pro, occurs naturally in albumens (human, bovine and rat), histatins, human sperm protamine P2a, and neuromedins (C and K).[1] In the albumens its prominent role is proposed to be the binding and transport of metal ions, usually copper(II) and nickel(II). These ions have been the most extensively studied for ATCUN and ATCUN-like systems.[2–6] The presence of the ATCUN motif in the other proteins raises the possibility that the binding of metal ions may have some influence, presumably adverse, upon the normal function of these systems. It is also worthy of note that although the copper(II) binding sites identified in the prion protein of Creutzfeld–Jakob disease (CJD) are not terminal, they are nevertheless structurally very similar to the ATCUN motif, and it has been proposed that this may indicate the function of the normal cellular form of this protein is copper(II) binding, storage and/or transport.[7]

The investigation of the role of the ATCUN and related motifs in biological systems is well established, but of particular chemical importance are: (i) The observations that both the copper(II) and nickel(II) bound forms of the ATCUN motif are able to mediate oxidative DNA damage, including cleavage and cross-linking, and (ii) even simple ATCUN-like complexes display selective binding to, and cleavage of, DNA and RNA.[1,2] Indeed this has inspired the synthesis and study of ATCUN-containing proteins as selective DNA binding/cleavage systems.[2,5,6] In addition, polydentate ligands predominantly based upon the ATCUN motif have been demonstrated to act as highly selective, fluorescent chemosensors for copper(II).[8,9]

We report herein the synthesis of novel copper(II) binding peptides (Scheme 1) that do not contain a His residue within the amino-terminal protein sequence. In the peptide systems (**7** and **8**) the heterocyclic *N*-donor ligand for the metal ion is provided by the straightforward condensation of (pyrazol-1-yl)acetic acid (**1**) or (pyridin-2-yl)acetic acid with the amino terminal of the peptide. In principle, this approach allows the generation of an ATCUN-like site at the amino terminal of any dipeptide. In the specific examples described here the chosen starting dipeptide was Phe−Gly and in the resulting tetradentate systems the terminal carboxylate group acts as the fourth ligand to the bound, square-planar copper(II) ion.

Results and Discussion

(Pyrazol-1-yl)acetic acid HL^1 (**1**) was prepared in good yield by the alkylation of pyrazole with bromoacetic acid, and X-ray quality crystals were obtained by recrystallisation from water. The structure of **1** (Figure 1) reveals that the pyrazole group is not sufficiently basic for the compound to crystallise in a zwitterionic form; the freely refined acidic proton H(1) is clearly located on the carboxylic acid

[a] Department of Chemistry, University of Hull, Cottingham Road, Kingston-upon-Hull, HU6 7RX, UK
Fax: +44-1482-466410
E-mail a.n.boa@hull.ac.uk
[b] EPSRC Multi-frequency EPR Service Centre, Department of Chemistry, The University of Manchester, Manchester M13 9PL
Supporting information for this article is available on the WWW under http://www.eurjic.com or from the author

 © 2005 Wiley-VCH Verlag GmbH & Co. KGaA, Weinheim DOI: 10.1002/ejic.200400437

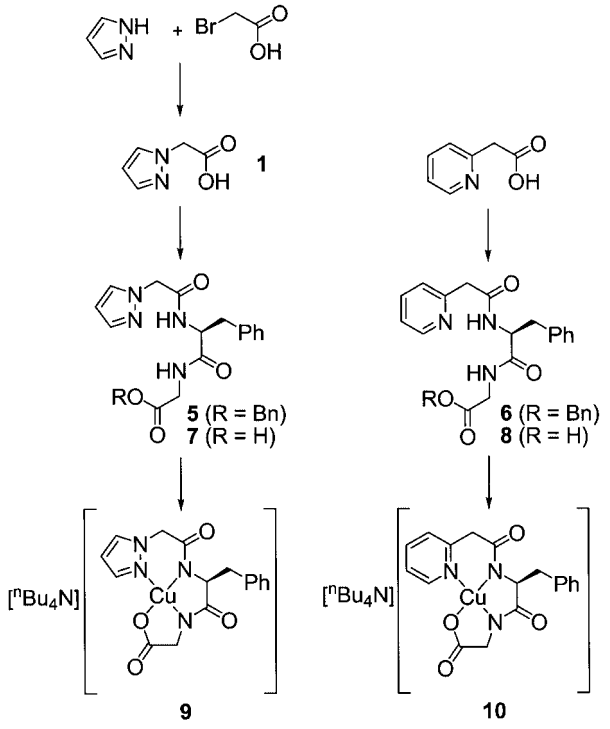

Scheme 1

group with a strong intermolecular hydrogen bond to N(1) of a neighbouring molecule. Thus **1** crystallises as parallel, 1-D, hydrogen-bonded chains that are helical and homochiral (non-centrosymmetric space group $P2_12_12_1$). The least-squares planes of the pyrazole and carboxylic acid groups are almost mutually perpendicular with a dihedral angle of 80.76(6)° and N(2) lies only 0.0276(14) Å out of the plane of the carboxylic group. In all these regards the structure is similar to that reported for the substituted analogue 3,5-dimethyl-(pyrazol-1-yl)acetic acid.[10]

The complexation of **1** with copper(II) yields the Jahn–Teller distorted, centrosymmetric, octahedral structure $Cu(L^1)_2(H_2O)_2$ (**2**), the molecular structure of which is shown in Figure 2. The ligand bite angle is 90.58(7)° and the neutral pyrazole Cu(1)–N(1) bond length of 1.954(2) Å is significantly shorter than the Cu(1)–O(1) bond length of 1.980(2) Å involving the anionic carboxylate ligand. This is consistent with the delocalisation of the carboxylate negative charge over both oxygen atoms as evinced by the similar C(5)–O(1) and C(5)–O(2) bond lengths of 1.274(3) and 1.246(2) Å respectively [Δd = 0.028(4) Å], and this delocalisation is stabilised by the presence of two hydrogen-bonds to the non-coordinated carboxylate oxygen atom O(2). Upon complexation the dihedral angle between the least-squares planes of the pyrazole and carboxylic acid groups has changed from 80.76(6)° in the free ligand (**1**) to 32.35(5)° in **2**. Due to the non-planarity of the ligand the dihedral angle between the pyrazole group and the copper square-plane is 22.55(4)°. The electronic absorption spectrum of **2** in aqueous solution is typical of axially elongated octahedral copper(II) with a single broad absorption band at 14700 cm^{-1} (ε = 32 $M^{-1}cm^{-1}$). There are no reported complexes of either (pyrazol-1-yl)acetic acid (**1**) or its simple derivatives in the literature, however several transition metal complexes (VO^{2+}, Mn^{2+}, Fe^{2+}, Co^{2+}, Ni^{2+} and Cu^{2+}) of the similar ligand imidazol-4-yl-acetic acid have been described.[11–16] The crystal structures of many of these have been reported,[17] but surprisingly not for Cu^{2+}. Furthermore, there is only one unequivocally characterised transition metal complex (Pt^{2+}) of (pyridin-2-yl)acetic acid or its simple derivatives.[18] To date, attempts to prepare and characterise other first row transition metal complexes of **1** have been unsuccessful, thus at present it is difficult to compare di-

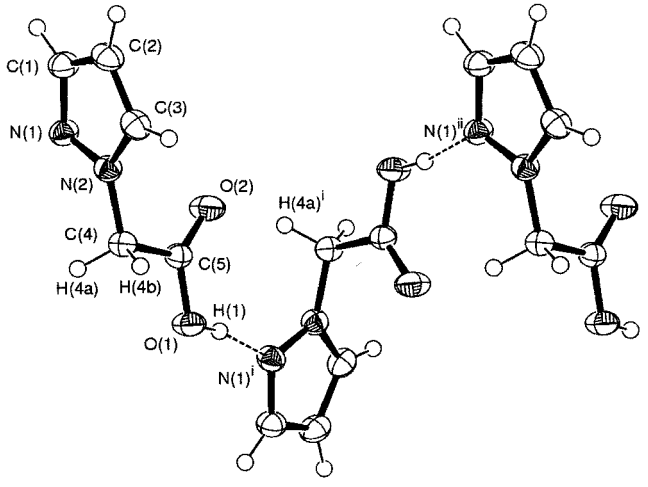

Figure 1. ORTEP[25] view of the molecular structure and hydrogen-bonding of **1** with thermal ellipsoids shown at 50 %. Selected bond lengths [Å] and angles [°]: O(1)–C(5), 1.309(2); O(2)–C(5), 1.207(2); O(1)–H(1), 0.95(3); H(1)···N(1)^i, 1.69(3); O(1)···N(1)^i, 2.628(2); O(1)–H(1)···N(1)^i, 170(3). Symmetry transformations: [i] $-x$, y + ½, $-z$ + 1½; [ii] x, y + 1, z.

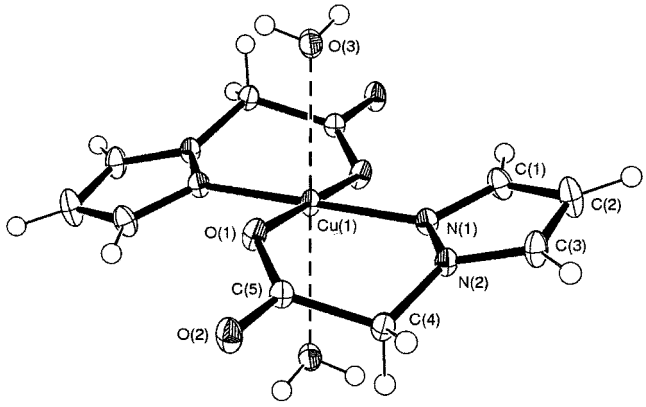

Figure 2. ORTEP[25] view of the molecular structure of **2** with thermal ellipsoids shown at 50 %. Selected bond lengths [Å] and angles [°]: Cu(1)–O(1), 1.980(2); Cu(1)–N(1), 1.954(2); Cu(1)–O(3), 2.503(2); O(1)–Cu(1)–N(1), 90.52(4); O(1)–Cu(1)–O(3), 92.57(4); N(1)–Cu(1)–O(3), 93.60(4); O(3)–H(3d), 0.80(2); H(3d)···O(2)^i, 2.11(2); O(3)···O(2)^i, 2.886(1); O(3)–H(3d)···O(2)^i, 167(2); O(3)–H(3e), 0.77(2); H(3e)···O(2)^{ii}, 2.03(2); O(3)···O(2)^{ii}, 2.801(1); O(3)–H(3e)···O(2)^{ii}, 176(2). Symmetry transformations: [i] x + ½, $-y$ + 1½, z + ½; [ii] $-x$ + 1½, y – ½, $-z$ – ½.

 © 2005 Wiley-VCH Verlag GmbH & Co. KGaA, Weinheim

rectly the coordination behaviour of these related ligand systems.

The two tetradentate square planar ligands H_3L^2 (**7**) and H_3L^3 (**8**) were prepared in two steps, from **1** and (pyridin-2-yl)acetic acid, respectively, by standard peptide coupling with the dipeptide H–Phe−Gly−OBn, followed by hydrolysis of the benzyl ester. The complexation of **7** with copper(II) yields the deep pink, square-planar complex $[Cu(L^2)]^-$ as the tetra-n-butylammonium salt **9**. The crystal structure of the complex anion of **9** (Figure 3) reveals that the copper(II) centre is close to planar; the sum of the angles subtended at the metal is 360.0° and the maximum deviation from the least-squares coordinate plane for Cu(1) and its four donor atoms is only 0.017(2) Å for N(4). There is a very slight tetrahedral distortion of the Cu(1) coordination geometry with the pairs of opposite donor atoms lying on opposite sides of the least-squares plane and N(1)–Cu(1)–N(4) and N(3)–Cu(1)–O(3) angles of 178.79(6) and 168.71(5)° respectively. As expected, the shortest bond lengths in the copper coordination sphere involve the deprotonated amide nitrogen atoms. The strength of these bonds is further illustrated by the short C=O [average 1.244(2) Å] and long C–N [average 1.324(2) Å] bond lengths within the amide groups showing very little delocalisation of the formal negative charge onto the oxygen atom, and hence relatively little contribution to the electronic structure by the oxy-imine [RN=C(R′)–O⁻] resonance form. Due to the square-planar geometry of the copper centre in **9** and the consequent absence of any axial ligand interactions, the neutral pyrazole Cu(1)–N(1) bond length of 1.9321(13) Å is shorter than in **2**, despite being *trans* to the shortest Cu(1)–N(amide) bond. The carboxylate Cu(1)–O(3) bond length is the longest in the coordination sphere, yet this is also shorter than the similar bond in **2**. In addition the carboxylate C(8)–O bond lengths are more dissimilar [Δd = 0.067(3) Å] than in **2**, consistent with the absence of any stabilisation of negative charge on O(4) by hydrogen bonding. Due to the non-planar nature of the (pyrazol-1-yl)acetyl group the dihedral angle between the pyrazole group and the copper square-plane is 17.81(5)°, similar to that found in **2**. The phenyl substituent of the ligand is positioned above one face of the copper square plane in the solid state and the angle between their respective least-squares planes is 61.59(5)°. Of the three possible staggered conformations about the C(6)–C(10) bond, this is the one that minimises the unfavourable steric interactions between the phenyl ring and the carbonyl oxygen atoms O(1) and O(2). The Flack parameter determined from the structure refinement confirms the known (*S*)-chirality of the ligand at C(6), being derived from (*S*)-phenylalanine. The pink colour of **9** is retained in dichloromethane solution and arises from a single absorption band at 19500 cm^{-1} in the visible region of the electronic absorption spectrum. There is no significant change to the spectrum either in dichloromethane/methanol (1:1) or upon the addition of ten equivalents of a good N-donor ligand (*N*-methylimidazole), indicating that the square-planar geometry is retained under these conditions. In aqueous solution however, the complex is pale violet and the absorption band shifts to 18000 cm^{-1}. This shift of 1500 cm^{-1} to lower energy is similar to that observed for the 1,4-diazacycloheptane (LL) complexes $[Cu(LL)_2]^{2+}$ and $[Cu(LL)_2(H_2O)]^{2+}$,[19] and may therefore indicate the coordination of one water ligand to give a five coordinate, square pyramidal complex in aqueous solution.

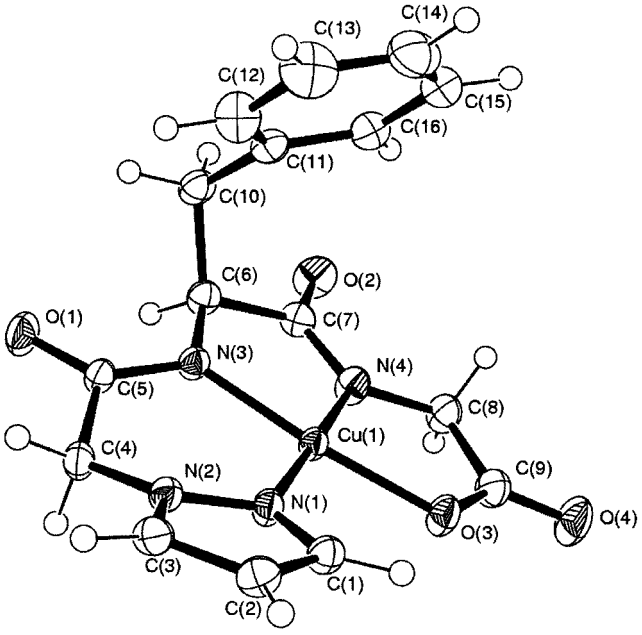

Figure 3. ORTEP[25] view of the structure of the complex cation of **9** with thermal ellipsoids shown at 50 %. Selected bond lengths [Å] and angles [°]: Cu(1)–O(3), 1.9606(12); Cu(1)–N(1), 1.9321(13); Cu(1)–N(3), 1.9299(13); Cu(1)–N(4), 1.8654(13); O(1)–C(5), 1.246(2); N(3)–C(5), 1.325(2); O(2)–C(7), 1.242(2); N(4)–C(7), 1.323(2); O(3)–C(9), 1.298(2); O(4)–C(9), 1.231(2); N(1)–Cu(1)–N(3), 94.42(5); N(3)–Cu(1)–N(4), 84.66(6); O(3)–Cu(1)–N(4), 84.09(6); O(3)–Cu(1)–N(1), 96.85(5).

The (pyridin-2-yl)acetyl analogue, **10**, could be prepared as a pink complex by the same method as used for **9**. Unfortunately, a pure or crystalline sample of **10** could not be obtained due to its slow decomposition during attempted recrystallisation, resulting in a pale green solution. Electronic absorption spectra of **10** in dichloromethane/methanol (3:1) and water were recorded for freshly prepared samples and were found to be almost identical to the corresponding spectra of **9**, consistent with the formation of a structurally very similar complex. Additionally, the negative ion electrospray mass spectrum of complex **10** in dichloromethane solution revealed the desired molecular ion. For further confirmation of the structure of **10**, and for comparison with **9**, the EPR spectra of both were measured at X-band. Complexes **9** and **10** gave near identical spectra in the same solvents systems (Figure 4).

At room temperature the Cu hyperfine (to both isotopes), as well as ligand superhyperfine splittings to ^{14}N and ^{1}H can be resolved, in both aqueous and in CH_2Cl_2 solution. In frozen solution at ca. 110 K (adding ca. 10 % glycerol to H_2O, or ca. 10 % toluene to CH_2Cl_2, to aid glassing) we observed well resolved spectra which are axial within the resolution of the X-band experiment. The ^{14}N

 © 2005 Wiley-VCH Verlag GmbH & Co. KGaA, Weinheim

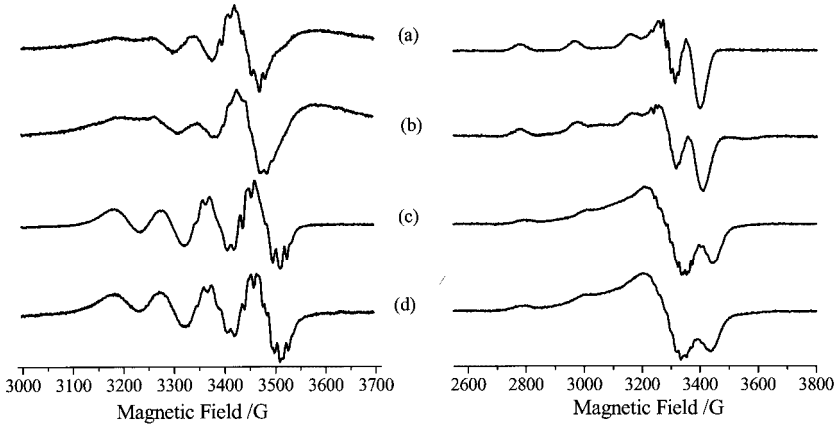

Figure 4. Fluid solution EPR spectra at 290 K and 9.773 GHz (left) and frozen solution EPR spectra at 120 K and 9.457 GHz (right). (a) **9** in H_2O/glycerol; (b) **10** in H_2O/glycerol; (c) **9** in CH_2Cl_2/toluene; (d) **10** in CH_2Cl_2/toluene.

Table 1. Simulation of EPR parameters for complex **9** (A in Gauss). Complex **10** gave nearly identical spectra in the same solvent systems.

Solvent	g_{iso}	A_{iso}^{Cu}	A_{iso}^{3N}	$A_{iso}^{2/3H}$	g_z	g_{xy}	A_z^{Cu}	A_{xy}^{Cu}	A_{xy}^{3N}
H_2O	2.104	79	14	8	2.206	2.040	190	20	16
CH_2Cl_2	2.088	90	16	8	2.165	2.050	216	35	16

Table 2. Comparison of visible and EPR parameters for complexes **9** and related Cu^{II} complexes (data taken from reference 1. *pH = 6.5; HSA, human serum albumin; DSA, dog serum albumin; A values in Gauss).

Complex*	$\lambda_{max.}$ (nm)	$\varepsilon_{max.}$ ($M^{-1}cm^{-1}$)	g_z	g_{xy}	A_z^{Cu}
9 (H_2O)	555	110	2.206	2.040	190
9 (CH_2Cl_2)	513	135	2.165	2.050	216
HSA−Cu^{II}	525	101	2.166	2.051	214
DSA−Cu^{II}	600 (br)	−	2.256	2.059	163
Gly−Gly−His−Cu^{II}	525	103	2.170	2.051	211
Asp−Ala−His−Cu^{II}	525	103	2.167	2.050	211

coupling in the "perpendicular" region of the spectra is also resolved. The frozen solution EPR spectra were modeled assuming coupling of the unpaired electron with Cu and to three equivalent in-plane coordinated ^{14}N nuclei (equivalent within the resolution of the EPR experiment). These simulations were sensitive to both the ^{14}N and Cu hyperfine coupling in the "perpendicular" region (the latter having been estimated initially from the values of A_z^{Cu} and A_{iso}^{Cu}). In order to simulate the isotropic spectra it was also necessary to include coupling to ^1H (this is not resolved in the anisotropic spectra). Simulation parameters are in Table 1. The large values of A_z^{Cu} are consistent with the N_3O in-plane coordination, and the A^N values are typical for (in-plane) N-bound Cu complexes. The important trends are that g_z increases in switching from CH_2Cl_2 to H_2O solution and A_z^{Cu} (and A_{xy}^{Cu}) decreases in going from CH_2Cl_2 to H_2O solution. These trends are consistent with going from a square-planar complex in dichloromethane to square pyramidal species in water and thus support the conclusions drawn from the electronic spectra. The EPR spectroscopic data from **9** in dichloromethane compared with data from human serum albumin, Gly−Gly−His−Cu^{II} and Asp−Ala−His−Cu^{II} are very similar, and are consistent with square-planar coordination in these systems (Table 2). The switch to a square pyramidal structure for complex **9** in water is clearly revealed with the expected changes in g_z, A_z^{Cu} and λ_{max}. Dog serum albumin does not show the ATCUN motif as it does not contain histidine as the third residue from the *N* terminus. The EPR and visible absorption data for this albumin is clearly divergent from the other complexes.

In conclusion, the condensation of (pyrazol-1-yl)acetic acid and (pyridin-2-yl)acetic acid with the terminal amino group of a dipeptide has been shown to generate copper(II) ion binding sites. The extension of this methodology to larger oligopeptides, the investigation of the chemical reactivity of the metal centre, the cytotoxicity of these complexes and their interaction/reaction with DNA are in progress.

Experimental Section

The protected dipeptide [(*S*)-2-*tert*-butoxycarbonylamino-3-phenylpropanoylamino]acetic acid benzyl ester (Boc−Phe−Gly−OBn, **3**) was prepared using standard procedures.[20] Elemental analyses were obtained with a Fisons EA1108 CHNS analyser. IR spectra were recorded as KBr disks with a Perkin–Elmer Paragon-100 FT-IR spectrophotometer. Electronic absorption spectra were recorded

 © 2005 Wiley-VCH Verlag GmbH & Co. KGaA, Weinheim

in the range 1100–300 nm with a Perkin–Elmer Lambda-40 spectrophotometer. NMR spectra were recorded with a Jeol JNM-LA400 spectrometer at room temperature (20 °C) and are reported relative to tetramethylsilane. Mass spectra were recorded with a Finnigan MAT-1020 or Thermo Finnigan LCQ ion trap spectrometer. EPR spectra were measured with a Bruker EMX X-band spectrometer.

(Pyrazol-1-yl)acetic Acid (HL^1, 1): Sodium hydroxide (16.2 g, 0.404 mol) was dissolved in water (185 mL) and pyrazole (12.5 g, 0.184 mol) was added. Next bromoacetic acid (28.1 g, 0.202 mol) was added in portions with stirring and the resulting mixture then heated at reflux for 2 hours. After cooling, the mixture was carefully acidified (2 M HCl) to about pH 3 whereupon the product crystallized from the solution. After drying under vacuum, **1** was isolated as a pale yellow crystalline solid. Yield: 15.26 g (67 %). ^{1}H NMR (400 MHz, $CDCl_3$): δ = 4.0–4.5 (br. s, 1 H, OH), 4.95 (s, 2 H, CH_2), 6.25 [dd, ^3J(H,H) = 2.3 and 1.8 Hz, 1 H, PzH], 7.42 (d, $^3J_{H,H}$ = 1.4 Hz, 1 H, PzH), 7.70 (d, $^3J_{H,H}$ = 2.3 Hz, 1 H, PzH) ppm. IR (KBr): $\tilde{\nu}$ = 3423, 2509, 1733, 1071, 780 cm^{-1}. MS (EI): *m*/*z* (%) = 126 (20) [M$^+$].

Synthesis of the Copper(II) Complex $Cu(L^1)_2(H_2O)_2$ (2): A solution of copper(II) acetate (0.39 g, 2 mmol) in water (15 mL) was added to a solution of (pyrazol-1-yl)acetic acid (**1**, 0.50 g, 4 mmol) in water (25 mL) with stirring. The blue solution was filtered and the solvent was evaporated slowly. Large, blue, X-ray quality crystals of the complex **2** deposited. Yield: 0.39 g (56 %). $C_{10}H_{14}CuN_4O_6$ (349.79): calcd. C 34.34, H 4.03, N 16.02; found C 34.11, H 3.98, N 15.86. UV/Vis (H_2O): λ = 14700 cm^{-1} (32 M^{-1}cm^{-1}). IR (KBr): $\tilde{\nu}$ = 3466, 1655, 1415, 1369, 1338, 1284, 1076, 926, 809, 755, 722, 614, 577 cm^{-1}.

(*S*)-[1-(Benzyloxycarbonylmethylcarbamoyl)-2-(phenylethyl)]ammonium Trifluoroacetate (TFA·H–Phe−Gly−OBn, 4): The dipeptide **3** (2.51 g 6.09 mmol) was dissolved in dichloromethane (10 mL) to which was added trifluoroacetic acid (3 mL). The mixture was stirred in an open flask for 2–3 h, and then the solvent and excess trifluoroacetic acid were evaporated in vacuo. The resulting oil was triturated thoroughly with diethyl ether/toluene to give **4** as a white solid. Yield: 2.26 g (87 %). ^{1}H NMR (400 MHz, $CDCl_3$/[D_6]DMSO): δ = 3.18 (ABX, $^2J_{H,H}$ = 13.9, $^3J_{H,H}$ = 6.2, 6.8 Hz, 2 H, $PhCH_2$), 3.98 (d, $^3J_{H,H}$ = 5.6 Hz, 2 H, CH_2NH), 4.31 (br. t, $^3J_{H,H}$ ≈ 6.7 Hz, 1 H, C*H*CH_2), 5.10 (s, 2 H, CH_2O), 7.21–7.47 (m, 10 H, PhH), 8.80 (br. t, $^3J_{H,H}$ ≈ 5.6 Hz, 1 H, NH) ppm.

Benzyl {(*S*)-3-Phenyl-2-[(2-pyrazol-1-yl)acetylamino]propionylamino}acetate ($PzCH_2CO$–Phe−Gly−OBn, 5): A sample of dipeptide **3** (3.0 g, 7.3 mmol) was deprotected as above and the resulting crude oil dissolved in dry dimethylformamide (50 mL). Next (pyrazol-1-yl)acetic acid (**1**, 1.08 g, 8.0 mmol) hydroxybenzotriazole (1.18 g, 8.8 mmol) and diisopropylethylamine (1.52 mL, 9.6 mmol) were added to the solution followed by 1-[3-(dimethylamino)propyl]-3-ethylcarbodiimide hydrochloride (1.54 g, 8.8 mmol). After stirring at room temperature overnight the dimethylformamide was removed by rotary evaporation under high vacuum and the oil dissolved in dichloromethane/water. After separation, the dichloromethane layer was washed with water, dried with anhydrous sodium sulfate, filtered then the solvent removed in vacuo. The resulting buff-coloured solid was dissolved in the minimum volume of hot ethyl acetate, and upon cooling an amorphous white solid precipitated. Filtration and thorough drying (to remove large amounts of ethyl acetate associated with the solid) under vacuum gave **5**. Yield: 2.34 g (76 %). $C_{23}H_{24}N_4O_4$ (420.18): calcd. C 65.70, H 5.75, N 13.33; found C 65.50, H 5.85, N 13.31. ^{1}H NMR (400 MHz, $CDCl_3$): δ = 3.02 (ABX, $^2J_{H,H}$ = 13.9, $^3J_{H,H}$ = 6.6, 7.3 Hz, 2 H, $PhCH_2$), 3.98 (ABX, $^2J_{H,H}$ = 18.3, $^3J_{H,H}$ = 5.2, 5.6 Hz, 2 H, CH_2NH), 4.68 (br. q, $^3J_{H,H}$ ≈ 7.3 Hz, 1 H, C*H*CH_2), 4.75 (AB, $^2J_{H,H}$ = 16.8 Hz, 2 H, CH_2Pz), 5.14 (s, 2 H, CH_2O), 6.30 (t, $^3J_{H,H}$ ≈ 2 Hz, 1 H, PzH), 6.63 (br. t, $^3J_{H,H}$ ≈ 5.6 Hz, 1 H, NH), 6.77 (br. d, $^3J_{H,H}$ ≈ 7.8 Hz, 1 H, NH), 7.04–7.06 (m, 2 H, PhH), 7.17–7.26 (m, 3 H, PhH), 7.32–7.39 (m, 6 H, PhH + PzH), 7.58 (d, $^3J_{H,H}$ ≈ 2 Hz, 1 H, PzH) ppm. ^{13}C NMR (100.6 MHz, $CDCl_3$): δ = 37.7, 41.3, 54.3, 54.7, 67.2, 106.8, 127.0, 128.4, 128.5(7), 128.6(3), 128.6(5), 129.2, 131.1, 135.1, 136.1, 141.3, 167.5, 169.2, 170.5 ppm. MS (EI): *m*/*z* (%) = 420 (1) [M$^+$]. HRMS found: [M]$^+$ 420.1798; $C_{23}H_{24}N_4O_4$ requires [M]$^+$ 420.1798.

Benzyl {(*S*)-3-Phenyl-2-[(2-pyridin-2-yl)acetylamino]propionylamino}acetate (2-$PyCH_2CO$–Phe−Gly−OBn, 6): A sample of the dipeptide salt **4** (5.0 g, 12.0 mmol) was coupled to (pyridin-2-yl) acetic acid hydrochloride (2.04 g, 12.0 mmol) as described above to give the title compound as a white solid. Yield: 3.40 g (67 %). ^{1}H NMR (400 MHz, $CDCl_3$): δ = 3.10 (ABX, $^2J_{H,H}$ = 14.0, $^3J_{H,H}$ = 5.9, 7.9 Hz, 2 H, $PhCH_2$), 3.66 (AB, $^2J_{H,H}$ = 15.7 Hz, 2 H, CH_2Py), 4.01 (ABX, $^2J_{H,H}$ = 18.2, $^3J_{H,H}$ = 5.0, 5.9 Hz, 2 H, CH_2NH), 4.77 (br. q, $^3J_{H,H}$ ≈ 8.0 Hz, 1 H, C*H*CH_2), 5.14 (s, 2 H, CH_2O), 7.09–7.20 (m, 8 H, ArH), 7.30–7.38 (m, 5 H, ArH), 7.60 (td, $^3J_{H,H}$ = 7.6, $^4J_{H,H}$ = 1.7 Hz, 1 H, ArH), 7.76 (br. d, $^3J_{H,H}$ ≈ 7.9 Hz, 1 H, NH), 8.41 (br. d, $^3J_{H,H}$ ≈ 4.8 Hz, 1 H, ArH) ppm. ^{13}C NMR (100.6 MHz, $CDCl_3$): δ = 37.4, 41.4, 44.7, 54.4, 67.1, 122.1, 124.0, 126.7, 128.3, 128.5 (two peaks), 128.6, 129.2, 135.2, 136.6, 137.2, 149.0, 155.1, 169.4, 169.6, 171.3 ppm. MS (EI): *m*/*z* (%) = 431 (2) [M$^+$], 340 (20), 239 (45), 120 (100).

{(*S*)-3-Phenyl-2-[(2-pyrazol-1-yl)acetylamino]propionylamino}acetic Acid (H_3L^2, 7): The modified tripeptide **5** (1.0 g, 2.38 mmol) was dissolved in H_2O/ethanol (1:1, 8.0 mL), and to this solution was added 1 M NaOH (7.2 mL, 7.2 mmol). The mixture was stirred at room temperature overnight, then carefully acidified to pH ≈ 2–3 with 2 M HCl causing precipitation of a white fluffy solid. After removal by filtration the solid obtained was dried in vacuo to yield **7**. Yield: 0.546 g (69 %). $C_{16}H_{18}N_4O_4$ (330.34): calcd. C 58.17, H 5.49, N 16.96; found C 58.15, H 5.53, N 16.74. ^{1}H NMR (400 MHz, [D_6]DMSO): δ = 2.90 (ABX, $^2J_{H,H}$ = 13.7, $^3J_{H,H}$ = 4.3, 9.5 Hz, 2 H, $PhCH_2$), 3.77 (d, $^3J_{H,H}$ = 6.1 Hz, 2 H, CH_2NH), 4.57 (br. dt, $^3J_{H,H}$ ≈ 9, 4.2 Hz, 1 H, C*H*CH_2), 4.75 (AB, $^2J_{H,H}$ = 16.0 Hz, 2 H, CH_2Pz), 6.20 (br. t, $^3J_{H,H}$ ≈ 2 Hz, 1 H, PzH), 7.16–7.27 (m, 5 H, PhH), 7.39 (d, $^3J_{H,H}$ = 1.7 Hz, 1 H, PzH), 7.55 (d, $^3J_{H,H}$ = 2.5 Hz, 1 H, PzH), 8.32 (br. d, $^3J_{H,H}$ ≈ 8.5 Hz, 1 H, NH), 8.49 (br. t, $^3J_{H,H}$ ≈ 5.8 Hz, 1 H, NH) ppm. ^{13}C NMR (100.6 MHz, [D_6]DMSO): δ = 37.9, 40.9, 53.6(8), 53.7(1), 106.3, 126.3, 128.1, 129.2, 131.2, 137.5, 138.8, 166.4 (2 peaks), 171.0 ppm. MS (EI): *m*/*z* (%) = 330 (2) [M$^+$].

{(*S*)-3-Phenyl-2-[(2-pyridin-2-yl)acetylamino]propionylamino}acetic Acid (H_3L^3, 8): The modified tripeptide ester **6** (3.0 g, 6.96 mmol) was hydrolysed by the method described for **7** to give three crops of a white solid. Total yield: 1.57 g (66 %). ^{1}H NMR (400 MHz, [D_6]DMSO + $CDCl_3$): δ = 2.77 (dd, $^2J_{H,H}$ = 13.9, $^3J_{H,H}$ = 10.4 Hz, 1 H, PhCH*H*CH), 3.10 (dd, $^2J_{H,H}$ = 13.9, $^3J_{H,H}$ = 3.9 Hz, 1 H, PhCH*H*CH), 3.59 (AB, $^2J_{H,H}$ = 14.6 Hz,, 2 H, CH_2Py), 3.80 (ABX, $^2J_{H,H}$ = 13.9, $^3J_{H,H}$ = 14.6, 14.6 Hz, 2 H, CH_2NH), 4.58 (br. dt, $^3J_{H,H}$ = 8.7, 4.2 Hz, 1 H, C*H*CH_2), 7.07 (d, $^3J_{H,H}$ = 7.9 Hz, 1 H, ArH), 7.15–7.24 (m, 6 H, ArH), 7.62 (td, $^3J_{H,H}$ = 7.6, $^4J_{H,H}$ = 1.7 Hz, 1 H, ArH), 8.42–8.46 (m, 2 H, NH + ArH), 8.52 (br. t, $^3J_{H,H}$ ≈ 5.9 Hz, 1 H, NH), 12.6 (br. s, 1 H, CO_2 H) ppm. ^{13}C NMR (100.6 MHz, [D_6]DMSO + $CDCl_3$): δ = 37.5, 40.7, 44.6, 53.8, 121.6, 123.4, 126.1, 127.9, 129.1, 136.4, 137.8, 148.6, 156.1, 168.8, 171.0, 171.4 ppm. MS (EI): *m*/*z* (%) = 341 (1) [M$^+$], 250 (15), 239 (20), 120 (90).

 © 2005 Wiley-VCH Verlag GmbH & Co. KGaA, Weinheim

Table 3. Crystal data and structure refinement for **1**, **2** and **9**.

Compound	**1**	**2**	**9**
Empirical formula	$C_5H_6N_2O_2$	$C_{10}H_{14}CuN_4O_6$	$C_{32}H_{51}CuN_5O_4$
M_r [g mol^{-1}]	126.12	349.79	633.32
Crystal system	orthorhombic	monoclinic	orthorhombic
Space group	$P2_12_12_1$	$C2/c$	$P2_12_12_1$
a [Å]	4.9166(4)	12.4705(16)	10.2652(3)
b [Å]	7.7232(9)	10.2272(10)	17.4034(6)
c [Å]	15.8610(15)	10.3266(12)	18.8660(8)
β [°]	90	99.298(10)	90
V [Å^3]	602.27(10)	1299.7(3)	3370.4(2)
Z, $D_{calcd.}$ [g cm^{-3}]	4, 1.391	4, 1.788	4, 1.248
μ (Mo-K$_\alpha$) [mm^{-1}]	0.110	1.716	0.689
$F(_{ooo})$	264	716	1356
Crystal dimensions [mm^3]	0.60 × 0.20 × 0.20	0.30×0.20×0.20	0.50×0.40×0.30
$\theta_{min.}$, $\theta_{max.}$ [°]	2.57, 34.81	2.59, 30.00	2.46, 34.77
h, k, l ranges	–7/6, –12/10, –25/25	–17/17, –12/14, –14/14	–16/14, –27/27, –30/30
Collected/unique reflections	8870/1525	6426/1862	50653/14515
Restraints, parameters	0, 87	0, 106	0, 380
$T_{min.}$, $T_{max.}$	–	0.6075, 0.7546	0.6962, 0.8495
R_{int}	0.0389	0.0195	0.0380
Goodness-of-fit on F^2	1.088	1.025	1.085
R indices [$I > 2\sigma(I)$]	R_1 = 0.0429, wR_2 = 0.1082	R_1 = 0.0212, wR_2 = 0.0563	R_1 = 0.0392, wR_2 = 0.0961
R indices (all data)	R_1 = 0.0529, wR_2 = 0.1148	R_1 = 0.0260, wR_2 = 0.0571	R_1 = 0.0475, wR_2 = 0.1029
Flack parameter	not determined	–	0.001(7)
Larg. diff. peak/hole [e·Å^{-3}]	0.219/–0.249	0.427/–0.362	0.696/–0.732

Synthesis of the Copper(II) Complex [Bu$_4$N][Cu(L^2)] (9): The modified tripeptide **7** (200 mg, 0.606 mmol) was added to potassium hydroxide (102.1 mg, 1.808 mmol) in water (2 mL) to give a pale yellow solution. To this was added dropwise a solution of cupric acetate monohydrate (120.7 mg, 0.606 mmol) in water (2 mL) and then the resulting royal blue solution was filtered through a cotton wool plug. (Tetra-*n*-butyl)ammonium bromide (194.3 mg, 0.606 mmol) was added and the solution evaporated to dryness giving a dark blue solid. Addition of chloroform (10 mL) resulted in the formation of a cherry red solution and white solid, the latter being removed by filtration. The red solution was evaporated and thoroughly dried in vacuo before crystallization from dichloromethane/ethyl acetate (1:6). Yield: 300 mg (78 %). Growth of crystals suitable for single-crystal X-ray diffraction was achieved by slow evaporation of dichloromethane from a dichloromethane/ethyl acetate solution, resulting in the isolation of red needle-like crystals. $C_{32}H_{51}CuN_5O_4$ (633.33): calcd. C 60.69, H 8.12, N 11.06; found C 60.48, H 7.84, N 11.05. MS (APCI): *m*/*z* (%) = 631.3 [M – H]$^+$. UV/Vis (CH_2Cl_2): λ = 19500 cm^{-1} (135 M^{-1} cm^{-1}); (H_2O): 18000 (110). IR (KBr): $\tilde{\nu}$ = 3090 (w), 2964 (m), 2935 (w), 2875 (m), 1623 (m), 1598 (s), 1387 (m), 1338 (m), 1081 (w), 1073 (w), 756 (w), 709 (w), 536 (w), 500 (w) cm^{-1}. EPR: See Table 1 and Figure 4. These spectra are available as Supporting Information (see also the footnote on the first page of this article).

Synthesis of the Copper(II) Complex [Bu$_4$N][Cu(L^3)] (10): The preparation of the copper(II) complex of the modified tripeptide **8** (200 mg, 0.606 mmol) was attempted using the method described above for **9**. Neither a pure sample nor X-ray quality crystals of **10** could be obtained due to the slow decomposition of the complex in solution over several days to give a pale green solution. The EPR and electronic absorption spectra were determined for freshly prepared solutions and the extinction coefficients were calculated with the assumption that all the ligand was successfully complexed to copper(II). UV/Vis [CH_2Cl_2/methanol (3:1)]: λ = 19200 cm^{-1} (125 M^{-1} cm^{-1}); (H_2O): 18000 (110). MS (negative ion electrospray) [CH_2Cl_2]: *m*/*z* (%) = 401.0 (100) ([M]$^-$ Cu^{63}), 403.0 (45) ([M]$^-$, Cu^{65}). EPR: see Figure 4 for the near identical spectra of complexes **9** and **10**. This data is available as Supporting information.

Crystal Structure Determinations: Data for **1**, **2** and **9** were collected at 150(2) K with graphite-monochromated Mo-K_α radiation (wavelength of 0.71073 Å) with a Stoe IPDS II image plate diffractometer (Table 3). Space groups were determined by an examination of the systematic absences in the data, and their correct identification was confirmed by the successful solution and refinement of the structures. Solutions were provided via direct methods using SHELXS-97 and refined by full-matrix least-squares on F^2 using SHELXL-97.[21] All non-hydrogen atoms were refined anisotropically. All hydrogen atoms on carbon were placed in calculated positions with U_{iso} set at 1.2 times the U_{eq} of the parent atom, and the positional and isotropic displacement parameters of all O–H groups were freely refined. Numerical absorption corrections were applied to **2** and **9** using X-RED/X-SHAPE.[22] The analysis of the structures was carried out with PLATON[23] and WinGX.[24]

Supplementary data for **1**, **2** and **9** (CCDC-239525, -239527 and -239526, respectively) are available free of charge from the Cambridge Crystallographic Data Centre (CCDC) via www.ccdc.cam.ac.uk/data_request/cif.

Acknowledgments

We acknowledge the University of Hull for financial support of this work and Dr E. J. L. McInnes, of the EPSRC Multi-frequency EPR Service Centre at The University of Manchester, for his contribution to the analysis of the EPR data.

[1] C. Harford, B. Sarkar, *Acc. Chem. Res.* **1997**, *30*, 123–130.
[2] E. C. Long, *Acc. Chem. Res.* **1999**, *32*, 827–836.
[3] L. W. Donaldson, N. R. Skrynnikov, W. Y. Choy, D. R. Muhandiram, B. Sarkar, J. D. Forman-Kay, L. E. Kay, *J. Am. Chem. Soc.* **2001**, *123*, 9843–9847.

 © 2005 Wiley-VCH Verlag GmbH & Co. KGaA, Weinheim

[4] W. Bal, G. N. Chmurny, B. D. Hilton, P. J. Sadler, A. Tucker, *J. Am. Chem. Soc.* **1996**, *118*, 4727.
[5] R. Nagane, T. Koshigoe, M. Chikira, *J. Inorg. Biochem.* **2003**, *93*, 204–212.
[6] R. Nagane, T. Koshigoe, M. Chikira, E. C. Long, *J. Inorg. Biochem.* **2001**, *83*, 17–23.
[7] G. L. Millhauser, *Acc. Chem. Res.* **2004**, *37*, 79–85.
[8] A. Torrado, G. K. Walkup, B. Imperiali, *J. Am. Chem. Soc.* **1998**, *120*, 609–610.
[9] Y. Zheng, K. M. Gattás-Asfura, V. Konka, R. M. Leblanc, *Chem. Commun.***2002**, 2350–2351.
[10] A. N. Boa, J. D. Crane, *Acta Crystallogr. Sect. E* **2004**, *60*, O966–O967.
[11] K. Kurdziel, T. Głowiak, S. Materazzi, J. Jezierska, *Polyhedron* **2003**, *22*, 3123–3128.
[12] P. Drożdżewski, B. Pawlak, T. Głowiak, *J. Mol. Struct.* **2003**, *654*, 111–118.
[13] S. Materazzi, E. Vasca, *Thermochim. Acta* **2001**, *373*, 7–12.
[14] K. Fukui, H. Ohya-Nishiguchi, H. Kamada, *Inorg. Chem.* **1998**, *37*, 2326–2327.
[15] D. Sanna, G. Micera, P. Buglyó, T. Kiss, T. Gajda, P. Surdy, *Inorg. Chim. Acta* **1998**, *268*, 297–306.
[16] M.-A. Martinez-Lorente, J.-P. Tuchagues, V. Pétrouléas, J. M. Savariault, R. Poinsot, M. Drillon, *Inorg. Chem.* **1991**, *30*, 3587–3589.
[17] The United Kingdom Chemical Database Service: D. A. Fletcher, R. F. McMeeking, D. Parkin, *J. Chem. Inf. Comput. Sci.* **1996**, *36*, 746–749.
[18] U. Bierbach, M. Sabat, N. Farrell, *Inorg. Chem.* **2000**, *39*, 1882–1890.
[19] W. K. Musker, M. S. Hussain, *Inorg. Nucl. Chem. Lett.* **1967**, *3*, 271–274.
[20] M. Bodansky, A. Bodansky, *The Practice of Peptide Synthesis*; Springer, New York, **1984**.
[21] G. M. Sheldrick, SHELXS-97 and SHELXL-97, *Programs for the Solution and Refinement of Crystal Structures*; University of Göttingen, **1997**.
[22] Stoe & Cie, *X-AREA and X-RED*, Stoe & Cie GmbH, Darmstadt, **2001**.
[23] A. L. Spek, *PLATON - A Multipurpose Crystallographic Tool*; Utrecht University, **2000**.
[24] *WinGX - An Integrated System of Windows Programs for the Solution, Refinement and Analysis of Single Crystal X-ray Diffraction Data*: L. J. Farrugia, *J. Appl. Crystallogr.* **1999**, *32*, 837–838.
[25] ORTEP-3 for Windows: L. J. Farrugia, *J. Appl. Crystallogr.* **1997**, *30*, 565.

Received: May 25, 2004

 © 2005 Wiley-VCH Verlag GmbH & Co. KGaA, Weinheim

Use of the Di-2-pyridyl Ketone/Acetate/Dicyanamide "Blend" in Manganese(II), Cobalt(II) and Nickel(II) Chemistry: Neutral Cubane Complexes

Giannis S. Papaefstathiou,[a] Albert Escuer,[b] Franz A. Mautner,[c] Catherine Raptopoulou,[d] Aris Terzis,[d] Spyros P. Perlepes,*[a] and Ramon Vicente*[b]

Keywords: Cobalt(II) cubanes / Dicyanamide complexes / Di-2-pyridyl ketone / Magnetic properties / Manganese(II) cubanes / Nickel(II) cubanes

The use of di-2-pyridyl ketone [$(2\text{-py})_2CO$]/dicyanamide "blend" in cobalt(II), manganese(II) and nickel acetate chemistry has yielded neutral cubane clusters. The preparation of $[Mn_4(O_2CMe)_2\{N(CN)_2\}_2\{(2\text{-py})_2C(OH)O\}_4]\cdot 2(2\text{-py})_2CO\cdot 4H_2O$ (**1**) and $[M_4(O_2CMe)_2\{N(CN)_2\}_2\{(2\text{-py})_2C(OH)O\}_4]\cdot 10H_2O$ [M = Ni (**2**), Co (**3**)] was achieved by the reaction of $[M(O_2CMe)_2]\cdot 4H_2O$ with $(2\text{-py})_2CO$ and $Na[N(CN)_2]$ in $MeOH/H_2O$ (1:5, v/v) at room temperature. The metal(II)-mediated hydrolysis of $(2\text{-py})_2CO$ to give the coordinated monoanion of the hydrate *gem*-diol form involves a nucleophilic attack of H_2O on the carbonyl group. In the case of the cobalt reaction system, there is a second product. Upon employing an excess of $(2\text{-py})_2CO$, long reaction times, reflux conditions and high dilution, slow oxidation of Co^{II} takes place leading to the isolation of the mononuclear cobalt(III) complex $[Co\{(2\text{-py})_2C(OH)O\}_2][N(CN)_2]\cdot 4H_2O$ (**4**) in yields higher than 70%. The structures of **1**, **2** and **4** have been solved by single-crystal X-ray diffraction studies, while a unit-cell determination indicated that complex **3** is isostructural with **2**. The tetranuclear cluster molecules of **1** and **2** have cubane $[M_4(\mu_3\text{-}OR)_4]^{4+}$ cores with divalent metal atoms and deprotonated oxygen atoms [originating from the $(2\text{-py})_2C(OH)O^-$ ligands] occupying alternate vertices. The centrosymmetric $[Co\{(2\text{-py})_2C(OH)O\}_2]^+$ cation of complex **4** has an octahedral structure with the $(2\text{-py})_2C(OH)O^-$ ligands adopting the tridentate *N*,*O*,*N*′-chelating coordination mode. The magnetic properties of **1**–**3** have been studied by variable-temperature dc magnetic susceptibility techniques. The studies indicate weak antiferromagnetic coupling for **1** and ferromagnetic behaviour for **2** and **3**. A three-*J* model was found to be adequate for describing the thermal variation of the molar magnetic susceptibilities of **1** and **2**. The magnetochemical results have been compared with literature data.

(© Wiley-VCH Verlag GmbH & Co. KGaA, 69451 Weinheim, Germany, 2005)

Introduction

There continues to be great interest in the synthesis and study of polynuclear metal complexes (clusters) containing paramagnetic 3d-metals in intermediate oxidation states.[1] There are various reasons for this, not least of which is the aesthetically pleasing nature of some of these species.[2] From an applications point of view, however, efforts in this area are part of the continuing search for new examples of molecular species which can function as nanoscale magnetic particles or so-called single-molecule magnets (SMMs).[3] These zero-dimensional (0D) systems display slow relaxation of their magnetisation vectors as a result of the combination of a large ground state (*S*) and an Ising (or easy-axis) type of magnetoanisotropy.[3] Thus, such molecules exhibit magnetisation hysteresis loops, i.e. the classical behaviour of a magnet. The unusual quantum phenomena[4] such molecules display have also led researchers to propose that the molecules could be used as Qbits in quantum computers.[5] The most studied examples of SMMs are the $[Mn_{12}O_{12}(O_2CR)_{16}(H_2O)_4]$ compounds with $S = 10$.[3] Another compound which has been intensely investigated for its SMM behaviour is $[\{Fe_8O_2(OH)_{12}(tacn)_6\}Br_7(H_2O)]Br\cdot 8H_2O$ (tacn = 1,4,7-triazacyclononane),[3] characterised by an $S = 10$ ground state. Since these first discoveries, other oxidation levels[6] in the Mn_{12} family and other Mn_x[2a,2d,3,7] and M_x (M = V^{III},[8] Fe^{II},[9] Fe^{III},[10] Co^{II},[11] Ni^{II}[12]) SMMs, including mixed-metal systems,[13] have been prepared with *S* values ranging from 3 to $5^1/_2$.

The future health of the field of high-spin molecules and the chances of identifying new SMMs will both benefit from the development of new synthetic methodologies for 3d-metal clusters. With this in mind, our group[9b,14,15] and

[a] Department of Chemistry, University of Patras, 265 04 Patras, Greece
E-mail: perlepes@patreas.upatras.gr
[b] Departament de Quimica Inorganica, Universitat de Barcelona, Diagonal 647, 08028 Barcelona, Spain
E-mail: ramon.vicente@qi.ub.es
[c] Institut für Physikalische und Theoretische Chemie, Technische Universität Graz, 8010 Graz, Austria
[d] Institute of Materials Science, NCSR "Demokritos", 153 10 Aghia Paraskevi Attikis, Greece

others[16] have been exploring "*binary* ligand blend" reactions involving (i) the monoanion $(2\text{-py})_2C(OH)O^-$ or the dianion $(2\text{-py})_2CO_2^{2-}$ of the *gem*-diol form of di-2-pyridyl ketone $(2\text{-py})_2CO$ (the formulae of these ligands are shown in Figure 1) *and* carboxylates, and (ii) the monoanion $(2\text{-py})_2C(OR)O^-$ of the hemiacetal form of $(2\text{-py})_2CO$ (Figure 1) *and* carboxylates, with the belief that they might foster formation of discrete polynuclear metal systems. The reactions of $(2\text{-py})_2CO$ with metal ions have been well studied over the years.[15–17] Water and alcohols (ROH) have been shown to add to the carbonyl group upon coordination of the 2-pyridyl ring to the ligands forming the ligands $(2\text{-py})_2C(OH)_2$ [the *gem*-diol form of $(2\text{-py})_2CO$] and $(2\text{-py})_2C(OR)(OH)$ [the hemiacetal form of $(2\text{-py})_2CO$], respectively. The neutral ligands $(2\text{-py})_2C(OH)_2$ and $(2\text{-py})_2C(OR)(OH)$ coordinate to the metal centres as tridentate N,N′,O chelates, with the M–O bond often being weak. Therefore, both neutral ligands do not hold much interest from the cluster formation point of view.[14] Completely different and much more interesting (for cluster chemistry) coordination modes are seen when the ligands $(2\text{-py})_2C(OH)_2$ and $(2\text{-py})_2C(OR)(OH)$ are deprotonated. Upon deprotonation the latter becomes monoanionic, while the former can exist either as monoanionic or dianionic. The presence of deprotonated hydroxyl group(s) leads to a great coordinative flexibility due to the well known ability of the negatively charged oxygen atom to bridge two or three metal ions. The immense structural diversity displayed by the complexes reported stems in part from the ability of $(2\text{-py})_2C(OH)O^-$, $(2\text{-py})_2CO_2^{2-}$ and $(2\text{-py})_2C(OR)O^-$ to exhibit no less than nine distinct bridging coordination modes ranging from μ_2 to μ_5.[14] Carboxylates are employed for two reasons in the above mentioned "ligand blends". Firstly, they are able to deprotonate the hydroxyl group(s) of $(2\text{-py})_2C(OH)_2$ and $(2\text{-py})_2C(OR)(OH)$ under mild conditions (the use of hydroxides often complicates the reactions). Secondly, they are flexible ligands, a consequence of their ability to adopt a number of different ligation modes, both terminal and bridging as well as both monodentate and bidentate. Thus, the $(2\text{-py})_2C(OH)O^-/R'CO_2^-$, $(2\text{-py})_2CO_2^{2-}/R'CO_2^-$ and $(2\text{-py})_2C(OR)O^-/R'CO_2^-$ "blends" (R = Me, Et; R′ = Me, CF_3, Ph) have led to a variety of Mn, Fe, Co, Ni and Cu clusters with nuclearities ranging from three to fourteen and with interesting magnetic properties.[14–16]

Three years ago we decided to incorporate azido ligands, N_3^-, into the 3d-metal carboxylate chemistry of $(2\text{-py})CO_2^{2-}$, $(2\text{-py})_2C(OH)O^-$ and $(2\text{-py})_2C(OR)O^-$, i.e. to study the "*ternary* ligand blend" reaction systems $(2\text{-py})_2C(OH)O^-$, $(2\text{-py})_2CO_2^{2-}$ or $(2\text{-py})_2C(OR)O^-/R'CO_2^-/N_3^-$, as a means of introducing specifically ferromagnetic components into the superexchange schemes, thus increasing the ground state *S* values of the clusters.[9b,18] For example, we reported[9b,18b,18c] that the reactions of $M(O_2CMe)_2{\cdot}xH_2O$ (M = Co, Ni, x = 4; M = Fe, x = 0) with (2-py)CO and N_3^- in DMF or MeCN with heating led to the nonanuclear cages $[M_9(N_3)_2(O_2CMe)_8\{(2\text{-py})_2CO_2\}]$ in which the nine M^{II} ions adopt a topology of two square pyramids sharing a common apex. Salient features of the similar structures are

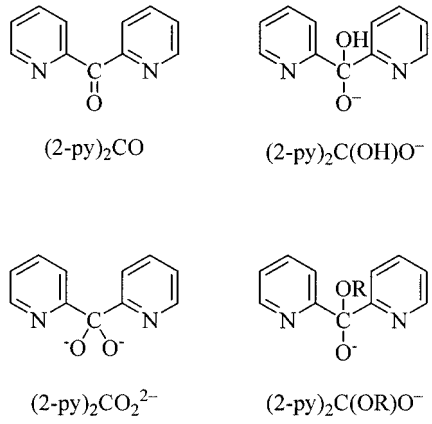

Figure 1. Some of the ligands discussed in the text. Note that the anionic ligands do not exist as free species, they exist only in metal complexes.

the unique $\eta^1{:}\mu_4$ coordination mode of the azido ligands, the μ_5 coordination mode of $(2\text{-py})_2CO_2^{2-}$ and the extremely rare coordination number 8 for the central M^{II} ion lying at the common apex of the pyramids. Magnetic studies revealed ferromagnetic coupling mediated by the azido bridges, giving a ground state total *S* value of seven times the local spin in the case of cobalt(II),[18c] 9 in the case of nickel(II)[18b] and 14 for the iron(II) cluster.[9b] It should be mentioned at this point that Mn^{II}, Co^{II} and Ni^{II} clusters containing *only* various anionic forms of $(2\text{-py})_2CO$ and N_3^- ligands, i.e. non-carboxylate species, are also known.[19]

Very recently we began a program which can be considered as a modification of the above "*ternary* ligand blend" approach. We have been exploring the use of the dicyanamido ligands, $N(CN)_2^-$ (Figure 2) instead of the azido ligands. The great coordinative flexibility and versatility of the $(2\text{-py})_2CO$-based anionic ligands and carboxylates, as well as the μ_2, μ_3, μ_4 or μ_5 potential of $N(CN)_2^-$,[20] prompted us to combine the three ligands to aim for new types of clusters and/or supramolecular architectures involving repeating cluster units. Our belief was that the simultaneous employment of the three classes of ligands in high-nuclearity 3d-metal chemistry would give extraordinary structural flexibility in the mixed $(2\text{-py})_2C(OH)O^-$, $(2\text{-py})_2CO_2^{2-}$ or $(2\text{-py})_2C(OR)O^-/R'CO_2^-/N(CN)_2^-$ ligand systems ("blends"). The loss of some degree of synthetic control[1b] may be more than compensated for by the vast diversity of structures expected using the combination of the three ligands. The advantages of using $N(CN)_2^-$ in place of N_3^- include (i) the possibility of triggering aggregation of preformed species into new, higher-nuclearity products and (ii) the possible diversion of known reaction systems developed using azides to new species as a result of the different flexibility of dicyanamides.

Dicyanamide is currently a ligand of great interest,[20,21] mainly due to the observation of long-range magnetic ordering in the binary α-$[\{M[N(CN)_2]_2\}_n]$ (M = Cr, Mn, Fe, Co, Ni) compounds.[20] Also of particular interest is the generation of new M^{II}-$N(CN)_2^-$ architectures through the introduction of coligands into the structures. These ternary

 © 2005 Wiley-VCH Verlag GmbH & Co. KGaA, Weinheim

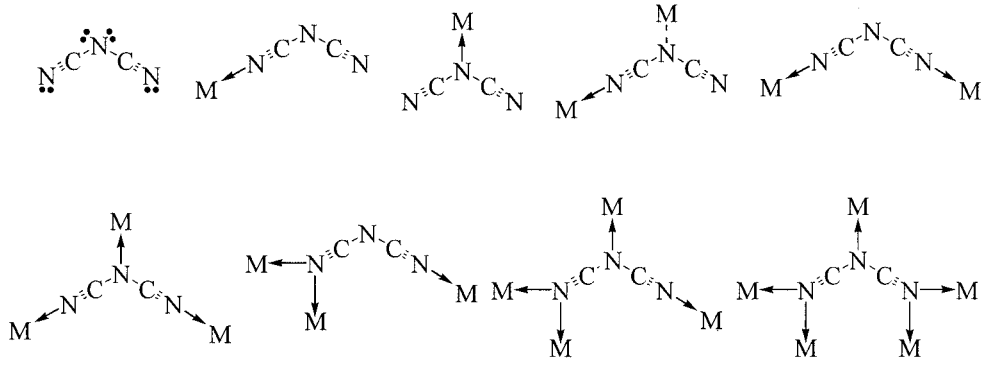

Figure 2. The dicyanamide ion and its crystallographically established coordination modes.

systems exhibit a wide variety of topologies and in a few cases long-range magnetic ordering has been observed at low temperatures.[20] This anion is a versatile ligand[20,22] which has been shown, by crystallography, to coordinate to metal ions in various modes (Figure 2), namely monodentate bonding through a nitrile nitrogen, end-to-end bridging through the two nitrile nitrogen atoms, bidentate bridging through one nitrile and the amide nitrogens or by strong coordination of one nitrile nitrogen and semicoordination of the amide nitrogen, tris(monodentate) bridging (μ_3), end-to-end μ_3 bridging with one nitrile nitrogen atom forming a monoatomic bridge as well as an unusual μ_4 mode where one nitrile nitrogen binds to two metal ions and an extremely rare μ_5 mode where each nitrile nitrogen binds to two metal ions. More generally, however, $N(CN)_2^-$ is also a very interesting ligand in the wider context of coordination chemistry due to its ability to undergo metal ion-assisted nucleophilic addition reactions with alcohols and pyrazole generating interesting polydentate ligands.[23]

The $N(CN)_2^-$ ligand has been used extensively in the synthesis of coordination polymers[20–22] but has been infrequently used for the synthesis of discrete 3d-metal clusters. We herein report the first use of $N(CN)_2^-$ in 3d-metal carboxylate/$(2\text{-py})_2CO$ chemistry which leads to neutral cubane manganese(II), cobalt(II) and nickel(II) clusters. The syntheses, structures, spectroscopic and magnetic properties of these species are described. A synthetically relevant cobalt(III) complex is also reported.

Results and Discussion

Synthesis

Our general synthetic approach for the isolation of heteroleptic $(2\text{-py})_2CO_2^{2-}$ or $(2\text{-py})_2C(OH)O^-$ or $(2\text{-py})_2C(OR)O^-/MeCO_2^-/N(CN)_2^-$ 3d-metal clusters was to treat an excess of the metal acetate with $(2\text{-py})_2CO$ and $N(CN)_2^-$ in various solvents. Obviously "$(2\text{-py})_2C(OH)_2$" and "$(2\text{-py})_2C(OR)(OH)$" can be fully/partially deprotonated by the basic acetate groups and polynuclear $M^{II}/(2\text{-py})_2CO_2^{2-}$, $(2\text{-py})_2C(OH)O^-$ or $(2\text{-py})_2C(OR)O^-/MeCO_2^-/N(CN)_2^-$ complexes may result from the reactions as long as the $MeCO_2^-$ to $(2\text{-py})_2CO$ ratio is high enough to leave an amount of $MeCO_2^-$ in the reaction mixture, given the fact that the anionic forms of $(2\text{-py})_2CO$, acetate and dicyanamide ligands can adopt a variety of terminal and bridging modes.

The preparation of compounds **1**, **2** and **3** can be achieved by the reaction of $M(O_2CMe)_2{\cdot}4H_2O$ with $(2\text{-py})_2CO$ and $Na[N(CN)_2]$ in $MeOH/H_2O$ ($\approx$ 1:5, v/v) at room temperature. The preparation of these complexes can be summarised by the general balanced Equation (1).

The metal(II)-mediated hydrolysis of $(2\text{-py})_2CO$ to give the monoanion of the hydrate *gem*-diol form involves a nucleophilic attack of H_2O on the carbonyl group. In such reactions it might not be necessary for the carbonyl atom to be coordinated to the metal centre. The induced polarisation from the pyridyl nitrogen atoms might be sufficient.[14]

A few features of the general chemical Equation (1) deserve comments. First, the incorporation of uncoordinated $(2\text{-py})_2CO$ molecules in **1** is not common and could not be predicted. Presumably, the presence of these molecules satisfies the requirements of the crystal lattice. However, the existence of ligand molecules in their ketone forms can be explained by the fact that the $(2\text{-py})_2C(OH)_2$ molecules do not exist as free species but exist only within the coordination sphere of metal ions.[14] The presence of lattice $(2\text{-py})_2CO$ has been established crystallographically[24] only in complexes $[Cu_2\{(2\text{-py})_2C(OMe)O\}_2(phen)_2]X_2{\cdot}2(2\text{-py})_2CO$, where phen = 1,10-phenanthroline and $X = PF_6^-$ or ClO_4^-. Secondly, the presence of MeOH in the solvent mixture might imply the presence of the monoanion of the hemiacetal form of di-2-pyridyl ketone, i.e. $(2\text{-py})_2C(OMe)$-

$$4\ M(O_2CMe)_2{\cdot}4H_2O + (4+n)\ (2\text{-py})_2CO + 2\ Na[N(CN)_2] + mH_2O \xrightarrow[20\ ^\circ C]{MeOH/H_2O}$$
$$[M_4(O_2CMe)_2\{N(CN)_2\}_2\{(2\text{-py})_2C(OH)O\}_4]{\cdot}n(2\text{-py})_2CO{\cdot}mH_2O + 2\ NaO_2CMe + 4\ MeCO_2H + 12\ H_2O \quad (1)$$

1: M = Mn^{II}, $n = 2$, $m = 4$
2: M = Ni^{II}, $n = 0$, $m = 10$
3: M = Co^{II}, $n = 0$, $m = 10$

 © 2005 Wiley-VCH Verlag GmbH & Co. KGaA, Weinheim

O^- in the complexes. This is a common synthetic feature in $(2\text{-py})_2CO$-based coordination chemistry.[14,17j–17l,19a,19c,19d] However, only $(2\text{-py})_2C(OH)O^-$ ligands are present in complexes **1**–**3**. This can be rationalised on the basis of the crystallisation method used. The complexes were crystallised by slow evaporation at room temperature of a solvent mixture consisting of MeOH and H_2O in a 1:5 volume ratio. This means that precipitation/crystallisation of the clusters was effected from *essentially aqueous media* (i.e., MeOH-free) and, thus, the coordination of *only* $(2\text{-py})_2C(OH)O^-$ might be expected. Thirdly, the "wrong" stoichiometry, i.e. $M(O_2CMe)_2{\cdot}4H_2O/(2\text{-py})_2CO/Na[N(CN)_2]$ = 2:1:1, employed for the preparation of **1**, **2** and **3** (see Exp. Sect.) compared with that required by Equation (1) was due to our desire to doubly deprotonate the *gem*-diol form of $(2\text{-py})_2CO$ and to prepare complexes of $(2\text{-py})_2CO_2^{2-}$. However, such efforts were in vain. Complexes **1**–**3** were isolated from $MeOH/H_2O$ or $MeCN/H_2O$ even employing a $M(O_2CMe)_2{\cdot}4H_2O/(2\text{-py})CO$ ratio of 3:1. With the identities of **1**–**3** established, the "correct" stoichiometries, i.e. $Mn(O_2CMe)_2{\cdot}4H_2O/(2\text{-py})_2CO/Na[N(CN)_2]$ = 1:1.5:0.5 and $M(O_2CMe)_2{\cdot}4H_2O/(2\text{-py})_2CO/Na[N(CN)_2]$ = 1:1:0.5 (M = Co, Ni), were employed and led to pure **1** and **2** but not to pure **3** (vide infra). It is worth mentioning that $(2\text{-py})_2CO_2^{2-}$ complexes are known in $M^{II}/(2\text{-py})_2CO/N_3^-$ chemistry.[18b,18c] Since these complexes contain $\eta^1{:}\mu_4$-azido ligands, the failure to isolate analogous dicyanamide complexes may be in part due to the inability of the $N(CN)_2^-$ anion to adopt an $\eta^1{:}\mu_4$ ligation mode. Lastly, in the case of the cobalt reaction systems *only*, there is a second product. The chemical and structural identity of the product depends on the $Co^{II}/(2\text{-py})_2CO$ ratio, reaction time, temperature and solution concentration. Upon employing an excess of $(2\text{-py})_2CO$, i.e. $Co^{II}/(2\text{-py})_2CO$ = 1:2, long reaction times, reflux conditions and high dilution (to avoid precipitation of the more insoluble tetranuclear Co^{II} cluster), slow oxidation of Co^{II} takes place under the normal laboratory atmosphere leading to the pure mononuclear complex $[Co^{III}\{(2\text{-py})C(OH)O\}_2]\{N(CN)_2\}{\cdot}4H_2O$ (**4**) in very good yields (≈ 70%). The source of the oxidising agent is oxygen from the air, facilitated by the mild reducing nature of Co^{II} in a nitrogen-rich environment. It is likely, as with other reactions in Co chemistry, that the reaction solution contains a mixture of two or more species in equilibrium, with factors such as relative solubility, reaction ratio, lattice energy, crystallisation kinetics and other factors determining the identity of the isolated product. Somewhat to our surprise, an analogous Mn^{III} complex (or a mixed-valent $Mn^{II/III}$ species) was not formed under the conditions employed.

Description of Structures

$[Mn_4(O_2CMe)_2\{N(CN)_2\}_2\{(2\text{-py})_2C(OH)O\}_4]{\cdot}2(2\text{-py})_2CO{\cdot}4H_2O$ (1)

A partially labelled plot of the tetranuclear molecule $[Mn_4(O_2CMe)_2\{N(CN)_2\}_2\{(2\text{-py})_2C(OH)O\}_4]$ present in compound **1** is shown in Figure 3. Selected interatomic distances and angles are listed in Table 1. The solvate $(2\text{-py})_2CO$ and H_2O molecules will not be further discussed.

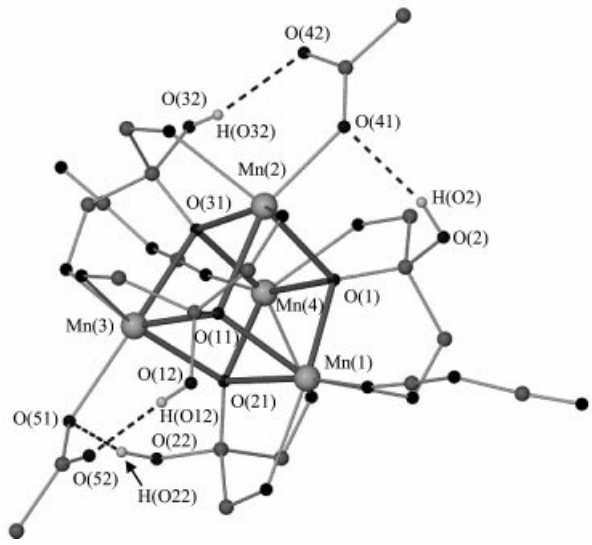

Figure 3. A partially labelled plot of the tetranuclear cluster molecule present in complex **1**. Many carbon atoms of the $(2\text{-py})_2C(OH)O^-$ ligands have been omitted for clarity. The intracubane hydrogen bonds are also shown.

The tetranuclear cluster molecule of **1** has a cubane $[Mn_4(\mu_3\text{-}OR)_4]^{4+}$ core with Mn^{II} and oxygen atoms occupying alternate vertices. Thus, the molecule consists of two interpenetrating tetrahedra, one of four Mn^{II} atoms and one of four μ_3-oxygen atoms originating form the $(2\text{-py})_2C(OH)O^-$ ligands. In addition to three μ_3 oxygen atoms, each Mn^{II} atom is coordinated to two N atoms belonging to two different $(2\text{-py})_2C(OH)O^-$ ligands and a single anion to complete an octahedral coordination environment. For Mn(1) and Mn(4), the anion is a monodentate $N(CN)_2^-$ group bonded through a nitrile nitrogen atom, whereas a monodentate acetate ligand completes the sixth coordination position at Mn(2) and Mn(3). Thus, the chromophores are $Mn(1,4)O_3N_3$ and $Mn(2,3)O_4N_2$. One octahedral face of each Mn^{II} atom is occupied by the three alkoxide-type oxygen atoms and the other contains the remaining donor atoms.

One oxygen atom of each $(2\text{-py})_2C(OH)O^-$ remains protonated and unbound to the metal ions. The resultant monoanion functions as an $\eta^1{:}\eta^3{:}\eta^1{:}\mu_3$ ligand (or as a 3.311 ligand using the Harris notation[25]) forming two five-membered MnNCCO chelating rings with two different metals (these rings share a common C–O edge) and an alkoxide-type bond to a third Mn^{II} atom (Figure 4). This ligation mode is common in the coordination chemistry of hydrated di-2-pyridyl ketone.[14] The large number of ligands involved results in a structure devoid of any point-group symmetry elements.[26]

There are two types for Mn–O (alkoxide-type) bonds for each metal ion: one bond is rather elongated to an average

 © 2005 Wiley-VCH Verlag GmbH & Co. KGaA, Weinheim

Table 1. Selected interatomic distances [Å] and angles [°] for $[Mn_4(O_2CMe)_2\{N(CN)_2\}_2\{(2\text{-py})_2C(OH)O\}_4]\cdot 2(2\text{-py})_2CO\cdot 4H_2O$ (**1**).

Mn(1)···Mn(2)	3.274(1)	Mn(3)–O(51)	2.137(3)
Mn(1)···Mn(3)	3.432(2)	Mn(3)–N(11)	2.223(3)
Mn(1)···Mn(4)	3.447(2)	Mn(3)–N(32)	2.271(3)
Mn(2)···Mn(3)	3.385(2)	Mn(4)–O(1)	2.308(3)
Mn(2)···Mn(4)	3.455(2)	Mn(4)–O(21)	2.170(3)
Mn(3)···Mn(4)	3.310(2)	Mn(4)–O(31)	2.186(3)
Mn(1)–O(1)	2.162(3)	Mn(4)–N(2)	2.213(4)
Mn(1)–O(11)	2.168(3)	Mn(4)–N(21)	2.276(4)
Mn(1)–O(21)	2.324(3)	Mn(4)–N(51)	2.171(4)
Mn(1)–N(1)	2.289(4)	C(92)–O(41)	1.274(5)
Mn(1)–N(22)	2.198(4)	C(92)–O(42)	1.237(5)
Mn(1)–N(41)	2.146(4)	C(94)–O(51)	1.269(5)
Mn(2)–O(1)	2.206(3)	C(94)–O(52)	1.227(6)
Mn(2)–O(11)	2.251(3)	N(43)–C(74)	1.123(8)
Mn(2)–O(31)	2.165(2)	N(42)–C(74)	1.294(8)
Mn(2)–O(41)	2.088(3)	C(73)–N(42)	1.284(7)
Mn(2)–N(12)	2.240(3)	N(41)–C(73)	1.133(6)
Mn(2)–N(31)	2.243(3)	C(76)–N(53)	1.115(8)
Mn(3)–O(11)	2.196(3)	N(52)–C(76)	1.281(8)
Mn(3)–O(21)	2.180(3)	N(52)–C(75)	1.284(6)
Mn(3)–O(31)	2.273(3)	C(75)–N(51)	1.135(6)
O(1)–Mn(1)–O(11)	83.3(1)	O(31)–Mn(3)–N(11)	100.8(1)
O(1)–Mn(1)–O(21)	78.7(1)	O(31)–Mn(3)–N(32)	70.6(1)
O(1)–Mn(1)–N(1)	72.1(1)	O(51)–Mn(3)–N(11)	97.9(1)
O(1)–Mn(1)–N(22)	146.2(1)	O(51)–Mn(3)–N(32)	91.9(1)
O(1)–Mn(1)–N(41)	111.2(1)	N(11)–Mn(3)–N(32)	96.9(1)
O(11)–Mn(1)–O(21)	77.0(1)	O(1)–Mn(3)–O(21)	78.9(1)
O(11)–Mn(1)–N(1)	155.2(1)	O(1)–Mn(3)–O(31)	75.9(1)
O(11)–Mn(1)–N(22)	106.4(1)	O(1)–Mn(4)–N(2)	72.4(1)
O(11)–Mn(1)–N(41)	98.1(1)	O(1)–Mn(4)–N(21)	99.9(1)
O(21)–Mn(1)–N(1)	100.9(1)	O(1)–Mn(4)–N(51)	164.8(1)
O(21)–Mn(1)–N(22)	72.4(1)	O(21)–Mn(4)–O(31)	81.7(1)
O(21)–Mn(1)–N(41)	168.6(1)	O(21)–Mn(4)–N(2)	146.3(1)
N(1)–Mn(1)–N(22)	96.2(1)	O(21)–Mn(4)–N(21)	72.3(1)
N(1)–Mn(1)–N(41)	87.9(1)	O(21)–Mn(4)–N(51)	115.0(1)
N(22)–Mn(1)–N(41)	99.6(1)	O(31)–Mn(4)–N(2)	107.4(1)
O(1)–Mn(2)–O(11)	80.4(1)	O(31)–Mn(4)–N(21)	154.0(1)
O(1)–Mn(2)–O(31)	78.5(1)	O(31)–Mn(4)–N(51)	99.2(1)
O(1)–Mn(2)–O(41)	89.0(1)	N(2)–Mn(4)–N(21)	95.3(1)
O(1)–Mn(2)–N(12)	112.4(1)	N(2)–Mn(4)–N(51)	95.9(1)
O(1)–Mn(2)–N(31)	150.9(1)	N(21)–Mn(4)–N(51)	90.8(1)
O(11)–Mn(2)–O(31)	80.4(1)	Mn(1)–O(1)–Mn(2)	97.1(1)
O(11)–Mn(2)–O(41)	154.8(1)	Mn(1)–O(1)–Mn(4)	100.9(1)
O(11)–Mn(2)–N(12)	72.5(1)	Mn(1)–O(11)–Mn(2)	95.6(1)
O(11)–Mn(2)–N(31)	103.1(1)	Mn(1)–O(11)–Mn(3)	103.7(1)
O(31)–Mn(2)–O(41)	120.0(1)	Mn(1)–O(21)–Mn(4)	100.1(1)
O(31)–Mn(2)–N(12)	148.0(1)	Mn(1)–O(21)–Mn(3)	99.2(1)
O(31)–Mn(2)–N(31)	73.8(1)	Mn(2)–O(1)–Mn(4)	99.8(1)
O(41)–Mn(2)–N(12)	91.0(1)	Mn(2)–O(11)–Mn(3)	99.1(1)
O(41)–Mn(2)–N(31)	97.3(1)	Mn(2)–O(31)–Mn(3)	99.4(1)
N(12)–Mn(2)–N(31)	95.9(1)	Mn(2)–O(31)–Mn(4)	105.1(1)
O(11)–Mn(3)–O(21)	79.5(1)	Mn(3)–O(21)–Mn(4)	99.1(1)
O(11)–Mn(3)–O(31)	79.3(1)	Mn(3)–O(31)–Mn(4)	95.8(1)
O(11)–Mn(3)–O(51)	121.3(1)	O(41)–C(92)–O(51)	124.4(4)
O(11)–Mn(3)–N(11)	73.1(1)	O(51)–C(94)–O(52)	125.6(4)
O(11)–Mn(3)–N(32)	146.1(1)	N(43)–C(74)–N(42)	171.0(8)
O(21)–Mn(3)–O(31)	79.5(1)	C(74)–N(42)–C(73)	122.7(6)
O(21)–Mn(3)–O(51)	91.1(1)	N(42)–C(73)–N(41)	171.7(6)
O(21)–Mn(3)–N(11)	151.9(1)	N(53)–C(76)–N(52)	171.2(7)
O(21)–Mn(3)–N(32)	109.4(1)	C(76)–N(52)–C(75)	127.0(5)
O(31)–Mn(3)–O(51)	155.8(1)	N(52)–C(75)–N(51)	172.2(6)

distance of 2.289 Å, whereas the two other bonds are shorter (average distance 2.179 Å). The cube deviates from the ideal geometry. The internal cube angles (RO–Mn–OR) at the metal vertices average 79.4°, whereas the comparable angles at the alkoxide corners (Mn–OR–Mn) are much larger averaging 99.6°. The Mn···Mn vectors in the complex reflect the different Mn–O (alkoxide-type) bond lengths, with the two Mn(1)···Mn(2) and Mn(3)···Mn(4) [3.274(1) and 3.310(2), respectively] cube face diagonals being shorter than the four other face diagonal vectors [3.385(2)–3.455(2) Å]. The bond distances around the Mn^{II} atoms are typical of those found in octahedrally coordinated high-spin manganese(II) complexes with *O*- and *N*-ligation.[16a,19d,27–29] A few Mn^{II} cubane structures containing $[Mn_4(\mu_3\text{-}OR_4)]^{4+}$ cores have been reported previously.[16a,28,29]

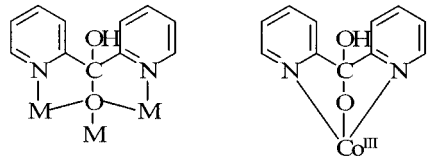

3.311 1.111

Figure 4. The crystallographically established coordination modes of the ligand $(2\text{-py})_2C(OH)O^-$ present in complexes **1**–**4** and the Harris notation[25] which describes these modes (M = Mn^{II}, Co^{II}, Ni^{II}).

$[Ni_4(O_2CMe)_2\{N(CN)_2\}_2\{(2\text{-py})_2C(OH)O\}_4]\cdot 10H_2O$ (2)

A partially labelled plot of the tetranuclear molecule present in compound **2** is shown in Figure 5. Selected interatomic distances and angles are listed in Table 2. Complex **2** crystallises in the triclinic space group $P\bar{1}$. Its structure consists of the tetranuclear $[Ni_4(O_2CMe)_2\{N(CN)_2\}_2\{(2\text{-py})_2C(OH)O\}_4]$ moiety and solvate H_2O molecules. The latter will not be further discussed.

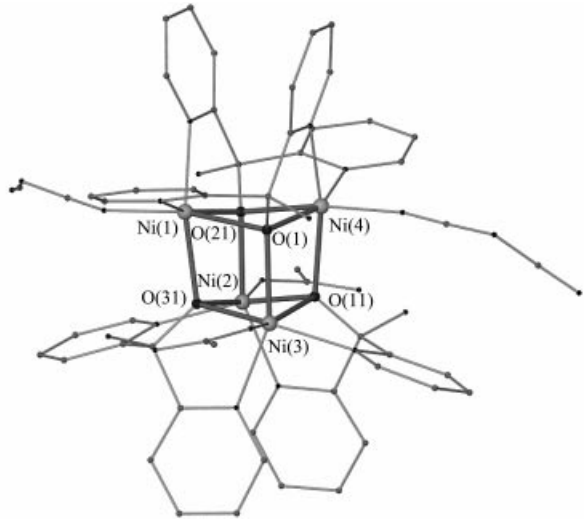

Figure 5. Partially labelled representation of the tetranuclear cluster molecule present in complex **2** emphasising its cubane structure.

The molecular structure of $[Ni_4(O_2CMe)_2\{N(CN)_2\}_2\{(2\text{-py})_2C(OH)O\}_4]$ is very similar to that of the tetranuclear cluster of complex **1**. Clearly, the replacement of Mn^{II} by Ni^{II} has little structural effect. The $[Ni_4(\mu_3\text{-}OR)_4]^{4+}$ core in **2** has almost all the geometric features found in the core of **1**, except that three Ni–O (alkoxide-type) distances are real-

 © 2005 Wiley-VCH Verlag GmbH & Co. KGaA, Weinheim

Table 2. Selected interatomic distances [Å] and angles [°] for $[Ni_4(O_2CMe)_2\{N(CN)_2\}_2\{(2\text{-py})_2C(OH)O\}_4]\cdot 10H_2O$ (**2**).

Ni(1)···Ni(2)	3.278(2)	Ni(3)–O(51)	2.039(4)
Ni(1)···Ni(3)	3.185(1)	Ni(3)–N(11)	2.068(4)
Ni(1)···Ni(4)	3.104(1)	Ni(3)–N(32)	2.076(5)
Ni(2)···Ni(3)	3.104(1)	Ni(4)–O(1)	2.018(3)
Ni(2)···Ni(4)	3.185(2)	Ni(4)–O(21)	2.150(3)
Ni(3)···Ni(4)	3.249(2)	Ni(4)–O(31)	2.094(3)
Ni(1)–O(1)	2.179(3)	Ni(4)–N(2)	2.122(4)
Ni(1)–O(11)	2.094(3)	Ni(4)–N(21)	2.019(4)
Ni(1)–O(21)	2.021(3)	Ni(4)–N(51)	2.026(5)
Ni(1)–N(1)	2.042(4)	C(81)–O(41)	1.264(6)
Ni(1)–N(22)	2.107(4)	C(81)–O(42)	1.255(7)
Ni(1)–N(41)	2.041(5)	C(91)–O(51)	1.264(7)
Ni(2)–O(1)	2.105(3)	C(91)–O(52)	1.252(8)
Ni(2)–O(11)	2.022(3)	N(43)–C(94)	1.148(9)
Ni(2)–O(31)	2.167(3)	C(94)–N(42)	1.323(10)
Ni(2)–O(41)	2.037(4)	N(42)–C(93)	1.309(8)
Ni(2)–N(12)	2.085(4)	C(93)–N(41)	1.137(7)
Ni(2)–N(31)	2.057(4)	N(53)–C(96)	1.152(13)
Ni(3)–O(11)	2.159(3)	C(96)–N(52)	1.304(13)
Ni(3)–O(21)	2.093(3)	N(52)–C(95)	1.301(8)
Ni(3)–O(31)	2.028(3)	C(95)–N(51)	1.130(7)
O(1)–Ni(1)–O(11)	75.6(1)	O(31)–Ni(3)–N(11)	156.5(2)
O(1)–Ni(1)–O(21)	82.0(1)	O(31)–Ni(3)–N(32)	78.3(2)
O(1)–Ni(1)–N(1)	77.3(2)	O(51)–Ni(3)–N(11)	91.6(2)
O(1)–Ni(1)–N(22)	104.8(1)	O(51)–Ni(3)–N(32)	92.4(2)
O(1)–Ni(1)–N(41)	169.3(2)	N(11)–Ni(3)–N(32)	96.8(2)
O(11)–Ni(1)–O(21)	81.5(1)	O(1)–Ni(4)–O(21)	82.8(1)
O(11)–Ni(1)–N(1)	103.7(2)	O(1)–Ni(4)–O(31)	82.2(1)
O(11)–Ni(1)–N(22)	158.3(2)	O(1)–Ni(4)–N(2)	77.1(2)
O(11)–Ni(1)–N(41)	95.3(2)	O(1)–Ni(4)–N(21)	158.0(2)
O(21)–Ni(1)–N(1)	156.5(2)	O(1)–Ni(4)–N(51)	102.9(2)
O(21)–Ni(1)–N(22)	77.2(2)	O(21)–Ni(4)–O(31)	76.6(1)
O(21)–Ni(1)–N(41)	102.5(2)	O(21)–Ni(4)–N(2)	102.9(1)
N(1)–Ni(1)–N(22)	97.5(2)	O(21)–Ni(4)–N(21)	77.9(1)
N(1)–Ni(1)–N(41)	99.2(2)	O(21)–Ni(4)–N(51)	169.0 (2)
N(22)–Ni(1)–N(41)	85.7(2)	O(31)–Ni(4)–N(2)	159.1(2)
O(1)–Ni(2)–O(11)	78.8(1)	O(31)–Ni(4)–N(21)	103.2(2)
O(1)–Ni(2)–O(31)	78.5(1)	O(31)–Ni(4)–N(51)	94.7(2)
O(1)–Ni(2)–O(41)	88.7(1)	N(2)–Ni(4)–N(21)	97.0(2)
O(1)–Ni(2)–N(12)	156.2(1)	N(2)–Ni(4)–N(51)	87.6(2)
O(11)–Ni(2)–N(31)	107.9(2)	N(21)–Ni(4)–N(51)	97.9(2)
O(11)–Ni(2)–O(31)	82.3(1)	Ni(1)–O(1)–Ni(2)	99.8(1)
O(11)–Ni(2)–O(41)	112.2(1)	Ni(1)–O(1)–Ni(4)	95.3(1)
O(11)–Ni(2)–N(12)	78.3(1)	Ni(1)–O(11)–Ni(2)	105.6(1)
O(11)–Ni(2)–N(31)	156.1(2)	Ni(1)–O(11)–Ni(3)	97.0(1)
O(31)–Ni(2)–O(41)	158.7(1)	Ni(1)–O(21)–Ni(3)	101.5(1)
O(31)–Ni(2)–N(12)	104.3(1)	Ni(1)–O(21)–Ni(4)	96.1(1)
O(31)–Ni(2)–N(31)	76.9(2)	Ni(2)–O(1)–Ni(4)	101.1(1)
O(41)–Ni(2)–N(12)	94.3(2)	Ni(2)–O(11)–Ni(3)	95.8(1)
O(41)–Ni(2)–N(31)	91.2(2)	Ni(2)–O(31)–Ni(3)	95.4(1)
N(12)–Ni(2)–N(31)	95.6(2)	Ni(2)–O(31)–Ni(4)	96.7(1)
O(11)–Ni(3)–O(21)	78.3(1)	Ni(3)–O(21)–Ni(4)	99.9(1)
O(11)–Ni(3)–O(31)	82.3(1)	Ni(3)–O(31)–Ni(4)	104.0(2)
O(11)–Ni(3)–O(51)	160.1(2)	O(41)–C(81)–O(42)	123.0(5)
O(11)–Ni(3)–N(11)	76.6(1)	O(51)–C(91)–O(52)	125.1(6)
O(11)–Ni(3)–N(32)	104.8(2)	N(43)–C(94)–N(42)	172.4(8)
O(21)–Ni(3)–O(31)	79.3(1)	C(94)–N(42)–C(93)	121.7(6)
O(21)–Ni(3)–O(51)	90.0(2)	N(42)–C(93)–N(41)	172.0(6)
O(21)–Ni(3)–N(11)	106.3(2)	N(53)–C(96)–N(52)	172.3(1)
O(21)–Ni(3)–N(32)	156.7(1)	C(96)–N(52)–C(95)	121.7(8)
O(31)–Ni(3)–O(51)	111.5(1)	N(52)–C(95)–N(51)	173.2(8)

ised for each metal ion. One bond is short with an average distance of 2.022 Å, one bond is relatively long with an average distance of 2.164 Å, while the third bond is of intermediate strength (average Ni–O distance of 2.097 Å). As in **1**, there are two chemically distinct metal sites in **2**. Two of them [Ni(1), Ni(4)] involve monodentate dicyanamides, while the other two [Ni(2), Ni(3)] are each bound to one monodentate acetate. The $\{Ni_4O_4\}$ cube also deviates from ideal geometry. The internal cube angles at the metal (OR–Ni–OR) average 80.0° whereas the analogous angles at the alkoxide-type corners (Ni–OR–Ni) are much larger averaging 99.0°. The Ni···Ni distances on opposite cubic faces are very similar, the pairs with the shortest distances being Ni(1)/Ni(4) and Ni(2)/Ni(3) (both distances are 3.104 Å). Average Ni–N and Ni–O bond lengths of 2.06 and 2.09 Å, respectively, lie well within the range of reported values for the corresponding bond lengths of other tetranuclear cubane Ni^{II} clusters.[2e,12b,12d,16a,26,29–31]

Many $\{Ni_4O_4\}$ cubanes have been reported previously.[2e,12b,12d,16a,26,29–31] Several[2e,29,30] have simple μ_3-alkoxides (CH_3O^-, $C_2H_5O^-$, ...) which provide the four oxygen centres. The first example which we were aware of involves terminal salicylaldehyde and ethanol ligands.[30a] Since that date, terminal ligands attached to the $[Ni_4(\mu_3\text{-}OR)_4]^{4+}$ core have included acetylacetonate,[30b] dibenzoylmethanate[30c,30d] and 6-chloro-2-pyridonate.[30e]

$[Co_4(O_2CMe)_2\{N(CN)_2\}_2\{(2\text{-py})_2C(OH)O\}_4]\cdot 10H_2O$ (3)

As mentioned in the Experimental Section, the unit-cell determination along with IR and elemental analysis data proved that complex **3** is isostructural with **2**. A full data set was therefore not collected for the cobalt(II) cluster. Compound **3** is a new member of the family containing tetranuclear cobalt(II) cubanes with the $[Co_4(\mu_3\text{-}OR)_4]^{4+}$ core.[11b,15c,16a,29,31b,32]

Intracubane Hydrogen Bonding in 1 and 2

There is a large amount of hydrogen bonding in **1** and **2**. We will briefly comment on the intracubane hydrogen bonds because they reinforce the framework of the cubes.[28a] Details of these bonds are listed in Table 3. Each $(2\text{-py})_2C(OH)O^-$ hydroxyl group is strongly intramolecularly hydrogen bonded to an O atom from an acetate ligand. A notable feature here is that both uncoordinated and coordinated oxygen atoms of the terminal acetate ligands participate in one intracubane hydrogen bond. The intracubane

Table 3. Intracubane hydrogen bonding details for complexes **1** and **2**.[a,b]

Complex	D-H···A	D···A [Å]	H···A [Å]	DHA [°]
1	O(2)–H(O2)···$O(41)_c$	2.756(1)	1.999(1)	161.5(1)
	O(12)–H(O12)···O(52)	2.704(1)	1.946(1)	177.2(1)
	O(22)–H(O22)···$O(51)_c$	2.801(2)	2.044(1)	154.6(1)
	O(32)–H(O32)···O(42)	2.842(1)	2.183(1)	167.6(1)
2	O(2)–H(O2)···O(41)	2.821(2)	2.190(1)	163.2(1)
	O(12)–H(O12)···O(42)	2.671(1)	1.955(1)	177.0(1)
	O(22)–H(O22)···O(51)	2.842(1)	2.168(1)	154.9(1)
	O(32)–H(O32)···O(52)	2.695(1)	2.044(1)	170.0(1)

[a] A = acceptor; D = donor. [b] The subscript c denotes a coordinated acetate oxygen.

 © 2005 Wiley-VCH Verlag GmbH & Co. KGaA, Weinheim

hydrogen bonds have the effect of lowering the symmetry of the $[M_4(\mu_3\text{-}OR)_4]^{4+}$ core.

Other (2-py)$_2$C(OH)O$^-$-Based Mn^{II}, Co^{II} and Ni^{II} Cubanes

Although several (2-py)C(OH)O$^-$-based, tetranuclear Mn^{II}, Co^{II} and Ni^{II} clusters have been reported,[14] only few have cubane structures in which the four μ_3-oxygen atoms originate from four deprotonated ligands. This group of compounds currently includes $[Co_4(O_2CMe)_4\{(2\text{-py})_2C(OH)O\}_4]$,[15c] $[Mn_4Cl_4\{(2\text{-py})_2C(OH)O\}_4]$,[16a] $[Mn_4(O_2CMe)_3(H_2O)\{(2\text{-py})_2C(OH)O\}_4](ClO_4)$,[16a] $[Co_4(O_2CMe)_3(H_2O)\{(2\text{-py})_2C(OH)O\}_4](ClO_4)$,[16a] $[Ni_4(O_2CMe)_3(H_2O)\{(2\text{-py})_2C(OH)O\}_4](ClO_4)$[16a] as well as **1**, **2** and **3**.

General Information on the Cubane 3d-Metal Clusters

The arrangement of four metal ions and four bridging ligands at alternating corners of a cube is a well-precedented unit in inorganic chemistry.[28d] There is great interest in the synthesis and study of cubanes featuring the first-row transition-metals.[30c,31b] Among the most thoroughly studied members of this class are $\{Fe_4S_4\}^{n+}$ clusters, many of which were prepared and characterised as models for the active site of iron-sulfur proteins.[33] Later, following the proposal of a cubic arrangement of Mn ions and bridging ligands for the oxygen evolving centre (OEC) of photosystem II (PS II),[34] several $\{Mn_4X_4\}^{n+}$ complexes with bridging oxo, chloro or alkoxo ligands were synthesised as models for this postulated unit.[35] More recently,[36] crystallographic data for a cyanobacterial PS II complex at 3.5 Å resolution strongly suggested that the OEC contains a cubane-like $\{Mn_3CaO_4\}$ cluster linked to a fourth Mn by a mono-μ-oxo bridge. However, higher resolution data are required to investigate whether some of the bridging oxygen atoms are protonated. It has also been suggested[31b,37] that these cubanes offer a way to model, and so better understand, the properties of extended networks which are often based on a cubane repeat unit.

[Co{(2-py)C(OH)O}$_2$]{N(CN)$_2$}·4H$_2$O (4)

A labelled plot of the structure of the mononuclear cation $[Co\{(2\text{-py})C(OH)O\}_2]^+$ present in complex **4** is shown in Figure 6. Selected bond lengths, angles and hydrogen bonding details are listed in Table 4 and Table 5, respectively. The structure consists of the above mentioned mononuclear cation, one disordered $N(CN)_2^-$ anion and H_2O solvate molecules; the latter two will not be further discussed. The Co^{III} ion sits on a crystallographic inversion centre.

The geometry of the *trans*-$Co^{III}N_4O_2$ chromophore is nearly octahedral, as would be expected for a Co^{III} species, with the $(2\text{-py})_2C(OH)O^-$ anions adopting the tridentate chelating coordination mode $\eta^1{:}\eta^1{:}\eta^1$ (or, 1.111 using Harris notation[25]) shown in Figure 4. The angle subtended by the off-axis coordination of the oxygen atom [O(1)] with the line normal to the equatorial N_4 plane is very small, with a value of 13.8° The Co–O and Co–N bond lengths agree well with values expected for low-spin Co^{III} in octahedral environments.[17b] There is a hydrogen bonding network among the H_2O molecules, the $N(CN)_2^-$ counterion and both protonated and deprotonated hydroxyl groups of $(2\text{-py})_2C(OH)O^-$ leading to a 2D assembly (Figure 7).

The structure of the cation of **4**, as detailed in the short discussion above and in Table 4, shows remarkable similar-

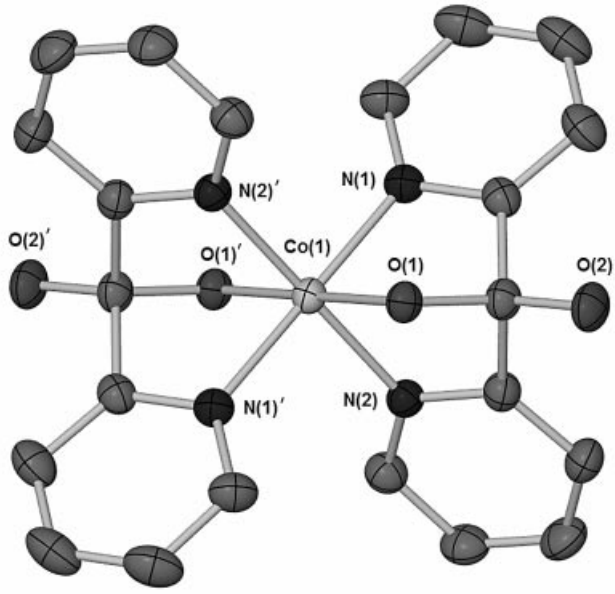

Figure 6. Partially labelled ORTEP plot of the mononuclear cation present in complex **4** with thermal ellipsoids at the 40% probability level. The primed atoms are related to the nonprimed ones by the crystallographic inversion centre.

Table 4. Selected bond lengths [Å] and angles [°] for $[Co\{(2\text{-py})_2C(OH)O\}_2]\{N(CN)_2\}\cdot 4H_2O$ (**4**).[a]

Co(1)–O(1)	1.887(2)	C(6)–O(1)	1.400(3)
Co(1)–N(1)	1.922(2)	C(6)–O(2)	1.376(3)
Co(1)–N(2)	1.915(2)		
O(1)–Co(1)–N(1)	82.84(7)	N(1)–Co(1)–N(2)	88.69(9)
O(1)–Co(1)–N(2)	83.31(8)	N(1)–Co(1)–N(2′)	91.32(9)
O(1)–Co(1)–N(1′)	97.16(7)	O(1)–C(6)–O(2)	114.0(2)
O(1)–Co(1)–N(2′)	96.69(8)		

[a] Primed atoms are related to the unprimed ones by the symmetry transformation $-x$, $1-y$, $1-z$.

Table 5. Hydrogen bonding details for complex $[Co\{(2\text{-py})_2C(OH)O\}_2]\{N(CN)_2\}\cdot 4H_2O$ (**4**).[a,b]

D–H···A	D···A [Å]	H···A [Å]	DHA [°]	Symmetry operator of A
O(2)–H(2A)···O(3)	2.669(3)	1.854	172.1	$x, y-1, z$
O(3)–H(31)···O(1)	2.730(3)	1.927	172.1	$-x, -y+1, -z+1$
O(3)–H(32)···O(4)	2.949(9)	2.136	170.2	$x-1, y+1, z$
O(4)–H(41)···N(11)	2.904(1)	2.062	179.3	$-x+1, -y+1, -z+2$
O(4)–H(42)···N(15)	2.903(1)	2.089	178.4	$-x+1, -y, -z+2$

[a] A = acceptor; D = donor. [b] Atoms O(3) and O(4) [not shown in Figure 6] belong to lattice water molecules, while N(11) and N(15) belong to the $N(CN)_2^-$ counterion. Only the highest occupancy atoms appear.

 © 2005 Wiley-VCH Verlag GmbH & Co. KGaA, Weinheim

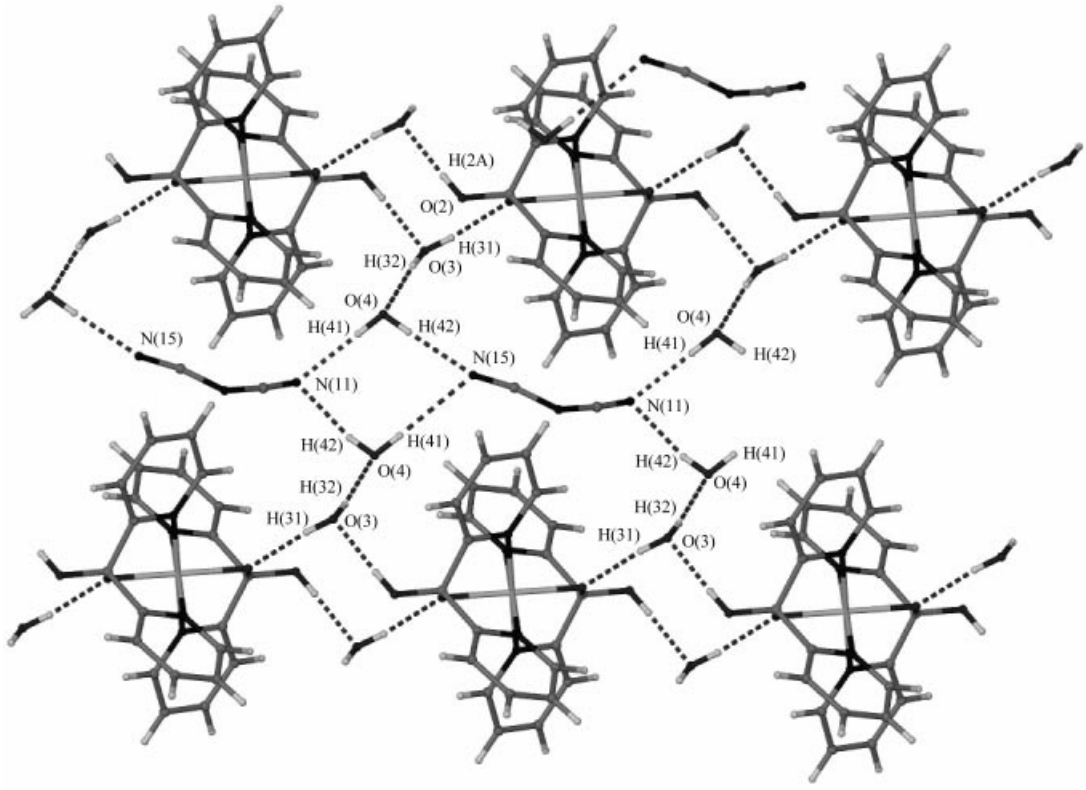

Figure 7. A view of the 2D network formed by hydrogen bonding in complex $[Co\{(2\text{-py})_2C(OH)O\}_2][N(CN)_2]\cdot 4H_2O$ (**4**).

ity to the structures of the cations in $[Co\{(2\text{-py})C(OH)O\}_2](NO_3)\cdot 2H_2O$,[38a] $[Co\{(2\text{-py})C(OH)O\}_2](ClO_4)\cdot 3H_2O$[38b] and $[Co\{(2\text{-py})C(OH)O\}_2](MeO)\cdot MeOH$.[38c] The latter was obtained from a reaction involving the oxidative degradation of bis[di(2-pyridyl)ethyl]amine in the presence of Co^{II}.

IR Spectra

Complexes **1** and **4** exhibit medium to strong intensity IR bands at 3419 (**1**) and 3500 (**4**) cm^{-1}, and 3329 (**1**) and ca. 3440 (**4**) cm^{-1}, assignable to ν(OH) vibrations for the $(2\text{-py})_2C(OH)O^-$ and H_2O groups, respectively.[15e] The broadness and relatively low frequencies of these bands are both indicative of hydrogen bonding. These two modes coincide at ca. 3450 cm^{-1} in the spectra of the isostructural compounds **2** and **3**.

The spectrum of **1** shows a medium band at 1685 cm^{-1}, suggesting that a certain amount of the organic ligand is present in its ketone form.[17e] This mode is situated at the same wavenumber (1684 cm^{-1}) in the spectrum of free $(2\text{-py})_2CO$, confirming the nonparticipation of the ketone group in the coordination in complex **1**. The spectra of **2**–**4** do not exhibit bands in the region expected for ν(C=O) absorptions, with the nearest strong IR absorptions at 1602 (**2**, **3**) and 1610 (**4**) cm^{-1} which can be assigned as 2-pyridyl stretching modes raised from 1582 cm^{-1} on coordination, as observed earlier[15e,19d] upon complex formation involving hydration of di-2-pyridyl ketone. The strong and rather broad band at 1602 cm^{-1} in **2** and **3** has $\nu_{as}(CO_2)$ character[39] since no other strong band can be observed in the 1600–1515 cm^{-1} region. The $\nu_s(CO_2)$ modes are difficult to assign due to the presence of 2-pyridyl stretching bands at 1440–1415 cm^{-1} and, thus, the application of the spectroscopic criterion of Deacon and Phillips[39] is extremely difficult.

The dicyanamide free anion in $Na[N(CN)_2]$ shows three sharp and medium to strong characteristic stretching bands in the 2290 to 2170 cm^{-1} region attributable to a $\nu_{as}(C\text{–}N) + \nu_s(C\text{–}N)$ combination mode (2286 cm^{-1}), $\nu_{as}(C\equiv N)$ (2232 cm^{-1}) and $\nu_s(C\equiv N)$ (2179 cm^{-1}).[22d] Monodentate coordination has been reported to have a minor effect on these features, whereas the bridging modes of $N(CN)_2^-$ cause a displacement of these bands towards higher frequencies, the effect increasing as one goes from bidentate to tridentate bonding.[22a] In compounds **1**–**3** the three bands occur at 2270–2279, 2210–2231 and 2156–2164 cm^{-1}. These features are indicative of terminal monodentate coordination and are consistent with the X-ray structures of **1** and **2** where $N(CN)_2^-$ was found to coordinate to the metal ions through one of its cyano nitrogen atoms. The $\nu_{as}(C\text{–}N) + \nu_s(C\text{–}N)$ (2275 cm^{-1}), $\nu_{as}(C\equiv N)$ (2238 cm^{-1}) and $\nu_s(C\equiv N)$ (2191 cm^{-1}) vibrations of **4** appear almost at the same frequencies as the corresponding ones in $Na[N(CN)_2]$, confirming the ionic nature of dicyanamide in the Co^{III} complex. The bands at ca. 1350 and 900–950 cm^{-1} in the spectra of **1**–**4** can be assigned to the $\nu_{as}(C\text{–}N)$ and

 © 2005 Wiley-VCH Verlag GmbH & Co. KGaA, Weinheim

ν_s(C–N) vibrations, respectively, with a satisfactory degree of certainty.[22a,22g,22i]

Magnetic Studies

Solid-state dc magnetic-susceptibility measurements were performed on polycrystalline samples of **1**–**3** in a 0.1 T field in the range 2.0–300 K. The $\chi_M T$ vs. T and χ_M vs. T plots for **1** are shown in Figure 8. The $\chi_M T$ value is 18.6 $cm^3 mol^{-1} K$ at room temperature, close to the expected value of 17.5 $cm^3 mol^{-1} K$ for four $S = {}^5/_2$ uncoupled spins with $g = 2$. The $\chi_M T$ value decreases slightly in the 300–40 K range and then decreases sharply, reaching a value of 1.0 $cm^3 mol^{-1} K$ at 2.0 K, whereas a maximum of 0.649 $cm^3 mol^{-1}$ in the χ_M vs. T plot is observed at 9 K. The data suggest that the complex appears to possess intramolecular antiferromagnetic interactions. Inspection of the molecular structure (Table 1) reveals that the Mn–O–Mn bond angles in the six faces of the cube are all different. However, if we divide the six faces into three pairs of opposite faces, each member of a given pair has a similar mean Mn–O–Mn bond angle with the other member of the same pair. Thus, the mean Mn–O–Mn bond angles for the faces Mn(1)O(1)Mn(2)O(11), Mn(3)O(21)Mn(4)O(31), Mn(1)O(11)Mn(3)O(21), Mn(2)O(1)Mn(4)O(31), Mn(1)O(1)Mn(4)O(21) and Mn(2)O(11)Mn(3)O(31) are 96.4, 97.5, 101.5, 102.5, 100.5 and 99.3°, respectively. Due to similarities of the mean Mn–O–Mn angles in opposite faces of the cubane motif, the experimental data were fitted using the expression derived from the isotropic Heisenberg Hamiltonian given by Equation (2). The fit of the scheme shown in Figure 9 was performed on $\chi_M$vs. T data by means of the computer program CLUMAG which uses the irreducible tensor operator formalism (ITO).[40] The best fit parameters were $J_1 = -1.71$ cm^{-1}, $J_2 = -0.81$ cm^{-1}, $J_3 = -0.27$ cm^{-1} and $g = 2.10$.

$$H = -J_1(S_1S_4 + S_2S_3) - J_2(S_1S_2 + S_3S_4) - J_3(S_1S_3 + S_2S_4) \quad (2)$$

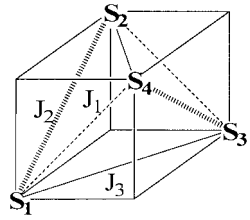

Figure 9. Assignments of J values to M···M interactions for the magnetic model with three coupling constants used for complexes **1** and **2** (M = Mn, Ni).

The J values of **1** are well within the narrow antiferromagnetic range (–0.22 to –4.11 cm^{-1}) reported for other cubane complexes containing the $[Mn_4(\mu_3\text{-}OR)_4]^{4+}$ core.[16a,28a,29]

The $\chi_M T$ vs. T and $\chi_M$vs. T plots for **2** are shown in Figure 10. The $\chi_M T$ value at 300 K is 5.70 $cm^3 mol^{-1} K$. As the temperature is lowered, $\chi_M T$ experiences a very slight increase, reaching a maximum value of 5.79 $cm^3 mol^{-1} K$ at 50 K followed by a much sharper decline at lower temperatures down to 0.84 $cm^3 mol^{-1} K$ at 2 K. On lowering the temperature, χ_M increases without a maximum to a value of 0.42 $cm^3 mol^{-1}$ at 2 K. The overall behaviour of **2** seems to have a ferromagnetic component. The structural parameters of **2** strongly suggest a lower symmetry than T_d for the molecule. As in compound **1**, if we divide the faces of the cube into three pairs of opposite faces, each face of a given pair has a similar mean Ni–O–Ni bond angle with the other member of the same pair. Thus, the mean Ni–O–Ni bond angles for the faces Ni(1)O(1)Ni(2)O(11), Ni(3)O21)Ni(4)O(31), Ni(1)O(11)Ni(3)O(21), Ni(2)O(1)Ni(4(O31), Ni(2)O(11)Ni(3)O(31) and Ni(1)O(1)Ni(4)O(21) are 102.7, 102.0, 99.3, 98.9, 95.6 and 95.7°, respectively. Again, as in **1**, the experimental data were fit using the expression derived from the isotropic Heisenberg Hamiltonian given by Equation (2). The fit on the scheme of Figure 9 was performed on $\chi_M T$ vs. T data by means of the computer program CLUMAG.[40] The best fit parameters were $J_1 = 8.63$ cm^{-1}, $J_2 = -4.43$ cm^{-1}, $J_3 = -0.53$ cm^{-1} and $g = 2.10$.

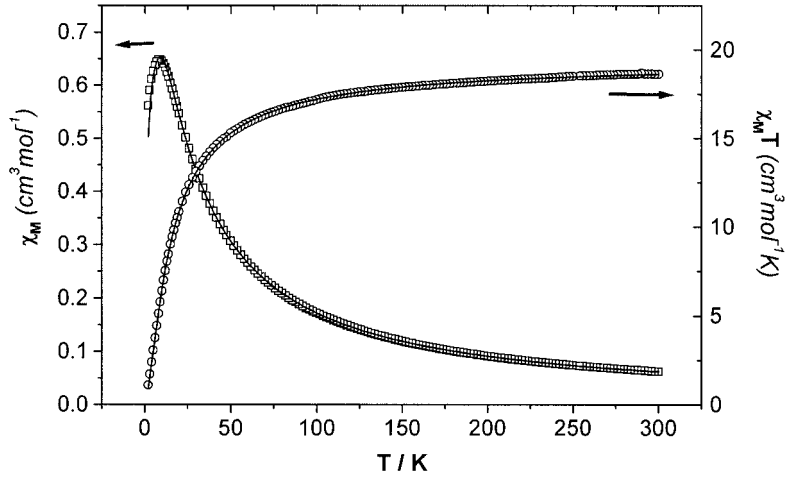

Figure 8. $\chi_M T$ vs. T and χ_M vs. T plots for complex **1**. The solid lines represent the best fit to the data as described in the text.

 © 2005 Wiley-VCH Verlag GmbH & Co. KGaA, Weinheim

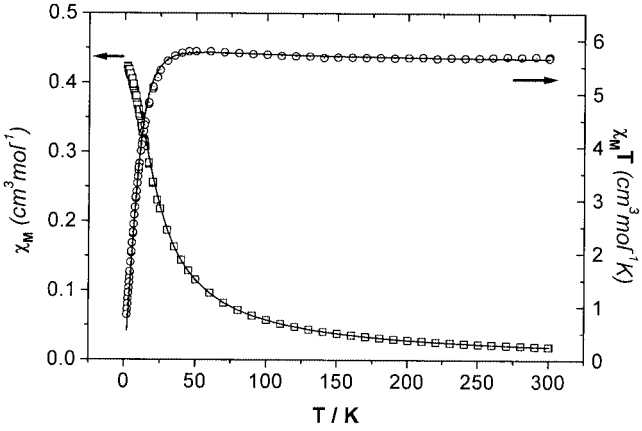

Figure 10. $\chi_M T$ vs. T and χ_M vs. T plots for complex **2**. The solid line represents the best theoretical fit of the data (see text for details).

It should be stressed at this point that the most important parameter in the magnetostructural correlation of tetranuclear nickel(II) complexes possessing the $[Ni_4(\mu_3\text{-}OR)_4]^{4+}$ cubane core has been reported[2e,26,29,30c,31a,41] to be the average Ni–O–Ni angle of a cubane face. A ferromagnetic exchange interaction can be observed for Ni–O–Ni angles lower than 99° and the J value increases as the angle decreases. On the other hand, Ni–O–Ni angles in the vicinity of, and larger than, 99° lead to an antiferromagnetic interaction and the $|J|$ value increases as the angle increases. Accordingly, a linear correlation between J and the Ni–O–Ni angle has been reported.[30c] The differences in sign and in absolute values among the J_1, J_2 and J_3 superexchange interactions are in good agreement with the three different types of faces present in the cubane core of **2** and support the 3-J model used which takes into account the reduced symmetry of the core observed in the X-ray structure of the complex. In **2**, the average Ni–O–Ni angles in the three different sets of faces are 102.4, 99.1 and 95.7°. Thus, the ferromagnetic coupling $J_1 = 8.63\ cm^{-1}$ should be associated with the faces [Ni(2)O(11)Ni(3)O(31), Ni(1)O(1)Ni(4)-O(21)] characterised by the mean angle of 95.7°. The J_2 value of $-4.43\ cm^{-1}$ can be assigned to the faces [Ni(1)O(1)-Ni(2)O(11), Ni(3)O(21)Ni(4)O(31)] with the mean angle of 102.4°, while the very weak antiferromagnetic coupling $J_3 = -0.53\ cm^{-1}$ should be assigned to the remaining two faces with the mean angle of 99.1°. The variable-temperature magnetic susceptibilities for most cubane Ni^{II} complexes have been interpreted on the basis of 1-J or 2-J models.[16a,29,30c,31b] Since the magnetic properties of only few $[Ni_4(\mu_3\text{-}OR)_4]^{4+}$ cubanes have necessitated a 3-J interpretation, Table 6 conveniently summarises some recent members of this small family.

The $\chi_M T$ vs. T plot for **3** is shown in Figure 11. The tetranuclear cluster exhibits a $\chi_M T$ value of $11.85\ cm^3 mol^{-1} K$ at 300 K which is higher than the spin-only value expected ($7.5\ cm^3 mol^{-1} K$) for four uncoupled Co^{II} centres in the $^4T_1$ ground state ($S = {}^3/_2$) with $g = 2$. One reason for this is that the orbital degeneracy of this state is not quenched and, consequently, there is a significant orbital contribution to the magnetic moment.[31b] As the temperature is lowered, $\chi_M T$ slightly increases to reach a broad maximum of $12.35\ cm^3 mol^{-1} K$ at 45 K, then decreases reaching a local minimum at about 25 K and below this temperature it sharply increases to a maximum value of $13.67\ cm^3 mol^{-1} K$ at 6 K, before dropping sharply to $11.58\ cm^3 mol^{-1} K$ at 2 K. χ_M increases continuously upon cooling from a value of $0.0395\ cm^3 mol^{-1}$ at room temperature to a value of $5.79\ cm^3 mol^{-1}$ at 2 K. The overall behaviour of **3** indicates a moderately weak ferromagnetic interaction. The shape of the $\chi_M T$ vs. T plot is probably due to the mixing of phenomena such as the ferromagnetic interaction with the depopulation of the $S = {}^3/_2$ spin levels due to zero-field splitting. The uncommon shape of the $\chi_M T$ vs. T plot is quite reproducible and was confirmed by measurements on different samples (microcrystalline powder, ground crystals, different batches). Analysis of the coupling constants for a high-spin rhombic cobalt(II) tetramer is not possible by me-

Table 6. J [cm^{-1}] as a function of the mean Ni–O–Ni angles [°] for selected $[Ni_4(\mu_3\text{-}OR)_4]^{4+}$-type cubanes the magnetic interpretation of which necessitated the employment of 3-J models.[a]

Complex[b]	mean Ni–O–Ni	J	Ref.
$[Ni_4(\mu_3\text{-}OH)_2(pypentO)(O_2CMe)_2(pym)(NCS)_2(H_2O]$	89.9	15.0	[26]
	92.9	6.7	
	100.5	–3.1	
$[Ni_4(\mu_3\text{-}OMe)_2(LH)_2(O_2CMe)_2(MeOH)_2]$	95.9	8.0	[31a]
	97.9	0.9	
	99.0	–3.9	
$[Ni_4(\mu_3\text{-}OMe)_4(L^{Se})_2(MeOH)_2(MeCN)_2]$	96.2	5.5	[2e]
	97.2	1.0	
	101.3	–4.1	
$[Ni_4(O_2CMe)_2\{N(CN)_2\}_2\{(2\text{-}py)_2C(OH)O\}_4]$	95.7	8.6	this work
	99.1	–0.5	
	102.4	–4.4	

[a] The 3-J models employed are not necessarily the same. [b] LH = the dianion of a Schiff base ligand derived from the [1+2] condensation of 2,6-diformyl-4-methylphenol and 6-amino-2,4-di-*tert*-butylphenol. L^{Se} = the dianion of 2,2′-selenobis(4,6-di-*tert*-butylphenol). Pym = the monoanion of 2-pyridylmethanol. PypentO = the monoanion of 1,5-bis[(2-pyridylmethyl)amino]pentan-3-ol.

 © 2005 Wiley-VCH Verlag GmbH & Co. KGaA, Weinheim

ans of an effective Hamiltonian based on four $S = {}^3/_2$ spins due to the large anisotropy of this ion.[19c,19d,29] Thus, several measurements were performed in order to characterise the ground state and the sign of the dominant interactions. To rule out any kind of long-range ordering phenomena, ac susceptibility measurements were performed. No out-of-phase response was obtained and dc susceptibility data were also collected under variable external fields (0.3, 0.1 and 0.02 T). The measurements revealed that the low temperature $\chi_M T$ values are field independent indicating a strictly molecular response. Magnetisation experiments show an increase of magnetisation at low fields (M is 6 in Nβ units at 1 T), reaching an Nβ value of 8.3 under the maximum external field of 5 T and clearly indicating a ferromagnetic interaction. Finally, the EPR spectrum of **3** at 4 K shows the typical transition between the ± 2 m_s levels at low fields (g = 15.5).

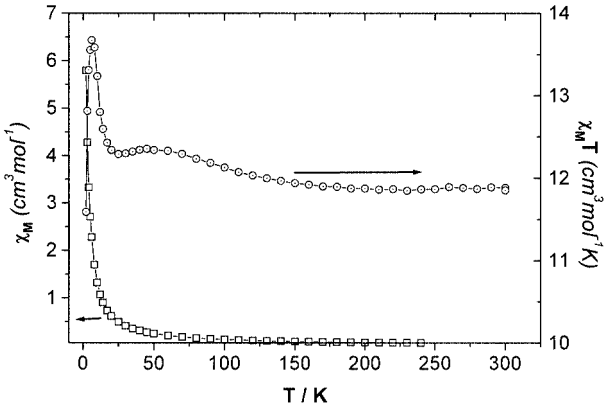

Figure 11. $\chi_M T$ (open circles) vs. T and χ_M (open squares) vs. T plot for complex **3**.

Based on the above data, the ground state of compound **3** can be adequately described as an effective, largely anisotropic, S' = 2 system, obtained from the ferromagnetic coupling of the four low-temperature local spins of the four Co^{II} (S = ½) ions. Complex **3** joins a handful of ferromagnetically coupled tetranuclear complexes consisting of a cubane $[Co_4(\mu_3\text{-}OR)_4]^{4+}$ core.[11b,15c,16a,29,42]

Conclusion and Perspectives

The first use of the dicyanamido ligand in manganese(II), cobalt(II) and nickel(II) acetate chemistry of $(2\text{-py})_2C(OH)O^-$, i.e. the study of the coordination chemistry of the $(2\text{-py})_2C(OH)O^-/MeCO_2^-/N(CN)_2^-$ "ternary ligand blend" has provided access to three new neutral cubane clusters and one mononuclear Co^{III} complex. The three $\{M_4(OR)_4\}$ cubes described are valuable additions to the chemistry of tetranuclear Mn^{II}, Co^{II} and Ni^{II} clusters. With the characterisation of **1**–**3**, the cubane geometry known for the 3d-metal/RCO_2^-/$(2\text{-py})_2C(OH)O^-$ systems can now be considered a feature of 3d-metal/RCO_2^-/pseudohalide/$(2\text{-py})_2C(OH)O^-$ chemistry as well. Complexes **1**–**3** contain low-symmetry cubane cores with different M···M distances and M–O–M angles, resulting in three types of $\{M_2O_2\}$ faces. The lower symmetry of the cubanes has necessitated the use of three discrete exchange parameters for the interpretation of the magnetic properties of **1** and **2**, a fact which is rare in the magnetochemical literature of 3d-metal cubanes. For Ni^{II}, it has recently been emphasised by Chaudhuri, Wieghardt and coworkers[31a] that other structural parameters such as Ni···Ni and Ni···O distances may be important in the magnetostructural correlation for the low-symmetry $[Ni_4(\mu_3\text{-}OR)_4]^{4+}$ cubane core. Thus, more such distorted cubane-type Ni^{II} complexes are needed to resolve this open question.

Analogues of compounds **1**–**3** with other pseudohalides, e.g. N_3^- and NCO^-, are not known, at least to date, and it is currently not evident whether the preparation and stability of these Mn^{II}, Co^{II} and Ni^{II} cubanes are dependent on the particular nature of the pseudohalide ligand. Work is in progress to clarify this matter. The dicyanamido and/or acetate terminal ligands present in **1**–**3** could have future utility as sites for facile incorporation of other monodentate ligands by metathesis or as a means of accessing higher-nuclearity cationic species by using bis(monodentate) bridging aromatic heterocycles. Finally, since the intended bridging behaviour of $N(CN)_2^-$ has not been achieved in **1**–**3**, we are intensively continuing our synthetic efforts to realise the bridging (μ_2-μ_5) potential of $N(CN)_2^-$ in the 3d-metal carboxylate/di-2-pyridyl ketone chemistry.

Experimental Section

Materials and Physical Measurements: All manipulations were performed under aerobic conditions using reagents and solvents (Merck, Aldrich) as received. Elemental analyses (C,H,N) were performed by the University of Ioannina (Greece) Microanalytical Service using an EA 108 Carlo–Erba analyser. IR spectra (400–450 cm^{-1}) were recorded in KBr pellets on Nicolet 520 and Perkin–Elmer PC 16 FTIR spectrometers. Magnetic susceptibility measurements under magnetic fields of approximately 0.1 T in the range 2–300 K and magnetisation measurements (only for complex **3**) in the field range of 1–5 T were performed with a Quantum Design MPMS-XL SQUID magnetometer at the Magnetochemistry Service of the University of Barcelona. All measurements were performed on polycrystalline samples. Pascal's constants were used to estimate the diamagnetic corrections which were subtracted from the experimental susceptibilities to give the corrected molar magnetic susceptibilities. EPR spectra were recorded on a Bruker ES200 spectrometer at X-band frequency.

$[Mn_4(O_2CMe)_2\{N(CN)_2\}_2\{(2\text{-py})_2C(OH)O\}_4]\cdot 2(2\text{-py})_2CO\cdot 4H_2O$ (1): A solution of $(2\text{-py})_2CO$ (0.099 g, 0.54 mmol) in MeOH (5 mL) was added to a stirred pale yellow aqueous solution (25 mL) of $Mn(O_2CMe)_2\cdot 4H_2O$ (0.270 g, 1.10 mmol) and $Na[N(CN)_2]$ (0.049 g, 0.55 mmol). The resultant yellow solution was stirred for about 10 min and was then allowed to slowly become more concentrated by evaporation at room temperature for a period of 10 days. Well-formed yellow crystals appeared which were collected by filtration, washed with MeOH (5 mL), Et_2O (3 mL) and dried in air. Yield (based on di-2-pyridyl ketone): 0.085 g (55%). $C_{74}H_{66}Mn_4N_{18}O_{18}$ (1715.21): calcd. C 51.8, H 3.9, N 14.7; found C 53.3, H 3.8, N 14.6. IR data (KBR pellet): $\tilde{\nu}$ = 3419 (s), 3329 (s, broad), 3070 (w), 2926 (w), 2270 (m), 2210 (m), 2156 (s), 1685 (m),

 © 2005 Wiley-VCH Verlag GmbH & Co. KGaA, Weinheim

1635 (w), 1600 (s), 1583 (s), 1474 (m), 1435 (m), 1386 (m), 1346 (m), 1320 (m), 1295 (w), 1247 (w), 1222 (m), 1155 (w), 1111 (m), 1080 (s), 1056 (s), 1016 (m), 995 (w), 946 (m), 908 (w), 828 (w), 804 (w), 781 (m), 751 (m), 694 (w), 678 (m), 663 (w), 652 (w), 638 (w), 616 (w), 589 (w), 524 (w), 484 (w), 453 (w) cm^{-1}.

$[Ni_4(O_2CMe)_2\{N(CN)_2\}_2\{(2\text{-py})_2C(OH)O\}_4]\cdot 10H_2O$ (2): This complex was prepared in a manner completely similar to complex **1** but using $Ni(O_2CMe)_2\cdot 4H_2O$ (0.269 g, 1.08 mmol) in place of $Mn(O_2CMe)_2\cdot 4H_2O$. Green crystals of the product were isolated. Yield (based on di-2-pyridyl ketone): 0.099 g (50%). $C_{52}H_{62}Ni_4N_{14}O_{22}$ (1470.00): calcd. C 42.5, H 4.3, N 13.3; found C 42.4, H 4.3, N 13.4. IR data (KBr pellet): $\tilde{\nu}$ = 3448 (s, broad), 2859 (w), 2279 (m), 2231 (m), 2164 (s), 1602 (s), 1511 (w), 1472 (m), 1438 (m), 1418 (m), 1338 (m), 1292 (w), 1260 (w), 1223 (m), 1157 (w), 1123 (m), 1086 (s), 1062 (m), 1048 (m), 1023 (m), 952 (w), 904 (w), 804 (w), 775 (m), 764 (m), 683 (m), 658 (m), 642 (m), 595 (w), 520 (m), 479 (w) cm^{-1}.

$[Co_4(O_2CMe)_2\{N(CN)_2\}_2\{(2\text{-py})_2C(OH)O\}_4]\cdot 10H_2O$ (3): A solution of $(2\text{-py})_2CO$ (0.099 g, 0.54 mmol) in MeOH (4 mL) was added to a stirred pink aqueous solution (20 mL) of $Co(O_2CMe)_2\cdot 4H_2O$ (0.269 g, 1.08 mmol) and $Na[N(CN)_2]$ (0.049 g, 0.55 mmol). The resultant red solution was allowed to slowly concentrate at room temperature for a period of 2 days only. X-ray quality reddish-pink crystals formed which were collected by filtration, washed with cold MeOH (3 mL), Et_2O (3 mL) and dried in air. Yield (based on di-2-pyridyl ketone): 0.069 g (35%). $C_{52}H_{62}Co_4N_{14}O_{22}$ (1471.00): calcd. C 42.5, H 4.3, N 13.3; found C 42.6, H 4.2, N 13.3. IR data (KBr pellet): $\tilde{\nu}$ = 3448 (s, broad), 2858 (w), 2279 (m), 2223 (m), 2162 (s), 1602 (s), 1511 (m), 1472 (m), 1436 (m), 1352 (m), 1338 (m), 1292 (w), 1260 (w), 1218 (m), 1157 (w), 1115 (m), 1093 (s), 1065 (m), 1045 (m), 1027 (m), 991 (m), 952 (w), 904 (w), 804 (w), 793 (m), 774 (m), 762 (m), 686 (m), 658 (m), 642 (m), 595 (w), 520 (m), 479 (w) cm^{-1}. In an attempt to obtain a second crop of the reddish-pink crystals of **3** (and thus to increase the yield), the filtrate obtained after separation of **3** was again allowed to slowly become more concentrated at room temperature. A gradual colour change to orange occurred over the course of 2–3 days. After several days reddish-pink and orange crystals were formed. They were carefully collected by filtration and rinsed with a small amount of cold MeOH. The two products were readily separable manually and the reddish-pink and orange crystals proved to be **3** and $[Co^{III}\{(2\text{-py})_2C(OH)O\}_2]\{N(CN)_2\}\cdot 4H_2O$ (4), respectively, by IR spectroscopy (**3**) and crystallography (**4**).

$[Co\{(2\text{-py})_2C(OH)O\}_2]\{N(CN)_2\}\cdot 4H_2O$ (4): A solution of $Co(O_2CMe)_2\cdot 4H_2O$ (0.112 g, 0.45 mmol) in H_2O (30 mL) was slowly added to a stirred solution of $(2\text{-py})_2CO$ (0.184 g, 1.00 mmol) in a mixture of MeOH and H_2O (30 mL, 1:3 v/v). The pink solution obtained was stirred while an aqueous solution (5 mL) of $Na[N(CN)_2]$ (0.049 g, 0.50 mmol) was added. The resultant pink solution was stirred overnight under reflux and during this time a noticeable colour change to orange occurred. Slow concentration of this solution at room temperature gave orange crystals suitable for crystallography. When precipitation was judged to be complete, the crystals were collected by filtration, washed with cold MeOH

Table 7. Crystal data and structure refinements for $[Mn_4(O_2CMe)_2\{N(CN)_2\}_2\{(2\text{-py})_2C(OH)O\}_4]\cdot 2(2\text{-py})_2CO\cdot 4H_2O$ (**1**), $[Ni_4(O_2CMe)_2\{N(CN)_2\}_2\{(2\text{-py})_2C(OH)O\}_4]\cdot 10H_2O$ (**2**) and $[Co\{(2\text{-py})_2C(OH)O\}_2]\{N(CN)_2\}\cdot 4H_2O$ (**4**).

	1	**2**	**4**
Empirical formula	$C_{74}H_{66}Mn_4N_{18}O_{18}$	$C_{52}H_{62}Ni_4N_{14}O_{22}$	$C_{24}H_{26}CoN_7O_8$
Mol. mass	1715.21	1470.00	599.45
Colour and habit	yellow prisms	green prisms	reddish-pink prisms
Crystal size [mm]	0.15×0.30×0.50	0.10×0.25×0.45	0.15×0.16×0.18
Crystal system	triclinic	triclinic	triclinic
Space group	$P\bar{1}$	$P\bar{1}$	$P\bar{1}$
a [Å]	18.00(1)	13.316(8)	8.148(4)
b [Å]	15.409(9)	19.31(1)	8.866(3)
c [Å]	14.913(9)	13.186(7)	10.316(3)
α [°]	86.26(2)	96.17(2)	70.23(2)
β [°]	66.89(2)	111.65(2)	71.84(3)
γ [°]	85.93(2)	98.35(2)	76.20(3)
V [Å^3]	3791(4)	3070(3)	658.9(4)
Z	2	2	1
$\rho_{calcd.}$ [Mg m^{-3}]	1.503	1.590	1.511
T [°C]	25	25	20
λ (Mo-K_α) [Å]	0.71073	0.71073	0.71069
μ [mm^{-1}]	0.734	1.297	0.713
F (000)	1760	1520	306
$2\theta_{max}$ [°]	47.0	47.5	53.0
Index ranges	$-20 \le h \le 18$	$0 \le h \le 15$	$-9 \le h \le 9$
	$-17 \le k \le 17$	$-21 \le k \le 21$	$-11 \le k \le 10$
	$-16 \le l \le 0$	$-14 \le l \le 13$	$-12 \le l \le 12$
No. of reflections collected	11718	9816	2978
No. of indep. refls./R_{int}	11213/0.0414	9330/0.0280	2645/0.033
Data with $I > 2\sigma(I)$	9082	7009	2465
Parameters refined	1239	977	191
$[\Delta/\sigma]_{max}$	0.001	0.068	0.005
GOF (on F^2)	1.123	1.083	1.051
R_1[a]	0.0492	0.0463	0.0383
wR_2[b]	0.1246	0.1130	0.1046
Residuals [e Å^{-3}]	0.938/-0.422	0.756/-0.420	0.48/-0.56

[a] $R_1 = \Sigma(|F_o| - |F_c|)/\Sigma(|F_o|)$. [b] $wR_2 = \{\Sigma w[(F_o^2 - F_c^2)^2]/\Sigma[w(F_o^2)^2]\}^{1/2}$.

 © 2005 Wiley-VCH Verlag GmbH & Co. KGaA, Weinheim

(1 mL), Et_2O (2× 3 mL) and dried in air. Yields (based on Co) as high as 0.19 g (≈ 70%) were obtained. $C_{24}H_{26}CoN_7O_8$ (599.46): calcd. C 48.1, H 4.4, N 16.4; found C 47.4, H 4.2, N 16.2. IR data (KBr pellet): $\tilde{\nu}$ = 3500 (s, broad), 3442 (m, broad), 3120 (w), 2821 (w), 2275 (m), 2238 (s), 2191 (m), 1642 (sh), 1610 (m), 1470 (sh), 1454 (m), 1390 (w), 1343 (w), 1312 (s), 1249 (s), 1233 (m), 1170 (m), 1029 (s), 950 (w), 903 (w), 824 (m), 762 (s), 699 (m), 683 (m), 573 (m), 525 (w), 494 (w), 479 (w), 455 (w) cm^{-1}.

X-ray Crystallographic Studies: Crystals of **1** and **2** were mounted in capillaries filled with drops of mother liquor while a crystal of **4** was mounted on a glass fibre. Diffraction measurements for **1** and **2** were made on a Crystal Logic Dual Goniometer diffractometer using graphite-monochromated Mo-K_α radiation. Data for **4** were collected on a modified STOE 4-circle diffractometer also with graphite-monochromated Mo-K_α radiation. Complete crystal data and parameters for data collection and refinements are listed in Table 7. Unit-cell dimensions were determined and refined using the angular settings of 25 (for **1** and **2**) or 36 (for **4**) automatically centred reflections in the ranges $11 < 2\theta < 23°$ (for **1** and **2**) or $10 < 2\theta < 15°$ (for **4**). Three standard reflections monitored every 97 (for **1** and **2**) or 100 (for **4**) reflections showed less than 3% variation and no decay. For **1** and **2**, Lorentz, polarisation and Ψ-scan absorption corrections were applied using the Crystal Logic software package whereas for **4** the data were processed without an absorption correction. The structures were solved by direct methods using SHELXS-86[43a] and refined by full-matrix least-squares techniques on F^2 with SHELXL-93[43b] or using the SHELXTL/PC program package[43c] (for **4**). For all three structures the ordered non-hydrogen atoms were refined anisotropically. In the case of **4**, disordered lattice water molecules containing O(4) and O(5) were refined anisotropically with split occupancies of 0.60(2) and 0.40(2), respectively. Further isotropic displacement parameters, split occupancies of 0.50 and geometrical constraints were applied to N(11), C(12), N(13), C(14) and N(15) of the disordered dicyanamide anion. For **1** and **2**, all hydrogen atoms [except those of the acetate ligands which were introduced in calculated positions as riding on their parent carbon atoms] were located from difference maps and refined isotropically. No hydrogen atoms of the solvate molecules were introduced in the refinements. In the case of **4**, hydrogen atoms of water molecules were fixed in positions located from difference maps. The remaining hydrogen atoms were introduced in calculated positions as riding on their parent atoms. Unit-cell determination (at 25 °C) proved that complex **3** is isostructural with **2**. The unit-cell dimensions of **3** are: a = 13.54, b = 19.13, c = 13.16 Å, α = 95.21, β = 111.09, γ = 98.07°, V = 3110 $Å^3$.

CCDC-246277 (for **1**), 246278 (for **2**) and 246279 (for **4**) contain the supplementary crystallographic data for this paper. These data can be obtained free of charge from The Cambridge Crystallographic Data Centre via www.ccdc.cam.ac.uk/data_request/cif.

Acknowledgments

A. E. and R. V. wish to thank the Spanish Ministerio de Ciencia y Technologia (BQU2003/0538 project) and G. S. P. and S. P. P. wish to thank the Research Committee of the University of Patras (K. CARATHEODORY Program No 1941) for financial support of this work. F. A. M. thanks Profs. C. Kratky and F. Belaj (Univ. Graz) for use of equipment.

[1] For reviews, see a) R. E. P. Winpenny, *Adv. Inorg. Chem.* **2001**, 52, 1–111; b) R. E. P. Winpenny, *Dalton Trans.* **2002**, 1–10.

[2] a) A. J. Tasiopoulos, A. Vinslava, W. Wernsdorfer, K. A. Abboud, G. Christou, *Angew. Chem. Int. Ed.* **2004**, *43*, 2117–2121; b) M. Murugesu, K. A. Abboud, G. Christou, *Dalton Trans.* **2003**, 4552–4556; c) S. Langley, M. Helliwell, J. Raftery, E. I. Tolis, R. E. P. Winpenny, *Chem. Commun.* 2004, 142–143; d) L. F. Jones, E. K. Brechin, D. Collison, A. Harrison, S. J. Teat, W. Wernsdorfer, *Chem. Commun.* **2002**, 2974–2975; e) T. K. Paine, E. Rentschler, T. Weyhermüller, P. Chaudhuri, *Eur. J. Inorg. Chem.* **2003**, 3167–3178; f) J. Overgaard, B. B. Iversen, S. P. Palii, G. A. Timco, N. V. Gerbeleu, F. K. Larsen, *Chem. Eur. J.* **2002**, *8*, 2775–2786; g) X. Liu, J. A. McAllister, M. P. de Miranda, E. J. L. McInnes, C. A. Kilner, M. A. Halcrow, *Chem. Eur. J.* **2004**, *10*, 1827–1837; h) T. S. M. Abedin, L. K. Thompson, D. O. Miller, E. Krupicka, *Chem. Commun.* **2003**, 708–709; i) M. Murugesu, C. E. Anson, A. K. Powell, *Chem. Commun.* **2002**, 1054–1055; j) G. L. Abati, A. Cornia, A. C. Fabretti, A. Caneschi, D. Gatteschi, *Inorg. Chem.* **1998**, *37*, 1430–1431.

[3] For excellent reviews see: a) D. Gatteschi, R. Sessoli, *Angew. Chem. Int. Ed.* **2003**, *42*, 268–297; b) G. Christou, D. Gatteschi, D. N. Hendrickson, *MRS Bull*. **2000**, *25*, 66–71.

[4] a) J. R. Friedman, M. P. Sarachik, J. Tejada, R. Ziolo, *Phys. Rev. Lett*. **1996**, *76*, 3830–3833; b) L. Thomas, F. Lionti, R. Ballou, D. Gatteschi, R. Sessoli, B. Barbara, *Nature* **1996**, *383*, 145–147; c) W. Wernsdorfer, R. Sessoli, *Science* **1999**, *284*, 133–135.

[5] M. N. Leuenberger, D. Loss, *Nature* **2001**, *410*, 789–793.

[6] a) H. J. Eppley, H. L.-Tsai, N. de Vries, K. Folting, G. Christou, D. N. Hendrickson, *J. Am. Chem. Soc.* **1995**, *117*, 301–317; b) M. Soler, S. K. Chandra, D. Ruiz, E. R. Davidson, D. N. Hendrickson, G. Christou, *Chem. Commun.* **2000**, 2417–2418.

[7] For recent examples, see: a) C. Dendrinou-Samara, M. Alexiou, C. M. Zaleski, J. W. Kampf, M. L. Kirk, D. P. Kessissoglou, V. L. Pecoraro, *Angew. Chem. Int. Ed.* **2003**, *42*, 3763–3766; b) C. P. Berlinguette, D. Vaughn, C. Canãda-Vilalta, J. R. Galán-Mascarós, K. R. Dunbar, *Angew. Chem. Int. Ed.* **2003**, *42*, 1523–1526; c) H. Zhao, C. P. Berlinguette, J. Bacsa, A. V. Prosvirin, J. K. Bera, S. E. Tichy, E. J. Schelter, K. R. Dunbar, *Inorg. Chem.* **2004**, *43*, 1359–1369; d) L. M. Wittick, K. S. Murray, B. Moubaraki, S. R. Batten, L. Spiccia, K. J. Berry, *Dalton Trans.* **2004**, 1003–1011; e) C. J. Milios, C. P. Raptopoulou, A. Terzis, F. Lloret, R. Vicente, S. P. Perlepes, A. Escuer, *Angew. Chem. Int. Ed.* **2004**, *43*, 210–212; f) E. C. Sanudo, W. Wernsdorfer, K. A. Abboud, G. Christou, *Inorg. Chem.* **2004**, *43*, 4137–4144, and references cited therein. g) M. Soler, W. Wernsdorfer, K. Folting, M. Pink, G. Christou, *J. Am. Chem. Soc.* **2004**, *126*, 2156–2165; h) V. Murugesu, M. Habrych, W. Wernsdorfer, K. A. Abboud, G. Christou, *J. Am. Chem. Soc.* **2004**, *126*, 4666–4767; i) N. E. Chakov, W. Wernsdorfer, K. A. Abboud, D. N. Hendrickson, G. Christou, *Dalton Trans.* **2003**, 2243–2248; j) S. Hill, R. S. Edwards, N. Aliaga-Alcalde, G. Christou, *Science* **2003**, *302*, 1015–1018; k) M. Soler, W. Wernsdorfer, Z. Sun, J. C. Huffman, D. N. Hendrickson, G. Christou, *Chem. Commun.* **2003**, 2672–2673; l) E. K. Brechin, M. Soler, G. Christou, M. Helliwell, S. J. Teat, W. Wernsdorfer, *Chem. Commun.* **2003**, 1276–1277; m) H. Miyasaka, R. Clérac, W. Wernsdorfer, L. Lecren, C. Bonhomme, K. Sugiura, M. Yamashita, *Angew. Chem. Int. Ed.* **2004**, *43*, 2801–2805.

[8] S. L. Castro, Z. Sun, C. M. Grant, J. C. Bollinger, D. N. Hendrickson, G. Christou, *J. Am. Chem. Soc.* **1998**, *120*, 2365–2375.

[9] a) H. Oshio, N. Hoshino, T. Ito, *J. Am. Chem. Soc.* **2000**, *122*, 12602–12603; b) A. K. Boudalis, B. Donnadieu, V. Nastopoulos, J. M. Clemente-Juan, A. Mari, Y. Sanakis, J.-P. Tuchagues, S. P. Perlepes, *Angew. Chem. Int. Ed.* **2004**, *43*, 2266–2270.

[10] a) A. L. Barra, A. Caneschi, A. Cornia, F. Fabrizi de Biani, D. Gatteschi, C. Sangregorio, R. Sessoli, L. Sorace, *J. Am. Chem. Soc.* **1999**, *121*, 5302–5310; b) A. Bouwen, A. Caneschi, D. Gatteschi, E. Goovaerts, D. Schoemaker, L. Sorace, M. Stefan, *J. Phys. Chem. B* **2001**, *105*, 2658–2663; c) R. W. Saalfrank, I.

 © 2005 Wiley-VCH Verlag GmbH & Co. KGaA, Weinheim

Bernt, M. M. Chowdry, F. Hampel, G. B. M. Yaughan, *Chem. Eur. J.* **2001**, *7*, 2765–2769; d) A. Cornia, A. C. Fabretti, P. Garrisi, C. Mortaló, D. Bonacchi, D. Gatteschi, R. Sessoli, L. Sorace, W. Wernsdorfer, A.-L. Barra, *Angew. Chem. Int. Ed.* **2004**, *43*, 1136–1139; e) C. Benelli, J. Cano, Y. Journaux, R. Sessoli, G. A. Solan, R. E. P. Winpenny, *Inorg. Chem.* **2001**, *40*, 188–189; f) J. C. Goodwin, R. Sessoli, D. Gatteschi, W. Wernsdorfer, A. K. Powell, S. L. Heath, *J. Chem. Soc., Dalton Trans.* **2000**, 1835–1840.

[11] a) M. Murrie, S. J. Teat, H. Stoeckli-Evans, H. U. Güdel, *Angew. Chem. Int. Ed.* **2003**, *42*, 4653–4656; b) E.-C. Yang, D. N. Hendrickson, W. Wernsdorfer, M. Nakano, L. N. Zakharov, R. D. Sommer, A. L. Rheingold, M. Ledezma-Gairaud, G. Christou, *J. Appl. Phys.* **2002**, *91*, 7382–7384.

[12] a) H. Andres, R. Basler, A. J. Blake, C. Cadiou, G. Chaboussant, C. M. Grant, H.-U. Güdel, M. Murrie, S. Parsons, C. Paulsen, F. Semadini, V. Villar, W. Wernsdorfer, R. E. P. Winpenny, *Chem. Eur. J.* **2002**, *8*, 4867–4876; b) E.-C. Yang, W. Wernsdorfer, S. Hill, R. S. Edwards, M. Nakano, S. Maccagnano, L. N. Zakharov, A. L. Rheingold, G. Christou, D. N. Hendrickson, *Polyhedron* **2003**, *22*, 1727–1733; c) S. T. Ochsenbein, M. Murrie, E. Rusanov, H. Stoeckli-Evans, C. Sekime, H. U. Güdel, *Inorg. Chem.* **2002**, *41*, 5133–5140; d) M. Moragues-Cánovas, M. Helliwell, L. Ricard, E. Riviére, W. Wernsdorfer, E. Brechin, T. Mallah, *Eur. J. Inorg. Chem.* **2004**, 2219–2222.

[13] J. J. Sokol, A. G. Hee, J. R. Long, *J. Am. Chem. Soc.* **2002**, *124*, 7656–7657.

[14] For a review, see: G. S. Papaefstathiou, S. P. Perlepes, *CommentsInorg. Chem.* **2002**, *23*, 249–274.

[15] a) C. J. Milios, E. Kefalloniti, C. P. Raptopoulou, A. Terzis, R. Vicente, N. Lalioti, A. Escuer, S. P. Perlepes, *Chem. Commun.* **2003**, 819–821; b) N. Lalioti, C. P. Raptopoulou, A. Terzis, A. E. Aliev, I. P. Gerothanassis, E. Manessi-Zoupa, S. P. Perlepes, *Angew. Chem. Int. Ed.* **2001**, *40*, 3211–3214; c) A. Tsohos, S. Dionyssopoulou, C. P. Raptopoulou, A. Terzis, E. G. Bakalbassis, S. P. Perlepes, *Angew. Chem. Int. Ed.* **1999**, *38*, 983–985; d) V. Tangoulis, C. P. Raptopoulou, S. Paschalidou, E. G. Bakalbassis, S. P. Perlepes, A. Terzis, *Angew. Chem. Int. Ed. Engl.* **1997**, *36*, 1083–1085; e) V. Tangoulis, C. P. Raptopoulou, A. Terzis, S. Paschalidou, S. P. Perlepes, E. G. Bakalbassis, *Inorg. Chem.* **1997**, *36*, 3996–4006.

[16] a) M.-L. Long, S.-L. Zheng, J.-X. Shi, Y.-X. Tong, H. K. Lee, X.-M. Chen, *Dalton Trans.* **2002**, 1727–1734; b) S. B. Jedner, H. Schwöppe, H. Nimir, A. Rompel, D. A. Brown, B. Krebs, *Inorg. Chim. Acta* **2002**, *340*, 181–186; c) S. R. Breeze, S. Wang, J. E. Greedan, N. P. Raju, *Inorg. Chem.* **1996**, *35*, 6944–6951.

[17] Representative literature: a) K. N. Crowder, S. J. Garcia, R. L. Burr, J. M. North, M. H. Wilson, B. L. Conley, P. E. Fanwick, P. S. White, K. D. Sienerth, R. M. Granger II, *Inorg. Chem.* **2004**, *43*, 72–78; b) G. Crundwell, B. L. Westcott, R. Coffey, M. Zeller, A. D. Hunter, *Inorg. Chim. Acta* **2003**, *355*, 432–437; c) J. Woltz, B. L. Westcott, G. Crundwell, M. Zeller, A. D. Hunter, S. O. Sommerer, *Acta Crystallogr., Sect. E* **2002**, *58*, 609–610; d) A. K. Boudalis, F. Dahan, A. Bousseksou, J.-P. Tuchagues, S. P. Perlepes, *Dalton Trans.* **2003**, 3411–3418; e) E. Katsoulakou, N. Lalioti, C. P. Raptopoulou, A. Terzis, E. Manessi-Zoupa, S. P. Perlepes, *Inorg. Chem. Commun.* **2002**, *5*, 719–723; f) S. Zhou, W. W. Brennessel, R. G. Harrison, L. Que, Jr., *Inorg. Chim. Acta* **2002**, *337*, 32–38; g) M. G. Barandika, Z. Serna, R. Cortes, L. Lezama, M. K. Urtiaga, M. I. Arriortua, T. Rojo, *Chem. Commun.* **2001**, 45–46; h) Z. E. Serna, R. Cortes, M. K. Urtiaga, M. G. Barandika, L. Lezama, M. I. Arriortua, T. Rojo, *Eur. J.Inorg. Chem.* **2001**, 865–872; i) M.-L. Tong, H. K. Lee, Y.-X. Tong, X.-M. Chen, T. C. W. Mak, *Inorg. Chem.* **2000**, *39*, 4666–4669; j) V. Tangoulis, C. P. Raptopoulou, S. Paschalidou, A. Tsohos, E. G. Bakalbassis, A. Terzis, S. P. Perlepes, *Inorg. Chem.* **1997**, *36*, 5270–5277; k) A. C. Deveson, S. L. Heath, C. J. Harding, A. K. Powell, *J. Chem. Soc., Dalton Trans.* **1996**, 3173–3178; l) A. N. Papadopoulos, V. Tangoulis, C. P. Raptopoulou, A. Terzis, D. P. Kessissoglou, *Inorg. Chem.* **1996**, *35*, 559–565.

[18] a) G. S. Papaefstathiou, A. Escuer, M. Font-Bardia, S. P. Perlepes, X. Solans, R. Vicente, *Polyhedron* **2002**, *21*, 2027; b) G. S. Papaefstathiou, A. Escuer, R. Vicente, M. Font-Bardia, X. Solans, S. P. Perlepes, *Chem. Commun.* **2001**, 2414–2415; c) G. S. Papaefstathiou, S. P. Perlepes, A. Escuer, R. Vicente, M. Font-Bardia, X. Solans, *Angew. Chem. Int. Ed.* **2001**, *40*, 884–886.

[19] a) Z. E. Serna, L. Lezama, M. K. Urtiaga, M. I. Arriortua, M. G. Barandika, R. Cortes, T. Rojo, *Angew. Chem. Int. Ed.* **2000**, *39*, 344–347; b) Z. E. Serna, M. G. Barandika, R. Cortes, M. K. Urtiaga, G. E. Barberis, T. Rojo, *J. Chem. Soc., Dalton Trans.* **2000**, 29–34; c) Z. E. Serna, M. K. Urtiaga, M. G. Barandika, R. Cortes, S. Martin, L. Lezama, M. I. Arriortua, T. Rojo, *Inorg. Chem.* **2001**, *40*, 4550–4555; d) G. S. Papaefstathiou, A. Escuer, C. P. Raptopoulou, A. Terzis, S. P. Perlepes, R. Vicente, *Eur. J. Inorg. Chem.* **2001**, 1567–1574.

[20] S. R. Batten, K. S. Murray, *Coord. Chem. Rev.* **2003**, *246*, 103–130.

[21] A. M. Kutasi, A. R. Harris, S. R. Batten, B. Moubaraki, K. S. Murray, *Cryst. Growth Des.* **2004**, *4*, 605–610, and references therein.

[22] Representative literature: a) B. Vangdal, J. Carranza, F. Lloret, M. Julve, J. Sletten, *Dalton Trans.* **2002**, 566–574, and references cited therein. b) A. M. Kutasi, S. R. Batten, B. Moubaraki, K. S. Murray, *Dalton Trans.* **2002**, 819–821; c) A. Escuer, F. A. Mautner, N. Sanz, R. Vicente, *Inorg. Chim. Acta* **2002**, *340*, 163–169; d) A. Escuer, F. A. Mautner, N. Sanz, R. Vicente, *Inorg. Chem.* **2000**, *39*, 1668–1673; e) J. L Manson, A. M. Arif, C. D. Incarvito, L. M. Liable-Sands, A. L. Rheingold, J. S. Miller, *J. Solid State Chem.* **1999**, *145*, 369–378; f) J. L. Manson, C. R. Kmety, Q.-Z. Huang, J. W. Lynn, G. M. Bendele, S. Pagola, P. W. Stephens, L. M. Liable-Sands, A. L. Rheingold, A. J. Epstein, J. S. Miller, *Chem. Mater.* **1998**, *10*, 2552–2560; g) M. Kurmoo, C. J. Kepert, *New J. Chem.* **1998**, *22*, 1515–1524; h) J. L. Manson, J. A. Schlueter, H.-J. Koo, M.-H. Whangbo, *Inorg. Chem.* **2004**, *43*, 4007–4011; i) B. Jürgens, H. A. Höppe, W. Schnick, *Solid State Sci.* **2002**, *4*, 821–825.

[23] M.-L. Tong, Y.-M. Wu, Y.-X. Tong, X.-M. Chen, H.-C. Chang, S. Kitagawa, *Eur. J. Inorg. Chem.* **2003**, 2385–2388.

[24] J. M. Seco, M. Quiros, M. J. González Garmendia, *Polyhedron* **2000**, *19*, 1005–1013.

[25] R. A. Coxall, S. G. Harris, D. K. Henderson, S. Parsons, P. A. Tasker, R. E. P. Winpenny, *J. Chem. Soc., Dalton Trans.* **2000**, 2349–2356.

[26] J. M. Clemente-Juan, B. Chansou, B. Donnadieu, J.-P. Tuchagues, *Inorg. Chem.* **2000**, *39*, 5515–5519.

[27] a) C. J. Milios, E. Kefalloniti, C. P. Raptopoulou, A. Terzis, A. Escuer, R. Vicente, S. P. Perlepes, *Polyhedron* **2004**, *23*, 83–95; b) C. J. Milios, T. C. Stamatatos, P. Kyritsis, A. Terzis, C. P. Raptopoulou, R. Vicente, A. Escuer, S. P. Perlepes, *Eur. J. Inorg. Chem.* **2004**, 2885–2901.

[28] a) L. E. Pence, A. Caneschi, S. J. Lippard, *Inorg. Chem.* **1996**, *35*, 3069–3072; b) S. Brooker, V. McKee, T. Metcalfe, *Inorg. Chim. Acta* **1996**, *246*, 171–79; c) P. Guerriero, S. Tamburini, P. A. Vigato, *Coord. Chem. Rev.* **1995**, *139*, 17–243; d) K. L. Taft, A. Caneschi, L. E. Pence, C. D. Delfs, G. C. Papaefthymiou, S. Lippard, *J. Am. Chem. Soc.* **1993**, *115*, 11753–11766; e) S. Brooker, V. McKee, W. B. Shepard, L. K. Pannell, *J. Chem. Soc., Dalton Trans.* **1987**, 255–2562.

[29] K. S. Murray, *Adv. Inorg. Chem.* **1995**, *43*, 261–358.

[30] a) J. E. Andrew, A. B. Blake, *J. Chem. Soc. A* **1969**, 1556–1560; b) V. G. Kessler, S. Golih, M. Kritikos, O. N. Korsak, E. E. Knyazeva, I. F. Moskovskaya, B. V. Romanovsky, *Polyhedron* **2001**, *20*, 915–922; c) M. A. Halcrow, J.-S. Sun, J. C. Huffman, G. Christou, *Inorg. Chem.* **1995**, *34*, 4167–4177; d) M. S. El Fallah, E. Rentschler, A. Caneschi, D. Gatteschi, *Inorg. Chim. Acta* **1996**, *247*, 231–235; e) A. J. Blake, E. K. Brechin, A. Gordon, R. O. Gould, C. M. Grant, S. Parsons, J. M. Rawson,

R. E. P. Winpenny, *J. Chem. Soc., Chem. Commun.* **1995**, 1983–1984.
[31] a) S. Mukherjee, T. Weyhermüller, E. Bothe, K. Wieghardt, P. Chaudhuri, *Eur. J. Inorg. Chem.* **2003**, 863–875; b) G. Aromi, A. S. Batsanov, P. Christian, M. Helliwell, O. Roubeau, G. A. Timco, R. E. P. Winpenny, *Dalton Trans.* **2003**, 4466–4471; c) A. K. Sah, C. P. Rao, P. K. Sarenketo, K. Rissanen, *Chem. Lett.* **2001**, 1296–1297; d) A. Escuer, M. Font-Bardia, S. B. Kumar, X. Solans, R. Vicente, *Polyhedron* **1999**, *18*, 909–914; e) W. Vreugdenhil, J. G. Haasnoot, J. Reedijk, A. L. Spek, *Inorg. Chim. Acta* **1987**, *129*, 205–216, and references therein.
[32] a) G. Aromi, A. S. Batsanov, P. Christian, M. Helliwell, A. Parkin, S. Parsons, A. A. Smith, G. A. Timco, R. E. P. Winpenny, *Chem. Eur. J.* **2003**, *9*, 5142–5161; b) K. E. Gubina, V. A. Ovchynnikov, J. Swiatek-Kozlowska, V. M. Amirkhanov, T. Yu. Silva, K. V. Domasevitch, *Polyhedron* **2002**, *21*, 963–967; c) M. M. Olmstead, P. P. Power, G. A. Sigel, *Inorg. Chem.* **1988**, *27*, 580–583; d) J. A. Bertrand, A. P. Ginsberg, R. I. Kaplan, C. E. Kirkwood, R. L. Martin, R. C. Sherwood, *Inorg. Chem.* **1971**, *10*, 240–246.
[33] R. H. Holm, S. Ciurli, J. A. Weigel, *Prog. Inorg. Chem.* **1990**, *38*, 1–74.
[34] G. W. Brudving, H. H. Thorp, R. H. Crabtree, *Acc. Chem. Res.* **1991**, *24*, 311–316.
[35] For example, see: a) K. Wieghardt, *Angew. Chem. Int. Ed. Engl.* **1989**, *28*, 1153–1172; b) M. W. Wemple, H.-L. Tsai, K. Folting, D. N. Hendrickson, G. Christou, *Inorg. Chem.* **1993**, *32*, 2025, and references cited therein. c) A. Rompel, J. C. Andrews, R. M. Cinco, M. W. Wemple, G. Christou, N. A. Law, V. L. Pecoraro, K. Sauer, V. K. Yachandra, M. P. Lein, *J. Am. Chem. Soc.* **1997**, *119*, 4465–4470.
[36] K. N. Ferreira, T. M. Iverson, K. Maghlaoui, J. Barber, S. Iwata, *Science* **2004**, *303*, 1831–1838.
[37] J. A. Bertrand, C. Marbela, D. G. Vanderneer, *Inorg. Chim. Acta* **1978**, *26*, 113–118.
[38] a) S. O. Sommerer, J. D. Baker, W. P. Jensen, A. Hamza, R. A. Jacobson, *Inorg. Chim. Acta* **1993**, *210*, 173–176; b) M.-L. Tong, G. Yang, X.-M. Chen, S. W. Ng, *Acta Crystallogr.*, Sect. C **1998**, *54*, 217–219; c) C. Hemmert, M. Renz, H. Gornitzka, S. Soulet, B. Meunier, *Chem. Eur. J.* **1999**, *5*, 1766–1774.
[39] G. B. Deacon, R. J. Phillips, *Coord. Chem. Rev.* **1980**, *33*, 227–250.
[40] D. Gatteschi, L. Pardi, *Gazz. Chim. Ital.* **1993**, *123*, 231–238.
[41] L. Ballestero, E. Coronado, A. Gutiérrez, A. Monge, M. F. Perpinan, E. Pinilla, T. Rico, *Inorg. Chem.* **1992**, *31*, 2053–2056.
[42] J. J. Smit, G. M. Nap, L. J. De Jongh, J. A. C. van Ooijen, J. Reedijk, *Physica B* **1979**, *97*, 365–371.
[43] a) G. M. Sheldrick, *SHELXS-86*, *Program for the Solution of Crystal Structures*, University of Göttingen, Germany, **1986**; b) G. M. Sheldrick, *SHELXL-93*, *Program for the Refinement of Crystal Structures*, University of Göttingen, Germany, **1993**; c) G. M. Sheldrick, SHELXTL/PC, Release 5.03, Siemens Analytical X-ray Instruments, Madison, WI, **1994**.

Received: August 2, 2004

 © 2005 Wiley-VCH Verlag GmbH & Co. KGaA, Weinheim

Coordination Chemistry of the Ditopic Ligand 4-[6-(2-Pyridyl)-2-pyridyl]-6-(2-pyridyl)pyrimidine: Encapsulation of Nitrate by [2×2]Grid Complexes

Larisa Kovbasyuk,[a] Hans Pritzkow,[a] and Roland Krämer*[a]

Keywords: Ligand design / Self-assembly / Nitrate recognition / Grids / Nickel(II) / Cobalt(II)

We describe herein the synthesis, physical properties and crystal structures of metal complexes with the new ligand 6-(2-pyridyl)-4-[6-(2-pyridyl)-2-pyridyl]pyrimidine (**L**). Reactions of **L** with Ni^{II}, Co^{II}, Fe^{II}, Zn^{II} and Cu^{II} nitrates in a 1:1 ratio leads to the self-assembled tetranuclear [2×2] grid complexes **1**–**5** with encapsulated NO_3^- ions, as confirmed by the X-ray crystal structures of $[Ni_4\mathbf{L}_4(DMSO)_2(H_2O)_2](NO_3)(ClO_4)_7\cdot 4\,DMSO\cdot 6\,H_2O$ (**1**) and $[Co_4\mathbf{L}_4(DMF)_4](NO_3)(ClO_4)_7$ (**2**). The mononuclear copper(I) complex $[Cu\mathbf{L}(PPh_3)_2]ClO_4\cdot 2\,(CH_3CN)$ (**6**) and the binuclear $[Cu_2\mathbf{L}_2(CN)(PPh_3)_2]ClO_4$ (**7**) were synthesized from **L** and $[Cu(PPh_3)_3]Cl$.

(© Wiley-VCH Verlag GmbH & Co. KGaA, 69451 Weinheim, Germany, 2005)

Introduction

Self-assembly of specially designed metal complexes may afford a variety of unusual topologies, e.g. molecular grids, boxes, ladders and helicates.[1] These highly ordered structures may have well defined cavities which can act as binding pockets for substrates. Self-assembled metal complexes may therefore be useful as receptors, sensors or catalysts. The sizes and shapes of such cavities may be tuned by varying both the ligand structure and the metal ion in order to achieve optimal interaction between the cavity and a substrate.

The development of anion selective receptors is an important topic in chemistry. Reported examples of anion binders based on polynuclear complexes include a "molecular square" assembled from four Ni^{II} ions and tetrazine-derived ligands with a tetrafluoroborate guest,[2] molecular Pd^{II}/Pt^{II} triangles containing ClO_4^- or PF_6^-[3] and a grid-like $Fe^{II}_2Ru^{II}_2$ complex of a 4,6-bis(2,2′-bipyridyl)pyrimidine ligand which encloses chloride in its central cavity.[4] We have recently demonstrated the usefulness of polynuclear metal complexes as ionophores for the construction of anion-selective electrodes.[5]

The selective recognition of nitrate is of particular interest since this ion has been implicated in groundwater contamination and is present in high concentrations in certain waste waters. The majority of reported receptors for nitrate are based on H-bonding interactions.[6] Funnel-shaped tri- and hexanuclear Pd^{II}/Pt^{II} complexes incorporating a nitrate at the bottom of the funnel by very weak coordinative bonds are a rare exception.[7] In a recent communication we reported the crystal structure of a tetranuclear nickel(II) complex forming a [2×2] grid structure and incorporating a nitrate in its cavity.[8]

Attempts to isolate the same complex with a Cl^- guest, as observed for the corresponding octahedral M^{II} complexes of the symmetric ligand 4,6-bis(2,2́-bipyridyl)pyrimidine,[4] failed. Interestingly, subtle structural modifications have a significant influence on the host-guest chemistry of the self-assembled complexes.

Herein we present a detailed investigation of the coordination chemistry and metal-induced self-assembly of **L** with the divalent 3d-metal ions Ni^{II}, Fe^{II}, Zn^{II}, Co^{II} and Cu^{II}. In addition, we have explored complex formation of **L** with Cu^{I} ions which prefers a tetrahedral over an octahedral metal coordination as observed in $\mathbf{L}_4M_4$ grid complexes.

Results and Discussion

Details of the synthesis and X-ray structure of the ditopic ligand **L** which has one tridentate and one bidentate metal binding site have been reported elsewhere.[9]

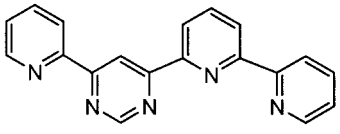

L

Complexes of **L** with Ni^{II}, Co^{II}, Fe^{II}, Cu^{II} and Zn^{II} were prepared by mixing the ligand and suitable metal salts in organic solvents or water. Crystalline compounds were filtered off, washed with isopropanol and dried under high vacuum. Sometimes recrystallisation from different solvents was necessary to obtain crystals suitable for X-ray analysis.

[a] Anorganisch-Chemisches Institut der Universität Heidelberg, Im Neuenheimer Feld 270, 69120 Heidelberg, Germany
Fax: +49-6221-548599
E-mail: roland.kraemer@urz.uni-heidelberg.de

 © 2005 Wiley-VCH Verlag GmbH & Co. KGaA, Weinheim **DOI: 10.1002/ejic.200400673**

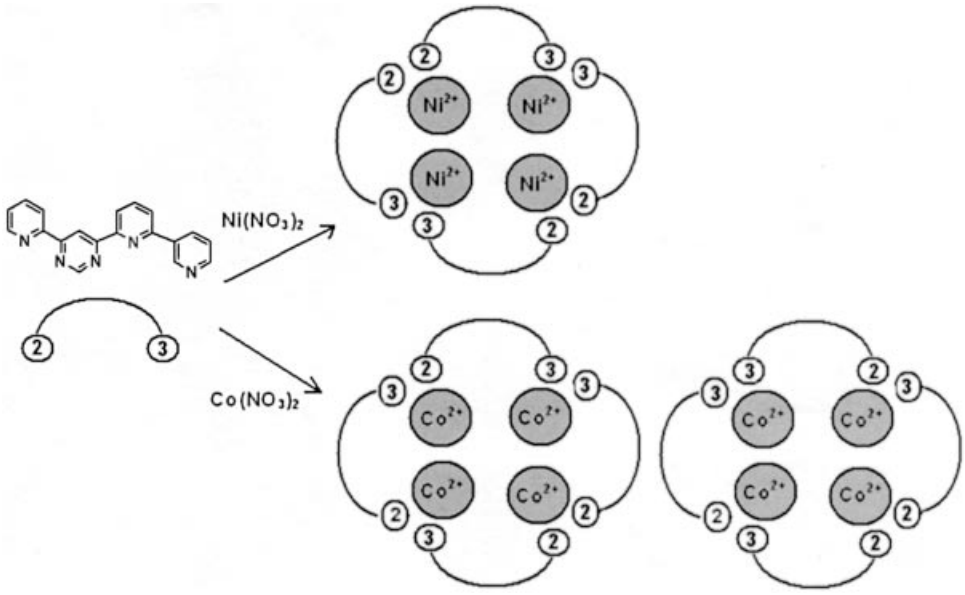

Scheme 1. Tetranuclear grid complexes **1** and **2** are pseudocoordination isomers.

Complex formation is accompanied by a colour change from colourless to yellow in the case of the Ni^{II} complex **1** to red-brown in the case of Co^{II} complex **2**, to dark-blue for the Fe^{II} complex **3** and to blue in the case of the Cu^{II} complex **5**. In the case of the Zn^{II} complex **4**, no significant colour changes were observed. C, H, N analyses of the isolated compounds were in agreement with following formulae: $[Ni_4\mathbf{L}_4(DMSO)_2(H_2O)_2](NO_3)(ClO_4)_7\cdot 4\,DMSO\cdot 6\,H_2O$ (**1**), $[Co_4\mathbf{L}_4(DMF)_4](NO_3)(ClO_4)_7$ (**2**), $[Fe_4\mathbf{L}_4(H_2O)_4](NO_3)(ClO_4)_7\cdot 6\,H_2O$ (**3**), $[Zn_4\mathbf{L}_4(H_2O)_4](NO_3)_4Cl_4\cdot 2\,H_2O$ (**4**) and $[Cu_4\mathbf{L}_4(H_2O)_4](NO_3)_4(ClO_4)_4\cdot 2\,H_2O$ (**5**). For **1** and **2** the tetranuclear structures were confirmed by X-ray analyses. Since **L** is unsymmetrical, isomerism of the metal complexes is possible (Scheme 1).

The complex cation of **1** displays C_2 symmetry and contains two crystallographically independent nickel ions (Figure 1). The four nitrogen atoms of two different molecules of **L** and two oxygen atoms of the *cis*-orientated DMSO and H_2O molecules, respectively, constitute the distorted octahedral environment of Ni(1).[8] Ni(2) is coordinated by six nitrogen atoms of the tridentate sites of two molecules of **L**. Four nickel atoms are arranged at the corners of an almost ideal square [Ni(1)···Ni(2) = 6.170 Å, Ni(1)···Ni(2a) = 6.235 Å, Ni(1)–Ni(2)–Ni(1a) = 88.4°, Ni(2)–Ni(1)–Ni(2a) = 91.6°].

The tetranuclear complex cation of **2**[10] is shown in Figure 2. There is disorder of the ligand connecting Co(1) and Co(2) through its bidentate/tridentate and tridentate/bidentate sites [the site occupation factor for the disordered **L**/DMF ligands on Co(1)–Co(3) is 50:50] and probably for the ligand between Co(2) and Co(3) as well. The DMF ligands could not be localised at these positions. The coordination environments of the cobalt atoms can be described as N_5O or N_6 for Co(1), N_5O or N_6 for Co(2) and N_5O or N_6 for Co(3). The coordination environment of Co(4) is N_4O_2 which is formed from four nitrogen atoms from two

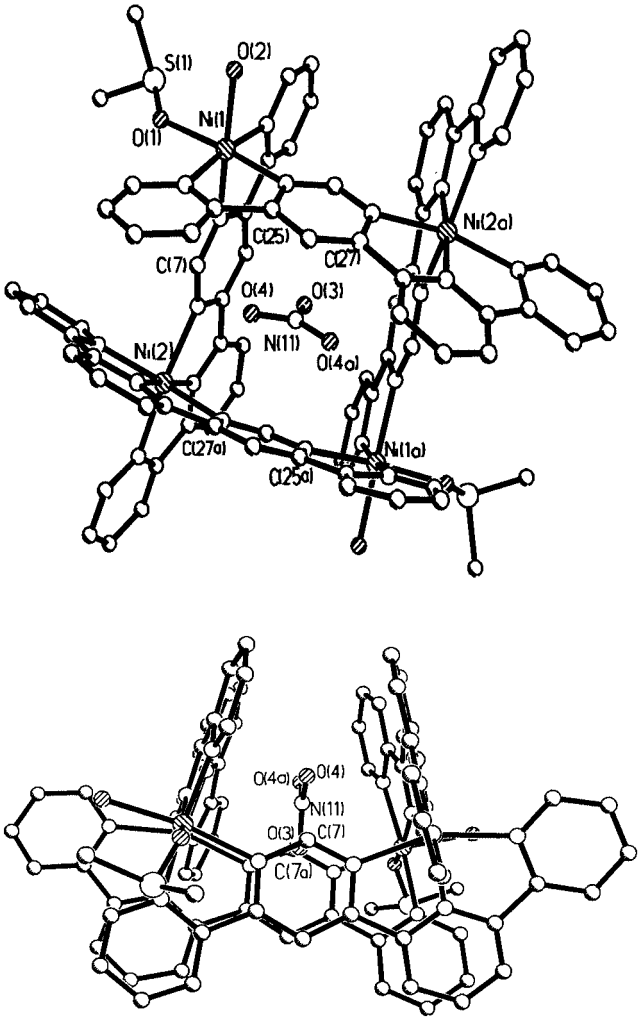

Figure 1. View of the structure of the complex cation of **1** with the enclosed nitrate ion. Hydrogen atoms are omitted for clarity.

 © 2005 Wiley-VCH Verlag GmbH & Co. KGaA, Weinheim

different molecules of **L** and two oxygen atoms from DMF molecules.

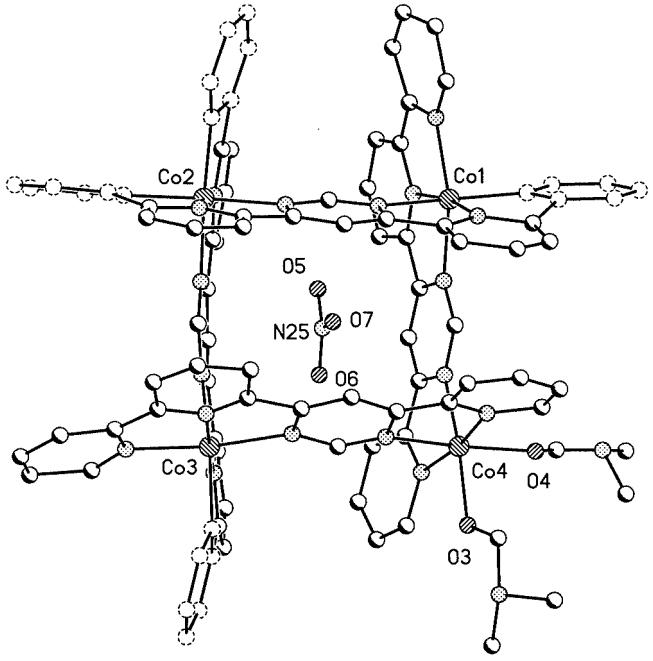

Figure 2. View of the structure of the complex cation of **2** with an enclosed nitrate ion.

The presence of two (depicted in Scheme 1) or more isomers in the crystal of **2** might be the origin of the disorder problems. The Co···Co distances average 6.25 Å which is slightly larger than Ni···Ni distances (6.20 Å) in **1** but significantly shorter than in a related tetracobalt (II) complex derived from a 4,6-bis(2,2′-bipyridyl)pyrimidine ligand (6.49 Å).[11] This illustrates that replacement of one of the two tridentate sites in the latter ligand by a bidentate site has a substantial effect on the cavity size of the self-assembled structure. The difference between the M···M distances in **1** and **2** corresponds to double the difference between the ionic radii of the corresponding metals. Consequently, both a variation in the ligand structure and metal ion size should enable fine tuning of the cavity size in complexes of this type. We have used a series of divalent transition-metals with different atomic radii for construction of [2×2] grids with different cavity sizes for guest binding. Crystallographic data for the Ni^{II} and Co^{II} grids allow us to estimate the M···M distances in the Fe^{II}, Zn^{II} and Cu^{II} [2×2] grids as 6.29, 6.14 and 6.08 Å, respectively, based on the published radii for the high-spin metal ions.[12]

A NO_3^- anion is trapped in the hydrophobic central cavity in both **1** and **2**, the latter being formed from the heterocyclic aromatic rings of the ligands. The molecular plane of the NO_3^- is coplanar to one ligand pair and perpendicular to the second (Figure 1). The close fit of the nitrate in **1** is confirmed by several short van der Waals contacts between the nitrate oxygens with the host, i.e. O(4)···C(25) = 2.814 Å, O(4a)···C(27) = 2.812 Å, O(4)···C(7) = 2.714 Å and O(3)···C(7) = 3.101 Å.[12] It is clear (Figure 1) that the mobility of nitrate within the cage is highly restricted since the two pairs of **L** are not exactly coplanar (interplanar angles are 38.2° and 33.4°) but display a roof-shaped arrangement. Binding of even slightly larger anions should be disfavoured since anion host contacts would be unfavourably short.

In the absence of crystallographic data for compounds **3**, **4** and **5**, a comparison of their solid state infrared spectra indicates that their structures might be related to those of **1** and **2**. Compounds **1**, **2** and **3** show characteristic strong bands of both nitrate (1384, 1384 and 1386 cm^{-1}) and perchlorate (1104, 1102 and 1107 cm^{-1}).[13] In the IR spectrum of **1** two $\nu_{(S=O)}$ peaks appear at 938 and 945 cm^{-1} confirming the presence of coordinated and uncoordinated molecules of DMSO. The presence of DMF molecules in **2** is indicated by presence in the IR spectrum of a strong peak at 1677 cm^{-1} which can be attributed to an amide $\nu_{(C=O)}$ vibration. Strong peaks in the IR spectra of **4** and **5** which are not observed in the spectrum of the free ligand with maxima at 1385, 1378, and 1386, 1378 cm^{-1}, respectively, can be assigned to $\nu_{(N=O)}$ vibrations of the expected two types of nitrate ion. The IR spectrum of **5** also exhibits a strong peak due to the perchlorate ions at 1105 cm^{-1}. All complexes **1**–**5** exhibit, in their IR spectra, a strong peak around 1385 cm^{-1} which in **1** and **2** can be unambiguously attributed to encapsulated nitrate. IR data support the assignment of the related tetranuclear structures of the cations of **3**, **4** and **5** with encapsulated nitrate ions.

To detect magnetic interactions between the metal centres, **2** was subjected to susceptibility measurements in the temperature range 1.7–300 K. Figure 3 shows the temperature dependence of $\chi_m \cdot T$. At 300 K, $\chi_m \cdot T$ equals 9.6 $cm^3 mol^{-1} K$ which roughly corresponds to the expected values for four uncoupled Co^{II} ions (d^7, S =). As T is lowered, $\chi_m \cdot T$ slowly decreases down to 50 K. Below this temperature, $\chi_m \cdot T$ drops abruptly down to 0.5 $cm^3 mol^{-1} K$. This behaviour indicates overall antiferromagnetic interactions between Co^{II} ions. The Curie temperature was evaluated as 23 K. For **3** a ^{57}Fe Mössbauer spectrum recorded at room temperature exhibited a major singlet characteristic of a low spin Fe^{II} species.

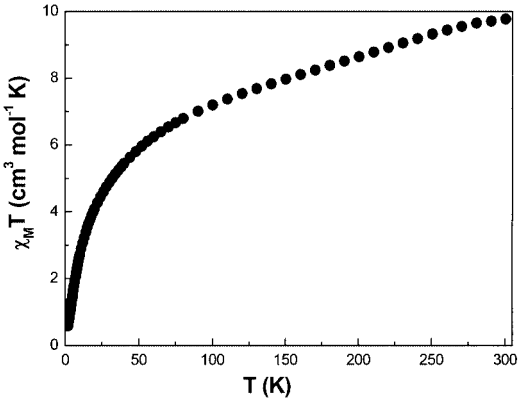

Figure 3. The temperature dependence of $\chi_m \cdot T$ for **2**.

 © 2005 Wiley-VCH Verlag GmbH & Co. KGaA, Weinheim

Spectrophotometric titrations of **L** with Co^{II} and Fe^{II} in an acetone/water mixture revealed fast formation of $[\mathbf{L}_2M]^{2+}$ (increase of absorbance at 390 nm) but no further changes were observed immediately after addition of more then 0.5 equiv. of the metal ion (Figure 4). Formation of $\mathbf{L}_2M$ complexes could be confirmed by MALDI mass spectra of solutions containing **L** and M^{II} in a 1:1 ratio. When a MALDI mass spectrum of the Fe^{II} complex solution was recorded several hours after sample preparation, however, new signal corresponding to an $Fe_3\mathbf{L}_2$ fragment appeared.

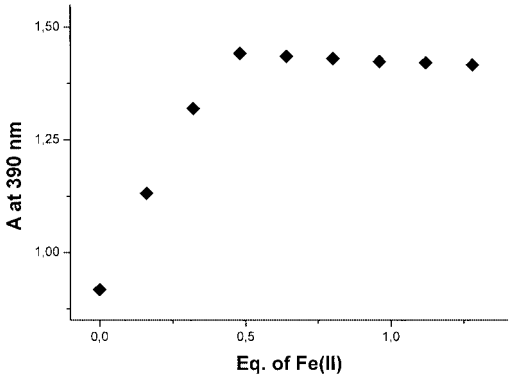

Figure 4. Increase of the 390 nm absorbance upon photometric titration of **L** (5×10^{-5} M) with Fe^{II}-tetrafluoroborate solution at 20 °C and pH 7.0 (spectra correspond to addition of Fe in steps of 0.16 equiv.).

These observations are consistent with fast formation of an $\mathbf{L}_2Fe$ species in which the terpyridine-like tridentate sites of **L** coordinate to the metal ion and slow conversion of this complex to the $\mathbf{L}_4Fe_4$ oligomer occurs. Any attempts to detect the intact $\mathbf{L}_4Fe_4$ complexes by mass spectrometric techniques (FAB, electrospray at variable concentrations, MALDI-TOF) failed, even for fresh solutions of crystalline samples of complexes **1** and **2**.

Complexes of L with Cu^I

While the tetranuclear [2×2] grid structure appears to be favoured with metal ions which can adopt octahedral coordination, **L** might form different types of self-assembled structures when metal ions with a preference for tetrahedral coordination are involved. We therefore explored the reaction of **L** with Cu^I ions which forms both tetrahedral complexes with 2,2′-bipyridyl type ligands and five coordinate complexes with *terpy* ligands, corresponding to the bidentate und tridentate sites of **L**, respectively.

The crystalline Cu^I complexes $[Cu\mathbf{L}(PPh_3)_2]ClO_4\cdot 2(CH_3CN)$ (**6**) and $[Cu_2\mathbf{L}_2(CN)(PPh_3)_2]ClO_4$ (**7**) could be obtained by treatment of **L** with $Cu^I(PPh_3)_3Cl$ followed by addition of $NaClO_4$ in acetone solution. Use of ClO_4^- promoted better crystallisation of the complexes.

The IR spectra of complexes **6** and **7** in the range 4000–400 cm^{-1} are quite similar and, as for **1**, **2**, **3**, **4** and **5**, show all the characteristic ligand peaks. The infrared spectra display bands for $\nu_{(C\equiv N)}$ at 2100 cm^{-1} (acetonitrile solvate) for **6** and 2080 cm^{-1} (bridging CN^-) for **7**, and bands for the perchlorate counterions at 1094 and 1098 cm^{-1} for **6** and **7**, respectively.[13] Crystals of **6** formed in acetonitrile appeared to lose solvent if left to stand in a solvent-free atmosphere.

ESI and MALDI mass spectra of solutions of **6** and **7** gave signals for mononuclear species. Major peaks in the spectra correspond to $[Cu\mathbf{L}]^+$ and $[Cu\mathbf{L}(OH)(OH_2)]^+$ with characteristic isotopic distributions for copper ions. Spectrophotometric titrations of ligand **L** with $[Cu(CH_3CN)_4]BF_4$ also indicate formation of a 1:1 **L**:Cu complex (Figure 5). Sharp isosbestic points were obtained in the range of 0 to 1 equiv. of Cu. The UV absorbance maxima of the complexes (about 330 nm) are shifted toward higher wavelengths relative to the free ligands (about 300 nm).

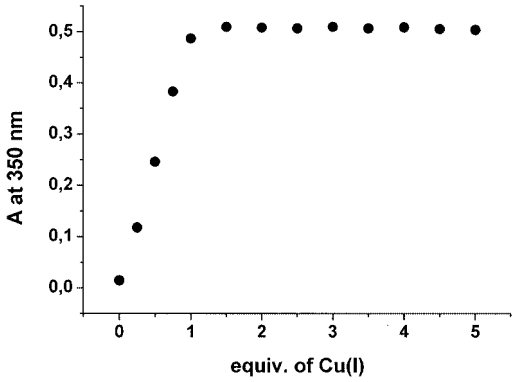

Figure 5. Increase of the 350 nm absorbance upon photometric titration of **L** (1×10^{-5} M) with $[Cu(CH_3CN)_4]BF_4$ solution at 20 °C (spectra correspond to addition of Cu in steps of 0.25 equiv.).

Crystal Structure of $[CuL(PPh_3)_2]ClO_4\cdot 2CH_3CN$ (6)

The solid-state structure of **6** was determined by X-ray crystallography (Table 1). The copper ion is four-coordinate (Figure 6) and bound to the two nitrogen atoms of **L** as well as two phosphorus atoms from PPh_3 groups. The geometry around the copper ion is distorted tetrahedral which is typical for Cu^I compounds, with angles ranging from 79.63(8) to 122.77(3)° (selected distances and angles are given in Table 1). The copper–phosphorus distances are nearly identical at 2.2461(8) and 2.2550(8) Å and are similar to the values in other Cu^I complexes.[14,15] The copper ion binds to the bidentate site of **L** with Cu–N distances of 2.052(2) and 2.083(2) Å. Very similar bonding parameters for the Cu^I ion were found in $[Cu(phen)(PPh_3)_2]^+$ and $[Cu(dmp)(PPh_3)_2]^+$ (where dmp is 2,9-dimethyl-1,10-phenanthroline).[16]

Table 1. Selected bond and lengths [Å] and angles [°] for **6**.

Cu(1)–N(1)	2.052(2)	N(1)–Cu(1)–P(1)	116.21(6)
Cu(1)–N(2)	2.083(2)	N(2)–Cu(1)–P(1)	107.82(6)
Cu(1)–P(1)	2.2461(8)	N(1)–Cu(1)–P(2)	109.08(6)
Cu(1)–P(2)	2.2550(8)	N(2)–Cu(1)–P(2)	113.24(6)
N(1)–Cu(1)–N(2)	79.63(8)	P(1)–Cu(1)–P(2)	122.77(3)

The heterocyclic fragments of **L** containing nitrogens N(3), N(4) and N(5) are coplanar whereas the heterocyclic fragment is tilted by 13.9°. The π-stacking (3.4 and 7.9 Å)

 © 2005 Wiley-VCH Verlag GmbH & Co. KGaA, Weinheim

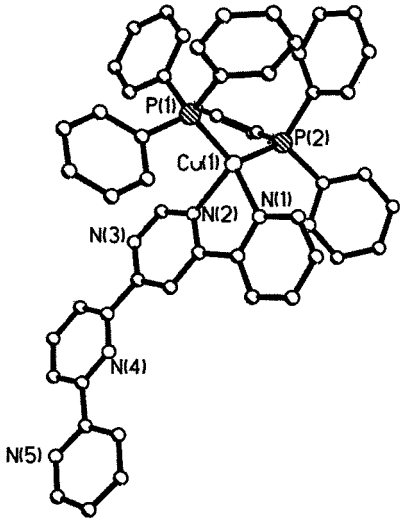

Figure 6. Molecular structure and numbering scheme for **6**. Hydrogen atoms are omitted for clarity.

of Cu**L** fragments can be observed in the crystal structure (Figure 7). The distances of the observed π-stacked units in **6** are approximately 3.4 and 7.9 Å.

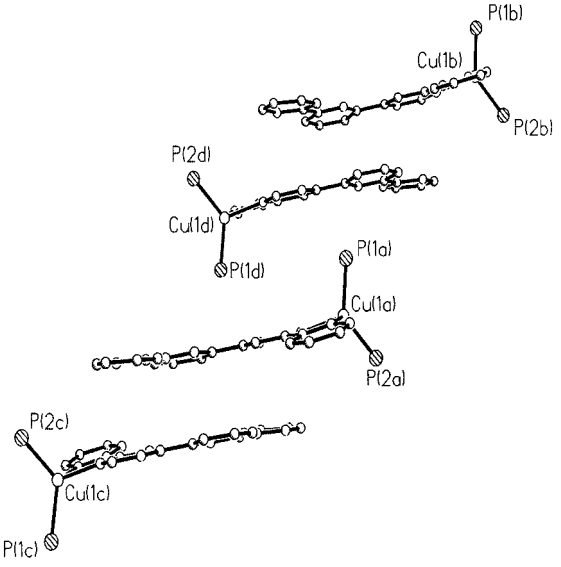

Figure 7. Stacking of complex cations in the crystal of **6**. Phenyl rings are omitted for clarity.

L contains both bi- and tridentate metal binding fragments. Interestingly, Cu^{I} prefers the bidentate bipyridyl-like binding site, although pentacoordinate Cu^{I} complexes with tridentate terpyridine and two monodentate coligands have been reported.[17] In each of the latter complexes, however, the metal ion coordination sphere is strongly distorted with one long metal–nitrogen contact and the complexes are not stable in solution and are spontaneously oxidised by air to the corresponding Cu^{II} complexes. In contrast, reported Cu^{I}-bipy-PPh_3 complexes are air stable in solution for days.[18] These facts indicate that bidentate bipyridyl is a better ligand for Cu^{I} than tridentate terpyridyl and explain the observed structures of **6** and **7** as well as the lack of oligomeric complex formation.

Sauvage and coworkers have designed a ligand system which consists of bidentate bipyridyl and tridentate terpyridyl fragments.[19] It was shown by electrochemical and spectroscopic methods that the preferred coordination mode for Cu^{I} is bidentate bipyridyl whereas for Cu^{II} it is tridentate terpyridyl. Similarly, the observation of a bidentate site preference for Cu^{I} should facilitate the design of mixed-metal self-assembled complexes of **L**.

Crystal Structure of $[Cu_2L_2(CN)(PPh_3)_2]ClO_4$ (7)

This structure (Table 2, Figure 8) reveals that the molecule of **7** contains two copper centres bridged by cyanide, traces of which were possibly present in the MeCN solvent. The bridging CN^- is disordered with respect to C/N coordination. Each copper ion exhibits a distorted tetrahedral geometry by binding to two nitrogen atoms from **L**, a phosphorus atom from PPh_3 and a nitrogen (carbon) atom from the CN group. The angles at the copper(I) atoms range from 78.84(9) to 127.87(7)°. In **7**, the copper–nitrogen distances are different, i.e. 2.089(2) and 2.090(2) Å to the heterocyclic nitrogen atoms and 1.930(2) Å to the nitrile nitrogen. The copper–phosphorus distance is 2.2094(8) Å. The copper–bpy nitrogen and copper–phosphorus distances are close to the corresponding values in **6**. The Cu–N(C)–C(N) angle is 164.5° and the Cu···Cu separation is 4.869 Å.

Table 2. Selected bond and lengths [Å] and angles [°] for **7**.

Cu(1)–N(1C)	1.930(2)	N(1C)–Cu(1)–N(3)	111.44(9)
Cu(1)–N(2)	2.089(2)	N(2)–Cu(1)–N(3)	78.84(9)
Cu(1)–N(3)	2.090(2)	N(1C)–Cu(1)–P(1)	127.87(7)
Cu(1)–P(1)	2.2094(8)	N(2)–Cu(1)–P(1)	105.10(6)
N(1C)–Cu(1)–N(2)	108.11(9)	N(3)–Cu(1)–P(1)	113.58(6)

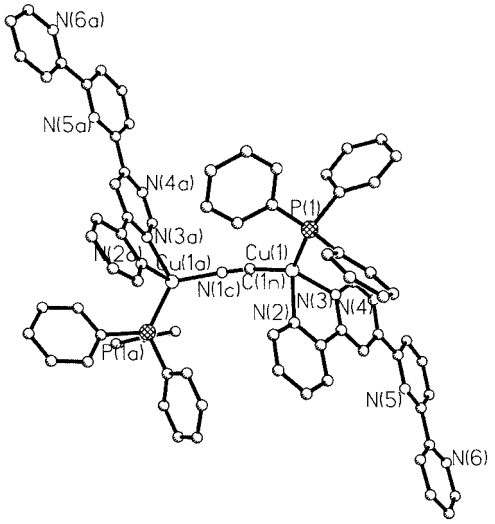

Figure 8. Molecular structure and numbering scheme for **7**. Hydrogen atoms are omitted for clarity.

 © 2005 Wiley-VCH Verlag GmbH & Co. KGaA, Weinheim

Conclusions

We have reported here a novel polynucleating ligand which forms [2×2] grids with divalent 3d metals having different electronic structures, i.e. Ni^{II}, Co^{II}, Fe^{II}, Zn^{II} and Cu^{II}. As shown by magnetic measurements and Mössbauer spectroscopy, no significant interactions between metal centres occur in these compounds. We have also shown that the grids are formed only in the presence of NO_3^- ions and with divalent metal ions. Monovalent metal ions (e.g. Cu^I) both in the presence and absence NO_3^- form mono and dinuclear complexes. In both cases Cu^I prefers the bidentate to the tridentate binding site of the ligand.

Experimental Section

Materials and Procedures: Reagents and solvents were obtained from Aldrich, Acros or Fluka and used as received. 6-(2-Pyridyl)-4-[6-(2-pyridyl)-2-pyridyl]pyrimidine (**L**) was synthesized as previously reported.[9] The iron(II) and copper(I) complexes were synthesized and purified using typical high vacuum and/or Schlenk techniques.

Physical Measurements: ^{1}H NMR spectra were recorded on Bruker AC-300 (300.13 MHz) and Bruker AC-400 (400.13 MHz) spectrometers and chemical shifts are reported in ppm. Tetramethylsilane was used as an internal standard. Absorbance UV/Vis spectra of solutions were recorded on a Specord S100 spectrophotometer (Carl Zeiss Jena). IR spectra were obtained on a Perkin–Elmer 983 G spectrometer (as KBr pellets). Matrix-assisted laser desorption ionisation time of flight (MALDI-TOF) and LDI-TOF mass spectra were recorded on a Bruker Biflex III MS spectrometer in negative and positive linear modes. Variable-temperature magnetic susceptibility data (1.7–300 K) were acquired on powdered samples using a Quantum Design MPMS-5 SQUID magnetometer. Corrections for the diamagnetism of the ligand and Co^{II} cations were applied using Pascal's[20] constants; the diamagnetic contribution from the sample holder was also taken into account. The ^{57}Fe Mössbauer measurements were carried out using a conventional constant-acceleration spectrometer and the spectra were fitted using the MOSSFUN program.[21] Elemental analyses were performed by the Microanalytisches Laboratorium des Organisch-Chemischen Instituts der Universität Heidelberg.

Crystallographic Studies: Intensity data were collected at 173 K with a Bruker AXS SMART 100 diffractometer (Mo-K_α radiation, λ = 0.71073 Å, graphite monochromator, ω scans, SADABS 10). Absorption corrections were applied. The structures were solved by direct methods using SHELXS-86[22,23] and refined by least-squares methods based on F^2 with all measured reflections using SHELX-97.[24] All non-hydrogen atoms were refined anisotropically. Hydrogen atoms were located and refined (Table 3).

CCDC-246323 (for **6**) and CCDC-246324 (for **7**) contain the supplementary crystallographic data for this paper. These data can be obtained free of charge from The Cambridge Crystallographic Data Centre via www.ccdc.cam.ac.uk/data_request/cif.

Caution! Transition-metal perchlorate complexes are potentially explosive and should be handled with due care and in small quantities!

Synthesis of 1: See ref.[8]

Synthesis of 2: To a stirred solution of **L** (77 mg, 0.246 mmol) in acetone (5 mL) was added a solution of $Co(NO_3)_2{\cdot}4H_2O$ (63 mg, 0.249 mmol) in water (5 mL). A dark-red precipitate formed within 12 h which was filtered, washed with acetone and dried. The complex crystallised from DMF upon layering with a solution of $NaClO_4$ in acetone. Yield: 119 mg, (79%). $C_{88}H_{80}Cl_7Co_4N_{25}O_{35}$ (2451.63) calcd. C 41.75, H 3.19, N 13.83; found C 41.39, H 3.88, N 13.91. MS (MALDI) *m*/*z* (%): 370.2 (100) $[^{59}Co\mathbf{L} + e]^+$, 387.2 (90) $[^{59}Co\mathbf{L}(OH)]^+$. IR (KBr): $\tilde{\nu}$ = 1384 (N=O), 1102 (Cl=O), 1677 (C=O) cm^{-1}.

Synthesis of 3: To a stirred solution of **L** (20 mg, 0.064 mmol) in acetone (5 mL) was added a solution of $Fe(NO_3)_2{\cdot}6H_2O$ (17 mg, 0.064 mmol) in water (5 mL). A solution of $NaClO_4$ in acetone was then added to the resultant dark blue solution over 24 h. Complex **3** started to crystallise from this solution after 24 h and was filtered, washed with diethyl ether and dried in a high vacuum. Yield 34.8 mg (90%). $C_{76}H_{72}Cl_7Fe_4N_{21}O_{41}$ (2407.05): calcd. C 37.92, H 3.01, N 12.22; found C 38.51, H 3.21, N 12.31. MS (MALDI) *m*/*z* (%): 678.5 (100) $[^{56}Fe\mathbf{L}_2 + e]^+$, 791.4 (70) $[^{56}Fe_3\mathbf{L}_2]^+$. IR (KBr): $\tilde{\nu}$ = 1386 (N=O), 1107 (Cl=O) cm^{-1}.

Synthesis of 4: To a stirred solution of **L** (65 mg, 0.21 mmol) in acetone (5 mL) was added a solution of $Zn(NO_3)_2{\cdot}4H_2O$ (58 mg, 0.21 mmol) in water and a solution of $ZnCl_2$ (31mg, 21 mmol) in water (5 mL). The white precipitate which formed was filtered off, washed with diethyl ether and dried in high vacuum. Yield 82.2 mg (79%). $Zn_4C_{76}H_{64}Cl_4N_{24}O_{18}$ (2004.8): calcd. C 45.53, H 3.22, N

Table 3. Crystal data and structure refinements for **6** and **7**.

	6	**7**
Formula	$[Cu\mathbf{L}(Ph_3P)_2](ClO_4){\cdot}2CH_3CN$	$[Cu_2\mathbf{L}_2(Ph_3P)_2(CN)](ClO_4)$
Empirical formula	$C_{59}H_{49}ClCuN_7O_4P_2$	$C_{75}H_{56}ClCu_2N_{11}O_4P_2$
M	1080.98	1399.78
Crystal system	monoclinic	orthorhombic
Space group	$P2_1/c$	*Pbcn*
a [Å]	14.2661(12)	21.7976(13)
b [Å]	28.741(2)	18.7664(12)
c [Å]	13.7571(12)	15.8443(10)
V [Å] ^{3}	5347.0(8)	6481.3(7)
Z	4	4
Scan range θ [°]	1.42 to 26.38	1.43 to 26.37
μ [mm^{-1}]	0.573	0.809
Unique reflections	10937	6633
Final *R* indices [$I > 2\sigma(I)$]	R_1 = 0.0449, wR_2 = 0.1046	R_1 = 0.0402, wR_2 = 0.0883

 © 2005 Wiley-VCH Verlag GmbH & Co. KGaA, Weinheim

16.77; found C 46.51, H 3.20, N 16.34. MS (MALDI) *m/z* (%): 375.74 (100) [^{64}Zn**L** + e]$^+$, 377.0 (60) [^{66}Zn**L** + e]$^+$, 379.74 (50) [^{68}Zn**L** + e]$^+$, 393.74 (54) [^{64}Zn**L**(H_2O) + e]$^+$, 395.0 (32) [^{66}Zn**L**(H_2O) + e]$^+$, 397.74 (26) [^{68}Zn**L**(H_2O) + e]$^+$. IR (KBr): $\tilde{\nu}$ = 1385 and 1378 (N=O) cm^{-1}.

Synthesis of 5: To a stirred solution of **L** (73 mg, 0.23 mmol) in acetone (5 mL) was added a solution of $Cu(NO_3)_2{\cdot}4H_2O$ (44 mg, 0.22 mmol). The blue precipitate was filtered off, washed with diethyl ether and dried. The complex crystallised from DMF upon layering with a solution of $NaClO_4$ in acetone. Yield 89.3 mg (68%). $C_{76}H_{64}Cl_4Cu_4N_{24}O_{34}$ (2253.46): calcd. C 40.51, H 2.06, N 14.92; found C 41.34, H 2.10, N 13.74. MS (MALDI) *m/z* (%): 374.0 (100) [^{63}Cu(**L**)]$^+$, 376.0 (60) [^{65}Cu(**L**)]$^+$, 392.0 (54) [^{63}Cu(**L**)(H_2O)]$^+$, 394.0 (32) [^{65}Cu(**L**)(H_2O)]$^+$. IR (KBr): $\tilde{\nu}$ = 1386 and 1378 (N=O), 1105 (Cl=O) cm^{-1}.

Synthesis of 6 and 7: To a stirred solution of **L** (45 mg, 0.14 mmol) in dry acetonitrile (3 mL) was added a solution of $Cu(PPh_3)_3Cl$ (90 mg, 0.15 mmol) in dry acetonitrile (5 mL). The clear orange solution was stirred for 30 min at 40 °C. After 15 min a small amount of a white precipitate started to form. This was filtered off and to the filtrate was added $NaClO_4$ in acetone (1 mL). Complex **6** was filtered off from this solution after 48 h. Complex **7** crystallised from the second solution after 24 h. For **6**: Yield 26 mg (17%). $C_{59}H_{49}ClCuN_7O_4P_2$ (1080.98): calcd. C 65.55, H 4.57, N 9.07; found C 64.75, H 3.98, N 8.51. MS (MALDI) *m/z* (%): 374.0 (100) [^{63}Cu**L** + e]$^+$, 376.0 (60) [^{65}Cu**L** + e]$^+$, 636.1 (10) [^{63}Cu**L**Ph_3P + e]$^+$, 638.1 (5) [^{65}Cu(**L**)(Ph_3P) + e]$^+$. IR (KBr): $\tilde{\nu}$ = 2100 (CN), 1094 (Cl=O) cm^{-1}. For **7**: Yield 39 mg (19%). $C_{69}N_{11}H_{56}P_2ClO_4Cu_2$ (1399.78): calcd. C 64.35, H 4.03, N 11.01; found C 62.97, H 3.88, N 10.79. MS (MALDI) *m/z* (%): 374.0 (100) [^{63}Cu(**L**)]$^+$, 376.0 (60) [^{65}Cu(**L**)]$^+$, 636.1 (10) [^{63}Cu**L**Ph_3P + e]$^+$, 638.1 (5) [^{65}Cu**L**(Ph_3P) + e]$^+$, 400.1 (10) [^{63}Cu**L**(CN) + e]$^+$, 402.1 (5) [^{65}Cu**L**(CN) + e]$^+$. IR (KBr): $\tilde{\nu}$ = 2080 (CN), 1098 (Cl=O) cm^{-1}.

Acknowledgments

This work was funded by the Deutsche Forschungsgemeinschaft (Gerhard-Hess-Programm) and supported by the Fonds der Chemischen Industrie.

[1] G. F. Swigers, T. J. Malefetse, C. Name, *Chem. Rev.* **2000**, *100*, 3483.
[2] C. S. Campos-Fernandez, R. Clerac, K. R. Dunbar, *Angew. Chem. Int. Ed.* **1999**, *38*, 3477.
[3] a) R.-D. Schnebeck, E. Freisinger, B. Lippert, *Chem. Commun*. **1999**, 675; b) R.-D. Schnebeck, E. Freisinger, B. Lippert, *J. Am. Chem. Soc.* **2000**, *122*, 1381.
[4] D. M. Bassani, J.-M. Lehn, K. Fromm, D. Fenske, *Angew. Chem. Int. Ed.* **1998**, *37*, 2364.
[5] B. Ahlers, K. Cammann, S. Warzeska, R. Krämer, *Angew. Chem. Int. Ed. Engl.* **1996**, *35*, 2141.
[6] a) L. H. Uppadine, M. G. B. Drew, P. D. Beer, *Chem. Commun.* **2001**, 291; b) K. Kavallieratos, R. A. Sachleben, G. J. Van Berkel, B. A. Moyer, *Chem. Commun.* **2000**, 187; c) K. Niikura, A. P. Bisson, E. V. Anslyn, *J. Chem. Soc., Perkin Trans. 2* **1999**, 1111; d) S. Mason, T. Clifford, L. Seib, K. Kuczera, K. Bowman-James, *J. Am. Chem. Soc.* **1998**, *120*, 8899; e) R. C. Jagessar, D. H. Burns, *Chem. Commun.* **1997**, 1685; f) J. Wiorkiewicz-Kuczera, K. Kuczera, C. Bazzicalupi, A. Bencini, B. Valtancoli, A. Bianchi, K. Bowman-James, *New J. Chem.* **1999**, *23*, 1007 and references cited therein; g) P. D. Beer, M. G. B. Drew, R. Jagessar, *J. Chem. Soc., Dalton Trans.* **1997**, 881; h) P. D. Beer, M. G. B. Drew, D. Hesek, R. Jagessar, *J. Chem. Soc., Chem. Commun.* **1995**, 1187; i) R. J. Motekaitis, A. E. Martell, J.-M. Lehn, E. I. Watanabe, *Inorg. Chem.* **1982**, *21*, 4253; j) Q. Qian, G. S. Wilson, K. Bowman-James, H. H. Girault, *Anal. Chem.* **2001**, *73*, 497 and references cited therein; k) Metalated calixarene receptor: M. Staffilani, K. S. B. Hancock, J. W. Steed, K. T. Holman, J. L. Atwood, R. K. Juneja, R. S. Burkhalter, *J. Am. Chem. Soc.* **1997**, *119*, 6324.
[7] R.-D. Schnebeck, E. Freisinger, B. Lippert, *Angew. Chem. Int. Ed.* **1999**, *38*, 168.
[8] R. Krämer, L. Kovbasyuk, H. Pritzkow, *New J. Chem.* **2002**, *26*, 516.
[9] L. Kovbasyuk, M. Hoppe, H. Pritzkow, R. Krämer, *Eur. J. Inorg. Chem.* **2001**, *5*, 1353.
[10] The quality of the crystals available did not allow a satisfactory structure determination but the connectivity could be determined. We have therefore refrained from publishing details of the structure. $P\bar{1}$, a = 16.0805(10), b = 6.7139(10), c = 25.3261(15) Å, α = 82.427(2), β = 78.958(2), γ = 67.935(1)°, V = 6178.10 Å^3, Z = 2, $\theta_{max.}$ = 20.82°, μ = 0.64 mm^{-1}, R_1 = 0.1599, wR_2 = 0.2341 [for $I > 2\sigma(I)$]. Two CH_3 groups belonging to DMF molecules are not localised because of high disorder.
[11] a) E. Breuning, U. Ziener, J.-M. Lehn, E. Wegelius, K. Rissanen, *Eur. J. Inorg. Chem.* **2001**, 1515; b) G. S. Hanan, D. Volkmer, U. S. Schubert, J.-M. Lehn, G. Baum, D. Fenske, *Angew. Chem. Int. Ed. Engl.* **1997**, *36*, N17, 1842 and references cited therein.
[12] S. S. Batsanov, *J. Chem. Soc., Dalton Trans.* **1998**, *10*, 1541.
[13] K. Nakamoto, *Infrared and Raman Spectra of Inorganic and Coordination Compounds*, 4th ed., Wiley, New York, **1986**.
[14] L. M. Engelhardt, C. Pakawatchai, A. H. White, P. C. Healy, *J. Chem. Soc., Dalton Trans.* **1985**, 125.
[15] K. T. Brooks, D. C. Finnen, J. R. Kirchhoff, A. A. Pinkerton, *Acta Crystallogr. Sect. C* **1994**, *50*, 1696.
[16] J. R. Kirchhoff, D. R. McMillin, W. R. Robinson, D. R. Powell, A. T. McKenzie, S. Chen, *Inorg. Chem.* **1985**, *24*, 3928.
[17] E. W. Ainscough, A. M. Brodie, S. L. Ingham, J. M. Waters, *J. Chem. Soc., Dalton Trans.* **1994**, 215.
[18] S. W. Keller, S. Lopez, *J. Am. Chem. Soc.* **1999**, *121*, 6306.
[19] A. Livoreili, C. O. Dietrich-Buchecker, J.-P. Sauvage, *J. Am. Chem. Soc.* **1994**, *116*, 9399.
[20] I. M. Kolthoff, P. J. Elving, *Treat. Anal. Chem.* **1963**, *4*, Part 1.
[21] D. Adler, H. Spiering, P. Gütlich, *Inorg. Chem.* **1987**, *26*, 3840.
[22] G. M. Sheldrick, SADABS, Bruker AXS, Madison, WI, USA, **1999**.
[23] G. M. Sheldrick, *SHELXS-97, Program for Crystal Structure Solution*, University of Göttingen, Germany, **1997**.
[24] G. M. Sheldrick, *SHELXL-97, Program for Crystal Structure Refinement*, University of Göttingen, Germany, **1997**.

Received: August 2, 2004

 © 2005 Wiley-VCH Verlag GmbH & Co. KGaA, Weinheim

New Access to Homodinuclear Half-Sandwich Vinylidenemanganese Complexes

Koushik Venkatesan,[a] Thomas Fox,[a] Helmut W. Schmalle,[a] and Heinz Berke*[a]

Keywords: Cyclopentadienyl ligands / Half-sandwich complexes / Phosphanes / Molecular devices / Vinylidene ligands

The d^6 low-spin Mn^I half-sandwich dinuclear complexes of the type [{Mn(MeC_5H_4)($R_2PCH_2CH_2PR_2$)=C=C($SnMe_3$)}$_2${X}] (X = {μ-1,4-C_6H_4}, R = Me, **2a**; X = {μ-1,4-C_6H_4}, R = Et, **2b**; X = {μ-1,3-C_6H_4}, R = Me, **3a**; X = {μ-1,3-C_6H_4}, R = Et, **3b**; X = {μ-4,4-C_6H_4-C_6H_4}, R = Me, **4a**; X = {μ-4,4-C_6H_4-C_6H_4}, R = Et, **4b**; X = {μ-1,4-C_4H_2S}, R = Me, **5a**; X = {μ-1,4-C_4H_2S}, R = Et, **5b**) were obtained by the treatment of [Mn(C_5H_4Me)(η^6-cycloheptatriene)] with 0.5 equiv. of the corresponding acetylene Me_3Sn–C≡C–X–C≡C–$SnMe_3$ (X = {μ-1,4-C_6H_4}, {μ-1,3-C_6H_4}, {μ-4,4-C_6H_4-C_6H_4}, {μ-1,4-C_4H_2S}) and $R_2PCH_2CH_2PR_2$ (R = Me, Et) at 50 °C for 12 h to yield the corresponding dinuclear complexes in very good yields. These dinuclear tin-substituted vinylidene complexes were further treated with an excess of MeOH to give the corresponding dinuclear parent vinylidene complexes of the type [{Mn(MeC_5H_4)($R_2PCH_2CH_2PR_2$)=C=C(H)}$_2${X}] (X = {μ-1,4-C_6H_4}, R = Me, **6a**; X = {μ-1,4-C_6H_4}, R = Et, **6b**; X = {μ-1,3-C_6H_4}, R = Me, **7a**; X = {μ-1,3-C_6H_4}, R = Et, **7b**; X = {μ-4,4-C_6H_4-C_6H_4}, R = Me, **8a**; X = {μ-4,4-C_6H_4-C_6H_4}, R = Et, **8b**). All dinuclear compounds were characterised by NMR and IR spectroscopy and elemental analysis. X-ray diffraction studies were performed on complexes **2b**, **3a**, **4a** and **6a**.
(© Wiley-VCH Verlag GmbH & Co. KGaA, 69451 Weinheim, Germany, 2005)

Introduction

Carbon-rich organometallics containing rigid, π-conjugated chains are of increasing interest due to their uses in the synthesis of unsaturated organic species,[1–4] organometallic polymers[5] and π-conjugated di- or multimetallic systems.[3,6–24] In particular, the dinuclear transition metal acetylide complexes offer an interesting perspective for the build-up of organometallic systems as molecular-level single-electron devices and the bottom-up construction of miniaturised components capable of performing specific electronic functions.[8–20] Our ongoing interest in such building blocks is devoted to the synthesis and physical properties of molecular species which might function as wires. Specifically, they should consist of an all-carbon chain capped by two redox-active metal termini.[6–17] We sought to explore reactions of dinuclear vinylidene precursor complexes which would ultimately lead to polyyne ligand containing complexes. We recently reported the chemistry and reactivity of Mn^{II} and Mn^{III} half-sandwich $Me_2PCH_2CH_2PMe_2$ (dmpe) alkynyl complexes and their conversion to (vinylidene)Mn^I species.[21,23,24] The first conclusion of this study was that vinylidene complexes gained considerable stability through the presence of the bis(dimethylphosphanyl)ethane ligand (dmpe) in comparison with the reported CO-substituted species [Mn(Cp)L^1L^2(C=CR_2)] (L^1 = L^2 = CO, PR'_3 or L^1 = CO, L^2 = PR'_3).[25] Although the dinuclear complexes with the CO ligands were reported earlier,[26] these complexes are not expected to possess low-energy work functions which is an important property required for the molecules to function as molecular wires.[23] In contrast, the complexes bearing electron-donating phosphane ligands can be expected to possess suitable electronic properties, i.e. a low energy work function. Similar types of dinuclear vinylidene complexes have been reported with terminal ends capped by various other transition metals such as Ru,[17b] Rh[27] or Fe.[7] We herein report access to new dinuclear half-sandwich complexes of the type [{Mn(MeC_5H_4)($R_2PCH_2CH_2PR_2$) = C=C(H)}$_2${X}] (R = Me, Et) (X = {μ-1,4-C_6H_4}, {μ-1,3-C_6H_4} and {μ-4,4-C_6H_4-C_6H_4}). It has been demonstrated by other groups that similar types of dinuclear vinylidene complexes can serve as valuable starting materials for obtaining access to dinuclear acetylide complexes.

Results and Discussion

A common method for obtaining vinylidene complexes is to make use of the high propensity of terminal acetylide derivatives to rearrange into vinylidene compounds.[28–36] Such principal possibilities have been corroborated by recent studies by our group.[18–23] For such a process to be initiated in half-sandwich Mn^I chemistry, we believed the complex [Mn(C_5H_4Me)(η^6-cycloheptatriene)] (**1**)[37] would be an excellent starting material, since facile cycloheptatriene exchange could be expected to occur with electron donating ligands such as phosphanes or acetylenes.[38,39] Further reactivity with disubstituted tin acetylides was anticipated, thus leading to the desired dinuclear vinylidene species.

[a] Anorganisch-Chemisches Institut der Universität Zürich, Winterthurerstrasse 190, 8057 Zürich, Switzerland
E-mail: hberke@aci.unizh.ch

 DOI: 10.1002/ejic.200400686 © 2005 Wiley-VCH Verlag GmbH & Co. KGaA, Weinheim

The reaction of [Mn(C_5H_4Me)(η^6-cycloheptatriene)] (**1**) with 0.5 equiv. of $Me_3Sn–C\equiv C–X–C\equiv C–SnMe_3$ (X = {μ-1,4-C_6H_4}, {μ-1,3-C_6H_4}, {μ-4,4-C_6H_4-C_6H_4},[40–42] {μ-1,4-C_4H_2S}) and $R_2PCH_2CH_2PR_2$ (R = Me, Et) at 50 °C for 12 h gave the corresponding vinylidene complexes of the type [{Mn(MeC_5H_4)($R_2PCH_2CH_2PR_2$)=C=C($SnMe_3$)}$_2$-{X}] (X = {μ-1,4-C_6H_4}, R = Me, **2a**; X = {μ-1,4-C_6H_4}, R = Et, **2b**; X = {μ-1,3-C_6H_4}, R = Me, **3a**; X = {μ-1,3-C_6H_4}, R = Et, **3b**; X = {μ-4,4-C_6H_4-C_6H_4}, R = Me, **4a**; X = {μ-4,4-C_6H_4-C_6H_4}, R = Et, **4b**; X = {μ-1,4-C_4H_2S}, R = Me, **5a**; X = {μ-1,4-C_4H_2S}, R = Et, **5b**) in quantitative yields (Scheme 1).

These reactions appear to require the initial formation of (alkyne)Mn species.[25] However, NMR studies of the reactions carried out in the temperature range of –70 to 20 °C did not reveal any intermediates. The ^{13}C NMR spectra of complexes **2**–**5** show the C_α and the C_β resonances between δ = 326–330 and 110–140 ppm, respectively. The ^{31}P NMR resonances appear at $\delta \approx 95$ ppm for complexes **2a**–**5a** and are thus comparable with those observed for the related [Mn($C_5H_4R^1$)($Me_2PCH_2CH_2PMe_2$)(=C=CR^2H)] complexes.[24,38,39] However, for complexes **2b**–**5b** a downfield shift to $\delta \approx 115$ ppm was observed in the ^{31}P NMR spectra. The resonances corresponding to the trimethyltin groups were observed in the ^{119}Sn NMR spectra as triplets at $\delta \approx -30$ ppm. The ^{31}P, ^{119}Sn and ^{13}C NMR spectroscopic data for the complexes **2**–**5** are summarised in Table 1.

Table 1. $^{31}P\{^1H\}$, $^{119}Sn\{^1H\}$ and $^{13}C\{^1H\}$ NMR spectroscopic data for compounds **2**–**5**

Compound	^{31}P NMR ($R_2PCH_2CH_2PR_2$) δ (ppm)	^{119}Sn NMR ($SnMe_3$) δ (ppm)	^{13}C NMR Mn=C_α=C_β	Mn=C_α=C_β
2a	94.9 (s)	–30.2 (t)	329.6 (t)	129.1
2b	115.0 (s)	–27.4 (t)	326.3 (t)	129.9
3a	94.3 (s)	–29.8 (t)	328.5 (t)	129.1
3b	115.0 (s)	–29.8 (t)	328.5 (t)	129.1
4a	93.0 (s)	–17.1 (t)	330.5 (t)	129.1
4b	113.5 (s)	–29.2 (t)	328.0 (t)	142.3
5a	93.7 (s)	–27.5 (t)	328.5 (t)	110.1
5b	115.1 (s)	–26.3 (t)	326.8 (t)	141.1

The structure of **2b** was additionally confirmed by an X-ray diffraction study (Figure 1). A pseudo-tetrahedral coordination environment of the manganese centre was revealed. The bond lengths of 1.763(4) Å and 1.345(2) Å for Mn–C11 and C11–C12, respectively, confirm the double-bond character of these bonds. The observed C12–Sn bond length of 2.159(4) Å is similar to that found in the mononuclear vinylidene complexes already reported.[38,39] The bond angles for Mn–C11–C12 and C11–C12–C13 were found to be 175.7(3)° and 125.8(4)°, respectively.

X-ray diffraction analysis confirmed the spectroscopically derived structures of **3a** and **4a** which are closely related to that of **2b** (Figures 2 and 3). The solid-state structures indicated the Mn–C_α and C_α–C_β bond lengths to be 1.769(4) and 1.299(6) Å, and 1.744(4) and 1.358(5) Å, for **3a** and **4a**, respectively. These values confirm the double-bond nature in these vinylidene complexes.

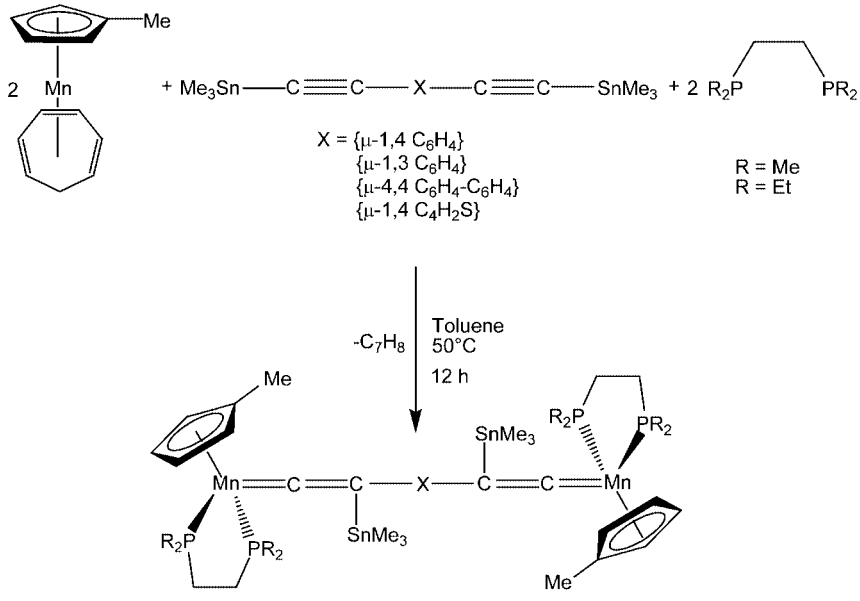

X = {μ-1,4 C_6H_4}, R = Me, **2a**;
X = {μ-1,4 C_6H_4}, R = Et, **2b**;
X = {μ-1,3 C_6H_4}, R = Me, **3a**;
X = {μ-1,3 C_6H_4}, R = Et, **3b**;
X = {μ-4,4 C_6H_4-C_6H_4}, R = Me, **4a**;
X = {μ-4,4 C_6H_4-C_6H_4}, R = Et, **4b**;
X = {μ-1,4 C_4H_2S}, R = Me, **5a**;
X = {μ-1,4 C_4H_2S}, R = Et, **5b**

Scheme 1.

 © 2005 Wiley-VCH Verlag GmbH & Co. KGaA, Weinheim

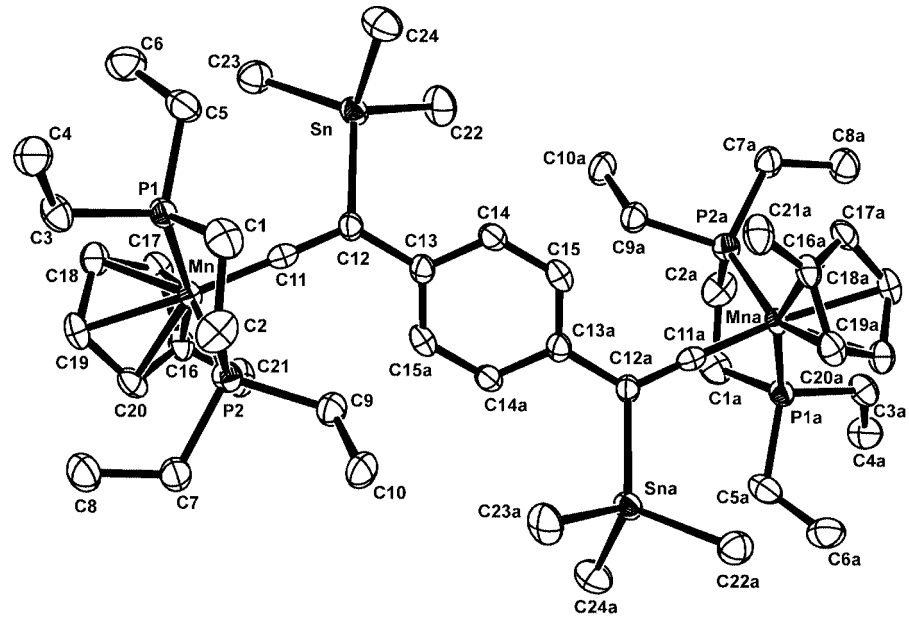

Figure 1. Molecular structure of **2b**; the symmetry operator $a = -x, 2 - y, 1 - z$ represents a centre of inversion in the middle of the benzene ring; the ellipsoids are at the 30% probability level and the hydrogen atoms are omitted for clarity; selected bond lengths [Å] and bond angles [°]: Mn–C11 1.763(4), C11–C12 1.345(5), C12–Sn 2.159(4), C12–C13 1.486(6), C13–C14 1.402(5), C14–C15 1.390(6), Mn–Cg1 1.7885(6); C12–C11–Mn 175.7(3), C11–C12–Sn 118.3(3), C13–C12–Sn 115.1(2), C11–C12–C13 125.8(4), P1–Mn–P2 83.59(5)

Complexes **2**–**4** were further transformed into their corresponding parent vinylidene species of the type $[\{Mn(MeC_5H_4)(R_2PCH_2CH_2PR_2)=C=C(H)\}_2\{X\}]$ (X = {μ-1,4-C_6H_4}, R = Me, **6a**; X = {μ-1,4-C_6H_4}, R = Et, **6b**; X = {μ-1,3-C_6H_4}, R = Me, **7a**; X = {μ-1,3-C_6H_4}, R = Et, **7b**; X = {μ-4,4-C_6H_4-C_6H_4}, R = Me, **8a**; X = {μ-4,4-C_6H_4-C_6H_4}, R = Et, **8b**) by treatment with an excess of MeOH for 2 h (Scheme 2). However, complexes **5a** and **5b** decomposed upon treatment either with MeOH or tbaf (5% H_2O). The ^1H NMR spectra of these complexes revealed charac-

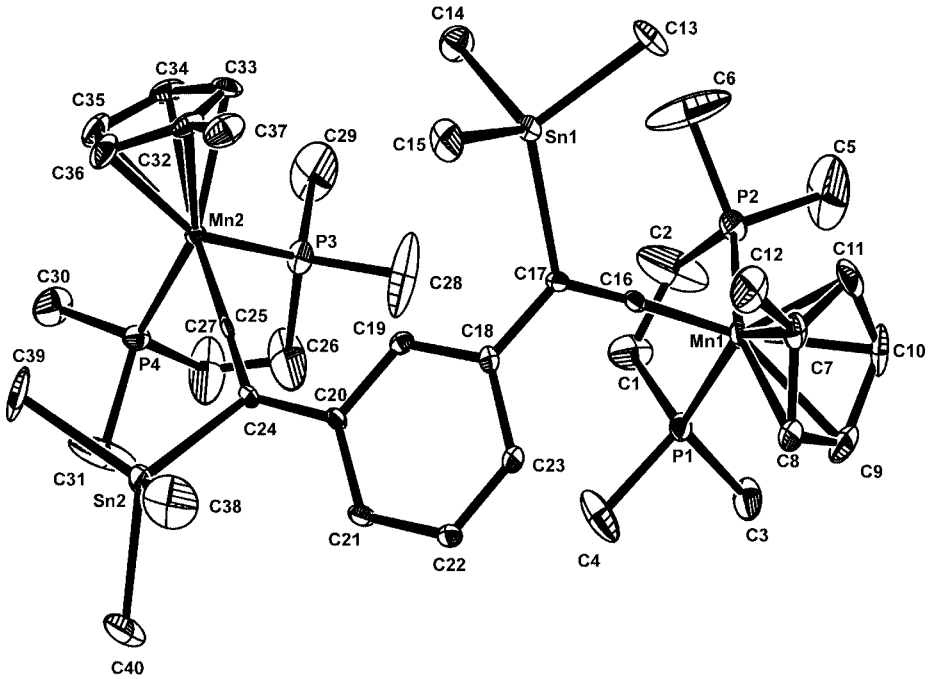

Figure 2. Molecular structure of **3a**; the ellipsoids are at the 30% probability level and the hydrogen atoms are omitted for clarity; selected bond lengths [Å] and bond angles [°]: Mn1–C16 1.769(4), C16–C17 1.299(6), C17–Sn1 2.161(4), C17–C18 1.481(6), C18–C19 1.392(5), C19–C20 1.418(5), Mn1–Cg1 1.8062(7), Mn2–Cg2 1.8045(7); C17–C16–Mn1 176.0(4), C16–C17–C18 124.2(4), C16–C17–Sn1 119.0(2), C17–C18–C19 122.5(4), C23–C18–C17 120.0(3)

 © 2005 Wiley-VCH Verlag GmbH & Co. KGaA, Weinheim

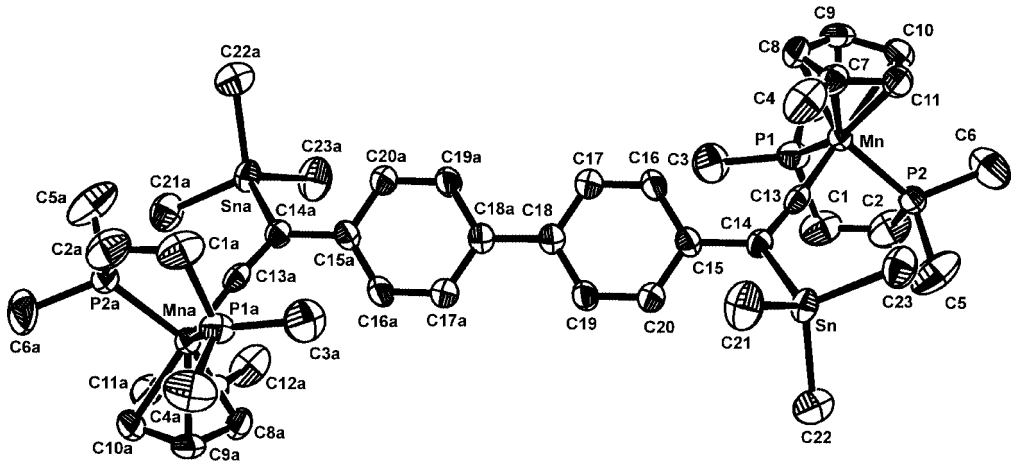

Figure 3. Molecular structure of **4a**; the symmetry operator $a = 2 - x, 1 - y, 1 - z$ represents a centre of inversion in the middle of the biphenyl bond; the ellipsoids are at the 30% probability level and the hydrogen atoms are omitted for clarity; selected bond lengths [Å] and bond angles [°]: Mn–C13 1.744(4), C13–C14 1.358(5), C14–Sn 2.154(4), C14–C15 1.490(5), C15–C16 1.397(5), C16–C17 1.368(5), C17–C18 1.393(5), Mn1–Cg1 1.8055(5); C14–C13–Mn 174.1(13), C13–C14–C15 123.0(3), C13–C14–Sn 117.7(3), C14–C15–C16 122.7(3), C14–C15–C20 122.5(3)

Table 2. $^{31}P\{^1H\}$ and $^{13}C\{^1H\}$ NMR spectroscopic data for compounds **6**–**8**

Compound	^{31}P NMR ($R_2PCH_2CH_2PR_2$) δ (ppm)	^{13}C NMR δ (ppm) Mn=C_α=C$_\beta$	Mn=C$_\alpha$=C_β
6a	96.1 (s)	325.4 (t)	133.9
6b	114.5 (s)	327.4 (t)	133.9
7a	94.9 (s)	343.4 (t)	141.3
7b	114.2 (s)	341.9 (t)	140.4
8a	94.5 (s)	342.2 (t)	139.9
8b	115.1 (s)	345.5 (t)	140.2

teristic triplet resonances at $\delta \approx 6.0$ ppm with $^4J_{P,H}$ values of 8.4 Hz. The ^{13}C NMR spectra of complexes **2**–**5** show the C$_\alpha$ and the C$_\beta$ resonances further downfield between δ = 325–350 and 130–140 ppm, respectively, in comparison with the tin derivatives. The ^{31}P NMR resonances appear at $\delta \approx 97$ ppm for complexes **6a**–**8a** and are thus comparable with those observed for the related $[Mn(C_5H_4R^1)(Me_2PCH_2CH_2PMe_2)(=C=CR^2H)]$ complexes.[24,38,39] However, the ^{31}P NMR resonances for complexes **6b**–**8b** were observed further downfield at $\delta \approx$ 114 ppm. The ^{31}P NMR and ^{13}C NMR spectroscopic data for complexes **6**–**8** are summarised in Table 2.

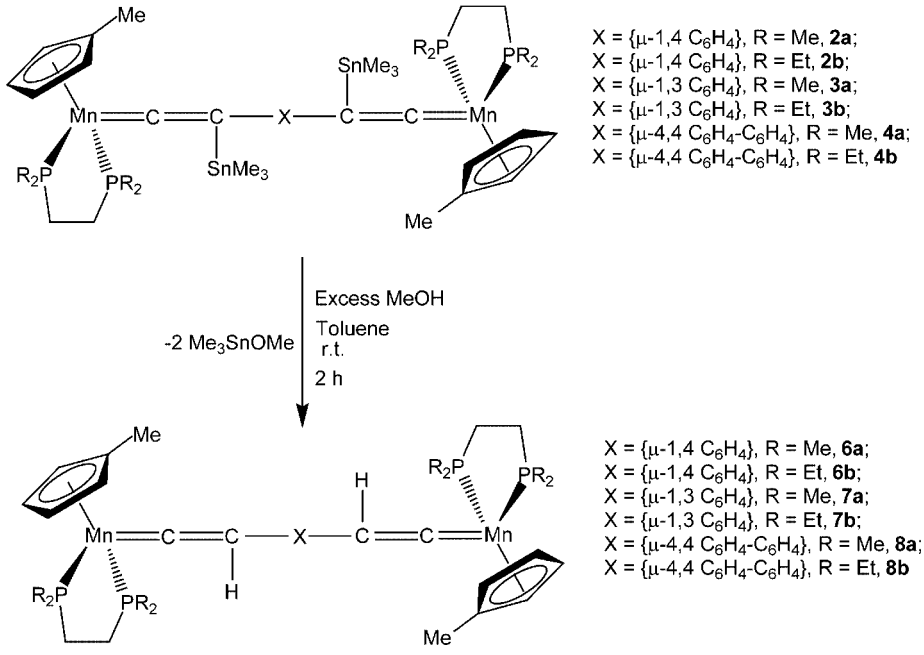

Scheme 2.

 © 2005 Wiley-VCH Verlag GmbH & Co. KGaA, Weinheim

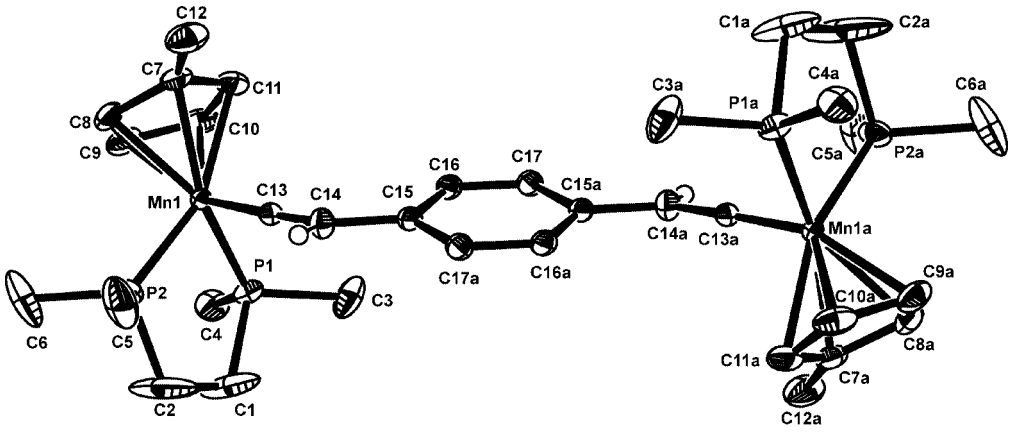

Figure 4. Molecular structure of **6a**; the symmetry operator $a = 2 - x, 2 - y, 1 - z$ represents a centre of inversion in the middle of the benzene ring; the ellipsoids are at the 30% probability level and selected hydrogen atoms are omitted for clarity; selected bond lengths [Å] and bond angles [°]: Mn(1)–C(13) 1.746(2), C(13)–C(14) 1.340(3), C(14)–C(15) 1.466(3), C(1)–C(2) 1.354(5), C(15)–C(16) 1.403(3), Mn1–Cg1 1.7769(3); C(14)–C(13)–Mn(1) 175.09(19), C(13)–C(14)–C(15) 127.8(2), C(14)–C(15)–C(16) 123.1(2), C(5)–P(2)–C(6) 99.17(16), C(3)–P(1)–Mn(1) 120.44(11)

The structure of **6a** was also confirmed by an X-ray diffraction study (Figure 4). A pseudo-tetrahedral coordination environment for each manganese centre was found. The bond lengths of 1.746(4) Å and 1.340(3) Å for Mn1–C13 and C13–C14, respectively, are similar to those found for the previous complexes **2b**, **3a** and **4a** and confirm the double-bond character of these bonds. The bond angles for Mn–C13–C14 and C13–C14–C15 were found to be 175.09(19)° and 127.8(2)°. The latter bond angle suggests that the bending is less pronounced in comparison with the tin derivative.

Conclusions

New dinuclear vinylidenetin complexes and the parent vinylidene complexes capped by Mn^{I} half-sandwich units have been synthesised. A series of these complexes has been structurally characterised. These complexes offer further possibilities for gaining access to the corresponding dinuclear acetylide complexes.

Experimental Section

X-ray Diffraction Studies on 2b, 3a, 4a and 6a: Single-crystal X-ray diffraction data were collected at measurement temperatures of 183(2) K for **2b** and **4a**, and 153(2) K for **3a** and **6a** using an imaging plate detector system (Stoe IPDS) with graphite-monochromated Mo-K_α radiation (λ = 0.71073 Å). A total of 200, 167, 154 and 200 images were exposed at constant times of 3.0, 5.0, 2.6 and 2.5 min per image for the structures of **2b**, **3a**, **4a** and **6a**.[43] The crystal-to-image distances were set to 50 mm for **3a**, **4a** and **6a** and to 60 mm for **2b** (θ_{max} range: 27.90–30.46°). φ-oscillation (**2b** and **3a**) and rotation modes (**4a** and **6a**) were chosen for the increments of 1.5, 1.2, 1.3 and 1.3° per exposure in each case. Total exposure times were 21, 24, 14 and 22.4 h. The intensities were integrated using a dynamic peak profile analysis and an estimated mosaic spread (EMS) check was performed to prevent overlapping intensities. For the cell parameter refinements, 8000 reflections with intensities $I > 6\sigma(I)$ were selected out of the whole limiting spheres for the four structures. A total of 18043, 53927, 29813 and 13632 reflections were collected of which 5603, 13101, 7610 and 4830 were unique after performing absorption corrections and data reductions (R_{int} = 8.79, 11.04, 8.02 and 3.92%). For the numerical absorption corrections of **2b**, **3a**, **4a** and **6a**, the numbers of indexed crystal faces used were 9, 10, 6 and 10.[44] All measurement procedures were performed using the stoe IPDS software.[43] The measurement temperatures were controlled by an Oxford cryogenic system. It should be noted that the structures of **2b**, **4a** and **6a** have crystallographically imposed inversion symmetry (see Figure 1, Figure 3 and Figure 4). The structures were solved with the unique data sets using the Patterson method of the program SHELXS-97.[45] The structures were refined with the program SHELXL-97.[46] The programs PLATON and PLUTON[47] were used to check the results of the X-ray analyses and also for the completion of the structures by checking the different electron density calculations. Relevant crystallographic data are collected in Table 3.

Preparations

General: Reagent grade benzene, toluene, hexane, pentane, diethyl ether and tetrahydrofuran were dried and distilled from sodium benzophenone ketyl prior to use. Dichloromethane was distilled first from P_2O_5 and then from CaH_2 prior to use. Literature procedures were used to prepare the following compounds: 1,2-bis(dimethylphosphanyl)ethane (dmpe),[48] 1,2-bis(diethylphosphanyl) ethane (depe),[48] [Mn(η^5-MeC_5H_4)(η^6-cycloheptatriene)],[37] Me_3Sn–C≡C–X–C≡C–$SnMe_3$ (X = {μ-1,4-C_6H_4}, {μ-1,3-C_6H_4}, {μ-4,4-C_6H_4-C_6H_4},[40–42] {μ-1,4-C_4H_2S}). *n*BuLi (1.6 M in hexane), MeLi·LiBr (1.5 M in diethyl ether) and Me_3SnCl were used as received. All manipulations were carried out under nitrogen using Schlenk techniques or in a drybox. IR spectra were obtained with a Bio-Rad FTS-45 instrument. NMR spectra were measured with a Varian Gemini-2000 spectrometer at 300 MHz for ^1H and 121.5 MHz for $^{31}P\{^1H\}$ and with a Bruker DRX-500 spectrometer the frequencies were 125.8 MHz for $^{13}C\{^1H\}$ and 186.5 MHz for ^{119}Sn. Chemical shifts for ^1H and ^{13}C NMR spectra are given in ppm with respect to the solvent signals. $^{31}P\{^1H\}$ NMR spectra were referenced to 98% external H_3PO_4 and the $^{119}Sn\{^1H\}$ NMR spectra are relative to $SnBu_4$.

[{Mn(MeC_5H_4)($Me_2PCH_2CH_2PMe_2$)=C=C($SnMe_3$)}$_2$(μ-1,4-C_6H_4)] (2a): To a toluene solution (10 mL) of [Mn(MeC_5H_4)(η^6-cycloheptatriene)] (50 mg, 0.22 mmol) was added a toluene solution

 © 2005 Wiley-VCH Verlag GmbH & Co. KGaA, Weinheim

Table 3. Crystallographic details of **2b**, **3a**, **4a** and **6a**

	2b	**3a**	**4a**	**6a**
Empirical formula	$C_{48}H_{84}Mn_2P_4Sn_2$	$C_{40}H_{68}Mn_2P_4Sn_2$	$C_{46}H_{72}Mn_2P_4Sn_2$	$C_{34}H_{52}Mn_2P_4$
Colour	Red plate	Red elongated block	Red-orange plate	Red block
Formula mass [g mol^{-1}]	1132.29	1020.08	1096.18	694.52
Crystal size [mm]	0.24 × 0.20 × 0.12	0.12 × 0.07 × 0.06	0.20 × 0.12 × 0.05	0.23 × 0.22 × 0.14
T [K]	183(2)	153(2)	183(2)	153(2)
λ(Mo-K_α) [Å]	0.71073	0.71073	0.71073	0.71073
Crystal system	triclinic	monoclinic	monoclinic	triclinic
Space group	$P\bar{1}$	$P2_1/c$	$P2_1/n$	$P\bar{1}$
a [Å]	9.5069(16)	14.9180(8)	10.3548(8)	8.3499(7)
b [Å]	9.8993(16)	17.8972(11)	15.9512(9)	8.3784(7)
c [Å]	14.425(2)	18.1653(10)	15.9948(13)	14.4569(11)
α [°]	104.729(18)	90	90	79.513(10)
β [°]	96.130(19)	108.609(6)	106.259(9)	80.926(10)
γ [°]	97.78(2)	90	90	63.470(9)
V [Å^3]	1286.6(4)	4596.4(5)	2536.2(3)	886.41(12)
Z	1	4	2	1
$\rho_{calcd.}$ [g·cm^{-3}]	1.461	1.474	1.435	1.301
μ [mm^{-1}]	1.594	1.776	1.615	0.914
F(000)	582	2072	1116	366
Transmission range	0.6157–0.8188	0.8326–0.9386	0.7581–0.9257	0.8837–0.9383
2θ range [°]	4.90 < 2θ < 55.80	5.14 < 2θ < 60.70	5.46 < 2θ < 60.92	5.48 < 2θ < 60.50
Measured reflections	18043	53927	29813	13632
Unique reflections	5603	13101	7610	4830
$I > 2\sigma(I)$ reflections	3790	5652	3291	3623
Parameters	261	448	252	186
Gof (for F^2)	0.973	0.718	0.759	1.052
$R_1[I > 2\sigma(I)]$, R_1(all data)[a]	0.0345, 0.0598	0.0338, 0.1070	0.0356, 0.0901	0.0411, 0.0588
$wR_2[I > 2\sigma(I)]$, wR_2(all data)[a]	0.0734, 0.0794	0.0562, 0.0635	0.0556, 0.0594	0.1033, 0.1109
$\Delta\rho_{max/min}$ [e·Å^{-3}]	0.719/–1.166	0.819/–1.192	0.735/–0.489	1.230/–1.174
hkl range	–12/12, –13/13, –18/18	–21/21, –25/25, –25/25	–14/14, –22/22, –22/22	–11/11, –11/11, –20/20

[a] $R_1 = \Sigma(F_o - F_c)/\Sigma F_o$; $I > 2\sigma(I)$; $wR_2 = \{\Sigma w(F_o^2 - F_c^2)^2/\Sigma w(F_o^2)^2\}^{1/2}$.

(10 mL) of dmpe (33 mg, 0.22 mmol) and Me_3Sn–C≡C–C_6H_4–C≡C–$SnMe_3$ (50mg, 0.11 mmol). The solution was stirred at 50 °C for 3 h to give a dark red solution. The solvent was removed under vacuum to afford a dark red solid. Then the solid was extracted with diethyl ether and filtered through Celite. The ether fraction was concentrated to give an orange red precipitate. Crystallisation from ether at –35 °C gave single orange-red crystals. Yield: 104 mg, 93%. ^{1}H NMR ([D$_8$]THF, 300 MHz, 20 °C): δ = 6.75 (4 H, C_6H_5), 4.26 (4 H, C_5H_4Me), 4.00 (4 H, C_5H_4Me), 1.98 (6 H, C_5H_4Me), 1.72 (4 H, PCH_2), 1.61 (4 H, PCH_2), 1.22 (24 H, $P[CH_3]_2$), –0.07 ppm (18 H, $SnMe_3$). ^{13}C{^{1}H} NMR ([D$_8$]THF, 125.8 MHz, 20 °C): δ = 329.6 (t, $^2J_{P,C}$ = 35 Hz, Mn-C_α), 136.7 (s, C_i-Ph), 129.1 (m, = C_β), 129.4 (s, 2 C, C_i-C_5H_4Me), 122.2 (s, C_6H_5), 120.5 (s, C_6H_5), 120.2 (s, C_6H_5), 83.9 (s, 4 C, C_5H_4Me), 81.3 (s, 4 C, C_5H_4Me), 32.1 (4 C, PCH_2), 24.5 (PCH_2), 21.9 ($P[CH_3]_3$), 14.8 ($P[CH_3]_3$), –6.1 ($SnMe_3$) ppm. ^{31}P{^{1}H} NMR ([D$_8$]THF, 121.5 MHz, 20 °C): δ = 94.9 (s, 4 P) ppm. ^{119}Sn NMR ([D$_8$]THF, 186.5 MHz, 20 °C): δ = –30.2 (t, J = 76 Hz) ppm. IR (CH_2Cl_2, 20 °C): $\tilde{\nu}$ = 1544 [ν(C=C)], 1552 [ν(C=C)] cm^{-1}. $C_{40}H_{68}Mn_2P_4Sn_2$ (1020.15): calcd. C 47.09, H 6.71; found C 47.08, H 6.74.

[{Mn(MeC$_5$H$_4$)(Et$_2$PCH$_2$CH$_2$PEt$_2$)=C=C(SnMe$_3$)}$_2$(μ-1,4-C$_6$H$_4$)] (2b): The same procedure as for **2a** was applied using [Mn(MeC$_5$H$_4$)(η^6-cycloheptatriene)] (50 mg, 0.22 mmol), depe (45 mg, 0.22 mmol) and 1,4-C_6H_4(C≡C–$SnMe_3$)$_2$ (50 mg, 0.11 mmol). Yield: 115 mg, 94%. ^{1}H NMR (C_6D_6, 300 MHz, 20 °C): δ = 7.09 (4 H, C_6H_5), 4.53 (4 H, C_5H_4Me), 3.97 (4 H, C_5H_4Me), 2.22 (6 H, C_5H_4Me), 1.82 (4 H, PCH_2), 1.23 (4 H, PCH_2), 1.58 (4 H, PCH_2CH_3), 1.46 (4 H, PCH_2CH_3), 0.98 (6 H, PCH_2CH_3), 0.67 (6 H, PCH_2CH_3), 0.35 (18 H, $SnMe_3$) ppm. ^{13}C{^{1}H} NMR (C_6D_6, 125.8 MHz, 20 °C): δ = 326.3 (t, $^2J_{P,C}$ = 30.5 Hz, Mn-C_α), 136.7 (s, C_i-Ph), 129.9 (m, = C_β), 119.4 (s, 2 C, C_i-C_5H_4Me), 96.3 (s, C_6H_5), 120.5 (s, C_6H_5), 81.9 (s, 4 C, C_5H_4Me), 79.3 (s, 4 C, C_5H_4Me), 30.8 (PCH_2), 22.2 (PCH_2), 21.8 (PCH_2CH_3), 19.7 (PCH_2CH_3), 14.5 (s, $C_5H_4CH_3$), –7.1 ($SnMe_3$) ppm. ^{31}P{^{1}H} NMR (C_6D_6, 121.5 MHz, 20 °C): δ = 115.0 (s, 4 P) ppm. ^{119}Sn NMR (C_6D_6, 186.5 MHz, 20 °C): δ = –27.4 (t, J = 76.0 Hz) ppm. IR (CH_2Cl_2, 20 °C): $\tilde{\nu}$ = 1545 [ν(C=C)], 1553 [ν(C=C)] cm^{-1}. $C_{48}H_{84}Mn_2P_4Sn_2$ (1132.37): calcd. C 50.91, H 7.47; found C 50.61, H 7.66.

[{Mn(MeC$_5$H$_4$)(Me$_2$PCH$_2$CH$_2$PMe$_2$)=C=C(SnMe$_3$)}$_2$(μ-1,3-C$_6$H$_4$)] (3a): The same procedure as for **2a** was applied using [Mn(MeC$_5$H$_4$)(η^6-cycloheptatriene)] (50 mg, 0.22 mmol), dmpe (33 mg, 0.22 mmol) and Me_3Sn–C≡C–C_6H_4–C≡C–$SnMe_3$ (50 mg, 0.11 mmol). Yield: 100 mg, 92%. ^{1}H NMR ([D$_8$]THF, 300 MHz, 20 °C): δ = 6.76 (1 H, C_6H_5), 6.62 (2 H, C_6H_5), 6.41 (1 H, C_6H_5), 4.27 (4 H, C_5H_4Me), 4.01 (4 H, C_5H_4Me), 1.99 (6 H, C_5H_4Me), 1.73 (4 H, PCH_2), 1.63 (4 H, PCH_2), 1.23 (24 H, $P[CH_3]_3$), 0.1 (18 H, $SnMe_3$) ppm. ^{13}C{^{1}H} NMR ([D$_8$]THF, 125.8 MHz, 20 °C): δ = 328.5 (t, $^2J_{P,C}$ = 30 Hz, Mn-C_α), 143.1 (s, C_i-Ph), 129.1 (m, =C_β), 125.4 (s, 2 C, C_i-C_5H_4Me), 122.2 (s, C_6H_5), 118.5 (s, C_6H_5), 98.2 (s, C_6H_5), 83.9 (s, 4 C, C_5H_4Me), 81.3 (s, 4 C, C_5H_4Me), 32.1 (4 C, PCH_2), 24.5 (PCH_2), 21.9 ($P[CH_3]_3$), 14.8 ($P[CH_3]_3$), –8.1 ($SnMe_3$) ppm. ^{31}P{^{1}H} NMR ([D$_8$]THF, 121.5 MHz, 20 °C): δ = 94.3 (s, 4 P) ppm. ^{119}Sn NMR ([D$_8$]THF, 186.5 MHz, 20 °C): δ = –29.8 (t, J = 77.0 Hz). IR (CH_2Cl_2, 20 °C): $\tilde{\nu}$ = 1545 [ν(C=C)], 1556 [ν(C=C)] cm^{-1}. $C_{40}H_{68}Mn_2P_4Sn_2$ (1020.15): calcd. C 47.09, H 6.71; found C 47.08, H 6.74.

[{Mn(MeC$_5$H$_4$)(Et$_2$PCH$_2$CH$_2$PEt$_2$)=C=C(SnMe$_3$)}$_2$(μ-1,3-C$_6$H$_4$)] (3b): The same procedure as for **2a** was applied using

[Mn(MeC$_5$H$_4$)(η^6-cycloheptatriene)] (50 mg, 0.22 mmol), depe (45 mg, 0.22 mmol) and 1,3-C$_6$H$_4$(C≡C–SnMe$_3$)$_2$ (50 mg, 0.11 mmol). Yield: 120 mg, 98%. ^{1}H NMR ([D$_8$]THF, 300 MHz, 20 °C): δ = 6.76 (1 H, C$_6$H$_5$), 6.62 (2 H, C$_6$H$_5$), 6.41 (1 H, C$_6$H$_5$), 4.27 (4 H, C$_5$H$_4$Me), 4.01 (4 H, C$_5$H$_4$Me), 1.99 (6 H, C$_5$H$_4$Me), 1.82 (4 H, PCH$_2$), 1.23 (4 H, PCH$_2$), 1.58 (4 H, PC*H*$_2$CH$_3$), 1.46 (4 H, PC*H*$_2$CH$_3$), 0.98 (6 H, PCH$_2$C*H*$_3$), 0.67 (6 H, PCH$_2$C*H*$_3$), 0.1 (18 H, SnMe$_3$) ppm. ^{13}C{^{1}H} NMR ([D$_8$]THF, 125.8 MHz, 20 °C): δ = 328.5 (t, $^2J_{P,C}$ = 30 Hz, Mn-*C*$_α$), 143.1 (s, *C*$_i$-Ph), 129.1 (m, =*C*$_β$), 125.4 (s, 2 C, *C*$_i$-C$_5$H$_4$Me), 122.2 (s, C$_6$H$_5$), 118.5 (s, C$_6$H$_5$), 98.2 (s, C$_6$H$_5$), 83.9 (s, 4 C, C$_5$H$_4$Me), 81.3 (s, 4 C, C$_5$H$_4$Me), 30.8 (P*C*H$_2$), 22.2 (P*C*H$_2$), 21.8 (P*C*H$_2$CH$_3$), 19.7 (PCH$_2$*C*H$_3$), 14.5 (s, C$_5$H$_4$*C*H$_3$), –7.1 (SnMe$_3$) ppm. ^{31}P{^{1}H} NMR ([D$_8$]THF, 121.5 MHz, 20 °C): δ = 115.0 (s, 4 P) ppm. ^{119}Sn NMR ([D$_8$]THF, 186.5 MHz, 20 °C): δ = –29.8 (t, *J* = 75.0 Hz) ppm. IR (CH$_2$Cl$_2$, 20 °C): ν̃ = 1549 [ν(C=C)], 1558 [ν(C=C)] cm^{-1}. C$_{48}$H$_{84}$Mn$_2$P$_4$Sn$_2$ (1132.37): calcd. C 50.91, H 7.47; found C 50.56, H 7.32.

[{Mn(MeC$_5$H$_4$)(Me$_2$PCH$_2$CH$_2$PMe$_2$)=C=C(SnMe$_3$)}$_2${μ-4,4-(C$_6$H$_4$)$_2$}] (4a): The same procedure as for **2a** was applied using [Mn(MeC$_5$H$_4$)(η^6-cycloheptatriene)] (50 mg, 0.22 mmol), dmpe (33 mg, 0.22 mmol) and Me$_3$Sn–C≡C–C$_6$H$_4$–C$_6$H$_4$–C≡C–SnMe$_3$ (58 mg, 0.11 mmol). Yield: 105 mg, 91%. ^{1}H NMR ([D$_8$]THF, 300 MHz, 20 °C): δ = 7.28 (m, 4 H, C$_6$H$_5$), 7.02 (m, 4 H, C$_6$H$_5$), 4.28 (4 H, C$_5$H$_4$Me), 4.03 (4 H, C$_5$H$_4$Me), 1.97 (6 H, C$_5$H$_4$Me), 1.72 (4 H, PCH$_2$), 1.61 (4 H, PCH$_2$), 1.23 (24 H, P(CH$_3$]$_3$), 0.09 (18 H, SnMe$_3$) ppm. ^{13}C{^{1}H} NMR ([D$_8$]THF, 125.8 MHz, 20 °C): δ = 330.5 (t, $^2J_{P,C}$ = 35 Hz, Mn-*C*$_α$), 143.3 (s, *C*$_i$-Ph), 135.8 (s, C$_6$H$_5$), 133.2 (s, 2 C, *C*$_i$-C$_5$H$_4$Me), 129.1 (m, =*C*$_β$), 125.4 (s, C$_6$H$_5$), 118.1 (s, C$_6$H$_5$), 83.4 (s, 4 C, C$_5$H$_4$Me), 81.3 (s, 4 C, C$_5$H$_4$Me), 32.05 (4 C, PCH$_2$), 24.5 (PCH$_2$), 21.9 (P[CH$_3$]$_3$), 14.8 (P[CH$_3$]$_3$), –6.1 (SnMe$_3$) ppm. ^{31}P{^{1}H} NMR ([D$_8$]THF, 121.5 MHz, 20 °C): δ = 93.0 (s, 4 P) ppm. ^{119}Sn NMR ([D$_8$]THF, 186.5 MHz, 20 °C): δ = –17.1 (t, *J* = 77.0 Hz) ppm. IR (CH$_2$Cl$_2$, 20 °C): ν̃ = 1545 [ν(C=C)], 1553 [ν(C=C)] cm^{-1}. C$_{46}$H$_{72}$Mn$_2$P$_4$Sn$_2$ (1096.25): calcd. C 50.39, H 6.61; found C 50.47, H 6.39.

[{Mn(MeC$_5$H$_4$)(Et$_2$PCH$_2$CH$_2$PEt$_2$)=C=C(SnMe$_3$)}$_2${μ-4,4-(C$_6$H$_4$)$_2$}] (4b): The same procedure as for **2a** was applied using [Mn(MeC$_5$H$_4$)(η^6-cycloheptatriene)] (50 mg, 0.22 mmol), dmpe (45 mg, 0.22 mmol) and 4,4-(C$_6$H$_4$)$_2$(C≡C–SnMe$_3$)$_2$ (58 mg, 0.11 mmol). Yield: 125 mg, 96%. ^{1}H NMR ([D$_8$]THF, 300 MHz, 20 °C): δ = 7.31 (m, 4 H, C$_6$H$_5$), 6.98 (m, 4 H, C$_6$H$_5$), 4.48 (4 H, C$_5$H$_4$Me), 4.02 (4 H, C$_5$H$_4$Me), 2.08 (6 H, C$_5$H$_4$Me), 1.89 (4 H, PCH$_2$), 1.73 (4 H, PCH$_2$), 1.43 (4 H, PC*H*$_2$CH$_3$), 1.14 (4 H, PC*H*$_2$CH$_3$), 1.02 (6 H, PCH$_2$C*H*$_3$), 0.92 (6 H, PCH$_2$C*H*$_3$), 0.11 (18 H, SnMe$_3$) ppm. ^{13}C{^{1}H} NMR ([D$_8$]THF, 125.8 MHz, 20 °C): δ = 328.0 (t, $^2J_{P,C}$ = 35 Hz, Mn-*C*$_α$), 142.3 (m, =*C*$_β$), 138.4 (s, *C*$_i$-Ph), 135.8 (s, C$_6$H$_5$), 133.2 (s, 2 C, *C*$_i$-C$_5$H$_4$Me), 125.4 (s, C$_6$H$_5$), 118.1 (s, C$_6$H$_5$), 83.4 (s, 4 C, C$_5$H$_4$Me), 81.3 (s, 4 C, C$_5$H$_4$Me), 30.8 (P*C*H$_2$), 22.2 (P*C*H$_2$), 21.8 (P*C*H$_2$CH$_3$), 19.7 (PCH$_2$*C*H$_3$), 14.5 (s, C$_5$H$_4$*C*H$_3$), –8.3 (SnMe$_3$) ppm. ^{31}P{^{1}H} NMR ([D$_8$]THF, 121.5 MHz, 20 °C): δ = 113.5 (s, 4 P) ppm. ^{119}Sn NMR ([D$_8$]THF, 186.5 MHz, 20 °C): δ = –29.2 (t, *J* = 75.1 Hz) ppm. IR (CH$_2$Cl$_2$, 20 °C): ν̃ = 1544 [ν(C=C)], 1559 [ν(C=C)] cm^{-1}. C$_{54}$H$_{88}$Mn$_2$P$_4$Sn$_2$ (1208.46): calcd. C 53.66, H 7.33; found C 53.77, H 7.36.

[{Mn(MeC$_5$H$_4$)(Me$_2$PCH$_2$CH$_2$PMe$_2$)=C=C(SnMe$_3$)}$_2$(μ-1,4-C$_4$H$_2$S)] (5a): The same procedure as for **2a** was applied using [Mn(MeC$_5$H$_4$)(η^6-cycloheptatriene)] (50 mg, 0.22 mmol), dmpe (33 mg, 0.22 mmol) and Me$_3$Sn–C≡C–C$_4$H$_2$S–C≡C–SnMe$_3$ (37 mg, 0.11 mmol). Yield: 105 mg, 94%. ^{1}H NMR (C$_6$D$_6$, 300 MHz, 20 °C): δ = 6.36 (4 H, C$_6$H$_5$), 4.36 (4 H, C$_5$H$_4$Me), 3.95 (4 H, C$_5$H$_4$Me), 2.18 (6 H, C$_5$H$_4$Me), 1.59 (4 H, PCH$_2$), 1.32 (12 H, P[CH$_3$]$_2$), 1.24 (4 H, PCH$_2$), 0.85 (12 H, P[CH$_3$]$_2$), 0.41 (18 H, SnMe$_3$) ppm. ^{13}C{^{1}H} NMR (C$_6$D$_6$, 125.8 MHz, 20 °C): δ = 328.5 (t, $^2J_{P,C}$ = 32.3 Hz, Mn-*C*$_α$), 139.7 (s, *C*$_i$-C$_4$H$_2$S), 120.2 (s, C$_4$H$_2$S), 110.1 (m, =*C*$_β$), 97.3 (s, 2 C, *C*$_i$-C$_5$H$_4$Me), 83.9 (s, 4 C, C$_5$H$_4$Me), 81.5 (s, 4 C, C$_5$H$_4$Me), 31.8 (2 C, PCH$_2$), 23.7 (2 C, PCH$_2$), 23.7 (P[CH$_3$]$_3$), 21.7 (P[CH$_3$]$_3$), 15.3 (2 C, C$_5$H$_4$Me), –6.2 (SnMe$_3$) ppm. ^{31}P{^{1}H} NMR (C$_6$D$_6$, 121.5 MHz, 20 °C): δ = 93.7 (s, 4 P) ppm. ^{119}Sn NMR (C$_6$D$_6$, 186.5 MHz, 20 °C): δ = –27.5 (t, *J* = 72.0 Hz) ppm. IR (CH$_2$Cl$_2$, 20 °C): ν̃ = 1545 [ν(C=C)], 1553 [ν(C=C)] cm^{-1}. C$_{38}$H$_{66}$Mn$_2$P$_4$Sn$_2$S (1026.18): calcd. C 44.47, H 6.48; found C 44.59, H 6.74.

[{Mn(MeC$_5$H$_4$)(Et$_2$PCH$_2$CH$_2$PEt$_2$)=C=C(SnMe$_3$)}$_2$(μ-1,4-C$_4$H$_2$S)] (5b): The same procedure as for **2a** was applied using [Mn(MeC$_5$H$_4$)(η^6-cycloheptatriene)] (50 mg, 0.22 mmol), depe (45 mg, 0.22 mmol) and 1,4-C$_4$H$_2$S(C≡C–SnMe$_3$)$_2$ (37 mg, 0.11 mmol). Yield: 120 mg, 94%. ^{1}H NMR (C$_6$D$_6$, 300 MHz, 20 °C): δ = 6.35 (4 H, C$_6$H$_5$), 4.61 (4 H, C$_5$H$_4$Me), 4.01 (4 H, C$_5$H$_4$Me), 2.31 (6 H, C$_5$H$_4$Me), 1.59 (4 H, PCH$_2$), 1.32 (8 H, P[CH$_2$CH$_3$]$_2$), 1.32 (8 H, P[CH$_2$CH$_3$]$_2$), 1.02 (12 H, P[CH$_3$]$_2$), 0.73 (4 H, PCH$_2$), 0.48 (18 H, SnMe$_3$) ppm. ^{13}C{^{1}H} NMR (C$_6$D$_6$, 125.8 MHz, 20 °C): δ = 326.8 (t, $^2J_{P,C}$ = 32.3 Hz, Mn-*C*$_α$), 141.1 (m, =*C*$_β$), 120.9 (s, *C*$_i$-C$_4$H$_2$S), 109.4 (s, C$_4$H$_2$S), 97.4 (s, 2 C, *C*$_i$-C$_5$H$_4$Me), 82.9 (s, 4 C, C$_5$H$_4$Me), 79.8 (s, 4 C, C$_5$H$_4$Me), 30.8 (P*C*H$_2$), 22.2 (P*C*H$_2$), 21.8 (P*C*H$_2$CH$_3$), 19.7 (PCH$_2$*C*H$_3$), 14.5 (s, C$_5$H$_4$*C*H$_3$), –6.2 ppm (SnMe$_3$). ^{31}P{^{1}H} NMR (C$_6$D$_6$, 121.5 MHz, 20 °C): δ = 115.1 ppm (s, 4 P). ^{119}Sn NMR (C$_6$D$_6$, 186.5 MHz, 20 °C): δ = –26.3 (t, *J* = 72.0 Hz). IR (CH$_2$Cl$_2$, 20 °C): ν̃ = 1548 [ν(C=C)], 1554 [ν(C=C)] cm^{-1}. C$_{38}$H$_{66}$Mn$_2$P$_4$Sn$_2$S (1138.40): calcd. C 44.47, H 6.48; found C 44.59, H 6.74.

[{Mn(MeC$_5$H$_4$)(Me$_2$PCH$_2$CH$_2$PMe$_2$)=C=C(H)}$_2$(μ-1,4-C$_6$H$_4$)] (6a): To a toluene solution (10 mL) of [{Mn(MeC$_5$H$_4$)(dmpe)=C=C(SnMe$_3$)}$_2$(μ-1,4-C$_6$H$_4$)] (120 mg, 0.17 mmol) was added an excess of methanol. The solution was stirred at room temperature for 2 h to give a dark red solution. The solvent was removed under vacuum to afford a dark red solid which was washed with pentane. The solid was extracted with toluene and filtered through Celite. The toluene fraction was concentrated to give an orange-red precipitate. Crystallisation from a mixture of tetrahydrofuran/ether at –35 °C gave single orange-red crystals. Yield: 105 mg, 90%. ^{1}H NMR ([D$_8$]toluene, 300 MHz, 20 °C): δ = 7.15 (4 H, C$_6$H$_5$), 5.91 (2 H, $^4J_{P,H}$ = 8.4 Hz, = C[H]), 4.30 (4 H, C$_5$H$_4$Me), 3.86 (4 H, C$_5$H$_4$Me), 1.93 (6 H, C$_5$H$_4$Me), 1.49 (4 H, PCH$_2$), 1.11 (12 H, P(CH$_3$]$_2$), 1.02 (4 H, PCH$_2$), 0.74 (12 H, P[CH$_3$]$_2$) ppm. ^{13}C{^{1}H} NMR ([D$_8$]toluene, 125.8 MHz, 20 °C): δ = 325.4 (t, $^2J_{P,C}$ = 37.5 Hz, Mn-*C*$_α$), 133.9 (m, =*C*$_β$), 132.3 (s, *C*$_i$-Ph), 129.4 (s, 2 C, *C*$_i$-C$_5$H$_4$Me), 123.1 (s, C$_6$H$_5$), 122.3 (s, C$_6$H$_5$), 121.9 (s, C$_6$H$_5$), 84.1 (s, 4 C, C$_5$H$_4$Me), 80.4 (s, 4 C, C$_5$H$_4$Me), 31.2 (2 C, PCH$_2$), 23.5 (2 C, PCH$_2$), 21.1 (P[CH$_3$]$_3$), 14.8 (P[CH$_3$]$_3$) ppm. ^{31}P{^{1}H} NMR ([D$_8$]toluene, 121.5 MHz, 20 °C): δ = 96.1 (s, 4 P) ppm. IR (CH$_2$Cl$_2$, 20 °C): ν̃ = 1545 [ν(C=C)], 1553 [ν(C=C)] cm^{-1}. C$_{34}$H$_{52}$Mn$_2$P$_4$ (694.54): calcd. C 58.79, H 7.54; found C 58.95, H 7.43.

[{Mn(MeC$_5$H$_4$)(Et$_2$PCH$_2$CH$_2$PEt$_2$)=C=C(H)}$_2$(μ-1,4-C$_6$H$_4$)] (6b): The same procedure as for **6a** was applied using [{Mn(MeC$_5$H$_4$)(depe)=C=C(SnMe$_3$)}$_2$(μ-1,4-C$_6$H$_4$)] (120 mg, 0.10 mmol). Yield: 80 mg, 98%. ^{1}H NMR (C$_6$D$_6$, 300 MHz, 20 °C): δ = 7.28 (4 H, C$_6$H$_5$), 5.91 (2 H, $^4J_{P,H}$ = 12.9 Hz, =C[H]), 4.51 (4 H, C$_5$H$_4$Me), 4.05 (4 H, C$_5$H$_4$Me), 2.17 (6 H, C$_5$H$_4$Me), 1.89 (4 H, PCH$_2$), 1.73 (4 H, PCH$_2$), 1.43 (4 H, PC*H*$_2$CH$_3$), 1.14 (4 H, PC*H*$_2$CH$_3$), 1.02 (6 H, PCH$_2$C*H*$_3$), 0.92 (6 H, PCH$_2$C*H*$_3$) ppm. ^{13}C{^{1}H} NMR (C$_6$D$_6$, 125.8 MHz, 20 °C): δ = 327.4 (t, $^2J_{P,C}$ = 37.5 Hz, Mn-*C*$_α$), 133.9 (m, =*C*$_β$), 132.3 (s, *C*$_i$-Ph), 129.4 (s, 2 C,

 © 2005 Wiley-VCH Verlag GmbH & Co. KGaA, Weinheim

C_i-C_5H_4Me), 123.1 (s, C_6H_5), 122.3 (s, C_6H_5), 121.9 (s, C_6H_5), 84.1 (s, 4 C, C_5H_4Me), 80.4 (s, 4 C, C_5H_4Me), 30.8 (P*C*H$_2$), 22.2 (P*C*H$_2$), 21.8 (P*C*H$_2$CH$_3$), 19.7 (PCH$_2$*C*H$_3$), 14.5 (s, C_5H_4*C*H$_3$) ppm. $^{31}P\{^1H\}$ NMR (C_6D_6, 121.5 MHz, 20 °C): δ = 114.5 (s, 4 P) ppm. IR (CH_2Cl_2, 20 °C): $\tilde{\nu}$ = 1548 [ν(C=C)], 1555 [ν(C=C)] cm^{-1}. $C_{42}H_{68}Mn_2P_4$ (806.76): calcd. C 62.52, H 8.49; found C 62.31, H 8.45.

[{Mn(MeC$_5$H$_4$)(Me$_2$PCH$_2$CH$_2$PMe$_2$)=C=C(H)}$_2$(μ-1,3-C$_6$H$_4$)] (7a): The same procedure as for **6a** was applied using [{Mn(MeC$_5$H$_4$)(dmpe)=C=C(SnMe$_3$)}$_2$(μ-1,3-C$_6$H$_4$)] (120 mg, 0.17 mmol). Yield: 105 mg, 90%. ^1H NMR ([D$_8$]toluene, 300 MHz, 20 °C): δ = 7.31 (1 H, C_6H_5), 7.25 (1 H, C_6H_5), 7.13 (2 H, C_6H_5), 6.01 (2 H, $^4J_{P,H}$ = 8.4 Hz, =C[H]), 4.42 (4 H, C_5H_4Me), 3.99 (4 H, C_5H_4Me), 2.07 (6 H, C_5H_4Me), 1.59 (4 H, PCH$_2$), 1.24 (12 H, P[CH$_3$]$_2$), 1.18 (4 H, PCH$_2$), 0.80 (12 H, P[CH$_3$]$_2$) ppm. $^{13}C\{^1H\}$ NMR ([D$_8$]toluene, 125.8 MHz, 20 °C): δ = 343.4 (t, $^2J_{P,C}$ = 37.5 Hz, Mn-C_α), 141.3 (m, =C_β), 132.3 (s, C_i-Ph), 122.4 (s, 2 C, C_i-C_5H_4Me), 123.1 (s, C_6H_5), 118.4 (s, C_6H_5), 116.7 (s, C_6H_5), 84.1 (s, 4 C, C_5H_4Me), 80.4 (s, 4 C, C_5H_4Me), 31.3 (2 C, PCH$_2$), 23.8 (2 C, PCH$_2$), 21.7 (P[CH$_3$]$_3$), 14.8 (P[CH$_3$]$_3$) ppm. $^{31}P\{^1H\}$ NMR (C_6D_6, 121.5 MHz, 20 °C): δ = 94.9 (s, 4 P) ppm. IR (CH_2Cl_2, 20 °C): $\tilde{\nu}$ = 1549 [ν(C=C)], 1558 [ν(C=C)] cm^{-1}. $C_{34}H_{52}Mn_2P_4$ (694.54): calcd. C 58.79, H 7.54; found C 58.95, H 7.43.

[{Mn(MeC$_5$H$_4$)(Et$_2$PCH$_2$CH$_2$PEt$_2$)=C=C(H)}$_2$(μ-1,3-C$_6$H$_4$)] (7b): The same procedure as for **6a** was applied using [{Mn(MeC$_5$H$_4$)(depe)=C=C(SnMe$_3$)}$_2$(μ-1,3-C$_6$H$_4$)] (190 mg, 0.17 mmol). Yield: 120 mg, 90%. ^1H NMR ([D$_8$]toluene, 300 MHz, 20 °C): δ = 7.31 (1 H, C_6H_5), 7.25 (1 H, C_6H_5), 7.13 (2 H, C_6H_5), 6.08 (2 H, $^4J_{P,H}$ = 8.4 Hz, =C[H]), 4.51 (4 H, C_5H_4Me), 4.05 (4 H, C_5H_4Me), 2.17 (6 H, C_5H_4Me), 1.89 (4 H, PCH$_2$), 1.73 (4 H, PCH$_2$), 1.43 (4 H, PC*H*$_2$CH$_3$), 1.14 (4 H, PC*H*$_2$CH$_3$), 1.02 (6 H, PCH$_2$C*H*$_3$), 0.92 (6 H, PCH$_2$C*H*$_3$) ppm. $^{13}C\{^1H\}$ NMR ([D$_8$]toluene, 125.8 MHz, 20 °C): δ = 341.9 (t, $^2J_{P,C}$ = 37 Hz, Mn-C_α), 140.4 (m, =C_β), 132.3 (s, C_i-Ph), 122.4 (s, 2 C, C_i-C_5H_4Me), 123.1 (s, C_6H_5), 118.4 (s, C_6H_5), 116.7 (s, C_6H_5), 84.1 (s, 4 C, C_5H_4Me), 80.4 (s, 4 C, C_5H_4Me), 30.8 (P*C*H$_2$), 22.2 (P*C*H$_2$), 21.8 (P*C*H$_2$CH$_3$), 19.7 (PCH$_2$*C*H$_3$), 14.5 (s, C_5H_4*C*H$_3$) ppm. $^{31}P\{^1H\}$ NMR (C_6D_6, 121.5 MHz, 20 °C): δ = 114.2 (s, 4 P) ppm. IR (CH_2Cl_2, 20 °C): $\tilde{\nu}$ = 1545 [ν(C=C)], 1553 [ν(C=C)] cm^{-1}. $C_{42}H_{68}Mn_2P_4$ (806.76): C 58.79, H 7.54; found C 58.89, H 7.89.

[{Mn(MeC$_5$H$_4$)(Me$_2$PCH$_2$CH$_2$PMe$_2$)=C=C(H)}$_2$(μ-4,4-(C$_6$H$_4$)$_2$)] (8a): The same procedure as for **6a** was applied using [{Mn(MeC$_5$H$_4$)(dmpe)=C=C(SnMe$_3$)}$_2${μ-4,4-(C$_6$H$_4$)$_2$}] (120 mg, 0.10 mmol). Yield: 70 mg, 92%. ^1H NMR ([D$_8$]toluene, 300 MHz, 20 °C): δ = 7.67 (m, 4 H, C_6H_5), 7.42 (m, 4 H, C_6H_5), 6.00 (2 H, $^4J_{P,H}$ = 7.9 Hz, =C[H]), 4.42 (4 H, C_5H_4Me), 3.95 (4 H, C_5H_4Me), 2.06 (6 H, C_5H_4Me), 1.56 (4 H, PCH$_2$), 1.20 (24 H, P[CH$_3$]$_3$), 1.05 (4 H, PCH$_2$), 0.79 (24 H, P[CH$_3$]$_3$) ppm. $^{13}C\{^1H\}$ NMR ([D$_8$]toluene, 125.8 MHz, 20 °C): δ = 342.2 (t, $^2J_{P,C}$ = 34.7 Hz, Mn-C_α), 139.9 (m, =C_β), 135.4 (s, C_i-Ph), 133.2 (s, C_6H_5), 126.7 (s, 2 C, C_i-C_5H_4Me), 126.2 (s, C_6H_5), 120.4 (s, C_6H_5), 84.6 (s, 4 C, C_5H_4Me), 80.3 (s, 4 C, C_5H_4Me), 30.8 (4 C, PCH$_2$), 23.3 (PCH$_2$), (P[CH$_3$]$_3$), 14.6 (P[CH$_3$]$_3$) ppm. $^{31}P\{^1H\}$ NMR ([D$_8$]toluene, 121.5 MHz, 20 °C): δ = 94.5 (s, 4 P) ppm. IR (CH_2Cl_2, 20 °C): $\tilde{\nu}$ = 1547 [ν(C=C)], 1553 [ν(C=C)] cm^{-1}. $C_{40}H_{56}Mn_2P_4$ (770.64): calcd. C 62.34, H 7.32; found C 62.47, H 7.39.

[{Mn(MeC$_5$H$_4$)(Et$_2$PCH$_2$CH$_2$PEt$_2$)=C=C(H)}$_2${μ-4,4-(C$_6$H$_4$)$_2$}] (8b): The same procedure as for **6a** was applied using [{Mn(MeC$_5$H$_4$)(depe)=C=C(SnMe$_3$)}$_2${μ-4,4-(C$_6$H$_4$)$_2$}] (130mg, 0.10 mmol). Yield: 82 mg, 95%. ^1H NMR ([D$_8$]toluene, 300 MHz, 20 °C): δ = 7.68 (m, 4 H, C_6H_5), 7.38 (m, 4 H, C_6H_5), 6.00 (2 H, $^4J_{P,H}$ = 8.4 Hz, =C[H]), 4.52 (4 H, C_5H_4Me), 4.03 (4 H, C_5H_4Me), 2.16 (6 H, C_5H_4Me), 1.73 (4 H, PCH$_2$), 1.66 (4 H, PCH$_2$), 1.43 (4 H, PC*H*$_2$CH$_3$), 1.14 (4 H, PC*H*$_2$CH$_3$), 1.02 (6 H, PCH$_2$C*H*$_3$), 0.92 (6 H, PCH$_2$C*H*$_3$) ppm. $^{13}C\{^1H\}$ NMR ([D$_8$]toluene, 125.8 MHz, 20 °C): δ = 345.5 (t, $^2J_{P,C}$ = 34.7 Hz, Mn-C_α), 140.2 (m, =C_β), 136.3 (s, C_i-Ph), 133.2 (s, C_6H_5), 127.8 (s, 2 C, C_i-C_5H_4Me), 123.2 (s, C_6H_5), 120.2 (s, C_6H_5), 83.1 (s, 4 C, C_5H_4Me), 80.4 (s, 4 C, C_5H_4Me), 30.8 (P*C*H$_2$), 22.2 (P*C*H$_2$), 21.8 (P*C*H$_2$CH$_3$), 19.7 (PCH$_2$*C*H$_3$), 14.5 (s, C_5H_4*C*H$_3$) ppm. $^{31}P\{^1H\}$ NMR ([D$_8$]toluene, 121.5 MHz, 20 °C): δ = 115.1 (s, 4 P) ppm. IR (CH_2Cl_2, 20 °C): $\tilde{\nu}$ = 1546 [ν(C=C)], 1559 [ν(C=C)] cm^{-1}. $C_{48}H_{52}Mn_2P_4$ (862.69): calcd. C 66.82, H 6.07; found C 66.93, H 6.04.

X-ray Crystallography: Crystallographic data (excluding structure factors) for the structures given in this paper have been deposited with the Cambridge Crystallographic Data Centre as Supplementary Publication Nos. CCDC-239735, -239736, -239737 and -239738. Copies of the data can be obtained free of charge on application to CCDC, 12 Union Road, Cambridge CB2 1EZ, UK (Fax: +44-1223-336-033; E-mail: deposit@ccdc.cam.ac.uk).

Acknowledgments

Funding from the Swiss National Science Foundation (SNSF) and from the University of Zürich is gratefully acknowledged.

[1] T. Bartik, B. Bartik, M. Brady, R. Dembinski, J. A. Gladysz, *Angew. Chem. Int. Ed. Engl.* **1996**, *35*, 414.
[2] U. H. F. Bunz, *Angew. Chem. Int. Ed. Engl.* **1994**, *33*, 1073.
[3] U. H. F. Bunz, Y. Rubin, Y. Tobe, *Chem. Soc. Rev.* **1999**, *28*, 107.
[4] F. Diederich, Y. Rubin, *Angew. Chem. Int. Ed. Engl.* **1992**, *31*, 1101.
[5] I. Manners, *Angew. Chem. Int. Ed. Engl.* **1996**, *35*, 1603.
[6] N. Le Narvor, L. Toupet, C. Lapinte, *J. Am. Chem. Soc.* **1995**, *117*, 7129.
[7] N. Le Narvor, C. Lapinte, *Organometallics* **1995**, *14*, 634.
[8] F. Paul, C. Lapinte, *Coord. Chem. Rev.* **1998**, *180*, 431.
[9] J. M. Tour, *Chem. Rev.* **1996**, *96*, 537.
[10] A. Harriman, R. Ziessel, *Coord. Chem. Rev.* **1998**, *171*, 331.
[11] R. L. Carroll, C. B. Groman, *Angew. Chem. Int. Ed.* **2002**, *41*, 4378.
[12] E. Viola, C. LoSterzo, F. Trezzi, *Organometallics* **1996**, *15*, 4352.
[13] W. G. Weng, T. Bartik, J. A. Gladysz, *Angew. Chem. Int. Ed. Engl.* **1994**, *33*, 2199.
[14] I. R. Whittall, M. G. Humphrey, D. C. R. Hockless, *Organometallics* **1995**, *14*, 3970.
[15] M. I. Bruce, M. Z. Ke, P. J. Low, *Chem. Commun.* **1996**, 2405.
[16] U. H. F. Bunz, V. Enkelmann, *Organometallics* **1994**, *13*, 3823.
[17] a) O. Lavastre, M. Even, P. H. Dixneuf, A. Pacreau, J. P. Vairon, *Organometallics* **1996**, *15*, 1530; b) H. Werner, P. Bachmann, M. Martin, *Can. J. Chem.* **2001**, *79*, 519.
[18] V. V. Krivykh, I. L. Eremenko, D. Veghini, I. A. Petrunenko, D. L. Pountney, D. Unseld, H. Berke, *J. Organomet. Chem.* **1996**, *511*, 111.
[19] V. V. Krivykh, H. Berke, *Abstr. Pap.- Am. Chem. Soc.* **1997**, *213*, 103.
[20] S. Kheradmandan, K. Heinze, H. W. Schmalle, H. Berke, *Angew. Chem. Int. Ed.* **1999**, *38*, 2270.
[21] F. J. Fernandez, M. Alfonso, H. W. Schmalle, H. Berke, *Organometallics* **2001**, *20*, 3122.
[22] F. J. Fernandez, O. Blacque, M. Alfonso, H. Berke, *Chem. Commun.* **2001**, 1266.
[23] F. J. Fernandez, K. Venkatesan, O. Blacque, M. Alfonso, H. W. Schmalle, H. Berke, *Chem. Eur. J.* **2003**, *9*, 6192.
[24] D. Unseld, V. V. Krivykh, K. Heinze, F. Wild, G. Artus, H. Schmalle, H. Berke, *Organometallics* **1999**, *18*, 1525.

 © 2005 Wiley-VCH Verlag GmbH & Co. KGaA, Weinheim

[25] M. R. Terry, C. Kelley, N. Lugan, G. L. Geoffroy, B. S. Haggerty, A. L. Rheingold, *Organometallics* **1993**, *12*, 3607.
[26] N. E. Kolobova, O. S. Zhvanko, L. L. Ivanov, A. S. Batsanov, Y. T. Struchkov, *J. Organomet. Chem.* **1986**, *302*, 235.
[27] H. Werner, P. Bachmann, M. Laubender, O. Gevert, *Eur. J. Inorg. Chem.* **1998**, 1217.
[28] R. D. Adams, A. Davison, J. P. Selegue, *J. Am. Chem. Soc.* **1979**, *101*, 7232.
[29] C. P. Casey, T. L. Dzwiniel, S. Kraft, M. A. Kozee, D. R. Powell, *Inorg. Chim. Acta* **2003**, *345*, 320.
[30] Y. Ortin, A. Sournia-Saquet, N. Lugan, R. Mathieu, *Chem. Commun.* **2003**, 1060.
[31] A. Davison J. P. Selegue, *J. Am. Chem. Soc.* **1978**, *100*, 7763.
[32] P. N. Nickias, J. P. Selegue, B. A. Young, *Organometallics* **1988**, *7*, 2248.
[33] T. Rappert, O. Nurnberg, H. Werner, *Organometallics* **1993**, *12*, 1359.
[34] H. Werner, *J. Organomet. Chem.* **1994**, *475*, 45.
[35] H. Werner, *Chem. Commun.* **1997**, 903.
[36] V. Cadierno, M. P. Gamasa, J. Gimeno, *Eur. J. Inorg. Chem.* **2001**, 571.
[37] P. L. Pauson J. A. Segal, *J. Chem. Soc., Dalton Trans.* **1975**, 2387.
[38] K. Venkatesan, F. J. Fernandez, O. Blacque, T. Fox, M. Alfonso, H. W. Schmalle, H. Berke, *Chem. Commun.* **2003**, 2006.
[39] K. Venkatesan, O. Blacque, T. Fox, M. Alfonso, H. W. Schmalle, H. Berke, *Organometallics* **2004**, *23*, 1183.
[40] S. Takahashi, Y. Kuroyama, K. Sonogashira, N. Hagihara, *Synthesis* **1980**, 627.
[41] W. B. Austin, N. Bilow, W. J. Kelleghan, K. S. Y. Lau, *J. Org. Chem.* **1981**, *46*, 2280.
[42] R. Nast, H. Grouhi, *J. Organomet. Chem.* **1979**, *182*, 197.
[43] STOE-IPDS Software package, version 2.87 5/1998, STOE & Cie, GmbH, Darmstadt, Germany, **1998**.
[44] P. Coppens, L. Leiserow, D. Rabinovi, *Acta Crystallogr.* **1965**, *18*, 1035.
[45] G. M. Sheldrick, *Acta Crystallogr., Sect. A* **1990**, *46*, 467.
[46] G. M. Sheldrick, *Program for the Refinement of Crystal Structures*, University of Göttingen, Germany, **1997**.
[47] A. L. Spek, *Acta Crystallogr., Sect. A* **1990**, *46*, 34.
[48] R. J. Burt, J. Chatt, W. Hussain, G. J. Leigh, *J. Organomet. Chem.* **1979**, *182*, 203.

Received: August 9, 2004

 © 2005 Wiley-VCH Verlag GmbH & Co. KGaA, Weinheim

First Complexes of a 4-Alkyl-3,5-di(2-pyridyl)-4*H*-1,2,4-triazole: Synthesis, X-ray Crystal Structures and Magnetic Properties of Dinuclear Cobalt(II), Nickel(II) and Copper(II) Complexes of 4-Isobutyl-3,5-di(2-pyridyl)-4*H*-1,2,4-triazole

Marco H. Klingele,[a] Peter D. W. Boyd,[b] Boujemaa Moubaraki,[c] Keith S. Murray,[c] and Sally Brooker*[a]

Keywords: 1,2,4-Triazole / Bridging ligands / N ligands / Magnetic properties / X-ray diffraction

The reaction of the new, bis(bidentate), potentially dinucleating ligand 4-isobutyl-3,5-di(2-pyridyl)-4*H*-1,2,4-triazole (ibdpt) with $M(ClO_4)_2{\cdot}6H_2O$ (M = Co^{II}, Ni^{II} or Cu^{II}) in a 1:1 molar ratio in MeCN affords the dinuclear complexes $[Co^{II}_2(ibdpt)_2(MeCN)_2(H_2O)_2](ClO_4)_4$ (**1**), $[Ni^{II}_2(ibdpt)_2(MeCN)_4](ClO_4)_4$ (**2**) and $[Cu^{II}_2(ibdpt)_2(MeCN)_2(ClO_4)_2](ClO_4)_2{\cdot}2MeCN$ (**3**). Complex **1** is obtained as a mixture of the red-orange polymorph **1a** and the yellow-orange polymorph **1b**, the main difference between the two forms being the hydrogen bonding patterns between the H_2O co-ligands and the ClO_4^- counterions. The mononuclear complex $[Cu^{II}(ibdpt)_2(ClO_4)_2]$ (**4**) was initially obtained as a minor by-product in the preparation of complex **3** but can also be deliberately prepared from $Cu(ClO_4)_2{\cdot}6H_2O$ and ibdpt in MeCN using a metal-to-ligand molar ratio of 1:2. All five complexes have been structurally characterised by X-ray diffraction. In the dinuclear complexes **1**–**3** the $(N',N^1,N^2,N'')_2$double bridging coordination mode is realised while the mononuclear complex **4** features the common *trans*-$(N',N^1)_2$ coordination mode. In all cases the metal centres reside in distorted octahedral N_4X_2 coordination spheres with axially bound co-ligands (X = H_2O, MeCN or ClO_4^-). The dinuclear complexes **1**–**3** readily lose solvent when taken out of their mother liquors giving rise to partially desolvated materials. Magnetic studies have been carried out on crystalline samples of the resulting complexes that analysed as $Co^{II}_2(ibdpt)_2(ClO_4)_4(MeCN)(H_2O)$ (**5**), $Ni^{II}_2(ibdpt)_2(ClO_4)_4(MeCN)$ (**6**) and $Cu^{II}_2(ibdpt)_2(ClO_4)_4(MeCN)$ (**7**). It was found that in these complexes the two 1,2,4-triazole bridges facilitate antiferromagnetic coupling between the two metal centres (J = –3.76 cm^{-1}, –13.0 cm^{-1} and –105 cm^{-1}, respectively). The coordination compounds described in this paper are the first to incorporate a 4-alkyl-substituted 3,5-di(2-pyridyl)-4*H*-1,2,4-triazole ligand.
(© Wiley-VCH Verlag GmbH & Co. KGaA, 69451 Weinheim, Germany, 2005)

Introduction

The strong current interest in the coordination chemistry of 1,2,4-triazole derivatives[1–3] is mainly due to the fact that their ligand strength is in the right region to give complexes with iron(II) salts that show the spin crossover phenomenon.[4–7] Because of their bistability such coordination compounds have potential applications in nano-technology as switches and memory devices, but also as materials for the construction of displays.[8–12] In order for a bistable molecular system to be used in nano-technology it must, however, fulfil certain requirements.[8,9] Most importantly, the transition between the two detectable states should be complete and abrupt with a relatively large thermal hysteresis, centred near room temperature.[13] Such behaviour is associated with cooperative interactions between the metal centres.[14] In mononuclear complexes cooperativity can be conferred by hydrogen bonding, π–π stacking, solvation and the nature of the counterion. These relatively weak interactions pass on the information from one unit to another that the spin transition is occurring. It has been suggested that more pronounced cooperativity could be achieved by the use of ligands capable of bridging metal centres, thus giving rise to oligo- or polynuclear assemblies rather than mononuclear complexes. The employment of mostly 4-substituted 4*H*-1,2,4-triazoles as bridging ligands has allowed the isolation and investigation of various, mainly tri- and polynuclear, spin crossover systems that show promising properties with regard to the requirements outlined above.[4–7] In light of this, we are particularly interested in the synthesis and study of discrete dinuclear iron(II) complexes.[15,16] As a result of these ongoing studies we were recently able to identify the nature of the [low spin–high spin] species of the doubly 1,2,4-triazole-bridged complex $[Fe^{II}_2(PMAT)_2](BF_4)_4{\cdot}DMF$

[a] Department of Chemistry, University of Otago,
P. O. Box 56, Dunedin, New Zealand
Fax: +64-3-479-7906
E-mail: sbrooker@alkali.otago.ac.nz
[b] Department of Chemistry, The University of Auckland,
Private Bag 92019, Auckland, New Zealand
[c] School of Chemistry, Building 23, Monash University,
Clayton, Victoria 3800, Australia
Supporting information for this article is available on the WWW under http://www.eurjic.org or from the author.

 © 2005 Wiley-VCH Verlag GmbH & Co. KGaA, Weinheim **DOI: 10.1002/ejic.200400780**

(PMAT = 4-amino-3,5-bis{[(2-pyridylmethyl)amino]-methyl}-4*H*-1,2,4-triazole) by means of X-ray diffraction[15] and thus to confirm the conclusions drawn by Real, Gütlich and co-workers[17,18] on the basis of magnetic and applied-field Mössbauer data about the pathway of the transition in their two-step spin crossover systems.

Structurally related to the bis(terdentate) ligand PMAT (Figure 1) are the bis(bidentate) 4-substituted 3,5-di(2-pyridyl)-4*H*-1,2,4-triazoles.[2] Within this class of potentially dinucleating ligands only two members, namely 4-amino-3,5-di(2-pyridyl)-4*H*-1,2,4-triazole (NH_2dpt)[19,20] and 3,5-di(2-pyridyl)-4-(1*H*-pyrrol-1-yl)-4*H*-1,2,4-triazole (pldpt)[21–23] (Figure 1), have actually produced dinuclear complexes while no 4-aryl-3,5-di(2-pyridyl)-4*H*-1,2,4-triazoles have ever been reported to do so.[24–29] We therefore hypothesised that the coordination behaviour of these bis(bidentate) ligands, i. e. their ability to bind and bridge two metal centres, is influenced not only by factors such as the reaction stoichiometry and product solubility but also by the electronic effects of the substituent on N^4.[2,22] Given that our goal is the preparation of dinuclear iron(II) complexes, it was desirable to test this hypothesis by investigating the coordination chemistry of the hitherto unknown 4-alkyl-3,5-di(2-pyridyl)-4*H*-1,2,4-triazoles which carry electron-donating substitutents on N^4. We recently succeeded in the synthesis of the first two members of this group, namely 4-methyl-3,5-di(2-pyridyl)-4*H*-1,2,4-triazole (medpt) and 4-isobutyl-3,5-di(2-pyridyl)-4*H*-1,2,4-triazole (ibdpt) (Figure 1).[22,30] In this paper we present the results of our investigation of the dinucleation behaviour of the new ligand ibdpt towards the *d*-block ions cobalt(II), nickel(II) and copper(II).

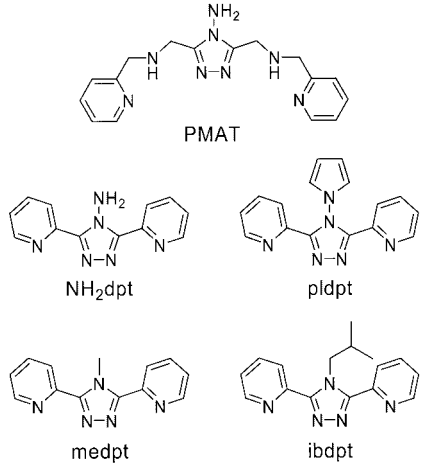

Figure 1. Structural drawings of the ligands 4-amino-3,5-bis{[(2-pyridylmethyl)amino]methyl}-4*H*-1,2,4-triazole (PMAT), 4-amino-3,5-di(2-pyridyl)-4*H*-1,2,4-triazole (NH_2dpt), 3,5-di(2-pyridyl)-4-(1*H*-pyrrol-1-yl)-4*H*-1,2,4-triazole (pldpt), 4-methyl-3,5-di(2-pyridyl)-4*H*-1,2,4-triazole (medpt) and 4-isobutyl-3,5-di(2-pyridyl)-4*H*-1,2,4-triazole (ibdpt).

Results and Discussion

Preparation of the Complexes

The reaction of ibdpt with $M(ClO_4)_2{\cdot}6H_2O$ (M = Co^{II}, Ni^{II} or Cu^{II}) in a 1:1 molar ratio in MeCN produced coloured solutions from which solid products were only obtained upon vapour diffusion of Et_2O. In the case of the cobalt(II) salt this led to the formation of a mixture of red-orange and yellow-orange crystals from the orange reaction mixture in virtually quantitative yield. On the basis of their elemental analyses both crystal types were found to have metal-to-ligand molar ratios of 1:1, not 1:2, and subsequent X-ray diffraction studies showed them to be the two polymorphs **1a** and **1b** of $[Co^{II}_2(ibdpt)_2(MeCN)_2(H_2O)_2](ClO_4)_4$ (**1**). From the purple solution obtained with the nickel(II) salt only one type of purple crystals formed, quantitatively, which were identified by X-ray diffraction as the dinuclear complex $[Ni^{II}_2(ibdpt)_2(MeCN)_4](ClO_4)_4$ (**2**). Using the copper(II) salt instead, blue-green crystals separated from the blue solution which, on prolonged vapour diffusion of Et_2O, were followed by a small amount of steel-blue crystals. Here too, the crystallisation was virtually quantitative. Both crystal types were studied by X-ray diffraction. The blue-green main component was thus identified as the desired dinuclear complex $[Cu^{II}_2(ibdpt)_2(MeCN)_2(ClO_4)_2](ClO_4)_2{\cdot}2MeCN$ (**3**) while the steel-blue minor component was found to be the mononuclear complex $[Cu^{II}(ibdpt)_2(ClO_4)_2]$ (**4**). Complex **4** was readily accessible by the direct reaction of ibdpt with $Cu(ClO_4)_2{\cdot}6H_2O$ in a 2:1 molar ratio in MeCN. Under these conditions it precipitated from the reaction mixture as a blue powder in 48% yield. Vapour diffusion of Et_2O into either the mother liquor or a solution of the powder in MeCN afforded crystals of complex **4** that were identical to those obtained as described above (Table 1).

The dinuclear complexes **1**–**3** readily lost solvent when taken out of their mother liquors. In the case of the yellow-orange polymorph **1b** this was accompanied by a colour change to red-orange while no colour change was observed for the red-orange polymorph **1a**. Subsequent drying of the crystalline samples in vacuo gave rise to partially desolvated materials which were found by elemental analysis to have the compositions $Co^{II}_2(ibdpt)_2(ClO_4)_4(MeCN)(H_2O)$ (**5**) (red-orange), $Ni^{II}_2(ibdpt)_2(ClO_4)_4(MeCN)$ (**6**) (purple) and $Cu^{II}_2(ibdpt)_2(ClO_4)_4(MeCN)$ (**7**) (blue-green). The latter materials were used for further characterisation and magnetic studies.

Description of the Structures

The molecular structures of the red-orange polymorph **1a** (Figure 2) and the yellow-orange polymorph **1b** (Figure S1, Supporting Information) of $[Co^{II}_2(ibdpt)_2(MeCN)_2(H_2O)_2](ClO_4)_4$ (**1**) are very similar, the most obvious difference between them being the orientation of the isobutyl groups of the respective ligand molecule (Figure S2, Supporting Information). The dinuclear $(N',N^1,N^2,N'')_2$ double bridging coordination mode realised in both of these complexes causes distortion of the CoN_5O coordination octahedra and longer Co–N_{pyr} than Co–N_{trz} bond lengths are observed (Table 2 and Table 3). The Co···Co separation in polymorphs **1a** and **1b** are 4.1481(7) and 4.1722(4) Å,

 © 2005 Wiley-VCH Verlag GmbH & Co. KGaA, Weinheim

Table 1. Crystallographic data for $[Co^{II}_2(ibdpt)_2(MeCN)_2(H_2O)_2](ClO_4)_4$ (**1**), $[Ni^{II}_2(ibdpt)_2(MeCN)_4](ClO_4)_4$ (**2**), $[Cu^{II}_2(ibdpt)_2(MeCN)_2(ClO_4)_2](ClO_4)_2\cdot 2MeCN$ (**3**) and $[Cu^{II}(ibdpt)_2(ClO_4)_2]$ (**4**).

	1a	**1b**	**2**	**3**	**4**
Empirical formula	$C_{36}H_{44}Cl_4Co_2N_{12}O_{18}$	$C_{36}H_{44}Cl_4Co_2N_{12}O_{18}$	$C_{40}H_{46}Cl_4N_{14}Ni_2O_{16}$	$C_{40}H_{46}Cl_4Cu_2N_{14}O_{16}$	$C_{32}H_{34}Cl_2CuN_{10}O_8$
Formula mass [g mol^{-1}]	1192.49	1192.49	1238.13	1247.79	821.14
Crystal system	monoclinic	monoclinic	monoclinic	triclinic	triclinic
Space group	$P2_1/n$	$P2_1/n$	$C2/c$	$P\bar{1}$	$P\bar{1}$
a [Å]	12.7535(1)	9.0719(1)	12.4932(2)	12.1370(2)	9.2380(5)
b [Å]	13.7125(1)	21.7150(1)	22.3110(1)	13.4873(1)	9.4059(5)
c [Å]	13.6380(2)	12.1300(1)	19.1890(2)	16.3988(1)	10.6591(6)
α [°]	90	90	90	79.678(1)	77.436(1)
β [°]	92.739(1)	99.614(1)	92.612(1)	79.926(1)	81.666(1)
γ [°]	90	90	90	76.488(1)	76.771(1)
V [Å^3]	2382.32(4)	2356.00(3)	5343.1(1)	2542.90(5)	875.59(8)
Z	2	2	4	2	1
$\rho_{calcd.}$ [g cm^{-3}]	1.662	1.681	1.539	1.630	1.557
μ [mm^{-1}]	1.007	1.018	0.983	1.129	0.843
Temperature [K]	83(2)	83(2)	83(2)	83(2)	83(2)
F(000)	1220	1220	2544	1276	423
Crystal colour and shape	red-orange plate	yellow-orange block	purple block	blue-green plate	steel-blue prism
Crystal size [mm^3]	0.20×0.16×0.03	0.40×0.28×0.18	0.42×0.16×0.08	0.24×0.20×0.04	0.35×0.20×0.15
$\Theta_{min.}/\Theta_{max.}$ [°]	2.11/25.69	1.88/25.72	1.83/25.74	1.27/25.68	1.97/25.67
h	–15 → 15	–11 → 10	–15 → 14	–14 → 14	–11 → 11
k	–16 → 6	0 → 26	–27 → 20	–16 → 16	–11 → 11
l	–16 → 15	0 → 14	–20 → 23	–19 → 19	–12 → 12
Reflections collected/R(int)	13076/0.0323	13549/0.0540	15006/0.0352	23025/0.0463	8017/0.0624
Data/restraints/parameter	4504/0/334	4477/0/334	5088/4/395	9523/9/709	3284/0/241
GOF	1.079	1.032	1.047	1.116	1.034
$R1/wR2$ [$I > 2\sigma(I)$]	0.0352/0.0715	0.0254/0.0626	0.0566/0.1543	0.0510/0.1011	0.0494/0.1222
$R1/wR2$ (all data)	0.0509/0.0793	0.0300/0.0647	0.0681/0.1645	0.0773/0.1130	0.0636/0.1313
Max. peak/hole [e·Å^{-3}]	0.344/–0.591	0.382/–0.469	1.606/–0.534	0.584/–0.503	0.647/–0.522

respectively, and thus are somewhat shorter than the corresponding bond length of 4.226(2) Å in $[Co^{II}_2(pldpt)_2(H_2O)_4]Cl_4\cdot 2MeOH\cdot 2H_2O$,[21] the only structurally characterised dinuclear cobalt(II) complex of any 4-substituted 3,5-di(2-pyridyl)-4*H*-1,2,4-triazole previously reported. The torsion angles between the mean planes of the pyridine rings and the central triazole ring in the red-orange polymorph **1a** [8.6(1) and 8.8(1)°] are slightly larger than in the yellow-orange polymorph **1b** [2.3(1) and 8.1(1)°]. In both polymorphs some doming of the ligands is observed. The most significant structural difference between the two polymorphs is found in their hydrogen bonding patterns. In the red-orange polymorph **1a** both ClO_4^- ions form hydrogen bonds to the axial H_2O co-ligand [O(1)···O(11) 2.79 and O(1)···O(21) 2.82 Å] (Figure S3, Supporting Information). In contrast, only one ClO_4^- ion is involved in hydrogen bonding in the yellow-orange polymorph **1b** while the other ClO_4^- ion resides independently within the lattice. A chain of dinuclear units is thus formed with the ClO_4^- ion hydrogen bonding to the H_2O co-ligands of its own and a neighbouring unit in a bridging fashion [O(1)···O(11) 2.76 and O(1)···O(12B) 2.88 Å] (Figure S4, Supporting Information). The shortest bond length between the metal centres of two dinuclear units across this $H_2O\cdots ClO_4^-\cdots H_2O$ link is 8.5770(5) Å while it is only 8.3822(4) Å between the metal centres of two independent chains.

The adoption of the $(N',N^1,N^2,N'')_2$ double bridging coordination mode in $[Ni^{II}_2(ibdpt)_2(MeCN)_4](ClO_4)_4$ (**2**) with MeCN molecules as the axial co-ligands (Figure 3) results in a distorted octahedral N_6 coordination environment about the nickel centres (Table 2 and Table 3). As can be expected for this coordination mode,[2] the Ni–N_{pyr} bond lengths are considerably longer than the Ni–N_{trz} bond lengths [2.139(3)–2.149(3) and 2.023(3)–2.031(3) Å, respectively]. The former are slightly shorter than the corresponding bond lengths observed in $[Ni^{II}_2(NH_2dpt)_2(H_2O)_2Cl_2]Cl_2\cdot 4H_2O$[19] [2.155(1)–2.164(1) Å] while the latter are very similar in both complexes. The Ni···Ni separation in complex **2** is 4.1107(9) Å which is also slightly less than in $[Ni^{II}_2(NH_2dpt)_2(H_2O)_2Cl_2]Cl_2\cdot 4H_2O$ [4.1348(3) Å].[19] The pyridine–triazole–pyridine moiety of the ligand is not completely flat but shows slight doming and torsion angles between the mean planes of the pyridine rings and the central triazole ring of 5.7(2) and 8.7(2)°.

The asymmetric unit of $[Cu^{II}_2(ibdpt)_2(MeCN)_2(ClO_4)_2](ClO_4)_2\cdot 2MeCN$ (**3**) contains two crystallographically independent but structurally very similar complex cations (Table 2 and Table 4), one of which is shown in Figure 4. The Cu···Cu separations in the two cations are 4.0701(10) and 4.0861(9) Å and are thus very similar to one another while they are dramatically shorter than the Cu···Cu separation of 4.415(1) Å found in the only other known dinuclear

 © 2005 Wiley-VCH Verlag GmbH & Co. KGaA, Weinheim

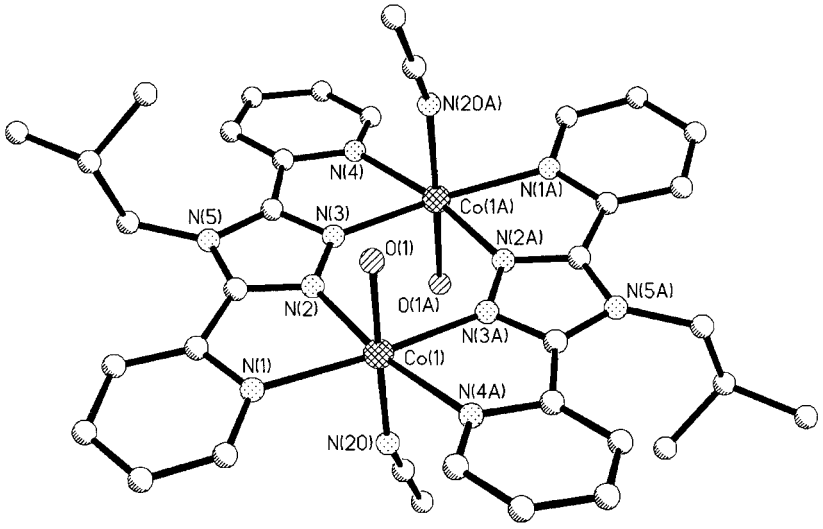

Figure 2. View of the molecular structure of the cation of the red-orange polymorph **1a** of $[Co^{II}_2(ibdpt)_2(MeCN)_2(H_2O)_2](ClO_4)_4$ (**1**). Hydrogen atoms have been omitted for clarity. Symmetry operation used to generate equivalent atoms: (A) $-x, -y, -z + 1$.

Table 2. Selected bond lengths [Å] for $[Co^{II}_2(ibdpt)_2(MeCN)_2(H_2O)_2](ClO_4)_4$ (**1**), $[Ni^{II}_2(ibdpt)_2(MeCN)_4](ClO_4)_4$ (**2**), $[Cu^{II}_2(ibdpt)_2(MeCN)_2(ClO_4)_2](ClO_4)_2 \cdot 2MeCN$ (**3**) and $[Cu^{II}(ibdpt)_2(ClO_4)_2]$ (**4**); values in square brackets refer to the second crystallographically independent complex cation within the asymmetric unit.

	1a	**1b**	**2**	**3**	**4**
M···M	4.1481(7)	4.1722(4)	4.1107(9)	4.0701(10) [4.0861(9)]	
M–N_{pyr}	N(1) 2.185(2)	N(1) 2.1988(14)	N(1) 2.139(3)	N(1) 2.070(3) [N(6) 2.068(3)]	N(1) 2.038(3)
	N(4) 2.164(2)	N(4) 2.1879(14)	N(4) 2.140(3)	N(4) 2.079(3) [N(9) 2.072(3)]	
M–N_{trz}	N(2) 2.069(2)	N(2) 2.0757(14)	N(2) 2.023(3)	N(2) 1.961(3) [N(7) 1.972(3)]	N(2) 1.962(3)
	N(3) 2.083(2)	N(3) 2.0815(14)	N(3) 2.031(3)	N(3) 1.972(3) [N(8) 1.965(3)]	
M–X	N(20) 2.117(2)	N(20) 2.1082(15)	N(20) 2.066(3)	N(50) 2.327(5) [N(60) 2.279(4)]	O(11) 2.471(2)
	O(1) 2.079(2)	O(1) 2.0539(14)	N(30) 2.070(3)	O(11) 2.413(3) [O(21) 2.583(3)]	

Table 3. Selected angles [°] for $[Co^{II}_2(ibdpt)_2(MeCN)_2(H_2O)_2](ClO_4)_4$ (**1**) and $[Ni^{II}_2(ibdpt)_2(MeCN)_4](ClO_4)_4$ (**2**).

1a		**1b**		**2**	
N(1)–Co(1)–N(2)	74.52(8)	N(1)–Co(1)–N(2)	74.46(5)	N(1)–Ni(1)–N(2)	76.61(12)
N(1)–Co(1)–N(3A)	169.33(8)	N(1)–Co(1)–N(3A)	169.14(5)	N(1)–Ni(1)–N(3A)	170.39(12)
N(1)–Co(1)–N(4A)	115.68(8)	N(1)–Co(1)–N(4A)	116.24(5)	N(1)–Ni(1)–N(4A)	113.30(12)
N(1)–Co(1)–N(20)	89.39(8)	N(1)–Co(1)–N(20)	88.61(5)	N(1)–Ni(1)–N(20)	90.02(13)
N(1)–Co(1)–O(1)	91.54(9)	N(1)–Co(1)–O(1)	85.69(6)	N(1)–Ni(1)–N(30)	88.26(13)
N(2)–Co(1)–N(3A)	95.34(8)	N(2)–Co(1)–N(3A)	94.73(5)	N(2)–Ni(1)–N(3A)	93.92(13)
N(2)–Co(1)–N(4A)	169.68(8)	N(2)–Co(1)–N(4A)	168.69(6)	N(2)–Ni(1)–N(4A)	169.91(13)
N(2)–Co(1)–N(20)	91.29(9)	N(2)–Co(1)–N(20)	95.29(6)	N(2)–Ni(1)–N(20)	90.00(13)
N(2)–Co(1)–O(1)	90.78(9)	N(2)–Co(1)–O(1)	93.18(6)	N(2)–Ni(1)–N(30)	93.51(13)
N(3A)–Co(1)–N(4A)	74.57(8)	N(3A)–Co(1)–N(4A)	74.62(5)	N(3A)–Ni(1)–N(4A)	76.22(12)
N(3A)–Co(1)–N(20)	87.50(9)	N(3A)–Co(1)–N(20)	91.39(6)	N(3A)–Ni(1)–N(20)	91.63(13)
N(3A)–Co(1)–O(1)	91.92(9)	N(3A)–Co(1)–O(1)	96.16(6)	N(3A)–Ni(1)–N(30)	90.73(13)
N(4A)–Co(1)–N(20)	90.44(8)	N(4A)–Co(1)–N(20)	88.87(5)	N(4A)–Ni(1)–N(20)	88.20(13)
N(4A)–Co(1)–O(1)	87.46(8)	N(4A)–Co(1)–O(1)	84.37(6)	N(4A)–Ni(1)–N(30)	88.79(13)
N(20)–Co(1)–O(1)	177.89(9)	N(20)–Co(1)–O(1)	168.15(6)	N(20)–Ni(1)–N(30)	175.63(13)
Co(1)–N(2)–N(3)	132.27(16)	Co(1)–N(2)–N(3)	132.26(11)	Ni(1)–N(2)–N(3)	133.5(2)
N(2)–N(3)–Co(1A)	132.38(16)	N(2)–N(3)–Co(1A)	132.97(11)	N(2)–N(3)–Ni(1A)	132.6(2)

copper(II) complex incorporating a 4-substituted 3,5-di(2-pyridyl)-4*H*-1,2,4-triazole, $[Cu^{II}_2(NH_2dpt)(H_2O)_2(SO_4)_2] \cdot H_2O$.[20] It should be pointed out, however, that due to the fact that $[Cu^{II}_2(NH_2dpt)(H_2O)_2(SO_4)_2] \cdot H_2O$ features the dinuclear N',N^1,N^2,N'' single bridging coordination mode with an additional bridging sulfato co-ligand rather than the $(N',N^1,N^2,N'')_2$ double bridging coordination mode, the geometrical parameters of the two complexes cannot really be compared directly. The Cu–N_{pyr} bond lengths in complex **3** vary over the range 2.068(3)–2.079(3) Å. The Cu–N_{trz} bond lengths are shorter, as can be expected from the realisation of the $(N',N^1,N^2,N'')_2$ double bridging coordination mode,[2] and are in the range of 1.961(3)–1.972(3) Å. As in the other dinuclear 2:2 complexes of ibdpt described

 © 2005 Wiley-VCH Verlag GmbH & Co. KGaA, Weinheim

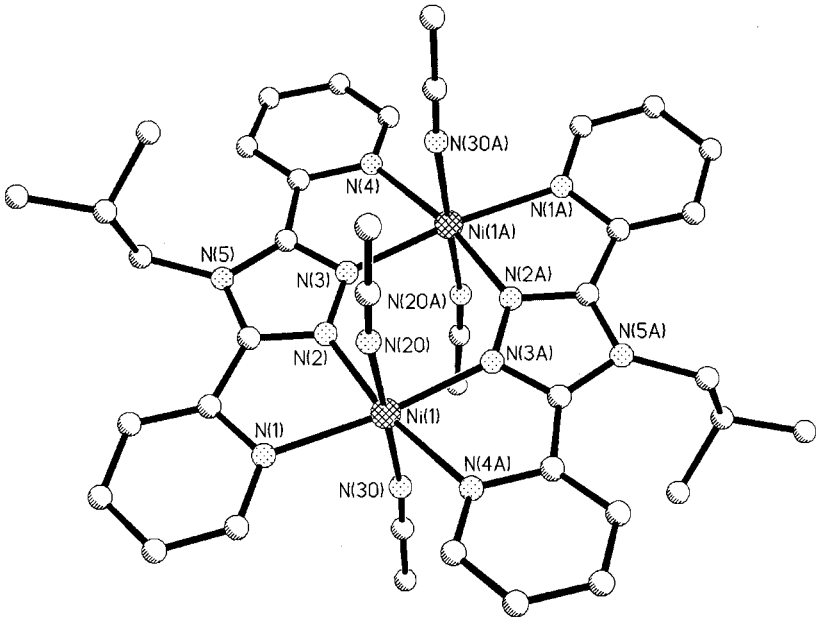

Figure 3. View of the molecular structure of the cation of $[Ni^{II}_2(ibdpt)_2(MeCN)_4](ClO_4)_4$ (**2**). Hydrogen atoms have been omitted for clarity. Symmetry operation used to generate equivalent atoms: (A) $-x + 1.5, -y + 0.5, -z + 1$.

Table 4. Selected angles [°] for $[Cu^{II}_2(ibdpt)_2(MeCN)_2(ClO_4)_2](ClO_4)_2 \cdot 2MeCN$ (**3**) and $[Cu^{II}(ibdpt)_2(ClO_4)_2]$ (**4**).

3				**4**	
N(1)–Cu(1)–N(2)	78.27(14)	N(6)–Cu(2)–N(7)	78.87(13)	N(1)–Cu(1)–N(2)	79.84(10)
N(1)–Cu(1)–N(3A)	169.46(14)	N(6)–Cu(2)–N(8B)	166.52(14)	N(1)–Cu(1)–N(1A)	180
N(1)–Cu(1)–N(4A)	111.21(13)	N(6)–Cu(2)–N(9B)	110.36(13)	N(1)–Cu(1)–N(2A)	100.16(10)
N(1)–Cu(1)–N(50)	86.75(15)	N(6)–Cu(2)–N(60)	96.57(13)	N(1)–Cu(1)–O(11)	89.13(9)
N(1)–Cu(1)–O(11)	89.83(12)	N(6)–Cu(2)–O(21)	84.54(11)	N(1)–Cu(1)–O(11A)	90.87(9)
N(2)–Cu(1)–N(3A)	92.70(14)	N(7)–Cu(2)–N(8B)	92.08(13)	N(2)–Cu(1)–N(2A)	180
N(2)–Cu(1)–N(4A)	169.92(13)	N(7)–Cu(2)–N(9B)	170.68(13)	N(2)–Cu(1)–O(11)	90.44(10)
N(2)–Cu(1)–N(50)	90.07(16)	N(7)–Cu(2)–N(60)	89.15(14)	N(2)–Cu(1)–O(11A)	89.56(10)
N(2)–Cu(1)–O(11)	96.85(13)	N(7)–Cu(2)–O(21)	86.69(12)	O(11)–Cu(1)–O(11A)	180
N(3A)–Cu(1)–N(4A)	78.17(13)	N(8B)–Cu(2)–N(9B)	78.61(13)		
N(3A)–Cu(1)–N(50)	98.81(16)	N(8B)–Cu(2)–N(60)	93.23(13)		
N(3A)–Cu(1)–O(11)	85.82(13)	N(8B)–Cu(2)–O(21)	84.98(11)		
N(4A)–Cu(1)–N(50)	87.17(15)	N(9B)–Cu(2)–N(60)	91.00(13)		
N(4A)–Cu(1)–O(11)	86.83(12)	N(9B)–Cu(2)–O(21)	92.80(11)		
N(50)–Cu(1)–O(11)	171.51(16)	N(60)–Cu(2)–O(21)	175.40(12)		
Cu(1)–N(2)–N(3)	133.5(3)	Cu(2)–N(7)–N(8)	134.0(3)		
N(2)–N(3)–Cu(1A)	133.8(3)	N(7)–N(8)–Cu(2B)	133.6(3)		

above, the pyridine–triazole–pyridine moieties of the ligands are not planar but show some doming and the torsion angles between the mean planes of the pyridine rings and the central triazole rings vary over the range 6.9(2)–9.0(2)°.

The overall architecture of $[Cu^{II}(ibdpt)_2(ClO_4)_2]$ (**4**) (Figure 5) is practically identical to that of $[Cu^{II}(pyppt)_2(ClO_4)_2] \cdot MeCN$ [pyppt = 3-phenyl-5-(2-pyridyl)-4-(4-pyridyl)-4*H*-1,2,4-triazole].[31] As a result of the realisation of the *trans*-$(N',N^1)_2$ coordination mode longer $Cu–N_{pyr}$ bond lengths [2.038(3) Å] than $Cu–N_{trz}$ bond lengths [1.962(3) Å] are observed in complex **4** (Table 2 and Table 4). The respective values are in good agreement with the corresponding bond lengths observed in $[Cu^{II}(pyppt)_2(ClO_4)_2] \cdot MeCN$ [2.045(2) and 1.989(2) Å, respectively]. This is also true for the Cu–O bond length which is 2.471(2) Å in complex **4** and 2.466(3) Å in $[Cu^{II}(pyppt)_2(ClO_4)_2] \cdot MeCN$.[31] The nitrogen atom of the non-coordinated pyridine ring points outwards towards the isobutyl group and the pyridine–triazole–pyridine moiety is almost perfectly planar, with the angles between the mean planes of the coordinated and the non-coordinated pyridine rings relative to the triazole mean plane being very small and identical within experimental error [2.0(2) and 1.9(2)°, respectively].

Magnetic Studies

The curves for the temperature dependence of the molar magnetic susceptibility and the effective magnetic moment for the dinuclear cobalt(II) complex **5** are shown in Figure S5 (Supporting Information). The maximum in susceptibility observed at 18 K (χ_m = 0.05383 $cm^3 mol^{-1}$) is due

 © 2005 Wiley-VCH Verlag GmbH & Co. KGaA, Weinheim

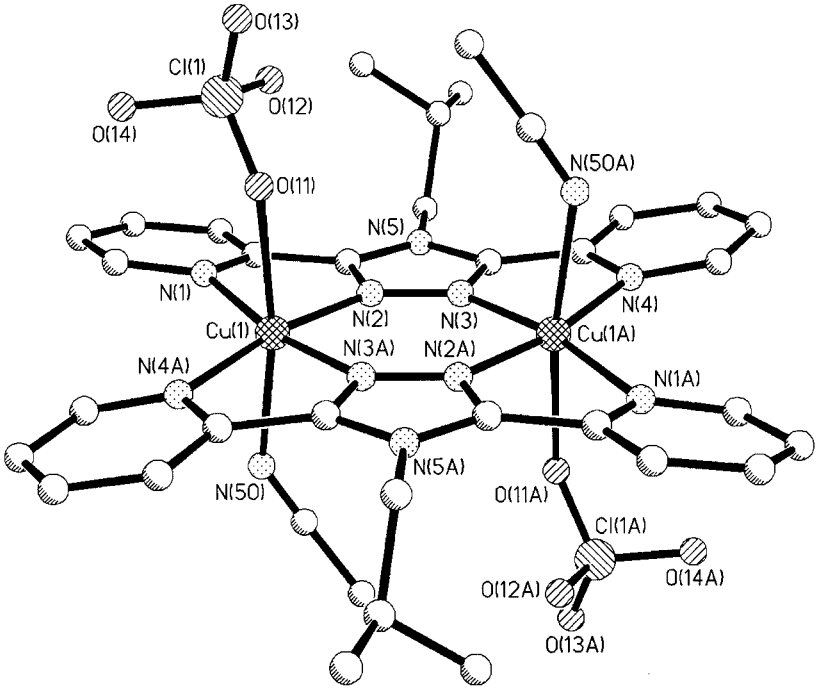

Figure 4. View of the molecular structure of one of the two crystallographically independent cations of $[Cu^{II}_2(ibdpt)_2(MeCN)_2(ClO_4)_2](ClO_4)_2 \cdot 2MeCN$ (**3**). Hydrogen atoms have been omitted for clarity. Symmetry operation used to generate equivalent atoms: (A) $-x + 1, -y, -z + 2$.

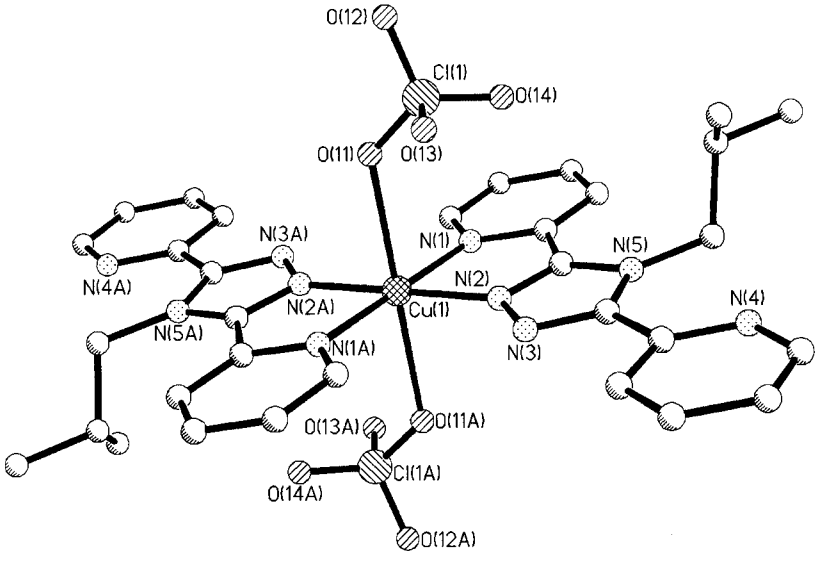

Figure 5. View of the molecular structure of $[Cu^{II}(ibdpt)_2(ClO_4)_2]$ (**4**). Hydrogen atoms have been omitted for clarity. Symmetry operation used to generate equivalent atoms: (A) $-x + 2, -y, -z + 2$.

to antiferromagnetic coupling across the two 1,2,4-triazole bridges. The corresponding magnetic moment data show a μ_{eff} value of 4.64 μ_B at room temperature which is a little reduced from typical weak-field octahedral cobalt(II) centres having $^4T_{1g}$ (d^7) ground states. Low symmetry ligand field effects, combined with spin-orbit coupling, cause splitting of these single-ion states and thus allow for the use of the Heisenberg–Van Vleck exchange Hamiltonian ($-2J\mathbf{S_1 \cdot S_2}$) for an $S = 3/2$ dimer as a reasonable approximation for fitting the data. A good fit was obtained using the parameters $J = -3.76$ cm^{-1}, $g = 2.45$, $TIP = 0$ cm^3 mol^{-1} and 0.2% monomer (in this and in all other cases all parameters were allowed to vary for the best fit except for *TIP* which was fixed). The high g value accounts for spin-orbit and orbital degeneracy effects. The value of J is similar to that obtained for related compounds incorporating NH_2dpt[19] and is somewhat less than observed for pyridazine-bridged systems.[32,33]

The dinuclear nickel(II) complex **6** also exhibits antiferromagnetic coupling. The fitted curve for the molar magnetic

 © 2005 Wiley-VCH Verlag GmbH & Co. KGaA, Weinheim

susceptibility reaches a maximum at 38 K (χ_m = 0.01142 $cm^3 mol^{-1}$) and the corresponding effective magnetic moment decreases from 2.81 μ_B at room temperature to 0.17 μ_B at 4.2 K (Figure S6, Supporting Information). The data were fitted extremely well to an $S = 1$ dimer–$2J\mathbf{S_1}\cdot\mathbf{S_2}$ model using $J = -13.0\ cm^{-1}$, $g = 2.08$, $TIP = 85\times10^{-6}\ cm^3 mol^{-1}$ and 0.3% monomer. The coupling is slightly stronger than that found in related doubly 1,2,4-triazole-bridged complexes incorporating NH_2dpt[19] but weaker than in doubly pyridazine-bridged derivatives ($J \approx -21\ cm^{-1}$).[33]

The analogous dinuclear copper(II) complex **7** shows quite strong antiferromagnetic coupling. Thus, the maximum in molar magnetic susceptibility is observed at 185 K (χ_m = 0.00093 $cm^3 mol^{-1}$) and the corresponding effective magnetic moment decreases from 1.39 μ_B at room temperature to 0.22 μ_B at 4.2 K (Figure 6). Monomer impurity is clearly evident in the susceptibility plot below ca. 50 K. Fitting to the Bleaney–Bowers $S = 1/2$ dimer model[34] yielded $J = -105\ cm^{-1}$, $g = 1.87$, $TIP = 60\times10^{-6}\ cm^3 mol^{-1}$ and 1.5% monomer. The g value is lower than expected for a tetragonally elongated copper(II) site which is probably due to the loss of the remaining MeCN solvate affecting the molar mass used in the calculation of the molar magnetic susceptibilities. The strong antiferromagnetic coupling is compatible with the triazole p orbitals of the two 1,2,4-triazole nitrogen donors coupling effectively with the $d(x^2–y^2)$ magnetic orbitals of the copper(II) centres within the planar six-membered $(Cu–N_{trz}–N_{trz})_2$ ring. Other doubly 1,2,4-triazole-bridged compounds with symmetrical bis(bidentate) ligands[35–37] have similar values of J while weaker coupling is found in systems incorporating the unsymmetrical anionic 3-(2-pyridyl)-1,2,4-triazolato ligand ($J \approx -50\ cm^{-1}$).[38,39] Interestingly, in $[Cu^{II}_2(NH_2dpt)(H_2O)_2(SO_4)_2]\cdot H_2O$,[20] containing a single 1,2,4-triazole bridge and an additional bridging sulfato co-ligand between the two copper(II) centres, the J value was found to be $-34.5\ cm^{-1}$, i. e. about one third of the value obtained here for the doubly 1,2,4-triazole-bridged system. Clearly, the poor superexchange pathway provided by a bidentate sulfate ion in combination with only one 1,2,4-triazole pathway leads to the diminution in J. The Cu···Cu separation in the present complex is significantly shorter than in the singly 1,2,4-triazole-bridged complex $[Cu^{II}_2(NH_2dpt)(H_2O)_2(SO_4)_2]\cdot H_2O$.[20] The $Cu–N_{trz}–N_{trz}$ angles of ca. 133–134° in the present complex are somewhat smaller than the corresponding angles of ca. 136–138° found in the unsymmetrical singly 1,2,4-triazole-bridged example. Haasnoot and coworkers[39] have concluded that $Cu–N_{trz}–N_{trz}$ angles of ca. 134° in symmetrical doubly 1,2,4-triazole-bridged systems lead to the largest possible coupling with $J \approx -120\ cm^{-1}$. The J value of $-105\ cm^{-1}$ observed here is only a little smaller than the predicted value.

Conclusions

The new ligand ibdpt was used to investigate the coordination chemistry of a 4-alkyl-substituted 3,5-di(2-pyridyl)-4*H*-1,2,4-triazole for the first time. We initially focused on the exploration of the dinucleation behaviour of this ligand. It has been found that, unlike with 4-aryl-substituted 3,5-di(2-pyridyl)-4*H*-1,2,4-triazoles, dinuclear complexes can be readily obtained. This result clearly supports our hypothesis that whether or not dinuclear complexes of bis(bidentate) 4-substituted 3,5-di(2-pyridyl)-4*H*-1,2,4-triazoles can be formed is strongly influenced by the nature of the actual substituent on N^4, including its electronic effect on the 1,2,4-triazole ring. In the resulting dinuclear doubly 1,2,4-triazole-bridged complexes the two metal centres have been found to be antiferromagnetically coupled. In light of these findings the synthesis of exchange-coupled dinuclear iron(II) spin crossover compounds of ibdpt and other 4-alkyl-3,5-di(2-pyridyl)-4*H*-1,2,4-triazoles[30] appears possible. Studies in this direction are currently underway and will be reported in due course.[16]

Experimental Section

General Remarks: All solvents used were laboratory reagent grade. $Co(ClO_4)_2\cdot 6H_2O$, $Ni(ClO_4)_2\cdot 6H_2O$ and $Cu(ClO_4)_2\cdot 6H_2O$ were purchased from Aldrich and used as received. 4-Isobutyl-3,5-di(2-pyridyl)-4*H*-1,2,4-triazole (ibdpt) was prepared as described elsewhere.[22,30] Elemental analyses were carried out by the Campbell Microanalytical Laboratory at the University of Otago. Infrared spectra were recorded over the range 4000–400 cm^{-1} with a Perkin–Elmer Spectrum BX FT-IR spectrophotometer. ESI mass spectra were run with a MicroMass LCT mass spectrometer at the University of Canterbury. X-ray data were collected with a Bruker SMART CCD area detector using graphite-monochromated Mo-K_α radiation (λ = 0.71073 Å). The structures were solved by direct methods with SIR-92[40] and refined against F^2 using all data by full-matrix least-squares techniques with SHELXL-97.[41] Magnetic data were recorded over the range 300–4.2 K with a Quantum Design MPMS5 SQUID magnetometer with an applied field of 1 T.

Caution: While no problems were encountered in the course of this work, ClO_4^- salts are potentially explosive and should be handled with appropriate care!

$[Co^{II}_2(ibdpt)_2(MeCN)_2(H_2O)_2](ClO_4)_4$ (1) and $Co^{II}_2(ibdpt)_2(ClO_4)_4(MeCN)(H_2O)$ (5): An orange solution of $Co(ClO_4)_2\cdot 6H_2O$ (366 mg, 1.00 mmol) in MeCN (5 mL) was added to a colourless solution of ibdpt (279 mg, 1.00 mmol) in MeCN (35 mL). The resulting orange solution was stirred at room temperature for 2 hours before it was subjected to vapour diffusion of Et_2O. This afforded crystalline $[Co^{II}_2(ibdpt)_2(MeCN)_2(H_2O)_2](ClO_4)_4$ (**1**) as a mixture of the red-orange polymorph **1a** and the yellow-orange polymorph **1b** which were both identified by X-ray diffraction. The ratio of the two crystal types was variable and they both readily lost solvent when taken out of their mother liquor which in the case of the yellow-orange polymorph **1b** was accompanied by a colour change to red-orange while no colour change was observed for the red-orange polymorph **1a**. A bulk sample of complex **1** was dried in vacuo to give 541 mg (95%) of $Co^{II}_2(ibdpt)_2(ClO_4)_4(MeCN)(H_2O)$ (**5**) as dull red-orange crystals. This material was used for further characterisation and magnetic studies. $C_{34}H_{39}Cl_4Co_2N_{11}O_{17}$ (1133.43): calcd. C 36.03, H 3.47, N 13.59; found C 35.81, H 3.56, N 13.66. IR (KBr): $\tilde{\nu}$ = 3374, 2966, 1607, 1579, 1511, 1498, 1467, 1436, 1394, 1299, 1280, 1248, 1145, 1117, 1083, 1027, 1002, 940, 928, 793, 760, 744, 709, 688, 668, 636, 626, 515, 417 cm^{-1}. ESI-

 © 2005 Wiley-VCH Verlag GmbH & Co. KGaA, Weinheim

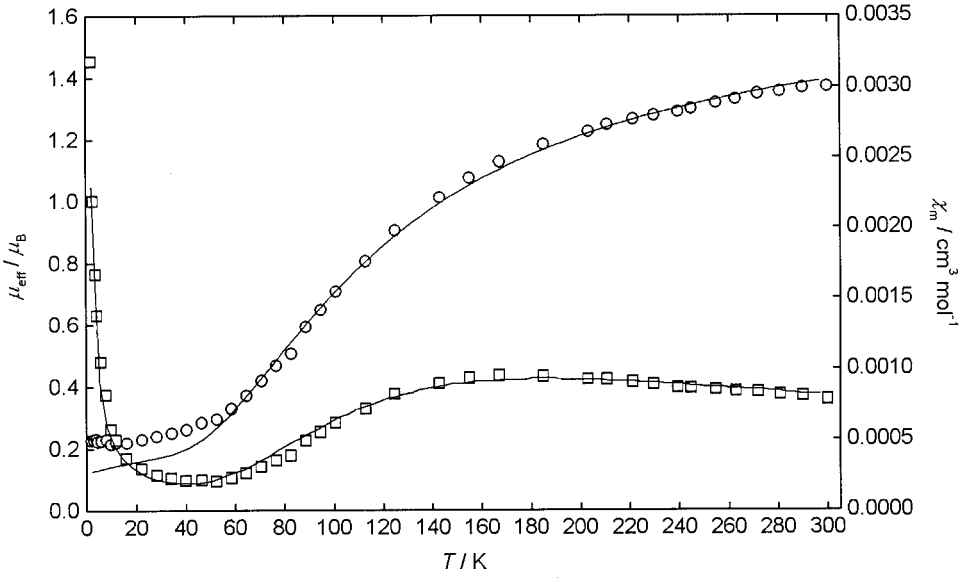

Figure 6. Temperature dependence of the effective magnetic moment μ_{eff} (○) and the molar magnetic susceptibility χ_m (□) per copper centre for $Cu^{II}_2(ibdpt)_2(ClO_4)_4(MeCN)$ (**7**). The solid line represents the best fit: $J = -105\ cm^{-1}$, $g = 1.87$, $TIP = 60 \times 10^{-6}\ cm^3 mol^{-1}$, 1.5% monomer.

MS (pos., MeCN): *m*/*z* = 308.6 $[Co(ibdpt)_2]^{2+}$, 329.1 $[Co(ibdpt)_2(MeCN)]^{2+}$, 448.2 $[Co(ibdpt)_3]^{2+}$, 478.1 $[Co(ibdpt)(MeCN)(ClO_4)]^+$, 716.2 $[Co(ibdpt)_2(ClO_4)]^+$, 973.0 $[Co_2(ibdpt)_2(ClO_4)_3]^+$, 995.4 $[Co(ibdpt)_3(ClO_4)]^+$, 1254.2 $[Co_2(ibdpt)_3(ClO_4)_3]^+$, 1531.5 $[Co_2(ibdpt)_4(ClO_4)_3]^+$.

$[Ni^{II}_2(ibdpt)_2(MeCN)_4](ClO_4)_4$ (2) and $Ni^{II}_2(ibdpt)_2(ClO_4)_4(MeCN)$ (6): A blue solution of $Ni(ClO_4)_2{\cdot}6H_2O$ (366 mg, 1.00 mmol) in MeCN (5 mL) was added to a colourless solution of ibdpt (279 mg, 1.00 mmol) in MeCN (35 mL). The resulting purple solution was stirred at room temperature for 2 hours before it was subjected to vapour diffusion of Et_2O. This afforded $[Ni^{II}_2(ibdpt)_2(MeCN)_4](ClO_4)_4$ (**2**) as purple crystals which were identified by X-ray diffraction. The crystals readily lost solvent when taken out of their mother liquor. A bulk sample of complex **2** was dried in vacuo to yield 547 mg (98%) of $Ni^{II}_2(ibdpt)_2(ClO_4)_4(MeCN)$ (**6**) as dull purple crystals. This material was used for further characterisation and magnetic studies. $C_{34}H_{37}Cl_4N_{11}Ni_2O_{16}$ (1114.92): calcd. C 36.63, H 3.34, N 13.82; found C 36.30, H 3.56, N 14.16. IR (KBr): $\tilde{\nu}$ = 3334, 2967, 1606, 1577, 1510, 1465, 1437, 1397, 1379, 1283, 1245, 1145, 1118, 1082, 1032, 1000, 940, 929, 791, 756, 710, 686, 668, 636, 626, 514, 418 cm^{-1}. ESI-MS (pos., MeCN): *m*/*z* = 308.1 $[Ni(ibdpt)_2]^{2+}$, 328.7 $[Ni(ibdpt)_2(MeCN)]^{2+}$, 447.7 $[Ni(ibdpt)_3]^{2+}$, 477.1 $[Ni(ibdpt)(MeCN)(ClO_4)]^+$, 715.2 $[Ni(ibdpt)_2(ClO_4)]^+$, 975.0 $[Ni_2(ibdpt)_2(ClO_4)_3]^+$, 994.4 $[Ni(ibdpt)_3(ClO_4)]^+$, 1252.2 $[Ni_2(ibdpt)_3(ClO_4)_3]^+$, 1533.5 $[Ni_2(ibdpt)_4(ClO_4)_3]^+$.

$[Cu^{II}_2(ibdpt)_2(MeCN)_2(ClO_4)_2](ClO_4)_2{\cdot}2MeCN$ (3) and $Cu^{II}_2(ibdpt)_2(ClO_4)_4(MeCN)$ (7): A blue solution of $Cu(ClO_4)_2{\cdot}6H_2O$ (371 mg, 1.00 mmol) in MeCN (5 mL) was added to a colourless solution of ibdpt (279 mg, 1.00 mmol) in MeCN (35 mL). The resulting blue solution was stirred at room temperature for 2 hours before it was subjected to vapour diffusion of Et_2O. This afforded $[Cu^{II}_2(ibdpt)_2(MeCN)_2(ClO_4)_2](ClO_4)_2{\cdot}2MeCN$ (**3**) as blue-green crystals along with a small amount of $[Cu^{II}(ibdpt)_2(ClO_4)_2]$ (**4**) as steel-blue crystals which were both identified by X-ray diffraction. The crystals of complex **3** readily lost solvent when taken out of their mother liquor. A bulk sample of complex **3** was dried in vacuo to give 485 mg (86%) of $Cu^{II}_2(ibdpt)_2(ClO_4)_4(MeCN)$ (**7**) as dull blue-green crystals. This material was used for further characterisation and magnetic studies. $C_{34}H_{37}Cl_4Cu_2N_{11}O_{16}$ (1124.64): calcd. C 36.31, H 3.32, N 13.70; found C 36.53, H 3.24, N 13.73. IR (KBr): $\tilde{\nu}$ = 3454, 2967, 1614, 1586, 1514, 1472, 1442, 1398, 1378, 1280, 1254, 1144, 1119, 1087, 1014, 929, 793, 763, 746, 710, 688, 667, 624, 507, 417 cm^{-1}. ESI-MS (pos., MeCN): *m*/*z* = 310.6 $[Cu(ibdpt)_2]^{2+}$, 331.1 $[Cu(ibdpt)_2(MeCN)]^{2+}$, 450.2 $[Cu(ibdpt)_3]^{2+}$, 482.1 $[Cu(ibdpt)(MeCN)(ClO_4)]^+$, 720.2 $[Cu(ibdpt)_2(ClO_4)]^+$, 983.0 $[Cu_2\text{-}(ibdpt)_2(ClO_4)_3]^+$, 1262.2 $[Cu_2(ibdpt)_3(ClO_4)_3]^+$, 1541.3 $[Cu_2\text{-}(ibdpt)_4(ClO_4)_3]^+$.

$[Cu^{II}(ibdpt)_2(ClO_4)_2]$ (4): A blue solution of $Cu(ClO_4)_2{\cdot}6H_2O$ (185 mg, 0.50 mmol) in MeCN (5 mL) was added to a colourless solution of ibdpt (279 mg, 1.00 mmol) in MeCN (5 mL). The resulting blue solution was stirred at room temperature for 24 hours during which time a precipitate formed. The solid was filtered off and washed with small amount of MeCN. Drying in vacuo gave 198 mg (48%) of $[Cu^{II}(ibdpt)_2(ClO_4)_2]$ (**4**) as a pale blue powder. $C_{32}H_{34}Cl_2CuN_{10}O_8$ (821.14): calcd. C 46.81, H 4.17, N 17.06; found C 46.64, H 4.10, N 16.98. IR (KBr): $\tilde{\nu}$ = 3447, 2971, 1612, 1584, 1497, 1460, 1428, 1395, 1310, 1280, 1247, 1171, 1131, 1054, 1021, 926, 796, 762, 751, 739, 712, 693, 668, 649, 623, 592 cm^{-1}. ESI-MS (pos., MeCN): *m*/*z* = 310.6 $[Cu(ibdpt)_2]^{2+}$, 383.1 $[Cu(ibdpt)(MeCN)]^+$, 621.2. $[Cu(ibdpt)_2]^+$, 785.1 $[Cu_2(ibdpt)_2(ClO_4)]^+$, 900.5 $[Cu(ibdpt)_3]^+$, 1064.3 $[Cu_2(ibdpt)_3(ClO_4)]^+$. Vapour diffusion of Et_2O into the mother liquor or a solution of the powder in MeCN gave steel-blue crystals of $[Cu^{II}(ibdpt)_2(ClO_4)_2]$ (**4**) which were identified by X-ray diffraction.

X-ray Crystallography: All non-hydrogen atoms, except N(90) to C(91) of the disordered MeCN solvate in complex **3**, were refined anistropically. All hydrogen atoms, except H(101) and H(102) of the axial H_2O co-ligands in complexes **1a** and **1b**, were placed at calculated positions using a riding model with thermal parameters 1.2 times the equivalent isotropic thermal parameters of the atom to which they were bonded. The hydrogen atoms of the H_2O co-ligands in complexes **1a** and **1b** were located from the difference maps and allowed to refine freely. In the structure of complex **2** one of the two methyl groups of the isobutyl moiety was disordered

 © 2005 Wiley-VCH Verlag GmbH & Co. KGaA, Weinheim

over two positions with site occupancy factors of 0.75 and 0.25 for C(17) and C(17′), respectively. One of the ClO_4^- ions was also disordered over two positions with a site occupancy factor of 0.50 for both Cl(2) to O(24) and Cl(3) to O(34). The structure of complex **3** featured two crystallographically independent moieties within the asymmetric unit. In one of the ClO_4^- ions three of the oxygen atoms were disordered over two positions with a site occupancy factor of 0.50 for both O(42) to O(44) and O(42′) to O(44′). One of the MeCN solvates was also disordered over two positions with site occupancy factors of 0.75 for N(80) to C(81) and 0.25 for N(90) to C(91). CCDC-250036 (**1a**), -250037 (**1b**), -250038 (**2**), -250039 (**3**) and -250040 (**4**) contain the supplementary crystallographic data for this paper. These data can be obtained free of charge from The Cambridge Crystallographic Data Centre via www.ccdc.cam.ac.uk/data_request/cif.

Supporting Information (see also the footnote on the first page of this article): A PDF file (five pages) with Supporting Information for this article is available on the internet under http://www.eurjic.org or from the authors. The file contains a view of the molecular structure of complex **1b** (Figure S1), an overlay of the molecular structures of complexes **1a** and **1b** (Figure S2), illustrations of the hydrogen bonding in complexes **1a** and **1b** (Figures S3 and S4, respectively) and the curves for the molar magnetic susceptibilities and effective magnetic moments of complexes **5** and **6** over the range 300–4.2 K (Figures S5 and S6, respectively).

Acknowledgments

This work was supported by a number of grants from the University of Otago (including a University of Otago Postgraduate Scholarship to MHK and a Bridging Grant) and the Australian Research Council (Discovery Grant). Mr. B. M. Clark (University of Canterbury) is thanked for running the ESI mass spectra and Dr. J. Hausmann (University of Otago) for helpful discussions. SB is grateful for the provision of sabbatical leave which has facilitated the completion of this manuscript and thanks her host Prof. A. K. Powell (University of Karlsruhe) for helpful discussions and the DFG Research Center for Functional Nanostructures (CFN) for the award of a Visiting Professorship.

[1] J. G. Haasnoot, *Coord. Chem. Rev.* **2000**, *200–202*, 131–185.
[2] M. H. Klingele, S. Brooker, *Coord. Chem. Rev.* **2003**, *241*, 119–132.
[3] U. Beckmann, S. Brooker, *Coord. Chem. Rev.* **2003**, *245*, 17–29.
[4] O. Kahn, E. Codjovi, *Phil. Trans. R. Soc. Lond. A* **1996**, *354*, 359–379.
[5] J. G. Haasnoot, in: *Magnetism: A Supramolecular Function* (Ed.: O. Kahn), Kluwer, Dordrecht, **1996**, pp. 299–321.
[6] L. G. Lavrenova, S. V. Larionov, *Koord. Khim.* **1998**, *24*, 403–420; *Russ. J. Coord. Chem.* **1998**, *24*, 379–395.
[7] P. J. van Koningsbruggen, *Top. Curr. Chem.* **2004**, *233*, 123–149.
[8] O. Kahn, J. P. Launay, *Chemtronics* **1988**, *3*, 140–151.
[9] J. Zarembowitch, O. Kahn, *New. J. Chem.* **1991**, *15*, 181–190.
[10] O. Kahn, J. Kröber, C. Jay, *Adv. Mater.* **1992**, *4*, 718–728.
[11] O. Kahn, C. J. Martinez, *Science* **1998**, *279*, 44–48.
[12] J.-F. Létard, P. Guionneau, L. Goux-Capes, *Top. Curr. Chem.* **2004**, *235*, 221–249.
[13] O. Kahn, Y. Garcia, J. F. Létard, C. Mathonière, in: *Supramolecular Engineering of Synthetic Metallic Materials: Conductors and Magnets* (Eds.: J. Veciana, C. Rovira, D. B. Amabilino), Kluwer, Dordrecht, **1998**, pp. 127–144.
[14] J. A. Real, A. B. Gaspar, V. Niel, M. C. Muñoz, *Coord. Chem. Rev.* **2003**, *236*, 121–141.
[15] M. H. Klingele, B. Moubaraki, J. D. Cashion, K. S. Murray, S. Brooker, *Chem. Commun.* **2005**, in press [DOI: 10.1039/b415891a].
[16] C. D. Brandt, M. Weitzer, B. Moubaraki, K. S. Murray, S. Brooker, unpublished results.
[17] V. Ksenofontov, A. B. Gaspar, V. Niel, S. Reiman, J. A. Real, P. Gütlich, *Chem. Eur. J.* **2004**, *10*, 1291–1298.
[18] J. A. Real, A. B. Gaspar, M. C. Muñoz, P. Gütlich, V. Ksenofontov, H. Spiering, *Top. Curr. Chem.* **2004**, *233*, 167–193.
[19] F. J. Keij, R. A. G. de Graaff, J. G. Haasnoot, J. Reedijk, *J. Chem. Soc., Dalton Trans.* **1984**, 2093–2097.
[20] P. J. van Koningsbruggen, D. Gatteschi, R. A. G. de Graaff, J. G. Haasnoot, J. Reedijk, C. Zanchini, *Inorg. Chem.* **1995**, *34*, 5175–5182.
[21] S. K. Mandal, H. J. Clase, J. N. Bridson, S. Ray, *Inorg. Chim. Acta* **1993**, *209*, 1–4.
[22] M. H. Klingele, PhD Thesis, University of Otago (New Zealand), **2004**.
[23] M. H. Klingele, P. D. W. Boyd, B. Moubaraki, K. S. Murray, S. Brooker, manuscript in preparation.
[24] S.-C. Shao, D.-R. Zhu, X.-H. Zhu, X.-Z. You, S. S. S. Raj, H.-K. Fun, *Acta Crystallogr. Sect. C* **1999**, *55*, 1412–1413.
[25] S. C. Shao, D. R. Zhu, T. W. Wang, Y. Zhang, S. S. S. Raj, H.-K. Fun, *Chin. Chem. Lett.* **2000**, *11*, 93–94.
[26] D. Zhu, Y. Song, Y. Liu, Y. Xu, Y. Zhang, X. You, *Transition Met. Chem.* **2000**, *25*, 589–593.
[27] D.-R. Zhu, Y. Song, Y. Xu, Y. Zhang, S. S. S. Raj, H.-K. Fun, X.-Z. You, *Polyhedron* **2000**, *19*, 2019–2025.
[28] D. Zhu, Y. Xu, Y. Mei, Y. Shi, C. Tu, X. You, *J. Mol. Struct.* **2001**, *559*, 119–125.
[29] D. Zhu, Y. Xu, Z. Yu, Z. Guo, H. Sang, T. Liu, X. You, *Chem. Mater.* **2002**, *14*, 838–843.
[30] M. H. Klingele, S. Brooker, *Eur. J. Org. Chem.* **2004**, 3422–3434.
[31] M. H. Klingele, S. Brooker, *Inorg. Chim. Acta* **2004**, *357*, 3413–3417.
[32] S. Brooker, D. J. de Geest, R. J. Kelly, P. G. Plieger, B. Moubaraki, K. S. Murray, G. B. Jameson, *J. Chem. Soc. Dalton Trans.* **2002**, 2080–2087.
[33] Y. Lan, D. K. Kennepohl, B. Moubaraki, K. S. Murray, J. D. Cashion, G. B. Jameson, S. Brooker, *Chem. Eur. J.* **2003**, *9*, 3772–3784.
[34] B. Bleaney, K. D. Bowers, *Proc. R. Soc. Lond. A* **1952**, *214*, 451–465.
[35] R. Prins, P. J. M. W. L. Birker, J. G. Haasnoot, G. C. Verschoor, J. Reedijk, *Inorg. Chem.* **1985**, *24*, 4128–4133.
[36] W. M. E. Koomen-van Oudenniel, R. A. G. de Graaff, J. G. Haasnoot, R. Prins, J. Reedijk, *Inorg. Chem.* **1989**, *28*, 1128–1133.
[37] P. J. van Koningsbruggen, J. G. Haasnoot, R. A. G. de Graaff, J. Reedijk, S. Slingerland, *Acta Crystallogr. Sect. C* **1992**, *48*, 1923–1926.
[38] P. M. Slangen, P. J. van Koningsbruggen, J. G. Haasnoot, J. Jansen, S. Gorter, J. Reedijk, H. Kooijman, W. J. J. Smeets, A. L. Spek, *Inorg. Chim. Acta* **1993**, *212*, 289–301.
[39] P. M. Slangen, P. J. van Koningsbruggen, K. Goubitz, J. G. Haasnoot, J. Reedijk, *Inorg. Chem.* **1994**, *33*, 1121–1126.
[40] A. Altomare, G. Cascarano, C. Giacovazzo, A. Guagliardi, M. C. Burla, G. Polidori, M. Camalli, *J. Appl. Crystallogr.* **1994**, *27*, 435.
[41] G. M. Sheldrick, T. R. Schneider, *Methods Enzymol.* **1997**, *277*, 319–343.

Received: September 21, 2004

Assisted Crystallization of Organometallic Cations by Interplay with Inorganic Anionic Clusters Units: Synthesis and Characterizations of the [Cp*(dppe)Fe–NCMe]$_2$·M_6L_{14} Series (M_6L_{14} = Cluster Unit: $[Re_6S_6Br_8]^{2-}$, $[Mo_6Br_{14}]^{2-}$ and $[Mo_6I_{14}]^{2-}$)

Guillaume Pilet,*[a–c] Kaplan Kirakci,[a] Frédéric de Montigny, Stéphane Cordier,[a] Claude Lapinte,[d] Christiane Perrin,[a] and André Perrin[a]

Keywords: Iron / Rhenium / Molybdenum octahedral clusters / M_6L_{14} units / Hybrid compounds / Inorganic organometallic chemistry / Single-crystal structures

Novel hybrid inorganic/organometallic compounds have been obtained from the crystallization of inorganic anionic clusters units with the [Cp*(dppe)Fe–NCMe]$^+$organometallic entity as the cationic counter part. After dissolution of $Cs_2M_6L_{14}$ (M_6L_{14} = $[Re_6S_6Br_8]^{2-}$, $[Mo_6Br_{14}]^{2-}$ and $[Mo_6I_{14}]^{2-}$) and [Cp*(dppe)Fe–NCMe]Cl precursors in acetonitrile at room temperature, the reaction proceeds by a metathesis of the Cl^- anion by $[M_6L_{14}]^{2-}$ anions and precipitation of CsCl. The crystal structures of the [Cp*(dppe)Fe–NCMe]$_2$[M_6L_{14}] series reveal that inorganic and organic entities can be assembled without any structural modifications to both partners whatever the M_6L_{14} unit. These properties of the M_6L_{14} cluster units could be extended for the crystallization of other novel organometallic cations when usual small counter anions do not lead to any crystallization with the new organometallic cation
(© Wiley-VCH Verlag GmbH & Co. KGaA, 69451 Weinheim, Germany, 2005)

Introduction

A wide variety of compounds based on M_6 clusters (M = Re, Mo) have been obtained by solid-state synthesis and extensively investigated.[1–5] Such compounds are built up from M_6L_{14} units (L = halogen, chalcogen) in which the M_6 cluster is face-capped by eight inner ligands (L^i) and six apical ligands (L^a) lie in terminal positions. The developed formula of the unit is then written as $M_6L^i{}_8L^a{}_6$ according to the H. Schäfer notation.[6] The condensation of units by means of apical-inner connections leads to solid-state compounds containing octahedral clusters with various physico-chemical properties such as superconductivity at high critical field,[7] catalytic[8] or redox intercalation behavior.[9] On the other hand, fascinating molecular and supramolecular assemblies based on axially substituted $M_6L^i{}_8$ cluster cores have been reported, particularly in rhenium cluster chemistry.[10] Their synthesis requires soluble cluster precursors with isolated $Re_6L^i{}_8L^a{}_6$ units. Numerous water-soluble cesium salts built up from isolated Re_6L_{14} units have been obtained from solid-state chemistry.[11] After dissolution in distilled water or acidic solutions, the $(TBA)_xRe_6L^i{}_8L^a{}_6$ series can be easily obtained by precipitation after addition of an excess of a TBA halide. The $(TBA)_xRe_6L^i{}_8L^a{}_6$ series, soluble in organic solvents, constitutes a set of relevant precursors for use in coordination chemistry.[1]

In this paper, we report the room-temperature synthesis and characterization of novel hybrid inorganic/organometallic compounds based on $[M_6L_{14}]^{2-}$ anionic units obtained by direct dissolution of $Cs_2M_6L_{14}$ in organic solvents ($[M_6L_{14}]^{2-}$ = $[Re_6S_6Br_8]^{2-}$, $[Mo_6Br_{14}]^{2-}$ and $[Mo_6I_{14}]^{2-}$). It will become evident that $[M_6L_{14}]^{2-}$ anionic units can be used to advantage in organometallic chemistry for the isolataton and characterization of new organometallic cations. Thus, the crystallization of large organometallic cations with small anions usually used in organometallic chemistry (for instance PF_6^-, BF_4^- or BPh_4^-), often affords single crystals with high mosaic spreads and low diffracting powers. Indeed, the quality of the single-crystal X-ray diffraction

[a] Institut de Chimie de Rennes, Laboratoire de Chimie du Solide et Inorganique Moléculaire, UMR 6511 CNRS – Université de Rennes 1,
Avenue du Général Leclerc, 35042 Rennes Cedex, France
[b] Arrhenius Laboratory, Department of Inorganic Chemistry, Stockholm University,
10691 Stockholm, Sweden
[c] Laboratoire des Multimatériaux et Interfaces, Université Claude Bernard Lyon 1, Bâtiment Berthollet,
43 Boulevard du 11 Novembre 1918, 69622 Villeurbanne Cedex, France
E-mail: guillaume@inorg.su.se
guillaume.pilet@univ-lyon1.fr
[d] Institut de Chimie de Rennes, Organométalliques et Catalyse: Chimie et Electrochimie Moléculaires, UMR 6509 CNRS – Université de Rennes 1,
Avenue du Général Leclerc, 35042 Rennes Cedex, France

 DOI: 10.1002/ejic.200400798 © 2005 Wiley-VCH Verlag GmbH & Co. KGaA, Weinheim

data often thwarts a structural solution or gives low reliability factors. The latter condition is the key point for obtaining accurate structural information on bond lengths and angles. In this work, we focused on the crystallization of the $[Cp^*(dppe)Fe–NCMe]^+$ organometallic cation with $[M_6L_{14}]^{2-}$ units ($[Re_6S_6Br_8]^{2-}$, $[Mo_6Br_{14}]^{2-}$ and $[Mo_6I_{14}]^{2-}$). The structures of the resultant $[Cp^*(dppe)Fe–NCMe]_2[M_6L_{14}]$ complexes, determined from single-crystal X-ray diffraction data, indicatee that inorganic and organic entities can be assembled without any structural modifications to both partners whatever the M_6L_{14} unit.

Single-Crystal X-ray Diffraction Analyses

Data Collection

Experimental details for $[Cp^*(dppe)FeNCCH_3]_2[Re_6(S_6Br_2)^iBr_6^a]$ (**1**), $[Cp^*(dppe)FeNCCH_3]_2[Mo_6Br_8{}^iBr_6^a]$ (**2**) and $[Cp^*(dppe)FeNCCH_3]_2[Mo_6I_8{}^iI_6^a]$ (**3**) are given in Table 1. Once the data processing had been performed by the KappaCCD analysis softwares,[12] the lattice constants were refined by least-squares refinements using 33851 reflections ($1.00° < \theta < 27.48°$), 10475 reflections ($2.55° < \theta < 27.48°$) and 14097 reflections ($2.72° < \theta < 30.03°$) for **1**, **2** and **3**, respectively. In each case, an absorption correction based on crystal shape was applied to the data sets with the ANALYTICAL program.[13]

Structure Solution and Refinement

The three compounds are isostructural and crystallize in the monoclinic system. According to the observed systematic extinctions, the structures were solved in the $P2_1/c$ space group (No. 14). The unit-cell parameters, crystal system, space group and refinement details are summarized in Table 1 for the three phases. The structures were solved by direct methods (SIR97 program[14]) combined with Fourier difference syntheses and refined against F using reflections with $I/\sigma(I) > 3$ (CRYSTALS program[15]).

In the case of the $[Cp^*(dppe)Fe–NCMe]_2[Re_6S_6Br_8]$ structure refinement, all ligand sites were at first considered as being occupied by bromine atoms. After several cycles of refinement, it turned out that only the inner sites were not fully occupied by bromine atoms. Sulfur atoms were then introduced to these inner sites with the same positions and the same atomic displacement parameters as those of the bromine atoms and for each crystallographic site the sum of the occupancies was restrained to the value corresponding to a fully occupied position. Afterwards, the two first constraints (on positional and atomic displacement parameters) were progressively relaxed during the convergence, leading to a final position in agreement with reliable Re–

Table 1. Crystallographic data[a] for $[Cp^*(dppe)Fe–NCCH_3]_2[Re_6S_6Br_8]$ (**1**), $[Cp^*(dppe)Fe–NCCH_3]_2[Mo_6Br_{14}]$ (**2**) and $[Cp^*(dppe)Fe–NCCH_3]_2[Mo_6I_{14}]$ (**3**).

	1	**2**	**3**
Refined formula	$Re_6S_{5.9(1)}S_{8.1(1)}Fe_2P_4N_2C_{76}$	$Mo_6Br_{14}Fe_2P_4N_2C_{76}$	$Mo_6I_{14}Fe_2P_4N_2C_{76}$
Formula mass (g mol^{-1})	3130.05	2870.80	3528.81
Crystallographic system	monoclinic	monoclinic	monoclinic
Unit-cell constants			
a [Å]	11.0059 (1)	10.9782 (1)	11.1154 (1)
b [Å]	24.0960 (3)	24.4768 (3)	25.3927 (2)
c [Å]	17.7444 (3)	17.6397 (2)	18.0104 (2)
β [°]	107.5597 (5)	107.1463 (8)	106.4890 (4)
V [Å^3]	4486.5 (1)	4529.32 (9)	4874.38 (8)
Space group	$P2_1/c$ (No. 14)	$P2_1/c$ (No. 14)	$P2_1/c$ (No. 14)
Z	2	2	2
T [K]	293	293	293
Density [g cm^{-3}]	2.32	2.10	2.40
μ [mm^{-1}]	122.29	73.98	55.70
θ range [°]	1.47; 27.48	2.55; 27.48	2.72; 30.03
Index range			
h	–14; 14	–14; 11	–15; 14
k	–30; 31	–31; 31	–35; 35
l	–23; 23	–21; 22	–25; 22
R[b]	0.0283	0.0362	0.0331
R_w[c]	0.0328	0.0422	0.0406
S	1.13	1.11	1.10
$\Delta\rho_{max}$ [e$^-$ Å^{-3}]	1.00	1.06	1.71
$\Delta\rho_{min}$ [e$^-$ Å^{-3}]	–1.12	–0.90	–1.22
No. of reflections used	4776	6617	8570
No. of parameters	514	470	470

[a] All data collected with Mo-K_α radiation (λ = 0.71069 Å). [b] $R = \Sigma(|F_o - F_c|)/\Sigma|F_o|$. [c] $R_w = \{\Sigma[w(|F_o - F_c|)^2]/\Sigma[w|F_o|^2]\}^{1/2}$.

 © 2005 Wiley-VCH Verlag GmbH & Co. KGaA, Weinheim

Br and Re–S interatomic distances. Therefore, the chemical formula deduced from the X-ray diffraction refinement, $[Cp^*(dppe)Fe–NCMe]_2[(Re_6S^i_{5.9(1)}S^i_{2.1(1)})Br^a_6]$, is in good agreement with the EDS analyses.

All atoms of the cationic unit are located in 4*e* general crystallographic Wyckoff positions and were successfully refined anisotropically for the three structures (Figure 1). The refined formulae for **1**, **2** and **3** are given in Table 1. Atomic positions, equivalent thermal factors and occupancy factors are given in Table 2, Table 4 and Table 6. Meaningful bond lengths are summarized in Table 3, Table 5 and Table 7. All the thermal atomic displacements were refined anisotropically.

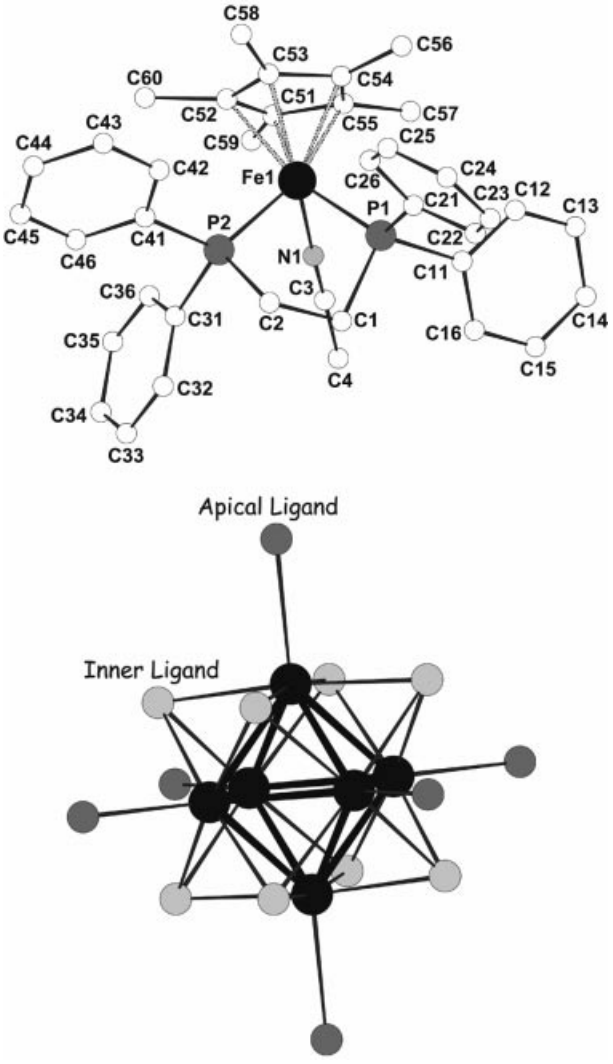

Figure 1. (a) Representation of the $[Cp^*(dppe)Fe–NCCH_3]^+$ cationic complex. The same labelling is used for the three structures. (b) Description of the $[Me_6L_{14}]$ (Me = Re, Mo; L = S, Br, I) anionic cluster entity.

Results

Structure of $[Cp^*(dppe)Fe–NCMe]_2[Re_6S_6Br_8]$

The structure of $[Cp^*(dppe)Fe–NCMe]_2[Re_6S_6Br_8]$ is based on a discrete $[Re_6S^i_6Br^i_2Br^a_6]^{2-}$ centrosymmetric cluster anion with an $(Re_6S^i_6Br^i_2)^{4+}$ cluster core. The Re_6 octahedron is slightly distorted and is inscribed into a cube of eight μ_3-S/Br atoms (inner ligands). Among the four independent inner ligand sites, all are randomly occupied by sulfur and bromine atoms [L^i1 = 0.39(1) S + 0.61(1) Br; L^i2 = 0.807(9) S + 0.193(9) Br; L^i3 = 0.903(8) S + 0.097(8) Br; L^i4 = 0.843(7) S + 0.157(7) Br]. The six apical positions are fully occupied by bromine atoms. The bond length ranges within the cluster unit are 2.5889(5)–2.6157(5) Å for Re–Re; 2.533(1)–2.5386(9) Å for Re–Br^a; 2.49(2)–2.66(5) Å for Re–Br^i and 2.403(7)–2.53(2) Å for Re–S^i (Table 3). These bond lengths correspond, within the s.u.'s, to those observed in the starting $Cs_2Re_6S_8Br_8$ cluster precursor. Indeed the substitution of $[Cp^*(dppe)Fe–NCMe]^+$ for Cs^+ does not influence the Re–Br^a bond length which is the most sensitive to a change in the counter cation in solid-state compounds.[16]

The bond lengths within the $[Cp^*(dppe)Fe–NCMe]^+$ cation in $[Cp^*(dppe)Fe–NCMe]_2[Re_6S_6Br_8]$ corresponds to those found in $[Cp^*(dppe)Fe–NCMe][PF_6]$.[17] The Fe^{II} atom is located in an environment built from a pentamethylcyclopentadienyl (Cp^*: $C_{10}H_{15}$), a P–$(CH_2)_2$–P bridge connected to four phenyl groups (dppe) and a molecule of acetonitrile (NCMe).

The Fe–C interatomic distances [2.097(9)–2.14(1) Å] and C–C bond lengths [1.41(2)–1.44(1) Å and 1.48(2)–1.55 (2) Å for C_5 ring and $C_5(CH_3)_5$, respectively] inside the Cp^* ligand are in good agreement with those generally observed for this kind of aromatic ring (average Fe–C distance equal to 2.11 Å, for example).[18–20]

Other selected interatomic distances are Fe–P [2.228(3)–2.258(3) Å], Fe–$NCCH_3$ [1.909(8) Å], P–C [1.833(9)–1.860(9) Å] and C–C [1.53(1) Å for the bridge, 1.34(2)–1.43(2) Å for aromatic rings inside the –P–$(CH_2)_2$–P– bridge], N–CCH_3 [1.15(1) Å] and NC–CH_3 [1.46(2) Å].

Structure of $[Cp^*(dppe)Fe–NCMe]_2[Mo_6Br_{14}]$

The anionic unit of the $[Cp^*(dppe)Fe–NCMe]_2[Mo_6Br_{14}]$ structure contains a slightly distorted Mo_6 octahedron. All the inner and apical positions of the cluster are occupied by bromine atoms. The chemical formula deduced from the X-ray diffraction refinement is $[Cp^*(dppe)Fe–NCMe]_2$-$[Mo_6Br_{14}]$ which fully corroborates with the EDS analysis. The ranges for the bond lengths within the cluster unit are 2.6358(6)–2.6437(6) Å for Mo–Mo, 2.5921(7)–2.6000(6) Å for Mo–Br^a and 2.5960(6)–2.6103(6) Å for Mo–Br^i (Table 5). Such values are comparable with data previously reported for the starting compound $Cs_2Mo_6Br_{14}$[23] (see Table 8). Indeed, the $[Cp^*(dppe)Fe–NCMe]^+$ cation does not influence the intra-unit bond lengths. The interatomic distances observed within the organometallic partner are very close to those observed in **1**.

Structure of $[Cp^*(dppe)Fe–NCMe]_2[Mo_6I_{14}]$

The structure of $[Cp^*(dppe)Fe–NCMe]_2[Mo_6I_{14}]$ is built from a slightly distorted Mo_6 octahedral cluster surrounded

 © 2005 Wiley-VCH Verlag GmbH & Co. KGaA, Weinheim

Table 2. Atomic positions for $[Cp^*(dppe)Fe–NCCH_3]_2[Re_6S_6Br_8]$ (**1**).

Atom	Wyckoff position	*x*/*a*	*y*/*b*	*z*/*c*	$U(iso)_{eq.}$	Occ.
Re1	4*e*	0.41878(3)	0.54389(1)	0.91480(2)	0.0397	1
Re2	4*e*	0.52424(3)	0.44678(1)	0.93159(2)	0.0406	1
Re3	4*e*	0.65319(3)	0.53265(1)	0.00322(2)	0.0390	1
Br1	4*e*	0.3091(1)	0.60362(4)	0.79586(6)	0.0589	1
Br2	4*e*	0.5566(1)	0.37343(5)	0.83721(7)	0.0674	1
Br3	4*e*	0.86506(9)	0.57564(4)	0.00619(6)	0.0529	1
S1[a]	4*e*	0.252(2)	0.560(1)	0.975(1)	0.1009	0.39(1)
Br11[a]	4*e*	0.2425(3)	0.5646(2)	0.9820(3)	0.0470	0.61(1)
S2[a]	4*e*	0.5420(7)	0.6223(3)	0.9859(5)	0.0439	0.807(9)
Br21[a]	4*e*	0.545(2)	0.6264(5)	0.991(1)	0.0774	0.193(9)
S3[a]	4*e*	0.3051(6)	0.4609(2)	0.8560(7)	0.0447	0.903(8)
Br31[a]	4*e*	0.297(3)	0.460(1)	0.841(3)	0.0679	0.097(8)
S4[a]	4*e*	0.5882(7)	0.5215(3)	0.8606(4)	0.0565	0.843(7)
Br41[a]	4*e*	0.595(2)	0.5221(4)	0.8538(8)	0.0521	0.157(7)
Fe1	4*e*	–0.1005(1)	0.31715(5)	0.58432(7)	0.0421	1
P1	4*e*	0.0904(2)	0.32193(9)	0.5655(1)	0.0420	1
P2	4*e*	–0.0989(2)	0.41082(9)	0.5824(1)	0.0451	1
C1	4*e*	0.1539(9)	0.3919(4)	0.6001(6)	0.0504	1
C2	4*e*	0.0480(9)	0.4330(4)	0.5596(6)	0.0536	1
N1	4*e*	–0.0035(7)	0.3187(3)	0.6934(5)	0.0467	1
C3	4*e*	0.055(1)	0.3180(4)	0.7588(6)	0.0539	1
C4	4*e*	0.133(2)	0.3194(6)	0.8413(7)	0.0919	1
C30	4*e*	0.2138(8)	0.2743(4)	0.6225(5)	0.0453	1
C31	4*e*	0.2144(9)	0.2186(4)	0.5980(6)	0.0553	1
C32	4*e*	0.3014(9)	0.1808(4)	0.6418(7)	0.0611	1
C33	4*e*	0.395(1)	0.1982(4)	0.7106(7)	0.0661	1
C34	4*e*	0.397(1)	0.2527(5)	0.7334(7)	0.0750	1
C35	4*e*	0.3087(9)	0.2904(4)	0.6903(6)	0.0596	1
C40	4*e*	0.1167(8)	0.3232(4)	0.4684(5)	0.0479	1
C41	4*e*	0.237(1)	0.3146(5)	0.4610(6)	0.0672	1
C42	4*e*	0.256(1)	0.3264(7)	0.3887(8)	0.0913	1
C43	4*e*	0.161(1)	0.3456(7)	0.3242(7)	0.0884	1
C44	4*e*	0.042(1)	0.3521(6)	0.3314(7)	0.0825	1
C45	4*e*	0.015(1)	0.3401(5)	0.4036(5)	0.0586	1
C50	4*e*	–0.0867(9)	0.4430(4)	0.6777(5)	0.0488	1
C51	4*e*	–0.009(1)	0.4891(5)	0.7071(6)	0.0629	1
C52	4*e*	–0.009(1)	0.5129(6)	0.7800(7)	0.0806	1
C53	4*e*	–0.084(1)	0.4933(6)	0.8206(7)	0.0776	1
C54	4*e*	–0.163(1)	0.4465(5)	0.7929(8)	0.0812	1
C55	4*e*	–0.162(1)	0.4228(5)	0.7225(7)	0.0720	1
C60	4*e*	–0.2196(9)	0.4544(4)	0.5135(6)	0.0524	1
C61	4*e*	–0.246(1)	0.4458(4)	0.4335(6)	0.0618	1
C62	4*e*	–0.339(1)	0.4789(5)	0.3776(7)	0.0718	1
C63	4*e*	–0.403(1)	0.5203(5)	0.4067(9)	0.0789	1
C64	4*e*	–0.374(1)	0.5292(5)	0.4866(8)	0.0730	1
C65	4*e*	–0.2826(9)	0.4962(4)	0.5407(7)	0.0641	1
C70	4*e*	–0.235(1)	0.2674(4)	0.6176(7)	0.0610	1
C71	4*e*	–0.2992(9)	0.3050(5)	0.5577(8)	0.0677	1
C72	4*e*	–0.262(1)	0.2932(5)	0.4886(7)	0.0709	1
C73	4*e*	–0.1725(9)	0.2488(4)	0.5068(6)	0.0543	1
C74	4*e*	–0.1540(8)	0.2339(4)	0.5880(6)	0.0494	1
C80	4*e*	–0.250(1)	0.2629(5)	0.6989(8)	0.0812	1
C81	4*e*	–0.406(1)	0.3452(6)	0.562(1)	0.0984	1
C82	4*e*	–0.329(1)	0.3136(6)	0.4044(8)	0.1026	1
C83	4*e*	–0.123(1)	0.2187(5)	0.4500(6)	0.0687	1
C84	4*e*	–0.070(1)	0.1869(5)	0.6298(7)	0.0705	1

[a] For inner ligands, these atoms correspond to a split position.

by eight inner iodine ligands and six apical iodine ligands. As expected, owing to the larger ionic radius of iodine face-capping ligands compared with bromine, the Mo–Mo bonds are longer in $[Cp^*(dppe)Fe–NCMe]_2[Mo_6I_{14}]$ than in $[Cp^*(dppe)Fe–NCMe]_2[Mo_6Br_{14}]$. The chemical formula deduced from the X-ray diffraction refinement is $[Cp^*(dppe)Fe–NCMe]_2[Mo_6I_{14}]$ which is fully consistent with the EDS analysis. The bond length ranges within the

 © 2005 Wiley-VCH Verlag GmbH & Co. KGaA, Weinheim

Table 3. Selected interatomic distances [Å] for $[Cp^*(dppe)Fe–NCCH_3]_2[Re_6S_6Br_8]$ (**1**).

Anionic unit: $[Re_6(S_6Br_2)^iBr^a_8]^{2-}$					
Re–Re bond lengths					
Re1–Re2	2.5890(5)	Re1–Re3	2.5979(5)	Re1–Re3	2.6154(5)
Re1–Re2	2.6157(5)	Re2–Re3	2.6000(5)	Re2–Re3	2.6118(5)
$Re–Br^a$ bond lengths (^{a}: apical ligand)					
Re1–Br1	2.5386(9)	Re2–Br2	2.533(1)	Re3–Br3	2.538(1)
$Re–Br^i$ bond lengths (^{i}: inner ligand)					
Re1–Br11	2.613(5)	Re1–Br21	2.56(1)	Re1–Br31	2.56(2)
Re1–Br41	2.54(1)	Re2–Br11	2.577(3)	Re2–Br21	2.49(2)
Re2–Br31	2.55(2)	Re2–Br41	2.54(1)	Re3–Br11	2.587(5)
Re3–Br21	2.53(1)	Re3–Br31	2.66(5)	Re3–Br41	2.55(1)
$Re–S^i$ bond lengths (^{i}: inner ligand)					
Re1–S1	2.42(2)	Re1–S2	2.442(7)	Re1–S3	2.422(5)
Re1–S4	2.403(7)	Re2–S1	2.53(2)	Re2–S2	2.467(7)
Re2–S3	2.404(5)	Re2–S4	2.421(7)	Re3–S1	2.45(2)
Re3–S2	2.455(7)	Re3–S3	2.41(1)	Re3–S4	2.428(7)
Cationic unit: $[Cp^*(dppe)Fe–NCCH_3]^+$					
Fe–X distances and bond lengths					
X = Cp*					
Fe1–C70	2.13(1)	Fe1–C71	2.11(1)	Fe1–C72	2.14(1)
Fe1–C73	2.138(9)	Fe1–C74	2.097(9)		
X = (dppe)					
Fe1–P1	2.228(3)	Fe1–P2	2.258(3)		
$X = NCCH_3$					
Fe1–N1	1.909(8)				
Cp* intra-bond lengths					
C70–C71	1.41(3)	C71–C72	1.43(2)	C72–C73	1.43(2)
C73–C74	1.44(1)	C74–C70	1.42(1)		
C70–C80	1.50(2)	C71–C81	1.55(2)	C72–C82	1.53(2)
C73–C83	1.48(2)	C74–C84	1.51(1)		
(dppe) intra-bond lengths					
P1–C1	1.857(9)	C1–C2	1.53(1)	C2–P2	1.860(9)
P1–C30	1.833(9)	P1–C40	1.831(9)	P2–C50	1.83(1)
P2–C60	1.839(9)				
C30–C31	1.41(1)	C31–C32	1.38(1)	C32–C33	1.40(1)
C33–C34	1.37(2)	C34–C35	1.38(1)	C35–C30	1.39(1)
C40–C41	1.39(1)	C41–C42	1.39(2)	C42–C43	1.38(2)
C43–C42	1.38(2)	C44–C45	1.43(2)	C45–C40	1.40(1)
C50–C51	1.40(1)	C51–C52	1.41(2)	C52–C53	1.34(2)
C53–C54	1.41(2)	C54–C55	1.38(2)	C55–C50	1.39(2)
C60–C61	1.38(1)	C61–C62	1.43(1)	C62–C63	1.40(2)
C63–C64	1.37(2)	C64–C65	1.41(1)	C65–C60	1.39(1)
$–NCCH_3$ intra-bond lengths					
N1–C3	1.15(1)	C3–C4	1.46(2)		

anionic unit are 2.6745(5)–2.6878(6) Å for Mo–Mo, 2.8408(5)–2.8467(5) Å for $Mo–I^a$ and 2.7665(5)–2.7889(5) Å for $Mo–I^i$ (Table 7). These distances are in good agreement with those found in the starting compound $Cs_2Mo_6I_{14}$[23] (see Table 8). The interatomic distances within the organometallic cation are identical to the values observed in **1** and **2**.

General Description of the Three Structures

The structures of the three original compounds are based on discrete $[M_6L_{14}]^{2-}$ anions (M = Mo, Re; L = Br, I, S) located at the corners and the centre of two opposite faces of the unit-cell (Figure 2), thus forming a pseudo-*A*-centered monoclinic unit-cell. Owing to the symmetry of the cationic $[Cp^*(dppe)Fe–NCMe]^+$ group, the space group is $P2_1/n$ and the systematic extinctions corresponding to the *A* lattice are not observed. The structural cohesion results from coulombic interactions between anionic inorganic units and cationic entities based on organo–iron molecules.

The structures of the compounds in the $[Cp^*(dppe)Fe–NCMe]_2{\cdot}M_6L_{14}$ series can be described in each case as a succession of $[M_6L_{14}]^{2-}$ anionic units layers and cationic layers. The layers of anionic entities are planar whilst the layers of $[Cp^*(dppe)Fe–NCMe]^+$ cations are puckered along the *a* axis of the unit-cell (Figure 3). The shortest Fe–Fe distances between two consecutive cationic planes are equal to 11.01, 10.98 and 11.12 Å for $[Cp^*(dppe)Fe–NCMe]_2[Re_6S_6Br_8]$, $[Cp^*(dppe)Fe–NCMe]_2[Mo_6Br_{14}]$ and $[Cp^*(dppe)Fe–NCMe]_2[Mo_6I_{14}]$, respectively. The shortest Fe–Fe distances within the puckered plane of cations are 9.44, 9.83 and 9.74 Å for these three compounds, respectively. For comparison, the Fe–Fe distance in $[Cp^*(dppe)Fe–NCMe][PF_6]$ is 9.099 Å.

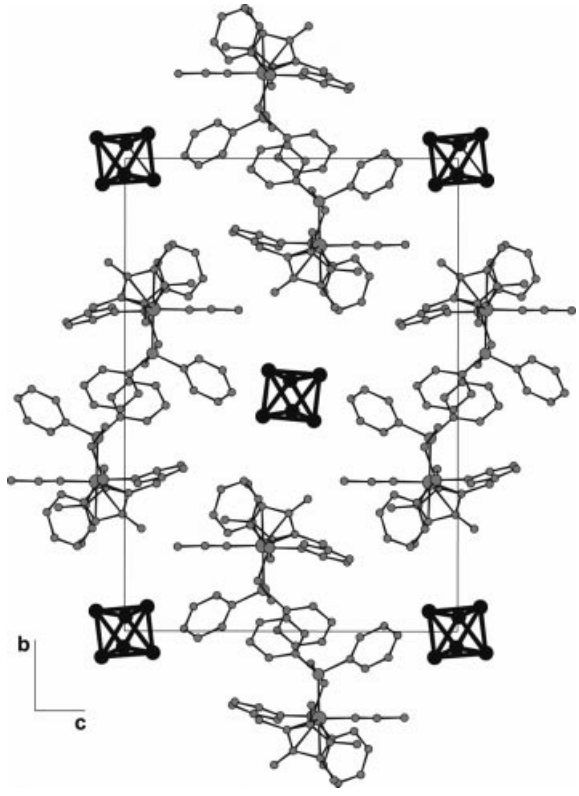

Figure 2. $[Cp^*(dppe)Fe–NCCH_3]_2[Me_6L_{14}]$ (Me = Re, Mo; L = S, Br, I) structure projection in the (*b*,*c*) plane of the unit-cell. For clarity, cluster ligands have been removed.

 © 2005 Wiley-VCH Verlag GmbH & Co. KGaA, Weinheim

Table 4. Atomic positions for $[Cp^*(dppe)Fe–NCCH_3]_2[Mo_6Br_{14}]$ (**2**).

Atom	Wyckoff position	*x/a*	*y/b*	*z/c*	$U(iso)_{equiv.}$	Occ.
Mo1	4*e*	0.47207(4)	0.05236(2)	0.06998(2)	0.0341	1
Mo2	4*e*	0.34605(4)	–0.03384(2)	–0.00290(2)	0.0334	1
Mo3	4*e*	0.58474(4)	–0.04383(2)	0.08587(2)	0.0339	1
Br1	4*e*	0.23650(5)	0.06150(2)	–0.01869(3)	0.0409	1
Br2	4*e*	0.40469(5)	–0.02484(2)	0.15091(3)	0.0403	1
Br3	4*e*	0.53910(5)	0.12851(2)	–0.01209(3)	0.0427	1
Br4	4*e*	0.70768(5)	0.04185(2)	0.15669(3)	0.0418	1
Br5	4*e*	0.13158(5)	–0.07986(2)	–0.00518(3)	0.0470	1
Br6	4*e*	0.69729(6)	–0.10414(2)	0.20771(3)	0.0510	1
Br7	4*e*	0.43641(6)	0.12481(2)	0.16849(4)	0.0585	1
Fe1	4*e*	0.10199(6)	0.18095(3)	0.41408(4)	0.0355	1
P1	4*e*	0.0984(1)	0.08889(5)	0.41616(8)	0.0393	1
P2	4*e*	–0.0893(1)	0.17715(5)	0.43394(7)	0.0364	1
C1	4*e*	–0.0495(5)	0.0677(2)	0.4388(4)	0.0461	1
C2	4*e*	–0.1517(5)	0.1090(2)	0.3992(3)	0.0448	1
N1	4*e*	0.0039(4)	0.1811(2)	0.3053(2)	0.0398	1
C3	4*e*	–0.0562(6)	0.1834(2)	0.2405(3)	0.0480	1
C4	4*e*	–0.1321(8)	0.1854(3)	0.1580(4)	0.0769	1
C30	4*e*	0.2185(5)	0.0458(2)	0.4848(3)	0.0425	1
C31	4*e*	0.2836(6)	0.0047(3)	0.4586(4)	0.0549	1
C32	4*e*	0.3740(6)	–0.0276(3)	0.5126(4)	0.0628	1
C33	4*e*	0.3996(6)	–0.0195(3)	0.5921(5)	0.0641	1
C34	4*e*	0.3333(7)	0.0204(3)	0.6204(4)	0.0653	1
C35	4*e*	0.2421(6)	0.0525(3)	0.5663(4)	0.0560	1
C40	4*e*	0.0838(5)	0.0557(2)	0.3205(3)	0.0426	1
C41	4*e*	0.0166(6)	0.0074(3)	0.2968(4)	0.0564	1
C42	4*e*	0.0150(7)	–0.0173(3)	0.2251(4)	0.0615	1
C43	4*e*	0.0786(7)	0.0067(3)	0.1767(4)	0.0639	1
C44	4*e*	0.1452(7)	0.0538(3)	0.1983(4)	0.0639	1
C45	4*e*	0.1492(6)	0.0786(3)	0.2716(4)	0.0548	1
C50	4*e*	–0.2125(5)	0.2239(2)	0.3776(3)	0.0406	1
C51	4*e*	–0.2085(5)	0.2788(2)	0.4009(3)	0.0484	1
C52	4*e*	–0.2972(6)	0.3157(3)	0.3578(4)	0.0562	1
C53	4*e*	–0.3931(6)	0.2999(3)	0.2923(4)	0.0610	1
C54	4*e*	–0.3991(6)	0.2455(3)	0.2687(4)	0.0637	1
C55	4*e*	–0.3096(6)	0.2075(2)	0.3112(3)	0.0511	1
C60	4*e*	–0.1168(5)	0.1760(2)	0.5309(3)	0.0458	1
C61	4*e*	–0.2383(6)	0.1839(3)	0.5383(4)	0.0619	1
C62	4*e*	–0.2582(7)	0.1745(4)	0.6127(4)	0.0768	1
C63	4*e*	–0.1613(8)	0.1558(4)	0.6767(4)	0.0790	1
C64	4*e*	–0.0407(7)	0.1495(3)	0.6697(4)	0.0646	1
C65	4*e*	–0.0184(6)	0.1591(3)	0.5969(3)	0.0502	1
C70	4*e*	0.1586(5)	0.2633(2)	0.4125(3)	0.0442	1
C71	4*e*	0.1792(6)	0.2466(2)	0.4926(3)	0.0489	1
C72	4*e*	0.2651(6)	0.2028(3)	0.5079(4)	0.0564	1
C73	4*e*	0.3011(5)	0.1917(3)	0.4373(4)	0.0553	1
C74	4*e*	0.2360(6)	0.2289(2)	0.3796(4)	0.0510	1
C80	4*e*	0.0782(7)	0.3102(3)	0.3717(4)	0.0625	1
C81	4*e*	0.1321(7)	0.2768(3)	0.5536(4)	0.0690	1
C82	4*e*	0.3372(7)	0.1819(3)	0.5919(5)	0.0822	1
C83	4*e*	0.4043(6)	0.1529(3)	0.4305(6)	0.0825	1
C84	4*e*	0.2507(8)	0.2369(3)	0.2974(5)	0.0711	1

Discussion and Conclusion

The crystal structures of the $[Cp^*(dppe)Fe–NCMe]_2 \cdot M_6L_{14}$ series reveal that inorganic and organic entities can be assembled without any structural modifications to each-partner whatever the M_6L_{14} unit (Table 8). Indeed, the interatomic distances within the M_6L_{14} units do not significantly vary between the starting $Cs_2M_6L_{14}$ solid-state compound and the final $[Cp^*(dppe)Fe–NCMe]_2 \cdot M_6L_{14}$ series. Furthermore, the interatomic distances within the $[Cp^*(dppe)Fe–NCMe]^+$ entity correspond to those found in the previously reported $[Cp^*(dppe)Fe–NCMe][PF_6]$. The compound $[Cp^*(dppe)Fe–NCMe]PF_6$ was obtained by photolysis of $[Cp^*Fe–(CO)_3]PF_6$ in acetonitrile with 1 equiv. of dppe. After the reaction, single crystals were ob-

 © 2005 Wiley-VCH Verlag GmbH & Co. KGaA, Weinheim

Table 5. Selected inter-atomic distances [Å] for $[Cp^*(dppe)Fe–NCCH_3]_2[Mo_6Br_{14}]$ (**2**).

Anionic unit: $[Mo_6Br^i_8Br^a_6]^{2-}$					
Mo–Mo bond lengths					
Mo1–Mo2	2.6402(5)	Mo1–Mo2	2.6429(6)	Mo1–Mo3	2.6358(6)
Mo1–Mo3	2.6419(5)	Mo2–Mo3	2.6379(5)	Mo2–Mo3	2.6437(6)
$Mo–Br^a$ bond lengths (^{a}: apical ligand)					
Mo1–Br7	2.5921(7)	Mo2–Br5	2.5996(7)	Mo3–Br6	2.6000(6)
$Mo–Br^i$ bond lengths (^{i}: inner ligand)					
Mo1–Br1	2.6076(6)	Mo1–Br2	2.6037(6)	Mo1–Br3	2.5960(6)
Mo1–Br4	2.6007(6)	Mo2–Br1	2.6024(6)	Mo2–Br2	2.6067(6)
Mo2–Br3	2.6139(6)	Mo2–Br4	2.6081(6)	Mo3–Br1	2.6103(6)
Mo3–Br2	2.6031(6)	Mo3–Br3	2.6068(6)	Mo3–Br4	2.6050(6)
Cationic unit: $[Cp^*(dppe)Fe–NCCH_3]^+$					
Fe–X distances and bond lengths					
X = Cp*					
Fe1–C70	2.112(5)	Fe1–C71	2.128(5)	Fe1–C72	2.118(6)
Fe1–C73	2.118(6)	Fe1–C74	2.108(5)		
X = (dppe)					
Fe1–P1	2.254(2)	Fe1–P2	2.231(1)		
X = $NCCH_3$					
Fe1–N1	1.903(4)				
Cp* intra-bond lengths					
C70–C71	1.422(8)	C71–C72	1.400(9)	C72–C73	1.44(1)
C73–C74	1.396(9)	C74–C70	1.435(8)		
C70–C80	1.497(9)	C71–C81	1.516(9)	C72–C82	1.547(9)
C73–C83	1.51(1)	C74–C84	1.517(9)		
(dppe) intra-bond lengths					
P1–C1	1.858(5)	C1–C2	1.520(8)	C2–P2	1.838(5)
P1–C30	1.837(5)	P1–C40	1.836(5)	P2–C50	1.826(5)
P2–C60	1.822(5)				
C30–C31	1.390(8)	C31–C32	1.399(9)	C32–C33	1.36(1)
C33–C34	1.40(1)	C34–C35	1.402(9)	C35–C30	1.393(9)
C40–C41	1.393(8)	C41–C42	1.396(9)	C42–C43	1.38(1)
C43–C44	1.36(1)	C44–C45	1.418(9)	C45–C40	1.391(8)
C50–C51	1.401(8)	C51–C52	1.381(8)	C52–C53	1.370(9)
C53–C54	1.390(9)	C54–C55	1.400(8)	C55–C50	1.390(7)
C60–C61	1.392(8)	C61–C62	1.411(9)	C62–C63	1.38(1)
C63–C64	1.37(1)	C64–C65	1.397(9)	C65–C60	1.398(8)
$–NCCH_3$ intra-bond lengths					
N1–C3	1.141(7)	C3–C4	1.449(8)		

tained by slowly cooling the solution to 233K. This procedure cannot guarantee a rigorous control of the crystallization and cannot be extended to brittle entities or those unstable at lowtemperatures. On the other hand, [Cp*(dppe)Fe–NCMe] is easily crystallized at room temperature with M_6L_{14} units. The reaction proposed here for the synthesis of the $[Cp^*(dppe)Fe–NCMe]_2 \cdot M_6L_{14}$ series is based on the exchange, in solution, of the chlorine atom from the Cp*(dppe)FeCl precursor by the more strongly coordinating acetonitrile group.[21] The charge is then compensated for by the M_6L_{14} dianionic unit. Using an organic solvent, it is more easy to separate CsCl than TBACl from $[Cp^*(dppe)Fe–NCMe]_2[Mo_6L_{14}]$. TBACl results from the reaction between [Cp*(dppe)Fe–NCMe]Cl and $(TBA)_2$-Mo_6L_{14} indicating that $Cs_2Mo_6L_{14}$ solid-state compounds must be preferentially chosen instead of the $(TBA)_2Mo_6L_{14}$ series usually used in coordination chemistry. M_6L_{14} anionic units could be used for the crystallization of other novel cationic organometallic entities when usual anionic counterparts give unfruitful results. In particular, the $Cs_2M_6L_{14}$ series could be used to advantage instead of $MReX_6$ salts for the crystallization of organic or organometallic cations from chloride precursors by precipitation of CsCl.

Finally, it is noteworthy that a solubile cation needs to counterbalance an insolubile anion to favour the crystal growing process.

Experimental Section

General: Unless otherwise specified, all reagents and solvents were purchased from commercial suppliers and used without further purification. The complex (η^2-dppe)(η^5-C_5Me_5)FeCl was prepared as described.[21][1]H NMR spectra were recorded with a Bruker Avance 200 (200 MHz) spectrometer. ^1H and ^{31}P NMR chemical shifts are reported in units of parts per million relative to the residual protio solvent and H_3PO_4, respectively.Transmittance-FTIR spectra were recorded with a Bruker IFS28 spectrometer (400–4000 cm^{-1}). $Cs_2Re_6S_6Br_8$, as well as $Cs_2Mo_6Br_{14}$ and $Cs_2Mo_6I_{14}$ were prepared by solid-state reactions as described in refs.[22,23], respectively. Chemical analyses were performed by energy dispersive spectrometry (EDS), using a scanning electron microscope JEOL JSM 6400 equipped with a microprobe EDS Oxford Link ISIS. Single-crystal X-ray diffraction data collections were performed at room temperature with a Nonius KappaCCD diffractometer. CCDC-244494, -250568 {for $[Cp^*(dppe)Fe–NCMe]_2[Re_6S_6Br_8]$, $[Cp^*(dppe)Fe–NCMe]_2[Mo_6Br_{14}]$} and CCDC-250569 {for $[Cp^*(dppe)Fe–NCMe]_2[Mo_6I_{14}]$} contain the supplementary crystallographic data for this paper. These data can be obtained free of charge from The Cambridge Crystallographic Data Centre via www.ccdc.cam.ac.uk/data_request/cif.

Synthesis of $[Cp^*(dppe)Fe–NCMe]_2[Re_6S_6Br_8]$ (1): [Cp*(dppe)FeCl] (0.312 g; 0.5 mmol) and $Cs_2Re_6S_6Br_8$ (0.609 g; 0.25 mmol) were separately dissolved in degassed MeCN (10 mL and 50 mL, respectively) in Schlenk tubes. The solutions were then mixed together with magnetic stirring for 1 h. The solvent was subsequently removed. $[Cp^*(dppe)Fe–NCMe]_2[Re_6S_6Br_8]$ was extracted from the resultant product by addition of acetone. The orange solution was then separated from the CsCl precipitate by filtration. After evaporation of acetone, $[Cp^*(dppe)Fe–NCMe]_2[Re_6S_6Br_8]$ was obtained as a brown powder (yield 40 %). Single crystals suitable for X-ray diffraction studies were obtained by diffusion of pentane into an acetone solution. No traces of chlorine or cesium were apparent in the final product from the EDS analysis (experimental atomic percentages: Fe, P, Re, S, Br: 7.0, 17.3, 24.1, 23.8, 27.8; calculated for $[Cp^*(dppe)Fe–CMe]_2[Re_6S_6Br_8]$: 7.7, 15.4, 23.1, 23.1, 30.8). This result is consistent with a complete cationic exchange between $[Re_6S_6Br_8]$ dianionic units and Cl^- with precipitation of CsCl in an organic solvent. In agreement with previous data reported with the related PF_6 salt,[24] the ^{31}P NMR spectrum exhibits only one signal at δ = 91.13 ppm characteristic for the two P atoms of the –P–$(CH_2)_2$–P– chain bridging the central iron atom. The presence of a

 © 2005 Wiley-VCH Verlag GmbH & Co. KGaA, Weinheim

Table 6. Atomic positions for $[Cp^*(dppe)Fe–NCCH_3]_2[Mo_6I_{14}]$ (**3**).

Atom	Wyckoff position	*x*/*a*	y/*b*	*z*/*c*	$U(iso)_{equiv.}$	Occ.
Mo1	4*e*	–0.97087(4)	0.54948(2)	0.42827(2)	0.0296	1
Mo2	4*e*	–1.08147(4)	0.45503(2)	0.41714(2)	0.0293	1
Mo3	4*e*	–0.84480(3)	0.46681(2)	0.50508(2)	0.0288	1
I1	4*e*	–0.72438(3)	0.56333(1)	0.51756(2)	0.0377	1
I2	4*e*	–1.21536(3)	0.53925(1)	0.33469(2)	0.0383	1
I3	4*e*	–0.89424(3)	0.47067(1)	0.34503(2)	0.0369	1
I4	4*e*	–1.19610(4)	0.38744(2)	0.29125(2)	0.0479	1
I5	4*e*	–1.04416(3)	0.63242(1)	0.50508(2)	0.0386	1
I6	4*e*	–0.61208(3)	0.41816(2)	0.50963(2)	0.0440	1
I7	4*e*	–0.92918(4)	0.62303(2)	0.31917(3)	0.0543	1
Fe1	4*e*	–0.39819(7)	0.17697(3)	0.41956(5)	0.0371	1
P1	4*e*	–0.4039(1)	0.08851(6)	0.42454(9)	0.0401	1
P2	4*e*	–0.5869(1)	0.17556(6)	0.44063(8)	0.0390	1
N1	4*e*	–0.4940(5)	0.1770(2)	0.3137(3)	0.0440	1
C1	4*e*	–0.5486(6)	0.0707(2)	0.4493(4)	0.0474	1
C2	4*e*	–0.6514(5)	0.1096(2)	0.4092(4)	0.0448	1
C3	4*e*	–0.5522(7)	0.1808(3)	0.2498(4)	0.0534	1
C4	4*e*	–0.623(1)	0.1856(4)	0.1687(4)	0.0879	1
C30	4*e*	–0.2856(6)	0.0467(3)	0.4918(4)	0.0465	1
C31	4*e*	–0.2671(7)	0.0526(3)	0.5716(4)	0.0569	1
C32	4*e*	–0.1774(9)	0.0210(3)	0.6230(5)	0.0700	1
C33	4*e*	–0.1098(7)	–0.0167(3)	0.5960(6)	0.0727	1
C34	4*e*	–0.1301(7)	–0.0222(3)	0.5168(5)	0.0670	1
C35	4*e*	–0.2172(6)	0.0099(3)	0.4651(4)	0.0571	1
C40	4*e*	–0.4190(5)	0.0539(2)	0.3326(3)	0.0423	1
C41	4*e*	–0.4790(7)	0.0058(3)	0.3152(4)	0.0547	1
C42	4*e*	–0.4821(7)	–0.0209(3)	0.2475(5)	0.0633	1
C43	4*e*	–0.4259(6)	0.0011(3)	0.1945(5)	0.0597	1
C44	4*e*	–0.3662(7)	0.0495(3)	0.2112(5)	0.0616	1
C45	4*e*	–0.3612(6)	0.0759(3)	0.2799(4)	0.0512	1
C50	4*e*	–0.6137(5)	0.1776(3)	0.5360(4)	0.0453	1
C51	4*e*	–0.5198(6)	0.1638(3)	0.6015(4)	0.0513	1
C52	4*e*	–0.5418(8)	0.1577(4)	0.6735(4)	0.0679	1
C53	4*e*	–0.6625(9)	0.1657(4)	0.6799(5)	0.0793	1
C54	4*e*	–0.7577(8)	0.1804(5)	0.6146(5)	0.0853	1
C55	4*e*	–0.7349(7)	0.1862(4)	0.5434(4)	0.0638	1
C60	4*e*	–0.7057(5)	0.2210(2)	0.3848(3)	0.0417	1
C61	4*e*	–0.7017(6)	0.2736(3)	0.4071(4)	0.0523	1
C62	4*e*	–0.7868(7)	0.3103(3)	0.3636(5)	0.0601	1
C63	4*e*	–0.8786(7)	0.2951(3)	0.2978(5)	0.0603	1
C64	4*e*	–0.8839(8)	0.2424(3)	0.2758(5)	0.0725	1
C65	4*e*	–0.7989(7)	0.2051(3)	0.3186(4)	0.0575	1
C70	4*e*	–0.2361(6)	0.1977(3)	0.5103(4)	0.0540	1
C71	4*e*	–0.2016(6)	0.1858(3)	0.4410(5)	0.0553	1
C72	4*e*	–0.3417(6)	0.2560(2)	0.4164(4)	0.0488	1
C73	4*e*	–0.2647(6)	0.2221(2)	0.3834(4)	0.0506	1
C74	4*e*	–0.3205(6)	0.2410(3)	0.4947(4)	0.0488	1
C80	4*e*	–0.1710(9)	0.1779(4)	0.5919(6)	0.0894	1
C81	4*e*	–0.0996(7)	0.1477(4)	0.4343(7)	0.0859	1
C82	4*e*	–0.2497(9)	0.2283(3)	0.3034(5)	0.0716	1
C83	4*e*	–0.4184(7)	0.3005(3)	0.3748(5)	0.0614	1
C84	4*e*	–0.3648(8)	0.2715(3)	0.5531(5)	0.0678	1

unique singlet is evidence the formation of only one organometallic complex with an η^2-dppe ligand. The ^{1}H NMR spectrum exhibits several peaks, i.e. a group between δ = 7.34 and 7.70 ppm (20 hydrogen atoms of the four phenyl groups connected to the two P atoms), a manifold between 2.15 ppm and 2.45 ppm [4 hydrogen atoms of the CH_2 groups of the –P–$(CH_2)_2$–P– bridge], a singlet at δ = 2.15 ppm (3 hydrogen atoms of the $NCCH_3$ solvent molecule connected to the metal atom) and a singlet at δ = 1.38 ppm (15 hydrogen atoms of the methyl groups of the Cp* ligand). In addition, the coordination of an $NCCH_3$ molecule on the iron atom is indicated by the presence of a characteristic ν_{CN} band stretch at 2249 cm^{-1} in the IR spectrum. This value is in agreement with those observed in other iron complexes with this same solvent molecule.[24] FT-IR (Nujol): $\tilde{\nu}$ = 2249 (m, $\nu_{C\equiv N}$) cm^{-1}. ^{1}H NMR (200 MHz $CDCl_3$): δ = 7.70–7.34 (m, 20 H, Ph), 2.45–2.45 (m, 4 H, CH_2dppe), 2.15 (s, 3 H, CH_3CN), 1.90 (s, 15 H, Cp*) ppm. ^{31}P NMR (81 MHz, $CDCl_3$): δ = 91.1 (s, dppe) ppm.

Synthesis of $[Cp^*(dppe)Fe–NCMe]_2[Mo_6Br_{14}]$ (2): [Cp*(dppe)FeCl] (0.115 g, 0.36 mmol) and $Cs_2Mo_6Br_{14}$ (0.360 g, 0.18 mmol) were

 © 2005 Wiley-VCH Verlag GmbH & Co. KGaA, Weinheim

Table 7. Selected interatomic distances [Å] for [Cp*(dppe)Fe–NCCH$_3$]$_2$[Mo_6I_{14}] (**3**).

Anionic unit: $[Mo_6I^i_8I^a_6]^{2-}$					
Mo–Mo bond lengths					
Mo1–Mo2	2.6765(6)	Mo1–Mo2	2.6802(6)	Mo1–Mo3	2.6801(6)
Mo1–Mo3	2.6844(5)	Mo2–Mo3	2.6745(5)	Mo2–Mo3	2.6878(6)
Mo–I^a bond lengths (^{a}: apical ligand)					
Mo1–I7	2.8427(5)	Mo2–I4	2.8408(5)	Mo3–I6	2.8467(5)
Mo–I^i bond lengths (^{i}: inner ligand)					
Mo1–I1	2.7776(5)	Mo1–I2	2.7736(5)	Mo1–I3	2.7753(5)
Mo1–I5	2.7665(5)	Mo2–I1	2.7745(5)	Mo2–I2	2.7819(5)
Mo2–I3	2.7766(5)	Mo2–I5	2.7808(5)	Mo3–I1	2.7710(5)
Mo3–I2	2.7755(5)	Mo3–I3	2.7788(5)	Mo3–I5	2.7889(5)
Cationic unit: [Cp*(dppe)Fe–NCCH$_3$]$^+$					
Fe–X distances and bond lengths					
X = Cp*					
Fe1–C70	2.127(6)	Fe1–C71	2.121(6)	Fe1–C72	2.108(6)
Fe1–C73	2.118(6)	Fe1–C74	2.135(6)		
X = (dppe)					
Fe1–P1	2.250(2)	Fe1–P2	2.236(2)		
X = NCCH$_3$					
Fe1–N1	1.902(5)				
Cp* intra-bond lengths					
C70–C71	1.44(1)	C71–C72	1.41(1)	C72–C73	1.455(9)
C73–C74	1.414(9)	C74–C70	1.42(1)		
C70–C80	1.53(1)	C71–C81	1.52(1)	C72–C82	1.51(1)
C73–C83	1.48(1)	C74–C84	1.50(1)		
(dppe) intra-bond lengths					
P1–C1	1.843(6)	C1–C2	1.527(9)	C2–P2	1.847(6)
P1–C30	1.850(6)	P1–C40	1.840(6)	P2–C50	1.825(6)
P2–C60	1.826(6)				
C30–C31	1.402(9)	C31–C32	1.40(1)	C32–C33	1.39(1)
C33–C34	1.39(1)	C34–C35	1.40(1)	C35–C30	1.375(9)
C40–C41	1.385(8)	C41–C42	1.39(1)	C42–C43	1.40(1)
C43–C44	1.39(1)	C44–C45	1.40(1)	C45–C40	1.404(9)
C50–C51	1.381(9)	C51–C52	1.39(1)	C52–C53	1.39(1)
C53–C54	1.39(1)	C54–C55	1.38(1)	C55–C50	1.408(9)
C60–C61	1.391(9)	C61–C62	1.40(1)	C62–C63	1.38(1)
C60–C61	1.39(1)	C64–C65	1.40(1)	C65–C60	1.399(8)
–NCCH$_3$ intra-bond lengths					
N1–C3	1.152(8)	C3–C4	1.45(1)		

separately dissolved in degassed MeCN (10 mL and 50 mL, respectively) in Schlenk tubes. The solutions were then mixed together with magnetic stirring. In contrast to [Cp*(dppe)Fe–NCMe]$_2$[$Re_6S_6Br_8$], [Cp*(dppe)Fe–NCMe]$_2$[Mo_6Br_{14}] is not soluble in acetone. Consequently, the solution volume was reduced to 10 mL in order to precipitate all the CsCl which was then separated by filtration. Subsequently, the solvent was removed to provide [Cp*(dppe)Fe–NCMe]$_2$[Mo_6Br_{14}] as an orange crystalline powder (yield 34 %). Suitable single crystals for X-ray diffraction studies were obtained by diffusion of pentane into an acetonitrile solution. EDS analysis did not indicate any traces of Cl or Cs. Heavy-element analyses are in good agreement with the stoichiometry determined from structural data. Spectroscopic characterization (^{31}P NMR, IR) of [Cp*(dppe)Fe–NCMe]$_2$[Mo_6Br_{14}] was carried out and no significant shifts in the band maxima in the IR spectrum or shifts in the NMR peaks could be observed compared with those of [Cp*(dppe)Fe–NCMe]$_2$[$Re_6S_6Br_8$].

Synthesis of [Cp*(dppe)Fe–NCMe]$_2$[Mo_6I_{14}] (3): [Cp*(dppe)Fe–NCMe]$_2$[Mo_6I_{14}] was prepared according to a similar experimental procedure to that described for [Cp*(dppe)Fe–NCMe]$_2$[Mo_6Br_{14}] using Cp*(dppe)FeCl (0.110 g, 0.18 mmol) and $Cs_2Mo_6I_{14}$ (0.230 g, 0.09 mmol). After drying under vacuum, [Cp*(dppe)Fe–NCMe]$_2$[Mo_6I_{14}] was obtained as an orange powder (yield 50 %). Single crystals suitable for X-ray diffraction studies were obtained by diffusion of pentane into an acetonitrile solution. EDS analysss did not suggest any traces of Cl or Cs. Heavy-element analyses are in good agreement with the stoichiometry determined from structural data. Spectroscopic characterization (^{31}P NMR, IR) of [Cp*(dppe)Fe–NCMe]$_2$[Mo_6I_{14}] was carried out and no significant shifts in the band maxima in the IR spectrum or shifts in the NMR peaks could be observed compared with those of [Cp*(dppe)Fe–NCMe]$_2$[$Re_6S_6Br_8$].

Acknowledgments

This work has been supported in part by three research grants from the French Ministry of Research and Education (F. d. M., K. K., G. P.). We would like to thank the Scanning Electron Microscopy Center at the University of Rennes 1 for microanalyses and the Diffraction Center of the University of Rennes 1 for the data collection with the Nonius KappaCCD X-ray diffractometer. In particular, the useful advice of Dr. Thierry Roisnel is gratefully acknowledged. We are also indebted to the French Research Ministry for "ACI Nanosciences 2001 – No. 18-01" contract and to "Fondation Langlois" for financial support.

[1] A. Perrin, M. Sergent, *New J. Chem.* **1988**, *12*, 337.
[2] A. Perricone, A. Slougui, A. Perrin, *Solid State Sci.* **1999**, *1*, 657.
[3] J. P. Gabriel, K. Boubekeur, S. Uriel, P. Batail, *Chem. Rev.* **2001**, *101*, 2037.
[4] A. Perrin, C. Perrin, M. Sergent, *J. Less-Common. Met.* **1988**, *137*, 241.
[5] C. Perrin, *J. Alloys Compd.* **1997**, *262–263*, 10, and references cited therein.
[6] H. Schäfer, H. G. von Schnering, *Angew. Chem.* **1964**, *76*, 833.
[7] R. Chevrel, M. Sergent, "Superconductivity in Ternary Compounds", in *Topics in Current Physics* (Eds.: Ø. Fischer, M. P. Maple), Springer Verlag, Berlin, Heidelberg, New York, **1982**.
[8] *Metal Clusters in Chemistry*, vol. II (Eds.: P. Braunstein, L. A. Oro, P. R. Raithby), Wiley-VCH, Weinheim, **1999**.
[9] J. M. Tarascon, F. J. Di Salvo, D. W. Murphy, G. W. Hull, E. A. Rietman, S. V. Waszczak, *J. Solid State Chem.* **1984**, *54*, 104.
[10] H. D. Selby, B. K. Roland, Z. Zheng, *Acc. Chem. Res.* **2003**, *36*, 933.
[11] M. W. Willer, J. R. Long, C. C. McLauhan, R. Holm, *Inorg. Chem.* **1998**, *37*, 328.
[12] Nonius, *COLLECT, DENZO, SCALEPACK, SORTAV: KappaCCD Program Package*, Nonius B. V., Delft, The Netherlands, **1999**.
[13] J. De Meulenaar, H. Tompa, *Acta Crystallogr., Sect A* **1965**, *19*, 1014.
[14] G. Cascarano, A. Altomare, C. Giacovazzo, A. Guagliardi, A. G. G. Moliterni, D. Siliqi, M. C. Burla, G. Polidori, M. Camalli, *Acta Crystallogr., Sect A* **1996**, *52*, C-79.
[15] D. J. Watkin, C. K. Prout, J. R. Carruthers, P. W. Betteridge, *CRYSTAL*, Chemical Crystallography Laboratory, Oxford, UK, **1999**, issue 11.
[16] A. Slougui, A. Perrin, M. Sergent, *J. Solid State Chem.* **1999**, *147*, 358.

 © 2005 Wiley-VCH Verlag GmbH & Co. KGaA, Weinheim

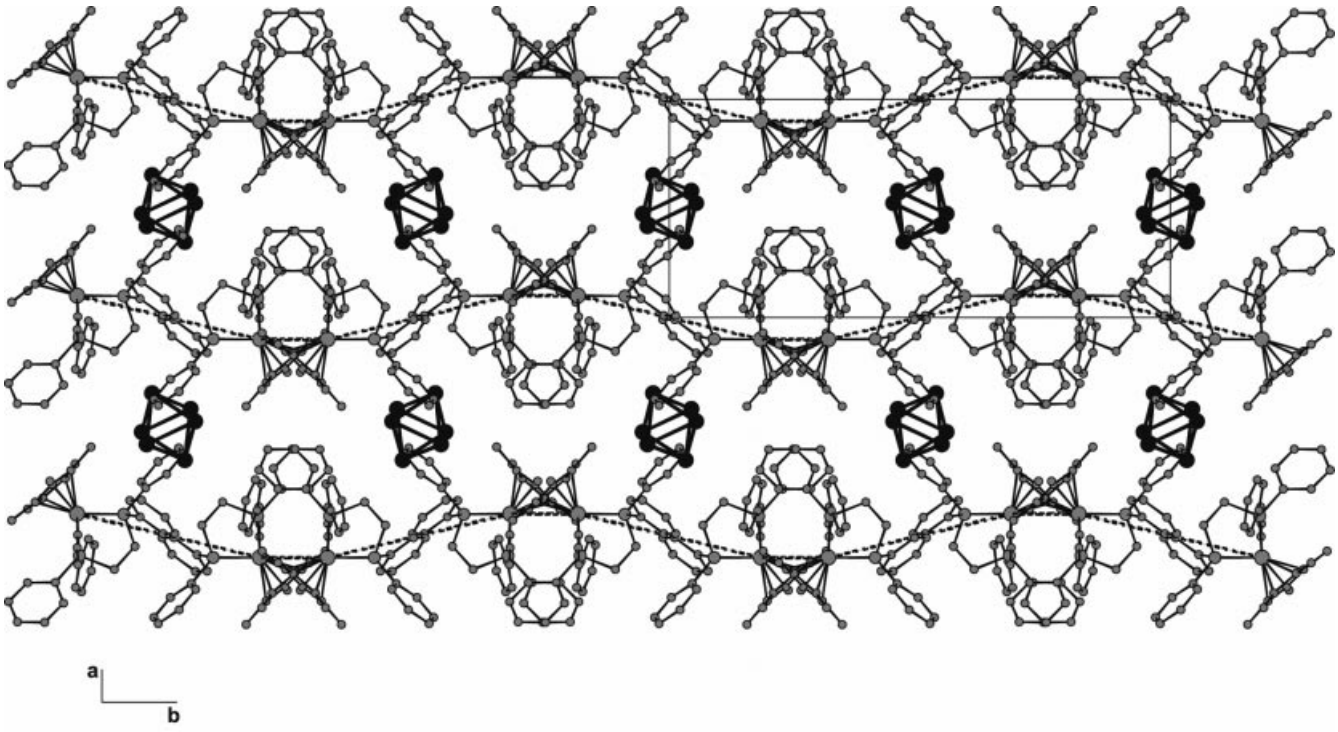

Figure 3. $[Cp^*(dppe)Fe–NCCH_3]_2[Me_6L_{14}]$ (Me = Re, Mo; L = S, Br, I) structure projection in the (*a*,*b*) plane of the unit-cell. Illustration of the anionic/waved cationic layers succession along the *a* axis of the nit-cell.

Table 8. Average bond lengths or interatomic distances [Å] in the structure of the three title compounds, for $[Cp^*(dppe)Fe–NCMe]PF_6$ and for the precursor cesium salts of $[Re_6S_6Br_8]^{2-}$, $[Mo_6Br_{14}]^{2-}$, $[Mo_6I_{14}]^{2-}$ (X = halogen atoms; Y = chalcogen atoms; A = organometallic cation: $[Cp^*(dppe)Fe–NCMe]^+$).

		$A_2[Re_6S_6Br_8]$ (**1**)	$A_2[Mo_6Br_{14}]$ (**2**)	$A_2[Mo_6I_{14}]$ (**3**)	APF_6	$Cs_2[Re_6S_6Br_8]$[22]	$Cs_2[Mo_6Br_{14}]$[23]	$Cs_2[Mo_6I_{14}]$[23]
	M–M	2.605	2.640	2.679		2.592	2.636	2.679
	$M–L^a$	2.537	2.597	2.843		2.520	2.600	2.851
$M–L^i$	$M–X^i$	2.56	2.605	2.777		2.525	2.601	2.779
	$M–Y^i$	2.44	–	–		2.407	–	–
	Fe–C (Cp*)	2.12	2.12	2.12	2.12			
	Fe–N (NCMe)	1.909	1.903	1.902	1.906			
	Fe–P (dppe)	2.24	2.24	2.24	2.23			
	C–C (C_5)	1.43	1.42	1.43	1.42			
Cp*	C–C (C_5–C_5H_{15})	1.51	1.52	1.51	1.51			
	P–C (C_2H_2)	1.86	1.85	1.84	1.84			
(dppe)	C–C (C_2H_2)	1.53	1.52	1.53	1.54			
	P–C (C_6H_6)	1.83	1.83	1.84	1.84			
	C–C (C_6H_6)	1.39	1.39	1.39	1.38			
N≡C–CH_3	N–CCH_3	1.15	1.14	1.15	1.13			
	NC–CH_3	1.46	1.45	1.45	1.45			

[17] J. Ruiz, D. Astruc, J.-P. Bideau, M. Cotrait, *Acta Crystallogr., Sect.C: Cryst. Struct. Commun.* **1990**, *46*, 2367.
[18] F. Paul, C. Lapinte, *Coord. Chem. Rev.* **1998**, *178–180*, 427.
[19] R. Denis, L. Toupet, F. Paul, C. Lapinte, *Organometallics* **2000**, *19*, 4240.
[20] K. Costuas, F. Paul, L. Toupet, J.-F. Halet, C. Lapinte, *Organometallics* **2004**, *23*, 2053.
[21] C. Roger, P. Hamon, L. Toupet, H. Rabaâ, J.-Y. Saillard, J.-R. Hamon, C. Lapinte, *Organometallics* **1991**, *10*, 1045.
[22] G. Pilet, PhD Dissertation, Rennes, France, **2003**.
[23] K. Kirakci, S. Cordier, C. Perrin, *Z. Anorg. Allgem. Chem.*, in press.
[24] D. Catheline, D. Astruc, *Organometallics* **1984**, *3*, 1094.
Received September 24, 2004

 © 2005 Wiley-VCH Verlag GmbH & Co. KGaA, Weinheim

Evolution of the Structural Parameters and Magnetic Properties in a Series of Di(μ-hydroxy)bis(nitrilotriacetato)dichromium(III) Complexes

Ghenadie Novitchi,*[a,c] Jean-Pierre Costes,[b] Victor Ciornea,[c] Sergiu Shova,[b,c] Irina Filippova,[d] Yurii A. Simonov,[d] and Aurelian Gulea[c]

Dedicated to Prof. André E. Merbach (EPFL, Lausanne, Switzerland) on the occasion of 65th birthday

Keywords: Chromium / Alkaline earth metals / N,O ligands / Magnetic properties

Four heterometallic complexes $\{Mg(H_2O)_6\}[Cr_2(\mu\text{-}OH)_2(nta)_2]\cdot 4H_2O$ (**I**), $\{Ca(H_2O)_3\}[Cr_2(\mu\text{-}OH)_2(nta)_2]\cdot 3H_2O$ (**II**), $\{Sr(H_2O)_3\}[Cr_2(\mu\text{-}OH)_2(nta)_2]\cdot 3H_2O$ (**III**) and $\{Ba(H_2O)_3dmso\}[Cr_2(\mu\text{-}OH)_2(nta)_2]\cdot 2H_2O$ (**IV**) containing dinuclear *bis*(μ-hydroxo) chromium(III) complex ions, where *nta* is the nitrilotriacetate ligand and *dmso* is dimethyl sulfoxide, have been prepared and crystallographically characterised. Compound **I** displays an ionic type structure, **II** and **III** are 3D coordination polymers and **IV** behaves like a 2D coordination polymer. In these compounds, the chromium(III) dimeric unit exhibits different structural features. It forms a polymeric structure by coordination of alkaline earth metal ions and/or formation of hydrogen-bonding interactions. The temperature dependencies of the magnetic susceptibilities of **I**–**IV** were fitted on the basis of the expression derived from the isotropic Hamiltonian including a biquadratic exchange term, $\hat{H} = -2J(\vec{S}_1\,\vec{S}_2) - j(\vec{S}_1\,\vec{S}_2)^2$. The values of the coupling interaction (J) range from –17.38 cm^{-1} to –5.80 cm^{-1} and the biquadratic terms (j) from +0.71 to 2.02 cm^{-1}. The experimental and theoretical values of J (calculated, using the Glerup–Hodgson–Pedersen model) have been discussed.

(© Wiley-VCH Verlag GmbH & Co. KGaA, 69451 Weinheim, Germany, 2005)

Introduction

The magnetic interactions between the unpaired electrons located at different metal atoms in polynuclear compounds are an important characteristic of magnetic materials.[1] The interest in this arises from the essential contribution of the exchange coupling constant to the magnetic properties of compounds containing coupled paramagnetic centres.[2] Among the transition-metal binuclear complexes known, many bridged complexes of transition metals with a wide variety of bridging ligands such as mono-cyanide[3] (CN^-, $S\text{–}CN^-$, $O\text{–}CN^-$), chloro,[4] azido,[5] oxo,[6,7] hydroxo,[8] oxalato[9] or even more complex bridges have been already described. The magnetic behaviour of these compounds depends on the ligand nature, the metal coordination number and the geometrical structure of the bridge. For closely related complexes such as alkoxo- and hydroxo-bridged $V^{II}O$[10] or oxo-bridged dimers,[11] magneto-structural correlations have been established. Many[12] studies have been devoted to chromium(III) dimers $[Cr_2(\mu\text{-}OH)_2L_x]^y$ with a *bis*(μ-hydroxo) bridge, where L are bidentate or polydentate ligands. For these types of dimer, Hoffmann and coworkers[12a] have characterised the exchange coupling constant J as the sum of ferromagnetic (J_f) and antiferromagnetic (J_{af}) terms where $J = J_{af} + J_f$. The two contributions J_f and J_{af} can be correlated to structural parameters: the metal-oxygen distance r, the in plane bridge angle φ as well as the out-of-plane distortions θ of the hydroxide ligand (Scheme 1).[12]

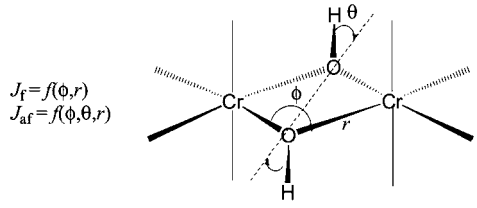

Scheme 1.

In the development of this correlation, Pedersen and coworkers[12b,12c] demonstrated that the magnetic exchange is highly sensitive to both θ and r or to the hybridisation state of the bridging oxygen atom.

[a] Institut des Sciences et Ingénierie Chimiques, EPFL, BCH, Laboratoire de Chimie Inorganique et Bioinorganique
1015 Lausanne, Switzerland
Fax: +412-16-9398-75
E-mail: novitchi@usm.md
[b] Laboratoire de Chimie de Coordination du CNRS,
205 route de Narbonne, 31077 Toulouse Cedex, France
[c] Department of Chemistry Moldova State University,
A.Mateevici str. 60. 2009 Chisinau, Moldova
[d] Institute of Applied Physics, Academy of Sciences of Moldova,
Academiei str. 3. 2028 Chisinau, Moldova
Supporting information for this article is available on the WWW under http://www.eurjic.org or from the author.

In this paper, we report the synthesis, structures and magnetic characterisation of four chromium(III) alkaline earth heterometallic complexes: $\{Mg(H_2O)_6\}[Cr_2(\mu\text{-}OH)_2(nta)_2]\cdot 4H_2O$, (**I**), $\{Ca(H_2O)_3\}[Cr_2(\mu\text{-}OH)_2(nta)_2]\cdot 3H_2O$ (**II**), $\{Sr(H_2O)_3\}[Cr_2(\mu\text{-}OH)_2(nta)_2]\cdot 3H_2O$ (**III**) and $\{Ba(H_2O)_3\text{-}dmso\}[Cr_2(\mu\text{-}OH)_2(nta)_2]\cdot 2H_2O$ (**IV**) where *nta* is the nitrilotriacetate ligand and *dmso* is dimethyl sulfoxide.

Results and Discussion

Synthesis and Characterisation of the Complexes

The heterometallic complexes **I**–**IV** containing dinuclear bis(μ-hydroxo)chromium(III) complex ions were prepared by the interaction of $CrCl_3\cdot 6H_2O$ and $M_3(nta)_2$ (where M = Ca^{2+}, Sr^{2+} or Ba^{2+}). The reactions proceed in aqueous solutions and the pH was adjusted with a solution of $M(OH)_2$. $M_3(nta)_2$ was previously obtained by an exchange reaction between MCO_3 and nitrilotriacetic acid (H_3nta). As usual, the formation of the dinuclear complex ion (**4**) (Scheme 2) results from a hydrolysis reaction which is characteristic of chromium(III) ions.[13] The reversibility of the protolytic reaction between **1** and **2** and also between **2** and **3** has already been demonstrated byspectroscopic (UV/Vis, ^2H NMR) and pH-metric investigations of different Co^{III} and Cr^{III}-*nta* complexes.[14]

This work reveals that the dimeric ions (**4**) are broken in an irreversible protonation step to form diaqua complexes (**1**). The very slow dimerisation steps **2**↔**4** and **3**↔**4** proceed over several days.[15] Compound **I** was obtained by an exchange reaction between the barium compound **IV** and $MgSO_4$.

In order to establish the coordination modes of the carboxylic groups of the nitrilotriacetate ligands, the IR absorption spectra of **I**–**IV** were determined. In the IR spectra, the difference between the asymmetric and the symmetric stretching frequencies [$\Delta = \nu_{as}(COO^-) - \nu_s(COO^-)$] characterises the coordination modes of the carboxylic groups.[15] In the IR spectrum of **I**, three intensive bands were found, namely one at ca. 1623 cm^{-1} related to $\nu_{as}(COO^-)$ and two at 1363 and 1335 cm^{-1} attributable to $\nu_s(COO^-)$. The differences between the asymmetric and symmetric frequencies are equal to 260 and 287 cm^{-1}. Differences higher than 250 cm^{-1} indicate two different monodentate modes of coordination for the carboxylate groups. In the IR spectra of compounds **II** and **III**, three intense bands corresponding to carboxylate moieties do exist: for **II** they are $\nu_{as}(COO^-)$ = 1596 cm^{-1} and $\nu_s(COO^-)$ = 1385 and 1345 cm^{-1} whereas for complex **III** these bands appear at 1597, 1386 and 1345 cm^{-1}. The related frequency differences Δ = 252 cm^{-1} and 211 cm^{-1} support the presence of monodentate and bidentate bridging modes of coordination, respectively. The similarities of the values for complexes **II** and **III** suggest isostructural arrangements for the nitrilotriacetate ligands. Two coordination modes are also present in **IV**: monodentate (Δ = 255 cm^{-1}) and bridging or chelating (Δ = 231 cm^{-1}).

The electronic spectra of complexes **I**–**IV** in aqueous solution (in the 300–1100 nm range) show two bands $\nu_1(^4A_{2g}\rightarrow{}^4T_{2g})$ = 17069 cm^{-1} (ε = 40 $L\,mol^{-1}\,cm^{-1}$) and $\nu_2[^4A_{2g}\rightarrow{}^4T_{1g}(F)]$ = 24510 cm^{-1} (ε = 63 $L\,mol^{-1}\,cm^{-1}$), characteristic for an $\{NO_5\}$ octahedral environment for chromium(III) with ligand field parameters $10Dq$ = 17069 cm^{-1} and B = 745 cm^{-1}.[16] The configuration interaction (x) between

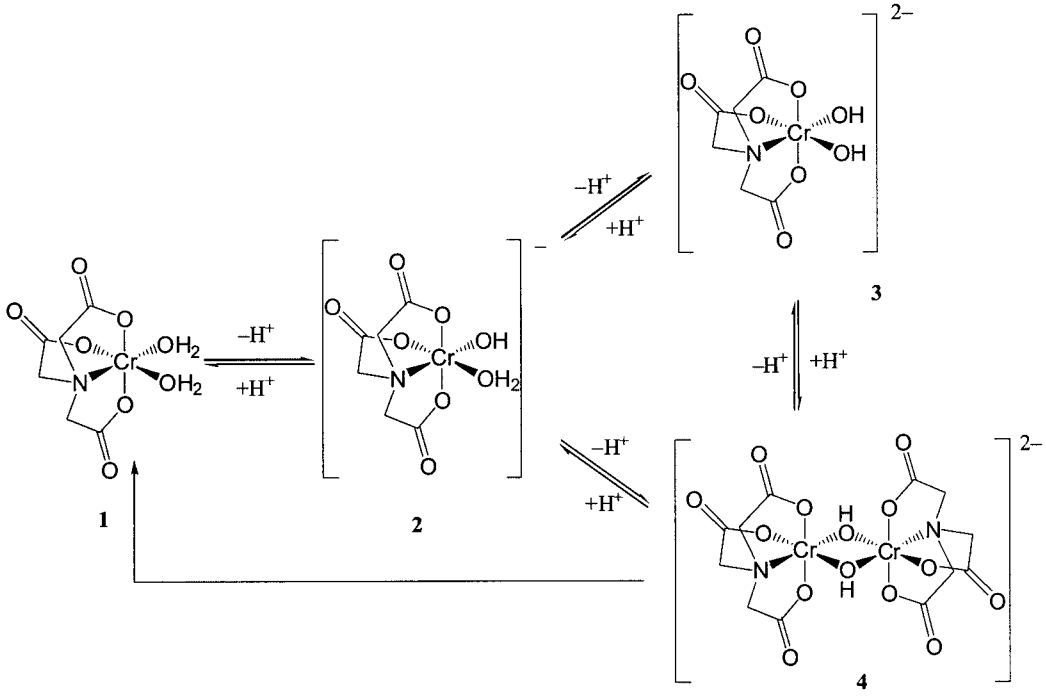

Scheme 2.

the $^4T_{1g}(F)$ and $^4T_{1g}(P)$ states of the same symmetry is 6214 cm^{-1}. The similarities in the wave numbers for **I–IV** indicate that the complexes dissociate in solution, keeping the dianionic dichromium structure unchanged.

Structures

A perspective view of the centrosymmetric dinuclear complex anion **I** is shown in Figure 1. A similar $[Cr_2(\mu\text{-}OH)_2(nta)_2]^{2-}$ unit is present in the four complexes **I–IV** as well as in the $Cs_2[M_2(\mu\text{-}OH)_2(nta)_2]\cdot 4H_2O$ entities already reported (M = Cr, Co).[14a,14b] In compounds **II–IV**, the asymmetric part of the unit-cell contains two crystallographically independent nitrilotriacetate molecules which generate two different centrosymmetric dimeric anions (named **A** and **B** hereafter) (Figure 2).The octahedral coordination of the chromium atoms implies four donor atoms from the nta^{3-} ligands (N,O,O,O) and two bridging OH groups. For **I–IV**, the average Cr–N bond length is 2.060 Å [from 2.052(3) to 2.069(2) Å, Table 1] while a more significant dispersion is observed for the Cr–O bonds [from 1.952(1) to 2.015(2) Å]. The nta^{3-} ligand forms three five-membered ring chelates with the central atom. According to ref.[17] these rings can be classified as one *R* ring {N(1) CrO(6)C(6)C(5)N(1)} and two *G* rings (Figure 1). For complexes **I–IV**, the sums of the endocyclic angles vary in the ranges 537.5–540.0° and 524.9–536.2° for the *R* and *G* rings, respectively. Two oxygen atoms from hydroxy groups act as bridges in the $[Cr_2(\mu\text{-}OH)_2(nta)_2]^{2-}$ anion (Figure 1 and Figure 2).The Cr–(μ-OH) bond lengths are in the range 1.942(3)–1.979(1) Å, as in the previously published $Cr_2(\mu\text{-}OH)_2$ fragments.[12,14a,14b,18b] Slight differences characterise the Cr–O(1)–Cr* angles (φ) [96.0(1)–101.2(8)°] (Table 1). As a consequence, the Cr–Cr distances vary from 2.928(1) to 3.014(1) Å. Significant differences can also be observed for the angles defined by the O–H and O(1)–O(1)* vectors (θ angles in Scheme 1 and Table 1). These angles are essential for differentiating the dimeric units and are 51(2)° (dimer **A**) and 8(3)° (dimer **B**) in compound **II.**

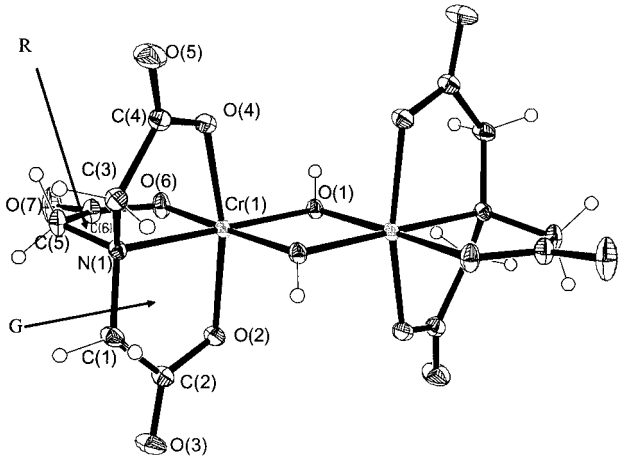

Figure 1. Perspective view of $[Cr_2(\mu\text{-}OH)_2(nta)_2]^{2-}$ with the numbering scheme for **I**. Thermal ellipsoids are drawn at the 30% probability level.

The sizes of the alkaline earth metal ions from Mg^{2+} (0.72 Å) to Ba^{2+} (1.35 Å)[18a] lead to a change in the coordi-

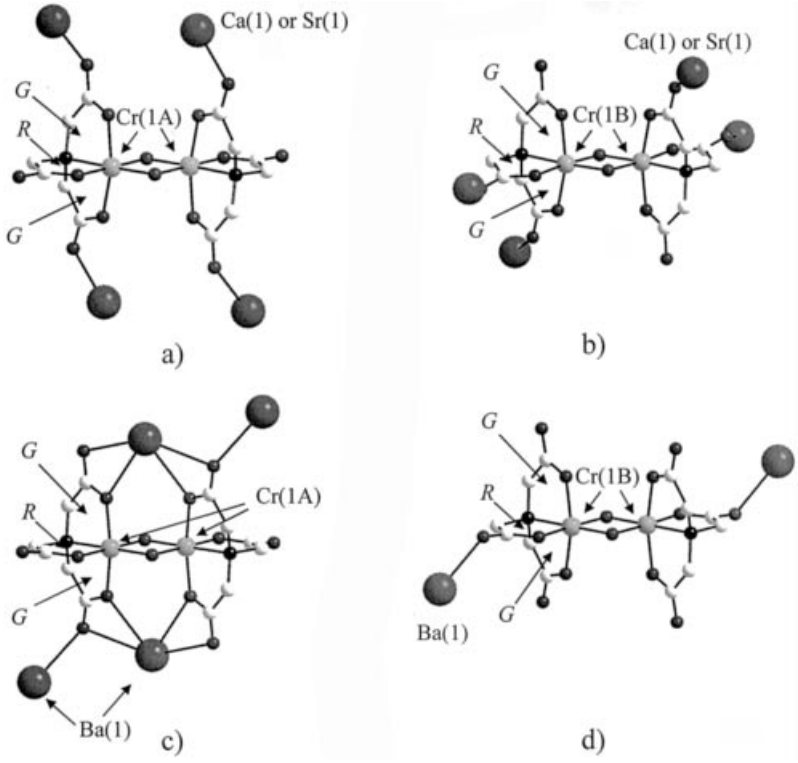

Figure 2. Ball and stick representations of the **A** and **B** type chromium(III) dimers in **II–IV**. a) **IIA** or **IIIA**, b) **IIB** or **IIIB**, c) **IVA** and d) **IVB**.

 © 2005 Wiley-VCH Verlag GmbH & Co. KGaA, Weinheim

Table 1. Selected bond lengths [Å] and angles [°] in the $[Cr_2(\mu\text{-}OH)_2(nta)_2]^{2-}$ dimers in **I**–**IV**.

	I	**II**		**III**		**IV**	
		A[a]	B	A	B	A	B
Cr–O(1)	1.966(1)	1.950(2)	1.950(2)	1.950(2)	1.942(3)	1.961(2)	1.943(2)
Cr–O(1)*	1.979(1)	1.958(2)	1.951(2)	1.949(2)	1.954(3)	1.978(2)	1.948(2)
Cr–O(2)	1.995(1)	1.989(2)	1.993(2)	1.999(2)	1.970(3)	1.959(2)	1.975(2)
Cr–O(4)	1.993(1)	1.987(2)	2.015(2)	1.975(2)	2.007(2)	1.976(2)	2.003(2)
Cr–O(6)	1.952(1)	1.983(2)	1.965(2)	1.965(2)	1.963(2)	1.953(2)	1.967(2)
Cr–N(1)	2.060(1)	2.065(2)	2.069(2)	2.063(3)	2.064(3)	2.052(3)	2.058(3)
Cr···Cr	2.985(1)	2.935(1)	3.014(1)	2.919(1)	2.993(1)	2.928(1)	2.929(1)
O(1)–Cr–O(2)	97.53(5)	98.43(7)	97.19(8)	100.3(1)	96.1(1)	96.9(1)	97.5(1)
O(1)–Cr–O(4)	99.10(5)	97.94(7)	101.43(8)	96.7(1)	101.7(1)	96.7(1)	99.4(1)
O(1)–Cr–N(1)	179.36(4)	179.76(7)	177.66(8)	178.3(1)	177.1(1)	178.8(2)	178.9(1)
O(1)*–Cr–O(2)	90.69(5)	91.77(8)	91.67(9)	91.8(1)	91.7(1)	89.8(1)	91.2(1)
O(1)*–Cr–O(4)	88.81(5)	88.92(8)	91.44(8)	88.3(1)	90.4(1)	87.6(1)	89.1(1)
O(1)*–Cr–N(1)	98.94(4)	97.12(7)	100.45(7)	97.1(1)	99.7(1)	97.3(1)	98.6(1)
O(2)–Cr–O(4)	163.11(4)	163.57(7)	161.38(7)	162.9(1)	162.2(1)	165.8(1)	163.0(1)
O(2)–Cr–O(6)	89.67(6)	89.46(8)	90.20(8)	89.3(1)	91.7(1)	90.4(1)	89.8(1)
O(2)–Cr–N(1)	82.72(5)	81.57(7)	80.59(8)	81.4(1)	81.1(1)	83.3(1)	82.0(1)
O(4)–Cr–N(1)	80.68(5)	82.05(7)	80.79(8)	81.6(1)	81.2(1)	83.2(1)	81.1(1)
O(6)–Cr–O(1)	94.77(4)	95.85(7)	95.99(7)	94.9(1)	96.1(1)	94.6(1)	93.6(1)
O(6)–Cr–O(1)*	176.43(4)	178.18(6)	174.65(7)	177.8(1)	174.8(1)	178.6(1)	175.9(1)
O(6)–Cr–O(4)	91.88(6)	90.28(8)	88.38(7)	91.2(1)	87.7(1)	92.5(1)	91.1(1)
O(6)–Cr–N(1)	84.63(4)	84.39(7)	84.80(7)	84.9(1)	84.8(1)	84.2(2)	85.5(1)
Cr–O(1)–Cr (φ)	98.34(4)	97.36(7)	101.20(8)	96.9(1)	100.4(1)	96.0(1)	97.7(1)
θ [°]	50(2)	51(2)	8(3)	50(4)	28(4)	50(3)	37(4)
Symm. transf. for *	$-x, -y + 1, -z$	$-x + 1, -y + 1, -z$	$-x + 3, -y, -z + 1$	$-x + 1, -y + 1, -z$	$x + 3, -y, -z + 1$	$-x + 1, -y + 1, -z + 1$	$-x + 2, -y + 1, -z$

[a] Two crystallographically independent *nta* molecules are named as **A** and **B**.

nation polyhedron and induce different assemblies of the dinuclear units in the polymer networks. In **I** the Mg^{2+} ion is surrounded by six water molecules and has an octahedral coordination geometry. The Mg–O distances vary between 2.049(1) Å and 2.072(2) Å, with the O–Mg–O angles close to 90°. Distances and bond angles (Table S2) are similar to those found in other $[Mg(H_2O)_6]^{2+}$ containing compounds.[18] Multiple hydrogen bonds involving coordinated and solvated water molecules link the $[Cr_2(\mu\text{-}OH)_2(nta)_2]^{2-}$ anions with the $[Mg(H_2O)_6]^{2+}$ cations in a 3D network (Figure S1).

The isostructural compounds **II** and **III** are 3D coordination polymers (Figure 3). In this framework, four bridging carboxylic groups ($\eta^1{:}\eta^1{:}\mu_2$) arising from four *G* rings from the **A** type dimers form bonds with seven-coordinate Ca or Sr ions (see a in Figure 2). On the other hand, two *G* and two *R* rings are used for the **B** type dimers (see b in Figure 2). The coordination polyhedron of Ca^{2+} is completed by four carboxylate oxygen atoms belonging to four Cr dimers with Ca–O lengths ranging from 2.395(2) to 2.431(2) Å and by three water molecules with bond lengths ranging from 2.410(2) to 2.427(2) Å (Figure 3). The corresponding bond lengths to the Sr centres in **III** increase with the ionic radius of Sr^{2+}. The Sr–O(*w*) bond lengths are in the range of 2.526(2)–2.573(2) Å and the Sr–O_{carb} distances vary from 2.507(2) to 2.561(2) Å. The 3D structure is stabilised by O–H···O hydrogen bonds (Table S1). The increase in the Sr–O bond lengths in comparison with the Ca–O distances leads to small modifications in the orientations of some of the H-bonds.

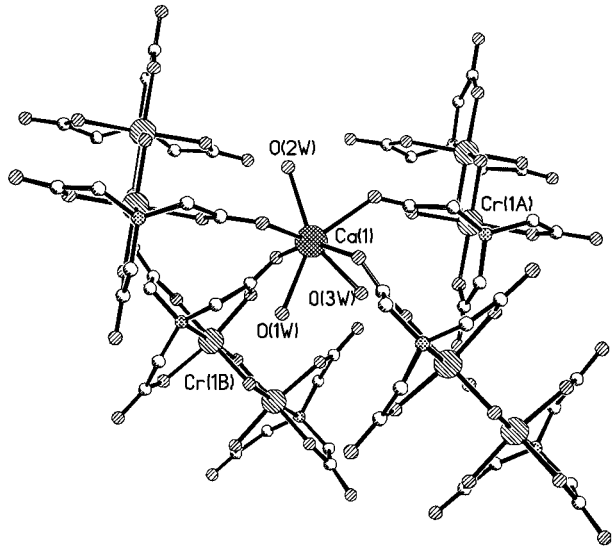

Figure 3. Coordination environment of Ca^{2+} in the 3D network of compound **II**.

In compound **IV**, the **A** type dimers have four *G* carboxylic groups chelating the ten- coordinate Ba^{2+} ions (see c in Figure 2). In **IV-A**, the carboxylic groups exhibit different bridging functions: two are tridentate bridging groups ($\eta^2{:}\eta^1{:}\mu_2$) whereas the other two are tetradentate ($\eta^2{:}\eta^2{:}\mu_2$). In contrast, only two *trans* (*R*) carboxylic bridging groups ($\eta^1{:}\eta^1{:}\mu_2$) are bound to the Ba^{2+} ions in the **B** type dimers, (see d in Figure 2). The coordination sphere of barium is composed of six oxygen atoms from two nta^{3-} ligands [dis-

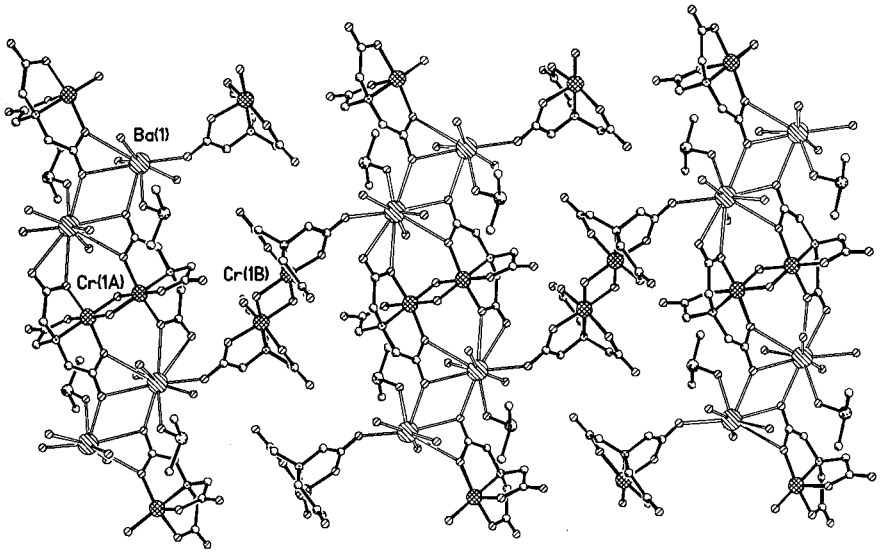

Figure 4. View of the 2D polymeric layer in compound **IV**. Hydrogen atoms and solvated water molecules have been omitted for clarity.

tances: 2.697(2)–3.094(3) Å], one dimethyl sulfoxide molecule [Ba(1)–O(1S) = 2.751(3) Å] and three H_2O molecules [2.786(3)–2.813(3) Å]. A centrosymmetric dimer **B** joins two atoms [Ba(1) and Ba(1*)] through two oxygen atoms [Ba(1)–O(7B) = 2.697(2) Å] whereas the second dimer (**A**) has five short contacts [2.827(2)–3.094(3) Å] with Ba(1). Furthermore, the carboxylate oxygen atoms O(5A) form a bridge between two centrosymmetric Ba^{2+} ions yielding dimers with Ba···Ba distances of 4.691(1) Å (Figure 4). Decadentate chelate-bridging dimeric anions enable the formation of chains with alternating of Cr(1A) and Ba(1) dimers along the *b* axis while Cr(1B)-dimers join the adjacent chains to give 2D polymeric layers (Figure 4). The layers are held together by hydrogen bonds (Table S1).

Magnetic Studies

The magnetic behaviour of compounds **I**–**IV** has been studied in the 2–300 K temperature range. As an example, the magnetic behaviour of **II** is shown in Figure 5 in the form of the thermal variation of χ_M, where χ_M is the molar susceptibility corrected for diamagnetism. At 300 K, χ_M is equal to 1.1×10^{-2} $cm^3 mol^{-1}$ which corresponds to the expected value for two uncoupled metal ($S = {}^3/_2$) ions both in the $^4A_{2g}$ ground state. As usual, the appropriate model for obtaining a fairly good agreement between the theoretical and experimental data may include a biquadratic exchange term [Equation (1)]. The resultant Hamiltonian is:[11e,11f,19]

$$\hat{H} = -2J(\vec{S}_1 \cdot \vec{S}_2) - j(\vec{S}_1 \cdot \vec{S}_2)^2 \quad (1)$$

and this leads to the following expression [Equation (2)].

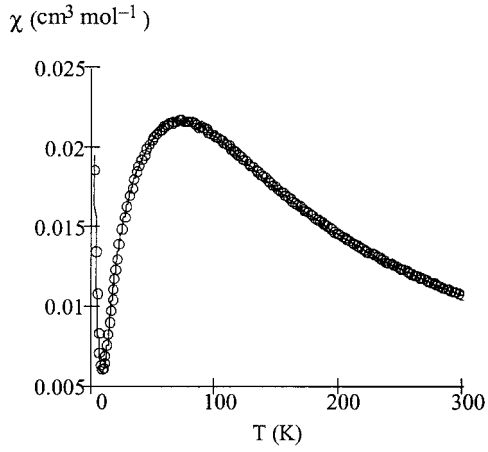

Figure 5. Magnetic susceptibility data for **II**. The solid line corresponds to the best fit for a pair of exchange-coupled $S = {}^3/_2$ spins including biquadratic exchange.

where the variable magnetic parameters *J* and *j* determine triplet, quintet and septet electronic ground states $E(^3A_2'') = -2J + 6.5j$, $E(^5A_1') = -6J + 13.5j$ and $E(^7A_2'') = -12J + 9j$, respectively (Scheme S1). C_{pi} represents the paramagnetic impurity factor. Least-squares fittings of the experimental data lead to the parameters collected in Table 2 with the agreement factors defined by $R = \Sigma(\chi_{calc} - \chi_{obs})^2/\Sigma(\chi_{obs})^2$. The negative *J* value indicates that the main exchange interaction in the dimeric building block fragments is antiferromagnetic. On the contrary, however, the biquadratic exchange *j* is positive but of lower amplitude with a

$$\chi_m = \frac{2Ng^2\mu_B^2(1-C_{pi})}{kT} \cdot \frac{\exp\left[\frac{(2J-6,5j)}{kT}\right] + 5\exp\left[\frac{(6J-13,5j)}{kT}\right] + 14\exp\left[\frac{(12J-9j)}{kT}\right]}{1 + 3\exp\left[\frac{(2J-6,5j)}{kT}\right] + 5\exp\left[\frac{(6J-13,5j)}{kT}\right] + 7\exp\left[\frac{(12J-9j)}{kT}\right]} \quad (2)$$

 © 2005 Wiley-VCH Verlag GmbH & Co. KGaA, Weinheim

j/2*J* ratio equal to 0.05.[20] In our complexes, a parallel evolution of *J* and *j* can be observed, with an increase of |*J*| occurring as |*j*| increases and a ratio varying from 0.05 to 0.06.

Table 2. Best parameters obtained from magnetic susceptibility data fitting.

Parameters	I	II	III	IV
J	–5.80(1)	–12.59(1)	–13.85(1)	–17.38(1)
j	0.71(2)	1.29(2)	1.31(2)	2.02(2)
Cp	–0.006	–0.039	–0.012	–0.0063
R	7×10^{-5}	7×10^{-5}	9×10^{-7}	9×10^{-7}

The exchange interaction in chromium(III) dimers with $S = 0, 1, 2$ and 3 concerns two coupled $(^4A_{2g})a(^4A_{2g})b$ states derived from the $|t_{2g}^3(a)t_{2g}^3(b)>$ configuration where $^4A_{2g}$ and t_{2g}^3 characterise two d^3-metal centres *a* and *b*. The chromium(III) t_{2g} orbitals containing the unpaired electrons and the p orbitals of the bridging OH-ligands are both involved in the superexchange interactions. In this pathway, the magnetic interactions also depend upon the orientation of the oxygen atom orbitals which determine the dominant contributions between the two paramagnetic centres. The resultant expression for *J* in the Heisenberg's Hamiltonian may be calculated using the Glerup–Hodgson–Pedersen model [Equation (3)].[12]

$$J = J_{af} - J_f = e^{-a(r-1,8)}\left[\frac{b\cdot\cos^4\theta}{\left\{(1-\sin^2\theta)\Big/\tan^2(\phi/2)\right\}^2} - \frac{c\cdot\sin\phi}{(1-\cos\phi)^2}\right] \quad (3)$$

where *r*, φ and θ are defined as represented in Scheme 1. The calculated *J* values with $a = 19$ Å^{-1}, $b = 611$ cm^{-1} and $c = 172$ cm^{-1} [12b] and the experimental ones for **I**–**IV** are presented in Figure 6. Theoretical *J* values with their standard deviations were calculated using distances and angles obtained from X-ray experiments. For compound **I** and for **II-A** and **III-A** type dimers, experimental and theoretical estimations of *J* values are in fair agreement. For dimers **II-B** and **III-B**, the theoretical values are overestimated compared with the experimental measurements. This difference may be explained by a supplementary interaction between dimers through Ca or Sr ions. Indeed, the carboxylate groups bridge Cr and Ca or Sr ions in a *syn-anti* conformation for dimers **A** and in an *anti-anti* conformation for dimers **B**.

The Hamiltonian used in our calculations assumes that the chromium dimers are well isolated from each other. A look at the structural determinations indicates that this assumption is only true for complex **I**. In complexes **II**–**IV**, the Ca, Sr and Ba ions bridge these dinuclear units but we have no experimental evidence to suggest that such bridges are able to transmit magnetic interactions. On the contrary, the quality of the fits obtained for the entire set of complexes agrees with the accuracy of the retained Hamiltonian and the absence of magnetic interactions through the alkaline-earth metal ions.

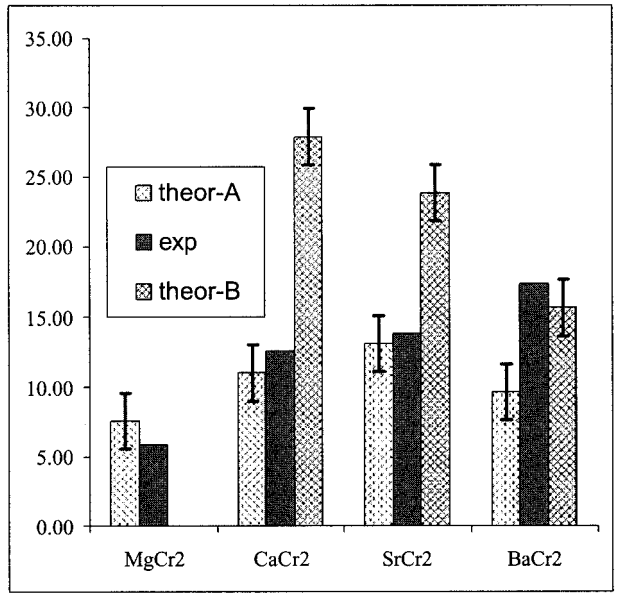

Figure 6. Experimental (best fit of Eq. 2) and theoretical (Glerup–Hodgson–Pedersen model, Eq. 3) *J* values for compounds **I**–**IV** (**theor-A** and **theor-B** correspond to the values calculated with the crystallographic data of the **A** and **B** dimers).

Conclusion

Four new heterometallic chromium nitrilotriacetate complexes have been synthesized and structurally characterised by X-ray analysis. The dinuclear di-(μ-hydroxo) chromium anion $[Cr_2(\mu\text{-}OH)_2(nta)_2]^{2-}$ is present in each complex. Thus, the effect of substitution of one alkaline earth metal with another, while preserving the basic composition and inducing a variation in the number of solvated water molecules, affords dramatic alterations in the molecular structures which range from an ionic type in compound **I** to coordination polymers in **II**–**IV**. This is predetermined by the coordination function of $[Cr_2(\mu\text{-}OH)_2(nta)_2]^{2-}$ and its binding to give 2D or 3D coordination polymers.

The IR spectra confirm, with help of the Δ parameters [$\Delta = \nu_{as}(COO^-) - \nu_s(COO^-)$], that monodentate, bidentate bridging or chelating coordination modes of the carboxylate groups are present. This is consistent with the structural features of the studied complexes.

The magnetic properties of this series of di-μ-hydroxo bridged chromium(III) complexes containing the nitrilotriacetic ligand include antiferromagnetic coupling interactions with *J* values ranging from –5.80 to –17.38 cm^{-1}. A comparison of the best fit magnetic parameters with theoretical values calculated using the Glerup–Hodgson–Pedersen model clearly shows a fair correlation with the structural parameters of the dinuclear units, with only a minute influence from the hydrogen bonds and the alkaline earth metal bridges.

 © 2005 Wiley-VCH Verlag GmbH & Co. KGaA, Weinheim

Experimental Section

Materials: All starting materials and solvents were purchased from Aldrich and were used without further purification. Elemental analyses (C, H, N) were carried out by the Service de Microanalyse du Laboratoire de Chimie de Coordination, Toulouse.

Syntheses: Calcium [Di-μ-hydroxy-bis(nitrilotriacetato)dichromium(III)] Hexahydrate $\{Ca(H_2O)_3\}[Cr_2(\mu\text{-}OH)_2(nta)_2]\cdot 3H_2O$ (II): Water (100 mL) was added to a mixture of H_3nta (0.76 g, 4 mmol) and dispersed $CaCO_3$ (0.6 g, 6 mmol). The resultant solution was warmed to 95 °C. After complete dissolution of $CaCO_3$, $CrCl_3\cdot 6H_2O$ (1.07 g, 4 mmol) in water (50 mL) was added to the initial solution (the temperature was maintained at about 95 °C). Heating was stopped after 1 h and a saturated solution of $Ca(OH)_2$ was added dropwise in order to raise the pH value to 6.5–7.0. As a result, the solution changed from violet to navy blue-green. The reaction mixture was filtered and concentrated to 30 mL. After 24 h, the crystals which appeared were separated by filtration, washed with cold water, ethanol and diethyl ether. Yield 70%. $C_{12}H_{26}CaCr_2N_2O_{20}$: calcd. C 21.76, H 3.96, N 4.23; found C 21.63, H 4.03, N 4.21.IR (KBr): $\tilde{\nu}$ = 3318 (br,m) ν(OH), 1596 (vs) $\nu_{as}(CO_2)$, 1455 (w) 1429 (w) $\delta(CH_2)$, 1385 (s) 1345 (s) $\nu_s(CO_2)$, 1272 (m) 1216 (m) $\rho_\omega(CH_2)$, 1098 (m) 1010 (m) ν(CN), 974 (w) ρ_r, 953 (m) 941 (m) ν(CC), 748 (s) $\delta(CO_2)$, 624 (s) $\rho_\omega(CO_2)$ cm^{-1}.

Strontium [Di-μ-hydroxy-bis(nitrilotriacetato)dichromium(III)] Hexahydrate $\{Sr(H_2O)_3\}[Cr_2(\mu\text{-}OH)_2(nta)_2]\cdot 3H_2O$ (III)andBarium [Di-μ-hydroxy-bis(nitrilotriaacetato)dichromium(III)] Dimethyl Sulfoxide Pentahydrate $\{Ba(H_2O)_3dmso\}[Cr_2(\mu\text{-}OH)_2(nta)_2]\cdot 2H_2O$ (IV): The syntheses were analogous to that of **II** except for neutralisation of the reaction mixture (pH = 6.5–7) that was carried out with concentrated NH_4OH.Compound **IV** was recrystallised from dimethyl sulfoxide. $\{Sr(H_2O)_3\}[Cr_2(\mu\text{-}OH)_2(nta)_2]\cdot 3H_2O$ (**III**) Yield 65%. $C_{12}H_{26}Cr_2N_2O_{20}Sr$: calcd. C 20.30, H 3.69, N 3.95; found C 20.35, H 3.89, N 3.71. IR (KBr): $\tilde{\nu}$ = 3319 (m, br) ν(OH), 1597 (vs) $\nu_{as}(CO_2)$, 1455 (w) 1430 (w) $\delta(CH_2)$, 1386 (s) 1345 (s) $\nu_s(CO_2)$, 1274 (m) $\rho_\omega(CH_2)$, 1100 (m) 1011 (m) ν(CN), 941 (m) ν(CC), 744 (s) $\delta(CO_2)$, 621 (s) $\rho_\omega(CO_2)$ cm^{-1}.$\{Ba(H_2O)_3dmso\}[Cr_2(\mu\text{-}OH)_2(nta)_2]\cdot 2H_2O$(**IV**) Yield 55%. $C_{14}H_{30}BaCr_2N_2O_{20}S$: calcd. C 20.51, H 3.69, N 3.42; found C 20.50, H 3.42, N 3.48. IR (KBr): $\tilde{\nu}$ = 3421 (s, br) ν(OH), 1653 (vs) 1617 (vs) $\nu_{as}(CO_2)$, 1456 (w) $\delta(CH_2)$, 1386 (vs) $\nu_s(CO_2)$, 1268 (m) 1212 (w) $\rho_\omega(CH_2)$, 1104 1093 (w) ν(CN), 951 (m) ν(CC), 754 (s) $\delta(CO_2)$, 621 (m) $\rho_\omega(CO_2)$ cm^{-1}.

Magnesium [Di-μ-hydroxy-bis(nitrilotriacetato)dichromium(III)] Decahydrate$\{Mg(H_2O)_6\}[Cr_2(\mu\text{-}OH)_2(nta)_2]\cdot 4H_2O$ (I): $MgSO_4\cdot 7H_2O$ (0.25 g, 1 mmol) was dissolved in water (50 mL) and the crystalline complex **IV** (0.74 g, 1 mmol) was added. The mixture was stirred for 2 h at 70°C. The solution was then filtered and concentrated to a volume of 20 mL. A substance crystallised from the navy blue-green solution over 24 h and this was separated by filtration. The crystals obtained were washed with cold water, alcohol and eventually with acetone and were dried at room temperature. Yield 67%. $C_{12}H_{34}Cr_2MgN_2O_{24}$: calcd. C 20.05, H 4.78, N 3.89; found C 20.91, H 4.56, N 4.05. IR (KBr): $\tilde{\nu}$ = 3356 (s, br) ν(OH), 1623 (vs) $\nu_{as}(CO_2)$, 1457 (w) 1420 (w) $\delta(CH_2)$, 1363 (s) 1335 (s) $\nu_s(CO_2)$, 1268 (m) 1220 (m) $\rho_\omega(CH_2)$, 1107 (m) 1092 (m) ν(CN), 934 (m) ν(CC), 746 (s) $\delta(CO_2)$, 620 (s) $\rho_\omega(CO_2)$ cm^{-1}.

The substances **I–IV** are soluble in water, slightly soluble in DMSO and DMF but insoluble in ethanol and acetone.

Physical Measurements: TheIR spectra (KBr pellets) were recorded on a GX system 2000 Perkin–Elmer spectrophotometer. Electronic absorption spectra were recorded on a Perkin–Elmer UV/Vis-NIR-

Table 3. Crystal data and details of structural determinations.

	I	II	III	IV
Empirical formula	$C_{12}H_{34}Cr_2MgN_2O_{24}$	$C_{12}H_{26}CaCr_2N_2O_{20}$	$C_{12}H_{26}Cr_2N_2O_{20}Sr$	$C_{14}H_{30}BaCr_2N_2O_{20}S$
Formula mass	718.72	662.43	709.97	819.80
Temperature (K)	293	293	180	293
Crystal system	triclinic	triclinic	triclinic	triclinic
Space group	$P\bar{1}$	$P\bar{1}$	$P\bar{1}$	$P\bar{1}$
a [Å]	6.555(1)	9.711(2)	9.761(3)	9.787(2)
b [Å]	10.144(2)	10.576(2)	10.587(3)	10.974(2)
c [Å]	11.430(2)	13.041(3)	13.076(4)	12.876(3)
α [°]	111.52(3)	88.68(3)	89.05(2)	99.02(3)
β [°]	101.26(3)	75.03(3)	76.28(2)	90.96(3)
γ [°]	91.94(3)	64.23(3)	64.01(3)	102.45(3)
V [Å^3]	688.8(2)	1159.1(4)	1174.2(6)	1331.9(5)
D_{calc} [Mg m^{-3}]	1.733	1.898	2.008	2.044
Z	1	2	2	2
μ [mm^{-1}]	0.915	1.258	3.271	2.434
F(000)	372	680	716	816
Crystal size [mm]	0.35 × 0.35 × 0.3	0.40 × 0.20 × 0.07	0.37 × 0.15 × 0.12	0.40 × 0.2 × 0.2
θ range for data collection[°]	3.652–9.50	3.712–9.93	3.213–2.14	2.893–2.03
Limiting indices	$-8 \le h \le 6$, $-13 \le k \le 13$, $-15 \le l \le 15$	$-13 \le h \le 13$, $-8 \le k \le 14$, $-17 \le l \le 17$	$-12 \le h \le 14$, $-15 \le k \le 15$, $-18 \le l \le 19$	$-14 \le h \le 12$, $-15 \le k \le 15$, $-18 \le l \le 18$
Reflections collected	6581 [R_{int} = 0.0156]	14862 [R_{int} = 0.0239]	12499[R_{int} = 0.0474]	14140[R_{int} = 0.0367]
Completeness to θ	90.1%	88.7%	90.0%	90.4%
Data/restraints/parameters	3449/0/255	5961/19/426	7478/20/378	8402/16/417
Goodness-of-fit on F^2	1.070	1.059	0.850	0.982
T_{max} and T_{min}	0.809 and 0.737	0.805 and 0.698	0.988 and 0.559	0.980 and 0.705
R_1, wR_2 [$I > 2\sigma(I)$]	0.0270, 0.0715	0.0378, 0.0982	0.0466, 0.0879	0.0399, 0.0890
R_1, wR_2 (all data)	0.0292, 0.0733	0.0428, 0.1025	0.0790, 0.0962	0.0550, 0.0965
Largest diff. peak and hole (e Å^{-3})	0.321 and –0.496	0.684 and –0.695	1.760 and –1.207	1.727 and –1.331

 © 2005 Wiley-VCH Verlag GmbH & Co. KGaA, Weinheim

Lambda-19 spectrophotometer. Magnetic susceptibility data (2–300 K) were collected on powdered samples using a SQUID-based sample magnetometer on a Quantum Design model MPMS instrument in an applied magnetic field of 0.1 T. All data were corrected for the diamagnetism of the ligands as estimated from Pascal's constants.[21]

Single-Crystal X-ray Analyses: X-ray diffraction data were collected with a KUMA KM4CCD-κ-axis diffractometer for compounds **I** and **II**, anOxford-Diffraction XCALIBUR CCD instrument for **III** and a Stoe Imaging Plate Diffractometer System (IPDS)[22a] for **IV** using graphite-monochromated Mo-K_α radiation. Absorption corrections were introduced for **I**–**IV** using semi-empirical methods from symmetry equivalent reflections.[22b,22c] Crystal data, details of data collections and refinements for **I**–**IV** are given in Table 3. The structures were solved by direct methods with SHELXS-97[22d] and refined on F^2 with SHELXL-97[22e] with an anisotropic approach for non-hydrogen atoms. In the crystal structure of **IV**, two water molecules O(2*w*) and O(4*w*) are disordered over two positions in the unit cell. The ratios of the site occupancy factors of the major and minor components *sof* O(2*w*)/*sof* O(2*w**) and *sof* O(4*w*)/*sof* O(4*w**) are 3:1. The positional parameters for the hydrogen atoms of bridging OH groups in **I**–**IV** were located objectively from the difference syntheses of electronic density and were refined in isotropic approximation. The accuracy of the determinations of H-atom coordinates guarantees that the estimated standard deviations of O–H bonds are no more than 0.05 Å and those of the bond angles no more than 4° (these data are used for interpretation of magnetic properties, see above). Other hydrogen atoms were also located from the difference syntheses of electronic density, except for the H-atoms of the minor components water molecules O(2*w**) and O(4*w**) for **IV**. H-atoms were refined in an isotropic approximation for **I** and **II**, except for the H-atoms of the H_2O molecules of **II**. In all other cases the positions of H atoms were allowed to ride on a pivot atom with isotropic displacement parameters fixed at $1.5 \times U_{eq}$ for H_2O and CH_3, and $1.2 \times U_{eq}$ for CH_2 groups where U_{eq} is the equivalent isotropic displacement parameter for the pivot atom.

CCDC-244108, -244109, -244110 and -244111 contain the supplementary crystallographic data for this paper. These data can be obtained free of charge from The Cambridge Crystallographic Data Centre via www.ccdc.cam.ac.uk/data_request/cif.

Supporting Information Available: Figure S1. Packing diagram of compound **I**. Hydrogen atoms are omitted for the sake of clarity and hydrogen bonds are indicated by dotted lines. Figure S2. Magnetic susceptibility data for **I**, **III** and **IV**. Table S1. Hydrogen bonding interactions in the crystal structures of **I**–**IV**. Table S2. Bond lengths [Å] in coordination polyhedra of the alkaline-earth metals in structures **I**–**IV**. Scheme S1. Energy level diagram for di(μ-hydroxo)chromium(III) dimers ($S = {}^3/_2$).

Acknowledgments

The authors thank Professor M. Gdaniec (Department of Chemistry, A. Mickiewicz University, Poznań, Poland) for the X-ray structure determinations of compounds **I** and **II**. Gh. Novitchi is grateful to the Swiss Federal Institute of Technology, Lausanne, for financial support. This work was also supported by the Superior Council for Sciences and Technology Developing of the R. Moldova (Project 45.003p).

[1] a) *Magnetism: Molecules to Materials*, vol I. *Models and Experiments*, vol. II *Molecule-Based Materials* (Eds.: J. S. Miller, M. Drillon), Wiley-VCH, Weinheim, **2001**; b) C. Benelli, D. Gatteschi, *Chem. Rev.* **2002**, *102*, 2369; c) *Molecular Magnetic Materials* (Eds.: D. Gatteschi, O. Kahn, J. S. Miller, F. Palacio), NATO ASI Series, Kluwer, Dordrecht, The Netherlands, **1991**.

[2] a) O. Kahn, *Molecular magnetism*, VCH Publishers, New York, **1993**; b) *Magnetism: A Supramolecular Function* (Ed.: O. Kahn), *NATO ASI series C484*, Kluwer Academic Publishers, Dordrecht, **1996**; c) O. Kahn, *Adv. Inorg. Chem.* **1996**, *4*, 179; d) O. Kahn, *Struct. Bonding, Berlin* **1987**, *68*, 89; e) P. Chaudhuri, *Coord. Chem. Rev.* **2003**, *243*, 143; f) M. Drillon, J. Darriet, *Progress. Struct. Bonding, Berlin* **1992**, *79*, 55.

[3] a) M. Ohba, H. Okawa, *Coord. Chem. Rev.* **2000**, *198*, 313–328; b) S. R. Batten, R. Robson, *Angew. Chem. Int. Ed.***1998**, *37*, 1460–1494; c) S. R. Batten, K. S. Murray, *Coord. Chem. Rev.* **200**3, *246*, 103–130; d) L. Ouahab, *Coord. Chem. Rev.* **1998**, *178–180*, 1501–1531; e) G. Wrzeszcz, L. Dobrzanska, A. Wojtczak, A. Grodzicki, *Dalton Trans.* **2002**, 2862–2867.

[4] a) K. O. Joung, C. J. O'Connor, E. Sinn, R. L. Carlin, *Inorg. Chem.* **1979**, *18*, 804; b) R. D. Willet, in *Magneto structural Correlations in Exchange Coupled Systems* (Eds.: R. D. Willet, D. Gatteschi, O. Kahn), NATO Advanced studies Series C, Reidel, Dordecht, **1985**, vol. 140, 389 and references therein.

[5] a) J. Comarmond, P. Pluméré, J.-M. Lehn, Y. Agnus, R. Louis, R. Weiss, O. Kahn, I. Morgenstern-Badarau, *J. Am. Chem. Soc.* **1982**, *104*, 6330; b) O. Kahn, S. Sikorav, J. Gouteron, S. Jeannin, Y. Jeannin, *Inorg. Chem.* **1983**, *22*, 2883; c) C. G. Pierpont, D. N. Hendrickson, D. M. Duggan, F. Wagner, E. K. Barefield, *Inorg. Chem.* **1975**, *14*, 604; d) J. Ribas, M. Monfort, C. Diaz, C. Bastos, X. Solans, *Inorg. Chem.* **1993**, *32*, 3557; e) M. I. Arriortua, A. R. Cortés, L. Lezama, T. Rojo, X. Solans, M. Font-Bardia, *Inorg. Chim. Acta.* **1990**, *174*, 263; f) R. Vincente, A. Escuer, J. Ribas, M. Salah-el-Fallah, X. Solans, M. Font-Bardia, *Inorg. Chem.* **1993**, *32*, 1920.

[6] a) B. G. Gafford, C. O'Rear, J. H. Zhang, C. J. O'Connor, R. A. Holwerda, *Inorg. Chem.* **1989**, *28*, 1720; b) B. G. Gafford, R. E. Marsh, W. P. Schaefer, J. H. Zhang, C. J. O'Connor, R. A. Holwerda, *Inorg. Chem.* **1990**, *29*, 4652; c) A. Harton, K. Terrell, J. C. Huffman, C. MacDonald, A. Beatty, S. Li, C. J. O'Connor, J. B. Vincent, *Inorg. Chem.* **1997**, *36*, 4875; d) C. Blanchet- Boiteux, J.-M. Mouesca, *Theor. Chem. Acc.* **2000**, *104*, 257; e) J. H. Rodriguez, K. McCusker, *J. Chem. Phys.* **2002**, *116*, 6253.

[7] a) L. L. Martin, K. Wieghardt, G. Blondin, J.-J. Girerd, B. Nuber, J. Weiss, *J. Chem. Soc., Chem. Commun.* **1990**, 1767; b) P. Knopp, K. Wieghardt, B. Nuber, J. Weiss, W. S. Sheldrick, *Inorg. Chem.* **1990**, *29*, 363; c) P. Knopp, K. Wieghardt, *Inorg. Chem.* **1991**, *30*, 4061; d) A. Bodner, S. Drüeke, K. Wieghardt, B. Nuber, J. Weiss, *Angew. Chem. Int. Ed. Engl.* **1990**, *29*, 68; e) A. Bodner, B. S. P. C. Della-Vedova, K. Wieghardt, B. Nuber, J. Weiss, *J. Chem. Soc., Chem. Commun.* **1990**, 1042; f) A. Bodner, P. Jeske, T. Weyhermüller, K. Wieghardt, E. Dubler, H. Schmalle, B. Nuber, *Inorg. Chem.* **1992**, *31*, 3737; g) P. Jeske, K. Wieghardt, B. Nuber, *Inorg. Chem.* **1994**, *33*, 47; h) S. G. Brand, N. Edelstein, C. J. Hawkins, G. Shalimoff, M. Snow, E. R. T. Tiekink, *Inorg. Chem.* **1990**, *29*, 434.

[8] a) W. W. Lukens, R. A. Anderson, *Inorg. Chem.* **1995**, *34*, 3440; b) K. T. McGregor, N. T. Watkins, D. L. Lewis, R. F. Drake, D. J. Hodgson, W. E. Hatfield, *Inorg. Nucl. Chem. Lett.* **1973**, *9*, 423; c) D. L. Lewis, W. E. Hatfield, D. J. Hodgson, *Inorg. Chem.* **1972**, *11*, 2216; d) K. T. McGregor, W. E. Hatfield, D. J. Hodgson, *Inorg. Chem.* **1974**, *13*, 1013; e) E. D. Estes, W. E. Hatfield, D. J. Hodgson, *Inorg. Chem.* **1974**, *13*, 1654; f) V. H. Crawford, H. W. Richardson, J. R. Wasson, D. J. Hodgson, W. E. Hatfield, *Inorg. Chem.* **1976**, *15*, 2107; g) O. Kahn, *Inorg. Chim. Acta.* **1982**, *62*, 3; h) E. Ruiz, J. Cano, S. Alvarez, P. Alemany, *J. Comput. Chem.* **1999**, *20*, 1391.

 © 2005 Wiley-VCH Verlag GmbH & Co. KGaA, Weinheim

[9] a) L. P. Battaglia, A. Bianchi, A. Bonamartini-Corradi, E. Garcia-Espana, M. Micheloni, M. Julve, *Inorg. Chem.* **1988**, *27*, 4174; b) A. Bencini, A. Bianchi, E. Garcia-Espana, Y. Jeannin, M. Julve, V. Marcelino, M. Philoche-Leviasalles, *Inorg. Chem.* **1990**, *29*, 963; c) J. Glerup, P. A. Goodson, D. J. Hodgson, K. Michelsen, *Inorg. Chem.* **1995**, *34*, 6255.

[10] a) A. Rodriguez-Fortea, P. Alemanu, S. Alvares, E. Ruiz, *Eur. J. Inorg. Chem.* **2004**, 143; b) H. Weihe, H. U. Güdel, *J. Am. Chem. Soc.* **1998**, *120*, 2870.

[11] a) P. Andersen, *Coord. Chem. Rev.* **1989**, *94*, 47; b) P. A. Lay, A. Levina, "Chromium" in *Comprehensive Coordination Chemistry II* Vol. 4 (Ed.: A. G. Wedd), Amsterdam, **2004**, p. 313; c) D. M. Stearns W. H. Armstrong, *Inorg. Chem.* **1992**, *31*, 5178; d) W. E. Hatfield, J. J. MacDougall R. E. Shepherd, *Inorg. Chem.* **1981**, *20*, 4216; e) S. J. Cline, S. Kallesoe, E. Pedersen, D. J. Hodgson, *Inorg. Chem.* **1979**, *18*, 796; f) M. A. Heinrichs, D. J. Hodgson, K. Michelsen, E. Pedersen, *Inorg. Chem.* **1984**, *23*, 3174; g) K. Michelsen, E. Pedersen, S. R. Wilson, D. J. Hodgson, *Inorg. Chim. Acta* **1982**, *63*, 141; h) F. Teixidor, J. Colomer, J. Casabo, E. Molins, C. Miravitlles, F. Palacio, *Inorg. Chim. Acta* **1988**, *147*, 151.

[12] a) P. J. Hay, J. C. Thibeault, R. Hoffmann, *J. Am. Chem. Soc.* **1975**, *97*, 4884; b) J. Glerup, D. J. Hodgson, E. Pedersen, *Acta Chem. Scand., Sect. A* **1983**, *A37*, 161; c) S. J. Cline, D. J. Hodgson, S. Kallesoe, S. Larsen, E. Pedersen, *Inorg. Chem.* **1983**, *22*, 637; d) D. Hodgson, in *Magneto Structural Correlations in Exchange Coupled Systems* (Eds.: R. D. Willet, D. Gatteschi, O. Kahn), NATO Advanced studies Series C, Reidel, Dordecht, **1985**, vol. 140, p. 497.

[13] a) F. P. Rotzinger, H. Stunzi, W. Marty, *Inorg. Chem.* **1986**, *25*, 489; b) L. Spiccia, H. Stoeckli-Evans, W. Marty, R. Giovanoli, *Inorg. Chem.* **1987**, *26*, 474; c) L. Spiccia, W. Marty, *Polyhedron* **1991**, *10*, 619; d) L. F. Larkworthy, K. B. Nolan, P. O'Brien, "Chromium"in *Comprehensive Coordination Chemistry*, vol. 3 (Eds.: G. Wilkinson, R. D. Gillard, J. A. McCleverty), Pergamon Press, Oxford, **1987**, p. 699.

[14] a) G. H. Visser, W. Purcell, S. S. Basson, *Polyhedron* **1999**, *18*, 2795; b) G. H. Visser, W. Purcell, S. S. Basson, Q. Claassen, *Polyhedron* **1997**, *16*, 2851; c) G. H. Visser, J. G. Leipoldt, W. Purcell, D. Mostert, *Polyhedron* **1994**, *13*, 1051; d) N. Koime, J. Bianchimi, I. Legg, *Inorg. Chem.* **1986**, *25*, 2835.

[15] a) K. Nakamoto, *Infrared and Raman Spectra of Inorganic and Coordination Compound*, 5th ed., Wiley, **1997**; b) G. B. Deacon, R. J. Phillips, *Coord. Chem. Rev.* **1980**, *33*, 227.

[16] a) J. R. Perumareddi, *Coord. Chem. Rev.* **1969**, *4*, 73; b) A. B. P. Lever, *Inorganic Electronic Spectroscopy*, 2nd ed., Elsevier Publishing Co., Amsterdam, **1984**; c) J. A. Huheey, *Inorganic Chemistry*, 3rd ed., Harper & Row, New York, **1983**; d) $10Dq$, B and x were calculated using the following equations: $\nu_1 = 10Dq$; $B = \frac{2\nu_1^2 + \nu_2^2 - 3\nu_1\nu_2}{15\nu_2 - 27\nu_1}$; $\nu_2 = 9/5\nu_1 - x$; e) C. L. Sharma, P. K. Jain, T. K. De, *J. Inorg. Nucl. Chem.* **1980**, *42*, 1681; f) Y. Dou, *J. Chem. Ed.* **1990**, *67*, 134; g) A. B. P. Lever, *J. Chem. Educ.* **1968**, *45*, 711.

[17] a) T. Fujihara, A. Fuyuhiro, S. Kaizaki, *J. Chem. Soc., Dalton Trans.* **1995**, 1813; b) H. A. Wiakliem, J. L. Hoard, *J. Am. Chem. Soc.* **1959**, *81*, 549.

[18] a) A. F. Wells, *Structural Inorganic Chemistry*, Oxford: Clarendon Press, **1984**; b) U. Ruchlewska, D. D. Radanovic, V. S. Jevtovic, D. J. Radanovic, *Polyhedron* **2000**, *19*, 1.

[19] a) R. Basler, C. Boskovic, G. Chaboussant, H. U. Gudel, M. Murrie, S. T. Ochsenbein, A. Sieber, *Chem. Phys. Chem.* **2003**, *4*, 910; b) D. E. Bolter, Ph. Gutlich, W. E. Hatfield, S. Kremer, E. W. Muller, K. Wieghardt, *Inorg. Chem.* **1983**, *22*, 1725; c) S. Kremer, *Inorg. Chem.* **1985**, *24*, 887; d) S. J. Cline, J. Glerup, D. J. Hodgson, G. S. Jensen, E. Pedersen, *Inorg. Chem.* **1981**, *20*, 2229.

[20] E. A. Boudreaux, L. N. Mulay, *Theory and Applications of Molecular Paramagnetism*, John Wiley, New York, **1976**.

[21] P. Pascal, *Ann. Chim. Phys.* **1910**, *19*, 5.

[22] a) *STOE*, IPDS Manual, Version 2.93, Stoe & Cie, Darmstadt, Germany, **1997**; b) R. H. Blessing, *Acta Crystallogr., Sect. A* **1995**, *51*, 33; c) XEMP Ver. 4.2 Siemens Analytical X-ray Inst. Inc., **1990**; d) G. M. Sheldrick, *SHELXS-97*, *Program for the Solution of Crystal Structures*, University of Göttingen, Germany, **1997**; e) G. M. Sheldrick, *SHELXL-97*, *Program for the Refinement of Crystal Structures*, University of Göttingen, Germany, **1997**.

Received: November 10, 2004

 © 2005 Wiley-VCH Verlag GmbH & Co. KGaA, Weinheim

Selective C–H and C–F Bond Activation Reactions of Pyridine and Fluoropyridines – Formation of Binuclear μ-X Titanocene Complexes (X = H, F) with α-Functionalized N-Heterocycles

Ingmar M. Piglosiewicz,[a] Susanne Kraft,[a] Rüdiger Beckhaus,*[a] Detlev Haase,[a] and Wolfgang Saak[a]

Keywords: Titanium / Bridging ligand / Fluorinated ligands / Nitrogen heterocycles / C–H activation / C–F activation

Titanocene synthons react with pyridine (**2**), fluorosubstituted pyridines [pentafluoropyridine (**3**), 2-fluoropyridine(**4**)] and cyanuric fluoride, by C–H and C–F bond activation, respectively, to afford interesting novel binuclear titanium(III) complexes. C–H bond activation requires high temperatures (110 °C), whereas C–F bond activation occurs at room temperature. X-ray structure analysis showed that the two titanium(III) centres are hydride-bridged when pyridine was reacted with the titanocene fragment and fluoride-bridged if a 2-fluoro-substituted derivative of pyridine was used. The reactivities of a C–F and a C–H bond in the 2-position toward the titanocene fragment have been compared in a competition experiment using 2-fluoropyridine – revealing a preference for C–F bond cleavage. Primary mononuclear C–F bond activation products have been proved in solution by NMR measurements using [$Cp^*_2Ti\{\eta^2$-$C_2(SiMe_3)_2\}$] instead of the non-methylated titanocene source.

(© Wiley-VCH Verlag GmbH & Co. KGaA, 69451 Weinheim, Germany, 2005)

Introduction

We recently reported that N-heterocycles such as pyrimidine, pyrazine and triazine may undergo amazing C–C couplings when reacted with the titanocene fragments [Cp_2Ti] or [Cp^*_2Ti].[1] With this kind of reaction we presume a single electron transfer from the titanium(II) centre to the N-heterocycles, as in the case of 2,2′-bipyridine and comparable chelating ligands.[2–4] Here we report reactions of low valent titanium complexes with pyridines. Examples of C–C coupling reactions of pyridine via low valent early transition metal complexes are rare.[5] As well as simple pyridine (C_5H_5N) we also wanted to use fluorinated pyridines. The electronegative fluorine substituents lower the energy of the LUMOs and increase the electron affinities,[6] which could be helpful in C–C coupling reactions. In particular, C–H or C–F bond activation reactions could also be possible.

Carbon–fluorine bond activation of several fluoroaromatics mediated by transition metal complexes has been thoroughly investigated in the last two decades. Especially, late transition metal complexes have been employed to cleave aromatic carbon–fluorine bonds by oxidative addition.[7] There are few examples for C–F bond activation reactions via electron-deficient transition metal complexes.[7–26] For titanium compounds, Burk and co-workers showed, as one of the first examples, that tetrakis(trifluoromethyl)cyclopentadienone reacts with d^0 bis(cyclopentadienyl)-titanacyclobutanes to produce titanium fluoride products.[26] Our group has given an example of complete defluorination of a CF_3 moiety, employing a titanium amide.[18] Kiplinger and Richmond reported the first hydrogenolysis of an aromatic C–F bond at ambient temperature, using an in situ generated, low-valent zirconocene fragment [Cp_2Zr].[25] They also reported the conversion of several saturated perfluorohydrocarbon compounds into the corresponding aromatic derivatives by reductive defluorination, using the Cp_2TiF_2/Al/$HgCl_2$ system.[25] Jones et al. found that zirconocene hydrides ([$Cp_2ZrH_2]_2$, [$Cp^*_2ZrH_2$]) can activate a C–F bond of perfluorobenzene at room temperature.[22,27] They suggested the reaction proceeded by oxidative addition to a low valent zirconocene intermediate[22] and an S_NAr2 of fluorinated aromatics to give either reduced fluoroaromatics or new zirconium-aryl bonds.[12] Metallation of polyfluorinated pyridines and other fluorine-containing N-heterocycles in the 2-position via C–F activation is of special interest. Perutz et al. prepared the nickel complex [$NiF(2\text{-}C_5NF_4)(PEt_3)_2$] by reacting pentafluoropyridine with [$Ni(COD)(PEt_3)_2$][28] and provided new pathways for the synthesis of uncommon tetrafluoropyridines substituted at the 2-position.[29] Substitution reactions of unsubstituted pyridines at the 2-position are common and well known.[30] There are fewer examples of the synthesis of 2-

[a] Institut für Reine und Angewandte Chemie, Fakultät für Mathematik und Naturwissenschaften
Carl von Ossietzky Universität Oldenburg
Postfach 2503, 26111 Oldenburg, Germany,
Fax: +49-441-798-3581
E-mail: ruediger.beckhaus@uni-oldenburg.de

 DOI: 10.1002/ejic.200400252

substituted pyridines mediated by early transition metal complexes.[31,32] Teuben et al. have also synthesized a 6-substituted 2-methylpyridine by hydrogen transfer using a titanium complex.[33]

This paper describes the reactions of pyridine (**2**) and fluorosubstituted pyridines [pentafluoropyridine (**3**), 2-fluoropyridine (**4**)] with the titanocene fragments [Cp_2Ti] and [Cp^*_2Ti], generated in situ by using the corresponding bis(trimethylsilyl)acetylene complexes **10** and **13**.[34]

We also report the structure and facile synthesis of complexes **5**–**8** by activation of the 2-C–H and 2-C–F bonds of pyridine (**2**) and the fluorosubstituted pyridines **3** and **4**, respectively, using an in situgenerated titanocene fragment [Cp_2Ti] (**1**). Due to the facile preparation and its versatility the titanocene complex of bis(trimethylsilyl)acetylene (**10**)[34] was used as well as the reaction between magnesium and titanocene dichloride to generate the titanocene fragment.

Results and Discussion

Reactivity

Upon refluxing for 3 h, a solution of [$Cp_2Ti\{\eta^2$-$C_2(SiMe_3)_2\}$] (**10**) and C_5H_4N (**2**) in toluene the color changes from yellow to red-brown. Slow evaporation leads to precipitation of dark brown crystals of the fulvalene titanium complex **6** (Scheme 1). Stirring a suspension of [Cp_2TiCl_2], Mg and an excess of **2** in THF for 48 h yields a brown solution. Brown crystals of the binuclear titanocene complex **5** can then be obtained after filtration from the magnesium chloride pyridine adduct, removal of the solvent and recrystallization of the residue from toluene. Treatment of a solution of **10** in *n*-hexane with pentafluoro- (**3**) and monofluoropyridine (**4**)at ambient temperature leads to a color change from yellow to slightly green and to the slow crystallization of the fluoride-bridged binuclear titanium derivatives **7** and **8**, respectively. All these compounds were isolated as thermally robust solids with high melting points (207–217 °C) but they decomposed rapidly upon exposure to air and moisture. Complexes **5**–**8**, isolated in 25–75% yield, have been characterized by X-ray structure analysis, mass spectrometry and elemental analysis.

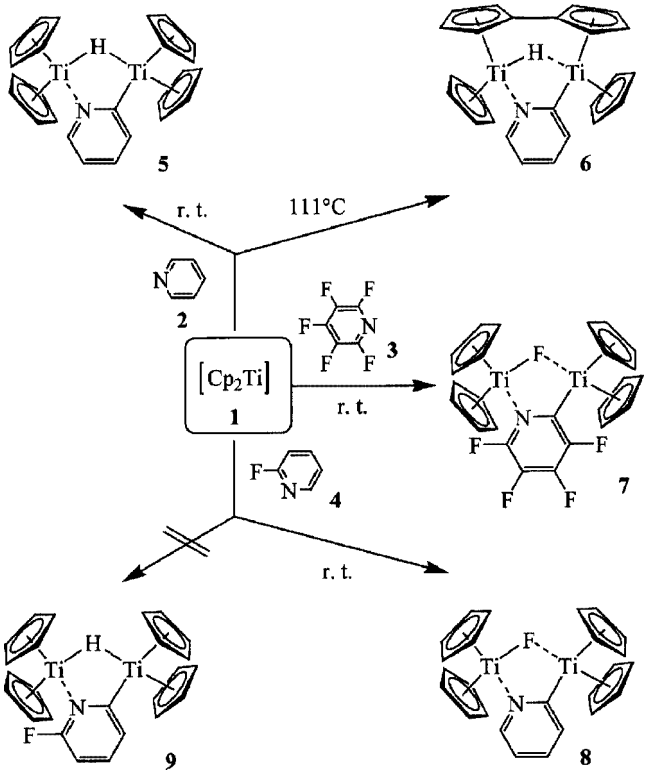

Scheme 1. Reaction of **1** (generated in situ from [$Cp_2Ti\{\eta^2$-$C_2(SiMe_3)_2\}$] or [Cp_2TiCl_2]/Mg) with pyridines **2**–**4**.

In all reactions of the in situ generated titanocene fragment **1** and N-heterocycles **2**–**4** we observed C–H or C–F bond activation at the 2-position and transfer of hydrogen or fluorine, respectively, into the titanium coordination sphere. The titanium(III) centres of the resulting dimeric complexes are bridged by a hydride and a fluoride, respectively, and the metallated pyridyl ligand. As expected for compounds with unpaired electrons the ^1H NMR spectra (300 MHz, 25 °C, C_6D_6) of the Ti^{III} complexes show either no or paramagnetically broadened signals. The positions of the signals are reproducible and provide a characteristic fingerprint. For the syntheses of complexes **6**–**8** the titanocene complex of bis(trimethylsilyl)acetylene (**10**) was used as the source of titanocene fragment **1**.[35] The reaction of **10** with pyridine (**2**) requires higher temperatures and results in the coupling of two Cp ligands, leading to fulvalene complex **6**. Conversely, **2** reacts with the titanocene generating system [Cp_2TiCl_2/Mg] at room temperature[36] to give complex **5** with no Cp ligand coupling (Scheme 2).

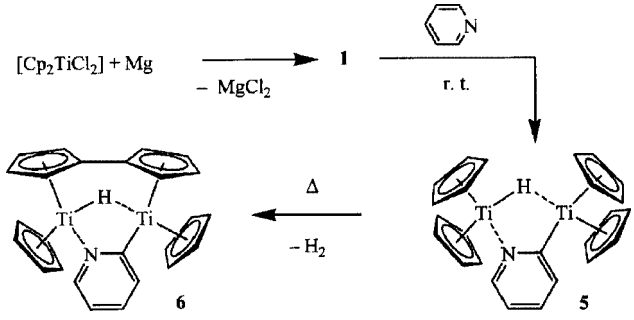

Scheme 2. Formation of fulvalene-bridged titanocene complex **6**.

Complex **5** has been isolated as an intermediate in the hydrosilylation of pyridines with silanes catalyzed by low valent titanocene complexes.[37] In this reaction the silane provides the bridging hydride of **5**, and the pyridine undergoes the ortho-metallation under liberation of H_2. The reaction between the titanocene fragment (**1**) and pyridine (**2**) shows that **5** can also be synthesized by C–H activation without an external hydride source. Several facts indicate that the reaction to **6** probablyproceeds via a preliminary hydride transfer from the pyridine and a subsequent coupling of the Cp ligands. The mass spectrum of **5** has no molecular peak, but one at [$M^+ - H_2$] (40% intensity) shows that this complex easily loses H_2, which suggests that the

 © 2005 Wiley-VCH Verlag GmbH & Co. KGaA, Weinheim

higher reaction temperature could explain the Cp ligand coupling and the formation of **6** instead of **5** if acetylene complex **10** is used to generate titanocene **1**. This is supported by the spectra of the product isolated after refluxing a solution of **5** for 3 h in toluene. IR and ^{1}H NMR spectra are identical to those of the fulvalene-bridged complex **6**, while the characteristic signals of **5** have vanished. For **5** a broad signal at δ = 31 ppm in the ^{1}H NMR spectrum is consistent with investigations by Harrod and Samuel, who assigned this signal to Cp ligands.[37] The ^{1}H NMR spectrum of **6** shows weaker broad signals at δ = 8.9,9.5, 10.9, 11.1,16.2 and 21.5 ppm. Accordingly, it seems reasonable to propose **5** as an intermediate in the reaction of **10** with **2** to give **6** because the coupling reaction follows its formation if the reaction is carried out at a higher temperature (Scheme 2).

The fact that [$Cp_2Ti\{\eta^2$-$C_2(SiMe_3)_2\}$] (**10**) reacts with perfluorinated pyridine (**3**) to afford complex **7** at room temperature, whereas pyridine only reacts at >100 °C, indicates that fluorine transfer is a favored reaction pathway. This has been confirmed by a C–H/C–F competition experiment with 2-fluoropyridine (**4**), which bears hydrogen as well as fluorine in the 2-position. In this reaction the selective transfer of fluorine occurs, and only the C–F activation product **8** is observed. The alternative C–H activation product **7** is not found. Under preparative conditions **8** could be isolated in 71% yield. A comparison of C–F and C–H bond activation by zerovalent nickel and platinum complexes shows, by DFT calculation, a preferred exothermic C–F bond activation, owing to a strong thermodynamic preference for C–F over C–H bond activation and a relatively low kinetic barrier.[38] Generally, ortho-substituted aryl fluorides undergo C–F bond activation. In such a way [Cp^*_2Zr(o-C_6H_4F)H] reacts by β-fluoride elimination to give [$Cp^*_2Zr(C_6H_5)$F].[20] The selectivity of C–F versus C–H activation depends on the nature of the transition metal system. Late transition metal complexes (Rh,[39] Os[40,41]) often prefer C–H over C–F activation reactions, whereas [Ru(dmpe)$_2H_2$] and partially fluorinated arenes produce only C–F bond activation products.[42] The insertion of tungsten in a C–F bond in the presence of C–H bonds was one of the first examples.[43]

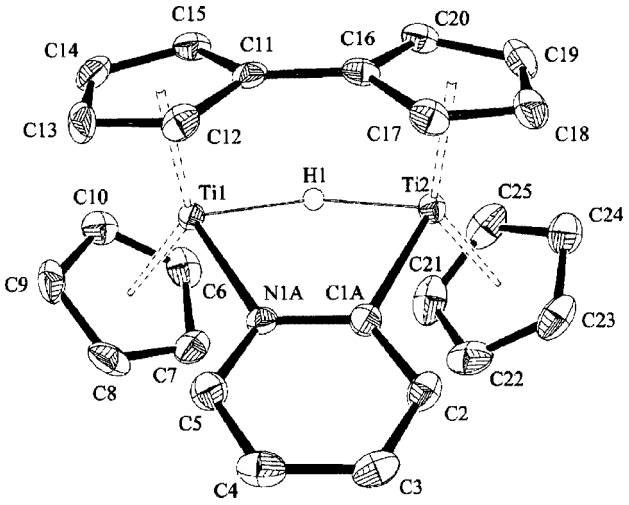

Figure 1. Molecular structure of **6**: ORTEP plot with 50% probability thermal ellipsoids; hydrogen atoms omitted for clarity.Thebridging H-atom has been freely refined. Selected bond lengths [Å] and angles [°]: Ti1–Ti2 3.324, Ti1–H1 1.85(3), Ti1–N1A 2.205(3), Ti2–H1 1.79(3), Ti2–C1A 2.205(3), Ti1–Ct1 2.062, Ti1–Ct2 2.040, Ti2–Ct3 2.050, Ti2–Ct4 2.065; Ct1–Ti1–Ct2 139.79, Ct3–Ti2–Ct4 137.21, H1–Ti1–N1A 84.6(9), H1–Ti2–C1A 84.7, Ti1–H1–Ti2 131.64, Ct1 = centroid of C6–C10, Ct2 = centroid of C11–C15, Ct3 = centroid of C16–C20, Ct4 = centroid of C21–C25.

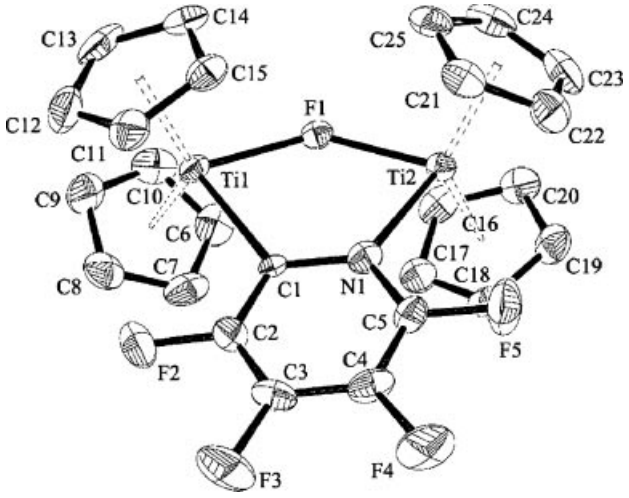

Figure 2. Molecular structure of **7**: ORTEP plot with 50% probability thermal ellipsoids. The asymmetric unit contains two independent molecules A and B; only data for A are given; hydrogen atoms omitted for clarity.Selected bond lengths [Å] and angles [°]: Ti1–Ti2 3.829, Ti1–F1 2.0487(13), Ti1–C1 2.277(2), Ti2–N1 2.288(2), Ti2–F1 2.0448(15), Ti1–Ct1 2.076, Ti1–Cpt 2.075, Ti2–Ct3 2.071, Ti2–Ct4 2.078; Cp1–Ti1–Ct2 132.72, Ct3–Ti2–Ct4 131.86, F1–Ti1–C1 78.31(7), F1–Ti2–N1 77.79(7), Ti1–F1–Ti2 138.62(8), Ct1 = centroid of C6–C10, Ct2 = centroid of C11–C15, Ct3 = centroid of C16–C20, Ct4 = centroid of C21–C25.

Crystal Structures of 6–8

Crystals suitable for X-ray structure analysis were obtained either directly from the reaction mixtures or after recrystallization from toluene for complex **5** and from fluorobenzene for complex **7**. Figure 1, Figure 2 and Figure 3 show the molecular structures of **6**–**8**, respectively.

Due to slight disorder of the pyridyl ligands in **6**–**8**, the Ti1–C1 and Ti2–N1 bond lengths could not be determined reliably. The asymmetric unit of **7** contains two independent molecules, A and B. Since the two molecules do not exhibit significant differences only the structure of A will be discussed. The bridging H-atom of **6** could be freely refined and the bond lengths between titanium and hydrogen, which average 1.82(3) Å, are in the same range as in the published structure of **5**[37] but shorter than in the analogue fulvalene hydrido chloride complex.[44] Ti–F bond lengths for **7** (2.047 Å) and **8** (2.051 Å) (average) are in the range expected for bent bridging Ti–F–Ti bonds.[45–48] The Ti–Ti distance in **6** (3.324 Å) is considerably shorter than in **7** (3.829 Å) and **8** (3.788 Å), probably due to the minor steric

 © 2005 Wiley-VCH Verlag GmbH & Co. KGaA, Weinheim

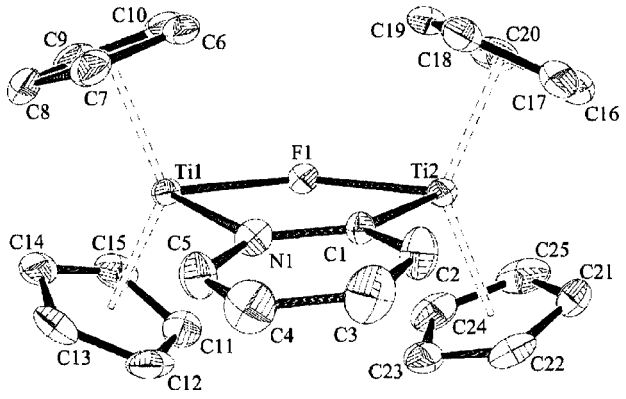

Figure 3. Molecular structure of **8**. ORTEP plot with 50% probability thermal ellipsoids; hydrogen atoms omitted for clarity. Selected bond lengths [Å] and angles [°]: Ti1–Ti2 3.788, Ti1–F1 2.0507(11), Ti1–N1 2.2271(18), Ti2–F1 2.0504(11), Ti2–C1 2.2252(18), Ti1–Ct1 2.081, Ti1–Ct2 2.078, Ti2–Ct3 2.084, Ti2–Ct4 2.083; Ct1–Ti1–Ct2 131.67, Ct3–Ti2–Ct4 132.91, F1–Ti1–N1 79.27(5), F1–Ti2–C1 79.60(6), Ti1–F1–Ti2 134.91, Ct1 = centroid of C6–C10, Ct2 = centroid of C11–C15, Ct3 = centroid of C16–C20, Ct4 = centroid of C21–C25.

demand of the hydride and the presence of the fulvalene bridge. In all three complexes the distance is beyond the range of a direct Ti–Ti interaction.

Reaction of 10 with Cyanuric Fluoride

Reactions between **10** and fluorinated and non-fluorinated triazine further support the cleavage of a C–F bond as a favored pathway in reactions of fluorinated N-heterocycles and low-valent titanium complexes. Scheme 3 shows the two reaction pathways.

Triazine reacts with **10**, through C–C coupling, to give a dimeric chelate ligand,[1] whereas the fluorinated analogue reacts through α-F-activation to form a complex similar to those obtained in the reactions with pyridines (Scheme 3).

Crystal Structure of 11

Figure 4 shows the molecular structure of **11**. Unlike the disordered pyridyl ligands in **6**–**8**,the N-heterocyclic ligand in **11** showed no disorder. The fluoride-bridge in **11** is approximately symmetric. Ti–F distances [Ti1–F1 = 2.0413(18) Å; Ti2–F1 2.0619(18) Å] are typical for fluoride-bridged Ti complexes[45] (Ti–F = 2.046 Å in $[(\eta^5\text{-}C_5H_5)Ti(\mu\text{-}F)]_2(\mu\text{-}\ \eta5\text{:}\ \eta5\text{-}C_{10}H_8)]$;[48] Ti–F = 2.092 Å in $[(C_5H_4Me)_2\text{-}TiF]_2$[49]). The Ti–Ti distance (3.831 Å) is similar to those in **6**–**8**. The Ti2–C1 bond [2.229(3) Å] is slightly shorter than the Ti1–C1 bond [2.293(3) Å]. Generally, **11** has the same structural characteristics as **6**–**8**.

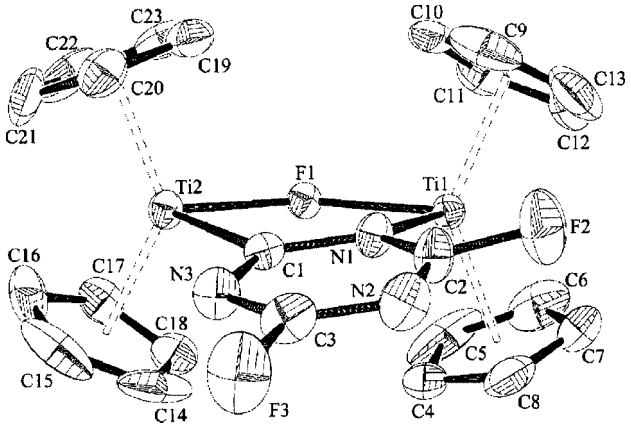

Figure 4. Molecular structure of **11**: ORTEP plot with 50% probability thermal ellipsoids; hydrogen atoms omitted for clarity. Selected bond lengths [Å] and angles [°]: Ti1–Ti2 3.831, Ti1–F1 2.0413(18), Ti1–N1 2.293(3), Ti2–F1 2.0619(18), C1–N1 1.391(4), N1–C2 1.324(4), C2–N2 1.310(4), N2–C3 1.318(5), C3–N3 1.299(4), N3–C1 1.373(4), Ti2–C1 2.229(3), Ti1–Ct1 2.067, Ti1–Ct2 2.073, Ti2–Ct3 2.067, Ti2–Ct4 2.072; Ct1–Ti1–Ct2 132.18, Ct3–Ti2–Ct4 133.66, F1–Ti1–N1 77.39, F1–Ti2–C1 78.62, Ti1–F1–Ti2 138.02(9), Ct1 = centroid of C4–C8, Ct2 = centroid of C9–C13, Ct3 = centroid of C14–C18, Ct4 = centroid of C19–C23.

Reactions of $[Cp^*_2Ti\{\eta^2\text{-}C_2(SiMe_3)_2\}]$ (13) with Fluorinated N-Heterocycles

To understand the formation of binuclear complexes **7**, **8** and **11** reactions were performed using the permethylated complex $[Cp^*_2Ti\{\eta^2\text{-}C_2(SiMe_3)_2\}]$ (**13**)[34] instead of the non-methylated analogue **10**.

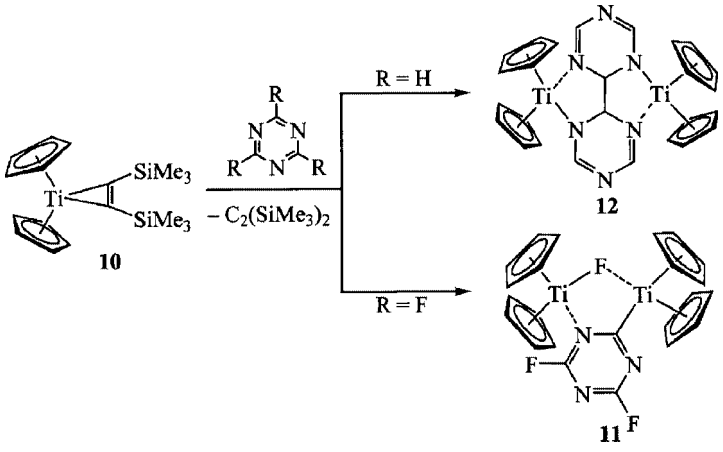

Scheme 3. Reaction of **10** with triazine and cyanuric fluoride.

 © 2005 Wiley-VCH Verlag GmbH & Co. KGaA, Weinheim

Both fluorosubstituted pyridines and cyanuric fluoride react with **13** to give $[Cp^*_2TiF_2]$ (**16**) as the final product and not binuclear, fluoride-bridged titanocene complexes. Mass spectroscopic investigations, as well as ^1H, ^{13}C and ^{19}F NMR experiments, revealed the intermediate formation of mononuclear Ti^{IV} complexes, which react further with fluorinated starting material to form **16** (Scheme 4).

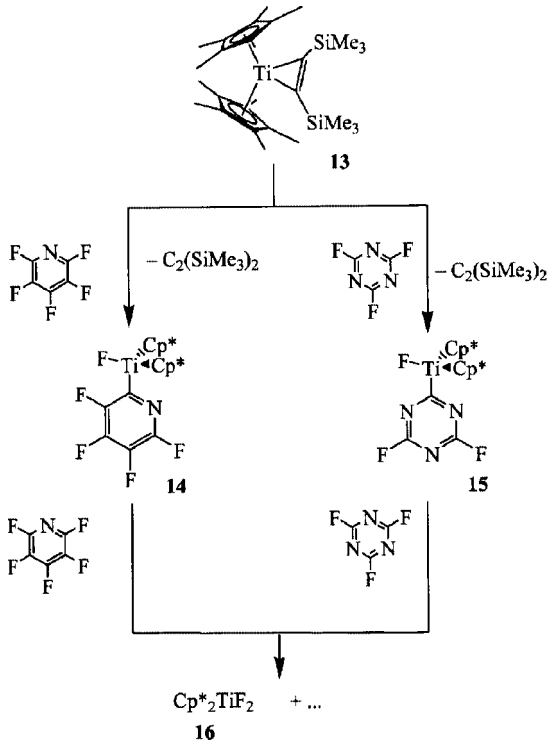

Scheme 4. Reaction of $[Cp^*_2Ti\{\eta^2\text{-}C_2(SiMe_3)_2\}]$ (**13**) with pentafluoropyridine and cyanuric fluoride, with intermediate formation of mononuclear complexes **14** and **15**.

^1H, ^{13}C and ^{19}F NMR spectroscopic data of **14** were obtained by recording NMR spectra of a corresponding reaction mixture. Therefore, the acetylene complex **13** was reacted with pentafluoropyridine for 2 h at 60 °C in *n*-hexane. The volatiles were then removed and the resulting solid was redissolved in C_6D_6. The ^{19}F NMR spectrum of the reaction mixturedisplaysfour multiplets of equal integration in the fluoroaromatic region at δ = –170.31, –147.48, –130.08 and –87.61, which are assignable to the fluoro nuclei of the pyridyl ligand of complex **14**. These δ are in excellent agreement with ^{19}F NMR spectroscopic data given for the complex $[NiF(2\text{-}C_5NF_4)(PEt_3)_2]$, which contains a fluorosubstituted pyridyl ligand with an analogous substitution pattern (δ –173.38, –150.75, –131.33, –84.70).[50] The spectrum also shows a singlet for the metal fluoride of **14** at δ = 128.82. Another ^{19}F resonance at δ = 74.14 was assigned to the final product $[Cp^*_2TiF_2]$ (**16**), which is consistent with the NMR spectroscopic data of pure **16** in C_6D_6 prepared according to the literature.[51] The proton spectrum of the reaction mixture shows a singlet at δ = 1.56, assigned to **14**, and, as expected, a further singlet at δ = 1.82, which was assigned to **16**. The single resonance seen for the protons of **14** reveals that the Cp*–Ti–Cp* plane is orthogonal to that of the pyridyl ligand. Consistently, only two signals assigned to the Cp* ligands of **14** arise in the ^{13}C NMR spectrum, at δ = 11.3 and 124.4, respectively. Two further signals, at δ = 11.2 and 124.9, are as expected for **16**. To determine that **14** is formed as an intermediate that reacts with pentafluoropyridine to give the final product **16** the reaction was monitored by following the increase of the ^1H resonance of **14** at δ = 1.56 as the reaction starts and the decrease of this resonance while that assigned to **16** at δ = 1.82 increases. Analogues NMR investigations revealed the formation of the intermediate complex **15** and, subsequently, **16** in the reaction between **13** and cyanuric fluoride (Scheme 4). Besides **16**, NMR investigations could characterize no further products. The fate of the fluoroaromatic ligands could not be clarified. The fluoroaromatic region of the ^{19}F spectra showed several additional signals of very low intensity, probably due to the formation of multiple compounds in low concentration. Table 1 summarizes the ^1H and ^{19}F NMR spectroscopic data of intermediates **14** and **15**.

Table 1. NMR spectroscopic data of **14**, **15** (C_6D_6, 298 K).[a]

Complex	^1H	^{19}F
14	1.56 (s, 30 H, CH_3)	128.82 (s, 1 F, Ti–F)
		–87.61 (m, 1 F)
		–130.08 (m, 1 F)
		–147.48 (m, 1 F)
		–70.31 (m, 1 F)
15	1.53 (s, 30 H, CH_3)	128,71 (s, 1 F, Ti–F)
		–41.00 (d, J_{FF} = 12, 1 F)
		–45.31 (d, J_{FF} = 12, 1 F)

[a] Reported in ppm (δ) and *J* values in Hz.

Mass spectra (MS CI, *iso*-butane) of reaction mixtures prepared analogously to those used for the NMR investigations also showed evidence for the intermediate formation of mononuclear Ti^{IV} complexes **14** and **15**. The spectra show the characteristic fragments $[M + 1]^+$, $[M - F]^+$, $[Cp^*_2TiF_2]^+$, $[Cp^*_2TiF]^+$ and $[Cp^*]^+$ (M = molecular mass of **14** and **15**, respectively). Due to their similarly high solubilities, **14** and **15** could not be separated from the final product **16**.

Intermediate formation of mononuclear Ti^{IV} complexes can also be assumed in the reactions to **6**–**8**, and **11**. The Ti^{IV} species might subsequently react further with in situ generated titanocene $[Cp_2Ti^{II}]$ in terms of a comproportion reaction that results in Ti^{III} complexes **6**–**8** and **11** (Scheme 5).

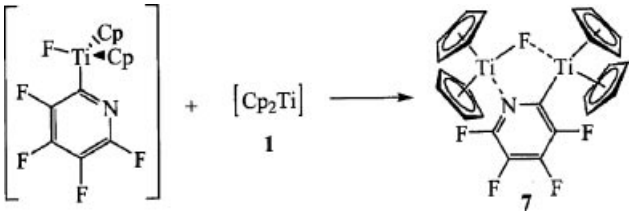

Scheme 5. Proposed formation of binuclear Ti^{III} complex **7**.

 © 2005 Wiley-VCH Verlag GmbH & Co. KGaA, Weinheim

The observed preference for C–F activation at the 2-position of the fluoropyridines provides indirect evidence for concerted oxidative addition of the heterocycles via a three-centered transition state, as proposed for nickel-mediated C–F bond activation reactions.[52] A primary electron transfer reaction pathway, as expected from the reducing properties of titanium(II) derivatives, can be excluded due to the absence of reactions at the 4-position, which are found as a result of the formation of ion pairs or Meisenheimer type intermediates.[53–56]

Conclusions

Titanocene-generating systems can selectively activate 2-C–H and 2-C–F bonds of pyridine and fluorosubstituted pyridines, respectively, in reactions that yield dimeric, hydride-bridged Ti^{III} complexes. C–F activation reactions at room temperature between the titanocene source $[Cp_2Ti\{\eta^2\text{-}C_2(SiMe_3)_2\}]$ and the fluorosubstituted N-heterocycles pentafluoropyridine and 2-fluoropyridine, as well as cyanuric fluoride, afforded dimeric, fluoride-bridged titanocene complexes that were isolated in good yields. The reaction of $[Cp_2Ti\{\eta^2\text{-}C_2(SiMe_3)_2\}]$ with 2-fluoropyridine showed that 2-C–F activation is preferred over 2-C–H activation. The ease synthesis of polyfluorinated pyridines metallated at the 2-position, via C–F activation reactions, may offer new opportunities to synthesize polyfluorinated pyridines substituted at the 2-position. Such compounds are very difficult to prepare by either electrophilic or nucleophilic substitution.[53,57–60]

Experimental Section

General Remarks: All operations were performed under nitrogen with rigorous exclusion of oxygen and moisture using glove box or Schlenk techniques. Solvents were thoroughly dried and saturated with nitrogen. ^1H and ^{19}F NMR spectra were recorded with a Bruker AVANCE 300 spectrometer (^1H, 300.1 MHz; ^{19}F, 282.4 MHz). ^1H NMR chemical shifts were referenced to residual protons of the solvent; ^{13}C and ^{19}F NMR spectra were referenced to C_6D_6 and $CFCl_3$ (externally), respectively. Electron impact (EI) mass spectra were recorded with a Finnigan-MAT 95 Spectrometer. IR spectra were recorded with a BIO-RAD FTS-7 Spectrometer using KBr pellets. Elemental analyses were carried out by the Analytischen Laboratorien in Lindlar (Germany). $[Cp_2Ti\{\eta^2\text{-}C_2(SiMe_3)_2\}]$ (**10**) and $[Cp^*_2Ti\{\eta^2\text{-}C_2(SiMe_3)_2\}]$ (**13**) were prepared according to the literature.[34] All heterocyclic compounds (Aldrich) were used as received.

Preparation of Complex 5: A suspension of Cp_2TiCl_2 (1 g, 4 mmol), magnesium (96 mg, 4 mmol) and pyridine (2 mL, excess) in THF (40 mL) was stirred for 48 h. The solution turned dark brown and a white solid precipitated. The mixture was then concentrated and the resultant brown solid was dissolved in toluene (20 mL) and filtered. Concentrating the solution to a few mL afforded 420 mg (48%) of **5** as brown crystals that were washed with *n*-hexane and dried in vacuo. M.p. 217–219 °C; ^1H NMR (C_6D_6): δ = 31.0, 16.3, 14.0, 11.1, 10.9 ppm broad signals. IR (KBr): $\tilde{\nu}$ = 3075, 1601, 1441, 1217, 1067, 1009, 793, 758, 698, 629 cm^{-1}. $C_{25}H_{25}NTi_2$ (435.24 $g\,mol^{-1}$); MS (70 eV): *m*/*z* (rel. intensity) 433 (40) [$M^+ - H_2$], 354 (100) [$M^+ - C_5H_7N_2$], 288 (20), 260 (15), 178 (85) [$Cp_2Ti]^+$, 113 (20) [$CpTi]^+$, 66 (15) [$CpH]^+$ The experimental data, including the molecular structure determined by single crystal X–ray diffraction, agree with published results.[37]

Preparation of Complex 6: A solution of **10** (1 g, 2.87 mmol) and pyridine (2 mL, excess) in toluene (30 mL), heated under reflux for 3 h, turned dark brown. Concentrating the solution to a few mL afforded 150 mg (24%) of **6** as brown crystals that were washed with *n*-hexane and dried in vacuo. M.p. 203–205 °C; ^1H NMR (C_6D_6): δ = 16.2, 11.0, 10.9, 9.5, 8.9 ppm broad paramagnetic signals. IR (KBr): $\tilde{\nu}$ = 3079, 1576, 1520, 1435, 1242, 1042, 1009, 8097, 799, 735, 631, 586 cm^{-1}. MS (70 eV): *m*/*z* (rel. intensity) 433 (50) [M^+], 354 (100) [$M^+ - C_5H_5N$], 288 (25), 260 (18), 178 (25) [$Cp_2Ti]^+$, 113 (25) [$CpTi]^+$. HR-MS: calcd 433.0789; found 433.0793. $C_{25}H_{23}NTi_2$ (433.22 $g\,mol^{-1}$): calcd H 5.35, C 69.31, N 3.23; found H 5.39, C 69.06, N 3.11.

Preparation of Complex 7: 10 (300 mg, 0.86 mmol) and pentafluoropyridine (**3**) (72.8 mg, 0.43 mmol) were dissolved in *n*-hexane (60 mL) at room temperature. After 24 h crystals precipitated, and the reaction was complete after one week. The mixture changed from yellow to slightly green during the reaction. Crystals, separated from the solution by decanting, were washed twice with *n*-hexane (20 mL) and subsequently dried in vacuo. The yield of **7** was 158 mg (70%) as green-yellow crystals. Crystals suitable for X-ray structure analysis were obtained from fluorobenzene. M.p. 207 °C, IR (KBr): $\tilde{\nu}$= 3937, 3090, 2955, 1715, 1620, 1588, 1505, 1478, 1437, 1373, 1252, 1090, 1013, 795, 691, 592, 471, 395, 226 cm^{-1}. MS (70 eV): *m*/*z* (rel. intensity) 328 (95) [$M^+ - Cp_2TiF$], 197 (80) [$Cp_2TiF]^+$, 178 (85) [$Cp_2Ti]^+$, 132 (100) [$CpTiF]^+$. $C_{25}H_{20}F_5NTi_2$ (525.19 $g\,mol^{-1}$): calcd. H 3.84, C 57.18, F 18.09; found H 3.78, C 56.97, F 18.01.

Preparation of Complex 8: 10 (300 mg 0.86 mmol) and 2-fluoropyridine (41.8 mg 0.43 mmol) (**4**) were dissolved in *n*-hexane (60 mL) at room temperature. After one week, the solution was cooled to 0 °C and tawny crystals precipitated. During the reaction the mixture changed from yellow to slightly green. Crystals, separated from the solution by decanting, were washed twice with *n*-hexane (20 mL) and subsequently dried in vacuo. The yield of **8** was 139 mg (71%) as tawny crystals. Crystals suitable for X-ray structure analysis were obtained from the reaction mixture. M.p. 211 °C, IR (KBr): $\tilde{\nu}$= 3090, 2955, 2724, 2367, 2276, 2081, 1651, 1578, 1532, 1449, 1441,1398,1362, 1260, 1154, 1065, 1013, 795, 727, 667, 590, 485, 451, 422, 378 cm^{-1}. MS (70 eV): *m*/*z* (rel. intensity) 256 (100) [$M^+ - Cp_2TiF$], 197 (70) [$Cp_2TiF]^+$, 178 (60) [$Cp_2Ti]^+$, 132 (95) [$CpTiF]^+$. $C_{25}H_{24}FNTi_2$ (453,23 $g\,mol^{-1}$): calcd. H 5.34, C 66.26, F 4.02; found H 5.23, C 65.91, F 4.19.

Preparation of Complex 11: 10 (300 mg, 0.86 mmol) and cyanuric fluoride (**9**) (58.1 mg, 0.43 mmol) were dissolved in *n*-hexane (60 mL) at room temperature. After 6 h a brown solid and dark brown crystals precipitated; the reaction was completed after 3 days. The solid, separated from the solution by decanting, was washed twice with *n*-hexane (20 mL) and subsequently dried in vacuo. The yield of **9** was 148 mg (70%) as a brown solid. Crystals suitable for X-ray structure analysis were obtained from the reaction mixture. M.p. 160 °C (dec.), IR (KBr): $\tilde{\nu}$= 3740, 3104, 2955, 2864, 2733, 2517, 2367, 2338, 1615, 1580, 1495, 1398, 1260, 1094, 1017, 804, 689, 590, 463, 397, 328, 303, 280 cm^{-1}. MS (70 eV): *m*/*z* (rel. intensity) 197 (60) [$Cp_2TiF]^+$, 178 (20) [$Cp_2Ti]^+$, 132 (100) [$CpTiF]^+$, 65 (50) [$Cp]^+$. $C_{23}H_{20}F_3N_3Ti_2$ (491.19 $g\,mol^{-1}$): H 4.10, C 56.24, F 11.60; found H 4.13, C 55.99, F 11.32.

Crystal Structure Determinations: Data for structures **6**–**8** and **11** were collected with a STOE-IPDS diffractometer with graphite-

 © 2005 Wiley-VCH Verlag GmbH & Co. KGaA, Weinheim

Table 2. Crystal structure data for complexes **6**–**8**, and **11**.

	6	**7**	**8**	**11**
Empirical formula	$C_{25}H_{23}NTi_2$	$C_{56}H_{45}F_{11}N_2Ti_4$	$C_{28}H_{31}FNTi_2$	$C_{23}H_{20}F_3N_3Ti_2$
Formula mass	433.24	1146.54	496.34	491.22
Diffractometer	STOE IPDS	STOE IPDS	STOE IPDS	STOE IPDS
Crystal dimensions [mm]	0.5 × 0.13 × 0.04	0.88 × 0.11 × 0.06	1.00 × 0.18 × 0.08	0.17 × 0.11 × 0.06
Color, habit	brown	yellow	tawny	brown
Crystal system	orthorhombic	orthorhombic	orthorhombic	monoclinic
a [Å]	14.1436(7)	7.9100(2)	17.7395(5)	14.5571(9)
b [Å]	16.1737(4)	18.2720(4)	17.3790(5)	9.7461(3)
c [Å]	17.2637(7)	33.6745(12)	7.81280(10)	15.5543(9)
α [°]	90	90	90	90
β [°]	90	90	90	114.017(7)
γ [°]	90	90	90	90
V [Å^3]	3949.1(3)	4867.0(2)	2408.65(10)	2015.71(18)
Space group	*Pbca*	$P2_12_12_1$	$P2_12_12$	$P2_1/c$
Z	8	4	4	4
$D_{calcd.}$ [Mg m^{-3}]	1.457	1.565	1.369	1.619
ν [mm^{-1}]	0.819	0.716	0.686	0.835
F_{000}	1792	2328	1036	1000
λ (Mo-*Kα*, graphite) [Å]	0.71073	0.71073	0.71073	0.71073
Temp. [K]	193(2)	193(2)	193(2)	193(2)
θ Range for collection [°]	2.25 to 25.94	2.13 to 26.01	2.30 to 26.01	2.53 to 25.96
No. reflns. collected	327242	42160	25102	20089
No. obsd. reflns. [$I > 2\sigma(I)$]	2186	7586	3919	2199
No. independent reflns.	3649	9058	4506	3921
Absorption corr. method	numerical	none	numerical	none
Max., min. transmission	0.9680, 0.6850	0.9583, 0.5713	0.9471, 0.5469	0.9516, 0.8710
No. data/restraints/parameters	3649/0/344	9058/0/662	4506/0/382	3921/0/280
R indices (all data)	*R*1 = 0.0801, *wR*2 = 0.0663	*R*1 = 0.0410, *wR*2 = 0.0644	*R*1 = 0.0308, *wR*2 = 0.0538	*R*1 = 0.0959, *wR*2 = 0.0808
Final *R* indices [$I > 2\sigma(I)$]	*R*1 = 0.0368, *wR*2 = 0.0586	*R*1 = 0.0305, *wR*2 = 0.0618	*R*1 = 0.0241, *wR*2 = 0.0522	*R*1 = 0.0395, *wR*2 = 0.0694
GoF on F^2	0.837	0.939	0.968	0.801
Fleck parameter	–	–0.003(15)	–0.001(18)	–
Largest diff. peak, hole [e Å^{-3}]	0.268, –0.264	0.229, –0.266	0.333, –0.203	0.316, –0.370

monochromated Mo-Kα radiation (*λ* = 0.71073 Å). Table 2 summarizes the crystal data and intensity collection and refinement parameters. Intensity measurements were performed at 193(2) K. The structure of each complex was solved by direct phase determination (SHELXL 97)[61] and refined on F^2 (SHELXL 97)[61] with anisotropic thermal parameters for all non-hydrogen atoms. CCDC-223097 (**6**), -223098 (**7**), -223099 (**8**), and CCDC-243696 (**11**) contain the supplementary crystallographic data for this paper. These data can be obtained free of charge from The Cambridge Crystallographic Data Centre via www.ccdc.cam.ac.uk/data_request/cif.

Acknowledgments

This work was supported by the Fonds der Chemischen Industrie and by the Karl-Ziegler-Stiftung der Gesellschaft Deutscher Chemiker.

[1] S. Kraft, R. Beckhaus, D. Haase, W. Saak, *Angew. Chem.* **2004**, *116*, 1609–1614; *Angew. Chem. Int. Ed.* **2004**, *43*, 1583–1587.
[2] P. T. Witte, R. Klein, H. Kooijman, A. L. Spek, M. Polasek, V. Varga, K. Mach, *J. Organomet. Chem.* **1996**, *519*, 195–204.
[3] D. R. Corbin, W. S. Willis, E. N. Duesler, G. D. Stucky, *J. Am. Chem. Soc.* **1980**, *102*, 5969–5971.
[4] A. M. McPherson, B. F. Fieselmann, D. L. Lichtenberger, G. L. McPherson, G. D. Stucky, *J. Am. Chem. Soc.* **1979**, *101*, 3425–3430.
[5] L. D. Durfee, P. E. Fanwick, I. P. Rothwell, K. Folting, J. C. Huffman, *J. Am. Chem. Soc.* **1987**, *109*, 4720–4722.
[6] D. M. W. van den Ham, G. F. S. Harrison, A. Spaans, D. van der Meer, *Recl. Trav. Chim. Pays-Bas* **1975**, *94*, 168–173.
[7] General aspects and reviews;[7–10] mechanistic aspects using early transition metals,[11–13] selected examples using early transition metals:[14–16] J. L. Kiplinger, T. G. Richmond, C. E. Osterberg, *Chem. Rev.* **1994**, *94*, 373–431.
[8] T. G. Richmond, *Angew. Chem.* **2000**, *112*, 3378–3380; *Angew. Chem. Int. Ed.* **2000**, *39*, 3241–3243.
[9] T. Richmond, *Metal Reagents for Activation and Functionalization of Carbon-Fluorine Bonds* (Ed.: Murai, S.), Springer, Berlin, **1999**, vol. 3.
[10] J. Burdeniuc, B. Jedlicka, R. H. Crabtree, *Chem. Ber./Recueil* **1997**, *130*, 145–154.
[11] E. Clot, C. Megret, B. M. Kraft, O. Eisenstein, W. D. Jones, *J. Am. Chem. Soc.* **2004**, *126*, 5647–5653.
[12] W. D. Jones, *J. Chem. Soc., Dalton Trans.* **2003**, 3991–3995.
[13] B. M. Kraft, W. D. Jones, *J. Am. Chem. Soc.* **2002**, *124*, 8681–8689.
[14] P. A. Deck, M. M. Konaté, B. V. Kelly, C. Slebodnick, *Organometallics* **2004**, *23*, 1089–1097.
[15] P. E. O'Connor, D. J. Berg, T. Barclay, *Organometallics* **2002**, *21*, 3947–3954.
[16] M. W. Bouwkamp, J. de Wolf, I. del Hierro Morales, J. Gercama, A. Meetsma, S. I. Troyanov, B. Hessen, J. H. Teuben, *J. Am. Chem. Soc.* **2002**, *124*, 12956–12957.
[17] B. M. Kraft, R. J. Lachicotte, W. D. Jones, *Organometallics* **2002**, *21*, 727–731.
[18] C. Santamaria, R. Beckhaus, D. Haase, W. Saak, R. Koch, *Chem. Eur. J.* **2001**, *7*, 622–626.
[19] L. A. Watson, D. V. Yandulov, K. G. Caulton, *J. Am. Chem. Soc.* **2001**, *123*, 603–611.

 © 2005 Wiley-VCH Verlag GmbH & Co. KGaA, Weinheim

[20] B. M. Kraft, R. J. Lachicotte, W. D. Jones, *J. Am. Chem. Soc.* **2001**, *123*, 10973–10979.
[21] B. M. Kraft, R. J. Lachicotte, W. D. Jones, *J. Am. Chem. Soc.* **2000**, *122*, 8559–8560.
[22] B. L. Edelbach, A. K. F. Rahman, R. J. Lachicotte, W. D. Jones, *Organometallics* **1999**, *18*, 3170–3177.
[23] M. J. Nelsen, G. S. Girolami, *J. Organomet. Chem.* **1999**, *585*, 275–284.
[24] J. L. Kiplinger, T. G. Richmond, *Chem. Commun.* **1996**, 1115–1116.
[25] J. L. Kiplinger, T. G. Richmond, *J. Am. Chem. Soc.* **1996**, *118*, 1805–1806.
[26] M. J. Burk, D. L. Staley, W. Tumas, *J. Chem. Soc., Chem. Commun.* **1990**, 809–810.
[27] B. M. Kraft, W. D. Jones, *J. Organomet. Chem.* **2002**, *658*, 132–140.
[28] T. Braun, S. Parsons, R. N. Perutz, M. Voith, *Organometallics* **1999**, *18*, 1710–1716.
[29] T. Braun, R. N. Perutz, M. I. Sladek, *Chem. Commun.* **2001**, *21*, 2254–2255.
[30] H. Vorbrüggen, *Adv. Heterocycl. Chem.* **1990**, *49*, 117–192.
[31] E. Klei, J. H. Teuben, *J. Organomet. Chem.* **1981**, *214*, 53–64.
[32] B. Klei, J. H. Teuben, *J. Chem. Soc., Chem. Commun.* **1978**, 659–660.
[33] J. W. Pattiasina, F. van Bolhuis, J. H. Teuben, *Angew. Chem.* **1987**, *99*, 342–343; *Angew. Chem. Int. Ed. Engl.* **1987**, *26*, 330–331.
[34] V. V. Burlakov, A. V. Polyakov, A. I. Yanovsky, Y. T. Struchkov, V. B. Shur, M. E. Vol′pin, U. Rosenthal, H. Görls, *J. Organomet. Chem.* **1994**, *476*, 197–206.
[35] U. Rosenthal, V. V. Burlakov, P. Arndt, W. Baumann, A. Spannenberg, *Organometallics* **2003**, *22*, 884–900.
[36] For different titanocene generating systems and literature therein: R. Beckhaus, *Titanocenes* (Eds.: R. L. Halterman, A. Togni), VCH, Weinheim, **1998**, chapter 4, p. 153.
[37] L. Hao, J. F. Harrod, A.-M. Lebuis, Y. Mu, R. Shu, E. Samuel, H.-G. Woo, *Angew. Chem.* **1998**, *110*, 3314–3318; *Angew. Chem. Int. Ed.* **1998**, *37*, 3126-3129.
[38] M. Reinhold, J. E. McGrady, R. N. Perutz, *J. Am. Chem. Soc.* **2004**, *126*, 5268–5276.
[39] A. D. Selmeczy, W. D. Jones, M. G. Partridge, R. N. Perutz, *Organometallics* **1994**, *13*, 522–532.
[40] P. Barrio, R. Castarlenas, M. A. Esteruelas, A. Lledos, F. Maseras, E. Onate, J. Tomas, *Organometallics* **2001**, *20*, 442–452.
[41] R. Bosque, E. Clot, S. Fantacci, F. Maseras, O. Eisenstein, R. N. Perutz, K. B. Renkema, K. G. Caulton, *J. Am. Chem. Soc.* **1998**, *120*, 12634–12640.
[42] M. K. Whittlesey, R. N. Perutz, M. H. Moore, *Chem. Commun.* **1996**, 787–788.
[43] B. L. Lucht, M. J. Poss, M. A. King, T. G. Richmond, *J. Chem. Soc., Chem. Commun.* **1991**, 400–401.
[44] E. G. Perevalova, I. F. Uranzowski, D. A. Lemenovskii, Y. L. Slovokhotov, Y. T. Struchkov, *J. Organomet. Chem.* **1985**, *289*, 319–329.
[45] Bridging Ti–F–Ti bonds: overview;[45] selected examples: $[(TiF_6)(TiCp_2)_3]$ 2.097(2) Å;[46] $[\{Cp^*Ti(F)_2(\mu\text{-}F)\}_2]$ 2.002 Å;[47] $[(\eta^5\text{:}\eta^5\text{-}C_{10}H_8)Ti_2(\mu\text{-}F)_2Cp_2]$ 2.046(4) Å;[48] H. W. Roesky, I. Haiduc, *J. Chem. Soc., Dalton Trans.* **1999**, 2249–2264.
[46] F.-Q. Liu, A. Künzel, A. Herzog, H. W. Roesky, M. Noltemeyer, R. Fleischer, D. Stalke, *Polyhedron* **1997**, *16*, 61–65.
[47] M. Sotoodeh, I. Leichtweis, H. W. Roesky, M. Noltemeyer, H.-G. Schmidt, *Chem. Ber.* **1993**, *126*, 913–919.
[48] P. Yu, E. F. Murphy, H. W. Roesky, P. Lubini, H.-G. Schmidt, M. Noltemeyer, *Organometallics* **1997**, *16*, 313–316.
[49] A. Herzog, F.-Q. Liu, H. W. Roesky, A. Demsar, K. Keller, M. Noltemeyer, F. Pauer, *Organometallics* **1994**, *13*, 1251–1256.
[50] L. Cronin, C. L. Higgitt, R. Karch, R. N. Perutz, *Organometallics* **1997**, *16*, 4920–4928.
[51] P. G. Gassman, W. H. Campbell, D. W. Macomber, *Organometallics* **1984**, *3*, 385–387.
[52] T. Braun, R. N. Perutz, *Chem. Commun.* **2002**, 2749–2757.
[53] Compare discussion[52] and examples,[53–56] G. M. Brooke, *J. Fluorine Chem.* **1997**, *86*, 1–76.
[54] P. L. Coe, A. J. Rees, *J. Fluorine Chem.* **2002**, *101*, 45–60.
[55] A. J. Adamson, W. J. Jondi, A. E. Tipping, *J. Fluorine Chem.* **1996**, *76*, 67–78.
[56] H. Benmansour, R. D. Chambers, P. R. Hoskin, G. Sandford, *J. Fluorine Chem.* **2001**, *112*, 133–137.
[57] R. E. Banks, W. Jondi, A. E. Tipping, *J. Chem. Soc., Chem. Commun.* **1989**, 1268–1269.
[58] R. D. Chambers, J. S. Waterhouse, D. L. H. Williams, *J. Chem. Soc., Perkin Trans. 2* **1977**, 585–588.
[59] R. E. Banks, R. N. Haszeldine, K. H. Legge, F. E. Rickett, *J. Chem. Soc., Perkin Trans. 1* **1974**, 2367–2369.
[60] R. E. Banks, W. J. Jondi, A. E. Tipping, *J. Fluorine Chem.* **1996**, *99*, 87–92.
[61] G. M. Sheldrick, *SHELXL-97, A program for refining crystal structures*, University of Göttingen, **1997**..

Received: March 29, 2004

 © 2005 Wiley-VCH Verlag GmbH & Co. KGaA, Weinheim

Two Novel Transition-Metal Phosphite Compounds with 4-, 6- and 12-Membered Rings: Hydrothermal Syntheses, Crystal Structures and Magnetic Properties of $Na_2[M(HPO_3)_2]$ (M = Fe, Co)

Wei Liu,[a] Hao-Hong Chen,[a] Xin-Xin Yang,[a] and Jing-Tai Zhao*[a]

Keywords: Synthesis / Structure / Cobalt / Iron / Phosphites / Magnetic properties

Two transition-metal phosphites, $Na_2[M(HPO_3)_2]$ (M = Fe, Co) with a new structure type have been synthesised under mild hydrothermal conditions and the solid-state structures have been elucidated by single-crystal X-ray diffraction studies. The structures are of a new type with the following data: orthorhombic, *Pnma*, a = 12.169(4), b = 5.441(2) and c = 9.146(3) Å for the iron species **1** and a = 12.091(3), b = 5.400(4) and c = 9.115(2) Å for the cobalt compound **2**, with Z = 4. The crystal structures of these compounds are isotypic and built up from a 3D open framework with 4-, 6- and 12-membered polyhedral rings of vertex-linked MO_6 and HPO_3 building units. The inorganic frameworks contains 12-membered ring channel systems in which the sodium ions are located. The topology of this structure type is remarkably similar to that of the aeschynite $CaTa_2O_6$ with much larger channels. Magnetic measurements of $Na_2[Co(HPO_3)_2]$ show different magnetic features in the low-temperature (5–30 K) and high-temperature ranges (100–320 K) suggesting the possible existence of a complex magnetic structure. Antiferromagnetic ordering can be observed as a broadened cusp in χ^{-1} at θ = 2.6 K. For $Na_2[Fe(HPO_3)_2]$, the magnetic behavior follows the Curie–Weiss law with μ_{eff} = 5.41 μ_B, fitted for 100–320 K.

(© Wiley-VCH Verlag GmbH & Co. KGaA, 69451 Weinheim, Germany, 2005)

Introduction

Transtion-metal phosphates with open-framework structures are of great interest from both an industrial and an academic point of view due to their applications as catalysts, ion-exchangers and molecular sieves.[1] Although attention has focused initially on the phosphates of aluminium and gallium because of their structural similarities with zeolites and clays, numerous open-framework transition-metal phosphates with novel properties are also known.[2–17] Besides, in the past few years, considerable efforts have been devoted to exploratory work on the possibilities of incorporating the phosphorus atom as a pseudo-pyramidal HPO_3^{2-} hydrogen phosphite group into extended structures and these studies have yielded a structurally diverse range of transition-metal phosphites, e.g. $(VO)(HPO_3)(H_2O)_5$ with isolated single chains,[18] $ZnCa(HPO_3)_2(H_2O)_2$,[19] $Fe(HPO_3H)_3$,[20] $M(HPO_3)(H_2O)$ (M = Co, Ni)[21] and $(NH_4)_2Zn_5(HPO_3)_6(H_2O)_4$[22] with layered structures as well as $NaM(H_2PO_3)_3(H_2O)$ (M = Mn, Co),[23] $[Zn_2(H_2O)_4](HPO_3)_2(H_2O)$,[24] $Na_2Zn_3(HPO_3)_4$[24] and $M_{11}(HPO_3)_8(OH)_6$ (M = Co, Ni, Zn)[25] with 3D structures. A few examples of inorganic-organic hybrid phosphites with transition-metal elements (V, Cr, Co, Mn, Fe) have also been reported in the literature.[26–30] However, phosphites with transition-metal elements have not been studied widely when compared with the related phosphates. In order to further examine the structural chemistry of these types of materials containing the first series of transition elements, we synthesised two new transition-metal phosphites of formula $Na_2[M(PO_3H)_2]$ (M = Fe, Co). The crystal structures of these compounds and their magnetic properties are also reported in this paper.

[a] The State Key Laboratory of High Performance Ceramics and Superfine Microstructure, Shanghai Institute of Ceramics, Chinese Academy of Science,
Shanghai 200050, P. R. China
Fax: +86-21-52413122
E-mail: jtzhao@mail.sic.ac.cn

Results and Discussion

Synthesis

Reactions of phosphorous acid with the transition-metal salts in the presence of NaOH under mild hydrothermal conditions afforded two new isostructural complexes with 3D open-frameworks. According to experimental investigations, we noted that the pH value has a significant influence on the reaction products. To obtain information about the reactive process of $Na_2[M(HPO_3)_2]$ (M = Fe, Co), an in-depth study at various pH values was carried out. Different experiments were performed with the pH = 1.0, 3.0, 5.0, 7.0 and 9.0 but all other conditions were kept constant. The study of the final products by X-ray powder diffraction measurements revealed that when the pH ≤ 5.0, the reactions lead to an unknown powder for $Na_2[Fe(HPO_3)_2]$ (**1**)

 DOI: 10.1002/ejic.200400644

and a known compound, $Co(PO_3H)\cdot H_2O$ (JCPDS: 44-1323) for $Na_2[Co(HPO_3)_2]$ (**2**) while with a pH > 5.0 the title compounds were isolated as pure phases (Scheme 1). When thinking about the synthesis of transition-metal derivatives of this low-oxidation-state phosphorous acid, it becomes necessary to consider the problems resulting from the hydrolytic processes of phosphorous acid which would be essentially controlled by the pH of the solution.[31] In this context, it becomes possible to understand the experimental results obtained when the syntheses of the title compounds were performed. Since the protons of the phosphorous acid are easily removed under alkaline conditions, the phosphorus atom is suitable for simultaneously binding to three M^{II} atoms to form the polyhedral network of alternating MO_6 and PO_3H units in the title compounds. On the contrary, with a decrease in the pH value, less protons from the phosphorous acid can be removed which correspondingly reduces the degree of coordination of the phosphorus atoms to the M^{II} atoms. Therefore, the cationic groups in the solution tend to aggregate themselves under suitable conditions, leading to the resultant cationic network in the final solid $Co(PO_3H)\cdot H_2O$. Similar results have also been reported by Marcos et al. in their synthetic process.[25] For example, they were also able to prepare $M(HPO_3)(H_2O)$ (M = Co, Ni, Zn) at low pH whereas by carrying out the synthesis at intermediate pH values, other compounds with a different structure type were obtained, namely $M_{11}(HPO_3)_8(OH)_6$ (M = Zn, Co, Ni). All the above observations indicate that the pH of the solution indeed plays a crucial role in the reactive process and mainly determines the stability ranges of the various compounds.

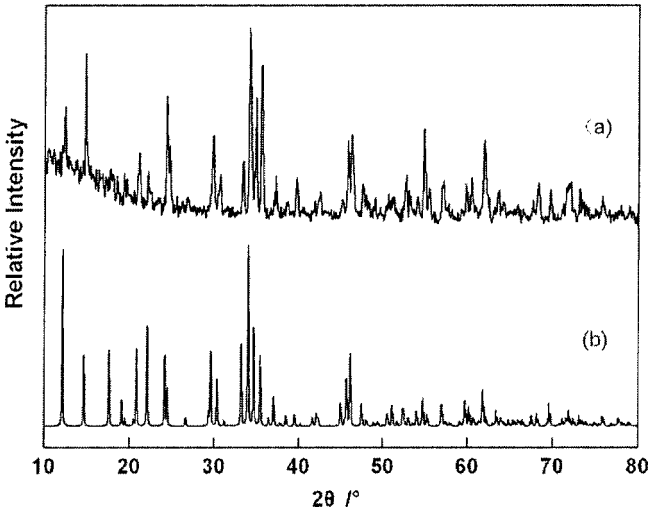

Scheme 1. Observed (a) and calculated (b) X-ray powder diffraction profiles for $Na_2[(CoPO_3H)_2]$

Crystal Structures of $Na_2[M(HPO_3)_2]$ (M = Fe and Co)

The crystal structures of the two isotypic compounds both contain a 3D anionic framework made from polyhedral linkages between MO_6 and HPO_3 units sharing common O-corners. Such connectivities between these units produce numerous six-membered rings which connect to each other by sharing common edges giving rise to an infinite honeycomb-like six-membered sheet in the *bc* plane [see Figure 1 (left)]. Pairs of phosphite groups are distributed between these sheets and bridge the sheets into the whole 3D open-framework. An offset between the sheets in the [001] direction destroys the formation of a six-membered ring channel system along the *a* axis [see Figure 1 (right)] but the 4- and 12-membered ring channel systems are distributed alternately in the structure along the *b* axis which is enclosed by the 4- and 6- membered ring walls [see Figure 2 (d)]. The shape of the 12-membered ring channel is close to rhombohedral with the largest length being 12.8 Å and the smallest being 6.8 Å. Therefore, the structures of the title compounds examined here can also be characterised by the presence of an infinite number of 4-, 6- and 12-membered polyhedral rings.

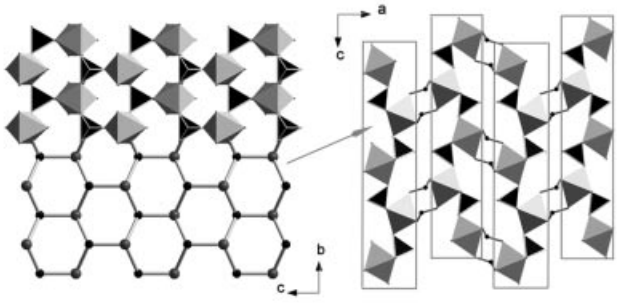

Figure 1. (left) The 6-membered ring polyhedral sheet in the *bc* plane constructed from alternating MO_6 and HPO_3 polyhedra. (right) The parallel stack of 6-membered ring sheets along the [010] direction showing the offset along the *c* axis between the sheets (MO_6, grey octahedron; PO_3H, dark tetrahedron; M atom, gray sphere; P atom, dark sphere).

More importantly, a detailed analysis of the structures allows the entire framework in each case to be described as an assembly of multiple ribbons running along the *b* axis. Such multiple ribbons are built up from two distinct types of single polyhedral ribbons: the linear chain possessing corner-shared four-membered rings [Figure 2(a)] and the ladders with edge-sharing four-membered rings [Figure 2 (b)]. The centred ladder interconnects with two neighbouring linear chains through edge sharing and forms a novel unbranched multiple-chain running along the *b* axis [Figure 2 (c)]. Such multiple-ribbons repeat themselves in parallel along the *c* axis in a zigzag-like manner with an angle of approximately 120° along the *a* axis [Figure 2 (d)], giving rise to a fish backbone-type arrangement in the *bc* plane. Such multiple-chains connect to each other through the M–O–P bridges to form the entire open-framework [Figure 2 (e)].

The guest Na^+ ions occupy the open spaces in the framework to maintain the structural stability and satisfy the charge balance. The $Na(1)^+$ ions are located in the twelve-membered ring channels and the $Na(2)^+$ ions occupy the centres of the six-membered rings, respectively (see Figure 3).

 © 2005 Wiley-VCH Verlag GmbH & Co. KGaA, Weinheim

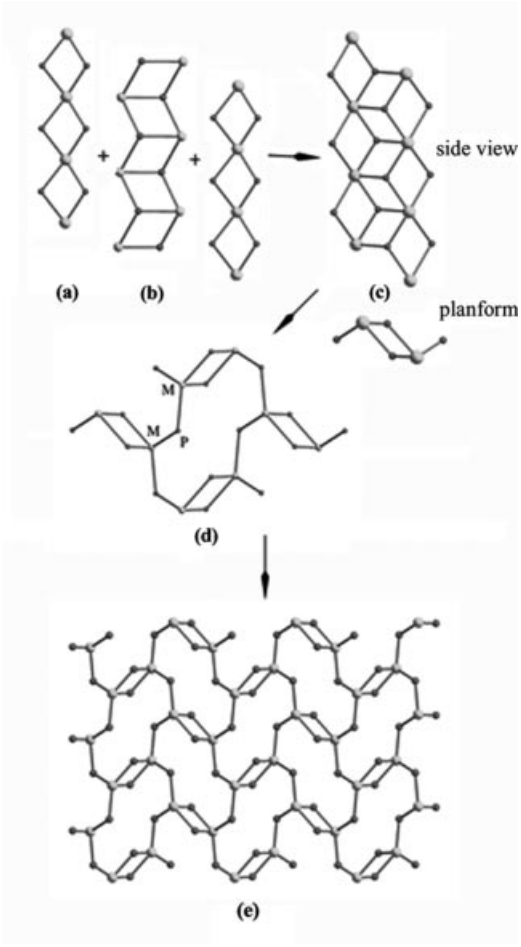

Figure 2. Schematic representation of the formation of the open-framework structure of $Na_2[M(HPO_3)_2]$ (M = Fe, Co). (a) The linear chain possessing corner-shared four-membered rings. (b) The ladders with edge-shared four-membered rings. (c) The loop-branched multiple ribbon. (d) The combination of four multiple ribbons to form a 12-membered ring via the M–O–P bridge. (e) The infinite 3D open-framework.

The topology of this structure is remarkably similar to that of the aeschynite $CaTa_2O_6$ (see Figure 4). According to the concept of scale chemistry,[32,33] the two structures can be considered as though they have the same walls (topology) but are built from different bricks (BUs). The latter has the double rows of TaO_6 octahedra as BUs, while the former has an upper analogue in which the BUs are the multiple ribbons made of corner-shared tetrahedra and octahedra. The *trans* corner linkage of the BUs givs rise to zigzag chains and Na^+ and Ca^{2+}cations are located in similarly oriented tunnels in these phosphites and in the aeschynite, respectively. The augmentation of the 4,6 net in the aeschynite structure largely increases the porosity of the structure. The channels (12.8 × 6.8 Å) in the title compounds are more expanded compared with those (7.67 × 4.93 Å) in the aeschynite as a result of the adoption of larger BUs which is consistent with the principle of scale chemistry, i.e. the larger the brick, the larger the pore. Thus, the present structural type, in addition to being a new member of the family of $CaTa_2O_6$, also demonstrates that many structures can readily be designed and preformed to basic topologies dictated by the shapes (triangle, square, tetrahedron, etc.) and connectivities of the structural building units.

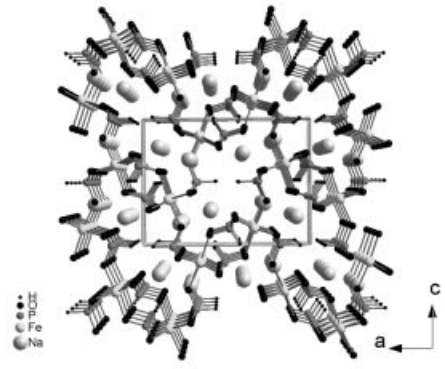

Figure 3. Structure of $Na_2[M(HPO_3)_2]$ (M = Fe, Co) along the [010] direction showing the 4-, 6-, and 12-membered polyhedral rings. The $Na(1)^+$ ions and $Na(2)^+$ ions are located in the channels and the centre of six-membered rings, respectively.

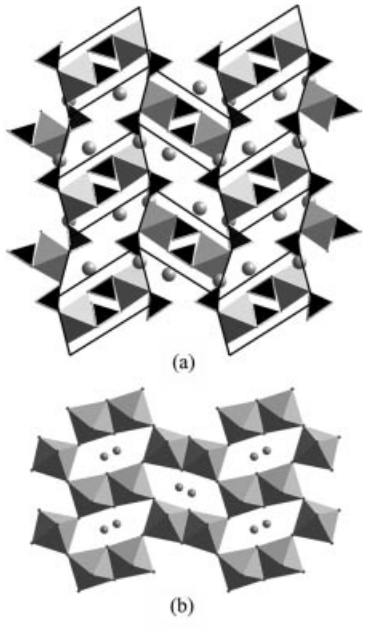

Figure 4. (a) The stacking of the multiple ribbons in $Na_2[M(HPO_3)_2]$ (M = Fe, Co) leading to a aeschynite-like framework. (b) The aeschynite ($CaTa_2O_6$) frameworks (Na atom, large gray sphere; Ca atom, small gray sphere).

For **1**, the FeO_6 octahedra have Fe–O distances in the range of 2.113(2)–2.171(2) Å whereas the *cis* and *trans* bond angles are in the ranges of 84.29(5)–96.04(4)° and 172.39(5)–174.64(7)°, respectively. For **2**, the Co–O distances vary from 2.079(2) Å to 2.147(2) Å and the *cis* and *trans* angles are in the ranges of 83.95(6)–95.77(4)° and 172.57(6)–174.99(7)°, respectively. These values are typical for Fe and Co in an octahedral oxygen environment. The

 © 2005 Wiley-VCH Verlag GmbH & Co. KGaA, Weinheim

tetrahedral P atoms have P–O bond lengths in the ranges of 1.517(2)–1.522(2) Å for **1** and 1.518(2)–1.523(2) Å for **2** and the P–H distances vary between 1.31(7) and 1.46(5) Å [P(1)–H(2) = 1.31(7) Å, P(2)–H(1) = 1.396(1) Å in **1**; P(1)–H(2) = 1.34(7) Å, P(2)–H(1) = 1.46(5) Å in **2**]. These values are within the expected ranges. The Na cations reside in the irregular $Na(1)O_5$ and $Na(2)O_9$ environments and are coordinated to neighbouring phosphite groups by sharing common corners or edges. Additionally, Na(1) bonds to two hydrogen atoms of the HPO_3 groups with distances in the range of 2.608–2.872 Å. The Na–O bond lengths are quite diverse with Na(1)–O in the range of 2.36–2.41 Å and Na(2)–O in the range of 2.29–2.78 Å for compound **1**. For **2** the Na(1)–O distances are in the range of 2.35–2.39 Å and the Na(2)–O distances are in the range of 2.29–2.76 Å.

Magnetic Properties

Magnetic measurements of $Na_2[M(HPO_3)_2]$ (M = Fe, Co) were performed on crystalline samples in the temperature range of 1.8–320 K. The temperature dependence of the inverse molar magnetic susceptibilities, χ^{-1}, of compounds **1** and **2** in the range of 1.8–320 K are show in Figure 5 and Figure 6, respectively. Compound $Na_2[Co(HPO_3)_2]$ displays a magnetic susceptibility not obeying a simple Curie–Weiss law. If one separates the low- and the high-temperature ranges, the Curie–Weiss can be fit in the ranges of 100–320 K (HT) and 5–30 K (LT). For the low-temperature interval, an effective magnetic moment of 4.47 μ_B and θ = –21 K can be obtained. The effective magnetic moment per Co atom obtained from the LT fit is well within the range reported in the literature for octahedrally coordinated Co^{2+} ions (but also near to the value of 4.3 μ_B reported for Co^{3+}).[34] The effective magnetic moment for the high-temperature range is 5.30 μ_B which, while significantly larger than the spin-only value for spin S = centres (3.87 μ_B), indicates especially strong deviations of Co^{2+} from the spin-only value due to strong orbital contributions. A Weiss temperature θ = –50 K can be obtained, demonstrating dominant antiferromagnetic interactions between the magnetic centres at low temperature. The zero-field cooled samples measured under an external field of 100 Oe show a broadened cusp at 1 and 4 K in the χ^{-1} vs T curve, indicating antiferromagnetic ordering at low field [Figure 5 (inset)]. The different magnetic features at low and high temperatures indicate that the magnetic structure is complex. Similar magnetic properties can also be observed in $[Co_3(pyz)(HPO_4)_2F_2]$ and $[Co_3(4,4'\text{-bpy})(HPO_4)_2F_2]\cdot xH_2O$ (Figure 5).[35] For $Na_2[Fe(HPO_3)_2]$, the magnetic behaviour follows the Curie–Weiss law in the temperature range of 100–320 K (Figure 6). A fit in the range of 100–320 K gives an effective magnetic moment of 5.41 μ_B which is well within the range reported in the literature for octahedrally coordinated Fe^{2+} ions.[34] The asymptotic Curie–Weiss temperature θ is equal to –20.3 K, indicating antiferromagnetic exchange in compound **2**. There is possible magnetic ordering observed in fields as low as 1 kOe and above 1.8 K [Figure 6 (inset)].

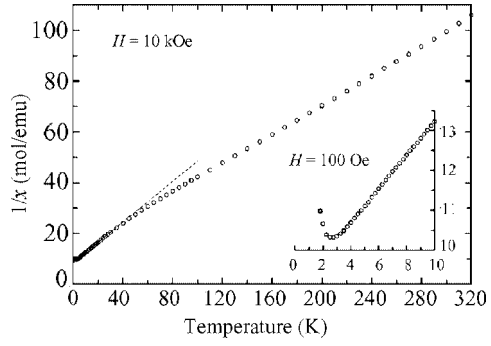

Figure 5. Inverse magnetic susceptibility (χ^{-1}, open circles) plotted as a function of temperature for powder samples of $Na_2[Co(HPO_3)_2]$. The inset shows the antiferromagnetic ordering at low temperature.

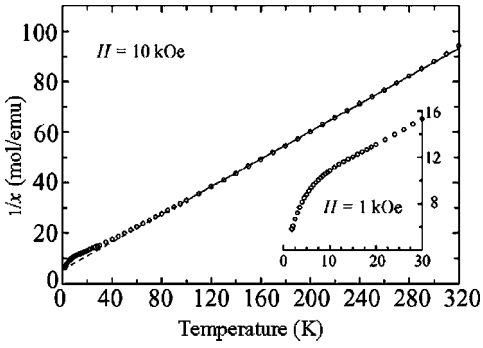

Figure 6. Inverse magnetic susceptibility (χ^{-1}, open circles) plotted as a function of temperature for powder samples of $Na_2[Fe(HPO_3)_2]$. The inset shows the possible magnetic ordering at low temperature.

Conclusions

Two new transition-metal phosphites with 4-, 6- and 12-membered polyhedral rings have been synthesised under mild hydrothermal conditions. Both of the compounds are constructed from strictly alternating MO_6 octahedra and HPO_3 tetrahedra through sharing the O-vertexes. Such connectivities between the units also form 4- and 12-membered ring channel systems in the framework structures in which the sodium ions are located. The topology of this structure is remarkably similar to that of the aeschynite $CaTa_2O_6$ and the augmentation of the BUs largely increases the channel size in the new compounds. Magnetic studies for $Na_2[Co(HPO_3)_2]$ show interesting features suggesting the possible existence of a complex magnetic structure at low temperature. For $Na_2[Fe(HPO_3)_2]$, the magnetic susceptibility obeys the Curie–Weiss law in the temperature range of 100–320 K with μ_{eff} = 5.41 μ_B which indicates Fe^{2+} character.

 © 2005 Wiley-VCH Verlag GmbH & Co. KGaA, Weinheim

Table 1. Crystal structure refinement data for $Na_2[M(HPO_3)_2]$ (M = Fe, Co).

	1	2
Empirical formula	$H_2FeNa_2O_6P_2$	$H_2CoNa_2O_6P_2$
Formula weight	261.79	264.87
Wavelength [Å]	0.71073	0.71073
Crystal system	orthorhombic	orthorhombic
Space group	*Pnma* (no. 62)	*Pnma* (no. 62)
a [Å]	12.169(4)	12.091(3)
b [Å]	5.441(2)	5.400(4)
c [Å]	9.164(3)	9.115(2)
V [Å^3]	606.7(4)	595.1(3)
Z	4	4
D_c [g cm^{-3}]	2.866	2.956
μ(Mo-K_α) [mm^{-1}]	3.124	3.534
F(000)	512	516
θ range [°]	2.78–27.11	2.80–27.09
Total data	2760	2814
Unique data	727	724
Observe data	704	689
GOF on F^2	1.17	1.14
Final *R* indices	R_1[a] = 0.0224,	R_1[a] = 0.0210,
[$I > 2\sigma(I)$]	wR_2[b] = 0.0611	wR_2[b] = 0.0587
R indices	R_1[a] = 0.0230,	R_1[a] = 0.0222,
(all data)	wR_2[b] = 0.0615	wR_2[b] = 0.0592

[a] $R_1 = \Sigma||F_o| - |F_c||/\Sigma|F_o|$. [b] $wR_2 = \{\Sigma[w(F_o^2 - F_c^2)^2]/\Sigma[w(F_o^2)^2]\}^{1/2}$, $w = 1/[\sigma^2(F_o^2) + (0.0302P)^2 + 5.74P]$, $P = (F_o^2 + F_c^2)/3$.

Table 2. Selected bond lengths [Å] and angles [°] in $Na_2[Fe\text{-}(HPO_3)_2]$.

Fe(1)–O(4)	2.113(2)	Na(1)–O(1)[d]	2.363(2)
Fe(1)–O(1)	2.118(1)	Na(1)–O(2)[k]	2.386(3)
Fe(1)–O(1)[a]	2.118(1)	Na(1)–O(3)[k]	2.408(2)
Fe(1)–O(2)	2.130(2)	Na(1)–O(3)[l]	2.408(2)
Fe(1)–O(3)[a]	2.171(2)	Na(1)–H(1)	2.872(2)
Fe(1)–O(3)	2.171(2)	Na(1)–H(2)	2.620(2)
P(1)–O(4)[e]	1.517(2)	Na(2)–O(4)	2.291(2)
P(1)–O(1)	1.522(1)	Na(2)–O(1)[l]	2.657(2)
P(1)–O(1)[f]	1.522(1)	Na(2)–O(1)[n]	2.657(2)
P(1)–H(2)	1.31(7)	Na(2)–O(3)[n]	2.670(2)
P(2)–O(2)[h]	1.517(2)	Na(2)–O(3)[l]	2.670(2)
P(2)–O(3)[c]	1.517(2)	Na(2)–O(2)[k]	2.731(1)
P(2)–O(3)[h]	1.517(2)	Na(2)–O(2)[n]	2.731(1)
P(2)–H(1)	1.396(1)	Na(2)–O(3)[a]	2.784(2)
Na(1)–O(1)[j]	2.363(2)	Na(2)–O(3)	2.784(2)
O(4)–Fe(1)–O(1)[a]	95.98(4)	O(4)[e]–P(1)–O(1)[f]	113.22(6)
O(4)–Fe(1)–O(1)	95.98(4)	O(1)–P(1)–O(1)[f]	110.38(9)
O(1)[a]–Fe(1)–O(1)	87.97(6)	O(4)[e]–P(1)–H(2)	107.51(6)
O(4)–Fe(1)–O(2)	174.68(8)	O(1)–P(1)–H(2)	105.97(6)
O(1)[a]–Fe(1)–O(2)	87.84(4)	O(1)[f]–P(1)–H(2)	105.97(6)
O(1)–Fe(1)–O(2)	87.84(4)	O(3)[g]–P(2)–O(3)[c]	112.84(9)
O(4)–Fe(1)–O(3)	91.31(4)	O(3)[g]–P(2)–O(2)	112.20(7)
O(1)[a]–Fe(1)–O(3)	172.41(6)	O(3)[c]–P(2)–O(2)	112.20(7)
O(2)–Fe(1)–O(3)	84.75(4)	O(3)[g]–P(2)–H(1)	104.62(6)
O(1)–Fe(1)–O(3)	93.39(6)	O(3)[c]–P(2)–H(1)	104.62(6)
O(4)[e]–P(1)–O(1)	113.22(6)	O(2)–P(2)–H(1)	109.75(10)

[a] $x, -y + ½, z$. [b] $-x + ½, -y + 1, z + ½$. [c] $-x + ½, -y, z + ½$. [d] $-x, -y + 1, -z + 1$. [e] $-x, -y, -z + 1$. [f] $x, -y - ½, z$. [g] $-x + ½, y + ½, z + ½$. [h] $x, y, z + 1$. [i] $-x, y + ½, -z + 1$. [j] $-x + ½, -y + 1, z - ½$. [k] $-x + ½, y + ½, z - ½$. [l] $x, y + 1, z$. [m] $-x + ½, -y, z - ½$. [n] $x, y, z - 1$.

Table 3. Selected bond lengths [Å] and angles [°] in $Na_2[Co\text{-}(HPO_3)_2]$.

Co(1)–O(4)	2.080(2)	Na(1)–O(1)[d]	2.346(2)
Co(1)–O(1)[a]	2.094(2)	Na(1)–O(2)[k]	2.383(3)
Co(1)–O(1)	2.094(2)	Na(1)–O(3)[k]	2.390(2)
Co(1)–O(2)	2.099(2)	Na(1)–O(3)[l]	2.390(2)
Co(1)–O(3)	2.147(2)	Na(1)–H(1)	2.764(1)
Co(1)–O(3)[a]	2.147(2)	Na(1)–H(2)	2.608(2)
P(1)–O(4)[e]	1.518(2)	Na(2)–O(4)	2.287(2)
P(1)–O(1)[f]	1.523(2)	Na(2)–O(1)[l]	2.640(2)
P(1)–O(1)	1.523(2)	Na(2)–O(1)[n]	2.640(2)
P(1)–H(2)	1.34(7)	Na(2)–O(3)[n]	2.663(2)
P(2)–O(2)	1.516(2)	Na(2)–O(3)[l]	2.663(2)
P(2)–O(3)[d]	1.516(2)	Na(2)–O(2)[k]	2.709(1)
P(2)–O(3)[g]	1.516(2)	Na(2)–O(2)[n]	2.709(1)
P(2)–H(1)	1.46(5)	Na(2)–O(3)[a]	2.757(2)
Na(1)–O(1)[j]	2.346(2)	Na(2)–O(3)	2.757(2)
O(4)–Co(1)–O(1)[a]	95.71(5)	O(4)[e]–P(1)–O(1)[f]	113.04(6)
O(4)–Co(1)–O(1)	95.71(5)	O(1)P–(1)–O(1)[f]	110.24(9)
O(1)[a]–Co(1)–O(1)	87.72(6)	O(4)[e]–P(1)–H(2)	110.76(2)
O(4)–Co(1)–O(2)	175.05(8)	O(4)–P(1)–H(2)	104.55(6)
O(1)[a]–Co(1)–O(2)	87.85(4)	O(4)[f]–P(1)–H(2)	104.55(6)
O(1)–Co(1)–O(2)	87.85(4)	O(3)[h]–P(2)–O(3)[d]	112.87(9)
O(4)–Co(1)–O(3)	91.36(5)	O(3)[h]–P(2)–O(2)	112.24(7)
O(1)[a]–Co(1)–O(3)	172.62(6)	O(3)[d]–P(2)–O(2)	112.24(7)
O(2)–Co(1)–O(3)[a]	172.62(6)	O(3)[h]–P(2)–H(1)	104.88(6)
O(1)[a]–Co(1)–O(3)[a]	93.69(5)	O(3)[d]–P(2)–H(1)	104.88(6)
O(4)[e]–P(1)–O(1)	113.04(6)	O(2)–P(2)–H(1)	109.13(1)

[a] $x, -y + ½, z$. [b] $-x + ½, -y + 1, z + ½$. [c] $-x + ½, -y, z + ½$. [d] $-x, -y + 1, -z + 1$. [e] $-x, -y, -z + 1$. [f] $x, -y - ½, z$. [g] $-x + ½, y + ½, z + ½$. [h] $x, y, z + 1$. [i] $-x, y + ½, -z + 1$. [j] $-x + ½, -y + 1, z - ½$. [k] $-x + ½, y + ½, z - ½$. [l] $x, y + 1, z$. [m] $-x + ½, -y, z - ½$. [n] $x, y, z - 1$.

Experimental Section

General Remarks: All chemicals were obtained from commercial sources and used as received. The products were examined by powder X-ray diffraction (Rigaku D/max 2550V diffractometer, Cu-K_α radiation) in order to confirm their phase identity and purity. IR spectra were recorded with a Digilab-FTS-80 spectrophotometer from 4000 to 400 cm^{-1} using pressed KBr pellets of the samples. The magnetic susceptibility measurements were carried out with a SQUID magnetometer (Quantum-Design, MPMS XL-7) in the temperature range 1.8 K–320 K. The elemental analyses were performed with an ICP-AES (Vista AX ICP-AES) instrument.

$Na_2[Fe(HPO_3)_2]$ (1): $FeCl_2{\cdot}6H_2O$ (0.29 g), NaOH (0.125 g), H_3PO_3 (solid state, 2.56 g) and deionised water (15 mL) were mixed in a molar ratio of 2:2.5:25:667. A solution of $NH_3{\cdot}H_2O$ (40 wt.-%) was added to adjust the pH to 7.0 and the resultant solution was sealed in a 25-mL Teflon-lined stainless steel autoclave and heated under autogenous pressure at 433 K for 5 d. The resultant pink rod-like water-soluble crystals from the reaction were recovered by filtration, washed with ethanol and dried at room temperature. Yield: 0.258 g (80% based on $FeCl_2{\cdot}6H_2O$). $H_2FeNa_2O_6P_2$ (261.79): calcd. Fe 21.3, Na 17.6, P 23.6; found Fe 21.0, Na, 17.7, P 23.2. IR (KBr disk): $\tilde{\nu}$ = 2388 (m), 1170 (s), 1085 (s), 1025 (s), 998 (m), 591 (m), 501 (m) cm^{-1}.

$Na_2[Co(HPO_3)_2]$ (2): $CoCl_2{\cdot}6H_2O$ (0.3 g), NaOH (0.125 g), H_3PO_3 (solid state, 2.56 g) and deionised water (15 mL) were mixed in a molar ratio of 2:2.5:25:667. A solution of $NH_3{\cdot}H_2O$ (40 wt.-%) was added to adjust the pH to 7.0 and the resultant solution was sealed in a 25-mL Teflon-lined stainless steel autoclave and heated under autogenous pressure at 433 K for 5 d. The resultant pink rod-like water-soluble crystals from the reaction were recovered by filtration, washed with ethanol and dried at room temperature. Yield: 0.234 g (70% based on $CoCl_2{\cdot}6H_2O$). $H_2CoNa_2O_6P_2$ (264.87): calcd. Co 22.2, Na 17.4, P 23.7; found Co 21.7, Na 17.0, P 23.3.

 © 2005 Wiley-VCH Verlag GmbH & Co. KGaA, Weinheim

IR (KBr disk): $\tilde{\nu}$ = 2383 (m), 1172 (s), 1095 (s), 1025 (s), 995 (m), 586 (m), 493 (m) cm^{-1}.

X-ray Crystallographic Study: Crystals of each compound were selected under a polarising microscope, glued to a thin glass fibre with cyanoacrylate (superglue) adhesive and inspected for singularity. Two of them with regular rod-like shapes were chosen ($0.40 \times 0.20 \times 0.20$ mm for **1** and $0.40 \times 0.15 \times 0.15$ mm for **2**) and data sets were collected with a Nonius Kappa CCD diffractometer (Mo-K_α radiation, λ = 0.71073 Å) at 293 K. For **1**, the θ range for data collection was from 2.79 to 27.12° and an absorption correction was applied with maximum and minimum transmission factors of 0.732 and 0.694, respectively. A total of 2760 reflections were collected with ω scans, yielding 727 unique observed reflections(R_{int} = 0.0233). For **2** the θ range for data collection was from 2.80 to 27.09° and an absorption correction was applied with maximum and minimum transmission factors of 0.702 and 0.661, respectively. A total of 2814 reflections were collected with ω scans, yielding 724 unique observed reflections(R_{int} = 0.0210). The intensity data were corrected for Lorentz and polarisationeffects. The structures were solved by direct methods and refined against $|F^2|$ with the aid of the SHELXTL-PLUS package.[36] The iron, cobalt, sodium, phosphorus and oxygen atoms were initially found and refined. The coordinates of hydrogen atoms on the phosphorus centres were obtained from difference Fourier maps. Additional information concerning the data collection and structure refinements is presented in Table 1 while selected interatomic distances are given in Table 2 and Table 3 for **1** and **2**, respectively. Further details of the crystal-structure investigations may be obtained from the Fachinformationszentrum Karlsruhe, 76344 Eggenstein-Leopoldshafen, Germany, on quoting the depository numbers CSD-414247 (**1**) and -414248 (**2**).

Acknowledgments

This work was supported by the Fund for Distinguished Young Scholars (No. 20025101) and a Key Project from the NNSF of China (No.50332050), State "863" project (No. 2002AA324070) and a fund from Shanghai Optical Science and Technology (No. 022261015).

[1] A. K. Cheetham, G. Ferey, T. Loiseau, *Angew. Chem. Int. Ed.* **1999**, *38*, 3268–3292.
[2] S. B. Harmon, S. C. Sevov, *Chem. Mater.* **1998**, *10*, 3020–3023.
[3] C. H. Lin, S. L. Wang, K. H. Lii, *J. Am. Chem. Soc.* **2001**, *123*, 4649–4650.
[4] G. Y. Yang, S. C. Sevov, *J. Am. Chem. Soc.* **1999**, *121*, 8389–8390.
[5] J. Do, R. P. Bontchev, A. J. Jacobson, *Inorg. Chem.* **2000**, *39*, 3230–3237.
[6] S. Fernandez, J. L. Mesa, J. L. Pizarro, L. Lezama, M. I. Arriortua, R. Olazcuaga, T. Rojo, *Chem. Mater.* **2000**, *12*, 2092–2098.
[7] W. Tong, G. G. Xia, Z. R. Tian, J. Liu, J. Cai, S. L. Suib, J. C. Hanson, *Chem. Mater.* **2002**, *14*, 615–620.
[8] S. S. Bao, L. M. Zheng, Y. J. Liu, W. Xu, S. H. Feng, *Inorg. Chem*. **2003**, *42*, 5037–5039.
[9] M. B. Korzenski, J. W. Kolis, *Inorg. Chem.* **2000**, *39*, 5663–5668.
[10] C. D. Peloux, A. Dolbecq, P. Mialane, J. Marrot, E. Rivière, F. Sécheresse, *Angew. Chem. Int. Ed.* **2001**, *40*, 2455–2457.
[11] A. Natarajan, K. Cheetham, *J. Solid State Chem.* **1998**, *140*, 435–439.
[12] S. Ekambaram, S. C. Sevov, *J. Mater. Chem.* **2000**, *10*, 2522–2525.
[13] K. H. Lii, Y. F.Huang, *Inorg. Chem.* **1999**, *38*, 1348–1350.
[14] X. Q. Wang, L. M. Liu, H. D. Cheng, K.Ross, A. J. Jacobson, *J. Mater. Chem.* **2000**, *10*, 1203–1208.
[15] S. Y. Mao, Y. X. Huang, Z. B. Wei, J. X. Mi, Z. L. Huang, J. T. Zhao, *J. Solid State Chem.* **2000**, *149*, 292–297.
[16] Y. P. Chiang, H. M. Kao, K. H. Lii, *J. Solid State Chem.* **2001**, *162*, 168–175.
[17] B. G. Shpeizer, X. Ouyang, J. M. Heising, A. Clearfield, *Chem. Mater.* **2001**, *13*, 2288–2296.
[18] B. S. Zakharova, A. B. Ilyukhin, N. N. Chudinova, *Zh. Neorg. Khim.* **1994**, *39*, 1443–1445.
[19] M. Shieh, K. J. Martin, P. J. Squattrito, A. Clearfield, *Inorg. Chem.* **1990**, *29*, 958–963.
[20] M. Sghyar, J. Durand, L. Cot, M. Rafiq, *Acta Crystallogr., Sect. C* **1991**, *47*, 2515–2517.
[21] F. Sapina, P. Gomez-Romero, M. D. Marcos, P. Amoros, R. Ibanez, D. Beltran, R. Navarro, C. Rillo, F. Lera, *Eur. J. Solid State Inorg. Chem.* **1989**, *26*, 603–617.
[22] L. E. Gordon, W. T. A. Harrison, *Acta Crystallogr., Sect. E* **2002**, *58*, i41–i43.
[22] R. Chmelikova, J. Loub, V. Petricek, *Acta Crystallogr., Sect. C* **1986**, *42*, 1281–1283.
[24] C. Y. Ortiz-Avila, P. J. Squattrito, M. Shieh, A. Clearfield, *Inorg. Chem.* **1989**, *28*, 2608–2615.
[25] M. D. Marcos, P. Amoros, A. Beltrh-Porter, R. Martinez-Mfiez, J. P. Attfields, *Chem. Mater.* **1993**, *5*, 121–128.
[26] S. Fernandez, J. L. Pizarro, J. L. Mesa, L. Lezama, M. I. Arriortua, R. Olazcuaga, T. Rojo, *Inorg. Chem.* **2001**, *40*, 3476–3483.
[27] S. Fernandez, J. L. Mesa, J. L. Pizarro, L. Lezama, M. I. Arriortua, T. Rojo, *Chem. Mater.* **2003**, *15*, 1204–1209.
[28] G. Bonavia, J. DeBor, R. C. Haushalter, D. Rose, J. Zubieta, *Chem. Mater.* **1995**, *7*, 1995–1998.
[29] S. Fernandez, J. L. Mesa, J. L. Pizarro, L. Lezama, M. I. Arriortua, R. Olazcuaga, T. Rojo, *Chem. Mater.* **2000**, *12*, 2092–2098.
[30] S. Fernandez, J. L. Mesa, J. L. Pizarro, L. Lezama, M. I. Arriortua, T. Rojo, *Chem. Mater.* **2002**, *14*, 2300–2307.
[31] J. Durand, M. Loukili, N. Tijani, M. Wiq, L. Cot, *Eur. J.Solid State Inorg. Chem.* **1988**, *25*, 297.
[32] G. Férey, *J. Solid State Chem.* **2000**, *152*, 37–48.
[33] G. Férey, C. Mellot-Draznieks, T. Loiseau, *Solid State Sci.* **2003**, *5*, 79–94.
[34] R. L. Carlin, *Magneto-Chemistry*, Springer-Verlag, New York, **1986**.
[35] W. K. Chang, R. K. Chiang, Y. C. Jiang, S. L. Wang, S. F. Lee, K. H. Lii, *Inorg. Chem.* **2004**, *43*, 2564–2568.
[36] G. M. Sheldrick, *SHELXTL Programs*, Release Version 5.1, Bruker AXS, Madison, WI, **1998**.

Received: July 23, 2004

 © 2005 Wiley-VCH Verlag GmbH & Co. KGaA, Weinheim

(Cyanocyclopentadienyl)potassium and -cesium

Eberhardt Herdtweck,[a] Frank H. Köhler,*[a] and Rüdiger Mölle[a]

Keywords: Cyanocyclopentadienide / Crystal structure / ^{133}Cs NMR spectroscopy

(Cyanocyclopentadienyl)potassium and -cesium have been synthesized and subsequently characterized by single-crystal X-ray structure determinations, ^{1}H and ^{13}C NMR spectroscopy in solution as well as by ^{133}Cs NMR spectroscopy in solution and the solid-state. Both salts crystallize in zigzag chains which are crosslinked differently through the cyano substituents. There is significant distortion of the cyanocyclopentadienide ion toward a fulvalene-like structure because the alkali-metal ions do not only interact with the five-membered ring but also with the cyano groups. The ^{133}Cs NMR spectra reflect the bending of the [CpCsCp]$^{-}$ fragments of the chains.
(© Wiley-VCH Verlag GmbH & Co. KGaA, 69451 Weinheim, Germany, 2005)

Introduction

The cyclopentadienyl (Cp) ligand is ubiquitous in organometallic chemistry and substitution has been widely used for generating special properties of its (transition) metal compounds such as better solubility, increased stability and asymmetry.[1] More recently, donor substituents have been introduced[2] mainly for providing (planar-)chiral[2b,2c] or C_2-symmetric[2a,2d] catalysts. For the latter derivatives, the substituted Cp groups have been designed such that intramolecular coordination of the Cp-attached donor occurs owing to dangling substituents. If intermolecular or bridging coordination is to be achieved, a donor function bonded directly to the Cp ring is advantageous. An example is the cyanocyclopentadienyl ligand (CpCN) which has been synthesised by various routes.[3] As for alkali-metal cyclopentadienides, these may be assumed to be simple compounds but, in fact, there is surprising structural diversity among them[4] and this might be particularly true for structural implications of the cyano substituent in the solid and liquid state. Therefore, we synthesized the title compounds CpCNK and CpCNCs and investigated them by techniques including X-ray diffraction and solid-state ^{133}Cs NMR spectroscopy.

Results and Discussion

Synthesis

When choosing Webster's synthetic approach,[3b] (see Scheme 1) special attention is warranted. Thus, the reaction between CpNa and ClCN is clean if the latter has been freshly prepared. The resultant isomeric cyanocyclopentadienes react almost instantaneously to give dimers (not only those in Scheme 1) which must be cracked thermally just before the reaction with an alkali carbonate. The overall yield (5–6%) of the alkali-metal cyanocyclopentadienides, CpCNK and CpCNCs, according to the sequence in Scheme 1 is mainly limited by interfering polymerization of cyanocyclopentadiene. Both compounds are colorless to brown powders which are air-sensitive and soluble in donor solvents such as propionitrile, DMSO and THF. The ^{1}H and ^{13}C NMR spectra of both salts in solution show similar signal patterns and confirm the expected structure of the anion. An example is the AA′BB′ spin system of the five-membered ring protons which gives rise to two pseudo-triplets. These and other signals of the nuclei in positions 2/5 and 3/4 of the ring could be distinguished by considering the contribution of a fulvene-type limiting structure (cf. discussion below and Figure 2b) and the fact that in fulvenes and the related cyclopentadienones the signal of C-3/4 is always more shifted than that of C-2/5.[5] Nevertheless, this assignment is tentative. The new cesium derivative was characterised in addition by mass spectrometry and IR spectroscopy, and its purity was checked.

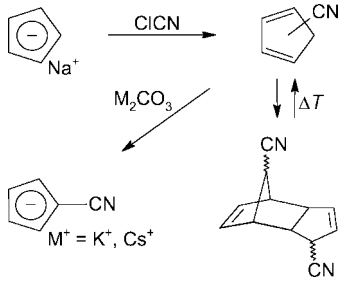

Scheme 1.

[a] Department Chemie, Technische Universität München,
85747 Garching, Germany
Fax: +49-89-28913109
E-mail: F.H.Koehler@lrz.tu-muenchen.de

 DOI: 10.1002/ejic.200400663

Crystal Structures of CpCNK and CpCNCs

An issue which arises during structural work on solid-state alkali-metal cyclopentadienides is whether solvent molecules are incorporated into the lattice or not. Because of the low solubilities of these salts, only few solvent-free structures are known[6] and most of them have been determined from powders. It is, therefore, unsurprising that the rich structural chemistry of alkali cyclopentadienides stems from crystals usually containing solvating amines or ethers. In contrast, the potassium and cesium salts of cyanocyclopentadiene form solvent-free crystals from THF or propionitrile because the anion contains its own donor.

The potassium salt CpCNK forms monoclinic crystals in which the anions and cations are arranged in zigzag chains running almost parallel to the *a* axis as illustrated in Figure 1. The chains can be broken down into inverse sandwich cations $[K(CpCN)K]^+$ highlighted by the broken frame and separated by $CpCN^-$ anions. The corresponding solvated and hence isolated lithium species $[(TMEDA)Li(MeCp)Li(TMEDA)]^+$ has been established previously.[7] Alternatively, the chains may be broken down into bent metallocene anions (solid frame in Figure 1) separated by potassium anions thereby enabling a structural analogy with bent metallocenes such as $[Cp_2Ti(NCCH_3)_2]^+$[8] which are well known in transition-metal organometallic chemistry. As for titanium in $[Cp_2Ti(NCCH_3)_2]^+$, the coordination sphere of potassium in CpCNK is completed by two neutral ligands, i.e. the cyano groups of adjacent CpCN anions. The metallocene bending angles (D–K1–D′ 135.86° and D–K2–D′ 135.14°) are very similar to that in $[Cp_2Ti(NCCH_3)_2]^+$ [134.8(5)°] but the angles N–K–N′ [90.00(4)° for K1 and 88.84(4)° for K2] and N–Ti–N′ [80.6(5)°] are somewhat different. It follows that the cyano groups of CpCNK force bent chains while for the cyclopentadienides of other alkali-metal ions, the chains may be linear or bent[6c–e] depending on the radius of the cation.[4a] When crystallizing with one molecule of diethyl ether, CpK also forms bent chains in which the angle is about 10° wider.[9]

The CpCN···K interaction links neighbouring chains to give a 3D network through slightly distorted squares K1,N,K2,N′ lying approximately in the *bc* plane as shown in Figure 2a. The angles between the best plane of K1,N,K2,N′ and the Cp groups on the left and the right are 22.6°. Unlike in $[Cp_2Ti(NCCH_3)_2]^+$, the metal–Cp bonding in CpCNK should be almost purely ionic as in all alkali-metal cyclopentadienides.[4] This implies a polarisation of the $CpCN^-$ anion in such a way that the negative charge is not only localised in the Cp π system but also at the N atom. Therefore, it can be expected that the limiting electronic structure B in Figure 2b plays a significant role. The crystal structure confirms this in two ways. Firstly, the

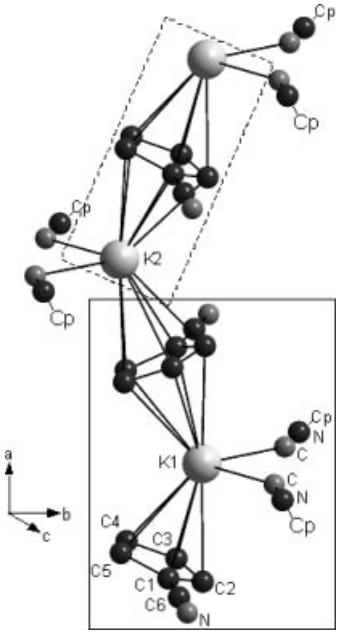

Figure 1. Inverse sandwich motif (broken frame) and bent-metallocene motif (solid frame) within the polymeric chains of CpCNK (detail with three formula units complemented by full coordination at the potassium ion); hydrogen atoms have been omitted for clarity; selected bond lengths [Å]: K1–C1 3.036(1), K1–C2 3.092(2), K1–C3 3.125(2), K1–C4 3.100(2), K1–C5 3.049(2), K2–C1 3.008(1), K2–C2 3.079(2), K2–C3 3.133(2), K2–C4 3.115(2), K2–C5 3.043(2), K1–D 2.840, K2–D 2.835, where D is the centre of gravity of the five-membered ring.

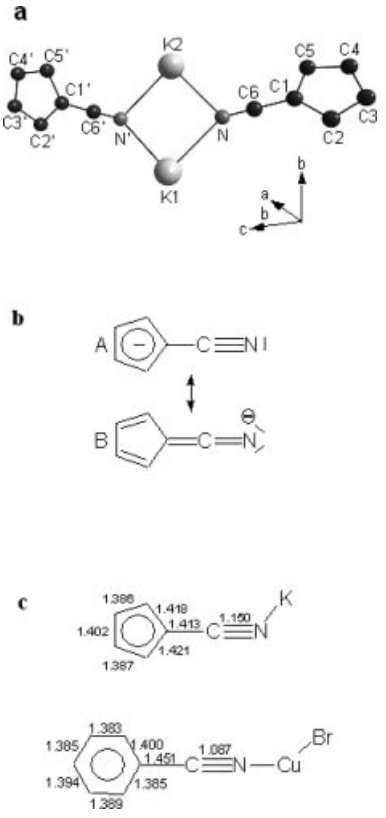

Figure 2. (a) Detail of the structure of CpCNK showing the K1, N, K2, N′ interactions between adjacent chains shown in Figure 1; selected bond lengths [Å] and angles [°]: C1–C2 1.418(2), C2–C3 1.386(2), C3–C4 1.402(2), C4–C5 1.387(2), C5–C1 1.421(2), C1–C6 1.413(2), C6–N 1.150(2), N–K1 2.7760(12), N–K2 2.8045(12), C1–C6–N 179.51(15), C6–N–K1 149.01(11), C6–N–K2 119.71(10), N–K1–N′ 90.00(4), N–K2–N′ 88.84(4); (b) limiting electronic structures of the CpCN anion; (c) bond lengths [Å] in CpCNK and $C_6H_5CNCuBr$.

 © 2005 Wiley-VCH Verlag GmbH & Co. KGaA, Weinheim

CNK fragments in Figure 2a are bent rather than linear and secondly, the $CpCN^-$ anion is distorted toward a fulvene-type structure. A comparison of the bond lengths of CpCNK with those of the benzonitrile complex of CuBr[10] in Figure 2c shows that the C–C bond lengths of the phenyl group are very similar, whereas in CpCNK the bonds C3–C2 and C4–C5 are significantly shorter than C1–C2, C3–C4 and C5–C1. Also, compared with $C_6H_5CNCuBr$, C1–C6 of CpCNK is shorter while C6–N is longerand both are towards double bonds. It is worth noting that structure B in Figure 2b is the deprotonation product of the transient species 6-iminofulvene.[11]

The cesium salt CpCNCs forms orthorhombic crystals again featuring zigzag chains (along the *c* direction of the unit cell) which may also be decomposed into inverse sandwich cations (Figure 3, broken frame) or bent sandwich anions (Figure 3, solid frame). However, compared with the potassium salt, there are remarkable differences. The mean metal–Cp distance in CpCNCs is 0.37 Å longer than in CpCNK which is more than the difference of the coordination number adjusted radii of Cs^+ and K^+ (0.23 Å[12]) and which, therefore, points to additional factors contributing to that distance. There is a striking decrease in the sandwich bending angles from 135.14° and 135.86° to 107.3° when passing from CpCNK to CpCNCs. While in the latter salt the angle is still 8.3° smaller than in the isolated anion $[Cp_3Cs_2]^-$[13] and 22.4° smaller than in CpCs,[6c] the bending of the alkali-metal cyclopentadienides is most pronounced for Cs. Bending of Cp sandwich compounds as an intrinsic molecular property has been addressed for main-group element derivatives.[14] In particular, the salts CpCNK and CpCNCs correspond to the general tendency that the deviation from linearity in main-group compounds MX_2 increases when M becomes heavier.[15] In mostly ionic solids, another driving force is the need to optimise coulombic interactions and to complete the coordination spheres of the ions. Incomplete coordination of alkali-metal–organic compounds becomes more critical when the radius of the metal ion increases.[16] In the present case this means that upon additional coordination of the cyano groups, the Cp_2Cs^- fragment bends more strongly than Cp_2K^-.

The linkage of the chains in CpCNCs is also different from that in CpCNK. As can be seen in Figure 4, the CpCN···Cs interaction occurs in such a way that the $CpCN^-$ anions on both sides of the cation chain bridge different pairs of cations, whereas in CpCNK they bridge the same pair (Figure 2a). This does not prevent the CN group of CpCNCs from interacting with two cesium ions, thereby stretching the anion toward a fulvene limiting structure (Figure 2) much in the same way as in the case of CpCNK. An additional linkage between adjacent chains of CpCNCs occurs between one edge of the cyclopentadienyl and Cs′ (see inset of Figure 4). This is indicated by the large angle between the plane formed by C2,C3,Cs and the Cp plane (152.0°), and by the distances Cs′–C2 [3.654(3) Å] and Cs′–C3 [3.654(3) Å] which are only slightly longer than the Cs–C distances within the chains. The contribution of the η^2 interaction to the overall bonding energy of CpCNCs is probably substantial because, for the Cp^- and Li^+ pair, it has been calculated that such η^2 interactions are only about 1.4 times smaller than η^5 interactions.[4a]

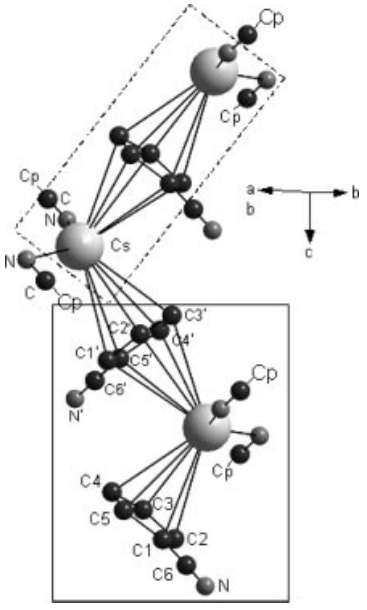

Figure 3. Inverse sandwich motif (broken frame) and bent-metallocene motif (solid frame) within the polymeric chains of CpCNCs (detail with three formula units complemented by full coordination at the potassium ion); hydrogen atoms have been omitted for clarity; selected bond lengths [Å] and angles [°]: Cs–C1 3.541(3), Cs–C2 3.436(3), Cs–C3 3.309(3), Cs–C4 3.334(3), Cs–C5 3.486(3), Cs–C1′ 3.426(3), Cs–C2′ 3.464(3), Cs–C3′ 3.438(3), Cs–C4′ 3.403(3), Cs–C5′ 3.389(3), C1–C6–N 179.4(3), C6–N–Cs 117.7(3), C6′–N′–Cs 149.0(3), Cs–D 3.207, Cs–D′ 3.209, D–Cs–D′ 107.32, where D is the centre of gravity of the five-membered ring.

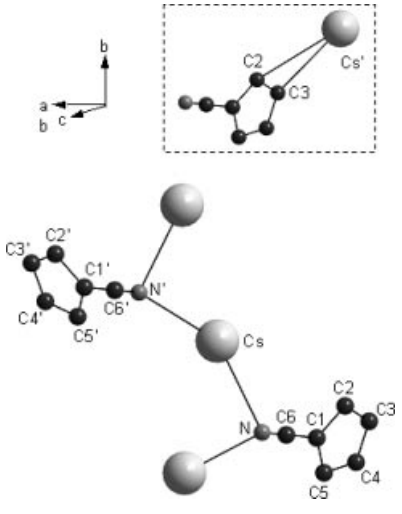

Figure 4. Detail of the structure of CpCNCs showing the Cs···N interactions between adjacent chains shown in Figure 3; inset: η^2 interaction between $CpCN^-$ and Cs^+; selected bond lengths [Å] and angles [°]: C1–C2 1.417(5), C2–C3 1.390(5), C3–C4 1.406(5), C4–C5 1.389(5), C5–C1 1.418(5), C1–C6 1.428(5), C6–N 1.151(5), N–Cs 3.236(3), N′–Cs 3.292(3), Cs′–C2 3.654(3), Cs′–C3 3.654(3), N–Cs–N′ 145.48(8), Cs–N–Cs 87.21(7), C2–Cs′–C3 21.93(7).

 © 2005 Wiley-VCH Verlag GmbH & Co. KGaA, Weinheim

^{133}Cs NMR Spectroscopy

Since crystal structures of alkali-metal–organic compounds are sometimes difficult to obtain, we wanted to find out whether ^{133}Cs NMR spectroscopy would be a useful method of characterization. Alkali-metal ions have neither p nor d valence electrons and this makes qualitative signal shift interpretation as straightforward as for proton signals because simple electron density arguments can be used. The disadvantage is that the signal shift range of an alkali-metal nucleus is much smaller than that of its neighbours in the same row of the periodic table. For instance, ^{7}Li NMR signal shifts are much smaller than those of ^{11}B which are in turn smaller than those of ^{19}F. The disadvantage is partly compensated for by the fact that the shift range increases rapidly when passing from a light to a heavy nucleus in a given group. Therefore, ^{133}Cs should be the nucleus of choice for studying small changes of the bonding in alkali-metal cyclopentadienides. Figure 5 shows the ^{133}Cs MAS NMR spectra of microcrystalline samples of CpCNCs and CpCs. The envelope of the spinning sideband pattern corresponds to the typical signal shape of a spin nucleus with low chemical shift anisotropy.[17] At the given spinning frequency, the six satellite transitions flanking the central m = ±½ transition are best seen in the case of CpCs from the modulation of the sideband intensities. At lower spinning frequencies, some chemical shift anisotropy and its orientation relative to the quadrupolar interaction leads to additional spectroscopic features as has been worked out in detail previously.[18] In this study we were interested in the isotropic signal shifts which turned out to be rather different for solid CpCNCs (δ = –128.2 ppm) and CpCs (δ = –247.6 ppm). Similar shifts were found in solution for CpCNCs (δ = –50.7 ppm in MeCN) and CpCs (δ = –253.7 ppm in THF). One may think of attributing the shift difference of both salts to additional CN coordination in CpCNCs. This would be equivalent to solvation which has been shown to actually shift ^{133}Cs NMR signals to high frequency when the solvent is acetonitrile.[19] However, these shifts are much smaller even for fully solvated ions. Another reason for the low-frequency signal shift is the fact that Cs^+ sits above the center of the Cp ring and hence experiences the additional field induced by the π electrons of the aromatic ligand. This scenario applies to mapping protons of transition-metal compounds[20] and to determining the interaction of Li^+ with Cp and Cp-like anions.[21] In fact, for $^{6/7}$Li, as for ^{133}Cs in this work, the metal resonance is shifted to a lower frequency upon interacting with Cp anions and these shifts are much larger than solvation-induced shifts. In the case of ^{133}Cs NMR spectroscopy, the Cp-induced signal shift is so large that structural changes of CpCs derivatives should be visible. On this basis we suggest that the ^{133}Cs NMR signal shift depends on the bending angle α of the $[Cp_2Cs]^-$ fragment (see Figure 1 and Figure 3). When adding the field vectors induced at both Cp groups, the ^{133}Cs NMR signal shift can be expected to behave as cos(180 – α). A linear sandwich fragment can thus be expected to give the largest ^{133}Cs signal shift. Upon bending the sandwich, the angle α decreases and the signal should move to high frequency. This is true for CpCNCs [α = 107.3°, δ(^{133}Cs) = –128.2 ppm] and CpCs [α = 129.7°, δ(^{133}Cs) = –247.6 ppm] although the correlation is not perfect. The reason is that the signal shift also depends on other factors such as the Cp–Cs distance, additional ligands such as the CN groups and the neighbors in the lattice. In solution, the structural parameters may be different and solvation cannot be neglected.

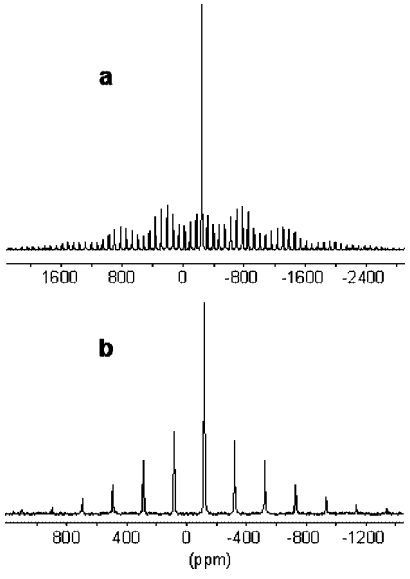

Figure 5. ^{133}Cs MAS NMR spectra of CpCNCs (a) and CpCs (b) at a spinning frequency of 8 kHz and a temperature of 301 K.

Conclusions

The potassium and cesium salts of cyanocyclopentadiene are soluble compounds and yet they do not form solid-state solvates. The arrangement of CpCN anions and alkali-metal cations in the lattice may be viewed as chains or *n*-decker sandwiches which are bent and which consist of linear inverse sandwich (M–Cp′–M) fragments and bent sandwich $[Cp'_2M(NCCp)_2]$ fragments. The chains are crosslinked through CN···M interactions which at the same time polarize the CpCN anion such that it is distorted from a cyclopentadienyl- toward a fulvene-type geometry. Different crosslinking patterns exist for CpCNK and CpCNCs and the latter features an additional η^2 interaction between Cs^+ and $CpCN^-$. ^{133}Cs NMR spectroscopy proved to be a sensitive probe for structural changes of the $[Cp_2Cs]^-$ fragment.

Experimental Section

Caution: *Cyanogen chloride used as reagent in this work is a very toxic gas at room temperature and should be handled with proper precautions!* All manipulations involving alkali-metal cyclopentadienides were carried out under nitrogen using Schlenk tech-

 © 2005 Wiley-VCH Verlag GmbH & Co. KGaA, Weinheim

niques and dry, oxygen-free solvents. Cesium cyclopentadienide was synthesized as described by Harder.[13] The spectroscopic results were obtained with a Varian Mat 50 mass spectrometer, a Perkin–Elmer IR spectrometer 1600 FTIR as well as Jeol JNM GX 400 and Bruker Avance 300 NMR spectrometers for solution and solid-state NMR spectra, respectively. The solid samples were packed in ZrO_2 rotors and sealed with Kel-F caps in a glovebox. All referencing was done relative to TMS except for the ^{133}Cs NMR spectroscopic data which are relative to external CsCl as a solid or highly diluted in water for MAS and solution spectra, respectively. The sample temperature under MAS conditions was obtained from a previous calibration.[22]

Dicyanotricyclo[5.2.1.0^{2,6}]deca-4,8-diene Isomers: By modifying Webster's procedure,[3b] freshly prepared cyanogen chloride[23] (30.0 g, 0.488 mol) was dissolved at –78 °C in THF (150 mL). The colourless solution was warmed to 0 °C and a THF solution of sodium cyclopentadienide (208 mL, 2.35 M, 0.49 mol) was added dropwise while cooling with an ice bath. The reaction was apparent from the immediate formation of a colourless precipitate and colour changes first to yellow and subsequently to red-brown. The reaction mixture was allowed to warm to room temperature and was then stirred for 2 h. After removing the solvent at 10^{-4} bar, the brown solid was dissolved in water (100 mL), the pH was adjusted to 7 using a solution of 0.1 N hydrochloric acid and the product was extracted with diethyl ether (4 × 100 mL). The combined organic phases were dried with sodium sulfate, the solvent was removed under reduced pressure and the resultant deep red oil of cyanocyclopentadiene dimers (60.2 g, 67% yield relative to cyanogen chloride) was subjected immediately to further reaction.

Potassium Cyanocyclopentadienide: Similar to the procedure described previously,[3b] a mixture of dicyanotricyclo[5.2.1.0^{2,6}]deca-4,8-dienes (20.0 g, 0.110 mol) was cracked to cyanocyclopentadienes by heating to 170–180 °C and distilled at 15 mbar by using a short bridge directly into a suspension of potassium carbonate (11.1 g, 0.110 mol) in propionitrile (200 mL). The resultant pink suspension was stirred for 2 h and the solid removed by filtration. The solvent was then removed at 10^{-4} bar leaving behind microcrystalline CpCNK. Yield 1.71 g, yield 6%. Colourless crystals suitable for X-ray analysis were obtained by covering a solution of the solid in THF with hexane at room temperature. ^1H NMR (400 MHz, [D$_6$]DMSO, 305 K): δ = 5.51 (pseudo-t, $^{2+4}J_{H,H}$ = 5.6 Hz, 2 H, 2/5-H), 5.92 (pseudo-t, $^{2+4}J_{H,H}$ = 5.6 Hz, 2 H, 3/4-H) ppm. ^{13}C NMR (100 MHz, [D$_6$]DMSO, 305 K): δ = 80.7 (C-1), 107.7 (C-2/5), 111.4 (C-3/4), 126.4 (CN) ppm.

Cesium Cyanocyclopentadienide: The procedure described for the potassium analogue was carried out with dicyanotricyclo[5.2.1.0^{2,6}]deca-4,8-dienes (9.11 g, 50 mmol) and cesium carbonate (16.3 g, 50 mmol) in propionitrile (100 mL). Crystallization of the resultant powder from acetonitrile at room temperature gave CpCNCs as brown crystals which were analytically pure and suitable for X-ray analysis. Yield 1.11 g, 5%. M.p. 170–175 °C (dec.). IR (KBr): $\tilde{\nu}$ = 3037, 3095 [m, ν(CH)], 2191 [s, ν(CN)] cm^{-1}. CI$^+$ MS: *m*/*z* (%) = 223 (75) [M]$^+$, 196 (10) [M – CHN]$^+$, 133 (78) [M – C_6H_4N]$^+$. ^1H NMR (400 MHz, [D$_6$]DMSO, 305 K): δ = 5.67 (pseudo-t, $^{2+4}J_{H,H}$ = 5.6 Hz, 2 H, 2/5-H), 6.07 (pseudo-t, $^{2+4}J_{H,H}$ = 5.6 Hz, 2 H, 3/4-H) ppm. ^{13}C NMR (100 MHz, [D$_6$]DMSO, 305 K): δ = 84.1 (C-1), 110.3 (C-2/5), 114.0 (C-3/4), 126.5 (CN) ppm. C_6H_4CsN (223.0): calcd. C 32.32, H 1.81, N 6.28; found C 32.79, H 1.91, N 6.18.

Single Crystal X-ray Structure Determination of CpCNK and CpCNCs

CpCNK: Crystal data and details of the structure determination are presented in Table 1. Suitable single-crystals for the X-ray diffraction study were grown from THF/hexane. A clear colorless fragment was stored under perfluorinated ether, transferred to a Lindemann capillary, fixed and sealed. Preliminary examinations and data collection were carried out with an area detecting system (NONIUS, MACH3, κ-CCD) at the window of a rotating anode (NONIUS, FR951) with graphite-monochromated Mo-K_α radiation (λ = 0.71073 Å). The unit-cell parameters were obtained by a full-matrix least-squares refinement of 1331 reflections. Data collection was performed at 173 K within a θ-range of 3.33° < θ < 25.34°. Nine data sets were measured in rotation scan mode with $\Delta\varphi/\Delta\Omega$ = 1.0°. A total number of 16425 intensities were integrated. Raw data were corrected for Lorentz, polarisation and latent decay and absorption effects (arising from the scaling procedure). After merging (R_{int} = 0.042), a sum of 1266 (all data) and 1173 [$I > 2\sigma(I)$] reflections remained and all data were used. The structure was solved by a combination of direct methods and difference Fourier syntheses. All non-hydrogen atoms were refined with anisotropic displacement parameters. All hydrogen atom positions were found in the difference map calculated from the model containing all non-hydrogen atoms. The hydrogen positions were refined with individual isotropic displacement parameters. Full-matrix least-squares refinements with 90 parameters were carried out by minimizing $\Sigma w(F_o^2 - F_c^2)^2$ with the SHELXL-97weighting scheme and the refinements were stopped at shift/err < 0.001. The final residual electron density maps showed no remarkable features. Neutral atom scattering factors for all atoms and anomalous dispersion corrections for the non-hydrogen atoms were taken from the *International Tables for Crystallography.* All calculations were performed with an Intel Pentium II PC with the STRUX-V system including the programs PLATON, SIR92 and SHELXL-97.[24]

CpCNCs: Crystal data and details of the structure determination are presented in Table 1. Suitable single-crystals for the X-ray diffraction study were grown from acetonitrile. A clear light brown fragment was stored under perfluorinated ether, transferred to a Lindemann capillary, fixed and sealed. Preliminary examinations and data collection were carried out with an area detecting system (NONIUS, MACH3, κ-CCD) at the window of a rotating anode (NONIUS, FR951) with graphite-monochromated Mo-K_α radiation (λ = 0.71073 Å). The unit-cell parameters were obtained by a full-matrix least-squares refinement of 759 reflections. Data collection was performed at 173 K within a θ-range of 3.08° < θ < 25.36°. Eight data sets were measured in rotation scan mode with $\Delta\varphi/\Delta\Omega$ = 2.0°. A total number of 13279 intensities were integrated. Raw data were corrected for Lorentz, polarisation and latent decay and absorption effects (arising from the scaling procedure). After merging (R_{int} = 0.046), a sum of 1238 (all data) and 1215 [$I > 2\sigma(I)$] reflections remained and all data were used. The structure was solved by a combination of direct methods and difference Fourier syntheses. All non-hydrogen atoms were refined with anisotropic displacement parameters. All hydrogen atom positions were calculated in ideal positions (riding model). Full-matrix least-squares refinements with 75 parameters were carried out by minimizing $\Sigma w(F_o^2 - F_c^2)^2$ with the SHELXL-97weighting scheme and were stopped at shift/err < 0.001. The final residual electron density maps showed no remarkable features. As shown by Flack's parameter ε = 0.15(3), the crystal is slightly twinned. A correction for extinction was applied using the SHELXL-97 procedure with a final ε value of 0.0125(4). Neutral atom scattering factors for all atoms and anomalous dispersion corrections for the non-hydrogen atoms were taken from the *International Tables for Crystallography.* All calculations were performed with an Intel Pentium II PC with the STRUX-V system including the programs PLATON, SIR92, and SHELXL-97.[24]

 © 2005 Wiley-VCH Verlag GmbH & Co. KGaA, Weinheim

Table 1. Summary of the crystal data, details of data collections and refinements for the compounds CpCNK and CpCNCs.

	CpCNK	CpCNCs
Empirical formula	C_6H_4KN	C_6H_4CsN
Formula mass	129.20	223.01
Crystal system	monoclinic	orthorhombic
Space group	*C*2/*c* (no. 15)	$P2_12_12_1$ (no. 19)
a [Å]	10.4879(1)	7.5274(1)
b [Å]	12.2297(2)	8.6227(2)
c [Å]	11.6318(1)	10.3183(2)
β [°]	111.4875(6)	90
V [Å^3]	1388.25(3)	669.72(2)
Z	8	4
$\rho_{calcd.}$ [g cm^{-3}]	1.236	2.212
μ [mm^{-1}]	0.658	5.418
T [K]	173	173
F(000)	528	408
Crystal size [mm]	0.61×0.19×0.08	0.56×0.28×0.18
θ-range [°]	3.33/25.34	3.08/25.36
Index ranges	$h = \pm12$, $k = \pm14$, $l = \pm13$	$h = \pm9$, $k = \pm10$, $l = \pm12$
Reflections collected	16425	13279
Independent reflections [$I_o>2\sigma(I_o)$/all data/R_{int}]	1173/1266/0.042	1215/1238/0.046
Data/restraints/parameters	1266/0/90	1238/0/75
R_1 [$I_o>2\sigma(I_o)$/all data]	0.0235/0.0259	0.0128/0.0133
wR_2 [$I_o>2\sigma(I_o)$/all data]	0.0613/0.0628	0.0308/0.0309
GoF	1.085	1.146
Weights *a*/*b*	0.0305/0.5258	0.0095/0.7628
$\Delta\rho_{max/min}$ [e Å^{-3}]	0.13/–0.20	0.49/–0.38

[1] a) D. W. Macomber, W. P. Hart, M. D. Rausch, *Adv. Organomet. Chem.* **1982**, *21*, 1–55; b) R. L. Halterman, *Chem. Rev.* **1992**, *92*, 965–994; c) C. Janiak, H. Schumann, *Adv. Organomet. Chem.* **1991**, *33*, 291–379; d) J. Okuda, *Top. Curr. Chem.* **1992**, *160*, 97–145; e) N. B. Ivchenko, P. V. Ivchenko, I. E. Nifant'ev, *Russ. J. Org. Chem.* **2000**, *36*, 609–637.

[2] a) J. Okuda, *Comments Inorg. Chem.* **1994**, *16*, 185–205; b) G. Wagner, R. Herrmann, in *Ferrocenes* (Eds.: A. Togni, T. Hayashi), VCH, Weinheim, **1995**, chapter 4; c) R. L. Halterman, in *Metallocenes* (Eds.: A. Togni, R. L. Halterman), Wiley-VCH, Weinheim, **1998**, vol. 1, chapter 8; d) U. Siemeling, *Chem. Rev.***2000**, *100*, 1495–1526.

[3] a) D. Peters, *J. Chem. Soc., Dalton Trans.* **1960**, 1832–1837; b) O. W. Webster, *J. Am. Chem. Soc.* **1966**, *88*, 3046–3050; c) W. Neukam, W. Grimme, *Tetrahedron Lett.***1978**, 2201–2204; d) K. Banert, F. Köhler, B. Meier, *Tetrahedron Lett.* **2003**, *44*, 3781–3783.

[4] a) S. J. Harder, *Coord. Chem. Rev.* **1998**, *176*, 17–66; b) P. Jutzi, N. Burford, *Chem. Rev.* **1999**, *99*, 969–990. Selected recent examples of heavy alkali-metal cyclopentadienides: c) S. Neander, F. E. Tio, R. Buschmann, U. Behrens, F. Olbrich, *J. Organomet. Chem.* **1999**, *582*, 58–65; d) M. J. Harvey, T. P. Hanusa, M. Pink, *J. Chem. Soc., Dalton Trans.* **2001**, 1128–1130; e) W. J. Evans, J. C. Brady, C. H. Fujimoto, D. G. Giarikos, J. W. Ziller, *J. Organomet. Chem.* **2002**, *649*, 252–257; f) G. Bai, H. W. Roesky, P. Muller, *Bull. Pol. Acad. Sci. Chem.* **2002**, *50*, 1–10; g) S. Kheradmandan, H. W. Schmalle, H. Jacobsen, O. Blacque, T. Fox, H. Berke, M. Gross, S. Decurtins, *Chem. Eur. J.* **2002**, *8*, 2526–2533; h) M. L. Cole, C. Jones, P. C. Junk, *J. Chem. Soc., Dalton Trans.* **2002**, 896–905; i) W. J. Evans, D. G. Giarikos, J. W. Ziller, *J. Organomet. Chem.* **2003**, *688*, 200–205.

[5] H.-O. Kalinowski, S. Berger, S. Braun, *^{13}C NMR-Spektroskopie*, Georg Thieme Verlag, Stuttgart, **1984**, p. 124 and 277.

[6] a) P. Jutzi, W. Leffers, B. Hampel, S. Pohl, W. Saak, *Angew. Chem.* **1987**, *99*, 563–564; *Angew. Chem. Int. Ed. Engl.* **1987**, *26*, 583–584; b) W. J. Evans, T. J. Boyle, J. W. Ziller, *Organometallics* **1992**, *11*, 3903–3907; c) R. E. Dinnebier, F. Olbrich, G. M. Bendele, *Acta Crystallogr., Sect. C* **1997**, *53*, 699–701; d) R. E. Dinnebier, F. Olbrich, S. van Smaalen, P. W. Stephens, *Acta Crystallogr., Sect. B* **1997**, *53*, 153–158; e) R. E. Dinnebier, U. Behrens, F. Olbrich, *Organometallics* **1997**, *16*, 3855–3858.

[7] S. D. Stults, R. A. Anderson, A. Zalkin, *J. Am. Chem. Soc.* **1989**, *111*, 4507–4508.

[8] P. A. Seewald, G. S. White, D. W. Stephan, *Can. J. Chem.* **1988**, *66*, 1147–1152.

[9] V. Jordan, U. Behrens, F. Olbrich, E. Weiss, *J. Organomet. Chem.* **1996**, *517*, 81–88.

[10] M. Massaux, M.-T. Le Bihan, *Acta Crystallogr., Sect. B* **1976**, *32* 1586–1589.

[11] a) C. Thétaz, C. Wentrup, *J. Am. Chem. Soc.* **1976**, *98*, 1258–1259; b) T. Sakaizumi, H. Kikuchi, O. Ohashi, I. Yamaguchi, *Bull. Chem. Soc. Jpn.* **1987**, *60*, 3903–3909.

[12] R. D. Shannon, *Acta Crystallogr., Sect. A* **1976**, *32* 751–767.

[13] S. J. Harder, M. H. Prosenc, *Angew. Chem.* **1996**, *108*, 101–103; *Angew. Chem. Int. Ed. Engl.* **1996**, *35*, 97–99.

[14] a) T. K. Hollis, J. K. Burdett, B. Bosnich, *Organometallics* **1993**, *12*, 3385–3386; b) T. V. Timofeeva, J.-H. Lii, N. L. Allinger, *J. Am. Chem. Soc.* **1995**, *117*, 7452–7459; c) E. P. F. Lee, P. Soldan, T. G. Wright, *Inorg. Chem.* **2001**, *40*, 5979–5984; d) V. N. Sapunov, K. Kirchner, R. Schmid, *J. Organomet. Chem.* **2001**, *214*, 143–185.

[15] M. Kaupp, *Angew. Chem.* **2001**, *113*, 3642–3677; *Angew. Chem. Int. Ed.* **2001**, *40*, 3535–3565.

[16] C. Schade, P. von R. Schleyer, *Adv. Organomet. Chem.* **1987**, *27*, 169–278.

[17] a) S. Mooibroek, R. E. Wasylishen, R. Dickson, G. Facey, B. A. Pettitt, *J. Magn. Reson.* **1986**, *66*, 542–545; b) P. W. France, *J. Magn. Reson.* **1991**, *92*, 30–44.

[18] a) W. P. Power, R. E. Wasylishen, S. Mooibroek, B. A. Pettitt, W. Danchura, *J. Phys. Chem.* **1990**, *94*, 591–598; b) J. Skipsted, T. Vosegaard, H. Bildsøe, H. J. Jakobsen, *J. Phys. Chem.* **1996**, *100*, 14872–14881.

[19] W. J. DeWitte, L. Liu, E. Mei, J. L. Dye, A. I. Popov, *J. Solution Chem.* **1977**, *6*, 337–348.

[20] C. Elschenbroich, J. Schneider, H. Prinzbach, W.-D. Fessner, *Organometallics* **1986**, *5*, 2091–2096.

[21] a) L. A. Paquette, W. Bauer, M. R. Sivik, M. Bühl, M. Feigel, P. von R. Schleyer, *J. Am. Chem. Soc.* **1990**, *112*, 8776–8789; b)

 © 2005 Wiley-VCH Verlag GmbH & Co. KGaA, Weinheim

N. Hertkorn, F. H. Köhler, *Z. Naturforsch., Teil B* **1990**, *45*, 848–856; c) D. Johnels, A. Boman, U. Edlund, *Magn. Reson. Chem.* **1998**, *36*, S151–S156.
[22] F. H. Köhler, X. Xie, *Magn. Reson. Chem.* **1997**, *35*, 487–492.
[23] G. Brauer, A. Haas, *Handbuch der Präparativen Anorganischen Chemie*, Ferdinand Enke Verlag, Stuttgart, **1978**, p. 630.
[24] a) Data Collection Software for NONIUS κ-CCD devices, Delft, The Netherlands, **1997**; b) Z. Otwinowski, W. Minor, *Methods Enzymol.* **1997**, *276*, 307; c) *International Tables for Crystallography*, vol. C, 3rd ed. (Eds.: T. Hahn, A. J. C. Wilson), Kluwer Academic Publisher, Dordrecht, Boston, London, **1992**; d) G. Artus, W. Scherer, T. Priermeier, E. Herdtweck, *STRUX-V: A Program System to Handle X-ray Data*, TU München, Garching, Germany, **1997**; e) A. L. Spek, *PLATON: A Multipurpose Crystallographic Tool*, Utrecht University, Utrecht, The Netherlands, **2001**; f) *SIR92*: A. Altomare, G. Cascarano, C. Giacovazzo, A. Guagliardi, M. C. Burla, G. Polidori, M. Camalli, *J. Appl. Crystallogr.* **1994**, *27*, 435–436; g) G. M. Sheldrick, *SHELXL-97*, University of Göttingen, Göttingen, Germany, **1998**; h) CCDC-246097 (CpCNK) and -246098 (CpCNCs) contain the supplementary crystallographic data for this paper. These data can be obtained free of charge from The Cambridge Crystallographic Data Centre via www.ccdc.cam.ac.uk/data_request/cif.

Received: July 29, 2004
Published Online January 26, 2005

 © 2005 Wiley-VCH Verlag GmbH & Co. KGaA, Weinheim

Crystallographic Proof of Double Walden Inversion in Nucleophilic Substitution Reactions of Macrocyclic Cyclotriphosphazene Derivatives

Serap Beşli,[a] Simon J. Coles,[b] David B. Davies,[c] Robert J. Eaton,[c] Michael B. Hursthouse,[b] Adem Kılıç,*[a] and Robert A. Shaw[c]

Keywords: Nucleophilic substitution / Inversion of configuration / Cyclotriphosphazenes / Crystal structures / Configuration determination

Using X-ray crystallography it is demonstrated unambiguously that a double Walden inversion reaction occurs for successive nucleophilic substitution of the mono-spiropropanoxyamino derivative of the *cis*-ansa-macrocyclic cyclophosphazene compound $N_3P_3[O(CH_2)_3NH][O(CH_2CH_2O)_4]Cl_2$ (**3**). The spiropropanoxyamino moiety enables groups above and below the plane of the N_3P_3 ring to be distinguished. The first nucleophilic substitution of compound **3** with X^- (e.g., X = 2-naphthoxy) gives $N_3P_3[O(CH_2)_3NH][O(CH_2CH_2O)_4]XCl$ (**4a**), which has a *trans*-ansa-macrocyclic ring as a result of the inversion reaction, and then subsequent reaction of **4a** with the same nucleophile gives $N_3P_3[O(CH_2)_3NH][O(CH_2CH_2O)_4]X_2$ (**5a**), in which the macrocyclic ring is *cis*-ansa again, but it is now on the *opposite side* of the N_3P_3 ring from that of the starting material **3** as a result of the second inversion reaction. Structures stereochemically analogous to compound **5a** were also obtained upon reaction with other monofunctional nucleophiles, such as phenol, pyrrolidine and aniline, to give compounds **5b**, **5c** and **5d**, respectively, and with the difunctional nucleophile 2,2,3,3-tetrafluorobutanediol to give the di-ansa derivative **6**. Compound **3** was also sequentially treated with two different mononucleophiles – phenol and aniline – to give the unsymmetrically disubstituted compound **7**, in which the macrocyclic ring is also *cis*-ansa again and on the *opposite side* of the N_3P_3 ring from that of the starting material, as a result of the double Walden inversion reactions.

(© Wiley-VCH Verlag GmbH & Co. KGaA, 69451 Weinheim, Germany, 2005)

Introduction

The Walden inversion[1] has played an important part in the study of reaction mechanisms in organic chemistry.[2] For S_N2 reactions involving four-coordinate carbon atoms, attack by a nucleophile leads to an inversion of configuration, which is usually confirmed by starting with an optically active compound so that the product has the opposite optical rotation.[3] A similar approach has been taken for reactions involving four-coordinate phosphorus atoms; unless pseudorotation or steric constraints intervene, nucleophilic attack generally leads to inversion of configuration, if the reaction is associative, via either a five-coordinate transition state $S_N2(P)$ or intermediate.[4,5] Pentacoordinate intermediates with fluoride ions have been reported for $(NPF_2)_n$ (n = 4, 5 and 6) and crystallographically characterised as the $(N_4P_4F_9)^-$ and $(N_6P_6F_{13})^-$ anions.[6]

Instead of using changes in optical rotation to investigate reaction mechanisms involving inversion of configuration, we have used a different approach involving reactions of *meso* compounds to give racemates, which can react further to give either another *meso* compound or another racemate depending on the second substituent.[7,8] In recent years macrocyclic derivatives of cyclotriphosphazene have been isolated and X-ray crystallographic investigations of the initial products with polyether macrocyclic rings in the ansa configuration have been found, so far without exception, to have *cis*-ansa structures.[9,10] In macrocyclic cyclophosphazene compounds such as **1** (Scheme 1), the two P atoms carrying the macrocyclic ring, P(Om)Cl (where Om = macrocyclic residue), are stereogenic and, because compound **1** is symmetrically substituted, it is the *meso* form.[7] The first reaction of compound **1** with a nucleophile (X^-) takes place at either of the two P(Om)Cl groups to give the P(Om)X moiety, in which the macrocyclic ring now exists in a *trans*-ansa configuration and the molecule is racemic.[7,8] Further reaction with the same nucleophile X^- then converts the second P(Om)Cl group into another P(Om)X moiety and the resulting derivative has regained a *cis*-ansa structure and is *meso* again.[7] On the other hand, reaction of **1** with

[a] Department of Chemistry, Gebze Institute of Technology, Gebze, Turkey
Fax: +90-262-754-2385
E-mail: kilic@gyte.edu.tr
[b] Department of Chemistry, University of Southampton, Highfield, Southampton, UK
[c] School of Biological and Chemical Sciences, Birkbeck College (University of London), Malet Street, London, UK

Supporting information for this article is available on the WWW under http://www.eurjic.org or from the author.

 DOI: 10.1002/ejic.200400745 © 2005 Wiley-VCH Verlag GmbH & Co. KGaA, Weinheim

the first nucleophile X^- and then further reaction with a different nucleophile Y^- converts the second P(Om)Cl group into a P(Om)Y moiety and the resulting derivative has regained a *cis*-ansa structure, but is now racemic.[8] These structures have been confirmed crystallographically for single-bridged and double-bridged macrocyclic cyclophosphazene compounds, thus supporting the postulate of Walden inversions for both steps of the reaction.[7] However, only the first step was proven crystallographically; the second was assumed by analogy based mainly on ^{31}P NMR measurements.[7,8]

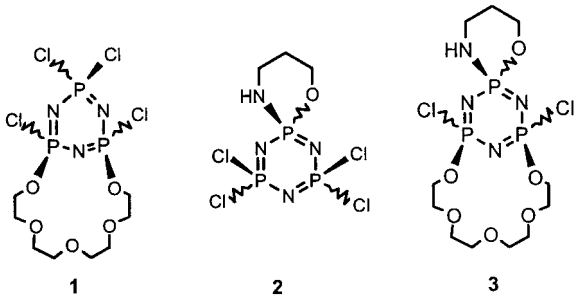

Scheme 1. Wedge-based structure representation of compounds **1**–**3** in order to emphasise that the macrocyclic ring of compound **3** is in the *cis-ansa* configuration with respect to the cyclophosphazene ring and is *cis* to the NH group of the spirocyclic ring.

Although there is good evidence of inversion of configuration at each step of the reaction, we could not prove by X-ray crystallography that the second Walden inversion led to a *cis*-ansa structure in which the macrocyclic ring was now on the *opposite side* of the N_3P_3 ring to that of the starting material. In order to distinguish groups that are above and below the plane of the N_3P_3 ring, a marker is needed having non-identical substituents on the third phosphorus atom, i.e. the one not involved in the ansa segment. This was achieved by using the mono-spiro derivative $N_3P_3Cl_4[O(CH_2)_3NH]$ (**2**; Scheme 1), whose synthesis[11,12] and crystal structure[12] have been reported previously. The spiropropanoxyamino group is approximately perpendicular to the cyclophosphazene ring[12] and, because it is linked by two different groups (O and NH) to the N_3P_3 ring, a distinction can be be made between the two sides (above and below) of the planar cyclophosphazene ring. Reaction of **2** with the sodium derivative of tetraethylene glycol, $NaO(CH_2CH_2O)_4Na$, gives $N_3P_3[O(CH_2)_3NH][O(CH_2CH_2O)_4]Cl_2$ (**3**), which is a suitable starting material for further nucleophilic substitution reactions of the two remaining P–Cl bonds in a *cis*-ansa relationship. Compound **3** (Scheme 1) was chosen as an easily accessible starting material with no more than two P–Cl bonds in the molecule (to avoid side-reactions) and because the two P–Cl bonds had to exist in a definite *cis* relationship; suitably substituted *cis*-ansa compounds provide such a juxtaposition of bonds.

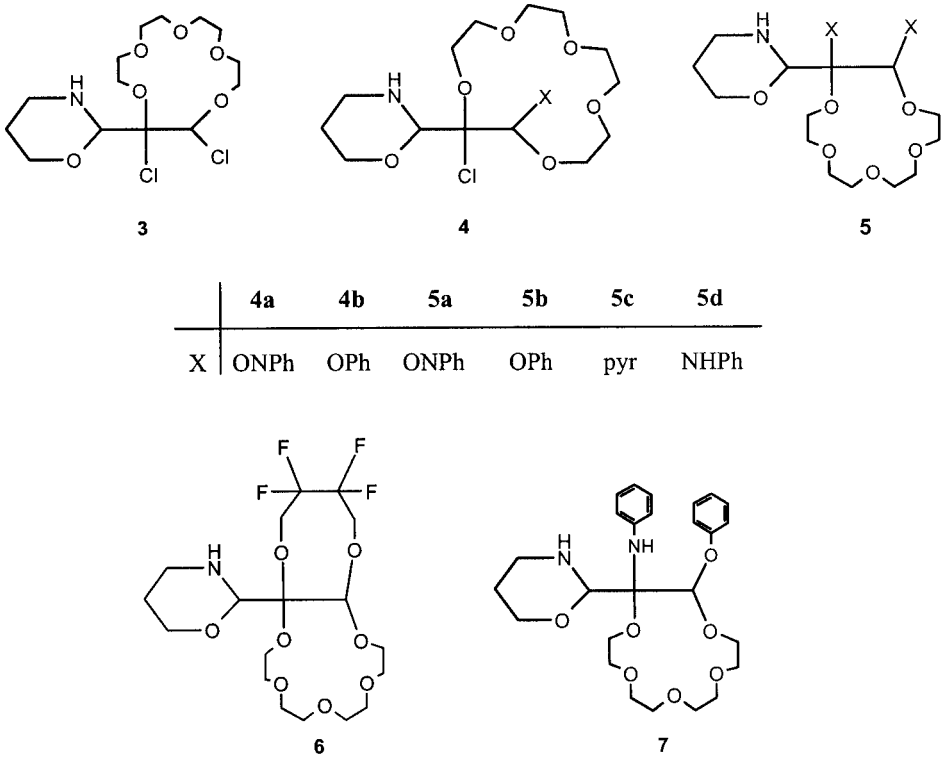

	4a	4b	5a	5b	5c	5d
X	ONPh	OPh	ONPh	OPh	pyr	NHPh

Scheme 2. Diagrammatic representation of the structure of compound **3** showing the macrocyclic ring in the *cis-ansa* configuration with respect to the cyclophosphazene ring and *cis* to the NH group of the spirocyclic ring. The structure of compound **4** shows the macrocyclic ring in the *trans-ansa* configuration with respect to the cyclophosphazene ring, resulting from one inversion reaction of compound **3** with a mono(nucleophile). The structure of compounds **5**–**7** shows the macrocyclic ring in the *cis-ansa* configuration with respect to the cyclophosphazene ring but it is now *trans* to the NH group of the spirocyclic ring as a result of double inversion reactions.

 © 2005 Wiley-VCH Verlag GmbH & Co. KGaA, Weinheim

However, if the length of the *cis*-ansa chain is too short, reaction could lead to retention of configuration, as recently observed in two systems containing nine-membered ansa rings.[13] Previous work has shown that the sixteen-membered ring of the *cis*-ansa macrocyclic cyclophosphazene derivative **1** is sufficiently large and flexible to take up both *cis* and *trans* configurations as a result of nucleophilic substitution reactions,[7,8] and so this same macrocyclic ring was incorporated into compound **3**. Reaction of compound **3** with a range of mononucleophiles (2-naphthol, phenol, pyrrolidine and aniline) with different steric demands and different nucleophilicities gave examples of the monosubstituted compound **4** (**4a**, X = 2-naphthoxy; **4b**, X = phenoxy) and of the disubstituted compounds **5a**, **5b**, **5c** and **5d**, respectively. Compound **3** was also treated with the difunctional nucleophile 2,2,3,3-tetrafluorobutanediol, to give the diansa derivative **6**, and also treated sequentially with two different mononucleophiles − phenol and aniline − to give the unsymmetrically disubstituted compound **7**. The products (**3**, **4a**, **5a**, **5b**, **5c**, **6** and **7**, summarised in diagrammatic form in Scheme 2) were characterised by X-ray crystallography to show that double Walden inversion reactions had taken place.

Results and Discussion

Macrocyclic cyclophosphazene derivatives are difficult to crystallise and, even when they do, often give rise to disordered structures. Many mono- and disubstituted derivatives (such as **4** and **5**, respectively) remained stubbornly as oils, even though they were shown to be pure by chromatography, elemental analyses, mass spectrometry and ^{31}P NMR spectroscopy. Other derivatives gave solids that were unsuitable for crystallography. The most probable cause of these difficulties is the conformational flexibility of the macrocyclic ring. In particular, the monosubstituted macrocyclic cyclophosphazene derivatives caused major experimental problems, though we eventually succeeded in obtaining a good crystalline product for one compound $\{N_3P_3Cl[O(CH_2CH_2O)_4][NH(CH_2)_3O]X$ (**4a**), X = 2-naphthoxy$\}$. We had more success in crystallisation of the symmetrically disubstituted derivatives $N_3P_3[O(CH_2CH_2O)_4][NH(CH_2)_3O]X_2$ [X = 2-naphthoxy (**5a**), X = phenoxy (**5b**),X = pyrrolidino (**5c**)],though not with X = anilino(**5d**). Crystal structures were also obtained for the symmetrically disubstituted derivative **6**, which is the diansa compound formed from reaction of compound **3** with thedifunctional nucleophile 2,2,3,3-tetrafluorobutanediol, and for the unsymmetrically disubstituted derivative **7**), formed from sequential reaction of compound **3** with phenol and aniline. The X-ray data for compounds **3**, **4a**, **5a**, **5b**, **5c**, **6** and **7** are summarised in the Exp. Sect. and the molecular crystal structures are given below.

Treament of compound **3** with the Na derivative of 2-naphthol gave, successively, the mono- (**4a**) and dinaphthoxy derivatives (**5a**). The same product (**5a**) was obtained in a one-pot reaction with 2 equiv. of thereagent**.** The crystal structure of the starting compound (**3**; Figure 1) shows that the *cis*-ansa macrocyclic ring is on the same side of the cyclophosphazene ring as the NH moiety of the spiropropanoxyamino ring, whereas that for the monosubstituted naphthoxy compound **4a** (Figure 2) shows that the macrocyclic ring is in a *trans*-ansa configuration as a result of a Walden inversion. The crystal structure of the disubstituted naphthoxy compound **5a** (Figure 3) shows that the macrocyclic ring again has a *cis*-ansa configuration as a result of a second Walden inversion, and that the macrocyclic ring is now on the opposite side of the cyclophosphazene ring to the NH moiety of the spiropropanoxyamino ring. These results prove conclusively that we are dealing in this reaction with two successive Walden inversions, which give rise to derivatives with a c*is*-ansa ring on the opposite side of the N_3P_3 ring to that of the starting material. It should be noted that the two P(OR)Cl groups in **3** have the opposite stereogenic configuration and the compound is therefore *meso* (Figure 1).Reaction of a mononucleophile with **3** can take place with equal probability at either P(OR)Cl group to form compound **4a**, which has been shown by X-ray crystallography to have a *trans*-ansa macrocyclic configuration (Figure 2) and exist as a racemate. Further reaction of **4a** with the same nucleophile gives the symmetrical compound **5a**, which has regained a *cis*-ansa structure and is *meso* (Figure 3).

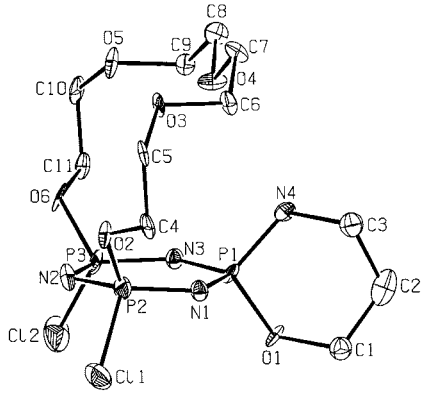

Figure 1. The molecular structure and atomic numbering scheme for one of the independent molecules of compound **3**, with hydrogen atoms (except for NH) and disorder omitted for clarity

In order to ensure that the double Walden inversion reaction does not depend on a bulky, anionic oxygen nucleophile (i.e. 2-naphthol), it was important to show the generality of the phenomenon with a variety of reagents with different steric demands and different nucleophilicities. Therefore we investigated the reaction of **3** with two smaller anionic analogues, phenol, to form the diphenoxide derivative **5b**, and the difunctional aliphatic nucleophile tetrafluorobutanediol, to give the diansa derivative **6**. The crystal structures of **5b** (Figure 4) and **6** (Figure 5) both demonstrate that double inversion has taken place because the macrocyclic ring is found to exist in the *cis*-ansa configuration that was *trans* to the NH group of the spiropropanoxy-

 © 2005 Wiley-VCH Verlag GmbH & Co. KGaA, Weinheim

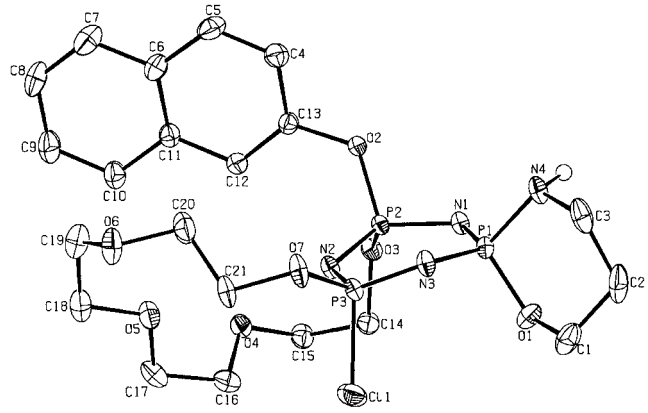

Figure 2. The molecular structure and atomic numbering scheme for compound **4a**, with hydrogen atoms (except for NH) and solvent omitted for clarity

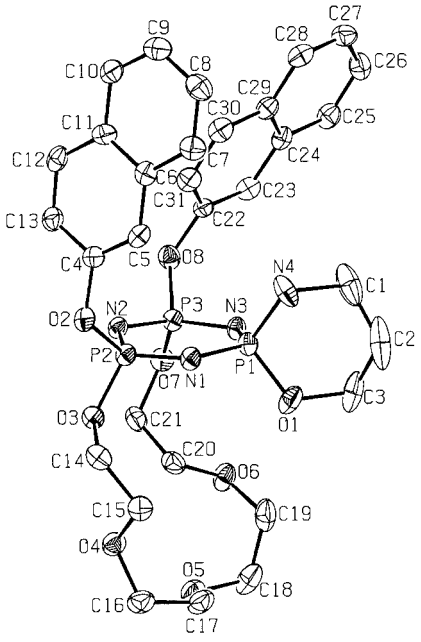

Figure 3. The molecular structure and atomic numbering scheme for one of the independent molecules of compound **5a**, with hydrogen atoms (except for NH) omitted for clarity

amino group. The investigation was then extended to test the inversion reaction with neutral nucleophiles. Reaction of **3** with the fairly strong nucleophilic secondary aliphatic amine pyrrolidine gave **5c**, whose crystal structure (Figure 6) again showsthat a double inversion has taken place as the macrocyclic ring is on the opposite side of the cyclophosphazene ring compared to the starting compound. It should be noted that reaction of primary amines with the P(OR)Cl group of **1**, which is analogous to **3**, takes place with inversion of configuration,although double inversion could not be conclusively proved in the absence of a stereochemical marker group.[7]

All of the symmetrically disubstituted compounds (**5a**–**c**, **6**; Scheme 2) have the ansa ring in a *cis* configuration and are *meso*. It therefore remained to synthesise an unsymmetrically disubstituted compound, which has a *cis*-ansa ring

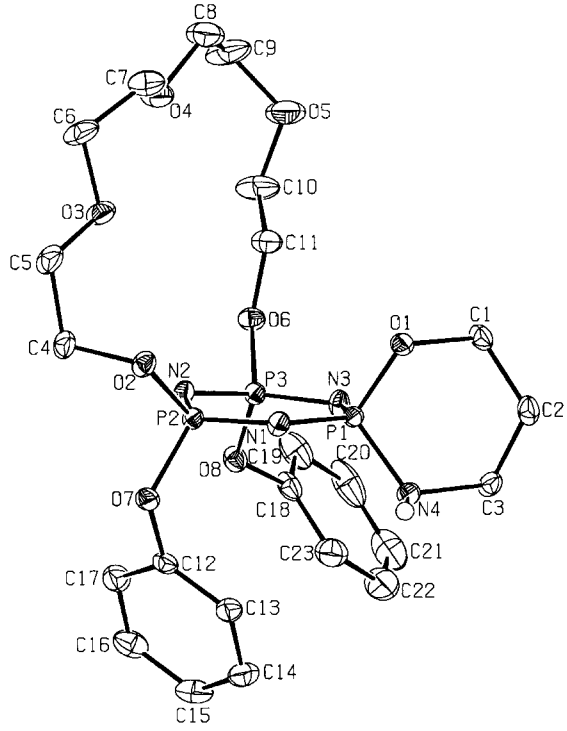

Figure 4. The molecular structure and atomic numbering scheme for compound **5b**, with hydrogen atoms (except for NH) omitted for clarity

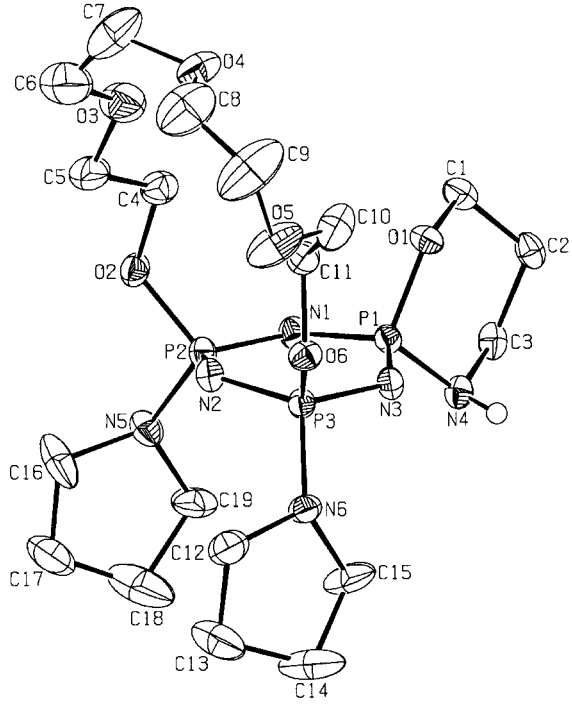

Figure 5. The molecular structure and atomic numbering scheme for one of the independent molecules of compound **6**, with hydrogen atoms (except for NH) and minor component disorder omitted for clarity

 © 2005 Wiley-VCH Verlag GmbH & Co. KGaA, Weinheim

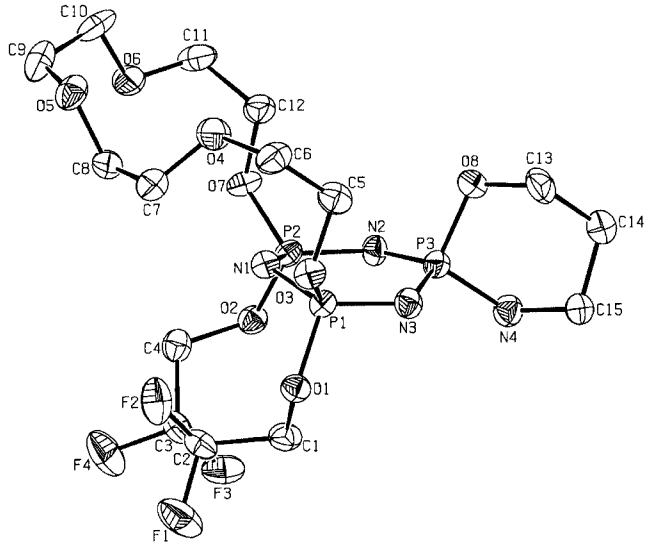

Figure 6. The molecular structure and atomic numbering scheme for compound **5c**, with hydrogen atoms (except for NH) and minor component disorder omitted for clarity

but exists as a racemate, by a double Walden inversion reaction. This was achieved by introducing two different substituents, viz. OPh and NHPh in compound **7**, whose molecular structure is shown in Figure 7 and diagrammatic representation in Scheme 2. This compound also confirms that the weak primary aromatic amine aniline reacts with the P(OR)Cl group with inversion of configuration, which could not be proved with the dianilino derivative **5d** because suitable crystals were not obtained.

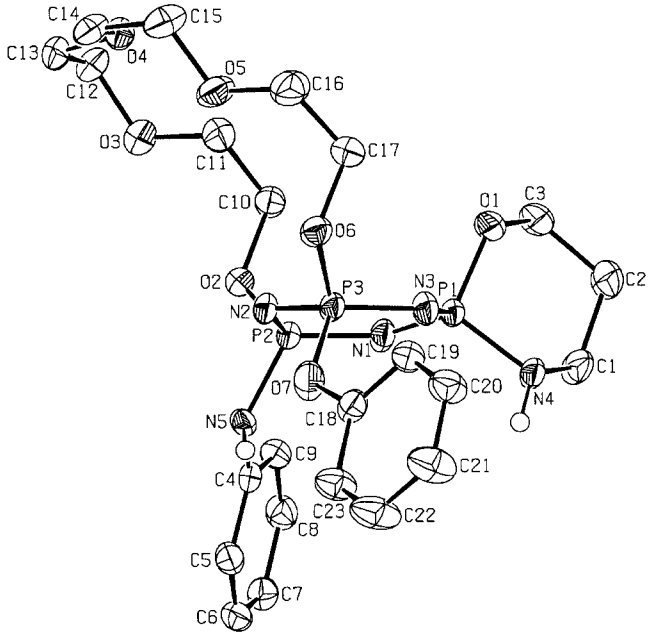

Figure 7. The molecular structure and atomic numbering scheme for compound **7**, with hydrogen atoms (except for NH) and the hydrogen-bonded water molecule omitted for clarity

Discussion of Crystal Structures

In all the crystal structures summarised in Figures 1–7, the bond lengths and bond angles of the N_3P_3 moieties are within the normal range found for cyclophosphazenes.[14] The shape of the cyclophosphazene ring varies from planar in compound **3**,through almost planar in **5b**, **5c** and **7**,to quite puckered in **4a**, **5a** and **6**. The really interesting features in this series of molecules are the hydrogen bonding and the conformation of the macrocyclic substituent with respect to the cyclophosphazene ring. Compound **3** is the only structure reported in this work that exhibits intramolecular hydrogen bonding; the other compounds exhibit intermolecular hydrogen bonding, except **5a**, which does not exhibit any significant hydrogen bonding at all. In compound **3** the macrocycle is pulled back over the N_3P_3 ring, probably because of the intramolecular hydrogen bonding of the NH group of the spiro ring to a central oxygen atom of the macrocycle. In compound **4a**, by contrast, the macrocycle is now pulled away from the N_3P_3 ring and the NH group is involved in intermolecular hydrogen bonding to the ring nitrogen atom of a second molecule to form discrete dimers. The sole 2-naphthoxy group adopts an edge-on conformation with respect to the N_3P_3 ring. A disordered Et_2O molecule is present in the crystal lattice. In the more symmetrical structure of compound **5a** the two 2-naphthoxy groups adopt quite different conformations with respect to the N_3P_3 ring, one being face-on and the other edge-on.The macrocycle is placed over the phosphazene ring, but here no hydrogen bonding is involved and, in fact, there are no close hydrogen bonds in this structure.In compound **5b** the macrocyclic moiety adopts an intermediate position, being neither pulled over or away from the phosphazene ring, even though, as in compound **4a**, the NH group is involved in intermolecular hydrogen bonding to the ring nitrogen atom of a second molecule to form discrete dimers. The structure of compound **5c** resembles that of **5b**,except that the macrocycle is pulled a bit further back from the N_3P_3 ring. In the diansa compound **6** the macrocycle is strongly pulled away from the N_3P_3 ring and the NH group is involved in intermolecular hydrogen bonding to one of the central oxygen atoms of the macrocycle of a second molecule to form infinite chains. In compound **7** the NH group hydrogen bonds intermolecularly to the oxygen atom of the macrocycle of another molecule to again form infinite chains. There is also a molecule of water present, which hydrogen bonds to a ring nitrogen atom and to an oxygen atom of the macrocycle.

Summary

It has been demonstrated by X-ray crystallography that all the nucleophilic reactions so far studied with the macrocyclic cyclophosphazene compound **3**, which contains a sixteen-membered tetraethylene glycol ansa moiety, give rise on monosubstitution, by a Walden inversion, to a racemic *trans*-ansa derivative, and on disubstitution, by a double Walden inversion, to *cis*-ansa compounds. The double

 © 2005 Wiley-VCH Verlag GmbH & Co. KGaA, Weinheim

Walden inversion has been verified with a wide variety of nucleophiles (mono- and difunctional reagents with different steric demands and different nucleophilicities). It is also found that compound **3** is *meso*, the symmetrically disubstituted derivatives of **3** (viz. **5a**, **5b**, **5c** and **6**) are *meso* and the unsymmetrically substituted derivative of **3** (viz. **7**) is, as expected, a racemate.

In all nucleophilic substitution reactions studied in this work, inversion of configuration is the preferred mechanism of reaction, though the possibility cannot be excluded that under some conditions there might be a product with retention of configuration. It has now been demonstrated crystallographically that inversion of configuration takes place in nucleophilic substitution reactions of macrocyclic phosphazene compounds containing a sixteen-membered ansa ring system, whereas retention of configuration occurs in cyclophosphazenes containing nine-membered ansa rings.[13] We are currently investigating analogous *cis*-ansa cyclophosphazene compounds with ring sizes intermediate between nine and sixteen to determine at which point or in which range of ring sizes retention changes to inversion. The work will be greatly facilitated by using a marker, such as the spiro-propanoxyamino group, which can be used to distinguish above and below the plane of the cyclophosphazene ring, and hence to investigate retention versus inversion mechanisms.

Experimental Section

Materials: Hexachlorocyclotriphosphazene (a gift from Shin Nisso Kako Co. Ltd.) was purified by fractional crystallization from hexane. Sodium hydride (60% dispersion in mineral oil, Merck) was washed with dry heptane, followed by decantation, to remove the oil prior to use. 2-Naphthol, phenol, pyrrolidine and aniline were obtained from Merck. 2,2,3,3-Tetrafluorobutanediol was obtained from Aldrich. Tetraethylene glycol (Fluka) and 3-amino-1-propanol (Merck) were dried with molecular sieves (4 Å). All solvents used in this work were purified by conventional methods. THF was distilled from a sodium/potassium alloy under dry argon. All reactions were carried out under dry argon. Products were subjected to separation by column chromatography using silica gel (230–400 mesh, Merck). Deuterated $CDCl_3$ for NMR spectroscopy was obtained from Goss Scientific.

NMR Measurements: 200 MHz ^{31}P NMR spectra of all compounds were recorded at 25 °C in $CDCl_3$ solutions with a Bruker DRX 500 MHz spectrometer using 85% H_3PO_4 as an external reference. In some cases both proton-coupled and proton-decoupled ^{31}P NMR spectra were recorded to aid assignment of spectra.

Synthesis of 3: Compound **2** was synthesised by the reaction of hexachlorocyclophosphazene with 3-amino-1-propanol, as described in the literature.[11,12] Compound **2** (3.5 g, 10 mmol) and tetraethylene glycol (2.91g, 15 mmol) were dissolved in 650 mL of dry THF in a 1-L, three-necked, round-bottomed flask. The reaction mixture was cooled in an ice-bath and NaH (1.2 g, 30 mmol) in 100 mL of dry THF was quickly added to the stirred solution under argon. The reaction mixture was stirred at room temperature for a further 2 h and was followed by TLC on silica gel plates with hexane/THF (1:1) as eluent. The reaction mixture was filtered to remove the sodium chloride formed, the solvent was removed under reduced pressure, and the resulting colourless oil was subjected to column chromatography with THF/hexane (2:1) as eluent. $N_3P_3[O(CH_2)_3NH][O(CH_2CH_2O)_4]Cl_2$ (**3**) was isolated as a colourless oil and crystallised from chloroform/hexane (1:2) to give white crystals, m.p. 137 °C (yield: 0.94 g, 20%). ^{31}P NMR (analysed as A_2X): δ = 13.8 [t, $^2J_{P,P}$ = 65 Hz, 1 P, P(spiro)], 23.4 [d, $^2J_{P,P}$ = 65 Hz, 2 P, P(OR)Cl] ppm. $C_{11}H_{23}Cl_2N_4O_6P_3$ (471): calcd. C 28.04, H 4.92, N 11.89; found C 28.04, H 4.88, N 12.5.

Reaction of 3 with 2-Naphthol To Give 4a: Compound **3** (0.47 g, 1 mmol) and 2-naphthol (0.216 g, 1.5 mmol) were dissolved in 50 mL of dry THF in a 100-mL, three-necked, round-bottomed flask. The reaction mixture was cooled in an ice-bath and NaH (0.06 g, 1.5 mmol) in 25 mL of dry THF was quickly added to the stirred solution under argon. The reaction mixture was stirred at room temperature for a further 4 h and followed by TLC on silica gel plates with hexane/THF (1:1) as eluent. The reaction mixture was filtered to remove the sodium chloride formed, the solvent ws removed under reduced pressure, and the resulting colourless oil was subjected to column chromatography with THF/hexane (1:1) as eluent. $N_3P_3[O(CH_2)_3NH][O(CH_2CH_2O)_4]$(2-naphthoxy)Cl] (**4a**) was isolated as a colourless oil and crystallised from dichloromethane/light petroleum (boiling range 40–60°C) to give white crystals, m.p. 75°C (yield 1.13 g, 60%). ^{31}P NMR (analysed as AMX): δ = 12.8 [dd, 1 P, P(OR)(2-naphthoxy), A], 16.9 [dd, 1 P, P(spiro), M], 26.4 ppm [dd, 1 P, P(OR)Cl, X]; $^2J_{P,P}$ = 79.4 Hz, AM; $J_{P,P}$ = 71.8 Hz, AX; $J_{P,P}$ = 79.4 Hz, MX. $C_{21}H_{30}ClN_4O_7P_3$ (578.8): calcd. C 43.57, H 5.22, N 9.68; found C 43.60, H 5.20, N 9.70.

Reaction of 3 with 2-Naphthol To Give 5a: Compound **3** (0.47 g, 1 mmol) and 2-naphthol (0.3 g, 2.1 mmol) were dissolved in 30 mL of dry THF in a 100-mL, three-necked, round-bottomed flask. The reaction mixture was cooled in an ice-bath and NaH (0.084 g, 2.1 mmol) in 25 mL of dry THF was quickly added to the stirred solution under argon. The reaction mixture was stirred at room temperature for a further 18 h and followed by TLC on silica gel plates with hexane/THF (1:1) as eluent. The reaction mixture was filtered to remove the sodium chloride formed, the solvent was removed under reduced pressure, and the resulting colourless oil was subjected to column chromatography with THF/hexane (1:1) as eluent. $N_3P_3\{[O(CH_2)_3NH][O(CH_2CH_2O)_4](2\text{-Naphthoxy})_2\}$ (**5a**) was isolated as a colourless oil and crystallised from (1:1) chloroform/light petroleum (boiling range 40–60°C) to give white crystals, m.p. 116 °C (yield 0.3 g, 43%). ^{31}P NMR (analysed as A_2X): δ = 18.6 [t, 1 P, P(spiro)], 14.6 ppm [d, 2 P, P(OR)(2-naphthoxy)$_2$]; $^2J_{P,P}$ = 73.1 Hz. $C_{31}H_{37}N_4O_8P_3$ (686.94): calcd. C 54.23, H 5.43, N 8.16; found C 54.21, H 5.40, N 8.10.

Reaction of 3 with Monofunctional Nucleophiles To Give Symmetrically Disubstituted Compounds 5b–d: Compound **3** was treated with phenol, pyrollidine and aniline to give compounds **5b**, **5c** and **5d**, respectively. Experimental and analytical details are provided as Supporting Information.

Reaction of 3 with 2,2,3,3-Tetrafluorobutanediol To Give the Monospiro-diansa Compound 6: Compound **3** (0.95 g, 2 mmol) and 2,2,3,3-tetrafluorobutanediol (0.33 g, 2 mmol) were dissolved in 50 mL of dry THF in a 100-mL, three-necked, round-bottomed flask. NaH (1.2 g, 30 mmol) in 20 mL of dry THF was quickly added to the stirred solution under argon and the reaction mixture was stirred at room temperature for a further 5 d and followed by TLC on silica gel plates with THF as eluent. The reaction mixture was filtered to remove the sodium chloride formed, the solvent was removed under reduced pressure, and the resulting colourless oil was subjected to column chromatography with THF/hexane (3:1) as eluent. The solvent was removed under reduced pressure and the

 © 2005 Wiley-VCH Verlag GmbH & Co. KGaA, Weinheim

Table 1. X-ray crystallographic data for compounds **3**, **4a**, **5a**, **5b**, **5c**, **6** and **7**

	3	**4a**	**5a**	**5b**	**5c**	**6**	**7**
Empirical formula	$C_{11}H_{23}Cl_2N_4O_6P_3$	$C_{22.50}H_{33.75}ClN_4O_{7.75}P_3$	$C_{31}H_{37}N_4O_8P_3$	$C_{23}H_{33}N_4O_8P_3$	$C_{19}H_{39}N_6O_6P_3$	$C_{15}H_{26}F_4N_4O_8P_3$	$C_{23}H_{36}N_5O_8P_3$
Formula weight	471.14	612.65	686.56	586.44	540.47	559.31	603.48
Crystal system	monoclinic	triclinic	monoclinic	triclinic	monoclinic	orthorhombic	monoclinic
Space group	$P2_1/c$	$P\bar{1}$	$P2_1$	$P\bar{1}$	$C2/c$	$P2_12_12_1$	$P2_1/c$
a [Å]	15.846(3)	7.8459(2)	9.0346(14)	10.2889(3)	31.3856(10)	9.9411(3)	14.232(3)
b [Å]	14.991(3)	12.8968(3)	20.006(3)	12.4494(3)	9.3691(3)	17.6912(5)	19.571(4)
c [Å]	16.895(3)	14.6925(4)	17.882(3)	12.7523(3)	17.9477(6)	26.1432(7)	10.326(2)
α [°]	90	105.5030(10)	90	64.6480(10)	90	90	90
β [°]	97.73(3)	94.6410(10)	91.955(2)	75.2640(10)	99.322(2)	90	97.57(3)
γ [°]	90	95.7200(10)	90	71.6650(10)	90	90	90
V [Å^3]	3976.9(14)	1416.47(6)	3230.2(9)	1387.50(6)	5207.9(3)	4597.8()	2851.2(10)
Z	8	2	4	2	8	8	4
Density (calcd.) [Mg/m^3]	1.574	1.436	1.412	1.404	1.379	1.616	1.406
Crystal size [mm]	0.15×0.12×0.12	0.26×0.20×0.06	0.04×0.04×0.03	0.30×0.12×0.09	0.20×0.08×0.02	0.24×0.20×0.08	0.22×0.03×0.02
Independent reflections	4463	6256	11030	6254	5914	5344	6503
R(int)	0.0591	0.0212	0.0487	0.0862	0.1108	0.0636	0.0730
Final R indices	$R1$ = 0.0980	$R1$ = 0.0438	$R1$ = 0.0556	$R1$ = 0.0481	$R1$ = 0.0870	$R1$ = 0.0425	$R1$ = 0.0564
$F^2 > 2\sigma(F^2)$	$wR2$ (all) = 0.2497	$wR2$ (all) = 0.1220	$wR2$ = 0.1401	$wR2$ = 0.1311	$wR2$ = 0.1902	$wR2$ = 0.0992	$wR2$ = 0.1506
$\Delta\rho$(max/min) [e•Å^{-3}]	0.778/–2.065	0.906/–0.678	0.509/–0.5456	0.586/–0.636	0.852/–0.682	0.378/–0.281	1.256/–0.397

product crystallized from dichloromethane/hexane (1:1) to give **6** as white crystals, m.p. 110 °C (yield 0.13 g, 12%). ^{31}P NMR (analysed as A_2B): δ = 20.5 [1 P, P(spiro)], 21.2 ppm [2 P, P(OR)-($OCH_2CF_2CF_2CH_2O$)]; $^2J_{P,P}$ = 72.0 Hz. $C_{15}H_{27}F_4N_4O_8P_3$ (561.1): calcd. C 32.15, H 4.86, N 10.00; found C 32.11, H 4.87, N 9.97.

Sequential Reaction of 3 with Phenol and Aniline To Give the Unsymmetrically Disubstituted Compound 7. (i) Reaction of 3 with Phenol To Give 4b: Compound **3** (0.95 g, 2 mol) and phenol (0.188 g, 2 mmol) were dissolved in 50 mL of dry THF in a 100-mL, three-necked, round-bottomed flask. The reaction mixture was cooled in an ice-bath and NaH (0.08 g, 2 mmol) in 20 mL of dry THF was quickly added to the stirred solution under argon. The reaction mixture was stirred at room temperature for a further 4 h and followed by TLC on silica gel plates with hexane/THF (1:1) as eluent. The reaction mixture was filtered to remove the sodium chloride formed, the solvent was removed under reduced pressure, and the resulting colourless oil was subjected to column chromatography with THF/hexane (1:1) as eluent. $N_3P_3\{[O(CH_2)_3NH][O(CH_2CH_2O)_4](OPh)Cl\}$ (**4b**) was isolated as a colourless oil (yield 0.78 g, 74%). ^{31}P NMR (analysed as AMX): δ = 12.6 [dd, 1 P, P(OR)-(OPh), A], 16.9 [dd, 1 P, P(spiro), M], 26.4 ppm [dd, 1 P, P(OR)Cl, X]; $^2J_{P,P}$ = 79.1 Hz, AM; $J_{P,P}$ = 72.1 Hz, AX; $J_{P,P}$ = 69.3 Hz, MX. $C_{17}H_{28}ClN_4O_7P_3$ (529): calcd. C 38.61, H 5.34, N 10.59; found C 38.65, H 5.35, N 10.55. **(ii) Reaction of 4b with Aniline To Give 7:** Aniline (2.79g, 30mmol) was added dropwise from an addition funnel to a solution of **4b** (0.53 g, 1 mmol) in 15 mL of dry THF in a 50-mL, three-necked, round-bottomed flask. The reaction mixture was heated to reflux for 4 h and followed by TLC on silica gel plates with THF/hexane (2:1) as eluent. The reaction mixture was then cooled to room temperature, filtered and the solvent removed under reduced pressure. Distilled water (30 mL) was added to the reaction mixture and the mixture was extracted with dichloromethane. The organic layer was dried with anhydrous Na_2SO_4 and concentrated to 5 mL. The crude product was poured into 750 mL of hexane to give $N_3P_3\{[O(CH_2)_3NH][O(CH_2CH_2O)_4](OPh)(NHPh)\}$ (**7**) as white crystals, m.p. 76°C (yield 0.38 g 65%). ^{31}P NMR (analysed as ABX): δ = 14.7 [dd, 1 P, P(spiro), A], 14.0 [dd, 1 P, P(OR)(NPh), B], 18.1 ppm [t, 1 P, P(OR)(OPh), X]; $^2J_{P,P}$ = 72.3 Hz, AB; $J_{P,P}$ = 65.2 Hz, AX; $J_{P,P}$ = 65.4 Hz, BX. $C_{23}H_{34}N_5O_7P_3$ (586): calcd. C 47.18, H 5.85, N 11.96; found C 47.18, H 5.86, N 11.90.

X-ray Crystallography: Data were collected at low temperature with a Nonius KappaCCD area-detector diffractometer located at the window of a Nonius FR591 rotating anode X-ray generator, equipped with a molybdenum target (Mo-K_α, λ = 0.71073 Å). Structures were solved and refined using the SHELX-97 suite of programs.[15] Data were corrected for absorption effects by means of comparison of equivalent reflections using the program SORTAV.[16] Non-hydrogen atoms were refined anisotropically; NH hydrogen atoms were determined experimentally, whilst the other hydrogen atoms were generally fixed in idealised positions with their thermal parameters riding on the values of their parent atoms. Compound **3** exhibits 50:50 disorder at many sites in one of the two independent molecules, whilst **5c** and **6** show minor disorder in the macrocycle moiety and compound **4a** contains a disordered Et_2O solvent molecule. The absolute structure of **5a** was confirmed by refinement of the Flack parameter to a value of 0.01(9). The macrocycle moiety of **7** encapsulates a water molecule by means of hydrogen bonding. Details are given in Table 1. CCDC-189494 (**3**), -189495 (**4a**), -189496 (**5a**), -238735 (**5b**), -238736 (**5c**), -238737 (**6**) and-238738 (**7**) contain the supplementary crystallographic data for this paper. These data can be obtained free of charge from The Cambridge Crystallographic Data Centre via www.ccdc.cam.ac.uk/data_request/cif.

Supporting Information: Details of the preparation and analytical data for compounds **5b**, **5c** and **5d** are provided as Supporting Information (see also footnote on the first page of this article).

Acknowledgments

The authors would like to thank the Gebze Institute of Technology (GIT) Research Fund for partial support (S. B. and A. K.), the Shin Nisso Kako Co. Ltd. for gifts of $N_3P_3Cl_6$ and the EPSRC for funding the National Crystallographic Service (Southampton, UK).

[1] a) B. Walden, *Ber. Dtsch. Chem. Ges.* **1893**, *26*, 210; b) B. Walden, *Ber. Dtsch. Chem. Ges.***1896**, *29*, 133; c) B. Walden, *Ber. Dtsch. Chem. Ges.* **1899**, *32*, 1855.

[2] J. March, *Advanced Organic Chemistry: Reactions, Mechanisms and Structures*, 4th ed., Wiley Interscience, New York, **1992**.

[3] E. L. Eliel, S. H. Wilen, L. N. Mander, *Stereochemistry of Organic Compounds*, John Wiley and Sons, Inc., New York, **1994**.

[4] a) A. J. Kirby, S. G. Warren, *The Organic Chemistry of Phosphorus*, Elsevier Publ. Co., New York, **1967**, p. 307; b) J. Emsley, D. Hall, *The Chemistry of Phosphorus*, Harper & Row, New York, **1976**, p. 323; c) L. D. Quin, *A Guide to Organophosphorus Chemistry*, Wiley Interscience, New York, **2000.**

 © 2005 Wiley-VCH Verlag GmbH & Co. KGaA, Weinheim

[5] K. V. Katti, S. S. Krishnamurthy, *J. Chem. Soc., Dalton Trans.* **1985**, 285–289.
[6] E. Lork, D. Böhler, R. Mews, *Angew. Chem. Int. Ed.* **1995**, *34*, 2696–2698.
[7] D. B. Davies, T. A. Clayton, R. E. Eaton, R. A. Shaw, A. Egan, M. B. Hursthouse, G. D. Sykara, I. Porwolik-Czomperlik, M. Siwy, K. Brandt, *J. Am. Chem. Soc.* **2000**, *122*, 12447–12457.
[8] I. Porwolik-Czomperlik, M. Siwy, K. Brandt, D. B. Davies, T. A. Clayton, R. E. Eaton, R. A. Shaw, *Inorg. Chem.* **2002**, *41*, 4944–4951.
[9] K. Brandt, T. Kupka, J. Drodz, J. C. van de Grampel, A. Meetsma, A. P. Jekel, *Inorg. Chim. Acta* **1995**, *228*, 187–192.
[10] S. Beşli, S. J. Coles, D. B. Davies, M. B. Hursthouse, A. Kılıç, T. A. Mayer, R. A. Shaw, *Acta Crystallogr. Sect. B* **2002**, *58*, 1067–1073.
[11] a) K. C. Kumara Swamy, S. S. Krishnamurthy, *Indian J. Chem., Sect. A* **1984**, *3*, 717–723, b) F. Sourne, K. Zai, V. Vercruysse, M.-C. Labarre, J.-F. Labarre, *J. Mol. Struct.* **1997**, *412*, 19–26.
[12] A. H. Alkubaisi, H. A. Al-Madfa, W. F. Deutsch, M. B. Hursthouse, H. G. Parkes, L. S. Shaw (née Gözen), R. A. Shaw, *Phosphorus Sulfur* **1986**, *28*, 277–288.
[13] S. Beşli, S. J. Coles, D. B. Davies, M. B. Hursthouse, H. İbişoğlu, A. Kılıç, R. A. Shaw, *Chem. Eur. J.* **2004**, *10*, 4915–4920.
[14] C. W. Allen, *Chem. Rev.* **1991**, *91*, 119–135.
[15] G. M. Sheldrick, *SHELX-97: Programs for structure solution and refinement*, University of Göttingen, Germany, **1997**.
[16] R. H. Blessing, *J. Appl. Crystallogr.* **1997**, *30*, 421–426.

Received September 6, 2004
Published Online January 26, 2005

 © 2005 Wiley-VCH Verlag GmbH & Co. KGaA, Weinheim

Synthesis, Structural and Magnetic Characterization of a New Scheelite Related Compound: $Eu_2Mo_3O_{12}$

Khalid Boulahya,[a] Marina Parras,[a] and José M. González-Calbet*[a]

Keywords: Molybdate / X-ray diffraction / High resolution electron microscopy / Magnetic properties

Polycrystalline $Eu_2Mo_3O_{12}$ has been synthesized and characterized by X-ray and electron diffraction, high resolution electron microscopy and magnetic measurements. This oxide shows a complex scheelite superstructure whose essential feature is the existence of isolated Mo tetrahedra. Each Mo atom has four oxygen neighbors at distances ranging from 1.75 to 1.91 Å, whereas each Eu atom has eight oxygen neighbors at 2.43 Å. The temperature dependence of the inverse magnetic susceptibility shows that $Eu_2Mo_3O_{12}$ behaves as a Curie–Weiss paramagnet at high temperature (160–300 K), whereas in the range 100–20 K it shows Van Vleck paramagnetism.
(© Wiley-VCH Verlag GmbH & Co. KGaA, 69451 Weinheim, Germany, 2005)

Introduction

Rare earth molybdates constitute a large family of materials with interesting physical properties which depend on the crystal structure, rare earth element and molybdenum oxidation state. Initial interest was developed due to fluorescence properties.[1] Later on, new applications were reported for the molybdenum highest oxidation state (VI). Ferroelectric/ferroelastic properties have been described for $Gd_2Mo_3O_{12}$,[2] whereas La_2MoO_6[3] shows catalytic behavior and $La_2Mo_2O_9$[4] is a fast ionic conductor. More reduced molybdates present some interesting transport properties such as metal–insulator transitions, as is the case of $La_2Mo_2O_7$[5,6] which exhibits short Mo–Mo distances.

The chemical nature of the lanthanide element strongly influences its structural type. For instance, at least three polymorphs have been described for the $Ln_2Mo_3O_{12}$ complex. The $La_2Mo_3O_{12}$[7] structure is formed by a network of corner-sharing square-antiprismatic and tetrahedral sites, with La having eightfold and Mo slightly distorted tetrahedral oxygen coordination. The structure is related to the scheelite ($CaWO_4$) type,[8] from which it can be derived through vacancy ordering of one third of the Ca sites. Nearest-neighbor environments of the cations resemble those of the scheelite. $Gd_2Mo_3O_{12}$[2] presents two polymorphs with different symmetries; both structures contain a network of corner-sharing polyhedra in which Gd and Mo cations are coordinated by seven and four oxygen atoms, respectively. Tb and Mo stabilize the same oxygen environment in $Tb_2Mo_3O_{12}$.[9]

[a] Departamento de Química Inorgánica, Facultad de Químicas, Universidad Complutense,
28040 Madrid, Spain
Fax: +34-91-394-43-52
E-mail: jgcalbet@quim.ucm.es

The europium-molybdenum systems are attractive as a result of their structural and compositional variation. Such variation arises from the ability of isolated MoO_4 tetrahedra and Mo_nO_m structural units to be incorporated, in an ordered manner, giving rise to the stabilization of phases with different Eu/Mo ratios. For instance, the crystal structure of $Eu_6Mo_{12}O_{45}$[10] comprises four MoO_4 tetrahedra, and Mo_2O_8 and $Mo_{12}O_{11}$ structural units which, connected by sharing corners, form polymeric $[Mo_4O_{17}]$ chains. $Eu_6Mo_{10}O_{39}$[11] and $Eu_2Mo_5O_{18}$[12] are formed by MoO_4 and Mo_2O_7 units, which are three-dimensionally arranged. $Eu_4Mo_7O_{27}$[11] is a layered compound consisting of MoO_4 and Mo_3O_{11} units, while $EuMoO_4$[13] adopts the scheelite structural type where isolated MoO_4 tetrahedra constitute the three-dimensional structure. Finally, the crystal structure of $Eu_6Mo_{10}O_{39}$[11] is characterized by bioctahedral Mo_{10} clusters forming extended chains.

In this work, we report the synthetic conditions and characterization, by means of X-ray Rietveld refinement, electron diffraction (ED), high resolution electron microscopy (HREM), electrical resistivity and magnetic susceptibility, of a new europium molybdate with the composition $Eu_2Mo_3O_{12}$. The structural relationship between this phase and the scheelite structural type is reported.

Results and Discussion

The cationic composition, as analyzed by energy-dispersive X-ray spectroscopy, is in agreement with the nominal composition, $Eu_2Mo_3O_{12}$. The corresponding X-ray powder diffraction pattern (Figure 1) can be fully indexed on the basis of a monoclinic unit cell with space group, *C*2/*c,* and lattice parameters a = 7.5613(3) Å, b = 11.4685(5) Å, c = 11.5055(5) Å and β = 109.309(3)°, no extra reflections being detected.

 DOI: 10.1002/ejic.200400662 © 2005 Wiley-VCH Verlag GmbH & Co. KGaA, Weinheim

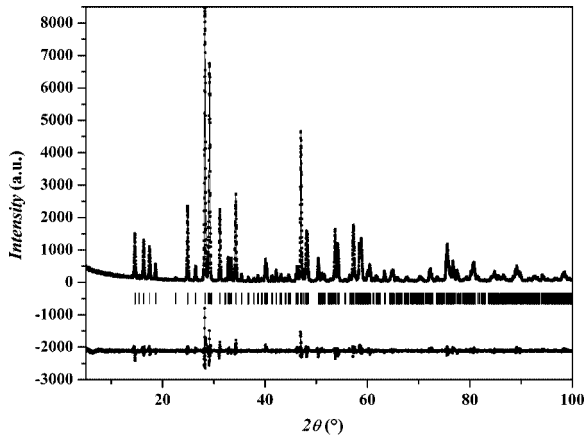

Figure 1. Experimental, calculated and difference X-ray diffraction patterns for $Eu_2Mo_3O_{12}$

The $Eu_2Mo_3O_{12}$ structure has been initially determined by ED and HREM (Figure 2). The HREM micrograph along the [100] zone axis (Figure 2b) shows an apparently well ordered material with d-spacings 5.7 and 3.6 Å, corresponding to d_{020} and d_{003}, respectively. Following the *b* axis, a layer of bright dots alternate with brighter ones in an ordered manner. This contrast can be associated with rows of tetrahedrally coordinated Mo atoms arranged at different heights along the *a* axis. These structural features are those presented by $Eu_2W_3O_{12}$[14] which can be described as a three-dimensional distribution of WO_4 tetrahedra linked by EuO_8 units. Therefore, from the $Eu_2W_3O_{12}$ atomic coordinates, an image calculation was performed in the *C*2/*c* space group. The simulated image (shown in the inset) compare well with the experimental one at Δt = 6 nm and Δf = –70 nm.

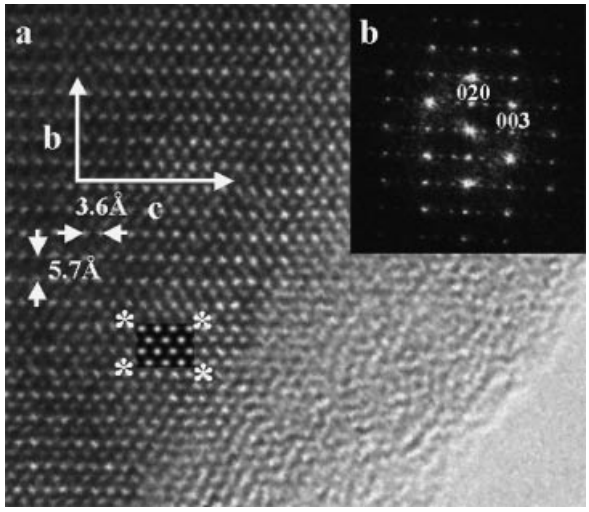

Figure 2. (a) HRTEM image of $Eu_2Mo_3O_{12}$ along [100], (b) corresponding FT. Simulated image is shown in the inset

On the basis of these results, an X-ray profile refinement was performed. The structure was solved in the ***C2/c*** space group taking the $Eu_2W_3O_{12}$ crystallographic data as the starting point. Peak shapes were described by pseudo-Voigt functions. Figure 1 shows the graphic results of the fitting of the experimental X-ray diffraction pattern and the difference between observed and calculated data. The refinement was stable and it was possible to refine the positions of oxygen atoms, provided a temperature factor for each type of atom was used. The structural model is depicted in Figure 3. The final structural parameters are collected in Table 1, whereas Table 2 shows some selected inter-atomic distances. The structure refinement confirms isotypism with $Eu_2W_3O_{12}$.[14] The crystal structure of the $Eu_2Mo_3O_{12}$ is formed by isolated $Mo(1)O_4$ tetrahedra and $Mo_2(2)O_8$ groups constituted by very irregular $Mo(2)O_5$ trigonal bipyramids. Mo1 forms a MoO_4 tetrahedron with M-O average distances of 1.78 or 1.83 Å. The Mo_2O_8 group comprises of two $Mo(2)O_5$ trigonal bipyramids sharing one edge. They are formed by three oxygen neighbors at distances of 1.79, 1.76, and 1.75 Å, a fourth one at 1.91 Å, and a fifth at 2.4 Å. Figure 4 shows a view of the Mo_2O_8 group. Such a dimeric group is also present in isostructural $Eu_2W_3O_{12}$ but, in this case, the distance to the fifth neighbor is smaller, close to 2.19 Å. However, a similar

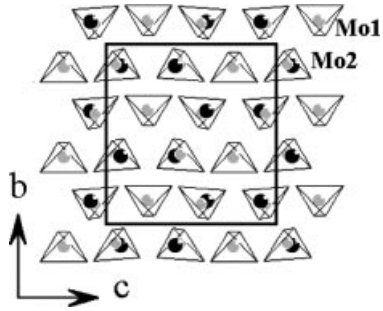

Figure 3. Structural model along *a*-axis of $Eu_2Mo_3O_{12}$. Black dots represent Eu atoms whereas grey dots correspond to Mo atoms

Table 1. Final structural parameters of $Eu_2Mo_3O_{12}$

Atom	*x*/*a*	*y*/*b*	*z*/*c*	*B* (Å^2)	Occ.
Eu1	0.3325(6)	0.3771(3)	0.4089(2)	1.106(85)	1
Mo1	0	0.1293(5)	1/4	1.75(11)	1
Mo2	0.1491(8)	0.3885(3)	0.0594(2)	1.75(11)	1
O1	0.173(3)	0.046(1)	0.214(2)	1.36(21)	1
O2	0.136(3)	0.211(2)	0.387(2)	1.36(21)	1
O3	0.250(3)	0.313(2)	0.198(2)	1.36(21)	1
O4	0.346(3)	0.461(1)	0.039(2)	1.36(21)	1
O5	0.033(3)	0.475(2)	0.394(2)	1.36(21)	1
O6	0.449(3)	0.208(2)	0.064(2)	1.36(21)	1

S.G. C 2/c (15), a = 7.5613(3) Å, b = 11.4685(5) Å, c = 11.5055(5) Å,
β = 109.309(3)° V = 941.598(63) Å^3,
R_B = 0.041, R_{exp} = 0.064, R_{wp} = 0.113, χ^2 = 3.12.

Table 2. Selected inter-atomic distances (Å) in $Eu_2Mo_3O_{12}$

Eu1–O1: 2.39 (2)	Mo1–O1: 1.78 (2)
Eu1–O2: 2.38 (2)	Mo1–O2: 1.83 (2)
Eu1–O2: 2.49 (2)	Mo2–O3: 1.75 (2)
Eu1–O3: 2.41 (2)	Mo2–O4: 1.79 (2)
Eu1–O4: 2.49 (2)	Mo2–O5: 1.91 (2)
Eu1–O4: 2.37 (2)	Mo2–O6: 1.76 (2)
Eu1–O5: 2.48 (3)	Mo2–O5: 2.40 (2)[a]
Eu1–O6: 2.49 (2)	Mo2–Mo2: 3.38 (2)

 © 2005 Wiley-VCH Verlag GmbH & Co. KGaA, Weinheim

value (2.39 Å) is observed in the related oxide $Eu_4Mo_7O_{27}$.[11] The Eu atom has eight oxygen neighbors at an average distance of 2.43 Å with a distorted square-antiprismatic coordination as observed in related europium oxides.[11]

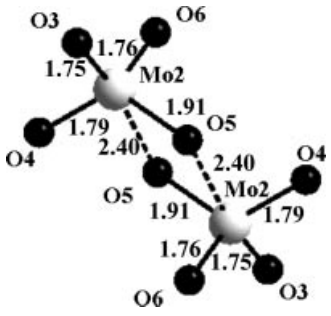

Figure 4. Structural details of the Mo_2O_8 group

The $EuMoO_4$,[13] scheelite related structure is depicted in Figure 5a. The analogy with $Eu_2Mo_3O_{12}$ can be clearly seen by comparing Figures 5a and b. Both structures are formed by similar [MoO_4] units of isolated tetrahedra. The essential structural difference is related to the europium atoms planes. In the scheelite $EuMoO_4$ structure, the three crystallographic Eu planes, indicated by solid lines in Figure 5a, are fully occupied and equidistant along the [120] direction. The ordered elimination of one of every three Eu planes in $EuMoO_4$, leads to the $Eu_2Mo_3O_{12}$ structure (Figure 5b). This Eu elimination process has less influence on the Eu coordination than in the Mo one. Whereas in the scheelite structure Mo only adopts tetrahedral coordination, in the $Eu_2Mo_3O_{12}$ oxide, Mo is also trigonal bipyramidally coordinated.

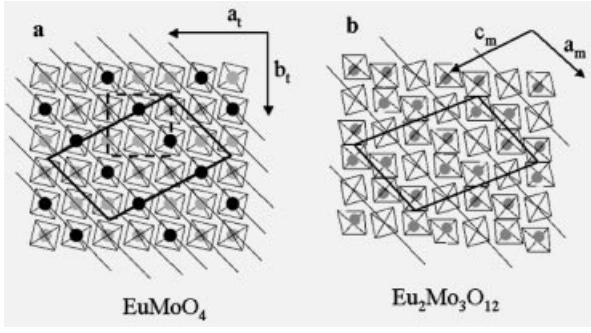

Figure 5. Schematic representation of the structural relationship between (a) $EuMoO_4$ and (b) $Eu_2Mo_3O_{12}$. Both structures are projected along the *c* axis of the scheelite cell, which is outlined by broken lines. Black dots represent the Eu atoms, which are eliminated in $Eu_2Mo_3O_{12}$. The steps involving the $EuMoO_4$ to $Eu_2Mo_3O_{12}$ transformation are shown

From the crystallographic point of view, monoclinic (*C*2/*c*) $Eu_2Mo_3O_{12}$ can be considered as a superstructure of tetragonal ($I4_1/a$) $EuMoO_4$ as depicted in Figure 5a. The monoclinic cell parameters a_m, b_m, and c_m can be related to the tetragonal ones a_t and c_t by means of the expression: $a_m \approx a_t\sqrt{2}$, $b_m \approx c_t$ and $c_m \approx a_t\sqrt{5}$. Furthermore, the symmetry *C*2/*c* is a subgroup of $I4_1/a$.

On the other hand, different physical properties have also been explored. First, from an electrical point of view, $Eu_2Mo_3O_{12}$ behaves as an insulator at room temperature.

The temperature dependence of the molar susceptibility is shown in Figure 6. The curve shape resembles that reported by Holsa et al.[15] but χ is smaller by 14–30% than their data at all the temperatures measured. The χ^{-1} value follows the Curie–Weiss law down to about 160 K and then is constant for the lower temperature range between 100 and 20 K. Finally, below 20 K, a sharp decrease in the inverse susceptibility is observed. This behavior can be qualitatively explained by the exceptional ^7F_J (J = 0–6) ground term energy level Scheme of the Eu^{3+} ion.[16,17] The $^7F_0$–$^7F_1$ energy gap is large enough to induce a *plateau* in the inverse paramagnetic susceptibility curve due to the constant temperature independent paramagnetism, since practically only the ground level $^7F_0$ is populated. The $^7F_0$ ground level is non-magnetic and gives no contribution to the $Eu_2Mo_3O_{12}$ susceptibility at low temperatures. At the higher temperature range, the population of the closely spaced higher ^7F_J (J = 1–6) levels leads to the normal Curie–Weiss paramagnetism. It can be concluded that for Eu^{3+}, the crystal field plays a significant role in the susceptibility. Below 15 K, a sharp decrease in the inverse susceptibility is observed. This has been already been observed with other Eu compounds, as in the oxychloride EuOX (X = Br, Cl),[15,16] and attributedto the presence of a slight amount of Eu^{2+} impurity, since Eu^{2+} with the $^4f_7$ electron configuration has high paramagnetic susceptibility. In order to understand this phenomenon, a study on partially reduced Eu^{3+} samples is in progress.

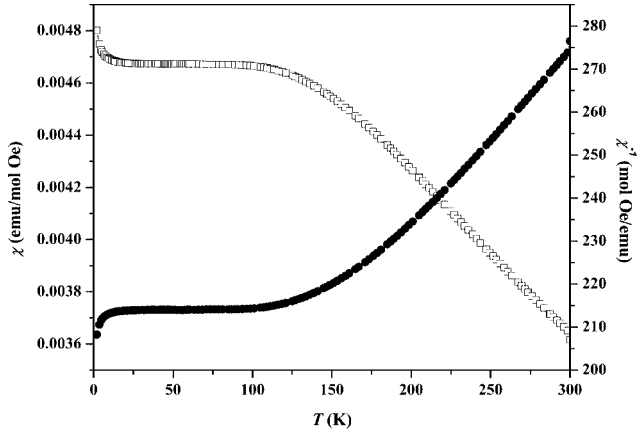

Figure 6. Temperature evolution of the magnetic susceptibility χ (squares) and χ^{-1} (black dots) of $Eu_2Mo_3O_{12}$

Experimental Section

Polycrystalline $Eu_2Mo_3O_{12}$ was synthesised by heating stoichiometric amounts of Eu_2O_3 (Aldrich; 99.98%) and MoO_2 (Aldrich; 99+%) in air at 900 °C for 4 days and then quenched to room temperature.

Powder X-ray diffraction patterns were collected with CuKα radiation at room temperature on a PHILIPS X'PERT diffractometer

 © 2005 Wiley-VCH Verlag GmbH & Co. KGaA, Weinheim

equipped with a graphite monochromator. Diffraction data were analyzed by the Rietveld method[18] using the Fullprof program.[19]

The sample was characterized by ED and HREM using a PHILIPS CM200 FEG electron microscope, fitted with a double tilting goniometer stage (±40°, ±24°). Local composition was analyzed with an EDAX DX-4 analyzer system attached to the above microscope. Simulated HREM images were calculated by the multislice method using the MacTempas software package. Magnetic properties were measured with a SQUID magnetometer, over the temperature range 2 to 300 K, and magnetic fields up to 5 T.

Acknowledgments

Financial support through research project MAT2001-1440 is acknowledged. K. B. thanks the MCYT (Spain) for financial support under the "Ramón y Cajal" Program.

[1] R. MacDonald, M. Vogel, J. Brookman, *IBM J. Res. Dev.* **1962**, *6*, 363.
[2] E. T. Keve, S. C. Abrahams, J. L. Berstein, *J. Chem. Phys.* **1971**, *54*, 3185–3194; W. Jeitschko, *Acta Crystallogr., Sect. B* **1972**, *28*, 60–76.
[3] J. S. Xue, M. R. Antonio, L. Soderholm, *Chem. Mater.* **1995**, *7*, 333–340.
[4] P. Lacorre, F. Goutenoire, R. Retoux, Y. Laligant, *Nature* **2000**, *404*, 856–858.
[5] A. Moini, M. A. Subramanian, A. Clearfield, F. J. DiSalvo, W. H. McCaroll, *J. Solid State Chem.* **1987**, *66*, 136–143.
[6] T. Mingliang, M. Zhiqiang, Z. Yuheng, *J. Phys.*: *Condens. Matter* **1996**, *8*, 3413–3418.
[7] W. Jeitschko, *Acta Crystallogr. Sect. B* **1973**, *29*, 2074–2078.
[8] L. G. Sillen, A. Nylander, *Ark. Kem.* **1943**, *17A*, 1.
[9] C. Svensson, S. C. Abrahams, J. L. Berstein, *J. Chem. Phys.* **1979**, *71*, 5191–5195.
[10] H. Naruke, T. Yamase, *Inorg. Chem.* **2002**, *41*, 6514–6520.
[11] H. Naruke, T. Yamase, *J. Solid State Chem.* **2001**, *161*, 85–92.
[12] P. Gougeon, P. Gall, J. F. Halet, R. Gautier, *Acta Crystallogr., Sect. B* **2003**, *59*, 472–79.
[13] G. J. McCarthy, *Mater. Res. Bull.* **1971**, *6*, 31–39.
[14] H. D. Templeton, A. Zalkin, *Acta Crystallogr.* **1963**, *16*, 762–766.
[15] J. Holsa, M. Lastusaari, J. Niittykoski, R. Saez Puche, *Phys. Chem. Chem. Phys.* **2002**, *4*, 3091–3097.
[16] T. Aitasalo, J. Holsa, M. Lastusaari, J. Legendziewicz, L. Lehto, J. Linden, M. Marysko, *J. Alloys Compd.*, in press.
[17] S. Ebisu, T. Sogabe, H. Morita, S. Nagata, *J. Magn. Magn. Mater.* **1998**, *177*, 1073–1074.
[18] H. V. Rietveld, *J. Appl. Crystallogr.* **1969**, *2*, 65–71.
[19] J. Rodríguez-Carvajal, *J. Physica* **1993**, *B192*, 55–69.

Received: July 29, 2004
Published Online January 26, 2005

 © 2005 Wiley-VCH Verlag GmbH & Co. KGaA, Weinheim

Reaction Chemistry of the Carbenoid Butadienyl Complex Ion $[CpCo(\sigma,\eta^4\text{-}C_4HMe_4)]^+$ Formed by Protonation of the Cyclobutadiene Complex $[CpCo(C_4Me_4)]$

Mikhail V. Butovskii,[a] Ulli Englert,[a] Gerhard E. Herberich,*[a] and Ulrich Koelle[a]

Keywords: Cobalt / Cyclobutadiene / Butadienyl / Carbene

The protonation of $[CpCo(C_4Me_4)]$ (**1**) with excess acid, which produces the carbenoid ion $\mathbf{3}^+$, is shown to be reversible under conditions of low proton activity. Treatment of $\mathbf{3}^+$ with *one equivalent* of NEt_3 mainly produces **1** (60 %, isolated yield), and in DMSO the solvent acts as base transforming $[\mathbf{3}]BF_4$ into **1** (67 %, isolated yield). Deprotonation of $[\mathbf{3}]BF_4$ with *excess* NEt_3 affords (cyclopentadienyl)[(2–5-η)-(3Z,4Z)-3,4-dimethylhexa-1,2,4-triene]cobalt (**5**) in high yield (83 %). The structure of **5** has been determined by X-ray work. In the reaction of $\mathbf{3}^+$ with pyridine four reaction channels could be unveiled by low-temperature NMR spectroscopy: i) Reversible deprotonation to form **5** in a kinetic shunt; ii) reversible nucleophilic addition at the carbenoid center to form a pyridinium ion complex $\mathbf{6}^+$ as a low-temperature species with a terminal *anti*-Me group; iii) irreversible isomerization of $\mathbf{6}^+$ to the more stable stereoisomer $\mathbf{7}^+$ with a terminal *syn*-Me group; iv) very slow formation of **1**. Using very high concentrations of pyridine (mixing at –60 °C, slowly warming to 20 °C) allowed the preparation of $[\mathbf{7}]BF_4$ in near quantitative yield (97 %). The pyridine rings in $\mathbf{6}^+$ and $\mathbf{7}^+$ display hindered rotation (NMR), and the structure of $[\mathbf{7}]CF_3SO_3$ shows considerable steric crowding. On treatment with a large excess of CF_3CO_2H (≥ 7 equiv.) the hexatriene complex **5** quantitatively reverts to the carbenoid $\mathbf{3}^+$. Reaction of **5** with $(C_5H_5NH)CF_3SO_3$ (–80 °C, 3 weeks) produced $[\mathbf{6}]CF_3SO_3$ with retention of the stereochemistry at C-4 (NMR), while the same reaction at ambient temperature and in presence of a large excess of pyridine is accompanied by stereoisomerization and afforded $[\mathbf{7}]CF_3SO_3$ (94 %). Nucleophilic addition of excess PPh_3 to $\mathbf{3}^+$ gave a phosphonium salt $[\mathbf{8}]BF_4$, again with stereoisomerization, in near quantitative yield (98 %). Addition of CN*t*Bu with concomitant rearrangement produced a (*tert*-butylamino)cobaltocenium salt $[\mathbf{9}]CF_3SO_3$ (90 %). Nucleophilic substitution of the pyridine moiety of $\mathbf{7}^+$ with 4-picoline gave the 4-picoline addition product $[\mathbf{10}]CF_3SO_3$ (96 %). With CN^- a hexa-2,4-dienenitrile complex $[CpCo(\eta^4\text{-}C_4HMe_4CN)]$ (**11**) was obtained (85 %), which on protonation gave an aminocobaltocenium ion $[CpCo\{C_5Me_4(NH_2)\}]^+$ ($\mathbf{12}^+$), isolated as $[\mathbf{12}]BF_4$ (94 %). Acid removes the pyridine moiety from $\mathbf{7}^+$ to produce a carbenoid ion $\mathbf{13}^+$ with a 4-Me group in *syn*-position (a stereoisomer of $\mathbf{3}^+$) which was characterized by NMR spectroscopy. Deprotonation of $\mathbf{13}^+$ affords a hexatriene complex **14** (a stereoisomer of **5**) in good yield (57 %). Thermolyses of **5** and **14** show that **14** is the lower-energy isomer and produce a dinuclear complex $[(\mu\text{-}C_5H_3Me_3)(CoCp)_2\textit{(Co–Co)}]$ (**15**) (91 %) with a bridging penta-2,4-dienylidene ligand.

(© Wiley-VCH Verlag GmbH & Co. KGaA, 69451 Weinheim, Germany, 2005)

Introduction

In an earlier communication[1] we described the protonation of (cyclopentadienyl)(tetramethylcyclobutadiene)cobalt [CpCoCb*] (Cb* = C_4Me_4) (**1**).[1,2] According to a DFT study this protonation takes place from the *endo*-side to give a primary agostic intermediate $\mathbf{2}^+$. This intermediate rearranges by way of a stereospecific ring-opening reaction to give a carbenoid cation $\mathbf{3}^+$ with a σ,η^4-butadienyl substructure and an *anti*-Me group. While $\mathbf{2}^+$ has not been observed experimentally, the rearranged cation $\mathbf{3}^+$ was isolated as tetrafluoroborate in quantitative yield (97%) and has fully been characterized.[1]

If this protonation reaction is performed with a large excess of acid (for instance with 9 equivalents of HBF_4 in Et_2O at –50 °C or in neat CF_3CO_2H), product formation is fast and clean. At lower proton activity some solid material is formed, possibly by some decomposition processes. These observations suggest that the protonation reaction of **1** might be reversible, but only in this paper can we present straightforward experimental evidence for the reversibility of the sequence $\mathbf{1} \rightarrow \mathbf{2}^+ \rightarrow \mathbf{3}^+$.

The carbenoid cation $\mathbf{3}^+$ is a highly reactive species. At temperatures above –10 °C it undergoes thermal rearrangement with formation of [(cyclopentadienyl){η^5-(2*Z*,3*Z*,4*E*)-

[a] Institut für Anorganische Chemie, Technische Hochschule Aachen,
52056 Aachen, Germany
Fax: +49-241-809 22 88
E-mail: gerhard.herberich@ac.rwth-aachen.de

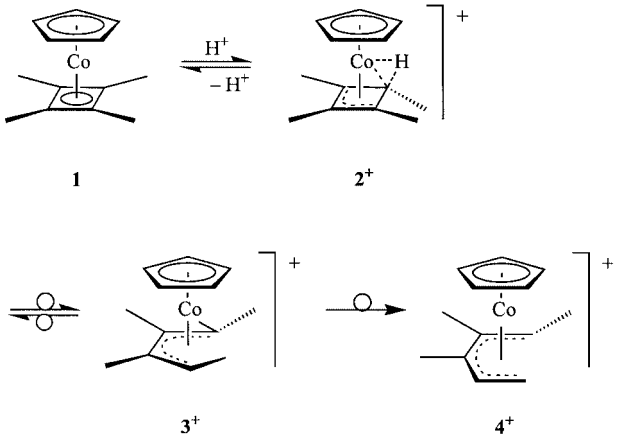

Scheme 1. Primary protonation equilibrium/rearrangement.

3,4-dimethylhexa-2,4-dienyl}cobalt] cation (**4**$^+$), a half-open cobaltocenium ion. This chemistry is summarized in Scheme 1.[1]

Early papers on (cyclobutadiene)(cyclopentadienyl)cobalt derivatives describe electrophilic H/D-exchange as well as some other electrophilic aromatic substitution reactions as characteristic reactions in this family of complexes,[3] the most notable examples being the parent complex [CpCo(C_4H_4)][4] and the tetraphenyl derivative CpCo(C_4Ph_4).[5] The boratabenzene analogue of **1**, [Cb*Co(C_5H_5BMe)],[6] which is less electron-rich than **1**, displays similar reactivity with very fast H/D exchange, but ring opening of the Cb* ring has never been observed. We conclude that only the most electron-rich complexes of the [CpCoCb]-type can undergo the protonation/rearrangement sequence of Scheme 1.

Complexes with σ,η^4-butadienyl-type ligands are known in some variety, for instance of the fragments CpRu,[7] Cp*Ru,[8] CpRe,[9] and CpMo[10] as well as of other complexes of Nb,[11] Mo,[12] and W.[12] To the best of our knowledge, cation **3**$^+$ is the first such complex of a 3d metal. Since the ion **3**$^+$ originates from a protonation reaction, it seemed particularly interesting to study its reactions with bases and/or nucleophiles. During our work, it quickly turned out that the reactions of **3**$^+$ depend in a subtle manner on the nature of the attacking reagents and on the reaction conditions. In this paper we describe the deprotonation of **3**$^+$, conditions which result in a reversal of the ring opening of complex **1** (in Scheme 1), furthermore nucleophilic addition to **3**$^+$, and some closely related chemistry of the products obtained.

Results and Discussion

Deprotonation of the Carbenoid Complex 3$^+$

Reaction of [**3**]BF_4 in dichloromethane with a large excess of triethylamine effects deprotonation and produces (cyclopentadienyl)[(2–5-η)-(3*Z*,4*Z*)-3,4-dimethylhexa-1,2,4-triene]cobalt (**5**). For instance, an NMR experiment with a 1:5 ratio of the reactants showed the formation of the hexatriene complex **5** as the sole complex product and of $NHEt_3^+$; no further change was seen at ambient temperature after 16 h. Preparative runs yielded **5** as air-sensitive, low-melting, orange-red crystals. Other strongly basic reagents, as for instance allylmagnesium chloride in ether, gave the same product **5**. Note that **5** is an isomer of **1**, but does not spontaneously convert to **1** under the conditions given here.

^{1}H NMR spectra of **5** show that the terminal MeCH= moiety of **3**$^+$ with an *anti*-Me group is retained in **5** and that one methyl group is now replaced with a noncoordinated methylene function. This result was later confirmed by a single-crystal structure determination (see below). Marked C–H acidity at a carbon atom ß to a carbene center is well known for Fischer carbene complexes,[13] and has previously been observed for some of the known σ,η^4-butadienyl complexes.[10,14]

When **3**$^+$ was deprotonated with NEt_3 in a 1:1 ratio, i.e. under conditions where a low proton activity is retained, some unidentified solid material was deposited. The ^{1}H NMR of the solution, recorded without delay, indicated the presence of two complex products, the hexatriene complex **5** and the cyclobutadiene complex **1** in roughly a 1:1 ratio. Upon standing at ambient temperature, the concentration of **1** grew at the expense of **5**, and after 16 h, complex **1** had become the sole complex product. Conventional workup of the NMR tube contents including chromatography on alumina with hexane as eluent afforded a 60% yield of spectroscopically pure **1**. In a related experiment [**3**]BF_4 was dissolved in CH_2Cl_2/DMSO (2:1, v/v) and kept at 30 °C for 30 min; in this case the basicity of the medium is sufficient to allow the transformation of **3**$^+$ into complex **1** which was isolated in 67% yield.

These observations imply reversibility of the deprotonation of **3**$^+$ (Scheme 2) and of the ring-opening reaction of **1** (Scheme 1). Protonation of **5** by protic reagents other than the relatively weak acid $NHEt_3^+$ will be described below.

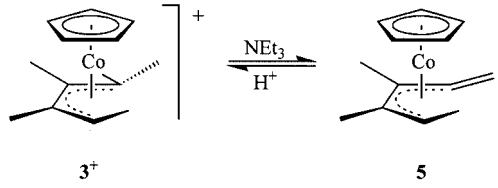

Scheme 2. Protonation/deprotonation equilibrium.

We summarize and conclude: i) In strongly acidic medium the stable complex species is the carbenoid ion **3**$^+$ which is formed either from the cyclobutadiene complex **1** (Scheme 1)[1] or from the hexatriene complex **5** (Scheme 2). ii) In strongly basic medium, i.e. with a large excess of base or with strong bases, a kinetically controlled deprotonation of **3**$^+$ affords the hexatriene complex **5**. iii) Under conditions of low, but noticeable proton activity reversibility comes into play. The product now is the cyclobutadiene complex **1**, both in the reaction of **3**$^+$ with bases and in the

 © 2005 Wiley-VCH Verlag GmbH & Co. KGaA, Weinheim

protonation of **5**; thus the cyclobutadiene complex **1** is seen to be thermodynamically more stable than its isomer **5**.

Structure of 5

The structure of **5** was determined by single-crystal X-ray diffraction (Figure 1) and confirms the presence of an η^4-bonded vinylallene-type ligand and the *anti*-position of the terminal Me group. Related structures are known for $[Fe(CO)_3]$[16] and CpRu compounds[14c] and a $[RhCl(PPh_3)]$ complex.[17] We note the short bond length C3–C4 [1.408(11) Å] of the central diene bond, which is now shorter than the former diene double bonds C2–C3 [1.449(9) Å] and C4–C5 [1.438(11) Å], furthermore the remarkably short bond length Co–C2 [1.883(5) Å], and the bond angle C1–C2–C3 [137.2(6)°]; the methyl group at C5 is bent away from the metal. These details are all indicative of pronounced metal-to-ligand back-bonding, as expected for a complex which belongs to the CpCo(diene) family in a broad sense.

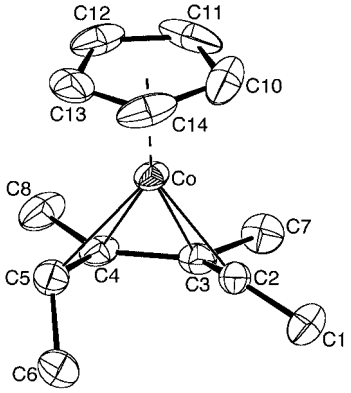

Figure 1. Molecular structure of **5** in the crystal (PLATON plot[15] at the 30% probability level); selected bond lengths (Å) and angles (°): Co–C2 1.883(5), Co–C3 1.988(5), Co–C4 1.979(5), Co–C5 2.050(6), Co–C(Cp) 2.053 (av.), C1–C2 1.316(8), C2–C3 1.449(9), C3–C4 1.408(11), C4–C5 1.438(11); C1–C2–C3 137.2(6), C4–C5–C6 126.3(6), C2–C3–C4–C5 9.5, C3–C4–C5–C6 56.3, C1–C2–C3–C4 147.1.

Nucleophilic Addition to the Carbenoid Complex 3^+

In this chapter we describe nucleophilic addition reactions which are the preferred reactions for weak bases such as pyridine, PPh_3, and CN*t*Bu. The case of pyridine addition, which revealed an unexpected complexity of the reaction system, was investigated by means of low-temperature NMR experiments and by varying the substrate/base ratio.

Addition of Pyridine

In one NMR tube experiment pyridine (1 equiv.) was added to a solution of $[\mathbf{3}]BF_4$ in CD_2Cl_2 at –80 °C and the reaction mixture was kept at this temperature for several days. Four different cobalt complexes were observed as products: i) The hexatriene complex **5**, ii) a primary addition product $[\mathbf{6}]BF_4$, iii) an isomeric addition product $[\mathbf{7}]BF_4$, and iv) the cyclobutadiene complex **1**. In the early stages of the reaction (up to 30 h) the major product was the hexatriene complex **5**; after 30 h at –80 °C the product ratios (normalized to 100%) were $\mathbf{5}:\mathbf{6}^+:\mathbf{7}^+:\mathbf{1}$ = 53:37:8:2. Later the primary addition product $\mathbf{6}^+$ grew at the expense of **5** and amounted to 80% of the product mixture after 7 days; the product ratios now were $\mathbf{5}:\mathbf{6}^+:\mathbf{7}^+:\mathbf{1}$ = 5:80:10:6. It is remarkable that **1** already appears at –80 °C with its concentration very slowly increasing with time at this temperature.

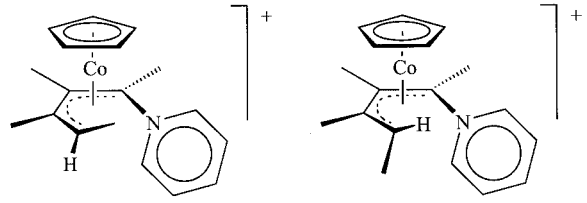

$\mathbf{6}^+$ $\mathbf{7}^+$

In a second NMR tube experiment the temperature of the reaction mixture ($\mathbf{3}^+/C_5H_5N$, 1:1) was increased in steps of 10 K. Under these conditions the hexatriene complex **5** was the major product up to –60 °C, but had disappeared completely below –30 °C. The primary addition product $\mathbf{6}^+$ reached its maximum concentration at –30 °C. At higher temperatures the concentration of **1** grew quickly at the expense of $\mathbf{6}^+$; at 10 °C ratios of $\mathbf{5}:\mathbf{6}^+:\mathbf{7}^+:\mathbf{1}$ = 0:0:14:86 were observed. A similar experiment with a higher pyridine concentration ($\mathbf{3}^+/C_5H_5N$, 1:7) differed in two respects. Above –50 °C the isomerization $\mathbf{6}^+ \rightarrow \mathbf{7}^+$ was clearly seen and was the main process above –25 °C, while the formation of **1** was markedly slowed down; at 10 °C ratios of $\mathbf{5}:\mathbf{6}^+:\mathbf{7}^+:\mathbf{1}$ = 0:1.5:76:23 were reached. In all these experiments the primary addition product $\mathbf{6}^+$ seemed to be the sole source for the formation of **1**. We may conclude i) that the pyridine addition to $\mathbf{3}^+$ is reversible allowing the formation of **1**, and ii) that the isomerization $\mathbf{6}^+ \rightarrow \mathbf{7}^+$ is an irreversible reaction (Scheme 3).

Scheme 3. Pyridine addition equilibrium and stereoisomerization.

The primary addition product $[\mathbf{6}]BF_4$ could, of course, only be characterized by its ^1H NMR and ^{13}C NMR spectra. For the preparation of the more stable isomeric addition product $[\mathbf{7}]BF_4$ a very high concentration of pyridine $[CH_2Cl_2/C_5H_5N$, 1:1 (v/v)] has to be used. Mixing the reagents at –60 °C effected an immediate color change from dark red to orange-red; while the temperature was slowly increased the color began to deepen and was burgundy at ambient temperature. From this solution the product was isolated in near quantitative yield.

The ^1H NMR spectra of the isomeric ions $\mathbf{6}^+$ and $\mathbf{7}^+$ are rather similar, but differ conspicuously in the doublet/quartet pattern of the terminal MeCH= moiety [for $\mathbf{6}^+$: δ = –0.49 ppm (d, J = 7.6 Hz, 4-Me) and 3.76 ppm (q, J = 7.6 Hz, 4-H); for $\mathbf{7}^+$: δ = 1.18 (d, J = 6.1 Hz, 4-Me) and –0.37 ppm (q, J = 6.1 Hz, 4-H)]. These data show that $\mathbf{6}^+$

 © 2005 Wiley-VCH Verlag GmbH & Co. KGaA, Weinheim

still possesses an *anti*-Me group (with a negative chemical shift) which has become a *syn*-Me group in **7**$^+$. This result is in agreement with the structure determination of [**7**]CF_3SO_3 (see below). In contrast to **6**$^+$ the cation **7**$^+$ displays an additional long-range coupling (^4J = 0.7 Hz) between the proton 4-H_{anti} and the methyl group 3-Me which are in a zigzag arrangement in this isomer. Both ions **6**$^+$ and **7**$^+$ display separate signals for the proton pairs 2-H/6-H and 3-H/5-H of the pyridine ring. This indicates hindered rotation of the pyridine ring. When the solution of [**7**]BF_4 in $MeNO_2$ was warmed, five sharp lines were observed up to 50 °C; at higher temperatures the spectra deteriorated due to decomposition, but even at 80 °C five signals were seen. Hindered rotation of pyridine ligands has occasionally been observed, albeit only at low temperatures.[18] We comment on the origin of this barrier in the context of the structure description of the structure of [**7**]CF_3SO_3.

We noted above that low concentration of pyridine and higher temperatures favor the formation of the cyclobutadiene complex **1** while very high concentrations of pyridine favor the stereoisomerization **6**$^+$ → **7**$^+$. Excess pyridine and low temperature will suppress the dissociation of the primary addition product **6**$^+$ → **3**$^+$ and hence the formation of **1** (cf. Scheme 1 and Scheme 3). As a consequence, the slow stereoisomerization can come into play. Note also, that in the preparation of [**7**]BF_4 mixing at low temperature and slow warm up are features which are essential for the excellent yields obtained. We consider this interpretation as the most likely one. However, in the absence of kinetic data we cannot exclude that pyridine does actively participate in the stereoisomerization; in such a case high pyridine concentrations would directly accelerate the formation of **7**$^+$.

Addition of Triphenylphosphane

Under the same reaction conditions used for the preparation of [**7**]BF_4, the carbenoid complex [**3**]BF_4 reacts with excess PPh_3 (7 equiv.) to undergo nucleophilic addition, again with stereoisomerization of the diene chain. The resulting complex phosphonium ion **8**$^+$ was isolated as tetrafluoroborate [**8**]BF_4 in quantitative yield. The ion **8**$^+$ has a remarkably small direct coupling constant $^1J_{PC}$ = 46.0 Hz as has the related ion [CpCo{η^4-$C_4HPh_4(PPh_3)$}]$^+$ ($^1J_{PC}$ = 36.6 Hz).[19] If only 1 equivalent of PPh_3 was used the familiar complications appeared again: Formation of **1** and of insoluble material. Trimethylphosphane reacted unselectively to produce several unidentified [CpCo(PMe_3)] species (NMR).

Addition of tert-Butyl Isocyanide

The reaction of [**3**]CF_3SO_3 with CN*t*Bu is fast at –35 °C, showing a fast color change from dark red to yellow, and produced the (*tert*-butylamino)cobaltocenium derivative [**9**]CF_3SO_3 (Scheme 4). The new cobaltocenium ion was readily identified and characterized by its simple NMR spectra which show effective lateral symmetry for the cation. This fascinating ring formation has precedence in M. Green's chemistry,[19] and will be discussed below.

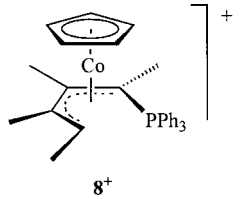

8$^+$

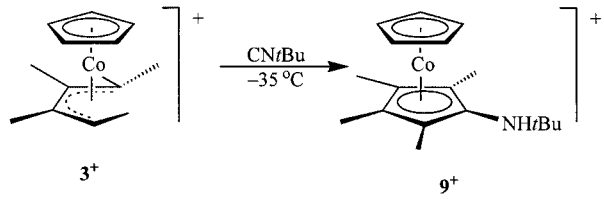

3$^+$ **9**$^+$

Scheme 4. Reaction with CN*t*Bu.

Protonation of the Hexatriene Complex 5

The protonation of **5** (Scheme 2) had first been deduced from the evolution of the system **3**$^+$/C_5H_5N with time, but can be confirmed by independent experiments. Indeed, when **5** was treated with a large excess CF_3CO_2H (≥ 7 equiv., NMR tube experiment), the reverse protonation reaction took place and produced **3**$^+$ in a very clean reaction; no species other than **3**$^+$ and CF_3CO_2H were seen. With only stoichiometric quantities (**5**/CF_3CO_2H, 1:1) we found again formation of **1** and of insoluble material.

The protonation of **5** by the pyridinium salt (C_5H_5NH) CF_3SO_3 in CD_2Cl_2 was monitored by low-temperature NMR spectroscopy. When the reaction mixture was kept at –80 °C, the main process was the slow formation of [**6**]CF_3SO_3, and both [**7**]CF_3SO_3 and **1** remained trace products. After 3 weeks at –80 °C the product ratios were **5**:**6**$^+$:**7**$^+$:**1** = 0:93:5:2. In contrast to this low-temperature situation, the synthetic version of this experiment required high concentrations of pyridine in CH_2Cl_2 (4:6 v/v) to ensure high chemoselectivity, and at ambient temperature afforded the complex triflate [**7**]CF_3SO_3 in excellent yield (94%).

Structure of [7]CF_3SO_3

The structure determination of [**7**]CF_3SO_3 confirms the constitution of **7**$^+$ and specifically the *syn*-position of the Me group at C4 (in chemical notation C-4′) and the *anti*-stereochemistry of the pyridinio substituent at C1 (Figure 2). Thus, the cation **7**$^+$ is a CpCo(diene) derivative with the unusual feature of a positively charged substituent in the terminal *anti*-position of the diene ligand. The short central bond of the diene substructure [C2–C3 1.384(4) Å] and the long former double bonds [C1–C2 1.441(3) and C3–C4 1.443(4) Å] show again that metal-to-diene back bonding is rather pronounced as in **5**. We also note that the bond N–C1 [1.498(3) Å] is longer than expected. A search in the CSD database[20] for structures with comparable ge ometry[21] resulted in 692 hits with an average C–N distance

 © 2005 Wiley-VCH Verlag GmbH & Co. KGaA, Weinheim

of 1.392(1) Å; only six of the 692 matches showed a C–N distance longer than the one observed in **7**$^+$. We explain the unusual length of the N–C1 bond by a steric labilization caused by two short interactions between the pentadienyl chain and the pyridinium N atom, namely N···H5–C5 of 2.61 and N···H4–C4 of 2.19 Å. Of course, we cannot exclude an additional electronic effect due to the neighboring metal center.

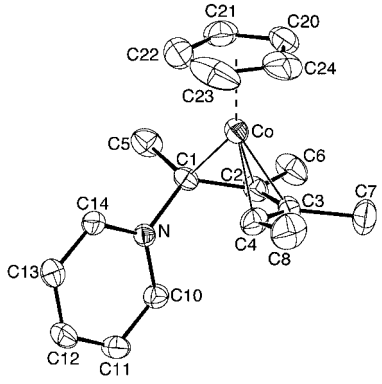

Figure 2. Structure of the ion **7**$^+$ in the crystal of [**7**]CF_3SO_3 (PLATON plot[15] at the 30% probability level); selected bond lengths (Å) and angles (°): Co–C1 1.975(2), Co–C2 1.971(2), Co–C3 1.966(3), Co–C4 2.053(3), Co–C(Cp) 2.057 (av.), N–C1 1.498(3), C1–C2 1.441(3), C2–C3 1.384(4), C3–C4 1.443(4); C2–C1–N 118.5(2), C2–C1–C5 120.8(2), N–C1–C5 106.31(19); C1–C2–C3–C4 2.1, N–C1–C2–C3 59.0, C5–C1–N–C10 100.6, C5–C1–N–C14 76.6.

If the (trimethylpentadienyl)pyridinium ligand of **7**$^+$ were planar we would have a prohibitively strong repulsive 1,6-interaction between a C atom in the *ortho*-position of the pyridinium ring and C4 of the pentadienyl chain. In the structure this 1,6-interaction is reduced by a bending of the ring out of the pentadienyl plane and away from the metal [dihedral angle N–C1–C2–C3 59.0°] and by a near orthogonal rotational position of the ring. This situation explains the unusually high barrier to internal rotation of the pyridine ring which is seen in the NMR spectra.

Nucleophilic Substitution of the Pyridine Moiety of 7$^+$

In the system **3**$^+$/pyridine we had observed the slow formation of the cyclobutadiene complex **1** from the pyridine addition product **6**$^+$, most likely via the carbenoid ion **3**$^+$ (cf. Scheme 1 and Scheme 3). Given the low thermal stability of **6**$^+$, it would be difficult to verify the reversibility of the pyridine addition to **3**$^+$ directly. However, the more stable isomer **7**$^+$ is prone to reactions which suggest that pyridine can dissociate from the complex.

A Pyridine/4-Picoline Exchange Reaction

When 4-picoline (4-methylpyridine) was added to a solution of [**7**]CF_3SO_3 in CD_2Cl_2 a new species **10**$^+$ was seen in a slow exchange reaction at ambient temperature (NMR, two Cp signals) with a slight preference of **3**$^+$ for 4-picoline over pyridine (Scheme 5). The pure 4-picoline addition product [**10**]BF_4 could be prepared in CH_2Cl_2 by repeated removal of the volatiles and addition of fresh CH_2Cl_2 and 4-picoline.

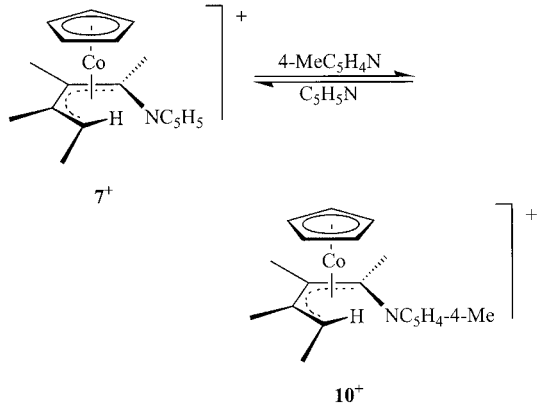

Scheme 5. Pyridine/4-picoline exchange.

Substitution Reaction of 7$^+$ with Cyanide

Attempted nucleophilic addition of cyanide to **3**$^+$ produced the hexatriene complex **5** because of the high basicity of CN^- in an aprotic medium. However, the reaction of **7**$^+$ with $(NBu_4)CN$ resulted in a smooth substitution of pyridine with cyanide and afforded the neutral complex **11** as a robust crystalline compound (Scheme 6). This nitrile **11** could readily be protonated in an NMR tube experiment. The reaction with CF_3CO_2H (3 equiv.) in CD_2Cl_2 effected a fast color change from red to yellow. The cation so formed was precipitated from aqueous solution as hexafluorophosphate [**12**]PF_6 (Scheme 6). A synthetically more

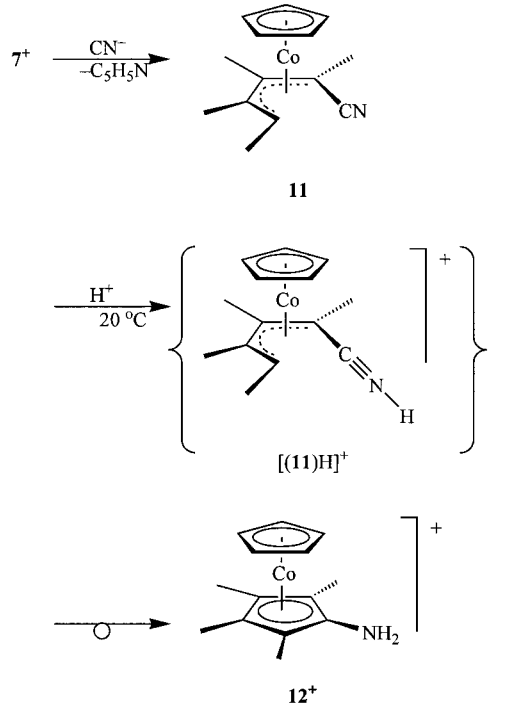

Scheme 6. Cyanide reaction, protonation, rearrangement.

 © 2005 Wiley-VCH Verlag GmbH & Co. KGaA, Weinheim

convenient reaction with HBF_4 in ether afforded [**12**]BF_4 in near quantitative yield. Mechanistically, this transformation is thought to involve protonation at the nitrilic nitrogen of **11** forming a nitrilium intermediate [(**11**)H]$^+$, which by way of an electrocyclic ring closure and subsequent proton migration rearranges into the aminocobaltocenium cation **12**$^+$. Details of the metal-participation involved and potential further intermediates must at present remain undefined.

Substitution Reaction of 7$^+$ with tert-Butyl Isocyanide

Isocyanides are much less basic than cyanide ion. Therefore, the direct nucleophilic addition of CN*t*Bu to **3**$^+$ described above was feasible. We then found that [**7**]CF_3SO_3 also reacts with CN*t*Bu, though much slower than **3**$^+$, and also gave the (*tert*-butylamino)cobaltocenium derivative [**9**]CF_3SO_3. Both reactions, that of CN*t*Bu with **3**$^+$ (Scheme 4) and that with **7**$^+$ follow the same mechanistic pattern exemplified Scheme 6.

Abstraction of Pyridine from the Pyridinium Ion 7$^+$

The demonstrated lability of the pyridine moiety in **7**$^+$ suggested that acid should be able to remove pyridine from **7**$^+$, thereby producing the carbenoid ion **13**$^+$, the alternative stereoisomer of **3**$^+$. Indeed, treatment of the triflate [**7**]CF_3SO_3 with a large excess of CF_3CO_2H (1:7) at ambient temperature resulted in the formation of **13**$^+$ and pyridinium ion $C_5H_5NH^+$ (Scheme 7). The new complex ion is labile and decomposes above –20 °C. It could be characterized by its NMR spectra by recording the spectra a few minutes after mixing the reagents. The ^{1}H NMR spectra of **13**$^+$ and **3**$^+$ are remarkably similar, except for the doublet/quartet patterns of the terminal MeCH= moiety [for **13**$^+$: δ = 2.37 (d, J = 6.6 Hz, 4-Me) and 3.13 ppm (q, J = 6.6 Hz, 4-H); for **3**$^+$: δ = 0.55 (d, J = 6.7 Hz, 4-Me) and 6.49 ppm (q, J = 6.7 Hz, 4-H)] which readily distinguish the two stereoisomers. In the ^{13}C NMR spectrum of **13**$^+$ a signal at very high chemical shift [for **13**$^+$$\delta$ = 288.4 and for **3**$^+$$\delta$ = 292.1 ppm] indicates the presence of a carbenoid center at C-1 as in **3**$^+$, and small shifts to lower chemical shifts for 3-Me, C-4, and C-5 reflect the presence of steric strain in **3**$^+$, but not in **13**$^+$.

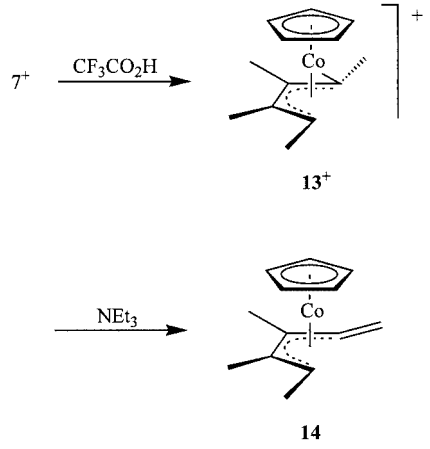

Scheme 7. Reaction with acid / deprotonation.

One would expect that the new isomer **13**$^+$ should be amenable to deprotonation in the same way that was successful in the case of **3**$^+$. To verify this expectation [**7**]BF_4 was treated with excess of CF_3CO_2H (1:8) and subsequently with a very large excess of NEt_3. Workup afforded the hexatriene complex **14** (57%), the alternative stereoisomer of **5**, as a low-melting red solid (Scheme 7). As may be verified by inspection, the NMR spectra of **14** and **5** are largely similar and, as discussed above in detail for the pair **13**$^+$/**3**$^+$, allow a straightforward distinction of the respective stereochemistries.

Thermolysis Reactions of the Hexatriene Complexes 5 and 14

It is intuitively clear that complex **14** with its terminal methyl group in *syn* position should be more stable than its stereochemical counterpart **5** with a terminal *anti*-Me group. Experimental support for this notion comes from the thermal behavior of **5**. Monitoring a solution of **5** in [D_8]-toluene showed the onset of a slow thermolysis reaction around 80 °C. Complex **5** partially isomerized to produce its stereoisomer **14**, and partially decomposed with formation of a new dinuclear complex **15** and free olefins. After three days at 80 °C the molar product ratio amounted to **5**:**14**:**15** = 2.8:3.4:4.8 and after seven days it was 0.3:4.2:6.1. This result demonstrates that **14** is indeed more stable than **5**. Unfortunately it was not possible to selectively produce the isomer **14** by a meticulous choice and control of the reaction temperature. A stereoisomerization related to the transformation **5** → **14** has been described for vinylallene complexes of the [RhCl(PPh_3)] fragment.[17] M. Murakami et al. argue that the isomerization occurs via a 14e complex with a 2,5-σ^2-coordinated vinylallene (1,2,4-pentatriene) ligand and present an example where this arrangement becomes the groundstate of the molecular system. Most likely the isomerization **5** → **14** follows the same path.

Thermolysis of **14** in [D_8]toluene was found to be markedly slower and again produced the dinuclear complex **15** and free olefins. Complex **5** was not found in the product mixtures. For the practical synthesis of **15** the more readily accessible complex **5** was used as starting material. Heating **5** in toluene at 110 °C for 4 days gave, after workup, **15** as black crystals in high yield (91%) (Scheme 8).

The ^{1}H NMR spectrum of **15** displayed two singlets of equal intensity for two CoCp moieties, three doublets of doublets for a coordinated vinyl group, and three singlets for methyl groups. These observations suggested the presence of a 1,2,3-trimethylpenta-2,4-dien-1-ylidene ligand in a dinuclear complex. The ^{13}C NMR spectrum of **15** was in agreement with this conclusion, and the signal with the highest chemical shift (δ = 166.1 ppm) indicated that the ylidene carbon was in a bridging position between the two metal centers. It was then found that complexes of this type have previously been obtained from the thermolysis of (cyclopentadienyl)[(1–4-η)-(2Z,3*E*)-1,3,5-hexatriene]cobalt and have structurally been characterized.[22]

 © 2005 Wiley-VCH Verlag GmbH & Co. KGaA, Weinheim

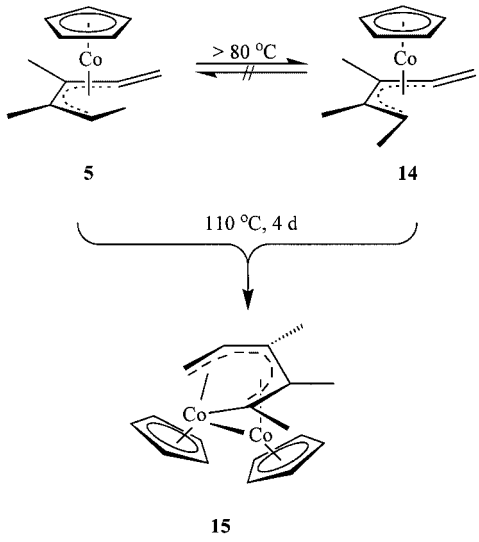

Scheme 8. **5** → **14** + **15** and **14** → **15** at higher temperature.

Conclusion

In this paper we have demonstrated that the carbenoid complex ion **3**$^+$ can react to give the cyclobutadiene complex **1**. Thus we have now a kind of acid/base equilibrium between **1** and **3**$^+$ as already expressed in Scheme 1. According to our earlier theoretical analysis by means of DFT calculations the forward reaction consists of a protonation step followed by a ring-opening step.[1] The principle of microscopic reversibility suggests that the reverse transformation begins with a ring closure (**3**$^+$ → **2**$^+$), and subsequent deprotonation (**2**$^+$ → **1**) gives the cyclobutadiene complex **1**.

As we have seen the experimental situation is much more complicated. i) At temperatures above –20 °C the acid **3**$^+$ rearranges irreversibly to give the half-open cobaltocenium ion **4**$^+$ (Scheme 1). ii) Bases effect reversible deprotonation of **3**$^+$ with formation of the hexatriene complex **5** (Scheme 2) at a rate which is higher than the rate of the reverse reaction of Scheme 1; alternatively they may undergo competing nucleophilic addition reactions (Scheme 3). iii) The formation of **3**$^+$ from **1** is a clean reaction only under strongly acidic conditions. Likewise the formation of **5** from **3**$^+$ is a clean reaction only under strongly basic conditions. Whenever the acid **3**$^+$ is allowed to coexist for some time (minutes to several hours at ambient temperature) with its deprotonated forms (**1** or **5**) we observed undefined decomposition.

The irreversible isomerization of the low-temperature pyridine addition product **6**$^+$ with formation of the more robust stereoisomer **7**$^+$ (Scheme 3) opened a route to sterically less crowded complexes with the terminal methyl group in *syn*-position. Thus we have pairs of stereoisomers, the pyridine addition products **6**$^+$ and **7**$^+$, the carbenoid complex ions **3**$^+$ and **13**$^+$, and the hexatriene complexes **5** and **14**. In the cases **6**$^+$/**7**$^+$ and **5**/**14**, the species with the *syn*-Me group are the more stable isomers, in agreement with expectation.

Experimental Section

General: All manipulations were carried out under nitrogen by means of standard Schlenk techniques. THF and Et_2O were distilled from sodium benzophenone ketyl and CH_2Cl_2 was distilled from CaH_2. Hexane was distilled from potassium and toluene from sodium. Alumina for chromatography was deactivated with 5% water. Elemental analyses were performed by Analytische Laboratorien, 51789 Lindlar, Germany. Melting points were determined with a Büchi 510 melting point apparatus and are uncorrected. NMR spectra were recorded with a Varian 200 (^{1}H, 200.0 MHz; ^{13}C{^{1}H}, 50.29 MHz; ^{31}P{^{1}H}, 80.96 MHz), with a Varian Unity 500 (^{1}H, 499.6 MHz; ^{13}C, 125.6 MHz; ^{31}P{^{1}H}, 202.2 MHz) or with a Varian Inova 400 (^{1}H, 400.0 MHz; ^{13}C, 100.6 MHz). Chemical shifts are given in ppm; they were measured at ambient temperature and are referenced to internal TMS for ^{1}H and ^{13}C, and relative to H_3PO_4 (85%) as external reference for ^{31}P. IR spectra were measured with a Nicolet Avatar 360 FT-IR instrument.

Deprotonation of [3]BF$_4$ and Synthesis of (Cyclopentadienyl)[(2–5-η)-(3*Z*,4*Z*)-3,4-dimethylhexa-1,2,4-triene]cobalt (5): Triethylamine (20 mL) was added to [**3**]BF_4 (1.28 g, 4 mmol) in CH_2Cl_2 (30 mL) at –60 °C. The color of the solution changed immediately from deep wine-red to orange. After dilution with hexane (150–200 mL) the reaction mixture was filtered through a short column of alumina at –80 °C. Thorough removal of all volatiles under vacuum left **5** (0.775 g, 83%) as orange-red crystalline product. The product was recrystallized by cooling Et_2O or hexane solutions to –80 °C; m.p. 37–39 °C. $C_{13}H_{17}Co$ (232.21): calcd. C 67.24, H 7.38; found C 67.07, H 7.42. ^{1}H NMR (500 MHz, CD_2Cl_2): δ = 0.47 (d, J = 7.02 Hz, 5-Me), 1.83 (s, 3-Me), 2.09 (s, 4-Me), 3.37 (q, J = 7.02 Hz, 5-H), 4.68 (s, Cp), 4.72 (d, J = 2.14 Hz, 1-H$_{anti}$), 4.95 (d, J = 2.14 Hz, 1-H$_{syn}$) ppm. ^{13}C{^{1}H} NMR (126 MHz, CD_2Cl_2): δ = 17.9 (3-Me), 18.5 (5-Me), 21.1 (4-Me), 49.4 (C-5), 77.2 (C-3), 82.6 (Cp), 97.5 (C-1), 99.0 (C-4), 175.6 (C-2) ppm.[23]

Deprotonation of 3$^+$ by an Allyl Grignard Reagent: Allylmagnesium chloride (0.87 mL, 1.74 mmol, 2 M solution in THF) was added with stirring to [**3**]BF_4 (279 mg, 0.87 mmol) in CH_2Cl_2 (20 mL) at –90 °C. After warming to ambient temperature overnight, evaporation to dryness, extraction of the residue with hexane, filtration of the combined extracts through a plug of alumina, and finally removal of the hexane afforded **5** (165 mg, 81%) which was identified by its ^{1}H NMR spectrum.

Deprotonation of 3$^+$ with One Equivalent of NEt$_3$ and Formation of the Cyclobutadiene Complex 1: In an NMR tube a sample of [**3**]BF_4 (109 mg, 0.34 mmol) was dissolved in CD_2Cl_2 (0.7 mL). One equivalent of NEt_3 (47 μL, 0.34 mmol, d = 0.73 g·mL^{-1}) was added at ambient temperature. After shaking the mixture vigorously some insoluble material was separated utilizing a centrifuge. The ^{1}H NMR (200 MHz, CD_2Cl_2) spectrum, recorded without delay, displayed three species in the mixture: the cyclobutadiene complex **1** and the hexatriene complex **5** in roughly equal amounts, and $NHEt_3^+$ [δ = 1.32 (t, Me), 3.18 (q, CH_2), 6.75 (broad, H) ppm]. After 16 h **5** had disappeared completely. Chromatography of the reaction mixture on alumina (20 cm) with hexane, followed by removal of the eluent under vacuum gave **1** (47 mg, 60%) as deep yellow crystalline solid.

Deprotonation of 3$^+$ in CH$_2$Cl$_2$/DMSO and Formation of the Cyclobutadiene Complex 1: A Schlenk tube was charged with [**3**]BF_4 (253 mg, 0.79 mmol), CH_2Cl_2 (10 mL), and finally with dimethylsulfoxide (5 mL) at ca. –40 °C. Then the solution was warmed to 30 °C and stirred for 30 min. Concentrating the solution under vacuum, extraction of the yellow product with hexane, followed by

 © 2005 Wiley-VCH Verlag GmbH & Co. KGaA, Weinheim

filtration of the combined extracts through short plug of alumina, and finally removal of the hexane afforded **1** (124 mg, 67%) as deep yellow crystalline solid.

The System [3]BF_4/C_5H_5N in the NMR Tube: A solution of [**3**]BF_4 (26 mg, 0.08 mmol) in CD_2Cl_2 (0.7 mL) was prepared in an NMR tube at –50 °C. The ^1H NMR spectrum of the sample showed the spectrum of [**3**]BF_4 and impurity signals due to traces of Et_2O and of [**4**]BF_4. One equivalent of pyridine (6.5 μL, 0.08 mmol, d = 0.98 g·mL^{-1}) was then added at –80 °C. The reagents were mixed utilizing an ultrasonic bath at –80 °C. ^1H NMR spectra were recorded on a 200 MHz spectrometer. In one experiment the temperature was kept below –70 °C for 7 d. In a second experiment the temperature was increased in 10 K steps over the range from –80 to 10 °C, and the sample was kept at the chosen temperature for 10 minutes before the spectrum was recorded. Integral intensities of the pertinent Cp ring signals were measured using the signal of the residual solvent protons as internal standard.

Data for 6^+: ^1H NMR (200 MHz, CD_2Cl_2, –30 °C): δ = –0.45 (d, J = 7.6 Hz, 4-Me), 1.95 (s, Me), 2.12 (s, Me), 2.20 (s, Me), 3.78 (q, J = 7.6 Hz, 4-H), 4.90 (s, Cp); pyridine: 7.61 (t, J = 6.4 Hz, 1 H, β-H_{exo}), 7.97 (t, J = 6.4 Hz, 2 H, β-H_{endo} + α-H_{exo}), 8.23 (t, J = 7.8 Hz, γ-H), 9.26 (d, J = 5.6 Hz, 1 H, α-H_{endo}) ppm; partial assignments by analogy to 7^+. Multiplets at δ = 8.08 (t), 8.47 (t), 8.83 (d) ppm were assigned to the pyridine/pyridinium mixture. For $^{13}C\{^1H\}$ NMR spectroscopic data see below.

Synthesis of [(Cyclopentadienyl){*N*-[η^4-(1′*Z*,2′*Z*,3′*E*)-1′,2′,3′-trimethylpenta-1′,3′-dienyl]pyridinium}cobalt] Tetrafluoroborate ([7]BF_4): Pyridine (10 mL) was added to a solution of [**3**]BF_4 (640 mg, 2.00 mmol) in CH_2Cl_2 (10 mL) at –60 °C. The reaction mixture was warmed to ambient temperature overnight. Addition of Et_2O precipitated a raw product which was purified by re-precipitation from CH_2Cl_2 solutions yielding [**7**]BF_4 (775 mg, 97%) as deep red, crystalline solid; m.p. 112 °C (dec). $C_{18}H_{23}BCoF_4N$ (399.12): calcd. C 54.17, H 5.80, N 3.51; found C 54.09, H 5.70, N 3.71. ^1H NMR (500 MHz, CD_2Cl_2): δ = –0.37 (qq, J = 6.1, 0.7 Hz, 4-H), 1.18 (d, J = 6.1 Hz, 4-Me), 1.94 (s, 1-Me), 2.17 (d, J = 0.7 Hz, 3-Me), 2.21 (s, 2-Me), 4.82 (s, Cp); pyridine: 7.52 (t, J = 6.7 Hz, β-H_{exo}), 7.66 (d, J = 6.1 Hz, α-H_{exo}), 8.00 (t, J = 6.7 Hz, β-H_{endo}), 8.23 (t, J = 7.6 Hz, γ-H), 9.34 (d, J = 6.1 Hz, α-H_{endo}) ppm. Note the ^4J coupling between 4-H and 3-Me which can be observed under favorable conditions and which is absent in 6^+; the coupling constant was measured applying digital filtering with a Lorentz Gauss function. $^{13}C\{^1H\}$ NMR (126 MHz, CD_2Cl_2): δ = 16.0 (3-Me), 16.3 (2-Me), 20.2 (4-Me), 32.3 (1-Me), 53.7 (C-4), 80.4 (C-2), 81.8 (C-1), 84.6 (Cp), 100.0 (C-3); pyridine: 126.8 (β-C_{exo}), 129.3 (β-C_{endo}), 143.3 (α-C_{exo}), 143.9 (γ-C), 147.6 (α-C_{endo}) ppm.[23]

Synthesis of [(Cyclopentadienyl){*P*,*P*,*P*-triphenyl-*P*-[η^4-(1′*Z*,2′*Z*,3′*E*)-1′,2′,3′-trimethylpenta-1′,3′-dienyl]phosphonium}-cobalt] Tetrafluoroborate ([8]BF_4): Triphenylphosphane (3.67 g, 14 mmol) in CH_2Cl_2 (50 mL) was added to [**3**]BF_4 (640 mg, 2.00 mmol) in CH_2Cl_2 (10 mL) at –60 °C. The reaction mixture was warmed to ambient temperature overnight. The solution was concentrated to a small volume (ca.10 mL) and THF (100 mL) was added. A raw product precipitated, which was purified by re-precipitation from CH_2Cl_2 solution to give [**8**]BF_4 (1.14 g, 98%) as a dark red powder; m.p. 145 °C, dec. 150 °C. $C_{31}H_{33}BCoF_4P$ (582.30): calcd. C 63.94, H 5.71; found C 64.00, H 5.70. ^1H NMR (500 MHz, CD_2Cl_2): δ = 0.85 (d, J = 6.4 Hz, 4-Me), 1.24 (q, J = 6.4 Hz, 4-H), 1.34 (d, $^3J_{PH}$ = 16.2 Hz, 1-Me), 1.83 (s, 3-Me), 2.56 (d, $^4J_{PH}$ = 2.4 Hz, 2-Me), 4.76 (s, Cp); PPh_3: 7.63 (m, α-H), 7.73 (m, β-H), 7.75 (m, γ-H) ppm. $^{13}C\{^1H\}$ NMR (126 MHz, CD_2Cl_2): δ = 14.9 (3-Me), 17.5 (2-Me), 18.4 (4-Me), 29.0 (C-1) 30.0 (d, $^2J_{PC}$ = 12.4 Hz, 1-Me), 52.1 (C-4), 85.2 (Cp), 92.3 (C-2), 97.3 (C-3); PPh_3: 122.4 (d, $^1J_{PC}$ = 80.6 Hz, C_i), 129.9 (d, $^2J_{PC}$ = 11.5 Hz, C_o), 134.0 (d, $^3J_{PC}$ = 8.6 Hz, C_m), 134.2 (d, $^4J_{PC}$ = 2.8 Hz, C_p) ppm. $^{13}C\{^1H\}$ NMR (50 MHz, CD_2Cl_2): δ = 14.8 (3-Me), 17.4 (d, $^3J_{PC}$ = 2.75 Hz, 2-Me), 18.3 (4-Me), 29.4 (d, $^1J_{PC}$ = 46.0 Hz, C-1), 29.9 (d, $^2J_{PC}$ = 13.05 Hz, 1-Me), 52.0 (d, J_{PC} = 3.43 Hz, C-4), 84.9 (Cp), 92.0 (d, $^2J_{PC}$ = 1.48 Hz, C-2), 97.0 (d, $^3J_{PC}$ = 1.96 Hz, C-3); PPh_3: 122.1 (d, $^1J_{PC}$ = 80.23 Hz, C_i), 129.7 (d, $^2J_{PC}$ = 11.9 Hz, C_o), 133.8 (d, $^3J_{PC}$ = 8.45 Hz, C_m), 134.0 (d, $^4J_{PC}$ = 2.98 Hz, C_p) ppm. $P\{^1H\}$ NMR (202 MHz, CD_2Cl_2): δ = 25.91 (PPh_3) ppm.

Synthesis of [{1-(*tert*-Butylamino)-2,3,4,5-tetramethylcyclopentadienyl}(cyclopentadienyl)cobalt] Trifluoromethanesulfonate ([9]CF_3SO_3): A solution of [CpCoCb*] (**1**) (237 mg, 1.02 mmol) in CH_2Cl_2 (10 mL) was treated with CF_3SO_3H (90 μL, 1.02 mmol, d = 1.708 g·mL^{-1}) at –35 °C. After 5 min *tert*-butyl isocyanide (0.12 mL, 1.06 mmol, d = 0.736 g·mL^{-1}) was added to the solution of [**3**]CF_3SO_3 so obtained, resulting in an immediate color change from dark red to yellow. Addition of Et_2O (35 mL) and cooling to –80 °C overnight gave a yellow powder which was recrystallized from CH_2Cl_2 to afford analytically pure [**9**]CF_3SO_3 (430 mg, 90%) as yellow powder; m.p. 274–276 °C (dec.). $C_{19}H_{27}CoF_3NO_3S$ (465.42): calcd. C 49.03, H 5.85, N 3.01; found C 48.69, H 5.87, N 2.98. ^1H NMR (500 MHz, CD_3CN): δ = 1.41 (s, *t*Bu), 2.08 (s, 3-/4-Me), 2.26 (s, 2-/5-Me), 5.53 (s, Cp), 9.34 (s, N*H*) ppm. $^{13}C\{^1H\}$ NMR (126 MHz, CD_3CN): δ = 10.9 (3-/4-Me), 12.0 (2-/5-Me), 26.7 (C*Me*$_3$), 70.9 (*C*Me$_3$), 89.2 (Cp), 94.7 (C-2,5), 100.4 (C-3,4), 97.3 (C-1) ppm; in CD_2Cl_2 solution some C atoms were not observed.[23]

The System 5/(C_5H_5NH)CF_3SO_3 in the NMR Tube: A solution of **5** (22 mg, 0.095 mmol) in CD_2Cl_2 (0.8 mL) was added into an NMR tube containing [C_5H_5NH]CF_3SO_3 (21 mg, 0.095 mmol) at –80 °C. The reagents were mixed utilizing an ultrasonic bath at this temperature. ^1H NMR spectra were recorded after one, two, and three weeks at –80 °C. As some solid [C_5H_5NH]CF_3SO_3 had formed, the mixing process was repeated. After three weeks the product ratio was **5**:6^+:7^+:**1** = 0:93:5:2, and a good ^{13}C NMR spectrum of 6^+ could be recorded from this reaction mixture.

^{13}C NMR Data for 6^+: $^{13}C\{^1H\}$ NMR (50.3 MHz, CD_2Cl_2, –80 °C): δ = 13.2 (4-Me), 17.2 (Me), 24.2 (Me), 35.6 (1-Me), 49.3 (C-4), 82.7 (C-2), 83.8 (Cp), 87.8 (C-1), 100.0 (C-3); pyridine: 128.0 (β-C_{exo}), 128.3 (β-C_{endo}), 143.1 (α-C_{exo}), 144.0 (γ-C), 147.7 (α-C_{endo}) ppm; tentative and partial assignments by analogy to the case of 7^+.

Addition of Pyridinium Triflate to the Hexatriene Complex 5 and Synthesis of [7]CF_3SO_3: To a mixture of **5** (649 mg, 2.79 mmol) and (C_5H_5NH)CF_3SO_3 (640 mg, 2.79 mmol) was added pyridine (10 mL) and thereafter CH_2Cl_2 (15 mL). The reaction mixture was stirred for 1 h. Concentrating the solution and addition of Et_2O precipitated the raw product, which was purified by re-precipitation from CH_2Cl_2 solution to give [**7**]CF_3SO_3 (1.21 g, 94%) as spectroscopically pure, red, microcrystalline powder, with ^1H NMR spectroscopic data identical to those for [**7**]BF_4.

Pyridine/4-Picoline Exchange of [7]BF_4 and Synthesis of [10]BF_4: A sample of the pyridinium derivative [**7**]BF_4 (112 mg, 0.28 mmol) was dissolved in CH_2Cl_2 (10 mL) and 4-picoline (1 mL) was added with stirring. After 20 min the solution was concentrated to a small volume and Et_2O was added to precipitate the complex salts which were dried in a vacuum for 0.5 h. This procedure was repeated three more times to give a spectroscopically pure sample of [**10**]BF_4 (111 mg, 96%). ^1H NMR (200 MHz, CD_2Cl_2): δ = –0.36 (q, J = 6.1 Hz, 4-H), 1.17 (d, J = 6.1 Hz, 4-Me), 1.89 (s, 1-Me), 2.15 (s, 3-Me), 2.19 (s, 2-Me), 4.80 (s, Cp); 4-picoline: 2.48 (s, 4-Me), 7.27 (dd, J = 6.22, 1.95 Hz, α-H_{exo}), 7.48 (dd, J = 6.22, 1.46 Hz, β-H_{exo}), 7.75 (dd, J = 6.22, 1.95 Hz, α-H_{endo}), 9.13 (dd, J = 6.22, 1.46 Hz,

 © 2005 Wiley-VCH Verlag GmbH & Co. KGaA, Weinheim

β-H_{endo}) ppm; assignments by analogy with the assignments for [7]BF_4.

Nucleophilic Substitution of Pyridine in [7]BF_4 with Cyanide and Synthesis of (Cyclopentadienyl)[η⁴-(2*Z*,3*Z*,4*E*)-2,3,4-trimethylhexa-2,4-dienenitrile]cobalt (11): A solution of [7]BF_4 (395 mg, 0.99 mmol) in CH_2Cl_2 (10 mL) was mixed with a solution of $(Bu_4N)CN$ (531 mg, 1.98 mmol) in CH_2Cl_2 (10 mL) at –80 °C. The mixture was stirred and warmed to ambient temperature within 24 h. Then all volatiles were removed. The residue was extracted several times with a hexane/ether (4:1) mixture. The combined extracts were filtered through a layer of alumina (2 cm). Removal of the volatiles and crystallization from CH_2Cl_2/hexane at –80 °C yielded **11** (218 mg, 85%) as dark red crystalline solid; m.p. 90–91 °C, dec. 126 °C. $C_{14}H_{18}CoN$ (259.23): calcd. C 64.86, H 6.99, N 5.40; found C 64.92, H 7.08, N 5.37. ^{1}H NMR (500 MHz, CD_2Cl_2): δ = 1.33 (d, J = 6.1 Hz, 5-Me), 1.43 (s, 2-Me), 1.84 (q, J = 6.1 Hz, 5-H), 2.06 (s, 4-Me), 2.15 (s, 3-Me), 4.61 (s, Cp) ppm. ^{13}C{^{1}H} NMR (126 MHz, CD_2Cl_2): δ = 15.6 (4-Me), 16.2 (3-Me), 19.7 (5-Me), 24.2 (C-2), 25.7 (2-Me), 51.2 (C-5), 83.2 (Cp), 88.4 (C-3), 95.0 (C-4), 125.5 (C-1) ppm.[23] IR (CH_2Cl_2): $\tilde{\nu}$(CN) = 2183.0 cm^{-1}.

Synthesis of [(1-Amino-2,3,4,5-tetramethylcyclopentadienyl)(cyclopentadienyl)cobalt] Salts: a) Trifluoroacetic acid CF_3CO_2H (25 μL, d = 1.48 g·mL^{-1}, 0.33 mmol) was added to a solution of the nitrile complex **11** (30 mg, 0.11 mmol) in CD_2Cl_2 (0.7 mL). The color of the reaction mixture rapidly changed from dark red to lemon-yellow. Removal of the volatiles and precipitation from aqueous solution (10 mL) with NH_4PF_6 (57 mg, 0.33 mmol) gave, after recrystallization from CH_2Cl_2/Et_2O, [**12**]PF_6 (42 mg, 90%) as a yellow powder. b) A solution of HBF_4 in Et_2O (87 μL, 54%, d = 1.18 g·mL^{-1}, 0.636 mmol) was added to a solution of the nitrile complex **11** (55 mg, 0.212 mmol) in CH_2Cl_2 (10 mL). The color immediately changed to lemon-yellow and a precipitate formed within seconds. Ether (30 mL) was added to complete the precipitation. The solid was collected on a frit, thoroughly washed with diethyl ether, and reprecipitated several times from acetone/ether to yield [**12**]BF_4 (69 mg, 94%) as a yellow powder. $C_{14}H_{19}BCoF_4N$ (347.05): calcd. C 48.45, H 5.52, N 4.04; found C 48.39, H 5.59, N 4.13.

Data for [12]PF_6: ^{1}H NMR (500 MHz, CD_2Cl_2): δ = 1.98 (s, 3-/4-Me), 1.99 (s, 2-/5-Me), 4.25 (s, NH), 4.97 (s, Cp) ppm. ^{13}C{^{1}H} NMR (126 MHz, CD_2Cl_2): δ = 9.5 (3-/4-Me), 10.4 (2-/5-Me), 79.7 (C-2/-5), 85.6 (Cp), 92.4 (C-3/-4), 122.7 (C-1) ppm.[23]

Reaction of [7]CF_3SO_3 with Excess CF_3CO_2H and Formation of the Carbenoid Cation 13⁺: In an NMR tube a solution of [7]CF_3SO_3 (93 mg, 0.20 mmol) in CD_2Cl_2 (0.7 mL) was combined with CF_3CO_2H (109 μL, d = 1.48 g·mL^{-1}, 1.41 mmol) at ambient temperature and kept for several minutes. NMR spectra were then measured with a 500 MHz spectrometer at –20 °C. ^{1}H NMR (500 MHz, –20 °C, CD_2Cl_2): δ = 1.80 (s, 2-Me), 2.37 (d, J = 6.6 Hz, 4-Me), 2.53 (s, 1-Me), 2.56 (s, 3-Me), 3.13 (q, J = 6.6 Hz, 4-H), 5.36 (s, Cp) ppm. ^{13}C{^{1}H} NMR (126 MHz, –20 °C, CD_2Cl_2): δ = 11.5 (2-Me), 17.5 (3-Me), 20.0 (C-5 = 4-Me), 31.3 (1-Me), 77.6 (C-4), 88.7 (Cp), 100.3 (C-2), 117.3 (C-3), 288.4 (C-1) ppm.[23]

Synthesis of (Cyclopentadienyl)[(2–5-η)-(3*Z*,4*E*)-3,4-dimethylhexa-1,2,4-triene]cobalt (14): A large excess of CF_3CO_2H (3.1 mL, 40 mmol) was added to [7]BF_4 (2.02 g, 5.06 mmol) in CH_2Cl_2 (20 mL) at 0 °C. The mixture was stirred for 30 min and then added slowly to a slurry of alumina (ca. 30 g) in NEt_3/hexane (22 mL/80 mL) at 0°. After stirring for 30 min the orange-red solution was filtered with the help of a plug of alumina (2–3 cm). Removal of the volatiles in a vacuum left a red oil which was crystallized from a minimal amount of hexane at –80 °C overnight to give the hexatriene complex **14** (0.668 g, 57%) as red crystalline material; m.p. 30 °C. $C_{13}H_{17}Co$ (232.21): calcd. C 67.24, H 7.38; found C 67.01, H 7.26. ^{1}H NMR (500 MHz, CD_2Cl_2): δ = 0.50 (q, J = 6.45 Hz, 5-H), 1.31 (d, J = 6.47 Hz, 5-Me), 1.86 (s, 3-Me), 2.18 (s, 4-Me), 4.63 (s, Cp), 4.72 (d, J = 2.08 Hz, 1-H_{anti}), 4.88 (d, J = 2.08 Hz, 1-H_{syn}) ppm. ^{13}C{^{1}H} NMR (126 MHz, CD_2Cl_2): δ = 14.0 (4-Me), 16.9 (3-Me), 19.2 (5-Me), 49.6 (C-5), 72.4 (C-3), 83.2 (Cp), 97.2 (C-4), 97.3 (C-1), 171.9 (C-2) ppm.[23]

Synthesis of Bis(cyclopentadienyl)[μ-2(1–3-η):1(4,5-η)-(1*Z*,2*Z*,3*Z*)-1,2,3-trimethylpenta-2,4-dien-1-ylidene-1κ(*C*¹)]dicobalt(*Co–Co*)] (15): A solution of **5** (694 mg, 2.98 mmol) in toluene (15 mL) was heated to 110 °C for 4 d. Then all volatiles were removed in a vacuum leaving a black oily residue which was chromatographed on alumina (35-cm column) using hexane as eluent. Removal of the solvent afforded spectroscopically pure **15** (487 mg, 91%) as black microcrystalline solid; m.p. 67 °C. $C_{18}H_{22}Co_2$ (356.23): calcd. C 60.69, H 6.22; found C 61.28, H 6.25. ^{1}H NMR (500 MHz, CD_2Cl_2): δ = –0.43 (dd, $^2J_{5anti,5syn}$ = 1.1, $^3J_{4,5anti}$ = 10.01 Hz, 5-H_{anti}), 1.28 (s, 2-Me), 1.58 (dd, $^2J_{5anti,5syn}$ = 1.1, $^3J_{4,5syn}$ = 6.72 Hz, 5-H_{syn}), 2.00 (s, 3-Me), 2.59 (s, 1-Me), 3.05 (dd, $^3J_{4,5anti}$ = 10.01, $^3J_{4,5syn}$ = 6.72 Hz, 4-H), 4.60 [s, Cp(Co-2)], 4.87 [s, Cp(Co-1)] ppm. ^{13}C{^{1}H} NMR (126 MHz, CD_2Cl_2): δ = 14.5 (2-Me), 23.0 (3-Me), 26.8 (C-5), 30.5 (1-Me), 55.0 (C-4), 69.5 (C-3), 81.7 [Cp(Co-2)], 85.0 [Cp(Co-1)], 87.1 (C-2), 161.1(C-1) ppm.[23]

X-ray Crystal Structure Determinations: Suitable crystals of **5** were obtained by slow vacuum sublimation (40–50 °C, 1–2 days) as orange-red platelets. Crystallization of [7]CF_3SO_3 from acetone/ether afforded well-shaped red rods. Geometry and intensity data were collected with ENRAF-Nonius CAD4 diffractometers

Table 1. Crystal data, data collection parameters, and convergence results for **5** and [7]CF_3SO_3.

	5	[7]CF_3SO_3
Empirical formula	$C_{13}H_{17}Co$	$C_{19}H_{23}CoF_3NO_3S$
Formula mass	232.21	461.37
Crystal system	orthorhombic	monoclinic
Space group	$P2_12_12_1$ (no. 19)	$P2_1/n$ (no. 14)
a [Å]	8.945(3)	8.208(2)
b [Å]	9.2280(10)	16.585(2)
c [Å]	13.732(2)	15.663(4)
β [°]		101.28(2)
V [Å^3]	1133.5(4)	2091.0(8)
Z	4	4
$d_{calcd.}$ [g/cm^3]	1.361	1.466
F(000)	488	952
μ [mm^{-1}]	1.472	0.965
Absorption correction	empirical	empirical
Max./min. transmission	0.855/0.448	0.644/0.551
θ range [°]	2–27	2–27
Temperature [K]	223	223
Scan mode	ω	ω-2θ
Crystal size [mm]	0.65×0.50×0.11	0.7×0.7×0.5
Reflections collected	10810	12703
Reflections unique	2480	4565
Refls observed $I > 2\sigma(I)$	1944	3763
Variables	131	257
R_1[a], observed (all data)	0.0679 (0.0844)	0.0429 (0.0534)
wR_2[b], observed (all data)	0.1601 (0.1670)	0.1163 (0.1221)
GOF[c]	1.049	1.052
Max. resd. density (e/Å^3)	2.772 (0.8 Å from Co)	0.503

[a] $R_1 = \Sigma||F_o| - |F_c||/\Sigma|F_o|$. [b] $wR_2 = [\Sigma w(F_o^2 - F_c^2)^2/\Sigma w(F_o^2)^2]^{1/2}$, where $w = 1/[\sigma^2(F_o^2) + (aP)^2]$ and $P = [\max(F_o^2,0) + 2F_c^2]/3$. [c] GOF = $[\Sigma w(F_o^2 - F_c^2)^2/\Sigma(n - p)]^{1/2}$

 © 2005 Wiley-VCH Verlag GmbH & Co. KGaA, Weinheim

(graphite-monochromated Mo-K_α). Crystal data, data collection parameters, and convergence results for the compounds **5** and [**7**]-CF_3SO_3 are listed in Table 1. Note that the crystal of **5** turned out to be an inversion twin. CCDC-251060 (for **5**) and CCDC-251061 (for [**7**]CF_3SO_3) contain the supplementary crystallographic data for this paper. These data can be obtained free of charge from The Cambridge Crystallographic Data Centre via www.ccdc.cam.ac.uk/data_request/cif.

[1] M. V. Butovskii, U. Englert, G. E. Herberich, K. Kirchner, U. Koelle, *Organometallics* **2003**, *22*, 1989–1991.

[2] a) U. Koelle, *Inorg. Chim. Acta* **1981**, *47*, 13–18; b) R. Bruce, P. M. Maitlis, *Can. J. Chem.* **1967**, *45*, 2017–2022.

[3] A. Efraty, *Chem. Rev.* **1977**, *77*, 691–744.

[4] a) R. G. Amiet, R. Pettit, *J. Am. Chem. Soc.* **1968**, *90*, 1059–1060; b) M. Rosenblum, B. North, *J. Am. Chem. Soc.* **1968**, *90*, 1060–1061; c) M. Rosenblum, B. North, D. Wells, W. P. Gierig, *J. Am. Chem. Soc.***1972**, *94*, 1239–1246; d) P. E. Riley, R. A. Davis, *J. Organomet. Chem.* **1976**, *113*, 157–166.

[5] a) A. Nakamura, N. Hagihara, *Bull. Chem. Soc. Jpn.* **1961**, *34*, 452–453; b) M. D. Rausch, R. A. Genetti, *J. Am. Chem. Soc.* **1967**, *89*, 5502–5503; c) M. D. Rausch, R. A. Genetti, *J. Org. Chem.* **1970**, *35*, 3888–3897.

[6] G. E. Herberich, A. K. Naithani, *J. Organomet. Chem.* **1983**, *241*, 1–14.

[7] a) M. Crocker, M. Green, K. R. Nagle, A. G. Orpen, H.-P. Neumann, C. E. Morton, C. J. Schaverien, *J. Chem. Soc. Chem. Commun.* **1984**, 1351–1353; b) M. Crocker, M. Green, K. R. Nagle, A. G. Orpen, H.-P. Neumann, C. E. Morton, C. J. Schaverien, *Organometallics* **1990**, *9*, 1422–1434; c) K. Mauthner, K. M. Soldouzi, K. Mereiter, R. Schmid, K. Kirchner, *Organometallics* **1999**, *18*, 4681–4683.

[8] a) E. Rüba, K. Mereiter, R. Schmid, K. Kirchner, E. Bustelo, M. C. Puerta, P. Valerga, *Organometallics* **2002**, *21*, 2912–2920; b) C. Ernst, O. Walter, E. Dinjus, *J. Organomet. Chem.* **2001**, *627*, 249–254.

[9] a) R. J. Deeth, S. J. Dossett, M. Green, M. F. Mahon, S. J. Rumble, *J. Chem. Soc. Chem. Commun.* **1995**, 593–595; b) S. J. Dossett, M. Green, M. F. Mahon, J. M. McInnes, *J. Chem. Soc. Chem. Commun.* **1995**, 767–768.

[10] A. Fries, M. Green, M. F. Mahon, T. D. McGrath, C. B. M. Nation, A. P. Walker, C. M. Woolhouse, *J. Chem. Soc. Dalton Trans.* **1996**, 4517–4532.

[11] F. Biasotto, M. Etienne, F. Dahan, *Organometallics* **1995**, *14*, 1870–1874.

[12] a) J. R. Morrow, T. L. Tonker, J. L. Templeton, *J. Am. Chem. Soc.* **1985**, *107*, 5004–5005; b) S. G. Feng, A. S. Gamble, J. L. Templeton, *Organometallics* **1989**, *8*, 2024–2031; c) W.-Y. Yeh, S.-M. Peng, L.-K. Liu, *Inorg. Chem.* **1993**, *32*, 2965–2967.

[13] a) C. G. Kreiter, *Angew. Chem.* **1968**, *80*, 402; *Angew. Chem. Int. Ed. Engl.* **1968**, *7*, 390; b) H. Fischer, F. R. Kreissl, U. Schubert, P. Hofmann, K. H. Dötz, K. Weiss, *Transition Metal Carbene Complexes*, VCH Publishers, Weinheim, Germany, **1984**.

[14] a) G. C. Conole, M. Green, M. McPartlin, C. Reeve, C. M. Woolhouse, *J. Chem. Soc. Chem. Commun.* **1988**, 1310–1313; b) M. Green, M. F. Mahon, K. C. Molloy, C. B. M. Nation, C. M. Woolhouse, *J. Chem. Soc. Chem. Commun.* **1991**, 1587–1588; c) E. Becker, K. Mereiter, M. Puchberger, R. Schmid, K. Kirchner, *Organometallics* **2003**, *22*, 2124–2133.

[15] A. L. Spek, *Acta Crystallogr. Sect. A* **1990**, *46*, C34.

[16] a) C. E. Kerr, B. E. Eaton, J. A. Kaduk, *Organometallics* **1995**, *14*, 269–273; b) S. P. Saberi, S. E. Thomas, *J. Chem. Soc.Perkin Trans. 1* **1992**, 259–265; c) L. S. Trifonov, A. S. Orahovats, R. Prewo, H. Heimgartner, *Helv. Chim. Acta* **1988**, *71*, 551–561.

[17] M. Murakami, K. Itami, Y. Ito, *Organometallics* **1999**, *18*, 1326–1336.

[18] a) M. L. H. Green, A. K. Hughes, *J. Chem. Soc. Dalton Trans.* **1992**, 527–536; b) S. C. Dunn, P. Mountford, D. A. Robson, *J. Chem. Soc. Dalton Trans.* **1997**, 293–304; c) S. C. Dunn, P. Mountford, O. V. Shishkin, *Inorg. Chem.* **1996**, *35*, 1006–1012.

[19] L. Brandt, M. Green, A. W. Parkins, *Angew. Chem.* **1990**, *102*, 1062–1064; *Angew. Chem. Int. Ed. Engl.* **1990**, *29*, 1046–1048.

[20] F. H. Allen, *Acta Crystallogr.Sect. B* **2002**, *58*, 380–388.

[21] With a single bond between C (total coordination number four, bonded to at least one transition metal and at least one other carbon atom) and N (total coordination number three) resulted in 692 hits (coordinates available, no disorder, $R < 0.1$, error-free).

[22] J. A. King, Jr., K. P. C. Vollhardt, *J. Organomet. Chem.* **1994**, *470*, 207–222.

[23] For these spectra all assignments are based on relative intensities and on various 2D NMR techniques.

Received: October 4, 2004

 © 2005 Wiley-VCH Verlag GmbH & Co. KGaA, Weinheim

Dioxovanadium(V) Complexes of ONO Donor Ligands Derived from Pyridoxal and Hydrazides: Models of Vanadate-Dependent Haloperoxidases

Mannar R. Maurya,*[a] Shalu Agarwal,[a] Cerstin Bader,[b] and Dieter Rehder*[b]

Keywords: Vanadium / Hydrazones / Catalytic bromination / Pyridoxal

Figure 1 has been depicted twice in the original article (as Figure 1 and Figure 5).[1] For the correct Figure 5, see below.

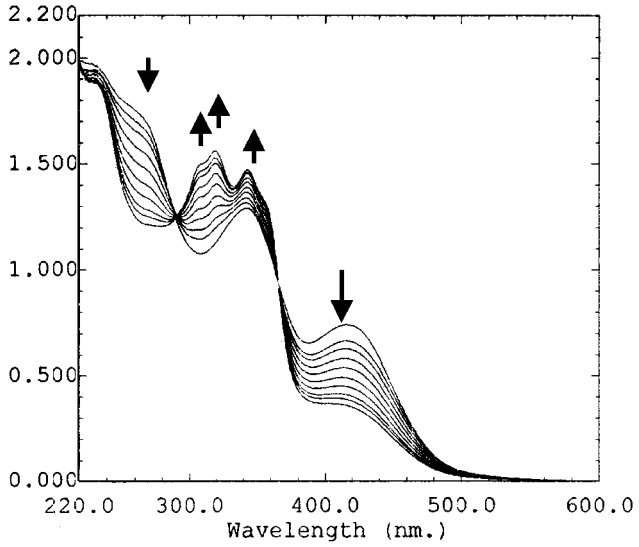

Figure 5. Titration of $[K(H_2O)_2][VO_2(pydx\text{-}bhz)]$ (**8**) with a saturated solution of HCl in MeOH; the spectra were recorded after addition of 2-drops portions MeOH/HCl to 10 mL of ca. 10^{-4} M solution of **8** in MeOH

[1] M. R. Maurya, S. Agarwal, C. Bader, D. Rehder, *Eur. J. Inorg. Chem.* **2005**, 147−157.

Received: January 18, 2005
The Editors

[a] Department of Chemistry, Indian Institute of Technology Roorkee,
Roorkee 247667, India
E-mail: rkmanfcy@iitr.ernet.in
[b] Institut für Anorganische und Angewandte Chemie, Universität Hamburg,
Martin-Luther-King-Platz 6, 20146 Hamburg, Germany
E-mail: dieter.rehder@chemie.uni-hamburg.de

 DOI: 10.1002/ejic.200500051 © 2005 Wiley-VCH Verlag GmbH & Co. KGaA, Weinheim

EurJIC
European Journal of Inorganic Chemistry

Issue 6/2005

Pages 985–1192

Papers available ahead of print in Early View at www.interscience.wiley.com

Earliest available Table of Contents:
Automatically, free of charge by e-mail through
www.interscience.wiley.com/alerts

COVER PICTURE

The cover picture shows a high-yield, one-step synthesis of end-on bridged dinuclear titanium–dinitrogen complexes using Cp^*TiCl_3, N_2 and pentafulvenes under reductive conditions. The Cp* as well as the fulvene ligands are arranged in a stereoregular manner along the Ti–N≡N–Ti axis, both in the solid state as well as in solution, as proved by extensive NMR measurements. Details are discussed in the article by R. Beckhaus et al. on p. 1003ff. In a similar way a nitrogen-free, low-coordinated titanium complex is obtained by using sterically demanding benzofulvenes. We thank the Fonds der Chemischen Industrie for a kindly granted scholarship (A. S.).

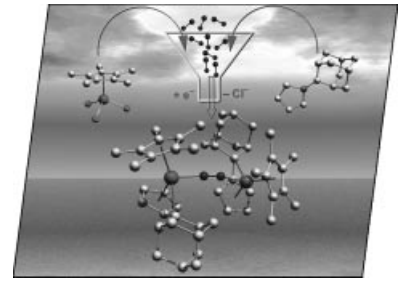

SHORT COMMUNICATION

Contents

999 **Laurent Bénisvy, J.-C. Chottard, J. Marrot, Y. Li***

Iron-Assisted Oxidative Radical C–C Bond Cleavage

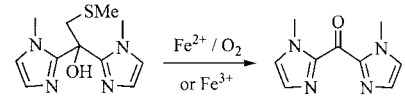

Keywords: Iron / Multidentate ligand / Imidazole ligand / Thioether ligand / Radical fragmentation / X-ray diffraction

 © 2005 Wiley-VCH Verlag GmbH & Co. KGaA, Weinheim

FULL PAPERS

1003 **A. Scherer, K. Kollak, A. Lützen, M. Friedemann, D. Haase, W. Saak, R. Beckhaus***

Low-Valent Titanium−Pentafulvene Complexes − Formation of Dinuclear Titanium−Nitrogen Complexes

Keywords: Titanium / Bridging ligands / Nitrogen / Metallocenes / Fulvene ligands

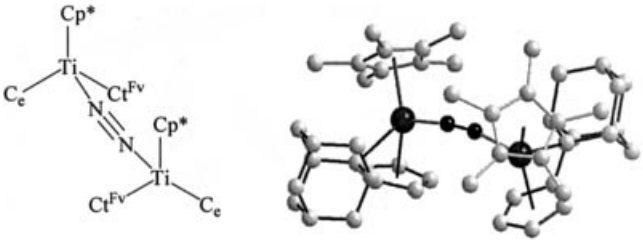

1011 **D. Lucas,* F. Lemaître, B. Gallego-Gómez, C. Cugnet, P. Richard, Y. Mugnier, P. D. Harvey***

New Insights into the Stoichiometric and Catalytic Reactivity of Unsaturated $Pd_3(dppm)_3$-CO^{n+} Clusters (n = 0, 1) Towards Halocarbons − First Evidence for Inorganic By-Products

Keywords: Palladium cluster / Alkyl halide / Reduction / Electrocatalysis / Alkyl radicals

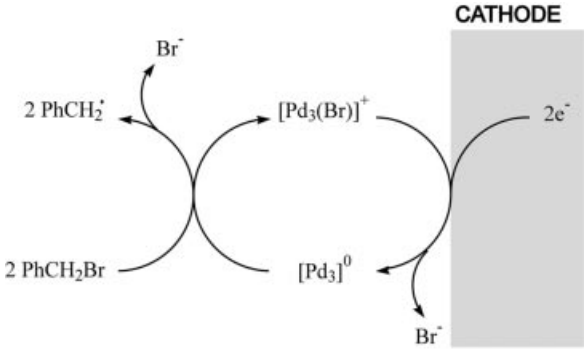

1019 **E. Iengo, E. Zangrando, E. Baiutti, F. Munini, E. Alessio***

Synthesis and Structural and Spectroscopic Characterization of New Ru^{II}-dmso Precursors with Face-Capping Ligands for Use in Self-Assembly Reactions

Keywords: Facial coordination / Ruthenium / Self-assembly / Tridentate ligands / Tripodal ligands

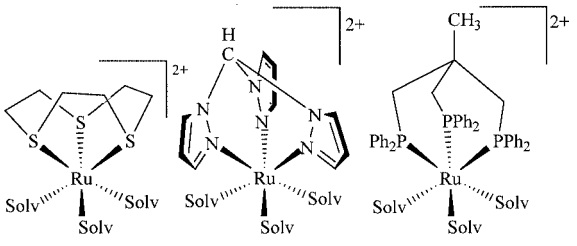

Solv = dmso or H_2O

1032 **J.-M. Barbe,* F. Burdet, E. Espinosa, R. Guilard***

Synthesis and Physicochemical Characterization of Bis(macrocycles) Involving a Porphyrin and a *meso*-Substituted Corrole − X-ray Crystal Structure of a [(Free-base porphyrin)−corrole]-bis(pyridine)cobalt Complex

Keywords: Bis(macrocycles) / Porphyrins / Corroles / Synthetic methods / X-ray diffraction

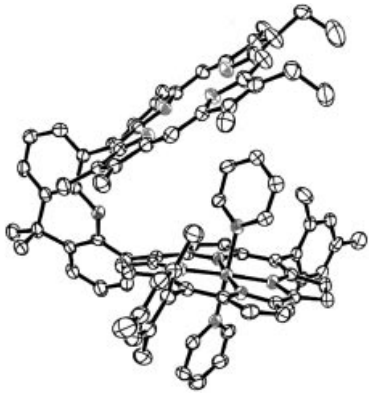

 © 2005 Wiley-VCH Verlag GmbH & Co. KGaA, Weinheim

1042 **A. Uslu,* S. J. Coles, D. B. Davies, R. J. Eaton, M. B. Hursthouse, A. Kılıç, R. A. Shaw**

Stereoisomerism in Pentaerythritol-Bridged Cyclotriphosphazene Tri-Spiranes: Spiro and Ansa 1,3-Propanediyldioxy Disubstituted Derivatives

Keywords: Cyclotriphosphazene derivatives / Tri-spiranes

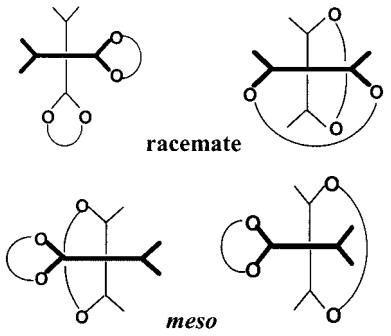

1048 **R. C. Jones, R. L. Madden, B. W. Skelton, V.-A. Tolhurst,* A. H. White, A. M. Williams, A. J. Wilson, B. F. Yates**

Solution, Structural and Catalytic Studies of Neutral MCl_2 (M = Pd, Pt) Complexes of the N/E Mixed-Donor Ligands 2-$(RECH_2)C_5H_4N$ (RE = MeS, PhS, MeSe)

Keywords: Palladium / Platinium / N,S ligands / Homogeneous catalysis / Fluxional processes

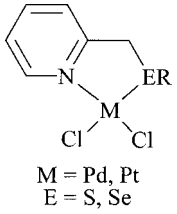

1056 **W. Uhl,* A. El-Hamdan, A. Lawerenz**

Investigations into the Reactivity of Organoelement Gallium and Indium Subhalides − Syntheses of Digallium and Diindium Acetylacetonates

Keywords: Gallium / Indium / Subvalent compounds / Acetylacetonate ligands

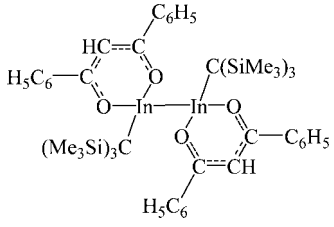

1063 **Z. Janas,* L. B. Jerzykiewicz, K. Przybylak, P. Sobota, K. Szczegot, D. Wiśniewska**

Titanium Complexes of Chelating, Dianionic O,S,O-Bisphenolato Ligands: Syntheses, Characterisation, and Catalytic Activity

Keywords: Polymerization / Titanium / O,S ligands

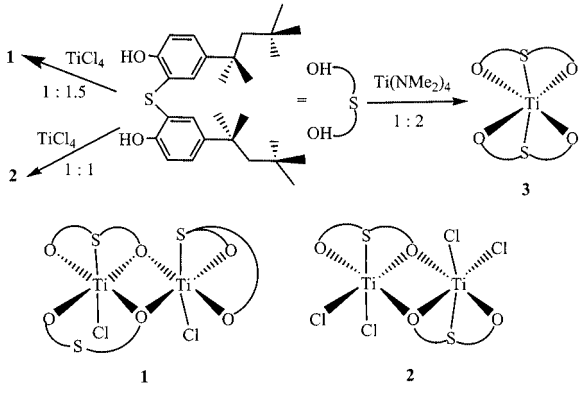

1071 **C. Vedder, F. Schaper, H.-H. Brintzinger,* M. Kettunen, S. Babik, G. Fink**

Chiral Iron(II) and Cobalt(II) Complexes with Biphenyl-Bridged Bis(pyridylimine) Ligands − Syntheses, Structures and Reactivities

Keywords: Iron(II) / Cobalt(II) / Bianiline / Pyridylimine

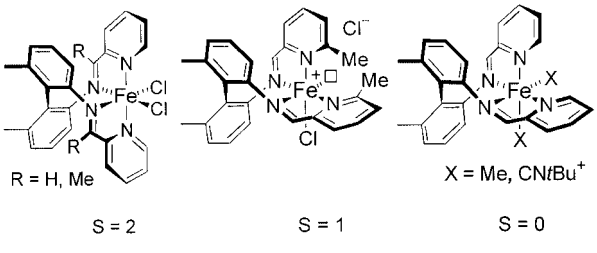

 © 2005 Wiley-VCH Verlag GmbH & Co. KGaA, Weinheim

1081 **M. Kettunen, C. Vedder, H.-H. Brintzinger, I. Mutikainen, M. Leskelä, T. Repo***

Alternative Coordination Modes in Palladium(II)-Diimino-Bispyridine Complexes with an Axially Chiral Biphenyl Backbone

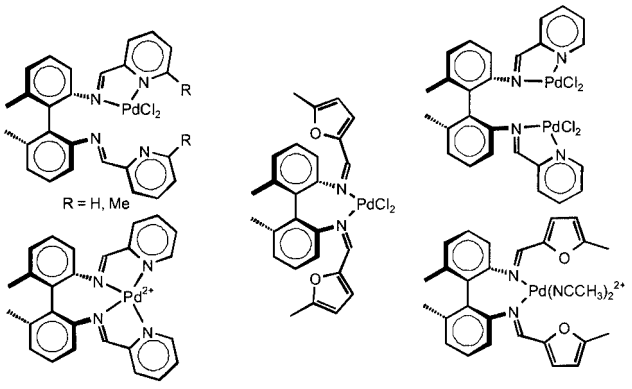

Keywords: Chiral biaryl ligands / Palladium imino complexes / Binuclear complexes

1090 **M. L. Cole, G. B. Deacon,* P. C. Junk, K. Konstas, P. W. Roesky**

Novel Mercury Phosphanylamides

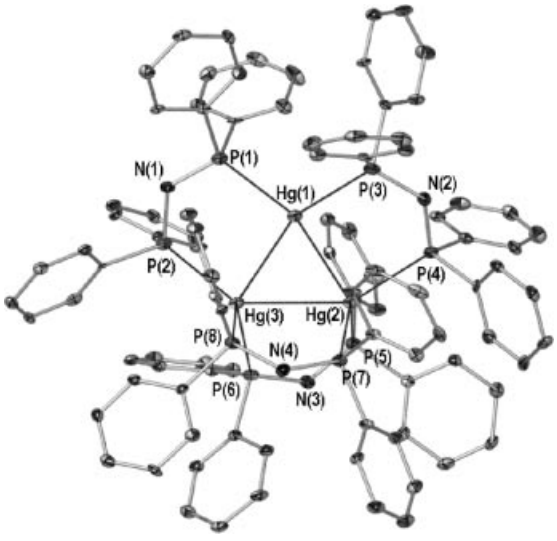

Keywords: Mercury / Redox transmetallation / Phosphanylamide ligands / Subvalent complexes / P Donors

1099 **K. Knabel, T. M. Klapötke, H. Nöth,* R. T. Paine, I. Schwab**

A Bicyclic P−P-Bridged 1,3,2,4-Diphosphadiboretane Cation and an Imino(phosphinidene)-borane−$AlBr_3$ Adduct

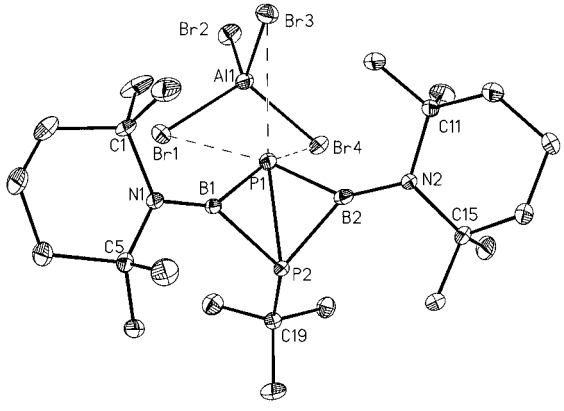

Keywords: 1,3-Di(*tert*-butyl)-2,4-bis(2,2,6,6-tetramethylpiperidino)-1,3,2,4-diphosphadiboretane / 1-*tert*-Butyl-2,4-bis(2,2,6,6-tetramethylpiperidino)-1,3-diphospha-2,4-diborabicyclo[1.1.0]butane cation / 2,2,6,6-Tetramethylpiperidino-*tert*-butylphosphinideneborane−$AlBr_3$ adduct / X-ray structures / ab initio calculations

 © 2005 Wiley-VCH Verlag GmbH & Co. KGaA, Weinheim

1109 **G. C. Nemes, H. Ranaivonjatovo, J. Escudié,* I. Silaghi-Dumitrescu, L. Silaghi-Dumitrescu, H. Gornitzka**

A Surprisingly Stable 1-(Chlorosilyl)-2-phosphaethenyllithium Compound, $RCl_2SiC(Li)=PMes^*$

Keywords: Phosphaalkenes / (Chlorosilyl)phosphaethenyllithium / Chlorophosphasilaallene / Molecular modelling / Cation-π interaction

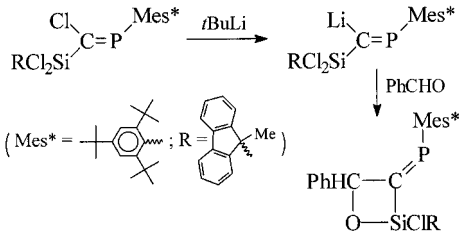

1114 **A. Panda, S. C. Menon, H. B. Singh,* C. P. Morley, R. Bachman, T. M. Cocker, R. J. Butcher**

Synthesis, Characterization and Coordination Chemistry of Some Selenium-Containing Macrocyclic Schiff Bases

Keywords: Macrocycles / Selena-aza macrocycles / Palladium / Nickel / Cobalt

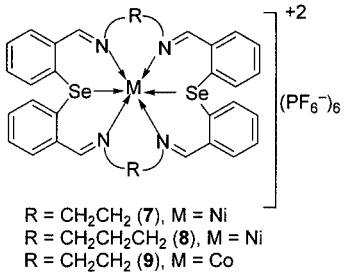

R = CH_2CH_2 (**7**), M = Ni
R = $CH_2CH_2CH_2$ (**8**), M = Ni
R = CH_2CH_2 (**9**), M = Co

1127 **P. A. Brayshaw, A. K. Hall, W. T. A. Harrison, J. M. Harrowfield,* D. Pearce, T. M. Shand, B. W. Skelton, C. R. Whitaker, A. H. White**

Structural Studies of Rare Earth/Transition Metal Complex Ion Systems as a Basis for Understanding Their Thermal Decomposition to Mixed Oxides

Keywords: Dipicolinates / Rare earths / Crystal structures / Mixed oxides / Thermochemistry

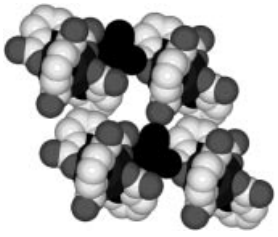

1142 **L. Vander Elst, I. Raynal, M. Port, P. Tisnès, R. N. Muller***

In vitro Relaxometric and Luminescence Characterization of P792 (Gadomelitol, Vistarem®), an Efficient and Rapid Clearance Blood Pool MRI Contrast Agent

Keywords: P792 / MRI contrast agent / NMRD / Luminescence / Oxygen-17 relaxometry

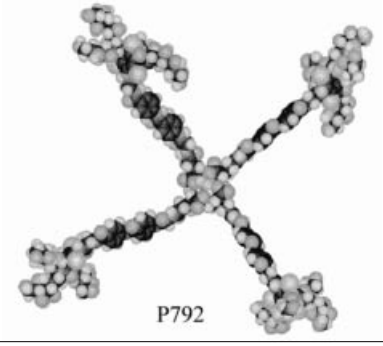

1149 **R. W. Saalfrank,* T. Nakajima, N. Mooren, A. Scheurer, H. Maid, F. Hampel, C. Trieflinger, J. Daub**

Syntheses and Properties of Metal-Centered Mixed-Valent $[NEt_4]\{Mn^{II}\subset[Mn^{II}_3Mn^{III}_3Cl_6(L)_6]\}$ Manganese Wheels

Keywords: Manganese clusters / Self-assembly / Mixed valency / X-ray diffraction / Cyclic voltammetry

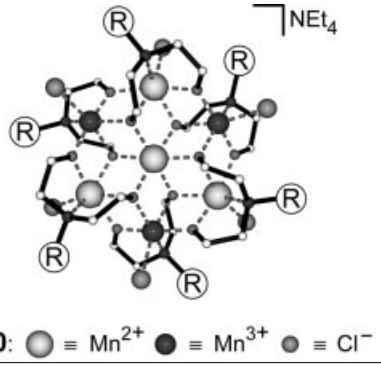

 © 2005 Wiley-VCH Verlag GmbH & Co. KGaA, Weinheim

1154 **G. Košová, S. Ernst, M. Hartmann, J. Čejka***

Incorporation of Aluminium and Iron into the Zeolite MCM-58

Keywords: Acidity / Aluminum / Iron / Kinetics / Zeolites

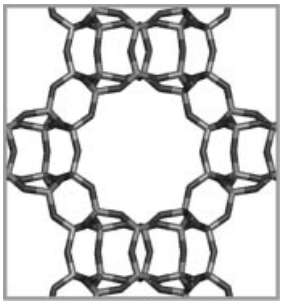

1162 **M. Rietjens,* P. A. Steenbergen**

Crosslinking Mechanism of Boric Acid with Diols Revisited

Keywords: Boric acid / Borate / Diols / Guaran / Crosslinking / Rheology

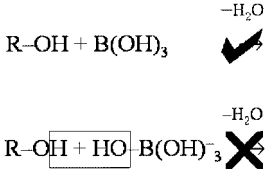

1175 **J. K. Eberhardt, T. Glaser,* R.-D. Hoffmann, R. Fröhlich, E.-U. Würthwein***

A Tetranuclear Hydroxo-Bridged Copper(II) Complex with Primary *N*-Acylamidines as Ligands: Preparation, Structural and Magnetic Characterisation

Keywords: *N*-Acylamidines / Copper(II) complexes / Magnetic susceptibility / N ligand / O ligand

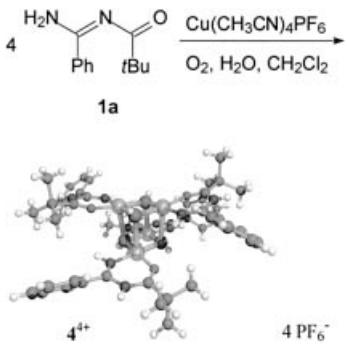

1182 **D. Yuan, Y. Xu, M. Hong,* W. Bi, Y. Zhou, X. Li**

A Novel Two-Dimensional Layer Structure Built from a Tetracobalt(II)-*p*-sulfonatothiacalix[4]-arene Cluster Unit

Keywords: *p*-Sulfonatothiacalix[4]arene / Cobalt / Magnetic properties / Coordination polymer

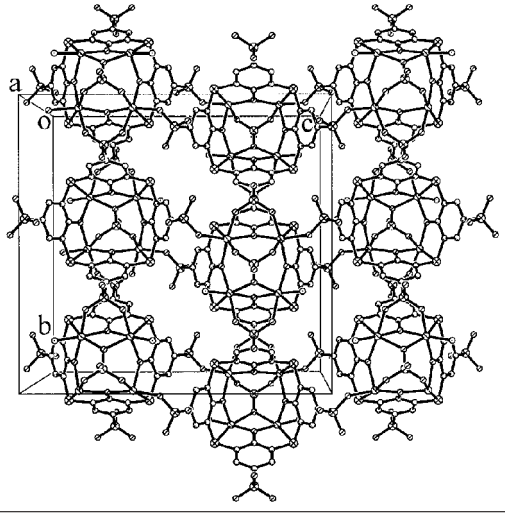

CORRECTION

1189 **M. A. Carreon, V. V. Guliants***

Ordered Meso- and Macroporous Binary and Mixed Metal Oxides

Keywords: Mesoporous / Macroporous / Transition metal oxides / Catalytic applications

 © 2005 Wiley-VCH Verlag GmbH & Co. KGaA, Weinheim

Iron-Assisted Oxidative Radical C–C Bond Cleavage

Laurent Bénisvy,[a,c] Jean-Claude Chottard,[a] Jérôme Marrot,[b] and Yun Li*[a]

Keywords: Iron / Multidentate ligand / Imidazole ligand / Thioether ligand / Radical fragmentation / X-ray diffraction

The N_2SO ligand, bis(*N*-methylimidazol-2-yl)-2-methylthioethanol (**L**), when coordinated to Fe^{3+} or Fe^{2+}, undergoes a radical C–C bond cleavage in air, to form bis(*N*-methylimidazol-2-yl) ketone (Me_2-BIK).

(© Wiley-VCH Verlag GmbH & Co. KGaA, 69451 Weinheim, Germany, 2005)

Introduction

Model complexes play an important role in the comprehension of mechanistic studies of metalloproteins. Iron complexes with polyimidazole and benzimidazole ligands are commonly used to mimic the active sites of various iron-containing proteins with histidine residues.[1,2] A variety of protein residues other than His also coordinate a metal ion in enzyme active sites. For example, a relatively unusual metal site [$N_2SM^{II}(H_2O)$] (N = Histidine, S = Cysteine, M = Zn, Co, Ni and Fe) is found in peptide deformylase (PDF).[3,4] Peptide deformylase (PDF) is responsible for the hydrolysis of an N-terminal formyl group during bacterial protein synthesis and has been under investigation as a new target for antibiotics. Our initial goal was to look at the coordination behavior of a mixed N,S,O multidentate ligand to Fe^{2+} or Fe^{3+}. However, because of the frustrating propensity of thiolato (RS^-) ligands to yield sulfur-bridged polymeric metal species and disulfide derivatives by radical coupling reactions, we chose to work with thioethers to avoid undesired side reactions. We have prepared the new tripodal N_2SO ligand, bis(*N*-methylimidazol-2-yl)-2-methylthioethanol (**L**, see Scheme 1), comprising donor atoms from *N*-methylimidazole, methylthioether and alcohol functionalities. **L** is an analogue of the previously reported N_2S ligands (N = imidazole, S = thiolate), that have been studied for Hg^{2+}, Cu^{2+}, Zn^{2+} and Fe^{2+} coordination.[5,6] These thiolato ligands presented both synthetic difficulties and the above-mentioned undesirable side reactions. In principle, **L** could coordinate to $Fe^{2+/3+}$ as a tridentate (N_2S or *NOS*), or as a bidentate (N_2 or *NO*). We have found that in aerated MeOH, in the presence of Fe^{2+} or Fe^{3+}, this ligand was converted into bis(*N*-methylimidazol-2-yl) ketone (Me_2-BIK). This reaction could be compared to the iron-catalyzed oxidations of bis(*N*-methylimidazol-2-yl)methanol (Me_2-BICOH)[7] and bis(*N*-methylimidazol-2-yl)methane (Me_2-BIM)[8] into Me_2-BIK. However, in the case of **L**, the formation of Me_2-BIK requires a carbon–carbon bond scission (Scheme 1).

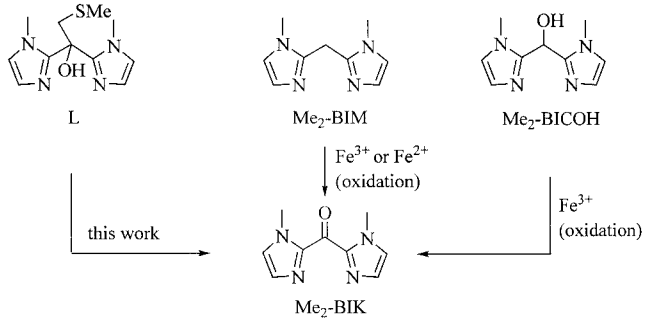

Scheme 1. Different pathways for the formation of Me_2-BIK.

Results and Discussion

The synthesis of **L** was straightforward and was achieved in only one step by condensation of the anion of *N*-methylimidazole with ethyl (methylthio)acetate ($MeSCH_2COOEt$).

Under argon, the reaction of **L** with $Fe(ClO_4)_2{\cdot}xH_2O$ in degassed MeOH in a 3:1 ratio, led to a pale-yellow Fe^{II} complex (EPR silent). Its cyclic voltammogram in MeOH clearly shows the formation of an Fe^{II} complex, as there is an irreversible oxidation peak at ca. 0.180 V (vs. Fc^+/Fc) (Figure S1, see Supporting Information). In the presence of air, the Fe^{II} complex oxidized into a yellow, paramagnetic Fe^{3+} species. Its EPR spectrum in MeOH at 10 K is typical of rhombic high-spin Fe^{3+} species (g = 4.25). The cyclic voltammogram of this yellow complex in MeOH exhibits an irreversible reduction wave at –0.62 V (vs. Fc^+/Fc), con-

[a] Laboratoire de Chimie et Biochimie Pharmacologiques et Toxicologiques (CNRS UMR8601), Université René Descartes, 45, Rue des Saints Pères, 75270 Paris Cedex 06, France
E-mail: yun.xu-li@univ-paris5.fr
[b] Institut Lavoisier, Université Versailles Saint-Quentin, 45, Avenue des Etats-Unis, 78035 Versailles, France
[c] Present address: Max-Planck Institut für Bioanorganische Chemie, Stiftstrasse 34-36, 45470 Mülheim, Germany
Supporting information for this article is available on the WWW under http://www.eurjic.org or from the author.

firming the +3 oxidation state (Figure S1 top, see Supporting Information). This yellow complex turned blue at room temperature. After several days, deep-blue crystals precipitated. The IR spectrum of the solid indicates the presence of a ketone function ($\nu_{C=O}$ = 1637 cm^{-1}). The cyclic voltammogram in CH_3CN solution shows a fully reversible one-electron oxidation process at $E_{1/2}$ = 0.44 V (vs. Fc^+/Fc) (Figure S2, see Supporting Information).

The X-ray structural determination of the blue complex revealed it to be $[Fe^{II}(Me_2\text{-}BIK)_3](ClO_4)_2$. The Me_2-BIK ligand resulted obviously from the fragmentation of the CH_2SMe arm during the oxidation of **L**. An ORTEP[9] view of the $[Fe(Me_2\text{-}BIK)_3]^{2+}$ cation at 298 K is shown in Figure 1. The unit cell includes eight mononuclear complex molecules. The iron is hexacoordinated in an N_6 environment with a distorted octahedral geometry. The six nitrogen donors originate from three Me_2-BIK molecules. The significant departure of the FeN_6 core from octahedral geometry is evidenced by the values of the bond angles, e.g. 83.91° for the N(26)–Fe–N(15) angle. The Fe–N distances range from 2.123 to 2.159 Å, clearly demonstrating that the iron is high-spin (HS, S = 2). For low-spin (LS, S = 0) octahedral $[Fe^{II}N_6]$ complexes, the average bond lengths are ca. 1.97 Å.[10] Moreover, the paramagnetism of $[Fe^{II}(Me_2\text{-}BIK)_3](ClO_4)_2$ was also observed in the ^{1}H NMR spectrum (250 MHz, CN_3CN, 300 K), which spread over the range from 17 to 4 ppm (see Experimental Section).

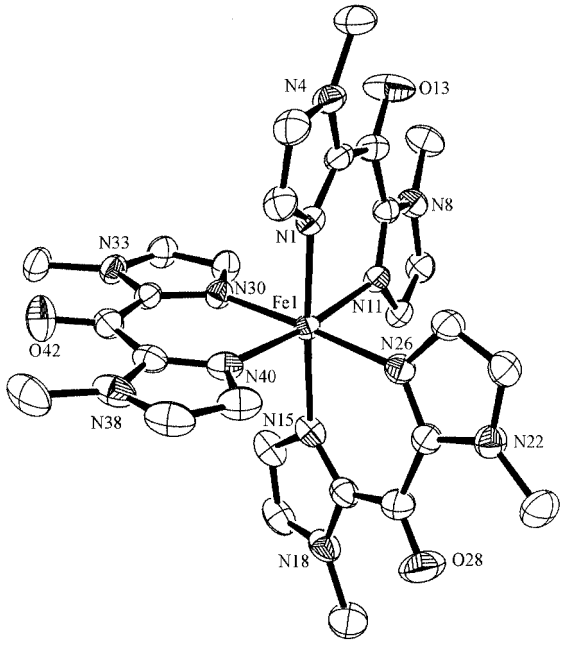

Figure 1. ORTEP view (ellipsoid at the 30% probability level) of $[Fe(Me_2\text{-}BIK)_3]^{2+}$. H atoms are omitted for clarity. Selected bond distances (Å): Fe–N(1) 2.143(2), Fe–N(11) 2.125(2), Fe–N(15) 2.159(3), Fe–N(26) 2.132(2), Fe–N(30) 2.140(2), Fe–N(40) 2.123(3). Selected bond angles (°): N(1)–Fe–N(11) 84.53(9), N(1)–Fe–N(26) 92.88(9), N(1)–Fe–N(15) 176.61(9), N(1)–Fe–N(40) 90.56(9), N(1)–Fe–N(30) 91.02(9), N(11)–Fe–N(26) 91.07(9), N(11)–Fe–N(15) 94.45(8), N(11)–Fe–N(40) 172.67(9), N(11)–Fe–N(30) 88.92(8), N(26)–Fe–N(15) 83.91(9), N(26)–Fe–N(40) 94.62(9), N(26)–Fe–N(30) 176.09(9), N(15)–Fe–N(40) 90.75(9), N(15)–Fe–N(30) 92.19(9), N(40)–Fe–N(30) 85.71(9).

It is well-known that some octahedral iron(II)-N_6 complexes exhibit temperature-dependent "spin-equilibrium" (LS ↔ HS) behavior. This active research area has been widely reviewed.[11] The spin-crossover property of $[Fe(Me_2\text{-}BIK)_3](BF_4)_2$, prepared classically from $Fe(BF_4)_2$ and 3 equiv. of Me_2-BIK[12] in CH_3CN, has been investigated earlier by Mössbauer spectroscopy in cooperation with our group.[13]

When Fe^{3+} or Fe^{3+}/Et_3N (3 equiv.) in MeOH were used instead of Fe^{2+}, the same cleavage reaction was observed. The addition of Et_3N accelerated the reaction and gave a better yield.

It has been previously reported that $[Fe(Me_2\text{-}BIK)_3]^{2+}$ was a side-product formed during the complexation of Fe^{3+} by the N_2OH ligand (Me_2-BICOH) (Scheme 1).[7] We have also found that Me_2-BIM was converted into Me_2-BIK by $Fe^{2+/3+}$ under oxygen upon base catalysis (Scheme 2).[8] A comparable reaction has been observed with Cu^{II}-catalyzed oxidation of *bis*(*N*-methylbenzimidazol-2-yl)methane and *bis*(2-pyridyl)methane into the corresponding ketones.[14,15] In all these cases, the ligands present "benzylic"-type oxidizable hydrogen atom(s), and the mechanism involves most likely the "benzylic" radicals. However, the mechanism ought to be different in the present instance, since the "benzylic" carbon is fully substituted.

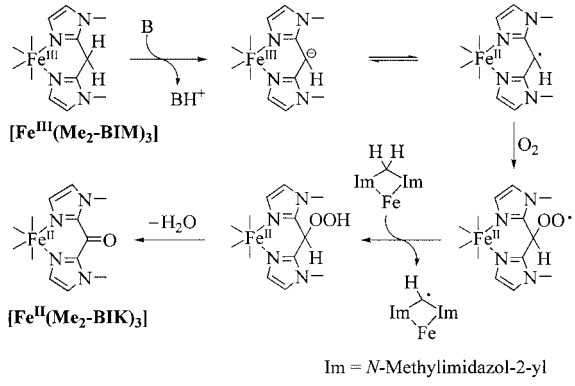

Scheme 2. Iron-assisted oxidation of Me_2-BIM into Me_2-BIK upon base catalysis (ref.[8]).

When the reaction was run under $^{18}O_2$ instead of air, no ^{18}O atom incorporation was found by electrospray mass spectroscopy. This result means that the oxygen atom in $[Fe^{II}(Me_2\text{-}BIK)_3]^{2+}$ comes from the ligand. We suggest a radical mechanism for this C–C bond fragmentation which involves the following sequence (Scheme 3): [1] oxidation of the very unstable Fe^{II} complex **1** by O_2 to generate the intermediate Fe^{III} complex **2** with a switch of ligand in the coordination sphere, in agreement with the preference of Fe^{III} for the alcoholate rather than the imidazole ligand; [2] homolytic C–C bond cleavage, forming the (methylthio) methyl radical, assisted by the homolytic fragmentation of the Fe^{III}–O bond, to give the corresponding ketone function. The (methylthio)methyl radical is stabilized by the presence of the sulfur atom in the α-position of the radical and dimerizes into $CH_3SCH_2CH_2SCH_3$. The latter was detected in the mother liquor after the reaction, by electro-

 © 2005 Wiley-VCH Verlag GmbH & Co. KGaA, Weinheim

spray MS (m/z = 123, M + H^+) and ^1H NMR spectroscopy ($CDCl_3$, δ = 2.653, and 2.151 ppm in a 2:3 ratio); the spectrum agreed with the literature data.[16] The driving force of the fragmentation likely results from the stability of $[Fe(Me_2\text{-BIK})_3]^{2+}$ ($E_{1/2}$ = +0.44 V vs. Fc^+/Fc, CH_3CN), as well as the relative stability of the thioether α-carbon radicals.

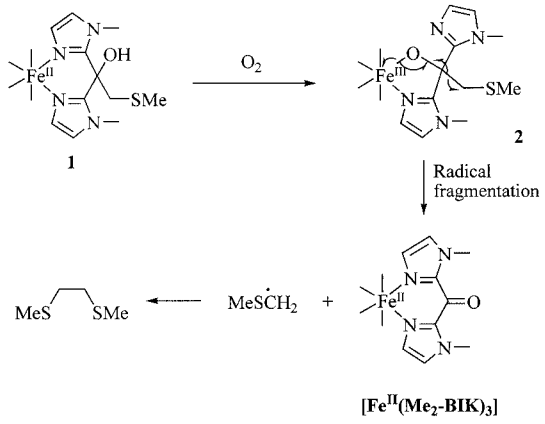

Scheme 3. Proposed iron-assisted radical fragmentation mechanism for the formation of Me_2-BIK.

Conclusion

This study has shown that whatever the substituents on the "benzylic" type bridge of the bis(*N*-methylimidazol-2-yl)methane core, either H/H, H/OH or OH/CH_2SMe, its Fe(III)-catalyzed oxidation takes an appropriate pathway to form bis(*N*-methylimidazol-2-yl) ketone (Me_2-BIK). To avoid this fragmentation, a new ligand with one more carbon in the side arm (CH_2CH_2SMe instead of CH_2SMe) was synthesized. Its complexation towards Fe^{2+} and Fe^{3+} is under investigation.

Experimental Section

Synthesis of Ligand L: A solution of *n*BuLi (1.6 M *in* hexane, 7.3 mL, 11.7 mmol) was added dropwise to a solution of *N*-methylimidazole (0.96 g, 11.7 mmol) in anhydrous THF (10 mL) cooled to 0 °C. After 30 min at 0 °C under argon, $MeSCH_2CO_2Et$ (0.5 mL, 520 mg, 3.9 mmol) was added dropwise to the yellow solution at 0 °C. The temperature was allowed to rise slowly to room temperature and maintained at room temperature for 1 night. The mixture was extracted with EtOAc (3 × 50 mL), and the combined organic layers were washed with saturated aq. NaCl (2 × 50 mL), dried ($MgSO_4$), and the solvents evaporated to dryness. The crude product was filtered through silica gel (MeOH-CH_2Cl_2-conc. aq. NH_3 = 5:95:0.25 as the eluent). The pale-yellow solid obtained was recrystallized from EtOAc/cyclohexane (1:1) to give **L** as colorless crystals (403 mg, 41%). M.p. (EtOAc/cyclohexane) 133 °C. MS (CI, NH_3): m/z = 253 (M + 1). ^1H NMR (250 MHz, $CDCl_3$): δ = 6.97 (s, 2 H, H_{im}), 6.80 (s, 2 H, H_{im}), 5.40 (s, 1 H, D_2O exchangeable, OH), 3.66 (S, 2 H, CH_2), 3.29 (s, 6 H, NMe), 1.92 (s, 3 H, SMe) ppm. ^{13}C NMR (63 MHz, $CDCl_3$): δ = 146.6 (C-2_{im}), 126.3 + 123.5 (C-4_{im} + C-5_{im}), 77.8 (C-OH), 44.6 (CH_2), 33.5 (NCH_3), 17.1 (SCH_3) ppm. $C_{11}H_{16}N_4OS$ (252.34): calcd. C 52.36, H 6.39, N 22.20, S 12.71; found: C 52.47, H 6.47, N 22.12, S 12.57.

$[Fe^{II}(Me_2BIK)_3](ClO_4)_2$: A solution of **L** (83 mg, 0.33 mmol) and $Fe^{II}(ClO_4)_2.xH_2O$ (37 mg, 0.11 mmol) in degassed MeOH (2.5 mL) was stirred under Ar. The initial pale-yellow solution turned yellow after 10 min at room temperature. Stirring was continued for 15 h, and the solvent was evaporated to dryness under reduced pressure. The yellow-brown solid was dissolved in MeOH (6 mL). Et_2O (12 mL) was carefully added to the surface of the MeOH solution, and the mixture was left unperturbed for 24 h. The blue precipitate was filtered, rinsed with Et_2O and vacuum-dried to afford $[Fe^{II}(Me_2BIK)_3](ClO_4)_2$ as a crystalline powder (40 mg, 44%). UV/Vis (CH_3CN): λ_{max} (ε) = 591 (4305), 329 (40200), 284 (21607), 236 nm (15185 $M^{-1}cm^{-1}$). IR [KBr (cm^{-1})]: 1637 (ν_{CO}). ^1H NMR (250 MHz, CD_3CN, 300 K): δ = 17.00 (1 H, H_{im}), 7.22 (3 H, NCH_3), 4.06 (1 H, H_{im}) ppm. $C_{27}H_{30}Cl_2FeN_{12}O_{11}$ (825.35): calcd. C 39.29, H 3.66, N 20.36; found: C 39.12, H 3.81, N 20.53.

To produce the crystals of $[Fe^{II}(Me_2BIK)_3](ClO_4)_2$, the same procedure was used without addition of Et_2O. The MeOH solution was kept at room temperature for 1 week and deep-blue single crystals suitable for X-ray diffraction were collected.

X-ray intensity data were collected on a Bruker X8-APEX2 CCD area-detector diffractometer using Mo-K_α radiation (λ = 0.71073 Å). Seven sets of narrow data frames were collected using 0.5° increments of ω or φ. Data reduction was accomplished with SAINT V7.03.[17] The substantial redundancy in the data allowed a semi-empirical absorption correction (SADABS V2.10)[17] to be applied, on the basis of multiple measurements of equivalent reflections. The structure was solved by direct methods, developed by successive-difference Fourier syntheses, and refined by full-matrix least-squares on all F^2 data using SHELXTL V6.12.[18] Hydrogen atoms were included in calculated positions and allowed to ride on their parent atoms.

Crystal Data for $[Fe^{II}(Me_2BIK)_3](ClO_4)_2$: $C_{27}H_{30}Cl_2FeN_{12}O_{11}$, M = 825.35, blue parallelepipeds, orthorhombic, space group *pbca*, a = 15.2718(3), b = 11.8490(2), c = 38.3903(7) Å, Z = 8, $\alpha = \beta = \gamma$ = 90.00°, V = 6946.9(2) $Å^3$, D_c = 1.578 $g\,cm^{-3}$, T = 298 K, Mo-K_α radiation (λ = 0.71073 Å), 95217 reflections were measured, 6373 independent reflections [5466 $I > 2\sigma(I)$] were used in all calculations. R = 0.0492, R_w = 0.1385. G.O.F. = 1.038.

CCDC-240407 contains the supplementary crystallographic data for this paper. These data can be obtained free of charge from The Cambridge Crystallographic Data Centre via www.ccdc.cam.ac.uk/data_request/cif.

Supporting Information (see also footnote on the first page of this article): cyclic voltammograms of **1**, **2** (Figure S1) and $[Fe^{II}(Me_2\text{-}BIK)_3](ClO_4)_2$ (Figure S2).

[1] E. Y. Tshuva, S. J. Lippard, *Chem. Rev.* **2004**, *104*, 987–1011.
[2] M. Costas, M. P. Mehn, M. P. Jensen, L. Que, *Chem. Rev.* **2004**, *104*, 939–986.
[3] M. K. Chan, W. M. Gong, P. T. R. Rajagopalan, B. Hao, C. M. Tsai, D. H. Pei, *Biochemistry* **1997**, *36*, 13904–13909.
[4] P. T. R. Rajagopalan, S. Grimme, D. H. Pei, *Biochemistry* **2000**, *39*, 779–790.
[5] J. M. Downes, J. Whelan, B. Bosnich, *Inorg. Chem.* **1981**, *20*, 1081–1086.
[6] V. V. Karambelkar, R. C. diTargiani, C. D. Incarvito, L. N. Zakharov, A. L. Rheingold, C. L. Stern, D. P. Goldberg, *Polyhedron* **2004**, *23*, 471–480.
[7] S. M. Gorun, S. J. Lippard, *Inorg. Chem.* **1988**, *27*, 149–156.

 © 2005 Wiley-VCH Verlag GmbH & Co. KGaA, Weinheim

[8] G. Guillot, E. Mulliez, P. Leduc, J. C. Chottard, *Inorg. Chem.* **1990**, *29*, 577–579.
[9] L. J. Farrugia, *J. Appl. Crystallogr.* **1997**, *30*, 565–565.
[10] E. Konig, *Prog. Inorg. Chem.* **1987**, *35*, 527–622.
[11] P. Gütlich, A. Hauser, *Angew. Chem. Int. Ed. Engl.* **1994**, *33*, 2024–2054.
[12] S. M. Gorun, G. C. Papaefthymiou, R. B. Frankel, S. J. Lippard, *J. Am. Chem. Soc.* **1987**, *109*, 4244–4255.
[13] A. Bousseksou, C. Place, J. Linares, F. Varret, *J. Magn. Magn. Mater.* **1992**, *104–107*, 225–226.
[14] C. A. Sprecher, A. D. Zuberbühler, *Angew. Chem. Int. Ed. Engl.* **1977**, *16*, 189–189.
[15] F. L. Urbach, U. Knopp, A. D. Zuberbühler, *Helv. Chim. Acta* **1978**, *61*, 1097–1106.
[16] R. C. Chambers, G. L. Hill, *J. Am. Chem. Soc.* **1990**, *112*, 8427–8433.
[17] APEX2 version 1.0-8, Bruker AXS, Madison, WI, **2003**.
[18] SHELXTL version 6.12, Bruker AXS, Madison, WI, **2001**.
Received: September 23, 2004

 © 2005 Wiley-VCH Verlag GmbH & Co. KGaA, Weinheim

Low-Valent Titanium–Pentafulvene Complexes − Formation of Dinuclear Titanium–Nitrogen Complexes

Axel Scherer,[a] Kay Kollak,[a] Arne Lützen,[a] Marion Friedemann,[a] Detlev Haase,[a] Wolfgang Saak,[a] and Rüdiger Beckhaus*[a]

Dedicated to Prof. Dr. Jan H. Teuben

Keywords: Titanium / Bridging ligands / Nitrogen / Metallocenes / Fulvene ligands

Sodium amalgam reduction of $[(\eta^5\text{-}C_5Me_5)TiCl_3]$ (**1**) in the presence of the pentafulvenes $\{C_5H_4{=}CR_2$, R: *p*-tol (**2**), *p*-FPh (**3**), CR_2: adamantyl (**4**)$\}$ under nitrogen smoothly produces dark green or dark blue dinuclear low-valent titanium complexes $[\{(\eta^5\text{-}C_5Me_5)Ti(\eta^6\text{-}C_5H_4{=}CR_2)\}_2(\mu_2,\eta^1,\eta^1\text{-}N_2)]$ {R: *p*-tol (**6**), *p*-FPh (**7**), CR_2: adamantyl (**8**)}, characterized by a bridging end-on coordinated dinitrogen ligand, in high yield. In the same way, the nitrogen-free, low-coordinated complex $[(\eta^5\text{-}C_5Me_5)Ti(\eta^6\text{-}C_9H_6{=}C(p\text{-tol})_2)]$ (**10**) is obtained by using the more sterically demanding benzofulvene $C_9H_6{=}C(p\text{-tol})_2$ (**5**) instead of **2**–**4**. The solid-state structures of the dinitrogen compounds reveal weakly activated end-on bound N_2 ligands with identical N–N distances of 1.160(3) Å (**6**) and 1.160(5) Å (**8**). The dinitrogen complexes **6**, **7** and **8** show diamagnetic behaviour, which allowed a complete NMR spectroscopic characterization. So a correlation between the situation in solution, measured by NMR, and in the solid state (X-ray diffraction) becomes possible and shows a congruent picture. A broad range of reactions can be imagined concerning the easily replaceable dinitrogen ligand as well as the known reactivity of fulvene ligands in complexes of early transition metals.
(© Wiley-VCH Verlag GmbH & Co. KGaA, 69451 Weinheim, Germany, 2005)

Introduction

Low-valent titanium complexes are of great importance in the complexation and activation of molecular nitrogen. Different bonding modes are found in early transition metals, depending on the nature of the other ligands.[1–5] Titanocene- as well as zirconocene-based systems have been and are still being extensively investigated. It was found that the cyclopentadienyl substituent patterns have a strong influence on the N_2 coordination and activation modes.[6–11] In such a way, for example, the permethylated $[(\eta^5\text{-}C_5Me_5)_2Zr]$ fragment coordinates the N_2 molecules by end-on bridging as well as in a terminal mode.[12–14] On the other hand, using the tetramethylcyclopentadiene ligand instead of the pentamethyl derivative, a side-on bridging coordination mode, characterized by an efficient N_2 activation, is found.[15,16] Results like this initiated further studies in order to obtain a detailed understanding of the field of N_2 activation reactions. In addition to the metallocene-based systems, Cp alternatives based on multidentate anionic ligands bearing N, O and P donor atoms were successfully used in order to obtain nitrogen complexes.[17–25] It was also shown that the introduction of nitrogen into organic substrates becomes possible under reductive conditions.[26–29]

Recently we were able to demonstrate that pentafulvene complexes of early transition metals are easily available from the reaction of titanium halides, reducing agents (Mg, Na/Hg), and free pentafulvenes.[30] Using fulvenes exhibiting asymmetric exocyclic carbon centres, a diastereoselective complexation of the fulvene ligand at different cyclopentadienyltitanium fragments is possible.[31]

Here we wish to report the one-step formation of dinitrogen-containing titanium complexes by reactions of $[(\eta^5\text{-}C_5Me_5)TiCl_3]$ (**1**) with the pentafulvenes **2**, **3**, **4** and Na/Hg as reducing agent in the presence of dinitrogen. Using the bulky benzofulvene **5**, a low-coordinated mononuclear titanium compound is formed.

Results and Discussion

Treatment of a THF solution of equimolar amounts of $[(\eta^5\text{-}C_5Me_5)TiCl_3]$ (**1**) [Equation (1)] and **2**, **3**, or **4** with three equivalents of Na (20% Na/Hg) under nitrogen leads to intensely coloured solutions. After removal of

[a] Institut für Reine und Angewandte Chemie, Fakultät für Mathematik und Naturwissenschaften, Carl von Ossietzky Universität Oldenburg,
Postfach 2503, 26111 Oldenburg, Germany
Fax: +49-441-798-3581
E-mail: ruediger.beckhaus@uni-oldenburg.de
Supporting information for this article is available on the WWW under http://www.eurjic.org or from the author.

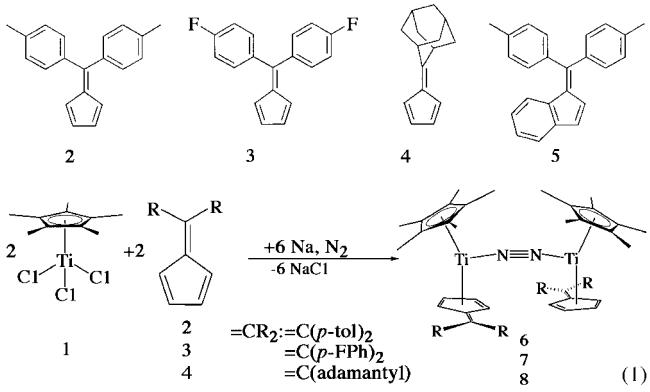

the solvent, addition of *n*-hexane to the residue and separation from the insoluble NaCl and mercury by filtration, **6**, **7**, and **8** can be isolated as dark green (**6**, **7**) or dark blue (**8**) crystals showing a fascinating cupric lustre. All complexes were isolated in high yields (**6**, **8** 90%; **7** 80%). It is also possible to use magnesium as the reducing agent, but the products could only be isolated in lower yields (40%), because the formation of $MgCl_2$ containing adducts with the dinitrogen complexes made it difficult to separate $MgCl_2$ quantitatively. All three dinitrogen complexes are thermally stable; melting points are found at 125 °C (**6**), 138–140 °C (**7**), and 175 °C (**8**). They are easily soluble in inert solvents like ethers and saturated or aromatic hydrocarbons.

Suitable crystals for X-ray diffraction were obtained from *n*-hexane/toluene (1:1) (**6**) or *n*-hexane (**8**) solutions at ambient temperature. In the case of **6** the asymmetric unit contains a disordered *n*-hexane molecule, which was refined on 3 positions (1/3, 1/3, 1/3) in idealised geometry; **8** shows two independent molecules in the asymmetric unit. Figure 1 and Figure 2 show ORTEP plots of the molecules with 50% probability ellipsoids, the hydrogen atoms, solvent molecules and the second molecule in the asymmetric unit (**8**) are omitted for clarity. Due to similarities of the structural values, we will limit our discussion mainly on the data of molecule one (Ti1, Ti2). Selected structural data are given in Table 1 and Table 2. The dinuclear structures consist of two [(η^5-C_5Me_5)(η^6-C_5H_4=CR_2)Ti] moieties bridged by N_2 in an almost linear Ti–N≡N–Ti arrangement. However, a deviation from linearity of about 9–10° was found (**6** Ti1–Ti2–N2 9.4°, Ti2–Ti1–N1 9.0°; **8** Ti1–Ti2–N2 9.9°, Ti2–Ti1–N1 10°). In accordance with this observation, the Ti–N–N angles were found to be slightly smaller than 180° [**6** 171.0(2)°, 169.1(2)°; **8** 170.0(4)°, 169.6(4)°]. These values correspond well to the lower range of values found in comparable μ_2,η^1,η^1-N_2 titanium complexes (168–180°, Table 1). The N–N bond lengths of 1.160(3) Å (**6**) and 1.160(5) Å (**8**) are also consistent with a just slightly activated N_2 molecule, since the N–N distance is not significantly different from that of free N_2 (1.0976 Å[32]). Thus, these values are in good agreement with metallocene type dinitrogen–titanium complexes (Table 1). Also, the Ti–N bond lengths are in the range of end-on coordinated dinitrogen–titanocene complexes [**6** 1.997(3), 2.001(3) Å; **8** 2.012(4), 2.003(4) Å]. Only in non-titanocene–nitrogen complexes derived from titanium amides are shorter Ti–N and longer N–N bonds found (Ti–N av. 1.72–1.76 Å, N–N 1.26–1.29 Å[17,24,25]).

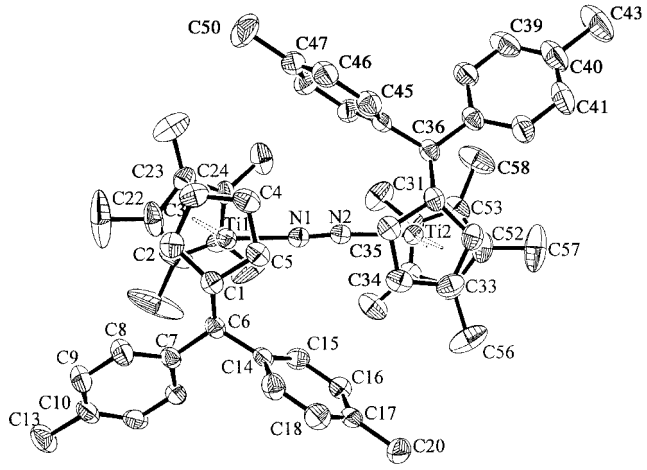

Figure 1. Solid state structure of **6** (50% probability ellipsoids). Selected bond lengths [Å] and angles [°]: Ti(1)–C(1) 2.195(3), Ti(1)–C(2) 2.253(3), Ti(1)–C(5) 2.303(3), Ti(1)–C(3) 2.375(3), Ti(1)–C(4) 2.409(3), Ti(1)–C(6) 2.601(3), C(1)–C(6) 1.436(4), C(1)–C(2) 1.439(4), C(1)–C(5) 1.434(4), C(2)–C(3) 1.416(5), C(4)–C(5) 1.412(4), C(3)–C(4) 1.393(5), Ti(1)–N(1) 1.997(3), N(1)–N(2) 1.160(3), Ti(1)–Ct(1) 2.056(3), Ti(1)–Ct(2) 1.968(3), Θ 28.4, Ct(1)–Ti(1)–Ct(2) 139.0 [Ct(1) = Centroid of Cp*, Ct(2) = centroid of the fulvene ring, Θ = tilt of C(6) out of the plane of C(11)–C(15)].

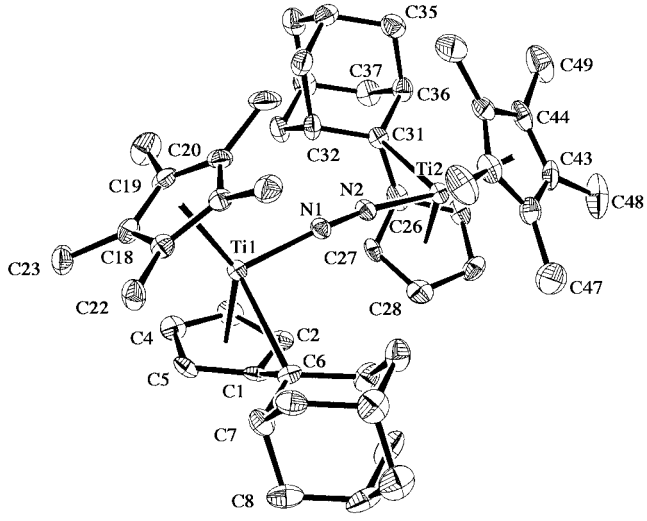

Figure 2. Solid state structure of **8** (50% probability ellipsoids). Selected bond lengths [Å] and angles [°]: Ti(1)–C(1) 2.179(5), Ti(1)–C(2) 2.301(5), Ti(1)–C(5) 2.291(5), Ti(1)–C(3) 2.424(5), Ti(1)–C(4) 2.426(5), Ti(1)–C(6) 2.511(5), C(1)–C(6) 1.441(6), C(1)–C(2) 1.437(6), C(1)–C(5) 1.448(7), C(2)–C(3) 1.413(8), C(4)–C(5) 1.419(7), C(3)–C(4) 1.397(7), Ti(1)–N(1) 2.012(4), N(1)–N(2) 1.160(5), Ti(1)–Ct(1) 2.061(4), Ti(1)–Ct(2) 1.986(4), Θ 30.4, Ct(1)–Ti(1)–Ct(2) 138.8 [Ct(1) = Centroid of Cp*, Ct(2) = centroid of the fulvene ring, Θ = tilt of C(6) out of the plane of C(1)–C(5)].

6 as well as **8** show similarities but also some marked differences compared with titanocene complexes. Probably the most striking point is the well-defined arrangement of the pentafulvene ligands which are located on the same side of the molecule. In general, a selective *trans* orientation of

 © 2005 Wiley-VCH Verlag GmbH & Co. KGaA, Weinheim

Table 1. Selected bond lengths [Å] and angles [°] of **6** and **8**, compared with related dinitrogen complexes.

Compound	N–N	Ti–N	Ti–N–N	Ref.
6	1.160(3)	1.997(3), 2.001(3)	171.0(2), 169.1(2)	
8	1.160(5)	2.012(4), 2.003(4)	170.0(4), 169.6(4)	
$[\{(\eta^5\text{-}C_5Me_5)_2Ti\}_2(\mu_2,\eta^1,\eta^1\text{-}N_2)]$	1.165(14)	2.005(10), 2.016(10)	176.8(4), 178.1(4)	[33]
$[\{(\eta^5\text{-}C_5Me_4H)_2Ti\}_2(\mu_2,\eta^1,\eta^1\text{-}N_2)]$	1.170(4)	1.987(3)	178.5(3)	[8]
$[\{(\eta^5\text{-}C_5H_5)_2Ti(PMe_3)\}_2(\mu_2,\eta^1,\eta^1\text{-}N_2)]$	1.191(8)	1.920(6), 1.921(5)	169.0(5), 172.6(5)	[9]
$[\{(\eta^5\text{-}C_5H_5)_2Ti(p\text{-Tol})\}_2(\mu_2,\eta^1,\eta^1\text{-}N_2)]$	1.162(12)	1.962(6)	176.5(5)	[11]
$[\{(\eta^5\text{-}C_5H_3(SiMe_3)_2)_2Ti\}_2(\mu_2,\eta^1,\eta^1\text{-}N_2)]$	1.164(5)	1.991(4)	176.0(3)	[7]
$[\{((Me_3Si)_2N)TiCl(TMEDA)\}_2(\mu_2,\eta^1,\eta^1\text{-}N_2)]$	1.289(9)	1.762(5)	168.5(2)	[25]
$[\{((Me_3Si)_2N)TiCl(Py)_2\}_2(\mu_2,\eta^1,\eta^1\text{-}N_2)]$	1.263(7)	1.759(3)	175.5(3)	[24]
$[\{((Me_2N)C(N\textit{i}Pr)_2)_2Ti\}_2(\mu_2,\eta^1,\eta^1\text{-}N_2)]$	1.280(8)	1.723(8), 1.744(8)	180.0	[17]

Table 2. Selected bond lengths [Å] and angles [°] of **6**, **8**, **10** compared with **2**,[30] **4**[35] and **5**.

	6	**2**	**8**	**4**	**10**	**5**
Ti–Ci	2.195(3)		2.179(5)		2.116(2)	
	2.195(2)		2.188(4)			
Ti–Ce	2.601(3)		2.511(5)		2.351(2)	
	2.612(3)		2.471(5)			
Ti–C_a	2.253(3)		2.291(5)		2.220(2)	
	2.258(3)		2.282(5)			
Ti–C'_a	2.303(3)		2.301(5)		2.350(3)	
	2.296(3)		2.310(4)			
Ti–C_b	2.375(3)		2.426(5)		2.360(2)	
	2.362(3)		2.428(6)			
Ti–C'_b	2.409(3)		2.424(5)		2.461(2)	
	2.399(3)		2.424(5)			
Ti–Ct* [a]	2.056(3)		2.061(4)		2.006(2)	
	2.056(3)		2.068(4)			
$Ti–Ct^{Fv}$ [a]	1.968(3)		1.986(4)		1.956(2)	
	1.963(3)		1.986(4)			
Ci–Ce	1.436(4)	1.359(2)	1.441(6)	1.342(2)	1.465(3)	1.359(2)
	1.435(4)		1.427(8)			
Ci–C_a	1.439(4)	1.465(2)	1.448(7)	1.459(2)	1.449(4)	1.467(2)
	1.441(4)		1.459(8)			
Ci–C'a	1.434(4)	1.458(3)	1.437(6)	1.459(2)	1.465(3)	1.488(2)
	1.430(4)		1.454(7)			
$C_a–C_b$	1.416(5)	1.340(3)	1.419(7)	1.327(3)	1.401(3)	1.340(3)
	1.406(5)		1.411(8)			
$C'_a–C'_b$	1.412(4)	1.344(3)	1.413(8)	1.337(3)	1.437(4)	1.416(2)
	1.412(4)		1.404(8)			
$C_b–C'_b$	1.393(5)	1.445(3)	1.397(7)	1.451(3)	1.414(4)	1.454(2)
	1.396(5)		1.416(8)			
Θ[b]	28.4	0	30.4	0	34.9	0
	28.2		32.8			
Ct*–Ti–Ct^{Fv} [a]	139.0		138.8		150.9	
	138.7		138.8			

[a] Ct*: ring centroid of C_5Me_5 ligand; Ct^{Fv}: ring centroid of C_i, C_a, C'_a, C_b, C'_b.

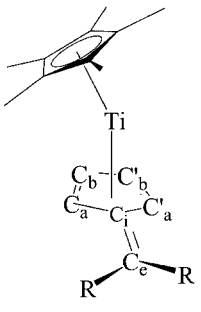

[b] Deviation angle.

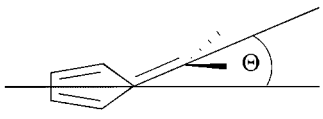

the non-Cp-type ligands is found in dinuclear, μ_2,η^1,η^1-dinitrogen-bridged titanocene complexes with tetrahedral coordinated titanium centres like $[\{(\eta^5\text{-}C_5H_5)_2Ti(p\text{-tol})\}_2(\mu_2,\eta^1,\eta^1\text{-}N_2)]$[11] and $[\{(\eta^5\text{-}C_5H_5)_2Ti(PMe_3)\}_2(\mu_2,\eta^1,\eta^1\text{-}N_2)]$.[9] In the case of **6** and **8**, in principle, four different stereoisomers are possible with respect to the position of the exocyclic fulvene carbon atoms (C_e) to each other (Scheme 1). Again, the formation of the "*cis* isomers" **A** and **B** was not observed, whereas of the two possible "*trans* isomers" **C** was found to be formed exclusively. This was confirmed not only in the solid state but also in solution (vide infra).

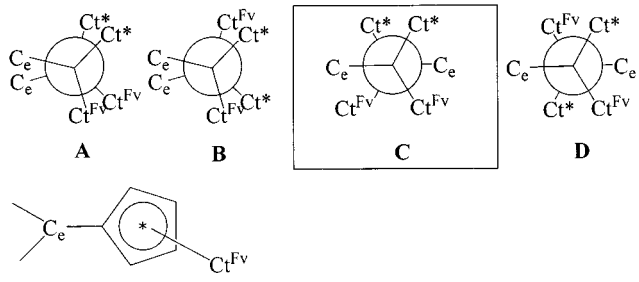

Scheme 1. Possible isomers of $[\{(\eta^5\text{-}C_5Me_5)(\eta^6\text{-}C_5H_4{=}CR_2)Ti\}_2(\mu^2,\eta^1,\eta^1\text{-}N_2)]$ complexes (Ct*: ring centroid of C_5Me_5; Ct^{Fv}: ring centroid of Ci, C_a, C'_a, C_b, C'_b; C_e *exo*-cyclic carbon of the fulvene ligand, see also Table 2).

The formal titanocene moieties $[(\eta^5\text{-}C_5Me_5)Ti(\eta^6\text{-}C_5H_4{=}CR_2)]$ are canted towards each other, forming a dihedral angle of 3.2° in **6** and 19.1° in **8** between the planes defined by the metallocene wedges, respectively (a value of 20.0° was found for the second molecule of **8** in the asymmetric unit). This is again in the same range as it was observed for similar complexes as, for example, in the case of $[\{(\eta^5\text{-}C_5H_3(SiMe_3)_2)_2Ti\}_2(\mu_2,\eta^1,\eta^1\text{-}N_2)]$ where a dihedral angle of 9.6° was found.[7]

However, this behaviour is different from that of the Ti(II) dinitrogen complexes showing twisted metallocene units $[\{(\eta^5\text{-}C_5Me_5)_2Ti\}_2(\mu_2,\eta^1,\eta^1\text{-}N_2)]$ (av. 90°)[33] and $[\{(\eta^5\text{-}C_5H_5)_2Ti(PMe_3)\}_2(\mu_2,\eta^1,\eta^1\text{-}N_2)]$ (P–Ti–Ti–P 109°).[9] A nearly perpendicular twist was found also for tantalum–dinitrogen complexes $[\{(\eta^5\text{-}C_5Me_5)_2TaCl\}_2(\mu_2,\eta^1,\eta^1\text{-}N_2)]$ (90.8°).[34] Nevertheless, structural parameters that are com-

 © 2005 Wiley-VCH Verlag GmbH & Co. KGaA, Weinheim

parable to those of **6** and **8** were found in the case of the diamagnetic Ti^{III} derivative $[\{(\eta^5\text{-}C_5H_5)_2Ti(p\text{-Tol})\}_2(\mu_2,\eta^1,\eta^1\text{-}N_2)]$[11] exhibiting a coplanar arrangement of both aryl groups and the centrosymmetric titanocene complex $[\{(\eta^5\text{-}C_5Me_4H)_2Ti\}_2(\mu_2,\eta^1,\eta^1\text{-}N_2)]$.[8]

Indeed, the N_2 coordination in our complexes is comparatively weak, and nitrogen is thus released quantitatively under reduced pressure or vacuum (0.49 moles per mole of Ti), forming the paramagnetic fulvene complex **9** [Equation (2)], characterized by elementary analysis ($C_{30}H_{33}Ti$ (M_τ = 441.47 g mol^{-1}): calcd. C 81.62, H 7.53; found: C 81.46, H 7.42). This observation is confirmed by MS analysis (EI, 70 eV) of **6**, **7**, and **8**, where only the monomeric $[(\eta^5\text{-}C_5Me_5)Ti(\eta^6\text{-}C_5H_4{=}CR_2)]$ units are detectable.

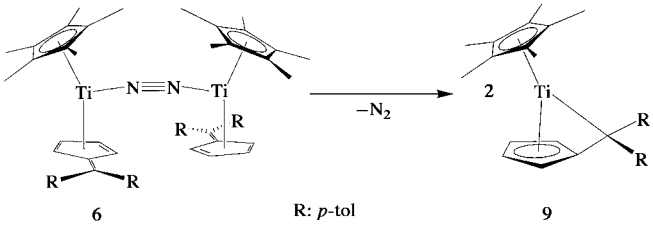

(2)

Unfortunately, crystals of **9** suitable for X-ray diffraction were not available up to now. However, using **5** instead of **2** under the reaction conditions described in Equation (1), the nitrogen-free fulvene complex **10** became available in a one-step synthesis. The low-coordinated complex **10** [Equation (3)] was isolated in the form of black, needle-shaped crystals (85%). In the mass spectrum, the peak of the molecular ion (*m*/*z* 491) was observed as the base peak. Suitable crystals for X-ray structure determination were obtained from *n*-hexane solutions at –20 °C. Due to the paramagnetic behaviour of the complex caused by the odd number of electrons at the titanium, it was not possible to record NMR spectra with distinct signals.

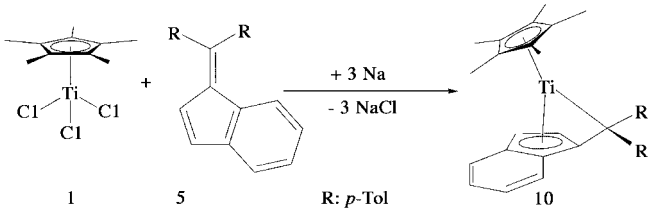

(3)

The molecular structure of **10** is given in Figure 3. The structure of the free ligand **5** was determined for comparison by X-ray diffraction (Figure 4). Selected structural parameters are summarized in Table 2.

Due to the two quite different π-ligands, (η^5-C_5Me_5) and (η^6-$C_5H_4{=}CR_2$), in **6** and **8** the bonding situation is remarkably different compared to bent-titanocene-derived dinitrogen complexes. The complexation of pentafulvenes to low-valent titanium fragments is generally assumed to be accompanied by electron transfer to the π-acceptor ligand. This leads to a situation that can probably be best described

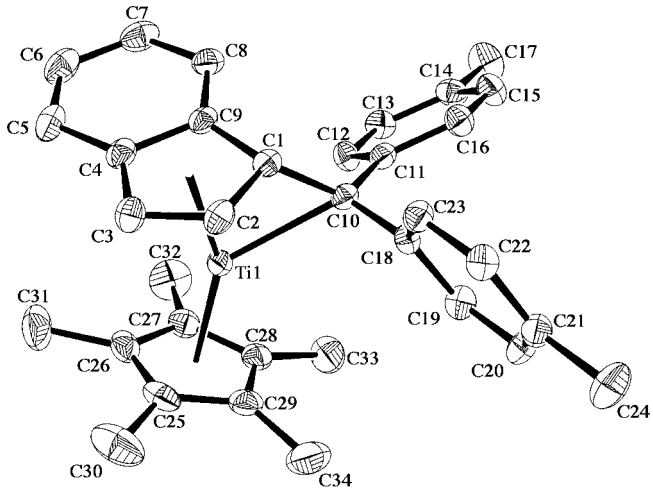

Figure 3. Solid-state structure of **10** (50% probability ellipsoids). Selected bond lengths [Å] and angles [°]: Ti(1)–C(1) 2.116(2), Ti(1)–C(2) 2.220(2), Ti(1)–C(9) 2.350(3), Ti(1)–C(3) 2.360(3), Ti(1)–C(4) 2.461(2), Ti(1)–C(10) 2.351(2), C(1)–C(10) 1.465(3), C(1)–C(2) 1.449(4), C(1)–C(9) 1.465(3), C(2)–C(3) 1.401(3), C(4)–C(9) 1.437(4), C(3)–C(4) 1.414(4), C(5)–C(6) 1.355(4), C(6)–C(7) 1.415(4), C(7)–C(8) 1.367(4), C(8)–C(9) 1.408(4), Ti(1)–Ct(1) 2.006(3), Ti(1)–Ct(2) 1.956(3), Θ 34.9, Ct(1)–Ti(1)–Ct(2) 150.9 [Ct(1) = Centroid of Cp*, Ct(2) = centroid of the fulvene ring, Θ = tilt of C(10) out of the plane of C(1)–C(9)].

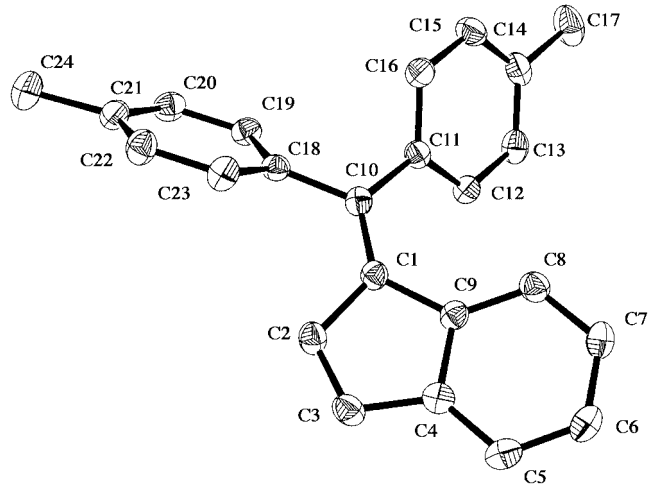

Figure 4. Solid-state structure of **5** (50% probability ellipsoids). Selected bond lengths [Å] and angles [°]: C(1)–C(10) 1.359(2), C(1)–C(2) 1.467(2), C(1)–C(9) 1.488(2), C(2)–C(3) 1.340(3), C(3)–C(4) 1.454(2), C(4)–C(5) 1.390(3), C(4)–C(9) 1.416(2), C(5)–C(6) 1.382(3), C(6)–C(7) 1.387(3), C(7)–C(8) 1.390(3), C(8)–C(9) 1.387(2).

by the formation of a dianionic fulvene ligand coordinated in a π-η^5:σ-η^1 manner.[31,30] Thus, the five-membered ring of the pentafulvene becomes aromatic, the C_i–C_e bond is elongated, and the C_e atom is bent out of the ring plane (Θ, see footnote Table 2). A comparison of the structural data of the free ligands **2**,[30] **4**[35] and **5** with the titanium complexes **6**, **8** and **10** is given in Table 2. The exocyclic C_i–C_e distances in **2** [1.359(2) Å], **4** [1.342(2) Å][35] and **5** [1.359(2) Å] are elongated to av. 1.436 Å (**6**), av. 1.434 Å (**8**) and 1.465(3) Å (**10**) after complexation. The strongest

 © 2005 Wiley-VCH Verlag GmbH & Co. KGaA, Weinheim

elongation and, simultaneously, the shortest Ti–C_e bond lengths [2.351(2) Å] were observed in the mononuclear titanium complex **10**. On the other hand, the Ti–C_e distances in **6** and **8** were found to be av. 2.606 Å and av. 2.491 Å. A comparable value was found for [(η^5-C_5Me_5)Ti(η^6-C_5H_4=C(*p*-tol)$_2$)Cl] [2.535(5) Å].[30] In fulvene complexes substituted with one or two protons at the C_e-atom of the fulvene ligand, Ti–C_e distances close to typical bond lengths between titanium and sp^3-hybridized C-atoms were found as in [(η^5-C_5Me_5)Ti(η^6-C_5Me_4=CH_2)] [2.281(14) Å][36] and [(η^5-C_5Me_5)Ti(η^6-C_5H_4=CH(*t*Bu))Cl] [2.355(2) Å].[31] The fulvene ligands in **6**, **8** and **10** show characteristic deviations (Θ) of the C_e-atom from the plane of the five-membered ring (**6** av. 28.3°, **8** av. 31.6°, **10** 34.9°). The Ct*–Ti–Ct^{Fv} angles of **6** (av. 138.8°) and **8** (138.8°) were found in a typical range of bent-titanocene derivatives[37] {Ti^{IV}: [(η^5-C_5Me_5)(η^5-C_5H_5)$TiCl_2$] 132.0°,[38] Ti^{III}: [(η^5-C_5Me_4H)$_2$TiCl] 139.1°,[39] [(η^5-C_5Me_5)$_2$TiCl] 143.6°[40]}. In contrast, the Ct*–Ti–Ct* angles in permethylated titanium(II) complexes are usually significantly larger {[{(η^5-C_5Me_5)$_2$Ti}$_2$(μ_2,η^1,η^1-N_2)] 145.7(3)°,[33] [(η^5-C_5Me_5)$_2$Ti(CO)$_2$] 147.9°[41]}. Also, in the case of the bulky fulvene complex **10** a larger value of 150.9° was found. Compared to free fulvene **5**, the two double bonds of the six-membered ring are significantly shortened from av. 1.39 Å to av. 1.36 Å in **10** and therefore seem to be more localised, indicating a loss of aromaticity. This is in agreement with an η^5 complexation mode of the five-membered ring, thus no hints for a typical indenyl effect are found.[42,43]

The isolated dinitrogen complexes **6**, **7**, and **8** showed diamagnetic behaviour, which allowed a complete NMR spectroscopic characterization (Table 3). The magnetic behaviour is comparable to the titanium(III)–dinitrogen complex [{(η^5-C_5H_5)$_2$Ti(*p*-tol)}$_2$(μ_2,η^1,η^1-N_2)].[44] On the other hand the titanium(II)–dinitrogen complexes like [{(η^5-C_5Me_5)$_2$Ti}$_2$(μ_2,η^1,η^1-N_2)] are often paramagnetic compounds (μ_{eff} = 2.18 BM per titanium atom[33]), showing broad downfield-shifted signals at room temperature[45] and dynamic properties in solutions. In such a way, detailed ^{1}H NMR measurements of [{(η^5-C_5Me_5)$_2$Ti(N_2)}$_2$(μ_2,η^1,η^1-N_2)] in [D_8]toluene at low temperatures (–78 to –42 °C) are in full accord with an η^5-C_5Me_5 ring site exchange.[13]

However, strong upfield shifts of proton and carbon signals, e.g. of up to 3 ppm for H_a of **8**, clearly show the presence of low-valent titanium complexes. This is especially pronounced for the exocyclic fulvene carbon atoms of all titanium complexes compared to the free ligands. Interestingly, the signals for these carbons were found at almost the same chemical shifts in all complexes although the free fulvenes do show significant differences. Furthermore, a complete loss of symmetry indicated by separated signals for all protons and carbons of the fulvenes in the dinuclear titanium complexes compared to the highly symmetrical fulvenes themselves and the absence of saturation transfer phenomena clearly show the formation of conformationally rigid dinitrogen complexes in benzene solution at room temperature. This is in sharp contrast to the conformational behaviour found for the mononuclear fulvene complexes [(η^5-C_5Me_5)Ti(η^6-C_5H_4=C(*p*-tol)$_2$)Cl][30] and [(η^5-C_5Me_5)-Ti(η^6-C_5H_4=C(*p*-C_6H_4F)$_2$)Cl][46], where a fast rotation of the fulvene ligand was observed under similar conditions. Obviously, a free rotation of the fulvene ligand is hindered by the dimeric structure, although the Ti–C_e distances are in a similar range. NOE measurements at room temperature indicate that the favoured isomer C (Scheme 1) in the solid state is also found in benzene solution because strong NOE contacts were observed between fulvene ring protons H'_b–H'_a of **8** which do not only result from the interaction of these protons attached to one fulvene ring but also from the interaction of protons attached to different fulvenes.

Table 3. Selected ^{1}H- (C_6D_6, 500 MHz, 300 K) and ^{13}C NMR spectroscopic data (C_6D_6, 125 MHz, 300 K) of **6**, **7** and **8**, compared with **2**,[30] **3** and **4**[47] (assignment of the proton and carbon signals in accordance with footnote[b] in Table 2).

	6	**2**	**7**	**3**	**8**	**4**
^{1}H NMR data						
H_a	4.38 (m, 2 H)	6.57 (m, 1 H)	4.17 (m, 2 H)	6.29 (m, 1 H)	3.64 (m, 2 H)	6.66 (m, 1 H)
H'_a	3.98 (m, 2 H)	6.57 (m, 1 H)	3.87 (m, 2 H)	6.29 (m, 1 H)	4.20 (m, 2 H)	6.66 (m, 1 H)
H_b	4.79 (m, 2 H)	6.65 (m, 1 H)	4.86 (m, 2 H)	6.58 (m, 1 H)	5.10 (m, 2 H)	6.61 (m, 1 H)
H'_b	4.07 (m, 2 H)	6.65 (m, 1 H)	4.17 (m, 2 H)	6.58 (m, 1 H)	5.69 (m, 2 H)	6.61 (m, 1 H)
^{13}C NMR data						
C_e	108.5	152.2	105.7	149.0	107.9	164.8
C_a	104.0	124.8	104.1	124.4	103.2	119.8
C'_a	106.5	124.8	105.9	124.4	104.5	119.8
C_b	111.9	132.4	112.3	133.2	113.3	131.0
C'_b	108.4	132.4	108.0	133.2	103.7	131.0

Conclusion

An efficient type of one-step synthesis of end-on bridged dinuclear cyclopentadienyltitaniumfulvene complexes was presented. These complexes are formed in high yields from [(η^5-C_5Me_5)$TiCl_3$], bulky substituted pentafulvenes, and sodium amalgam as reducing agent under nitrogen. Along the Ti–N≡N–Ti axis the C_5Me_5 as well as the fulvene ligands are arranged in a stereoregular manner. The weak activation of the dinitrogen ligand suggests that the dinuclear [(η^5-C_5Me_5)Ti(η^6-C_5H_4=CR_2)] dinitrogen complexes serve as synthons for interesting titanocenes, derived from the displacement of the nitrogen molecule in combination with the known possibilities to functionalize the strongly nucleophilic exocyclic carbon atom of the fulvene ligand by electrophilic attack.

Experimental Section

General Remarks: All operations were performed under nitrogen with rigorous exclusion of oxygen and moisture by using glove box or Schlenk techniques. Solvents were thoroughly dried and saturated with nitrogen. ^{1}H- and ^{13}C NMR spectra were recorded with a Bruker AVANCE 500 spectrometer (^{1}H, 500.1 MHz; ^{13}C

 © 2005 Wiley-VCH Verlag GmbH & Co. KGaA, Weinheim

125.8 MHz) or a Bruker AVANCE 300 spectrometer for ^{19}F- (282.4 MHz) and ^{1}H- or ^{13}C nuclei. The ^{1}H NMR chemical shifts were referenced to residual protons of the solvent. The ^{13}C NMR spectra were referenced to the signals of the solvent. The ^{19}F NMR spectra were referenced externally to $CFCl_3$. Assignment of the signals was done on the basis of ^{1}H, ^{13}C, H,H-COSY, HMQC, HMBC, and sel-1D NOESY NMR experiments.[48] Electron impact (EI) mass spectra were taken with a Finnigan-MAT 95 Spectrometer. IR spectra were recorded with a BIO-RAD FTS-7 Spectrometer by using KBr pellets. Elemental analyses were carried out by the Analytischen Laboratorien in Lindlar (Germany). [(η^5-C_5Me_5)$TiCl_3$] (**1**) was prepared according to the literature.[49] Sodium amalgam was purchased as 20% pellets from Aldrich. The fulvenes **2** and **3** were prepared according to general literature procedures.[48,50] **5**[48,51] was obtained in a similar way under only slightly modified conditions. Compound **4** was prepared according to the literature.[47,48]

[Bis{[η^6-6,6-bis(*p*-tolyl)pentafulvene](η^5-pentamethylcyclopentadienyl)titanium}-μ^2,η^1,η^1-dinitrogen] (6): Sodium amalgam (2.38 g, 20% Na, 20.73 mmol Na), di-*para*-tolylfulvene (**2**) (1.78 g, 6.91 mmol) and [(η^5-C_5Me_5)$TiCl_3$] (**1**) (2.00 g, 6.91 mmol) were placed in a Schlenk tube. At a temperature of 0 °C (ice bath) of THF (100 mL) was added under an excess nitrogen pressure of 200 mbar. The reaction mixture was stirred for 16 h. A colour change from red to dark green occurred. The reaction mixture was filtered twice (first P4/Celite, then P5). Removing the solvent under vacuum led to a brown residue, which became dark green again after adding N_2. After recrystallisation from of *n*-hexane (50 mL) at –20 °C, complex **6** could be isolated as dark green crystals showing a cupric lustre. Yield: 2.83 g (90%). M.p. 125 °C. ^{1}H NMR (500.1 MHz, C_6D_6, 300 K):[48] δ = 1.69 [s, 30 H, $C_5(CH_3)_5$], 2.14 (s, 6 H, outer CH_3), 2.16 (s, 6 H, inner CH_3), 3.98 (m, 2 H, H′$_a$), 4.07 (m, 2 H, H′$_b$), 4.38 (m, 2 H, H$_a$), 4.79 (m, 2 H, H$_b$), 6.83 (m, 4 H, inner C_6H_4), 6.92 (m, 4 H, outer C_6H_4), 6.98 (m, 4 H, inner C_6H_4), 7.28 (m, 4 H, outer C_6H_4) ppm. ^{13}C NMR (125.8 MHz, C_6D_6, 300 K):[48] δ = 12.5 [$C_5(CH_3)_5$], 21.0 (each C_6H_4-CH_3), 104.0 (C$_a$), 106.5 (C′$_a$), 108.4 (C′$_b$), 108.5 (C$_e$), 111.9 (C$_b$), 113.5 [$C_5(CH_3)_5$], 125.6 (Ci), 126.3 (outer C_6H_4), 128.5 (outer C_6H_4), 128.8 (inner C_6H_4), 132.0 (outer *i*-C_6H_4-C6), 132.2 (inner C_6H_4), 133.9 (inner *i*-C_6H_4-CH_3), 141.7 (outer *i*-C_6H_4-C6), 144.1 (inner *i*-C_6H_4-C6) ppm. IR (KBr): $\tilde{\nu}$ = 2915 (m), 2859 (m), 2745 (m), 1894 (w), 1746, 1605, 1505 (s), 1460 (s), 1375 (s), 1296, 1260 (w), 1159, 1103, 1067, 1020 (m), 905, 804, 731 cm^{-1}. MS (70 eV): *m*/*z* (%) = 441 (100) [M^+ – N_2 – Cp*Ti(*p*-Tolfv)], 307 (28). $C_{60}H_{66}N_2Ti_2$ (910.56): calcd. C 79.11, H 7.30, N 3.08; found C 78.93, H 7.42, N 3.05.

[Bis{[η^6-6,6-bis(*p*-fluorophenyl)pentafulvene](η^5-pentamethylcyclopentadienyl)titanium}-μ^2-η^1,η^1-dinitrogen] (7): Sodium amalgam (2.38 g, 20% Na, 20.73 mmol Na), di-*para*-fluorofulvene **3** (1.84 g, 6.91 mmol) and [(η^5-C_5Me_5)$TiCl_3$] (**1**) (2.00 g, 6.91 mmol) were placed in a Schlenk tube. At a temperature of 0 °C (ice bath) THF (100 mL) was added under an excess nitrogen pressure of 200 mbar. The reaction mixture was stirred for 16 h. A colour change from red to dark green occurred. The reaction mixture was filtered twice (first P4/Celite, then P5). Removing the solvent under vacuum led to a brown residue, which became dark green again after adding N_2. After recrystallisation from *n*-hexane (20 mL) at –20 °C, **7** could be isolated as dark green crystals with a cupric lustre. Yield: 2.56 g (80%). M.p. 138–140 °C. ^{1}H NMR (500.1 MHz, C_6D_6, 300 K):[48] δ = 1.56 [s, 30 H, $C_5(CH_3)_5$], 3.87 (m, 2 H, H′$_a$), 4.17 (m, 4 H, H$_a$ and H′$_b$), 4.86 (m, 2 H, H$_b$), 6.68 [m, *J* = 8.1 Hz, 4 H, ^{3}J(H,F) = 8.5 Hz, inner C_4H_6F], 6.75 (m, *J* = 8.4 Hz, 4 H, $^{3}J_{H,F}$ = 8.5 Hz, outer C_4H_6F), 6.81 (m, 4 H, inner C_4H_6F), 7.05 (m, 4 H, outer C_4H_6F) ppm. ^{13}C NMR (125.8 MHz, C_6D_6, 300 K):[48] δ = 12.4 [$C_5(CH_3)_5$], 104.1 (C$_a$), 105.7 (C$_{exo}$), 105.9 (C′$_a$), 108.0 (C′$_b$), 112.3 (C$_b$), 114.0 [$C_5(CH_3)_5$], 114.6 (outer C_4H_6F, d, $^{2}J_{C,F}$ = 21 Hz), 114.7 (inner C_4H_6F, d, $^{2}J_{C,F}$ = 21 Hz), 125.4 (Ci), 133.5 (outer C_4H_6F, d, $^{3}J_{C,F}$ = 8 Hz), 133.5 (inner C_4H_6F, d, $^{3}J_{C,F}$ = 8 Hz), 140.4 (outer *i*-C_6H_4-C6, d, $^{4}J_{C,F}$ = 3 Hz), 142.8 (inner *i*-C_6H_4-C6, d, $^{4}J_{C,F}$ = 3 Hz), 159.9 (outer *i*-C_6H_4-F, d, $^{1}J_{C,F}$ = 244 Hz), 162.2 (inner *i*-C_6H_4-F, d, $^{1}J_{C,F}$ = 244 Hz) ppm. ^{19}F NMR (282.4 MHz, C_6D_6, 303 K): δ = –115.8 (2F) ppm.- MS (CI, isobutane): *m*/*z* (%) = 938 (65) [469 × 2], 469 (100) [M^+ – N_2 – Cp*Ti(*p*-Ffv) + HF], 450 (20) [M+ – N_2 – Cp*Ti(*p*-Ffv) + H]. $C_{56}H_{54}F_4N_2Ti_2$ (926.81): calcd. C 72.57, H 5.87, N 3.02; found C 72.16, H 6.11, N 2.37.

[Bis{(η^6-adamantylidenepentafulvene)(η^5-pentamethylcyclopentadienyl)titanium}-μ^2-η^1,η^1-dinitrogen] (8): Sodium amalgam (2.38 g, 20% Na, 20.73 mmol Na), adamantylidenepentafulvene **4** (1.37 g, 6.91 mmol) and [(η^5-C_5Me_5)$TiCl_3$] (**1**) (2.00 g, 6.91 mmol) were placed in a Schlenk tube. At a temperature of 0 °C (ice bath) THF (100 mL) was added under an excess nitrogen pressure of 200 mbar. The reaction mixture was stirred for 16 h. A colour change from red to dark blue occurred. The reaction mixture was filtered twice (first P4/Celite, then P5). Removing the solvent under vacuum led to a turquoise residue, which became dark blue again after adding N_2. After recrystallisation from *n*-hexane (20 mL) at –20 °C, **8** could be isolated as dark blue crystals with a cupric lustre. Yield: 2.46 g (90%). M.p. 175 °C. ^{1}H NMR (500.1 MHz, C_6D_6, 300 K):[48] δ = 1.75 (s, 30 H, $C_5(CH_3)_5$), 1.48–2.53 (m, 28 H, $H_{Adamantyl}$), 3.64 (m, 2 H, H$_a$), 4.20, (m, 2 H, H′$_a$), 5.10 (m, 2 H, H$_b$), 5.69 (m, 2 H, H′$_b$) ppm. ^{13}C NMR (125.8 MHz, C_6D_6, 300 K):[48] δ = 12.3 [$C_5(CH_3)_5$], 29.2, 30.2, 34.1, 34.9, 38.2, 38.8, 39.0, 43.4, 45.4 ($C_{Adamantyl}$), 103.2 (C$_a$), 103.7 (C′$_b$), 104.5 (C′$_a$), 113.3 (C$_b$), 107.9 (C$_e$), 112.8 [$C_5(CH_3)_5$], 125.2 (Ci) ppm. MS (70 eV): *m*/*z* (%) = 381 (100) [M^+ – N_2 – Cp*Ti{$C_5H_4(C_{10}H_{14})$}]. $C_{50}H_{66}N_2Ti_2$ (790.85): calcd. C 75.94, H 8.41, N 3.54; found C 75.76, H 8.45, N 3.47.

[{η^6-10,10-Bis(*p*-tolyl)benzofulvene}(η^5-pentamethylcyclopentadienyl)titanium] (10): Sodium amalgam (2.38 g, 20% Na, 20.73 mmol Na), di-*p*-tolylbenzofulvene (**5**) (2.13g, 6.91 mmol) and [(η^5-C_5Me_5)$TiCl_3$] (**1**) (2.00 g, 6.91 mmol) were placed in a Schlenk tube. At a temperature of 0 °C (ice bath) THF (100 mL) was added under an excess nitrogen pressure of 200 mbar. The reaction mixture was stirred for 16 h. A colour change from red to brownish green occurred. The reaction mixture was filtered twice (first P4/Celite, then P5). Removing the solvent under vacuum led to a brown residue, which was recrystallised from *n*-hexane (20 mL) at –20 °C. Compound **10** could be isolated as black needle-shaped crystals. Yield: 2.8 g (85%). M.p. 115 °C. MS (70 eV): *m*/*z* (%) = 491 (100) [M^+], 308 (80) [di-*para*-tolylbenzofulvene$^+$]. $C_{34}H_{35}Ti$ (491.51): calcd. C 83.08, H 7.18; found C 83.04, H 7.21.

Di-*p*-tolylbenzofulvene (5): During 30 minutes, *n*BuLi (40.5 mL, 1.6 M) was added dropwise to a cooled solution (0 °C) of freshly distilled indene (9.8 mL, 0.082 mol) in THF (170 mL). The mixture was cooled to –60 °C, and 4,4′-dimethylbenzophenone (17.24 g, 0.082 mol) dissolved in THF (120 mL) was added. The reaction mixture was stirred overnight at room temperature. Then, water and diethyl ether were added, and the ether phase was extracted with water until pH 7 was reached. The ether phase was dried with $MgSO_4$, and the solvent was evaporated. After that the residue was dissolved in *n*-hexane (200 mL) and cooled rapidly. The precipitated crystalline solid was filtered and dried. Finally, the product could be isolated as orange crystals after recrystallisation from *n*-hexane/dichloromethane (2:1). Yield: 19.0 g (75%). M.p. 130–131 °C. ^{1}H NMR (500 MHz, $CDCl_3$, 300 K):[48] δ = 2.46 (s, 3 H, H-20), 2.52 (s, 3 H, H-15), 6.75 (m, 1 H, H-2), 6.79 (m, 1 H, H-8),

Table 4. Crystal structure data for compounds **6**, **8**, **10** and **5**.

	6	**8**	**10**	**5**
Empirical formula	$C_{66}H_{80}N_2Ti_2$	$C_{50}H_{66}N_2Ti_2$	$C_{34}H_{35}Ti$	$C_{24}H_{20}$
Formula mass	997.12	790.85	491.52	308.40
Diffractometer	STOE IPDS	STOE IPDS	STOE IPDS	STOE IPDS
Crystal dimensions [mm]	0.45×0.38×0.36	0.52×0.04×0.04	0.30×0.16×0.13	0.21×0.19×0.18
Colour, habit	dark green, red	dark blue, red	black	orange
Crystal system	triclinic	monoclinic	triclinic	triclinic
a [Å]	11.0985(6)	29.2685(18)	8.1648(5)	9.2556(10)
b [Å]	12.9268(5)	10.0234(4)	12.5378(9)	9.3584(12)
c [Å]	19.5985(10)	29.713(2)	13.9286(10)	11.0345(14)
α [°]	86.095(5)	90	74.338(8)	71.141(14)
β [°]	87.996(6)	104.619(8)	74.302(8)	67.960(13)
γ [°]	81.364(5)	90	77.604(8)	85.793(14)
V [Å]^3	2772.6(2)	8434.7(9)	1306.19(15)	837.12(18)
Space group	$P\bar{1}$	$P2_1/n$	$P\bar{1}$	$P\bar{1}$
Z	2	8	2	2
D_{calcd} [Mg·m^{-3}]	1.194	1.246	1.250	1.224
μ [mm^{-1}]	0.330	0.415	0.348	0.069
F(000)	1068	3392	522	328
λ (Mo-K_α, graphite) [Å]	0.71073	0.71073	0.71073	0.71073
Temperature [K]	193(2)	193(2)	193(2)	193(2)
θ range for data collection [°]	2.11 to 25.90	2.09 to 26.06	2.62 to 25.97	2.30 to 26.02
Number of reflections collected	33979	69268	16076	10252
Number of observed reflections [$I > 2\sigma(I)$]	6285	5786	3308	1760
Number of independent reflections	10040	15703	4750	3057
Absorption correction method	none	none	none	None
Max. and min. transmission	0.8906 and 0.8659	0.9836 and 0.8131	0.9562 and 0.9028	0.9877 and 0.9857
Number of data/restraints/parameters	10040/27/634	15703/0/973	4750/0/316	3057/0/297
R indices (all data)	$R1$ = 0.0868, $wR2$ = 0.1370	$R1$ = 0.1626, $wR2$ = 0.1392	$R1$ = 0.0693, $wR2$ = 0.1131	$R1$ = 0.0824, $wR2$ = 0.0770
Final R indices [$I > 2\sigma(I)$]	$R1$ = 0.0510, $wR2$ = 0.1245	$R1$ = 0.0494, $wR2$ = 0.0946	$R1$ = 0.0427, $wR2$ = 0.1047	$R1$ = 0.0374, $wR2$ = 0.0680
GoF on F^2	0.908	0.601	0.958	0.816
Largest difference peak and hole [e·Å^{-3}]	0.556 and –0.383	0.307 and –0.280	0.414 and –0.424	0.160 and –0.161

6.94 (m, 1 H, H-3), 6.94 (m, 1 H, H-7), 7.20 (m, 1 H, H-6) 7.24 (m, 2 H, H-18), 7.27 (m, 2 H, H-17), 7.30 (m, 2 H, H-13), 7.34 (m, 2 H, H-12), 7.35 (m, 1 H, H-5) ppm. ^{13}C NMR (125.8 MHz, $CDCl_3$, 300 K):[48] δ = 21.3 (C-20), 21.4 (C-15), 120.7 (C-5), 123.4 (C-8), 124.3 (C-7), 126.8 (C-6), 128.5 (C-18), 129.2 (C-13), 130.4 (C-12), 130.7 (C-2, C-3), 131.7 (C-17), 136.0 (C-4), 138.1 (C-19*), 138.2 (C-9*), 138.4 (C-14), 138.7 (C-11), 139.7 (C-16), 144.3 (Ci), 147.4 (C_e) ppm (*assignment might be interchanged).

X-ray Crystallographic Study: Data for the structures **6**, **8**, **10** and **5** were collected on a STOE-IPDS diffractometer with graphite-monochromated Mo-K_α radiation (λ = 0.71073 Å). A summary of crystal data and intensity collection and refinement parameters is reported in Table 4. Intensity measurements were performed at 193(2) K. The structure of all complexes was solved by direct phase determination (SHELXL 97) and refined on F^2 (SHELXL 97)[52] with anisotropic thermal parameters for all non-hydrogen atoms.

Additionally crystallographic data for the structures **6**, **8**, **10**, and **5** have been deposited. CCDC-161093 (**6**), -252794 (**8**), -252795 (**10**), and -252796 (**5**) contain the supplementary crystallographic data for this paper. These data can be obtained free of charge from The Cambridge Crystallographic Data Centre via www.ccdc.cam.ac.uk/data_request/cif.

Supporting Information Available (see also footnote on the first page of this article).

Acknowledgments

We thank the Fonds der Chemischen Industrie for a kindly granted scholarship (A. S.).

[1] For reviews see [1–5], S. Gambarotta, J. Scott, *Angew. Chem.* **2004**, *116*, 5412–5422; *Angew. Chem. Int. Ed.* **2004**, *43*, 5293–5295.
[2] B. A. MacKay, M. D. Fryzuk, *Chem. Rev.* **2004**, *104*, 385–402.
[3] C. M. Kozak, P. Mountford, *Angew. Chem.* **2004**, *116*, 1206–1209; *Angew. Chem. Int. Ed.* **2004**, *43*, 1186–1189.
[4] M. E. Volpin, *J. Organomet. Chem.* **1980**, *200*, 319–334.
[5] M. D. Fryzuk, S. A. Johnson, *Coord. Chem. Rev.* **2000**, *200*, 379–409.
[6] T. E. Hanna, E. Lobkovsky, P. J. Chirik, *J. Am. Chem. Soc.* **2004**, *126*, 14688–14689.
[7] T. E. Hanna, I. Keresztes, E. Lobkovsky, W. H. Bernskoetter, P. J. Chirik, *Organometallics* **2004**, *23*, 3448–3458.
[8] J. M. deWolf, R. Blaauw, A. Meetsma, J. H. Teuben, R. Gyepes, V. Varga, K. Mach, N. Veldman, A. L. Spek, *Organometallics* **1996**, *15*, 4977–4983.
[9] D. H. Berry, L. J. Procopio, P. J. Carroll, *Organometallics* **1988**, *7*, 570–572.
[10] G. P. Pez, P. Apgar, R. K. Crissey, *J. Am. Chem. Soc.* **1982**, *104*, 482–490.
[11] J. D. Zeinstra, J. H. Teuben, F. Jellinek, *J. Organomet. Chem.* **1979**, *170*, 39–50.

 © 2005 Wiley-VCH Verlag GmbH & Co. KGaA, Weinheim

[12] J. M. Manriquez, R. D. Sanner, R. E. Marsch, J. E. Bercaw, *J. Am. Chem. Soc.* **1976**, *98*, 3042.
[13] J. M. Manriquez, D. R. McAlister, E. Rosenberg, A. M. Shiller, K. L. Williamson, S. I. Chan, J. E. Bercaw, *J. Am. Chem. Soc.* **1978**, *100*, 3078–3083.
[14] R. D. Sanner, J. M. Manriquez, R. E. Marsch, J. E. Bercaw, *J. Am. Chem. Soc.* **1976**, *98*, 8351–8357.
[15] J. A. Pool, E. Lobkovsky, P. J. Chirik, *Nature* **2004**, *427*, 527–530.
[16] J. A. Pool, E. Lobkovsky, P. J. Chirik, *Organometallics* **2003**, *22*, 2797–2805.
[17] S. M. Mullins, A. P. Duncan, R. G. Bergman, J. Arnold, *Inorg. Chem.* **2001**, *40*, 6952–6963.
[18] R. Baumann, W. M. Stumpf, M. W. Davis, L.-C. Liang, R. R. Schrock, *J. Am. Chem. Soc.* **1999**, *121*, 7822–7832.
[19] J. R. Hagadorn, J. Arnold, *Organometallics* **1998**, *17*, 1355–1368.
[20] J. R. Hagadorn, J. Arnold, *Inorg. Chem.* **1997**, *36*, 2928–2929.
[21] J. R. Hagadorn, J. Arnold, *J. Am. Chem. Soc.* **1996**, *118*, 893–894.
[22] J. D. Cohen, M. Mylvaganam, M. D. Fryzuk, T. M. Loehr, *J. Am. Chem. Soc.* **1994**, *116*, 9529–9534.
[23] M. D. Fryzuk, T. S. Haddad, M. Mylvaganam, D. H. McConville, S. J. Rettig, *J. Am. Chem. Soc.* **1993**, *115*, 2782–2792.
[24] N. Beydoun, R. Duchateau, S. Gambarotta, *J. Chem. Soc., Chem. Commun.* **1992**, 244–246.
[25] R. Duchateau, S. Gambarotta, N. Beydoun, C. Bensimon, *J. Am. Chem. Soc.* **1991**, *113*, 8986–8988.
[26] M. Hidai, Y. Mizobe in *Activation of the N–N Triple Bond in Molecular Nitrogen: Toward its Chemical Transformation into Organo-Nitrogen Compounds* (Ed.: S. Murai), Springer, Berlin, Heidelberg, New York, **1999**, vol. 3.
[27] M. Akashi, Y. Sato, M. Mori, *J. Org. Chem.* **2001**, *66*, 7873–7874.
[28] K. Hori, M. Mori, *J. Am. Chem. Soc.* **1998**, *120*, 7651–7652.
[29] M. Mori, K. Hori, M. Akashi, M. Hori, Y. Sato, M. Nishida, *Angew. Chem.* **1998**, *110*, 659–661; *Angew. Chem. Int. Ed.* **1998**, *37*, 636–637.
[30] J. Stroot, M. Friedemann, A. Lützen, W. Saak, R. Beckhaus, *Z. Anorg. Allg. Chem.* **2002**, *628*, 797–802.
[31] R. Beckhaus, A. Lützen, D. Haase, W. Saak, J. Stroot, S. Becke, J. Heinrichs, *Angew. Chem.* **2001**, *113*, 2112–2115; *Angew. Chem. Int. Ed.* **2001**, *40*, 2056–2058.
[32] M. D. Fryzuk, J. B. Love, S. J. Rettig, V. G. Young, *Science* **1997**, *275*, 1445–1447 and the references cited therein.
[33] R. D. Sanner, D. M. Duggan, T. C. McKenzie, R. F. Marsh, J. E. Bercaw, *J. Am. Chem. Soc.* **1976**, *98*, 8358–8365.
[34] D. C. Bregel, S. M. Oldham, R. J. Lachicotte, R. Eisenberg, *Inorg. Chem.* **2002**, *41*, 4371–4377.
[35] J. G. Garcia, M. L. McLaughlin, F. R. Fronczek, *Acta Crystallogr.* **1989**, *C45*, 1099–1100.
[36] J. M. Fischer, W. E. Piers, V. G. Young, Jr., *Organometallics* **1996**, *15*, 2410–2412.
[37] R. Beckhaus in *Titanocenes* (Eds.: R. L. Halterman, A. Togni), VCH, Weinheim, **1998**, chapter 4.
[38] R. D. Rogers, M. M. Benning, L. K. Kurihara, K. J. Moriarty, M. D. Rausch, *J. Organomet. Chem.* **1985**, *293*, 51–60.
[39] S. I. Troyanov, V. B. Rybakov, U. Thewalt, V. Varga, K. Mach, *J. Organomet. Chem.* **1993**, *447*, 221–225.
[40] J. W. Pattiasina, H. J. Heeres, F. Van Bolhuis, A. Meetsma, J. H. Teuben, A. L. Spek, *Organometallics* **1987**, *6*, 1004–1010.
[41] D. J. Sikora, M. D. Rausch, R. D. Rogers, J. L. Atwood, *J. Am. Chem. Soc.* **1981**, *103*, 1265–1267.
[42] M. J. Calhorda, C. A. Gamelas, C. C. Romão, L. F. Veiros, *Eur. J. Inorg. Chem.* **2000**, 331–340.
[43] J. M. O'Connor, C. P. Casey, *Chem. Rev.* **1987**, *87*, 307–318.
[44] J. H. Teuben, *J. Organomet. Chem.* **1973**, *57*, 159–167.
[45] J. E. Bercaw, *J. Am. Chem. Soc.* **1974**, *96*, 5087–5095.
[46] W. Küppers, Dissertation, Universität Oldenburg, **2003**, 1–126.
[47] M. B. Abrams, J. C. Yoder, C. Loeber, M. W. Day, J. E. Bercaw, *Organometallics* **1999**, *18*, 1389–1401.
[48] For further details, see Supporting Information.
[49] G. Hidalgo, M. Mena, F. Palacios, P. Royo, R. Serrano in *Herrmann/Brauer: Synthetic Methods of Organometallic and Inorganic Chemistry* (Ed.: W. A. Herrmann), Georg Thieme Verlag, Stuttgart, **1996**, vol. 1, p. 95.
[50] J. Jeffery, E. J. Probitts, R. J. Mawby, *J. Chem. Soc., Dalton Trans.* **1984**, 2423–2427.
[51] M. Neuenschwander in *The Chemistry of Double-Bonded Functional Groups*, vol. 2 chapter 16 ("Fulvenes") (Ed.: S. Patai), John Wiley & Sons Ltd., Chichester, **1989**.
[52] G. M. Sheldrick *SHELXL-97. A Program for Refining Crystal Structures*, University of Göttingen, Germany, **1997**.

Received November 8, 2004

 © 2005 Wiley-VCH Verlag GmbH & Co. KGaA, Weinheim

New Insights into the Stoichiometric and Catalytic Reactivity of Unsaturated $Pd_3(dppm)_3CO^{n+}$ Clusters (n = 0, 1) Towards Halocarbons – First Evidence for Inorganic By-Products

Dominique Lucas,*[a] Frédéric Lemaître,[a,b] Beatriz Gallego-Gómez,[a] Cyril Cugnet,[a] Philippe Richard,[a] Yves Mugnier,[a] and Pierre D. Harvey*[b]

Keywords: Palladium cluster / Alkyl halide / Reduction / Electrocatalysis / Alkyl radicals

The title clusters, $Pd_3(dppm)_3(CO)^+$ and $Pd_3(dppm)_3(CO)^0$ can be electrochemically generated from the 1- and 2-electron reductions, respectively, of the $Pd_3(dppm)_3(CO)^{2+}$ cluster [dppm = bis(diphenylphosphanyl)methane; Pd_3^{2+}]. Pd_3^+ reacts in a stoichiometric ratio with methyl iodide, MeI, and benzyl bromide, BzBr, in THF to provide the corresponding $Pd_3(X)^+$ adducts (X = I, Br respectively) as inorganic products. Other products are Bz_2 and PhMe for BzBr but, for MeI, no organic product was observed (since they are too volatile). In the presence of the same substrates, Pd_3^0 also reacts in a stoichiometric ratio to form the same organics and the $Pd_3(X)^+$ adducts (X = I and Br). However for MeI, the major inorganic product is the A-frame $Pd_2(dppm)_2(Me)_2I^+$ binuclear complex. For BzBr, the corresponding A-frame complex $Pd_2(dppm)_2(Bz)_2Br^+$ could not be detected. The spin-trap agents, 2,2,6,6-tetramethylpiperidin-1-oxyl (TEMPO) and 5,5′-dimethyl-1-pyrroline *N*-oxide (DMPO), have been used to demonstrate the intermediacy of the radical Bz˙. The catalytic generation of "Bz˙" was performed using two methods, i.e. 1) using a copper anode as the working electrode [$Pd_3(Br)^+ + Cu - e^- \rightarrow Pd_3^{2+} + CuBr$ (s)] and 2) using a carbon cathode as the working electrode [$Pd_3(Br)^+ + 2e^- \rightarrow Pd_3^0 + Br^-$]. The chemical yields for Bz_2 vary between 50 and 56 % and the Faradic yield is of the order of 90 % for method 1 and between 52 and 59 % for method 2 [taking into account the quantity of electricity necessary to reduce the catalyst $Pd_3(Br)^+$]. The X-ray structure of $Pd_3(dppm)_3(CO)(Br)^+$ is presented and the following parameters were recorded: monoclinic space group $P2_1/n$, a = 10.6546(2), b = 37.1091(7), c = 21.2714(7) Å, β = 91.55(1)°, V = 8407.3(4) Å^3, Z = 4, R_1 = 0.0581 [$I > 2\sigma(I)$], wR_2 = 0.1478 (all data).

(© Wiley-VCH Verlag GmbH & Co. KGaA, 69451 Weinheim, Germany, 2005)

Introduction

The C–X bond activation is an important process in organic synthesis.[1–7] In this respect, our groups have investigated numerous thermal and electrochemical reactions between $Pd_3(dppm)_3(CO)^{2+}$ (**1**; Pd_3^{2+})[8–10] and halocarbons (RX) and some important electrochemically induced organic catalyses have been reported.[11–13] The direct thermal reaction (Pd_3^{2+} + RX) quantitatively produces the corresponding adducts $Pd_3(X)^+$ and "R^+".

The elucidation of the mechanism of C–X bond cleavage for alkyl halides and acid chlorides has been studied in some detail.[14] However, whereas the reactivity of Pd_3^{2+} towards RX has been fully investigated under both stoichiometric and catalytic conditions, the corresponding reduced species Pd_3^+ and Pd_3^0 have only been briefly studied under catalytic conditions.

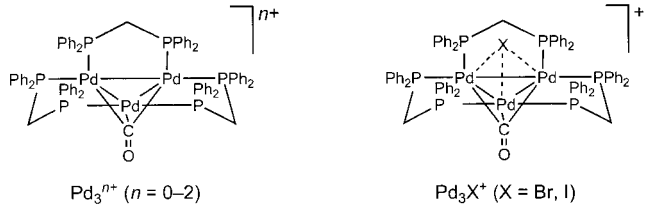

Pd_3^{n+} (n = 0–2) Pd_3X^+ (X = Br, I)

We now wish to report the reactivity of the Pd_3^+ and Pd_3^0 species under stoichiometric conditions towards MeI and BzBr and evidence for the slow formation of the d^8–d^8 A-frame $Pd_2(dppm)_2(Me)_2I^+$ complex during the Pd_3^0 + MeI reactions has been obtained for the first time, indicating the presence of a parallel process which may explain the catalyst poisoning in some cases.

The use of BzBr was made since the presence of the potential Bz^+ and Bz˙ intermediates can easily be deduced from the lesser volatile products, hence providing key information on the mechanism. Similarly, the MeI substrate is well known to undergo facile oxidative addition with Pd species in the low oxidation states, often resulting in the

[a] Laboratoire de Synthèse et d'Electrosynthèse Organométalliques, CNRS UMR 5188, Faculté des Sciences Mirande, Université de Bourgogne,
9 avenue Alain Savary, 21100 Dijon, France
Fax: +33-380-39-36-64
E-mail: lucasd@u-bourgogne.fr
[b] Département de Chimie, Université de Sherbrooke, Sherbrooke, Québec, Canada J1K 2R1
Fax: +1-819-821-8017
E-mail: pharvey@courrier.usherb.ca

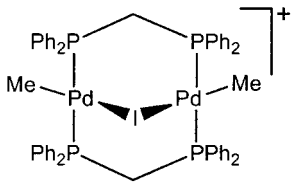

formation of a Pd–Me bond.[15–18] Finally, the efficient catalytic generation of "Bz˙" was examined.

Results and Discussion

Stoichiometric Reactivity of Pd_3^+

As reported earlier,[11,14,19] Pd_3^+ can be quantitatively obtained from a 1-electron reduction of the corresponding dicationic compound. Its RDE voltammogram is depicted in Figure 1 (trace a) and exhibits two closely spaced waves for oxidation and reduction labelled A'_1 and A_2, respectively [$E_{1/2}$ (A_1') = –0.24 V and $E_{1/2}$ (A_2) = –0.51 V vs. SCE]. Line 1b results from the addition of an excess of methyl iodide to Pd_3^+. The disappearance of waves A'_1 and A_2 can be observed, demonstrating that the Pd_3^+ complex has completely reacted. On the other hand, the current waves A_3 and A_4 indicate the formation of the previously known iodide coordination cluster $Pd_3(I)^+$ [$E_{1/2}$ (A_3) = –0.80 V and $E_{1/2}$ (A_4) = –1.25 V vs. SCE] which was confirmed by ^{31}P NMR spectroscopic analysis of the reaction solution in which only the signal of $Pd_3(I)^+$ can be seen (δ = –6.4 ppm).[20–22]

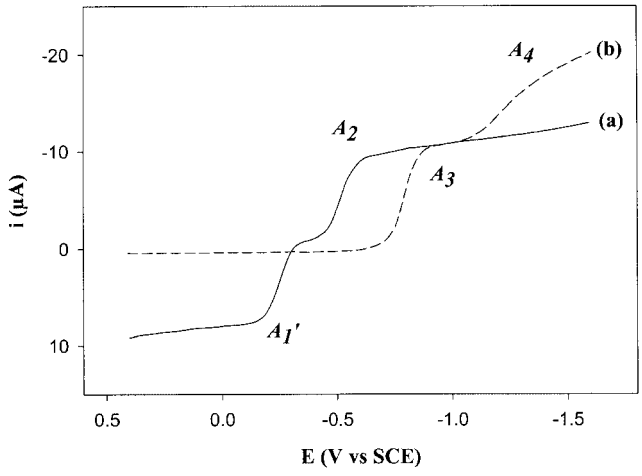

Figure 1. RDE voltammogram of Pd_3^+ (0.81 mM) in THF with 0.2 M Bu_4NPF_6: (a) alone, (b) immediately after addition of 1.1 molar equiv. of CH_3I.

Addition of BzBr (1.1 equiv.) to Pd_3^+ produces $Pd_3(Br)^+$ as confirmed by the comparison of the electrochemical [$E_{1/2}$ = –0.7 V (A_3)] and ^{31}P NMR spectroscopic data (δ = –6.14 ppm in [D_6]acetone) as well as the formation of Bz_2 (44% based upon GCMS data) and PhMe.[23] During the course of this investigation, crystals of $Pd_3(Br)^+$ suitable for X-ray analysis were obtained and investigated (see below). The organic products indicate a radical-type reactivity involving the "Bz˙" species which produces Bz_2 by homocoupling and PhMe by hydrogen abstraction from the solvent.[24] The addition of an excess of the spin trap agent 5,5′-dimethyl-1-pyrroline *N*-oxide (DMPO, 10 equiv.) to the Pd_3^+/BzBr reaction yields the stable Bz-DMPO spin adduct as readily observed by EPR spectroscopy which exhibits the expected 6-line signal:[25] a_β^H = 20.66 G, a^N = 14.16 G.[26,27] The absence of Bz_2 in reaction (1) suggests a quantitative reaction.

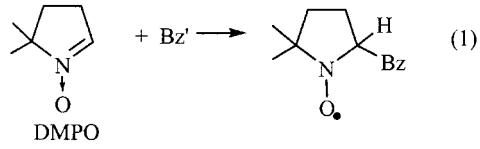

The two possible mechanisms for the production of the organic radical [$Pd_3^+ + RX \rightarrow Pd_3(X)^+ + R^{\cdot}$] are 1) an outer-sphere electron transfer from Pd_3^+ to RX, followed by X^- elimination from the intermediate $R–X^{\cdot-}$ (X^- is then trapped by the resultant Pd_3^{2+}) or 2) a halide abstraction process occurring within a host-guest $Pd_3\cdots(RX)^+$ assembly in which the homolytic C–X bond cleavage takes place, as described by reactions (2) and (3).

$$Pd_3^+ + RX \rightleftharpoons Pd_3\text{---}(XR)^+ \quad (2)$$

$$Pd_3\text{---}(XR)^+ \longrightarrow Pd_3(X)^+ + \text{"R}^{\cdot}\text{"} \quad (3)$$

The driving force in reaction (3) is the formation of the very stable $Pd_3(X)^+$ adduct. The former outer-sphere mechanism is highly unlikely since the oxidation ($E_{1/2}$ = –0.29 V) and reduction potentials ($E_{1/2} \approx$ –2.5 V vs. SCE)[28,29] for Pd_3^+ and R–X, respectively, are not thermodynamically favourable for such a process. On the other hand, the second proposal is more likely to occur based upon the well-established mechanism reported for the Pd_3^{2+} cluster [$Pd_3^{2+} + RX \rightarrow Pd_3\cdots(XR)^{2+} \rightarrow Pd_3(X)^+ +$ "R^+"].[11–14]

Going back to the Pd_3^+/MeI reaction, the absence of observed organics is due to their high volatility and, based on the observation made for the Pd_3^+/BzBr reaction, one can suggest that these are Me_2 and MeH.

Reactivity with Pd_3^0

The 2-electron reduction of Pd_3^{2+} leads to Pd_3^0 quantitatively. Addition of an excess of MeI to the electrochemically generated Pd_3^0-containing solution monitored by RDE voltammetry (Figure 2) results in the complete disappearance of the two 1-electron oxidation waves of the Pd_3^0 species (waves A_1' and A_2') and the appearance of waves A_3 and B_1 (–1.18 V vs. SCE) which are due to the anticipated $Pd_3(I)^+$ species and the known dinuclear d^8–d^8 A-frame complex $Pd_2(dppm)_2(Me)_2I^+$, respectively.[30] Based upon the current amplitudes of waves A_3 and B_1 and the relative intensity of the corresponding ^{31}P NMR signals (at –6.40 and +19.76 ppm), the relative proportions are ≈ 20–25% and ≈ 80–75%, respectively. This result is different from that of Pd_3^+ for which no A-frame complex was observed and

 © 2005 Wiley-VCH Verlag GmbH & Co. KGaA, Weinheim

suggests the presence of oxidative addition of MeI to Pd_3^0 as a parallel pathway.

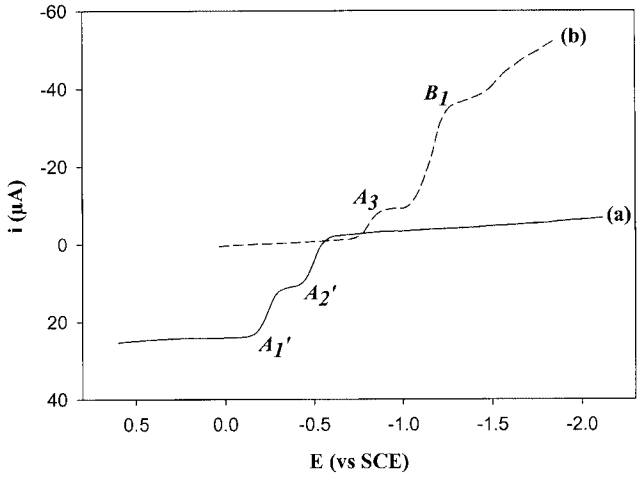

Figure 2. RDE voltammogram of Pd_3^0 (1.2 mM) in THF with 0.2 M Bu_4NPF_6: (a) alone, (b) immediately after addition of an excess (4 molar equiv.) of CH_3I.

The addition of BzBr (2 equiv.) to a Pd_3^0-containing solution leads to a slower reaction with respect to that of a similar reaction with Pd_3^+ (as monitored by the RDE method; Figure 3) but the presence of Bz_2 (GC-MS yields $\approx$ 44%) and PhMe as organic products could be detected in about the same relative amount.

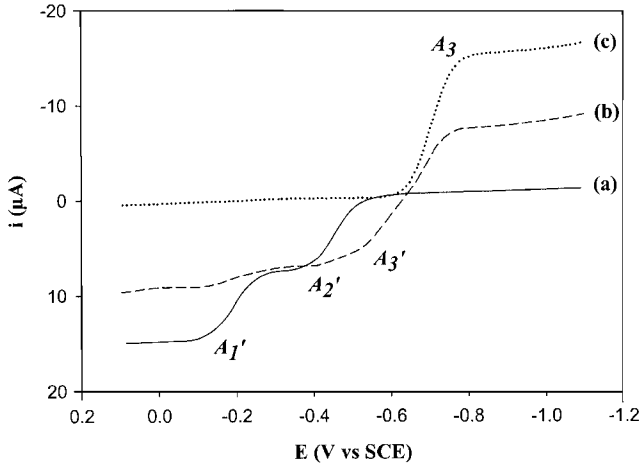

Figure 3. RDE voltammogram of Pd_3^0 (0.75 mM) in THF with 0.2 M Bu_4NPF_6: (a) alone, (b) immediately after addition of 2 molar equiv. of $PhCH_2Br$, (c) after 15 min at room temperature.

On the other hand, $Pd_3(Br)^+$ was quantitatively obtained and no trace of the d^8–d^8 $Pd_2(dppm)_2(Bz)_2Br^+$ complex was detected on this occasion (see below). The addition of DMPO to the solution prior to reaction leads to the same spin adduct as described above and no Bz_2 was observed, also suggesting completion of the spin-trap reaction. The overall reaction for the radical formation can be written as in reaction (4).

$$Pd_3^0 + 2\,RX \longrightarrow Pd_3(X)^+ + 2\,R^{\cdot} + X^- \quad (4)$$

A similar mechanism to that for Pd_3^+ can be proposed; see reaction (7).

$$Pd_3^0 + RX \rightleftharpoons Pd_3\text{---}(XR)^0 \quad (5)$$

$$Pd_3\text{---}(XR)^0 \longrightarrow Pd_3(X)^0 + \text{"}R^{\cdot}\text{"} \quad (6)$$

$$Pd_3(X)^0 \longrightarrow Pd_3^+ + X^- \quad (7)$$

The halocarbon molecule penetrates inside the cluster cavity forming a transient reactive host-guest complex $Pd_3\cdots(XR)^0$ [reaction (5)], in which a homolytic C–X bond cleavage takes place, giving the corresponding alkyl radical "$R^{\cdot}$" [reaction (6)]. The resultant $Pd_3(X)^0$ intermediate is unstable and eliminates X^- to form Pd_3^+ [reaction (7)]. This latter process is well known and has been previously established for X^- = Br^- and I^-.[8,22] Finally, the paramagnetic Pd_3^+ cluster undergoes reactions (2) and (3).

A second mechanism can also be considered and this involves the heterolytic C–X bond cleavage of the species $Pd_3\cdots(RX)^0$ followed by the reductive elimination of "$R^{\cdot}$"; see reactions (8) and (9).

$$Pd_3\text{---}(RX)^0 \longrightarrow Pd_3(R)^+ + X^- \quad (8)$$

$$Pd_3(R)^+ \longrightarrow Pd_3^+ + \text{"}R^{\cdot}\text{"} \quad (9)$$

Again, Pd_3^+ undergoes reactions (2) and (3). Reaction (8), which differs from reaction (6), finds its driving force from the electrostatic attraction of a potential carbocation "R^+" with the electron-rich Pd_3^0 centre. However, reactions 8 and 9 are both unlikely. The postulated $Pd_3(R)^+$ intermediate exhibits a Pd_3^{2+} centre and a carbanion which follows the octet rule similar to the Pd_3X^+ adducts. Its dissociation into Pd_3^+ and "$R^{\cdot}$" [reaction (9)] would be far too high in energy. In addition, the formation of the $Pd_3(R)^+$ species would prove difficult since the approach of the Pd_3^0 cluster towards the alkyl carbon atom in BzBr is sterically encumbered. Finally, such alkyl adducts of Pd_3^{2+} have never been observed and appear highly reactive.[31]

In order to support this hypothesis, DFT computations were performed on the model compounds $Pd_3(H_2PCH_2PH_2)_3(CO)(Me)^+$ and $Pd_3(H_2PCH_2PH_2)_3(CO)(Br)^+$. The first observation is that the computed total energies are –17067.91 and –19590.39 a. u. (arbitrary units), respectively, indicating the greater stability of the $Pd_3(Br)^+$ species. The second observation pointing in the same direction is that the computed energies for individual MOs are systematically higher for the $Pd_3(Me)^+$ species. As an example, a partial comparative MO diagram for the LUMO and HOMO is presented in Figure 4. The MO's have been described previously elsewhere and this is not within the scope of this work.[32,33] In conclusion, DFT supports the hypothesis that $Pd_3(Me)^+$ is a less stable species than $Pd_3(Br)^+$, Br^- or Pd_3^{2+}.

 © 2005 Wiley-VCH Verlag GmbH & Co. KGaA, Weinheim

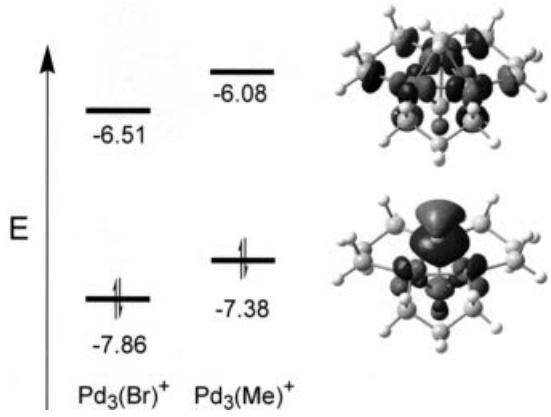

Figure 4. Left: Partial MO diagram of the HOMO and LUMO of the model compounds $Pd_3(H_2PCH_2PH_2)_3(CO)(Me)^+$ and $Pd_3(H_2PCH_2PH_2)_3(CO)(Br)^+$. Right: MO drawing for the HOMO and LUMO for $Pd_3(H_2PCH_2PH_2)_3(CO)(Me)^+$.

Two new questions now arise. Firstly, why can the radical Bz˙ intermediate be observed in quantitative amounts (based upon observed Bz_2 and PhMe) for both Pd_3^0 and Pd_3^+ species and, secondly, why can two inorganic products be observed for the Pd_3^0/MeI reaction (Pd_3 adduct and A-frame) while the Pd_3^+/MeI reaction leads to only one inorganic product (Pd_3 adduct)? These observations imply that another competitive process must occur which can be formalised as shown in reaction (10).

$$Pd_3(dppm)_3(CO)^0 + 3\ MeI \longrightarrow 3/2\ Pd_2(dppm)_2(Me)_2(I)^+ + CO + 3/2\ I^- \quad (10)$$

The answer to the first question can be found in the considerable stability of the $Pd_3(X)^+$ adducts[22] [reaction (3)] which readily drives the reactions. Thus, the same driving force may be present in the case of Pd_3^+. The answer to the second question can be found in the synthesis of Pd_3^0 itself.[34] The reduction of $Pd(dppm)Cl_2$ or $Pd_2(dppm)_2Cl_2$ leads to the zero-valent "$Pd_2(dppm)_2$" species. In the presence of a source of CO, this very reactive binuclear complex provides Pd_3^0.[35,36] On the other hand, the synthesis of $Pd_2(dppm)_2(Me)_2(I)^+$ can be performed by addition of MeI to $Pd_2(dppm)_3$[37] and the latter can dissociate into "$Pd_2(dppm)_2$" and dppm.[38] These previous results suggest that Pd_3^0 should dissociate to form the highly reactive species "$Pd_2(dppm)_2$" which would react with MeI.

On the other hand, the absence of reactivity in the case of BzBr, to form the A-frame product, suggests an important difference between the rates of the Pd_3^0/BzBr and "$Pd_2(dppm)_2$"/BzBr reactions which would favour the first reaction. It should be noted that the A-frame product $Pd_2(dppm)_2(Bz)_2(Br)^+$ has been previously reported in the literature[39] but the synthesis was not through the BzBr oxidative addition pathway as for MeI. This method was attempted but with no success which is consistent with our results. The preferred route was the reaction between $Pd(dppm)Br_2$ and the Grignard reagent BzMgBr.

Some questions remain such as how does the structure of the halogenated substrate affect the occurrence of the A-frame product? What is the main factor between the halogen and the alkyl group? In order to address these points, Pd_3^0 was treated with a slight excess of BzI in a cross experiment. This led to quantitative formation of $Pd_3(I)^+$ meaning that reaction (4) proceeds solely.

Thus, the steric hindrance of the alkyl group is likely playing an important role in the oxidative addition of RX to Pd_3^0. In order to confirm this proposal, a series of alkyl iodides, RI, were tested in the reaction with Pd_3^0 (R = Et, *i*Pr, *t*Bu). In no case was the A-frame product observed and $Pd_3(I)^+$ was always the sole inorganic product. Hence, reaction (10) may be extremely sensitive to the steric encumbrance of the alkyl group since it operates only when R = Me.

Catalytic Formation of "Bz˙" Radicals

The chemistry of free radicals has experienced an important growth in recent years[40,41] but the use of organotin compounds such as R_3SnH remains the first choice for radical generation.[42] However, because their use must be stoichiometric, their toxicity has encouraged chemists to find alternate and more environmentally friendly methods.[43] Thus, the indirect reduction of RX using an electron transfer catalyst mediating the RX conversion to "R˙" is appealing.[44]

$$RX + e^- \longrightarrow "R^{\cdot}" + X^- \quad (11)$$

In an attempt to render the stoichiometric reactions for "Bz˙" described above catalytic, two methodologies were examined. The first involves $Pd_3(Br)^+$ as a precatalyst in a single compartment electrochemical cell equipped with a copper anode as the controlled-potential working electrode, a platinum cathode as the counter-electrode and CH_2Cl_2 as the solvent. The electrolysis proceeds as shown in Scheme 1. The 1-electron oxidation at the copper anode produces CuBr(s) and Pd_3^{2+} from $Pd_3(Br)^+$. Pd_3^{2+} diffuses towards the cathode where it is reduced to Pd_3^+ which itself diffuses in the solution and reacts with BzBr to generate $Pd_3(Br)^+$ and "Bz˙". Bz_2 is the sole organic product observed and no PhMe is formed. The reason is that, unlike THF, CH_2Cl_2 is not an H-donor. Table 1 summarises the results (entry

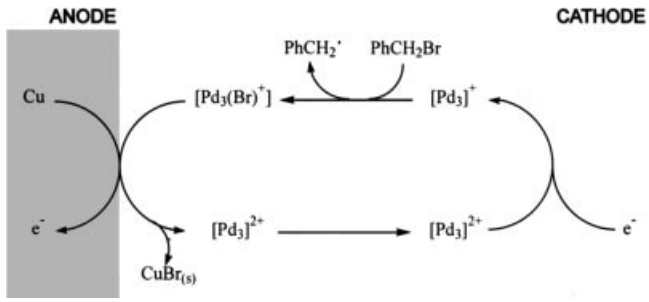

Scheme 1.

 © 2005 Wiley-VCH Verlag GmbH & Co. KGaA, Weinheim

Table 1. Controlled-potential electrolysis of $Pd_3(Br)^+$ in the presence of BzBr.

Entry	Working electrode (WE)	E_{WE} (V vs. SCE)	Solvent[a]	Molar ratio BzBr/cluster	Q (F per mol of BzBr)	Spin trap	Product(s)	% Chemical yield	% Faradic yield[b]
1	Cu anode[c]	+0.6	CH_2Cl_2	25	0.84	none	dibenzyl	76[d]	90
2	C cathode[e]	–0.9	THF	14	1.24	none	dibenzyl	70[d]	56
3	C cathode[e]	–1.3	THF	14	1.21	none	dibenzyl	60[d]	50
4	C cathode[e]	–0.9	THF	14	1.14	DMPO[f]	spin adduct	[g]	
5	C cathode[e]	–0.9	THF	14	1.09	TEMPO[f]	dibenzyl	42[d]	38
							spin Adduct	30[h]	28

[a] In the case of entry 1, CH_2Cl_2 was used as the solvent and no PhMe was observed; for entries 2–5, THF was used and PhMe was detected by GC–MS but not quantified because of strong overlap with the solvent peak in the chromatogram. [b] Faradic yield = Chemical Yield/Q. [c] The platinum counter-electrode was not separated, being directly immersed in the solution in order for it to electrolyse. [d] Measured by gas chromatography. [e] Standard assembly with an isolated platinum counter-electrode located in a separate compartment. [f] Quantity = 1 molar equivalent with respect to BzBr. [g] Only observed by ESR with no quantification. [h] Isolated yield.

1). Both the chemical (76%) and Faradic (90%) yields are good.

The second method involves the use of a carbon cathode where the single 2-electron reduction of $Pd_3(Br)^+$ in Pd_3^0 (at about –1 V vs. SCE) occurs in THF. The catalytic cycle is shown in Scheme 2 based on the findings of the stoichiometric reactions above. This method leads to slightly lower chemical yields of Bz_2 and the presence of PhMe was noted. The data are summarised in Table 1.

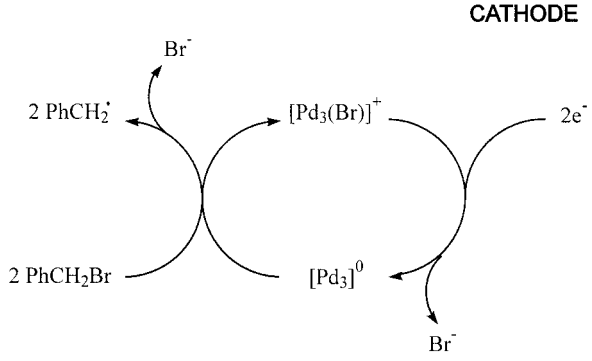

Scheme 2.

The addition of the spin trap DMPO to the solution during catalysis (entry 4) leads to the formation of the spin adduct as shown in reaction (1). On the other hand, addition of 2,2,6,6-tetramethylpiperidin-1-oxyl (TEMPO) [45–48] (entry 5) leads to a partial trapping where Bz_2 and the diamagnetic spin adduct can be observed [reaction (12)].

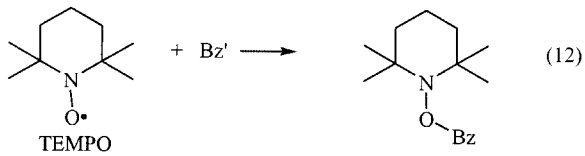

(12)

X-ray Structure of $Pd_3(Br)^+$

This compound completes the series for $Pd_3(X)^+$ (Figure 5 and Table 2) where X = Cl[49,50] and I.[21] A comparison of the skeleton (Table 3) indicates a fairly robust core in which the nature of the halide does not perturb the bond distances within the experimental uncertainties. In all cases, the Pd–X distances indicate strong ionic interactions and vary as expected (Cl < Br < I).

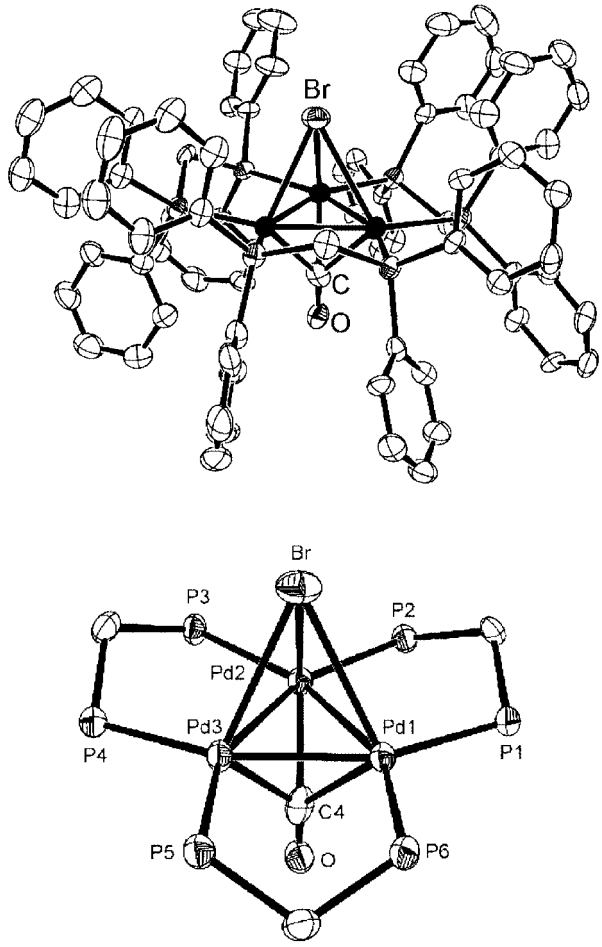

Figure 5. Top: ORTEP representation of $Pd_3(Br)^+$. The PF_6^- counter-anion, crystallisation toluene molecules and H-atoms are not shown for clarity. The ellipsoids are shown at the 50% probability level. Bottom: Drawing showing the skeleton of the cluster and the atom numbering.

Conclusions

The stoichiometric reactivity toward halocarbons of the Pd_3^+ and Pd_3^0 species has been investigated for the first

 © 2005 Wiley-VCH Verlag GmbH & Co. KGaA, Weinheim

Table 2. Selected bond distances [Å] and angles [°] for $Pd_3(Br)^+$.

Distances		Angles	
Pd(1)–C(4)	2.143(10)	Pd(1)–Pd(2)–Pd(3)	59.63(2)
Pd(2)–C(4)	2.139(10)	Pd(1)–Pd(3)–Pd(2)	60.26(2)
Pd(3)–C(4)	2.145(9)	Pd(2)–Pd(1)–Pd(3)	60.11(2)
Pd(1)–Br	3.027(9)	O–C(4)–Pd(1)	132.7(9)
Pd(2)–Br	2.8276(10)	O–C(4)–Pd(2)	141.0(9)
Pd(3)–Br	2.9666(11)	O–C(4)–Pd(3)	132.9(10)
Pd(1)–Pd(2)	2.5991(8)	C(4)–Pd(1)–P(1)	114.8(2)
Pd(1)–Pd(3)	2.5826(8)	C(4)–Pd(1)–P(6)	112.3(2)
Pd(2)–Pd(3)	2.5950(8)	C(4)–Pd(2)–P(2)	115.2(2)
Pd(1)–P(1)	2.315(2)	C(4)–Pd(2)–P(3)	118.4(2)
Pd(1)–P(6)	2.314(2)	C(4)–Pd(3)–P(4)	113.6(2)
Pd(2)–P(2)	2.315(2)	C(4)–Pd(3)–P(5)	112.1(2)
Pd(2)–P(3)	2.311(2)	P(1)–Pd(1)–P(6)	109.55(7)
Pd(3)–P(4)	2.309(2)	P(2)–Pd(2)–P(3)	108.44(7)
Pd(3)–P(5)	2.305(2)	P(4)–Pd(3)–P(5)	108.97(7)
C(4)–O	1.104(10)	P(1)–Pd(1)–Br	104.46(6)
		P(6)–Pd(1)–Br	113.22(6)
		P(2)–Pd(2)–Br	104.95(6)
		P(3)–Pd(2)–Br	98.83(6)
		P(5)–Pd(3)–Br	113.85(6)
		P(4)–Pd(3)–Br	104.09(6)

Table 3. Comparison of selected bond distances [Å] for the $Pd_3(X)^+$ clusters.

Average distance[a]	X = Cl[49]	X = Cl[50]	X = Br (this work)	X = I[21]
d(Pd–Pd)	2.595(17)	2.591(11)	2.592(10)	2.596(5)
d(Pd–P)	2.311(30)	2.310(11)	2.311(6)	2.314(9)
d(Pd–C)	2.103(10)	2.133(50)	2.142(3)	2.163(29)
d(Pd–X)	2.861	2.899	2.940	3.022

[a] The uncertainties are based on the maximum difference between the average value and experimental data.

time and has allowed the discovery of a new reactivity, particularly with respect to the inorganic products evolved from the Pd_3^0 species. The resultant A-frame product is stable since its reduction potential is higher than that for Pd_3^+ and Pd_3^0. Although there is no evidence in this work, the parallel pathway leading to the A-frame product may cause catalyst poisoning. Moreover, the catalytic generation of free radicals has been performed in good yields and the electrochemical methods may represent interesting alternatives to other stoichiometric reagents such as R_3SnH which may exhibit some undesired toxicity. Applications of such species in organic syntheses, especially those relative to C–X bond activation, are many. Due to the nature of the radical-type reactions that these species lead to, many other applications should be possible.

Experimental Section

Materials: The $[Pd_3(dppm)_3(CO)](PF_6)_2$ complex was prepared according to the literature.[20,51] Dichloromethane was distilled under Ar over P_2O_5 and tetrahydrofuran (THF) was distilled under Ar over Na (Aldrich). Benzyl bromide (BzBr), methyl iodide (MeI) and the spin trap agents TEMPO (2,2,6,6-tetramethylpiperidin-1-oxyl) and DMPO (5,5′-dimethyl-1-pyrroline *N*-oxide) were purchased from Aldrich and used as received. Benzyl iodide (BzI) was prepared according to a literature method.[52] The Bu_4NPF_6 salt was synthesized by mixing stoichiometric amounts of Bu_4NOH (40% in water) and HPF_6 (60% in water). After filtration, the salt was recrystallised twice from ethanol and dried at 80 °C for at least two days.

Apparatus: NMR spectra were measured on a Bruker WM 300 spectrometer (^{31}P NMR: 121.497 MHz). The chemical shifts are reported with respect to H_3PO_4 (^{31}P NMR). The GC–MS data were collected on a Hewlett–Packard 6890 Series instrument. EPR measurements were carried out on a Bruker ESP 300 spectrometer; field calibration was made with DPPH (g = 2.0037).

Electrochemical Experiments: All manipulations were performed using Schlenk techniques in an atmosphere of dry oxygen-free argon. The supporting electrolyte was degassed under vacuum before use and then dissolved to a concentration of 0.2 M. For cyclic voltammetry experiments, the concentration of the analyte was almost 10^{-3} M. Voltammetric analyses were carried out in a standard three-electrode cell with a Tacussel PJT24–1 potentiostat connected to a Tacussel GSTP4 waveform generator. The reference electrode was a saturated calomel electrode(SCE)separated from the solution by a sintered glass disk. The auxiliary electrode was a platinum wire. For all voltammetric measurements, the working electrode was a vitreous carbon electrode (φ = 3 mm). Under these conditions, when operating in THF, the formal potential for the ferrocene$^{+/-}$ couple was found to be +0.56 V versus the SCE. The controlled potential electrolysis was performed with an Amel 552 potentiostat coupled with an Amel 721 electronic integrator. High scale electrolyses were performed in a cell with three compartments separated with fritted glasses of medium porosity. Carbon gauze was used as the working electrode, a platinum plate as the counter-electrode and a saturated calomel electrode as the reference electrode. The electrolyses corresponding to the copper method were performed with a copper plate as the working electrode (anode), a platinum plate as the counter-electrode (cathode) and a saturated calomel electrode as the reference electrode, the latter being separated from the others in a two-compartment cell.

Procedures for the Electrochemical Experiments. Conventional High-Scale Electrolysis: The $[Pd_3(dppm)_3(CO)](PF_6)_2$ cluster (12.5 mg, 7×10^{-3} mmol, 6 mol-% per mol of BzBr) and BzBr (12.45 μL, 0.105 mmol) were added to the cathodic compartment of the cell containing a 0.2 M solution of Bu_4NPF_6 in THF (10 mL). The anodic compartment and the reference electrode compartment were filled with the Bu_4NPF_6–THF solution. The potential was set to –0.9 V vs. SCE. The electrolysis was stopped after the current had dropped to less than 0.5 mA. After filtration of the mixture, the solvent was removed and the residue extracted with diethyl ether (3× 5 mL). The internal standard method was used to measure the GC yields of the products. These were identified by comparison of the GC–MS spectra and GC retention times with those of available authentic samples. The electrolysis was also performed in the presence of TEMPO (in an equimolar amount to BzBr) which led to the isolation of the spin adducts Bz–DMPO (30%) and Bz_2 (42%). These were separated by column chromatography (solvent: CH_2Cl_2) and identified by mass spectrometry, ^1H NMR spectroscopy and by comparison with literature data.[53]

High-Scale Electrolysis. The Copper Method: Pd_3^{2+} cluster (11.6 mg, 6.5×10^{-3} mmol, 4 mol-% per mol of BzBr) and BzBr (20 μL, 0.168 mmol) were added to the anodic compartment containing a 0.2 M solution of Bu_4NPF_6 in CH_2Cl_2 (10 mL). The Bu_4NPF_6–CH_2Cl_2 solution (10 mL) was poured into the reference electrode compartment. The copper anode potential was set to +0.6 V vs. SCE and the electrolysis was stopped after one Faraday

 © 2005 Wiley-VCH Verlag GmbH & Co. KGaA, Weinheim

per mol of BzBr had passed. The quantification procedure was the same as described above.

Theoretical Computations: The Density Functional Theory calculations (DFT) were performed using the commercially available Gaussian 98[54] software and a Pentium 4 (1.6 GHz) computer. The computations were performed at the RB3LYP level [Becke's three parameter hybrid functional[55] using the LYP (Lee–Yang–Parr) correlation functional].[56,57] The basis set for the polarisation and diffuse function was the 3-21G* set.[58–60] To save computation time, $H_2PCH_2PH_2$ was selected instead of dppm. In order to test the methodology, the computed bond distances and angles of the model cluster $Pd_3(H_2PCH_2PH_2)_3(CO)(Br)^+$ were checked against those of the crystal structure of $Pd_3(dppm)_3(CO)(Br)^+$ [denoted as $Pd_3(Br)^+$ in the text]. The comparison was satisfactory.

X-ray Structure of $[Pd_3(dppm)_3(CO)Br](PF_6)$: Single crystals of Pd_3Br^+ (as its PF_6^- salt) were obtained from acetone/toluene/hexane, mounted in inert oil and transferred to the cold gas stream (110 K) of a Nonius Kappa CCD diffractometer located at the Université de Bourgogne. The structure was solved by the heavy atoms method (SHELXS-97) and refined by full-matrix least-squares methods (SHELXL-97)[61] with the aid of the WINGX program.[62] The capping CO molecule and the capping Br atom were found to be slightly disordered (inversion of both ligands with respect to the Pd_3 plane), the occupancies converged to 0.93/0.07. The minor component of the disorder was isotropically refined with some least-squares restraints to ensure equivalent geometrical parameters for both components. Among the three toluene solvate molecules, only one was anisotropically refined, the others were each refined with an overall isotropic thermal parameter and one of them, close to an inversion centre, was refined with an occupancy of 0.5. All other non-hydrogen atoms were anisotropically refined and the hydrogen atoms were included using a riding model. Crystallographic data are reported in Table 4.

Table 4. Crystallographic data.

	$[Pd_3(dppm)_3(CO)Br]PF_6$·2.5 toluene
Empirical formula	$C_{76}H_{66}BrF_6OP_7Pd_3$·2.5 C_7H_8
F_w	1955.52
Description	red prism
Crystal size [mm]	0.3 × 0.1 × 0.1
Temperature [K]	110(2)
Crystal system	monoclinic
Space group	$P21/n$
a [Å]	10.6546(2)
b [Å]	37.1091(7)
c [Å]	21.2714(7)
α [°]	90
β [°]	91.55(1)
γ [°]	90
V [Å^3]	8407.3(4)
Z	4
ρ(calcd.) [g cm^{-3}]	1.545
Scan mode	ω and φ
F(000)	3948
μ(Mo-K_α) [mm^{-1}]	1.305
θ-range [°]	2.96–23.77
Limiting indices	$-11 \le h \le 11$ $-42 \le k \le 32$ $-24 \le l \le 24$
Reflections collected	15640
Independent reflections	11002
Data/restraints/parameters	11002/25/949
Goodness-of-fit on F^2	1.038[c]
Final R indices [$I > 2\sigma(I)$]	R_1[a] = 0.0581 wR_2[b] = 0.1325
R indices (all data)	R_1[a] = 0.0816 wR_2[b] = 0.1479
Largest diff. peak and hole (e Å^{-3})	1.14 –1.12

[a] $R_1 = \Sigma||F_o| - |F_c||/\Sigma|F_o|$. [b] $wR_2 = (\Sigma[w(F_o^2 - F_c^2)^2]/\Sigma[F_o^4])^{1/2}$. [c] Goodness of fit = $[\Sigma w(F_o^2 - F_c^2)^2/(N_o - N_v)]^{1/2}$. Weight for $[Pd_3(dppm)_3(CO)Br]PF_6$·2.5 toluene = $1/[\sigma^2(F_o^2) + (0.051 \times P)^2 + 54.0 \times P]$ where $P = [\mathrm{Max}(F_o^2,0) + 2 \times F_c^2]/3$.

CCDC-243382 contains the supplementary crystallographic data for this paper. These data can be obtained free of charge from The Cambridge Crystallographic Data Centre via www.ccdc.cam.ac.uk/data_request/cif.

Acknowledgments

P. D. H. thanks the NSERC (Natural Sciences and Engineering Research Council) for funding. Y. M. is grateful to the CNRS (Centre National de la Recherche Scientifique) and the Conseil Régional de Bourgogne for funding.

[1] *Comprehensive Organometallic Chemistry II: A Review of the Literature 1982–1994* (Eds.: E. W. Abel, F. G. A. Stone, G. Wilkinson), 14-volume set, **1995**.
[2] R. J. Kulawiec, R. H. Crabtree, *Coord. Chem. Rev.* **1990**, *99*, 89–115.
[3] J. K. Kochi, *Organometallic Mechanisms and Catalysis*; Academic Press, New York, **1978**.
[4] J. K. Stille, K. S. Y. Lau, *Acc. Chem. Res.* **1977**, *10*, 434–442.
[5] J. P. Collman, L. S. Hegedus, J. R. Norton, R. G. Finke, *Organometallic Chemistry of Transition Metals: Principles and Use, Part 2*, University Science Books, Mill Valley, **1989**.
[6] *Applied Homogeneous Catalysis with Organometallic Compounds: Developments*, 2nd ed., vols. 2 and 3 (Eds.: B. Cornils, W. A. Herrmann), Wiley-VCH, Weinheim, Germany, **2002**.
[7] J. Tsuji, *Transition Metal Reagents and Catalysts: Innovations in Organic Synthesis*; Wiley: Chichester, U.K., **2000**.
[8] P. D. Harvey, Y. Mugnier, D. Lucas, D. Evrard, F. Lemaitre, A. Vallat, *J. Clust. Sci.* **2004**, *15*, 63–90.
[9] P. D. Harvey, *J. Clust. Sci.* **1993**, *4*, 377–402.
[10] R. J. Puddephatt, L. Manojlovic-Muir, K. W. Muir, *Polyhedron* **1990**, *9*, 2767–2802.
[11] D. Brevet, D. Lucas, H. Cattey, F. Lemaitre, Y. Mugnier, P. D. Harvey, *J. Am. Chem. Soc.* **2001**, *123*, 4340–4341.
[12] D. Brevet, Y. Mugnier, F. Lemaitre, D. Lucas, S. Samreth, P. D. Harvey, *Inorg. Chem.* **2003**, *42*, 4909–4917.
[13] F. Lemaitre, D. Lucas, Y. Mugnier, P. D. Harvey, *J. Org. Chem.* **2002**, *67*, 7537–7540.
[14] F. Lemaitre, D. Lucas, K. Groison, P. Richard, Y. Mugnier, P. D. Harvey, *J. Am. Chem. Soc.* **2003**, *125*, 5511–5522.
[15] R. van Asselt, K. Vrieze, C. J. Elsevier, *J. Organomet. Chem.* **1994**, *480*, 27–40.
[16] P. K. Byers, A. J. Canty, B. W. Skelton, A. H. White, *J. Chem. Soc. Chem. Commun.* **1986**, 1722–1724.
[17] R. S. Paonessa, A. L. Prignano, W. C. Trogler, *Organometallics* **1985**, *4*, 647–657.
[18] K. J. Klabunde, J. S. Roberts, *J. Organomet. Chem.* **1977**, *137*, 113–130.
[19] I. Gauthron, Y. Mugnier, K. Hierso, P. D. Harvey, *Can. J. Chem.* **1997**, *75*, 1182–1187.
[20] L. Manojlovic-Muir, K. W. Muir, B. R. Lloyd, R. J. Puddephatt, *J. Chem. Soc. Chem. Commun.* **1983**, 1336–1337.
[21] B. R. Lloyd, L. Manojlovic-Muir, K. W. Muir, R. J. Puddephatt, *Organometallics* **1993**, *12*, 1231–1237.
[22] F. Lemaitre, D. Brevet, D. Lucas, A. Vallat, Y. Mugnier, P. D. Harvey, *Inorg. Chem.* **2002**, *41*, 2368–2373.

 © 2005 Wiley-VCH Verlag GmbH & Co. KGaA, Weinheim

[23] PhMe was not quantified because its peak was not resolved from that of the solvent in the chromatogram.
[24] T. Nishino, T. Watanabe, M. Okada, Y. Nishiyama, N. Sonoda, *J. Org. Chem.* **2002**, *67*, 966–969.
[25] EPR hyperfine splitting for the benzyl spin adduct: found (THF): $a_{\beta H}$ = 20.47 G, a_N= 14.12 G; literature values refs.[26,27]
[26] E. G. Janzen, J. I. P. Liu, *J. Magn. Reson.* **1973**, *9*, 510–512.
[27] E. G. Janzen, Y.-K. Zhang, D. L. Haire, *J. Am. Chem. Soc.* **1994**, *116*, 3738–3743.
[28] $E_{1/2,ox}$ = –0.29 V and $E_{1/2,red}$ = –2.5 V vs. SCE and the outer-sphere mode is not feasible at the limit of –0.3 V.[29]
[29] O. N. Efimov, V. V. Strelets, *Coord. Chem. Rev.* **1990**, *99*, 15–53.
[30] D. Evrard, M. Drouin, Y. Mugnier, P. D. Harvey, *Inorg. Chim. Acta* **2003**, *350*, 442–448.
[31] Attempts to prepare $Pd_3(R)^+$ from Pd_3^{2+} and *n*-butyllithium failed, leading only to cluster dissociation.
[32] P. D. Harvey, S. M. Hubig, T. Ziegler, *Inorg. Chem.* **1994**, *33*, 3700–3710.
[33] P. D. Harvey, R. Provencher, *Inorg. Chem.* **1993**, *32*, 61–65.
[34] I. Gauthron, Y. Mugnier, K. Hierso, P. D. Harvey, *New J. Chem.* **1998**, *22*, 237–246.
[35] This reactive complex has not been isolated so far but the related and crystallographically characterised $Pd_2(iPr_2PCH_2P iPr_2)_2$ complex has been known for ten years.[36]
[36] A. Doehring, R. Goddard, G. Hopp, P. W. Jolly, N. Kokel, C. Krueger, *Inorg. Chim. Acta* **1994**, *222*, 179–192.
[37] A. L. Balch, C. T. Hunt, C.-L. Lee, M. M. Olmstead, J. P. Farr, *J. Am. Chem. Soc.* **1981**, *103*, 3764–3772.
[38] R. U. Kirss, R. Eisenberg, *Inorg. Chem.* **1989**, *28*, 3372–3378.
[39] R. A. Stockland Jr., G. K. Anderson, N. P. Rath, *Organometallics* **1997**, *16*, 5096–5101.
[40] W. B. Motherwell, D. Crich, *Free Radical Chain in Organic Synthesis*, Academic, London, **1992**.
[41] C. P. Jasperse, D. P. Curran, T. L. Fevig, *Chem. Rev.* **1991**, *91*, 1237–1286.
[42] A. G. Davies, *Organotin Chemistry*, Wiley-VCH, Weinheim, **1997**.
[43] P. A. Baguley, J. C. Walton, *Angew. Chem. Int. Ed.* **1998**, *37*, 3072–3082.
[44] E. Dunach, D. Franco, S. Olivero, *Eur. J. Org. Chem.* **2003**, 1605–1622.
[45] A. R. Forrester, J. M. Hay, R. H. Thomson, *Organic Chemistry of Stable Free Radicals*, Academic Press, New York, **1968**.
[46] E. G. Rozantsev, *Free Nitroxyl Radicals*, Plenum Press, New York, **1970**.
[47] *Molecular Biology: Spin Labelling. Theory and Applications* (Ed.: L. J. Berliner), Academic Press, New York, **1976**.
[48] S. Yamago, H. Miyazoe, J.-I. Yoshida, *Tetrahedron Lett.* **1999**, *40*, 2339–2342.
[49] P. D. Harvey, R. Provencher, J. Gagnon, T. Zhang, D. Fortin, K. Hierso, M. Drouin, S. M. Socol, *Can. J. Chem.* **1996**, *74*, 2268–2278.
[50] L. Manojlovic-Muir, K. W. Muir, B. R. Lloyd, R. J. Puddephatt, *J. Chem. Soc., Chem. Commun.* **1985**, 536–537.
[51] B. R. Lloyd, R. J. Puddephatt, *Inorg. Chim. Acta* **1984**, *90*, 77–78.
[52] A. Kowalczuk-Bleja, B. Trzebicka, H. Komber, B. Voit, A. Dworak, *Polymer* **2004**, *45*, 9–18.
[53] V. F. Patel, G. Pattenden, D. M. Thompson, *J. Chem. Soc. Perkin Trans. 2* **1990**, 2729–2734.
[54] M. J. Frisch, G. W. Trucks, H. B. Schlegel, G. E. Scuseria, M. A. Robb, J. R. Cheeseman, V. G. Zakrzewski, J. A. Jr. Montgomery, R. E. Stratmann, J. C. Burant, S. Dapprich, J. M. Millam, A. D. Daniels, K. N. Kudin, M. C. Strain, O. Farkas, J. Tomasi, V. Barone, M. Cossi, R. Cammi, B. Mennucci, C. Pomelli, C. Adamo, S. Clifford, J. Ochterski, G. A. Petersson, P. Y. Ayala, Q. Cui, K. Morokuma, D. K. Malick, A. D. Rabuck, K. Raghavachari, J. B. Foresman, J. Cioslowski, J. V. Ortiz, A. G. Baboul, B. B. Stefanov, G. Liu, A. Liashenko, P. Piskorz, I. Komaromi, R. Gomperts, R. L. Martin, D. J. Fox, T. Keith, M. A. Al-Laham, C. Y. Peng, A. Nanayakkara, C. Gonzalez, M. Challacombe, P. M. W. Gill, B. G. Johnson, W. Chen, M. W. Wong, J. L. Andres, M. Head-Gordon, E. S. Replogle, J. A. Pople, *Gaussian 98* (Revision A.6), Gaussian, Inc., Pittsburgh PA, **1998**.
[55] A. D. Becke, *J. Chem. Phys.* **1993**, *98*, 5648–5652.
[56] C. Lee, W. Yang, R. G. Parr, *Phys. Rev. B* **1988**, *37*, 785–789.
[57] A. D. Miehlich, A. Savin, H. Stoll, H. Preuss, *Chem. Phys. Lett.* **1989**, *157*, 200.
[58] K. D. Dobbs, W. J. Hehre, *J. Comput. Chem.* **1986**, *7*, 359–378.
[59] K. D. Dobbs, W. J. Hehre, *J. Comput. Chem.* **1987**, *8*, 880–893.
[60] K. D. Dobbs, W. J. Hehre, *J. Comput. Chem.* **1987**, *8*, 861–879.
[61] G. M. Sheldrick, SHELX-97 (Includes SHELXS-97, SHELXL-97), Release 97–2, *Programs for Crystal Structure Analysis*, University of Göttingen, Germany, **1998**.
[62] L. J. Farrugia, *J. Appl. Crystallogr.* **1999**, *32*, 837.

Received: July 9, 2004

 © 2005 Wiley-VCH Verlag GmbH & Co. KGaA, Weinheim

Synthesis and Structural and Spectroscopic Characterization of New Ru^{II}-dmso Precursors with Face-Capping Ligands for Use in Self-Assembly Reactions

Elisabetta Iengo,[a] Ennio Zangrando,[a] Edi Baiutti,[a] Fabio Munini,[a] and Enzo Alessio*[a]

Keywords: Facial coordination / Ruthenium / Self-assembly / Tridentate ligands / Tripodal ligands

The aim of this work is the preparation of new, easy-to-make, octahedral Ru^{II} precursors with facial geometry to be used in self-assembly reactions. We chose dmso as a leaving group and 1,4,7-trithiacyclononane ([9]aneS$_3$), tris(pyrazolyl)methane [CH(pz)$_3$, pz = pyrazol-1-yl], or triphos [CH$_3$C(CH$_2$PPh$_2$)$_3$] as the face-capping ligand (fcl). We describe here the preparation and structural characterization of three new dicationic Ru^{II} complexes (as triflate salts) of the type *fac*-[Ru(fcl)(solv)$_3$]$^{2+}$, namely *fac*-[Ru([9]aneS$_3$)(dmso-O)(dmso-S)$_2$]$^{2+}$ (**3b**), which equilibrates in solution with the linkage isomer *fac*-[Ru([9]aneS$_3$)(dmso-O)$_2$(dmso-S)]$^{2+}$ (**3a**), *fac*-[Ru{CH(pz)$_3$}(dmso-O)(dmso-S)$_2$]$^{2+}$ (**7**), and *fac*-[Ru(triphos)(dmso-O)$_2$(H$_2$O)]$^{2+}$ (**9**). In all cases the preferred synthetic procedure involved coordination of the face-capping ligand to *cis*-[RuCl$_2$(dmso)$_4$] first, followed by replacement of the chlorides with dmso (or water) molecules assisted by addition of AgCF$_3$SO$_3$ (AgOTf). NMR investigations showed that hydrolysis of the dmso ligands occurs very easily for **3** in water and for **9** in chloroform, while for complex **7** only the O-bound dmso ligand is replaced in water. In the course of this work, the following complexes were also isolated and structurally characterized: *fac*-[Ru([9]aneS$_3$)Cl(dmso-S)$_2$][OTf] (**2**), *trans*,*cis*,*cis*-[RuCl$_2$(dmso-S)$_2${CH(pz)$_2$(pz)}] (**4**), *trans*,*cis*,*cis*-[RuCl$_2$(dmso-S)$_2$(pzH)$_2$] (**5**), *fac*-[Ru{CH(pz)$_3$}Cl$_2$(dmso-S)] (**6**), *fac*-[Ru([9]aneS$_3$)(py)$_3$][OTf]$_2$ (**11**), *fac*-[Ru([9]aneS$_3$)(py)$_2$(CH$_3$CN)][OTf]$_2$ (**13**), and *fac*-[Ru([9]aneS$_3$O)(dmso-O)$_2$(dmso-S)][OTf]$_2$ ([9]aneS$_3$O = 1,4,7-trithiacyclononane 1-oxide); in **4** the tripodal tris(pyrazolyl)methane acts as a bidentate ligand.

(© Wiley-VCH Verlag GmbH & Co. KGaA, 69451 Weinheim, Germany, 2005)

Introduction

Metal-mediated synthetic procedures involving the self-assembly of electron-donor building blocks (polytopic organic ligands) and electron-acceptor components (naked ions or coordination compounds with some labile ligands) are increasingly being exploited for the preparation of stable, shape-persistent supramolecular assemblies of nanoscopic dimensions.[1] Fascinating three-dimensional systems have been reported by several groups.[2,3] Compared to naked ions, in which the number of available coordination sites for self-assembly and their geometry is determined by the nature of the ion, the use of suitable coordination compounds allows, in principle, a better control of the number and geometry of such sites. In addition, useful properties can be introduced into the supramolecular systems by the nonparticipating ligands. Also, the solubility of the products can be largely influenced by the nature of the ancillary ligands at the metal centers.

However, a literature survey shows that, while a large number of polytopic organic ligands have been employed for the construction of metal-mediated supramolecular assemblies, the number of metal-containing components is relatively limited. Most frequently used are the square-planar complexes [Pd(en)(ONO$_2$)$_2$] (en = ethylenediamine),[3e–3g,3k,4] [Pd(bipy)(ONO$_2$)$_2$] (both soluble in water),[5] and [Pd(dppp)(OTf)$_2$] [soluble in chlorinated solvents, dppp = 1,2-bis(diphenylphosphanyl)propane, OTf = CF$_3$SO$_3$, triflate],[3d,6] which yield *cis* bifunctional dicationic metal fragments after dissociation of the two weakly coordinated anions. Square-planar complexes with labile neutral ligands, such as *cis*-[PtCl$_2$(PhCN)$_2$] and *trans*-[PdCl$_2$(PhCN)$_2$], which yield the bifunctional metal fragments *cis*-PtCl$_2$ and *trans*-PdCl$_2$, respectively, have also been employed in self-assembly reactions.[7] The use of octahedral coordination complexes is more rare and, in most cases, concerns complexes such as [ReX(CO)$_5$] (X = Cl, Br)[8] or *trans*-[RuCl$_2$(dmso)$_2$(L)$_2$] (L = CO, dmso)[9] that yield the *cis* bifunctional neutral fragments *fac*-ReX(CO)$_3$ and *trans*,*cis*-RuCl$_2$(L)$_2$, respectively.

Even though the two coordination sites available in these metal fragments define a linear or planar geometry, 3D adducts have been obtained; tridimensionality can be induced by flexible organic polytopic ligands or by a noncoplanar mutual orientation of planar rigid fragments. In general, in both cases, the shape of the 3D product is rarely predictable a priori.

We believe that the field of coordination-driven self-assembly would greatly benefit from the introduction of new,

[a] Dipartimento di Scienze Chimiche, Università di Trieste, Via L. Giorgieri 1, 34127 Trieste, Italy
E-mail: alessi@mail.univ.trieste.it

Supporting information for this article is available on the WWW under http://www.eurjic.org or from the author.

easy-to-make, coordination compounds having three (or more) readily available coordination sites for self-assembly. In particular, we are interested in the development of low-valent metal fragments with three sites in facial geometry occupied by good leaving groups, either weak neutral ligands (e.g. solvent molecules) or weakly coordinating anions. In such cases the tridimensionality of the adduct would be inherently determined by that of the metal fragment. The remaining three positions must be firmly held by nonparticipating ligands, so that neither dissociation nor isomerization occur during the substitution reaction with the bridging building blocks. Thus, the three permanent facial atoms may be conveniently embedded in a face-capping ligand (fcl), either a heterocycle,[10–12] a tripodal ligand,[13,14] or an organometallic fragment such as η^5-cyclopentadienyl or η^6-arene.[15]

Even though most of the low-valent, half-sandwich complexes described in the literature were not specifically developed for use in self-assembly reactions (for example, they have been widely investigated as homogeneous catalysts),[16] there are some remarkable exceptions.[3a,12,17] For example, Ru^{II}-, Rh^{III}-, and Ir^{III}-arene fragments have been exploited as building blocks for the construction of supramolecular cubes and metallamacrocyclic complexes.[3a,17] One striking example with a nonorganometallic fragment is that of the molecular cube $[\{Ru([9]aneS_3)\}_8(\mu\text{-}4,4'\text{-bipy})_{12}][OTf]_{16}$ ([9]aneS$_3$ = 1,4,7-trithiacyclononane), which is obtained by treatment of *fac*-[Ru([9]aneS$_3$)Cl$_2$(dmso-S)] with the linear ditopic ligand 4,4′-bipy in an 8:12 stoichiometry in noncoordinating solvents. The *fac*-Ru([9]aneS$_3$) and 4,4′-bipy fragments form the corners and edges of the cube, respectively.[12a] However, this synthetic procedure requires prolonged reaction times and heating (four weeks in nitromethane at refluxing temperature), and the addition of AgOTf to remove chlorides. In an ideal metal-mediated self-assembly process, two (or more) components are mixed in solution in the appropriate ratio and react spontaneously with each other to afford the desired product; external interventions, such as addition of silver salts to remove coordinated halides and filtration of precipitates (other than the product), should be avoided. Therefore, precursors with more-labile leaving ligands, such as those mentioned above, would be much preferred for self-assembly purposes.

In this work we report our results concerning the preparation of three new, easy-to-make [Ru(fcl)(solv)$_3$][OTf]$_2$ complexes {fcl = [9]aneS$_3$, tris(pyrazolyl)methane [CH-(pz)$_3$, pz = pyrazol-1-yl], or triphos [CH$_3$C(CH$_2$PPh$_2$)$_3$]; solv = dmso or H$_2$O} (Scheme 1); dmso was chosen as, in our experience with ruthenium precursors, it is normally a better leaving group than the widely used CH$_3$CN. The three face-capping ligands were chosen with the aim of investigating a range of electronic, steric, and solubility properties; in addition, they are either commercially available or very easily prepared and, unlike the organometallic fragments, their reactions do not require the use of Schlenk techniques. In the case of triphos, we partially revisited the work of Venanzi and co-workers on the Ru/dmso/triphos systems.[13]

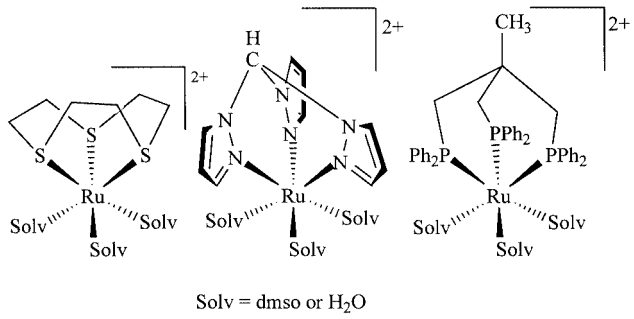

Scheme 1. Schematic representations of the Ru^{II} complexes with face-capping ligands discussed in this work.

Results

The main ruthenium precursor used in this work is the well known complex *cis*-[RuCl$_2$(dmso)$_4$]. Several examples in the literature indicate that the reaction of *cis*-[RuCl$_2$(dmso)$_4$] with one equivalent of a neutral, face-capping ligand usually leads to *fac*-[Ru(fcl)Cl$_2$(dmso-S)] complexes after replacement of three facial sulfoxides (one O-bonded and two S-bonded).[18] Treatment of *fac*-[Ru(fcl)-Cl$_2$(dmso-S)] with two equivalents of a soluble silver salt, such as AgOTf, in a weakly coordinating solvent (solv) is expected to yield the desired *fac*-[Ru(fcl)(solv)$_3$][OTf]$_2$ complexes.[11a,13,18] For example, the reaction of *fac*-[Ru([9]-aneS$_3$)Cl$_2$(dmso-S)] (**1**) with AgOTf in refluxing acetonitrile produces *fac*-[Ru([9]aneS$_3$)(CH$_3$CN)$_3$][OTf]$_2$ in excellent yield.[11a]

As an alternative, in some cases we also employed the dicationic precursor *fac*-[Ru(dmso-S)$_3$(dmso-O)$_3$][OTf]$_2$. In this synthetic approach removal of the chlorides from *cis*-[RuCl$_2$(dmso)$_4$] occurred first and was followed by coordination of the face-capping ligand (see also Scheme 5).

Compounds with 1,4,7-Trithiacyclononane ([9]aneS$_3$)

The complex *fac*-[Ru([9]aneS$_3$)Cl$_2$(dmso-S)] (**1**), despite being an excellent precursor for inorganic synthesis,[11,12] is not suitable *as such* for facial self-assembly reactions with neutral, monodentate bridging ligands, as chloride replace-

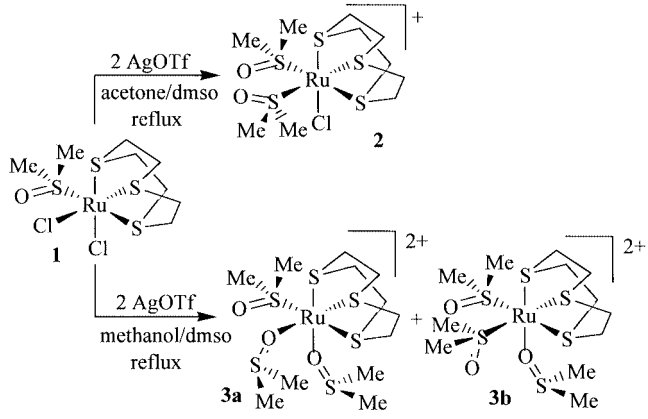

Scheme 2.

 © 2005 Wiley-VCH Verlag GmbH & Co. KGaA, Weinheim

ment needs the assistance of Ag^+.[12d–12f] For example, *fac*-[Ru([9]aneS$_3$)(L)$_3$][PF$_6$]$_2$ complexes (L = py or 4,4′-bipy) can be obtained by treatment of **1** with $AgPF_6$ and a large excess of ligand (L/Ru = in the range from 14 to 25) in refluxing ethanol/water mixtures.[12b,12c]

With the aim of preparing *fac*-[Ru([9]aneS$_3$)(dmso)$_3$][OTf]$_2$, we found that the reaction of **1** with two equivalents of AgOTf in refluxing acetone in the presence of dmso afforded a crystalline product (**2**) that, according to spectroscopic investigations and X-ray diffraction analysis, was established to be the monocationic complex *fac*-[Ru([9]aneS$_3$)Cl(dmso-S)$_2$][OTf] (**2**) (Scheme 2, Figure 1).[19] The same product was also obtained when the above reaction was performed in pure dmso at 100 °C.

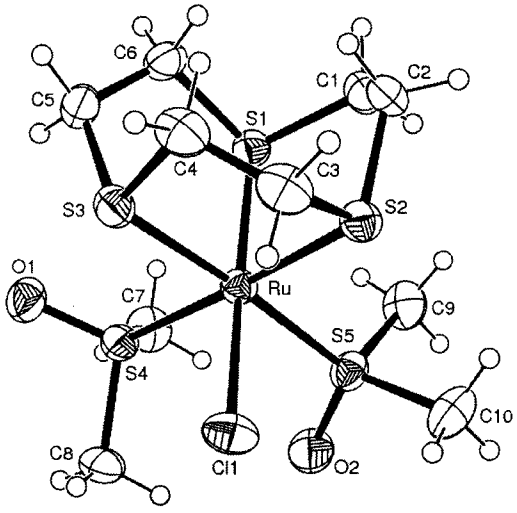

Figure 1. Molecular structure of the cation of *fac*-[Ru([9]aneS$_3$)Cl(dmso-S)$_2$][OTf] (**2**) with thermal ellipsoids at the 40% probability level. Selected bond lengths [Å] and angles [°]: Ru–S(1) 2.313(1), Ru–S(2) 2.346(1), Ru–S(3) 2.351(1), Ru–S(4) 2.325(1), Ru–S(5) 2.339(1), Ru–Cl(1) 2.420(1); S(2)–Ru–S(4) 174.69(3), S(3)–Ru–S(5) 175.21(3), S(1)–Ru–Cl(1) 173.03(3).

Replacement of both chlorides of **1** with dmso molecules was accomplished by performing the reaction with a slight excess of AgOTf in refluxing methanol in the presence of dmso (Scheme 2).

The IR spectrum of the product, which analyzed correctly for [Ru([9]aneS$_3$)(dmso)$_3$][OTf]$_2$ (**3**), showed the presence of both S-bonded (S=O stretching at $\tilde{\nu}$ = 1088 cm^{-1}) and O-bonded (S=O stretching at $\tilde{\nu}$ = 933 and 914 cm^{-1}) dmso molecules. The ^{1}H NMR spectrum of **3** in noncoordinating solvents (e.g. CD_3NO_2 or [D$_6$]acetone), besides many, low-intensity multiplets for the [9]aneS$_3$ protons between δ = 2.8 and 3.4 ppm, contains two sets of signals in an approximate 2.5 to 1 ratio in the region of dmso resonances; the most abundant has two singlets for dmso-O and one for dmso-S ligands, while the less abundant one has one singlet for dmso-O and two for dmso-S ligands (Figure 2). These two sets were attributed to the linkage isomers *fac*-[Ru([9]aneS$_3$)(dmso-O)$_2$(dmso-S)]$^{2+}$ (**3a**) and *fac*-[Ru([9]aneS$_3$)(dmso-O)(dmso-S)$_2$]$^{2+}$ (**3b**), respectively. In each isomer there are two equivalent dmso ligands with diastereotopic methyl groups; accordingly, their NMR resonances are slightly broader than that of the other dmso because of the long-range coupling ($^4J_{H,H} \approx 0.5$ Hz).[20]

X-ray structural determinations performed on crystals selected both from the raw material and from a sample recrystallized from acetone (at room temperature, upon addition of diethyl ether) gave the same results: in both cases the solid-state structure corresponded to *fac*-[Ru([9]aneS$_3$)(dmso-O)(dmso-S)$_2$][OTf]$_2$ (**3b**), i.e. the less-abundant isomer in solution (Figure 3).[21] It is noteworthy that the Ru–S distance in **3b***trans* to dmso-O [2.298(1) Å] is shorter than the values observed for the other S atoms of [9]aneS$_3$ [mean value 2.352(1) Å].

Dissolution of the crystals in CD_3NO_2 or [D$_6$]acetone afforded the usual NMR spectrum, with the same ratio between **3a** and **3b**, thus suggesting that an equilibrium between the two linkage isomers occurs in solution. However, saturation of the dmso resonances of one isomer did not result in any appreciable transfer of saturation to those of the other one, thus indicating that the equilibrium must be quite slow on the NMR timescale. As progressive hydrolysis

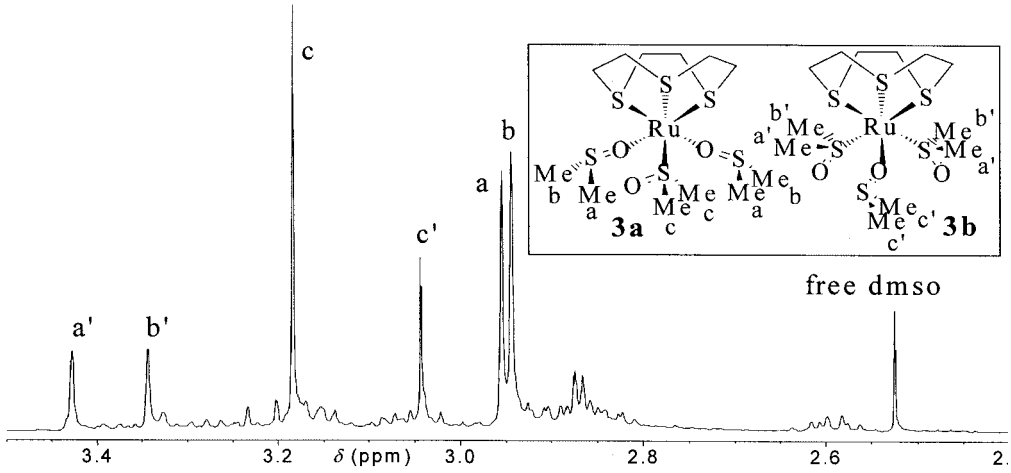

Figure 2. ^{1}H NMR spectrum (CD_3NO_2) of the mixture of the two linkage isomers **3a** and **3b**; dmso singlets are labeled (see insert for labeling scheme). The other small resonances belong to [9]aneS$_3$ protons.

 © 2005 Wiley-VCH Verlag GmbH & Co. KGaA, Weinheim

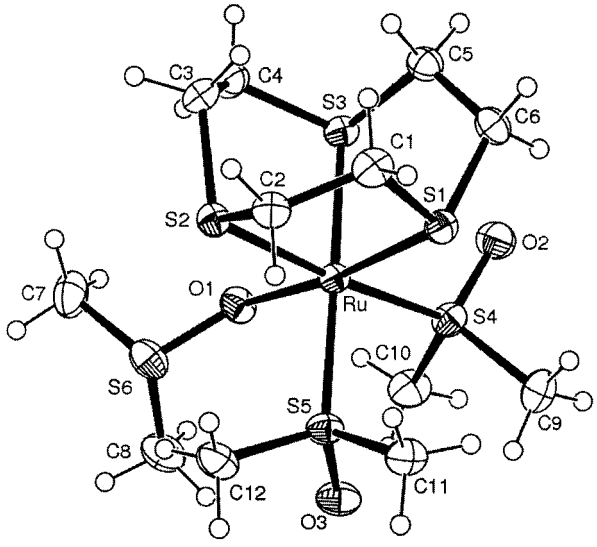

Figure 3. Molecular structure of the cation of *fac*-[Ru([9]aneS$_3$)(dmso-O)(dmso-S)$_2$][OTf]$_2$ (**3b**) with thermal ellipsoids at the 40% probability level. Selected bond lengths [Å] and angles [°]: Ru–O(1) 2.169(3), Ru–S(1) 2.298(1), Ru–S(2) 2.350(1), Ru–S(3) 2.355(1), Ru–S(4) 2.326(1), Ru–S(5) 2.307(1); O(1)–Ru–S(1) 171.49(10), S(2)–Ru–S(4) 174.15(5), S(3)–Ru–S(5) 176.64(5).

of coordinated dmso was observed (minutes), it was not possible to perform a saturation-transfer experiment (and/or line-shape analysis) above room temperature.

We also found that the reaction of *fac*-[Ru(dmso-S)$_3$(dmso-O)$_3$][OTf]$_2$ with *one* equivalent of [9]aneS$_3$ in a number of refluxing solvents (nitromethane, methanol, chloroform, and chloroform/acetone mixtures) yielded only mixtures of the unreacted precursor and of the fully substituted product [Ru([9]aneS$_3$)$_2$][OTf]$_2$, identified by elemental analysis and by comparison with the NMR spectrum reported in the literature.[22]

The ^{1}H NMR spectrum of *fac*-[Ru([9]aneS$_3$)(dmso)$_3$]$^{2+}$ (mixture of the two isomers) in D$_2$O showed that hydrolysis of the dmso ligands occurs within minutes after dissolution (the resonance of a species with one coordinated dmso-S, δ = 3.31 ppm, that integrates for 1/3 of the free dmso appears and remains unchanged for longer observation times, up to 2 days). Under the same conditions only very slow hydrolysis of acetonitrile from *fac*-[Ru([9]aneS$_3$)(CH$_3$CN)$_3$]$^{2+}$ was observed (ca. 30% after one week at ambient temperature).

Compounds with Tris(pyrazolyl)methane [CH(pz)$_3$]

The reaction of *cis*-[RuCl$_2$(dmso)$_4$] with tris(pyrazolyl)methane, CH(pz)$_3$, has not been described so far. We found that treatment of *cis*-[RuCl$_2$(dmso)$_4$] with one equivalent of CH(pz)$_3$ in refluxing methanol yielded a yellow precipitate and large, deep-orange crystals. The mixture was found to contain three products, **4**–**6**, in approximately equimolar amounts (NMR ratio measured in [D$_6$]DMSO, in which the mixture is well soluble), which were separated and obtained in pure form (see Experimental Section).

The elemental analysis of compound **4** was consistent with the formula [RuCl$_2$(dmso)$_2$CH(pz)$_3$], and the solid-state IR spectrum indicated the presence of S-bonded dmso exclusively. The ^{1}H NMR spectrum of **4** in CDCl$_3$ shows two singlets for dmso-S, integrating for six protons each, which is consistent with two geometries, each featuring a bidentate coordination for the tris(pyrazolyl)methane, CH(pz)$_2$(pz): either *trans,cis,cis*-[RuCl$_2$(dmso-S)$_2${CH(pz)$_2$(pz)}] or *cis,trans,cis*-[RuCl$_2$(dmso-S)$_2${CH(pz)$_2$(pz)}] (Scheme 3).[23] In the first hypothesis the two dmso-S ligands are equivalent but have diastereotopic methyls, while in the second hypothesis the two *trans* dmso-S ligands have enantiotopic methyl groups but are not equivalent as the N$_2$Cl$_2$ plane is not a plane of symmetry for the complex.

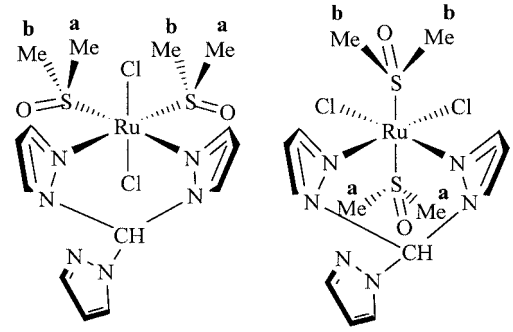

Scheme 3. The two possible geometries of compound **4** that are compatible with the observed ^{1}H NMR spectrum.

A *cis,cis,cis* geometry can be excluded since four methyl resonances for the two sulfoxides would be expected. The *trans,cis,cis*-[RuCl$_2$(dmso-S)$_2${CH(pz)$_2$(pz)}] geometry was eventually confirmed by an X-ray structural investigation (Figure 4), which showed that the tris(pyrazolyl)methane in **4** indeed acts as a bidentate ligand, with a chelating angle of 81.61(13)°.

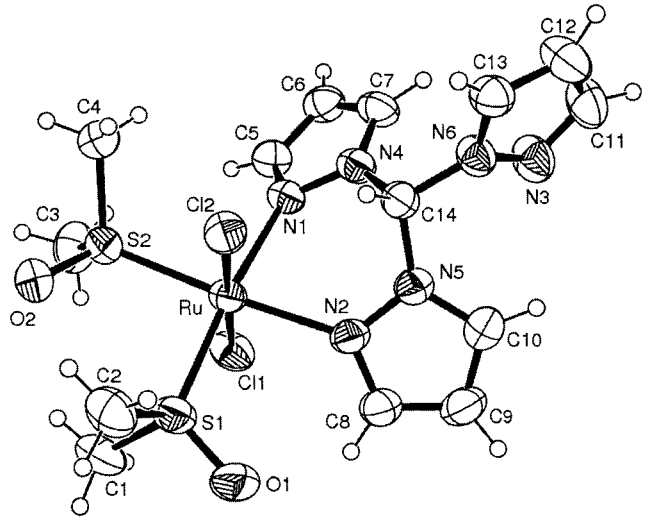

Figure 4. Molecular structure of *trans,cis,cis*-[RuCl$_2$(dmso-S)$_2${CH(pz)$_2$(pz)}] (**4**) with thermal ellipsoids at the 40% probability level. Selected bond lengths [Å] and angles [°]: Ru–N(1) 2.119(3), Ru–N(2) 2.148(4), Ru–S(1) 2.278(1), Ru–S(2) 2.262(1), Ru–Cl(1) 2.402(1), Ru–Cl(2) 2.416(1); N(1)–Ru–N(2) 81.61(13), N(1)–Ru–S(1) 173.84(10), N(2)–Ru–S(2) 176.01(9), Cl(1)–Ru–Cl(2) 179.04(5).

 © 2005 Wiley-VCH Verlag GmbH & Co. KGaA, Weinheim

Complex **4** was also selectively prepared in good yield by reaction of *trans*-[$RuCl_2$(dmso-S)$_4$] with one equivalent of $CH(pz)_3$ in chloroform at ambient temperature. It is in fact well known that *trans*-[$RuCl_2$(dmso-S)$_4$] replaces two *cis* dmso-S ligands to affording the *trans,cis*-$RuCl_2$(dmso-S)$_2$ fragment selectively.[24]

The ^{1}H NMR spectrum of **5** in $CDCl_3$ is very simple (see Experimental Section), suggesting that the complex must be highly symmetrical and that, most likely, simple pyrazole ligands (pzH), derived from the decomposition of tris(pyrazolyl)methane, are bound to ruthenium. X-ray analysis confirmed this hypothesis, indicating that the molecular structure of **5** is *trans,cis,cis*-[$RuCl_2$(dmso-S)$_2$(pzH)$_2$] (see Supporting Information). Complex **5**, which had been already prepared by Taqui Khan and co-workers by treatment of *cis*-[$RuCl_2$(dmso)$_4$] with two equivalents of pyrazole in acetonitrile at 60 °C,[25] is structurally similar to **4**, as it contains two *cis* pyrazole ligands instead of the two *cis* pyrazole units belonging to $CH(pz)_3$ found in **4**.

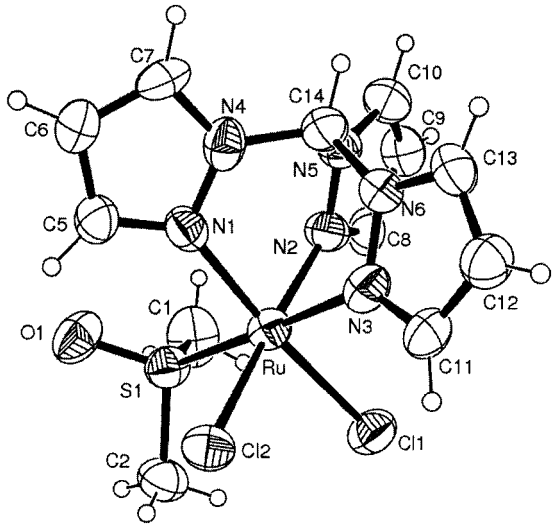

Figure 5. Molecular structure of *fac*-[Ru{CH(pz)$_3$}Cl$_2$(dmso-S)] (**6**) with thermal ellipsoids at the 40% probability level. Selected bond lengths [Å] and angles [°]: Ru–N(1) 2.052(9), Ru–N(2) 2.049(11), Ru–N(3) 2.078(10), Ru–S(1) 2.251(4), Ru–Cl(1) 2.419(3), Ru–Cl(2) 2.406(3); N(1)–Ru–N(2) 87.8(4), N(1)–Ru–N(3) 84.4(4), N(2)–Ru–N(3) 83.3(4), N(1)–Ru–Cl(1) 174.8(4), N(2)–Ru–Cl(2) 172.4(3), N(3)–Ru–S(1) 177.1(3).

Elemental analysis of the third product, **6**, suggested an [$RuCl_2$(dmso)CH(pz)$_3$] stoichiometry. The pattern of the downfield region of the ^{1}H NMR spectrum of **6** in noncoordinating solvents (CD_3NO_2) is similar to that of complex **4**, as it shows two sets of pyrazole resonances with a 2:1 intensity ratio and a singlet at δ = 8.87 ppm for the CH proton of tris(pyrazolyl)methane. The region of the dmso resonances contains one singlet for dmso-S (δ = 3.41 ppm), integrating for six protons. The NMR spectrum of **6** is thus consistent with a *fac*-[Ru{CH(pz)$_3$}Cl$_2$(dmso-S)] geometry in which the two pz units *trans* to the chlorides are equivalent and the methyl groups of dmso-S are enantiotopic. This geometry was confirmed by an X-ray investigation (Figure 5).

As anticipated in the Introduction, complex **6** is the product expected from the reaction of *cis*-[$RuCl_2$(dmso)$_4$] with one equivalent of a face-capping ligand. We found that compound **6** can also be obtained in almost pure form and in good yield by performing the reaction between *cis*-[$RuCl_2$(dmso)$_4$] and $CH(pz)_3$ at slightly higher temperature (in refluxing ethanol rather than methanol), as the product precipitates spontaneously from the reaction mixture. The reactivity of *cis*-[$RuCl_2$(dmso)$_4$] towards $CH(pz)_3$ is summarized in Scheme 4.

Treatment of **6** with two equivalents of AgOTf in refluxing methanol in the presence of dmso afforded *fac*-[Ru{CH(pz)$_3$}(dmso-O)(dmso-S)$_2$][OTf]$_2$ (**7**; Scheme 5). The IR spectrum of **7** clearly indicates the presence of both

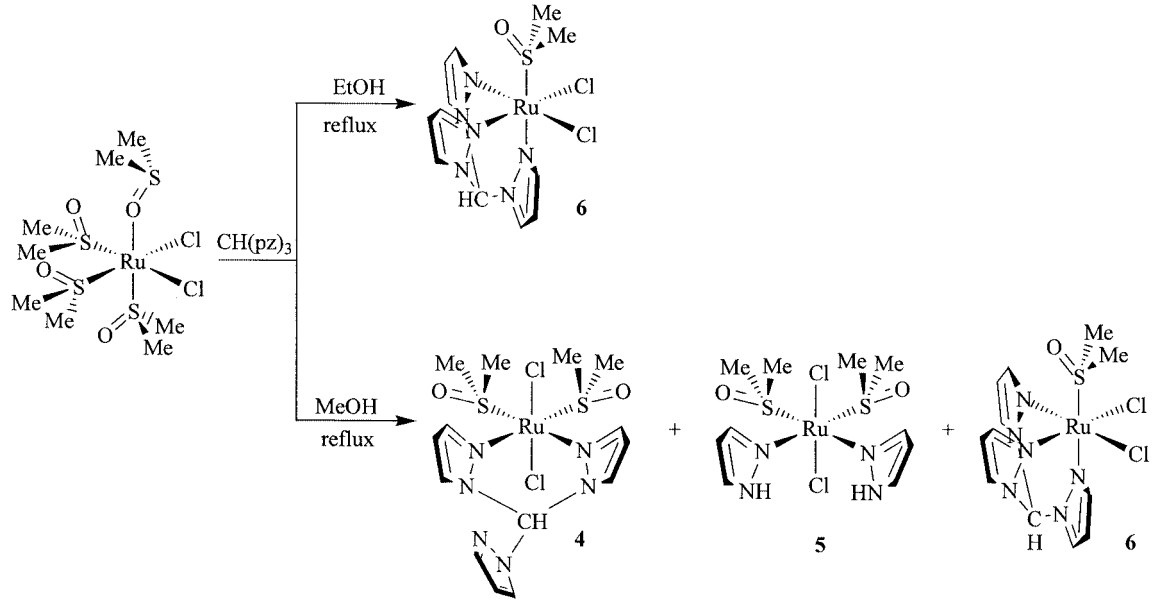

Scheme 4.

 © 2005 Wiley-VCH Verlag GmbH & Co. KGaA, Weinheim

S-bonded (S–O stretching at $\tilde{\nu}$ = 1155 cm^{-1}) and O-bonded (S–O stretching at $\tilde{\nu}$ = 938 cm^{-1}) dmso ligands. Its ^1H NMR spectrum in noncoordinating solvents ([D_6]acetone or CD_3NO_2) shows three singlets for the dmso ligands, integrating for six protons each, one O-bonded and two S-bonded; the resonances for coordinated $CH(pz)_3$ consist of two sets of pyrazole protons with a 2:1 intensity ratio and a singlet for the CH proton. X-ray diffraction studies confirmed the molecular structure of complex **7** (Figure 6); the two equivalent dmso-S ligands have diastereotopic methyl groups, which are responsible for the two NMR resonances in the dmso-S region.

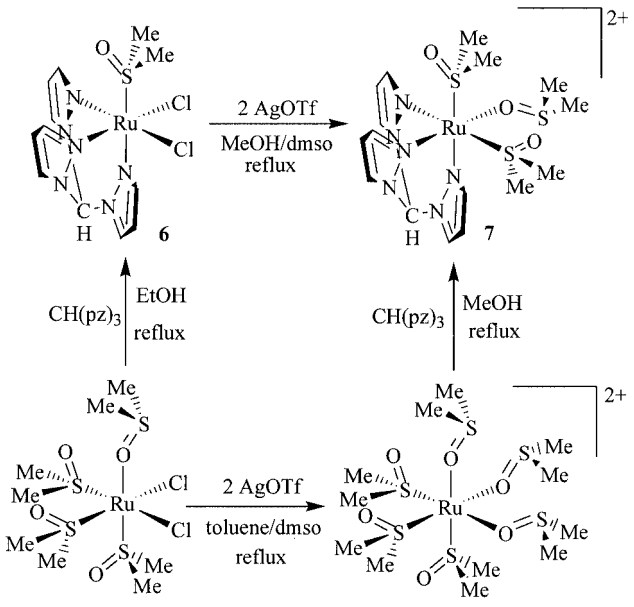

Scheme 5.

When **7** was dissolved in D_2O the O-bonded dmso was rapidly and completely hydrolyzed as, in this solvent, the dmso-O resonance was replaced by the signal of free dmso at δ = 2.72 ppm; hydrolysis of the dmso-S ligands was not observed. In addition, in D_2O the resonance of the CH proton of coordinated $CH(pz)_3$ decreased rather rapidly (minutes) because of exchange with the deuterated solvent. This result suggests that, as might be expected, the acidity of this proton in **7** is greater than in the neutral precursor **6**, for which this phenomenon was not observed.

As an alternative, complex **7** was also obtained by reaction of *fac*-[Ru(dmso-S)$_3$(dmso-O)$_3$][OTf]$_2$ with one equivalent of $CH(pz)_3$ in refluxing methanol (Scheme 5). In this case, unlike with [9]aneS_3 (see above), we found no evidence of the formation of the homoleptic sandwich adduct *fac*-[Ru{$CH(pz)_3$}$_2$][OTf]$_2$.

The structural characterizations indicated that the metal in complexes **4**–**7** displays a distorted octahedral geometry with coordination bond lengths falling in a range already observed for similar ruthenium species.[26] Interestingly, the mean Ru–N bond length found in *fac*-[Ru{$CH(pz)_3$}Cl_2(dmso-S)] (**6**) is shorter (by about 0.1 Å) than those found in the other structures, but similar to that *trans* to the dmso-O in *fac*-[Ru{$CH(pz)_3$}(dmso-O)(dmso-S)$_2$][OTf]$_2$ (**7**).

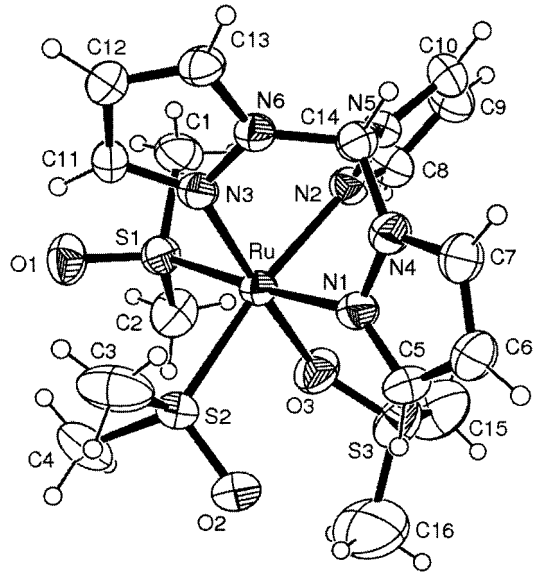

Figure 6. Molecular structure of the cation of *fac*-[Ru{$CH(pz)_3$}(dmso-O)(dmso-S)$_2$][OTf]$_2$ (**7**) with thermal ellipsoids at the 40% probability level. Selected bond lengths [Å] and angles [°]: Ru–N(1) 2.130(5), Ru–N(2) 2.123(4), Ru–N(3) 2.051(4), Ru–S(1) 2.272(2), Ru–S(2) 2.283(2), Ru–O(3) 2.110(4); N(1)–Ru–N(2) 81.89(17), N(1)–Ru–N(3) 86.70(18), N(2)–Ru–N(3) 85.42(17), N(3)–Ru–O(3) 174.32(18), N(1)–Ru–S(1) 175.61(12), N(2)–Ru–S(2) 169.52(13).

The different binding mode of $CH(pz)_3$ in **4** (bidentate) compared to **6** and **7** (tripodal) is reflected in the values of the Ru–N–N and Ru–N–C bond angles. Those found in **4** (131.0° and 123.6°, respectively) are quite different from those found in **6** and **7** (mean values of 136.6° and 118.0°, respectively).

Compounds with $CH_3C(CH_2PPh_2)_3$ (triphos)

We reinvestigated the reaction between *cis*-[$RuCl_2$-(dmso)$_4$] and $CH_3C(CH_2PPh_2)_3$ with the aim of obtaining a more detailed characterization of the *fac*-[Ru(triphos)(dmso)$_3$]$^{2+}$ and *fac*-[Ru(triphos)(dmso)$_2$(H_2O)]$^{2+}$ complexes described by Venanzi and co-workers.[13] Initially, we found that the reaction of *cis*-[$RuCl_2$(dmso)$_4$] with one equivalent of triphos, even when performed under milder conditions than those reported in the literature (4 h in refluxing chloroform vs. 24 h in refluxing toluene),[13] led to the isolation of the dinuclear species [(triphos)Ru(μ-Cl)$_3$Ru(triphos)]Cl (**8**) exclusively (Scheme 6). Formation of the mononuclear complex *fac*-[$RuCl_2$(triphos)(dmso-S)] was not observed. Then, we found that treatment of **8** with four equivalents of AgOTf in refluxing methanol in the presence of dmso led exclusively to the isolation of crystalline *fac*-[Ru(triphos)(dmso-O)$_2$(H_2O)][OTf]$_2$ (**9**) in good yield (Scheme 6).

 © 2005 Wiley-VCH Verlag GmbH & Co. KGaA, Weinheim

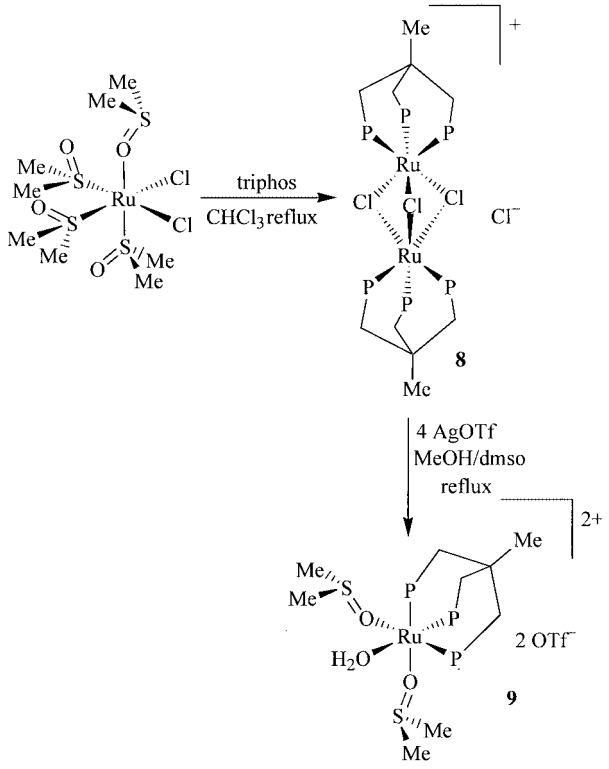

Scheme 6.

The molecular structure of **9** was determined by X-ray analysis (Figure 7). The dimensions of the triphos ligand reflect a small degree of geometrical distortions, with Ru–P distances of 2.272(2), 2.296(2), 2.280(2) Å (the latter *trans* to the aqua ligand), and P–Ru–P bond angles that average 87.4°. Overall, the structural parameters of the tripodal ligand are very similar to those found in the dinuclear complex cation $[(triphos)Ru(\mu\text{-}Cl)_3Ru(triphos)]^+$.[13]

We found no evidence of the formation of *fac*-[Ru(triphos)(dmso-O)$_3$][OTf]$_2$ (**10**); compound **9** was the only product that we isolated, even under the conditions (dmso at 110 °C) that, according to the literature,[13] should afford **10**. Our synthetic procedure leading to **9** is simpler than that described by Venanzi and co-workers[13] in that it avoids the tedious removal of dmso. Several attempts to prepare either **9** or **10** by reaction of *fac*-[Ru(dmso-S)$_3$(dmso-O)$_3$][OTf]$_2$ with triphos in a number of refluxing solvents (e.g. acetone, methanol, toluene) were unsuccessful and led to the isolation of small amounts of unreacted precursor only.

Complex **9** was found to be insoluble in water but soluble in a range of organic solvents, including chloroform. The ^{1}H NMR spectrum of **9** in $CDCl_3$ shows, besides the resonances of coordinated triphos, only the singlet of free dmso at δ = 2.62 ppm, thus indicating that both dmso-O ligands are rapidly released and probably replaced by water molecules. The ^{31}P NMR spectrum shows a singlet at δ = 38.2 ppm, in agreement with the equivalence of the three P atoms in the hydrolyzed species.

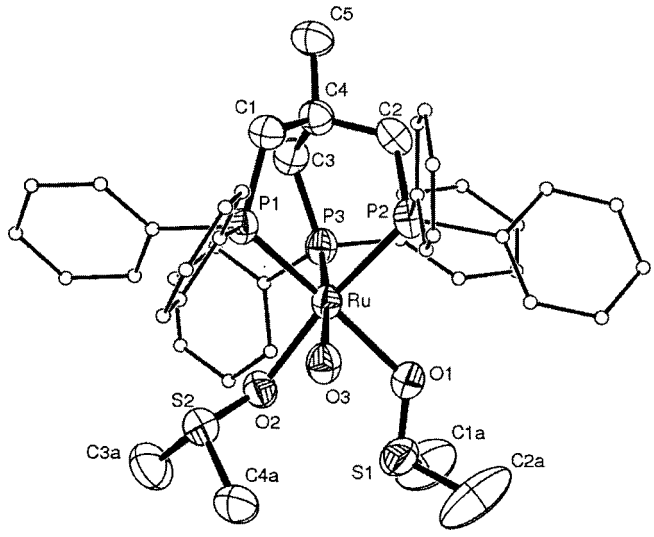

Figure 7. Molecular structure of the cation of *fac*-[Ru(triphos)(dmso-O)$_2$(H_2O)][OTf]$_2$ (**9**) with thermal ellipsoids the 40% probability level. For the sake of clarity the phenyl carbon atoms are indicated as spheres of fixed radius. Selected bond lengths [Å] and angles [°]: Ru–O(1) 2.215(4), Ru–O(2) 2.190(4), Ru–O(3) 2.197(4), Ru–P(1) 2.272(2), Ru–P(2) 2.296(2), Ru–P(3) 2.280(2); O(1)–Ru–P(1) 173.25(12), O(2)–Ru–P(2) 172.80(12), O(3)–Ru–P(3) 174.41(12).

Reactivity of the New Precursors

The reactivity of the new precursors with facial geometry, **3**, **7** and **9**, is currently being investigated in our laboratory and will be the subject of a subsequent paper. We report here only one example concerning the reactivity of the [9]aneS$_3$ complex **3** towards the model ligand pyridine.

The reaction between **3** and a slight excess of pyridine (py/Ru = 4) in refluxing methanol led selectively to the isolation of *fac*-[Ru([9]aneS$_3$)(py)$_3$][OTf]$_2$ (**11**) in excellent yield (Scheme 7). As expected from literature data,[12d–12f] reaction of **1** with pyridine under the same conditions did not yield complex **11**. By comparison, we found that the reaction between the known acetonitrile-containing precursor *fac*-[Ru([9]aneS$_3$)(CH_3CN)$_3$][OTf]$_2$ (**12**) and pyridine, despite being performed at higher temperature (refluxing ethanol) and with a larger excess of ligand (py/Ru = 8), always led to mixtures of **11** and of the disubstituted species *fac*-[Ru([9]aneS$_3$)(py)$_2$(CH_3CN)][OTf]$_2$ (**13**; Scheme 7); both

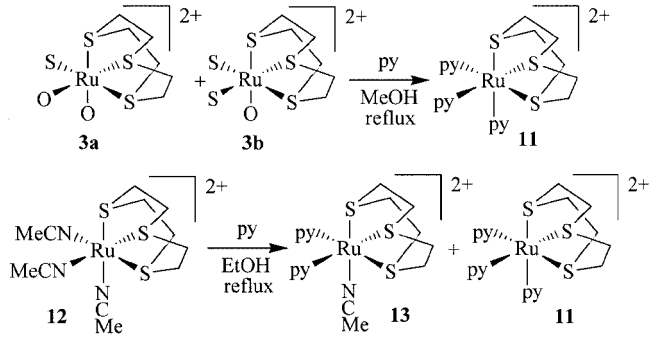

Scheme 7. For simplicity, in **3a** and **3b** O = dmso-O and S =dmso-S.

 © 2005 Wiley-VCH Verlag GmbH & Co. KGaA, Weinheim

products were isolated in pure form and characterized spectroscopically and by X-ray diffraction analysis (see Supporting Information).[27]

Thus, owing to the greater lability of dmso than acetonitrile bound to the $Ru([9]aneS_3)^{2+}$ fragment (see above), complex **3** proved to be a better precursor than **12** in reactions involving the selective replacement of all three leaving groups with monodentate ligands.

Discussion and Conclusions

In summary, we have prepared and structurally characterized three new, easy-to-make, complexes of the type *fac*-$[Ru(fcl)(solv)_3][OTf]_2$, namely *fac*-$[Ru([9]aneS_3)(dmso\text{-}O)(dmso\text{-}S)_2][OTf]_2$ (**3b**), which equilibrates in solution of noncoordinating solvents with the linkage isomer *fac*-$[Ru([9]aneS_3)(dmso\text{-}O)_2(dmso\text{-}S)]^{2+}$ (**3a**), *fac*-$[Ru\{CH(pz)_3\}(dmso\text{-}O)(dmso\text{-}S)_2][OTf]_2$ (**7**), and *fac*-$[Ru(triphos)(dmso\text{-}O)_2(H_2O)][OTf]_2$ (**9**). In all cases the preferred synthetic procedure involves coordination of the face-capping ligand to *cis*-$[RuCl_2(dmso)_4]$ first, followed by replacement of chlorides with dmso (or water) molecules assisted by addition of AgOTf. The isolated yields of compounds **3** and **9** were satisfactory {ca. 80% for **3**, and ca. 50% for **9**, both calculated with respect to *cis*-$[RuCl_2(dmso)_4]$}, while that of **7** was quite low (18–24% depending on the synthetic route). In addition, unlike $[9]aneS_3$ and triphos, tris(pyrazolyl)methane is not commercially available and it is the only fcl, among the three tested, that undergoes decomposition rather easily and shows a tendency to coordinate in a bidentate rather than a tridentate manner.

It should be noted that while in the dications **3b** and **7** there are two S-bonded and one O-bonded dmso ligands, in **9** both dmso ligands are bonded through oxygen and, according to Venanzi and co-workers,[13] the third one also binds in the same manner when it replaces the water molecule to give **10**. The preferential O-bonding of dmso in **9** might be due to both steric and electronic reasons: the steric bulk of the phenyl groups of coordinated triphos might favor coordination of dmso through oxygen, as dmso-O is less sterically demanding than dmso-S. In addition, dmso might coordinate through oxygen to avoid competition for π-electrons with the *trans* phosphane, as is already well established for the coordination of dmso *trans* to other strong π-accepting ligands such as CO and NO.[18]

A comparison of the structural data of the dmso ligands in the three dicationic species *fac*-$[Ru([9]aneS_3)(dmso\text{-}S)_2(dmso\text{-}O)]^{2+}$ (**3b**), *fac*-$[Ru\{CH(pz)_3\}(dmso\text{-}O)(dmso\text{-}S)_2]^{2+}$ (**7**), and *fac*-$[Ru(triphos)(dmso\text{-}O)_2(H_2O)]^{2+}$ (**9**) shows the following trend for Ru–O(dmso) distances: *trans* to N [2.110(4) Å in **7**] < *trans* to S [2.169(3) Å in **3b**] < *trans* to P [2.202(4) Å, mean value in **9**]. In addition, the Ru–S(dmso) bonds *trans* to pyrazole N atoms in **7** are also significantly shorter (0.04 Å) than the corresponding bonds *trans* to the S atoms in **3b**. As both coordinated $CH(pz)_3$ and $[9]aneS_3$ have a small steric bulk in the region of space occupied by the dmso ligands, the reason for the longer Ru–dmso bond distances in **3b** compared to **7** might be found in the greater *trans* influence of trithiacyclononane than tris(pyrazolyl)methane. This consideration might also explain why the S/O linkage isomerization of one sulfoxide was observed for the trithiacyclononane complex **3**, but not in the case of the corresponding tris(pyrazolyl)methane complex **7**.

As the new complexes were prepared with the aim of being employed in self-assembly reactions, the lability of the coordinated dmso molecules is an important parameter to be assessed. NMR investigations showed that hydrolysis of the dmso ligands occurred very easily from **3** in waterand from **9** in chloroform. In the case of complex **7**, only the O-bound dmso ligand was found to be replaced in water. In general, the lability of the dmso ligands of the three dicationic precursors reflects the trend of Ru–dmso bond distances. In addition, NMR investigations of the two similar complexes *fac*-$[Ru([9]aneS_3)(dmso)_3]^{2+}$ (**3**) and *fac*-$[Ru([9]aneS_3)(CH_3CN)_3]^{2+}$ (**12**) in coordinating solvents such as water have shown that coordinated dmso is much more labile than acetonitrile. Accordingly, replacement of the three dmso ligands of **3** with pyridine occurs more easily than that of the acetonitrile ligands of **12**.

In conclusion, a number of experimental results (total yield, structural considerations in the solid state, the lability of the dmso ligands in solution, preliminary results on the reactivity towards model ligands) agree that *fac*-$[Ru([9]aneS_3)(dmso)_3][OTf]_2$ (**3**) and *fac*-$[Ru(triphos)(dmso\text{-}O)_2(H_2O)][OTf]_2$ (**9**) are the most promising complexes for further use in self-assembly reactions with polytopic ligands. Their solubility, a fundamental parameter to be considered in self-assembly reactions, is strongly influenced by the nature of the face-capping ligand. Taken together, they cover a broad range of solvents: while both complexes are soluble in nitromethane, acetone and methanol, **3** is also well soluble in water, while **9** is soluble in chloroform.

It may be argued that the steric demand of triphos in **9** might disfavor coordination of bulkier ligands in place of the dmso and water molecules; however, the steric bulk of dppp, which may be considered as the bidentate analog of triphos, has not prevented the use of $Pd(dppp)^{2+}$ and $Pt(dppp)^{2+}$ fragments in the construction of many 2D and 3D supramolecular adducts through self-assembly procedures.[3d,6]

Experimental Section

Infrared spectra (KBr) were obtained on a Perkin–Elmer 2000 NIR FT-Raman spectrometer. ^1H and $^{31}P\{^1H\}$ NMR spectra were collected at room temperature at 400 and 161.9 MHz, respectively, on a Jeol Eclipse 400 FT spectrometer, with 2,2-dimethyl-2,2-silapentane-5-sulfonate (DSS) as an internal standard for D_2O solutions and the residual non-deuterated solvent signal as reference for spectra recorded from [D_6]acetone (δ = 2.04 ppm), CD_3NO_2 (δ = 4.33 ppm), and $CDCl_3$ (δ = 7.26 ppm) solutions. ^{31}P NMR spectra were referenced to external H_3PO_4 set at δ = 0 ppm. ES-MSdata were obtained on a Perkin–Elmer AP1 spectrometer. Samples were dissolved in acetonitrile; the spectra were recorded in the positive-ion mode at 5.6 kV accelerating potential. Elemental analyses were

 © 2005 Wiley-VCH Verlag GmbH & Co. KGaA, Weinheim

performed at the Dipartimento di Scienze Chimiche, University of Trieste.

Trithiacyclononane, triphos, and deuterated solvents were purchased from Aldrich and used as received. Tris(pyrazolyl)methane,[28] *fac*-[Ru([9]aneS$_3$)(CH$_3$CN)$_3$][OTf]$_2$ (**12**),[11a] *fac*-[Ru([9]aneS$_3$)Cl$_2$(dmso-S)] (**1**),[11a] *cis*-[RuCl$_2$(dmso)$_4$],[29] and *trans*-[RuCl$_2$(dmso)$_4$][29] were prepared as described in the literature. *fac*-[Ru(dmso-O)$_3$(dmso-S)$_3$][OTf]$_2$ was prepared by an improved method compared to those reported in the literature for similar *fac*-[Ru(dmso-O)$_3$(dmso-S)$_3$][X]$_2$ (X = ClO$_4$, BF$_4$) compounds:[30,31] *cis*-[RuCl$_2$(dmso)$_4$] (0.48 g, 1 mmol) was treated with a slight excess of AgOTf in refluxing toluene in the presence of dmso (dmso/Ru = 4) for 30 min; the precipitate was extracted with methanol. Solvent removal afforded the product, which was recrystallized from acetone upon addition of diethyl ether. Yield: 0.6 g (70%).

***fac*-[Ru([9]aneS$_3$)Cl(dmso-S)$_2$][OTf] (2):** *fac*-[Ru([9]aneS$_3$)Cl$_2$(dmso-S)] (**1**; 0.18 g, 0.41 mmol) was dissolved in acetone (10 mL); dmso (75 μL, 1 mmol) and AgOTf (0.21 g, 0.82 mmol) were added and the light-protected mixture was heated to reflux for 1 h. After removal of AgCl by filtration through fine paper, the yellow solution was concentrated in vacuo to ca. 3 mL and stored at room temperature after dropwise addition of diethyl ether until saturation. A light-yellow precipitate formed within 24 h and was removed by filtration, washed with diethyl ether, and vacuum dried. Yield: 55 mg (20%). $C_{11}H_{24}ClF_3O_5RuS_6$ (622.19): calcd. C 21.2, H 3.88; found C 21.6, H 3.63. Selected IR (Nujol): $\tilde{\nu}$ = 1093 (s, νSO dmso-S), 428 cm^{-1} (w, νRu–S). ^{1}H NMR (400 MHz, D_2O, 25 °C): δ = 3.3–2.8 (m, 12 H, [9]aneS$_3$), 3.38 (s, 6 H, dmso-S), 3.46 (s, 6 H, dmso-S) ppm. ^{1}H NMR (400 MHz, CD_3NO_2, 25 °C): δ = 3.3–2.8 (m, 12 H, [9]aneS$_3$), 3.29 (s, 6 H, dmso-S), 3.38 (s, 6 H, dmso-S) ppm.

Crystals suitable for X-ray diffraction were obtained by diffusion of diethyl ether into an acetone solution of **2**.

***fac*-[Ru([9]aneS$_3$)(dmso)$_3$][OTf]$_2$ (3):** *fac*-[Ru([9]aneS$_3$)Cl$_2$(dmso-S)] (**1**; 0.43 g, 1 mmol) was partially dissolved in MeOH (10 mL); dmso (250 μL, 3.5 mmol) and AgOTf (0.60 g, 2.3 mmol) were added and the light-protected mixture was heated to reflux for 3 h. After removal of AgCl by filtration, the yellow solution was concentrated in vacuo to ca. 5 mL. A yellow crystalline precipitate was obtained within 24 h from the solution stored at room temperature after dropwise addition of diethyl ether until saturation. It was removed by filtration, washed with diethyl ether, and vacuum dried. Yield: 0.71 g (88%). $C_{14}H_{30}F_6O_9RuS_8$ (813.93): calcd. C 20.6, H 3.71; found C 20.7, H 3.77. Selected IR (Nujol): $\tilde{\nu}$ = 1088 (s, νSO dmso-S), 933 and 914 (s, νSO dmso-O), 517 (w, νRu–O), 418 cm^{-1} (w, νRu–S). ^{1}H NMR (400 MHz, CD_3NO_2, 25 °C): δ = 2.94 (s, 6 H, dmso-O **3a**), 2.96 (s, 6 H, dmso-O **3a**), 3.04 (s, 6 H, dmso-O **3b**), 3.18 (s, 6 H, dmso-S **3a**), 3.34 (s, 6 H, dmso-S **3b**), 3.43 (s, 6 H, dmso-S **3b**), 3.4–2.8 (m, 12 H, [9]aneS$_3$) ppm. ^{1}H NMR (400 MHz, [D$_6$]acetone, 25 °C): δ = 3.03 (s, 6 H, dmso-O **3a**), 3.04 (s, 6 H, dmso-O **3a**), 3.13 (s, 6 H, dmso-O **3b**), 3.22 (s, 6 H, dmso-S **3a**), 3.42 (s, 6 H, dmso-S **3b**), 3.49 (s, 6 H, dmso-S **3b**), 3.5–2.7 (m, 12 H, [9]aneS$_3$) ppm. Recrystallization: the product was dissolved in acetone and then diethyl ether was added dropwise until saturation.

***trans*,*cis*,*cis*-[RuCl$_2$(dmso-S)$_2${CH(pz)$_2$(pz)}] (4) and *trans*,*cis*,*cis*-[RuCl$_2$(dmso-S)$_2$(pzH)$_2$] (5):** *cis*-[RuCl$_2$(dmso)$_4$] (0.20 g, 0.41 mmol) was partially dissolved in MeOH (15 mL); CH(pz)$_3$ (0.09 g, 0.41 mmol) was added and the mixture was heated to reflux for 2 h. The resulting orange solution was concentrated in vacuo to ca. 2 mL and stored at room temperature after dropwise addition of diethyl ether until saturation. A yellow microcrystalline precipitate containing big orange crystals formed within 12 h. It was removed by filtration, washed with diethyl ether, and vacuum dried (yield: 0.15 g). The mixture was found to contain approximately equimolar amounts of **4**, **5**, and **6** by NMR spectroscopy. The orange crystals of **4** were manually separated under a microscope, washed with cold methanol and diethyl ether, and vacuum dried. $C_{14}H_{22}N_6Cl_2O_2RuS_2$ (542.46): calcd. C 31.0, H 4.09, N 15.49; found C 31.4, H 4.01 N 15.23. Selected IR (Nujol): $\tilde{\nu}$ = 1086 (s, νSO dmso-S), 424 (w, νRu–S), 341 cm^{-1} (m, νRu–Cl). ^{1}H NMR (400 MHz, $CDCl_3$, 25 °C): δ = 3.45 (s, 6 H, dmso-S), 3.47 (s, 6 H, dmso-S), 6.39 (m, 2 H, H4 bound pz), 6.60 (m, 1 H, H4 unbound pz), 7.79 (m, 2 H, H5 bound pz), 8.03 (m, 2 H, H3 + H5 unbound pz), 8.26 (m, 2 H, H3 bound pz), 10.97 (s, 1 H, C*H*) ppm.

The remaining yellow solid, according to ^{1}H NMR analysis, was a mixture of **5** and **6** (and some residual **4**). Treatment of the mixture with chloroform (twice 5 mL) afforded a small amount of almost pure **6** as an insoluble solid residue (see below). Diffusion of diethyl ether into the chloroform solution afforded yellow crystals of **5**. $C_{10}H_{20}N_4Cl_2O_2RuS_2$ (464.39): calcd. C 25.8, H 4.34, N 12.06; found C 25.3, H 4.18, N 12.02. ^{1}H NMR (400 MHz, $CDCl_3$, 25 °C): δ = 3.21 (s, 12 H, dmso-S), 6.38 (m, 2 H, H4 pzH), 7.63 (m, 2 H, H5 pzH), 7.98 (m, 2 H, H3 pzH), 12.6 (br. s, 2 H, N*H* pzH) ppm.

***trans*,*cis*,*cis*-[RuCl$_2$(dmso-S)$_2${CH(pz)$_2$(pz)}] (4):** As an alternative, complex **4** was selectively prepared in good yield by the following route: *trans*-[RuCl$_2$(dmso-S)$_4$] (0.1 g, 0.2 mmol) was dissolved in $CHCl_3$ (20 mL) and CH(pz)$_3$ (45 mg, 0.21 mmol) was added. After standing 24 h at room temperature, the resulting orange solution was concentrated in vacuo to ca. 5 mL and stored at room temperature after dropwise addition of diethyl ether until saturation. Orange crystals formed within 24 h and were removed by filtration, washed with diethyl ether, and vacuum dried. Yield: 65 mg (60%). See above for elemental analysis and spectroscopic characterization.

***fac*-[Ru{CH(pz)$_3$}Cl$_2$(dmso-S)] (6):** *cis*-[RuCl$_2$(dmso)$_4$] (0.30 g, 0.62 mmol) was partially dissolved in absolute EtOH (20 mL); CH(pz)$_3$ (0.14 g, 0.62 mmol) was added and the mixture was heated to reflux for 2 h. A yellow precipitate formed from the hot orange solution. After cooling the mixture to room temperature, it was removed by filtration, washed with cold ethanol and diethyl ether, and vacuum dried. Yield: 0.13 g (45%). Concentration of the mother liquor and addition of diethyl ether afforded a further yellow precipitate that, according to ^{1}H NMR spectroscopy, was a mixture of **5** and **6**. Recrystallization: the product was dissolved in the minimum amount of dmso (e.g. 0.15 g of **6** in 0.5 mL dmso), the solution was diluted with acetone (5 mL) and diethyl ether was added dropwise until saturation. Crystals of **6** suitable for X-ray diffraction were obtained by diffusion of diethyl ether into the dmso/acetone solution. $C_{12}H_{16}N_6Cl_2ORuS$ (464.33): calcd. C 31.0, H 3.47, N 18.09; found C 30.9, H 3.37, N 17.85. Selected IR (Nujol): $\tilde{\nu}$ = 1078 (s, νSO dmso-S), 424 cm^{-1} (w, νRu–S). ^{1}H NMR (400 MHz, D_2O, 25 °C): δ = 3.49 (s, 6 H, dmso-S), 6.56 (m, 2 H, H4), 6.65 (m, 1 H, H4), 8.01 (m, 2 H, H5), 8.23 (m, 1 H, H5), 8.36 (m, 2 H, H3), 8.40 (m, 1 H, H3), 9.47 (s, 1 H, C*H*) ppm. ^{1}H NMR (400 MHz, CD_3NO_2, 25 °C): δ = 3.41 (s, 6 H, dmso-S), 6.49 (m, 2 H, H4), 6.60 (m, 1 H, H4), 8.07 (m, 2 H, H5), 8.23 (m, 1 H, H5), 8.28 (m, 2 H, H3), 8.31 (m, 1 H, H3), 8.87 (s, 1 H, C*H*) ppm.

***fac*-[Ru{CH(pz)$_3$}(dmso-O)(dmso-S)$_2$][OTf]$_2$ (7):** This complex was prepared by two different routes: a) by treatment of **6** with two equivalents of AgOTf in the presence of dmso; b) by reaction of *fac*-[Ru(dmso-S)$_3$(dmso-O)$_3$][OTf]$_2$ with CH(pz)$_3$. The yield of **7** with respect to the common precursor *cis*-[RuCl$_2$(dmso)$_4$] is similar in the two procedures: 18% via route a, and 24% via route b.

 © 2005 Wiley-VCH Verlag GmbH & Co. KGaA, Weinheim

Route a: *fac*-[Ru{CH(pz)$_3$}Cl$_2$(dmso-S)] (**6**; 0.10 g, 0.21 mmol) was dissolved in MeOH (5 mL); dmso (46 μL, 0.65 mmol) and AgOTf (0.11 g, 0.43 mmol) were added and the light-protected mixture was heated to reflux for 3 h. After removal of AgCl by filtration, the yellow solution was concentrated in vacuo to ca. 2 mL and stored at room temperature after dropwise addition of diethyl ether until saturation. A pale-yellow microcrystalline precipitate formed within 24 h and was removed by filtration, washed with diethyl ether, and vacuum dried. Yield: 72 mg (40%). $C_{18}H_{28}N_6F_6O_9RuS_5$ (847.82): calcd. C 25.5, H 3.33, N 9.91; found C 25.0, H 3.12, N 9.76. Selected IR (Nujol): $\tilde{\nu}$ = 1092 (s, νSO dmso-S), 938 (s, νSO dmso-O), 518 (w, νRu–O), 428 cm^{-1} (w, νRu–S). ^{1}H NMR (400 MHz, [D$_6$]acetone, 25 °C): δ = 2.94 (s, 6 H, dmso-O), 3.27 (s, 6 H, dmso-S), 3.35 (s, 6 H, dmso-S), 6.75 (m, 1 H, H4 pz *trans* to dmso-O), 6.83 (m, 2 H, H4 pz *trans* to dmso-S), 8.22 (m, 1 H, H5 pz *trans* to dmso-O), 8.69 (m, 2 H, H5 pz *trans* to dmso-S), 8.75 (m, 3 H, H3), 10.19 (s, 1 H, C*H*) ppm. ^{1}H NMR (400 MHz, CD_3NO_2, 25 °C): δ = 2.83 (s, 6 H, dmso-O), 3.17 (s, 6 H, dmso-S), 3.22 (s, 6 H, dmso-S), 6.68 (m, 1 H, H4 pz *trans* to dmso-O), 6.75 (m, 2 H, H4 pz *trans* to dmso-S), 8.09 (m, 1 H, H5 pz *trans* to dmso-O), 8.46 (m, 2 H, H5 pz *trans* to dmso-S), 8.62 (m, 3 H, H3), 9.61 (s, 1 H, C*H*) ppm. ^{1}H NMR (400 MHz, D_2O, 25 °C): δ = 2.72 (s, 6 H, free dmso), 3.20 (s, 6 H, dmso-S), 3.29 (s, 6 H, dmso-S), 6.71 (m, 1 H, H4 pz *trans* to dmso-O), 6.75 (m, 2 H, H4 pz *trans* to dmso-S), 8.03 (m, 1 H, H5 pz *trans* to dmso-O), 8.42 (m, 2 H, H5 pz *trans* to dmso-S), 8.53 (m, 3 H, H3), 9.84 (s, 1 H, C*H*) ppm.
Route b: *fac*-[Ru(dmso-S)$_3$(dmso-O)$_3$][OTf]$_2$ (0.10 g, 0.11 mmol) was dissolved in MeOH (5 mL); CH(pz)$_3$ (25 mg, 0.11 mmol) was added and the mixture was heated to reflux for 30 min. During reflux the initially colorless solution turned yellow; it was then concentrated in vacuo to ca. 1.5 mL and stored at room temperature after dropwise addition of diethyl ether until saturation. A pale-yellow microcrystalline precipitate formed within a few days and was removed by filtration, washed with diethyl ether, and vacuum dried. Yield: 32 mg (35%). $C_{18}H_{28}N_6F_6O_9RuS_5$ (847.82): calcd. C 25.5, H 3.33, N 9.91; found C 26.0, H 3.23, N 10.06. Crystals suitable for X-ray diffraction were obtained by diffusion of diethyl ether into an acetone solution of **7** (15 mg in 2 mL).

[(triphos)Ru(μ-Cl)$_3$Ru(triphos)]Cl (8): *cis*-[RuCl$_2$(dmso)$_4$] (0.48 g, 1 mmol) was dissolved in CHCl$_3$ (20 mL); triphos (0.62 g, 1 mmol) was added and the mixture was heated to reflux for 4 h under a stream of Ar. A yellow precipitate formed from the hot orange solution. After cooling the mixture to room temperature, this precipitate was removed by filtration, washed with diethyl ether, and vacuum dried. Yield: 0.6 g (75%). $C_{82}H_{78}Cl_4P_6Ru_2$ (1593.29): calcd. C 61.8, H 4.93; found C 60.5, H 4.90. ^{1}H NMR (400 MHz, $CDCl_3$, 25 °C): δ = 1.59 (br. s, 6 H, CH_3), 2.40 (br. s, 12 H, CH_2), 6.83 (m, 24 H, *m*-Ph), 7.18 (t, 12 H, *p*-Ph), 7.37 (t, 24 H, *o*-Ph) ppm.

***fac*-[Ru(triphos)(dmso-O)$_2$(H$_2$O)][OTf]$_2$ (9):** [(triphos)Ru(μ-Cl)$_3$Ru-(triphos)]Cl (**8**; 0.20 g, 0.12 mmol) was dissolved in MeOH (10 mL); dmso (60 μL, 0.84 mmol) and AgOTf (0.13 g, 0.52 mmol) were added and the light-protected mixture was heated to reflux for 2 h. AgCl was removed by filtration and thoroughly washed with MeOH. The pale-orange solution was concentrated in vacuo to ca. 2 mL and stored at room temperature after dropwise addition of diethyl ether until saturation. A pale-yellow microcrystalline precipitate formed within 24 h and was removed by filtration, washed with diethyl ether, and vacuum dried. Yield: 0.2 g (70%). $C_{47}H_{53}F_6O_9P_3RuS_4$ (1198.1): calcd. C 47.1, H 4.46; found C 46.4, H 4.56. ^{1}H NMR (400 MHz, $CDCl_3$, 25 °C): δ = 1.63 (br. s, 3 H, CH_3), 2.40 (br. s, 6 H, CH_2), 2.61 (s, 12 H, free dmso), 7.13 (m, 12 H, *m*-Ph), 7.27 (m, 18 H, *o*+*p*-Ph) ppm. ^{31}P{^{1}H} NMR (161.9 MHz, $CDCl_3$, 25 °C): δ = 38.2 ppm.

***fac*-[Ru([9]aneS$_3$)(py)$_3$][OTf]$_2$ (11) and *fac*-[Ru([9]aneS$_3$)(py)$_2$-(CH$_3$CN)][OTf]$_2$ (13):** *fac*-[Ru([9]aneS$_3$)(CH$_3$CN)$_3$][OTf]$_2$ (**12**; 0.1 g, 0.14 mmol) was partially dissolved in EtOH (20 mL); pyridine (92 μL, 1.13 mmol) was added and the mixture was heated to reflux for 4 h. The resulting yellow-green solution was filtered through fine paper to remove a small amount of a dark precipitate and then concentrated in vacuo to ca. 2 mL and stored at room temperature after dropwise addition of diethyl ether until saturation. A yellow crystalline precipitate containing two types of crystals (big prisms and small needles) formed within 24 h and was then removed by filtration, washed with chloroform and diethyl ether, and vacuum dried (yield 80 mg). The precipitate was shown to be an approximate 1:3 mixture of **11** and **13** by ^{1}H NMR spectroscopy. The large yellow prisms were manually separated from the mixture under a microscope and were found to be **13** (by X-ray diffraction and ^{1}H NMR spectroscopy). $C_{20}H_{25}N_3F_6O_6RuS_5$ (778.80): calcd. C 30.8, H 3.23, N 5.39; found C 31.0, H 3.17, N 5.41. ^{1}H NMR (400 MHz, D_2O, 25 °C): δ = 2.52 (s, 3 H, CH_3CN), 2.80 (m, 8 H, [9]aneS$_3$), 3.05 and 2.85 (m, 2 H each, [9]aneS$_3$), 7.45 (m, 4 H, *m*H py), 7.98 (t, 2 H, *p*H py), 8.61 (d, 4 H, *o*H py) ppm.

Recrystallization of the remaining mixture from ethanol by diffusion of diethyl ether afforded yellow crystals of pure **11**. $C_{23}H_{27}N_3F_6O_6RuS_5$ (816.85): calcd. C 33.8, H 3.33, N 5.14; found C 33.9, H 3.27, N 5.27. ^{1}H NMR (400 MHz, D_2O, 25 °C): δ = 2.80 (s, 12 H, [9]aneS$_3$), 7.44 (m, 6 H, *m*H py), 7.98 (t, 3 H, *p*H py), 8.48 (d, 6 H, *o*H py) ppm.

As an alternative, *fac*-[Ru([9]aneS$_3$)(py)$_3$][OTf]$_2$ (**11**) was selectively prepared as follows: *fac*-[Ru([9]aneS$_3$)(dmso)$_3$][OTf]$_2$ (**3**; 0.1 g, 0.12 mmol) was dissolved in MeOH (5 mL); pyridine (41 μL, 0.5 mmol) was added and the mixture was heated to reflux for 2 h. The resulting yellow-green solution was concentrated in vacuo to ca. 2 mL and stored at room temperature after dropwise addition of diethyl ether until saturation. A yellow crystalline precipitate formed within 24 h and was then removed by filtration, washed with chloroform and diethyl ether, and vacuum dried. Yield: 68 mg (70%). $C_{23}H_{27}N_3F_6O_6RuS_5$ (816.85): calcd. C 33.8, H 3.33, N 5.14; found C 34.3, H 3.41, N 5.22. ^{1}H NMR (400 MHz, CD_3NO_2, 25 °C): δ = 2.89 (m, 12 H, [9]aneS$_3$), 7.52 (m, 6 H, *m*H py), 8.04 (t, 3 H, *p*H py), 8.50 (d, 6 H, *o*H py) ppm. ES-MS: *m*/*z* (calcd.) = 667.8 (667.8) [M – OTf]$^+$, 259.4 (259.2) [M – 2OTf]$^{2+}$.

X-ray Crystallography: All diffraction data, with the exception of **3b** [150(2) K] were collected at room temperature on a Nonius DIP-1030H system with graphite-monochromated Mo-K_α radiation. For each crystal, a total of 30 frames were collected (exposure time of 15–30 min, rotation angle of 6° about φ, with the detector at a distance of 80–90 mm from the crystal). Cell refinement, indexing, and scaling of the data sets were done using the programs Mosflm and Scala.[32] All the structures were solved by Patterson and Fourier analyses and refined by the full-matrix least-squares method based on F^2 with all observed reflections.[33] The choice of the non-centrosymmetric space group $Pna2_1$ for **7** was confirmed by the successful final refinement; the Flack parameter of 0.49(10) indicates racemic twinning of the crystal. A difference Fourier map of **6** revealed a molecule of dmso and one of water. A residual in **3b** was assigned to a water oxygen (occupancy = 0.5, H atoms omitted). All the calculations were performed using the WinGX System, Ver. 1.64.05.[34]

Crystallographic Data for 2: $C_{11}H_{24}ClF_3O_5RuS_6$, M = 622.18, triclinic, space group $P\bar{1}$, a = 8.031(3), b = 9.501(3), c = 14.890(4) Å, α = 94.48(2)°, β = 104.01(3)°, γ = 89.12(2)°, V = 1099.0(6) Å^3, Z =

 © 2005 Wiley-VCH Verlag GmbH & Co. KGaA, Weinheim

2, D_c = 1.880 g cm^{-3}, μ(Mo-K_α) = 1.450 mm^{-1}, F_{000} = 628, θ range = 2.65–29.01°. Final $R1$ = 0.0424, $wR2$ = 0.1130, S = 1.059 for 248 parameters and 8340 reflections, 5152 unique [R(int) = 0.0463], of which 4233 with $I > 2\sigma(I)$; max positive and negative peaks in ΔF map 0.678, –0.590 e Å^{-3}.

Crystallographic Data for 3b·0.5H$_2$O: $C_{14}H_{31}F_6O_{9.50}RuS_8$, M = 822.94, triclinic, space group $P\bar{1}$, a = 11.795(3), b = 12.115(3),c = 12.878(4) Å, α = 64.96(2)°, β = 66.88(3)°, γ = 71.14(2)°, V = 1505.8(7) Å^3, Z = 2, D_c = 1.815 g cm^{-3}, μ(Mo-K_α) = 1.155 mm^{-1}, F_{000} = 834, θ range = 1.83–27.48°. Final $R1$ = 0.0475, $wR2$ = 0.1234, S = 1.032 for 384 parameters and 10 769 reflections, 6407 unique [R(int) = 0.0626], of which 5004 with $I > 2\sigma(I)$; max positive and negative peaks in ΔF map 0.621, –1.267 e Å^{-3}.

Crystallographic Data for 4: $C_{14}H_{22}Cl_2N_6O_2RuS_2$, M = 542.47, orthorhombic, space group $Pbca$, a = 16.158(3), b = 13.456(3), c = 21.605(4) Å, V = 4697.4(16) Å^3, Z = 8, D_c = 1.534 g cm^{-3}, μ(Mo-K_α) = 1.093 mm^{-1}, F_{000} = 2192, θ range = 2.52–28.28°. Final $R1$ = 0.0494, $wR2$ = 0.1495, S = 1.079 for 249 parameters and 11 332 reflections, 5780 unique [R(int) = 0.0331], of which 4413 with $I > 2\sigma(I)$; max positive and negative peaks in ΔF map 1.164,–0.474 e Å^{-3}.

Crystallographic Data for 5: $C_{10}H_{20}Cl_2N_4O_2RuS_2$, M = 464.41, monoclinic, space group $P2_1/n$, a = 8.807(3), b = 16.668(4), c = 12.416(4) Å, β = 104.97(2)°, V = 1760.8(9) Å^3, Z = 4, D_c = 1.752 g cm^{-3}, μ(Mo-K_α) = 1.438 mm^{-1}, F_{000} = 936, θ range = 2.09–29.92°. Final $R1$ = 0.0363, $wR2$ = 0.0925, S = 1.055 for 194 parameters and 8455 reflections, 4950 unique [R(int) = 0.0335], of which 4326 with $I > 2\sigma(I)$; max positive and negative peaks in ΔF map 0.951, –0.604 e Å^{-3}.

Crystallographic Data for 6·dmso·H$_2$O: $C_{14}H_{24}Cl_2N_6O_3RuS_2$, M = 560.48, orthorhombic, space group $Pna2_1$, a = 18.614(4), b = 13.631(4), c = 8.585(3) Å, V = 2178.3(11) Å^3, Z = 4, D_c = 1.709 g cm^{-3}, μ(Mo-K_α) = 1.185 mm^{-1}, F_{000} = 1136, θ range = 2.65–26.37°. Final $R1$ = 0.0656, $wR2$ = 00.1486, S = 1.039 for 258 parameters and 4527 reflections, 4238 unique [R(int) = 0.0749], of which 2385 with $I > 2\sigma(I)$; max positive and negative peaks in ΔF map 0.733, –0.803 e Å^{-3}.

Crystallographic Data for 7: $C_{18}H_{28}F_6N_6O_9RuS_5$, M = 847.83, triclinic, space group $P\bar{1}$, a = 9.831(3), b = 13.378(4), c = 14.050(4) Å, α = 72.72(2)°, β = 69.29(3)°, γ = 72.05(3)°, V = 1607.3(8) Å^3, Z = 2, D_c = 1.752 g cm^{-3}, μ(Mo-K_α) = 0.901 mm^{-1}, F_{000} = 856, θ range = 2.37–26.37°. Final $R1$ = 0.0571, $wR2$ = 0.1509, S = 1.027 for 412 parameters and 10 399 reflections, 6148 unique [R(int) = 0.0494], of which 4620 with $I > 2\sigma(I)$; max positive and negative peaks in ΔF map 0.733, –0.792 e Å^{-3}.

Crystallographic Data for 9: $C_{47}H_{53}F_6O_9P_3RuS_4$, M = 1198.11, monoclinic, space group $P2_1/n$, a = 18.847(4), b = 15.173(4), c = 18.941(5) Å, β = 97.09(2)°, V = 5375(2) Å^3, Z = 4, D_c = 1.481 g cm^{-3}, μ(Mo-K_α) = 0.608 mm^{-1}, F_{000} = 2456, θ range = 1.73–27.48°. Final $R1$ = 0.0623, $wR2$ = 0.1703, S = 1.056 for 637 parameters and 22 951 reflections, 12 105 unique [R(int) = 0.0746], of which 6332 with $I > 2\sigma(I)$; max positive and negative peaks in ΔF map 0.477, –1.011 e Å^{-3}.

Crystallographic Data for 13: $C_{20}H_{25}F_6N_3O_6RuS_5$, M = 778.80, triclinic, space group $P\bar{1}$, a = 7.563(2), b = 10.777(3), c = 19.310(4) Å, α = 97.40(2)°, β = 86.63(3)°, γ = 104.66(3)°, V = 1509.4(7) Å^3, Z = 2, D_c = 1.714 g cm^{-3}, μ(Mo-K_α) = 0.942 mm^{-1}, F_{000} = 784, θ range = 2.34–27.10°. Final $R1$ = 0.0550, $wR2$ = 0.1558, S = 1.040 for 371 parameters and 8918 reflections, 5644 unique [R(int) = 0.0431], of which 4898 with $I > 2\sigma(I)$; max positive and negative peaks in ΔF map 1.446, –0.499 e·Å^{-3}.

CCDC-238841 (for **13**), -238842 ... -238847 (for **2**–**8**) and -238848 (for **9**) contain the supplementary crystallographic data forthis paper. These data can be obtained free of charge from The Cambridge Crystallographic Data Centre via www.ccdc.cam.ac.uk/data_request/cif.

Supporting Information: The molecular structures of *trans,cis,cis*-[$RuCl_2$(dmso-S)$_2$(pzH)$_2$] (**5**) and the cations of *fac*-[Ru([9]aneS_3)(py)$_3$][OTf]$_2$·CH_3OH (**11**), *fac*-[Ru([9]aneS_3)(py)$_2$(CH_3CN)][OTf]$_2$ (**13**), and of one of the two crystallographically independent cations of *fac*-[Ru([9]aneS_3O)(dmso-O)$_2$(dmso-S)][OTf]$_2$ are reported. Of these, only the data for compounds **5** and **13** have been deposited, as the other structures are of poor resolution mainly because of the disordered triflate anions. The preparation of *fac*-[Ru([9]aneS_3O)(dmso-O)$_2$(dmso-S)][OTf]$_2$ is also reported (see also footnote on the first page of this article).

Acknowledgments

Acknowledgments are made for financial support to the donors of The Petroleum Research Fund, administered by the ACS, (grant ACS PRF# 38892-AC3), to MIUR (PRIN no. 2003035553), and to Regione Autonoma Friuli-Venezia Giulia (L. R. 3/98). We wish to thank Engelhard Italiana S.p.A. for a generous loan of hydrated $RuCl_3$.

[1] For recent reviews see: a) C. A. Schalley, A. Lützen, M. Albrecht, *Chem. Eur. J.* **2004**, *10*, 1072–1080; b) E. Iengo, E. Zangrando, E. Alessio, *Eur. J. Inorg. Chem.* **2003**, 2371–2384; c) G. F. Swiegers, T. J. Malefetse, *Coord. Chem. Rev.* **2002**, *225*, 91–121; d) S. R. Seidel, P. J. Stang, *Acc. Chem. Res.* **2002**, *35*, 972–983; e) F. A. Cotton, C. Lin, C. A. Murillo, *Acc. Chem. Res.* **2001**, *34*, 759–771.

[2] For selected examples of 3D systems mediated by naked ions, see: a) Z. R. Bell, L. P. Harding, M. D. Ward, *Chem. Commun.* **2003**, 2432–2433; b) M. Hong, Y. Zhao, W. Su, R. Cao, M. Fujita, Z. Zhou, A. S. C. Chan, *J. Am. Chem. Soc.* **2000**, *122*, 4819–4820; c) B. F. Abrahams, S. J. Egan, R. Robson, *J. Am. Chem. Soc.* **1999**, *121*, 3535–3536; d) R. W. Saalfrank, U. Reimann, M. Göritz, F. Hampel, A. Scheurer, F. W. Heinemann, M. Büschel, J. Daub, V. Schünemann, A. X. Trautwein, *Chem. Eur. J.* **2002**, *8*, 3614–3619; e) T. Beissel, R. E. Powers, K. N. Raymond, *Angew. Chem. Int. Ed. Engl.* **1996**, *35*, 1084–1086; f) M. Barboiu, G. Vaughan, R. Graff, J.-M. Lehn, *J. Am. Chem. Soc.* **2003**, *125*, 10 257–10 265; g) C.-Y. Su, Y.-P. Cai, C.-L. Chen, M. D. Smith, W. Kaim, H.-C. zur Loye, *J. Am. Chem. Soc.* **2003**, *125*, 8595–8613; h) D. K. Chand, M. Fujita, K. Biradha, S. Sakamoto, K. Yamaguchi, *Dalton Trans.* **2003**, 2750–2756.

[3] For selected examples of 3D systems mediated by coordination or organometallic compounds, see: a) M. L. Kuhlman, T. B. Rauchfuss, *Inorg. Chem.* **2004**, *43*, 430–435 and refs. therein; b) J.-P. Lang, Q.-F. Xu, Z.-N. Chen, B. F. Abrahams, *J. Am. Chem. Soc.* **2003**, *125*, 12 682–12 683; c) J. J. Sokol, M. P. Shores, J. R. Long, *Inorg. Chem.* **2002**, *41*, 3052–3054; d) A. Ikeda, M. Ayabe, S. Shinkai, S. Sakamoto, Y. Yamaguchi, *Org. Lett.* **2000**, *2*, 3707–3710; e) K. Kumazawa, K. Biradha, T. Kusukawa, T. Okano, M. Fujita, *Angew. Chem. Int. Ed.* **2003**, *42*, 3909–3913; f) S. Tashiro, M. Tominaga, T. Kusukawa, M. Kawano, S. Sakamoto, K. Yamaguchi, M. Fujita, *Angew. Chem. Int. Ed.* **2003**, *42*, 3267–3270; g) M. Yoshizawa, Y. Takeyama, T. Kusukawa, M. Fujita, *Angew. Chem. Int. Ed.* **2002**, *41*, 1347–1349; h) K.-W. Chi, C. Addicott, Y. K. Kryschenko, P. J. Stang, *J. Org. Chem.* **2004**, *69*, 964–966; i) Y. K. Kryschenko, S. R. Seidel, D. C. Muddiman, A. I. Nepomuceno, P. J. Stang, *J. Am. Chem. Soc.* **2003**, *125*, 9647–9652; j) C. J. Kuhel, Y. K. Kryschenko, U. Radhakrishnan, S. R. Siedel, S. D. Huang, P. J. Stang,

 © 2005 Wiley-VCH Verlag GmbH & Co. KGaA, Weinheim

Proc. Natl. Acad. Sci. USA **2002**, *99*, 4932–4936; k) S. C. Johannessen, R. G. Brisbois, J. P. Fischer, P. A. Grieco, A. E. Counterman, D. E. Clemmer, *J. Am. Chem. Soc.* **2001**, *123*, 3818–3819; l) D. A. McMorran, P. J. Steel, *Angew. Chem. Int. Ed.* **1998**, *37*, 3295–3297.

[4] a) A. Orita, L. Jiang, T. Nakano, N. Ma, J. Otera, *Chem. Commun.* **2002**, 1362–1363; b) T. Moriuchi, M. Miyaishi, T. Hirao, *Angew. Chem. Int. Ed.* **2001**, *40*, 3042–3045.

[5] a) S.-Y. Yu, H. Huang, H.-B. Liu, Z.-N. Chen, R. Zhang, M. Fujita, *Angew. Chem. Int. Ed.* **2003**, *42*, 686–690; b) T. Kusukawa, M. Fujita, *J. Am. Chem. Soc.* **2002**, *124*, 13 576–13 582.

[6] a) M. Ferrer, M. Mounir, O. Rossell, E. Ruiz, M. A. Maestro, *Inorg. Chem.* **2003**, *42*, 5890–5899; b) F. Würthner, A. Sautter, *Chem. Commun.* **2000**, 445–446; c) U. Radhakrishnan, M. Schweiger, P. J. Stang, *Org. Lett.* **2001**, *3*, 3141–3143.

[7] a) C. M. Drain, F. Nifiatis, A. Vasenko, J. D. Batteas, *Angew. Chem. Int. Ed.* **1998**, *37*, 2344–2347; b) D. Sun, F. S. Tham, C. A. Reed, L. Chaker, M. Burgess, P. D. Boyd, *J. Am. Chem. Soc.* **2000**, *122*, 10 704–10 705; c) H. Yuan, L. Thomas, L. K. Woo, *Inorg. Chem.* **1996**, *35*, 2808–2817; d) A. P. H. J. Schenning, F. B. G. Benneker, H. P. M. Geurts, X. Y. Liu, R. J. M. Nolte, *J. Am. Chem. Soc.* **1996**, *118*, 8549–8552.

[8] a) T. Brasey, A. Buryak, R. Scopelliti, K. Severin, *Eur. J. Inorg. Chem.* **2004**, 964–967; b) T. Rajendran, B. Manimaran, R.-T. Liao, R.-J. Lin, P. Thanasekaran, G.-H. Lee, S.-M. Peng, Y.-H. Liu, I.-J. Chang, S. Rajagopal, K.-L. Lu, *Inorg. Chem.* **2003**, *42*, 6388–6394; c) B. Manimaran, P. Thanasekaran, R.-J. Lin, I.-J. Chang, G.-H. Lee, S.-M. Peng, S. Rajagopal, K.-L. Lu, *Inorg. Chem.* **2002**, *41*, 5323–5325; d) K. E. Splan, M. H. Keefe, A. M. Massari, K. A. Walters, J. T. Hupp, *Inorg. Chem.* **2002**, *41*, 619–621; e) G. A. Mines, B.-C. Tzeng, K. J. Stevenson, J. Li, J. T. Hupp, *Angew. Chem. Int. Ed.* **2002**, *41*, 154–157; f) H. Hartmann, S. Berger, R. Winter, J. Fiedler, W. Kaim, *Inorg. Chem.* **2000**, *39*, 4977–4980; g) S.-S. Sun, A. J. Lees, *J. Am. Chem. Soc.* **2000**, *122*, 8956–8967.

[9] a) E. Iengo, E. Zangrando, R. Minatel, E. Alessio, *J. Am. Chem. Soc.* **2002**, *124*, 1003–1013; b) E. Iengo, E. Zangrando, S. Geremia, R. Graff, B. Kieffer, E. Alessio, *Chem. Eur. J.* **2002**, *8*, 4670–4674; c) E. Iengo, B. Milani, E. Zangrando, S. Geremia, E. Alessio, *Angew. Chem. Int. Ed.* **2000**, *39*, 1096–1099.

[10] a) M. Schröder, *Pure Appl. Chem.* **1988**, *60*, 517–524; b) A. J. Blake, M. Schröder, *Adv. Inorg. Chem.***1990**, *35*, 1–80; c) S. R. Cooper, *Acc. Chem. Res.* **1988**, *21*, 141–146; d) N. W. Alcock, J. C. Cannadine, G. R. Clark, A. F. Hill, *J. Chem. Soc., Dalton Trans.* **1993**, 1131–1135; e) A. J. Blake, M. A. Halcrow, M. Schröder, *J. Chem. Soc., Chem. Commun.* **1991**, 253–256; f) S.-M. Yang, W.-C. Cheng, S.-M. Peng, K.-K. Cheung, C.-M. Che, *J. Chem. Soc., Dalton Trans.* **1995**, 2955–2959.

[11] a) C. Landgrafe, W. S. Sheldrick, *J. Chem. Soc., Dalton Trans.* **1994**, 1885–1893; b) K. Brandt, W. S. Sheldrick, *J. Chem. Soc., Dalton Trans.* **1996**, 1237–1243; c) B. J. Goodfellow, V. Félix, S. M. D. Pacheco, J. Pedrosa de Jesus, M. G. B. Drew, *Polyhedron* **1997**, *16*, 393–401.

[12] a) S. Roche, C. Haslam, H. Adams, S. L. Heath, J. A. Thomas, *Chem. Commun.* **1998**, 1681–1682; b) S. Roche, H. Adams, S. E. Spey, J. A. Thomas, *Inorg. Chem.* **2000**, *39*, 2385–2390; c) S. Roche, S. E. Spey, H. Adams, J. A. Thomas, *Inorg. Chim. Acta* **2001**, *323*, 157–162; d) S. Roche, L. J. Yellowlees, J. A. Thomas, *Chem. Commun.* **1998**, 1429–1430; e) C. S. Araujo, M. G. B. Drew, V. Felix, L. Jack, J. Madureira, M. Newell, S. Roche, T. M. Santos, J. A. Thomas, L. Yellowlees, *Inorg. Chem.* **2002**, *41*, 2250–2259; f) N. Shan, S. J. Vickers, H. Adams, M. D. Ward, J. A. Thomas, *Angew. Chem. Int. Ed.* **2004**, *43*, 3938–3941.

[13] L. F. Rhodes, C. Sorato, L. M. Venanzi, F. Bachechi, *Inorg. Chem.* **1988**, *27*, 604–610.

[14] a) W. Levason, S. D. Orchard, G. Reid, *J. Chem. Soc., Dalton Trans.* **2000**, 4550–4554; b) W. Levason, S. D. Orchard, G. Reid, J. M. Street, *J. Chem. Soc., Dalton Trans.* **2000**, 2537–2543; c) D. P. Riley, J. D. Oliver, *Inorg. Chem.* **1986**, *25*, 1814–1821.

[15] a) H. Brunner, A. Köllnberger, A. Mehmood, T. Tsuno, M. Zabel, *Organometallics* **2004**, *23*, 4006–4008 and refs. therein; b) L. A. Huxham, E. L. S. Cheu, B. O. Patrick, B. R. James, *Inorg. Chim. Acta* **2003**, *352*, 238–246; c) H. Chen, J. A. Parkinson, S. Parsons, R. A. Coxall, R. O. Gould, P. J. Sadler, *J. Am. Chem. Soc.* **2002**, *124*, 3064–3082; d) C. S. Allardyce, P. J. Dyson, D. J. Ellis, S. L. Heath, *Chem. Commun.* **2001**, 1396–1397; e) W. Luginbühl, P. Zbinden, P. A. Pittet, T. Armbruster, H.-B. Bürgi, A. E. Merbach, A. Ludi, *Inorg. Chem.* **1991**, *30*, 2350–2355; f) W. S. Sheldrick, S. Heeb, *Inorg. Chim. Acta* **1990**, *168*, 93–100; g) A. M. McNair, D. C. Boyd, K. R. Mann, *Organometallics* **1986**, *5*, 303–310; h) M. A. Bennett, A. K. Smith, *J. Chem. Soc., Dalton Trans.* **1974**, 233–241.

[16] a) B. M. Trost, F. D. Toste, A. B. Pinkerton, *Chem. Rev.* **2001**, *101*, 2067–2096; b) G. Jia, C. P. Lau, *J. Organomet. Chem.* **1998**, *565*, 37–48; c) S. G. Davies, J. P. McNally, A. J. Smallridge, *Adv. Organomet. Chem.* **1990**, *30*, 1–77; d) H. A. Meyer, W. C. Kaska, *Chem. Rev.* **1994**, *94*, 1239–1272; e) C. Bianchini, A. Meli, M. Peruzzini, F. Vizza, F. Zanobini, *Coord. Chem. Rev.* **1992**, *120*, 193–208.

[17] a) R. H. Fish, *Coord. Chem. Rev.* **1999**, *185–186*, 569–584; b) K. Severin, *Coord. Chem. Rev.* **2003**, *245*, 3–10; c) M.-L. Lehaire, R. Scopelliti, L. Herdeis, K. Polborn, P. Mayer, K. Severin, *Inorg. Chem.* **2004**, *43*, 1609–1617; d) K. Yamanari, S. Yamamoto, R. Ito, Y. Kushi, A. Fuyuhiro, N. Kubota, T. Fukuo, R. Arakawa, *Angew. Chem. Int. Ed.* **2001**, *40*, 2268–2271; e) K. Yamanari, R. Ito, S. Yamamoto, T. Konno, A. Fuyuhiro, K. Fujioka, R. Arakawa, *Inorg. Chem.* **2002**, *41*, 6824–6830; f) S. Korn, W. S. Sheldrick, *J. Chem. Soc., Dalton Trans.* **1997**, 2191–2199; g) H. Amouri, M. N. Rager, F. Cagnol, J. Vaissermann, *Angew. Chem. Int. Ed.* **2001**, *40*, 3636–3638; h) Y. Tanabe, S. Kuwata, Y. Ishii, *J. Am. Chem. Soc.* **2002**, *124*, 6528–6529; i) W. S. Han, S. W. Lee, *Dalton Trans.* **2004**, 1656–1663.

[18] E. Alessio, *Chem. Rev.* **2004**, *104*, 4203–4242.

[19] A poorly characterized complex formulated as $[Ru([9]aneS_3)Cl(dmso)_2]^+$ has apparently been obtained by treatment of hydrated $RuCl_3$ with $[9]aneS_3$ in dmso: M. N. Bell, A. J. Blake, M. Schröder, H.-J. Küppers, K. Wieghardt, *Angew. Chem. Int. Ed. Engl.* **1987**, *26*, 250–251.

[20] J. R. Barnes, P. L. Goggin, R. J. Goodfellow, *J. Chem. Res. (M)* **1979**, 1610–1656.

[21] Slow recrystallization of the raw product **3** from dmso/acetone mixtures (days) yielded crystals of a new product, *fac*-$[Ru([9]aneS_3O)(dmso\text{-}O)_2(dmso\text{-}S)][OTf]_2$ ($[9]aneS_3O$ = 1,4,7-trithiacyclononane 1-oxide), whose X-ray structure was determined (see Supporting information). In this complex one of the S atoms of the face-capping ligand has been oxidized to SO; the remaining three coordination positions are occupied by one S-bonded and two O-bonded dmso ligands (one is *trans* to the SO function of $[9]aneS_3O$).

[22] S. C. Rawle, T. J. Sewell, S. R. Cooper, *Inorg. Chem.* **1987**, *26*, 3769–3775.

[23] The *trans*-$Ru(dmso\text{-}S)_2$ fragment is seldom found in Ru^{II} complexes. The best known examples are *trans*-$[RuCl_2(dmso\text{-}S)_4]$ and *cis*,*trans*,*cis*-$[RuCl_2(dmso\text{-}S)_2(CO)_2$ (see ref.[18]).

[24] a) E. Alessio, E. Iengo, E. Zangrando, S. Geremia, P. A. Marzilli, M. Calligaris, *Eur. J. Inorg. Chem.* **2000**, 2207–2219; b) M. Henn, E. Alessio, G. Mestroni, M. Calligaris, W. M. Attia, *Inorg. Chim. Acta* **1991**, *187*, 39–50.

[25] M. M. Taqui Khan, P. S. Roy, K. Venkatasubramanian, N. H. Khan, *Inorg. Chim. Acta* **1990**, *176*, 49–55.

[26] a) M. Calligaris, *Coord. Chem. Rev.* **2004**, *248*, 351–375; b) M. Calligaris, *Croat. Chem. Acta* **1999**, *72*, 147–169; c) M. Calligaris, O. Carugo, *Coord. Chem. Rev.* **1996**, *153*, 83–154.

[27] The structural determinations of the analogous *fac*-$[Ru([9]aneS_3)(py)_2(CH_3CN)][PF_6]_2$ and *fac*-$[Ru([9]aneS_3)(py)_3][PF_6]_2$ derivatives have been already described by J. A. Thomas and coworkers.[12b]

 © 2005 Wiley-VCH Verlag GmbH & Co. KGaA, Weinheim

[28] D. L. Reger, T. C. Grattan, K. J. Brown, C. A. Little, J. J. S. Lamba, A. L. Rheingold, R. D. Sommer, *J. Organomet. Chem.* **2000**, *607*, 120–128.
[29] E. Alessio, G. Mestroni, G. Nardin, W. M. Attia, M. Calligaris, G. Sava, S. Zorzet, *Inorg. Chem.* **1988**, *27*, 4099–4106.
[30] I. P. Evans, A. Spencer, G. Wilkinson, *J. Chem. Soc., Dalton Trans.* **1973**, 204–209.
[31] A. R. Davies, F. W. B. Einstein, N. P. Farrell, B. R. James, R. S. McMillan, *Inorg. Chem.* **1978**, *17*, 1965–1969.
[32] Collaborative Computational Project, Number 4, *Acta Crystallogr., Sect. D* **1994**, *50*, 760–763.
[33] G. M. Sheldrick, *SHELX97, Programs for Crystal Structure Analysis*, Release 97-2, University of Göttingen, Germany, **1998**.
[34] L. J. Farrugia, *J. Appl. Crystallogr.* **1999**, *32*, 837–838.
Received: August 25, 2004

 © 2005 Wiley-VCH Verlag GmbH & Co. KGaA, Weinheim

Synthesis and Physicochemical Characterization of Bis(macrocycles) Involving a Porphyrin and a *meso*-Substituted Corrole – X-ray Crystal Structure of a [(Free-base porphyrin)–corrole]bis(pyridine)cobalt Complex

Jean-Michel Barbe,*[a] Fabien Burdet,[a] Enrique Espinosa,[a] and Roger Guilard*[a]

Keywords: Bis(macrocycles) / Porphyrins / Corroles / Synthetic methods / X-ray diffraction

A very efficient, simple synthesis of face-to-face porphyrin–corrole free-bases bearing substituents at the *meso* positions of the corrole ring is reported. Starting from the (porphyrin–aldehyde)zinc species **1Zn**, porphyrin–corrole free-bases (**3M**, **3C**) are obtained in two steps, in fairly good yields (40–43 %), compared to 11 steps for their corrole β-pyrrole-substituted counterparts. Moreover, the possibility to directly synthesize the free-base (porphyrin–corrole)cobalt complex (**5M** or **5C**) allows for the further preparation of heterodimetallic derivatives. Crystals of the bis(pyridine) adduct of **5M** have been grown; the molecular structure clearly shows that the two pyridine molecules are coordinated to the cobalt ion in *endo* and *exo* positions, leading to an open-mouth geometry of the bis(macrocycle). The structure of **5M(py)$_2$**also shows intermolecular π–π interactions along the [1 0 0] direction, leading to stacking of the complexes.
(© Wiley-VCH Verlag GmbH & Co. KGaA, 69451 Weinheim, Germany, 2005)

Introduction

Enzyme mimics have always been of great interest. For example, considerable studies of heme/copper terminal oxidases have led to several models of the active site. In addition, several reviews have been published recently.[1–3] Concurrently, cofacial bis(porphyrins) were proposed as synthetic models of the dioxygen reduction site and, particularly, face-to-face bis(porphyrin)bis(cobalt) complexes appeared to be very efficient catalysts for the four-electron reduction of O_2 to water in acidic media.[1,2,4,5] Cofacial heterodimetallic bis(porphyrins) containing one cobalt atom were later reported, and also proved to be good catalysts for O_2 reduction.[1,6–8] Numerous studies on the synthetic models indicate that the catalytic activity originates from intermetallic cooperation between the two metal atoms of the bis(porphyrin) complex, tuned by the nature of the spacer.[1,5] Moreover, the Lewis acid character of one of the two metals in the bis(porphyrin) complex is a key factor in stabilizing the dioxygen adduct during catalysis.[1]

Our research in this domain has focused on cofacialbis(-macrocycles) where a porphyrin and a corrole are held together by a rigid spacer.[9,10] The originality of this approach lies in the difference in coordination properties between the porphyrin and the corrole rings. Indeed, corroles can coordinate metal ions in higher oxidation states than porphyrins.[11,12] Therefore, complexation of the bis-(macrocycle) by a cobalt ion could directly generate the active species in the O_2 four-electron catalytic cycle, i.e. cobalt(II) in the porphyrin and cobalt(III) in the corrole ring.[13] We recently demonstrated that this mixed-valence species is a good catalyst for the 4e reduction of O_2 to water.[14]

Most investigated porphyrin–corrole bis(macrocycles) were substituted at the β-pyrrole positions by electron-donating groups.[9] However, recent syntheses of *meso*-substituted corroles allow significant variation of the substituents on the corrole ring, particularly at the *meso* positions.[15–23] Electron-withdrawing substituents on the bis(macrocycle) corrole ring enhance the Lewis acid character of the complexed metal ion [namely cobalt(III)], the main parameter in stabilizing the dioxygen adduct. Therefore, the stability of the dioxygen adduct formed during the catalytic process increases with the Lewis acid character of the corrole-coordinated metal ion. By adapting the new procedures, involving the reaction of dipyrromethanes with an aromatic aldehyde, we could prepare new porphyrin–corrole derivatives with the corrole counterpart substituted at the *meso* positions with mesityl or 2,6-dichlorophenyl groups. Moreover, the corrole ring is formed in only two steps, allowing for the synthesis of gram quantities of these model catalysts.

Here we describe the synthesis of these new bis(macrocycles), and show the possibility of selectively metalating the corrole ring by cobalt (or another metal) to access heterodimetallic derivatives.

[a] Laboratoire d'Ingénierie Moléculaire pour la Séparation et les Applications des Gaz (LIMSAG, CNRS UMR 5633), Faculté des Sciences, Université de Bourgogne,
6 boulevard Gabriel, 21100 Dijon, France
Fax: +33-3-80396117
E-mail: Roger.Guilard@u-bourgogne.fr

Results and Discussion

Synthesis and Physicochemical Characterization

We recently reported a significant improvement in the syntheses of β-substituted porphyrin–corrole and bis(corrole) bis(macrocycles), allowing the yield in final free-bases to be almost tripled.[10] However, even if one can introduce electron-withdrawing substituents (i.e. phenyl groups) at the β-pyrrole positions of the corrole ring, the synthetic pathway affording the final free-bases is somewhat long. As an example, Scheme 1 shows the synthesis of a β-phenyl-substituted porphyrin–corrole derivative.

When starting from the porphyrin–aldehyde precursor (**1** in Scheme 1), the target compound is obtained in 11 steps due to the step-by-step nature of this approach, which firstly requires the formation of a dipyrromethane. This dipyrromethane is then coupled with a pyrrole–aldehyde to obtain the final corrole ring by formation of an *a*,*c*-biladiene. Each pyrrole precursor is obtained in three to five steps, depending upon the substitution at the β-pyrrole positions (Scheme 1). Notably, a symmetrical corrole ring is prepared in only eight steps since only one pyrrole derivative is needed. Another drawback of this multistep synthetic route is that any variation in the structure of the desired bis(macrocycle) requires the synthesis of a new pyrrole precursor (Scheme 1). Nevertheless, this is still the only method that allows the insertion of electron-donating substituents at the β-pyrrole positions of the corrole ring.[9,10]

An alternative to these β-substituted derivatives would be the *meso*-substituted ones. Indeed, the new methods leading to *meso*-substituted corrole rings[15–23] can be adapted to the synthesis of porphyrin–corrole derivatives. In the present case, starting from **1Zn**, the porphyrin–corrole bis(macrocycle) is obtained in only two steps. Scheme 2 gives the overall procedure.

5-Mesityldipyrromethane and 5-(2,6-dichlorophenyl)dipyrromethane were obtained from a previously described procedure[24] and used for reaction with **1Zn**. **1Zn** was used in the condensation instead of **1** since the reaction requires the presence of trifluoroacetic acid (TFA), which can protonate the porphyrin moiety. For **1**, larger quantities of TFA must be used for the condensation reaction, and acidolysis of the reacting dipyrromethane can occur. Therefore, **1Zn** is a more appropriate precursor because no protonation of the porphyrin core can occur and the final derivatives **2M** and **2C** are much easier to purify by column chromatography than their non-metalated counterparts.

1Zn was obtained in 87% yield in classical conditions by simple metalation of **1** by zinc acetate dihydrate in chloroform/methanol (Scheme 2). The remaining aldehyde function of **1Zn** was treated further, with either 5-mesityldipyrromethane or 5-(2,6-dichlorophenyl)dipyrromethane, in dichloromethane in the presence of a catalytic amount of TFA (aldehyde/TFA = 17:1.3 mmol).[19] Under the best experimental conditions, in which dipyrromethane was added in twice the stoichiometric amount (66 mmol, 4 equiv.) with respect to **1Zn**, both **2M** and **2C** were obtained in yields close to 30% compared to ca. 6% for stoichiometric amounts (33 mmol, 2 equiv.).[19] To recover **2M** and **2C**, the final reoxidation process was performed using 2,3-dichloro-5,6-dicyano-1,4-benzoquinone (DDQ) after a 25× dilution in dichloromethane.[21] **2M** and **2C** were isolated in 27 and 33% yield, respectively. Corrole ring formation is easily evidenced in MALDI/TOF by a distribution of peaks centered at 1253.92 (**2M**) and 1307.34 (**2C**), and by ^{1}H NMR resonance signals of the corrole (Table 1). Notably, no signal

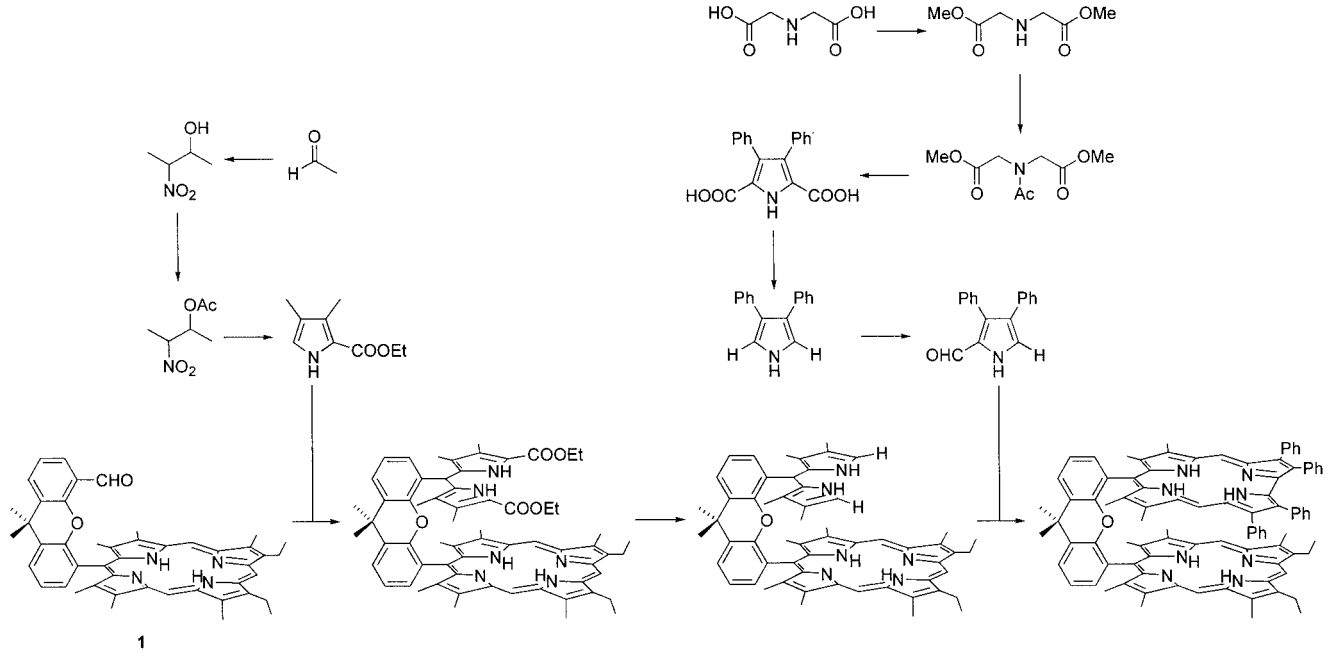

Scheme 1.

 © 2005 Wiley-VCH Verlag GmbH & Co. KGaA, Weinheim

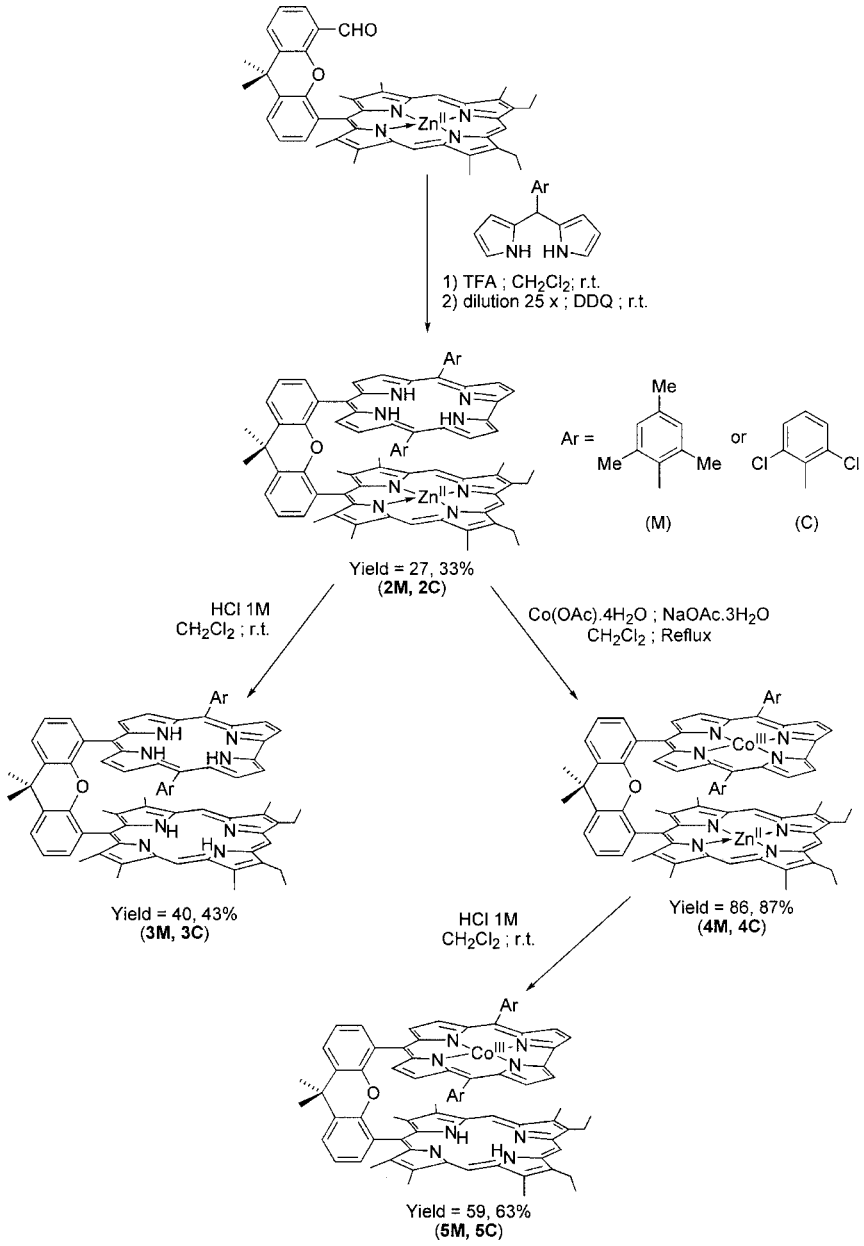

Scheme 2.

could be attributed to the inner NH protons of the corrole ring.

Similarly, the corrole ring is evidenced in UV/Vis spectroscopy by two extra Q bands at 610 and 638 nm, and 617 and 636 nm for **2M** and **2C**, respectively. At the same time, the unique Soret band is slightly blue-shifted by 7 nm for both derivatives compared to that of **1Zn** (Table 2). This shift is generally interpreted in terms of the mutual influence of the porphyrin and corrole rings, thus increasing the HOMO–LUMO gap and therefore shifting the transition at lower wavelengths.[25,26]

Corrole ring formation is further indicated by the disappearance of the C=O stretching band at 1680 cm^{-1} of the aldehyde function of **1Zn** and the concomitant appearance of a new band around 3360 cm^{-1} relative to the vibration of the NH groups of the corrole ring of **2M** and **2C** (see Exp. Sect.).

2M and **2C** can be demetalated by washing with one molar hydrochloric acid solution to afford the free bases **3M** and **3C** in 43 and 40% yield, respectively (Scheme 2). UV/Vis spectroscopy reveals **3M** and **3C** formation by one extra Q band at ca. 510 nm when compared to **2M** and **2C** (Table 2). ^{1}H NMR spectra of **3M** and **3C** feature two signals corresponding to the NH protons of the porphyrin free-base at δ = –5.43 and –4.69 ppm, and at δ = –5.63 and –4.97 ppm, for **3M** and **3C**, respectively. Again, no signal is observed for the same protons in the corrole ring.

When treated with excess cobalt acetate tetrahydrate and sodium acetate in dichloromethane/methanol, **2M** and **2C** lead to **4M** and **4C** in ca. 85% yield, as confirmed by the

 © 2005 Wiley-VCH Verlag GmbH & Co. KGaA, Weinheim

Table 1. ^{1}H NMR spectroscopic data of the investigated compounds.

Compound[a,b]	Solvent	Porphyrin ring[c]					Corrole ring[c]		
		NH	CH_2CH_3	CH_3	CH_2CH_3	H_{meso}	$CH_{3mesityl}$	$H_{mesityl}$	H_β
1	$CDCl_3$	–3.24, –3.04	1.89	2.50, 3.50, 3.65	4.26	9.99, 10.16			
1Zn	$CDCl_3$		1.88	2.48, 3.48, 3.63	4.08	10.02, 10.12			
2M[d]	C_6D_6		1.83	2.60, 2.92, 3.19	3.86	9.07, 9.66	0.93, 1.48, 2.36	7.23	7.51, 7.81, 8.04, 8.28
3M[d]	C_6D_6	–5.43, –4.69	1.85	2.25, 2.56, 3.07	3.88	7.55, 9.44	0.84, 1.45, 2.20	6.97	7.55, 7.55, 8.11, 8.39
4M	C_5D_5N		1.72	3.00, 3.36, 3.51	3.97	9.92, 10.00	0.80, 2.14, 2.65	7.35	8.22, 8.58, 8.69, 9.00
5M	C_5D_5N	–3.72, –3.38	1.68	2.93, 3.33, 3.49	3.89	9.94, 9.94	0.71, 2.17, 2.29	7.33	8.23, 8.55, 8.73, 8.96
							$H_{dichlorophenyl}$		H_β
2C[d]	C_6D_6		1.75	2.68, 3.16, 3.28	3.81	9.31, 9.56	6.87, 7.09, 7.43		7.49, 7.91, 7.93, 8.43
3C[d]	C_6D_6	–5.63, –4.97	1.88	2.31, 2.84, 3.12	3.89	8.66, 9.39	7.24, 7.41, 7.64		7.41, 7.64, 8.16, 8.37
4C	C_5D_5N		1.70	2.97, 3.46, 3.50	3.94	9.89, 9.95	7.70, 7.86, 8.01		8.30, 8.59, 8.81, 9.12
5C	C_5D_5N	–4.10, –3.49	1.67	2.88, 3.39, 3.47	3.88	9.90, 9.91	7.71, 7.86, 8.00		8.32, 8.64, 8.78, 9.09

[a] Dimethylxanthene unit protons omitted. [b] See Schemes 1 and 2 for structures of the compounds. [c] Coupling constants given in the Exp. Sect. [d] Corrole NH protons not detected.

Table 2. UV/Vis data of the investigated compounds in CH_2Cl_2.

Compound	λ_{max} [nm] ($\varepsilon \times 10^{-3}$ L mol^{-1} cm^{-1})						
1		403 (141)	502 (11.2)	535 (6.1)	571 (5.2)		625 (2.)
1Zn	332 (23.6)	406 (346)		536 (16.9)	572 (16.0)		
2M		399 (252)		540 (14.6)	574 (18.1)	610 (5.9)	638(4.2)
3M		397 (238)	508 (12.7)	544 (11.9)	574 (17.4)	608 (8.3)	633 (5.2)
4M		393 (231)		538 (19.0)	575 (16.7)		
5M		389 (189)	507 (14.6)	541 (9.9)	576 (8.2)		628 (4.5)
2C		399 (296)		538 (16.1)	573 (20.7)	617 (5.8)	636 (3.8)
3C		396 (217)	509 (10.9)	543 (10.1)	574 (15.6)	616 (6.8)	
4C		389 (197)	501 (11.1)	539 (19.3)	575 (15.4)		
5C		389 (160)	506 (16.7)	540 (11.9)	573 (9.2)		627 (4.7)

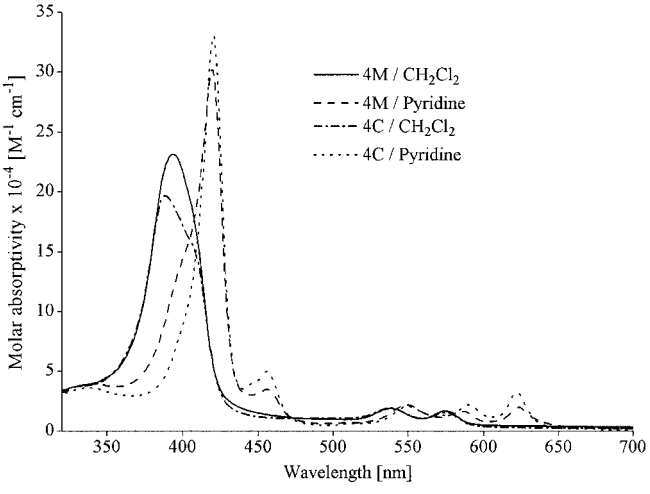

Figure 1. UV/Vis spectra of **4M** and **4C** recorded in CH_2Cl_2 and pyridine.

hypsochromic shift of the Soret band and by the presence of only two major Q bands (Scheme 2 and Table 2). The spectra of the two species recorded in pyridine are interesting (see Exp. Sect. for data). Figure 1 shows the UV/Vis spectra of both **4M** and **4C** in CH_2Cl_2 and pyridine. In dichloromethane, the data are close to those of pure zinc monoporphyrins, the only difference being the shoulder on the Soret band of the porphyrin corresponding to that of the corrole ring. In contrast, major differences arise when pyridine is used as a solvent. For example, all Q bands are red-shifted and a new absorption appears in the range 620–625 nm. Such a band is specific of the coordination of two pyridine molecules on the cobalt(III) ion of the corrole moiety.[10,27–29] Therefore, the coordination of two pyridine molecules is expected on the cobalt atom in *endo* and *exo* positions. The spectra in pyridine exhibit another band, at 456 nm, for both **4M** and **4C** complexes, corresponding to the Soret band of the corrole ring. In ^{1}H NMR spectra recorded in deuterated pyridine all resonance signals appear

 © 2005 Wiley-VCH Verlag GmbH & Co. KGaA, Weinheim

in the diamagnetic region (δ = 0–10 ppm) while in non-coordinating solvents ($CDCl_3$ or C_6D_6) broad signals appear over a wider range for the corrole counterpart. This behavior is attributed to the presence, in non-coordinating solvents, of a high-spin Co^{III} (S = 1) species while in coordinating solvents a low-spin Co^{III} (S = 0) is expected.[11] A detailed study of these spectral characteristics will be published separately.[30]

Demetalation of **4M** and **4C** using 1 M hydrochloric acid affords **5M** and **5C** in yields ranging from 59 to 63% (Scheme 2). No demetalation of the (corrole)cobalt moiety occurs, as demonstrated in MALDI/TOF mass spectrometry by single ionic patterns at m/z = 1246.98 and 1300.8, which correspond to the **5M** and **5C** molecular ions, respectively. The relative "protective action" of the cobalt-containing corrole ring during metalation is interesting. Indeed, direct demetalation from **2M** and **2C** affords **3M** and **3C** in lower yields (around 40%). Other porphyrin–corrole and bis(corrole) bis(macrocycles) show such behavior; the free-bases exhibiting instability relative to the metalated derivatives.[31,32]^{1}H NMR spectra of **5M** and **5C**, recorded in [D_5]-pyridine, do not differ significantly from those of **4M** and **4C**, apart from the NH proton resonances of the porphyrin pyrrole units, which are centered at δ = –3.72 and –3.38 ppm for **5M**, and δ = –4.10 and –3.49 ppm for **5C** (Table 1). The UV/Vis spectrum of **5M** recorded in CH_2Cl_2 closely resembles that of **5C** (Figure 2). Due to the lower molar absorptivity of the absorption bands on the corrole, both spectra exhibit characteristic features of free-base monoporphyrins, with four Q bands between 500 and 630 nm and a Soret band at 389 nm. This latter band is broadened slightly by overlap with the Soret band of the corrole ring. With pyridine as solvent, similar UV/Vis spectra are again obtained for **5M** and **5C** (Figure 2). The band close to 620–625 nm increases in intensity, in accordance with the coordination of two pyridine molecules on the cobalt atom in the corrole. As observed for **4M** and **4C**, **5M** and **5C** exhibit a band at 456 nm in pyridine corresponding to the Soret band of the corrole moiety. Finally, crystallization of **5M** in cyclohexane/pyridine furnished crystals of **5M(py)$_2$**.

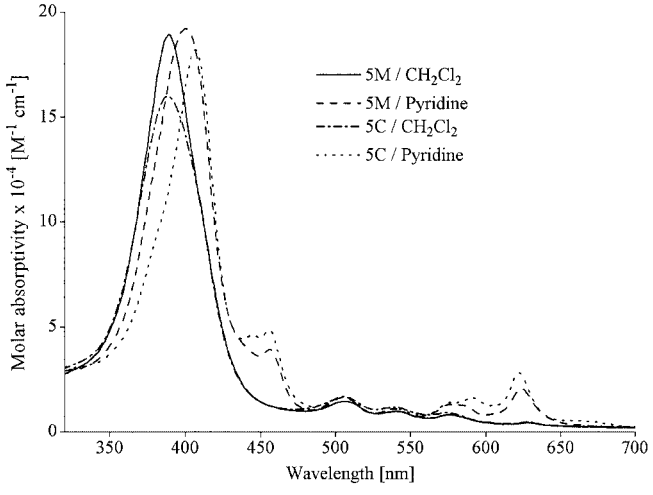

Figure 2. UV/Vis spectra of **5M** and **5C** recorded in CH_2Cl_2 and pyridine.

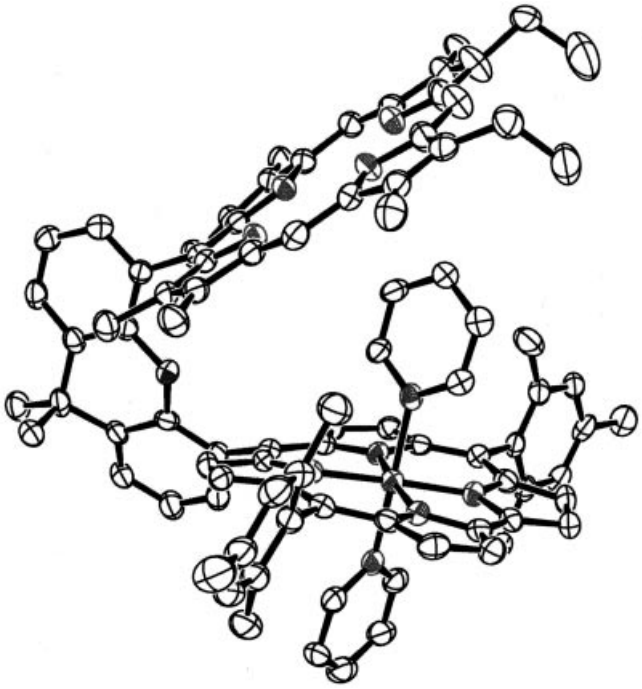

Figure 3. ORTEP view of the **5M(py)$_2$** complex. Ellipsoids drawn at 50% probability level; hydrogen atoms omitted for clarity.

Structural Study

A single-crystal X-ray diffraction analysis of **5M(py)$_2$** revealed the molecular structure of the monometallic cobalt(III) complex (Figure 3). The Co^{III} ion is coordinated to the four pyrrole nitrogen atoms ($4N_{pyrrole}$) in a planar conformation (the metal ion is only 0.011 Å out of the $4N_{pyrrole}$ mean plane), lying slightly out of the $4N_{pyrrole}$ centroid Ct_1 at 0.070 Å. Two kinds of Co–$N_{pyrrole}$ distances are observed in the complex [1.869(4)–1.875(4) and 1.896(4)–1.898(4) Å, each group involving the nitrogen atoms in *trans* positions], indicating a slightly distorted $4N_{pyrrole}$ square coordination. In addition, two pyridine (py) nitrogen atoms (N_{py}) are in apical positions from the metal centre at 1.969(4) and 1.978(4) Å, completing a close square-bipyramidal coordination geometry. These coordination distances and geometry are very similar to those reported for related complexes. Thus, for the [5,10,15-tris-(pentafluorophenyl)corrole]cobalt(III) complex,[33] M–$N_{pyrrole}$ and M–N_{py} distances are 1.873–1.900 and 1.994 Å for the monomer, and 1.868–1.899 and 1.989–2.000 Å for the dimer. In the face-to-face homodimetallic bis(corrole) complex [(BCA)$Co_2(py)_3$],[28] bearing three coordinated pyridine molecules (one inside and two out of the complex cavity), M–$N_{pyrrole}$ and M–N_{py} distances are 1.879–1.905 and 1.976–1.979 Å for the hexacoordinate metal centre. In this latter structure, the coordination distances of the pentacoordinate metal centre, [1.875(4)–1.894(4) for $N_{pyrrole}$ and 1.946(5) Å for N_{py}], compare well with those of the mono-

 © 2005 Wiley-VCH Verlag GmbH & Co. KGaA, Weinheim

metallic (corrole–porphyrin)cobalt(III) complex, where the spacer is a biphenylenyl unit, [(PCB)H_2Co(py)],[10] which binds one pyridine molecule out of the complex cavity. The corresponding distances were 1.882(3)–1.902(3) ($N_{pyrrole}$) and 1.945(4) Å (N_{py}). Thus, from penta- to hexacoordinate (corrole)cobalt(III) species having pyridine in apical positions, the most relevant difference in coordination geometry concerns: (i) elongation of M–N_{py} by about 0.03 Å and (ii) displacement of the metal centre towards the $4N_{pyrrole}$ mean plane (<$4N_{pyrrole}$>); the Co···<$4N_{pyrrole}$> distance being 0.202(1) and 0.252(1) Å for pentacoordinate cases in [(PCB)H_2Co(py)] and [(BCA)$Co_2(py)_3$] and 0.009(1) and 0.011(1) Å for hexacoordinate ones in [(BCA)$Co_2(py)_3$] and **5M(py)$_2$**.

In the molecular structure of the **5M(py)$_2$**complex both macrocycles exhibit a small distortion from planarity, the root mean square deviation of the 23 and 24 atoms from the corrole and porphyrin least-squares planes being 0.112 and 0.078 Å, respectively. While the corrole macrocycle shows a ruffled conformation, as indicated by the displacements of the alternated *meso*-carbon atoms above and below the corrole mean plane, the porphyrin moiety is closely planar. Thus, for the corrole ring, the *meso*-carbon atom C10 lies 0.210(4) Å above the mean plane, whereas C5 and C15 lie –0.159(4) and –0.175(4) Å below this plane. With the porphyrin, only five atoms lie more than 0.1 Å out of the mean plane [C55, C60, C61, C68, and C71 at 0.128(4), –0.108(4), –0.122(4), –0.105(4), and –0.207(4) Å, respectively]. [(BCA)$Co_2(py)_3$] and [(PCB)H_2Co(py)] complexes have similar macrocycle conformations.[10,28]

Both H(–N) hydrogen atoms were found unambiguously in the porphyrin cavity, on N7 and N5, and are involved in hydrogen-bonding interactions with N6 and N8 pyrrole nitrogen atoms [d(N–H) = 0.95(5) and 0.99(5) Å, d(H···N) = 2.23(5) and 2.11(5) Å and α(N–H···N) = 120(4) and 127(4)°, respectively].

The coordination of one of the pyridine molecules within the complex cavity leads to a large open-mouth face-to-face geometry (the interplanar angle between the macrocycle mean planes β is 43.2°) due to the important steric effects with the porphyrin moiety. Nevertheless, the spacer is folded through the Csp^3–O direction (the dihedral angle between both half parts is 28.9°), allowing for a short pyridine–porphyrin contact that balances the repulsive steric effect by the attractive (C_{py}–)H···π-system interaction (the $4N_{pyrrole}$ porphyrin centroid Ct_2 distance to the closest H_{py} atom is 2.22 Å, and the four H···Ct_2···$N_{pyrrole}$ angles range between 80 and 100°). The anchored sites of both macrocycles at the spacer and at the corrole–porphyrin moieties are 4.64 and 4.79 Å, respectively, apart. The small difference in distances (0.15 Å) suggests that, while steric repulsion mainly drives the corrole macrocycle orientation (leading to the large β angle), both the spacer folding and the attractive H···π–porphyrin interaction avoid a larger difference. Further support for both this attractive interaction and the role of the spacer follows from a comparison of the molecular structures of (BCA)$Co_2(py)_3$ and **5M(py)$_2$**, where the distances from the hexacoordinate metal centre to the centroid of the other macrocycle are 7.23 and 6.86 Å, respectively. Thus, the latter complex exhibits a short "macrocycle-to-macrocycle" distance due to the folding of its spacer, which in the relaxed planar conformation corresponds to the distance observed for the anthracenyl moiety. Therefore, thanks to its flexibility, the dimethylxanthene spacer is of great interest for tuning potential metal···metal or metal···molecule···metal interactions in face-to-face macrocyclic complexes.

In **5M(py)$_2$**, the slip angle α, defined as the average angle between the vector joining Ct_1···Ct_2 and the unit vectors normal to the two macrocyclic least-squares planes [$\alpha = (\alpha_1 + \alpha_2)/2$], is 24.0° and the lateral shift $L = \sin\alpha \cdot d(Ct_1 \cdots Ct_2)$ is 2.80 Å [$d(Ct_1 \cdots Ct_2)$ = 6.90 Å]. These values are larger than those found in [(BCA)$Co_2(py)_3$] (α = 14.7°, L = 1.84 Å), even if α and L slightly differ in their definitions in the two complexes.[28]

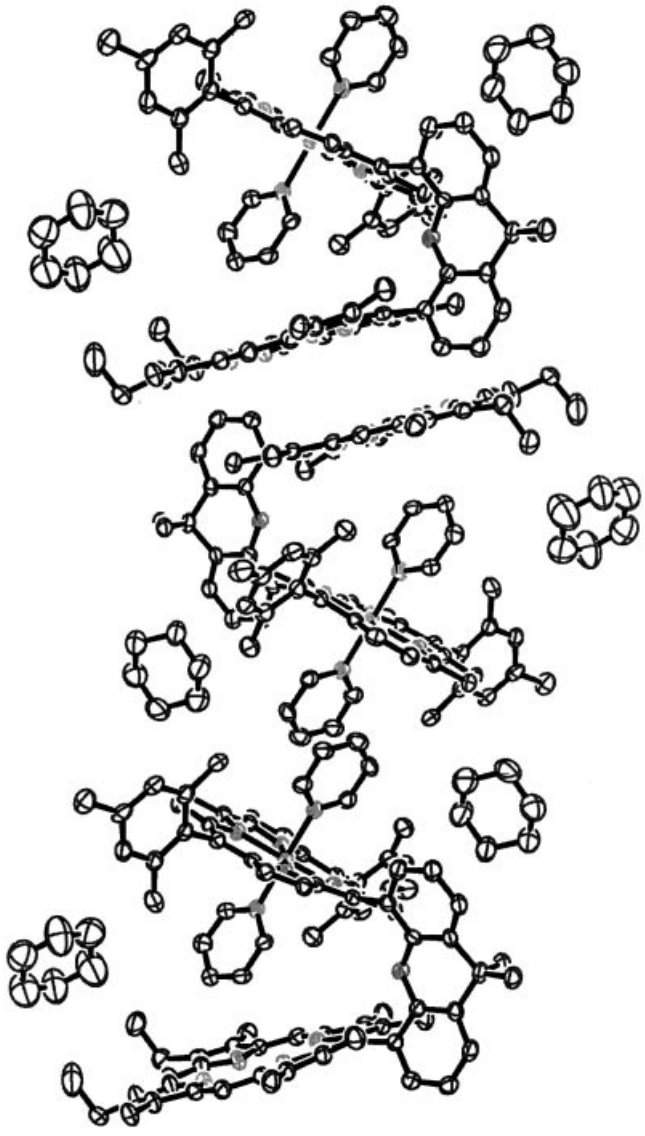

Figure 4. Stacking of **5M(py)$_2$** complexes along the [1 0 0] direction, including solvent molecules. Ellipsoids drawn at 50% probability level; hydrogen atoms omitted for clarity.

 © 2005 Wiley-VCH Verlag GmbH & Co. KGaA, Weinheim

Moreover, the pyridine molecules are almost staggered around the metal centre; the dihedral angle between their mean planes being 87.9°. While this almost perpendicular orientation has also been observed in [(BCA)$Co_2(py)_3$] (88.2°)[28] and [(Me_4Ph_5Cor)Co$(py)_2$] (83.7°),[27] in the [5,10,15-tris(pentafluorophenyl)corrole]cobalt(III) complex a mutually parallel arrangement between both pyridine molecules is found for the monomer and dimer.[33]

In the **5M(py)$_2$** crystal structure, the stacking of complexes is driven by two kinds of π–π interactions along the [1 0 0] direction (Figure 4). Hence, while the porphyrin ring interacts with the adjacent equivalent moiety of another molecule (the shortest distance is 3.57 Å for two equivalent *meso*-C atoms), at the other side of the complex the outer pyridine molecule makes a π–π interaction with an equivalent molecule of the closest complex (the shortest C–C distance being 3.33 Å). In the former case, the centroid–centroid distance is quite large (7.50 Å), indicating an important lateral shift between the macrocycles. In the second case, the centroid–centroid distance is 3.63 Å, reflecting significant overlap between the π-systems of both pyridine molecules.

The relative orientation of the inner pyridine in front of two methyl groups of the mesityl substituents (C_{methyl}···Ct_{py}···C_{methyl} = 160°) seems to indicate a further stabilisation by two quite weak C–H···aromatic ring interactions (H···Ct_{py} distances are 3.83 and 4.41 Å). A variable ^{1}H NMR analysis down to 220 K, to visualize tentatively any interaction involving a methyl proton of a mesityl group with a pyridine molecule, found no significant variation in signal shape or chemical shift for the protons concerned.

Summary and Conclusion

1Zn reacts with an aryldipyrromethane to afford good yields of (free-base corrole–porphyrin)zinc complexes (**2M** and **2C**). Further metalation of the corrole ring by cobalt followed by demetalation of the porphyrin moiety gives the (free-base porphyrin–corrole)cobalt complex, which is a precursor of heterodimetallic derivatives. The "protective" effect of the zinc ion in the porphyrin ring is evidenced throughout the synthetic pathway and, especially, during the first step, leading to the formation of the corrole, where lower amounts of TFA are required than for the reaction carried out from **1**. Therefore, acidolysis of the dipyrromethane reactant avoided, and reaction yields in bis(macrocycle) are obviously increased.

In the presence of pyridine, the bis(pyridine) adduct of **5M** crystallized. The structure of **5M(py)$_2$**was solved, exhibiting coordination of the two pyridine molecules on the cobalt atom of the corrole ring in *endo* and *exo* positions. Another interesting feature is that the complexes are stacked along the [1 0 0] direction through π–π interactions.

Work towards the preparation of heterodimetallic complexes and their use as catalysts for the reduction of dioxygen is being carried out.

Experimental Section

General Remarks: All analytical grade reagents, obtained from commercial suppliers, were used without further purification. 5-Mesityldipyrromethane, 5-(2,6-dichlorophenyl)dipyrromethane,[24] 5-(13,17-diethyl-2,3,7,8,12,18-hexamethylporphyrin-5-yl)-4-formyl-9,9-dimethylxanthene[13,31,32] (**1**) were synthesized according to reported procedures. ^{1}H NMR spectra were recorded at 500 MHz with a Bruker DRX-500 Avance spectrometer of the "Centre de Spectrométrie Moléculaire de l'Université de Bourgogne" of the FR 2604. Chemical shifts are expressed in ppm relative to residual peaks of chloroform (δ = 7.26 ppm), pyridine (δ = 7.19, 7.55, 8.71 ppm) or benzene (δ = 7.16 ppm). UV/Vis spectra were collected with a Varian Cary 1 spectrophotometer in dichloromethane solution. Infrared spectra were measured in the attenuated total reflectance mode (ATR) with a Bruker Vector 22 Fourier transform spectrometer. MALDI/TOF mass spectra were obtained with a Bruker ProFLEX III spectrometer using dithranol as matrix. Microanalyses were performed with a Fisons EA 1108 CHNS instrument.

[13,17-Diethyl-5-(5-formyl-9,9-dimethylxanthen-4-yl)-2,3,7,8,12,18-hexamethylporphyrin]zinc(II) (1Zn): A solution of porphyrin **1** (0.200 g, 0.291 mmol, 1 equiv.), zinc acetate dihydrate (0.128 g, 0.582 mmol, 2 equiv.), and sodium acetate trihydrate (0.396 g, 2.91 mmol, 10 equiv.) in a chloroform (35 mL)/methanol (15 mL) mixture was heated to reflux for 15 min. After cooling to room temperature, dichloromethane (50 mL) was added. The reaction mixture was then washed with water (3 × 100 mL), dried with magnesium sulfate, filtered and the solvents were evaporated. The resulting solid was chromatographed on silica gel using first toluene as eluent and then dichloromethane to collect a pink fraction. After concentration, the solid was recrystallized from dichloromethane/heptane. **1Zn** was obtained in 87% yield (0.190 g, 0.253 mmol). ^{1}H MNR ($CDCl_3$, 300 K): δ = 1.88 (t, $^3J_{H,H}$ = 7.85 Hz, 6 H, $CH_3$$CH_2$-porphyrin), 1.92 (s, 6 H, CH_3-dimethylxanthene) 2.48 (s, 6 H, CH_3-porphyrin), 3.48 (s, 6 H, CH_3-porphyrin), 3.63 (s, 6 H, CH_3-porphyrin), 4.08 (m, 4 H, $CH_3$$CH_2$-porphyrin), 7.05 (t, $^3J_{H,H}$ = 7.68 Hz, 1 H, H-dimethylxanthene), 7.30 (dd, $^3J_{H,H}$ = 7.39, $^4J_{H,H}$ = 1.19 Hz, 1 H, H-dimethylxanthene), 7.51 (s, 1 H, CHO), 7.60 (t, $^3J_{H,H}$ = 7.71 Hz, 1 H, H-dimethylxanthene), 7.71 (dd, $^3J_{H,H}$ = 7.90, $^4J_{H–H}$ = 1.43 Hz, 1 H, H-dimethylxanthene), 7.87 (d, $^3J_{H,H}$ = 6.40 Hz, 1 H, H-dimethylxanthene), 7.93 (dd, $^3J_{H,H}$ = 7.95, $^4J_{H,H}$ = 1.01 Hz, 1 H, H-dimethylxanthene), 10.02 (s, 1 H, H_{meso}-porphyrin), 10.12 (s, 2 H, H_{meso}-porphyrin). MS (MALDI/TOF): *m*/*z* = 747.30 [M – H]$^+$; 748.28 calcd. for $C_{46}H_{44}N_4O_2Zn$. UV/Vis (CH_2Cl_2): λ_{max} ($\varepsilon \times 10^{-3}$ L mol^{-1} cm^{-1}) = 332.0 (23.6), 406.0 (346), 536.1 (16.9), 572.1 (16.0) nm. IR $\tilde{\nu}$ = 2959 (C–H), 2923 (C–H), 2861 (C–H), 1680 (C=O) cm^{-1}. $C_{46}H_{44}N_4O_2Zn$ (750.27): calcd. C 73.64, H 5.91, N 7.47; found C 73.63, H 6.07, N 7.48.

{5-[5-(5,15-Dimesitylcorrol-10-yl)-9,9-dimethylxanthen-4-yl]-13,17-diethyl-2,3,7,8,12,18-hexamethylporphyrin}zinc(II) (2M): (Porphyrin)zinc complex **1Zn** (0.20 g, 0.27 mmol, 1 equiv.) and mesityldipyrromethane (0.28 g, 1.07 mmol, 4 equiv.) were dissolved in 16 mL of a solution of trifluoroacetic acid (0.02 mmol, 0.08 equiv.) in CH_2Cl_2 (10 μL of TFA in 100 mL of CH_2Cl_2). The reaction mixture was then stirred for 5 h, diluted 25× with CH_2Cl_2 (400 mL) and a solution of 2,3-dichloro-5,6-dicyano-1,4-benzoquinone (DDQ; 0.182 g, 0.80 mmol, 3 equiv.) in toluene (4 mL) was added with stirring. After a further 5 min, the reaction mixture was chromatographed on silica gel and eluted with CH_2Cl_2. The first collected, violet, fraction was concentrated, washed with pentane and dried under vacuum, yielding 0.091 g (27%, 0.07 mmol) of **2M**. ^{1}H MNR (C_6D_6, 330 K): δ = 0.93 (s, 6 H, CH_3-mesityl), 1.48 (s, 6 H,

CH_3-mesityl), 1.83 (t, $^3J_{H,H}$ = 7.71 Hz, 6 H, CH_3CH_2-porphyrin), 2.11 (s, 6 H, CH_3-dimethylxanthene), 2.36 (s, 6 H, CH_3-mesityl), 2.60 (s, 6 H, CH_3-porphyrin), 2.92 (s, 6 H, CH_3-porphyrin), 3.19 (s, 6 H, CH_3-porphyrin), 3.86 (m, 4 H, CH_3CH_2-porphyrin), 6.81 (s, 2 H, H_{meta}–mesityl), 7.01 (dd, $^3J_{H,H}$ = 7.18, $^4J_{H,H}$ = 1.46 Hz, 1 H, H-dimethylxanthene), 7.15 (t, $^3J_{H,H}$ = 7.50 Hz, 1 H, H-dimethylxanthene), 7.17 (t, $^3J_{H,H}$ = 7.86 Hz, 1 H, H-dimethylxanthene), 7.23 (s, 2 H, H_{meta}-mesityl), 7.34 (dd, $^3J_{H,H}$ = 7.28, $^4J_{H,H}$ = 1.51 Hz, 1 H, H-dimethylxanthene), 7.51 (br. d, $^3J_{H,H}$ = 3.06 Hz, 2 H, H_β-corrole), 7.72 (dd, $^3J_{H,H}$ = 7.91, $^4J_{H,H}$ = 1.53 Hz, 1 H, H-dimethylxanthene), 7.75 (dd, $^3J_{H,H}$ = 7.97, $^4J_{H,H}$ = 1.52 Hz, 1 H, H-dimethylxanthene), 7.81 (d, $^3J_{H,H}$ = 4.38 Hz, 2 H, H_β-corrole), 8.04 (d, $^3J_{H,H}$ = 3.88 Hz, 2 H, H_β-corrole), 8.28 (d, $^3J_{H,H}$ = 4.58 Hz, 2 H, H_β-corrole), 9.07 (s, 2 H, H_{meso}-porphyrin), 9.66 (s, 1 H, H_{meso}-porphyrin). MS (MALDI/TOF): *m*/*z* = 1253.92 ([M]$^{+\cdot}$); 1254.54 calcd. for $C_{82}H_{76}N_8OZn$. UV/Vis (CH_2Cl_2): λ_{max} ($\varepsilon \times 10^{-3}$ L mol^{-1} cm^{-1}) = 399.0 (252), 540.0 (14.6), 574.0 (18.1), 610.0 (5.91), 638.0 (4.17) nm. IR $\tilde{\nu}$ = 3366 (N–H), 2960 (C–H), 2918 (C–H), 2850 (C–H) cm^{-1}. $C_{82}H_{76}N_8OZn$ (1254.95): calcd. C 78.48, H 6.10, N 8.93; found C 78.21, H 6.21, N 8.87.

(5-{5-[5,15-Bis(2,6-dichlorophenyl)corrol-10-yl]-9,9-dimethylxanthen-4-yl}-13,17-diethyl-2,3,7,8,12,18-hexamethylporphyrin)-zinc(II) (2C): This compound was synthesized as described above for **2M**, starting from **1Zn** (0.20 g, 0.27 mmol, 1 equiv.) and (2,6-dichlorophenyl)dipyrromethane (0.31 g, 1.07 mmol, 4 equiv.), in 33% yield (0.12 g, 0.09 mmol). ^{1}H NMR (C_6D_6, 330 K): δ = 1.75 (t, $^3J_{H,H}$ = 7.74 Hz, 6 H, CH_3CH_2-porphyrin), 2.14 (s, 6 H, CH_3-dimethylxanthene), 2.68 (s, 6 H, CH_3-porphyrin), 3.16 (s, 6 H, CH_3-porphyrin), 3.28 (s, 6 H, CH_3-porphyrin), 3.81 (m, 4 H, CH_3CH_2-porphyrin), 6.87 (t, $^3J_{H,H}$ = 8.31 Hz, 2 H, H_{para}-dichlorophenyl), 6.89 (dd, $^3J_{H,H}$ = 7.19, $^4J_{H,H}$ = 1.30 Hz, 1 H, H-dimethylxanthene), 7.09 (dd, $^3J_{H,H}$ = 8.24, $^4J_{H,H}$ = 1.15 Hz, 2 H, H_{meta}-dichlorophenyl), 7.11 (t, $^3J_{H,H}$ = 7.63 Hz, 1 H, H-dimethylxanthene), 7.18 (t, $^3J_{H,H}$ = 7.69 Hz, 1 H, H-dimethylxanthene), 7.28 (dd, $^3J_{H,H}$ = 7.25, $^4J_{H,H}$ = 1.54 Hz, 1 H, H-dimethylxanthene), 7.43 (dd, $^3J_{H,H}$ = 8.38, $^4J_{H,H}$ = 1.02 Hz, 2 H, H_{meta}-dichlorophenyl), 7.49 (br. d, $^3J_{H,H}$ = 3.12 Hz, 2 H, H_β-corrole), 7.75 (m, 2 H, H-dimethylxanthene), 7.91 (br. d, $^3J_{H,H}$ = 3.86 Hz, 2 H, H_β-corrole); 7.93 (d, $^3J_{H,H}$ = 4.51 Hz, 2 H, H_β-corrole), 8.43 (d, $^3J_{H,H}$ = 4.61 Hz, 2 H, H_β-corrole), 9.31 (s, 2 H, H_{meso}-porphyrin), 9.56 (s, 1 H, H_{meso}-porphyrin). MS (MALDI/TOF): *m*/*z* = 1307.34 ([M]$^{+\cdot}$); 1308.29 calcd. for $C_{76}H_{60}Cl_4N_8OZn$. UV/Vis (CH_2Cl_2): λ_{max} ($\varepsilon \times 10^{-3}$ L mol^{-1} cm^{-1}) = 399.0 (296), 538.0 (16.1), 573.0 (20.7), 616.9 (5.81), 636.1 (3.81) nm. IR $\tilde{\nu}$ = 3357 (N–H), 2960 (C–H), 2918 (C–H), 2850 (C–H) cm^{-1}. $C_{76}H_{60}Cl_4N_8OZn$ (1308.57): calcd. C 69.76, H 4.62, N 8.56; found C 69.97, H 4.82, N 8.32.

4-(13,17-Diethyl-2,3,7,8,12,18-hexamethylporphyrin-5-yl)-5-(5,15-dimesitylcorrol-10-yl)-9,9-dimethylxanthene (3M): A solution of **2M** (0.06 g, 0.048 mmol) in dichloromethane (60 mL) was stirred vigorously in the presence of hydrochloric acid (1 M, 3 × 60 mL) in a separating funnel. The organic layer was washed with water (3 × 60 mL), dried with magnesium sulfate, filtered and the solvents were evaporated. The resultant solid residue was chromatographed on basic alumina and eluted with CH_2Cl_2. The first eluting fraction was concentrated and recrystallized from dichloromethane/methanol to yield **3M** as a violet solid (43%, 0.024 g, 0.02 mmol). ^{1}H NMR ($CDCl_3$, 300 K): δ = –5.43 (br. s, 1 H, NH-porphyrin), –4.69 (br. s, 1 H, NH-porphyrin), 0.84 (br. s, 6 H, CH_3-mesityl), 1.45 (br. s, 6 H, CH_3-mesityl), 1.85 (t, $^3J_{H,H}$ = 7.76 Hz, 6 H, CH_3CH_2-porphyrin), 2.20 (s, 6 H, CH_3-dimethylxanthene), 2.25 (s, 6 H, CH_3-porphyrin), 2.43 (s, 6 H, CH_3-mesityl), 2.56 (br. s, 6 H, CH_3-porphyrin), 3.07 (br. s, 6 H, CH_3-porphyrin), 3.88 (m, 4 H, CH_3CH_2-porphyrin), 6.81 (br. s, 2 H, H_{meta}-mesityl), 6.97 (br. s, 2 H, H_{meta}-mesityl), 7.09 (br. s, 1 H, H-dimethylxanthene), 7.33 (t, $^3J_{H,H}$ = 7.62 Hz, 1 H, H-dimethylxanthene), 7.37 (t, $^3J_{H,H}$ = 7.50 Hz, 1 H, H-dimethylxanthene), 7.42 (br. dd, $^3J_{H,H}$ = 6.32 Hz, 1 H, H-dimethylxanthene), 7.55 (m, 6 H, H_β-corrole + H_{meso}-porphyrin), 7.91 (dd, $^3J_{H,H}$ = 7.73, $^4J_{H,H}$ = 1.74 Hz, 1 H, H-dimethylxanthene), 7.94 (br. dd, $^3J_{H,H}$ = 8.03 Hz, 1 H, H-dimethylxanthene), 8.11 (br. s, 2 H, H_β-corrole), 8.39 (br. s, 2 H, H_β-corrole), 9.44 (s, 1 H, H_{meso}-porphyrin) ppm. MS (MALDI/TOF): *m*/*z* = 1191.06 [M]$^+$; 1190.63 calcd. for $C_{82}H_{78}N_8O$. UV/Vis (CH_2Cl_2): λ_{max} ($\varepsilon \times 10^{-3}$ L mol^{-1} cm^{-1}) = 397.0 (238), 508.0 (12.7), 544.0 (11.9), 574.0 (17.4), 608.1 (8.35), 633.0 (5.24) nm. IR $\tilde{\nu}$ = 3388 (N–H), 3349 (N–H), 3278 (N–H), 2960 (C–H), 2921 (C–H), 2859 (C–H) cm^{-1}. $C_{82}H_{78}N_8O$·2MeOH (1255.66): calcd. C 80.35, H 6.90, N 8.92; found C 80.77, H 6.68, N 8.73.

4-[5,15-Bis(2,6-dichlorophenyl)corrol-10-yl]-5-(13,17-diethyl-2,3,7,8,12,18-hexamethyl porphyrin-5-yl)-9,9-dimethylxanthene (3C): This compound was obtained as described for **3M**, starting from **2C** (0.06 g, 0.046 mmol), in 40% yield (0.023 g, 0.018 mmol). ^{1}H NMR ($CDCl_3$, 300 K): δ = –5.63 (br. s, 1 H, NH-porphyrin), –4.97 (br. s, 1 H, NH-porphyrin), 1.88 (t, $^3J_{H,H}$ = 7.77 Hz, 6 H, CH_3CH_2-porphyrin), 2.21 (s, 6 H, CH_3-dimethylxanthene), 2.31 (s, 6 H, CH_3-porphyrin), 2.84 (br. s, 6 H, CH_3-porphyrin), 3.12 (br. s, 6 H, CH_3-porphyrin), 3.89 (m, 4 H, CH_3CH_2-porphyrin), 7.17 (br. d, $^3J_{H,H}$ = 7.07 Hz, 1 H, H-dimethylxanthene), 7.24 (m, 5 H, H-dimethylxanthene + H_{meta}-dichlorophenyl), 7.41 (m, 4 H, H_{para}-dichlorophenyl + H_β-corrole), 7.64 (br. s, 4 H, H_{meta}-dichlorophenyl + H_β-corrole), 7.90 (dd, $^3J_{H,H}$ = 6.55, $^4J_{H,H}$ = 2.96 Hz, 1 H, H-dimethylxanthene), 7.95 (dd, $^3J_{H,H}$ = 8.06, $^4J_{H,H}$ = 1.51 Hz, 1 H, H-dimethylxanthene), 8.16 (br. s, 2 H, H_β-corrole), 8.37 (br. s, 2 H, H_β-corrole), 8.66 (br. s, 2 H, H_{meso}-porphyrin), 9.39 (s, 1 H, H_{meso}-porphyrin) ppm. MS (MALDI/TOF): *m*/*z* = 1244.43 [M]$^{+\cdot}$; 1244.38 calcd. for $C_{76}H_{62}Cl_4N_8O$. UV/Vis (CH_2Cl_2): λ_{max} ($\varepsilon \times 10^{-3}$ L mol^{-1} cm^{-1}) = 395.9 (217), 509.0 (10.9), 543.0 (10.1), 574.0 (15.6), 616.0 (6.77) nm. IR $\tilde{\nu}$ = 3359 (N–H), 3312 (N–H), 3280 (N–H), 2960 (C–H), 2922 (C–H), 2859 (C–H) cm^{-1}. $C_{76}H_{62}Cl_4N_8O$·CH_2Cl_2·H_2O (1348.14): calcd. C 68.60, H 4.93, N 8.31; found C 68.55, H 4.58, N 8.02.

Mixed Cobalt(III)–Zinc(II) Complex 4M: Two solutions, one of **3M** (0.050 g, 0.040 mmol, 1 equiv.) in dichloromethane (7 mL) and another of cobalt(II) acetate tetrahydrate (0.025 g, 0.1 mmol, 2.5 equiv) and sodium acetate trihydrate (0.027 g, 0.2 mmol, 5 equiv.) in methanol (3 mL), were combined and the mixture was heated to reflux for 15 min. After cooling, dichloromethane (50 mL) was added and the resulting solution was washed with water (3 × 50 mL), dried with magnesium sulfate, filtered and the solvents were evaporated under vacuum. The residue was then chromatographed on basic alumina and eluted with CH_2Cl_2/MeOH (98:2). The violet solid collected from concentration of the first fraction was recrystallized from CH_2Cl_2/MeOH, leading to **4M** in 86% yield (0.045 mg, 0.034 mmol). ^{1}H NMR (C_5D_5N, 330 K): δ = 0.80 (s, 6 H, CH_3-mesityl), 1.72 (t, $^3J_{H,H}$ = 7.61 Hz, 6 H, CH_3CH_2-porphyrin), 2.14 (s, 6 H, CH_3-mesityl), 2.36 (s, 6 H, CH_3-dimethylxanthene), 2.65 (s, 6 H, CH_3-mesityl), 3.00 (s, 6 H, CH_3-porphyrin), 3.36 (s, 6 H, CH_3-porphyrin), 3.51 (s, 6 H, CH_3-porphyrin), 3.97 (m, 4 H, CH_3CH_2-porphyrin), 6.46 (dd, $^3J_{H,H}$ = 7.25, $^4J_{H,H}$ = 1.57 Hz, 1 H, H-dimethylxanthene), 6.77 (dd, $^3J_{H,H}$ = 7.26, $^4J_{H,H}$ = 1.58 Hz, 1 H, H-dimethylxanthene), 7.23 (m, 2 H, 2 H-dimethylxanthene), 7.31 (s, 2 H, H_{meta}-mesityl), 7.35 (s, 2 H, H_{meta}-mesityl), 7.97 (dd, $^3J_{H,H}$ = 8.04, $^4J_{H,H}$ = 1.42 Hz, 1 H, H-dimethylxanthene), 8.04 (dd, $^3J_{H,H}$ = 7.89, $^4J_{H,H}$ = 1.58 Hz, 1 H, H-dimethylxanthene), 8.22 (d, $^3J_{H,H}$ = 3.96 Hz, 2 H, H_β-corrole), 5.58 (d, $^3J_{H,H}$ = 4.61 Hz, 2 H, H_β-corrole), 8.69 (m, partially overlapped by a C_5D_4HN signal, H_β-corrole), 9.00 (d, $^3J_{H,H}$ = 4.64 Hz, 2 H, H_β-

 © 2005 Wiley-VCH Verlag GmbH & Co. KGaA, Weinheim

corrole), 9.92 (s, 2 H, H_{meso}-porphyrin), 10.00 (s, 1 H, H_{meso}-porphyrin). MS (MALDI/TOF): *m/z* = 1309.84 $[M]^{+\cdot}$; 1310.45 calcd. for $C_{82}H_{73}N_8OZnCo$. UV/Vis (CH_2Cl_2): λ_{max} ($\varepsilon \times 10^{-3}$ L mol^{-1} cm^{-1}) = 393.0 (231), 538.0 (19.0), 575.1 (16.7) nm. UV/Vis (pyridine): λ_{max} ($\varepsilon \times 10^{-3}$ L mol^{-1} cm^{-1}) = 340.0 (39.4), 420.0 (302), 456.0 (34.7), 510.1 (6.96), 550.1 (21.8), 587.0 (16.3), 623.0 (19.8) nm. IR $\tilde{\nu}$ 2958 (C–H), 2920 (C–H), 2858 (C–H) cm^{-1}. $C_{82}H_{73}CoN_8OZn$ (1310.86): calcd. C 75.13, H 5.61, N 8.55; found C 75.40, H 5.70, N 8.80.

Mixed Cobalt(III)–Zinc(II) Complex 4C:4C was prepared as described for **4M**, starting from **3C** (0.050 g, 0.038 mmol, 1 equiv.), cobalt(II) acetate tetrahydrate (0.024 g, 0.095 mmol, 2.5 equiv.) and sodium acetate trihydrate (0.026 g, 0.191 mmol, 5 equiv.). It was obtained as a violet solid in 87% yield (0.045 g, 0.033 mmol). ^{1}H NMR (C_5D_5N, 330 K): δ = 1.70 (t, $^3J_{H,H}$ = 7.64 Hz, 6 H, CH_3CH_2-porphyrin), 2.34 (s, 6 H, CH_3-dimethylxanthene), 2.97 (s, 6 H, CH_3-porphyrin), 3.46 (s, 6 H, CH_3-porphyrin), 3.50 (s, 6 H, CH_3-porphyrin), 3.94 (m, 4 H, CH_3CH_2-porphyrin), 6.12 (dd, $^3J_{H,H}$ = 7.30, $^4J_{H,H}$ = 1.61 Hz, 1 H, H-dimethylxanthene), 6.91 (dd, $^3J_{H,H}$ = 7.33, $^4J_{H,H}$ = 1.62 Hz, 1 H, H-dimethylxanthene), 7.11 (t, $^3J_{H,H}$ = 7.62 Hz, 1 H, H-dimethylxanthene), 7.24 (t, $^3J_{H,H}$ = 7.66 Hz, 1 H, H-dimethylxanthene), 7.70 (t, $^3J_{H,H}$ = 8.23 Hz, 2 H, H_{meta}-dichlorophenyl), 7.86 (dd, $^3J_{H,H}$ = 8.22, $^4J_{H,H}$ = 1.17 Hz, 2 H, H_{meta}-dichlorophenyl), 7.96 (dd, $^3J_{H,H}$ = 7.93, $^4J_{H,H}$ = 1.63 Hz, 1 H, H-dimethylxanthene), 7.99 (dd, $^3J_{H,H}$ = 7.95, $^4J_{H,H}$ = 1.73 Hz, 1 H, H-dimethylxanthene), 8.01 (dd, $^3J_{H,H}$ = 8.17, $^4J_{H,H}$ = 1.21 Hz, 1 H, H_{meta}-dichlorophenyl), 8.30 (d, $^3J_{H,H}$ = 4.08 Hz, 2 H, H_β-corrole), 8.59 (d, $^3J_{H,H}$ = 4.10 Hz, 2 H, H_β-corrole), 8.81 (d, $^3J_{H,H}$ = 4.69 Hz, 2 H, H_β-corrole), 9.12 (d, $^3J_{H,H}$ = 4.68 Hz, 2 H, H_β-corrole), 9.89 (s, 2 H, H_{meso}-porphyrin), 9.95 (s, 1 H, H_{meso}-porphyrin). MS (MALDI/TOF): *m/z* = 1364.16, $[M]^{+\cdot}$; 1364.20 calcd. for $C_{76}H_{57}Cl_4N_8OZnCo$. UV/Vis (CH_2Cl_2): λ_{max} ($\varepsilon \times 10^{-3}$ L mol^{-1} cm^{-1}) = 389.0 (197), 501.0 (11.1), 538.9 (19.3), 575.1 (15.4) nm. UV/Vis (pyridine): λ_{max} ($\varepsilon \times 10^{-3}$ L mol^{-1} cm^{-1}) = 337.9 (36.4), 420.0 (323), 456.0 (48.6), 515.1 (6.15), 550.1 (20.0), 590.0 (21.3), 621.9 (31.4) nm. IR $\tilde{\nu}$ 2961 (C–H), 2927 (C–H), 2862 (C–H) cm^{-1}. $C_{76}H_{57}Cl_4CoN_8OZn$·MeOH (1396.52): calcd. C 66.23, H 4.40, N 8.02; found C 66.48, H 4.38, N 8.38.

{10-[5-(13,17-Diethyl-2,3,7,8,12,18-hexamethylporphyrin-5-yl)-9,9-dimethylxanthen-4-yl]-5,15-dimesitylcorrole}cobalt(III) (5M): A solution of **4M** (35 mg, 26.7 μmol) in dichloromethane (35 mL) was vigorously stirred with hydrochloric acid (1 M; 3 × 50 mL) in a separating funnel. The organic layer was then washed with distilled water (3 × 50 mL), dried with magnesium sulfate, filtered and the solvents were evaporated under vacuum. The resultant solid residue was chromatographed on basic alumina and eluted with dichloromethane/methanol (98:2). The first eluting fraction was concentrated and then recrystallized from dichloromethane/methanol, yielding **5M** (59%, 0.020 g, 0.016 mmol). ^{1}H NMR (C_5D_5N, 330 K): δ = –3.72 (br. s, 1 H, NH-porphyrin), –3.38 (br. s, 1 H, NH-porphyrin), 0.71 (s, 6 H, CH_3-mesityl), 1.68 (t, $^3J_{H,H}$ = 7.59 Hz, 6 H, CH_3CH_2-porphyrin), 2.17 (s, 6 H, CH_3-mesityl), 2.29 (s, 6 H, CH_3-dimethylxanthene), 2.65 (s, 6 H, CH_3-mesityl), 2.93 (s, 6 H, CH_3-porphyrin), 3.33 (s, 6 H, CH_3-porphyrin), 3.49 (s, 6 H, CH_3-porphyrin), 3.89 (m, 4 H, CH_3CH_2-porphyrin), 6.62 (m, 2 H, H-dimethylxanthene), 7.29 (t, $^3J_{H,H}$ = 7.57 Hz, 1 H, H-dimethylxanthene), 7.33 (m, 5 H, 4 H_{meta}-mesityl + 1 H-dimethylxanthene), 7.96 (dd, $^3J_{H,H}$ = 8.01, $^4J_{H,H}$ = 1.53 Hz, 1 H, H-dimethylxanthene), 8.08 (dd, $^3J_{H,H}$ = 7.53, $^4J_{H,H}$ = 1.54 Hz, 1 H, H-dimethylxanthene), 8.23 (d, $^3J_{H,H}$ = 3.88 Hz, 2 H, H_β-corrole), 8.55 (d, $^3J_{H,H}$ = 4.64 Hz, 2 H, H_β-corrole), 8.73 (d, $^3J_{H,H}$ = 4.01 Hz, 2 H, H_β-corrole), 8.96 (d, $^3J_{H,H}$ = 4.56 Hz, 2 H, H_β-corrole), 9.94 (s, 3 H, H_{meso}-porphyrin) ppm. MS (MALDI/TOF): *m/z* = 1246.98 $[M]^{+\cdot}$; 1246.54 calcd. for $C_{82}H_{78}N_8O$. UV/Vis (CH_2Cl_2): λ_{max} ($\varepsilon \times 10^{-3}$ L mol^{-1} cm^{-1}) = 389.0 (189), 507.0 (14.6), 541.0 (9.91), 576.0 (8.20), 628.0 (4.50) nm. UV/Vis (pyridine): λ_{max} ($\varepsilon \times 10^{-3}$ L mol^{-1} cm^{-1}) = 399.9 (192), 456.0 (39.2), 505.1 (16.4), 538.9 (11.1), 576.0 (br.) (13.1), 582.1 (br.) (12.9), 624.0 (20.5) nm. IR $\tilde{\nu}$ = 3276 (N–H), 2961 (C–H), 2918 (C–H), 2858 (C–H) cm^{-1}. $C_{82}H_{75}CoN_8O$ (1247.48): calcd. C 80.35, H 6.90, N 8.92; found C 80.77, H 6.68, N 8.73.

{5,15-Bis(2,6-dichlorophenyl)-10-[5-(13,17-diethyl-2,3,7,8,12,18-hexamethylporphyrin-5-yl)-9,9-dimethylxanthen-4-yl]corrole}-cobalt(III) (5C):5C was obtained in 63% yield (0.021 g, 0.016 mmol) using the same procedure as described for **5M**, starting from **4C** (0.035 g, 0.026 mmol). ^{1}H NMR (C_5D_5N, 330 K): δ = –4.10 (br. s, 1 H, NH-porphyrin), –3.49 (br. s, 1 H, NH-porphyrin), 1.67 (t, $^3J_{H,H}$ = 7.66 Hz, 6 H, CH_3CH_2-porphyrin), 2.33 (s, 6 H, CH_3-dimethylxanthene), 2.88 (s, 6 H, CH_3-porphyrin), 3.39 (s, 6 H, CH_3-porphyrin), 3.47 (s, 6 H, CH_3-porphyrin), 3.88 (m. 4 H, CH_3CH_2-porphyrin), 6.27 (dd, $^3J_{H,H}$ = 7.28, $^4J_{H,H}$ = 1.61 Hz, 1 H, H-dimethylxanthene), 6.83 (dd, $^3J_{H,H}$ = 7.34, $^4J_{H,H}$ = 1.62 Hz, 1 H, H-dimethylxanthene), 7.14 (t, $^3J_{H,H}$ = 7.63 Hz, 1 H, H-dimethylxanthene), 7.22 (t, $^3J_{H,H}$ = 7.63 Hz, 1 H, H-dimethylxanthene), 7.71 (t, $^3J_{H,H}$ = 8.22 Hz, 2 H, H_{meta}-dichlorophenyl), 7.86 (dd, $^3J_{H,H}$ = 8.16, $^4J_{H,H}$ = 1.03 Hz, 2 H, H_{meta}-dichlorophenyl), 8.00 (m, 4 H, 2 H-dimethylxanthene + 2 H_{meta}-dichlorophenyl), 8.32 (d, $^3J_{H,H}$ = 4.10 Hz, 2 H, H_β-corrole), 8.64 (d, $^3J_{H,H}$ = 4.09 Hz, 2 H, H_β-corrole), 8.78 (d, $^3J_{H,H}$ = 4.68 Hz, 2 H, H_β-corrole), 9.09 (d, $^3J_{H,H}$ = 4.68 Hz, 2 H, H_β-corrole), 9.90 (s, 1 H, H_{meso}-porphyrin), 9.91 (s, 2 H, H_{meso}-porphyrin) ppm. MS (MALDI/TOF): *m/z* = 1300.80 $[M]^{+\cdot}$; 1300.29 calcd. for $C_{76}H_{59}Cl_4N_8OCo$. UV/Vis (CH_2Cl_2): λ_{max} ($\varepsilon \times 10^{-3}$ L mol^{-1} cm^{-1}) = 389.0 (160), 506.0 (16.7), 540.0 (11.9), 573.0 (9.22), 627.0 (4.70) nm. UV/Vis (pyridine): λ_{max} ($\varepsilon \times 10^{-3}$ L mol^{-1} cm^{-1}) = 406.0 (182), 444.0 (46.1), 456.0 (48.6), 506.0 (16.9), 541.0 (11.1), 577.0 (b.) (14.1), 591.0 (16.2), 621.9 (28.2) nm. IR $\tilde{\nu}$ = 3275 (N–H), 2960 (C–H), 2920 (C–H), 2860 (C–H) cm^{-1}. $C_{76}H_{59}Cl_4CoN_8O$·MeOH (1333.14): calcd. C 69.37, H 4.76, N 8.41; found C 69.11, H 5.11, N 8.04.

Table 3. Crystal data and structure refinement details for **5M(py)$_2$**

Formula	$C_{92}H_{85}CoN_{10}O·2C_6H_{12}$
M_w	1573.94
Crystal system	triclinic
Space group	$P\bar{1}$
a [Å]	13.6160(4)
b [Å]	15.8720(5)
c [Å]	20.1957(7)
α [°]	83.092(1)
β [°]	79.587(1)
γ [°]	81.574(1)
V [Å^3]	4226.6(2)
Z	2
$d_{calcd.}$ [g cm^{-3}]	1.237
T [K]	115(2)
μ (Mo-K_α) [mm^{-1}]	0.260
θ range [°]	$1.74 < \theta < 24.02$
Index ranges	$-15 \le h \le 15$
	$-18 \le k \le 12$
	$-23 \le l \le 20$
Collected reflns	17425
Unique reflns	11702 (R_{int} = 0.0524)
Data/parameters	11702/1088
R indices [$I \ge 2\sigma(I)$]	R_1 = 0.0700; wR_2 = 0.1523
(all data)	R_1 = 0.1385; wR_2 = 0.1853
GOF	1.024
$\Delta\rho_{max}/\Delta\rho_{min}$ [e·Å^{-3}]	0.373/-0.454

[a] $R_1 = \Sigma||F_o| - |F_c||/\Sigma|F_o|$; $wR_2 = \{\Sigma[w(F_o^2 - F_c^2)^2]/\Sigma[wF_o^4]\}^{1/2}$. [b] $GOF = [\Sigma w(|F_o| - |F_c|)^2/(N_o - N_v)]^{1/2}$.

 © 2005 Wiley-VCH Verlag GmbH & Co. KGaA, Weinheim

X-ray Crystallography: X-ray diffraction experiment and data processing: Dark green single-crystals of prismatic morphology were grown in a mixture of pyridine and cyclohexane. A specimen of good quality was selected for low-temperature [T = 115(2) K] X-ray diffraction. The X-ray source was graphite-monochromatized Mo-K_α radiation (λ = 0.71073 Å) from a sealed tube. Data were collected with a Nonius KappaCCD diffractometer, equipped with a nitrogen jet-stream low-temperature system (Oxford Cryosystems).[34] Lattice parameters were obtained by a least-squares fit to the optimised setting angles of all collected reflections observed up to the maximum diffraction angle $2\theta_{max}$ = 48°. Intensity data were recorded as φ and ω scans with κ offsets. Data reduction was performed using the DENZO program.[35] Table 3 shows crystal data and some experimental details. Structure solution and refinement: The structure was solved by direct methods using the SIR97 program.[36] Refinements were carried out by full-matrix least squares on F^2 using the SHELXL97 program[37] and the complete set of reflections. The applied weighting scheme was $w = 1/[\sigma^2(F_o^2) + (AP)^2 + BP]$ where $P = (F_o^2 + 2F_c^2)/3$, A and B being updated parameters (at convergence, A = 0.0715 and B = 4.8787). Anisotropic thermal parameters were used for non-H atoms. Most hydrogen atoms were observed from Fourier synthesis. Hydrogen atoms were placed at calculated positions using a riding model [except both H(–$N_{pyrrole}$) atoms belonging to the free porphyrin moiety, for which the structural parameters were refined]. All H atoms were refined with a global isotropic thermal factor. One ethyl group belonging to the porphyrin moiety was disordered over two positions, showing sites occupation factors of 0.58(2)/0.42(2). Two cyclohexane solvent molecules co-crystallized with the complex. CCDC-240510 contains the supplementary crystallographic data for this paper. These data can be obtained free of charge at www.ccdc.cam.ac.uk/conts/retrieving.html [or from the Cambridge Crystallographic Data Centre, 12 Union Road, Cambridge CB2 1EZ, UK, Fax: +44-1223/336-033, E-mail: deposit@ccdc.cam.ac.uk].

Acknowledgments

This work was supported by the CNRS and Air Liquide. F. B. gratefully acknowledges the "Région Bourgogne" and CNRS for financial support. The authors also thank Mr. Marcel Soustelle for his assistance in the synthesis of pyrrole precursors.

[1] J. P. Collman, R. Boulatov, C. J. Sunderland, *The Porphyrin Handbook* (Eds.: K. M. Kadish, K. M. Smith, R. Guilard), Academic Press, New York, **2003**, vol. 11, p. 1–49.
[2] J. P. Collman, R. Boulatov, C. J. Sunderland, L. Fu, *Chem. Rev.* **2004**, *104*, 561–588.
[3] E. Kim, E. E. Chufan, K. Kamaraj, K. D. Karlin, *Chem. Rev.* **2004**, *104*, 1077–1133.
[4] J. M. Barbe, R. Guilard, *The Porphyrin Handbook* (Eds.: K. M. Kadish, K. M. Smith, R. Guilard), Academic Press, New York, **2000**, vol. 3, p. 211–244.
[5] J. P. Collman, P. S. Wagenknecht, J. E. Hutchison, *Angew. Chem. Int. Ed. Engl.* **1994**, *33*, 1537–1554.
[6] R. Guilard, M. A. Lopez, A. Tabard, P. Richard, C. Lecomte, S. Brandès, J. E. Hutchison, J. P. Collman, *J. Am. Chem. Soc.* **1992**, *114*, 9877–9889.
[7] R. Guilard, S. Brandès, A. Tabard, N. Bouhmaida, C. Lecomte, P. Richard, J. M. Latour, *J. Am. Chem. Soc.* **1994**, *116*, 10202–10211.
[8] R. Guilard, S. Brandès, C. Tardieux, A. Tabard, M. L'Her, C. Miry, P. Gouerec, Y. Knop, J. P. Collman, *J. Am. Chem. Soc.* **1995**, *117*, 11721–11729.
[9] R. Guilard, J. M. Barbe, C. Stern, K. M. Kadish, *The Porphyrin Handbook* (Eds.: K. M. Kadish, K. M. Smith, R. Guilard), Academic Press, New York, **2003**, vol. 18, p. 303–349.
[10] J. M. Barbe, F. Burdet, E. Espinosa, C. P. Gros, R. Guilard, *J. Porphyrins Phthalocyanines* **2003**, *7*, 365–374.
[11] C. Erben, S. Will, K. M. Kadish, *The Porphyrin Handbook* (Eds.: K. M. Kadish, K. M. Smith, R. Guilard), Academic Press, New York, **2000**, vol. 2, p. 233–300.
[12] R. Paolesse, *The Porphyrin Handbook* (Eds.: K. M. Kadish, K. M. Smith, R. Guilard), Academic Press, New York, **2000**, vol. 2, 201–232.
[13] R. Guilard, F. Jérôme, C. P. Gros, J. M. Barbe, Z. P. Ou, J. G. Shao, K. M. Kadish, *C. R. Acad. Sci. Ser. IIc* **2001**, *4*, 245–254.
[14] K. M. Kadish, L. Frémond, Z. P. Ou, J. Shao, C. Shi, F. C. Anson, F. Burdet, C. P. Gros, J. M. Barbe, R. Guilard, *J. Am. Chem. Soc.*, submitted.
[15] Z. Gross, N. Galili, I. Saltsman, *Angew. Chem. Int. Ed.* **1999**, *38*, 1427–1429.
[16] L. Simkhovich, N. Galili, I. Saltsman, I. Goldberg, Z. Gross, *Inorg. Chem.* **2000**, *39*, 2704.
[17] R. Paolesse, S. Nardis, F. Sagone, R. G. Khoury, *J. Org. Chem.* **2001**, *66*, 550–556.
[18] D. T. Gryko, *Chem. Commun.* **2000**, 2243–2244.
[19] D. T. Gryko, K. Jadach, *J. Org. Chem.* **2001**, *66*, 4267–4275.
[20] C. V. Asokan, S. Smeets, W. Dehaen, *Tetrahedron Lett.* **2001**, *42*, 4483–4485.
[21] D. T. Gryko, K. E. Piechota, *J. Porphyrins Phthalocyanines* **2002**, *6*, 81–97.
[22] D. T. Gryko, B. Koszarna, *Org. Biomol. Chem.* **2003**, *1*, 350–357.
[23] R. Guilard, D. T. Gryko, G. Canard, J.-M. Barbe, B. Koszarna, S. Brandès, M. Tasior, *Org. Lett.* **2002**, *4*, 4491–4494.
[24] B. J. Littler, M. A. Miller, C. H. Hung, R. W. Wagner, D. F. O'Shea, P. D. Boyle, J. S. Lindsey, *J. Org. Chem.* **1999**, *64*, 1391–1396.
[25] J. W. Buchler, D. P. K. Ng, *The Porphyrin Handbook* (Eds.: K. M. Kadish, K. M. Smith, R. Guilard), Academic Press, New York, **2000**, vol. 3, p. 245–294.
[26] K. M. Kadish, G. Moninot, Y. Hu, D. Dubois, A. Ibnlfassi, J. M. Barbe, R. Guilard, *J. Am. Chem. Soc.* **1993**, *115*, 8153–8166.
[27] R. Guilard, C. P. Gros, F. Bolze, F. Jérôme, Z. P. Ou, J. G. Shao, J. Fischer, R. Weiss, K. M. Kadish, *Inorg. Chem.* **2001**, *40*, 4845–4855.
[28] R. Guilard, F. Jérôme, J. M. Barbe, C. P. Gros, Z. P. Ou, J. Shao, J. Fischer, R. Weiss, K. M. Kadish, *Inorg. Chem.* **2001**, *40*, 4856–4865.
[29] K. M. Kadish, Z. P. Ou, J. G. Shao, C. P. Gros, J. M. Barbe, F. Jérôme, F. Bolze, F. Burdet, R. Guilard, *Inorg. Chem.* **2002**, *41*, 3990–4005.
[30] F. Burdet, J.-M. Barbe, Z. P. Ou, J. Shao, K. M. Kadish, E. Espinosa, C. P. Gros, R. Guilard, manuscript in preparation.
[31] F. Jérôme, C. P. Gros, C. Tardieux, J. M. Barbe, R. Guilard, *New J. Chem.* **1998**, *22*, 1327–1329.
[32] F. Jérôme, C. P. Gros, C. Tardieux, J. M. Barbe, R. Guilard, *Chem. Commun.* **1998**, 2007–2008.
[33] A. Mahammed, I. Giladi, I. Goldberg, Z. Gross, *Chem. Eur. J.* **2001**, *7*, 4259–4265.
[34] *COLLECT Program, Data Collection Software*, Nonius, Delft, The Netherlands, **1998**.
[35] Z. Otwinowski, W. Minor, *Methods Enzymol.* **1997**, *276*, 307–326.
[36] A. Altomare, M. C. Burla, M. Camalli, G. L. Cascarano, C. Giacovazzo, A. Guagliardi, A. G. Moliterni, G. Polidori, R. Spagna, *J. Appl. Crystallogr.* **1999**, *32*, 115–119.
[37] *SHELXL97 Program, Program for the Refinement of the Crystal Structures*, University of Göttingen, Germany, **1997**.

Received September 13, 2004

 © 2005 Wiley-VCH Verlag GmbH & Co. KGaA, Weinheim

Stereoisomerism in Pentaerythritol-Bridged Cyclotriphosphazene Tri-Spiranes: Spiro and Ansa 1,3-Propanediyldioxy Disubstituted Derivatives

Aylin Uslu,*[a] Simon J. Coles,[b] David B. Davies,[c] Robert J. Eaton,[c] Michael B. Hursthouse,[b] Adem Kılıç,[a] and Robert A. Shaw[c]

Keywords: Cyclotriphosphazene derivatives / Trispiranes

Four isomeric products were isolated and purified from the reaction of 1,3-propanediol with the tri-spirane cyclophosphazene-organophosphate compound **1**: viz. the di-monospiro (**2a**), di-monoansa (**2b**) and two monospiro-monoansa derivatives (**2c** and **2d**). It is shown by ^{31}P NMR spectroscopy on addition of a chiral solvating agent (CSA) that both the di-monospiro **2a** and di-monoansa **2b** derivatives are racemates, as expected, whereas no splitting of NMR signals occurred on addition of CSA to solutions of **2c** and **2d**. It is found by X-ray crystallography that the two monospiro-monoansa spirane derivatives, **2c** and **2d**, are *meso* diastereoisomers, which represent a new case of the stereochemistry of bis(disubstituted) cyclophosphazene derivatives of **1**. It is also observed from the ^{31}P NMR spectrum of the reaction mixture, supported by the yields of pure compounds, that formation of a spiro group is about 4.5 times more likely than that of an ansa moiety under the conditions of the reaction.

(© Wiley-VCH Verlag GmbH & Co. KGaA, 69451 Weinheim, Germany, 2005)

Introduction

Difunctional reagents with cyclophosphazenes can give rise to four structural types: spiro, ansa, bridged and open chain.[1] For example, the reaction of 1,3-propanediol with cyclotriphosphazene, $N_3P_3Cl_6$, gave spiro, $N_3P_3[O(CH_2)_3O]_xCl_{6-x}$ (x = 1,2,3); ansa, $N_3P_3[O(CH_2)_3O]Cl_4$; spiro-ansa, $N_3P_3[O(CH_2)_3O]_2Cl_2$; open chain, $N_3P_3[O(CH_2)_3OH]Cl_5$ and bridged, $N_3P_3Cl_5[O(CH_2)_3O]N_3P_3Cl_5$ compounds, in which spiro derivatives are by far the major product.[2] It is known that reaction of cyclotriphosphazene with a tetrafunctional alcohol such as pentaerythritol, $C(CH_2OH)_4$, gives a spirane-bridged compound **1**, whose structure (Figure 1) consists of four six-membered rings, each joined by a tetrahedral atom (phosphorus or carbon atom) to the next ring, with each six-membered ring being orthogonal to its neighbours.[3] The stereochemistry of bis(disubstituted) cyclophosphazene derivatives of **1** has recently been elucidated;[4] it was shown that racemates were observed for bis(geminal) derivatives, as well as for non-geminally disubstituted *cis* and *trans* (the latter has two diastereoisomers) derivatives. In the present work, the reaction of the spirane-bridged compound **1** with 1,3-propanediol was investigated and four isomeric disubstituted spiro and ansa derivatives **2a**–**d** were isolated (Figure 1).

Two of the products **2a**–**b** gave rise to chiral compounds corresponding to cases observed previously [bis(disubstitution that is geminal or *cis* non-geminal],[4] whereas the other two derivatives **2c**–**d** have geminal disubstitution in one cyclophosphazene ring and *cis* non-geminal disubstitution in the other cyclophosphazene ring, giving rise to a new case of chirality in such systems, in which both compounds are *meso* diastereoisomers.

Results and Discussion

The spirane-bridged compound **1**, was allowed to react with 1,3-propanediol in a 1:2 mol ratio to give four disubstituted isomers **2a**–**d**, which were separated by column chromatography. Overall, there was a yield of about 25% with compound **2a** (14.9%) being the major product, and with minor yields of **2b** (2.5%) **2c** (4%) and **2d** (3.5%). The products were characterised by elemental analysis, mass spectrometry and ^{31}P NMR spectroscopy. Elemental analysis and mass spectrometry give the same results for the four compounds, as expected for isomers.

The proton-decoupled ^{31}P NMR spectra of **2a** and **2b** are observed (Figure 2, a and b, respectively) as ABX spin systems resulting from the two phosphazene rings in each compound having the same substitution pattern. However, the two ABX spin systems are quite different as in **2a** the X-part is ca. 26–27 ppm and the AB portion is 8–11 ppm, whereas the X-part of **2b** is ca. 11 ppm and the AB portion is 30–32 ppm. The assignment of signals of **2a** was assisted

[a] Department of Chemistry, Gebze Institute of Technology, Gebze, Kocaeli, Turkey
Fax: +90-262-754-2385
E-mail: aylin@gyte.edu.tr
[b] University of Southampton, Highfield, Southampton SO17 1BG, UK
[c] School of Biological and Chemical Sciences, Birkbeck College (University of London), Malet Street, London WC1E 7HX, UK

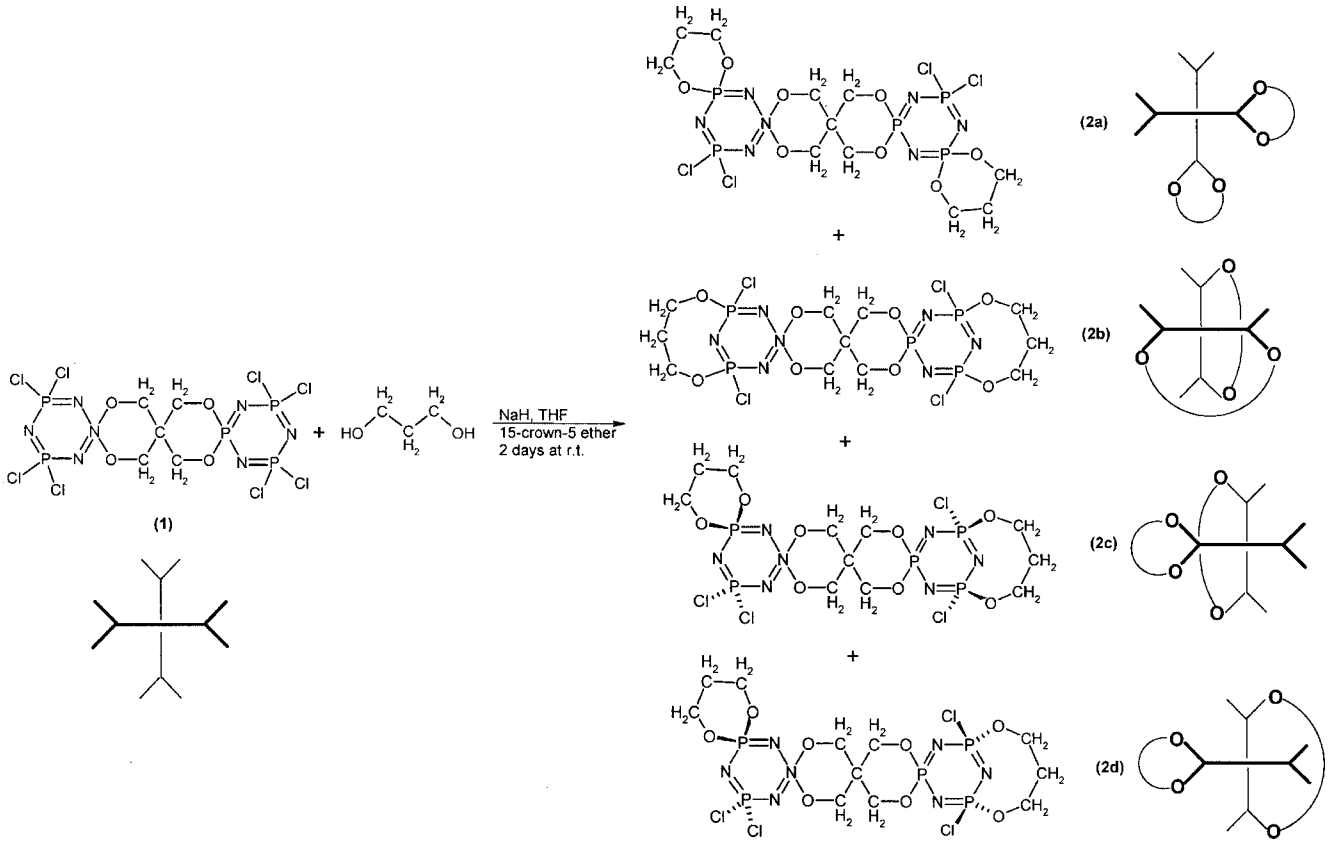

Figure 1. Structures of spirane-bridged unsubstituted, **1**, and disubstituted cyclotriphosphazene derivatives; di-monospiro **2a**, di-monoansa **2b**, and two monospiro-monoansa derivatives (**2c**, *syn*) and (**2d**, *anti*). A diagrammatic representation is also shown for compounds **1** and **2a**–**2d**. For clarity the inner organophosphate rings have been omitted and the outer cyclophosphazene rings, which are orthogonal to each other, are shown in the same projection with the ring to the front in bold type.

by proton-coupled ^{31}P NMR spectra [not shown], which indicates that the 26–27 ppm signal corresponds to a $>PCl_2$ group (no coupling) and the AB portion results from the >P(bridge) and >P(spiro) groups. The ^{31}P NMR spectrum of **2b** at 30–32 ppm is characteristic of a cyclotriphosphazene dioxy-ansa derivative with a relatively small ansa ring[5] and the signal at δ = 11 ppm is given by the >P(bridge) group; the ansa moiety is observed as an AB spin system because **2b** is a chiral diastereoisomer (see below). The ^{31}P NMR spectra are consistent with **2a** being the di-monospiro compound and **2b** being the di-monoansa compound. The ^{31}P NMR spectra of **2c** and **2d** (Figure 2, c and d, respectively) are very similar to each other and consist of five multiplets resulting from the superposition of an A_2X and an ABX spin system; the ABX spin system is similar to that for the spiro derivative **2a**, and the A_2X has similar chemical shifts and coupling constants to those found for the ansa derivative **2b**, but is A_2 rather than AB because compounds **2c** and **2d** are a *meso* diastereoisomers (see below). ^{31}P NMR indicates that both, **2c** and **2d**, are monospiro-monoansa compounds, having slightly different chemical shifts and coupling constants, especially for the spiro-substituted ring. The ^{31}P NMR spectroscopic data for compounds **2a**–**2d** are summarised Table 1.

By analogy with previous work on the stereochemistry of bis(disubstituted) cyclophosphazene derivatives of **1**,[4] it is expected that both compounds **2a** and **2b** are chiral and exist as racemates. The di-monospiro compound **2a** is the case of a bis(geminal) derivative and the di-monoansa compound **2b** has non-geminal disubstitutents that are *cis*.[4] On addition of a chiral solvating agent [CSA, (*S*)-(+)-2,2,2-trifluoro-1-(9′-anthryl)ethanol] it was found that all the ^{31}P NMR signals of compounds **2a** and **2b** exhibit chemical shift changes indicating complexation with the CSA, and that all signals, except the >P(bridge) group of compound **2b**, separate into two lines of equal intensity consistent with compounds **2a** and **2b** existing as racemates. The change in ^{31}P NMR chemical shifts and separation of signals of compounds **2a** and **2b** at a 20:1 mol ratio of CSA:**2a** or **2b** are summarised Table 1. Addition of CSA to compounds **2c** and **2d** also caused changes in chemical shifts of each signal (Table 1), but no separation of signals even at higher mol ratios of 50:1 (**2c**) and 40:1 (**2d**). These results indicate that CSA complexes to compounds **2c** and **2d** in solution, and that both molecules may be *meso*, because CSA does not cause extra splitting of the NMR peaks. Such a caveat needs to be made, in the first instance, because previous NMR work has shown splitting of peaks for *meso* com-

 © 2005 Wiley-VCH Verlag GmbH & Co. KGaA, Weinheim

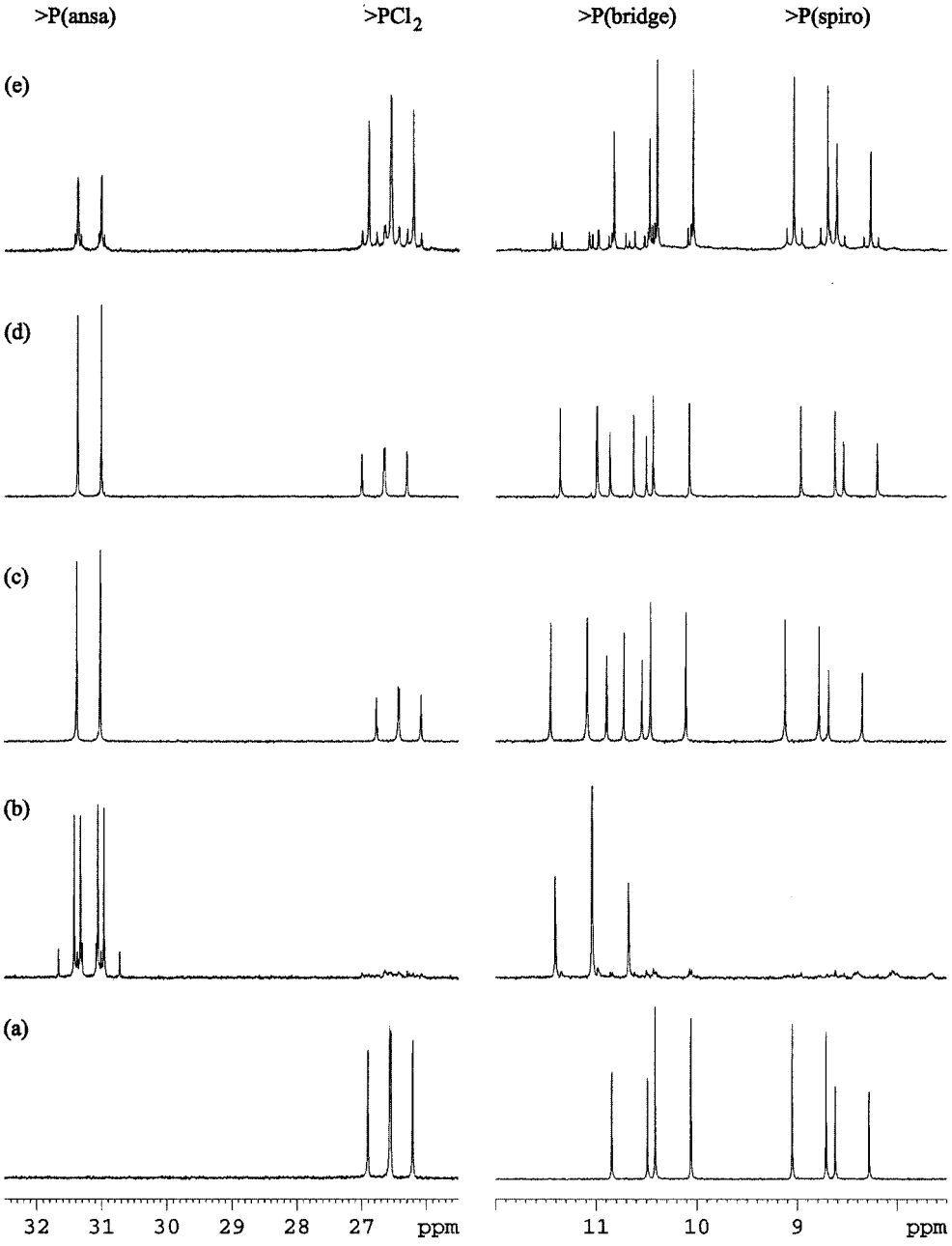

Figure 2. ^{31}P NMR spectra of the reaction mixture and the isolated four isomers of 1,3-propanediyldioxy derivatives of pentaerythritol-bridged cyclotriphosphazenes. (a) **2a**, spiro-spiro, (b) **2b**, ansa-ansa, (c) **2c**, *syn*-spiro-ansa, (d) **2d**, *anti*-spiro-ansa, (e) reaction mixture.

pounds with remote stereogenic centres on addition of CSA (and Chiral Shift Reagents, CSR).[6] However, in the case of compounds **2c** and **2d** the centres of chirality in the cyclophosphazene ansa moiety are part of the same ring and only two bonds apart and so complexation with CSA will affect both centres at the same time, as is normally found for other analogous systems,[6] i.e. the anomalous ^{31}P NMR effect with CSA is not expected for compounds **2c** and **2d** and so both are expected to be *meso* compounds.

Although NMR spectroscopy has been used to show that both compounds **2c** and **2d** are different monospiro-monoansa derivatives, such data cannot be used to assign an absolute structure and hence compounds **2c** and **2d** were characterised by X-ray crystallography.

The crystal structures of **2c** and **2d** (Figure 3) show that both molecules contain six rings, two phosphazene units bridged by a pentaerythritol molecule in a spirane arrangement, a spiro-$O(CH_2)_3O$ unit in one cyclophosphazene ring and an ansa-$O(CH_2)_3O$ moiety in the *cis*-configuration in the other cyclophosphazene ring.[7]

In both **2c** and **2d** the cyclophosphazene ring is essentially planar for the spiro-containing moiety, whereas for the ansa-substituted moiety the cyclophosphazene ring is non-planar, indicating strain which is relieved by the ring

 © 2005 Wiley-VCH Verlag GmbH & Co. KGaA, Weinheim

Table 1. ^{31}P NMR parameters of compounds **2a**–**2d** and the effect of addition of CSA.

Compound[a]		Ansa moiety Chemical shifts /ppm		^2J(P,P)/Hz	Spiro moiety Chemical shifts /ppm			Coupling constants ^2J(P,P) /Hz		
	Struct.	>P(ansa)	>P(bridge)		$>PCl_2$	>P(bridge)	>P(spiro)			
		1,2	3	1,3; 2,3	1	2	3	1,2	1,3	2,3
(i) ^{31}P NMR parameters of spirane compounds										
2a	sp–sp				26.55	10.43	8.69	71.7	68.8	87.1
2b	an–an	31.31; 31.08	11.05	74.3; 72.8 48.6 (1,2)[b]						
2c	sp–an *syn*	31.21; 31.21	11.09	73.5	26.42	10.48	8.77	71.0	68.5	87.9
2d	sp–an *anti*	31.20; 31.20	11.00	73.5	26.65	10.45	8.61	72.5	68.9	86.5
(ii) Effect of addition of CSA on chemical shifts (ppb) and ^2J(P,P) at 20:1 mol ratio										
2a	sp–sp $\Delta\delta$[c]				43 (35)	–75 (8)	–13 (15)	71.6	68.5	86.8
2b	an–an $\Delta\delta$[c]	10; 22 (4); (7)	–76 [d]	73.8; 72.5 48.6 (1,2)[b]						
2c	sp–an *syn*[d]	12	–108	73.2	53	–77	–22	70.9	68.3	87.6
2d	sp–an *anti*[e]	16	–82	73.4	24	–60	–5	72.3	68.6	86.2

[a] 202.45 MHz ^{31}P NMR measurements in $CDCl_3$ solutions at 298K. CSA is chiral solvating agent, (*S*)-(+)-2,2,2-trifluoro-1-(9′-anthryl) ethanol. [b] AB coupling for ^2J(P,P)/Hz in ansa ring. [c] $\Delta\delta$ is the difference in chemical shift (ppb) of racemic signals at a mol ratio of CSA:**2** of 20:1. [d] No separation of signals observed up to a mol ratio of CSA:**2** of 50:1. [e] No separation of signals observed up to a mol ratio of CSA:**2** of 40:1.

nitrogen atom containing the ansa moiety being significantly out of plane; 0.262 Å **2c** and 0.289 Å **2d**.[8] The difference between the two structures is that in **2c** the ansa- and spiro-propanediyldioxy units are in a *syn* arrangement, whereas in **2d** there is an *anti* arrangement of the ansa- and spiro-propanediyldioxy units. The *syn* and *anti* structures are shown in Figure 1 for **2c** and **2d**, respectively, from which it can be clearly seen that both molecules have a plane of symmetry and so are not chiral, confirming the ^{31}P NMR results. The stereochemistry of bis(disubstituted) cyclophosphazene derivatives of **1** has recently been elucidated[4] and compounds **2c** and **2d** give rise to a new case of stereochemistry of these spirane derivatives.

The ^{31}P NMR spectrum of the reaction mixture of compound **2** is shown in Figure 2(e). Using the NMR spectroscopic data in Table 1, it is possible to assign all the ^{31}P NMR signals in the reaction mixture to the four disubstituted compounds **2a**–**2d** (i.e. there is no evidence of the starting material, mono-substituted or higher substituted compounds). Assuming similar relaxation times for ^{31}P NMR signals of phosphorus nuclei with similar substitution patterns, the analysis gives spiro-spiro **2a** (ca. 70%), *syn*-spiro-ansa **2c** = *anti*-spiro-ansa **2d** (ca. 12%) and ansa-ansa **2b** (ca. 6%), which corresponds to the formation of a spiro being about 4.5 times more likely than that of an ansa moiety. This was confirmed by the similar relative distribution of compounds observed as a result of isolation and purification after column chromatography (**2a**, ca. 60%; **2b** ca. 10%; **2c** ca. 16%; **2d** ca.14%), though the results do not match exactly, because there are likely to be small differences in the efficiency of isolation and purification of the four compounds. The preference for spiro over ansa 1,3-propanediyldioxy derivatives of cyclophosphazene is not surprising given that the spiro ring is a six-membered thermodynamically stable chair form, in contrast to the eight-membered strained ansa ring.[8] In fact, it is somewhat surprising that significant quantities of the ansa derivatives are formed. However, in the reactions of cyclophosphazenes with diols in THF solution it has been observed[9–12] that the formation of ansa derivatives is promoted by using the more reactive sodium alkoxides (rather than the less reactive neutral pentaerythritol and tertiary base used previously[3]). It was also expected[11,12] that addition of 15-crown-5 ether (which should make the nucleophilic alkoxide more reactive by reducing ion-pairing) might also assist in the formation of ansa derivatives with 1,3-propanediol in this work. The reaction conditions for the formation of spiro and ansa derivatives of cyclophosphazenes with diols are currently being investigated.

Experimental Section

Materials: Hexachlorocyclotriphosphazene (Shin Nisso Kako Co Ltd.) was purified by fractional crystallisation from hexane. The following chemicals were obtained from Merck: Pentaerythritol (> 98%), 1,3-propanediol (> 98%), silica gel 60, tetrahydrofuran (≥ 99.0%), dichloromethane (≥ 99.0%), ethyl acetate (≥ 99.0%), *n*-hexane (>96%), sodium hydride (> 60%), 15-crown-5 ether (> 98%). The deuteriated solvent ($CDCl_3$) for NMR spectroscopy was obtained from Apollo Scientific and the chiral solvating agent (CSA), (*S*)-(+)-2,2,2-trifluoro-1-(9′-anthryl)ethanol, from Aldrich Chem. Co.

 © 2005 Wiley-VCH Verlag GmbH & Co. KGaA, Weinheim

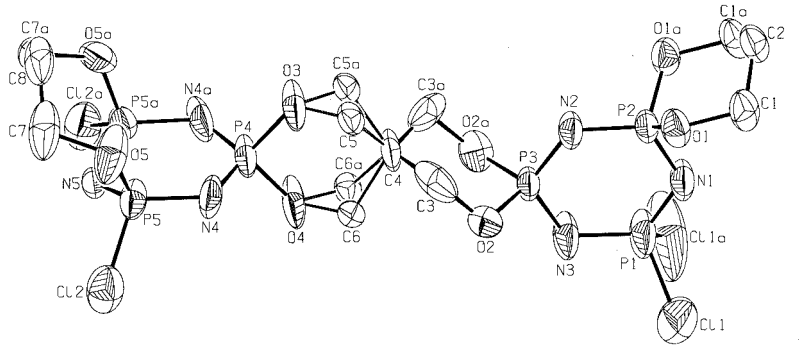

2c (*syn*)

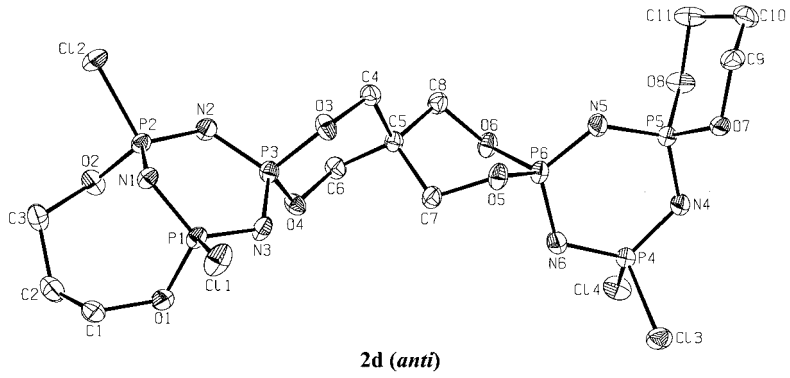

2d (*anti*)

Figure 3. X-ray crystal structures of the two monospiro-monoansa derivatives **2c** and **2d**.

Methods: Elemental analyses were obtained with a Carlo–Erba 1106 Instrument. Mass spectra were recorded with a VG Zab Spec GC-MS spectrometer using the fast atom bombardment (FAB) method (35 kV) with MNBA as the matrix; ^{35}Cl values were used for calculated masses. Analytical thin layer chromatography (TLC) was performed on Merck Silica gel plates (Merck, Kieselgel 60, 0.25 mm thickness) with F_{254} indicator. Column chromatography was performed on silica gel (Merck, Kieselgel 60, 230–400 mesh; for 3 g. crude mixture, 100g. silica gel was used in a column of 3 cm in diameter and 60 cm in length). ^{31}P NMR spectra were recorded in $CDCl_3$ solutions with a Bruker DRX 500 MHz spectrometer using 85% H_3PO_4 as an external reference for ^{31}P. In order to assign the signals of some compounds both proton-coupled and proton-decoupled ^{31}P NMR spectra were recorded. Experiments involving the chiral solvating agent (CSA) were performed by addition of small aliquots of a concentrated solution of CSA in the solvent used for NMR spectroscopy and the proton-decoupled ^{31}P NMR spectrum recorded at each addition.

X-ray Crystallography: X-ray structure determination and crystallographic data were collected by means of combined phi and omega scans with a Bruker–NoniusKappaCCD area detector situated at the window of a rotating anode (λ, Mo-K_α = 0.71073 Å). The structures were solved by direct methods, SHELXS-97 and refined by using SHELXL-97.[13] Hydrogen atoms were included in the refinement, but thermal parameters and geometry were constrained to ride on the atom to which they are bonded. The data were corrected for absorption effects using SORTAV.[14] The structure of **2c** exhibits crystallographic disorder about the mirror axis in the space group. In addition a disordered solvent molecule was also present, but was too disordered to resolve and was therefore removed from the model using the SQUEEZE[15] procedure from within the PLATON[16] suite of programs (Table 2).

Table 2. X-ray data for compounds **2c** and **2d**.

	2c	**2d**
Empirical formula	$C_{11}H_{20}Cl_4N_6O_8P_6$	$C_{11}H_{20}Cl_4N_6O_8P_6$
Formula mass	691.95	691.95
Crystal system	orthorhombic	monoclinic
Space group	*Pnma*	$P2_1/c$
a [Å]	12.1255(3)	14.7211(3)
b [Å]	10.7597(3)	11.9459(3)
c [Å]	23.7161(5)	14.9661(4)
β [°]	90	105.089(2)
V [Å^3]	3094.16(13)	2541.15(11)
Z	4	4
Density (calcd.) [Mg/m^3]	1.720	1.809
Absorption coefficient [mm^{-1}]	0.751	0.895
F(000)	1400	1400
Crystal size [mm]	0.45 × 0.40 × 0.40	0.12 × 0.10 × 0.01
$\theta_{max.}$ [°]	27.49	27.46
Reflections collected	25948	34251
Independent reflections	3716	5808
Final *R* indices $F^2 > 2\sigma F^2$	*R*1 = 0.1102 *wR*2 = 0.2708	*R*1 = 0.0362 *wR*2 = 0.0754
$\Delta\rho_{max./min.}$ [e·Å^{-3}]	1.333/–1.104	0.369/–0.427

CCDC-245906 and CCDC-245907 contain the supplementary crystallographic data for this paper. These data can be obtained free of charge from The Cambridge Crystallographic Data Centre via www.ccdc.cam.ac.uk/data_request/cif.

Reaction of Compound 1 with 1,3-Propanediol To Give Compounds 2a–d: Compound **1** was prepared as in the literature.[3] To a stirred solution of compound **1** (2 g, 2.92 mmol) dissolved in dry tetrahydrofuran (20 mL) at –15 °C under argon was first added dropwise 1,3-propanediol (0.4 g, 5.84 mmol) in dry tetrahydrofuran (20 mL), then sodium hydride (0.28 g, 11.68 mmol) in dry tetrahydrofuran (20 mL) was added dropwise and finally 15-crown-5 (0.5 g) was

 © 2005 Wiley-VCH Verlag GmbH & Co. KGaA, Weinheim

added. The reaction mixture was stirred for a further 2 days at room temperature and the reaction was followed by TLC indicating four products and no starting material remaining. The precipitated salt (NaCl) was then filtered off, the solvent was removed under reduced pressure and four products were isolated by column chromatography [silica gel 60 (70–230 mesh) as adsorbent and ethyl acetate/*n*-hexane (1:2) as eluent]. The order of compounds eluted is **2d**, **2b**, **2a** and **2c** . Compound **2c** was crystallized from benzene and **2d** was crystallized from dichloromethane/hexane (3:1). **2a:** Yield 0.30 g (14.85%), m.p. 208 °C. (found: C 18.96, H 2.85, N 12.05. MS: *m*/*z* = 690.8 $[M + 1]^+$). **2b:** Yield 0.05 g (2.47%), decomp. 200 °C, (found: C 21.06, H, 2.86, N 12.11. MS: *m*/*z* = 691.0 $[M + 1]^+$). **2c:** Yield 0.08 g (3.97%), m.p. 170 °C, (found: C 20.25, H 2.89, N 12.12. MS: *m*/*z* = 690.7 $[M + 1]^+$). **2d:** Yield 0.07 g (3.47%), decomp. 140 °C, (found: C 20.21, H 2.74, N 11.96. MS: *m*/*z* = 690.7 $[M + 1]^+$). $C_{11}H_{20}Cl_4N_6O_8P_6$: calcd. C 19.09, H 2.91, N 12.15. MS: *m*/*z* = 690.0 $[M^+]$.

Acknowledgments

We thank the Shin Nisso Kako Co Ltd. for gifts of $N_3P_3Cl_6$, the EPSRC for the National Crystallographic Service (Southampton, UK) and Gebze Institute of Technology Research Fund for partial support (AK, AU).

[1] a) R. A. Shaw, *Pure Appl. Chem.* **1980**, *52*, 1063; b) J-F. Labarre, *Topics Curr. Chem*. **1985**, *129*, 173–230; c) V. Chandrasekhar, V. Krishnan, in *Advances in Inorganic Chemistry Including Bioinorganic Studies*, *53* (Ed.: A. G. Sykes), Academic Press, Amsterdam, **2002**.

[2] A. H. Alkubaisi, H. G. Parkes, R. A. Shaw, *Heterocycles* **1989**, *28*, 347–358.

[3] a) H. A. Al-Madfa, L. S. Shaw (neé Gözen), R. A. Shaw, *Phosphorus*, *Sulfur, Silicon* **1991**, *56*, 133; b) H. A. Al-Madfa, *Ph. D. Thesis*, University of London, **1988**.

[4] S. J. Coles, D. B. Davies, R. J. Eaton, M. B. Hursthouse, A. Kılıç, R. A. Shaw, A. Uslu, *Eur. J. Org. Chem.* **2004**, 1881–1886.

[5] a) S. R. Contractor, M. B. Hursthouse, H. G. Parkes, L. S. Shaw (neé Gözen), R. A. Shaw, H. Yılmaz, *Chem. Commun.* **1984**, 675; b) H. R. Allcock, K. D. Lavin, G. H. Riding, P. R. Susko, R. R. Whittle, *J. Am. Chem. Soc.* **1984**, *106*, 2337; c) S. R. Contractor, M. B. Hursthouse, H. G. Parkes, L. S. Shaw (née Gözen), R. A. Shaw, H. Yılmaz, *Phosphorus Sulfur* **1986**, *28*, 267–275.

[6] S. Beşli, S. J. Coles, D. B. Davies, R. J. Eaton, M. B. Hursthouse, A. Kılıç, R. A. Shaw, G. Yenilmez Çiftçi, S. Yeşilot, *J. Am. Chem. Soc.* **2003**, *125*, 4943–4950.

[7] The starting material, compound **1**, is a linear tri-spirane, in which all the organophosphate and cyclotriphosphazene spirane moieties are six-membered and the shape of the ring system may be described as planar/chair/chair/planar. The introduction of spiro substituents creates further six-membered spirane rings, whereas ansa substituents form eight-membered rings giving rise to fused bicyclic systems. Thus the spiro-spiro derivative, **2a**, is a penta-spirane with the two terminal spirane rings at an angle to the linear central four. The ansa-ansa compound, **2b**, is a tri-spirane with both ends having fused bicyclic units. The two spiro-ansa isomers, **2c** and **2d**, are tetra-spiranes and have one end with a fused bicyclic structure. The ring system of the *syn* compound **2c** may be described as chair/planar/chair/disordered-chair/fused-envelope and the *anti* compound **2d** as chair/planar/twisted-chair/chair/fused-envelope. All the CH_2 groups are staggered with respect to their nearest neighbours and eclipsed with those two bonds away, except in the twisted chair, where they are staggered.

[8] The fused bicyclic ansa structures exhibit a boat-chair form. The ring N atom sandwiched between the two P–O ansa segments is forced out of the rest of the plane of the N_2P_3 ring to such an extent that it is nearly parallel with the adjacent P–Cl bonds. This distortion causes a ring compression. The respective non-bonded P···P distances for the spiro and ansa N_3P_3 rings for these two diastereoisomers are for the *syn* compound **2c** (spiro 2.724, 2.729 and 2.763 Å and ansa **2.636**, 2.725 and 2.726 Å) and for the *anti* compound **2d** (spiro 2.745, 2.760 and 2.764 Å and ansa **2.637**, 2.735 and 2.741 Å).

[9] a) K. Brandt, T. Kupka, J. Drozd, J. C. van de Grampel, A. Meetsma, A. P. Jekel, *Inorg. Chim. Acta* **1995**, *228*, 187; b) K. Brandt, I. Porwolik, T. Kupka, A. Olejnik, R. A. Shaw, D. B. Davies, *J. Org. Chem.* **1995**, *60*, 7433–7438; c) K. Brandt, I. Porwolik-Czomperlik, M. Siwy, T. Kupka, R. A. Shaw, D. B. Davies, M. B. Hursthouse, G. D. Sikara, *J. Am. Chem. Soc.* **1997**, *119*, 12432–12440.

[10] K. Muralidharan, P. Venugopalan, A. J. Elias, *Inorg. Chem.* **2003**, *42*, 3176−3182.

[11] K. Muralidharan, A. J. Elias, *Inorg. Chem.* **2003**, *42*, 7535–7543.

[12] A. Uslu, unpublished results.

[13] G. M. Sheldrick, SHELX suite of programs for crystal structure solution and refinement, University of Göttingen, Germany, **1997**.

[14] R. H. Blessing, *J. Appl. Crystallogr.* **1997**, *30*, 421.

[15] P. v. d. Sluis, A. L. Spek, *Acta Crystallogr. Sect A* **1990**, *46*, 194–201.

[16] a) A. L. Spek, *Acta Crystallogr. Sect. A* **1990**, *46*, C34; b) A. L. Spek, *PLATON, A Multipurpose Crystallographic Tool*, Utrecht University, Utrecht, The Netherlands, **1998**.

Received: September 24, 2004

 © 2005 Wiley-VCH Verlag GmbH & Co. KGaA, Weinheim

Solution, Structural and Catalytic Studies of Neutral MCl_2 (M = Pd, Pt) Complexes of the N/E Mixed-Donor Ligands 2-$(RECH_2)C_5H_4N$ (RE = MeS, PhS, MeSe)

Roderick C. Jones,[a] Rachael L. Madden,[a] Brian W. Skelton,[b] Vicki-Anne Tolhurst,*[a] Allan H. White,[b] Alan M. Williams,[a] Adele J. Wilson,[a] and Brian F. Yates[a]

Keywords: Palladium / Platinium / N,S ligands / Homogeneous catalysis / Fluxional processes

The reaction of MCl_2 (M = Pd, Pt) with one mole-equivalent of **L** [**L** = 2-$(MeSCH_2)C_5H_4N$ (**L**^{1}), 2-$(PhSCH_2)C_5H_4N$ (**L**^{2}), 2-$(MeSeCH_2)C_5H_4N$ (**L**^{3})] in MeCN gave the monomeric complexes [MCl_2**L**] in good yields. Single-crystal X-ray diffraction studies of [MCl_2**L**^{2}] confirmed the complexes to be monomeric with square-planar geometry about the metal centre. Variable-temperature NMR spectroscopy showed that the complexes undergo fluxional processes in solution, which were confirmed, by DFT calculations, to be (*E*)-pyramidal inversion at the chalcogen centre rather than ring-flip or (*E*)-dissociation processes. The calculations showed that the barrier to inversion increases in the order S<Se<Te. All complexes were characterised using ^{1}H NMR, UV/Vis and IR spectroscopy and microanalysis.
(© Wiley-VCH Verlag GmbH & Co. KGaA, 69451 Weinheim, Germany, 2005)

Introduction

Palladium(II) and platinum(II) complexes containing dithioether ligands have been extensively studied in recent years,[1–3] leading to an understanding of the *S*-pyramidal inversion process in solution. Reports of similar compounds containing diselenoether and ditelluroether ligands are now more prevalent and include solution properties ascertained by using multinuclear NMR spectroscopy.[4] In contrast, complexes containing mixed-N/S or N/Se donor groups have not been as extensively studied, nor have these studies generally included systematic investigations into the complexes' behaviour in solution.

The use of hemilabile ligands in catalysis is gaining interest, as these ligands are thought to give better catalyst stability and higher yields compared to catalysts containing homoleptic ligands.[5] It has been suggested that the enantioselectivity observed in Pd-catalysed enantioselective allylic alkylation may be related to the pyramidal inversion at the sulfur donor atom in complexes containing thioether ligands.[6] Organo-palladium(II) complexes containing the mixed-donor ligand 2-$(RSCH_2)C_5H_4N$ (R = Me, Ph) undergo allene insertion into Pd–C bonds.[7,8]

Herein we report the preparation of a number of palladium(II) and platinum(II) complexes containing the mixed-donor ligands 2-$(RECH_2)C_5H_4N$ [E = S, R = Me (**L**^{1}), Ph (**L**^{2}); E = Se, R = Me (**L**^{3})] and the single-crystal structure determinations of isomorphous [$PdCl_2$**L**^{2}] and [$PtCl_2$**L**^{2}]. We have investigated the solution behaviour of these complexes using variable-temperature NMR spectroscopy. Density Functional Theory calculations have been employed to determine the likely processes being observed. Trends in (*E*)-pyramidal inversion barriers for the complexes have been compared with those associated with Pd^{II} and Pt^{II} complexes containing homoleptic dithio- and diselenoether ligands. Studies into the solid-state structures and solution properties are important for understanding the usefulness of these complexes as catalysts as they infer information on the strength of the ligand-metal interactions. We also report the catalytic activity of the Pd^{II} complexes [$PdCl_2$**L**^{1}] and [$PdCl_2$**L**^{2}] in the Heck reaction, by using various aryl halides and olefins. The efficiencies of these complexes in this reaction are compared to those for the analogous complexes containing the homoleptic ligands 2,5-dithiahexane ($MeS(CH)_2SMe$) and bipyridine (bipy).

Results and Discussion

Neutral [MCl_2L] Complexes (M = Pd, Pt)

The reactions of **L**^{1}, **L**^{2} and **L**^{3} with $PdCl_2$ or $PtCl_2$ in MeCN at ambient temperature afforded the complexes

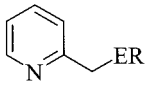

ER = SMe (**L**^{1}), SPh (**L**^{2}), SeMe (**L**^{3})

[a] School of Chemistry, University of Tasmania, Private Bag 75, Hobart TAS, 7001, Australia
Fax: +61-3-6226-2858
E-mail: VickiAnne.Tolhurst@utas.edu.au
[b] Department of Chemistry, University of Western Australia, Crawley WA, 6009, Australia
Supporting information for this article is available on the WWW under http://www.eurjic.org or from the author.

 © 2005 Wiley-VCH Verlag GmbH & Co. KGaA, Weinheim DOI: 10.1002/ejic.200400514

$[MCl_2L]$ {M = Pd, **L** = $\mathbf{L^1}$ (**1a**), $\mathbf{L^2}$ (**2a**), $\mathbf{L^3}$ (**3a**); M = Pt, **L** = $\mathbf{L^1}$ (**1b**), $\mathbf{L^2}$ (**2b**), $\mathbf{L^3}$ (**3b**)} in good to high yields as yellow powders (Scheme 1). All complexes were air stable and had poor solubility in most solvents except DMSO. Liquid-secondary-ionisation (LSI) mass spectra of all complexes exhibited ions corresponding to the molecular ion with loss of one halide atom. The IR spectra for all compounds showed all observed stretches corresponding to those of the coordinated ligand. The UV/Vis spectra of these compounds exhibited peaks consistent with square-planar geometries.

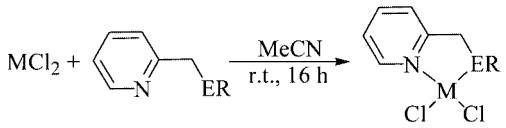

ER = SMe, M = Pd (**1a**), Pt (**1b**)
ER = SPh, M = Pd (**2a**), Pt (**2b**)
ER = SeMe, M = Pd (**3a**), Pt (**3b**)

Scheme 1. Preparation of Pd(II) and Pt(II) chloride complexes.

Room-temperature ^{1}H NMR spectra of the complexes in [D_6]DMSO exhibit resonances between 9.13–6.63 ppm, ascribed to the pyridyl rings of the ligands. A second-order AB spin system is observed for the methylene protons of the α-carbon upon coordination to the metal centre for each compound. This is due to the formation of a new stereogenic centre at each chalcogen upon coordination. The methyl protons in complexes **1(a,b)** and **3(a,b)** are obscured by the [D_6]DMSO resonance.

Fluxional Behaviour and Theoretical Calculations

The appearance of a second-order AB spin system at ambient temperature in the ^{1}H NMR spectra for all complexes led us to undertake variable-temperature ^{1}H NMR studies. On warming the complexes in solution, the resonances of the methylene protons coalesced for most complexes to form broad singlets. Coalescence temperatures of the methylene protons in the complexes are listed in Table 1. Three fluxional processes can occur in these complexes: (a) conformational changes of the chelate ring (ring flip, Figure 1a) where the transition state contains a nearly flat five-membered chelate ring which is quasi-coplanar with the coordination plane of the metal, (b) pyramidal inversion at the chalcogen, where the transition state has a planar five-membered ring, and the terminal substituent is also in the same plane as the coordination plane of the metal centre (Figure 1b), and (c) dissociation of the chalcogen donor atom from the palladium centre (Figure 1c). Variable-temperature NMR studies of palladium(II) and platinum(II) complexes containing chelating dichalcogenoether ligands have established that the coalescence of resonances at high temperatures is due to pyramidal inversion at the chalcogen.[2,3,9,10]

Table 1. Coalescence temperatures for compounds.

Complex	Coalescence temperature [°C]
$\mathbf{L^1}$ 2-$(MeSCH_2)C_5H_3N$	
$PdCl_2L$	95
$PtCl_2L$	>160
$\mathbf{L^2}$ 2-$(PhSCH_2)C_5H_3N$	
$PdCl_2L$	90
$PtCl_2L$	157
$\mathbf{L^3}$ 2-$(MeSeCH_2)C_5H_3N$	
$PdCl_2L$	82
$PtCl_2L$	110[a]

[a] Decomposes at this temperature in solution.

Density Functional Theory (DFT) calculations confirm that the fluxional process observed for the complexes described here is not a ring-flip process, which has a calculated activation energy of 2.7 kJ mol^{-1} for the complex $PdCl_2\mathbf{L^1}$ (in contrast, sulfur-pyramidal-inversion and sulfur-dissociation processes for $PdCl_2\mathbf{L^1}$ have calculated activation energies of 71.7 and 92.0 kJ mol^{-1}, respectively). This suggests that the ring inversion process is already occurring at room temperature, thus explaining the presence of only one AB spin system rather than two, as would be expected for two possible conformers given the similar energies of the two.

The calculated energy difference between the two conformers, the barrier to (*E*)-pyramidal inversion and the barrier to (*E*)-dissociation for $[MCl_2L]$ {M = Pd, Pt; **L** = 2-$(MeECH_2)C_5H_4N$ where E = S ($\mathbf{L^1}$), Se ($\mathbf{L^3}$), Te ($\mathbf{L^4}$)} are listed in Table 2. All $\Delta H^{\ddagger}$ values listed here have been zero-point corrected for enthalpy. Structures **II** and **III** are enantiomers, so the energy for only one enantiomer was calculated, as both are of equal energy.

Trends observed in the calculated energy barriers to (*E*)-pyramidal inversion for the Pd^{II} and Pt^{II} complexes containing the mixed-donor ligands are similar to those seen for the analogous complexes containing dichalcogenoether ligands. Pyramidal inversion at the chalcogen centres of the palladium complexes occurs at lower energies relative to those of the platinum compounds, consistent with a stronger Pt–E bond compared with Pd–E, as is also observed in the solid-state structures of $[MCl_2\mathbf{L^2}]$ (**2a**, **2b**). There is also an increase in the barrier to chalcogen pyramidal inversion in the order S < Se < Te. This trend is also observed in the compounds containing the homoleptic ligands. However, the relative increase in the energy barrier is considerably larger for the heteroleptic complexes compared with the homoleptic complexes. For instance, the energy difference between the complexes $[PtClMe\{MeS(CH_2)_2SMe\}]$ and $[PtClMe\{MeSe(CH_2)_2SeMe\}]$ is 10.9 kJ mol^{-1} where inversion occurs *trans* to the coordinated methyl group,[2] whereas the increase in inversion energy between the complexes $[PtCl_2\mathbf{L^1}]$ and $[PtCl_2\mathbf{L^3}]$ calculated here is 29.8 kJ mol^{-1}. However, this could be consequent on the difference in the *trans*-effect of the methyl compared to the chloride group on the chalcogen.

Energies associated with the full dissociation of the chalcogen donor atom from the metal centre are generally

 © 2005 Wiley-VCH Verlag GmbH & Co. KGaA, Weinheim

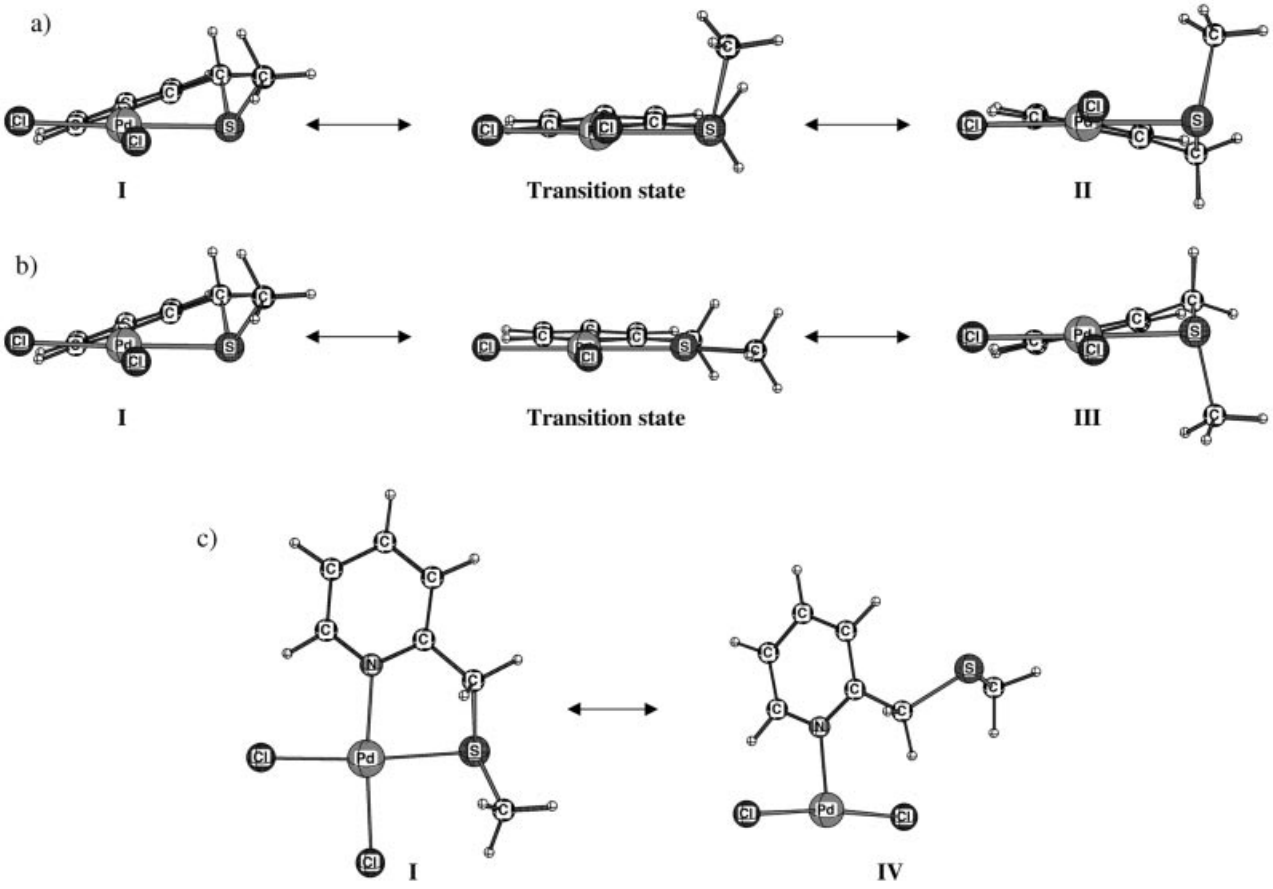

Figure 1. Calculated structures of conformers and transition states for a) ring inversion, b) pyamidal S-inversion and c) S-dissociation for [$PdCl_2$**L**^{1}]. Structures are viewed side-on and through the coordination planes of the metals with the pyridine rings distant from the reader.

Table 2. DFT calculated (*E*)-pyramidal inversion barriers and (*E*)-dissociation energies.

Complex	Energy of **III** [kJ mol^{-1}][a]	$\Delta H^{\ddagger}$ [(*E*)-Pyramidal Inversion] [kJ mol^{-1}]	ΔH (Dissociation Energy) [kJ mol^{-1}]
2-($MeSCH_2$)C_5H_3N (**L**^{1})			
$PdCl_2$L	1.5	71.7	92.0
$PtCl_2$L	0.4[c]	92.1	130.7
2-($MeSeCH_2$)C_5H_3N (**L**^{3})			
$PdCl_2$L	2.2	97.5	95.3
$PtCl_2$L	2.0	119.1	131.1
2-($MeTeCH_2$)C_5H_3N (**L**^{4}) [b]			
$PdCl_2$L	3.5	118.7	119.2
$PtCl_2$L	1.75	141.2	150.8

[a] Energy relative to **I** (0 kJ mol^{-1}). [b] Synthesis of **L**^{4} and its compounds have not been reported. [c] Energy of **I** relative to **III** (0 kJ mol^{-1}).

higher than those of the (*E*)-inversion processes by 10–40 kJ mol^{-1} except for [$PdCl_2$**L**] (**L** = **L**^{3}, **L**^{4}) where the two processes have similar energies. This is consistent with the better orbital overlap between the softer selenium and tellurium donor atoms with platinum compared to the harder palladium centre affording stronger M–Se and M–Te bonds for platinum.

Structures of [$PdCl_2$**L**^{2}] (2a) and [$PtCl_2$**L**^{2}] (2b)

The solid-state structures of **2a** and **2b** are isomorphous, with both complexes crystallising in the monoclinic space group $P2_1/n$, and the molecules being discrete monomers, one comprising the asymmetric unit of each. The structure of [$PdCl_2$**L**^{2}] is shown in Figure 2. Crystallographic data of

 © 2005 Wiley-VCH Verlag GmbH & Co. KGaA, Weinheim

2a and **2b** are listed in Table 3, with important bond distances and angles given in Table 4. The molecules of **2a** and **2b** contain four-coordinate metal centres with square-planar geometry with slight tetrahedral distortion, with the ligand acting as a bidentate.

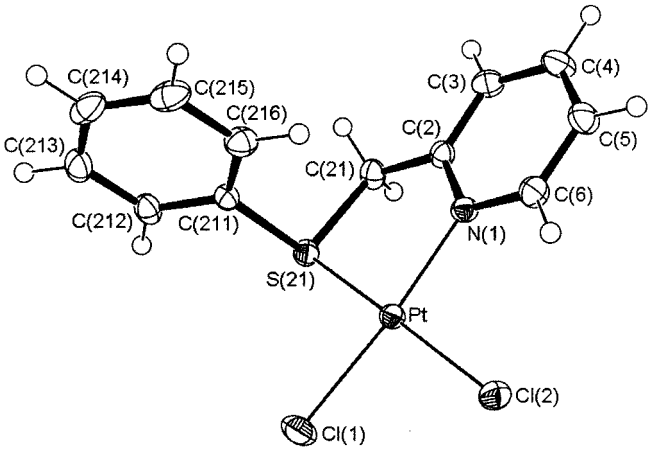

Figure 2. Molecular projection of $[PtCl_2\mathbf{L^2}]$ showing the atom labelling scheme. Thermal ellipsoids are drawn at the 50% probability level. $[PdCl_2\mathbf{L^2}]$ is isostructural.

Table 3. Crystallographic data of $[MCl_2\mathbf{L^3}]$ {M = Pd (**2a**), Pt (**2b**)}.

	$[PdCl_2\mathbf{L^2}]$ (**2a**)	$[PtCl_2\mathbf{L^2}]$ (**2b**)
Formula	$C_{12}H_{11}NSPdCl_2$	$C_{12}H_{11}NSPtCl_2$
M	378.62	467.28
Crystal system	monoclinic	monoclinic
Space group	$P2_1/n$	$P2_1/n$
a [Å]	9.232(2)	9.176(2)
b [Å]	12.997(3)	13.035(3)
c [Å]	10.847(3)	10.895(2)
β [°]	96.306(5)	95.822(5)
D_c [g cm^{-3}]	1.944	2.394
Z	4	4
μ [mm^{-1}]	1.98	11.4
$T_{min/max}$	0.71	0.65
N_t	26827	9548
$N(R_{int})$	6828 (0.027)	6017 (0.028)
N_O	5776	4500
R	0.025	0.032
R_w	0.032	0.034
GooF	1.09	1.12

Table 4. Selected bond distances and angles of $[MCl_2\mathbf{L^3}]$ {M = Pd (**2a**), Pt (**2b**)}.

	M = Pd	M = Pt
Bond distances [Å]		
M–Cl(1)	2.2887(6)	2.296(1)
M–Cl(2)	2.3162(5)	2.316(1)
M–N(1)	2.045(1)	2.034(3)
M–S(21)	2.2540(5)	2.235(1)
Bond angles [°]		
Cl(1)–M–Cl(2)	90.90(2)	89.79(4)
Cl(1)–M–N(1)	172.95(3)	174.73(9)
Cl(1)–M–S(21)	88.74(1)	89.70(4)
Cl(2)–M–N(1)	94.50(3)	94.2(1)
Cl(2)–M–S(21)	174.40(1)	175.15(3)
N(1)–M–S(21)	86.32(3)	86.6(1)
Dihedral angles [°]		
M–N(1)–C(6)–C(5)	–179.71(1)	179.5(3)
N(1)–M–S(21)–C(211)	–93.12(6)	–92.5(2)
M–N(1)–C(2)–C(21)	–2.7(2)	–3.1(5)
N(1)–C(2)–C(21)–S(21)	16.9(2)	18.0(5)
C(2)–C(21)–S(21)–M	–20.1(1)	–21.4(3)

The Pd–N bond distance of 2.045(1) Å is shorter than that found in $[Pd(\eta^3\text{-allyl})\mathbf{L^2}](ClO_4)$ (2.088(5) Å).[11] This can be attributed to the difference in the *trans* effect of the chloride ion compared to that of the allyl group. The Pd–S bond distance of 2.2540(5) Å is similar to those observed in the similar compounds $[PdClMe(2\text{-}(MeSCH_2)C_5H_4N)]$ (2.257(5), 2.255(6) Å)[8] and $[PdClMe(2\text{-}(t\text{Bu}SCH_2)C_5H_4N)]$ (2.2589(13) Å)[7], where the sulfur atom is *trans* to a chloride group. The Pd–Cl bond distances of 2.2887(6) and 2.3162(5) Å, are similar to those seen in complexes where chloride is *trans* to nitrogen and sulfur, respectively.[12–14]

Pt–Cl bond distances of 2.296(1) and 2.316(1) Å, are again similar to those seen in complexes where the chloride atom is *trans* to nitrogen and sulfur, respectively.[14] They are also similar to those seen in the palladium complex **2a**, which is not surprising given that the ionic radii of Pd^{II} and Pt^{II} are the same within experimental error. The Pt–N bond distance of 2.034(3) Å is also similar to that in complex **2a** within experimental error. Interestingly, the Pt–S bond distance of 2.235(1) Å is significantly shorter than the Pd–S bond distance observed in **2a** [Δ_S = –0.019 Å, where Δ_S = *d*(Pt–S)-*d*(Pd–S)] while the Pt–Cl bond for the chloride *trans* to the sulfur atom is the same as the analogous Pd–Cl bond [2.316(1) vs 2.3162(5) Å]. Similar trends in bond distances in isomorphous structures of palladium and platinum complexes containing homoleptic and heteroleptic ligands have been observed, and theoretical calculations have been performed to explain the trend.[14–19] Results from theoretical calculations for the geometry optimisations of the complexes $[MMe_3\{(H_2C{=}N{-}NH)_3CH\}]^+$ compared well with the X-ray studies of isostructural $[MMe_3\{(pz)_3CH\}]^+$ (M = Pd, Pt), where the M–C bond distances are identical or slightly shorter for palladium and platinum while the Pd–N bonds are longer than the Pt–N bonds.[19] The explanation for this trend is attributed to the softer acidity of platinum compared with palladium. Steric influences on the trends in bond lengths, which were previously suggested as having an additional effect,[16,17] were eliminated after similar trends were found in the optimised geometries of *trans*-$[M(H)_2(CH_3)(NH_3)]^-$.[19]

The five-membered chelate ring formed by the bidentate ligand in both the palladium and the platinum complexes is puckered, with the sulfur atom lying out of the M, N, C(2), C(21) plane [χ^2 205 (Pd), 28 (Pt)] by 0.415(2) and 0.434(5) Å, respectively. This distortion and the larger Cl(2)–M–N(1) bond angle [94.50(3) (Pd), 94.2(1)° (Pt)] offset the smaller angles about the metal centre, including the small bite angle of the ligand [86.32(3) (Pd), 86.6(1)° (Pt)]. The ligand chelates the metal centre, with the pyridyl ring

 © 2005 Wiley-VCH Verlag GmbH & Co. KGaA, Weinheim

of the ligand lying almost in the same plane as the coordination plane of the metal centre {τ[M–N–C(6)–C(5)] 179.70(1) (Pd), 179.5(3)° (Pt)} and the phenyl substituent of the thioether almost perpendicular to this plane {τ[N–M–S(21)–C(211)] –93.12(6) (Pd), –92.5(2)° (Pt)}.

Catalytic Activity of $[PdCl_2L^1]$ (2a) and $[PdCl_2L^2]$ (2b)

The catalytic activity of $[PdCl_2\mathbf{L}]$ in the Heck reaction was investigated. The versatility of the compounds in this reaction was tested by using both an activated and deactivated aryl bromide, and terminal mono- and disubstituted alkenes, and an internal alkene. The catalytic results are listed in Table 5 and Table 6.

Table 5. Catalytic data for the Heck reaction of various aryl halides and alkenes.[a]

Aryl halide	Alkene	Conversion (%)[b]	TON
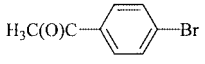	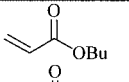	>99	1,000,000[c]
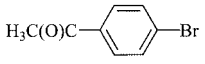	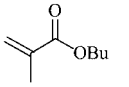	>99	1,000,000[c]
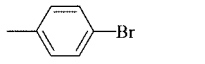	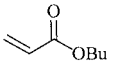	94	94[d]
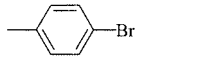	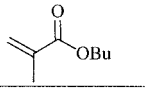	>99	100[d]

[a] The reactions were carried out with 1.5 mol aryl halide, excess alkene, 2.2 mol NaOAc in 7 mL DMAc for 48 h. [b] Determined by GC (standard: diethylene glycol monobutyl ether). [c] Reaction carried out at 100 °C with 0.001 mol-% $[PdCl_2\mathbf{L^2}]$. [d] Reaction carried out at 120 °C with 1 mol-% $[PdCl_2\mathbf{L^2}]$.

Table 6. Catalytic data for the Heck reaction of 4-bromoacetophenone and ethyl *trans*-cinnamate.[a]

Catalyst	Time [h]	Conversion [%][b]	*E*/*Z* Ratio[c]
$[PdCl_2\mathbf{L^1}]$	6	68	4.3:1
$[PdCl_2\mathbf{L^2}]$	6 (3)	83 (>99[d])	4.2:1 (>99:1)
$[PdCl_2(bipy)]$	6 (6)	56 (46)	4.3:1 (>99:1)
$[PdCl_2(MeS(CH_2)_2SMe)]$	6 (6)	64 (90)	4.6:1 (>99:1)

[a] The reactions were carried out with 1.5 mol 4-bromoacetophenone, 4.2 mol ethyl *trans*-cinnamate, 1 mol-% catalyst, 2.2 mol NaOAc in 7 mL DMAc at 140 °C for 6 h. Data in brackets correspond to reactions carried out with addition of 1.1 equiv. nBu$_4$NCl, 1.1 equiv. HCO_2Na at 80 °C for 6 h. [b] Determined by GC (standard: diethylene glycol monobutyl ether). [c] Determined by GC. [d] Conversion after 3 h.

The complex $[PdCl_2\mathbf{L^2}]$ was found to facilitate high turnover numbers (1,000,000) in the reaction between 4-bromoacetophenone and both *n*-butylacrylate and *n*-butylmethacrylate. In both reactions, only one product was observed by using GC. These turnover numbers are comparable to those of Herrmann's palladacycle, $\{Pd_2[P(o\text{-tol})_3]_2(\mu\text{-OAc})_2\}$, although this reaction is undertaken at 130 °C.[20] The reaction between 4-bromotoluene and *n*-butylacrylate and *n*-butylmethacrylate resulted in excellent conversion of the aryl halide with 94 and >99 % conversion achieved, respectively; however, the turnover number for neither reaction was as good as those for 4-bromoacetophenone.

More significantly, the reaction between 4-bromoacetophenone and ethyl *trans*-cinnamate was undertaken to see if the complexes facilitated the reaction using 1,2-disubstituted alkenes (Scheme 2). Intermolecular Heck reactions of internal alkenes are not often due to their low reactivity using typical catalysts.[21–23] The difficulty of this reaction is reflected in the high catalyst loadings and long reaction times required as well as other complications such as the possibility of both (*E*)- and (*Z*) isomers of the product being formed because of the high temperatures often required to undertake the reaction. Full conversion of 4-bromoacetophenone is achieved within 3 hours with $[PdCl_2\mathbf{L^2}]$, resulting in the formation of (*E*)-ethyl-3-(4-acetylphenyl)-3-phenyl-2-propenoate regio- and stereoselectively. This occurs at lower catalyst loadings relative to other similar reactions reported in the literature.[21,22] Fu and Littke have reported the reaction of deactivated aryl bromides with methyl *trans*-cinnamate at room temperature achieving 80 % isolated yield after 72 h with >20:1 *E*/*Z* selectivity by using 1.0 mol-% $Pd_2(dba)_3$ and 2.0 mol-% P(tBu)$_3$.[21]

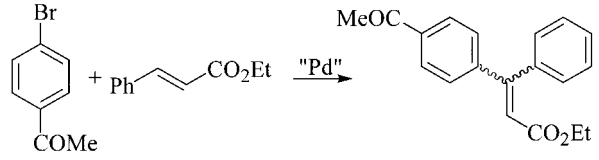

Scheme2. Reaction of 4-bromoacetophenone and ethyl *trans*-cinnamate.

Modification of the hemilable ligands also results in significant differences in activity. When the reaction shown in Scheme 2 is conducted without the aid of phase-transfer agents and reducing agents, the phenylthioether-containing complex, $[PdCl_2\mathbf{L^2}]$, achieves higher conversion of the 4-bromoacetophenone (83 %) compared to the methylthioether-containing complex, $[PdCl_2\mathbf{L^1}]$ (68 %) after 16 hours at 140 °C, suggesting that the presence of a softer S-donor atom enhances the reactivity. This is consistent with theoretical calculations investigating the electronic and steric ligand effects on the activity of the Heck reaction, by using a substituted phenylpalladium(II) diimine complex.[24] Similar reactivity comparisons have been observed for the insertion reaction of allenes into Pd–C bonds.[7,8]

We also compared the catalytic activity in the Heck reaction of the heteroleptic complex $[PdCl_2\mathbf{L^2}]$ with that of $[PdCl_2(bipy)]$ (bipy = 2,2′-dipyridyl), a complex containing a homoleptic bidentate N-donor ligand, and $[PdCl_2(MeS(CH_2)_2SMe)]$, a complex containing a homoleptic bidentate S-donor ligand, again using the reaction shown in Scheme 2. As mentioned previously, the complex $[PdCl_2\mathbf{L^2}]$ facilitates the full conversion of 4-bromoacetophenone in 3 hours to form (*E*)-ethyl-3-(4-acetylphenyl)-3-phenyl-2-propenoate regio- and stereoselectively. In contrast, complexes containing the homoleptic nitrogen and sulfur ligands only achieved 46 and 90 % conversion, respectively, after 6 hours under the same conditions. If the

 © 2005 Wiley-VCH Verlag GmbH & Co. KGaA, Weinheim

reaction is done at higher temperatures, Pd black is produced in the two homoleptic systems, with significant amounts in the [$PdCl_2(MeS(CH_2)_2SMe)$] catalysed system, which indicates that catalyst degradation occurs readily. Degradation of catalysts containing the hemilable ligands was also observed, but probably occurred after the reaction was complete.

Conclusions

Neutral palladium(II) and platinum(II) complexes have been prepared containing the mixed-N/E donor ligands 2-$(RECH_2)C_5H_4N$ [E = S, R = Me (**L**^{1}), Ph (**L**^{2}); E = Se, R = Me (**L**^{3})].

DFT calculations have shown that the process observed in variable-temperature ^{1}H NMR studies is most probably due to either the (*E*)-pyramidal inversion process or (*E*)-dissociation processes rather than ring flip. For all platinum complexes and the palladium complex [$PdCl_2$**L**^{1}] the fluxionality is most probably due to the (*E*)-pyramidal inversion process, which is 10–40 kJ mol^{-1} lower in energy than the (*E*)-dissociation process. The cause of the fluxional process for the complexes [$PdCl_2$**L**] (**L** = **L**^{2}, **L**^{3}) is not as clear based on the DFT calculations. Both the (*E*)-pyramidal inversion and (*E*)-dissociation processes involve a weakening of the M–E bond. In the case of the heavier chalcogenoether-containing palladium complexes, the orbital overlap between the softer chalcogen atom and the harder palladium atom becomes mismatched, leading to a destabilising effect on the Pd–E bond during the processes. As a result, it is plausible that full (*E*)-dissociation may occur in these complexes rather than just a partial weakening of the Pd–E bond during the (*E*)-pyramidal inversion process. The trends observed in the barrier to (*E*)-pyramidal inversion for the complexes containing the mixed-donor ligand complexes reported here are the same as those observed for complexes containing homoleptic dichalcogenoether ligands. These include the barrier to (*E*)-inversion increasing in the order S<Se<Te, and Pd<Pt.

The isomorphous solid-state structures of [MCl_2**L**^{2}] (M = Pd, Pt) show that the thioether functional group is more strongly bound to the platinum than to the palladium as seen by a shorter Pt–S bond compared to the Pd–S bond, probably due to the softness of the platinum centre.

The complexes [$PdCl_2$**L**] (**L** = **L**^{1}, **L**^{2}) were found to facilitate the Heck reaction of various aryl bromides with terminal and internal alkenes with excellent conversions. In the case of the reaction of 4-bromoacetophenone with ethyl *trans*-cinnamate, full conversion of the aryl bromide is achieved to form (*E*)-ethyl-3-(4-acetylphenyl)-3-phenyl-2-propenoate regio- and stereoselectively. The complex [$PdCl_2$**L**^{2}] was found to have higher catalytic activity compared to [$PdCl_2$**L**^{1}], suggesting that activity is promoted by the presence of the softer ligand. Both complexes containing the hemilabile ligands had higher catalytic activity than complexes containing homoleptic N- and S-donor containing ligands. At this stage it can not be discounted that the difference in catalytic activities is due to a difference in induction period and/or the efficiency in the reduction of the complexes to a Pd^0 catalytically active species. This is under further investigation.

Experimental Section

General Remarks: All reactions were done under nitrogen gas using standard Schlenk techniques. Palladium(II) chloride and platinum(II) chloride were obtained as a loan from Johnson Matthey, and used without purification. The ligands 2-$(RECH_2)C_5H_4N$ [E = S, R = Me (**L**^{1}), Ph (**L**^{2}); E = Se, R = Me (**L**^{3})] were prepared according to literature procedures.[25,11] All solvents were degassed prior to use. Infrared spectra were recorded as a KBr disc on a Bruker IF55 Infra-Red Spectrometer. LSIMS mass spectra of the complexes were recorded on a Kratos Analytical Concept ISQ mass spectrometer. ^{1}H NMR spectra were recorded on a Varian Gemini (200 MHz) or Unity (400 MHz) NMR spectrometer, in deuterated dimethylsulfoxide and referenced to the residual resonances of the solvent (δ = 4.33 ppm). Microanalyses (C,H,N,S) were determined by The Microanalysis Services, Central Science Laboratory, University of Tasmania.

[$PdCl_2$L**^{1}] (1a):** **L**^{1} (43 mg, 0.309 mmol) was added to a degassed solution of $PdCl_2$ (50 mg, 0.28 mmol) in MeCN (20 mL), and the reaction was stirred at room temperature for 16 hours. An orange precipitate formed over this time. The MeCN volume was reduced in vacuo (to about 2 mL) to afford a yellow precipitate. The solid was collected and washed with Et_2O (56 mg, 62 %). ^{1}H NMR (200 MHz, [D_6]DMSO): δ = 4.51, 4.85 (AB spin system, 2 H, CH_2), 7.60 (m, 1 H, C_6H_4N), 7.78 (m, 1 H, C_6H_4N), 8.13 (m, 1 H, C_6H_4N), 9.13 (m, 1 H, C_6H_4N) ppm. IR (KBr): $\tilde{\nu}$ = 3079 (m), 2987 (m), 2945 (vs), 2902 (s), 1606 (vs), 1481 (s), 1446 (s), 1381 (m), 1320 (w), 1274 (s), 1166 (s), 1111 (m), 1060 (m), 1030 (m), 978 (m), 863 (w), 825 (w), 769 (vs), 657 (w), 428 (w) cm^{-1}. *m*/*z* = 280 (M-Cl)$^+$ [^{106}Pd($^{12}C_7H_9N^{32}S$)^{35}Cl 280]. UV/Vis (DMSO)/cm^{-1}: $\tilde{\nu}_{max}$ (ε_{mol}/dm^3 mol^{-1} cm^{-1}) = 26170 (1113), 33600 (3537). $C_7H_9Cl_2PdNS$ (316.51): calcd. C 26.56, H 2.87, N 4.43; found C 26.99, H 2.83, N 4.63.

[$PtCl_2$L**^{1}] (1b):** The procedure described above using $PtCl_2$ afforded an off-white solid (75 %). ^{1}H NMR (200 MHz, [D_6]DMSO): δ = 4.50, 4.78 (AB spin system, 2 H, CH_2), 7.60 (m, 1 H, C_6H_4N), 7.87 (m, 1 H, C_6H_4N), 8.22 (m, 1 H, C_6H_4N), 9.45 (m, 1 H, C_6H_4N) ppm. IR (KBr): $\tilde{\nu}$ = 3116 (w), 3087 (m), 3000 (m), 2959 (vs), 2903 (s), 1612 (s), 1475 (s), 1427 (s), 1397 (m), 1321 (m), 1272 (m), 1168 (s), 1113 (w), 1063 (w), 996 (m), 977 (m), 901 (w), 773 (vs), 710 (w), 473 (w), 435 (w) cm^{-1}. *m*/*z* = 369 (M-Cl)$^+$ [^{195}Pt($^{12}C_7H_9N^{32}S$)^{35}Cl 369]. UV/Vis (DMSO)/cm^{-1}: $\tilde{\nu}_{max}$ (ε_{mol}/dm^3 mol^{-1} cm^{-1}) = 34400 (2502). $C_7H_9Cl_2NPtS$ (405.21): calcd. C 20.75, H 2.43, N 3.46; found C 20.91, H 2.26, N 3.44.

[$PdCl_2$L**^{2}] (2a):** Procedure as for [$PdCl_2$**L**^{1}]using **L**^{2} (64 %). ^{1}H NMR (200 MHz, [D_6]DMSO): δ = 4.84, 5.40 (AB spin system, 2 H, CH_2), 7.47–7.52 (m, 4 H, C_6H_4N, C_6H_5), 7.77–7.85 (m, 3 H, C_6H_4N, C_6H_5), 8.12 (m, 1 H, C_6H_4N), 9.13 (m, 1 H, C_6H_4N) ppm. IR (KBr): $\tilde{\nu}$ = 3085 (w), 3058 (w), 2969 (s), 2902 (s), 1604 (m), 1475 (s), 1439 (s), 1400 (m), 1276 (m), 1165 (m), 1060 (w), 1030 (w), 1002 (w), 914 (w), 827 (w)m 781 (s), 738 (s), 705 (w), 684 (m), 656 (w), 600 (w), 480 (m) cm^{-1}. UV/Vis (DMSO)/cm^{-1}: $\tilde{\nu}_{max}$ (ε_{mol}/dm^3 mol^{-1} cm^{-1}) = 25650 (1163), 33900 (6415). *m*/*z* = 344 (M-Cl)$^+$ [^{106}Pd($^{12}C_{12}H_{11}N^{32}S$)^{35}Cl 344]. $C_{12}H_{11}Cl_2NPdS$ (378.58): calcd. C 38.07, H 2.93, N 3.70; found C 38.00, H 3.03, N 3.46.

[$PtCl_2$L**^{2}] (2b):** Procedure as for [$PtCl_2$**L**^{1}] using **L**^{2} (79 %). ^{1}H NMR (200 MHz, [D_6]DMSO): δ = 4.85, 5.21 (AB spin system, 2

 © 2005 Wiley-VCH Verlag GmbH & Co. KGaA, Weinheim

H, CH_2), 7.46–7.63 (m, 4 H, C_6H_4N, C_6H_5), 7.76–7.85 (m, 3 H, C_6H_4N, C_6H_5), 8.19 (m, 1 H, C_6H_4N), 9.45 (m, 1 H, C_6H_4N) ppm. IR (KBr): $\tilde{\nu}$ = 3085 (w), 3052 (w), 2974 (m), 2905 (m), 2854 (w), 1608 (m), 1476 (s), 1439 (s), 1396 (m), 1310 (w), 1273 (w), 1163 (m), 1113 (w), 1063 (w), 1022 (w), 998 (w), 914 (w), 780 (s),m 739 (s), 704 (w), 684 (m), 611 (w), 484 (m) cm^{-1}. UV/Vis (DMSO)/cm^{-1}: $\tilde{\nu}_{max}$ (ε_{mol}/$dm^3\,mol^{-1}\,cm^{-1}$) = 33950 (4698). *m*/*z* = 432 (M-Cl)$^+$ [^{195}Pt($^{12}C_{12}H_{11}N^{32}S$)^{35}Cl 432]. $C_{12}H_{11}Cl_2NPtS$ (467.28): calcd. C 30.84, H 2.37, N 3.00; found C 30.99, H 2.40, N 2.97.

[$PdCl_2L^3$] (3a): Procedure as for [$PdCl_2L^1$] using **L^3** (82 %). ^{1}H NMR (200 MHz, [D_6]DMSO): δ = 4.52, 4.75, (AB spin system, 2 H, CH_2), 7.55 (m, 1 H, C_6H_4N), 7.71 (m, 1 H, C_6H_4N), 8.08 (m, 1 H, C_6H_4N), 9.21 (m, 1 H, C_6H_4N) ppm. IR (KBr): $\tilde{\nu}$ = 3076 (m), 3000 (w), 2983 (w), 2958 (s), 2908 (m), 1652 (w), 1606 (s), 1558 (w), 1540 (w), 1480 (s), 1446 (s), 1421 (m), 1381 (m), 1265 (m), 1111 (m), 1060 (w), 1029 (w), 924 (m), 839 (w), 815 (w), 762 (vs), 650 (w), 467 (w), 425 (w) cm^{-1}. UV/Vis (DMSO)/cm^{-1}: $\tilde{\nu}_{max}$ (ε_{mol}/$dm^3\,mol^{-1}\,cm^{-1}$) = 25920 (1100), 32800 (4295). *m*/*z* = 328 (M-Cl)$^+$ [^{106}Pd($^{12}C_7H_9N^{80}Se$)^{35}Cl 328]. $C_7H_9Cl_2NPdSe$ (363.41): calcd. C 23.13, H 2.50, N 3.86; found C 23.41, H 2.83, N 3.58.

[$PtCl_2L^3$] (3b): Procedure as for [$PtCl_2$L1] using **L^3** (45 %). ^{1}H NMR (200 MHz, [D_6]DMSO): δ = 4.47, 4.70 (AB spin system, 2 H, CH_2), 7.53 (m, 1 H, C_6H_4N), 7.81(m, 1 H, C_6H_4N), 8.15 (m, 1 H, C_6H_4N), 9.50 (m, 1 H, C_6H_4N) ppm. IR (KBr): $\tilde{\nu}$ = 3111 (w), 3080 (w), 3005 (w), 2987 (w), 2964 (m), 2910 (m), 1610 (s), 1480 (s), 1447 (s), 1421 (m), 1382 (m), 1270 (m), 1113 (m), 1064 (w), 924 (m), 838 (m), 819 (w), 651 (w)m 560 (w), 468 (w), 433 (w) cm^{-1}. UV/Vis (DMSO)/cm^{-1}: $\tilde{\nu}_{max}$ (ε_{mol}/$dm^3\,mol^{-1}\,cm^{-1}$) = 33450 (2071). *m*/*z* = 416 (M-Cl)$^+$ [^{195}Pt($^{12}C_7H_9N^{80}Se$)^{35}Cl 416]. $C_7H_9Cl_2NPtSe$ (452.11): calcd. C 18.59, H 2.01, N 3.10; found C 18.56, H 1.99, N 3.01.

General Procedure for Heck Reactions: A degassed solution of aryl halide in dimethylacetamide (5.0 mL, 0.30 mol L^{-1}) was added to the alkene (0.70 mL), NaOAc (2.2 mmol), catalyst, $n$$Bu_4NCl$ (1.1 equiv.) and HCO_2Na (1.1 equiv.) in a Schlenk vessel under argon. The reaction was heated at the appropriate temperature for 3–48 hours. The reaction was then cooled to room temperature, after which 0.20 mL diethylene glycol monobutyl ether was added. An aliquot (1.00 mL) was taken from the reaction, diluted with CH_2Cl_2, and washed three times with a saturated aqueous solution of NaCl. The organic layer was dried over $MgSO_4$. The conversion of aryl halide and the *E*/*Z* product ratio of ethyl 3-(4-acetylphenyl)-3-phenyl-2-propenoate were then determined by GC.

X-ray Crystallographic Study: Suitable crystals for X-ray diffraction studies of [$PdCl_2$**L^2**] and [$PtCl_2$**L^2**] were grown from $MeNO_2$/Et_2O (vapour diffusion). Spheres of CCD area-detector diffractometer data for [$PdCl_2$**L^2**] and [$PtCl_2$**L^2**] were measured (Bruker AXS, ω-scans, monochromatic Mo-K_α radiation, λ = 0.7107$_3$ Å, $2\theta_{max}$ = 75°). $N_{t(otal)}$ reflections merging to N unique (R_{int} cited) after "empirical"/multiscan absorption correction (proprietary software), N_o with $F > 4\sigma(F)$ being considered "observed" and used in the full-matrix least-squares refinements. (x, y, z, U_{iso})$_H$ were refined for **2a** only, constrained in **2b**. Neutral atom complex scattering factors were employed within the context of the Xtal 3.7 program system.[26] Pertinent results are given above and in the Tables and Figures, the latter showing the 50 % probability amplitude displacement ellipsoids for the non-hydrogen atoms, hydrogen atoms having arbitrary radii of 0.1 Å.

Computational Methods: Full geometry optimisations were carried out with the use of the B3LYP[27,28] density functional level of theory combined with the LANL2DZ basis set (which incorporates the Hay and Wadt[29,30] small-core relativistic effective core potential and double-zeta valence basis set on palladium, platinum, sulphur, selenium and tellurium together with the Dunning/Huzinaga[31] double zeta basis set on other atoms). Sets of five d-functions were used in the basis sets throughout these calculations. For the optimised geometries, harmonic vibrational frequencies were calculated at the B3LYP level. All transition structures possessed one and only one imaginary frequency, and they were further characterised by following the corresponding normal mode towards each product and reactant. Single-point energies on B3LYP/LANL2DZ optimised geometries were calculated at the B3LYP level with the LANL2augmented:6-311+G(2d,p) basis set,[32] which incorporates the LANL2 effective core potential and augmented basis sets on the metals (the large f-polarised valence basis set of Bauschlicher and coworkers[33] was used for palladium and the LANL2TZ+(3f) basis set for platinum[34]) together with the 6-311+G(2d,p) basis set[35–37] on all other atoms (3–11G basis set was used for tellurium). Energies from these single-point calculations were combined with the zero-point vibrational energy corrections from the lower level of theory to yield ΔH_0 numbers. Unless otherwise noted all computed energies quoted in this paper refer to these final ΔH_0 numbers. All calculations were carried out with the Gaussian 03[38] program.

CCDC-228118 and CCDC-228119 contain the supplementary crystallographic data for this paper. These data can be obtained free of charge from The Cambridge Crystallographic Data Centre via www.ccdc.cam.ac.uk/data_request/cif.

XYZ Cartesian coordinates for all optimised structures described in this article are available as Supporting Information (see also the footnote on the first page of this article).

Acknowledgments

We acknowledge the Australian Research Council for funding this project. We also thank Johnson-Matthey for the generous loan of $PtCl_2$ and $PdCl_2$, and Prof. W. Levason and Dr. G. Reid for the [$PdCl_2$(MeS(CH_2)$_2$SMe)] sample.

[1] S. G. Murray, F. R. Hartley, *Chem. Rev.* **1981**, *81*, 365–414 and references cited therein.
[2] E. W. Abel, S. K. Bhargava, K. Kite, K. G. Orrell, V. Šik, B. L. Williams, *Polyhedron* **1982**, *1*, 289–298.
[3] F. Hartley, S. G. Murray, W. Levason, H. E. Soutter, C. A. McAuliffe, *Inorg. Chim. Acta* **1979**, *35*, 265–277.
[4] W. Levason, S. D. Orchard, G. Reid, *Coord. Chem. Rev.* **2002**, *225*, 159–199 and references cited therein.
[5] M. Casey, J. Lawless, C. Shirran, *Polyhedron* **2000**, *19*, 517–520.
[6] K. Boog-Wick, P. S. Pregosin, M. Wörle, *Helv. Chim. Acta* **1998**, *81*, 1622–1633.
[7] L. Canovese, F. Visentin, G. Chessa, P. Uguagliati, G. Bandoli, *Organometallics* **2000**, *19*, 1461–1463.
[8] L. Canovese, F. Visentin, G. Chessa, C. Santo, P. Uguagliati, G. Bandoli, *J. Organomet. Chem.***2002**, *650*, 43–56.
[9] R. J. Cross, T. H. Green, R. Keat, *J. Chem. Soc. Chem. Commun.* **1974**, 207–208.
[10] R. Cross, T. H. Green, R. Keat, *J. Chem. Soc. Dalton Trans.* **1976**, 382–384.
[11] L. Canovese, F. Visentin, P. Uguagliati, G. Chessa, V. Lucchini, G. Bandoli, *Inorg. Chim. Acta***1998**, *275–276*, 385–394.
[12] A. Caubet, V. Moreno, E. Molins, C. Miravitlles, *J. Inorg. Biochem.* **1992**, *48*, 135–152.
[13] H. A. Ankersmit, N. Veldman, A. L. Spek, K. Eriksen, K. Goubitz, K. Vrieze, G. van Koten, *Inorg. Chim. Acta* **1996**, *252*, 203–219.

 © 2005 Wiley-VCH Verlag GmbH & Co. KGaA, Weinheim

[14] S. Chattopadhyay, C. Sinha, P. Basu, A. Chakravorty, *Organometallics* **1991**, *10*, 1135–1139.
[15] J. M. Wisner, T. J. Bartczak, J. A. Ibers, *J. Am. Chem. Soc.* **1986**, *108*, 347–348.
[16] J. M. Wisner, T. J. Bartczak, J. A. Ibers, *Organometallics* **1986**, *5*, 2044–2050 and references therein.
[17] W. Kläui, M. Glaum, T. Wagner, M. A. Bennett, *J. Organomet. Chem.* **1994**, *472*, 355–358.
[18] R. E. Marsh, W. P. Schaefer, D. K. Lyon, J. A. Labinger, J. E. Bercaw, *Acta Crystallogr. Sect. C* **1992**, *48*, 1603–1606.
[19] A. L. Canty, A. Dedieu, H. Jin, A. Milet, B. W. Skelton, S. Trofimenko, A. H. White, *Inorg. Chim. Acta* **1999**, *287*, 27–36.
[20] W. A. Herrmann, C. Brossmer, K. Ofele, C.-P. Reisinger, T. Priermeier, M. Beller, *Angew. Chem. Int. Ed. Engl.* **1995**, *34*, 1844.
[21] A. F. Littke, G. C. Fu, *J. Am. Chem. Soc.* **2001**, *123*, 6989–7000.
[22] C. Gürther, S. L. Buchwald, *Chem. Eur. J.* **1999**, *5*, 3107–3112.
[23] S. Bräse, A. De Meijere, in: *Metal-Catalyzed Cross-Coupling Reactions* (Eds.: F. Diederich, P. J. Stang), Wiley, New York, **1998**.
[24] H. von Schenck, B. Åkermark, M. Svensson, *Organometallics* **2002**, *21*, 2248–2253.
[25] B. W. Skelton, V.-A. Tolhurst, A. H. White, A. M. Williams, A. J. Wilson, *J. Organomet. Chem.* **2003**, *674*, 38–44.
[26] S. R. Hall, D. J. du Boulay, R. Olthof-Hazekamp, *The Xtal 3.7 System*, University of Western Australia, **2000**.
[27] A. D. Becke *J. Chem. Phys.* **1993**, *98*, 5648–5652.
[28] P. J. Stephens, J. F. Devlin, C. F. Chabalowski, M. J. Frisch, *J. Phys. Chem.* **1994**, *98*, 11623–11627.
[29] R. H. Hertwig, W. Koch, *Chem. Phys. Lett.* **1997**, *268*, 345–351.
[30] P. J. Hay, W. R Wadt, *J. Chem. Phys.* **1985**, *82*, 299–310.
[31] T. H. Dunning, P. J. Hay, in: *Modern Theoretical Chemistry* (Ed.: H. F. Schaefer), Plenum, New York, **1976**, vol. 3, p. 1–27.
[32] K. E. Frankcombe, K. J. Cavell, B. F. Yates, R. B. Knott, *J. Phys. Chem.* **1996**, *100*, 18363–18370.
[33] S. R. Langhoff, L. G. Petterson, C. W. Bauschlicher, H. J. Partridge, *J. Chem. Phys.* **1987**, *86*, 268–278.
[34] B. F. Yates, *J. Mol. Struct. (Theochem)* **2000**, *506*, 223–232.
[35] R. Krishnan, J. S. Binkley, R. Seeger, J. A. Pople, *J. Chem. Phys.* **1980**, *72*, 650–654.
[36] A. D. McLean, G. S. Chandler, *J. Chem. Phys.* **1980**, *72*, 5639–5648.
[37] M. J. Frisch, J. A. Pople, J. S. Binkley *J. Chem. Phys.* **1984**, *80*, 3265–3269.
[38] M. J. Frisch, G. W. Trucks, H. B. Schlegel, G. E. Scuseria, M. A. Robb, J. R. Cheeseman, J. A. Montgomery Jr., T Vreven, K. N. Kudin, J. C. Burant, J. M. Millam, S. S. Iyengar, J. Tomasi, V. Barone, B. Mennucci, M. Cossi, G. Scalmani, N. Rega, G. A. Petersson, H. Nakatsuji, M. Hada, M. Ehara, K. Toyota, R. Fukuda, J. Hasegawa, M. Ishida, T. Nakajima, Y. Honsa, O. Kitao, H, Nakai, M. Klene, X. Li, J. E. Knox, H. P. Hratchian, J. B. Cross, C. Adamo, J. Jaramillo, R. Gomperts, R. E. Stratmann, O. Yazyev, A. J. Austin, R. Cammi, C. Pomelli, J. W. Ochterski, P. Y. Ayala, K. Morokuma, G. A. Voth, P. Salvador, J. J. Dannenberg, V. G. Zakrzewski, S. Dapprich, A. D. Rabuck, K. Raghavachari, J. B. Foresman, J. V. Ortiz, Q. Cui, A. G. Baboul, S. Clifford, J. Cioslowski, B. B. Stefanov, G. Liu, A. Liashenko, P. Piskorz, I. Komaromi, R. L. Martin, D. J. Fox, T. Keith, M. A. Al-Laham, C. Y. Peng, A. Nanayakkara, M. Challacombe, P. M. W. Gill, B. Johnson, W. Chen, M. W. Wong, C. Gonzalez, J. A. Pople, *Gaussian 03, Revision B.04*, Gaussian, Inc., Pittsburgh, PA, **2003**.

Received: June 15, 2004

 © 2005 Wiley-VCH Verlag GmbH & Co. KGaA, Weinheim

Investigations into the Reactivity of Organoelement Gallium and Indium Subhalides – Syntheses of Digallium and Diindium Acetylacetonates

Werner Uhl,*[a] Abdelhakim El-Hamdan,[a] and Andreas Lawerenz[a]

Keywords: Gallium / Indium / Subvalent compounds / Acetylacetonate ligands

The organoelement subhalides $R_2Ga_2I_2$ (**1**) and $[R_2In_2Cl_2]_2$ (**2**) [R = $C(SiMe_3)_3$] react with silver acetylacetonate Ag(acac) (acac = $[OC(CH_3)]_2CH$) and lithium acetylacetonate Li(acac), respectively, to yield the di(acetylacetonato)dielement compounds $R_2E_2(acac)_2$ (**3**: E = Ga; **4**: E = In). Both products possess E–E single bonds with relatively long E–E distances of 251.1 (Ga–Ga) and 278.0 pm (In–In). The gallium or indium atoms are terminally coordinated by an alkyl and a bidentate acetylacetonato group. Similar reactions of the subhalides **1** and $[R_2In_2Br_2]_2$ with lithium diphenyltriazenide $LiN_3(C_6H_5)_2$ did not result in the formation of dielement compounds analogous with **3** and **4** but in the cleavage of the E–E bonds with formation of element(III) compounds of the type R–E(X)$[N_3(C_6H_5)_2]$ (E = Ga, In; X = Br, I).
(© Wiley-VCH Verlag GmbH & Co. KGaA, 69451 Weinheim, Germany, 2005)

Introduction

Organoelement subhalides of the heavier elements of the third main-group, i.e. aluminum, gallium, indium and thallium form an interesting class of compounds. They possess the elements in unusually low oxidation states with direct E–E interactions and are valuable starting materials for the generation of secondary products by salt elimination reactions. Their synthesis can be accomplished by several different methods such as (i) the treatment of tetrahalogenosubhalides of the type $X_2(L)E–E(L)X_2$ with aryl or silyl alkali-metal compounds in molar ratios of 1:1 or 1:2[1–4] (ii) the reduction of organogallium(III) compounds by alkali metals[5] (iii) the treatment of GaBr or "GaI" with organo lithium or sodium compounds accompanied by disproportionation of the third main-group element[1,6,7] (iv) the reduction of an indium(III) compound with an aminoborole[8] (v) the insertion of AlCp* into Al–I bonds of the aluminum triiodide dimer[9] and (vi) the careful oxidation of tetragallium or tetraindium clusters $E_4[C(SiMe_3)_3]_4$ with halogens or halogen donors.[10–13] The last method was introduced by our group and affords subhalides possessing different structures in reasonable yields. The transfer of one bromine molecule to the tetrahedral tetraindium cluster affords the compound $In_4Br_2[C(SiMe_3)_3]_4$ in which the tetrahedral arrangement of the indium atoms is retained but one triangular face of the In_4 tetrahedron and one edge of that face are bridged by bromine atoms.[11] The oxidation of all element(I) atoms of the starting clusters to an oxidation state of +II yields the element(II) halides R(X)E–E(X)R (E = Ga, In; X = Cl, Br, I) which possess E–E single bonds.[11–13] They remain monomeric even in the solid state for gallium whereas they form dimers with all halogen atoms in bridging positions for the indium derivatives. A chain of three indium atoms connected by two In–In single bonds was observed for the subhalide $In_3I_2[C(SiMe_3)_3]_3$[10] which resulted from the oxidation of the tetraindium cluster with elemental iodine in the presence of AlI_3.

These subhalides proved to be very effective starting compounds for the synthesis of secondary products by salt elimination reactions. For instance, several transition-metal gallium or indium compounds possessing quite different and interesting structures can be obtained by such a route on treatment with transition-metal carbonylate anions such as $[Fe(CO)_4]^{2-}$ or $[Fe_2(CO)_8]^{2-}$.[14–17] Silver or lithium carboxylates give dialkyldicarboxylatodielement compounds in which the carboxylato ligands occupy bridging positions across the relatively short E–E bonds.[18] Whereas the corresponding digallium compounds are easily available by the direct treatment of a tetraalkyldigallium(4) derivative $R_2Ga–GaR_2$ [R = $CH(SiMe_3)_2$] with carboxylic acids,[19–24] the In–In bonds of the diindium analogue $R_2In–InR_2$ are completely cleaved by oxidation of the indium atoms under similar conditions.[25] Thus, the reactions of these organoelement subhalides of gallium and, in particular, indium seem to offer a valuable route for the syntheses of new compounds which contain the elements in unusually low oxidation states and are not accessible by other methods. The behaviour of the dielement compounds $R_2E–ER_2$ towards acetylacetones is similar to that described for carboxylic acids. While substituent exchange with retention of the Ga–Ga bonds was observed for the digallium derivative, oxidation and cleavage of the In–In bond occurred with the diindium compound.[26,27] Diindium acetylacetonates containing an In–In bond may, however, be accessible by use

[a] FachbereichChemie der Philipps-Universität,
Hans-Meerwein-Straße, 35032 Marburg, Germany
Fax: +49-6421-2825653

 © 2005 Wiley-VCH Verlag GmbH & Co. KGaA, Weinheim **DOI: 10.1002/ejic.200400554**

of the corresponding subhalides. We report here on the continuation of our systematic investigations into the reactivities of these subhalides and on their reactions with acetylacetonate and diphenyltriazenide anions.

Results and Discussion

Syntheses and Molecular Structures of the Di(acetylacetonato)digallium and-diindium Compounds 3 and 4

Treatment of the monomeric dialkyldigallium subiodide $R_2Ga_2I_2$ (**1**) [R = $C(SiMe_3)_3$] with lithium acetylacetonate gave a mixture of unknown products, none of which could be isolated in a pure form. We therefore employed silver acetylacetonate in order to enhance the driving force of the reaction with the formation of silver iodide. A suspension of the silver salt was treated with **1** at low temperature (–90 °C) and it appeared that the reaction was complete upon warming to –70 °C. Filtration was carried out at that temperature and subsequent workup yielded yellow crystals of the product **3** in 67% yield [Equation (1)]. In contrast, the corresponding reaction of the dimeric diindium subchloride $(R_2In_2Cl_2)_2$**2** with silver acetylacetonate gave decomposition only. Probably, the In–In bond was cleaved by oxidation of the indium atoms with the formation of unknown products. A silver mirror formed at the glass wall of the Schlenk tube. Lithium acetylacetonate now gave a clean reaction although reproducible yields after reasonable reaction times were obtained only upon warming of the mixtures in toluene to 50 °C. Pale yellow crystals of the product **4** were isolated in 66% yield after recrystallisation from *n*-hexane. The chemical shifts of the trimethylsilyl protons of both products **3** and **4** (δ = 0.44 and 0.42 ppm, respectively) are in the characteristic range for $C(SiMe_3)_3$ groups attached to Ga–Ga or In–In single bonds possessing coordinatively saturated Ga or In atoms (about δ = 0.4 to 0.5 ppm).[11,18] The integration ratios in the ^{1}H NMR spectra, too, were in accordance with the formulae given schematically in Equation (1) with intact Ga–Ga or In–In bonds and the replacement of both halogen atoms of the starting dielementdihalides by chelating acetylacetonato groups. We were not able to detect the resonance of the inner carbon atoms of the $C(SiMe_3)_3$ groups attached to the In–In bond, probably as a result of the quadrupole moment of indium. The corresponding ^{13}C NMR signal of the gallium compound appeared at δ = 5.0 ppm which is characteristic of compounds possessing coordination numbers of four at their gallium atoms. Usually, tetraalkyl- or tetraaryldielement compounds of the type R_2E–ER_2 (E = Ga, In) containing Ga–Ga or In–In single bonds and an empty p-orbital at each Ga or In atom are deeply coloured.[28] However, upon coordinative saturation of the central gallium atoms by introduction of chelating ligands such as a carboxylato[19–24] or imidotetraphenyldiphosphinato groups,[29] colourless digallium products were isolated. Colours observed for those compounds in some cases are caused by transitions within ligands which possess electronically delocalised bonding systems such as diphenyltriazenide.[30,31] Similar to the acetylacetonato digallium derivatives[26,27] cited in the introduction, compounds **3** and **4** are yellow. The longest wavelengths were observed at 345 and 355 nm, respectively, the absorption of the gallium compound **3** is broader than that of the diindium diacetylacetonate **4**. The mononuclear E(III) compounds $E(acac)_3$ (E = Al, Ga, In) were reported to be colourless to orange.[32–34] Absorptions in the UV/Vis spectra were assigned to π-π transitions within the ligands.[35]

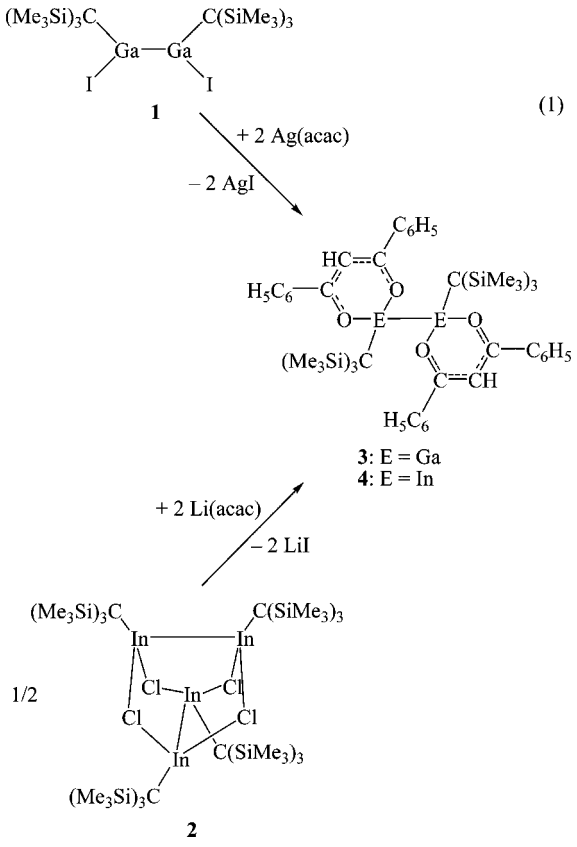

The molecular structures of **3** and **4** determined by single-crystal X-ray diffraction studies are depicted in Figure 1 and Figure 2. The compounds are not isostructural. While the molecules of **3** are in general positions, the molecules of **4** reside on crystallographic twofold rotation axes. The chelating acetylacetonato ligands of both compounds are terminally coordinated to the gallium or indium atoms of the unsupported Ga–Ga or In–In single bonds. Each central atom is further attached to an alkyl group so that coordination numbers of four result. Although an approach to the *trans* arrangement of the ligands is observed for both structures, the molecules deviate more or less significantly from an ideal centrosymmetric conformation. The torsion angles across the E–E bonds (C–E–E–C) are 151.4(3)° and 146.4(1)°, respectively. The Ga–Ga and In–In bond lengths (251.1 and 278.0 pm) are relatively long and similar to those of tetraalkyldielement derivatives R_2E–ER_2 [R = $CH(SiMe_3)_2$].[28,36,37] Thus, the shortening usually detected

 © 2005 Wiley-VCH Verlag GmbH & Co. KGaA, Weinheim

upon coordination of electronegative atoms to the E–E bonds[28] is not observed in these cases. Two dialkyldigallium compounds containing terminal acetylacetonato groups attached to their Ga–Ga bonds have been reported in the literature.[26,27,38] They show shorter Ga–Ga bond lengths of 244.3 pm on average. Owing to the smaller alkyl groups employed in these compounds [$CH(SiMe_3)_2$ compared with $C(SiMe_3)_3$ in **3** and **4**], we suppose that the long E–E distances of **3** and **4** may be caused by some steric interactions between their very bulky substituents. Accordingly, the Ga–C distances are longer in the tris(trimethylsilyl)methyl compounds described here (199 versus 204 pm). In contrast, the Ga–O distances are unaffected by the different alkyl groups and, at 195 pm,are almost indistinguishable between the compounds. An analogous dialkyldiindium compound was not obtained before so that a sound comparison of bond distances is difficult. However, the In–C bonds appear to be relatively long (221.2 pm).[37]

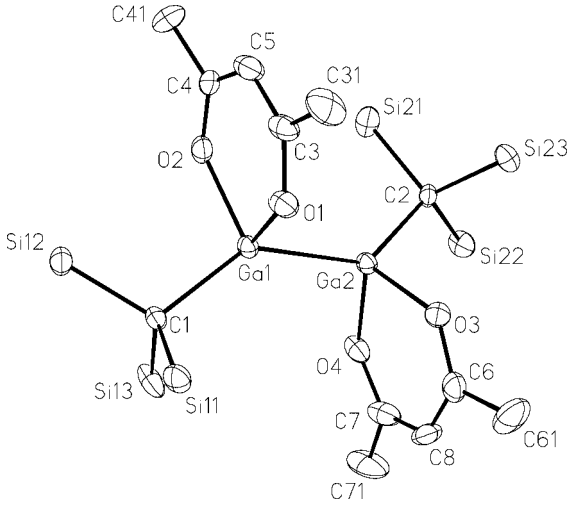

Figure 1. Molecular structure and numbering scheme of compound **3**. Thermal ellipsoids are drawn at the 40% probability level. Methyl groups of $SiMe_3$ substituents and hydrogen atoms are omitted. Selected bond lengths [pm] and angles [°]: Ga1–Ga2 251.12(8), Ga1–C1 204.0(5), Ga2–C2 204.5(6), Ga1–O1 195.1(3), Ga1–O2 195.7(4), Ga2–O3 195.1(3), Ga2–O4 195.1(4), Ga1–Ga2–C2 134.1(1), Ga2–Ga1–C1 133.8(1), O1–Ga1–O2 91.3(2), O3–Ga2–O4 91.3(2).

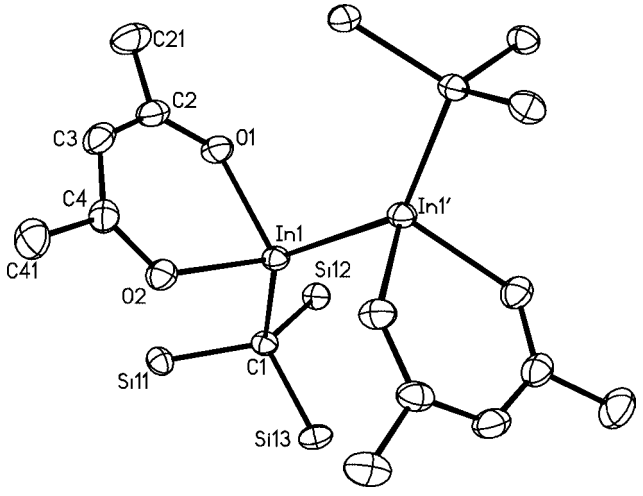

Figure 2. Molecular structure and numbering scheme of compound **4**. Thermal ellipsoids are drawn at the 40% probability level. Methyl groups of $SiMe_3$ substituents and hydrogen atoms are omitted. Selected bond lengths [pm] and angles [°]: In1–In1′ 278.04(7), In1–C1 221.3(2), In1–O1 216.3(1), In1–O2 216.0(1), In1′–In1–C1 136.73(5), O1–In1–O2 85.31(5); In1′ generated by $-x, y, -z + 1/2$.

Reactions of the Subhalides with Lithium Diphenyltriazenide

As was shown before, the subhalides of gallium and indium are excellent starting compounds for the generation of secondary products containing Ga–Ga or In–In bonds. Carboxylato and acetylacetonato ligands could be introduced by such a route and the products were generally isolated in reasonable yields. Another ligand which is able to stabilise the Ga–Ga bond of bis(trimethylsilyl)methyl compounds is diphenyltriazenide. However, the direct reaction of $R_2Ga–GaR_2$ [$R = CH(SiMe_3)_2$] with diphenyltriazene by release of two equivalents of bis(trimethylsilyl)methane gave partial cleavage of the Ga–Ga bond as an undesired side-reaction and the separation of both products by recrystallisation did not succeed.[30] Owing to their different colours, the crystalline products could be separated in very small quantities under a microscope only. Later, the bis(triazenido)digallium compound containing a Ga–Ga bond was isolated in an almost quantitative yield by the reaction of an acetato derivative, $R_2Ga_2(\mu\text{-}O_2C\text{-}CH_3)_2$ [$R = CH(SiMe_3)_2$], with lithium diphenyltriazenide.[31] The driving force was the precipitation of lithium acetate. Such a procedure is similar to the method described here. Diindium compounds bearing triazenido ligands are unknown and so we tried to introduce triazenido groups into digallium or diindium compounds starting with our subhalides. Treatment of the digallium subhalide $R_2Ga_2I_2$**1** with lithium diphenyltriazenide (easily obtained by deprotonation of diphenyltriazene with *n*-butyllithium) in *n*-hexane afforded a mixture of products. Recrystallisation from diisopropyl ether yielded a small quantity of orange crystals of compound **5** which was identified from a crystal structure determination (see below) as the mononuclear compound $IGa[C(SiMe_3)_3][N_3(C_6H_5)_2]$ (Scheme 1) possessing gallium atoms in the +III oxidation state. Compound **5** was formed by the cleavage of the Ga–Ga bond. Although the ^1H NMR spectrum of the crude product of the reaction showed that **5** (δ = 0.31 ppm, $SiMe_3$) had formed in a considerable amount, no second fraction could be isolated after concentration and cooling of the mother liquor. Furthermore, a second main product was detected (δ = 0.25 ppm) which could not be isolated in a pure form at all. Its constitution remains unknown and we do not have any suitable information to allow a sound discussion of the reaction course. A similar situation holds for the reactions of the diindium subhalides $(R_2In_2X_2)_2$ [X = Cl: **2**; X = Br] with lithium diphenyltriazenide. Mixtures were formed in which $HC(SiMe_3)_3$ and the protonated triazenide $N_3(C_6H_5)_2H$

 © 2005 Wiley-VCH Verlag GmbH & Co. KGaA, Weinheim

could be detected by NMR spectroscopy. Both compounds may indicate the occurrence of radical intermediates. Another product formed was indium tris(diphenyltriazenide) **6** (Scheme 1) which could be isolated as yellow crystals in a low yield from the reaction of the dibromide but was also clearly identified in the NMR spectrum of the crude product from the reaction of **2**. The mother liquor remaining after the separation of **6** showed one resonance of relatively high intensity in the trimethylsilyl range of the ^{1}H NMR spectrum at δ = 0.22 ppm which is characteristic of $C(SiMe_3)_3$ groups attached to gallium or indium in the +III oxidation state. It may result from the cleavage of the In–In bond and, in accordance with the integration ratio, may be described as $BrIn[C(SiMe_3)_3][N_3(C_6H_5)_2]$ similar to the gallium compound **5** described before. We did not succeed in isolating this compound in a pure form. However, a few crystals of a similar indium compound were isolated from the reaction of lithium diphenyltriazenide with the triindium subiodide $In_3I_2[C(SiMe_3)_3]_3$. This product, $InI[C(SiMe_3)_3][N_3(C_6H_5)_2]$ **7**, was identified by a crystal structure determination (see below) and by ^{1}H NMR spectroscopy (δ = 0.28 pm for the trimethylsilyl groups). It was obtained as well as $HC(SiMe_3)_3$ and several other compounds. The main resonances in the ^{1}H NMR spectrum of the crude product were observed at δ = 0.22, 0.50 and 0.68 ppm. We did not succeed in isolating any of these components in a pure form.

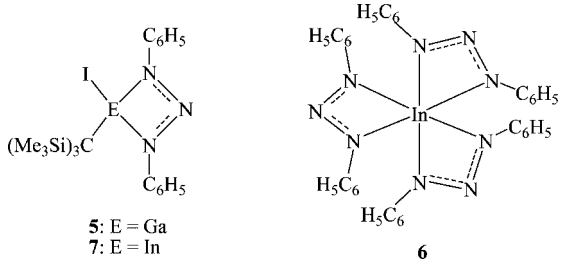

Scheme 1.

Three triazenido compounds (**5**, **6** and **7**) were characterised by single-crystal X-ray diffraction studies. The structure of the tris(triazenido)indium compound **6**, containing an indium atom coordinated by six nitrogen atoms in a distorted octahedral coordination sphere, was determined before.[39] We observed the occurrence of another space group and crystal system (monoclinic instead of orthorhombic). Therefore, we include some details of the structure determination in Table 1 but omit a pictorial presentation of the molecular structure. The bond parameters (In–N 224.1 pm on average; N–In–N within the chelate 56.4° on average; N–N–N 108.6° on average) are almost identical to those reported in the literature and do not need a further discussion. The structures of compounds **5** and **7** (Figures 3 and 4) are quite similar but they do not crystallise isotypically. They possess central gallium or indium atoms with oxidation numbers of +III which are coordinated by an iodine atom, a tris(trimethylsilyl)methyl group and a chelating triazenido ligand. The E–I distances (Ga–I 252.7 pm; In–I 269.5 pm) are in the expected ranges for terminal Ga–I or In–I bonds (some examples are given in refs.[12,40–54]). The same holds for the E–C (197.7 and 217.3 pm, respectively) and E–N distances (203.9 and 223.7 pm, respectively).[30,31,39,55,56] The N–N bond lengths of the triazenido groups are almost indistinguishable in both compounds (130.4 pm on average) while the N–N–N angle is slightly enlarged in the indium derivative **7** (107.5 compared with 109.6°) which may be caused by the larger covalent radius of indium.

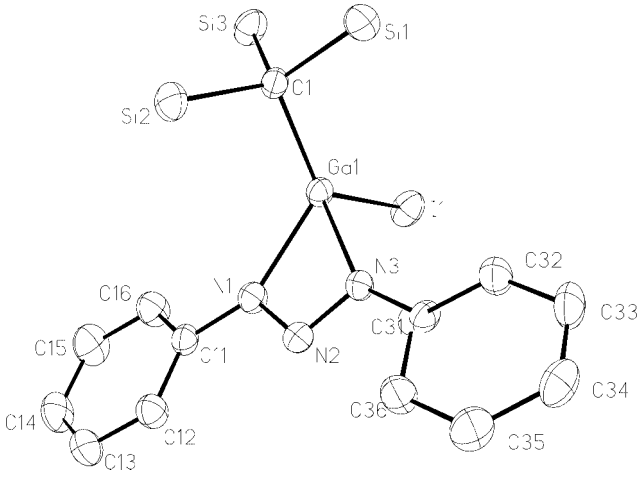

Figure 3. Molecular structure and numbering scheme of compound **5**. Thermal ellipsoids are drawn at the 40% probability level. Methyl groups of $SiMe_3$ substituents and hydrogen atoms are omitted. Selected bond lengths [pm] and angles [°]: Ga1–I1 252.7(1), Ga1–C1 197.7(4), Ga1–N1 203.6(3), Ga1–N3 204.2(3), N1–N2 130.7(5), N2–N3 130.0(4), N1–Ga1–N3 62.1(1), N1–N2–N3 107.5(3).

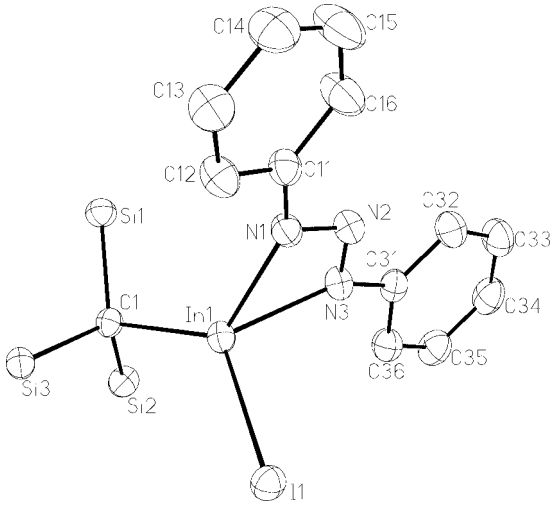

Figure 4. Molecular structure and numbering scheme of compound **7**. Thermal ellipsoids are drawn at the 40% probability level. Methyl groups of $SiMe_3$ substituents and hydrogen atoms are omitted. Selected bond lengths [pm] and angles [°]: In1–I1 269.49(3), In1–C1 217.3(2), In1–N1 223.8(2), In1–N3 223.6(2), N1–N2 130.5(3), N2–N3 130.2(3), N1–In1–N3 56.85(9), N1–N2–N3 109.6(2).

 © 2005 Wiley-VCH Verlag GmbH & Co. KGaA, Weinheim

Experimental Section

General: All procedures were carried out under purified argon in dried solvents (toluene and diisopropyl ether over Na/benzophenone; *n*-hexane and cyclopentane over $LiAlH_4$; 1,2-difluorobenzene over molecular sieves). The compounds $R_2Ga_2I_2$ (**1**),[12] $(R_2In_2Cl_2)_2$ (**2**),[11] $(R_2In_2Br_2)_2$[11] and $R_3In_3I_2$[10] were synthesised according to literature procedures. Commercially available silver acetylacetonate Ag(acac) (STREM), acetylacetone acacH (Aldrich) and diphenyltriazene (Aldrich) were employed without further purification. Lithium diphenyltriazenide was prepared by treatment of diphenyltriazene with an equimolar quantity of *n*-butyllithium in *n*-hexane. The insoluble product was filtered off and dried in vacuo.

Synthesis of $R_2Ga_2(acac)_2$ (3) [R = C(SiMe$_3$)$_3$]: A suspension of silver acetylacetonate (68 mg, 0.328 mmol) in toluene (25 mL) was cooled to –90 °C and treated with the diiodide **1** (141 mg, 0.165 mmol) dissolved in toluene (10 mL). The mixture was stirred and warmed to –70 °C (20 min). The precipitate was filtered off at –70 °C and the solvent was subsequently removed in vacuo at room temperature. The yellowish solid residue was recrystallised from cyclopentane (temp. range +20 to +8 °C). Yield: 89 mg of yellow crystals, 67%. M.p. (argon, sealed capillary): 194 °C (dec.). ^{1}H NMR (C_6D_6, 300 MHz, 298 K): δ = 0.44 (s, 27 H, $SiMe_3$), 1.64 (s, 6 H, acac-Me), 5.03 (s, 1 H,acac-CH) ppm. ^{13}C NMR (C_6D_6, 75.5 MHz, 298 K): δ = 5.0 (GaC), 6.2 ($SiMe_3$), 27.7 (acac-Me), 103.1 (acac-C, inner), 192.2 (CO) ppm. IR (CsBr, paraffin): $\tilde{\nu}$ = 1644 (vw), 1580 (w), 1555 (vw), 1525 (w, νCO, νCC), 1461 (vs), 1377 (vs, paraffin), 1304 (vw), 1260 (s, νCO, δCH_3), 1125 (s), 1095 (s), 1026 (s, δCH, νCC), 934 (vw), 843 (s), 804 [s, ρCH_3(Si)], 720 (w, paraffin), 699 (w), 677 (w), 659 (vw, ν_{as}SiC), 618 (vw, ν_sSiC), 514 (w), 464 (vw), 404 (vw), 390 (vw, νGaC, νGaO) cm^{-1}. UV/Vis (*n*-hexane): λ_{max} (log ε) = 250 (4.0), 275 (sh, 3.7), 345 (sh, 3.0) nm.

Synthesis of $R_2In_2(acac)_2$ (4) [R = C(SiMe$_3$)$_3$]: Acetylacetone (27.5 mg, 0.275 mmol) was dissolved in toluene (10 mL), cooled to –30 °C and treated with a solution of *n*-butyllithium (1.6 M, 17.2 μL) in *n*-hexane. After warming to room temperature the mixture was stirred for 30 min. A solution of the diindium dichloride (**2**) (105 mg, 0.138 mmol) in toluene (15 mL) was then added at room temperature. After stirring for 1 h the mixture was heated in a prewarmed oil-bath at 50 °C for a further hour. The solvent was removed in vacuo and the residue was treated with *n*-hexane. After filtration, the solution was cooled to –15 °C to give the solid, yellowish product **4**. Yield: 81 mg of yellowish crystals, 66%. M.p. (argon, sealed capillary): 178–182 °C. ^{1}H NMR (C_6D_6, 300 MHz, 298 K): δ = 0.42 (s, 27 H, $SiMe_3$), 1.71 (s, 6 H, acac-Me), 5.09 (s, 1 H, acac-CH) ppm. ^{13}C NMR (C_6D_6, 75.5 MHz, 298 K): δ = 6.3 ($SiMe_3$), 29.0 (acac-Me), 102.7 (acac-C, inner), 193.0 (CO) ppm, InC not detected. IR (CsBr, paraffin): $\tilde{\nu}$ = 1577 (s), 1543 (m), 1517 (s, νCO, νCC), 1459 (vs), 1375 (vs, paraffin), 1260 (s), 1248 (s, νCO, δCH_3), 1019 (ν_{as}Me-CO), 927 (ν_sMe-CO), 858 (vs), 777 [s, ρCH_3(Si)], 724 (w, paraffin), 676 (m), 653 (m, ν_{as}SiC), 615 (w), 600 (m, ν_sSiC), 555 (w), 417 (w), 399 (w, νInC, νInO) cm^{-1}. UV/Vis (*n*-hexane): λ_{max} (log ε) = 250 (3.4), 300 (sh, 3.6), 355 (3.7) nm.

Reaction of $R_2Ga_2I_2$ 1 with Lithium Diphenyltriazenide: A cooled (–80 °C) mixture of lithium diphenyltriazenide (57 mg, 0.281 mmol) and *n*-hexane (20 mL) was treated with a solution of **1** (117 mg, 0.137 mmol) in *n*-hexane (10 mL). The suspension was warmed to room temperature and stirred overnight. After filtration and evaporation of the solvent, the red residue was recrystallised twice from diisopropyl ether (temp. range +20 to –45 °C) to afford a small quantity of the pure compound IGa[C(SiMe$_3$)$_3$][N$_3$(C$_6$H$_5$)$_2$] (**5**) as orange crystals. ^{1}H NMR (C_6D_6, 300 MHz, 298 K): δ = 0.31 (s, 27 H, $SiMe_3$), 6.92 (pseudo-t, 2 H, *para*-PhH), 7.09 (pseudo-t, 4 H, *meta*-PhH), 7.52 (pseudo-d, 4 H, *ortho*-PhH) ppm.

Table 1. Crystal data, data collection parameters and structure refinement of compounds **4** to **8**.[a]

	3	**4**	**5**	**6**	**7**
Formula	$C_{30}H_{68}Ga_2O_4Si_{16}$	$C_{30}H_{68}In_2O_4Si_6$	$C_{22}H_{37}GaIN_3Si_3$	$C_{42}H_{30}F_2InN_9$	$C_{22}H_{37}IIn_2N_3Si_3$
Crystal system	monoclinic	monoclinic	monoclinic	monoclinic	monoclinic
Space group	$P2_1$ (No. 4)[57]	$C2/c$ (No. 15)[57]	$P2_1/n$ (No. 14)[57]	$P2_1/c$ (No. 14)[57]	$P2_1/c$ (No. 14)[57]
Z	2	4	4	4	4
T [K]	193(2)	193(2)	193(2)	193(2)	193(2)
$d_{calcd.}$ [g cm^{-3}]	1.248	1.360	1.468	1.422	1.538
a [pm]	901.02(9)	2117.3(4)	1322.7(3)	929.10(9)	900.24(4)
b [pm]	1437.22(9)	899.0(2)	1322.2(3)	1182.77(8)	1829.60(7)
c [pm]	1646.0(2)	2286.5(5)	1717.4(3)	3467.5(4)	1758.50(8)
β [°]	90.24(1)	91.75(3)	109.87(3)	94.36(1)	93.197(4)
V [10^{-30} m^3]	2131.5(3)	4350(2)	2824(1)	3799.4(6)	2891.9(2)
μ [mm^{-1}]	1.462	1.254	2.209	0.675	2.023
Crystal size [mm]	0.26 × 0.07 × 0.15	0.45 × 0.35 × 0.30	0.30 × 0.24 × 0.09	0.80 × 0.60 × 0.40	0.21 × 0.12 × 0.09
Diffractometer	STOE IPDS				
Radiation	Mo-K_α radiation; graphite monochromator				
θ range [°]	1.88 to 25.95	2.46 to 26.16	1.99 to 26.03	2.09 to 26.01	1.61 to 26.26
Index ranges	–11 ≤ h ≤ 10	–26 ≤ h ≤ 26	–16 ≤ h ≤ 16	–11 ≤ h ≤ 11	–11 ≤ h ≤ 11
	–17 ≤ k ≤ 16	–11 ≤ k ≤ 11	–16 ≤ k ≤ 16	–14 ≤ k ≤ 14	–22 ≤ k ≤ 22
	–20 ≤ l ≤ 20	–28 ≤ l ≤ 28	–21 ≤ l ≤ 21	–42 ≤ l ≤ 42	–21 ≤ l ≤ 21
Independent reflections	7709 [R(int) = 0.0492]	4271 [R(int) = 0.0856]	5523 [R(int) = 0.0677]	7312 [R(int) = 0.0751]	5814 [R(int) = 0.0351]
Reflections $I > 2\sigma(I)$	5758	4035	4371	4524	5080
Parameters	402	201	280	459	280
$R = \Sigma\|\|F_o\| - \|F_c\|\|/\Sigma\|F_o\|$ [$I > 2\sigma(I)$]	0.0429	0.0201	0.0407	0.0635	0.0284
$wR_2 = \{\Sigma w(F_o^2 - F_c^2)^2/\Sigma w(F_o^2)^2\}^{1/2}$ (all data)	0.0965	0.0579	0.1236	0.1764	0.0840
Max./min. residual [10^{30} e/m^3]	0.497/–0.599	0.547/–0.819	2.051/–0.776	1.936/–1.289	0.425/–0.941

[a]Programs: SHELXTL-Plus and SHELXL-97.[58] Solutions by direct methods. Full-matrix refinement with all independent structure factors.

 © 2005 Wiley-VCH Verlag GmbH & Co. KGaA, Weinheim

^{13}C NMR (C_6D_6, 75.5 MHz, 298 K): δ = 5.2 ($SiMe_3$), 6.0 (GaC?), 120.0, 126.4, 129.6 and 144.0 (phenyl) ppm.

Reaction of $(R_2In_2Br_2)_2$ with Lithium Diphenyltriazenide: Diphenyltriazene (69 mg, 0.35 mmol) was dissolved in *n*-hexane (20 mL), cooled to –30 °C and treated with a solution of *n*-butyllithium (0.2 mL, 1.6 M, 0.32 mmol) in *n*-hexane. The resultant suspension was stirred for 30 min at room temperature, cooled again to –30 °C and treated with a solution of the dibromide (130 mg, 1.53 mmol based on the monomeric formula) in *n*-hexane (25 mL). The mixture was warmed to room temperature and stirred for 30 min. A black precipitate formed which probably contained elemental indium. After filtration, the yellow-orange solution was concentrated and cooled to –30 °C. Only a few crystals of $In[N_3(C_6H_5)_2]_3$ (**6**) sufficient for a crystal structure determination could be isolated. All attempts to crystallise a second component from the reaction mixture failed.

Reaction of $R_3In_3I_2$ with Lithium Diphenyltriazenide: A cooled (–80 °C) suspension of lithium diphenyltriazenide (35 mg, 0.172 mmol) in *n*-hexane (25 mL) was treated with a solution of the triindiumdiiodide (101 mg, 0.078 mmol) in *n*-hexane (10 mL). The mixture was stirred for 1 h at room temperature. After filtration, the red solution was concentrated and cooled to –15 °C. Only a few crystals of $InI[C(SiMe_3)_3][N_3(C_6H_5)_2]$ (**7**) could be isolated. ^1H NMR (C_6D_6, 200 MHz, 298 K): δ = 0.28 (s, 27 H, $SiMe_3$), 6.92 (pseudo-t, 2 H, *para*-PhH), 7.10 (pseudo-t, 4 H, *meta*-PhH), 7.46 (pseudo-d, 4 H, *ortho*-PhH) ppm.

Crystal Structure Determinations: Single crystals of the compounds **3** to **7** were obtained by cooling solutions in cyclopentane (temp. range from +20 to +8 °C, **3**), *n*-hexane (temp. range from +20 to +8 °C, **4**), diisopropyl ether (temp. range from +20 to –45 °C, **5**), 1,2-difluorobenzene (temp. range from +20 to –30 °C, **6**) or *n*-hexane (temp. range +20 to 0 °C, **7**). Crystal data and structure refinement parameters are given in Table 1.[59] The molecules of compound **4** reside on a crystallographic twofold rotation axis. The crystals of **6** contain one molecule of 1,2-difluorobenzene per formula unit of **6**. These solvent molecules are strongly disordered.

Acknowledgments

We are grateful to the Deutsche Forschungsgemeinschaft and the Fonds der Chemischen Industrie for generous financial support.

[1] M. Kehrwald, W. Köstler, A. Rodig, G. Linti, T. Blank, N. Wiberg, *Organometallics* **2001**, *20*, 860.
[2] C. Klemp, C. Üffing, E. Baum, H. Schnöckel, *Z. Anorg. Allg. Chem.* **2000**, *626*, 1787.
[3] G. Linti, W. Köstler, *Angew. Chem.* **1996**, *108*, 593; *Angew. Chem. Int. Ed. Engl.* **1996**, *35*, 550.
[4] A. H. Cowley, A. Decken, C. A. Olazábal, *J. Organomet. Chem.* **1996**, *524*, 271.
[5] N. Wiberg, T. Blank, M. Westerhausen, S. Schneiderbauer, H. Schnöckel, I. Krossing, A. Schnepf, *Eur. J. Inorg. Chem.* **2002**, 351.
[6] N. J. Hardman, R. J. Wright, A. D. Phillips, P. P. Power, *Angew. Chem.* **2002**, *114*, 2966; *Angew. Chem. Int. Ed.* **2002**, *41*, 2842.
[7] N. J. Hardman, R. J. Wright, A. D. Pillips, P. P. Power, *J. Am. Chem. Soc.* **2003**, *125*, 2667.
[8] V. Lomeli, B. G. McBurnett, A. H. Cowley, *J. Organomet. Chem.* **1998**, *562*, 123.
[9] C. Üffing, E. Baum, R. Köppe, H. Schnöckel, *Angew. Chem.* **1998**, *110*, 2488; *Angew. Chem. Int. Ed.* **1998**, *37*, 2397.
[10] W. Uhl, S. Melle, G. Geiseler, K. Harms, *Organometallics* **2001**, *20*, 3355.
[11] W. Uhl, S. Melle, *Chem. Eur. J.* **2001**, *7*, 4216.
[12] W. Uhl, A. El-Hamdan, M. Prött, P. Spuhler, G. Frenking, *Dalton Trans.* **2003**, 1360.
[13] W. Uhl, A. El-Hamdan, G. Geiseler, K. Harms, *Z. Anorg. Allg. Chem.* **2004**, *630*, 821.
[14] G. Linti, W. Köstler, *Chem. Eur. J.* **1998**, *4*, 942.
[15] G. Linti, G. Li, H. Pritzkow, *J. Organomet. Chem.* **2001**, *626*, 82.
[16] W. Uhl, F. Schmock, W. Petz, *Z. Naturforsch. Teil B* **2003**, *58*, 385.
[17] W. Uhl, A. El-Hamdan, W. Petz, G. Geiseler, K. Harms, *Z. Naturforsch. Teil B* **2004**, *59*, 789.
[18] W. Uhl, A. El-Hamdan, *Eur. J. Inorg. Chem.* **2004**, 969.
[19] W. Uhl, I. Hahn, H. Reuter, *Chem. Ber.* **1996**, *129*, 1425.
[20] W. Uhl, T. Spies, W. Saak, *Eur. J. Inorg. Chem.* **1998**, 1661.
[21] W. Uhl, T. Spies, D. Haase, R. Winter, W. Kaim, *Organometallics* **2000**, *19*, 1128.
[22] W. Uhl, I. Hahn, A. Jantschak, T. Spies, *J. Organomet. Chem.* **2001**, *637–639*, 300.
[23] W. Uhl, L. Cuypers, M. Prött, K. Harms, *Polyhedron* **2002**, *21*, 511.
[24] W. Uhl, A.-C. Fick, T. Spies, G. Geiseler, K. Harms, *Organometallics* **2004**, *23*, 72.
[25] W. Uhl, R. Graupner, S. Pohl, W. Saak, W. Hiller, M. Neumayer, *Z. Anorg. Allg. Chem.* **1997**, *623*, 883.
[26] W. Uhl, R. Graupner, I. Hahn, T. Spies, W. Frank, *Eur. J. Inorg. Chem.* **1998**, 355.
[27] W. Uhl, L. Cuypers, K. Schüler, T. Spies, C. Strohmann, K. Lehmen, *Z. Anorg. Allg. Chem.* **2000**, *626*, 1526.
[28] Review: W. Uhl, *Adv. Organomet. Chem.* **2004**, *51*, 53.
[29] W. Uhl, T. Spies, W. Saak, *Z. Anorg. Allg. Chem.* **1999**, *625*, 2095.
[30] W. Uhl, I. Hahn, R. Wartchow, *Chem. Ber./Recueil* **1997**, *130*, 417.
[31] W. Uhl, T. Spies, R. Koch, *J. Chem. Soc. Dalton Trans.* **1999**, 2385.
[32] L. Pang, M. A. Whitehead, E. A. C. Lucken, *Inorg. Chim. Acta* **1993**, *203*, 239.
[33] K. Dymock, G. J. Palenik, *Acta Crystallogr. Sect. B* **1974**, *30*, 1364.
[34] G. J. Palenik, K. R. Dymock, *Acta Crystallogr. Sect. B* **1980**, *36*, 2059.
[35] C. A. Fleming, D. A. Thornton, *J. Mol. Struct.* **1975**, *25*, 271.
[36] W. Uhl, M. Layh, T. Hildenbrand, *J. Organomet. Chem.* **1989**, *364*, 289.
[37] W. Uhl, M. Layh, W. Hiller, *J. Organomet. Chem.* **1989**, *368*, 139.
[38] A di(acetylacetonato)digallium dichloride has been reported: O. T. Beachley Jr., J. R. Gardinier, M. R. Churchill, *Organometallics* **2000**, *19*, 4544.
[39] J. T. Leman, H. A. Roman, A. R. Barron, *Organometallics* **1993**, *12*, 2986.
[40] G. Gerlach, W. Hönle, A. Simon, *Z. Anorg. Allg. Chem.* **1982**, *486*, 7.
[41] B. Beagley, S. M. Godfrey, K. J. Kelly, S. Kungwankunakorn, C. A. McAuliffe, R. G. Pritchard, *Chem. Commun.* **1996**, 2179.
[42] A. Schnepf, C. Doriat, E. Möllhausen, H. Schnöckel, *Chem. Commun.* **1997**, 2111.
[43] C. U. Doriat, M. Friesen, E. Baum, A. Ecker, H. Schnöckel, *Angew. Chem.* **1997**, *109*, 2057; *Angew. Chem. Int. Ed. Engl.* **1997**, *36*, 1969.
[44] W. Hönle, G. Miller, A. Simon, *J. Solid State Chem.* **1988**, *75*, 147.
[45] R. C. Crittendon, B. C. Beck, J. Su, X.-W. Li, G. H. Robinson, *Organometallics* **1999**, *18*, 156.
[46] P. Jutzi, B. Neumann, G. Reumann, H.-G. Stammler, *Organometallics* **1998**, *17*, 1305.
[47] M. Wilkinson, I. J. Worrall, *J. Organomet. Chem.* **1975**, *93*, 39.
[48] S. M. Godfrey, K. J. Kelly, P. Kramkowski, C. A. McAuliffe, R. G. Pritchard, *Chem. Commun.* **1997**, 1001.

 © 2005 Wiley-VCH Verlag GmbH & Co. KGaA, Weinheim

[49] M. A. Khan, C. Peppe, D. G. Tuck, *Can. J. Chem.* **1984**, *62*, 601.
[50] M. A. Khan, C. Peppe, D. G. Tuck, *J. Organomet. Chem.* **1985**, *280*, 17.
[51] A. H. Cowley, F. P. Gabbaï, H. S. Isam, A. Decken, R. D. Culp, *Main Group Chem.* **1995**, *1*, 9.
[52] T. Viefhaus, W. Schwarz, J. Weidlein, *Z. Anorg. Allg. Chem.* **2002**, *628*, 333.
[53] J. T. Leman, J. W. Ziller, A. R. Barron, *Organometallics* **1991**, *10*, 1766.
[54] A. Meller, C. Kümmel, M. Noltemeyer, *Z. Naturforsch. Teil B* **1996**, *51*, 107.
[55] J. T. Leman, A. R. Barron, J. W. Ziller, R. M. Kren, *Polyhedron* **1989**, *8*, 1909.
[56] J. T. Leman, H. A. Roman, A. R. Barron, *J. Chem. Soc. Dalton Trans.* **1992**, 2183.
[57] *International Tables for Crystallography, Space Group Symmetry* (Ed.: T. Hahn), Kluwer Academic Publishers, Dordrecht, Boston, London, **1989**, vol. A.
[58] *SHELXTL-Plus, Release 4.2* for Siemens R3 Crystallographic Research Systems, Siemens Analytical X-ray Instruments Inc., Madison, USA, **1990**; G. M. Sheldrick, *SHELXL-97*, *Program for the Refinement of Structures*, University of Göttingen, **1997**.
[59] CCDC-241978 (for **3**), -241981 (for **4**), -241979 (for **5**), -242176 (for **6**) and -241980 (for **7**) contains the supplementary crystallographic data for this paper (excluding structure factors). These data can be obtained free of charge from The Cambridge Crystallographic Data Centre via www.ccdc.cam.ac.uk/data_request/cifThe crystallographic data of the compounds 3 to 7 (excluding structure factors) were deposited with the Cambridge Crystallographic Data Centre as supplementary publication no. CCDC-241978 (**3**), -241981 (**4**), -241979 (**5**), -242176 (**6**), and -241980 (**7**). Copies of the data can be obtained free of charge on application to The Director, CCDC, 12 Union Road, Cambridge CB2 1EZ, UK (Fax: +1223-336-033; E-mail: deposit@chemcrys.cam.ac.uk).

Received: June 25, 2004

 © 2005 Wiley-VCH Verlag GmbH & Co. KGaA, Weinheim

Titanium Complexes of Chelating, Dianionic O,S,O-Bisphenolato Ligands: Syntheses, Characterisation, and Catalytic Activity

Zofia Janas,*[a] Lucjan B. Jerzykiewicz,[a] Katarzyna Przybylak,[a] Piotr Sobota,[a] Krzysztof Szczegot,[b] and Dorota Wiśniewska[a]

Keywords: Polymerization / Titanium / O,S ligands

Titanium complexes based on 2,2′-thiobis[4-(1,1,3,3-tetramethylbutyl)phenolato] (tbop) are prepared by reaction of $TiCl_4$ or $Ti(NMe_2)_4$ with the parent biphenol. Three new complexes are reported: $[Ti_2(\mu\text{-tbop-}\kappa^3O,S,O)(\mu\text{-tbop-}\kappa^2O,O)(\text{tbop-}\kappa^3O,S,O)Cl_2]$ (**1**)·2CH_3CN, $[Ti_2(\mu\text{-tbop-}\kappa^3O,S,O)_2Cl_4]$ (**2**) and $[Ti(\text{tbop-}\kappa^3O,S,O)_2]$ (**3**). Substitution of the chlorides in **1** and **2** by 2,6-diisopropylphenolato and imido (N*t*Bu) ligands generates the new compounds $[Ti_2(\mu\text{-tbop-}\kappa^3O,S,O)_2Cl_2(dipp)_2]$ (**4**)·Et_2O and $[Ti_2(\mu\text{-tbop-}\kappa^3O,S,O)_2(N\text{t}Bu)_2(NH_2\text{t}Bu)_2]$ (**5**), respectively. Treatment of **5** with crude Me_3SiCl, containing Me_3SiOH, produces $[Ti(\text{tbop-}\kappa^3O,S,O)Cl(OSiMe_3)(NH_2\text{t}Bu)]$ (**6**). Reaction of **2** with an excess of $NHiPr_2$ provides a mixture of compounds: ionic $[NH_2iPr_2][Ti(\text{tbop-}\kappa^3O,S,O)Cl_3]$ (**7**)·CH_2Cl_2 and molecular $[Ti_2(\mu\text{-tbop-}\kappa^3O,S,O)_2Cl_2(NiPr_2)_2]$ (**8**). The structures of **1**–**8** were confirmed by NMR spectroscopy; complexes **1**, **5**, **6** and **7** were further investigated by X-ray crystallography. Compounds **1**, **2**, **4** and **5**, when supported on $MgCl_2$ and activated with alkylaluminiums, effectively polymerise ethene.

(© Wiley-VCH Verlag GmbH & Co. KGaA, 69451 Weinheim, Germany, 2005)

Introduction

Titanium complexes $[Ti_2(\mu\text{-}X)_2X_2(\text{tbmp-}\kappa^3O,S,O)_2]$ derived from the sulfide-linked bisphenol $\text{tbmp}H_2$ [$\text{tbmp}H_2$ = 2,2′-thiobis(6-*tert*-butyl-4-methylphenol); X = Cl, O*i*Pr] were first reported by Kakugo et al. to be highly active for the polymerisation of ethene, propene, styrene and dienes, as well as the copolymerisation of ethene with styrene, upon activation with methylalumoxane (MAO).[1–3] These titanium complexes were found to be an order of magnitude more active than the methylene-bridged chelating aryloxide complexes of the type $[TiX_2(\text{mbmp})]$ [mbmp = 2,2′-methylenebis(6-*tert*-butyl-4-methylphenolato)].[4] This is in qualitative agreement with theoretical studies that showed the S-bridged chelating phenolates to have lower insertion barriers than their methylene-bridged or directly bridged analogues.[5–7] Although the Ti–S interaction in $[Ti_2(\mu\text{-}X)_2X_2(\text{tbmp-}\kappa^3O,S,O)_2]$ is weak, it is likely to be of importance in stabilizing the active cationic species, facilitating its formation from the former and MAO and making the coordination of the counterion less tight.[8] Bisphenolato- and bisnaphtholatotitanium complexes have been well characterised both structurally and spectroscopically, and the kinetics and thermodynamics of intra- and intermolecular rearrangement in bisnaphtholates has been described as well.[9,10] However, there are very few reports of structural data on S-bridged titanium analogues, especially of their ligand modifications.[5,11,12] This encouraged us to investigate the titanium compounds with the tridentate O,S,O-thiobisphenolato ligand 2,2′-thiobis[4-(1,1,3,3-tetramethylbutyl)phenolato] (tbop). In addition to the S bridge, the tbop ligand seemed to have one more attractive feature: the long, sterically hindered auxiliary group on the thiobisphenolato ligand sufficiently increases solubility of the catalyst in hydrocarbons.

Recently we described the synthesis and structural characterisation of the mixed-ligand complexes $[Ti_2(\mu\text{-}OR)_2(X)_2(\text{tbop-}\kappa^3O,S,O)_2]$ (R = Me, Et; X = OR or Me).[13] In these complexes the tbop ligand was found to coordinate to the titanium in a *fac* fashion. $[Ti_2(\mu\text{-}OR)_2(X)_2(\text{tbop-}\kappa^3O,S,O)_2]$ complexes supported on $MgCl_2$ and activated with $AlEt_2Cl$ or $AlEt_2Cl/AlEt_3$ show very high activity in ethene polymerisation. The narrow molecular-weight distribution obtained for these systems is indicative of the operation of typical heterogeneous single-site catalyst behaviour.

We have been exploringthe use of the tbop ligand for the preparation of new titanium complexes that might serve as catalysts for the ethene polymerisation process. We report here their syntheses and structures, along with catalytic behaviour in ethene polymerisation.

Results and Discussion

The reaction between $TiCl_4$ and $\text{tbop}H_2$ in *n*-hexane, depending on the stoichiometry (1:1.5 and 1:1), produces

[a] Faculty of Chemistry, University of Wrocław,
14 F. Joliot-Curie Street, 50-383 Wrocław, Poland
Fax: +48-71-3282348
E-mail: zj@wchuwr.chem.uni.wroc.pl
[b] Institute of Chemistry, University of Opole
48 Oleska Street, 45-052 Opole, Poland

compounds [Ti_2(μ-tbop-κ^3O,S,O)(μ-tbop-κ^2O,O)(tbop-κ^3O,S,O)Cl_2] (**1**·2CH_3CN and [Ti_2(μ-tbop-κ^3O,S,O)$_2Cl_4$] (**2**) with concomitant elimination of three and two equivalents of HCl, respectively (Scheme 1). Surprisingly, reaction of $TiCl_4$ with two equivalents of $tbopH_2$ in diethyl ether did not lead to the anticipated [Ti(tbop-κ^3O,S,O)$_2$] (**3**) but to a good yield of complex **2**. Fortunately, compound **3** is available by simple addition of $tbopH_2$ to [$Ti(NMe_2)_4$]. When the reaction of $tbopH_2$ with neat $TiCl_4$ is carried out in toluene, a mixture of **1**, **2** and **3** is formed, from which only compound **1** could be isolated as an analytically pure product. The IR spectra of **1** and **2** show characteristic modes for terminal coordinated chlorides at 380 and 378 cm^{-1}, respectively.

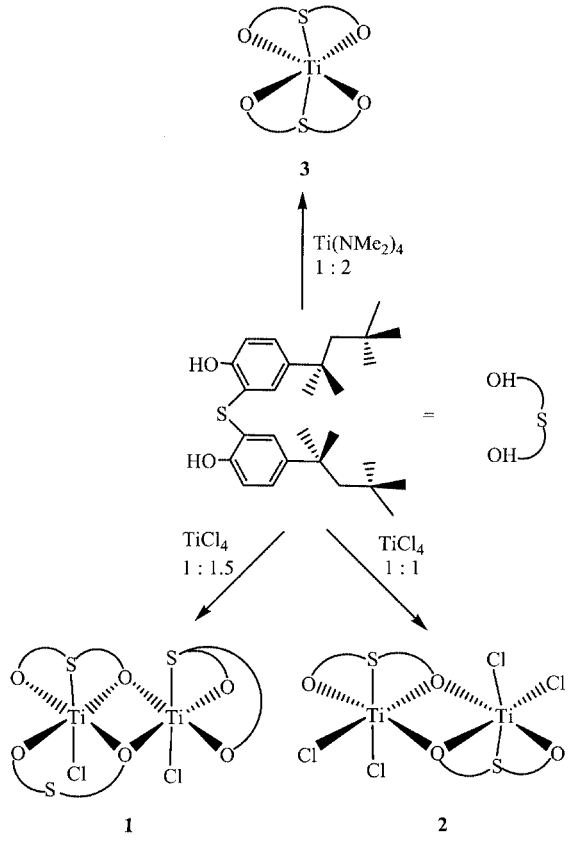

Scheme 1.

The structure of **1** (Figure 1) consists of discrete molecules of dimer [Ti_2(μ-tbop-κ^3O,S,O)(μ-tbop-κ^2O,O)(tbop-κ^3O,S,O)Cl_2] together with two MeCN molecules of crystallisation. The coordination environment about the Ti centres bridged by two oxygen atoms of tbop ligands is best described as highly distorted octahedral. The major distortions from idealised octahedral geometry are for the O(41)–Ti(1)–O(61), O(21)–Ti(1)–S(1), O(31)–Ti(2)–O(61), O(41)–Ti(2)–O(61) and O(61)–Ti(2)–S(3) angles, with values of 71.88(11)°, 75.72(9)°, 149.18(12)°, 71.54(10)° and 74.19(8)°, respectively. Two tbop ligands in **1** bridge titanium centres and the third one is facially coordinated to Ti(1). All the oxygen atoms of the tbop ligands are engaged in the formation of the equatorial planes, while the terminal chlorides and two sulfur links [S(1), S(3)] of the tbop ligands occupy the apical sites. The third sulfur atom [S(2)] isnot bonded to any Ti atom. The average titanium–sulfur bond length of 2.735(2) Å is longer than those found in other complexes, for example[Ti_2(μ-O*i*Pr)$_2$(O*i*Pr)$_2$(tbmp-κ^3O,S,O)$_2$] [tbmp = 2,2′-thiobis(6-*tert*-butyl-4-methylphenolato; 2.719(1) Å],[Ti(tbmp-κ^3O,S,O)($C_6H_4CH_2NMe_2$-2-κ^2C,N)Cl] [2.704(1) Å]and [Ti(tbmp-κ^3O,S,O)Cl(O*i*Pr)(HO*i*Pr)] [2.693(1) Å],[5,11] and shorter than those in [Ti_2(μ-OEt)$_2$(OEt)$_2$(tbop-κ^3O,S,O)$_2$] [2.800(1) Å] and [{Ti_2(μ-OEt)$_2$(tbop-κ^3O,S,O)$_2$}$_2$-(μ-O)$_2$] [2.762(2) Å].[13] The average Ti–O distances of 1.832(3) Å and 2.040(3) Å are in the expected range for Ti^{IV} complexes with non-bridging and bridging aryloxo ligands, respectively.[4] The terminal Ti–Cl distances of 2.254(2) Å and 2.265(2) Å are slightly shorter (by less than 0.01 Å) than those in [Ti_2(μ-Cl)$_2Cl_2$(tbmp-κ^3O,S,O)$_2$].[12]

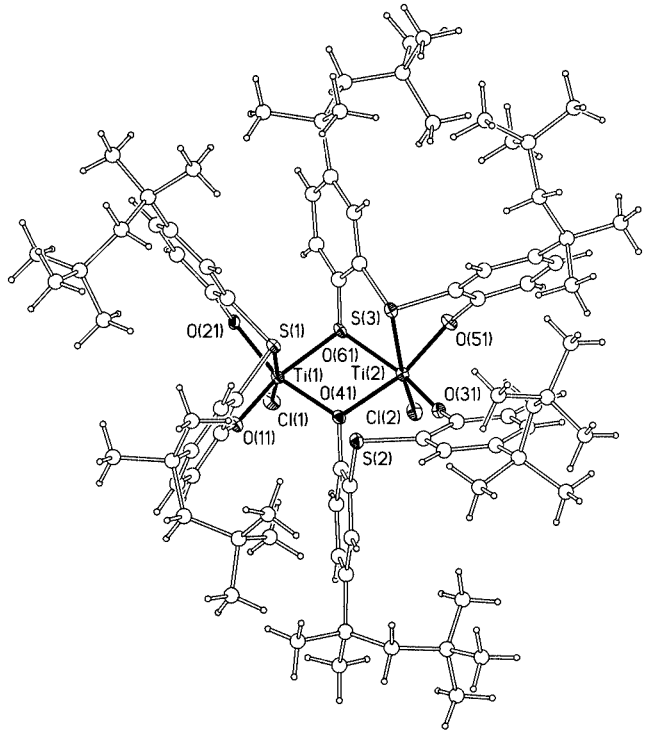

Figure 1. Molecular structure of **1**·2CH_3CN. Selected bond lengths [Å] and angles [°]: Ti(1)–O(11) 1.833(3), Ti(1)–O(21) 1.839(3), Ti(1)–O(41) 2.024(3), Ti(1)–O(61) 2.048(3), Ti(1)–Cl(1) 2.254(2), Ti(1)–S(1) 2.752(2), Ti(2)–Cl(2) 2.265(2), Ti(2)–O(31) 1.793(3), Ti(2)–O(41) 2.041(3), Ti(2)–O(51) 1.863(3), Ti(2)–O(61) 2.048(3), Ti(2)–S(3) 2.728(2); O(41)–Ti(1)–O(61) 71.88(11), O(21)–Ti(1)–S(1) 75.72(9), O(31)–Ti(2)–O(61) 149.18(12), O(41)–Ti(2)–O(61) 71.54(10), O(61)–Ti(2)–S(3) 74.19(8).

The ^1H NMR spectra of **1** in C_6D_6 show more peaks corresponding to the tbop ligand than would be expected from the crystal structure. These data suggest that the structure of **1** does not stay intact in solution at room temperature. It is most likely that compound **1** undergoes an intramolecular rearrangement in solution probably to the chloride- and oxygen-bridged dinuclear derivative **A** (Scheme 2). This closely corresponds to the well-documented mechanism for intramolecular exchange in [(R_2bino)Ti(O*i*Pr)$_2$]$_2$

 © 2005 Wiley-VCH Verlag GmbH & Co. KGaA, Weinheim

(R_2bino = 3,3′-disubstituted-1,1′-bi-2-naphtholates)[10] and [(tartrate)Ti(O*i*Pr)$_2$]$_2$ proposed by Sharpless and Finn.[14]

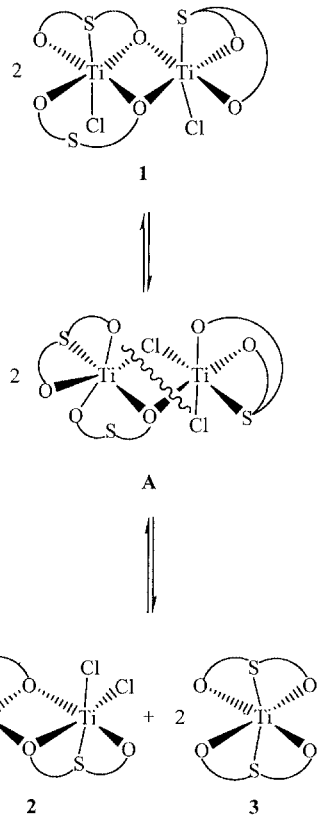

Scheme 2.

Fragmentation of **A** through the interruption of chloride and oxygen bridges would produce compounds [Ti$_2$(μ-tbop-κ^{3}O,S,O)$_2$Cl$_4$] (**2**) and [Ti(tbop-κ^{3}O,S,O)$_2$] (**3**). All these compoundscould participate in a facile equilibrium involving the interconversion of chemically distinct compounds. Partial confirmation of this hypothesis is the fact that compound **1** gives the same products upon substitution of its chlorides as **2** (described below). The presence of compound **3** was confirmed from the ^{1}H NMR spectrum.

Attempts to grow crystals of **2** suitable for X-ray diffraction proved unsuccessful. Therefore, we tried to examine its structure by indirect methods, by investigating the products of substitution of the chlorides in **2** (Scheme 3).

We found that the reaction of **2** with Li(dipp) (dipp = 2,4-diisopropylphenolato) in diethyl ether provides orange-red crystals of [Ti$_2$(μ-tbop-κ^{3}O,S,O)$_2$Cl$_2$(dipp)$_2$] (**4**)·Et$_2$O in good yield. The ^{1}H NMR spectrum of **4** contains septet and doublet resonances for the isopropyl substituents of the dipp groups and similar resonance sets for the tbop ligand to those detected for **2**, together with resonances corresponding to the free diethyl ether. Single-crystal X-ray diffraction of **4** showed it to be composed of dimeric [Ti$_2$(μ-tbop-κ^{3}O,S,O)$_2$Cl$_2$(dipp)$_2$] and one Et$_2$O molecule of crystallisation. Two titanium centres are linked by a double bridge formed from the oxygen atoms of the tbop ligands. The chloride atoms and dipp ligands are terminally coordinated to each titanium atom to complete the octahedral

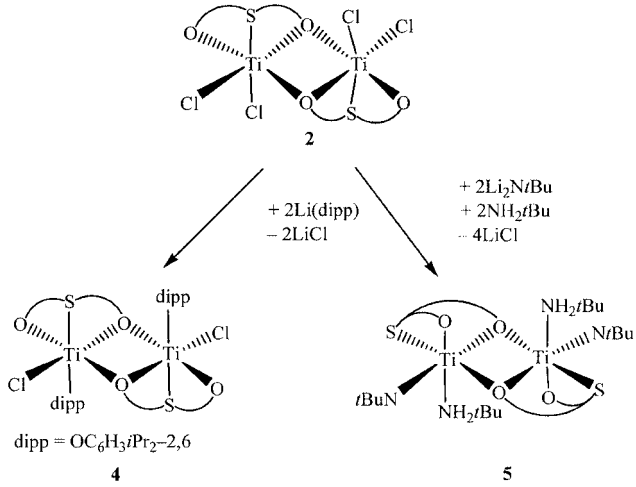

Scheme 3.

coordination sphere. Unfortunately, the poor-quality X-ray data for **4** do not allow a discussion of bond lengths and angles.[15]

Treatment of **2** with one equivalent of Li$_2$N*t*Bu and NH$_2$*t*Bu per titanium atom in diethyl ether produced [Ti$_2$(μ-tbop-κ^{3}O,S,O)$_2$(N*t*Bu)$_2$(NH$_2$*t*Bu)$_2$] (**5**) in high yield. The coordination of both amine (NH$_2$*t*Bu) and imido (N*t*Bu) ligands to the titanium centres is implied by the presence of two inequivalent *t*Bu groups and the broad resonance for the NH$_2$ group in the ^{1}H NMR spectrum and by ν(NH) bands in the IR spectra (see Experimental Section). Single-crystal X-ray diffraction clearly confirms (Figure 2) that **5** contains an approximately linear Ti=N*t*Bu linkage [166.4(3)°], with a Ti–N$_{imido}$ distance [1.710(3) Å] consistent with a formal metal–nitrogen triple bond ($\sigma^2\pi^4$),[16] and a

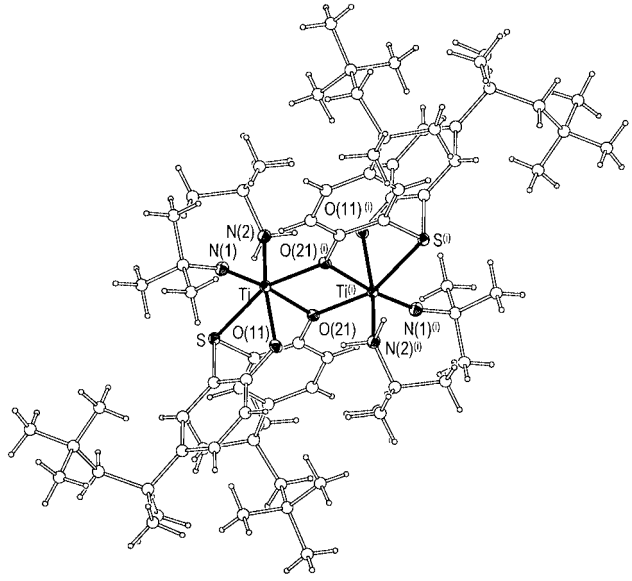

Figure 2. Molecular structure of **5**. Selected bond lengths [Å] and angles [°]: Ti–N(1) 1.710(3), Ti–O(11) 2.013(2), Ti–O(21)^i 2.010(3), Ti–N(2) 2.255(3), Ti–O(21) 2.298(2), Ti–S 2.587(2); Ti–N(1)–C(51) 166.4(3), Ti–N(2)–C(61) 126.5(2). Symmetry operation: (*i*) –*x* + 1, –*y*, –*z*.

 © 2005 Wiley-VCH Verlag GmbH & Co. KGaA, Weinheim

bent Ti–NH_2tBu unit with a Ti–N bond length and a Ti–N–C angle of 2.255(3) Å and 126.5(2)°, respectively.

The amine and imido groups are terminally coordinated to the titanium centres. A similar coordination of both amine and imido groups to the titanium centres is found in the tetramer $[Ti_4(\mu\text{-}Cl)_4(\mu^3\text{-}Cl)_2Cl_2(NtBu)_4(NH_2tBu)_4]$, which is obtained from the direct reaction of $TiCl_4$ and four equivalents of tBuN(H)$SiMe_3$.[17] The octahedral titanium centres in **5** are bridged by two oxygen atoms [O(21), O(21)$^{(i)}$] of the tbop ligands. These two oxygens form the equatorial planes together with sulfur and imido nitrogen atoms, while the remaining oxygens [O(11), O(11)$^{(i)}$] and amine nitrogens [N(2) and N(2)$^{(i)}$] occupy the apical sites. The Ti–S bond length of 2.587(2) Å is significantly shorter than that in **1** and is one of the shortest Ti–S lengths so far reported in the literature of titanium S-bridged bisaryloxo complexes.[5,11–13] Typically, it is observed that the Ti-μ-O_{Ar} distances are a minimum of 0.1 Å longer than terminal Ti–O_{Ar} bonds, as was found for **1**. However, the Ti–O bond distances in **5** do not reveal this tendency and show a significant variation. These variations could be caused by the *trans* interactions of bridging O(21) and O(21)$^{(i)}$ atoms with imido N(1), N(1)$^{(i)}$ atoms and S, S$^{(i)}$ atoms, respectively, as well as terminal O(11) and O(11)$^{(i)}$ atoms situated in axial positions with amine N(2) and N(2)$^{(i)}$ atoms, respectively. On the other hand, an increased axial Ti–O distance is expected, because axial ligands generally engender more severe steric interactions and experience greater competition for empty dπ-bonding orbitals than analogous equatorial ligands.[18] These two effects sufficiently influence the variation in Ti–O bond distances, although the influence of crystal packingcannot be excluded.

On the basis of structures **4** and **5** it seems most likely that complex **2** is a dimer in which the titanium centres are doubly bridged by oxygen atoms of the tbop ligands and the chlorides are coordinated terminally. This is in contrast to $[Ti_2(\mu\text{-}Cl)_2Cl_2(tbmp\text{-}\kappa^3O,S,O)_2]$, reported by Nakamura and Okuda, which has a chloro-bridged binuclear structure with tbmp ligands facially coordinated to each titanium centre,[12] probably because of the bulky tBu substituents in the tbmp ligands.

Addition of four equivalents of crude Me_3SiCl to **5** in diethyl ether led unexpectedly to yellow crystals of [Ti(tbop-κ^3O,S,O)Cl($OSiMe_3$)(NH_2tBu)] (**6**) in low yield. The X-ray structure of **6** (Figure 3) displays a distorted octahedral geometry around the titanium centre with the tbop ligand coordinated in a *fac* fashion. The oxygen atom [O(3)] of the $OSiMe_3$ ligand and the sulfur atom of the tbop group occupy the apical positions, while oxygens atoms O(1) and O(2) of the tbop ligand, together with the nitrogen atom of NH_2tBu, occupy the equatorial plane. The Ti–S distance of 2.757(1) Å is similar to those found in **1** and significantly longer than those detected in **5**. The Ti–$O_{aryloxo}$ [av. 1.87(2) Å], Ti–O_{alkoxo} [1.7758(2) Å] and Ti–Cl [2.385(1) Å] distances are in the expected range for Ti^{IV} complexes with non-bridging aryloxo[4] and alkoxo ligands[12] and terminal chlorides.Interestingly, intramolecular N–H···Cl [d(N···Cl): 3.4179 Å; N–H–Cl: 169.00°] and C(44)–H(44C)···O(2) [d(C···O): 3.3033 Å; C–H–O: 136.00°]hydrogen bonds are observed. One may suppose that compound **6** might be an-intermediate species in the Ti=NtBu linkage formation.

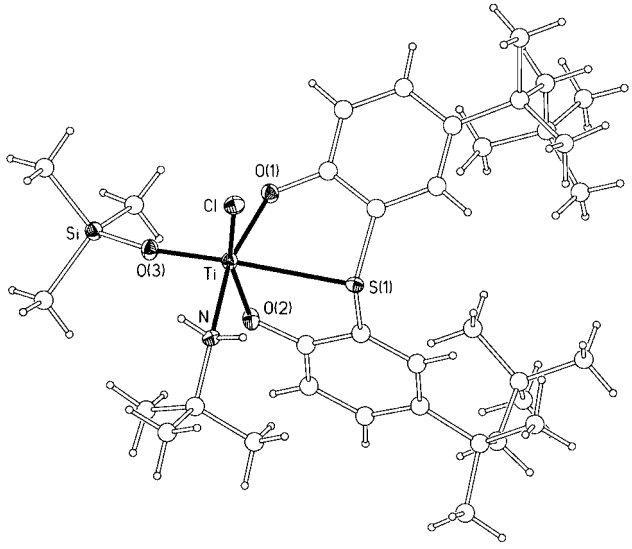

Figure 3. Molecular structure of **6**. Selected bond lengths [Å] and angles [°]: Ti–Cl 2.385(1), Ti–S(1) 2.757(1), Ti–N 2.232(2), Ti–O(1) 1.866(2), Ti–O(2) 1.874(2), Ti–O(3) 1.7758(2); S(1)–Ti–O(3) 174.32, O(2)–Ti–Cl 159.18(6), N–Ti–O(1) 158.69(9), Ti–N–C(41) 130.43(17).

We suggest that the interaction of **5** with crude Me_3SiCl generates a monomeric compound **B** (Scheme 4), which immediately reacts with Me_3SiOH (a product of the hydrolysis of Me_3SiCl that is present in the crude sample) to form **6**

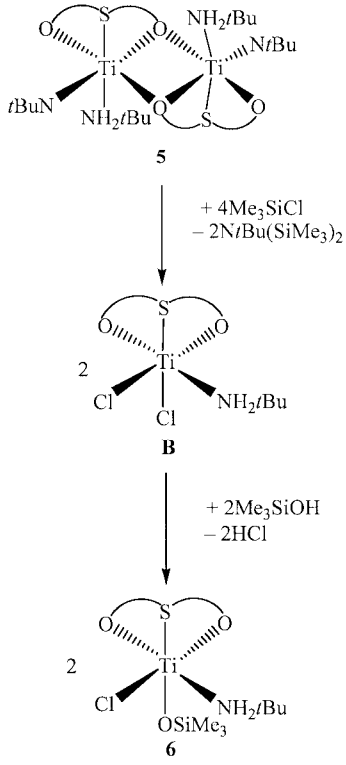

Scheme 4.

 © 2005 Wiley-VCH Verlag GmbH & Co. KGaA, Weinheim

with elimination of HCl. However, when freshly distilled Me_3SiCl was used, no formation of **6** was observed and a mixture of **B**, $NH_2tBu{\cdot}HCl$, amido and imido products was identified by ^1H NMR and IR spectroscopy.

The reaction of **2** with two equivalents of $NHiPr_2$ in diethyl ether results in the formation of two products: the ionic complex $[NH_2iPr_2][TiCl_3(tbop\text{-}\kappa^3O,S,O)]$ (**7**) and the molecular complex $[Ti_2(\mu\text{-}tbop\text{-}\kappa^3O,S,O)_2Cl_2(NiPr_2)_2]$ (**8**) (Scheme 5).

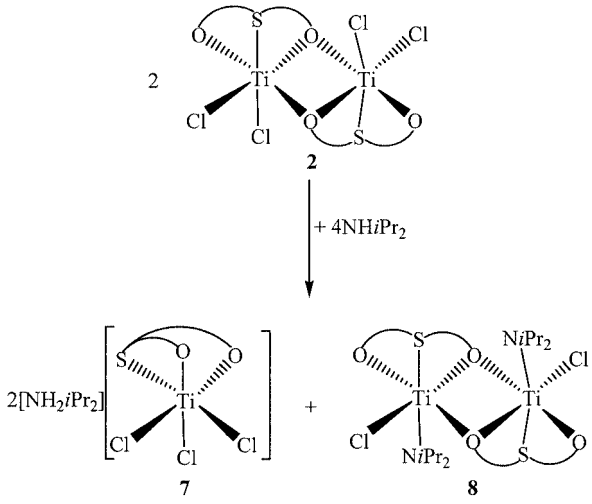

Scheme 5.

Crystals of **7** consist of $[NH_2iPr_2]^+$ cations and $[Ti(tbop\text{-}\kappa^3O,S,O)Cl_3]^-$ anions in a 1:1 ratio and one CH_2Cl_2 molecule of crystallisation. The molecular structure of the $[Ti(tbop\text{-}\kappa^3O,S,O)Cl_3]^-$ anion in **7** is shown in Figure 4. This anion evidently maintains a mononuclear octahedral environment with a facially capped tbop ligand. The oxygen atom O(12) of the tbop ligand and chloride Cl(2) occupy an apical coordination sphere, while the remaining donor atoms form the equatorial plane. The Ti–O distances of 1.863(2) and 1.884(2) Å are relatively short and comparable to the terminal aryloxide oxygens found in **1** and **5**. The Ti–Cl bond lengths, disposed *trans* to Ti–O and Ti–S, vary from 2.270(2) to 2.380(2) Å, presumably due to the *trans* influence. The structure of the cation $[NH_2iPr_2]^+$ is well known.[19]

The ^1H NMR spectrum of compound **8** shows similar sets of resonances for the tbop ligand to **5** and additional resonances (septet and doublet) for the deprotonated amido $NiPr_2$ groups. The IR spectrum of **8** also confirms the lack of the ν(NH) frequencies in the expected region. In compounds **1**–**7** thetitanium atom prefers to be six-coordinate. This suggests that complex **8**, which is isolated from non-donor solvents, might be a dimer, as shown in Scheme 5. By analogy to **5**, we propose that the titanium atoms in **8** are joined through the oxygen donors of the tbop ligand rather than the amido $NiPr_2$ groups. Terminal coordination of the amido $NiPr_2$ group to the titanium centre has been observed and crystallographically characterised in $[CpTiCl_2(NiPr_2)]$[20] and $[Li(tmeda)][TiPh_2(NiPr_2)_2]$.[21]

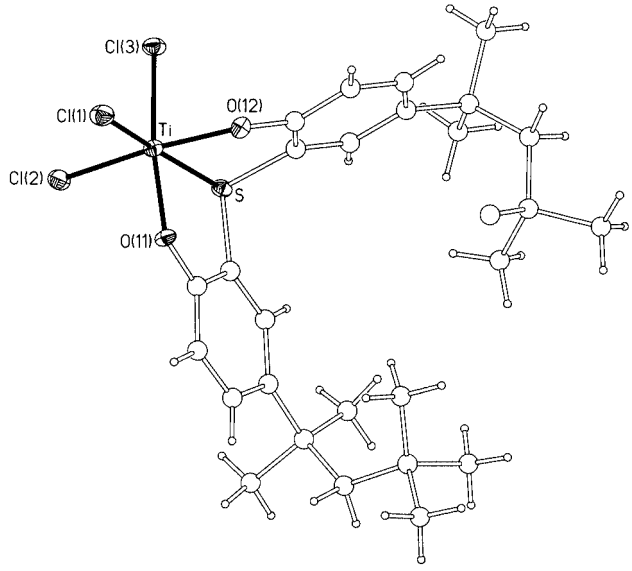

Figure 4. Molecular structure of the $[Ti(tbop\text{-}\kappa^3O,S,O)Cl_3]^-$ anion in **7**·CH_2Cl_2. Selected bond lengths [Å]: Ti–Cl(1) 2.270(2), Ti–Cl(3) 2.369(2), Ti–Cl(2) 2.380(2), Ti–S 2.652(2), Ti–O(11) 1.863(2), Ti–O(12) 1.884(2).

Complexes **1**, **2**, **4** and **5** were tested in ethene polymerisation. Catalysts based on these compounds were prepared in *n*-hexane by milling (see Experimental Section) a slurry of $[MgCl_2(THF)_2]$ with the titanium compound (10:1) and $AlEt_2Cl$ as cocatalyst. Prior to the polymerisation, ethene was passed through a suspension of the catalyst. Then, an additional amount of organoaluminium compound [$Al(iBu)_3$ or MAO] was added to the catalyst dispersed in the prepolymer to form a highly active catalyst. Thus, the polymerisation of ethene was performed in a two-step process. The aim of the first step (very low Al:Ti molar ratio, normal pressure of monomer, very low rate of polymerisation) was to prepare granules of polymer containing dispersed catalyst. These granules act as a "microreactor" in the second step of the polymerisation with a high rate (Granular Reactor Technology). This method gave PE yields twice as high as those obtained with a one-stage activation process. The ethene polymerisation results and polymer characterisation data are summarised in Table 1.

Table 1.Ethylene polymerisation.[a]

Entry	Complex	Cocatalyst	Activity[b]	M_w/M_n
1	**1**	MAO	110	3.73
2	**1**	$Al(iBu)_3$	345	4.23
3	**2**	MAO	465	4.36
4	**2**	$Al(iBu)_3$	322	4.67
5	**4**	MAO	357	3.05
6	**4**	$Al(iBu)_3$	707	5.48
7	**5**	MAO	207	3.32
8	**5**	$Al(iBu)_3$	402	4.74
9	$[Cp_2TiCl_2]$	MAO	137	2.80
10	$[Cp_2TiCl_2]$	$Al(iBu)_3$	123	3.16

[a] Polymerisation conditions: for MAO $[Ti]_0$ = 0.05 mmol dm^{-3}, [Al]/[Ti] = 4000; for $Al(iBu)_3$ $[Ti]_0$ = 0.01 mmol dm^{-3}, [Al]/[Ti] = 2000, time 30 min. [b] kg PE/g Ti/h.

 © 2005 Wiley-VCH Verlag GmbH & Co. KGaA, Weinheim

For comparison of catalyst activities, titanocene dichloride [Cp_2TiCl_2] was used as a reference under the same conditions (Table 1, entries 9 and 10). It turned out that the catalyst based on complex **4** (entry 6) exhibits the highest catalytic activity (707 kg PE/g Ti/h) for ethene polymerisation. This is about two- and sevenfold more than catalysts basedon[$Ti_2(\mu\text{-}OEt)_2(Me)_2(tbop\text{-}\kappa^3O,S,O)_2$] (344 kg PE/g Ti/h; 323 K, 0.5 MPa, 0.005 mmol catalyst)[13]and the species formulated as [Ti(tbmp)X_2] (100 kg PE/g Ti/h; 293 K, 3 MPa, 0.2 mmol catalyst, 25 mmol MAO, toluene),[2b] respectively, but is comparable with [Ti(tbmp)X_2]/MAO (820 kg PE/g Ti/h for X = Cl and 677 kg PE/g Ti/h for X = O*i*Pr; 293 K, 3 MPa, 0.001 mmol catalyst, 5.17 mmol MAO, toluene) originally reported by Kakugo.[1b,1c] The molecular weights of the polymers produced with complexes **1**, **2**, **4** and **5** under these conditions range from 924 000 to 1 269 000.The polydispersities, M_w/M_n, for **1**, **2**, **4** and **5** (see Table 1) are narrower than those reported for ethylenepolymerisation with catalysts based on [$Ti_2(\mu\text{-}OEt)_2(OEt)_4$-(maltolato-$\kappa^2O,O)_2$] (6.11)[22] and [Ti(tbmp)X_2] (11.9).[2b] It would appear that for polymerisation of ethene, activation of these systems affords a single, well-defined active species. This indicates that the cocatalyst does not abstract the tbop ligand from the titanium centre.

The preliminary polymerisation results on our Ziegler–Natta-like systems are promising on account of the production of a polymer with a sufficiently narrow particle-size distribution.

Conclusions

Reaction of $TiCl_4$ with $tbopH_2$ results in the formation of dimeric, mixed-ligand complexes **1** and **2** depending on the stoichiometry. Analytically pure compound **3** can be only obtained by the protonolysis reaction of $tbopH_2$ with [$Ti(NMe_2)_4$]. The extremely high solubility of **3** makes its isolation in the solid state difficult. Treatment of **1** and **2** with Li(dipp) or Li_2NtBu leads to the partial or complete substitution of chlorides to form dimeric compounds **4** and **5**, respectively. The monomeric complex **6** is a casual product of the reaction of **5** with crude Me_3SiCl containing Me_3SiOH. The use of the secondary amine $NHiPr_2$ in the reaction with **2** produces a mixture of the ionic compound **7** and the molecular species **8**. The solid-state crystal structures of **1**, **4** and **5** showthat their dimeric nature is due to oxygen bridges from the tbop ligands. This is in contrast to the complexes containing a tbmp ligand. It is likely that the bulky substituents in the *ortho* positions of the tbmp ligand are the main reason why chloride bridges are favoured in [$Ti_2(\mu\text{-}Cl)_2Cl_2(tbmp\text{-}\kappa^3O,S,O)_2$].

The complexes **1**, **2**, **4** and **5** are highly effective ethene polymerisation catalysts upon activation with alkylaluminium compounds. The narrow molecular-mass distribution for these systems suggests the operation of heterogeneous, well-defined, single-site catalysts.

Experimental Section

General Remarks: All operations were carried out under a dry dinitrogen atmosphere using standard Schlenk techniques. All the solvents were distilled under dinitrogen from the appropriate drying agents prior to use. The compounds $TiCl_4$, $Al(iBu)_3$, MAO, NH_2tBu, $NHiPr_2$, Me_3SiCl and 2,2′-thiobis[4-(1,1,3,3-tetramethylbutyl)phenol] ($tbopH_2$) were obtained from the Aldrich Chemical Co. and used without further purification, unless stated otherwise. Infrared spectra were recorded on a Perkin–Elmer 180 spectrophotometer in Nujol mulls. NMR spectra were performed on a Bruker ARX 300 spectrometer. Microanalysis was conducted with a ASA-1 (GDR, Carl-Zeiss-Jena) instrument (in-house).

[$Ti_2(\mu\text{-}tbop\text{-}\kappa^3O,S,O)(\mu\text{-}tbop\text{-}\kappa^2O,O)(tbop\text{-}\kappa^3O,S,O)Cl_2$](1)·2$CH_3CN$: $tbopH_2$ (6.05 g, 13.67 mmol) was addedto a solution of $TiCl_4$ (1.73 g, 9.11 mmol) in *n*-hexane (60 mL), and the mixture was stirred at room temperature until the evolution of HCl had ceased (48 h). All volatiles were then removed under reduced pressure. The resulting brown solid was washed with *n*-hexane (60 mL), and then the brown precipitate was filtered off, washed with *n*-hexane (3 × 5 mL) and dried under vacuum. The resultant solid was dissolved in warm CH_3CN, from which bright-red crystals suitable for the structure determination were isolated after standing at room temperature for two days. Yield: 5.83 g (86%). $C_{84}H_{120}Cl_2O_6S_3Ti_2$ (1488.67): calcd. C 67.80, H 8.13, Cl 4.70, S 6.45; found C 68.01, H 8.26, Cl 5.32, S 6.13. IR (Nujol mull): $\tilde{\nu}$ = 380 (s), 412 (w), 438 (s), 454 (w), 488 (w), 546 (m), 580 (s), 628 (s), 682 (m), 734 (w), 766 (m), 828 (s), 890 (m), 1060 (w), 1100 (w), 1144 (w), 1250 (s), 1288 (s), 1592 (w) cm^{-1}. ^1H NMR (300 MHz, C_6D_6, 25 °C): δ = 7.78–5.98 (m, 3 H, C_6H_3), 1.54–0.71 [multiplet, signals of $C(CH_3)_2$-$CH_2C(CH_3)_3$] ppm. The crystal structure shows the presence of two CH_3CN molecules in the unit cell. However, the elemental analysis indicates that these are absent from the powder sample analysed; they are presumably removed by the vacuum drying to which the sample was subjected.

[$Ti_2(\mu\text{-}tbop\text{-}\kappa^3O,S,O)_2Cl_4$] (2): $tbopH_2$ (4.05 g, 9.11 mmol) was added to a solution of $TiCl_4$ (1.73 g, 9.11 mmol) in Et_2O or *n*-hexane (60 mL) and the mixture was refluxed until the evolution of HCl had ceased (48 h). The resulting dark-red solid was filtered off, washed with cold Et_2O (3 × 5 mL), and dried under vacuum. Yield: 4.07 g (80%). $C_{56}H_{80}Cl_4O_4S_2Ti_2$ (1118.99): calcd. C 60.20, H 7.22, Cl 12.53, S 5.73; found C 60.86, H 6.96, Cl 12.02, S 5.92. IR (Nujol mull): $\tilde{\nu}$ = 324 (vw), 340 (vw), 378(vs, sh), 420 (s), 448 (m), 466 (m), 500 (w), 542 (w), 568 (m), 578 (m), 628 (vw), 670 (vw), 720 (m), 748 (w), 780 (m), 824 (s), 840 (vs), 888 (m), 916 (m), 936 (vs), 1048 (w), 1064 (w), 1100 (w), 1150 (w), 1192 (m), 1262 (vs), 1324 (m), 1588 (w) cm^{-1}. ^1H NMR (300 MHz, C_6D_6, 25 °C): δ = 7.71–6.89 (m, 12 H, C_6H_3), 1.58 [s, 8 H, $C(CH_3)_2CH_2C(CH_3)_3$], 1.19 [s, 24 H, $C(CH_3)_2CH_2C(CH_3)_3$], 0.77 [s, 36 H, $C(CH_3)_2$-$CH_2C(CH_3)_3$] ppm.

[Ti(tbop-$\kappa^3O,S,O)_2$] (3): $tbopH_2$ (2.19 g, 5.44 mmol) was added to a solution of [$Ti(NMe_2)_4$] (0.5 g, 2.72 mmol) in hexane (30 mL). After refluxing the reaction mixture for 6 h, all volatiles were evaporated in vacuo and the residue was dissolved in *n*-hexane (10 mL). The resulting solution was allowed to stand at room temperature for several days, upon which orange microcrystals of **3** separated. Yield: 0.4 g (15.8%). The extremely good solubility of this complex in organic solvents did not allow us to separate pure **3** with higher yield. Removal of solvent under vacuum gave a sticky product. $C_{56}H_{80}O_4S_2Ti$ (929.30): calcd. C 72.38, H 8.68, S 6.90; found C 71.99, H 8.65, S 7.11. IR (Nujol mull): $\tilde{\nu}$ = 446 (m), 460 (m), 502 (w), 539 (w), 566 (m), 575 (m), 627 (vw), 669 (vw), 722 (m), 747 (w), 781 (m), 822 (s), 838 (vs), 882 (m), 915 (m), 934 (vs), 1046 (w),

 © 2005 Wiley-VCH Verlag GmbH & Co. KGaA, Weinheim

1060 (w), 1100 (w), 1151 (w), 1190 (m), 1260 (vs), 1320 (m), 1588 (w) cm^{-1}. ^1H NMR (300 MHz, C_6D_6, 25 °C): δ = 8.35–6.24 (m, 12 H, C_6H_3), 1.70 [br, 8 H, $C(CH_3)_2CH_2C(CH_3)_3$], 1.40 [br, 24 H, $C(CH_3)_2CH_2C(CH_3)_3$], 0.95, 0.90, 0.84 [s, 36 H, $C(CH_3)_2CH_2C(CH_3)_3$] ppm.

[Ti$_2$(μ-tbop-κ^{3}O,S,O)$_2$Cl$_2$(dipp)$_2$] (4)·Et$_2$O: A solution of Li(dipp) (0.50 g, 2.70 mmol) in diethyl ether (20 mL) was added to a solution of **2** (2.52 g, 2.70 mmol) in diethyl ether (30 mL). The mixture was stirred over a period of 12 h and then filtered to remove LiCl. Reduction of the filtrate volume to 10 mL and storage at 253 K for 1 week provided red crystals of complex **4**. Yield: 1.24 g (65%). $C_{80}H_{114}Cl_2O_6S_2Ti_2$ (1402.65): calcd. C 68.54, H 8.20, Cl 4.99, S 4.57; found C 67.99, H 8.01, Cl 5.05, S 4.68. IR (Nujol mull): $\tilde{\nu}$ = 350 (m), 386 (s), 416 (m), 428 (m), 456 (m), 488 (m), 544 (w), 572 (m), 588 (m), 616 (w), 628 (w), 640 (w), 684 (m), 724 (s), 736 (s), 748 (s), 796 (m), 830 (s), 890 (m), 922 (s), 976 (w), 1044 (w), 1050 (m), 1100 (m), 1122 (m), 1146 (s), 1194 (s), 1250 (m), 1274(s), 1326 (s) cm^{-1}. ^1H NMR (300 MHz, C_6D_6, 25 °C): δ = 8.5–7.15 (m, 18 H, C_6H_3), 3.21 [sept, 4 H, $C_6H_3\{CH(CH_3)_2\}_2$], 1.43 [s, 8 H, $C(CH_3)_2CH_2C(CH_3)_3$], 1.35 [d, 24 H, $C_6H_3\{CH(CH_3)_2\}_2$], 0.95 [s, 24 H, $C(CH_3)_2CH_2C(CH_3)_3$], 0.77 [s, 36 H, $C(CH_3)_2CH_2C(CH_3)_3$] ppm. The crystal structure shows the presence of one Et_2O molecule in the unit cell. However, the elemental analysis indicates that this is absent from the powder sample analysed; presumably it is removed by the vacuum drying to which the sample was subjected.

[Ti$_2$(μ-tbop-κ^{3}O,S,O)$_2$(N*t*Bu)$_2$(NH$_2$*t*Bu)$_2$] (5): BuLi (2.19 mL, 3.52 mmol) was added to a cooled (233 K) solution of NH_2tBu (0.13 g, 1.76 mmol) in diethyl ether (40 mL). The mixture was allowed to warm to room temperature. After 3 h of stirring, **2** (0.98 g, 0.88 mmol) was added. The orange mixture was stirred for 24 h and then filtered to remove LiCl. Then, NH_2tBu (0.13 g, 1.76 mmol) was added to the filtrate and stirred for 2 h. Concentration of the reaction mixture to 10 mL gave yellow crystals of **5** after standing at room temperature for 2 d. These were filtered off and dried in vacuo. Yield: 0.86 g (76%). $C_{72}H_{120}N_4O_4S_2Ti_2$ (1265.64): calcd. C 68.33, H 9.56, N. 4.43, S, 5.07; found C 68.98, H 10.16, N 4.31, S 5.37. IR (Nujol mull): $\tilde{\nu}$ = 346 (vw), 402 (w), 420 (w), 444 (w), 492 (w), 530 (w), 560 (w), 574 (w), 604 (w), 672 (m), 748 (m), 758 (m), 824 (vs), 886 (m), 874 (s), 1018 (s), 1060 (s), 1112 (s), 1146 (s), 1194 (m), 1232 (s), 1260 (vs), 1308 (vs), 1536 (w), 1592 (m), 3104 (m), 3180 (w) cm^{-1}. ^1H NMR (300 MHz, C_6D_6, 25 °C): δ = 7.94–6.60 (m, 12 H, C_6H_3), 4.22 [br. s, 4 H, $NH_2C(CH_3)_3$], 1.48 [s, 8 H, $C(CH_3)_2CH_2C(CH_3)_3$], 1.27 [s, 18 H, $NH_2C(CH_3)_3$], 1.26 [s, 24 H, $C(CH_3)_2CH_2C(CH_3)_3$], 1.04 [s, 18 H, $NC(CH_3)_3$], 0.73 [s, 36 H, $C(CH_3)_2CH_2C(CH_3)_3$] ppm.

[Ti(tbop-κ^{3}O,S,O)Cl(OSiMe$_3$)(NH$_2$*t*Bu)] (6): Crude Me_3SiCl (0.86 g, 7.90 mmol) was added to a solution of **2** (2.5 g, 1.97 mmol) in diethyl ether (30 mL). The reaction mixture was stirred at room temperature, upon which the solution changed colour from orange to dark red. After filtration the solution was concentrated to 10 mL and allowed to stand at room temperature for 4 d. After that time red crystals of **6** suitable for X-ray structural analysis separated. Yield: 1.73 g (72%). $C_{35}H_{60}ClNO_3SiSTi$ (686.34): calcd. C 61.28, H 8.82, Cl 5.10, N 2.04, S 4.67; found C 61.91, H 8.53, Cl 5.28, N 2.16, S 5.03%. IR (Nujol mull): $\tilde{\nu}$ = 340 (vw), 472 (w), 492 (w), 584 (m), 622 (w), 680 (m), 736 (m), 762 (s), 836 (s), 892 (s), 928 (vs), 1028 (m), 1056 (m), 1148 (m), 1248 (s), 1280 (s), 1296 (s), 1568 (m), 3216 (s), 3280 (s) cm^{-1}. ^1H NMR (300 MHz, C_6D_6, 25 °C): δ = 7.38–6.79 (m, 6 H, C_6H_3), 4.15 [br. s, 2 H, $NH_2C(CH_3)_3$], 1.47 [s, 4 H, $C(CH_3)_2CH_2C(CH_3)_3$], 1.21 [s, 9 H, $NH_2C(CH_3)_3$], 1.09 [s, 12 H, $C(CH_3)_2CH_2C(CH_3)_3$], 0.65 [s, 18 H, $C(CH_3)_2CH_2C(CH_3)_3$], 0.13 [s, 9 H, $Si(CH_3)_3$] ppm.

[NH$_2$*i*Pr$_2$][Ti(tbop-κ^{3}O,S,O)Cl$_3$] (7)·CH$_2$Cl$_2$ and [Ti$_2$(μ-tbop-κ^{3}O,S,O)$_2$Cl$_2$(N*i*Pr$_2$)$_2$] (8): $NHiPr_2$ (0.16 mL, 1.94 mmol) was addedto a solution of **2** (1.09 g, 1.94 mmol) in toluene (20 mL) and the mixture was stirred for 12 h. Then, solvent was removed under vacuum and the residue extracted with Et_2O. CH_2Cl_2 (5 mL) was added to the dark-red ether solution, and left at room temperature for a few days. After that time red crystals of **7** suitable for X-ray analysis had settled out. They were filtered off and dried under vacuum. Yield: 0.89 g (66%). $C_{34}H_{56}Cl_3NO_2STi$ (697.10): calcd. C 58.68, H 8.12, Cl 15.09, N 2.01, S 4.60; found C 58.58, H 8.09, Cl 14.89, N 1.96, S 4.48. IR (Nujol mull): $\tilde{\nu}$ = 316 (s), 352 (m), 416 (m), 450 (m), 468 (m), 492 (m), 578 (s), 588 (m), 680 (m), 740 (s), 754 (m), 834 (s), 879 (m), 892 (m), 1100 (w), 1140 (w), 1248 (s), 1258 (s), 1272 (s), 1290 (s), 1334 (s), 1568 (m), 1579 (m) cm^{-1}. ^1H NMR (300 MHz, C_6D_6, 25 °C): δ = 7.75 (br., 2 H, NH_2iPr_2), 7.63–6.50 (m, 6 H, C_6H_3), 2.88 [m, 2 H, $NCH(CH_3)_2$], 1.63 [s, 4 H, $C(CH_3)_2CH_2C(CH_3)_3$], 1.28 [d, 12 H, $NCH(CH_3)_2$], 1.25 [s, 12 H, $C(CH_3)_2CH_2C(CH_3)_3$], 0.81 [s, 18 H, $C(CH_3)_2CH_2C(CH_3)_3$] ppm. The crystal structure shows the presence of one CH_2Cl_2 molecule in the unit cell. However, the elemental analysis indicates that this is absent from the powder sample analysed; presumably it is removed by the vacuum drying to which the sample was subjected.

The dark-orange, solid residue from the separation of **7** was dissolved in toluene (20 mL) and Et_2O (20 mL) was added. After standing for 2 d at room temperature, orange microcrystals of **8** precipitated. These were filtered off, washed with Et_2O and dried under vacuum. Yield: 0.58 g (48%). $C_{68}H_{108}Cl_2N_2O_4S_2Ti_2$ (1248.47): calcd. C 65.42, H 8.72, Cl 5.68, N 2.24, S 5.14; found C 65.02, H 8.41, Cl 5.52, N 2.01, S 5.21. IR (Nujol mull): $\tilde{\nu}$ = 338 (w), 456 (m), 486 (m), 576 (s), 625 (w), 675 (m), 735 (s), 750 (s), 799 (s), 879 (s), 890 (m), 1105 (w), 1139 (w), 1245 (s), 1251 (s), 1269 (s), 1287 (s), 1330 (s), 1579 (m) cm^{-1}. ^1H NMR (300 MHz, C_6D_6, 25 °C): δ = 7.63–6.50, (m, 6 H, C_6H_3), 3.37 [sept, 2 H, $N\{CH(CH_3)_2\}_2$], 1.63 [s, 4 H, $C(CH_3)_2CH_2C(CH_3)_3$], 1.28 [s, 12 H, $C(CH_3)_2CH_2C(CH_3)_3$], 1.01 [d, 12 H, $N\{CH(CH_3)_2\}_2$], 0.81 [s, 18 H, $C(CH_3)_2CH_2C(CH_3)_3$] ppm.

Polymerisation Test: A slurry of [$MgCl_2(THF)_2$] (10 mmol) in *n*-hexane was milled under argon in a glass mill (capacity 250 mL, with 20 balls of diameter 5–15 mm) at room temperature for 6 h. Then, the titanium compound (1 mmol) and *n*-hexane (50 mL) were added, and the mixture was milled for a further 24 h. The sample of precatalyst suspension (containing 0.01 mmol of titanium) was activated with $AlEt_2Cl$ (Al:Ti = 120) for 15 min at 323 K under argon. Prior to polymerisation, ethene was passed through the suspension of the catalyst (10 mL) in a Schlenk ampoule for 15 min at room temperature and normal pressure to form the prepolymer (about 1 g). An additional amount of organoaluminium compound [$Al(iBu)_3$ or MAO] was then added to the catalyst dispersed in the prepolymer (Al:Ti = 2000) to form a highly active catalyst. The polymerisation of ethylene was carried out in *n*-hexane at 323 K in a stainless-steel reactor (1 L), equipped with a stirrer, at 0.5 MPa pressure. The polymerisation was quenched with a 5% solution of HCl in methanol and dried under vacuum.

Crystal Data and Refinement Details for 1·2CH$_3$CN, 5, 6, and 7·CH$_2$Cl$_2$: Preliminary examination and intensity data collections were carried out on a CCD KUMA KM4 κ-axis diffractometer with graphite-monochromated Mo-K_α. Data were corrected for Lorentz, polarisation and absorption effects. The structures were solved by direct methods and refined by the full-matrix least-squares method on all F^2 data using the SHELXTL-NT v. 5.1 software package.[23] Carbon-bound hydrogen atoms were included in calculated positions and refined in the riding mode. Other hydrogen

 © 2005 Wiley-VCH Verlag GmbH & Co. KGaA, Weinheim

Table 2. Details of data collection and structural refinements for **1**·2CH_3CN, **5**, **6** and **7**·CH_2Cl_2.

	1·2CH_3CN	**5**	**6**	**7**·CH_2Cl_2
Empirical formula	$C_{88}H_{126}Cl_2N_2O_6S_3Ti_2$	$C_{72}H_{120}N_4O_4S_2Ti_2$	$C_{35}H_{60}ClNO_3SSiTi$	$C_{35}H_{58}Cl_5NO_2STi$
M	1570.77	1265.64	686.34	782.03
T [K]	100(1)	100(1)	100(1)	100(2)
λ [Å]	0.71073	0.71073	0.71073	0.71073
Crystal system	triclinic	monoclinic	triclinic	monoclinic
Space group	$P\bar{1}$	$C2/c$	$P\bar{1}$	$P2_1/c$
a [Å]	16.029(2)	17.312(5)	10.761(2)	17.770(3)
b [Å]	17.208(2)	23.068(4)	11.943(2)	15.272(2)
c [Å]	18.016(2)	22.075(6)	15.433(2)	15.207(3)
α [°]	110.19(1)	90	78.54(1)	90
β [°]	103.27(1)	112.47(5)	88.54(1)	98.26(1)
γ [°]	92.05(1)	90	82.00(1)	90
D_c [Mg m^{-3}]	1.147	1.029	1.184	1.272
μ [mm^{-1}]	0.355	0.289	0.409	0.618
Reflections collected	31389	17731	13320	26620
Independent reflections (R_{int})	19801 (0.0576)	9489 (0.0483)	8476 (0.0323)	9602 (0.0553)
R_1, wR_2 [$I > 2\sigma(I)$]	0.0717, 0.1292	0.0752, 0.1665	0.0502, 0.1047	0.0734, 0.1200

atoms were located in a difference map and refined free. All non-hydrogen atoms were refined with anisotropic displacement parameters. Crystal data are summarised in Table 2.

CCDC-243718 to -243721 (for **1**·2CH_3CN, **5**, **6**, and **7**·CH_2Cl_2) contain the supplementary crystallographic data for this paper. These data can be obtained free of charge from The Cam-bridge Crystallographic Data Centre via www.ccdc.cam.ac.uk/data_request/cif.

Acknowledgments

The authors thank the State Committee for Scientific Research (Poland) for financial support of this work (grant no. 4 T09A 137 24).

[1] a) M. Kakugo, T. Miyatake, K. Mizunuma, *Chem. Express* **1987**, *2*, 445; b) T. Miyatake, K. Mizunuma, Y. Seki, M. Kakugo, *Macromol. Chem. Rapid Commun.* **1989**, *10*, 349; c) T. Miyatake, K. Mizunuma, M. Kakugo, *Macromol. Symp.* **1993**, *66*, 203.
[2] a) C. J. Schaverien, A. J. van der Linden, A. G. Orpen, *Polym. Prepr. (Am. Chem. Polym. Div.)* **1994**, *35*, 672; b) A. J. van der Linden, C. J. Schaverien, N. Meijboom, C. Ganter, A. G. Orpen, *J. Am. Chem. Soc.* **1995**, *117*, 3008.
[3] Patent, Mitsui Toatsu Chem. Inc., JP 05230133-A, **1992**.
[4] a) C. Floriani, F. Corazza, W. Lesueur, A. Chiesi-Villa, C. Guastini, *Angew. Chem. Int. Ed. Engl.* **1989**, *101*, 93; b) F. Corazza, C. Floriani, A. Chiesi-Villa, C. Guastini, *Inorg. Chem.* **1991**, *30*, 146; c) J. Okuda, S. Fokken, H.-C. Kang, W. Massa, *Chem. Ber.* **1995**, *128*, 221.
[5] L. Porri, A. Ripa, P. Colombo, E. Miano, S. Capelli, S. V. Meille, *J. Organomet. Chem.* **1996**, *514*, 213.
[6] R. D. J. Froese, D. G. Musaev, T. Matsubara, K. Morokuma, *J. Am. Chem. Soc.* **1997**, *119*, 7190.
[7] R. D. J. Froese, D. G. Musaev, T. Matsubara, K. Morokuma, *Organometallics* **1999**, *18*, 373.
[8] E. Y.-X, Chen, T. J. Marks, *Chem. Rev.* **2000**, *100*, 1391.
[9] a) M. Mazzanti, C. Floriani, A. Chesi-Villa, C. Guastini, *J. Chem. Soc., Dalton Trans.* **1989**, 1793; b) P. J. Toscano, E. J. Schermerhorn, C. Dettelbacher, D. Macherone, J. Zubieta, *J. Chem. Soc., Chem. Commun.* **1991**, 933.
[10] T. J. Boyle, D. L. Barnes, J. A. Heppert, L. Morales, F. Takusagawa, J. W. Connolly, *Organometallics* **1992**, *11*, 1112.
[11] a) S. Fokken, T. P. Spaniol, H.-Ch. Kang, W. Massa, J. Okuda, *Organometallics* **1996**, *15*, 5069; b) H.-J. Krüger, *Angew. Chem. Int. Ed.* **1999**, *38*, 627; c) Y. Nakayama, H. Saito, N. Ueyama, A. Nakamura, *Organometallics* **1999**, *18*, 3149; d) P. L. Arnold, L. S. Natrajan, J. J. Hall, S. J. Bird, C. Wilson, *J. Organomet. Chem.* **2002**, *647*, 205.
[12] Y. Nakayama, K. Watanabe, N. Ueyama, A. Nakamura, A. Harada, J. Okuda, *Organometallics* **2000**, *19*, 2498.
[13] Z. Janas, L. B. Jerzykiewicz, K. Przybylak, P. Sobota, K. Szczegot, *Eur. J. Inorg. Chem.* **2004**, 1639.
[14] M. B. Finn, K. B. Sharpless, in *AsymmetricSynthesis* (Ed.: J. D. Morrison), Academic Press, New York, **1985**; vol. 5, chapter 8.
[15] Triclinic, space group $P\bar{1}$, a = 11.799(5) Å, b = 13.128(5) Å, c = 14.969(5) Å, α = 70.17(8)°, β = 87.39(8)°, γ = 87.42(8)°.
[16] For reviews, see: D. E. Wigley, *Prog. Inorg. Chem.* **1998**, *42*, 239; P. Mountford, *Chem. Commun.* **1997**, 2127.
[17] C. J. Carmalt, A. C. Newport, I. P. Parkin, A. J. P. White, D. J. Williams, *J. Chem. Soc., Dalton Trans.* **2002**, 4055.
[18] M. H. Chisholm, J. C. Huffman, N. S. Marchant, *J. Am. Chem. Soc.* **1983**, *105*, 6162.
[19] a) G. J. Reiss, B. Koppelhuber-Bitschnau, *Acta Crystallogr., Sect. E* **2002**, *58*, 1309; b) G. J. Reiss, *Acta Crystallogr., Sect. C* **1998**, *54*, 1489; c) S. Daniel, D. M. Hoffman, *Inorg. Chem.* **2002**, *41*, 3843.
[20] R. M. Pupi, J. N. Coalter, J. L. Petersen, *J. Organomet. Chem.* **1995**, *497*, 17.
[21] R. K. Minhas, L. Scoles, S. Wong, S. Gambarotta, *Organometallics* **1996**, *15*, 1113.
[22] P. Sobota, K. Przybylak, J. Utko, L. B. Jerzykiewicz, A. J. L. Pombeiro, M. F. C. Guedes da Silva, K. Szczegot, *Chem. Eur. J.* **2001**, *7*, 951.
[23] G. M. Sheldrick, *SHELXTL* Version 5.1. Bruker AXS Inc., Madison, Wisconsin, USA, **1998**.

Received: August 23, 2004

Chiral Iron(II) and Cobalt(II) Complexes with Biphenyl-Bridged Bis(pyridylimine) Ligands – Syntheses, Structures and Reactivities

Christoph Vedder,[a] Frank Schaper,[a] Hans-Herbert Brintzinger,*[a] Mika Kettunen,[b] Sebastian Babik,[c] and Gerhard Fink[c]

Keywords: Iron(II) / Cobalt(II) / Bianiline / Pyridylimine

A new class of iron(II) and cobalt(II) complexes with neutral, tetradentate bis(pyridylimine) chelate ligands bridged by a chiral 6,6′-dimethylbiphenyl backbone has been synthesized. Their dihalogen derivatives gave spectral, magnetic and X-ray diffraction results in agreement with a C_2-symmetric, approximately octahedral geometry with *cis*-positioned halide ligands and high-spin d-electron configuration. ^{1}H NMR signals of these paramagnetic complexes were assigned by correlating line widths with reciprocal proton-metal distances. Methyl substitution in 6-position of the pyridyl rings lead to a different, presumably square-pyramidal coordination geometry under dissociation of one chloride ion. Fe^{II} dimethyl and diisocyanide derivatives were shown to have low-spin configuration and C_1-symmetric geometry. With respect to MAO-activated olefin polymerization, significant catalytic activities were reproducibly obtained only under conditions, where the original complex structure was degraded.
(© Wiley-VCH Verlag GmbH & Co. KGaA, 69451 Weinheim, Germany, 2005)

Introduction

Complexes of late transition metals such as Pd, Ni, Fe, or Co are interesting targets for olefin polymerization catalysis,[1,2] none the least since these catalysts are relatively tolerant towards polar substrates and might thus allow copolymerization of α-olefins with polar monomers.[3] Iron-based catalysts in particular have shown activities for ethene polymerization which are comparable to those of the most active group(IV) metallocene catalysts. The excellent stereoselectivity of metallocene-catalyzed propene polymerization,[4] however, is still lacking for late transition metal catalysts. Low-temperature polymerizations have afforded polypropene with only partially syndiotactic or isotactic microstructures induced by chain-end stereocontrol.[5]

Most iron- or cobalt-based polymerization catalysts employ symmetric tridentate pyridyldiimine ligands, which form C_{2v}-symmetric bipyramidal complex species with homotopic coordination sites (Scheme 1).[1c,2c] Enantiotopic coordination sites, as required for olefin insertion under catalytic-site control, might be obtained by use of axially chiral, tetradentate ligands, from which C_2-symmetric octahedral complexes would be generated on coordination to MX_2 (Scheme 1). Chiral complexes with two N ligand atoms have previously been applied in enantioselective homogeneous catalysis.[6] Here we report on the synthesis of chiral Fe^{II} and Co^{II} complexes with C_2-symmetric, bianiline-bridged tetradentate nitrogen ligands, and on the properties of these complexes in homogeneous olefin polymerization.

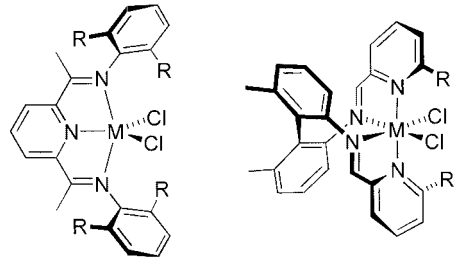

Scheme 1. Pyridyldiimine complexes with C_{2v} symmetry (left) and biphenyl-bridged bis(pyridylimine) complexes with axial C_2 symmetry (right)

Results and Discussion

Ligand Syntheses

The neutral, potentially tetradentate ligands *N*,*N*′-(biphenyl-2,2′-diyl)bis(2-pyridylmethyl)diimine (**1**), and *N*,*N*′-(6,6′-dimethylbiphenyl-2,2′-diyl)bis[(6-R′′-2-pyridyl)methyl]diimine [R′′ = H (**2**), Me (**3**)], were prepared by condensation of the known *N*,*N*′-(biphenyl-2,2′-diyl)diamines **4** and **5**,[7] with the appropriate heteroaromatic aldehyde in

[a] Fachbereich Chemie, Universität Konstanz,
78457 Konstanz, Germany
Fax: +49-7531-883137
E-mail: hans.brintzinger@uni-konstanz.de
[b] Laboratory of Inorganic Chemistry, University of Helsinki,
00014 Helsinki, Finland
[c] Max-Planck-Institut für Kohlenforschung,
45470 Mülheim/Ruhr, Germany
Supporting information for this article is available on the WWW under http://www.eurjoc.com or from the author.

ethanol at room temperature [Equation (1)]. Ligand **1** was reacted directly, without prior isolation, with iron(II) chloride (vide infra). Reaction of **5** with 2-acetylpyridine, be it in ethanol, methanol or dichloromethane with catalytic amounts of acetic, formic or hydrochloric acid, or in benzene over molecular sieves or in diethyl ether/pentane mixtures in the presence of excess $TiCl_4$, did not afford the desired ligand **6**. Refluxing a toluene solution of **5** and 2-acetylpyridine with a catalytic amount of *p*-toluenesulfonic acid in a Dean–Stark apparatus, however, yielded after three days a mixture which contained, apart from the starting materials, *N*,*N*′-(6,6′-dimethylbiphenyl-2,2′-diyl)bis[1-(2-pyridyl)ethane]diimine (**6**), in ca. 45% yield as determined by ^{1}H NMR spectroscopy. This reaction mixture was used without purification for further complex syntheses.

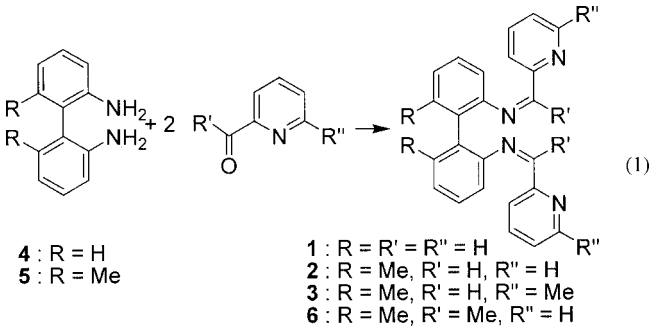

(1)

Complex Syntheses, Structures, and Spectroscopic Properties

Reaction of $FeCl_2$ or $FeBr_2$ with the dipyridyldiimine ligands **1**, **2**, or **6** in THF afforded, after evaporation of solvent and extraction with CH_2Cl_2, the blue to turquoise iron(II) complexes **7**–**10** [Equation (2)].[8] Since **7**–**10** were found to be insoluble in non-chlorinated solvents, excess ligand (and starting materials of the ligand synthesis in the case of **6**) was removed by washing with diethyl ether and pentane to yield analytically and spectroscopically pure products. The light brown cobalt(II) complex **11** was obtained by an analogous reaction of $CoCl_2$ with **2**.

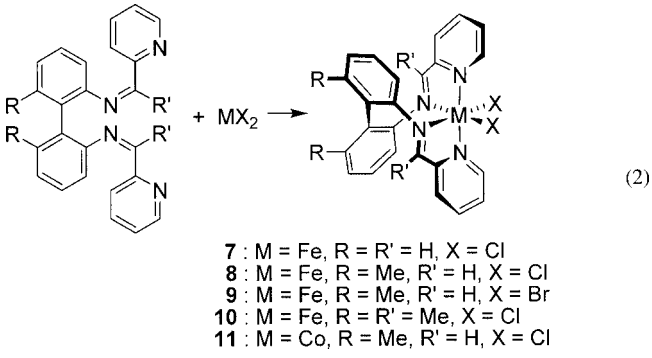

(2)

Single crystals of the dichloro complexes **8** and **11** were obtained by layering their dichloromethane solutions with pentane or toluene, respectively. The complexes are isostructural and crystallize in the monoclinic space group *C*2/*c* with cell constants deviating by less than 0.2 Å and less than 0.5° (Figure 1, Table 1). The distorted octahedral complexes, with *cis*-positioned chlorine atoms, both possess crystallographic C_2-symmetry. Co–N bonds are approximately 0.05 Å shorter than their Fe–N counterparts (Table 1), presumably a consequence of higher nuclear charge and more strongly contracted metal d-orbitals of cobalt. Fe–N distances are within the range generally observed in neutral, octahedral iron complexes.[9] The bond angles ∠N1–M–Cl1, ∠N2–M–Cl1 and ∠N2–M–Cl1A (M = Fe, Co) at each of the metal centers deviate by less than 2° from each other and from the value of 90° expected for octahedral coordination. The bite angles of the twisted seven-membered chelate ring, ∠N1–M–N1A = 73–74°, and of the five-membered chelate rings, ∠N1–M–N2 = 73–74°, however, are both significantly smaller than 90° and lead to a distortion of the octahedral coordination, i.e. to an opening of the angle ∠Cl1–M–Cl1A to a value of 110–112° (Table 1). Due to the twisted bianiline backbone, the planes formed by N1, N1A, and M and by M, Cl1, and Cl1A deviate from each other by 26–28°.

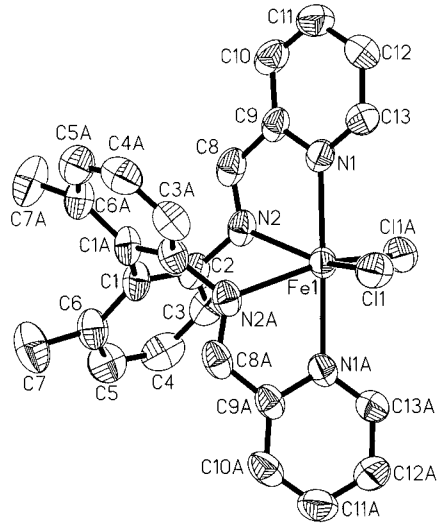

Figure 1. Crystal structures of complex **8**; hydrogen atoms omitted for clarity, thermal ellipsoids drawn at the 50% probability level

Table 1. Selected bond lengths [Å] and bond angles [°] for complexes **8** and **11**

	8[a]	**11**[b]
M–N1 (imine)	2.296(4)	2.235(2)
M–N2 (pyridine)	2.214(3)	2.175(2)
M–Cl1	2.397(2)	2.401(1)
N1–M–N1A	72.8(2)	73.8(1)
N2–M–N2A	178.6(2)	178.8(1)
X1–M–Cl1A	111.6(1)	109.8(1)
N1–M–N2	72.9(1)	74.0(1)
N1–M–N2A	106.0(1)	107.0(1)
N1–M–Cl1	91.0(1)	91.1(1)
N1–M–Cl1A	152.6(1)	154.2(1)
N2–M–Cl1	89.4(1)	88.1(1)
N2–M–Cl1A	91.4(1)	91.3(1)

[a] **8**: M = Fe, [b] **11**: M = Co.

 © 2005 Wiley-VCH Verlag GmbH & Co. KGaA, Weinheim

For the magnetic moments of complexes **8** and **11**, high-spin values of μ_{eff} = 5.47 μ_B and μ_{eff} = 4.96 μ_B, respectively, were measured by the SQUID method at 300 K. No indication for any thermally induced spin-crossover between 90 K and 300 K was obtained in either case. In this regard, complex **8** falls in line with related Fe^{II} complexes such as [bis(bipyridyl)$FeCl_2$] or bis(phenanthrolin)$FeCl_2$, for which high-spin configurations have likewise been reported.[10]

In the ^{1}H NMR spectrum of the paramagnetic iron(II) complex **8** in $CDCl_3$ solution, nine signals are detected over a range of nearly 190 ppm (Figure 2), in agreement with a time-averaged C_2-symmetric complex geometry. Based on the observed signal intensities, the resonance at δ = –6.72 ppm is clearly identified as being due to the methyl groups. Since no signal above δ = 120 is displayed in the NMR spectrum of complex **10**, which contains, instead of the aldimine ligand **2**, the analogous ketimine ligand **6**, we can conclude that the resonance of complex **8** at $\delta \approx$ 180 ppm must be due to its aldimine protons.

Assignments of further signals are based on their relative line widths: Up to a distance of ca. 5 Å from the metal center, relative line widths of two nuclei A and B depend reciprocally on the ratio of their distances from the metal center, $v_2(A)/v_2(B) \approx (d_B/d_A)^6$.[11] The remaining signals can thus be assigned as shown in Figure 2 and Table 2.

^{1}H NMR spectra of complexes **7** and **9**–**11** in $CDCl_3$ solution, which are likewise in agreement with time-averaged C_2 symmetry, were assigned in a manner similar to that used for **8** (see Exp. Sect.). Complexes **7**, **9**, and **10**, for which crystal structure determinations are not available, could in principle adopt the C_2-symmetric geometries indicated by their ^{1}H NMR spectra with their two chlorine ligands either in *trans*- or in *cis*-configuration. In order to ascertain, whether these complexes have the same *cis*-halide geometry as found for **8** and **11**, we have characterized these complexes also by their far-infrared vibrational spectra.

For a C_{2v}-symmetric complex of the type [*cis*-N_4FeCl_2], four Fe–N and two Fe–Cl vibrations are expected to be IR-active. For [*trans*-N_4FeCl_2] with approximate D_{4h} symmetry, however, only one Fe–N and one Fe–Cl vibration would be IR-active, if no distinction is made between imine and pyridine N atoms.[12] In the IR spectra of solid **8**, **9**, and **11**

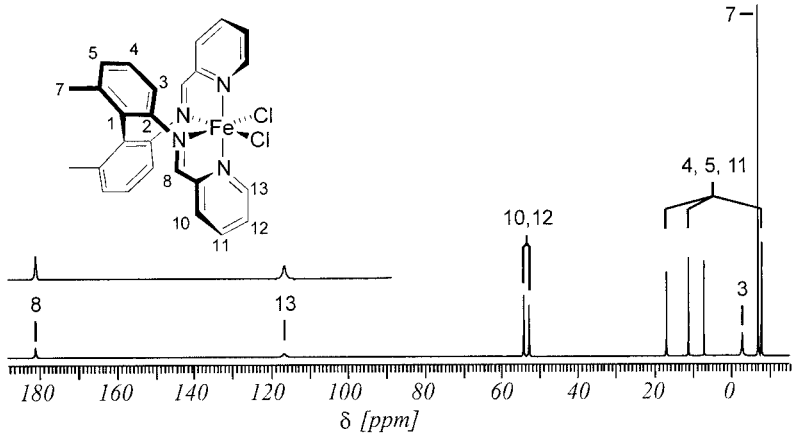

Figure 2. ^{1}H NMR spectrum of the paramagnetic complex **8** in $CDCl_3$ solution at 25 °C (600 MHz; numbering as in the crystal structure represented in Figure 1)

Table 2. Assignment of ^{1}H NMR resonances of complex **8**[a]

	d(H-Fe)/Å[b]	$d^{-6}\cdot10^5\cdot$Å^6	$\nu_{½,calcd}$/Hz[c]	$\nu_{½,exp}$ /Hz	δ/ppm[d]
13-H	3.250	84,86	703	520	116.2
3-H	3.977	25.27	210	149	–2.6
8-H	4.110	20.75	172	172[e]	180.7
10-H	5.218	4.95	41	} 66/57	52.8/54.20
12-H	5.311	4.46	37		
4-H	5.918	2.33	19		
11-H	6.074	1.99	17	} 42/36/30	17.1/11.4/–7.6
5-H	6.678	1.13	9		
7-CH_3	6.665	1.14	9	29[e]	–6.7

[a] Numbering corresponding to that used for the crystal structure in Figure 1. [b] Taken from the crystal structure of **8**. [c] Calculated relative to 8-H. [d] For temperature dependence of these paramagnetic shift values see Supporting Information. [e] Assigned independently (see text).

 © 2005 Wiley-VCH Verlag GmbH & Co. KGaA, Weinheim

(Table 3) four medium to strong vibrations are observed between ca. 180 and 350 cm^{-1}.[13] We assign these bands, which are absent in the IR spectrum of the free ligand **2**, to metal–N vibrations.

Table 3. Far-infrared absorption bands of ligand **2** and of complexes **8**, **9**, and **11** (positions in cm^{-1})

2	**8**	**9**	**11**	Assignment
590 (s)	590 (w)	588 (m)	591 (m)	ligand
549 (m)	555 (m)	557 (s)	558 (m)	ligand
520 (m)	536 (w)	535 (w)	496 (m)	ligand
	515 (m)	522 (w)		
		512 (w)		
475 (s)	474 (m)	479 (s)	484 (s)	ligand
440 (w)	437 (w)	423 (w)	430 (m)	ligand
404 (s)	416 (s)	414 (m)		ligand
368 (m)	386 (w)	371 (w)	379 (w)	ligand
	337 (m)	339 (m)	341 (m)	M–N
316 (m)		318 (w)		ligand
	300 (s)	297 (s)	308 (s)	M–N
260 (m)	271 (w)	269 (m)	270 (m)	ligand
240 (m)	244 (vs)	241 (m)	242 (s)	ligand, M–Cl in **8** and **11**
	c. f. [13]	223 (s)	225 (m)	M–N
	192 (m)	191 (s)	181 (m)	M–N
		174 (s)		Fe–Br
	144 (s)		135 (s)	M–Cl
		104 (s)		Fe–Br

Two further strong peaks are observed at 244 and 144 cm^{-1} for complex **8** and at 174 and 104 cm^{-1} for its dibromo homologue **9**. The 1.4:1 ratio of these wavenumbers, which is close to the theoretical value of 1.5 estimated from the ratio of reduced masses of Fe–Cl and Fe–Br, supports the assignment of these bands to the symmetric and asymmetric stretching modes of a *cis*-FeX_2 unit. The Co–Cl vibrations of **11** were found at 242 and 135 cm^{-1}, as expected only slightly below those of **8**. Analogous assignments hold for **7** and **10**. Complexes **7**–**11** thus all contain *cis*-coordinated halogen ligands in the solid state.

While the chiral, C_2-symmetric complexes **7**–**11** have the *cis*-positioned homotopic sites required for enantioselective olefin insertion, substituents bigger than hydrogen would be desirable in the 6-positions of the pyridine rings, so as to transfer the axial chirality of the biphenyl backbone most effectively to the coordination sites of the complex (Figure 3).

In order to obtain a homologue of complex **8** with methyl substituents in both pyridyl 6-positions, $FeCl_2$ was reacted with ligand **3**. Reactions in THF yielded **12**·THF as a brown solid. The same product, without THF, was obtained from reactions in CH_2Cl_2. In contrast to complexes **7**–**11**, complex **12** gives a ^1H NMR spectrum with only three broad signals centered at δ = 3.45, –4.91, and –11.39. Only two strong and one medium vibration at 367, 319, and 268 cm^{-1}, respectively, are apparent in its far-infrared spectrum, again in contrast to complexes **7**–**11**, where four M–N and two M–X vibrations have been observed. The C_2-symmetric geometry found for these complexes is thus unlikely to be adopted by complex **12**.

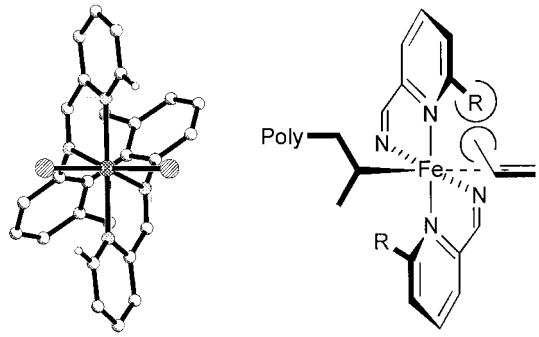

Figure 3. Front view of complex **8** (left) and of a putative Fe-polymeryl π complex (right) with propene coordinated by its disfavored enantioface (biphenyl bridge omitted for clarity)

The only useful structural clue is derived from SQUID measurements, which yielded for complex **12** an effective magnetic moment of μ_{eff} = 3.41 μ_B, indicative of 2–3 unpaired electrons, i.e. of a configuration with partly paired electron spins. The ligand field separation ΔE = 10 *Dq* of the octahedral complexes **7**–**11** is clearly insufficient to induce any spin pairing, and the same holds, a fortiori, for tetrahedral or trigonal bipyramidal geometries (Figure 4). The only plausible coordination geometry, which would be in agreement with the partial spin pairing observed for **12**, is that of a square pyramidal complex, e. g. of a species [(**3**)FeCl]$^+$Cl$^-$, in which one of the chloride ligands has been eliminated from the metal center due to steric repulsions by the methyl-substituted pyridyl ligands. To reach a square pyramidal geometry, at least three of the four N ligand atoms must be positioned in the square base plane of the complex (Scheme 2). Rearrangements between alternative connectivities, which are likely to occur quite rapidly, as well as chloride dissociation and re-association equilibria would plausibly explain the observed broadening of the NMR signals of **12**.[14]

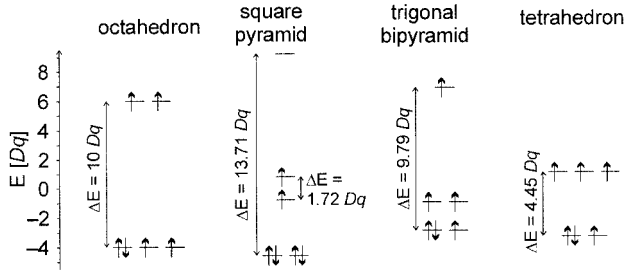

Figure 4. Effects of different complex geometries with moderately strong ligand field on d^6 electron configurations (values taken from ref.[15])

In order to obtain also bona-fide low-spin complexes with the bianiline-bridged ligand framework under consideration, complex **8** was reacted with methylmagnesium chloride [Equation (3)]. The diamagnetic dimethyl complex **13** was obtained from this reaction as a brown powder.[16] Its ^1H NMR spectrum revealed a C_1-symmetric geometry in solution. The same geometry was also found for its counterpart with isocyanide instead of methyl ligands. This sec-

 © 2005 Wiley-VCH Verlag GmbH & Co. KGaA, Weinheim

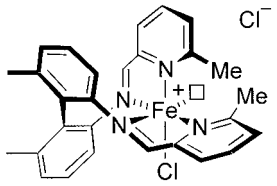

12

Scheme 2. Structure proposed for complex **12**

ond low-spin derivative, the orange-red complex **14** was obtained by reaction of complex **8** with two equivalents each of AgOTf and *tert*-butyl isocyanide [Equation (3)].[17] The ^{1}H NMR spectrum of **14** (see Exp. Sect.) confirmed the coordination of two isocyanide ligands, and indicated, again, a C_1-symmetric geometry.

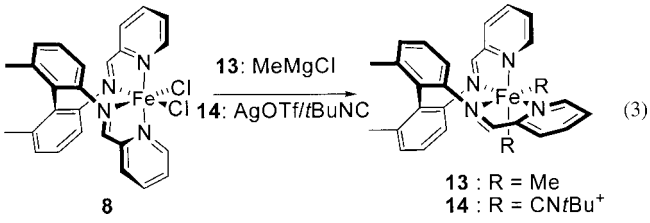

(3)

This structural assignment is supported by the results of an X-ray diffraction study (Figure 5, Table 4): In the cationic diisocyanide complex **14**, three of the four N ligand atoms reside in one meridional plane; in the second meridional plane, one of the pyridyl moieties and the two *tert*-butyl isocyanide ligands are coordinated to the iron center.[18]

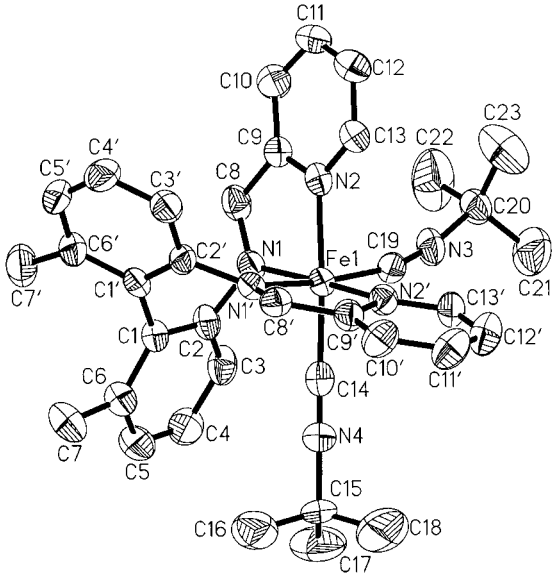

Figure 5. Crystal structure of the complex cation **14**; hydrogen atoms, triflate anions and co-crystallized solvent omitted for clarity, thermal ellipsoids drawn at the 50% probability level

The overall C_1 symmetry of this complex appears to be stabilized by one or more of the following factors: Close

Table 4. Selected bond lengths [Å] and angles [°] for complex **14**

Fe–N1 (imine)	1.940(5)	N1′–Fe–N2	89.7(2)
Fe–N1′ (imine)[a]	2.001(4)	N1′–Fe–N2′	81.5(2)
Fe–N2 (pyridine)	2.014(4)	N1′–Fe–C14	90.1(2)
Fe–N2′ (pyridine)[a]	2.002(5)	N1′–Fe–C19	172.8(2)
Fe–C14	1.904(6)	N2–Fe–N2′	99.8(2)
Fe–C19	1.884(6)	N2–Fe–C14	176.0(2)
		N2–Fe–C19	84.1(2)
N1–Fe–N1A	90.0(2)	N2′–Fe–C14	84.1(2)
N1–Fe–N2	80.4(2)	N2′–Fe–C19	96.0(2)
N1– Fe–N2A	171.4(2)	C14–Fe–C19	96.4(2)
N1–Fe–C14	95.7(2)	C14–N4–C15	175.4(7)
N1–Fe–C19	92.5(2)	C19–N3–C20	167.8(5)

adherence to idealized octahedral geometry and a shortening of the Fe–N bonds, which is presumably required by the low-spin configuration of **14**, is more easily adopted by a C_1- than by a C_2-symmetric geometry, as indicated by the ligand–metal–ligand bite angles in **14** (Table 4), which are much closer to 90° than those of the C_2-symmetric complex **8** (Table 1). In addition, the pyridyl ligands are likely to prefer a *cis* over a *trans* arrangement in order to utilize different d orbitals for backdonation. A possible preference of isocyanide ligands to coordinate *trans* to pyridine, finally, can be satisfied, for at least one of the isocyanide ligands, only in the C_1-symmetric geometry shown in Figure 5.[19]

Polymerization Experiments

Reaction conditions suitable for catalytic polymerization of ethene were sought in particular using complex **8** as precatalyst. When very finely dispersed suspensions of 10–20 mg (ca. 20–40 μmol) of turquoise **8** in 120 mL of toluene, prepared by extended exposure to an ultrasound bath, were reacted with a toluene solution of methylalumoxane (MAO) in a glass-walled reactor, with [Al]/[Fe] ratios varying between 30:1 and 1000:1, dark green solutions were obtained. Exposure of such a solution to 2–4 bar of ethene or propene yielded only miniscule flakes of polymer (if any), which escaped any isolation attempts. Neither particularly careful exclusion of air and moisture from the reaction mixture nor its deliberate exposure to the atmosphere or even addition of oxidizing reagents, such as $[NO][BF_4]$ or Meerwein salt, which are capable of oxidizing Fe^{II} complexes,[20] gave any more positive results, nor was this the case when the Fe^{III} complex $[\mathbf{8}]^+Cl^-$ was separately synthesized (see Exp. Sect.) and tested with regard to its catalytic activity after reaction with MAO or with trityl perfluorotetraphenyl borate and $(i\text{Bu})_3\text{Al}$.[21]

Remarkably, however, significant amounts of polymer were obtained, when 20–50 mg (ca. 40–100 μmol) of solid complex **8** in toluene were activated, *without* being finely dispersed by ultrasound treatment, by addition of a toluene solution of MAO, at [Al]/[Fe] ratios of ca. 55–85:1. When the black viscous tar, obtained from this activating procedure, was introduced into a stainless-steel reactor and then immediately exposed to 30 bar of ethene at reaction temperatures of 0–40 °C, yields of 40–160 mg polyethene

 © 2005 Wiley-VCH Verlag GmbH & Co. KGaA, Weinheim

were reproducibly isolated after a reaction time of 4 hours,[22] corresponding to productivities of ca. 160–1000 g polymer/(mol Fe≅h) (Table 5). In analogous experiments with complexes **10** and **12**, no polymer was obtained although these experiments followed a protocol which had proven successful for complex **8**.

Table 5.Conditions and results of olefin polymerization reactions[a]

Run	Catalyst [μmol]	MAO [Al]:[Fe]	T_p [°C]	Monomer [bar]	Ultra-sound treatment	Polymer yield
1	**8**, 38.7	30:1	20	ethene, 4	yes	traces
2	**8**, 29.8	100:1	30	ethene, 2	yes	60 mg
3	**8**, 27.5	300:1	40	ethene, 4	yes	traces
4	**8**, 18.4	1000:1	40	ethene, 2	yes	traces
5	**8**, 34.0	70:1	30	propene, 2	yes	0
6	**8**, 26.3	T-FPB[b]	30	propene, 2	yes	0
7	**8**, 94.7	100:1	25	ethene, 30	yes	traces
8	**8**, 73.5	70:1	40	ethene, 30	yes	0
9	**8**, 40.8	85:1	25	ethene, 30	no	160 mg
10	**8**, 69.4	73:1	10	ethene, 30	no	60 mg
11	**8**, 47.4	55:1	0	ethene, 30	no	100 mg
12	**10**, 50.1	100:1	25	ethene, 30	no	0
13	**12**, 42.2	120:1	25	ethene, 30	no	0

[a] Reaction conditions: 120 mL of toluene; reaction time, 4 hours; 1–5 min. pre-incubation with cocatalyst. [b] Trityl (perfluorotetraphenyl)borate (1 equiv.) and triisobutylaluminum (0.5 mL).

Conclusions

The results described above indicate that complex **8** undergoes some transformation upon exposure to MAO; this does not lead to an active species, capable of inducing catalytic olefin polymerization, however, when the reaction is conducted in homogeneous solution. While no direct clues indicate the nature of the green species formed under these conditions, we can surmise, in analogy to results obtained with related reaction systems,[23] that metal alkyl cations of the type N_4FeMe^+, most likely stabilized by uptake of a MAO-derived $AlMe_3$ unit, dominate in these solutions and would thus be responsible for the strongly red-shifted UV/Vis absorption of these reaction systems. If indeed present in these solutions, these species are obviously not capable of inducing chain growth by olefin insertion. Their 16-valence electron configuration is apparently not sufficiently electron-deficient to coordinate and insert an olefin substrate, in distinction to related 14-electron cations of the type N_3FeMe^+, which are considered to be catalytically active in MAO-activated Fe^{II} pyridyldiimine systems.[23]

The reaction of MAO with solid particles of complex **8**, on the other hand, seems to favour some other reaction paths, most likely some intermolecular ligand exchange reaction. Formation of the viscous, tarry product is likely to arise from a transfer of some of the N ligand atoms, e. g. of a pyridyl moiety, from one complex molecule to another, such that the resulting oligomeric or polymeric complex species now contains metal centers, which are coordinated to less than four N ligand atoms. More likely than not, such a reaction would lead to a collection of different coordination patterns each with its own catalytic property, rather than to a unique complex geometry.

In accord with this assumption, a gel-permeation chromatography (GPC) analysis of the polyethene samples obtained from runs 10–12 reveals in all cases a molecular mass distribution with three distinct fractions (see Supporting Information) with M_n values of 130–180 ($M_w/M_n \approx 1.25$), ca. 3600–7000 ($M_w/M_n \approx 1.7$) and ca. 160000–320000 ($M_w/M_n \approx 6.2–7.1$), respectively. Clearly, several catalytic species contribute to chain growth in these reaction systems. The component with highest M_n is remarkably similar, in its mean chain length as well as in its rather broad molar mass distribution, to polyethene samples obtained with typical MAO-activated iron pyridyldiimine complexes,[1c,2d] in agreement with the assumption that some related catalyst species with reduced coordination number might be generated from complex **8** by the heterogeneous activation procedure described above. The observations presented here, in particular the lack of reactivity of any of our reaction systems vis-à-vis propene,[21] let the probability of observing catalytic-site-controlled, stereoselective olefin polymerization by precatalyst structures of the type investigated in this report, appear rather remote.

Experimental Section

All preparations were performed under an argon atmosphere using standard Schlenk techniques. Solvents were dried prior to use by refluxing over and distillation from sodium (THF, hydrocarbons) or calcium hydride (dichloromethane). Deuterated solvents were dried over 4-Å molecular sieves. All other chemicals were commercially obtained and used without further purification. Melting points were determined with a Sanyo–Gallenkamp MFB-600–010F thermometer, magnetic susceptibilities with a Quantum Design Superconducting Quantum Interference Device (SQUID) MPMS-XL5. NMR spectra were collected on Bruker AC 250 FT NMR or Bruker Avance DRX 600 spectrometers, IR spectra measured with a Perkin–Elmer 2000 FT-IR spectrometer, either as KBr or polyethene (PE) pellets, UV spectra of 1.0 mM solutions in a 1-cm cuvette with a Varian–Cary 50 and mass spectra with Finnigan MAT 312 (EI) or Finnigan AMD MAT 312/AMD 5000 (FAB) mass spectrometers. Elemental compositions were analyzed with an Elementar Vario EL device. Ligands **2** and **3** were prepared as described earlier.[24]

***N,N′*-(Biphenyl-2,2′-diyl)bis(2-pyridylmethyl)diimine (1):** A solution of **4** (361 mg, 1.96 mmol) in ethanol (10 mL) was stirred for 1 h with pyridine-2-carbaldehyde (373 μL, 420 mg, 3.92 mmol). After evaporation of solvent, **1** was obtained as a solid residue in almost quantitative yield. ^{1}H NMR (250 MHz, $CDCl_3$, ppm): δ = 7.11 [d, ^3J (H-H) = 7.9 Hz, 2 H; Ar-H], 7.23–7.48 (m, 8 H, Ar-H), 7.66 [t, ^3J (H-H) = 7.3 Hz, 2 H; Ar-H], 7.79 [d, ^3J (H-H) = 7.9 Hz, 2 H; Ar-H], 8.34 (s, 2 H, N=CH), 8.49 [d, ^3J (H-H) = 4.3 Hz, 2 H; 6′′-H]. Since **1** was not obtainable in powdered form, the solid residue was dissolved in THF and used for further reactions.

***N,N′*-(6,6′-Dimethylbiphenyl-2,2′-diyl)bis[1-(2-pyridyl)ethyl]diimine (6):** To a solution of **5** (4.45 g, 21.0 mmol) in toluene (100 mL) was added 2-acetylpyridine (4.70 mL, 5.08 g, 41.9 mmol) and *para*-toluenesulfonic acid hydrate (797 mg, 4.19 mmol). After refluxing the reaction mixture in a Dean–Stark aparatus for 3 days, the solvent

was evaporated. The residue was suspended in 200 mL of diethyl ether, freed from solids by filtration and the solids washed with diethyl ether. The combined ether fractions were extracted with diluted sodium hydroxide solution (200 mL) and subsequently dried with $MgSO_4$. After evaporation of solvent, a brown crude product was obtained (6.97 g), which contained, according to its ^1H NMR, 24% toluene, 6% **5**, 12% 2-acetylpyridine, 21% of the mono condensation product, and 37% of **6**. Attempted purification by column chromatography on silica gel lead to decomposition of **6** to the starting materials. Since this crude ligand was suitable for complex formation, no further attempts were undertaken to purify it. Yield (calculated on ^1H NMR basis) 2.58 g (6.16 mmol, 29%). ^1H NMR (250 MHz, $CDCl_3$, ppm): δ = 2.14 (s, 6 H, 6-CH_3/6′-CH_3), 2.28 (s, 6 H, N=C–CH_3), 6.57 [d, ^3J (H-H) = 7.9 Hz, 2 H; 3-H/3′-H], 7.03 [d, ^3J (H-H) = 7.3 Hz, 2 H; 5-H/5′-H], 7.15–7.30 (m, 4 H, 4-H/4′-H, 5′′-H), 7.56–7.67 (m, 4 H, 3′′-H, 4′′-H), 8.55 [d, ^3J (H-H) = 4.9 Hz, 2 H; 6′′-H].

General Procedure for the Synthesis of Dihalogeno Metal(II) Complexes 7–11: To a stirred suspension of the metal halide in THF (10 mL/mmol), a solution of 1.02 equiv. of the ligand in THF (10 mL/mmol) was slowly added. After stirring overnight, the solvent was evaporated and the residue extracted four times with CH_2Cl_2 (4 × 20 mL/mmol). The combined extracts were evaporated to dryness and the remaining solids suspended in diethyl ether (15 mL/mmol). The complex was collected by filtration, washed with diethyl ether (3 × 5 mL/mmol), once with pentane (5 mL/mmol), and finally dried in vacuo.

Dichloro[*N*,*N*′-(biphenyl-2,2′-diyl)bis(2-pyridylmethyl)diimine]-iron(II)·0.5 CH_2Cl_2 (7·0.5 CH_2Cl_2): A solution of **1**, obtained from **4** (361 mg, 1.96 mmol) and pyridine-2-carbaldehyde (373 µL, 420 mg, 3.92 mmol), in THF (20 mL) was reacted, following the general procedure, with $FeCl_2$ (246 mg, 1.94 mmol) to yield blue **7**·0.5 CH_2Cl_2 (858 mg, 1.61 mmol, 83%). ^1H NMR (600 MHz, $CDCl_3$, ppm): δ = –8.29 (s, $\Delta\nu_{1/2}$ = 72.3 Hz, 2 H; 4-H/4′-H or 5-H/5′-H or 4′′-H), –4.20 (s, $\Delta\nu_{1/2}$ = 179 Hz, 2 H; 3-H/3′-H), 5.34 (s, $\Delta\nu_{1/2}$ = 61.5 Hz, 1 H; CH_2Cl_2), 6.42 (s, $\Delta\nu_{1/2}$ = 78.8 Hz, 2 H; 6-H/6′-H), 11.07 (s, $\Delta\nu_{1/2}$ = 76.9 Hz, 2 H; 4-H/4′-H or 5-H/5′-H or 4′′-H), 17.61 (s, $\Delta\nu_{1/2}$ = 94.9 Hz, 2 H; 4-H/4′-H or 5-H/5′-H or 4′′-H), 55.12 (s, $\Delta\nu_{1/2}$ = 119 Hz, 2 H; 3′′-H or 5′′-H), 56.01 (s, $\Delta\nu_{1/2}$ = 113 Hz, 2 H; 3′′-H or 5′′-H), 116.53 (s, $\Delta\nu_{1/2}$ = 575 Hz; 2 H), 180.40 (s, $\Delta\nu_{1/2}$ = 230 Hz, 2 H; N=CH). ^{13}C NMR (151 MHz, $CDCl_3$, ppm): δ = 14.59, 71.37 (C-6/C-6′), 160.91 (C-4/C-4′ or C-5/C-5′ or C-4′′), 193.84, 193.95, 198.96, 218.13 (C-4/C-4′ or C-5/C-5′ or C-4′′), 244.74, 421.96 (C-3′′ or C-5′′), 544.79 (C-3′′ or C-5′′), other expected ^{13}C signals were not observable due to the low solubility and the low intensity of the broad ^{13}C signals. IR (KBr, cm^{-1}): $\tilde{\nu}$ = 3054, 3045, 3019 (m, m, w, Ar-H), 2978, 2964 (m, w, C–H), 1632, 1593, 1564 (s, s, m, C=N, C=C), 1471 (m, C–H_{def}), 1304 (m), 1011 (m). IR (PE, cm^{-1}): $\tilde{\nu}$ = 560 (m), 542 (m), 503 (m), 495 (m), 451 (m), 419 (m), 397 (w), 328 (w, Fe–N), 295 (m, Fe–N_{imine}), 251 (vs, Fe–Cl), 214 (w), 202 (w), 146 (m, Fe–Cl). Further $\tilde{\nu}$(Fe–N) bands could not be identified. UV/Vis (CH_2Cl_2): λ_{max} (ε) = 653 (1290). $C_{24.5}H_{19}Cl_3FeN_4$ (531.65): calcd. C 55.35, H 3.60, N 10.54; found C 55.24, H 3.75, N 10.58 (%).

Dichloro[*N*,*N*′-(6,6′-dimethylbiphenyl-2,2′-diyl)bis(2-pyridylmethyl)-diimine]iron(II) (8): Following the general procedure, **2** (2.10 g, 5.38 mmol) and $FeCl_2$ (668 mg, 5.27 mmol) yielded turquoise **8** (2.54 g, 4.91 mmol, 93%). SQUID: μ_{eff} = 5.47 μ_B. ^1H NMR (600 MHz, $CDCl_3$, ppm): δ = –7.62(s, $\Delta\nu_{1/2}$ = 30.3 Hz, 2 H; 4-H/4′-H or 5-H/5′-H or 4′′-H), –6.72 (s, $\Delta\nu_{1/2}$ = 28.7 Hz, 6 H; CH_3), –2.65 (s, $\Delta\nu_{1/2}$ = 149 Hz, 2 H; 3-H/3′-H), 11.35 (s, $\Delta\nu_{1/2}$ = 36.3 Hz, 2 H; 4-H/4′-H or 5-H/5′-H or 4′′-H), 17.08 (s, $\Delta\nu_{1/2}$ = 42.1 Hz, 2 H; 4-H/4′-H or 5-H/5′-H or 4′′-H), 52.77 (s, $\Delta\nu_{1/2}$ = 66.4 Hz, 2 H; 3′′-H or 5′′-H), 54.20 (s, $\Delta\nu_{1/2}$ = 56.6 Hz, 2 H; 3′′-H or 5′′-H), 116.21 (s, $\Delta\nu_{1/2}$ = 520 Hz, 2 H; 6′′-H), 180.74 (s, $\Delta\nu_{1/2}$ = 172 Hz, 2 H; N=CH). ^{13}C NMR (151 MHz, $CDCl_3$, ppm): δ = –181.44, 0.41, 39.30 (CH_3), 71.79 (C-4/C-4′ or C-5/C-5′ or C-4′′), 80.22, 157.30 (C-4/C-4′ or C-5/C-5′ or C-4′′), 194.91 (C-4/C-4′ or C-5/C-5′ or C-4′′), 195.76, 199.13, 232.31, 418.95, 533.17, 908.63 (C=N). IR (KBr, cm^{-1}): $\tilde{\nu}$ = 3065, 3012 (w, w, Ar–H), 2962, 2916, 2850 (w, w, w, C–H), 1627, 1594, 1563 (m, s, m, C=N, C=C), 1475, 1450 (m, m, C–H_{def}), 1012 (m). IR (PE, cm^{-1}): $\tilde{\nu}$ = 590 (w), 555 (m), 536 (w), 515 (m), 488 (m), 474 (m), 437 (w), 416 (s), 386 (w), 337 (m, Fe–N), 300 (s, Fe–N_{imine}), 271 (w), 244 (vs, Fe–Cl), 192 (m, Fe–N), 144 (s, Fe–Cl), one $\tilde{\nu}$(Fe–N) was probably hidden by $\tilde{\nu}$ = 244 cm^{-1}. UV/Vis (CH_2Cl_2): λ_{max} (ε) = 641 (1140). MS (FAB): *m*/*z* (%): 516/518/520 (11/8/2) [M^+], 481/483 (100/43) [M^+ – Cl], 446 (22) [481/483 – Cl]; for $C_{26}H_{22}Cl_2FeN_4$ (517.24). calcd. C 60.38, H 4.29, N 10.83; found C 60.37, H 4.38, N 10.95 (%).

Dibromo[*N*,*N*′-(6,6′-dimethylbiphenyl-2,2′-diyl)bis(2-pyridylmethyl)-diimine]iron(II) (9): Following the general procedure, **2** (506 mg, 1.30 mmol) and $FeBr_2$ (274 mg, 1.27 mmol) yielded blue **9** (398 mg, 657 µmol, 52%). ^1H NMR (600 MHz, $CDCl_3$, ppm): δ = –9.14 (s, $\Delta\nu_{1/2}$ = 16.4 Hz, 2 H; 4-H/4′-H or 5-H/5′-H or 4′′-H), –7.09 (s, $\Delta\nu_{1/2}$ = 20.1 Hz, 6 H; CH_3), –6.55 (s, $\Delta\nu_{1/2}$ = 110 Hz, 2 H; 3-H/3′-H), 11.15 (s, $\Delta\nu_{1/2}$ = 20.9 Hz, 2 H; 4-H/4′-H or 5-H/5′-H or 4′′-H), 17.43 (s, $\Delta\nu_{1/2}$ = 22.0 Hz, 2 H; 4-H/4′-H or 5-H/5′-H or 4′′-H), 53.48 (s, $\Delta\nu_{1/2}$ = 37.3 Hz, 2 H; 3′′-H or 5′′-H), 57.97 (s, $\Delta\nu_{1/2}$ = 34.2 Hz, 2 H; 3′′-H or 5′′-H), 119.70 (s, $\Delta\nu_{1/2}$ = 425 Hz, 2 H; 6′′-H), 191.20 (s, $\Delta\nu_{1/2}$ = 128 Hz, 2 H; N=CH); due to the very low solubility no signals were observed in the ^{13}C NMR spectrum. IR (KBr, cm^{-1}): $\tilde{\nu}$ = 3089, 3057, 3015 (w, m, m, Ar-H), 1636, 1598, 1564 (m, m, m, m, m, C=N, C=C), 1476, 1448 (m, m, C–H_{def}), 1306 (m), 1217 (m), 1013 (m). IR (PE_{THF}, cm^{-1}): $\tilde{\nu}$ = 588 (m), 557 (s), 535 (w), 522 (w), 512 (w), 479 (s), 423 (w), 414 (m), 371 (w), 339 (m, Fe–N), 318 (w), 297 (s, Fe–N_{imine}), 269 (m), 241 (m), 223, 191 (s, s, Fe–N), 174 (s, Fe–Br), 104 (s, Fe–Br). UV/Vis (CH_2Cl_2): λ_{max} (ε) = 630 (1000). $C_{26}H_{22}Br_2FeN_4$ (606.14): calcd. C 51.52, H 3.66, N 9.24; found C 52.07, H 3.63, N 9.19 (%).

Dichloro{*N*,*N*′-(6,6′-dimethylbiphenyl-2,2′-diyl)bis[1-(2-pyridyl)-ethane]diimine}iron(II) (10): Following the general procedure, crude **6** (1.59 g, 1.41 mmol, based on ^1H NMR) and $FeCl_2$ (157 mg, 1.24 mmol) yielded blue **10** (608 mg, 1.12 mmol, 90%). ^1H NMR (600 MHz, $CDCl_3$, ppm): δ = –10.43 (s, $\Delta\nu_{1/2}$ = 16.8 Hz (2 signals), 4 H; 3-H/3′-H and 4-H/4′-H or 5-H/5′-H or 4′′-H), –7.45 (s, $\Delta\nu_{1/2}$ = 12.6 Hz, 6 H; 6-CH_3/6′-CH_3), 0.07 (s, $\Delta\nu_{1/2}$ = 43.1 Hz, 6 H; N=C-CH_3), 10.13 (s, $\Delta\nu_{1/2}$ = 21.4 Hz, 2 H; 4-H/4′-H or 5-H/5′-H or 4′′-H), 17.19 (s, $\Delta\nu_{1/2}$ = 22.9 Hz, 2 H; 4-H/4′-H or 5-H/5′-H or 4′′-H), 52.32 (s, $\Delta\nu_{1/2}$ = 38.0 Hz, 2 H; 3′′-H or 5′′-H), 71.49 (s, $\Delta\nu_{1/2}$ = 48.0 Hz, 2 H; 3′′-H or 5′′-H), 112.82 (s, $\Delta\nu_{1/2}$ = 552 Hz, 2 H; 6′′-H). ^{13}C NMR (151 MHz, $CDCl_3$, ppm): δ = –344.57 (N=C-*C*H_3), –169.06, –10.31, 30.66, 58.11, 66.02 (C-3′′ or C-5′′), 163.12, 185.37, 194.82, 198.83 (C-4/C-4′ or C-5/C-5′ or C-4′′), 207.07, 347.97, 449.81, 522.34. IR (KBr, cm^{-1}): $\tilde{\nu}$ = 3091, 3057, 3021 (m, m, m, Ar–H), 2985, 2965, 2946, 2921, 2860 (w, w, w, m, w, C–H), 1629, 1593, 1565 (m, m, m, C=N, C=C), 1436 (m, C–H_{def}), 1366 (m), 1318 (m), 1258 (m), 1009 (m). IR (PE, cm^{-1}): $\tilde{\nu}$ = 595 (w), 590 (m), 575 (m), 569 (m), 559 (m), 537 (m), 420 (m), 372 (w), 345 (m, Fe–N), 245, 235 (s, s, Fe–N, Fe–Cl), 192 (w), 179 (m, Fe–N), 150 (w), 141 (m, Fe–Cl), one (Fe–N) signal was probably hidden by peaks at $\tilde{\nu}$ = 245 and 235 cm^{-1}. UV/Vis (CH_2Cl_2): λ_{max} (ε) = 625 (1430). $C_{28}H_{26}Cl_2FeN_4$ (545.29): calcd. C 61.67, H 4.81, N 10.27; found C 61.78, H 4.95, N 10.23 (%).

Dichloro[*N*,*N*′-(6,6′-dimethylbiphenyl-2,2′-diyl)bis(2-pyridylmethyl)-diimine]cobalt(II) (11): Following the general procedure, **2** (512 mg,

 © 2005 Wiley-VCH Verlag GmbH & Co. KGaA, Weinheim

1.31 mmol) and $CoCl_2$ (167 mg, 1.29 mmol) yielded light brown **11** (542 mg, 1.04 mmol, 81%). SQUID: μ_{eff} = 4.96 μ_B. ^{1}H NMR (600 MHz, $CDCl_3$, ppm): δ = –16.17 (s, $\Delta\nu_{1/2}$ = 137 Hz, 2 H; 3-H/3′-H), –10.57 (s, $\Delta\nu_{1/2}$ = 14.1 Hz, 2 H; 4-H/4′-H or 5-H/5′-H or 4′′-H), –2.17 (s, $\Delta\nu_{1/2}$ = 11.5 Hz, 6 H; CH_3), 6.46 (s, $\Delta\nu_{1/2}$ = 18.7 Hz, 2 H; 4-H/4′-H or 5-H/5′-H or 4′′-H), 12.94 (s, $\Delta\nu_{1/2}$ = 22.8 Hz, 2 H; 4-H/4′-H or 5-H/5′-H or 4′′-H), 38.15 (s, $\Delta\nu_{1/2}$ = 39.8 Hz, 2 H; 3′′-H or 5′′-H), 54.23 (s, $\Delta\nu_{1/2}$ = 54.2 Hz, 2 H; 3′′-H or 5′′-H), 70.38 (s, $\Delta\nu_{1/2}$ = 472 Hz, 2 H; 6′′-H), 230.67 (s, $\Delta\nu_{1/2}$ = 215 Hz, 2 H; N=CH). ^{13}C NMR (151 MHz, $CDCl_3$, ppm): δ = 15.75, 51.37 (C-4/C-4′ or C-5/C-5′ or C-4′′), 53.44 (CH_3), 73.51, 130.72 (C-4/C-4′ or C-5/C-5′ or C-4′′), 219.72 (C-4/C-4′ or C-5/C-5′ or C-4′′), 225.22, 258.22, 296.55, 411.81, other expected ^{13}C signals were not detectable due to the low solubility and the low intensity of the broad ^{13}C signals. IR (KBr, cm^{-1}): $\tilde{\nu}$ = 3093, 3061 , 3042, 3013 (w, m, w, m, Ar–H), 1639, 1598, 1568 (s, s, m, C=N, C=C), 1479, 1448 (m, s, C–H_{def}), 1307 (s), 1219 (s), 1014 (s). IR (PE, cm^{-1}): $\tilde{\nu}$ = 591 (m), 558 (m), 496 (m), 484 (s), 430 (m), 379 (w), 341, 308 (m, s, Co–N), 270 (m), 242 (s, Co–Cl), 225, 181 (m, m, Co–N), 135 (s, Co–Cl). UV/Vis (CH_2Cl_2): no maxima observed. $C_{26}H_{22}Cl_2CoN_4$ (520.33): calcd. C 60.02, H 4.26, N 10.77; found C 59.32, H 4.47, N 10.64 (%).

Dichloro{*N*,*N*′-(6,6′-dimethylbiphenyl-2,2′-diyl)bis[(6-methyl-2-pyridyl)methyl]diimine}iron(II)·THF (12·THF): According to the general procedure for complexes **7**–**11**, ligand **3** (1.04 g, 2.48 mmol) and $FeCl_2$ (308 mg, 2.43 mmol) yielded brown **15**·THF (891 mg, 1.44 mmol, 59%). ^{1}H NMR (250 MHz, $CDCl_3$, ppm): δ = –11.39 (s, $\Delta\nu_{1/2}$ = 325 Hz), –4.91 (s, $\Delta\nu_{1/2}$ = 75.3 Hz), 3.45 (s, $\Delta\nu_{1/2}$ = 94.2 Hz). MS (FAB): *m*/*z* (%): 509/511 (100/50) [M^+ – THF – Cl], 474 (38) [509/511 – Cl], 406 (77), 371 (71); $C_{32}H_{34}Cl_2FeN_4O$ (617.40): calcd. C 62.25, H 5.55, N 9.07; found: C 62.42, H 5.41, N 8.99 (%).

Dichloro{*N*,*N*′-(6,6′-dimethylbiphenyl-2,2′-diyl)bis[(6-methyl-2-pyridyl)methyl]diimine}iron(II) (12): A solution of ligand **3** (1.01 g, 2.42 mmol) in CH_2Cl_2 (30 mL) was added to a suspension of $FeCl_2$ (301 mg, 2.37 mmol) in CH_2Cl_2 (30 mL). After 2 days, the reaction mixture was filtered, the filtrate evaporated to dryness and the residue suspended in diethyl ether (20 mL). The solid was collected by filtration, washed with diethyl ether (3 × 5 mL) and dried in vacuo. Yield 872 mg (1.60 mmol, 68%) of brown **15**. SQUID (CH_2Cl_2):[a] μ_{eff} = 3.41 μ_B; SQUID (diethyl ether):[a] μ_{eff} = 5.23 μ_B. IR (PE, diethyl ether, cm^{-1}):[a] $\tilde{\nu}$ = 595 (w), 580 (m), 568 (w), 560 (m), 550 (w), 541 (m), 526 (m), 488 (w), 477 (m), 444 (m), 435 (w), 362 (m), 327 (s), 307 (m), 269 (m), 202 (m). IR (PE, CH_2Cl_2, cm^{-1}):[a] $\tilde{\nu}$ = 586 (m), 565 (m), 541 (m), 528 (m), 512 (m), 448 (m), 431 (w), 408 (w), 367 (vs), 319 (vs), 268 (m). $C_{28}H_{26}Cl_2FeN_4$ (545.29): calcd. C 61.67, H 4.81, N 10.27; found C 61.82, H 5.01, N 10.31 (%).[a]

Dimethyl[*N*,*N*′-(6,6′-dimethylbiphenyl-2,2′-diyl)bis(2-pyridylmethyl)diimine]iron(II) (13): Complex **8** (700 mg, 1.35 mmol) was suspended in THF (20 mL) and cooled to –78 °C. At this temperature MeMgCl (451 μL of a 3.0 M solution in THF, 1.35 mmol) was added and the reaction mixture was allowed to warm to room temperature within 3 h. After stirring overnight, solvent was removed by distillation and the residue extracted with toluene (40 mL). Evaporating the solvent yielded complex **13** as a brown powder (289 mg, 607 μmol, 45%). ^{1}H NMR (600 MHz, CD_2Cl_2, ppm): δ = –0.47(s, 3 H, Fe–$CH_{3,ax}$), 1.15 (s, 3 H, Fe–$CH_{3,eq}$), 2.04 (s, 3 H, 6-CH_3), 2.09 (s, 3 H, 6′-CH_3), 6.70 [d, ^3J (H-H) = 7.6 Hz, 1 H; 3′-H], 6.72 [d, ^3J (H-H) = 7.9 Hz, 1 H; 3-H], 6.88 [t, ^3J (H-H) = 6.5 Hz, 1 H; 5′′′-H], 6.99 [t, ^3J (H-H) = 7.6 Hz, 1 H; 4-H], 7.03 [d, ^3J (H-H) = 7.6 Hz, 1 H; 5′-H], 7.05 [d, ^3J (H-H) = 5.6 Hz, 1 H; 6′′′-H], 7.09 [d, ^3J (H-H) = 7.3 Hz, 1 H; 5-H], 7.19 [t, ^3J (H-H) = 7.6 Hz, 1 H; 4′-H], 7.30 [t, ^3J (H-H) = 7.9 Hz, 1 H; 4′′′-H], 7.40 [t, ^3J (H-H) = 6.3 Hz, 1 H; 5′′-H], 7.47 [t, ^3J (H-H) = 7.5 Hz, 1 H; 4′′-H], 7.51 [d, ^3J (H-H) = 7.9 Hz, 1 H; 3′′′-H], 7.70 [d, ^3J (H-H) = 8.2 Hz, 1 H; 3′′-H], 8.63 (s, 1 H, 2′-N=CH), 8.87 [d, ^3J (H-H) = 5.9 Hz, 1 H; 6′′-H], 9.68 (s, 1 H, 2-N=CH). ^{13}C NMR (151 MHz, CD_2Cl_2, ppm): δ = 18.13 (Fe–$CH_{3,ax}$), 19.75 (6′-CH_3), 20.43 (6-CH_3), 22.22 (Fe–$CH_{3,eq}$), 115.18 (C-3′), 115.87 (C-5′′), 118.90 (C-5′′′), 121.84 (C-3), 123.57 (C-3′′), 124.80 (C-3′′′), 126.61 (C-5′), 126.66 (C-5, C-4′), 128.25, 128.27 (C-4, C-4′′), 128.52 (C-1), 129.17 (C-1′), 130.28 (C-4′′′), 137.19 (C-6′), 139.04 (C-6), 148.28 (C-6′′′), 148.54 (2-N=C), 149.90 (2′-N=C), 151.85 (C-6′′), 152.27 (C-2), 154.41 (C-2′), 157.48 (C-2′′′), 157.92 (C-2′′). IR (KBr, cm^{-1}): $\tilde{\nu}$ = 3054, 3008 (m, w, Ar–H), 2963, 2916, 2856 (w, w, m, C–H), 1584, 1567 (s, s, C=N, C=C), 1467, 1441 (s, s, C–H_{def}), 1407 (s), 997 (m), 991 (m). IR (PE, cm^{-1}): $\tilde{\nu}$ = 588 (m), 551 (w), 539 (w), 520 (s), 476 (s), 452 (m), 405 (m). UV/Vis (THF): λ_{max} (ε) = 834 (3200). $C_{28}H_{28}FeN_4$ (476.40): calcd. C 70.59, H 5.92, N 11.76; found C 67.48, H 5.49, N 11.15 (%).

Di(*tert*-butylisocyano)[*N*,*N*′-(6,6′-dimethylbiphenyl-2,2′-diyl)bis-(2-pyridylmethyl)diimine]iron(II)-bis(trifluoromethanesulfonate) (14): To a suspension of **8** (300 mg, 580 μmol) in THF (20 mL) was added *tert*-butylisocyanide (131 μL, 96.4 mg, 1.16 mmol) and a solution of AgOTf (298 mg, 1.16 mmol) in THF (15 mL). A red suspension formed immediately. After stirring overnight the solvent was evaporated and the residue dissolved in CH_2Cl_2 (40 mL). The solution was filtered via cannula and the solvents evaporated to dryness and the solid residue suspended in diethyl ether (20 mL). The solid was collected by filtration and washed with diethyl ether (3 × 5 mL). Yield 407 mg (447 μmol, 77%) orange 14. ^{1}H NMR (600 MHz, $CDCl_3$, ppm): δ = 1.04 [s, 9 H; $C(CH_3)_{3,ax}$], 1.57 [s, 9 H; $C(CH_3)_{3,eq}$], 2.03 (s, 3 H, 6-CH_3), 2.22 (s, 3 H, 6′-CH_3), 6.85 [d, ^3J (H-H) = 7.9 Hz, 1 H; 3-H], 7.05 [d, ^3J (H-H) = 7.9 Hz, 1 H; 3′-H], 7.14 [t, ^3J (H-H) = 7.9 Hz, 1 H; 4-H], 7.34 [d, ^3J (H-H) = 7.9 Hz, 2 H; 5-H, 5′-H], 7.45 [t, ^3J (H-H) = 7.8 Hz, 1 H; 4′-H], 7.58 [t, ^3J (H-H) = 6.2 Hz, 1 H; 5′′′-H], 7.83 [d, ^3J (H-H) = 5.3 Hz, 1 H; 6′′′-H], 7.89 [t, ^3J (H-H) = 6.5 Hz, 1 H; 5′′-H], 7.98 [t, ^3J (H-H) = 7.3 Hz, 1 H; 4′′′-H], 8.15 [t, ^3J (H-H) = 7.3 Hz, 1 H; 4′′-H], 8.23 [d, ^3J (H-H) = 7.6 Hz, 1 H; 3′′′-H], 8.50 (s, 1 H, 2′-N=CH), 8.58 [d, ^3J (H-H) = 7.6 Hz, 1 H; 3′′-H], 8.89 [d, ^3J (H-H) = 5.0 Hz, 1 H; 6′′-H], 9.37 (s, 1 H, 2-N=CH). ^{13}C NMR (151 MHz, $CDCl_3$, ppm): δ = 20.03 (6′-CH_3), 20.29 (6-CH_3), 30.06 [$C(CH_3)_{3,ax}$], 30.54 [$C(CH_3)_{3,eq}$], 58.91, 60.70 [$C(CH_3)_3$], 115.37 (C-3′), 122.56 (C-3), 126.54 (C-1′), 129.03 (C-4′, C-5′′′), 129.58 (C-1), 129.81 (C-3′′′), 129.95 (C-5′′), 130.00 (C-5′), 130.04 (C-4), 131.47 (C-3′′), 132.74 (C-5), 139.18 (C-4′′′), 139.27 (C-4′′), 140.00 (C-6′), 140.26 (C-6), 143.79 (C-2), 151.44 (C-2′), 153.09 (C-6′′′), 156.03 (C-2′′′), 156.19 (C-6′′), 157.01 (C-2′′), 169.08 (2-N=C), 171.86 (2′-N=C), the CF_3 and C≡N signals could not be detected. ^{19}F NMR (376 MHz, $CDCl_3$, ppm): δ = –77.44. IR (KBr, cm^{-1}): $\tilde{\nu}$ = 3075, 3033 (w, w, Ar–H), 2984, 2939, 2879 (m, w, w, C–H), 2184, 2160 (s, s, C≡N), 1619, 1603, 1594, 1569 (m, m, m, m, C=N, C=C), 1477, 1462, 1451 (m, w, m, C–H_{def}), 1276, 1262, 1223, 1149 (s, s, s, s, S=O, C–F), 1031 (s), 636 (s). IR (PE, cm^{-1}): $\tilde{\nu}$ = 571 (s), 550 (m), 516 (s), 464 (m), 445 (m), 394 (m), 348 (m), 320 (m), 293 (m), 270 (m), 227 (w), 209 (m), 188 (w), 177 (w). UV/Vis (CH_2Cl_2): no maxima observed. MS (FAB): *m*/*z* (%): 761 (5) [M^+ – OSO_2CF_3], 595 (100) [761 – 2 $CNC(CH_3)_3$], 529 (10) [761 – OSO_2CF_3 – $CNC(CH_3)_3$], 446 (63) [529 – $CNC(CH_3)_3$]. $C_{38}H_{40}F_6FeN_6O_6S_2$ (910.79): calcd. C 50.11, H 4.43, N 9.23; found C 50.29, H 4.60, N 9.27 (%).

Bis(trifluoromethanesulfonato)[*N*,*N*′-(6,6′-dimethylbiphenyl-2,2′-diyl)bis(2-pyridylmethyl)diimine]iron(II): A solution of AgOTf (289 mg, 1.12 mmol) in THF (15 mL) was added to complex **8** (0.55 mmol) suspended in THF (15 mL). After stirring overnight,

 © 2005 Wiley-VCH Verlag GmbH & Co. KGaA, Weinheim

Table 6. Details of crystal structure determinations

	8	**11**	**14**[a]
Empirical formula	$C_{26}H_{22}Cl_2FeN_4$	$C_{26}H_{22}Cl_2CoN_4$	$[C_{36}H_{40}N_6Fe]\ [CF_3O_3S]_2{\cdot}C_7H_8$
CCDC number[b]	229184	229186	229185
Mw (g/mol); *F*(000)	517.23; 1064	520.31; 1068	1002.77; 1040
Crystal color and form	blue plate	red prism	red prism
Crystal size (mm)	0.5×0.3×0.3	0.5×0.5×0.4	0.4×0.4×0.3
T (K); $d_{calcd.}$ (g/cm^3)	243; 1.380	238; 0.933	243; 1.351
Crystal system	monoclinic	monoclinic	triclinic
Space group	*C*2/*c*	*C*2/*c*	*P*–1
Unit cell: *a* [Å]	14.598(4)	14.396(2)	12.564(7)
b [Å]	10.657(2)	10.6835(15)	13.497(6)
c [Å]	17.304(6)	17.3013(18)	15.876(8)
α [°]	90	90	97.95(3)
β [°]	112.40(3)	111.955(7)	101.67(5)
γ [°]	90	90	106.93(3)
V [Å^3]; *Z*	2488.8(11); 4	2468.0(6); 4	2465.9(22); 2
θ range [°]	2.44–25.00	2.44–26.99	1.34–25.00
Reflections: collected	2375	3262	9284
independent	1874	2700	7860
R_{int}	4.90%	1.67%	6.12%
μ (mm^{-1}); absorption corr.	0.842; ψ-scan	0.933; ψ-scan	0.464; ψ-scan
$R1(F)$; $wR(F^2)$ [$I > 2\sigma(I)$]	5.54%; 12.44%	3.39%; 8.31%	7.19%; 18.57%
$R1(F)$; $wR(F^2)$ (all data)	8.55%; 13.98%	4.30%; 8.79%	11.57%; 23.16%
$GoF(F^2)$	1.086	1.052	1.051
Residual electron density	0.406 e$^-$·Å^{-3}	0.352 e$^-$·Å^{-3}	0.644 e$^-$·Å^{-3}

[a] One disordered triflate anion was refined with geometrical restraints applied; occupation factors were refined to 0.66 and 0.34, respectively. [b] CCDC-229184 to -229186 contain the supplementary crystallographic data for this paper. These data can be obtained free of charge from The Cambridge Crystallographic Data Centre via www.ccdc.cam.ac.uk/data_request/cif.

the solvent was evaporated to dryness and the residue extracted with CH_2Cl_2 (6×40 mL). The combined extracts were evaporated to dryness, the solids suspended in diethyl ether (20 mL), collected by filtration and washed with diethyl ether (10 mL). Yield 318 mg (427 μmol, 76%) of violet product. ^{1}H NMR (250 MHz, $CDCl_3$): no signals detected. IR (KBr, cm^{-1}): $\tilde{\nu}$ = 3109, 3084, 3062, 3034 (m, w, m, w, Ar-H), 2963, 2928, 2854 (m, m, w, C–H), 1640, 1602, 1571 (s, s, m, C=N, C=C), 1477, 1453 (m, s, C–H_{def}), 1315, 1306, 1237, 1220, 1184, 1172, 1158 (s, m, s, s, s, m, s, S=O, C–F), 1029 (s), 1016 (s), 780 (s), 628 (s). IR (PE, cm^{-1}): $\tilde{\nu}$ = 584 (s), 571 (m), 558 (m), 515 (s), 473 (m), 435 (m), 418 (s), 358 (m), 349 (w), 336 (m), 315 (m), 292 (s), 249 (m), 235 (m), 212 (m), 187 (m), 171 (m), 139 (w), 123 (w). UV/Vis (CH_2Cl_2): λ_{max} = 492. $C_{28}H_{22}F_6FeN_4O_6S_2$ (744.48): calcd. C 45.17, H 2.98, N 7.53; found C 45.37, H 3.31, N 7.53 (%). For crystal structure data see CCSD no 229183.

Dichloro[*N*,*N*′-(6,6′-dimethylbiphenyl-2,2′-diyl)bis(2-pyridylmethyl)diimine]iron(III) chloride·CH_2Cl_2 (8Cl·CH_2Cl_2): A solution of ligand **2** (894 mg, 2.29 mmol) in THF (20 mL) was added to $FeCl_3$ (364 mg, 2.24 mmol) in THF (30 mL). After stirring overnight, the solution was evaporated to dryness, the residue dissolved in CH_2Cl_2 (20 mL), filtered via cannula, and the solvent removed by evaporation again. The solid residue was suspended in diethyl ether (20 mL), collected by filtration, washed with diethyl ether (3×10 mL) and dried in vacuo. Yield 865 mg (1.36 mmol, 61%) of dark violet **8**Cl·CH_2Cl_2. SQUID: μ_{eff} = 6.69 μ_B. ^{1}H NMR (250 MHz, $CDCl_3$): no signals detected. IR (KBr, cm^{-1}): $\tilde{\nu}$ = 3062, 3014 (m, m, Ar-H), 2964, 2924, 2863 (m, w, m, C–H), 1631, 1595, 1567 (m, s, m, C=N, C=C), 1467, 1449 (m, s, C–H_{def}), 1017 (s). IR (PE, cm^{-1}): $\tilde{\nu}$ = 591 (m), 557 (m), 518 (m), 483 (m), 460 (m), 416 (w), 379 (s), 331 (w), 278 (m), 236 (m), 136 (m). UV/Vis (CH_2Cl_2): λ_{max} (ε) = 591 (1980). MS (FAB): *m*/*z* (%): 483/481 (64/33) [M^+ – CH_2Cl_2 – 2 Cl], 446 (93) [481/483 – Cl], 391 (100) [446 – Fe + H]. $C_{27}H_{24}Cl_5FeN_4$ (637.63): calcd. C 50.86, H 3.79, N 8.79; found C 50.87, H 3.94, N 8.88 (%).

Diffractometric Structure Determination: Diffraction data for complexes **8**, **11**, and **14** were collected on a Siemens P4 diffractometer by using graphite-monochromatized Mo-*Kα* radiation with λ = 0.71073 Å (Table 6). Three check reflections were measured every 97 reflections. The structures were solved by direct methods (SHELXS97).[25] All non-hydrogen atoms were refined based on F_{obs}^2 (SHELXL97),[25] while hydrogen atoms were refined on calculated positions with fixed isotropic *U*, using riding model techniques.

Supporting Information: Far-infrared spectra of compounds **2**, **8**, **9**, **12**, and **12b**, temperature dependence of paramagnetic NMR shifts for complex **8**, GPC elution diagrams of polyethene samples obtained from entries 9–11 in Table 5.

Acknowledgments

For contributions to this work at the University of Konstanz we thank Anke Friemel (for 2D NMR spectra), Marie-Jose Quelle and Klaus Hägele (for EI and FAB mass spectra) and Dirk Haffke (for elemental analyses). For helpful comments we thank Professor Ulrich Steiner, for diffractometric structure determinations Dr. Ulrich Wieser (both University of Konstanz) and Dr. Christian Eichhorn (University of Würzburg). Encouragement for this work byProfessor Wolf-Dieter Schenk (University of Würzburg) and by Professor Markku Leskälä (University of Helsinki) and financial support by BMBF and BASELL GmbH are gratefully acknowledged.

[1] a) L. K. Johnson, C. M. Killian, M. Brookhart, *J. Am. Chem. Soc.* **1995**, *117*, 6414– 6415; b) B. L. Small, M. Brookhart, A. M. A. Bennett, *J. Am. Chem. Soc.* **1998**, *120*, 4049–4050; c) S. D. Ittel, L. K. Johnson, M. Brookhart, *Chem. Rev.* **2000**, *100*, 1169–1203.

[2] a) G. J. P. Britovsek, V. C. Gibson, B. S. Kimberley, P. J. Maddox, S. J. McTavish, G. A. Solan, A. J. P. White, D. J. Williams,

 © 2005 Wiley-VCH Verlag GmbH & Co. KGaA, Weinheim

Chem. Commun. **1998**, 849–850; b) G. J. P. Britovsek, V. C. Gibson, D. F. Waas, *Angew. Chem.* **1999**, *111*, 448–468; *Angew. Chem. Int. Ed.* **1999**, *38*, 428–447; c) G. J. P. Britovsek, M. Bruce, V. C. Gibson, B. S. Kimberley, P. J. Maddox, S. Mastroianni, S. J. McTavish, C. Redshaw, G. A. Solan, S. Strömberg, A. J. P. White, D. J. Williams, *J. Am. Chem. Soc.* **1999**, *121*, 8728–8740; d) V. C. Gibson, S. K. Spitzmesser, *Chem. Rev.* **2003**, *103*, 283–316.

[3] a) L. K. Johnson, S. Mecking, M. Brookhart, *J. Am. Chem. Soc.* **1996**, *118*, 267–268; b) S. Mecking, *Angew. Chem.* **2001**, *113*, 550–557; *Angew. Chem. Int. Ed.* **2001**, *40*, 534–540; c) L. S. Boffa, B. M. Novak, *Chem. Rev.* **2000**, *100*, 1479–1494.

[4] L. Resconi, L. Cavallo, A. Fait, F. Piemontesi, *Chem. Rev.* **2000**, *100*, 1253–1346.

[5] a) C. Pellecchia, A. Zambelli, *Macromol. Rapid Commun.* **1996**, *17*, 333–338; b) C. Pellecchia, M. Mazzeo, D. Pappalardo, *Macromol. Rapid Commun.* **1998**, *19*, 651–655; c) B. L. Small, M. Brookhart, *Macromolecules* **1999**, *32*, 2120–2132.

[6] a) A. Togni, L. M. Venanzi, *Angew. Chem.* **1994**, *106*, 517–547; *Angew. Chem. Int. Ed. Engl.* **1994**, *33*, 497–527; b) F. Fache, E. Schulz, M. L. Tommasino, M. Lemaire, *Chem. Rev.* **2000**, *100*, 2159–2231.

[7] a) W. B. Smith, *J. Heterocycl. Chem.* **1987**, *24*, 745–748; b) S. Flanagan, J. Dong, K. Haller, S. Wang, W. R. Scheidt, R. A. Scott, T. R. Webb, D. M. Stanbury, L. J. Wilson, *J. Am. Chem. Soc.* **1997**, *119*, 8857–8868; c) H. Suda, S. Kanoh, N. Murose, S. Goka, M. Motoi, *Polym. Bull.* **1983**, *10*, 162–167.

[8] Complex **8** was also prepared from $FeCl_2 \cdot 4H_2O$, but approximately one equivalent of water remained in the product, as judged by its elemental analysis and IR spectrum.

[9] a) F. H. Allen, *Acta Crystallogr., Sect. B* **2002**, *58*, 380–388; b) I. J. Bruno, J. C. Cole, P. R. Edington, M. Kessler, C. F. Macrae, P. McCabe, J. Pearson, R. Taylor, *Acta Crystallogr., Sect. B* **2002**, *58*, 389–397.

[10] a) D. A. Buckingham, F. P. Dwyer, H. A. Goodwin, A. M. Sargeson, *Austr. J. Chem.* **1964**, *17*, 325–336; b) P. Spacu, M. Teodorescu, C. I. Lepadatu, *Z. Phys. Chem. (Muenchen Ger.)* **1974**, *88*, 285–289; c) T. J. Hubin, J. M. McCormick, S. R. Collinson, M. Buchalova, C. M. Perkins, N. W. Alcock, P. K. Kahol, A. Raghunathab, D. H. Busch, *J. Am. Chem. Soc.* **2000**, *122*, 2512–2522.

[11] a) G. La Mar, J. S. de Ropp, in: *NMR of Paramagnetic Molecules* (Eds.: L. J. Berliner, J. Reuben), Plenum Press, New York, **1993**, p. 1–73; b) I. Bertini, C. Luchinat, *Coord. Chem. Rev.* **1996**, *150*, 77–110; c) T. E. Lehmann, L.-J. Ming, M. E. Rosen, L. Que, Jr., *Biochemistry* **1997**, *36*, 2807–2816.

[12] K. Nakamoto, *Infrared and Raman Spectra of Inorganic and Coordination Compounds, Part B: Applications in Coordination, Organometallic, and Bioinorganic Chemistry*, 5th ed., John Wiley & Sons, Inc., New York, **1997**, p. 23–30, 183–190.

[13] The Fe–N vibration of **8** at ca. 223 cm^{-1} is probably obscured by the broad and intense peak at 244 cm^{-1}.

[14] When brown **12** or **12**·THF was stirred overnight in an apolar solvent such as toluene or diethyl ether, it was transformed to a pink-colored solid (**12b**). Stirring **12b** in THF or CH_2Cl_2 regenerates brown **12**. Complex **12b** has a high-spin value of $\mu_{eff} = 5.23\ \mu_B$. Formation of **12b** in non-polar solvents indicates that both chloride ligands are coordinated, but **12b** differs from the C_2-symmetric complexes **7**–**11** in its FIR bands at 327 (s), 269 (m) and 202 (m) cm^{-1}. In the absence of suitable single crystals, its coordination geometry cannot be reliably assigned.

[15] a) J. J. Zuckermann, *J. Chem. Educ.* **1965**, *42*, 315–317; b) R. Krishnamurthy, W. B. Schaap, *J. Chem. Educ.* **1969**, *46*, 799–810.

[16] We were not able to obtain satisfactory elemental analyses for complex **13**. Although no other species were detected in its NMR spectra, elemental analysis consistently gave carbon values too low by 3–4%; this might be caused by the presence of small amounts of $MgCl_2$.

[17] Reactions of **8** with 2 equiv. of silver triflate gave the analytically pure bistriflate derivative (see Exp. Sect.). A diffractometric structure determination revealed a C_2-symmetric geometry rather similar to that of **8** (for details see CCDC-229183).

[18] Vibrations of the isocyanide ligands were observed at 2160 and 2184 cm^{-1}, significantly higher than $\nu_{CN} = 2138\ cm^{-1}$ measured for free isocyanide. Back-bonding from the metal to the isocyanide ligand thus appears negligible.

[19] Coordination of both σ-donors *trans* to pyridine is prohibited by the obligatory *cis*-coordination of the diimine nitrogen atoms.

[20] a) H. K. Gupta, S. Brydges, M. J. McGlinchey, *Organometallics* **1999**, *18*, 115–122; b) V. C. Gibson, P. J. Maddox, C. Newton, C. Redshaw, G. A. Solan, A. J. P. White, D. J. Williams, *Chem. Commun.* **1998**, 1651–1652.

[21] Further propene polymerization experiments with **8**/MAO, **12**/MAO, or **13**/MAO in CH_2Cl_2 or toluene, at temperatures between 40 and 80 °C, propene pressures ranging from 2 to 10 bar and polymerization times up to 23 hours failed in all cases to produce even traces of polypropene.

[22] We assume that the unexpected formation of 60 mg of polyethene in polymerization run no. 2 (and in occasional other polymerization experiments) is caused by incomplete homogeneous dispersion of **8** due to insufficient exposure to the ultrasound pretreatment.

[23] H.-K. Luo, Z.-H. Yang, B.-Q. Mao, D.-S. Yu, R. G. Tang, *J. Mol. Catalysis A: Chem.* **2002**, *177*, 195; K. P. Bryliakov, N. V. Semikolenova, V. N. Zudin, V. A. Zakharov, E. P. Talsi, *Catal. Commun.* **2004**, *5*, 45–48.

[24] M. Kettunen, C. Vedder, F. Schaper, M. Leskelä, I. Mutikainen, H.-H. Brintzinger, *Organometallics* **2004**, *23*, 3800–3807.

[25] a) G. M. Sheldrick, *SHELXS97*, *Program for the Solution of Crystal Structures*, University of Göttingen, Göttingen, Germany, **1997**; b) G. M. Sheldrick, *SHELXL97*, *Program for Crystal Structure Refinement*, University of Göttingen, Göttingen, Germany, **1997**.

Received: October 28, 2004

 © 2005 Wiley-VCH Verlag GmbH & Co. KGaA, Weinheim

Alternative Coordination Modes in Palladium(II)-Diimino-Bispyridine Complexes with an Axially Chiral Biphenyl Backbone

Mika Kettunen,[a] Christoph Vedder,[b] Hans-Herbert Brintzinger,[b] Ilpo Mutikainen,[a] Markku Leskelä,[a] and Timo Repo*[a]

Keywords: Chiral biaryl ligands / Palladium imino complexes / Binuclear complexes

The chiral biphenyl-bridged diimino-bispyridine ligands *N*,*N*′-(6,6′-dimethylbiphenyl-2,2′-diyl)bis(2-pyridylmethyl)-diimine(**1**)and *N*,*N*′-(6,6′-dimethylbiphenyl-2,2′-diyl)bis[(6-methyl-2-pyridyl)methyl]diimine (**2**) react with Pd(COD)Cl_2 to give, depending on the reaction conditions, either mono- or binuclear $PdCl_2$ complexes. In the binuclear complex **1**-$(PdCl_2)_2$, the Pd nuclei are held at a distance of 3.37 Å by the ligand backbone. *N*,*N*′-(6,6′-dimethylbiphenyl-2,2′-diyl) bis[(5-methyl-2-furyl)methyl]diimine (**3**), with furyl instead of pyridyl rings, gives mononuclear, C_2-symmetric complexes only. Reactions of $[Pd(NCCH_3)_4]^{2+}(BF_4^-)_2$ with ligand **1** or **3** give the C_2-symmetric cations [**1**-Pd]$^{2+}$or [**3**-Pd$(NCCH_3)_2]^{2+}$, respectively, as their BF_4^- salts. Solid-state structures of the chloride complexes **1**-$PdCl_2$, **1**-$(PdCl_2)_2$ and **3**-$PdCl_2$, and of the complex cations [**1**-Pd]$^{2+}$ and [**3**-Pd$(NCCCH_3)_2]^{2+}$ with tetradentate and bidentate ligand coordination, respectively, all show square-planar coordination, with some distortion toward tedrahedral geometry due to the twisted biaryl-backbone. Preliminary observations on norbornene polymerization with the catalysts **1**-$PdCl_2$/MAO, **2**-$PdCl_2$/MAO and [(**3**-Pd$(NCCH_3)_2]^{2+}$ suggest that a certain degree of stereoregularity of the polymers is induced by these chiral catalysts.
(© Wiley-VCH Verlag GmbH & Co. KGaA, 69451 Weinheim, Germany, 2005)

Introduction

Considerable attention has lately been focused on binuclear organometallic compounds, based on expectations that their reactivity in synthesis and catalysis may differ significantly from that of analogous mononuclear species.[1] Interactions between closely adjacent metal centers might cause increased reaction rates or transformations not occurring with monometallic species, as was recently shown for copolymerization of styrene and ethene by binuclear titanocene complexes.[2] The distance between two metal centers and their orientation to each other can be important for catalytic performance, as had been noted for binuclear rhodium hydroformylation catalysts[3] and for palladium complexes that catalyze hydration reactions.[4] Additional oxidation states might also be accessible in binuclear complexes as a result of stabilizing metal–metal interactions.[5]

Late transition metal complexes with nitrogen-based ligands have found a wide range of applications in homogeneous catalysis including polymerization of olefins or acrylates as well as hydrogenation reactions.[6] Pyridylimine-Pd^{II} chelates as dendrimeric complexes and binuclear Pd^{II} complexes with long aliphatic spacers have recently been described as effective catalyst precursors for Heck coupling[7] and for ethene polymerization,[8] respectively, as well as with shorter chiral spacers to produce optically active polyketones.[9] Palladium complexes with chiral bidentate bis(oxazoline) ligands have been shown to be efficient in asymmetric allylic alkylation,[10] while biaryl Schiff base Cu complexes catalyze the aziridination of alkenes.[11]

With a structurally rigid 6,6′-disubstituted biaryl ligand backbone, the configuration of the ligand is fixed and its axial chirality can efficiently be transmitted to the stereotopicity of the active site.[12] Biphenyl-bridged ligands form, in general, mononuclear complexes,[13] but binuclear complexes, e. g. with Cu^{II}, have also been reported.[14] Tetradentate N_4, N_2O_2 and N_2P_2 ligands are known to form both mono- and binuclear Pd^{II} complexes,[15,16,17] but only few of these have chiral biaryl backbones.[16a,17c]

Since cationic Pd^{II} complexes bearing diimine ligands with bulky substituents have been discovered to catalyze copolymerizations of α-olefins with functional vinyl monomers,[18] significant amounts of research have been aimed at tuning the electronic and steric properties of these ligands. Bulky aryls disfavor associative displacement and chain transfer reactions by steric protection of the electrophilic metal center; ligands with labile donor atoms like oxygen or sulfur in their side arms might likewise hinder β-H elimination by temporarily occupying a vacant site on the metal center.[19] Interesting featuresmight thus be expected for C_2-symmetric Pd^{II} diimine complexes with side-arm donors bridged by a chiral ligand backbone.

[a] Laboratory of Inorganic Chemistry, University of Helsinki, 00014 Helsinki, Finland
Fax: +358-9-1915-0198
E-mail: timo.repo@helsinki.fi
[b] Fachbereich Chemie, Universität Konstanz, 78457 Konstanz, Germany

In previous contributions, we have studied complexes of tetradentate 6,6′-dimethylbianiline-based ligands with metals such as Zr, Fe, Co or Cr in regard to their structures and catalytic activities.[20] In this work, we extend these studies to mono- and bimetallic Pd^{II} complexes bearing chiral diimino ligands with a biphenyl backbone.

Results and Discussion

Ligands **1**, **2** and **3** were prepared, as described earlier,[20] by imine condensation of *N*,*N*′-(6,6′-dimethylbiphenyl-2,2′-diyl)diamine with the required aldehydes. Reaction of *N*,*N*′-(6,6′-dimethylbiphenyl-2,2′-diyl)bis(2-pyridylmethyl)di-imine (**1**) with one equivalent of $Pd(COD)Cl_2$ at 0 °C gave **1**-$PdCl_2$, which precipitated from the reaction mixture in almost quantitative yield [Equation (1)]. When the reaction was repeated in an NMR tube, starting at 0 °C and continuing at room temperature, the rate of the reaction was found to be quite fast; 95% of the $Pd(COD)Cl_2$ was consumed after 30 minutes. Ligand **2** likewise reacted readily with $Pd(COD)Cl_2$ under similar reaction conditions, but **2**-$PdCl_2$ was isolated with lower yield due to its higher solubility.

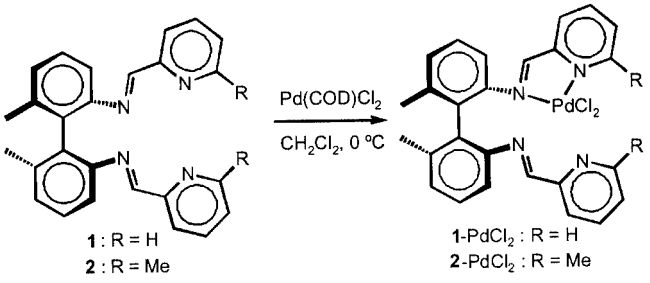

(1)

A single-crystal X-ray structure analysis of **1**-$PdCl_2$ confirms an approximately square-planar coordination of the Pd^{II} *cis*-dichloro unit to one of the pyridylimine moieties of ligand **1** (Figure 1), which thus forms a five-membered pyridylimine chelate, with Pd–N and Pd–Cl distances (Table 1) close to values reported for similar complexes.[15–17] In the solid state, the non-coordinated pyridylimine moiety lies on the backside of the biphenyl bridge, pointing away from the $PdCl_2$ unit.

The ^1H NMR spectrum of **1**-$PdCl_2$ in [D_6]DMSO solution reveals, instead of two singlets expected for the non-equivalent methyl groups in 6- and 6′-positions of the biaryl backbone, three sharp CH_3 signals at δ = 1.82, 2.02 and 2.23 ppm with an integral ratio of 1:2:1.[21] The occurrence of these three CH_3 signals, as well as non-integer ratios for the aromatic proton signal integrals (see Experimental section), indicate the presence of two isomers in [D_6]DMSO solution of **1**-$PdCl_2$, each with one Pd-coordinated and one non-coordinated ligand moiety. Related phenomena in connection with possible isomers of **1**-$(PdCl_2)_2$ will be discussed below.

For **2**-$PdCl_2$ in [D_6]DMSO solution, however, only two singlets are observed, in agreement with the presence of a

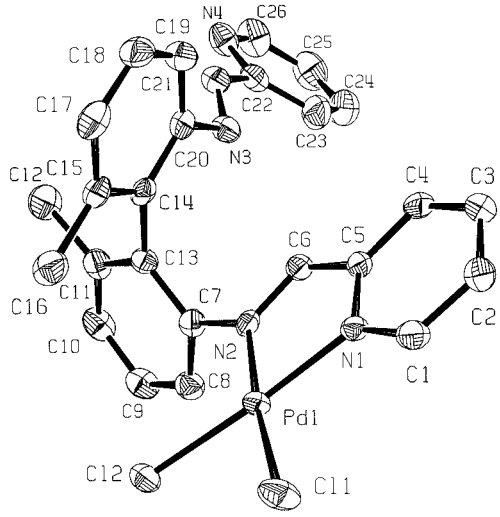

Figure 1. Crystal structure of **1**-$PdCl_2$ (ORTEP plot, thermal ellipsoids drawn at 50% probability, H atoms and CH_2Cl_2 solvent molecules omitted for clarity).

Table 1. Selected bond lengths (Å) and angles [°] for **1**-$PdCl_2$ (c.f. Figure 1).

Pd(1)–N(1)	2.022(3)	N(1)–Pd(1)–N(2)	80.38(12
Pd(1)–N(2)	2.037(3)	N(1)–Pd(1)–Cl(2)	175.56(9)
Pd(1)–Cl(2)	2.2893(11)	N(2)–Pd(1)–Cl(2)	95.26(9)
Pd(1)–Cl(1)	2.2916(11)	N(1)–Pd(1)–Cl(1)	93.28(9)
		N(2)–Pd(1)–Cl(1)	173.61(9)
		Cl(2)–Pd(1)–Cl(1)	91.06(4)

Pd-coordinated and an uncoordinated ligand moiety, for the methyl groups at the biphenyl bridge (1.96 and 2.05 ppm), for the methyl groups in 6-position of each pyridyl ring (2.47 and 2.80 ppm) and for the imine protons (8.21 and 8.69 ppm).

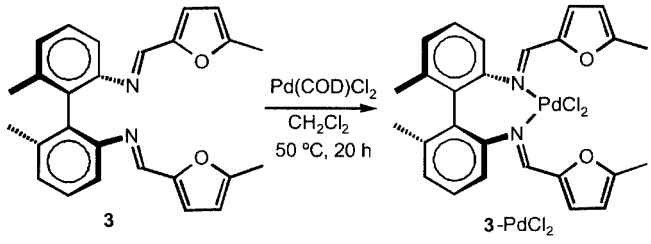

(2)

With ligand **3**, where the side-arm pyridyl groups are replaced by furyl rings, a significantly longer reaction time (20 h) was required for complex formation with $Pd(COD)Cl_2$ [Equation (2)]. As shown by the crystal structure of **3**-$PdCl_2$ (Figure 2, Table 2), ligand **3** is bound in a bidentate manner again. Here, however, the two imino nitrogens form a seven-membered chelate with the *cis*-dichloro Pd unit to give an approximately square-planar and C_2-symmetric geometry. Due to the dihedral angle of 67° between the phenyl rings of the biphenyl bridge, the ligand plane at the Pd center is somewhat distorted, with an angle of 5.9(2)° spanned by the planes Cl1–Pd–N1 and Cl2–Pd–N2. The furyl oxy-

 © 2005 Wiley-VCH Verlag GmbH & Co. KGaA, Weinheim

gen atoms are located at non-bonding distances of 5.0 and 5.1 Å from the Pd center, from which the side arms are pointing away.[22] The preference of the Pd center for N over O ligand atoms obviously overrides its preference for five-membered over seven-membered chelate rings to such an extent that a C_2-symmetric geometry becomes favored for **3**-$PdCl_2$ over the C_1-symmetric structures of **1**-$PdCl_2$ and **2**-$PdCl_2$.

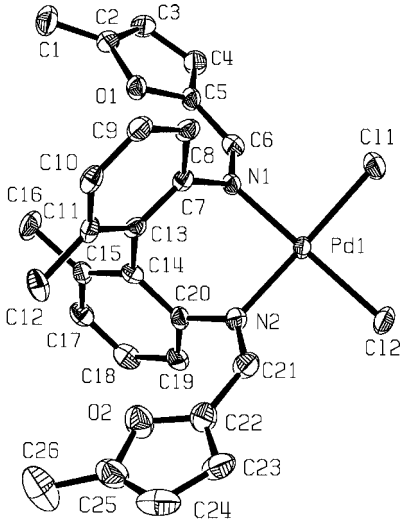

Figure 2. Crystal structure of **3**-$PdCl_2$ (ORTEP plot, thermal ellipsoids drawn at 50% probability, H atoms and CH_2Cl_2 solvent molecule omitted for clarity).

Table 2. Selected bond lengths (Å) and angles [°] for **3**-$PdCl_2{\cdot}CH_2Cl_2$ (c.f. Figure 2).

Pd(1)–N(1)	2.029(3)	N(1)–Pd(1)–N(2)	90.26(11)
Pd(1)–N(2)	2.057(3)	N(1)–Pd(1)–Cl(1)	89.26(8)
Pd(1)–Cl(1)	2.2944(9)	N(2)–Pd(1)–Cl(1)	174.45(9)
Pd(1)–Cl(2)	2.2973(9)	N(1)–Pd(1)–Cl(2)	177.96(9)
		N(2)–Pd(1)–Cl(2)	90.17(8)
		Cl(1)–Pd(1)–Cl(2)	90.51(4)

$CDCl_3$ solutions of **3**-$PdCl_2$ give ^1H NMR spectra in agreement with an apparent C_2 symmetry, with a singlet at δ = 1.88 ppm due to the two methyl groups in the biphenyl backbone, another singlet at δ = 2.18 ppm due to the methyl groups at the furyl rings, and a singlet at δ = 8.32 ppm assigned to the imine protons. These signals are accompanied, however, by a set of smaller signals located slightly up-field, at δ = 1.82, 2.12 and 8.29 ppm, which integrate to ratios of ca. 1:10 relative to the respective main peaks. The observation of this additional signal set in solutions of **3**-$PdCl_2$ would indicate that some minor isomer is present, in addition to the structure represented in Figure 2. From our data it is not clear, which alternative geometry prevails in this isomer, whether (and how) e. g. furyl oxygen atoms might be coordinated to the Pd^{II} center.[19]

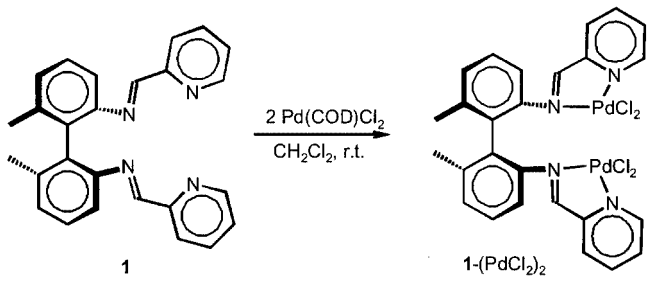

(3)

In **1**-$PdCl_2$ one halve of ligand **1** remains available for further coordination and provides a possibility for the preparation of bimetallic complexes. The dipalladium complex **1**-$(PdCl_2)_2$ was indeed isolated in 97% yield when ligand **1** was treated with two equivalents of $Pd(COD)Cl_2$ at room temperature [Equation (3)].[23] In the solid-state structure of binuclear **1**-$(PdCl_2)_2$, one $PdCl_2$ unit is coordinated, as expected, to each of the biphenyl-bridged pyridylimine moieties (Figure 3, Table 3). The two square-planar N_2PdCl_2 units are almost parallel to each other, stacking under an angle of 7.40(2)°. Viewed along the Pd–Pd axis, the two $PdCl_2$ units are rotated by an angle of 104.9° relative to each other. The Pd(1)–Pd(2) distance of 3.37 Å is in the range of quite a number of binuclear Pd^{II} complexes with relatively short (2−4 atom) bridging ligands.[24] Apparently a similarly favorable situation for a close $Pd^{II}\cdots Pd^{II}$ contact is created by the preference of the biaryl bridge for a twist angle of ca. 70°. In addition, some attractive interaction between Pd–Cl dipoles might contribute to keep the Pd centers at a distance close to the sum of their van-der-Waals radii.

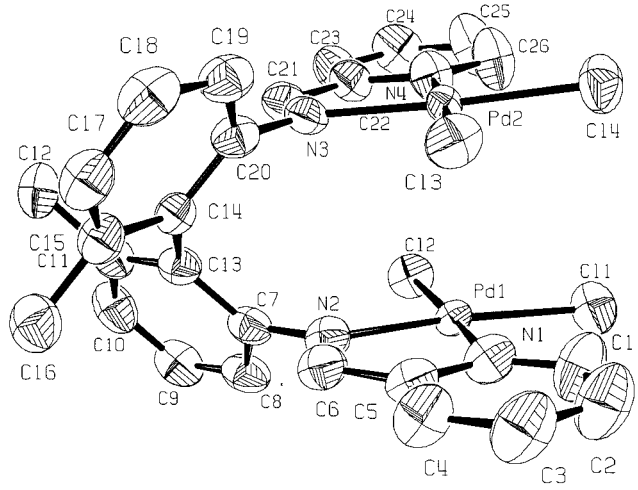

Figure 3. Crystal structure of **1**-$(PdCl_2)_2$ (ORTEP plot, thermal ellipsoids drawn at 50% probability, H atoms and CH_2Cl_2 solvent molecules omitted for clarity).

In the ^1H NMR spectra of **1**-$(PdCl_2)_2$ in $[D_6]$DMSO solution, the methyl groups at the biphenyl bridge give rise to a sharp signal at δ = 2.02 ppm and a broader one at δ = 2.12 ppm, each corresponding to 3 protons; the 6-posi-

 © 2005 Wiley-VCH Verlag GmbH & Co. KGaA, Weinheim

Table 3. Selected bond lengths (Å) and angles [°] for **1**-$(PdCl_2)_2$·$2CH_2Cl_2$ (c.f. Figure 3).

Pd(1)–N(1)	2.034(6)	N(1)–Pd(1)–N(2)	79.8(3)
Pd(1)–N(2)	2.048(6)	N(1)–Pd(1)–Cl(1)	94.4(2)
Pd(1)–Cl(1)	2.292(2)	Cl(1)–Pd(1)–Cl(2)	88.56(7)
Pd(1)–Cl(2)	2.2930(19)	N(2)–Pd(1)–Cl(1)	173.42(19)
		N(1)–Pd(1)–Cl(2)	176.94(19)
		N(2)–Pd(1)–Cl(2)	97.31(18)
		C(1)–N(1)–Pd(1)	127.1(6)
		C(5)–N(1)–Pd(1)	113.7(5)
Pd(2)–N(3)	2.044(6)	N(3)–Pd(2)–N(4)	80.3(2)
Pd(2)–N(4)	2.056(6)	N(3)–Pd(2)–Cl(4)	173.60(18)
Pd(2)–Cl(3)	2.300(2)	N(3)–Pd(2)–Cl(3)	97.19(18)
Pd(2)–Cl(4)	2.281(2)	N(4)–Pd(2)–Cl(4)	93.44(19)
		Cl(4)–Pd(2)–Cl(3)	89.04(8)

tioned protons of the pyridyl rings likewise appear as two doublets at 8.83 and at δ = 9.04 ppm representing one proton each and the other aromatic and imine signals are also grouped in a manner incompatible with a C_2-symmetric complex. These observations can be explained either by the occurrence of two diastereomers, e.g. *meso*- and *rac*-like conformers of the two complex moieties, in a ratio of ca. 1:1 or by some nonequivalence of the two complex moieties in solution, caused e.g. by co-ordination of a solvent molecule to one of the Pd centers. Our data do not allow us to estimate the lifetimes of isomers of this kind.

The *cis*-$PdCl_2$ unit considered so far obviously favors formation of a five-membered pyridyl-imine chelate over that of a seven-membered diimine chelate; complexes such as **1**-$PdCl_2$ or **2**-$PdCl_2$ are thus of C_1 symmetry. In order to synthesize complexes which fully exploit the axialsymmetry inherent in the biaryl backbone to generate C_2-symmetric complexes suitable for asymmetric catalysis,[25] we have sought to induce tetradentate coordination of ligands **1** and **2** with formation of cationic complexes by use of the more electron-deficient Pd precursor $[Pd(NCCH_3)_4]^{2+}(BF_4^-)_2$ [Equation (4)].

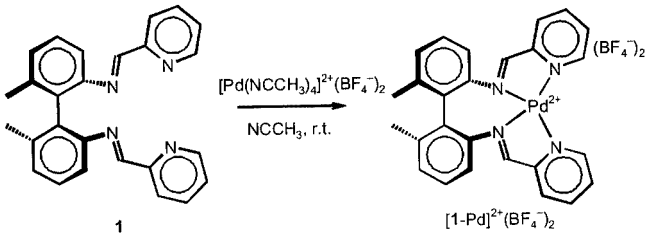

(4)

Reaction of ligand **1** with one equivalent of $[Pd(NCCH_3)_4]^{2+}(BF_4^-)_2$ in acetonitrile at room temperature gave the ion pair $[\mathbf{1}\text{-Pd}]^{2+}(BF_4^-)_2$ in high yield. The expected tetradentate coordination of ligand **1** in $[\mathbf{1}\text{-Pd}]^{2+}(BF_4^-)_2$ was verified by single-crystal structure determination (Figure 4). The Pd center forms an approximately C_2-symmetric seven-membered chelate ring with the biphenyl-bridged imine nitrogens and one five-membered chelate ring with each of the pyridylimine moieties, with Pd–N distances (Table 4) in the range reported for other Pd-imino complexes.[15–17] Due to the dihedral angle of 71° in the 2,2′-dimethyl-substituted biphenyl backbone, the square-planar coordination at the Pd atom shows some tetrahedral distortion, so that the planes N1–Pd–N2 and N3–Pd–N4 span an angle of 12.9(5)°.[26]

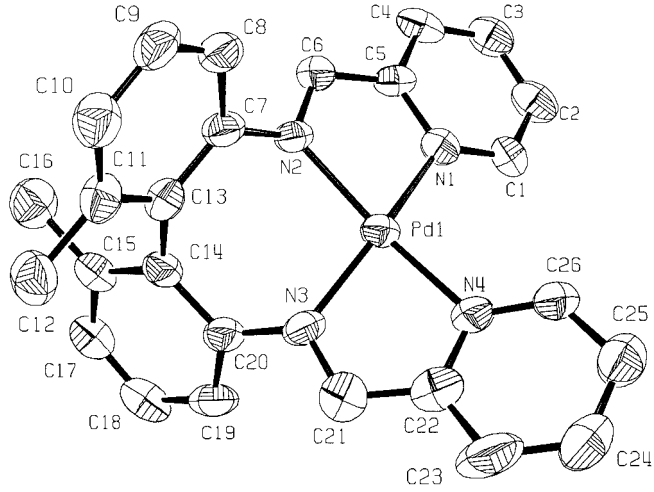

Figure 4. Crystal structure of $[\mathbf{1}\text{-Pd}]^{2+}(BF_4^-)_2$ (ORTEP plot, thermal ellipsoids drawn at 50% probability, H atoms, 0.5 H_2O and BF_4^- omitted for clarity).

Table 4. Selected bond lengths (Å) and angles [°] for $[\mathbf{1}\text{-Pd}]^{2+}(BF_4^-)_2$ (c.f. Figure 4).

Pd(1)–N(3)	2.012(7)	N(3)–Pd(1)–N(2)	99.0(3)
Pd(1)–N(2)	2.017(6)	N(3)–Pd(1)–N(4)	80.4(3)
Pd(1)–N(4)	2.021(7)	N(2)–Pd(1)–N(4)	161.7(3)
Pd(1)–N(1)	2.044(7)	N(3)–Pd(1)–N(1)	164.5(3)
		N(2)–Pd(1)–N(1)	79.7(3)
		N(4)–Pd(1)–N(1)	105.6(3)

^{1}H NMR spectra in CD_3CN solution indicate, again, some deviations of the cation $[\mathbf{1}\text{-Pd}]^{2+}$ from the approximate C_2 symmetry found in the solid state. The 6,6′-positioned methyl groups of the ligand backbone give rise to a multiplet with two maxima at δ = 1.72 and 1.76 ppm, and the aromatic protons are likewise grouped in multiplets which do not appear to be compatible with an overall C_2 symmetry. Even though we do not have any direct evidence in this regard, we would assume that the equivalence of both halves of the complex molecule might be destroyed, as in the cases discussed above, by coordination of a solvent molecule.

In order to test whether a tetradentate coordination similar to that achieved for ligand **1** might also be accessible for the furyl-substituted ligand **3**,[27] the latter was likewise reacted with $[Pd(NCCH_3)_4]^{2+}(BF_4^-)_2$ in acetonitrile solution. The reaction proceeded fast and with high yield, but gave, instead of a product with tetracoordinate ligand **3**, $[\mathbf{3}\text{-Pd}]^{2+}(BF_4^-)_2$, the bis(acetonitrile) adduct $[\mathbf{3}\text{-Pd-}(NCCH_3)_2]^{2+}(BF_4^-)_2$ [Equation (5)].

 © 2005 Wiley-VCH Verlag GmbH & Co. KGaA, Weinheim

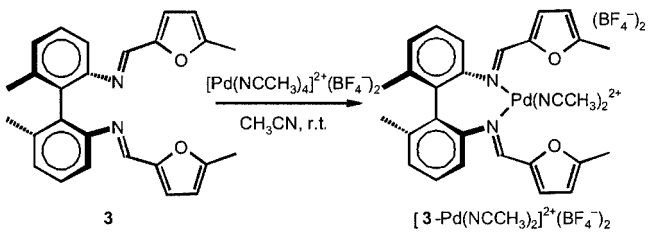

(5)

In the crystal structure of [**3**-Pd(NCCH$_3$)$_2$]$^{2+}$(BF$_4^-$)$_2$ (Figure 5, Table 5), square-planar coordination at the cationic Pd center is found to involve two *cis*-positioned acetonitrile ligands and the two imino nitrogen atoms of ligand **3**; as in **3**-PdCl$_2$, the ligand **3** forms again a seven-membered chelate ring with the Pd center. In distinction to **3**-PdCl$_2$, however, where the furyl oxygen atoms point away from the Pd center, they are now turned towards the latter and lie rather close to it, in pseudo-axial positions at Pd–O distances of 3.0(1) Å. Some (presumably weak) coordination or dipolar attraction of the furyl oxygen atoms to the Pd^{II} center thus appears to be stabilized by the cationic nature of the metal.[27,28]

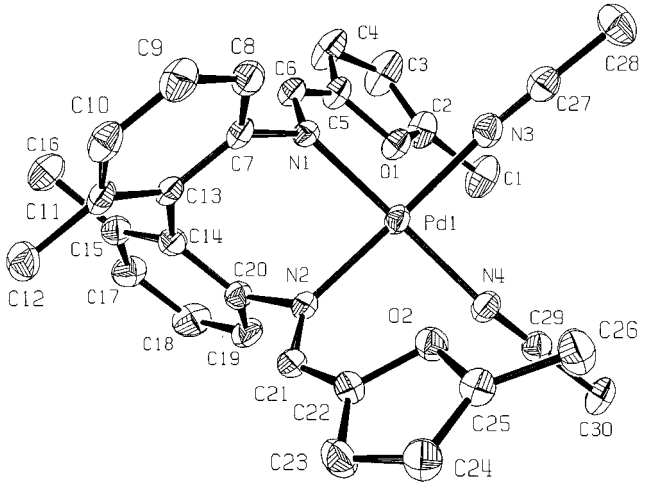

Figure 5. Crystal structure of [**3**-Pd(NCCH$_3$)$_2$]$^{2+}$(BF$_4^-$)$_2$ (ORTEP plot, thermal ellipsoids drawn at 50% probability, H atoms, CH$_3$CN solvent molecule and BF$_4^-$ omitted for clarity).

Table 5. Selected bond lengths (Å) and angles [°] for [**3**-Pd(NCCH$_3$)$_2$]$^{2+}$(BF$_4^-$)$_2$ (c.f. Figure 5).

Pd(1)–N(1)	2.006(2)	N(1)–Pd(1)–N(4)	171.03(8)
Pd(1)–N(4)	2.009(2)	N(1)–Pd(1)–N(2)	86.35(9)
Pd(1)–N(2)	2.016(2)	N(4)–Pd(1)–N(2)	93.37(9)
Pd(1)–N(3)	2.022(2)	N(1)–Pd(1)–N(3)	91.97(9)
		N(4)–Pd(1)–N(3)	89.15(9)
		N(2)–Pd(1)–N(3)	174.21(8)

The ^{1}H NMR spectrum of [**3**-Pd(NCCH$_3$)$_2$]$^{2+}$ is entirely in agreement with the overall C_2 symmetry expected from its solid-state structure. Its NCCH$_3$ ligands and its biphenyl and furyl methyl substituents give rise to only one singlet signal each, at δ = 2.08, 2.20 and 2.63 ppm, respectively. Apparently, the binding of the furyl groups to the cationic Pd^{II} center, however weak, protects the latter from interaction with a solvent donor, which might otherwise destroy the overall C_2 symmetry of the complex molecule in solution.

Since two nitrogen ligand atoms are sufficient for the formation of a cationic di-acetonitrile complex, ligand **1** was also treated with two equivalents of [Pd(NCCH$_3$)$_4$](BF$_4$)$_2$ to prepare the binuclear cationic complex **1**-([Pd(NCCH$_3$)$_2$]$^{2+}$)$_2$(BF$_4^-$)$_4$ [Equation (6)]. The reaction yielded an oily product, the elemental analysis and ^{1}H NMR spectra of which indicated formation of the expected complex. As no crystals suitable for X-ray diffraction were obtained, it was not possible to study the effect of the increased charges on the mutual arrangement of the metal centers in this binuclear complex.

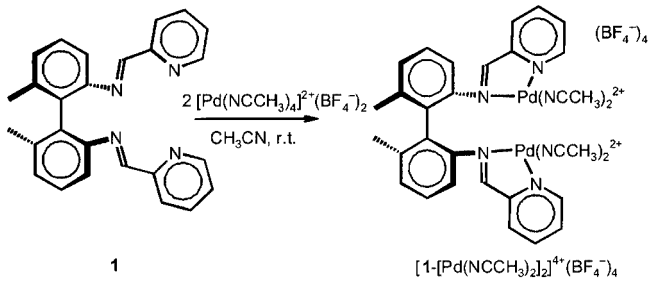

(6)

Preliminary data concerning catalytic activities of the new Pd^{II} complexes described above were obtained with regard to polymerization of norbornene at room temperature.[29] When activated by addition of methylaluminoxane (MAO), the dichloro complexes **1**-PdCl$_2$, **2**-PdCl$_2$ and **3**-PdCl$_2$ gave polymers which were insoluble in organic solvents such as trichlorobenzene even at elevated temperatures. The cationic complex [**3**-Pd(NCCH$_3$)$_2$]$^{2+}$(BF$_4^-$)$_2$ gave, without activation by MAO,[29] polymers with good solubility, e.g. in toluene or chloroform, in moderate yield. For these polynorbornenes, a molar mass of 33800 g/mol and a polydispersity index of 1.26 were determined. Complex [**1**-Pd]$^{2+}$(BF$_4^-$)$_2$, in which the Pd center is bound to all four N atoms of the tetradentate ligand, was found to be inactive for polymerization of norbornene at room temperature.

Decomposition temperatures, determined by thermogravimetric analysis, of the polymers obtained with MAO-activated **1**-PdCl$_2$, **2**-PdCl$_2$ and **3**-PdCl$_2$ as well as of those obtained with [(**3**-Pd(NCCH$_3$)$_2$]$^{2+}$(BF$_4^-$)$_2$, were found to be exceptionally high (ca. 450 °C), i.e. more than 100 °C higher than that (335 °C) determined for the polymer obtained with [Pd(NCCH$_3$)$_4$](BF$_4$)$_2$.[29] This might suggest that a certain degree of stereoregularity is induced in the polymer by the chiral ligands of the catalysts **1**-PdCl$_2$/MAO, **2**-PdCl$_2$/MAO, **3**-PdCl$_2$/MAO and [(**3**-Pd(NCCH$_3$)$_2$]$^{2+}$.[30]

 © 2005 Wiley-VCH Verlag GmbH & Co. KGaA, Weinheim

Conclusions

Axially symmetric, biphenyl-bridged diimino ligands with additional pyridyl or furyl side arms are highly versatile with respect to Pd^{II} complex formation. Depending on the Pd precursors and the reaction conditions used, mononuclear-bidentate complexes of C_1 or C_2 symmetry, as well as binuclear and mononuclear-tetradentale Pd^{II} complexes can be obtained in a controlled manner and with high yields. Preliminary observations indicate distinctly different properties of cationic species derived from them as norbornene polymerization catalysts.

Experimental Section

All complex preparation and polymerization reactions were performed under argon atmosphere using standard Schlenk techniques. *N,N′*-(6,6′-Dimethylbiphenyl-2,2′-diyl)diamine,[31] the ligands **1**–**3**[20] and dichloro(1,5-cyclooctadiene)palladium(II) [Pd(COD)Cl_2],[32] were prepared as reported earlier. Solvents were dried prior to use by refluxing over and distillation from sodium (hydrocarbons), magnesium (alcohols), P_2O_5 (acetonitrile) or calcium hydride (dichloromethane). Deuterated solvents were dried over 4-Å molecular sieves. All other chemicals were purchased from commercial suppliers and used without further purification. Elemental analyses were performed with an EA 1110 CHNS-O CE instrument. NMR spectra were collected with a Varian Gemini 200 spectrometer. Polymer molar mass and molar mass distributions were measured by gel permeation chromatography (GPC) relative to polystyrene standards.

***N,N′*-(6,6′-Dimethylbiphenyl-2,2′-diyl)bis(2-pyridylmethyl)-diimine-$PdCl_2$ (1-$PdCl_2$):** A solution of ligand **1** (0.59 g, 1.52 mmol) and Pd(COD)Cl_2 (0.39 g, 1.38 mmol) in CH_2Cl_2 (25 mL) was stirred at 0 °C. The product started to precipitate as a light yellow powder after 1 h. After stirring for another 20 h at room temperature, the product was filtered, washed with diethyl ether and dried in vacuo. Yield 658 mg, 84%. ^{1}H NMR (200 MHz, [D$_6$]DMSO): δ = 1.82, 2.02 and 2.23 (3 lines, 6 H, CH_3), 7.02 (d, J = 8.0 Hz, 0.5 H, Ar-*H*), 7.25−7.39 (m, 3.5 H, Ar-*H*), 7.5 (m, 2 H, Ar-*H*), 7.71−7.94 (m, 3.5 H, Ar-*H*), 8.21−8.27 (m, 2.5 H, C*H*), 8.5 (s, 0.5 H, imine-C*H*), 8.64−8.71 (m, 1 H, C*H*), 8.83−8.97 (m, 1.5 H, C*H*), 8.88 ppm (s, 1 H, imine-C*H*); elemental analysis (%) calcd. for $C_{26}H_{22}Cl_2N_4Pd$ (567.81): C 55.00, H 3.91, N 9.87; found: C 54.70, H 3.71, N 10.25.

***N,N′*-(6,6′-Dimethylbiphenyl-2,2′-diyl)bis[(6-methyl-2-pyridyl)methyldiimine-$PdCl_2$ (2-$PdCl_2$):** This complex was prepared in the same manner as described above for complex **1**-$PdCl_2$. Yield 0.16 g, 50%. ^{1}H NMR (200 MHz, [D$_6$]DMSO): δ = 1.96 (s, 3 H, biaryl-CH_3), 2.05 (s, 3 H, biaryl-CH_3 on Pd-coordinated side), 2.47 (s, 3 H, pyridine-CH_3), 2.80 (s, 3 H, pyridine-CH_3 on Pd-side), 6.96 (d, J = 8 Hz, 1 H, pyridine-C*H*), 7.16 (d, J = 8 Hz, 1 H, pyridine-C*H*), 7.24−7.48 (m, 6 H, 1 pyridine-C*H* and 2 biaryl-C*H* on non-coordinated side, and 3 Ar-C*H* on Pd-coordinated side), 7.65−7.73 (m, 2 H, 1 pyridine-C*H* from Pd-free side and 1 Ar-*H* from Pd-coordinated side), 7.97−8.11 (br., 2 H, Ar-*H* on Pd-side), 8.21 (s, 1 H, imine-C*H*), 8.69 ppm (br., 1 H, Pd-coordinated imine-C*H*); elemental analysis (%) calcd. for $C_{28}H_{26}Cl_2N_4Pd$ (595.86): C 56.44, H 4.40, N 9.40; found: C 55.85, H 4.34, N 9.21.

***N,N′*-(6,6′-Dimethylbiphenyl-2,2′-diyl)bis[(5-methyl-2-furyl)methyl]-diimine-$PdCl_2$ (3-$PdCl_2$):** Ligand **3** (0.49 g, 1.25 mmol) and Pd(COD)Cl_2 (0.36 g, 1.25 mmol) were refluxed in CH_2Cl_2 (20 mL) for 20 h. Diethyl ether (20 mL) was added to reaction mixture, which was then filtered and kept at –20 °C. The product was collected as orange crystals by filtration after 24 h. Yield 0.36 g, 50%. ^{1}H NMR (200 MHz, $CDCl_3$): δ = 1.88 (s, 6 H, furyl-CH_3), 2.18 (s, 6 H, biaryl-CH_3), 6.01 (d, J = 3.6 Hz, 2 H, furyl-C*H*), 6.16 (d, J = 3.2 Hz, 2 H, furyl-C*H*), 7.09 (d, J = 7.8 Hz, 2 H, biaryl-C*H*), 7.22 (d, J = 7.0 Hz, 2 H, biaryl-C*H*), 7.29 (pt, J = 7.6 Hz, 2 H, biaryl-C*H*), 8.32 ppm (s, 2H imine-C*H*). Minor isomer: 1.82 (s, biaryl-CH_3), 2.12 (s, furyl-CH_3), 8.29 ppm (s, imine-C*H*). ^{13}C NMR (50 MHz, $CDCl_3$): δ = 13.9, 18.7, 109.9, 120.3, 124.5, 127.7 129.3, 129.7, 138.5, 145.9, 146.4, 156.3, 159.5 ppm; elemental analysis (%) calcd. for $C_{26}H_{24}Cl_2N_2O_2Pd{\cdot}CH_2Cl_2$ (658.75): C 49.23, H 3.98, N 4.25; found: C 48.26, H 4.57, N 4.06.

***N,N′*-(6,6′-Dimethylbiphenyl-2,2′-diyl)bis(2-pyridylmethyl)diimine-$(PdCl_2)_2$ [1-$(PdCl_2)_2$]:** A solution of ligand **1** (0.43 g, 1.10 mmol) and Pd(COD)Cl_2 (0.63g, 2.20 mmol) in CH_2Cl_2 (35 mL) was stirred at room temperature for 20 h. The product precipitated as a yellow powder, which was collected by filtration, washed with diethyl ether and dried in vacuo. Yield 0.80 g, 97%. ^{1}H NMR (200 MHz, [D$_6$]DMSO): δ = 2.02 (s, 3 H, CH_3), 2.12 (s, 3 H, CH_3), 7.31−7.38 (m, 3.5 H, Ar-*H*), 7.48−7.51 (m, 2.5 H, Ar-*H*), 7.80 (br., 3.5 H, Ar-*H*), 8.21 (m, 3.5 H, C*H*), 8.83 (d, J = 5.2 Hz, 1 H, C*H*), 8.88 (s, 1 H, imine-C*H*), 9.04 ppm (br., 1 H, pyridine-C*H*). ^{13}C NMR (50 MHz, $CDCl_3$): δ = 19.30, 120.23, 128.90−130.16 (m), 131.39, 144.01, 150.91, 171.36 ppm; elemental analysis (%) calcd. for $C_{26}H_{22}N_4Pd_2Cl_4$ (745.14): C 41.91, H 2.97, N 7.51; found: C 41.25, H 2.78, N 7.67.

[*N,N′*-(6,6′-Dimethylbiphenyl-2,2′-diyl)bis(2-pyridylmethyl)diimine-Pd]$^{2+}$ $(BF_4^-)_2$ {[1-Pd]$^{2+}$ $(BF_4^-)_2$}: A filtered solution of ligand **1** (0.29 g, 0.74 mmol) in acetonitrile (15 mL) was added to a solution of $[Pd(NCCH_3)_4]^{2+}(BF_4^-)_2$ (0.33 g, 0.74 mmol) in acetonitrile (15 mL) and the reaction mixture stirred at room temperature for 5 h. Reaction was then evaporated and dried in vacuo. Yield 0.49 g, 98%. ^{1}H NMR (200 MHz, CD_3CN): δ = 1.67−1.81 (m, 6 H, CH_3), 7.16−7.45 (m, 7 H, Ar-*H*), 7.65−7.82 (m, 2 H, Ar-*H*), 7.93−7.97 (m, 2 H, Ar-*H*), 8.09−8.16 (m, 3 H, Ar-*H*), 8.37−8.39 ppm (m, 2 H, imine-C*H*); elemental analysis (%) calcd. for $C_{26}H_{22}B_2F_8N_4Pd{\cdot}CH_3CN$ (711.57): C 47.26, H 3.54, N 9.84; found: C 47.44, H 3.31, N 9.92.

[*N,N′*-(6,6′-Dimethylbiphenyl-2,2′-diyl)bis[(5-methyl-2-furyl)methyl-]diimine-Pd$(NCCH_3)_2]^{2+}$ $(BF_4^-)_2$ {[(3-Pd$(NCCH_3)_2]^{2+}$ $(BF_4^-)_2$}: This complex was prepared in the same manner as described above for complex [(1-Pd]$^{2+}$ $(BF_4^-)_2$. Yield 0.53 g, 94%. ^{1}H NMR (200 MHz, CD_3CN): δ = 2.08 (s, 6 H, $NCCH_3$), 2.20 (s, 6 H, biaryl-CH_3), 2.63 (s, 6 H, furyl-CH_3), 6.52−6.55 (m, 2 H, furyl-C*H*), 7.30−7.39 and 7.48−7.50 ppm (m, 10 H, Ar-H); elemental analysis (%) calcd. for $C_{28}H_{30}B_2F_8N_4O_2Pd$ (734.60): C 45.78, H 4.11, N 7.62; found: C 45.62, H 3.97, N 7.66.

[*N,N′*-(6,6′-Dimethylbiphenyl-2,2′-diyl)bis(2-pyridylmethyl)diimine-{Pd$(NCCH_3)_2\}_2]^{4+}$ $(BF_4^-)_4$ {[1-{Pd$(NCCH_3)_2\}_2]^{4+}$ $(BF_4^-)_4$}: This complex was prepared in the same manner as described for complex [**1**-Pd]$^{2+}$ $(BF_4^-)_2$ above except for the use of only 0.15 g (0.37 mmol) of ligand **1** for reaction with 0.33 g (0.74 mmol) of $[Pd(NCCH_3)_4]^{2+}(BF_4^-)_2$. Yield 0.41 g, 95%. ^{1}H NMR (200 MHz, CD_3CN): δ = 1.72 (s, 6 H, biaryl-CH_3), 2.05 (br., 12 H, $NCCH_3$), 7.35−7.37 (m, 8 H, Ar-*H*), 7.77 (t, 2 H, Ar-*H*), 7.97 (d, 2 H, Ar-*H*), 8.21 (t, 2 H, Ar-*H*), 8.58 ppm (d, 2 H, Ar-*H*); elemental analysis (%) calcd. for $C_{34}H_{34}B_4F_{16}N_8Pd_2$, (1114.75): C 36.63, H 3.07, N 10.05; found: C 36.00, H 3.16, N 10.74%.

Crystal Structure Determinations: Single crystals of complexes **1**-$PdCl_2$, **1**-$(PdCl_2)_2$,[(**1**-Pd]$^{2+}$ $(BF_4^-)_2$ and [(**3**-Pd$(NCCH_3)_2]^{2+}$ $(BF_4^-)_2$ were obtained as yellow-orange blocks upon layering a filtered re-

 © 2005 Wiley-VCH Verlag GmbH & Co. KGaA, Weinheim

Table 6. Details for the crystal structure determinations

	1-$PdCl_2$·$2CH_2Cl_2$	**3**-$PdCl_2$	**3**-$PdCl_2$·CH_2Cl_2	**1**-$(PdCl_2)_2$·$2CH_2Cl_2$	[**1**-Pd]$^{2+}$(BF_4^-)$_2$·$(H_2O)_{0.5}$	[**3**-Pd($NCCH_3$)$_2$]$^{2+}$(BF_4^-)$_2$
CCDC number	243264	243267	243268	243265	243266	243269
Formula	$C_{26}H_{22}Cl_2N_4Pd$·$(CH_2Cl_2)_2$	$C_{26}H_{25}Cl_2N_2O_2Pd$	$C_{26}H_{24}Cl_2N_2O_2Pd$·(CH_2Cl_2)	$C_{25}H_{20}Cl_4N_4Pd_2$·$(CH_2\ Cl_2)_2$	$C_{26}H_{24}N_4Pd(BF_4)_2$·$(H_2O)_{0.5}$	$C_{30}H_{30}N_4O_2Pd(BF_4)_2$·$(C_2H_3N)$
Formula mass	737.63	574.78	658.70	999.85	680.51	799.65
Temperature	173(2)K	173(2)K	173(2)K	173(2)K	173(2)K	173(2)K
Crystal system	monoclinic	monoclinic	monoclinic	triclinic	monoclinic	triclinic
Space group	*P*21/*c*	*P*21/*c*	*P*21/*c*	$P\bar{1}$	*P*21/*c*	$P\bar{1}$
a (Å)	14.003(2)	8.4180(8)	10.7960(7)	9.0280(12)	12.593(4)	12.023(2)
b (Å)	14.360(1)	15.2480(17)	17.573(2)	14.6330(17)	14.363(5)	12.9240(7)
c (Å)	17.917(2)	18.679(3)	17.484(2)	15.5050(19)	19.361(4)	14.341(3)
α (°)	90	90	90	113.074(11)	90	104.178(8)
β (°)	121.844(14)	99.244(8)	122.895(5)	98.359(13)	128.47(3)	99.756(11)
γ (°)	90	90	90	90.177(9)	90	117.483(6)
V (Å^3); *Z*	3060.5(6); 4	2366.5(5); 2	2785.2(5); 4	1860.4(4); 2	2741.6(14); 4	1810.4(5); 2
$d_{calcd.}$ [g/cm^3]	1.601	1.613	1.571	1.785	1.649	1.467
μ [mm^{-1}], *F*(000)	1.156; 1480	1.037; 1164	1.078; 1328	1.713; 984	0.758; 1360	0.590; 808
Crystal size (mm)	0.25 × 0.15 × 0.12	0.30 × 0.25 × 0.20	0.25 × 0.18 × 0.12	0.20 × 0.05 × 0.05	0.18 × 0.04 × 0.02	0.20 × 0.20 × 0.20
Theta range (°)	5.03 to 27.51	5.03 to 27.51	5.01 to 27.53	2.66 to 27.57	3.04 to 25.25	3.10 to 27.50
Reflections collected/unique	24160 / 6960 [*R*(int) = 0.0714]	16675 / 5352 [*R*(int) = 0.1057]	29085 / 6210 [*R*(int) = 0.0456]	28531 / 8435 [*R*(int) = 0.0572]	39662 / 4875 [*R*(int) = 0.1233]	26221 / 8243 [*R*(int) = 0.0459]
T_{max}, T_{min}	0.8737, 0.7609	0.8194, 0.7461	0.8816, 0.7744	0.9193, 0.7258	0.9850, 0.8757	0.9127, 0.8932
Data/restraints/parameters	6960 / 0 / 352	5352 / 0 / 302	6210 / 0 / 325	8435 / 80 / 462	4875 / 74 / 416	8243 / 0 / 463
GoF(F^2)	0.989	0.963	0.628	1.050	1.033	1.030
Final *R* indices [$I > 2\sigma(I)$]	*R*1 = 0.0471, *wR*2 = 0.0883	*R*1 = 0.0649, *wR*2 = 0.1009	*R*1 = 0.0344, *wR*2 = 0.1232	*R*1 = 0.0597, *wR*2 = 0.1530	*R*1 = 0.0726, *wR*2 = 0.1781	*R*1 = 0.0381, *wR*2 = 0.0823
R indices (all data)	*R*1 = 0.0993, *wR*2 = 0.1025	*R*1 = 0.1561, *wR*2 = 0.1236	*R*1 = 0.0537, *wR*2 = 0.1545	*R*1 = 0.0863, *wR*2 = 0.1698	*R*1 = 0.1163, *wR*2 = 0.1990	*R*1 = 0.0584, *wR*2 = 0.0887
Largest diff. peak	0.671 eA^{-3}	0.539 eA^{-3}	0.997 eA^{-3}	1.136 eA^{-3}	1.047 eA^{-3}	0.572 eA^{-3}

action solution with diethyl ether at ambient temperature. Crystals of **3**-$PdCl_2$ were obtained at 4 °C; at room temperature, **3**-$PdCl_2$ gave crystals with a different unit cell. Crystals selected for X-ray measurements were mounted on a glass fiber using the oil-drop method. Data were collected on a Nonius–Kappa CCD diffractometer using Mo-*Kα* radiation (71.073 pm) and a graphite monochromator. Structures were solved by direct methods. All non-hydrogen atoms were refined anisotropically.[33] Hydrogen atoms were introduced at calculated positions and refined with fixed geometry with respect to their carrier atoms. Cell parameters and data collection parameters are summarized in Table 6. CCDC-243264 (for **1**-$PdCl_2$), CCDC-243267 and CCDC-243268 (for **3**-$PdCl_2$, two crystals with different structures), CCDC-243265 (for **1**-$(PdCl_2)_2$), CCDC-243266 (for [**1**-Pd]$^{2+}$(BF_4^-)$_2$) and CCDC-243269 (for [**3**-Pd($NCCH_3$)$_2$]$^{2+}$(BF_4^-)$_2$) contain the supplementary crystallographic data for this paper. These data can be obtained free of charge from The Cambridge Crystallographic Data Centre via www.ccdc.cam.ac.uk/data_request/cif.

Norbornene Polymerizations: The dichloro complexes **1**-$PdCl_2$, **2**-$PdCl_2$ and **3**-$PdCl_2$ (20 μmol) were suspended in toluene (60 mL), MAO (4 mL, 20 mmol) and 2-norbonene (2.1 g, 22.3 mmol) were added and the reaction solution stirred at room temperature for 1 h. Conversions measured from the isolated products were 64, 71 and 38%, respectively. In the case of complexes [**1**-Pd]$^{2+}$(BF_4^-)$_2$, and [**3**-Pd($NCCH_3$)$_2$]$^{2+}$(BF_4^-)$_2$ norbornene was added to a solution of the complex (50 mg, 66 μmol) in CH_2Cl_2 (50 mL), chlorobenzene (5 mL) and nitrobenzene (1 mL) and stirred at room temperature for 1 h. Conversions were 0 and 44%, respectively. After quenching the reaction by addition of methanol (200 mL), acidified with HCl (1 mL), the precipitate was collected by filtration, washed with methanol and dried at 60 °C. Decomposition points were determined with thermogravimetric balance under N_2 flow. ^{1}H NMR (200 MHz, $CDCl_3$): δ = 0.87−2.23 (br. m, 10 H) ppm. ^{13}C NMR (50 MHz, $CDCl_3$): δ = 28−44 (br. m), 48−55 ppm (br. m).

Acknowledgments

M. K. thanks the foundation of Alfred Kordelin for support. The Academy of Finland is acknowledged for financial support via Centre of Excellence (Bio- and Nanopolymer Research Group, project 77317).

[1] a) E. L. Mutterties, M. J. Krause, *Angew. Chem. Int. Ed. Engl.* **1983**, *22*, 135−148; b) D. A. Roberts, G. L. Geoffroy in *Comprehensive Organometallic Chemistry*, vol. 6 (Eds.: E. Wilkinson, F. G. A. Stone, E. W. Abel), Pergamon, Oxford, **1982**, chapter 40, pp. 763−877; c) W. Beck, B. Niemer, M. Wieser, *Angew. Chem.* **1993**, *105*(7), 969−996; *Angew. Chem. Int. Ed. Engl.* **1993**, *32*, 923−949; d) E. K. van den Beuken, B. L. Feringa, *Tetrahedron* **1998**, *54*, 12985−13011; e) S. Barlow, D. O'Hare, *Chem. Rev.* **1997**, *97*, 637−670.

[2] N. Guo, L. Li, T. J. Marks, *J. Am. Chem. Soc.* **2004**, *126*, 6542−6543.

 © 2005 Wiley-VCH Verlag GmbH & Co. KGaA, Weinheim

[3] a) M. E. Broussard, B. Juma, S. G. Train, W.-J. Peng, S. A. Laneman, G. G. Stanley, *Science* **1993**, *260*, 1784−1788; b) R. C. Matthews, D. K. Howell, W.-J. Peng, S. G. Train, W. D. Treleaven, G. G. Stanley, *Angew. Chem.* **1996**, *108*, 2402−2405; *Angew. Chem. Int. Ed. Engl.* **1996**, *35*, 2253−2256; c) W. J. Peng, S. G. Train, D. K. Howell, F. R. Fronczek, G. G. Stanley, *Chem. Commun.* **1996**, 2607−2612; d) G. Süss-Fink, *Angew. Chem.* **1994**, *106*, 71−73; *Angew. Chem. Int. Ed. Engl.* **1994**, *33*, 67−69.

[4] C. J. McKenzie, R. Robson, *J. Chem. Soc., Chem. Commun.* **1988**, 112−114.

[5] B.-H. Xia, H.-X. Zhang, C.-M. Che, K.-H. Leung, D. L. Phillips, N. Zhu, Z.-Y. Zhou, *J. Am. Chem. Soc.* **2003**, *125*, 10362−10374.

[6] A. Togni, L. M. Venanzi, *Angew. Chem.***1994**, *106*, 517−547; *Angew. Chem. Int. Ed. Engl.* **1994**, *33*, 497−526.

[7] G. S. Smith, S. F. Mapolie, *J. Mol. Cat. A: Chem.* **2004**, *213*,187–192.

[8] R. Chen, S. F. Mapolie, *J. Mol. Cat. A: Chem.* **2003**, *193*, 33–40.

[9] C. R. Baar, M. C. Jennings, R. J. Puddephatt, *Organometallics* **2001**, *20*, 3459−3465.

[10] a) O. Hoarau, H. Ait-Haddou, J.-C. Daran, D. Cramailere, G. G. A. Balavoine, *Organometallics* **1999**, *18*, 4718−4723; b) H. Ait-Haddou, O. Hoarau, D. Cramailere, F. Pezet, J.-C. Daran, G. G. A. Balavoine, *Chem. Eur. J.* **2004,***10*, 699−707; c) For a recent review about Pd-catalyzed enantioselective transformations, see L. F. Tietze, H. Ila, H. P. Bell, *Chem. Rev.* **2004**, *104*, 3453–3516.

[11] a) H. Suga, A. Kakehi, S. Ito, T. Ibata, T. Fudo, Y. Watanabe, Y. Kinoshita, *Bull. Chem. Soc. Jpn.* **2003**, *76*, 189−199; b) K. M. Gillespie, C. J. Sanders, P. O'Shaughnessy, I. Westmoreland, C. P. Thickitt, P. Scott, *J. Org. Chem.* **2002**, *67*, 3450−3458.

[12] a) H.Takaya, T. Ohta, R. Noyori in *Catalytic Asymmetric Synthesis* (Ed.: I. Ojima), VCH, Weinheim, Germany, **1993**; b) H. B. Kagan, O. Riant, *Chem. Rev.* **1992**, *92*, 1007−1019; c) H. Suga, T. Fudo, T. Ibata, *Synlett* **1998**, *8*, 933−935; c) N. Yoshikawa, Y. M. A. Yamada, J. Das, H. Sasai, M. Shibasaki, *J. Am. Chem. Soc.* **1999**, *121*, 4168−4178; d) H. Ishitani, M. Ueno, S. Kobayashi, *J. Am. Chem. Soc.* **2000**, *122*, 8180−8186; e) A. H. Hoveyda, R. R. Schrock, *Chem. Eur. J.* **2001**, *7*, 945−950; f) D. R. Cefalo, A. F. Kiely, M. Wuchrer, M. Jamieson, R. R. Schrock, A. H. Hoveyda, *J. Am. Chem. Soc.* **2001**, *123*, 3139−3140.

[13] a) F. Lions, K. V. Martin, *J. Am. Chem. Soc.* **1957**, *79*, 1273−1275; b) S. Knapp, T. P. Keenan, X. Zhang, R. Fikar, J. A. Potenza, H. Schugar, *J. Am. Chem. Soc.* **1987**, *109*, 1882−1883; c) E. Müller, C. Piquet, G. Bernadinella, A. F. Williams, *Inorg. Chem.* **1988**, *27*, 849−855; d) H. Frydendahl, H. Toftlund, J. Becher, J. C. Dutton, K. S. Murray, L. F. Taylor, O. P. Anderson, E. R. T. Tiekink, *Inorg. Chem.* **1995**, *34*, 4467−4476; e) R. Noyori, H. Takaya, *Acc. Chem. Res.* **1990**, *23*, 345−350; f) M. Kitamura, T. Ohkuma, S. Inoue, N. Sayo, H. Kumobayashi, S. Akutagawa, T. Ohta, H. Takaya, R. Noyori, *J. Am. Chem. Soc.* **1988**, *110*, 629−631; g) J. M. Brown, S. Woodward, *J. Org. Chem.* **1991**, *56*, 6803−6809; h) N. W. Alcock, J. M. Brown, D. I. Hulmes, *Tetrahedron: Asym.* **1993**, *4*, 743−756.

[14] M. Réglier, C. Jorand, B. Waegell, *J. Chem. Soc., Chem. Commun.* **1990**, *24*, 1752−1755.

[15] a) M. Gomez, G. Muller, D. Panyella, M. Rocamora, E. Dunach, S. Olivero, J.-C. Clinet, *Organometallics* **1997**, *16,* 5900−5908; b) A. S. Abu-Surrah, U. Thewalt, B. Rieger, *J. Organomet. Chem.* **1999**, *587*,58−66; c) R. Feldhaus, J. Koeppe, R. Mattes, U. Voet, *Z. Naturforsch. Teil B: Chem. Sci.* **1996**, *51*, 1449−1458; d) F. Gomez-de la Torre, A. de la Hoz, F. A. Jalon, B. R. Manzano, A. M. Rodriguez, J. Elguero, M. Martinez-Ripoll, *Inorg. Chem.* **2000**, *39*, 1152−1162.

[16] a) X.-G. Zhou, J.-S. Huang, X.-Q. Yu, Z.-Y. Zhou, C.-M. Che, *J. Chem. Soc., Dalton Trans.* **2000**, 1075−1080; b) R. Kivekas, A. Pajunen, A. Navarrete, E. Colacio, *Inorg. Chim. Acta* **1999**, *284*, 292−295; c) M. R. A. Pillai, C. L. Barnes, C. S. John, D. E. Troutner, E. O. Schlemper, *J. Crystallogr. Spectr. Res.***1993**, *23*, 949−953; d) N. Ahmad, *Inorg. Chim. Acta* **1989**, *155*, 237−241.

[17] a) M. Gomez, S. Jansat, G. Muller, D. Panyella, P. W. N. M. van Leeuwen, P. C. J. Kamer, K. Goubitz, J. Fraanje, *Organometallics* **1999**, *18*, 4970−4981; b) U. Burckhardt, M. Baumann, G. Trabesinger, V. Gramlich, A. Togni, *Organometallics* **1997**, *16*, 5252−5259; c) A. G. J. Ligtenbarg, E. K. van den Beuken, A. Meetsma, N. Veldman, W. J. J. Smeets, A. L. Spek, B. L. Feringa, *J. Chem. Soc., Dalton Trans.* **1998**, 263−270; d) E. K. van den Beuken, A. Meetsma, H. Kooijman, A. L. Spek, B. L. Feringa, *Inorg. Chim. Acta* **1997**, *264*, 171−183; e) T. G. Schenck, J. M. Downes, C. R. C. Milne, P. B. Mackenzie, T. G. Boucher, J. Whelan, B. Bosnich, *Inorg. Chem.* **1985**, *24*, 2334−2337.

[18] L. K. Johnson, C. M. Killian, M. Brookhart, *J. Am. Chem. Soc.* **1995**, *117*, 6414−6415.

[19] Labile coordination of diimine ligands with oxygen- or sulfur-containing side arms has been reported: a) X.-G. Fang, B. L. Scott, J. G. Watkin, G. J. Kubas, *Organometallics* **2000**, *19*, 4193−4195; b) X. Fang, J. G. Watkin, B. L. Scott, G. J. Kubas, *Organometallics* **2001**, *20*, 3351−3354.

[20] a) M. Kettunen, C. Vedder, F. Schaper, M. Leskelä, I. Mutikainen, H.-H. Brintzinger, *Organometallics* **2004**, *23*, 3800−3807; b) C. Vedder, Doctoral dissertation, University of Konstanz, Germany, **2002**.

[21] The ratio of the integrals of the methyl proton signals changed gradually when the NMR sample was heated. DMSO as a solvent did not allow low-temperature NMR studies.

[22] When grown from CH_2Cl_2/Et_2O solution at room temperature, **3**-$PdCl_2$ crystallized in another modification without a solvent molecule in the unit cell. The coordination geometry of this modification is practically superimposable to that of **3**-$PdCl_2$ described above, but it contains one of the uncoordinated furyl side arms in a different orientation.

[23] When ligand **1** was reacted with one equivalent of Pd(COD)Cl_2 at room temperature, complex **1**-$[PdCl_2]_2$didprecipitate first under partial consumption of the ligand, while mononuclear **1**-$PdCl_2$ was isolated later by recrystallization.

[24] a) S. Cosar, M. B. L. Janik, M. Flock, E. Freisinger, E. Farkas, B. Lippert, *J. Chem. Soc., Dalton Trans.* **1999**, 2329−2336; b) W. Wong-Ng, P. T. Cheng, V. Kocman, H. Luth, S. C. Nyburg, *Inorg. Chem.* **1979**, *18*,2620−2623; c) B. Oskui, W. S. Sheldrick, *Eur. J. Inorg. Chem.* **1999**, 1325−1333.

[25] C.-M. Che, J.-S. Huang, *Coord. Chem. Rev.* **2003**, *242*, 97−113 and references cited therein.

[26] Dihedral angles of ca.10.5° between two adjacent N–Pd–O(phenoxide)planes have been reported for binaphtyl salen Pd complexes (see ref.[16a]).

[27] To the best of our knowledge, no structurally characterized Pd^{II} complexes with oxygen-coordinated furyl ligands have been reported so far.

[28] Pentacoordinate Pd^{II} centers have been reported to occur in complexes with constrained ligand frameworks: a) T. J. Hubin, N. W. Alcock, D. H. Busch, *Acta Crystallogr. Sect. C* **1999** *55,* 1404; b) R. Garrone, A. M. Romano, R. Santi, R. Millini, *Organometallics* **1998**, *17*, 4519−4522.

[29] Other studies on norbornene polymerisation with neutral or cationic Pd complexes: a) C. Mehler, W. Risse, *Makromol. Chem. Rapid Commun.* **1991**, *12*, 255−259; b) C. Mehler, W. Risse, *Macromolecules* **1992**, *25*, 4226−4228; c) A. Sen, T. W. Lai, *Organometallics* **1982**, *1*, 415−417; d) A. S. Abu-Surrah, B. Rieger, *J. Mol. Catal.* **1998**, *128*, 239−243.

[30] Use of an enantiomerically pure Pd^{II} complex with a (1*R*,2*R*)-(−)-*N*,*N*′-bis(quinoline-2-methylene)diiminocyclohexane backbone for MAO-activated norbornene polymerization has been

reported to give, under similar conditions, polynorbornene with an elevated decomposition temperature of 415 °C (see ref.[15b]).
[31] S. Kanoh, S. Goka, N. Murose, H. Kubo, M. Kondo, T. Sugino, M. Motoi, H. Suda, *Polym. J.* **1987**, *19*, 1047−1065.
[32] D. Drew, J. R. Doyle, *Inorg. Synth.* **1972**, *13*, 47−55.
[33] G. M. Sheldrick, *SHELXTL*, **1990**, and *SHELXTL*, **1997**, University of Göttingen, Germany. G. M. Sheldrick, *SADABS*, **1996**, University of Göttingen, Germany. G. M. Sheldrick, *SHELX97*, **1997**, University of Göttingen, Germany.
Received: October 28, 2004

 © 2005 Wiley-VCH Verlag GmbH & Co. KGaA, Weinheim

Novel Mercury Phosphanylamides

Marcus L. Cole,[a,b] Glen B. Deacon,*[a] Peter C. Junk,[a] Kristina Konstas[a] and Peter W. Roesky[c]

Keywords: Mercury / Redox transmetallation / Phosphanylamide ligands / Subvalent complexes / P Donors

The reactions of bis(pentafluorophenyl)mercury, bis(diphenylphosphanyl)amine and neodymium or erbium metal in toluene yielded the subvalent mercury(1.33) complex $[Hg_3\{\mu_2\text{-}(Ph_2P)_2N\}_4]\cdot 3C_7H_8$ (**1**·3 C_7H_8) as a toluene solvate. The complex was also prepared in high yield from $Hg(C_6F_5)_2$, $(PPh_2)_2NH$ and mercury metal in toluene at room temperature. From reaction of $Hg(C_6F_5)_2$ and $HN(PPh_2)_2$ in toluene with no added metal, $[Hg_2\{\mu_2\text{-}(Ph_2P)_2N\}_2\{(Ph_2P)(OPPh_2)N\}_2]\cdot 2C_7H_8$ (**3**·2 C_7H_8) has been obtained, and **3**·2 $C_4H_{10}O_2$ has also been isolated in low yield. From a related reaction, a solution of the product in $CDCl_3$ deposited $[Hg_2\{\mu_2\text{-}(Ph_2P)_2N\}_3Cl]\cdot 3/2\,CDCl_3$ (**4**·3/2 $CDCl_3$). The structure of **1**·3 C_7H_8 contains a Hg–Hg bonded Hg_3 triangle with adjacent metals bridged (P,P′) by either one or two phosphanylamide ligands. One mercury is four coordinate, and the other two are five coordinate. In $[Hg_2\{\mu_2\text{-}(Ph_2P)_2N\}_2\{(Ph_2P)(OPPh_2)\text{-}N\}_2]\cdot 2S$ [S = C_7H_8 or $C_4H_{10}O_2$ (1,2-dimethoxyethane)], the mercury atoms are bridged (P,P′) by two phosphanylamide ligands, whilst the hemi-oxidised ligands are chelating (O,P) in a *transoid* disposition to each other leading to four coordination. There is unsymmetrical ligation in $[Hg_2\{\mu_2\text{-}(Ph_2P)_2N\}_3Cl]\cdot 3/2\,CDCl_3$ (**4**·3/2 $CDCl_3$) with one mercury four coordinate and the other three. Three phosphanylamide ligands bridge (P,P′) the metals with a non-bonding Hg···Hg separation of 3.0042(7) Å. Each HgP_3 array has a triangular arrangement, little affected in one case by the attachment of a chloride approximately normal to HgP_3.

(© Wiley-VCH Verlag GmbH & Co. KGaA, 69451 Weinheim, Germany, 2005)

Introduction

In recent years the bidentate bis(diphenylphosphanyl) amine (Hdppa) ligand has received considerable attention.[1] This interest partly emanates from the electronic and structural similarity to the widely used and hugely successful bis(diphenylphosphanyl)methane (dppm) ligand,[2] which gives a wide range of binuclear and metal cluster complexes with transition metals.[3] Such diphosphane ligands are attractive due to their ability to bridge or flexibly chelate (for dppm an aspect furnished by distortion of the central sp^3 hybridised methylene PCP angle), offering coordination geometries that can be tailored to the metal at hand. This often permits short metal–metal contacts, thereby increasing the likelihood of high nuclearity metal complexes.[2,4] Deprotonation of bis(diphenylphosphanyl) amine is readily achieved by treatment with group 1 alkyls (e.g. butyllithium) or alkoxides.[5] The resulting bis(diphenylphosphanyl)amide ligand is an isoelectronic analogue of dppm that has so far demonstrated an ability to bridge, chelate or act as a terminal ligand for transition metals[5–7] and, more recently, lanthanoid metals by coordination through the amide and the phosphorus donor sets.[1b,8]

Another interesting feature of the bis(diphenylphosphanyl)amine ligand is the ability of the phosphorus atoms to be sequentially oxidised by selected chalcogen elements (E = O, S, Se), thereby forming the new derivatives $(PPh_2)[P(E)Ph_2]NH$ and $[P(E)Ph_2]_2NH$.[7] The neutral ligands, or their anionic forms generated by deprotonation,[1a] can also behave as unidentate N/P/E-bonded, E,E/P-chelating or E,E/P-bridging ligands. This class of ligand is capable of acting simultaneously as both a hard and soft Lewis base donor.[1c] Herein we report the synthesis and structures of some unusual and unexpected mercury complexes resulting initially from redox transmetallation/ligand exchange reactions involving lanthanoid metals, bis(pentafluorophenyl)mercury and bis(diphenylphosphanyl)amine. These reactions normally provide a "one-pot" route to numerous organo, organoamido and aryloxo complexes of the lanthanoids[9–10] and appeared attractive for bis(diphenylphosphanyl)amide complexes as a complementary synthesis to the existing metathesis and protolysis routes.[1b,8]

Results and Discussion

Synthesis

The preparation of lanthanoid (Ln) complexes with chelating phosphanylamide ligands was attempted using redox

[a] School of Chemistry, Monash University, Clayton Campus, Victoria 3800, Australia
Fax: +61-3-9905-4597
E-mail: glen.deacon@sci.monash.edu.au
[b] Current Address: Department of Chemistry, University of Adelaide,
South Australia 5005, Australia
[c] Institut für Chemie, Freie Universität Berlin, Fabeckstrasse 34–36, 14195 Berlin, Germany

transmetallation/ligand exchange with bis(pentafluorophenyl)mercury and bis(diphenylphosphanyl)amine [Equation (1); Ln = Nd].

$$Ln + 1.5[Hg(C_6F_5)_2] + 3(Ph_2P)_2NH \rightarrow [Ln\{(Ph_2P)_2N\}_3] + 1.5\,Hg + 3\,C_6F_5H \quad (1)$$

Treatment of neodymium metal [Equation (1); Ln = Nd) with the reactants in the non-coordinating solvent toluene, did not yield the target $[Nd\{(Ph_2P)_2N\}_3]$ but rather an orange crystalline product that was identified as a subvalent mercury complex, $[Hg_3\{\mu_2\text{-}(Ph_2P)_2N\}_4]\cdot 3\,C_7H_8$ (**1**·3 C_7H_8), by an X-ray structure determination (Figure 1 and i in Scheme 1). Compound **1**·3 C_7H_8 was also characterised by $^{31}P\{^1H\}$ NMR, ^1H NMR and infrared spectroscopy (below). Despite repeated attempts, $[Nd\{(Ph_2P)_2N\}_3]$ could not be isolated. A similar attempt with erbium metal [Equation (1); Ln = Er] also gave no isolable lanthanoid complex. The $^{31}P\{^1H\}$ NMR spectra of the reaction mixture indicated the presence of the same trinuclear complex **1**. Single crystals isolated from the Er reaction mixture were also identified by X-ray crystallography as **1**·3 C_7H_8 (see Experimental Section: Method 2). Attempts to effect reaction (1) were accompanied by formation of insoluble precipitates containing Ln and F.

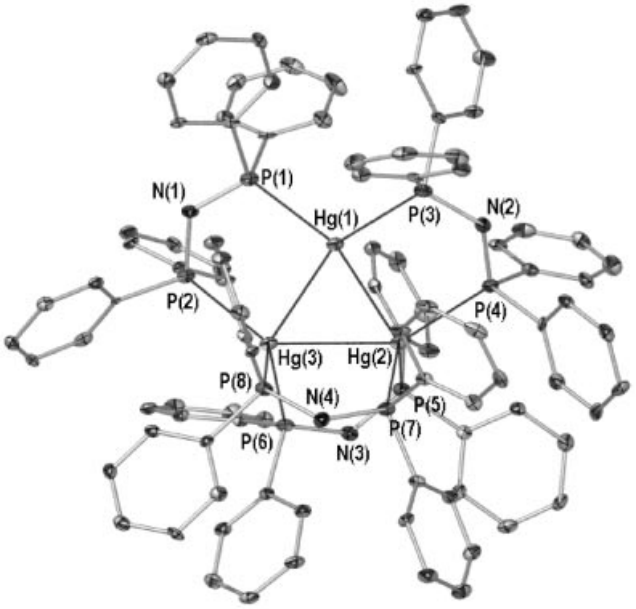

Figure 1. The molecular structure of $[Hg_3\{\mu\text{-}(Ph_2P)_2N\}_4]\cdot 3\,C_7H_8$ (**1**·3C_7H_8). POV-Ray graphic (www.povray.org), 40% thermal ellipsoids. All solvent molecules are removed for clarity.

As mercury metal is a sufficient reductant to give the subvalent $[Hg_3(\mu\text{-dmpm})_4][O_3SCF_3]_4$ [dmpm = bis(dimethylphosphanyl)methane] complex,[11] the reaction of $Hg(C_6F_5)_2$ with $(Ph_2P)_2NH$ was attempted in the presenceof mercury metal (and no lanthanoid) [see i in Scheme 1 and Equation (2)] and compound **1**·3 C_7H_8 was isolated in excellent yield.

$$2[Hg(C_6F_5)_2] + 4(Ph_2P)_2NH + Hg^0 \rightarrow [Hg_3\{\mu_2\text{-}(Ph_2P)_2N\}_4] + 4\,C_6F_5H \quad (2)$$

Since the first step in redox transmetallation/ligand exchange reactions with Nd or Er can be formulated as in Equation (3), the mercury metal produced may well be the reductant in reactions with lanthanoid metals.

$$2\,Ln + 3[Hg(C_6F_5)_2] \rightarrow 2[Ln(C_6F_5)_3] + 3\,Hg^0 \quad (3)$$

Independent attempts to prepare $[Ln(C_6F_5)_3]$ by Equation (3) resulted in decomposition to LnF_3,[9,12] by contrast with isolation of $[Ln(C_6F_5)_2(THF)_n]$ (Ln = Eu, n = 5; Ln = Yb, n = 4),[13] and decomposition of such species accounts for the formation of intractable Ln/F containing precipitates in attempted reaction (1).

Although no direct reaction could be induced between Nd metal and $(Ph_2P)_2NH$ in toluene, it was evident that the amine reacts with $Hg(C_6F_5)_2$ at room temperature since an immediate orange colour developed. When this reaction was carried out on a 2:1 mole ratio, pentafluorobenzene was formed, indicative of ligand exchange. However, the expected exchange product $[Hg\{(Ph_2P)_2N\}_2]$ **2** (see iv in Scheme 1) was not isolated but instead a partly oxidised species, $[Hg_2\{\mu_2\text{-}(Ph_2P)_2N\}_2\{(Ph_2P)(OPPh_2)N\}_2]\cdot 2\,C_7H_8$ (**3**·2 C_7H_8), (Figure 2 and ii in Scheme 1), which was initially identified by X-ray crystallography.

$$2[Hg(C_6F_5)_2] + 4(Ph_2P)_2NH \xrightarrow{O_2} [Hg_2\{\mu_2\text{-}(Ph_2P)_2N\}_2\{(Ph_2P)(OPPh_2)N\}_2] + 4\,C_6F_5H \quad (4)$$

Multiple preparations of **2** were attempted under dry anaerobic conditions but all resulted in the isolation solely of **3**·2 C_7H_8, which was additionally characterised by $^{31}P\{^1H\}$ NMR, ^1H NMR and IR spectroscopy (below). Since four phosphane sites are unaffected by oxidation, the amount of oxygen present must have been extremely small. This compound was also isolated as a DME solvate in low yield from DME washings of a similar reaction mixture involving Nd metal, and was identified by X-ray crystallography as $[Hg_2\{\mu_2\text{-}(Ph_2P)_2N\}_2\{(Ph_2P)(OPPh_2)N\}_2]\cdot 2\,C_4H_{10}O_2$ (**3**·2 $C_4H_{10}O_2$).

Protolysis (see iv in Scheme 1) implies that the phosphanylamine ligand is more acidic than pentafluorobenzene (pK_a = 25.6, in THF),[9,14] but this reaction is highly unexpected given that bis(pentafluorophenyl)mercury is very resistant to electrophilic attack, as evidenced by successful recrystallisation from concentrated sulphuric acid and the very slow reaction with bromine.[15] By contrast bis(pentafluorophenyl)mercury is prone to nucleophilic attack, being readily cleaved by nucleophiles, for example by I^- to give $[HgI_4]^{2-}$ and pentafluorobenzene,[16] (see also recent isolation of a $[Hg(C_6F_5)_2I]^-$ intermediate).[17] This may suggest that coordination of the neutral $(Ph_2P)_2NH$ ligand through phosphorus provides nucleophilic assistance for

 © 2005 Wiley-VCH Verlag GmbH & Co. KGaA, Weinheim

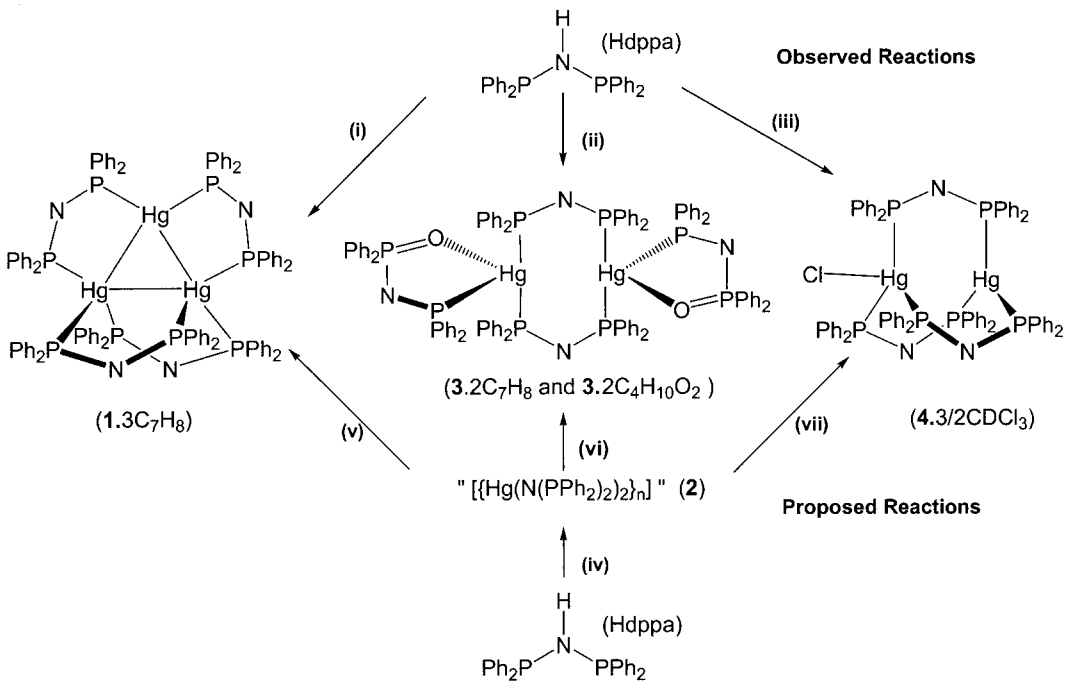

Scheme 1. (i) $Hg(C_6F_5)_2$, Er, Nd, Hg metal, toluene, 20 °C (ii) $Hg(C_6F_5)_2$, toluene, trace of O_2, 20 °C or DME extraction after (i), (iii) $Hg(C_6F_5)_2$, toluene, 20 °C, and crystallisation from $CDCl_3$ (iv) $Hg(C_6F_5)_2$ (v) Hg (vi) trace of O_2 (vii) $CHCl_3/CDCl_3$, $-(Ph_2P)_2NH$.

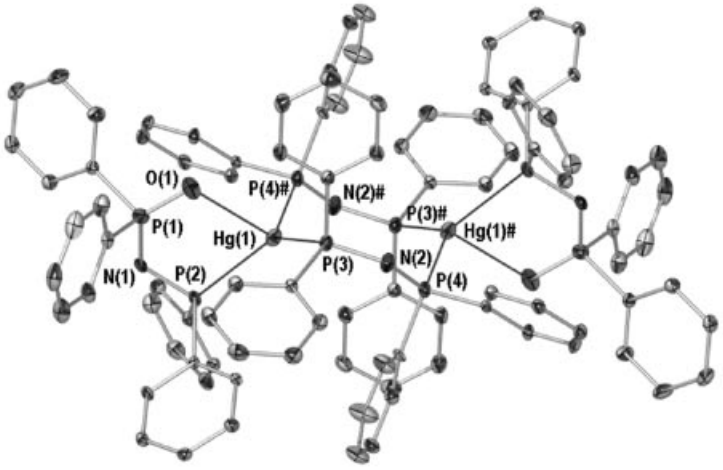

Figure 2. The crystal structure of $[Hg_2\{\mu_2\text{-}(Ph_2P)_2N\}_2\{(Ph_2P)(OPPh_2)N\}_2]\cdot 2C_4H_{10}O_2$ (**3**·$2C_4H_{10}O_2$), (POV-Ray, 40% thermal ellipsoids). All solvent molecules are removed for clarity.

protolysis by generation of partial carbanion character in the C_6F_5 group. Complexation of $Hg(C_6F_5)_2$ by phosphanes is known though the coordination is weak.[15,18] In previous studies of redox transmetallation/ligand exchange, blank reactions between $Hg(C_6F_5)_2$ and the protic ligand have failed, but no soft donor has been present to support X–H scission.[19]

In an attempt to stem the oxidation of **2** that yields **3** (see vi in Scheme 1) the preparation of **2** was attempted under even more strenuously anaerobic conditions (see Experimental Section) and spectroscopic characterisation of the initially deposited material was undertaken rapidly. Attempts to dissolve this material in C_4D_8O or C_7D_8 gave poor data, due to sparing solubility. Thus deuteriochloroform was employed, and gave NMR spectra suggesting a species with two separate ligand environments of equal resonance intensity, see below, as well as $(PPh_2)_2NH$ and the still persistent **3**. Slow evaporation of the NMR solution rendered a deep orange crystalline material suitable for X-ray structure analysis. This indicated the formation of a non-oxidised mercury(II) phosphanylamide chloride complex; $[Hg_2\{\mu_2\text{-}(Ph_2P)_2N\}_3Cl]\cdot 3/2\,CDCl_3$, **4**·$3/2\,CDCl_3$ (Figure 3, iii in Scheme 1). Further crystallization from the reaction mixture filtrate gave **3**·$2C_7H_8$.

 © 2005 Wiley-VCH Verlag GmbH & Co. KGaA, Weinheim

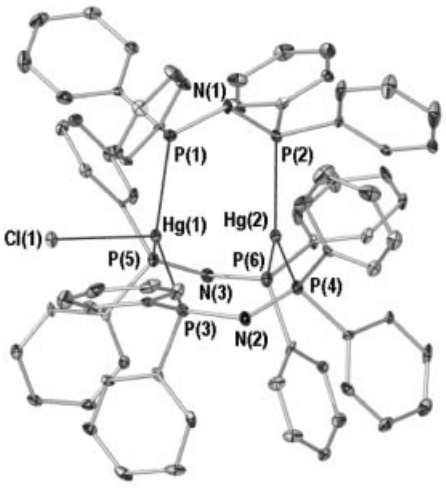

Figure 3. The crystal structure of $[Hg_2\{\mu_2\text{-}(Ph_2P)_2N\}_3Cl]\cdot 3/2CDCl_3$ (**4**·3/2 $CDCl_3$), (POV-Ray 40% thermal ellipsoids). All solvent molecules removed for clarity.

X-ray Crystal Structures and Characterisation

Compound **1**·3 C_7H_8 crystallises in the triclinic space group $P\bar{1}$ with three Hg metal ions and four deprotonated ligands in the asymmetric unit (Figure 1, Table1 and Table 2). The structure is a neutral homoleptic trinuclear complex with mercury atoms in a triangular array and considered to be linked by metal–metal bonds (below). This core is supported by four bridging phosphanylamide ligands. Hg(1) is coordinated by two phosphorus atoms [P(1,3)] from two ligands, while Hg(2) and Hg(3) are coordinated to three phosphorus atoms [P(2,5,7) and P(4,6,8)], respectively, from three different ligands. Including Hg–Hg bonds, Hg(2) and Hg(3) are five-coordinate and Hg(1) is four-coordinate. Different bond lengths are observed for all Hg–P contacts; these range from 2.526(2)–2.630(2) Å. Mercury to phosphorus interactions associated with Hg(2) and Hg(3) have an average length of 2.560 Å. Counterintuitively, this is smaller than to the analogous bonds of lower coordinate Hg(1) (mean 2.598 Å), as lower coordination numbers are usually associated with shorter bond lengths.[20] A similar dmpm based compound,[11] $[Hg_3(\mu\text{-dmpm})_4][O_3SCF_3]_4$, with a triangular Hg_3 cation and similar connectivity to the neutral compound **1**·3 C_7H_8 has a mean Hg–P bond length of 2.539 Å. Neutrality and the increased steric bulk at phosphorus of **1**·3 C_7H_8 results in lengthening of the Hg–P interactions overall. In $[Hg_3(\mu_2\text{-}(Ph_2P)_2NH)_3][O_3SCF_3]_4$,[21] a decrease in the number of ligands and the cationic nature offset lack of deprotonation leading to shorter Hg–P bond lengths (2.506–2.536 Å) than in **1**·3 C_7H_8.

Overall charge neutrality indicates that the formal oxidation state of Hg in **1**·3 C_7H_8 is +4/3. The Hg–Hg bond

Table 1. Selected (i) bond lengths [Å] and (ii) angles [°] for $[Hg_3\{\mu\text{-}(Ph_2P)_2N\}_4]\cdot 3C_7H_8$ (**1**·3 C_7H_8).

(i) Atoms	Bond lengths	Atoms	Bond lengths
Hg(1)–Hg(2)	2.7785(10)	Hg(1)–Hg(3)	2.8986(10)
Hg(2)–Hg(3)	3.0721(8)	Hg(1)–P(1)	2.566(2)
Hg(1)–P(3)	2.630(2)	Hg(2)–P(4)	2.571(2)
Hg(2)–P(5)	2.526(2)	Hg(2)–P(7)	2.562(2)
Hg(3)–P(2)	2.572(2)	Hg(3)–P(3)	2.573(2)
Hg(3)–P(8)	2.559(2)	P(1)–N(1)	1.606(7)
P(2)–N(1)	1.647(6)	P(3)–N(2)	1.627(7)
P(4)–N(2)	1.617(6)	P(5)–N(3)	1.620(6)
P(6)–N(3)	1.609(7)	P(7)–N(4)	1.614(7)
P(8)–N(4)	1.618(7)		

(ii) Atoms	Angles	Atoms	Angles
Hg(2)–Hg(1)–Hg(3)	65.48(2)	Hg(1)–Hg(2)–Hg(3)	59.14(3)
Hg(1)–Hg(3)–Hg(2)	55.37(3)	P(1)–Hg(1)–Hg(2)	152.49(5)
P(3)–Hg(1)–Hg(2)	91.88(5)	P(3)–Hg(1)–Hg(3)	154.77(5)
P(1)–Hg(1)–P(3)	114.03(7)	P(4)–Hg(2)–Hg(1)	89.26(5)
P(5)–Hg(2)–Hg(1)	120.38(5)	P(7)–Hg(2)–Hg(1)	108.85(6)
P(4)–Hg(2)–Hg(3)	148.36(5)	P(5)–Hg(2)–Hg(3)	85.68(6)
P(7)–Hg(2)–Hg(3)	88.20(6)	P(4)–Hg(2)–P(5)	112.04(8)
P(4)–Hg(2)–P(7)	105.01(8)	P(5)–Hg(2)–P(7)	116.97(7)
P(2)–Hg(3)–Hg(1)	88.67(5)	P(6)–Hg(3)–Hg(1)	133.06(5)
P(8)–Hg(3)–Hg(1)	96.78(6)	P(2)–Hg(3)–Hg(2)	140.52(5)
P(6)–Hg(3)–Hg(2)	85.70(6)	P(8)–Hg(3)–Hg(2)	86.74(6)
P(2)–Hg(3)–P(6)	114.40(7)	P(2)–Hg(3)–P(8)	116.10(8)
P(6)–Hg(3)–P(8)	106.98(7)	N(1)–P(1)–Hg(1)	115.3(2)
N(1)–P(2)–Hg(3)	115.0(2)	N(2)–P(3)–Hg(1)	112.4(2)
N(2)–P(4)–Hg(2)	116.9(3)	N(3)–P(5)–Hg(2)	113.8(2)
N(3)–P(6)–Hg(3)	116.4(2)	N(4)–P(7)–Hg(2)	116.4(2)
N(4)–P(8)–Hg(3)	116.5(3)	P(1)–N(1)–P(2)	123.1(4)
P(3)–N(2)–P(4)	126.3(4)	P(5)–N(3)–P(6)	125.4(4)
P(7)–N(4)–P(8)	127.8(4)		

 © 2005 Wiley-VCH Verlag GmbH & Co. KGaA, Weinheim

Table 2. Crystallographic data for compounds **1**·3 C_7H_8, **3**·2 C_7H_8, **3**·2 $C_4H_{10}O_2$ and **4**·3/2 $CDCl_3$.

	1·3 C_7H_8	**3**·2 C_7H_8	**3**·2 $C_4H_{10}O_2$	**4**·3/2 $CDCl_3$
Empirical formula	$C_{117}H_{104}Hg_3N_4P_8$	$C_{55}H_{48}Hg_1N_2O_1P_4$	$C_{52}H_{50}Hg_1N_2O_3P_4$	$C_{73.5}H_{60}Cl_{5.5}D_{1.5}Hg_2N_3P_6$
Mol. mass	2415.57	1077.42	1075.41	1770.33
Temperature (K)	123(2)	123(2)	123(2)	123(2)
Space group	$P\bar{1}$	$P\bar{1}$	$P\bar{1}$	$P\bar{1}$
a [Å]	13.178(3)	12.177(2)	12.304(3)	11.653(2)
b [Å]	18.779(4)	12.605(3)	12.640(3)	13.129(3)
c [Å]	21.029(4)	16.196(3)	16.019(3)	24.457(5)
α [°]	88.38(3)	101.52(3)	101.31(3)	93.09(3)
β [°]	84.61(3)	96.07(3)	93.95(3)	98.91(3)
γ [°]	77.52(3)	101.52(3)	103.08(3)	109.27(3)
V [Å^3]	5058.5(18)	2369.6(8)	2362.8(8)	3467.1(12)
Z	2	2	2	2
$D_{calcd.}$ (g·cm^{-3})	1.586	1.510	1.512	1.694
μ (mm^{-1})	4.720	3.425	3.437	4.819
Reflections collected	24316	33655	40868	36967
Unique reflections	12336	11542	10186	16268
Parameters varied	1218	569	552	829
R(int.)	0.1257	0.0546	0.0768	0.1249
R_1	0.0618	0.0968	0.0361	0.0741
wR_2	0.0983	0.2130	0.0643	0.1267

lengths vary within the complex, the shortest being 2.7785(10) Å [Hg(1)–Hg(3)] and the longest 3.0721(8) Å [Hg(2)–Hg(3)]. The upper value is larger than the Hg–Hg bond lengths in $[Hg_3(\mu\text{-dmpm})_4][O_3SCF_3]_4$ (2.767(1) to 2.955(1) Å],[11] owing to the uncharged nature of **1** and greater crowding. The van der Waals radius of Hg (1.73 Å)[22] gives an upper limit of 3.46 Å for a dimercury bonding contact. Reported Hg^I–Hg^I bonds range from 2.48 to 2.60 Å,[23] while the closed shell configuration of Hg^{2+} does not favour participation in Hg^{II}–Hg^{II} bonds. Thus, the Hg–Hg bond lengths of **1**·3C_7H_8, are indicative of subvalent mercury between Hg^I and Hg^{II} oxidation states. With a $Hg^{4/3+}$ oxidation state there are two electrons in excess of the d^{10} Hg^{II} configuration. These electrons bind the trinuclear core of **1**·3 C_7H_8, and presumably occupy a molecular orbital within the triangle. For the Hg_3^{4+} ion of $[Hg_3(dppm)_3(SO_4)_2]$,[24a] the bonding electrons are considered to occupy a molecular orbital from overlap of the 6s orbitals of the mercury atoms.[24b,24c] The Hg–Hg distances suggest the bonding electrons are more associated with Hg(1) than Hg(2,3), and greater Hg^I character might explain the longer Hg–P bonds to Hg(1). The triangular planes described by the triphosphorus donor ensembles [P(2,6,8) and P(4,5,7)] lie roughly perpendicular [76.24(5) and 85.97(5)°, respectively] to the plane of the trinuclear core. Hg(2) resides 0.7659(14) Å out of its triphosphorus plane [P(4,5,7)] and Hg(3) 0.7168(14) Å out of the analogous plane [P(2,6,8)]. The neutral homoleptic compound **1**·3 C_7H_8 is the first crystallographically characterised triangular mercury complex of a phosphanylamide ligand. The P–N distance (1.606–1.647 Å) shows values between P–N single and double bond range as in phosphazines, (range of 1.60–1.65 Å).[25]

Examination of **1**·3 C_7H_8 by $^{31}P\{^1H\}$ NMR spectroscopy indicates three very broad signals at 130.4, 95.6 and 81.9 ppm, which are characteristic of $[Hg_3(\mu\text{-dmpm})_4][O_3SCF_3]_4$[11] but at much higher chemical shifts than observed for $[Hg_3\{(\mu\text{-}Ph_2P)_2NH\}_3][O_3SCF_3]_4$.[21] The highest frequency resonance is attributed to the phosphorus atoms [P(1,3)] from two different ligands bound to the mercury of lowest coordination number. The next is assigned to the other two phosphorus atoms P(2,4) of these ligands, and the lowest frequency signal to P(5–8) of the two equivalent ligands linking Hg(2,3). These assignments are supported by intensities. Low solubility precluded low temperature measurements and resulted in very broad resonances, hence ^{199}Hg satellites could not be detected. The ^1H NMR spectrum of **1**·3 C_7H_8 shows three broad peaks situated at δ = 7.42, 6.91 and 6.81 ppm resulting from aromatic resonances associated with the ligands, as well as toluene resonances from lattice solvent. The IR spectrum of **1**·3 C_7H_8 is devoid of an N–H stretching band at 3300–3400 cm^{-1}, thus eliminating the possibility of remnant starting material or protonation of any of the coordinated ligands. Distinct bands at 1147 and 1229 cm^{-1} can be assigned as PNP stretching, which are typically found in the range of 1100 to 1300 cm^{-1}.[26] This is consistent with deprotonation of $(Ph_2P)_2NH$, resulting in delocalisation of the anionic charge across the PNP backbone. Characterisation of **1**·3 C_7H_8 by ^{199}Hg NMR spectroscopy proved unsuccessful due to insufficient solubility of this compound in suitable solvents.

Discussion of the structures of **3**·2 C_7H_8 and **3**·2 $C_4H_{10}O_2$ is centred on the latter, as it gave a more precise refinement than compound **3**·2 C_7H_8. Both contain the same complex and differ only in solvation. The crystallographic data are in Table 2 and selected bonds lengths and angles for **3**·2 $C_4H_{10}O_2$ in Table 3, whilst geometric values for **3**·2 C_7H_8 have been deposited.

Compound **3**·2 $C_4H_{10}O_2$ crystallises as a centrosymmetric dimer (triclinic, space group $P\bar{1}$) and consists of two mercury atoms bridged by two unoxidised phosphanylamide ligands. The metal coordination is completed by two terminal $[(Ph_2P)(OPPh_2)N]^-$ ligands which are *transoid* across the centre of symmetry (Figure 2). The Hg atom resides

 © 2005 Wiley-VCH Verlag GmbH & Co. KGaA, Weinheim

Table 3. Selected (i) bond lengths [Å] and (ii) angles [°] for $[Hg_2\{\mu_2\text{-}(Ph_2P)_2N\}_2\{(Ph_2P)(OPPh_2)N\}_2]\cdot 2C_4H_{10}O_2$ ($\mathbf{3}\cdot 2C_4H_{10}O_2$).

(i)			
Atoms	Bond lengths	Atoms	Bond lengths
Hg(1)–P(2)	2.5242(12)	Hg(1)–P(3)	2.4953(12)
Hg(1)–P(4#)	2.5123(12)	Hg(1)–O(1)	2.624(3)
P(1)–N(1)	1.513(3)	P(1)–O(1)	1.513(3)
P(2)–N(1)	1.618(3)	P(3)–N(2)	1.598(3)
P(4#)–P(2)	1.609(3)		
(ii)			
Atoms	Angles	Atoms	Angles
P(2)–Hg(1)–P(3)	126.10(4)	P(2)–Hg(1)–P(4#)	109.37(4)
P(3)–Hg(1)–P(4#)	124.14(3)	P(2)–Hg(1)–O(1)	76.55(6)
P(3)–Hg(1)–O(1)	94.04(6)	P(4#)–Hg(1)–O(1)	105.34(7)
P(1)–N(1)–P(2)	121.55(19)	P(3)–N(2)–P(4)	133.1(2)
N(1)–P(2)–Hg(1)	108.91(12)	N(2)–P(3)–Hg(1)	118.52(12)
N(2#)–P(4#)–Hg(1)	117.41(12)	P(1)–O(1)–Hg(1)	111.96(13)
O(1)–P(1)–N(1)	118.10(15)		

Symmetry transformation used to generate # atoms $-x + 1, -y + 1, -z + 1$.

0.0893(15) Å out of the plane defined by the three associated P atoms with the O atom in an apical position completing four coordination. Thus, the geometry of mercury is best described as a distorted triangular-based pyramid [P(3)–Hg(1)–P(4*) 124.14(3)°, P(3)–Hg(1)–P(2) 126.10(4)°, P(4*)–Hg(1)–P(2) 109.37(4)°]. Unlike $\mathbf{1}\cdot 3C_7H_8$, the Hg···Hg distance in $\mathbf{3}\cdot 2C_4H_{10}O_2$ of 4.487(2) Å is well outside the sum of the van der Waals radii (3.46 Å).[22]

Comparison with the structure of $[Hg\{(OPPh_2)NPPh_2\}_2]$, which has two chelating diphenylphosphanyl(diphenylphosphoryl)amide ligands, shows this has much shorter Hg–P distances, 2.4042(7) Å, but longer Hg–O lengths, 2.7135(15) Å.[27] This arises from the different stereochemistry (square planar) which is skewed towards two short and two long bonds in accordance with the preference of mercury for digonal two coordination.[23,28] Similarly Hg–P distances in the dinuclear phosphanylamine complex $[Hg_2\{\mu\text{-}(Ph_2P)_2NH\}_2(O_3SCF_3)_4]$ are short [2.421(1)–2.426(1) Å] with longer Hg–O bond lengths [2.679(4)–2.893(5) Å],[27] again owing to the tendency of mercury to have two short colinear bonds. This factor is not in evidence in $\mathbf{3}\cdot 2C_7H_8$ and $\mathbf{3}\cdot 2C_4H_{10}O_2$ with the three soft P and one hard O donors giving rise to the trigonal pyramidal geometry.

The $^{31}P\{^1H\}$ NMR spectrum of bulk $\mathbf{3}\cdot 2C_7H_8$ exhibits three broad resonances at δ = 60.1, 28.3 and 12.4 ppm with intensities in approximately a 2:4:2 ratio, corresponding to the three types of phosphorus atoms in the structure. The oxidised phosphorus P(1) should resonate at the highest chemical shift, since P^V centres are more deshielded than P^{III} centres. The ^{31}P resonance of the P=O group in the free (protonated) ligand, $(Ph_2P)(OPPh_2)NH$ occurs at δ = 21.4 ppm,[29] and the large shift of P(1) (60.1 ppm) can be attributed to chelation as observed for other phosphorus based systems that have five membered chelate rings.[30] The larger intensity indicates the middle resonance should be assigned to the four bridging phosphorus atoms [P(3,4,3#,4#)]. This leaves the remaining resonance to be assigned to P(2) (δ =12.4 ppm). The ^1H NMR spectrum of $\mathbf{3}\cdot 2C_7H_8$ is unremarkable, while the IR spectrum exhibits a band at 1128 cm^{-1} characteristic of an *O*-coordinated phosphoryl group.[31] Other characteristic features include bands at 1228 and 1148 cm^{-1} attributed to P=N stretching.[26]

The structure of $\mathbf{4}\cdot 3/2CDCl_3$ (Figure 3) consists of two mercury atoms bridged by three phosphanylamide ligands with a chloride coordinated to Hg(1). Each mercury is coordinated by three phosphorus atoms, Hg(1) being four coordinate and Hg(2) three coordinate. The latter has an average Hg–P bond length of 2.482 Å and four coordinate Hg(1) has an average Hg–P bond length of 2.593 Å (Table 4). This is consistent with the higher coordination of Hg(1). The Hg(1)–Cl(1) terminal bond length in $\mathbf{4}\cdot 3/2CDCl_3$, 2.624(2) Å, is considerably extended relative to those in $[HgCl_4]^{2-}$ complexes, which possess an average Hg–Cl bond length of 2.472 Å,[32] but well inside the sum (3.58 Å) of the van der Waals radii of Hg and Cl. In $[Hg_2(\mu\text{-}dppm)_2(\mu\text{-}Cl)Cl_2][Cl]\cdot H_2O$[33] which has a somewhat similar structural core to $\mathbf{4}\cdot 3/2CDCl_3$, the mean terminal Hg–Cl bond length is 2.587 Å, similar to that of $\mathbf{4}\cdot 3/2CDCl_3$.

The HgP_3 geometry of Hg(1) and Hg(2) can be considered equilateral triangular with all P–Hg–P angles close to 120° (Table 4). Hg(1) is 0.3280 (14) Å out of the P(1,3,5) plane, *exo* to the Hg···Hg vector. The chloride ligand lies perpendicular to this plane. Overall the stereochemistry for Hg(1) is trigonal pyramidal. Hg(2) is 0.1260(13) Å out of the analogous P(2,4,6) plane being *endo* to the Hg···Hg vector and has triangular geometry. The two triphosphorus donor P(1,3,5) and P(2,4,6) ensembles are very close to coplanar with an interplanar angle of 0.68(3)°. Although the Hg···Hg distance [3.0042(7) Å] is well within two van der Waals radii (3.46 Å),[22] this does not indicate the presence of a mercury–mercury bond as there are no valence electrons available for bonding, unless some electron density is transmitted from the *trans* Hg–Cl bond. A closer nonbonding Hg···Hg contact has been reported in $[Hg_2(1,8\text{-}C_{10}H_6)_2]$ [2.797(1) Å],[34] whilst Hg···Hg [3.2805(7) Å] of $[Hg_2\{\mu\text{-}(Ph_2P)_2NH\}_2(O_3SCF_3)_4]$ is not considered bonding.[27] It has been claimed on the basis of a low frequency

 © 2005 Wiley-VCH Verlag GmbH & Co. KGaA, Weinheim

Table 4. Selected (i) bond lengths [Å] and (ii) angles [°] for $[Hg_2\{\mu_2\text{-}(Ph_2P)_2N\}_3Cl]\cdot 3/2\,CDCl_3$ (**4**·3/2 $CDCl_3$).

(i) Atoms	Bond lengths	Atoms	Bond lengths
Hg(1)–Hg(2)	3.0042(7)	Hg(1)–Cl(1)	2.624(2)
Hg(1)–P(1)	2.599(3)	Hg(1)–P(3)	2.583(3)
Hg(1)–P(5)	2.599(2)	Hg(2)–P(2)	2.483(3)
Hg(2)–P(4)	2.464(3)	Hg(2)–P(6)	2.468(3)
P(1)–N(1)	1.635(7)	P(2)–N(1)	1.618(7)
P(3)–N(2)	1.607(7)	P(4)–N(2)	1.605(7)
P(5)–N(3)	1.624(7)	P(6)–N(3)	1.612(8)

(ii) Atoms	Angles	Atoms	Angles
P(1)–Hg(1)–Hg(2)	84.67(6)	P(3)–Hg(1)–Hg(2)	81.55(6)
P(5)–Hg(1)–Hg(2)	82.01(6)	Cl(1)–Hg(1)–Hg(2)	177.86(6)
P(1)–Hg(1)–Cl(1)	96.85(8)	P(3)–Hg(1)–Cl(1)	96.38(8)
P(5)–Hg(1)–Cl(1)	98.59(8)	P(1)–Hg(1)–P(3)	119.44(8)
P(1)–Hg(1)–P(5)	117.24(9)	P(3)–Hg(1)–P(5)	118.59(9)
P(2)–Hg(2)–Hg(1)	90.49(6)	P(4)–Hg(2)–Hg(1)	94.30(6)
P(6)–Hg(2)–Hg(1)	93.87(6)	P(2)–Hg(2)–P(4)	121.33(9)
P(2)–Hg(2)–P(6)	115.63(9)	P(4)–Hg(2)–P(6)	122.27(10)
N(1)–P(1)–Hg(1)	119.3(3)	N(1)–P(2)–Hg(2)	116.7(3)
N(2)–P(3)–Hg(1)	120.7(3)	N(2)–P(4)–Hg(2)	111.5(3)
N(3)–P(5)–Hg(1)	122.0(3)	N(3)–P(6)–Hg(2)	114.1(3)

Raman absorption (46 to 48 cm^{-1}) assigned to ν(Hg–Hg) that there is a weak mercury–mercury bond in $[Hg_2(\mu\text{-dppm})_2(\mu\text{-Cl})Cl_2][Cl]\cdot H_2O$, where the separation is 3.343(3) Å.[33] We find this difficult to sustain for an $Hg^{II}\cdots Hg^{II}$ interaction, unless electron density is transmitted from Hg–Cl bonds.

The crude product from which crystals of **4**·3/2 $CDCl_3$ were obtained was characterised by $^{31}P\{^1H\}$ NMR and ^1H NMR spectroscopy. Two equal intensity and very broadened resonances in the $^{31}P\{^1H\}$ NMR spectrum at δ = 71.0 and 37.2 ppm, can be assigned to P(2,4,6) on the lower coordinate mercury and P(1,3,5) of **4** respectively. There is also a resonance at δ = 45.8 ppm attributable to (protonated) $(Ph_2P)_2NH$,[5] in the appropriate ratio to **4** consistent with the formation of **4**·3/2 $CDCl_3$ by protolysis/deuterolysis (see vii in Scheme 1). The ^1H NMR spectrum of the crude product displays solely the expected protons from phenyl groups (7.8 to 6.9 ppm) and a resonance attributable to the amine proton of $(Ph_2P)_2NH$ (δ = 3.1 ppm).

Conclusions

The attempted synthesis of homoleptic lanthanoid chelating phosphanylamide complexes by redox transmetallation/ligand exchange, gave instead the unusual subvalent mercury compound **1**·3 C_7H_8, attributable to formation of intermediate $[Hg\{(Ph_2P)_2N\}_2]$ **2** followed by reduction by mercury metal. Consistent with this, reaction of $Hg(C_6F_5)_2$ with $(Ph_2P)_2NH$ in the presence of mercury metal provided a higher yielding route to **1**·3 C_7H_8. Attempted preparation of **2** yielded **3**·2 C_7H_8 and **3**·2 $C_4H_{10}O_2$ containing hemi-oxidised phosphanylamide as well as the unoxidised phosphanylamide ligands.

Experimental Section

Mercury complexes, lanthanoid metal filings and the phosphanylamine ligand were handled and stored under purified nitrogen (activated BASF R3/11 copper oxide "catalyst" and 4-Å molecular sieves). Toluene, tetrahydrofuran, 1,2-dimethoxyethane and hexane were pre-dried with sodium wire and then distilled from sodium benzophenone under purified nitrogen. The reagents $Hg(C_6F_5)_2$ and $(Ph_2P)_2NH$ were prepared as reported.[35] The former was recrystallised from hot methanol/water, followed by drying under reduced pressure for several hours. The latter was shown free of P=O species by ^{31}P NMR spectroscopy. $^{31}P\{^1H\}$, ^{19}F and ^1H nuclear magnetic resonance (NMR) spectra were recorded with a Bruker AC 300 spectrometer. ^{199}Hg NMR could not be recorded due to the low solubility of the mercury compounds. Deuterated solvents (C_6D_6 and C_4D_8O) were dried with calcium hydride (powdered) for 24 h. Deuterated $CDCl_3$ was dried with 4-Å molecular sieves. All dried deuterated solvents were degassed by three cycles of freezing, evacuating, and backfilling with nitrogen and thawing and were then vacuum transferred and stored under nitrogen. Infrared spectra (4000–650 cm^{-1}) of Nujol mulls (prepared in a drybox) were recorded with a Perkin–Elmer 1600 Fourier transform infrared spectrometer. Melting points were determined in sealed glass capillaries under nitrogen. Elemental analyses were by the Campbell Microanalytical Laboratory, University of Otago, New Zealand. The complicated isolation/preparation and solvation of **4**·3/2 $CDCl_3$ frustrated all attempts to obtain satisfactory elemental analyses.

$[Hg_3\{\mu_2\text{-}(Ph_2P)_2N\}_4]\cdot 3\,C_7H_8$(1·3 C_7H_8).Method1: Bis(diphenylphosphanyl)amine (1.01 g, 2.56 mmol) and $Hg(C_6F_5)_2$ (0.68 g, 1.28 mmol) were dissolved in toluene (40 mL). Nd metal (1.23 g, 8.5 mmol) was added and the mixture was stirred at 80 °C for 96 h. The resulting suspension was filtered through a cannula and a light green/blue precipitate remained. This was subsequently washed with 2 × 10 mL of toluene. The orange-coloured solution was then evaporated under reduced pressure to yield a bright orange solid. Dissolution in a mixture of toluene (15 mL) and hex-

 © 2005 Wiley-VCH Verlag GmbH & Co. KGaA, Weinheim

ane (5 mL) and concentration to 5 mL gave single rectangular orange crystals. These were filtered off, washed with hexane (5 mL) and dried in vacuo giving $[Hg_3\{\mu_2\text{-}(Ph_2P)_2N\}_4]\cdot 3C_7H_8$ (**1**·3C$_7$H$_8$). Yield 0.70 g (26%), and the crystals were used for the structure determination. EDAX analysis of the green/blue precipitate detected C, F, O, Nd, P and no Hg.

Method 2: A suspension of bis(diphenylphosphanyl)amine (0.10 g, 0.25 mmol), $Hg(C_6F_5)_2$ (0.07 g, 0.13 mmol) and Er metal (0.14 g, 0.85 mmol) in toluene (30 mL) was stirred for 15 d at room temperature. The resulting suspension was filtered through a cannula and a yellow/blue precipitate remained. The orange filtrate was evaporated under reduced pressure to yield a bright orange solid. Crystallisation from toluene/hexane gave a few orange crystals which were identified by X-ray crystallography as $[Hg_3\{\mu_2\text{-}(Ph_2P)_2N\}_4]\cdot 3C_7H_8$ (**1**·3C$_7$H$_8$). Yield 0.068g (22%), m.p. 253 °C. Unit cell data: a = 13.17, b = 18.79, c = 21.04 Å, α= 88.43, β= 84.61, γ= 77.52°. V = 5063.83 Å^3. $^{31}P\{^1H\}$ NMR (C$_7$H$_8$, 25 °C): δ = 80.5 (br. s, 4 P), 95.8 (br. s, 2 P), 130.1 (br. s, 2 P) ppm. The IR spectrum was in agreement with that of the analytically pure sample (Method 3).

Method 3: To bis(diphenylphosphanyl)amine (0.31 g, 0.80 mmol) dissolved in toluene (40 mL) was added $Hg(C_6F_5)_2$ (0.21 g, 0.40 mmol) and the solution turned yellow. Two drops of liquid mercury were added. The solution became bright orange, was left at room temperature overnight under nitrogen and filtered. The solvent was evaporated to 20 mL and left to crystallise, yielding **1**·3C$_7$H$_8$ (0.69 g, 80%). M.p. 250–252 °C. Unit cell data: a = 13.15, b = 18.76, c = 21.06 Å, α= 88.40, β= 84.61, γ= 77.53°. V = 5064.53 Å^3. ^{1}H NMR (300 MHz, C$_6$D$_6$, 25 °C): δ = 2.11 (s, 9 H, *Me*Ph), 6.83–6.89 (m, 15 H, *Ph*Me), 6.81 [br. m, 16 H, *p*-H (PhP)], 6.91 [br. m, 32 H, *m*-H (PhP)], 7.42 [br. m, 32 H, *o*-H (PhP)] ppm. $^{31}P\{^1H\}$ NMR (C$_6$D$_6$, 25 °C): δ = 81.9 (br. s, 4 P, P5,6,7,8), 95.6 (br. s, 2 P, P2,4), 130.4 (br. s, 2 P, P1,3) ppm. IR (Nujol): $\tilde{\nu}$ = 3020 m, 1229 s, 1147 s, 1098 m, 1025 w, 950 w, 755 m, 697 s cm^{-1}. $C_{117}H_{104}Hg_3N_4P_8$ (2415.57): calcd. C 58.17, H 4.34, N 2.32; found C 57.95, H 4.86, N 2.95.

$[Hg_2\{\mu_2\text{-}(Ph_2P)_2N\}_2\{(Ph_2P)(OPPh_2)N\}_2]\cdot 2C_7H_8$ (3·2C$_7$H$_8$): To bis(diphenylphosphanyl)amine (0.31 g, 0.80 mmol) dissolved in toluene (50 mL) was added $Hg(C_6F_5)_2$ (0.21 g, 0.40 mmol) and the solution turned yellow. After 1 h the yellow solution became bright orange and was left at room temperature overnight under nitrogen. Yellow crystals formed and were filtered from the mother liquor and characterised by X-ray crystallography as $[Hg_2\{\mu_2\text{-}(Ph_2P)_2N\}_2\{(Ph_2P)(OPPh_2)N\}_2]\cdot 2C_7H_8$ (**3**·2C$_7$H$_8$). Yield 0.60 g (77%). M.p. 242–245 °C. ^{1}H NMR (300 MHz, C$_4$D$_8$O, 25 °C): δ = 2.04 (s, 6 H, *Me*Ph), 6.8–8.2 (m , 90 H, PhP and *Ph*Me) ppm. $^{31}P\{^1H\}$ NMR (C$_4$D$_8$O, 25 °C): δ = 12.4 (s, 2 P, Hg–P chelating) 28.3 (s, 4 P, Hg–P bridging) 60.1 (s, 2 P, PO) ppm. IR (Nujol): $\tilde{\nu}$ = 3055 w, 1228 br. s, 1178 w, 1149 m, 1128 m, 1101 m, 1080 m, 1063 m, 1026 m, 998 m, 793 s, 731 m, 694 vs cm^{-1}. $C_{110}H_{96}Hg_2N_4O_2P_8$ (2154.9): calcd. C 61.31, H 4.49, N 2.60; found C 60.60, H 4.65, N 2.84. The presence of C_6F_5H in the filtrate was established by ^{19}F NMR spectroscopy.[36]

$[Hg_2\{\mu_2\text{-}(Ph_2P)_2N\}_2\{(Ph_2P)(OPPh_2)N\}_2]\cdot 2C_4H_{10}O_2$ (3·2C$_4$H$_{10}$O$_2$): Bis(diphenylphosphanyl)amine (0.10 g, 0.26 mmol) and $Hg(C_6F_5)_2$ (68 mg, 0.13 mmol) were dissolved in toluene (30 mL). Nd metal (12 mg, 0.09 mmol) was added and the mixture sonicated for 4 d. The resulting suspension was filtered through a cannula and a light green/blue precipitate remained. Evaporation of the filtrate yielded a bright orange solid, which on crystallisation from toluene/hexane gave single crystals, which were unsatisfactory for X-ray diffraction. The precipitate was washed with 1,2-dimethoxyethane (20 mL) which on partial evaporation deposited single crystals of $[Hg_2\{\mu_2\text{-}(Ph_2P)_2N\}_2\{(Ph_2P)(OPPh_2)N\}_2]\cdot 2C_4H_{10}O_2$ (**3**·2C$_4$H$_{10}$O$_2$). Yield 0.04 g (16%). IR (Nujol): $\tilde{\nu}$ = 1230 s, 1149 m, 1128 m, 1101 m, 1080 m, 983 w, 939 m, 830 w, 780 w-m, 754 m-s, 698 s, 668 s, 648 w cm^{-1}.

$[Hg_2\{\mu_2\text{-}(Ph_2P)_2N\}_3Cl]\cdot 3/2CDCl_3$ (4·3/2CDCl$_3$): Solid bis(diphenylphosphanyl)amine (0.39 g, 1.0 mmol) and $Hg(C_6F_5)_2$ (0.27 g, 0.50 mmol) were mixed in the dry box (O_2 < 0.1 ppm) whereupon onset of reaction was indicated by a developing yellow colour. After connection to a vacuum/N_2 line with a recently regenerated purification train, addition of toluene (50 mL) gave a yellow solution which intensified to orange in 10 min. After 24 h an orange solid deposited, m.p. 205–208 °C. IR (Nujol): $\tilde{\nu}$ = 3034 w, 1495 m, 1164 s, 1097 m, 1025 s, 998 s, 769 s, 727 s, 692 s, 525 w cm^{-1}. This material when dissolved in $CDCl_3$ was shown to be a mixture of **3**, **4** and $(Ph_2P)_2NH$ by $^{31}P\{^1H\}$ NMR ($CDCl_3$, 25 °C): δ = 15.7 (s, 2 P, Hg–P chelating of 3), 26.7 (s, 4 P, Hg–P bridging of 3), 37.2 (br. m, 3 P, P1,3,5 of **4**) 45.8 [s, $(Ph_2P)_2NH$], 64.0 (m, 2 P, PO of **3**), 71.03 (br. m, 3 P, P2,4,6 of **4**), together with further minor impurity signals. Single crystals formed in the $CDCl_3$ solution and were identified by X-ray crystallography as **4**·3/2CDCl$_3$. The mother liquor was evaporated to 5 mL. The resulting orange precipitate was dissolved on gentle heating and slow cooling deposited crystals of **3**·2C$_7$H$_8$ (unit cell data a = 12.19, b = 12.61, c = 16.19 Å, α= 101.53, β= 96.07, γ= 101.52°, V = 2370.3 Å^3).

X-ray Crystallography: Crystalline samples of compounds $[Hg_3\{\mu\text{-}(Ph_2P)_2N\}_4]\cdot 3C_7H_8$ (**1**·3C$_7$H$_8$), $[Hg_2\{\mu_2\text{-}(Ph_2P)_2N\}_2\{(Ph_2P)\text{-}(OPPh_2)N\}_2]\cdot 2C_7H_8$ (**3**·2C$_7$H$_8$), $[Hg_2\{\mu_2\text{-}(Ph_2P)_2N\}_2\{(Ph_2P)\text{-}(OPPh_2)N\}_2]\cdot 2C_4H_{10}O_2$ (**3**·2C$_4$H$_{10}$O$_2$), and $[Hg_2\{\mu_2\text{-}(Ph_2P)_2N\}_3Cl]\cdot 3/2CDCl_3$ (**4**·3/2CDCl$_3$) were mounted on glass fibres, in viscous hydrocarbon oil. Crystal data were obtained using an Enraf–NoniusKappa CCD at –150 °C (123 K). X-ray data were processed using the DENZO program.[37] Structural solution and refinement was carried out using the SHELX suite of programs[38,39] with the graphical interface X-Seed.[40] All hydrogen atoms were placed in calculated positions using the riding model.

CCDC-241398 (for **1**·3C$_7$H$_8$), CCDC-241399 (for **3**·2C$_4$H$_{10}$O$_2$), CCDC-241400 (for **3**·2C$_7$H$_8$) and CCDC-241401 (for **4**·3/2CDCl$_3$) contain the supplementary crystallographic data for this paper. These data can be obtained free of charge from The Cambridge Crystallographic Data Centre via www.ccdc.cam.ac.uk/data_request/cif.

Compound $[Hg_3\{\mu\text{-}(Ph_2P)_2N\}_4]\cdot 3C_7H_8$ (1·3C$_7$H$_8$): For compound $[Hg_3\{\mu\text{-}(Ph_2P)_2N\}_4]\cdot 3C_7H_8$ (**1**·3C$_7$H$_8$), one toluene molecule of solvation was disordered "tip-to-toe" over two sites of partial occupancy. These were satisfactorily modelled with half occupancy. No hydrogen atoms were appended to this disordered molecule and an ISOR 0.01 refinement was used to obtain satisfactory thermal parameters for atoms C(112), C(114), C(118) and C(120).

Compound $[Hg_2\{\mu_2\text{-}(Ph_2P)_2N\}_2\{(Ph_2P)(OPPh_2)N\}_2]\cdot 2C_7H_8$ (3·2C$_7$H$_8$): For compound $[Hg_2\{\mu_2\text{-}(Ph_2P)_2N\}_2\{(Ph_2P)(OPPh_2)N\}_2]\cdot 2C_7H_8$ (**3**·2C$_7$H$_8$), the poor R_1 value (see Table 2) can be attributed to a peak of residual electron density (20.086) located 0.829 Å from Hg(1). Incorporation of this density led to extension of the Hg(1)–O(1) and Hg(1)–P(2) bonds (lesser occupancy relative to greater Hg(1) occupancy) of greater than 0.16 and 0.80 Å, respectively. Accordingly, the disorder was not modelled.

Compound $[Hg_2\{\mu_2\text{-}(Ph_2P)_2N\}_2\{(Ph_2P)(OPPh_2)N\}_2]\cdot 2C_4H_{10}O_2$ (3·2C$_4$H$_{10}$O$_2$): For compound $[Hg_2\{\mu_2\text{-}(Ph_2P)_2N\}_2\{(Ph_2P)(OPPh_2)N\}_2]\cdot 2C_4H_{10}O_2$ (**3**·2C$_4$H$_{10}$O$_2$), a peak of residual electron density (3.97) is located 0.882 Å from Hg(1). Modelling of this electron density as a partial Hg occupancy led to extension of the original

 © 2005 Wiley-VCH Verlag GmbH & Co. KGaA, Weinheim

Hg(1)–O(1) and Hg(1)–P(2) bonds, new occupancy less relative to Hg(1) of greater than 0.12 and 0.8 Å, respectively. Accordingly, the disorder was not modelled.

Compound $[Hg_2\{\mu_2\text{-}(Ph_2P)_2N\}_3Cl]\cdot 3/2\,CDCl_3$ ($4\cdot 3/2\,CDCl_3$): For compound $[Hg_2\{\mu_2\text{-}(Ph_2P)_2N\}_3Cl]\cdot 3/2\,CDCl_3$ ($\mathbf{4}\cdot 3/2\,CDCl_3$), ISOR 0.01 refinement was required for atoms C(25), C(55) and N(1) in order to obtain satisfactory thermal parameters. Due to computational constraints the deuterium atoms of the lattice solvent were refined as hydrogen.

Acknowledgments

We thank the Australian Research Council for continued financial support. Dr. Craig Forsyth, David Evans and Stuart Leary are acknowledged for X-ray crystallography input to this publication.

[1] a) T. Q. Ly, J. D. Woollins, *Coord. Chem. Rev.* **1998**, *176*, 451–481; b) P. W. Roesky, M. T. Gamer, M. Puchner, A. Greiner, *Chem. Eur. J.* **2002**, *8*, 5265–5271; c) P. Bhattacharyya, J. D. Woollins, *Polyhedron***1995***14*, 3367–3388; d) P. W. Roesky, *Heteroatom Chem.* **2002**, *13*, 514–520.
[2] a) M. Valderrama, R. Contreras, P. Muñoz, M. P. Lamata, D. Carmona, F. J. Lahoz, S. Elipe, L. A. Oro, *J. Organomet. Chem.* **2001**, *633*, 182–188; b) B. Chaudret, B. Delavaux, R. Poilblanc, *Coord. Chem. Rev.* **1988**, *86*, 191–243.
[3] a) I. Bachert, P. Braunstein, M. K. McCart, F. Fabrizizi de Biani, F. Laschi, P. Zanello, G. Kickelbick, U. Schubert, *J. Organomet. Chem.* **1999**, *573*, 47–59; b) A. Knoepfler-Mühlecker, B. Scheffter, H. Kopacka, K. Wurst, P. Peringer, *J. Chem. Soc.-Dalton Trans.* **1999**, 2525–2528.
[4] a) F. A. Cotton, F. E. Kühn, *Inorg. Chim. Acta* **1996**, *252*, 257–264; b) L. Han, L. Shi, L. Zhang, Z. Chen, M. Hong, *Inorg. Chem. Commun.* **2003**, *6*, 281–283.
[5] O. Kühl, T. Koch, F. B. Somoza, Jr, P. C. Junk, E. Hey-Hawkins, D. Plat, M. S. Eisen, *J. Organomet. Chem.* **2000**, *604*, 116–125.
[6] O. Kühl, P. C. Junk, E. Hey-Hawkins, *Z. Anorg. Allg. Chem.* **2000**, *626*, 1591–1594.
[7] H. Liu, M. Calhorda, M. G. B Drew, V. Félix, J. Novosad, L. F. Veiros, F. Fabrizizi de Biani, P. Zanello, *J. Chem. Soc. Dalton Trans.* **2002**, 4365–4375.
[8] T. G. Wetzel, S. Dehnen, P. W. Roesky, *Angew. Chem. Int. Ed.* **1999**, *38*, 1086–1088.
[9] G. B. Deacon, C. M. Forsyth, S. Nickel, *J. Organomet. Chem.* **2002**, *647*, 50–60.
[10] G. B. Deacon, C. M. Forsyth, *Inorganic Chemistry Highlights*, Wiley-VCH, Weinheim, **2002**, chapter 7.
[11] A. Knoepfler-Mühlecker, E. Ellmerer-Müller, R. Konrat, K. Ongania, K. Wurst, P. Peringer, *J. Chem. Soc. Dalton Trans.* **1997**, 1607–1610.
[12] G. B. Deacon, A. J. Koplick, W. D. Raverty, D. G. Vince, *J. Organomet. Chem.* **1979**, *182*, 121–141.
[13] G. B. Deacon, C. M. Forsyth, *Organometallics* **2000**, *19*, 1205–1207; **2003**, *22*, 1349–1352.
[14] a) G. B. Deacon, C. M. Forsyth, B. M. Gatehouse, P. A. White, *Aust. J. Chem.* **1990**, *43*, 795–806; b) G. B. Deacon, R. H. Newnham, *Aust. J. Chem.* **1985**, *38*, 1757–1765.
[15] R. D. Chambers, G. E. Coates, J. G. Livingstone, W. K. R. Musgrave, *J. Chem. Soc.* **1962**, 4367–4371.
[16] a) G. B. Deacon, *J. Organomet. Chem.* **1967**, *9*, P1–P2; b) H. B. Albrecht, G. B. Deacon, M. J. Tailby, *J. Organomet. Chem.* **1974**, *70*, 313–321.
[17] F. Schulz, I. Pantenburg, D. Naumann, *Z. Anorg. Allg. Chem.* **2003**, *629*, 2312–2316.
[18] a) J. E. Connett, A. G. Davies, G. B. Deacon, J. H. S. Green, *J. Chem. Soc. (C)* **1966**, 106–111; b) A. J. Canty, G. B. Deacon, *Aust. J. Chem.* **1971**, *24*, 489–499.
[19] a) J. E. Cosgriff, G. B. Deacon, B. M. Gatehouse, *Aust. J. Chem.* **1993**, *46*, 1881–1896; b) G. B. Deacon, S. Nickel, P. MacKinnon, E. R. T. Tiekink, *Aust. J. Chem.* **1990**, *43*, 1245–1257.
[20] R. D. Shannon, *Acta Crystallogr. Sect. A* **1976**, *32*, 751–767.
[21] W. Schuh, G. Hägele, R Olschner, A. Lindner, P. Dvortsak, H. Kopacka, K. Wurst, P. Peringer, *J. Chem. Soc. Dalton Trans.* **2002**, 19–27.
[22] A. J. Canty, G. B. Deacon, *Inorg. Chim Acta* **1980**, *45*, 225–227.
[23] J. L. Wardell, *Mercury*, in Comprehensive Organometallic Chemistry (Eds.: G. Wilkinson, F. G. A. Stone, E. W. Abel), Pergamon, Oxford, **1982**, chapter 17; D. Breitinger, *Cadmium and Mercury*, in Comprehensive Coordination Chemistry II, Elsevier Pergamon, **2004**, vol. 6, chapter 6.9.
[24] a) B. Hammerle, E. P. Müller, D. L. Wilkinson, G. Müller, P. Peringer, *J. Chem. Soc. Chem. Commun.* **1989**, 1527–1528; b) W. R. Mason, *Inorg. Chem.* **1997**, *36*, 1164–1167; c) H. Kunkely, A. Vogler, *Chem. Phys. Lett.* **1993**, *206*, 467–469.
[25] M. Enlow, *Polyhedron* **2003**, *22*, 473–482.
[26] L. J. Bellamy, *The Infra-red Spectra of Complex Molecules*, 2nd ed., Methuen, London, **1958**, chapter 18.
[27] R. Haid, R. Gutmann, G. Czermak, C. Langes, W. Oberhauser, H. Kopacka, K. Ongania, P. Brüggeller, *Inorg. Chem. Commun.* **2003**, *6*, 61–67.
[28] D. Grdenic, *Quart. Rev. Chem. Soc.* **1965**, *19*, 303–328.
[29] P. Bhattacharyya, A. M. Z. Slawin, M. B. Smith, J. D. Woollins, *Inorg. Chem.* **1996**, *35*, 3675–3682.
[30] a) W. Oberhauser, C. Bachmann, T. Stampfl, R. Haid, C. Langes, A. Rieder, P. Brüggeller, *Polyhedron* **1998**, *17*, 3211–3220; b) W. Oberhauser, C. Bachmann, T. Stampfl, R. Haid, C. Langes, A. Rieder, P. Brüggeller, *Inorg. Chem. Commun.* **1998**, *1*, 185–189; c) W. Oberhauser, C. Bachmann, P. Brüggeller, *Inorg. Chim. Acta* **1995**, *238*, 35–43.
[31] K. Nakamoto, *Infra-red and Raman Spectra of Inorganic and Coordination compounds*, 5th ed., John Wiley & Sons, New York, **1997**.
[32] a) A. B. Salah, J. W. Bats, R. Kalus, H. Fuess, A. Daoud, *Z. Anorg. Allg. Chem.* **1982**, *493*, 178–186; b) A. B. Salah, J. W. Bats, R. Kalus, H. Fuess, A. Daoud, *Inorg. Chim. Acta* **1982**, *63*, 169–175.
[33] P. D. Harvey, K. T. Aye, K. Hierso, E. Isabel, I. Iognot, Y. Mugnier, F. D. Rochon, *Inorg. Chem.* **1994**, *33*, 5981–5982.
[34] H. Schmidbaur, H-J. Öller, D. L. Wilkinson, B. Huber, G. Müller, *Chem. Ber.* **1989**, *122*, 31–36.
[35] a) G. B. Deacon, J. E. Cosgriff, E. T. Lawrenz, C. M. Forsyth, D. L. Wilkinson, in Herrmann/Brauer, *Synthetic Methods of Organometallic and Inorganic Chemistry* (Ed.: W. A. Herrmann), G. Thieme, Stuttgart, **1997**, vol. 6 (Ed.: F. T. Edelmann), pp. 48, 49; b) H. Nöth, L. Mernel, *Z. Anorg. Allg. Chem.* **1967**, *349*, 225–240.
[36] M. I. Bruce, *J. Chem. Soc. (A)* **1968**, 1459.
[37] Z. Otwinowski, W. Minor, in *Processing of X-ray Diffraction Data Collected in Oscillation Mode*, Methods in Enzymology, 276: Macromolecular Crystallography, Part A (Eds.: C. W. Cater, R. M. Sweet), Academic Press, New York, **1997**, 307.
[38] G. M. Sheldrick, SHELXL-97, University of Göttingen, Germany, **1997**.
[39] G. M. Sheldrick, SHELXS-97, University of Göttingen, Germany, **1997**.
[40] L. J. Barbour, *J. Supramol. Chem.* **2001**, *1*, 189–191.

Received: November 4, 2004

 © 2005 Wiley-VCH Verlag GmbH & Co. KGaA, Weinheim

A Bicyclic P–P-Bridged 1,3,2,4-Diphosphadiboretane Cation and an Imino(phosphinidene)borane–$AlBr_3$ Adduct[‡]

Klaus Knabel,[a] Thomas M. Klapötke,[a] Heinrich Nöth,*[a] Robert T. Paine,[b] and Ingo Schwab[a]

Dedicated to Prof. Dr. Alfred Schmidpeter on the occasion of his 70th birthday

Keywords: 1,3-Di(*tert*-butyl)-2,4-bis(2,2,6,6-tetramethylpiperidino)-1,3,2,4-diphosphadiboretane / 1-*tert*-Butyl-2,4-bis(2,2,6,6-tetramethylpiperidino)-1,3-diphospha-2,4-diborabicyclo[1.1.0]butane cation / 2,2,6,6-Tetramethylpiperidino-*tert*-butylphosphinideneborane–$AlBr_3$ adduct / X-ray structures / ab initio calculations

Depending on reaction conditions the 1,3,2,4-diphosphadiboretane **1** reacts with $AlBr_3$ to give the unstable adduct tmp=B=P(*t*Bu)$AlBr_3$, **3**, and/or the somewhat more stable salt $[(tmpB)_2(PtBu)P]^+[AlBr_4]$, **2**. The X-ray structure determination of **3** shows an almost linear NBP array with BN and BP double bonds resembling an allene type structure. NBO analysis shows the presence of BN- and BP-π-bonds. On the other hand, the cation of compound **2** has a bicyclic structure with a long P–P bond [2.349(2) Å]. The B–P bonds to the phosphonium type P2 atom [av. 1.939(5) Å] are longer than those to the tri-coordinated P1 atom [1.889(6) Å]. NBO analysis of the model compound $(H_2NB)_2(PMe)P^+$, **9**, show that the P–P bond in **2** is formed from *p*-orbitals.

(© Wiley-VCH Verlag GmbH & Co. KGaA, 69451 Weinheim, Germany, 2005)

Introduction

In contrast to boron nitrogen chemistry, the development of the chemistry of B–P compounds began much later, but has attracted increasing attention during the last two decades. The state of the art has been summarized in a review.[2] Particularly 1,3,2,4-diphosphadiboretanes[3–11] offer many interesting aspects as ligands as well as a source for amino-phosphinidene-boranes $R_2N{=}B{=}PR$[8,11] having a boron atom of coordination number 2 and B=N as well as B=P double bonds. They also react with many Lewis acids often in rather unusual ways,[12] and we report here on the reaction of $[tmpB\text{-}PtBu]_2$, **1**, (tmp = 2,2,6,6-tetramethylpiperidino) with $AlBr_3$.

Results

Synthesis and Reactions

The chemistry of 1,3,2,4-diphosphadiboretanes is well developed. Many derivatives have been synthesized, characterized, and their chemistry studied to some extent.[2] For example, in most cases reactions with metal carbonyl fragments lead simply to coordination of the P atoms of the intact four-membered ring.[6,7] More interesting are reactions where cycloreversion produces phosphinidene boranes with dicoordinated B atoms as shown for $(tmpB\text{-}PCEt_3)_2$,[11] which gives the complex tmp=B=PR–$Cr(CO)_5$.[5] This suggests that other Lewis acidic compounds or fragments might behave similarly. Another ideal candidate for cycloreversion reactivity is the diphosphadiboretane $(tmpB\text{-}PtBu)_2$, **1**. The synthesis of this compound has already been reported.[4] We now find that the reaction sequence Equation (1) allows the synthesis of **1** in a one pot reaction with yields of up to 81%.

The subsequent reaction of **1** with $AlBr_3$ in a 1:2 ratio in toluene solution at room temperature proceeds unexpectedly by P–C bond cleavage, according to Equation (2), to give compound **2**, which crystallized from toluene at –30 °C as yellow prisms. The compound is stable for more than a week in toluene below –20 °C. However, compound **2** is not the primary reaction product. Monitoring the reaction by ^{31}P and ^{11}B NMR spectroscopy at –30 °C we find that the primary reaction leads to the yellow 1:1 adduct tmp=B=P*t*Bu·$AlBr_3$, **3**, on rapid addition of an excess of $AlBr_3$ to **1** (ratio 2:1) as shown in Equation (3). Compound **3** quickly converts, at room temperature, from a solid into an orange oil which finally yields the golden yellow compound **2** after addition of toluene. At low temperatures (below –20 °C) both **2** and **3** are stable for some hours in tolu-

[‡] Contribution to the Chemistry of Boron, 255. Part 254: Ref.[1]

[a] Department of Chemistry, University of Munich, Butenandtstr. 5–13, 81377 München, Germany
[b] Department of Chemistry, University of New Mexico, Albuquerque, NM 87131, USA

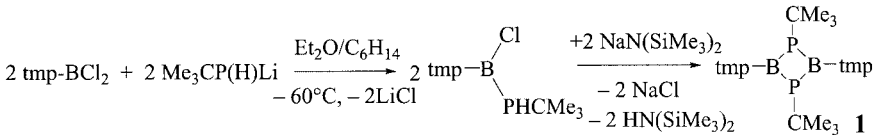

(1)

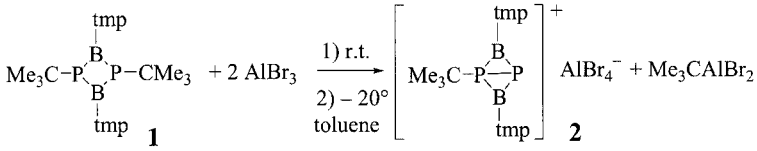

(2)

ene. In the solution of **2** the formation of tBuAlBr$_2$ was detected by its ^{27}Al NMR signal at δ = 152.5 ppm. Compound **2** is nearly insoluble in pentane but reacts with $CDCl_3$ and more slowly in CD_2Cl_2 solution.

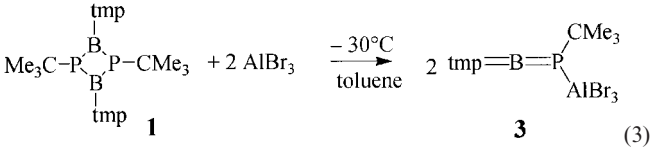

(3)

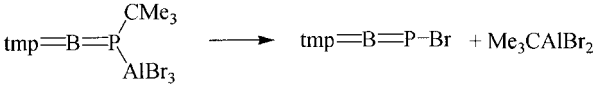

(4)

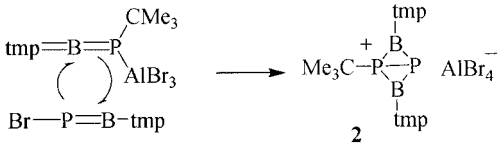

(5)

There are at least two conceivable mechanisms for the formation of the salt **2**. We prefer the one that is shown in Equation (4) and Equation (5) as **3** is one of the isolated products, i.e. we assume a decomposition of **3** with elimination of tBuAlBr$_2$ [Equation (4)] and cycloaddition of the proposed intermediate BrP=Btmp with **3** [Equation (5)].

The reaction of **1** with $AlCl_3$ in toluene produced a yellow powder that was insoluble in nonpolar solvents. Elemental analyses of products from several experiments ranged from 6.74 to 8.38% for Al, and from 29.80 to 34.70% for Cl. These data show that the Cl:Al ratio is close to 3. However, IR data are not conclusive as to whether the product is an analogue of **2** or **3** or something else**.** With $GaCl_3$ the same observation was made for toluene solutions. The colorless powder which forms decomposes at about 185°C. The ^{11}B NMR spectrum of the solution showed the presence of tmpBCl$_2$ (δ^{11}B = 33.8 ppm) besides a signal at δ^{11}B = 44.5 ppm. In the ^{31}P NMR spectrum of the $GaCl_3$ reaction five signals are observed at –181.4 [d, $J(^1H^{31}P)$= 110 Hz], –148.7 [d, $J(^1H^{31}P)$= 110 Hz], 91.9, 7.9, and 1.8 ppm, indicating that no single species is present in solution. In contrast, $InCl_3$ in the toluene suspension did not react at all with **1**. This demonstrates the unique behavior of $AlBr_3$.

NMR Spectra

The rapid decomposition of **3** made the recording and interpretation of the NMR spectra difficult, particularly for the ^{1}H and ^{13}C NMR spectra due to the presence of **2** and other by-products.

It is surprising to note that the shielding of the ^{11}B nucleus in **3** is only 4.6 ppm, less than in the starting diphosphadiboretane **1** in spite of the fact that the boron atom is now dicoordinate. However, in agreement with this, the line width has increased from 400 (for, **1**) to 530 Hz for **3**. The small amount of deshielding is most likely due to the presence of BN- and weaker BP-π-bonding which leads to a comparatively high electron density at the boron atom (see results of calculations). Moreover, the δ^{11}B value is very close to those of tmp=B=P(tBu)M(CO)$_5$ (M = Cr, W)[5] which are 67.0 and 62.9 ppm. The ^{31}P NMR signal of **3** is broad ($h_{1/2}$ = 900 Hz) and found at δ = –59.8 ppm. This P atom environment is better shielded than in the M(CO)$_5$ complexes (δ^{31}P = –32.7 and –45.3 ppm for M = Cr and W, respectively). Its ^{27}Al NMR spectrum contains a doublet at δ = 98.3 ppm due to AlP coupling with $^1J(^{31}P^{27}Al)$ = 140 Hz. The small line width of 20 Hz, as well as the chemical shift, is typical of a tetracoordinate Al atom.

Due to the low solubility the ^{13}C NMR spectroscopic data of **3** could not be recorded in deuterated benzene. Reliable assignment of the ^{1}H NMR spectrum was also not possible. Similarly, the very low solubility of **2** in deuterobenzene or deuterotoluene resulted in the detection of ^{1}H NMR resonances only for the *tert*-butyl group. In $CDCl_3$ rapid decomposition of **2** occurred. In CD_2Cl_2 the decomposition was slow enough to allow the measurement of several NMR resonances. Nevertheless, even under these circumstances the compound decomposed completely within 15 to 20 min. Thus, the measurements had to be done very quickly with as few pulses as possible. For this reason we were unable to get ^{13}C NMR spectroscopic data of compound **2**, and only the ^{1}H resonance for the tBu group could be reliably assigned as a doublet due to $^3J(^{31}P^1H)$ = 11 Hz.

 © 2005 Wiley-VCH Verlag GmbH & Co. KGaA, Weinheim

The boron atoms in the cation of **2** are more shielded by 30 ppm compared with **3.** As expected, the line width is much smaller (280 Hz) since the B atoms are tricoordinate. The observed two ^{31}P signals were doublets with $^{1}J(^{31}P^{31}P)$ = 62 Hz in accordance with the calculations, and the shift difference of 40 ppm is 6 ppm from the calculated value.[13] The small coupling constant suggests that the bond between the two P atoms does not represent a normal P–P single bond as found e.g. in 3-(diisopropylamino)-4-(dimethylamino)-1,2-di(*tert*-butyl)-1,2,3,4-diphosphadiboretane.[14] The presence of the tetrabromoaluminate anion in **2** is manifested by a sharp ^{27}Al NMR signal at δ = 80.3 ppm.[15]

The IR spectrum of **3** is characterized by two strong bands at 1633 and 1590 cm^{-1}. These heteroallene bands are 26 and 23 cm^{-1} higher than those observed for tmp=B=P(*t*Bu)M(CO)$_5$[5] indicating stronger BN and BP bonds. In tmp=B=N(*t*Bu)$AlBr_3$ these bands are found at 1800 and 1850 cm^{-1}.[16] This is due to a better coupling of the two BN vibrations, and obviously stronger BN bonds.

The mass spectrum of **3** shows few peaks, and there is no peak for the molecular ion. The most intense peak is found at *m*/*z* = 298. It can be assigned to the $PAlBr_3$ fragment due to the isotopic pattern. A peak at *m*/*z* = 426 (22%) results from loss of a Br atom from the molecular ion. Loss of a Me group from this ion, either from the *t*Bu group or the tmp substituent, leads to a peak at *m*/*z* = 411 (35%).

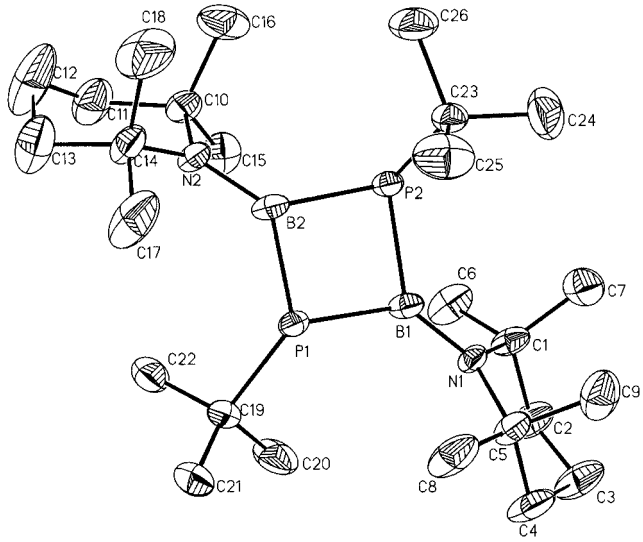

Figure 1. The molecular structure of **1** in ORTEP description. Thermal ellipsoids are represented on a 25% probability level. Selected bond lengths (Å): P1–B1 1.876(9), P1–B2 1.865(6), P1–C19 1.895(7), P2–B2 1.943(8), P2–B1 1.948(6), P2–C23 1.880(7), B1–N1 1.408(8), B2–N2 1.419(8), N1–C1 1.503(7), N1–C5 1.492(7), N2–C10 1.494(8), N2–C14 1.492(7). Selected bond angles (°): B1–P1–B2 90.1(3), B1–P1–C19 124.1(3), B2–P1–C19 124.9(3), B1–P2–B2 85.9(3), B1–P2–C23 111.1(3), B2–P2–C23 112.1(3), N1–B1–P1 134.7(5), N1–B1–P2 133.5(6), P1–B1–P2 91.6(3), P1–B2–P2 92.1(3), N2–B2–P2 133.3(5), N2–B2–P1 134.4(6), B1–N1–C1 118.5(5), B1–N1–C5 122.8(5), C1–N1–C5 118.4(5), B1–N2–C10 118.5(5), B2–N2–C14 143.8(5), C10–N2–C14 118.1(5).

Molecular Structures

Figure 1 shows the molecular structure of the diphosphadiboretane **1**. The compound crystallizes in orange prisms in the monoclinic system, space group $P2_1/c$ with Z = 4. The four-membered ring is asymmetric with unequal B–P bond lengths spanning a range from 1.865(6) to 1.948(6) Å. This results in endocyclic bond angles also being different with P–B–P angles of 91.6(2)° at B1 and 92.1(3)° at B2 and B–P–B bond angles of 90.1(3)° at P1, and 85.9(3)° at P2. As expected, the B and N atoms reside in planar environments, e.g. the sum of bond angles for N1 is 359.7°, and 359.8° for N2. The B–N bonds are on the upper end of the range of B(sp^2)–N(sp^2) bonds in monoaminoboranes. The reason for this is that the tmp groups are twisted against the respective P_2B planes by 47.8° for the C1N1C5 plane and by 51.1° for the C10N2C14 plane. This twisting is due to steric repulsion of the bulky organyl groups. Actually, the BN bond lengths found for **1** are intermediate with those determined for (tmpB-$PCEt_3$)$_2$ (1.431 Å)[11] and (tmpB-$PH)_2$ (1.405 Å).[7] In contrast to most other 1,3,2,4-diphosphadiboretanes, the four-membered ring of **1** is not planar whereas calculations (v. i.) predict a planar ring structure: the two P_2B planes are bent by 7.1° (roof angle 172.9°). The angle that the PC bonds form with their respective P_2 bonds are also unusual: for P2–P1–C19 this angle is 149.7° while an angle of 126.7° is found for P2–P1–C23.

The molecular structure of **3** is depicted in Figure 2. This compound also crystallizes in the monoclinic system, space group $P2_1/n$ with Z = 4. The molecule is characterized by a dicoordinated B atom and by tricoordinate N and P atoms. The plane C1N1C5 lies almost perpendicular to the plane Al1P1C10 as expected for an allene type configuration. This is in agreement with an N–B–P bond angle of 170.4(3)°. Similar deviation from the ideal linearity has been observed for compounds of type tmp=B=N(*t*Bu)(Cr[CO)$_5$[16] or tmp=B=N(*t*Bu)ECl_3 (E = Ga, In).[17] While atom N1 sits in the center of the C1C5B1 plane, the sum of bond angles at atom P1 is only 334.4°. Thus, the geometry about the P1 atom is pyramidal. The bond angle C10–P1–Al1 is 118.2(2)° and the other two angles, B1–P1–C10 and B1–P1–Al1 are 110.6(2) and 105.6(2)°, respectively. This corresponds with a distorted trigonal pyramid. Consequently, this geometry is not optimal for BP-π-bonding. One can indeed note that the B–P bond length in **3** [1.787(4) Å] is somewhat longer than in tmp=B=P(*t*Bu)Cr(CO)$_5$[5] [1.742(5) Å] where the P atom resides in a planar environment. Nevertheless, the B–P bond length in **3** is shorter than expected for B–P single bonds for which a range from 1.81 to 1.91 Å has been determined in agreement with covalent radii and taking the Shoemaker–Stevenson correction into account.[18] It should be noted, however, that in most cases a covalent bond length increases as the coordination number of an atom decreases, thus the B–P bond in **3** can still be considered to have multiple bond characteristics. However it does not show the

 © 2005 Wiley-VCH Verlag GmbH & Co. KGaA, Weinheim

geometry of a classical pp–π-bond in contrast to the model compound $Me_2N{=}B{=}P(Me)AlBr_3$ (**10**), see below.

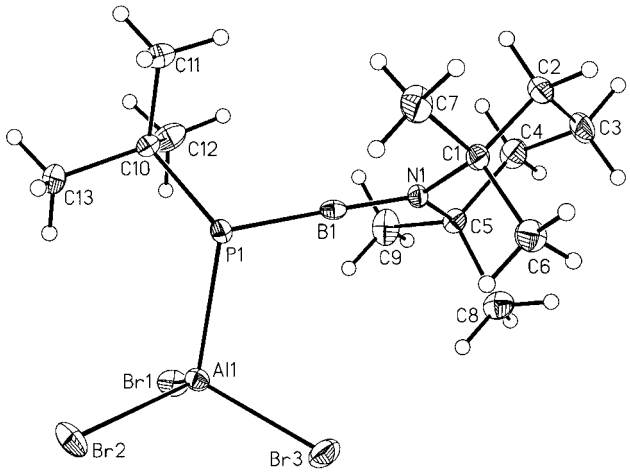

Figure 2. The molecular structure of **3** in ORTEP description. Thermal ellipsoids are shown on a 25% probability level. Selected bond lengths (Å): Al1–Br1 2.279(1), Al1–Br2 2.302(1). Al1–Br3 2.281(1), Al1–P1 2.67(1), P1–B1 1.787(4), P1–C10 1.892(3), N1–B1 1.331(4), N1–C1 1.529(4), N1–C5 1.527(4). Selected bond angles (°): Br1–Al1–Br2 109.40(4), Br1–Al1–Br3 112.49(4), Br1–Al1–P1 111.95(4), Br2–Al1–P1 107.66(5), Br3–Al1–P1 104.36(4), B1–P1–C10 110.6(2), B1–P1–Al1 105.6(1), Al1–P1–C10 118.2(1), N1–B1–P1 170.4(3), B1–N1–C1 119.5(3), B1–N1–C5 119.7(3), B1–N1–C5 120.7(2).

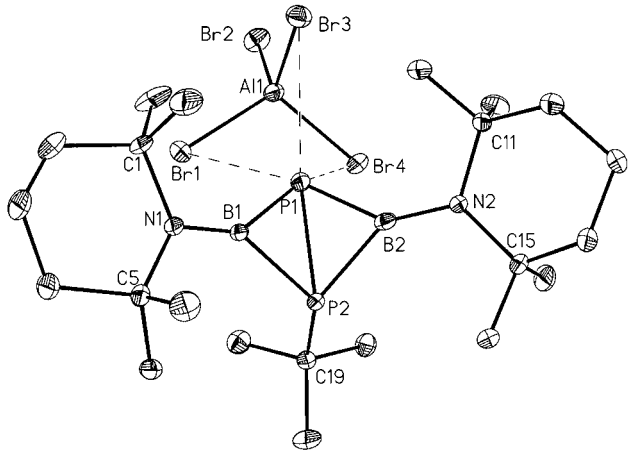

Figure 3. The molecular structure of **2** in ORTEP description. Thermal ellipsoids are depicted on a 25% probability level. Selected bond lengths (Å): Al1–Br1 2.310(2), Al1–Br2 2.293(2), Al1–Br3 2.297(2), Al1–Br4 2.308(2), P1–P2 2.315(2), P1–B1 1.894(6), P2–B1 1.944(5), P1–B2 1.884(7), P2–B2 1.931(6), B1–N1 1.360(6), B2–N2 1.377(8), N1–C1 1.532(6), N1–C5 1.534(6), N2–C10 1.537(6), N2–C14 1.519(6). Selected bond angles (°): B1–P1–B2 90.4(3), B2–P1–P2 53.6(2), B1–P1–P2 53.9(2), B1–P2–B2 87.6(2), B2–P2–P1 51.7(2), B1–P2–P1 51.9(2), B1–P2–C19 123.9(3), B2–P2–C19 124.6(2), N1–B1–P1 143.9(4), N1–B1–P2 141.9(4), P1–B1–P2 74.2(2), P1–B2–P2 74.7(2), N2–B2–P1 142.1(4), N2–P–B2–P2 142.9(4), B1–N1–C1 118.0(4), B1–N1–C5 121.8(4), C1–N1–C5 118.5(4), B2–N2–C10 118.3(4), B2–N2–C14 122.1(4), C10–N2–C14 118.8(4), P1–P2–C110.1(4).

The molecular structure of compound **2** is shown in Figure 3. The bicyclic ring has a butterfly configuration with the P atoms at the roof and an angle of 123.4° between the two P_2B planes. This fold angle differs enormously from that in **1** (172.9°), but corresponds with the bicyclo[1.1.0]-butane structure with a "roof" angle of 126°.[19] The B and N atoms of **2** have a planar environment, demonstrating their sp^2 type character which allows good BN-π-bonding. This is not only shown by short BN bonds [1.360(6) Å for B1–N1, and 1.377(8) Å for B2–N2] but also by the fact that the torsion angles τ of C1–N1–B1–P1 and C14–N2–B2–P2 are only 16.3 and 15.4°, respectively.

The P–B bonds in the cation of **2** are shorter for P1 (1.894(6) and 1.884(7) Å) than those at atom P2 which show bond lengths of 1.944(5) and 1.931(6) Å. These longer bonds are in line with the higher coordination number at atom P2. Of particular interest is the P1–P2 distance, 2.315(2) Å. This is longer than the usual P–P single bond length, 2.15(2) Å, but compared with the PP separation in the related diphosphadiboretane (tmpB-P*t*Bu)$_2$, **1**, there is a shortening by 0.427 Å. This is consistent with the presence of a weak P–P bond in **2**. The two B–P–B bond angles are close to 90° [90.4(3)° for P1 and 87.6(2)° for P2]. On the other hand, we find the P–B–P bond angle at B1 to be 74.2(2)°, and 74.7(2)° for B2, while the B1–P1–P2 and B2–P1–P2 angles are 53.9(2)° and 53.6(2)°.

Twhere is a very weak interaction of atom P1 with the bromine atom Br3 of the tetrabromoaluminate anion (P1···Br3 3.720 Å). The other two "contacts", P1···Br1 and P1···Br4 show distances of 3.965 and 4.166 Å, respectively. The Al–Br bonds lie in the range of 2.293 to 2.310 Å and the Br–Al–Br bond angles range from 108.6 to 110.1°. The Br3···P1 interaction has no elongating effect on the Al1–Br3 bond (Al1–Br3 2.297 Å).

Theoretical Studies

The formation of the $(tmpB)_2P_2tBu^+$ cation in **2** is not only unusual but also of interest considering bonding situation and structure. Therefore, we performed ab initio and density functional calculations at various levels not only for the gas phase structure of compound **2** but also for the model compounds **5** to **10**, **5** being a model for the cation in compound **2**. Moreover, ELF calculations were performed for the model compounds **9** and **10** (see Figures 7 and 8, molecule **8** is not depicted but calculations have been performed for comparison).

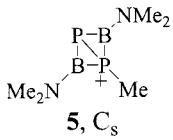

5, C_s

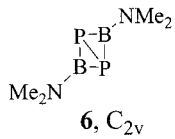

6, C_{2v}

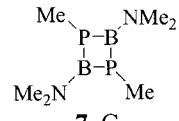

7, C_1

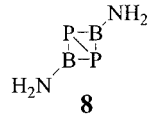

8

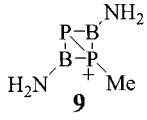

9

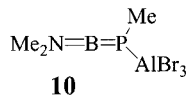

10

 © 2005 Wiley-VCH Verlag GmbH & Co. KGaA, Weinheim

Compound **1** is an analogue of **7**. While **1** has a slightly bent ring structure and shows two differently *trans*-oriented P–C bonds with respect to the P1/P2 atoms, the calculations for model **7** in the *trans*-configuration reveal a planar ring structure with longer P–B bonds, and, more noticeably, the P–B–P bond angle is 8° larger than that calculated for the *cis*-isomer of **7** (see Figure 4). Compound **1** has only been observed as the *trans*-isomer which is obviously the more stable structure, and this has been ascertained for *cis*-**7** which is 611.6 kJ/mol less stable than the *trans*-isomer. Figure 5 shows the results of the calculations for the *trans*-isomer.

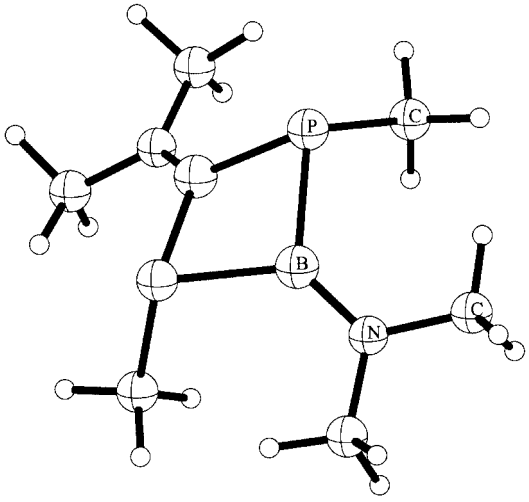

Figure 4. Optimized structure for the model compound *cis*-[$(Me_2B)_2$-$(PMe)_2$], **7** (C_{2v}) at the RI-MP2/TZVP level of theory. Bond lengths (Å) and angles (°): P–B 1.943, P–C 1.885, B–N 1.399*N*–C 1.455; P–B–P 98.60, B–P–B 74.15, B–P–C 106.51, P–B–N 130.67, B–N–C 123.71; torsion angle P–B–B–P 143.9.

Table 1 contains calculated data for compound **6** and experimental data for compound **4**, respectively. It also shows selected experimental and calculated data for the cation in compound **2** as well as calculated values for the model **5**

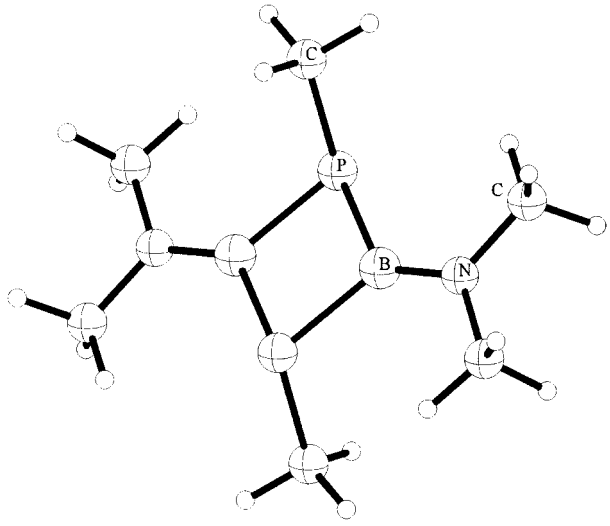

Figure 5. Optimized structure for the model compound *trans*-[$(Me_2B)_2(PMe)_2$], **7** (C_1) at the RI-MP2/TZVP level of theory. Bond lengths (Å) and angles (°): P–N 1.924, P–C 1.875, B–N 1.395, N–C 1.452; P–B–P 97.95, B–P–B 82.05, B–P–C 114.26, P–B–N 131.03, B–N–C 123.28; torsion angle 0.01.

(C_1 and C_s; see also Figure 6). It also contains experimental and calculated ^{31}P chemical shifts. The ^{31}P spectrum of the cation of **2** showed two doublets with $^1J(^{31}P^{31}P)$ = 62 Hz and a separation of the two signals by 40 ppm. These data are roughly in agreement with the calculated values for the model cation **5** with C_1 or C_s symmetry. The largest deviation between experimental and calculated data results for the bond angle P1–P2–C, most likely a result of the different steric requirements of the tmp and Me_2N groups.

Selected data from the NBO analysis of **9** and **10** are listed in Table 2 and Table 3. It is noteworthy that the P–P bond in **9** is built almost exclusively from the *p*-orbitals of the phosphorus atoms. While the P1–B bond results from a boron sp^2 and a phosphorus *p*-orbital (86% p character),

Table 1. Experimental parameters from X-ray diffraction and ^{31}P NMR shifts for compounds **2** and **4** together with the calculated parameters of the cation of **2** and the model compounds **5** and **8**.

Compound	**4**	**6** (C_{2v})		**2**	**2** calcd. (C_1)		**5** (C_s)	
Method	exp.	RI-MP2 [a]	RI–CC2	exp.	RI–BP86	RI-MP2/SV(P)	RI-MP2	RI–CC2
P1–P2	2.349(2)	2.459	2.465	2.315(2)	2.331	2.328	2.385	2.393
P1–B	1.904(6)/1.907(5)	1.898	1.901	1.884(7)/1.894(6)	1.908/1.911	1.897/1.901	1.890	1.891
P2–B	–	–	–	1.931(6)/1.944(5)	1.947/1.955	1.925/1.932	1.925	1.926
B–N	1.385(7)/1.381(9)	1.390	1.395	1.360(6)/1.377(8)	1.386/1.387	1.381/1.382	1.366	1.372
N–C	1.528(7)/ 1.525(7)	1.455	1.456	1.519(6)–1.537(6)	1.535–1.546	1.517–1.524	1.466	1.470
P2–C	–	–	–	1.884(5)	1.943	1.892	1.846	1.850
B–P–P	51.9(1)/52.0(1)	49.64	49.58	90.4(3)	51.97/53.82	51.86/52.05	50.66/51.97	50.56/51.80
P–B–P	76.0(2)/76.2(3)	80.73	80.84	74.2(2)/74.7(2)	74.21/74.34	74.89/74.96	77.37	77.63
P–B–N	141.4(1)/141.6(2)	139.51	139.48	87.6(2)	141.78–144.00	140.40–144.69	137.83/144.25	137.78/144.01
P1–P2–C	–	–	–	123.9(3)	111.32	109.41	110.42	110.58
B–P2–C	–	–	–	123.9(3)/124.6(2)	124.60/125.16	124.2/124.9	122.82	122.68
Roof angle	104.1	101.9	101.28	123.4	123.36	121.56	127.46	128.06
$\delta = {}^{31}P$[b]	–290 ppm [3]	–280 ppm		not reproducible	–121.6/187.6–ppm		–223/–257 ppm	

[a] TZVP basis sets used unless noted otherwise. [b] NMR shifts at the GIAO/MP2 level, except for [(tmpB)2(P*t*Bu)P]$^+$ (**2**) which has been calculated at the BP86 level because of exceedingly high memory requirements for MP2.

 © 2005 Wiley-VCH Verlag GmbH & Co. KGaA, Weinheim

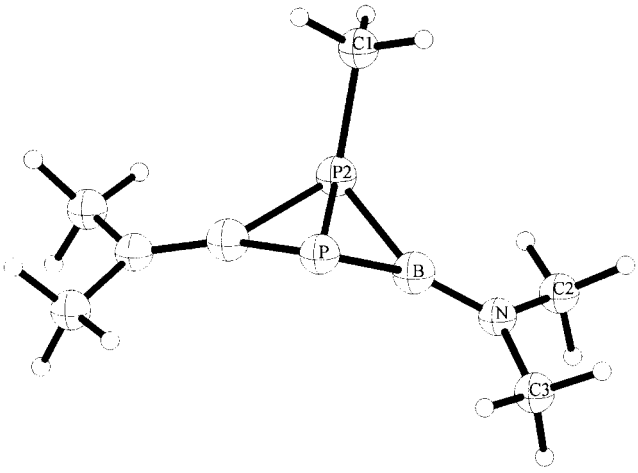

Figure 6. Optimized geometry (C_s) for the model cation **5** at the RI-MP2/TZVP level of theory. Bond lengths (Å) and angles (°): P–P2 2.385, P–B 1.890, P2–B 1.925, P2–C1 1.846, B–N 1.366, N–C2 1.466, N–C3 1.468; P–P2–B 50.66, P–B–P2 77.37, B–P–P2 51.97, P–P2–C1 110.42, P–B–N 137.83, B–N–C2 124.17, B–N–C3 122.13

the P2–B bond is formed from a boron sp^3 orbital and a phosphorus sp^2 orbital. The positive charge of the cation resides mainly on the tetracoordinate P atom (see data in Figure 6). As expected, the B–N bonds are double bonds.

A similar situation is present in the $AlBr_3$ adduct **10**. Both, the B–N and the B–P bonds are double bonds.

Finally, the bonding situation in **2** and **3** as calculated for the model compounds **9** and **10** is illustrated by the use of topological ELF analysis (electron localization function),[20] as depicted in Figure 7 and Figure 8, calculated for C_s and C_1 symmetry, respectively. There are four B–P bonds and a weak P–P bond that form the B_2P_2 core of **9**. The corresponding attractors are above the two BP_2 planes. The disynaptic basins of these attractors are merged in the case of the alkyl-substituted atoms P2. Regarding the location of positive charges: the tetracoordinate atom P2 carries a higher positive charge than atom P1, which is almost neutral, and as expected the boron atoms also carries a positive charge while negative charges are primarily located at the N atoms. Figure 8, on the other hand, clearly shows the allene type structure of the $AlBr_3$ adduct **10** (orthogonal attractor positions) and also reveals BN- and BP-π-bonding.

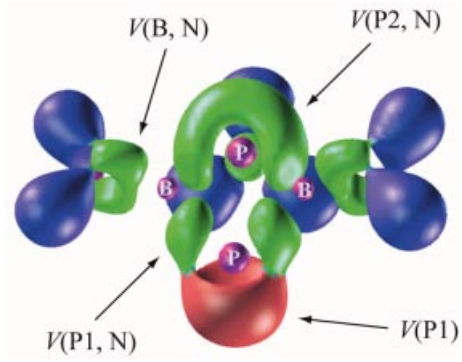

Figure 7. Rendered *ELF* isosurface and basin assignment for $[(H_2NB)_2(PMe]P)]^+$ (**9**C_s) with disynaptic basins (green) and monosynaptic basin *V*(P1) (red). Representation at η = 0.80, 150^3 grid points, core basins in purple, protonated basins in blue. The *V*(P1, P2) for the weak interaction between the two phosphorus atoms has a maximum *ELF* value of 0.645 and is therefore difficult to visualize. AIM basin populations (charges): P1 15.04 (–0.04), P2 14.76 (+0.24), B1/B2 3.89 (+1.11), N 8.54 (–1.54).

Discussion

1,3,2,4-Diphosphadiboretanes (RB–PR′)$_2$ are more readily accessible than the six-membered 1,3,5,2,4,6-triphosphatriboranes but need bulky groups R for stabilization. The 2,2,6,6-tetramethylpiperidino is such a group as shown e.g. by (tmpB-PH)$_2$.[17] Another one is the mesityl group

Table 2. Selected data from the NBO analysis of the model compound **8** at the MP2/TZVP level of theory, reflecting the bonding situation in **2.**

Bond	Degree of occupation	Bonding in % electrons		Share in % of AO′s	
P1–P2	1.66	P1: 41	P2: 59	P1:s 1 p 98 d 1	p2:s 2 p 97 d 1
P1–B	1.85	P: 53	B: 47	P:s 14 p 86	B:s 35 P 65
P2–B	1.87	P: 59	B: 41	P:s 33 p 67	B:s 25 p 75
B–N (σ)	1.97	N: 74	B: 26	N:s 48 p 52	B:s 40 p 60
B–N (π)	1.95	N: 81	B: 19	N:s 0 p 100	B:s 0 p 100
P–C	1.94	P: 45	C: 55	P:s 33 p 67	C:s 23 p 77

Table 3. Selected data from the NBO analysis of the model compound **10** at the MP2/TZVP level of theory, reflecting the bonding situation in **2**.

Bond	Type	Degree of occupation	Bonding in % electrons		Share in % of AO′s	
P–B	σ	1.97	P: 57	B: 42	P:s 33 p 67	B:s 51 p 49
P–B	π	1.93	P: 74	B: 26	P:s 3 p 97	B:s 7 P 93
B–N	σ	1.99	N: 79	B: 21	N:s 41 p 59	B:s 42 p 58
B–N	π	1.95	N: 82	B: 18	N:s 0 p 100	B:s 0 p 100
P–Al	π-donor	1.87	P: 81	Al: 19	P:s 35 p 65	Al:s 19 p 81
P–C	σ	1.97	P: 47	C: 53	P:s 29 p 71	C:s 22 p 78

 © 2005 Wiley-VCH Verlag GmbH & Co. KGaA, Weinheim

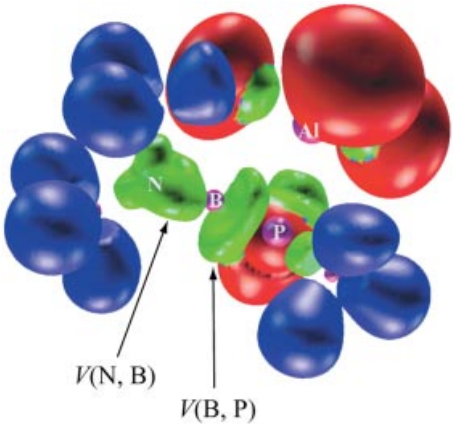

Figure 8. Rendered *ELF* isosurface and basin assignment for $AlBr_3$ adduct (**10**) with disynaptic basins (green). Representation at η = 0.75, grid increment 0.2 Å, core basins in purple, protonated basins in blue. The *ELF* surface illustrates the allene type character of the N–B–P moiety. Attractor distances (Å): P–*V*(P, Al)–Al: 1.026, 1.503; P–V(P, B)–B: 1.083, 0.775; P–V(P, C)–C: 1.024, 0.859; B–V(B, N)–N: 0.738/0.747, 0.701/0.718. AIM basin populations (charges): N 8.37 (–1.37), B 4.41 (+0.59), P 14.66 (+0.34), Al 11.02 (+1.98).

attached to the B atom.[21,22] Table 4 lists some typical structural features as well as ^{11}B and ^{31}P NMR spectroscopic data of some 2,4-diamino-1,3,2,4-diphosphadiboretanes. A more complete survey is given in a review.[2] A small range is observed for the B–P bond lengths (1.865 to 1.97 Å) which is typical for a B–P single bond between tricoordinate B and P atoms. In almost all cases the BN bonds are close to 1.4 Å with extremes of 1.37(1) to 1.431(2) Å. It appears that the B–P bond lengths are influenced by the steric requirements of the amino groups at the boron atoms: the smaller the amino group the longer is the B–P bond. This is coupled with the lengths of the B–N bonds and coplanarity of the C_2N plane with the BP_2 plane, e.g. the strength of the BN bond. Moreover, this also becomes apparent in the respective $\delta^{11}B$ values where deshielding is noted for the diphosphadiboretanes (tmpB-PR)$_2$ with an increasing steric demand of the R substituents (R = H, $\delta^{11}B$ = 47.1 ppm; R = CMe_3, $\delta^{11}B$ = 50.2 ppm; R = CEt_3,$\delta^{11}B$ = 66.1 ppm). Most of the four-membered rings are planar, and many of them show C_i point group symmetry. Therefore, the nonplanar rings of **1** as well as (tmpB-PSiMe$_3$)$_2$[4] are exceptional, particularly in comparison with the planar ring in (tmpB-PCEt$_3$)$_2$ where the P substituent is more bulky.[11] Nonplanarity is also observed for the two B_2P_2 rings of $Et_3CP(Btmp)_2P$–P(tmpB)$_2$PCEt$_3$,[23] whose angles between the P_2B planes are 157.2° within a bicyclic ring, and 98.4° between adjacent rings. The P–P bond length joining the two four-membered rings is 2.189(1) Å. In compound **4**, which results from the photolysis of (tmpB-PCEt$_3$)$_2$ [Equation (6)], the P–P distance is 2.349(2) Å, while in compound **2** a length of 2.315(2) Å is observed. The shrinking is significant and obviously due to the positive charge.

A noteworthy feature of diphosphadiboretanes (see Table 4) is that the sum of bond angles at the P atoms (average values of the two P atoms) is decreasing with increasing steric requirement of the organyl group as shown

Table 4. Selected NMR spectroscopic data of 2,4-amino-1,3-diorganyl-(silyl or hydrido)-1,3,2,4-diphophadiboretanes.

Compound	$\delta^{11}B$	$\Delta^{31}P$	B–P (Å)	B–N (Å)	B–P–B (°)	P–B–P (°)	Σ°P	Ref.
(tmpB-P*t*Bu)$_2$	63.2	4.4	1.865(2)	1.408(8)	90.1(3)	91.6(3)	339.1	
			1.876(8)	1.419(8)	8.8(3)	92.1(3)	308.5	
			1.943(8)					
			1.948(6)					
(Me$_2$NB-P*t*Bu)$_2$	50.2	–46.8	1.923(4)	1.395(5)	82.4(2)	97.6(2)	309.0	4
			1.925(4)					
(*i*Pr$_2$NB-P*t*Bu)$_2$	45.8	–48.0	1.92(1)	1.37(1)	85.0(4)	95.0(4)	313.5	6
			1.939(9)					
(Et$_2$NB-P*t*Bu)$_2$	48.9	–49.6						6
(tmpB-PCEt$_3$)	66.1	–20.0	1.916(2), 1.933(2)	1.431(2)	88.9(1)	91.1(1)	329.2	3
(tmpB-PSiMe$_3$)$_2$	60.8	–55.0	1.95(1)	1.42(1)	83.2(5)	95.9(5)	292.8	10
			1.97(1)	1.40(1)	83.5(5)	95.4(5)		
			1.95(1)					
			1.96(1)					
(tmpB-PH)$_2$	50.8	–127.2	1,913(4)	1.405(5)	89.4(2)	90.6(2)		7
			1.934(4)					
(tmpB-Pmes)$_2$	[a]	[a]	1.916(3)	1.393(3)	90.2	89.8	329.0	22

[a] No NMR spectroscopic data reported.

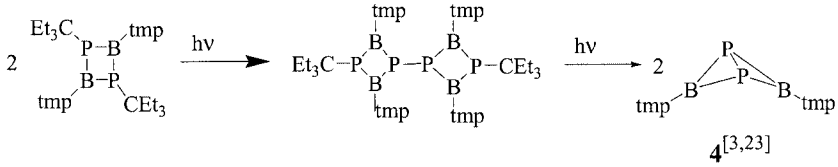

(6)

 © 2005 Wiley-VCH Verlag GmbH & Co. KGaA, Weinheim

by the following data: R = CEt_3, 329.2°; R = CMe_3, 323.1°; $SiMe_3$ = 287.9°. On the other hand, in the series of compounds $(R_2NB\text{-}PtBu)_2$ this sum of bond angles decreases in the series from R_2N = tmp (332.8°) > iPr_2N (313.5°) > Me_2N (309°). Thus, the *p*-character at the P atoms increases. The result of the ring of compound **1** being nonplanar in contrast to $(tmpB\text{-}PCEt_3)_2$ is puzzling. In the latter compound the higher steric requirement of the CEt_3 group is compensated by a stronger twist of the tmp group which obviously allows ring planarity while in compound **1** the structure prefers a stronger BN bond at the expense of loss of planarity. Although the solid-state structure of **1** has two nonequivalent P atoms, in solution only one ^{31}P NMR signal is observed as well as only one each for the protons of the CMe_3 group but two ^{13}C resonances for this group. Therefore, the two P atoms are equivalent in solution.

It has been shown that $(tmpB\text{-}PCEt_3)_2$ reacts with $M(CO_5)$ fragments to yield $tmp{=}B{=}P(CEt_3)M(CO)_5$ (M = Cr, MoW).[5] In analogy, **1** reacts with $AlBr_3$ to give **3**. In contrast to compounds $tmp{=}B{=}N(tBu)EX_3$ (E = Al, Ga, In; X = Cl, Br),[17] **3** is unstable and decomposes to **2** which, however, is more conveniently obtained from **1** and $AlBr_3$ at ambient temperature followed by rapid cooling to prevent decomposition. The formation of Me_3CAlBr_2 in this process indicates that this is most likely not a radical reaction although this has not been proven definitely.

Experimental Section

All experiments were performed under anhydrous conditions using Schlenk techniques. Solvents were dried by conventional methods. $TmpBCl_2$,[23] LiPH*t*Bu,[24] and $NaN(SiMe_3)_2$[25] were prepared by literature methods. $AlBr_3$ was freshly sublimed before use. NMR: Bruker WP 200 and JEOL EX 400, IR: Nicolet FT-IR, MS: Atlas CH-7 (70 eV), X-ray: Siemens P4 four circle diffractometer operated with Mo-*Kα*-radiation, graphite monochromator, CCD detector, and the low temperature device Siemens LT2. NMR references: $SiMe_4$ for ^1H and ^{13}C; $BF_3{\cdot}OEt_2$ (ext. for ^{11}B), 1 M aqueous $HAlCl_4$ solution (ext.), 85% H_3PO_4 (ext.) for ^{31}P.

***tert*-Butylchlorophosphanyl-(2,2,6,6-tetramethylpiperidino)borane and 1,3-Di(*tert*-butyl)-2,4-(2,2,6,6-tetramethylpiperidino)-1,3,2,4-diphosphadiboretane (1):** LiPH(*t*Bu) (9.2 g, 95.8 mmol) were dissolved in diethyl ether (100 mL) – slight warming of the stirred suspension may be necessary. The clear, yellowish solution was then cooled to –60 °C, and a solution of $tmpBCl_2$, (21.2 g, 95.5 mmol) in hexane (300 mL) was added over a period of 3 h under rapid stirring. Stirring was continued overnight. After allowing the suspension to attain room temperature the orange solution was separated by a cannula from the white precipitate which was washed twice with hexane (50 mL). All solvent was evaporated in vacuo from the solution, which contained only tmpBCl–PH*t*Bu ($\delta^{11}B$ = 45.6 ppm, $\delta^{31}P$ = –52.6 ppm), leaving behind a very viscous to waxy material to which benzene (100 mL) was added. The solution was then treated with a solution of $NaN(SiMe_3)_2$ (20.9 g, 114 mmol) in benzene (200 mL). Within a few minutes a white precipitate formed. After stirring overnight the benzene was removed in vacuo and the residue treated with hexane (200 mL). According to NMR data ($\delta^{11}B$ = 63.8 ppm, $\delta^{31}P$ = 4.6 ppm) the filtrate contains only compound **1**. After reduction of the filtrate by 2/3 of its volume and cooling to –30 °C orange crystals separated within 2 d. Yield: 18.4 g of **1** (81%), m.p. 129–131 °C. ^1H NMR (C_6D_6): δ = 1.42 [t, *N* = 11 Hz, 18 H, $C(CH_3)_3$], 1.52 [m, 8 H, βCH_2], 1.61 [s, br., 16 H, γCH_2 + $C(CH_3)_2$], 1.67 [s, 12 H, $N(CH_3)_2$] ppm. ^{13}C NMR: δ = 17.1 [s, γCH_2], 32.4 [t, *N* = 6 Hz, $C(CH_3)_2$], 33.2 [t, *N* = 9 Hz, $C(CH_3)_2$], 36.1 [t, *N* = 6 Hz, $C(CH_3)_2$),], 38.6 [d, $^1J(^{31}P^{13}C)$ = 16 Hz, $C(CH_3)_3$], 54. [t, *N* = 8 Hz, $N(CH_3)_2$] ppm. ^{11}B NMR: δ = 63.8 ($h_{1/2}$ = 400 Hz) ppm. ^{31}P NMR: δ = 4.6 ($h_{1/2}$ = 90 Hz) ppm. MS: (*m*/*z*, rel. %) 421 (100), 365 (54), 316 (6), 239 (25), 224 (11), 182 (29), 126 (36), 70 (55), 57 (56). $C_{26}H_{54}B_2N_2P_2$ (478.27): calcd. C 65.29, H 11.38, N 5.86; found C 64.28, H 11.44, N 5.81

***tert*-Butylphosphinidene-2,2,6,6-tetramethylpiperidino-borane Aluminium Tribromide (3):** A solution of $AlBr_3$ (1.28 g, 4.80 mmol) in toluene (30 mL) was rapidly added to a stirred solution of compound **1** (1.12 g, 2.34 mmol, dissolved in toluene, 30 mL) at –30 °C. The mixture turned deep yellow. About 2/3 of the solvent was then removed in vacuo. From the solution, which was kept at –30 °C, golden yellow prisms separated (most of them as single crystals) within a few hours. Yield: 1.23 g, (47%), m.p. 112 °C. Additional material was retained in the filtrate including an excess of $AlBr_3$ (NMR). The compound decomposed on standing at room temperature to give an orange oil. Treatment of the oil with toluene resulted in a deep yellow solution. At –20 °C yellow crystals of **3** separated. ^1H NMR (C_6D_6): δ = 0.48, 1.40, 1.46, 1.53, 1.55 ppm. ^{13}C NMR: δ = 16.3 [s, γ-CH_2], 31.3 [s, ß-CH_2], 34.8 [d, $^2J(^{31}P^{13}C)$ = 7 Hz $C(CH_3)_3$], 37.4 [s, $N(CH_3)_2$], 57.2 [s, $C(CH_3)_2$]), 58.2 [d, $^1J(^{31}P^{13}C)$ = 8 Hz $C[CH_3)_3]$ ppm. ^{11}B NMR: δ = 68.4 ($h_{1/2}$ = 530 Hz) ppm. ^{31}P NMR: δ = –59.8 ($h_{1/2}$ = 900 Hz) ppm. MS: (*m*/*z*, rel. %) 426 (22), 411 (35), 298 (100). $C_{13}H_{27}AlBBr_3NP$ (505.85): calcd. C 30.87, H 5.38, N 2.77; found C 29.92, H 4.87, N 2.79

1-*tert*-Butyl-2,4-bis(2,2,6,6-tetramethylpiperidino)-1-phosphonia-3-phospha-2,4-dibora-bicyclo[1.1.0]butane Tetrabromoaluminate (2): A solution of $AlBr_3$ (1.0 g, 3.8 mmol) in toluene (20 mL) was slowly (1 h) added to a stirred solution of 1 (0.90 g, 1.9 mmol) in toluene (15 mL) at ambient temperature. During addition the color of the solution became light yellow. The solution was reduced in volume to about 20 mL and then stored at –20 °C. Within two weeks golden yellow crystals of **2** separated. Yield (0.2 g, 16%). Most of the crystals had single crystal quality. At room temperature the crystals turned into an oily material within a few hours. The crystals were insoluble in hexane, only slightly soluble in benzene, and dissolved in $CDCl_3$ and CD_2Cl_2 with decomposition within several minutes. ^1H NMR (CD_2Cl_2): δ = 1.41 [9 H, $^3J(^{31}P^1H)$ = 11 Hz, $C(CH_3)_3$)], 1.47, 1.56 [24 H, $N(CH_3)_2$)], 1.60, 1.61 (appr. 12 H) ppm. ^{11}B NMR: δ = 37.8 ($h_{1/2}$ = 280 Hz) ppm. ^{27}Al NMR: δ = 80.3 ($h_{1/2}$ = 50 Hz) ppm. $C_{22}H_{45}AlB_2Br_4N_2P_2$ (767.78): calcd. C 34.42, H 5.19, N 3.65; Br 41.63, found C 29.25, H 5.45, N 1.27, Br 40.9 (C and N values were always too low due to possible formation of AlN).

X-ray Structure Analysis: Single crystals were selected under perfluoro ether oil and mounted on the a glass fiber. Graphite-monochromatized Mo-*Kα* radiation was used in all cases. Compound **1** was measured on a Siemens P4 diffractometer with a scintillation counter and an LT2 low-temperature device at –80 °C in the ω/2θ mode. For compounds **2** and **3** a CCD detector was applied, and data collection was performed in the hemisphere mode.[26] For data reduction the program SAINT was used.[27] The structures were solved by direct methods implemented in SHELXTL Plus.[27] This program was also used in the refinement and SADABS for absorption correction. Non-hydrogen atoms were refined in anisotropic description, and although most H atom positions were found in the difference Fourier they were placed in calculated positions and

 © 2005 Wiley-VCH Verlag GmbH & Co. KGaA, Weinheim

Table 5. Crystallographic data and data related to data collection and structure solution of compounds **1**, **2**, and **3**.

Compound	**1**	**3**	**2**
Empirical formula	$C_{26}H_{54}B_2N_2P_2$	$C_{13}H_{27}AlBBr_3NP$	$C_{22}H_{45}AlB_2Br_4N_2P_2$
Formula mass	478.27	505.85	767.78
Crystal size [mm]	0.3 × 0.3 × 0.5	0.1 × 0.2 × 0.3	0.1 × 0.1 × 0.2
Crystal system	monoclinic	monoclinic	triclinic
Space group	$P2_1/c$	$P2_1/n$	$P\bar{1}$
a [Å]	10.417(4)	8.3848(2)	10.8617(6)
b [Å]	15.482(7)	14.3300(1)	11.3177(7)
c [Å]	18.758(8)	17.5006(2)	14.7818(9)
α [°]	90.00	90.00	95.810(1)
β [°]	100.04(2)	98.04(1)	97.094(1)
γ [°]	90.00	90.00	115.114(1)
V [Å^3]	2979(2)	2082.12(6)	1608.7(2)
Z	4	4	2
ρ(calcd.), [Mg/m^3]	1.066	1.614	1.585
μ [mm^{-1}]	0.162	5.923	5.145
F(000)	1056	1000	768
Index range	$0 \le h \le 11$	$-11 \le h \le 8$	$-11 \le h \le 14$
	$0 \le k \le 17$	$-17 \le k \le 17$	$-14 \le k \le 12$
	$-21 \le l \le 21$	$-22 \le l \le 22$	$-17 \le l \le 18$
2 θ (°)	48.10	58.52	57.52
Temp. [K]	293(2)	193	193
Reflections collected	4651	12057	9046
Reflections unique	4475	3473	4862
Reflections observed (4σ)	2503	2039	3759
R(int.)	0.0585	0.0272	0.0303
Number of variables	303	188	308
Weighting scheme[a] x/y	0.0660/9.7473	0.0248/1.7484	0.0419/3.1643
GOOF	1.031	1.151	1.171
Final R(4σ)	0.0783	0.0226	0.0427
Final wR_2	0.1713	0.0537	0.0987
Largest res. peak [e/Å^3]	0.445	0.440	0.714

[a] $w^{-1} = \sigma^2 F_o^2 + (xP)^2 + yP$; $P = (F_o^2 + 2F_c^2)/3$.

incorporated into the refinement as riding on their respective C atoms. Table 5 contains the relevant information related to the crystallography, data acquisition and structure solution. CCDC-237980 to -237982 contain the supplementary crystallographic data for this paper. These data can be obtained free of charge from The Cambridge Crystallographic Data Centre via www.ccdc.cam.ac.uk/data_request/cif.

Computational Details: Geometries of the model compounds and **2** were optimized with internal redundant coordinates (total energy converged to $\le 1\times10^{-7}$ a. u., max norm of BP86/MP2/CC2 energy gradient converged to $\le1\times10^{-4}$ a. u.) with TURBOMOLE5.[29–32] using density functional (Becke–Perdew86 exchange correlation functional[33,34] for **2** and second order Møller-Plesset theory (frozen core) as well as a second-order approximated coupled cluster model for the model compounds **5**, **6**, **7** and **10** with the resolution of the identity (RI) approximation employing TZVP sets for all atoms.[35,36] For all structures, frequency calculations with SNF (MPI-parallel for **2**[37] or TURBOMOLE[38] (for the model compounds) were carried out. The geometries were re-optimized until the imaginary no imaginary frequencies remained (NIMAG = 0). NMR shift calculations were performed with the MPSHIFT module of TURBOMOLE.[39,40] ELF and AIM analyses were performed with the ToPMoD package,[41] NBO(NPA analysis with Gaussian 03 at the equilibrium geometries).[42]

Acknowledgments

We thank the University of Munich and Fonds der Chemischen Industrie as well as Chemetall GmbH for financial support. We also thank Dr. T. Seifert, and Prof. I. Krossing for recording X-ray data sets and for their help in determining the X-ray structures, Mr. P. Mayer for NMR spectra, and Mrs. D. Ewald for the MS spectra.

[1] U. Braun, T. Habereder, H. Nöth, *Eur. J. Inorg. Chem.* **2004**, 3629–3643.
[2] R. T. Paine, H. Nöth, *Chem. Rev.* **1995**, *95*, 343–379.
[3] P. Kölle, G. Linti, H. Nöth, K. Polborn, *J. Organomet. Chem.* **1988**, *355*, 7–18.
[4] P. Kölle, G. Linti, H. Nöth, G. L. Wood, C. K. Narula, R. T. Paine, *Chem. Ber.* **1988**, *121*, 871–879.
[5] G. Linti, H. Nöth, K. Polborn, R. T. Paine, *Angew. Chem.* **1990**, *102*, 715–716; *Angew. Chem. Int. Ed. Engl.* **1990**, *29*, 682–684.
[6] G. Linti, H. Nöth, R. T. Paine, *Chem. Ber.* **1993**, *126*, 875–889.
[7] M. Westerhausen, D. Dou, G. L. Wood, G. Linti, E. N. Duesler, H. Nöth, R. T. Paine, *Chem. Ber.* **1993**, *126*, 379–397.
[8] B. Kaufmann, H. Nöth, R. T. Paine, K. Polborn, M. Thomann, *Angew. Chem.***1993**, *105*, 1534–1536; *Angew. Chem. Int. Ed. Engl.* **1994**, *32*, 1446–1448.
[9] D. Dou, E. N. Duesler, R. T. Paine, H. Nöth, *J. Am. Chem. Soc.* **1992**, *114*, 9691–9692.
[10] P. Kölle, G. Linti, H. Nöth, G. L. Wood, C. K. Narula, R. T. Paine, *Chem. Ber.* **1987**, *121*, 871–876.
[11] P. Kölle, H. Nöth, R. T. Paine, *Chem. Ber.* **1986**, *119*, 2681–2685.
[12] K. Knabel, *Ph. D. Thesis*, University of Munich, **2000**.
[13] There is ambiguity about the ^{31}P chemical shifts. Therefore no data are given.
[14] S. Grundei, H. Nöth, R. T. Paine, *Chem. Ber.* **1996**, *129*, 1233–1242.

 © 2005 Wiley-VCH Verlag GmbH & Co. KGaA, Weinheim

[15] J. Mason, *Multinucelar NMR*, Plenum Press, New York, London, **1987**.
[16] H. Nöth, S. Weber, *Chem. Ber.* **1985**, *118*, 2554–2556.
[17] B. Böck, U. Braun, T. Habereder, H. Nöth, *Z. Naturfosch. Teil B* **2004**, *59*, 681–684.
[18] V. Shoemaker, P. D. Stevenson, *J. Am. Chem. Soc.* **1941**, *63*, 37–40.
[19] I. Haller, R. Srivasan, *J. Chem. Phys.* **1964**, *14*, 2745–2752.
[20] B. Silvi, A. Savin, *Nature* **1994**, *371*, 683–686.
[21] H. V. Rasika Dias, P. P. Power, *J. Am. Chem. Soc.* **1989**, *111*, 144–148.
[22] A. M. Arif, A. H. Cowley, J.-G. Pakulski, M. Power, *J. Chem. Soc.Chem. Commun.* **1986**, 889–890.
[23] B. Kaufmann, H. Nöth, R. T. Paine, *Chem. Ber.* **1996**, *129*, 557–560.
[24] H. Nöth, S. Weber, *Z. Naturforsch. Teil B* **1983**, 38, 1460–1465.
[25] K. Issleib, F. Krech, M. Riemer, *Phosphorus Sulfur* **1985**, *22*, 349–352.
[26] C. Krüger, H. Niederprüm, *Inorg. Synth.* **1966**, *8*, 15–23.
[27] SMART and SAINT, Programs for data collection and data reduction, Bruker Analytical Instruments, Madison, version 5.1.
[28] SHELXTL Plus, Program for structure solution, Bruker Analytical Instruments, Madison, version 5.1.
[29] R. Ahlrichs, M. Bär, M. Häser, H. Horn, C. Kölmel, *Chem. Phys. Lett.* **1989**, *162*, 165–169.
[30] K. Eichkorn, O. Treutler, H. Öhm, M. Haeser, R. Ahlrichs, *Chem. Phys. Lett.* **1995**, *242*, 652–660.
[31] K. Eichkorn, O. Treutler, H. Öhm, M. Haeser, R. Ahlrichs, *Chem. Phys. Lett.* **1995**, *240*, 283–290.
[32] K. Eichkorn, F. Weigand, O. Treutler, R. Ahlrichs, *Theor. Chem.* **1997**, *97*, 119 –124.
[33] J. P. Perdew, *Phys. Rev. B* **1986**, *33*, 8822–8824.
[34] A. D. Becke, *Phys. Rev. A* **1988**, *38*, 3098–3100.
[35] A. Schäfer, C. Huber, R. Ahlrichs, *J. Chem. Phys.* **1994**, *100*, 5829–5835.
[36] A. Schäfer, H. Horn, R. Ahlrichs, *J. Chem. Phys.* **1992**, *97*, 2571–2577.
[37] C. Kind, M. Reiher, J. Neugebauer, B. A. Hess, *J. Comput. Chem.* **2002**, *23*, 895 –910.
[38] P. Deglmann, F. Furche, R. Ahlrichs, *Chem. Phys. Lett.* **2002**, *362*, 511–518.
[39] M. Kollwitz, J. Gauss, *Chem. Phys. Lett.* **1996**, *260*, 639–646.
[40] M. Kollwitz, M. Häser, J. Gauss, *J. Chem. Phys.* **1998**, *260*, 8295–8301.
[41] S. Noury, X. Krokidis, F. Fuster, B. Silvi, *Computers and Chemistry*, Oxford Press, **1999**, *23*, 597.
[42] M. J. Frisch, G. W. Trucks, H. B. Schlegel, G. E. Scuseria, M. A. Robb, J. R. Cheeseman, J. A. Montgomery, Jr., T. Vreven, K. N. Kudin, J. C. Burant, J. M. Millam, S. S. Iyengarm, J. Tomasi, V. Barone, B. Mennucci, M. Cossi, G. Scalmani, N. Rega, G. A. Petersen, H. Nakatsuji, M. Hada, M. Ehara, K. Toyota, R. Fukuda, J. Hasegawa, M. Ishida, T. Nakajima, Y. Hond, O. Kitao, H. Nakai, M. Klene, X. Li, J. E. Knox, H. P. Hratshian, J. B. Cross, C. Adamo, J. Jaramillo, R. Gomperts, R. E. Stratmann, O. Yazyev, A. J. Austin, R. Dammi, C. Pomelli, J. W. Ochtersi, P. Y. Ayala, K.Morokuma, G. A. Voth, P. Salvador, J. J. Dannenberg, V. G. Zakrzewski, S. Dapprich, A. D. Daniels, M. C. Strain, O. Farkas, D. K. Malick, A. D. Rabuck, K. Raghavavhari, J. B. Foresman, J. V. Ortiz, Q. Cui, A. G. Baboul, S. Clifford, J. Cioslowski, B. B. Stefanov, G. Kiu, A. Liashenkon, P. Piskorz, A. Nanayakkara, M. Challacombe, P. M. W. Gill, B. Johnson, W. Chen, M. W. Wong, C. Gonzalez, J. A. Pople, Revision B01, Gaussian Inc., Pittsburgh, PA, USA, **2003**.

Received: May 6, 2004

 © 2005 Wiley-VCH Verlag GmbH & Co. KGaA, Weinheim

A Surprisingly Stable 1-(Chlorosilyl)-2-phosphaethenyllithium Compound, $RCl_2SiC(Li)=PMes^*$

Gabriela Cretiu Nemes,[a,b] Henri Ranaivonjatovo,[b] Jean Escudié,*[b] Ioan Silaghi-Dumitrescu,[a] Luminita Silaghi-Dumitrescu,[a] and Heinz Gornitzka[b]

Keywords: Phosphaalkenes / (Chlorosilyl)phosphaethenyllithium / Chlorophosphasilaallene / Molecular modelling / Cation-π interaction

$RCl_2Si–C(Li)=PMes^*$ (**1**) (R = 9-methylfluoren-9-yl, Mes* = 2,4,6-tri-*tert*-butylphenyl), considered as a key intermediate in the synthesis of the heteroallene $RClSi=C=PMes^*$, was obtained from $RCl_2Si–C(Cl)=PMes^*$ by lithium/chlorine exchange with *n*BuLi and evidence for its identity was obtained by hydrolysis. Remarkably, however, it failed to undergo a lithium salt elimination to form the corresponding chlorophosphasilaallene, $RClSi=C=PMes^*$, even under prolonged heating in toluene. As shown by theoretical studies (RHF/3-21G* and RHF/6-31G**//RHF/3-21G* level), interactions between the lithium ion and the π-systems of the substituents at the phosphorus and silicon atoms could partly account for this stability. The lithium compound **1** reacts with methanol or chlorotrimethylsilane leading to new silylphosphaalkenes. The reaction of the lithium derivative **1** with benzaldehyde gave a four-membered heterocycle with an exocyclic P=C bond which virtually corresponds to the product of a [2+2] cycloaddition between the Si=C and C=O double bonds.
(© Wiley-VCH Verlag GmbH & Co. KGaA, 69451 Weinheim, Germany, 2005)

Introduction

Silenes, the silicon counterparts of olefins, have challenged chemists for many years. Although the initial claim for producing an Si=C linkage dates back to 1912,[1] isolation of a stable silene was first achieved in 1981.[2] This major breakthrough, combined with the syntheses of the stable disilene $Mes_2Si=SiMes_2$ (Mes = 2,4,6-trimethylphenyl)[3] and diphosphene Mes*P=PMes* (Mes* = 2,4,6-tri-*tert*-butylphenyl)[4] paved the way for the remarkable and thriving chemistry of heavier multiple-bonded main group elements from which other bonding patterns such as heterocumulative double-bond systems have emerged.[5] A stable 1-silaallene >Si=C=C<, in which the carbon atom involved in the double bond to the silicon atom adopts sp-hybridisation, was reported a decade later.[6] We have been interested in 1,3-phosphasilaallenes, i.e. compounds with phosphorus and silicon atoms (thus, two heavier group 14 and 15 elements) at the terminal positions of the heteroallene skeleton and reported the hitherto unique >Si=C=P– derivative some years ago.[7] The latter readily undergoes dimerisation above –30 °C. Clearly, the steric shielding of the bulky groups in PhTipSi=C=PMes* (Tip = 2,4,6-triisopropylphenyl) is not sufficient to prevent the target molecule from coupling with itself and, consequently, the study of its chemical behaviour was limited. Due to the presence of three reaction sites (the Si=C and P=C double bonds as well as the phosphorus lone pair), such compounds should be extremely interesting from a synthetic point of view. Various cycloadducts could be obtained with unsaturated species, making these allenic derivatives powerful building blocks in heterocyclic and organometallic chemistry. In order to increase the synthetic utility of such compounds, we have tried to attach a chlorine atom to the silicon atom which could allow functionalisation of SiCP systems. Thus, it seemed interesting to prepare a phosphasilaallene, the main objective being to obtain a stable derivative to facilitate the study of its reactivity.

Herein we describe the synthesisof the stable chloro-lithio compound $RCl_2Si–C(Li)=PMes^*$ (R = 9-methylfluoren-9-yl) **1** from dichlorophosphasilapropene **2**, along with its characterisation showing that it exhibits a chemical behaviour which could be theoretically expected from the target phosphasilaallene $RClSi=C=PMes^*$ **3**.

[a] Universitatea Babes-Bolyai Cluj, Facultatea de Chimie si Inginerie Chimica,
Kogalniceanu Nr. 1, 400084 Cluj-Napoca, Romania
Fax: +40-264-190818
E-mail: isi@chem.ubbcluj.ro
[b] Hétérochimie Fondamentale et Appliquée, UMR 5069, Université Paul Sabatier,
118 Route de Narbonne, 31062, Toulouse cedex 04, France
Fax: +33-561558204
E-mail: escudie@chimie.ups-tlse.fr

Results and Discussion

Vicinal dihalophosphametallapropenes >M(X)–C(Cl)=P– (X = F, Cl; M = Si,[7] Ge[8]) are suitable precursors to the corresponding heteroallenes. Lithiation of the central carbon atom occurs smoothly at low temperature through a lithium/halogen exchange and the subsequent

lithium salt elimination gives rise to a metal–carbon double bond adjacent to the existing P=C bond which remains intact throughout the whole procedure. The final step in the synthesis of stable 1-silaallenes also involves lithium salt elimination from the closely related 3-fluoro-2-lithio-3-silapropenes >Si(F)–C(Li)=C<.[5e,6,9]

The above-described synthetic approach was applied for the target chlorophosphasilaallene. Substitution with the 9-methylfluorenyl group at the silicon atom was intended to provide extra steric protection for the desired double bond. The coupling of the carbenoid Cl(Li)C=PMes*[10] with trichloro(9-methylfluoren-9-yl)silane[11] afforded the anticipated trichlorophosphasilapropene **2** in good yield. A ^{31}P NMR analysis of the reaction mixture suggested that only one isomer of compound **2** was formed (δ_P = 328.1 ppm). Because of the severe steric hindrance of the Mes* group, the more accessible *trans*-chlorine atom in Cl_2C=PMes* can be expected to undergo an easier lithium/halogen exchange with *n*BuLi. This favours the formation of the (*E*)-carbenoid Cl(Li)C=PMes* which hence led to the (*Z*)-phosphasilapropene **2** when mixed with the starting trichlorosilane. The (*Z*) configuration of derivative **2** was confirmed by an X-ray diffraction study (Figure 1). The P=C distance [1.669(3) Å] matches the average value reported for such bonds (1.67 Å).[5c]

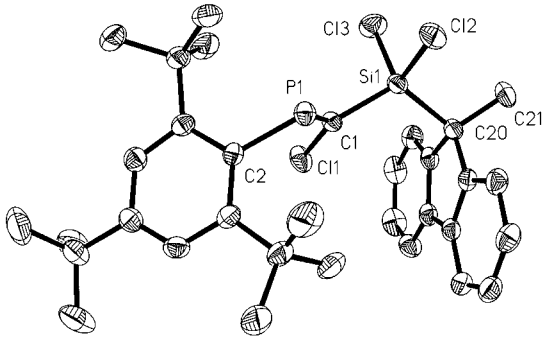

Figure 1. Molecular structure of **2** (thermal ellipsoids at the 50% probability level; H atoms are omitted for clarity); selected bond lengths [Å] and angles [°]: C(1)–P(1) 1.669(3), C(1)–Cl(1) 1.747(2), C(1)–Si(1) 1.850(3), P(1)–C(2) 1.833(3), Si(1)–C(20) 1.883(3), Si(1)–Cl(2) 2.0404(9), Si(1)–Cl(3) 2.0524(10); P(1)–C(1)–Cl(1) 125.92(15), P(1)–C(1)–Si(1) 119.65(14), C(1)–P(1)–C(2) 104.42(11), C(1)–Si(1)–C(20) 115.89(11), C(20)–Si(1)–Cl(2) 109.47(8), C(20)–Si(1)–Cl(3) 109.97(8)

Treatment of **2** with *tert*-butyllithium resulted in the expected metallation and caused the ^{31}P NMR signal to shift downfield (δ_P = 441.4 ppm). Further evidence for the ensuing lithium derivative $RCl_2SiC(Li)$=PMes* **1** was obtained by formation of its hydrolysis product (Scheme 1).

Compound **1** is stable under a rigorously maintained inert gas at room temperature and fails to eliminate lithium chloride to give **3** even under prolonged heating at reflux in toluene. However, attempts to isolate the highly air- and moisture-sensitive **1** by crystallisation at –30 °C led to the hydrolysis product **4** due to adventitious water. The (*E*) isomer was exclusively obtained, as expected from the configuration of starting **1** and was proved by the $^1J_{P=C}$ coupling

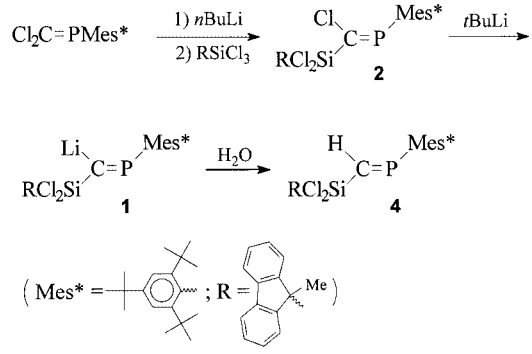

Scheme 1.

constant (67.9 Hz). A similar value (66.4 Hz) was reported by Bickelhaupt et al. for the (*E*) isomer of Mes*P=C(H)$SiMe_3$[10a] whereas the coupling constant for the (*Z*) isomer is smaller (54.4 Hz).

According to Wiberg, the 1,2-elimination of LiX to form an Si=C double bond involves dipolar intermediates B (Scheme 2).[12]

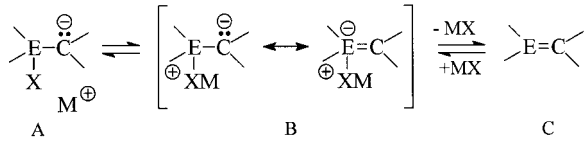

Scheme 2.

In our case, the non-elimination of LiCl means that the position of the equilibrium is shifted to form A, probably because of the presence of two chlorine atoms on the silicon atom. The natural charges on the carbon atom in the model carbanions $[Cl_{3-x}H_xSi–C=PH]^-$ at the RHF/6-31+G** level (Table 1) show that by increasing the number of chlorine atoms on the silicon atom, the negative charge on the carbon atom increases. This in turn favours the A form in Scheme 2.

Table 1.Natural charges on the carbon atom in the $[Cl_{3-x}H_xSi–C=PH]^-$ anions

Model	Natural charge on the carbon atom
$[H_3Si–C=PH]^-$	–1.224
$[ClH_2Si–C=PH]^-$	–1.315
$[Cl_2HSi–C=PH]^-$	–1.362
$[Cl_3Si–C=PH]^-$	–1.393

In order to obtain a deeper understanding of the observed reluctance of **1** to lose LiCl, molecular orbital calculations on various conformers of the model $Cp'Cl_2SiC(Li)$=PMes* system (Cp′ = 1-methylcyclopentadienyl) were carried out at the RHF/3-21G* level of theory, with full optimisation of the geometry. Note that this model retains the main steric and electronic features of **1** (through the Mes* group on P and the Cp′ group on Si). The influence of the solvent on the relative stability of these conformers has been inferred from single point calculations with the PCM solvation model of Tomasi by using two sol-

 © 2005 Wiley-VCH Verlag GmbH & Co. KGaA, Weinheim

Table 2. Relative energies [kJ mol^{-1}] and natural charges on Li in **1a** and **1b**

Conformer	Gas phase		DMSO		Toluene	
	Relative energy	Natural charge	Relative energy	Natural charge	Relative energy	Natural charge
1a	30.00	0.897	47.00	0.900	40.42	0.898
1b	0.0	0.885	0.0	0.887	0.0	0.886

vents (DMSO and toluene). The two lowest energy conformers (**1a** and **1b**) are shown in Figure 2. Table 2 includes the relative energies of these conformers calculated in the gas phase and in the two solvents as well as the natural charges on Li.

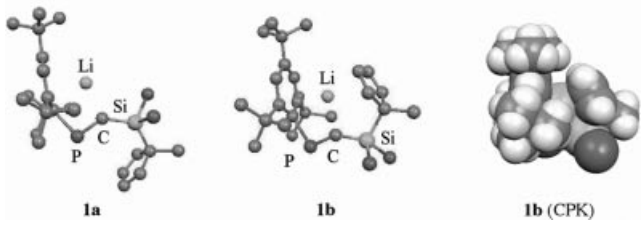

Figure 2. Lowest energy conformers of Cp′Cl_2SiC(Li)=PMes* (hydrogen atoms omitted); note the special position of Li in **1b** allowing for strong cation–π interactions

The lowest energy conformer **1b** exhibits strong electrostatic interactions between Li and both π systems (Mes* and Cp′) as shown by the following distances: Li–*ipso*-C(Mes*) 2.357 Å, Li–centroid(Mes*) 2.380 Å, Li–*ipso*-C(Cp′) 2.325 Å, Li–centroid(Cp′) 2.247 Å. These distances are in good agreement with those determined from X-ray analyses of similar interactions.[13]

The chlorine atoms in **1b** are located in unfavourable positions for intramolecular elimination of LiCl. Intermolecular condensation is also quite improbable due to the very efficient steric protection of the Li cation (see the CPK representation of **1b** in Figure 2). Note also that because of these cation···π interactions, the natural charge on Li does not change on going from gas phase to DMSO or toluene solution. Conformer **1a** is higher in energy both in the gas phase and in solution and, presumably, this arrangement is more difficult to achieve in the real system **1**. This order is also maintained at the RHF/6-31G**//RHF/3-21G* level where **1a** is still higher by 15.22 kJ mol^{-1}. Thus, cation···π interactions between Li and the Mes* and fluorenyl groups in **1** could account for its failure to eliminate lithium chloride. Such interactions have been recently highlighted by an X-ray diffraction analysis of a lithium (difluorosilyl)phosphide –Si(F_2)–P(Li)– which failed to undergo lithium fluoride elimination up to 100 °C.[14]

Lithium···π interactions in the case of $RCl_2SiC(Li)$=PMes* **1** also favour a shift in the position of the equilibrium to form A in accordance with the calculations and this could also explain the lack of elimination of LiCl. A similar reluctance to form an Si=C double bond by salt elimination has been previously reported.[15]

The lithio compound **1** reacts with excess methanol or chlorotrimethylsilane to give the silylphosphaalkenes **5** and **6**, respectively. The same derivatives should also be obtainable from the chlorophosphasilaallene **3** with these reactants (Scheme 3).

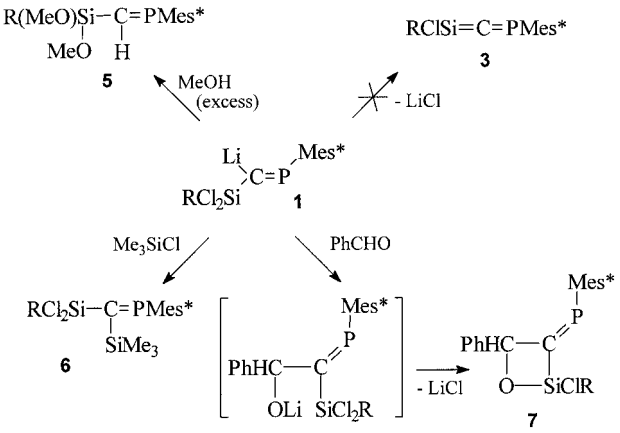

Scheme 3.

Interestingly, compound **1** readily reacts with benzaldehyde to afford oxasiletane **7** with an exocyclic P=C double bond in the form of one isomer as shown by ^{31}P NMR spectroscopy (δ_P = 339.4 ppm) (Scheme 3). From the $^2J_{P,CO}$ coupling constant (10.2 Hz) it seems that **7** exists as the (*E*) isomer (Mes* and Si *trans* to each other). This stereochemistry is in agreement with the postulated configuration of **1** and the mechanism of the reaction. Similar values were obtained by Appel and Bickelhaupt [16] for $^2J_{P,C}$ in Mes*P=C–C systems [(*E*) isomer 10–15 Hz, (*Z*) isomer 20–60 Hz]. In the closely related germanium compound **8c**, the structure of which was established by an X-ray determination, a $^2J_{P,CO}$ coupling constant of 38.7 Hz was observed for the (*Z*) isomer (Scheme 4). In the absence of an X-ray structural study, the stereochemistry of the four-membered ring (Ph and Cl in *cis* or *trans* positions) could not be determined.

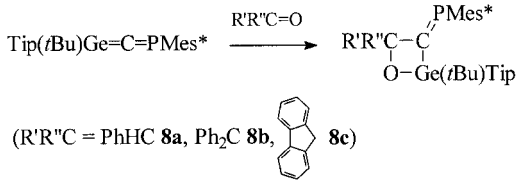

Scheme 4.

Though the latter reaction likely proceeds through an addition/elimination pathway, the four-membered ring **7** virtually conforms to the cycloaddition product of the Si=C double bond of the corresponding chlorophosphasilaallene with the starting aldehyde without participation of the contiguous P=C double bond as was found earlier for the Ge congener *t*BuTipGe=C=PMes*.[8]

 © 2005 Wiley-VCH Verlag GmbH & Co. KGaA, Weinheim

Similarly, a silenoid, >Si(Cl)–C(Li)<, has already been observed to behave as a synthetic equivalent of the corresponding silene in its reaction with carbonyl compounds.[15e] The study of the chemical behaviour of **1** towards various unsaturated species is now under investigation.

Experimental Section

General Remarks: All manipulations were carried out under N_2 or Ar using standard Schlenk techniques with solvents freshly distilled from sodium/benzophenone. ^1H, ^{13}C and ^{31}P NMR spectra were recorded in $CDCl_3$ with a Bruker AC 200 instrument at 200.1, 50.1 and 81.01 MHz, respectively, except for compound **1** which was measured in [D_8]toluene with a Bruker AC 400 spectrometer at 100.6 MHz. Mass spectra were recorded with a Hewlett–Packard 5989 A spectrometer by EI at 70 eV. Melting points were determined using a Leitz microscope heating stage 250. Elemental analyses were performed by the "Service de Microanalyse de l'Ecole de Chimie de Toulouse". The carbon atoms of the fluorenyl group are numbered as shown in Scheme 5.

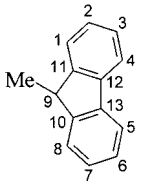

Scheme 5.

Synthesis of RCl_2Si–C(Cl)=PMes* (2): A sample of Cl_2C=PMes* (1.14 g, 3.18 mmol) was dissolved in THF (15 mL) and cooled to –80 °C. Under nitrogen, *t*BuLi (2 mL of a 1.7 M hexane solution, 1 equiv.) was added to form ClLiC=PMes*. This solution was slowly added to a solution of trichloro(9-methylfluoren-9-yl)silane (1.00 g, 3.18 mmol) in THF (10 mL) at –80 °C. The mixture was slowly warmed to room temperature with magnetic stirring over 2 h. After filtration, the solution was concentrated in vacuo and pentane (10 mL) was added. Cooling to –20 °C led to **2** as a crystalline product. Yield 1.49 g (78%). M.p. 131 °C. ^1H NMR ($CDCl_3$): δ = 1.12 (s, 18 H, *o*-CMe_3), 1.23 (s, 9 H, *p*-CMe_3), 1.88 (s, 3 H, Me), 7.28–7.85 (m, 10 H, arom. H of R and *m*-CH of Mes*) ppm. ^{13}C NMR ($CDCl_3$): δ = 21.4 (br., Me), 30.3 (br., C*Me*$_3$), 35.0 (*p*-*C*Me_3), 37.8 (*o*-*C*Me_3), 46.2 (C-9), 120.3 and 122.0 (C-4, -5 and *m*-CH of Mes*), 125.2 and 127.2 (C-1–3, C-6–8), 134.0 (d, $J_{P,C}$ = 63.0 Hz, *i*-C of Mes*), 141.1 and 146.1 (C-10–13), 151.0 and 153.1 (*o*- and *p*-C of Mes*), 155.7 (d, $J_{P,C}$ = 83.5 Hz, P=CCl) ppm. ^{31}P NMR ($CDCl_3$): δ = 328.1 ppm. MS (EI): *m*/*z* (%) = 602 (5) $[M]^+$, 587 (10) $[M – Me]^+$, 565 (5) $[M – Cl]^+$, 423 (30) $[M – R]^+$, 179 (95) $[R]^+$, 57 (100) $[t\text{Bu}]^+$. $C_{33}H_{40}Cl_3PSi$ (602.09): calcd. C 65.83, H 6.70; found C 66.10, H 6.91.

Synthesis of RCl_2Si–C(Li)=PMes* (1): A solution of RCl_2Si–C(Cl)=PMes* (1.30 g, 2.16 mmol) in diethyl ether (20 mL) was cooled to –80 °C under nitrogen. To the stirred solution was slowly added *t*BuLi (1.27 mL of a 1.7 M hexane solution, 1 equiv.) and the solution was then warmed to room temperature with magnetic stirring over 2 h. ^{13}C and ^{31}P NMR spectroscopic analyses of the brown solution showed nearly quantitative formation of **1**. ^{13}C NMR (400 MHz, [D_8]toluene): δ = 18.6 (Me), 31.2 and 33.9 (C*Me*$_3$), 33.3 (*C*Me_3), 38.4 (C-9), 120.0 (C-4, -5), 124.7, 126.7 and 127.1 (C-1–3, C-6–8), 141.0 and 145.7 (C-10–13), 144.4 (d, $J_{P,C}$ = 74.6 Hz, P=C or *i*-C of Mes*), 149.1 and 151.6 (*o*- and *p*-C of Mes*) ppm. ^{31}P NMR (Et_2O, [D_8]toluene): δ = 441.4 ppm.

Formation of RCl_2Si–C(H)=PMes* (4): A white waxy solid of **4** (95% purity) was obtained due to hydrolysis when a solution of the lithium compound **1** in Et_2O, prepared as described previously from **2** (1.00 g, 1.66 mmol), was kept at –30 °C for a week. Yield 0.85 g (90%). ^1H NMR ($CDCl_3$): δ = 1.25 (s, 18 H, *o*-CMe_3), 1.32 (s, 9 H, *p*-CMe_3), 1.85 (s, 3 H, Me), 6.75 (d, $^2J_{P,H}$ = 22.5 Hz, 1 H, CH), 7.28–7.91 (m, 10 H, arom. H of R and *m*-CH of Mes*) ppm. ^{13}C NMR ($CDCl_3$): δ = 19.1 (br. s, Me), 31.6 and 34.3 (br., C*Me*$_3$), 35.0 and 35.2 (*o*- and *p*-*C*Me_3), 38.1 (C-9), 120.2 and 122.0 (C-4, -5 and *m*-CH of Mes*), 124.9 and 127.2 (C-1–3, C-6–8), 141.0, 146.0, 150.2 and 152.6 (*o*- and *p*-C of Mes*, C-10–13), 156.6 (d, $^1J_{P,C}$ = 67.9 Hz,P=C) ppm. ^{31}P NMR ($CDCl_3$): δ = 375.3 ($^2J_{P,H}$ = 22.5 Hz) ppm.

Synthesis of $R(OMe)_2Si$–C(H)=PMes* (5): RCl_2Si–C(Li)=PMes* (1.66 mmol) prepared as previously described was treated with excess methanol (1 mL). The reaction mixture was filtered and the solution concentrated in vacuo followed by addition of pentane. Cooling to –20 °C gave **5** as a white solid (90% purity). Yield 0.87 g (88%). ^1H NMR ($CDCl_3$): δ = 1.28 (s, 18 H, *o*-CMe_3), 1.34 (s, 9 H, *p*-CMe_3), 1.66 (s, 3 H, Me), 3.27 (s, 6 H, OMe), 6.98 (d, $^2J_{P,H}$ = 22.0 Hz, 1 H, CH), 7.20–7.80 (m, 10 H, arom. H of R and *m*-CH of Mes*) ppm. ^{13}C NMR ($CDCl_3$): δ = 19.1 (Me), 31.5 and 33.8 (br., C*Me*$_3$), 35.1, 38.1 and 38.9 (*o*- and *p*-*C*Me_3, C-9), 45.5 (br., OMe), 119.9 (br., C-4, -5 and *m*-CH of Mes*), 124.8 and 126.5 (C-1–3, C-6–8), 140.4, 145.8, 152.2 and 153.1 (*o*- and *p*-C of Mes*, C-10–13) ppm. ^{31}P NMR ($CDCl_3$): δ = 362.2 (d, $^2J_{P,H}$ = 22.0 Hz) ppm. MS (EI): *m*/*z* (%) = 558 (5) $[M]^+$, 527 (1) $[M – OMe]^+$, 379 (40) $[M – R]^+$, 323 (33) $[M – R – t\text{Bu} + 1]^+$, 179 (100) $[R]^+$.

Synthesis of RCl_2Si–C($SiMe_3$)=PMes* (6): RCl_2Si–C(Li)=PMes* (1.66 mmol) in Et_2O (10 mL) was treated with excess chlorotrimethylsilane (0.5 mL) at room temperature. The lithium salt was removed by filtration and the solution concentrated in vacuo followed by addition of pentane. Cooling to –20 °C afforded **6** as a white solid. Yield 0.90 g(85%). M.p. 116 °C. ^1H NMR ($CDCl_3$): δ = –0.33(s, 9 H, $SiMe_3$), 1.12 (s, 18 H, *o*-CMe_3), 1.28 (s, 9 H, *p*-CMe_3), 1.92 (s, 3 H, Me), 7.23–7.91 (m, 10 H, arom. H of R and *m*-CH of Mes*) ppm. ^{13}C NMR ($CDCl_3$): δ = 0.4 ($SiMe_3$), 19.6 (Me), 29.9 and 31.6 (br., C*Me*$_3$), 37.1 and 37.6 (*o*- and *p*-*C*Me_3), 45.3 (C-9), 118.3 and 119.6 (C-4, -5 and *m*-CH of Mes*), 125.1 and 127.2 (C-1–3, C-6–8), 141.0, 146.0, 150.1 and 153.2 (*o*- and *p*-C of Mes*, C-10–13), 177.2 (d, $^1J_{P,C}$ = 90.5 Hz, P=CSi) ppm. ^{31}P NMR ($CDCl_3$): δ = 433.7 ppm. MS (EI): *m*/*z* (%) = 638 (15) $[M]^+$, 623 (15) $[M – Me]^+$, 566 (20) $[M – SiMe_3 + 1]^+$, 459 (20) $[M – R]^+$, 403 (15) $[M – R – t\text{Bu} + 1]^+$, 275 (22) $[ArP – 1]^+$, 179 (65) $[R]^+$, 57 (100) $[t\text{Bu}]^+$. $C_{36}H_{49}Cl_2PSi_2$ (638.83): calcd. C 67.58, H 7.72; found C 67.81, H 7.88.

Synthesis of Oxasiletane 7: A solution of RCl_2Si–C(Li)=PMes*, prepared from **2** (1.00 g, 1.66 mmol) in diethylether (20 mL), was cooled to –60 °C under nitrogen. To the stirred solution was slowly added benzaldehyde (0.19 g, 1.75 mmol). The solution was warmed to room temperature with magnetic stirring over 2 h. The reaction mixture was then filtered to remove LiCl and the solution concentrated in vacuo. Addition of pentane and cooling to –20 °C gave a waxy yellow solid which could not be obtained completely pure (90% purity) but was unambiguously identified as **7** by NMR spectroscopy and mass spectrometry. Yield 0.85 g (77%). ^1H NMR ($CDCl_3$): δ = 1.35 (br., 27 H, CMe_3), 1.80 (s, 3 H, Me), 5.80 (d, $^3J_{P,H}$ = 13.6 Hz, 1 H, OCH), 6.75–8.10 (m, 15 H, Ph, arom. H of R and *m*-CH of Mes*) ppm. ^{13}C NMR ($CDCl_3$): δ = 13.8 (Me), 31.4 and 33.6 (br., C*Me*$_3$), 37.1 and 38.3 (*o*- and *p*-*C*Me_3) 47.7 (C-

 © 2005 Wiley-VCH Verlag GmbH & Co. KGaA, Weinheim

9), 113.1 (d, $^2J_{P,CO}$ = 10.2 Hz, OCH), 120.2–130.0 (C-1–8 and *m*-CH of Mes*), 140.8–154.0 (*o*- and *p*-C Mes*, C-10–13) ppm. ^{31}P NMR ($CDCl_3$): δ = 339.4 (d, $^3J_{P,H}$ = 13.6 Hz) ppm. MS (EI): *m*/*z* (%) = 636 (2) $[M]^+$, 545 (3) $[M - PhCH - 1]^+$, 456 (5) $[M - R - 1]^+$, 394 (3) $[M - ClSiR]^+$, 379 (3) $[ArP{=}CCHPh]^+$, 350 (8) $[ArP{=}C{-}SiCl + 1]^+$, 179 (35) $[R]^+$, 105 (30) $[PhCO]^+$, 57 (100) $[t\text{Bu}]^+$.

Computational Details: A complete search of the conformational space of **1** was carried out using Spartan02[17] and the conformers thus obtained were further subjected to complete geometry optimisation at the RHF/3-21G* level with the same package. Single point calculations, taking into account the effect of solvents with the PCM model of Tomasi,[18] were performed using the G98 system Gaussian98, revision A.11.3.[19] The NBO analysis[20] was carried out within the NBO module implemented in G98.

Crystal Data for 2: $C_{33}H_{40}Cl_3PSi$, M = 602.06, monoclinic, $C2/c$, a = 16.661(2) Å, b = 10.730(1) Å, c = 36.380(3) Å, β = 90.284(2)°, V = 6504.0(11) Å^3, Z = 8, T = 193(2) K. 18162 reflections (6577 independent, R_{int} = 0.0340) were collected at low temperature using an oil-coated shock-cooled crystal with a Bruker-AXS CCD 1000 diffractometer with Mo-K_α radiation (λ = 0.71073 Å). The structure was solved by direct methods (SHELXS-97)[21] and all non-hydrogen atoms were refined anisotropically using the least-squares method on F^2.[22] Largest electron density residue: 0.403 e·Å^{-3}, $R_1[I > 2\sigma(I)]$ = 0.0511 and wR_2 (all data) = 0.1187 with $R_1 = \Sigma||F_o| - |F_c||/\Sigma|F_o|$ and $wR_2 = [\Sigma w(F_o^2 - F_c^2)^2/\Sigma w(F_o^2)^2]^{0.5}$. CCDC-233371 contains the supplementary crystallographic data for this paper. These data can be obtained free of charge at www.ccdc.cam.ac.uk/conts/retrieving.html [or from the Cambridge Crystallographic Data Centre, 12, Union Road, Cambridge CB2 1EZ, UK; Fax: +44-1223-336-033; E-mail: deposit@ccdc.cam.ac.uk].

Acknowledgments

G. C. N. thanks the NATO for support through the postdoctoral grant no. 376651J.

[1] W. Schlenk, *Justus Liebigs Ann. Chem.* **1912**, *394*, 178–223.
[2] A. G. Brook, F. Abdesaken, B. Gutekunst, G. Gutekunst, R. K. Kallury, *J. Chem. Soc., Chem. Commun.* **1981**, 191–192.
[3] R. West, M. J. Fink, J. Michl, *Science* **1981**, *214*, 1343–1344.
[4] M. Yoshifuji, I. Shima, N. Inamoto, K. Hirotsu, T. Higuchi, *J. Am. Chem. Soc.* **1981**, *103*, 4587–4589.
[5] a) M. Yoshifuji, K. Toyota, N. Inamoto, *J. Chem. Soc., Chem. Commun.* **1984**, 689–690; b) H. H. Karsch, H.-U. Reisacher, G. Müller, *Angew. Chem. Int. Ed. Engl.* **1984**, *23*, 618–619; for reviews see: c) R. Appel, in *Multiple Bonds, Low Coordination in Phosphorus Chemistry* (Eds.: M. Regitz, O. J. Scherer), Thieme, Stuttgart, **1990**, part D, p. 157–219; d) J. Escudié, H. Ranaivonjatovo, L. Rigon, *Chem. Rev.* **2000**, *100*, 3639–3696; e) B. Eichler, R. West, *Adv. Organomet. Chem.* **2000**, *46*, 1–46.
[6] G. E. Miracle, J. L. Ball, D. R. Powell, R. West, *J. Am. Chem. Soc.* **1993**, *115*, 11598–11599.
[7] L. Rigon, H. Ranaivonjatovo, J. Escudié, A. Dubourg, J.-P. Declercq, *Chem. Eur. J.* **1999**, *5*, 774–781.
[8] Y. El Harouch, H. Gornitzka, H. Ranaivonjatovo, J. Escudié, *J. Organomet. Chem.* **2002**, *643–644*, 202–208.
[9] a) M. Trommer, G. E. Miracle, B. E. Eichler, D. R. Powell, R. West, *Organometallics* **1997**, *16*, 5737–5747; b) B. E. Eichler, G. E. Miracle, D. R. Powell, R. West, *Main Group Met. Chem.* **1999**, *22*, 147–162
[10] a) S. J. Goede, F. Bickelhaupt, *Chem. Ber.* **1991**, *124*, 2677–2684; b) E. Niecke, M. Nieger, O. Schmidt, D. Gudat, W. W. Schoeller, *J. Am. Chem. Soc.* **1999**, *121*, 519–522; c) M. Yoshifuji, S. Ito, *Topics in Current Chem.* **2003**, *223*, 67–89.
[11] M. Schneider, B. Neumann, H.-G. Stammler, P. Jutzi, *Monatsh. Chem.* **1999**, *130*, 33–44.
[12] N. Wiberg, *J. Organomet. Chem.* **1984**, *273*, 141–177.
[13] a) K. Jonas, W. Rüsseler, K. Angermund, C. Krüger, *Angew. Chem. Int. Ed. Engl.* **1986**, *25*, 927–928; b) C. Üffing, R. Köppe, H. Schnöckel, *Organometallics* **1998**, *17*, 3512–3515; c) K. Ruhlandt-Senge, J. J. Ellison, R. J. Wehmschulte, F. Pauer, P. P. Power, *J. Am. Chem. Soc.* **1993**, *115*, 11353–11357; d) B. Schiemenz, P. P. Power, *Angew. Chem. Int. Ed. Engl.* **1996**, *35*, 2150–2151.
[14] A. S. Ionkin, W. J. Marshall, *Organometallics* **2003**, *22*, 4136–4144.
[15] a) N. Wiberg, G. Wagner, G. Mueller, J. Riede, *J. Organomet. Chem.* **1984**, *271*, 381–391;b) N. Wiberg, G. Wagner, *Chem. Ber.* **1986**, *119*, 1455–1466; c) N. Wiberg, C. M. M. Finger, T. Passler, S. Wagner, K. Polborn, *Z. Naturforsch. Teil B* **1996**, *51*, 1744–1760; d) N. Wiberg, H.-S. Hwang-Park, P. Mikulcik, G. Mueller, *J. Organomet. Chem.* **1996**, *511*, 239–253; e) C. Couret, J. Escudié, G. Delpon-Lacaze, J. Satgé, *J. Organomet. Chem.* **1992**, *440*, 233–242.
[16] a) R. Appel, J. Kochta, V. Winkhaus, *Chem. Ber.* **1988**, *121*, 631–635; b) S. J. Goede, L. de Vries, F. Bickelhaupt, *Bull. Soc. Chim. Fr.* **1993**, *130*, 185–188.
[17] *Spartan02*, Wavefunction, Inc., Irvine, CA.
[18] S. Miertus, J. Tomasi, *Chem. Phys.* **1982**, *65*, 239–245.
[19] M. J. Frisch, G. W. Trucks, H. B. Schlegel, G. E. Scuseria, M. A. Robb, J. R. Cheeseman, V. G. Zakrzewski, J. A. Montgomery Jr., R. E. Stratmann, J. C. Burant, S. Dapprich, J. M. Millam, A. D. Daniels, K. N. Kudin, M. C. Strain, O. Farkas, J. Tomasi, V. Barone, M. Cossi, R. Cammi, B. Mennucci, C. Pomelli, C. Adamo, S. Clifford, J. Ochterski, G. A. Petersson, P. Y. Ayala, Q. Cui, K. Morokuma, N. Rega, P. Salvador, J. J. Dannenberg, D. K. Malick, A. D. Rabuck, K. Raghavachari, J. B. Foresman, J. Cioslowski, J. V. Ortiz, A. G. Baboul, B. B. Stefanov, G. Liu, A. Liashenko, P. Piskorz, I. Komaromi, R. Gomperts, R. L. Martin, D. J. Fox, T. Keith, M. A. Al-Laham, C. Y. Peng, A. Nanayakkara, M. Challacombe, P. M. W. Gill, B. Johnson, W. Chen, M. W. Wong, J. L. Andres, C. Gonzalez, M. Head-Gordon, E. S. Replogle, J. A. Pople, *Gaussian98*, revision A.11.3, Gaussian, Inc., Pittsburgh, PA, **2002**.
[20] J. E. Carpenter, F. Weinhold, *J. Mol. Struct. (Theochem)* **1988**, *169*, 41–62.
[21] G. M. Sheldrick, *Acta Crystallogr., Sect. A* **1990**, *46*, 467–473.
[22] G. M. Sheldrick, *SHELXL-97, Program for Crystal Structure Refinement*, University of Göttingen, **1997**.

Received July 9, 2004

 © 2005 Wiley-VCH Verlag GmbH & Co. KGaA, Weinheim

Synthesis, Characterization and Coordination Chemistry of Some Selenium-Containing Macrocyclic Schiff Bases

Arunashree Panda,[a] Saija C. Menon,[a] Harkesh B. Singh,*[a] Christopher P. Morley,[b] Robert Bachman,[c] T. Matthew Cocker,[c] and Ray J. Butcher[d]

Keywords: Macrocycles / Selena-aza macrocycles / Palladium / Nickel / Cobalt

The condensation of bis(*o*-formylphenyl) selenide with 1,2-diaminoethane or 1,3-diaminopropane yielded the new macrocyclic ligands **1** and **2** in very good yields. Crystals of **1** are monoclinic, space group $P2_1/c$ with a = 10.0648(10) Å, b = 37.390(4) Å, c = 8.0073(11) Å, Z = 4 and those of **2** are triclinic, space group $P\bar{1}$ with a = 7.200(3), b = 9.137(3), c = 12.780(6) Å, Z = 1. The coordination chemistry of **1** and **2** has been studied with the "soft" metal ion Pd^{II} and "hard" metal ions Ni^{II} and Co^{II}. Reaction of $[PdCl_2(COD)]$ with 1 mol-equiv. of **1** or **2** in refluxing methanol and addition of NH_4PF_6 afforded the Pd^{II} complexes **5** and **6**, respectively. Compound **5** is an unexpected partially hydrolyzed complex. It crystallizes in the tetragonal space group $P4_12_12$ with a = 10.7737(10) Å, b = 10.7737(10) Å, c = 28.190(5) Å, Z = 4. The structure shows the Pd^{II} ion coordinated to a square-planar arrangement of two selenium and two nitrogen atoms. Reaction of $NiCl_2{\cdot}6H_2O$ with **1** or **2** and NH_4PF_6 yielded complexes **7** and **8**, respectively. The assignment of octahedral geometries to $[Ni(L)](PF_6)_2]$ (**7**: L = **1**; **8**: L = **2**) follows from their paramagnetism [μ_{eff} = 3.23 (**7**), 1.81 (**8**) B.M.] and their UV/Vis spectra. This was also confirmed by single-crystal X-ray studies. The crystal structures of **7** and **8** showed a distorted octahedral nickel center coordinated by two selenium and four nitrogen atoms. **7**: Monoclinic, space group $P2_1/c$; a = 9.979(2) Å, b = 18.901(4) Å, c = 19.333(4) Å; Z = 4. **8**:Orthorhombic, space group $Pna2_1$; a = 20.277(5), b = 20.865(5), c = 9.416(2) Å; Z = 4. The cyclic voltammograms of **7** and **8** in MeCN solution show well-behaved quasi-reversible Ni^{III}/Ni^{II} couples. The analogous Co^{II} complex, $[Co(\mathbf{1})](PF_6)_2]$ (**9**) also shows a quasi-reversible Co^{III}/Co^{II} couple.
(© Wiley-VCH Verlag GmbH & Co. KGaA, 69451 Weinheim, Germany, 2005)

Introduction

Currently, a great deal of attention is being focused on macrocyclic ligands because they play an important role in many aspects of chemistry, medicine and the chemical industry.[1] The contrast-enhancing properties of their lanthanide complexes in NMR imaging,[2] their suitability as antibiotics in radioimmunotherapy,[2] their high selectivity in the binding of metal ions,[1,2] and nucleotide bases,[3] and their unique structural features as spacers for crystal engineering[4] are some of the notable applications. In seeking optimum efficiency in their existing and potential applications, numerous macrocyclic ligands with a wide spectrum of electronic and structural features have been designed and synthesized. To date, the majority of these synthetic cyclic ligands contain oxygen,[5] nitrogen,[6] phosphorus[7] and sulfur[8] donor atoms.

[a] Department of Chemistry, Indian Institute of Technology, Powai, Bombay 400076, India
Fax: +91-22-2572-3480
E-mail: chhbsia@chem.iitb.ac.in
[b] Department of Chemistry, University of Wales Swansea, Singleton Park, Swansea, SA2 8PP, UK
[c] Department of Chemistry, Georgetown University, Washington DC 20057, USA
[d] Department of Chemistry, Howard University, Washington DC 20059 USA

The chemical and structural features of macrocyclic metal complexes can be tuned by incorporating different "soft" and "hard" donor atoms in the chelating ring, thereby promoting the stabilization of both low and high oxidation states of the metal center, as well as forcing metal ions to adopt an atypical coordination geometry. In this context, thia[8] and mixed aza-thia[9] crown ethers have been the subject of intense interest in the last few years, particularly as their complexes are useful model compounds for biological systems.[10]

Pinto and co-workers pioneered work on the synthesis of the cyclic selenium ligands. They have reported a series of selena crowns, including [14]aneSe$_4$, [16]aneSe$_4$, and [24]aneSe$_4$.[11] The Pd^{II} complex $[Pd([16]aneSe_4)]^{2+}$ has been shown to possess the *c*,*c*,*c* configuration by Pinto et al.[12] They have also reported the complexes of Cu^{I} and Cu^{II} with [16]-aneSe$_4$ and some new selenium-containing coronands.[13] Reid et al. have reported complexes with a variety of platinum metal centers, viz. $[M([16]aneSe_4)]^{2+}$ (M = Pd or Pt),[14] $[PtX_2([16]aneSe_4)]^{+}$ (X = Cl, Br),[15] $[MX_2([16]-aneSe_4)]^{+}$ (M = Rh or Ir),[16,17] $[RuX_2([16]aneSe_4)]^{n+}$ (n = 0 or 1), and $[MX(PPh_3)([16]aneSe_4)]^{+}$ (M = Ru or Os).[18] There are limited examples on Ni^{II}[19] and Co^{II}[17] complexes of these selenoethers. Reid et al. have also reported a range of complexes of Cr,[20] Mo, W, Mn, Re Cu, Ag and

 © 2005 Wiley-VCH Verlag GmbH & Co. KGaA, Weinheim **DOI: 10.1002/ejic.200400757**

Au involving [8]aneSe_2(1,5-diselenacyclooctane), 1,6-diselena-3,4-benzocyclononane, and [16]aneSe_4,[21,22] The main group metal complexation of these selenoethers are only reported for As^{III}, Sb^{III} and Bi^{III}.[23] Recently, Levason et al. have developed some mixed donor selenoether and telluroether macrocyclic ligands and studied their complexation property towards various metal ions.[24]

Cyclic polyselenoethers have also been prepared and their extraction abilities towards transition metal and heavy metal cations determined.[25] The first host molecule containing an Se–Se bond has been synthesized by Tomoda et al.[26] Muralidharan et al. have described a selenium-containing cyclophane and also studied its complexation.[27] Another novel tetraselenide macrocycle has been synthesized by Furukawa and co-workers.[28] Polyselenoether macrocycles have also been synthesized from 3,3-dimethylselenatane which is cyclooligomerized catalytically at 115 °C in the presence of $[Re_2(CO)_9(SeCH_2CMe_2CH_2)]$.[29] Jackson and co-workers have designed and synthesized a novel macrobicyclic cage incorporating N/Se (N_3Se_3) atoms and its Co^{III} complex.[30] Meunier et al. have reported the synthesis of a diselena crown ether[31] and tetraselena crown ethers of three different sizes incorporating several oxygen atoms in the bridge.[32] The complexation of these selenoethers has been achieved by their reaction with mercury(II) iodide. Very recently, they have reported the preparation of new cationic palladium complexes binding to two selena macrocyclic ligands.[33] Zeng et al. has synthesized a calix[4]diselena crown ether which has been tested as sensor for ion selective electrodes.[34] Meng et al. have synthesized a phospha-selena macrocycle and studied their complexation with $Pd^{II}Cl_2$.[35]

In continuation of our work on tellurium-[36] and selenium-containing aza macrocycles[37] we report here the facile synthesis, structure and reactivity of the new 22- and 24-membered Schiff-base macrocycles **1** and **2** along with their coordination chemistry. We also compare their structural behavior and relative donor abilities with their tellurium analogs.

Results and Discussion

Macrocyclic Schiff-Base Ligands

The 22- and 24-membered macrocyclic Schiff bases **1** and **2** with N and Se donor sets were isolated in 91 and 89% yield as colorless solids by use of the [2+2] condensation reaction of bis(*o*-formylphenyl) selenide[37] with 1,2-diaminoethane or 1,3-diaminopropane, respectively, in CH_3CN at room temperature without recourse to a metal ion template (Scheme 1). Secondary intramolecular Se···N interaction (vide infra) plays an important role in the formation of the macrocycles by reducing the unfavorable lone pair−lone pair repulsion between nitrogen atoms. These compounds are soluble in $CHCl_3$ and CH_2Cl_2 but show poor solubility in other common organic solvents and in polar solvents like CH_3OH and DMSO. They could be recrystallized from a $CHCl_3/CH_3CN$ (1:1) mixture.

The IR spectra of the crystals of **1** and **2** showed that cyclization had occurred; an imine C=N stretch was present at 1636 and 1632 cm^{-1}, respectively, and no absorptions corresponding to unreacted carbonyl or primary amine were observed. Both the ^1H and ^{13}C NMR spectra of compounds **1** and **2** show resonances corresponding to one quarter of the molecule, suggesting very symmetric structures for the macrocyles. The CH=N proton signals were observed at δ = 8.52 and 8.46 ppm, respectively, being shifted ca.1.8 ppm upfield of the signal of the formyl proton in the starting bis(*o*-formylphenyl) selenide[37] (δ = 10.28 ppm).

The observation of a single signal in the ^{77}Se NMR spectra of the macrocycles confirms the equivalence of the two selenium atoms in **1** and **2**. On comparing the values for **1** and **2** (δ = 407, 413 ppm) with those for the corresponding saturated compounds **3** and **4** (δ = 329, 326 ppm), prepared as shown in Scheme 1, a considerable decrease in ^{77}Se chemical shift is noticed. This indicates poorer shielding of the selenium nucleus in the former cases, due to the delocalization of the selenium lone pairs in the five-membered ring formed by the strong Se···N interactions. In **3** and **4**, the Se···N interactions are not significant and hence delocalization of the electron pair is not possible.

The fast electron bombardment (FAB) mass spectra of **1** and **2** were recorded in order to confirm the formation of the [2+2] cyclocondensation products. The selenium-containing fragments could easily be recognized because of their characteristic isotope distribution pattern. In addition to the molecular ion peaks at m/z = 627 and 657 as the base peaks, the FAB mass spectra clearly show peaks due to the successive loss of groups from the macrocyclic framework.

Crystal Structures of 1 and 2

The crystal structure of **1** consists of discrete molecules and the unit cell contains four of them. The bond lengths and bond angles for a representative molecule are given in

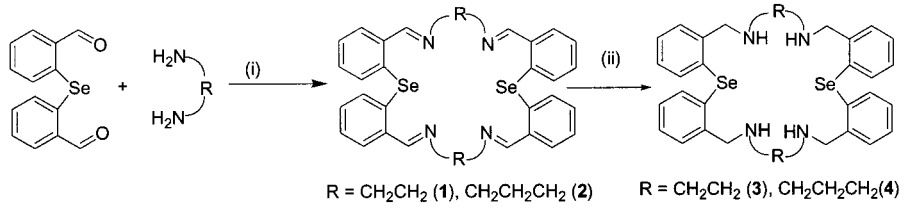

Scheme 1. (i) $NH_2CH_2CH_2NH_2$ or $NH_2CH_2CH_2CH_2NH_2$; (ii) $NaBH_4$, EtOH, reflux.

 © 2005 Wiley-VCH Verlag GmbH & Co. KGaA, Weinheim

Table 1. Selected bond lengths [Å] and angles [°] for **1**.

Se(1)–C(1A)	1.929(6)	Se(1)–C(1B)	1.941(6)
Se(2)–C(1D)	1.923(7)	Se(2)–C(1C)	1.933(7)
N(1A)–C(7A)	1.261(9)	N(1A)–C(8A)	1.455(9)
N(1B)–C(7B)	1.251(9)	N(1B)–C(8B)	1.472(10)
N(1C)–C(7C)	1.271(9)	N(1C)–C(8C)	1.440(10)
N(1D)–C(7D)	1.233(9)	N(1D)–C(8D)	1.458(9)
C(1A)–Se(1)–C(1B)	100.2(3)	C(1D)–Se(2)–C(1C)	100.9(3)
C(7A)–N(1A)–C(8A)	121.0(6)	C(7B)–N(1B)–C(8B)	117.5(6)
C(7C)–N(1C)–C(8C)	118.8(7)	C(7D)–N(1D)–C(8D)	119.6(6)
C(2A)–C(1A)–Se(1)	121.3(5)	C(6A)–C(1A)–Se(1)	119.3(5)
N(1A)–C(7A)–C(6A)	123.3(6)	N(1A)–C(8A)–C(8C)	111.4(6)
C(2B)–C(1B)–Se(1)	116.2(5)	C(6B)–C(1B)–Se(1)	123.9(5)
N(1B)–C(7B)–C(6B)	122.3(6)	N(1B)–C(8B)–C(8D)	108.7(6)
C(6C)–C(1C)–Se(2)	123.9(5)	C(2C)–C(1C)–Se(2)	116.5(6)
N(1C)–C(7C)–C(6C)	122.0(7)	N(1C)–C(8C)–C(8A)	110.8(6)
C(2D)–C(1D)–Se(2)	123.1(5)	C(6D)–C(1D)–Se(2)	117.9(5)
N(1D)–C(7D)–C(6D)	122.5(7)	N(1D)–C(8D)–C(8B)	111.5(6)

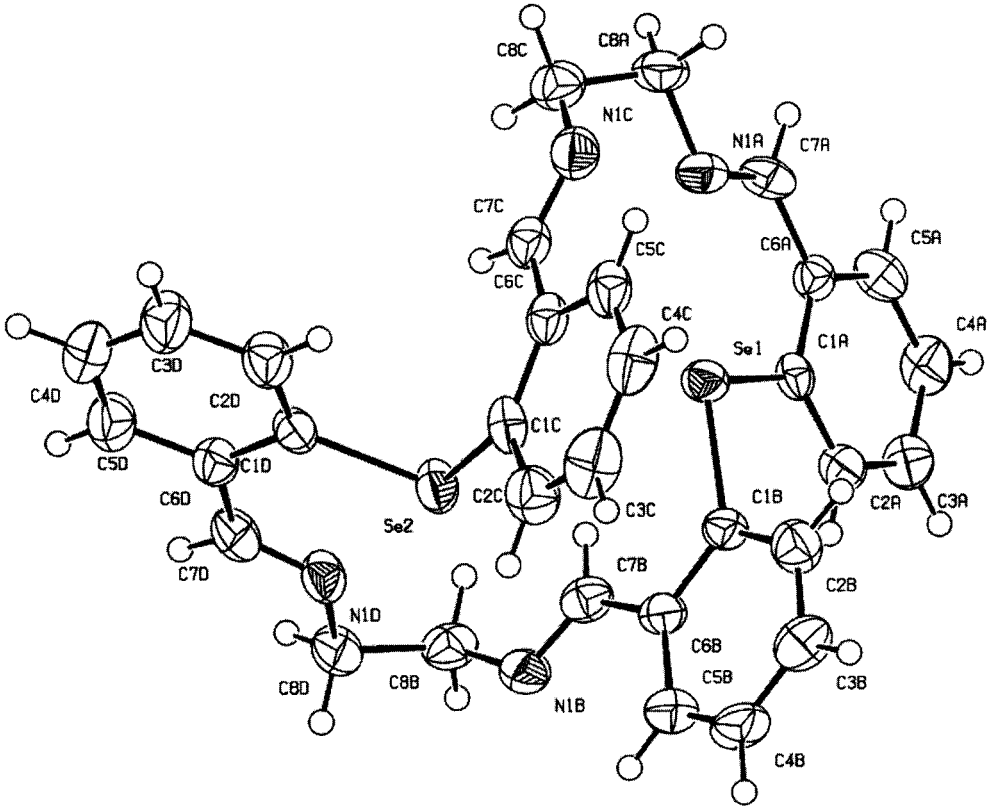

Figure 1. ORTEP diagram for **1**.

Table 1, and the ORTEP diagram is shown in Figure 1. The Se(1)···N(1A) and Se(2)···N(1C) intramolecular distances of 2.723 Å and 2.729 Å are shorter than the sum of the van der Waals radii of Se (2 Å) and sp^2-hybridized N (1.5 Å).[38] Although there are equal chances of coordination of N(1A), N(1B) to the Se(1) atom and N(1C), N(1D) to the Se(2) atom, the N(1B) and N(1D) atoms are not coordinated to Se(1) and Se(2), respectively. Thus, the solid-state geometry of the molecule indicates the presence of only one attractive interaction per selenium atom, i.e. it corresponds to the structure of 10-Se-3 selenurane. The bond configuration at the selenium atom is T-shaped. The C(1B)–Se–C(1A) angle is 100.2(3)°.

The transannular Se···Se distance (3.808 Å) is shorter than the sum of the van der Waals radii (4 Å). Interestingly, the transannular Te···Te bond length (4.979 Å)[36] in the case of the tellurium analog is greater than the sum of the van der Waals radii (4.4 Å). However, the transannular Se···Se distance in **1** is comparable to the Se1···Se2 distance of 3.9315(8) Å in 22-diselenasapphyrin.[39]

Compound **2** crystallized in the triclinic space group $P\bar{1}$. The unit cell contains one molecule. Selected bond lengths

 © 2005 Wiley-VCH Verlag GmbH & Co. KGaA, Weinheim

Table 2. Selected bond lengths [Å] and angles [°] for **2**.

Se–C(1B)	1.924(8)	Se–C(1A)	1.930(9)
N(1A)–C(7A)	1.271(11)	N(1A)–C(8A)	1.477(11)
N(1B)–C(7B)	1.242(11)	N(1B)–C(8B)	1.470(10)
C(1B)–Se–C(1A)	97.7(4)	C(7A)–N(1A)–C(8A)	118.0(7)
C(7B)–N(1B)–C(8B)	119.3(8)	C(6A)–C(1A)–Se	122.8(6)
C(2A)–C(1A)–Se	118.3(7)	N(1A)–C(7A)–C(6A)	120.1(8)
N(1A)–C(8A)–C(9)	107.9(7)	C(2B)–C(1B)–Se	122.5(7)
C(6B)–C(1B)–Se	119.6(6)	N(1B)–C(7B)–C(6B)	123.7(8)
N(1B)–C(8B)–C(9)#1	110.0(7)		

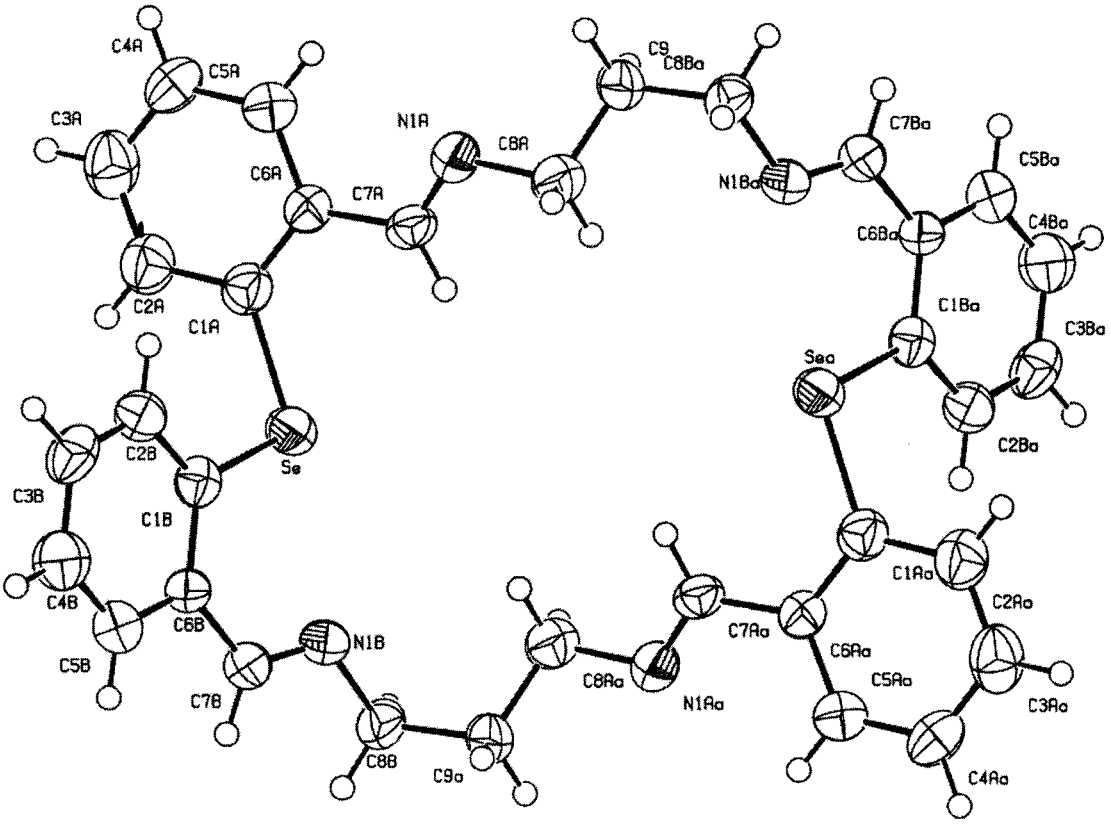

Figure 2. ORTEP diagram for **2**.

and angles are provided in Table 2. The ORTEP view is given in Figure 2. The solid-state geometry of the molecule indicates the presence of only one attractive Se···N interaction per selenium atom, i.e. it corresponds to the structure of 10-Se-3 selenurane. The intramolecular Se···N(1B) distance is 2.773 Å slightly longer than the equivalent distances in **1**. The geometry around the selenium atom is T-shaped, with the C(1B)–Se(1)–C(1A) angle being 97.7(4)°. The transannular Se···Se distance (7.229 Å) is much longer than the sum of van der Waals radii (4 Å) and also greater than the corresponding Se···Se distance (3.808 Å) observed in the 22-membered macrocycle **1**.

Reactions of 1 and 2 with Pd^{II}

The reaction of **1** or **2** with 1 equiv. of $[PdCl_2(COD)]$ (COD = 1,5-cyclooctadiene) in refluxing methanol afforded a yellow solution, which gave a yellow precipitate of complex **5** or **6**, respectively, in quantitative yield upon addition of PF_6^- counterions (Scheme 2). Slow concentration of an MeCN solution of **5** yielded yellow crystals of the complex. These complexes are air-stable in the solid state. They are insoluble in chlorinated solvents and hydrocarbons but soluble in MeCN, $MeNO_2$, acetone, DMF and DMSO.

The IR spectra of the complexes confirm the presence of PF_6^- anion {836 [ν(P–F)], 556 [δ(F–P–F)] cm^{-1}} and display the characteristic ν(C=N) stretching frequency around 1640 and 1637 cm^{-1}, respectively, shifted slightly compared with the ν(C=N) stretching frequencies of 1650 (**1**) and 1653 cm^{-1} (**2**) for the free ligands. The ^1H NMR spectrum of **5** shows a peak at δ = 10.1 ppm corresponding to two aldehydic protons and at δ = 8.89 ppm corresponding to two azomethine protons. The IR spectrum also shows a peak corresponding to ν(C=O) stretching at 1667 cm^{-1}, which implies that of the four CH=N bonds, two are hydrolyzed to −CHO groups. This hydrolysis may be due to excessive strain in the ring due to the planar geometry en-

 © 2005 Wiley-VCH Verlag GmbH & Co. KGaA, Weinheim

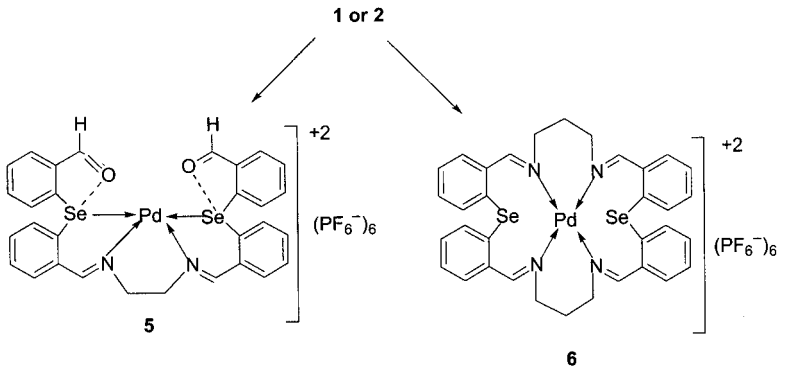

Scheme 2. Reagents: (i) $Pd(COD)Cl_2$, MeOH, reflux; (ii) NH_4PF_6.

forced by the metal ion. However, a similar reaction of the Pd^{II} precursor with the 22-membered tellurium analog gives the cationic complex $[Pd(L)](PF_6)_2$ [L = macrocycle derived from bis(*o*-formylphenyl) telluride and 1,2-diaminoethane] without any hydrolysis.[36] This may be due to the larger hole size of the tellurium analog. The ^{77}Se NMR spectrum of **5** exhibits a single signal at δ = 411 ppm showing that the selenium atoms are equivalent. The FAB mass spectrum of the complex shows peaks with the correct isotope distribution pattern at *m*/*z* = 855, 709, 605 corresponding to [**5** − PF_6], [**5** − 2PF_6] and [**5** − Pd − 2 PF_6]. The formulation of the product **5** as $[Pd\{(C_6H_4(CHO)SeC_6H_4CHNCH_2)_2\}](PF_6)_2$ was confirmed by a crystal structure determination (vide infra).

The elemental analysis data for **6** were in accordance with the formation of a 1:1 product. The ^1H NMR spectrum of **6** shows a single peak at δ = 8.66 ppm for the azomethine protons and the ^{13}C NMR spectrum shows a peak at δ = 170 ppm for the azomethine carbon atoms, confirming the equivalence of the four azomethine groups. The quintuplet and the triplet for the CH_2–C*H*$_2$–CH_2 and the NH–C*H*$_2$–CH_2 protons are found in the deshielded region at δ = 3.64 and 4.83 ppm compared with δ = 2.00 and 3.61 ppm for the free ligand **2**, thus confirming the coordination of all the nitrogen atoms to the Pd^{II} ion. The large ring size of **2** (24-membered and Se···Se distance 7.229 Å) probably mitigates against coordination of the selenium atoms to Pd^{II}. A single signal was observed in the ^{77}Se NMR spectrum at δ = 441 ppm, which confirmed the identical environment around each selenium atom. The molecular ion peak was not observed in the FAB mass spectrum of **6**. However, the highest recorded peak was found at *m*/*z* = 905, corresponding to [$\mathbf{6}^+$ − PF_6]. Similar observations have been reported by Reid et al.,[14,17] The peak at *m*/*z* = 761 was assignable to [**6** – 2 PF_6]. The base peak at *m*/*z* = 434 corresponded to $[(CH_2)_2N{=}CH(C_6H_4)Se(C_6H_4)CH{=}NCH_2Pd]$. In addition, the spectrum clearly shows peaks due to the fragmentation of the macrocyclic framework. The crystal structure of **6**, which was isolated as yellow needles, could not be solved due to a crystallographic problem. The formulation of **6** as $[Pd(\mathbf{2})](PF_6)_2$ is, however, assured on the basis of the analytical data, IR, ^1H, ^{13}C, ^{77}Se NMR spectroscopy and mass spectrometry.

Crystal Structure of 5

Complex **5** crystallizes in a tetragonal crystal system with four molecules in the unit cell. Figure 3 shows the structure of a representative molecule and confirms the hydrolysis of two of the azomethine bonds in the starting material **1**. Selected bond lengths and angles are given in Table 3. The structure of **5** shows that the palladium ion is bound to two selenium and two nitrogen atoms. The average Pd–N distance, 2.019(6) Å, is in excellent agreement with the sum of the Pauling single bond covalent radii for palladium (1.31 Å) and nitrogen (0.7 Å).[38] The average Pd–Se bond length 2.3973(11) Å is close to that reported in a range of other palladium complexes of selenium-containing ligands.[40–42] It is also comparable to the Pd–Se distances [2.4191(5), 2.4183(5) Å] in $[PdL](PF_6)_2$ (L = diselena macrocycle),[33] although shorter than the Pd–Se bond lengths of 2.428(1) Å and 2.435(2) Å in $[Pd([16]aneSe_4)](PF_6)_2{\cdot}2\,MeCN$.[14] The Se–Pd–N and N–Pd–Se angles are 93.3(2)° and 169.7(2)°, respectively, which implies that the complex has a distorted square-planar geometry. The Se···O distance 2.855 Å shows that selenium atom is weakly coordinated to the oxygen atom. This bond length can be compared to the selenium···oxygen contacts 2.888(3) Å in α-selenazofurin.[44] The geometry around the Se atom is V-shaped. The C(1A)–Se–C(1B) angle of 96.7(4)° is 3.5° smaller than the C(1A)–Se–C(1B) angle (100.2(3)°] in **1**.

Reactions of 1 and 2 with Ni^{II}

The reaction of $NiCl_2{\cdot}6H_2O$ with 1 equiv. of **1** or **2** in refluxing methanol followed by the addition of an excess of PF_6^- afforded air-stable, brown and greenish yellow paramagnetic complexes **7** or **8**, respectively (Scheme 3). Complex **7** could be recrystallized by the slow diffusion of diethyl ether into an MeCN solution. Complex **8** was isolated as green needles from methanol. The compounds are soluble in MeCN, $MeNO_2$, acetone, DMSO and DMF. The elemental analysis data of the complexes **7** and **8** suggested the formation of a 1:1 product in each case. The infrared spectroscopic measurements showed the presence of the PF_6^- anion. The $\nu_{C=N}$ absorption for **7** and **8** was found at 1650 and 1628 cm^{-1}, respectively. The electronic spectra of

 © 2005 Wiley-VCH Verlag GmbH & Co. KGaA, Weinheim

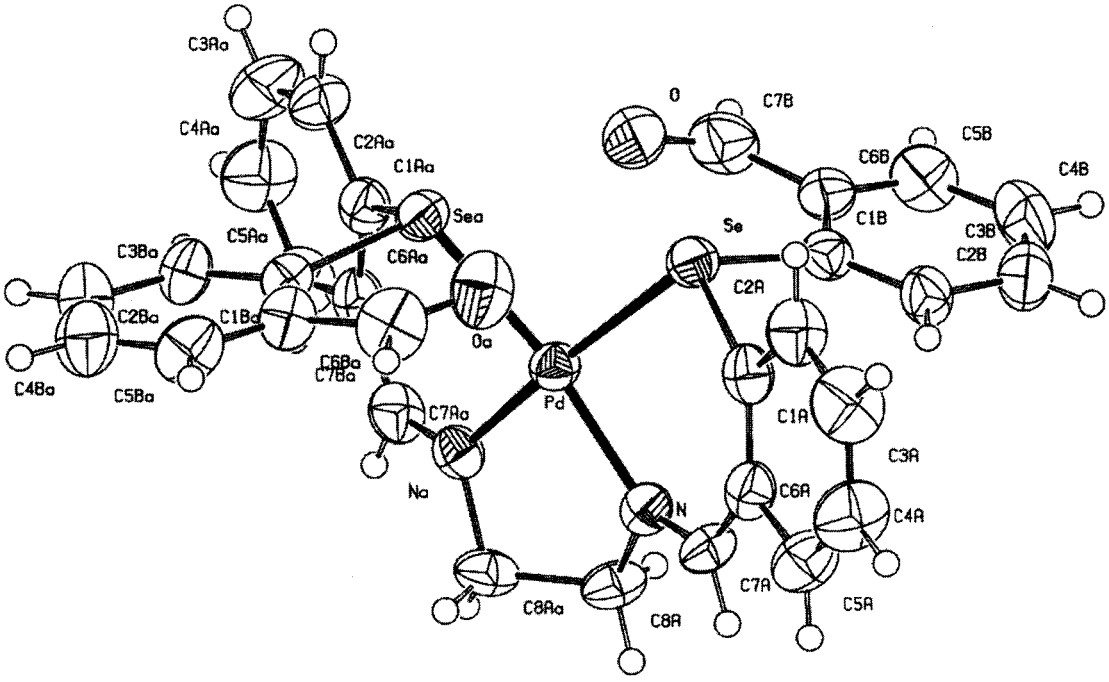

Figure 3. ORTEP diagram for **5**.

Table 3. Selected bond lengths [Å] and angles [°] for **5**.

Pd–N	2.019(6)	Pd–Se	2.3973(11)
Se–C(1A)	1.924(8)	Se–C(1B)	1.954(9)
N–C(7A)	1.297(9)	N–C(8A)	1.470(10)
O–C(7B)	1.197(13)	C(1B)–Se–Pd	106.7(2)
N–Pd–N#1	83.7(4)	N–Pd–Se	93.3(2)
N#1–Pd–Se	169.7(2)	N–Pd–Se#1	169.7(2)
N#1–Pd–#Se1	93.3(2)	Se–Pd–Se#1	91.24(5)
C(1A)–Se–C(1B)	96.7(4)	C(1A)–Se–Pd	101.7(3)
C(7A)–*N*–C(8A)	118.7(7)	C(7A)–*N*–Pd	128.3(6)
C(8A)–*N*–Pd	111.2(5)	C(2A)–C(1A)–Se	115.1(7)
C(6A)–C(1A)–Se	124.0(6)	N–C(7A)–C(6A)	128.7(8)
N–C(8A)–C(8A) #1	108.5(6)	C(2B)–C(1B)–Se	119.7(6)
C(6B)–C(1B)–Se	121.1(6)	O–C(7B)–C(6B)	126.4(10)

the complexes **7** and **8** were recorded at room temperature in CH_3CN in the range of 190–900 nm. The solution-phase electronic spectra (> 200 nm) of the ligands **1** and **2** consist of two intense bands centered at 290 and 335 nm which can be assigned to π–π* transitions. The intense peak found at 295 nm in each case may be attributed to a charge-transfer transition. Three spin-allowed transitions are expected for d^8 Ni^{II} complexes in an octahedral field. For the complex **7** there are three intense bands at 310, 452, and 804, which may be assigned to the interligand π–π* and d–d transitions. The solid-state UV/Vis spectrum also shows similar peaks at 800, 458, and 312 nm confirming the stability of the complex in the solution state. Complex **8** shows peaks at 872 (7.3), 560 (8.2) and 446 (24.3) nm in acetonitrile solution. These may be assigned to a combination of intraligand π–π* and d–d transitions. The solid-state UV/Vis spectra shows peaks at 866, 552 and 452 nm confirming the stability of complex in solution.

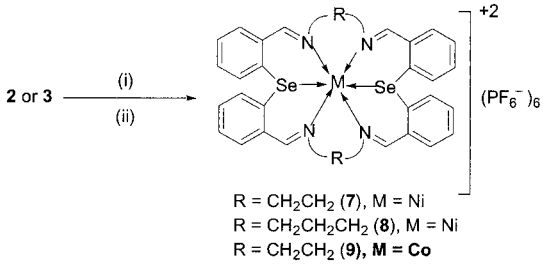

Scheme 3. Reagents: (i) $NiCl_2 \cdot 6H_2O$ or $CoCl_2 \cdot 6H_2O$; (ii) MeOH, reflux, NH_4PF_6.

In the FAB mass spectrum the highest recorded peak for complex **7** was found at *m*/*z* = 997. This was assigned to [**7** + H_2O]. The peak at *m*/*z* = 831 corresponds to [**7** − PF_6]. The base peak was found at *m*/*z* = 686 and can be assigned to [**7** – 2 PF_6]. For complex **8** a peak at *m*/*z* = 733 was found as the base peak, which can be assigned to [**8** − 2

 © 2005 Wiley-VCH Verlag GmbH & Co. KGaA, Weinheim

PF_6 + H_2O]. A peak at m/z = 712 corresponds to [**8** – 2 PF_6]. The cyclic voltammograms of **7** and **8** revealed well-behaved quasi-reversible (ΔE = 100 mV at scan rate = 100 $mV \cdot s^{-1}$) Ni^{III}/Ni^{II} couples, with $E_{1/2}$ = 1.42 V and 1.55 V, respectively.

The assignment of octahedral geometries to [Ni(**1**)]-$(PF_6)_2$ (**7**) and [Ni(**2**)]$(PF_6)_2$ (**8**) follows from their paramagnetism, μ_{eff} = 3.06 and 3.25 B.M., respectively, which indicates S = 1. This was confirmed by single-crystal X-ray studies (vide infra).

Crystal Structures of 7 and 8

Complex **7** crystallizes as a monohydrate in the monoclinic system (space group $P2_1/c$) with four molecules in the

Table 4. Selected bond lengths [Å] and angles [°] for **7**.

Ni–N(2B)	2.048(5)	Ni–N(2A)	2.053(5)
Ni–N(1B)	2.055(5)	Ni–N(1A)	2.073(5)
Ni–Se(1)	2.4890(10)	Ni–Se(2)	2.5517(10)
Se(1)–C(11B)	1.920(6)	Se(1)–C(11A)	1.937(6)
Se(2)–C(21A)	1.933(6)	Se(2)–C(21B)	1.942(6)
N(1A)–C(17A)	1.269(7)	N(1A)–C(18A)	1.471(7)
N(2A)–C(27A)	1.275(7)	N(2A)–C(28A)	1.481(7)
N(1B)–C(17B)	1.274(7)	N(1B)–C(18B)	1.489(8)
N(2B)–C(27B)	1.271(7)	N(2B)–C(28B)	1.478(8)
N(2B)–Ni–N(2A)	98.8(2)	N(2B)–Ni–N(1B)	79.0(2)
N(2A)–Ni–N(1B)	177.7(2)	N(2B)–Ni–N(1A)	95.3(2)
N(2A)–Ni–N(1A)	77.9(2)	N(1B)–Ni–N(1A)	101.3(2)
N(2B)–Ni–Se(1)	167.6(2)	N(2A)–Ni–Se(1)	93.37(13)
N(1B)–Ni–Se(1)	88.72(13)	N(1A)–Ni–Se(1)	85.26(13)
N(2B)–Ni–Se(2)	84.57(14)	N(2A)–Ni–Se(2)	86.62(14)
N(1B)–Ni–Se(2)	94.11(13)	N(1A)–Ni–Se(2)	164.32(14)
Se(1)–Ni–Se(2)	98.24(3)	C(11B)–Se(1)–C(11A)	97.7(2)
C(11B)–Se(1)–Ni	98.3(2)	C(11A)–Se(1)–Ni	99.1(2)
C(21A)–Se(2)–C(21B)	97.7(3)	C(21A)–Se(2)–Ni	95.1(2)
C(21B)–Se(2)–Ni	95.8(2)	C(17A)–N(1A)–C(18A)	119.2(5)
C(17A)–N(1A)–Ni	133.6(4)	C(18A)–N(1A)–Ni	106.8(4)
C(27A)–N(2A)–C(28A)	115.9(5)	C(27A)–N(2A)–Ni	129.6(4)
C(28A)–N(2A)–Ni	112.6(4)	C(17B)–N(1B)–C(18B)	116.3(5)
C(17B)–N(1B)–Ni	128.5(4)	C(18B)–N(1B)–Ni	112.5(4)
C(27B)–N(2B)–C(28B)	119.9(5)	C(27B)–N(2B)–Ni	132.2(4)
C(28B)–N(2B)–Ni	107.8(4)	C(12A)–C(11A)–Se(1)	118.2(5)
C(16A)–C(11A)–Se(1)	121.4(4)	N(1A)–C(17A)–C(16A)	125.8(6)
N(1A)–C(18A)–C(28A)	108.9(5)	C(22A)–C(21A)–Se(2)	115.6(5)
C(26A)–C(21A)–Se(2)	123.2(5)	N(2A)–C(27A)–C(26A)	125.5(6)
N(2A)–C(28A)–C(18A)	110.9(5)	N(1B)–C(17B)–C(16B)	127.8(5)
C(22B)–C(21B)–Se(2)	117.6(5)	C(26B)–C(21B)–Se(2)	122.2(5)
N(2B)–C(27B)–C(26B)	124.4(6)	N(2B)–C(28B)–C(18B)	109.5(6)

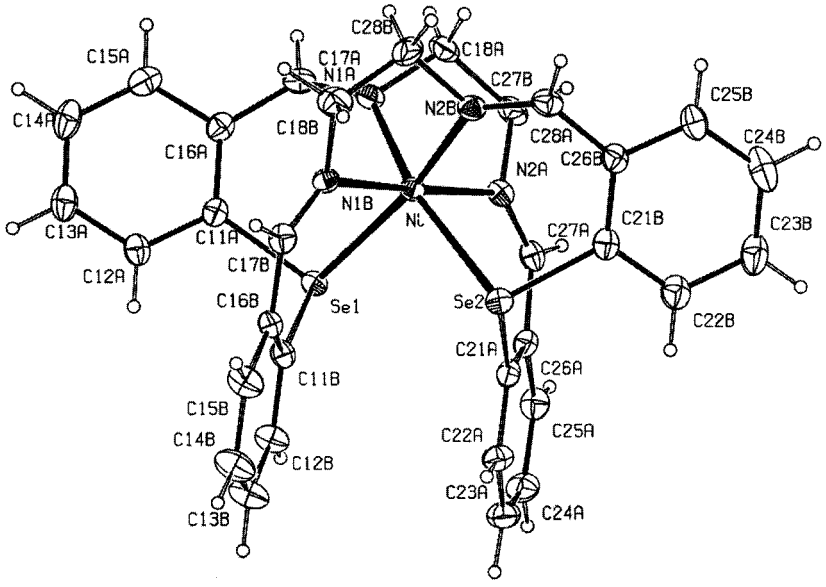

Figure 4. ORTEP diagram for **7**.

 © 2005 Wiley-VCH Verlag GmbH & Co. KGaA, Weinheim

unit cell. Selected bond lengths and bond angles for a representative molecule are listed in Table 4. The ORTEP diagram is shown in Figure 4. The structure shows the nickel(II) ion occupying the macrocyclic cavity, bound through the four nitrogen and two selenium donor atoms. The angles around the nickel ion lie in the range 84.57(14)–98.24(3)° and 164.32(14)–177.7(2)° deviating only slightly from those expected for regular octahedral geometry. The two selenium atoms are mutually *cis* to each other. The Ni–Se distances [2.489(10) and 2.552(10) Å] are significantly

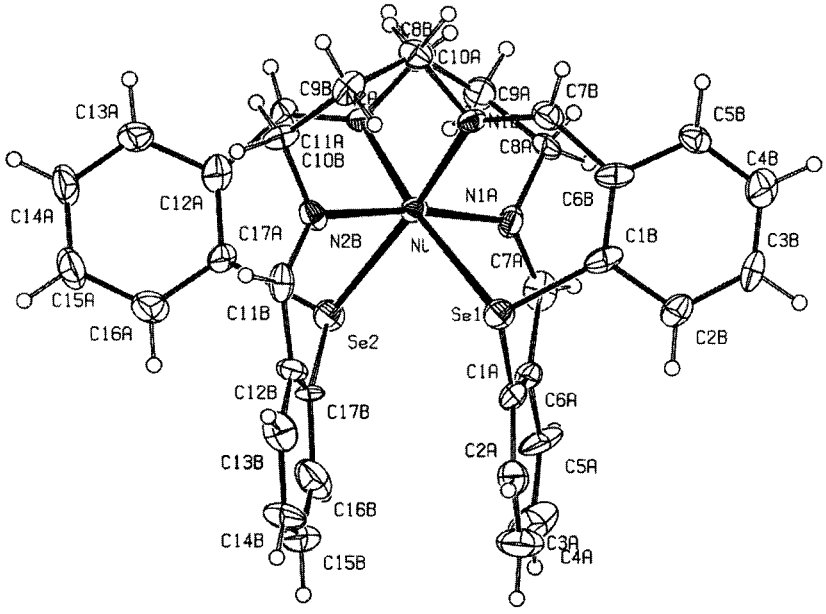

Figure 5. ORTEP diagram for **8**.

Table 5. Selected bond lengths [Å] and angles [°] for **8**.

Ni–N(2A)	2.072(12)	Ni–N(1A)	2.079(13)
Ni–N(2B)	2.086(13)	Ni–N(1B)	2.104(12)
Ni–Se(1)	2.558(2)	Ni–Se(2)	2.578(3)
Se(1)–C(1A)	1.874(19)	Se(1)–C(1B)	1.907(18)
Se(2)–C(17B)	1.927(16)	Se(2)–C(17A)	1.939(17)
N(1A)–C(7A)	1.29(2)	N(1A)–C(8A)	1.471(18)
N(2A)–C(11A)	1.283(19)	N(2A)–C(10A)	1.466(19)
N(1B)–C(7B)	1.281(19)	N(1B)–C(8B)	1.495(18)
N(2B)–C(11B)	1.281(19)	N(2B)–C(10B)	1.486(18)
N(2A)–Ni–N(2B)	94.6(5)	N(1A)–Ni–N(2B)	172.1(5)
N(2A)–Ni–N(1B)	93.4(4)	N(1A)–Ni–N(2A)	88.8(5)
N(1A)–Ni–N(1B)	97.2(5)	N(2B)–Ni–N(1B)	89.7(5)
N(2A)–Ni–Se(1)	172.2(4)	N(1A)–Ni–Se(1)	84.4(4)
N(2B)–Ni–Se(1)	92.6(4)	N(1B)–Ni–Se(1)	83.7(3)
N(2A)–Ni–Se(2)	85.4(3)	N(1A)–Ni–Se(2)	88.8(4)
N(2B)–Ni–Se(2)	84.4(3)	N(1B)–Ni–Se(2)	173.9(4)
Se(1)–Ni–Se(2)	98.29(9)	C(1A)–Se(1)–C(1B)	97.1(7)
C(1A)–Se(1)–Ni	97.9(5)	C(1B)–Se(1)–Ni	95.7(4)
C(17B)–Se(2)–C(17A)	96.7(7)	C(17B)–Se(2)–Ni	95.8(5)
C(17A)–Se(2)–Ni	96.8(5)	C(7A)–N(1A)–C(8A)	114.3(14)
C(7A)–N(1A)–Ni	125.7(12)	C(8A)–N(1A)–Ni	119.9(10)
C(11A)–N(2A)–C(10A)	117.5(13)	C(11A)–N(2A)–Ni	128.0(11)
C(10A)–N(2A)–Ni	114.4(10)	C(7B)–N(1B)–C(8B)	115.1(13)
C(7B)–N(1B)–Ni	129.6(11)	C(8B)–N(1B)–Ni	115.3(9)
C(11B)–N(2B)–C(10B)	114.9(13)	C(11B)–N(2B)–Ni	124.7(11)
C(10B)–N(2B)–Ni	119.8(9)	C(2A)–C(1A)–Se(1)	116.5(14)
C(6A)–C(1A)–Se(1)	122.9(12)	N(1A)–C(7A)–C(6A)	129.4(18)
N(1A)–C(8A)–C(9A)	111.5(14)	N(2A)–C(10A)–C(9A)	111.6(13)
N(2A)–C(11A)–C(12A)	128.0(15)	C(12A)–C(17A)–Se(2)	121.2(13)
C(16A)–C(17A)–Se(2)	117.6(13)	C(6B)–C(1B)–Se(1)	123.0(13)
C(2B)–C(1B)–Se(1)	118.4(12)	N(1B)–C(7B)–C(6B)	126.2(16)
C(9B)–C(8B)–N(1B)	112.5(13)	N(2B)–C(10B)–C(9B)	112.5(13)
N(2B)–C(11B)–C(12B)	130.7(15)	C(12B)–C(17B)–Se(2)	124.7(12)
C(16B)–C(17B)–Se(2)	116.0(14)		

 © 2005 Wiley-VCH Verlag GmbH & Co. KGaA, Weinheim

different, but comparable to those in [NiPyPySe$_2$(H$_2$O)$_2$](ClO$_4$)$_2$ [2.479(2), 2.477(2) [Å][27] and *trans*-[NiCl$_2$(MeSeCH$_2$CH$_2$SeMe)$_2$] [2.5581(9), 2.5536(9) Å],[19] respectively.

The single-crystal X-ray structure determination of **8** alsoshowed a distorted octahedral arrangement of the four nitrogen atoms and two selenium atoms around the central metal ion. Figure 5 shows the coordination sphere around the Ni^{II} ion and Table 5 summarizes selected bond lengths and bond angles. The complex crystallizes in a chiral space group *Pna*2$_1$ with four molecules in the unit cell. The Ni–Se distances [2.558(2), 2.578(3) Å] are slightly longer than those in **7**, and resemble those [2.568(2), 2.567(2) Å] in [(CO)$_3$Mn(μ-2-SC$_4$H$_3$S)$_3$Ni(μ-SePh)$_3$Fe(CO)$_3$]$^-$.[45] The C(1A)–Se(1)–C(1B) angle of 97.1(7)° deviates slightly (0.6°) from that in the ligand **2**.

Reaction of 1 with Co^{II}

The reaction of CoCl$_2$·6H$_2$O with 1 equiv. of **1** in refluxing methanol afforded a black solution. Addition of excess NH$_4$PF$_6$ yielded a black crystalline precipitate of complex **9** (Scheme 3). The air-stable complex **9** is insoluble in chlorocarbons and hydrocarbons. However, it dissolves in coordinating solvents such as MeCN, DMF, or DMSO. Rapid decomposition by displacement of the aza-selena macrocycle **1** occurs in the solvent DMSO. This was confirmed by ^{1}H NMR spectroscopic studies on the compound in [D$_6$]DMSO. A similar type of observation has been made by Reid et al. for the seven-coordinate Mo^{II} and W^{II} species derived from the selenoether ligands 1,5,9,13-tetraselenacyclohexadecane ([16]aneSe$_4$) and 1,6-diselena-3,4-benzocyclononane.[21] The elemental analysis data confirmed a 1:1 stoichiometry for the complex. The peaks at 838 and 554 cm^{-1} in the infrared spectrum were assigned to ν(P–F), δ(F–P–F). The peak at 1644 cm^{-1} was due to ν(C=N) stretching. In the UV/Vis spectrum of **9** an intense band was found centered at 290 nm, which may be due to a charge-transfer transition. Two further bands at 340 and 515 nm may be attributed to a combination of π–π* and d–d transitions. The FAB mass spectrum shows a low-intensity peak at *m*/*z* = 975 corresponding to the molecular ion [M]. The peak at *m*/*z* = 832 is for [**9** − PF$_6$]. The base peak at *m*/*z* = 687 corresponds to [**9** − 2 PF$_6$].

A powder sample of the paramagnetic black Co^{II} complex had μ_{eff} = 1.81 B.M., which indicates that it has a low-spin configuration (S = 1/2). Elemental analysis data, IR, UV/Vis, ^{77}Se NMR and FAB mass spectra, and magnetic susceptibility data are consistent with the formula of the complex **9** being [Co(**1**)](PF$_6$)$_2$. Cyclic voltammetry in acetonitrile solution reveals a well-behaved quasi-reversible (ΔE = 72 mV) Co^{III}/Co^{II} couple having $E_{1/2}$ = 0.17 V.

Conclusions

The Schiff-base condensation reaction of 1,2-diaminoethane or 1,3-diaminopropane with bis(*o*-formylphenyl) selenide yields the 22- and 24-membered [2+2] ligands **1** and **2**, respectively. Here the Se···N intramolecular interaction acts as a template in the formation of the ring. Macrocycles **1** and **2** have contrasting conformations. Whereas the transannular Se···Se distance in **1** is 3.808 Å, in **2** the distance is 7.229 Å. The Pd^{II} complex of **1** is isolated as a partially hydrolyzed complex. This is in contrast to the tellurium analog where the macrocycle is intact. The hydrolysis probably occurs due to the ring strain imposed by the square-planar geometry. The Ni^{II} complexes of **1** and **2** also show contrasting behavior. The former crystallises in an achiral space group ($P2_1/c$) whereas the latter crystallises in a chiral space group (*Pna*2$_1$).

Experimental Section

General: Bis(*o*-formylphenyl) selenide[37] and [PdCl$_2$(COD)][46] were prepared according to reported procedures. Air-sensitive reactions were carried out under inert conditions. Solvents were purified by standard techniques and were freshly distilled prior to use. 1,2-Diaminoethane (en) and 1,3-diaminopropane (pn) were reagent grade and were distilled prior to use. Melting points were recorded in capillary tubes and are uncorrected. IR spectra were recorded as KBr pellets with a Nicolet Impact 400 FT-IR spectrometer (4000–400 cm^{-1}). Electronic absorption spectra were obtained in CHCl$_3$/CH$_3$CN at 25 °C in a 1-cm quartz cuvette with a thermostatted Shimadzu UV-2100 apparatus and reflectance spectra was recorded with a UV-160A spectrophotometer. ^{1}H, ^{13}C and ^{77}Se NMR spectra were recorded with a Varian VXR 300S spectrometer at the indicated frequencies. Chemical shifts cited were referenced to TMS (^{1}H, ^{13}C NMR) as internal, Me$_2$Se (^{77}Se) as external standard. Elemental analyses were performed with a Carlo–Erba model 1106 elemental analyzer. Fast atom bombardment (FAB) mass spectra were recorded at room temperature with a JEOL SX 102 DA-6000 mass spectrometer/data system using xenon (6 kV, 10 mV) as the bombarding gas. The acceleration voltage was 10 kV and *m*-nitrobenzyl alcohol was used as the matrix with positive-ion detection. In the case of clusters due to the presence of more than one isotope, the value given is for the most intense peak. Magnetic susceptibilities of powdered samples were determined at room temperature with a Faraday balance, standardized with mercury tetracyanocobaltate(II) [$\chi = 16.44 \times 10^{-6}$ cm^3·mol^{-1}]. The molar susceptibilities were corrected for diamagnetism using Pascal's constants. The effective magnetic moments were calculated using the expression $\mu_{eff} = 2.83(\chi_m \times T)^{1/2}$. Cyclic Voltammetry (CV) experiments were performed with a Scanning Potentiostat EG and G PARC Model 362 instrument which consists of a one-compartment cell with platinum working and counter electrodes and a standard Ag/AgCl reference electrode. Tetrabutylammonium tetrafluoroborate (Aldrich) was used as the supporting electrolyte. All solutions were purged with nitrogen before the CV data were recorded. Measurements were conducted in 0.1 mol·dm^{-3} Bu$_4$NBF$_4$ in acetonitrile with sample concentration 0.05 mM. Ferrocene was taken as standard.

Synthesis of Macrocyclic Schiff Base 1: A solution of bis(*o*-formylphenyl) selenide (0.15g, 0.5 mmol) in acetonitrile (100 mL) was added to a stirred solution of 1,2-diaminoethane (0.030 g, 0.5 mmol) in acetonitrile (100 mL) over a period of 1 h. The mixture was stirred overnight and the precipitated colorless powder was filtered off, washed with acetonitrile and recrystallized from CHCl$_3$/CH$_3$CN (1:1). Yield: 0.14g, 91%. M.p. 218–220 °C. C$_{32}$H$_{28}$N$_4$Se$_2$ (627.31): calcd. C 61.35, H 4.50, N 8.94; found C

 © 2005 Wiley-VCH Verlag GmbH & Co. KGaA, Weinheim

61.18, H 4.71, N 8.63. IR (KBr): $\tilde{\nu}$ = 636 ν(C=N) cm^{-1}. ^1H NMR (300 MHz, $CDCl_3$, 25 °C): δ = 8.52 (s, 4 H), 7.72 (dd, J = 7.7 H, 4 Hz), 7.28 (t, J = 7.37 Hz, 4 H), 7.16 (t, J = 7.29 Hz, 4 H), 7.09 (dd, J = 7.93 Hz, 4 H), 3.67 (s, 8 H, CH_2) ppm. ^{13}C NMR (75.42 MHz, $CDCl_3$, 25 °C): δ = 163.72 (*C*H=N), 136.25, 134.65, 133.88, 130.74, 130.16, 127.31 (aromatic C), 62.24 (N–*C*H_2) ppm. ^{77}Se NMR (57.22 MHz, $CDCl_3$): δ = 407 ppm. MS (FAB): m/z = 627 [M^+], 307, 298, 284, 272, 245, 233, 184, 165, 154, 136, 117, 104, 91, 71.

Synthesis of Macrocyclic Schiff Base 2: This was prepared as described for **1** from bis(*o*-formylphenyl) selenide (0.15g, 0.5 mmol) and 1,3-diaminopropane (0.037g, 0.5 mmol). The colorless powder was washed with acetonitrile and recrystallized from $CHCl_3$/CH_3CN (1:1). Yield: 0.15 g, 89%. M.p. 225–227 °C (dec.). $C_{34}H_{32}N_4Se_2$ (654.57): calcd. C 62.39, H 4.93, N 8.56; found C 62.18, H 5.04, N, 8.69. IR (KBr): $\tilde{\nu}$ = 1653 ν(C=N), 1632 ν(C=N) cm^{-1}. ^1H NMR (300 MHz, $CDCl_3$): δ = 8.46 (s, −C*H*=N−, 4 H), 7.64–7.16 (m, 16 H, aromatic H), 3.61 (t, 8 H, N–CH_2–CH_2), 2.01 (quint, 4 H, –CH_2–CH_2–CH_2–) ppm. ^{13}C NMR (75.42 MHz, $CDCl_3$): δ = 162.58 (azomethine C), 136.92, 134.34, 133.78, 130.60, 130.18, 127.18 (aromatic C), 56.87 (N–*C*H_2–CH_2), 30.07 (N–CH_2–*C*H_2–) ppm. ^{77}Se NMR (57.22 MHz, $CDCl_3$): δ = 413 ppm. MS (FAB): m/z = 657 [M^+], 327, 307, 284, 245, 204, 165, 154, 136, 117, 107, 91, 77, 65, 41.

Synthesis of Complex 5: The ligand **1** (0.1 g, 0.16 mmol) was taken up in a two-necked round-bottomed flask with 20 mL of methanol. This was brought to reflux and then [$PdCl_2$(COD)] (0.045 g, 0.16 mmol) was added. The suspension immediately changed color to a clear yellow solution. This was allowed to reflux for an additional 15 min. Then it was filtered and an excess of NH_4PF_6 was added to the filtrate. Immediately a yellow powder precipitated. This could be recrystallized by slow concentration of an MeCN solution of the complex. Yield: 0.12 g, 76%. M.p. 208–210 °C (dec.). $C_{30}H_{24}F_1N_2O_2P_{22}PdSe_2$ (998.78): calcd. C 36.08, H 2.42, N 2.80; found C 35.92, H 2.46, N 2.55. IR (KBr): $\tilde{\nu}$ = 1667 ν(C=O), 1640 ν(C=N) cm^{-1}. ^1H NMR (300 M Hz, [D_6]DMSO): δ = 10.05 (s, 2 H, aldehydic H), 8.88 (s, 2 H, azomethine H), 8.34–6.61 (m, 16 H, aromatic H), 3.81–3.52 (m, 4 H, =NCH_2–CH_2N=) ppm. ^{77}Se NMR (57.22 M Hz, [D_6]DMSO): δ = 411 ppm. MS (FAB): m/z = 855 [M^+− PF_6], 709 [M^+ – 2 PF_6], 525, 495, 467, 439, 420, 391, 329, 307, 289, 245.

Synthesis of Complex 6: This was prepared as described for **5** by the addition of [$PdCl_2$(COD)] (0.043 g, 0.15 mmol) to the ligand **2** (0.1 g, 0.15 mmol) in methanol. Recrystallization by the slow diffusion of diethyl ether into a nitromethane solutionas afforded **6** as yellow needles. Yield: 0.14 g, 87.5%. M.p. 220–222 °C (dec.). $C_{34}H_{32}F_{12}N_4P_2PdSe_2$ (1050.90): calcd. C 38.86, H 3.07, N 5.33; found C 39.11, H 2.93, N 5.39. IR (KBr): $\tilde{\nu}$ = 1637 ν(C=N), 836 ν(P–F), 556 δ(F–P–F) cm^{-1}. ^1H NMR (300 MHz, [D_6]DMSO): δ = 8.66 (s, 4 H, azomethine H), 7.60–8.06 (m, 24 H, aromatic H), 3.64 (quint, 4 H, NCH_2–CH_2–CH_2N), 4.82 (t, 8 H, NCH_2–CH_2–CH_2N) ppm. ^{13}C NMR (75.42 MHz, [D_6]DMSO): δ = 170.18 (azomethine C), 137.60, 135.38, 135.18, 131.84, 130.75, 119.08 (aromatic C), 62.46 (N–*C*H_2–CH_2), 32.22 (CH_2–*C*H_2–CH_2) ppm. ^{77}Se NMR (57.22 MHz, [D_6]DMSO): δ = 441 ppm. MS (FAB): m/z = 905 [M^+ − PF_6], 761 [M^+ − 2 PF_6], 577, 551, 539, 512, 487, 469, 434 (base peak), 247.

Synthesis of Complex7: The ligand **1** (0.1 g, 0.16 mmol) was added to methanol (20 mL) under nitrogen. This was brought to reflux and then $NiCl_2 \cdot 6H_2O$ (0.038 g, 0.16 mmol) was added. The suspension changed to a clear red solution within 5 min. It was allowed to reflux for an additional 15 min. The solution was filtered and to the filtrate an excess of NH_4PF_6 was added. Immediately a brown precipitate was obtained which was filtered and washed with methanol. Yield: 0.15 g, 96%. M.p. 258–260 °C (dec). $C_{32}H_{28}F_{12}N_4NiP_2Se_2 \cdot H_2O$ (993.17): calcd. C 38.70, H 3.04, N 5.64; found C 38.25, H 3.04, N 5.95. IR (KBr): $\tilde{\nu}$ = 1650 ν(C=N), 830 ν(P–F), 555 δ(F–P–F) cm^{-1}. UV/Vis (MeCN): $\lambda_{max.}$ (ε) = 295 (14 330), 345 (2950), 435 (579), 805 nm (58 $mol^{-1} \cdot dm^3 \cdot cm^{-1}$); μ_{eff} = 3.23 B.M.. MS (FAB): m/z = 831 [M^+ − PF_6], 686 [M^+ − 2 PF_6], 372, 343, 291, 273, 242, 178, 153, 120.

Table 6. Crystal data and structure refinement for **1**, **2** and **5**.

	1	**2**	**5**
Empirical formula	$C_{32}H_{28}N_4Se_2$	$C_{34}H_{32}N_4Se_2$	$C_{30}H_{24}F_{12}N_2O_2P_2PdSe_2$
Formula mass	626.50	654.56	998.77
Crystal system	monoclinic	triclinic	tetragonal
Space group	$P2_1/c$	$P\bar{1}$	$P4_12_12$
a [Å]	10.0648(10)	7.200(3)	10.7737(10)
b [Å]	37.390(4)	9.137(3)	10.7737(10)
c [Å]	8.0073(11)	12.780(6)	28.190(5)
α [°]	90	72.78(3)	90
β [°]	112.978(8)	76.40(4)	90
γ [°]	90	69.00(3)	90
V [Å^3]	2774.3(6)	741.8(5)	3272.1(7)
Z	4	1	4
d(calcd.) [Mg/m^3]	1.500	1.465	2.027
Temp. [K]	293(2)	293(2)	293(2)
λ [Å]	0.71073	0.71073	0.71073
Range of θ [°]	2.74–25.00	2.46–27.49	2.67–29.99
Data collected	$\pm h$, $+k$, $+l$		$+h$, $+k$, $-l$
Abs. coeff. [mm^{-1}]	2.694	2.522	2.993
Obsd. reflections [$I > 2\sigma$]	4782	2581	2677
Final $R(F)$ [$I > 2\sigma$][a]	0.0556	0.0717	0.0499
$wR(F^2)$ indices [$I > 2\sigma$]	0.1270	0.1769	0.0837
Data/restraints/parameters	4718/0/371	2581/0/198	2677/64/358
Goodness of fit on F^2	1.045	1.098	1.039

[a] Definitions: $R(F_o) = \Sigma||F_o| - |F_c||/\Sigma|F_o|$ and $wR(F_o^2) = \{\Sigma[w(F_o^2 - F_c^2)^2]/\Sigma[w(F_c^2)^2]\}^{1/2}$.

 © 2005 Wiley-VCH Verlag GmbH & Co. KGaA, Weinheim

Table 7. Crystal data and structure refinement for **7** and **8**.

	7	**8**
Empirical formula	$C_{32}H_{30}F_{12}N_4NiOP_2Se_2$	$C_{34}H_{32}F_{12}N_4NiP_2Se_2$
Formula mass	993.17	1003.21
Crystal system	monoclinic	orthorhombic
Space group	$P2_1/c$	$Pna2_1$
a [Å]	9.979(2)	20.277(5)
b [Å]	18.901(4)	20.865(5)
c [Å]	19.333(4)	9.416(2)
α [°]	90	90
β [°]	100.94(2)	90
γ [°]	90	90
V [Å^3]	3580.4(13)	3983.5(17)
Z	4	4
d(calcd) [Mg/m^3]	1.842	1.673
Temp. [K]	293(2)	293(2)
λ [Å]	0.71073	0.71073
Range of θ [°]	2.69–27.50	2.37–26.24
Data collected	$+h$, $+k$, $\pm l$	$+h$, $+k$, $+l$
Abs. coeff. [mm^{-1}]	2.762	2.482
Obsd. reflections [$I > 2\sigma$]	8074	2792
Final $R(F)$ [$I > 2\sigma$][a]	0.0586	0.0561
$wR(F^2)$ indices [$I > 2\sigma$]	0.1108	0.1225
Data/restraints/parameters	8073/0/516	2792/1/496
Goodness of fit on F^2	1.030	1.025
Absolute structure parameter	–	0.01(3)

[a] Definitions: $R(F_o) = \Sigma||F_o| - |F_c||/\Sigma|F_o|$ and $wR(F_o^2) = \{\Sigma[w(F_o^2 - F_c^2)^2]/\Sigma[w(F_c^2)^2]\}^{1/2}$.

Synthesis of Complex 8: This was prepared similarly from ligand **2** (0.1 g, 0.15 mmol) and $NiCl_2{\cdot}6H_2O$ (0.036 g, 0.15 mmol). It was recrystallized by the slow diffusion of diethyl ether into a nitromethane solution. Yield: 0.13 g, 87%. M.p. 258–260 °C (dec.). $C_{34}H_{32}F_{12}N_4NiP_2Se_2{\cdot}H_2O$ (1021.23): calcd. C 39.99, H 3.30, N 5.48; found C 39.57, H 3.22; N 5.98. IR (KBr): $\tilde{\nu}$ = 1628 ν(C=N) 834, 753, 557 cm^{-1}. UV/Vis (MeCN): $\lambda_{max.}$ (ε) = 295 (12 200), 335 (3650), 565 nm (24 mol^{-1}·dm^3·cm^{-1}); μ_{eff} = 3.25 B.M.. MS (FAB): m/z = 733 [M$^+$ − PF_6 + H_2O], 712 [M$^+$ − PF_6], 577, 407, 386, 327, 306, 251, 224.

Synthesis of Complex 9: This was prepared according to the method used for the preparation of the complex **7** by adding $CoCl_2{\cdot}6H_2O$ (0.038 g, 0.16 mmol) to the ligand **1** (0.1 g, 0.16 mmol) in 20 mL methanol. Yield: 0.12 g, 75%. M.p. 226–228 °C (dec.). $C_{32}H_{28}CoF_{12}N_4P_2Se_2$ (975.38): calcd. C 39.41, H 2.89, N 5.74; found C 38.50, H 2.96, N 5.66. IR (KBr): $\tilde{\nu}$ = 1644 ν(C=N), 838 ν(P–F), 554 (δ(F–P–F) cm^{-1}. UV/Vis: (MeCN): $\lambda_{max.}$ (ε) = 290 (13 240), 340 (6640), 515 nm (1100 mol^{-1}·dm^3·cm^{-1}); μ_{eff} = 1.81 B.M. MS (FAB): m/z = 975 [M$^+$], 832 [M$^+$ − PF_6], 687 [M$^+$ − 2 PF_6, base peak], 373, 343, 309, 291, 242, 152, 120.

X-ray Crystallographic Study: The diffraction measurements for compound **1**, **2**, **5**,**7** and **8** were performed at room temperature (293 K) with a Siemens R3m/V diffractometer using graphite-monochromated Mo-K_α radiation (λ = 0.71073 Å). The unit cell was determined from 25 randomly selected reflections using the automatic search index and least-squares routine. The data were corrected for Lorentz, polarization and absorption effects. A semiempirical absorption correction from ψ-scans was applied to the data of **5** and **7**. The maximum and minimum transmission values of the correction factors for compounds **5** and **7** were 0.2761 and 0.2170 and 0.5048 and 0.4442, respectively. The structures were solved by routine heavy-atom (using SHELXS[47]) and Fourier methods and refined by full-matrix least squares, the non-hydrogen atoms with anisotropic and the hydrogen atoms with fixed isotropic thermal parameters of 0.07 Å^2 using SHELXL93.[48] The hydrogen atoms were partially located from difference electron-density maps and the rest were fixed at calculated positions. Scattering factors were from common sources.[49] Some details of data collection and refinement are given in Tables 6 and 7. CCDC-148626 (**1**), -148627 (**2**), -148630 (**5**), -148631 (**7**) and -148632 (**8**) contain the supplementary crystallographic data for this paper. These data can be obtained free of charge from The Cambridge Crystallographic Data Centre via www.ccdc.cam.ac.uk/data_request/cif.

Acknowledgments

We are grateful to the Department of Science and Technology (DST), New Delhi and Board of Research in Nuclear Sciences (BRNS), Department of Atomic Energy, Bombay for funding this work. Additional help from the Regional Sophisticated Instrumentation Center (RSIC), Indian Institute of Technology (IIT), Bombay for 300 MHz NMR spectroscopy, and RSIC, CDRI Lucknow for mass spectrometry, is gratefully acknowledged. R. J. B. wishes to acknowledge the DOD-ONR program for funds to upgrade the diffractometer.

[1] a) L. F. Lindoy, in: *The Chemistry of Macrocyclic Ligand Complexes*, Cambridge University Press, Cambridge, **1989**; b) B. Dietrich, P. Viout, J.-M. Lehn, *Macrocyclic Chemistry: Aspects of Organic and Inorganic Supramolecular Chemistry*, Wiley-VCH, Weinheim, **1993**; c) J.-M. Lehn, *Supramolecular Chemistry: Concepts and Perspectives*, Wiley-VCH, Weinheim, **1995**; d) J. W. Steed, J. L. Atwood, in: *Supramolecular Chemistry*, Wiley, Chichester, **2000**; e) H. Dodziuk, *Introduction to Supramolecular Chemistry*, Kluwer Academic Pub., Dordrecht, **2002**.
[2] V. Alexander, *Chem. Rev.* **1995**, *95*, 273.
[3] S. Goswami, A. D. Hamilton, *J. Am. Chem. Soc.* **1989**, *111*, 3425.
[4] A. J. Blake, W. Li, V. Lippolis, M. Schröder, *Chem. Commun.* **1997**, 1943.

 © 2005 Wiley-VCH Verlag GmbH & Co. KGaA, Weinheim

[5] a) G. W. Gokel, L. J. Barbour, S. L. De Wall, E. S. Meadows, *Coord. Chem. Rev.* **2001**, *222*, 127; b) K. Gloe, H. Graubaum, M. Wust, T. Rambusch, W. Seichter, *Coord. Chem. Rev.* **2001**, *222*, 103; c) J. W. Steed, *Coord. Chem. Rev.* **2001**, *215*, 171.

[6] a) A. Bianchi, E. Garcia-España, K. Bowman-James (Eds.), *Supramolecular Chemistry of Anions*, Wiley-VCH, New York, **1997**; b) H. Elias, *Coord. Chem. Rev.* **1999**, *187*, 37; c) C. L. Kranemann, B. Costisella, P. Eilbracht, *Tetrahedron Lett.* **1999**, *40*, 7773; d) J. Nelson, V. McKee, G. Morgan, *Prog. Inorg. Chem.* **1998**, *47*, 167; R. Ibrahim, S. Tsuchiya, S. Ogawa, *J. Am. Chem. Soc.* **2000**, *122*, 12174; e) D. Utz, F. W. Heinemann, F. Hampel, D. T. Richens, S. Schindler, *Inorg. Chem.* **2003**, *42*, 1430.

[7] a) K. Brandt, I. Porwolik-Czomperlik, M. Siwy, T. Kupka, R. A. Shaw, D. B. Davies, M. B. Hursthouse, G. D. Sykara, *J. Am. Chem. Soc.* **1997**, *119*, 12432; b) M. Dreiss, M. Faulhaber, H. Pritzkow, *Angew. Chem. Int. Ed. Engl.* **1997**, *36*,1892; c) F. Mercier, F. Laporte, L. Richard, F. Mathey, M. Schröder, M. Regitz, *Angew. Chem. Int. Ed. Engl.* **1997**, *36*, 947; d) K. Brandt, I. Porwolik-Czomperlik, M. Siwy, T. Kupka, R. A. Shaw, S. Ture, A. Clayton, D. B. Davies, M. B. Hurdthouse, G. D. Sykara, *J. Org. Chem.* **1999**, *64*, 7299; e) L. Escriche, J. A. Munoz, R. Kivekas, R. Sillampaa, J. Casabo, *Eur. J. Inorg. Chem.* **2002**, 3258; f) R. J. Baker, P. G. Edwards, *J. Chem. Soc., Dalton Trans.* **2002**, 2960; g) L. Escriche, J. A. Munoz, R. Kivekas, R. Sillampaa, J. Casabo, *Eur. J. Inorg. Chem.* **2002**, 3258; h) S. Ekici, M. Nieger, R. Glaum, E. Niecke, *Angew. Chem. Int. Ed.* **2003**, *42*, 435.

[8] a) R. Schibli, R. Alberto, U. Abram, S. Abram, A. Egli, P. A. Schubiger, T. A. Kaden, *Inorg. Chem.* **1998**, *37*, 3509; b) A. J. Blake, W. Li, V. Lippolis, M. Schröder, *Chem. Commun.* **1998**, 1943; c) S. Brooker, T. C. Davidson, *Chem. Commun.* **1997**, 2007; d) T. Tsuchiya, T. Shimizu, K. Hirabayashi, N. Kamigata, *J. Org. Chem.* **2003**, *68*, 3480 .and references cited therein; e) M. Vetrichelvan, Yee-Hing Lai, K. F. Mok, *Dalton Trans.* **2003**, 295 .and references cited therein.

[9] a) P. Comba, A. Kühner, *Eur. J. Inorg. Chem.* **1999**, 509; b) P. Comba, A. Kühner, A. Peters, *J. Chem. Soc. Dalton Trans.* **1999**, 509; c) P. Comba, J. Ensling, P. Gütlich, A. Kühner, A. Peters, H. Pritzkow, *Inorg. Chem.* **1999**, *38*, 3316 .and references cited therein; d) P. D. Metelski, Y. Fu, K. Khan, T. W. Swaddle, *Inorg. Chem.* **1999**, *38*, 3103; e) P. Osvath, A. M. Sargeson, A. McAuley, R. E. Mendelez, S. Subramanian, M. J. Zaworotko, L. Broge, *Inorg. Chem.* **1999**, *38*, 3634; f) S. Galijasevic, K. Krylova, M. J. Koenigbauer, G. S. Jaeger, J. D. Bushendorf, M. J. Heeg, L. A Ochrymowycz, M. J. Taschner, D. B. Rorabacher, *Dalton Trans.* 2003, 1577; g) M. Arca, A. J. Blake, V. Lippolis, D. R. Montesu, J. McMaster, L. Tei, M. Schröder, *Euro. J. Inorg. Chem.* **2003**, 1232; h) P. J. Wilson, A. J. Blake, P. Mountford, M. Schröder, *Inorg. Chim. Acta* **2003**, *345*, 44; i) C. Ma, F. Li, D. Wang, H. Yin, *J. Organomet. Chem.* **2003**, *667*, 5.

[10] V. McKee, *Adv.Inorg. Chem.* **1993**, *40*, 323.

[11] R. J. Batchelor, F. W. B. Einstein, I. D. Gay, J-H. Gu, B. D. Johnston, B. M. Pinto, *J. Am. Chem. Soc.* **1989**, *111*, 6582.

[12] R. J. Batchelor, F. W. B. Einstein, I. D. Gay, J. Gu, B. M. Pinto, X. Zhou, *Inorg. Chem.* **1996**, *35*, 3667.

[13] a) R. J. Batchelor, F. W. B. Einstein, I. D. Gay, J. Gu, B. M. Pinto, *J. Organomet. Chem.* **1991**, *411*, 147; b) R. J. Batchelor, F. W. B. Einstein, I. D. Gay, J. Gu, B. M. Pinto, X. Zhou, *J. Am. Chem. Soc.* **1990**, *112*, 3706; c) R. J. Batchelor, F. W. B. Einstein, I. D. Gay, J-H. Gu, S. Mehta, B. M. Pinto, X-M. Zhou, *Inorg. Chem.* **2000**, *39*, 2558.

[14] a) N. R. Champness, P. F. Kelly, W. Levason, G. Reid, A. M. Z. Slawin, D. J. Williams, *Inorg. Chem.* **1995**, *34*, 651; b) N. R. Champness, W. Levason, J. J. Quirk, G. Reid, *Polyhedron* **1995**, *14*, 2753.

[15] W. Levason, J. J. Quirk, G. Reid, C. S. Frampton, *Inorg. Chem.* **1994**, *33*, 6120.

[16] P. F. Kelly, W. Levason, G. Reid, D. J. Williams, *J. Chem. Soc., Chem. Commun.* **1993**, 1716.

[17] W. Levason, J. J.Quirk, G. Reid, *J. Chem. Soc., Dalton Trans.* **1996**, 3713.

[18] W. Levason, J. J. Quirk, G. Reid, S. M. Smith, *J. Chem. Soc., Dalton Trans.* **1997**, 3719.

[19] M. K. Davies, W. Levason, G. Reid, *J. Chem. Soc., Dalton Trans.* **1998**, 2185.

[20] W. Levason, G. Reid, S. M. Smith, *Polyhedron* **1997**, *16*, 4253.

[21] M. K. Davies, M. C. Durrant, W. Levason, G. Reid, R. L. Richards, *J. Chem. Soc., Dalton Trans.* **1999**, 1077.

[22] D. G. Booth, W. Levason, J. J. Quirk, G. Reid, S. M. Smith, *J. Chem. Soc., Dalton Trans.* **1997**, 3493.

[23] a) A. J. Barton, A. R. J. Genge, W. Levason, G. Reid, *J. Chem. Soc., Dalton Trans.* **2000**, 2163; b) A. J. Barton, N. J. Hill, W. Levason, B. Patel, G. Reid, *Chem. Commun.* **2001**, 95; c) A. J. Barton, N. J. Hill, W. Levason, G. Reid, *J. Chem. Soc., Dalton Trans.* **2001**, 1621; d) J. Barton, N. J. Hill, W. Levason, G. Reid, *J. Am. Chem. Soc.* **2001**, *123*, 11801; e) N. J. Hill, W. Levason, G. Reid, *Inorg. Chem.* **2002**, *41*, 2070; f) N. J. Hill, W. Levason, R. Patel, G. Reid, M. Webster, *Dalton Trans.* **2004**, 980.

[24] a) W. Levason, S. D. Orchard, G. Reid, *Chem. Commun.* **2001**, 427; b) M. J. Hesford, W. Levason, M. L. Matthews, S. D. Orchard, G. Reid, *Dalton Trans.* **2003**, 2434; c) M. J. Hesford, W. Levason, M. L. Matthews, G. Reid, *Dalton Trans.* **2003**, 2852.

[25] T. Kumagi, S. Akabori, *Chem. Lett.* **1989**, 1667.

[26] S. Tomoda, M. J. Iwaoka, *J. Chem. Soc., Chem. Commun.* **1990**, 231.

[27] S. Muralidharan, M. Hojjatie, M. Firestone, H. Freiser, *J. Org. Chem.* **1989**, *54*, 393.

[28] a) H. Fujihara, M. Yabe, M. Ikemori, N. Furukawa, *J. Chem. Soc. Perkin. Trans. 1* **1993**, 2145; b) H. Fujihara, M. Yabe, N. Furukawa, *J. Chem. Soc., Perkin. Trans. 1* **1996**, 1783.

[29] R. Adams, K. T. McBride, *J. Chem. Soc., Chem. Commun.* **1997**, 525.

[30] R. Bhula, A. P. Arnold, G. J. Gainsford, W. G. Jackson, *J. Chem. Soc., Chem. Commun.* **1996**, 143.

[31] A. Mazouz, J. Bodiguel, P. Meunier, B. Gautheron, *Phosphorus, Sulfur Silicon* **1991**, *61*, 247.

[32] A. Mazouz, P. Meunier, M. M. Kubicki, B. Hanquet, R. Amardeil, C. Bornet, A. Zahidi, *J. Chem. Soc., Dalton Trans.* **1997**, 1043.

[33] C. Bornet, R. Amardeil, P. Meunier, J. C. Daran, *J. Chem. Soc., Dalton Trans.* **1999**, 1039.

[34] X. Zeng, X. Han, L. Chen, Q. Li, F. Xu, X. He, Z. Zhang, *Tetrahedron Lett.* **2002**, *43*, 131.

[35] J. L. Li, J. B. Meng, Y. M. Wang, J. T. Wang, T. Matsuura, *J. Chem. Soc., Perkin Trans. 1* **2001**, 1140.

[36] a) S. C. Menon, H. B. Singh, R. P. Patel, S. K. Kulshereshtha, *J. Chem. Soc., Dalton Trans.* **1996**, 1203; b) S. C. Menon, A. Panda, H. B. Singh, R. J. Butcher, *J. Chem. Soc., Chem. Commun.* **2001**, 143; c) S. C. Menon, A. Panda, H. B. Singh, R. P. Patel, S. K. Kulshereshtha, W. L. Darby, R. J. Butcher, *J. Organomet. Chem.* **2004**, *689*, 1452.

[37] a) A. Panda, S. C. Menon, H. B. Singh, R. J. Butcher, *J. Organomet. Chem.* **2001**, *623*, 87; b) S. Panda, H. B. Singh, R. J. Butcher, *Chem. Commun.* **2004**, 322.

[38] J. E. Huheey, E. A. Keiter, R. L. Keiter, in *Inorganic Chemistry: Principles of structure and reactivity*, HarperCollins College Publishers, New York, **1993**.

[39] S. J. Narayanan, B. Sridevi, T. K. Chandrashekar, A. Vij, R. Roy, *Angew. Chem. Int. Ed.* **1998**, *37*, 3394.

[40] S. Ford, P. K. Khanna, C. P. Morley, M. D. Vaira, *J. Chem. Soc., Dalton Trans.* **1999**, 791.

[41] R. Cao, W. Su, M. Hong, W. Zhang, W. Wong, J. Lu, *J. Chem. Soc., Chem. Commun.* **1998**, 2083.

[42] R. Oilunkaniemi, R. S. Laitinen, M. Ahlgrén, *J. Chem. Soc., Chem. Commun.* **1999**, 585.

[43] a) W. Nakanishi, S. Hayashi, S. Toyota, *J. Chem. Soc., Chem. Commun.* **1996**, 371; b) W. Nakanishi, S. Hayashi, S. Toyota,

 © 2005 Wiley-VCH Verlag GmbH & Co. KGaA, Weinheim

J. Org. Chem. **1998**, *63*, 8790; c) P. G. Jones, M. C. Ramirez de Arellano, *J. Chem. Soc., Dalton Trans.* **1996**, 2713.
[44] B. M.Goldstein, F. Takusagawa, H. M. Berman, P. C. Srivastava, R. K. Robins, *J. Am. Chem. Soc.* **1985**, *107*, 1394.
[45] W. Liaw, C. Lee, L. Horng, G. Lee, S. Peng, *Organometallics* **1999**, *18*, 782.
[46] D. Drew, J. R. Doyle, *Inorg. Synth.* **1972**, *13*, 47.
[47] G. M. Sheldrick, *Crystallographic Computing 3*, Oxford University Press, Oxford, **1985**, p. 175.
[48] G. M. Sheldrick, *SHELX93, Program for Crystal Structure Determination*, University of Göttingen, **1993**.
[49] *International Tables for X-ray Crystallography*, Kynoch Press, Birmingham, **1974**, vol. 4, p. 99.

Received: September 13, 2004

 © 2005 Wiley-VCH Verlag GmbH & Co. KGaA, Weinheim

Structural Studies of Rare Earth/Transition Metal Complex Ion Systems as a Basis for Understanding Their Thermal Decomposition to Mixed Oxides

Philippa A. Brayshaw,[a] Annegret K. Hall,[a] William T. A. Harrison,[a,b] Jack M. Harrowfield,*[a,c] Dierdre Pearce,[a] Todd M. Shand,[a] Brian W. Skelton,[d] Claire R. Whitaker,[a,e] and Allan H. White[d]

Keywords: Dipicolinates / Rare earths / Crystal structures / Mixed oxides / Thermochemistry

Thermal decomposition in air of the series of complexes $[Co(NH_3)_6][Ln(dipic)_3]\cdot x H_2O$, $[Cr(en)_3][Ln(dipic)_3]\cdot y H_2O$ and $[Cr(urea)_6][Ln(dipic)_3]\cdot z H_2O$ (Ln = La – Lu, excluding Pm but plus Y; dipic = 2,6-pyridinedicarboxylate) to give oxide phases has been examined. The products were characterised by powder X-ray diffraction, magnetic and surface area measurements. From the Co-containing species, either Co_3O_4 + Ln_2O_3 or perovskite ($CoLnO_3$) products result, while the Cr-containing species provide $CrLnO_4$ phases in addition, the monazite form of $CrNdO_4$ being detected for the first time in this way. Underpinning consideration of the solid state decomposition mechanisms, single-crystal X-ray structure determinations have been performed on $[Co(NH_3)_6][Ln(dipic)_3]\cdot n H_2O$ across the Ln series, defining differing phases (all triclinic $P\bar{1}$) for n = 5 (encompassing Ln = La–Pr), n = 8(.5) (Ln = Tm – Eu) and n = 10 (Ln = Pr – Er, including Y), and also on one of the low-temperature decomposition products, $[Co(NH_3)_6]Cl\cdot dipic\cdot 2H_2O$ (**1**). The structure of **1** provides evidence that conventional π-stacking of the dipicolinate anions may be of some importance in determining the solid state array, whereas consideration of all structures involving $[Ln(dipic)_3]^{3-}$ anions indicates that "edge-to-face" interactions between dipicolinate ligands of adjacent complex anions may also be determinants of the formation of sheet-like arrays of the trianions commonly observed in these compounds.
(© Wiley-VCH Verlag GmbH & Co. KGaA, 69451 Weinheim, Germany, 2005)

Introduction

In the hope of gaining some understanding of the complicated events which must be involved in the thermal decomposition reactions of mixed-metal solids in which a transition metal is present in a cationic complex and a lanthanide (Ln) in an anionic complex, we have conducted a detailed crystallographic study of one family of reactants, $[Co(NH_3)_6][Ln(dipic)_3]\cdot x H_2O$, [dipic = dipicolinate = 2,6-pyridinedicarboxylate; x = 5, 8(.5), 10] and some related materials. Solids containing tris(dipicolinato)lanthanide(III) anions ($[Ln(dipic)_3]^{3-}$) have been of interest for many reasons,[1–5] but thermal decomposition reactions of their derivatives with transition metal cations to give "mixed" oxides have not been investigated. Analogous reactions, however, have been explored in numerous systems[6–11] and frequently have been found superior to those based on reactions between separate solid phases such as the monometallic oxide constituents (or their simple precursors). While mixed lanthanide/transition metal oxides have long been of interest in regard to their structural, spectroscopic, magnetic and catalytic properties, which are consequently rather well understood,[12] there remains a need to provide more efficient syntheses and better methods of control of particle size.[13] We provide herein evidence that this need may be met to some extent through the use of thermal decomposition of solids containing $[Ln(dipic)_3]^{3-}$ in association with cobalt(III) or chromium(III) complex cations. One reason for studying compounds involving a cation such as $[Co(NH_3)_6]^{3+}$ in the presence of $[Ln(dipic)_3]^{3-}$ anions was to see if the aspects of three-fold symmetry present in both species would lead to particular modes of association in their lattices which might be seen to control solid-state reactions. Interpretation of features of the supramolecular chemistry of these lattices which may be deduced from detailed analysis of their structures is enhanced by structural studies of $[Co(NH_3)_6]dipic\cdot Cl\cdot 2H_2O$ and $[Eu(dipicH)(dipic)(OH_2)_2]\cdot 4H_2O$, the latter being a member of a known

[a] Research Centre for Advanced Mineral and Materials Processing, University of Western Australia,
35 Stirling Highway, W. A. 6009, Australia
[b] Current address: Department of Chemistry University of Aberdeen,
AB24 3UE, Scotland
[c] Current address: Institut de Science et de l'Ingénierie Supramoléculaires,
8 allée Gaspard Monge, 67083 Strasbourg, France
Fax: +33-3-90245140
E-mail: harrowfield@isis.u-strasbg.fr
[d] Chemistry M313, University of Western Australia,
Nedlands, W. A. 6907, Australia
[e] Institut de Ciència de Materials de Barcelona, Campus de la Universitat Autònoma de Barcelona,
08193 Bellaterra, Cerdanyola del Valles (Barcelona), Spain
Supporting information for this article is available on the WWW under http://www.eurjic.org or from the author.

series of lanthanide complexes,[14] though both complexes were presently isolated through unintended solution decomposition reactions of two of the mixed-oxide precursor species, $[Co(NH_3)_6][La(dipic)_3]\cdot x\,H_2O$ and $[Cr(urea)_6][Eu(dipic)_3]\cdot x\,H_2O$, respectively.

Results and Discussion

1. Cobalt/Rare Earth Systems

Structure Determinations: Various hydrates, $[Co(NH_3)_6][Ln(dipic)_3]\cdot x\,H_2O$, are obtained when $[Co(NH_3)_6]^{3+}$ is precipitated from aqueous solutions by the addition of tris(dipicolinato)lanthanate(III) anions, $[Ln(dipic)_3]^{3-}$. Any given lanthanide may be a member of more than one hydrate family, thus rendering extremely complicated any attempt to fully characterise the systems. This situation is exacerbated by the fact that, although the very insoluble compounds may be readily recrystallised, the crystals obtained are often small and needle-like, thus being less than optimal for diffraction studies. To find that some adducts, slowly crystallised over periods as long as years, underwent apparent desolvation within seconds of separation from their supernatant solution was a further significant handicap. In combination, these difficulties were more acute for the heavier than the lighter rare earths. Overall, nonetheless, the gamut of the rare earth array (including Y) appears to be encompassed within three dominant series, a pentahydrate ($x = 5$) phase being defined for La – Pr, a decahydrate form for Pr – Er, Y, and an octahydrate (more precisely, an 8.5-hydrate) for Tm − Lu, these limiting members (with some intermediates) being structurally characterised herein. A broader survey, focussed particularly on hydrogen bonding in these hydrates and defining further sporadic phases, will be reported elsewhere.[15]

In all $[Co(NH_3)_6][Ln(dipic)_3]\cdot x\,H_2O$, a triclinic $P\bar{1}$ cell obtains, with one formula unit comprising the asymmetric unit of the structure. The space group $P\bar{1}$ necessarily implies a racemic mixture of the chiral anions in each case. In the penta- and "octa-"hydrate phases, the asymmetric unit of the structure is devoid of any symmetry but in the decahydrate phase, the cations lie with their cobalt atoms disposed on crystallographic inversion centres, there being two such independent species. The similarity between crystallographic *a*, *b*, *c* of the deca- and "octa"-hydrate species is noted but, seemingly, carries no deeper significance (see below). The geometries of the $[Co(NH_3)_6]^{3+}$ cations are "normal"[16] and do not justify further comment. The anions, one representative being shown in Figure 1, are also of a form already known from studies of the sodium salts,[17–20] as well as from more recent work,[1–5] with the three ligands tridentate through ONO donor atoms about the metal, making up a three-bladed propeller array of putative *32* symmetry. Their geometries are tabulated comparatively and in summary in Table 1, the most obvious trend being that expected of the "lanthanide contraction", <Ln−N> diminishing by ca. 0.22 Å across the series, and <Ln−O> by rather less, ca. 0.18 Å. The components of the geometries vary rather widely, particularly in the angles and particularly at the lighter end of the series, where it might be expected that, in the context of nine-coordination throughout, the constraints on the packing of the three ligands about the metal are less demanding. The carboxylate groups are essentially coplanar with their parent pyridine rings, albeit not rigidly so, and out-of-plane Ln deviations are substantial, even relative to the pyridine ring and most particularly among the complexes containing the lighter rare earths. There is no association of the cations and anions into intimate pairs or columns of alternating species which simply reflects common aspects of threefold symmetry.

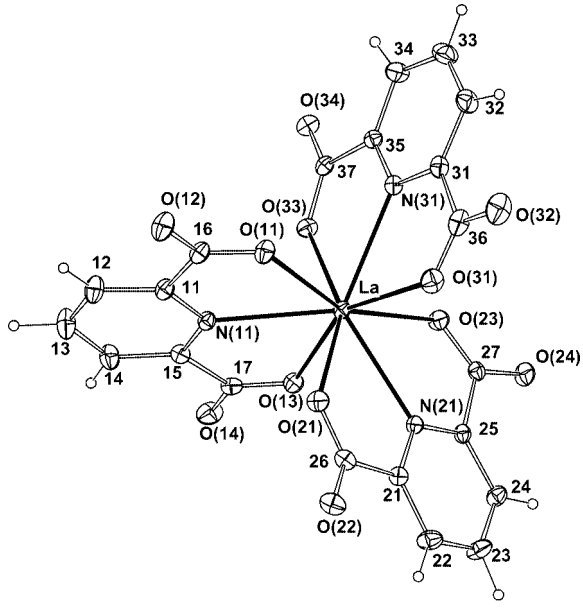

Figure 1. A view of the $[La(dipic)_3]^{3-}$ anion present within the lattice of $[Co(NH_3)_6][La(dipic)_3]\cdot 5\,H_2O$ (**2**), showing the numbering system which provides the basis for Table 1.

The component water molecules are described with variable definitiveness, those in the penta- and deca-hydrate families, respectively, being most and least precisely defined. The first structure solved was that of the pentahydrate phase of the Ce species **3**, a significant result at the time in confirming the Ce^{III} oxidation state, since the orange colour of the precursor $Na_3[Ce(dipic)_3]\cdot 15\,H_2O$ complex had led to some suspicion that it might in fact be a Ce(IV) species (as has been obtained, apparently, with a Ca^{II} counter cation[21]). A superior structural characterisation of the pentahydrate phase was ultimately obtained for the Pr (**4a**) species, where the precision of the determination is such that all hydrogen atoms in the structure have been resolved and refined in (x, y, z, U_{iso}) and are taken as indicative of the basic hydrogen bonding scheme for this family, the La species making up a third member. Powder XRD studies (see below) indicate, however, that the pentahydrate phase may well be common to the whole rare earth series, upon partial desolvation of the higher hydrates.

The decahydrate phase has been structurally characterised for Pr (**4b**), Sm (**5**), Tb (**6**), Er (**7**) and Y (**8**) and is

 © 2005 Wiley-VCH Verlag GmbH & Co. KGaA, Weinheim

Table 1. Minimum, maximum and average interatomic distances [Å] and angles [°] of the lanthanoid environments for the terminal members of each phase. Atom numbering herein uses the Scheme of Figure 1 as a reference/basis.

	2	**4a**	**4b**	**8**	**7**	**9**	**10**
Ln	La-5H_2O	Pr-5H_2O	Pr-10H_2O	Y-10H_2O	Er-10H_2O	Tm-8·5H_2O	Lu-8·5H_2O
Distances							
Ln−N	2.631(2)	2.589(7)	2.580(7)	2.469(5)	2.455(4)	2.420(3)	2.404(8)
	2.656(2)	2.609(9)	2.594(9)	2.478(6)	2.469(4)	2.474(2)	2.42(1)
Average	2.64(1)	2.60(1)	2.588(6)	2.474(5)	2.463(6)	2.45(3)	2.42(2)
Ln–O	2.525(2)	2.490(2)	2.492(7)	2.391(5)	2.382(3)	2.360(3)	2.337(8)
	2.571(2)	2.537(2)	2.526(6)	2.419(4)	2.419(3)	2.408(2)	2.381(5)
Average	2.54(2)	2.50(2)	2.50(1)	2.40(1)	2.39(1)	2.38(5)	2.36(2)
Angles							
N–Ln−N	116.96(6)	117.13(6)	118.4(3)	118.1(2)	118.3(1)	117.28(8)	117.7(3)
	125.22(6)	124.65(6)	122.7(2)	122.6(2)	122.6(2)	121.80(9)	121.5(3)
Average	120(5)	120(4)	120(2)	120(2)	120(2)	120(2)	120(2)
O*n*1−Ln−O*n*+13	153.2(1)	151.26(6)	149.4(2)	145.4(1)	145.2(1)	145.58(9)	144.8(3)
	157.2(1)	154.85(5)	153.3(2)	148.4(1)	147.7(1)	147.18(7)	146.0(3)
Average	155(2)	153(2)	151(1)	147(2)	146(1)	146.5(8)	145(1)
N*n*1–Ln–O*n*1,3	60.98(7)	61.81(6)	61.9(2)	64.2(1)	64.6(1)	64.45(8)	64.7(3)
	62.05(7)	62.92(6)	62.8(2)	64.9(2)	65.1(1)	65.96(9)	66.5(3)
Average	61.4(4)	62.4(4)	62.4(3)	64.5(4)	64.9(2)	65.6(9)	65.7(8)
O*n*1–Ln–O*n*3	122.09(7)	123.87(6)	124.1(2)	129.0(2)	129.6(1)	129.01(7)	129.6(2)
	122.93(7)	125.02(5)	125.3(2)	129.3(1)	129.9(1)	131.80(8)	132.5(3)
Average	122.6(4)	124.6(6)	124.7(6)	129.2(2)	129.7(2)	130(1)	131(2)
O*nm*−Ln−O*n*±1*m*	73.36(7)	73.69(6)	73.6(2)	73.4(2)	73.3(1)	73.89(8)	74.8(3)
	80.72(8)	80.18(7)	80.4(2)	79.1(2)	78.9(1)	77.84(8)	78.0(3)
Average	77(3)	76(3)	77(3)	77(3)	76.2(12)	76.0(15)	76(5)
O*n*1−Ln−O*n*−13	87.79(8)	87.58(7)	84.0(2)	84.2(1)	84.3(1)	87.64(9)	87.3(3)
	93.18(8)	92.56(6)	93.0(2)	92.1(1)	92.1(1)	93.32(8)	93.1(2)
Average	91(3)	91(3)	90(5)	89(4)	89(4)	89(3)	90(3)
N*n*1−Ln−O*n*+11;*n*−13	73.25(7)	72.96(6)	74.3(2)	72.1(1)	72.0(1)	72.47(8)	71.9(3)
	80.55(8)	78.71(7)	79.8(2)	74.6(2)	74.3(1)	73.93(9)	73.5(2)
Average	74(3)	76(3)	76(2)	74(1)	73(1)	73.3(5)	72.7(6)
N*n*1−Ln−O*n*+13;*n*−11	131.5(1)	132.1(1)	131.7(2)	132.6(1)	132.9(1)	133.05(7)	133.4(2)
	140.0(1)	139.6(1)	139.0(2)	138.7(2)	138.8(1)	137.37(9)	135.8(3)
Average	134(3)	134(3)	135(3)	135(2)	135(2)	135(2)	135(1)
Interplanar dihedral angles							
$C_5N(1)/C_5N(2)$	86.4(1)	86.5(1)	87.7(4)	87.5(3)	87.6(2)	89.3(1)	89.4(5)
$C_5N(2)/C_5N(3)$	87.0(1)	81.8(1)	84.1(4)	82.7(3)	82.6(2)	81.7(1)	81.3(4)
$C_5N(3)/C_5N(1)$	81.7(1)	87.7(1)	83.9(4)	81.8(2)	81.6(2)	86.6(1)	87.0(5)
$C_5N(1)/CCO_2(11)$	4.8(1)	5.6(1)	1.6(3)	1.0(2)	0.6(2)	8.8(1)	2.7(5)
$C_5N(1)/CCO_2(13)$	4.6(1)	5.5(1)	3.9(4)	3.9(3)	4.2(2)	12.2(1)	9.0(5)
$C_5N(2)/CCO_2(21)$	5.5(1)	6.3(1)	8.0(4)	7.0(3)	6.6(2)	5.8(1)	6.2(5)
$C_5N(2)/CCO_2(23)$	5.6(1)	7.7(1)	7.6(4)	8.1(3)	7.8(2)	6.4(1)	6.7(5)
$C_5N(3)/CCO_2(31)$	3.0(1)	3.5(1)	4.4(4)	3.7(3)	4.1(2)	10.4(1)	10.7(4)
$C_5N(3)/CCO_2(33)$	4.4(1)	4.4(1)	1.7(4)	2.0(3)	2.5(2)	2.7(1)	2.8(5)
Ln out of plane deviations [Å]							
$C_5N(1)$	0.192(5)	0.176(4)	0.08(1)	0.05(1)	0.032(8)	0.015(6)	0.04(2)
$C_5N(2)$	0.297(4)	0.280(4)	0.01(1)	0.04(1)	0.030(8)	0.043(5)	0.06(2)
$C_5N(3)$	0.051(5)	0.042(4)	0.12(2)	0.10(1)	0.112(8)	0.228(5)	0.24(2)

presumed accessible to at least the intervening rare earths (Table 1). For this family, site occupancy refinement of water molecule oxygen sites is indicative of full occupancy of all postulated sites across the series; for all, however, the displacement parameters, possibly a foil for minor disorder, are high for a number of these, and for some no hydrogen atom locations were definitively established. Throughout the x = 8(.5) series also, solvent displacement parameters generally are high, possibly indicative of or associated with the difficulties in the crystallisation of adducts containing heavy Ln, with site occupancy refinement suggestive of some fragment populations. Unit cell projections for the various phases are shown in Figures 2(a)–(c), representative in general for each phase, although there may be variations in the fine detail of the modelling of the hydration. The complex anions, as in other structures (discussed ahead), may be considered to be disposed in homochiral columns lying side-by-side, with chirality alternating, to form sheets, viewed edge-on here, interspersed by layers of cations and associated water molecules, the two systems being interconnected by hydrogen bonds between cation, solvent and anions, in the last via the uncoordinated carboxylate oxygen atoms. In the "octa"-hydrates, the cations lie in between translation-related anions in projection down *b*, generating a CoLn column up that axis. In similar projections of the penta- and deca-hydrates, the cations lie between the anions with the axes of the Co and Ln chains parallel but not collinear. A similar motif of parallel-column/sheet formation

 © 2005 Wiley-VCH Verlag GmbH & Co. KGaA, Weinheim

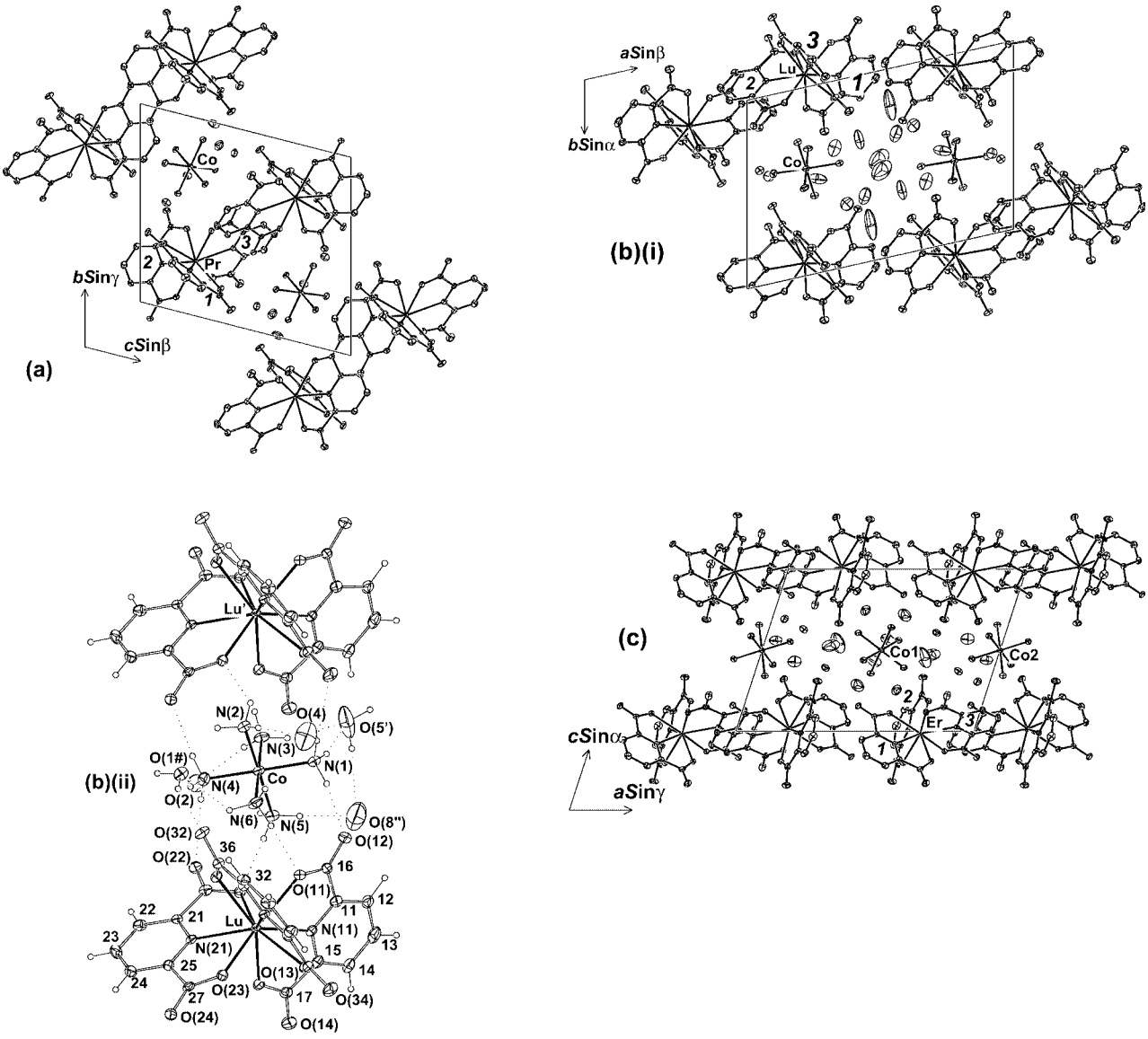

Figure 2. Representative unit cell projections for the various hydrate types $[Co(NH_3)_6][Ln(dipic)_3]\cdot x\,H_2O$, x = 5, 8(.5), 10. (a) Ln = Pr, x = 5 (**4a**), down *a*; (b) Ln = Lu, x = 8.5 (**10**), (i) down *c* and (ii) down *b*, showing the column stacking; (c) Ln = Er, x = 10 (**7**), down *b*.

is seen for the more highly charged anions of the complex $Na_5[Gd(chelidamate)_3]\cdot 16\,H_2O$[22] (chelidamic acid = 4-hydroxy-2,6-pyridinedicarboxylic acid), where approaches between anions of opposite chirality involve chelate units on the separate centres very closely parallel but with no atom separations for these rings being <3.9 Å and the closest atom approaches (3.1–3.2 Å) in fact being between uncoordinated carboxylate-*O* and C(2) of a near-orthogonal chelate ring on the adjacent centre. (Contact between anions of the same chirality appears to be mediated by H-bonding involving the 4-phenol/phenoxide groups.) In terms of the details of possible interactions, the present systems exhibit similarities but with further complications.

Thus, in the precisely defined pentahydrate-phase structure of $[Co(NH_3)_6][Pr(dipic)_3]\cdot 5\,H_2O$, the anion sheets (in planes parallel to [0,−1,1]), seen edge-on in the view down *a* [Figure 2(a)], involve each anion having two near neighbours (as part of a column) of the same chirality, with Pr···Pr 10.4500(7) Å (= *a*; homochiral contact), and three near-neighbours of opposite chirality, with Pr···Pr 8.4476(4), 8.6449(4) and 9.3568(4) Å (heterochiral contacts). The homochiral pairs are rather remote, with the only close approaches involving atoms in near orthogonal chelate units, so that they are perhaps best described as of a "edge-to-face" type,[23] (or possibly as a bent CH···O interaction) involving O(uncoordinated)···C(2) 3.458(4) Å and O(coordinated)···C(3) 3.576(4) Å. For the heterochiral pairs, interpenetration of the coordination spheres involves pairs of chelates being closely parallel but this is duplicitous evidence for stacking in that either ring atoms are not overlapped in projection or the ring planes are separated by >3.6 Å. Thus, both the 8.4476 and 8.6449 Å pairs involve

 © 2005 Wiley-VCH Verlag GmbH & Co. KGaA, Weinheim

parallel rings for which only the C–O(uncoordinated) units overlap in projection, involving C···O separations of 3.020(3) and 2.911(3) Å, respectively. For the 9.3568 Å pair, while the parallel ring overlap in projection is more extensive, all interatomic separations are >3.6 Å and possible edge-to-face interactions involving coordinated-*O* to C(4) and C(3) of a nonparallel ring lead to significantly shorter contacts [3.566(3) and 3.585(3) Å, respectively]. In an "octa"hydrate species such as $[Co(NH_3)_6][Lu(dipic)_3]\cdot 8.5H_2O$, where the anion sheets are seen edge-on in the view down *c* [Figure 2(b)], both homochiral [10.419(5) Å] and heterochiral [8.571(4), 8.860(5) and 9.328(4) Å] unit separations involve quite similar juxtapositioning of the anions to those in the Pr pentahydrate compound, though involving differences in specific interatomic approaches consistent with a very complicated balance of forces being involved. The closest contact in the homochiral pair, 3.291(2) Å, is that of a dipicolinate C(3) to an uncoordinated-*O* of a near-orthogonal chelate unit, again possibly an edge-to-face aromatic or a bent CH···O interaction. The adjacent C(4) is 3.46(1) and 3.58(2) Å, respectively, from uncoordinated- and coordinated-*O* of the same carboxylate and these are the only contacts which could be termed close. For the heterochiral pair at 8.571 Å, stacking C···O contacts are apparent at 3.24(1) Å but the 8.860 Å pair is less like its Pr analogue in that the closest (stacking) contacts are C(aromatic)···C(carboxylate) at 3.406(2) Å and two C(aromatic)···C(aromatic) at 3.461(2) Å. The closest contact in the heterochiral 9.328 Å pair is a C(4)···O(coordinated) separation of 3.461(2) Å, again involving atoms in nonparallel rings. In a decahydrate such as $[Co(NH_3)_6][Er(dipic)_3]\cdot 10H_2O$, where the anion sheets are seen edge-on in the view down *b* [Figure 2(c)], there are no contacts <3.7 Å between atoms in the homochiral pairs [11.227(1) Å = *b* apart] and while in the closest heterochiral pair [8.468(9) Å apart], there are stacking contacts C(carboxylate)···O(uncoordinated) of 3.422(8) Å, the closest atomic separation is 3.310(7) Å for O(uncoordinated)···O(coordinated). For the more remote pair 8.588(7) Å apart, the parallel ring positions are very similar but just sufficiently different to those of the 8.468 Å pair for C(carboxylate)···O(uncoordinated) at 3.226(8) Å to now be shorter than C(carboxylate)···O(uncoordinated) (3.313(8) Å] and O(uncoordinated)···O(coordinated) [3.346(8) Å]. For the longest heterochiral pair separation [9.269(9) Å], despite two rings being closely parallel and having significant overlap in projection, no interatomic separations are <3.6 Å, though several are close to this value. All these subtleties in the detail of what can be grossly termed "aromatic-aromatic" interactions can also be discerned in many structures of simpler materials such as metal nitrophenoxides and other aza-aromatic carboxylates,[24,25] as well as in structures of complexes of neutral aza-aromatic ligands.[23] How significant particular separations may be and how they may be related to lattice energies are nontrivial issues but the individual interaction energies are presumably small[23] and it may be noted that, across the various $[Co(NH_3)_6][Ln(dipic)_3]\cdot xH_2O$ phases, the cell dimensions are not too dissimilar, suggestive of a relatively facile passage from one form to another, possibly with rather minimal energy differences, in the course of crystallisation.

While the segregation of $[Ln(dipic)_3]^{3-}$ anions into sheet-like structures in all the cases described above might be taken as indicative of energetically important interactions, particularly those involving heterochiral pairs, between the anions, it is instructive to apply a similar analysis to the structures of other known derivatives. First structurally characterised were the sodium compounds and in $Na_3[Nd(dipic)_3]\cdot 15H_2O$,[18] for example, while again anion sheets generated from a side-by-side, alternating arrangement of homochiral columns can be discerned, one heterochiral pair involves closely parallel rings but with no ring atom separations <4 Å and another closely parallel rings with no separation <3.5 Å, suggesting any stacking to be of minimal importance. For the closest homochiral pair [10.353(15) Å = *a* apart], the only close contacts are C(3)···O(uncoordinated) and C(4)···C(carboxylate) of 3.25 and 3.30 Å, respectively. In the monoclinic form of $Na_3[Yb(dipic)_3]\cdot 13H_2O$,[17] racemic anion sheets are present but can no longer be regarded as built up from side-by-side positioning of homochiral columns containing anions in a common orientation. Concomitantly, heterochiral pairs involve closely parallel ring arrangements but none of this apparent stacking involves atomic approaches <3.6 Å and only for one pair is there a close edge-to-face contact [C(3)···O(uncoordinated)] of 3.37 Å. The closest homochiral pair involves a relative orientation unlike that in the Nd compound which results in one C(4)···C(4′) contact of 3.46 Å. In orthorhombic $Na_3[Yb(dipic)_3]\cdot 14H_2O$,[17] an anion sheet built up of adjacent homochiral columns is recovered but no pair within it involves short interatomic contacts aside from C(4)···C(carboxylate) and C(4)···O(uncoordinated), both close to 3.5 Å in the heterochiral pair 9.76 Å apart. In the similar anion sheet of $Na_4[Yb(dipic)_3][ClO_4]\cdot 10H_2O$,[19] close contacts are again rare, only edge-to-face C(3,5)···O(uncoordinated) at 3.31 Å in the homochiral pair 10.37 Å apart being obvious. Such results may mean that the anion sheet is a flexible motif, adjusting to restraints imposed by other components of the lattice. Consistent with this is the presence of homochiral sheets in $Cs_3[Eu(dipic)_3]\cdot 9H_2O$[1a] [with closest interatomic contacts being C(3,5)···O(uncoordinated) 3.44(2) Å] and the presence of racemic sheets in $[Co(sar)][Eu(dipic)_3]\cdot 13H_2O$[1a] (sar = "sarcophagine" = 3,6,10,13,16,19-hexaazabicyclo[6.6.6]icosane) where there is no evidence of any significant stacking. $[N(CH_2CH_3)_4]_3[Eu(dipic)_3]\cdot 4H_2O$[1c] provides a complicated system in which sheets of anions can be discerned which alternate in the sense that the orientations of the anion, common within a sheet, are nearly orthogonal from one sheet to the next. In one sheet, only homochiral pairs involve any close interatomic approaches, very similar to those in $Na_4[Yb(dipic)_3][ClO_4]\cdot 10H_2O$, with C(3,5)···O(uncoordinated) 3.33 Å. In the other sheet, homochiral pair contacts are similar, with a separation of 3.39 Å but the heterochiral pairs 10.29 Å apart appear to involve stacking, with C(3)···C(3′) 3.42 and C(4)···C(4′) 3.43 Å. The tet-

 © 2005 Wiley-VCH Verlag GmbH & Co. KGaA, Weinheim

raethylammonium cation is, of course, unlike all other countercations discussed so far in that it is formally neither an H-bond donor nor a coordinating centre, properties shared with cations such as $[Co(bipy)_3]^{3+}$ and $[Co(phen)_3]^{3+}$. These cations also give $[Ln(dipic)_3]^{3-}$ derivatives with rather different anion arrays, their properties being described in detail elsewhere.[26] $[NEt_4]^+$ is not like these cations in having an aliphatic exterior and there are approaches indicating possible CH···O interactions with dipicolinate carboxylate-*O*, as in fact there are for the butyl chain in the complex $[Co(3\text{-butyldiamsar})][Sm(dipic)_3]\cdot 15H_2O$ ("diamsar" = 1,8-diaminosarcophagine).[27]

Of the various forces in addition to anion−anion (aromatic) interactions which may determine the lattice arrays, important in the present systems would appear to be familiar H-bonding (discussed in more detail elsewhere[15]) and metal ion coordination. In addition to the columnar arrays of anions referred to above, it is possible to discern in many instances columns in which anions are bridged by cations and/or water. In all $[Co(NH_3)_6][Ln(dipic)_3]\cdot x H_2O$, as well as $Na_3[Nd(dipic)_3]\cdot 15H_2O$,[17] $Na_3[Yb(dipic)_3]\cdot NaClO_4\cdot 10H_2O$[19] and $Cs_3[Eu(dipic)_3]\cdot 9H_2O$,[1a] the metal ions align in such a way that the lanthanide and the other cation alternate in a chain, with the C_3 axes of the $[Ln(dipic)_3]^{3-}$ anions being oriented along the chain and with the structural indications being that coordination (of an alkali metal) or H-bonding (of Co–NH_3) to the "*exo*" dipicolinate oxygens atoms determines or assists this feature of the total crystalline array. In orthorhombic $Na_3[Yb(dipic)_3]\cdot 14H_2O$,[17] however, no such "mixed" chains are found and the C_3 axes of the anions appear to lie in the *bc* plane with alternating tilts towards Na^+ columns parallel to *c*. This may be associated with size differences between Nd^{3+} and Yb^{3+} in this hydrate series, where it is apparent also that the $[Yb(dipic)_3]^{3-}$ species is significantly distorted from true D_3 symmetry and the Yb columns can be regarded as forming pairs parallel to *b*. The Yb environment appears more symmetrical in monoclinic $Na_3[Yb(dipic)_3]\cdot 14H_2O$[19] and the C_3 axes of the complex anions seem more closely aligned (here, parallel to *a*) but again sodium cations are not directly interposed between Yb ions in columns. Although it is possible for $[Co(NH_3)_6]^{3+}$ to orient three NH bonds on a trigonal face parallel to the threefold axis of the octahedron, it does not adopt this mode to interact with the threefold symmetric dipicolinate *exo*-O_3 array of a given anion, presumably because of dimensional mismatching, but it is nonetheless apparent from the structure of $[Co(sar)][Eu(dipic)_3]\cdot 13H_2O$[1a] that in this case the fixed orientations of the NH bonds of the cation away from its C_3 axis are the likely cause of the juxtaposition (down *b*) of columns of the cations adjacent to columns of the anions (with their C_3 axes oriented down *b*). A similar feature is apparent in the structure of the $[Cr((NH_2)_2sar)][Ln(dipic)_3]\cdot 8H_2O$ series,[1b] even though here some differences might be expected because of the presence of the terminal primary amino groups. In both cases, anyway, the interactions between a given cation-anion pair are only part of an extended structure involving lattice water as well. Any asymmetry in the overall formal charge distributions on the cation and anion must of course be considered as another influence on cation-anion orientation and the rather beautiful sinusoidally undulating cation and anion sheets observed in $[Cr((NH_3)NH_2sar)][Cr((NH_3)_2sar)][La(dipic)_3]_3\cdot 32H_2O$[1b] provide evidence of its possible effects.

A specific aspect of interest in the solid-state structures of mixed transition metal/rare earth compounds is the influence of particular features of the structure on the separation and consequent degree of interaction between the different metal centres. The least separation of the Co and Ln centres within the asymmetric units of the present series varies from 5.752(3) Å in the 8.5 hydrate of the Lu species to 6.169(4) Å in the pentahydrate of the La species, all such Co···Ln separations being significantly shorter than the Cr···Ce separation in $[Cr\{(NH_2)_2sar\}][Ce(dipic)_3]\cdot 8H_2O$ (7.054(2) Å)[1b] and the Co–Eu separation in $[Co(sar)][Eu(dipic)_3]\cdot 13H_2O$ [6.733(3) Å – note an incorrect minimum of 7.408(3) Å was quoted in ref.[1a]], though still much longer than the Cs–Eu separation in $Cs_3[Eu(dipic)_3]\cdot 9H_2O$ [4.584(2) Å][1a] (where the Cs is directly coordinated to dipicolinate oxygen atoms). The relatively short Co···Ln approaches in the present compounds (and note that, for all, there is another only slightly longer) presumably reflects the fact that some of the coordinated ammonia ligands appear to be involved in direct hydrogen bonding to dipicolinate oxygen atoms though, as indicated by the Co···Pr separations in the pentahydrate and decahydrate species, 6.1629(6) and 5.9143(9) Å, respectively, water also acts as a "glue" which is more effective the greater its abundance. It is also notable that in the series of hydrated sodium salts, $Na_3[Ln(dipic)_3]\cdot x H_2O$,[17–20] the shorter Ln..Ln separations occur in the lattices of the earlier and larger Ln^{3+} ions, again in association with a (here, slightly) higher degree of hydration. The subtleties of these issues are further illustrated by the facts that: (i) in the $[Cr\{(NH_2)_2sar\}][Ln(dipic)_3]\cdot 8H_2O$ series,[1b] Cr···Lu [7.097(5) Å] is longer than its counterpart Cr···La [7.051(7) Å], while Cr···La (x, $y-1$, z), at 7.097(9) Å contracts to a counterpart Cr···Lu value of 6.991(6) Å; (ii) that in the present $[Co(NH_3)_6][Ln(dipic)_3]\cdot 10H_2O$ family, the minimum Co···Ln [5.9143(5) (Pr), 5.880(1) (Sm), 5.8747(9) (Tb), 5.8719(4) Å (Er)] decreases in agreement with the lanthanide contraction but by an amount which is les than half the change in Ln-donor atom bond lengths. The lanthanide-transition metal ion separations observed in the present system must be close to the minima possible if both metals are to retain independent coordination environments but they considerably exceed the separations found between lanthanide ions in binuclear calixarene complexes where significant but very weak metal-metal interactions can be detected.[28]

Crystals of $[Co(NH_3)_6]dipic\cdot Cl\cdot 2H_2O$ (**1**) were first isolated as a result of decomposition reactions occurring during first attempts to recrystallise $[Co(NH_3)_6][La(dipic)_3]$, though it was discovered after the structural study had been completed that orange, needle-like crystals of the same material slowly deposited on simply mixing solutions of $[Co(NH_3)_6]Cl_3$ and disodium dipicolinate. A representation

 © 2005 Wiley-VCH Verlag GmbH & Co. KGaA, Weinheim

of the structure, viewed down *a*, is given in Figure 3(a). An unusual feature is that three formula units constitute the asymmetric unit. Viewed parallel to the *a* axis, the three inequivalent units appear to be related by pseudo-2_1-screw operations parallel to *c* but this is only approximately true for one of the units, and both the number of "observed" reflections and systematic absences are inconsistent with a smaller cell. Throughout the cell, in a sheet about $y = 0.5$,

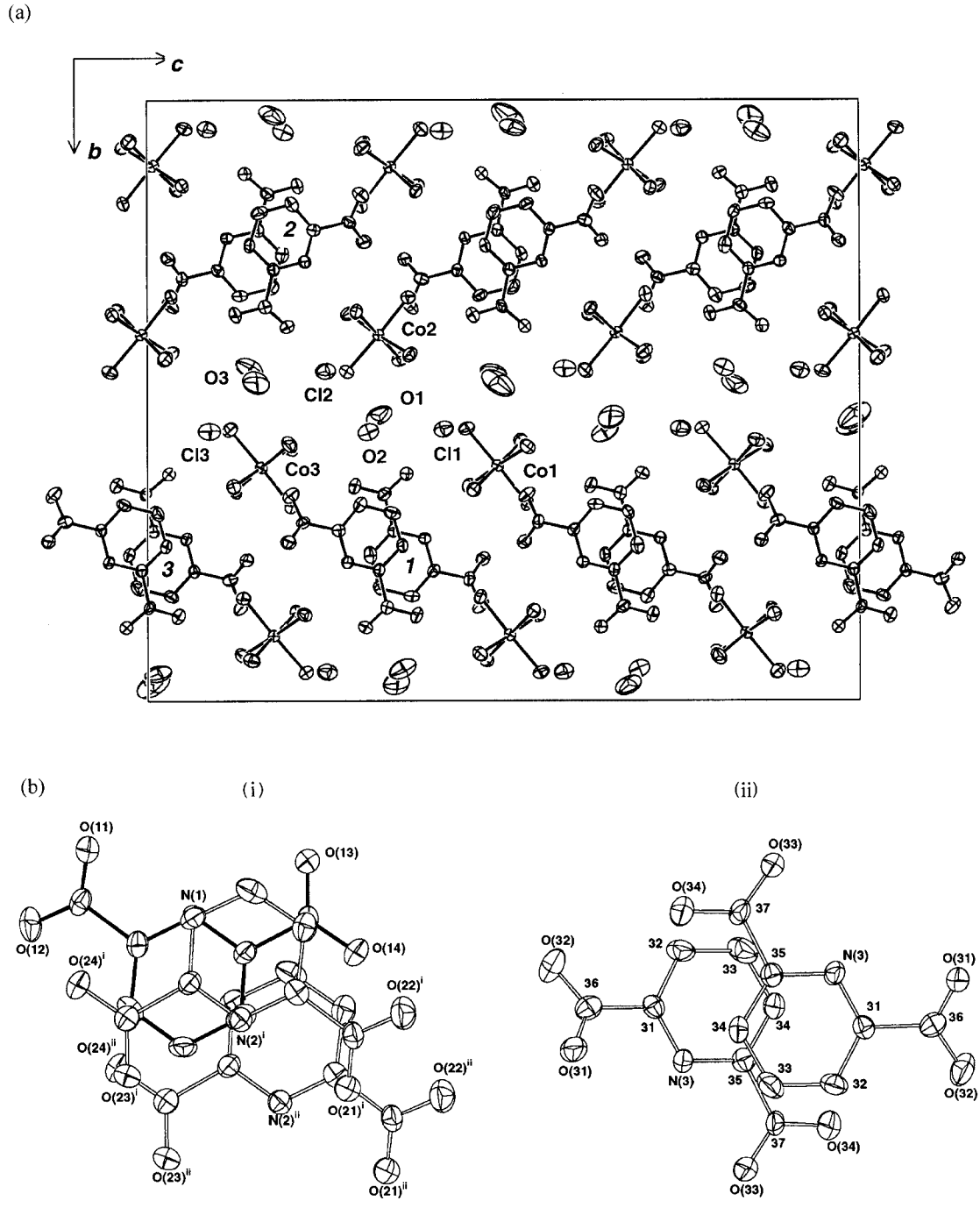

Figure 3. (a) Unit cell contents of $[Co(NH_3)_6]$dipic·Cl·$2H_2O$ (**1**), projected down *a*. (b) Interanion overlaps between; (i) anions 1 and 2, perpendicular to the aromatic plane of anion 1 (i: $1 - x$, $^1/_2 + y$, $^1/_2 - z$; ii: $2 - x$, $^1/_2 + y$, $^1/_2 - z$). N(1) contacts C(Ar) of ligand 2^i at 3.360(9), N(2^i) C(Ar) of ligand 1 at 3.387(9), the latter also contacting C(Ar) of ligand 2^{ii} at 3.54(1) Å.; (ii) anion 3 and its image ($x - ^1/_2$, $^3/_2 + y$, $\bar{z}$); C(34)···C(35) is 3.496(9) Å.

 © 2005 Wiley-VCH Verlag GmbH & Co. KGaA, Weinheim

there is a complicated hydrogen-bonding network involving the water molecules, chloride and carboxylate anions and the ammonia groups of the cations. This is a common situation in "crystallised ion pairs" of polycarboxylate anions and amine complexes[29] and the very complicated nature of the system contrasts with the rather elegant simplicity of other systems incorporating polyamidinium cations and polycarboxylates.[30] by (presumed) hydrogen-bonding interactions, the "inner" oxygen atoms of a dipicolinate anion *quasi*-chelate one hexamminecobalt(III) cation while the outer oxygen atoms bridge to other hexammine cations. In the view presented in Figure 3(a), it is apparent that the dipicolinate entities lie in columns, with one molecule projecting upon the next in its column in a manner suggestive of π-stacking interactions, consistent with the fact that when viewed down *b*, the dipicolinates form undulating sheets *a*/2 = 3.56 Å apart. This is to ignore some subtleties of the array, however, in that there are dipicolinate columns down *a* of three types, two with the dipicolinate ring planes close to parallel but with their ring plane vectors oppositely oriented relative to *a* and one where the ring plane orientations alternate down the column between those of the other columns. These are associated with three types of adjacent ring projections and thus different short interatomic approaches, as shown in Figure 3(b). The anion array is quite reminiscent of that known for the sodium complex, [Na(dipicH)(dipicH$_2$)(OH$_2$)$_3$],[31] where layers are separated by *a*/2 = 3.44 Å. Dipicolinate stacking is also apparent in the lattice of [Eu(dipicH)(dipic)(OH$_2$)$_2$] and its congeners.[14]

Powder Diffraction Studies of Hydration

The powder diffraction pattern predicted[32–34] from the single crystal structure determined for [Co(NH$_3$)$_6$][Ce(dipic)$_3$]·5H$_2$O (**3a**) was in good agreement with that observed for the bulk sample rapidly crystallised from water and stored under ambient (low humidity) conditions, indicating that the pentahydrate phase may be readily isolated. On the first occasion that several members of the complete [Co(NH$_3$)$_6$][Ln(dipic)$_3$]·*x*H$_2$O series were isolated under essentially identical conditions, the La (**2**), Ce (**3**) and Pr (**4a**) compounds all gave this powder pattern. However, a clearly different powder pattern was observed for the Sm (**5**) and Eu derivatives and yet another for the Dy, Ho and Yb derivatives. The 2θ angles of the most intense peak in these powder spectra were found to be 8.70–8.80° for La, Ce, Pr, 8.25–8.30° for Sm and Eu, and 9.35–9.40° for Dy, Ho and Yb but after the Sm and Ho compounds, for example, had been heated at 50 °C under vacuum for several hours, both provided a powder pattern with the most intense peak having 2θ = 8.75°. Extended, later studies of the complete series showed that if the samples were thoroughly ground prior to the recording of powder diffraction spectra (so, presumably, allowing rapid equilibration of crystal hydrate water with atmospheric humidity), the powder patterns for all compounds were close to that predicted for the pentahydrate phase. The facts that subsequent crystal structure determinations (described above and to be reported elsewhere) showed that other (higher) hydrates could be isolated at least as larger crystals and that the predicted powder pattern for the Lu species[33] closely corresponded to that first observed for the Dy, Ho and Yb compounds we interpret, in conjunction with the first observations, as indicating that the [Co(NH$_3$)$_6$][Ln(dipic)$_3$] compounds may precipitate as various hydrate mixtures but that the pentahydrate phase is preferred for the solid materials stored under ambient conditions.

Thermogravimetry

Qualitatively, thermograms over the range of ca. 25–800 °C obtained for all the [Co(NH$_3$)$_6$][Ln(dipic)$_3$]·*x*H$_2$O compounds were identical, showing the features expected from the behaviour of related, simpler compounds. Data for the Ln = La and Lu compounds are shown in Figure 4(a). The major mass change between 400–470 °C is associated with evolution of heat and corresponds with the major exotherm observed for [Co(NH$_3$)$_6$]dipic·Cl·2H$_2$O (**1**), so that

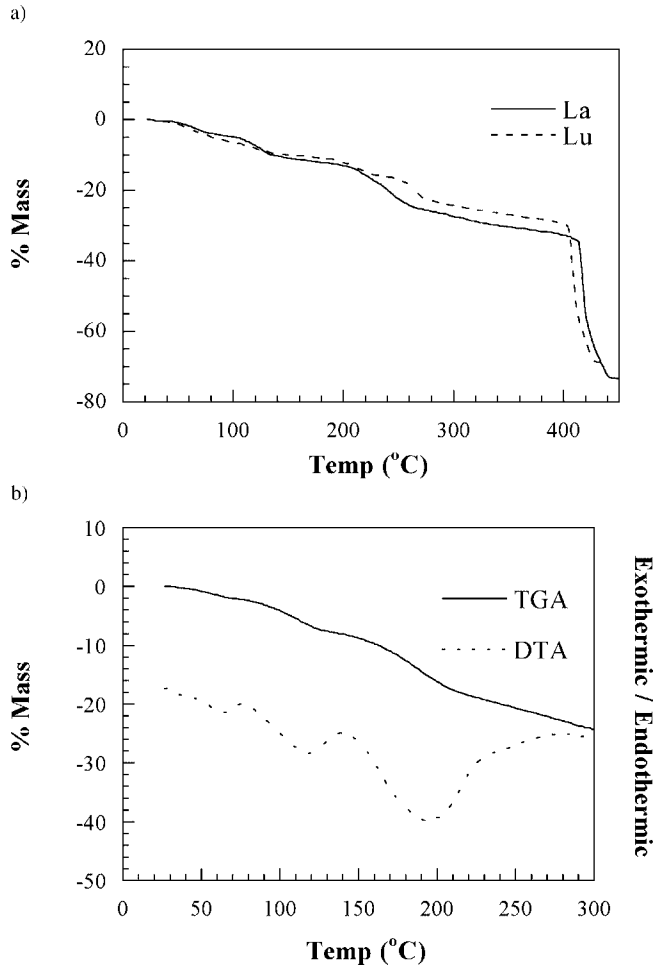

Figure 4. (a) Mass changes during thermal decomposition of [Co(NH$_3$)$_6$][Ln(dipic)$_3$]·*x*H$_2$O (Ln = La, Lu) in air. (b) Initial mass changes during thermal decomposition of [Co(NH$_3$)$_6$][Ce(dipic)$_3$] ≈ 6H$_2$O in air.

 © 2005 Wiley-VCH Verlag GmbH & Co. KGaA, Weinheim

we assume it to reflect the oxidative decomposition of dipicolinate.[10] The significantly endothermic events occurring between ca.200 and 300 °C are similar to those of both **1** and $[Co(NH_3)_6]Cl_3$ in this range (note that the latter complex displays no strong exotherm at higher temperatures) and are thus associated with at least the final steps in the decomposition of the $[Co(NH_3)_6]^{3+}$ moiety. The mass changes below ca. 200 °C, all of them associated with weak endotherms, were of particular interest given the crystallographic characterisation of different hydrates across the rare earth series but from observation of the mass changes alone and without monitoring of the evolved gases, it is not possible to clearly distinguish water and ammonia loss processes in this range. However, the most readily induced changes (below 100 °C) can be reversed by exposure of the solids to humid air, so that it is assumed that these are simply associated with reversible dehydration. A thermogram for the Ln = Ce compound between ambient temperature and 250 °C is shown in Figure 4(b). The starting material for this experiment was previously equilibrated in air of 75% relative humidity (298 K)[36] to ensure a reproducible composition, though microanalyses (C, H, N) indicated a formulation intermediate between that of a hexahydrate and a pentahydrate and presumably the bulk sample may have contained several phases. Repetitive thermograms provided the mean results of a near mass plateau at 75 ± 10 °C corresponding to a weight loss of 4.8 ± 0.9% (i.e., ≈ $2H_2O$) and another at 113 ± 5 °C corresponding to a total weight loss of 12.2 ± 1.4% (i.e., ≈ $6H_2O$ overall, though a contribution from ammonia loss cannot be excluded). The stepwise loss of water is consistent with the fact that the crystal structure determination on the pentahydrate shows that the lattice water molecules are in inequivalent sites, so that some differences in their rates of thermal release would be expected.

After being heated to 600 °C or higher in air, all the $[Co(NH_3)_6][Ln(dipic)_3]\cdot x H_2O$ solids were converted to black powders for which microanalysis showed negligible carbon and nitrogen contents. Powder diffractometry (see below) confirmed that these powders were metal oxides. Scanning electron micrographs of the products obtained after ca. 15 min at 600 °C from the Pr and Lu compounds showed the different products to have different particle morphologies but with a similar mean particle size ca.2 μm.

Powder Diffractometry of Thermal Decomposition Products

Phase equilibria in Co/Ln/O systems have been thoroughly studied,[12] so that it was anticipated that perovskite, $CoLnO_3$, materials might be observed as the products of the thermal decomposition reactions. Powder diffractometry showed this expectation to be justified, though, again as expected, generation of the perovskite phase from the separate monometallic oxides appeared to become more difficult in progressing from the lighter to the heavier rare earths. Thus, under the conditions of our experiments, only Co_3O_4 and Ln_2O_3 could be detected as products for Ln = Yb, Lu. In fact, Co_3O_4 and Ln_2O_3 were the initial products in all cases, indicating that there could be no particular advantage to synthesis of the perovskites by thermal decomposition of $[Co(NH_3)_6][Ln(dipic)_3]\cdot x H_2O$ rather than by direct reaction of the oxides. This initial formation of separate oxide phases may be consistent with the observed decomposition during attempted recrystallisation in that dipicolinate release could result from the (solid state) hydrolysis reaction

$$[Ln(dipic)_3]^{3-} + 3H_2O \rightarrow [Ln(OH)_3] + 3Hdipic^-$$

giving a separate rare earth phase prior to any decomposition of the $[Co(NH_3)_6]^{3+}$ unit. The self-association of "free" dipicolinate units through π-stacking may be a factor favouring the early occurrence of this reaction. The kinetic inertness and high stability of the $[Co(NH_3)_6]^{3+}$ cation is probably another reason why a dipicolinate-bridged Co/Ln species which might smoothly transform to a mixed oxide is not formed.

2. Chromium/Rare Earth Systems

The $[Cr(en)_3][Ln(dipic)_3]\cdot x H_2O$ solids are all light-sensitive and the initially clear-yellow crystals precipitated from aqueous solution turn violet within several hours on exposure to normal ambient levels of illumination. For this reason, we have made a study of only a few members of the series to ensure that there are no dramatic differences in thermal behaviour from that of their $[Cr(urea)_6][Ln(dipic)_3]\cdot x H_2O$ analogues (which, as expected, are much less light-sensitive). The green $[Cr(urea)_6][Ln(dipic)_3]\cdot x H_2O$ compounds are particularly insoluble, precipitating very rapidly as powders, and we have been unable yet to grow crystals suitable for single-crystal structure determinations. However, their powder diffractograms show a common pattern of lines for the whole series, indicating a common hydrate stoichiometry (x = 7 on the basis of microanalysis).

Thermogravimetry

Weight losses and heat exchanges occurring on heating samples of both $[Cr(en)_3][Ln(dipic)_3]$ and $[Cr(urea)_6][Ln(dipic)_3]$ compounds are unremarkable and, as with the $[Co(NH_3)_6][Ln(dipic)_3]$ compounds, the most prominent feature of the thermograms is the major mass loss and exotherm initiated near 450 °C, again assumed to be associated with decomposition of the dipicolinate units. The chemical properties of the oxide products obtained at this point appeared to be independent of the particular precursor used (at least in the cases of Ln = La, Pr, Eu, Yb and Y) but the changes occurring on further heating at higher temperatures were considerably more complicated than in the Co systems. They were studied in detail for the products from the $[Cr(urea)_6][Ln(dipic)_3]$ precursors using powder diffractometry of the solids after periods of oven-heating at various temperatures between 450 and 900 °C.

 © 2005 Wiley-VCH Verlag GmbH & Co. KGaA, Weinheim

Powder Diffractometry of Thermal Decomposition Products

Phase equilibria are again well-characterised for Cr/Ln/O systems,[12] so that the formation of both "chromate", $LnCrO_4$, and "chromite" (perovskite), $LnCrO_3$, solids was expected. Excepting only $[Cr(urea)_6][Ce(dipic)_3]$, which gave rise to a stable mixture of CeO_2 and Cr_2O_3, this was the case for all the compounds studied. A significant difference from the Co systems, however, was that the separate monometallic oxide phases could not be detected as intermediate products prior to the formation of the chromate or chromite phases. This may reflect a greater lability of the Cr^{III} cations compared to $[Co(NH_3)_6]^{3+}$, so that a dipicolinate-oxygen-bridged species, say, may be produced early on in the decomposition, although another significant observation is that the chromates, formally containing a Cr^{V} species, appear to be produced prior to the chromites, formally containing Cr^{III} (as in the reactant). It is difficult to establish the exact sequence of events near the actual point of oxide formation, since the product formed between 450 and 500 °C (following the major dipicolinate exotherm) is black or very dark green in colour and apparently amorphous, giving very broad lines in its X-ray diffraction pattern and an increase in temperature and/or prolonged heating are required to form materials giving identifiable powder diffraction lines. In general, nonetheless, the amorphous black initial product undergoes a conversion to a dark green, crystalline chromate phase (which is dimorphic) and then to an olive-green, crystalline chromite phase. Table 2 contains a summary of observations across the full series of compounds. Included are our measurements made to date of surface areas of the oxides, showing that high surface area materials can be readily produced through these decomposition reactions. Also interesting in relation to catalytic activity of the mixed oxides is the fact that in early experiments conducted in crucibles with (loose fitting) lids, the chromate species were observed to persist to higher temperatures. Assuming the lid to cause retention of CO_2 generated during the dipicolinate decomposition, this may indicate that the oxides effectively catalyse the CO_2/CO interconversion.

In the particular case of the thermal decomposition of $[Cr(urea)_6][Nd(dipic)_3]$, careful observation of the powder patterns of the products produced between 450 °C and 550 °C provided evidence for the hitherto unknown monazite phase of neodymium chromate being produced along with the known zircon phase. Rietveld refinement confirmed the presence of both monoclinic monazite-type [a = 6.9226(7), b = 7.1148(7), c = 6.6088(6) Å, β = 105.318(6)°, V = 313.94(7) Å^3] and tetragonal zircon-type [a = 7.3101(3), c = 6.3982(3) Å, V = 341.91(4) Å^3] in a sample prepared

Table 2. Reaction conditions and product characteristics for thermal decomposition of $[Cr(urea)_6][Ln(dipic)_3]\cdot 7H_2O$ in air.

Ln	Time / temperature	Product	Phase[a]	BET surface area [m^2 g^{-1}]
La	1 h / 550 °C	$LaCrO_4$	M	12.2
La	1 h / 600 °C	$LaCrO_4$	M	14.2
La	1 h / 700 °C	$LaCrO_3$	P	5.0
Ce	all conditions	$CeO_2 + Cr_2O_3$	–	–
Pr	1 h / 500 °C + 1 h / 550 °C	$PrCrO_4$	M / Z	11.5
Pr	1 h / 550 °C	$PrCrO_4$	M (traces Z)	15.0
Pr	1 h / 700 °C	$PrCrO_3$	P	8.1
Nd	1 h / 550 °C + 1 h / 580 °C	$NdCrO_4$	Z	8.7
Nd	1 h / 530 °C	$NdCrO_4$	M / Z	13.4
Nd	1 h / 700 °C	$NdCrO_3$	P	7.1
Sm	1 h / 600 °C	$SmCrO_4$	Z	12.7
Sm	1 h / 700 °C	$SmCrO_3$	P	19.3
Eu	1 h / 600 °C	$EuCrO_4$	Z	9.7
Eu	1 h / 700 °C	$EuCrO_3$	P	10.1
Gd	1 h / 600 °C	$GdCrO_4$	Z	7.7
Gd	1 h / 700 °C	$GdCrO_3$	P	10.2
Tb	1 h / 550 °C + 1 h / 580 °C	$TbCrO_4$	Z	13.5
Tb	1 h / 700 °C	$TbCrO_3$	P	5.5
Dy	1 h / 580 °C + 1 h / 600 °C	$DyCrO_4$	Z	18.0
Dy	1 h / 700 °C	$DyCrO_3$	P	15.2
Ho	4 h / 600 °C	$HoCrO_4$	Z	7.6
Ho	1 h / 700 °C	$HoCrO_3$	P	12.7
Er	6 h / 600 °C	$ErCrO_4$	Z	6.5
Er	24 h / 620 °C	$ErCrO_3$	P	16.5
Er	3 h / 700 °C	$ErCrO_3$	P	7.4
Tm	9 h / 600 °C	$TmCrO_4$	Z	7.9
Tm	3 h / 700 °C	$TmCrO_3$	P	14.7
Yb	5 h / 700 °C	$YbCrO_3$ (traces of Yb_2O_3)	P	13.1
Lu	3 h / 700 °C	$LuCrO_3$ (traces of Lu_2O_3)	P	11.4
Y	4 h / 600 °C	$YCrO_4$	Z	28.6
Y[b]	4 h / 600 °C	$YCrO_4$	Z	15.0
Y	5 h / 700 °C	$YCrO_3$	P	4.5

[a] M = monazite type, Z = zircon type, P = perovskite. [b] $[Cr(en)_3][Ln(dipic)_3]$ reactant.

 © 2005 Wiley-VCH Verlag GmbH & Co. KGaA, Weinheim

under optimum conditions of one hour's heating at 530 °C. These well-known ABO_4-type structures, which consist of alternating [001] stacks of AO_9 polyhedra and BO_4 tetrahedra (monazite) or AO_8 and BO_4 groups (zircon) have been described in detail elsewhere.[37,38] In both structures, which are nominally related by tetrahedral rotations about [001], the O atoms are three coordinate to two rare earth cations and one tetrahedral cation. This is the first report of the monazite form of $NdCrO_4$, though the precision of the atomic positional parameters and derived geometrical data is only mediocre and neutron diffraction data would be required for a high-precision structure determination of monoclinic $NdCrO_4$. The tetragonal $NdCrO_4$ cell parameters are in good accordance with those determined earlier (a = 7.315, c = 6.399 Å) from X-ray powder data.[39] Comparison of phase fraction scale factors indicated that the ratios of the two phases in the mixture analysed was approximately 1:1. So far, we have not been able to prepare the monazite form in greater purity.

Thus, the monazite structure is now confirmed for $LnCrO_4$ (Ln = La, Pr and Nd) and the zircon structure for Ln = Pr to Yb (excluding Pm and Tm). A plot[40] of ^3V (V = unit cell volume) vs. ionic radius of the rare earth cations (Figure 5) shows smooth, approximately linear relationships for each of the two structure types. The overall trend for the $LnCrO_4$ phases is comparable to the situation for the $LnPO_4$ family,[37] where the break point between the large lanthanide (monazite) and small lanthanide (xenotime/zircon) structures occurs between Gd and Tb. Unlike the phosphates, two of the chromates, $PrCrO_4$ and $NdCrO_4$, show polymorphism between these two forms. The monazite-type polymorphs of $PrCrO_4$ and $NdCrO_4$ have smaller unit cell volumes (by ≈ 8.4 and 9.0%, respectively) than their zircon modifications, even though the rare earth cations have a higher coordination number in the monazite phases. This phenomenon has also been observed for the monazite and zircon polymorphs of thorium silicate, $ThSiO_4$, and correlated with void space and short O..O contacts in the zircon-type phase.[41] Another phase which shows polymorphism between monazite and zircon forms is $CeVO_4$.[38] The stable room-temperature polymorph of this material is monazite, with the zircon form stable above ≈ 1300 °C at ambient pressure. Under more extreme conditions ($T >$ ≈ 500 °C, $P >$ ≈ 27 kbar), $CeVO_4$ transforms again to the scheelite ($CaWO_4$) structure.

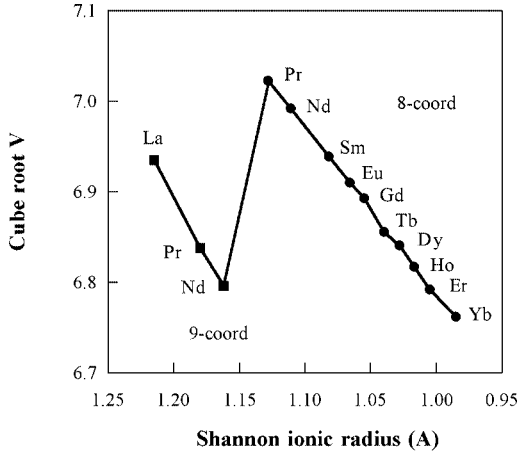

Figure 5. The relationship between unit cell volume and estimated cation radius for the monazite and zircon families of rare earth chromates.

Oxide Phase Magnetic Properties

Measurements (deposited as Supporting information; for supporting information see also the footnote on the first page of this article) of magnetic susceptibility on a selection for both the Co and Cr containing mixed oxides provided no evidence of significant differences from known data[42] for the same oxides prepared by conventional methods, and hence were not pursued in detail.

Conclusions

The work described herein provides evidence that the dipicolinate anion, whether coordinated to the proton or to metal ions, can undergo self-association through mechanisms[22–24] associated with its aromatic character, which do not directly involve the formally recognised donor and acceptor groups (N, O and hydroxy H atoms). There is, of course, very substantial evidence in solid-state structures[1,5,17–21,28,43] of its capacity to promote oligomerisation through bridging coordination of the carboxylate groups, and facts such as the solvatochromism of the complex $[Fe(dipic)_2]^{2-}$[31] show that at least some other association mechanisms must remain effective in solution. A substantial remaining problem, recently recognised in general terms for both solid[23] and solution[44] systems, is to conduct a quantitative partitioning of the factors operative in any particular case of "supermolecule" formation. The present work provides at least circumstantial evidence that the energies of inter-dipicolinate interactions are sufficiently great to influence solid state reaction rates.

Experimental Section

General: Thermogravimetry: Weight loss and associated thermal changes resulting when ca. 20 mg samples of the complexes were heated between ca. 25 and 800 °C under air were monitored with a Rigaku "Thermoflex" instrument. Magnetometry: Measurements were made with a SQUID magnetometer (Quantum Design MPMS-7) at a magnetic field strength of 12 T in the temperature range 5–300 K. Samples were formed as small discs by compression of the powdered solids. Surface Area Determination: Surface areas for nitrogen adsorption were determined by the BET method on a Micrometer Gemini 2360 Surface Area Analyser, with a free space correction made using He.

Synthesis of the Precursor Complexes: Precipitation of $[Ln(dipic)_3]^{3-}$ anions from aqueous solution by the addition of cations such as $[Co(NH_3)_6]^{3+}$, $[Cr(en)_3]^{3+}$ and $[Cr(urea)_6]^{3+}$ is very efficient and we have previously described[1] the very simple syntheses of the resulting microcrystalline materials. In early attempts to prepare larger crystals of the various $[Co(NH_3)_6][Ln(dipic)_3]\cdot x\,H_2O$ solids

 © 2005 Wiley-VCH Verlag GmbH & Co. KGaA, Weinheim

by digestion in the preparative supernatant solution and by recrystallisation from water, the Ln = La compound, in particular, was observed to be rather readily decomposed. In one apparently decomposed sample, however, orange crystals were found to be present and were then identified through crystallographic study as $[Co(NH_3)_6]$dipic·Cl·2 H_2O (**1**). In fact, this material is rather readily precipitated by simple addition of a molar equivalent of Na_2dipic to an aqueous solution of $[Co(NH_3)_6]Cl_3$, analysis of the bulk solid suggesting a slightly higher degree of hydration than deduced from the structure solution. (Found C 20.8, H 6.3, N 24.4; calculated for $C_7H_{21}ClCoN_7O_4$·2 H_2O: C 21.14, H 6.34, N 24.65; for $C_7H_{21}ClCoN_7O_4$·2.5 H_2O: C 20.67, H 6.44, N 24.11.)

Attempts, by numerous variations on liquid and vapour diffusion procedures, to obtain diffraction quality specimens of $[Co(NH_3)_6]$-$[Ln(dipic)_3]$·x H_2O for the full Ln series in an effort to systematically define phases present and their domains of existence yielded results that are erratic, the factors which determine the form of the solids remaining obscure. The principal method adopted for the growth of quite large crystals (sometimes 1 mm on edge) of all the $[Co(NH_3)_6][Ln(dipic)_3]$·$x$ H_2O compounds was to form a solution of the initial precipitate by slow addition of dilute HCl to its slurry with water until dissolution just occurred. (This was readily achieved with all the compounds up to Ln = Nd but with the heavier lanthanides it was apparent that an acid insoluble species, probably $[Ln(dipicH)(dipic)(OH_2)_2]$,[14] was formed, so that the initial solution, even when as dilute as 20 mg in 10 mL, was slightly cloudy. Fortunately, this did not seem to affect the quality of the crystals ultimately formed, though removal of this faint precipitate presumably decreased the recovery). After gravity filtration, this solution was then placed in a vapour diffusion cell with dilute aqueous ammonia in the outer compartment and the system allowed to stand under ambient conditions for extended periods. Several of the crystals used (particularly those involving the heavier rare earths, where there was a tendency for very long, thin needles to form) in the present structural studies were obtained only after more than a year of standing in contact with their supernatant solutions. Even then, for some elements no useful material was obtained at all.

Attempts to apply the above procedure for the growth of larger crystals of the $[Cr(urea)_6][Ln(dipic)_3]$ series were successful to the extent that materials obviously crystalline to the naked eye could be obtained but the crystals remained too small for single-crystal X-ray studies. Prolonged standing in the reaction mixture was to no advantage due to the hydrolysis of the $[Cr(urea)_6]^{3+}$ cation, which caused the initially deposited green crystals to redissolve and colourless crystalline solids to form under a violet supernatant solution. In the case of $[Cr(urea)_6][Eu(dipic)_3]$, a crystal drawn from the final product mass was characterised as [Eu(dipicH)(dipic)-$(OH_2)_2$]·4 H_2O, at the time of its isolation a new member of this Ln series, though its structure has since been determined.[14]

Powder Diffractometry: Measurements were made with a Siemens "Kristalloflex" D5000 diffractometer. For determination of the neodymium chromate structure, step-scan powder data were collected for 15°< 2θ < 100° (step size 0.02°, 8 s counting time per point) with Cu-K_α radiation, $\lambda = 1.5417_8$ Å, $T = 298(2)$ K. Rietveld refinement was carried out using the GSAS[35] suite of programs, with starting atomic models for the monazite (space group $P2_1/n$) and zircon (space roup $I4_1/amd$) forms of $NdCrO_4$ taken from the structures of monoclinic $PrPO_4$[37] and tetragonal $NdCrO_4$,[45] repectively. The profile (unit cells, zero-point error, 6-term background polynomial descriptors, pseudo-Voigt peak-shape parameters) and atomic parameters were progressively added to the model as variables in the usual fashion. The refinement converged to yield residuals, as defined in ref.[35] of $R_p = 8.75\%$, $R_{wp} = 11.94\%$, $R(F^2) = 5.78\%$ and $\chi^2 = 2.33$ (50 parameters, 424 reflections, 4248 profile points). The final observed, calculated and difference profiles are illustrated in Figure 6.

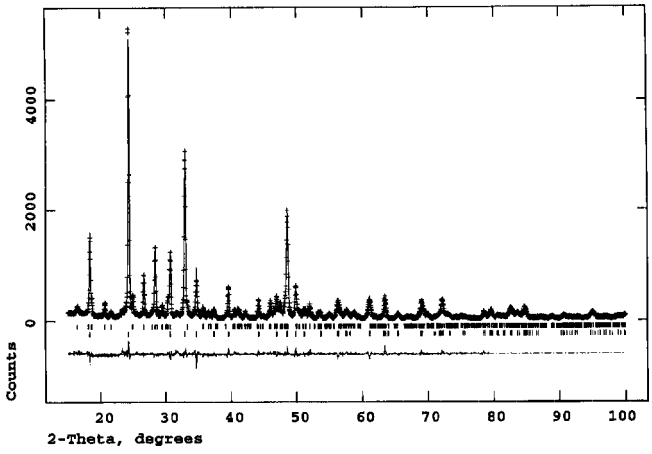

Figure 6. Observed, calculated (Rietveld) and difference intensity profiles for the powder X-ray diffraction pattern of $NdCrO_4$.

Room Temperature Single Crystal X-ray Structure Determinations: The structures of $[Co(NH_3)_6]$dipic·Cl·2 H_2O (**1**) and $[Co(NH_3)_6]$-$[Ce(dipic)_3]$·5 H_2O (**3a**) were determined first in Barcelona. Data sets (Enraf–Nonius CAD4 diffractometer; ω-scan mode; graphite-filtered Mo-K_α radiation, $\lambda = 0.7107_3$ Å) were measured at 293(2) K, with ψ-scan absorption corrections.

Structural studies of the $[Co(NH_3)_6][Ln(dipic)_3]$·$x$ H_2O series were extended in Western Australia (Ln = La(**2**), Ce(**3**), Pr(**4a**) (x = 5); Ln = Pr(**4b**), Sm(**5**), Tb(**6**), Er(**7**), Y(**8**) (x = 10); Ln = Tm(**9**), Lu(**10**) (x = 8.5). The frequent assumption that arrays of rare earth complexes can be adequately represented by studies of a single member or, alternatively, "early" and "late" members, has been effectively demolished as a reasonable presumption by studies of series such as the picrates[47–50] or chloride/terpyridyl[51] complexes (which is not to say that there are not series, such as the triflates,[52] which are represented by a single invariant, unambiguous structural type). The present array is no exception, offering suggestions of a series of subtlety comparable to that of the picrates, though more severe practical difficulties in respect of accessing appropriately crystalline specimens intrude here. As noted above, the gadolinium, terbium and lutetium specimens, for example, were grown by digestion at room temperature on a time scale of years (following slow precipitation over days by pH variation), and in most other cases several months' wait was involved. For several early samples, room temperature, single counter "four circle" diffractometer data sets were measured ($2\theta_{max}$ as specified; $2\theta/\theta$ scan mode; monochromatic Mo-K_α radiation, $\lambda = 0.7107_3$ Å; $T \approx$ 295 K), $N_{t(otal)}$ symmetry-equivalent reflections (where appropriate) being merged to N_r (unique) (R_{int} as quoted), N_o with $I > 3\sigma(I)$ being considered "observed" and used in the full-matrix, least-squares refinement on $|F|$ after Gaussian absorption correction. Conventional residuals R, R_w [statistical weights derivative of $\sigma^2(I) = \sigma^2(I_{diff}) + 0.0004\sigma^4(I_{diff})$] are quoted at convergence, neutral atom complex scattering factors being employed, computation using the Xtal 3.4 program system.[53] Significant nontrivial difference map residues were modelled as water molecule oxygen fragments, site occupancies being established by refinement; not infrequently, hydrogen atom dispositions could not be established with any cer-

 © 2005 Wiley-VCH Verlag GmbH & Co. KGaA, Weinheim

tainty in association with fractionally occupied or "thermally smeared" fragments. For the extrema of the three major families, pertinent results are presented in the Figures and Tables, the latter showing the displacement envelopes for the non-hydrogen atoms at the 50% probability amplitude level, hydrogen atoms (where shown) having arbitrary radii of 0.1 Å.

A number of the determinations presented here were only finally accessible with the advent of an area-detector facility (Bruker AXS CCD instrument), spheres of data being measured at $T \approx 300$ K; preliminary data processing was carried out using proprietary software incorporating "empirical"/multiscan absorption correction, refinement using the Xtal 3.7 program system.[53]

Crystal/Refinement Data

1: $[Co(NH_3)_6]$dipic·Cl·2 H_2O, $C_7H_{25}ClCoN_7O_6$, M = 397.7, orthorhombic, space group $P2_12_12_1$ (D_2^4, No. 19), Z = 12, a = 7.123(1), b = 24.099(1), c = 28.670(2) Å, V = 4921 Å^3. $D_{calcd.}$ = 1.61$_1$ g cm^{-3}; μ_{Mo} = 12.5 cm^{-1}; specimen: 0.54 × 0.31 × 0.10 mm; $T_{min./max.}$ = 0.84. $2\theta_{max.}$ = 61°; N_t = 8408, N_r = 8623 (R_{int} = 0.107), N_o = 6408; R = 0.048, R_w = 0.121; n_v = 493, $|\Delta\rho_{max}|$ = 0.78 e Å^{-3}, $x_{abs.}$ = 0.24(2).

$[Co(NH_3)_6][Ln(dipic)_3]\cdot x\,H_2O$, $C_{21}H_{27}CoLnN_9O_{12}\cdot x\,H_2O$, triclinic, space group $P\bar{1}$ (C_i^1, No. 2), Z = 2.

(a) x = 5

2: Ln = La. M = 885.4. a = 10.454(5), b = 12.593(9), c = 13.438(7) Å, α = 102.69(5), β = 94.48(4), γ = 104.39(5)°, V = 1655 Å^3. $D_{calcd.}$ = 1.77$_6$ g cm^{-3}; μ_{Mo} = 18.6 cm^{-1}; specimen: 0.58 × 0.32 × 0.65 mm; $T_{min/max}$ = 0.63. $2\theta_{max}$ = 55°; N_t = 10703, N_r = 7591 (R_{int} = 0.025), N_o = 7064; R = 0.026, R_w = 0.037; n_v = 575, $|\Delta\rho_{max}|$ = 1.4 e Å^{-3}.

Variata: (x, y, z, U_{iso})$_H$ were refined throughout, except O(4,5) (water), for which they could not be definitively established. A further hemisphere of data was measured to $2\theta_{max}$ = 45°, hence R_{int} is quoted.

3: Ln = Ce. M = 886.6. a = 10.432(2), b = 12.583(2), c = 13.427(4) Å, α = 102.72(2), β = 94.32(2), γ = 104.27(2)°, V = 1651 Å^3. $D_{calcd.}$ = 1.78$_4$ g cm^{-3}; μ_{Mo} = 19.5 cm^{-1}; specimen: 0.24 × 0.19 × 0.14 mm; $T_{min/max}$ = 0.79 × $2\theta_{max}$ = 61°; N_t ($2\theta_{max}$ = 61°) = 10430, N_r = 9929, N_o = 4197; R = 0.071, R_w = 0.153; n_v = 448, $|\Delta\rho_{max}|$ = 1.4 e Å^{-3}.

Variata: Study of this complex (and of $[Co(NH_3)_6]$dipic·Cl·2 H_2O), undertaken in Barcelona, initiated the present series of determinations, the precision of which is improved for other Ln extending the domain of this phase. One attempt to improve crystal quality for the Ce species yielded better material but of a new, nonahydrate phase, described elsewhere.[15]

4a: Ln = Pr. M = 887.4. a = 10.4500(7), b = 12.5988(8), c = 13.4262(9) Å, α = 102.750(1), β = 94.180(1), γ = 104.305(1)°, V = 1655 Å^3. $D_{calcd.}$ = 1.78$_0$ g cm^{-3}; μ_{Mo} = 20.4 cm^{-1}; specimen: 0.30 × 0.20 × 0.12 mm; $T_{min/max}$ = 0.77. $2\theta_{max}$ = 58°; N_t (CCD data) = 22325, N_r = 8116 (R_{int} = 0.021), N_o [$F > 4\sigma(F)$] = 6830; R = 0.024, R_w = 0.030; n_v = 590, $|\Delta\rho_{max}|$ = 1.4 e Å^{-3}.

Variata: (x, y, z, U_{iso})$_H$ (all H) were refined. The unit cell dimensions of the Pr derivative are surprisingly similar to those of the La derivative, notwithstanding the clear and expected differences found in the Ln-N,O distances of the Ln coordination environments.

(b) x = 10

4b: Ln = Pr. M = 977.5. a = 16.416(1), b = 11.374(1), c = 11.0082(7) Å, α = 88.300(1), β = 72.577(1), γ = 70.863(1)°, V = 1847 Å^3. $D_{calcd.}$ = 1.75$_7$ g cm^{-3}; μ_{Mo} = 18.5 cm^{-1}; specimen: 0.29 × 0.20 × 0.18 mm; $T_{min/max}$ = 0.59 × $2\theta_{max}$ = 58°; N_t (CCD data) = 20623, N_r = 8994 (R_{int} = 0.068), N_o [$F > 4\sigma(F)$] = 7160; R = 0.078, R_w = 0.100; n_v = 481, $|\Delta\rho_{max}|$ = 5.9 e Å^{-3}.

Variata: Determinations of the members of this phase, although generally with larger specimen size, are inherently less precise than those of some other phases. Displacement parameters throughout the water molecules are generally high, some being modelled only with difficulty; associated hydrogen atoms were defined with reasonable certainty [though not for O(5,9)] but not refined, for the Ln = Er study, the present heavy and most precisely defined extremum.

5: Ln = Sm. M = 986.9. a = 16.302(6), b = 11.237(2), c = 10.978(2) Å, α = 88.26(1), β = 72.54(2), γ = 71.07(2)°, V = 1810 Å^3. $D_{calcd.}$ = 1.81$_1$ g cm^{-3}; μ_{Mo} = 21.6 cm^{-1}; specimen: 0.50 × 0.15 × 0.30 mm; $T_{min/max}$ = 0.83. $2\theta_{max}$ = 50°; N_t (sphere) = 12239, N_r = 6351 (R_{int} = 0.041), N_o [$I > 3\sigma(I)$] = 5735; R = 0.054, R_w = 0.074; n_v = 491, $|\Delta\rho_{max}|$ = 3.4 e Å^{-3}.

6: Ln = Tb. M = 995.5. a = 16.250(3), b = 11.227(1), c = 10.977(2) Å, α = 88.36(1), β = 72.48(2), γ = 71.23(1)°, V = 1803 Å^3. $D_{calcd.}$ = 1.83$_3$ g cm^{-3}; μ_{Mo} = 25.0 cm^{-1}; specimen: 0.55 × 0.18 × 0.45 mm; $T_{min/max}$ = 0.64. N_t (hemisphere to $2\theta_{max}$ = 50°, further hemisphere to 40°) = 11179, N_r = 8356 (R_{int} = 0.079), N_o [$I > 3\sigma(I)$] = 6851; R = 0.052, R_w = 0.068; n_v = 494, $|\Delta\rho_{max}|$ = 2.2 e Å^{-3}.

Variata: Hydrogen atoms were located in association with water molecule oxygen atoms O(1–3) only, for this adduct and for O(6–8) in addition for the Er adduct, for the Pr, Y and Sm adducts not at all.

7: Ln = Er. M = 1003.8. a = 16.216(2), b = 11.225(1), c = 10.982(1) Å, α = 88.377(2), β = 72.414(2), γ = 71.307(2)°, V = 1800 Å^3. $D_{calcd.}$ = 1.85$_2$ g cm^{-3}; μ_{Mo} = 28.8 cm^{-1}; specimen: 0.74 × 0.40 × 0.15 mm; $T_{min/max}$ = 0.54. $2\theta_{max}$ = 58°; N_t (CCD data) = 20903, N_r = 8768 (R_{int} = 0.035), N_o [$F > 4\sigma(F)$] = 7851; R = 0.039, R_w = 0.049; n_v = 491, $|\Delta\rho_{max}|$ = 3.0 e Å^{-3}.

8: Ln = Y. M = 925.5. a = 16.259(2), b = 11.275(1), c = 10.981(1) Å, α = 88.370(2), β = 72.389(2), γ = 71.239(2)°, V = 1811.$_5$ Å^3. $D_{calcd.}$ = 1.69$_7$ g cm^{-3}; μ_{Mo} = 21.5 cm^{-1}; specimen: 0.50 × 0.30 × 0.30 mm; $T_{min/max}$ = 0.66. $2\theta_{max}$ = 58°; N_t (CCD data) = 20168, N_r = 8886 (R_{int} = 0.036), N_o [$F > 4\sigma(F)$] = 5187; R = 0.060, R_w = 0.067; n_v = 491, $|\Delta\rho_{max}|$ = 2.1 e Å^{-3}.

(c) x = 8.5

9: Ln = Tm. M = 978.5. a = 16.250(6), b = 11.584(4), c = 10.449(4) Å, α = 110.905(9), β = 104.743(9), γ = 96.206(9)°, V = 1733 Å^3. $D_{calcd.}$ = 1.87$_5$ g cm^{-3}; μ_{Mo} = 31.2 cm^{-1}; specimen: 0.17 × 0.11 × 0.07 mm; $T_{min/max}$ = 0.79. $2\theta_{max}$ = 76°; N_t (CCD data) = 34830, N_r = 17907 (R_{int} = 0.033), N_o [$F > 4\sigma(F)$) = 12897; R = 0.041, R_w = 0.043; $|\Delta\rho_{max}|$ = 1.9 e Å^{-3}.

10: Ln = Lu. M = 984.5. a = 16.242(9), b = 11.591(5), c = 10.419(5) Å, α = 110.87(4), β = 104.96(5), γ = 96.05(4)°, V = 1728 Å^3. $D_{calcd.}$ = 1.91$_4$ g cm^{-3}; μ_{Mo} = 34.2 cm^{-1}; specimen: 0.18 × 0.30 × 0.35 mm; $T_{min/max}$ = 0.76. $2\theta_{max}$ = 50°; N_t (sphere) = 12081, N_r = 6091 (R_{int} = 0.069), N_o [$I > 3\sigma(I)$] = 4337; R = 0.048, R_w = 0.061; n_v = 480, $|\Delta\rho_{max}|$ = 2.9 e Å^{-3}.

Variata: The crystal decomposed isotropically by ca. 10% (as determined by periodic measures of standards), compensated by scaling. Water molecule hydrogen atoms were located in association with water molecule oxygen atoms O(1,5) only. O(9) has site occupancy 0.5; in the model for the Tm analogue, O(3–7) were modelled in terms of pairs of resolved fragments, with an additional fragment, "O(10)", hydrogen atoms only being located in association with O(1,2).

 © 2005 Wiley-VCH Verlag GmbH & Co. KGaA, Weinheim

11: $[Eu(dipicH)(dipic)(OH_2)_2]_{(\infty|\infty)}\cdot 4H_2O = C_{14}H_{19}EuN_2O_{14}$, M = 591.3. Monoclinic, space group $P2_1/c$ (C_{2h}^5, No. 14), a = 14.002(1), b = 11.2293(9), c = 12.845(1) Å, β = 102.492(1)°, V = 1972 Å^3. $D_{calcd.}$ (Z = 4) = 1.99$_1$ g cm^{-3}; μ_{Mo} = 32.6 cm^{-1}; specimen: 0.15 × 0.15 × 0.15 mm; $T_{min/max}$ = 0.84. $2\theta_{max}$ = 50°; N_t (CCD data) = 21787, N_r = 4999 (R_{int} = 0.025), N_o [$F > 4\sigma(F)$] = 4290; R = 0.025, R_w = 0.019; $|\Delta\rho_{max}|$ = 1.15(6) e Å^{-3}.

Variata: (x, y, z, U_{iso})$_H$ (all H) were refined. At the time of this determination, cell and coordinate settings were based upon those of the known La analogue.[14a,14b] In the present, Eu–N are 2.566(2), 2.564(2) Å, Eu−O(dipic) 2.433(2)–2.512(2) and Eu−O(water) 2.390(2)–2.440(2) Å.

CCDC-252240 to -252251 contain the supplementary crystallographic data for this paper. These data can be obtained free of charge from The Cambridge Crystallographic Data Centre via www.ccdc.cam.ac.uk/data_request/cif.

Acknowledgments

We thank Dr Jordi Rius (Barcelona) for calculation of the powder X-ray diffraction pattern expected for $[Co(NH_3)_6][Ce(dipic)_3]\cdot 5H_2O$, and the Australian Research Council for partial support of this work.

[1] a) P. A. Brayshaw, J-C. G. Bünzli, P. Froidevaux, J. M. Harrowfield, Y. Kim, A. N. Sobolev, *Inorg. Chem.* **1995**, *34*, 2068–2076; b) J. M. Harrowfield, Y. Kim, B. W. Skelton, A. H. White, *Aust. J. Chem.* **1995**, *48*, 807–823; c) P. A. Brayshaw, J. M. Harrowfield, A. N. Sobolev, *Acta Crystallogr. Sect. C* **1995**, *51*, 1799–1802.

[2] E. Hukowska, J. P. Riehl, *Inorg. Chem.* **1995**, *34*, 5615–5621 and references cited therein.

[3] J. Dexpert-Ghys, C. Picard, A. Taurines, *J. Incl. Phenom. Macrocyclic Chem.* **2001**, *39*, 261–267.

[4] N. Ouali, B. Bocquet, S. Rigault, P-Y. Morgantini, J. Weber, C. Piguet, *Inorg. Chem.* **2002**, *41*, 1436–1445; see also references given in ref.[1a]

[5] Structural studies of various hydrated salts of the tris(dipicolinato)lanthanide(III) anions not acknowledged in our earlier publications include a) S. Hu, Z. Dong, H. Zhang, Q. Liu, *J. Xi'an Med. Univ.* **1989**, *28*, 279–283, 514–518; b) T. Gin, J. Liu, H. Zhang, C. Huang, G. Xu, Y. Han, N. Shi, *J. Chin. Rare Earth Soc.* **1991**, *9*, 97–100. Recent spectroscopic work has included corroboration of early structural data (see references [17–20] on $Na_3[Ln(dipic)_3]\cdot 13H_2O$ species; c) C. Reinhard, H. U. Güdel, *Inorg. Chem.* **2002**, *41*, 1048–1055. Some related $Ln_2(dipic)_3$ species have been recently characterised by structural studies, see d) S. K. Ghosh, P. K. Bharadwaj, *Inorg. Chem.* **2004**, *43*, 2293–2298.

[6] A. Roy, K. Nag, *J. Inorg. Nucl. Chem.* **1978**, *40*, 1501–1505.

[7] P. S. Devi, M. S. Rao, *Mater. Lett.* **1993**, *16*, 14–21.

[8] M. Insausti, M. K. Urtiaga, R. Cortés, J. L. Mesa, M. I. Arriortua, T. Rojo, *J. Mater. Chem.* **1994**, *4*, 1867–1870.

[9] Y. Sadaoka, E. Traversa, M. Sakamoto, *Chem. Lett.* **1996**, 177–178.

[10] P. S. Devi, M. S. Rao, *J. Therm. Anal.* **1997**, *48*, 909–916.

[11] A. Gonzalez, E. Martinez Tamayo, A. Beltran Porter, V. Cortes Corberan, *Catal. Today* **1997**, *33*, 361.

[12] See, for example: L. G. Tejuca, J. L. G. Fierro, J. M. D. Tascon, *Adv. Catal.* **1989**, *36*, 237–328; D. J. M. Bevan, E. Summerville (chapter 28), C. P. Khattak, F. F. Y. Wang (chapter 29), in: *Handbook on the Chemistry and Physics of the Rare Earths* (Eds.: K. A. Geschneidner, Jr., L. Eyring), vol. 3, North-Holland, Amsterdam, **1978**.

[13] M. Chen, H-Q. Huang, X-M. Zheng, M. A. Morris, *Aust. J. Chem.* **2002**, *55*, 757–760.

[14] a) (Ln = La) P. Gurriero, U. Castellato, S. Sitran, P. A. Vigato, R. Graziani, *Inorg. Chim. Acta* **1987**, *133*, 337–345; b) (Ln = Nd) J-L. Wang, T-Z. Jin, J-K. Liu, H-Z. Zhang, C-H. Huang, *Chinese J. Inorg. Chem. (Wuji Huaxe Xuebao)* **1992**, *8*, 180–183; c) (Ln = Eu, Gd, Tb, Dy, Ho, Er, Yb) A. Fernandes, J. Dexpert-Ghys, C. Brouca-Cabarrecq, *Polyhedron* **2001**, *20*, 2385–2391; d) (Ln = Ce, Pr) S. K. Ghosh, P. K. Bharadwaj, *Inorg. Chem.* **2003**, *42*, 8250–8254.

[15] J. M. Harrowfield, B. W. Skelton, A. H. White, submitted to *Cryst. Growth Des.* **2004**.

[16] D. A. House, in: *Comprehensive Coordination Chemistry* (Eds.: J. A. McCleverty, R. D. Gillard, G. Wilkinson), Pergamon Press, Oxford, **1987**, vol. 2, Ch. 13.1, p. 21, provides a summary of structural data relating to various $[Co(NH_3)_6]^{3+}$ salts.

[17] J. Albertsson, *Acta Chem. Scand.* **1970**, *24*, 1213–1229.

[18] J. Albertsson, *Acta Chem. Scand.* **1972**, *26*, 1023–1044.

[19] J. Albertsson, *Acta Chem. Scand.* **1972**, *26*, 1005–1017.

[20] J. Albertsson, *Acta Chem. Scand.* **1972**, *26*, 985–1004.

[21] G. Swarnabala, M. V. Rajasekharan, *Inorg. Chem.* **1998**, *37*, 1483–1485.

[22] A. K. Hall, J. M. Harrowfield, B. W. Skelton, A. H. White, *Acta Crystallogr., Sect. C* **2000**, *56*, 407–411.

[23] Comprehensive analyses of both "offset face-to-face" (conventional π- stacking) and "edge-to-face" interactions between aromatic groups in metal complexes have been given by a) W. B. Jennings, B. M. Farrell, J. F. Malone, *Acc. Chem. Res.* **2001**, *34*, 885–895; b) V. Russell, M. L. Scudder, I. G. Dance, *J. Chem. Soc. Dalton Trans.* **2001**, 789–799; b) I. G. Dance, M. L. Scudder, *J. Chem. Soc. Chem. Commun.* **1995**, 1039–1040; *Chem. Eur. J.* **1996**, *2*, 481–486; *J. Chem. Soc. Dalton Trans.* **1996**, 2755–2769; **1998**, 1341–1350, 3155–3166, 3167–3176; c) C. Janiak, *J. Chem. Soc. Dalton Trans.* **2000**, 3885; d) Z-H. Liu, C-Y. Duan, J-H. Li, Y-J. Liu, Y-H. Mei, X-Z. You, *New J. Chem.* **2000**, *24*, 1057–1062.

[24] a) See:J. M. Harrowfield, *J. Chem. Soc. Dalton Trans.* **1996**, 3165–3171 and references cited therein; b) L. Troxler, J. M. Harrowfield, G. Wipff, *J. Phys. Chem. A* **1998**, *102*, 6821–6830; c) J. M. Harrowfield, R. P. Sharma, T. M. Shand, B. W. Skelton, A. H. White, *Aust. J. Chem.* **1998**, *51*, 707–722; d) J. M. Harrowfield, R. P. Sharma, B. W. Skelton, A. H. White, *Aust. J. Chem.* **1998**, *51*, 723–734; e) J. M. Harrowfield, R. P. Sharma, B. W. Skelton, A. H. White, *Aust. J. Chem.* **1998**, *51*, 735–745; f) J. M. Harrowfield, R. P. Sharma, B. W. Skelton, A. H. White, *Aust. J. Chem.* **1998**, *51*, 747–760; g) J. M. Harrowfield, R. P. Sharma, B. W. Skelton, A. H. White, *Aust. J. Chem.* **1998**, *51*, 761–774; h) J. M. Harrowfield, R. P. Sharma, B. W. Skelton, P. Vengulopalam, A. H. White, *Aust. J. Chem.* **1998**, *51*, 775–784; i) J. M. Harrowfield, R. P. Sharma, B. W. Skelton, A. H. White, *Aust. J. Chem.* **1998**, *51*, 785–793.

[25] a) S. Burnet, A. K. Hall, J. M. Harrowfield, G. A. Koutsantonis, V. Sanford, D. Sauter, B. W. Skelton, A. H. White, *Supramol. Chem.* **2003**, *15*, 291–312; b) A. A. Soudi, J. M. Harrowfield, G. H. Shahverdizadeh, *Supramol. Chem.* **2003**, *15*, 367–373.

[26] J. M. Harrowfield, G. A. Koutsantonis, B. W. Skelton, A. J. Strong, A. H. White, submitted to *Cryst. Growth Des.* **2004**.

[27] J. M. Harrowfield, G. A. Koutsantonis, G. L. Nealon, B. W. Skelton, A. H. White, submitted to *Inorg. Chem.* **2004**.

[28] J-C. G. Bünzli, P. Froidevaux, J. M. Harrowfield, *Inorg. Chem.* **1993**, *32,* 3306–3311.

[29] See, for example: R. J. Geue, M. R. Snow, *Inorg. Chem.* **1977**, *16*, 231–241; H. Okazaki, U. Sakaguchi, H. Yoneda, *Inorg. Chem.* **1983**, *22*, 1539–1542 and references cited therein.

[30] M. W. Hosseini, R. Ruppert, P. Schaeffer, A. De Cian, N. Kyritsakas, J. Fischer, *J. Chem. Soc. Chem. Commun.* **1994**, 2135–2136.

[31] P. Lainé, A. Gourdon, J-P. Launay, *Inorg. Chem.* **1995**, *34*, 5129–5137.

[32] D. B. Wiles, R. A. Young, *J. Appl. Crystallogr.* **1981**, *14*, 149–151.

 © 2005 Wiley-VCH Verlag GmbH & Co. KGaA, Weinheim

[33] R. J. Hill, C. J. Howard, *AAEC Report* **1986**, *M112*.
[34] I. C. Madsen, R. J. Hill, *Powder Diffraction* **1990**, *5*, 195–199.
[35] A. C. Larson, R. V. von Dreele, *GSAS User Guide*, Los Alamos National Laboratory, New Mexico, USA, **1995**.
[36] A. S. Wexler, J. H. Seinfeld, *Atmospheric Environment* **1991**, *25A*, 2731–2748.
[37] Y. Ni, J. M. Hughes, A. N. Mariano, *Amer. Miner.* **1995**, *80*, 21–26.
[38] K. J. Range, H. Meister, U. Klement, *Zeit. Naturforsch.* **1990**, *B45*, 598–602.
[39] JCPDS Card 16–880.
[40] R.D Shannon, *Acta Crystallogr. Sect. A* **1976**, *32*, 751–767.
[41] M. Taylor, R. C. Ewing, *Acta Crystallogr. Sect. B* **1978**, *34*, 1074–1079.
[42] A. Morales-Sanchez, F. Fernandez, *J. Alloys and Compounds* **1963**, *201*, 161–165; H. Walter, H. G. Kahle, K. Mulder, H. C. Schopper, H. Schwarz, *Int. J. Magnetism* **1973**, *5*, 129–135;E. F. Bertraut, G. Bassi, G. Buisson, P.Burlet, J. Chappert, A. Delapalme, J. Mareschal, G. R. Rault, R. Aleonard, R. Pauthenet, J. B. Rebouillat, *J. Appl. Phys.* **1966**, *37*, 1038–1039.
[43] P. Lainé, A. Gourdon, J-P. Launay, *Inorg. Chem.* **1995**, *34*, 5138–5149, 5150–5155, 5156–5165.
[44] R. B. Martin, *Chem. Rev.* **1996**, *96*, 3043–3064.
[45] G. Buisson, F. Bertaut, J. Mareschal, *C. R. Acad. Sci. Paris* 19**64**, *259*, 411–415.
[46] A. J. C. Wilson (Ed.), *International Tables for Crystallography*, vol. C, Kluwer Academic Publishers, Dordrecht, **1992**.
[47] J. M. Harrowfield, Lu Weimin, B. W. Skelton, A. H. White, *Aust. J. Chem.* **1994**, *47*, 321–337.
[48] J. M. Harrowfield, Lu Weimin, B. W. Skelton, A. H. White, *Aust. J. Chem.* **1994**, *47*, 339–348.
[49] J. M. Harrowfield, Lu Weimin, B. W. Skelton, A. H. White, *Aust. J. Chem.* **1994**, *47*, 349–358.
[50] J. M. Harrowfield, Lu Weimin, B. W. Skelton, A. H. White, *Aust. J. Chem.* **1994**, *47*, 359–364.
[51] C. J. Kepert, Lu Weimin, B. W. Skelton, A. H. White, *Aust. J. Chem.* **1994**, *47*, 365–384.
[52] J. M. Harrowfield, D. L. Kepert, J. M. Patrick, A. H. White, *Aust. J. Chem.* **1983**, *36*, 483–492.
[53] a) S. R. Hall, G. S. D. King, J. M. Stewart (Eds.), *The Xtal 3.4 User's Manual* (University of Western Australia: **1995**); b) S. R. Hall, D. J. Du Boulay, R. Olthof-Hazekamp (Eds.) *The Xtal 3.7 System*, University of Western Australia, **2000**.

Received: October 14, 2004

 © 2005 Wiley-VCH Verlag GmbH & Co. KGaA, Weinheim

In vitro Relaxometric and Luminescence Characterization of P792 (Gadomelitol, Vistarem®), an Efficient and Rapid Clearance Blood Pool MRI Contrast Agent

Luce Vander Elst,[a] Isabelle Raynal,[b] Marc Port,[b] Pierre Tisnès,[c] and Robert N. Muller*[a]

Keywords: P792 / MRI contrast agent / NMRD / Luminescence / Oxygen-17 relaxometry

P792 (Gadomelitol, Vistarem®), a hydrophilic high molecular weight (MW = 6473 g/mol) derivative of DOTA-Gd is a rapid clearance blood pool agent (RCBPA) characterized by high proton relaxivities r_1 and r_2 at 310 K in the current range of clinical imaging magnetic fields. Luminescence data of the Eu^{III} complex, as expected for this type of DOTA derivative, agree with the presence of one water molecule in the first coordination sphere of the lanthanide ion. The stability of the water proton longitudinal relaxation rate in the presence of zinc(II) and phosphate ions showed that the transmetallation by Zn^{II} ions is negligible. The temperature dependence of the water oxygen-17 transverse relaxation rate gave a τ_M smaller than 100 ns at 310 K. No significant increase of longitudinal or transverse relaxation rates in serum or HSA solution was noticed, precluding association with high molecular weight blood components. The proton Nuclear Magnetic Relaxation Dispersion (NMRD) profile of the water solution showed a maximum of longitudinal relaxivity between 20 and 40 MHz ($r_1 \approx 40\ s^{-1}\,mM^{-1}$ at 310 K). Fitting of the proton NMRD curve by the classical outersphere and innersphere models, including or not additional second sphere water molecules, gave a rotational correlation time of approximately 2 to 3 ns and a large value of the electronic relaxation time at low field ($\tau_{SO} \approx 500$ ps).
(© Wiley-VCH Verlag GmbH & Co. KGaA, 69451 Weinheim, Germany, 2005)

Introduction

The development of new paramagnetic MRI contrast agents with high relaxivity usually involves the decrease of their rotational mobility by covalent or non-covalent binding to endogenous or exogenous macromolecules.[1–5] The resulting bulky contrast agents are confined in the vascular space and their renal excretion is reduced. Recently, medium molecular weight ($MW > 5000$ g/mol) contrast agents based on the DOTA-Gd structure tetra-substituted by hydrophilic arms have been developed. For example, P760 (MW = 5.3 kDa) is a low diffusion agent which extravasates at a slow rate through the vascular endothelium but is freely excreted by the kidneys.[6–8] Due to a long rotational correlation time ($\tau_R \approx 2$ ns at 310 K) its proton relaxivity is quite large, with a maximum around $25\ s^{-1}\,mM^{-1}$ observed between 0.35 and 1.4 T.[9]

Another macromolecular DOTA-Gd structure, P792 (Gadomelitol, Vistarem®, MW = 6.47 kDa) has proved also to be a rapid clearance blood pool agent (RCBPA) (Figure 1) with a limited diffusion across the normal endothelium.[6,8] It is mainly excreted by glomerular filtration and has been reported to be well suited for high-quality first-pass and equilibrium-phase MR angiography,[10] visualization of the coronary arteries and their branches,[11] assessment of viability of infarcted myocardium,[12] differentiation of tumor-bearing lymph nodes from reactive inflammatory and normal nodes,[13] and for the distinction between metastatic and relatively benign cancers.[14] A phase I clinical trial has established its safety in humans.[15] In a previous study,[8] some physicochemical parameters were reported like its high proton relaxivity at 20, 40, and 60 MHz and at body temperature. This work aims at extending these preliminary data with a comprehensive in vitro physicochemical characterization encompassing luminescence and oxygen-17 relaxometry and an investigation of the possible non-covalent interaction with blood proteins as well as the analysis of the proton NMRD profile and the determination of related physical parameters.

[a] Department of Organic and Biomedical Chemistry, NMR and Molecular Imaging Laboratory, University of Mons-Hainaut, 7000 Mons, Belgium
Fax: +32-65-37-35-20
E-mail: robert.muller@umh.ac.be
[b] Guerbet, Research Department, 95943 Roissy Cdg Cedex, France
[c] Laboratoire de Synthèse et Physicochimie de Molécules d'Interêt Biologique / UMR 5068, Université Paul Sabatier, 118 route de Narbonne 31062 Toulouse Cedex 4, France

Results and Discussion

Luminescence of the Europium Complex

According to Horrocks and Sudnick,[16] the difference in the decay rate of Eu^{3+} luminescence in H_2O ($1/\tau_{H_2O(ms)}$) and

 DOI: 10.1002/ejic.200400919

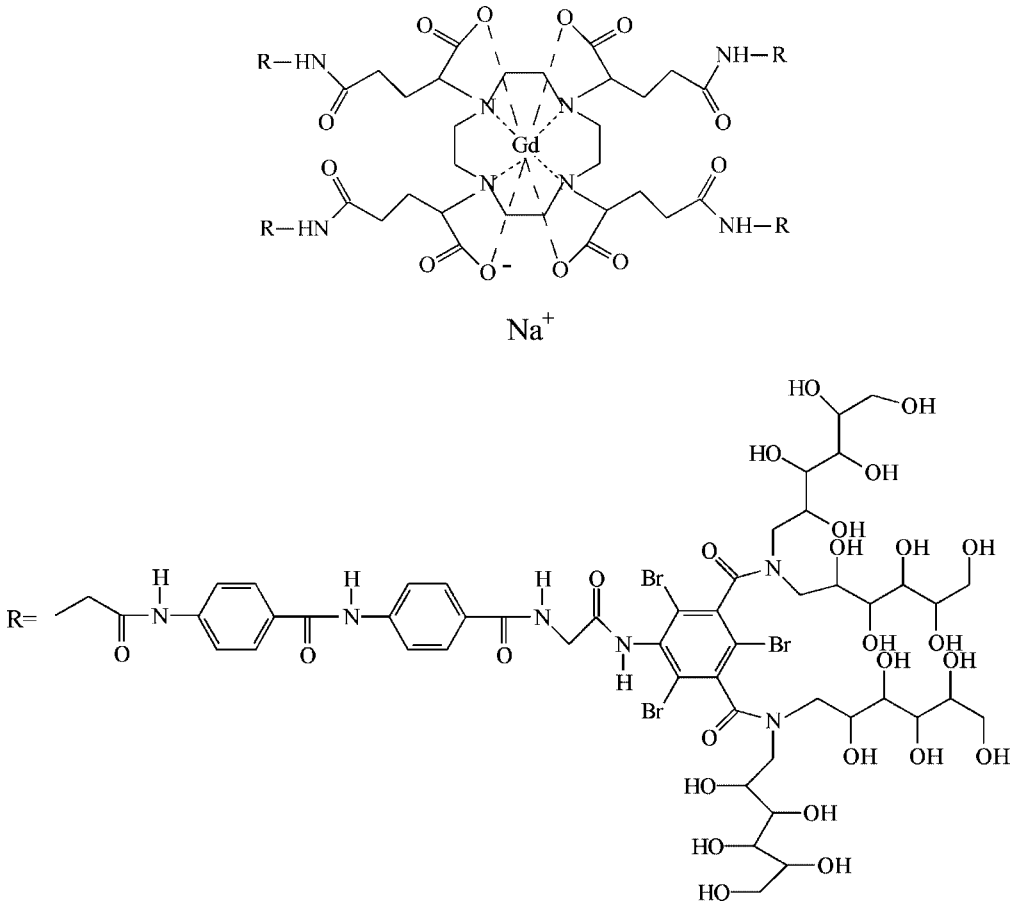

Figure 1. Chemical structure of P792.

D_2O ($1/\tau_{D_2O(ms)}$) solutions depends on the number of water molecules (q) in the first coordination sphere of the complex [Equation (1)]. More recently, Beeby et al.[17] included in the relevant equation the contribution from water molecules diffusing close to the Ln^{3+} complex and from other protons behaving as exchangeable oscillators [Equation (2)]. The measured luminescence lifetimes of P792-Eu in H_2O and D_2O were 0.71 ms and 2.32 ms, respectively. The corresponding calculated q values are 1.02 using Horrock's equation or 0.87 according to Beeby et al.

$$q = 1.05 \cdot \left(\frac{1}{\tau_{H_2O}} - \frac{1}{\tau_{D_2O}}\right) \quad (1)$$

$$q_{corr} = 1.2 \cdot \left(\frac{1}{\tau_{H_2O}} - \frac{1}{\tau_{D_2O}} - 0.25\right) \quad (2)$$

where τ is the lifetime (in ms) of the complex in H_2O and D_2O.

These values agree with the q value reported for the precursor P730.[18,19] As expected, the Gd^{III} ion is thus coordinated to the four nitrogen atoms of the macrocycle, the four carboxylate groups, and one water molecule.

Oxygen-17 Relaxometry of the Gadolinium Complex

The residence time of the coordinated water molecule is a very important parameter likely to limit the innersphere relaxivity of gadolinium complexes and more particularly of bulky structures. In such complexes, the expected enhancement in relaxivity resulting from the slow tumbling of the complex can indeed be quenched by a too slow water exchange.

It is well established that the exchange rate of the water molecule in the first coordination sphere of Gd^{3+} can be determined by analyzing the temperature dependence of the paramagnetic transverse relaxation rate ($R_2p = 1/T_2p$) of the oxygen-17 NMR signal of the aqueous solution.[20–22] The temperature dependence of ^{17}O R_2 was, therefore studied from 290 K to 357 K (Figure 2). Lower temperatures were not investigated to avoid problems related to an increase in viscosity. The qualitative analysis of the transverse relaxation rate data indicates that the water exchange

 © 2005 Wiley-VCH Verlag GmbH & Co. KGaA, Weinheim

is quite fast. Moreover, the much larger values obtained for the longitudinal relaxation rates of P792 as compared to those of DOTA-Gd[22] agree with a complex of higher molecular weight.

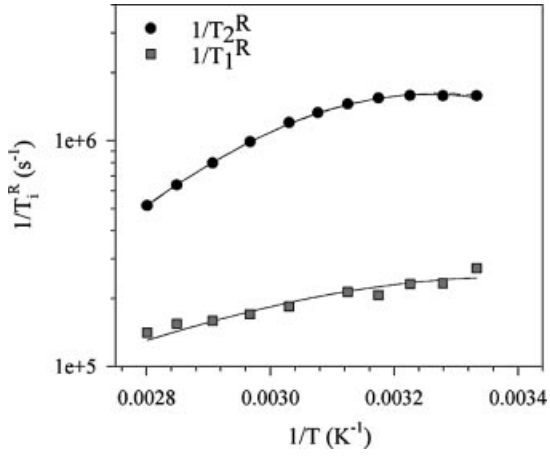

Figure 2. Reduced transverse $\{1/T_2R = 55.55/(T_2p^*[Gd\ complex])\}$ and longitudinal ^{17}O relaxation rate of water in P792 solution as a function of the reciprocal of temperature.

Quantitative analyses of the experimental data were performed with or without quadrupolar contribution, leading to 2 sets of values (Table 1). The first fitting of the experimental data was performed on the transverse relaxation rates with a model where the transverse relaxation rate of the bound nuclei of ^{17}O ($1/T_{2M}$) results mainly from scalar interaction with the gadolinium ion as described in ref.[20]. The second fitting was performed simultaneously on the transverse and longitudinal relaxation rate data with a model taking into account quadrupolar and dipolar contributions for $1/T_{1M}$ and quadrupolar and scalar contributions for $1/T_{2M}$.[9]

Table 1. Parameters obtained from the fitting of the transverse and longitudinal relaxation rates of oxygen-17.

	Without quadrupolar contribution	With quadrupolar contribution
τ_V^{298} [ps]	11.8 ± 0.3	12.8 ± 1.1
B [10^{20} s^{-2}]	4.06 ± 0.10	3.45 ± 0.41
E_v [kJ/mol]	0.9 ± 44.0	1.4 ± 1.5
$2\pi A/h$ [10^6 rad s^{-1}]	–4.46 ± 0.03	–3.95 ± 0.36
$\Delta H^{\#}$ [kJ/mol]	46.3 ± 0.09	46.9 ± 0.3
$\Delta S^{\#}$ [J/mol·K]	40.3 ± 1.3	40.6 ± 0.3
τ_M^{310} [ns]	79.6 ± 5.0	95.7 ± 14.9
τ_R^{298} [ns]		3.2 ± 0.2
τ_R^{310} [ns]		2.4 ± 0.2
E_R [kJ/mol]		17.0 ± 0.2
χ [MHz]		6.60 ± 0.35

The following parameters are simultaneously determined:
i) The hyperfine coupling constant between the oxygen-17 nucleus and the electronic spin of Gd^{3+} ($2\pi A/h$);
ii) the parameters related to the electronic relaxation times (τ_{S1} and τ_{S2}), i.e. the correlation time for the modulation of the zero field splitting (τ_V), the activation energy for this process (E_V), and B which depends on the trace of the square of the zero field splitting tensor (Δ^2) and on the electron spin S ($B = \Delta^2\{4S(S + 1) - 3\}/25$);
iii) the parameters of the water exchange rate, i.e. the enthalpy ($\Delta H^{\neq}$) and the entropy ($\Delta S^{\neq}$) of activation;
iv) the rotational correlation time τ_R and the activation energy for the rotation (E_R), as well as a term related to the quadrupolar coupling constant and the asymmetry parameter of ^{17}O ($\chi = [1 + \eta^2/3]^{1/2}[2\pi e^2qQ/h]$) when the quadrupolar contribution is taken into account.

The fitted value of τ_M obtained with the first model is approximately 80 ns at 310 K, a value close to that of the parent complex DOTA-Gd ($\tau_M^{310} \approx 97$ ns[22]). When the quadrupolar contribution is taken into account, the data from both longitudinal and transverse relaxation rates were fitted simultaneously and the distance between the gadolinium ion and the oxygen nucleus of the coordinated water molecule was set to 0.25 nm.[22] The fitted value of τ_M^{310} was then slightly larger (≈ 96 ns) and the τ_R^{310} value was equal to 2.4 ns, a value slightly larger than that obtained for P760 a compound of rather similar size and shape.[9] Such values of τ_M^{310} although not optimal to ensure a maximum relaxivity are not too large and, if any, their influence on the proton relaxivity should be small or moderate.

Transmetallation by Zn^{2+} Ions

The suitability of paramagnetic complexes as MRI contrast agents depends not only on their relaxivity but also on various other factors, among which is their inertness towards transmetallation by endogenous ions like Zn^{2+}. This can be assessed in vitro by H-1 relaxometry since, as already reported, transmetallation of gadolinium complexes by Zn^{2+} ions induces a release of Gd^{3+} ions which are trapped in a buffered solution containing phosphate ions. The subsequent decrease of the water proton relaxation rate quantitatively reflects the extent of the transmetallation process.[23] In the context of this protocol, the relaxation rate of macrocyclic gadolinium complexes like DOTA-Gd, HPDO3A-Gd [tris(carboxymethyl)-10-(2-hydroxypropyl)-1,4,7,10-tetraazacyclododecane gadolinium(III)], and P760 does not vary, whereas R_1p drops to about 53% of its initial value for DTPA-Gd, 18% for DTPA-BMA-Gd, and 85% for MS-325 after 1900 minutes showing that a significant transmetallation takes place for these open-chain gadolinium complexes.[9,23,24] For P792, lower concentrations of the complex and of Zn^{2+} were used (0.8 mM and 0.87 mM, respectively, instead of 2.5 mM in the original protocol). The data were thus compared to those obtained for DTPA-Gd at identical concentration ([DTPA-Gd] = 0.8 mM and [Zn^{2+}] = 0.87 mM). No significant evolution of the proton paramagnetic relaxation rate was observed for P792 over a period of more than 3000 minutes. This agrees with the absence of transmetallation by Zn^{2+} ions. In the same conditions, the R_1p of DTPA-Gd decreased by about 60% during the same period (Figure 3). These data confirm the very high kinetic and thermodynamic stabilities of DOTA-like

 © 2005 Wiley-VCH Verlag GmbH & Co. KGaA, Weinheim

complexes of gadolinium as compared to DTPA-like complexes.[23,24]

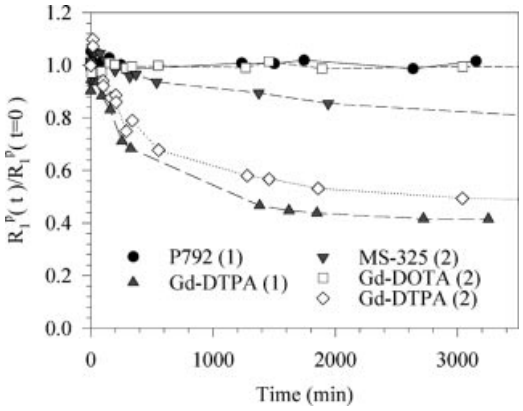

Figure 3. Evolution of the ratio $R_1p(t)/R_1p(t = 0)$ with time for solutions containing $ZnCl_2$ and P792 (circles), DTPA-Gd (up triangles and diamonds), MS-325 (down triangles), DOTA-Gd (squares). The experimental conditions are: (1): $ZnCl_2$ (0.87 mM) and complex-Gd (0.80 mM) at pH 7.0 and 37 °C (B_0 = 0.47 T) and (2): $ZnCl_2$ 2.5 mM and complex-Gd (2.5 mM) at pH 7.0 and 310 K (B_0 = 0.47 T).

Proton NMRD Profile

The proton longitudinal relaxation rates were measured at 310 K between 0.01 MHz and 300 MHz on 0.285 mM and 1 mM solutions of P792; the transverse relaxation rates were measured at 20 MHz, 60 MHz and 300 MHz. The calculated relaxivities (the relaxation rate enhancement brought by one millimol per liter of the gadolinium complex) vs. proton Larmor frequencies (proton NMRD profile) are shown on Figure 4.

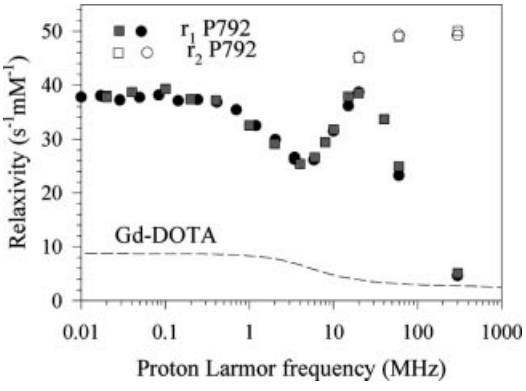

Figure 4. Proton NMRD data obtained at 310 K on a 0.285 mM solution (closed squares: r_1, open squares: r_2) and on a 1 mM solution (closed circles: r_1, open circles: r_2). The proton NMRD profile of DOTA-Gd (dashed line) has been added for comparison.

The longitudinal relaxivities show a hump at high magnetic fields in good agreement with the large size of the gadolinium complex and thus with its slow rotation. The values are remarkably larger, not only as compared to the parent complex DOTA-Gd, but also with respect to another large molecular weight derivative, the P760.[9] Longitudinal relaxivity reaches its maximum (38–40 s^{-1} mM^{-1}) between 15 and 40 MHz (0.35 and 0.94 T) while the transverse relaxivity levels off above 50 MHz (1.18 T).

In a first approach, ^1H NMRD curves were fitted according to the classical innersphere model described by Solomon[25] and Bloembergen[26] and to the outersphere model described by Freed.[27] In these fittings, the number of water molecules coordinated to the Gd^{3+} ion was fixed to 1 in agreement with the luminescence data. Some other parameters were also fixed: r, the distance between the proton nuclei of the innersphere water molecule and the Gd^{3+} (0.31 nm); D, the relative diffusion constant (3×10^{-9} $m^2 s^{-1}$); and d, the distance of closest approach for the outersphere contribution (0.36 nm[28,29]). τ_V and τ_{SO} (the electronic relaxation time at zero field), describing the elec-

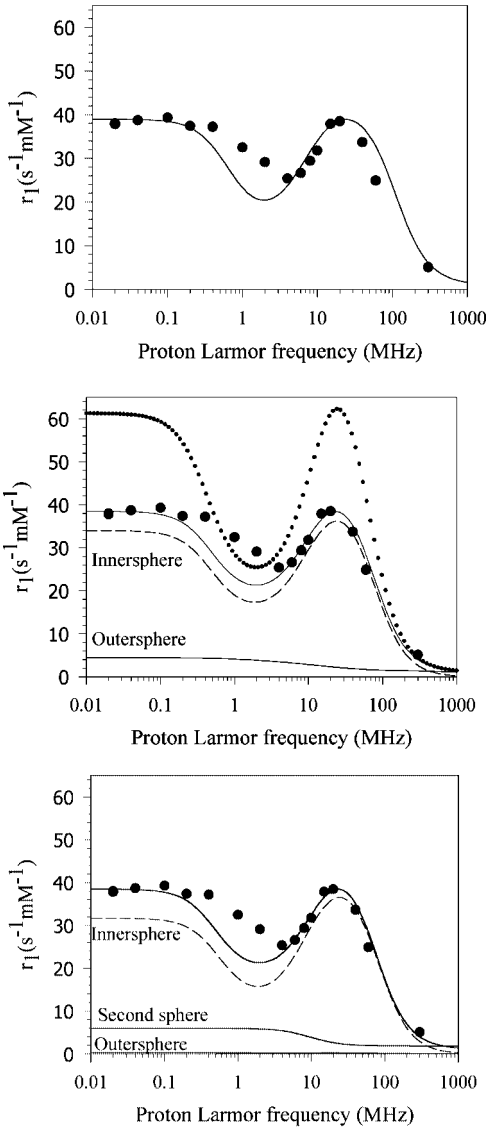

Figure 5. Theoretical fittings of the proton NMRD data obtained at 310 K using outersphere and innersphere models with τ_M fixed to 96 ns or τ_M adjusted (top and middle graphs; respectively) and using outersphere and innersphere models with second sphere water molecules included (bottom graph). The dotted line in the middle graph corresponds to the theoretical optimal relaxivity calculated with τ_M optimum (τ_M = 20–30 ns).

 © 2005 Wiley-VCH Verlag GmbH & Co. KGaA, Weinheim

tronic relaxation times, were optimized for the outersphere and the innersphere contributions simultaneously. τ_R was allowed to fluctuate around the values obtained by ^{17}O NMR and τ_M was fixed to 96 ns. A $\tau_R{}^{310}$ value of 1.7 ns and a τ_{SO} value of 538 ps were obtained but in the high field region, the fitted values are larger than the experimental ones (Figure 5 and Table 2). A second adjustment was therefore performed in which τ_M was adjusted. A satisfactory fit of the data could be obtained at low fields and at high fields with a $\tau_R{}^{310}$ value of 3.2 ns and a τ_M value of 240 ns (Figure 5 and Table 2). These values are significantly larger than those determined by ^{17}O NMR (2.4 ns and 80–96 ns, respectively). The τ_{SO} value is also larger than that reported for the parent compound DOTA-Gd ($\tau_{SO}{}^{310}$ = 480 ps).[22] These discrepancies could be explained by the fact that the model used to fit the ^1H NMRD curve is not the most appropriate to describe the behavior of slowly tumbling paramagnetic molecules.[30] They also could result from the presence of a second sphere of water molecules due to the hydrophilic nature of the substituents of the macrocyclic core of P792.

Table 2. Parameters obtained from the fitting of the proton NMRD profile of P792 at 310 K.

	Theoretical model with innersphere and outersphere water molecules; τ_M set to 96 ns	Theoretical model with innersphere and outersphere water molecules; τ_M adjusted	Theoretical model with innersphere, outersphere and second sphere water molecules
d [nm]	0.36	0.36	0.45
D [10^{-9} m^2 s^{-1}]	3.0	3.0	3.0
r [nm]	0.31	0.31	0.31
τ_R [ns]	1.7	3.2	2.7
τ_M [ns]	96	240	200
τ_{SO} [ps]	538	730	520
τ_V [ps]	40	26	29
τ_{SS} [ps]			25
r_{ss} [nm]			0.40
q_{ss}			10

In a third approach, the interaction between the gadolinium ion and water molecules in its second sphere was therefore included in the theoretical model.[31] The hydrogen atoms of these water molecules were assumed to be at a distance of 0.4 nm and the distance of closest approach was set to 0.45 nm. The experimental data were fitted, as shown in Figure 5, with a $\tau_R{}^{310}$ value of 2.7 ns which is similar to the value obtained above by the analysis of the paramagnetic longitudinal rate of oxygen-17. The value found for τ_M (200 ns) is closer to the value obtained by oxygen-17 NMR spectroscopy. The τ_{SO} (520 ps) and τ_V (29 ps) values are also in better agreement with those reported for the parent compound DOTA-Gd. In this fitting, 10 water molecules are found in the second sphere. Their interaction with the paramagnetic center is modulated by a correlation time called τ_{SS} which depends on the rotational correlation time and on the residence time of the second sphere water molecules. A value of 25 ps was found. However, it should be pointed out that both last fittings give similar results and that the choice of the "best" theoretical model is quite subjective.

Nevertheless, it emerges from these data that the rotational correlation time is approximately equal to 2–3 ns at 310 K and that the value of the electronic relaxation rate at low fields is similar to that of the parent complex DOTA-Gd.

Finally, it can be calculated that the observed relaxivity is not optimal and that values of the order of 60 s^{-1} mM^{-1} between 20–60 MHz could be obtained if the water residence time was of the order of 20–30 ns (Figure 5).

Interaction of P792 with Blood Proteins

When small gadolinium complexes bind non-covalently to HSA, an increase of their paramagnetic relaxation rate is usually observed at magnetic fields ranging from 10 to 60 MHz due to the slowing down of the rotational motion of the bound complex. Proton relaxation rate measurements were thus performed at 20 and 60 MHz and 310 K on P792 (0.46 mM) solutions in human serum (Table 3). The increase of the longitudinal and transverse apparent relaxivities is minimal and can be explained by the slight increase in viscosity of the medium as compared to water solution. Alternatively, these data show either the absence of interaction between P792 and blood proteins, or that there is an interaction but that the rotational correlation time of the paramagnetic center is not significantly modified by the binding.

Table 3. Apparent relaxivities in water and human serum solutions of 0.46 mM of P792 at 310 K.

	20 MHz	60 MHz
r_1 [s^{-1} mM^{-1}] (water)	42 ± 1.5	26.7 ± 0.6
$r_1$app [s^{-1} mM^{-1}] (serum)	47.7 ± 1.0	26.9 ± 0.5
r_2 [s^{-1} mM^{-1}] (water)	50 ± 1.4	53.3 ± 2.9
$r_2$app [s^{-1} mM^{-1}] (serum)	59.4 ± 1.3	65.1 ± 1.5

The influence of HSA 4% on the longitudinal and transverse NMRD profiles was also investigated (Figure 6). The

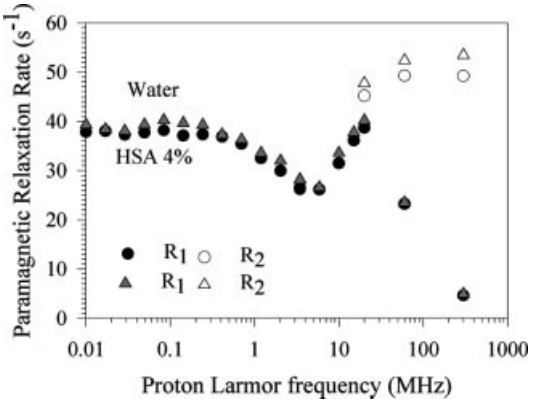

Figure 6. Proton NMRD data obtained at 310 K on a 1 mM solution in water (closed circles: R_1p, open circles: R_2p) and HSA 4% (closed triangles: R_1p, open triangles: R_2p).

 © 2005 Wiley-VCH Verlag GmbH & Co. KGaA, Weinheim

similarity of the paramagnetic R_1 data over the whole range of magnetic fields and of the paramagnetic R_2 data at high fields confirms that P792 does not bind to serum albumin.

The absence of a significant interaction with blood proteins must be related to the observed relatively fast clearance of P792 from mice plasma ($t_{1/2}\beta$ = 22 min)[6] or from rabbit plasma ($t_{1/2}\beta$ = 41 min)[8] as compared to the much larger values reported for MRI contrast agents like MS-325 ($t_{1/2}\beta$ = 155 min in rabbits)[32] and MP2269 ($t_{1/2}\beta$ = 142 min in rabbits);[33] known for their interaction with HSA.

Conclusions

P792, a new tetra-substituted macromolecular DOTA-Gd derivative, is a very interesting MRI contrast agent due to its hydrophilic properties, its very high longitudinal and transverse relaxivities in the imaging magnetic fields (> 30 $s^{-1}mM^{-1}$), and its very high stability with respect to Zn^{II} transmetallation. This complex, which does not bind significantly to serum proteins, is consequently cleared very rapidly by the kidneys. On the other hand, its in vivo relaxivity is independent of concentration; unlike what is observed for contrast agents binding to serum albumin.[34,35]

Experimental Section

Chemicals: All commercial chemicals [$ZnCl_2$ (Merck) and Titrisol buffer pH 7.0 (Merck)] were used without further purification. Non-defatted human albumin (fraction V) was purchased from Sigma (Bornem, Belgium). The synthesis of P792 has been described previously.[7]

Luminescence Studies on the Eu Complex: The Eu^{III} phosphorescence emission spectra were acquired with an LS-50B Perkin–Elmer spectrofluorimeter equipped with a pulsed Xenon lamp and a Hamamatsu R928 photomultiplier tube operating in time-resolved mode. 7×10^{-3} M and 5.5×10^{-3} M solutions of the Eu^{III} complex in H_2O and D_2O, respectively, were used in these experiments. Lifetimes (τ) were obtained by monitoring the emission intensity at 616 nm, resulting from pulsed excitation at 395 nm. Excitation and emission slit widths of 5 nm and 20 nm were used, respectively, and the gate time was 0.4 ms. 160 (H_2O) or 260 (D_2O) different delay times were used. The decays of the europium emitting state were fitted by an equation of the form $I(t) = I(0)\exp(-t/\tau)$ using a current software fitting procedure (Excel). High correlation coefficients were observed in each case (typically 0.999). Error limits on the lifetime are equal to 5%. The number of water molecules (q) bound to the inner coordination sphere of the europium ion was quantified by using either the original equation proposed by Horrocks and Sudnick[16] or the equation reported by Beeby et al.[17]

NMR Spectroscopy: Proton Nuclear Magnetic Relaxation Dispersion (NMRD) profiles extending from 0.24 mT to 1.2 T were recorded with Field Cycling Relaxometers (Field Cycling Systems, Oradell, New Jersey, USA and Stelar, Mede, Italy) on 0.6 mL solutions contained in 10-mm o.d. tubes. Proton relaxation rates were also measured at 0.47 T, 0.94 T, 1.5 T and 7.05 T with Minispec PC-120, PC-140, mq-60 and AMX-300 spectrometer. All these instruments were from Bruker (Karlsruhe, Germany). ^1H NMRD data were fitted according to the theoretical innersphere model described by Solomon[25] and Bloembergen[26] and to the outersphere contribution described by Freed.[27] Calculations were performed with previously described software.[36,37]

Transmetallation by Zn^{II} ions was evaluated at 310 K by the decrease of the water proton longitudinal relaxation rate at 20 MHz (Bruker Minispec PC 120) of buffered solutions (pH 7, phosphate buffer: [KH_2PO_4] = 26 mM, [Na_2HPO_4] = 41 mM) containing the gadolinium complex and Zn^{II} according to a procedure previously described.[23]

^{17}O spectra were recorded on 2 mL samples (10-mm o.d. tubes) on a Bruker AMX-300 spectrometer (Bruker, Karlsruhe, Germany) using a broadband probe and a Bruker BVT-2000 unit for temperature control. ^{17}O transverse relaxation times of distilled water (pH = 6.5) were measured using a CPMG sequence and a subsequent two parameters fit of the data points. The 90° and 180° pulse lengths were respectively 25 μs and 50 μs. ^{17}O T_2 of water in P792 ([P792] = 7 mM, pH = 6.0–7.0) was obtained from linewidth measurement. All ^{17}O spectra were proton decoupled. The procedures for the analysis of the ^{17}O data have been described elsewhere.[20]

All T_1 measurements at 7.05 T (^1H, ^{17}O) were performed with an inversion recovery or fast inversion recovery Fourier transform technique and a subsequent three parameters fit of the peak heights.

Acknowledgments

The authors thank Mrs Patricia de Francisco for her help in preparing the manuscript, and Dr. Claude Picard and Dr. Chantal Galaup (UMR, 5068 Toulouse) for their contribution to luminescence studies. This work was supported by the FNRS and the ARC Program 00/05–258 of the French Community of Belgium. The support and sponsorship concerted by COST Action D18 "Lanthanide Chemistry for Diagnosis and Therapy" are kindly acknowledged.

[1] C. Curtet, F. Maton, T. Havet, M. Slinkin, A. Mishra, J. F. Chatal, R. N. Muller, *Invest. Radiol.* **1998**, *3*, 752–761.
[2] N. Sato, H. Kobayashi, A. Hiraga, T. Saga, K. Togashi, J. Konishi, M. W. Brechbiel, *Magn. Reson. Med.* **2001**, *46*, 1169–1173.
[3] M. G. Duarte, M. H. Gil, J. A. Peters, J. M. Colet, L. Vander Elst, R. N. Muller, C. F. Geraldes, *Bioconjugate Chem.* **2001**, *12*, 170–177.
[4] L. Vander Elst, F. Chapelle, S. Laurent, R. N. Muller, *J. Biol. Inorg. Chem.* **2001**, *6*, 196–200.
[5] T. J. McMurry, D. J. Parmelee, H. Sajiki, D. M. Scott, H. S. Ouellet, R. C. Walovitch, Z. Tyeklar, S. Dumas, P. Bernard, S. Nadler, K. Midelfort, M. Greenfield, J. Troughton, R. B. Lauffer, *J. Med. Chem.* **2002**, *45*, 3465–3474.
[6] F. Bourasset, A. Dencausse, P. Bourrinet, M. Ducret, C. Corot, *Magn. Reson. Mater. Phys. Biol. Med.* **2001**, *12*, 82–87.
[7] M. Port, C. Corot, O. Rousseaux, I. Raynal, L. Devoldere, J. M. Idée, A. Dencausse, *Magn. Reson. Mater. Phys. Biol. Med.* **2001**, *12*, 121–127.
[8] M. Port, C. Corot, I. Raynal, J. M. Idée, A. Dencausse, E. Lancelot, D. Meyer, B. Bonnemain, J. Lautrou, *Invest. Radiol.* **2001**, *36*, 445–454.
[9] L. Vander Elst, M. Port, I. Raynal, C. Simonot, R. N. Muller, *Eur. J. Inorg. Chem.* **2003**, 2495–2501.
[10] S. G. Ruehm, H. Christina, X. Violas, C. Corot, J. F. Debatin, *Magn. Reson. Med.* **2002**, *48*, 844–851.
[11] M. Taupitz, J. Schnorr, S. Wagner, D. Kivelitz, P. Rogalla, B. Claaβen, M. Dewey, P. Robert, C. Corot, B. Hamm, *Magn. Reson. Med.* **2001**, *46*, 932–938.

 © 2005 Wiley-VCH Verlag GmbH & Co. KGaA, Weinheim

[12] M. Dewey, N. Kaufels, M. Laule, J. Schnorr, S. Wagner, D. Kivelitz, J. S. Raynaud, P. Robert, B. Hamm, M. Taupitz, *Magn. Reson. Med.* **2004**, *51*, 703–709.
[13] C. U. Herborn, F. M. Vogt, T. C. Lauenstein, M. Goyen, O. Dirsch, C. Corot, J. F. Debatin, S. G. Ruehm, *J. Magn. Reson. Imaging* **2003**, *18*, 328–335.
[14] X. Fan, M. Medved, J. N. River, M. Zamora, C. Corot, P. Robert, P. Bourrinet, M.Lipton, R. M. Culp, G. S. Karczmar, *Magn. Reson. Med.* **2004**, *51*, 487–494.
[15] S. Gaillard, C. Kubiak, C. Stolz, B. Bonnemain, D. Chassard, *Invest. Radiol.* **2002**, *37*, 161–166.
[16] W. De W. Horrocks Jr., D. R. Sudnick, *J. Am. Chem. Soc.* **1979**, *101*, 334–340.
[17] A. Beeby, I. M. Clarkson, R. S. Dickins, S. Faulkner, D. Parker, L. Boyle, A. S. de Sousa, J. A. G. Williams, M. Woods, *J. Chem. Soc., Perkin Trans. 1***999**, *2*, 493–503.
[18] M. Port, O. Rousseaux, I. Raynal, M. Woods, D. Parker, J. Moreau, J. Rimbault, J. C. Pierrard, M. Aplincourt, *Acad. Radiol.* **2002**, *9*, suppl. 2, S300–303.
[19] J. Moreau, E. Guillon, P. Aplincourt, J. C. Pierrard, J. Rimbault, M. Port, M. Aplincourt, *Eur. J. Inorg. Chem.* **2003**, 3007–3020.
[20] L. Vander Elst, F. Maton, S. Laurent, F. Seghi, F. Chapelle, R. N. Muller, *Magn. Reson. Med.* **1997**, *38*, 604–614.
[21] K. Micskei, L. Helm, E. Brücher, A. E. Merbach, *Inorg. Chem.* **1993**, *32*, 3844–3850.
[22] D. H. Powell, O. M. Ni Dhubhghaill, D. Pubanz, L. Helm, Y. S. Lebedev, W. Schlaepfer, A. E. Merbach, *J. Am. Chem. Soc.* **1996**, *118*, 9333–9346.
[23] S. Laurent, L. Vander Elst, F. Copoix, R. N. Muller, *Invest. Radiol.* **2001**, *36*, 115–122.
[24] R. N. Muller, B. Raduchel, S. Laurent, J. Platzek, C. Piérart, P. Mareski, L. Vander Elst, *Eur. J. Inorg. Chem.* **1999**, 1949–1955.
[25] I. Solomon, *Phys. Rev.* **1955**, *99*, 559–565.
[26] N. Bloembergen, *J. Chem. Phys.* **1957**, *27*, 572–573.
[27] J. H. Freed, *J. Chem. Phys.* **1978**, *68*, 4034–4037.
[28] S. Aime, M. Botta, M. Fasano, S. Paoletti, P. L. Anelli, F. Uggeri, M. Virtuani, *Inorg. Chem.* **1994**, *33*, 4707–4711.
[29] F. Uggeri, S. Aime, P. L. Anelli, M. Botta, M. Brocchetta, C. de Haën, G. Ermondi, M. Grandi, P. Paoli, *Inorg. Chem.* **1995**, *34*, 633–642.
[30] I. Bertini, O. Galas, C. Luchinat, G. Parigi, *J. Magn. Reson. A* **1995**, *113*, 151–158.
[31] S. Aime, M. Botta, F. Fedeli, E. Gianolio, E. Terreno, P. Anelli, *Chem. Eur. J.* **2001**, *7*, 5262–5269.
[32] R. B. Lauffer, D. J. Parmelee, H. S. Ouellet, D. P. Dolan, H. Sajiki, D. M. Scott, P. J. Bernard, E. M. Buchanan, K. Y. Ong, Z. Tyeklar, K. S. Midelfort, T. J. McMurry, R. C. Walovitch, *Acad. Radiol.* **1996**, *3*, S356–S358.
[33] R. A. Wallace, J. P. Haar Jr., D. B. Miller, S. R. Woulfe, J. A. Polta, K. P. Galen, M. R. Hynes, K. Adzamli, *Magn. Reson. Med.* **1998**, *40*, 733–739.
[34] C. Corot C, X. Violas, P. Robert, G. Gagneur, M. Port, *Invest. Radiol.* **2003**, *38*, 311–319.
[35] M. Port, C. Corot, X. Violas, P. Robert, I. Raynal, G. Gagneur, submitted to *Invest. Radiol*..
[36] R. N. Muller, D. Declercq, P. Vallet, F. Giberto, B. Daminet, H. W. Fischer, F. Maton, Y. Van Haverbeke, *Implementation and operation of an integrated and comprehensive relaxometric data bank* in "Proc., ESMRMB, 7th Annual Congress, Strasbourg, France ", **1990**, p. 394.
[37] P. Vallet, "Relaxivity of nitroxide stable free radicals. Evaluation by the field cycling method and optimisation", Ph. D. Dissertation, Univ. of Mons-Hainaut, Belgium, **1992**.

Received: October 31, 2004

 © 2005 Wiley-VCH Verlag GmbH & Co. KGaA, Weinheim

Syntheses and Properties of Metal-Centered Mixed-Valent $[NEt_4]\{Mn^{II}\subset[Mn^{II}_3Mn^{III}_3Cl_6(L)_6]\}$ Manganese Wheels[‡]

Rolf W. Saalfrank,*[a] Takayuki Nakajima,[a] Nicolai Mooren,[a] Andreas Scheurer,[a] Harald Maid,[a] Frank Hampel,[a] Christian Trieflinger,[b] and Jörg Daub[b]

In memoriam Professor Bernd A. Heß

Keywords: Manganese clusters / Self-assembly / Mixed valency / X-ray diffraction / Cyclic voltammetry

Upon reaction of *N*-substituted diethanolamines H_2L^{2-4} (**4**, **6**, **7**) with cesium carbonate and bis(tetraethylammonium) tetrachloromanganate(II) in acetonitrile in the presence of air, the metal-centered mixed-valent manganese wheels $[NEt_4]\{Mn^{II}\subset[Mn^{II}_3Mn^{III}_3Cl_6(L^{2-4})_6]\}$ (**8**–**10**) were generated. X-ray crystallographic structure analyses revealed, that **8**–**10** are principally isostructural and consist of an alternating ring of three Mn^{II} and three Mn^{III} ions, centered by an additional Mn^{II} ion. The cyclic voltammograms of **8** and **10** displayed three quasi-reversible oxidation processes, which are attributed to the subsequent one electron-oxidations of the three peripheral Mn^{II} ions to Mn^{III}. Oxidation of the central Mn^{II} ion is not observed within the applied potential.

(© Wiley-VCH Verlag GmbH & Co. KGaA, 69451 Weinheim, Germany, 2005)

Introduction

Despite their unpredictable nature, polyoxometalates have become the focus of intense research activities.[2] Recently, distinct supramolecular metal clusters have become accessible by rational design rather than by serendipity[3] and oxo-bridged polynuclear iron and manganese metal clusters have been the subject of numerous detailed magnetic studies, which have been rewarded by the discovery of single molecule magnets (SMMs).[4,5] In this context, we reported on the template-mediated self-assembly of six- and eight-membered iron-coronates, $\{Na\subset[Fe_6(L^1)_6]\}^+$ (**2**) and $\{Cs\subset[Fe_8(L^1)_8]\}^+$ (**3**), which were prepared from triethanolamine H_3L^1 (**1**) with iron(III) chloride and sodium hydride or cesium carbonate, respectively (Scheme 1).[6] A common feature of complexes **2** and **3** is that the μ_1-oxygens of the $(L^1)^{3-}$ ligands do not participate in the formation of the hexa- or octanuclear structures. They solely function as ligands for the coordinative saturation of the iron centers. For this reason, further mono-anionic donors, such as chloride ions, should also be candidates for this function. Therefore, reaction of *N*-methyldiethanolamine H_2L^2 (**4**) with cal-

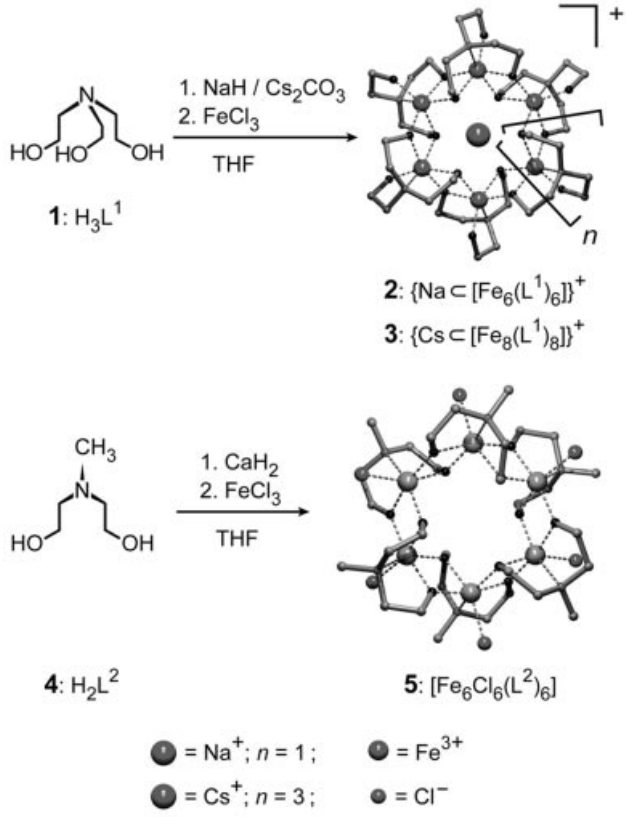

Scheme 1. Top: Synthesis of ferric wheels **2** and **3** with triethanolamine. Bottom: Synthesis of ferric wheel **5** with *N*-methyldiethanolamine.

[‡] Chelate Complexes, Part 28. Part 27: Ref.[1]

[a] Institut für Organische Chemie der Universität Erlangen-Nürnberg,
Henkestraße 42, 91054 Erlangen, Germany
Fax: +49-9131-852-1165
E-mail: saalfrank@chemie.uni-erlangen.de
http://www.organik.uni-erlangen.de/saalfrank
[b] Institut für Organische Chemie der Universität Regensburg, 93053 Regensburg

cium hydride and iron(III) chloride yielded the unoccupied neutral iron coronand $[Fe_6Cl_6(L^2)_6]$ (**5**) (Scheme 1).[6] In **5**, the μ_2-oxygen donors of the $(L^2)^{2-}$ ligands are structure determining, whereas their *N*-methyl groups are not. In addition, six chloride coligands are necessary for coordinative saturation at the iron centers and for charge compensation. Consequently, a series of ferric wheels was generated with *N*-substituted diethanolamines.[1,7]

In this communication we report on the synthesis of metal-centered, heptanuclear, mixed-valent manganese wheels **8**–**10**.

Results and Discussion

Synthesis

The metal-centered, heptanuclear, mixed-valent, six-membered manganese wheels **8**–**10** were generated in good yields in a one-pot reaction. For that purpose, *N*-substituted diethanolamines **4**, **6** and **7** were deprotonated with cesium carbonate in acetonitrile under nitrogen for 1 h. After addition of soluble bis(tetraethylammonium) tetrachloromanganate(II), the resulting reaction mixture was stirred for an extra 4 d. Workup in air, and crystallization from suitable solvent systems afforded black parallelepipeds (Scheme 2).

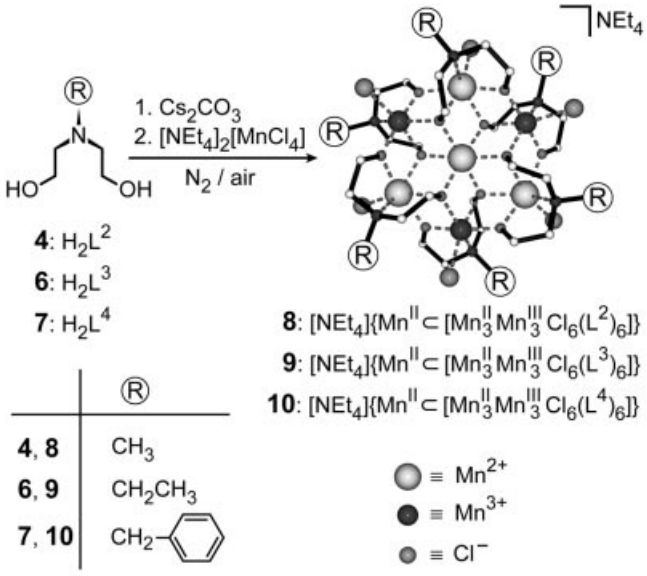

Scheme 2. Synthesis of manganese wheels **8**–**10** with *N*-substituted diethanolamines.

X-ray Analyses

X-ray crystallographic structure determinations were carried out for **8**–**10** (Table 2).[8,9] According to these analyses all three clusters are principally isostructural with idealized S_6 molecular symmetry, and for that reason, only the structure of **8** is discussed in detail. In the crystal, **8** is present as a cyclic manganese complex, consisting of an alternating ring of three Mn^{II} and three Mn^{III} ions[10] centered by an additional Mn^{II} ion, and tetraethylammonium is the counterion. Charge considerations and bond valence calculations require six doubly deprotonated methyldiethanolate amine ligands and six chloride ions. For the idealized consideration, the six equivalent manganese ions of the centrosymmetric anion $\{Mn^{II} \subset [Mn^{II}_3 Mn^{III}_3 Cl_6(L^2)_6]\}^-$ of **8** are located in the corners of a regular hexagon. The Mn–Mn distance is 3.3 Å. The diameter of the hexagon, defined as

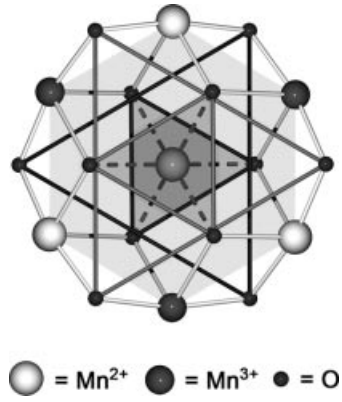

Figure 1. Schematic presentation of the central $[Mn^{II}_3 Mn^{III}_3 \mu_2\text{-}O_6]$ scaffold of $[\mathbf{8}]^-$ together with the octahedral μ_3-O environment of the encapsulated Mn^{II} ion. View along the idealized molecular S_6 axis, neglecting the valency of manganese.

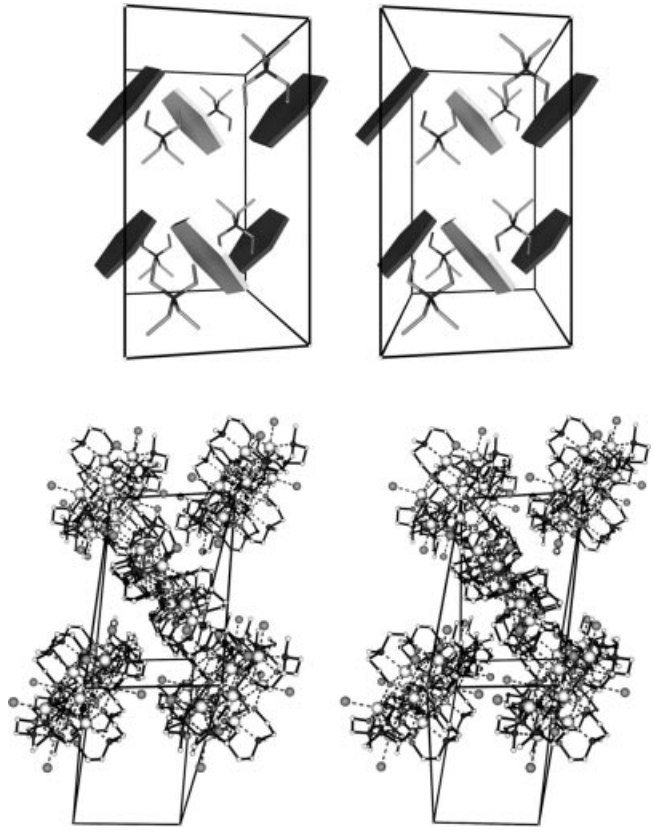

Figure 2. Top: Schematic stereo presentation of the crystal packing of **8** along the *a* axis. Bottom: Stereo view of the crystal packing of manganese wheel **8** along the *a*,*b* plane diagonal of the unit cell.

 © 2005 Wiley-VCH Verlag GmbH & Co. KGaA, Weinheim

the distance between two opposite manganese ions, is 6.6 Å. The distorted octahedral coordination sphere of the manganese ions is composed of one nitrogen donor, two μ_2- and two μ_3-oxygen donors and one chloride ion. Consequently, doubly deprotonated methyldiethanolate amine acts as a tetratope tridentate ligand and links three manganese ions. There is a set of six outer μ_2-O donors and a set of six inner μ_3-O donors. The six oxygen donors of each set are located at the corners of a pair of regular triangles, rotated by 60° relative to each other. The pairs of triangular faces are arranged parallel and equidistant in pairs from the central one, with one plane above and one below this hexagonal plane, generated by the peripheral manganese ions. These two pairs of six oxygen donors are related by an S_6 axis. The Mn^{II} ion located in the center of $[\mathbf{8}]^-$ has a distorted octahedral coordination sphere with respect to the six μ_3-O donors (Figure 1). The diameter of the cavity d[11] marked by opposite μ_3-O donors almost corresponds to double the ionic radius of Mn^{II}.

Manganese wheel $[NEt_4]\{Mn^{II}\subset[Mn^{II}_3Mn^{III}_3Cl_6(L^2)_6]\}$ (**8**) crystallizes with four molecules in the unit cell. The disklike clusters are all arranged in parallel (shortest midpoint distance d = 11.2 Å), but in two orientations (mean included angle φ = 85°), and are piled in cylindrical columns, with all the manganese centers superimposed (Figure 2).

Cyclic Voltammetry

The cyclic voltammogram of **8** and **10** were recorded under anaerobic and aprotic conditions and displayed three quasi-reversible oxidation processes, which are attributed to the subsequent one-electron oxidations of the three Mn^{II} ions to Mn^{III}, which are located at the ring positions (Figure 3, Table 1). Oxidation of the central Mn^{II} ion is not observed within the applied potential range.[12] In multisweep experiments under thin layer conditions the first oxidation shows complete reversibility over several cycles, whereas the second and third oxidations lead to degradation of the complex indicating irreversible chemical side reactions. The large potential displacement between the individual oxidations of several hundred mV is indication of a strong electronic coupling between the crystallographically equivalent manganese ions, whereas in a noncoupled system a simultaneous threefold oxidation within one oxidation wave would have been expected.

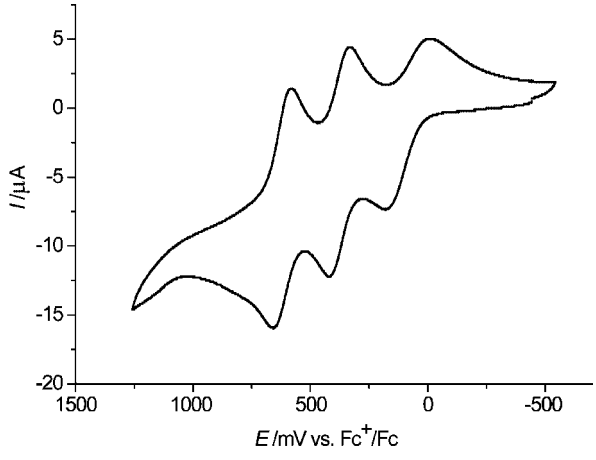

Figure 3. Cyclic voltammogram of **8**.

Table 1. Data of the cyclic voltammogram of **8** and **10** in CH_3CN {0.1 M $[(n\text{Bu})_4N](PF_6)$} versus Fc/Fc^+ at 20 °C; scan rate 200 mV s^{-1}.

Complex	$E_{1/2}{}^1$ [mV]	$E_{1/2}{}^2$ [mV]	$E_{1/2}{}^3$ [mV]
8	85	375	630
10	119	396	650

Conclusion

We are still far from understanding the template effect on the mysterious rules of the self-assembling processes leading to metallic wheels. Whereas triethanolamine with iron(III) chloride affords homovalent metal-centered cationic wheels like $\{Na\subset[Fe_6(L^1)_6]\}^+$ (**2**), methyldiethanolamine yields the unoccupied neutral homovalent species $[Fe_6Cl_6(L^2)_6]$ (**5**). However, when manganese(II) instead of iron(III) was reacted under aerobic conditions with methyldiethanolamine, the mixed-valent metal-centered anionic wheel $\{Mn^{II}\subset[Mn^{II}_3Mn^{III}_3Cl_6(L^2)_6]\}^-$ $(\mathbf{8})^-$ was formed.

Experimental Section

General Techniques: Metal salts, and H_2L^2[2,3] (**4**, **6**) were used as obtained from Aldrich. All solvents used were purified and dried according to standard procedures. $[NEt_4]_2[MnCl_4]$ and H_2L^4 (**7**) were prepared according to literature methods.[13,7] IR spectra were recorded from KBr pellets with a Bruker IFS 25 spectrometer. FAB-MS spectra were recorded with a Micromass ZAB-Spec spectrometer. Elemental analyses were performed with an EA 1110 CHNS-Microautomat. Single-crystal X-ray structure analyses: details for crystal data, data collection and refinement are given in Table 2. X-ray data for **8**–**10** were collected with a Nonius Kappa CCD area detector, using Mo-K_α radiation (λ = 0.71073 Å). Scalepack absorption correction was employed. The structure was solved by direct methods with SHELXS-97 and refined with full-matrix least-squares against F^2 with SHELXL-97.[8]

General Method: Methyldiethanolamine H_2L^2 (**4**) (1.7 mmol, 0.200 g), ethyldiethanolamine H_2L^3 (**6**) (1.7 mmol, 0.230 g), or benzyldiethanolamine H_2L^4 (**7**) (1.7 mmol, 0.330 g) were added to a suspension of Cs_2CO_3 (2 mmol, 0.650 g) in CH_3CN (70 mL). After stirring for 1 h at room temperature $[NEt_4]_2[MnCl_4]$ (2 mmol, 0.915 g) was added. The reaction mixture was stirred for 4 d at room temperature. For **8** and **9**, the resulting black precipitate was filtered off, extracted with $CHCl_3$ (100 mL) and concentrated. Black crystals were obtained from $CHCl_3/Et_2O$ (for **8**) or CH_3CN/Et_2O (for **9**). For **10**, the resulting black suspension was filtered, and the filtrate was concentrated in vacuo to dryness. A mixture of Et_2O (5 mL) and EtOH (5 mL) was added. After standing for 12 h, the black precipitate that had formed was filtered off and extracted with $CHCl_3$ (100 mL). Black crystals were obtained from $CHCl_3/Et_2O$.

 © 2005 Wiley-VCH Verlag GmbH & Co. KGaA, Weinheim

Table 2. Details of X-ray structure determinations for complexes **8**–**10**.

	8	**9**	**10**
Formula	$C_{38}H_{86}Cl_6Mn_7N_7O_{12}$	$C_{44}H_{98}Cl_6Mn_7N_7O_{12}$	$C_{74}H_{110}Cl_6Mn_7N_7O_{12}\cdot 7\,CHCl_3$
*M*r	1430.42	1514.57	2722.55
Crystal size (mm)	0.30 × 0.30 × 0.10	0.30 × 0.30 × 0.20	0.35 × 0.30 × 0.15
Crystal system	monoclinic	cubic	monoclinic
Space group	*C*2/*c*	*Pa*3	$P2_1$
T [K]	173(2)	173(2)	173(2)
a [Å]	30.4649(13)	18.600(2)	13.917(3)
b [Å]	18.9810(11)		25.151(5)
c [Å]	11.1999(5)		16.410(3)
α [°]			
β [°]	107.237(3)		96.82(3)
γ [°]			
V [Å^3]	6185.5(5)	6434.3(13)	5703(2)
Z	4	4	2
$\rho_{calcd.}$ [Mg m^{-3}]	1.536	1.563	1.585
θ range [°]	2.12 to 24.99	2.19 to 27.45	1.25 to 27.47
Reflections collected	9455	4636	21343
Unique reflections	5427	2460	21343
[R_{int}]	0.0348	0.0256	0.0000
Reflections observed [$I > 2\sigma(I)$]	3706	1682	15862
Parameters	318	126	1208
Final *R*1 [$I > 2\sigma(I)$]	0.0673	0.0557	0.0614
*wR*2 (all data)	0.2451	0.1755	0.1786
Largest residuals [e Å^{-3}]	1.971/–0.706	1.217/–0.554	1.499/–1.186

Compound [NEt$_4$]{Mn^{II}⊂[Mn$^{II}_3$Mn$^{III}_3$Cl$_6$(L^2)$_6$]} (8): Starting material: H_2L^2, $MeN(CH_2CH_2OH)_2$ (**4**): Yield 153 mg (32%) black crystals from chloroform/Et_2O; m.p. > 250 °C (decomp.). IR (KBr): $\tilde{\nu}$ = 3464, 2855, 2363, 2345 cm^{-1}. FAB-MS (*m*-NBA): *m*/*z* (%) = 1394 (5) $[NEt_4][Mn_7Cl_5(L^2)_6]^+$, 1300 (15) $[Mn_7Cl_6(L^2)_6]^+$, 1265 (40) $[Mn_7Cl_5(L^2)_6]^+$, 1229 (40) $[Mn_7Cl_4(L^2)_6]^+$, 1146 (40) $[Mn_7Cl_6(L^2)_5]^+$, 1100 (40) $[Mn_7Cl_5(L^2)_5]^+$, 1075 (50) $[Mn_7Cl_4(L^2)_5]^+$, 1030 (100) $[Mn_7Cl_6(L^2)_4]^+$. $C_{38}H_{86}Cl_6Mn_7N_7O_{12}$ (1430.42): calcd. C 31.91, H 6.06, N 6.85; found C 31.59, H 6.06, N 6.76.

Compound [NEt$_4$]{Mn^{II}⊂[Mn$^{II}_3$Mn$^{III}_3$Cl$_6$(L^3)$_6$]} (9): Starting material: H_2L^3, $EtN(CH_2CH_2OH)_2$ (**6**): Yield 212 mg (42%) black crystals from CH_3CN/Et_2O; m.p. > 250 °C (decomp.). IR (KBr): $\tilde{\nu}$ = 3434, 2969, 2936, 2903, 2856, 1623 cm^{-1}. FAB-MS (*m*-NBA): *m*/*z* (%) = 1515 (5) $[NEt_4][Mn_7Cl_6(L^3)_6]^+$, 1478 (5) $[NEt_4][Mn_7Cl_5(L^3)_6]^+$, 1382 (20) $[Mn_7Cl_6(L^3)_6]^+$, 1349 (60) $[Mn_7Cl_5(L^3)_6]^+$, 1313 (70) $[Mn_7Cl_4(L^3)_6]^+$, 1218 (50) $[Mn_7Cl_5(L^3)_5]^+$, 1181 (50) $[Mn_7Cl_4(L^3)_5]^+$, 1145 (60) $[Mn_7Cl_3(L^3)_5]^+$, 1085 (100) $[Mn_7Cl_5(L^3)_4]^+$. $C_{44}H_{98}Cl_6Mn_7N_7O_{12}$ (1514.57): calcd. C 34.89, H 6.52, N 6.47; found C 33.80, H 6.67, N 6.13.

Compound [NEt$_4$]{Mn^{II}⊂[Mn$^{II}_3$Mn$^{III}_3$Cl$_6$(L^4)$_6$]} (10): Starting material: H_2L^4, $BnN(CH_2CH_2OH)_2$ (**7**): Yield 277 mg (44%) black crystals from chloroform/Et_2O; m.p. > 250 °C (decomp.). IR (KBr): $\tilde{\nu}$ = 3548, 3028, 2904, 2858, 2367 cm^{-1}. FAB-MS (*m*-NBA): *m*/*z* (%) = 1887 (5) $[NEt_4][Mn_7Cl_6(L^4)_6]^+$, 1850 (10) $[NEt_4][Mn_7Cl_5(L^4)_6]^+$, 1755 (10) $[Mn_7Cl_6(L^4)_6]^+$, 1720 (20) $[Mn_7Cl_5(L^4)_6]^+$, 1685 (15) $[Mn_7Cl_4(L^4)_6]^+$, 1527 (20) $[Mn_7Cl_5(L^4)_5]^+$, 1334 (50) $[Mn_7Cl_5(L^4)_4]^+$, 1030 (20) $[Mn_5Cl_5(L^4)_3]^+$. $C_{74}H_{110}Cl_6Mn_7N_7O_{12}\cdot 7\,CHCl_3$ (2722.55).[14]

Acknowledgments

This work was supported by the Deutsche Forschungsgemeinschaft Sa 276/26-1, SFB 583, GK 312, SPP 1137, the Bayerisches Langzeitprogrammm "Neue Werkstoffe", and the Fonds der Chemischen Industrie. T. N. thanks the Alexander von Humboldt-Stiftung for a postdoctoral fellowship. N. M. thanks the Freistaat Bayern for a scholarship.

[1] R. W. Saalfrank, C. Deutscher, S. Sperner, T. Nakajima, Ayuk M. Ako, E. Uller, F. Hampel, F. W. Heinemann, *Inorg. Chem.* **2004**, *43*, 4372–4382.

[2] a) R. E. P. Winpenny, in *Perspectives in Supramolecular Chemistry*, vol. 5 ("Transition Metals in Supramolecular Chemistry") (Ed.: J. P. Sauvage), Wiley-VCH, Weinheim, **1999**, pp. 193–223; b) A. D. Cutland, R. G. Malkani, J. W. Kampf, V. L. Pecoraro, *Angew. Chem.* **2000**, *112*, 2801–2803; *Angew. Chem. Int. Ed.* **2000**, *39*, 2689–2691; c) H. Oshio, N. Hoshino, T. Ito, M. Nakano, F. Renz, P. Gütlich, *Angew. Chem.* **2003**, *115*, 233–235; *Angew. Chem. Int. Ed.* **2003**, *42*, 223–225; d) O. L. Sydora, P. T. Woleczanski, E. B. Lobkovsky, *Angew. Chem.* **2003**, *115*, 2789–2791; *Angew. Chem. Int. Ed.* **2003**, *42*, 2685–2687; e) C. Benelli, S. Parsons, G. A. Solan, R. E. P. Winpenny, *Angew. Chem.* **1996**, *108*, 1967–1970; *Angew. Chem. Int. Ed. Engl.* **1996**, *35*, 1825–1827; f) A. Caneschi, A. Cornia, A. C. Faretti, D. Gatteschi, *Angew. Chem.* **1999**, *111*, 1372–1374; *Angew. Chem. Int. Ed.* **1999**, *38*, 1295–1297; g) S. P. Watton, P. Fuhrmann, L. E. Pence, A. Caneschi, A. Cornia, G. L. Abbati, S. J. Lippard, *Angew. Chem.* **1997**, *109*, 2917–2919; *Angew. Chem. Int. Ed. Engl.* **1997**, *36*, 2774–2776.

[3] a) R. W. Saalfrank, B. Demleitner, in *Perspectives in Supramolecular Chemistry*, vol. 5 ("Transition Metals in Supramolecular Chemistry") (Ed.: J. P. Sauvage), Wiley-VCH, Weinheim, **1999**, pp. 1–51; b) E. Uller, B. Demleitner, I. Bernt, R. W. Saalfrank, in: *Structure and Bonding*, vol. 96 (Ed.: M. Fujita), Springer, Berlin, **2000**, pp. 149–175; c) D. L. Caulder, K. N. Raymond, *Acc. Chem. Res.* **1999**, *32*, 975–982; d) M. Fujita, *Chem. Soc. Rev.* **1998**, *27*, 417–425; e) S. L. James, M. P. Mingos, A. J. P. White, D. J. Williams, *Chem. Commun.* **1998**, 2323–2324; f) C. J. Jones, *Chem. Soc. Rev.* **1998**, *27*, 289–299; g) S. Leininger, B. Olenyuk, P. J. Stang, *Chem. Rev.* **2000**, *100*, 853–908; h) F. Hof, S. L. Craig, C. Nuckolls, J. Rebek, Jr., *Angew. Chem.* **2002**, *114*, 1556–1578; *Angew. Chem. Int. Ed.* **2002**, *41*, 1488–1508; i) B. J. Holliday, C. A. Mirkin, *Angew. Chem.* **2001**, *113*,

2076–2097; *Angew. Chem. Int. Ed.* **2001**, *40*, 2022–2043; j) S. R. Seidel, P. J. Stang, *Acc. Chem. Res.* **2002**, *35*, 972–983; k) J. L. Atwood, L. R. MacGillivray, *Angew. Chem.* **1999**, *111*, 1080–1096; *Angew. Chem. Int. Ed.* **1999**, *38*, 1018–1033; l) E. Barea, J. A. R. Navarro, J. M. Salas, M. Quirós, M. Willermann, B. Lippert, *Chem. Eur. J.* **2003**, *9*, 4414–4421.

[4] a) D. Gatteschi, R. Sessoli, A. Cornia, *Chem. Commun.* **2000**, 725–732; b) D. Gatteschi, A. Caneschi, L. Pardi, R. Sessoli, *Science* **1994**, *265*, 1054–1058; c) R. W. Saalfrank, S. Trummer, U. Reimann, M. M. Chowdhry, F. Hampel, O. Waldmann, *Angew. Chem.* **2000**, *112*, 3634–3636; *Angew. Chem. Int. Ed.* **2000**, *39*, 3492–3494; d) E. Coronado, J. R. Galán-Mascarós, C.-J. Gómez-García, J. Ensling, P. Gütlich, *Chem. Eur. J.* **2000**, *6*, 552–563; e) E. Coronado, M. Clemente-León, J. R. Galán-Mascarós, C. Giménez-Saiz, C. J. Gómez-García, E. Martínez-Ferrero, *J. Chem. Soc. Dalton Trans.* **2000**, 3955–3961; f) A. Cornia, A. C. Fabretti, P. Garrisi, C. Mortalò, D. Bonacchi, D. Gatteschi, R. Sessoli, L. Sorace, W. Wernsdorfer, A.-L. Barra, *Angew. Chem.* **2004**, *116*, 1156–1159; *Angew. Chem. Int. Ed.* **2004**, *43*, 1136–1139; g) B. Pilawa, *Ann. Phys. (Leipzig)* **1999**, *8*, 191–254; h) V. Marvaud, C. Decroix, A. Scuiller, C. Guyard-Duhayon, J. Vaisermann, J. Gonnet, M. Verdaguer, *Chem. Eur. J.* **2003**, *9*, 1677–1691; i) R. Sessoli, D. Gatteschi, *Angew. Chem.* **2003**, *115*, 278–309; *Angew. Chem. Int. Ed.* **2003**, *42*, 268–297; j) R. Koch, S. Schromm, J. Schülein, P. Müller, I. Bernt, R. W. Saalfrank, F. Hampel, E. Balthes, *Inorg. Chem.* **2001**, *40*, 2986–2995; k) A. Müller, F. Peters, M. T. Pope, D. Gatteschi, *Chem. Rev.* **1998**, *98*, 239–271; l) O. Waldmann, R. Koch, S. Schromm, P. Müller, I. Bernt, R. W. Saalfrank, *Phys. Rev. Lett.* **2002**, *89*, 246401-1–246401-4.

[5] a) M. A. Bolcar, S. M. J. Aubin, K. Folting, D. N. Hendrickson, G. Christou, *Chem. Commun.* **1997**, 1485–1486; b) B. Pilawa, M. T. Kelemen, S. Wanka, A. Geisselmann, A. L. Barra, *Europhys. Lett.* **1998**, *43*, 7–12; c) L. M. Wittick, K. S. Murray, B. Moubaraki, S. R. Batten, L. Spiccia, K. J. Berry, *Dalton Trans.* **2004**, *1*, 1003–1011.

[6] a) R. W. Saalfrank, I. Bernt, E. Uller, F. Hampel, *Angew. Chem.* **1997**, *109*, 2596–2599; *Angew. Chem. Int. Ed. Engl.* **1997**, *36*, 2482–2485; b) R. W. Saalfrank, I. Bernt, M. M. Chowdhry, F. Hampel, G. B. M. Vaughan, *Chem. Eur. J.* **2001**, *7*, 2765–2769.

[7] R. W. Saalfrank, C. Deutscher, H. Maid, A. M. Ako, S. Sperner, T. Nakajima, W. Bauer, F. Hampel, B. A. Hess, N. J. R. van Eikema Hommes, R. Puchta, F. W. Heinemann, *Chem. Eur. J.* **2004**, *10*, 1899–1905.

[8] a) G. M. Sheldrick, C. Krüger, P. Goddard, *Crystallographic Computing 3*, Oxford University Press, Oxford, **1985**, p. 175; b) G. M. Sheldrick, SHELXL-97, *Program for Crystal Structure Refinement*, University of Göttingen, **1997**.

[9] CCDC-247134 (**8**), CCDC-247135 (**9**) and CCDC-247133 (**10**) contain the supplementary crystallographic data for this paper. These data can be obtained free of charge from The Cambridge Crystallographic Data Centre via www.ccdc.cam.ac.uk/data_request/cif.

[10] The alternation of Mn^{II} and Mn^{III} ions in **8**–**10** is explicitly confirmed by the coordination geometry of the Mn^{II} and Mn^{III} centers in compound **10**; cf.: CCDC-247133.

[11] $d = d_{\mu3O-\mu3O} - 2r_O = 4.4 - 2.3$ Å almost corresponds to double the ionic radius (1.9 Å) of high-spin Mn^{II}.

[12] Cf.: a) M. Ruben, J. Rojo, F. J. Romero-Saluero, L. H. Uppadine, J.-M. Lehn, *Angew. Chem.* **2004**, *116*, 3728–3747; *Angew. Chem. Int. Ed.* **2004**, *43*, 3644–3662; b) L. Zhao, C. J. Matthews, K. Thompson, S. L. Heath, *Chem. Commun.* **2000**, 265–266.

[13] N. S. Gill, R. S. Nyholm, *J. Chem. Soc.* **1959**, 3997–4007.

[14] The microanalytical data for **10** deviate from theory due to varying amounts of crystal solvents and are not recorded here.

Received: September 20, 2004

 © 2005 Wiley-VCH Verlag GmbH & Co. KGaA, Weinheim

Incorporation of Aluminium and Iron into the Zeolite MCM-58

Gabriela Košová,[a] Stefan Ernst,[b] Martin Hartmann,[b] and Jiří Čejka*[a]

Keywords: Acidity / Aluminum / Iron / Kinetics / Zeolites

The hydrothermal synthesis of zeolite MCM-58 is investigated with *N*-benzylquinuclidinium bromide as a structure-directing agent in order to isomorphously substitute aluminium or iron for silicon. Al-MCM-58 was synthesised in a wide range of n_{Si}/n_{Al} ratios (from 19 to 56), and Fe-MCM-58 was successfully prepared in a narrower range of n_{Si}/n_{Fe} ratios (from 18 to 36). The obtained products were characterised by XRD, SEM, ^{27}Al MAS NMR, ^{29}Si MAS NMR, FTIR, and ESR spectroscopy. Two different calcination procedures, viz. in a stream of nitrogen and air or in a stream of ammonia, were used in order to modify the acid sites in the zeolite. FTIR spectroscopy before and after the adsorption of [D_3]acetonitrile and pyridine was employed to determine the concentration and type of the acid sites. The acid forms of Al(Fe)-MCM-58 are characterised by the vibrations of bridging Si–OH–Al(Fe) groups at 3628 cm^{-1} and 3564 cm^{-1} (Al-MCM-58) or 3646 cm^{-1} and 3520 cm^{-1} (Fe-MCM-58). The acid sites of both zeolites Al-MCM-58 and Fe-MCM-58 are accessible for [D_3]acetonitrile and pyridine, and all materials contain substantial numbers of Lewis sites (Al-MCM-58: 50 % of the total acid sites; Fe-MCM-58: 90 %) over the whole range of n_{Si}/n_{Al} (n_{Si}/n_{Fe}) ratios studied. Only a small increase in the concentration of Brønsted acid sites was achieved after calcination of the as-synthesised samples in a flow of ammonia.
(© Wiley-VCH Verlag GmbH & Co. KGaA, 69451 Weinheim, Germany, 2005)

Introduction

Zeolite-based molecular sieves are a very important group of inorganic materials with a variety of applications, such as adsorption, ion-exchange and, particularly, heterogeneous catalysis.[1,2] The catalytic activity and selectivity of zeolites is attributed to their large internal surface, with active sites that are accessible through uniformly sized pores. The shape and the size of the pore system influence the diffusion of reactants and products and also the path of the reaction. The successful substitution of trivalent heteroatoms into the silicate framework results in a negative charge compensated by protons that are essential for the catalytic activity of zeolites in acid-catalysed reactions. The hydrophobic/hydrophilic properties of high silica zeolites can be varied enormously by suitable variation of the concentration and location of the trivalent cations. Several detailed studies of the feasibility of trivalent cation incorporation into zeolite frameworks, the distribution of these cations among different sites and the location of the charge compensating metal cations in high silica zeolites have been reported that combine experimental and theoretical approaches.[3–6] In the past decade, isomorphous substitution of trivalent cations into various zeolite structures has been reported.[7,8] In addition to aluminosilicate zeolite, ferrisilicate analogues have already been commercially applied as catalysts.[9] Ferrisilicates are less acidic than aluminosilicates, which results in improved selectivity in some acid-catalysed reactions, such as oligomerisation of C_2-C_4 olefins and catalytic dewaxing. Ferrisilicate analogues of molecular sieves can also serve as precursors for the preparation of redox catalysts with a homogeneous distribution of active iron oxide particles, for example in the synthesis of phenol from benzene.[10]

Nowadays, more than 130 framework types have been described[11] and it is still a big challenge to rationally design the synthesis of new structural types of zeolites.[12] The synthesis of zeolites is usually performed under hydrothermal conditions in the presence of various organocationic structure-directing agents (SDA). It is believed that the size and shape of the SDA predefine the shape and dimensions of the zeolite pore system.[13] The synthesis efforts using novel types of SDA in many laboratories around the world have resulted recently in the successful synthesis of new types of zeolites, for example ITQ-21, a large-pore, three-dimensional zeolite,[14] ITQ-13, with 9- and 10-membered rings,[15] a zeolite having 8-, 10- and 12-membered rings,[16] SSZ-58, a zeolite with previously unseen double 5-ring subunits,[17] MCM-68, in which 12-membered-rings channel are intersected by two independent tortuous 10-membered-ring channel systems,[18] or the novel, extra-large-pore zeolites SSZ-53 and SSZ-59, which possess 14-membered rings in a one-dimensional channel system.[19] Other strategies have been developed for the synthesis of micro/meso-composite molecular sieves.[20,21]

[a] J. Heyrovský Institute of Physical Chemistry, Academy of Sciences of the Czech Republic,
Dolejškova 3, 182 23 Prague, Czech Republic
Fax: +420-28658-2307
E-mail: jiri.cejka@jh-inst.cas.cz
[b] Department of Chemistry, Chemical Technology, University of Kaiserslautern,
Erwin-Schrödinger-Strasse 54, 67663 Kaiserslautern, Germany

 © 2005 Wiley-VCH Verlag GmbH & Co. KGaA, Weinheim **DOI: 10.1002/ejic.200400743**

Zeolite MCM-58, which was described for the first time in 1994 by Valyocsik as a high-silica zeolite, can be synthesised with n_{Si}/n_{Al} ratios from 15 to 50.[22] Zeolite MCM-58 (IZA structure code IFR) is isostructural with SSZ-42 and ITQ-4 and is characterised by an undulating, one-dimensional, 12-membered-ring channel system.[23] Due to the relatively large pore diameter of 0.64 nm at the narrowest point and a cage at the widest point with a diameter of 1.0 nm, zeolite MCM-58 could be an interesting catalyst for the conversion of relatively bulky molecules. For example, MCM-58 has been used as catalyst in the gas-phase alkylation of toluene with propylene giving large amount of *n*-propyltoluenes,[24] or ethylbenzene disproportionation and hydroconversion of *n*-decane.[25] Several organic SDAs have been used for the synthesis of MCM-58, including benzyltropanium salts, *N*-benzyl-1-azabicyclo[2.2.2]octane cations (benzylquinuclidinium) and *N*-benzyl-1,4-diazabicyclo[2.2.2] cations.[22]

In the present work, we report on the synthesis of aluminosilicate MCM-58 with n_{Si}/n_{Al} ratios from 20 to 60 and of ferrisilicate MCM-58 with n_{Si}/n_{Fe} ratios from 20 to 40 using *N*-benzylquinuclidinium bromide (BQ) as the templating agent. In particular, we were interested in the isomorphous substitution of iron for silicon in the framework of MCM-58, which has not yet been described. The kinetics of the crystallisation and the effect of incorporated trivalent atoms on concentrations and types of acid sites of this zeolite were also investigated.

Results and Discussion

The progress of crystallisation of MCM-58 from molar gel compositions of $(0.016–0.025)\,Al_2O_3$:SiO_2:$38\,H_2O$:$0.30\,K_2O$:$0.10\,BQ$ for Al-MCM-58 and $(0.0125–0.025)\,Fe_2O_3$:SiO_2:$38\,H_2O$:$0.30\,K_2O$:$0.20\,BQ$ for Fe-MCM-58 was followed by X-ray powder diffraction. By optimising the synthesis conditions and time at 170 °C it was possible to reproducibly synthesise highly crystalline zeolite Al-MCM-58 (Figure 1) with initial n_{Si}/n_{Al} ratios from 20 to 60. Because BQ, which is used as an SDA in the synthesis of MCM-58, is relatively expensive, the amount of BQ in the reaction mixture for Al-MCM-58 was further lowered from the original BQ/SiO_2 molar ratio of 0.2 to 0.1. Even with a reduced amount of SDA, MCM-58 can be synthesised without any loss of quality. When the BQ/SiO_2 ratio is lower then 0.1, or BQ is omitted completely, α-quartz is obtained as a pure phase.[26] A similar effect occurs when the amount of aluminium in the reaction mixture is decreased. When the initial n_{Si}/n_{Al} ratio exceeds 60, α-quartz begins to crystallise as well. Valyocsik has reported that mordenite can be formed as an impurity phase if either the n_{Si}/n_{Al} ratio is less then 10 in the initial gel or sodium cations are used instead of potassium cations in the synthesis gel.[27]

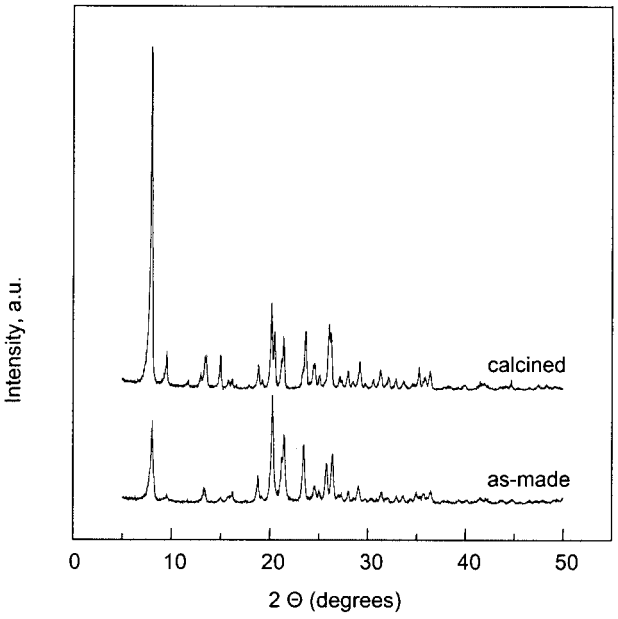

Figure 1. X-ray powder-diffraction patterns of as-synthesised and calcined Al-MCM-58 (n_{Si}/n_{Al} = 36).

The MCM-58 reflections were first observed after three days of synthesis (Figure 2) and the crystallisation was complete after six to eight days, depending on the n_{Si}/n_{Al} ratio (n_{Si}/n_{Al} = 60, 40, 30 and 20, respectively). The rate of crystallisation increases with decreasing amount of aluminium. A relative decrease in the crystallisation rate with reduced aluminium concentration in the synthesis gel has also been reported for other zeolites, such as Al-ZSM-12.[28]

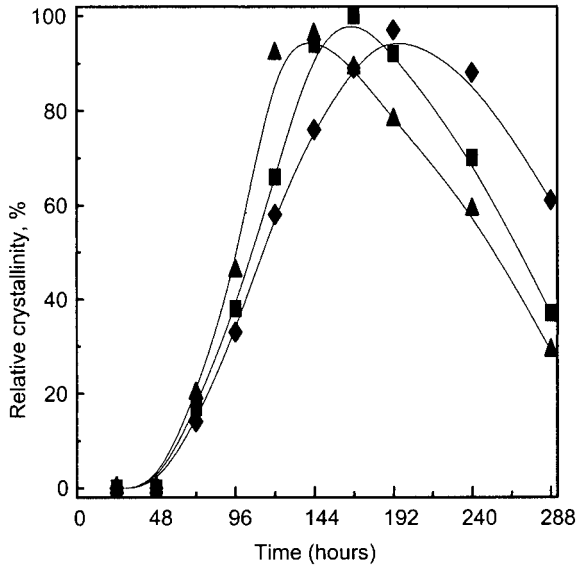

Figure 2. The dependence of relative crystallinity of Al-MCM-58 on the initial n_{Si}/n_{Al} ratio. Temperature: 170 °C; n_{Si}/n_{Al} = 20 (▲), 30 (■), 40 (♦).

In contrast to the synthesis of Al-MCM-58, which was carried out at 170 °C and yielded the phase-pure zeolite, in the case of Fe-MCM-58 it was not possible to synthesise

 © 2005 Wiley-VCH Verlag GmbH & Co. KGaA, Weinheim

this zeolite as a pure phase under the same conditions: the sample was always contaminated with α-quartz. After six days, α-quartz was the sole product (see Figure 3). To prevent the formation of α-quartz, the reaction temperature for the synthesis of Fe-MCM-58 was lowered to 155 °C and the synthesis time was optimised. The optimal synthesis time was found to be between 4.5 and 5.5 days independent of the n_{Si}/n_{Fe} ratio in the gel. The molar ratio BQ/SiO_2 was kept at 0.2 as in the original recipe for Al-MCM-58. It was not possible to lower it as in the synthesis of Al-MCM-58. Under these conditions, pure Fe-MCM-58 was synthesised. Moreover, we found that the silicon source is of uttermost importance in order to obtain phase-pure Fe-MCM-58. Three different silica sources were tested, namely Ludox AS-30, Ludox AM-30 and Levasil, all of them as 30 wt-% SiO_2 solutions in water. Phase-pure zeolite Fe-MCM-58 was obtained only with Levasil as the silica source (Figure 3). The shape of the crystallisation curves (Figure 4) reveals that crystallisation starts after two days and increases to 70–80% after 96 h. The crystallisation curves for Fe-MCM-58 are characterised by a sharp maximum at about 120 h irrespective of the n_{Si}/n_{Fe} ratio. Thereafter, α-quartz starts to be formed as well, and later on Fe-MCM-58 is completely transformed into α-quartz, which is the thermodynamically most stable phase. The zeolite synthesis obeys the Ostwald ripening law. As described for zeolite A, the initial metastable phase is converted into a thermodynamically more stable sodalite until the most stable SiO_2 is formed.[29] Thus, the successful synthesis of Fe-MCM-58 requires the control of the optimum synthesis time, which was found to be close to 5.5 days for the conditions used (Figure 5).

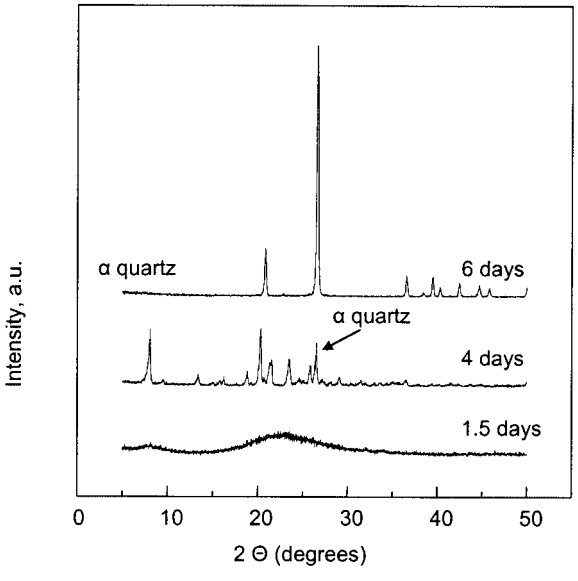

Figure 3. X-ray powder diffraction pattern of Fe-MCM-58 (n_{Si}/n_{Fe} = 28, T = 170 °C). After six days α-quartz is formed.

The scanning electron micrographs (Figure 6) of Al-MCM-58 (n_{Si}/n_{Al} = 36) and Fe-MCM-58 (n_{Si}/n_{Fe} = 36) show that no amorphous phase is present. Crystals of Al-

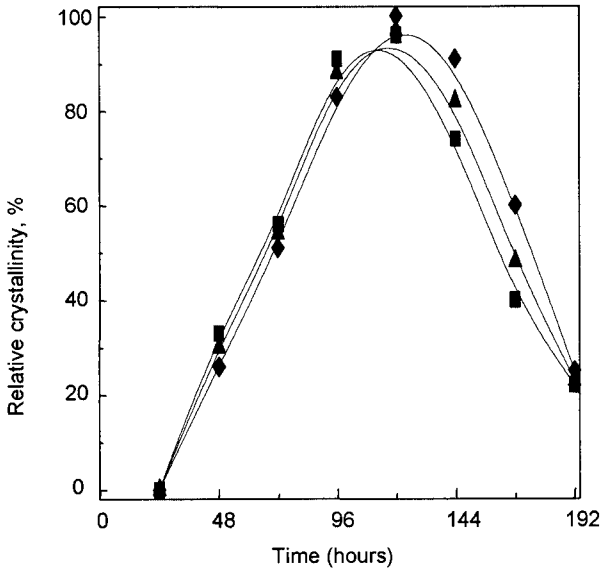

Figure 4. The dependence of relative crystallinity of Fe-MCM-58 on the initial n_{Si}/n_{Fe} ratio. Temperature: 155 °C; n_{Si}/n_{Fe} = 20 (▲), 30 (■), 40 (♦).

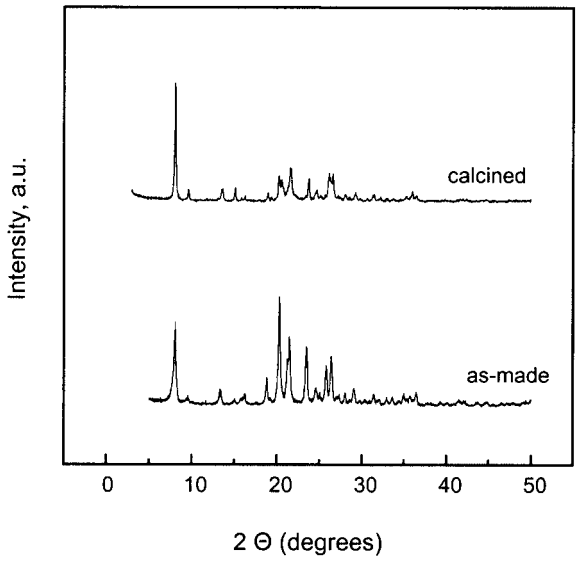

Figure 5. X-ray powder-diffraction pattern of Fe-MCM-58 (n_{Si}/n_{Fe} = 28; T = 155 °C; crystallisation time: 5 days).

MCM-58 (A and B) are represented by elongated particles with lengths ranging from 1 to 5 μm depending on the n_{Si}/n_{Al} ratio in the synthesis gel. The size of the crystals increases with a decreasing amount of aluminium in the reaction mixture. No uniform distribution of crystal sizes was observed for Al-MCM-58. The crystals of Fe-MCM-58 (n_{Si}/n_{Fe} = 36) (see C,D in Figure 6) are smaller than those of Al-MCM-58, with sizes between 0.5 and 3.0 μm. Some agglomeration of Fe-MCM-58 crystals to form stars was found (see C in Figure 6), which is also typical for Fe-ZSM-12.[28]

In agreement with our previous data,[25,31] two resonance signals at about δ = 58 and 61 ppm, reflecting tetrahedrally coordinated Al atoms, are observed in the ^{27}Al MAS NMR

 © 2005 Wiley-VCH Verlag GmbH & Co. KGaA, Weinheim

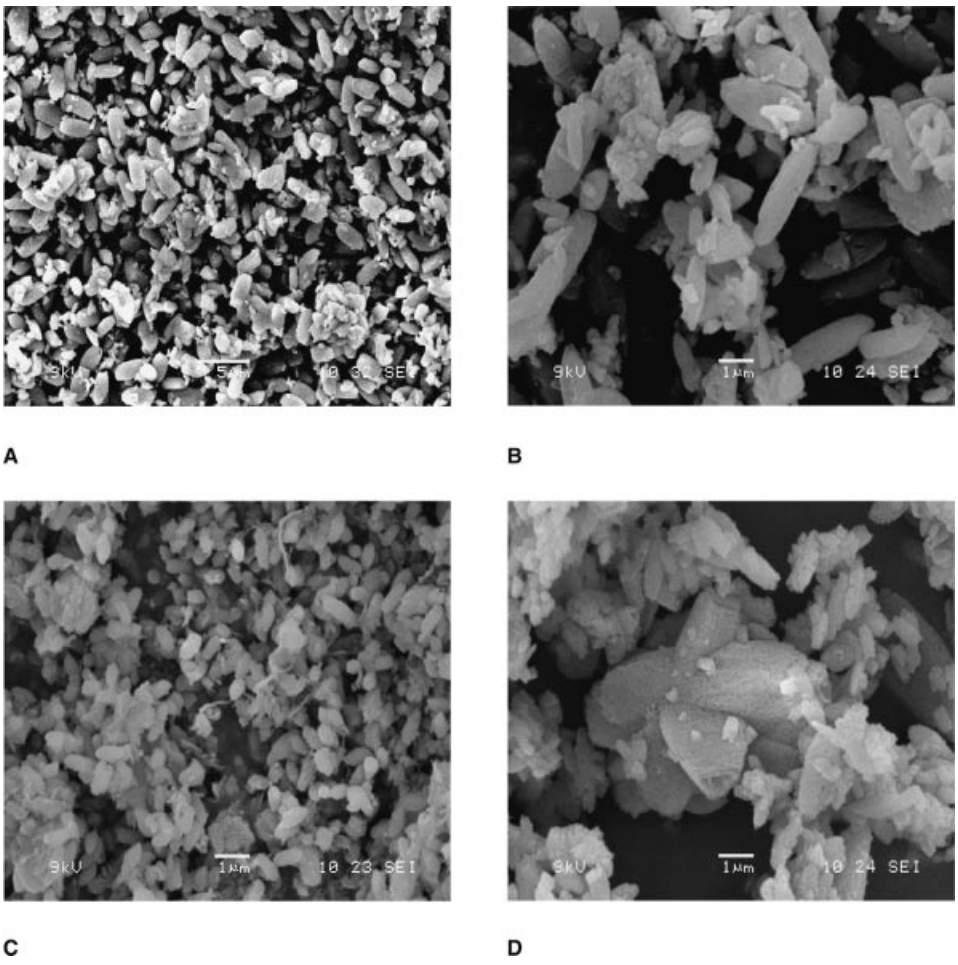

Figure 6. Scanning electron micrographs of zeolites Al-MCM-58 (A, B) and Fe-MCM-58 (C, D).

spectra of Al-MCM-58 with n_{Si}/n_{Al} ratios from 19 to 56 (Figure 7). No resonance around δ = 0 ppm, corresponding to octahedrally coordinated aluminium at extra-framework positions, was observed. This indicates that only tetrahedrally coordinated aluminium is present in Al-MCM-58. The two resonances in the tetrahedral region are explained by the presence of two crystallographically inequivalent aluminium atoms in T1–T4 sites.[31,37] The relative amount of the two different kinds of aluminium (δ = 60.9 and 58.2 ppm) changes with the n_{Si}/n_{Al} ratio: with increasing amount of aluminium in the zeolite, the intensity of the resonance at δ = 60.9 ppm decreases.

The ^{29}Si NMR spectrum of Al-MCM-58 (n_{Si}/n_{Al} ratio = 56) is composed of two broad, complex bands centred around δ = –110 and –102 ppm corresponding to tetrahedrally coordinated silicon atoms with different local environments (see a in Figure 8). The band around δ = –110 ppm can be attributed to Si(4Si) atoms, and is a superposition of four resonances at δ = –107.7, –109.3, –110.7 and –111.8 ppm. These resonances correspond to Si(4Si) atoms at four crystallographically inequivalent positions (T1–T4). The observed chemical shifts are in good agree-

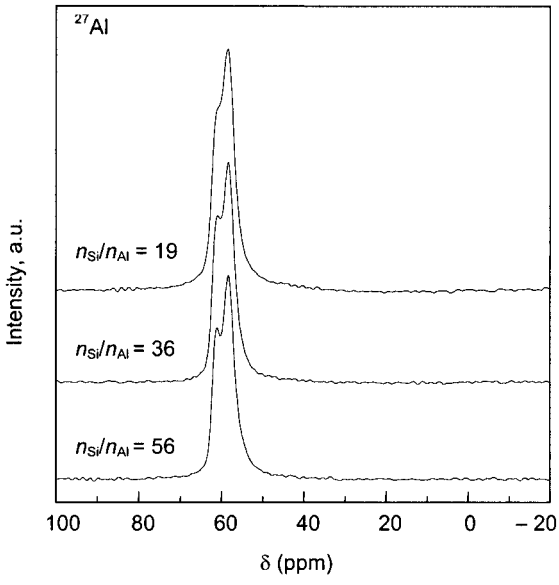

Figure 7. ^{27}Al MAS NMR spectra of Al-MCM-58 samples with different n_{Si}/n_{Al} ratios.

 © 2005 Wiley-VCH Verlag GmbH & Co. KGaA, Weinheim

ment with those reported for ITQ-4, which is isostructural with MCM-58 (δ = –108.0, –109.7, –110.9 and –111.5 ppm).[30] The higher resolution of the ^{29}Si NMR spectrum of Al-MCM-58 than that in the literature[31,37] is explained by the decrease in the perturbation of the Si environment due to a lower framework aluminium content. The broad band centred at δ = –102 ppm is ascribed to a superposition of the resonances corresponding to Si(3Si, 1Al) atoms and Si(3Si,OH) atoms. Decomposition of the spectrum to the Gaussian curves (not shown) indicated the presence of two resonances at δ = –101.1 and –104.0 ppm. The resonance at δ = –101.1 ppm can be attributed to Si(3Si, OH) atoms, as indicated by a CP experiment (see a in Figure 8). The resonance at δ = –104.0 ppm corresponds to Si(3Si, 1Al) atoms. Note that the intensity correction factor of Si(3Si, OH) is 1, compared to a value of 0.25 for Si(3Si, 1Al). Thus the relatively high intensity of the resonance at δ = –101.1 ppm compared to that at δ = –104.0 ppm indicates a higher amount of silanol groups than framework Al in the sample. A high amount of silanol groups has also been reported in previous papers from Ernst et al.[31,37]

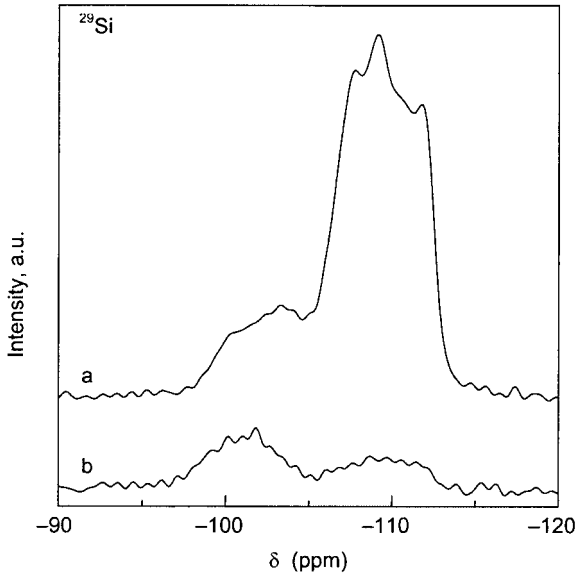

Figure 8. ^{29}Si HP (a) and CP (b) MAS NMR spectra of hydrated Al-MCM-58 (n_{Si}/n_{Al} = 56).

The type and concentration of the acid sites were determined after adsorption of probe molecules such as [D_3]acetonitrile and pyridine on the activated zeolites Al-MCM-58 and Fe-MCM-58, respectively. The spectra of Al-MCM-58 in the region of OH groups before and after adsorption of [D_3]acetonitrile are depicted in part A of Figure 9. The absorption band at 3746 cm^{-1} belongs to terminal Si–OH groups and the two bands at 3630 and 3564 cm^{-1} are characteristic of bridging OH groups. After the interaction with [D_3]acetonitrile, the bands of the hydroxyls groups are significantly reduced and new bands at 2327 cm^{-1} (Lewis sites) and 2297 cm^{-1} (Brønsted sites) are formed (see B in Figure 9).

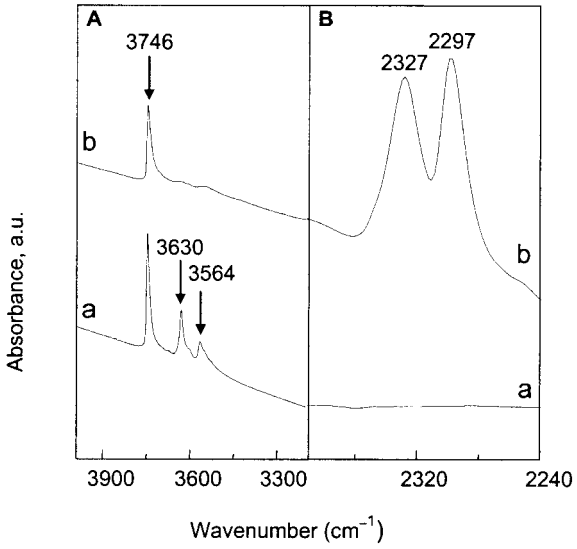

Figure 9. IR spectra of hydroxyl vibration region of Al-MCM-58 with n_{Si}/n_{Al} = 36 before (a) and after (b) [D_3]acetonitrile adsorption (A) and spectra of acetonitrile region before (a) and after (b) its adsorption (B).

In the case of Fe-MCM-58, absorption bands with maxima at 3746 cm^{-1} for terminal Si–OH groups and 3646 and 3520 cm^{-1} for bridging Si–OH–Fe groups (see A,a in Figure 10) were detected. Pyridine adsorption leads to the consumption of all bridging Si–OH–Fe groups (see A,b in Figure 10) and the formation of a band at 1545 cm^{-1} characteristic of the presence of the pyridinium ion, which reflects the interaction of pyridine with Brønsted sites. The band at 1448 cm^{-1} originates from coordinatively bonded pyridine on Lewis sites (see B,b in Figure 10).

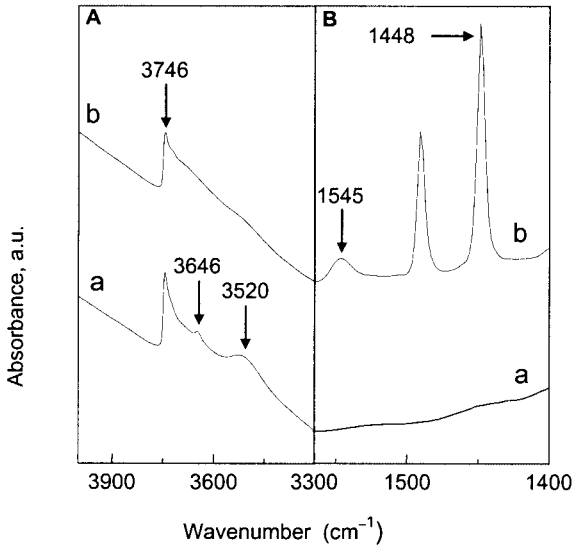

Figure 10. IR spectra of hydroxyl vibration region of Fe-MCM-58 with n_{Si}/n_{Fe} = 28 before (a) and after (b) pyridine adsorption (A) and spectra of pyridine region before (a) and after (b) its adsorption (B).

 © 2005 Wiley-VCH Verlag GmbH & Co. KGaA, Weinheim

The type, strength and concentration of acid sites control the rate and pathway of acid-catalysed reactions such as hydrocarbon cracking and rearrangement. It is evident that Lewis and Brønsted acid sites play a role in catalytic processes; however, their role is still not completely clear. In *n*-butene skeletal isomerisation, it has been shown that an increasing concentration of Lewis sites enhances the rate of deactivation.[32] We tried to modify the concentration of different types of acid sites in MCM-58 by using different methods of calcination. Besides the classical two-step calcination procedure in a stream of nitrogen and air at a calcination temperature of 540 °C, calcination in a stream of ammonia at a temperature of 450 °C was also used. The latter procedure has been described for zeolite beta by Kunkeler et al.,[33] who showed that this treatment results in a reduced formation of Lewis acid sites. They supposed that ammonia ions substitute the leaving organic template cations occluded in the channel system of the zeolite and thus stabilise the zeolite structure. Furthermore, Bourgeat-Lami et al.[34] have proposed that ammonium cations could hinder the formation of octahedrally coordinated aluminium and thus stabilise the structure of the zeolite. In the case of Al-MCM-58 (n_{Si}/n_{Al} = 19), the relative concentration of Brønsted acid sites amounts to about 47% and that of Lewis acid sites to bout 53%. After calcination of this zeolite in a stream of ammonia (5% of NH_3 in N_2) the relative concentration of Brønsted sites increased to 53%. Similar trends were also observed for Fe-MCM-58 (Table 1).

Table 1. n_{Si}/n_{Al} and n_{Si}/n_{Fe} ratios of zeolites Al-MCM-58 and Fe-MCM-58 in the initial gel and in the synthesised zeolite, as determined by X-ray fluorescence (XRF) and FTIR spectroscopy, and the relative amounts of Lewis and Brønsted acid sites.

Calcination	Si/Al[a]	Si/Al (XRF)	Si/Al (FTIR)	LS [%][b]	BS [%][b]
calcd. N_2/air	20	19	19	53	47
	40	36	36	53	47
	60	56	53	55	45
calcd. NH_3	20	19	19	47	53
	40	37	35	48	52
	60	56	52	49	51
Calcination	Si/Fe[a]	Si/Fe (XRF)	Si/Fe (FTIR)	LS [%][c]	BS [%][c]
calcd. N_2/air	20	18	18	86	14
	30	28	27	89	11
	40	36	32	94	6
calcd. NH_3	20	18	18	84	16
	30	28	26	86	14
	40	36	31	92	8

[a] Initial n_{Si}/n_M ratio in the reaction gel. [b] Adsorption of acetonitrile. [c] Adsorption of pyridine.

The determined concentrations of Brønsted and Lewis acid sites for Al- and Fe-MCM-58 are summarised in Table 1. From a comparison of the n_{Si}/n_{Al} (n_{Si}/n_{Fe}) ratios in the initial reaction mixture and in the synthesised zeolite we found that the obtained product was always richer in aluminium (iron) than the initial gel. The increase in the Al (Fe) content in the zeolite is more notable for Fe-MCM-58 than for Al-MCM-58.

The concentration of the Brønsted acid sites in Al-MCM-58 is practically constant despite the n_{Si}/n_{Al} ratio, while it decreases slightly with an increasing n_{Si}/n_{Fe} ratio. In other words, the higher the concentration of trivalent atoms in the zeolite, the higher the concentration of Lewis sites. The concentration of Brønsted sites depends strongly on the type of trivalent cation. While about 50% of the acid sites are of the Brønsted type in the Al-containing MCM-58 samples, only about 8–16% of the total acid sites are Brønsted sites in Fe-MCM-58. On one side, the concentration of trivalent cations in the synthesised sample is larger for Fe than for Al, whereas the concentration of Brønsted sites is significantly lower for Fe-MCM-58 than for Al-MCM-58. Due to the relatively large ionic radius of Fe^{3+} (0.063 nm) compared to Si^{4+} and Al^{3+} (0.040 nm and 0.053 nm,[35] respectively), the incorporation of iron into the framework is expected be much more complicated. Some evidence for the incorporation of iron into the Fe-MCM-58 framework can be obtained from the ESR spectra. The X-band EPR spectra (not shown) recorded at –196 °C for the calcined Fe-MCM-58 materials with different n_{Si}/n_{Fe} ratios show a sharp signal at g = 4.3 with shoulders at g = 9.1 and g = 2.3 and an intense broad signal at g = 2. The relative proportion of the signal at g = 4.3 decreases from n_{Si}/n_{Fe} = 40 to 20. The signal intensity is directly proportional to the iron content in the materials with different n_{Si}/n_{Fe} ratio. The assignment of the EPR signals to various species is still a matter of debate and is beyond the scope of this paper. Details can be found in our subsequent publication.[36]

Conclusions

Zeolite MCM-58 containing trivalent metal cations such as Al and Fe in the framework can be readily synthesised with *N*-benzylquinuclidinium bromide as the structure directing agent and Levasil (30% SiO_2 in water) as the silica source. The synthesis of Al-MCM-58 was accomplished at an SiO_2/BQ concentration of 0.1 in a wide range of initial n_{Si}/n_{Al} ratios (20 to 60) under dynamic conditions at 170 °C.

Incorporation of iron into the zeolite framework is not as straightforward. The synthesis requires a lower temperature, higher concentration of the template, and the suitable range of initial n_{Si}/n_{Fe} ratios is narrower (20 to 40). The synthesis was carried out with a SiO_2/BQ ratio of 0.2, under dynamic conditions at 155 °C.

The acid forms of both Al-MCM-58 and Fe-MCM-58 contain substantial amounts of Brønsted and Lewis acid sites. After calcination in a stream of ammonia, the amount of Brønsted sites was slightly greater than after conventional calcination in nitrogen and air.

Experimental Section

Abbreviations: BQ = *N*-benzylquinuclidinium bromide, CP = cross polarisation.

 © 2005 Wiley-VCH Verlag GmbH & Co. KGaA, Weinheim

The syntheses of MCM-58 with n_{Si}/n_{Al} ratios in the initial synthesis gel ranging from 20 to 60 and n_{Si}/n_{Fe} ratios ranging from 20 to 40 were investigated under hydrothermal conditions in Teflon-lined, stainless-steel autoclaves (35 and 90 mL) under autogenous pressure. *N*-Benzylquinuclidinium bromide (BQ) was used as structure-directing agent in a modified version of the procedure for the synthesis of zeolite MCM-58 described previously.[37]

N-Benzylquinuclidinium bromide was prepared by refluxing an equimolar mixture of benzyl bromide (from Fluka) and quinuclidine (from Fluka) in ethanolic solution for 24 h. Crystals were recovered after cooling the reaction mixture in an ice bath. The chemical composition and structure of the template were confirmed by elemental analysis and NMR spectroscopy.

The synthesis gels were prepared in polyethylene beakers at ambient temperature. In a typical synthesis of Al-MCM-58, 3.69 g of $Al_2(SO_4)_3 \cdot 18\,H_2O$ (from Fluka) was dissolved in 88.00 g of distilled water. To this solution, 3.24 g of KOH (from Lachema, CZ) and subsequently 4.02 g of *N*-benzylquinuclidinium bromide (as made) were added whilst stirring. Later on, 30.00 g of colloidal silica sol (30 wt.-% SiO_2 in water, Ludox AS-30, from Aldrich) was added slowly with vigorous stirring to the reaction mixture, which was finally homogenised for 2 min. The resulting gel was loaded into 90-mL, Teflon-lined, stainless steel autoclaves. The synthesis was carried out with agitation at 170 °C for Al-MCM-58 and at 155 °C for Fe-MCM-58 for 4 to 9 days. For the synthesis of Fe-MCM-58, the aluminium source was replaced by $Fe(NO_3)_3 \cdot 9\,H_2O$ (from Fluka) and instead of Ludox AS-30, Levasil VP 4038 (30% SiO_2 in water, from Bayer AG) was used. After crystallisation, the autoclaves were cooled to room temperature by quenching in cold water; the solid product was recovered by filtration, washed with distilled water, and dried at 80 °C overnight.

To remove the template, the as-synthesised sample was heated to 200 °C in a stream of nitrogen with a temperature ramp of 1 °C min^{-1} and kept at the same temperature for 4 h. Thereafter, the sample was heated to 540 °C with the same heating rate and kept for 2 h at this temperature. Finally, the material was calcined for 24 h in a stream of air at 540 °C.

In a second set of experiments the as-synthesised sample was treated in a stream of ammonia at 470 °C for 8 h with a heating rate of 1 °C min^{-1}. The samples were then ion-exchanged twice with a 0.5 M $NaNO_3$ solution for 8 h and once with 1.0 M $NaNO_3$ for 8 h using 100 mL of solution per gram of zeolite at room temperature. Finally, the sample was calcined again as described above.

The ammonium forms of both zeolites were prepared by fourfold repeated ion-exchange of the zeolite in a 0.5 M aqueous solution of ammonium nitrate at ambient temperature.

X-ray powder diffraction was used for identification of as-synthesised zeolites and the determination of their crystallinity to follow the kinetics of the crystallisation process. The XRD patterns were collected on a Siemens D5005 X-ray powder diffractometer equipped with a graphite monochromator and scintillation counter using Cu-K_α radiation in Bragg–Brentano geometry. Relative crystallinity is defined as the intensity of the peak at $2\theta = 20.53°$ compared to that of the MCM-58 sample with the highest crystallinity obtained in this study.

^{29}Si and ^{27}Al MAS NMR experiments were performed on a Bruker Avance 500 MHz (11.7 T) Wide Bore spectrometer operating at Larmor frequencies of 130.3 MHz for aluminium and 99.35 MHz for silicon using 4 mm and 7 mm o.d. rotors, respectively. Prior to the NMR experiments, all calcined samples were ion-exchanged three times with a 0.5 M NaCl solution for 8 h using 100 mL of solution per gram of zeolite at room temperature. In order to monitor Si coordination and local environment in the samples, ^{29}Si MAS NMR high-power decoupling (HPDec) and cross-polarisation (CP) experiments were carried out. In the case of high-power decoupling, pulse sequences with a $\pi/6$ (1.7 μs) excitation pulse and relaxation delay of 30 s were applied. 1024 FIDs were accumulated to obtain a sufficiently good signal-to-noise ratio. In the case of cross-polarisation spectra, pulse sequences with 50% ramp CP pulse, contact time 2 ms, high-power decoupling and a relaxation delay of 5 s were applied. 10 240 FIDs were accumulated to obtain the spectrum. Rotors were spun at a speed of 5 kHz; chemical shifts are referenced to the chemical compound Q8M8 as a standard. ^{29}Si high-power decoupling spectra were decomposed to the Gaussian bands using Microcall Origin 4.1 software (Microcall Software Inc., U.S.A.).

In order to measure the ^{27}Al MAS NMR spectra, high-power decoupling pulse sequences with a $\pi/12$ (0.7 μs) excitation pulse and relaxation delay of 1 s were applied; 1024 FIDs were accumulated to obtain the spectrum. Rotors were spun at a speed of 12 kHz;chemical shifts are referenced to an aqueous solution of $Al(NO_3)_3$.

The shape and the size of zeolite crystals were determined by scanning electron microscopy (JEOL, JSM-03). X-ray fluorescence spectroscopy was employed to estimate the chemical composition of Al- and Fe-MCM-58.

The concentrations of Brønsted and Lewis acid sites in Al-MCM-58 and Fe-MCM-58 were determined after the adsorption of [D_3]-acetonitrile and pyridine, respectively, followed by FTIR spectroscopy using a Nicolet FTIR Protégé 460 spectrometer. For this purpose, the zeolite powders were pressed binder-free into self-supporting wafers with a density from 4.0 to 10.0 mg cm^{-2}. [D_3]Acetonitrile was degassed by repeated freeze-thaw cycles before use. Prior to the adsorption of [D_3]acetonitrile, the zeolites were activated in situ by overnight evacuation at 400 °C. All measured spectra were recalculated to a normalised wafer thickness of 10 mg cm^{-2}. For a quantitative characterisation of the Brønsted acid sites (B), the C≡N–B vibration at about 2296 cm^{-1} was used with an extinction coefficient of $\varepsilon_B = 2.05 \pm 0.1$ cm μmol^{-1}. For a quantitative evaluation of Lewis acid sites (L), the C≡N–L vibration at 2323 cm^{-1} was used with an extinction coefficient of $\varepsilon_L = 3.6 \pm 0.1$ cm μmol^{-1}.[38] To determine the concentrations of acid sites in Fe-MCM-58, pyridine was used as a probe molecule. From the integral intensities of individual bands at 1545 cm^{-1} (Brønsted sites) and at 1448 cm^{-1} (Lewis sites) and using extinction coefficients of $\varepsilon_L = 1.67 \pm 0.1$ and $\varepsilon_B = 2.22 \pm 0.1$ cm μmol, respectively, concentrations of both types of acid sites were calculated according to ref.[39]

Acknowledgments

This study was supported by the Grant Agency of the Czech Republic (203/02/0804) and by the Volkswagen-Stiftung (I/75 886). G. K. thanks the Grant Agency of the Academy of Sciences of the Czech Republic (B4040402). S. E. and M. H. gratefully acknowledge financial support by the Deutsche Forschungsgemeinschaft and the Fonds der Chemischen Industrie. The authors thank Dr. L. Brabec for recording SEM pictures and Dr. J. Dědeček for running the MAS NMR experiments (both J. Heyrovský Institute, Prague).

[1] J. Čejka, B. Wichterlová, *Catal. Rev.* **2002**, *44*, 375–421.

 © 2005 Wiley-VCH Verlag GmbH & Co. KGaA, Weinheim

[2] C. S. Cundy, P. A. Cox, *Chem. Rev.* **2003**, *103*, 663–701.
[3] V. Gábová, J. Dědeček, J. Čejka, *Chem. Commun.* **2003**, *10*, 1196–1197.
[4] J. Kučera, P. Nachtigall, *Phys. Chem. Chem. Phys.* **2003**, *15*, 3311–3317.
[5] Q. Li, A. Navrotsky, F. Rey, A. Corma, *Microporous Mesoporous Mater.* **2003**, *64*, 127–133.
[6] J. Yu, J. Li, R. Xu, *Microporous Mesoporous Mater.* **2001**, *48*, 47–56.
[7] G. Bellussi, M. S. Rigutto, *Stud. Surf. Sci. Catal.* **1994**, *85*, 177–213.
[8] G. Perego, R. Millini, G. Bellussi, in *Molecular Sieves: Science and Technology* (Eds.: H. G. Karge, J. Weitkamp), Springer, *Molecular Sieves* **1998**, *1*, 187.
[9] P. Ratnasamy, R. Kumar, *Catal. Today* **1991**, *9*, 329–416.
[10] B. Liptakova, M. Hronec, Z. Cvengrosova, *Catal. Today* **2000**, *61*, 143–148.
[11] W. M. Meier, D. H. Olson, C. Baerlocher, *Atlas of Zeolite Structure Types*, 5th ed., Elsevier, Amsterdam **2001**.
[12] M. Tagliabue, L. C. Carluccio, D. Ghisletti, C. Perego, *Catal. Today* **2003**, *81*, 405–412.
[13] M. E. Davis, F. R. Lobo, *Chem. Mater.* **1992**, *4*, 756–768.
[14] A. Corma, M. Diaz-Cabanas, J. Martinez-Triguero, F. Rey, J. Rius, *Nature* **2002**, *418*, 514–517.
[15] A. Corma, M. Puche, F. Rey, G. Sankar, S. J. Teat, *Angew. Chem. Int. Ed.* **2003**, *42*, 1156–1159.
[16] A. Corma, F. Rey, S. Valencia, J. L. Jorda, J. Ruis, *Nat. Mater.* **2003**, *2*, 493–497.
[17] A. Burton, S. Elomari, R. C. Medrud, I. Y. Chan, C.-Y. Chen, L. M. Bull, E. S. Vittoratos, *J. Am. Chem. Soc.* **2003**, *125*, 1633–1642.
[18] D. C. Calabro et al., *US Patent 6,049,018*, assigned to Mobil Oil Corp **2000**.
[19] A. Burton, S. Elomari, C. Y. Chen, *Chem. Eur. J.* **2003**, *9*, 5737–5748.
[20] P. Prokešová, S. Mintova, J. Čejka, T. Bein, *Microporous Mesoporous Mater.* **2003**, *64*, 165–174.
[21] C. J. H. Jacobsen, C. Madsen, J. Houžvička, *J. Am. Chem. Soc.* **2000**, *122*, 7116–7117.
[22] E. W. Valyocsik, *WO Patent 95/11196* assigned to Mobil Oil Corp. **1994**.
[23] C. Y. Chen, L. W. Finger, R. C. Medrud, C. L. Kibby, P. A. Crozier, I. Y. Chan, T. V. Harris, L. W. Beck, S. I. Zones, *Chem. Eur. J.* **1998**, *4*, 1312–1323.
[24] J. Čejka, A. Krejčí, N. Žilková, J. Kotrla, S. Ernst, A. Weber, *Microporous Mesoporous Mater.* **2002**, *53*, 121–133.
[25] S. Ernst, M. Hartmann, T. Hecht, A. Weber, *Stud. Surf. Sci. Catal.* **2001**, *135*, 315–317.
[26] S. Ernst, in *Molecular Sieves: Science and Technology* (Eds.: H. G. Karge, J. Weitkamp), Springer, *Molecular Sieves*, **1998**, *1*, 66.
[27] E. W. Valyocsik, *US Patent 5,441,721*, assigned to Mobil Oil Corp. **1994**.
[28] G. Košová, J. Čejka, *Collect. Czech. Chem. Commun.* **2002**, *67*, 1760–1778.
[29] J. R. Francis, D. O'Hare, *J. Chem. Soc., Dalton Trans.* **1998**, *19*, 3133–3148.
[30] M. C. Camblor, A. Corma, L. A. Villaescusa, *Chem. Commun.* **1997**, *8*, 749-750.
[31] S. Ernst, M. Hartmann, T. Hecht, A. Weber, *Prepr. Petrol. Div. Am. Chem. Soc., 221st National Meeting, American Chemical Society, San Diego*, **2001**, 37–38.
[32] B. Wichterlová, N. Žilková, E. Uvarová, J. Čejka, Ch. Paganini, J. A. Lercher, *Appl. Catal. A* **1999**, *182*, 297–308.
[33] O. J. Kunkeler, B. J. Zuurdeeg, J. C. van der Waal, J. A. van Bokhoven, D. C. Koningsberger, H. van Bekkum, *J. Catal.* **1998**, *180*, 234–244.
[34] E. Bourgeat-Lami, P. Massiani, F. di Renzo, P. Espiau, F. Fajula, T. des Courieres, *Appl. Catal.* **1991**, *72*, 139–152.
[35] http://www.webelements.com.
[36] V. Umamaheswari, M. Hartmann, A. Pöppl, *J. Phys. Chem.* submitted.
[37] S. Ernst, M. Hunger, J. Weitkamp, *Chem. Ing. Tech.* **1997**, *6*, 77–79.
[38] B. Wichterlová, Z. Tvarůžková, Z. Sobalík, P. Sarv, *Microporous Mesoporous Mater.* **1998**, *24*, 223.
[39] C. A. Emeis, *J. Catal.* **1993**, *141*, 347–354.

Received: September 6, 2004

 © 2005 Wiley-VCH Verlag GmbH & Co. KGaA, Weinheim

Crosslinking Mechanism of Boric Acid with Diols Revisited

Marcel Rietjens*[a,b] and Peter A. Steenbergen[a,c]

Keywords: Boric acid / Borate / Diols / Guaran / Crosslinking / Rheology

Complex formation of boric acid with diol functional groups is well known and many papers have been published assuming borate is the reactive species. Based on the high reactivity of boric acid towards nucleophiles, this paper assumes boric acid is the reactant. We prove this hypothesis by presenting a study of the reaction of the polymer guaran with boric acid under various conditions. A thermodynamic analysis of the underlying reactions does not show any differences between either crosslinking species. Thermodynamics shows that the concentration of the 2:1 crosslinks, that give rise to the enhanced viscosity, is proportional to [B], the boric acid concentration, [X^2], the concentration of available crosslink sites and inversely proportional to [H^+]. These predictions were all confirmed by experiment. However, a difference between the mechanisms is demonstrated in a kinetic analysis: Longer gel times are predicted with the mechanism based on boric acid as the pH of the fluid increases, that is exactly what is observed in practice. Evidence is provided from visco-elastic measurements. A new approach to describe inter- and intramolecular crosslink formation is introduced and evidence for the correctness of this description is provided.
(© Wiley-VCH Verlag GmbH & Co. KGaA, 69451 Weinheim, Germany, 2005)

Introduction

Gelled fluids based on the natural polysaccharide guaran, crosslinked with for example borate, are generally used to fracture oil and gas wells to improve productivity. These fractures start at the well bore and can extend up to several hundred meters into the formation. Basically, this process tremendously increases the surface area of the well bore. In the preparation of borate crosslinked gels, pH (control) is crucial to the success of fracture treatments. The effects of pH and temperature on borate equilibriums have been well described and summarized by Harris.[1] Interestingly, when these gels are prepared the crosslink time depends on the pH of the solution: the higher the pH, the longer it takes to form a gel. At a pH value of 12 and above, the crosslink time may be an hour or longer. This cannot be explained by assuming borate as the reactive species. An additional interesting feature of borate crosslinked gels is their self-healing property: i.e. when exposed to high shear stresses, the network breaks up (shear thinning) but reheals quickly when it comes to rest.[1–3]

Guaran consists of a (1→4) linked mannosepyranosyl backbone with single galactosepyranosyl units connected by (1→6) linkages. The ratio between mannose and galactose is about 2:1.[4,5] Both monomers are capable of forming complexes with boric acid. The complex formation constant strongly depends on the stereochemistry of the diol functionality and their relative positions, 1,2 or 1,3. These aspects have been treated in detail by van den Berg et al.[6] Nuclear Magnetic Resonance (NMR) experiments have shown that complex formation constants of 1,2-diols are larger than 1,3-diols whereas 1,2 complex formation constants of mannose and galactose 1:1 complexes are comparable.[7,8] Combined with the known ratio of mannose to galactose in guaran, boric acid preferentially forms crosslinks with mannose in a ratio of 2:1 in agreement with experiment.[5]

Many authors have assumed borate is the reactive species[1,2,5,8–15] while others have assumed cations to be involved.[14] In a few cases boric acid was proposed as the reactant but merely because the reactions took place at very low pH values.[13] Tetraborate was assumed to be the crosslinking reactant by Khomutov et al., which is more in line with the proposed mechanism covered in this paper because it contains trivalent boron.[16] Van Duin[17,18] realized, based on similar arguments as given below, that boric acid could also be the reactive species and takes both boric acid and borate into account in the reaction equations.

In principle, reaction of an alcoholic group with borate is similar to the formation of an ether and requires dehydration. These types of reactions require time and specific conditions such as heat, to overcome the activation energy, and the removal of water. Properties like self-healing and the fact that equilibrium between boric acid and borate is faster than the NMR time scale can only be explained provided the reactions are fast, in contradiction with the above observations for ether formation. Thus the reaction must

[a] Halliburton,
Treubstraat 1H, 2288 EG Rijswijk, Netherlands
[b] Current address: Cimcool Industrial Products B.V.,
Schiedamsedijk 20, 3134 KK, Vlaardingen,
E-mail: marcel.rietjens@tiscali.nl
[c] Current address: Panterra Geoconsultants,
Leiderdorp, The Netherlands
E-mail: p.steenbergen@panterra.nl

have a very low activation energy. A determination of this latter value shows that it is indeed low and was reported to be 20.5 kJ/mol.[15] The trivalent B atom in boric acid has an empty p orbital that is very electrophilic in nature; it rapidly reacts with various nucleophiles to form complexes.[19] Therefore, a much more likely alternative mechanism is to assume boric acid as the reactant.

Theory

First, the two models based on boric acid and based on borate will be described. We assume that all crosslink sites are available for reaction and, for the moment, we do not differentiate between inter- and intramolecular crosslinks (Mxl). This issue will be dealt with later because we are primarily interested in the concentration of inter-Mxls because these give rise to visco-elasticity. We further assume similar behavior of guar (G) and hydroxypropylguar (HPG). Thus values for K_1 and K_2 are expected to be similar in magnitude. In the equations below, the following abbreviations are used:

X: Free crosslink site on guar polymer chain

B: $B(OH)_3$

B^-: $B(OH)_4^-$

X_1B/X_1B^-: 1:1 Complex with B in the boric acid/borate form crosslinked with one guar chain.

X_2B^-: 2:1 Complex in which two guar chains are crosslinked by one borate molecule and which is always negatively charged. X_2B^- includes both inter- and intramolecular crosslinks.

Boric Acid as the Reactive Species. Thermodynamics: The fundamental equilibriums are:

$$B + H_2O \rightleftarrows B^- + H^+ \quad (1a)$$

$$B + X \underset{k_{-1}}{\overset{k_1}{\rightleftarrows}} X_1B^- + H^+ + H_2O \quad (2a)$$

$$X_1B^- + H^+ \rightleftarrows X_1B + H_2O \quad (3a)$$

$$X_1B + X \underset{k_{-2}}{\overset{k_2}{\rightleftarrows}} X_2B^- + H^+ + H_2O \quad (4a)$$

Further, the mass balance is given by:

$$[B_{total}] = [B_t] = [B] + [B^-] + [X_1B] + [X_1B^-] + [X_2B^-] \quad (5a)$$

When substituting the expressions for B^-, X_1B^- etc. into Equation (5a) and rearranging we get:

$$[B_t] = [B]\cdot\left[1 + \frac{K_a}{[H^+]} + \frac{K_1\cdot[X]}{[H^+]} + \frac{K_1\cdot[X]}{K_a^{1:1}} + \frac{K_1\cdot K_2\cdot[X^2]}{[H^+]\cdot K_a^{1:1}}\right] = [B]\cdot M \quad (6a)$$

here K_a is the acid dissociation constant of boric acid, $K_a^{1:1}$ the acid dissociation constant of the complex X_1B, K_1 the equilibrium constant for the formation of the 1:1 complex and K_2 the formation constant of the 2:1 complex. The concentration of 2:1 complexes is then given as:

$$[X_2B^-] = \frac{K_1\cdot K_2\cdot[B_t]\cdot[X^2]}{[H^+]\cdot K_a^{1:1}\cdot M} \quad (7a)$$

Equation (7a) is the fundamental thermodynamic expression that describes the concentration of the 2:1 crosslinked products as a function of X, B and pH.

Borate Anion as the Reactive Species. Thermodynamics: In this case Equation (2a) and (4a) are defined as:

$$B^- + X \underset{k_{-1}}{\overset{k_1}{\rightleftarrows}} X_1B^- + 2H_2O \quad (2b)$$

$$X_1B^- + X \underset{k_{-2}}{\overset{k_2}{\rightleftarrows}} X_2B^- + 2H_2O \quad (4b)$$

The mass balance is now defined as:

$$[B_t] = [B^-]\cdot\left[\frac{[H^+]}{K_a} + 1 + \frac{K_1\cdot[H^+]\cdot[X]}{K_a^{1:1}} + K_1\cdot[X] + K_1\cdot K_2\cdot[X^2]\right] = [B^-]\cdot N \quad (6b)$$

The concentration of 2:1 complexes is now given by:

$$[X_2B^-] = \frac{K_1\cdot K_2\cdot[B_t]\cdot[X^2]}{N} \quad (7b)$$

Equation (7a) and (7b) show $[X_2B^-]$ is linear in $[X^2]$ and $[B_t]/M$ or $[B_t]/N$ in both models. In fact Equation (7a) and (7b) are exactly equivalent and therefore thermodynamics *cannot* differentiate between both mechanisms.

Boric Acid as the Reactive Species. Kinetics: The basic general rate equations for the formation of 1:1 and 2:1 complexes are:

$$Rate = \frac{d([X_2B^-])}{dt} = k_2\cdot[X_1B]\cdot[X] - k_{-2}\cdot[X_2B^-]\cdot[H^+] \quad (8a)$$

$$\frac{d([X_1B])}{dt} = k_{-a}^{1:1}\cdot[X_1B^-]\cdot[H^+] - k_a^{1:1}\cdot[X_1B] - k_2\cdot[X]\cdot[X_1B] + k_{-2}\cdot[X_2B^-]\cdot[H^+] \quad (9a)$$

$$\frac{d([X_1B^-])}{dt} = k_1\cdot[B]\cdot[X] - k_{-1}\cdot[X_1B^-]\cdot[H^+] - k_{-a}^{1:1}\cdot[X_1B^-]\cdot[H^+] + k_a^{1:1}\cdot[X_1B] \quad (10a)$$

A steady state is assumed for the formation of X_1B and X_1B^-. In other words $d([X_1B])/dt = d([X_1B^-])/dt = 0$. The justification for these assumptions is that reaction rates in-

 © 2005 Wiley-VCH Verlag GmbH & Co. KGaA, Weinheim

volving free boric acid, which is a small molecule, are much greater than reaction rates involving two polymer chains.

An expression for $[X_1B]$ in terms of [B], [X] and $[X_2B^-]$ can now be derived from Equation (9a) and (10a). Substitution in Equation (8a) yields:

$$\frac{d([X_2B^-])}{dt} = C_1 + C_2 \cdot [X_2B^-] \quad (11a)$$

with

$$C_1 = \frac{k_{-a}^{1:1} \cdot k_1 \cdot k_2 \cdot [B] \cdot [X^2]}{k_{-1} \cdot k_a^{1:1} + k_{-1} \cdot k_2 \cdot [X] + k_{-a}^{1:1} \cdot k_2 \cdot [X]} \quad (12a)$$

and

$$C_2 = \frac{(k_{-1} \cdot k_{-2} + k_{-a}^{1:1} \cdot k_{-2}) \cdot k_2 \cdot [X] \cdot [H^+]}{k_{-1} \cdot k_a^{1:1} + k_{-1} k_2 \cdot [X] + k_{-a}^{1:1} \cdot k_2 \cdot [X]} - k_{-2} \cdot [H^+] \quad (13a)$$

After applying the initial condition $X_2B^- = 0$ for $t = 0$, the solution of Equation (11a) is:

$$[X_2B^-] = \left(e^{C_2 \cdot t} - 1\right) \cdot (C_1 / C_2) \quad (14a)$$

Borate Anion as the Reactive Species. Kinetics: The derivation is very similar and the solution of the differential equations has the same form with C_1 and C_2 expressed as:

$$C_1 = \frac{k_1 \cdot k_2 \cdot [B^-] \cdot [X]^2}{k_{-1} + k_2 \cdot [X]} \quad (12b)$$

$$C_2 = \frac{k_2 \cdot k_{-2} \cdot [X]}{k_{-1} + k_2 \cdot [X]} - k_{-2} \quad (13b)$$

As t approaches infinity, both kinetic expressions yield the thermodynamic relation. The main difference is that the term C_2 is independent of pH in the borate model whereas it is a function of pH in the boric acid model.

Results and Discussion

In the calculations and discussions that follow we introduce [X*], the critical concentration of crosslink sites in mol/L, similarly defined as the critical overlap concentration of a polymer, [P*]. Likewise, the concentrations of 1:1 and 2:1 complexes are expressed in mol reacted crosslink sites/L. In plots or when dealing with critical concentrations, we sometimes use the polymer concentrations [P] and [P*] in g/L because these are more familiar in use. No precautions were made to minimize effects due to charge repulsion by the addition of salt.

Chemistry of Borate Complexes: Both 1,2- and 1,3-diols can form 1:1 and 2:1 complexes with boric acid. Each reaction is assumed to proceed in two steps, and because the second step, ring closure, is relatively fast due to the chelate effect, the first step is rate limiting.[17] Paál[20,21] discusses effects of induction, solvation, and H-bonding, in the case that multiple OH groups are present, on the value of K_1. Boric acid complexes with 1,2-diols are well known to possess higher acidities as opposed to 1,3-diols.[15,21,22] The stronger acidity is primarily caused by ring strain. Complexes formed from 1,3-diols form six rings and are slightly more acidic compared to boric acid[15,22] but complexes from 1,2-diols are five rings and have considerable ring strain. In the neutral form, the hybridization of the B nucleus is sp^2 vs. sp^3 in the borate form. In the transition to the borate form, the ring strain is relieved and the activation energy decreases to even lower values.

The stability of 1:1 and 2:1 borate complexes has been shown to be optimum in a certain pH range. Below and above this range no complexes are formed.[17,23] The reason that has been forwarded at high pH values, > 13, is charge repulsion because of deprotonation of the diol group.[13,23] Although we propose compounds containing trivalent boron, B and X_1B, as the reactant species, B and X_1B are still in rapid equilibrium with B^- and X_1B^- respectively. As a consequence, the boron nucleus will be negatively charged on average and therefore subject to charge repulsion.

Inter/intramolecular Crosslinking: In the derivation of the equations above no account was given to inter- and intra-Mxls. Because visco-elasticity is a function of the concentration of inter-Mxl only this must be incorporated in the model. We assume that the polymer coils have a fixed radius of gyration that is independent of the polymer concentration. Thus at [P] > [P*] the coils mix instead of compressing each other. The first step, formation of the 1:1 complex, is the same for both inter- and intra-Mxls. Basically, this formation is a reaction between a crosslink site and boric acid. Because the latter is able to move freely throughout the fluid, all potential crosslink sites are available for reaction. The concentration of 1:1 complexes is than proportional to [X]·[B].

The formation of 2:1 intra-Mxl complexes is a reaction between a 1:1 complex and a free crosslink site in the same polymer chain. At [P] < [P*], the available number of crosslink sites equals the number of crosslink sites within the individual coil. Effectively, this is the same (bulk) concentration as when the coils just touch each other, i.e. at [P] = [P*]. Therefore, the effective concentration of crosslink sites within each coil is equal to [X*]. For intra-Mxls, this relation applies also to concentrations above [P*] because we have assumed the radius of gyration as constant and because reaction with other coils are counted separately as inter-Mxls. Therefore, the concentration of intra-Mxls is proportional to [X]·[X*].

At [P] > [P*] coils of different polymer chains touch each other and reactions between different polymer coils lead to inter-Mxls. Formation of inter-Mxls are assumed to commence at [P] > [P*]. As with intra-Mxls, inter-Mxls are the reaction products from a 1:1 complex and an available crosslink site. Now the number of available crosslink sites is proportional to ([X] – [X*]) because only that portion is able to react with other coils. It follows that the concentration of inter-Mxls is proportional to [X]·{[X] – [X*]}. The ratio of inter- and intra-Mxls is then simply calculated as {[X] – [X*]}/[X*] and is > 0 at [P] > [P*]. However, at polymer concentrations higher than P* deviations can be

 © 2005 Wiley-VCH Verlag GmbH & Co. KGaA, Weinheim

anticipated. For example, due to excluded volume effects, compression of the coils can be expected to some extent. This leads to an effective higher concentration of P*. Overall, the concentration of 2:1 complexes can be calculated as the sum of inter- and intra-Mxls and is proportional to $[X]^2$ [see Equation (7a)]. The fractions F of the inter- and intra-Mxls are calculated as:

$$F_{Inter} = \frac{P - P^*}{P} \quad (15a)$$

$$F_{Intra} = \frac{P^*}{P} \quad (15b)$$

having a ratio of

$$\frac{Inter}{Intra} = \frac{P - P^*}{P^*} \quad (15c)$$

Pezron et al. derived a different equation for the ratio between inter- and intra-Mxls.[9] They relate a critical concentration C_0 to the average size of a loop or an intra-Mxl. The ratio inter/intra is calculated as $(C/C_0)^{5/4}$. For guar of similar molecular weight they assessed a value for C_0 of 4%. In their view, the concentration of inter-Mxls is always > 0, assuming a $[P] > 0$, and steadily grows. However, even at a polymer concentration twice as large as [P*], the ratio is barely 0.05, whereas in our case it is 1, that is twenty times as large. This issue is further discussed in the model parameter section that follows. We do agree with the statement of Pezron et al. that the ratio inter/intra is dependent on the flexibility of the polymer coils. The more flexible, the closer the segments are to each other favoring intra-Mxl. In our view this is accounted for in the higher value of [P*] because a more flexible coil has a smaller radius of gyration.

Model Parameters: We have deduced the model parameters from first principles and available date of equilibrium constants published in the literature. Further, we have applied the concept of reduced diffusion coefficient in analogy with the reduced mass and is defined as: $D_{reduced} = D_1 + D_2$, where D_1 and D_2 are the diffusion coefficients of the species 1 and 2.

***K*$_a$:** The equilibrium between boric acid and borate is known to be very fast, even faster then the NMR time scale. The reverse rate constant, k_{-a}, was determined by Gilkerson as $1.3 \cdot 10^{10}$ L·mol^{-1}·s^{-1}.[24] Based on this value and the known value of K_a of boric acid,[25] $5.8 \cdot 10^{-10}$ mol·L^{-1}, the forward rate constant, k_a, is calculated as 7.5 s^{-1}. The value of k_{-a} will be used as a basis for the rate constants k_{-1} and k_{-2}.

[P], [P*]: The critical concentration P* was determined by measuring G' as a function of [P] down to the lowest measurable concentration of 1.7 g/L, with and without additional crosslinker. The value of [P*] was taken as the concentration where the two curves merge and was assessed at 2.04 g L^{-1}. This value is in good agreement with published values.[5]

[X], [X*]: At a polymer concentration of 3 g/L, the concentration of [X] is calculated as $0.73 \cdot 3/179 = 0.012$ mol·L^{-1}. The average Mw of a monomer in HPG is about 179 and 0.73 is the fraction of crosslink sites available per monomer due to the HP groups. The value of X* is 0.0083 mol·L^{-1}.

***K*$_1$, *k*$_{-1}$, *k*$_1$:** The value for k_{-1} is deduced from k_{-a}. Three effects influence its value: 1) Compared to the borate anion, which has four OH groups, the 1:1 complex has two OR groups thus a statistical chance of 2/4 to become protonated followed by elimination of H_2O. 2) Compared to OH groups, OR groups have a twofold lower basicity thus have equally less chance to become protonated.[26] 3) The 1:1 complex dissociates into boric acid and a polymer chain and, compared to water, as in the reverse reaction of B^- to B, boric acid has a roughly threefold smaller diffusion coefficient. In summary, the value of k_{-1} is calculated as $1.3 \cdot 10^{10}/(2 \cdot 2 \cdot 3) = 1.08 \cdot 10^9$ L·mol^{-1}·s^{-1}. The value of the equilibrium constant K_1 is calculated from literature data based on dialysis measurements: $K'_1 = 11$ L·mol^{-1} and is defined as $K'_1 = [X_1B^-]/([B^-] \cdot [X])$.[8] In this paper K_1 is defined as $K_1 = [X_1B^-] \cdot [H^+]/([B] \cdot [X])$. Because $K_1 = K'_1 \cdot K_a$ its value is $6.4 \cdot 10^{-9}$. The value of k_1 is then calculated as 6.9 L·mol^{-1}·s^{-1}.

***K*$_a^{1:1}$, *k*$_{-a}^{1:1}$, *k*$_a^{1:1}$:** The acidity of the (neutral) 1:1 complex is defined by $K_a^{1:1}$. Its value is required to calculate K_2. It is well known that the acidity of boric acid increases upon the addition of a 1,2-diol. Sugars such as mannitol and sorbitol are widely used for this purpose in analytical chemistry. Based on titration data with these sugars, apparent K_a values were calculated for boric acid complexes.[27] Based on these data, we estimate an apparent $K_a^{1:1}$ value for the 1:1 complex of $1 \cdot 10^{-5}$ mol·L^{-1}. The absolute value is in fact not relevant for the calculated crosslink density because $K_a^{1:1}$ cancels out in the equation for $[X_2B^-]$. However, it does point out that X_1B complexes are much more acidic and that the concentration of the neutral 1:1 complex decreases very rapidly with increasing pH. The value of $k_{-a}^{1:1}$ is based on the value of k_{-a}. Because there are two OH groups vs. four in borate, the statistical factor is 2/4. We neglect any effect on the basicity of the OH groups due to the complexed diol. Because the values of $k_a^{1:1}$ and $k_{-a}^{1:1}$ are of no concern for the result, ring strain caused by complexation with an 1,2-diol is accounted for only in an increase in the value of $k_a^{1:1}$, not in $k_{-a}^{1:1}$. The reduced diffusion coefficient is that for water and does not change. The value for $k_{-a}^{1:1}$ is then $1.3 \cdot 10^{10}/2 = 6.5 \cdot 10^9$ L·mol^{-1}·s^{-1} and $k_a^{1:1} = K_a^{1:1} \cdot k_{-a}^{1:1} = 6.5 \cdot 10^4$ s^{-1}.

***K*$_2$:** Similar to K_1 we can express K_2 as $K'_2 \cdot K_a^{1:1}$. Pezron[8] defined K'_2 as $K'_2 = [X_2B^-]/([X_1B^-] \cdot [X])$. Two sets of data are available that should allow for the calculation of K_2, NMR spectroscopic data and rheological data. Because the NMR spectroscopic data have a high level of uncertainty, we used the data based on rheological experiments.[2] A critical note to place is that these data have not been corrected for physical crosslinks (see below). The value of K'_2 was obtained from the slope of G' vs. $[P]^{2.6} \cdot [B^-]$ (Figure 6 in ref.[2]), although it is unclear why they have used a power

 © 2005 Wiley-VCH Verlag GmbH & Co. KGaA, Weinheim

of 2.6 instead of 2. The same analysis, but based on a power of 2, yields a slightly better fit. Further, they state that the slope is equal to $2{\cdot}K'_2{\cdot}RT$ but substitution of the appropriate definitions for $[X_2B^-]$ in Equation (16) below, results in $2{\cdot}K'_1{\cdot}K'_2{\cdot}RT$. Using a power of 2.6 the value of K'_2 yields 0.43 mol·L^{-1} whereas with a power of 2 the value of K'_2 is only 0.09 mol·L^{-1}. Model calculations with a value of K'_2 = 0.09 mol·L^{-1} give smaller values for G' than observed experimentally and consequently the deviations, see Table 1, are < 1. The strange observation we then make is that the deviations become even larger (thus $<< 1$) in tests with higher polymer concentrations, whereas at higher polymer concentrations a gel behaves more rubber-like in line with model requirements. Therefore we have decided to use the value of 0.43 mol·L^{-1} instead. The value of K_2 is calculated as $4.3{\cdot}10^{-6}$.

In calculating the value of k_{-2}, the statistical factor is now 4/4 = 1, because there are four possibilities to break a bond of a diol as in B^-. The basicity is still twofold smaller than OH in B^-. At this point dissociation is between two polymer chains that have considerably smaller diffusion coefficients. From data of Brandrup,[28] the value of D for a guar sample with a M_w of 657.000 is $0.54{\cdot}10^{-11}$ m^2·s^{-1}. The molecular weight of the sample we used is approximately $2.0{\cdot}10^6$. Based on the data given in Brandrup, an empirical relation between D and M_w could be set up and based on this relation a value of D for the HPG sample used is calculated as 0.10 10^{-11} m^2·s^{-1}. Compared to the value for water ($D = 2.26{\cdot}10^{-9}$ m^2·s^{-1}), this value is about 2000-fold smaller. The value of k_{-2} is then calculated as $1.3{\cdot}10^{10}/(2{\cdot}2000) = 3.2{\cdot}10^6$ L·mol^{-1}·s^{-1}. From K_2 and k_{-2}, k_2 is finally calculated as 14 L·mol^{-1}·s^{-1}.

Physical Crosslinking: Solutions of guaran are very viscous and possess some degree of visco-elasticity caused by physical crosslinks or entanglements.[29] Because the model outlined above is based on chemical crosslinks, G' data must be corrected for contributions due to physical crosslinks (G'_{phys}). Experiments showed that physical crosslinks form very fast as plateau values were attained within few minutes. The value of G'_{phys} can be expected to be a function of polymer concentration and pH.[29] Figure 1 shows that the value of G'_{phys} is constant up to a pH of about 12, after which it decreases with increasing pH.

This observation is in line with data presented by Goycoolea et al.,[29] and is thought to be caused by charge up on the polymer chain due to deprotonation. In principle, the polymer behaves like a polyelectrolyte at very high pH values.[30] Assuming a pK_a value of 14.7 for the OH groups, it can be calculated that about 1% is dissociated at a pH value of 12.5.[26,30] The acquired charge leads to repulsion between chains, and therefore, partial disruption of the weak physical crosslinks. Charge up of the polymer is also caused by 1:1 complexes (the concentration of 2:1 complexes is relatively small). In the determination of the values for G'_{phys}, fructose was added to mask boric acid. A consequence is that 1:1 complexes are also not formed, whereas they are formed in the other experiments. This means that the values for G'_{phys} are overestimated, and therefore G′ values for chemical crosslinks are overcorrected. Model calculations, however, show that at the highest polymer and borate concentrations used, the concentration of 1:1 complexes is only 0.4% (relative to the total number of crosslink sites) so the magnitude of the overcorrection should be small. This observation is in agreement with calculations by Ochiai.[31] The effect of polymer concentration on G'_{phys} is shown in Figure 2.

In principle, one could expect G'_{phys} to be proportional to [P]·{[P] – [P*]}, the reason being similar to chemical

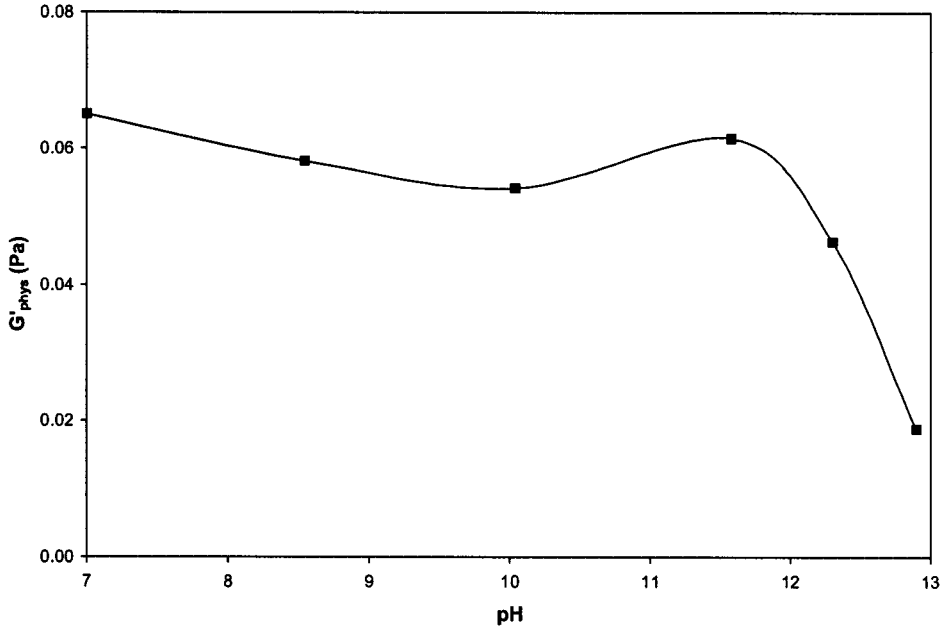

Figure 1. Effect of pH on visco-elasticity due to physical crosslinking.

 © 2005 Wiley-VCH Verlag GmbH & Co. KGaA, Weinheim

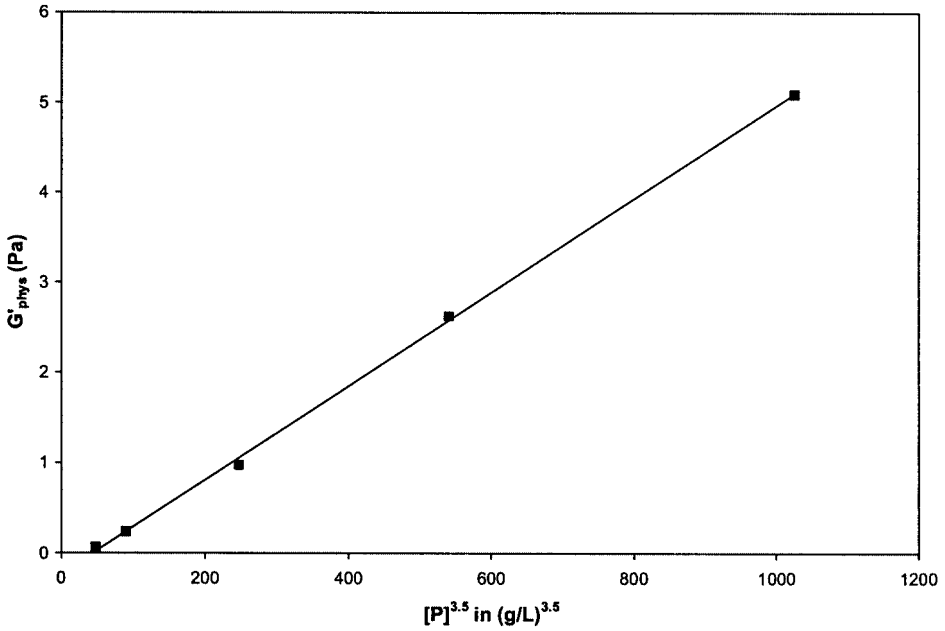

Figure 2. Effect of polymer concentration on visco-elasticity due to physical crosslinking.

crosslinking. This was not confirmed by an analysis, instead we found excellent correlations with the relations $G'_{phys} \approx [P]^{3.5}$ and $G'_{phys} \approx [P]^2 \cdot \{[P] - [P^*]\}$.

Model Validation. Thermodynamics: The dependence of G' as a function of total boron concentration is shown in Figure 3. Because these experiments were run at the same pH value, no account needed to be given to M. A straight line is observed in agreement with theory and published data.[2,3,14]

Equation (7a) further predicts a linear relationship between G' and $[P] \cdot \{[P] - [P^*]\}$. This relation is shown in Figure 4. This curve is clearly not linear but has some curvature because we assume

$$G' = 2\,[X_2B^-]_{Inter}RT \quad (16)$$

to be valid at very low values of G'. Schultz and Myers,[3] however, indicate that a minimum value for $[X_2B^-]_{inter}$ is required for this relation to be valid. Thus Equation (16) is true only if the gel behaves like an ideal rubber. The gels in our experiments have a very low crosslink density and cannot be considered a real rubber. However, this argument

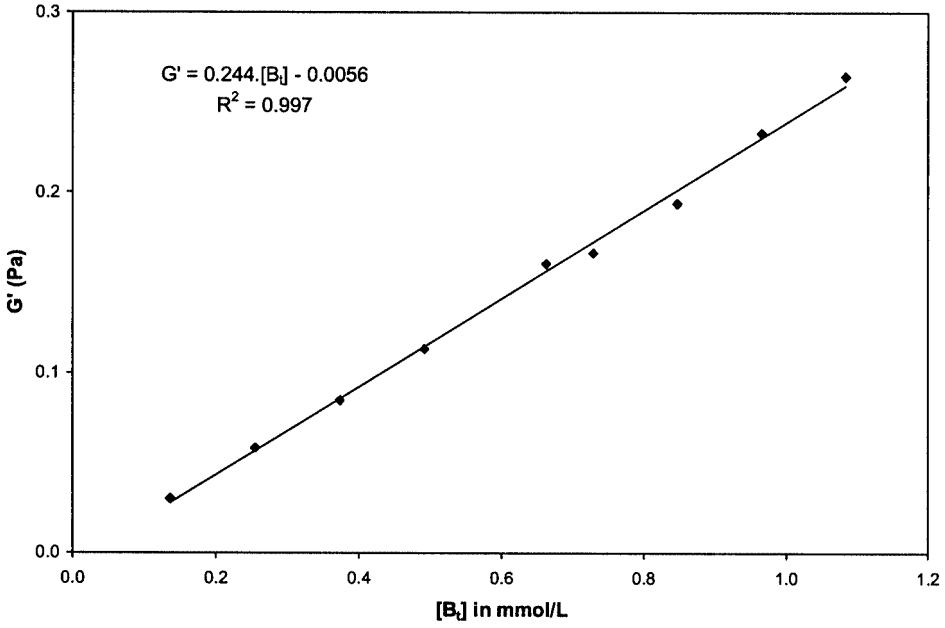

Figure 3. Correlation between visco-elasticity and total boron concentration; 3 g HPG/L, pH 10.04 ± 0.04.

 © 2005 Wiley-VCH Verlag GmbH & Co. KGaA, Weinheim

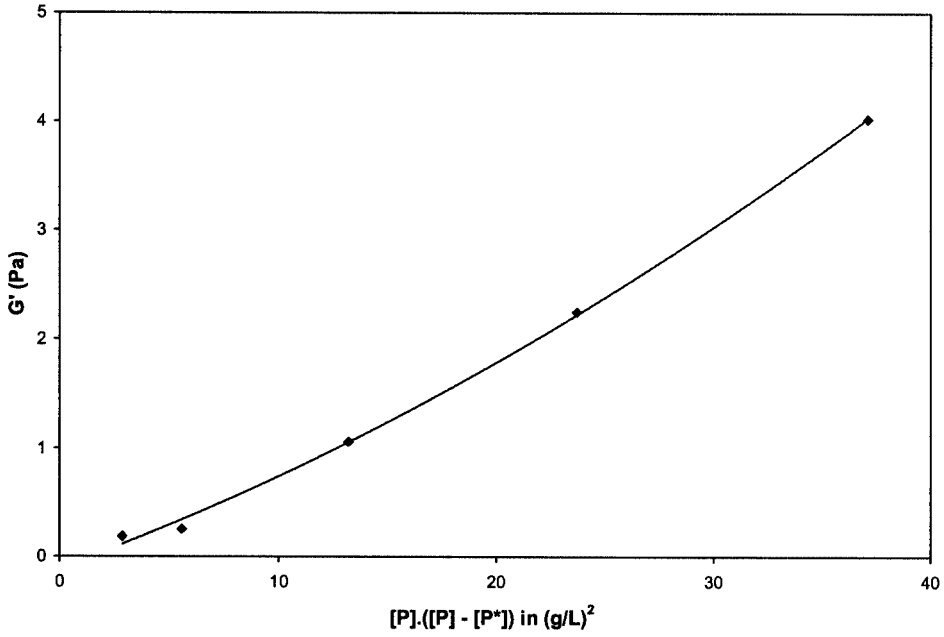

Figure 4. Correlation between visco-elasticity and [P]·([P] − [P*]); 300 μL crosslinker solution, pH 10.0 ± 0.08.

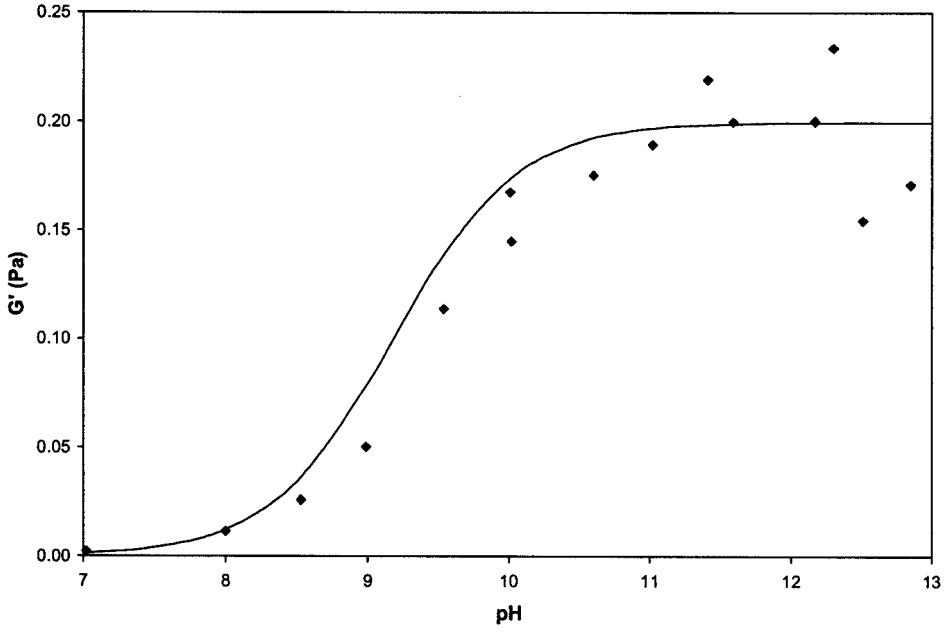

Figure 5. Visco-elasticity as a function of pH. The solid line is the theoretical curve with a deviation factor of 3.6 applied (see text); 500 μL crosslinker solution, [P] is 3 g/L.

is equally true for the data shown Figure 3. Because the corrections due to physical crosslinks in Figure 4 were up to 50% and were not a constant value, as opposed to data in Figure 3, and are subject to error also, the observed curvature may be misleading. Note that similar deviations from ideal behavior are shown in data published by Pezron et al. in gels with low B_t content and low polymer concentration: compare parts a–d in Figure 5 in ref.[2]

In Figure 5, G' is plotted as a function of pH at fixed concentrations of polymer and $[B_t]$. In the same Figure, the calculated model curve is included as well using a deviation factor of 3.6 (see later). Although there is some scatter in the experimental data at high pH values, the match with the theoretical curve is quite reasonable. Effects of deprotonation of the polymer chain could be anticipated at the highest pH value tested, 12.8, but because of the amount of scatter, it is difficult to state that the experimental curve drops below the theoretical curve. Experiments by van Duin et al.[23] do show that at deprotonation conditions, 0.5 M NaOH, the complex formation constant K_2 drops to zero

 © 2005 Wiley-VCH Verlag GmbH & Co. KGaA, Weinheim

Table 1. Master Table showing the calculated and experimentally observed visco-elasticity values at the conditions specified. The deviation factor is defined as the theoretical value divided by the experimental value.

pH	$[B_t]$ (mol/L)	[P] (g/L)	[X] (mol xl sites/L)	# xl/ chain	$G'_{calcd.}$ (Pa)	$G'_{obsd.}$ (Pa)	Deviation
10.02	0.49	2.99	$1.22\cdot10^{-2}$	0.06	0.42	0.13	3.2
9.99	0.51	3.59	$1.47\cdot10^{-2}$	0.09	0.83	0.23	3.6
10.19	0.54	4.79	$1.96\cdot10^{-2}$	0.18	2.10	1.28	1.6
10.10	0.57	6.00	$2.45\cdot10^{-2}$	0.25	3.77	2.59	1.5
10.10	0.61	7.20	$2.94\cdot10^{-2}$	0.34	6.01	4.99	1.2
10.00	0.14	2.99	$1.22\cdot10^{-2}$	0.02	0.12	0.03	3.9
10.00	0.25	2.99	$1.22\cdot10^{-2}$	0.03	0.22	0.06	3.7
10.00	0.37	2.99	$1.22\cdot10^{-2}$	0.04	0.32	0.08	3.8
10.09	0.49	2.99	$1.22\cdot10^{-2}$	0.06	0.43	0.11	3.8
10.01	0.66	2.99	$1.22\cdot10^{-2}$	0.08	0.57	0.16	3.5
10.01	0.73	2.99	$1.22\cdot10^{-2}$	0.08	0.62	0.17	3.7
10.08	0.85	2.99	$1.22\cdot10^{-2}$	0.10	0.74	0.19	3.8
10.07	0.97	2.99	$1.22\cdot10^{-2}$	0.11	0.84	0.23	3.6
10.08	1.08	2.99	$1.22\cdot10^{-2}$	0.13	0.94	0.26	3.6
7.02	0.73	2.99	$1.22\cdot10^{-2}$	0.00	0.00	0.00	2.2
8.00	0.73	2.99	$1.22\cdot10^{-2}$	0.01	0.04	0.01	3.8
8.53	0.73	2.99	$1.22\cdot10^{-2}$	0.02	0.13	0.03	5.0
8.99	0.73	2.99	$1.22\cdot10^{-2}$	0.04	0.28	0.05	5.6
9.54	0.73	2.99	$1.22\cdot10^{-2}$	0.07	0.49	0.11	4.4
10.01	0.73	2.99	$1.22\cdot10^{-2}$	0.08	0.62	0.17	3.7
10.60	0.73	2.99	$1.22\cdot10^{-2}$	0.09	0.68	0.17	3.9
11.02	0.73	2.98	$1.22\cdot10^{-2}$	0.09	0.70	0.19	3.7
11.41	0.73	2.98	$1.22\cdot10^{-2}$	0.09	0.70	0.22	3.2
12.03	0.73	2.98	$1.22\cdot10^{-2}$	0.09	0.70	0.19	3.6
12.17	0.73	2.98	$1.21\cdot10^{-2}$	0.09	0.70	0.20	3.6
12.30	0.73	2.98	$1.21\cdot10^{-2}$	0.09	0.70	0.23	3.1
12.40	0.73	2.98	$1.21\cdot10^{-2}$	0.09	0.70	0.23	3.0
12.85	0.73	2.96	$1.21\cdot10^{-2}$	0.09	0.68	0.16	4.2

and estimates that effects of pH are noticeable at a pH > 13.

The data are summarized in Table 1. The deviation factor, defined as the ratio of calculated and observed values, is 3.6 on average but decreases to 1.2 in the experiments with the highest polymer concentration.

In Table 2 some data points published by Pezron et al.[2] are shown that were calculated through also. We used a molecular mass of $2.2\cdot10^6$ Daltons, a [P*] of 1.5 $g\cdot L^{-1}$, and assumed one crosslink site per monomer, each with a M_w of 156.[2] Even though the gels examined in their case were reasonably representative of a true rubber, the deviations from model calculations are quite similar to our results.

Model Validation. Kinetics: Figure 6 shows the results of model calculations of the concentration of X_2B^- vs. time. The calculated gel times vary from 100 seconds at a pH of 7 up to $10\cdot10^6$ seconds at a pH of 13. Compared to experimental data these numbers are about two orders in magnitude too large and are likely to be due to the estimated value for the diffusion coefficient D of polymer segments. The constant C_1 in Equation (14a) contains two terms but is in fact dominated by the last term: $k_{-2}\cdot H^+$. The value of k_{-2} is proportional to $D_{reduced}$ and the value used for guaran was calculated from sedimentation experiments. In such experiments, the entire molecule settles in a gravitational field, whereas the mobility of chain segments is expected to be

Table 2. Data from Pezron et al. re-calculated[2], see text for details.

pH	$[B_t]$ (mol/L)	[P] (g/L)	[X] (mol xl sites/ L)	# xl/ chain	$G'_{calcd.}$ (Pa)	$G'_{obsd.}$ (Pa)	Deviation
9.2	3.5	4.4	$2.8\cdot10^{-2}$	2	18	4	4.5
9.2	8.2	4.4	$2.8\cdot10^{-2}$	4	42	19	2.3
9.2	3.9	5.5	$3.5\cdot10^{-2}$	3	34	13	2.7
9.2	8.8	5.5	$3.5\cdot10^{-2}$	6	75	38	2.0
9.2	4.2	7.7	$4.9\cdot10^{-2}$	4	72	29	2.5
9.2	9.7	7.7	$4.9\cdot10^{-2}$	10	168	100	1.7
9.2	4.7	11.0	$7.1\cdot10^{-2}$	7	163	100	1.6
9.2	11.0	11.0	$7.1\cdot10^{-2}$	15	384	255	1.5

 © 2005 Wiley-VCH Verlag GmbH & Co. KGaA, Weinheim

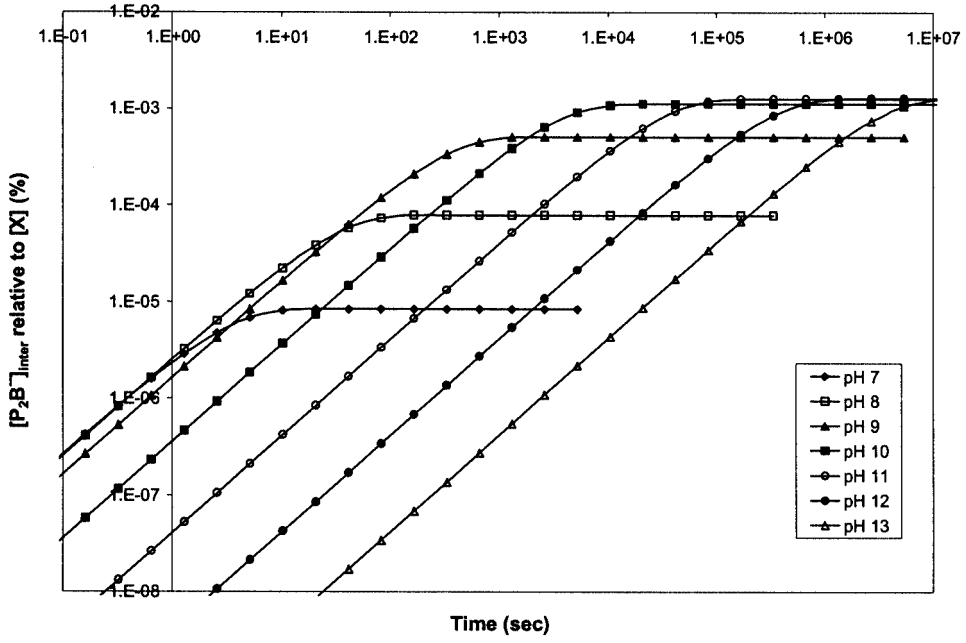

Figure 6. Results of calculated concentrations of $[X_2B^-]$ relative to the concentration of available crosslink sites X vs. time. Curves for pH values from 7 up to 13 are shown.

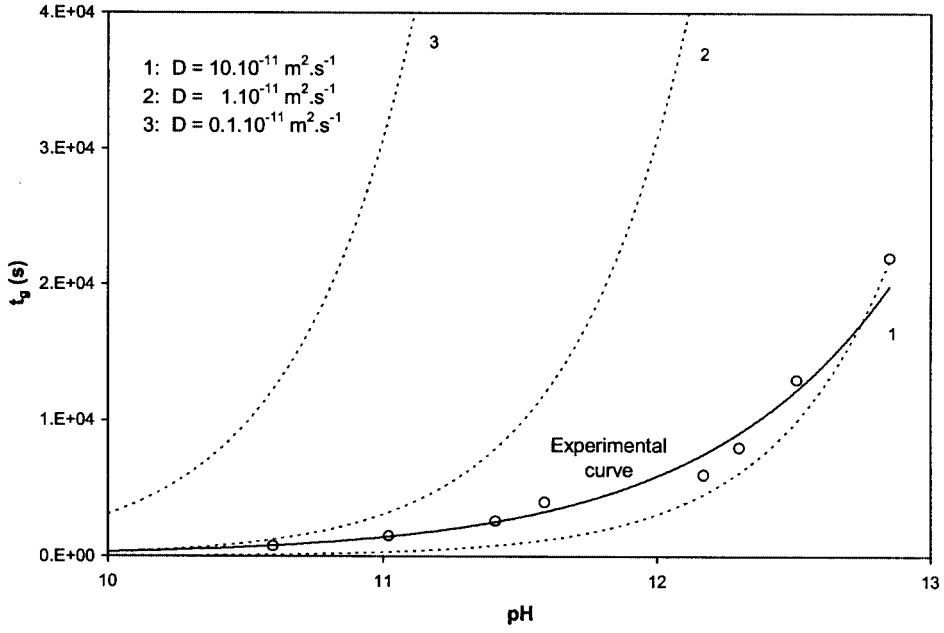

Figure 7. Results of experimental gel times as a function of pH and diffusion coefficient. Three curves (dashed) are shown based on diffusion coefficients ranging from $0.1 \cdot 10^{-11}$ $m^2 \cdot s^{-1}$ up to $10 \cdot 10^{-11}$ $m^2 \cdot s^{-1}$. The solid curve is based on experimental data.

greater. Leibler et al.[32] have made detailed calculations of these effects in reversible networks. Crosslink reactions take place between chain segments with a value for D of roughly two orders greater than the value based on sedimentation, in line with experimental data shown in Figure 7.

On the other hand, as more crosslinks form, the network becomes more rigid and consequently the mobility of the chain segments decreases.[32] As exemplified in Table 1, network formation is not much of an issue here, but it should be taken into account in experiments with more rigid gels.

The time it takes for the gel to reach maximum viscoelasticity is called the gel time, t_g, and can be calculated theoretically. The curves in Figure 6 all show the same value of the slope in a log-log plot. The value of the slope is derived by taking the ln of Equation (14a) and calculating the derivative to ln(t). Using the approximation $e^{C_2 t} \approx 1 +$

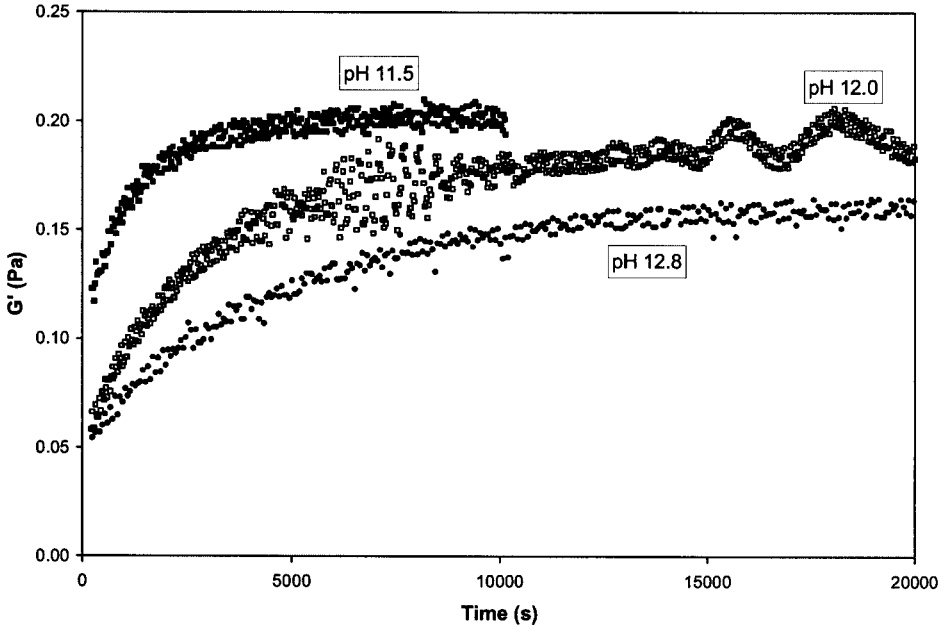

Figure 8. Results of experimental G' values as a function of time. Only a few curves measured at different pH values are shown as examples. Note that only the initial parts of the curves at pH values of 12.0 and 12.8 are shown.

$C_2 \cdot t$, it turns out that the slope is exactly 1. In Figure 6 we can draw two imaginary lines, one through the first part of the curve with a slope of 1 and one through the horizontal part with a slope of zero. The gel time is defined as the intersection of the two lines and yields:

$$t_g = \frac{1}{k_{-2} \cdot [H^+]} \tag{17}$$

These results can be translated to gel times as a function of pH and D_{guaran}. In Figure 7, three curves (dashed) are shown for different diffusion coefficients of chain segments (0.1-, 1- and $10 \cdot 10^{-11}$ $m^2 \cdot s^{-1}$). The resemblance with the experimental curve is quite reasonable, with a value of D close to $10 \cdot 10^{-11}$ $m^2 \cdot s^{-1}$, i.e., about 2 orders in magnitude greater than based on the sedimentation value but in agreement with calculations published by Leibler et al.[32]

Example experimental gel time curves are shown in Figure 8 to demonstrate the increase of gel times in tests at higher pH values. A log-log plot of the initial part of these curves shows a straight line as shown in Figure 9. The re-

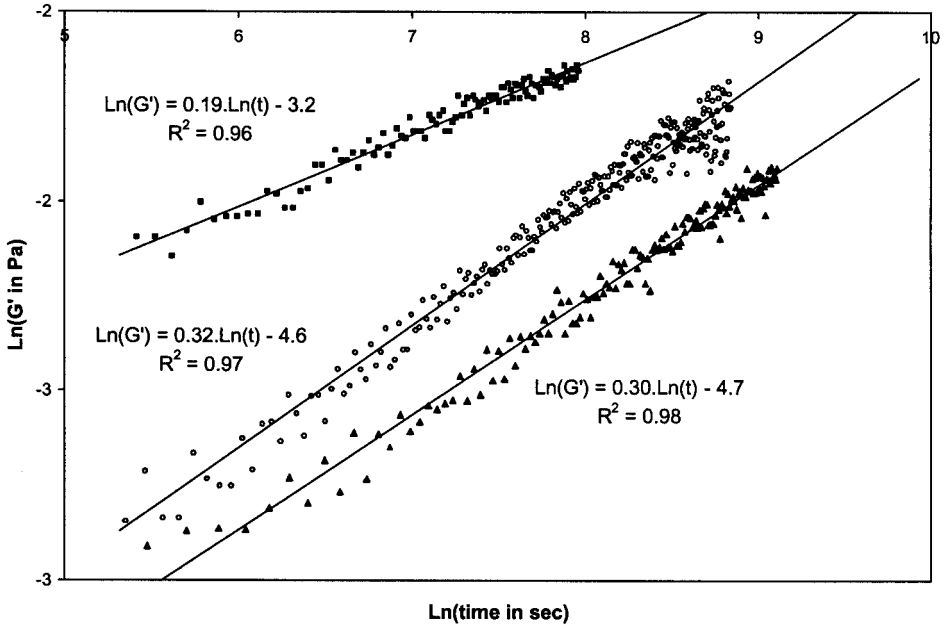

Figure 9. Calculations of the slopes of the initial parts of the curves for the examples shown in Figure 8.

 © 2005 Wiley-VCH Verlag GmbH & Co. KGaA, Weinheim

sults for the gel times and the slopes of tests run at pH values >10.5, which have sufficiently long gel times, are shown in Table 3 (corrected for physical crosslinking).

Table 3. Values of the slopes of the initial part of the experimental curves and the gel times t_g

pH	Slope	Gel time (s)
10.60	0.12	750
11.02	0.19	1500
11.41	0.16	2600
11.59	0.19	4000
12.17	0.32	6000
12.30	0.30	8000
12.51	0.24	13000
12.85	0.30	22000

Compared to the theoretical value of the slope, which is exactly 1, the experimental values are < 1. The slopes of the lines increase as the pH increases but level off at a pH around 12. At low pH values, the gel time is short, and therefore the slopes could have already leveled off to some extent. This is also true in the theoretical curves. At high pH values, 12 for instance, where deprotonation of the polymer is not expected to play any role and where the network is not built up fully because the gel time is at least one hour, the value of the slope is only 0.3. This reason for this discrepancy is not clear.

Data presented in a paper by Pezron et al.[2] provide further indication of the overall correctness of the proposed mechanism. They measured G' curves as a function of frequency for gels with pH values of 8.7, 9.2, and 11. At the highest pH value tested, the plateau extends to lower frequencies and indicates longer life times of the crosslinks, in accordance with the proposed model.

Verification of Assumptions and Improvements: In the derivation of Equation (14a), the steady state assumption was applied to d([X_1B])/dt and d([X_1B^-])/dt. Using the appropriate values for k_1, k_{-1} and others the forward and reverse reaction rates were calculated for reactions 1a through 4a at pH values of 9 and 13. Compared to the B/B^- equilibrium, the relative reaction rates for the forward and reverse reactions of reaction (2a) is two orders slower, and for reaction (3a), one order slower. The forward and reverse reaction rates for reaction (4a) are five orders slower relative to the B/B^- equilibrium. Thus the assumption that the formation of X_2B^- is rate-limiting was indeed valid. Note that X_1B is replenished rapidly because X_1B^- is present in excess. A second assumption made, was constancy of [X] and [B]. As with X_1B, the concentration of B is small relative to [B^-] and readily replenished. A problem could be the amount of free available crosslink sites because a relatively large part is in the form of X_1B^-. However, relative to concentrations of available crosslink sites, model calculations show that [X_1B^-] is not even 1% at a polymer concentration of 10 g/L and a [B_t] of $1\cdot10^{-3}$M. However, in rigid gels reduction of available crosslink sites X needs to be taken into account.

Although the model has been shown to be reasonably accurate, it does have a few shortcomings: 1) in the calculation of k_{-2} application of the diffusion coefficient based on the entire polymer is unrealistic, 2) no effects due to network formation are taken into account 3) effects for the charge up of the polymer chain due to 1:1 complexes and deprotonation are not accounted for and, 4) the relation between G' and [X_2B^-] is not well defined in weakly crosslinked gels.

Verification with Results by Pezron et al.:[10] Interesting results have been compiled by Pezron et al. for borate complexes with poly(glyceryl methacrylate) by using NMR spectroscopy. This polymer was shown to have a critical polymer concentration of 20 g/L. It was observed that the ratio [X_1B^-]/[B_t] varied linearly with [P] whereas the ratio

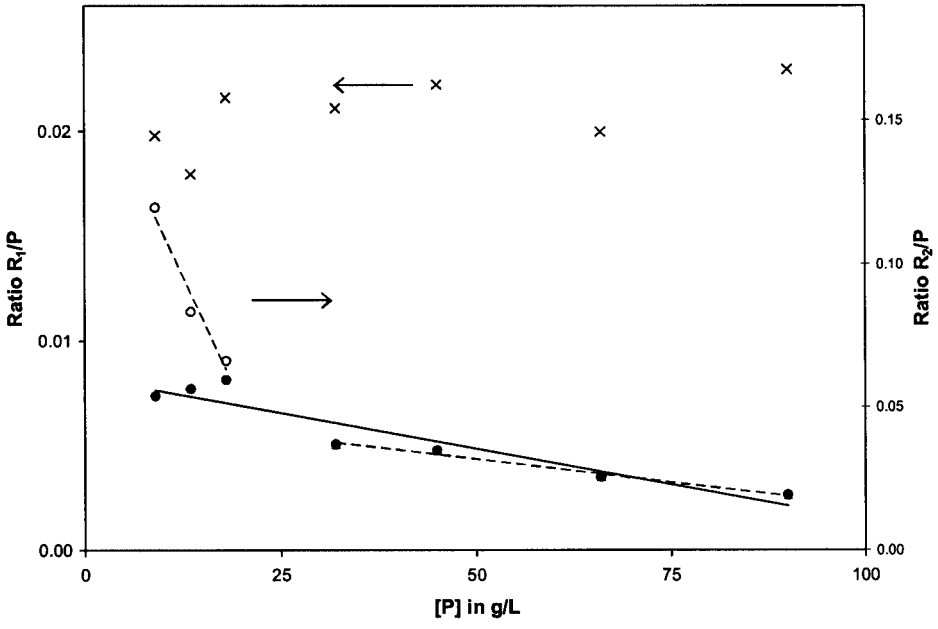

Figure 10. Results of an analysis of data published by Pezron et al.[10]; see text for details.

 © 2005 Wiley-VCH Verlag GmbH & Co. KGaA, Weinheim

$[X_2B^-]/[X_1B^-]$ was independent of [P] at [P] < [P*] but dependent on [P] at [P] > [P*]. These observations are in agreement with the proposed theory, and the latter observation is especially convincing evidence for the proposed scheme of inter/intra-Mxl formation. Note that NMR does not distinguish between inter- and intra-Mxl. Thus the peak representing free boron is the sum of [B] and $[B^-]$ and the peak representing the 1:1 complex is the sum of $[X_1B^-]$ and $[X_1B]$. The first relation, $[X_1B^-]/[B_t]$, is calculated as:

$$R_1 = \frac{[X_1B^-]}{([B]+[B^-])} = \left(\frac{K_1}{K_a+[H^+]}\right)\cdot[X] \quad (18)$$

Thus R_1 divided by [P] is constant as shown in Figure 10. The second ratio R_2 is calculated as:

$$R_2 = \frac{[X_2B^-]}{[X_1B^-]+[X_1B]} = \left(\frac{K_2}{K_a^{1:1}+[H^+]}\right)\cdot[X] \quad (19)$$

and therefore R_2/[P] is constant also. However, note that the concentration of X in Equation (18) originates from the formation of 1:1 complexes and is always [X] whereas the concentration of X in Equation (19) is based on the formation of 2:1 complexes and is [X*] at [P] < [P*] and [X] at [P] > [P*], in agreement with Pezron's observations.

The dashed lines in Figure 10 represent the uncorrected data, that is, the value of [P] is used in Equation (19) for all data points. The solid line represents the corrected data, i.e., for the first three data points [P*] was used and for the remaining data points [P]. The slight decrease of the slope could be due to a reduction of the dielectric constant of the solvent at high polymer concentrations.[15]

The data shown by Pezron et al. for 1,2-propanediol are in perfect agreement with Equation (18) and (19). In this case the value of [P] can be used throughout because small molecules are able to diffuse through the entire fluid as 1:1 and as 2:1 complexes.

Verification with Results by Pizer et al.:[11–13] Attempts to clarify the mechanism have been undertaken by the group of Pizer. One observation that can be explained directly from the mechanism above is the relation between the acidity of boric acid derivatives and the value of K_1. Some data published by Pizer et al.[11] are shown graphically in Figure 11 including the results from regression analysis. A linear relationship between the pK_1 and the pK_a is observed with a slope of almost equal to 1. Note that the 95% confidence interval for the slope is quite broad and about ±0.3. Thus even though smaller slopes are suggested, its values are not statistically different from 1, the theoretical value. This latter value is readily seen if we express K_1 as $K'_1 \cdot K_a$ or $\log K_1 = \log K_a + \log K'_1$. Of course, deviations can be expected in case boron is hybridized differently.

Experimental Section

Materials: Hydroxpropyl guaran (HPG) with a molecular weight of about $2.0 \cdot 10^6$ Daltons and an MS of 0.4 was used. The HPG sample is coated with a small amount of Na-borate to improve its dispersability in water. The B-content was determined with Inductively Coupled Plasmaspectrometry (ICP) as 0.328 mg B/g polymer. As a borate source $Na_2B_8O_{13} \cdot 4H_2O$ was used in a concentration of exactly 6 g/100 g in deionized water. This solution has a density of 1.036 g/mL and contains 13.97 g B/L. For the preparation of gels, tap water was used which contains small amounts of Na^+, K^+, Mg^{2+}, Ca^{2+} and B. The content of these elements, as determined with ICP, were 49.5, 4.10, 10.2, 49.0, and 0.624 mg/L, respectively. It is known that Ca^{2+}, and probably Mg^{2+} as well, can be sequestered by 2:1 polysaccharide-borate complexes. This leads to increased values of the complex formation constant K_2. However, at these low concentrations, the effect is negligible and is therefore of no concern.[33] In the calculations, the total B content was taken into account from all three sources: tap water, polymer coating, and crosslinker solution. A 25% (w/v) solution of NaOH was used for pH adjustments. $NaHCO_3$ was added to the gels as a buffer in

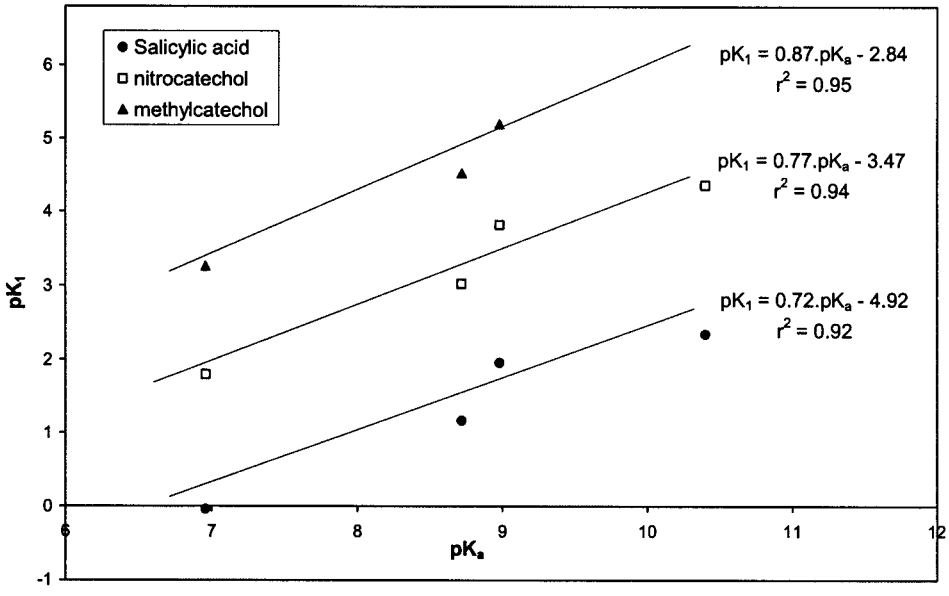

Figure 11. Results of an analysis of data published by Pizer et al.[11]; see text for details.

 © 2005 Wiley-VCH Verlag GmbH & Co. KGaA, Weinheim

a concentration of exactly 3 g/kg. The reagents mentioned above were all of technical purity.

ICP Analysis: ICP was used to analyze the polymer for B and the tap water for Na^+, K^+, Mg^{2+}, Ca^{2+}, and B. The measurements were performed on a Philips PU7000 ICP. Plastic measure flaks were used to minimize the uptake of B from glassware. Exactly 10 mL of a 30% HNO_3 (p.a. quality) solution was added to the tap water samples together with 1.000 mL of a 1000 mg/L solution in Y (Merck) as an internal standard. The HPG sample was analyzed by adding 50.00 g of a base gel containing exactly 3 g/kg in DI water to a measure flask of 100 mL and adding HNO_3 and Y as above. These samples were mixed and, prior to work up, the polymer was allowed to de-polymerize in the course of about two days.

Gel Preparation: Base gels were prepared using a blade stirrer to first disperse the polymer. HPG masses from 15 to 36 g, but exactly known, were mixed in 5.000 kg tap water To initiate hydration of the polymer, the Na-borate coating was removed by adding acetic acid until a pH value of 6.5. The gel was allowed to hydrate for 15 minutes while being stirred before the sample was put in a refrigerator to further hydrate overnight. Then, the gel was homogenized and approximately 950 g of the base gel was added to a Waring blender followed by the required amount of crosslinker solution (see above), usually 500 μL. After 1 minute of stirring, 3.000 g of $NaHCO_3$ was added as a buffer, and after dissolution the pH was adjusted to the desired value with a 25% NaOH solution. In cases where gel formation was followed at high pH values (>11.5) about 75% of the required amount of NaOH was added very quickly to prevent premature gel formation. The Waring blender was then weighted off to exactly 1 kg with base gel and allowed to fully homogenize for 2 more minutes. Then the timer was started, and a sample was injected into the cup of the rheometer. Only in cases where the pH > 10.5 and the [polymer] > 3 g/L, volume and density effects due to additions of NaOH and polymer were signficant and corrected for.

The procedure above is similar for the determination of visco-elasticity due to physical crosslinks but no additional crosslinker was added and 10.0 g fructose per kg base gel was added to absolutely ascertain masking of present borate. The complex formation constant of borate with fructose (F) was determined at K'_1 = 6000 L/mol, defined as $[F_1B^-]/([B^-]\cdot[F])$, which is much higher than the constant for mannose.[6] Effective masking of borate by fructose was verified experimentally by adding 500 μL crosslinker solution to these gels: no crosslinking took place. The data were corrected for volume and density effects caused by fructose addition.

Rheology: A Reologica Stresstech rheometer was used. After the cylindrical cone plate bob was positioned, the sample was covered with a thin layer of aliphatic oil (Shellsol D90) to prevent dehydration of the gel. The gel properties G', G'' and the viscosity were followed in time by oscillating the bob at a frequency of 1 Hz and a strain of 0.3. Previous work by Pezron[2] has shown that a frequency of 1 Hz is sufficiently fast compared to the live time of the crosslinks, i.e., $(\omega.\tau)^2 >> 1$ and G' values are determined at the plateau level in all experiments. The temperature was fixed at 25.0 °C ± 0.2. The gels prepared contained relatively low concentrations of B and polymer to extend reaction times as much as possible.

Acknowledgements

We thank Drs. Gerard Glasbergen and Dr. Marco Verlaan for the useful discussions and remarks. Dr. Diederik van Batenburg and Dr. Jim Weaver are appreciated for reviewing the manuscript and the suggestions they have made. Finally, we appreciate and thank Halliburton management for permission to publish this paper.

[1] P. C. Harris, *J. Petr. Technology* **1993**, 264–269.
[2] E. Pezron, A. Ricard, L. Leibler, *J. Polym. Sci.: Polym. Phys. Ed.* **1990**, *28*, 2445–2461.
[3] R. K. Schultz, R. R. Myers, *Macromolecules* **1969**, *2*, 281–285.
[4] H. Maier, M. Anderson, K. Karl, K. Magnuson, in: *Industrial gums: polysaccharides and their derivatives*, (Eds.: R. L. Whistler, J. N. BeMiller,), Academic Press, San Diego, 3rd ed., **1993**, chapter 8.
[5] J. C. Dawson, *Soc. Petr. Eng.*, paper no. 22837, Annual Conference and exhibition of the Society of Petroleum Engineers, Dallas, Texas, October 6–9, **1991**.
[6] R. van den Berg, J. A. Peters, H. van Bekkum, *Carbohydr. Res.* **1994**, *253*, 1–12.
[7] M. van Duin, J. A. Peters, A. P. G. Kieboom, H. van Bekkum, *Tetrahedron* **1985**, *41*, 3411–3421.
[8] E. Pezron, A. Ricard, F. Lafuma, R. Audebert, *Macromolecules* **1988**, *21*, 1121–1125.
[9] E. Pezron, L. Leibler, F. Lafuma, *Macromolecules* **1989**, *22*, 2656–2662.
[10] E. Pezron, L. Leibler, A. Ricard, F. Lafuma, R. Audebert, *Macromolecules* **1989**, *22*, 1169–1174.
[11] L. Babcock, R. Pizer, *Inorg. Chem.* **1980**, *19*, 56–61.
[12] R. Pizer, L. Babcock, *Inorg. Chem.* **1977**, *16*, 1677–1681.
[13] S. Friedman, R. Pizer, *J. Am. Chem. Soc.* **1975**, *97*, 6059–6062.
[14] T. Y. Cheng, F. Rodriquez, *J. Appl. Polym. Sci.* **1981**, *26*, 3895–3908.
[15] S. W. Sinton, *Macromolecules* **1987**, *20*, 2430–2441.
[16] L. L. Khomutov, N. K. Kolnibolotchuk, E. P. Korchagina, S. A. Glikman, *J. Appl.Chem. USSR* **1967**, *40*, 1395–1399.
[17] M. van Duin, J. A. Peters, A. P. G. Kieboom, H. van Bekkum, *Tetrahedron* **1984**, *40*, 2901–2911.
[18] J. A. Peters, Technical University of Delft, private communication.
[19] F. A. Cotton, G. Wilkinson, *Advanced inorganic chemistry*, 4th ed., John Wiley & Sons, New York, **1980**, chapter 9.
[20] L. Paál, *Acta Chim. Acad. Sci. Hung.* **1977**, *95*, 31–40.
[21] T. L. Paál, *Acta Chim. Acad. Sci. Hung.* **1980**, *103*, 181–191.
[22] J. L. Frahn, *J. Chromatogr.* **1984**, *314*, 167–181.
[23] M. van Duin, J. A. Peters, A. P. G. Kieboom, H. van Bekkum, *J. Chem. Soc. Dalton Trans.* **1987**, *8*, 2051–2057.
[24] W. R. Gilkerson, *J. Chem. Phys.* **1957**, *61*, 914–917.
[25] K. Skoog, D. M. West, *Fundamentals of analytical chemistry*, 3rd ed. (Eds.: Holt, Reinhart, Winston), New York, **1976**, p. 784.
[26] J. March, *Advanced organic chemistry*, 3rd ed., John Wiley & Sons, New York, **1985**, p. 220, 221.
[27] R. Belcher, G. W. Tully, G. Svelha, *Anal. Chim. Acta* **1970**, *50*, 261–267.
[28] M. D. Lechner, E. N. Nordmeier, D. G. Steinmeier, in: *Polymer Handbook* (Eds.: J. Brandrup, E. H. Immergut, E. A. Grulke), John Wiley & Sons, New York, 4th ed., **1999**, chapter VII, p. 156.
[29] F. M. Goycoolea, E. R. Morris, M. J. Gidley, *Carbohydr. Polym.* **1995**, *27*, 69–71.
[30] F. Oosawa, *Polyelectrolytes*, Marcel Dekker, Inc., New York, **1971**, chapter 6.
[31] H. Ochiai, Y. Kurita, I. Murakami, *Makromol. Chem.* **1984**, *185*, 167–172.
[32] L. Leibler, M. Rubinstein, R. H. Colby, *Macromolecules* **1991**, *24*, 4701–4707.
[33] M. van Duin, J. A. Peters, A. P. G. Kieboom, H. van Bekkum, *J. Chem. Soc. Perkin Trans. 2* **1987**, *4*, 473–478.

Received: August 3, 2004

 © 2005 Wiley-VCH Verlag GmbH & Co. KGaA, Weinheim

A Tetranuclear Hydroxo-Bridged Copper(II) Complex with Primary *N*-Acylamidines as Ligands: Preparation, Structural, and Magnetic Characterisation

Jan K. Eberhardt,[a] Thorsten Glaser,*[b] Rolf-Dieter Hoffmann,[b] Roland Fröhlich,[a] and Ernst-Ulrich Würthwein*[a]

Keywords: *N*-Acylamidines / Copper(II) complexes / Magnetic susceptibility / N ligand / O ligand

The reaction of *N*-pivaloylbenzamidine (**1a**) and tetrakis(acetonitrile)copper(I) hexafluorophosphate in the presence of air yields a hydroxo-bridged copper(II) complex (**4**). The product was characterised by X-ray diffraction analysis and found to be a cubane-like dimeric complex consisting of two square dimers with the formula $[\{(\mathbf{1a})_2Cu_2(OH)_2\}_2](PF_6)_4 \cdot 4\,CH_2Cl_2$ ($\mathbf{4}\cdot 4\,CH_2Cl_2$) with cupric ions and hydroxyl oxygen atoms at alternating vertices of a cube. The complex can be described as consisting of two [ligand-Cu-$(OH)_2$-Cu-ligand] units held together by long out-of-plane Cu–O bonds, creating a tetrameric entity with a $Cu_4(OH)_4$ core. Each cupric ion is essentially square-pyramidally coordinated, being bound to three OH bridges, one N atom of the amidine and one *N*-acylamidine O atom. The magnetic properties of this compound have been studied in the 2–300 K temperature range. The measurements revealed that the cupric ions in the cube are antiferromagnetically coupled. This observation has been rationalised on the basis of the structural data.
(© Wiley-VCH Verlag GmbH & Co. KGaA, 69451 Weinheim, Germany, 2005)

Introduction

Alkoxo-bridged Cu^{II} tetramers with cubane-like Cu_4O_4 cores are well-known. A number of complexes with this moiety have been reported and their magnetic properties have been compared with those of the corresponding binuclear compounds.[1–7] These studies have shown that oxygen-bridged tetrameric copper(II) complexes may exhibit ferromagnetic[8] as well as antiferromagnetic interactions. The correlation between structural parameters and magnetic properties seems to be well established.[9]

In contrast to the alkoxy-bridged complexes, hydroxo-bridged $Cu_4(OH)_4$ tetramers are rather rare. To the best of our knowledge, which is based on a recent CCDC database search, only two examples have been structurally characterised, one containing bidentate 2,2′-bipyridyl ligands[10] and the other bearing tris(2-pyridyl)amine in a bidentate coordination mode.[11]

We report here the synthesis and solid-state molecular structure of a cubane-like hydroxo-bridged *N*-acylamidine copper(II) complex of formula $[\{(\mathbf{1a})_2Cu_2(OH)_2\}_2](PF_6)_4$ (**4**) as well as its magnetic properties measured down to 2 K. The organic ligand employed for the synthesis of this copper complex is *N*-pivaloyl benzamidine (**1a**). *N*-Acylamidines (**1**) offer coordination sites for the formation of six membered chelates, namely the oxygen atom of the acyl functionality and the nitrogen atom of the amino group. Compounds **1** carrying an $-NH_2$ (primary *N*-acylamidines) or an -NHR group (secondary *N*-acylamidines) undergo tautomerism involving 1,3 proton shifts (tautomer **A** and **B**, Scheme 1).

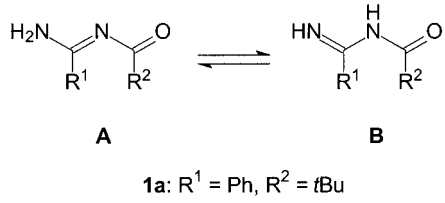

Scheme 1. *N*-Acylamidine **1**, Tautomerism **A/B**.

Spectroscopic data[12] as well as crystal structure determinations[13,14] show that the tautomer **A** dominates, while the other tautomer **B** with the two protons located on different nitrogen atoms plays, if at all, only a minor role in the equilibrium.

In earlier work we were able to characterise four monomeric copper(II) complexes with these ligands which display rather versatile coordination chemistry depending on the ligand-to-metal ion stoichiometry, the charges on the complexes and the properties of the solvents used for the syntheses (Scheme 2).[13] For example, the reaction of *N*-piva-

[a] Organisch-Chemisches Institut der Westfälischen Wilhelms-Universität Münster,
Corrensstraße 40, 48149 Münster, Germany
Fax: +49-251-83-39772
E-mail: wurthwe@uni-muenster.de
[b] Institut für Anorganische und Analytische Chemie der Westfälischen Wilhelms-Universität Münster,
Wilhelm-Klemm-Straße 8, 48149 Münster, Germany
Fax: +49-251-83-33108
E-mail: tglaser@uni-muenster.de

loyl benzamidine (**1a**) with $CuCl_2 \cdot 2H_2O$ in acetonitrile and diethyl ether yielded a mononuclear 1:1 complex **2** consisting of a neutral *N*-acylamidine in its C=NH tautomeric form complexed to a central copper(II) ion. The reaction of two equivalents of *N*-pivaloyl benzamidine (**1a**) with one equivalent of $Cu(CF_3SO_3)_2$ in acetonitrile and diethyl ether led to the formation of the mononuclear 2:1 copper(II) complex **3**. In complex **2** the copper(II) ion is four coordinate leading to a distorted tetrahedral structure. The 2:1 compound **3** possesses an approximate square plane around the central metal ion. Two oxygen atoms of the triflate counterions complement the coordination sphere of the copper(II) ion in axial positions.

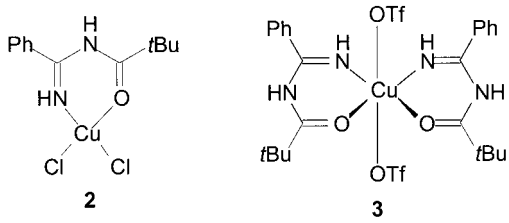

Scheme 2. Two *N*-Pivaloyl benzamidine-Cu complexes from ref.[13]

In another publication we presented experimental and theoretical results concerning the complexation of substituted *N*-acylamidine ligands **1** towards palladium(II), the structures of the complexes as well as their catalytic properties in cross-coupling reactions.[15]

Results and Discussion

Synthesis

N-Acylamidines (**1**) are interesting yet rarely used ligands for metal complexation. They resemble β-dialkylamino-acroleine derivatives which have found various applications in coordination chemistry.[16] The nitrogen atom in the 3-position of *N*-acylamidines (**1**) has a distinct influence on the electronic properties and on the reactivity of these ligands towards metal ions. A major advantage of the *N*-acylamidines (**1**) is that they are easily prepared by simple acylation of the corresponding amidines with acyl chlorides in yields of up to 97%.[12,17] Amidines are readily available from the reactions of nitriles with amines.[18,19]

In a new experiment, we studied the reaction of *N*-pivaloyl benzamidine (**1a**) with copper(I) hexafluorophosphate. Equimolar amounts of **1a** and tetrakis(acetonitrile)copper(I) hexafluorophosphate were dissolved in dichloromethane, resulting in a colourless solution. A small amount of water was then added. The reaction was stirred without protection from the air leading to oxidation of the copper(I). The solution slowly turned blue due to the formation of a copper(II) complex.

Addition of an excess of diethyl ether yielded blue crystals of $[\{(\mathbf{1a})_2Cu^{II}_2(OH)_2\}_2](PF_6)_4 \cdot 4CH_2Cl_2$ (**4**·$4CH_2Cl_2$) (Scheme 3, 43% yield). The crystals lose solvent molecules indicating that the dichloromethane molecules of solvation are only weakly bound. Elemental analysis of a sample of **4**·$4CH_2Cl_2$ dried in air indicated the loss of one dichloromethane molecule. In a SQUID magnetometer, a high vacuum is applied to the sample to remove water and paramagnetic dioxygen. Thus, it is important to know the exact nature of the sample which is measured after the application of the high vacuum. For this purpose, it is routine to study the behaviour of samples which loose solvents of crystallization under a high vacuum before measuring such a sample in a SQUID magnetometer. Thus, a sample of **4**·$4CH_2Cl_2$ was dried in a high vacuum and subsequent elemental analysis indicated the presence of two molecules of dichloromethane. Detailed infrared spectroscopy indicated that no structural changes occurred in the tetranuclear complexes. Thus, the formula **4**·$2CH_2Cl_2$ was used for the calculation of the molecular mass and the diamagnetic correction for the analysis of the magnetic data.

The hexafluorophosphate counterion is bound to **4** via weak H–F interactions (see below). It possibly acts as a template favouring the formation of polynuclear entities. In contrast to the copper(II) chloride complex **2**, the copper ions in **4** are able to use two more coordination sites to interact with other molecules rather than with the counterions. In one of the other known examples (Sletten et al.) of a hydroxo-bridged $Cu_4(OH)_4$ tetramer, hexafluorophosphate counterions were also used.[10] In this case the hexafluorophosphate ions bridge two copper atoms within the

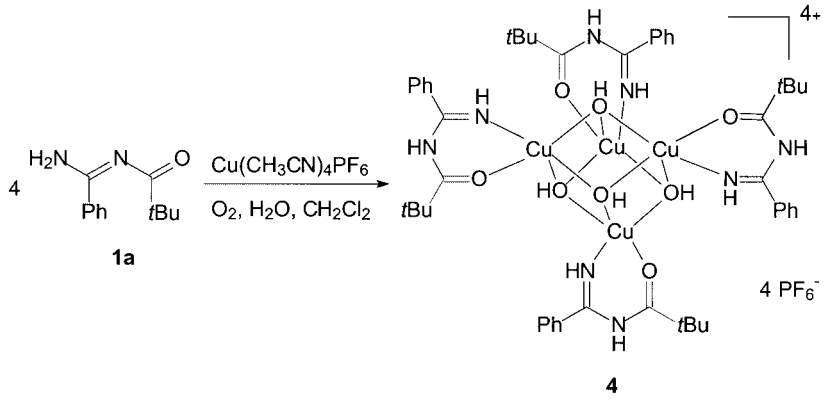

Scheme 3. Synthesis of **4**.

 © 2005 Wiley-VCH Verlag GmbH & Co. KGaA, Weinheim

dinuclear units through loose Cu–F interactions. The tetramer reported by Marks, Ibers et al. has triflate counterions bridging two copper(II) centres.[11]

The complexes **2** and **3** were precipitated from acetonitrile using diethyl ether. In contrast, **4** was synthesized in the less strongly coordinating solvent dichloromethane (with traces of water) and again precipitated using diethyl ether. Thus, dichloromethane offers better possibilities for interactions between metal ions and polynuclear entities are formed more easily.

From these three examples it is clear that there is a strong influence on the complex composition and molecular structure by the counterion and the solvent.

Description of the Structure

The crystal structure of $[\{(\mathbf{1a})_2Cu^{II}_2(OH)_2\}_2](PF_6)_4 \cdot 4CH_2Cl_2$ was determined by single-crystal X-ray diffraction. Figure 1 and Figure 2 show the molecular structure of the tetranuclear tetracation in crystals of $\mathbf{4}\cdot 4CH_2Cl_2$. Two dinuclear copper(II) entities are connected by long axial Cu–(OH) bonds forming a tetranuclear entity with a cubane-like $Cu_4(OH)_4$ core. The Cu^{II} ions and the oxygen atoms of the hydroxy groups are located at alternating corners of a pseudo-cube.

The copper atoms are (4+1)-coordinated showing an approximate square-pyramidal geometry. One oxygen atom and one nitrogen atom from the bidentate organic ligand **1a** and two hydroxide oxygen atoms act as equatorial donors. The equatorial Cu–OH bonds are short (1.930 Å), as are the bonds to the *N*-acylamidine ligand (Cu–O 1.978 Å, Cu–N 1.935 Å). The N–Cu–O bond angles amount to 89.11°. Hence, a rhombic dimeric $Cu_2(OH)_2$ entity results which interacts with a second dimer to form the observed cubane-like structure through longer axial Cu–OH bonds (2.359 Å). In the other known $Cu_4(OH)_4$ cubanes, the equatorial Cu–OH distances were 1.947–1.971 Å, while the axial distances were slightly longer at 2.382–2.585 Å[10,11] when compared with those in **4**. Within each binuclear unit, the Cu–O–Cu bridging angle is 98.84° which is similar to the values found in the literature.[10,11] There is a slight bending within the units, the dihedral angle between the O–Cu–O planes being 6.5°.

In the $Cu_4(OH)_4$ core there is one short Cu1–Cu2 separation of 2.953 Å (within the dimeric entity) and one long distance of 3.226 Å. The long separation is an interdimer copper–copper distance measured along a plane parallel to the $\bar{4}$ axis.

In compound **4**, four neutral *N*-acylamidines (**1**) in their C=NH tautomeric form **B** coordinate to one copper(II) ion each (analogous to **2** and **3**). As in the former examples (see Scheme 2), conjugated six-membered chelate rings are formed by coordination of the oxygen atoms and terminal nitrogen atoms of the *N*-acylamidines (**1**) to the metal centre. Due to the complexation, the former amino group of the ligand is transformed into an imine moiety by a formal 1,3-shift of one of the amino hydrogen atoms to the nitro-

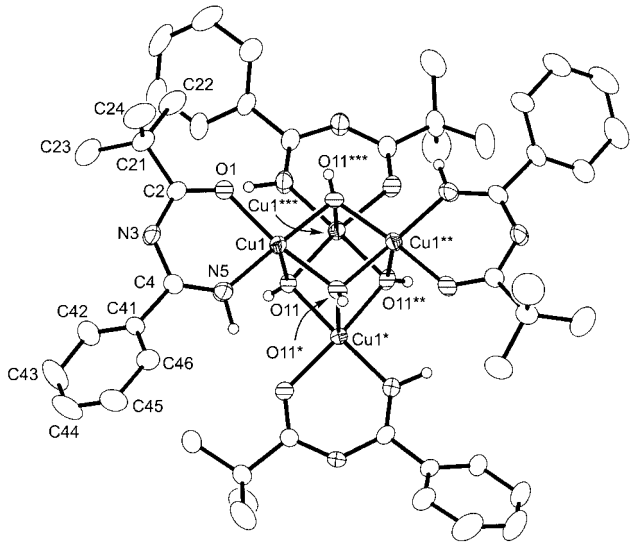

Figure 1. Molecular structure of the tetracation of **4** (Ortep plot) with crystallographic numbering; selected structural parameters: bond lengths [Å] Cu(1)–O(11) 1.930(3), Cu(1)–N(5) 1.935(3), Cu(1)–O(11) 1.957(3), Cu(1)–O(1) 1.978(3), Cu(1)–O(11) 2.359(3), Cu(1)–Cu(1) 2.9526(8), O(1)–C(2) 1.224(5), C(2)–N(3) 1.362(5), C(2)–C(21) 1.528(5), C(21)–C(24) 1.525(8), C(21)–C(23) 1.525(7), C(21)–C(22) 1.533(6), N(3)–C(4) 1.393(5), C(4)–N(5) 1.269(5), P(1)–F 1.558(4)–1.612(4); bond angles [°] O(11)–Cu(1)–N(5) 177.96(13), O(11)–Cu(1)–O(11) 80.79(11), N(5)–Cu(1)–O(11) 97.32(12), O(11)–Cu(1)–O(1) 92.85(11), N(5)–Cu(1)–O(1) 89.11(13), O(11)–Cu(1)–O(1) 170.98(11), O(11)–Cu(1)–O(11) 83.03(11), N(5)–Cu(1)–O(11) 96.01(15), O(11)–Cu(1)–O(11) 82.47(11), O(1)–Cu(1)–O(11) 103.22(11), O(11)–Cu(1)–Cu(1) 40.92(8), N(5)–Cu(1)–Cu(1) 137.28(10), O(11)–Cu(1)–Cu(1) 40.24(7), O(1)–Cu(1)–Cu(1) 132.47(8), O(11)–Cu(1)–Cu(1) 84.73(6), Cu(1)–O(11)–Cu(1) 98.84(11), Cu(1)–O(11)–Cu(1) 97.04(11), Cu(1)–O(11)–Cu(1) 96.29(10), C(2)–O(1)–Cu(1) 129.3(3), O(1)–C(2)–N(3) 122.4(3), O(1)–C(2)–C(21) 120.4(3), N(3)–C(2)–C(21) 17.2(3), C(24)–C(21)–C(23) 110.2(5), C(24)–C(21)–C(2) 107.2(4), C(23)–C(21)–C(2) 112.3(4), C(24)–C(21)–C(22) 109.0(5), C(23)–C(21)–C(22) 109.9(5), C(2)–C(21)–C(22) 108.3(3), C(2)–N(3)–C(4) 128.4(3), N(5)–C(4)–N(3) 121.1(3), N(5)–C(4)–C(41) 123.1(3), N(3)–C(4)–C(41) 115.8(3), C(42)–C(41)–C(46) 120.6(4), C(42)–C(41)–C(4) 121.1(4), C(46)–C(41)–C(4) 118.3(4), C(4)–N(5)–Cu(1) 129.2(3).

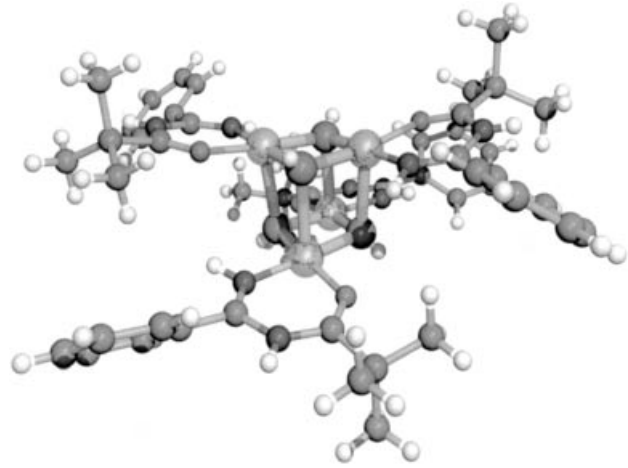

Figure 2. Povray plot of the tetracation of **4** (for numbering see Figure 1).

 © 2005 Wiley-VCH Verlag GmbH & Co. KGaA, Weinheim

gen atom N(3). The lone pair of the sp^2 hybridised imine type nitrogen atom N(5) acts as the coordination site. Thus, the ligand **1a** presents as a conjugated 6π/5z ligand, carrying a central planar sp^2 amino group. This result is in good agreement with former experiments.[13]

The hexafluorophosphate ions are weakly coordinated to the cationic cluster via N–H···F hydrogen bonds (2.215 Å). The H atoms of the OH groups are at a distance of 2.404 Å from the closest fluorine atom of the PF_6^- counterion, the O–H–F bond angle amounts to 146.3°.

Infrared and UV/Vis Spectra

The IR spectra of hydroxo-bridged copper(II) compounds have been studied thoroughly.[20] The IR spectrum of **4** (KBr pellet) exhibits a characteristic doublet at 3620 and 3615 cm^{-1} which can be assigned to the bridging OH stretch in full accordance with the literature. Three sharp absorptions at 3390, 3380 and 3340 cm^{-1} can be assigned to the =NH and –NH stretching vibrations (isomer **B** of the *N*-acylamidine). In contrast, the free ligand shows bands at 3320 and 3160 cm^{-1} which can be attributed to the asymmetric and symmetric NH_2 stretching vibrations (isomer **A**), respectively.[13] The other absorptions of the complex can be observed at common frequencies. A signal at 970 cm^{-1} has been described in the literature as a bending OH vibration.[20] A very intense band at 845 cm^{-1} can be assigned to the stretching and bending modes of the hexafluorophosphate anions. Low intensity UV absorptions may be observed at 625 nm. These are due to d→d transitions at the metal ion which cause the blue colour of solutions of **4**.

Magnetic Susceptibility

Magnetic susceptibility data of complex **4**·2 CH_2Cl_2 were measured on a microcrystalline sample in the temperature range 2–300 K with an applied field of 1 T. Note that the sample for the susceptibility measurements was dried in vacuo resulting in loss of two solvent molecules and no structural changes of **4** as demonstrated by infrared spectroscopy. A composition **4**·2 CH_2Cl_2 was used for the calculation of the molecular mass and the diamagnetic correction based on elemental analysis.

Figure 3 shows the effective magnetic moment, μ_{eff}, calculated per tetranuclear unit as a function of the temperature. The temperature dependence shows a monotonic decrease from 3.60 μ_B at 300 K to 2.10 μ_B at 50 K. Below 50 K, a change in the curvature occurs. The value at 2 K is 0.66 μ_B. This behaviour is in accordance with an antiferromagnetically coupled spin-system and a total spin ground state of $S_t = 0$. The magnetic properties of the core of **4**, $[Cu^{II}_4(OH)_4]^{4+}$, were analysed with the spin Hamiltonian for four coupled spins $S_i = ½$ including the isotropic Heisenberg–Dirac–van Vleck (HDvV) exchange Hamiltonian and the single-ion Zeeman interaction using a full-matrix diagonalisation approach [Equation (1)].[21]

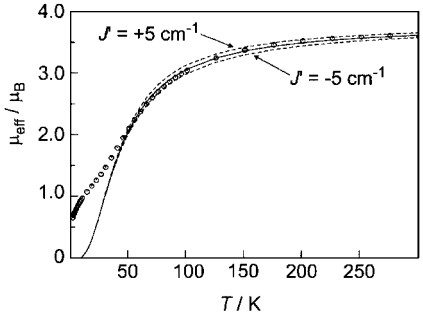

Figure 3. Temperature dependence of the effective magnetic moment, μ_{eff}, of **4**·2 CH_2Cl_2 at 1 T. The solid line represents a simulation using the spin-Hamiltonian given in the text with $J = –41$ cm^{-1}, $J' = 0$, $g = 2.21$ and $\chi_{TIP} = 500 \times 10^{-6}$ $cm^3 mol^{-1}$. The dashed lines represent simulations using the same parameter set but using $J' = +5$ cm^{-1} and $J' = –5$ cm^{-1}, respectively.

$$H = H_{HDvV} + \sum_{i=1}^{4} \mu_B g_i S_i B \quad (1)$$

The spin topology of the $[Cu^{II}_4(OH)_4]^{4+}$ cubane is shown in Figure 4. The crystallographically imposed S_4 axes lead to the equivalence of $J = J_{13} = J_{24}$ as well as $J' = J_{12}$, J_{14}, J_{23} and J_{34}. Thus, the HDvV part of the Hamiltonian becomes [Equation (2)].

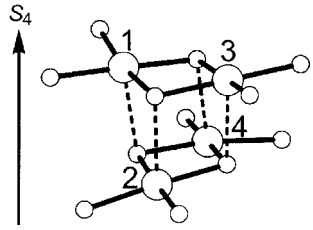

Figure 4. Spin system of **4** imposed on its molecular structure. Copper centres 1 and 3 as well as 2 and 4 both form subdimeric units. The S_4 axes yield the equivalence of the coupling constants J_{13} and J_{24} as well as the coupling constants J_{12}, J_{14}, J_{23} and J_{34}. Note that the magnetic orbitals of the Cu^{II} ions ($d_{x^2-y^2}$) are oriented in the subdimer plane perpendicular to the bond of the apical ligands.

$$H_{HDvV} = -2J(\mathbf{S_1S_3} + \mathbf{S_2S_4}) - 2J'(\mathbf{S_1S_2} + \mathbf{S_1S_4} + \mathbf{S_2S_3} + \mathbf{S_3S_4}) \quad (2)$$

The coupling constant J describes the interactions in the dinuclear subunits (intradimer exchange), whereas J' describes the interactions between the dimeric subunits (interdimer exchange). Dinuclear $Cu^{II}(\mu_2\text{-}OH)_2Cu^{II}$ cores are classics in magnetochemistry. A magneto-structural correlation describing the coupling constant J as a function of the Cu–O–Cu angle was established by Hodgson, Hatfield and coworkers.[22] Applying this correlation to the dimeric subunits of complex **4** with an angle of 98.84° results in $J = –44$ cm^{-1}. The overall spin topology of the tetramer $[Cu^{II}_4(OH)_4]^{4+}$ has been found in several complexes with a

 © 2005 Wiley-VCH Verlag GmbH & Co. KGaA, Weinheim

central $[Cu^{II}_4(OR)_4]^{4+}$ cubane core.[4–7,9–11] Reasonable values have been established for the intradimer coupling constants depending on the subdimer geometry. Differing magnitudes and signs have been reported for the interdimer coupling constant J'.[4–7,9] Fallon et al. already pointed out that the interdimer interaction should be very small due to the large interdimer Cu–O distances (apical Cu–O bond of a square-pyramidal coordination geometry) when compared with the shorter intradimer Cu–O distances (equatorial Cu–O bonds of a square-pyramidal coordination geometry).[4] They were able to fit their magnetic data only without the use of an interdimer coupling constant. Moreover, by explicitly using the appropriate tetramer model, they obtained an interdimer coupling constant of zero.[4]

Simulation of the magnetic data of **4** using only the intradimer coupling constant J, i.e. $J' = 0$, results in a good reproduction of the experimental data above 50 K with $J = -41\ cm^{-1}$, $g = 2.21$ and $\chi_{TIP} = 500 \times 10^{-6}\ cm^3\,mol^{-1}$ (solid line in Figure 3). The value of J pleasingly corroborates the value obtained from the magneto-structural correlation (vide supra). The resultant spin ladder consists of an $S_t = 0$ spin ground state, two $S_t = 1$ spin states at $+82\ cm^{-1}$, one $S_t = 0$, one $S_t = 1$ and one $S_t = 2$ spin state at $+164\ cm^{-1}$ (Figure 5, centre). Incorporation of an interdimer coupling constant J' does not result in a splitting of the first two excited $S_t = 1$ states but only in a splitting of the excited states at $+164\ cm^{-1}$. Inclusion of $J' = -5\ cm^{-1}$ splits them into $S_t = 0$ at $+144\ cm^{-1}$, $S_t = 1$ at $154\ cm^{-1}$ and $S_t = 2$ at $+174\ cm^{-1}$ (Figure 5, left). On the other hand, inclusion of $J' = +5\ cm^{-1}$ splits them into $S_t = 2$ at $+154\ cm^{-1}$, $S_t = 1$ at $174\ cm^{-1}$ and $S_t = 0$ at $+184\ cm^{-1}$ (Figure 5, right). These splittings do not affect the population of the spin levels at low temperatures. Thus, even taking into account an interdimer coupling, it is not possible to explain the unusual curvature of μ_{eff} below 50 K.

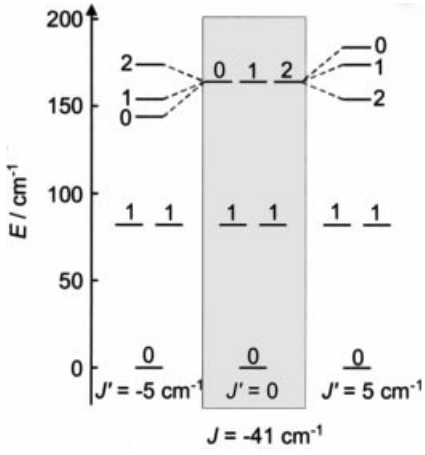

Figure 5. Spin ladder of **4** using $J = -41\ cm^{-1}$. Incorporation of $J' = -5\ cm^{-1}$ (left) or $J' = +5\ cm^{-1}$ (right) only induces a splitting of the degenerate spin states $S_t = 0$, 1 and 2 at $164\ cm^{-1}$ above the spin ground state.

It seems that the deviation of μ_{eff} below 50 K originates from a paramagnetic impurity. Taking into account a paramagnetic impurity leads to minor changes in J ($\pm 2\ cm^{-1}$) and g (± 0.02). However, this uncertainty prohibits a detailed analysis of the influence of J'. Simulations using a constant intradimer coupling constant $J = -41\ cm^{-1}$ and interdimer couplings constants $J' = +5\ cm^{-1}$ and $J' = -5\ cm^{-1}$, respectively, (dashed lines in Figure 3) indicate that the interdimer coupling should be restricted to the range $-5\ cm^{-1} < J' < +5\ cm^{-1}$. Hence, the coupling between the two dimers appears to be small.

This is in agreement with the argument of Fallon et al. whereby the interdimer distances are larger than the intradimer distances which leads to weaker superexchange pathways (vide supra).[4] The interdimer Cu–O distances in **4** are larger (2.36 Å) when compared with the intradimer Cu–O distances ($\approx$ 1.95 Å). Independent of the distance point of view, the orientation of the magnetic orbitals leads to weak couplings. The magnetic orbital of each Cu^{II} ($d_{x^2-y^2}$) is oriented towards the four ligands of the dimeric subunit (Figure 4). This leads to an effective superexchange pathway across the bridging hydroxides of the subdimer. On the other hand, the magnetic orbital of each Cu^{II} ($d_{x^2-y^2}$) is of δ-type symmetry with regard to the Cu–O interaction with its apical ligand. Since these oxygen atoms do not have δ-type symmetry orbitals, there is no interaction with the magnetic orbitals of the Cu^{II} ions. Hence, the superexchange pathway through the apical ligand must be rather weak.

Conclusions

Copper(I) ions, which are important as catalysts in both enzymatic and non-enzymatic chemical systems,[23,24,25] can be easily oxidised by molecular oxygen to Cu^{II}. Consequently, during the reaction of *N*-acylamidine **1a** with tetrakis(acetonitrile)copper(I) hexafluorophosphate in the presence of oxygen, copper(I) is transformed into copper(II) to form the tetrameric Cu^{II} complex **4** with its cubane like structure. The magnetic properties of this compound have been studied in the 2–300 K temperature range. The measurements reveal that the cupric ions in the cube are antiferromagnetically coupled.

This observation can be rationalised on the basis of the structural data. These examples clearly demonstrate that *N*-acylamidines (**1**) are very versatile ligands for copper(II) complexation. In general, they tend to form thermodynamically favourable cyclic six-membered chelates. In earlier work we found that independent of the stoichiometry used, ligand **1a** forms mononuclear 1:1 (**2**) and 2:1 (**3**) complexes with copper(II) chloride and copper(II) triflate, respectively,[13] whereas complex **4** is formed when tetrakis(acetonitrile)copper(I) hexafluorophosphate is used. Besides the counterions, the solvent has a pronounced influence on the nature of the complexes, since the application of acetonitrile leads to complexes **2** and **3**, whereas **4** was obtained using dichloromethane.

To summarise, this series of closely related Cu^{II} complexes demonstrates well the ability of the *N*-acylamidine ligand to form structurally quite diverse copper(II) com-

 © 2005 Wiley-VCH Verlag GmbH & Co. KGaA, Weinheim

plexes and underlines the intriguing role of the counterions and solvents used for the structures obtained.

Experimental Section

Materials and Methods: Compound **1a** was prepared as described previously.[15,26] Commercially available solvents (p.a. quality) were used without further purification. The CHN analysis was performed with a Vario El III (Elementar) instrument. The melting point was measured with a differential scanning calorimeter type 910 (DuPont Instruments) with a Thermal Analyst 2000 (TA Instruments) instrument. IR spectra were recorded on a Nicolet 5DXC FTIR spectrometer as KBr pellets. UV/Vis spectra were recorded on a Cary 1 Bio spectrometer (Varian). The ^{1}H spectrum was obtained by using a Bruker WM 300 spectrometer.

***N*-Pivaloylbenzamidinecopper(II) Hexafluorophosphate Hydroxide Tetramer (4·4 CH_2Cl_2):** *N*-Pivaloylbenzamidine (**1a**, 20 mg, 0.100 mmol) was treated at room temperature with tetrakis(acetonitrile)copper(I) hexafluorophosphate (37 mg, 0.100 mmol) in dichloromethane (5.0 mL). Deionised water (0.1 mL) was then added. After stirring for 10 min, a slight precipitate was removed by filtration. Diethyl ether (7.0 mL) was carefully added to the filtrate to form an upper layer. After five days blue crystals of **4**·4 CH_2Cl_2 were collected. Yield: 22 mg, 0.011 mmol (43%). M.p. 171.1 °C (dec).IR (KBr): $\tilde{\nu}$ = 3620 (vs, OH), 3615 (vs, OH), 3425 (sh), 3390 (s, NH), 3380 (s, NH), 3340 (vs, NH), 3070 (w, $CH_{arom.}$), 2980 (s, $CH_{aliph.}$), 2970 (s, $CH_{aliph.}$), 2940 (m, $CH_{aliph.}$), 2920 (w, $CH_{aliph.}$), 2880 (w, $CH_{aliph.}$), 1680 (vs, C=O/C=N), 1645 (s), 1585 (w), 1555 (w), 1495 (vs), 1450 (m), 1405 (w), 1390 (m), 1375 (w), 1285 (w), 1275 (w), 1230 (m), 1190 (s), 1030 (w), 970 (w, OH), 935 (sh), 845 (vs, PF), 785 (w), 760 (s), 740 (w), 700 (s) cm^{-1}. UV/Vis (acetonitrile): λ_{max} (ε) = 625 (278), 247 (70367), 202 (112200) nm. ^{1}H NMR (300.13 MHz, CD_3CN): δ = 1.61 (m), 2.42 (m), 2.92 (br), 3.90 (m), 5.35 (br), 5.93 (s), 7.82 (br), 8.04 (br), 8.55 (m), 10.28 (br) ppm. MS (ESI, acetonitrile): *m*/*z* (%) = 616–619 (4) $[C_{24}H_{32}CuF_6N_4O_2P]^+$, 470–473 (25) $[C_{24}H_{31}CuN_4O_2]^+$, 236 (46) $[C_{24}H_{32}CuN_4O_2]^{2+}$, 205 (100) $[C_{12}H_{16}N_2O+H]^+$. $C_{48}H_{68}Cu_4N_8O_8$·4 PF_6·4 CH_2Cl_2 (2058.88): calcd. C 30.34, H 3.72, N 5.44; calcd. (after loss of one equivalent of dichloromethane) C 31.03, H 3.78, N 5.68; found C 31.16, H 3.84, N 5.32.

X-ray Crystal Structure Analysis for 4·4 CH_2Cl_2:[27] Formula $C_{48}H_{68}Cu_4N_8O_8$·4 PF_6·4 CH_2Cl_2, M = 2058.84, blue crystal 0.40 × 0.30 × 0.30 mm, a = 17.585(1), c = 13.726(1) Å, V = 4244.5(5) Å^3, ρ_{calc} = 1.611 g cm^{-3}, μ = 14.17 cm^{-1}, empirical absorption correction (0.601 ≤ T ≤ 0.676), Z = 2, tetragonal, space group $I\bar{4}$ (No. 82), λ = 0.71073 Å, T = 198 K, ω and φ scans, 7923 reflections collected (±h, ±k, ±l), sinθ/λ = 0.66 Å^{-1}, 4633 independent (R_{int} = 0.032) and 4332 observed reflections [$I \geq 2\sigma(I)$], 256 refined parameters, R = 0.048, wR_2 = 0.124, max. residual electron density 069 (–0.66) e Å^{-3} close to the disordered CH_2Cl_2 molecules, hydrogen atoms at N3, N5 and O11 from difference Fourier calculations, others calculated and all refined as riding atoms.

Magnetic Measurements: Temperature-dependent magnetic susceptibilities of a sample of **4**·4 CH_2Cl_2, dried in a high vacuum, were measured in a gelatine capsule using a SQUID magnetometer (Quantum Design) at 1.0 T in the temperature range 2–300 K. This sample was analysed as **4**·2 CH_2Cl_2 indicating the loss of two solvated dichloromethane molecules. Infrared spectroscopic analyses before and after the drying process exhibited no changes, i.e. no structural change in the tetranuclear entity in **4** is associated with the loss of the two dichloromethane molecules. For calculations of the molar magnetic susceptibility, χ_M, the measured susceptibilities were corrected for the susceptibilities of the sample holder and for the underlying diamagnetism of the sample using tabulated Pascal's constants and for the temperature independent paramagnetism (χ_{TIP}) which was obtained by a fitting procedure.

Acknowledgments

Financial support by the Deutsche Forschungsgemeinschaft (Sonderforschungsbereich 424) and the Fonds der Chemischen Industrie (Doktorandenstipendium for JKE) is gratefully acknowledged.

[1] L. Walz, H. Paulus, W. Haase, H. Langhof, F. Nepveu, *J. Chem. Soc. Dalton Trans.* **1983**, 657–664.
[2] H. Astheimer, F. Nepveu, L. Walz, W. Haase, *J. Chem. Soc. Dalton Trans.* **1985**, 315–320.
[3] H. Oshio, Y. Saito, T. Ito, *Angew. Chem.* **1997**, *109*, 2789–2791; *Angew. Chem. Int. Ed. Engl.* **1997**, *36*, 2673–2675.
[4] G. D. Fallon, B. Moubaraki, K. S. Murray, A. M. van den Bergen, B. O. West, *Polyhedron* **1993**, *12*, 1989–2000.
[5] L. Schwabe, W. Haase, *J. Chem. Soc. Dalton Trans.* **1985**, 1909–1913.
[6] R. Wegner, M. Gottschaldt, H. Görls, E.-G. Jäger, D. Klemm, *Chem. Eur. J.* **2001**, *7*, 2143–2157.
[7] L. Merz, W. Haase, *J. Chem. Soc. Dalton Trans.* **1978**, 1594–1598.
[8] N. Matsumoto, T. Kondo, M. Kodera, H. Okawa, S. Kida, *Bull. Soc. Chem. Jpn.* **1989**, *62*, 4041–4043.
[9] L. Merz, W. Haase, *J. Chem. Soc. Dalton Trans.* **1980**, 875–879.
[10] J. Sletten, A. Sørensen, M. Julve, Y. Journaux, *Inorg. Chem.* **1990**, *29*, 5054–5058.
[11] P. L. Dedert, T. Sorrell, T. J. Marks, J. A. Ibers, *Inorg. Chem.* **1982**, *21*, 3506–3517.
[12] S.-O. Chua, M. J. Cook, A. R. Katritzky, *J. Chem. Soc. Perkin Trans. 2* **1974**, 546–552.
[13] J. K. Eberhardt, R. Fröhlich, S. Venne-Dunker, E.-U. Würthwein, *Eur. J. Inorg. Chem.* **2000**, 1739–1743.
[14] J. Prigge, E.-U. Würthwein, unpublished results.
[15] J. K. Eberhardt, R. Fröhlich, E.-U. Würthwein, *J. Org. Chem.* **2003**, *68*, 6690–6694.
[16] L. Kakaliou, W. J. Scanlon IV, B. Qian, S. W. Baek, M. R. Smith III, D. H. Motry, *Inorg. Chem.* **1999**, *38*, 5964–5977 and references cited therein.
[17] J. K. Eberhardt, *Diploma Thesis*, Universität Münster, **1999**.
[18] P. Oxley, M. W. Partridge, W. F. Short, *J. Chem. Soc.* **1947**, 1110–1116.
[19] T. Konakahara, M. Matsuki, S. Sugimoto, K. Sato, *J. Chem. Soc. Perkin Trans. 1* **1987**, 1489–1493.
[20] J. R. Ferraro, W. R. Walker, *Inorg. Chem.* **1965**, *4*, 1382–1386 and references cited therein.
[21] The routine JULIUS was used for spin Hamiltonian simulations of the data (C. Krebs, F. Birkelbach, V. Staemmler, E. Bill, unpublished results).
[22] V. H. Crawford, H. W. Richardson, J. R. Wasson, D. J. Hodgson, W. E. Hatfield, *Inorg. Chem.* **1976**, *15*, 2107–2110.
[23] R. H. Holm, P. Kennepohl, E. I. Solomon, *Chem. Rev.* **1996**, *96*, 2239–2314.
[24] N. Oishi, Y. Nishida, K. Ida, S. Kida, *Bull. Chem. Soc. Jpn.* **1980**, *53*, 2847–2850.
[25] *Modern Organocopper Chemistry* (Ed.: N. Krause), Wiley-VCH, Weinheim, **2002**.
[26] M. Buhmann, *Diploma Thesis*, Universität Münster, **1989**.
[27] Data set was collected with a Nonius KappaCCD diffractometer, equipped with a rotating anode generator. Programs used: data collection COLLECT (Nonius B.V., 1998), data reduction Denzo-SMN [a) Z. Otwinowski, W. Minor, *Methods in Enzymology* **1997**, *276*, 307–326], absorption cor-

 © 2005 Wiley-VCH Verlag GmbH & Co. KGaA, Weinheim

rection SORTAV [b) R. H. Blessing, *Acta Crystallogr.Sect. A* **1995**, *51*, 33–37; c) R. H. Blessing, *J. Appl. Crystallogr.* **1997**, *30*, 421–426], structure solution SHELXS-97 [d) G. M. Sheldrick, *Acta Crystallogr. Sect. A* **1990**, *46*, 467–473], structure refinement SHELXL-97 [e) G. M. Sheldrick, University of Göttingen, **1997**].

[28] CCDC-249168 contains the supplementary crystallographic data for this paper. These data can be obtained free of charge from The Cambridge Crystallographic Data Centre via www.ccdc.cam.ac.uk/data_request/cif.

Received: September 21, 2005

 © 2005 Wiley-VCH Verlag GmbH & Co. KGaA, Weinheim

A Novel Two-Dimensional Layer Structure Built from a Tetracobalt(II)-*p*-sulfonatothiacalix[4]arene Cluster Unit

Daqiang Yuan,[a] Yanqing Xu,[a] Maochun Hong,*[a] Wenhua Bi,[a] Youfu Zhou,[a] and Xing Li[a]

Keywords: *p*-Sulfonatothiacalix[4]arene / Cobalt / Magnetic properties / Coordination polymer

The novel coordination polymer $[Co_4(TCAS)(\mu_4\text{-}SO_4)(4,4'\text{-}Hbipy)_2]_n$ (TCAS = the octaanion of *p*-sulfonatothiacalix[4]arene) (**1**) has been synthesized hydrothermally and characterized. X-ray diffraction analyses reveal a two-dimensional (2D) layer structure built from the $[Co_4(TCAS)(\mu_4\text{-}SO_4)]^{2-}$ unit. The tetranuclear cobalt(II) clusters bridged by the μ_4-SO_4^{2-} and phenoxy groups of the same TCAS provide a unique trapeziform magnetic mode; magnetic studies in the temperature range 2–300 K show weak antiferromagnetic interactions between the four cobalt(II) centers.
(© Wiley-VCH Verlag GmbH & Co. KGaA, 69451 Weinheim, Germany, 2005)

Introduction

Water-soluble *p*-sulfonatocalix[4]arene (H_4CAS^{4-}, Scheme 1) is a versatile host for molecules of relevance in areas of materials science such as separation technology, biomimetics, and structural biology.[1] As a multifunctional supramolecular synthon, H_4CAS^{4-} can form capsules, nano-scale spheres, tubes and bi-layer structures with cavities.[2] A new water-soluble *p*-sulfonatothiacalix[4]arene (H_4TCAS^{4-}, Scheme 1) was then obtained by replacing the methylene junctions with thioether sulfur.[3] The sulfur donor atoms in H_4TCAS^{4-} add four new potential coordination sites and has provided a new type of complex.[4] Although many metal-TCAS complexes have been synthesized and studied by X-ray crystallography,[5] complexes possessing a polynuclear structure seem to have been almost neglected.[6] Currently, there is much interest in transition-metal coordination polymers as magnetic, electronic or photooptical molecular materials.[7] One strategy used to obtain such interesting new materials is to increase the structural dimensionality by combining recognizable polynuclear repeating units to form chains, layers or three-dimensional (3D) networks.[8,9] We recently introduced $TCAS^{8-}$ as a polydentate ligand to synthesize polynuclear clusters, and expected the clusters to link into novel structural coordination polymers with special properties. Fortunately, we have successfully synthesized a novel 2D layer coordination polymer with a tetranuclear cobalt(II) cluster unit $[Co_4(TCAS)(\mu_4\text{-}SO_4)(4,4'\text{-}Hbipy)_2]$ (**1**) (4,4′-Hbipy = monocation of 4,4′-H-bipyridine). Herein, we report its synthesis, structural analysis and magnetic properties.

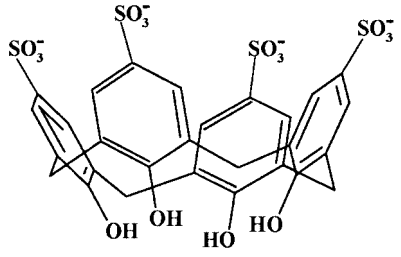

H_4CAS^{4-}

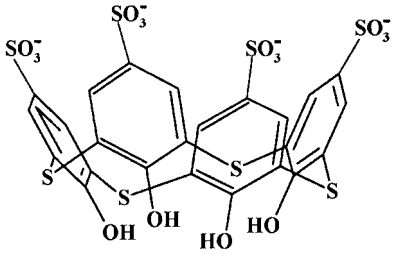

H_4TCAS^{4-}

Scheme 1. Molecular structures of H_4CAS^{4-} and H_4TCAS^{4-}.

Results and Discussion

Synthesis

The hydrothermal reaction of cobalt(II) salt with Na_4H_4TCAS and 4,4′-bipyridine (molar ratio 4:1:2) at

[a] State Key Laboratory of Structural Chemistry, Fujian Institute of Research on the Structure of Matter, Chinese Academy of Sciences,
Fuzhou, Fujian, China
Fax: +86-591-8379-4946
E-mail: hmc@ms.fjirsm.ac.cn

160 °C for 3 days afforded red crystalline compound **1**, which is insoluble in water and common organic solvents. The preparation is summarised in Equation (1).

$$4n\ CoSO_4{\cdot}6\ H_2O + n\ Na_4H_4TCAS + 2n\ 4,4'\text{-bipy} \xrightarrow[T = 160\ ^\circ C]{pH = 3} [Co_4(TCAS)(SO_4)(4,4'\text{-Hbipy})_2]_n + 2n\ Na_2SO_4 + n\ H_2SO_4 + 24n\ H_2O \quad (1)$$

Structural Description

An X-ray structure analysis showed that **1** exhibits a 2D layer structure built from the $[Co_4(TCAS)(\mu_4\text{-}SO_4)]^{2-}$ anion complex unit and 4,4′-Hbipy cation (Figure 1). Table 1 lists selected bond lengths and bond angles. The structure of the anion complex unit, like a bowl, consists of a trapezoid of four cobalt(II) centers between one TCAS unit and one sulfate ligand. In the complex unit, there is only one $TCAS^{8-}$ ligand arranged about the metal cluster, which differs greatly from the metal-thiacalix[4]arene clusters.[4] Furthermore, a mirror plane is imposed on the complex unit and passes through S(3), S(5), S(6), O(1), O(2), O(8), O(9), O(11), O(12), C(1), C(4), C(12), and C(15). A disordered water molecule is included within the cavity of the $TCAS^{8-}$ unit. The fully deprotonated $TCAS^{8-}$ unit, maintaining a conventional cone conformation, utilizes its phenoxy groups as μ_2-phenoxy bridges to bind four cobalt(II) ions to form the tetracobalt cluster with an average $Co–O_{(phenoxy)}$ distance of 2.073(4) Å. The array of four cobalt(II) ions is close to an isosceles trapezoid, and the Co(1)···Co(2), Co(1A)···Co(2A), Co(1)···Co(1A), and Co(2)···Co(2A) distances are 3.645(1), 3.645(1), 3.604(2), and 3.285(2) Å, respectively. Interestingly, at the lower rim of $TCAS^{8-}$, the $\mu_4\text{-}SO_4^{2-}$ anion binds with the four Co^{II} ions in a rare tridentate coordination mode to form the base of the bowl. There are two types of coordination environments for the four cobalt(II) ions: Co(1) and Co(1A) are in a O_5S octahedral geometry, while Co(2) and Co(2A) are in a NO_4S donor-atom environment. Co(1)–S(1) and Co(2)–S(2) have bond lengths of 2.445(2) and 2.499(2) Å, respectively. The oxygen atoms from sulfonate and sulfate oxygen and/or nitrogen atoms from 4,4′-Hbipy complete the six-coordinate cobalt(II) spheres with average $Co–O_{(sulfonate)}$ $Co–O_{(sulfate)}$, and Co–N distances of, respectively, 2.132(5), 2.124(5) and 2.107(6) Å. The 4,4′-Hbipy acts as terminal ligand rather than common bridging ligand, in which uncoordiated nitrogen is protonated, for charge balance, and shows hydrogen bonding with sulfonate and sulfate oxygen [$N···O_{(sulfonate)}$ 3.161(11) Å; $N···O_{(sulfate)}$ 2.851(12) Å]. Notably, further aggregation of the tetracobalt clusters is directed by the coordination of sulfonate groups of $TCAS^{8-}$ in **1**, where the sulfonate groups adopt two types of coordination modes, one half in monodentate and the other half in O,O′-η^1:η^1:μ_2 bridging bidentate mode (Scheme 2).

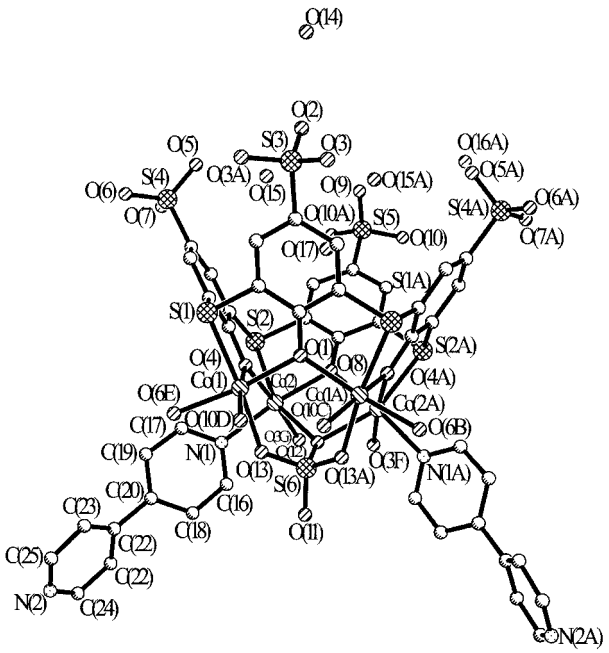

Figure 1. X-ray crystallographic structure of **1**; hydrogen atoms omitted for clarity. Symmetry transformations used to generate equivalent atoms A: *x*, *y*, ½ – *z*; B: 1 – *x*, 1 – *y*, ½ + *z*; C: 1 – *x*, ½ + *y*, *z*; D: 1 – *x*, ½ + *y*, ½ – *z*; E: 1 – *x*, 1 – *y*, – *z*; F: 1 – *x*, *y* – ½, *z*; G: 1 – *x*, *y* – ½, ½ – *z*.

Table 1. Selected bond lengths [Å] and angles [°] in **1**.

Co(1)–O(13)	2.078(4)	O(13)–Co(1)–O(4)	92.10(17)
Co(1)–O(4)	2.085(4)	O(13)–Co(1)–O(1)	103.4(2)
Co(1)–O(1)	2.089(3)	O(4)–Co(1)–O(1)	93.3(2)
Co(1)–O(6E)	2.091(4)	O(13)–Co(1)–O(6E)	86.04(18)
Co(1)–O(10D)	2.147(5)	O(4)–Co(1)–O(6E)	96.44(17)
Co(1)–S(1)	2.4460(19)	O(1)–Co(1)–O(6E)	166.2(2)
Co(2)–O(8)	2.018(4)	O(13)–Co(1)–O(10D)	81.01(18)
Co(2)–O(4)	2.100(4)	O(4)–Co(1)–O(10D)	172.65(17)
Co(2)–N(1)	2.101(6)	O(1)–Co(1)–O(10D)	85.9(2)
Co(2)–O(3G)	2.157(5)	O(6E)–Co(1)–O(10D)	85.70(17)
Co(2)–O(12)	2.174(4)	O(13)–Co(1)–S(1)	172.76(14)
Co(2)–S(2)	2.5004(19)	O(4)–Co(1)–S(1)	83.75(12)
S(1)–C(2)	1.773(6)	O(1)–Co(1)–S(1)	82.82(15)
S(1)–C(6)	1.788(6)	O(6E)–Co(1)–S(1)	88.53(13)
S(2)–C(10)	1.783(7)	O(10D)–Co(1)–S(1)	103.36(13)
S(2)–C(13)	1.796(6)	O(8)–Co(2)–O(4)	95.8(2)
S(3)–O(2)	1.430(7)	O(8)–Co(2)–N(1)	172.5(2)
S(3)–O(3)	1.474(5)	O(4)–Co(2)–N(1)	90.8(2)
S(3)–C(4)	1.769(10)	O(8)–Co(2)–O(3G)	88.2(2)
S(4)–O(5)	1.442(5)	O(4)–Co(2)–O(3G)	175.39(18)
S(4)–O(7)	1.448(6)	N(1)–Co(2)–O(3G)	85.3(2)
S(4)–O(6)	1.480(5)	O(8)–Co(2)–O(12)	75.35(19)
S(4)–C(8)	1.775(7)	O(4)–Co(2)–O(12)	98.5(2)
S(5)–O(9)	1.437(7)	N(1)–Co(2)–O(12)	100.2(2)
S(5)–O(10)	1.470(5)	O(3G)–Co(2)–O(12)	84.7(2)
S(5)–C(15)	1.777(9)	O(8)–Co(2)–S(2)	81.02(15)
S(6)–O(11)	1.433(7)	O(4)–Co(2)–S(2)	82.39(12)
S(6)–O(12)	1.490(7)	N(1)–Co(2)–S(2)	103.39(17)
S(6)–O(13)	1.490(5)	O(3G)–Co(2)–S(2)	96.05(14)
		O(12)–Co(2)–S(2)	156.34(14)

Symmetry transformations used to generate equivalent atoms: D: 1 – *x*, ½ + *y*, ½ – *z*; E: 1 – *x*, 1 – *y*, – *z*; G: 1 – *x*, *y* – ½, ½ – *z*

Each $[Co_4(TCAS)(\mu_4\text{-}SO_4)]^{2-}$ bowl links four other bowl units through $Co–O_{(sulfonate)}$ bonds to generate a layer structure in an alternating up-down bowl alignment (Figure 2). Moreover, each $TCAS^{8-}$ unit forms π–π interactions

 © 2005 Wiley-VCH Verlag GmbH & Co. KGaA, Weinheim

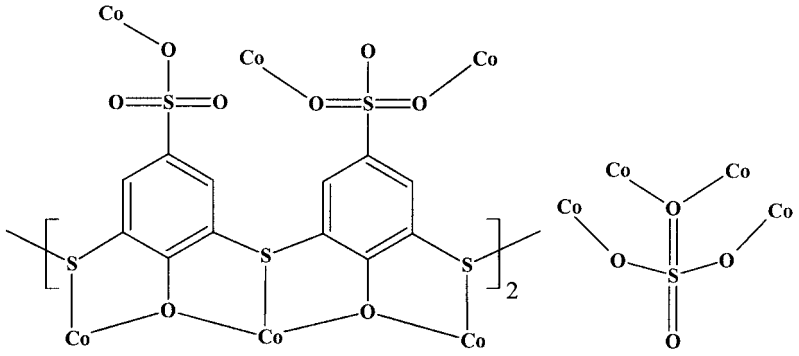

Scheme 2. Schematic of the coordination modes of $TCAS^{8-}$ and SO_4^{2-}.

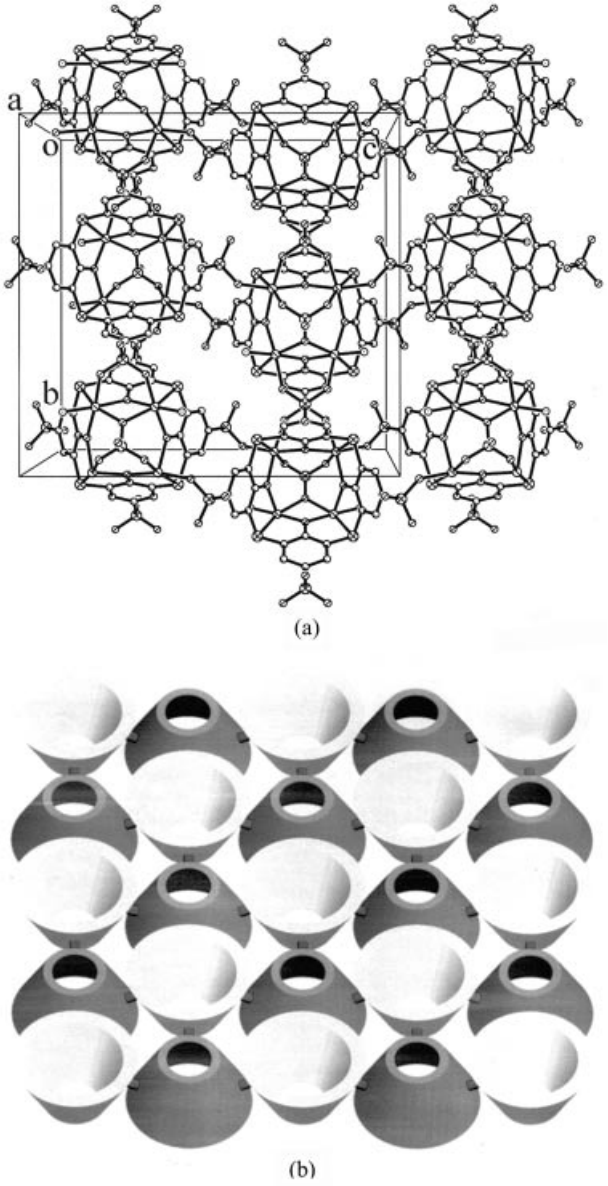

Figure 2. View of the 2D layer structure of **1** (a) and a schematic showing the regular structure with bowl alignment (b).

with four other $TCAS^{8-}$ units within the crystal lattice at ring centroid separations of 3.34, 4.48, 3.34, and 4.48 Å.[10] To date, although many reports have described TCAS complexes, this is the first example showing a 2D layer structure with tetranuclear Co^{II} clusters from $TCAS^{8-}$.

It is pertinent to mention that a disordered water molecule that resides in the cavity of the $TCAS^{8-}$ is located by the OH–aromatic π-hydrogen bonds between the water and aromatic rings, and the O···π centroid distances are 3.45, 3.83, 3.68 and 3.79 Å. Aromatic π-hydrogen bonding to water has been reported for the complex $Na_4H_4CAS{\cdot}13.5\,H_2O$ in which the O···π centroid distances are 3.48, 3.83, 4.78, 4.00 Å.[11] The water molecule penetrates 2.582 Å into the cavity, as measured by how far the water molecule is from the plane of the thiacalix[4]arene bridging sulfur atoms.

Thermal Stability

Thermogravimetric analysis (TGA) was performed on polycrystalline samples of **1**, under nitrogen, to study their stability. The data show two weight loss steps (Figure 3). The first occurs from 30 to 130 °C, with a weight loss of 6.83%, which corresponds to the loss of water molecules. The weight then remains almost unchanged in the plateau from 130 to 510 °C. The second step occurs in the range 510 to 595 °C (weight loss of 29.25%), corresponding to the loss of the 4,4′-bipyridine ligands and the SO_4^{2-}. The compound begins to decompose at 595 °C. The thermogravimetric results demonstrate that the compound is rather stable under nitrogen.

Magnetic Properties

The temperature-dependent magnetic susceptibility of complex **1** was investigated in the range 2–300 K at a 10 kOe applied field. The χ_m and $\chi_m T$ per four Co^{II} ions versus T curves are shown in Figure 4. At 300 K, $\chi_m T$ is 9.80 $cm^3\,mol^{-1}\,K$, which is larger than the expected 7.50 $cm^3\,mol^{-1}\,K$ for four magnetically isolated high-spin Co^{II} ions (S_{Co} = 3/2, g = 2.0). This larger value is the result of contributions to the susceptibility from orbital angular

 © 2005 Wiley-VCH Verlag GmbH & Co. KGaA, Weinheim

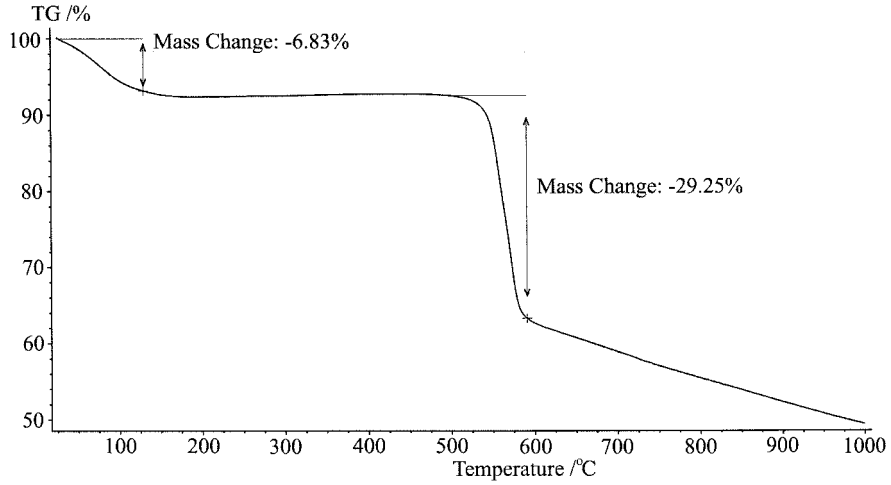

Figure 3. TGA plot for **1** between 30 and 1000 °C.

momentum at high temperature. As the temperature is lowered χ_m increases, reaching a maximum at ca. 14 K. Between 50 and 300 K, χ_m follows the Curie–Weiss law, $\chi_m = C_m/(T - \theta)$, with $C_m = 2.71 \pm 0.01$ cm^{3}kmol (per Co) and $\theta = -28.9 \pm 0.4$ K. These results indicate the antiferromagnetic interactions between cobalt(II) centers.

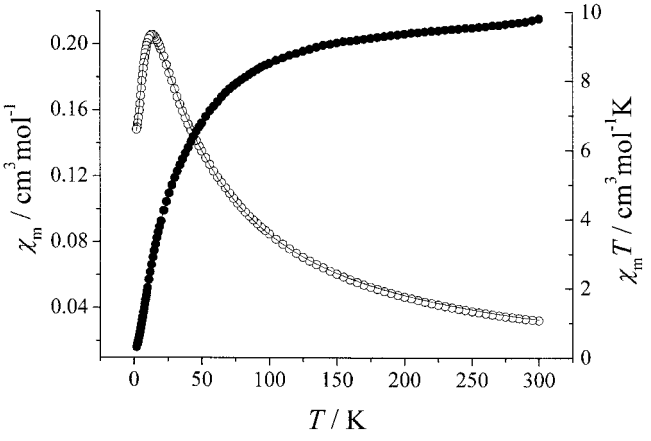

Figure 4. Experimental temperature dependences of χ_m (○) and $\chi_m T$ (●) for **1**; solid lines correspond to the best fit obtained for **1**.

Considering cluster topology and connectivity (Figure 5), an exchange pathway of four cobalt(II) centers of **1** was taken into account. However, we failed to fit the behavior of an array of four orbital degeneration Co^{II} centers by means of an effective spin-Hamiltonian, proposing a four-*J* model, due to the large magnetic anisotropy and spin–orbit coupling of these ions.[12] Therefore, the simplest treatment was carried, considering only isotropic exchange interactions and assuming $J_1 = J_2 = J_3$. The magnetic data were analyzed with the spin Hamiltonian shown in Equation (2).

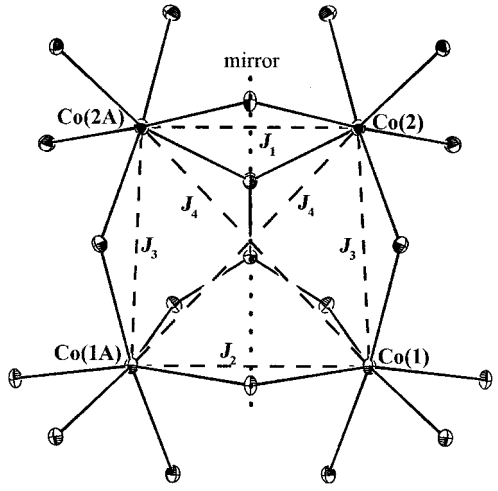

Figure 5. Spin topology for **1** assuming four different *J* values.

The total spin states (S_T) and their energies [$E(S_T)$] can be obtained using the vector-coupling method of Kambe,[13] and substituted into the Van Vleck equation in Equation (3). A Weiss-like temperature correction (θ') to account for intermolecular exchange effects has been applied. The magnetic data were fitted to Equation (3), and gave best-fit parameters of $g = 2.40 \pm 0.01$, $J_1 = -3.07 \pm 0.02$ cm^{-1}, $J_4 = -1.36 \pm 0.06$ cm^{-1}, $\theta' = 1.66 \pm 0.01$ K and an agreement factor $R = 6.12 \times 10^{-6}$. These results show the presence of two kinds of weak antiferromagnetic interactions (J_1 and J_4) associated with the interactions of μ_2-PhO$^-$ and μ_4-SO_4^{2-}. The antiferromagnetic interactions between Co(1) and Co(2) or Co(1) and Co(1A) or Co(2) and Co(2A) through the μ_2-PhO$^-$ originate, presumably, from the high Co–O–Co angles of 121.2° or 119.3° or 108.8°, which differ considerably from 90°.[14]

$$\hat{H}_{ex} = -2J_1(\hat{S}_{Co(2A)}\hat{S}_{Co(2)} + \hat{S}_{Co(1A)}\hat{S}_{Co(1)} + \hat{S}_{Co(2A)}\hat{S}_{Co(1A)} + \hat{S}_{Co(2)}\hat{S}_{Co(1)}) - 2J_4(\hat{S}_{Co(2A)}\hat{S}_{Co(1)} + \hat{S}_{Co(2)}\hat{S}_{Co(1A)}) \quad (2)$$

$$\chi_m = \frac{N\beta^2 g^2}{3k(T-\theta')} \frac{\sum S_T(S_T+1)(2S_T+1)e^{-E(S_T)/kT}}{\sum (2S_T+1)e^{-E(S_T)/kT}} \quad (3)$$

 © 2005 Wiley-VCH Verlag GmbH & Co. KGaA, Weinheim

Conclusions

We have successfully used $TCAS^{8-}$ to produce a novel 2D coordination polymer consisting of antiferromagnetically coupled tetranuclear Co^{II} building units. This work suggests that the TCAS-based anion is a versatile ligand with various advantages, including high-nuclearity cluster formation, linking of cluster into polymer arrays, mixed-metal chemistry and ferromagnetic exchange interaction.

Experimental Section

General Remarks: Na_4H_4TCAS was prepared according to a literature method.[3] All other starting chemicals and solvent were commercially available with analytical purity and were used as received. IR spectra were recorded on a Magna 750 FT-IR spectrophotometer (using KBr disks). C, H and N elemental analyses were determined on an Elementary Vario ELIII elemental analyzer and the Co content was determined by atomic absorption. Thermogravimetric analyses (TGA) were performed with a NETSCHZ STA-449C thermoanalyzer under N_2 (30–1000 °C) at a heating rate of 10 °C min^{-1}. Temperature-dependent magnetic-susceptibility measurements on powdered solid samples were performed on Quantum Design MPMS-7 SQUID magnetometer in the range 2–300 K. The magnetic field applied was 10 kOe. Observed susceptibility data were corrected for underlying diamagnetism using Pascal's constants.[15]

Synthesis of 1: The pH of an aqueous mixture (15 mL) containing Na_4H_4TCAS (90.48 mg, 0.1 mmol), 4,4′-bipyridine (31.20 mg, 0.2 mmol) and $CoSO_4{\cdot}6H_2O$ (105.2 mg, 0.4 mmol) was preadjusted to about 3 with 0.1 M H_2SO_4 aqueous solution. The mixture was then transferred to a Teflon-lined stainless vessel (20 mL) that was sealed, heated in an autoclave to 160 °C for 72 h, and then cooled to room temperature at 10 °C h^{-1}. Red crystal of $1{\cdot}3.5H_2O$ were obtained (79.24 mg, yield 52.2% based on Co). Anal. calcd. for $1{\cdot}3.5H_2O$, $C_{44}H_{33}N_4O_{23.5}S_9Co_4$ (1518.00): C 34.81, H 2.19, N 3.69, Co 15.54; found: C 34.53, H 2.11, N 3.82, Co 15.27. IR (KBr): $\tilde{\nu}$ = 3464, 3222, 3116, 3066, 3033, 1637, 1614, 1454, 1423, 1247, 1157, 1141, 1029, 881, 804, 754, 613 cm^{-1}.

Table 2. Crystal data for **1**.

Empirical formula	$C_{44}H_{33}N_4O_{23.5}S_9Co_4$
Formula mass	1518.00
Temperature [K]	298(2)
Wavelength [Å]	0.71073
Crystal system	orthorhombic
Space group	*Pbcm* (No. 57)
a [Å]	15.3120(4)
b [Å]	18.9858(2)
c [Å]	19.8374(4)
α [°]	90
β [°]	90
γ [°]	90
V [Å^3]	5766.9(2)
Z	4
$D_{calcd.}$ [Mg m^{-3}]	1.748
M(Mo-K_α) [mm^{-1}]	1.540
F_{000}	3060
θ range [°]	2.52 to 25.03
Measured reflections	13675
Unique reflections	5222
Observed reflections	3680
R_{int}	0.0614
Goodness-of-fit on F^2	1.131
R_1, wR_2 [$I > 2\sigma(I)$]	0.0636, 0.1379
[all data]	0.1041, 0.1580
Res. electron density [e Å^{-3}]	+0.871, –0.609

X-ray Crystallography Determination: A block crystal (ca. 0.28 × 0.22 × 0.18 mm) of **1** was selected for X-ray diffraction analysis. Data collection was performed on a Siemens SMART-CCD diffractometer equipped with a graphite monochromated Mo-K_α radiation (λ = 0.71073 Å), using the ω-scan mode at 293 K. All absorption corrections were applied using the SADABS program.[16] Structures were solved by direct methods, the metal atoms were located from the E-maps, and other non-hydrogen atoms were derived from successive difference Fourier syntheses. Hydrogen atoms were positioned geometrically, and allowed to ride on their parent C or N atoms. The structure was refined on F^2 by full-matrix least-squares using the SHELXTL-97 program package.[17] Crystallographic data of **1** is summarized in Table 2, and selected bond lengths and bond angles are listed in Table 1. CCDC-221212 (for **1**) contains the supplementary crystallographic data for this paper. These data can be obtained free of charge from The Cambridge Crystallographic Data Centre via www.ccdc.cam.ac.uk/data_request/cif.

Acknowledgments

We are grateful for financial support from NSFC (No. 20231020), the Natural Foundation of Fujian Province and the key project of CAS. We also thank Professor Song Gao for collecting the magnetism data.

[1] a) L. J. Barbour, G. W. Orr, J. L. Atwood, *Nature* **1998**, *393*, 671–673; b) D. A. Dougherty, *Science* **1996**, *271*, 163–168; c) J. C. Ma, D. A. Dougherty, *Chem. Rev.* **1997**, *97*, 1303–1324; d) J. M. Lehn, R. Meric, J. P. Vigneron, M. Cesario, J. Guilhem, C. Pascard, Z. Asfari, J. Vicens, *Supramol. Chem.* **1995**, *5*, 97–103; e) J. L. Atwood, L. J. Barbour, E. S. Dawson, P. C. Junk, J. Kienzle, *Supramol. Chem.* **1996**, *7*, 271–274; f) J. L. Atwood, T. Ness, P. J. Nichols, C. L. Raston, *Cryst. Growth Des.* **2002**, *2*, 171–176.

[2] a) J. L. Atwood, L. J. Barbour, M. J. Hardie, C. L. Raston, *Coord. Chem. Rev.* **2001**, *222*, 3–32; b) A. W. Coleman, S. Bott, G. S. D. Morley, C. M. Means, K. D. Robinson, H. Zhang, J. L. Atwood, *Angew. Chem. Int. Ed. Engl.* **1988**, *27*, 1361–1362; c) S. G. Bott, A. W. Coleman, J. L. Atwood, *J. Am. Chem. Soc.* **1988**, *110*, 610–611; d) J. L. Atwood, G. W. Orr, F. Hamada, R. L. Vincent, S. G. Bott, K. D. Robinson, *J. Am. Chem. Soc.* **1991**, *113*, 2760–2761; e) J. L. Atwood, G. W. Orr, N. C. Means, F. Hamada, H. Zhang, S. G. Bott, K. D. Robinson, *Inorg. Chem.* **1992**, *31*, 603–606; f) J. W. Steed, C. P. Johnson, C. L. Barnes, R. K. Juneja, J. L. Atwood, S. Reilly, R. L. Hollis, P. H. Smith, D. L. Clark, *J. Am. Chem. Soc.* **1995**, *117*, 11426–11433; g) C. P. Johnson, J. L. Atwood, J. W. Steed, C. B. Bauer, R. D. Rogers, *Inorg. Chem.* **1996**, *35*, 2602–2610; h) G. W. Orr, L. J. Barbour, J. L. Atwood, *Science* **1999**, *285*, 1049–1052.

[3] a) H. Kumagai, M. Hasegawa, S. Miyanari, Y. Sugawa, Y. Sato, T. Hori, S. Ueda, H. Kamiyama, S. Miyano, *Tetrahedron Lett.* **1997**, *38*, 3971–3972; b) N. Iki, C. Kabuto, T. Fukushima, H. Kumagai, H. Takeya, S. Miyanari, T. Miyashi, S. Miyano, *Tetrahedron* **2000**, *56*, 1437–1443; c) N. Iki, T. Fujimoto, S. Miyano, *Chem. Lett.* **1998**, 625–626.

[4] a) N. Iki, N. Morohashi, C. Kabuto, S. Miyano, *Chem. Lett.* **1999**, 219–220; b) G. Mislin, E. Graf, M. W. Hosseini, A. Bilyk, A. K. Hall, J. M. Harrowfield, B. W. Skelton, A. H. White, *Chem. Commun.* **1999**, 373–374; c) A. Bilyk, A. K. Hall, J. M. Harrowfield, M. W. Hosseini, G. Mislin, B. W. Skelton, C. Tay-

 © 2005 Wiley-VCH Verlag GmbH & Co. KGaA, Weinheim

lor, A. H. White, *Eur. J. Inorg. Chem.* **2000**, 823–826; d) H. Akdas, E. Graf, M. W. Hosseini, A. D. Cian, A. Bilyk, B. W. Skelton, G. A. Koutsantonis, I. Murray, J. M. Harrowfield, A. H. White, *Chem. Commun.* **2002**, 1042–1043; e) A. Bilyk, A. K. Hall, J. M. Harrowfield, M. W. Hosseini, B. W. Skelton, A. H. White, *Aust. J. Chem.* **2000**, *53*, 895–898.

[5] a) Q. L. Guo, W. X. Zhu, S. L. Ma, S. J. Dong, M. Q. Xu, *Polyhedron* **2004**, *23*, 1461–1466; b) Q. L. Guo, W. X. Zhu, S. L. Ma, D. Q. Yuan, S. J. Dong, M. Q. Xu, *J. Mol. Struct.* **2004**, *690*, 63–68; c) B. Wanno, W. Sang-aroon, T. Tuntulani, B. Polpoka, V. Ruangpornvisuti, *J. Mol. Struct.-Theochem.* **2003**, *629*, 137–150; d) Q. L. Guo, W. X. Zhu, S. J. Dong, S. L. Ma, X.Yan, *J. Mol. Struct.* **2003**, *650*, 159–164; e) T. Horiuchi, N. Iki, H. Oka, S. Miyano, B. Chem. *Soc., Jpn*. **2002**, *75*, 2615–2619; f) D. Yuan, W. X. Zhu, S. Ma, X. Yan, *J. Mol. Struct.* **2002**, *616*, 241–246.

[6] Q. L. Guo, W. X. Zhu, S. Gao, S. L. Ma, S. J. Dong, M. Q. Xu, *Inorg. Chem. Commun.* **2004**, *7*, 467–470.

[7] a) S. Kitagawa, R. Kitaura, S. Noro, *Angew. Chem. Int. Ed.* **2004**, *43*, 2334–2375; b) C. N. R. Rao, S. Natarajan, R. Vaidhyanathan, *Angew. Chem. Int. Ed.* **2004**, *43*, 1466–1496; c) S. L. James, *Chem. Soc. Rev.* **2003**, *32*, 276–288; d) C. Janiak, *J. Chem. Soc.*, *Dalton Trans.* **2003**, 2781–2804; e) O. M. Yaghi, M. O'Keeffe, N. W. Ockwig, H. K. Chae, M. Eddaoudi, J. Kim, *Nature* **2003**, *423*, 705–714; f) K. M. Park, D. Whang, E. Lee, J. Heo, K. Kim, *Chem. Eur. J.* **2002**, *8*, 498–508; g) S. R. Batten, *Curr. Opin. Solid State Mater. Sci.* **2001**, *5*, 107–114; h) B. Moulton, M. J. Zaworotko, *Chem. Rev.* **2001**, *101*, 1629–1658; i) M. Eddaoudi, D. B. Moler, H. L. Li, B. L. Chen, T. M. Reineke, M. O'Keeffe, O. M. Yaghi, *Acc. Chem. Res.* **2001**, *34*, 319–330.

[8] a) J. H. Yang, S. L. Zheng, X. L. Yu, X. M. Chen, *Cryst. Growth Des.* **2004**, *4*, 831–836; b) A. Fragoso, M. L. Kahn, A. Castiñeiras, J. P. Sutter, O. Kahn, R. Cao, *Chem. Commun.* **2000**, 1547–1548; c) X. J. Zheng, L. P. Jin, S. Gao, *Inorg. Chem.* **2004**, *43*, 1600–1602; d) B. K. Roland, H. D. Selby, J. R. Cole, Z. P. Zheng, *J. Chem. Soc.*, *Dalton Trans.* **2003**, 4307–4312; e) H. D. Selby, B. K. Roland, Z. P. Zheng, *Acc. Chem. Res.* **2003**, *36*, 933–944; f) D. F. Sun, R. Cao, Y. Q. Sun, W. H. Bi, D. Q. Yuan, Q. Shi, X. Li, *Chem. Commun.* **2003**, 1528–1529; g) S. Q. Xia, T. L. Sheng, S. M. Hu, G. Leibeling, F. Meyer, X. T. Wu, S. C. Xiang, R. B. Fu, *Chem. Commun.* **2004**, 1186–1187; h) W. F. Fu, X. Gan, C. M. Che, Q. Y. Cao, Z. Y. Zhou, N. N. Y. Zhu, *Chem. Eur. J.* **2004**, *10*, 2228–2236.

[9] a) Y. V. Mironov, N. G. Naumov, K. A. Brylev, O. A. Efremova, V. E. Fedorov, K. Hegetschweiler, *Angew. Chem. Int. Ed.* **2004**, *43*, 1297–1300; b) H. Chun, D. Kim, D. N. Dybtsev, K. Kim, *Angew. Chem. Int. Ed.* **2004**, *43*, 971–974; c) J. Tao, X. Yin, Z. B. Wei, R. B. Huang, L. S. Zheng, *Eur. J. Inorg. Chem.* **2004**, 125–133; d) Z. Shi, G. H. Li, L. Wang, L. Gao, X. B. Chen, J. Hua, S. Feng H, *Cryst. Growth Des.* **2004**, *4*, 25–27; e) X. S. Wang, H. Zhao, Z. R. Qu, Q. Ye, J. Zhang, R. G. Xiong, X. Z. You, H. K. Fun, *Inorg. Chem.* **2003**, *42*, 5786–5788; f) Y. G. Li, N. Hao, E. B. Wang, Y. Lu, C. W. Hu, L. Xu, *Eur. J. Inorg. Chem.* **2003**, 2567–2571; g) C. L. Pan, J. Q. Xu, G. H. Li, D. Q. Chu, T. G. Wang, *Eur. J. Inorg. Chem.* **2003**, 1514–1517; h) W. Chen, J. Y. Wang, C. Chen, Q. Yue, H. M. Yuan, J. S. Chen, S. N. Wang, *Inorg. Chem.* **2003**, *42*, 944–946.

[10] C. Janiak, *J. Chem. Soc.*, *Dalton Trans.* **2000**, 3885–3896.

[11] J. L. Atwood, F. Hamada, K. D. Robinson, G. W. Orr, R. L. Vincent, *Nature* **1991**, *349*, 683–684.

[12] a) M. G. Barandika, Z. Serna, R. Cortes, L. Lezama, M. K. Urtiaga, M. I. Arriortua, T. Rojo, *Chem. Commun.* **2001**, 45–46; b) G. S. Papaefstathiou, A. Escuer, M. Font-Bardia, S. P. Perlepes, X. Solans, R. Vicente, *Polyhedron* **2002**, *21*, 2027–2032; c) Z. E. Serna, M. K. Urtiaga, M. G. Barandika, R. Cortes, S. Martin, L. Lezama, M. I. Arriortua, T. Rojo, *Inorg. Chem.* **2001**, *40*, 4550–4555; d) C. Boskovic, G. Labat, A. Neels, H. U. Gudel, *J. Chem. Soc.*, *Dalton Trans.* **2003**, 3671–3672; e) G. S. Papaefstathiou, A. Escuer, C. P. Raptopoulou, A. Terzis, S. P. Perlepes, R. Vicente, *Eur. J. Inorg. Chem.* **2001**, 1567–1574.

[13] K. Kambe, *J. Phys. Soc. Jpn.* **1950**, *5*, 48–51.

[14] P. Jaitner, J. Veciana, C. Sporer, H. Kopacka, K. Wurst, D. Ruiz-Molina, *Organometallics* **2001**, *20*, 568–571.

[15] O. Kahn, *Molecular Magnetism*, VCH Publishers, New York, **1993**.

[16] G. M. Sheldrick, *SADABS*, University of Göttingen, **1996**.

[17] a) G. M. Sheldrick, *SHELXS-97, program for the solution of crystal structure*, University of Göttingen, **1997**; b) G. M. Sheldrick, *SHELXL-97, program for the solution of crystal structure*, University of Göttingen, **1997**.

Received: July 12, 2004

 © 2005 Wiley-VCH Verlag GmbH & Co. KGaA, Weinheim

Ordered Meso- and Macroporous Binary and Mixed Metal Oxides

Moises A. Carreon[a,b] and Vadim V. Guliants*[a]

Keywords: Mesoporous / Macroporous / Transition metal oxides / Catalytic applications

The caption of Figure 8 on page 32 of the original article[1] was reporduced incompletely; the correct caption should read as follows:

Figure 8. Nitrogen adsorption−desorption isotherms and BJH pore-size distribution plot (inset) for mesoporous niobium oxide (L. Yuan, V. V. Guliants, unpublished data).

[1] M. A. Carreon, V. V. Guliants, *Eur. J. Inorg. Chem.* **2005**, 27−43.

Received February 16, 2005
The Editors

[a] Department of Chemical and Materials Engineering, University of Cincinnati,
Cincinnati, OH 45221-0012, USA
E-Mail: Vadim.Guliants@uc.edu
[b] Current address: Materials Chemistry Research Group, Chemistry Department, University of Toronto,
80 Saint George Street, Toronto, Ontario, Canada M5S 3H6

 DOI: 10.1002/ejic.200500137 © 2005 Wiley-VCH Verlag GmbH & Co. KGaA, Weinheim

EurJIC
European Journal of Inorganic Chemistry

Issue 7/2005

Pages 1193–1408

Papers available ahead of print in Early View at www.interscience.wiley.com

Earliest available Table of Contents:
Automatically, free of charge by e-mail through
www.interscience.wiley.com/alerts

COVER PICTURE

The cover picture shows the crystal structures of free radicals of the type $(t\mathrm{Bu_2MeSi})_3\mathrm{E}^{\cdot}$ (E = Si, Ge, Sn) representing the first stable tricoordinate acyclic radicals of the heavier group 14 elements. All of these radicals have a perfect trigonal-planar geometry, being truly π radicals, both in the crystalline form and in solution, accommodating an odd-electron on the p_z(E) orbitals. The synthesis of such stable radicals has been achieved nearly a century after the historical discovery of the first free radical species, triphenylmethyl $\mathrm{Ph_3C}^{\cdot}$ by Gomberg in 1900. The recent developments in the field of stable Si-, Ge-, and Sn-centered free radicals include the synthesis and physico-chemical characterization of the neutral (cyclic and acyclic radicals) and charged (anion radicals of heavy carbene analogues, heavy alkene analogues and heavy alkyne analogues) compounds. The details of this chemistry are described and discussed in the Microreview by V. Ya. Lee and A. Sekiguchi on p. 1209 ff.

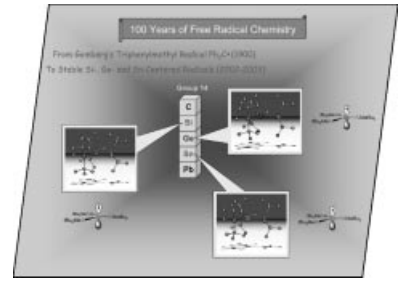

MICROREVIEW

Contents

1209 **V. Ya. Lee, A. Sekiguchi***

Si-, Ge-, and Sn-Centered Free Radicals: From Phantom Species to Grams-Order-Scale Materials

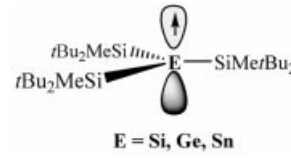

Keywords: Free radical / X-ray diffraction / EPR spectroscopy / Silicon / Germanium / Tin

 © 2005 Wiley-VCH Verlag GmbH & Co. KGaA, Weinheim

SHORT COMMUNICATIONS

1223 **E. A. Medlycott, I. Theobald, G. S. Hanan***

Co^{II} Complexes of Triazine-Based Tridentate Ligands with Positive and Attractive $Co^{II/III}$ Redox Couples

Keywords: Tridentate N ligands / Cobalt complexes / Electrochemistry / Triazine

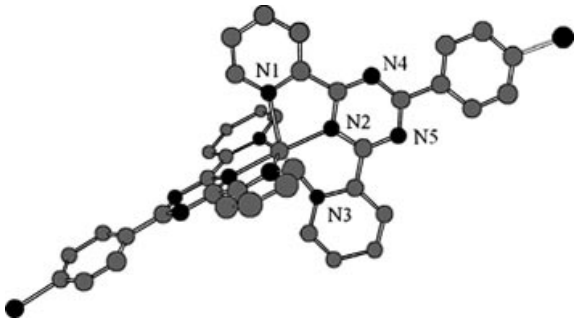

1227 **I. Rusonik, H. Cohen, D. Meyerstein***

Reduction of CCl_4 by Iron Powder in Aqueous Solution

Keywords: Carbon tetrachloride / Reduction / Iron / Mechanism

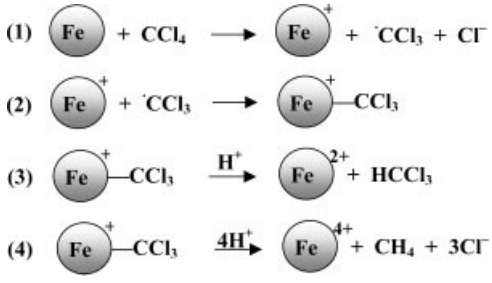

1230 **B.-H. Ye,* A.-P. Sun, T.-F. Wu, Y.-Q. Weng, X.-M. Chen***

Tapes of Cyclic Water Tetramers in the Double-Helical Complex $[Cd_2(bpa)_2Cl_4]\cdot 6\ H_2O$

Keywords: Cadmium / Helical structures / N ligands / Water

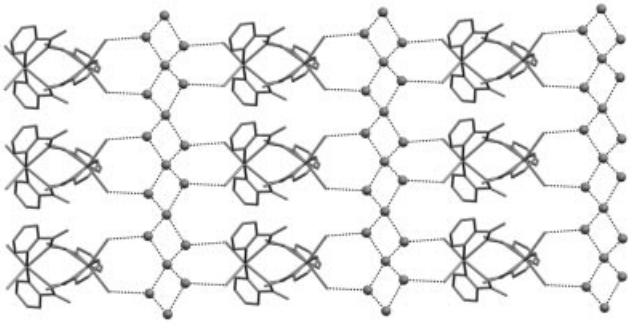

1235 **H. Tanaka,* E. Kwon, S. Tsutsui, S. Matsumoto, K. Sakamoto***

Relationship between the Molecular Structure and the $\pi-\pi^*$ Transition Energy of a Lattice-Framework Disilene: A DFT Study

Keywords: Density functional calculations / Disilenes / UV/Vis spectroscopy / Electronic structure / Electron transition

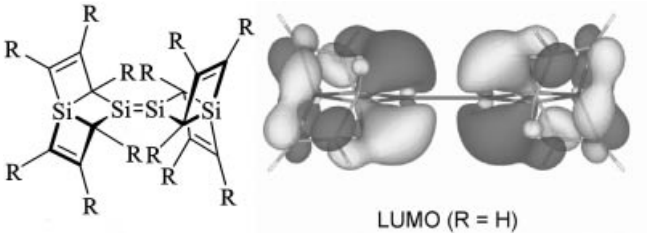

FULL PAPERS

1239 **Y. Lu, Y. Li, E. Wang,* J. Lü, L. Xu, R. Clérac***

$[H_2bpy]_2[\{Cu(bpy)_2\}Mo_5P_2O_{23}]\cdot 4H_2O$: A Three-Dimensional Framework Built from Transition-Metal Coordination Polymer Sheets Pillared by Polyoxomolybdophosphate Clusters

Keywords: Coordination polymers / Magnetic properties / Hydrothermal synthesis / Polyoxometallates

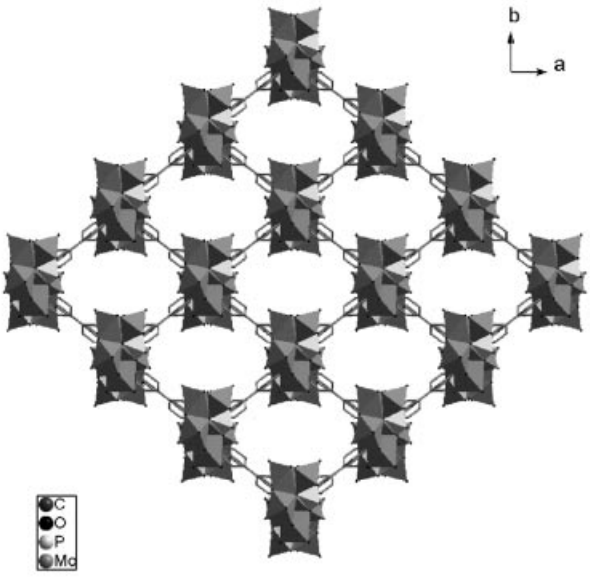

1245 **A. Eichhöfer***

Thermal Properties of $[M_{10}Se_4(SePh)_{12}(PR_3)_4]$ (M = Zn, Cd, Hg) Cluster Molecules − Synthesis and Structure of $[Cd_{32}Se_{14}(SePh)_{36}(L)_4]$; L = $OPPh_3$, OC_4H_8

Keywords: Cluster compounds / Cadmium / Selenium / X-ray structure analysis / Thermogravimetric analysis

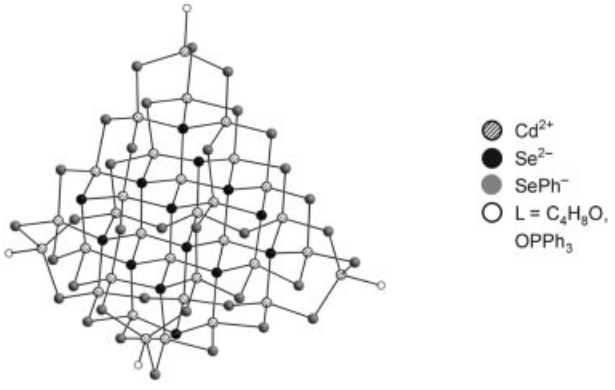

1254 **A. Mukherjee, U. Subramanyam, V. G. Puranik, T. P. Mohandas, A. Sarkar***

Pyrazole-Tethered Heteroditopic Ligands and Their Transition Metal Complexes: Synthesis, Structure, and Reactivity

Keywords: Pyrazole / Hemilabile ligands / Nickel / Copper / Cobalt / Oligomerization

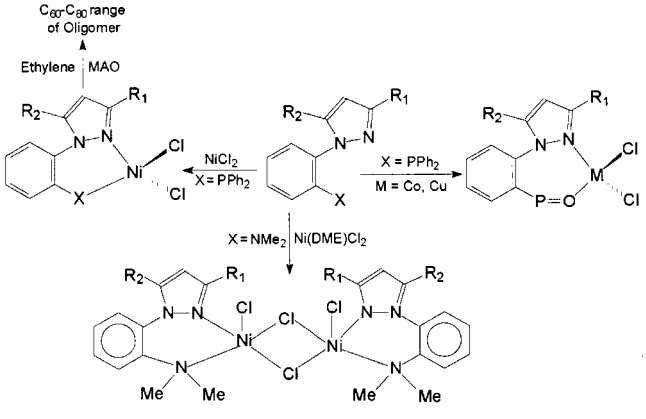

 © 2005 Wiley-VCH Verlag GmbH & Co. KGaA, Weinheim

1264 **M. Carlone,* L. G. Marzilli, G. Natile**

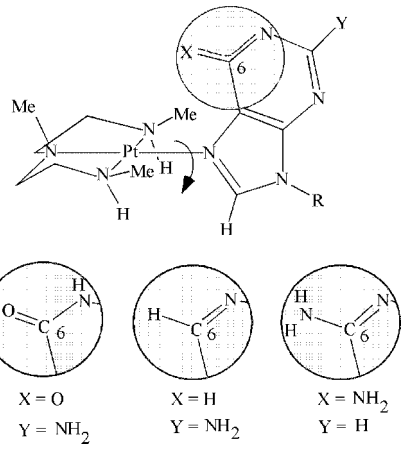

Platinum Complexes with Only One Purine Ligand (Guanine, Deoxyguanine, or Adenine) Flanked by Two *cis*-$NH(CH_3)$ Groups − Informative Models for Assessing the Interaction of Purine C6 Substituents with *cis*-Amines

Keywords: Penciclovir / Platinum / Anticancer drugs

1274 **C. Schaefer, G. Scholz, R. Gleiter,* T. Oeser, F. Rominger**

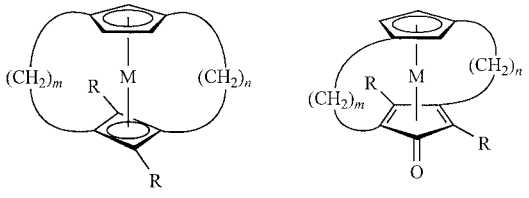

Endohedral Metallocenophanes of Rhodium and Cobalt

Keywords: Cage compounds / Sandwich complexes / Alkynes / Rhodium / Cobalt

1282 **B. S. Creaven,* M. Deasy, C. McKenna, B. A. Murray, D. Tobin**

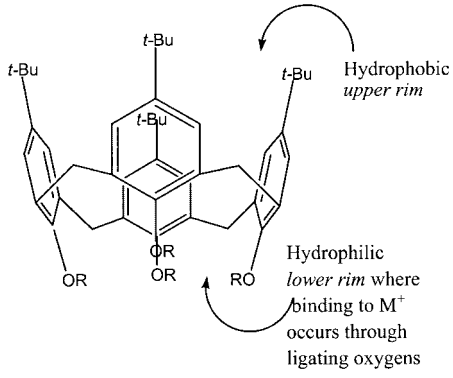

R = $CH_2COOCH_2CH_3$

Photocontrol of Complexation of Neutral and Cationic Species by *p*-*tert*-Butylcalix[4]arene Tetraethyl Ester

Keywords: Calixarene / Photocontrol / Anion effect / Solvent effect / Sodium complexes

1293 **T. Sheng, S. Dechert, A. C. Stückl, F. Meyer***

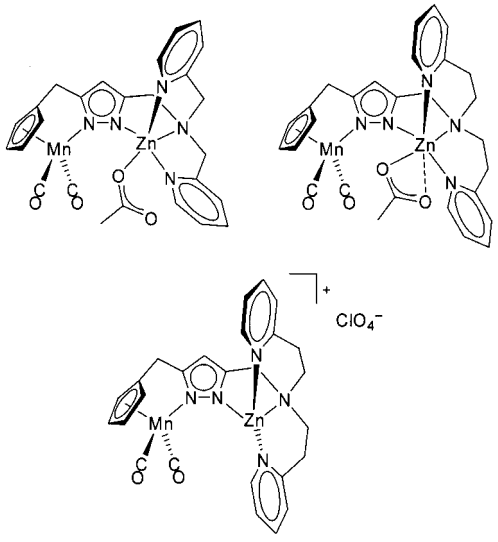

Heterobimetallic Systems Containing Organometallic and Classical Coordination Sites: Effects of Subtle Changes in the Werner-Type Site

Keywords: Bridging ligands / Cyclopentadienyl ligands / Heterometallic complexes / N ligands / Manganese / Zinc

 © 2005 Wiley-VCH Verlag GmbH & Co. KGaA, Weinheim

1303 **B. Wu, D. Yuan, F. Jiang, L. Han, B. Lou, C. Liu, M. Hong***

Effect of Conformation and Combination of 1,3-Bis(4-pyridylthio)propan-2-one upon Coordination Architectures: Syntheses, Characterizations and Properties

Keywords: Coordination polymer / Interpenetration / Conformation analysis / Magnetic property / Fluorescence

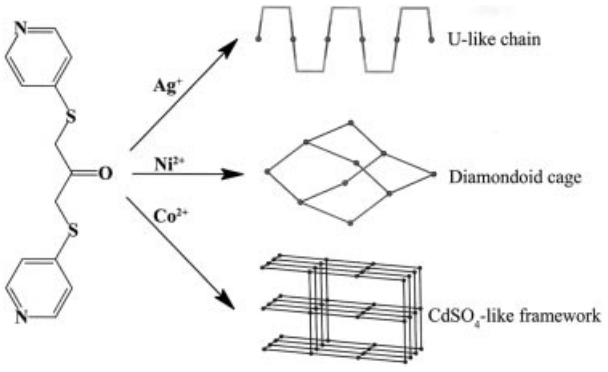

1312 **L. Flamigni,* B. Ventura, F. Barigelletti,* E. Baranoff, J.-P. Collin,* J.-P. Sauvage***

Luminescent Iridium(III)-Terpyridine Complexes − Interplay of Ligand Centred and Charge Transfer States

Keywords: Iridium / Photochemistry / Luminescence / Charge transfer / Electron transfer

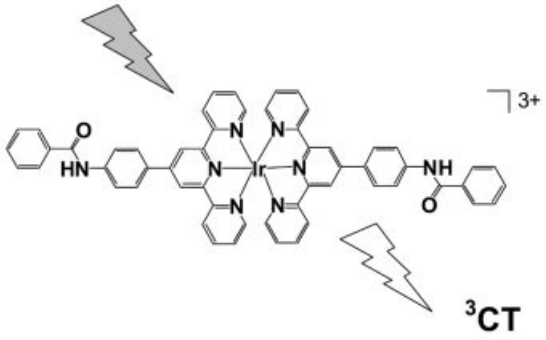

1319 **N. M. Scott, R. Kempe***

Di- and Trivalent Lanthanide Complexes Stabilized by Sterically Demanding Aminopyridinato Ligands

Keywords: minopyridinato ligands / Lanthanides / Neodymium / N ligands / Olefin polymerization / Samarium / Ytterbium

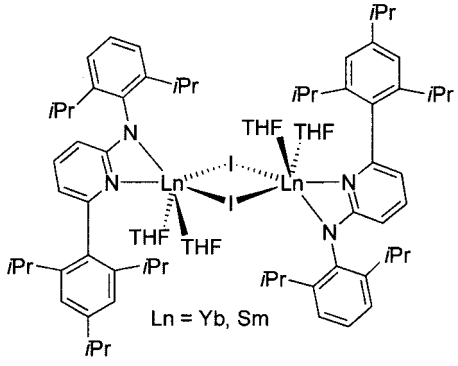

1325 **G. Steiner, H. Kopacka, K.-H. Ongania, K. Wurst, P. Preishuber-Pflügl, B. Bildstein***

Heteroditopic Imino N-Heterocyclic Carbenes and Their Sulfur, Selenium, and Tungsten Tetracarbonyl Derivatives

Keywords: Carbene ligands / N ligands / Selenium / Sulfur / Tungsten

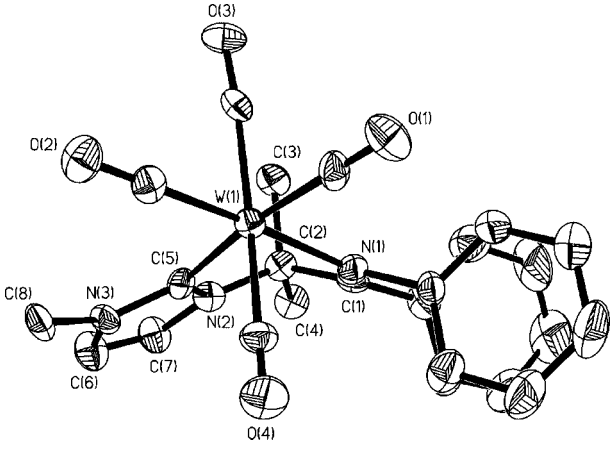

 © 2005 Wiley-VCH Verlag GmbH & Co. KGaA, Weinheim

1334 C.-C. Wang,* C.-H. Yang, G.-H. Lee, H.-L. Tsai

Syntheses, Structures, and Magnetic Properties of Two 1D, Mixed-Ligand, Metal Coordination Polymers, $[M(C_4O_4)(dpa)(OH_2)]$ (M = Co^{II}, Ni^{II}, and Zn^{II}; dpa = 2,2′-dipyridylamine) and $[Cu(C_4O_4)(dpa)(H_2O)]_2\cdot(H_2O)$

Keywords: Hydrogen bonds / Hydrothermal synthesis / Magnetic properties / Self-assembly / Squarate

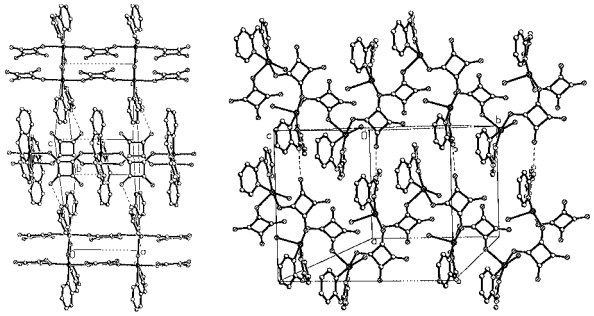

$[M(dpa)(C_4O_4)(H_2O)]$ $[Cu(dpa)(C_4O_4)(H_2O)]_2\cdot(H_2O)$

1343 A. J. Nielson,* C. Shen, P. Schwerdtfeger, J. M. Waters

Synthesis, Structure, Coordination Expansion and Theoretical Modelling of Dichlorobis(phenoxo) Titanium(IV) Complexes

Keywords: Complexes / Phenoxo ligands / Structure elucidation / Theoretical structure / Titanium

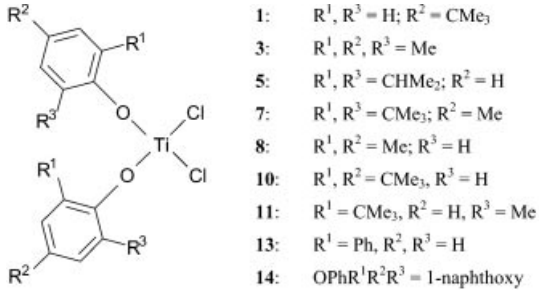

1: R^1, R^3 = H; R^2 = CMe_3
3: R^1, R^2, R^3 = Me
5: R^1, R^3 = $CHMe_2$; R^2 = H
7: R^1, R^3 = CMe_3; R^2 = Me
8: R^1, R^2 = Me; R^3 = H
10: R^1, R^2 = CMe_3, R^3 = H
11: R^1 = CMe_3, R^2 = H, R^3 = Me
13: R^1 = Ph, R^2, R^3 = H
14: $OPhR^1R^2R^3$ = 1-naphthoxy

1353 M. Barth, X. Kästele, P. Klüfers*

Nitrosyl Ruthenium Diolato Complexes

Keywords: Ruthenium / Nitrosyl / Diols / Carbohydrate complexes

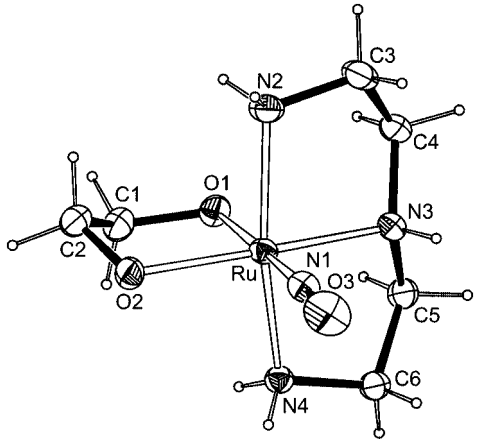

1360 P. Barbaro, M. Di Vaira, M. Peruzzini, S. Seniori Costantini, P. Stoppioni*

Adducts of Cyclotriphosphorus Complexes with Cyclopentadienyl Ruthenium Fragments: Synthesis, Solid-State Structure and Solution Behaviour

Keywords: Cyclotriphosphorus / Ruthenium / Cyclopentadienyl / Monodentate P ligands

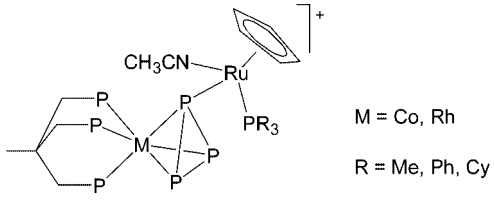

 © 2005 Wiley-VCH Verlag GmbH & Co. KGaA, Weinheim

1369 **E. Garribba,* E. Lodyga-Chruscinska, G. Micera,* A. Panzanelli, D. Sanna**

Binding of Oxovanadium(IV) to Dipeptides Containing Histidine and Cysteine Residues

Keywords: Vanadium / Peptides / Bioinorganic chemistry / EPR spectroscopy / Coordination modes / Bond theory

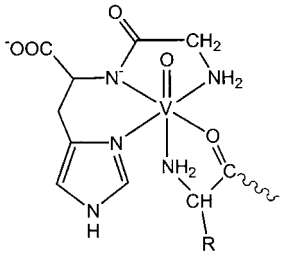

$[VO(GlyHis)_2H_{-1}]^-$

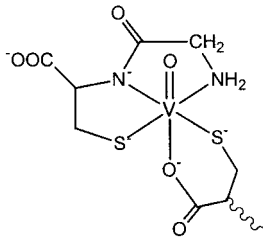

$[VO(GlyCys)_2H_{-1}]^{3-}$

1383 **R. W. Saalfrank,* A. Scheurer, K. Pokorny, H. Maid, U. Reimann, F. Hampel, F. W. Heinemann, V. Schünemann, A. X. Trautwein**

Trinuclear Oxo-Centered Iron and Iron/Nickel Clusters − Ligand-Controlled Homo/Hetero Valency

Keywords: Trinuclear complexes / Iron / Nickel / Mixed-valent complexes / Heteronuclear complexes

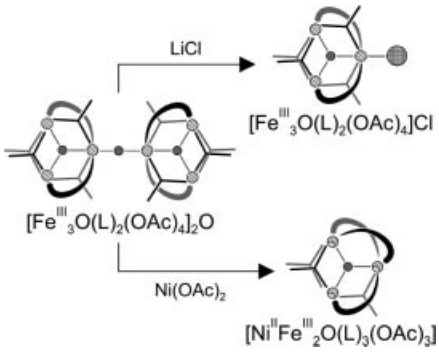

1388 **M. M. Ibrahim, M. Shu, H. Vahrenkamp***

New Tris(thioimidazolyl)borate Ligands and Some Zinc Complexes Thereof

Keywords: Alcohol ligands / Alkoxide ligands / S ligands / Tripodal ligands / Zinc

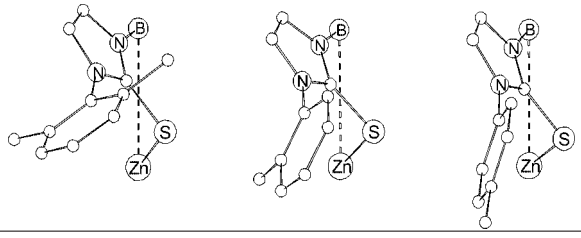

1398 **M. Ji, H. Vahrenkamp***

Zinc Thiolate Complexes of (N,N,S)-Tridentate Ligands for the Modeling of Thiolate Alkylating Enzymes

Keywords: Bioinorganic chemistry / S ligands / Tridentate ligands / Zinc

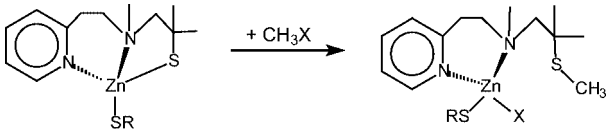

 © 2005 Wiley-VCH Verlag GmbH & Co. KGaA, Weinheim

Si-, Ge-, and Sn-Centered Free Radicals: From Phantom Species to Grams-Order-Scale Materials

Vladimir Ya. Lee[a] and Akira Sekiguchi*[a]

Keywords: Free radicals / X-ray diffraction / EPR spectroscopy / Silicon / Germanium / Tin

Recent developments in the field of the stable free radicals of heavier group 14 elements are reviewed, covering both neutral and charged radical species. The electronic and crystal structural features of these radicals, both in the solid state and in solution, are compared with each other. The most important parameters affecting the stability, geometry and electronic configuration of the radicals are discussed on the basis of the latest experimental and computational data.
(© Wiley-VCH Verlag GmbH & Co. KGaA, 69451 Weinheim, Germany, 2005)

1. Introduction

Free radicals, that is, compounds featuring a trivalent carbon atom having only seven valence electrons, have been known for more than one hundred years, since the groundbreaking discovery of the triphenylmethyl radical. Such a departure from the fundamental octet rule causes an intrinsic electronic unsaturation of the radical species expressed in the existence of the unpaired electron, resulting in the extremely high reactivity of free radicals compared with that of normal tetravalent carbon compounds.[1] Together with carbocations and carbanions (and later, carbenes), the most fundamental species in organic chemistry, free radicals were always among the most desired and challenging synthetic goals. The two most historically significant discoveries are worth mentioning in this review. The first one commemorates the starting point of free radical chemistry: in 1900 Gomberg provided convincing evidence for the existence of $Ph_3C^{\cdot}$ species obtained by the treatment of triphenylmethyl chloride with metallic silver.[2] This was the first representative of a new class of organic compounds, which were later named free radicals. At the beginning of the era of free radical chemistry, another fundamental breakthrough was achieved by Paneth, who reported in 1929 the first proof for the generation of the simplest methyl radical by the thermal decomposition of tetramethyllead.[3] Since then, and during the last one hundred years, a great deal of experimental information supporting the real existence and participation in chemical reactions of free radical species has been developed. In the early stage, free radicals were speculated to be reactive intermediates with

[a] Department of Chemistry, Graduate School of Pure and Applied Sciences,
University of Tsukuba, Tsukuba, Ibaraki 305-8571, Japan

Vladimir Ya. Lee was born in Russia (Sakhalin). He graduated from the chemistry department of the Far-Eastern State University in 1982. He received his Ph.D. degree in chemistry from the Institute of Organic Chemistry of the Academy of Sciences of the USSR (Moscow) in 1987. He has then worked as a postdoctoral researcher at the Korea Institute of Science and Technology (Korea) in 1996 and at the Université Paul Sabatier (France) in 1997. Since 1998 he is working at the University of Tsukuba. His research interests lie in the field of highly reactive species: carbene analogues, cations, free radicals, anions, multiply bonded compounds and small rings.

Akira Sekiguchi is Professor of Organic Chemistry at the University of Tsukuba. He was born in Gunma, Japan, in 1952. He obtained his B. Eng. and M. Eng. from Gunma University in 1974 and 1976, respectively. He received his D. Sc. from the University of Tsukuba in 1981. He became a research fellow in 1978, an assistant in 1981, and an assistant professor in 1982 at the University of Tsukuba. In 1987, he moved to the organosilicon research laboratory at Tohoku University as an associate professor. He worked as a research fellow at the University of Wisconsin, Madison in 1985–1986. In 1996, he returned to the University of Tsukuba as a full professor. He received the Japan IBM Science Award in 1996, the Divisional Award of the Chemical Society of Japan (Organic Chemistry) in 1997, and the Alexander von Humboldt Research Award in 2004. His research interests are organosilicon and organolithium chemistry, organogermanium chemistry, and reactive intermediates.

MICROREVIEWS: This feature introduces the readers to the authors' research through a concise overview of the selected topic. Reference to important work from others in the field is included.

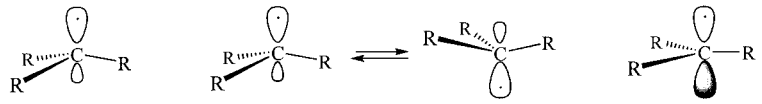

Scheme 1. Geometry of organic free radicals.

very short lifetimes, often undetectable by physico-chemical methods. However, researchers quickly realized that such ephemeral radical species could gain extra stability through the electronic and steric effects of substituents. This greatly extended the lifetime of those radicals, enabling them to be detected and identified directly by means of spectroscopic methods, mainly by EPR and CIDNP techniques.[1] Many so-called persistent radicals have been prepared and characterized since then, and a review dealing with this topic has been published.[4] As a major development in this field, one should mention the synthesis of stable free radicals, whose isolation and structural identification has been possible in a limited number of cases in the past few years.[5]

One of the most fundamental characteristics of free radicals, directly associated with their ground-state electronic structure, is their geometry in the solid state and in solution. It is now well-established that free radicals can adopt one of three possible geometries, known as rigid pyramidal (**A**), flexible pyramidal (**B**), and planar (**C**) (Scheme 1).[1] Planar radicals are also flexible.

In the first two cases, the unpaired electron is accommodated in an orbital with some degree of s-character (tetrahedral configuration), whereas in the latter case the SOMO (singly occupied molecular orbital) is represented by an orbital with essentially p-character (trigonal-planar configuration). The arrangement of the odd electron in an orbital of either s- or p-character is totally governed by the substitution pattern at the radical center. For example, the structure of the methyl radical was found by EPR studies to be either planar or in the form of a very shallow pyramid,[6] whereas the trifluoromethyl radical was found to be markedly pyramidal.[7] The general tendency of the σ-accepting and π-donating substituents to favor the pyramidal structure is explained by the attractive interaction of the SOMO and the central element–electronegative substituent antibonding σ* orbital, increasing the electron density on the more electronegative atom. Accordingly, electropositive σ-donating and π-accepting substituents (such as silyl groups) have the opposite influence on the geometry of the radical center, causing a significant flattening of the radical structure. A great deal of information about the geometry and consequently the electronic structure of free radicals in solution can be obtained from their EPR spectra. The geometry of free radicals in solution can thus be reliably elucidated on the basis of the value of the hyperfine coupling constant (hfcc), since the latter arises from the spin density in the *n*s-orbitals, markedly increasing with increased s-character of the SOMO.[8] In other words, the higher the hfcc value, the more pyramidal is the radical (σ-type radical), the lower the hfcc value, the more planar is the radical (π-type radical).

The chemistry of the heavy analogues of free radicals, centered on the Si, Ge, Sn, and Pb atoms, was developed much later than its carbon counterpart, although the participation of radicals of the type $R_3E^{\cdot}$ (E = heavier group 14 element) in a number of organometallic reactions was postulated and debated several decades ago.[9] Later, the right combination of both steric and electronic stabilizing effects of substituents enabled the preparation of heavier group 14 element centered radicals with lifetimes long enough to be detected directly by EPR spectroscopy.[10] Such compounds have been known since the important publication of the first EPR spectrum of the persistent stannyl radical $[(Me_3Si)_2CH]_3Sn^{\cdot}$ by Lappert et al. nearly 30 years ago.[11] The progress in this field, made after this first discovery, was thoroughly described in a most recent review, to which we refer our readers.[12] The culmination of this steady progress in the field of heavier group 14 element centered radicals was reached just in the past few years, expressed in the publication of the papers describing the first crystal structures of the Si-, Ge- and Sn-centered free radicals. In this review we will deal with the chemistry of such stable (that is, isolable) compounds only, leaving the vast area of the transient and limitedly stable radical species outside the framework of the present article.

The chemistry of stable free radicals centered on the heavier group 14 elements (Si, Ge, Sn, Pb) can be divided into two main areas: the first one concerns the chemistry of the stable *neutral* radical species, whereas the second one is devoted to the *charged* radical species, that is, ion radicals (namely, anion radicals). Below, we will deal with the radicals of both groups, emphasizing the synthetic methods for each class as well as their structural peculiarities, first of all geometry and electronic structure. A remark concerning the terminology used throughout the text: In the literature two main terms for the long-lived radical species are currently used: **persistent** radicals, with a relatively long lifetime enabling them to be detected either by spectroscopic means or chemically, and **stable** radicals, which are indefinitely stable and isolable.[4,12] However, such confusing terminology, particularly with respect to the "relatively" or "indefinitely" long lifetime, may cause conflicting situations when the same radicals are sometimes treated as persistent ones, and sometimes as stable ones. In order to avoid such contradictions, in our review we will use only the term "stable" for those radical species that can be isolated and characterized as individual compounds, in the majority of cases by means of X-ray crystallography.

 © 2005 Wiley-VCH Verlag GmbH & Co. KGaA, Weinheim

2. Neutral Si-, Ge- and Sn-Centered Radicals

The area of neutral radical species of heavier group 14 elements can be subdivided into the chemistry of cyclic and acyclic compounds. The electronic composition, structural features and stability of these two subgroups differ from each other greatly, since the cyclic radicals can gain extra stability from the cyclic π delocalization of the odd electron over the cyclic π-bond system, whereas the simple acyclic tricoordinate silyl-substituted radicals mainly take advantage of the stabilization through the σ delocalization of the odd electron over the σ* orbitals of the neighboring silyl substituents. The chemistry of both of these groups of neutral radicals will be considered below.

2.1 Cyclic Neutral Radicals

The first example of a stable compound featuring a radical center on a heavier group 14 element, the cyclotrigermenyl radical **1** stabilized by the very bulky 2,6-Mes_2–C_6H_3 groups, was reported by Power's group in 1996.[13] Compound **1** was synthesized by the reduction of chlorogermylene :Ge(Cl)(2,6-Mes_2–C_6H_3)[14] with KC_8 in THF (Scheme 2). Although the exact structural determination of **1** was prevented by skeletal disorder problems, its structure was reliably refined to reveal a Ge analogue of the cyclopropenyl radical, that is, a three-membered ring involving a double bond between the two Ge atoms and an odd electron on the remaining Ge atom.

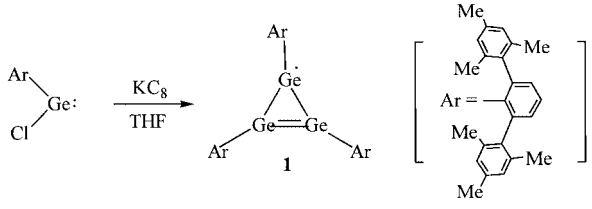

Scheme 2. Synthesis of cyclotrigermenyl radical **1**.

The EPR spectrum of **1** displayed a resonance with a *g* value of 2.0069 and an hfcc, $a(^{73}Ge)$, of 1.6 mT, suggesting a location for the unpaired electron in an orbital of π symmetry, which in turn means essential planarity at the Ge radical centers. Further reduction of radical **1** resulted in the formation of the corresponding anion species accompanied with the ring-opening process to produce finally the acyclic trigermaallyl anion **2** (Scheme 3).[13]

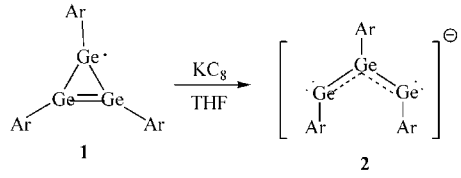

Scheme 3. Synthesis of trigermaallyl anion **2**.

The cyclic silicon analogue of the delocalized allyl radical, cyclotetrasilenyl radical **3**, was recently reported by Sekiguchi et al.[15] This compound, representing the first stable Si-centered radical, was synthesized by the one-electron reduction of the precursor compound, cyclotetrasilenylium ion **4**,[16] with either silylsodium tBu_3SiNa or KC_8 in Et_2O (Scheme 4).

X-ray crystallography disclosed the free radical structure of **3** (Figure 1). As expected, the four-membered-ring core of **3** was nearly planar (folding angle 4.7°) in contrast to the precursor cation **4**,[16] which had a largely folded cyclic skeleton (folding angle 46.6°) due to the homoaromatic 1,3-

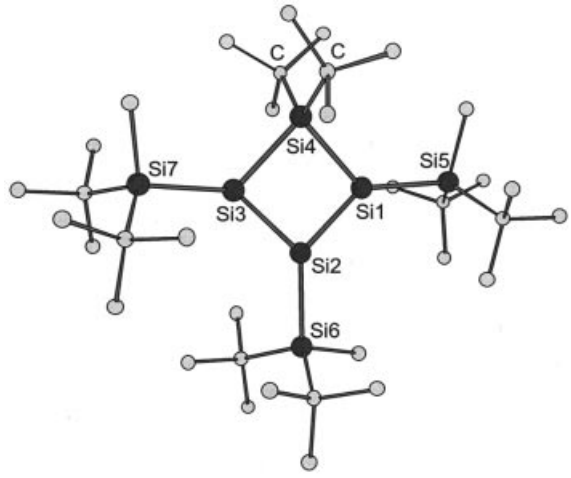

Figure 1. Crystal structure of cyclotetrasilenyl radical **3**.

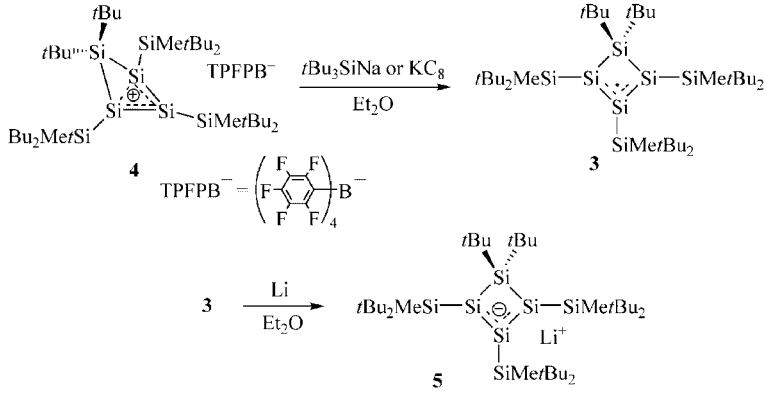

Scheme 4. Synthesis of cyclotetrasilenyl radical **3**.

 © 2005 Wiley-VCH Verlag GmbH & Co. KGaA, Weinheim

orbital interaction. The Si1–Si2 and Si2–Si3 bond lengths were slightly different [2.226(1) and 2.263(1) Å, respectively]. This was consistent with some insignificant pyramidalization of the Si3 atom (the sum of the bond angles was 356.2°). However, the lengths of both the Si1–Si2 and the Si2–Si3 bonds were intermediate between those of the typical Si–Si single and Si=Si double bonds, which proved the allylic-radical-type structure of **3**.

The EPR spectrum of **3** displayed a strong signal with a *g* value of 2.0058 (typical for silyl-substituted silyl radicals: 2.0053–2.0063).[10i–10l] The three pairs of satellite signals with the largest spin densities [hfcc values: $a(^{29}Si)$ = 4.07, 3.74, and 1.55 mT] were assigned to the coupling of an unpaired electron with the terminal Si1, terminal Si3, and the central Si2 nuclei, respectively, which also agreed well with the delocalized-allylic-type structure of radical **3**. The small values of the hfcc's are consistent with the planarity of the radical unit, that is, the planarity of the four-membered ring of **3** is also retained in solution. The cyclic radical **3** can be smoothly reduced with metallic Li in Et_2O to form the corresponding cyclotetrasilenide ion **5**, which preserves the allylic-type structure of its predecessor (Scheme 4).[17] Such stability of the four-membered ring of **3** upon reduction is amazing, in contrast to the above-mentioned ring-opening reduction of the cyclotrigermenyl radical **1**.[13]

The first, and still the sole, example of a stable bicyclic radical of heavier group 14 elements was reported just recently by Sekiguchi et al.[18] Such a Ge-centered free radical, 1,6,7-trigermabicyclo[4.1.0]hept-3-en-7-yl (**6**), was synthesized by the selective one-electron oxidation of the corresponding precursor, bicyclic anion **7**, generated by the reduction of iodide **8**, with tris(pentafluorophenyl)boron in THF (Scheme 5).

The crystal structure of **6** was determined by means of X-ray crystallographic analysis (Figure 2), which showed that the radical center was specifically accommodated on the Ge3 atom having a nearly planar geometry (sum of the bond angles: 357°). The bridgehead Ge1–Ge2 bond was slightly longer than the bridging Ge1–Ge3 and Ge2–Ge3 bonds: 2.4864(4) Å vs. 2.4254(5) and 2.4326(4) Å. A particularly important observation is that compound **6** has *endo* conformation, in contrast to all other structurally

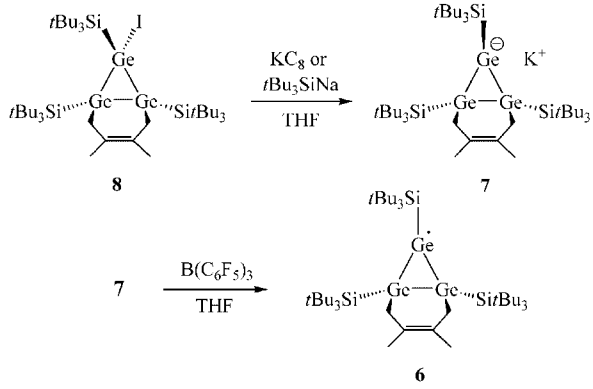

Scheme 5. Synthesis of bicyclic germyl radical **6**.

characterized compounds of this type, which have exclusively *exo* conformation.[19] This fact indicates some degree of intramolecular Ge radical–π(C=C) interaction in **6**; this is deduced from the relative proximity of the two species: the interatomic distance between the Ge radical and the C=C bond is 3.632 Å, which lies in the range of van der Waals interactions.

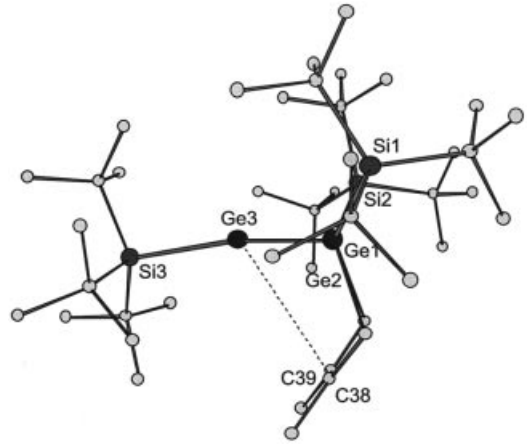

Figure 2. Crystal structure of bicyclic germyl radical **6**.

Surprisingly, the EPR spectrum of **6** revealed two signals of almost identical intensity, with *g* values of 2.0210 and 2.0223. Again, as in all of the above cases of cyclic radicals,

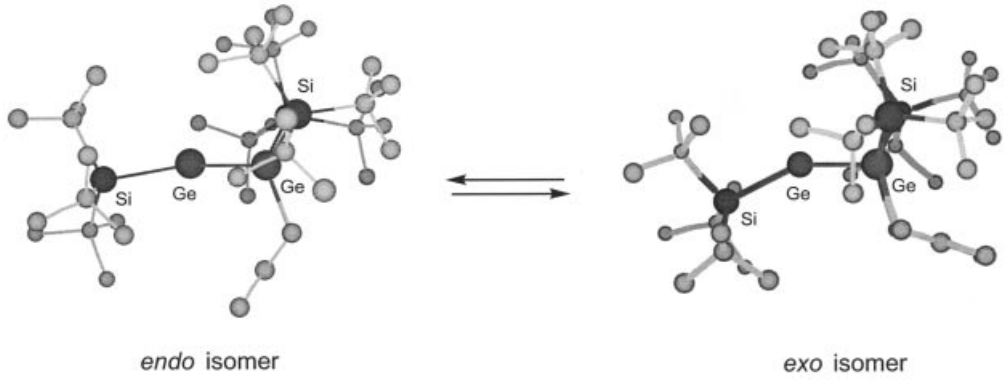

Figure 3. *endo–exo* isomerization of bicyclic germyl radical **6**.

 © 2005 Wiley-VCH Verlag GmbH & Co. KGaA, Weinheim

the planarity of these Ge radical centers was maintained also in the condensed phase, which was clearly manifested by their small hfcc's (3.4 and 2.6 mT, respectively), indicating also the sp^2-type hybridization of the Ge radical center. The existence of two signals in the EPR spectrum was explained in terms of the *endo–exo* isomerization taking place in the solution of **6** on the EPR time scale (Figure 3).[18] Apparently, in the solid state such isomerization is suppressed in favor of the *endo* isomer, stabilized by the intramolecular Ge radical–C=C interaction, which was supported by theoretical calculations (the *endo* isomer is more stable than the *exo* isomer by 0.59 kcal/mol).

One can easily notice that, in contrast to the allylic-type cyclotrigermenyl radical **1**[13] and cyclotetrasilenyl radical **3**,[15] the bicyclic radical **6**[18] has a localized structure caused by the absence of the π bond in the proximity necessary for effective through-bond interaction and by the insufficiency of the through-space interaction with the C=C double bond to enable the remarkable delocalization of the odd-electron density.

2.2 Acyclic Tricoordinate Neutral Radicals

Although the above-mentioned cyclic Si- and Ge-centered radicals were synthesized as the remarkable first representatives of this class of organometallic compounds, their structural features were significantly affected by their particular and unique cyclic skeletons. However, the properties and stability of the acyclic radicals of the type $R_3E^{\cdot}$ (E = heavier group 14 element) without stabilization through cyclic π delocalization were expected to be greatly different and even more challenging. Therefore, despite the evident progress in the development of the stable-free-radical chemistry described in the previous section, the search for stable, tricoordinate, acyclic radicals of heavier group 14 elements turned out to be a problem of great importance.

The first breakthrough in the development of such chemistry was achieved just a couple of years ago by Sekiguchi et al., who reported the synthesis and structural identification of the first stable acyclic silyl, germyl, and stannyl radicals lacking conjugation with π bonds. Of particular importance was the fact that all compounds were prepared by a similar and very simple method, which demonstrated the generality of the synthetic approach. All synthesized $R_3E^{\cdot}$ (E = Si, Ge, Sn) radicals had the same silyl substituents (R = SiMe*t*Bu$_2$), which provided a unique possibility to prepare a homologous series of the compounds and trace the regularities and tendencies inside this series, on descending group 14.

The tris(silyl)substituted silyl radical **7** was synthesized by the oxidation of the in situ generated silylsodium derivative (*t*Bu$_2$MeSi)$_3$SiNa, prepared by the reaction of dibromosilane (*t*Bu$_2$MeSi)$_2$SiBr$_2$ and silylsodium *t*Bu$_2$MeSiNa with dichlorogermylene–dioxane complex GeCl$_2$·dioxane in Et$_2$O (Scheme 6).[20]

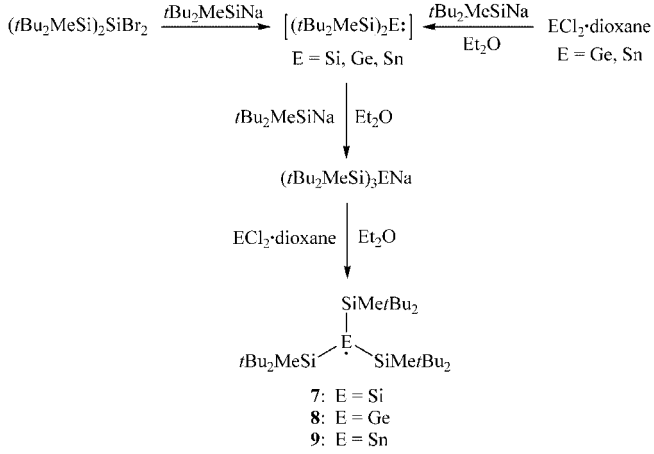

Scheme 6. Synthesis of tris(di-*tert*-butylmethylsilyl)-substituted silyl-, germyl-, and stannyl radicals **7**, **8**, and **9**.

Radical **7** has a trigonal-planar configuration of the Si radical center, implying that the odd electron is accommodated in the 3p$_z$ orbital of the Si atom (Figure 4). Both steric and electronic factors contribute significantly to the planarity of the radical center: Sterically, for example, all methyl substituents at the peripheral Si atoms are arranged in a clockwise manner exactly in the Si1–Si2–Si3–Si4 plane, thus minimizing the steric repulsion of the bulky *t*Bu groups. Electronically, electropositive silyl substituents significantly lower the inversion barrier at the Si radical center, also resulting in its planarization. On the other hand, the bulky substituents sterically protect the free-radical species, enabling it to be isolated. Another important factor enhancing the stability of **7** is the possibility of delocalization of the unpaired-electron density over the antibonding σ* orbitals of the Si–C(*t*Bu) bonds (hyperconjugation effects).

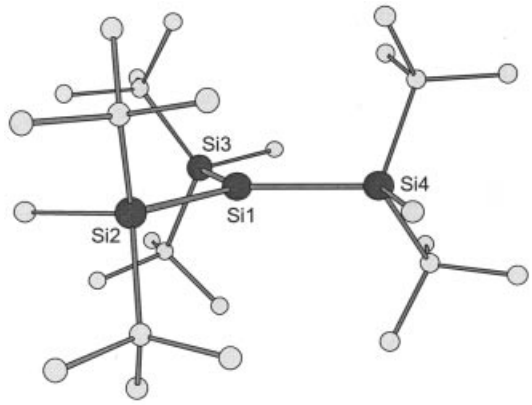

Figure 4. Crystal structure of tris(di-*tert*-butylmethylsilyl)silyl radical **7**.

Radical **7** exhibited an intense signal in the EPR spectrum with a *g* value of 2.0056 and two pairs of satellite signals with the hfcc's $a(^{29}Si)$ = 5.80 mT (α-Si) and 0.79 mT (β-Si) (Figure 5). The small coupling with the central Si atom of 5.80 mT definitely manifests the arrangement of the unpaired electron in an orbital of predominantly p-character, implying that the Si radical center is sp^2-hy-

 © 2005 Wiley-VCH Verlag GmbH & Co. KGaA, Weinheim

bridized and planar. Thus, both in the solid state and in solution the persilyl-radical **7** behaves as a π radical, whose SOMO is mainly represented by the $3p_z$(Si) orbital.

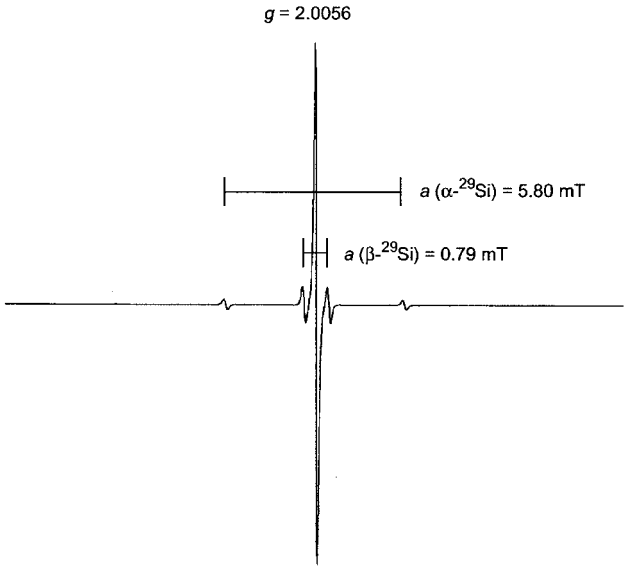

Figure 5. EPR spectrum of tris(di-*tert*-butylmethylsilyl)silyl-radical **7**.

The corresponding Ge analogue (tBu$_2$MeSi)$_3$Ge· (**8**) was prepared in a similar, and even simpler, procedure: by the direct reaction of tBu$_2$MeSiNa with GeCl$_2$·dioxane in Et$_2$O (Scheme 6).[20] At first, the intermediate germylene (tBu$_2$MeSi)$_2$Ge**:** was generated in situ, followed by the formation of the germylsodium derivative (tBu$_2$MeSi)$_3$GeNa, and its subsequent oxidation with a second equivalent of GeCl$_2$·dioxane. It is worth mentioning that in the above reactions the GeCl$_2$·dioxane complex behaved as a very mild and selective oxidizing reagent, whose high oxidizing ability was documented in the previous electrochemical studies [$E_{1/2}$(red) = –0.41 V].[21]

Being a heavy homologue of silyl radical **7**, germyl radical **8** exhibited quite similar structural and electronic features. Its crystal structure was isomorphous to that of **7**: an absolutely planar configuration of the Ge center with the same in-plane and clockwise arrangement of the methyl groups.[20] The EPR spectrum of **8** displayed a strong central signal (*g*-factor = 2.0229) with the very characteristic picture of ten satellite signals with the hfcc a(^{73}Ge) = 2.00 mT (Figure 6). Again, one should recognize that Ge radical **8** is a planar π radical, parallel to the above case of silyl radical **7**.

Employing the same synthetic approach, Sekiguchi et al., recently succeeded in the preparation of the first stable Sn-centered radical, (tBu$_2$MeSi)$_3$Sn· (**9**), by the reaction of tBu$_2$MeSiNa with SnCl$_2$·dioxane in Et$_2$O (Scheme 6).[22] The crystal structure of **9** is identical to those of the silyl and germyl radicals **7** and **8** discussed above: a planar Sn radical center with the same orientation of the silyl substituents. The EPR spectrum of **9** revealed a central signal with a *g* value of 2.0482 and two pairs of satellite signals with the hfcc a(^{119,117}Sn) = 32.9 mT (Figure 7).

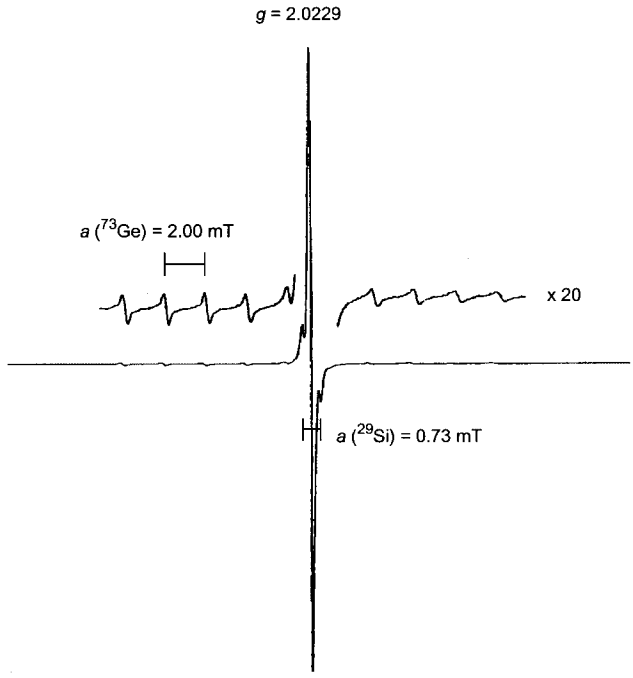

Figure 6. EPR spectrum of tris(di-*tert*-butylmethylsilyl)germyl radical **8**.

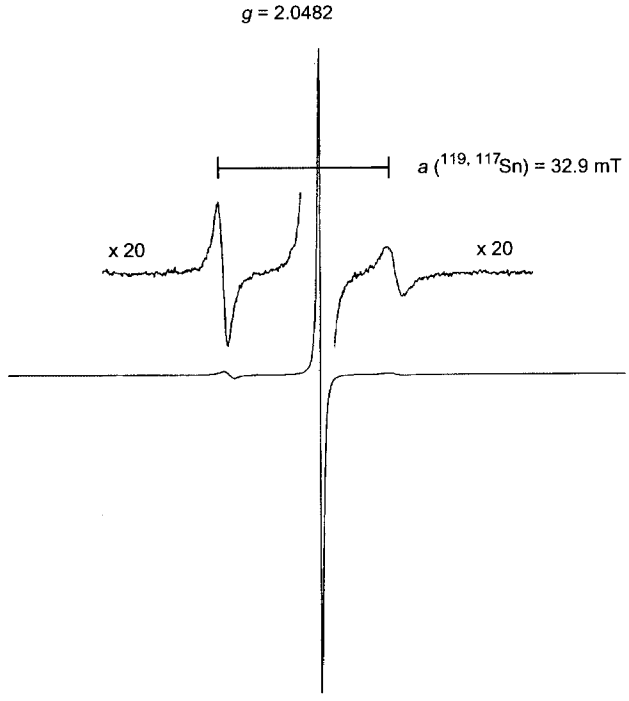

Figure 7. EPR spectrum of tris(di-*tert*-butylmethylsilyl)stannyl-radical **9**.

Most importantly, in the series of silyl, germyl and stannyl radicals **7**, **8**, and **9** the structural features are absolutely identical both in the solid state and in solution, that is, all radicals should be described as truly π radicals with the characteristic sp^2-hybridization and trigonal-planar configuration of the central element. Since the substitution

 © 2005 Wiley-VCH Verlag GmbH & Co. KGaA, Weinheim

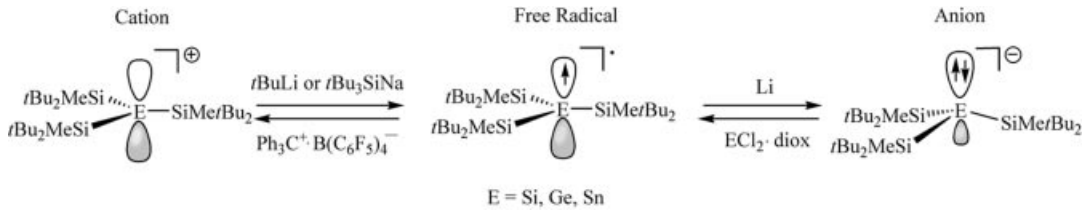

Scheme 7. Reversible redox system of the $(t\mathrm{Bu_2MeSi})_3\mathrm{E}$ (E = Si, Ge, Sn) species: cations–free radicals–anions.

pattern is the same in all cases, one should attribute such uniform behavior of the $(t\mathrm{Bu_2MeSi})\mathrm{E}^{\cdot}$ (E = Si, Ge, Sn) radical homologues to the determining influence of the bulky electropositive silyl substituents, in contrast to simple alkyl and aryl substituents causing a highly pronounced pyramidalization around the metal radical centers, in which the unpaired electron occupies the orbital with a high degree of s-character (σ radicals).

In addition to the evident simplicity of the preparation and hence the easy accessibility of radicals **7**, **8**, and **9**, another striking peculiarity of these compounds is their reactivity. All these radicals easily and quantitatively undergo one-electron oxidation or reduction to form the corresponding cation and anion species (Scheme 7).[23,24] This allowed the synthesis of the first stable free germyl and stannyl cations $(t\mathrm{Bu_2MeSi})_3\mathrm{Ge}^+$ and $(t\mathrm{Bu_2MeSi})_3\mathrm{Sn}^+$, recently described by Sekiguchi et al.[23b,23c]

3. Charged Si-, Ge-, and Sn-Centered Radicals

Another name for charged radicals is ion radicals, either anion radicals or cation radicals of the heavier group 14 elements. Although the existence of such molecules as transient species has been discussed for a long while, being sometimes experimentally demonstrated by special spectroscopic techniques such as low-temperature EPR spectroscopy,[25] significant progress in this field has been achieved only in the last few years, with the synthesis of stable representatives of this class of highly reactive compounds. In reviewing these latest developments, we will also subdivide these radicals into two groups: cyclic and acyclic ones.

3.1 Cyclic Ion Radicals of Heavier Group 14 Elements

Only one example of a stable cyclic anion radical of heavier group 14 elements has been reported very recently, the cyclotetrasilane anion radical **10**.[26] This compound was formed, together with the more extensively reduced species, the cyclotetrasilane dianion **12**, upon reduction of the heterocyclic dichlorosilane precursor **11** with metallic potassium in THF (Scheme 8).

In the crystal state of **10** the potassium ion is solvent-separated from the anion radical part (Figure 8). The four-membered Si_4 ring is square-planar with endocyclic Si–Si bond lengths of 2.347(2) Å, which are slightly shorter than those of known cyclopolysilanes.[27] The EPR spectrum of **10** showed a multiplet signal with $g = 2.0025$ and $a(^{14}\mathrm{N}) = 0.35$ mT, consisting of 15 of the expected 17 lines due to

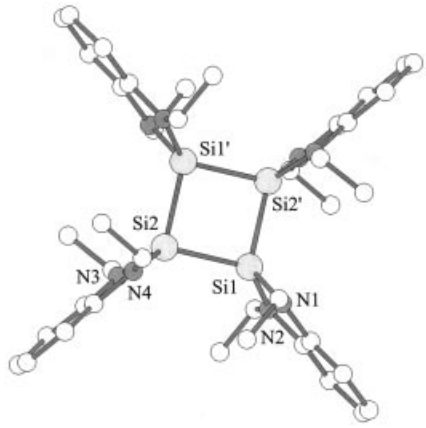

Figure 8. Crystal structure of cyclotetrasilane anion radical **10** (only the anionic part of the molecule is shown).

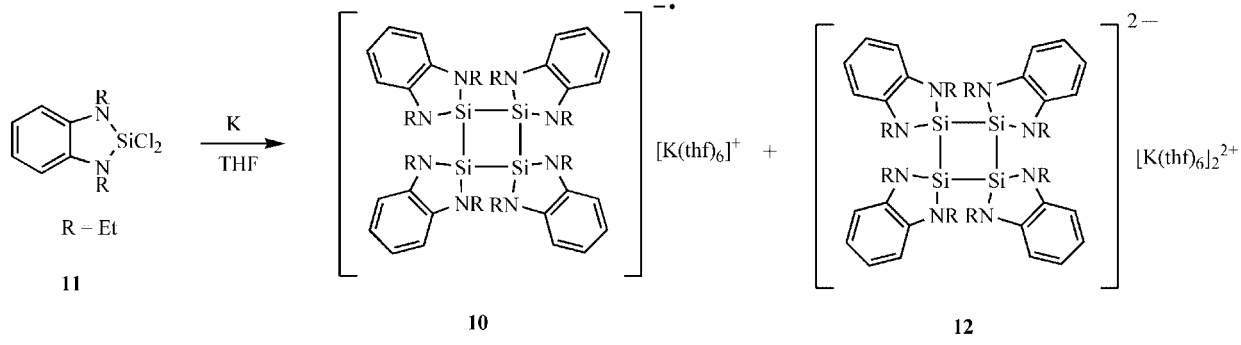

Scheme 8. Synthesis of the cyclotetrasilane anion radical **10**.

 © 2005 Wiley-VCH Verlag GmbH & Co. KGaA, Weinheim

coupling of the unpaired electron with the eight ^{14}N nuclei ($I = 1$). Such an EPR spectrum pattern agrees well with the formulation of odd-electron delocalization over the Si_4 ring, which is supported by the EPR spectrum simulation.

3.2 Acyclic Ion Radicals of Heavier Group 14 Elements

Until now, no examples of stable cation radicals based on the heavier group 14 elements have been reported in the scientific literature. As for stable anion radicals, there were just a few papers devoted to this subject, published mainly in the past few years. Among them, one can recognize the following subtopics: (1) anion radicals of heavy carbene analogues, (2) anion radicals of heavy alkene analogues, (3) anion radicals of heavy alkyne analogues. Each one will be briefly considered below.

3.3 Anion Radicals of Heavy Carbene Analogues

It is now well established that the heavy analogues of carbenes, that is, silylenes, germylenes, stannylenes and plumbylenes, have a singlet ground state with a σ^2 electronic configuration, implying that the two paired electrons are accommodated in the orbital of σ symmetry, corresponding to the a $^1A_1$ electronic ground state (Scheme 9).[28] However, upon either oxidation or reduction, the electronic configuration of heavy carbene analogues may be changed or may be retained depending on the substitution pattern. For example, the silylene cation radical was experimentally found to be a σ-type radical, whereas the silylene anion radical was calculated to be a π radical.[29] The anion radicals of dichlorogermylene, as well as its complexes with Lewis bases, were also calculated to be π radicals, in contrast to their cation radicals of σ type.[21]

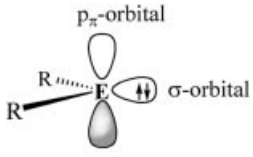

Scheme 9. Electronic configuration of the heavy analogues of carbenes.

Although experimental data on the stable (isolable) anion radicals of heavy carbene analogues are still lacking in the scientific literature, there were several papers on the generation of such anion-radical species with lifetimes long enough to be detected and identified by EPR. The first report on the generation of anion radicals of heavy carbene analogues was published by Sita et al., who described the room-temperature EPR spectrum of the reaction mixture obtained upon the reduction of hexakis(2,6-diethylphenyl)-cyclotristannane with potassium amalgam in THF.[30] This EPR signal, exhibiting an $^{119,117}Sn$ hyperfine coupling of 15.2 mT, was reasonably assigned to the bis(2,6-diethylphenyl)stannylene anion radical; however, the assignment was not unambiguously proved. More recent developments in the field involve the direct reduction of the stable heavy carbene analogues (silylenes, germylenes, and stannylenes) with the alkali metals, providing more convincing evidence for the generation of the relatively stable anion-radical species of the heavy carbenes. The latter achievements will be briefly overviewed below.

The first paper on the generation of germylene and stannylene anion radicals was published by Egorov and Gaspar in 1995.[31] These anion radicals were prepared by the reduction of Lappert's germylene $[(Me_3Si)_2CH]_2Ge$**:** and stannylene $[(Me_3Si)_2CH]_2Sn$**:** with sodium mirror in THF (Scheme 10). Although both germylene anion radical **13** and stannylene anion radical **14** were not indefinitely stable in solution at room temperature (the lifetime for **13** was about 1.5 h, whereas for **14** it was several minutes), it was possible to characterize them by EPR spectroscopy. Germylene anion radical **13** exhibited a strong EPR resonance ($g = 2.0125$) as a triplet due to the coupling of the unpaired electron with the two α-protons of the alkyl substituents [$a(^1H) = 0.26$ mT]. The characteristic coupling with the ^{73}Ge nuclei was manifested in the observation of eight (of the total of ten) weak satellite signals with $a(^{73}Ge) = 1.25$ mT. The disappearance of the anion radical **13** in solution obeys second-order kinetics, implying that **13** dimerizes to form the diamagnetic dianion species.

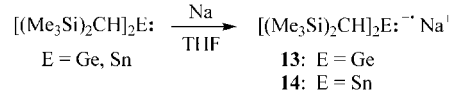

Scheme 10. Generation of the germylene and stannylene anion radicals **13** and **14**.

The stannylene anion radical **14** was also identified by its EPR spectrum, which revealed a broad singlet ($g = 2.0177$) having a pair of unresolved satellite signals arising from the coupling of the unpaired electron with both ^{119}Sn and ^{117}Sn nuclei [$a(^{119,117}Sn) = 11.6$ mT].[31] The small values of the hfcc's [$a(^{73}Ge) = 1.25$ mT and $a(^{119,117}Sn) = 11.6$ mT] make possible a reliable assignment of both anion radicals **13** and **14** to a class of π radicals with the $^2B_1$ ground electronic state.

A study on the generation of the silylene anion radical was published several years later than that for germylene and stannylene anion radicals. The silylene anion radical **15** with a lifetime of about 20 minutes at room temperature was generated similarly by the direct reduction of the stable silylene **16** with potassium mirror in dimethoxyethane (Scheme 11).[32] The one-electron reduction of **16** to form anion radical **15** was also achieved by reduction with other alkali metals such as Li, Na, Rb, and Cs, to produce essentially the same EPR spectra (Scheme 11). The identification and assignment of **15** was made on the basis of its EPR spectrum, which revealed a multiplet signal ($g = 2.0077$) composed of more than 20 lines due to the coupling of the unpaired electron with the 36 protons of the Me_3Si groups [$a(^1H) = 0.0189$ mT] and the 4 protons of the CH_2 groups

 © 2005 Wiley-VCH Verlag GmbH & Co. KGaA, Weinheim

of the cyclopentane skeleton [$a(^1H)$ = 0.0378 mT]. The satellite signals due to the coupling with ^{29}Si nuclei were observed as three sets of doublets, corresponding to the coupling with the central Si atom [$a(^{29}Si)$ = 2.99 mT] and the two types of Si atoms of the Me_3Si groups [$a(^{29}Si)$ = 1.66 and 1.30 mT]. These EPR parameters of **15** are similar to those of the transient silylene anion radical $[(iPr_3Si)_2LiSi]^{-\cdot}$, generated together with other silyl-radical species by the photolysis of $[(iPr_3Si)_2Li(THF)_2Si]_2Hg$, g = 2.0073, $a(^{29}Si_\alpha)$ = 3.20 mT.[33]

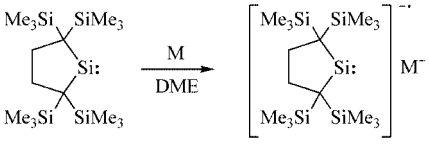

16 **15**

Scheme 11. Generation of the silylene anion radical **15**.

3.4 Anion Radicals of Heavy Alkene Analogues

The heavy analogues of alkenes of the type >E=E< (E = Si, Ge, Sn and Pb) are expected to be oxidized or reduced much more easily than the corresponding alkenes >C=C< because of the high-lying HOMOs and low-lying LUMOs of the former relative to those of the latter. There have been several reports on the formation and EPR identification of the anion radicals of heavy alkene analogues generated either by the reduction of the 1,2-dichlorodisilane precursors or by the direct reduction of disilenes with alkali metals. Weidenbruch et al. reported in 1985 the generation of the first representatives of disilene anion radicals of the type $[R_2Si{=}SiR_2]^{-\cdot}$ (R = *i*Pr, *t*Bu), which were generated by the reduction of the 1,2-dihalo precursors $R_2(X)Si{-}Si(X)R_2$ with alkali metals in THF.[34] The assignment of a lifetime of several minutes at room temperature to the above-mentioned anion radical species was based on its EPR spectrum, which had an hfcc, $a(^{29}Si)$, of 3.36 mT. Following this original report, Kira et al. briefly commented on the generation of disilene anion radicals by the direct reduction of stable tetrasilyldisilenes with potassium in DME; the EPR spectral parameters for these radicals were listed.[35] However, the final isolation and unambiguous structural elucidation of anion radicals of the heavy alkene analogues were achieved only in 2004.

The first virtually stable disilene anion radical **17** was synthesized by the reduction of the disilene $(tBu_2MeSi)_2Si{=}Si(SiMetBu_2)_2$ (**18**) with *t*BuLi in THF (Scheme 12).[36]

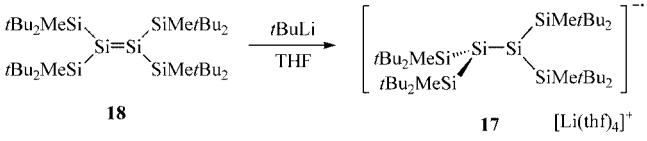

18 **17**

Scheme 12. Synthesis of the disilene anion radical **17**.

The crystal structure analysis of **17** revealed a solvent-separated ion pair with a highly twisted (88°) central Si–Si bond with a bond length of 2.341(5) Å (about 4% longer than that of the neutral precursor **18**) (Figure 9). The geometry around the two central Si atoms was different, nearly planar at Si2 (sum of the bond angles 359.9°) and pyramidal at Si1 (sum of the bond angles 352.7°), implying that the odd electron and the negative charge were separated, hence the radical character of Si2 and the anionic character of Si1. The EPR spectrum of **17** exhibited a central signal with g = 2.0061 accompanied by a pair of satellites due to the coupling of the unpaired electron with the ^{29}Si nuclei, $a(^{29}Si)$ = 2.45 mT (Figure 10). However, this hfcc is less than half that of the structurally very similar tris(di-*tert*-butylmethylsilyl)silyl radical **7** (5.80 mT).[20] This variation in magnitude was explained by the delocalization of the unpaired-electron-spin density over the Si1 and Si2 atoms of **17** on the EPR time scale (Scheme 13). At low temperature (120 K), the observed coupling constant in the EPR spectrum of **17** increased to 4.50 mT, indicating that the fast spin exchange was suppressed under glass matrix conditions.

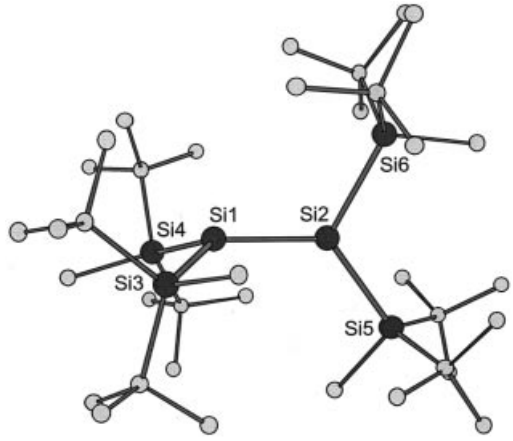

Figure 9. Crystal structure of disilene anion radical **17**.

The tin homologue of the above-mentioned compound, distannene anion radical **19**, was also synthesized by Sekiguchi et al., using the same synthetic protocol, that is, the direct reduction of the precursor distannene $(tBu_2MeSi)_2Sn{=}Sn(SiMetBu_2)_2$ (**20**) with potassium mirror in THF in the presence of [2.2.2]cryptand (Scheme 14).[37]

The crystal structure of **19** is reminiscent of that of the silicon analogue **17**:[36] a highly twisted (74°) Sn–Sn skeleton with a bond length of 2.8978(3) Å, which is 0.2295 Å longer than that in the starting distannene **20** because of the decrease in bond order upon one-electron reduction (Figure 11). As in the case of **17** mentioned above, the geometry around the two Sn atoms is different: one of them is essentially planar (355.4°), whereas the other one is highly pyramidal (323.2°), again assuming that the negative charge and the unpaired electron are effectively separated between the two Sn atoms. However, in contrast to disilene anion radical **17**,[36] such charge–electron separation is also maintained in the solution of distannene anion radical **19**. This was demonstrated by the EPR spectrum of **19** showing a signal (g = 2.0517) with two distinct pairs of $^{119,117}Sn$-satel-

 © 2005 Wiley-VCH Verlag GmbH & Co. KGaA, Weinheim

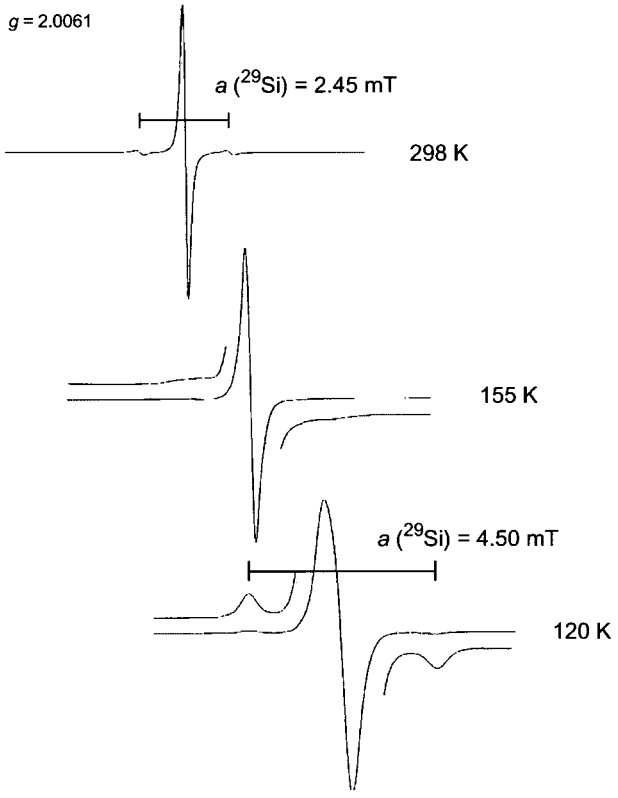

Figure 10. VT-EPR spectra of disilene anion radical **17**.

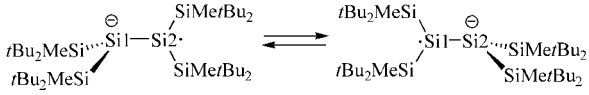

Scheme 13. Delocalization of unpaired electron over Si1 and Si2 atoms in **17**.

lite signals with hfcc values of 34.0 mT ($^{119,117}Sn_{\alpha}$) and 18.7 mT ($^{119,117}Sn_{\beta}$), respectively, implying that the odd electron localized on only one of the two Sn atoms (Figure 12).[37]

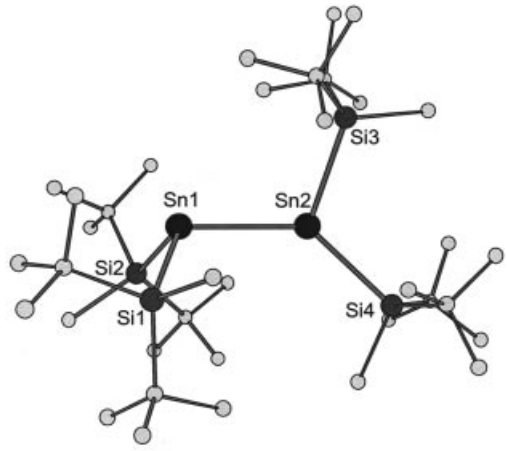

Figure 11. Crystal structure of distannene anion radical **19**.

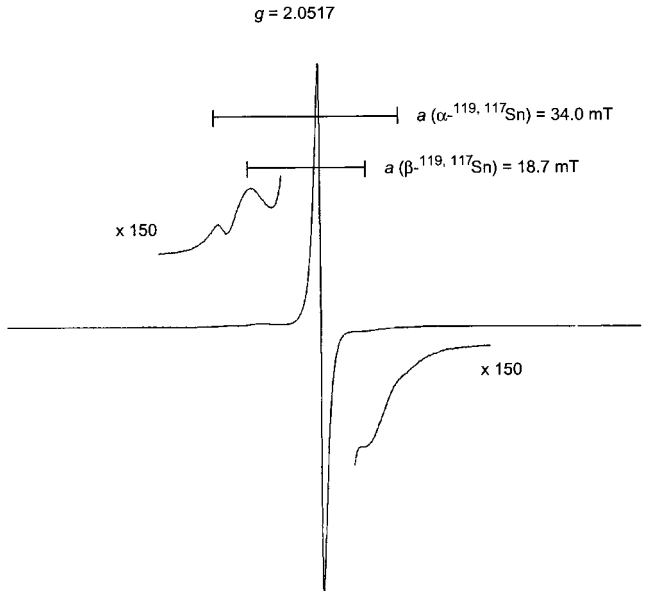

Figure 12. ERP spectrum of distannene anion radical **19** in 2-Me-THF at 310 K.

3.5 Anion Radicals of Heavy Alkyne Analogues

Further increasing the degree of unsaturation of the precursors, one can imagine the triply bonded compounds of heavier group 14 elements as possible candidates for one-electron reduction to produce their corresponding anion radicals. However, until very recently such heavy alkyne analogues were not available as stable species because of their intrinsic instability and high reactivity. Just a few years ago, the first compounds of this class containing a formal triple bond between elements heavier than carbon were synthesized, making possible the study of their reduction.[38] The synthesis of the first, and still the only, example of a singly reduced heavy alkyne analogue was recently reported by Power et al. This product, compound **21-K**, representing the anion radical of the valence isomer of distannyne, was produced by reduction of the precursor chlorostannylene **22** with potassium graphite in THF (Scheme 15).[39]

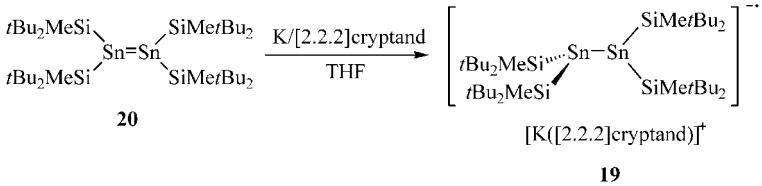

20 **19**

Scheme 14. Synthesis of the distannene anion radical **19**.

 © 2005 Wiley-VCH Verlag GmbH & Co. KGaA, Weinheim

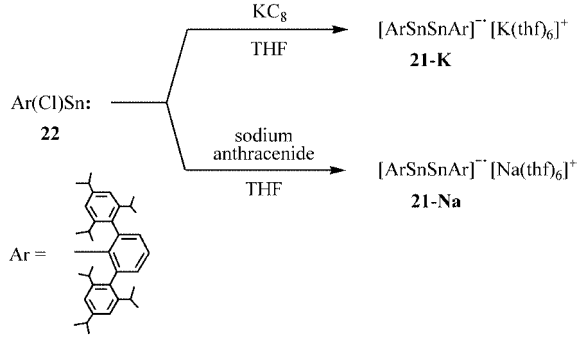

Scheme 15. Synthesis of the distannyne valence isomer anion radicals **21-K** and **21-Na**.

The crystal-structure analysis of **21-K** revealed a highly *trans*-bent configuration of the substituents at both Sn atoms with an Sn–Sn–C bond angle of 95.20(13)° and an Sn–Sn bond length of 2.8123(9) Å (Figure 13). The EPR spectrum of **21-K** displayed a signal with g = 2.0069 and hyperfine coupling with both ^{119}Sn and ^{117}Sn nuclei, which were simulated to produce the values $a(^{117}Sn)$ = 0.83 mT and $a(^{117}Sn)$ = 0.85 mT. The small hfcc values provide evidence for the localization of the unpaired electron in an orbital of π symmetry. Such structural and spectral properties of **21-K** are most consistent with the *trans*-bent structure **23**, in which each tin atom bears a lone pair and the unpaired electron is accommodated in a (5p-5p) π orbital of the tin atoms (Figure 14). The species **23**, with a formal Sn–Sn bond order of 1.5 and highly pronounced *trans*-bending of substituents, was suggested to have little hybridization between the tin atoms, implying poor overlap of the 5p-orbitals to form a weak π bond.

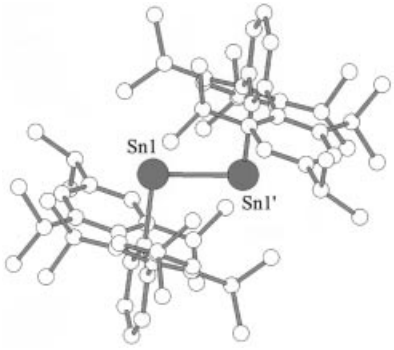

Figure 13. Crystal structure of the distannyne valence isomer anion radical **21-K** (only the anionic part of the molecule is shown).

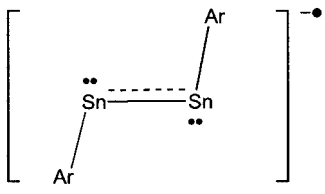

Figure 14. Bonding model of [ArSnSnAr]$^{-\cdot}$ anion radical **23** (Ar = 2,6-Tip$_2$C$_6$H$_3$).

The anion radical **21-Na**, having a sodium counterion, was also prepared by the reduction of chlorostannylene **22** with sodium anthracenide in THF (Scheme 15).[40] Although **21-Na** was isolated as a contact ion pair, in contrast to the potassium salt **21-K** obtained as a solvent-separated ion pair,[39] the EPR spectral and X-ray structural parameters of the two salts were almost completely identical, not being notably affected by the difference in their counterions. Thus, although the Sn–Sn–C bond angles in **21-Na**[40] were just a little bit wider than those in **21-K**:[39] 98.0(4) vs. 95.20(13)°, the Sn–Sn bond lengths in **21-Na** and **21-K** were practically the same, 2.8107(13) vs. 2.8123(9) Å, respectively. That is, the bonding model description **23** is fully applicable to the sodium derivative **21-Na**.

4. Heavier Group 14 Elements Centered Biradicals

The last class of free radicals based on the heavier group 14 elements has just very recently become synthetically accessible and is represented by compounds featuring the singlet biradical character. Such biradicals (or, more precisely speaking, biradicaloids, that is, the closed-shell derivatives of singlet biradicals exhibiting a weak partial coupling between the radical centers) were expected to be more stable than their carbon analogues.[41] Although several papers devoted to the stable carbon- and boron-centered biradicaloids incorporated in four-membered rings have been reported in the scientific literature since 1995,[42] there are very few examples of the stable compounds of heavier group 14 elements with some degree of biradical character. The two latest examples of stable biradicaloids, representing very attractive heteroatom analogues of the classical organic cyclobutane-1,3-diyl, were simultaneously reported in 2004 by research groups of Power and Lappert.[43,44] Both compounds have similar four-membered-ring skeletons composed of the two 1,3-nitrogen atoms and the 2,4-heavier group 14 elements (Ge in Power's paper and Sn in Lappert's paper) with the two radical centers localized on the group 14 elements. In this review, we will highlight the properties of only these two latter compounds.

The first biradicaloid, 1,3-diaza-2,4-digermacyclobutane-1,3-diyl **24**, was synthesized by the reduction of the digermyne **25** with trimethylsilyl azide in hexane (Scheme 16).[43] The crystal structure of **24** revealed a perfectly planar Ge_2N_2 four-membered ring, in which both nitrogen atoms are trigonal-planar [359.97(8)°], whereas the two germanium atoms are pyramidal [322.10(7)°] and the two aryl substituents at the germanium atoms are *trans* to each other (Figure 15). The Ge–Ge separation of 2.755 Å is nearly 0.3 Å longer than the typical Ge–Ge single bond (av. 2.44 Å),[45] indicating no Ge–Ge bonding in the Ge_2N_2 skeleton of **24**. Such tricoordination of both Ge atoms is consistent with the localization of the unpaired electrons on them, that is, with the formulation of **24** as a singlet biradicaloid. Accordingly, no signals were detected in the EPR spectrum of **24** in the temperature range 77–300 K, whereas the usual NMR spectra were observed. The biradical structure of **24** was supported by theoretical calculations, which revealed

 © 2005 Wiley-VCH Verlag GmbH & Co. KGaA, Weinheim

the absence of the Ge–Ge bonding, showing that the HOMO of the molecule consisted mainly of a nonbonding combination of the two lone-pair p-orbitals centered on the two Ge atoms.

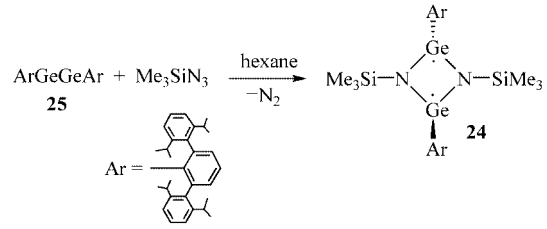

Scheme 16. Synthesis of 1,3-diaza-2,4-digermacyclobutane-2,4-diyl **24**.

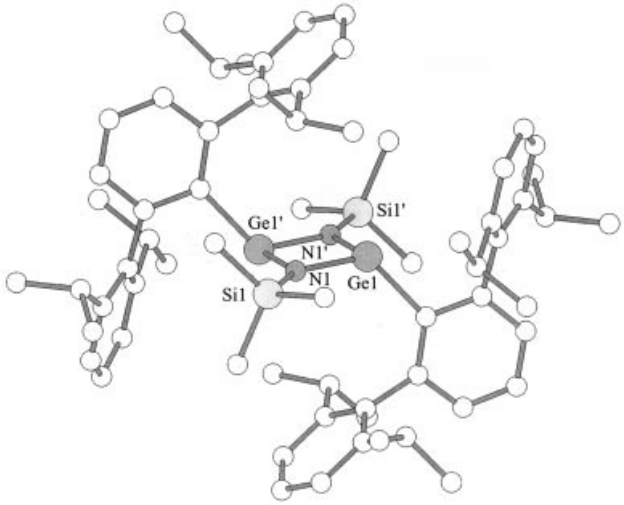

Figure 15. Crystal structure of 1,3-diaza-2,4-digermacyclobutane-2,4-diyl **24**.

The second biradicaloid, 1,3-diaza-2,4-distannacyclobutane-1,3-diyl **26**, was prepared by the rather unusual reaction of the chloro(amino)stannylene dimer $[Sn\{N(SiMe_3)_2\}(\mu\text{-}Cl)]_2$ (**27**) and AgOCN in diethyl ether (Scheme 17).[44] This compound featured an unusual solvent-dependent behavior of its ^{119}Sn NMR chemical shift: δ = –87 (C_6D_6), –83 (toluene/C_6D_6), –102 (CD_2Cl_2), –140 (THF/C_6D_6), –285 (HMPA/toluene/C_6D_6). This was explained by the increasing electron-donating ability of the solvents to the Sn centers in the order C_6D_6 < toluene < CD_2Cl_2 < THF < HMPA, which progressively shifted the ^{119}Sn NMR resonance to higher field. Similar to the above-mentioned Ge_2N_2 biradicaloid **24**, the four-membered ring of **26** is planar, the two *trans*-silyl substituents are nearly in the same plane, and the two Cl atoms are positioned perpendicular to this Sn_2N_2 plane (Figure 16). The central Sn–Sn separation of 3.398 Å is well outside the range of covalent interaction, which indicates the absence of transannular 2,4-bonding. Such pyramidalization and tricoordination of both Sn atoms implies that each Sn atom represents a radical center, therefore simple electron counting provides the overall value of six electrons for the Sn_2N_2 ring: each N atom contributes two electrons (lone pair) to the ring and each Sn atom one (odd) electron. Thus, the most appropriate bonding description of **26** is a six-π-electron-four-center system. The biradicaloid **26** is diamagnetic, being EPR-silent both in the solid state and in solution, which is typical for singlet biradicaloids. Indeed, the theoretical calculations have demonstrated that the singlet state of **26** is more stable than its triplet state with a singlet–triplet energy separation [Δ(S–T)] of 13.6 kcal/mol. This is in agreement with the recent calculations on 2,4-diphosphacyclobutane-1,3-diyl, which revealed that the σ-donating substituents at the phosphorus atoms increase the Δ(S–T) value in favor of the singlet ground state.[46] As one can see, the structural and bonding peculiarities of both 1,3-diaza-2,4-digermacyclobutane-1,3-diyl **24** and 1,3-diaza-2,4-distannacyclobutane-1,3-diyl **26** are very similar to each other, and both of them can be reliably included in the new class of singlet biradicaloids of heavier group 14 elements.

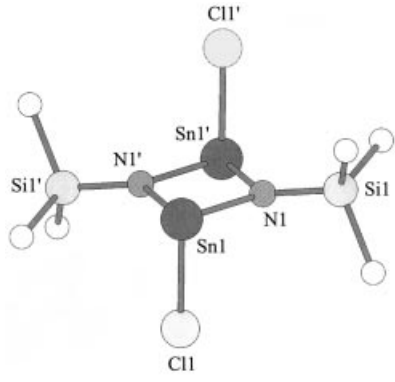

Figure 16. Crystal structure of 1,3-diaza-2,4-distannacyclobutane-2,4-diyl **26**.

5. Summary and Outlook

The evolution of our knowledge of free radicals centered on group 14 elements heavier than carbon is rather spectacular: those molecules which were originally treated several decades ago as very short-lived elusive transient species

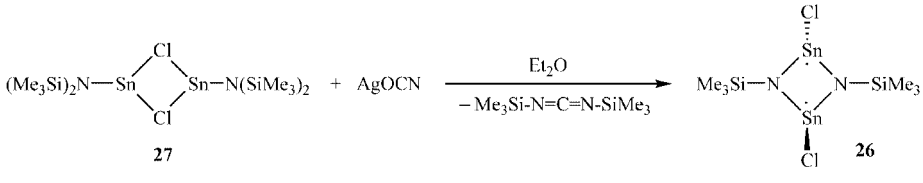

Scheme 17. Synthesis of 1,3-diaza-2,4-distannacyclobutane-2,4-diyl **26**.

 © 2005 Wiley-VCH Verlag GmbH & Co. KGaA, Weinheim

only, were later stabilized as "persistent" radicals with a *relatively* long lifetime, and were finally synthesized as absolutely stable crystalline individual compounds, whose identity was unambiguously verified by X-ray structural determination. The latest developments in the field of stable free radicals of heavier group 14 elements enable the relatively easy synthesis, isolation, and investigation of compounds of this type in the preparative (sometimes in the order of grams) scale. The most prominent achievements in this area, offering deep insight into the electronic and crystal structure of the stable radical species (primarily by means of X-ray crystallography and EPR spectroscopy accompanied by theoretical calculations), should stimulate further interest in this field of organometallic chemistry. Despite the evident and important progress that has been made in this area in just the past few years, there are still many "white spots" to be uncovered on the spacious "map" of free radical chemistry. This concerns, first of all, the synthetic availability of the stable radicals of heavier group 14 elements: these compounds are still not widespread in organometallic chemistry. More general and sophisticated synthetic methods for the preparation of stable Si-, Ge-, Sn-, and Pb-centered radicals are definitely required; for the Pb radicals such experimental procedures should be discovered for the first time, since no stable examples of such compounds have been reported to date. Another great challenge is the synthesis of the charged radical compounds: cationic and anionic. Both stable cation radicals and anion radicals of low-coordinated species, such as heavy carbene analogues or heavy alkene analogues, are among the research goals of primary importance. Deeper and more fundamental theoretical elucidation of the structural peculiarities, bonding nature, multiplicity, and hybridization of free radical species of group 14 elements, both already synthesized and theoretically predicted, is certainly necessary to verify and clarify the recent experimental findings. In the very young and promising field of stable biradicals of group 14 elements (or their combinations with group 13 or 15 elements), new synthetic breakthroughs are also expected in the near future, which could even be extended to the chemistry of stable polyradicals. As one of the most logical and very important developments in the field, the possible applications of stable radicals and polyradicals in the design of new advanced materials with a variety of prospective (for example, magnetic) properties can also be anticipated as an impressive example of the real interplay between fundamental and applied organometallic chemistry.

Acknowledgments

We wish to thank all our coworkers, whose names are listed in the references, for their important experimental contribution to this work. We are also grateful for the permanent financial support of the Ministry of Education, Science, and Culture of Japan (Nos. 147078204, 16205008), and COE (Center of Excellence) program funds.

[1] F. A. Carey, R. J. Sundberg, *Advanced Organic Chemistry, Part A: Structure and Mechanisms*, 4th ed., Kluwer Academic/Plenum Publishers, New York, **2000**.
[2] M. Gomberg, *J. Am. Chem. Soc.* **1900**, *22*, 757–771.
[3] F. Paneth, W. Hofeditz, *Ber. Dtsch. Chem. Ges.* **1929**, *62*, 1335–1347.
[4] D. Griller, K. U. Ingold, *Acc. Chem. Res.* **1976**, *9*, 13–19.
[5] a) P. Andersen, B. Klewe, *Acta Chem. Scand.* **1967**, *21*, 2599–2607; b) O. Armet, J. Veciana, C. Rovira, J. Riera, J. Castaner, E. Molins, J. Rius, C. Miravitlles, S. Olivella, J. Brichfeus, *J. Phys. Chem.* **1987**, *91*, 5608–5616; c) H. Sitzmann, R. Boese, *Angew. Chem. Int. Ed. Engl.* **1991**, *30*, 971–973; d) B. T. King, B. C. Noll, A. J. McKinley, J. Michl, *J. Am. Chem. Soc.* **1996**, *118*, 10902–10903; e) Y. Apeloig, D. Bravo-Zhivotovskii, M. Bendikov, D. Danovich, M. Botoshansky, T. Vakul'skaya, M. Voronkov, R. Samoilova, M. Zdravkova, V. Igonin, V. Shklover, Y. Struchkov, *J. Am. Chem. Soc.* **1999**, *121*, 8118–8119.
[6] M. Karplus, *J. Chem. Phys.* **1959**, *30*, 15–18.
[7] a) R. W. Fessenden, R. H. Schuler, *J. Chem. Phys.* **1965**, *43*, 2704–2712; b) G. A. Carlson, G. C. Pimentel, *J. Chem. Phys.* **1966**, *44*, 4053–4054.
[8] J. Iley, *The Chemistry of Organic Germanium, Tin and Lead Compounds* (Eds.: S. Patai, Z. Rappoport), John Wiley & Sons Ltd., Chichester, **1995**, Chapter 5.
[9] H. Sakurai, *Free Radicals* (Ed.: J. K. Kochi), John Wiley & Sons Ltd., New York, Vol. II, **1973**, 741–808.
[10] Persistent silyl and germyl radicals: a) S. W. Bennett, C. Eaborn, A. Hudson, R. A. Jackson, K. D. J. Root, *J. Chem. Soc. (A)* **1970**, 348–351; b) J. D. Cotton, C. S. Cundy, D. H. Harris, A. Hudson, M. F. Lappert, P. W. Lednor, *J. Chem. Soc., Chem. Commun.* **1974**, 651–652; c) M. J. S. Gynane, M. F. Lappert, P. I. Riley, P. Riviére, M. Riviére-Baudet, *J. Organomet. Chem.* **1980**, *202*, 5–12; d) H. Sakurai, H. Umino, H. Sugiyama, *J. Am. Chem. Soc.* **1980**, *102*, 6837–6840; e) A. Hudson, R. A. Jackson, C. J. Rhodes, A. L. D. Vecchio, *J. Organomet. Chem.* **1985**, *280*, 173–176; f) A. J. McKinley, T. Karatsu, G. M. Wallraff, R. D. Miller, R. Sooriyakumaran, J. Michl, *Organometallics* **1988**, *7*, 2567–2569; g) A. J. McKinley, T. Karatsu, G. M. Wallraff, D. P. Thompson, R. D. Miller, J. Michl, *J. Am. Chem. Soc.* **1991**, *113*, 2003–2010; h) C. Chatgilialoglu, C. Ferreri, D. Vecchi, M. Lucarini, G. F. Pedulli, *J. Organomet. Chem.* **1997**, *545/546*, 475–481; i) S. Kyushin, H. Sakurai, T. Betsuyaku, H. Matsumoto, *Organometallics* **1997**, *16*, 5386–5388; j) S. Kyushin, H. Sakurai, H. Matsumoto, *Chem. Lett.* **1998**, 107–108; k) M. Kira, T. Obata, I. Kon, H. Hashimoto, M. Ichinohe, H. Sakurai, S. Kyushin, H. Matsumoto, *Chem. Lett.* **1998**, 1097–1098; l) Y. Apeloig, D. Bravo-Zhivotovskii, M. Yuzefovich, M. Bendikov, A. I. Shames, *Appl. Magn. Reson.* **2000**, *18*, 425–434. Reviews: m) C. Chatgilialoglu, *Chem. Rev.* **1995**, *95*, 1229–1251; n) See ref.[8]; o) C. Chatgilialoglu, C. H. Scheisser, *The Chemistry of Organic Silicon Compounds* (Eds.: Z. Rappoport, Y. Apeloig), John Wiley & Sons Ltd., Chichester, **2001**, Vol. 3, Chapter 4.
[11] A. Hudson, M. F. Lappert, P. Lednor, *J. Chem. Soc., Dalton Trans.* **1976**, 2369–2375.
[12] P. P. Power, *Chem. Rev.* **2003**, *103*, 789–809.
[13] M. M. Olmstead, L. Pu, R. S. Simons, P. P. Power, *Chem. Commun.* **1997**, 1595–1596.
[14] R. S. Simons, L. Pu, M. M. Olmstead, P. P. Power, *Organometallics* **1997**, *16*, 1920–1925.
[15] A. Sekiguchi, T. Matsuno, M. Ichinohe, *J. Am. Chem. Soc.* **2001**, *123*, 12436–12437.
[16] A. Sekiguchi, T. Matsuno, M. Ichinohe, *J. Am. Chem. Soc.* **2000**, *122*, 11250–11251.
[17] T. Matsuno, M. Ichinohe, A. Sekiguchi, *Angew. Chem. Int. Ed.* **2002**, *41*, 1575–1577.
[18] Y. Ishida, A. Sekiguchi, K. Kobayashi, S. Nagase, *Organometallics* **2004**, *23*, 4981–4986.

 © 2005 Wiley-VCH Verlag GmbH & Co. KGaA, Weinheim

[19] a) A. Sekiguchi, Y. Ishida, N. Fukaya, M. Ichinohe, N. Takagi, S. Nagase, *J. Am. Chem. Soc.* **2002**, *124*, 1158–1159; b) N. Fukaya, M. Ichinohe, A. Sekiguchi, *Angew. Chem. Int. Ed.* **2000**, *39*, 3881–3884.
[20] A. Sekiguchi, T. Fukawa, M. Nakamoto, V. Ya. Lee, M. Ichinohe, *J. Am. Chem. Soc.* **2002**, *124*, 9865–9869.
[21] V. Ya. Lee, A. A. Basova, I. A. Matchkarovskaya, V. I. Faustov, M. P. Egorov, O. M. Nefedov, R. D. Rakhimov, K. P. Butin, *J. Organomet. Chem.* **1995**, *499*, 27–34.
[22] A. Sekiguchi, T. Fukawa, V. Ya. Lee, M. Nakamoto, *J. Am. Chem. Soc.* **2003**, *125*, 9250–9251.
[23] Cations: a) Silyl cation: M. Nakamoto, T. Fukawa, A. Sekiguchi, *Chem. Lett.* **2004**, *33*, 38–39; b) Germyl cation: A. Sekiguchi, T. Fukawa, V. Ya. Lee, M. Nakamoto, M. Ichinohe, *Angew. Chem. Int. Ed.* **2003**, *42*, 1143–1145; c) Stannyl cation: see ref.[22] .
[24] Anions: a) Silyl and germyl anions: M. Nakamoto, T. Fukawa, V. Ya. Lee, A. Sekiguchi, *J. Am. Chem. Soc.* **2002**, *124*, 15160–15161; b) Stannyl anion: T. Fukawa, M. Nakamoto, V. Ya. Lee, A. Sekiguchi, *Organometallics* **2004**, *23*, 2376–2381.
[25] The topic of the spectroscopic detection of ion radicals of heavier group 14 elements was not specially reviewed, however it was briefly discussed in the recent reviews on group 14 radical chemistry. See, for example, references [8] and [12].
[26] B. Gehrhus, P. B. Hitchcock, L. Zhang, *Angew. Chem. Int. Ed.* **2004**, *43*, 1124–1126.
[27] M. Kaftory, M. Kapon, M. Botoshansky, *The Chemistry of Organic Silicon Compounds* (Eds.: Z. Rappoport, Y. Apeloig), John Wiley & Sons Ltd., **1998**, Vol. 2, Part 1, Chapter 5.
[28] Reviews on heavy carbene analogues (R_2E:; E = Si, Ge, Sn): a) P. P. Gaspar, R. West, *The Chemistry of Organic Silicon Compounds* (Eds.: Z. Rappoport, Y. Apeloig), John Wiley & Sons Ltd., **1998**, Vol. 2, Part 3, Chapter 43; b) W. P. Neumann, *Chem. Rev.* **1991**, *91*, 311–334.
[29] L. B. Knight, M. Winiski, P. Kudelko, C. A. Arrington, *J. Chem. Phys.* **1989**, *91*, 3368–3377.
[30] L. R. Sita, I. Kinoshita, *J. Am. Chem. Soc.* **1992**, *114*, 7024–7029.
[31] M. P. Egorov, O. M. Nefedov, *Organometallics* **1995**, *14*, 1539–1541.
[32] S. Ishida, T. Iwamoto, M. Kira, *J. Am. Chem. Soc.* **2003**, *125*, 3212–3213.
[33] D. Bravo-Zhivotovskii, M. Yuzefovich, N. Sigal, G. Korogodsky, K. Klinkhammer, B. Tumanskii, A. Shames, Y. Apeloig, *Angew. Chem. Int. Ed.* **2002**, *41*, 649–651.
[34] M. Weidenbruch, K. Kramer, A. Schäfer, J. K. Blum, *Chem. Ber.* **1985**, *118*, 107–115.
[35] M. Kira, T. Iwamoto, *J. Organomet. Chem.* **2000**, *611*, 236–247.
[36] A. Sekiguchi, S. Inoue, M. Ichinohe, Y. Arai, *J. Am. Chem. Soc.* **2004**, *126*, 9626–9629.
[37] T. Fukawa, V. Ya. Lee, M. Nakamoto, A. Sekiguchi, *J. Am. Chem. Soc.* **2004**, *126*, 11758–11759.
[38] P. P. Power, *Chem. Commun.* **2003**, 2091–2101.
[39] M. M. Olmstead, R. S. Simons, P. P. Power, *J. Am. Chem. Soc.* **1997**, *119*, 11705–1706.
[40] L. Pu, S. T. Haubrich, P. P. Power, *J. Organomet. Chem.* **1999**, *582*, 100–102.
[41] H. Grützmacher, F. Breher, *Angew. Chem. Int. Ed.* **2002**, *41*, 4006–4011.
[42] a) E. Niecke, A. Fuchs, F. Baumeister, M. Nieger, W. W. Schoeller, *Angew. Chem. Int. Ed. Engl.* **1995**, *34*, 555–557; b) T. Baumgartner, D. Gudat, M. Nieger, E. Niecke, T. J. Schiffer, *J. Am. Chem. Soc.* **1999**, *121*, 5953–5960; c) E. Niecke, A. Fuchs, M. Nieger, *Angew. Chem. Int. Ed.* **1999**, *38*, 3028–3031; d) E. Niecke, A. Fuchs, M. Nieger, O. Schmidt, W. W. Schoeller, *Angew. Chem. Int. Ed.* **1999**, *38*, 3031–3034; e) E. Niecke, A. Fuchs, O. Schmidt, M. Nieger, *Phosphorus Sulfur Silicon Relat. Elem.* **1999**, *144–146*, 41–44; f) H. Sugiyama, S. Ito, M. Yoshifuji, *Angew. Chem. Int. Ed.* **2003**, *42*, 3802–3804; g) D. Scheschkewitz, H. Amii, H. Gornitzka, W. W. Schoeller, D. Bourissou, G. Bertrand, *Science* **2002**, *295*, 1880–1881; h) W. W. Schoeller, A. Rozhenko, D. Bourissou, G. Bertrand, *Chem. Eur. J.* **2003**, *9*, 3611–3617; i) D. Scheschkewitz, H. Amii, H. Gornitzka, W. W. Schoeller, D. Bourissou, G. Bertrand, *Angew. Chem. Int. Ed.* **2004**, *43*, 585–587; j) H. Amii, L. Vranicar, H. Gornitzka, D. Bourissou, G. Bertrand, *J. Am. Chem. Soc.* **2004**, *126*, 1344–1345.
[43] C. Cui, M. Brynda, M. M. Olmstead, P. P. Power, *J. Am. Chem. Soc.* **2004**, *126*, 6510–6511.
[44] H. Cox, P. B. Hitchcock, M. F. Lappert, L. J.-M. Pierssens, *Angew. Chem. Int. Ed.* **2004**, *43*, 4500–4504.
[45] a) K. M. Mackay, *The Chemistry of Organic Germanium, Tin and Lead Compounds* (Eds.: S. Patai, Z. Rappoport), John Wiley & Sons Ltd., Chichester, **1995**, Chapter 2; b) K. M. Baines, W. G. Stibbs, *Coord. Chem. Rev.* **1995**, *145*, 157–200.
[46] W. W. Schoeller, C. Begemann, E. Niecke, D. Gudat, *J. Phys. Chem. A* **2001**, *105*, 10731–10738.

Received: December 2, 2004

 © 2005 Wiley-VCH Verlag GmbH & Co. KGaA, Weinheim

Co^{II} Complexes of Triazine-Based Tridentate Ligands with Positive and Attractive $Co^{II/III}$ Redox Couples

Elaine A. Medlycott,[a] Isabelle Theobald,[a] and Garry S. Hanan*[a]

Keywords: Tridentate N ligands / Cobalt complexes / Electrochemistry / Triazine

Co^{II} complexes based on the triazine ligand 2,4-di(2′-pyridyl)-6-(*p*-R-C_6H_4)-1,3,5-triazine have been synthesized and characterized. Cyclic voltammetry shows that the $Co^{II/III}$ redox couple is more positive than previously described Co complexes of tridentate ligands. The $Co^{II/III}$ redox couple may be varied depending on the nature of the substituent on the phenyl ring of the triazine ligand.

(© Wiley-VCH Verlag GmbH & Co. KGaA, 69451 Weinheim, Germany, 2005)

Introduction

Dye-sensitized solar cells (DSSCs) have been intensely studied in the last fifteen years since Grätzel published his landmark work.[1,2] In order to advance the field, many groups have focused their efforts on improving the excited-state properties of the polypyridine Ru^{II} complexes that act as the photosensitizers in the Grätzel cell.[3] Much less attention has been paid to the redox mediator, even though it contributes directly to the maximum photocurrent attainable by the DSSC.[2,3] Whereas the classic redox mediator in such systems is the volatile and corrosive I^-/I_3^- couple, its redox potential is fixed and, therefore, cannot be varied to improve the efficiency of the DSSC.[4] Recently, Co^{II} complexes of heterocyclic ligands have been shown to be effective redox mediators in DSSCs, as they are non-corrosive, non-volatile and modifiable.[5–7] Herein we report on a new family of Co^{II} complexes based on tridentate triazine ligands that are easily synthesized and modified. Their considerably more positive $Co^{II/III}$ redox couples than previously reported Co^{II} complexes of polypyridine ligands favors their use in DSSCs.[5,6]

Results and Discussion

The synthesis of triazines ligands **1a**[8] and **1b**[9] has previously been reported. Ligand **1c** was synthesized by the addition of *p*-bromobenzonitrile to a solution of $LiNMe_2$ in anhydrous diethyl ether.[9,10] The amidinate intermediate that forms reacts with two equivalents of 2-cyanopyridine to afford ligand **1c** after loss of dimethylamide. A series of homoleptic Co^{II} complexes of ligands **1a**–**c** were synthesized by allowing the ligands to react with $CoCl_2{\cdot}6H_2O$ followed by precipitation of complexes **2a**–**c** from the reaction mixture by the addition of NH_4PF_6 [see (a) in Scheme 1].[11] Heteroleptic complexes **3a**–**c** may be obtained directly by treating ligands **1a**–**c** with one equivalent of $CoCl_2{\cdot}6H_2O$ in the presence of tetrabutylammonium chloride (Bu_4NCl) [see (b) in Scheme 1] or indirectly when Bu_4NCl is introduced into an acetone solution of complexes **2a**–**c** [see (c) in Scheme 1].[12] It has previously been established that an equilibrium exists between the homo- and heteroleptic state of Co^{II} complexes of 2,4,6-tripyridyl-*s*-triazine in acidic solution.[13] In this case, heteroleptic Co^{II} complexes **3a**–**c** could be obtained by the addition of Bu_4NCl to complexes **2a**–**c**.

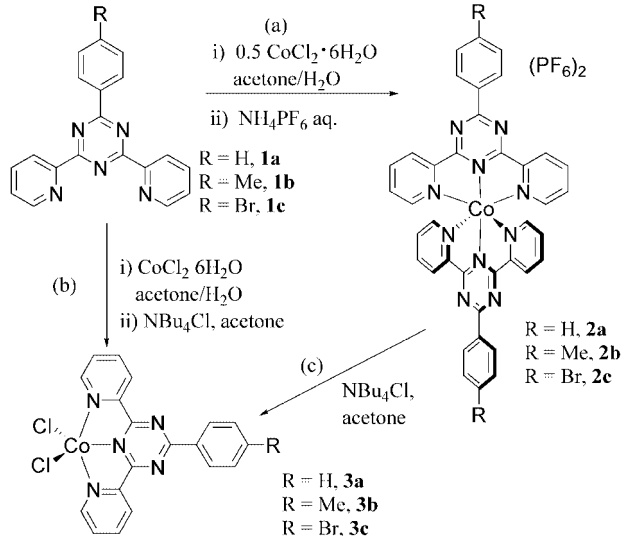

Scheme 1. Synthesis of Co^{II} homo- and heteroleptic complexes.

The ^1H NMR chemical shifts of the homoleptic complexes are typical of paramagnetic Co^{II} complexes that are low spin, with chemical shifts ranging over approximately

[a] Département de Chimie, Université de Montréal,
2900 Edouard-Montpetit, Montreal, Quebec, H3T 1J4, Canada
Fax: +001-514-343-7586
E-mail: garry.hanan@umontreal.ca

110 ppm (Table 1).[14] The signals are broadened considerably, and therefore no coupling constants could be obtained from the spectra. The greatest shifts are observed for the protons *ortho* to the pyridine nitrogen atoms and, therefore, closest to the paramagnetic Co^{II} center. The protons farthest from the paramagnetic center, those on the phenyl ring, have the smallest shift as compared to the free ligands.[9]

Table 1. ^1H NMR chemical shifts of homoleptic complexes **2a**, **2b** and **2c** in CD_3CN.

	δ [ppm]						
	Pyridyl				Phenyl		CH_3
1c	8.99	8.87	8.74	7.60	8.74	7.73	
2a	115.08	80.09	37.54	22.87	13.51	6.17	
2b	113.39	78.56	37.13	21.99	13.27	6.13	5.83
2c	111.88	79.38	36.28	22.96	13.36	6.66	

The X-ray crystal structure of **2c** is shown in Figure 1.[15] The Co^{II} ion is bound by two orthogonal ligands **1c** in a pseudo-octahedral coordination environment as the peripheral pyridines in each ligand pinch in to form N–Co–N angles of 151.79°. The Co–N bond length to the central triazine (1.986 Å) is shorter than the Co–N bond length in homoleptic terpyridine complex (2.022 Å) and the homoleptic triazine complex of 2,4,6-tris(2′-pyridyl)-1,3,5-triazine ligand (2.058 Å).[16,17] The Co–N bond lengths to the peripheral pyridine rings range from 2.134 Å to 2.158 Å, similar to those found in terpyridine complexes of Co^{II}.

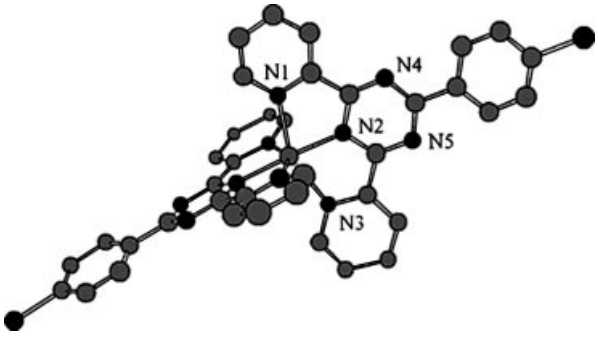

Figure 1. Ball-and-stick representation of the X-ray crystal structure of **2c**. The counteranions and solvent of crystallization have been omitted for clarity.

The phenyl ring is twisted by 13.3° relative to the central triazine ring (Figure 1). This near planar arrangement is due to favorable N-to-CH hydrogen bonding interactions between the N lone pairs and the hydrogen atoms *ortho* to the interannular bond. The slight twist in the interannular bond is a result of edge-to-face packing between the phenyl rings in different molecules of **2c**, which are separated by 3.514 Å (Figure 2). A planar arrangement should easily be adopted in solution which would permit greater electron delocalization between the triazine and the phenyl ring. The two PF_6 counterions are found above and below the planes of the triazine rings and do not interfere with the phenyl packing arrangement, consistent with other extended packing arrangements in the solid state.[18] There is also a short Br1···Br2′ distance of 3.395 Å between adjacent molecules which is indicative of favorable van der Waals interactions which give rise to a linear one-dimensional tape in the solid state (Figure 2).

In the electronic spectra of complexes **2a**–**c**, a very weak metal-centered transition is found at approximately 470 nm (Figure 3). The $\lambda_{max.}$ for these d–d transitions are difficult to identify due to the low energy tail from the ligand-based transitions but the extinction coefficients are in the order of 500 M^{-1} cm^{-1} for all three complexes. For applications in DSSC, a low extinction coefficient is desirable so as to minimise the competition between the redox mediator and sensitiser for absorption in the visible region.[5–7] Intense ligand-based $\pi\rightarrow\pi^*$ transitions are observed in the UV region. Lower energy $\pi\rightarrow\pi^*$ transitions are observed for the Me- and Br-substituted complexes as compared to the complex with R = H. In **2b**, the electron donating methyl groups destabilise the ligand π orbitals to a greater extent than the ligand π^* orbitals. Conversely, in **2c** the ligand π^* orbitals

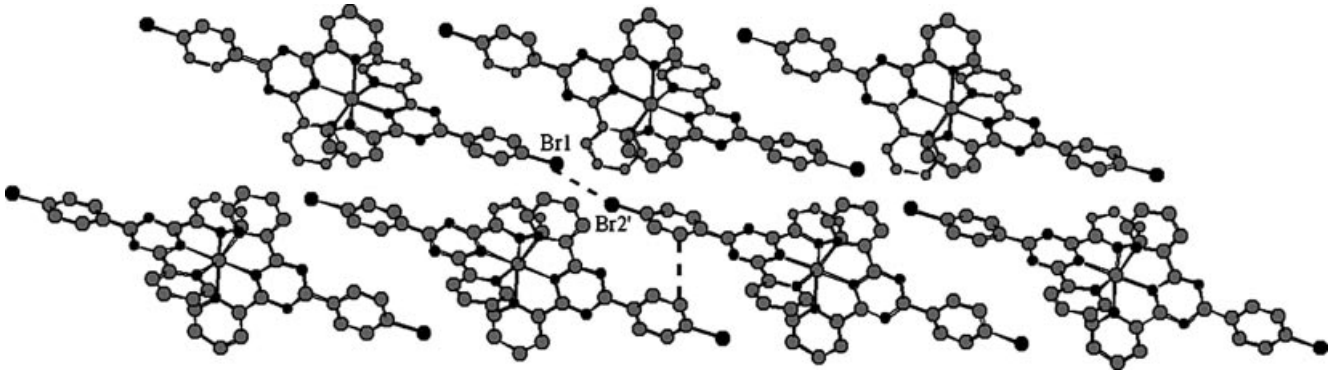

Figure 2. Intermolecular packing forces in the solid-state structure of **2c**. Phenyl-to-phenyl distance = 3.514 Å and the Br1···Br2′ distance = 3.395 Å. The PF_6 counteranions and solvent of crystallization have been removed for clarity.

 © 2005 Wiley-VCH Verlag GmbH & Co. KGaA, Weinheim

are stabilized to a greater extent than ligand π orbitals due to the electron withdrawing nature of the bromine substituent.

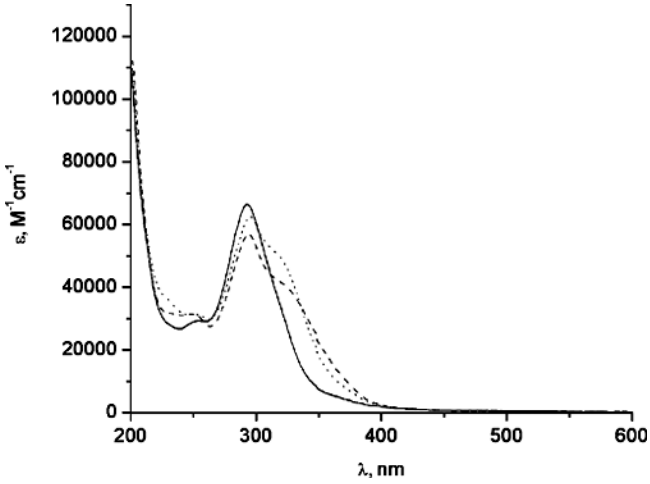

Figure 3. Electronic absorption spectra of complexes **2a** (solid line), **2b** (dashed line) and **2c** (dotted line).

The electrochemical parameters of complexes **2a**, **2b** and **2c** were measured in acetonitrile vs. tetrabutylammonium PF_6 using a Pt electrode and ferrocene as the internal standard. The data (reported vs. SCE) are gathered in Table 2. The $Co^{II/III}$ couples are centered at approximately +0.75 V, which is considerably more positive than previously reported Co^{II} of heterocyclic ligands.[5–7] In each case, oxidative processes are irreversible, which may be a result of limited solubility of the Co^{III} species. It had previously been noted that irreversibility of the $Co^{II/III}$ couple does not necessarily translate into inefficient redox mediators, but sometimes give rise to the most efficient redox mediators.[6] The more positive oxidation potential of **2a**–**c** as compared to terpyridine complexes of Co^{II} is favorable with respect to an increased photocurrent in DSSCs.[7] The $Co^{II/III}$ couple is only slightly affected by substituent on the phenyl ring, with complex **2c** being the most difficult to oxidise as a result of the electron withdrawing Br substituent and **2b** being the easiest as a result of the electron donating Me substituent. The $Co^{II/I}$ couple is also affected by the various substitutents, with **2b** being the hardest to reduce and **2c** the easiest to reduce. The greater variability in the $Co^{II/I}$ reduction potential is a reflection of the increased backbonding of the metal center to the ligand upon reduction. The two remaining reductions are independent triazine-based reductions and follow the electron-withdrawing effect of the substitutents.

Table 2. Electrochemical redox potentials for complexes **2a**–**c** in argon-purged acetonitrile solutions (vs. SCE).

Compound	$E_{1/2}$ (V) [ΔE_p (mV)] $Co^{II/III}$	$Co^{II/I}$	Triazine reductions	
2a	0.76 [irr]	–0.42 [73]	–1.06 [72]	–1.47 [85]
2b	0.74 [irr]	–0.47 [64]	–1.11 [66]	–1.52 [64]
2c	0.77 [irr]	–0.40 [52]	–1.04 [56]	–1.46 [66]

Conclusions

Co^{II} complexes of tridentate triazine-based ligands, either heteroleptic or homoleptic, are readily synthesized and isolated. The electrochemical properties of the homoleptic complexes indicate that the $Co^{II/III}$ redox couples are more positive and more favorable for DSSC than those of Co^{II} terpyridine-based complexes. The $Co^{II/III}$ couple exhibits small shifts in oxidation potential upon modification of the phenyl ring substituents, whereas the $Co^{II/I}$ reduction potential is more readily modified. Further modifications to substitute electron withdrawing and donating groups directly on the triazine ring will be reported in due course.

Acknowledgments

We thank the Natural Sciences and Engineering Research Council (NSERC) of Canada and the Université de Montréal for financial support. E. A. M. thanks the Canadian Commonwealth Scholarship and Fellowship Program. I. T. thanks NSERC of Canada for an undergraduate research award.

[1] B. O'Regan, M. Grätzel, *Nature* **1991**, *353*, 737.
[2] A. Hagfeldt, M. Grätzel, *Acc. Chem. Res.* **2000**, *33*, 269.
[3] C. A. Bignozzi, E. Argazzi, C. J. Kleverlaan, *Chem. Soc. Rev.* **2000**, *29*, 87.
[4] M. K. Nazeeruddin, A. Kay, I. Rodicio, R. Humphry-Baker, E. Müller, P. Liska, N. Vlachopoulos, M. Grätzel, *J. Am. Chem. Soc.* **1993**, *115*, 6382.
[5] H. Nusbaumer, J.-E. Moser, S. M. Zakeeruddin, M. K. Nazeeruddin, M. Grätzel, *J. Phys. Chem. B* **2001**, *105*, 10461.
[6] S. A. Sapp, C. M. Elliott, C. Contado, S. Caramori, C. A. Bignozzi, *J. Am. Chem. Soc.* **2002**, *124*, 11215.
[7] H. Nusbaumer, S. M. Zakeeruddin, J.-E. Moser, M. Grätzel, *Chem. Eur. J.* **2003**, *9*, 3756.
[8] M. I. J. Polson, N. J. Taylor, G. S. Hanan, *Chem. Commun.* **2002**, 1356.
[9] M. I. J. Polson, E. A. Medlycott, G. S. Hanan, L. Mikelsons, N. J. Taylor, M. Watanabe, Y. Tanaka, F. Loiseau, R. Passalacqua, S. Campagna, *Chem. Eur. J.* **2004**, *10*, 3640.
[10] Synthesis of 2,4-di(2′-pyridyl)-6-(*p*-bromophenyl)-1,3,5-triazine **1c:** *para*-bromobenzonitrile (0.68 g, 3.73 mmol) was added to a stirred mixture of $LiNMe_2$ (0.19 g, 3.73 mmol) in anhydrous diethyl ether. After 30 min, 2-cyanopyridine (0.77 g, 7.46 mmol) was added to the mixture. After an hour the reaction mixture was diluted with H_2O (250 mL) and the precipitate was collected. Recrystallization of the solid from ethanol afforded **1c** (0.90 g, 62%) as a white solid. ^1H NMR ($CDCl_3$): δ = 8.99 (d, J = 4.1 Hz, 2 H), 8.87 (d, J = 7.8 Hz, 2 H), 8.74 (d, J = 8.4 Hz, 2 H), 8.0 (t, J = 7.1 Hz, 2 H), 7.73 (d, J = 8.4 Hz, 2 H), 7.60 (t, 2 H, J = 5.0 Hz) ppm.
[11] General procedure for the synthesis of homoleptic Co^{II} complexes **2a**, **2b**, **2c**: The triazine ligand (0.42 mmol) was stirred in acetone (25 mL) and added to a solution of $CoCl_2 \cdot 6H_2O$ (0.38 mmol, 91 mg). After heating at reflux for 75 min and precipitation in aqueous NH_4PF_6, complexes **2a** (110 mg, 54%), **2b** (127 mg, 61%) and **2c** (103 mg, 43%) were collected.
[12] Synthesis of heteroleptic complexes **3a**, **3b** and **3c** followed the same procedure for complexes **2**. After heating for 75 min the acetone/water mix was removed under reduced pressure and the solution was dissolved in a small amount of acetone and precipitated by the addition of Bu_4NCl. Complexes **3a** (44%), **3b** (33%) and **3c** (23%) were collected. **3a**·$2H_2O$: calcd. C 47.82, H 3.59 N 14.68; found C 47.67, H 3.33, N 14.66. **3b**·H_2O: calcd. C 50.76, H 3.62, N 14.80; found C 51.38, H

 © 2005 Wiley-VCH Verlag GmbH & Co. KGaA, Weinheim

3.46, N 15.09. **3c**·4 H_2O: calcd: C 38.54 H 3.40; N 11.83, found C 38.55, H 2.78, N 11.81.

[13] J. Prasad, N. C. Peterson, *Inorg. Chem.* **1971**, *10*, 88.

[14] E. C. Constable, C. E. Housecroft, T. Kulke, C. Lazzarini, E. R. Schofield, Y. Zimmermann, *J. Chem. Soc., Dalton Trans.* **2001**, 2864.

[15] Orange crystals of **2c** suitable for X-ray analysis could be grown by slow diffusion of isopropyl ether into a solution of the complex in acetonitrile. Crystal data for **2c**: $C_{38}H_{24}CoN_{10}$·2(PF_6) was collected with a Bruker APEX at 100 K using Cu-K_α radiation (λ = 1.54178 Å). Full-matrix, least-squares refinements on F^2 using all data. 3198 reflections, M = 1129.36, monoclinic, space group $C2/c$, a = 14.7467(4), b = 20.8588(6), c = 16.6451(5) Å, α = 90°, β = 96.2640(10)°, γ = 90°, V = 5089.4(3) Å^3, Z = 4, $R1$ [$I > 2\sigma(I)$] = 4.28, $wR2$ = 8.36. CCDC-252138 contains the supplementary crystallographic data for this paper. These data can be obtained free of charge from The Cambridge Crystallographic Data Centre via otherwww.ccdc.cam.ac.uk/data_request/cif.

[16] T. Yutaka, I. Mori, M. Kurihara, N. Tamai, H. Nishihara, *Inorg. Chem.* **2003**, *42*, 6306.

[17] B. N. Figgis, E. S. Kucharski, S. Mitra, B. W. Skelton, A. H. White, *Aust. J. Chem.* **1990**, *43*, 1269.

[18] N. W. Alcock, P. R. Barker, J. M. Haider, M. J. Hannon, C. L. Painting, Z. Pikramenou, E. A. Plummer, K. Rissanen, P. Saarenketo, *J. Chem. Soc., Dalton Trans.* **2000**, 1447.

Received: October 06, 2004
Published Online: February 22, 2005

 © 2005 Wiley-VCH Verlag GmbH & Co. KGaA, Weinheim

Reduction of CCl_4 by Iron Powder in Aqueous Solution

Irena Rusonik,[a] Haim Cohen,[a,b] and Dan Meyerstein*[a,b]

Keywords: Carbon tetrachloride / Reduction / Iron / Mechanism

$^{\cdot}CCl_3$ radicals formed in the first step of the CCl_4 degradation react with iron powder to form an intermediate with an Fe–C σ bond. In the absence of iron powder, $^{\cdot}CCl_3$ radicals formed by γ-irradiation react with 2-propanol in a chain reaction toward dechlorination. When the irradiated solution contains iron powder, the iron scavenges the $^{\cdot}CCl_3$ radicals, thus inhibiting the chain reaction. The minor product of the dechlorination of CCl_4 by iron powder in aqueous solution is CH_4, contrary to the results reported in the literature for the electrochemical reduction of CCl_4 on iron electrodes.
(© Wiley-VCH Verlag GmbH & Co. KGaA, 69451 Weinheim, Germany, 2005)

Introduction

The widespread use of chlorinated solvents in commerce has led to considerable groundwater contamination. Halocarbons, including carbon tetrachloride, have a cumulative toxicity and are carcinogenic. Research on the biological degradation of carbon tetrachloride has received much attention.[1,2] Nevertheless, the microbial degradation of CCl_4 can be relatively slow[3] and may be inhibited by the toxicity of CCl_4.

Many recent studies have focused on the abiotic transformation of CCl_4[4,5] and other ground-water pollutants[6,7] by naturally occurring soil minerals such as iron sulfide (FeS). This weak reducing agent reacts slowly with some halo-aliphatic compounds.[8] However, the mechanism of the process has not been elucidated.[8] Consequently, abiotic reductive dechlorination with reduced metals has received increased attention. The use of zero-valent metals has been an active research area[9–11], and most efforts have been concentrated on iron because of the success encountered with iron subsurface permeable walls[12] and the acceptance of zero-valent iron as being safe for the environment. The results indicate that significant CCl_4 reduction occurred at pits rather than on the passive oxide film on the metal.[13] Least-oxidized Fe^0 is the most reactive in CCl_4 degradation.[14]

The combination of ultrasound and Fe^0 has a positive synergistic effect on the dehalogenation of CCl_4. A mechanism involving the formation of $^{\cdot}CCl_3$ radicals was proposed.[15]

The electrochemical reduction of CCl_4 on Fe^0 electrodes was reported to yield CH_4 directly without the formation of $CHCl_3$, CH_2Cl_2, and CH_3Cl as intermediates,[16] though the latter compounds are reduced slower than CCl_4 by the Fe^0 electrode.[9,17–19] Iron is a reasonably strong reducing agent, thus it is not surprising that iron powder can reduce chloro-organic compounds.[20] Therefore it was of interest to investigate the mechanism of the dechlorination reaction of CCl_4 by iron powder, as this method is economically preferable to the electrochemical one.

[a] Department of Chemistry, Ben-Gurion University of the Negev, Beer-Sheva, Israel
[b] Department of Biological Chemistry, College of Judea and Samaria, Ariel, Israel
Fax: +972-3-906-7440
E-mail: danmeyer@bgumail.bgu.ac.il

Results and Discussion

The mechanism proposed to explain the latter results, involves the formation of carbenes.[16] However, this mechanism seems to be too complicated, and alternative simpler mechanisms can be proposed. In principle, the following mechanism is proposed (Scheme 1).

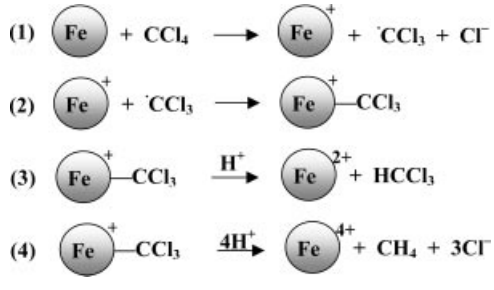

Scheme 1. Plausible mechanism of reduction of CCl_4 by iron powder immersed in aqueous solution.

The first reaction in this scheme is identical to that proposed in the literature.[16] However the second one is different; it is proposed that the radical formed in the first reaction, that is, the one near the iron surface, reacts with the resultant $\mathbf{1}^+$ particle to form an intermediate having an Fe–C σ bond, that is, a $–CCl_3$ bound to the iron powder.

 DOI: 10.1002/ejic.200400979 © 2005 Wiley-VCH Verlag GmbH & Co. KGaA, Weinheim

1
Fe powder particles

Analogous transients are formed in the fast reaction of Fe^0 powder with CH_3.[21] The intermediate $\mathbf{1^+–CCl_3}$ thus formed might decompose by two alternative mechanisms:
1. Heterolysis of the Fe–C bond, reaction (3), as observed[21] for $\mathbf{1^+–CH_3}$.
2. The iron particle can be considered as a microelectrode that can supply many electrons, which can reduce the $–CCl_3$ substituent directly to form methane, reaction (4).

In order to check the relative contribution of reactions (3) and (4) it was decided to study the reaction of $^{\cdot}CCl_3$ radicals with iron powder and measure the relative yields of $Cl^–$ and CH_4. The radicals were formed by γ-irradiating an aqueous solution containing CCl_4 (0.01 M) and 2-propanol (2.6 M). This solution was placed between the grains of iron powder.

$^{\cdot}CCl_3$ radicals formed in the first step of the CCl_4 degradation might react by two pathways:
1. Initiate a chain reaction by hydrogen abstraction from 2-propanol.[22–24]

$$^{\cdot}CCl_3 + HC(CH_3)_2OH \rightarrow HCCl_3 + {}^{\cdot}C(CH_3)_2OH$$
$$^{\cdot}C(CH_3)_2OH + CCl_4 \rightarrow C(CH_3)_2O + {}^{\cdot}CCl_3 + Cl^– + H_3O^+$$

2. React with the iron powder surface to form $CHCl_3$ or directly CH_4, as proposed in Scheme 1.

Therefore, dehalogenation of CCl_4 was investigated in three different systems (Table 1). Two of them contained iron powder and an aqueous solution containing CCl_4 and 2-propanol. One of these samples was irradiated, and the second served as a thermal blank. The light alkanes formed in the latter samples are due to traces of carbon in the analytical iron.[21] The main idea was to study the reaction of $^{\cdot}CCl_3$ radicals with the iron powder, where, in the nonirradiated system, the source of radicals is the dehalogenation process, and in the irradiated system, $^{\cdot}CCl_3$ radicals are derived from γ-irradiation in addition to the dehalogenation process. The third system contained the aqueous solution of CCl_4 and 2-propanol in the absence of iron powder and was irradiated. The latter blank system contributes to the investigation of the reaction of $^{\cdot}CCl_3$ radicals with 2-propanol in aqueous solution. The results of this blank experiment clearly demonstrate (Table 1) that indeed the chain process occurs, as the yield of $Cl^–$ is $G \sim 50–60$, even though the total primary radical yield is $G(\text{radicals}) \sim 6$.[25] G is defined as the number of molecules of each product per 100 eV of radiation absorbed by the solution. When the same solution is brought in contact with the iron powder, the yield of methane is approximately 1% of the $Cl^–$ yield (Table 1). This result clearly demonstrates that CH_4 is not the major product of the thermal dechlorination reaction and suggests that this process involves reactions (1), (2), and (3) in Scheme 1. This result clearly differs from that reported for the reduction of CCl_4 on Fe^0 electrodes.[16]

When the solution is irradiated in contact with the iron powder, the results (Table 1) point out that the $Cl^–$ yield is considerably smaller than the sum of the two blank experiments. The irradiation of the Fe^0-containing system adds only about 3×10^{-4} M to the $Cl^–$ yield when compared to the

Table 1. The relative yields of the organic gases and $Cl^–$ formed in the reduction of CCl_4 (radiation 3.3 Gy/min, 120 min).

[a]

Sample	Radiation	CH_4 [ppm]	CH_4[d] [M]	C_2H_4 [ppm]	C_2H_6 [ppm]	C_3H_6 [ppm]	C_3H_8 [ppm]	$Cl^–$[d] [M]	G
Fe^0(activ.), CCl_4, 2-propanol	+	143	2.0×10^{-5}	7.2	6.4	21.7	8.9	1.9×10^{-3}	–
Fe^0(activ.), CCl_4, 2-propanol	–	110	1.5×10^{-5}	5.2	4	10	3.4	1.6×10^{-3}	–
CCl_4, 2-propanol	+	80.6	1.1×10^{-5}	–	1.5	6.6	–	2.2×10^{-3}	55.6

[b]

Sample	Radiation	CH_4 [ppm]	CH_4[d] [M]	C_2H_4 [ppm]	C_2H_6 [ppm]	C_3H_6 [ppm]	C_3H_8 [ppm]	$Cl^–$[d] [M]	G
Fe^0(activ.), CCl_4, 2-propanol	+	127	1.8×10^{-5}	7	8	24	8.9	1.7×10^{-3}	–
Fe^0(activ.), CCl_4, 2-propanol	–	91.9	1.3×10^{-5}	6.4	5.9	4	3	1.3×10^{-3}	–
CCl_4, 2-propanol	+	64.3	9.0×10^{-6}	–	1	4.2	–	2.0×10^{-3}	50.5

[c]

Sample	Radiation	CH_4 [ppm]	CH_4[d] [M]	C_2H_4 [ppm]	C_2H_6 [ppm]	C_3H_6 [ppm]	C_3H_8 [ppm]	$Cl^–$[d] [M]	G
Fe^0(activ.), CCl_4, 2-propanol	+	184	2.6×10^{-5}	8.9	8.5	21.6	12	2.3×10^{-3}	–
Fe^0(activ.), CCl_4, 2-propanol	–	110.4	1.5×10^{-5}	7.4	7.4	5.6	7.5	2.0×10^{-3}	–
CCl_4, 2-propanol	+	69.5	9.7×10^{-6}	–	1.2	11	1.6	2.6×10^{-3}	65.7

[a] Activated Fe^0 powder (10 g), solution (2.5 mL) containing CCl_4 (0.01 M) and 2-propanol (2.6 M), phosphate buffer (0.01 M, pH 7.0), He sat., t = 3 h. [b] Activated Fe^0 powder (10 g), solution (2.5 mL) containing CCl_4 (0.01 M) and 2-propanol (2.6 M), phosphate buffer (0.01 M, pH 3.0), He sat., t = 3 h. [c] Activated Fe^0 powder (10 g), solution (2.5 mL) containing CCl_4 (0.01 M) and 2-propanol (2.6 M, pH 7.0), He sat., t = 3 h. [d] Error limit ±15%.

 © 2005 Wiley-VCH Verlag GmbH & Co. KGaA, Weinheim

nonirradiated sample, that is, $G(Cl^-)$ under these conditions is $G(Cl^-) = 7.6$. This result clearly demonstrates that the Fe^0 powder scavenges the $\cdot CCl_3$ and partially the $\cdot C(CH_3)_2OH$ radicals, thus inhibiting the chain reaction. Also under these conditions where $G(\cdot CCl_3) \geq 2.5$, as all the e^-_{aq} is expected to react with CCl_4, $G(CH_4) \leq 2\%$ of $G(Cl^-)$. This result clearly proves that reaction (4) in Scheme 1 is at most a side reaction in the process, and that reaction (3) is the major pathway.

The results are pH-independent in the range pH 3–7 (Table 1). Therefore, it was decided to omit the phosphate buffer from the solution. This action slightly increased the radiolytic yield of Cl^-. This result suggests that one of the reactions,

$\cdot C(CH_3)_2OH + H_2PO_4^- \rightarrow (CH_3)_2CHOH + HPO_4^{\cdot -}$

$\cdot CCl_3 + H_2PO_4^- \rightarrow HCCl_3 + HPO_4^{\cdot -}$

probably the latter, shortens the chain reaction. The effect of phosphate on the reduction of CCl_4 by Fe^0 is probably due to the precipitation of $Fe_3(PO_4)_2$ or $Fe(PO_4)$ on the surface of the iron particles, which decreases their activity.[21]

Finally it is suggested that, in the electrochemical reduction of CCl_4[16] on Fe^0, the potential of the cathode was negative enough to reduce the $-CCl_3$ groups bound to the surface by reaction (4). The redox potential of the iron particle is smaller; therefore $CHCl_3$ is obtained as the main product of the reduction of CCl_4 by the iron powder. This conclusion is highly complementary to the early studies of the reductive dehalogenation of CCl_4 by elementary iron.[9]

Experimental Section

The metal powder used in this study was Fe^0 powder Merck 99%, ≤10 μm. The solution was deaerated by bubbling He through it for 15 min by the syringe technique. The solution (2.5 mL) was then added over 2 min to a glass bulb (15 mL) sealed with a rubber septum and containing the Fe^0 powder (10 g), which was previously activated by H_2SO_4 (0.1 M), and then washed with water (7–8×8 mL). The bulb was also deaerated with He prior to the injection of the solution. Some of the samples were irradiated for 2 h in a ^{60}Co γ source with a dose rate of 3.3 Gy/min, within a 3-h reaction time span. After 3 h of reaction, the gas phase above the metal was analyzed with an HP 5890 GC fitted with an FID detector [Porapak QS GC column, 10 ft, 1/8 in; He (30 mL/min), T = 70 °C]. Concentrations of chloride ions were analyzed by a colorimetric method.[26]

Acknowledgments

This study was supported in part by a grant from the Budgeting and Planning Committee of The Council of Higher Education and the Israel Atomic Energy Commission. D. M. wishes to express his thanks to Mrs. Irene Evens for her ongoing interest and support.

[1] G. R. Chaudhry, S. Chapalamadugu, *Microbiol. Rev.* **1991**, *55*, 59–79.
[2] W. W. Mohn, J. M. Tiedje, *Microbiol. Rev.* **1992**, *56*, 482–507.
[3] E. J. Bouwer, P. L. McCarty, *Appl. Environ. Microbiol.* **1983**, *45*, 1286–1294.
[4] E. Lipczynska-Kochany, S. Harms, R. Milburn, G. Sprah, N. Nadarajah, *Chemosphere* **1994**, *29*, 1477–1489.
[5] J. F. Devlin, D. Muller, *Environ. Sci. Technol.* **1999**, *33*, 1021–1027.
[6] E. C. Butler, K. F. Hayes, *Environ. Sci. Technol.* **1999**, *33*, 2021–2027.
[7] R. A. Doong, S. C. Wu, *Chemosphere* **1992**, *24*, 1063–1075.
[8] E. C. Butler, K. F. Hayes, *Environ. Sci. Technol.* **2000**, *34*, 422–429.
[9] L. J. Matheson, P. G. Tratnyek, *Environ. Sci. Technol.* **1994**, *28*, 2045–2053.
[10] A. L. Roberts, L. A. Totten, W. A. Arnold, D. R. Boris, T. J. Campbell, *Environ. Sci. Technol.* **1996**, *30*, 2654–2659.
[11] B. Deng, T. J. Campbell, D. R. Burris, *Environ. Sci. Technol.* **1997**, *31*, 1185–1190.
[12] R. W. Gillham, *Natl. Meet. Am. Chem. Soc., Div. Environ. Chem.* **1995**, *35*, 691–693.
[13] D. J. Gaspar, A. S. Lea, M. H. Engelhard, D. R. Baer, R. Miehr, P. G. Tratnyek, *Langmuir* **2002**, *18*, 7688–7693.
[14] M. L. Tamara, E. C. Butler, *Environ. Sci. Technol.* **2004**, *38*, 1866–1876.
[15] H. M. Hung, M. R. Hoffmann, *Environ. Sci. Technol.* **1998**, *32*, 3011–3016.
[16] T. Li, J. Farrell, *Environ. Sci. Technol.* **2000**, *34*, 173–179.
[17] R. Muftikian, Q. Fernando, N. Korte, *Water Res.* **1995**, *29*, 2434–2439.
[18] B. R. Helland, P. J. J. Alvarez, J. L. Schnoor, *J. Hazardous Mater.* **1995**, *41*, 205–216.
[19] K. D. Warren, R. G. Arnold, T. L. Bishop, L. C. Lindholm, E. A. Betterton, *J. Hazardous Mater.* **1995**, *41*, 217–227.
[20] W. A. Arnold, A. L. Roberts, *Environ. Sci. Technol.* **2000**, *34*, 1794–1805.
[21] I. Rusonik, H. Polat, H. Cohen, D. Meyerstein, *Eur. J. Inorg. Chem.* **2003**, 4227–4233.
[22] D. Brault, P. Neta, *J. Phys. Chem.* **1983**, *87*, 3320–3327.
[23] W. C. Choi, M. R. Hoffmann, *Environ. Sci. Technol.* **1995**, *29*, 1646–1654.
[24] W. C. Choi, M. R. Hoffmann, *J. Phys. Chem.* **1996**, *100*, 2161–2169.
[25] J. C. Russell, G. R. Freeman, *J. Phys. Chem.* **1968**, *72*, 808–815.
[26] T. M Florence, Y. J. Farrar, *Anal. Chim. Acta* **1971**, *54*, 373–377.

Received: November 25, 2004

 © 2005 Wiley-VCH Verlag GmbH & Co. KGaA, Weinheim

Tapes of Cyclic Water Tetramers in the Double-Helical Complex $[Cd_2(bpa)_2Cl_4]\cdot 6H_2O$

Bao-Hui Ye,*[a] Ai-Ping Sun,[a] Tong-Fei Wu,[a] Yan-Qin Weng,[a] and Xiao-Ming Chen*[a]

Keywords: Cadmium / Helical structures / N ligands / Water

The new complex $[Cd_2(bpa)_2Cl_4]\cdot 6H_2O$ [bpa = *N*,*N*′-bis(picolinamide)azine] has been synthesized in which each bpa ligand is twisted into a spiral-like conformation and the two Cd^{II} ions are ligated by two bpa ligands to form a double-stranded binuclear helicate. Unprecedented water chains featuring cyclic water tetramers composed of three independent water molecules are trapped by $[Cd_2(bpa)_2Cl_4]$ double helicates by hydrogen bonds. The binuclear chiral helicates are interlinked into homochiral layers by hydrogen bonds with the water tapes. The layers are alternately stacked in a heterochiral fashion to yield the final racemic structure. The complex shows an endotherm at 65.7 °C in the DSC due to loss of water molecules, giving an enthalpy value of 47 kJ mol^{-1} per water molecule.
(© Wiley-VCH Verlag GmbH & Co. KGaA, 69451 Weinheim, Germany, 2005)

Introduction

Considerable attention has been paid in the past decades to theoretical and experimental studies of small water clusters.[1,2] These studies facilitate an understanding of the structures and functions of liquid water and ice.[3] Among the water clusters, the cyclic $(H_2O)_4$ is very interesting as it is a simple two-structure model for liquid water.[4] Moreover, water chains are of great interest since many fundamental biological processes[5] and material properties[6] appear to depend on the unique properties of water chains. Structural studies have shown that water chains exist in gramicidin A membrane channels,[7] bacteriorhodopsin,[8] and α-amylase[9] for rapid transport of protons and act as "proton wires". The observation of water chains in porous materials[10] and organic hosts[11] exhibiting supramolecular interactions has significantly advanced the understanding of the structures and functions of water chains in biological systems. Furthermore, the homochiral units could assemble into higher dimensionalities and yield a conglomerate with coordination bonds[12] and/or hydrogen bonds.[13] Herein, we report the crystal structure of the double-helical complex $[Cd_2(bpa)_2Cl_4]\cdot 6H_2O$ (**1**) [bpa = *N*,*N*′-bis(picolinamide)azine], in which the lattice water molecules form an unprecedented water tape involving cyclic $(H_2O)_4$ units. Such a tape is relatively rare[14] and is further stabilized by hydrogen bonds to the host molecules. The chiral binuclear helicates are assembled into homochiral layers by the water tapes.

[a] School of Chemistry and Chemical Engineering, Sun Yat-Sen University,
Guangzhou 510275, China
Fax: +86-20-8411-2245
E-mail: cesybh@zsu.edu.cn
cescxm@zsu.edu.cn

Results and Discussion

Complex **1** was obtained by the reaction of $CdCl_2$ and bpa in the molar ratio of 1:1 in a methanol/water solution. The crystal structure reveals that complex **1** consists of a neutral $[Cd_2(bpa)_2Cl_4]$ molecule and six lattice water molecules. As shown in Figure 1, each bpa ligand is twisted into a spiral-like conformation and the two Cd^{II} ions are ligated by two bpa ligands to form a double-stranded binuclear helicate. Two chloride anions complete a distorted octahedral coordination in a *cis* arrangement for each Cd^{II}, featuring potential chirality.

The two octahedra are bridged by two N–N single bonds in a twisted arrangement (Cd–N–N–Cd = 86.0° and Cd···Cd = 4.817 Å) with the diazine nitrogen atoms [Cd(1)–N(3) = 2.409(1) Å] in the metal equatorial plane and the pyridine nitrogen atoms [Cd(1)–N(1) = 2.421(1) Å] in the axial positions, resulting in a double helicate with each metal coordination environment having the same helicity (delta-delta or lambda-lambda), although both optical isomers coexist in the lattice. Notably, these binuclear chiral units are interlinked into homochiral units through hydrogen bonds [Cl···O(3w) = 3.23 Å] between the water chains, as shown in Figure 2.

The layers are alternately stacked in a heterochiral fashion to yield the final racemic structure. Although the bpa ligand bearing two bidentate sites have been used to construct binuclear triple helicates,[15] only three examples of double helicates have been prepared with competing counteranions and/or solvent molecules such as NO_3^-, N_3^- and H_2O.[16] The chloride ions arranged in the *cis* fashion in **1** not only serve as ligands, but also form hydrogen bonds with the water tapes. The homochiral helicates are interlinked into homochiral layers through the water tapes. This

 © 2005 Wiley-VCH Verlag GmbH & Co. KGaA, Weinheim DOI: 10.1002/ejic.200400956

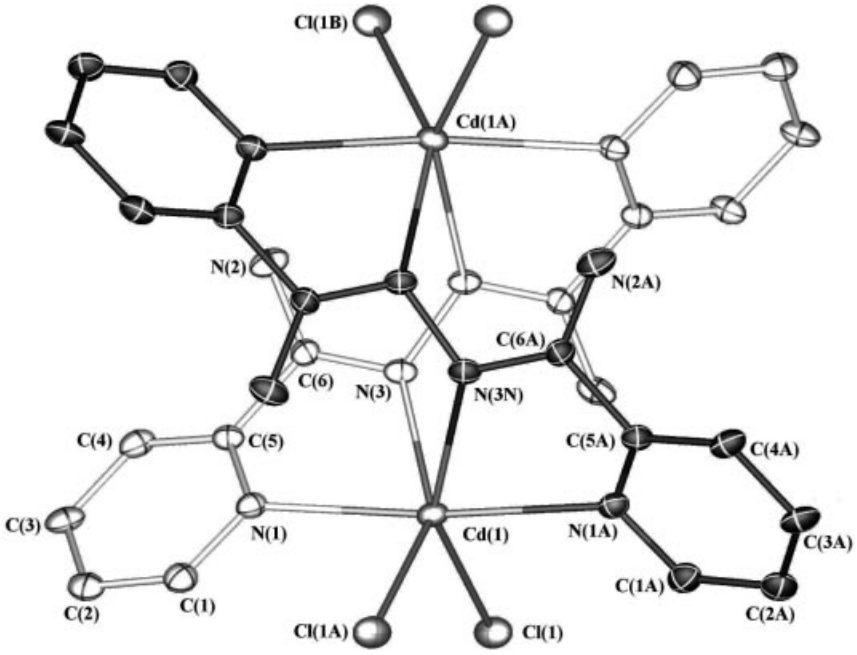

Figure 1. ORTEP view of the Cd^{II} coordination environments. Selected bond lengths [Å] and angles [°]: Cd(1)–N(1) 2.416(2), Cd(1)–N(3) 2.397(2), Cd(1)–Cl(1) 2.553(1); Cl(1)–Cd(1)–Cl(1a) 107.24(2), Cl(1)–Cd(1)–N(1) 97.29(6), Cl(1)–Cd(1)–N(3) 92.33(6), N(1)–Cd(1)–N(3) 68.59(7), C(6)–N(3)–N(3b)–C(6b) 147.4(2), Cd(1)–N(3)–N(3b)–Cd(1a) 86.0. Symmetry codes: a: 1/2 – *x*, 1/2 – *y*, *z*; b: 1/2 – *x*, *y*, 3/2 – *z*; c: *x*, 1/2 – *y*, 3/2 – *z*.

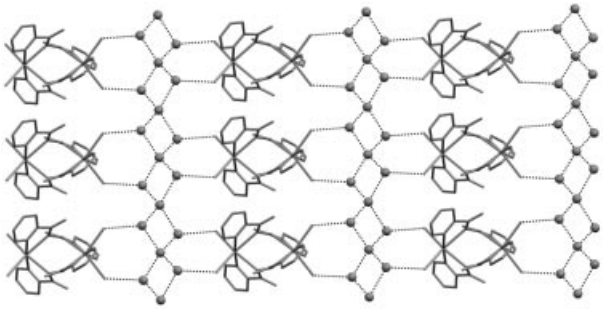

Figure 2. View of the hydrogen-bonded homochiral layer in the *ac* plane. The grey spheres represent the water oxygen atoms; all hydrogen atoms have been omitted for clarity.

Table 1. Selected bond lengths and angles associated with the water tape and the host structure (D: donor atom; A: acceptor atom).

D–H···A	D–H [Å]	H···A [Å]	D···A [Å]	D–H···A [°]
293 K				
O(3w)–H···Cl	0.850	2.380	3.231	178
O(2w)–H···O(3w)	0.850	2.030	2.854	164
O(1w)–H···O(3w)	0.850	2.150	2.968	161
O(3w)–H···O(2w)	0.850	2.100	2.854	148
O(3w)–H···O(1w)	0.850	2.200	2.968	150
173 K				
O(3w)–H···Cl	0.850	2.380	3.228	172
O(2w)–H···O(3w)	0.850	2.000	2.829	163
O(1w)–H···O(3w)	0.850	2.080	2.919	168
O(3w)–H···O(2w)	0.850	2.110	2.829	141
O(3w)–H···O(1w)	0.850	2.260	2.919	136

is markedly different from the related complex $[Cd_2(bpa)_2(NO_3)_2(H_2O)_2](NO_3)_2{\cdot}4H_2O$, in which no water chain was found due to the involvement of the NO_3^- anion in hydrogen bonds with water molecules.[16b]

Interestingly, infinite water tapes involving cyclic $(H_2O)_4$ units consisting of three types of water molecules extended along the *a* axis (Table 1, Figure 3) are observed in the solid state.

To the best of our knowledge, such an arrangementhas not been experimentally observed so far, althoughcyclic $(H_2O)_4$ units consisting of two[4c,4e,4g–4i,14] andfour[4a,4b,4d,4f] independent water molecules have been reported. However, cyclic water pentamers and hexamers containing three independent water molecules have been observed.[17,18] Both the O(1w) and O(2w) atoms are located on the axis of the water chain and are hydrogen bonded to four neighboring O(3w) water molecules [O(1w)···O(3w) = 2.969 or 2.919 Å, and O(2w)···O(3w) = 2.854 or 2.829 Å at 293 or 173 K] in a tetrahedral arrangement [∠O(3w)–O(1w)–O(3wc) = 91.3° and ∠O(3w)–O(2w)–O(3wc) = 96.1°, symmetry code c: *x*, 3/2 – *y*, 1/2 + *z*] to form a cyclic water tetramer. In contrast, the O(3w) molecule is trigonally distorted, in which hydrogen atom H(1wa) has a full occupancy and is hydrogen bonded to Cl(1d) [Cl(1d)···O(3w) = 3.23 Å, symmetry code d: –*x*, 1 – *y*, 1 – *z*]. The other hydrogen atoms H(1wb) and H(1wc) are positionally disordered and were treated as half occupancy atoms during the refinement. The average hydrogen bond length [2.912 (293 K) or 2.874 (173 K) Å] within the water tetramer in **1** is shorter than that (2.950 Å) observed in tac·3H$_2$O (tac = 1,4,7,10-tetraazacyclododecane),[14] but significantly longer than those in other known cases (2.768–2.834 Å).[4f,4g,4i,4j] The four oxygen atoms in the tetramer are coplanar, with nonbonding dis-

 © 2005 Wiley-VCH Verlag GmbH & Co. KGaA, Weinheim

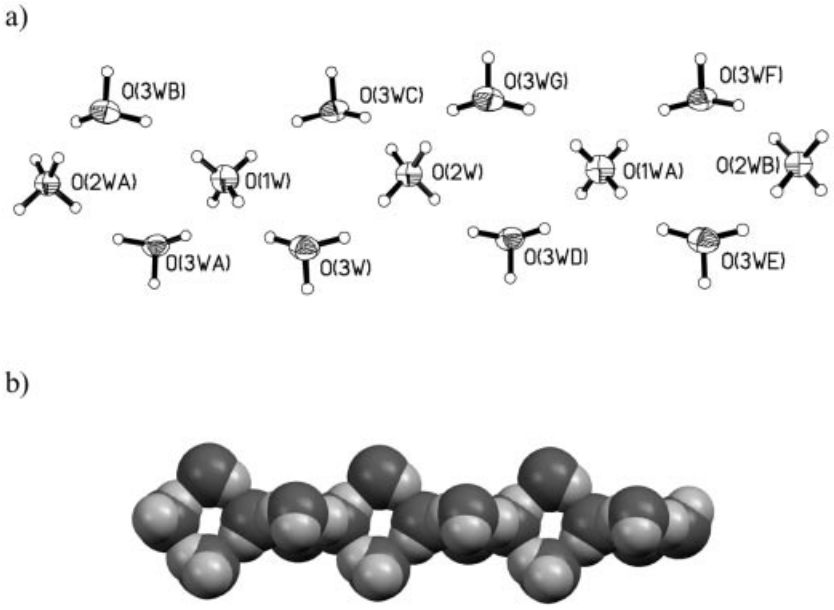

Figure 3. ORTEP (top) and CKP (bottom) plots showing a water chain involving the cyclic water tetramers running along the *a* axis. Symmetry codes: A: 1/2 – *x*, 3/2 – *y*, *z*; B: 1/2 – *x*, *y*, 3/2 – *z*; C: *x*, 3/2 – *y*, 1/2 – *z*; D: –1/2 – *x*, *y*, 3/2 – *z*; E: –1 + *x*, *y*, *z*; F: –1 + *x*, 3/2 – *y*, 3/2 – *z*; G: –1/2 – *x*, 3/2 – *y*, *z*.

tances O(1w)···O(2w) = 3.984 (293 K) or 3.947 (173 K) and O(3w)···O(3wc) = 4.254 (293 K) or 4.177 (173 K) Å, and an O(1w)–O(3w)–O(2w) angle of 92.3° (293 K) or 86.7° (173 K). Adjacent tetramers lie in a perpendicular fashion and are further assembled into a water tape by sharing corners. In fact, the water tape in **1** is very different from the only other example of a water tape involving cyclic water tetramers, which consists of two independent water molecules (O···O = 2.896 Å) that are further bridged by the third type of water molecule by hydrogen bonds (O···O = 3.004 Å) into a water chain with each water molecule tetracoordinate.[14] The nonbonding distances in the cyclic tetramer (O···O = 3.968 Å) and the successive tetramer (O···O = 4.923 Å) are markedly longer than those observed here. These differences may arise from the different hosts and the organization of the water molecules. This observation can help us understand the structure and formation of water clusters and tapes. Another significant phenomenon in **1** is that the water chains arranged in this unique fashion link the homochiral helicates into homochiral layers.

Thermogravimetric analysis (TGA) and differential scanning calorimetry (DSC) (Figure 4) were also performed to observe the thermal stability of the water chain in **1**.

The TGA curve shows a weight loss of 11.0% in the temperature range 25–130 °C, which is consistent with the theoretical value of 11.3% for the loss of six water molecules. The DSC measurement done at 0–150 °C heating at a rate of 5 °C min^{-1} shows a single, sharp endotherm centered at 65.5 °C. The enthalpy is 47 kJ per water molecule, which is larger than that observed in infinite water chains (16 and 36 kJ mol^{-1}),[11e,11g] but similar to those in 4,4′-methylenebis(2,5-dimethylimidazole) dihydrate (44 kJ),[11e] tripeptides hydrates (53 kJ),[19] and theophylline monohydrate (47.3 kJ).[20] Obviously, these data can be correlated to the

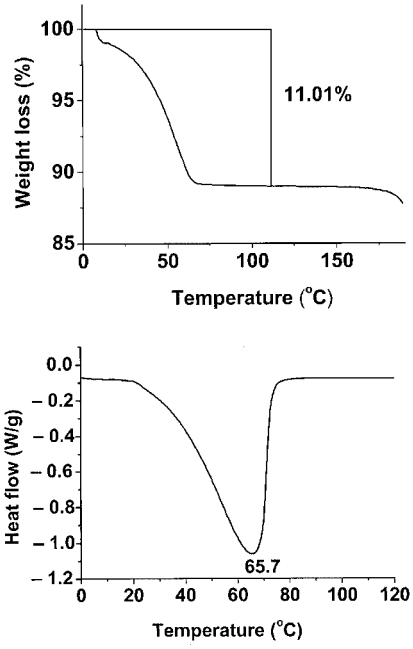

Figure 4. TG plot showing the weight loss of the sample on increasing the temperature (top) and a DSC plot displaying an endotherm for the loss of water molecules (bottom).

number and strength of hydrogen bonds per water molecule. In comparison with the IR spectrum of the free ligand (around 3464 and 3275 cm^{-1}), the peaks at 3234 and 3182 cm^{-1} of the complex can be assigned to the O–H stretching vibration of the water molecules of the tapes. These bands are close to the value reported for ice (3220 cm^{-1}),[21] but lower than those observed for the helical water chain in [Ni(Hsglu)$(H_2O)_2$]·3 H_2O [3368 and 3429 cm^{-1}, H_2sglu = *N*-(2-hydroxybenzyl)-L-glutamic acid][11h]

 © 2005 Wiley-VCH Verlag GmbH & Co. KGaA, Weinheim

and the cyclic tetramer water in $[Fe_3(\mu_3\text{-}O)(\mu_2\text{-}CH_3COO)_6(2\text{-pyridone})_2(H_2O)]ClO_4{\cdot}4H_2O$ (3500 cm^{-1}).[4f]

Conclusions

In conclusion, we have described a new water tape featuring cyclic $(H_2O)_4$ units consisting of three independent water molecules, which is trapped by double-helical hosts through hydrogen bonds that link homochiral helicates into homochiral layers. This observation may provide an insight into the formation of water clusters and chains in nature and biological systems, and help our understanding of the mechanism of proton transport in living systems.

Experimental Section

General Remarks: The reagents and solvents employed were commercially available and used as received without further purification. The C, H and N microanalyses were carried out with a Vario EL elemental analyzer. The FT-IR spectra were recorded from KBr pellets in the range 4000–400 cm^{-1} on a Bruker Equinox 55 FT-IR spectrometer. ^1H NMR spectra were recorded on a Varian 300 MHz spectrometer at 25 °C. ESI-MS was carried out with a LCQ DECA XP. TGA analysis was performed on a NETZSCH TG 209 thermal analyzer under nitrogen atmosphere at a scan rate of 10 °C min^{-1}. The DSC curve was obtained with a NETZSCH DSC 204 Differential Scanning Calorimeter at a scan rate of 5 °C min^{-1}.

Synthesis of bpa: The bpa ligand was synthesized in accordance with a published procedure.[22] $C_{12}H_{12}N_6$ (240.11): calcd. C 59.99, H 5.03, N 34.98; found C 59.94, H 5.14, N 34.94. FT-IR (KBr): $\tilde{\nu}$ = 3464 cm^{-1} (vs), 1610 (vs), 1559 (vs), 1465 (s), 376 (s), 799 (s), 746 (vs), 672 (s). ^1H NMR (300 MHz, CD_3OD): δ = 8.58 (d, J = 3.0 Hz, 2 H), 8.34 (d, J = 5.1 Hz, 2 H), 7.84 (t, 2 H), 7.41 (t, 2 H) ppm. ^{13}C NMR (300 MHz, CD_3OD): δ = 1532, 150.8, 148.2, 136.0, 124.3, 120.7 ppm.

Synthesis of 1: $CdCl_2{\cdot}2.5H_2O$ (0.3 mmol) and bpa were added in a 1:1 molar ration to a methanol/water solution (8:2 v/v) and the solution was stirred for 30 min. Crystals of **1** were obtained after one week (48% yield). $C_{24}H_{36}Cl_4Cd_2N_{12}O_6$ (955.27): calcd. C 30.18, H 3.80, N 17.60; found C 29.79, H 3.59, N 17.21. FT-IR (KBr): $\tilde{\nu}$ = 3396 cm^{-1} (m), 3303 (m), 3224 (m), 3182 (m), 1625 (vs), 1604 (s), 1582 (s), 1563 (s), 1483 (m), 1412 (vs), 1301 (m), 1011 (m), 796 (m),749 (m), 678 (m). ESI-MS: m/z = 810.67 $[Cd_2(bpa)_2Cl_3]^+$.

X-ray Crystallographic Study: Diffraction intensities of **1** were collected on a Bruker Smart Apex CCD diffractometer with graphite-monochromated Mo-K_α radiation (λ = 0.71073 Å) at 293 and 173 K. Absorption corrections were applied using SADABS.[23] The structures were solved by direct methods and refined with a full-matrix least-squares technique based on F^2 using the SHELXTL program package.[24] Crystal data at 293 K: orthorhombic, space group *Pnnn*, a = 7.9680(4), b = 13.4830(7), c = 16.9690(8) Å, V = 1823.02(16) Å^3, Z = 2, D_c = 1.740 g cm^{-3}, F_{000} = 952, μ(Mo-K_α) = 1.514 mm^{-1}. Of the 2188 independent reflections ($1.9° \le \theta \le 28.3°$), 2022 reflections were observed [$I \ge 2\sigma(I)$]. On the basis of all reflections and 111 refined parameters, $R1$ = 0.0207, $wR2$ = 0.0521, and GOOF on F^2 of 1.06 were obtained. At 173 K: orthorhombic, space group *Pnnn*, a = 7.8940(12), b = 13.418(2), c = 16.911(3) Å, V = 1791.2(5) Å^3, Z = 2, D_c = 1.771 g cm^{-3}, F_{000} = 952, μ(Mo-K_α) = 1.541 mm^{-1}. Of the 2097 independent reflections ($1.9° \le \theta \le 28.3°$), 1815 reflections were observed [$I \ge 2\sigma(I)$]. On the basis of all reflections and 140 refined parameters, $R1$ = 0.0309, $wR2$ = 0.0761, and GOOF on F^2 of 1.04 were obtained. Anisotropic thermal parameters were applied to all non-hydrogen atoms. The organic hydrogen atoms were generated geometrically (C–H = 0.96 Å) and refined with isotropic temperature factors. The hydrogen atoms of the water molecule are disordered. One full-occupancy hydrogen atom H(3wa) and two half-occupancy hydrogen atoms H(3wb) and H(3wc) were located by difference maps and refined isotropically in a trigonal arrangement about O(3w). Water molecules O(1w) (1/4, 3/4, 3/4) and O(2w) (–1/4, 3/4, 3/4) are located on special positions with 0.25 occupancy; only two hydrogens [H(1w) and H(2w)] were located by difference map and refined isotropically as half-occupancy atoms and restrained using the DFIX command.

CCDC-253594 (at 293 K) and -253595 (at 173 K) contain the supplementary crystallographic data for this paper. These data can be obtained free of charge from The Cambridge Crystallographic Data Centre via www.ccdc.cam.ac.uk/data_request/cif.

Acknowledgments

This work was supported by the NSFC (no. 20371052 and 20131020), NSF of Guangdong (no. 031581), and the Creative Experimental Foundation of the School of Chemistry Chemical Engineering, Sun Yat-Sen University.

[1] a) S. S. Xantheas, T. H. Dunning, Jr. *J. Chem. Phys.* **1993**, *999*, 8774–8792; b) J. Kim, D. Majumbur, H. M. Lee, K. S. Kim, *J. Chem. Phys.* **1999**, *110*, 9128–9134.

[2] a) R. Ludwig, *Angew. Chem. Int. Ed.* **2001**, *40*, 1808–1827 and refs cited therein; b) L. Infantes, S. Motherwell, *CrystEngCommun* **2002**, *4*, 454–461; c) A. L. Gillon, N. Feeder, R. J. Davey, R. Storey, *Cryst. Growth Des.* **2003**, *3*, 663–673; d) R. J. Doedens, E. Yohannes, M. I. Khan, *Chem. Commun.* **2002**, 62–23; e) J. N. Moorthy, R. Natarajan, P. Venugopalan, *Angew. Chem. Int. Ed.* **2002**, *41*, 3417–3420; f) K. Raghuraman, K. K. Katti, L. J. Barbour, N. Pillarsetty, C. L. Barnes, K. V. Katti, *J. Am. Chem. Soc.* **2003**, *125*, 6955–6961; g) S. K. Ghosh, P. K. Bharadwaj, *Angew. Chem. Int. Ed.* **2004**, *43*, 3577–3580; h) P. Rodríguez-Cuamatzi, G. Vargas-Díaz, H. Höpfl, *Angew. Chem. Int. Ed.* **2004**, *43*, 3041–3044.

[3] a) K. A. Udachin, J. A. Ripmeester, *Nature* **1999**, *397*, 420–423; b) C. Janiak, T. G. Scharamann, *J. Am. Chem. Soc.* **2002**, *124*, 14010–14011; c) A. Müller, E. Krickemeyer, H. Bögge, M. Schmidtmann, B. Botar, M. O. Talismanova, *Angew. Chem. Int. Ed.* **2003**, *42*, 2085–2090; d) B.-Q. Ma, H.-L. Sun, S. Gao, *Angew. Chem. Int. Ed.* **2004**, *43*, 1374–1376.

[4] a) K. K. Chacko, W. Saenger, *J. Am. Chem. Soc.* **1981**, *103*, 1708–1715; b) V. Zabel, W. Saenger, S. A. Mason, *J. Am. Chem. Soc.* **1986**, *108*, 3664–3673; c) F. C. Stephens, R. S. Vagg, *Inorg. Chim. Acta* **1982**, *57*, 43–46; d) J. Xu, E. Radkov, M. Ziegler, K. N. Raymond, *Inorg. Chem.* **2000**, *39*, 4156–4164; e) M. C. Favas, D. L. Kepert, B. W. Skelton, A. H. White, *J. Chem. Soc., Dalton Trans.* **1980**, 454–460; f) S. Supriya, S. K. Das, *New J. Chem.* **2003**, *27*, 1568–1574; g) L.-S. Long, Y.-R. Wu, R.-B. Huang, L.-S. Zheng, *Inorg. Chem.* **2004**, *43*, 3798–3800; h) D. R. Turner, M. B. Hursthouse, M. E. Light, J. W. Steed, *Chem. Commun.* **2004**, 1354–1355; i) J. Tao, Z.-J. Ma, R.-B. Huang, L.-S. Zheng, *Inorg. Chem.* **2004**, *43*, 6133–6135; j) J. D. Cruzan, L. B. Braly, K. Liu, M. G. Brown, J. G. Loeser, R. J. Saykally, *Science* **1996**, *271*, 59–62; k) M. T. Ng, T. C. Deivaraj, W. T. Klooster, G. J. McIntyre, J. J. Vittal, *Chem. Eur. J.* **2004**, *10*, 5853–5859.

[5] a) K. M. Jude, S. K. Wright, C. Tu, D. N. Silverman, R. E. Viola, D. W. Christianson, *Biochemistry* **2002**, *41*, 2485–2491; b)

 © 2005 Wiley-VCH Verlag GmbH & Co. KGaA, Weinheim

Y. S. Lee, M. Krauss, *J. Am. Chem. Soc.* **2004**, *126*, 2225–2230.
[6] a) G. Hummer, J. C. Rasaiah, J. P. Noworyta, *Nature* **2001**, *414*, 188–190; b) K. Koga, G. T. Gao, X. C. Zeng, *Nature* **2001**, *412*, 802–805.
[7] F. Kovacs, J. Quine, T. A. Cross, *Proc. Natl. Acad. Sci. USA* **1999**, *96*, 7910–7915.
[8] Y.-S. Lee, M. Krauss, *J. Mol. Struct.* **2004**, *700*, 243–246.
[9] N. Ramasubbu, K. Sundar, C. Ragunath, M. M. Rafi, *Arch. Biochem. Biophys.* **2004**, *421*, 115–124.
[10] Y. Lee, T. Vogt, J. A. Hriljac, J. B. Parise, G. Artioli, *J. Am. Chem. Soc.* **2002**, *124*, 5466–5475.
[11] a) S. Rau, M. Ruben, T. Büttner, C. Temme, S. Dautz, H. Görls, M. Rudolph, D. Walther, A. Brodkorb, M. Duati, C. O'Connor, J. G. Vos, *J. Chem. Soc., Dalton Trans.* **2000**, 3649–3657; b) A. J. Lough, R. M. Gregson, G. Ferguson, C. Glidewell, *Acta Crystallogr., Sect. B* **2000**, *56*, 85–93; c) D. Cheng, M. A. Khan, R. P. Houser, *Inorg. Chem.* **2001**, *40*, 6858–6859; d) C. Q. Sun, D. L. Zhou, D. J. W. Grant, V. G. Young, *Acta Crystallogr., Sect. E* **2002**, *58*, o368–o370; e) L. E. Cheruzel, M. S. Pometun, M. R. Cecil, M. S. Mashuta, R. J. Wittebort, R. M. Buchanan, *Angew. Chem. Int. Ed.* **2003**, *42*, 5452–5455; f) S. Banerjee, R. Murugavel, *Cryst. Growth Des.* **2004**, *4*, 545–552; g) A. Mukherjee, M. K. Saha, M. Nethaji, A. R. Chakravarty, *Chem. Commun.* **2004**, 716–717; h) B. Sreenivasulu, J. J. Vittal, *Angew. Chem. Int. Ed.* **2004**, *43*, 5769–5772.
[12] A. von Zelewsky, U. Knof, *Angew. Chem. Int. Ed.* **1999**, *38*, 302–322.
[13] L. Pérez-García, D. B. Amabilino, *Chem. Soc. Rev.* **2002**, *31*, 342–356.
[14] S. Pal, N. B. Sankaran, A. Samanta, *Angew. Chem. Int. Ed.* **2003**, *42*, 1741–1743.
[15] L. K. Thompson, *Coord. Chem. Rev.* **2002**, *233*, 193–206.
[16] a) Z.-Q. Xu, L. K. Thompson, C. J. Matthews, D. O. Miller, A. E. Goeta, C. Wilson, J. A. K. Howard, M. Ohba, S. Ōkawa, *J. Chem. Soc., Dalton Trans.* **2000**, 69–77; b) Z.-Q. Xu, L. K. Thompson, D. A. Black, C. Ralph, D. O. Miller, M. A. Leech, J. A. K. Howard, *J. Chem. Soc., Dalton Trans.* **2001**, 2042–2048; c) E.-Q. Gao, Y.-F. Yue, S.-Q. Bai, Z. He, C.-H. Yan, *J. Am. Chem. Soc.* **2004**, *126*, 1419–1429.
[17] B.-Q. Ma, H.-L. Sun, S. Gao, *Chem. Commun.* **2004**, 2220–2221.
[18] B.-H. Ye, B.-B. Ding, Y.-Q. Weng, X.-M. Chen, *Inorg. Chem.* **2004**, *43*, 2866–2868.
[19] M. S. Pometun, U. M. Gundusharma, J. F. Richardson, R. J. Wittebort, *J. Am. Chem. Soc.* **2002**, *124*, 2345–2351.
[20] E. Suihko, J. Ketolainen, A. Poso, M. Ahlgren, J. Gynther, P. Paronen, *Int. J. Pharm.* **1997**, *158*, 47–55.
[21] D. Eisenberg, W. Kauzmann, *The Structure and Properties of Water*, Oxford University Press, Oxford, **1969**.
[22] Z. Xu, L. K. Thompson, D. O. Miller, *Inorg. Chem.* **1997**, *36*, 3985–3995.
[23] R. Blessing, *Acta Crystallogr., Sect. A* **1995**, *51*, 33.
[24] G. M. Sheldrick, *SHELXL-97, Program for Crystal Structure Refinement*; Göttingen University, **1997**.

Received: November 17, 2004

 © 2005 Wiley-VCH Verlag GmbH & Co. KGaA, Weinheim

Relationship between the Molecular Structure and the π–π* Transition Energy of a Lattice-Framework Disilene: A DFT Study

Hiromasa Tanaka,*[a] Eunsang Kwon,[a] Shinobu Tsutsui,[a] Shigeki Matsumoto,[a] and Kenkichi Sakamoto*[a,b]

Keywords: Density functional calculations / Disilenes / UV/Vis spectroscopy / Electronic structure / Electron transition

The origin of a significantly red-shifted π–π* transition observed in a unique lattice-framework disilene, 2,3,4,6,7,8,2′,3′,4′,6′,7′,8′-dodeca-*tert*-butyl[5,5′]bi{1,5-disilatricyclo[4.2.0.0^{1,4}]octylidene}-2,7,2′,7′-tetraene, has been elucidated by time-dependent density functional calculations and MO energy calculations. An intramolecular through-space interaction between the $\pi^*_{Si=Si}$ orbital and the $\pi^*_{C=C}$ orbitals in the lattice framework strongly stabilizes the LUMO, resulting in a small HOMO–LUMO energy gap.

(© Wiley-VCH Verlag GmbH & Co. KGaA, 69451 Weinheim, Germany, 2005)

Introduction

Silicon–silicon doubly-bonded species (disilenes)[1–4] are pale yellow to red-orange, while carbon–carbon doubly bonded species, such as ethylene, are colorless. The longest wavelength absorptions of disilenes, which correspond to the HOMO–LUMO transition, are generally assigned to the $\pi_{Si=Si}$–$\pi^*_{Si=Si}$ transition and are responsible for the color of the disilenes. It has been postulated that the π–π* transition energy of disilenes is governed by both geometric and electronic effects. For example, steric repulsion caused by the bulkiness of the substituents and electron delocalization between the Si=Si bond and substituents result in a shift of the π–π* absorption wavelength of the disilenes.[4] Substituent effects on the geometry and bond energy of disilenes are of particular interest in theoretical calculations, because of large the differences in the bonding nature between the Si=Si bond and the C=C bond.[5–11] However, to the best of our knowledge, there are few theoretical investigations on the relationship between molecular structures and electron-transition energies of disilenes.[12,13]

Very recently, we reported the synthesis of a novel lattice-framework disilene **1** (Scheme 1).[14] An X-ray crystallographic analysis of **1** reveals that the geometry around the Si=Si bond is almost planar (177.8° for the Si···Si=Si angle) and the Si=Si bond is relatively long (2.262 Å) and slightly twisted (12.1°). Surprisingly, this unique tetraalkyldisilene has the π–π* absorption maximum at 493 nm (2.52 eV) in hexane, which is significantly red-shifted relative to the absorption maximum of tetramethyldisilene (344 nm or 3.60 eV)[15] measured in an argon matrix. The small π–π* transition energy of **1** suggests that the lattice framework surrounding the Si=Si bond should strongly influence the energy levels of the HOMO and LUMO. In this study, to elucidate factors controlling the π–π* transition energy of **1**, we have performed density functional theory (DFT) calculations. The electron transition energies of **1** are evaluated by using a time-dependent DFT (TD-DFT) calculation. The HOMO and LUMO energies of **1** are compared with those of four model disilenes **2**–**5** (Scheme 1).

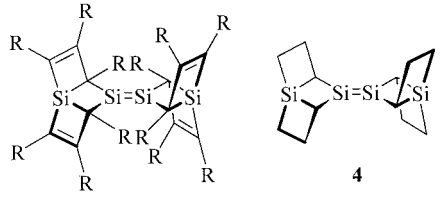

1: R = *tert*-Butyl
2: R = CH_3
3: R = H

4

$(H_3C)_2Si{=}Si(CH_3)_2$

5

Scheme 1.

Results and Discussion

As described in our previous report, **1-opt** reproduces the experimental crystal structure of **1** well.[16] The result of the TD-DFT calculation of **1-opt** is shown in Figure 1, together with the experimental UV/Vis absorption spectrum of **1**. It is noteworthy that the TD-B3LYP calculation of **1-opt** with moderate-size basis sets quantitatively reproduce not only

[a] Photodynamics Research Center, RIKEN,
519-1399 Aoba, Aramaki, Aoba-ku, Sendai 980-0845, Japan
Fax: +81-22-228-2017
E-mail: hirotana@riken.jp
[b] Department of Chemistry, Graduate School of Science, Tohoku University,
Aoba-ku, Sendai 980-8578, Japan
E-mail: sakamoto@si.chem.tohoku.ac.jp
Supporting information for this article is available on the WWW under http://www.eurjic.org or from the author.

the positions of the absorption bands but also the relative intensity of the bands.[17] Also, this calculation demonstrates that the longest-wavelength absorption of **1** is assigned to the π–π* transition.

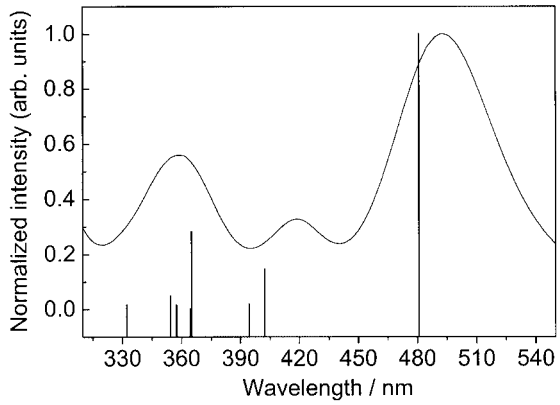

Figure 1. Electron transition energies of **1-opt** calculated by the TD-B3LYP method (vertical line). The UV/Vis spectrum of **1**, in which the intensities are nomalized, is also shown for comparison. Normalized oscillator strengths are used for the calculated intensities.

Although the red-shifted π–π* absorption of **1** was successfully reproduced using the TD-B3LYP method, this calculation does not give information on the factors determining the small π–π* transition energies of **1**. Here we chose four model disilenes **2**–**5** (Scheme 1) and compared the MO energies of the model disilenes with those of **1**. The π–π* transition energies calculated by the TD-B3LYP method are listed in Table 1. The HOMO–LUMO energy gaps (HLGs) as well as the HOMO and LUMO energies are also summarized in Table 1.

Table 1. π–π* transition energies, MO energies, and HOMO–LUMO energy gaps (HLGs) of disilenes **1**–**5** (in eV).

Disilene	π–π* Transition energy[a]	HOMO energy[b]	LUMO energy[b]	HLG
1-fix	2.58[c] (2.52)[d]	–4.18 (0)	–1.24 (0)	2.94
2-fix	2.63	–4.40 (–0.22)	–1.38 (–0.14)	3.03
3-fix	2.56	–4.62 (–0.44)	–1.89 (–0.65)	2.89
4-fix	3.53	–4.77 (–0.59)	–1.15 (+0.09)	3.47
5-fix	4.07	–4.85 (–0.67)	–1.18 (+0.06)	3.67
5-opt	3.45 (3.60)[e]	–4.85 (–0.67)	–1.31 (–0.07)	3.54

[a] Obtained by the TD-B3LYP method. The employed basis sets are described in the text. Experimental values are presented in parentheses. [b] Calculated at the B3LYP/6-311+G(d,p) level. The MO energies relative to **1-fix** are presented in parentheses. [c] Calculated for **1-opt**. [d] Ref.[14] [e] Ref.[15]

Firstly, the result of the DFT calculations for disilenes **1**–**3** are compared in order to evaluate electronic properties depending on the bulkiness of the substituents R (R = *tert*-butyl, CH_3, H). Disilenes **2-fix** and **3-fix** have a structure in which the geometric parameters for the lattice framework are fixed to those of **1-fix**. All the *tert*-butyl groups in **1-fix** are replaced by methyl groups in **2-fix** and by hydrogen atoms in **3-fix**. The π–π* transition energies of **1-fix** (2.58 eV) are almost similar to those of **2-fix** (2.63 eV) and **3-fix** (2.56 eV). The HLGs of these molecules are also very similar to each other, while both the HOMO and LUMO energy levels gradually become lower as the size of the substituents increases in all the molecules. The order of the lowering of the MO energy levels corresponds to the order of the electron-donating ability of the substituents (*tert*-butyl group > methyl group > hydrogen atom). Thus, reducing the size of the substituent R lowers the energy levels of the HOMO and LUMO, whereas it does not change the π–π* transition energy and the HLGs.

Secondly, to discuss how the lattice-framework structure influences the MO energy levels and the π–π* transition energy, the results for **3-fix** are compared with those for **4-fix**, **5-fix** and **5-opt**. Disilene **4-fix** has a lattice-framework structure like **3-fix**, but the C=C bonds are replaced by CH–CH bonds. In **4-fix**, the geometric parameters for doubly bonded silicon atoms and four carbon atoms bound to the silicon atoms are fixed to the parameters of **1-fix** during optimization. Tetramethyldisilene **5-fix** has a structure in which the Si=Si and Si–C bond lengths as well as the C–Si–C bond angle are fixed to those of **1-fix**. The other parameters are optimized in **5-fix**. Tetramethyldisilene **5-opt** has the lowest-energy structure with a trans-bent Si=Si bond.

For a comparison between **3-fix** and **4-fix**, the HLG of **4-fix** (3.47 eV) is significantly larger than that of **3-fix** (2.89 eV), due to the increasing LUMO energy of **4-fix** (+0.71 eV relative to **3-fix**). Thus, the presence of the C=C bonds in the lattice framework is essential for reproducing the small π–π* transition energy observed for **1**. The HOMO and LUMO energies of **4-fix** are calculated to be –4.77 and –1.15 eV, respectively. These values are comparable with the HOMO and LUMO energies of **5-fix** (–4.85 and –1.18 eV, respectively) and **5-opt** (–4.85 and –1.31 eV, respectively). This comparison reveals that geometric changes around the Si=Si bond, such as elongation, flattening, and twisting of the Si=Si bond, play a minor role in changing the HOMO and LUMO energies. Also, replacement of the methyl groups in **5** by the condensed four-membered ring has only a slight influence on the shift in the

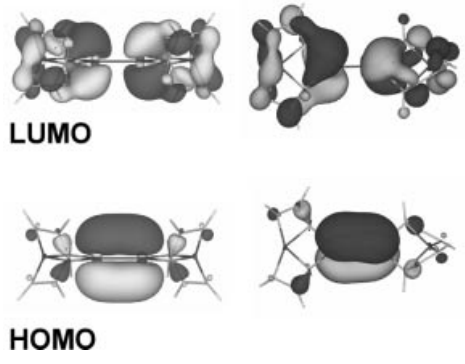

Figure 2. Spatial distribution of the HOMO and LUMO of **3-fix**. Both the side-view (left) and top-view (right; tilted by 60°) images are presented to clarify the interaction between the Si=Si bond and the C=C bonds in the lattice framework.

 © 2005 Wiley-VCH Verlag GmbH & Co. KGaA, Weinheim

HOMO and LUMO energies. To explain the large difference in the π–π* transition energy between **3-fix** and **4-fix**, the frontier orbitals of **3-fix** are shown in Figure 2. In the LUMO of **3-fix**, an intramolecular through-space interaction can be found between the Si=Si bond and the four C=C orbitals surrounding the Si=Si bond. The $\pi^*_{C=C}$ orbital overlaps with the $\pi^*_{Si=Si}$ orbitals, as depicted in Figure 3. This π*–π* overlap strongly stabilizes the LUMO of **3-fix**. In the HOMO of **3-fix**, on the other hand, no significant interactions are found between the Si=Si bond and the lattice framework. Because the shape of the frontier orbitals of **1-fix** (or **1-opt**) is almost similar to **3-fix** and the calculated π–π* transition energy of **1-opt** is very close to that of **3-fix**,[18] we can conclude that the stabilization of the LUMO significantly contributes to the small π–π* transition energy of **1**.

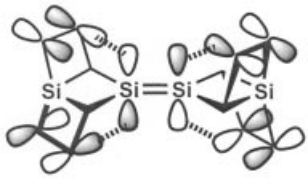

Figure 3. Schematic view of an intramolecular through-space interaction between $\pi^*_{Si=Si}$ and $\pi^*_{C=C}$ orbitals in the LUMO of **1**.

Conclusions

The TD-B3LYP calculation of the lattice-framework disilene **1** combined with moderate-size basis sets quantitatively reproduces the experimental UV/Vis spectrum. The TD-B3LYP calculation would be useful for a full characterization of the electron transitions of "real" disilenes. The red-shifted π–π* absorption maximum observed for **1** can be ascribed to the stabilization of the LUMO. A comparison of the MO energies of **1** and model disilenes **2-5** reveals that an intramolecular through-space interaction between the $\pi^*_{Si=Si}$ and $\pi^*_{C=C}$ orbitals lowers the LUMO energy of **1**. This π*–π* overlap is effectively achieved in **1**, because the four C=C bonds surrounding the Si=Si bond locate nearly perpendicularly to the Si=Si bond. Geometric changes around the Si=Si bond play a minor role in shifting the energy levels of the HOMO and LUMO of **1**.

Computational Methods

All calculations were carried out with the Gaussian98 program.[19] The optimized structure of **1** (**1-opt**) was computed with the B3LYP hybrid functional.[20,21] The 6-31G(d) basis sets were used for the Si and C atoms, except for the atoms consisting of 12 *tert*-butyl groups. For the C and H atoms included in the *tert*-butyl groups, the 3-21G basis sets were employed. The TD-B3LYP calculation[22–25] for **1-opt** was performed at the same level of theory. For model disilenes **2**–**5**, all calculations including the TD calculations were performed at the B3LYP/6-311+G(d,p) level.[25] The MO energies of **1** were also obtained with the B3LYP/6 311+G(d,p) level calculation at the geometry of the experimental crystal structure[14] (represented as **1-fix**). The MO energy calculation of **1** required large basis sets to give converged results, unlike the TD-B3LYP calculation.

[1] A. Sekiguchi, V. Y. Lee, *Chem. Rev.* **2003**, *103*, 1429–1447.
[2] M. Weidenbruch, *J. Organomet. Chem.* **2002**, *646*, 39–52.
[3] M. Kira, T. Iwamoto, *J. Organomet. Chem.* **2000**, *611*, 236–247.
[4] R. Okazaki, R. West, *Adv. Organomet. Chem.* **1996**, *39*, 231–273.
[5] Y. Apeloig, *The Chemistry of Organic Silicon Compounds* (Eds.: S. Patai, Z. Rappoport), Wiley, Chichester, **1989**, pp. 129–136.
[6] M. Karni, Y. Apeloig, *J. Am. Chem. Soc.* **1990**, *112*, 8589–8590.
[7] L. Andersen, M. Dabney, H. A. Harris, *Main Group Metal Chemisty* **1994**, *17*, 403–408.
[8] P. P. Power, *Chem. Rev.* **1999**, *99*, 3463-3503.
[9] G. Trinquier, J.-P. Malrieu, *J. Phys. Chem.* **1990**, *94*, 6184–6196.
[10] H. Jacobsen, T. Ziegler, *J. Am. Chem. Soc.* **1994**, *116*, 3667–3679.
[11] N. O. J. Malcolm, R. J. Gillespie, P. L. A. Popelier, *J. Chem. Soc. Dalton Trans.* **2002**, 3333–3341.
[12] M. Takahashi, M. Kira, K. Sakamoto, T. Müller, Y. Apeloig, *J. Comput. Chem.* **2001**, *22*, 1536–1541.
[13] M. Takahashi, S. Tsutsui, K. Sakamoto, M. Kira, T. Müller, Y. Apeloig, *J. Am. Chem. Soc.* **2001**, *123*, 347–348.
[14] S. Matsumoto, S. Tsutsui, E. Kwon, K. Sakamoto, *Angew. Chem. Int. Ed.* **2004**, *43*, 4610–4612.
[15] A. Sekiguchi, I. Maruki, K. Ebata, C. Kabuto, H. Sakurai, *J. Chem. Soc. Chem. Commun.* **1991**, 341–343.
[16] S. Tsutsui, H. Tanaka, E. Kwon, S. Matsumoto, K. Sakamoto, *Organometallics* **2004**, *23*, 5659–5661.
[17] UV/Vis spectrum (hexane): λ_{max} in nm (normalized intensity) = 359 (0.56), 419 (0.33), 493 (1); calculated transition energy in nm (normalized oscillator strength): 365 (0.28), 402 (0.15), 481 (1) for **1-opt**, 357 (0.12), 389 (0.17), 485 (1) for **3-fix**.
[18] Spatial distribution of the HOMO and LUMO of **1-opt** is presented in Supporting Information.
[19] M. J. Frisch, G. W. Trucks, H. B. Schlegel, G. E. Scuseria, M. A. Robb, J. R. Cheeseman, V. G. Zakrzewski, J. J. A. Montgomery, R. E. Stratmann, J. C. Burant, S. Dapprich, J. M. Millam, A. D. Daniels, K. N. Kudin, M. C. Strain, O. Farkas, J. Tomasi, V. Barone, M. Cossi, R. Cammi, B. Mennucci, C. Pomelli, C. Adamo, S. Clifford, J. Ochterski, G. A. Petersson, P. Y. Ayala, Q. Cui, K. Morokuma, D. K. Malick, A. D. Rabuck, K. Raghavachari, J. B. Foresman, J. Cioslowski, J. V. Ortiz,A. G. Baboul, B. B. Stefanov, G. Liu, A. Liashenko, P. Piskorz, I. Komaromi, R. Gomperts, R. L. Martin, D. J. Fox, T. Keith, M. A. Al-Laham, C. Y. Peng, A. Nanayakkara, C. Gonzalez, M. Challacombe, P. M. W. Gill, B. Johnson, W. Chen, M. W. Wong, J. L. Andres, C. Gonzalez, M. Head-Gordon, E. S. Replogle, J. A. Pople, *Gaussian 98, Revision A.11*, Gaussian Inc., Pittsburgh PA, **1998**.
[20] A. D. Becke, *J. Chem. Phys.* **1993**, *98*, 5648–5652.
[21] C. Lee, W. Yang, R. Parr, *Phys. Rev. B* **1988**, *37*, 785–789.
[22] R. E. Stratmann, G. E. Scuseria, M. J. Frisch, *J. Chem. Phys.* **1998**, *109*, 8218–8224.
[23] R. Bauernschmitt, R. Ahlrichs, *Chem. Phys. Lett.* **1996**, *256*, 454–464.
[24] M. E. Casida, C. Jamorski, K. C. Casida, K. D. R. Salahub, *J. Chem. Phys.* **1998**, *108*, 4439–4449.
[25] The geometric parameters for disilenes **1**–**5** are presented in the Supporting Information.

Received: November 9, 2004

 © 2005 Wiley-VCH Verlag GmbH & Co. KGaA, Weinheim

$[H_2bpy]_2[\{Cu(btepy)_2\}Mo_5P_2O_{23}]\cdot 4H_2O$: A Three-Dimensional Framework Built from Transition-Metal Coordination Polymer Sheets Pillared by Polyoxomolybdophosphate Clusters

Ying Lu,[a] Yangguang Li,[a,b] Enbo Wang,*[a] Jian Lü,[a] Lin Xu,[a] and Rodolphe Clérac*[b]

Keywords: Coordination polymers / Magnetic properties / Hydrothermal synthesis / Polyoxometallates

$[H_2bpy]_2[\{Cu(bpy)_2\}Mo_5P_2O_{23}]\cdot 4H_2O$ (**1**; bpy = 4,4′-bipyridine) contains the first three-dimensional framework based on two-dimensional transition metal coordination polymer sheets pillared by polyoxomolybdophosphate clusters. It crystallises in the *C*2/*c* monoclinic space group with a = 17.630(4) Å, b = 13.670(3) Å, c = 25.111(5) Å, and β = 106.61(3)°. Thermogravimetric analysis shows that guest molecules (H_2O and free bpy ligands) can be easily removed from **1** by simple heat treatment without losing the three-dimensional framework. Moreover, the paramagnetic properties of the $\{Cu(bpy)_2\}$ arrays, make this material an interesting magnetic solid based on polyoxometallate clusters.
(© Wiley-VCH Verlag GmbH & Co. KGaA, 69451 Weinheim, Germany, 2005)

Introduction

Porous materials have attracted much attention due to their potential applications in gas storage, ion exchange or heterogeneous catalysis.[1] A promising approach toward the synthesis of these porous materials is the design of metal–organic frameworks built from transition metal ions and bridging organic ligands.[2] In this field, the synthesis of robust three-dimensional (3D) frameworks with high porosity and thermal stability has become an important issue.[3] Pillared-layer structures have been proven to be an effective route to design 3D frameworks with large channels. In the known pillared-layer structure, bidentate linear organic ligands such as 4,4′-bipyridine, pyrazine and 1,2-bis(4-pyridyl)ethylene play the role of pillars.[4] An alternative choice of pillars may be the polyoxometallate (POM) clusters. Indeed, the occupation of their surface by oxygen atoms offers the possibility of coordination to other transition metals[5] and hence their use as pillars to link transition metal coordination polymer sheets. In addition, POMs possess interesting properties, for example in catalysis, magnetism and nonlinear optics,[6] and also have a higher thermal stability than organic ligands, which may strengthen the thermal stability of the pillared-layer structures formed. Hence, the combination of POMs and transition metal coordination polymer appears to be an appealing route to design multifunctional porous hybrid materials. Unfortunately, this strategy remains unexplored due to the difficulties in combining appropriate POM clusters and 2D transition metal coordination polymer networks while controlling their interactions to form a three-dimensional architecture.

Among the possible POMs, polyoxomolybdophosphate clusters of general formula, $[H_xMo_5P_2O_{23}]^{(6-x)-}$ (x = 0, 1, 2)[7] have recently proved their ability to form organic–inorganic hybrid materials through their coordination to transition-metal complexes.[5c,8] Although the number of organic–inorganic hybrid materials based on these clusters is limited in the literature, $[H_xMo_5P_2O_{23}]^{(6-x)-}$ clusters can be regarded as valuable building units due to their ability to link transition-metal complexes in diverse coordination modes[5c,8] and their chemical versatility − they can easily be modified at the molecular level by substitution of phosphate groups by organophosphate functions.[9] In our quest for the right polyoxometallate cluster to assemble two dimensional arrays into 3D porous materials, $[H_xMo_5P_2O_{23}]^{(6-x)-}$ clusters appeared to be good candidates. This idea was reinforced by the chemistry of these clusters, which can be easily performed under hydrothermal conditions by mixing Na_2MoO_4 (or MoO_3) and H_3PO_4 in water; they are also stable over a wide pH range (3–6).

We report here the novel compound $[H_2bpy]_2[\{Cu(bpy)_2\}Mo_5P_2O_{23}]\cdot 4H_2O$ (**1**; bpy = 4,4′-bipyridine) which exhibits a 3D framework of 1D channels built from $\{Cu(bpy)_2\}_n^{2n+}$ coordination polymer sheets pillared by $[Mo_5P_2O_{23}]^{6-}$ clusters.

[a] Institute of Polyoxometallate Chemistry, Department of Chemistry, Northeast Normal University,
Changchun, 130024, P. R. China
Fax: +86-431-509-8787
E-mail: wangenbo@public.cc.jl.cn
[b] Centre de Recherche Paul Pascal, CNRS UPR 8641,
115 Avenue du Dr. A. Schweitzer, 33600 Pessac, France
Fax: +33-556-855-600
E-mail: clerac@crpp-bordeaux.cnrs.fr
Supporting information for this article is available on the WWW under http://www.eurjic.org or from the author.

Results and Discussion

Synthesis

The successful isolation of compound **1** depends on the exploitation of hydrothermal techniques. Hydrothermal synthesis has recently been proved to be a particularly useful technique in the preparation of inorganic–organic hybrid materials.[10] In the hydrothermal environment, the reduced viscosity of the solvent results in enhanced rates of solvent extraction of solids and crystal growth from solution. Furthermore, since different solubility problems can be minimised, a variety of organic and inorganic precursors can be introduced. However, hydrothermal synthesis is still a relatively complex process because many factors can influence the outcome of reaction, such as the type of initial reactants, starting concentrations, pH values, reaction time and temperature.[11]

Compound **1** was separated from the hydrothermal reaction of $Na_2MoO_4{\cdot}2H_2O$, H_3PO_4, $Cu(MeCO_2)_2{\cdot}H_2O$, 4,4′-bpy and water in the molar ratio of 4:4:1:1:550 at 160 °C for six days. Parallel experiments showed that the pH value of the reaction system is crucial for the crystallisation of compound **1**: blue crystals of compound **1** could only be obtained in the pH range 4–5. At pH 3–4 no crystalline phase was formed and the products were a mixture of blue and white powders. However, at lower pH (2.5–3) another novel compound reported by our group could be synthesised, which shows a two dimensional structure constructed from interconnecting polyoxomolybdate chains $\{HPCuMo_{11}O_{39}\}_n^{4n-}$ and transition metal coordination polymer chains $\{Cu(bpy)\}_n^{n+}$.[5a] In addition, the nature of the divalent transition metal is crucial for the formation of the pillared-layer structure of compound **1**. We tried to replace $Cu(MeCO_2)_2{\cdot}H_2O$ with $Co(MeCO_2)_2{\cdot}4H_2O$, $Ni(MeCO_2)_2{\cdot}4H_2O$ or $Zn(MeCO_2)_2{\cdot}2H_2O$ in the synthesis of compound **1**, but no isostructural compounds were obtained.

Crystal Structure

A single-crystal X-ray diffraction analysis was performed on **1**; the basic motif of the structure is shown in Figure 1. The $[Mo_5P_2O_{23}]^{6-}$ cluster can be described as a ring of five distorted MoO_6 octahedra with two capped PO_4 tetrahedra on each side. Each phosphate subunit shares three oxo groups with the molybdate ring. One of these oxo-groups (O8) adopts a μ_2-bridging mode, linking Mo1 to P1, and the two others (O2 and O6) adopt a μ_3-bridging mode, linking Mo2, Mo3 (or Mo1) and the P1 site. The fourth oxygen (O3) of the PO_4 is dangling. The Cu1 site adopts a "4+2" axially distorted geometry, characteristic of a d^9 Jahn–Teller distortion.[8b,12] Its equatorial and axial positions are occupied by four nitrogen donors from the four distinct bpy ligands and two oxo groups (O5) from adjacent $[Mo_5P_2O_{23}]^{6-}$ clusters, respectively. The Cu–N and Cu–O bond lengths are 2.062 Å (Cu1–N1), 2.041 Å (Cu1–N2) and 2.423 Å (Cu1–O5).

The three-dimensional structure of **1** is composed of square-grid $\{Cu(bpy)_2\}_n^{2n+}$ layers pillared by $[Mo_5P_2O_{23}]^{6-}$ clusters. The $\{Cu(bpy)_2\}_n^{2n+}$ layers lie parallel to the *ab* plane (Figure 2). Each layer consists of a square lattice of Cu^{II} and bpy located at the corners and the edges, respec-

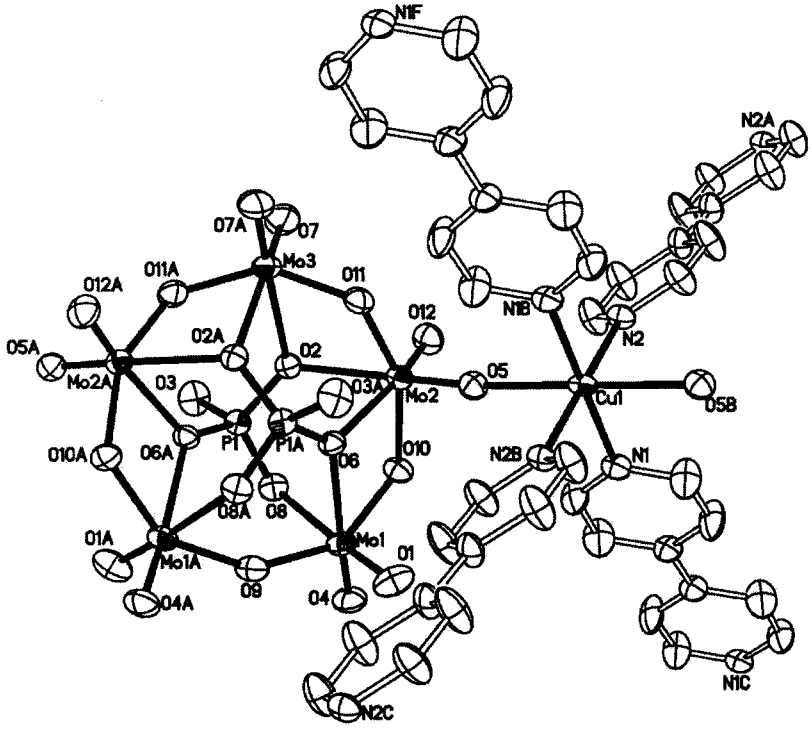

Figure 1. ORTEP drawing of the basic crystallographic unit in **1**. All the hydrogen atoms, H_2bpy^{2+} and H_2O have been omitted for clarity.

 © 2005 Wiley-VCH Verlag GmbH & Co. KGaA, Weinheim

tively. As observed in related materials,[13] this type of arrangement leads to a square cavity of about 11.2×11.2 Å^2. Moreover, it is noteworthy that the layers are perfectly planar with the equatorial plane of the Cu coordination sphere. Adjacent square-grid layers are connected by $[Mo_5P_2O_{23}]^{6-}$ clusters through the axial positions of the Cu site to form the 3D open framework (Figure 3). This organisation leads to the formation of channels in two directions: along the *c* axis the channels have an elliptical shape of about 11.2×6.5 Å^2 (Figure 4) and along the *b* axis rectangular channels can be observed with dimensions of about 10.0×3.7 Å^2. Free bipyridine and H_2O molecules are located in these channels. According to the consideration of the charge balance and weak acidic conditions of the synthesis, the free bipyridines are doubly protonated.

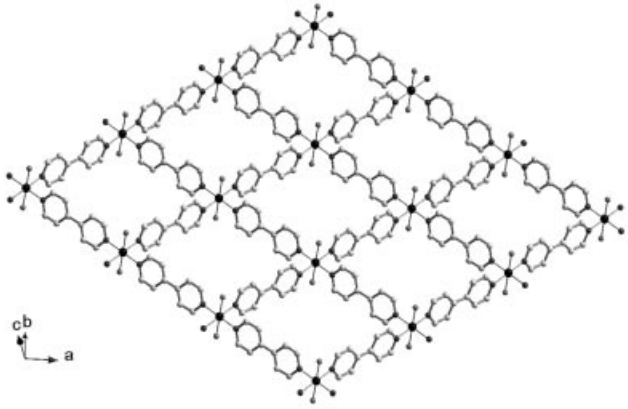

Figure 2. View of the 2D square-grid layer in **1**.

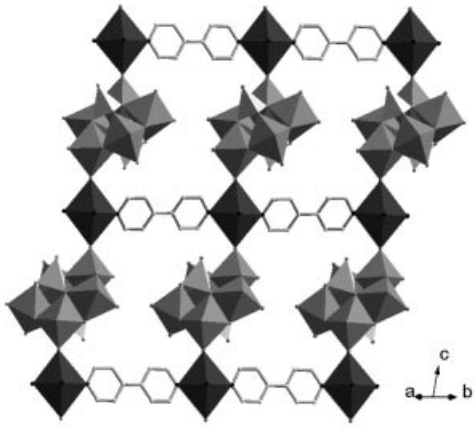

Figure 3. Polyhedral representation of the 3D network in **1**. Guest molecules included in the channels have been omitted for clarity.

Thermogravimetric analysis (TGA) was performed in air at a heating rate of 10 °C min^{-1} on a polycrystalline sample of **1** (Figure 5). A first weight loss of 4.4% occurred between 40 and 150 °C, corresponding to the loss of four water molecules (calcd. 4.3%). In the range 240–340 °C, a second weight loss of 18.6% is observed corresponding to the loss of two free bpy molecules (calcd. 18.8%). Between 390 and 610 °C a weight loss of 19.5% is due to loss of the

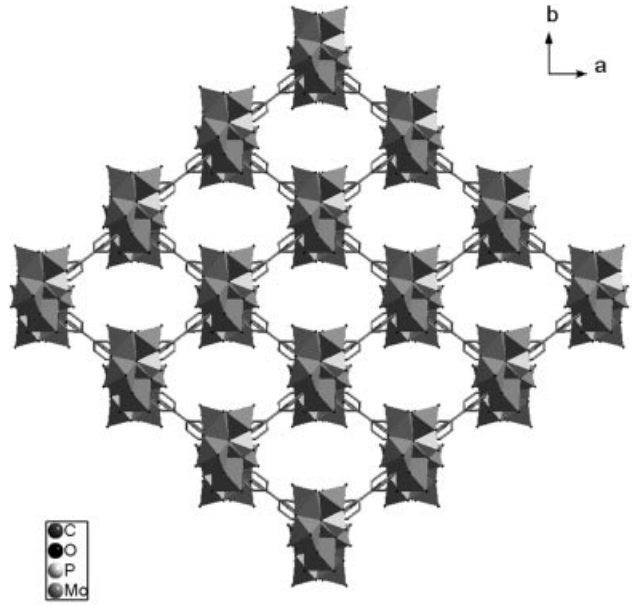

Figure 4. View of the 3D network along the *c* aixs. Guest molecules included in the channels have been omitted for clarity.

coordinated bpy ligands. Above 610 °C and up to 750 °C no further weight loss is observed. Over the whole range of temperature explored, the total weight loss (42.5%) agrees well with the calculated value (41.8%). The final product was found to be amorphous by powder X-ray diffraction.

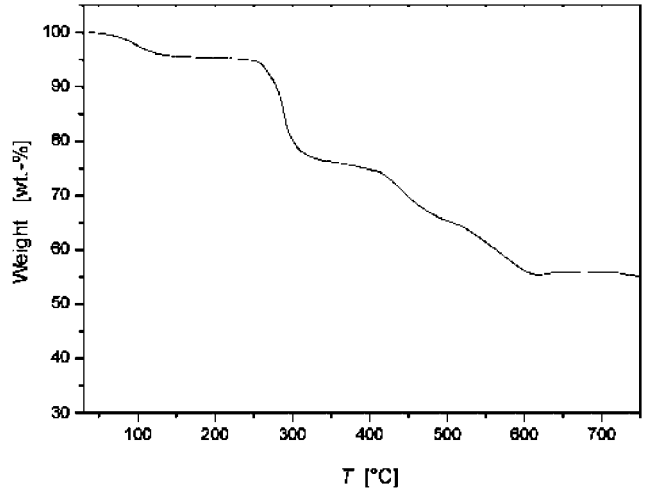

Figure 5. Thermogravimetric analysis curve of **1**.

Based on the TG analysis, **1** was heated in air at 350 °C for six hours to remove the free bpy ligands and water molecules and form **1′**. The elemental analysis of **1′** (C 18.9, H 1.5, N 4.6) agrees well with the expected formula for the opened $[H_4\{Cu(bpy)_2\}Mo_5P_2O_{23}]$ network (calcd. C 18.6, H 1.6, N 4.3). The TG curve of **1′** also confirms that water molecules and free bpy ligands have been removed (Supporting Information, Figure S1). The X-ray powder diffraction spectra of **1** and **1′** (Figure S2) were compared and found to be very similar, thereby confirming that the framework of **1** is retained after the loss of the guest molecules.

 © 2005 Wiley-VCH Verlag GmbH & Co. KGaA, Weinheim

This phenomenon, where a compound retains its framework structure after guest organoamine molecules have been removed, has been reported by several groups.[14]

Magnetic Properties

The magnetic susceptibility of **1** was studied from 300 K to 1.83 K at 1000 Oe on a polycrystalline sample. The χT vs. T plot, shown in Figure 6, decreases continuously from 0.42 $cm^3 K mol^{-1}$ at 300 K to reach 0.24 $cm^3 K mol^{-1}$ at 1.83 K. Based on the structure analysis, the spins are carried by the Cu^{II} centres, which are organized into well-separated, 2D square arrays. Therefore, the magnetic susceptibility was analysed using an $S = 1/2$ Heisenberg 2D square lattice model. A high temperature series-expansion for the susceptibility of this model has been reported by Rushbrooke and Wood.[15a] To fit the experimental data, the compact expression of Lines[15b] was used, with the following spin Hamiltonian:

$$H = -2J \sum_{<i,j>} S_i S_j$$

$$\frac{Ng^2\mu_B^2}{2\chi J} = 3\theta + \sum_{n=1}^{6} \frac{C_n}{\theta^{n-1}}$$

where $\theta = k_B T/|2J|S(S + 1)$, $C_1 = 4$, $C_2 = 2.667$, $C_3 = 1.185$, $C_4 = 0.149$, $C_5 = -0.191$, $C_6 = 0.001$ and N, g, and μ_B have their usual meanings. The best set of parameters are $J/k_B = -0.53(1)$ K and $g = 2.11(1)$. The fitting procedure was performed down to 1.83 K as the validity condition $k_B T \approx 0.9JS(S + 1)$ for this model was not reached.[15b] The J value obtained confirms that the interaction through the bridging bpy is weak, in agreement with the large Cu–Cu distance (ca. 11.2 Å).

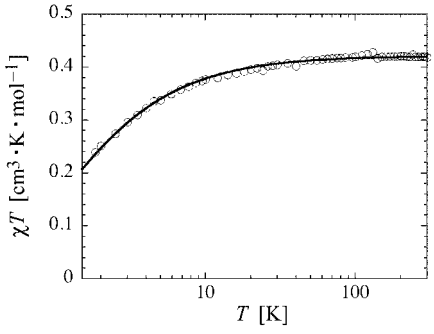

Figure 6. Temperature dependence of the χT product measured at 1000 Oe in the temperature range 1.83–300 K. The solid line is the best fit obtained with the $S = 1/2$ Heisenberg two-dimensional antiferromagnetic square lattice model.[15]

The room-temperature EPR spectrum of **1** (Supporting Information, Figure S3) shows a typical Cu^{2+} signal in an elongated octahedral coordination geometry, as expected from the crystal structure. The eigenvalues of the g tensor can be calculated as $g_{\parallel} = 2.1538(1)$ and $g_{\perp} = 2.0539(1)$; they are in relatively good agreement with the average value ($g = 2.11$) found by susceptibility measurements.

Conclusion

In summary, we have reported here the first 3D structure based on a transition-metal coordination polymer sheet linked by polyoxomolybdophosphate clusters. The successful synthesis of **1** provides an interesting illustration of the use of polyoxometallate clusters to obtain new magnetic materials. Since chemical modifications of the polyoxometallate cluster and the transition-metal coordination polymer sheet may be easily achieved, a complete new family of magnetic solids should be accessible in the near future.

Experimental Section

Materials and General Methods: Reagents were purchased commercially and used without further purification. Elemental analyses (C, H and N) were performed on a Perkin–Elmer 2400 CHN Elemental Analyzer. Mo, Cu and P were determined with a Leeman inductively coupled plasma (ICP) spectrometer. The IR spectrum was obtained on an Alpha Centaurt FT/IR spectrometer with pressed KBr pellet in the 4000–400 cm^{-1} regions. A Perkin–Elmer TGA7 thermogravimetric analyzer was used to obtain TGA curves under N_2 with a temperature increasing rate of 10 °C min^{-1}. X-ray powder diffraction (XRPD) patterns were recorded on a Siemens D5005 diffractometer with Cu-K_α (λ = 1.5418 Å) radiation. The EPR spectrum was recorded on a Bruker ER 200D spectrometer at room temperature. The magnetic susceptibility data were measured with a Quantum Design SQUID magnetometer MPMS-XL.

Synthesis of 1: In a typical synthesis of compound **1**, $Cu(MeCO_2)_2 \cdot H_2O$ (1 mmol) and 4,4′-bpy (1 mmol) were added to a stirred solution of $Na_2MoO_4 \cdot 2H_2O$ (4 mmol) and H_3PO_4 (4 mmol) in water (10 mL). The resultant mixture was sealed in a 23-mL, Teflon-lined autoclave and heated at 160 °C for 6 d. The initial pH value of the reaction solution was ca. 4.6 and the final pH value was ca. 5.5. Blue, block-like crystals of **1** were obtained from the solid product in a yield of 60% (0.65g) with respect to 4,4′-bpy. $C_{40}H_{44}CuMo_5N_8O_{27}P_2$ (1674.0): calcd. C 28.70, H 2.65, Cu 3.80, Mo 28.66, N 6.69, P 3.70; found C 28.58, H 2.59, Cu 3.67, Mo 28.81, N 6.65, P 3.62. IR (KBr pellet): $\tilde{\nu}$ = 3448 (s), 3100 (w), 1607

Table 1. Crystal data and structure refinement for **1**.

Empirical formula	$C_{40}H_{44}CuMo_5N_8O_{27}P_2$
Formula mass	1673.97
Temperature [K]	293(2)
Wavelength [Å]	0.71073
Crystal system	monoclinic
Space group	*C*2/*c*
a [Å]	17.630(4)
b [Å]	13.670(3)
c [Å]	25.111(5)
β [°]	106.61(3)
V [Å^3]	5799(2)
Z	4
$D_{calcd.}$ [g cm^{-3}]	1.912
μ [mm^{-1}]	1.553
F_{000}	3280
Data/restraints/parameters	6582/158/516
Goodness-of-fit on F^2	1.039
$R1$[a] [$I > 2\sigma(I)$]	0.0555
w$R2$[b]	0.1365
Largest diff. peak and hole [e·Å^{-3}]	0.680 and –0.978

[a] $R1 = \Sigma||F_o| - |F_c||/\Sigma|F_o|$. [b] $wR_2 = \Sigma[w(F_o^2 - F_c^2)^2]/\Sigma[w(F_o^2)^2]^{1/2}$.

 © 2005 Wiley-VCH Verlag GmbH & Co. KGaA, Weinheim

(m), 1535 (w), 1512 (w), 1488 (w), 1411 (w), 1126 (m), 1066 (w), 1032 (m), 1012 (m), 914 (vs), 884 (s), 827 (w), 803 (w), 700 (vs), 671 (vs), 558 (m) cm^{-1} (see Supporting Information, Figure S4).

X-ray Crystallography: A blue single crystal of **1** was carefully selected under a polarizing microscope and glued to the tip of a thin glass fibre with cyanoacrylate (super glue) adhesive. Single-crystal structure determination by X-ray diffraction was performed on an R-axis RAPID IP diffractometer equipped with a normal focus, 18 kW sealed tube X-ray source (Mo-K_α radiation, λ = 0.71073 Å) operating at 50 kV and 200 mA. Data processing was accomplished with the RAXWISH processing program.[16] An empirical absorption correction was applied. The structure was solved by direct methods and refined by full-matrix least-squares on F^2 using the SHELXL 97 software.[17] All the non-hydrogen atoms were refined anisotropically. The hydrogen atoms were located from difference Fourier maps. Further details of the X-ray structural analysis are given in Table 1. Selected bond lengths and angles are listed in Table 2.

CCDC-239758 contains the supplementary crystallographic data for this paper. These data can be obtained free of charge from The Cambridge Crystallographic Data Centre via www.ccdc.cam.ac.uk/data_request/cif.

Supporting Information Available (see also footnote on the first page of this article): The TG curve of **1′**, the XRPD patterns for **1** and **1′**, IR and ESR spectra for **1**, space-filling diagram of the three-dimensional framework of **1** and a view of the 3D network of **1** along the *b* axis.

Table 2. Bond lengths [Å] and angles [°] for **1**.[a]

Mo(1)–O(4)	1.713(4)	Mo(1)–O(1)	1.723(5)
Mo(1)–O(9)	1.8990(18)	Mo(1)–O(10)	1.938(4)
Mo(1)–O(8)	2.279(4)	Mo(1)–O(6)	2.367(4)
Mo(2)–O(12)	1.697(4)	Mo(2)–O(5)	1.740(4)
Mo(2)–O(11)	1.905(4)	Mo(2)–O(10)	1.960(4)
Mo(2)–O(6)	2.214(4)	Mo(2)–O(2)	2.353(4)
Mo(3)–O(7)#1	1.714(5)	Mo(3)–O(7)	1.714(5)
Mo(3)–O(11)#1	1.916(4)	Mo(3)–O(11)	1.916(4)
Mo(3)–O(2)	2.362(4)	Mo(3)–O(2)#1	2.362(4)
Cu(1)–N(2)	2.041(5)	Cu(1)–N(2)#2	2.041(5)
Cu(1)–N(1)#2	2.062(5)	Cu(1)–N(1)	2.062(5)
Cu(1)–O(5)#2	2.423(4)	Cu(1)–O(5)	2.423(4)
P(1)–O(8)	1.509(4)	P(1)–O(6)#1	1.536(4)
P(1)–O(2)	1.547(4)	P(1)–O(3)	1.574(4)
O(4)–Mo(1)–O(1)	102.7(2)	O(4)–Mo(1)–O(9)	102.4(2)
O(1)–Mo(1)–O(9)	98.7(2)	O(4)–Mo(1)–O(10)	99.8(2)
O(1)–Mo(1)–O(10)	101.5(2)	O(9)–Mo(1)–O(10)	145.8(2)
O(4)–Mo(1)–O(8)	84.1(2)	O(1)–Mo(1)–O(8)	173.2(2)
O(9)–Mo(1)–O(8)	79.94(15)	O(10)–Mo(1)–O(8)	76.80(17)
O(4)–Mo(1)–O(6)	167.65(19)	O(1)–Mo(1)–O(6)	86.2(2)
O(9)–Mo(1)–O(6)	84.50(18)	O(10)–Mo(1)–O(6)	69.65(15)
O(8)–Mo(1)–O(6)	87.05(14)	O(12)–Mo(2)–O(5)	104.8(2)
O(12)–Mo(2)–O(11)	101.2(2)	O(5)–Mo(2)–O(11)	95.94(19)
O(12)–Mo(2)–O(10)	96.4(2)	O(5)–Mo(2)–O(10)	98.96(19)
O(11)–Mo(2)–O(10)	153.13(18)	O(12)–Mo(2)–O(6)	159.87(19)
O(5)–Mo(2)–O(6)	93.75(17)	O(11)–Mo(2)–O(6)	84.14(17)
O(10)–Mo(2)–O(6)	72.73(16)	O(12)–Mo(2)–O(2)	89.44(19)
O(5)–Mo(2)–O(2)	163.61(17)	O(11)–Mo(2)–O(2)	72.99(17)
O(10)–Mo(2)–O(2)	87.18(16)	O(6)–Mo(2)–O(2)	73.46(14)
O(7)#1–Mo(3)–O(7)	104.2(4)	O(7)#1–Mo(3)–O(11)#1	102.3(2)
O(7)–Mo(3)–O(11)#1	98.9(2)	O(7)#1–Mo(3)–O(11)	98.9(2)
O(7)–Mo(3)–O(11)	102.3(2)	O(11)#1–Mo(3)–O(11)	145.2(3)
O(7)#1–Mo(3)–O(2)	166.4(2)	O(7)–Mo(3)–O(2)	88.2(2)
O(11)#1–Mo(3)–O(2)	80.87(17)	O(11)–Mo(3)–O(2)	72.58(16)
O(7)#1–Mo(3)–O(2)#1	88.2(2)	O(7)–Mo(3)–O(2)#1	166.4(2)
O(11)#1–Mo(3)–O(2)#1	72.58(16)	O(11)–Mo(3)–O(2)#1	80.87(17)
O(2)–Mo(3)–O(2)#1	80.05(19)	N(2)–Cu(1)–N(2)#2	180.0(3)
N(2)–Cu(1)–N(1)#2	92.50(19)	N(2)#2–Cu(1)–N(1)#2	87.50(19)
N(2)–Cu(1)–N(1)	87.50(19)	N(2)#2–Cu(1)–N(1)	92.50(19)
N(1)#2–Cu(1)–N(1)	180.0(3)	N(2)–Cu(1)–O(5)#2	92.63(17)
N(2)#2–Cu(1)–O(5)#2	87.37(17)	N(1)#2–Cu(1)–O(5)#2	87.58(17)
N(1)–Cu(1)–O(5)#2	92.42(17)	N(2)–Cu(1)–O(5)	87.37(17)
N(2)#2–Cu(1)–O(5)	92.63(17)	N(1)#2–Cu(1)–O(5)	92.42(17)
N(1)–Cu(1)–O(5)	87.58(17)	O(5)#2–Cu(1)–O(5)	180.0(2)
O(8)–P(1)–O(6)#1	108.6(2)	O(8)–P(1)–O(2)	111.5(2)
O(6)#1–P(1)–O(2)	110.5(2)	O(8)–P(1)–O(3)	110.8(3)
O(6)#1–P(1)–O(3)	105.9(2)	O(2)–P(1)–O(3)	109.3(3)
P(1)–O(2)–Mo(2)	127.9(2)	P(1)–O(2)–Mo(3)	126.7(2)
Mo(2)–O(2)–Mo(3)	91.01(14)	Mo(2)–O(5)–Cu(1)	174.7(2)
P(1)#1–O(6)–Mo(2)	129.7(2)	P(1)#1–O(6)–Mo(1)	133.4(2)
Mo(2)–O(6)–Mo(1)	95.80(14)	P(1)–O(8)–Mo(1)	120.6(2)
Mo(1)–O(9)–Mo(1)#1	148.1(4)	Mo(1)–O(10)–Mo(2)	121.5(2)
Mo(2)–O(11)–Mo(3)	123.3(2)		

[a] Symmetry transformations used to generate equivalent atoms: #1: $-x$, y, $-z$ + 1/2; #2: $-x$, $-y$, $-z$.

Acknowledgment

The authors thank the National Natural Science Foundation of China (20371011) for financial support.

[1] a) K. Biradha, Y. Hongo, M. Fujita, *Angew. Chem. Int. Ed.* **2000**, *39*, 3843–3845; b) B. Moulton, M. J. Zaworotko, *Chem. Rev.* **2001**, *101*, 1629–1658; c) M. Eddaoudi, D. B. Moler, H. L. Li, B. L. Chen, T. M. Reineke, M. O'Keeffe, O. M. Yaghi, *Acc. Chem. Res.* **2001**, *34*, 319–330; d) U. Kortz, S. S. Hamzeh, N. A. Nasser, *Chem. Eur. J.* **2003**, *9*, 2945–2952; e) C. N. R. Rao, S. Natarajan, R. Vaidhyanathan, *Angew. Chem. Int. Ed.* **2004**, *43*, 1466–1496.

[2] a) S. S.-Y. Chui, S. M.-F. Lo, J. P. H. Charmant, A. G. Orpen, I. D. Williams, *Science* **1999**, *283*, 1148–1150; b) S. Kitagawa, R. Kiaura, S.-I. Noro, *Angew. Chem. Int. Ed.* **2004**, *43*, 2334–2375; c) Y.-Q. Tian, C.-X. Cai, X.-M. Ren, C.-Y. Duan, Y. Xu, S. Gao, X. Z. You, *Chem. Eur. J.* **2003**, *9*, 5673–5685.

[3] a) X.-H. Bu, M.-L. Tong, H.-C. Chang, S. Kitagawa, S. R. Batten, *Angew. Chem. Int. Ed.* **2004**, *43*, 192–195; b) C.-Y. Su, A. M. Goforth, M. D. Smith, P. J. Pellechia, H.-C. zur Loye, *J. Am. Chem. Soc.* **2004**, *126*, 3576–3586; c) B. Zhao, P. Cheng, X. Y. Chen, C. Cheng, W. Shi, D. Z. Liao, S. P. Yan, Z. H. Jiang, *J. Am. Chem. Soc.* **2004**, *126*, 3012–3013.

[4] a) S. Subramanian, M. J. Zaworotko, *Angew. Chem. Int. Ed. Engl.* **1995**, *34*, 2127–2130; b) S.-I. Noro, S. Kitagawa, M. Kondo, K. Seki, *Angew. Chem. Int. Ed.* **2000**, *39*, 2081–2084; c) X. L. Wang, C. Qin, E. B. Wang, Y. Y. Li, C. W. Hu, L. Xu, *Chem. Commun.* **2004**, 378–379.

[5] a) Y. Lu, Y. Xu, E. Wang, J. Lü, C. Hu, L. Xu, *Cryst. Growth Des.* **2004** *in press*; b) A. Dolbecq, P. Mialane, L. Lisnard, J. Marrot, F. Sécheresse, *Chem. Eur. J.* **2003**, *9*, 2914–2920; c) J.-J. Lu, Y. Xu, N. K. Goh, L. S. Chia, *Chem. Commun.* **1998**, 2733–2734; d) C.-M. Liu, D.-Q. Zhang, M. Xiong, D.-B. Zhu, *Chem. Commun.* **2002**, 1416–1417; e) A. Tripathi, T. Hughbanks, A. Clearfield, *J. Am. Chem. Soc.* **2003**, *125*, 10 528–10 529; f) D. Hagrman, J. Zubieta, *Chem. Commun.* **1998**, 2005–2006; g) U. Kortz, S. Matta, *Inorg. Chem.* **2001**, *40*, 815–817; h) J. R. Galán-Mascarós, C. Giménez-Saiz, S. Triki, C. J. Gómez-García, E. Coronado, L. Ouahab, *Angew. Chem. Int. Ed. Engl.* **1995**, *34*, 1460–1462.

[6] D. E. Katsoulis, *Chem. Rev.* **1998**, *98*, 359–388.

[7] a) R. Strandberg, *Acta Chem. Scand.* **1973**, *27*, 1004–1018; b) B. Hedman, *Acta Chem. Scand.* **1973**, *27*, 3335–3354.

[8] a) J. Chen, S. F. Lu, R. M. Yu, Z. N. Chen, Z. X. Huang, C. Z. Lu, *Chem. Commun.* **2002**, 2640–2641; b) E. Burkholder, J. Zubieta, *Chem. Commun.* **2001**, 2056–2057.

[9] a) U. Kortz, C. Marquer, R. Thouvenot, M. Nierlich, *Inorg. Chem.* **2003**, *42*, 1158–1162; b) R. C. Finn, E. Burkholder, J. Zubieta, *Chem. Commun.* **2001**, 1852–1853.

 © 2005 Wiley-VCH Verlag GmbH & Co. KGaA, Weinheim

[10] a) M. Yuan, Y. G. Li, E. B. Wang, C. G. Tian, L. Wang, C. W. Hu, N. H. Hu, H. Q. Jia, *Inorg. Chem.* **2003**, *42*, 3670–3676; b) D.-Q. Chu, J.-Q. Xu, L.-M. Duan, T.-G. Wang, A.-Q. Tang, L. Ye, *Eur. J. Inorg. Chem.* **2001**, 1135–1137.
[11] P. J. Hagrman, D. Hagrman, J. Zubieta, *Angew. Chem. Int. Ed.* **1999**, *38*, 2638–2684.
[12] a) V. Shivaiah, M. Nagaraju, S. K. Das, *Inorg. Chem.* **2003**, *42*, 6604–6606; b) C.-Z. Lu, C.-D. Wu, S.-F. Lu, J.-C. Liu, Q.-J. Wu, H.-H. Zhuang, J.-S. Huang, *Chem. Commun.* **2002**, 152–153.
[13] a) M.-L. Tong, B.-H. Ye, J.-W. Cai, X.-M. Chen, S. W. Ng, *Inorg. Chem.* **1998**, *37*, 2645–2650; b) S. Kawata, S. Kitagawa, M. Kondo, I. Furuchi, M. Munakata, *Angew. Chem. Int. Ed. Engl.* **1994**, *33*, 1759–1761.
[14] a) C.-H. Huang, L.-H. Huang, K.-H. Lii, *Inorg. Chem.* **2001**, *40*, 2625–2627; b) J. H. Lou, M. C. Hong, R. H. Wang, R. Cao, L. Han, D. Q. Yuan, Z. Z. Lin, Y. F. Zhou, *Inorg. Chem.* **2003**, *42*, 4486–4488; c) X.-M. Zhang, M.-L. Tong, M.-L. Gong, X.-M. Chen, *Eur. J. Inorg. Chem.* **2003**, 138–142.
[15] a) G. S. Rushbrooke, P. J. Wood, *Mol. Phys.* **1958**, *1*, 257–283; b) M. E. Lines, *J. Phys. Chem. Solids* **1970**, *31*, 101–106; c) J. Darriet, M. S. Haddad, E. N. Duesler, D. N. Hendrickson, *Inorg. Chem.* **1979**, *18*, 2679–2682.
[16] H. Uekusa, *J. Crystallogr. Soc. Jpn.* **1999**, *41*, 82–91.
[17] G. M. Sheldrick, *SHELXS-97, Program for Crystal Structure Solution*, University of Göttingen, Germany, **1997**.

Received: September 06, 2004

 © 2005 Wiley-VCH Verlag GmbH & Co. KGaA, Weinheim

Thermal Properties of $[M_{10}Se_4(SePh)_{12}(PR_3)_4]$ (M = Zn, Cd, Hg) Cluster Molecules – Synthesis and Structure of $[Cd_{32}Se_{14}(SePh)_{36}(L)_4]$; L = $OPPh_3$, OC_4H_8

Andreas Eichhöfer*[a]

Keywords: Cluster compounds / Cadmium / Selenium / X-ray structure analysis / Thermogravimetric analysis

A series of four different M_{10} selenide cluster molecules of the general formula $[M_{10}Se_4(SePh)_{12}(PR_3)_4]$ (M = Zn, Cd, Hg; R = organic group) have been synthesized by the reaction of metal chlorides MCl_2 (M = Zn, Cd, Hg) with phosphanes PR_3, $Se(SiMe_3)_2$ and $PhSeSiMe_3$ in organic solvents. The investigations of the thermal properties by thermogravimetric analysis (TGA) reveal that $[Zn_{10}Se_4(SePh)_{12}(PnPr_2Ph)_4]$, $[Cd_{10}Se_4(SePh)_{12}(PEt_3)_4]$, $[Cd_{10}Se_4(SePh)_{12}(PnPr_3)_4]$ and $[Hg_{10}Se_4(SePh)_{12}(PnPrPh_2)_4]$ form the corresponding bulk chalcogenides in mainly two- or three-step processes. From the intermediate product of the first step of the vacuum thermolysis of $[Cd_{10}Se_4(SePh)_{12}(PnPr_3)_4]$ we were able to obtain in solution the larger cluster molecule $[Cd_{32}Se_{14}(SePh)_{36}(OC_4H_8)_4]$ and upon addition of $OPPh_3$ its homologue $[Cd_{32}Se_{14}(SePh)_{36}(OPPh_3)_4]$. The structures of both molecules have been determined by single-crystal XRD. Obviously, the smaller Cd_{10} cluster grows upon thermal treatment in the solid state to form larger cluster cores. However, optical spectra and dynamic light scattering of the dissolved residues reveal that this growth is not totally specific.
(© Wiley-VCH Verlag GmbH & Co. KGaA, 69451 Weinheim, Germany, 2005)

Introduction

Semiconductor cluster molecules that are composed of a defined number of atoms are of particular interest for investigations concerning the variation of properties related to a change in size. For example, recent optical studies have shown that CdSe cluster molecules can be seen, not only with respect to their structure but also to their electronic properties, as molecular models for the bulk semiconductor.[1–4] But although a few well-defined molecular clusters formed by group 12 and 16 elements do exist, these tend to be on the smaller end of the size spectrum. Up to now the largest CdSe cluster compound that has been synthesized and characterized by single-crystal X-ray analysis contains thirty two cadmium atoms with the common formula $[Cd_{32}E_{14}(E'R)_{36}(L)_4]$ (E = Se, S; E′ = Se, S; L = neutral ligand).[5–7] Weller and coworkers found evidence from extended X-ray absorption fine structure (EXAFS) and UV/Vis[8] that the next stable cluster molecule in size is $[Cd_{54}Se_{32}(SeR)_{52}]^{8-}$, but no crystal structure from single-crystal XRD has been reported to date. It is therefore, a major goal to find new synthetic routes to enlarge the number of species in this class of materials. Most of the cluster syntheses are done in solution, but especially for one of the largest clusters $[Cd_{32}S_{14}(SC_6H_5)_{36}(DMF)_4]$, Herron et al. developed a combined solid-state/solution process in which a smaller cluster, namely $(NMe_4)_2[Cd_{10}S_4(SPh)_{16}]$, acts as a precursor for the synthesis of the larger compound.[5,9] With regard to the synthesis of 12–16 nanomaterials, Cumberland et al. have shown recently that similar smaller cluster molecules can also act in solution as convenient single-source precursors for controlled preparation of 2–9 nm CdSe and CdSe/ZnS nanocrystals.[10]

This paper reports on the investigations of the thermal properties of a series of four different M_{10}-selenide cluster molecules of the general formula $[M_{10}Se_4(SePh)_{12}(PR_3)_4]$ (M = Zn, Cd, Hg; R = organic group) by TGA. Recrystallisation of the intermediate product of the first step of the vacuum thermolysis of $[Cd_{10}Se_4(SePh)_{12}(PnPr_3)_4]$ led to the isolation of the larger cluster molecules $[Cd_{32}Se_{14}(SePh)_{36}(L)_4]$ (L = $OPPh_3$, OC_4H_8), which were characterised by single-crystal XRD.

Results and Discussion

Synthesis and Structure of the Precursor Cluster Molecules

The reaction of MCl_2 (M = Zn, Cd, Hg) with PR_3 (R = organic group), $PhSeSiMe_3$ and $Se(SiMe_3)_2$ in organic solvents results, according to Scheme 1, in the formation of crystals of $[Zn_{10}Se_4(SePh)_{12}(PnPr_2Ph)_4]$ (**1**), $[Cd_{10}Se_4(SePh)_{12}(PnPr_3)_4]$ (**2**),[1] $[Cd_{10}Se_4(SePh)_{12}(PEt_3)_4]$ (**3**, **3a**) and $[Hg_{10}Se_4(SePh)_{12}(PnPrPh_2)_4]$ (**4**).[11]

[a] Institut für Nanotechnologie (INT), Forschungszentrum Karlsruhe,
Postfach 3640, 76021 Karlsruhe, Germany
Fax: +49-7247-82-6368
E-mail: eichhoefer@int.fzk.de

$MCl_2 + PR_3$ (M = Zn, Cd, Hg)

organic solvent ↓ $PhSeSiMe_3$/ $Se(SiMe_3)_2$

$[Zn_{10}Se_4(SePh)_{12}(PnPr_2Ph)_4]$ **(1)**
$[Cd_{10}Se_4(SePh)_{12}(PnPr_3)_4]$ **(2)**
$[Cd_{10}Se_4(SePh)_{12}(PEt_3)_4]$ **(3, 3a)**
$[Hg_{10}Se_4(SePh)_{12}(PnPrPh_2)_4]$ **(4)**

Scheme 1.

Figure 1 shows, as an example, the molecular structure of a $[M_{10}Se_4(SePh)_{12}(PR_3)_4]$ (M = Zn, Cd, Hg; R = organic group) cluster core; these have been determined for all four compounds by single-crystal X-ray diffraction (Table 1). The cluster core, which comprises four adamantane cages each of which is formed by six selenium and four group 12 metal atoms, is a macrotetrahedral fragment of the sphalerite structure, which can be found in ZnSe, CdSe and HgSe. The four phosphane atoms occupy the apex positions of the resultant tetrahedron. The metal atoms are all four coordinate with distorted tetrahedral coordination geometry. Whilst most of them are bonded to either μ_3-Se^{2-}- or μ_2-$SePh^-$ ligands, those at the apex positions are also coordinated to phosphorus atoms. Mean interatomic distances vary in **1–4** because of the increasing covalent radii of zinc, cadmium and mercury (Table 2). The solution absorption spectrum for cluster **1** in THF features one maximum in the UV region at 246 nm ($\varepsilon = 2.9 \cdot 10^5\ M^{-1}\,cm^{-1}$).

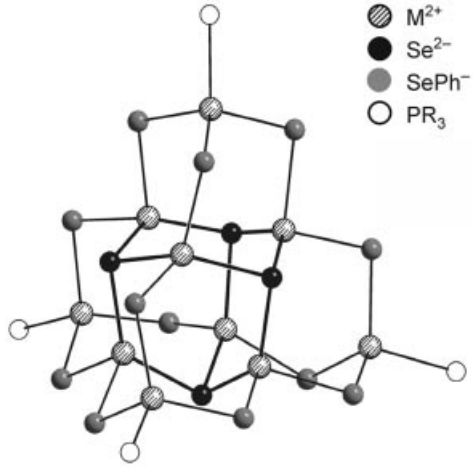

Figure 1. The $M_{10}Se_{16}P_4$ cluster core as a section of the molecular structures of $[M_{10}Se_4(SePh)_{12}(PR_3)_4]$; M = Zn (**1**), Cd (**2**, **3**, **3a**), Hg (**4**); R = organic group.

Thermogravimetric Analysis

The decomposition of **1–4** upon heating was followed by combined thermogravimetric analysis (TGA) and mass spectrometry (Figure 2). In the DTG, the mass change of **1** shows one sharp feature at 204 °C immediately followed by two further steps at 262 °C and 334 °C. The weight change in the first step corresponds to the cleavage of four $PPhnPr_2$ (calcd. 21.5%), while the added mass loss of the second and third step is equivalent to six $SePh_2$ (calcd. 38.7%) leading to the formation of ZnSe. A powder diffraction pattern proves the cubic structure of the formed material.

Thermogravimetric analysis of **2** in vacuo shows that the thermal decomposition occurs in two successive steps represented by two well-resolved peaks in the DTG curve (Figure 2). While the peak at 175 °C displays only one maximum, the other is split into two closely neighbouring maxima at 282 °C and 308 °C. The mass change of the first reaction corresponds to 16.9% which is equivalent in mass to four $PnPr_3$ (calcd. 16.2%) and some additional toluene incorporated in the crystal lattice. The intermediate product '$Cd_{10}Se_4(SePh)_{12}$' then undergoes a second reaction, beginning at around 220 °C. The mass loss is equivalent to six $SePh_2$ (calcd. 35.4%), leaving a solid residue with the formula CdSe. X-ray diffraction indicates that this solid is phase-pure CdSe in the zincblende structure. This interpretation is in good agreement with simultaneously recorded mass spectra. Starting from 40 °C, two peaks at *m/e* = 91, 92 evolve, which indicate small amounts of remaining toluene in the crystal powder. The principal product of the low-temperature weight loss event is identified to be $PnPr_3$ (*m/e* = 161, 133, 104/105, 91, 77, 62, 41, 27). The highest peaks in mass in the spectra of the second step are located between *m/e* = 150–161 and can be assigned to $(C_6H_5)_2$ (*m/e* = 154), HSePh (*m/e* = 158) and 'SePh' as a fragmentation product of $SePh_2$, although molecular peaks (*m/e* = 234; 312) of this latter compound were not detected. Therefore, the volatile products of the second step of the vacuum thermolysis of **5** were collected in a cool trap and investigated by GC-MS as a solution in THF. $SePh_2$ was found to be the main product accompanied by HSePh, $(C_6H_5)_2$ and PhSe–SePh, all with lower concentrations by approximately one-tenth.

Nearly the same decomposition sequence is observed for **3**; the second step that corresponds to the cleavage of six $SePh_2$ (calcd. 36.96%) is quite similar to that of **2** (Figure 2). However, the differential peak for the first event in the TGA of **3** appears to be much broader than that of **2** with an indicated splitting into two subprocesses. As a consequence the mean temperature for the cleavage of four PEt_3 (calcd. 12.49%) is found to be by approximately 30 °C higher than that of $PnPr_3$ in **2**. Therefore, the two steps of the thermolysis of **3** are not as well separated as for **2**. Accordingly the measured weight loss in the mass spectra indicate that PEt_3 (*m/e* = 118) and 'SePh' (*m/e* = 157) are the main decomposition products of either step 1 (low temperature) and step 2 (high temperature).

The investigations of the thermal properties of **4** reveal that it decomposes rapidly in a two-step process between 40 °C and 140 °C to yield a black residue of 12% in mass of the starting cluster with C: 0.61% and H: 0.04% (Figure 2). Powder X-ray diffraction analysis shows it to be HgSe in its cubic form, which then further decomposes at a mean

 © 2005 Wiley-VCH Verlag GmbH & Co. KGaA, Weinheim

Table 1. Crystallographic Data for $[Zn_{10}Se_4(SePh)_{12}(PPhnPr_2)_4]$ (**1**), $[Cd_{10}Se_4(SePh)_{12}(PEt_3)_4]$ (**3**, **3a**), $[Cd_{32}Se_{14}(SePh)_{36}(C_4H_8O)_4]$ (**5**) and $[Cd_{32}Se_{14}(SePh)_{36}(OPPh_3)_4]$ (**6**).

	1·5C_6H_6	**3**	**3a**	**5**	**6**·9.5C_4H_8O
Formula mass	4009.77	3785.16	3785.16	10608.82	11830.05
Crystal system	triclinic	trigonal	tetragonal	trigonal	monoclinic
Space group	$P\bar{1}$	$R\bar{3}c$	$P\bar{4}$	$R\bar{3}c$	$C2/c$
a [pm]	1870.6(4)	5103.5(7)	2694.3(4)	2317.6(3)	2504.1(5)
b [pm]	1999.3(4)				4436.5(9)
c [pm]	2439.6(5)	3156.9(6)	1629.0(3)	22119(4)	3514.8(7)
α [°]	69.14(3)				
β [°]	68.54(3)				91.43(3)
γ [°]	85.77(3)				
V [10^6pm^3]	7919(3)	71209(20)	11825(3)	102888	39036(14)
Z	2	24	4	12	4
T [K]	190	190	190	190	160
$d_{calcd.}$ [g cm^{-3}]	1.682	2.118	2.126	2.055	2.013
μ(Mo-K_α) [mm^{-1}]	5.249	6.754	6.778	7.280	6.424
F[000]	3940	42700	7120	58464	22064
$2\Theta_{max}$ [°]	50	48	50	40	48
Measured reflections	39100	39426	38771	47186	66696
Unique reflections	25167	18859	20626	10616	26715
R_{int}	0.0771	0.0574	0.0477	0.0815	0.0901
Reflections with $I > 2\sigma(I)$	17284	14249	13333	8174	15726
Refined parameters	887	873	672	577	1053
$R1[I > 2\sigma(I)]$[a]	0.0753	0.0450	0.0503	0.0932	0.0660
$wR2$(all data)[b]	0.2052	0.1272	0.1420	0.2935	0.2037
Abs. struct. param.		–0.008(9)	0.474(9)		

[a] $R1 = \Sigma||F_o| - |F_c||/\Sigma|F_o|$. [b] $wR2 = \{\Sigma[w(F_o^2 - F_c^2)^2]/\Sigma[w(F_o^2)^2]\}^{1/2}$.

Table 2. Selected ranges of interatomic distances [pm] for $[Zn_{10}Se_4(SePh)_{12}(PnPr_2Ph)_4]$ (**1**), $[Cd_{10}Se_4(SePh)_{12}(PnPr_3)_4]$ (**2**) $[Cd_{10}Se_4(SePh)_{12}(PEt_3)_4]$ (**3**, **3a**) and $[Hg_{10}Se_4(SePh)_{12}(PnPrPh_2)]$ (**4**).

	1 (M = Zn)	**2** (M = Cd)	**3** (M = Cd)	**3a** (M = Cd)	**4** (M = Hg)
M–μ_3-Se	240.1–244.0(2)	257.8–259.9(1)	257.6–262.2(2)	257.0–261.2(2)	256.0–262.8(1)
M–μ_2-SePh	244.6–254.6(2)	263.1–271.6(1)	262.3–274.3(2)	263.3–274.1(2)	262.1–277.7(1)
M–P	241.3–243.4(4)	260.6(2)	257.2–261.2(6)	259.4–261.4(4)	257.5(3)
P–P	1164.6–1188.9	1246.0–1258.3	1226.6–1309.4	1229.3–1296.9	1221.4–1293.4

temperature of 226 °C; this is in rough agreement with the reported value for the beginning of the sublimation of HgSe in an evacuated quartz crucible at 226 °C.[12] However, the observed mass changes in the three-step TGA of **4** cannot be simply assigned to the cleavage of a certain amount of product like in **1–3**, as a theoretical cleavage of four PPh_2nPr (calcd. 17.88%) and six $SePh_2$ (calcd. 27.4%) should yield a residue of 54.72 mass-% of HgSe. Similar to observations of Corrigan et al. on the TGA of $[Hg_{15}Cu_{20}S_{25}(PnPr_3)_{18}]$,[13] we assume that more complex redox processes including the reduction of Hg^{2+} may take place during the thermal treatment of **4**. For the first step, the recorded mass spectra only display the peaks associated to the fragmentation products of PPh_2nPr (m/e = 152 = PPh*n*Pr and 108 = PPh). Starting with the second step, a group of peaks between m/e = 150 and 161 evolves, which is indicative of the cleavage of SePh groups. Any other products could not be clearly identified in the mass spectra.

Characterization of the Intermediate '$Cd_{10}Se_4(SePh)_{12}$'

Bulk samples of the yellow '$Cd_{10}Se_4(SePh)_{12}$' were prepared according to Scheme 2 in a porcelain boat inside a glass tube, connected to a high vacuum pump.

The X-ray powder pattern of the yellow crude powder (Figure 3) shows one strong peak at d = 1.78 nm in the low 2θ range, and three further broad and weaker peaks at higher angles (25.4°, 43.3°), the latter of which has a distinct shoulder at 47.8°. The pattern of the three weaker peaks can be successfully fitted on the basis of the cubic bulk structure of CdSe, and the broad peaks indicating the small sizes of the crystallites. An estimation of the particle size on the basis of the Scherrer equation[14] yields a mean diameter of 1.5 nm, which suggests a growth of the originally 0.7-nm sized CdSe cluster cores in **2** (size is taken as the distance of the cadmium atom at one vertex to the opposite tetrahedral face; see Figure 1). The peak at d = 1.78 nm depicts some long-range order in the powder, which most probably originates from the nanostructuring of the material.

Yellow '$Cd_{10}Se_4(SePh)_{12}$' dissolves fairly well in THF, whilst the solubility is enhanced upon addition of aliquots of tertiary phosphanes. By comparison of the UV/Vis spectra of **2** and '$Cd_{10}Se_4(SePh)_{12}$' in THF it can clearly be seen that the absorption features of **2** have changed upon thermal treatment (Figure 4a). While the characteristic peaks for **2** at 297 nm and 316 nm have disappeared, new, weakly resolved absorption maxima are detected at higher wave-

 © 2005 Wiley-VCH Verlag GmbH & Co. KGaA, Weinheim

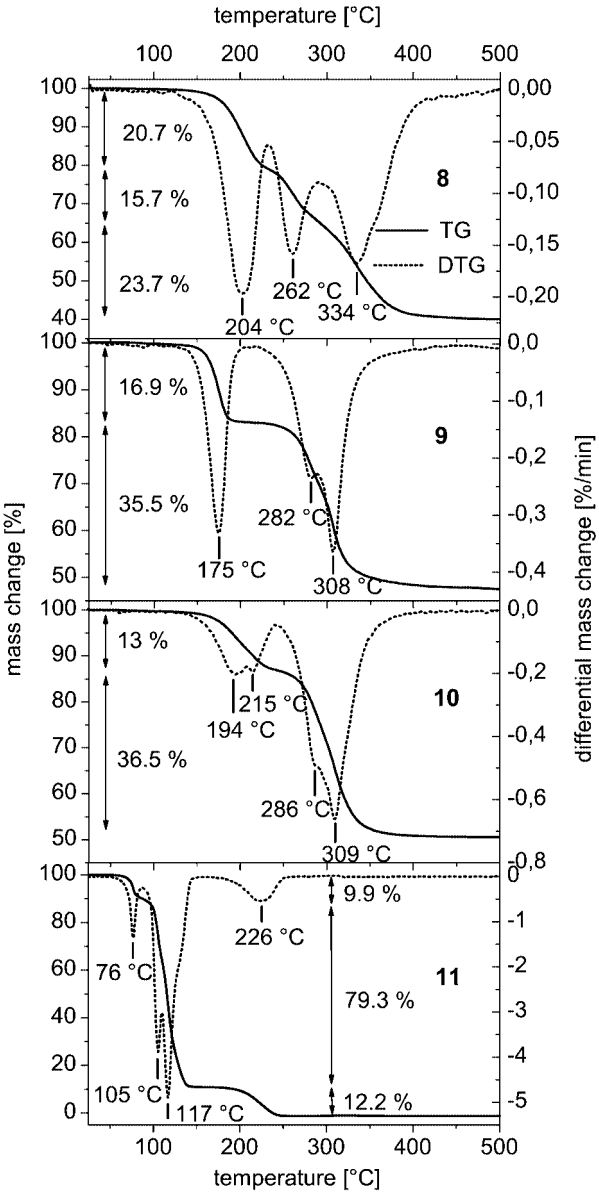

Figure 2. Thermogravimetric analysis of $[Zn_{10}Se_4(SePh)_{12}(PnPr_2Ph)_4]$ (**1**), $[Cd_{10}Se_4(SePh)_{12}(PnPr_3)_4]$ (**2**), $[Cd_{10}Se_4(SePh)_{12}(PEt_3)_4]$ (**3**, **3a**) and $[Hg_{10}Se_4(SePh)_{12}(PnPrPh_2)]$ (**4**) (straight lines). The corresponding differential thermogravimetric curves are drawn as dashed lines.

$$[Cd_{10}Se_4(SePh)_{12}(PnPr_3)_4] \quad (\mathbf{2})$$

$$\Delta / 210\ ^\circ C \;\Big|\; -4\ PnPr_3$$

$$\downarrow$$

$$`Cd_{10}Se_4(SePh)_{12}'$$

Scheme 2.

lengths suggesting a growth of the original CdSe cluster cores of **2**, which is in agreement with the particle sizes derived from powder X-ray data.

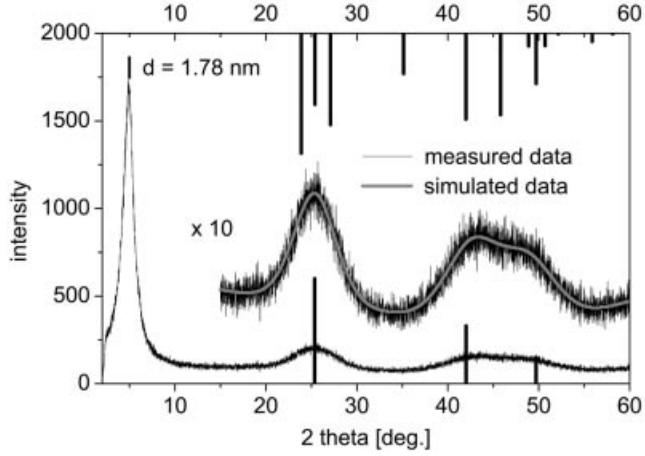

Figure 3. Powder XRD pattern for the intermediate product '$Cd_{10}Se_4(SePh)_{12}$' formed by TGA of $[Cd_{10}Se_4(SePh)_{12}(PnPr_3)_4]$ (**2**). The solid line represents a fit to the experimental data based on the peaks of cubic CdSe. Also shown are the peak patterns of cubic (downward sticks) and hexagonal (upward sticks up) CdSe.

Similar observations are made in a dynamic light scattering experiment (Figure 4b). For solutions of '$Cd_{10}Se_4(SePh)_{12}$' in THF, a broad peak for the hydrodynamic radius (resulting from the fit of the autocorrelation function) is observed, which is shifted by 0.7 nm relative to that of the precursor cluster **2** (the total diameter of **2** is estimated from a space-filling model to be 2.2 nm).[15] The increased width of the peak for the '$Cd_{10}Se_4(SePh)_{12}$' solutions results from a distribution of particle sizes, which is in agreement with the detection of several weakly resolved maxima in the UV/Vis spectrum. The shift of the peak maxima however supports the suggested growth of the '$Cd_{10}Se_4(SePh)_{12}$' cluster cores of **2** during thermal treatment.

Synthesis and Structure of $[Cd_{32}Se_{14}(SePh)_{36}(L)_4]$; L = OC_4H_8 (5), $OPPh_3$ (6)

Dissolution of the crude yellow powder resulting from the thermal treatment of **2** with the formal composition '$Cd_{10}Se_4(SePh)_{12}$' in THF yields pale yellow crystals after one night. Although some of these crystals appear to be perfect, they diffract only up to 25° in 2θ, and the determination of a hexagonal cell was only possible on the basis of 60% of the reflections being indexed ($a = b = 3929.1$, $c = 3017.1$ pm). Additionally, one axis shows a superstructure splitting of the reflections, which altogether makes a solution of the structure impossible. The separation of the supernatant solution from the crystals and subsequent concentration by evaporation of more than half of the solvent yielded other more suitable crystals for X-ray analysis, with the composition $[Cd_{32}Se_{14}(SePh)_{36}(OC_4H_8)_4]$ (**5**) (Scheme 3). Immediate addition of six equiv. triphenylphosphineoxide during the dissolution of '$Cd_{10}Se_4SePh_{12}$' inTHF avoided the formation of the initially formed weak diffracting crystals. Instead, pale yellow pinlike crystals of $[Cd_{32}Se_{14}(SePh)_{36}(OPPh_3)_4]$ (**6**) grew upon indirect layering of the solution with acetone (Scheme 3). However, the theo-

 © 2005 Wiley-VCH Verlag GmbH & Co. KGaA, Weinheim

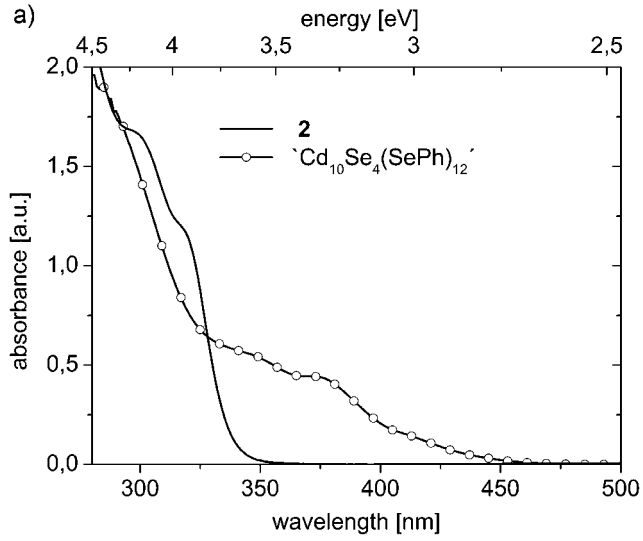

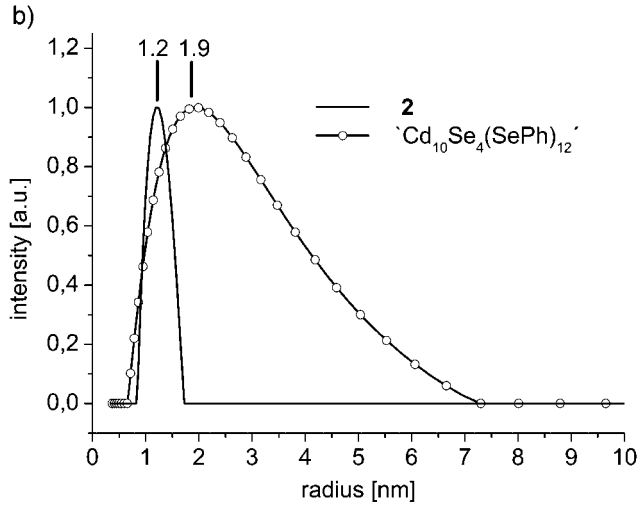

Figure 4. a) UV/Vis spectra of $[Cd_{10}Se_4(SePh)_{12}(PnPr_3)_4]$ (**2**) and the intermediate product '$Cd_{10}Se_4(SePh)_{12}$' of the TGA of **2** in THF; b) resulting peaks for the hydrodynamic radii of **2** and '$Cd_{10}Se_4(SePh)_{12}$' in THF from the fit of the autocorrelation function.

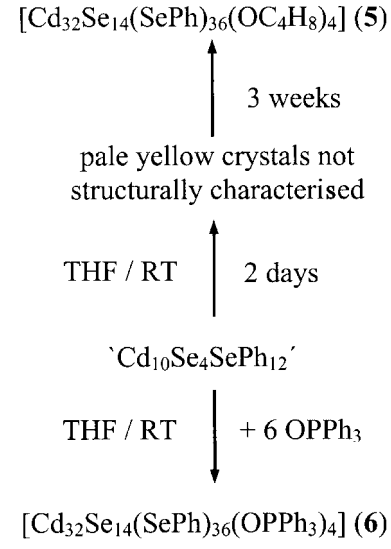

Scheme 3.

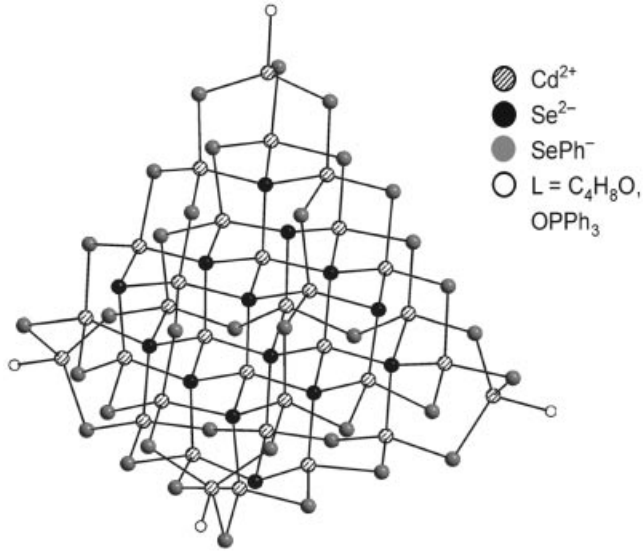

Figure 5. The $Cd_{32}Se_{50}O_4$ cluster core as a section of the molecular structures of $[Cd_{32}Se_{14}(SePh)_{36}(OC_4H_8)_4]$ (**5**) and $[Cd_{32}Se_{14}(SePh)_{36}(OPPh_3)_4]$ (**6**).

retical stoichiometric formation of **5** and **6** from '$Cd_{10}Se_4SePh_{12}$' produces a slight excess of cadmium atoms and phenylselenolate ligands with respect to the composition of the precursor compound, which suggests the formation of unidentified by-products in the reaction as represented by the unknown crystals (see also discussion of powder XRD and UV/Vis below).

Both compounds, **5** which crystallises in the space group $R\bar{3}c$ and **6** which crystallises in $C2/c$, exhibit the same tetrahedral cluster core structure $[Cd_{32}Se_{14}(SePh)_{36}L_4]$, with either C_4H_8O (**5**) or $OPPh_3$ (**6**) at the apex positions (Figure 5). This cluster framework is built up of 13-fused CdSe adamantane cages with four barrelene CdSe cages at each of the corners. Adamantane cages are the building blocks of the cubic zincblende structure of CdSe, while barrelene cages are those of the hexagonal wurtzite type. Thus, it is similar to the known M_{32} chalcogenide cluster molecules such as $[Cd_{32}S_{14}(SPh)_{36}(DMF)_4]$ (DMF = *N*,*N*-dimethylformamide),[5] $[Cd_{32}S_{14}(SCH_2CH(OH)CH_3)_{36}(H_2O)_4]$[6] and $[Hg_{32}Se_{14}(SePh)_{36}]$,[7] but slightly different to the closely related cluster $[Cd_{32}Se_{14}(SePh)_{36}(PPh_3)_4]$[7] and distinctly dif-ferent to a recently characterized cluster of composition $[Hg_{34}Te_{16}(SePh)_{36}(PPhnPr_2)_4]$.[16] The difference in structure in relative to that found in **5** and **6** (Figure 6) lies with the build up of the CdSe framework. A rotation of a corner part of the structure in **5** or **6** that consists of one barrelene cage and three adamantane cages by 120° (around the threefold axis pointing from this corner to the opposite triangular face) converts these three adamantane cages into three barrelene cages and thus leads to the structure of

 © 2005 Wiley-VCH Verlag GmbH & Co. KGaA, Weinheim

$[Cd_{32}Se_{14}(SePh)_{36}(PPh_3)_4]$ without changing the stoichiometry and the overall charge of the cluster. This cluster therefore comprises an increased number of seven barrelene cages and only ten adamantane cages in comparison to the numbers found in **5** and **6**. In principle this twisting should be possible at all four corners of the '$Cd_{32}Se_{14}(SePh)_{36}$' cluster core, which would result in a build up of one adamantane cage and 16 barrelene cages, a structure which has not yet been synthesized and characterized. The problems in crystallizing these compounds are maybe due to this geometric isomerism which reflects the dimorphism of bulk CdSe, together with a huge theoretical amount of isomeric-structures caused by the two possible positions for the phenyl groups of each μ_2-SePh$^-$ ligand.[17] Another tetrahedral cluster composed of elements of group 12 and 16 with a closely related composition and size but different structure is $[Hg_{34}Te_{16}(SePh)_{36}(PPhnPr_2)_4]$.[16] The '$Hg_{34}Te_{16}Se_{36}$' cluster core is completely formed by 20 adamantane cages and can be considered as an idealized fragment of the cubic sphalerite lattice, but with a mercury vacancy in the centre. Although the cluster cores of **5** and **6** are also formed by adamantane cages, except the barrelane cages at the four corners, both structures differ in their geometric centres. Whilst at the centre of $[Hg_{34}Te_{16}(SePh)_{36}(PPhnPr_2)_4]$, there is a mercury vacancy on what should be a formal atomposition, the centre of **5** and **6** lies within the centre of theinner adamantane cage and thus on a tetrahedral hole. This situation shows, in principle, the two possibilities of nucleation of a CdSe crystal, one where it grows regularly on all sides from a preformed 'Cd_4Se_6' adamantane cage and the other from a tetrahedral '$HgTe_4$' unit. The CdSe bond distances for **5** and **6** listed in Table 3 display slightly different ranges for the different bridging modes of the selenium ligands, either μ_4-Se^{2-}, μ_3-Se^{2-} or μ_2-Se^-, which are in analogy to those ranges found in the similar cluster, $[Cd_{32}Se_{14}(SePh)_{36}(PPh_3)_4]$.[7]

A comparison of the measured and calculated X-ray powder diffraction patterns for **5** and **6** reveal their reason-

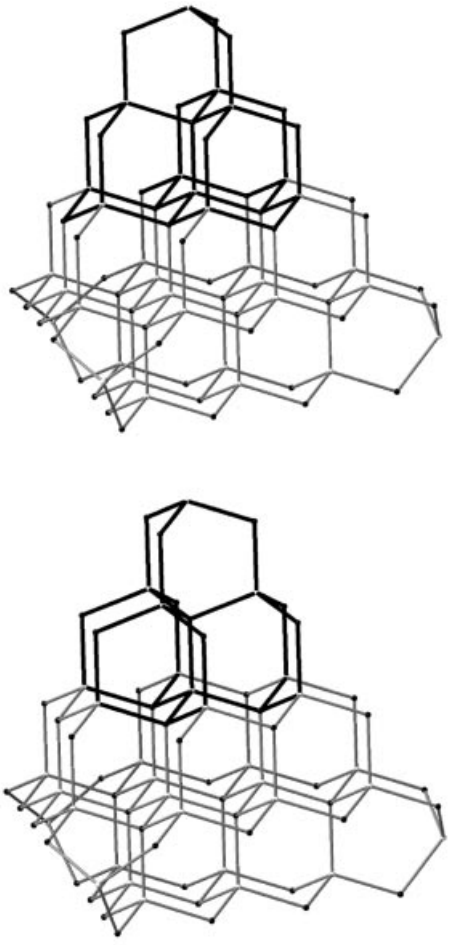

Figure 6. Schematic drawing of the different build up of the $Cd_{32}Se_{50}$ cluster cores in $[Cd_{32}Se_{14}(SePh)_{36}(OC_4H_8)_4]$ (**5**), $[Cd_{32}Se_{14}(SePh)_{36}(OPPh_3)_4]$ (**6**) (above) and $[Cd_{32}Se_{14}(SePh)_{36}(PPh_3)_4]$[7] (below) with the differing part highlighted in black.

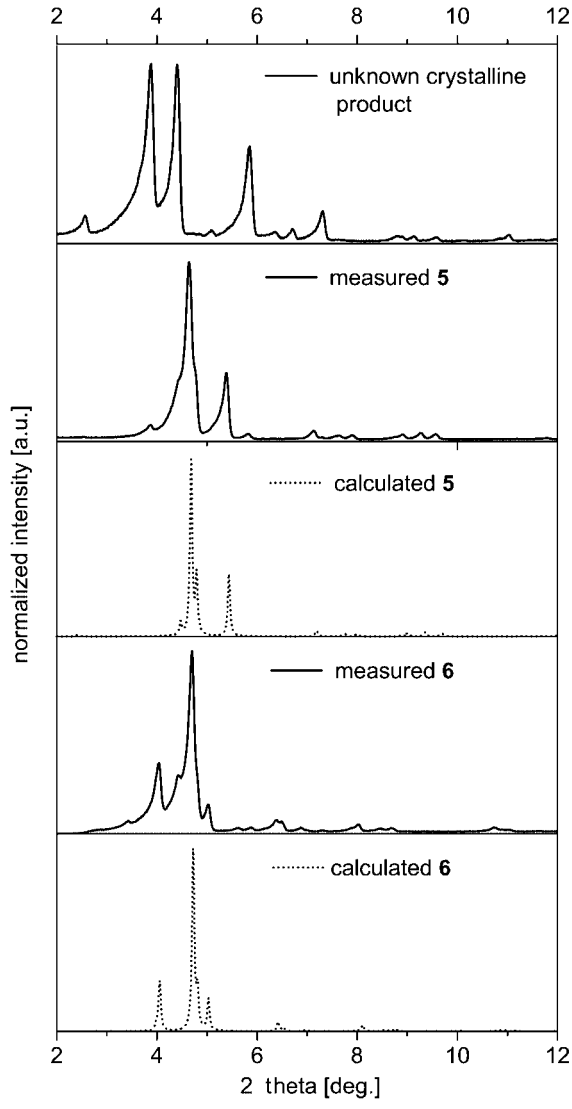

Figure 7. Measured (straight line) and calculated (dotted line) X-ray powder patterns for $[Cd_{32}Se_{14}(SePh)_{36}(OC_4H_8)_4]$ (**5**) and $[Cd_{32}Se_{14}(SePh)_{36}(OPPh_3)_4]$ (**6**) which can be compared to the pattern of the unknown crystalline preproduct resulting from the recrystallisation of the intermediate product '$Cd_{10}Se_4(SePh)_{12}$' of the TGA of $[Cd_{10}Se_4(SePh)_{12}(PnPr_3)_4]$ (**2**) (Scheme 3).

 © 2005 Wiley-VCH Verlag GmbH & Co. KGaA, Weinheim

Table 3. Selected ranges and mean values for bond distances [pm] for $[Cd_{32}Se_{14}(SePh)_{36}(OC_4H_8)_4]$ (**5**) and $[Cd_{32}Se_{14}(SePh)_{36}(OPPh_3)_4]$ (**6**).

Bond	No. of bonds	**5**		**6**	
		Range	Mean value	Range	Mean value
μ_4-Se^{2-}–Cd	40	261.8–267.4(3)	264.6	261.7–266.6(2)	264.0
μ_3-Se^{2-}–Cd	12	257.6–259.1(3)	258.0	257.5–258.7(2)	258.3
μ_2-$SePh^-$–Cd	72	258.2–269.9(4)	264.4	260.0–270.1(2)	265.1
O–Cd	4	236.7–237.7(30)	237.5	222.7–225.9(11)	224.3

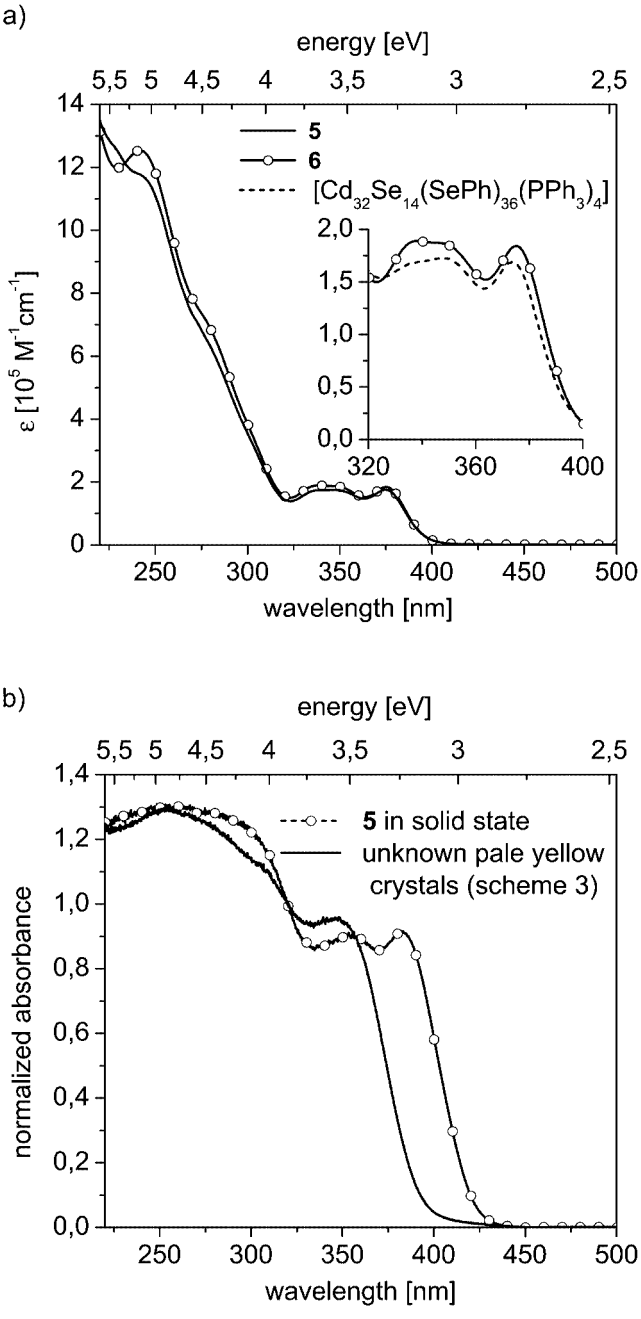

Figure 8. a) UV/Vis spectra of $[Cd_{32}Se_{14}(SePh)_{36}(OC_4H_8)_4]$ (**5**) and $[Cd_{32}Se_{14}(SePh)_{36}(OPPh_3)_4]$ (**6**) in THF. The inset displays a magnification of the absorption bands of **5** between 320 and 400 nm relative to the bands of the very similar cluster $[Cd_{32}Se_{14}(SePh)_{36}(PPh_3)_4]$; b) UV/Vis spectra of **5** and the unknown pale yellow crystals (see Scheme 3) in solid state.

able crystalline purity with respect to the formation of a mixture of compounds (Figure 7), although weak additional reflections in the patterns of **5** and **6** indicate cocrystallisation of small amounts of an unknown crystalline product in both compounds. However, the location of the strong reflections in the powder pattern of these unknown crystals at low 2θ values reflect long-range ordering in a size range comparable to **5** and **6**.

The UV/Vis spectra in THF (Figure 8a) are quite similar for **5** and **6**. Starting from higher wavelengths, the first absorption maximum is observed at 375 nm (3.3 eV) [the extinction coefficient for **5** in THF is $1.84 \cdot 10^5$ $M^{-1}cm^{-1}$ and for **6**, $1.76 \cdot 10^5$ $M^{-1}cm^{-1}$] followed by a broad peak centred at 343 nm (3.6 eV) which most probably consists of two closely neighbouring transitions at either 338 nm (3.7 eV) and 348 nm (3.6 eV). The following increase in absorbance in the region from 321 nm to 210 nm indicates further weakly resolved maxima and shows a last peak for **5** at 241 nm (5.12 eV) and a related shoulder for **6** at a similar position. The inset in Figure 8a displays a comparison of the spectra of **5** and the very similar cluster $[Cd_{32}Se_{14}(SePh)_{36}(PPh_3)_4]$, which has a slightly shifted first absorption maximum at 373 nm. In contrast to **5**, the unknown crystalline pale yellow product according to Scheme 3 is mostly insoluble in THF. The solid-state UV/Vis spectrum in Figure 8b shows the lowest energy absorption peak at 346 nm (3.58 eV), while under similar conditions, the spectrum for **5** shows the first maximum at 383 nm (3.24 eV). Therefore, the position of the lowest-energy transition between that of **2** and **5** points to an intermediate cluster size, for example, a cluster cage with 17 cadmium atoms such as '$Cd_{17}Se_4(SePh)_{24}$', which was found in $[Cd_{17}Se_4(SePh)_{24}(PnPr_2Ph)_4]^{2+}$.[1] The low solubility suggests an ionic or polymeric species. These findings are also in agreement with the elemental analysis (C: 30.2, H: 2.1%) of the preliminary crystallizing powder, which displays higher values than those calculated for **5** (C: 26.3, H 2.0%).

Experimental Section

Synthesis

Standard Schlenk techniques were employed throughout the syntheses using a double manifold vacuum line with high purity dry nitrogen. The solvents tetrahydrofuran (THF), dimethylethyleneglycol (DME) and benzene were dried over sodium benzophenone, and toluene, over $LiAlH_4$, and distilled under nitrogen. Anhydrous $ZnCl_2$, $CdCl_2$ and $HgCl_2$ were purchased from Aldrich. $PhSeSiMe_3$[18] and $Se(SiMe_3)_2$[19] were prepared according to stan-

 © 2005 Wiley-VCH Verlag GmbH & Co. KGaA, Weinheim

dard literature procedures. $Se(SinBu_3)_2$ was prepared according to the synthesis of $Se(SiMe_3)_2$ with $ClSinBu_3$ instead of $ClSiMe_3$.

1: $ZnCl_2$ (0.28 g, 2.05 mmol) was dissolved in benzene (50 mL) with the addition of $PPhnPr_2$ (0.43 mL, 2.05 mmol). $PhSeSiMe_3$ (0.55 mL, 2.87 mmol) was then added, and the resulting clear solution was stirred for 2 h. Addition of $Se(SiMe_3)_2$ (0.18 mL, 0.82 mmol) led to the formation of some droplets of colourless oil, which dissolves again upon standing for two days. Layering with *n*-pentane leads to the formation of colourless crystals of $[Zn_{10}Se_4(SePh)_{12}(PnPr_2Ph)_4]$ (**1**). Yield: 0.66 g, 80%. $C_{120}H_{136}Zn_{10}P_4Se_{16}$ (3619.45): calcd. C 39.82, H 3.79; found C 40.06, H 3.74%.

2: according to ref.[1].

3, **3a:** $CdCl_2$ (0.32 g, 1.75 mmol) was dissolved in DME (30 mL) with the addition of PEt_3 (0.64 mL, 4.36 mmol). $PhSeSiMe_3$ (0.54 mL, 2.8 mmol) was then added at 0 °C, and the resulting clear solution was stirred for 2.5 h. Addition of $Se(SiMe_3)_2$ (0.12 mL, 0.53 mmol) at 0 °C and subsequent standing at room temperature led to the formation of a mixture of colourless crystals of $[Cd_{10}Se_4(SePh)_{12}(PEt_3)_4]$ (**3**, **3a**). Yield: 0.50 g, 76%. $C_{96}H_{120}Cd_{10}P_4Se_{16}$ (3785.36): calcd. C 30.46, H 3.20; found C 30.43, H 3.31%.

4: according to ref.[11].

'$Cd_{10}Se_4(SePh)_{12}$': Bulk samples of the intermediate '$Cd_{10}Se_4(SePh)_{12}$', identified from the TGA experiments, were prepared by heating **2** in a porcelain boat inside a glass tube connected to a high vacuum pump via a cool trap. Samples of **2** (up to 0.5 g) were heated at 3 °C/min to 210 °C and then immediately cooled down by opening of the oven. The originally white/colourless crystals changed to give an intense-coloured yellow powder. $C_{72}H_{60}Cd_{10}Se_{16}$ (3312.73): calcd. C 26.11, H 1.82; found C 26.01, H 1.87%.

5: '$Cd_{10}Se_4(SePh)_{12}$' (0.043 g, 0.013 mmol) was dissolved in THF (12 mL). Hexagonal shaped crystals of poor diffraction quality were obtained after overnight standing. After two days the clear supernatant solution was separated from the crystals and this flask connected to another flask which contains Diglyme (50 mL). Slow evaporation of more than half of the THF solution into the Diglyme solution over a period of 3 weeks yielded pale yellow crystals of $[Cd_{32}Se_{14}(SePh)_{36}(C_4H_8O)_4]$ (**5**) as well as small amounts of the hexagonal ones with unknown composition. Yield: 0.018 g, 45% calculated for reaction of 3.5 equiv. '$Cd_{10}Se_4(SePh)_{12}$' to yield 1 equiv. **5**, according to Scheme 3. $C_{232}H_{212}Cd_{32}O_4Se_{50}$ (10609.35): calcd. C 26.27, H 2.01; found C 26.11, H 2.02%.

6: '$Cd_{10}Se_4(SePh)_{12}$' (0.097 g, 0.0293 mmol) was dissolved in THF (10 mL). Then $OPPh_3$ (1.21 mL of a 0.176 M solution in THF) was added and layered with acetone through slow diffusion by evaporation via a connected flask to give pale yellow crystals of $[Cd_{32}Se_{14}(SePh)_{36}(OPPh_3)_4]$ (**6**). Yield: 0.048 mg, 50% calculated for reaction of 3.5 equiv. '$Cd_{10}Se_4(SePh)_{12}$' to yield 1 equiv. **6** according to Scheme 3. $C_{288}H_{240}Cd_{32}O_4P_4Se_{50}$ (11434.09): calcd. C 30.25, H 2.12; found C 29.95, H 2.09%.

Crystallography

Crystals suitable for single-crystal X-ray diffraction were taken directly from the reaction solutions of the compounds and then selected in perfluoroalkylether oil.

Single-crystal X-ray diffraction data were collected with the use of graphite-monochromatised Mo-K_α radiation (λ = 0.71073 Å) on a STOE IPDS II (Imaging Plate Diffraction System) equipped with a Schneider rotating anode. The structures were solved with the direct methods program SHELXS[20] of the SHELXTL PC suite programs, and were refined with the use of the full-matrix least-squares program SHELXL.[20] Molecular diagrams were prepared by using the program SCHAKAL 97[21] and DIAMOND.[22]

All Zn, Cd, Se and P atoms were refined with anisotropic displacement parameters, whilst all C and O atoms were refined isotropically with the exception of **6** where the O atoms were treated anisotropically. Some of the phenyl rings were refined with a model of disorder **1**: C43–C48 and C103–C108, **3a**: C43–C48 and C91–C96, **5**: C1–C6 and C55–C60. The phenyl group C67–C72 in **5** could only be refined as a rigid group with half occupancy. One THF ligand (O2, C77, C78) in **5**, which coordinates to Cd2 at one apex position of the cluster core resides on a threefold axis. It was refined as a threefold degenerate solvent molecule but could also in general indicate a twinning of the crystals. Only two of the solvent THF molecules in **6** were refined with half occupancy. Residual electron density in the difference Fourier map of **1**, **5** and **6** indicates the existence of additional disordered solvent molecules in the crystal lattice that could not be refined successfully. Problems in the X-ray structural analysis of **5** arise from the very long *c* axis of the unit cell. In order to avoid an overlapping of reflections, a maximum detector distance (200 mm, $2\Theta_{max}$ = 40°) was chosen during the measurement together with a small effective mosaic spread and a small reflection box in the integration.

CCDC-250987 (**1**), CCDC-250988 (**3**), CCDC-250989 (**3a**), CCDC-250990 (**5**) and CCDC-250991 (**6**) contain the supplementary crystallographic data for this paper. These data can be obtained free of charge from The Cambridge Crystallographic Data Centre via www.ccdc.cam.ac.uk/data_request/cif.

X-ray powder diffraction patterns (XRD) were measured on a STOE STADI P diffractometer (Cu-K_α radiation, Germanium monochromator, Debye–Scherrer geometry) in sealed glass capillaries. Theoretical powder diffraction patterns for **1** and **2** were calculated on the basis of the atom coordinates obtained from single-crystal X-ray analysis by using the program package STOE WinXPOW.[23]

Physical Measurements

UV/Vis absorption spectra of cluster molecules in solution were measured on a Varian Cary 500 spectrophotometer in quartz cuvettes. Solid-state spectra were measured as micron-sized crystalline powders in mineral oil between quartz plates with a Labsphere integrating sphere.

Light scattering experiments were carried out with an ALV-NIBS particle sizer. The time correlation functions were measured with an ALV-5000/E Multiple Tau Digital Correlator. The light source a 3 mW He/Ne-Laser (632.8 nm) is therein combined with a focusing optic and a highly sensitive single photon detector in back-scattering geometry. All of the measurements were carried out at a temperature of 25 °C ± 0.1 °C in quartz cuvettes sealed with a septum to avoid decontamination of the samples with oxygen and water.

Thermogravimetric analyses were run on a thermobalance STA 409 from Netzsch in vacuo (heating rate 2 K/min). The balance was coupled with a quadrupole mass spectrometer QMG 422 from Balzers.

GC-MS spectra were performed on an Agilent Technologies 6869N Network GC System equipped with an Agilent 5973 Network Mass Selective Detector using 30 m DB5 columns.

Acknowledgments

This work was supported by the Deutsch-Israelisches Programm (DIP) and the Deutsche Forschungsgemeinschaft (centre for func-

tional nanostructures CFN). The author is grateful to Prof. Dr. D. Fenske for helpful discussions and for providing excellent working conditions, E. Tröster for her invaluable assistance in the practical work, Dr. P. Scheer for running the TGA and Dr. Dale Cave for careful revision of the manuscript.

[1] V. Soloviev, A. Eichhöfer, D. Fenske, U. Banin, *J. Am. Chem. Soc.* **2000**, *122*, 2673–2674.
[2] V. Soloviev, A. Eichhöfer, D. Fenske, U. Banin; *J. Am. Chem. Soc.* **2001**, *123*, 2354–2364.
[3] A. Eichhöfer, A. Aharoni, U. Banin, *Z. Anorg. Allg. Chem.* **2002**, *628*, 2415–2421.
[4] A. Aharoni, A. Eichhöfer, D. Fenske, U. Banin, *Opt. Mat.* **2003**, *24*, 43–49.
[5] N. Herron, J. C. Calabrese, W. E. Farneth, Y. Wang, *Science* **1993**, *259*, 1426–1428.
[6] T. Vossmeyer, G. Reck, L. Katsikas, E. T. K. Haupt, B. Schulz, H. Weller, *J. Am. Chem. Soc.* **1995**, *117*, 12881–12882.
[7] S. Behrens, M. Bettenhausen, A. C. Deveson, A. Eichhöfer, D. Fenske, A. Lohde, U. Woggon, *Angew. Chem.* **1996**, *108*, 2360–2363; *Angew. Chem. Int. Ed. Engl.* **1996**, *35*, 2215–2218.
[8] J. Rockenberger, L. Tröger, A. L. Rogach, M. Tischer, M. Grundmann, A. Eychmüller, H. Weller, *J. Chem. Phys.* **1998**, *108*(18), 7807–7815.
[9] W. E. Farneth, N. Herron, Y. Wang, *Chem. Mater.* **1992**, *4*, 916–922.
[10] S. L. Cumberland, K. M. Hanif, A. Javier, G. A. Khitrov, G. F. Strouse, S. M. Woessner, C. S. Yun, *Chem. Mater.* **2002**, *14*, 1576–1584.
[11] A. Eichhöfer, E. Tröster, *Eur. J. Inorg. Chem.* **2002**, 2253–2256.
[12] H. Gobrecht, U. Gerhardt, B. Peinemann, A. Tausend, *J. Appl. Phys.* **1961**, *32*, 2246–2250.
[13] D. T. T. Tran, L. M. C. Beltran, C. M. Kowalchuk, N. R. Trefiak, N. J. Taylor, J. F. Corrigan, *Inorg. Chem.* **2002**, *41*(22) 5693–5698.
[14] P. Scherrer, *Göttinger Nachrichten* **1918**, *2*, 98; H. Krischner, *Einführung in die Röntgenfeinstrukturanalyse*, 4te überarbeitete Auflage, Vieweg, Braunschweig, **1990**, 108.
[15] A. Eichhöfer, C. v. Hänisch, M. Jacobsohn, U. Banin, *Mat. Res. Soc. Symp.* **200**1, 636, D9.53.1–D9.53.9.
[16] A. Eichhöfer, P. Deglmann, *Eur. J. Inorg. Chem.* **2004**, 349–355.
[17] I. G. Dance, A. Choy, M. L. Scudder, *J. Am. Chem. Soc.* **1984**, *106*, 6285–6295.
[18] N. Miyoshi, H. Ishii, K. Kondo, S. Mui, N. Sonoda, *Synthesis* **1979**, 301–304.
[19] H. Schmidt, H. Ruf, *Z. Anorg. Allg. Chem.* **1963**, *321*, 270–273.
[20] G. M. Sheldrick, *SHELXTL PC version 5.1 An Integrated System for Solving, Refining, and Displaying Crystal Structures from Diffraction Data*, Bruker Analytical X-ray Systems, Karlsruhe, **2000**.
[21] E. Keller, *SCHAKAL 97, A Computer Program for the Graphic Representation of Molecular and Crystallographic Models*, University of Freiburg, **1997**.
[22] K. Brandenburg, *DIAMOND version 2.1d, Visual Crystal Structure Information System*, Bonn, **2000**.
[23] STOE, *WinXPOW*, STOE & Cie GmbH, Darmstadt, **2000**..

Received: September 24, 2004

 © 2005 Wiley-VCH Verlag GmbH & Co. KGaA, Weinheim

Pyrazole-Tethered Heteroditopic Ligands and Their Transition Metal Complexes: Synthesis, Structure, and Reactivity

Anuradha Mukherjee,[a] U. Subramanyam,[b] Vedavati G. Puranik,[c] Thekke P. Mohandas,[b] and Amitabha Sarkar*[a]

Keywords: Pyrazole / Hemilabile ligands / Nickel / Copper / Cobalt / Oligomerization

Various pyrazole-based P,N (**2a–c**) and N,N (**3a–b**) ligands have been synthesized. Using representative ligands, Ni^{II}, Co^{II}, Cu^{II}, and Cu^{I} complexes have been prepared and structurally characterized by crystallography. During complexation of Co^{II} and Cu^{II} salts, the phosphane part of the P,N ligand oxidized to phosphane oxide. For N,N donor ligands, a dimeric chloro-bridged Ni^{II} complex was obtained. Ni^{II} complex **4** is an active catalyst for ethylene oligomerization. (© Wiley-VCH Verlag GmbH & Co. KGaA, 69451 Weinheim, Germany, 2005)

Introduction

Trofimenko[1] introduced pyrazole as a unique donor in coordination chemistry as tris(pyrazolyl)borate (Tp) and related ligands during late 1960s and early 1970s. A rich and parallel chemistry of Tp and its analogs[2] (often called 'scorpionates') developed subsequently in relation to metal-cyclopentadienyl complexes. Bidentate bis-pyrazolyl ligands are also known[3] and mixed donor ligands (pyrazole in combination with another type of donor atom or group) are currently gaining prominence, especially for their ability to stabilize different metals in diverse oxidation states.

The use of hemilabile ligands in coordination and organometallic chemistry has increased recently because of their potential application in catalysis. They are multidentate ligands that feature one weakly coordinating donor. This donor atom readily dissociates from the metal during catalysis, to accommodate reacting groups on the metal, but recombines with the metal when a coordinative unsaturation develops to stabilize the catalytic intermediate. Mixed ligands containing phosphorus along with oxygen, nitrogen or sulfur donor atoms have been designed in catalytic reactions such as ethylene polymerization,[4] the Heck reaction,[5] Suzuki coupling.[6] Hybrid P,N-type ligands confer high reactivity and selectivity in several catalytic reactions.[7] In continuation of our interest in developing pyrazole-based chelates,[8] we initiated a program for the design and synthesis of mixed donor ligands featuring substituted pyrazoles.

We intended to examine a set of new ligands for late transition elements, especially those relevant for catalysis of C–C (polymerization, Suzuki, Heck, Sonogashira) and C–N (aromatic amination) bond formation. We recently reported preliminary results of Suzuki and amination reactions featuring pyrazole-tethered phosphanes.[9a] Here, we report in detail the synthesis and complete characterization of those ligands and their late transition metal complexes, and initial observations on the application of a typical nickel complex in ethylene oligomerization.

[a] Indian Association for the Cultivation of Science, Jadavpur, Kolkata-700 032, India
[b] Polymer Chemistry Division, National Chemical Laboratory, Pune-411 008, India
[c] Physical Chemistry Division, National Chemical Laboratory, Pune-411 008, India

Results and Discussions

Synthesis of Ligands

Of the two sets of bidentate ligands used in the present study, one has a phosphane (**2a–c)** and other an amine (**3a–b**) in combination with pyrazole moiety.

3,5-Dimethyl-*N*-phenylpyrazole was synthesized by the action of acetylacetone with phenylhydrazine[10] (Scheme 1). This method was suitable when 3 and 5 substituents of pyrazole were identical. To synthesize unsymmetrically substituted pyrazoles (**1b** and **1c**) we followed an alternative route whereby substituted pyrazoles are coupled with phenylboronic acid by copper acetate in the presence of pyridine[11] (Scheme 2). This procedure provided regiochemically pure derivatives – the bulky substituent (*t*Bu or mesityl) is confined to 3-position of the pyrazole. Compounds **1a–c**, were characterized unambiguously by their ^{1}H and ^{13}C NMR spectroscopic data.

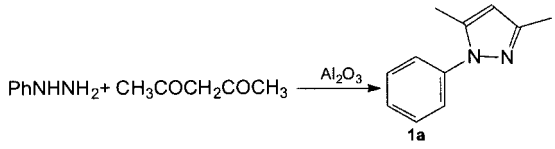

Scheme 1.

 © 2005 Wiley-VCH Verlag GmbH & Co. KGaA, Weinheim DOI: 10.1002/ejic.200400818

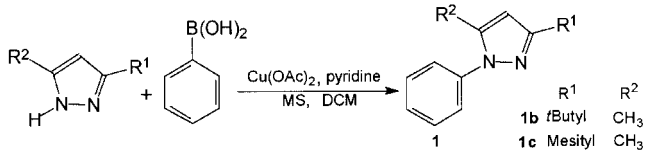

Scheme 2.

Directed lithiation on **1a** and **1b** at 0 °C using *n*BuLi and quenched with PPh_2Cl afforded the potentially bidentate ligands **2a** and **2b** (Scheme 3). Lithiation of **1c** proved difficult and required *s*BuLi. Compounds **2a**–**c** are solids that were purified by column chromatography or crystallization and characterized by spectroscopic data and elemental analysis.[9b] ^{31}P NMR absorptions appear at –23.89 (**2a**), –13.23 (**2b**) and –20.70 (**2c**) ppm.

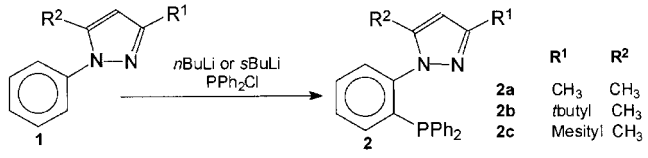

Scheme 3.

To prepare a set of ligands with nitrogen as a donor in place of phosphane we treated 2-nitrophenylhydrazine with acetylacetone or benzoylacetone followed by reduction of the nitro group with Pd/C. Reductive methylation of the resulting amine afforded the desired ligand (**3**) (Scheme 4). Reaction of benzoylacetone yielded only one product regioisomer, indicating that the hydrazine preferentially attacks the acetyl group.

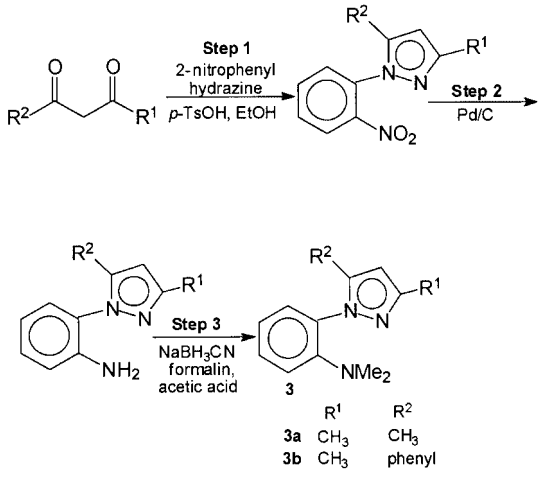

Scheme 4.

Preparation of Metal Complexes

Ligand **2a** was used to synthesize representative transition metal complexes. Addition of a solution of ligand **2a** in acetonitrile to anhydrous $NiCl_2$ dissolved in acetonitrile resulted in a change of colour from yellow to violet after refluxing for 6 h, affording a violet precipitate as product. Complex **4** was isolated by filtration and recrystallized from acetonitrile to provide an analytically pure sample (Scheme 5). The NMR spectrum of this high-spin complex could not be recorded.

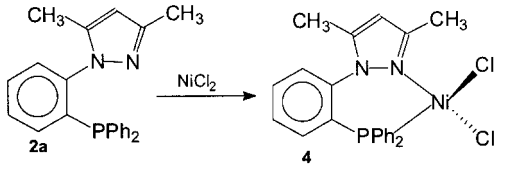

Scheme 5.

A single crystal of complex **4** suitable for structure analysis was grown in acetonitrile solution. Figure 1 depicts an ORTEP view of the so-determined molecular structure of **4**. A distorted tetrahedral geometry is seen around the nickel in a six-membered ring. It is strongly similar to a phosphanylaryl oxazoline complex[12] in terms of geometrical parameters, except that the difference in bond lengths of two Ni–halide bonds [0.021 Å between Ni–Cl1, 2.180(2) Å, and Ni–Cl, 2 2.201(2) Å] in **4** is more pronounced than in the reported complex (0.008 Å).

Nickel(II) complexes **5a** and **5b** were synthesized by the addition of ligands **3a** and **3b** to a solution of [Ni(DME)-Cl_2] in dichloromethane, resulting in an instant colour change from yellow to bright orange. A reddish orange solid was then filtered off and purified by crystallization from acetonitrile (Scheme 6). The crystal structure of **5b** (Figure 2) was then determined, revealing a bridged dinuclear species. The N3–Ni–Cl2A [170.4(4)°] bond angle is close to 180° while N1–Ni–N3 [83.18(5)°], Ni–Cl2–Ni1A [91.44(2)°] and N3–Ni–Cl1 [94.74(4)°] are close to 90°, establishing a square-pyramidal structure of complex **5b**. The Ni–Ni1A bond is 3.44 Å long.

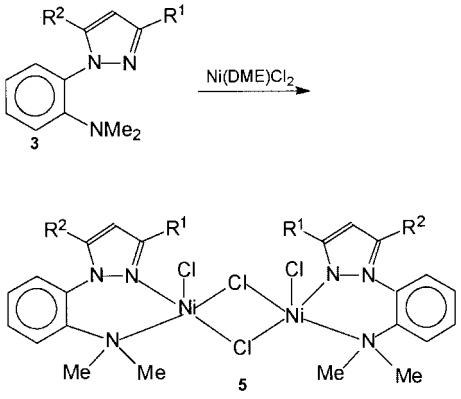

Scheme 6.

Addition of a solution of ligand **2a** in acetonitrile to anhydrous $CoCl_2$ dissolved in acetonitrile resulted in an instant color change, from pale blue to deep blue. The reaction mixture was then stirred and heated under reflux for 6 h. Complex **6** was collected by filtration and crystallized from hot acetonitrile to afford blue needle-shaped crystals. The NMR spectra could not recorded, as the product was paramagnetic. Ligand **2a** reacts with anhydrous $CuCl_2$ in

 © 2005 Wiley-VCH Verlag GmbH & Co. KGaA, Weinheim

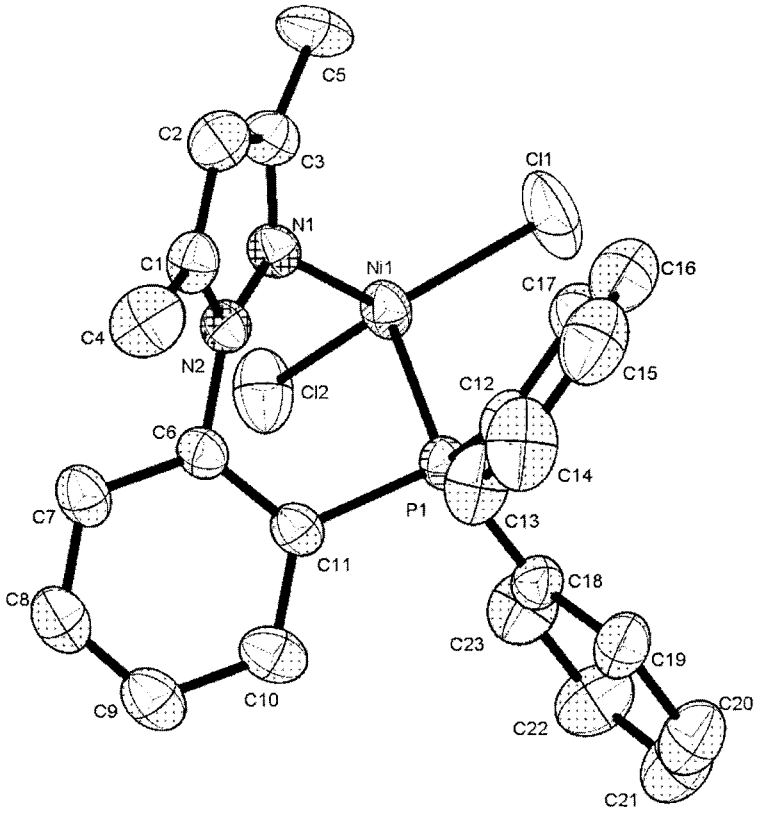

Figure 1. ORTEP diagram of Ni^{II} complex 4; ellipsoids drawn at 50% probability. Selected bond lengths [Å] and bond angles [°]: N1–N2 1.373(5), Ni–N1 2.003(4), Ni–Cl1 2.180(2), Ni–Cl2 2.201(2), Ni–P1 2.281(2). N1–Ni–P1 88.22(12), Cl1–Ni–Cl2 121.29(8), N2–N1–Ni 123.0(3), N1–Ni–Cl1 123.82 (14), N1–Ni–Cl2 104.07(13).

acetonitrile under identical conditions to furnish bright green, paramagnetic crystals of complex **7** (Scheme 7). Conversely, the reaction of ligand **2a** with CuCl in acetonitrile took 12 h to ensure a substantial reaction. Product **8** was obtained as a pale yellow powder, which was recrystallized from acetonitrile to obtain X-ray grade crystals.

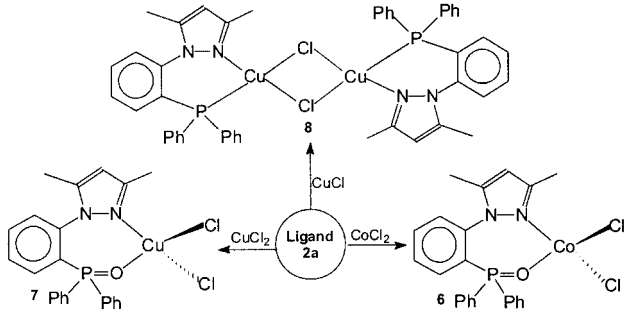

Scheme 7.

Crystal structures of complexes **6**–**8** were determined. Interestingly, the Co^{II} and Cu^{II} complexes **6** and **7** are both seven-membered chelates, where the phosphane has been converted into phosphane oxide and the ligand **2a** is coordinated to the metal through the oxygen rather than phosphorus (Figure 3 and Figure 4). For complex **7**, the angle Cu–O–P [122.40(11)°] is suggestive of an sp^2-hybridized oxygen, unlike in $Cu(TPPO)_2Cl_2$ where the angle is considerably greater [Cu–O–P 150.9(3)°].[13a] The Co–O–P bond angle in **6** is 121.72(6)°, which is comparable with that in **7**, but smaller than the Co–O–P angle (153°) in $CoCl_2(OPPh_3)_2$.[13b] Co–O [1.991(11) Å] and P–O [1.507(12) Å] bond lengths in **6** are also comparable with those in **7** {Cu–O [1.995(18) Å] and P–O [1.506(18) Å]}. The P–O bonds of **6** [1.507(12) Å] and 7 [1.506(18) Å] are longer than that of free Ph_3PO [1.46(1) Å].

The Cu^I complex **8**, however, revealed a chloro-bridged, dimeric structure (Figure 5) that has an inversion symmetry overall, and a molecule of the solvent acetonitrile. The copper centers of **8** are 3.101 Å apart, which is comparable with the Cu–Cu′ bond length [3.066(1) Å] of the complex $[(PCy_3)CuCl]_2$.[13c] The Cu–P bond length [2.220(9) Å] of **8** is longer than Cu–P [2.183(2) Å] that of $[(PCy_3)CuCl]_2$. The ^1H NMR spectrum of this diamagnetic complex **8** displays sharp signals – three-proton methyl signals appear at different positions compared to the parent ligand (2.40 and 1.81 ppm in **8** vis-a-vis 2.19 and 2.00 ppm in ligand **2a**). One of the methyl signals in the complex is broad, indicating stereochemical non-rigidity in the molecule. The relative shielding of the methyl signal (δ = 1.81 ppm vs. 2.00 ppm) is possibly a reflection of the anisotropic effect – one methyl group lies in the shielding zone of a neighboring phenyl ring The pyrazole-4H appears at δ = 5.69 ppm, shifted upfield

 © 2005 Wiley-VCH Verlag GmbH & Co. KGaA, Weinheim

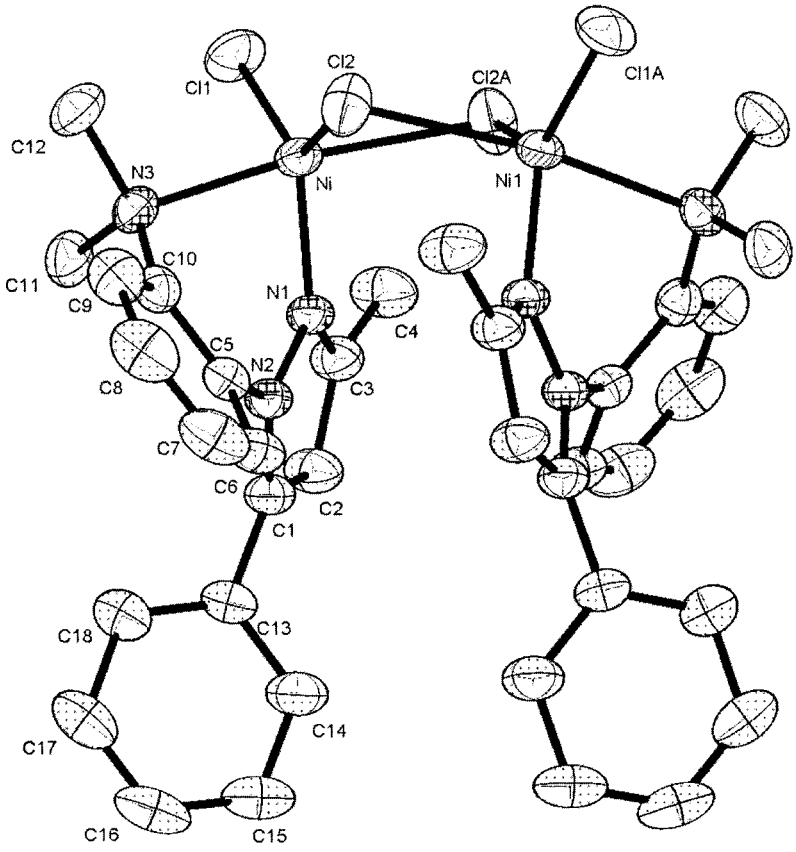

Figure 2. ORTEP diagram of Ni complex **5b**; ellipsoids drawn at 50% probability. Selected bond lengths [Å] and bond angles [°]: Ni–N1 2.025(2), Ni–N3 2.210(2), Ni–Cl1 2.281(7), Ni–Cl2 2.349(9), Ni–Cl2A 2.461(9), Cl2–Ni2A 2.461(9). N1–Ni–N3 83.18(5), Ni–Cl2–Ni1A 91.44(2), N3–Ni–Cl1 94.74(4), N1–Ni–Cl2 121.61(4), N1–Ni–Cl1 108.03(5), Cl1–Ni–Cl2 130.36(3), N3–Ni–Cl2A 170.4(4).

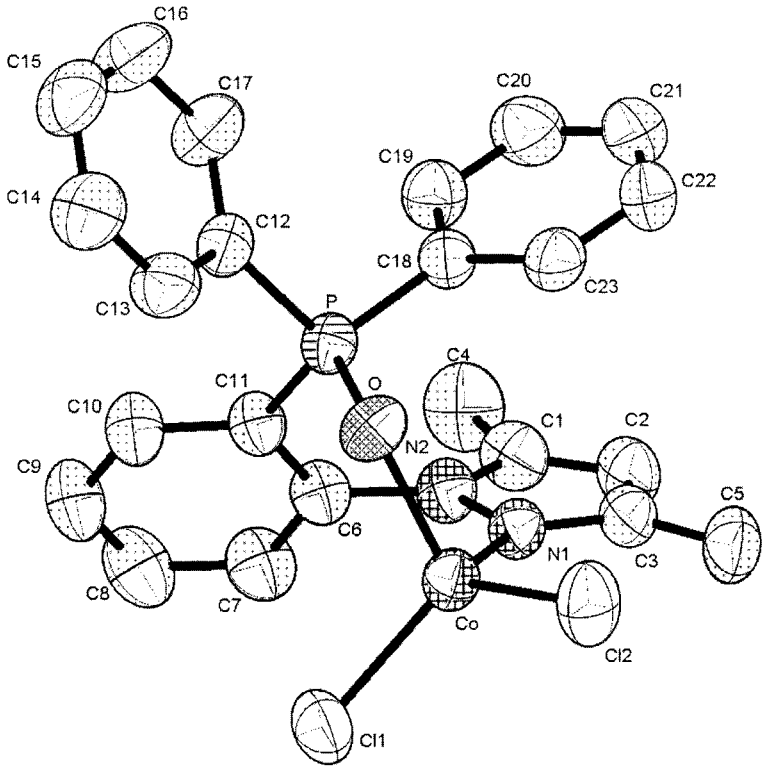

Figure 3. ORTEP diagram of complex **6**; ellipsoids drawn at 50% probability. Selected bond lengths [Å] and bond angles [°]: Co–O 1.9911(11), P–O 1.5075(12), P–O–Co 121.72(6), O–Co–Cl1 112.29(4), O–Co–Cl2 103.70(4), Cl1–Co–Cl2 116.54(2).

 © 2005 Wiley-VCH Verlag GmbH & Co. KGaA, Weinheim

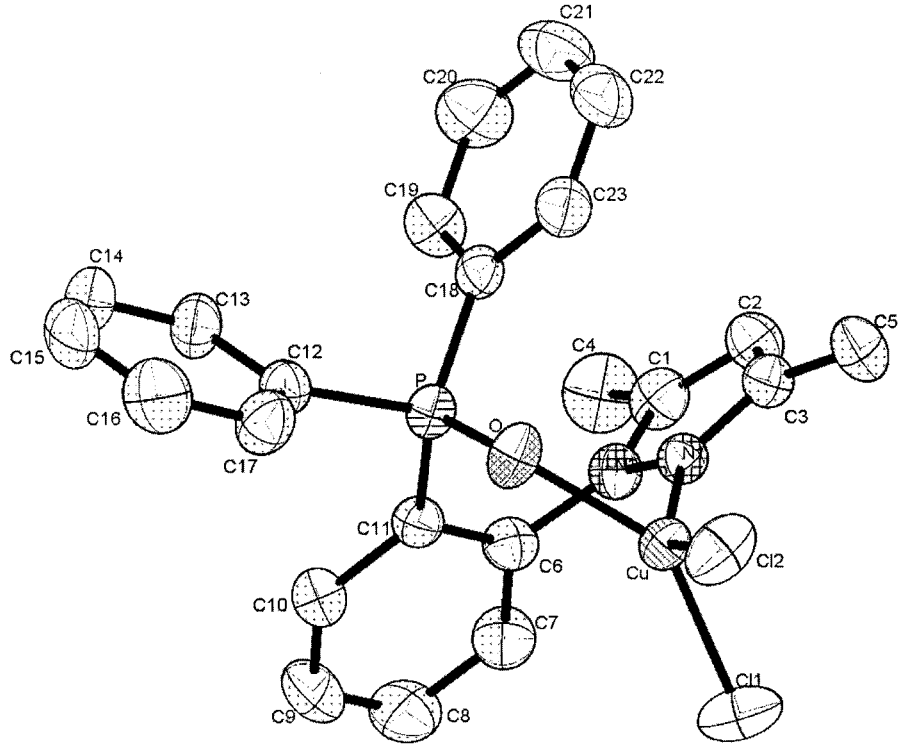

Figure 4. ORTEP diagram of complex **7**; ellipsoids drawn at 50% probability. Selected bond lengths [Å] and bond angles [°]: Cu–O 1.9952(18), P–O 1.5064(18), P–O–Cu 122.40(11), O–Cu–Cl1 144.91(7), O–Cu–Cl2 93.09(6), Cl2–Cu–Cl1 100.84(3).

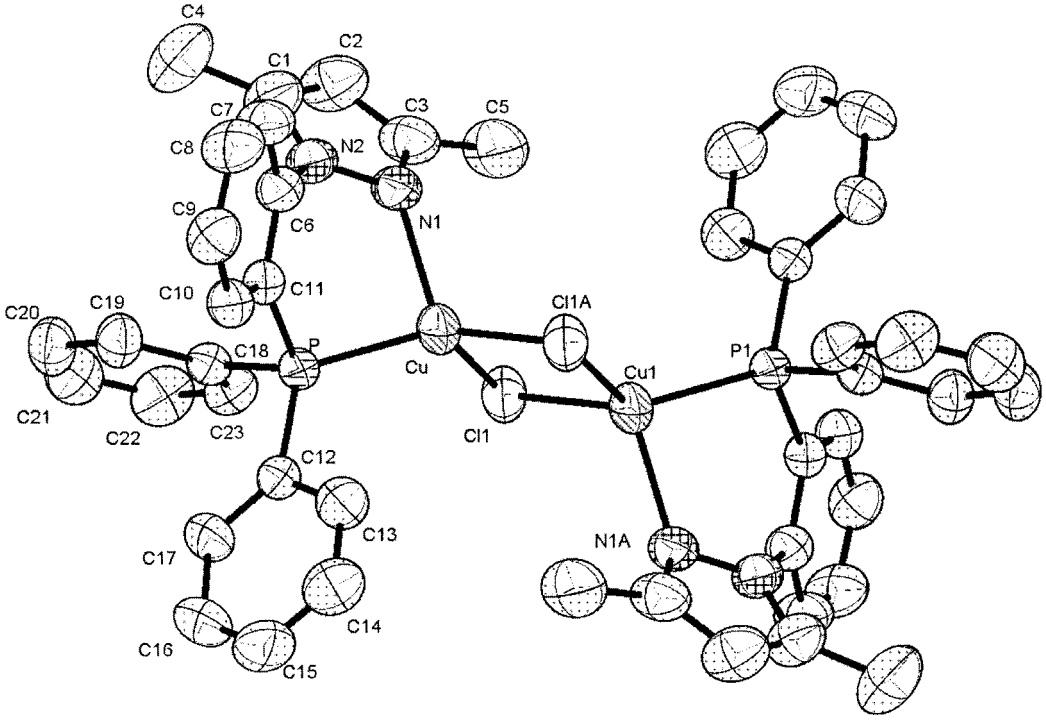

Figure 5. ORTEP diagram of complex **8**; ellipsoids drawn at 50% probability. Selected bond lengths [Å] and bond angles [°]: Cu–P 2.2205(9), Cu–Cl1 2.4140(9), Cu–Cl1A 2.4111(8), Cu–N1 2.186(2), N1–Cu–P 91.07(5), N1–Cu–Cl1 113.31(6), N1–Cu–Cl1A 111.96(7), Cl1A–Cu–Cl1 100.03(2), P–Cu–Cl1 118.83(3).

 © 2005 Wiley-VCH Verlag GmbH & Co. KGaA, Weinheim

compared to 5.86 in the free ligand **2a**. Similarly, the ^{31}P NMR of **8** is at –16.37 ppm, compared with δ = –23.89 ppm for the free ligand **2a**. The relative shielding of the pyrazole-4H signal with respect to corresponding signal in the parent ligand can possibly be attributed to the π-acceptor property of pyrazole in combination with a d^{10} metal nucleus.

Since complexation was performed under argon, the oxidation of phosphane was not anticipated. Elemental analyses of complexes **6** and **7** were not consistent with the formulation of the desired phosphane complexes. After the crystal structures were determined, the presence of phosphane oxide as ligand was established beyond doubt. The observed P=O absorption bands, it was then realized, were typical of a bent M–O–P structure, which differs from that of a complex with linear M–O–P arrangement.[14]

The mechanism of oxidation by a trace amount of oxygen is probably akin to the oxidation of tributylphosphane catalyzed by Co^{II} reported earlier. Yet, the facile oxidation of triarylphosphane in this instance presents an intriguing contrast to a previous report that described difficulty in oxidizing Ph_3P by $Co(acac)_2$.[15]

The unpaired electron of such a metal center (d^7 or d^9) probably readily interacts with the paramagnetic oxygen molecules present in trace amounts to generate the reactive intermediate that eventually transfers oxygen to the phosphane.[16] Once the structures were known, the reactions were repeated in an open vessel and yields were improved considerably (up to 90%).

Complexation of $CoCl_2$ and $CuCl_2$ was repeated using fourfold an excess of the ligand **2a**. Recovered ligand showed no evidence of oxidation while the complexes indeed featured the P=O group. This suggests that these metals do not catalytically oxidize the phosphorus to phosphane oxide.

Cu^{II} coordination chemistry is dominated by N or O as donor atom followed by chlorine, bromine and sulfur. The soft donor atom P is uncommon for Cu^{II} despite its frequent occurrence in Cu^{I} coordination chemistry. In a dimeric structure, phosphane can be present as a ligand, as seen in the dinuclear complex $[Cu_2(MeCO_2)_4(PPh_3)_2]$.[17] For mononuclear complexes, this is indeed rare. Therefore, complex **7** attains stability by oxidation of the phosphane to a phosphane oxide in the presence of oxygen. To the best of our knowledge, no precedent for such an oxidation within the coordination sphere of the Cu^{II} exists. Conversely, the dimeric structure of the Cu^{I} complex **7** is unexceptional.

Ethylene Oligomerization

Several nickel or palladium complexes are efficient catalysts for the oligomerization of ethylene.[18a] The degree of branching in ethylene oligomers is an important parameter for catalyst optimization since highly branched oligomers in the C_6–C_{20} range find wide use in lubrication and other applications. Mohring and Fink reported[18b] that aminobis(imino)phosphorane nickel complexes polymerize ethylene to low molecular weight branched polyethylene. More recently, Brookhart and co-workers described a neutral, SHOP-type catalyst, featuring an anionic P–N chelating ligand,[19] that can produce branched polymers/oligomers. The synthesis and coordination behavior of new P,N ligands, therefore, continues to attract interest,[20–22] owing to the possibility of independently tuning the steric and electronic attributes of different donor groups.

Our new nickel complex **4**, featuring a chelating pyrazole ligand, is an active catalyst for ethylene oligomerization. It efficiently polymerizes ethylene under mild conditions in the presence of methylaluminoxane (MAO) to yield highly branched oligomers with a relatively narrow molecular weight distribution. Table 1 and Table 2 display the results. Nickel complexes **5a** and **5b** show no activity for ethylene polymerization in the presence of MAO.

Table 1. Oligomerization of ethylene using a nickel-based catalyst system.

Entry	Ethylene [bar]	Catalyst [mol] × 10^5	MAO [mol] × 10^2	[Al/Ni]	Temp. [°C]	Yield [mg]	TOF[a]
1	1	2.1	2.1	1000	25	600	1045
2	5	2.1	2.1	1000	25	700	1219
3	5	2.1	2.1	1000	40	800	1365
4	1	2.1	1.05	500	25	500	871

Solvent: toluene [a] TOF (turn over frequency) = mol of polymer per mol of catalyst per hour.

Table 2. Characterization of oligomers.

Entry	GPC[a]			DP	DB[b]		Branch distribution[c]				End group [mol%][d]		
	M_n	M_w	MWD	(^{1}H NMR)	^{1}H NMR	^{13}C NMR	C_1	C_2	C_3	≥ C_4	–CH=CH–	–CH=CH_2	–CH=CMe_2
1	1630	3120	1.9	40	113	134	63	16	5	48	93	5	2
2	1560	2460	1.6	33	109	136	63	19	7	49	94	3	3
3	1440	2325	1.6	36	109	132	63	17	5	45	95	3	2
4	1600	2600	1.6	39	107	130	60	14	5	51	94	4	2

[a] For GPC, polystyrene was used as standard. [b] DB (degree of branching): branches per 1000 C atoms. [c] Calculated from ^{13}C NMR spectra. [d] Calculated from ^{1}H NMR spectra.

 © 2005 Wiley-VCH Verlag GmbH & Co. KGaA, Weinheim

Preliminary experiments indicate that the turnover frequency marginally increases with increasing ethylene pressure (entries 1 and 2), polymerization temperature (entries 2 and 3) and MAO concentration (entries 1 and 4).

The degree of polymerization (DP) and degree of branching were determined from the ^{1}H NMR spectrum of the oligomers following a reported method.[4a,19] The oligomers feature predominantly internal alkenes (ca. 90%), while the rest consists of 1-alkenes and some with CH_2=C(Me)C– end groups. An average of 125 branches per 1000 carbon atoms, a significant number, is estimated from the ^{1}H and ^{13}C NMR spectra (Table 2).

The average chain length of C_{60}–C_{80} and extensive branching are two noteworthy features of this new nickel catalyst. Extensive branching probably results from the 'chain running' behavior[4a] of nickel.

Conclusions

Two sets of new pyrazole-tethered bidentate ligands can form stable complexes with late transition metals such as Co^{II}, Cu^{II}, Ni^{II}, and Cu^{I}. Representative complexes were structurally characterized by crystal structure determination. For the first two metal ions, the phosphane of the ligand was readily oxidized to phosphane oxide, presumably within the metal coordination sphere. The new nickel complex activated by MAO is a highly active catalyst for ethylene oligomerization. Pyrazole-derived ligands seem to offer an alternative and viable motif for ligand design. The results are encouraging and warrant a systematic variation of donor groups and tuning of steric and electronic factors on this ligand skeleton in relation to catalytic performance and microstructure of polymer products, which is currently being pursued in our laboratory.

Experimental Section

General Procedure: All manipulations were carried out under argon. Dried solvents were used. Reagents and chemicals were used as received from Aldrich and Lancaster. M.p.s (°C) (recorded on a Thermonik Campbell melting point apparatus) are uncorrected. IR spectra were recorded on a Shimadzu FTIR-8400 spectrometer. NMR spectra (^{1}H, ^{13}C and ^{31}P) were recorded on Bruker AC200, MSL300 or DRX500 spectrometers. All crystal data were corrected for Lorentzian, polarization and absorption effects. SHELX-97 (ShelxTL)[24] was used for structure solution and full-matrix least-squares refinement on F^2 (see also Table 3 and Table 4). Hydrogen atoms were included in the refinement as per the riding model. CCDC-250550 (for **5b**), -250551 (for **6**), -250552 (for **7**), -250553 (for **8**) and -250554 (for **4**) contain supplementary crystallographic data for this paper. These data can be obtained free of charge from The Cambridge Crystallographic Data Centre via www.ccdc.cam.ac.uk/data_request/cif.

Oligomerization of Ethylene: Toluene (S.D. Fine Chemicals, India) was refluxed over sodium/benzophenone and distilled under nitrogen before use. Polymerization grade ethylene was obtained from the gas cracker complex of the Indian Petrochemical Corporation, Nagothane, India. Methylaluminoxane from Witco, Germany, was used as received. NMR Spectroscopy: ^{1}H and ^{13}C NMR spectra are recorded on a high-resolution Bruker 500 MHz spectrometer. Samples were dissolved in $CDCl_3$ in 5 mm tubes at 30 °C. Quantitative ^{13}C NMR spectra were recorded with a 40° flip angle and a delay of 8 s. GC: Gas Chromatograms were obtained on a Perkin–Elmer GC 2001. The following parameters were used for analysis of oligomer. Column: Poly Wax. Operating conditions: over: 100–300 °C, ramp rate: 7 °C min^{-1}, injector: 300 °C, detector: 320 °C, carrier gas (nitrogen): 0.7 psi. GPC: molecular weight and molecular weight distribution (MWD) of the oligomers were determined using a Thermofinnigan gel permeation chromatograph equipped with a refractive index detector and μ-styraged columns (10^5 to 50 Å), based on polystyrene standards, at 25 °C using chloroform as solvent with a 1 mL min^{-1} flow rate. Data were processed using the software PSS WinGPC scientific.

Table 3. Crystal data and structure refinement of complexes **4** and **5b**.

	Complex **4**	Complex **5b**
Empirical formula	$C_{23}H_{21}Cl_2N_2NiP$	$C_{19}H_{21}Cl_2N_{3.50}Ni$
Formula mass	486.10	428.00
Temperature [K]	293(2)	293(2)
Wavelength [Å]	0.71073	0.71073
Crystal system, space group	monoclinic, $P2_1/C$	monoclinic, $P2_n$
a [Å]	18.739 (2)	10.873(3)
b [Å]	10.812 (8)	12.749(4)
c [Å]	24.418 (2)	15.409(5)
β [°]	113.238(5)	109.640(5)
Volume [Å^3]	4545.9 (6)	2011.8(11)
Absorption coefficient [mm^{-1}]	1.172	1.238
$F_{(000)}$	2104	886
Crystal size [mm]	0.154 × 0.144 × 0.10	0.42 × 0.26 × 0.17
θ range for data collection (°)	1.18 to 28.20	1.60 to 28.16
Limiting indices	$-24 \le h \le 13$ $-13 \le k \le 13$ $-26 \le l \le 32$	$-14 \le h \le 13$ $-16 \le k \le 16$ $-20 \le l \le 20$
Data/restraints/parameters	10336/0/591	4735/0/243
Goodness of fit on F^2	0.860	1.059
Final R indices [$I > 2\sigma(I)$]	R1 = 0.0575, $wR2$ = 0.1359	R1 = 0.0328, $wR2$ = 0.0864
R indices (all data)	R1 = 0.1440, $wR2$ = 0.1602	R1 = 0.0368, $wR2$ = 0.0893
Largest diff. peak and hole [e Å^{-3}]	0.504 and –0.319	0.640 and –0.341

Preparation of Ligand 2a: nBuLi (15 mL 1.41 M, 21.15 mmol) was added dropwise at 0 °C to a solution of N-phenyl-3,5-dimethylpyrazole (**1a**)[10] (3.44 g, 20 mmol) in dry THF (40 mL). The solution was, initially, yellow but changed successively to blue, yellow, and brown. The reaction mixture was then stirred for 4 to 5 h followed by addition of PPh_2Cl (3.6 mL, 20 mmol) at 0 °C. Stirring was continued for an additional 3 h. The reaction was quenched with water and extracted with ethyl acetate (40 mL × 3). The combined organic phase was dried over Na_2SO_4 and concentrated. Crude semi-solid product was purified by flash chromatography followed by crystallization to obtain **2a** as a yellowish white solid (4 g, 56%). M.p. 110 °C. IR (Nujol): 1552 cm^{-1}. ^{1}H NMR ($CDCl_3$, 200 MHz): δ = 2.00 (s, 3 H, CH_3), 2.19 (s, 3 H, CH_3), 5.86 (s, 1 H, PzH), 7.31 (br. s, 14 H, PhH) ppm. ^{13}C NMR ($CDCl_3$, 50.32 MHz): δ = 11.4, 13.2, 105.1, 127.7, 127.9, 128.1, 128.4, 129.1, 133.5, 133.9, 134.0, 135.9, 136.1, 137.4, 137.8, 139.9, 142.8, 143.2, 147.7 ppm. ^{31}P

 © 2005 Wiley-VCH Verlag GmbH & Co. KGaA, Weinheim

Table 4. Crystal data and structure refinement of complexes **6**–**8**.

	Complex **6**	Complex **7**	Complex **8**
Empirical formula	$C_{23}H_{21}Cl_2CoN_2OP$	$C_{23}H_{21}Cl_2CuN_2OP$	$2[C_{23}H_{21}Cl_2CuN_2P]C_2H_3N$
Formula mass	502.25	506.86	951.87
Temperature [K]	293(2)	293(2)	293(2)
Wavelength [Å]	0.71073	0.71073	0.71073
Crystal system, space group	triclinic, $P\bar{1}$	orthorhombic, $P2_1P2_1P2_1$	triclinic, $P\bar{1}$
a [Å]	8.987(6)	8.771(1)	9.300(3)
b [Å]	10.199(7)	13.573(2)	10.701(3)
c [Å]	12.862(9)	19.334(2)	13.859(4)
α [°]	98.303(1)	–	72.466(4)
β [°]	91.904(1)	90	71.323(4)
γ [°]	95.825(1)	–	79.023(5)
Volume [Å^3]	1159.13(14)	2301.6(5)	1239.1(6)
Z, calculated density [mg m^{-3}]	2, 1.439	4, 1.463	2, 1.331
Absorption coefficient [mm^{-1}]	1.057	1.268	1.070
$F(_{000})$	514	1036	512
Crystal size [mm]	0.39 × 0.34 × 0.09	0.31 × 0.26 × 0.21	0.80 × 0.32 × 0.21
θ range for data collection [°]	1.60–28.26	1.83–27.69	1.61–27.87
Limiting indices	$-11 \le h \le 11$ $-13 \le k \le 13$ $-16 \le l \le 16$	$-11 \le h \le 11$ $-17 \le k \le 9$ $-24 \le l \le 24$	$-11 \le h \le 12$ $-13 \le k \le 14$ $-17 \le l \le 17$
Reflections collected/ unique	13222/ 5225 [R(int) = 0.0290]	13181/ 4983 [R(int) = 0.0246]	13601/5423 [R(int) = 0.0327]
Completeness to θ	= 28.26, 91.1%	= 27.69, 95.0%	= 27.87, 91.7%
Max. and min. transmission	0.9155 and 0.6833	0.7740 and 0.6931	0.8049 and 0.4819
Refinement method	full matrix least-squares on F^2	full matrix least-squares on F^2	full matrix least-squares on F^2
Data/restraints/parameters	5225/0/273	4983/0/273	5423/0/283
Goodness-of-fit on F^2	1.055	0.955	1.077
Final R indices [$I > 2\sigma(I)$]	$R1$ = 0.0331, $wR2$ = 0.0925	$R1$ = 0.0309, $wR2$ = 0.0646	$R1$ = 0.0434, $wR2$ = 0.1280
R indices (all data)	$R1$ = 0.0374, $wR2$ = 0.0950	$R1$ = 0.0369, $wR2$ = 0.0665	$R1$ = 0.0506, $wR2$ = 0.1333
Absolute structure parameter	–	–0.018(10)	–
Largest diff. peak and hole [e Å^{-3}]	0.335 and –0.281	0.433 and –0.190	1.082 and –0.384

NMR ($CDCl_3$, 81.02 MHz): δ = –23.89 ppm. $C_{23}H_{21}N_2P$ (356.40): calcd. C 77.52, H 5.89, N 7.26; found C 77.29, H 5.64, N 7.24.

Preparation of 1b: First we prepared pivaloylacetone, which on reaction with hydrazine hydrate yielded 3(5)-*tert*-butyl-5(3)-methylpyrazole.[23] Copper acetate (3.32 g, 16.62 mmol), pyridine (1.8 mL, 22.17 mmol), phenyl boronic acid (2.67 g, 22.17 mmol) and molecular sieve, dichloromethane (30 mL) were then added to the mixture of 3(5)-*tert*-butyl-5(3)-methylpyrazole (1.53 g, 11.08 mmol), and the resultant mixture was stirred for 2 days under air. Crude product was purified by column chromatography. Yield: 1.6 g (70%). ^{1}H NMR ($CDCl_3$, 200 MHz): δ = 1.43 [s, 9 H, $C(CH_3)_3$], 2.32 (s, 3 H, CH_3), 6.12 (s,1 H, PzH), 7.36–7.48 (m, 5 H, PhH). ^{13}C NMR ($CDCl_3$, 50.32 MHz): δ = 12.4, 30.5, 32.0, 103.6, 124.7, 126.9, 128.8, 138.6, 140.2, 162.0. $C_{14}H_{18}N_2$ (214.31): calcd. C 78.5, H 8.41, N 13.08; found: C 78.3, H 8.39, N 13.07.

Preparation of Ligand 2b: *n*BuLi (2.3 mL of 1.6 M, 2.55 mmol) was added dropwise to *N*-phenyl-3-*tert*-butyl-5-methylpyrazole (0.53 g, 2.48 mmol) in THF (3 mL) at 0 °C. The ice bath was removed after addition of *n*BuLi. The reaction mixture gradually changed to yellow and then brown, and stirring was continued for 6 h. PPh_2Cl (0.56 mL, 2.55 mmol) was then added at 0 °C and stirring continued for another 4 h. After the usual work up, semi-solid product was obtained that was purified by column chromatography. Yield: 0.47 g (48%); m.p. 99.5 °C. IR (neat): 1552 cm^{-1}. ^{1}H NMR ($CDCl_3$, 200 MHz): δ = 1.22 [s, 9 H, $C(CH)_3$], 2.21 (s, 3 H, CH_3), 6.04 (s, 1 H, PzH), 7.29–7.46 (m, 14 H, PhH) ppm. ^{13}C NMR ($CDCl_3$, 50.32 MHz): δ = 11.9, 30.3, 31.8, 102.2, 127.8, 128.2, 128.5, 129.3, 133.7, 134.2, 134.7, 136.9, 137.6, 137.9, 139.3, 143.6, 144.1, 161.3 ppm. ^{31}P NMR ($CDCl_3$, 81.02 MHz): δ = –13.23 ppm. $C_{26}H_{27}N_2P$ (398.48): calcd. C 78.39, H 6.78, N 7.03; found C 78.32, H 6.67, N 6.98.

Preparation of Compound 1c: 3-Mesityl-5-methyl-*N*-phenylpyrazole (**1c**) was prepared by *N*-phenylation of 3(5)-mesityl-5(3)-methylpyrazole (0.759 g, 3.79 mmol) using phenyl boronic acid (0.918 g, 7.59 mmol) following the above procedure [copper acetate (1.14 g, 5.68 mmol), pyridine (0.61 mL, 7.59 mmol)]. Yield: 0.9 g (86%); m.p. 73–75 °C. ^{1}H NMR ($CDCl_3$, 300 MHz): δ = 2.24 (s, 6 H, $2CH_3$), 2.34 (s, 3 H, CH_3), 2.46 (s, 3 H, CH_3), 6.14 (s, 1 H, PzH), 6.95 (s, 2 H, PhH), 7.03–7.58 (m, 5 H, PhH) ppm. ^{13}C NMR ($CDCl_3$, 75.47 MHz): δ = 12.7, 20.5, 21.0, 108.1, 118.8, 122.4, 123.2, 124.5, 128.0, 128.3, 128.9, 129.7, 137.2, 137.4, 138.8, 140.0, 151.0 ppm. $C_{19}H_{20}N_2$ (276.38): calcd. C 82.60, H 7.24, N 10.14; found C 81.90, H 7.44, N 10.12.

Preparation of Ligand 2c: The lithiation procedure was the same as that mentioned above, using 3-mesityl-5-methyl-*N*-phenylpyrazole (0.2 g, 0.72 mmol), *s*BuLi (1.5 M, 0.5 mL, 0.72 mL) and PPh_2Cl: (0.13 mL, 0.72 mmol). Yield: 0.065 g (26%); m.p. 107 °C. ^{1}H NMR ($CDCl_3$, 300 MHz): δ = 2.02 (s, 6 H, 2 CH_3), 2.13 (s, 3 H, CH_3), 2.28 (s, 3 H, CH_3), 6.04 (s, 1 H, PzH), 7.10–7.52 (m, 14 H, PhH) ppm. ^{13}C NMR ($CDCl_3$, 75.47 MHz): δ = 12.6, 20.5, 20.9, 108.1, 122.3, 124.4, 125.9, 126.0, 126.9, 127.9, 128.2, 128.4, 128.5, 128.8, 129.3, 130.8, 137.0, 137.3, 138.3, 138.7, 139.9, 140.2, 141.4, 149.2, 150.9 ppm. ^{31}P NMR ($CDCl_3$, 202.46 MHz): δ = –20.70 ppm.

 © 2005 Wiley-VCH Verlag GmbH & Co. KGaA, Weinheim

$C_{31}H_{29}N_2P$ (460.55): calcd. C 80.86, H 6.30, N 6.08; found C 80.53, H 5.97, N 6.23.

Preparation of 3,5-Dimethyl-1-(2-nitrophenyl)-1*H*-pyrazole: A solution of 2-nitrophenylhydrazine (1.5 g, 9.98 mmol), one pinch of *p*-toluenesulfonic acid and acetylacetone (1.5 mL, 14.98 mmol) in dry EtOH (50–60 mL) were refluxed for 20–24 h (reaction monitored by TLC). The reaction mixture was then cooled to room temperature and the solvent was evaporated. The resultant residue was taken up in ethyl acetate and washed with aq. $NaHCO_3$ and brine. The organic layer was dried over Na_2SO_4, concentrated and purified by column chromatography using 10% acetone/petroleum ether. Yield: 2 g (62%); m.p. 178–181 °C. IR (KBr): 790, 1529, 1355 cm^{-1}. ^1H NMR (200 MHz, $CDCl_3$) δ = 2.17 (s, 3 H, CH_3), 2.23 (s, 3 H, CH_3), 6.01 (s, 1 H, PzH), 7.45–7.59 (m, 2 H, PhH), 7.65–7.73 (m, 1 H, PhH), 7.94–7.98 (m, 1 H, PhH) ppm. ^{13}C NMR (50.32 MHz, $CDCl_3$): δ = 11.2, 13.4, 106.8, 125.0, 129.3, 129.4, 132.9, 133.2, 141.0, 146.3, 150.3 ppm. $C_{11}H_{11}N_3O_2$ (217.22): calcd. C 60.82, H 5.07, N 19.35; found: C 60.11 H 5.37, N 19.18.

Preparation of 2-(3,5-Dimethylpyrazol-1-yl)phenylamine: Dry ethanol (10 mL) was added to a mixture of 3,5-dimethyl-1-(2-nitrophenyl)-1*H*-pyrazole (0.4 g, 1.84 mmol) and 10% Pd–C (45 mg) and the resultant mixture was stirred under hydrogen until the starting material was consumed (3 h, monitored by TLC). The catalyst was filtered off and the solvent was evaporated. The reaction mixture was extracted with ethyl acetate and washed with water. Subsequent removal of the solvent afforded a yellow solid. The product was pure enough to proceed to the next step. Yield: 0.28 g (70%); m.p. 75–77 °C. IR (KBr) 1629, 1550, 3207, 3315, 3413 cm^{-1}. ^1H NMR (200 MHz, $CDCl_3$) δ = 2.67 (s, 3 H, CH_3), 2.85 (s, 3 H, CH_3), 4.60 (br., 2 H, NH), 6.53 (s, 1 H, PzH), 7.24–7.31 (m, 2 H, PhH), 7.58–7.70 (m, 2 H, PhH). ^{13}C NMR (50.32 MHz, $CDCl_3$) δ = 10.9, 13.1, 105.1, 116.0, 117.2, 124.8, 127.0, 128.9, 140.2, 143.1, 148.7. $C_{11}H_{13}N_3$ (187.24): calcd. C 70.59, H 6.95, N 22.45; found C 70.27, H 6.80, N 22.42.

Preparation of [2-(3,5-Dimethylpyrazol-1-yl)phenyl]dimethylamine (Ligand 3a): Sodium cyanoborohydride (0.215 g, 3.42 mmol), and then acetic acid, were added dropwise to a solution of 2-(3,5-dimethylpyrazol-1-yl)phenylamine (0.213 g, 1.14 mmol) in acetonitrile (4 mL) and formalin (37%) (0.912 mL, 11.40 mmol). Stirring was continued for 3 h (monitored by TLC). The reaction mixture was then poured into diethyl ether (20 mL) and then washed with brine solution. The so-obtained liquid compound was purified by column chromatography. Yield: 0.161 g (66%). ^1H NMR (300 MHz, $CDCl_3$): δ = 2.06 (s, 3 H, CH_3), 2.26 (s, 3 H, CH_3), 2.46 [s, 6 H, $N(CH_3)_2$], 5.91 (s, 1 H, PzH), 6.89–6.94 (m, 2 H, PhH), 7.19–7.28 (m, 2 H, PhH) ppm. ^{13}C NMR (50.32 MHz, $CDCl_3$): δ = 10.8, 13.3, 41.5, 105.0, 117.3, 120.2, 128.9, 129.4, 130.6, 140.9, 148.5. $C_{13}H_{17}N_3$ (215.29): calcd. C 72.56, H 7.91, N 19.53; found C 72.44, H 7.88, N 19.43.

Preparation of 3-Methyl-1-(2-nitrophenyl)-5-phenyl-1*H*-pyrazole: The same procedure as above was used; this time with benzoyl acetone (2 g, 12.34 mmol) and 2-nitrophenylhydrazine: (1.26 g, 8.23 mmol). Yield: 1 g (45%); m.p. 169–171 °C. IR: 765, 1350, 1527 cm^{-1}. ^1H NMR (300 MHz, $CDCl_3$): δ = 2.35 (s, 3 H, CH_3), 6.34 (s, 1 H, PzH), 7.19–7.28 (m, 6 H, PhH), 7.30–7.52 (m, 2 H, PhH), 7.54 (d, J = 2 Hz, 1 H, PhH) ppm. ^{13}C NMR (50.32 MHz, $CDCl_3$): 13.5, 107.6, 118.3, 124.9, 128.0, 128.3, 128.4, 128.5, 129.1, 129.3, 129.4, 133.0, 133.6, 144.9, 150.9 ppm. $C_{16}H_{13}N_3O_2$ (279.29): calcd. C 68.82 H 4.65, N 19.35; found 68.37, H 4.62, N 19.18.

Preparation of 2-[3-Methyl-5-phenylpyrazol-1-yl)]phenylamine: Using the same procedure as above, 3-methyl-1-(2-nitrophenyl)-5-phenyl-1*H*-pyrazole (0.280 g) and 10% Pd/C (30 mg) were used to obtain the desired product in 96% yield (0.240 g). M.p. 73–75 °C. IR: 1504, 1635, 3209, 3321, 3450 cm^{-1}. ^1H NMR (300 MHz, $CDCl_3$): δ = 2.40 (s, 3 H, CH_3), 3.97 (br., 1 H, NH), 6.37 (s, 1 H, PzH), 6.59–6.64 (m, 1 H, PhH), 6.79–6.85 (m, 2 H, PhH), 7.11–7.29 (m, 6 H, PhH) ppm. ^{13}C NMR (75.47 MHz, $CDCl_3$): δ = 13.6, 106.1, 116.7, 118.1, 128.0, 128.2, 129.1, 130.1, 142.7, 144.7, 149.8 ppm. $C_{16}H_{15}N_3$ (249.31): calcd. C 77.08, H 6.06, N 16.85; found C 77.19, H 6.14, 16.01.

Preparation of Dimethyl[2-{3-methyl-5-phenylpyrazol-1-yl)}-phenyl]amine (Ligand 3b): Ligand **3b** was prepared, by the same procedure as the previously, from 2-[3-methyl-5-phenylpyrazol-1-yl)]phenylamine (0.180 g, 0.72 mmol), $NaBH_3CN$ (0.14 g, 2.16 mmol) and formalin (7.2 mmol, 0.6 mL) in 95% yield (0.19 g). IR (neat): 1552 cm^{-1}. ^1H NMR (300 MHz, $CDCl_3$): δ = 2.07 (s, 6 H, NMe_2), 2.27 (s, 3 H, CH_3), 6.21 (s, 1 H, PzH), 6.67–6.84 (m, 2 H, PhH), 6.86–7.14 (m, 6 H, PhH), 7.28–7.31 (s, 1 H, PhH) ppm. ^{13}C NMR (75.47 MHz, $CDCl_3$) δ = 13.7, 41.9, 103.8, 116.6, 122.3, 124.9, 125.0, 126.5, 127.0, 132.8, 134.5, 136.4, 154.6 ppm. $C_{18}H_{19}N_3$ (277.16): calcd. C 77.97, H 6.86, N 15.16; found C 77.85, H 6.89, N 15.13.

Preparation of Nickel Complex 4: A solution of ligand **2a** (0.356 g, 1 mmol) in acetonitrile (15 mL) was added to a yellow suspension of anhydrous $NiCl_2$ (0.128 g, 1 mmol) in acetonitrile (15 mL) at room temperature. The suspension initially turned red, and during reflux over 6–8 h a violet precipitate was formed, which was filtered off and dried under vacuum to afford violet, crystalline complex **4** (0.3 g, 62%). X-ray grade crystals were obtained from a dilute solution of the complex **4** in acetonitrile. M.p. >240 °C. $C_{23}H_{21}Cl_2N_2NiP$ (485.69): calcd. C 56.26, H 4.28, N 5.70; found C 55.74, H 4.41, N 5.41.

Preparation of Nickel Complex 5a: A solution of ligand **3a** (0.17 g, 0.8 mmol) in dichloromethane (10 mL) was added to a hazy yellow solution of $Ni(DME)Cl_2$ (0.17 g, 0.8 mmol) in dry dichloromethane (5 mL); the resultant solution immediately turned violet, and gradually changed to yellowish violet. Stirring was continued for 12 h. After removal of solvent, an orange solid was obtained, which was purified by recrystallization from hot acetonitrile. Yield: 0.199 g (82%); m.p. >240 °C. IR (Nujol): 1504, 1556 cm^{-1}. $C_{13}H_{17}Cl_2N_3Ni$ (309.2): calcd. C 50.45, H 5.49, N 13.58; found C 50.57, H 5.46, N 13.29.

Preparation of Nickel Complex 5b: A solution of **3b** (0.190 g, 0.685 mmol) in dichloromethane (10 mL) was added to a hazy yellow solution of $Ni(DME)Cl_2$ in dry dichloromethane (5 mL); immediately, the hazy yellow solution turned violet and then orange. Stirring was continued for 12 h. After removal of solvent, an orange solid was obtained that was purified by recrystallization from hot acetonitrile. Yield: 0.453 g (79%); m.p. >240 °C. IR (Nujol): 1506, 1562 cm^{-1}. $C_{36}H_{38}Cl_4N_6Ni_2 \cdot 0.5CH_3CN$ (833.9): calcd. C 53.24, H 4.74, N 10.9; found C 52.99, H 4.32, N 10.88.

Preparation of Co Complex 6: An acetonitrile solution of **2a** (0.7 g, 1.93 mmol) was added to a solution of anhydrous $CoCl_2$ (0.25 g, 1.93 mmol) in acetonitrile (10 mL); the resultant solution become deep blue and, immediately, a blue precipitate formed. After 6 h of reflux reaction, the mixture was filtered, the residue was collected and dried under vacuum to give blue solid **6** (0.5 g, 51%). X-ray quality crystals were obtained from slow evaporation of acetonitrile. When the reaction was carried out in air the yield was better (0.83 g, 84%). M.p. >240 °C. IR ($CHCl_3$): 1215, 1438, 1477 cm^{-1}. $C_{23}H_{21}Cl_2CoN_2OP$ (502.25): calcd. C 55.00, H 4.21, N 5.57; found C 55.13, H 4.21, N 5.78.

Preparation of Cu^{II} Complex 7: An acetonitrile solution (20 mL) of **2a** (0.712 g, 2 mmol) was added to a brownish yellow solution of

 © 2005 Wiley-VCH Verlag GmbH & Co. KGaA, Weinheim

anhydrous $CuCl_2$ (0.27 g, 2 mmol) in acetonitrile (10 mL) at room temperature. Immediately, the solution was change color, to light yellow. It was then refluxed for 6 h; the solution turned greenish yellow. After removal of solvent, greenish compound **7** (0.42 g, 41%) was formed, which was purified by recrystallization from acetonitrile. When the reaction was performed under air the yield was improved (0.95 g, 94%). M.p. >240 °C. IR (Nujol) 1132, 1554, 1589 cm^{-1}. Microanalysis $C_{23}H_{21}Cl_2CuN_2OP$ (506.86): calcd. C 54.50, H 4.17, N 5.52; found C 54.42, H 4.32, N 5.51.

Preparation of Cu^I Complex 8: An acetonitrile solution (10 mL) of **2a** (0.356 g, 1 mmol) was added to a suspension of CuCl (0.093 g, 1 mmol) in acetonitrile (12 mL). The reaction mixture was refluxed for 12 h. The reaction slurry was filtered and the filtrate was concentrated under vacuum to give yellow solid **8** (0.40 g, 44%). Crystals suitable for X-ray analysis were obtained from an acetonitrile solution of Cu^I complex **8**. M.p. >240 °C. IR (Nujol): 1552, 1587 cm^{-1}. ^1H NMR ($CDCl_3$, 200 MHz): δ = 1.81 (s, 3 H, CH_3), 2.40 (br. s, 3 H, CH_3), 5.69 (s, 1 H, pzH), 7.24–7.54 (m, 14 H, PhH) ppm. ^{13}C NMR ($CDCl_3$, 50.32 MHz): δ = 11.90, 14.00, 107.77, 128.13, 128.76, 129.20, 130.15, 131.22, 133.68, 142.02, 150.92 ppm. ^{31}P ($CDCl_3$, 80.02 MHz): δ –16.37 ppm. $C_{46}H_{42}Cl_2Cu_2N_4P_2{\cdot}CH_3CN$ (951.87): calcd. C 60.57, H 4.76, N 7.36; found C 60.46, H 4.69, N 7.02.

Ethylene Polymerization: Ethylene polymerization was performed in a 100-mL Büchi AG miniclave. Catalyst was suspended in dry toluene (30 mL) and the solvent was saturated with ethylene. Polymerization was initiated by addition of a toluene suspension of MAO. After 60 min, polymerization was terminated by the addition of methanol (5 mL). The resultant oligomeric mixture, obtained as an oil, was dried under vacuum.

Acknowledgments

Financial support from Reliance Industries Ltd., India, is gratefully acknowledged; A. M. thanks CSIR, India, for a research fellowship.

[1] a) S. Trofimenko, *J. Am. Chem. Soc.* **1966**, *88*, 1842–1844; b) S. Trofimenko, *J. Am. Chem. Soc.* **1967**, *89*, 3170–3177; c) S. Trofimenko, *J. Am. Chem. Soc.* **1967**, *89*, 6288–6294.

[2] a) S. Trofimenko, *Scorpionates: The Coordination Chemistry of Polypyrazolylborate Ligands*, Imperial College Press, London, **1999**; b) S. Trofimenko, *Chem. Rev.* **1993**, *93*, 943–980.

[3] a) V. S. Joshi, A. Sarkar, P. R. Rajamohanan, *J. Organomet. Chem.* **1991**, *409*, 341 and references cited therein; b) V. S. Joshi, M. Nandi, H. Zhang, B. S. Haggerty, A. Sarkar, *Inorg. Chem* **1993**, *32*, 1301–1303; c) T. C. Higgs, C. J. Carrano, *Inorg. Chem.* **1997**, *36*, 291–297; d) T. C. Higgs, K. Spartalian, C. J. O'Connor, B. F. Matzanke, C. J. Carrano, *Inorg. Chem.* **1998**, *37*, 2263–2272; e) S. Tsuji, D. C. Swenson, R. F. Jordan, *Organometallics* **1999**, *18*, 4758–4764.

[4] a) S. D. Ittel, L. K. Johnson, M. Brookhart, *Chem. Rev.* **2000**, *100*, 1169–1203; b) G. J. P. Britovsek, V. C. Gibson, D. F. Wass, *Angew. Chem. Int. Ed.* **1999**, *38*, 428–447.

[5] a) R. F. Heck, J. P. Nolley, Jr., *J. Org. Chem.* **1972**, *37*, 2320; b) R. F. Heck, *Acc. Chem. Res.* **1979**, *12*, 146–151; c) R. F. Heck, *Org. React.* **1982**, *27*, 345–390; d) A. de Meijere, F. E. Meyer, *Angew. Chem. Int. Ed. Engl.* **1994**, *33*, 2379–2411; e) R. F. Heck, *Palladium Reagents in Organic Synthesis* Academic Press, London, **1985**; f) A. de Meijere, F. E. Meyer, *Angew. Chem.* **1994**, *106*, 2473–2506.

[6] a) N. Miyaura, A. Sujuki, *Chem. Rev.* **1995**, *95*, 2457–2483; b) A. Suzuki, *J. Organomet. Chem.* **1999**, *576*, 147–168.

[7] F. Fache, E. Schulz, M. L. Tommasino, M. Lemaire, *Chem. Rev.* **2000**, *100*, 2159–2231 and references cited therein.

[8] a) V. S. Joshi, V. K. Kale, K. M. Sathe, A. Sarkar, S. S. Tavale, C. G. Suresh, *Organometallics* **1991**, *10*, 2898–2907; b) V. S. Joshi, S. K. Chowdhury, A. Sarkar, *Proc. Indian Acad. Sci.* **1995**, *107*, 447–458; c) S. K. Chowdhury, V. S. Joshi, A. G. Samuel, V. G. Puranik, S. S. Tavale, A. Sarkar, *Organometallics* **1994**, *13*, 4092–4096.

[9] a) A. Mukherjee, A. Sarkar, *Arkivoc* **2003**, 87–95; b) The crystal structure of ligand **2a** is reported in ref. [9a].

[10] T. Boullet, B. Klein, J. Hamelin, *Synthesis* **1986**, 409–411.

[11] a) D. M. T. Chan, K. L. Monaco, R. P. Wang, M. P. Winters, *Tetrahedron Lett.* **1998**, *39*, 2933–2936; b) P. V. S. Lam, C. G. Clark, S. Saubern, J. Adams, M. P. Winters, D. M. T. Chan, A. Combs, *Tetrahedron Lett.* **1998**, *39*, 2941–2944; c) S. Yu, J. Saenz, J. K. Srirangam, *J. Org. Chem.* **2002**, *67*, 1699–1702.

[12] G. C. Lloyd-Jones, C. P. Butts, *Tetrahedron* **1998**, *54*, 901–914.

[13] a) J. A. Bertrand, A. R. Kalyanaraman, *Inorg. Chim. Acta* **1971**, 341–345; b) M. M. Manigon, R. Smith, S. G. Shore, *Cryst. Struct. Commun.* **1979**, *8*, 261; c) M. R. Churchill, F. J. Rotella, *Inorg. Chem.* **1979**, *18*, 166–171.

[14] J. A. Bertrand, *Inorg. Chem.* **1967**, *6*, 495–497.

[15] R. P. Hanzlik, D. Williamson, *J. Am. Chem. Soc.* **1976**, *98*, 6570–6573.

[16] D. A. Buckingham, C. R. Clark, in *Comprehensive Coordination Chemistry* (Eds.: G. Wilkinson, R. D. Gillard, J. A. McCleverty), Pergamon Press, Oxford, New York, **1987**, vol. 4, p. 724.

[17] R. McCrindle, G. Ferguson, A. J. Mc Alees, P. J. Roberts, *J. Chem. Soc., Dalton Trans.* **1981**, 1406–1414.

[18] a) S. Mecking, *Coord. Chem. Rev.* **2000**, *203*, 325–351; b) V. M. Mohring, G. Fink, *Angew. Chem. Int. Ed. Engl.* **1985**, *24*, 1001–1002.

[19] M. J. Rachita, R. L. Huff, J. L. Bennett, M. Brookhart, *J. Polym. Sci.: Part A*, *Polym. Chem*. **2000**, *38*, 4627–4640.

[20] a) L. K. Johnson, C. M. Killian, M. Brookhart, *J. Am. Chem. Soc.* **1995**, *117*, 6414–6415; b) L. K. Johnson, S. Mecking, M. Brookhart, *J. Am. Chem. Soc.* **1996**, *118*, 267–268; c) C. M. Killian, D. J. Tempel, L. K. Johnson, M. Brookhart, *J. Am. Chem. Soc.* **1996**, *118*, 11664–11665; d) C. M. Killian, L. K. Johnson, M. Brookhart, *Organometallics* **1997**, *16*, 2005–2007; e) S. Mecking, L. K. Johnson, L. Wang, M. Brookhart, *J. Am. Chem. Soc.* **1998**, *120*, 888–899; f) F. A. Hicks, M. Brookhart, *Organometallics* **2001**, *20*, 3217–3219.

[21] a) G. J. P. Britovsek, V. C. Gibson, B. S. Kimberley, P. J. Maddox, S. J. McTavish, G. A. Solan, A. J. P. White, D. J. Williams, *Chem. Commun.* **1998**, 849–850; b) G. J. P. Britovsek, V. C. Gibson, D. F. Wass, *Angew. Chem. Int. Ed.* **1999**, *38*, 428–447; c) G. J. P. Britovsek, M. Bruce, V. C. Gibson, B. S. Kimberley, P. J. Maddox, S. Mastroianni, S. J. McTavish, C. Redshaw, G. A. Solan, S. Stromberg, A. J. P. White, D. J. Williams, *J. Am. Chem. Soc.* **1999**, *121*, 8728–8740.

[22] a) S. Tsuji, D. C. Swenson, R. F. Jordan, *Organometallics* **1999**, *18*, 4758–4764; b) S. Murtuza, O. L. Casagrane, R. F. Jordan, *Organometallics* **2002**, *21*, 1882–1890.

[23] F. W. Swamer, C. R. Hauser, *J. Am. Chem. Soc.* **1950**, *72*, 1352–1356.

[24] G. M. Sheldrick, *SHELX-97, program for crystal structure solution and refinement*, University of Göttingen, Germany, **1997**.

Received: September 30, 2004

 © 2005 Wiley-VCH Verlag GmbH & Co. KGaA, Weinheim

Platinum Complexes with Only One Purine Ligand (Guanine, Deoxyguanine, or Adenine) Flanked by Two *cis*-NH(CH_3) Groups – Informative Models for Assessing the Interaction of Purine C6 Substituents with *cis*-Amines

Maria Carlone,*[a] Luigi G. Marzilli,[a] and Giovanni Natile[b]

Keywords: Penciclovir / Platinum / Anticancer drugs

syn-(*R*,*S*)-Me_3dienPtL complexes (Me_3dien = *N*,*N*′,*N*′′-trimethyldiethylenetriamine; L = a guanine, a 6-deoxyguanine, or an adenine derivative) represent useful models for assessing the influence of the purine C6 substituent on the rate of rotation about the Pt–N7 bond. Because of the unsymmetric nature of the *syn*-(*R*,*S*)-Me_3dien carrier ligand with respect to the coordination plane (all *N*–Me groups on one side of this plane), two rotamers are possible; they are defined as *endo* or *exo* for the six-membered ring of the purine on the same or opposite side of the coordination plane as the *N*–Me groups, respectively. The derivatives of guanine (Pen), 6-deoxyguanine (deoxy-Pen), and adenine (MeA) used are distinguished by their C6 substituent (O, H, or NH_2, respectively). At ambient temperature the rate of rotation of the purine about the Pt–N7 bond is slow on the NMR time scale for all three complexes. However, for Pen and deoxy-Pen, an increase of the temperature from 293 to 353 K led to coalescence of the ^{1}H NMR signals, indicating fast interconversion between rotamers and allowing evaluation of the rate constants and activation parameters ($\Delta H^{\neq}$ and $\Delta S^{\neq}$) for rotation. In contrast, for MeA raising the temperature to 353 K caused only a very slight broadening of the NMR signals, thus precluding a kinetic analysis of this complex by NMR methods. The rate of interconversion between the rotamers was comparable for the Pen and deoxy-Pen complexes, notwithstanding the greater bulk of the C6 substituent in the Pen complex. On the other hand, the far slower rate of rotation for MeA, as compared to Pen, cannot be explained solely on the basis of C6 substituent bulk. Activation parameters for rotation (average values for the two rotamers: $\Delta H^{\neq}$ = 57 ± 4 and 108 ± 3 kJ·mol^{-1}, $\Delta S^{\neq}$ = –18 ± 11 and 170 ± 11 J·K^{-1}·mol^{-1} for Pen and deoxy-Pen, respectively) suggest a plausible explanation for the observed trend.

(© Wiley-VCH Verlag GmbH & Co. KGaA, 69451 Weinheim, Germany, 2005)

Introduction

Cisplatin[1–3] and related drugs (carboplatin,[4] nedaplatin,[5] oxaliplatin[6–7]) are effective anticancer drugs widely used in the treatment of several human carcinomas. Nevertheless, limitations due to low activity toward some very common tumors (such as breast and colon carcinomas[6,8]), a variety of adverse side effects, and the development of resistance after an initial sensitivity to the treatment have fostered the search for new platinum drugs having improved therapeutic properties. There is a consensus that the antitumor efficacy of cisplatin stems from interaction with DNA and formation of intrastrand cross-links involving adjacent purines.[9–12]

Complexes of platinum with antiviral agents containing purine bases have also been investigated as potential drugs.[13–17] Although the antiviral potency of these compounds did not appear to increase with respect to that of the free base, very promising results were obtained from the viewpoint of antitumor activity. In particular, the complex *cis*-[PtCl(NH_3)$_2$(Acv)]Cl [Acv = Acyclovir = 9-(2-hydroxyethoxymethyl)guanine] proved to be active against sensitive and cisplatin-resistant tumor cells in mice.[18,19] Penciclovir {9-[4-hydroxy-3-(hydroxymethyl)butyl]guanine, Pen}, an agent similar to Acyclovir, is also used as an antiviral drug. 6-Deoxy-Penciclovir (deoxy-Pen) is similar to Penciclovir but carries a hydrogen atom instead of the oxo group on position six of the purine. Cellular enzymes can oxidize the C6 position, introducing an oxygen atom; therefore, deoxy-Pen can be considered a pro-drug of Pen (Scheme 1).[20,21] Having available Pen, deoxy-Pen, and 9-methyladenine (MeA), we used these three bases for investigating the role of the C6 substituent in the interaction between a coordinated purine base and the *cis*-amine(s), a possible key factor affecting the formation and stability of platinum adducts with DNA.

Moreover, in order to simplify the investigation, we looked for a model system having just one purine base and symmetrical *cis*-amine groups. MedienPtL (Medien = 4-

[a] Department of Chemistry, Louisiana State University, Baton Rouge, LA 70803, USA
Fax: +1-225-578-3458
E-mail: mcarlone@lsu.edu
[b] Dipartimento Farmaco-Chimico, Università degli Studi di Bari, Via E. Orabona, 4, 70125 Bari, Italy
Fax: +39-080-544-2230

Supporting information for this article is available on the WWW under http://www.eurjic.org or from the author.

 © 2005 Wiley-VCH Verlag GmbH & Co. KGaA, Weinheim **DOI: 10.1002/ejic.200400824**

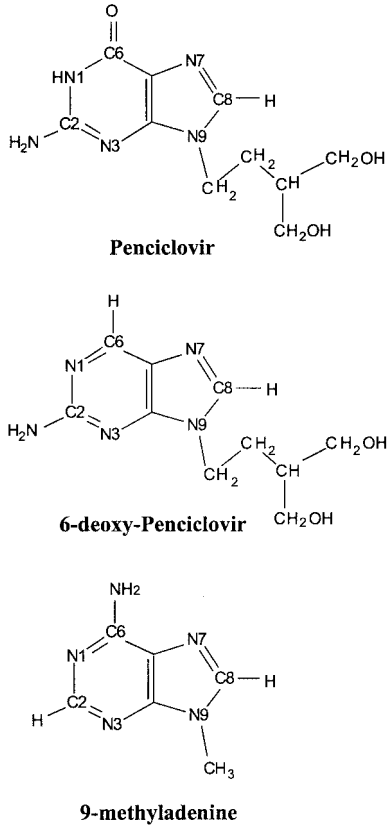

Scheme 1. Schematic drawing of purine derivatives used in this study: Penciclovir (Pen), 6-deoxy-Penciclovir (deoxy-Pen), and 9-methyladenine (MeA).

methyl-1,4,7-triazaheptane = *N*′-methyldiethylenetriamine) was the first candidate. However, the system was too dynamic for investigation by NMR (fast rotation about the Pt–N7 bond even at the lowest temperature). The rotation could be slowed by introducing methyl substituents on the terminal nitrogen atoms, and this led to the synthesis of Me_3dienPtL complexes.

The Me_3dien ligand can assume four different configurations when coordinated to the platinum atom (Scheme 2),

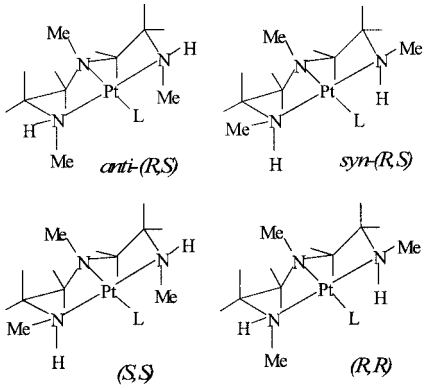

Scheme 2. Possible configurations for Me_3dien coordinated to platinum.

two of these are symmetrical [C_{2v} symmetry; *syn*-(*R*,*S*) and *anti*-(*R*,*S*), respectively], and two are non-symmetrical [C_s symmetry; (*R*,*R*) and (*S*,*S*), respectively].[22] [Pt(Me_3dien)-(NO_3)](NO_3) can be isolated, in the solid state, as the pure *syn*-(*R*,*S*) isomer,[23] and under acidic conditions no change of ligand configuration is observed in aqueous solution after several days at 300 K. Because of the unsymmetrical nature of the Me_3dien ligand with respect to the coordination plane, two possible rotamers are observable for restricted rotation of a coordinated purine base about the Pt–N7 bond. The two rotamers are designated as *endo* or *exo* for the six-membered ring of the purine and the central *N*–Me on the same side or on opposite sides with respect to the platinum coordination plane (Scheme 3).

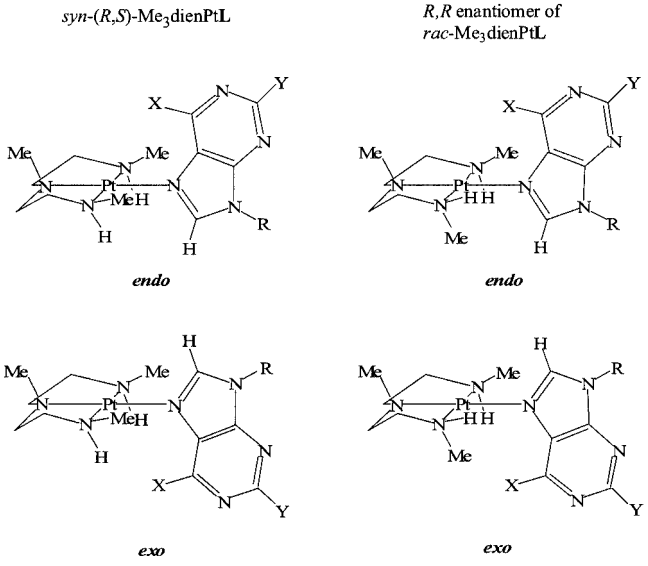

Scheme 3. Possible rotamers for a coordinated purine (L) in Me_3dienPtL complexes (L = Pen, deoxy-Pen, and MeA).

In previous studies we reported the preparation and characterization by ^{1}H NMR spectroscopy of Me_3dienPtG complexes (G = guanine or inosine derivatives).[22,24] These studies established the great relevance of H-bond formation between the NH group of the carrier ligand and the 5′-phosphate of a guanine nucleotide, in comparison with a negligible interaction between an amine NH group and the guanine O6 atom. The latter interaction becomes significant only at basic pH, when deprotonation at N1 takes place.

In the present work we have chosen the same platinum substrate to investigate the effect of the substituent in position 6 of a purine base (L) upon the stability and dynamic behavior of Me_3dienPtL complexes, and we have assessed how steric, solvation, and electronic factors influence the stability and dynamic behavior.

 © 2005 Wiley-VCH Verlag GmbH & Co. KGaA, Weinheim

Results

Me_3dienPtPen

The reaction of *syn*-(*R*,*S*)-[Pt(Me_3dien)(NO_3)](NO_3) with a slight excess of Pen (D_2O, pH* = 1 and 6; the asterisk denotes that no correction was made for the deuterium effect) was complete after 5 d at 298 K. At pH* = 6 (Figure 1) partial isomerization of the Me_3dien ligand from its original *syn*-(*R*,*S*) configuration to the (*S*,*S*) + (*R*,*R*) configurations (*rac*-Me_3dien) also takes place. Assignment of the resonance peaks to the *syn*-(*R*,*S*) or *rac* configurations could be performed easily by comparison with the analogous experiment performed at pH* = 1, in which case the initial *syn*-(*R*,*S*) configuration is preserved (Figure 2 for the H8 region).

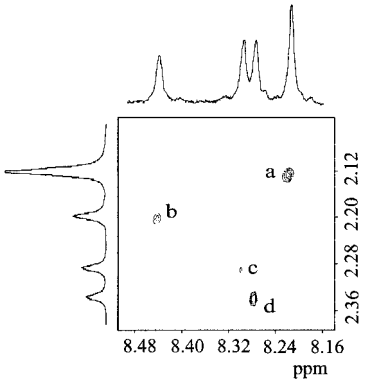

Figure 1. Selected regions of the ROESY spectrum (263 K, pH* = 6) for Me_3dienPtPen. NOE cross-peaks between purine H8 and terminal *N*–Me signals of Me_3dien are labeled. *syn*-(*R*,*S*) isomer: **a** = H8/*N*–Me for *endo* rotamer, **b** = H8/*N*–Me for *exo* rotamer. *rac* Isomer: **c** = H8/*syn*-*N*–Me for *exo* rotamer, **d** = H8/*anti*-*N*–Me for *endo* rotamer.

For both the *syn*-(*R*,*S*) and *rac* isomers two rotamers are possible (Scheme 3). The *endo* rotamer has the six-membered ring of the purine on the same side as the central *N*–Me group of Me_3dien with respect to the platinum coordination plane. In contrast, the *exo* rotamer has the six-membered ring of the purine on the opposite side of the central *N*–Me group with respect to the coordination plane. At 263 K (20% CD_3OD added to the D_2O solution) the exchange between rotamers is slow on the NMR time scale for both isomers; therefore, two relatively sharp and well-separated H8 signals are observed for each isomer (Figure 1, Table 1).

syn-(*R*,*S*)-Me_3dienPtPen has one major and one minor rotamer. In the ROESY spectrum (Figure 1) the H8/*N*–Me-(terminal) cross-peak for the major rotamer (a) was twice the size of that for the minor rotamer (b).

The H8/*N*–Me distance is expected to be shorter in the *exo* rotamer (H8 near the *N*–Me groups) than in the *endo* rotamer; however, in the present case the size of each cross-peak is proportional to the intensity of the parent resonances and therefore cannot be diagnostic for the *endo* or *exo* conformation of a given rotamer. However, for *syn*-(*R*,*S*)-Me_3dienPtG complexes, extensively investigated in a previous work, it was demonstrated that the H8 resonance at higher field (the most intense) belongs to the *endo* rotamer while the resonance at lower field (the less intense) belongs to the *exo* rotamer.[22,24] Thus, on this basis, the major rotamer has the *endo* conformation.

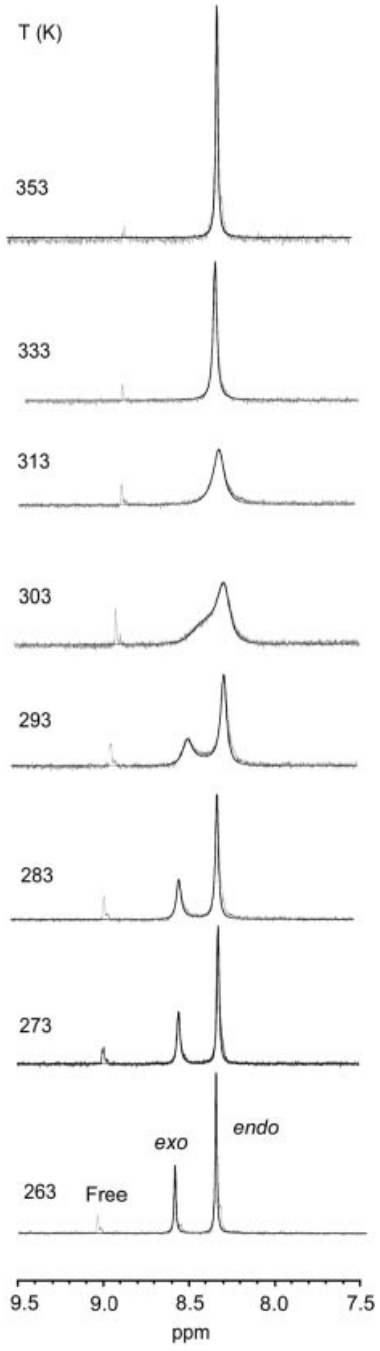

Figure 2. Experimental (pH* = 1, gray line) and simulated (dark line) NMR spectra in the H8 region for *syn*-(*R*,*S*)-Me_3dienPtPen at sample temperatures indicated.

For the adduct with the *rac* configuration of Me_3dien, the two rotamers were formed in equal amounts (equal intensity of the H8 signals). *rac*-Me_3dien has one terminal *N*–Me on the same side of the coordination plane (*syn*-*N*–Me) and the other on the opposite side (*anti*-*N*–Me) as the cen-

 © 2005 Wiley-VCH Verlag GmbH & Co. KGaA, Weinheim

Table 1. ^{1}H NMR shifts (ppm) and distribution ratios for Me_3dienPtL complexes (L = Pen, deoxy-Pen, and MeA).

L	Rotamer	H6/H2	H8	Central *N*–CH_3	*anti* *N*–CH_3	*syn* *N*–CH_3	*endo*/*exo* ratio
Pen[a]			7.74				
syn-(*R*,*S*)	*endo*		8.22	3.06		2.13	2.3
	exo		8.45	3.02		2.20	
rac	*endo*		8.28	3.00	2.34	2.29	1
	exo		8.30	3.00	2.34	2.29	
deoxy-Pen[b]		8.52	8.09				
syn-(*R*,*S*)	*endo*	9.10	8.58	3.10		2.17	1.4
	exo	8.91	8.83	3.08		2.18	
rac	*endo*	9.01	8.67	3.05	2.37	2.10	1.4
	exo	8.96	8.73	3.01	2.37	2.08	
MeA[c]		8.45	8.31				
syn-(*R*,*S*)	*endo*	8.62	9.03	3.24		2.34	2.9
	exo	8.62	9.30	3.21		2.33	
rac	*endo*	8.62	9.11	3.22	2.54	2.28	2.2
	exo	8.62	9.22	3.16	2.51	2.28	

[a] pH* = 6, 263 K, proton signal of HOD set at δ = 5.1 ppm. [b] pH* = 5.3, 258 K, proton signal of HOD set at δ = 5.2 ppm. [c] pH* = 1, 278 K, proton signal of HOD set at δ = 5.0 ppm.

tral *N*–Me. An NOE cross-peak between the central *N*–Me and one terminal *N*–Me (δ = 2.29 ppm) assigns the latter signal to the *syn*-*N*–Me; the remaining terminal *N*–Me signal at δ = 2.34 ppm is consequently assigned to the *anti*-*N*–Me. The *endo* rotamer is expected to give an H8/*anti*-*N*–Me NOE cross-peak (both groups on the same side of the coordination plane), while the *exo* rotamer is expected to give a cross-peak between the H8 and the *syn*-*N*–Me signals. The H8 signal at δ = 8.30 ppm has a cross-peak with the *syn*-*N*–Me signal at δ = 2.29 ppm (c in Figure 1), while the H8 signal at δ = 8.28 ppm has a cross-peak with the *anti*-*N*–Me signal at δ = 2.34 ppm (d in Figure 1). Therefore, the signal at δ = 8.30 ppm is assigned to H8 of the *exo* rotamer and that at δ = 8.28 ppm to H8 of the *endo* rotamer.

Cross-peak d is considerably more intense than cross-peak c (Figure 1), indicating that when the six-membered ring of the guanine is adjacent to the "quasi equatorial" *syn*-*N*–Me (*endo* rotamer), the H8 atom can come close to the "quasi axial" *anti*-*N*–Me. In contrast, when the six-membered ring of the guanine is adjacent to the "quasi axial" *anti*-*N*–Me (*exo* rotamer), the H8 atom is kept at some distance from the "quasi equatorial" *syn*-*N*–Me. This finding is in line with a recent observation indicating that there is greater steric interaction between O6 (of an N7-coordinated guanine) and a "quasi axial" *N*–Me than between O6 and a "quasi equatorial" *N*–Me.[25]

In *syn*-(*R*,*S*)-Me_3dienPtPen, rate constants and activation parameters for interconversion between rotamers were evaluated by simulation of ^{1}H NMR spectra recorded at pH* = 1 and at various temperatures between 258 and 353 K (Figure 2, Table 2). The enthalpy and entropy of activation ($\Delta H^{\neq}$ and $\Delta S^{\neq}$, respectively) were estimated from plots of $\ln(k/T)$ vs. $1/T$, which were linear within experimental error (Supporting information; for Supporting information see also the footnote on the first page of this article, Table 4). With respect to the transition state, the *endo* rotamer is lower in enthalpy by 61 ± 2 kJ·mol^{-1} and slightly higher in entropy by 8 ± 2 J·K^{-1}·mol^{-1}. Also the *exo* rotamer is lower in enthalpy by 54 ± 2 kJ·mol^{-1} but significantly higher in entropy by 29 ± 2 J·K^{-1}·mol^{-1}.

From the activation parameters, it is possible to calculate the difference in enthalpy (ΔH) and entropy (ΔS) between *endo* and *exo* rotamers. Compared to the *exo* rotamer, the *endo* rotamer is lower in both enthalpy and entropy (by 7 ± 2 kJ·mol^{-1} and 21 ± 2 J· K^{-1}·mol^{-1}, respectively).

Me_3dienPtdeoxy-Pen

The reaction of *syn*-(*R*,*S*)-[Pt(Me_3dien)(NO_3)](NO_3) with deoxy-Pen in D_2O solution at 298 K was performed at pH* = 1 and 6 for 5 d. In the experiment performed at the higher pH partial isomerization of the Me_3dien ligand from its original *syn*-(*R*,*S*) configuration to the *rac* configuration was observed. Assignment of the resonance peaks to the *syn*-(*R*,*S*) and *rac* isomers was facilitated by comparison with the results of the analogous experiment performed at pH* = 1, for which no isomerization of the *syn*-(*R*,*S*) ligand configuration took place (Figure 4). In order to distinguish between the H6 and H8 set of signals, an aliquot of the NMR samples was heated at 70 °C for several hours to allow H8 exchange with D_2O. The signals that disappeared were assigned as H8 signals.

Coordination of deoxy-Pen took place only through N7 at both pH* values. This conclusion is supported by several pieces of evidence such as: i) formation of the platinum adduct under conditions (pH* = 1) in which the N1 atom is fully protonated ($pK_a \approx 4.3$ as determined by NMR experiments); ii) upfield shift (ca. 0.25 ppm) of the H6 signal (but not of the H8 signal, which instead remained constant) as the pH* was raised from 1 to 6 (reflecting deprotonation at N1); iii) coalescence of the two H6 signals and of the two H8 signals of each isomer [only the *syn*-(*R*,*S*) isomer for the experiment performed at pH* = 1; the *syn*-(*R*,*S*) and the *rac* isomers for the experiment performed at pH* = 6] as the temperature was raised from 255 to 353 K. Coalescence could not be possible if the two H6 signals or the two H8 signals originated from isomers with a different mode of coordination of deoxy-Pen (N7- and N1-coordination).

The coordination, at the same pH* = 6 (where N1 is not protonated), of deoxy-Pen exclusively through N7 and of MeA through both N7 and N1 can be easily understood if we consider the position of the NH_2 substituent on the six-membered ring. In deoxy-Pen the NH_2 substituent is on position 2 of the ring and it can inhibit Pt binding at N1 but not N7; thus N7 binding is preferred. In MeA, in contrast, the NH_2 substituent is on position 6 and it can inhibit Pt binding at both N1 and N7. Thus, binding at both sites is still competitive, and two isomers that cannot interchange rapidly are formed.

The assignment of proton signals to the *endo* and *exo* conformers of each isomer [*syn*-(*R*,*S*) and *rac*] has been achieved by a ROESY experiment carried out at pH* = 5.3 and 258 K (30% CD_3OD added to the D_2O solution); the

 © 2005 Wiley-VCH Verlag GmbH & Co. KGaA, Weinheim

Table 2. Rate constants and percentages of rotamers used to simulate NMR spectra (pH* = 1) of *syn*-(*R*,*S*)-Me_3dienPtPen at different temperatures.

T [K]	Rate constants [s^{-1}]		Percentages of rotamers	
	k_1 (*endo* → *exo*)	k_{-1} (*exo* → *endo*)	*endo*	*exo*
258	–	–	71.20	28.80
263	–	–	69.87	30.13
268	2.00	4.42	68.18	31.82
273	3.80	7.69	66.93	33.07
278	6.00	11.61	65.93	34.07
283	9.50	17.18	64.39	35.61
288	15.50	26.60	63.18	36.82
293	28.00	45.40	61.85	38.15
298	39.85	61.56	60.71	39.29
303	66.70	97.00	59.25	40.75
308	102.00	142.60	58.30	41.70
313	137.00	181.00	56.92	43.08
323	268.00	323.00	54.65	45.35
333	614.00	672.00	52.26	47.74
343	1140.00	1164.00	50.52	49.48
353	2230.00	2240.00	50.11	49.89

low temperature ensures the observation of relatively sharp signals (Figure 3). The most upfield signals in the aliphatic region (δ = 2.0–2.2 ppm) are assigned to the terminal *syn*-*N*–Me signals, all of them having NOE cross-peaks with the central *N*–Me signals falling in the δ = 3.0–3.2 ppm region (Supporting information). The signals at δ = 2.17 and 2.18 ppm (one signal for each rotamer) belong to the *syn*-(*R*,*S*) isomer, while the signals at δ = 2.08 and 2.10 ppm (one signal for each rotamer) belong to the *syn*-*N*–Me of the *rac* isomer. The *anti*-*N*–Me signals of the two rotamers of *rac*-Me_3dienPtdeoxy-Pen overlap at δ = 2.37 ppm. Terminal *N*–Me signals were used to assign the signals of the aromatic protons. The a,b and a′,b′ pairs of resonances in the 1D trace (Figure 3) belonging to the *syn*-(*R*,*S*) isomer are assigned to the H8 and H6 protons, respectively, because of the presence of EXSY cross-peaks between a and b and between a′ and b′ resonances (not shown). The more intense pair of signals (a,a′) is characterized by having a stronger NOE between the H6 and terminal *N*–Me signals (cross-peak a′ in the 2D spectrum) than between the H8 and terminal *N*–Me signals (cross-peak a); therefore, this intense pair is assigned to the *endo* rotamer (H6 adjacent to *N*–Me groups). The weaker pair of signals (b,b′) is thus assigned to the *exo* rotamer. The *endo*/*exo* ratio is ca. 1.4.

For the *rac* isomer, again two rotamers of slightly different abundances are observed (pairs of H8,H6 signals, c,c′ and d,d′). For the more intense pair of signals (c,c′) the H8 signal (c) has a cross-peak to the *anti*-*N*–Me signal, and the H6 signal (c′) has a cross-peak to the *syn*-*N*–Me signal; thus, c,c′ are assigned to the *endo* rotamer. In contrast, for the weaker pair of signals (d,d′) the H8 signal (d) has a cross-peak to the *syn*-*N*–Me signal, and the H6 signal (d′) has a cross-peak to the *anti*-*N*–Me signal; therefore d,d′ are assigned to the *exo* rotamer.

Within the set of H8 signals for the two isomers (Figure 3), the most upfield signals belong to *endo* rotamers, while the most downfield signals belong to *exo* rotamers, as found previously.[24] In contrast, the H6 signals show the reverse trend (the most upfield signals belong to the *exo* rotamers, while the most downfield signals belong to the *endo* rotamers).

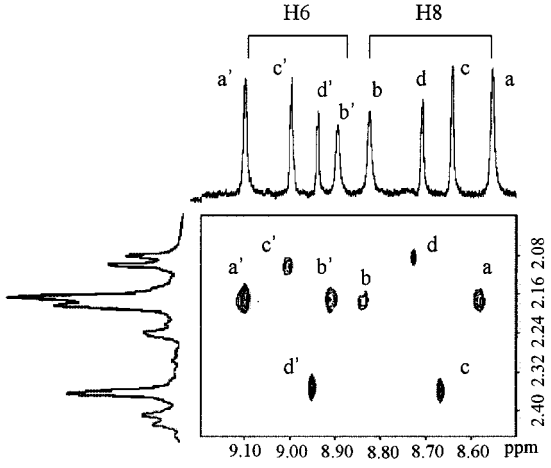

Figure 3. Selected regions of the ROESY spectrum (258 K, pH* = 5.3) for Me_3dienPtdeoxy-Pen. Protons H8 (a−d) and H6 (a′−d′) are labeled.

For *syn*-(*R*,*S*)-Me_3dienPtdeoxy-Pen, the rate constants for interconversion between rotamers were evaluated by spectral simulation between 255 K and 353 K performed at pH* = 1 (Figure 4, Table 3).

It is noteworthy that for the *exo* rotamer the chemical shifts of the H8 and H6 signals are rather close. One-dimensional NMR experiments show that a change of pH* from 1 (protonated N1) to 5.3 (non-protonated N1) causes a change in the relative positions of these two resonances (the H8 signal downfield to the H6 signal at pH* = 1 and upfield at pH* = 5.3). ROESY experiments performed at the two pH* values confirmed the correctness of all 1D assignments.

The enthalpy and entropy of activation ($\Delta H^{\neq}$ and $\Delta S^{\neq}$, respectively) were estimated from plots of ln(k/T) vs. 1/T, which were linear within experimental error (Supporting information, Table 4). With respect to the transition state, both the *endo* and *exo* rotamers are lower in enthalpy (by

 © 2005 Wiley-VCH Verlag GmbH & Co. KGaA, Weinheim

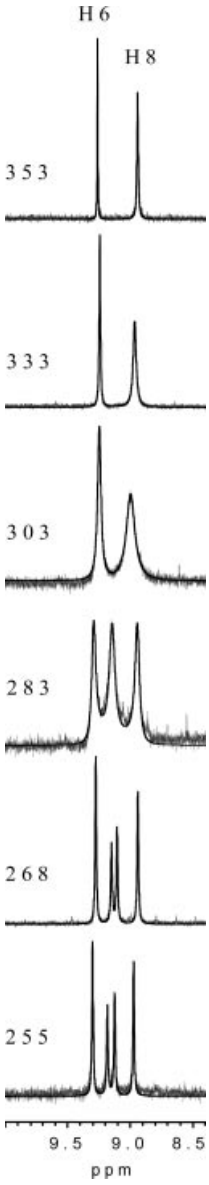

Figure 4. Experimental (pH* = 1, gray line) and simulated (dark line) NMR spectra in the H8 region for *syn*-(*R*,*S*)-Me_3dienPtdeoxyPen at sample temperatures indicated.

111 ± 2 and 105 ± 2 kJ·mol^{-1}, respectively) and entropy (by 181 ± 4 and 159 ± 4 J·K^{-1}·mol^{-1}, respectively). The *endo* rotamer is lower in enthalpy (6 kJ·mol^{-1}) and entropy (22 J·K^{-1}·mol^{-1}) than the *exo* rotamer. An analogous trend was already noted for the Pen complex (ΔH of 7 kJ·mol^{-1} and ΔS of 21 J·K^{-1}·mol^{-1}).

Me_3dienPtMeA

The reaction of *syn*-(*R*,*S*)-[Pt(Me_3dien)(NO_3)](NO_3) with a slight excess of MeA (molar ratio 1:1.4) was carried out in D_2O, pH′ = 1. The low pH ensures not only the absence of isomerization of the carrier ligand from its original *syn*-(*R*,*S*) configuration, but also coordination of adenine through N7 because N1 is fully protonated (pK_a = 4.3).[26] After 3 d at 298 K, 80% of the initial platinum complex had reacted, and another aliquot of MeA was added (Figure 5).

On the basis of their different intensities, the resonances can be grouped into two sets. The most intense set includes signals at δ = 3.82, 8.53, and 8.94 ppm; the second set, less intense, includes signals at δ = 3.84, 8.51, and 9.19 ppm. The intensity ratio between the two sets is ca. 3. The presence of two sets of resonances can be explained by the presence of two rotamers.

For each set of resonances the intensity of the most downfield signal decreased with time (δ = 8.94 and 9.19 ppm, respectively). Such a decrease in intensity is expected to take place for signals belonging to H8 protons, which are known to undergo exchange with deuterium of the solvent.[27,28] The downfield shift of the H8 and H2 resonances, consequent to coordination to the platinum atom (ca. 0.7 and 0.15 ppm, respectively), and the differences in chemical shift between the two H8 ($\Delta\delta$ = 0.25 ppm) and the two H2 resonances ($\Delta\delta$ = 0.02 ppm) are in agreement with N7 coordination of MeA. In fact, the H8 proton, being much closer to the donor atom (N7) than H2, will not only be more deshielded by the metal center, but will also experience more different chemical environments in the two rotamers.

The correct assignment of the H8 and H2 resonances was also confirmed by an inversion recovery experiment (Supporting information): the longitudinal relaxation time (T_1) of the H2 protons was about three times longer than that of the H8 protons, as previously reported for adenine derivatives.[29]

Although the coordinated *syn*-(*R*,*S*)-Me_3dien configuration is rather stable at low pH, a sample of Me_3dienPtMeA kept at 298 K for 30 d showed partial isomerization from the initial *syn*-(*R*,*S*)-Me_3dienPtMeA to the *rac*-Me_3dienPtMeA. A NOESY experiment was performed on this sample (pH* = 1, 278 K) in order to assign the *endo* or *exo* conformation to the two rotamers of the *syn*-(*R*,*S*) and *rac* species.

NOE cross-peaks between central and terminal *N*–Me signals (Figure 6 A) allow us to distinguish between *syn*- and *anti*-*N*–Me groups. For *syn*-(*R*,*S*)-Me_3dienPtMeA the NOE cross-peaks between central and terminal *N*–Me resonances (labeled a) fall at δ = 2.33/3.21 ppm (for the minor rotamer) and at δ = 2.34/3.24 ppm (for the major rotamer). For the *rac* isomer, the terminal *N*–Me signal at δ = 2.28 ppm gives an NOE cross-peak with the central *N*–Me signal at δ = 3.16 ppm (coincident peaks for the two rotamers, b); therefore, the resonance at δ = 2.28 ppm is assigned to the *syn*-*N*–Me group of both rotamers. As a consequence, the resonances of the terminal *N*–Me groups at δ = 2.51 and 2.54 ppm (two distinct signals for the two rotamers), which do not give NOE cross-peaks with the central *N*–Me resonances, are assigned to the *anti*-*N*–Me signals of the minor and major rotamer of the *rac* isomer, respectively.

For *syn*-(*R*,*S*)-Me_3dienPtMeA the minor rotamer has an intense NOE cross-peak between H8 and the terminal *N*–Me signals (δ = 9.30/2.33 ppm, c in Figure 6 B). In contrast, the major rotamer (H8; δ = 9.03 ppm) lacks such a cross-

 © 2005 Wiley-VCH Verlag GmbH & Co. KGaA, Weinheim

Table 3. Rate constants and percentages of rotamers used to simulate NMR spectra (pH* = 1) of *syn*-(*R*,*S*)-Me_3dienPtdeoxy-Pen at different temperatures.

T [K]	Rate constants [s^{-1}]		Percentages of rotamers	
	k_1 (*endo* → *exo*)	k_{-1} (*exo* → *endo*)	*endo*	*exo*
255	–	–	59.80	40.20
258	0.55	0.76	58.20	41.80
263	1.32	1.83	58.00	42.00
268	3.53	4.53	57.50	42.50
273	10.17	13.19	56.50	43.50
278	21.92	25.73	54.00	46.00
283	53.27	58.88	52.60	47.40
288	123.09	130.71	51.50	48.50
293	278.71	281.51	50.20	49.80
298	612.22	594.13	49.30	50.70
303	1317.82	1204.39	47.80	52.20
313	5631.90	4751.44	45.90	54.10
323	21974.81	17114.00	43.80	56.20
333	79074.24	57419.69	42.10	57.90
343	265065.02	177678.40	40.20	59.80
353	827751.32	522545.87	38.80	61.20

Table 4. Activation enthalpy [kJ·mol^{-1}] and entropy [J·K^{-1}·mol^{-1}] for interconversion between rotamers in *syn*-(*R*,*S*)-Me_3dienPtL, at pH′ = 1.

L	$\Delta H^{\neq}_{endo}$	$\Delta H^{\neq}_{exo}$	$\Delta S^{\neq}_{endo}$	$\Delta S^{\neq}_{exo}$
Pen	61 ± 2	54 ± 2	–8 ± 2	–29 ± 2
EtG[24]	65 ± 2	56 ± 2	2 ± 2	–28 ± 2
deoxy-Pen	111 ± 2	105 ± 2	181 ± 4	159 ± 4

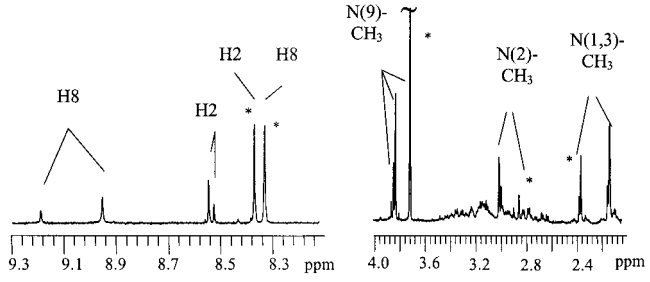

Figure 5. ^{1}H NMR spectrum (295 K, pH* = 1) of *syn*-(*R*,*S*)-Me_3dienPtMeA in the presence of an excess of MeA and some unchanged *syn*-(*R*,*S*)-$[Pt(Me_3dien)(H_2O)]^{2+}$ substrate (signals labeled with an asterisk).

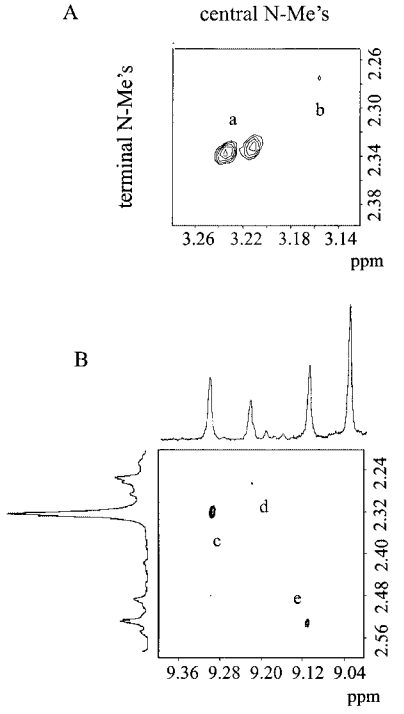

Figure 6. Selected regions of the NOESY spectrum (278 K, pH* = 1) of Me_3dienPtMeA. Spectrum A: Equatorial *N*–Me/central *N*–Me region; NOE cross-peaks are labeled a and b for the *syn*-(*R*,*S*) and *rac*-Me_3dienPtMeA, respectively. Spectrum B: Terminal *N*–Me/aromatic proton region; NOE cross-peaks are labeled c, d, and e for the *exo* rotamer of *syn*-(*R*,*S*)-Me_3dienPtMeA and for the *exo* and *endo* rotamers of the *rac* isomer, respectively.

peak. Thus, it is possible to assign the *exo* conformation to the minor rotamer (H8 near the terminal *N*–Me group with respect to the coordination plane) and the *endo* conformation to the major rotamer.

For *rac*-Me_3dienPtMeA, NOE cross-peaks were observed between the H8 signal of the minor rotamer and the *syn*-*N*–Me signal (δ = 9.22/2.28 ppm, d in Figure 6 B), and between the H8 signal of the major rotamer and one *anti*-*N*–Me signal (δ = 9.11/2.54 ppm, e in Figure 6 B); therefore, the *exo* form is assigned to the minor rotamer and the *endo* form to the major rotamer.

For *syn*-(*R*,*S*)-Me_3dienPtMeA, ^{1}H NMR spectra recorded between 268 and 353 K did not show significant broadening of the resonance peaks, indicating that the rotation around the Pt–N7 bond is slow on the NMR time scale, even at 353 K.

Discussion

In a previous study the Me_3dienPtL system (L = 9-ethylguanine, 5′-guanosine monophosphate, and 3′-guanosine monophosphate; EtG, 5′-GMP, and 3′-GMP, respectively) was used to investigate the effect of the substituent in position 9 of a guanine base upon the rotamer ratio and the

 © 2005 Wiley-VCH Verlag GmbH & Co. KGaA, Weinheim

rate of rotamer interconversion. The most interesting result of that investigation was the great tendency of the 5′-phosphate to form an H bond to the NH group of a *cis*-amine when phosphate and N–H are on the same side of the platinum coordination plane. As a consequence, the *endo* rotamer was the exclusive form for the *syn*-(*R*,*S*) species (at neutral and basic pH). In contrast, for the EtG and 3′-GMP complexes, in which such an interaction cannot take place, the *endo* and *exo* rotamers were present in comparable amounts with a slight preference for the *endo* rotamer. Moreover, in one case (EtG complex) the rate of interconversion between *endo* and *exo* rotamers was investigated by ^{1}H NMR and the activation parameters ($\Delta H^{\neq}$ and $\Delta S^{\neq}$) evaluated. Because the rate of rotation is expected to be very much dependent upon the substituent in position 6 of the ring system, we looked for purine bases differing in the nature of this substituent. Penciclovir, deoxy-Penciclovir, and 9-methyladenine appeared to be most appropriate because two of them have moderately bulky hydrophilic substituents of opposite surface charge (electron-rich oxygen in Penciclovir and electron-poor amine protons in adenine), and deoxy-Penciclovir has a sterically much less demanding H substituent.

Factors Influencing Rotation Around the Pt–N(7) Bond

Most notably, the behavior of the Pen derivative is very similar to that of the EtG derivative previously investigated.[24] The Pen and EtG complexes have not only very similar ratios between *endo* and *exo* rotamers, but also very similar rate constants and activation parameters for interconversion (Table 4). This finding indicates that the different nature of the N9 substituents [Et and 4-hydroxy-3-(hydroxymethyl)butyl for EtG and Pen, respectively] does not influence the ratio and interconversion rate of rotamers. The N9 substituents project in a direction opposite to that of the platinum core, and there is little chance for interaction with the *cis*-amine groups [except in the case of 5′-phosphate-(deoxy)ribo derivatives].

Quite surprising are the comparable rates of rotation observed in the compounds with Pen and deoxy-Pen. We expected a much faster rate of rotation in the deoxy-Pen derivative because of the much smaller steric bulk of the proton, as compared to an oxygen atom, at position 6 of the purine system. A possible explanation for this apparent paradox is suggested by the activation parameters for rotation about the Pt–N7 bond. In the deoxy-Pen complex the transition state is much higher in both enthalpy (average 108 ± 3 kJ·mol^{-1}) and entropy (average 170 ± 11 J·K^{-1}·mol^{-1}), with respect to the *endo* and *exo* ground states, than in the Pen complex (average $\Delta H^{\neq}$ and $\Delta S^{\neq}$ of 57 ± 4 kJ·mol^{-1} and -18 ± 11 J·K^{-1}·mol^{-1}, respectively). It is therefore rather surprising that in the case of Pen, carrying a rather bulky substituent in position 6 of the purine ring (O), the enthalpy of activation is ca. 50 kJ·mol^{-1} lower than in the case of deoxy-Pen, carrying a much smaller group (H).

We believe that the charge of the C6 substituent, in addition to its steric bulk, is very important also. It has been observed that the H8 of a purine carries a partial positive charge and also H6 (in the case of deoxy-Pen), although to a lesser extent, is likely to carry a partial positive charge.[30] In contrast, the O6 of Pen is electron rich. In the transition state, the purine is dragged through the platinum coordination plane, and H8 and X6 (X = O or H) approach the *cis*-amines. Because of the electronegativity of the nitrogen atom, the amine H and Me groups are expected to bear a partial positive charge. For Pen the opposite charge of O6 and of the *cis*-amine substituents (H or Me) evidently favors the bulky O6 group passing through the coordination plane. In other words, the O6 of Pen is an H bond acceptor while the amine group is an H-bond donor, and the attractive interaction between the two groups is likely to lower the rotational barrier. Pen also has very little entropy of activation. If, as we believe for an intramolecular process, the entropy of activation is mainly related to solvation/desolvation phenomena, we must conclude that in the present case (attractive interaction between the two groups passing by) there is only a reorganization of the solvation shells, without release of water molecules.

For deoxy-Pen, the purine H6 and the *cis*-amine substituents (H or Me) both carry a partial positive charge. The electrostatic repulsion between the two positively charged moieties, coming close to one another, will increase the rotational barrier, notwithstanding the small size of H6 compared to O6 of Pen. Moreover, deoxy-Pen (unlike Pen) has a very large entropy of activation (average 170 ± 11 J·K^{-1}·mol^{-1}). We propose that, in the presence of an electrostatic repulsion between the two groups passing by, there is a large desolvation process with consequent release of water molecules. This desolvation process will result in a large activation entropy and a further increase of activation enthalpy.

The explanation given above for the Pen and deoxy-Pen complexes fully accounts for the behavior of the MeA derivative, in which the substituent in position 6 of the purine ring is bulky (even more than O6 of Pen) and positively charged (like the substituents on the *cis* amine). Under these circumstances the barrier to rotation is expected to be far greater than that observed for Pen or deoxy-Pen, with the consequence that the interconversion between rotamers remains slow on the NMR time scale, even at the highest temperature explored (353 K).

Strong support in favor of the explanation given above comes from a parallel investigation regarding the rotation of guanine or adenine derivatives in platinum substrates in which the groups *cis* to the purine are H bond acceptors rather than H bond donors. In this case the trend is reversed and rotation is faster for adenine than guanine.

Factors Determining Conformer Distribution

The rotamer distribution found for the Me_3dienPtPen complex is, as expected, identical to that observed for Me_3-

 © 2005 Wiley-VCH Verlag GmbH & Co. KGaA, Weinheim

dienPtEtG.[24] For the *syn*-(*R*,*S*) isomer, the preference is for the *endo* rotamer having the bulky six-membered ring on the same side of the platinum coordination plane as the *N*–Me groups (*endo*/*exo* ratio of 2 at 273 K). The *exo* conformation, which could form H bonds between the N–H group of *cis*-amines and O6 of the purine, is less favored. This evidence is contrary to a long-held belief that H bonds between purine derivatives and the NH group of platinum-carrier ligands are of primary importance in stabilizing the complexes in solution.[31] On the other hand, for the *rac*-Me_3dienPtPen isomer the *endo*/*exo* ratio is 1, as observed for the *rac* isomer of the complex with EtG. The *rac* isomer has one N–H and one *N*–Me group on each side of the platinum coordination plane; therefore, it is plausible that the two rotamers have similar stability.

In the Me_3dienPtdeoxy-Pen complex, the *syn*-(*R*,*S*) isomer again has a slight preference for the *endo* rotamer (*endo*/*exo* ratio of 1.3 at 273 K). Therefore, in this case also the *endo* rotamer, in which the six-membered ring of Pen is on the more crowded side of the platinum coordination plane, is more favored. Moreover, this *endo*/*exo* ratio of 1.3 is also observed for the *rac* isomer.

The *endo*/*exo* ratio, which is in the range of 2–2.5 for G derivatives (Pen and EtG complexes), is ca. 2.9 for the MeA complex (Table 1). In the case of MeA, the racemic isomer also shows a net preference for the *endo* rotamer (*endo*/*exo* ratio of ca. 2.2), while such a preference is much smaller for G complexes (*endo*/*exo* ratio in the range 1–1.2). Moreover, because for MeA the interconversion between rotamers is still very slow (on the NMR time scale) at the highest temperature explored, we do not know if the observed *endo*/*exo* ratio represents the thermodynamic equilibrium or is a kinetically determined composition.

In summary, at 298 K all complexes show a preference for the more crowded *endo* rotamer; moreover, the preference for such a rotamer appears to increase as the size of the substituent in position 6 of the purine ring system increases, independently of its charge. We do not have a good explanation for such a preference; however, we wish to point out that, in terms of free energy, the difference between the two rotamers is very small (less than 2.5 kJ·mol^{-1} at 300 K) and thus very difficult to account for.

For cases in which it has been possible, from kinetic data, to evaluate the difference in ΔH and ΔS between *endo* and *exo* rotamers (EtG, Pen, and deoxy-Pen complexes), the *endo* rotamer is lower in both enthalpy and entropy with respect to the *exo* rotamer (average 7 ± 2 kJ·mol^{-1} and 26 ± 4 J·K^{-1}·mol^{-1} for ΔH and ΔS, respectively). For the *syn*-(*R*,*S*)-Me_3dienPtEtG complex[24] we hypothesized that in the less abundant *exo* rotamer, interference between solvation shells of the purine C6 substituent and the *cis*-amine NH groups could lead to release of water molecules with a consequent slight increase in enthalpy and entropy. The stabilizing effect of the greater ΔS would not compensate for the destabilizing effect of the greater ΔH. The same explanation could also apply to the present case. We hope to gain a deeper insight in the *endo*/*exo* preference of rotamers by extending the investigation to purine bases carrying different substituents in position 8 of the purine ring system, so as to counterbalance the effect of substituents in position 6 of the purine.

Experimental Section

Materials: [Pt(Me_3dien)(NO_3)](NO_3) was prepared as previously reported.[22] Penciclovir [9-(4-hydroxy-3-hydroxymethylbut-1-yl) guanine, Pen] and 6-deoxy-Penciclovir (deoxy-Pen) were a gift of the Institute of Chemistry of Ljubljana, Slovenia. 9-Methyladenine (MeA) was prepared according to a literature method.[32]

Preparation of Adducts: Solutions of the adducts were prepared by treatment of [Pt(Me_3dien)(NO_3)](NO_3) (5 mM solution in D_2O at pH* = 1 or ca. 6) with a stoichiometric amount of L (L = Pen, deoxy-Pen, or MeA). Reactions were monitored by ^{1}H NMR until the disappearance of free L (or constant intensity ratio between free and complexed L in the case of an excess of L). Standard DNO_3 and NaOD solutions (in D_2O) were used to adjust the pH* of each sample directly in the NMR tube when necessary. 1D NMR studies were normally performed at 295 K. NOESY experiments were performed at 263 K (solvent D_2O/CD_3OD, 80:20 v/v) or 258 K (solvent D_2O/CD_3OD, 70:30 v/v).

1D NMR Spectroscopy: 1D NMR spectra were collected with a Varian Unity 600 spectrometer (spectral width, 6 kHz). The residual HOD peak was used as reference. In a typical experiment, a selective presaturation pulse (10 dB) was applied for 1 s to the residual HOD resonance. The FID was accumulated for 64 transients in blocks containing 16 K data points. Before Fourier transformation, the FIDs were baseline-corrected for DC offset before an exponential multiplication apodization function with a 0.2 Hz line broadening was applied. Selected ^{1}H chemical shifts of the purine base and the Me_3dien ligand are reported in Table 1.

2D NMR Spectroscopy: 2D NMR spectra (512×2048 matrices with a spectral window of 6–7 kHz in each dimension) were recorded with a Varian Unity 600 Spectrometer.[33] For the NOESY and ROESY experiments, a 500-ms mixing time was used. A 1-s presaturation pulse was typically used to saturate the HOD resonance. Spectra were processed using Felix 97.0 (MSI) with a Silicon Graphics INDY R4400 workstation. Typical processing involved zero filling of the t_1 dimension to 2048 points, exponential multiplication (0.4 Hz line broadening) in t_2, and applying a sine bell function shifted 90° over all points in t_1.

Line-Shape Analysis: For *syn*-(*R*,*S*)-Me_3dienPtL complexes (L = Pen or deoxy-Pen), the rate constants for interconversion between the *endo* and *exo* rotamers at different temperatures were calculated from line-shape analyses of ^{1}H NMR spectra collected with a Bruker AVANCE 300 MHz spectrometer. The simulation of the spectra was performed in the temperature range 255–353 K using DNMR6, a dynamic NMR spectra simulation FORTRAN code.[34] Rate constants for interconversion at different temperatures are reported in Table 2 and Table 3 for Pen and deoxy-Pen complexes, respectively. By applying the Eyring equation, the enthalpy and the entropy of activation ($\Delta H^{\neq}$ and $\Delta S^{\neq}$) were evaluated (Table 4).[35] In order to avoid ligand isomerization, a pH* value of 1 was used.

Supporting Information: See also footnote on the first page of this article. ln(k/T) as a function of 1/T for *syn*-(*R*,*S*)-Me_3dienPtPen at pH* = 1; selected regions of the ROESY spectrum (258 K, pH* = 5.3) for Me_3dienPtdeoxy-Pen; ln(k/T) as a function of 1/T for *syn*-(*R*,*S*)-Me_3dienPtdeoxy-Pen at pH* = 1; inversion recovery experiment for *syn*-(*R*,*S*)-Me_3dienPtMeA at pH* = 1.

 © 2005 Wiley-VCH Verlag GmbH & Co. KGaA, Weinheim

Acknowledgments

This work was supported by the Ministero dell'Università e della Ricerca Scientifica e Tecnologica of Italy (MURST) Cofin. N. 2001053898 (to G. N.) and NIH Grant GM 29222 (to L. G. M.). The authors wish to thank the Institute of Chemistry of Ljubljana, Slovenia, for providing Penciclovir and 6-deoxy-Penciclovir, Dr. P. A. Marzilli for her valuable suggestions, Dr. N. G. Di Masi for NMR simulations, and Dr. F. Cannito for assistance in the manuscript preparation.

[1] E. Wong, C. M. Giandomenico, *Chem. Rev.* **1999**, *99*, 2451–2466.
[2] G. Giaccone, *Drugs* **2000**, *59*, 9–17.
[3] R. B. Weiss, M. C. Christian, *Drugs* **1993**, *46*, 360–377.
[4] K. R. Harrap, *Cancer Res.* **1995**, *55*, 2761–2768.
[5] K. Ito, S. Adachi, Y. Itani, M. Koyama, K. Hori, R. Chin, M. Shintani, K. Beppu, S. Kawai, K. Saito, *Jpn. J. Clin. Oncol.* **1999**, *29*, 299–302.
[6] J. L. Misset, *Br. J. Cancer* **1998**, *77*, 4–7.
[7] J. Lokich, *Cancer Invest.* **2001**, *19*, 756–760.
[8] N. Uchida, H. Kasai, Y. Takeda, R. Maekawa, K. Sugita, T. Yoshioka, *Anticancer Res.* **1998**, *18*, 247–252.
[9] S. E. Sherman, D. Gibson, A. H. J. Wang, S. J. Lippard, *Science* **1985**, *230*, 412–417.
[10] P. M. Takahara, A. C. Rosenzweig, C. F. Frederick, S. J. Lippard, *Nature* **1995**, *377*, 649–652.
[11] F. Legendre, V. Bas, J. Kozelka, J.-C. Chottard, *Chem. Eur. J.* **2000**, *6*, 2002–2010.
[12] F. Legendre, J. Kozelka, J.-C. Chottard, *Inorg. Chem.* **1998**, *37*, 3964–3967.
[13] M. R. Harnden, R. L. Jarvest, M. R. Boyd, D. Sutton, R. A. Vere Hodge, *J. Med. Chem.* **1989**, *32*, 1738–1743.
[14] E. de Clercq, *Clin. Microbiol. Rev.* **1997**, *10*, 674–693.
[15] S. Grabner, J. Plavec, N. Bukovec, D. Di Leo, R. Cini, G. Natile, *J. Chem. Soc. Dalton Trans.* **1998**, 1447–1451.
[16] R. Cini, S. Grabner, N. Bukovec, L. Cerasino, G. Natile, *Eur. J. Inorg. Chem.* **2000**, *7*, 1601–1607.
[17] L. Cerasino, F. P. Intini, J. Kobe, E. de Clercq, G. Natile, *Inorg. Chim. Acta* **2003**, *344*, 174–182.
[18] M. Coluccia, A. Boccarelli, C. Cermelli, M. Portolani, G. Natile, *Metal-Based Drugs* **1995**, *2*, 249–256.
[19] Z. Balcarová, J. Kaspárková, A. Zákovská, O. Nováková, M. F. Sivo, G. Natile, V. Brabec, *Mol. Pharmacol.* **1998**, *53*, 846–855.
[20] M. J. Abrams, C. M. Giandomenico, J. F. Vollano, D. A. Schwartz, *Inorg. Chim. Acta* **1987**, *131*, 3–4.
[21] L. Cavallo, R. Cini, J. Kobe, L. G. Marzilli, G. Natile, *J. Chem. Soc., Dalton Trans.* **1991**, *8*, 1867–1873.
[22] M. Carlone, F. P. Fanizzi, F. P. Intini, N. Margiotta, L. G. Marzilli, G. Natile, *Inorg. Chem.* **2000**, *39*, 634–641.
[23] N. G. Di Masi, F. P. Intini, C. Pacifico, L. Maresca, G. Natile, *Inorg. Chim. Acta* **2000**, *310*, 27–33.
[24] M. Carlone, L. G. Marzilli, G. Natile, *Inorg. Chem.* **2004**, *43*, 584–592.
[25] M. Benedetti, G. Tamasi, R. Cini, G. Natile, *Chem. Eur. J.* **2003**, *9*, 6122–6132.
[26] G. Kampf, L. E. Kapinos, R. Griesser, B. Lippert, H. Sigel, *J. Chem. Soc., Perkin Trans. 2* **2002**, *7*, 1320–1327.
[27] N. Hadjiliadis, T. Theophanides, *Inorg. Chim. Acta* **1976**, *16*, 67–75.
[28] B. Noszál, V. Scheller-Krattiger, R. B. Martin, *J. Am. Chem. Soc.* **1982**, *104*, 1078–1081.
[29] A. P. Zens, T. J. Williams, J. C. Wisowaty, R. R. Fisher, R. B. Dunlap, T. A. Bryson, P. D. Ellis, *J. Am. Chem. Soc.* **1975**, *97*, 2850–2857.
[30] L. G. Marzilli, P. A. Marzilli, E. Alessio, *Pure Appl. Chem.* **1998**, *70*, 961–968.
[31] S. O. Ano, F. P. Intini, G. Natile, L. G. Marzilli, *Inorg. Chem.* **1999**, *38*, 2989–2999.
[32] P. J. Toscano, C. C. Chiang, T. J. Kistenmacher, L. G. Marzilli, *Inorg. Chem.* **1981**, *20*, 1513–1519.
[33] Two-Dimensional NMR Spectroscopy. Applications for Chemists and Biochemists, VCH Publisher, Weinheim, **1987**, p. 303–309.
[34] D. S. Stephenson, G. Binsch, *J. Magn. Reson.* **1978**, *30*, 625–626.
[35] H. Eyring, *J. Chem. Phys.* **1935**, *3*, 107–115.

Received: October 01, 2004

 © 2005 Wiley-VCH Verlag GmbH & Co. KGaA, Weinheim

Endohedral Metallocenophanes of Rhodium and Cobalt

Carsten Schaefer,[a] Gerald Scholz,[a] Rolf Gleiter,*[a] Thomas Oeser,[a] and Frank Rominger[a]

Dedicated to Professor Paul von Ragué Schleyer on the occasion of his 75th birthday

Keywords: Cage compounds / Sandwich complexes / Alkynes / Rhodium / Cobalt

The synthesis of seven endohedral metallocenophanes of rhodium (**7b**, **8b**) and cobalt (**1d**−**h**) with a cyclopentadienyl unit as one of the π-systems and a cyclobutadiene or cyclopentadienone unit as the second π-system is described, including the synthesis of the unsubstituted parent compound of the [CpCo(cbd)]-derived endohedral phanes, [3.3]-η^5-(1,1′,3,3′)-cyclopentadienyl–η^4-(cyclobutadienophane)cobalt(I) (**1h**). This compound could be obtained by deprotection of the corresponding trimethylsilyl-substituted endohedral phane **1g**. The X-ray structures of **7b**, **1e**, **1g** and **1h** could be obtained. This paper compares their structural properties to the complexes reported in previous short communications.
(© Wiley-VCH Verlag GmbH & Co. KGaA, 69451 Weinheim, Germany, 2005)

Introduction

In [*n.n*]phanes[1−4] the cyclic conjugated π-systems which are held in place by at least two bridges, such as hydrocarbon chains, offer a variety of bonding modes for metal centres. The cage structures of these phanes exhibit an inside and an outside face leading to two binding modes for a metal atom or metal fragment to the π-systems: inside the cage (endohedral, **A**) or outside the cage (exohedral, **B**) as shown in Figure 1.[5]

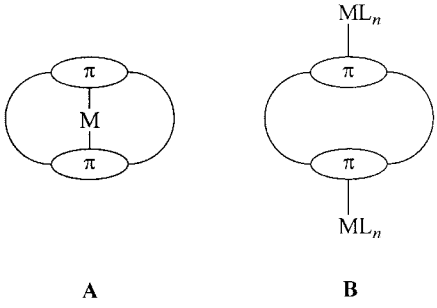

Figure 1. Endohedral (**A**) and exohedral (**B**) bonding modes of metallocenophanes.

In comparison to the numerous examples of the exohedral metallocenophanes reports of endohedral phanes are much rarer because of their limited accessibility. However, they deserve special interest because the hydrocarbon cage is able to stabilize low oxidation states of the incorporated metals. This has been demonstrated by complexing Ga^{I} and Ge^{II} in [2.2.2]paracyclophane.[6] In the literature there are reports of two protocols for the synthesis of endohedral metallocenophanes:

Either by reacting metal atoms or metal ions directly with the appropriate cyclophanes (path **I** in Scheme 1),[6,7] or by building the tethers on a metallocene in a stepwise fashion (path **II**).[8] Recently, we developed a third path (**III**) by utilizing substituted half-sandwich complexes which are able to form the second π-system by an intramolecular metal mediated cyclization of alkyne units (Scheme 1).[9]

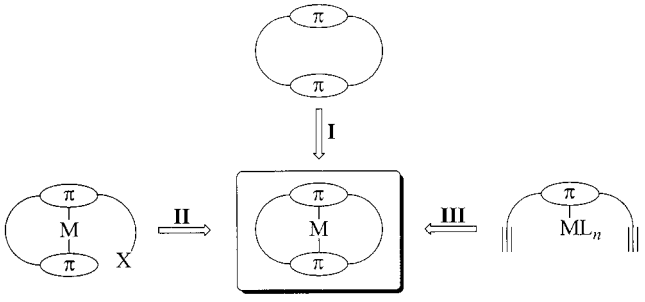

Scheme 1. Protocols **I**–**III** for the synthesis of endohedral metallocenophanes.

Using this third synthetic pathway we were able to synthesize the cobalt and rhodium complexes **1a**−**h**, **2c**, **3a**–**b**, **4a**–**b**, **5a**, and **6a** (Figure 2), of which **1a**, **1b**, **1e**, **1g**, **1h**, **5a**, and **6a** were investigated by X-ray diffraction.[9,10]

In this paper we report the synthesis of two endohedral rhodium phanes **7b** and **8b** (Figure 3), four endohedral co-

[a] Organisch-Chemisches Institut, Universität Heidelberg, INF 270, 69120 Heidelberg, Germany
Fax: +49-6221-544205
E-mail: Rolf.Gleiter@urz.uni-heidelberg.de

 © 2005 Wiley-VCH Verlag GmbH & Co. KGaA, Weinheim DOI: 10.1002/ejic.200400851

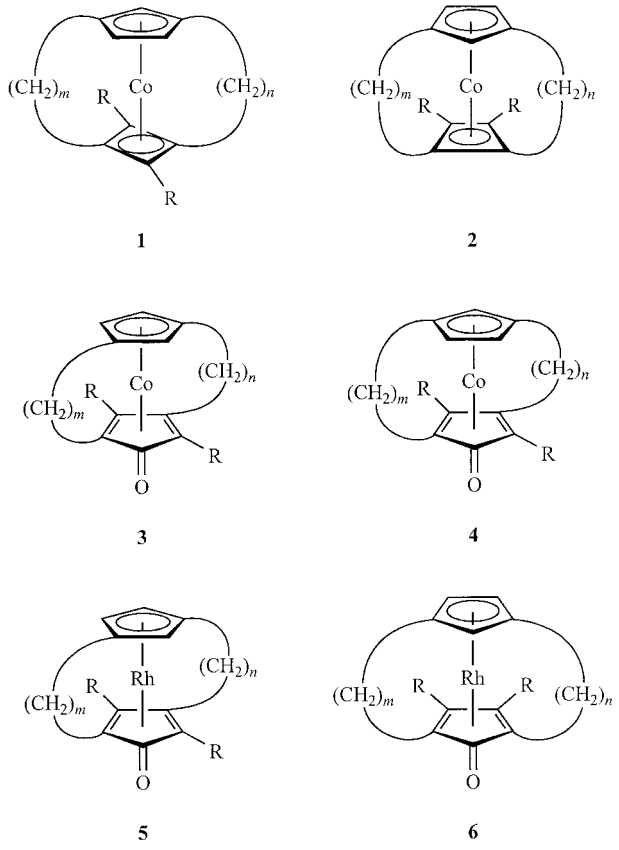

Figure 2. Endohedral metallocenophanes **1a**–**h**, **2c**, **3a**–**b**, **4a**–**b**, **5a**, and **6a** synthesized by route **III** [$m = n = 3$, R = *t*Bu (**a**); $m = n = 4$, R = *t*Bu (**b**); $m = n = 5$, R = *t*Bu (**c**); $m = 3$, $n = 4$, R = *t*Bu (**d**); $m = 3$, $n = 5$, R = *t*Bu (**e**); $m = 4$, $n = 5$, R = *t*Bu (**f**); $m = n = 3$, R = $SiMe_3$ (**g**); $m = n = 3$, R = H (**h**)].

balt phanes **1d**–**g** (Figure 2) and of the unsubstituted parent compound **1h** of phane **1a**.

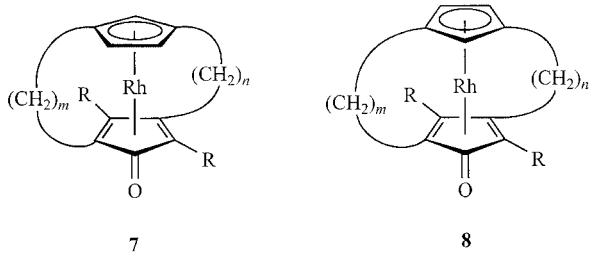

Figure 3. Isomeric rhodium phanes **7b** and **8b** ($m = n = 4$, R = *t*Bu).

Results and Discussion

Synthesis

The synthesis of the ω-haloalkynes **11a**–**d** necessary as building blocks for the tethers in the endohedral phanes was achieved by the substitution of tosylated ω-chloro alcohols **10a**–**c** by lithiated *tert*-butylacetylene or (trimethylsilyl)acetylene, respectively (Scheme 2).

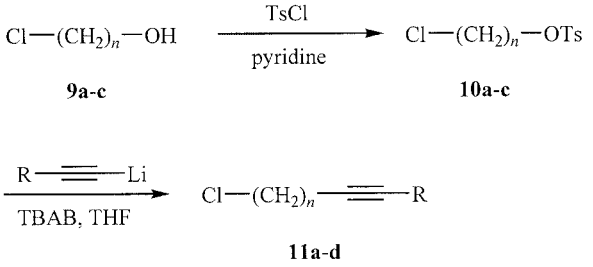

Scheme 2. Synthesis of ω-haloalkynes **11a**–**d** [$n = 3$, R = *t*Bu (**a**); $n = 4$, R = *t*Bu (**b**); $n = 5$, R = *t*Bu (**c**); $n = 3$, R = $SiMe_3$ (**d**)] from ω-hydroxy alcohols **9a**–**c** [$n = 3$, R = *t*Bu (**a**); $n = 4$, R = *t*Bu (**b**); $n = 5$, R = *t*Bu (**c**)].

The disubstituted cyclopentadiene derivatives that we used as ligands for the half-sandwich complexes were synthesized by a two step procedure (Scheme 3).[9] In the first step the first alkyne substituent was introduced by treatment of 3-ethoxycyclopent-2-ene-1-one (**12**) with a Grignard reagent of an ω-chloroalkyne **11**. Acidic workup of the reaction mixture yielded the respective 3-alkynylcyclopent-2-enones **13**. The second alkyne substituent was introduced in a similar reaction and again acidic workup led to the desired disubstituted cyclopentadienes. The resulting cyclopentadiene derivatives were deprotonated with *n*-butyllithium in THF shortly before their complexation with metal dicarbonyl fragments.

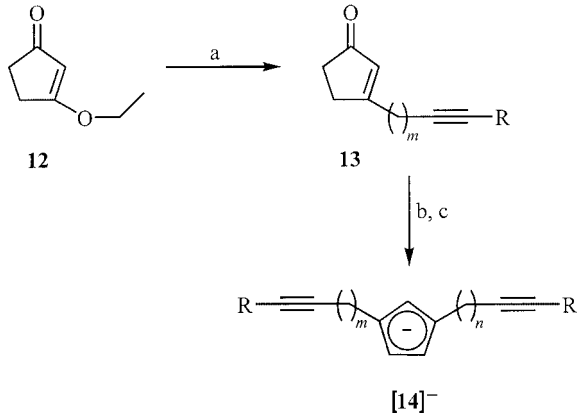

Scheme 3. Two step synthesis of 1,3-difunctionalized cyclopentadienyllithium salts [**14b**]⁻ ($n = m = 4$, R = *t*Bu) and [**14d**–**g**]⁻ [$n = 3$, $m = 4$, R = *t*Bu (**d**); $n = 3$, $m = 5$, R = *t*Bu (**e**); $n = 4$, $m = 5$, R = *t*Bu (**f**); $m = n = 3$, R = $SiMe_3$ (**g**)]. Reagents: (a) $ClMg–(CH_2)_mC{\equiv}CR$ in THF, then HCl (aq); (b) $ClMg–(CH_2)_nC{\equiv}R$ in THF, then HCl (aq); (c) *n*-butyllithium in THF.

In the case of the rhodium complexes, the lithium salt [**14b**]⁻ was treated with the dicarbonyl(chloro)rhodium dimer in THF to yield the dicarbonyl rhodium complex **15b** (Scheme 4) as an orange oil in 77% yield.

The thermolytic reaction of the dicarbonyl rhodium complex **15b** in refluxing cyclooctane yielded two isomeric endohedral products, **7b** and **8b** (Figure 3). While **7b** was formed in an acceptable yield of 16%, **8b** was only produced in minor quantities (0.5% yield). We were able to grow single crystals of **7b** which were suitable for X-ray diffraction analysis. This allowed us to confirm the structure

 © 2005 Wiley-VCH Verlag GmbH & Co. KGaA, Weinheim

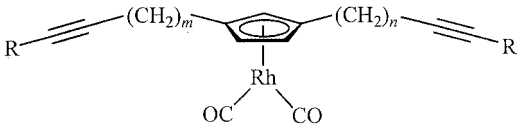

15

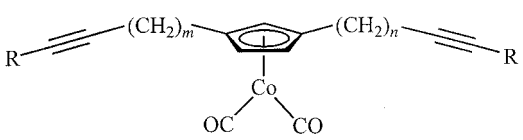

16

Scheme 4. Synthesized dicarbonyl metal complexes **15b** (n = m = 4, R = tBu) and **16d**–**g** [n = 3, m = 4, R = tBu (**d**); n = 3, m = 5, R = tBu (**e**); n = 4, m = 5, R = tBu (**f**); m = n = 3, R = $SiMe_3$ (**g**)].

of **7b** and also to assign the structure of **8b**. For the isomeric endohedral products six isomers are possible, of which four are C_s and two C_1 symmetric. The NMR spectroscopic data for **7b** and **8b** prove the C_1 symmetry of both isolated complexes **7b** and **8b**. As we were able to confirm the structure of **7b** by X-ray analysis the structure of **8b** could also be assigned unambiguously.

Until now only endohedral cobalt phanes bearing alkyl chains of the same length (m = n) had been synthesized.[9,10] To investigate the amount of distortion resulting from two different alkyl chains, the endohedral cobalt phanes **1d** (m = 3, n = 4, R = tBu), **1e** (m = 3, n = 5, R = tBu), **1f** (m = 4, n = 5, R = tBu) were envisaged. To obtain the dicarbonyl cobalt complexes **16d**–**f** we reacted the deprotonated cyclopentadiene derivatives [**14d**–**f**]$^-$ with $[Co_2(CO)_8]/I_2$. The thermolytic reaction of these half-sandwich complexes in refluxing cyclooctane resulted in the formation of the endohedral complexes **1d**–**f** in 5% (**1d**), 30% (**1e**) and 15% (**1f**) yield.

For the synthesis of the parent compound **1h** of the recently published endohedral [3.3]phane **1a** we made use of TMS as protecting groups on the cyclobutadiene unit (Scheme 5).[11] The twofold TMS substituted phane **1g** was obtained in 35% yield analogously to **1a** by refluxing the dicarbonyl cobalt complex **16g** in cyclooctane. The removal of the TMS groups was achieved in 74% yield by stirring a solution of **1g** with Me_4NF at 80 °C.

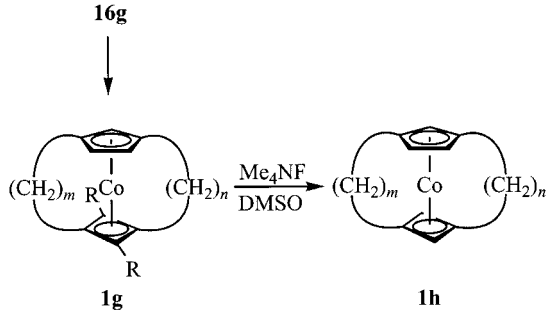

1g 1h

Scheme 5. Synthesis of unsubstituted phane **1h** by deprotection.

Structural Investigations

Crystals suitable for X-ray crystallographic studies could be obtained for the complexes **7b**, **1e**, **1g** and **1h**. In Figure 4, the molecular structures of these endohedral phanes are shown.

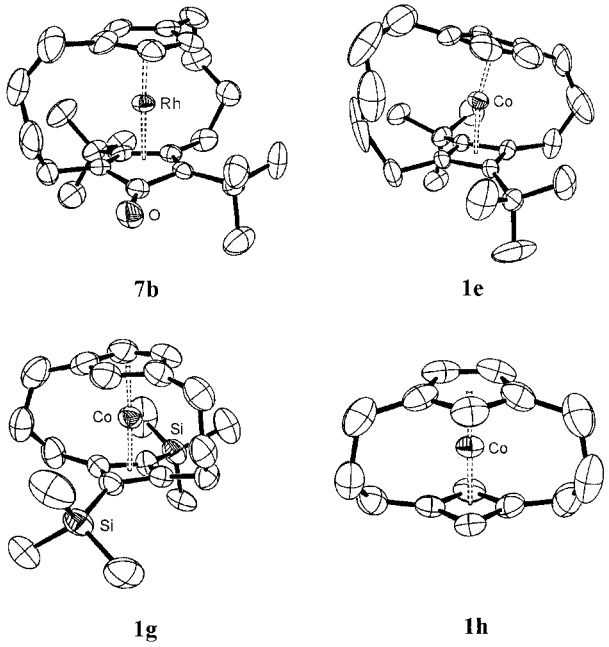

7b 1e

1g 1h

Figure 4. ORTEP plots (50% ellipsoid probability) of the molecular structures of **7b**, **1g** (left), **1e** and **1h** (right).

Including the previously described molecular structures,[9,10] a total number of eight crystallographically studied endohedral phanes synthesized with our protocol are available and can now be compared. Selected structural properties of these complexes are listed in Table 1.

Table 1. Structural properties of endohedral metallocenophanes **1a**, **1b**, **1g**, **1h**, **5a**, **6a** and **7b**.[a]

	Interplanar angle α [°]	Angle β [°]	(η^5-Cp)–M distance [Å]	M–(η^4-ligand) distance [Å]
1a[9]	6.6	174.2	1.604	1.645
1b[9]	4.0	178.3	1.670	1.692
1e	13.6	166.9	1.677	1.678
1 g[b]	6.8/7.2	173.6/173.1	1.609/1.604	1.645/1.650
1h	9.9	170.8	1.590	1.631
5a[10]	4.3	175.6	1.777	1.742
6a[10]	22.2	170.9	1.806	1.751
7b	5.1	174.8	1.857	1.791

[a] For the calculation of angles and centroids, all five C atoms of the Cp rings were used, but only the four coordinated C atoms of the η^4-ligands (cyclopentadienone or cyclobutadiene). [b] The two different values refer to two independent molecules in the unit cell.

The larger atomic radius of rhodium results in larger distances between the metal centre and the coordinated η^5-Cp ligand as well as the η^4-coordinated unit. While these distances for the rhodium complexes range from 1.78–1.86 Å [(η^5-Cp)···M distance] and 1.74–1.79 Å [M···(η^4-ligand) distance], the cobalt complexes show values of 1.59–1.68 Å [(η^5-Cp)···M distance] and 1.63–1.69 Å [M···(η^4-ligand) distance]. Within these limits the distances vary ac-

 © 2005 Wiley-VCH Verlag GmbH & Co. KGaA, Weinheim

cording to the lengths of the alkyl chains and to the substitution pattern. First, the structural features of the rhodium complexes shall be compared. Generally there exist six possible isomers for endohedral [*n.n*]phanes with a Cp and a cyclopentadienone unit, namely two C_1- and four C_s-symmetric. Of these six isomers three are represented by the complexes **5a** (C_1), **6a** (C_s) and **7b** (C_1). Because of the shorter alkyl bridges the two [3.3]phanes **5a** and **6a** are more strained than the [4.4]phane **7b**, which has the largest distances between the rhodium centre and the π-ligands. The two [3.3]phanes also differ in the strain of the carbon cage. The substitution pattern of the π-ligands in the C_s-symmetric phane **6a** allows the molecule to reduce the strain by increasing the interplanar angle α (22.2°), which is the largest of all the investigated complexes (Figure 5). The C_1-symmetric [3.3]phane **5a** does not have that much flexibility to reduce strain because of the substitution pattern of the alkyl chains and, therefore, shows a small interplanar angle (α = 4.3°) as well as the shortest rhodium···π-ligand distances.

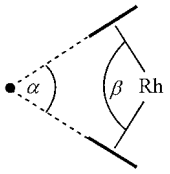

Figure 5. Illustration of the interplanar angle α and angle β.

In the row of the cobalt complexes the shortest bonding lengths between the cobalt centre and the π-ligands are found in the unsubstituted [3.3]phane **1h** [1.590 Å (η^5-Cp)−M distance, 1.631 Å M−(η^4-ligand) distance]. These distances are shorter than those reported for the unbridged species [(η^5-Cp)−M 1.660 Å and M−(η^4-ligand) 1.681 Å].[12] Addition of sterically demanding substituents on the cbd-unit increases these distances, with TMS groups [1.609/1.604 Å (η^5-Cp)−M distance, 1.645/1.650 Å M−(η^4-ligand) distance] having practically the same effect as *t*Bu groups [1.604 Å (η^5-Cp)−M distance, 1.645 Å M−(η^4-ligand) distance]. The metal-ligand distances for **1b** and **1e** are rather close to the parent system.[12] All the symmetrically bridged endohedral cobalt phanes (*n* = *m*) **1a**, **1b**, **1g** and **1h** show nearly parallel π-systems, with the interplanar angles α ranging from 4.0 to 9.9°. In the unsymmetrically bridged **1e** the distortion leads to an enlarged interplanar angle α (13.6°) and to a remarkably small angle β (166.9°), the smallest in all investigated phanes.

Conclusions

Our method of synthesizing metallocenophanes in situ by generating one ligand out of tethered precursors provided us with endohedral complexes of cobalt and rhodium. The yields were low (5%) to moderate (35%). In the case of the cobalt complexes, the generation of a cyclobutadiene or a cyclopentadienone ring is dependent on the reaction temperature. From the dicarbonyl rhodium complexes only the cyclopentadienone ligand was generated. A comparison of five endohedral (η^5-Cp)Co(η^4-Cbd) metallocenophanes revealed the anticipated shortest metal–ligand distances for the [3.3]cyclophane, whereas the other bridges led to metal−ligand distances close to the unbridged species. The relatively short metal−ligand distances for the [3.3]bridged species are also encountered in the case of the rhodium species **5a** and **6a**.

Experimental Section

General Remarks: All melting points are uncorrected. Elemental analyses were carried out by the Mikroanalytisches Laboratorium der Universität Heidelberg. UV/Vis absorption data were recorded with a Hewlett Packard HP 8452A Diode Array-spectrometer. IR spectra were recorded with a Bruker Vector 22 FT-IR spectrometer. The NMR spectra were measured with a Bruker WH 300 or Avance 500 spectrometer (^{1}H NMR at 300 or 500 MHz and ^{13}C NMR at 75 or 125 MHz) using the solvent as internal standard (δ). Standard symbols for signal multiplicities are used; p = pseudo. FAB and FD mass spectra refer to data from a Jeol JMS-700 instrument. All reactions were carried out in dried glassware under argon using dried and oxygen-free solvents.

X-ray Crystallographic Study: Data were collected with a Bruker Smart CCD-diffractometer at 200 K (**7b** and **1e**) and a Bruker Smart Apex-diffractometer at 295 K (**1g** and **1h**). Relevant crystal and data collection parameters are given in Table 2. The structures were solved by direct methods and refined against F^2 with a full-matrix least-square algorithm by using SHELXTL[13] software. In all cases an absorption correction was applied by using SADABS,[14] based on the Laue symmetry of the reciprocal space.

CCDC-249232 (for **1e**), -249234 (for **1g**), -249233 (for **1h**), and -249231 (for **7b**) contain the supplementary crystallographic data for this paper. These data can be obtained free of charge from the Cambridge Crystallographic Data Centre via www.ccdc.cam.ac.uk/data_request/cif.

General Procedure for the Preparation of ω-Chloroalkynes 11a−d: A dry 100-mL flask was charged with the respective 4-toluenesulfonate, dry THF and *tert*-butylammonium bromide (TBAB) and the mixture was cooled to 0 °C. Alkynyllithium (prepared by the addition of *n*-butyllithium to 1-alkyne in THF) was then added with a cannula. The mixture was stirred at 0 °C (1 h) then allowed to reach room temp. overnight. The solvent was removed, water was added to the residue and the solution was extracted with diethyl ether. The organic layer was washed with brine, dried ($MgSO_4$), filtered and the solvent was evaporated under reduced pressure. The products were purified by distillation.

1-Chloro-6,6-dimethylhept-4-yne (11a): Reaction mixture: 3-chloropropyl-1-tosylate (**10a**) (2.49 g, 10 mmol) and TBAB (3.22 g, 10 mmol) in THF (20 mL), 3,3-dimethylbut-1-yne (0.82 g, 10 mmol) and *n*-butyllithium (3.6 mL, 2.8 M) in THF (20 mL). Yield 1.19 g (75%). Colorless liquid, b.p. 49 °C (2 mbar). ^{1}H NMR (300 MHz, $CDCl_3$): δ = 1.18 (s, 9 H, CH_3), 1.90 (pquint, ^3J = 6.6 Hz, 2 H, CH_2), 2.31 (t, ^3J = 6.8 Hz, 2 H, CH_2), 3.63 (t, ^3J = 6.5 Hz, 2 H, CH_2) ppm. ^{13}C NMR (75 MHz, $CDCl_3$): δ = 16.9 (CH_2), 28.0 (C), 32.0 (CH_3), 32.6 (CH_2), 44.5 (CH_2), 77.0 (C), 90.8 (C) ppm. IR (film) $\tilde{\nu}$ = 2968, 2929, 2867, 1477, 1456 cm^{-1}. HRMS (positive EI) calcd. for $C_9H_{15}Cl$ ([M]$^+$), 160.0833; found, 160.0875 (+4.2 mmu).

1-Chloro-7,7-dimethyloct-5-yne (11b): Reaction mixture: 4-chlorobutyl-1-tosylate (**10b**) (2.63 g, 10 mmol) and TBAB (3.22 g,

 © 2005 Wiley-VCH Verlag GmbH & Co. KGaA, Weinheim

Table 2. Crystal data and structural refinement for **7b**, **1e**, **1g** and **1h**.

	7b	**1e**	**1g**	**1h**
Empirical formula	$C_{26}H_{37}ORh$	$C_{25}H_{37}Co$	$C_{21}H_{33}CoSi_2$	$C_{15}H_{17}Co$
Formula mass	468.47	396.48	400.58	256.22
Wavelength [Å]	0.71073	0.71073	0.71073	0.71073
Crystal system	tetragonal	monoclinic	monoclinic	orthorhombic
Space group	$I4_1/a$	$P2_1/n$	$P2_1/n$	$Pbca$
Temp. [K]	200	200	295	295
Z	16	4	8	8
a	14.3272(3)	9.1546(2)	8.925(2)	7.5187(8)
b	14.3272(3)	16.4597(3)	25.475(7)	16.561(2)
c	42.901(1)	14.1320(3)	19.307(5)	18.839(2)
α	90	90	90	90
β	90	91.063(1)	94.448(6)	90
γ	90	90	90	90
V [Å^3]	8806.2(4)	2129.07(8)	4377(2)	2345.7(4)
$D_{calcd.}$ [g/cm^3]	1.413	1.24	1.22	1.45
Abs. coeff. μ [mm^{-1}]	0.789	0.81	0.89	1.43
Max./min. transmission	0.95/0.88	0.93/0.59	0.76/0.97	0.56/0.96
Crystal shape	polyhedron	polyhedron	plate	needle
Crystal size [mm^3]	0.17×0.15×0.06	0.48×0.42×0.10	0.33×0.22×0.03	0.45×0.11×0.03
θ range for data collection [°]	1.5–24.7	1.9–27.5	1.92–28.36	2.16–28.35
Index ranges	$-16 \le h \le 16$	$-11 \le h \le 11$	$-11 \le h \le 11$	$-9 \le h \le 10$
	$-16 \le k \le 16$	$-21 \le k \le 21$	$-34 \le k \le 11$	$-10 \le k \le 22$
	$-50 \le l \le 50$	$-18 \le l \le 18$	$-22 \le l \le 25$	$-25 \le l \le 25$
Reflections collected	37141	21428	21679	16177
Independent reflections [R(int.)]	3763 (0.108)	4883 (0.035)	10521 (0.173)	2906 (0.046)
Observed reflections	2466 [$I > 2\sigma(I)$]	3835 [$I > 2\sigma(I)$]	5773 [$I > 2\sigma(I)$]	2443 [$I > 2\sigma(I)$]
Data/restraints/parameters	3763/10/278	4883/0/241	10521/0/445	2906/0/213
Goodness-of-fit on F^2	1.02	1.06	1.05	1.26
$R(F)$	0.054	0.078	0.088	0.055
$R_W(F^2)$	0.116	0.209	0.247	0.111
$(\Delta\rho)_{max.}$, $(\Delta\rho)_{min.}$ [e·Å^{-3}]	2.70 and –1.39	1.54 and –0.70	0.94 and –1.95	0.34 and –0.46

10 mmol) in THF (20 mL), 3,3-dimethylbut-1-yne (0.82 g, 10 mmol) and *n*-butyllithium (3.6 mL, 2.8 M) in THF (20 mL). Yield 1.21 g (70%). Colorless liquid, b.p. 54 °C (1 mbar). ^{1}H NMR (500 MHz, $CDCl_3$): δ = 1.18 (s, 9 H, CH_3), 1.62 (pquint, ^3J = 7.2 Hz, 2 H, CH_2), 1.87 (pquint, ^3J = 7.1 Hz, 2 H, CH_2), 2.18 (t, ^3J = 7.0 Hz, 2 H, CH_2), 3.56 (t, ^3J = 6.6 Hz, 2 H, CH_2) ppm. ^{13}C NMR (125 MHz, $CDCl_3$): δ = 18.7 (CH_2), 26.9 (CH_2), 28.0 (C), 32.0 (CH_3), 32.3 (CH_2), 45.4 (CH_2), 78.2 (C), 90.4 (C) ppm. IR (film) $\tilde{\nu}$ = 2968, 2866, 1477, 1779, 1476, 1362 cm^{-1}. HRMS (positive EI) calcd. for $C_{10}H_{17}Cl$ ([M]$^+$), 172.1019; found, 172.1023 (+0.4 mmu).

1-Chloro-8,8-dimethylnon-6-yne (11c): Reaction mixture: 5-chloropentyl-1-tosylate (**10c**) (2.77 g, 10 mmol) and TBAB (3.22 g, 10 mmol) in THF (20 mL), 3,3-dimethylbut-1-yne (0.82 g, 10 mmol) and *n*-butyllithium (3.6 mL, 2.8 M) in THF (20 mL). Yield 1.31 g (70%). Colorless liquid, b.p. 63 °C (2 mbar). ^{1}H NMR (300 MHz, $CDCl_3$): δ = 1.17 (s, 9 H, CH_3), 1.45–1.55 (m, 4 H, CH_2), 1.72–1.85 (m, 2 H, CH_2), 2.13 (t, ^3J = 6.5 Hz, 2 H, CH_2), 3.51 (t, CH_2, ^3J = 6.7 Hz, 2 H) ppm. ^{13}C NMR (75 MHz, $CDCl_3$): δ = 19.2 (CH_2), 26.7 (CH_2), 28.0 (C), 29.0 (CH_2), 32.1 (CH_3), 32.8 (CH_2), 45.6 (CH_2), 78.6 (C), 90.1 (C) ppm. IR (film) $\tilde{\nu}$ = 2968, 2864, 1476, 1361 cm^{-1}. HRMS (positive EI) calcd. for $C_{11}H_{19}Cl$ ([M]$^+$), 186.1175; found, 186.1171 (–0.4 mmu).

5-Chloropent-1-ynyltrimethylsilane (11d): Reaction mixture: 3-chloropropyl-1-tosylate (**10a**) (2.49 g, 10 mmol) and TBAB (3.22 g, 10 mmol) in THF (20 mL), (trimethylsilyl)acetylene (0.98 g, 10 mmol) and *n*-butyllithium (3.6 mL, 2.8 M) in THF (20 mL). Yield 1.36 g (78%). Colorless liquid, b.p. 80 °C (28 mbar). ^{1}H NMR (500 MHz, $CDCl_3$): δ = 0.14 (s, 9 H, CH_3), 1.95 (pquint, ^3J = 6.6 Hz, 2 H, CH_2), 2.40 (t, ^3J = 6.9 Hz, 2 H, CH_2), 3.63 (t, ^3J = 6.4 Hz, 2 H, CH_2) ppm. ^{13}C NMR (125 MHz, $CDCl_3$): δ = 0.2 (CH_3), 17.4 (CH_2), 31.5 (CH_2), 43.7 (CH_2), 85.8 (C), 105.3 (C) ppm. IR (film) $\tilde{\nu}$ = 2960, 2176, 1431, 1361 cm^{-1}. HRMS (positive EI) calcd. for $C_8H_{15}ClSi$ ([M]$^+$), 174.0632; found, 174.0567 (–6.5 mmu).

General Procedure for the Synthesis of Cyclopent-2-enones 13a–c: In a dry 50-mL flask a Grignard reagent was prepared from chloroalkyne and magnesium in dry THF. The resulting solution was cooled to 0 °C and 3-ethoxycyclopent-2-enone, dissolved in dry THF, was added dropwise. The reaction mixture was stirred at 0 °C (1 h) and then warmed to room temp. overnight. The reaction mixture was poured into ice, and the solution was acidified with 5% hydrochloric acid to pH 5. After extraction with diethyl ether the organic layer was washed with brine, dried ($MgSO_4$), filtered and the solvent was evaporated under reduced pressure. The products were purified by flash column chromatography (silica gel, petroleum ether/diethyl ether, 3:1).

3-(6,6-Dimethylhept-4-ynyl)cyclopent-2-enone (13a): Reaction mixture: 1-chloro-6,6-dimethylhept-4-yne (**11a**) (6.03 g, 38 mmol) and magnesium (0.92 g, 38 mmol) in THF (10 mL), 3-ethoxycyclopent-2-enone (3.0 g, 23.8 mmol) in THF (10 mL). Yield 3.11 g (64%). Colorless oil. ^{1}H NMR (300 MHz, $CDCl_3$): δ = 1.17 (s, 9 H, CH_3), 1.68–1.76 (pquint, ^3J = 7.1 Hz, 2 H, CH_2), 2.19 (t, ^3J = 6.9 Hz, 2 H, CH_2), 2.38 (m, 2 H, CH_2), 2.47–2.52 (m, 2 H, CH_2), 5.94 (s, 1 H, CH) ppm. ^{13}C NMR (125 MHz, $CDCl_3$): δ = 18.3 (CH_2), 26.4 (CH_2), 27.3 (C), 31.3 (CH_3), 31.5 (CH_2), 32.3 (CH_2), 35.2 (CH_2), 77.3 (C), 90.1 (C), 129.6 (CH), 182.3 (C), 210.0 (C) ppm. IR (film) $\tilde{\nu}$ = 2967, 2866, 1710, 1675, 1616, 1437, 1361 cm^{-1}. HRMS (positive

 © 2005 Wiley-VCH Verlag GmbH & Co. KGaA, Weinheim

EI) calcd. for $C_{14}H_{20}O$ ([M]$^+$), 204.1514; found, 204.1511 (–0.3 mmu). $C_{14}H_{20}O$ (204.31): calcd. C 82.30, H 9.87, found C 82.02, H 10.32.

3-(7,7-Dimethyloct-5-ynyl)cyclopent-2-enone (13b): Reaction mixture: 1-chloro-7,7-dimethyloct-5-yne (**11b**) (6.56 g, 38 mmol) and magnesium (0.92 g, 38 mmol) in THF (10 mL), 3-ethoxycyclopent-2-enone (3.0 g, 23.8 mmol) in THF (10 mL). Yield 2.65 g (51%). Colorless oil. ^{1}H NMR (300 MHz, $CDCl_3$): δ = 1.14 (s, 9 H, CH_3), 1.44–1.49 (m, 2 H, CH_2), 1.62–1.68 (m, 2 H, CH_2), 2.13 (t, ^3J = 6.9 Hz, 2 H, CH_2), 2.34–2.41 (m, 4 H, CH_2), 2.53–2.55 (m, 2 H, CH_2), 5.91–5.92 (m, 1 H, CH) ppm. ^{13}C NMR (75 MHz, $CDCl_3$): δ = 19.0 (CH_2), 26.6 (CH_2), 27.9 (C), 29.2 (CH_2), 32.0 (CH_3), 32.1 (CH_2), 33.6 (CH_2), 35.9 (CH_2), 78.2 (C), 90.2 (C), 130.2 (CH), 183.4 (C), 210.7 (C) ppm. IR (film) $\tilde{\nu}$ = 2966, 2930, 2864, 1710, 1675, 1616, 1437, 1361 cm^{-1}. UV/Vis (CH_2Cl_2): $\lambda_{max.}$ (log ε) = 276 (2.56), 310 (1.82) nm. HRMS (positive EI) calcd. for $C_{15}H_{22}O$ ([M]$^+$), 218.1671; found, 218.1672 (+0.1 mmu). $C_{15}H_{22}O$ (218.33): calcd. C 82.52, H 10.16; found C 82.11, H 10.36.

3-[5-(Trimethylsilyl)pent-4-ynyl]cyclopent-2-enone (13g): Reaction mixture: (5-chloropent-1-ynyl)trimethylsilane (**11d**) (6.64 g, 38 mmol) and magnesium (0.92 g, 38 mmol) in THF (10 mL), 3-ethoxycyclopent-2-enone (3.0 g, 23.8 mmol) in THF (10 mL). Yield 4.14 g (79%). Colorless oil. ^{1}H NMR (500 MHz, $CDCl_3$): δ = 0.14 (s, 9 H, CH_3), 1.79 (pquint, ^3J = 7.3 Hz, 2 H, CH_2), 2.28 (t, ^3J = 6.9 Hz, 2 H, CH_2), 2.39–2.41 (m, 2 H, CH_2), 2.51 (t, ^3J = 7.7 Hz, 2 H, CH_2), 2.57–2.59 (m, 2 H, CH_2), 5.94–5.96 (m, 1 H, CH) ppm. ^{13}C NMR (125 MHz, $CDCl_3$): δ = 0.2 (CH_3), 19.6 (CH_2), 26.0 (CH_2), 31.7 (CH_2), 32.5 (CH_2), 35.4 (CH_2), 85.9 (C), 106.0 (C), 129.9 (CH), 181.9 (C), 210.0 (C) ppm. HRMS (positive EI) calcd. for $C_{13}H_{20}OSi$ ([M]$^+$), 220.1283; found, 220.1283 (±0.0 mmu). IR (film) $\tilde{\nu}$ = 2957, 2174, 1710, 1675, 1616, 1438, 1409, 1249, 1183, 842, 760 cm^{-1}. $C_{13}H_{20}OSi$ (220.38): calcd. C 70.85, H 9.15; found C 70.91, H 9.32.

General Procedure for the Synthesis of Cyclopentadienes 14b and 14d–g: In a dry 50-mL flask a Grignard reagent was prepared from chloroalkyne and magnesium in dry THF. The resulting solution was cooled to 0 °C, cyclopent-2-enone dissolved in dry THF, was added. The mixture was stirred at 0 °C (1 h) and then allowed to reach room temp. overnight. The reaction mixture was poured into ice, the solution was acidified with 5% hydrochloric acid to pH 5 and extracted with diethyl ether. The organic layer was washed with brine, dried ($MgSO_4$), filtered and the solvent was evaporated under reduced pressure. The product was purified by flash column chromatography [alox III (neutral), petroleum ether] and used directly for the complexation after the removal of solvent.

1,3-Bis(7,7-dimethyloct-5-ynyl)cyclopentadiene (14b): Reaction mixture: 1-chloro-7,7-dimethyloct-5-yne (**11b**) (5.01 g, 29 mmol) and magnesium (0.70 g, 29 mmol) in THF (6 mL), 3-(7,7-dimethyloct-5-ynyl)cyclopent-2-enone (**13b**) (3.21 g, 14.7 mmol) in THF (10 mL). Yield 3.19 g (64%).

1-(6,6-Dimethylhept-4-ynyl)-3-(7,7-dimethyloct-5-ynyl)cyclopentadiene (14d): Reaction mixture: 1-chloro-7,7-dimethyloct-5-yne (**11b**) (5.01 g, 29 mmol) and magnesium (0.70 g, 29 mmol) in THF (6 mL), 3-(7,7-dimethylhept-4-ynyl)cyclopent-2-enone (**13a**) (3.00 g, 14.7 mmol) in THF (10 mL). Yield 0.91 g (19%).

1-(6,6-Dimethylhept-4-ynyl)-3-(8,8-dimethylnon-6-ynyl)cyclopentadiene (14e): Reaction mixture: 1-chloro-8,8-dimethylnon-6-yne (**11c**) (5.41 g, 29 mmol) and magnesium (0.70 g, 29 mmol) in THF (6 mL), 3-(7,7-dimethylhept-4-ynyl)cyclopent-2-enone (**13a**) (3.00 g, 14.7 mmol) in THF (10 mL). Yield 3.53 g (71%).

1-(7,7-Dimethyloct-5-ynyl)-3-(8,8-dimethylnon-6-ynyl)cyclopentadiene (14f): 1-Chloro-8,8-dimethylnon-5-yne (**11c**) (5.41 g, 29 mmol) and magnesium (0.70 g, 29 mmol) in THF (6 mL), 3-(7,7-dimethyloct-5-ynyl)cyclopent-2-enone (**13b**) (3.21 g, 14.7 mmol) in THF (10 mL). Yield 2.44 g (47%).

1,3-Bis[5-(trimethylsilyl)pent-4-ynyl]cyclopentadi-ene (14g): (5-Chloropent-1-ynyl)trimethylsilane (**11d**) (5.07 g, 29 mmol) and magnesium (0.70 g, 29 mmol) in THF (6 mL), 3-[5-(trimethylsilyl) pent-4-ynyl]cyclopent-2-enone (**13g**) (3.24 g, 14.7 mmol) in THF (10 mL). Yield 2.37 g (64%).

Dicarbonyl-η^5-[1,3-bis(7,7-dimethyloct-5-ynyl)cyclopentadienyl]rhodium(I) (15b): *n*-Butyllithium (2.6 mL, 1.6 M in hexane, 2.68 mmol) was added to a solution of cyclopentadiene **14b** (1.12 g, 3.30 mmol) in 10 mL of THF at –40 °C. After warming up to room temperature the solution was added to a solution of dicarbonyl(chloro) rhodium(I) dimer (0.50 g, 0.83 mmol) in 100 mL of THF and stirred for 24 h. The solvents were removed under vacuum and the products purified by flash column chromatography on silica gel using pentanes/diethyl ether (20:1) as eluent. Yield 636 mg (77%). Orange oil. ^{1}H NMR (500 MHz, $CDCl_3$): δ = 1.17 (s, 18 H, CH_3), 1.50 (m, 4 H, CH_2), 1.58 (m, 4 H, CH_2), 2.13 (m, 4 H, CH_2), 2.25 (m, 4 H, CH_2), 5.25 (ps, 2 H, CH), 5.38 (ps, 1 H, CH) ppm. ^{13}C NMR (125 MHz, $CDCl_3$): δ = 18.5 (CH_2), 27.4 (C), 27.9 (CH_2), 28.9 (CH_2), 31.4 (CH_2), 31.5 (CH_3), 78.0 (C), 86.0 (CH, $J_{Rh,C}$ = 3.8 Hz), 89.1 (CH, $J_{Rh,C}$ = 3.8 Hz), 89.5 (C), 110.6 (C, $J_{Rh,C}$ = 3.8 Hz), 192.7 (CO, $J_{Rh,C}$ = 83.8 Hz) ppm. IR (film) $\tilde{\nu}$ = 2967, 2862, 2034, 1969, 1476, 1456, 1361 cm^{-1}. UV/Vis (CH_2Cl_2): $\lambda_{max.}$ (log ε)= 240 (4.18), 296 (3.62) nm. MS (positive FD): m/z = 468 ([M – CO]$^+$).

General Procedure for the Synthesis of Dicarbonylcobalt Complexes 16d–g: A dry flask was charged with [$Co_2(CO)_8$] and dry THF, I_2 was added and the green mixture stirred at room temp. for 1 h. The green solution was cooled to 0 °C and a solution of cyclopentadienyllithium (prepared by the addition of *n*-butyllithium to a solution of cyclopentadiene in dry THF at –40 °C) was added. The brown mixture was stirred at 0 °C (1 h), then allowed to warm to room temp. overnight. The solvent was evaporated under reduced pressure and the product was purified by flash column chromatography [alox III (neutral), petroleum ether].

Dicarbonyl-η^5-[1-(6,6-dimethylhept-4-ynyl)-3-(7,7-dimethyloct-5-ynyl)cyclopentadienyl]cobalt(I) (16d): Reaction mixture: [$Co_2(CO)_8$] (402 mg, 1.2 mmol) and I_2 (299 mg, 1.2 mmol) in THF (25 mL), 1-(6,6-dimethylhept-4-ynyl)-3-(7,7-dimethyloct-5-ynyl)cyclopentadiene (**14d**) (0.9 g, 2.8 mmol) and *n*-butyllithium (2.4 mL, 1.6 M in hexane) in THF (5 mL). Yield 285 mg (55%). Orange oil. ^{1}H NMR (300 MHz, C_6D_6): δ = 1.32 (s, 9 H, CH_3), 1.34 (s, 9 H, CH_3), 1.50–1.64 (m, 6 H, CH_2), 2.10–2.56 (m, 8 H, CH_2), 4.57 (s, 2 H, CH), 4.70 (s, 1 H, CH) ppm. ^{13}C NMR (75 MHz, C_6D_6): δ = 18.7 (CH_2), 18.9 (CH_2), 27.4 (CH_2), 27.7 (C), 28.0 (CH_2), 29.2 (CH_2), 30.1 (CH_2), 30.3 (CH_2), 31.7 (CH_3), 78.1 (C), 78.5 (C), 83.5 (CH), 83.6 (CH), 85.6 (CH), 89.5 (C), 90.0 (C), 105.4 (C), 106.1 (C) ppm. IR (film) $\tilde{\nu}$ = 2964, 2862, 2044, 1952, 1475, 1453, 1360 cm^{-1}. UV/Vis (CH_2Cl_2): $\lambda_{max.}$ (log ε)= 252 (6.71), 336 (2.76), 360 (2.49).

Dicarbonyl-η^5-[1-(6,6-dimethylhept-4-ynyl)-3-(8,8-dimethylnon-6-ynyl)cyclopentadienyl]cobalt(I) (16e): Reaction mixture: [$Co_2(CO)_8$] (388 mg, 1.1 mmol) and I_2 (288 mg, 1.1 mmol) in THF (25 mL), 1-(6,6-dimethylhept-4-ynyl)-3-(8,8-dimethylnon-6-ynyl)cyclopentadiene (**14e**) (1.0 g, 3.0 mmol) and *n*-butyllithium (2.6 mL, 1.6 M in hexane) in THF (5 mL).Yield 130 mg (25%). Orange oil. ^{1}H NMR (500 MHz, C_6D_6): δ = 1.20 (s, 9 H, CH_3), 1.25 (s, 9 H, CH_3), 1.35–1.53 (m, 6 H, CH_2), 2.03–2.40 (m, 10 H, CH_2), 4.49 (s, 1 H, CH), 4.50 (s, 1 H, CH), 4.61 (s, 1 H, CH) ppm. ^{13}C NMR (125 MHz, C_6D_6): δ = 18.7 (CH_2), 19.0 (CH_2), 27.4 (CH_2), 27.7 (C), 28.3 (CH_2), 28.8 (CH_2), 29.2 (CH_2), 30.2 (CH_2), 30.3 (C), 30.6 (CH_2),

 © 2005 Wiley-VCH Verlag GmbH & Co. KGaA, Weinheim

31.5 (CH_3), 31.6 (CH_3), 78.1 (C), 78.8 (C), 83.5 (CH), 83.6 (CH), 85.6 (CH), 89.3 (C), 90.0 (C), 105.3 (C), 106.2 (C) ppm. IR (film) $\tilde{\nu}$ = 2964, 2920, 2850, 2015, 1955, 1474, 1455 cm^{-1}. UV/Vis (CH_2Cl_2): $\lambda_{max.}$ (log ε) = 250 (3.77), 306 (3.00), 330 (2.85) nm.

Dicarbonyl-η⁵-[1-(7,7-dimethyloct-5-ynyl)-3-(8,8-dimethylnon-6-ynyl)cyclopentadienyl]cobalt(I) (16f): Reaction mixture: [$Co_2(CO)_8$] (458 mg, 1.3 mmol) and I_2 (340 mg, 1.3 mmol) in THF (28 mL), 1-(7,7-dimethyloct-5-ynyl)-3-(8,8-dimethylnon-6-ynyl)cyclopentadiene (**14f**) (1.1 g, 3.2 mmol) and *n*-butyllithium (1.8 mL, 2.5 M in hexane) in THF (6 mL).Yield 250 mg (40%). Orange oil. ^1H NMR (300 MHz, C_6D_6): δ = 0.80–0.87 (m, 4 H, CH_2), 1.24 (s, 18 H, CH_3), 1.30–1.50 (br., 6 H, CH_2), 1.86–1.91 (m, 4 H, CH_2), 2.01–2.09 (m, 4 H, CH_2), 4.48 (s, 2 H, CH), 4.60 (s, 1 H, CH) ppm. ^{13}C NMR (75 MHz, C_6D_6): δ = 18.9 (CH_2), 19.1 (CH_2), 27.7 (C), 28.0 (CH_2), 28.4 (CH_2), 28.9 (CH_2), 29.2 (CH_2), 29.3 (CH_2), 30.1 (C), 30.3 (CH_2), 30.6 (CH_2), 31.6 (CH_3), 31.7 (CH_3), 78.6 (C), 78.8 (C), 83.4 (CH), 83.5 (CH), 85.6 (CH), 89.3 (C), 89.6 (C), 106.0 (C), 106.2 (C) ppm. IR (film) $\tilde{\nu}$ = 2967, 2930, 2860, 2016, 1955, 1475, 1455, 1388 cm^{-1}. UV/Vis (CH_2Cl_2): $\lambda_{max.}$ (log ε) = 246 (4.27), 294 (2.87) nm.

Dicarbonyl-η⁵-[1,3-bis(5-trimethylsilylpent-4-ynyl)cyclopentadienyl]-cobalt(I) (16g): Reaction mixture: [$Co_2(CO)_8$] (1.2 g, 3.5 mmol) and I_2 (896 mg, 3.5 mmol) in THF (75 mL), 1,3-bis[5-(trimethylsilyl) pent-4-ynyl]cyclopentadiene (**14g**) (2.7 g, 7.8 mmol) and *n*-butyllithium (6.3 mL, 1.6 M in hexane) in THF (15 mL). Yield 696 mg (57%). Orange oil. ^1H NMR (300 MHz, C_6D_6): δ = 0.17 (s, 18 H, CH_3), 1.37–1.46 (m, 4 H, CH_2), 1.94–2.07 (m, 8 H, CH_2), 4.40 (s, 2 H, CH), 4.48 (s, 1 H, CH) ppm. ^{13}C NMR (75 MHz, C_6D_6): δ = 0.4 (CH_3), 19.8 (CH_2), 27.3 (CH_2), 29.7 (CH_2), 83.5 (CH), 85.4 (CH), 85.5 (C), 105.1 (C), 106.9 (C) ppm. IR (film) $\tilde{\nu}$ = 2858, 2174, 2046, 2016, 1955, 1427, 1326 cm^{-1}. UV/Vis (CH_2Cl_2): $\lambda_{max.}$ (log ε) = 250 (4.03), 330 (3.21) nm.

Synthesis of Endohedral Rhodium Complexes 7b and 8b: A dry 250-mL flask was charged with cyclopentadienyl(dicarbonyl)rhodium (**15b**, 636 mg, 1.28 mmol) and 120 mL cyclooctane. The solution was refluxed (72 h). The solvent was evaporated under reduced pressure and the products were purified by column chromatography [alox III (neutral)]. After eluting the column with petroleum ether in the beginning, dichloromethane was used to elute first complex **7b** and then complex **8b** as yellow bands.

Complex 7b: Yield 95 mg (16%). Yellow solid. ^1H NMR (500 MHz, $CDCl_3$): δ = 1.49 (s, 9 H, CH_3), 1.51 (s, 9 H, CH_3), 1.56 (m, 2 H, CH_2), 1.73 (m, 2 H, CH_2), 1.79 (m, 2 H, CH_2), 1.90 (m, 2 H, CH_2), 2.19 (m, 2 H, CH_2), 2.22 (m, 2 H, CH_2), 2.58 (m, 2 H, CH_2), 2.71 (m, 2 H, CH_2), 5.15 (ps, 1 H, CH), 5.28 (ps, 1 H, CH), 5.35 (ps, 1 H, CH) ppm. ^{13}C NMR (75 MHz, $CDCl_3$): δ = 26.0 (CH_2), 27.0 (CH_2), 27.2 (CH_2), 29.1 (CH_2), 29.7 (CH_2), 30.0 (CH_2), 30.8 (CH_2), 31.6 (CH_3), 32.1 (CH_2), 33.4 (C), 33.9 (C), 34.5 (CH_3), 83.2 (CH, $J_{Rh,C}$ = 5.6 Hz), 84.0 (CH, $J_{Rh,C}$ = 6.5 Hz), 85.7 (C, $J_{Rh,C}$ = 8.8 Hz), 86.2 (CH, $J_{Rh,C}$ = 6.8 Hz), 93.5 (C, $J_{Rh,C}$ = 9.3 Hz), 93.9 (C, $J_{Rh,C}$ = 10.1 Hz), 106.1 (C, $J_{Rh,C}$ = 5.5 Hz), 106.4 (C, $J_{Rh,C}$ = 6.3 Hz), 111.1 (C, $J_{Rh,C}$ = 11.4 Hz), 163.2 (CO) ppm. MS (positive FAB): *m*/*z* = 468 $[M]^+$. IR (KBr) $\tilde{\nu}$ = 2922, 2857, 2232, 1733, 1598, 1485, 1448, 1388 cm^{-1}. UV/Vis (CH_2Cl_2): $\lambda_{max.}$ (log ε) = 266 (5.05), 348 (4.42) nm. HRMS (positive FAB) calcd. for $C_{26}H_{37}ORhNa$ ($[M + Na]^+$), 491.1797; 491.1804 found, (+0.7 mmu).

Complex 8b: Yield 3 mg (0.5%). Yellow oil. ^1H NMR (500 MHz, $CDCl_3$): δ = 1.41 (s, 9 H, CH_3), 1.58 (s, 9 H, CH_3), 1.91–2.62 (m, 16 H, CH_2), 5.33 (ps, 1 H, CH), 5.38 (ps, 1 H, CH), 5.50 (ps, 1 H, CH) ppm. MS (positive FD): *m*/*z* = 468 $[M]^+$. IR (film) $\tilde{\nu}$ = 2925, 2856, 1562, 1446, 1362, 1261, 1029 cm^{-1}. HRMS (positive FAB) calcd. for $C_{26}H_{38}ORh$ ($[M]^+$), 469.1978; found, 469.1939 (–3.9 mmu).

General Procedure for the Synthesis of Endohedral Cobalt Complexes 1d–g: A dry 250-mL flask was charged with the dicarbonylcobalt complex and cyclooctane. The solution was refluxed (12 h). The solvent was evaporated under reduced pressure and the products were purified by column chromatography (alox III).

[3.4]-η⁵-(1,1′,3,3′)-Cyclopentadienyl-η⁴-[2,4-bis(*tert*-butyl)cyclobutadienophane]cobalt(I) (1d): Reaction mixture: complex **16d** (140 mg, 0.40 mmol) in cyclooctane (80 mL). Yield 20 mg (5%). Yellow solid, m.p. 110 °C. ^1H NMR (500 MHz, C_6D_6): δ = 1.20 (s, 18 H, CH_3), 1.54–1.81 (br., 8 H, CH_2), 2.03–2.12 (br., 4 H, CH_2), 2.24–2.27 (m, 1 H, CH_2), 2.53–2.61 (m, 1 H, CH_2), 4.56 (s, 1 H, CH), 4.79 (s, 1 H, CH), 5.00 (s, 1 H, CH) ppm. ^{13}C NMR (125 MHz, C_6D_6): δ = 23.5 (CH_2), 24.3 (CH_2), 29.3 (CH_2), 29.6 (CH_2), 29.7 (CH_2), 31.2 (CH_2), 31.6 (CH_3), 32.4 (C), 32.7 (C), 33.0 (CH_3), 39.0 (CH_2), 66.1 (C), 80.9 (CH), 81.1 (C), 81.3 (CH), 81.8 (CH), 92.7 (C), 93.2 (C), 95.3 (C), 95.5 (C) ppm. IR (KBr) $\tilde{\nu}$ = 3079, 2953, 2910, 2849, 1622, 1478, 1460, 1442, 1391 cm^{-1}. UV/Vis (CH_2Cl_2): $\lambda_{max.}$ (log ε) = 268 (4.16), 302 (3.24), 342 (2.80) nm. HRMS (positive EI) calcd. for $C_{24}H_{35}Co$ ($[M]^+$), 383.2071; found, 383.2057 (–1.4 mmu). $C_{24}H_{35}Co$ (382.47): calcd. C 75.37, H 9.22; found C 75.47, H 8.99.

[3.5]-η⁵-(1,1′,3,3′)-Cyclopentadienyl-η⁴-[2,4-bis(*tert*-butyl)cyclobutadienophane]cobalt(I) (1e): Reaction mixture: complex **16e** (130 mg, 0.29 mmol) in cyclooctane (50 mL). Yield 34 mg (30%). Yellow solid, m.p. 140 °C. ^1H NMR (300 MHz, C_6D_6): δ = 1.14 (s, 9 H, CH_3), 1.16 (s, 9 H, CH_3), 1.37–1.74 (m, 8 H, CH_2), 1.82–1.88 (m, 4 H, CH_2), 2.19–2.23 (m, 1 H, CH_2), 2.39–2.43 (m, 1 H, CH_2), 2.59–2.62 (m, 2 H, CH_2), 4.58 (s, 1 H, CH), 4.70 (s, 1 H, CH), 4.78 (s, 1 H, CH) ppm. ^{13}C NMR (125 MHz, C_6D_6): δ = 22.9 (CH_2), 23.1 (CH_2), 24.0 (CH_2), 24.3 (CH_2), 25.0 (CH_2), 26.1 (CH_2), 31.4 (CH_3), 32.1 (CH_3), 32.4 (C), 32.6 (C), 37.7 (CH_2), 66.4 (C), 73.4 (C), 78.8 (CH), 81.0 (CH), 81.3 (CH), 90.7 (C), 92.1 (C) 93.5 (C), 94.2 (C) ppm. IR (KBr) $\tilde{\nu}$ = 2955, 2919, 2855, 1478, 1455, 1372 cm^{-1}. UV/Vis (CH_2Cl_2): $\lambda_{max.}$ (log ε) = 270 (4.49), 300 (3.54), 374 (3.20) nm. HRMS (positive EI) calcd. for $C_{25}H_{37}Co$ ($[M]^+$), 396.2227; found, 396.2238 (+1.1 mmu). $C_{25}H_{37}Co$ (396.49): calcd. C 75.37, H 9.41; found C 75.37, H 9.28.

[4.5]-η⁵-(1,1′,3,3′)-Cyclopentadienyl-η⁴-[2,4-bis(*tert*-butyl)cyclobutadienophane]cobalt(I) (1f): Reaction mixture: complex **16f** (165 mg, 0.35 mmol) in cyclooctane (60 mL). Yield 22 mg (15%). Yellow solid, m.p. 151 °C. ^1H NMR (300 MHz, C_6D_6): δ = 1.22 (s, 9 H, CH_3), 1.23 (s, 9 H, CH_3), 1.25–1.56 (m, 4 H, CH_2), 1.44–1.61 (m, 4 H, CH_2), 1.88–1.89 (m, 1 H, CH_2), 1.89–1.95 (m, 2 H, CH_2), 2.09–2.14 (m, 1 H, CH_2), 2.21–2.28 (m, 1 H, CH_2), 2.30–2.34 (m, 1 H, CH_2), 2.41–2.49 (m, 1 H, CH_2), 2.53–2.55 (m, 2 H, CH_2), 2.65–2.71 (m, 1 H, CH_2), 4.65 (s, 1 H, CH), 4.76 (s, 1 H, CH), 4.84 (s, 1 H, CH) ppm. ^{13}C NMR (125 MHz, C_6D_6): δ = 23.4 (CH_2), 23.7 (CH_2), 23.9 (CH_2), 25.3 (CH_2), 25.4 (CH_2), 27.3 (CH_2), 27.5 (CH_2), 28.9 (CH_2), 31.6 (CH_2), 31.8 (CH_3), 31.9 (CH_3) 32.6 (C), 69.7 (C), 74.1 (C), 77.8 (CH), 79.5 (CH), 79.8 (CH), 87.7 (C), 89.6 (C), 95.4 (C), 95.6 (C) ppm. IR (KBr) $\tilde{\nu}$ = 2957, 2921, 2857, 2026, 1628, 1479, 1458 cm^{-1}. UV/Vis (CH_2Cl_2): $\lambda_{max.}$ (log ε) = 278 (4.34), 322 (3.18), 372 (2.98) nm. HRMS (positive EI) calcd. for $C_{26}H_{39}Co$ ($[M]^+$), 410.2384; found, 410.2336 (–4.8 mmu).

[3.3]-η⁵-(1,1′,3,3′)-Cyclopentadienyl-η⁴-[2,4-bis(trimethylsilyl)cyclobutadienophane]cobalt(I) (1g): Reaction mixture: complex **16g** (665 mg, 360 mmol) in cyclooctane (360 mL). Yield 207 mg (35%). Yellow solid, m.p. 55 °C. ^1H NMR (500 MHz, C_6D_6): δ = 0.14 (s, 9 H, CH_3), 0.24 (s, 9 H, CH_3), 1.41–1.56 (br., 4 H, CH_2), 1.73–1.85 (br., 6 H, CH_2), 2.04–2.14 (m, 2 H, CH_2), 4.55 (s, 1 H, CH), 4.56

 © 2005 Wiley-VCH Verlag GmbH & Co. KGaA, Weinheim

(s, 1 H, CH), 5.13 (s, 1 H, CH) ppm. ^{13}C NMR (125 MHz, C_6D_6): δ = 1.7 (CH_3), 1.9 (CH_3), 26.0 (CH_2), 26.9 (CH_2), 40.8 (CH_2), 77.3 (C), 79.5 (C), 80.1 (CH), 84.1 (C), 84.3 (CH), 95.0 (C) ppm. IR (KBr) $\tilde{\nu}$ = 2936, 2912, 2849, 1627, 1545, 1421, 1324 cm^{-1}. UV/Vis (CH_2Cl_2): $\lambda_{max.}$ (log ε)= 266 (4.01), 310 (3.31), 398 (2.71) nm. HRMS (positive EI) calcd. for $C_{21}H_{33}CoSi_2$ ([M]$^+$), 400.1453; found, 400.1477 (+2.4 mmu).

[3.3]-η^5-(1,1′,3,3′)-Cyclopentadienyl-η^4-(cyclobutadienophane)cobalt(I) (1h): A dry 25-mL flask was charged with complex **1g** (126 mg, 0.32 mmol), tetramethylammonium fluoride tetrahydrate (408 mg, 2.47 mmol) and DMSO (10 mL). The solution was stirred at 80 °C (15 h). Then the mixture was extracted with petroleum ether (8×). The organic layer was washed with water and dried ($MgSO_4$). The solvent was removed under reduced pressure and the product was purified by column chromatography [alox III (neutral)]. Yield 61 mg (74%). Yellow solid, m.p. 77 °C. ^{1}H NMR (300 MHz, C_6D_6): δ = 1.09–1.25 (m, 4 H, CH_2), 1.53 (pt, ^2J = 12.7 Hz, 2 H, CH_2), 1.77–1.93 (m, 4 H, CH_2), 2.17 (pd, ^2J = 14.4 Hz, 2 H, CH_2), 3.68 (pd, ^4J = 8.0 Hz, 1 H, CH), 4.45–4.47 (d, ^4J = 8.0 Hz, 1 H, CH), 4.53 (s, 2 H, CH), 4.66 (s, 1 H, CH) ppm. ^{13}C NMR (75 MHz, C_6D_6): δ = 25.4 (CH_2), 25.9 (CH_2), 37.7 (CH_2), 66.1 (CH), 67.9 (CH), 72.2 (C), 78.7 (CH), 83.2 (CH), 94.9 (C) ppm. IR (KBr) $\tilde{\nu}$ = 3072, 2910, 2867, 2831, 1627, 1428, 1407 cm^{-1}. UV/Vis (CH_2Cl_2): $\lambda_{max.}$ (log ε) = 254 (4.31), 284 (3.30), 362 (3.01) nm. HRMS (positive EI) calcd. for $C_{15}H_{17}Co$ ([M]$^+$), 265.0662; found, 265.0649 (–1.3 mmu).

Acknowledgments

We are grateful to the Deutsche Forschungsgemeinschaft, the Fonds der Chemischen Industrie, and the BASF Aktiengesellschaft, Ludwigshafen, Germany, for financial support.

[1] R. Gleiter, H. Hopf (Eds.), *Modern Cyclophane Chemistry*, Wiley-VCH, Weinheim, **2004**.
[2] F. Vögtle, Cyclophane Chemistry: *Synthesis Structures and Reactions*, Wiley, Chichester, **1993**.
[3] P. M. Keehn, S. M. Rosenfeld (Eds.), *Cyclophanes*, Academic Press, New York, **1983**.
[4] F. Diederich, *Cyclophanes*, The Royal Society of Chemistry, London, **1991**.
[5] a) J. Schulz, F. Vögtle, *Top. Curr. Chem.* **1994**, *172*, 41–86; b) R. Gleiter, B. J. Rausch, R. J. Schaller, in: *Modern Cyclophane Chemistry* (Eds.: R. Gleiter, H. Hopf), Wiley-VCH, Weinheim, **2004**, 159–188.
[6] H. Schmidbaur, *Angew. Chem.* **1985**, *97*, 893–904; *Angew. Chem. Int. Ed. Engl.* **1985**, *24*, 893–904.
[7] a) C. Elschenbroich, R. Möckel, U. Zenneck, *Angew. Chem.* **1978**, *90*, 560–561; *Angew. Chem. Int. Ed. Engl.* **1978**, *17*, 531–532; b) A. R. Koray, M. L. Ziegler, N. E. Blank, M. W. Haenel, *Tetrahedron Lett.* **1979**, *26*, 2465–2466.
[8] M. Hisatome, *Rev. Heteroatom Chem.* **1992**, *6*, 142–176.
[9] G. Scholz, R. Gleiter, F. Rominger, *Angew. Chem.* **2001**, *113*, 2559–2562; *Angew. Chem. Int. Ed.* **2001**, *40*, 2477–2479.
[10] G. Scholz, C. Schaefer, F. Rominger, R. Gleiter, *Org. Lett.* **2002**, *4*, 2889–2892.
[11] R. I. Duclos, K. P. C. Vollhardt, L. S. Yee, *J. Organomet. Chem.* **1979**, *174*, 109–114.
[12] P. E. Riley, R. E. Davis, *J. Organomet. Chem.* **1976**, *113*, 157–166.
[13] SHELXTL G. M. Sheldrick, Bruker Analytical X-ray-Division, Madison, Wisconsin, **2001**.
[14] G. M. Sheldrick, **1996**, unpublished work based on the method described in: R. H. Blessing, *Acta Crystallogr. Sect. A* **1995**, S1–S33.

Received: October 11, 2004

 © 2005 Wiley-VCH Verlag GmbH & Co. KGaA, Weinheim

Photocontrol of Complexation of Neutral and Cationic Species by *p-tert*-Butylcalix[4]arene Tetraethyl Ester

Bernadette S. Creaven,*[a] Mary Deasy,[a] Catherine McKenna,[a] Brian A. Murray,[a] and Darren Tobin[a]

Keywords: Calixarene / Photocontrol / Anion effect / Solvent effect / Sodium complexes

A number of sodium salt complexes of *p-tert*-butylcalix[4]arene tetraethyl ester (**1**) were isolated both with and without upper-rim encapsulated acetonitrile or methanol. Upon dissolution in $CDCl_3$, **1** remained largely complexed to the sodium cation but ca. 90 % of the upper-rim bound solvent was released, reflecting the relative values of the binding constants for complexation of the two guest species. Selective decomplexation of lower-rim bound sodium cations could be successfully achieved using low-pressure light sources, triggering the immediate expulsion of the upper-rim bound solvent. The extent of decomplexation at both rims is controlled both by the oxidation of the counter-anionic species at the lower rim and by the fate of the photoproducts generated. The calixarene host molecule, **1**, remains intact during the decomplexation process.

(© Wiley-VCH Verlag GmbH & Co. KGaA, 69451 Weinheim, Germany, 2005)

Introduction

Calixarenes are a widely studied class of macrocyclic ligands, obtained from the base-catalysed condensation reaction between *para*-substituted phenols and formaldehyde. The general structure of a calixarene is shown in Figure 1. Functionalisation at the lower rim of parent calixarenes (Figure 1, R = H) has led to a variety of derivatives, which have found use in a number of industrial and analytical applications.[1–3] We have been interested in the calix[4]arene esters in particular as their well-defined hydrophobic region, defined by the upper-rim aromatic moieties and lower-rim hydrophilic regions, allows for complexation of both neutral and cationic guests, respectively.[4–7] There have been a limited number of studies carried out on calixarene complexes, which bind guests at the upper and lower rims simultaneously. In one such study, Pochini et al. have shown that a conformationally mobile calixarene host did not show significant upper-rim complexation of a guest whereas its sodium complex, which is more rigid, strongly interacts with the same guest.[8] Stibor et al. investigated the factors influencing the stability of inclusion complexes of calix[4]arene derivatives with neutral molecules, specifically acetonitrile (MeCN). *p-tert*-Butylcalix[4]arene tetraethyl ester (**1**) (Figure 1: R = $CH_2COOCH_2CH_3$) was included in this study, and Stibor found that the presence of a sodium cation at the lower rim of the calixarene significantly enhanced the binding of neutral guests at the upper rim.[9] Stibor's work correlates well with thermodynamic studies in solution of compound **1** with a series of alkali metal salts in MeCN, MeOH, and benzonitrile carried out by other groups. This latter work had concluded that MeCN was seen to produce an "allosteric effect", whereby the interaction of MeCN with the hydrophobic cavity of **1** preorganises the hydrophilic cavity to interact with cations, and the authors had noted the increased stability of sodium complexes of **1** in MeCN.[10–15]

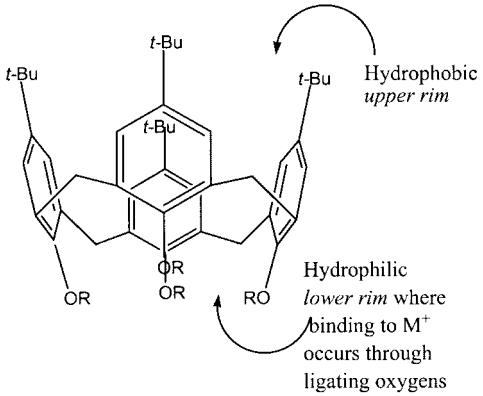

Figure 1. Structural formula of calixarene **1** indicating how it can bind guests.

Our main interest lies in the controlled decomplexation of alkali metal complexes of calixarene esters, specifically the sodium complexes. We have previously reported photodecomplexation studies on sodium iodide and tetraphen-

[a] Department of Applied Science, Institute of Technology, National Centre for Sensor Research, Institute of Technology, Tallaght, Dublin 24, Ireland
Fax: +353-1-4042700
E-mail: bernie.creaven@it-tallaght.ie

ylborate complexes of calixarenes in $CDCl_3$, including those of compound **1**,[16,17] and found the % decomplexation to be anion-dependent. Moreover, the decomplexation reaction did not appear to involve a structural change in the calixarene macrocycle. Most photoresponsive macrocyclic systems in the literature employ an *all or nothing* reaction, whereby complexation is controlled by a photoisomerisable moiety within the macrocycle. For example, Shinkai and his colleagues synthesised an azobenzene-containing crown ether, the *cis* form of which bound K^+, Rb^+, and Cs^+, whereas the *trans* isomer preferentially bound Li^+ and Na^+.[18] Our previous work had shown that decomplexation could be controlled to a pre-determined level for the complexes studied and hence was comparable to an analogue control mechanism or analogue switch. This work also showed that for complexes isolated from acetonitrile, rather than chloroform, the overall % decomplexation of the complexes was reduced by up to 20%.[17] The difference in % decomplexation was thought to be due to the inclusion of MeCN in the upper rim of the complexes, exerting a stabilising or allosteric effect on complexation of sodium at the lower rim.

While our previous work had noted both the anion dependency as well as the dependency on solvent inclusion on the extent of photodecomplexation of complexes of **1**, the exact reasons for either dependency were not fully understood. The present study details photodecomplexation studies on a range of sodium complexes of **1**, prepared with several different counter anions, which were isolated from a number of solvents. Our previous studies had also indicated that photodecomplexation of NaI-**1** and $NaBPh_4$-**1** only occurred in chloroform and not in methanol or acetonitrile. The photoreactivity of the complexes in the nonpolar solvent was though to be related to the existence of ion pairs in this solvent, which would allow for efficient energy transfer from the calixarene macrocycle to the associated counter anion. The role of the photolysis solvent in the decomplexation process was therefore also investigated in this study.

Results and Discussion

NMR Studies on NaX-1 and NaX-1·MeCN Complexes

The sodium salt complexes of **1**, NaX-**1** (X = iodide, thiocyanate, perchlorate, periodate, and tetraphenylborate) were isolated from a series of solvents. While it has been reported that calix[4]arenes tightly bind chloroform, benzene, toluene, xylene, anisole and acetonitrile,[19–23] the limited stability of the sodium complexes in some of these solvents precluded their use.[24] Microanalysis of the isolated complexes indicated that for each of the NaI, NaSCN, $NaIO_4$ and $NaBPh_4$ complexes isolated from MeCN, a solvent molecule was also present and these complexes are henceforth denoted as NaX-**1**·MeCN (X = I^-, SCN^-, BPh_4^-, IO_4^-). The integration of the ^1H NMR signals confirmed that the ratio of NaX-**1**:MeCN was 1:1 in all samples. However, the ^1H NMR signal of the methyl group in MeCN was moved upfield relative to free MeCN in $CDCl_3$. Solid-state studies have shown that an interaction between the calixarene and MeCN occurs possibly via a CH_3-π interaction where the methyl group of the MeCN is orientated toward the hydrophobic upper cavity resulting in a significant shielding effect on the MeCN alkyl hydrogen atoms.[23,25] The $NaIO_4$ complex of **1** isolated from MeOH also had an upper-rim bound solvent molecule, henceforth denoted as $NaIO_4$-**1**·MeOH. No encapsulated chloroform or dichloromethane complexes of **1** could be isolated and such complexes are denoted as NaX-**1** in this study. Sodium salt complexes of **1** have been widely reported in the literature[4,9–15] and NMR assignments in $CDCl_3$ were based on these reports (Table 1). All of the reported NMR spectra, including the ones reported here, and additional X-ray crystallo-

Table 1. ^1H NMR chemical shift data for NaX complexes of **1** (X = I^-, SCN^-, BPh_4^-, ClO_4^-, IO_4^-) isolated from different solvents. All spectra were recorded in $CDCl_3$.

Functional group	**1**	NaI-**1**·MeCN	NaI-**1**[a]	NaSCN-**1**·MeCN	NaSCN-**1**[a]
tert-Butyl	1.07	1.17 (s)	1.14 (s)	1.15 (s)	1.14 (s)
OCH_2CH_3	1.27	1.41 (t)	1.42 (t)	1.42 (t)	1.42 (t)
Solvent signal		1.67(s)		1.50 (s)	
H_B CH_2 bridge	3.19	3.42 (d)	3.40 (d	3.40 (d)	3.40 (d)
H_A CH_2 bridge	4.85	4.25 (d)	4.24 (d)	4.25 (d)	4.25 (d)
OCH_2CH_3	4.21	4.39 (q)	4.38 (q)	4.38 (q)	4.38 (q)
$OCH_2C{=}O$	4.8	4.48 (s)	4.47 (s)	4.48 (s)	4.48 (s)
Aromatic *H*	6.77	7.16 (s)	7.12 (s)	7.13 (s)	7.12 (s)
Functional group	$NaBPh_4$-**1**·MeCN	$NaBPh_4$-**1**[a]	$NaClO_4$-**1**[a]	$NaIO_4$-**1**·MeCN	$NaIO_4$-**1**·MeOH
tert-Butyl	1.16 (s)	1.14 (s)	1.14 (s)	1.15(s)	1.14 (s)
OCH_2CH_3	1.38 (t)	1.35 (t)	1.43 (t)	1.41 (t)	1.41 (t)
Solvent signal	1.43 (s)			1.47 (s)	3.39 (s)
H_B CH_2 bridge	3.36 (d)	3.34 (d)	3.38 (d)	3.40 (d)	3.40 (d)
H_A CH_2 bridge	4.19 (d)	4.18 (d)	4.26 (d)	4.26 (d)	4.26 (d)
OCH_2CH_3	4.32 (q)	4.33 (q)	4.38 (q)	4.38 (q)	4.38 (q)
$OCH_2C{=}O$	4.42 (s)	4.42 (s)	4.48 (s)	4.48 (s)	4.48 (s)
Aromatic *H*	7.12 (s)	7.11 (s)	7.12 (s)	7.13 (s)	7.12 (s)

[a] Complexes isolated with no encapsulated solvent

 © 2005 Wiley-VCH Verlag GmbH & Co. KGaA, Weinheim

graphic studies have indicated that the sodium complexes are in a fixed cone conformation in the solid and solution states. The complexation-induced shifts noted in Table 1 would indicate that the ion-pair interaction at the lower rim (as evidenced by ^{1}H NMR signals of the $OCH_2COCH_2CH_3$ and $OCH_2COCH_2CH_3$ moieties and the methylene bridges) was relatively similar for all the anions except for tetraphenylborate. This may be an indication that ion pairing with tetraphenylborate was weakest, which is consistent with the "non-coordinating" nature of this ligand, or that the phenyl groups of the anion are having an additional shielding effect at the lower rim.

^{1}H NMR signals at δ = 1.67 ppm, 1.50 ppm and 1.43 ppm in the ^{1}H NMR spectra of NaI-**1**·MeCN, NaSCN-**1**·MeCN, and $NaBPh_4$-**1**·MeCN, respectively, were assigned to MeCN in the upper rim of the complexes. In $CDCl_3$, free MeCN is known to have a chemical shift of 2.1 ppm.[26] The presence of MeCN resulted in small downfield shifts in the *tert*-butyl and aromatic signals for these complexes, relative to when MeCN was absent.

Stibor's study of the complexation of **1** with neutral molecules including MeCN in the presence and absence of sodium thiocyanate sets the context for our photolytic study of the same system in $CDCl_3$.[9] Scheme 1 shows the complexation equilibria that are set up when NaX-**1**·MeCN is dissolved in $CDCl_3$. The processes in which neutral guest MeCN complexes with **1** are fast on the NMR timescale, while Na^+ complexation processes are slow. However, the thermodynamics of these processes are reversed: Na^+ complexes very strongly with **1** with both $K_{\mathbf{1}:NaX}$ and $K_{\mathbf{1}\cdot MeCN:NaX}$ being of the order of 10^6–10^7 M^{-1}.[27] In contrast, the 1:1:1 complex formed from NaX-**1** and MeCN has a binding constant of 31 M^{-1}, while MeCN binds **1** extremely weakly with $K_{\mathbf{1}:MeCN} << 1$ M^{-1}.[9] Stibor has also determined the ^{1}H NMR properties of included MeCN in the ternary complex: from a free position of 2.1 ppm (i.e. δ_G^{MeCN}), the methyl group moves strongly upfield to a limiting value of δ_{GH}^{MeCN} = –3.9 ppm (associated with anisotropic shielding as the methyl group is inserted "head-first" into the upper rim of calixarene cavity and down into the inter-aryl space). This very large complexation-induced shift (CIS) of –6.0 ppm is probably also present in **1**·MeCN, as the geometry of NaX-**1**·MeCN and **1**·MeCN are similar, although the very weak binding precludes observation of this. If it is assumed that $K_{\mathbf{1}:MeCN}$ is < 0.3 M^{-1}, then the ratio $K_{NaX–\mathbf{1}:MeCN}/K_{\mathbf{1}:MeCN}$ is > 100; i.e. complexation of sodium at the lower rim favours complexation of MeCN at the upper rim by at least 11 kJ mol^{-1} in free energy terms.

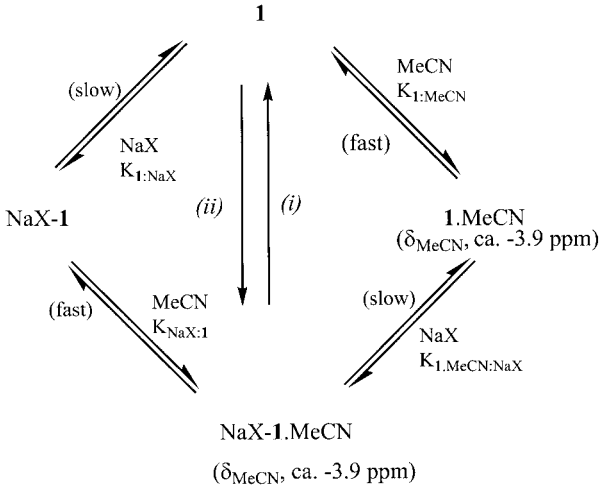

Scheme 1. Complexation equilibria established in $CDCl_3$ solution upon dissolution of NaSCN-**1**·MeCN. Processes (*i*) and (*ii*) are discussed in the text.

We can now:
(a) Estimate the position these equilibria will attain when 4.0 mmol of NaX-**1**·MeCN is dissolved per litre of $CDCl_3$;
(b) predict the expected ^{1}H NMR behaviour of the methyl signal of MeCN; and
(c) subsequently use this information to rationalize the effect of photolytic decomplexation of $Na^+(X^-)$ on (a) and (b).

Firstly consider the equilibrium:

NaX-**1** + MeCN ⇋ NaX-**1**·MeCN

with $K_{NaX–\mathbf{1}:MeCN}$ = 31 M^{-1}, dissolving compound to 4 mM will result in net dissociation of ca. 90%, leaving f_c^G (fraction of guest, MeCN, complexed) = 0.10, and $\delta_{obsd.}^G$ = 1.50 ppm, i.e. 10% of the way from 2.1 to –3.9 ppm. Neither complex should dissociate its sodium significantly; f_c^{Na} will be > 98%, assuming $K_{\mathbf{1}:NaX}$ and $K_{\mathbf{1}\cdot MeCN:NaX}$ are ca. 10^6 M^{-1}. Finally, any **1**·MeCN present will be 99.9% dissociated. Thus there will be effectively only two environments for MeCN: In the form of NaX-**1**·MeCN or free in solution.

Figure 2(a) shows the predicted ^{1}H NMR binding curve, based on Stibor's data, i.e. the movement of the MeCN methyl protons for a range of stoichiometric or initial concentrations of NaSCN-**1**·MeCN dissolved in $CDCl_3$. At low concentrations of NaSCN-**1**·MeCN, it shows linear behaviour (asymptotically). This is shown in the expansion of the range 0–5 mM in Figure 2(b) i.e $\delta_{obsd.}^G - \delta_G^{MeCN}$ (the observed CIS) is approximately proportional to $[NaSCN\text{-}\mathbf{1}\cdot MeCN]_{initial}$ in this region. When [NaSCN-**1**·MeCN] = 4.0 mM, the ternary complex is 90% dissociated and we observe δ_G^{MeCN} = 1.50 ppm, exactly as predicted by Stibor's data.

If we assume that the values of $K_{NaX\text{-}\mathbf{1}:MeCN}$ are of comparable magnitude, then all of the NaX-**1**·MeCN complexes would behave similarly once dissolved in $CDCl_3$, and $\delta_{obsd.}^{MeCN}$ for each of the complexes should also be of similar magnitude. In fact $\delta_{obsd.}^{MeCN}$ = 1.47, 1.43, 1.50 and 1.67 ppm upon dissolution of 4 mM $NaIO_4$-**1**·MeCN, $NaBPh_4$-**1**·MeCN, NaSCN-**1**·MeCN and NaI-**1**·MeCN, respectively.

The presence of encapsulated MeOH was also observed in $NaIO_4$-**1** complexes with a chemical shift of 3.39 ppm. Free MeOH in $CDCl_3$ has a chemical shift of 3.64 ppm.[25] Although crystals of suitable quality have not been isolated for solid-state structure analysis, a potassium complex of a calixarene tetraamide has been reported with a molecule of MeOH in its hydrophobic cavity.[28]

 © 2005 Wiley-VCH Verlag GmbH & Co. KGaA, Weinheim

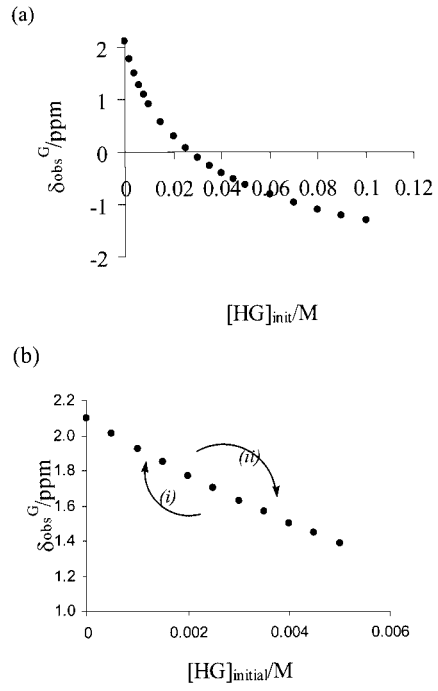

Figure 2. (a) Calculated plot of $\delta_{obsd.}{}^{MeCN}$ vs. [NaSCN-**1**·MeCN]$_{initial}$/M ($K_{NaSCN\text{-}\mathbf{1}:MeCN}$ = 31 M^{-1}, $\delta_G{}^{MeCN}$ to $\delta_{GH}{}^{MeCN}$ = 2.1 to –3.9 ppm). (b) Expansion of (a) shown in the range $\delta_{obsd.}{}^{MeCN}$ = 1.4 to 2.1 ppm, comparable to the range observed in our experiment.

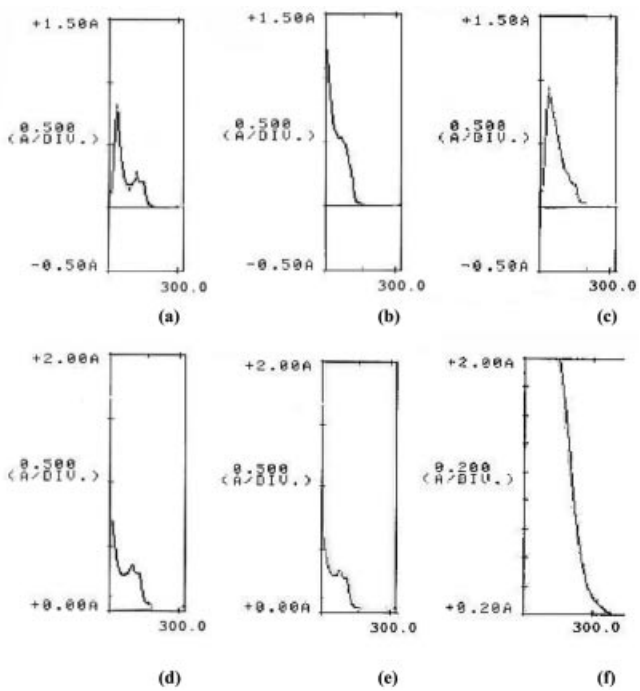

Figure 3. UV/Vis absorbance spectra recorded in $CDCl_3$ of (a) uncomplexed calixarene (**1**), (b) $NaBPh_4$-**1**·MeCN, (c) NaI-**1**·MeCN, (d) NaSCN-**1**·MeCN, (e) $NaIO_4$-**1**·MeCN, and (f) a pyrex NMR tube. Concentrations of complexes and calixarene approximately 1×10^{-5} M.

Photodecomplexation Studies of NaX-1, NaX-1·MeCN and $NaIO_4$-1·MeOH

Our previous work had shown that irradiation of $NaBPh_4$-**1** in $CDCl_3$ generated products consistent with the photooxidation of the tetraphenylborate anion.[17] In this study, we monitored the fate of the other anions upon photoexcitation of the macrocyclic complexes. The choice of excitation source was a low-pressure mercury lamp operating at room temperature, which emits primarily one band of radiation at 253.6 nm. Exposure of calixarene complexes to this wavelength leads to extensive photochemical reaction and breakdown of the host compound. However, the output of low-pressure mercury lamps includes a number of weak lines above 280 nm, including 289.4, 296.7, 302.2 and 312.6 nm. Use of this lamp with an appropriate UV filter, in this case a pyrex NMR tube, ensured that all photochemical decomplexations were clean and could be monitored over reasonable time-scales. Figure 3 shows the absorption spectra of the calixarene host compound **1** and some of its complexes, together with the transmission characteristic of a typical pyrex NMR tube.

The pyrex NMR tube effectively cuts out all radiation at the main excitation wavelength of the lamp and is only 10% transmitting at 280 nm, but increases thereafter. With this experimental set-up, decomplexation of the complexes of **1** could be monitored with good reproducibility over reasonable time scales.[29] The presence of the tetraphenylborate and iodide anions do alter the UV/Vis spectrum of its complexes, but for the remaining complexes the two main absorption bands of the calixarene varied little in position upon coordination; however, they varied somewhat in intensity. Table 2 gives the absorption data of free calixarene and its complexes at a number of wavelengths.

Table 2. UV/Vis absorbance data for host compound, **1**, and its NaI, NaSCN, and $NaIO_4$ complexes in $CDCl_3$.

Compound	λ (nm)	ε (cm^{-1} mol^{-1}) × 10^3
1	275	3.49
	281	3.54
	308	0.06
NaI-**1**·MeCN	272	4.73
	282	2.90
	308	0.25
NaI-**1**	272	4.71
	282	3.15
	308	0.28
NaSCN-**1**·MeCN	273	3.51
	282	3.41
	308	0.49
NaSCN-**1**	273	3.55
	282	3.44
	308	0.50
$NaIO_4$-**1**·MeCN	274	3.00
	283	2.58
	308	0.12
$NaIO_4$-**1**·MeOH	273	2.94
	282	2.59
	308	0.11

The unphotolysed samples of NaX-**1** had two main absorption bands at ca. 272 nm and 283 nm, characteristic of the complexed calixarene. The latter was assigned to the S_0

 © 2005 Wiley-VCH Verlag GmbH & Co. KGaA, Weinheim

$\rightarrow S_1$ transition of the aryl ether moiety.[30,31] The primary wavelengths of excitation, centred around 308nm, correspond to the shoulder of the $S_0 \rightarrow S_1$ transition and the anion-centred absorptions. Photoexcitation of aryl ethers usually leads to the ejection of an electron from the arene excited (π,π^*) state and the formation of a radical cation. The subsequent activation of the aromatic ring is primarily at the *para* position but also at the *ortho* position.[32] In our case, a *tert*-butyl and a methylene group occupy these two positions, and so the expected further reactions would be inhibited. The other chromophoric species in solution are the counter-anionic species i.e. the iodide, thiocyanate, tetraphenylborate or periodate ions that have weak absorptions at these wavelengths (perchlorate ions have no absorption bands in this region).[33]

The % decomplexations of NaX-**1** complexes upon irradiation in $CDCl_3$ at timed intervals are shown in Table 3. The values for % decomplexation are calculated from the ^{1}H NMR spectra of the photolysed solutions by the integration of the aryl protons of the free and complexed species, as distinct signals can be seen for both species in the spectrum. These results indicated a significant anion dependence on the extent of decomplexation with up to 85% decomplexation being achieved with BPh_4^- and SCN^- as anions, but no decomplexation occurring for the sodium perchlorate complex and little for the periodate complex (14%). There was no apparent relationship between the extent of ion pairing at the lower rim and the extent of photodecomplexation, a factor we had previously thought to be important.[17] If this were the case, a $NaBPh_4$-**1** complex, which from the NMR results looks to be the least ion-paired of the complexes, would show the least % decomplexation. However, this was not the case. If fresh solutions of salt were added to the NMR tubes, full recomplexation of **1** occurred, indicating the integrity of the calixarene host was maintained during decomplexation. The presence of encapsulated MeCN within the upper cavity reduced the initial % photodecomplexation of the tetraphenylborate and periodate complexes. In all cases at extended irradiation times, where MeCN was present in the sample, recomplexation was seen to occur to some extent. Irradiation over a two-hour period of the free host, **1**, showed that the calixarene remained intact throughout.

Interesting decomplexation behaviour was noticed upon irradiation of NaX-**1**·MeCN complexes. Figure 4 illustrates the relationship between the amount of calixarene remaining complexed to a sodium cation and the chemical shift of the ^{1}H NMR peak for MeCN measured for three sodium complexes. At the concentrations of NaX-**1**·MeCN used in these experiments, ca. 4.0 mM, the ternary complex is 90% dissociated. As stated earlier, for the NaSCN-**1**·MeCN complex we observe $\delta_G^{MeCN} = 1.50$ ppm. Photolysis now causes net decomplexation of Na^+, and the rapid nature of the reaction

1 + MeCN ⇋ **1**·MeCN

means MeCN dissociates too. Thus the degree to which the sodium is decomplexed can be represented as a movement up the binding curve shown in Figure 2(b): 50% decomplexation will cause $\delta_{obsd.}^{MeCN}$ to move to 1.80 ppm (halfway back to 2.1 ppm) while 100% decomplexation will completely free all the MeCN ($\delta_{obsd.}^{MeCN} = \delta_G^{MeCN} =$ 2.1 ppm). This is represented by process (i) of Figure 2(b) and in Scheme 1. The ordinate-intercept value of the graphs is consistent within experimental error with the value 2.1 ppm for free MeCN in $CDCl_3$,[26] although experimentally 100% decomplexation was not observed in any of the complexes studied. This is because on the slower timescale of many minutes post-photolysis, the sodium will recomplex, moving the acetonitrile position back down the binding curve, represented by process (ii) of Figure 2(b) and in

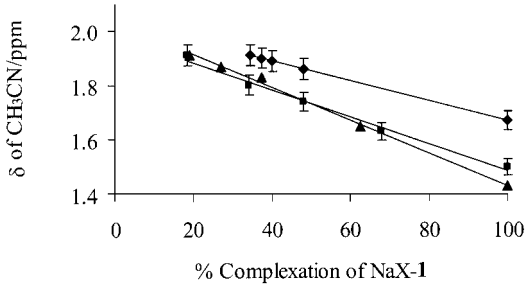

Figure 4. The relationship between the % complexation of NaX-**1** and the chemical shift, δ, of upper-rim bound acetonitrile; NaSCN-**1** (■), NaI-**1** (♦), $NaBPh_4$-**1** (▲). Concentration of each solution is 4 mM and each value is an average of 3 replicate experiments.

Table 3. Decomplexation (%) of NaX-**1** complexes (typical concentration 4.5 mM), before and after irradiation in $CDCl_3$ as determined by ^{1}H NMR spectroscopy. Each value is the average of 6 replicate experiments. Complexes with encapsulated MeCN and MeOH are indicated by NaX-**1**·MeCN or NaX-1·MeOH, respectively.

	% Decomplexation of NaX-**1** complexes								
Irradiation time [minutes]	NaI-**1**·MeCN	NaI-**1**	NaSCN-**1**·MeCN	NaSCN-**1**	$NaBPh_4$-**1**·MeCN	$NaBPh_4$-**1**	$NaClO_4$-**1**	$NaIO_4$-**1**·MeCN	$NaIO_4$-**1**·MeOH
0	0%	0%	0%	0%	0%	0%	0%	0%	0%
15	56±5%	55±6%	31±2%	25±1%	30±3%	44±9%	0%	7%	9%
30	64±2%	67±2%	62±4%	67±5%	65±5%	82±5%	0%	6%	16%
45	62±3%	65±2%	81±2%	81.5±3%	81±2%	87±1%	0%	10%	14%
60	53%	65%	68±3%	83.5±1%	72±3%	86±1%	0%	16%	14%

 © 2005 Wiley-VCH Verlag GmbH & Co. KGaA, Weinheim

Scheme 1. This recomplexation can be accelerated by adding fresh excess NaX.

The behaviour of the other anions should be similar with any variability being due to variation in $K_{NaX-1:MeCN}$ values due to the anion. This variability is reflected in the differing slopes of the plots in Figure 4 and Figure 5(b). Such variations would be expected to be small based on the observed values for $\delta_{obsd.}^{MeCN}$ for the four complexes isolated in this study. Determination of the value of K for NaX-**1** with MeCN in the presence of different anions at the lower rim is now a feature of a further study by our group.

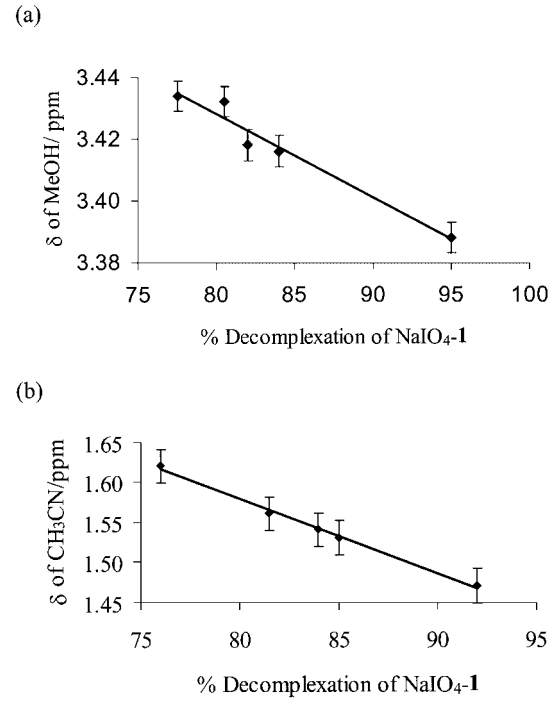

Figure 5. The relationship between (a) the % complexation of $NaIO_4$-**1**·MeOH and the chemical shift, δ, of upper-rim bound methanol and (b) the % complexation of $NaIO_4$-**1**·MeCN and the chemical shift, δ, of upper-rim bound acetonitrile. Concentration of each solution is 4 mM and each value is an average of 3 replicate experiments.

$NaIO_4$-**1** complexes with encapsulated solvent were also examined. The extent of decomplexation noted here was considerably less than in the thiocyanate, tetraphenylborate and iodide complexes. After irradiation of $NaIO_4$-**1**·MeOH, the MeOH peak shifted marginally downfield, consistent with the small extent of decomplexation noted for this anion, but again was found to be linearly dependent (presumably asymptotically) upon the extent of photodecomplexation [(a) in Figure 5]. A similar result was found for the corresponding $NaIO_4$-**1**·MeCN complex [(b) in Figure 5]. Stability constants for ternary complexes with methanol have not been determined yet but the behaviour of theses complexes upon irradiation would appear to be similar to the acetonitrile complexes of NaI-**1**, NaSCN-**1** and $NaBPh_4$-**1**.

From Table 3 it can be seen that the *extent* of neutral guest decomplexation depended on the identity of the counter anion at the lower rim, and the role of this anion in the decomplexation process was important to determine.

Photoreactivity of the Counter Anions of NaX-1

Potentiometric titration of aqueous extracts of the irradiated $CDCl_3$ solutions of NaI-**1** and NaI-**1**·MeCN (Table 4) indicated that the concentration of iodide was reduced upon irradiation, but that reduction did not correlate exactly with the decomplexation of the calixarene. In fact, while most of the iodide had reacted after 10 minutes, partial complexation of the calixarene at this and later times indicated the presence of another anion in solution. UV/Vis analysis indicated that triiodide was produced, presumably from the initial reaction of iodine radicals to form iodine followed by further reaction with iodide to form triiodide.[34] Chloride was also detected in reasonable concentrations (Table 4). A white precipitate isolated from the photolysed solutions was identified as NaCl. If a fresh source of counter anion, in the form of *tert*-butylammonium iodide was added to the NMR tubes, full recomplexation of **1** occurred. *tert*-Butylammonium is a cation that is too large to fit into the lower-rim hydrophilic cavity of **1**, and thus recomplexation of **1** must be with any sodium cation present (Table 4).

Replicate 1-mL samples of chloroform were irradiated for up to 90 minutes, under the same conditions described above, and in each case, no chloride was detected. Solutions of **1** in $CDCl_3$, irradiated for 60 minutes, showed no degradation of the calixarene. However, a potentiometric titration showed that chloride was present in these solutions, but at a significantly reduced level (1.69 ± 0.04 mM) than that recorded following irradiation of the sodium complexes of **1**. In a separate series of experiments *tert*-butylammonium iodide (TBAI) was irradiated for timed intervals and

Table 4. Autotitration results for NaI-**1** complexes before irradiation, and after irradiation for 10 (*) and 45 (#) minutes. Results are average of six replicate experiments (n.d. = not detectable).

	Complexed calixarene [%]	Complexed calixarene [mM]	Uncomplexed calixarene [mM]	Iodide concentration [mM]	Chloride concentration [mM]
NaI-**1**	100	8.76	0	8.56	n.d.
	74*	6.47 ± 0.65	2.29 ± 0.8	5.5 ± 1.5	0.92 ± 1
	36#	3.05 ± 0.14	5.70 ± 0.14	n.d.	6.63 ± 0.5
NaI-**1**·MeCN	100	8.76	0	8.64	n.d.
	66*	5.74 ± 0.2	3.02 ± 0.2	3.16 ± 0.6	n.d.
	38#	3.38 ± 0.2	5.38 ± 0.21	n.d.	6.53 ± 0.3

 © 2005 Wiley-VCH Verlag GmbH & Co. KGaA, Weinheim

analysed by both ^{1}H NMR and potentiometry; TBA cation has no absorption bands above 280 nm. After just 15 minutes no iodide could be detected in solution and chloride, in an equivalent amount to that of iodide initially present, was detected [(a) in Figure 6]. The presence of triiodide in these solutions was confirmed by UV/Vis spectroscopy. The results confirmed that direct photooxidation of the anion could result in the production of triiodide from iodide and lead to the generation of chloride from the solvent.

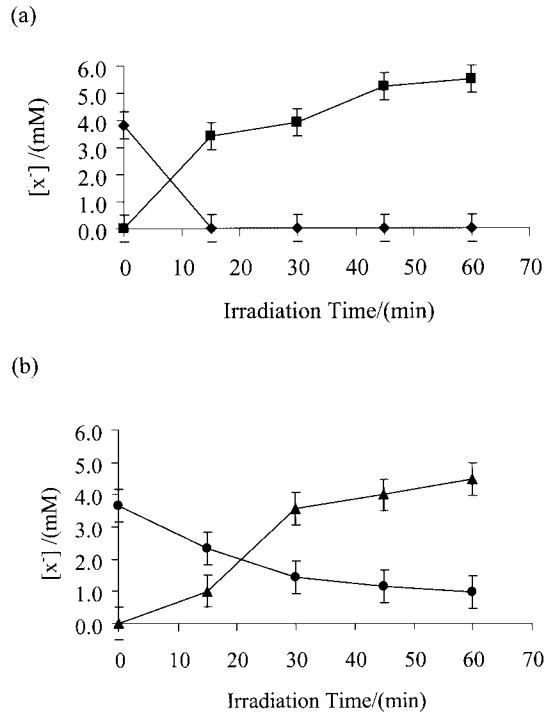

Figure 6. Plots showing (a) the relationship between concentration in mmol of iodide (♦) and chloride (■) ions in $CDCl_3$ solution on irradiation of 3.8 mmol TBAI at 15 minute intervals and (b) the relationship between concentration in mmol of thiocyanate (●) and chloride (▲) ions in solution on irradiation at 15 minute intervals of ca. 3.7 mmol TBASCN. Each value is an average of 3 replicate experiments.

GC and GC-MS analysis of the irradiated $CDCl_3$ solutions of both the calixarene and TBA iodide complexes showed that the primary organic products formed were deuterio-dichloromethane and -dichloroiodomethane ($CDCl_2I$) and traces of deuterio-1,1,2,2-tetrachloroethane. It is known that reduction of chloroform generates short-lived radical anions which eject chloride immediately upon formation.[35] The generated radicals can undergo disproportionation and recombination processes as well as further attack on solvent and this is evidenced by the photoproducts identified above. In all cases the photolysis by-products were present in much larger quantities for experiments carried out on the complexes rather than on the free ligand. In addition no organic photoproducts were identified upon extended irradiation of $CDCl_3$ solutions (or CD_2Cl_2 solutions, vide infra). In other studies, UV/Vis irradiation of metal coordination complexes where iodide is present either as an axial ligand or as a counter anion leads to the generation of an I$^{\cdot}$ radical, with concomitant reduction of the solvent by charge transfer to solvent (CTTS).[36–44] For those studies carried out in chlorinated solvents generation of iodide radicals has resulted in the production of chloride from chlorinated solvents.[40,41]

The pattern of destruction of counter anion and production of chloride can be seen again in the irradiation of NaSCN-**1** and NaSCN-**1**·MeCN This was shown firstly by quantitative FT-IR spectroscopy which indicated that irradiation of the NaSCN-**1** solutions resulted in the concentration of thiocyanate anions falling to undetectable levels after 30 minutes. A similar pattern was noted by potentiometric studies as shown in Figure 7. However, the complexes were once again noted by ^{1}H NMR spectroscopy to be only partially decomplexed over the same time period. The main anion present from photolysis of thiocyanate solutions, as detected by potentiometry, was again chloride and NaCl could be recovered as a precipitate from solution. Elemental sulfur also precipitated out of solution and was identified by microanalysis.

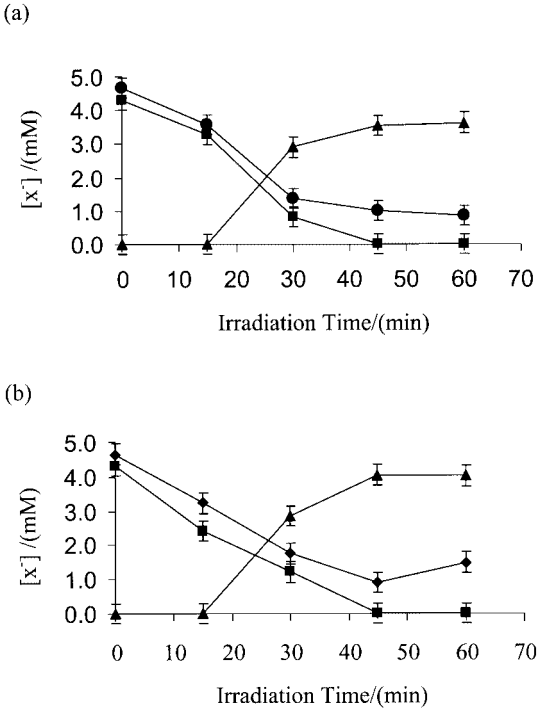

Figure 7. The relationship between (a) the concentration of NaSCN-**1** (●) and (b) the concentration of NaSCN-**1**·MeCN (♦) and those of chloride (▲) and thiocyanate (■) upon irradiation of the respective complexes in $CDCl_3$ at timed intervals. Each value is the average of six replicate measurements.

Irradiation of *tert*-butylammonium thiocyanate (TBASCN) over 60 minutes in $CDCl_3$ also showed the destruction of the SCN anion, though at lower levels than recorded for NaSCN-**1** [(b) in Figure 6]. Thus again the production of chloride in solution could be linked to the photoreaction of the counter-anionic species. GC-MS analysis of irradiated solutions of both TBASCN and NaSCN-**1** showed the formation of mainly deuterated dichloromethane as a photoproduct of the solvent.

 © 2005 Wiley-VCH Verlag GmbH & Co. KGaA, Weinheim

These results confirm what other workers have noted on irradiation of thiocyanate complexes in nonaqueous solvents.[39,40,42] Initially irradiation leads to production of thiocyanate radicals which can then form sulfur and cyanide anion. The proposed reaction is:

$$SCN^- + h\nu \rightarrow SCN^{\cdot} + e^-_{solvated} \quad (1)$$

$$SCN^- + h\nu \rightarrow S + CN^- \quad (2)$$

followed by complex reactions in which cage recombination and further reactions with SCN^- are central:

$$SCN^- + SCN^{\cdot} \leftrightharpoons (SCN)_2^{\cdot -} \quad (3)$$

$$2\ (SCN)_2^{\cdot -} \rightarrow (SCN)_2 + 2\ SCN^- \quad (4)$$

$$S + SCN^- \rightarrow S_2 + CN^- \quad (5)$$

$$2\ SCN^{\cdot} \rightarrow (SCN)_2 \quad (6)$$

Elemental sulfur was recovered following photolysis of both NaSCN-**1** and TBASCN, but there was no evidence for the presence of cyanide from auto-titration or FT-IR studies. The cyanide anion itself can be further photolysed to the cyano radical, which can oxidise the solvent or form cyanogen gas, and this may be what has happened here.[42]

Electrochemical Studies

The experiments on the thiocyanate and iodide complexes, taken together with our previous work on tetraphenylborate, has confirmed that the oxidation of the counter-anionic species is critical to the decomplexation process. The non-reaction of perchlorate and minimal reaction of periodate complexes would support this. The electrochemical oxidation of the anions in $CDCl_3$, as TBAX salts and as the complexes NaX-**1**, was examined by cyclic voltammetry. The results indicated that the iodide, thiocyanate and tetraphenylborate anions in the form of the TBAX salts had oxidation potentials at 0.86, 1.20 and 0.85 V, respectively. In the corresponding calixarene NaX-**1** complexes, these oxidation potentials were recorded at 0.55, 0.95, and 0.80 V, respectively. Thus complexation with the calixarene lowers the oxidation potential of the anion which is consistent with the anion being effectively shielded from the bound cation. The relative ease of electrochemical oxidation of the anions was approximately in the same order as their photochemical oxidation (taking irradiation results after 15 minutes in Table 3, which is before equilibrium is reached).

Irradiation of NaX-1 in Other Deuterated Solvents

The % decomplexation of NaI-**1** and NaSCN-**1** were recorded after irradiation in CD_3OD, CD_3CN, and CD_2Cl_2 (Figure 8). No decomplexation of the complexes occurred in CD_3OD or CD_3CN. While ion pairing is minimised in these solvents it should also be noted that these solvents are not easily reduced by CTTS. The extent of decomplexation of both complexes was significantly less in CD_2Cl_2 than in $CDCl_3$ and both autotitration and IR measurements indicated that, while destruction of the anions had occurred, it was to a far lesser extent than in $CDCl_3$. Although the extent of ion pairing would be similar for these solvents, this difference in reactivity is thought to reflect the relative ease of reduction of these solvents [chloroform, –1.67 V ($E_{1/2}$) vs. dichloromethane –2.33 V ($E_{1/2}$)][45] resulting in the formation of chloride as well as other photoproducts.

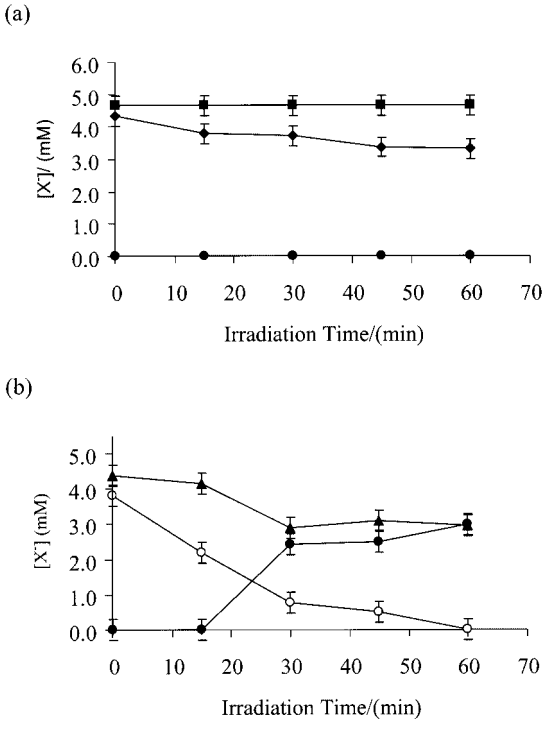

Figure 8. Variation in the concentrations of (a) NaSCN-**1** (■), thiocyanate (♦) and chloride (●) and (b) NaI-**1** (▲), iodide (○) and chloride (●) upon photolysis of the sodium complexes in CD_2Cl_2. Each value is an average of six replicate measurements.

Proposed Mechanism

In Scheme 2 the proposed mechanism for the decomplexation process is shown. Irradiation of NaX-**1** in $CDCl_3$ results in the possible generation of two excited species, a radical aryl cation and the direct oxidation of the counter-anionic species. While the experiments with TBA salts

 © 2005 Wiley-VCH Verlag GmbH & Co. KGaA, Weinheim

would indicate that excitation of the counter anion predominates, some excitation of the aryl cation does occur as evidenced by the production of chloride ions, albeit at low levels, from the solvent upon irradiation of **1** on its own. However, although a radical aryl cation may be generated initially, abstraction of an electron from the counter anion or solvent is likely to have occurred quickly, as no photoproducts of the host compound were detected in any of the experiments.

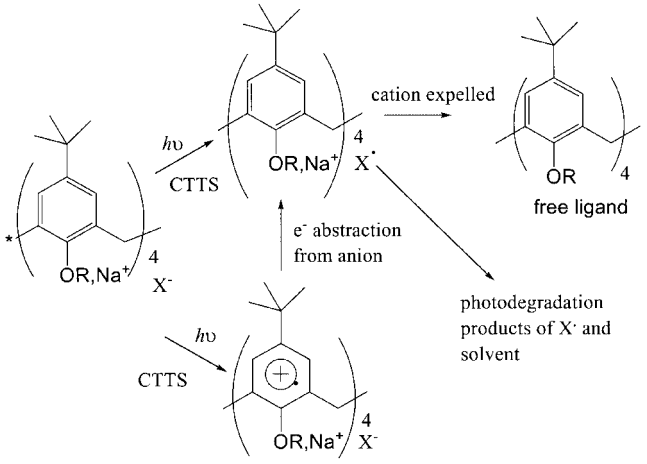

R = $CH_2OCOCH_2CH_3$

X = I^-, SCN^-, BPh_4^-

Scheme 2. Proposed decomplexation mechanism for the sodium salt complexes of **1**. Encapsulated solvent is omitted for clarity.

Excitation of the counter-anionic species resulted in a charge transfer to solvent with the subsequent generation of a number of photoproducts of both the solvent and anion. The generation of a radical from the anion leads to the break-up of the ion pair and the subsequent expulsion of the sodium cation. This cation remains available for recomplexation if a suitable counter anion is added to solution post-photolysis or indeed is generated during the photolysis process, i.e. triiodide, chloride.

The products of iodide oxidation were ultimately triiodide and iodine, sulfur was isolated from irradiated thiocyanate solutions, and chloride ion was generated from CTTS to the solvent in both cases. The poor solubility of sodium chloride in chloroform, even in the presence of the macrocycle, precluded full recomplexation. The NMR spectrum recorded after irradiation showed the complex peaks to be at slightly shifted positions relative to the initial complex and these positions are consistent with the complex being present as NaY-**1** (Y = product anion i.e. I_3^-, Cl^-).[17] While photoproducts of the solvent, including the deuterated forms of 1,1,2,2-tetrachloroethane, dichloromethane and dichloroiodomethane, could be detected by GC-MS, there were no photoproducts of the macrocycle itself indicated by NMR or GC-MS.

Conclusions

This study involved the irradiation of a series of sodium salt complexes of **1**. Some of the complexes were isolated in the solid sate with a moleclue of solvent bound at the upper rim. Upon dissolution, however, the upper-rim guest largely dissociated, with about 10% of the solvent molecule remaining associated with the upper rim at any given time. Decomplexation of the sodium cation and immediate subsequent expulsion of upper-rim bound guest could be triggered by the oxidation of the counter anion at the lower rim and the extent of decomplexation varied as a function of the anion. The lower the oxidation potential of the anion the greater the extent of initial decomplexation, with iodide, thiocyanate and tetraphenylborate complexes being easily decomplexed whereas the perchlorate complex was unreactive, as expected. Addition of fresh solutions of anion (in the form of *tert*-butylammonium iodide/thiocyanate etc.) allowed full recomplexation to occur, indicating that the integrity of both the cation and macrocycle were maintained during irradiation.

Potentiometric studies of the inorganic species in solution indicated that there was not a linear correlation between photooxidation of the anion and decomplexation of the calixarene. Photolysis of the anions resulted in the production of other anionic species which could allow recomplexation to occur to some extent. The overall % decomplexation measured was found to be determined by the amount of NaY-**1** present *in solution* at the end of the experiment.

These studies have also helped to understand the relationship between a guest binding at the lower rim of a calixarene and the "allosteric effect" that this confers on upper-rim binding of neutral species.[8,9,25,46] In the example studied here the difference in binding constant for the two guests confers essentially a "one-way allosterism" and removal of the lower-rim bound guest, in this case by photodecomplexation, results in the immediate expulsion of the upper-rim guest. Thus the possibility for a novel control mechanism for the complexation of neutral guest at the upper rim of calixarenes, by choice of lower rim counter anion or level of irradiation, has been identified. Importantly, the photoreaction of the nonchromophoric TBA salts followed similar patterns to the calixarene complexes suggesting that controlled photodecomplexation of bound guests by other macrocyclic systems such as cryptands or resorcinarenes should be possible. The development of high level control of switching systems is obviously desirable and such a system offers potential as an analogue switching device for the control of complexation of neutral species. The dependence of the binding constants at the upper and lower rim as a function of the nature of the counter anion, cation and upper-rim guest is currently being investigated.

Experimental Section

Complexes of *p-tert*-Butylcalix[4]arene Tetraethyl Ester: This calixarene was synthesised and supplied as pure from Prof. M. A. McKervey, Queen's University Belfast and from Loctite (Irl) Ltd. All salts used in this study were supplied by Sigma–Aldrich and were dried overnight at 110 °C prior to use. The following solvents were used in this study: HPLC MeCN, HPLC MeOH (Riedel de

 © 2005 Wiley-VCH Verlag GmbH & Co. KGaA, Weinheim

Haan); and HPLC chloroform, HPLC dichloromethane, [D_3]-MeCN, [D]chloroform, [D_2]dichloromethane and [D_4]MeOH (Aldrich). Anhydrous chloroform was supplied by Sigma–Aldrich. Hydrogen, air, nitrogen and helium were supplied by Air Products.

The complexes were prepared by mixing equimolar amounts of ligand and salt (typically 0.5 mmol) in ca.50 mL of MeCN, chloroform, dichloromethane or MeOH overnight in the dark. The solvent was allowed to evaporate naturally and passing a stream of N_2 over the complex dried the isolated salt. Full complexation was verified from ^{1}H NMR and FTIR data. Micro-analytical data, recorded at the micro-analytical laboratory at the National University of Ireland, Dublin, showed that the solid-state complexes, that contained solvent within the upper cavity, contained 1:1 mol ratios of solvent to complex in all cases.

Spectroscopic Techniques: Solutions of the analytes were typically 10^{-4} mol·L^{-1}. UV/Vis spectra were recorded with a double beam Shimadzu 160A Spectrophotometer. Their spectra were measured using a 10-mm path-length quartz cell. Infrared spectra were recorded with a Nicolet Impact 410 FTIR Spectrometer and the spectra processed on an attached PC using Omnic v.3.1a software. NMR spectra were recorded with a JEOL 300 MHz FT NMR spectrometer. Typically 20 mg of analyte was dissolved in 0.5 mL of a deuterated solvent and placed in a precision pyrex NMR tube.

Irradiation Procedure: The photolysis lamp used in this study was a Pen-Ray 5.5-Watt low-pressure cold cathode mercury vapour lamp with a 150 V (60 Hz) power supply. An external transformer was added to enable direct use of the mains power supply (220 V, 50 Hz). Previous irradiation studies with this lamp showed that a UV filter needed to be used in order to avoid ligand decomposition.[17] This filter was simply a glass NMR tube into which the irradiation sample was placed. Typically, 1 mL of a 4.5 mM solution of a complex in an appropriate solvent was placed into a Pyrex NMR tube. Another 1 mL aliquot of the irradiation sample was placed in the dark during the irradiation time as a reference sample. Before irradiation the solution was degassed for ca. 10 minutes to remove any dissolved oxygen from the sample.

Potentiometric Titration: A 1 mL aliquot of a 4 mM irradiated solution, in chloroform or dichloromethane, was washed with 5 mL ultra-pure water in order to extract all water-soluble inorganic species from the organic solvent. The aqueous layers were collected and transferred to a 50 mL plastic beaker where 2 mL of 2 M HNO_3 was added. The volume in the beaker was made up to ca. 25 mL with doubly distilled water. The solution was then titrated with 0.01 M $AgNO_3$ using a Metrohm 702 SM Titrino autotitrator with a Metrohm 703 Ti stand. The end point was determined potentiometrically using a combined silver ring electrode.

GC-MS Analysis: A GC method was developed using a Shimadzu GC system incorporating a GC-14A gas chromatograph fitted with an FID detector and a Supelco SBP-5 fused silica capillary column (15 m × 0.20 mm, 0.20 μm film thickness). Spectra were obtained from a Shimadzu C-R5A integrator. Samples were introduced to the GC with a Hamilton 10 μL syringe. A GC-MS method was developed using a Shimadzu GC system incorporating a GC-17A gas chromatograph, fitted with an FID detector and a Supelco SBP-5 fused silica capillary column (30 m × 0.25 mm, 0.25 μm film thickness), and a QP-5000 mass spectrometer. Spectra were obtained using the "Class-5000" software package, and samples were introduced to the system with a Shimadzu AOC-20i auto injector.

Electrochemical Analysis: A CHI630A Electrochemical Analyser was used with a Pt wire as the auxillary electrode, a Ag/Ag^+ non-aqueous reference electrode, and a glassy carbon working electrode. A 0.1 M solution of *tert*-butylammonium hexafluorophosphate in chloroform was used as the electrolyte. 0.1 M solutions of *tert*-butylammonium thiocyanate and iodide were prepared in chloroform, and the solution to be analysed contained 6 mL of the electrolyte + 1 mL of the individual anion solutions. A 1 mM solution of *tert*-butylammonium tetraphenylborate was prepared in the electrolyte and was analysed undiluted. All solutions were degassed using nitrogen for 10 minutes prior to analysis. The technique used was CV, sweeping in a positive direction, looking at oxidation between 0 and 1.8 V, and the reverse as far as –0.6 V. The scan rate was 0.1 V/s, four segments were carried out (two full sweeps forward and reverse from –0.6 to 1.8 V), and the sensitivity was 2×10^{-5} A/V.

Acknowledgments

We would like to thank Prof. M. A. McKervey and Loctite Ireland Ltd. for calixarene samples used in this work and J. McGinley for useful discussions. We would also like to thank E. M. Dempsey and T. McCormac for use of the electrochemical analyser. D. T. would like to thank Enterprise Ireland for financial assistance. C. McK. would like to thank the Postgraduate R&D Skills programme (Technological Sector Research, Strand I) and the PhD continuation fund of IT Tallaght for funding.

[1] R. Ungaro, L. Mandolini, *Calixarenes in Action*, Imperial College Press, London, **2000**.
[2] *Calixarenes 50th Anniversary: Commemorative Issue* (Ed.: J. Vicens), Kluwer Academic Publishers, Dordrecht, **1995**.
[3] *Calixarenes, a Versatile Class of Macrocyclic Compounds* (Eds.: J. Vincens, V. Bohmer), Kluwer, Dordrecht, **1991**.
[4] F. Arnaud-Neu, E. Collins, M. Deasy, G. Ferguson, S. J. Harris, B. Kaitner, A. J. Lough, M. A. McKervey, E. Marques, B. L. Ruhl, M. J. Schwing-Weill, E. M. Seward, *J. Am. Chem. Soc.* **1989**, *111*, 8681.
[5] G. Barrett, B. S. Creaven, S. Harris, B. Lynch, M. A. McKervey, M. Ryan, *Anal. Proc.* **1993**, *30*, 150.
[6] A. Arduini, A. Pochini, S. Reverberi, R. Ungaro, G. Andreeti, F. Ugozzoli, *Tetrahedron* **1986**, *42*, 2089.
[7] A. Yamada, T. Murase, K. Kikukawa, T. Arimura, S. Shinkai, *J. Chem. Soc. Perkin Trans. 2* **1991**, 793.
[8] A. Arduini, W. M. McGregor, D. Paganuzzi, A. Pochini, A, Secchi, F. Ugozzoli, R. Ungaro, *J. Chem. Soc. Perkin Trans. 2* **1996**, 839–846.
[9] S. Smirnov, V. Sidorov, E. Pinkhassik, J. Havlicek, I. Stibor, *Supramol. Chem.* **1997**, 187–196.
[10] A. F. Danil de Namor, N. Apaza de Sueros, M. A. McKervey, G. Barrett, F. Arnaud Neu, M. J. Schwing-Weill, *J. Chem. Soc. Chem. Commun.* **1991**, 1546.
[11] A. F. Danil de Namor, E. Gil, M. A. L. Tanco, D. A. P. Tanaka, L. E. P. Salazar, R. A. Schulz, J. Wang, *J. Phys. Chem.* **1995**, *99*, 16776.
[12] M. A. McKervey, F. Arnaud Neu, M. J. Schwing-Weill, in *Comprehensive Supramolecular Chemistry* (Ed.: G. W. Gokel), Pergamon Press, **1997**, vol. 1, p. 537.
[13] Y. Israël, C. Detellier, *J. Phys. Chem. B* **1997**, *101*, 1897–1901.
[14] R. Ungaro, A. Pochini, in *Topics in Inclusion Phenomena. Calixarenes, A Versatile Class of Macrocyclic Compounds* (Eds.: J. Vicens, V. Böhmer), Kluwer Academy: Dordrecht, **1990**.
[15] M. A. McKervey, M. J. Schwing-Weill, in *Topics in Inclusion Phenomena. Calixarenes, A Versatile Class of Macrocyclic Compounds* (Eds.: J. Vicens, V. Böhmer), Kluwer Academy: Dordrecht, **1990**.
[16] G. Barrett, B. S. Creaven, B. Lynch, D. Corry, B. Johnston, M. A. McKervey, *J. Chem. Soc. Chem. Commun.* **1995**, 363.
[17] M. Pitarch, A. Walker, J. F. Malone, M. A. McKervey, B. S. Creaven, D. Tobin, *Gazetta Chimica Italiana* **1997**, *127*, 717.

 © 2005 Wiley-VCH Verlag GmbH & Co. KGaA, Weinheim

[18] S. Shinkai, T. Nakaji, Y. Nishida, T. Ogawa, O. Manabe, *J. Am. Chem. Soc.* **1980**, *102*, 5860–5865.
[19] C. D. Gutsche, *Aldrichim. Acta* **1995**, *28*, 3.
[20] C. D. Gutsche, B. Dhavan, K. H. No, R. Muthukrish, *J. Am. Chem. Soc.* **1981**, *103*, 3782.
[21] G. D. Andreeti, R. Ungaro, A. Pochinni, *J. Chem. Soc. Chem. Commun.* **1979**, 1005.
[22] M. Coruzzi, G. D. Andreeti, V. Bocchi, A. Pochinni, R. Ungaro, *J. Chem. Soc. Perkin Trans.* **1982**, 1133.
[23] M. A. McKervey, E. Seward, G. Ferguson, B. L. Ruhl, *J. Org. Chem.* **1986**, *51*, 3581.
[24] In addition the high extinction coefficient of some of these solvents, at the wavelengths of excitation, precluded their use.
[25] A. Arduini, G. Giorgi, A. Pochini, A. Secchi, F. Ugozzoli, *Tetrahedron* **2001**, *57*, 2411–2417.
[26] M. E. Gottlieb, V. Kotlyar, A. Nudelman, *J. Org. Chem.* **1997**, *62*, 7512–7515.
[27] The values reported were typically determined in acetonitrile or methanol where ion-pairing is minimised (see refs.[10–15] above). The determination of binding constants in media of low dielectric constant, particularly chloroform, is complicated by the phenomenon of ion-pairing in this solvent and binding constants are likely to be higher in these solvents for charged species.
[28] A. Arduini, E. Ghidini, A. Pochini, R. Ungaro, G. D. Andreeti, F. Ugozzoli, *J. Inclusion Phenom.* **1988**, *6*, 119.
[29] A more logical choice of lamp might appear to be a medium pressure lamp, given the absorption spectra of the ligand and complexes detailed in Table 2 and shown in Figure 3. However use of such lamps resulted in complete photoreaction in short times, which would not allow for a comparison of extent of decomplexation as a function of time.
[30] A. Gilbert, J. Baggott, *Essentials of Molecular Photochemistry*, Blackwell Scientific Publications, Oxford, **1991**.
[31] A. Gilbert, in *Photochemistry in Organic Synthesis* (Ed.: J. D. Coyle), The Royal Society of Chemistry, Special Publication No 57, **1986**, 278.
[32] F. Galindo, M. A. Miranda, R. Tormos, *J. Photochem. Photobiol. A* **1998**, *117*, 17–19.
[33] All of the salts studied were soluble only in their complexed form in $CDCl_3$, but solutions of the salts in MeOH determined that they did have weak excitation spectra above 280 nm.
[34] UV/Vis spectra of the unphotolysed Na**I**-**1** complexes were recorded and had two main absorption bands at 274 nm and 283 nm. In the irradiated complexes a new peak at 368 nm was observed which was concomitant with the destruction of iodide and was assigned as an I_3^- absorption band by comparison with an authentic sample. Quantification of triiodide proved difficult due to the dilution effect on the equilibrium position between poly-iodide and monomeric iodide species in solution. Dilution to record UV/Vis spectra was necessary in order to compare NMR, UV/Vis and potentiometric readings on the same sample. While halides can form polyatomic species the likelihood of this occurring depends on the size of the counter cation and higher species than I_3^- are unlikely to occur with sodium cations in aqueous solution. However dilution in non-aqueous solution does affect the equilibrium between iodide, iodine and triiodide.
[35] J. Grimshaw, J. S. Ramsey, *J. Chem. Soc. Perkin Trans. 2* **1975**, 215.
[36] T. Donohue, *Lanthanide Actinide Res.* **1985**, 1, 89.
[37] T. Imamura, T. Jin, T. Suzuki, M. Fujimoto, *Chem. Lett.* **1985**, *6*, 847.
[38] F. Pina, M, Maestri, *Inorg. Chem.* **1986**, *25*, 4249–4252.
[39] J. Muchova, V. Holba, *Collect. Czech. Chem. Commun.* **1984**, *49*, 398–403.
[40] A. Vogler, H. Kunkely, *Inorg. Chem.* **1982**, *21*, 1172.
[41] A. Vogler, H. Kunkely, *Angew. Chem.* **1982**, *94*, 217.
[42] S. A. Vinogradov, K. P. Balashev, G. A.Shagisultanova, *Koord. Khim.* **1984**, *10*, 399.
[43] D. M. Dooley, B. M. Patterson, *Inorg. Chem.* **1982**, *21*, 4330.
[44] B. Kraut, L. Vincze, S. Papp, *Acta Chim. Hung.* **1986**, *122*, 203.
[45] A. J. Fry, *Synthetic Organic Electrochemistry*, 2nd Ed., Wiley-Interscience Publication, New York, **1989.**
[46] A. F. Danil de Namor, R. M. Cleverly, M. L. Zapata-Ormachea, *Chem. Rev.* **1998**, *98*, 2495–2525.

Received: August 18, 2004

 © 2005 Wiley-VCH Verlag GmbH & Co. KGaA, Weinheim

Heterobimetallic Systems Containing Organometallic and Classical Coordination Sites: Effects of Subtle Changes in the Werner-Type Site

Tianlu Sheng,[a] Sebastian Dechert,[a] A. Claudia Stückl,[a] and Franc Meyer*[a]

Keywords: Bridging ligands / Cyclopentadienyl ligands / Heterometallic complexes / N ligands / Manganese / Zinc

Several highly unsymmetrical heterodinuclear Mn/Zn complexes are reported, in which an organometallic $CpMn(CO)_2$ fragment and a classical Werner-type zinc coordination unit are arranged in close proximity by means of a bridging pyrazolate. Ligand scaffolds differing in the chelate size of the tripodal tetradentate $\{N_4\}$ binding site, and different co-ligands for zinc are employed. Both the zinc-devoid precursor compounds and the bimetallic complexes with zinc(II) nested in the tris(pyridylalkyl)amine type $\{N_4\}$ compartment have been characterized by X-ray crystallography. Structural and spectroscopic features as well as the redox potentials of the Mn^I/Mn^{II} couple indicate slight effects of the redox-inactive Werner-type subunit on the properties of the organometallic site. Oxidation is highly localized at the organometallic manganese site, as is evidenced by IR and EPR spectroscopy and supported by DFT calculations.
(© Wiley-VCH Verlag GmbH & Co. KGaA, 69451 Weinheim, Germany, 2005)

Introduction

Complexes of cyclopentadienyl (Cp) ligands bearing functional amino or amido side-chains are currently receiving enormous attention in organometallic chemistry.[1,2] While the donor substituent tethered to the Cp moiety might serve an intramolecular function, for example acting as a (sometimes hemilabile) chelate donor in generic type **A** complexes (Scheme 1),[3,4] it may also serve an intermolecular function, for example by anchoring to a solid support or providing solubility.[3] A further possibility is the introduction of a potentially bridging moiety that will lead to highly preorganized bimetallic systems formally composed of a type **A** Cp∩N fragment and an adjacent second metal ion. In this respect we have recently developed a synthetic approach for the construction of type **B** bimetallic complexes where a pyrazolate group linking two Cp units functions both as an intramolecular N-donor and as a bridging unit spanning two metals.[5,6] The dimanganese complex **1** has been studied in detail and has been shown to undergo two sequential, one-electron, metal-centered oxidations with fast intramolecular thermal-electron transfer ($k_{ET} \approx 2.6\times10^{10}\ s^{-1}$ at 298 K) in the mixed-valent Mn^IMn^{II} species.[6] In an extension of this concept, a first access to highly unsymmetrical heterobimetallic type **D** scaffolds has recently been developed.[7] These can be formally viewed as a combination of one type **A** and one type **C** subunit, i.e. as an assembly of both a Werner-type and an organometallic fragment in a preorganized bimetallic array. This description is corroborated by the structural characterization of the only such complex reported to date (**2**),[7] since inspection of its individual subunits reveals close similarities to related mononuclear complexes. In particular, the zinc subunit of **2** is reminiscent of the well-known $[(tmpa)ZnCl]^+$ complex, where tmpa is tripodal tetradentate tris(pyridylmethyl)amine. Oxidation of **2** occurs at around –0.66 V (versus the ferrocene couple), and IR spectroscopic evidence showed it to be Mn-centered.[7]

These findings suggest to probe type **D** systems in metal-mediated reactions that proceed by coordination of substrates to the M^2 metal ion in the classical Werner-type site, with the $CpMn(CO)_2$ subunit serving as an electron reservoir, but without direct involvement of the manganese in substrate binding. In the case of redox-active metal ions in the $\{N_4\}$ site, this approach may lead to well-defined systems capable of novel "one-site-addition-two-metal-oxidation" reactions.[8] Two characteristics of type **D** complexes are noteworthy in this regard: firstly, the rigid chelate arrangement precludes dissociation of the organometallic fragment from the bridging pyrazolate, and secondly, the π plane of the heterocycle roughly coincides with the mirror plane of the $Mn(CO)_2$ moiety. The latter situation is most favorable for Mn-pyrazolate π-interactions and hence for electronic communication between the Mn site and the second metal ion.[6,9,10]

It seems particularly attractive that type **D** compounds offer the potential to introduce various different ligand environments for the Werner-type coordination site. Fundamental to an understanding of bimetallic chemistry of those complexes is the knowledge of how different Werner-type

[a] Institut für Anorganische Chemie, Georg-August-Universität Göttingen,
Tammanstraße 4, 37077 Göttingen, Germany
Fax: +49-551-393063
E-mail: franc.meyer@chemie.uni-goettingen.de
Supporting information for this article is available on the WWW under http://www.eurjic.org or from the author.

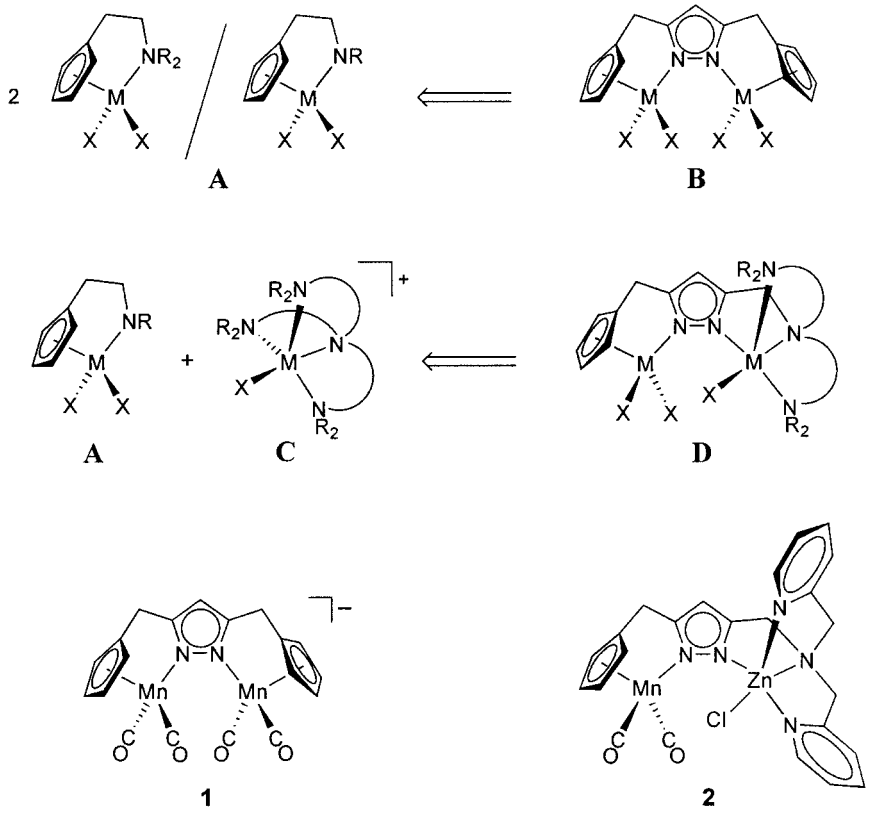

Scheme 1.

sites influence the properties of the redox-active $CpMn(CO)_2$ subunit, even in the absence of any M^2 or in the case of a redox-inactive M^2 ion such as zinc(II). The present contribution now reports two (Cp∩pyrazolate)$Mn(CO)_2$ systems with different chain lengths in the bis(pyridylalkyl) amine side-arms and several zinc complexes thereof. Effects of the different ligand side-arms and different anionic co-ligands (either coordinating or noncoordinating) on structural and electrochemical properties are investigated.

Results and Discussion

Synthesis and Structural Characterization of Complexes

The synthesis of pyrazole derivative **5a** with appended cyclopentadienyltricarbonylmanganese and bis(pyridylmethyl)amine substituents has been communicated previously and had been used for the direct synthesis of **2**.[7] Following the same synthetic strategy we have now prepared the analogous compound **5b** with a longer bis(pyridylethyl)amine side-arm (Scheme 2).

Starting from **3**, which is readily available in five steps from 3,5-dimethylpyrazole,[5,11] the $CpMn(CO)_3$ moiety was first introduced in a palladium-catalyzed cross-coupling reaction and the bis(pyridylmethyl)amine arm was subsequently attached to give 2-tetrahydropyranyl (thp)-protected **5b**. The thp group was then removed under acidic conditions. Irradiation of **5a**,**b** leads to elimination of one CO and intramolecular coordination of the pyrazole-N.[12] This reaction can be conveniently followed by IR spectroscopy. The resulting complexes **6a**,**b** were isolated and fully characterized, including by X-ray crystallography. Their molecular structures are depicted in Figure 1 and Figure 2, respectively, together with selected atom distances and bond angles.

The geometric parameters for the $CpMn(CO)_2$ fragments of **6a**,**b** are very similar to those of **1** and **2** reported previously.[6,7] The proton bound to the pyrazole-N(2) is involved in hydrogen bonding to the N-atoms of the pendent pyridine side-arms. Interestingly, it forms an intramolecular hydrogen bond in the case of **6b** [d{N(2)···N(5)} = 2.977(2) Å; Figure 2], while intermolecular hydrogen bonding that leads to a polymeric chain structure in the solid state is observed for **6a** [d{N(2)···N(5′)} = 2.825(2) Å; Figure 3]. Involvement of the pyrazole-NH in H-bonding has recently also been found to be crucial for unidentate pyrazole coordination.[13]

Heterobimetallic complexes with zinc ions in the $\{N_4\}$ donor compartment are best prepared in a one-pot procedure starting from **5a**,**b**. Thus, solutions of **6a**,**b** prepared in situ were treated with one equivalent of KO*t*Bu and one equivalent of $Zn(OAc)_2{\cdot}2H_2O$. Single crystals of **7a**·DMF·H_2O and **7b** (Scheme 3) were finally obtained by slow diffusion of Et_2O into DMF or CH_2Cl_2 solutions of the products, respectively. The constitution of both complexes was elucidated by X-ray crystallography. Molecular

 © 2005 Wiley-VCH Verlag GmbH & Co. KGaA, Weinheim

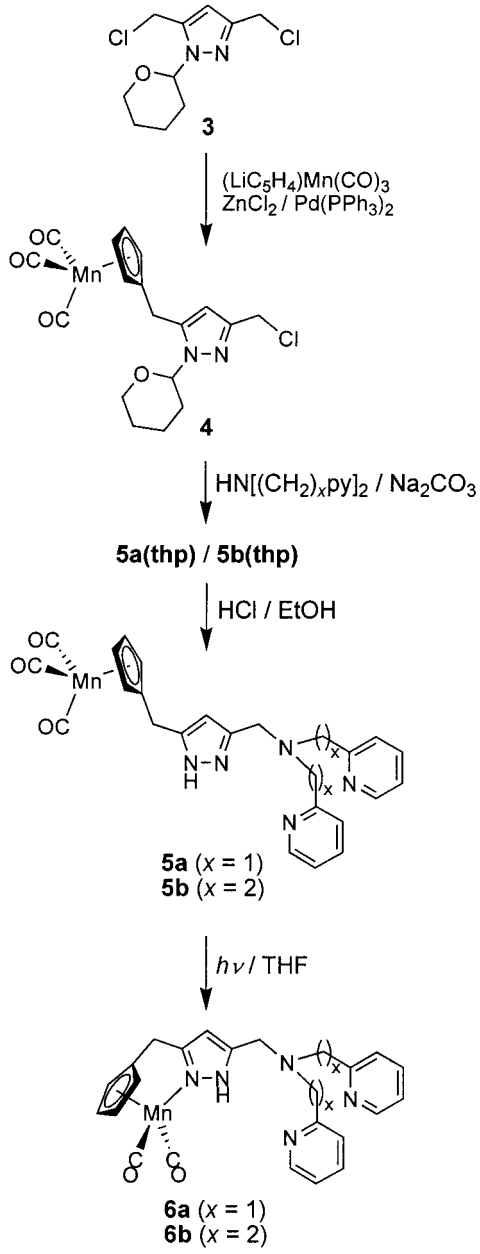

Scheme 2. Synthesis of **6a** and **6b**.

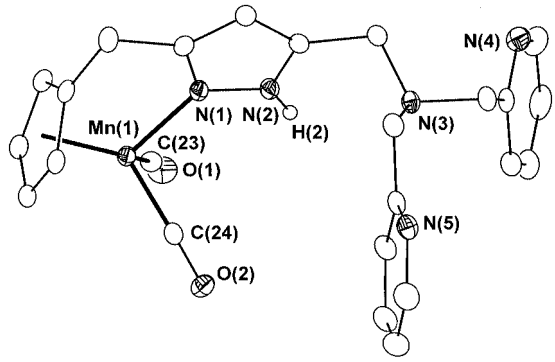

Figure 1. ORTEP plot (30% probability thermal ellipsoids) of the structure of **6a**. For the sake of clarity all hydrogen atoms, except H(2), have been omitted. Selected atom distances [Å] and angles [°] [Cg(1) defines the centroid of the Cp ring atoms]: Mn(1)–Cg(1) 1.7686(9), Mn(1)–N(1) 2.006(2), Mn(1)–C(23) 1.772(2), Mn(1)–C(24) 1.771(2), C(23)–O(1) 1.167(2), C(24)–O(2) 1.162(2); Cg(1)–Mn(1)–N(1) 111.24(5), Cg(1)–Mn(1)–C(23) 125.84(7), Cg(1)–Mn(1)–C(24) 125.04(7), C(23)–Mn(1)–C(24) 90.81(9), C(23)–Mn(1)–N(1) 102.15(8), C(23)–Mn(1)–N(1) 95.98(7), O(1)–C(23)–Mn(1) 173.5(2), O(2)–C(24)–Mn(1) 178.2(2).

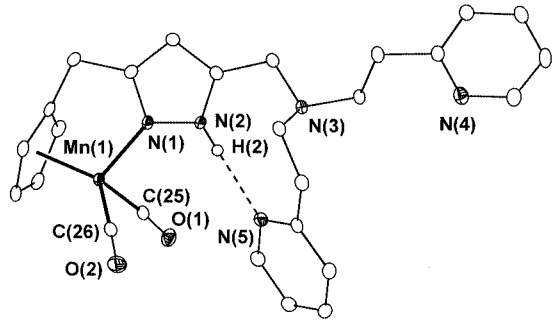

Figure 2. ORTEP plot (30% probability thermal ellipsoids) of the molecular structure of **6b**. For the sake of clarity all hydrogen atoms, except H(2), have been omitted. Selected atom distances [Å] and angles [°] [Cg(1) defines the centroid of the Cp ring atoms]: Mn(1)–Cg(1) 1.772(1), Mn(1)–N(1) 2.020(2), Mn(1)–C(25) 1.767(2), Mn(1)–C(26) 1.775(2), C(25)–O(1) 1.165(3), C(26)–O(2) 1.163(3); Cg(1)–Mn(1)–N(1) 111.16(6), Cg(1)–Mn(1)–C(25) 123.87(8), Cg(1)–Mn(1)–C(26) 127.21(8), C(25)–Mn(1)–C(26) 89.4(1), C(25)–Mn(1)–N(1) 100.45(8), C(26)–Mn(1)–N(1) 99.29(8), O(1)–C(25)–Mn(1) 174.8(2), O(2)–C(26)–Mn(1) 176.2(2); N(2)–H(2) 0.83(3), H(2)···N(5) 2.15(3), N(2)···N(5) 2.977(2); N(2)–H(2)···N(5) 170(2).

structures are depicted in Figure 4 and Figure 5, respectively, together with selected atom distances and bond angles.

The zinc ions in both **7a** and **7b** are nested in the classical $\{N_4\}$ coordination site and the pyrazolate bridge spans the $CpMn(CO)_2$ fragment and the zinc(II), as anticipated. Due to the rigid chelating ligand framework, the N(1)–Mn–CO bond angles of all complexes studied in this work are somewhat widened [95.2(1)–103.1(1)°]. A CSD search revealed that complexes of $CpMn(CO)_2$ fragments with N-donor ligands not tethered to the Cp usually have N–Mn–CO bond angles in the range 92.6–99.4°.

In **7a**, the zinc is five-coordinate with the bridgehead-N(3) and the carboxylate-O(3) in the apical positions of a distorted trigonal bipyramid [N(3)–Zn(1)–O(3) = 170.2(1)°; τ = 0.77].[14] This situation closely resembles the molecular structure of the mononuclear zinc benzoate complex of tmpa.[15] The remaining O(4) atom of the acetate in **7a** is involved in hydrogen bonding to a water molecule included in the crystal lattice (the water is further hydrogen bonded to a DMF solvent molecule; see Figure S1 in the Supporting Information). In contrast, the acetate ligand in **7b** adopts a semi-bidentate binding mode with one short and one significantly longer Zn–O bond [d\{Zn(1)–O(3)\} = 2.049(3) Å, d\{Zn(1)–O(4)\} = 2.447(2) Å]. This is accompanied by an increase in the metal–metal separation [d\{Mn(1)–Zn(1)\} = 4.1423(9) Å in **7a** versus d\{Mn(1)–Zn(1)\} = 4.3915(6) Å in **7b**] and a more drastic displacement of the metal ions out of the plane of the pyrazolate.

 © 2005 Wiley-VCH Verlag GmbH & Co. KGaA, Weinheim

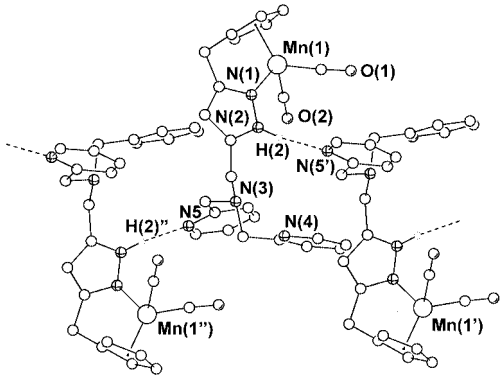

Figure 3. View of the hydrogen-bond structure of **6a**. Selected atom distances [Å] and angles [°]: N(2)–H(2) 0.90(2), H(2)···N(5′) 1.96(2), N(2)···N(5′) 2.825(2); N(2)–H(2)···N(5′) 161(2). Symmetry transformation used to generate equivalent atoms (′): 3/2 – *x*, *y* – 1/2, –*z* + 1/2.

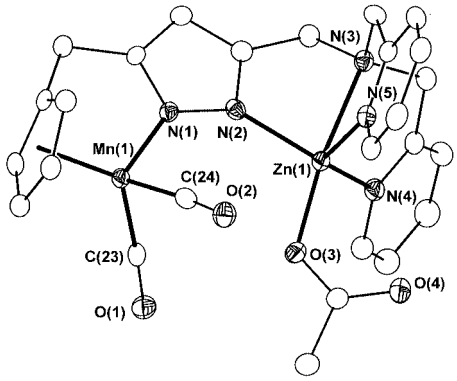

Figure 4. ORTEP plot (30% probability thermal ellipsoids) of the molecular structure of **7a**. For the sake of clarity all hydrogen atoms have been omitted. Selected atom distances [Å] and angles [°] [Cg(1) defines the centroid of the Cp ring atoms]: Mn(1)–Cg(1) 1.773(2), Mn(1)–N(1) 2.026(3), Mn(1)–C(23) 1.768(4), Mn(1)–C(24) 1.760(4), Mn(1)···Zn(1) 4.1423(9), Zn(1)–O(3) 1.947(3), Zn(1)–N(2) 2.008(3), Zn(1)–N(3) 2.312(3), Zn(1)–N(4) 2.143(3), Zn(1)–N(5) 2.074(3), O(1)–C(23) 1.166(5), O(2)–C(24) 1.185(4); Cg(1)–Mn(1)–N(1) 111.5(1), Cg(1)–Mn(1)–C(23) 125.3(2), Cg(1)–Mn(1)–C(24) 123.6(1), C(23)–Mn(1)–C(24) 90.3(2), C(23)–Mn(1)–N(1) 99.8(2), C(24)–Mn(1)–N(1) 101.4(2), O(1)–C(23)–Mn(1) 175.4(4), O(2)–C(24)–Mn(1) 172.8(3), N(2)–Zn(1)–N(3) 78.3(1), N(2)–Zn(1)–N(4) 111.3(1), N(2)–Zn(1)–N(5) 108.8(1), N(2)–Zn(1)–O(3) 108.0(1), N(3)–Zn(1)–N(4) 74.6(1), N(3)–Zn(1)–N(5) 77.1(1), N(3)–Zn(1)–O(3) 170.2(1), N(4)–Zn(1)–N(5) 124.0(1), N(4)–Zn(1)–O(3) 96.0(1), N(5)–Zn(1)–O(3) 107.1(1).

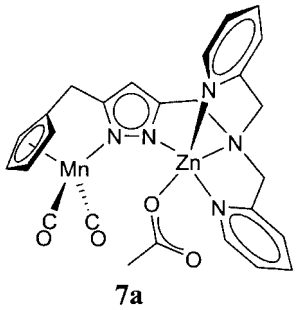

7a

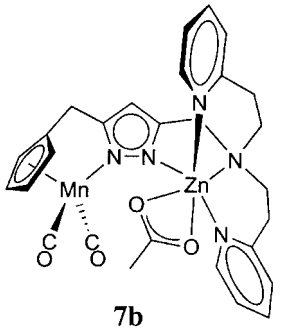

7b

Scheme 3. Heterobimetallic Mn/Zn complexes.

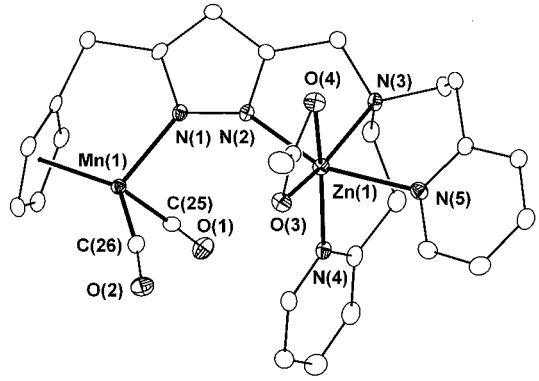

Figure 5. ORTEP plot (30% probability thermal ellipsoids) of the molecular structure of **7b**. For the sake of clarity all hydrogen atoms have been omitted. Selected atom distances [Å] and angles [°] [Cg(1) defines the centroid of the Cp ring atoms]: Mn(1)–Cg(1) 1.767(2), Mn(1)–N(1) 2.034(2), Mn(1)–C(25) 1.771(3), Mn(1)–C(26) 1.764(3), Mn(1)···Zn(1) 4.3915(6), Zn(1)–O(3) 2.049(2), Zn(1)–O(4) 2.447(2), Zn(1)–N(2) 2.088(2), Zn(1)–N(3) 2.176(2), Zn(1)–N(4) 2.068(2), Zn(1)–N(5) 2.290(3), O(1)–C(25) 1.160(4), O(2)–C(26) 1.174(4); Cg(1)–Mn(1)–N(1) 112.48(9), Cg(1)–Mn(1)–C(25) 122.4(1), Cg(1)–Mn(1)–C(26) 125.0(1), C(25)–Mn(1)–C(26) 93.2(1), C(25)–Mn(1)–N(1) 95.2(1), C(26)–Mn(1)–N(1) 103.1(1), O(1)–C(25)–Mn(1) 175.5(3), O(2)–C(26)–Mn(1) 172.7(3), N(2)–Zn(1)–N(3) 78.21(9), N(2)–Zn(1)–N(4) 103.0(1), N(2)–Zn(1)–N(5) 160.16(9), N(2)–Zn(1)–O(3) 105.18(9), N(2)–Zn(1)–O(4) 91.98(9), N(3)–Zn(1)–N(4) 99.97(9), N(3)–Zn(1)–N(5) 86.03(9), N(3)–Zn(1)–O(3) 158.66(9), N(3)–Zn(1)–O(4) 101.35(8), N(4)–Zn(1)–N(5) 91.4(1), N(4)–Zn(1)–O(3) 99.72(9), N(4)–Zn(1)–O(4) 156.03(9), N(5)–Zn(1)–O(3) 85.32(9), N(5)–Zn(1)–O(4) 79.27(9), O(3)–Zn(1)–O(4) 57.82(8).

Apparently, the six-membered chelate rings leave more space for anion coordination and allow for greater flexibility of the zinc coordination sphere. The different acetate binding modes are also discernible in the IR spectra, where **7a** features a high-energy $\nu_{as}(CO_2^-)$ vibration at $\tilde{\nu}$ = 1663 cm^{-1}, while $\nu_{as}(CO_2^-)$ of **7b** occurs around $\tilde{\nu}$ = 1607 cm^{-1}. The $\nu_s(CO_2^-)$ absorptions (expected around $\tilde{\nu}$ = 1400 cm^{-1})[16] cannot be clearly identified because of various other bands in that region.

The only known mononuclear zinc(II) complex of tris(pyridylethyl)amine (tpea), which provides longer alkyl spacers than tpma, is [(tpea)Zn](ClO$_4$)$_2$.[17] In contrast to the related zinc(II) complexes of tpma, however, the cationic portion of [(tpea)Zn](ClO$_4$)$_2$ contains four-coordinate zinc while the perchlorate remains uncoordinated. A similar sit-

 © 2005 Wiley-VCH Verlag GmbH & Co. KGaA, Weinheim

uation is now found in the heterobimetallic complex **8**, which was obtained from **6b** and $[Zn(H_2O)_6](ClO_4)_2$. The molecular structure of the cation of **8** is depicted in Figure 6, together with selected atom distances and bond angles.

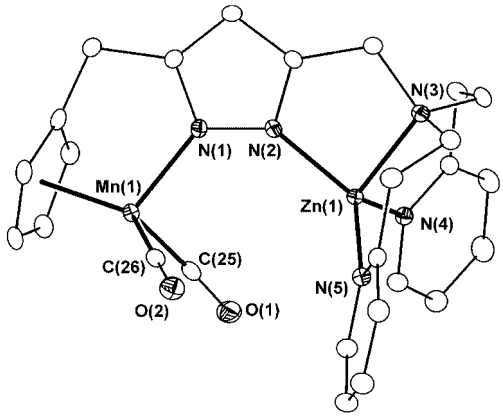

Figure 6. ORTEP plot (30% probability thermal ellipsoids) of the molecular structure of **8**. In the interests of clarity all hydrogen atoms and the ClO_4^- anion have been omitted. Selected atomic distances [Å] and angles [°] [Cg(1) defines the centroid of the Cp ring atoms]: Mn(1)–Cg(1) 1.773(1), Mn(1)–N(1) 1.991(2), Mn(1)–C(25) 1.761(3), Mn(1)–C(26) 1.774(3), Mn(1)···Zn(1) 4.0601(5), Zn(1)–N(2) 1.941(2), Zn(1)–N(3) 2.079(2), Zn(1)–N(4) 1.999(2), Zn(1)–N(5) 2.002(2), O(1)–C(25) 1.167(3), O(2)–C(26) 1.168(3); Cg(1)–Mn(1)–N(1) 110.81(7), Cg(1)–Mn(1)–C(25) 126.29(9), Cg(1)–Mn(1)–C(26) 128.3(1), C(25)–Mn(1)–C(26) 90.5(1), C(25)–Mn(1)–N(1) 99.16(9), C(26)–Mn(1)–N(1) 94.62(9), O(1)–C(25)–Mn(1) 177.2(2), O(2)–C(26)–Mn(1) 179.5(2), N(2)–Zn(1)–N(3) 85.24(8), N(2)–Zn(1)–N(4) 124.58(8), N(2)–Zn(1)–N(5) 114.46(8), N(3)–Zn(1)–N(4) 101.93(8), N(3)–Zn(1)–N(5) 103.88(8), N(4)–Zn(1)–N(5) 116.61(8).

The coordination geometry of Zn(1) in **8** is distorted tetrahedral, the strongest distortion resulting from the presence of an acute angle in the five-membered chelate ring [N(2)–Zn(1)–N(3) = 85.24(8)°]. Both the zinc and the manganese ions are located roughly within the plane of the pyrazolate heterocycle [out-of-plane displacement: 0.317(1) Å for Zn and 0.269(1) Å for Mn], indicating a relaxed bonding situation. The closest distance between Zn(1) and a CO ligand is almost 3.5 Å, which is clearly out of the bonding range.[18] Due to the absence of any coordinating counteranion, the Mn···Zn distance [4.0601(5) Å] is clearly shorter than in **7b**. Comparison of the structures of **7b** and **8** reveals that binding of small substrate molecules to the zinc ion in **8** should be feasible.

Spectroscopic and Electrochemical Trends

Incorporation of zinc in the $\{N_4\}$ compartment of **6a**,**b** to give **7a**,**b** induces a slight shift of the ν(CO) stretching frequencies to lower wavenumbers (Table 1; spectra of KBr pellets), thereby indicating an increase in π-backbonding from the manganese ion to the CO ligands. This is also reflected by a slight decrease of the $Mn–C_{CO}$ distance (mean value for **6a**,**b**: 1.771 Å; mean value for **7a**,**b**: 1.766 Å) and a slight increase of the C–O distance (mean value for **6a**,**b**: 1.164 Å; mean value for **7a**,**b**: 1.171 Å). The effects are less pronounced for **8**, which can be ascribed to the cationic charge of its MnZn entity. While mainly located at zinc, to a small extent the electronic unsaturation in **8** is apparently transmitted also towards the manganese.

Table 1. IR absorptions in the CO stretching range, along with *g* values and isotropic coupling constants derived from EPR spectra of the oxidized species.

	DMF solution [cm^{-1}]		KBr pellets [cm^{-1}]		g_{iso}	$a(^{55}Mn)_{iso}$ [mT]
6a	1915	1841	1910	1827	–	–
6a$^+$	2020	1934	–	–	2.036	6.10
6b	1913	1841	1912	1838	–	–
6b$^+$	2021	1935	–	–	2.038	6.04
7a	1910	1837	1901	1831	–	–
7a$^+$	2029	1950	–	–	2.044	6.16
7b	1914	1840	1898	1823	–	–
7b$^+$	2021	1935	–	–	2.040	6.17
8	1913	1838	1906	1833	–	–
8$^+$	2021	1935	–	–	–	–

The higher electron density at the manganese ions in **7a**,**b** should correspond to a more facile oxidation of manganese(I) in the heterobimetallic complexes than for the zinc-devoid precursors, which was confirmed by cyclic voltammograms of **6a**,**b** and **7a**,**b** (the cyclic voltammogram of **7a** is shown in Figure 7 as an example). The zinc-devoid compounds exhibit a reversible, one-electron oxidation wave at around $E_{1/2}$ = –0.35 V (versus the ferrocene/ferrocenium couple), while oxidation of the heterobimetallic complexes occurs around $E_{1/2}$ = –0.60 V (Table 2). This shift to more negative potentials is probably due to the higher electron-donating power of the ligand towards manganese as a consequence of the deprotonation of the pyrazole. In accordance with the spectroscopic results discussed above, the electron-poor **8** is clearly more difficult to oxidize than the corresponding acetate complex **7b** with a potential intermediate between those of **6b** and **7b** (the redox process is only quasi-reversible in the case of **8**).

The oxidation potentials of $CpMn(CO)_2L$ complexes are known to vary over a potential range of more than 2 V, depending on the nature of the ligand L.[9,10,19] The rather low oxidation potentials of **6a**,**b** and **7a**,**b** indicate significant stabilization of the Mn^{II} state by the anionic pyrazolate ligand and reflect the high nucleophilicity of the N-heterocycle, in particular in the heterobimetallic species.[19] However, a considerable cathodic shift is observed upon binding of the zinc ions. Zinc itself is redox inactive, but comparison of **7a** and **7b** reveals that the different Werner-type coordination subunits do indeed influence the redox properties of the $CpMn(CO)_2$ group, even though the effects are only minor (difference in $E_{1/2}$ of about 30 mV between **7a** and **7b**). Also, a certain degree of information about the type of coligand at zinc is transmitted to manganese, resulting in slight shifts in the Mn^I/Mn^{II} redox potential (**7b** versus **8**).

Chemical oxidation with $[Cp_2Fe]PF_6$ in DMF solution allowed the IR spectroscopic determination of the ν(CO) absorptions of the oxidized species (Table 1, Figure 8).

 © 2005 Wiley-VCH Verlag GmbH & Co. KGaA, Weinheim

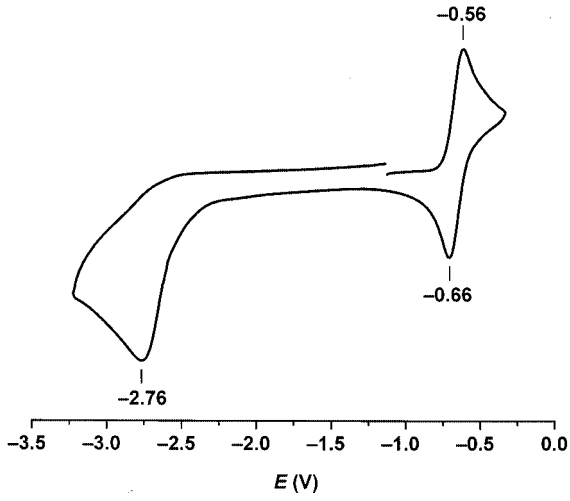

Figure 7. Cyclic voltammogram of **7a** in DMF. Potentials are given in volts versus the ferrocen/ferrocenium couple.

Table 2. Formal potentials for the Mn^{II}/Mn^{I} couple in DMF/0.1 M Bu_4NPF_6. Values are given in volts versus Fc/Fc^+.

6a	–0.33
6b	–0.35
7a	–0.61
7b	–0.58
8	–0.44 (quasi rev.)

Within minutes at room temperature, however, these bands gradually vanished without concomitant rise of any new bands in the CO stretching region, thus indicating irreversible decomposition of the oxidized $Mn^{II}Zn^{II}$ complexes. Solution EPR spectra at this point show an isotropic six-line signal around g = 2.009 with $a(^{55}Mn)_{iso}$ = 9.43 mT, suggesting extrusion of the manganese(II) ions and formation of $[Mn(DMF)_6]^{2+}$.[20] Unambiguous EPR characterization of the oxidized Mn^{II} (**6a**$^+$, **6b**$^+$) and $Mn^{II}Zn^{II}$ species (**7a**$^+$, **7b**$^+$, **8**$^+$) after chemical oxidation with $[Cp_2Fe]PF_6$ in a THF/DMF mixture was hampered by the immediate formation of a dominant signal for the $[Mn(DMF)_6]^{2+}$ decomposition product. In CH_2Cl_2 the product of decomposition seems to form less rapidly and is insoluble, which allows EPR spectroscopic characterization of the oxidized species (**6a**$^+$, **6b**$^+$, **7a**$^+$, **7b**$^+$) in solution. All EPR spectra after chemical oxidation with a substoichiometric amount of $[Cp_2Fe]PF_6$ in CH_2Cl_2 solution show a six-line pattern with only slightly differing g values around 2.040 and isotropic coupling constants around 6.12 mT (Table 1; the spectrum of **6b**$^+$ is shown in Figure 9 as an example). The magnitude of $a(^{55}Mn)_{iso}$ is typical for a $[CpMn^{II}(CO)_2L]^+$ species and suggest that the unpaired electron is mainly localized at the manganese atom, in accordance with electronic-structure calculations (see below). The spectrum of a frozen solution of **6b**$^+$ (Figure 9) compares well with those of other $[CpMn^{II}(CO)_2L]^+$ compounds with approximate axial symmetry of the g tensor and anisotropic hyperfine coupling to a single ^{55}Mn nucleus.[21] However, decomposition of the oxidized species occurred after a few minutes at room temperature. The product of decomposition in CH_2Cl_2 shows a very broad unstructured signal centered around g = 1.994. No EPR spectrum of the oxidized $Mn^{II}Zn^{II}$ species **8**$^+$ could be recorded because of the poor solubility of **8** in CH_2Cl_2.

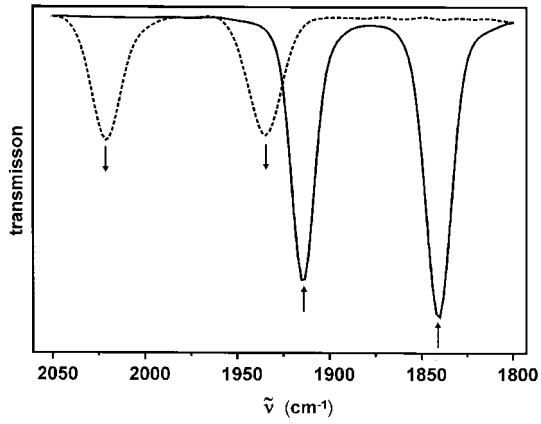

Figure 8. Stretching frequencies ν(CO) of **6b** (solid line) and after oxidation with $[Cp_2Fe]PF_6$ (**6b**$^+$, dashed line) in DMF.

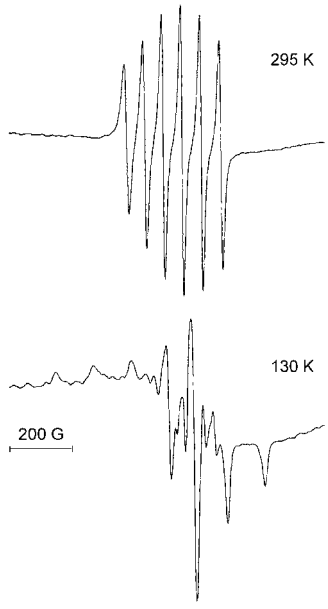

Figure 9. EPR spectra of **6b**$^+$ in CH_2Cl_2 at 295 and 130 K.

Since structural information about the oxidized species is not available, and in order to corroborate the spectroscopic findings, DFT calculations[22] were carried out for the doublet state of **8**$^+$. The geometry was DFT-minimized starting from the X-ray structure atomic coordinates for **8** to give the geometric information listed in Figure 10. The $Mn–N^{pz}$ and $Mn–C_{C\equiv O}$ bonds in **8**$^+$ were calculated to be 1.95 and 1.84 Å, respectively, which is clearly longer than the corresponding values of the $Mn^{I}Zn^{II}$ complex **8**. At the same time, the C–O distances of the Mn-bound carbonyls are significantly shortened at 1.15 Å, in agreement with diminished π-backbonding in the oxidized species and the observed shift of the IR stretching vibrations. The SOMO of **8**$^+$ is depicted in Figure 10, from which it is apparent that

 © 2005 Wiley-VCH Verlag GmbH & Co. KGaA, Weinheim

the SOMO has predominant Mn 3d character with some antibonding admixture from the π-pyrazolate system.

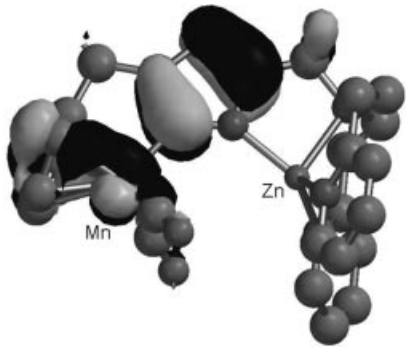

Figure 10. Calculated shape of the SOMO of **8**$^{+}$ (DFT, Spartan 02, UB3LYP/LACVP*). Selected structural parameters: Mn–N^{pz} 1.95 Å; Mn–$C_{C\equiv O}$ 1.84 Å; C–O 1.15 Å; Zn–N^{pz} 2.03 Å; Mn–N–N 139.2°; $C_{C\equiv O}$–Mn–N 98.1/98.2°; Zn–N–N 139.2°.

According to a Mulliken population analysis the spin is almost perfectly localized on manganese (ρMn = 1.017), while spin density on the pyrazolate-N is found to be negligible (ρN^{pz} = 0.009/–0.013), in accordance with the lack of any ^{55}Mn–^{14}N hyperfine coupling in the EPR spectra.

Conclusions

Highly unsymmetrical heterodinuclear Mn/Zn type **D** complexes based on a bridging pyrazolate with variable ligand environments for the classical Werner-type coordination site are accessible by the versatile synthetic approach outlined in Scheme 2. Structural characteristic of the two metal-containing subunits of the systems studied here are reminiscent of their corresponding mononuclear analogues, which supports the description of the present type **D** systems as hybrids of an organometallic $CpMn(CO)_2$ fragment and a classical Werner-type tris(pyridylalkyl)amine type $\{N_4\}$ metal site. Oxidation is highly localized at the organometallic manganese site, as is evidenced by IR and EPR spectroscopy and supported by DFT calculations. However, slight effects of the redox-inactive, Werner-type subunit of the Mn^{I}/Mn^{II} redox properties and of spectroscopic signatures of the organometallic site are revealed by comparing the zinc-devoid manganese compounds and the bimetallic Mn/Zn complexes, as well as by assessing the influence of the chelate size of the tripodal tetradentate $\{N_4\}$ binding site and of different coligands at zinc. Future work will focus on bimetallic type **D** complexes with a second redox-active metal ion other than zinc. It is hoped that application of the principles delineated in this work will allow modulation of the relative redox properties of the two distinct metal sites, and as a consequence will enable a tuning of the bimetallic redox reactivity of the "one-site-addition-two-metal-oxidation" type.

Experimental Section

General Remarks: All reagents were obtained from commercial sources (Aldrich, Fluka, or VWR) and used as received. Compounds **3**, **4**, and **5a** (Scheme 2) were prepared according to the literature methods.[5,7] Solvents were dried under reflux (CaH_2 for dichloromethane, Na/K alloy for diethyl ether and THF) and distilled prior to be used. All reactions were carried out under nitrogen using standard Schlenk techniques. IR spectra were recorded with a Digilab Excalibur, UV/Vis/NIR spectra with a Cary 5000, EPR spectra with a Bruker ELEXSYS 500. Cyclic voltammetry was performed with a potentiostat/galvanostat Perkin–Elmer Model 263A instrument with glassy-carbon working electrode and platinum reference and counter electrodes, in 0.1 M tetra-*n*-butylammonium hexafluorophosphate/DMF. Ferrocene (the potential being 0.45 V in DMF against SCE)[23] was used as internal standard. Elemental analyses were measured by the analytical laboratory of the Institut für Anorganische Chemie der Universität Göttingen using a Heraeus CHN-O-RAPID instrument.

Complex 5b(thp): Na_2CO_3 (4.0 g, 37 mmol) was dried at 100 °C under vacuum for 1 h. After cooling to room temperature, a solution of **4** (1.50 g, 3.60 mmol) and bis[2-(2-pyridyl)ethyl]amine (1.13 g, 3.80 mmol) in MeCN (100 mL) was added. The suspension was stirred overnight at 75 °C in the dark, then filtered and the residue washed several times with small portions of MeCN. Evaporation of the combined organic phases produced a red-brown oil that was purified by Kugelrohr distillation under vacuum to remove all volatile impurities and to give **5b(thp)** (yield 1.62 g, 89%). ^{1}H NMR ($CDCl_3$): δ = 1.55–1.66 (m, 3 H, CH_2^{thp}), 1.92 (d, J = 12.3 Hz, 1 H, CH_2^{thp}), 2.09 (br. s, 1 H, CH_2^{thp}), 2.41 (m, 1 H, CH_2^{thp}), 2.94 (s, 8 H, $PyCH_2CH_2N$), 3.61 (s, 2 H, CH_2Cp), 3.74 (s, 2 H, $PzCH_2$), 3.98 (d, J = 11.0 Hz, 1 H, CH_2^{thp}), 4.63 (d, J = 6.2 Hz, 2 H, CH^{Cp}), 4.69 (s, 2 H, CH^{Cp}), 5.21 (d, J = 8.7 Hz, 1 H, $CH^{thp,2}$), 5.87 (s, 1 H, $CH^{pz,4}$), 7.06 (br. s, 4 H, $CH^{py,3/5}$), 7.49 (t, J = 7.1 Hz, 2 H, $CH^{py,4}$), 8.46 (s, 2 H, $CH^{py,6}$) ppm; NH not observed. ^{13}C NMR ($CDCl_3$): δ = 22.4 ($CH_2^{thp,4}$), 24.3, 24.7 ($CH_2^{thp,5}$, CH_2Cp), 29.3 ($CH_2^{thp,3}$), 35.7 (NCH_2), 51.0, 53.5 ($PzCH_2$, $PyCH_2$), 67.2 ($CH_2^{thp,6}$), 81.4, 81.7, 83.1, 83.2 (CH^{Cp}), 84.4 ($CH^{thp,2}$), 101.9 (C^{Cp}), 106.1 ($CH^{pz,4}$), 120.6 ($CH^{py,5}$), 123.1 ($CH^{py,3}$), 135.7 ($CH^{py,4}$), 141.2 ($C^{pz,5}$), 148.8 ($CH^{py,6}$), 149.6 ($C^{pz,3}$), 160.6 ($C^{py,2}$), 224.6 (CO) ppm. MS (ESI): m/z (%) = 608 (50) [M^+], 501 (100) [M^+ – $pyCH_2CH_3$], 439 (80) [M^+ – 3CO – THP]. $C_{32}H_{34}MnN_5O_4$ (607.59): calcd. C 63.26, H 5.64, N 11.53; found C 62.86, H 5.82, N 11.34.

Complex 5b: A solution of **5b(thp)** (1.62 g, 2.67 mmol) in EtOH (20 mL) was treated with ethanolic HCl (10 mL) and stirred overnight in the dark. Addition of Et_2O (100 mL) caused precipitation of the hydrochloride salt of **5b** as a brownish solid. This was separated by filtration, neutralized with aqueous Na_2CO_3, and extracted with several portions of CH_2Cl_2. After drying the combined organic phases with $MgSO_4$, the solvent was evaporated to give the crude product as a red-brown oil that was purified by Kugelrohr distillation under vacuum to remove all volatile impurities (yield 1.28 g, 91.6%). ^{1}H NMR ($CDCl_3$): δ = 2.89 (br. s, 4 H, CH_2N), 2.99 (br. s, 4 H, $PyCH_2$), 3.59 (s, 2 H, CH_2Cp), 3.83 (br. s, 2 H, $PzCH_2$), 4.59 (s, 2 H, CH^{Cp}), 4.71 (s, 2 H, CH^{Cp}), 5.95 (br. s, 1 H, $CH^{pz,4}$), 6.97 (m, 2 H, $CH^{py,3}$), 7.07 (m, 2 H, $CH^{py,5}$), 7.51 (t, J = 7.2 Hz, 2 H, $CH^{py,4}$), 8.48 (s, 2 H, $CH^{py,6}$) ppm; NH not observed. ^{13}C NMR ($CDCl_3$): δ = 27.2, (CH_2Cp), 35.4 (NCH_2), 49.5 ($PzCH_2$), 54.0 ($PyCH_2$), 81.6, 83.2 (CH^{Cp}), 102.8 (br., $CH^{pz,4}$), 104.7 (C^{Cp}), 121.3 ($CH^{py,5}$), 123.5 ($CH^{py,3}$), 136.5 ($CH^{py,4}$), 148.9 ($CH^{py,6}$), 159.7 ($CH^{py,2}$), 225.1 (CO) ppm; $C^{pz,3/5}$ not observed. MS (ESI): m/z (%) = 524 (100) [M^+], 439 (43) [M^+ – 3CO – 1] 439. $C_{27}H_{26}MnN_5O_3$ (523.47): calcd. C 61.95, H 5.01, N 13.38; found C 62.78, H 5.36, N 13.14.

Complex 6a: A solution of **5a** (0.25 g, 0.50 mmol) in THF (200 mL) was irradiated with a high-pressure mercury lamp in a quartz tube

 © 2005 Wiley-VCH Verlag GmbH & Co. KGaA, Weinheim

at –40 °C. Within about 1 h the color of the solution had changed from light yellow to yellow. The solution was allowed to warm to room temperature and the solvent was removed under reduced pressure. The residue was extracted with 10 mL of CH_2Cl_2 and filtered. Slow diffusion of Et_2O into the red solution gradually gave red crystals of the product **6a** (yield 73 mg, 31%). IR (KBr): $\tilde{\nu}$ = 3060 w, 2920 w, 2849 w, 1910 vs, 1827 vs, 1592 m, 1571 m, 1474 m, 1435 m, 1231 m, 771 m, 657 m, 612 m, 585 m cm^{-1}. $C_{24}H_{22}MnN_5O_2 \cdot 0.5\,H_2O$ (476.42): calcd. C 60.51, H 4.65, N 14.70; found C 60.56, H 4.77, N 14.58.

Complex 6b: A solution of **5b** (0.26 g, 0.50 mmol) in THF (200 mL) was irradiated with a high-pressure mercury lamp in a quartz tube at –40 °C. After about 1 h the color of the solution had changed from light yellow to yellow. The solution was allowed to warm to room temperature and the solvent was removed under vacuum. The residue was extracted with 10 mL of CH_2Cl_2 and filtered. Slow diffusion of Et_2O into the red solution gradually gave red crystals of **6b**, which were filtered, washed with Et_2O, and dried under vacuum (yield 85 mg, 34%). IR (KBr): $\tilde{\nu}$ = 3127 w, 3061 w, 2968 w, 2851 w, 1912 vs, 1838 vs, 1595 m, 1568 m, 1465 m, 1433 m, 1352 m, 1260 m, 827 m, 803 m, 758 m, 658 m, 610 m, 590 m, 507 w, 472 w cm^{-1}. $C_{26}H_{26}MnN_5O_2$ (495.46): calcd. C 63.03, H 5.29, N 14.13; found C 62.69, H 5.41, N 14.23.

Complex 7a: A solution of **5a** (0.25 g, 0.50 mmol) in THF (200 mL) was irradiated with a high-pressure mercury lamp in a quartz tube at –40 °C. After about 1 h the color of the solution had changed from light yellow to yellow, and the solution was allowed to warm to room temperature. KO*t*Bu (0.056 g, 0.50 mmol) and Zn(OAc)$_2$·2H$_2$O (0.11 g, 0.50 mmol) were then added. The mixture was stirred overnight to give a yellow precipitate. The precipitate was separated by filtration, washed with light petroleum, and dried under vacuum. The crude material was dissolved in DMF (6 mL) to give an orange solution. Orange crystals of **7a**·DMF·H$_2$O were obtained by slow diffusion of Et_2O into that solution. The crystals were separated by filtration, washed with Et_2O, and dried under vacuum (yield 74 mg, 22%). IR (KBr): $\tilde{\nu}$ = 2926 w, 2855 w, 1901 vs, 1831 vs, 1663 s, 1606 s, 1582 m, 148 m, 1430 m, 1406 s, 1387 s, 1340 m, 1254 m, 1218 w, 1157 m, 1094 m, 1057 m, 1019 m, 918 w, 948 w, 889 w, 823 w, 774 m, 660 m, 611 m, 585 m, 412 m cm^{-1}. $C_{26}H_{24}MnN_5O_4Zn \cdot DMF$ (663.93): calcd. C 52.46, H 4.71, N 12.66; found C 52.08, H 4.75, N 12.59.

Complex 7b: A solution of **5b** (0.26 g, 0.50 mmol) in THF (200 mL) was irradiated with a high-pressure mercury lamp in a quartz tube at –40 °C. After about 1 h the color of the solution had changed from light yellow to yellow and the solution was allowed to warm to room temperature. KO*t*Bu (0.056 g, 0.50 mmol) and Zn(OAc)$_2$·2H$_2$0 (0.11 g, 0.50 mmol) were added and the mixture was stirred for 48 h. After removal of the solvent under reduced pressure, the residue was washed with light petroleum and dried under vacuum. Slow diffusion of Et_2O into a solution of the crude material in CH_2Cl_2 (8 mL) gradually gave orange-yellow crystals. These were separated by filtration, washed with Et_2O, and dried under vacuum (yield 57 mg, 19%). IR (KBr): $\tilde{\nu}$ = 308 w, 2975 w, 2911 w, 2850 w, 1898 vs, 1823 vs, 1607 m, 1578 m, 1483 w, 1443 m, 1416

Table 3. Crystal data and refinement details for **6a**, **6b**, **7a**, **7b**, and **8**

	6a	**6b**	**7a**·DMF·H$_2$O	**7b**	**8**
Formula	$C_{24}H_{22}MnN_5O_2$	$C_{26}H_{26}MnN_5O_2$	$C_{26}H_{24}MnN_5O_4Zn \cdot C_3H_7NO \cdot H_2O$	$C_{28}H_{28}MnN_5O_4Zn$	$[C_{26}H_{25}MnN_5O_2Zn]^+ \cdot ClO_4^-$
Mol. mass	467.41	495.46	681.95	618.88	659.29
Crystal size (mm)	0.43 × 0.38 × 0.32	0.32 × 0.23 × 0.21	0.49 × 0.12 × 0.11	0.42 × 0.34 × 0.26	0.32 × 0.19 × 0.18
Crystal system	monoclinic	monoclinic	triclinic	monoclinic	triclinic
Space group	*C*2/*c* (No. 15)	*P*2$_1$/*a* (No. 14)	*P*$\bar{1}$ (No. 2)	*P*2$_1$/*c* (No. 14)	*P*$\bar{1}$ (No. 2)
a [Å]	19.9753(12)	9.8267(7)	11.3286(12)	15.3470(12)	9.0716(8)
b [Å]	10.5765(7)	21.2521(17)	11.4389(13)	8.1298(4)	10.1812(8)
c [Å]	20.5310(15)	11.6223(8)	12.5080(16)	21.2398(17)	15.4600(12)
α [°]	90	90	91.908(10)	90	74.096(6)
β [°]	91.186(5)	111.457(5)	113.974(9)	97.390(6)	85.768(7)
γ [°]	90	90	97.228(9)	90	75.200(6)
V [Å^3]	4336.6(5)	2259.0(3)	1462.9(3)	2628.0(3)	1327.66(19)
$\rho_{calcd.}$ [g cm^{-3}]	1.432	1.457	1.548	1.564	1.649
Z	8	4	2	4	2
F_{000}	1936	1032	704	1272	672
μ(Mo-K$_\alpha$) [mm^{-1}]	0.641	0.619	1.305	1.438	1.531
T_{max}/T_{min}	0.9236/0.7724	0.8850/0.8036	0.8080/0.4746	0.7968/0.6055	0.8284/0.6161
hkl range	–21–23, ±12, –24–23	±11, ±24, ±13	±13, ±13, ±14	±18, –9–8, –24–25	–9–10, ±11, ±18
θ range [°]	1.98–24.81	1.88–24.74°	1.79–24.63	1.93–24.78°	2.15–24.80
Measured refl.	11939	10952	11941	14257	13460
Unique refl. [R_{int}]	3543 [0.0264]	3712 [0.0279]	4874 [0.0761]	4499 [0.0489]	4536 [0.0369]
Observed refl. $I > 2\sigma(I)$	3018	3180	3576	3503	3906
Refined parameters	293	311	397	353	361
Resid. electron density [e Å^{-3}]	0.281/–0.338	0.351/–0.246	0.408/–0.577	0.389/–0.534	0.478/–0.290
*R*1	0.0296	0.0310	0.0426	0.0350	0.0270
*wR*2 (all data)	0.0826	0.0786	0.0932	0.0790	0.0681
Goodness-of-fit	1.057	1.019	1.031	1.062	1.043

 © 2005 Wiley-VCH Verlag GmbH & Co. KGaA, Weinheim

m, 1331 w, 1256 m, 1161 m, 1112 m, 1059 m, 1017 m, 836 w, 764 m, 664 m, 592 m, 419 w cm^{-1}. $C_{28}H_{28}MnN_5O_4Zn·0.5H_2O$ (627.89): calcd. C 53.56, H 4.66, N 11.15; found C 53.41, H 4.67, N 11.15.

Complex 8: A solution of **5b** (0.26 g, 0.50 mmol) in THF (200 mL) was irradiated with a high-pressure mercury lamp in a quartz tube at –40 °C. After about 1 h the color of the solution had changed from light yellow to yellow. It was allowed to warm to room temperature, and KO*t*Bu (0.056 g, 0.50 mmol) and $Zn(ClO_4)_2·6H_2O$ (0.185 g, 0.50 mmol) were then added. The mixture was stirred overnight to give a yellow precipitate. The precipitate was separated by filtered, washed with light petroleum, and dried under vacuum. Orange crystals were obtained after several days by slow diffusion of diethyl ether into a DMF solution (10 mL) of the crude product. The crystals were separated by filtration, washed with diethyl ether, and dried under vacuum (yield 127 mg, 39%). IR (KBr): $\tilde{\nu}$ = 3098 w, 2917 w, 2883 w, 1906 vs, 1833 vs, 1613 m, 1569 w, 1492 m, 1447 m, 1329 w, 1310 w, 1102 s, 772 m, 659 w, 624 m, 593 w, 423 w cm^{-1}. $C_{26}H_{25}ClMnN_5O_6Zn·H_2O$ (677.31): calcd. C 46.11, H 4.02, N 10.34; found C 45.33, H 3.96, N 10.29.

X-ray Crystallographic Study: X-ray data were collected on a STOE IPDS II diffractometer (graphite-monochromated Mo-K_α radiation, λ = 0.71073 Å) by use of ω scans at –140 °C (Table 3). The structures were solved by direct methods and refined on F^2, using all reflections, with SHELX-97.[24] The non-hydrogen atoms were refined anisotropically. Hydrogen atoms which were not involved in hydrogen bonding were placed in calculated positions and assigned an isotropic displacement parameter of 0.08 $Å^2$. The positional and isotropic thermal parameters of the nitrogen-bonded hydrogen atom H(2) in **6a** and **6b** were refined without constraints. A DFIX (0.83 Å) restraint was applied to the H–O distances of the H_2O molecule in **7b** and the hydrogen atoms were refined with an isotropic displacement parameter of 0.08 $Å^2$. Face-indexed absorption corrections were performed numerically with the program X-RED.[25] The geometrical aspects of the structures were analyzed with the PLATON program.[26]

CCDC-248451 (for **6a**), -248452 (for **6b**), -248453 (for **7a**·DMF·H_2O), -248454 (for **7b**), and -248455 (for **8**) contain the supplementary crystallographic data for this paper. These data can be obtained free of charge from The Cambridge Crystallographic Data Centre via www.ccdc.cam.ac.uk/data_request/cif.

Supporting Information Available (see also the footnote on the first page of this article): View of the hydrogen-bonding interactions of **7a**·DMF·H_2O (Figure S1).

Acknowledgments

Financial support by the Fonds der Chemischen Industrie is gratefully acknowledged. We sincerely thank J. Teichgräber for CV measurements and M. Alvariño Gil for preparing some of the ligand side-arms.

[1] a) J. Okuda, *Comments Inorg. Chem.* **1994**, *16*, 185–205; b) C. Müller, D. Vos, P. Jutzi, *J. Organomet. Chem.* **2000**, *600*, 127–143; c) P. Jutzi, J. Dahlhaus, *Coord. Chem. Rev.* **1994**, *137*, 179–199.

[2] a) I. L. Fedushkin, S. Dechert, H. Schumann, *Organometallics* **2000**, *19*, 4066–4076; b) L. F. Groux, F. Bélanger-Gariépy, D. Zargarian, R. Vollmerhaus, *Organometallics* **2000**, *19*, 1507–1513; c) O. Segnitz, M. Winter, K. Merz, R. A. Fischer, *Eur. J. Inorg. Chem.* **2000**, 2077–2085; d) A. I. Philippopoulos, B. Donnadieu, R. Poilblanc, N. Hadjiliadis, *J. Organomet. Chem.* **1999**, *582*, 286–291; e) H. Schumann, E. C. Rosenthal, J. Demtschuk, G. A. Molander, *Organometallics* **1998**, *17*, 5324–5333; f) P. T. Gomes, M. L. H. Green, A. M. Martins, *J. Organomet. Chem.* **1998**, *551*, 133–138; g) P. Foster, J. C. W. Chien, M. D. Rausch, *J. Organomet. Chem.* **1997**, *545–546*, 35–38; h) Z. Ziniuk, I. Goldberg, M. Kol, *J. Organomet. Chem.* **1997**, *545–546*, 441–446; i) P.-J. Sinnema, L. van der Veen, A. L. Spek, N. Veldman, J. H. Teuben, *Organometallics* **1997**, *16*, 4245–4247; j) A. K. Hughes, J. A. Kingsley, *J. Chem. Soc., Dalton Trans.* **1997**, 4139–4142; k) M. Enders, R. Rudolph, H. Pritzkow, *Chem. Ber.* **1996**, *129*, 459–463; l) W. A. Herrmann, M. J. A. Morawietz, T. Priermeier, K. J. Mashima, *J. Organomet. Chem.* **1995**, *486*, 291–295.

[3] a) U. Siemeling, P. Jutzi, *J. Organomet. Chem.* **1995**, *500*, 175–185; b) P. Jutzi, T. Redeker, *Eur. J. Inorg. Chem.* **1998**, 663–674.

[4] a) P. J. Shapiro, E. Bunel, W. P. Schaefer, J. E. Bercaw, *Organometallics* **1990**, *9*, 867–869; b) A. L. McKnight, R. M. Waymouth, *Chem. Rev.* **1998**, *98*, 2587–2598 and references cited therein; c) R. Emrich, O. Heinemann, P. W. Jolly, C. Krüger, G. P. J. Verhovnik, *Organometallics* **1997**, *16*, 1511–1513; d) M. S. Blais, J. C. W. Chien, M. D. Rausch, *Organometallics* **1998**, *17*, 3775–3783; e) K. C. Hultzsch, T. P. Spaniol, J. Okuda, *Angew. Chem.* **1999**, *111*, 163–165; *Angew. Chem. Int. Ed.* **1999**, *38*, 227–230; f) P. T. Witte, A. Meetsma, B. Hessen, *Organometallics* **1999**, *18*, 2944–2946.

[5] J. C. Röder, F. Meyer, H. Pritzkow, *Organometallics* **2001**, *20*, 811–817.

[6] a) J. C. Röder, F. Meyer, E. Kaifer, *Angew. Chem.* **2002**, *114*, 2414–2417; *Angew. Chem. Int. Ed.* **2002**, *41*, 2304–2306; b) J. C. Röder, F. Meyer, I. Hyla-Kryspin, R. F. Winter, E. Kaifer, *Chem. Eur. J.* **2003**, *9*, 2636–2648.

[7] J. C. Röder, F. Meyer, R. F. Winter, E. Kaifer, *J. Organomet. Chem.* **2002**, *641*, 113–120.

[8] a) C. J. Qin, A. L. Gavrilova, B. Bosnich, *Pure Appl. Chem.* **2001**, *73*, 221–226; b) A. L. Gavrilova, B. Bosnich, *Inorg. Chim. Acta* **2003**, *352*, 24–30.

[9] K. G. Caulton, *Coord. Chem. Rev.* **1981**, *38*, 1–43.

[10] W. Kaim, R. Gross, *Comments Inorg. Chem.* **1988**, *7*, 269–285.

[11] T. G. Schenck, C. R. C. Milne, J. F. Sawyer, B. Bosnich, *Inorg. Chem.* **1985**, *24*, 2338–2344.

[12] Photolability of one CO ligand in $[CpMn(CO)_3]$ and its derivatives is well established: a) W. Strohmeier, *Angew. Chem.* **1964**, *76*, 873–881; *Angew. Chem. Int. Ed. Engl.* **1964**, *3*, 730–738; b) W. Strohmeier, F.-J. Müller, *Chem. Ber.* **1969**, *102*, 3608–3612.

[13] a) N. C. Mösch-Zanetti, M. Ferbinteanu, J. Magull, *Eur. J. Inorg. Chem.* **2002**, 950–956; b) G. B. Deacon, C. M. Forsyth, A. Gitlits, R. Harika, P. C. Junk, B. W. Skelton, A. H. White, *Angew. Chem.* **2002**, *114*, 3383–3385; *Angew. Chem. Int. Ed.* **2002**, *41*, 3249–3251; c) J. Hitzbleck, A. Y. O'Brien, C. M. Forsyth, G. B. Deacon, K. Ruhlandt-Senge, *Chem. Eur. J.* **2004**, *10*, 3315–3323.

[14] The degree of trigonality can be evaluated by means of the angular structural parameter $\tau = (\beta - \alpha)/60$, where α and β represent the two largest angles around the central atom with $\beta > \alpha$ (a perfect TB-5 structure is associated with τ = 1, while τ = 0 is expected for ideal SPY-5 geometry): A. W. Addison, T. N. Rao, J. Reedijk, J. van Rijn, G. C. Verschoor, *J. Chem. Soc., Dalton Trans.* **1984**, 1349–1356.

[15] H. Adams, N. A. Bailey, D. A. Fenton, Q.-Y. He, *J. Chem. Soc., Dalton Trans.* **1997**, 1533–1540.

[16] G. B. Deacon, R. J. Phillips, *Coord. Chem. Rev.* **1980**, *33*, 227–250.

[17] X. Xu, C. S. Allen, C.-L. Chuang, J. W. Canary, *Acta Crystallogr., Sect. C* **1998**, *54*, 600–601.

[18] An unusual side-on π-interaction has been observed for a nitrile moiety within the bimetallic pocket of a pyrazolate-based dinickel(II) complex, with Ni–N and Ni–C distances around 2.9 Å: F. Meyer, I. Hyla-Kryspin, E. Kaifer, P. Kircher, *Eur. J. Inorg. Chem.* **2000**, 771–781.

 © 2005 Wiley-VCH Verlag GmbH & Co. KGaA, Weinheim

[19] R. Gross, W. Kaim, *Angew. Chem.* **1985**, *97*, 869–870; *Angew. Chem. Int. Ed. Engl.* **1985**, *24*, 856–858.
[20] I. A. Veselov, V. G. Shtyrlin, V. A. Zakharov, *Koord. Khim. (Koordinatsionnaya Khimiya; Russ. J. Coord. Chem.)* **1988**, *14*, 943–947.
[21] Departures from first-order line-spacings result from coincidence of the *x* and z principal axes of the *g* and ^{55}Mn hyperfine tensors: R. D. Pike, A. L. Rieger, P. H. Rieger, *J. Chem. Soc., Faraday Trans. 1* **1989**, *85*, 3913–3925.
[22] *Spartan 02*, Wavefunction Inc.: Irvine, CA. The UB3LYP method with the LACVP* basis set was employed. Geometry optimization was started from the coordinates obtained from the X-ray structure of **8**. A doublet ground state was applied as the only constraint.
[23] N. G. Connelly, W. E. Geiger, *Chem. Rev.* **1996**, *96*, 877–910.
[24] G. M. Sheldrick, *SHELXL-97*, Program for Crystal Structure Refinement, Universität Göttingen, **1997**. G. M. Sheldrick, *SHELXS-97*, Program for Crystal Structure Solution, University of Göttingen, **1997**.
[25] STOE & CIE GmbH, *X-RED*, Darmstadt, **2002**.
[26] A. L. Spek, *PLATON*, A Multipurpose Crystallographic Tool, Utrecht University, **2003**.

Received: August 25, 2004

 © 2005 Wiley-VCH Verlag GmbH & Co. KGaA, Weinheim

Effect of Conformation and Combination of 1,3-Bis(4-pyridylthio)propan-2-one upon Coordination Architectures: Syntheses, Characterizations and Properties

Benlai Wu,[a] Daqiang Yuan,[a] Feilong Jiang,[a] Lei Han,[a] Benyong Lou,[a] Caiping Liu,[a] and Maochun Hong*[a]

Keywords: Coordination polymer / Interpenetration / Conformation analysis / Magnetic property / Fluorescence

Self-assemblies of the conformationally labile ditopic ligand 1,3-bis(4-pyridylthio)propan-2-one (L) with square-planer nodes Co^{II}, Ni^{II} and with linear nodes Ag^{I} have afforded three new coordination polymers, $\{[Ni(L)_2Cl_2]\}_\infty$ (**1**), $\{[Co(L)_2(SCN)_2]\cdot(DMF)_2\}_\infty$ (**2**) and $\{[AgL]NO_3\}_\infty$ (**3**), respectively. Structural analyses of these polymers and conformational analyses of L have revealed that metal-assisted conformational selectivity and unique combinations of conformational isomers of L around the metal nodes probably play the key role in determining the structural topologies. In **1**, a C_2 symmetric array of two sorts of conformational isomers of L around Ni^{II} centers results in a 3D interpenetrating framework, while in **2** a combination of two types of conformational isomers of L around the inversion center Co^{II} provides a 3D interpenetrating architecture of $CdSO_4$-like topology. In **3**, L presents only a typical conformation, with higher steric energy, that links linear nodes Ag^{I}, leading to a 1D U-like chain. The magnetic properties of **1** and **2**, as well as the interesting fluorescent properties of **3**, have also been investigated.
(© Wiley-VCH Verlag GmbH & Co. KGaA, 69451 Weinheim, Germany, 2005)

Introduction

Flexible ditopic or multitopic organic ligands that encode more variable chemical information, such as their flexibility and conformational freedoms, have attracted increasing interest in crystal engineering.[1–11] A combination of selective metal ions with tailored flexible ligands is very fruitful in building a large assortment of coordination polymers with unique architectures,[12–19] sometimes with interpenetrations[20–24] and interesting material properties.[25–29] Moreover, some conformational isomers of a flexible ligand in solution may be induced, enhanced, recognized and stabilized by numerous factors, especially by metal coordination preferences in a self-assembly process, providing additional opportunities to design and build unique coordination motifs as well as to separate an unfavorable conformation. This is clearly highlighted by Stang's rational design based on the conformationally defined dihedral angle of 4,4′-dithiodipyridine,[30] although such cases are still comparatively rare.

Recently, we have concentrated on the coordination chemistry of flexible ligands, particularly on metal-based supramolecular architectures of N-containing heterocyclic thioethers with various arene bridges, and have obtained several unique structural motifs.[31–34] While this work was in progress several reports of new Ag^{I} polymers coordinated by related N-containing heterocyclic thioethers with alkane bridges appeared.[35,36] Pursuing our work in this area, we deliberately designed dithioether ligand 1,3-bis(4-pyridylthio)propan-2-one (L) (Scheme 1). The advantages of this ligand are (i) as arene bridges are displaced by propan-2-one groups, the conformational transformation barrier is so low that some conformations of L may be induced by weak forces, such as solvent and electrostatic effects, and recognized by metal-coordination and further stabilized in crystallization; (ii) the relative rigidity resulting from the permanent planar requirement of the propan-2-one group, needed for sp^2 hybridization of its central carbon, enlarges conformational otherness, resultining in differences from analogs with simple alkane bridges; (iii) incorporating the ketone group into the alkane chain endows the ligand with a hydrogen-bond receptor, which will functionalize the resultant architecture. Consequently, using L to assemble with the square-planar nodes Ni^{II} and Co^{II} in solvothermal methanol or DMF/diethyl ether systems, we were able to prepare two new 3D interpenetrating polymers with distinctive topologies, owing to metal-assisted conformational selectivity and unique combinations of ligand L. In contrast, the assembly of L with linear node Ag^{I} in a three-layered diffusion system produced a 1D U-like polymer, where nitrate anions template both the architecture of the polymer and the typical conformation of L. We report here the resultant structures of $\{[Ni(L)_2Cl_2]\}_\infty$ (**1**), $\{[Co(L)_2(SCN)_2]$

[a] State Key Laboratory of Structural Chemistry, Fujian Institute of the Research on the Structure of Matter, Chinese Academy of Sciences,
Fuzhou, Fujian, 350002, China
Fax: +86-591-8371-4946
E-mail: hmc@ms.fjirsm.ac.cn
Supporting information for this article is available on the WWW under http://www.eurjic.org or from the author.

 DOI: 10.1002/ejic.200400734 © 2005 Wiley-VCH Verlag GmbH & Co. KGaA, Weinheim

·$(DMF)_2\}_\infty$ (**2**) and $\{[AgL]NO_3\}_\infty$ (**3**), along with conformational analysis of L. Furthermore, we also report quantitative magnetic characterizations of complexes **1** and **2**, and the fluorescence properties of ligand L and complex **3**.

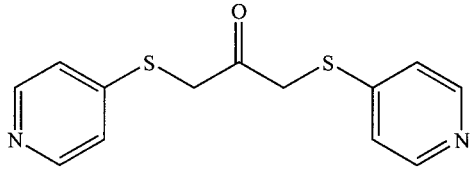

Scheme 1. Ligand L.

Results and Discussion

Synthesis and Conformational Analysis of 1,3-Bis(4-pyridylthio)propan-2-one (L)

Ligand L was prepared by the substitution reaction of 1,3-dichloro-2-propanone and sodium methylate, following the strategy we utilized previously to synthesize N-containing heterocyclic thioether ligands;[31–34] however, the separation of L from the oil phase was a key problem. Ultimately, the pure solid-phase of L was obtained through subtle use of its temperature-dependent solubility in water in the separation and purification process.

Propan-2-one is a planar molecule that shows no conformation due to sp^2 hybridization of its central carbon atom. However, as sulfur atoms are introduced at the 1 and 3 carbon atoms, the substituted compound displays three typical conformations, namely A, B and C isomers. In addition, as two 4-pyridyl groups are bound to the two sulfur atoms, three typical conformational isomers are expected, e.g. A1, A2 and A3 of conformation A (Scheme 2). Thus the resulting ligand L can adopt many conformational isomers. Generally, these conformational isomers will be balanced in solution due to their lower steric and larger solvation energy. Among them, five types of conformational isomers of L were obtained through assembly of L with tailored metal nodes (Scheme 2). The common feature of isomers A1, A2 and A3 is that the two sulfur atoms linked to propan-2-one group are almost coplanar with propan-2-one group (namely plane SCCCS). For the A1 conformation, the two nitrogen atoms of pyridyl groups are also located in the SCCCS plane, similar to the optimized conformational isomer L_{ideal} by Gaussian 03.[37] However, the combination of two pyridyl groups at either the same or each side of the SCCCS plane will afford isomer A2 or A3, respectively. For C1 and C2 isomers, their two 4-mercaptopyridine groups bind to each side of the propan-2-one plane to form the trans conformations, but the obvious distinction shown in

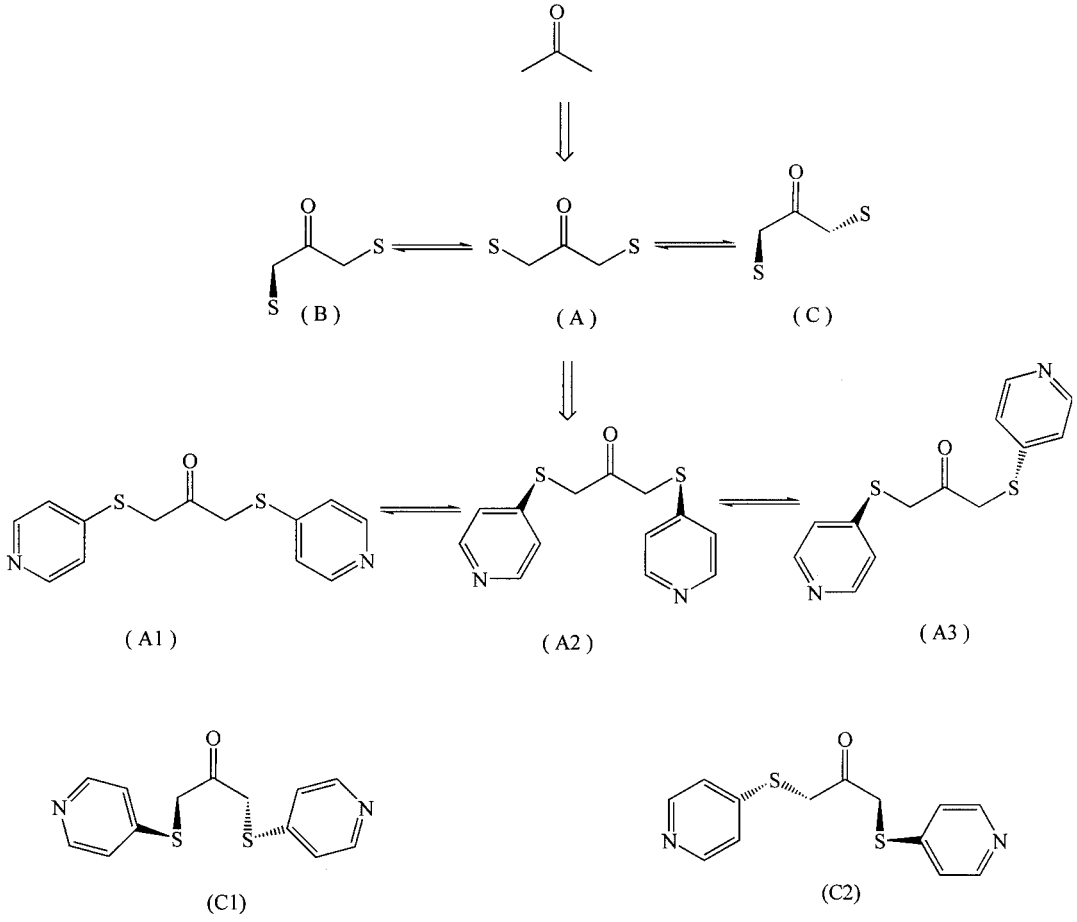

Scheme 2. Formation process of conformational isomers of L (with the A form as example) and representation of conformational isomers of ligand L obtained in its coordination complexes.

 © 2005 Wiley-VCH Verlag GmbH & Co. KGaA, Weinheim

Scheme 2 defines them as different conformations. Furthermore, using Gaussian 03 we calculated quantitatively their conformational energies (Table S1). Compared with the optimized conformational isomer L_{ideal} (the energy of L_{ideal} is arbitrarily regarded as the standard of zero), their steric energies (kJ mol^{-1}) are evaluated as $E^{A1}{}_{steric}$ 400.94, $E^{A2}{}_{steric}$ 411.65, $E^{A3}{}_{steric}$ 406.01, $E^{C1}{}_{steric}$ 389.86 and $E^{C2}{}_{steric}$ 724.51. Clearly, the energy gaps between those conformational isomers range from 5 to 22 kJ mol^{-1}, except for $E^{C2}{}_{steric}$ which is notably higher due to the relatively low statistical distribution of propan-2-one groups in this L. But as we will show, metal-induced conformational isomers A1, A2, C1 and C2 and their unique combinations around metal centers may play a crucial role in pre-defining the resultant polymeric architectures.

Crystal Structures of $\{[Ni(L)_2Cl_2]\}_\infty$ (1) and $\{[Co(L)_2(SCN)_2]\cdot(DMF)_2\}_\infty$ (2)

Complex **1** was obtained from a solvothermal methanol system. An X-ray structural analysis discloses that it crystallizes in orthorhombic space group *Ibca* and is a 3D sixfold interpenetrating diamondoid framework. Each Ni^{II} center is in a distorted octahedral environment surrounded by four pyridines that occupy equatorial sites in a paddlewheel array and two Cl^- that occupy axial sites (see a in Figure 1). The Ni–N bond distances range from 2.123(8) to 2.128(8) Å and Ni–Cl is 2.398(3) Å, while the in-plane andaxis-transition angles are 179.4(3) and 179.33(17)°, respectively. The Ni^{II} centers are linked by four L and act as square-planar nodes in the network. Exo-bidentate spacers L in **1** display A1 and C1 conformational isomers, and the unique array in A1A1C1C1 form around the metal centers produces a C_2 axis that passes through the Ni^{II} center and equally bisects the equatorial plane N1–N1A–N2A–N2. Furthermore, neighboring L around the Ni1 center extend above or below the equatorial plane, resulting in the sharp deviation of binding sites N1B, N1C, N2B and N2C from the least-squares plane N1–N1A–N2A–N2–Ni1, with deviation distances of N1B, N1C, N2B and N2C from the least-squares plane of 4.98771, –4.98771, –6.0371 and 6.0371 Å, respectively. Clearly, the four nickel(II) nodes bonded by N1B, N1C, N2B and N2C atoms are expected to be at the vertexes of a distorted tetrahedron. In this manner, a 3D diamondoid framework forms (b in Figure 1), which is indicative of a distinctive difference from widely encountered 2D grids constructed by square-planar nodes with other ditopic ligands.[38–41] Adjacent $Ni^{II}\cdots Ni^{II}$ bridged by A1 and C1 are separated by 16.435 and 14.869 Å, respectively (b in Figure 1). The long spacers between coordination sites result in large cavities within the diamondoid cages. However, due to the absence of large guest molecules to fill the void space, the potential voids are filled through mutual interpenetration of five independent equivalent frameworks, generating a sixfold interpenetrating 3D architecture (c in Figure 1).

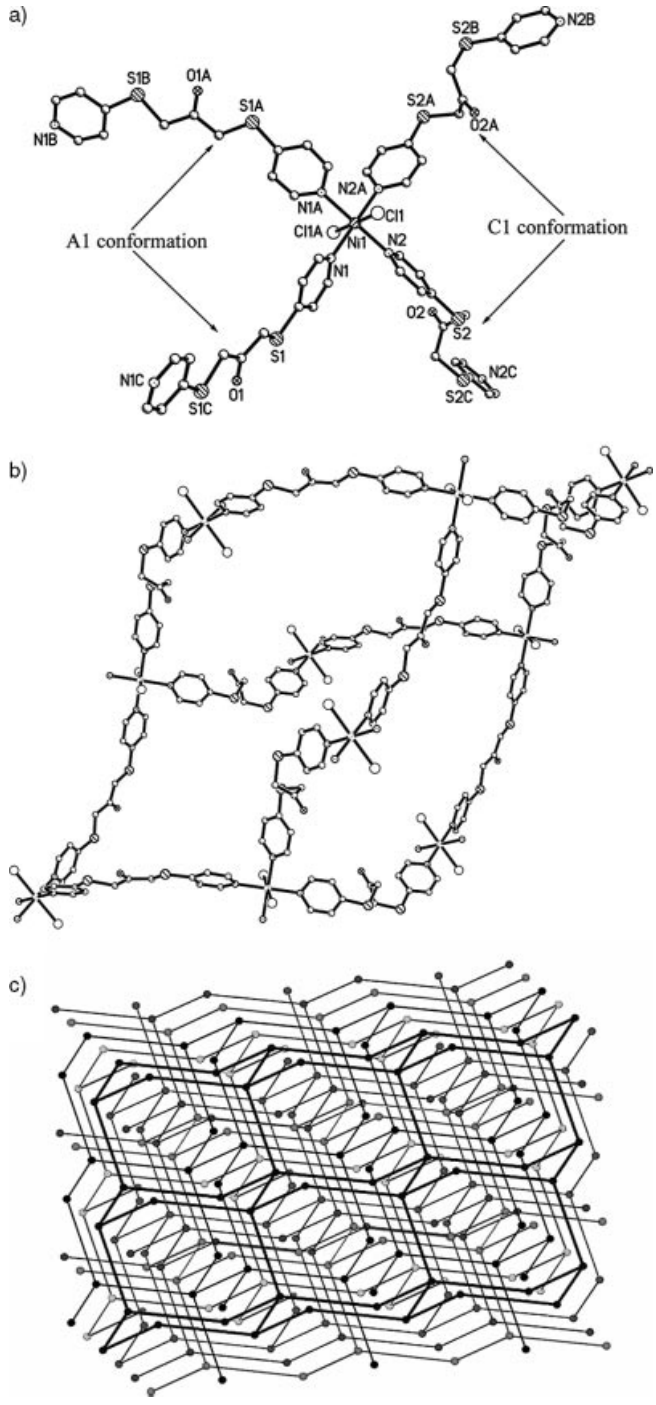

Figure 1. Views of the C_2 symmetric array of conformational isomers A1 and C1 around six-coordinate Ni^{II} centers (a), the single diamondoid cage generated through twelve L (six A1 and six C1) bridging ten Ni^{II} centers (b), and the sixfold interpenetrating diamondoid network with bridging and terminal ligands L and Cl^- omitted for clarity (c) in **1**.

Complex **2**, assembled in a DMF/diethyl ether system, crystallizes in monoclinic space group *C*2/*c* and possesses a 3D threefold interpenetrating network with $CdSO_4$-like topology. Each Co^{II} center in **2** is also in a compressed octahedral environment surrounded by four pyridines, which occupy equatorial sites, and by two SCN^- that occupy axial

 © 2005 Wiley-VCH Verlag GmbH & Co. KGaA, Weinheim

sites (a in Figure 2). The Co–N bond distances range from 2.087(6) to 2.210(5) Å while the in-plane and axis-transition angles are 180.0(3) and 180.0(2)°, respectively. In complex **2**, each Co^{II} center, linked by four L, plays the role of square-planar node, in the same way as the Ni^{II} node in complex **1**. Exo-bidentate spacers L in **2**, however, display A1 and C2 conformational isomers and array in A1C2A1C2 form around the inversion center Co^{II}. Moreover, two A1 isomers bound to the Co1 center extend either above or below the least-squares plane N1–N2–N1A–N2A–Co1, with their binding sites N1B and N1C deviating sharply from the least-squares plane, by –8.1064 and 8.1064 Å, respectively. In contrast the N2B and N2C binding sites of the two C2 isomers deviate comparatively slightly from the least-squares plane, by –1.9237 and 1.9237 Å, respectively. Consequently, the architecture of **2** is completely different from that of **1** with the diamondoid framework. As clearly shown in part b of Figure 2, the combination of A1 isomers and Co^{II} nodes forms 1D undulating chains, which are further alternately connected along two perpendicular directions by the coordination of C2 isomers with Co^{II} nodes. Consequently, a 3D network with a $CdSO_4$-type topology is generated. Furthermore, the $CdSO_4$-like architecture produces large channels that have an opening of about 30.720×14.722 $Å^2$ (see b and c in Figure 2). Part d in Figure 2 shows the threefold interpenetration of $CdSO_4$-like architecture in the crystal, which effectively reduces the void space. Even so, it has a porous rather than a close-packed structure, such that DMF molecules are entrapped within it.

A combination of four-connected nodes and ditopic ligands can provide 2D grids or novel 3D nets, some interesting architectures of which have been exploited recently.[42,43] Notably, both complex **1** and **2** are 3D nets bridged by the

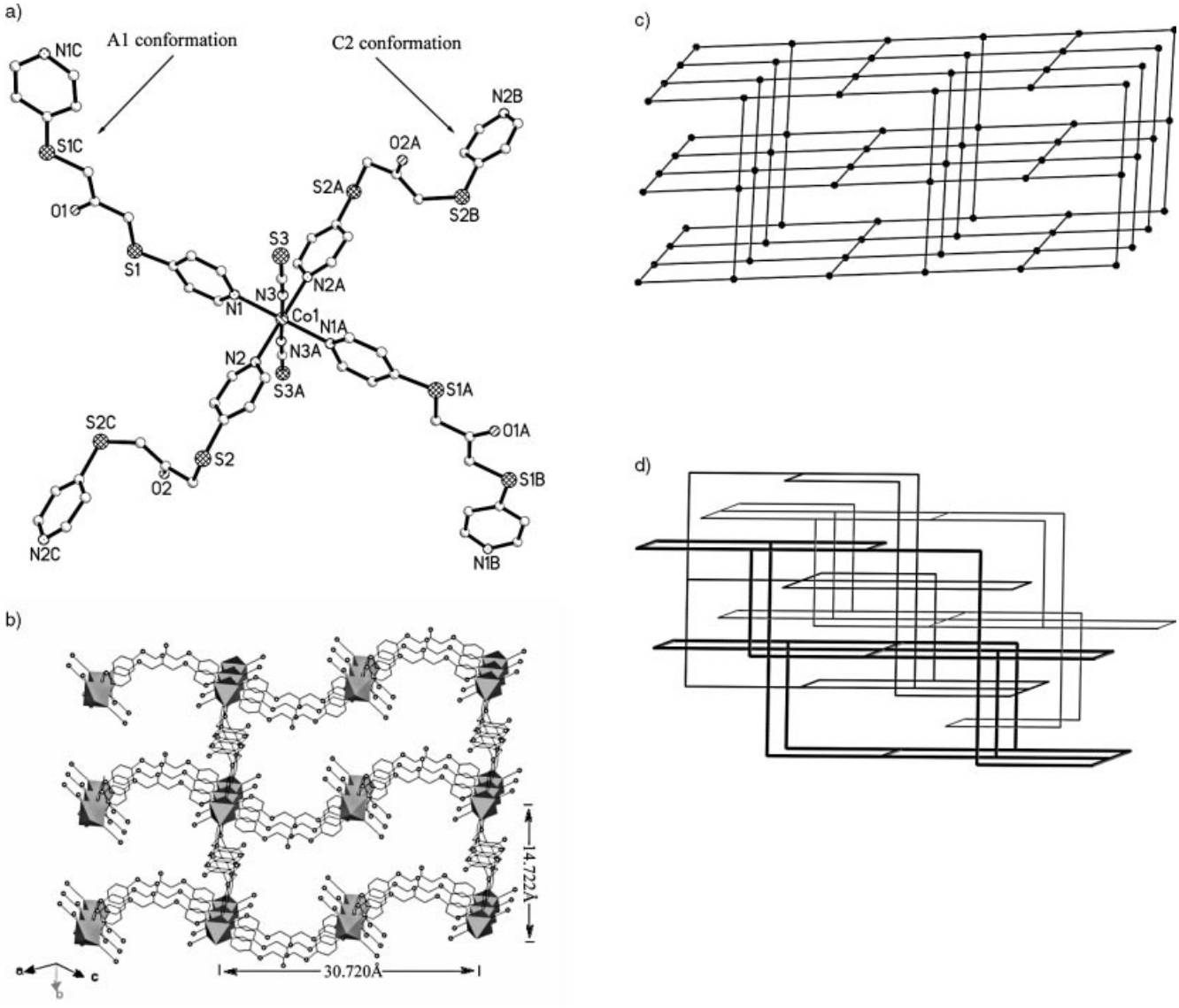

Figure 2. Combination of conformational isomers A1 and C2 around the inversion center of the six-coordinate Co^{II} (a), the 3D open framework containing large tunnels (b), schematic of the $CdSO_4$-like topology (c) and the 3D threefold interpenetrating network with bridging and terminal ligands L and SCN^- omitted for clarity (d) in **2**.

 © 2005 Wiley-VCH Verlag GmbH & Co. KGaA, Weinheim

same ditopic ligands L bonded to four-connected nodes Co^{II} or Ni^{II}, but possess different topologies. Although many factors are involved, conformational isomers of L and their unique combination around metal centers, as depicted above, presumably play the key role in determining the structural topologies.

Crystal Structure of $\{[AgL]NO_3\}_\infty$ (3)

Complex **3**, obtained through a three-layered diffusion method, crystallizes in orthorhombic space group *Pnma* and possesses a 1D U-like chain architecture. The Ag^I ion in **3** shows linear coordination, in which the N1–Ag1–N1A angle is 180.0(3)° and Ag1–N1 and Ag1–N1A bond lengths are 2.151(7) Å (Figure 3). Each L, similar to other dithioether ligands containing 4-pyridyl groups in Ag^I complexes we reported previously,[34] acts as an *exo*-bidentate ligand and bridges two Ag^I centers with its two pyridyl nitrogen atoms to construct a 1D chain structure. Interestingly, L in **3** only presents an A2-typical conformation with higher steric energy than that of isomers A1 and A3. The inversion array of A2 around Ag^I centers results in the unique U-like framework, with the $Ag^I\cdots Ag^I$ distance and deep length of the "U" chain (S···S) being 7.283 and 13.365 Å, respectively, which differ from the structures found in Ag^I and N-containing heterocyclic thioethers.[34,36] Notably, nitrate ions located in "U" chains stabilize the A2-typical conformation of L through weak interactions between its oxygen atoms and Ag^I (O3···Ag1A and O3···Ag1, 2.872 Å).

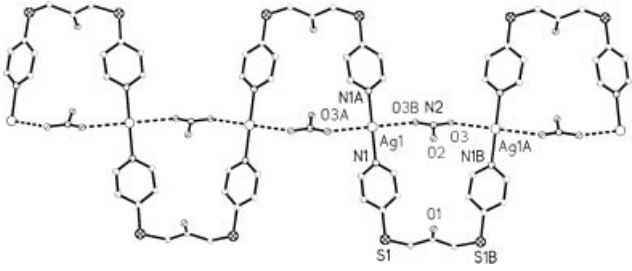

Figure 3. 1D U-like chain architecture in **3**, showing the weak interactions between the counter-anion and Ag^I as well as the template of counter-anions.

Magnetic Properties of Complexes 1 and 2

The temperature (T) dependencies of the magnetic susceptibility (χ_M) of complexes **1** and **2** were measured in the range 2–298 K under fixed fields of 5 and 10 kG, respectively; Figures 4 (see a and b) show the corresponding χ_M vs. T and μ_{eff} vs. T plots. For **1**, μ_{eff} decreases very slowly from 3.45 μ_B at 298 K to 3.29 μ_B at 8 K and then rapidly decreases to 2.53 μ_B at 2 K. The μ_{eff} of 3.45 μ_B per Ni^{II} at room temperature is larger than that calculated for the spin-only case (2.83 μ_B), revealing a significant orbital contribution, which always causes zero-field splitting. The magnetic behavior of complex **1** can be explained by large zero-field splitting, as well as a weak ferromagnetic interaction under the molecular field approximation. The best fit of Equation (1) to the data was achieved with $g = 2.31$, $D/k = 12.25$ K, $\theta = 0.94$ and $R = 4.5\times10^{-6}$ [$R = \sum(\chi_{obsd}-\chi_{cacld})^2/\sum\chi_{obsd}^2$].

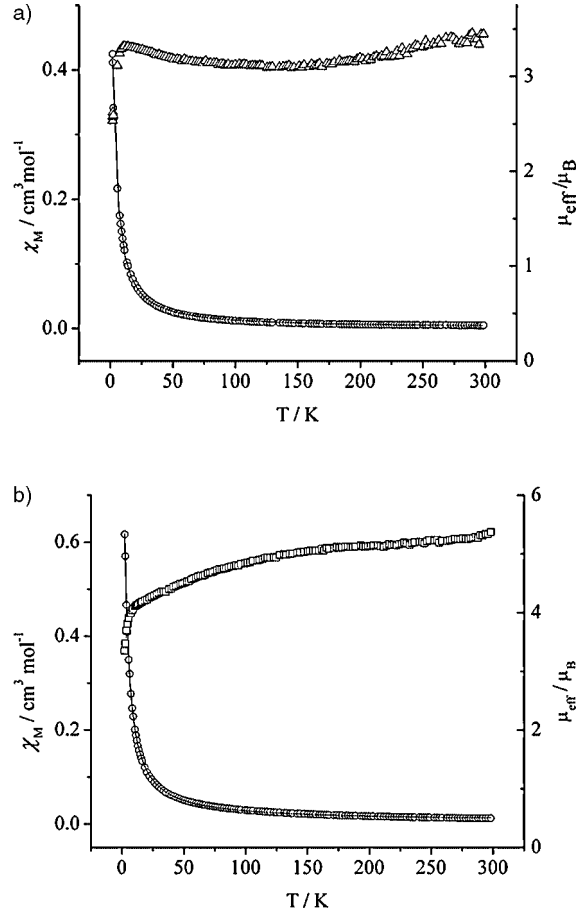

Figure 4. χ_M (○) and μ_{eff} (Δ) vs T with the theoretical fit (−) for **1** (a), and χ_M (○) and μ_{eff} (□) vs. T with the theoretical fit (−) for **2** (b).

$$\chi_M = \frac{2Ng^2\beta^2}{3k(T-\theta)}\left[\frac{2kT/D - 2kT\exp(-D/kT)/D + \exp(-D/kT)}{1+2\exp(-D/kT)}\right] \quad (1)$$

For complex **2**, the experimental μ_{eff} per Co^{II} ion at room temperature is ca. 5.38 μ_B, which is larger than that calculated for the spin-only case (3.87 μ_B), indicating a typical contribution of the orbital momentum for the $4T^1{}_g$ ground state.[44] Upon cooling, μ_{eff} gradually decreases to 4.06 μ_B at 9 K and then dramatically decreases to 3.35 μ_B at 2 K. The χ_M^{-1} vs. T plot is essentially linear, and least-squares fitting of the data to the Curie–Weiss law gives $C = 3.62$ cm^3 mol^{-1} K and $\theta = -17.50$ K. The negative value of θ may be attributed to antiferromagnetic interactions between Co^{II} ions. To date, quantitative magnetic analyses of cobalt(II) complexes have been a challenge due to the complexity of magnetic anisotropy originating from spin–orbit

 © 2005 Wiley-VCH Verlag GmbH & Co. KGaA, Weinheim

coupling and axial distortion. However, when cobalt(II) ions are located in a perfect or slightly distorted octahedral ligand field, the isotropic model proves to be preferable for describing the magnetic data.[45] As indicated in the structure description, each Co^{II} center in **2** is ligated by six nitrogen atoms in a slightly distorted octahedral geometry and these metal nodes are linked by long spacers L to build a 3D $CdSO_4$-like framework. Thus, a simplified analysis of this coupling system is based on considering the exchange coupling between two adjacent paramagnetic centers in an infinite chain and interchain interaction (zJ) under the molecular field approximation. Assuming an isotropic exchange between Co^{II} ions, the magnetic susceptibility per Co^{II} ion can be expressed as:

$$\chi_M^{J+J'} = \frac{\chi_M^{J}}{1-(2zJ'\times\chi_M^{J})/N\beta^2g^2}$$

$$\chi_M^{J} = \frac{N\beta^2g^2S(S+1)}{3kT}\frac{1+u}{1-u} \quad u = \coth\left[\frac{JS(S+1)}{kT}\right]-\left[\frac{kT}{JS(S+1)}\right] \qquad (2)$$

The best fit (assuming $zJ = 0$) of the experimental data to Equation 2 yields $J = -0.36\ cm^{-1}$, $g = 2.28$, with an agreement factor $R = \sum(\chi_{obsd}-\chi_{cacld})^2/\sum\chi_{obsd}^2) = 2.0\times10^{-5}$. It seems that the spin-only model gives quite a good fit.

On the basis of the molecular structures and the magnetic calculations of complexes **1** and **2**, we conclude that the interaction via the bridge L is very weak – indicative of the long and unconjugated ligand L being unfavorable for the electronic interactions needed for efficient superexchange between paramagnetic metal centers.

Fluorescence Properties of Ligand L and Complex 3

Figure 5 depicts solid-state photoluminescent spectra of **3** and free ligand L at room temperature. Free ligand L is strongly photoluminescent and exhibits intense green emission with a single broad band at λ_{max} = 537 nm, corresponding to an excitation at λ_{max} = 370 nm. The emission properties of **3** are complicated and very interesting. Although several Ag^I polymers that emit photoluminescence at room temperature have been reported,[46–49] complex **3** shows, unusually, multiple emission bands. When excited at 365 nm, it displays two weaker blue emission bands at λ_{max} = 416 and 442 nm and one stronger, broad, green emission band at λ_{max} = 541 nm. The low-energy band of 541 nm for **3** is very similar to that found for free ligand L in terms of position and band shape. Therefore, it is assigned to a silver(I)-perturbed intraligand transition. Perhaps, the two higher energy emission bands with weaker intensities, indicative of a slight modification in the photoluminescent activity in **3**, could be ascribed tentatively to either ligand-to-metal (LMCT) or metal-to-ligand charge-transfer transitions (MLCT), but further exact assignments have not carried out. Notably, free ligand L and its Ag^I complex **3** display useful photoluminescent activity in the blue/green region.

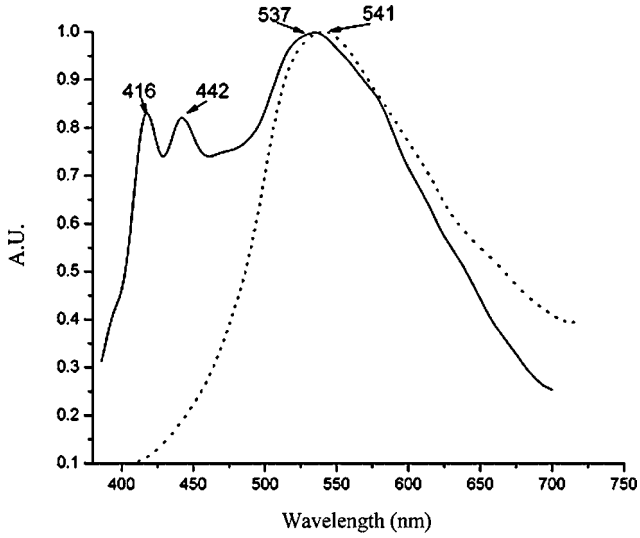

Figure 5. Fluorescence spectra of ligand L excited at 370 nm (dotted line) and complex **3** excited at 365 nm (solid line) in the solid state at room temperature.

Conclusions

We have synthesized flexible ligand L [L = 1,3-bis(4-pyridylthio)propan-2-one] and its three new coordination polymers $\{[Ni(L)_2Cl_2]\}_\infty$ (**1**), $\{[Co(L)_2(SCN)_2]\cdot(DMF)_2\}_\infty$ (**2**) and $\{[AgL]NO_3\}_\infty$ (**3**). Assemblies of L with four-connected square-planar nodes Ni^{II} and Co^{II} lead to two 3D interpenetrating nets with distinct topologies due to the metal-assisted conformational selectivity and unique combinations of ligand L around the metal centers. In **3**, L only presents a typical conformation, with higher steric energy, that links linear nodes Ag^I, leading to a 1D U-like chain, where counter-anions template both the architecture of the polymer and the A2-typical conformation of L. Clearly, L presents conformational lability that can be utilized in metal-assisted assemblies to affect the coordination architectures. Magnetic studies on complexes **1** and **2** show that the long, unconjugated ligand L is unfavorable for the electronic interactions needed for efficient superexchange between paramagnetic metal centers. Interestingly, complex **3** displays unusual fluorescent emission with multiple bands in the blue/green region. Moreover, as the ketone group incorporated into the ligand will functionalize the resultant architecture, further exploitation of such ligands in crystal engineering and material is underway.

Experimental Section

WARNING! Although we experienced no problems in handling these perchlorate compounds, they should be treated with great caution due to their potential for explosion.

General Remarks: All materials, reagents and solvents were purchased from commercial sources and used as received. Elemental

 © 2005 Wiley-VCH Verlag GmbH & Co. KGaA, Weinheim

Table 1. Crystal data and structure refinement for **1**–**3**.

	1	**2**	**3**
Empirical formula	$C_{26}H_{24}Cl_2N_4NiO_2S_4$	$C_{34}H_{38}CoN_8O_4S_6$	$C_{13}H_{12}AgN_3O_4S_2$
Formula mass	682.34	874.01	446.25
Temperature [K]	293(2)	130(2)	293(2)
Crystal system	orthorhombic	monoclinic	orthorhombic
Space group	*Ibca*	*C*2/*c*	*Pnma*
a [Å]	18.447(11)	22.65(4)	5.5447(5)
b [Å]	15.952(8)	16.34(2)	14.5664(15)
c [Å]	21.40(2)	12.57(5)	22.6241(22)
α [°]	90.00(0)	90.00(0)	90.00(0)
β [°]	90.00(0)	118.60(4)	90.00(0)
γ [°]	90.00(0)	90.00(0)	90.00(0)
V [A^3]	6297(8)	4086(18)	1827.3(0)
Z, $\rho_{calcd.}$ [Mg m^{-3}]	8, 1.439	4, 1.421	4, 1.622
μ (Mo-K_α) [mm^{-1}]	1.081	0.774	1.351
θ range [°]	2.54 to 22.50	1.61 to 22.50	3.60 to 22.50
Goodness-of-fit on F^2	0.974	1.090	1.301
*R*1, *wR* [$I > 2\sigma(I)$]	0.0944, 0.2329	0.0709, 0.1933	0.0660, 0.1578
(all data)	0.1372, 0.2728	0.0737, 0.1959	0.0695, 0.1601

Table 2. Selected bond lengths [Å] and angles [°] for **1**–**3**.

Complex **1**			
Ni1–N1	2.128(8)	Ni1–N1A	2.128(8)
Ni1–N2	2.123(8)	Ni1–N2A	2.123(8)
Ni1–Cl1	2.398(3)	Ni1–Cl1A	2.398(3)
N2–Ni1–N1	87.8(3)	N1–Ni1–N1A	92.4(5)
N2–Ni1–N2A	92.1(5)	N2A–Ni1–N1A	87.8(3)
N1–Ni1–Cl1A	90.1(2)	N1A–Ni1–Cl1	90.1(2)
N2–Ni1–Cl1A	91.2(2)	N2A–Ni1–Cl1A	89.3(2)
N1–Ni1–Cl1	89.5(2)	N1A–Ni1–Cl1A	89.5(2)
N2–Ni1–Cl1A	89.3(2)	N2A–Ni1–Cl1	91.2(2)
N2A–Ni1–N1	179.4(3)	N2–Ni1–N1A	179.4(3)
Cl1A–Ni1–Cl1	179.33(17)		
Complex **2**			
Co1–N1	2.210(5)	Co1–N1A	2.210(5)
Co1–N2	2.165(6)	Co1–N2A	2.165(6)
Co1–N3	2.087(6)	Co1–N3A	2.087(6)
N2–Co1–N1	88.7(2)	N3–Co1–N1	91.5(2)
N3–Co1–N2	89.7(3)	N3–Co1–N2A	90.3(3)
N3A–Co1–N2A	89.7(3)	N3A–Co1–N2	90.3(3)
N3–Co1–N1A	88.5(2)	N3A–Co1–N1A	91.5(2)
N2A–Co1–N1A	88.7(2)	N2–Co1–N1A	91.3(2)
N3A–Co1–N1	88.5(2)	N2A–Co1–N1	91.3(2)
N1A–Co1–N1	180.0(3)	N2A–Co1–N2	180.0(3)
N3–Co1–N3A	180.0(2)		
Complex **3**			
Ag1–N1	2.151(7)	Ag1–N1A	2.151(7)
N1A–Ag1–N1	180.0(3)		

Symmetry codes: A = ½ –*x*, *y*, –*z* for **1**; A = ½ –*x*, ½ –*y*, –*z* for **2**; A = –*x*, 1 –*y*, –*z* for **3**.

analyses were determined on an Elementary Vario ELIII elemental analyzer. IR spectra were measured as KBr pellets on a Nicolet Magna 750 FT-IR spectrometer in the range 400–4000 cm^{-1}. The NMR spectrum was recorded on a Varian Inova-500 spectrophotometer at room temperature and chemical shifts are quoted in δ (ppm) relative to the deuterated solvent used. Fluorescent spectra were measured with an Edinburgh FL-FS90 TCSPC system. Temperature-dependent magnetic measurements were determined on a Quantum Design SQUID-XL7 magnetometer.

Synthesis of 1,3-Bis(4-pyridylthio)propan-2-one (L): L was synthesized under nitrogen. Sodium methylate (0.540 g, 10 mmol) and 4-pyridinethiol (1.11 g, 10 mmol) were vigorously stirred in MeOH (50 mL) for 1 h before a quantitative amount of 1,3-dichloro-2-propanone (0.635 g, 5 mmol) was added. The resulting solution was heated at 60 °C for 12 h and then filtered after cooling to room temperature. Removal of the solvent from the resultant red filtrate gave a brown oil that afforded yellow needle crystals after recrystallization from warm water. The crystalline product was redissolved in warm water (20 mL) and neutralized with $NaHCO_3$ powder. The so-obtained pale yellow precipitate was filtered off, washed with cold water and a little methanol, and then dried in air to give 0.773 g (2.80 mmol) of L (56%). $C_{13}H_{12}N_2OS_2$ (276.4): calcd. C 56.50, H 4.38, N 10.14, S 23.20; found: C 56.42, H 4.35, N 10.00, S 23.05. ^{1}H NMR (500 MHz, [D$_6$]DMSO): δ = 8.481 [d, *J* (HH) = 6.0 Hz, 4 H, H^{2,6}py], 7.519 [d, *J* (HH) = 5.0 Hz, 4 H,

 © 2005 Wiley-VCH Verlag GmbH & Co. KGaA, Weinheim

$H^{3,5}$py], 4.594 (m, 4 H, -CH_2-) ppm. IR (KBr): $\tilde{\nu}$ = 3032 (w), 2942 (w), 1730 (vs), 1575 (vs), 1538 (s), 1482 (m), 1409 (vs), 1381 (s), 1220 (m), 1028 (s), 801 (vs), 702 (s), 497 (m) cm^{-1}.

Synthesis of $\{[Ni(L)_2Cl_2]\}_\infty$ (1): Solvothermal treatment of $NiCl_2 \cdot 6H_2O$ (0.024 g, 0.1 mmol), L (0.055 g, 0.2 mmol) and methanol (10 mL) at 80 °C for 1 day gave yellow-green prismatic crystals of **1** (0.048 g, 0.07 mmol, 70%). $C_{26}H_{24}Cl_2N_4NiO_2S_4$ (682.34): calcd. C 45.77, H 3.54, N 8.21, S 18.80; found: C 45.50, H 3.60, N 8.20, S 18.57. IR (KBr): $\tilde{\nu}$ = 3060 (w), 2916 (m), 1720 (m), 1601 (vs), 1535 (w), 1484 (s), 1417 (s), 1216 (m), 1072 (m), 806 (m), 718 (m), 502 (w) cm^{-1}.

Synthesis of $\{[Co(L)_2(SCN)_2]\cdot(DMF)_2\}_\infty$ (2): KSCN (0.019 g, 0.2 mmol) in DMF (5 mL) was added to a solution of $Co(ClO_4)_2 \cdot 6H_2O$ (0.037 g, 0.1 mmol) and L (0.055 g, 0.2 mmol) in DMF (5 mL) with stirring. The resulting mixture was stirred for 1 h and then filtered. Slow diffusion of diethyl ether (25 mL) into the blue filtrate for three weeks gave block orange crystals of **2** (0.065 g, 0.074 mmol, 74%). $C_{34}H_{38}CoN_8O_4S_6$ (874.01): calcd. C 46.72, H 4.38, N 12.82, S, 22.01; found: C 46.30, H 4.45, N 12.79, S 21.77. IR (KBr): $\tilde{\nu}$ = 3099 (w), 3059 (w), 2928 (w), 2873 (m), 2065 (vs), 1718 (w), 1664 (s), 1593 (vs), 1537 (w), 1485 (m), 1417 (m), 1221 (m), 1065 (m), 807 (m), 720 (m), 627 (w), 501 (m) cm^{-1}.

Synthesis of $\{[AgL]NO_3\}_\infty$ (3): A mixture of DMF (5 mL), methanol (5 mL) and CH_3CN (5 mL) was added dropwise along the wall of tube (50 mL) that contained a solution of $AgNO_3$ (0.017 g, 0.1 mmol) and DMF (5 mL) as the bottom layer. A solution of L (0.028 g, 0.1 mmol) and methanol (10 mL) as the top layer was then transferred into the tube in the same way. After slowly diffusing for two weeks, the mesosphere gave khaki needle crystals of **3** (0.023 g, 0.052 mmol, 52%). $C_{13}H_{12}AgN_3O_4S_2$ (446.25): calcd. C 34.99, H 2.71, N 9.42, S 14.37; found: C 35.10, H 2.64, N 9.17, S 14.50. IR (KBr): $\tilde{\nu}$ = 3091 (w), 2916 (w), 1720 (m), 1597 (s), 1535 (w), 1489 (m), 1422 (m), 1371 (vs), 1232 (m), 1114 (m), 1062 (m), 1026 (m), 806 (m), 718 (m), 636 (w), 487 (m) cm^{-1}.

X-ray Structure Determinations: Single-crystal data were collected on a Rigaku Mercury-CCD diffractometer at room temperature for **1** and **3,** and at 130 K for **2**, using graphite-monochromated Mo-K_α radiation (λ = 0.7107 Å). The structures were solved by direct methods and refined on F^2 by full-matrix least-squares procedures using the SHELXTL software suite.[50] All non-hydrogen atoms were refined anisotropically and the hydrogen atoms were treated as idealized contributions. For complex **2**, the propan-2-one groups of half L were split into two equivalent parts and the accommodated DMF solvent was treated as disordered; the maximum and minimum peaks in the final difference maps were 1.678 and –0.511 e $Å^{-3}$, respectively, and the largest residual density peak was close to the sulfur atom of SCN^-. Table 1 summarizes the crystallographic data of **1**–**3** and Table 2 lists selected bond lengths and angles. X-ray crystallographic data in CIF format for **1**–**3** have also been deposited. CCDC-247593 to -247595 (for **1**–**3)** contain the supplementary crystallographic data for this paper. These data can be obtained free of charge from The Cambridge Crystallographic Data Centre via www.ccdc.cam.ac.uk/data_request/cif.

Acknowledgments

This work was supported by grants from the National Nature Science Foundation of China and the Nature Science Foundation of Fujian Province.

[1] K. Kasai, M. Aoyagi, M. Fujita, *J. Am. Chem. Soc.* **2000**, *122*, 2140–2141.
[2] K.-W. Kim, M. G. Kanatzidis, *J. Am. Chem. Soc.* **1992**, *114*, 4878–4883.
[3] X.-H. Bu, W. Chen, S.-L. Lu, R.-H. Zhang, D.-Z. Liao, W.-M. Bu, M. Shionoya, F. Brisse, J. Ribas, *Angew. Chem. Int. Ed.* **2001**, *40*, 3201–3203.
[4] Z.-R. Qu, H. Zhao, Y.-P. Wang, X.-S. Wang, Q. Ye, Y.-H. Li, R.-G. Xiong, B. F. Abrahams, Z.-G. Liu, Z.-L. Xue, X.-Z. You, *Chem. Eur. J.* **2004**, *10*, 53–60.
[5] R. Horikoshi, T. Mochida, H. Moriyama, *Inorg. Chem.* **2001**, *40*, 2430–2433.
[6] N. Yoshida, H. Oshio, T. Ito, *Chem. Commun.* **1998**, 63–64.
[7] C.-Y. Su, Y.-P. Cai, C.-L. Chen, B.-S. Kang, *Inorg. Chem.* **2001**, *40*, 2210–2211.
[8] L. Raehm, L. Mimassi, C. Guyard-Duhayon, H. Amouri, *Inorg. Chem.* **2003**, *42*, 5654–5659.
[9] L. Carlucci, G. Ciani, P. Macchi, D. M. Proserpio, S. Rizzato, *Chem. Eur. J.* **1999**, *5*, 237–243.
[10] D. M. L. Goodgame, D. A. Grachvogel, I. Hussain, A. J. P. White, D. J. Williams, *Inorg. Chem.* **1999**, *38*, 2057–2063.
[11] J.-F. Ma, J. Yang, G.-L. Zheng, L. Li, J.-F. Liu, *Inorg. Chem.* **2003**, *42*, 7531–7534.
[12] X.-L. Wang, C. Qin, E.-B. Wang, Y.-G Li, C.-W. Hu, L. Xu, *Chem. Commun.* **2004**, 378–379.
[13] S. R Batten, A. R. Harris, P. Jensen, K. S. Murray, A. Ziebell, *J. Chem. Soc., Dalton Trans.* **2000**, 3829–3835.
[14] R. Horikoshi, T. Mochida, N. Maki, S. Yamada, H. Moriyama, *J. Chem. Soc., Dalton Trans.* **2002**, 28–33.
[15] X.-R. Meng, Y.-L. Song, H.-W. Hou, H.-Y. Han, B. Xiao, Y.-T. Fan, Y. Zhu, *Inorg. Chem.* **2004**, *43*, 3528–3536.
[16] M.-L. Tong, X.-M. Chen, B.-H. Ye, L.-N. Ji, *Angew. Chem. Int. Ed.* **1999**, *38*, 2237–2240.
[17] D. L. Reger, R. F. Semeniuc, V. Rassolov, M. D. Smith, *Inorg. Chem.* **2004**, *43*, 537–554.
[18] P. Borsting, P. J. Steel, *Eur. J. Inorg. Chem.* **2004**, 376–380.
[19] L. Mimassi, C. Guyard-Duhayon, L. Raehm, H. Amouri, *Eur. J. Inorg. Chem.* **2002**, 2453–2457.
[20] Y.-H. Liu, H.-C. Wu, H.-M. Lin, W.-H. Hou, K.-L. Lu, *Chem. Commun.* **2003**, 60–61.
[21] S. U. Son, B. Y. Kim, C. H. Choi, S. W. Lee, Y. S. Kim, Y. K. Chung, *Chem. Commun.* **2003**, 2528–2529.
[22] K. I. Na1ttinen, K. Rissanen, *Inorg. Chem.* **2003**, *42*, 5126–5134.
[23] K. A. Hirsch, S. R. Wilson, J. S. Moore, *Inorg. Chem.* **1997**, *36*, 2960–2968.
[24] D. M. Shin, I. S. Lee, Y. K. Chung, M. S. Lah, *Chem. Commun.* **2003**, 1036–1037.
[25] K. Uemura, S. Kitagawa, M. Kondo, K. Fukui, R. Kitaura, H.-Ch. Chang, T. Mizutani, *Chem. Eur. J.* **2002**, *8*, 3586–3560.
[26] C. M. Grunert, J. Schweifer, P. Weinberger, W. Linert, *Inorg. Chem.* **2004**, *43*, 155–165.
[27] O. R. Evans, W.-B. Lin, *Chem. Mater.* **2001**, *13*, 2705–2712.
[28] L. Han, M.-C. Hong, R.-H. Wang, J.-H. Luo, Z.-Z. Lin, D.-Q. Yuan, *Chem. Commun.* **2003**, 2580–2581.
[29] J. R. Black, N. R. Champness, W. Levason, G. Reid, *Inorg. Chem.* **1996**, *35*, 4432–4438.
[30] F. M. Tabellion, S. R. Seidel, A. M. Arif, P. J. Stang, *J. Am. Chem. Soc.* **2001**, *123*, 7740–7741.
[31] M.-C. Hong, W.-P. Su, R. Cao, M. Fujita, J.-X. Lu, *Chem. Eur. J.* **2000**, *6*, 437–431.
[32] M.-C. Hong, Y.-J. Zhao, W.-P. Su, R. Cao, M. Fujita, Z.-Y. Zhou, A. S. C. Chan, *Angew. Chem. Int. Ed.* **2000**, *39*, 2468–2470.
[33] Y.-J. Zhao, M.-C. Hong, D.-F. Sun, R. Cao, *J. Chem. Soc., Dalton Trans.* **2002**, 1354–1357.
[34] R.-H. Wang, M.-C. Hong, W.-P. Su, Y.-C. Liang, R. Cao, Y.-J. Zhao, J.-B. Weng, *Polyhedron* **2001**, *20*, 3165–3170.
[35] Y. Zheng, M. Du, J.-R. Li, R.-H. Zhang, X.-H. Bu, *J. Chem. Soc., Dalton Trans.* **2003**, 1509–1514.
[36] R.-Q. Zou, J.-R. Li, Y.-B. Xie, R.-H. Zhang, X.-H. Bu, *Cryst. Growth Des.* **2004**, *4*, 79–84.

[37] M. J. Frisch, G. W. Trucks, H. B. Schlegel, G. E. Scuseria, M. A. Robb, J. R. Cheeseman, J. A. Jr., Montgomery, T. Vreven, K. N. Kudin, J. C. Burant, J. M. Millam, S. S. Iyengar, J. Tomasi, V. Barone, B. Mennucci, M. Cossi, G. Scalmani, N. Rega, G. A. Petersson, H. Nakatsuji, M. Hada, M. Ehara, K. Toyota, R. Fukuda, J. Hasegawa, M. Ishida, T. Nakajima, Y. Honda, O. Kitao, H. Nakai, M. Klene, X. Li, J. E. Knox, H. P. Hratchian, J. B. Cross, C. Adamo, J. Jaramillo, R. Gomperts, R. E. Stratmann, O. Yazyev, A. J. Austin, R. Cammi, C. Pomelli, J. W. Ochterski, P. Y. Ayala, K. Morokuma, G. A. Voth, P. Salvador, J. J. Dannenberg, V. G. Zakrzewski, S. Dapprich, A. D. Daniels, M. C. Strain, O. Farkas, D. K. Malick, A. D. Rabuck, K. Raghavachari, J. B. Foresman, J. V. Ortiz, Q. Cui, A. G. Baboul, S. Clifford, J. Cioslowski, B. B. Stefanov, G. Liu, A. Liashenko, P. Piskorz, I. Komaromi, R. L. Martin, D. J. Fox, T. Keith, M. A. Al-Laham, C. Y. Peng, A. Nanayakkara, M. Challacombe, P. M. W. Gill, B. Johnson, W. Chen, M. W. Wong, C. Gonzalez, J. A. Pople, *Gaussian 03*, revision B.05; Gaussian, Inc.: Pittsburgh, PA, **2003**.

[38] D. M. Shin, I. S. Lee, Y. K. Chung, *Inorg. Chem.* **2003**, *42*, 8838–8846.

[39] D. M. Shin, I. S. Lee, Y. K. Chung, M. S. Lah, *Inorg. Chem.* **2003**, *42*, 2977–2982.

[40] N. G. Pschirer, D. M. Ciurtin, M. D. Smith, U. H. F. Bunz, H. C. Loye, *Angew. Chem. Int. Ed.* **2002**, *41*, 583–585.

[41] O. M. Yaghi, H. L. Li, T. L. Gory, *Inorg. Chem.* **1997**, *36*, 4292–4203.

[42] M. L. Tong, X. M. Chen, S. R. Batten, *J. Am. Chem. Soc.* **2003**, *125*, 16170–16171.

[43] B. Moulton, H. Abourahma, M. W. Bradner, J. J. Lu, G. J. McManus, M. J. Zaworotko, *Chem. Commun.* **2003**, 1342–1343.

[44] H. Sakiyama, R. Ito, H. Kumagai, K. Inoue, M. Sakamoto, Y. Nishida, M. Yamasaki, *Eur. J. Inorg. Chem.* **2001**, 2027–2032.

[45] G. De Munno, M. Julve, F. Lloret, J. Faus, A. Caneschi, *J. Chem. Soc., Dalton Trans.* **1994**, 1175–1183.

[46] B. L. Fei, W. Y. Sun, T. Okamura, W. X. Tanga, N. Ueyama, *New J. Chem.* **2001**, *25*, 210–212.

[47] M. L. Tong, X. M. Chen, B. H. Ye, L. N. Ji, *Angew. Chem. Int. Ed.* **1999**, *38*, 2237–2240.

[48] S. L. Zheng, M. L. Tong, S. D. Tan, Y. Wang, J. X. Shi, Y. X. Tong, H. K. Lee, X. M. Chen, *Organometallics* **2001**, *20*, 5319–5325.

[49] M. A. Omary, M. A. Rawashdeh-Omary, H. V. K. Diyabalanage, H. V. R. Dias, *Inorg. Chem.* **2003**, *42*, 8612–8614.

[50] G. M. Sheldrick, Bruker *SHELXTL-PC*, University of Göttingen, **1997**.

Received: September 01, 2004

 © 2005 Wiley-VCH Verlag GmbH & Co. KGaA, Weinheim

Luminescent Iridium(III)-Terpyridine Complexes – Interplay of Ligand Centred and Charge Transfer States

Lucia Flamigni,*[a] Barbara Ventura,[a] Francesco Barigelletti,*[a] Etienne Baranoff,[b] Jean-Paul Collin,*[b] and Jean-Pierre Sauvage*[b]

Keywords: Iridium / Photochemistry / Luminescence / Charge transfer / Electron transfer

Electrochemical properties, ground state absorption spectra, luminescence spectra and lifetimes (at room temperature and 77 K) as well as transient absorption spectra are reported herein for newly synthesized iridium(III) complexes in which benzamide units are appended to the coordinated terpyridine fragments. The nature of the luminescent excited states ($\Phi < 2\times10^{-3}$ and τ in the microsecond range, in air-equilibrated acetonitrile at 298 K) is discussed with regards to the ligand-centred (^{3}LC) or charge transfer (^{3}CT) nature. At room temperature, the excited state, a predominantly ligand-centred triplet (^{3}LC) for the iridium(III) terpyridine compounds, is switched for the benzamide-containing complexes to a charge transfer state (^{3}CT). Intense absorption in the visible range, high energy content, long excited states lifetimes at 298 and 77 K and good luminescence yields make these complexes very promising as photosensitisers (P). The CT nature of the excited states of the benzamide-containing complexes makes them ideal components for the construction of rigid, linear arrays of the Donor-P-Acceptor type for charge separation.
(© Wiley-VCH Verlag GmbH & Co. KGaA, 69451 Weinheim, Germany, 2005)

Introduction

Iridium(III) complexes of polypyridine ligands are increasingly being employed in relevant applications.[1–5] For iridium(III) terpyridine (2,2′:6′,2′′-terpyridine, tpy) complexes some interesting perspectives concern their use as biological labelling reagents[6] as well as the building up of dyads and triads as models for photoenergy conversion schemes.[7–9] $[Ir(tpy)_2]^{3+}$ and derivatives like those of the $Ir(ttpy)_2]^{3+}$ family (ttpy = 4′-tolyl-tpy) exhibit favourable optical properties which include intense luminescence ($\Phi \approx 10^{-2}$) and lifetimes in the μs time range.[10] Furthermore, the luminescent levels for these complexes come at ca. 2.5 eV so that they have potential to act as efficient photosensitisers. Indeed, the possibility of developing linear arrays by attaching suitable groups at the 4′-position of tpy groups coordinated at the Ir^{III} ion is very appealing.[8,9,11] The use of geometrically opposite photoactive and electroactive units (e.g. D and A, electron donor and acceptor units, respectively) has proven to be of importance within energy conversion schemes.[7] So far, the $[Ir(tpy)_2]^{3+}$ unit integrated within linear triad arrays has been used both as an electron relay[8a] and as a photosensitiser.[9] Whereas it has proven to be rather effective as an electron relay, its properties as a photosensitiser (P) are less satisfactory. For this latter role, in fact, in dyads (D-P and P-A) and triads (D-P-A) designed to perform photoinduced charge separation, it is relevant to gain control over the early events triggered by light absorption at P. In fact, primary formation of the lowest-lying charge transfer (CT) states within P could favour subsequent intercomponent hole and electron migration towards the D and A interacting partners, once the thermodynamic requirements are met. In contrast, for ligand centred (LC) excited states, holes and electrons reside in physically coincident sites and the expected intercomponent charge shift steps could be slowed down and be less competitive towards other processes, e.g. energy transfer.[9]

For the iridium(III) complexes of tpy derivatives studied up to now, the luminescent state has been found to be predominantly ligand centred, ^{3}LC.[10,11,13,14] This is in contrast to what happens for the closely investigated polypyridine complexes of transition metals such as ruthenium(II), osmium(II) and rhenium(I)[12] which are currently being employed as photosensitisers and the emitting states of which are triplet metal-to-ligand states (^{3}MLCT) in nature. In only one case, a scarcely emissive excited state in a 4-aminobiphenyl-substituted Ir(tpy) reported by Williams et al. was attributed to an intraligand charge transfer state, ILCT, where the appended group acts as a donor and the metal-

[a] Istituto ISOF-CNR,
Via P. Gobetti 101, 40129 Bologna, Italy
Fax: +39-051-639-9844
E-mail: flamigni@isof.cnr.it
franz@isof.cnr.it
[b] Laboratoire de Chimie Organo-Minérale, UMR 7513 CNRS, Université Louis Pasteur, Institut Le Bel,
4, rue Blaise Pascal, 67070 Strasbourg, France
Fax: +33-390-241-368
E-mail: sauvage@chimie.u-strasbg.fr
jpcollin@chimie.u-strasbg.fr

bond terpyridyl unit behaves as an acceptor.[11] The poor tendency of Ir(tpy) derivatives to form MLCT excited states can be understood on the basis of their electrochemical behaviour which is in contrast to that found for polypyridine complexes of transition metals such as ruthenium(II) and some others.[12] For the latter complexes, the free energy for the reaction of the one-electron oxidised and reduced forms, $\Delta E_{1/2}$, correlates with the energy of the lowest-lying absorption and emission bands. These are MLCT in nature as evaluated from the longest-wavelength portions of absorption spectra (^{1}MLCT) and from the characteristics of the emission spectra (^{3}MLCT).[15] For instance, for $[Ru(tpy)_2]^2$, the metal centred oxidation, $E_{1/2}^{ox}$ (3+/2+), and the ligand centred reduction, $E_{1/2}^{red}$ (2+/+), are +1.30 and –1.24 V, respectively, with respect to the SCE in MeCN.[16] The emission level, E_{em}, is ca. 2.0 eV so that $E_{em} \approx \Delta E_{1/2} - 0.5$ eV. On the other hand, for $[Ir(tpy)_2]^{3+}$, $E_{1/2}^{red}$ = –0.77 V but the oxidation of Ir(III) to Ir(IV) is not observed and $E_{1/2}^{ox} \geq +2.4$ V.[10] Based on these electrochemical results and the above correlation, the ^{3}MLCT level for $[Ir(tpy)_2]^{3+}$ can be estimated higher ($\geq$ 2.7 eV) than the luminescent ^{3}LC level which is ca. 2.5 eV.[1] It is worth mentioning here that a ligand-to-ligand excited state, LLCT, was identified as the emitting state in a related cyclometallated complex recently reported.[17]

We show below that newly prepared Ir(III)-tpy type species with appended *N*-phenyl-benzamide fragments, **2** and **3** Scheme 1, also feature ^{3}CT emission properties. Among other things, this CT character causes a low-energy shift of the main absorption bands in complexes **2** and **3** (bright yellow) in comparison with that observed in the prototype $[Ir(tpy)_2]^{3+}$ complex or **1** (colourless or yellowish). This makes this series more promising for the conversion of solar light into chemical energy.

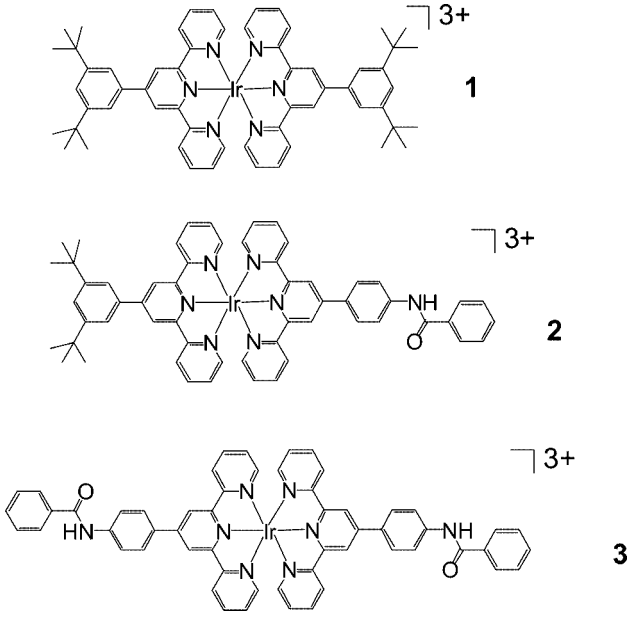

Scheme 1.

Results and Discussion

Synthesis and Electrochemistry

Complexes **1** and **2** were prepared as previously reported.[8,10] Complex **3** was synthesized straightforwardly in one step from 4′-(benzamidophenyl)-2,2′:6′,2"-terpyridine (bap-tpy) and $IrCl_3$.

The redox characteristics of complexes **1**, **2** and **3** examined by cyclic voltammetry in acetonitrile (MeCN) are reported in Table 1. The working electrode used was a glassy carbon electrode since irreproducible and poorly defined signals were obtained with a platinum electrode due to adsorption phenomena. Two reversible ligand-centred[10] one-electron waves followed by an irreversible peak at more negative potential were observed for the three complexes. As indicated by the values of the potentials, complex **1** is slightly more difficult to reduce than **2** and **3**. In fact, the presence of one (in **2**) or two (in **3**) benzamide groups leads to a very similar LUMO energy level in these two complexes. This fact is in agreement with the various spectroscopic properties observed for the three complexes (see below). Thus complex **1** has distinct characteristics compared with **2** and **3** which, in turn, are very similar to one another.

Table 1. Cyclic voltammetric data[a] for the complexes **1**, **2** and **3**.

	$E_{1/2}$ (V vs. SCE)		
	tpy/tpy$^-$	tpy$^-$/tpy^{2-}	tpy^{2-}/tpy^{3-}
1	–0.79	–0.93	–1.80[b]
2	–0.76	–0.92	–1.68[b]
3	–0.76	–0.92	–1.65[b]

[a] Solvent is MeCN, 0.1 M nBu_4NPF_6 and SCE as the reference electrode (v = 100 mV s^{-1}). [b] Irreversible peak.

Optical Spectroscopy

Figure 1 shows the absorption spectra in MeCN solutions for the complexes shown in Scheme 1. For complex **1**, the absorption onset is at 400 nm and the UV features are due to intraligand ^{1}LC transitions as previously established.[10] The spectra of complexes **2** and **3** are characterised by an additional, unstructured broad band extending

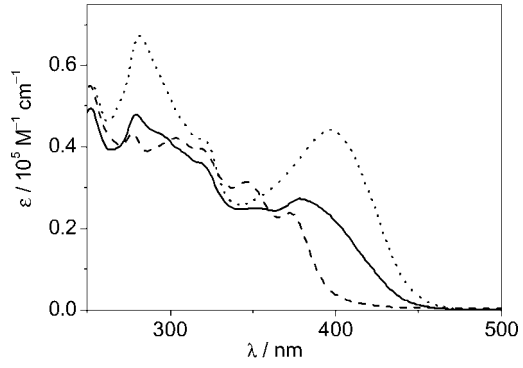

Figure 1. Absorption spectra in MeCN of **1** (dashed), **2** (solid) and **3** (dotted).

 © 2005 Wiley-VCH Verlag GmbH & Co. KGaA, Weinheim

well beyond 400 nm. This band is about twice as intense in **3** as it is in **2** with ε_{398nm} ca. 45000 $M^{-1}cm^{-1}$ and ε_{380nm} ca. 27000 $M^{-1}cm^{-1}$, respectively (see Figure 1).

Figure 2 shows the room temperature luminescence spectra in air-free MeCN. In the inset, the luminescence decays at 298 K of **2** and **3** are also displayed. While a structured luminescence profile can be observed for **1** at 298 K, a broad unstructured band was recorded for both **2** and **3**. The luminescence lifetimes at room temperature of **2** and **3**, which are 800 and 1990 ns, respectively, are shorter than the lifetime of 6800 ns for **1**. The poor solubility of **2** and **3** limits the use of solvents with different dielectric constants which could be helpful in the assignment of the nature of the luminescent state at room temperature. A comparison of emission data in MeCN (dielectric constant = 36), methanol (dielectric constant = 33) and acetone (dielectric constant = 21) shows band maxima in the range 566–570 nm and does not provide any clear evidence of the effect of solvent polarity on the luminescent state energy levels.

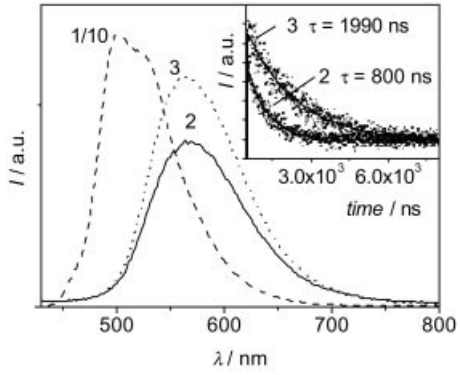

Figure 2. Corrected luminescence spectra (λ_{exc} = 379 nm) at 298 K of optically matched solutions in air-free MeCN of **1** (dashed), **2** (solid) and **3** (dotted). In the inset the luminescence decay in air-free MeCN for **2** and **3** is reported with the exponential fitting.

In contrast to room temperature data, the luminescence spectra at 77 K in glassy butyronitrile (BuCN) illustrated in Figure 3 display rather similar spectroscopic profiles for **1**, **2** and **3**. The luminescence lifetimes detected at 77 K in BuCN for **2** and **3** are 80 and 85 μs, respectively, as shown in the insets of Figure 3. These are longer than the lifetime of 39 μs for **1** under the same conditions. Luminescence data in aerated and air-free MeCN at 298 K and in BuCN at 77 K are collected in Table 2. The room temperature reaction rate constants with oxygen (O_2 solubility in air equilibrated MeCN is 1.9×10^{-3} M[18]) can be derived from the lifetime data shown in Table 2 and are 2.5×10^{8} $M^{-1}s^{-1}$, 4.2×10^{8} $M^{-1}s^{-1}$ and 6.4×10^{8} $M^{-1}s^{-1}$ for **1**, **2** and **3**, respectively, in agreement with previous reports.[19]

We noticed that complexes **2** and **3** exhibit spectroscopic features, both in the low-energy regions of the absorption spectra and in the luminescence spectra at room temperature, which suggest an electronic nature other than neat LC for the excited states involved in the concerned transitions. Thus, the absorption profile for these complexes, see Figure 1, is characterised by a broad, unstructured band extending beyond 400 nm with ε_{max} of the order of

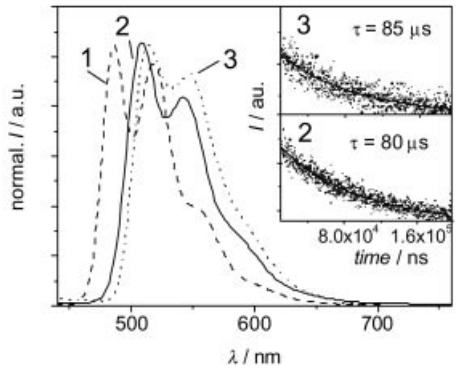

Figure 3. Normalised luminescence at 77 K in BuCN of **1** (dashed), **2** (solid) and **3** (dotted). In the inset the luminescence decay at 77 K in BuCN for **2** and **3** is reported with the exponential fitting.

Table 2. Luminescence data[a] for the complexes **1**, **2** and **3**.

	298 K					77 K			
	λ_{max} nm	Φ[b] $\times10^2$	τ[b] ns	Φ[c] $\times10^2$	τ[c] ns	λ_{max} nm	τ μs	E_0[d] eV	HS[e] cm^{-1}
1	506	9.3	6800	2.2	1600	486	39	2.55	810
2	570	0.55	800	0.21	490	510	80	2.43	2060
3	566	0.76	1990	0.27	580	514	85	2.41	1790

[a] Solvent is MeCN at room temperature, BuCN at 77 K; excitation performed at 379 and 373 nm for the luminescence spectra and lifetimes, respectively. [b] Air-free MeCN. [c] Air-equilibrated MeCN. [d] Estimated energy content of the emitting level from the energy of the emission maximum at 77 K. [e] Hypsochromic shift for the emission band maximum on going from 298 to 77 K.

10^4 $M^{-1}cm^{-1}$. These absorption features are consistent with a CT character for the implied electronic transitions. From the luminescence properties of the complexes at room temperature, further indications about the CT nature of the luminescent state can similarly be drawn, as discussed below.

The room temperature luminescence spectroscopic profiles of complexes **2** and **3** look fairly unstructured as opposed to that of complex **1**, Figure 2. For the latter complex, the extended conjugation at the phenyl-tpy ligand coupled with nuclear rearrangements at the torsional angle between the aromatic rings[20] is known to affect the spectroscopic profile.[10,11] For complexes **2** and **3**, therefore, it seems that further electronic effects must be taken into account. With regard to the low-temperature results, complex **1** on one hand and **2** and **3** on the other hand exhibit different behaviour in terms of the hypsochromic shift (HS) on going from fluid (298 K) to frozen (77 K) solvent, Table 2. Actually, HS amounts to 810 cm^{-1} for **1** but 2060 and 1790 cm^{-1} for **2** and **3**, respectively. The difference between the luminescence profiles of **1**, **2** and **3** recorded in frozen solvents appears less important (Figure 3) but some difference in peak positions and luminescence lifetimes still appears.

Inspection of Table 2 confirms that the luminescent behaviour of **1** at room temperature is different from that of **2** and **3**. Actually, the luminescence lifetimes at room temperature of **2** and **3**, which are 800 and 1990 ns, respectively, (O_2-free case) are well shorter than the lifetime of 6800 ns

 © 2005 Wiley-VCH Verlag GmbH & Co. KGaA, Weinheim

for **1** but still quite remarkable in comparison with other transition metal complexes widely used for light energy conversion, being of the same order of magnitude or greater than the prototype complex $[Ru(bpy)_3]^{2+}$.[21] The luminescence quantum yield, Φ (Table 2, room temperature, O_2-free) for **1** is one order of magnitude larger than for **2** and **3**. Furthermore, use of Φ and τ values from Table 2 yields radiative rate constants k_r of 1.4×10^4 s^{-1} for **1** (for $[Ir(tpy)_2]^{3+}$, k_r is 2.5×10^4)[10] and ca. 5×10^3 s^{-1} for **2** and **3**. This also points to a different nature for the emissive state at room temperature. Based on all these observations, we ascribe the luminescence of **2** and **3** to an excited state with CT character.

An assessment of the nature of the excited states responsible for the luminescence and the type of vibrations affecting their deactivation can further be obtained by studying the luminescence spectroscopic profiles in terms of Franck–Condon envelopes.[22–27] According to Equation (1a,b)[22–23] (see Experimental Section), vibronic analyses for complexes **1**, **2** and **3** reveal similarities and differences between them. Figure 4 provides a direct comparison of results obtained both at room temperature and at 77 K. Derived estimates for the indicated parameters are further listed in Table 3 (for **1**, at room temperature, no satisfactory analysis could be applied). The luminescence profiles at 77 K for **1**, **2** and **3** exhibit the same vibrational progression, with a frequency $\hbar\omega_v$ in the range 1200–1280 cm^{-1}, Table 3. The displacement parameter along this frequency, S, was found to be 0.90, 0.75 and 0.84 for **1**, **2** and **3**, respectively. The 0–0 energy of the luminescent level, E_0, is ≈ 2.8 eV for **1** and ≈ 2.7 eV for both **2** and **3**. This indicates that at 77 K, the luminescent state is deactivated via coupling with the same type of vibrational modes, which are likely to be C–N or C–C skeleton vibrations,[24–27] with a similar extent of electronic delocalisation for all three cases. According to previous assignments for the ^{3}LC emission for **1**,[1,10,11] this suggests that at 77 K the nature of the emitting state in **2** and **3** is likewise ^{3}LC.

With regards to the room temperature cases, analysis of the broad and unstructured luminescence shape for complexes **2** and **3** (Figure 4 and Table 3) yields a displacement parameter $S > 2$, supporting the view of a quite localised emitting level, with a coupled vibration $\hbar\omega_v \approx 600$–$700$ cm^{-1}. Because of their CT character, on passing from room temperature to the frozen solvent (77 K), these levels can be expected to be highly destabilised which explains why the luminescence of **2** and **3** in the glass has ^{3}LC origin, as for **1** (see Figure 4). This is supported by the large HS observed for **2** and **3** against a much smaller one for **1** on passing from room temperature to 77 K. We notice that the room temperature luminescence spectrum for **1** was not amenable to a profile analysis which might be explained by a *mixed* nature for the emission (presumably LC-CT) of this complex at this temperature.

Other interesting spectroscopic features which help to define useful spectroscopic differences among the investigated complexes are the excited state absorption spectra (ESA). Figure 5 shows the end of pulse spectra determined with

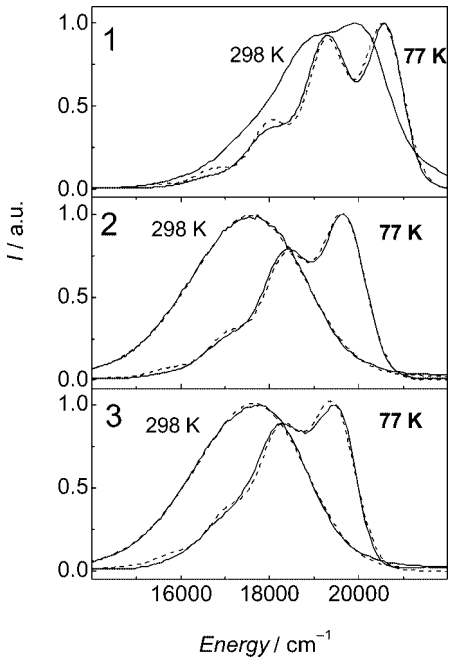

Figure 4. Vibronic analysis [dashed line, Equation (1a,b) of Experimental Section] of the corrected luminescence profiles (full line, an energy scale is employed) of complexes **1**, **2** and **3** as obtained in MeCN (room temperature) and BuCN (77 K); excitation was at 379 nm. For **1** at room temperature, the fit of the experimental profile was unsuccessful.

Table 3. Data from vibronic analyses of the luminescence spectra.[a]

	298 K		77 K		
	2	**3**	**1**	**2**	**3**
$\hbar\omega_v$ [cm^{-1}]	610	700	1270	1275	1190
λ_V [cm^{-1}]	1580	1450	1140	960	1000
λ_S [cm^{-1}]	1720	1430	1830	2270	2210
E_0 [eV]	2.57	2.52	2.78	2.72	2.69
S[b]	2.59	2.07	0.90	0.75	0.84

[a] According to Equation (1a,b) in the Experimental Section.[22,23] Solvent: MeCN at room temperature, BuCN at 77 K; excitation performed at 379 nm. The room temperature spectra of **1** could not be analysed. [b] Displacement parameter, $S = \lambda_V/\hbar\omega_v$, see text.

picosecond resolution upon excitation with a 355 nm laser pulse of the complexes in air-equilibrated MeCN. The ESA profiles are quite different. Complex **1** shows a peak at 670 nm whereas both **2** and **3** display more intense and broad bands peaking at 780 nm. This is indicative of the fact that excited states of a different nature are involved in the transitions of **1** on one hand and **2** and **3** on the other, i.e. a ^{3}LC state is involved in **1** and a ^{3}CT in is involved in both **2** and **3**. The time evolution of the transient absorption in aerated and air-free solutions, as determined by a nanosecond flash photolysis experiment for **2** and **3**, is reported in Figure 6. The decay has a lifetime of 440 ns in air-equilibrated and 740 ns in air-free solutions for **2** and 530 ns in air-equilibrated and 1.75 μs in air-free solutions for **3**. The good agreement[28] with the luminescence lifetimes indicates that the states responsible for the absorption are the same as those displaying luminescence. The molar

 © 2005 Wiley-VCH Verlag GmbH & Co. KGaA, Weinheim

absorption coefficient of the triplet state for **2** and **3** was determined against a benzophenone in benzene actinometer (see experimental section for details) and ε_{780nm} was of the order of 15 000 $M^{-1}cm^{-1}$. The characteristic and very strong ESA feature for **2** and **3**, in a spectroscopic region free from the absorbance of most D and A components, will prove very useful as a spectroscopic fingerprint during the study of the sequential events in the D-P-A arrays currently being designed.

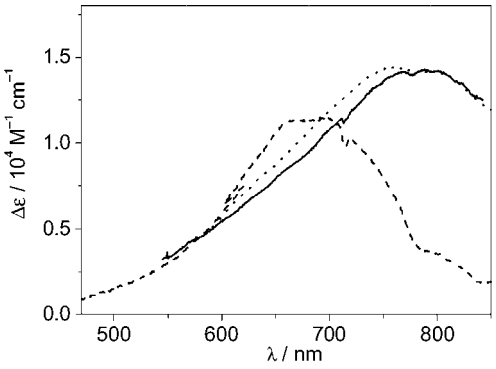

Figure 5. Excited state absorption spectra detected at the end of a laser pulse (35 ps, 355 nm, 3.5 mJ per pulse) in MeCN solutions. Symbols are: **1** (dashed), **2** (solid) and **3** (dotted).

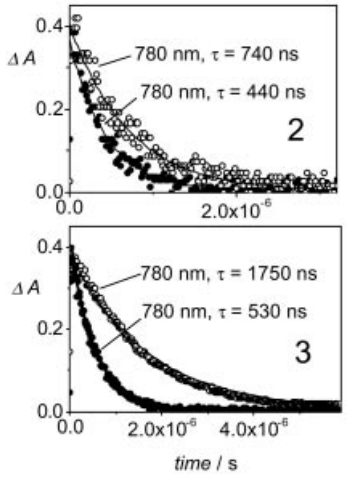

Figure 6. Time decay of excited state absorption spectra (full line results from exponential fit) detected at λ = 780 nm in air-free (o) and air-equilibrated (●) optically matched solutions of **2** (upper panel) and **3** (lower panel) in MeCN following nanosecond laser excitation (18 ns, 355 nm, 1.9 mJ per pulse)

All the above observations are consistent with a predominantly ^{3}LC-type emission for **1** whereas **2** and **3** qualify better at room temperature as ^{3}CT emitters. The differences between **1** on the one hand and **2** and **3** on the other tend to disappear at 77 K, indicating a common nature for the emitting states in frozen solutions. This can be easily understood if one keeps in mind that the rigid environment, which prevents molecular reorientation, effectively destabilises CT states whereas this effect is only minor for LC states. In fact, our results suggest that at 77 K the three complexes exhibit an LC emission. In this respect, the lower and lower energy of emission at 77 K upon passing from **1** to **2** and **3** could reflect a stabilisation induced by an increased delocalisation within the LC manifold.

While it is somewhat tempting to identify the CT state as a metal-to-ligand charge transfer, MLCT, in analogy to other photo- and electro-active transition metal complexes,[12] an ILCT state should in fact also be considered. An ILCT state with the appended benzamide group acting as a donor while the metal-bond terpyridyl unit functions as an acceptor, similar to that postulated by Williams et al. for a 4-aminobiphenyl-substituted $Ir(tpy)_2$ complex,[11] appears unlikely given the electrochemical inertness of the benzamide group which is rather difficult to oxidise.[29] Another possible source of an ILCT excited state could be connected with the intrinsic properties of the ligand, in particular of the benzamide unit. It is therefore useful to recall the spectroscopic properties of *N*-phenylbenzamide. The latter material has been investigated by Lewis at al. in aromatic solvents and at room temperature it displays dual fluorescence which can be assigned to an ^{1}n–π* transition (λ_{max} = 433 nm) and a twisted intramolecular charge transfer state, ^{1}TICT (λ_{max} = 510 nm), originating from a relaxed, higher energy ^{1}π–π* state.[30,31] The extended conjugation at the ligand, which occurs when benzamide units are appended to the tpy fragment coordinated to the metal centre, and the polar solvent could further stabilise the latter state so as to match the detected luminescent level in the present complexes. Accordingly, the low-lying CT transitions detected in the benzamide appended complexes **2** and **3** could be intra-ligand charge transfer in nature (^{3}ILCT) and localised on the *N*-phenyl benzamide fragment. This hypothesis, however, cannot explain the extremely large bathochromic shift, from 265 nm to ca. 400 nm, in the low energy absorption bands detected in these complexes with respect to *N*-phenylbenzamide.

So it seems that Ir^{III} to pab-tpy MLCT transitions could better explain the observed spectroscopic behaviour. However, we lack support from the electrochemistry for the occurrence of such CT transitions at low energy. As discussed above, with reference to the redox properties of $[Ir(tpy)_2]^{3+}$, estimated levels for an Ir^{III} →L CT emission could be too high in energy in comparison with experimental findings. Nonetheless, the estimated energy gap between ^{3}MLCT and luminescent levels is not exceedingly large and thermal redistribution might well mix some ^{3}MLCT character into the luminescent level at room temperature.

Conclusions

New Ir^{III}-bisterpyridine type complexes exhibiting a low-lying excited state with ^{3}CT nature at room temperature have been synthesized and spectroscopically characterised. The lifetimes of the excited states of these complexes are long, $\tau \approx$ 1–2 μs, given the CT nature of the excited species. In a rigid matrix at 77 K the emission, which is ^{3}LC in character, exhibits lifetimes $\tau \approx 10^2$ μs which is longer than recorded for other $[Ir(tpy)_2]^{3+}$ derivatives. In addition, with respect to previously investigated Ir^{III}-tpy type complexes,

 © 2005 Wiley-VCH Verlag GmbH & Co. KGaA, Weinheim

complex **2** and, even more, complex **3** feature an absorption spectrum the lowest-energy portion of which is shifted towards the visible region of the spectrum and is characterised by a high molar absorption coefficient. Because of their spectroscopic and photophysical properties, complexes **2** and **3** appear promising as photosensitisers and assembling units in D-P-A arrays designed for exploring photoinduced charge separation. In fact, they combine an advantageous geometry which allows the construction of linear and rigid arrays with the presence of a CT excited state (at room temperature) which, being characterised by a separation of charges with respect to an LC excited state, is much better suited to initiate a multistep electron transfer required to achieve charge separation over long distances.

Experimental Section

The syntheses and characterisations of **1** and **2** have been reported elsewhere.[8,10] Complex **3** was synthesized according to the following procedure: $IrCl_3$ and two equiv. of bap-tpy were heated at 196 °C in degassed ethylene glycol in the dark for 20 min. After precipitation with an aqueous solution of KPF_6, crude **3** was purified by column chromatography (silica, CH_3CN / water / saturated KNO_3 solution 100:10:1) to give **3** in 40% yield as a yellow solid. ^1H NMR (CD_3CN,300 MHz): δ = 9.17 (s, 2H, NH), 9.09 (s, 4H, $H_{3'5'}$), 8.73 (d, ^3J = 7.5 Hz, 4H, $H_{33''}$), 8.27 (d, ^3J = 8.9 Hz, 4H, H_{o1}), 8.25 (m, 4H, $H_{44''}$), 8.18 (d, ^3J = 8.9 Hz, 4H, H_{m2}), 8.04 (d, ^3J = 8.9 Hz, 4H, H_{o2}), 7.72 (d, ^3J = 8.8 Hz, 4H, $H_{66''}$), 7.66–7.57 (m, 6H, H_{m2}, H_{p2}), 7.51 (ddd, ^3J = 6.9 and ^4J = 1.2 Hz, 4H, $H_{55''}$) ppm. ES-MS, *m*/*z* (calcd.): 349.75 (349.76) $[M - 3PF_6]^{3+}$.

Spectrophotometric grade acetonitrile or butyronitrile solvents were used. Absorption and luminescence spectra were measured with a Perkin–Elmer Lambda 5 UV/Vis spectrophotometer and a Spex Fluorolog II spectrofluorimeter, respectively. Solutions were purged of air by bubbling with argon for 10 min. The samples were contained in home designed 10 mm fluorescence cells. Luminescence quantum yields (Φ) were evaluated, after correcting for the photomultiplier response, with reference to air-equilibrated $[Ir(ttpy)_2](PF_6)_3$ in aerated acetonitrile as a standard (Φ = 0.029).[10] Luminescence lifetimes (τ) were obtained with an IBH single photon counting instrument upon excitation at 373 nm from a pulsed diode source. Transient absorption spectra were determined by a pump-probe spectrograph with 30 ps resolution based on a Nd-YAG laser (355 nm, 10 Hz).[32] The lifetime of the absorbing excited state was determined by a laser flash photolysis system based on a Nd-YAG laser (355 nm, 18 ns pulse) previously described.[33] Molar absorption coefficients of the excited states were determined with the same nanosecond apparatus using the benzophenone in benzene actinometer (λ = 530 nm, ε = 7 220 M^{-1} cm^{-1}, Φ_T = 1).[34] The experimental uncertainty in the absorption and luminescence maxima is 2 nm. The uncertainties in the τ values and the Φ values are 10 and 20%, respectively.

The vibronic band profiles of the corrected luminescence spectra, $I(E)$, on an energy scale [E (cm^{-1})] were analysed according to Equations (1a) and (1b) which describe the relation between the Frank–Condon envelope, $FC(E)$, and some other pertinent parameters.[22–23]

$$I(E) = \cos t \times FC(E) \quad \text{(1a)}$$

$$FC(E) = \sum_{J=0}^{\infty} F_j (4\pi\lambda_s k_B T)^{-1/2} \exp\left(-\frac{(E - E_0 + j\hbar\omega_v + \lambda_s)^2}{4\lambda_s k_B T} \right) \quad \text{(1b)}$$

with $F_j = \exp(-S)\frac{S^j}{j!}$; and $S = \frac{\lambda_v}{\hbar\omega_v}$

In this equation, E_0 is the energy of the 0–0 transition (the energy gap between the 0–0 vibrational levels in the excited and ground states), j is a vibrational quantum number for high-frequency modes, $\hbar\omega_v$ (in practice an upper limit j = 5 is taken into account), λ_v and λ_s are internal and solvent reorganisation parameters, S is a displacement parameter and k_B is the Boltzmann constant. A nonlinear least-squares fit of Equation (1a,b)[35] to the experimental spectra provides estimates for E_0, λ_v, λ_s and the displacement parameter S along the $\hbar\omega_v$ vibrational mode (predominantly contributing to deactivation of the excited level). The magnitude of S (the electron-vibrational coupling constant or Huang–Rhys factor) is related to the relative intensities of the individual components in the vibrational progression. Analysis according to Equation (1a,b) allows, among other things, an assessment of the extent of delocalisation of the luminescent level which undergoes deactivation because of coupling with ground state $\hbar\omega_v$ vibrational modes. High values for S (typically in the range 0.7 to 1 and more)[27] indicate that the excited state is significantly distorted along the concerned vibrational mode because of electronic *localisation* effects. On the contrary, when the exited state undergoes extended electronic *delocalisation*, low S values are obtained (typically in the range 0.2 to 0.6)[24,36] indicating that the electronic curve for the excited level is not displaced much relative to that for the ground state.

Acknowledgments

We thank CNRS (France), CNR (Italy) and the Ministero dell'Istruzione, dell'Universita' e della Ricerca of Italy (FIRB, RBNE019H9K) for financial support. E. B. acknowledge support from the French Ministry of Education. We thank also Johnson Matthey Inc. for a loan of $IrCl_3$.

[1] I. M. Dixon, J. P. Collin, J.-P. Sauvage, L. Flamigni, S. Encinas, F. Barigelletti, *Chem. Soc. Rev.* **2000**, *29*, 385–391.
[2] X. Gong, J. C. Ostrowski, G. C. Bazan, D. Moses, A. J. Heeger, M. S. Liu, A. K. Y. Jen, *Adv. Mater.* **2003**, *15*, 45–49.
[3] K. K. W. Lo, C. K. Chung, T. K. M. Lee, L. H. Lui, K. H. K. Tsang, N. Y. Zhu, *Inorg. Chem.* **2003**, *42*, 6886–6897.
[4] V. I. Adamovich, S. R. Cordero, P. I. Djurovich, A. Tamayo, M. E. Thompson, B. W. D'Andrade, S. R. Forrest, *Organic Electronics* **2003**, *4*, 77–87.
[5] M. A. Baldo, S. Lamansky, P. E. Burrows, M. E. Thompson, S. R. Forrest, *Appl. Phys. Lett.* **1999**, *75*, 4–6.
[6] a) K. K. W. Lo, C. K. Chung, D. C. M. Ng, N. Y. Zhu, *New J. Chem.* **2002**, *26*, 81–88; b) K. K. W. Lo, C. K. Chung, N. Y. Zhu, *Chem. Eur. J.* **2003**, *9*, 475–483.
[7] E. Baranoff, J.-P. Collin, J.-P. Sauvage, L. Flamigni, *Chem. Soc. Rev.* **2004**, *33*, 147–155.
[8] a) I. M. Dixon, J.-P. Collin, J.-P. Sauvage, L. Flamigni, *Inorg. Chem.* **2001**, *40*, 5507–5517; b) E. Baranoff, I. M. Dixon, J.-P. Collin, J.-P. Sauvage, B. Ventura, L. Flamigni, *Inorg. Chem.* **2004**, *43*, 3057–3066.
[9] L. Flamigni, G. Marconi, I. M. Dixon, J.-P. Collin, J.-P. Sauvage, *J. Phys. Chem. B* **2002**, *106*, 6663–6671.

 © 2005 Wiley-VCH Verlag GmbH & Co. KGaA, Weinheim

[10] J.-P. Collin, I. M. Dixon, J.-P. Sauvage, J. A. G. Williams, F. Barigelletti, L. Flamigni, *J. Am. Chem. Soc.* **1999**, *121*, 5009–5016.
[11] W. Leslie, A. S. Batsanov, J. A. K. Howard, J. A. G. Williams, *Dalton Trans.* **2004**, 623–631.
[12] V. Balzani, A. Juris, M. Venturi, S. Campagna, S. Serroni, *Chem. Rev.* **1996**, *96*, 759–834.
[13] M. Licini, J. A. G. Williams, *Chem. Commun.* **1999**, 1943–1944.
[14] W. Goodall, J. A. G. Williams, *J. Chem. Soc., Dalton Trans.* **2000**, 2893–2895.
[15] A. A. Vlcek, E. S. Dodsworth, W. J. Pietro, A. B. P. Lever, *Inorg. Chem.* **1995**, *34*, 1906–1913.
[16] J.-P. Sauvage, J.-P. Collin, J. C. Chambron, S. Guillerez, C. Coudret, V. Balzani, F. Barigelletti, L. De Cola, L. Flamigni, *Chem. Rev.* **1994**, *94*, 993–1019.
[17] M. Polson, S. Fracasso, V. Bertolasi, M. Ravaglia, F. Scandola, *Inorg. Chem.* **2004**, *43*, 1950–1956.
[18] S. L. Murov, I. Carmichael, G. L. Hug, *Handbook of Photochemistry*, Marcel Dekker, New York, **1993**, p. 289, .
[19] N. P. Ayala, C. M. Flynn, Jr., L. A. Sacksteder, J. N. Demas, B. A. DeGraff, *J. Am. Chem. Soc.* **1990**, *112*, 3837–3844.
[20] Y. Kim, C. M. Lieber, *Inorg. Chem.* **1989**, *28*, 3990–3992.
[21] A. Juris, V. Balzani, F. Barigelletti, S. Campagna, P. Belser, A. von Zelewsky, *Coord. Chem. Rev.* **1988**, *84*, 85.
[22] I. R. Gould, S. Farid, *J. Photochem. Photobiol. A* **1992**, *65*, 133–147.
[23] I. R. Gould, R. H. Young, R. E. Moody, S. Farid, *J. Phys. Chem.* **1991**, *95*, 2068–2080.
[24] J. A. Treadway, G. F. Strouse, R. R. Ruminski, T. J. Meyer, *Inorg. Chem.* **2001**, *40*, 4508–4509.
[25] J. P. Claude, T. J. Meyer, *J. Phys. Chem.* **1995**, *99*, 51–54.
[26] Z. Murtaza, D. K. Graff, A. P. Zipp, L. A. Worl, W. E. Jones, W. D. Bates, T. J. Meyer, *J. Phys. Chem.* **1994**, *98*, 10504–10513.
[27] E. M. Kober, J. V. Caspar, R. S. Lumpkin, T. J. Meyer, *J. Phys. Chem.* **1986**, *90*, 3722–3734.
[28] It should be noticed that the absorbing species lifetimes detected by laser flash photolysis are, in general, shorter than those of the same luminescent species determined by single photon techniques. This is caused by the much higher photon flux which is used in laser flash photolysis experiments and this, increasing the concentration of excited states, introduces a second order component due to self annihilation in the decay which tends to shorten the lifetime compared with low intensity determinations.
[29] No oxidation of the benzamide fragment was observed in a scan of the complexes up to 1.6 V vs. SCE.
[30] D. D. Lewis, T. M. Long, *J. Phys. Chem. A* **1998**, *102*, 5327–5332.
[31] F. D. Lewis, W. Z. Liu, *J. Phys. Chem. A* **1999**, *103*, 9678–9686.
[32] L. Flamigni, N. Armaroli, F. Barigelletti, V. Balzani, J.-P. Collin, J.-O. Dalbavie, V. Heitz, J.-P. Sauvage, *J. Phys. Chem. B* **1997**, *101*, 5936–5943.
[33] L. Flamigni, *J. Phys. Chem.* **1992**, *96*, 3331–3337.
[34] S. L. Murov, I. Carmichael, G. L. Hug, *Handbook of Photochemistry*, Marcel Dekker, New York, **1993**, p. 107.
[35] P. R. Bevington, *Data Reduction and Error Analysis for the Physical Sciences*, chapter 11, McGraw-Hill, New York, **1969**.
[36] L. Hammarström, F. Barigelletti, L. Flamigni, M. T. Indelli, N. Armaroli, G. Calogero, M. Guardigli, A. Sour, J.-P. Collin, J.-P. Sauvage, *J. Phys. Chem. A* **1997**, *101*, 9061–9069.

Received: September 24, 2004

 © 2005 Wiley-VCH Verlag GmbH & Co. KGaA, Weinheim

Di- and Trivalent Lanthanide Complexes Stabilized by Sterically Demanding Aminopyridinato Ligands

Natalie M. Scott[a] and Rhett Kempe*[a,b]

Keywords: Aminopyridinato ligands / Lanthanides / Neodymium / N ligands / Olefin polymerization / Samarium / Ytterbium

Deprotonation of Ap*H {Ap*H = (2,6-diisopropylphenyl)-[6-(2,4,6-triisopropylphenyl)pyridin-2-yl]amine} and Ap′H {Ap′H = (2,6-diisopropylphenyl)-[6-(2,6-dimethylphenyl)pyridin-2-yl]amine} using KH leads to polymeric $[Ap^*K]_n$ and $[Ap'K]_n$ which undergo clean salt metathesis reactions with $NdCl_3$ in THF forming $[Nd(Ap^*)Cl_2(THF)_2]_2$ and $[Nd(Ap')_2Cl(THF)]$, respectively. Ethylene polymerization activities of the two chloro complexes (after activation with MAO) were studied. Derivatization of the chloro compounds proceeds without ate complex formation, for instance the reaction of $[Nd(Ap')_2Cl(THF)]$ with one equiv. of $[K\{N(SiMe_3)_2\}]$ leads to the "THF-free" silylamide $[Nd(Ap')_2\{N(SiMe_3)_2\}]$. Furthermore rare examples of heteroleptic amido-iodo complexes of selected divalent lanthanides can be stabilized by deprotonated Ap*H. Reaction of $[Ap^*K]_n$ with $[LnI_2(THF)_3]$ (Ln = Yb, Sm) in THF leads, after workup in hexane, to $[Yb(Ap^*)I(THF)_2]_2$ and $[Sm(Ap^*)I(THF)_2]_2$. All lanthanide complexes, four of them are paramagnetic, were characterized by X-ray crystal structure analysis. These compounds exhibit an excellent solubility in nonpolar solvents like hexane.
(© Wiley-VCH Verlag GmbH & Co. KGaA, 69451 Weinheim, Germany, 2005)

Introduction

During the renaissance[1] of amido[2] metal chemistry, aminopyridinato ligands (Ap)[3] have been used extensively to stabilize lanthanide (Ln) complexes. These compounds (Scheme 1) have been shown to exhibit unusual stoichiometric and catalytic reactivity.[4]

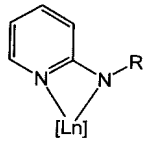

Scheme 1. An aminopyridinato ligand in its strained η^2 binding mode, typical for early transition metals and lanthanides ([Ln] = lanthanide moiety; R = aryl, silyl or alkyl substituent).

The size of the aminopyridinato ligands used thus far has been relatively small, resulting in a low steric demand of the metal, especially in the plane perpendicular to the pyridine moiety. This, in turn, gives rise to highly nitrogen-coordinated lanthanide complexes. Recently, we described the preparation of bulky aminopyridinato ligands by the introduction of 2,6-alkylphenyl substituents at the amido-N atom and also in the 6-position of the pyridine ring (Scheme 2).[5] Here, we report on synthesis, structure and reactivity of lanthanide complexes stabilized by deprotonated **1** and **2**.

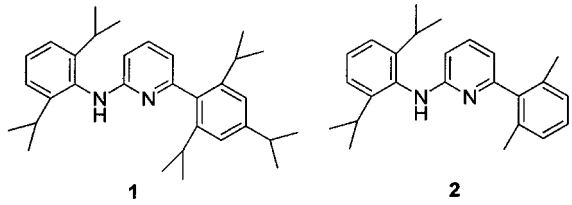

Scheme 2. Proligands Ap*H (**1**) and Ap′H (**2**).

The maximum atom-to-atom distance in deprotonated **1** (determined from its Li salt[5] is 15 Å (vector **a** in Scheme 3, top). Approximately perpendicular to it is vector ***b*** = 8 Å. Comparing these measurements with those of the bulky, η^5-coordinated Cp*-ligand[6] (Cp* = pentamethylcyclopentadienyl) (Scheme 3, bottom), which has a distance of **a** = ***b*** = 6.2 Å, indicates that deprotonated **1** would be effective for the protection of large metal ions such as lanthanides. Furthermore, the stabilization of mono-amide [mono-(aminopyridinato)] complexes, in which ligand redistribution is blocked, should become possible.

The size of deprotonated **2** is somewhat smaller than deprotonated **1** with ***a*** = 13 Å and ***b*** = 8 Å.

Results and Discussion

Synthesis and Structure of Neodymium Complexes

The reactions of the lithium salts of **1** or **2** (prepared by deprotonation in situ with BuLi) with $NdCl_3$ did not result

[a] Lehrstuhl für Anorganische Chemie II, Universität Bayreuth, 95440 Bayreuth, Germany
E-mail: kempe@uni-bayreuth.de
[b] Leibniz-Institut für Organische Katalyse, Buchbinderstrasse 5–6, 18055 Rostock, Germany

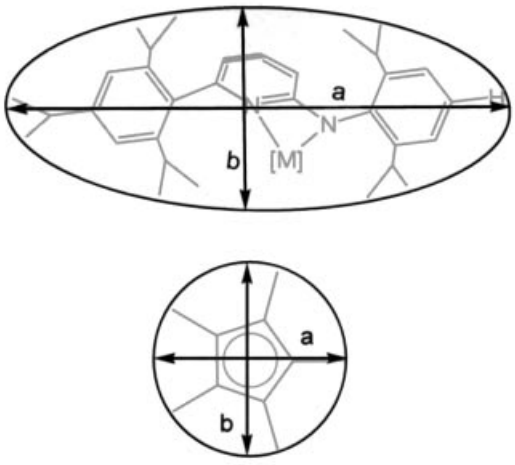

Scheme 3. Description of the steric demand of deprotonated **1** in comparison to Cp*.

in the isolation of a neodymium complex (only starting material was recovered). Deprotonation of **1** or **2** using KH gives rise to polymeric products **3** and **4**, as shown in Scheme 4.[5]

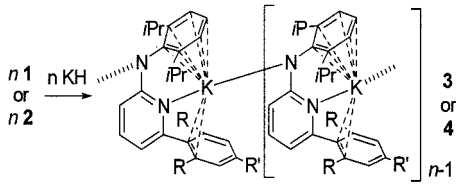

Scheme 4. Synthesis of **3** (R, R′, *i*Pr = isopropyl) and **4** (R = methyl, R′ = H).

Compounds **3** and **4** react with [$NdCl_3$] in a salt metathesis reaction affording **5** and **6**, see Scheme 5. No ate complex formation was observed. Compounds **5** and **6** were characterized by X-ray crystal structure analysis. Experimental details are summarized in Table 1. The molecular structure of **5** is shown in Figure 1.

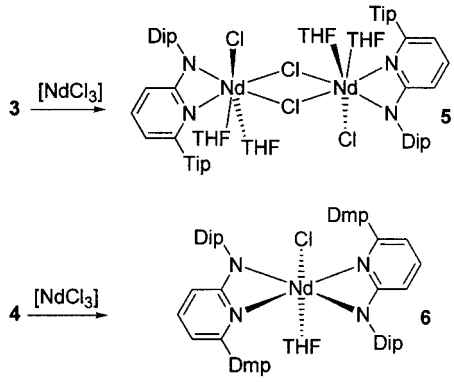

Scheme 5. Synthesis of **5** and **6** (Dip = 2,6-diisopropylphenyl, Tip = 2,4,6-triisopropylphenyl, Dmp = 2,6-dimethylphenyl).

These investigations revealed **5** to be a dinuclear mono(aminopyridinato) complex. Reacting K to Nd ratios of 1:1 or 2:1 gave rise to the same product. The steric bulk of deprotonated **1** seems to favor the formation of a one to one Ap to Ln ratio. The N–Nd–N angle (53°) underlines the strained nature of the aminopyridinato coordination and the different Nd–N distances indicate a localization of the anionic function of the ligand at the amido-N atom – a classic amido−metal bond and a standard pyridine–neodymium bond. The amido-*N*···neodymium distance (2.380 Å) is in accordance with the reported values from the literature (standard value 2.356 Å[7]), as is the pyridine-N···neodymium distance at 2.659 Å (standard value 2.670 Å[8]). This is in contrast to the coordination of silylaminopyridinato lanthanide complexes, where a delocalized binding mode, including equivalent metal···nitrogen distances, has been observered in all compounds described so far.[4] The molecular structure of **6** is shown in Figure 2.

Table 1. Details of the X-ray crystal structure analyses of **5**, **6**, **7**, **8**, and **9**.

Compound	**5**	**6**	**7**	**8**	**9**
Crystal system	triclinic	triclinic	monoclinic	triclinic	monoclinic
Space group	$P\bar{1}$	$P\bar{1}$	$P2_1/c$	$P\bar{1}$	$P2_1/c$
a [Å]	10.266(2)	12.985(3)	12.4893(4)	10.972(5)	12.059(5)
b [Å]	12.340(3)	14.336(3)	26.6564(7)	13.144(5)	17.584(5)
c [Å]	18.481(4)	14.377(3)	18.9051(6)	18.497(5)	19.978(5)
α [°]	84.31(3)	104.45(3)		84.183(5)	
β [°]	76.41(3)	91.17(3)	97.121(3)	78.661(5)	97.907(5)
γ [°]	71.98(3)	99.73(3)		82.795(5)	
V [Å^3]	2163	2549	6245	2587	4196
Z	1	2	4	1	2
Crystal size [mm^3]	0.36×0.31×0.15	0.21×0.18×0.16	0.29×0.22×0.20	0.45×0.31×0.28	0.11×0.06×0.05
$\rho_{calcd.}$ [g cm^{-3}]	1.251	1.260	1.176	1.340	1.389
μ [mm^{-1}]	1.355	1.110	0.909	2.443	2.167
T [K]	293	173	193	193	193
$\theta_{max.}$ [°]	26.06	25.99	26.05	25.95	26.34
No. of reflections unique	7737	9350	12305	10074	8264
No. of reflections obsd. [$I > 2\sigma(I)$]	6238	3982	8494	8504	2636
No. of parameters	426	562	631	455	195
wR_2 (all data)	0.142	0.127	0.073	0.131	0.366
R value [$I > 2\sigma(I)$]	0.057	0.056	0.030	0.042	0.131

 © 2005 Wiley-VCH Verlag GmbH & Co. KGaA, Weinheim

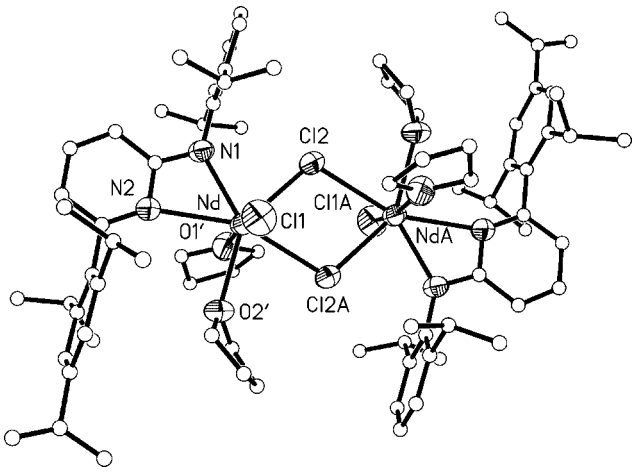

Figure 1. Molecular structure of **5** (ellipsoids correspond to the 50% probability level); selected bond lengths [Å] and angles [°]: Nd−N1 2.380(4), Nd−O2′ 2.510(4), Nd−O1′ 2.510(4), Nd−Cl1 2.6443(19), Nd−N2 2.659(4), Nd−Cl2 2.7919(17), Nd−Cl2A 2.8511(17); Nd−Cl2−NdA 108.37(5), Cl1−Nd−Cl2 99.81(6), N1−Nd−N2 53.25(14).

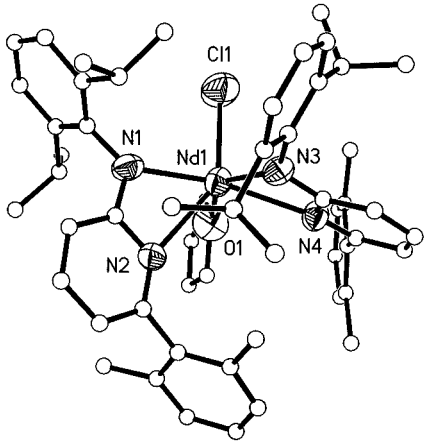

Figure 2. Molecular structure of **6** (ellipsoids correspond to the 50% probability level); selected bond lengths [Å] and angles [°]: Nd1−N1 2.361(6), Nd1−N3 2.386(7), Nd1−O1 2.442(7), Nd1−N4 2.569(6), Nd1−Cl1 2.599(3), Nd1−N2 2.622(6), Nd1−C1 2.936(8); N3−Nd1−N4 54.9(2), N1−Nd1−Cl1 90.50(17), N3−Nd1−Cl1 103.37(16), N4−Nd1−Cl1 107.91(15), N1−Nd1−N2 54.1(2), Cl1−Nd1−N2 142.91(14).

In contrast to **5** a bis(aminopyridinato) complex is formed which is monomeric in the solid state. Despite the fact that the differences of the steric bulk of deprotonated **1** and **2** are rather small in comparison to the size of the ligands, selective formation of mono- or bis(aminopyridinato) complexes are observed. The neodymium···N distances of **6** are indicative of a localization of the anionic function. This appears to be a general phenomenon and is illustrated by the 90° dihedral angle between the pyridine plane and arylamido plane. It is probable that the two alkyl substituents prevent an interaction between the two π-systems. In silylaminopyridinato lanthanide complexes the pyridine π-system may interact with the silicon atom to cause further delocalization. This delocalization may go some way to explain the parity of two N–Ln bonds in silylaminopyridinato ligands. Compound **5** and **6** are soluble in nonpolar solvents such as hexane and salt metathesis reactions proceed in this solvent without ate complex formation. The reaction of **6** with one equiv. of [K{N(SiMe$_3$)$_2$}] leads to the silylamide **7**, uncoordinated by THF (Scheme 6).

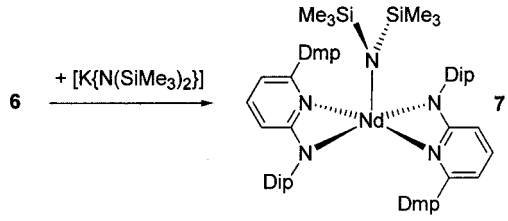

Scheme 6. Synthesis of **7**.

Compound **7** was characterized by X-ray crystal structure analysis. Experimental details are summarized in Table 1. The molecular structure of **7** is shown in Figure 3.

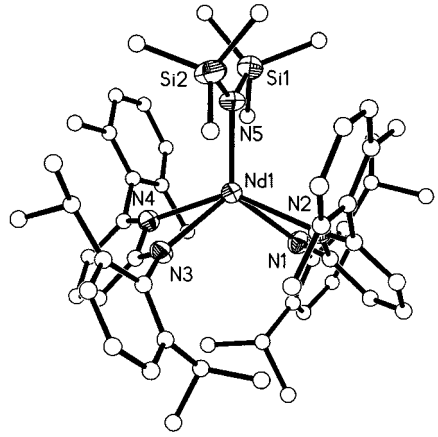

Figure 3. Molecular structure of **7** (ellipsoids correspond to the 50% probability level); selected bond lengths [Å] and angles [°]: Nd1−N5 2.280(2), Nd1−N3 2.407(2), Nd1−N1 2.414(2), Nd1−N2 2.544(2), Nd1−N4 2.552(2); N5−Nd1−N3 123.78(8), N5−Nd1−N1 125.18(8), N5−Nd1−N2 108.02(8), N1−Nd1−N2 54.56(7), N5−Nd1−N4 110.50(8), N3−Nd1−N4 54.57(7).

The coordination can be described as rectangular pyramidal with the four aminopyridinato-N atoms forming the rectangle. As far as we are aware the silylamido–Nd bond length represents the shortest observed so far and should indicate a highly Lewis-acidic metal center. Compounds **5** and **6** were tested as catalysts for ethylene polymerization after activation with MAO. The complexes were dissolved in toluene and treated with MAO (aluminium to catalyst ratio = 250:1). A 1-L laboratory autoclave was charged with the catalyst solution and an ethylene overpressure of 10 bar was applied at 60 °C for 30 minutes. Compounds **5** and **6** showed activities of 51.4 and 42.4 $kg_{polyethylene}\,mol_{cat}^{-1}\,h^{-1}\,bar^{-1}$, respectively. These moderate activities[9] indicate the potential of these compounds in olefin polymerization. Detailed studies of olefin insertion into neutral or cationic lanthanide complexes are underway.

 © 2005 Wiley-VCH Verlag GmbH & Co. KGaA, Weinheim

Synthesis and Structure of the Heteroleptic Ytterbium and Samarium Complexes

Pioneering work by Evans and coworkers[10,11] has shown that divalent lanthanide complexes exhibit a particularly rich reaction chemistry owing to the accessibility of different oxidation states;[12] for example, although $[Cp^*_2Sm]$ and $[Cp^*_2Sm(THF)_2]$ do not possess a metal–carbon bond they both show polymerization activity towards ethylene[13,14] The majority of this chemistry has been carried out utilizing homoleptic Cp* complexes. However, complexes incorporating a single Cp* ligand and a second anionic ligand (heteroleptic compounds), which may allow for further tuning of the reactivity, have received inadequate attention. This is partially due to the low stability of the mono-ligated starting materials. For example, the compounds $[(Cp^*)Sm(\mu\text{-}I)(THF)_2]_2$ [15] and $[(Me_3Si)_2NSm(\mu\text{-}I)(DME)(THF)]_2$ [16] (DME = dimethoxyethane) have been described and are reported to undergo facile ligand redistribution to give $[SmI_2(THF)_x]$ and $[SmL_2]$ [L = Cp*, $(Me_3Si)_2N$]. Divalent "heteroleptics" have been well documented in the case of donor-functionalized Cp-ligands but rarely described for alkoxy and amido ligands.[16,17] We expected deprotonated **1** to be an excellent candidate for the stabilization of such divalent complexes. The reaction of **3** with $[LnI_2(THF)_3]$ (Ln = Yb, Sm) in THF leads, after workup in hexane, to mono-iodido complexes, which prove to be binuclear in the solid state (Scheme 7). Experimental details of the X-ray crystal structure analyses are summarized in Table 1.

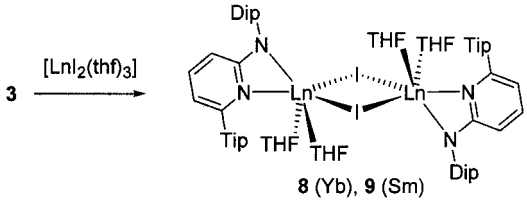

Scheme 7. Synthesis of **8** and **9**.

The molecular structures of **8** and **9** are shown in Figure 4 and Figure 5, respectively. The coordination of the two Yb centers of **8** is best described as octahedral with a dihedral angle of 95.1° between the Yb1–Yb1A–I1–I1A plane and the pyridine planes. Proton NMR spectra of **8** ([D_8]THF, [D_8]toluene) show a single signal set with well-resolved signals for the isopropyl groups in $C_6D_5CD_3$.

Since the paramagnetic nature of **9** prevents structural characterization by NMR spectroscopy, X-ray analysis was performed. Only very weak diffracting crystals of **9** could be obtained. However, the connectivity could be established. Owing to the low quality of structural data, a detailed discussion of bond length and angles is waived. The molecular structure of **9** is similar to that of **8** but the structures are not isomorphous.

Conclusions

Deprotonated **1** is an excellent ligand for the stabilization of mono(aminopyridinato) complexes of di- and trivalent lanthanides. The steric demands of this ligand result in a reduction of ligand redistribution during synthesis. Structurally, its lanthanide complexes can be compared to that of other bulky amide-containing compounds, such as troponiminate or amidate complexes but the chemistry should be somewhat different owing to higher ligand asymmetry. Surprisingly, deprotonated **2** gives selectively a bis(aminopyridinato) complex for neodymium, despite the relatively small difference in the structural size when compared with **1**. This study underlines the importance of fine-tuning, even surely in the "nano range".

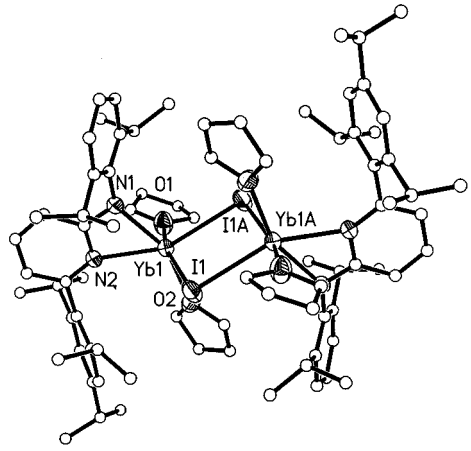

Figure 4. Molecular structure of **8** (ellipsoids correspond to the 50% probability level); selected bond lengths [Å] and angles [°]: Yb1−N1 2.423(4), Yb1−O2 2.432(4), Yb1−O1 2.445(4), Yb1−N2 2.508(4), Yb1−C1 2.922(5), Yb1−I1 3.1225(10), Yb1−I1 3.1241(8), I1−Yb1 3.1225(10); N1−Yb1−O2 156.82(14), N1−Yb1−O1 97.23(15), O2−Yb1−O1 81.22(15), N1−Yb1−N2 55.30(13), O2−Yb1−N2 101.54(13), O1−Yb1−N2 87.55(14), N1−Yb1−I1A 104.44(10), O2−Yb1−I1A 98.42(10), O1−Yb1−I1A 83.99(11), N2−Yb1−I1A 156.84(9), N1−Yb1−I1 97.46(10), O2−Yb1−I1 87.29(10), O1−Yb1−I1 164.43(10), N2−Yb1−I1 105.12(9), C1−Yb1−I1 102.77(9), I1−Yb1−I1A 87.36(3).

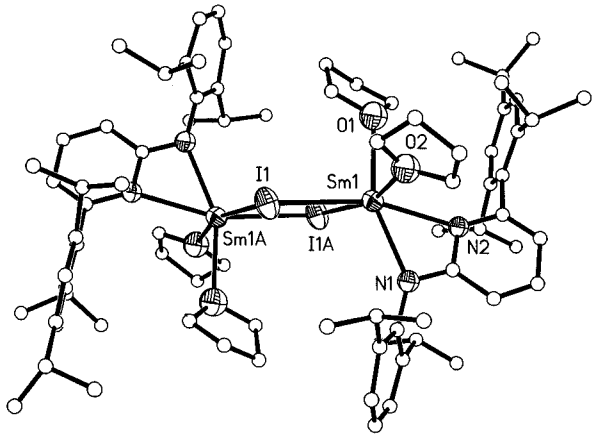

Figure 5. Molecular structure of **9** (ellipsoids correspond to the 50% probability level).

 © 2005 Wiley-VCH Verlag GmbH & Co. KGaA, Weinheim

Experimental Section

General Procedures: All reactions and manipulations with air-sensitive compounds were performed under dry argon, using standard Schlenk and drybox techniques. Solvents were distilled from sodium benzophenone ketyl. Deuterated solvents were obtained from Cambridge Isotope Laboratories and were degassed, dried (CaH_2) and distilled prior to use. NMR spectra were obtained using either a Bruker ARX 250, Bruker DRX 500, Varian Unity Inova 400 or 300 spectrometer. Chemical shifts are reported in ppm relative to the deuterated solvent. Elemental analyses were carried out with an Elementar Vario EL III. **1**, **2**, **3**, and **4**[5] as well as [$LnI_2(THF)_3$] (Ln = Yb, Sm)[18] were synthesized following literature procedures. Other starting materials were purchased from commercial suppliers. X-ray crystal structure analyses were performed with a STOE-IPDS I or II equipped with an Oxford Cryostream low-temperature unit. Structure solution and refinement was accomplished using SIR97,[19] SHELXL97,[20] and WinGX.[21] CCDC-251807 (for **5**), -251808 (for **6**), -251809 (for **7**), -251810 (for **8**), and CCDC-251811 (for **9**) contain the supplementary crystallographic data for this paper. These data can be obtained free of charge from The Cambridge Crystallographic Data Centre via www.ccdc.cam.ac.uk/data_request/cif.

Preparation of the Lanthanide Complexes

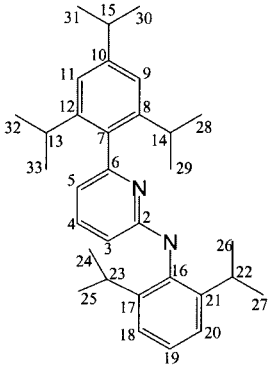

[Nd(Ap*)Cl_2(THF)$_2$]$_2$ (5): [$NdCl_3$] (0.38 g, 1.50 mmol), **3** (0.75 g, 1.50 mmol) and THF (40 cm^3) were added to a flask, and the mixture was stirred for 15 h. The solvent was removed under vacuum and hexane was added (30 cm^3). The light blue reaction mixture was filtered and on standing at room temperature for 2 h pale blue crystals of the title complex formed (0.80 g, 48%). $C_{80}H_{118}Cl_4N_4Nd_2O_4$ (1630): calcd. C 58.94, H 7.30, N 3.44; found C 58.95, H 7.14, N 3.05. Highly resolved NMR spectroscopic data could not be obtained. (2:1 Ligand/Nd reaction resulted in the formation of **5**.)

[Nd(Ap′)$_2$Cl(THF)] (6): [$NdCl_3$] (0.34 g, 0.93 mmol), **4** (0.74 g, 1.87 mmol) and THF (40 cm^3) were added to a flask, and the mixture was stirred for 24 h. The solvent was removed under vacuum and hexane was added (30 cm^3). The light blue reaction mixture was filtered and the filtrate allowed to stand at room temperature for 2 h whereupon small green-blue crystals of the title complex formed (0.37 g, 64%). $C_{54}H_{66}ClN_4NdO$ (967): calcd. C 67.08, H 6.88, N 5.79; found C 66.85 H 7.17, N 5.61. Highly resolved NMR spectroscopic data could not be obtained.

[Nd(Ap′)$_2${N(SiMe$_3$)$_2$}]•(hexane) (7): Hexane (30 cm^3) was added to **6** (0.11 g, 0.11 mmol) and [K{N(SiMe$_3$)$_2$}] (0.02 g, 0.11 mmol) and the mixture was stirred for 15 h. The reaction mixture was filtered and the filtrate concentrated to ca. 15 cm^3. The reaction mixture was cooled to –20 °C and on standing for 12 h pale blue crystals of the title complex were afforded (0.06 g, 42%). $C_{68}H_{104}N_5NdSi_2$ (1192): calcd. C 68.52, H 8.79, N 5.88; found C 68.85, H 7.98, N 6.31. Highly resolved NMR spectroscopic data could not be obtained.

[Yb(Ap*)I(THF)$_2$]$_2$ (8): [$YbI_2(THF)_3$] (0.70 g, 1.09 mmol), **3** (0.54 g, 1.09 mmol) and THF (40 cm^3) were added to a flask, and the mixture was stirred for 15 h. The solvent was removed under vacuum and a mixture of toluene (20 cm^3)/hexane (10 cm^3) was added. The red suspension was filtered and upon standing at –20 °C for 48 h, dark red crystals (suitable for X-ray analysis) of the title complex formed (0.80 g, 82%). $C_{80}H_{118}I_2N_4O_4Yb_2$ (1798): calcd. C 53.39, H 6.61, N, 3.11; found C 52.85, H 6.38, N 2.96. ^{1}H NMR (400 MHz, C_7D_8, 298 K): δ = 1.22 (d, ^3J = 7.0 Hz, 12 H, $H^{28,29,32,33}$), 1.27 (d, ^3J = 7.0 Hz, 6 H, $H^{24,25,26,27}$), 1.34 (d, ^3J = 7.0 Hz, 6 H, $H^{30,31}$), 1.35 (br, 8 H, β-CH_2, THF), 1.48 (d, ^3J = 7.0 Hz, 6 H, $H^{24,25,26,27}$), 2.78 (sept, ^3J = 7.0 Hz, 1 H, H^{15}), 3.28 (sept, ^3J = 7.0 Hz, 2 H, $H^{13,14}$), 3.41 (br, 8 H, α-CH_2, THF), 3.85 (sept, ^3J = 7.0 Hz, 2 H, $H^{22,23}$), 5.65 (d, ^3J = 8.4 Hz, 1 H, H^3), 5.85 (d, ^3J = 6.8 Hz, 1 H, H^5), 6.76 (dd, ^3J = 8.4 Hz, ^3J = 6.8 Hz, 1 H, H^4), 7.04 (s, 2 H, $H^{9,11}$), 7.11 (vt, ^3J = 8.0 Hz, 1 H, H^{19}), 7.23 (d, ^3J = 8.0 Hz, 2 H, $H^{18,20}$) ppm. ^{13}C NMR (100.5 MHz, C_7D_8, 298 K): δ = 25.3 (s, $C^{30,31}$), 25.7 (s, $C^{24,25,26,27}$), 26.3 (s, β-CH_2, THF), 26.5 (s, $C^{28,29,32,33}$), 26.6 (s, $C^{24,25,26,27}$), 26.7 (s, $C^{28,29,32,33}$), 28.9 (s, $C^{22,23}$), 31.3 (s, $C^{13,14}$), 35.7 (s, C^{15}), 70.1 (s, α-CH_2, THF), 108.5 (s, C^3), 109.0 (s, C^5), 121.7 (s, $C^{9,11}$), 123.5 (s, C^{19}), 124.7 (s, $C^{18,20}$), 138.3 (s, C^4), 139.3 (s, C^7), 144.8 (s, $C^{17,21}$), 147.9 (s, C^{10}), 149.26 (s, $C^{8,12}$), 149.32 (s, C^{16}), 156.9 (s, C^6), 171.0 (s, C^2) ppm.

[Sm(Ap*)I(THF)$_2$]$_2$ (9): THF (40 cm^3) was added to the solids [$SmI_2(THF)_3$] (0.62 g, 1.00 mmol) and **3** (0.99 g, 1.00 mmol) and the mixture was stirred for 15 h. The solvent was removed in vacuo and hexane (10 cm^3) was added. The dark blue suspension was filtered and on standing at –20 °C for 72 h small dark blue crystals (suitable for X-ray analysis) of the title complex formed (0.23 g, 26%). $C_{80}H_{118}I_2N_4O_4Sm_2$ (1754): calcd. C 54.77, H 6.78, N 3.19; found C 53.72, H 6.67, N 3.30. Highly resolved NMR spectroscopic data could not be obtained.

Polymerization of Ethylene: The complex (≈ 20 mg) was dissolved in 15 cm^3 of toluene and treated with MAO solution (30% in toluene; aluminium to catalyst ratio = 250:1). The catalyst mixture was transferred to a larger flask and *n*-pentane (250 cm^3) was added. A BÜCHI laboratory autoclave (1 L) was charged with the catalyst solution and an ethylene overpressure of 10 bar was applied at 60 °C for 30 minutes. The reaction was stopped by relieving the pressure in the reactor. The polymers were washed with hydrochloric acid and acetone and then air-dried.

Acknowledgments

We thank Wolfgang Milius for his support in the X-ray lab and Christine Denner for her help during the polymerization studies. Financial support from the Alexander von Humboldt Stiftung (N. M. S.), the Deutsche Forschungsgemeinschaft (Schwerpunktprogramm 1166 "Lanthanoidspezifische Funktionalitäten in Molekül und Material") and the Fonds der Chemischen Industrie is gratefully acknowledged.

[1] R. Kempe, *Angew. Chem.* **2000**, *112*, 478–504; *Angew. Chem. Int. Ed.* **2000**, *39*, 468–493.
[2] M. F. Lappert, P. P. Power, A. R. Sanger, R. C. Srivastava, *Metal and Metalloid Amides*, Ellis Norwood Ltd., Chichester, **1980**.

 © 2005 Wiley-VCH Verlag GmbH & Co. KGaA, Weinheim

[3] For a microreview on aminopyridinato ligands please see: R. Kempe, *Eur. J. Inorg. Chem.* **2003**, 791–803.
[4] For a review summarising lanthanide chemistry please see: R. Kempe, H. Noss, T. Irrgang, *J. Organomet. Chem.* **2002**, 647, 12–20.
[5] N. M. Scott, T. Schareina, O. Tok, R. Kempe, *Eur. J. Inorg. Chem.* **2004**, 3297–3304.
[6] R. Beckhaus, J. Oster, R. Kempe, A. Spannenberg, *Angew. Chem.* **1996**, *108*, 1636–1638; *Angew. Chem. Int. Ed. Engl.* **1996**, *35*, 1565–1567.
[7] Evaluation of all Nd−silylamido bond lengths stored in the Cambridge Crystallographic Data Base (November **2003**); number: 21, mean: 2.356, max.: 2.406, min.: 2.323.
[8] Evaluation of all Nd−pyridine (non-connected) bond lengths stored in the Cambridge Crystallographic Data Base (November **2003**); number: 10, mean: 2.670, max.: 2.741, min.: 2.555.
[9] G. J. P. Britovsek, V. C. Gibson, D. F. Wass, *Angew. Chem.* **1999**, *111*, 448–468; *Angew. Chem. Int. Ed.* **1999**, *38*, 428–447.
[10] W. J. Evans, *Polyhedron* **1987**, *6*, 803–835.
[11] W. J. Evans, *Coord. Chem. Rev.* **2000**, *206*, 263–283.
[12] L. R. Morss, *Chem. Rev.* **1976**, *76*, 827–841.
[13] W. J. Evans, T. A. Ulibarri, J. W. Ziller, *J. Am. Chem. Soc.* **1990**, *112*, 2314–2324.
[14] W. J. Evans, D. M. DeCoster, J. Greaves, *Macromolecules* **1995**, *28*, 7929–7936.
[15] W. J. Evans, J. W. Grate, H. W. Choi, I. Bloom, W. E. Hunter, J. L. Atwood, *J. Am. Chem. Soc.* **1985**, *107*, 941–946.
[16] W. J. Evans, D. K. Drummond, H. M. Zhang, J. L. Atwood, *Inorg. Chem.* **1988**, *27*, 575–579.
[17] a) L. Hasinoff, J. Takats, X. W. Zhang, A. H. Bond, R. D. Rogers, *J. Am. Chem. Soc.* **1994**, *116*, 8833–8834; b) G. H. Maunder, A. Sella, D. A. Tocher, A. Derek, *J. Chem. Soc., Chem. Comm.* **1994**, *23*, 2689–2690; c) G. R. Giesbrecht, C. Chunming, A. Shafir, J. A. R. Schmidt, J. Arnold, *Organometallics* **2002**, *21*, 3841–3844; d) E. A. Fedorova, N. V. Glushkova, M. N. Bochkarev, H. Schumann, H. Hemling, *Izv. Akad. Nauk, SSSR Ser. Khim. (Russ) (Russ. Chem. Bull.)* **1996**, *8*, 2101–2104; e) I. L. Fedushkin, S. Dechert, H. Schumann, *Organometallics* **2000**, *19*, 4066–4076;; f) D. J. Duncalf, P. B. Hitchcock, G. A. Lawless, *Chem. Commun.* **1996**, *2*, 269–271; g) A. A. Trifonov, E. N. Kirillov, S. Dechert, H. Schumann, M. N. Bochkarev, *Eur. J. Inorg. Chem.* **2001**, *12*, 3055–3058.
[18] F. T. Edelmann, *Lanthanoids and Actinides*, in: *Synthetic Methods of Organometallic and Inorganic Chemistry (Hermann/Brauer)* (Ed.: W. A. Hermann), Thieme Medical Publishers, New York, **1997**, *6*, pp. 40.
[19] A. Altomare, M. C. Burla, M. Camalli, G. L. Cascarano, C. Giacovazzo, A. Guagliardi, A. G. G. Moliterni, G. Polidori, R. Spagna, *J. Appl. Crystallogr.* **1999** *32*, 115–119.
[20] *SHELX97* Programs for Crystal Structure Analysis (Release 97–2). G. M. Sheldrick, Institut für Anorganische Chemie der Universität, Tammannstrasse 4, 3400 Göttingen, Germany, **1998**.
[21] L. J. Farrugia, *J. Appl. Crystallogr.* **1999**, *32*, 837–838.
Received: October 01, 2004

 © 2005 Wiley-VCH Verlag GmbH & Co. KGaA, Weinheim

Heteroditopic Imino N-Heterocyclic Carbenes and Their Sulfur, Selenium, and Tungsten Tetracarbonyl Derivatives

Georg Steiner,[a] Holger Kopacka,[a] Karl-Hans Ongania,[b] Klaus Wurst,[a] Peter Preishuber-Pflügl,[c] and Benno Bildstein*[a]

Keywords: Carbene ligands / N ligands / Selenium / Sulfur / Tungsten

New heterditopic imino N-heterocyclic carbenes for use as chelating ligands in homogeneous catalysis are the focus of this contribution. The synthesis of the corresponding imidazolium precursors is accomplished in three steps by alkylation of imidazole with ketoalkyl bromides, imination of the carbonyl functionality with anilines, either by conventional methods or by an aluminum-assisted condensation, and methylation using highly electrophilic methyl triflate. Deprotonation of the imidazolium triflates with potassium hydride gives a different outcome depending on the substitution pattern of the iminomethyl moiety: iminomethyl N-heterocyclic carbenes containing a methylene group between the imino moiety and the N-heterocycle are unstable because of tautomerization to the corresponding methylene-deprotonated ylides. In contrast, iminoisopropyl N-heterocyclic carbenes, where the acidic site of the methylene group is blocked by two methyl groups, are stable in solution, as proven by ^{1}H and ^{13}C NMR spectroscopy. First derivatives of these new [N,C]-ligands include their sulfur and selenium oxidation products (iminoisopropylimidazolin-2-thione and -selenone, respectively) as well as a tungsten tetracarbonyl complex with a six-membered [N,C] chelating moiety. All new products were fully characterized by multinuclear NMR (^{1}H, ^{13}C, ^{77}Se, ^{183}W) and IR spectroscopy, mass spectrometry, as well as by X-ray single crystal structures.

(© Wiley-VCH Verlag GmbH & Co. KGaA, 69451 Weinheim, Germany, 2005)

Introduction

The chemistry of N-heterocyclic carbenes (NHCs) and their metal complexes[1] is of great current interest for applications in homogeneous catalysis. The advantages of NHCs as steering ligands of catalytically active transition metal complexes arise from their synthetic, thermodynamic, and technical features. Synthetically, NHC ligands may be designed and more or less easily synthesized in great structural variety, including multidentate and chiral representatives. Thermodynamically, the metal–carbon bond of NHC complexes is stronger than the metal–phosphorus bond of phosphane complexes, which suggests that replacement of phosphanes by NHC ligands will lead to catalysts with improved stability and performance. Technically, NHC complexes are often quite stable towards oxygen and thereby allow catalytic reactions under noninert conditions without catalyst degradation. Up to now, successful applications of NHC catalysts include carbon-carbon cross-coupling reactions, olefin metathesis,[2] hydrosilylation, and CO/ethylene copolymerization.[1] In contrast, the use of NHC-derived catalysts for olefin homopolymerizations[3] have met with rather limited success so far. Established ligand lead structures in late transition metal olefin polymerization catalysis[4] include, inter alia, 1,2-diimines containing bulky peripheral imine donors (type **A**, Scheme 1). We therefore set out to explore new ligand architectures that combine the steric bulk of appropriately substituted imine donors with an electronically favorable NHC moiety.

In earlier work we showed that NHCs with a directly N-bonded imine group of type **B** (Scheme 1) are unstable because of a [1,2] rearrangement of the imidoyl moiety.[5] To avoid this difficulty, we reasoned that an electronically decoupled imine group with a spacer should be compatible with an NHC carbon. Note that type **B** ligands should form five-membered [N,C]-metal chelate rings, whereas type **C** ligands will form six-membered [N,C]-metal chelates due to the C_1 spacer unit. In this contribution we show that such [N,C] ligands are indeed accessible provided that the methylene hydrogens of the C_1 spacer are blocked by two additional methyl groups (type **D**), and we report on their group 6 metal carbonyl complexes and on their thio and seleno derivatives. In a comparable approach, Tilset and coworkers[6] as well as Coleman and coworkers[7] have recently published similar chemistry of type **C** ligands focusing on their monodentate silver and their labile κ^1/κ^2 palladium complexes.

[a] Institute of General, Inorganic and Theoretical Chemistry, University of Innsbruck,
Innrain 52a, 6020 Innsbruck, Austria
E-mail: benno.bildstein@uibk.ac.at
[b] Institute of Organic Chemistry, University of Innsbruck,
Innrain 52a, 6020 Innsbruck, Austria
[c] BASF Aktiengesellschaft,
67056 Ludwigshafen, Germany

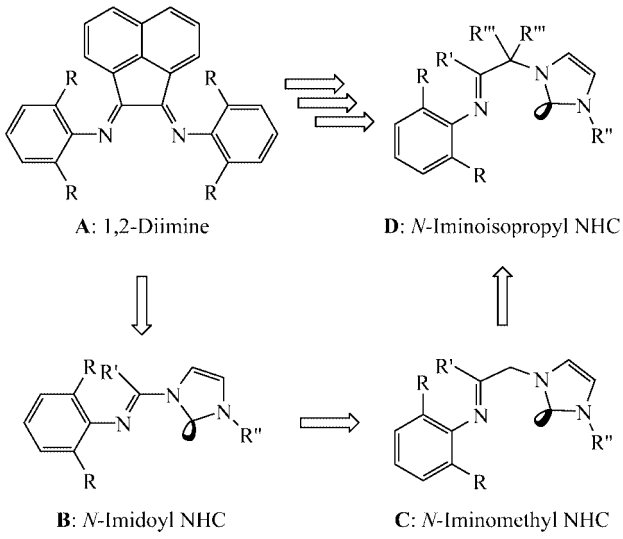

Scheme 1. Design concept for novel [N,C]-ligands.

Results and Discussion

N-Iminomethyl N-Heterocyclic Carbenes

In general, NHC ligands are generated most easily from their corresponding azolium salts (e.g. imidazolium salts) by deprotonation with suitable strong bases.[1] To get access to imino NHCs of type **C** (Scheme 1), the corresponding iminomethylimidazolium progenitors are therefore obvious synthetic targets. Such compounds may be obtained in a straightforward manner, as outlined in Scheme 2. First, a simple alkylation of imidazole with α-bromoacetophenone (**1**) afforded benzoylmethylimidazole **2** in a reasonable yield of 48%; for simplicity, one additional equivalent of imidazole was used as the base to bind the hydrogen bromide formed during the reaction. Secondly, conventional condensation of the carbonyl moiety of **2** with 2,6-diisopropylaniline with azeotropic removal of water gave iminomethylimidazole **3** as a yellow, air-stable oil. Finally, alkylation by the strongly electrophilic methyl trifluoromethanesulfonate afforded air-sensitive imidazolium triflate **4** in 29% overall yield starting from imidazole. Pertinent key NMR spectroscopic data of **4** include characteristic low-field signals for the imidazolium C(2)-bonded hydrogen [$\delta(^1H)$ = 9.17 ppm] as well as for the imine carbon [$\delta(^{13}C)$ = 161.2 ppm], observation of an imidazolium methyl group [$\delta(^1H)$ = 3.94 ppm, $\delta(^{13}C)$ = 35.8 ppm] and of an acceptor-substituted imidazolium methylene group [$\delta(^1H)$ = 5.85 ppm, $\delta(^{13}C)$ = 64.9 ppm], and detection of diastereotopic methyl groups of the isopropyl substituents [$\delta(^1H)$ = 0.83 and 0.91 ppm, $\delta(^{13}C)$ = 21.7 and 23.5 ppm] due to hindered rotation of the bulky 2,6-diisopropylphenyl substituent.

With the NHC precursor iminomethylimidazolium triflate **4** in hand, we anticipated that formation of the corresponding iminomethyl NHC would be easy to accomplish.

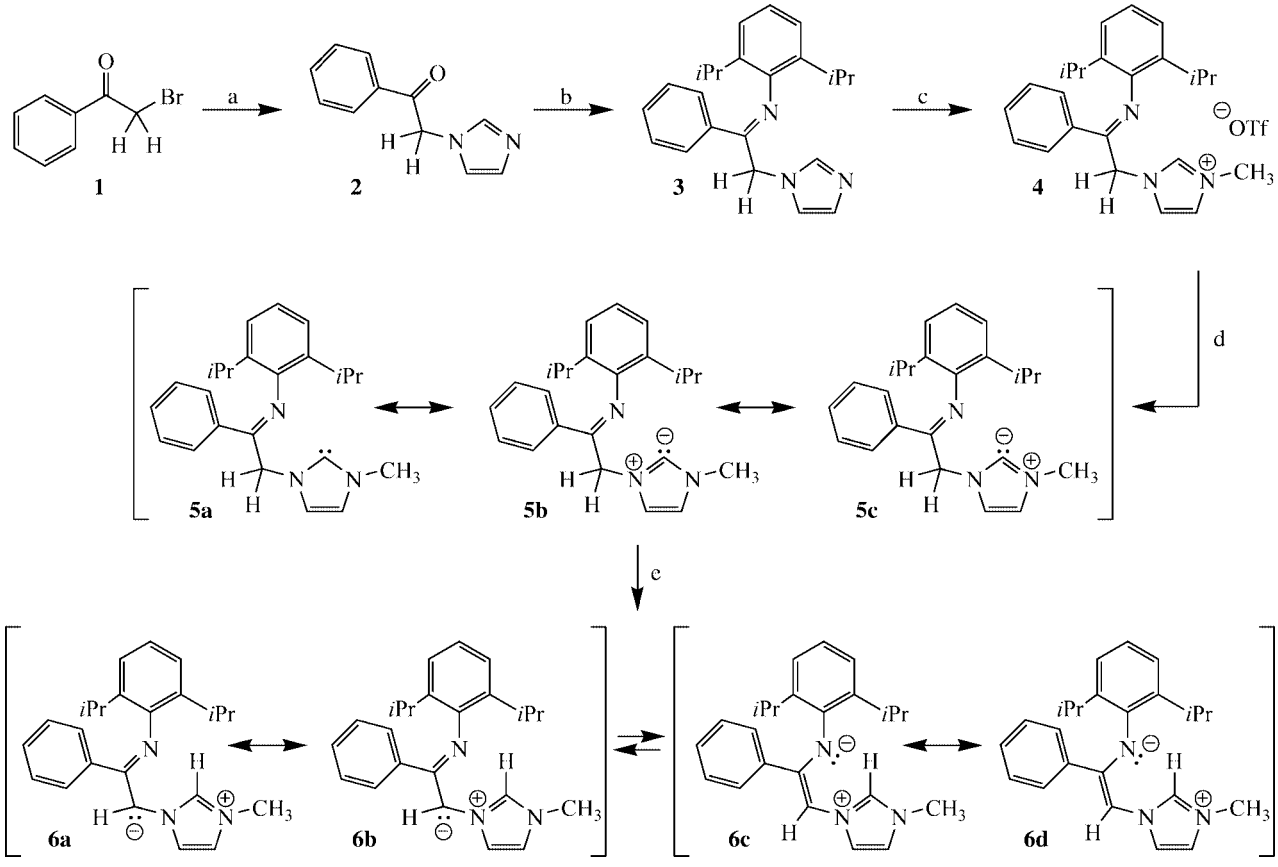

Scheme 2. Synthetic route to *N*-iminomethyl NHC ligands. Conditions: (a) imidazole; (b) 2,6-diisopropylaniline, H^+, reflux; (c) methyl triflate; (d) potassium hydride; (e) tautomerization.

 © 2005 Wiley-VCH Verlag GmbH & Co. KGaA, Weinheim

However, this is not the case. Upon reaction of **4** with one equivalent of potassium hydride as proton-abstracting reagent dihydrogen evolution was observed, as expected, and a dark red solution was obtained, presumably containing NHCs **5a**–**c**. Hydrolysis of this solution followed by TLC analysis showed that only the starting material **4** was present, indicating that deprotonation must have occurred without any decomposition, in contrast to earlier work[6] where intractable reaction mixtures were obtained on attempted deprotonation of iminomethylimidazolium salts. Closer inspection of the reactivity of this red solution indicated that no NHC was present, but instead its formal tautomer **6a**,**b** and/or its ylidic enamine **6c**,**d** must have been formed by deprotonation of the methylene group instead of the imidazolium C(2)-hydrogen. The intense red color of this new ylide is obviously due to the spread of charge over six unsaturated atoms, as indicated by formulas **6a**–**d**. In retrospect, this undesired deprotonation at the "wrong" site is not too surprising because similar behavior has been reported for some other imidazolium salts containing acidic methylene groups.[6–8] Based on these results we conclude that the free iminomethyl NHCs **5a**–**c** are unstable or rearrange to their tautomers. However, we note that such carbene ligands have been successfully incorporated into some silver and palladium complexes[6–8] using in situ deprotonation/complexation procedures which avoid the free carbenes as intermediates.

N-Iminoisopropyl N-Heterocyclic Carbenes

The problems associated with the acidic methylene hydrogens in NHCs of type **C** (Scheme 1) may be overcome by the use of appropriate protecting groups. As the most simple and sterically not too demanding groups we chose two methyl groups for this purpose, selecting NHCs of type **D** as our synthetic targets (Scheme 3). First, imidazole was alkylated with 2-bromo-2-methylpropiophenone (**7**) under reflux for three days in ethanolic solution to affording benzoylisopropylimidazole (**8**) in 61% yield. The longer reaction period and the increased temperature compared to the preparation of **2** reflect the steric shielding imposed by the two additional methyl groups. Besides the spectroscopic data, which are in line with expectations, the identity of **8** was further corroborated by a single crystal structure analysis (Table 2, Figure 1). In the second step, condensation of the carbonyl moiety of **8** with anilines was necessary to introduce the imine functionality. Attempts to perform this conversion under common condensation conditions (proton-catalyzed azeotropic removal of water) failed completely, but applying an aluminum-assisted protocol that was developed by us earlier for difficult substrates[9] worked nicely also in this case, affording iminoisopropylimidazoles **9a** and **9b** in over 75% yield. In the third step, imidazoles **9a** and **9b** were alkylated with methyl triflate to give the

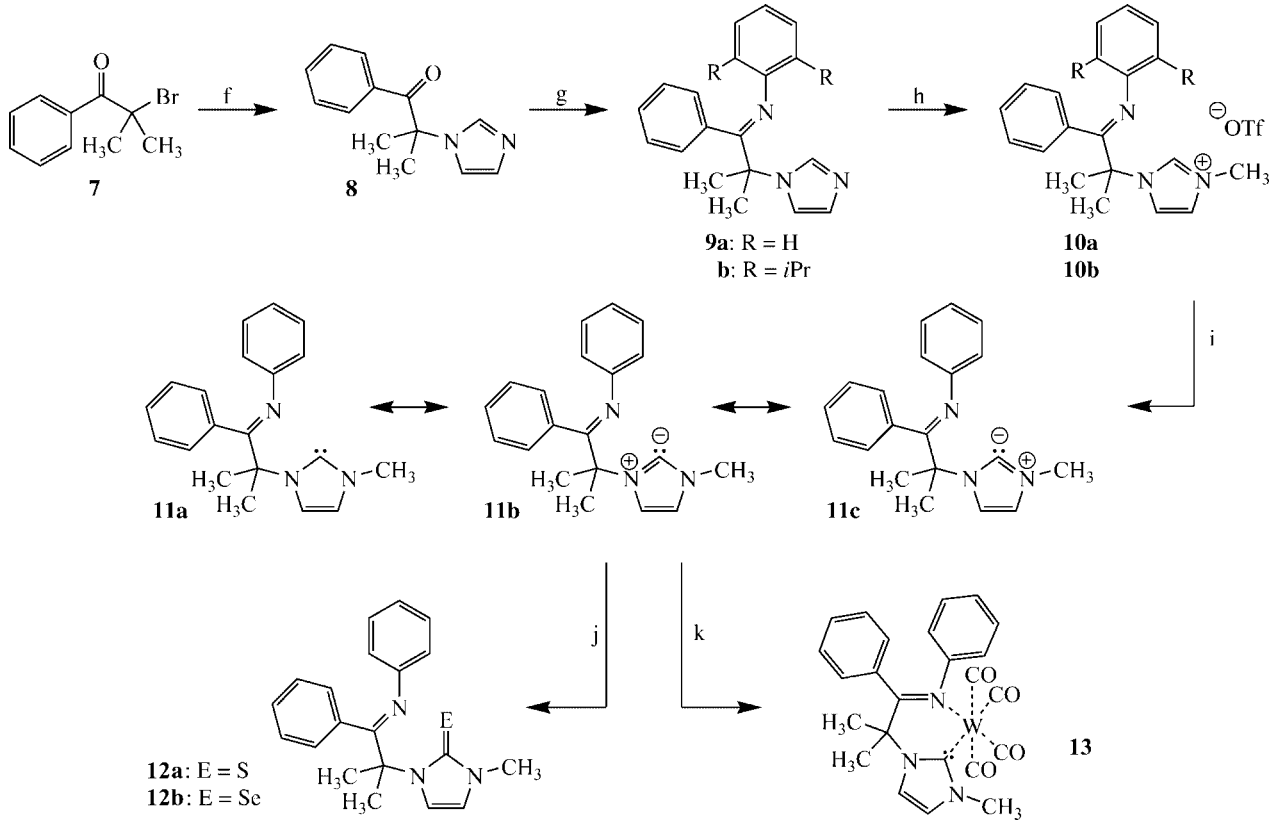

Scheme 3. Synthesis of *N*-iminoisopropyl NHC ligands and their derivatives. Conditions: (f) imidazole, reflux; (g) aniline or 2,6-diisopropylaniline, trimethylaluminum, reflux; (h) methyl triflate; (i) potassium hydride; (j) elemental sulfur or selenium; (k) $(CO)_5W(THF)$, hv.

 © 2005 Wiley-VCH Verlag GmbH & Co. KGaA, Weinheim

imidazolium salts **10a** and **10b** in over 40% overall yield starting from imidazole.

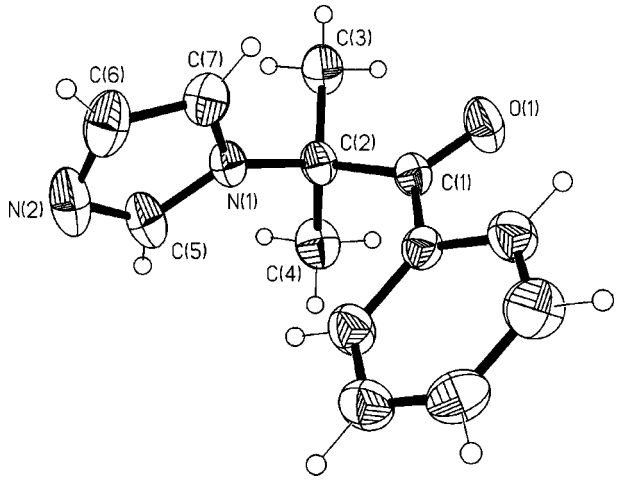

Figure 1. Molecular structure of **8**. Selected bond lengths (pm): C(5)–N(1) 135.24(17), C(5)–N(2) 131.1(2), N(1)–C(7) 137.36(17), N(2)–C(6) 137.4(2), C(6)–C(7) 134.7(2), N(1)–C(2) 147.49(16), C(2)–C(1) 154.95(17), C(1)–O(1) 121.61(15). Selected angles [°]: N(1)–C(5)–N(2) 112.66(13), N(1)–C(2)–C(1) 109.73(9), C(3)–C(2)–C(4) 109.52(11), C(2)–C(1)–O(1) 117.33(11).

Both imidazolium triflates **10a** and **10b** are yellow, slightly air-sensitive powders. Structurally, they differ only in the substitution pattern of the N-bonded aryl group. Because all further chemistry in this contribution was investigated with **10a** as precursor (vide infra), we will discuss only this triflate salt in more detail. Table 1 lists some key NMR spectroscopic data in comparison to its derivatives discussed below. Imidazolium salt **10a** shows a characteristic low-field resonance for the imidazolium C(2)-bonded hydrogen [$\delta(^1H)$ = 8.84 ppm] and an imine carbon signal [$\delta(^{13}C)$ = 171.6 ppm] in the expected range. The two methyl "protecting" groups of the isopropyl moiety are regular, nonshielded alkyl groups [$\delta(^1H)$ = 1.36 ppm, $\delta(^{13}C)$ = 25.7 ppm] as intended, ruling out a deprotonation at this site upon reaction with a strong base. The signals of the imidazolium *N*-methyl group [$\delta(^1H)$ = 3.33 ppm, $\delta(^{13}C)$ = 35.9 ppm] are similar in value to those observed for iminomethylmidazolium salt **4** containing a methylene spacer moiety (vide supra).

Imidazolium triflate **10a** serves as the precursor for the corresponding imino NHC **11a**–**c**. Treatment of **10a** with an equimolar amount of potassium hydride in THF solution caused effervescence due to dihydrogen evolution and the initially yellow solution gradually changed color to orange, which is notably different from the dark-red color of the deprotonation product of **4**. Performing this reaction on a small scale in deuterated THF solution and analyzing the outcome by NMR spectroscopy showed clearly that the desired imino-N-heterocyclic carbene **11a**–**c** had indeed been formed in quantitative yield (Table 1): the ^1H signal of the imidazole-C(2)-bonded hydrogen is absent and the ^{13}C resonance of the imidazole-C(2) carbon is detected at low field [$\delta(^{13}C)$ = 216.3 ppm] in the typical range [$\delta(^{13}C)$ = 205.9 to 231.5 ppm] of imidazolin-2-ylidene carbenes.[1e] All other NMR signals, including the imine carbon resonance [$\delta(^{13}C)$ = 175.0 ppm], are more or less similar to those of the formal conjugate acid **10a**, thus proving that carbene **11a**–**c** exists in solution. Some attempts were undertaken to crystallize NHC **11a**–**c**, but so far no suitable single crystals for an X-ray structure analysis have been obtained.

N-Iminoisopropyl N-Heterocyclic Carbene Derivatives

Having achieved a clean synthesis of the first free imino NHC **11a**–**c**, we explored its chemistry (Scheme 3). Oxidation with elemental sulfur afforded imidazolin-2-thione (**12a**) in 74% yield after workup. Spectroscopically, the sulfur-carbon double bond is clearly evident from the ^{13}C signal at δ = 161.0 ppm (Table 1) and an intense IR absorption ($\nu_{C=S}$ = 1224 cm^{-1}). The carbon resonance of the imine functionality [$\delta(^{13}C)$ = 173.3 ppm] is almost unshifted in comparison to **11a**–**c**, as expected. In addition, the C=N bond manifests itself by a strong IR band ($\nu_{C=N}$ = 1647 cm^{-1}). Further structural proof for **12a** was obtained from a single crystal structure analysis (Table 2, Figure 2); relevant bond lengths and angles are given in the caption.

Carbene **11a**–**c** reacts analogously with elemental selenium to afford the corresponding air-stable imidazolin-2-selenone (**12b**) in 43% isolated yield after workup. As expected, the spectroscopic features of **12b** are quite similar to those of its homologous thione **12a**. Due to the spin-1/2 ^{77}Se isotope further structural proof by ^{77}Se NMR spectroscopy was possible [$\delta(^{13}C)_{C=Se}$ = 153.8 ppm, $^1J(^{13}C\text{-}^{77}Se)$ = 232 Hz; $\delta(^{77}Se)$ = –1182 ppm; $\delta(^{13}C)_{C=N}$ = 172.8 ppm; $\nu_{C=Se}$ = 1222 cm^{-1}; $\nu_{C=N}$ = 1644 cm^{-1}]. These selenium NMR spectroscopic data compare well with those of the few other known imidazolin-2-selenones.[10] In the solid

Table 1. Relevant NMR spectroscopic data for **10a**, **11a**–**c**, **12a**, **12b**, and **13**.

Compound	**10a**	**11a–c**	**12a**	**12b**	**13**
Solvent	[D$_6$]DMSO	[D$_8$]THF	[D$_6$]DMSO	[D$_6$]DMSO	[D$_6$]DMSO
$\delta(^{13}C)$ of imidazole C(2)	149.3 ppm	216.3 ppm	161.0 ppm	153.8 ppm $^1J(^{13}C\text{-}^{77}Se)$ = 232 Hz	192.4 ppm $^1J(^{13}C\text{-}^{183}W)$ = 95 Hz
δ of atom bonded to imidazole C(2)	$\delta(^1H)$ = 8.84 ppm	–	$\delta(^{33}S)$: no data	$\delta(^{77}Se)$ = –1182 ppm	$\delta(^{183}W)$ = –2569 ppm
$\delta(^{13}C)$ of imine carbon	171.6 ppm	175.0 ppm	173.3 ppm	172.8 ppm	184.2 ppm
$\delta(^1H)$ of *N*-CH$_3$	3.33 ppm	3.69 ppm	3.49 ppm	3.59 ppm	3.84 ppm
$\delta(^{13}C)$ of *N*-CH$_3$	35.9 ppm	38.2 ppm	34.5 ppm	36.5 ppm	overlapped by solvent signal
$\delta(^1H)$ of *N*′-C(CH$_3$)$_2$	1.36 ppm	1.83 ppm	1.83 ppm	1.91 ppm	1.80 ppm
$\delta(^{13}C)$ of *N*′-C(CH$_3$)$_2$	25.7 ppm 66.7 ppm	28.4 ppm 64.8 ppm	26.3 ppm 64.6 ppm	26.7 ppm 65.7 ppm	27.6 ppm 64.4 ppm

 © 2005 Wiley-VCH Verlag GmbH & Co. KGaA, Weinheim

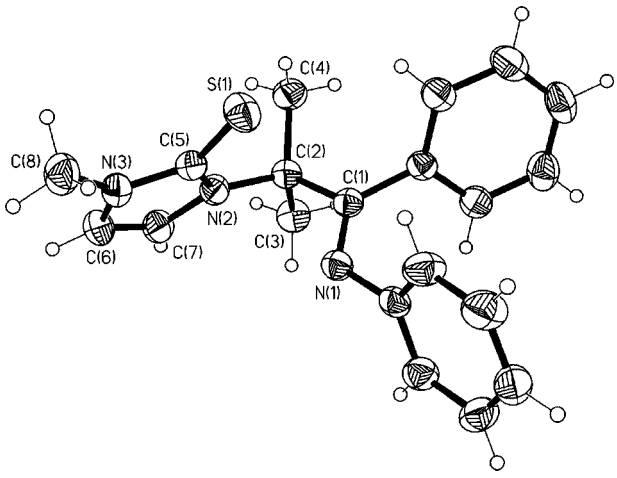

Figure 2. Molecular structure of **12a**. Selected bond lengths (pm): S(1)–C(5) 168.1(2), C(5)–N(2) 137.2(3), C(5)–N(3) 135.8(3), N(2)–C(7) 138.4(3), N(3)–C(6) 137.9(3), C(6)–C(7) 133.4(3), N(3)–C(8) 145.8(3), N(2)–C(2) 148.1(3), C(2)–C(1) 153.5(3), C(1)–N(1) 127.3(3). Selected angles [°]: N(2)–C(5)–N(3) 105.46(17), N(2)–C(2)–C(1) 108.49(16), C(3)–C(2)–C(4) 108.85(18), C(2)–C(1)–N(1) 116.60(18).

state, selenone **12b** (Table 2, Figure 3) is isomorphous with thione **12a**; only some minor differences in bond lengths and angles are observed. Most notable of these is the carbon-selenium bond length [184.0(2) pm] as compared to the shorter C=S bond [168.1(2) pm] of thione **12a**. The rather long C=Se bond length is similar in value to that of an imidazolinselenone published earlier[10] and suggests a reduced bond order due to significant contribution of the zwitterionic C^+-Se^- valence structure.

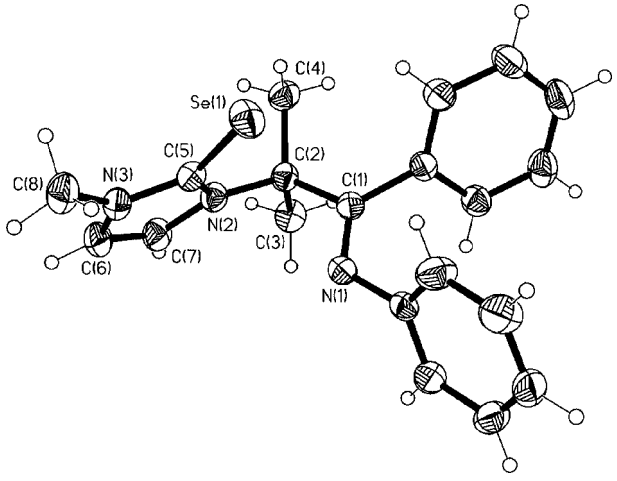

Figure 3. Molecular structure of **12b**. Selected bond lengths (pm): Se(1)–C(5) 184.0(2), C(5)–N(2) 136.7(2), C(5)–N(3) 135.4(3), N(2)–C(7) 138.7(3), N(3)–C(6) 137.5(3), C(6)–C(7) 133.7(3), N(3)–C(8) 146.0(3), N(2)–C(2) 148.2(3), C(2)–C(1) 153.9(3), C(1)–N(1) 127.2(2). Selected angles [°]: N(2)–C(5)–N(3) 105.84(17), N(2)–C(2)–C(1) 108.76(16), C(3)–C(2)–C(4) 108.55(17), C(2)–C(1)–N(1) 116.56(17).

In principal it would be interesting to synthesize the next higher homologue, iminoisopropylimidazolin-2-tellurone, by oxidation of carbene **11a**–**c** with elemental tellurium. However, because of the known sensitivity of such compounds at room temperature and towards sunlight,[11] and because of the obnoxious stench associated with organic tellurium compounds in general, we refrained from attempting this reaction. However, we note that both compounds **12a** and **12b** represent new heteroditopic [N,S]- and [N,Se]-ligands whose coordination chemistry remains unexplored at the moment.

As outlined in the introduction, carbene **11a**–**c** was designed as a member of a new family of heteroditopic [N,C]-imino NHC ligands for application in homogeneous catalysis. Consequently, it was of prime interest to study its coordination chemistry. Reaction with simple metal halides ($PdCl_2$, CuCl, AgCl, $NiCl_2$ etc.) gave, in general, polar products that are obviously [N,C]-bound metal complexes. Full characterization proved quite difficult, however, and the growth of suitable crystals for an unambiguous structural proof by single crystal structure analysis has not yet been possible. In contrast, the reaction with photochemically generated $W(CO)_5$(THF) afforded the air-stable tungsten complex **13**, which was fully characterized in solution by a range of spectroscopic methods as well as in the solid state by single crystal structure analysis. Its ^{13}C NMR spectrum (Table 1) shows the carbene carbon signal at δ = 192.4 ppm, with a one-bond ^{13}C-^{183}W coupling constant of 95 Hz, thereby proving the direct connectivity of the NHC-carbon to the metal center. The imine carbon is shifted to low field [$\delta(^{13}C)$ = 184.2 ppm] in comparison to the free carbene **11a**–**c** [$\delta(^{13}C)$ = 175.0 ppm], thus reflecting the coordination of the imine moiety to the tungsten metal center. The four carbonyl groups are evident from their strong IR absorptions and from three ^{13}C signals with ^{183}W satellites, indicating two magnetically equivalent axial carbonyl groups [$\delta(^{13}C)$ = 205.3 ppm, $^1J_{C,W}$ = 129 Hz] and two different equatorial CO ligands [$\delta(^{13}C)$ = 210.1 ppm, $^1J_{C,W}$ = 146 Hz; $\delta(^{13}C)$ = 218.2 ppm, $^1J_{C,W}$ = 169 Hz] due to the heteroditopic nature of the imino NHC ligand **11a**–**c**. The observation of only one ^{13}C signal for the two axial CO groups indicates rapid interconversion in solution of the two possible boat conformations of the six-membered chelate ring, which is further supported by the two isochronous methyl groups of the isopropyl moiety [$\delta(^{13}C)$ = 27.6 ppm, $\delta(^1H)$ = 1.80 ppm] (Table 1). Several NHC tungsten carbonyl complexes have been reported in the literature,[12] but only for one $(CO)_5$W(NHC) complex[12d] has a direct coupling of the NHC-carbon to the tungsten metal center been reported [$\delta(^{13}C)$ = 176.4 ppm, $^1J_{C,W}$ = 99 Hz];[12d] these data are in good agreement with ours. In addition, we were able to detect for the first time the ^{183}W chemical shift of an NHC-tungsten complex: **13** shows a weak but nevertheless significant ^{183}W signal at δ = –2569 ppm vs. aqueous Na_2WO_4 solution. In general, transition metal NMR spectroscopic data of tungsten metal complexes are very limited due to the unfavorable receptivity of ^{183}W (R^C = 0.0589), and only about 30 organometallic compounds have been investigated by this technique so far. Although the body of ^{183}W chemical shifts is therefore quite small for comparative purposes, the shift of **13** compares well with those of

 © 2005 Wiley-VCH Verlag GmbH & Co. KGaA, Weinheim

vinylidene-tungsten complexes $[(dppe)CO]_3W{=}C{=}CHR$] with signals in the range of δ = –2548 to –2596 ppm.[13]

In the solid state (Figure 4, Table 2), complex **13** shows the expected κ^2-coordination of the [N,C]-ligand in a boat conformation, with tungsten and the isopropylmethyl group occupying the apical sites. Pertinent bond lengths and angles are given in the caption of Figure 4. Due to geometrical constraints of the six-membered chelate ring, the coordination angle at the formally octahedral tungsten center is only 78.0° as compared to the idealized normal angle. In addition, due to the steric requirements of the [N,C]-ligand, the tungsten center shows a slightly distorted octahedron, indicated by an "umbrella-like" back-bending of the four carbonyl ligands. The W–N [226.5(8) pm] and W–C [221.8(9) pm] bond lengths of the tungsten-coordinated imino NHC ligand are in the normal range of other tungsten-imino and tungsten-NHC complexes.[12] As a consequence of the boat conformation of the [N,C] six-membered chelate the two axial carbonyl groups at the tungsten center are inequivalent. However, this is just a solid-state effect; in solution, a rapid ring flip process occurs as indicated by the simplicity of the NMR spectra discussed above. Overall the X-ray structure of **13** shows the desired heteroditopic imino NHC chelate metal structure and indicates that steric tuning will easily be possible in the future by altering the substitution pattern of the N-bonded aryl moiety.

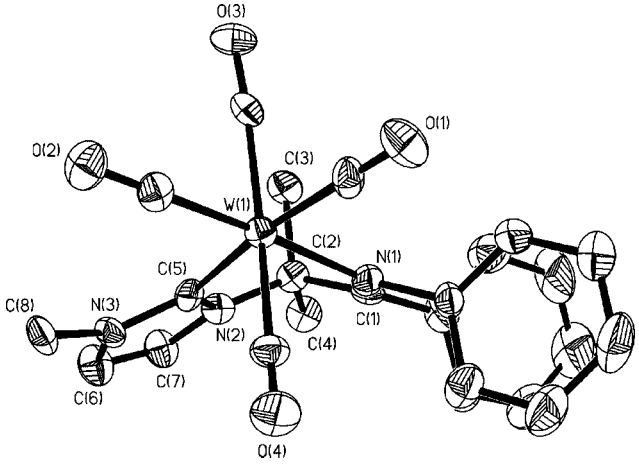

Figure 4. Molecular structure of **13**. Hydrogen atoms have been omitted for clarity. Selected bond lengths (pm): W(1)–C(5) 221.8(9), W(1)–N(1) 226.5(8), W(1)–C(01) 196.5(11), W(1)–C(02) 194.3(11), W(1)–C(03) 201.3(12), W(1)–C(04) 204.5(11), C(01)–O(1) 116.3(13), C(02)–O(2) 119.0(13), C(03)–(O3) 115.0(13), C(04)–O(4) 112.3(13), C(5)–N(2) 137.5(13), C(5)–N(3) 136.1(13), N(2)–C(7) 137.4(13), N(3)–C(6) 138.1(14), C(6)–C(7) 131.2(17), N(3)–C(8) 147.8(14), N(2)–C(2) 147.9(14), C(2)–C(1) 153.6(14), C(1)–N(1) 129.8(12). Selected angles [°]: N(1)–W(1)–C(5) 78.0(3), C(01)–W(1)–C(02) 88.3(4), C(03)–W(1)–C(04) 166.0(4), N(2)–C(5)–N(3) 102.7(8), N(2)–C(2)–C(1) 111.3(8), C(3)–C(2)–C(4) 106.8(9), C(2)–C(1)–N(1) 120.7(9).

Conclusions

New heteroditopic ligands combining the advantageous properties of N-heterocyclic carbenes and imine donors with *N*-aryl groups have been investigated. Such imino NHC systems can be prepared by alkylation of imidazole with a ketoalkyl bromide, condensation of the carbonyl group with anilines, alkylation of the iminoalkylimidazole with methyl trifluoromethanesulfonate, and deprotonation of the *N*-iminoalkyl-*N*′-methylimidazolium triflate with potassium hydride. For a successful generation of the imino NHC it is necessary to block the methylene group between the heterocycle and the imine group by two methyl substituents, otherwise deprotonation at this undesired "wrong" site occurs and an ylidic non-NHC product is observed. Spectroscopically, the imino NHC ligand is characterized by a typical low-field ^{13}C chemical shift of the NHC-carbene carbon together with an imine carbon signal. The chemical reactivity of the imino NHC comprises oxidation by elemental sulfur and selenium to afford the corresponding imidazolin-2-thione and selenone, which were fully characterized by solid state structures and multinuclear NMR spectroscopy, including ^{77}Se spectroscopy. A first transition metal complex of the imino NHC ligand was obtained by treatment with tungsten hexacarbonyl; the resulting [N,C] $W(CO)_4$ complex shows the anticipated six-membered metal [N,C] chelate in solution and in the solid state, as proven by an X-ray structure and by multinuclear NMR spectroscopy, including ^{183}W spectroscopy.

Experimental Section

General: Commercially available starting materials were used as obtained. Solvents were dried, deoxygenated, and saturated with argon according to standard procedures in organometallic chemistry. Reactions of air-sensitive materials were performed in Schlenk glassware under an atmosphere of argon using techniques common in organometallic chemistry.

Imidazole 2 (CA registry no. 24155-34-8): A round-bottomed flask was charged with imidazole (4.3 g, 62.8 mmol), α-bromoacetophenone (**1**; 5 g, 25.1 mmol), and 100 mL of THF. The yellow solution was stirred overnight at ambient temperature to give a yellow suspension of the product with precipitated imidazolium bromide. Aqueous workup and recrystallization from methanol/diethyl ether yielded pure, yellow **2** (2.24 g, 12 mmol, 48%). M.p.: 117–119 °C. IR (KBr): $\tilde{\nu}$ = 2965 cm^{-1} (w), 2919 (w), 1696 (vs), 1597 (s), 1503 (s), 1451 (s), 1360 (s), 1344 (m), 1288 (m), 1227 (vs), 1107 (s), 1074 (s), 1038 (s), 984 (s), 906 (s), 816 (s), 762 (s), 746 (vs), 692 (vs). ^1H NMR (300 MHz, CD_2Cl_2): δ = 5.43 (s, 2 H, CH_2), 6.94–7.99 (m, 8 H, C_6H_5, $C_3H_3N_2$) ppm. ^{13}C NMR (75.432 MHz, CD_2Cl_2): δ = 52.9 (CH_2), 120.7, 128.2, 129.3, 134.6, and 138.5 (C_6H_5, $C_3H_3N_2$), 192.4 (C=O) ppm.

Imidazole 3: A Dean–Stark apparatus was charged with **2** (940 mg, 5.05 mmol), 2,6-diisopropylaniline (2.80 mL, 15.1 mmol), *p*-toluenesulfonic acid monohydrate (2.9 g, 15.1 mmol), and 100 mL of toluene. The mixture was refluxed for 3 d, followed by aqueous workup. Chromatography on alumina with diethyl ether/*n*-hexane (v/v = 1:1) as eluent removed the excess of aniline, and elution with methanol yielded pure **3** (1.07 g, 3.1 mmol, 61.4%) as a yellow oil. MS (EI): *m*/*z* = 345.3 $[M]^+$. ^1H NMR (300 MHz, CD_2Cl_2): δ = 0.87–1.23 (m, 12 H, CH_3), 2.67 (m, 2 H, CH), 4.90 (s, 2 H, CH_2), 6.64–7.88 (m, 11 H, C_6H_5, C_6H_3, $C_3H_3N_2$) ppm. ^{13}C NMR (75.432 MHz, CD_2Cl_2): δ = 22.1, 23.7, and 28.8 [$CH(CH_3)_2$], 44.7 (CH_2), 119.4, 120.2, 123.2, 123.5, 124.2, 124.7, 127.6, 128.7, 129.1, 129.7, 130.2, 131.3, 135.7, 136.1, 136.9, 137.8, 138.2, and 145.1

 © 2005 Wiley-VCH Verlag GmbH & Co. KGaA, Weinheim

(C_6H_5, C_6H_3, $C_3H_3N_2$), 162.2, 162.9 (C=N) ppm. $C_{23}H_{27}N_3$ (345.48): calcd. C 79.96, H 7.88, N 12.16; found C 80.11, H 7.86, N 12.13.

Imidazolium Triflate 4: A Schlenk tube was charged with **3** (392 mg, 1.13 mmol) and dry dichloromethane (40 mL). The solution was cooled to –80 °C and methyl trifluoromethanesulfonate (124 μL, 1.13 mmol) was added from a syringe. After 90 min stirring at –80 °C, the cooling bath was removed and the mixture was stirred for a further 90 min. Workup: all volatile materials were removed on a vacuum line, the solid yellow residue was washed with two portions of dry diethyl ether, and dried in vacuo to afford 570 mg of **4** as a yellow, air-sensitive powder in 99% yield. MS (FAB): *m*/*z* = M of cation not observed due to hydrolysis. ^{1}H NMR [300 MHz, $(CD_3)_2SO$]: δ = 0.83 [d, $^3J_{H,H}$ = 6.9 Hz, 6 H, $CH(CH_3)_2$], 0.91 [d, $^3J_{H,H}$ = 6.6 Hz, 6 H, $CH(CH_3)_2$], 2.65 [m, 2 H, $2\times CH(CH_3)_2$], 3.94 (s, 3 H, CH_3), 5.85 (s, 2 H, CH_2), 6.95–7.82 (m, 10 H, C_6H_5, C_6H_3, $C_3H_3N_2$), 9.17 (s, 1 H, $C_3H_3N_2$) ppm. ^{13}C NMR [75.432 MHz, $(CD_3)_2SO$]: δ = 21.7, 23.5, and 27.4 [$CH(CH_3)_2$], 35.8 (N-CH_3), 64.9 (CH_2), 118.6, 122.6, 122.8, 123.2, 123.8, 124.1, 127.2, 128.5, 128.8, 130.4, 133.6, 134.8, 137.8, and 144.0 (C_6H_5, C_6H_3, $C_3H_3N_2$), 161.2 (C=N) ppm. The weak ^{13}C signals for the triflate anion [δ = 121 ppm, q, $^1J(^{13}C\text{-}^{19}F)$ = 322 Hz] were not observed due to insufficient concentration and/or too short an acquisition period. $C_{25}H_{30}F_3N_3O_3S$ (509.59): calcd. C 58.92, H 5.93, N 8.25; found C 58.69, H 5.95, N 8.22.

Imidazole 8: A round-bottomed flask was charged with imidazole (3.40 g, 49.9 mmol), 2-bromo-2-methylpropiophenone (**7**; 4 mL, 23.8 mmol), and 40 mL of ethanol. The yellow solution was refluxed for 3 d. Aqueous workup yielded a yellow oil which crystallized in the freezer. Recrystallization from dichloromethane/*n*-hexane (1:2) afforded pure, colorless **8** (3.11 g, 14.5 mmol, 61%). MS (EI): *m*/*z* = 214.1 $[M]^+$. IR (KBr): $\tilde{\nu}$ = 3145 cm^{-1} (w), 3000(w), 1672(vs), 1599(m), 1576(w), 1493(m), 1470(m), 1451(m), 1393(w), 1375(m), 1339(w), 1285(w), 1261(s), 1240(vs), 1177(s), 1167(s), 1153(m), 1082(s), 1013(s), 976(s), 906(s), 893(s), 820(s), 750(s). ^{1}H NMR [300 MHz, $(CD_3)_2SO$]: δ = 1.80 (s, 6 H, CH_3), 6.94–7.87 (m, 8 H, C_6H_5, $C_3H_3N_2$) ppm. ^{13}C NMR [75.432 MHz, $(CD_3)_2SO$]: δ = 26.6 and 64.7 [$C(CH_3)_2$], 118.1, 128.0, 128.5, 129.1, 132.6, 134.8, and 135.6 (C_6H_5, $C_3H_3N_2$), 199.3 (C=O) ppm. $C_{13}H_{14}N_2O$ (214.26): calcd. C 72.87, H 6.59, N 13.07; found C 72.95, H 6.57, N 13.03.

Imidazole 9a: A Schlenk tube was charged with aniline (524 μL, 5.75 mmol), 40 mL of toluene, and 2.87 mL of a 2.0 M toluene solution of trimethylaluminum (5.75 mmol). The stirred solution was heated to 80 °C. After 90 min methane evolution was complete and the solution was cooled to ambient temperature. Under protection from air, imidazole **8** (560 mg, 2.61 mmol) was added in one portion. The mixture was stirred overnight at ambient temperature and then heated to 80 °C for a further three hours to afford a bright-yellow solution. Workup: the solution was cooled to 0 °C, the mixture was carefully hydrolyzed with crushed ice, the organic product was extracted with three portions of dichloromethane, the combined organic layers were washed with three portions of a 5% aqueous NaOH solution, the dichloromethane solution was washed with two portions of water, the organic phase was dried with Na_2SO_4, and all volatile materials were removed in vacuo on a rotary evaporator to afford the crude product together with aniline. Chromatography on alumina with diethyl ether/*n*-hexane (v/v, 1:1) as eluent followed by methanol afforded 651 mg of pure **9a** in 86% yield as a yellow oil. MS (FAB): *m*/*z* = 290.2 $[M + H]^+$. ^{1}H NMR (300 MHz, CD_2Cl_2): δ = 1.85 (s, 6 H, CH_3), 6.39–7.53 (m, 13 H, C_6H_5, $C_3H_3N_2$) ppm. ^{13}C NMR (75.432 MHz, CD_2Cl_2): δ = 26.7 and 63.1 [$C(CH_3)_2$], 117, 8, 120.2, 123.6, 127.8, 128.1, 128.5, 128.7, 129.6, 134.6, 135.6, and 150.3 (C_6H_5, $C_3H_3N_2$), 173.0 (C=N) ppm. $C_{19}H_{19}N_3$ (289.37): calcd. C 78.86, H 6.62, N 14.52; found C 78.99, H 6.59, N 14.48.

Imidazole 9b: A Schlenk tube was charged with 2,6-diisopropylaniline (2.96 mL, 15.7 mmol), 40 mL of toluene, and 7.84 mL of a 2.0 M toluene solution of trimethylaluminum (15.7 mmol). The stirred solution was heated to 80 °C. After 90 min methane evolution was complete and the solution was cooled to ambient temperature. Under protection from air, imidazole **8** (1.12 g, 5.23 mmol) was added in one portion. The mixture was stirred overnight at ambient temperature and heated to 80 °C for a further three hours to afford a bright-yellow solution. Workup as described above for **9a** afforded 1.46 g of pure **9b** in 75% yield as a yellow oil. MS (EI): *m*/*z* = 373.3 $[M]^+$. ^{1}H NMR (300 MHz, CD_2Cl_2): δ = 1.06 [d, $^3J_{H,H}$ = 6.94 Hz, 6 H, $CH(CH_3)_2$], 1.14 [d, $^3J_{H,H}$ = 6.61 Hz, 6 H, $CH(CH_3)_2$], 2.74 [m, 2 H, $2\times CH(CH_3)_2$], 6.38–7.49 (m, 11 H, C_6H_5, C_6H_3, $C_3H_3N_2$) ppm. ^{13}C NMR (75.432 MHz, $CDCl_3$): δ = 21.3, 23.9, and 28.7 [$CH(CH_3)_2$], 27.3 and 63.4 [$C(CH_3)_2$], 117.8, 122.7, 126.4, 127.6, 128.0, 128.8, 129.5, 134.7, 135.5, 136.9, and 145.0 (C_6H_5, C_6H_3, $C_3H_3N_2$), 170.4 (C=N) ppm. $C_{25}H_{31}N_3$ (373.53): calcd. C 80.39, H 8.37, N 11.25; found C 80.52, H 8.34, N 11.20.

Imidazolium Triflate 10a: A Schlenk tube was charged with **9a** (650 mg, 2.25 mmol) and dry dichloromethane (40 mL). The solution was cooled to –80 °C and methyl trifluoromethanesulfonate (246 μL, 2.25 mmol) was added with a syringe. After 90 min stirring at –80 °C, the cooling bath was removed and the mixture was stirred for a further 90 min. Workup: all volatile materials were removed on a vacuum line, the solid yellow residue was washed with two portions of dry diethyl ether, and dried in vacuo to afford 920 mg of **10a** as a yellow, slightly air-sensitive powder in 90% yield. MS (FAB): *m*/*z* = 304.1 $[M]^+$ of cation. ^{1}H NMR [300 MHz, $(CD_3)_2SO$]: δ = 1.36 (s, 6 H, CH_3), 3.33 (s, 3 H, CH_3), 6.03–7.54 (m, 12 H, C_6H_5, $C_3H_3N_2$), 8.84 (s, 1 H, $C_3H_3N_2$) ppm. ^{13}C NMR [75.432 MHz, $(CD_3)_2SO$]: δ = 25.7 and 66.7 [$C(CH_3)_2$], 35.8 (N-CH_3), 119.4, 121.6, 121.8, 123.3, 123.6, 123.8, 127.8, 127.9, 128.3, 128.5, 128.6, 128.8, 133.4, 136.5, and 149.3 (C_6H_5, $C_3H_3N_2$), 171.6 (C=N), 120.7 (q, $^1J_{C,F}$ = 322 Hz, CF_3 of triflate) ppm. $C_{21}H_{22}F_3N_3O_3S$ (453.48): calcd. C 55.62, H 4.89, N 9.27; found C 55.34, H 4.91, N 9.24.

Imidazolium Triflate 10b: A Schlenk tube was charged with **9b** (1.47 g, 3.94 mmol) and dry dichloromethane (40 mL). The solution was cooled to –80 °C and methyl trifluoromethanesulfonate (432 μL, 3.94 mmol) was added with a syringe. After 90 min stirring at –80 °C, the cooling bath was removed and the mixture was stirred for a further 90 min. Workup: all volatile materials were removed on a vacuum line, the solid yellow residue was washed with two portions of dry diethyl ether, and dried in vacuo to afford 2.00 g of **10b** as a yellow, slightly air-sensitive powder in 95% yield. MS (FAB): *m*/*z* = 388.4 $[M]^+$ of cation. ^{1}H NMR [300 MHz, $(CD_3)_2SO$]: δ = 0.91 [d, $^3J_{H,H}$ = 6.61 Hz, 6 H, $CH(CH_3)_2$], 1.05 [d, $^3J_{H,H}$ = 6.93 Hz, 6 H, $CH(CH_3)_2$], 2.00 [s, 6 H, $C(CH_3)_2$], 2.65 [m, 2 H, $2\times CH(CH_3)_2$], 3.87 (s, 3 H, CH_3), 6.82–8.10 (m, 10 H, C_6H_5, C_6H_3, $C_3H_3N_2$), 8.94 (s, 1 H, $C_3H_3N_2$) ppm. ^{13}C NMR [75.432 MHz, $(CD_3)_2SO$]: δ = 21.2, 23.6, and 27.7 [$CH(CH_3)_2$], 26.1 and 66.9 [$C(CH_3)_2$], 35.8 (N-CH_3), 121.7, 122.2, 123.4, 123.8, 126.1, 126.8, 127.3, 127.5, 128.0, 129.1, 133.6, 134.6, 136.8, 143.7, and 143.8 (C_6H_5, C_6H_3, $C_3H_3N_2$), 170.5 (C=N), 120,7 (q, $^1J_{C,F}$ = 322 Hz, CF_3 of triflate) ppm. $C_{27}H_{34}F_3N_3O_3S$ (537.64): calcd. C 60.32, H 6.37, N 7.82; found C 60.04, H 6.40, N 7.78.

Imino N-Heterocyclic Carbene 11a–c: A small Schlenk tube was charged with imidazolium triflate **10a** (50 mg, 0.110 mmol) dis-

 © 2005 Wiley-VCH Verlag GmbH & Co. KGaA, Weinheim

solved in 1 mL of dry, deuterated THF. Under protection from air, potassium hydride (4.4 mg, 0.110 mmol) was added in one portion. The mixture was stirred at ambient temperature for 2 h. Dihydrogen evolution was observed and a white precipitate of potassium triflate formed during this period. The orange suspension was transferred under an atmosphere of argon to an NMR tube and analyzed spectroscopically: ^{1}H NMR (300 MHz, [D$_8$]THF): δ = 1.83 (s, 6 H, CH_3), 3.69 (s, 3 H, CH_3), 6.55–7.12 (m, 12 H, C_6H_5, $C_3H_2N_2$) ppm. ^{13}C NMR (75.432 MHz, [D$_8$]THF): δ = 28.4 and 64.8 [$C(CH_3)_2$], 38.2 (N-CH_3), 118.1, 120.7, 121.0, 123.3, 127.8, 128.2, 128.7, 129.4, 136.7, and 151.9 (C_6H_5, $C_3H_2N_2$), 175.0 (C=N), 216.3 (carbene C) ppm.

Imidazolin-2-thione 12a: A Schlenk tube was charged with imidazolium triflate **10a** (165 mg, 0.364 mmol), 40 mL of THF, and potassium hydride (15 mg, 0.364 mmol). The mixture was stirred for 2 h at ambient temperature. Dihydrogen evolution occurred during this period and the mixture gradually changed in color from yellow to orange. Elemental sulfur (93 mg, 0.364 mmol) was added to the stirred mixture and the reaction was allowed to proceed overnight at ambient temperature. Chromatography on alumina with diethyl ether/*n*-hexane (v/v, 1:1) and methanol as eluents afforded air-stable, yellow **12a** (90 mg, 0.268 mmol, 74%). MS (FAB): *m*/*z* = 335.0 [M]$^+$. IR (KBr): $\tilde{\nu}$ = 3140 cm^{-1} (w), 3071 (w), 2979 (w), 2928 (w), 1647 (vs) ($\nu_{C=N}$), 1591 (s), 1478 (s), 1453 (s), 1403 (s), 1386 (vs), 1362 (s), 1292 (m), 1265 (m), 1224 (vs) ($\nu_{C=S}$), 1149 (m), 989 (m), 778 (s), 704 (s), 697 (vs), 670 (vs). ^{1}H NMR [300 MHz, $(CD_3)_2SO$]: δ = 1.83 (s, 6 H, CH_3), 3.49 (s, 3 H, CH_3), 6.62–7.37 (m, 12 H, C_6H_5, $C_3H_2N_2$) ppm. ^{13}C NMR [75.432 MHz, $(CD_3)_2SO$]: δ = 26.3 and 64.6 [$C(CH_3)_2$], 34.5 (CH_3), 115.6, 117.9, 119.6, 122.4, 127.5, 128.0, 128.1, 128.6, 135.6, and 150.9 (C_6H_5, $C_3H_2N_2$), 161.0 (C=S), 173.3 (C=N) ppm. $C_{20}H_{21}N_3S$ (335.47): calcd. C 71.61, H 6.31, N 12.53; found C 71.34, H 6.33, N 12.48.

Imidazolin-2-selenone 12b: A Schlenk tube was charged with imidazolium triflate **10a** (220 mg, 0.485 mmol), 40 mL of THF, and potassium hydride (20 mg, 0.485 mmol). The mixture was stirred for 2 h at ambient temperature. Dihydrogen evolution occurred during this period and the mixture gradually changed in color from yellow to orange. Elemental selenium (40 mg, 0.507 mmol) was added to the stirred mixture and the reaction was allowed to proceed overnight at ambient temperature. Chromatography on alumina with diethyl ether/*n*-hexane (v/v, 1:1) and methanol as eluents afforded air-stable, yellow **12b** (80 mg, 0.209 mmol, 43%). MS (FAB): *m*/*z* = 383.1 [M]$^+$. IR (KBr): $\tilde{\nu}$ = 3141 cm^{-1} (w), 3072 (w), 2979 (w), 1644 (vs) ($\nu_{C=N}$), 1591 (s), 1478 (s), 1452 (vs), 1377 (vs), 1296 (s), 1222 (vs) ($\nu_{C=Se}$), 1131 (s), 938 (m), 778 (s), 733 (m), 697 (vs). ^{1}H NMR [300 MHz, $(CD_3)_2SO$]: δ = 1.91 (s, 6 H, CH_3), 3.59 (s, 3 H, CH_3), 6.70–7.48 (m, 12 H, C_6H_5, $C_3H_2N_2$) ppm. ^{13}C NMR [75.432 MHz, $(CD_3)_2SO$]: δ = 26.7 and 65.7 [$C(CH_3)_2$], 36.5 (CH_3), 118.2, 119.6, 119.8, 122.3, 127.4, 127.9, 128.8, 135.5, and 150.8 (C_6H_5, $C_3H_2N_2$), 153.8 ($^1J_{C,Se}$ = 232 Hz, C=Se), 172.8 (C=N) ppm. ^{77}Se NMR (57.203 MHz, $(CD_3)_2SO$, vs. H_2SeO_3): δ = –1182 (C=Se) ppm. $C_{20}H_{21}N_3Se$ (382.36): calcd. C 62.82, H 5.54, N 10.99; found C 62.62, H 5.56, N 10.95.

Tungsten Complex 13: A Schlenk tube was charged with imidazolium triflate **10a** (768 mg, 1.69 mmol), 50 mL of THF, and potassium hydride (86 mg, 1.69 mmol). The mixture was stirred for 2 h at ambient temperature. Dihydrogen evolution occurred during this period and the mixture gradually changed in color from yellow to orange. Tungsten hexacarbonyl (596 mg, 1.69 mmol) was added to

Table 2. Crystallographic data for **8**, **12a**, **12b**, and **13**.

Compound	**8**	**12a**	**12b**	**13**
Molecular formula	$C_{13}H_{14}N_2O$	$C_{20}H_2N_3S$	$C_{20}H_{21}N_3Se$	$C_{24}H_{21}N_3O_4W$
Molecular mass	214.26	335.46	382.36	599.29
Crystal system	triclinic	monoclinic	monoclinic	triclinic
Space group	*P*1 (no. 2)	*C*2/*c* (no. 15)	*C*2/*c* (no. 15)	*P*1 (No. 2)
a [pm]	626.64(3)	3330.04(5)	3344.67(2)	856.58(2)
b [pm]	792.77(4)	673.30(2)	680.17(4)	1363.90(5)
c [pm]	1238.73(6)	1626.7(2)	1622.54(5)	2014.61(7)
α [°]	97.332(2)	90	90	82.654(2)
β [°]	91.089(2)	101.313(6)	101.519(2)	79.147(2)
γ [°]	112.391(3)	90	90	89.959(2)
Z	2	8	8	4
V [nm^3]	0.56279(5)	3.5764(5)	3.6168(2)	2.29187(13)
ρ_{calcd} [Mg m^{-3}]	1.264	1.246	1.404	1.737
Temp. [K]	233(2)	233(2)	233(2)	233(2)
Absorption coeff. [mm^{-1}]	0.082	0.187	2.082	5.075
F_{000}	228	1424	1568	1168
Color, habit	colorless prism	colorless plate	colorless plate	yellow plate
Crystal size	0.4 × 0.2 × 0.15 mm	0.4 × 0.2 × 0.05 mm	0.35 × 0.15 × 0.07 mm	0.25 × 0.11 × 0.04 mm
θ range for data collection	1.66° to 24.00°	2.49° to 22.50°	2.49° to 25.00°	1.51° to 23.00°
Index ranges	$0 \le h \le 7$	$0 \le h \le 35$	$0 \le h \le 39$	$-9 \le h \le 0$
	$-9 \le k \le 8$	$-7 \le k \le 7$	$-8 \le k \le 8$	$-14 \le k \le 14$
	$-14 \le l \le 14$	$-17 \le l \le 16$	$-19 \le l \le 18$	$-22 \le l \le 21$
Reflections collected	2780	7515	10789	10971
Independent reflections	1754 (R_{int} = 0.0143)	2333 (R_{int} = 0.0293)	3180 (R_{int} = 0.0286)	6341 (R_{int} = 0.0370)
Reflections with $I > 2\sigma(I)$	1593	1909	2698	5407
Absorption correction	none	none	none	none
Refinement method	full-matrix least squares on F^2	full-matrix least squares on F^2	full-matrix least squares on F^2	full-matrix least squares on F^2
Data/restraints/parameters	1754/0/146	2333/0/219	3180/0/219	6341/0/581
Goodness-of-fit on F^2	1.065	1.028	1.040	1.025
Final *R* indices [$I > 2\sigma(I)$]	R_1 = 0.0341	R_1 = 0.0385	R_1 = 0.0274	R_1 = 0.0542
	wR_2 = 0.0874	wR_2 = 0.0957	wR_2 = 0.0640	wR_2 = 0.1352
R indices (all data)	R_1 = 0.0379	R_1 = 0.0518	R_1 = 0.0365	R_1 = 0.0630
	wR_2 = 0.0899	wR_2 = 0.1017	wR_2 = 0.0671	wR_2 = 0.1405
Extinction coefficient	0.171(18)	0.0017(3)	0.00029(11)	0.0043(10)
Largest diff. peak and hole	176 and –149 e nm^{-3}	168 and –200 e nm^{-3}	191 and –301 e nm^{-3}	6779 and –1654 e nm^{-3}

 © 2005 Wiley-VCH Verlag GmbH & Co. KGaA, Weinheim

the mixture and the reaction was stirred overnight at room temperature followed by irradiation at 0 °C with a 150 W high pressure mercury lamp for the period of 3 h. Chromatography on alumina with diethyl ether/*n*-hexane (v/v, 1:1) and methanol as eluents afforded air-stable, yellow **13** (253 mg, 0.422 mmol, 25%). M.p. 169 °C. MS (FAB): m/z = 600.9 $[M]^+$. IR (KBr): $\tilde{\nu}$ = 3206 cm^{-1} (w), 3057(w), 1990(vs), 1865 (vs), 1854 (vs), 1819 (vs), 1576 (m), 1466 (m), 1440 (s), 1390 (m), 1360 (s), 1287 (m), 1216 (s), 1125 (m), 1077 (m), 990 (m), 719 (s), 704 (s), 694 (s), 683 (s). ^{1}H NMR [300 MHz, $(CD_3)_2SO$]: δ = 1.80 (s, 6 H, CH_3), 3.84 (s, 3 H, CH_3), 6.69–7.19 (m, 10 H, C_6H_5), 7.54 (d, ^3J = 1.6 Hz, 1 H, $C_3H_2N_2$), 7.67 (d, ^3J = 1.6 Hz, 1 H, $C_3H_2N_2$) ppm. ^{13}C NMR [75.432 MHz, $(CD_3)_2SO$]: δ = 27.6 and 64.4 [$C(CH_3)_2$], 119.6, 121.2, 122.7, 124.3, 127.1, 127.4, 127.7, 128.1, 136.1, and 155.5 (C_6H_5, $C_3H_2N_2$), 184.2 (C=N), 192.4 ($^1J_{C,W}$ = 95 Hz, carbene C), 205.3 [$^1J_{C,W}$ = 129 Hz, $W(CO)_{axial}$], 210.1 [$^1J_{C,W}$ = 146 Hz, $W(CO)_{equatorial}$], 218.2 [$^1J_{C,W}$ = 169 Hz, $W(CO)_{equatorial}$] ppm. ^{183}W NMR [12.483 MHz, $(CD_3)_2SO$, vs. saturated aqueous Na_2WO_4]: δ = –2569 [$W(CO)_4$] ppm. $C_{24}H_{21}N_3O_4W$ (599.28): calcd. C 48.10, H 3.53, N 7.01; found C 47.97, H 3.52, N 6.97.

Crystallography: Crystallographic data for **8**, **12a**, **12b**, and **13** are given in Table 2. The data collection was performed on a Nonius Kappa-CCD equipped with graphite-monochromated Mo-K_α radiation (λ = 0.71073 Å) and a nominal crystal-to-area-detector distance of 36 mm. Intensities were integrated using DENZO and scaled with SCALEPACK.[14] Several scans in φ and ω direction were made to increase the number of redundant reflections, which were averaged in the refinement cycles. This procedure replaces an empirical absorption correction. The structures were solved by direct methods (SHELXS-86) and refined against F^2 (SHELX-97).[15] Hydrogen atoms at carbon atoms were added geometrically and refined using a riding model. All non-hydrogen atoms were refined with anisotropic displacement parameters.

The structure determination of **13** was complicated by two crystallographic characteristics. First, several crystals were examined and showed systematic twinning. The best crystal was measured and the 20 worst overlying reflections were omitted in the refinement. Second, the correct determination of the space group because of a possible transformation to bravais lattice higher in symmetry. In the triclinic space group were two identical molecules, which can be transferred into each other by refinement in the monoclinic space group *C*2/*c*. Nevertheless, the space group *C*2/*c* was excluded because the R_{int} value of 0.176 for 8154 symmetry-equivalent reflections is much higher than the R_{int} value of 0.038 for 4919 reflections in the triclinic space group. In addition, the conventional R_1 value of 0.0750 is also higher (0.0542). The unit cell constants of the transformed C-centered lattice are 3958.4, 856.6, 136.39 pm and 90.04, 97.48, 91.42°. The deviation of the angle γ from over 1° to the correct 90° angle is also too high for this monoclinic space group.

CCDC-252740 (for **8**), -252741 (for **12a**), -252742 (for **12b**), and -252743 (for **13**) contain the supplementary crystallographic data for this paper. These data can be obtained free of charge from The Cambridge Crystallographic Data Centre via www.ccdc.cam.ac.uk/data_request/cif.

Acknowledgments

Support from BASF Aktiengesellschaft, Ludwigshafen, Germany, is gratefully acknowledged.

[1] Reviews: a) *Carbene Chemistry* (Ed.: G. Bertrand), Marcel Dekker, Inc., New York, **2002**; b) W. A. Herrmann, *Angew. Chem.* **2002**, *114*, 1343; *Angew. Chem. Int. Ed.* **2002**, *41*, 1290; c) W. A. Herrmann, T. Weskamp, V. P. W. Böhm, *Adv. Organomet. Chem.* **2001**, *48*, 1; d) C. J. Carmalt, A. H. Cowley, *Adv. Inorg. Chem.* **2000**, *50*, 1; e) D. Bourissou, O. Guerret, F. P. Gabbai, G. Bertrand, *Chem. Rev.* **2000**, *100*, 39; f) A. J. Arduengo, *Acc. Chem. Res.* **1999**, *32*, 913; g) W. A. Herrmann, C. Köcher, *Angew. Chem.* **1997**, *109*, 2257; *Angew. Chem. Int. Ed. Engl.* **1997**, *36*, 2163.

[2] a) T. Weskamp, F. J. Kohl, W. A. Herrmann, *J. Organomet. Chem.* **1999**, *582*, 362; b) T. Weskamp, W. C. Schattenmann, M. Spiegler, W. A. Herrmann, *Angew. Chem.* **1998**, *110*, 2631; *Angew. Chem. Int. Ed.* **1998**, *37*, 2490; c) C. W. Bielawski, R. H. Grubbs, *Angew. Chem.* **2000**, *112*, 3025; *Angew. Chem. Int. Ed.* **2000**, *39*, 2903; d) Review: M. R. Buchmeiser, *Well-Defined Transition Metal Catalysts for Metathesis Polymerization*, in, *Late Transition Metal Polymerization Catalysis* (Eds.: B. Rieger, L. S. Baugh, S. Kacker, S. Striegler), Wiley-VCH, Weinheim, **2003**, chapter 5, p. 155.

[3] a) D. S. McGuiness, V. C. Gibson, D. F. Wass, J. W. Steed, *J. Am. Chem. Soc.* **2003**, *125*, 12 716; b) M. Tilset, O. Andell, A. Dhindsa, M. Froseth (Borealis Technology Oy, Finland), WO 2002049758; *Chem. Abstr.* **2002**, *137*, 63615.

[4] Recent reviews: a) *Late Transition Metal Polymerization Catalysis* (Eds.: B. Rieger, L. S. Baugh, S. Kacker, S. Striegler), Wiley-VCH, Weinheim, **2003**; b) V. C. Gibson, S. K. Spitzmesser, *Chem. Rev.* **2003**, *103*, 283; c) S. Mecking, *Angew. Chem.* **2001**, *113*, 550; *Angew. Chem. Int. Ed.* **2001**, *40*, 534; d) S. D. Ittel, L. K. Johnson, M. Brookhart, *Chem. Rev.* **2000**, *100*, 1169; e) S. Mecking, *Coord. Chem. Rev.* **2000**, *203*, 325; f) G. J. P. Britovsek, V. C. Gibson, D. F. Wass, *Angew. Chem.* **1999**, *111*, 448; *Angew. Chem. Int. Ed.* **1999**, *38*, 428.

[5] G. Steiner, A. Krajete, H. Kopacka, K.-H. Ongania, K. Wurst, P. Preishuber-Pflügl, B. Bildstein, *Eur. J. Inorg. Chem.* **2004**, 2827.

[6] M. Froseth, A. Dhindsa, H. Roise, M. Tilset, *Dalton Trans.* **2003**, 4516.

[7] K. S. Coleman, H. T. Chamberlayne, S. Turberville, M. L. H. Green, A. R. Cowley, *Dalton Trans.* **2003**, 2917.

[8] D. S. McGuiness, K. J. Cavell, *Organometallics* **2000**, *19*, 741.

[9] a) B. Bildstein, P. Denifl, *Synthesis* **1994**, 158; b) G. A. Luinstra, J. Queisser, B. Bildstein, H.-H. Görtz, C. Amort, M. Malaun, A. Krajete, G. Werne, M. O. Kristen, N. Huber, C. Gernert, *Highly Active Ethene Polymerization Catalysts with Unusual Imine Ligands*, in *Late Transition Metal Polymerization Catalysis* (Eds.: B. Rieger, L. S. Baugh, S. Kacker, S. Striegler), Wiley-VCH, Weinheim, **2003**, chapter 3, p. 59.

[10] N. Kuhn, G. Henkel, T. Kratz, *Z. Naturforsch. Teil B* **1993**, *48*, 973.

[11] N. Kuhn, G. Henkel, T. Kratz, *Chem. Ber.* **1993**, *126*, 2047.

[12] a) B. Bildstein, M. Malaun, H. Kopacka, K.-H. Ongania, K. Wurst, *J. Organomet. Chem.* **1999**, *572*, 177; b) B. Bildstein, M. Malaun, H. Kopacka, K.-H. Ongania, K. Wurst, *J. Organomet. Chem.* **1998**, *552*, 45; c) W. A. Herrmann, L. J. Goossen, G. R. J. Artus, C. Köcher, *Organometallics* **1997**, *16*, 2477; d) W. A. Herrmann, C. Köcher, L. J. Goossen, G. R. J. Artus, *Chem. Eur. J.* **1996**, *2*, 1627; e) W. A. Herrmann, L. J. Goossen, C. Köcher, G. R. J. Artus, *Angew. Chem.* **1996**, *108*, 2980; *Angew. Chem. Int. Ed. Engl.* **1996**, *35*, 2805; f) W. A. Herrmann, G. M. Lobmaier, M. Elison, *J. Organomet. Chem.* **1996**, *520*, 231; g) K. Öfele, W. A. Herrmann, D. Mihalios, M. Elison, E. Herdtweck, T. Priermeier, P. Kiprof, *J. Organomet. Chem.* **1995**, *498*, 1.

[13] R. J. Carbajo, L. Zhang, F. Lopez-Ortiz, *Magn. Reson. Chem.* **1998**, *36*, 807.

[14] Processing of X-ray diffraction data collected in oscillation mode: Z. Otwinowski, W. Minor, *Methods Enzymol.* **1997**, *276*, 307.

[15] G. M. Sheldrick, Program package *SHELXTL V.5.1*, Bruker Analytical X-ray Instruments Inc., Madison, USA, **1997**.

Received: October 14, 2004

 © 2005 Wiley-VCH Verlag GmbH & Co. KGaA, Weinheim

Syntheses, Structures, and Magnetic Properties of Two 1D, Mixed-Ligand, Metal Coordination Polymers, $[M(C_4O_4)(dpa)(OH_2)]$ ($M = Co^{II}$, Ni^{II}, and Zn^{II}; dpa = 2,2′-dipyridylamine) and $[Cu(C_4O_4)(dpa)(H_2O)]_2\cdot(H_2O)$

Chih-Chieh Wang,*[a] Cheng-Han Yang,[a] Gene-Hsiang Lee,[b] and Hui-Lien Tsai[c]

Keywords: Hydrogen bonds / Hydrothermal synthesis / Magnetic properties / Self-assembly / Squarate

Two metal coordination polymers with general formula $[M(dpa)(C_4O_4)(H_2O)]$ [M = Co (**1**), Ni (**2**), Zn (**3**); dpa = 2,2′-dipyridylamine] and $[Cu(dpa)(C_4O_4)(H_2O)]_2\cdot H_2O$ (**4**) have been synthesized under hydrothermal conditions. The single-crystal X-ray analyses reveal that compounds **1**–**3** are isostructural and possess distorted octahedral metal centers coordinated by two squarates, one dpa, and two water molecules. A 1D two-legged ladder-like framework is formed by interconnection of the water-bridged $[M(dpa)(\mu_2\text{-}OH_2)]_2^{4+}$ dimeric fragments and $\mu_{1,2}$-squarate ligands. Intra- and intermolecular hydrogen bonds between squarate, water, and dpa ligands, as well as the π-π stacking interaction of the pyridyl ring in the dpa ligands, provide extra forces to stabilize the extended network. Conversely, the molecular structure of compound **4** contains two distorted square-pyramidal Cu^{II} centers coordinated by two squarates, one dpa ligand, and one water molecule. The squarates adopt a $\mu_{1,2}$-binding mode to link the Cu centers and form a 1D helical chain. For compound **2**, the magnetic exchange couplings between metal centers are analyzed with a binuclear magnetic model. The resulting negative magnetic exchange coupling constant indicates an antiferromagnetic interaction within the dimers. The magnetic behavior of compound **4** is typical of paramagnetic Cu^{II} ions.
(© Wiley-VCH Verlag GmbH & Co. KGaA, 69451 Weinheim, Germany, 2005)

Introduction

Owing to its attractive topologies and intriguing structural features,[1–4] the crystal engineering of mixed-ligand metal coordination solids with functional building blocks has received much attention. Among various methodologies to construct novel 1-, 2-, and 3D frameworks, the hydrothermal method has been ubiquitously applied to the synthesis of metal–organic coordination polymers[5–9] and hydrogen-bonded systems.[10] Of significant important is the ability of the organic molecules to influence profoundly the structures of synthesized products, and to dictate their formation with particular structural and potential applications, such as magnetism, host-guest chemistry, shape specificity, and catalysis. The squarate dianion, $C_4O_4^{2-}$, has been widely used as a polyfunctional ligand, for example to induce hydrogen bonding or π-π interactions, for the construction of extended frameworks and has also been used as a bridging ligand to bind metal ions in various bonding modes to create many novel networks.[11–26] The most typical coordination modes of the squarate dianion are $\mu_{1,2}$- (*cis*) and $\mu_{1,3}$- (*trans*). Many squarate-bridged metal complexes with $\mu_{1,2}$-, $\mu_{1,3}$-, or $\mu_{1,2,3,4}$-binding modes combined with different nitrogen-based flexible ligands have been structurally characterized,[19–25] and their magnetic investigation shows that $\mu_{1,3}$-coordination gives a negligibly small coupling, while $\mu_{1,2}$-coordination induces a small antiferromagnetic coupling.[19,26] In this contribution, we describe the synthesis and structural characterization of two 1D coordination polymers, $[M(dpa)(C_4O_4)(H_2O)]$ [M = Co (**1**), Ni (**2**), Zn (**3**)] and $[Cu(dpa)(C_4O_4)(H_2O)]_2\cdot H_2O$ (**4**), by using flexible dpa (2,2′-dipyridylamine) and squarate ($C_4O_4^{2-}$) ligands as building units, as well as the studies of their thermal stability and magnetic properties.

Results and Discussion

Synthesis and IR Spectroscopy of Compounds 1–4

Compounds **1**–**4** were synthesized by mixing the divalent metal salt MCl_2 (M = Co, Ni, Cu, Zn), 2,2′-dipyridylamine (dpa), $H_2C_4O_4$, and H_2O. All reactions were carried out in 23-mL, acid-digestion bombs at 180 °C for three days. Low pH values were observed in all reactions (final pH = 2.82–3.91). The resulting products are very stable in air at ambient temperature and insoluble in common solvents such as water, alcohol, and acetonitrile. It is also worthy to note that the synthetic reproducibility is high. The appearance of N–H stretching vibrations in the region of 3000–

[a] Department of Chemistry, Soochow University, 111, Taipei, Taiwan
Fax: +886-2-2881-1053
E-mail: ccwang@mail.scu.edu.tw
[b] Instrumentation Center, National Taiwan University, Taipei, Taiwan
[c] Department of Chemistry, National Cheng Kung University, Tainan, Taiwan

3400 cm^{-1} in the IR spectrum is in agreement with that reported for hydrogen bonds between N–H and several H-acceptor groups. The most relevant IR features are those associated with the chelating squarate ligands. The coordinated CO groups are characterized by medium-strength absorptions at around 1664 cm^{-1}. A very strong band centered at around 1480 cm^{-1} is attributed to a combination mode of C–O and C–C stretchings and is in agreement with other $(CO)_n^{2-}$ salts.[27]

Crystal Structures of [M(dpa)(C_4O_4)(H_2O)] Complexes

Compounds **1**–**3** were found to be isostructural; a typical structure of **1** is shown in Figure 1. In **1**–**3**, each metal center is six-coordinate and adopts a slightly distorted octahedral coordination environment, being bonded to two nitrogen atoms from dpa ligands and four oxygen atoms from two squarate ligands and two water molecules. The corresponding M–N, M–O_w and M–O_{sq} bond lengths (see Table 1) are similar to those of relevant squarate-bridged metal complexes.[19–21,28,29] Two metal centers are linked together by two bridging water molecules to form an $[M(dpa)(H_2O)]_2^{4+}$ dimeric fragment (see Figure 1) in the equatorial plane. The squarate ligand adopts a $\mu_{1,2}$-binding mode to connect the neighboring $[M(dpa)(\mu_2\text{-}OH_2)]_2$ fragments at the axial sites, constructing a 1D linear two-legged ladder-like metal–organic framework (MOF) along the *a* axis [see (a) in Figure 2]. The M···M separations via μ_2-O_{water} and $\mu_{1,2}$-$C_4O_4^{2-}$ bridges are 3.459(1) and 7.416(1) Å

Table 1. Selected bond lengths [Å] and angles [°] for compounds **1**–**3**.[a]

	1 [M = Co]	**2** [M = Ni]	**3** [M = Zn]
M(1)–O(1)	2.081(1)	2.073(1)	2.096(1)
M(1)–O(2)	2.119(1)	2.096(1)	2.148(1)
M(1)–O(5)	2.155(2)	2.105(2)	2.133(1)
M(1)–$O(5)_i$	2.213(2)	2.175(2)	2.282(1)
M(1)–N(1)	2.121(2)	2.075(2)	2.117(2)
M(1)–N(3)	2.095(2)	2.056(2)	2.088(1)
C(1)–O(1)	1.256(3)	1.255(2)	1.261(2)
C(2)–$O(2)_{ii}$	1.251(3)	1.248(2)	1.256(2)
C(3)–O(3)	1.252(3)	1.257(2)	1.255(2)
C(4)–O(4)	1.270(2)	1.270(2)	1.270(2)
C(1)–C(2)	1.477(3)	1.475(3)	1.471(2)
C(2)–C(3)	1.474(3)	1.476(3)	1.471(2)
C(3)–C(4)	1.456(3)	1.449(3)	1.454(2)
C(4)–C(1)	1.454(3)	1.461(3)	1.452(2)
O(1)–M(1)–O(2)	176.37(6)	174.43(6)	174.35(5)
O(1)–M(1)–O(5)	91.53(6)	92.46(6)	92.06(5)
O(1)–M(1)–$O(5)_i$	90.11(6)	90.09(6)	89.32(5)
O(1)–M(1)–N(1)	92.50(6)	92.29(6)	93.66(5)
O(1)–M(1)–N(3)	90.55(6)	89.04(6)	90.34(5)
O(2)–M(1)–O(5)	90.54(6)	91.77(6)	90.22(5)
O(2)–M(1)–$O(5)_i$	87.54(6)	87.48(6)	86.27(5)
O(2)–M(1)–N(1)	90.07(6)	90.62(7)	91.03(5)
O(2)–M(1)–N(3)	86.93(6)	86.18(6)	86.47(5)
O(5)–M(1)–$O(5)_i$	75.25(6)	75.22(6)	75.15(5)
O(5)–M(1)–N(1)	100.01(7)	99.14(6)	99.99(5)
O(5)–M(1)–N(3)	170.54(7)	170.09(6)	169.01(5)
O(5)i–M(1)–N(1)	174.65(7)	173.98(6)	174.40(5)
O(5)i–M(1)–N(3)	95.52(7)	94.99(6)	94.17(5)
N(1)–M(1)–N(3)	89.12(7)	90.58(7)	90.55(6)

[a] Symmetry operations used to generate equivalent atoms: (i) $-x, -y, -z$; (ii) $x + 1, y, z$.

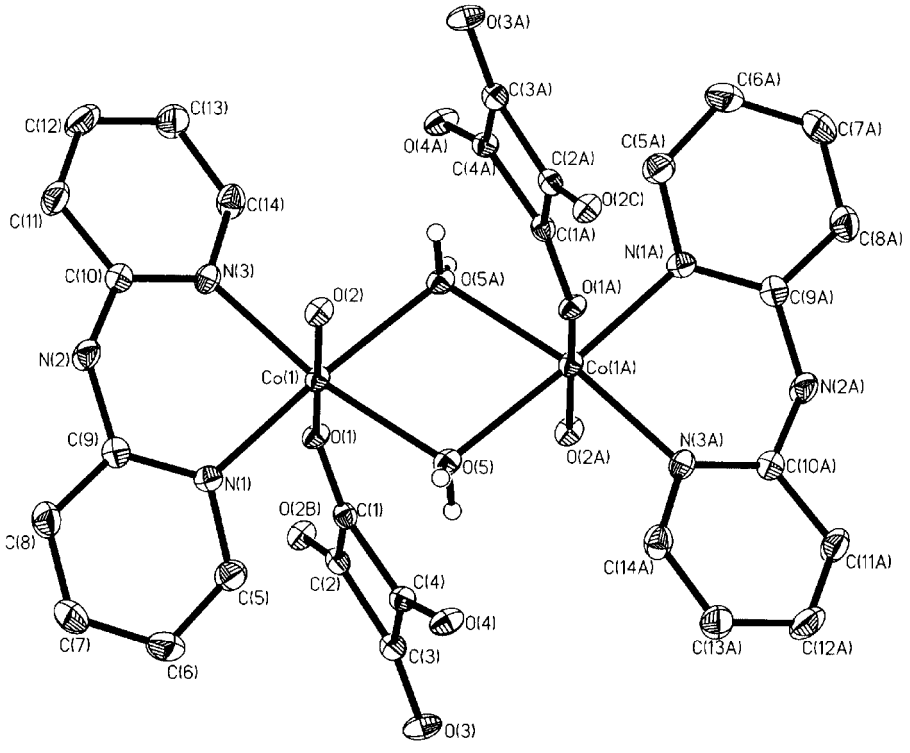

Figure 1. The basic building block of compound **1** showing the atom numbering scheme. Ellipsoids are drawn at the 50% probability level. Symmetry codes: A ($-x, -y, -z$), B ($1 + x, y, z$), C ($-1 - x, -y, -z$).

 © 2005 Wiley-VCH Verlag GmbH & Co. KGaA, Weinheim

for **1**, 3.391(1) and 7.377(1) Å for **2**, and 3.501(1) and 7.458(1) Å for **3**. The corresponding C–C and C–O bond lengths (see Table 1) of the squarate ligands show a roughly D_{4h} delocalized mode and fall in the same range as some analogous squarate-bridged complexes.[19–21,29] It should be noted that adjacent ladders are displaced by half a repeating unit along the *a* and *c* axes. This arrangement effectively prevents steric hindrance between the inter-ladder dpa ligands. As a result, compounds **1**–**3** favor the closer-packed building block shown in Figure 2. The centroids of the pyridine rings in the dpa ligands of adjacent ladders are generally parallel and adopt a face-to-face alignment with a separation distance within the range 3.59–3.82 Å, thus indicating a weak π–π stacking interaction[28,30] that may, in part, contribute to the stabilization of the extended framework. Hydrogen-bond formation is a very important aspect in constructing coordination polymers.[31–35] In compounds **1**–**3**, two strong O–H···O hydrogen bonds [O(5)–H(5a)···O(4) and O(5)–H(5b)···O(3)] are found between uncoordinated oxygen atoms of squarate and the coordinated water molecules, with O···O distances in the range of 2.528–2.600 Å, which are similar to those (2.589–2.748 Å) of O_{sq}···O_w-type hydrogen bonds found in other squarate-bridged compounds.[19–22,28b] In addition, the inter-ladder interactions are through one pair of N–H···O [N(2)–H(2a)···O(4)] and C–H···O [C(11)–H(11a)···O(4)] hydrogen bonds from the same dpa molecule linked to the oxygen atom of squarate in the neighboring ladders to form a mixed N–H···O and C–H···O hydrogen bond (dashed line in Figure 2(b)]. A similar hydrogen-bonding interaction has also been found in complexes such as [Fe(ox)(dpa)][28a] and $[M_2(dpa)_2(C_2O_4)(C_4O_4)]$.[28b] Relevant bond lengths and angles of the O–H···O, N–H···O and C–H···O hydrogen bonds for **1**–**3** are summarized in Table 2.

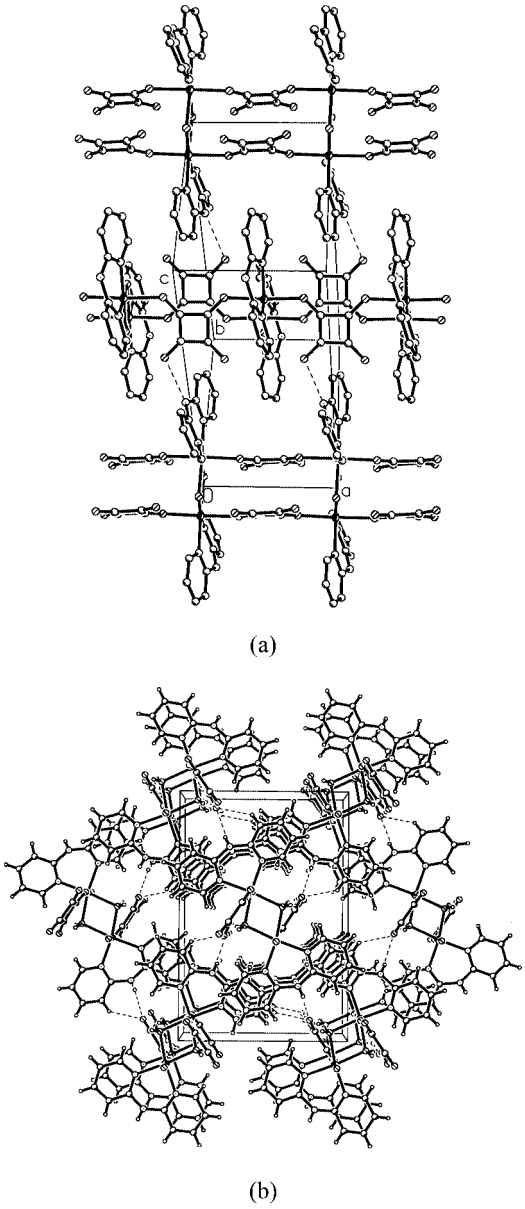

Figure 2. Perspective view of compound **1** along the crystallographic *b* axis (a) and the *a* axis (b).

Crystal Structure of $[Cu(dpa)(C_4O_4)(H_2O)]_2\cdot(H_2O)$ (4)

The asymmetric unit of compound **4** contains two copper ions, two squarates, two dpa ligands, and one solvated, doubly coordinated water molecule. Each of the two independent Cu centers adopts a slightly distorted square-pyramidal coordination environment, but is subject to different environments incorporating squarate and water molecules (Figure 3). In the equatorial plane, Cu(1) is bonded to two nitrogen atoms of dpa and two oxygen atoms of the two squarate ligands, while Cu(2) is bonded to two nitrogen atoms of dpa and two oxygen atoms, one from $C_4O_4^{2-}$ and the other from the water molecule. The axial ligand bonded to Cu(1) is the oxygen atom of a water molecule [O(9)], while that bonded to Cu(2) is an oxygen atom of a squarate [O(6)], forming a distorted square-pyramidal coordination environment. A 1D helical chain is observed in which the copper ions are alternately bridged by equatorial-axial and equatorial-equatorial $\mu_{1,2}$-$C_4O_4^{2-}$ ligands (Figure 4). The Cu···Cu separations across the equatorial-axial and equatorial-equatorial $C_4O_4^{2-}$ bridges are 4.832(4) Å and 5.392(4) Å, respectively. The former is longer than that of 4.328(1) Å in $[Cu(C_4O_4)(C_4H_4N_2)]_n$[36] but shorter than other relevant $\mu_{1,2}$- or $\mu_{1,2,3,4}$-$C_4O_4^{2-}$-bridged Cu complexes.[19a,22,26b,37] As expected, the axial Cu(1)–$O(9)_w$ and Cu(2)–$O(6)_{sq}$ distances of 2.242(2) and 2.174(2) Å are significantly longer than the equatorial Cu(1)–$O(1)_{sq}$ and Cu(1)–$O(5)_{sq}$ bond lengths [2.026(2) and 1.955(2) Å respectively] and the Cu(2)–$O(2)_{sq}$ and Cu(2)–$O(10)_w$ bond lengths [2.013(2) and 1.954(2) Å respectively] due to the Jahn–Teller distortion. The corresponding Cu–O_w, Cu–O_{sq}, and Cu–N bond lengths listed in Table 3 are similar to those found in some other squarate-bridged Cu complexes.[22–26,32,37] Hydrogen bonds also play an important role in the helical chain of compound **4**. These include three O–H···O hydrogen bonds [O(11)–H(11a)···O(8), O(10)–H(10b)···O(11), and O(9)–H(9b)···O(2)] between water molecules and squarate ligands, with O···O distances

 © 2005 Wiley-VCH Verlag GmbH & Co. KGaA, Weinheim

Table 2. Hydrogen bonds for compounds **1**–**3**.[a]

	Donor–H [Å]	Donor···Acceptor [Å]	H···Acceptor [Å]	∠Donor–H···Acceptor [°]
	O(5)–H(5a)	O(5)···O(4)	H(5a)···O(4)	∠O(5)–H(5a)···O(4)
1 [Co]	0.795(3)	2.574	1.784	172.6
2 [Ni]	0.812(3)	2.568	1.764	170.5
3 [Zn]	0.874(2)	2.584	1.712	174.8
	O(5)–H(5b)	O(5)···O(3)$_i$	H(5b)···O(3)$_i$	∠O(5)–H(5b)···O(3)$_i$
1 [Co]	0.760(4)	2.528	1.829	170.7
2 [Ni]	0.839(3)	2.574	1.738	174.6
3 [Zn]	0.891(3)	2.587	1.713	166.1
	N(2)–H(2a)	N(2)···O(4)$_{ii}$	H(2a)···O(4)$_{ii}$	∠N(2)–H(2a)···O(4)$_{ii}$
1 [Co]	0.860(2)	2.874	2.074	154.5
2 [Ni]	0.859(2)	2.871	2.080	152.6
3 [Zn]	0.860(2)	2.869	2.076	153.1
	C(11)–H(11a)	C(11)···O(4)$_{ii}$	H(11a)···O(4)$_{ii}$	∠C(11)–H(11a)···O(4)$_{ii}$
1 [Co]	0.929(3)	3.231	2.465	139.9
2 [Ni]	0.930(2)	3.248	2.486	139.3
3 [Zn]	0.931(2)	3.234	2.467	139.8

[a] Symmetry operations used to generate equivalent atoms: (i) –1 + *x*, *y*, *z*; (ii) –0.5 + *x*, 0.5 – *y*, 0.5 + *z*.

in the range 2.588–2.785 Å, similar to those (2.589–2.748 Å) of O_{sq}···O_w-type hydrogen bonds found in other squarate-bridged compounds.[19–22] The inter-chain interactions are through hydrogen bonds between the dpa nitrogen atoms in one chain and uncoordinated squarate oxygen atoms in the adjacent chain, with hydrogen-bonding distances N(2)–H(2a)···O(3)$_{ii}$ of 2.776 Å and N(5)–H(5a)···O(4)$_{iii}$ of 2.961 Å (dashed line in Figure 4). Relevant bond lengths and angles of the O–H···O and N–H···O hydrogen bonds for complex **4** are listed in Table 4.

Magnetic Properties

Compound 2

Plots of the magnetic susceptibility (χ_M and $\chi_M T$) in the temperature range of 5–300 K for **2** are shown in Figure 5. At room temperature, the $\chi_M T$ value is 2.31 emu K mol^{-1}, which, upon cooling, slowly decreases to a value of 2.05 emu K mol^{-1} at 75 K and then drops rapidly from 1.66 emu K mol^{-1} at 30 K to 0.35 emu K mol^{-1} at 5 K. This seems to be characteristic of weakly antiferromagnetic be-

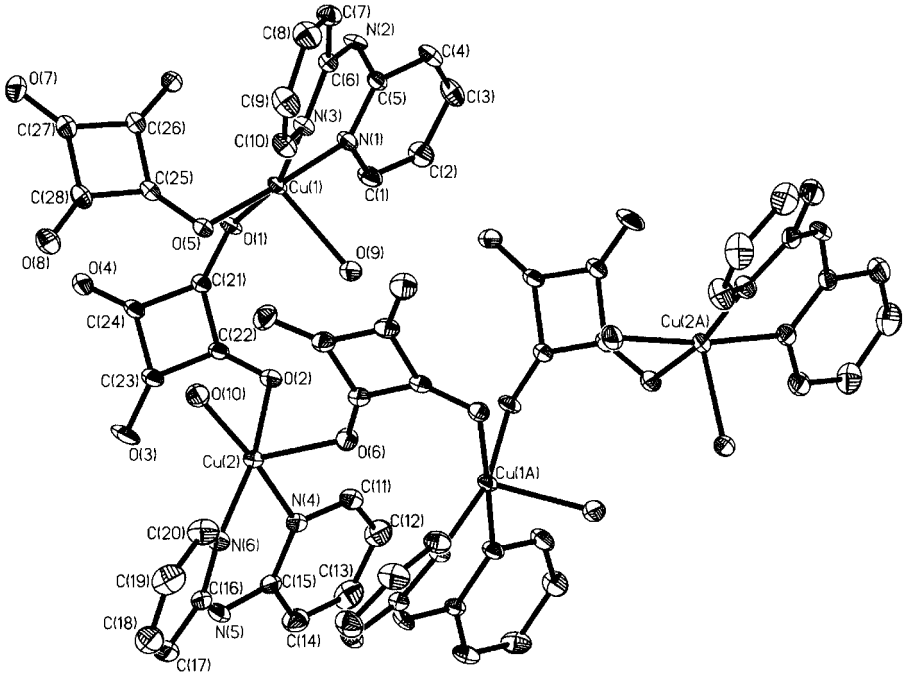

Figure 3. The basic building block of compound **4** showing the atom numbering scheme. Ellipsoids are drawn at the 50% probability level. Symmetry codes: A (–0.5 – *x*, –0.5 + *y*, *z*).

 © 2005 Wiley-VCH Verlag GmbH & Co. KGaA, Weinheim

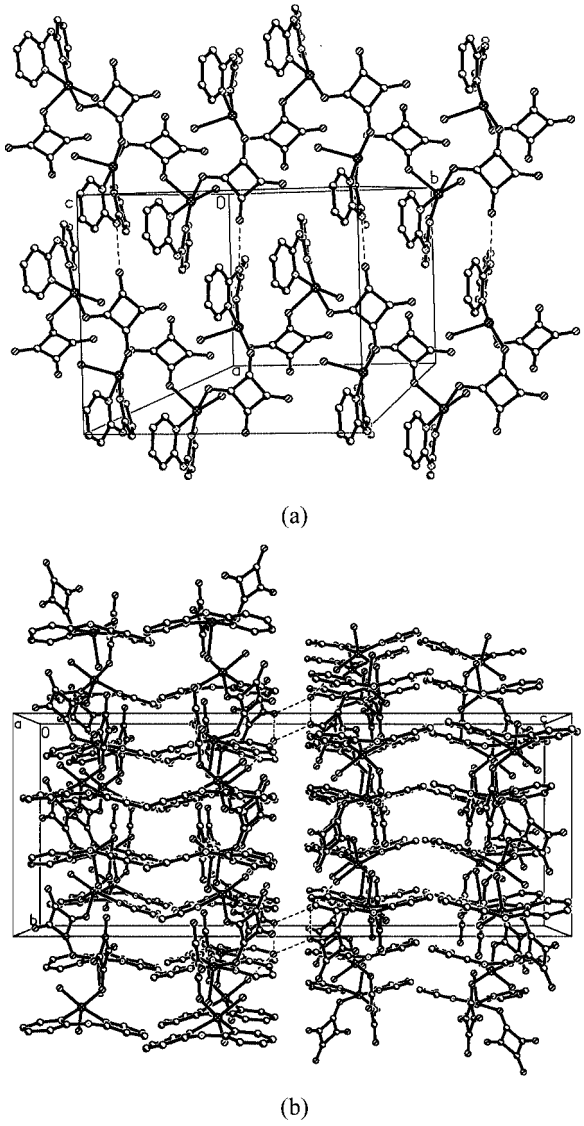

Figure 4. Perspective view of compound **4** along the crystallographic *c* axis (a) and the *a* axis (b).

havior. In order to analyze the magnetic exchange coupling interaction in **2**, the susceptibility data was fitted to a binuclear magnetic model, namely a dimer formed by double μ-OH_2 bridges, $[(dpa)Ni(\mu_2\text{-}OH_2)_2Ni(dpa)]^{4+}$. The corresponding molar susceptibility was calculated from the Hei-

Table 3. Selected bond length [Å] and angles [°] for compound **4**.[a]

Cu(1)–O(1)	2.026(2)	Cu(2)–O(2)	2.013(2)
Cu(1)–O(5)	1.955(2)	Cu(2)–O(6)	2.174(2)
Cu(1)–O(9)	2.242(2)	Cu(2)–O(10)	1.954(2)
Cu(1)–N(1)	1.984(2)	Cu(2)–N(4)	1.985(2)
Cu(1)–N(3)	2.014(2)	Cu(2)–N(6)	1.991(2)
C(21)–O(1)	1.274(3)	C(25)–O(5)	1.270(3)
C(22)–O(2)	1.272(3)	$C(26)–O(6)_i$	1.254(3)
C(23)–O(3)	1.237(3)	C(27)–O(7)	1.237(3)
C(24)–O(4)	1.249(3)	C(28)–O(8)	1.241(3)
C(21)–C(22)	1.444(3)	C(25)–C(26)	1.448(3)
C(22)–C(23)	1.449(3)	C(26)–C(27)	1.476(3)
C(23)–C(24)	1.477(3)	C(27)–C(28)	1.475(4)
C(24)–C(21)	1.464(3)	C(28)–C(25)	1.454(3)
O(5)–Cu(1)–N(1)	175.64(8)	O(10)–Cu(2)–N(4)	169.4(1)
O(5)–Cu(1)–N(3)	91.92(8)	O(10)–Cu(2)–N(6)	92.4(1)
N(1)–Cu(1)–N(3)	90.62(7)	N(4)–Cu(2)–N(6)	89.19(8)
O(5)–Cu(1)–O(1)	85.53(7)	O(10)–Cu(2)–O(2)	85.30(9)
N(1)–Cu(1)–O(1)	91.08(7)	N(4)–Cu(2)–O(2)	91.04(8)
N(3)–Cu(1)–O(1)	164.31(8)	N(6)–Cu(2)–O(2)	168.24(8)
O(5)–Cu(1)–O(9)	93.88(8)	O(10)–Cu(2)–O(6)	95.28(9)
N(1)–Cu(1)–O(9)	89.33(9)	N(4)–Cu(2)–O(6)	94.73(7)
N(3)–Cu(1)–O(9)	96.87(9)	N(6)–Cu(2)–O(6)	100.26(8)
O(1)–Cu(1)–O(9)	98.75(8)	O(2)–Cu(2)–O(6)	91.43(7)

[a] Symmetry operations used to generate equivalent atoms: (i) $-x + 1/2, y - 1/2, z$.

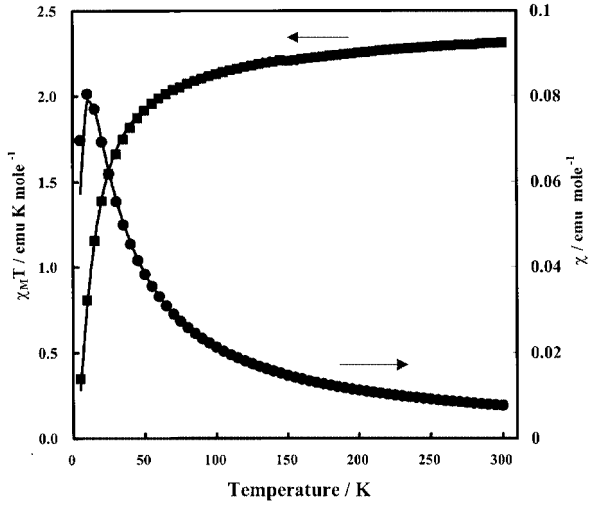

Figure 5. Plots of χ_M (●) and $\chi_M T$ (■) vs. T [K] for **2**. The solid line represents the best theoretical fit.

Table 4. Hydrogen bonds for compound **4**.[a]

Donor–H [Å]		Donor···Acceptor [Å]		H···Acceptor [Å]		∠ Donor–H···Acceptor [°]	
O(11)–H(11a)	0.950(4)	$O(11)\cdots O(8)_i$	2.759	$H(11a)\cdots O(8)_i$	1.939	$\angle O(11)–H(11a)\cdots O(8)_i$	143.1
O(11)–H(11b)	0.774(4)	O(11)···O(8)	2.785	H(11b)···O(8)	2.017	∠O(11)–H(11b)···O(8)	171.1
O(10)–H(10b)	0.895(4)	O(10)···O(11)	2.588	H(10b)···O(11)	1.707	∠O(10)–H(10b)···O(11)	167.3
O(9)–H(9b)	0.815(3)	O(9)···O(2)	2.768	H(9b)···O(2)	2.122	∠O(9)–H(9b)···O(2)	136.1
N(2)–H(2a)	0.860(2)	$N(2)\cdots O(3)_{ii}$	2.776	$H(2a)\cdots O(3)_{ii}$	2.033	$\angle N(2)–H(2a)\cdots O(3)_{ii}$	144.2
N(5)–H(5a)	0.860(2)	$N(5)\cdots O(4)_{iii}$	2.961	$H(5a)\cdots O(4)_{iii}$	2.263	$\angle N(5)–H(5a)\cdots O(4)_{iii}$	138.4

[a] Symmetry operations used to generate equivalent atoms: (i) $1 - x, -y, 1 - z$; (ii) $1 + x, y, z$; (iii) $1.5 - x, 0.5 + y, z$.

 © 2005 Wiley-VCH Verlag GmbH & Co. KGaA, Weinheim

senberg model ($H = -2JS_1S_2$, $S_1 = S_2 = 1$) given in Equation (1)[42]

$$\chi'_M = \frac{Ng^2\beta^2}{kT}\frac{2\exp(x)+10\exp(3x)}{1+3\exp(x)+5\exp(6x)} + TIP \quad (1)$$

where N, g, β, and x are the Avogadro number, g factor, Bohr magneton, and J/kT, respectively; TIP is the temperature-independent paramagnetism of the Ni^{2+} ion. The best fitting results for magnetic susceptibility data give $TIP = 4.00\times10^{-4}$ emu mol^{-1}, $g = 2.13$, $J = -3.9$ cm^{-1}, and $R = 2.80\times10^{-5}$ [$R = \Sigma[(\chi_M T)_{obs} - (\chi_M T)_{cal}]^2/\Sigma(\chi_M T)^2_{obs}$]. As shown in Figure 5, the solid lines obtained from the theoretical approach are in good agreement with the experimental results. The negative value of J, according to the crystallographic results, indicates an antiferromagnetic interaction through the water bridges between Ni^{II} ions in the [(dpa)-Ni(μ_2-OH$_2$)$_2$Ni(dpa)] dimer and the spin-orbit coupling contributes trivially to the g factor. The intermolecular exchange interactions through $\mu_{1,2}$-squarate bridges can be ignored since there is only a weak antiferromagnetic interaction through the squarate bridge in [Ni(C$_4$O$_4$)(tren)(H$_2$O)$_2$](ClO$_4$)$_2$ ($J = -0.4$ cm^{-1}).[19]

Compound 4

The temperature dependence of the magnetic susceptibilities of **4** in the form of χ_M and $\chi_M T$ vs. T plots is shown in Figure 6. At room temperature, the $\chi_M T$ value is 0.89 emu K mol^{-1}, which is equal to the spin-only $\chi_M T$ value of 0.89 when $g = 2.18$, expected for a doubly uncoupled $S = 1/2$ system. As the temperature decreases, the $\chi_M T$ value remains nearly unchanged and finally reaches a value of 0.88 emu K mol^{-1} at 5 K. This magnetic behavior indicates the existence of a very weak antiferromagnetic interaction between the Cu^{II} ions. Based on the framework of compound **4**, two possible origins of the magnetic properties are tentatively proposed, namely the magnetism induced from either the equatorial-axial squarate bridge with a separation distance of 4.832(4) Å or the equatorial-equatorial squarate bridge separated by 5.392(4) Å. In either case, the magnetic interaction is mainly dominated by the equatorial-axial squarate bridge. As a result, the magnetic susceptibility data can be fitted with the binuclear magnetic model to give $TIP = 0.0$ emu mol^{-1}, $g = 2.18$, $J = -0.08$ cm^{-1} and $R = 9.24\times10^{-6}$. The solid lines obtained from the theoretical model in Figure 6 demonstrate a good agreement between the theoretical and experimental results. For complex **4**, the magnetic interaction via the squarate bridge is rather small and it can thus be treated as a paramagnetic ion because of the weak overlap between the magnetic orbital through the $\mu_{1,2}$-bis-monodentate squarate bridging ligands.[24] However, the magnetic susceptibility data can be fitted to a Curie–Weiss law with $\theta = +0.224$ K, and $C = 0.444$ emu K mol^{-1}. The Curie constant agrees well with the value of $g = 2.18$ for a copper(II) one-spin electron configuration, which corresponds to a value of $\chi_M T$ per copper ion of 0.89 emu K mol^{-1}. The small, positive Weiss constant does not really reflect a weak ferromagnetic interaction but rather implies that there is a lack of strong metal–metal interactions within the frameworks.

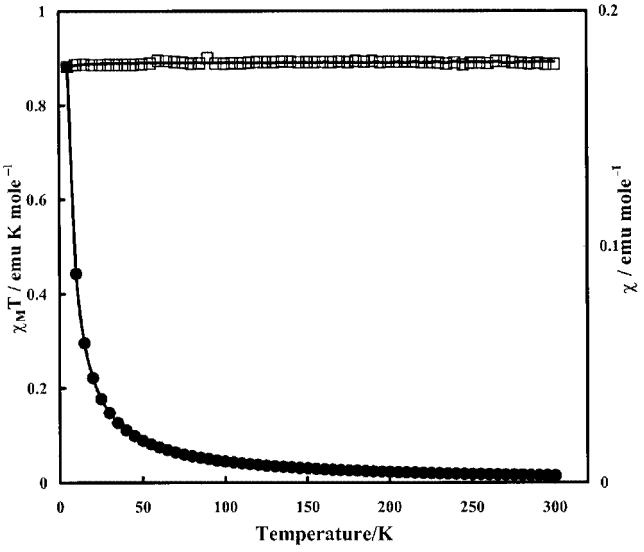

Figure 6. Plots of χ_M (●) and $\chi_M T$ (□) vs. T [K] for **4**. The solid line represents the best theoretical fit.

Compound 1

The magnetic behavior of **1** is illustrated in Figure 7 as a plot of $\chi_M T$ as a function of temperature in the range 5–300 K. At room temperature, the $\chi_M T$ value is 3.94 emu K mol^{-1}, which is close to the value (3.76 cm^3 K mol^{-1}) of a doubly uncoupled $S = 3/2$ spin system. The value of $\chi_M T$ slowly increases as the temperature decreases, and reaches a maximum (4.18 emu K mol^{-1}) near 125 K. It then decreases continuously and finally reaches a value of 1.52 emu K mol^{-1} at 5 K. For a weak-field configuration ($A = 1.5$) the value of $\chi_M T$ (3.94 emu K mol^{-1}) is unexpectedly large. Note that a similar phenomenon has been reported in the case of $CoBr_2$.[39] From the geometry point

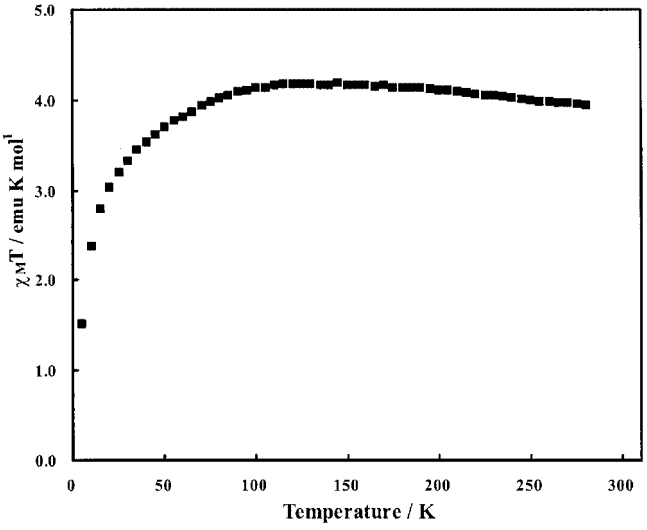

Figure 7. Plots of $\chi_M T$ (■) vs. T [K] for **1**.

 © 2005 Wiley-VCH Verlag GmbH & Co. KGaA, Weinheim

of view, the magnetic behavior may originate from the antiferromagnetic dimers $[(dpa)Co(\mu_2\text{-}OH_2)_2Co(dpa)]^{4+}$, bridged by H_2O ligands [Co···Co separation of 3.459(1) Å] similar to that of complex **2**. However, the susceptibility data could not be analyzed by using an expression for the magnetic susceptibility of a dinuclear cobalt(II) system because the dinuclear system does not take into account the effects of the zero-field splitting and/or spin-orbital coupling, which may be significant for cobalt(II) ions.[38,40]

Thermogravimetric Analysis

To assess the thermal stability of compounds **1**–**4** and their structural variation as a function of the temperature, thermogravimetric analysis (TGA) was performed on single-phase polycrystalline samples for each compound. The former three compounds (**1**–**3**) all undergo a continuous, single-step weight-loss process (losing coordinated water, followed by detachment of dpa and squarate groups) and are thermally stable up to at least 175 °C. The on-set temperatures for the weight losses are approximately 175 °C, 258 °C, and 180 °C for **1**–**3**, respectively. The decomposition processes were completed at approximately 454 °C for **1**, 361 °C for **2**, and 436 °C for **3**. These samples are then decomposed completely. The final products of the pyrolysis were identified as Co_3O_4, NiO, and ZnO, with remaining percentages of 20.25, 22.25, and 22.92%. The high thermal stability of these compounds can be mainly attributed to the intra- and intermolecular hydrogen bonds in combination with the π-π stacking interaction.

For compound **4**, the dehydration takes place in a temperature range 50–100 °C with a weight lost of 6.6%, corresponding to the calculated value (7.2%) for loss of one solvated and two coordinated water molecules. The loss of squarate groups occurs in the range 210–260 °C, with the weight loss of 30.0% corresponding to the calculated value of 30.5%. Above 290 °C the dpa ligand is degraded. The final pyrolysis product is CuO, with a remaining percentage of 20.98%.

Conclusions

In conclusion, under hydrothermal conditions, we have successfully synthesized two metal coordination polymer frameworks $[M(dpa)(C_4O_4)(H_2O)]$ [M = Co (**1**), Ni (**2**), Zn (**3**)] and $[Cu(dpa)(C_4O_4)(H_2O)]_2{\cdot}H_2O$ (**4**), the structures of which have been well characterized by X-ray diffraction. The squarate ligands afford a $\mu_{1,2}$-bridging coordination mode as well as hydrogen-bonding capability to build a 1D two-legged ladder-like MOF for compounds **1**–**3** and a 1D helical chain for compound **4**. The magnetic studies indicate a weak antiferromagnetic interaction via H_2O bridges for **1** and **2** and paramagnetism for **4**.

Experimental Section

Materials and Physical Techniques: All chemicals were of reagent grade and were used as received. The IR spectra were recorded on a Nicolet Fourier Transform IR, MAGNA-IR 500 spectrometer in the range of 500–4000 cm^{-1} using the KBr disc technique. The magnetic susceptibilities were measured on polycrystalline samples of compound **1** (Co), **2** (Ni), and **4** (Cu) at a field of 10000 G over a temperature range from 5 to 300 K with a SQUID magnetometer. Diamagnetic corrections were made with Pascal's constants for all constituent atoms, and the magnetic moments were calculated by the equation $\mu_{eff} = 2.828(\chi_M T)^{1/2}$. Thermogravimetric analyses (TGA) of the title compounds were performed on a computer-controlled Perkin–Elmer 7 Series/UNIX TGA7 analyzer. Single-phase powder samples of **1** (4.014 mg), **2** (5.079 mg), **3** (1.532 mg), and **4** (4.406 mg) were loaded into alumina pans and heated with a ramp rate of 5 °C min^{-1} from room temperature to 900 °C under nitrogen.

Synthesis of $[Co(dpa)(C_4O_4)(H_2O)]$ (1): Reaction of anhydrous $CoCl_2$ (0.0131 g, 0.1 mmol), $H_2C_4O_4$ (0.0114 g, 0.1 mmol), dpa (0.0348 g, 0.2 mmol), and deionized water (6 mL) in a molar ratio of 1:1:2:3333 at 180 °C for three days produced red, column-like crystals of **1** in a yield of 0.0198 g (54.9%) based on Co^{II}. The final pH value was 3.28. IR (KBr): $\tilde{\nu}$ = 3319 (w), 3204 (w), 3141 (w), 3041 (w), 1651 (m), 1582 (m), 1540 (s), 1480 (vs), 1425 (s), 1379 (m), 1235 (m), 1160 (m), 1011 (m), 847 (w), 763 (m), 646 (w) cm^{-1}. $C_{14}H_{11}CoN_3O_5$ (360.19): calcd. C 46.69, H 3.08, N 11.67; found C 46.78, H 3.01, N 11.64.

Synthesis of $[Ni(dpa)(C_4O_4)(H_2O)]$ (2): Reaction of $NiCl_2{\cdot}6H_2O$ (0.0241 g, 0.1 mmol), $H_2C_4O_4$ (0.0115 g, 0.1 mmol), dpa (0.0352 g, 0.2 mmol), and deionized water (6 mL) in a molar ratio of 1:1:2:3333 at 180 °C for three days produced light-blue, column-like crystals of **2** in a yield of 0.0194 g (53.9%) based on Ni^{II}. The final pH value was 2.82. IR (KBr): $\tilde{\nu}$ = 3319 (w), 3206 (w), 3143 (w), 3043 (w), 1652 (s), 1601 (s), 1580 (s), 1541 (vs), 1486 (vs, broad), 1434 (vs), 1381 (s), 1276 (m), 1236 (m), 1166 (m), 1160 (s), 1081 (m), 1047 (m), 1015 (m), 900 (m), 851 (m), 789 (m), 763 (m), 648 (w) cm^{-1}. $C_{14}H_{11}N_3NiO_5$ (359.97): calcd. C 46.72, H 3.08, N 11.67; found C 46.87, H 2.92, N 11.76.

Synthesis of $[Zn(dpa)(C_4O_4)(H_2O)]$ (3): Reaction of anhydrous $ZnCl_2$ (0.0136 g, 0.1 mmol), $H_2C_4O_4$ (0.0114 g, 0.1 mmol), dpa (0.0340 g, 0.2 mmol), and deionized water (6 mL) in a molar ratio of 1:1:2:3333 at 180 °C for three days produced light-brown, needle-like crystals of **3** in a yield of 0.0256 g (69.8%) based on Zn^{II}. The final pH value was 3.74. IR (KBr): $\tilde{\nu}$ = 3307 (w), 3210 (w), 3148 (w), 3037 (w), 1644 (m), 1586 (m), 1532 (s), 1483 (vs), 1379 (m), 1272 (w), 1236 (m), 1160 (m), 1013 (m), 765 (m), 648 (w) cm^{-1}. $C_{14}H_{11}N_3O_5Zn$ (366.63): calcd. C 45.86, H 2.02, N 11.46; found C 45.31, H 2.12, N 11.35.

Synthesis of $[Cu(dpa)(C_4O_4)(H_2O)]_2{\cdot}(H_2O)$ (4): Reaction of $CuCl_2{\cdot}6H_2O$ (0.0170 g, 0.1 mmol), $H_2C_4O_4$ (0.0114 g, 0.1 mmol), dpa (0.0170 g, 0.2 mmol), and deionized water (6 mL) in a molar ratio of 1:1:1:3333 at 180 °C for three days produced black, column-like crystals of **4** in a yield of 0.074 g (98.9%) based on Cu^{II}. The final pH value was 2.94. IR (KBr): $\tilde{\nu}$ = 3304 (w), 3204 (w), 3141 (w), 3106 (w), 3041 (w), 1652 (m), 1589 (m), 1520 (vs), 1483 (vs), 1463 (vs), 1434 (m), 1332 (m), 1241 (m), 1157 (m), 1082 (m), 1025 (m), 766 (m), 650 (m) cm^{-1}. $C_{28}H_{24}Cu_2N_6O_{11}$ (747.61): calcd. C 44.98, H 3.08, N 11.67; found C 44.58, H 2.89, N 11.15.

X-ray Crystallographic Study: Single-crystal structure analyses for compounds **1**–**4** were performed on a Siemens SMART diffractometer with a CCD detector with Mo-K_α radiation (λ = 0.71073 Å) at room temperature. A preliminary orientation matrix and unit-cell parameters were determined from three runs of 15 frames each, with each frame corresponding to a 0.3° scan in 10 s, following by spot integration and least-squares refinement. For each structure, data were measured using ω scans of 0.3° per frame

 © 2005 Wiley-VCH Verlag GmbH & Co. KGaA, Weinheim

Table 5. Crystal data for Compounds **1**–**4**.

	1	**2**	**3**	**4**
Empirical formula	$C_{14}H_{11}CoN_3O_5$	$C_{14}H_{11}N_3NiO_5$	$C_{14}H_{11}N_3O_5Zn$	$C_{28}H_{24}Cu_2N_3O_5$
Molecular mass	360.19	359.97	366.63	747.61
Crystal system	monoclinic	monoclinic	monoclinic	orthorhombic
Space group	$P2_1/n$	$P2_1/n$	$P2_1/n$	$Pbca$
a [Å]	7.4158(2)	7.3768(2)	7.4583(2)	11.7740(3)
b [Å]	11.1131(4)	11.0999(3)	11.1632(3)	13.8920(4)
c [Å]	16.3588(5)	16.1870(5)	16.2761(4)	35.1467(9)
β [°]	91.464(1)	91.337(1)	91.494(1)	
V [Å^3]	1347.73(7)	1325.06(6)	1354.66(6)	5748.7(3)
Z	4	4	4	8
$D_{calcd.}$ [g cm^{-3}]	1.775	1.804	1.798	1.728
T [K]	295(2)	295(2)	295(2)	295(2)
μ [mm^{-1}]	1.306	1.497	1.845	1.555
Refl. collected	11321	11512	13735	46336
Refl. unique/R_{int}	3102/0.0321	3048/0.0348	3120/0.0248	6606/0.0367
Refl. with [$I > 2\sigma(I)$]	2291	2269	2499	4894
N_v	216	216	216	448
R_F[a] R_w[b] (all data)	0.0516, 0.0772	0.0503, 0.0654	0.0339, 0.0615	0.0304, 0.0793
R_F[a] R_w[b] [$I > 2\sigma(I)$]	0.0308, 0.0726	0.0295, 0.0612	0.0235, 0.0592	0.0510, 0.0906
Goodness-of-fit	1.011	1.004	1.029	1.076
$\Delta\rho_{max./min.}$ [e Å^{-3}]	+0.377/–0.355	+0.344/–0.414	+0.335/–0.289	+0.332/–0.370

[a] $R_F = \Sigma||F_o| - |F_c||/\Sigma|F_o|$. [b] $R_w(|F|^2) = [\Sigma w(|F_o|^2 - |F_c^2|)^2/\Sigma w|F_o|^2]^{1/2}$.

for 20 s until a complete hemisphere had been collected. Cell parameters were retrieved with SMART[41] software and refined with SAINT[42] on all observed reflections. Data reduction was performed with SAINT and corrected for Lorentz and polarization effects. Absorption corrections were applied with the program SADABS.[43] Direct phase-determination and subsequent difference-Fourier map synthesis yielded the positions of non-hydrogen atoms, which were subjected to anisotropic refinements. For **1**–**4**, all hydrogen atoms were generated geometrically (C–H: 0.95) with the exception of the hydrogen atoms of the coordinated water molecules, which were located in the difference Fourier map with the corresponding positions and isotropic displacement parameters being refined. A final full-matrix, least-squares refinement method on F^2 was applied for all observed reflections [$I > 2\sigma(I)$]. All calculations were performed with the SHELXTL-PC V 5.03 software package.[44] Crystal data and details of the data collection and structure refinements for **1**–**4** are summarized in Table 5.

CCDC-205773 (for **1**), -205772 (for **2**), -172057 (for **3**) and -205774 (for **4**) contain the supplementary crystallographic data for this paper. These data can be obtained free of charge from The Cambridge Crystallographic Data Center via www.ccdc.cam.ac.uk/data_request/cif.

Acknowledgments

The authors are grateful for financial support from the National Science Council of the Republic of China (R.O.C).

[1] M. J. Zaworotko, *Chem. Commun.* **2001**, 1–9 and references cited therein.
[2] S. R. Batten, R. Robson, *Angew. Chem. Int. Ed.* **1998**, *37*, 1460–1494.
[3] O. M. Yaghi, H. Li, C. Davis, D. Richardson, T. L. Groy, *Acc. Chem. Res.* **1998**, *31*, 474–484.
[4] P. J. Hagrman, D. Hagrman, J. Zubieta, *Angew. Chem. Int. Ed.* **1999**, *38*, 2638–2684.
[5] O. R. Evans, R.-G. Xiong, Z. Wang, G. K. Wong, W. Lin, *Angew. Chem. Int. Ed.* **1999**, *38*, 536–538.
[6] W. Lin, O. R. Evans, R.-G. Xiong, Z. Wang, *J. Am. Chem. Soc.* **1998**, *120*, 13 272–13 273.
[7] W. Lin, Z. Wang, L. Ma, *J. Am. Chem. Soc.* **1999**, *121*, 11 249–11 250.
[8] Y. K. Shan, R. H. Huang, S. D. Huang, *Angew. Chem. Int. Ed.* **1999**, *38*, 1751–1755.
[9] J. Y. Lu, M. A. Lawandy, J. Li, T. Yuen, C. L. Lin, *Inorg. Chem.* **1999**, *38*, 2695–2704.
[10] A. Ranganathan, V. R. Pedireddi, C. N. R. Rao, *J. Am. Chem. Soc.* **1999**, *121*, 1752–1753.
[11] G. M. Frankenbach, M. A. Beno, A. M. Kini, J. M. Williams, U. Welp, J. E. Thompson, M.-H. Wangbo, *Inorg. Chim. Acta* **1992**, *192*, 195.
[12] A. Weiss, E. Riegler, I. Alt, H. Bohme, C. Robl, *Z. Naturforsch., Teil B* **1986**, *41*, 18.
[13] A. Weiss, E. Riegler, C. Robl, *Z. Naturforsch., Teil B* **1986**, *41*, 1333.
[14] C. Robl, A. Weiss, *Z. Naturforsch., Teil B* **1986**, *41*, 1341.
[15] B. C. Gerstein, M. Habenschuss, *J. Appl. Phys.* **1972**, *43*, 5155.
[16] S. O. H. Gutschke, M. Molinier, A. K. Powell, P. T. Wood, *Angew. Chem. Int. Ed. Engl.* **1997**, *36*, 991–992.
[17] K. J. Lin, K. H. Lii, *Angew. Chem. Int. Ed. Engl.* **1997**, *36*, 2076–2077.
[18] J. Spandl, I. Brüdgam, H. Hartl, *Angew. Chem. Int. Ed.* **2001**, *40*, 4018–4020.
[19] I. Castro, M. L. Calatayud, J. Sletten, F. Lloret, M. Julve, *J. Chem. Soc., Dalton Trans.* **1997**, 811–817.
[20] a) R. Soules, F. Dahan, J.-P. Laurent, P. Castan, *J. Chem. Soc., Dalton Trans.* **1988**, 587–590; b) M. Dan, C. N. R. Rao, *Solid State Sci.* **2003**, *5*, 615–620.
[21] J. A. C. van Ooijen, J. Reedijk, A. L. Spek, *Inorg. Chem.* **1979**, *18*, 1184–1189.
[22] C. E. Xanthopoulos, M. P. Sigalas, G. A. Katsoulos, C. A. Tsipis, C. C. Hadjikostas, A. Terzis, M. Mentzafos, *Inorg. Chem.* **1993**, *32*, 3743–3747.
[23] I. Castro, J. Faus, M. Julve, Y. Journaux, J. Sletten, *J. Chem. Soc., Dalton Trans.* **1991**, 2533–2538.
[24] X. Solans, M. Aguiló, A. Gieizes, J. Faus, M. Julve, *Inorg. Chem.* **1990**, *29*, 775–784.
[25] I. Castro, J. Faus, M. Julve, *Inorg. Chim. Acta* **1990**, *170*, 251–257.

 © 2005 Wiley-VCH Verlag GmbH & Co. KGaA, Weinheim

[26] a) P. S. Mukherjee, S. Konar, E. Zangrando, C. Diaz, J. Ribas, N. R. Chaudhuri, *J. Chem. Soc., Dalton Trans.* **2002**, 3471–3476; b) Y. Akhriff, J. Server-Carrió, A. Sancho, J. García-Lozano, E. Escrivá, L. Soto, *Inorg. Chem.* **2001**, *40*, 6832–6840.
[27] M. Ito, R. Weiss, *J. Am. Chem. Soc.* **1963**, *85*, 2580–2584.
[28] a) J. Y. Lu, A. M. Babb, *Inorg. Chim. Acta* **2001**, *318*, 186–190; b) J. Y. Lu, T. J. Schroeder, A. M. Babb, M. Olmstead, *Polyhedron* **2001**, *20*, 2445–2449.
[29] a) C. R. Lee, C. C. Wang, Y. Wang, *Acta Crystallogr, Sect. B* **1996**, *52*, 966–975; b) T. K. Maji, G. Mostafa, S. Sain, J. S. Prasad, N. R. Chaudhuri, *Cryst. Eng. Commun.* **2001**, 37.
[30] C. Janiak, *J. Chem. Soc., Dalton Trans.* **2000**, 3885–3896.
[31] S. B. Ferguson, E. M. Sanford, E. M. Seward, F. Diederich, *J. Am. Chem. Soc.* **1991**, *113*, 5410–5419.
[32] R. H. Groeneman, L. R. MacGillivray, J. L. Atwood, *Inorg. Chem.* **1999**, *38*, 208–209.
[33] J. Y. Lu, T. Paliwala, S. C. Lim, C. Yu, T. Niu, A. J. Jacobson, *Inorg. Chem.* **1997**, *36*, 923–929.
[34] A. J. Blake, S. J. Hill, P. Hubberstey, W. Li, *J. Chem. Soc., Dalton Trans.* **1997**, 913–914.
[35] O. M. Yaghi, H. Li, T. L. Groy, *J. Am. Chem. Soc.* **1996**, *118*, 9096–9101.
[36] C. Näther, I. Jeβ, *Acta Crystallogr., Sect. C* **2001**, *57*, 260–261.
[37] I. Castro, M. L. Calatayud, J. Sletten, F. Lloret, M. Julve, *Inorg. Chim. Acta* **1999**, *287*, 173–180.
[38] a) M. E. Fisher, *Am. J. Phys.* **1964**, *32*, 343; b) O. Kahn, *Molecular Magnetism*, VCH Publishers, New York, **1993**, p. 258.
[39] W. J. de Haas, B. H. Schultz, *Physica* **1939**, *6*, 481.
[40] F. E. Mabbs, D. J. Machin, *Magnetism and Transition Metal Complexes*, Chapman and Hall, London, **1973**.
[41] *SMART V 4.043 Software for CCD Detector System*; Siemens Analytical Instruments Division: Madison, WI, **1995**.
[42] *SAINT V 4.035 Software for CCD Detector System*; Siemens Analytical Instruments Division: Madison, WI, **1995**.
[43] G. M. Sheldrick, *Program for the Refinement of Crystal Structures*; University of Göttingen: Göttingen, Germany, **1993**.
[44] SHELXTL 5.03 (PC-Version), Program Library for Structure Solution and Molecular Graphics; Siemens Analytical Instruments Division: Madison, WI, **1995**.

Received: August 16, 2004

 © 2005 Wiley-VCH Verlag GmbH & Co. KGaA, Weinheim

Synthesis, Structure, Coordination Expansion and Theoretical Modelling of Dichlorobis(phenoxo) Titanium(IV) Complexes

Alastair J. Nielson,*[a] Chaohong Shen,[a] Peter Schwerdtfeger,[a] and Joyce M. Waters[a]

Keywords: Complexes / Phenoxo ligands / Structure elucidation / Theoretical structure / Titanium

Thermalisation of $TiCl_4$ and two equivalents of a phenol in toluene is found to be the best preparative method for quantitative yields of a variety of dichlorobis(phenoxo) complexes. $[TiCl_2(OC_6H_4CMe_3\text{-}4)_2]$ (**1**) is monomeric in benzene, a phenoxo-bridged dimer in the solid state and undergoes coordination expansion with 4,4′-dimethyl-2,2′-bipyridine (dmbipy) to give $[TiCl_2(OC_6H_4CMe_3\text{-}4)_2(dmbipy)]$ (**2**). Also monomeric are $[TiCl_2(OC_6H_2Me_3\text{-}2,4,6)_2]$ (**3**) and $[TiCl_2(OC_6H_3iPr_2\text{-}2,6)_2]$ (**5**) which expand their coordination with dmbipy to give $[TiCl_2(OC_6H_2Me_3\text{-}2,4,6)_2(dmbipy)]$ (**4**) and $[TiCl_2(OC_6H_3iPr_2\text{-}2,6)_2(dmbipy)]$ (**6**). In contrast $[TiCl_2(OC_6H_2\{CMe_3\}_2\text{-}2,6\text{-}Me\text{-}4)_2]$ (**7**) is only partially formed by the thermolysis reaction and does not coordinatively expand with dmbipy. $[TiCl_2(OC_6H_3Me_2\text{-}2,4)_2]$ (**8**) is monomeric in benzene and reacts to form $[TiCl_2(OC_6H_3Me_2\text{-}2,4)_2(dmbipy)]$ (**9**). $[TiCl_2(OC_6H_3\{CMe_3\}_2\text{-}2,4)_2]$ (**10**) forms along with the tri-phenoxo complex $[TiCl\{OC_6H_3(CMe_3)_2\text{-}2,4\}_3]$. $[TiCl_2(OC_6H_3CMe_3\text{-}2\text{-}Me\text{-}6)_2]$ (**11**) is monomeric in benzene and forms $[TiCl_2(OC_6H_3CMe_3\text{-}2\text{-}Me\text{-}6)_2(dmbipy)]$ (**12**). 2-Phenylphenol and 1-napthol form $[TiCl_2(OC_6H_4Ph\text{-}2)_2]$ (**13**) and $[TiCl_2(OC_{10}H_9)_2]$ (**14**) which are monomeric in benzene. DFT calculations give structural parameters for monomeric $[TiCl_2(OC_6H_5)_2]$ (**15**) in good agreement with the X-ray data for $[TiCl_2(OC_6H_3Me_2\text{-}2,6)_2]$. Each oxygen of the phenoxo ligand in **15** acts essentially as a 2π donor to titanium and there is substantial $p_\pi(O)\text{-}p_\pi^*(C{=}C)$ backbonding with the phenyl ring, which is absent in $[TiCl_2(OCH_3)_2]$ (**16**). The global minimum for the dimer $[(TiCl_2\{OC_6H_5\}\{\mu\text{-}OC_6H_5\})_2]$ is in almost perfect agreement with the crystal structure obtained for $[(TiCl_2\{OC_6H_5\}\{\mu\text{-}OC_6H_5\})_2]$ or $[(TiCl_2\{OC_6H_4CMe_3\text{-}4\}\{\mu\text{-}OC_6H_4CMe_3\text{-}4\})_2]$ (**1**). The dimerisation energy for **15** is $-26.2\ kJ{\cdot}mol^{-1}$.
(© Wiley-VCH Verlag GmbH & Co. KGaA, 69451 Weinheim, Germany, 2005)

Introduction

The relationship between dichlorobis(phenoxo) complexes $[TiCl_2(OAr)_2]$ and titanium metallocences $[TiCl_2Cp_2]$ is now very apparent[1,2] with the phenoxo complexes emerging as promising synthons and catalysts for organic reactions[2,3,4] and catalysts for olefin polymerisation.[5] Alkoxo complexes of titanium often form higher associates than monomers in solution[6] but the solution behavior of the bis(phenoxo) complexes and the coordination expansion properties have not been studied.[7] From the synthetic point of view, complexes containing *tert*-butyl or phenyl groups in the 2,6- positions of the aryloxo ring have received the most attention.[5,8–10] However, little is known about bis(phenoxo) complexes containing ligands which are less sterically demanding. For example, $[TiCl_2(OC_6H_5)_2]$ has a dimeric structure in the solid state[11] and there is conflicting evidence for the structure in solution,[12,13] $[TiCl_2(OC_6H_3Me_2\text{-}2,6)_2]$ has a monomeric solid-state structure,[9] and $[TiCl_2(OC_6H_2Me_3\text{-}2,4,6)_2]$ is monomeric in benzene and expands its co-ordination sphere forming the bis-adducts $[TiCl_2(OC_6H_2Me_3\text{-}2,4,6)_2(L)_2]$ (L = pyridine, $ArNH_2$ and tetrahydrofuran) which have been characterised only by analytical data and IR spectroscopy.[14] We have reported[15] a comprehensive systematic study of the mono(phenoxo) complexes $[TiCl_3(OAr)]$ (Ar = unsubstituted or substituted phenyl group) which included aspects of best synthetic method, co-ordination expansion and theoretical modelling. We report here a similar investigation for complexes of the type $[TiCl_2(OAr)_2]$ where changes are made to the size of the *ortho*-substituents of the phenyl rings. In particular we investigate the nature of the complexes in non-coordinating solvents to ascertain if co-ordinative unsaturation is maintained in solution. Some general comparisons of the bis(phenoxo) complexes with $[TiCl_2Cp_2]$ (Cp = cyclopentadienyl) are also made.

[a] Chemistry, Institute of Fundamental Sciences, Massey University at Albany,
Private Bag 102904, North Shore Mail Centre, Auckland, New Zealand

Results and Discussion

Synthetic Studies

Bis(phenoxide) complexes have been prepared by thermalising $TiCl_4$ and the phenol in a non-coordinating solvent[14,16] or more commonly by reacting the lithium phenolate with $TiCl_4$ in diethyl ether.[2–10] We have found that thermalisation in toluene of $TiCl_4$ and the phenol in 1:2 ratio is the best procedure for most phenols [Equation (1)].

$TiCl_4 + 2\ HOAr \rightarrow [TiCl_2(OAr)_2] + 2\ HCl$ (1)

HOAr = $HOC_6H_4CMe_3$-4, $HOC_6H_2Me_3$-2,4,6, $HOC_6H_3iPr_2$-2,6, $HOC_6H_3Me_2$-2,4, $HOC_6H_3(CMe_3)_2$-2,4, $HOC_6H_3CMe_3$-2-Me-6, HOC_6H_4Ph-2, $HOC_{10}H_9$ (naphthyl)

If the reaction is carried out to completion, then solid complexes can be obtained in virtually quantitative yield and in an analytically pure form. It is important to determine the end point of the reaction otherwise gummy materials often result which are difficult to purify. The last traces of HCl gas produced in the reaction are easily detected by a simple but very sensitive test which involves passing the exhaust gases close to concentrated ammonia solution or a liquid organic amine and observing any white hydrochloride cloud. On a 5–10 g scale in vigorously boiling toluene, the reactions are usually complete in less than 14 h and on a 50–100 g scale the reaction times are not much longer.

The crystal structure of $[TiCl_2(OC_6H_5)_2]$ has been determined,[11] but we have found the complex is not suitably soluble in benzene for an accurate cryoscopic molecular weight determination. However, reaction of $TiCl_4$ with 4-*tert*-butylphenol gave highly soluble $[TiCl_2(OC_6H_4CMe_3\text{-}4)_2]$ (**1**) and an X-ray crystal structure determination of the product crystallised from benzene showed a dimeric complex containing a phenoxo bridge in which each titanium atom adopts a distorted pentagonal bipyrimidal coordination geometry (Figure 1). The titanium atoms each have two *cis*-coordinated chloro ligands and two *cis*-coordinated phenoxo ligands, one of which bridges to the adjacent titanium atom where it lies *trans* to a terminal phenoxo ligand.

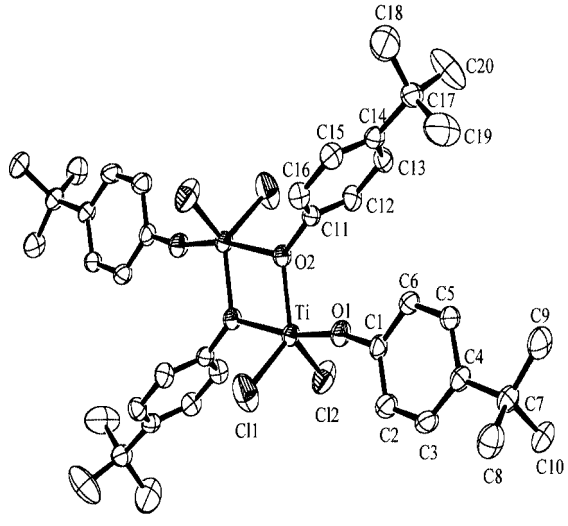

Figure 1.Thermal ellipsoid diagram (at the 50% probability level) for (**1**) showing the numbering system. Hydrogen atoms have been omitted for clarity.

The structure of **1** is essentially similar to that found for dimeric $[TiCl_2(OC_6H_5)_2]$,[11] but is described now in terms of modern bonding concepts. Selected bond lengths and angles are given in Table 1. The Ti–O(1) and O(1)–C(1) bond lengths [1.749(2) and 1.369(3) Å, respectively] and the Ti–O(1)–C(1) bond angle [165.2(2)°] are similar to those found for the mono(phenoxo) complex $[TiCl_3(OC_6H_2\{CMe_3\}_2\text{-}2,6\text{-}Me\text{-}4)]$ [1.750(2), 1.390(2) Å and 163.1°, respectively[15]]. Theoretical calculations on the model complex $[TiCl_3(OC_6H_2Me_3\text{-}2,4,6)]$ show that the terminal phenoxo ligand oxygen atom acts essentially as a 1-σ, 2-π donor to titanium but that there is also some O(2p) donation to the phenyl ring C=C(π*) orbital.[15] The Ti−O(2) bond length in **1** [1.912(2) Å], is significantly longer than the Ti–O(1) bond length [1.749(2) Å] as a consequence of O(2) forming a dative bond to the other titanium atom [Ti–O(2)′ bond length 2.142(2) Å] in the unsymmetrical bridge. The O(2) lone pair donation to Ti occurs *trans* to the strongly π-donating terminal phenoxo ligand so that the potentially π-donating chloro ligands do not have to compete for the same d orbitals. The increased length of the Ti–O(2) bond indicates that O(2)-to-Ti π-donation is much less than for the Ti–O(1) bond. Also the bridging phenoxo ligand O–C bond [O(2)–C(11) bond length 1.406(3) Å] is significantly longer than the terminal phenoxo ligand O–C bond [O(1)–C(1) bond length [1.369(3) Å] indicating there is less O(2p) donation to the phenyl ring C=C(π*) orbital for the bridging mode. This may be a consequence of the phenyl ring π-orbitals being unable to overlap to any significant extent with oxygen orbitals when the two oxygen lone pairs on O(2) are otherwise involved with bonding to Ti [possible O(2)p-to-Ti(1)d π-donation and O(2)p-to-Ti(2)d σ-donation].

Table 1. Selected bond lengths [Å] and angles [°] for **1**. Symmetry transformations used to generate equivalent atoms: #1: $-x + 1$, $-y + 1$, $-z + 1$).

Ti–O(1)	1.749(2)
Ti–O(2)	1.912(2)
Ti–O(2)#1	2.142(2)
Ti–Cl(1)	2.2186(11)
Ti–Cl(2)	2.2256(11)
Ti–Ti#1	3.282(2)
O(1)–C(1)	1.369(3)
O(2)–C(11)	1.406(3)
O(2)−Ti#1	2.142(2)
O(1)–Ti–O(2)	96.03(9)
O(1)–Ti–O(2)#1	167.96(9)
O(2)–Ti–O(2)#1	71.99(9)
O(1)–Ti–Cl(1)	96.52(8)
O(2)–Ti–Cl(1)	122.74(8)
O(2)#1−Ti–Cl(1)	89.25(6)
O(1)–Ti–Cl(2)	97.43(8)
O(2)–Ti–Cl(2)	119.23(7)
O(2)#1−Ti–Cl(2)	89.78(7)
Cl(1)–Ti–Cl(2)	114.06(5)
O(1)–Ti–Ti#1	134.38(7)
O(2)–Ti–Ti#1	38.36(6)
Cl(1)–Ti–Ti#1	107.85(4)
Cl(2)–Ti–Ti#1	106.38(4)
C(1)–O(1)–Ti	165.2(2)
C(11)–O(2)–Ti	123.5(2)
Ti–O(1)	1.749(2)
Ti–O(2)–Ti#1	108.01(9)

The Ti–Cl(1) and Ti–Cl(2) bond lengths in complex **1** [2.2186(11) and 2.2256(11) Å] are not very different from each other but are slightly longer than those found for

 © 2005 Wiley-VCH Verlag GmbH & Co. KGaA, Weinheim

$[TiCl_3(OC_6H_2\{CMe_3\}_2\text{-}2,6\text{-}Me\text{-}4)]$ [Ti–Cl bond lengths 2.1822(8), 2.1913(8) and 2.1945(9) Å] where π-donation from chloro ligands is needed to increase the overall electron count. The theoretical calculations made on the model complex $[TiCl_3(OC_6H_2Me_3\text{-}2,4,6)]$ show that significant Cl(2p) to Ti(3d) π-donation occurs in these tetrahedral molecules.[15] Assuming that O(2) in complex **1** makes a single π-donor interaction with the titanium atom then the overall (formal) electron count for the complex is 16 so an 18-electron count can be attained if Cl(2p) to Ti(3d) donation occurs.

The X-ray crystal structure indicates complex **1** exists in the solid state as a dimer but a molecular weight determination in benzene, the solvent from which the dimer crystallised, indicates a monomer (Scheme 1). The ^1H NMR spectrum in C_6D_6 shows a single resonance for the *tert*-butyl groups, a doublet for the *meta*-protons of the phenyl ring but a broadened resonance for the *ortho*-protons. In the $^{13}C\{^1H\}$ NMR spectrum the *tert*-butyl group methyl and quaternary carbons appear as single sharp resonances but the aromatic ring C resonances are somewhat broadened. Identical spectra are obtained for the complexes reported here whether the solvent is C_6D_6 or $CDCl_3$ but the resonances are slightly sharper in $CDCl_3$. Cooling $CDCl_3$ or $[D_8]$toluene solutions of **1** produced little change in the broadening observed leaving unclear the nature of any solution dynamics. The spectra are thus consistent with the monomeric structure shown by the molecular weight determination and not the dimer found in the solid state. The *ipso*-C resonance occurs at δ = 166.3 ppm, which lies slightly upfield to that observed for $[TiCl_3(OC_6H_4CMe_3\text{-}4)]$ (δ = 169.6 ppm[15]) and this may represent a small change in the O(2p)–C=C(π*) bonding system associated with the smaller need for tight O(2)p-to-Ti(1)d orbital donation on addition of the second phenoxide ligand which is a better π-bonder than Cl.[15]

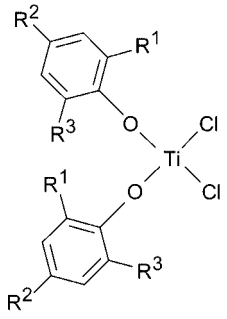

1: R^1, R^3 = H, R^2 = CMe_3
3: R^1, R^2, R^3 = Me
5: R^1, R^3 = $CHMe_2$, R^2 = H
7: R^1, R^3 = CMe_3, R^2 = Me
8: R^1, R^2 = Me, R^3 = H
10: R^1, R^2 = CMe_3, R^3 = H
11: R^1 = CMe_3, R^2 = H, R^3 = Me
13: R^1 = Ph, R^2, R^3 = H
14: $OPhR^1R^2R^3$ = 1-naphthoxo

Scheme 1.

The coordination expansion properties of complex **1** were studied using 4,4′-dimethyl-2,2′-bipyridine (dmbipy), as this ligand is useful in determining isomer structure by NMR spectroscopy.[15] $[TiCl_2(OC_6H_4CMe_3\text{-}4)_2(dmbipy)]$ (**2**) was readily formed in CH_2Cl_2 and the NMR spectra showed the presence of only one isomer. Both the ^1H and $^{13}C\{^1H\}$ NMR spectra indicate a symmetrical molecule based on a single set of resonances for the relevant position of the phenoxo and dmbipy ligands. Structure **I** (Scheme 2) is the preferred isomer since structure **II** contains *trans*-orientated phenoxo ligands, which would lead to an unfavourable competition for d-metal orbitals and structure **III** is an unsymmetrical molecule. A *trans*-chloro-*cis*-phenoxo configuration has been observed in the X-ray crystal structures $[TiCl_2(OC_6H_3Me_2\text{-}2,6)_2(THF)_2]$[17] [i.e. consistant with structure **I**, Scheme 2], where the THF ligands coordinate *cis* to each other and *trans* to the strongly π-donating phenoxo ligands. The NMR spectra for **2** show sharp resonances, which suggests that solution dynamics are not prevalent. The *ipso*-C resonance occurs at δ = 164.8 ppm, which lies slightly upfield to that observed for complex **1** (δ = 166.3 ppm) and again this may represent a small change in the O(2p)–C=C(π*) bonding system associated with the smaller need for tight O(2)p–to–Ti(1)d orbital donation on addition of the 4-electron donor bipy chelate. (see Table 2 for comparisons of the $^{13}C\{^1H\}$ spectra *ipso*-C resonance positions for complexes of the type $[TiCl_3(OAr)]$, $[TiCl_2(OAr)_2]$ and $[TiCl_2(OAr)_2(dmbipy)]$).

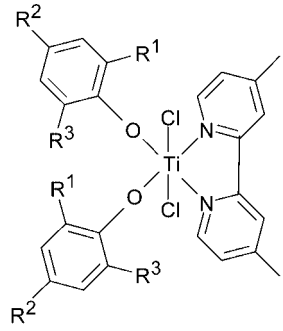

2: R^1, R^3 = H, R^2 = CMe_3
4: R^1, R^2, R^3 = Me
6: R^1, R^3 = $CHMe_2$, R^2 = H
9: R^1, R^2 = Me, R^3 = H
12: R^1 = CMe_3, R^2 = H, R^3 = Me

I

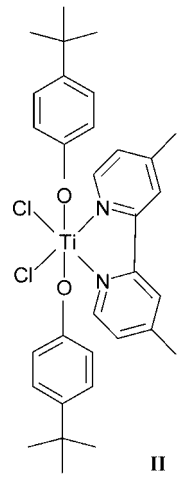

II

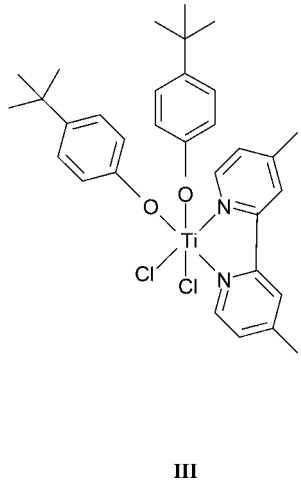

III

Scheme 2.

Thermalisation of 2,4,6-trimethylphenol and $TiCl_4$ gave $[TiCl_2(OC_6H_2Me_3\text{-}2,4,6)_2]$[14] (**3**) which is monomeric in

 © 2005 Wiley-VCH Verlag GmbH & Co. KGaA, Weinheim

Table 2. Comparison of $^{13}C\{^1H\}$ spectra *ipso*-C resonance positions for complexes of the type $[TiCl_3(OAr)]$, $[TiCl_2(OAr)_2]$ and $[TiCl_2(OAr)_2(dmbipy)]$.

Ligand (OAr)	Complex[a] $[TiCl_3(OAr)]$[b]	$[TiCl_2(OAr)_2]$	$[TiCl_2(OAr)_2(dmbipy)]$
$(OC_6H_4CMe_3\text{-}4)$	169.6	166.3 (**1**)	164.8 (**2**)
$(OC_6H_2Me_3\text{-}2,4,6)$	[c]	166.4 (**3**)	164.5 (**4**)
$(OC_6H_3iPr_2\text{-}2,6)$	170.5	165.7 (**5**)	162.6 (**6**)
$(OC_6H_3Me_2\text{-}2,4)$	169.9	165.2 (**8**)	164.3 (**9**)
$(OC_6H_3CMe_3\text{-}2\text{-}Me\text{-}6)$	172.8	168.3 (**11**)	166.4 (**12**)
$(OC_6H_3\{CMe_3\}_2\text{-}2,6\text{-}Me\text{-}4)$	174.9	170.0	[d]

[a] Spectra obtained in $CDCl_3$. [b] Data taken from ref.[15]. [c] *ipso*-C resonance not observed due to long relaxation times.[15] [d] Dmbipy complex does not form.

benzene and shows sharper NMR spectra than complex **1** suggesting again that solution dynamics are not prevalent. The complex reacts with dmbipy to give $[TiCl_2(OC_6H_2Me_3\text{-}2,4,6)_2(dmbipy)]$ (**4**) for which the NMR spectra indicate one isomer with a similar structure to **2**. The *ipso*-C resonance in the $^{13}C\{^1H\}$ NMR spectrum of **4** occurs at δ = 164.5 ppm compared with δ = 166.4 ppm in the parent complex **3** (Table 2). Both complexes **3** and **4** did not crystallise, so that comparisons of *ipso*-C resonance position with solid state bond length data cannot be made. However, complex **3** is closely related to $[TiCl_2(OC_6H_3Me_2\text{-}2,6)_2]$ for which an X-ray crystal structure determination has shown a monomeric tetrahedral structure with Ti–O bond lengths of 1.734(7) and 1.736(8) Å, Ti–Cl bond lengths of 2.192(4) and 2.211(4) Å[9] and an *ipso*-C resonance in the ^{13}C NMR spectrum at δ = 167.8 ppm.[8] In the octahedral adduct $[TiCl_2(OC_6H_3Me_2\text{-}2,6)_2(dpeda)]$ [dpeda = (1*S*,2*S*)-diphenylethylenediamine] the Ti–O bond lengths increase to 1.804(4) and 1.787(4) Å, the Ti–Cl bond lengths to 2.353(2) Å and the *ipso*-C resonance is at δ = 166.0 ppm.[7] The standard deviations for the C–O bond lengths do not allow reliable bond length comparisons to be made for these complexes.

The reaction of 2,6-diisopropylphenol with $TiCl_4$ gave an oil which failed to form a solid[9,18,19] but was identified as $[TiCl_2(OC_6H_3iPr_2\text{-}2,6)_2]$ (**5**) on the basis of its NMR spectra (*ipso*-C resonance δ = 165.7, cf. δ = 170.5 ppm for $[TiCl_3(OC_6H_3iPr_2\text{-}2,6)]$,[15] Table 2) being identical to an authentic sample.[19] Reaction of complex **5** with dmbipy gave $[TiCl_2(OC_6H_3iPr_2\text{-}2,6)_2(dmbipy)]$ (**6**) for which the NMR spectra showed one isomer with a similar structure to **2** [structure **I**, Scheme 2] and the *ipso*-C resonance at δ = 162.6 ppm. Refluxing a solution of 2,6-di-*tert*-butyl-4-methylphenol with $TiCl_4$ in toluene for 18 h, at which time HCl production had essentially ceased, gave a gum which NMR spectroscopy showed to be a mixture of $[TiCl_3(OC_6H_2\{CMe_3\}_2\text{-}2,6\text{-}Me\text{-}4)]$,[15] $[TiCl_2(OC_6H_2\{CMe_3\}_2\text{-}2,6\text{-}Me\text{-}4)_2]$[8] (**7**) and unreacted phenol. This indicated that the thermalisation reaction is not successful with this sterically demanding phenol.[8] A sample of $[TiCl_2(OC_6H_2\{CMe_3\}_2\text{-}2,6\text{-}Me\text{-}4)_2]$ prepared by the reaction of $TiCl_4$ and $LiOC_6H_2(CMe_3)_2\text{-}2,6\text{-}Me\text{-}4$[8] did not react with dmbipy and is reported not to react with pyridine.[8] These results indicate that 2,6-di-*tert*-butyl substituents represent the steric limit for coordination expansion about the titanium centre.

Several unsymmetrically substituted phenols were also thermalised with $TiCl_4$ in toluene giving bis(phenoxo) complexes which have not been reported before. $[TiCl_2(OC_6H_3Me_2\text{-}2,4)_2]$ (**8**) (*ipso*-C resonance at δ = 165.2 ppm, cf. δ = 169.9 ppm for $[TiCl_3(OC_6H_3Me_2\text{-}2,4)]$,[15] Table 2) is monomeric in benzene and reacts with dmbipy to give $[TiCl_2(OC_6H_3Me_2\text{-}2,4)_2(dmbipy)]$ (**9**) for which the NMR spectra show a single isomer similar to structure **I**, Scheme 2 and an *ipso*-C resonance at δ = 164.3ppm. Reaction of 2,4-di-*tert*-butylphenol and $TiCl_4$ gave a mixture of $[TiCl_2(OC_6H_3\{CMe_3\}_2\text{-}2,4)_2]$ (**10**) (identified as a monomer by NMR spectroscopy, one set of resonances in the NMR spectra, *ipso*-C resonance at δ = 165.7 ppm) and the tris-(phenoxo) complex $[TiCl(OC_6H_3\{CMe_3\}_2\text{-}2,4)_3]$, which could be crystallised from the solution and has a distinctly different *ipso*-C resonance position (δ = 163.2 ppm). NMR spectroscopy showed that a reaction of two equivalents of $LiOC_6H_3(CMe_3)_2\text{-}2,4$ with $TiCl_4$ in benzene also gave the tris(phenoxo) complex as the major product. The reason for the ease of formation of this tris-product in these reactions is unclear but appears to be related to the presence of the *para*-*tert*-butyl substituent. NMR spectral analysis of the reaction of two equivalents of 2-*tert*-butyl-4-methylphenol with $TiCl_4$ shows the product is exclusively the bis-(phenoxo) complex (*ipso*-C resonance at δ = 165.8 ppm).

Reaction of 2-*tert*-butyl-6-methylphenol and $TiCl_4$ gave $[TiCl_2(OC_6H_3CMe_3\text{-}2\text{-}Me\text{-}6)_2]$ (**11**) (*ipso*-C resonance at δ = 169.3 ppm, cf. δ = 172.8 ppm for $[TiCl_3(OC_6H_3CMe_3\text{-}2\text{-}Me\text{-}6)]$,[15] Table 2) which is monomeric in benzene. The complex is reported to be a liquid when prepared by thermolysis in CH_2Cl_2[18] and is formed in only 50% yield when $[Ti(NEt_2)_2(OC_6H_3CMe_3\text{-}2\text{-}Me\text{-}6)_2]$ is reacted with $SiCl_4$.[4b] Using the present thermolysis method, production of HCl appeared to have ceased after approximately 8 h of vigorous refluxing, but NMR spectroscopy indicated that the reaction was only about 80% complete. Starting the cooled solution refluxing again led to resumption of HCl gas production and further NMR spectral analysis at intervals showed that another 10 h of reaction time was needed for completion. On removing the solvent an oil remained but this solidified on standing. The reaction time can be compared with that when using 2,6-di-*tert*-butyl-4-methylphe-

 © 2005 Wiley-VCH Verlag GmbH & Co. KGaA, Weinheim

nol where HCl gas production appeared to cease after about 18 h but NMR spectral analysis showed the presence of $[TiCl_3(OC_6H_2\{CMe_3\}_2\text{-}2,6\text{-}Me\text{-}4)]$, $[TiCl_2(OC_6H_2\{CMe_3\}_2\text{-}2,6\text{-}Me\text{-}4)_2]$ (**7**) and unreacted phenol. This result emphasises the need to correctly identify the end-point of these reactions, especially in cases where the size of both *ortho*-substituents becomes larger. The X-ray crystal structure of **11** shows a distorted tetrahedral structure in the solid state with bond lengths and angles that are not significantly different from those found for $[TiCl_2(OC_6H_3Me_2\text{-}2,6)_2]$ except for the O–Ti–O bond angle which widens by ca. 3.5° in **11**.[4a] Complex **11** reacts readily with dmbipy to form $[TiCl_2(OC_6H_3CMe_3\text{-}2\text{-}Me\text{-}6)_2(dmbipy)]$ (**12**) for which the NMR spectra indicate a similar structure to complex (**2**). The *ipso*-C resonance occurs at δ = 166.4 ppm. $[TiCl_2(OC_2H_4Ph\text{-}2)_2]$ (**13**) and the 1-napthoxo complex $[TiCl_2(OC_{10}H_9)_2]$ (**14**) were also prepared and found to be monomeric in benzene.

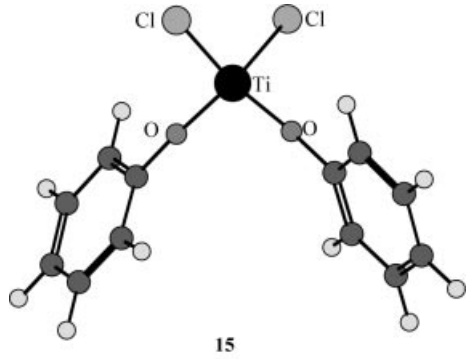

15

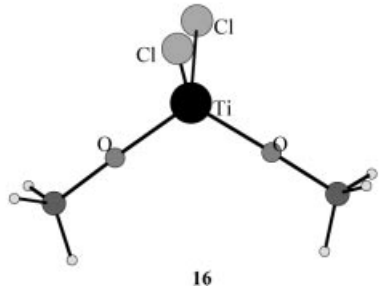

16

Figure 2. Optimized B3LYP structures of $[TiCl_2(OC_6H_5)_2]$ (**15**) and $[TiCl_2(OCH_3)_2]$ (**16**).

Theoretical Studies

Density functional theory (DFT) calculations were carried out on model complexes to study the electronic properties of the phenoxo and chloro ligand interactions with the titanium centre in the monomeric and dimeric complexes shown by the solution and solid-state structures. Unsubstituted phenoxo ligands were used in the models to simplify the calculations. The optimised geometry for the monomers $[TiCl_2(OC_6H_5)_2]$ (**15**) and $[TiCl_2(OCH_3)_2]$ (**16**) (used for comparisons) are shown in Figure 2. Bond lengths and angles for these two structures are given in Table 3 where they are compared with data obtained from the X-ray structure of the monomeric complexes $[TiCl_2(OC_6H_3Me_2\text{-}2,6)_2]$[9] and $[TiCl_2(OC_6H_3CMe_3\text{-}2\text{-}Me\text{-}6)_2]$.[3]

As expected, the ligands in **15** are tetrahedrally coordinated to titanium with the O–Ti–Cl, Cl–Ti–Cl and O–Ti–O bond angles (108.7 , 111.1 , and 111.0°, respectively) being very close to those found in the two X-ray structures. The Ti–O bond lengths in **15** [1.753 Å] are also similar to those found in the X-ray structures [Ti–O bond lengths 1.734(7) and 1.753(4) Å, respectively]. The model structures, however, indicate that the Ti–O bond lengths are longer in phenoxo model **15** (1.753 Å) than in the alkoxo model **16** (1.740 Å). Theoretical calculations have shown previously that a short Ti–O bond length of 1.750(2) Å in $[TiCl_3(OC_6H_2Me_3\text{-}2,4,6)]$ corresponds to a phenoxo ligand acting formally as a 2π-donor to Ti[15] but the Ti–O bonding is clearly stronger in **16**, where there is no $p_\pi(O)$-$p_\pi^*(C{=}C)$ backbonding with a phenyl ring (the C–O bond lengths in **15** and $[TiCl_2(OMe)_2]$ (**16**) are 1.384 and 1.436 Å,

Table 3. Comparison of the bond lengths [Å] and angles [°] for the X-ray structure of $[TiCl_2(OC_6H_3Me_2\text{-}2,6)_2]$ and $[TiCl_2(OC_6H_3CMe_3\text{-}2\text{-}Me\text{-}6)_2]$ with the calculated structures $[TiCl_2(OC_6H_5)_2]$ (**15**) and $[TiCl_2(OCH_3)_2]$ (**16**).

	$[TiCl_2(OC_6H_3Me_2\text{-}2.6)_2]$ (X-ray)[9]	$[TiCl_2(OC_6H_3CMe_3\text{-}2\text{-}Me\text{-}6)_2]$ (X-ray)[5]	$[TiCl_2(OC_6H_5)_2]$ (**15**) (calcd.)	$[TiCl_2(OCH_3)_2]$ (**16**) (calcd.)
Ti–O(1)	1.734(7)	1.753(4)	1.753	1.740
Ti–O(2)	1.736(8)	1.752(5)	1.753	1.740
Ti–Cl(1)	2.192(4)	2.217(3)	2.249	2.257
Ti–Cl(2)	2.211(4)	2.207(3)	2.249	2.257
C–O(1)	1.353(12)	1.403(7)	1.384	1.436
C–O(2)	1.365(15)	1.401(9)	1.384	1.436
O(1)–Ti–O(2)	109.1(4)	112.6(2)	111.1	112.2
O(1)–Ti–Cl(1)	109.4(3)	109.2(2)	108.7	108.6
O(1)–Ti–Cl(2)	108.1(3)	107.8(2)	108.7	108.2
O(2)–Ti–Cl(1)	109.2(3)	107.0(2)	108.7	108.6
O(2)–Ti–Cl(2)	110.1(3)	110.0(2)	108.7	108.3
Cl(1)–Ti–Cl(2)	111.0(2)	110.3(1)	111.1	111.1
Ti–O(1)–C(11)	167.3(7)	162.2(4)	175.8	178.3
Ti–O(2)–C(21)	168.9(8)	163.4(4)	175.8	178.3

 © 2005 Wiley-VCH Verlag GmbH & Co. KGaA, Weinheim

respectively). A similar situation was found for the models $[TiCl_3(OC_6H_2Me_3\text{-}2,4,6)]$ and $[TiCl_3(OMe)]$.[15]

The Ti–Cl bond lengths in **15** [2.249 Å] are somewhat longer than in $[TiCl_2(OC_6H_3Me_2\text{-}2,6)_2]$ [2.192(4) and 2.211(4) Å] and $[TiCl_2(OC_6H_3CMe_3\text{-}2\text{-}Me\text{-}6)_2]$ [2.217(3) and 2.207(3) Å], but this is to be expected from the level of theory applied, and they compare with 2.257 Å in $[TiCl_2(OMe)_2]$ where the strong Ti–O bonding allows the Ti–Cl bond to relax its π-bonding component somewhat when the electron count is maximised.

The Ti–O–C bond angle in model **15** [175.8°] is close to being linear which is also the case in the calculated structure of $[TiCl_3(OC_6H_2Me_3\text{-}2,4,6)]$ [177.7°][15] but the angles are smaller in the X-ray structures [e.g. 167.3(7)° in $[TiCl_2(OC_6H_3Me_2\text{-}2,6)_2]$ and 163.2(4)° in $[TiCl_2(OC_6H_3CMe_3\text{-}2\text{-}Me\text{-}6)_2]$. Ti–O–C bond angle linearity is also favoured by $p_\pi(O)$-$p_\pi^*(C{=}C)$ back bonding with the phenyl ring. However, the Ti–O–C bond angle in the model $[TiCl_2(OMe)_2]$ (**16**) in which there is no $p_\pi(O)$-$p_\pi^*(C{=}C)$ back bonding with a phenyl ring is 178.3°. In this molecule the bond angles about the titanium atom are similar to those in **15**, but more importantly the Ti–O bond lengths are slightly shorter in $[TiCl_2(OMe)_2]$ (1.740 Å, 1.753 Å in **15**), where the oxygen atom can bind to the metal without the influence of π-bonding to an aromatic ring. An angle scan reveals, however, that for the Ti–O–C bond angle in $[TiCl_3(OC_6H_2Me_3\text{-}2,4,6)]$ the energy difference between the calculated angle (177.7°) and the experimental value in the crystal [163.1(1)°] is only 3 kJ·mol^{-1}.[15] The reduced bond angle in the crystal structure is thus due to intermolecular effects similar to those apparent in the related organoimido complexes, where M–N–C bond angles can be as low as 150° without greatly effecting the electronic nature of the multiple bond.[20]

Interestingly, the phenyl rings in **15** face each other with the faces of the phenyl rings inclined to each other at an angle of 92.6°. This fact can be easily explained from electronic arguments. As there is strong π-overlap with both the Ti centre and the phenyl ring carbon atom (cummulene type arrangement), one oxygen atom overlaps with the d_{xz} orbital whilst the other overlaps with the d_{yz} orbital resulting in phenyl rings perpendicular to each other (Figure 3). The $p_\pi(O)$–$p_\pi^*(C{=}C)$ interaction extends the π system in the complexes which accounts for the deep red coloration observed. In comparison, bis(alkoxo) complexes which do not contain this feature are usually colourless.[6]

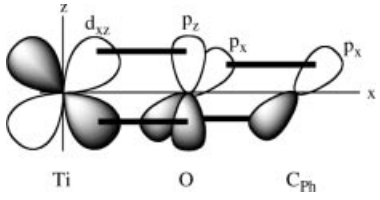

Figure 3. Op_z–Tid_{xz} and Op_x–Cp_x orbital overlaps in the Ti–O–Ar system.

A natural bond orbital (NBO) analysis[21] of **15** using second order perturbation analysis of the Fock matrix, which allows assignment of energetic contributions to individual donor acceptor pairs, shows there is substantial donation from the two oxygen 2p lone pairs on the phenoxo ligands to both the phenyl C=C (π*) orbital (E_2 = 104.6 kJ mol^{-1}) and more importantly to the unoccupied titanium 3d orbitals (E_2 = 376.6 kJ mol^{-1}). Both the $p_\pi(O)$-$p_\pi^*(C{=}C)$ and the $p_\pi(O)$-Ti interactions are stronger than that in the mono(phenoxo) model $[TiCl_3(OC_6H_2Me_3\text{-}2,4,6)]$ (E_2 = 54.4 kJ mol^{-1} and 230 kJ mol^{-1} per lone pair, respectively). Even so these values in **15** are clearly overestimated by the NBO procedure, but nevertheless it clearly points towards Ti–O multiple bonding. The O_{2p}-phenyl C=C (π*) back-bonding is also sufficiently strong to prevent rotation, so that at ambient temperatures the configuration of the two phenoxo ligands is essentially locked. A decrease in the Ti–O–C bond angle diminishes the backbonding into the Ti 3d-orbitals. This bonding situation would leave no orbitals available for π-donation from the two chloro ligands, which could build the electron count formally to 18. However, the perturbation analysis reveals that this picture is too simple as there is some orbital mixing of the Cl(3p) lone-pair on both chlorines via back donation into unoccupied titanium 3d orbitals. In comparison, for the complex $[TiCl_3(OC_6H_2Me_3\text{-}2,4,6)]$ in which there is only one phenoxo ligand and thus a greater need for Cl_p–Ti π-donation, calculations show that two of the lone pairs donate more strongly (E_2 = 108.8 kcal mol^{-1}.[15]) In $[TiCl_2(OMe)_2]$ (**16**) the calculations show that the contribution from the chloro ligands is much less than in **15** as without the $p_\pi(O)$-$p_\pi^*(C{=}C)$ interaction the strong Ti–O bonding allows the Ti–Cl bond to relax its π-bonding component and this is reflected in the longer Ti–Cl bond length in **16**.

Calculations were also carried out on models of the dimeric complex $[(TiCl_2\{OC_6H_4CMe_3\text{-}4\}\{\mu\text{-}OC_6H_4\text{-}CMe_3\text{-}4\})_2]$. For each titanium centre a trigonal bipyramidal arrangement for the ligands with the bridging oxygen atoms in the equatorial position was chosen in agreement with the crystal structure. With the 4-*tert*-butyl substituent replaced by H for computational convenience, a number of different structures according to all possible permutations was obtained. However, all the possible starting geometries optimised to only three different structures and these are shown in Figure 4. The global minimum (Figure 4A) is in almost perfect agreement with the crystal structures $[(TiCl_2\{OC_6H_4CMe_3\text{-}4\}\{\mu\text{-}OC_6H_4\text{-}CMe_3\text{-}4\})_2]$ (complex **1**) and $[(TiCl_2\{OC_6H_5\}\{\mu\text{-}OC_6H_5\})_2]$[11] (see Table 4). In particular the terminal Ti–O bond lengths are 1.747, 1.749 and 1.744 Å, respectively, and the Ti–O bridging bond lengths are 1.908, 1.912 and 1.910 Å, respectively. The C–O_t–Ti bond angles are also in reasonable agreement with experimental data (169.9, 165.2 and 165.9°, respectively) as are the C–O_b–Ti bond angles (126.6, 123.5 and 128.3°, respectively). It is clear that solid state effects and limitations in the computational procedure accounts for the small differences in the geometries. The other two structures (Figure 4 B and C) are 13.2 and 23.3 kJ·mol^{-1} above the global minimum (Figure 4, A). The dimerization energy for the reaction

 © 2005 Wiley-VCH Verlag GmbH & Co. KGaA, Weinheim

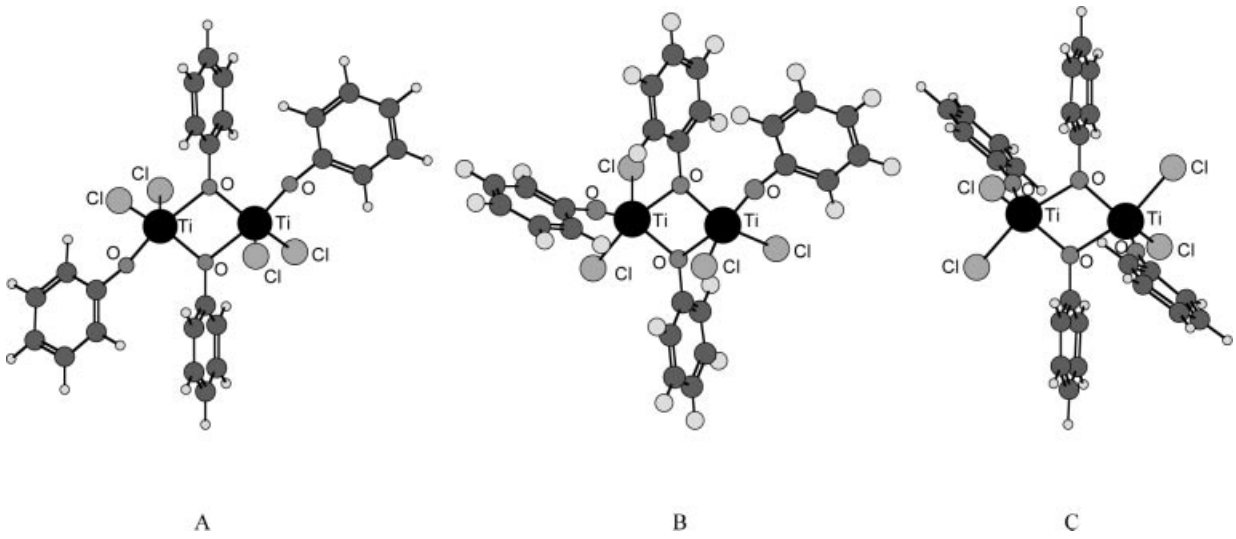

Figure 4. Optimized B3LYP structures of the dimeric titanium compound, $[TiCl_2(OC_6H_5)_2]_2$. (A) global minimum; (B); [ΔE = 13.2 kJ·mol^{-1} compared to (A)]; (C) [ΔE = 23.3 kJ·mol^{-1} compared to (A)].

Table 4. Comparison of the bond lengths [Å] and angles [°] for the calculated structure $[(TiCl_2\{OC_6H_5\}\{\mu\text{-}OC_6H_5\})_2]$ with the X-ray structures $[(TiCl_2\{OC_6H_5\}\{\mu\text{-}OC_6H_5\})_2]$[11]and $[(TiCl_2\{OC_6H_4CMe_3\text{-}4\}\{\mu\text{-}OC_6H_4CMe_3\text{-}4\})_2]$ (**1**).

Bond/angle[a]	$[(TiCl_2\{OC_6H_5\}\{\mu\text{-}OC_6H_5\})_2]$ (calcd.)	$[(TiCl_2\{OC_6H_5\}\{\mu\text{-}OC_6H_5\})_2]$ (X-ray[11])	$[(TiCl_2\{OC_6H_4CMe_3\text{-}4\}\{\mu\text{-}OC_6H_4CMe_3\text{-}4\})_2]$ (**1**) (X-ray)
Ti–O_b	2.151	2.122(9)	2.142(2)
Ti–O_t	1.747	1.744(10)	1.749(2)
Ti–O_b	1.908	1.910(9)	1.912(2)
Ti–Cl	2.270	2.209(6)	2.219(1)
Ti–Cl	2.276	2.219(6)	2.226(1)
C–O_t	1.382	1.359(19)	1.369(3)
C–O_b	1.423	1.422(14)	1.406(3)
C–O_t–Ti	169.9	165.9(6)	165.2(2)
C–O_b–Ti	126.6	128.3(4)	123.5(2)

[a] b = bridging. t = terminal.

$$2\ [TiCl_2(OC_6H_5)_2] \rightarrow [(TiCl_2\{OC_6H_5\}\{\mu\text{-}OC_6H_5\})_2]$$

[i.e. for dimer (A)] is only –26.2 kJ mol^{-1}. This supports the results obtained here indicating complex (**1**) is monomeric in solution but a dimer in the solid state and also gives insight as to why molecular weight studies could indicate either monomeric or dimeric structures in solution.[12,13] In the gas phase only the monomeric compound was found from mass spectroscopic studies.[13]

Conclusions

The results of this work show that a range of dichlorobis(phenoxo)titanium(IV) complexes can be prepared in essentially pure form and in quantitative yield if the end-point of thermalising $TiCl_4$ and two equivalents of a phenol in toluene is determined. This represents a major advance in the ease of preparing these complexes when larger quantities are required. In a non coordinating solvent such as benzene the complexes are monomeric and thus have a four-coordinate geometry typical of $[Cp_2TiCl_2]$ complexes. When there are no substituents in both *ortho*-positions of the phenoxo ligand phenyl rings, a dimeric phenoxo-bridged structure is possible in the solid state. Coordination expansion occurs where a ligand such as dmbipy is used but this ceases when both *ortho*-positions of the phenoxo ligand phenyl ring contain *tert*-butyl substituents. This compares with the dicyclopentadienyl complex $[Cp_2TiCl_2]$ which is not known to undergo coordination expansion easily and can be prepared in the presence of coordinating solvents.[22] The chloro ligands in the six-coordinate bis(phenoxo) adducts are expected to lie *trans* to each other which is not the orientation required for many catalytic reactions. It is thus important to keep potentially coordinating ligands away from the complexes if a *cis*-dichloro geometry is to be maintained. The *ipso*-C resonance position in the ^{13}C NMR spectra of the phenoxo ligand phenyl rings indicate that there is a trend towards less O(2p)-C=C(π^*) bonding component through the series $[TiCl_3(OAr)]$, $[TiCl_2(OAr)_2]$ and $[TiCl_2(OAr)_2(dmbipy)]$) and this would appear to be a sensitive probe for determining O_π-orbital-Ti_d orbital bonding tightness. The comparable feature in cyclopentadienyl complexes is ring slippage which is uncommon and is only found in circumstances where a strong π-donating ligand is

 © 2005 Wiley-VCH Verlag GmbH & Co. KGaA, Weinheim

able to compete for available metal orbitals.[23] DFT calculations on the model $[TiCl_2(OC_6H_5)_2]$ show that the structural parameters compare well with the X-ray structures of $[TiCl_2(OC_6H_3Me_2\text{-}2,6)_2]$ and $[TiCl_2(OC_6H_3CMe_3\text{-}2\text{-}Me\text{-}6)_2]$ and as already discussed, an NBO analysis indicates substantial donation from the two oxygen 2p lone pairs on the phenoxo ligands to the unoccupied titanium 3d orbitals. This is consistent with each ligand acting formally as a 5-electron donor and gives credence to the analogy with the 5-electron donor Cp ligand.[1] There is also sufficient O(2p)–C=C(π*) interaction to prevent rotation of the phenyl rings about the C–O bond at room temperature. The calculations also show that there is only a small dimerisation energy for $[TiCl_2(OC_6H_5)_2]$ and the global minimum structure is the one observed in the solid state. Overall the bis(phenoxo) complexes show a range of differences compared with $[Cp_2TiCl_2]$ and in the absence of cyclometallation involving the *ortho*-substituents on the aromatic rings[24] these differences may be exploited in tuning stoichiometric and catalytic reactions in organic synthesis. Such metal-mediated reactions are now emerging.[3]

Experimental Section

Syntheses: All preparations and manipulations were carried out under dry, oxygen-free nitrogen using standard bench-top techniques for air-sensitive substances. $TiCl_4$ and the phenols were used as received from commercial sources. 4,4′-Dimethyl-2,2′-bipyridine (dmbipy) was dried under vacuum before use. Light petroleum (b.p. 40–60 °C) and toluene were distilled from sodium wire and dichloromethane from freshly ground CaH_2. ^1H and $^{13}C\{^1H\}$ NMR spectra were recorded at 400 and 100 MHz respectively with a Bruker AM400 spectrometer. $CDCl_3$ and CD_2Cl_2 were dried with, and distilled from, freshly ground CaH_2 and $[D_6]$benzene from sodium wire. Molecular mass values were determined cryoscopically in benzene with a Knauer molecular weight determination apparatus under N_2 gas conditions using concentrations in the vicinity of 5.3×10^{-8} mol·L^{-1}. C, H and N analyses were determined by Dr A. Cunninghame and associates, University of Otago, New Zealand. Chlorine was determined by gravimetric measurements. The production of HCl gas in the thermalisation reactions was monitored by passing the exhaust gases from the nitrogen bubbler over *N*,*N*,*N*′,*N*′-teramethylethylenediamine and observing the white cloud produced.

$[TiCl_2(OC_6H_4CMe_3\text{-}4)_2]$ (1): 4-*tert*-Butylphenol (4.75 g, 31 6 mmol) in toluene (50 cm^3) was added to $TiCl_4$ (3.0 g, 15.8 mmol) in toluene (50 cm^3) and the mixture was refluxed vigorously until the production of HCl gas ceased (9 h). The solution was cooled, filtered and the solvent removed to give a deep red microcrystalline solid which was pumped on for several hours. Yield: 6.57 g, 100%. $C_{20}H_{26}Cl_2O_2Ti$: calcd. C 57.6, H 6.3, Cl 17.0; found C 57.5, H 6.3, Cl 17.3. Cryoscopic mol. mass: found 420.6; required: 417.2. ^1H NMR: δ = 1.25 (s, 18 H, CMe_3), 6.92 (b, 4 H, *o*-H), 7.18 (d, ^3J(H,H) = 7.7 Hz, 4 H, *m*-H) ppm. ^{13}C NMR: δ = 31.4 (CMe_3), 34.4 (C), 118.8 (*o*-C), 125.8 (*m*-C), 148.2 (*p*-C), 166.3 (*ipso*-C) ppm. Recrystallisation of a portion of the solid from benzene gave well formed crystals. [$C_{20}H_{26}Cl_2O_2Ti$: calcd. C 57.6, H 6.3; found C 57.5, H 6.5]. One of these crystals was used in the X-ray analysis.

$[TiCl_2(OC_6H_4CMe_3\text{-}4)_2(dmbipy)]$ (2): Dmbipy (0.24 g, 1.3 mmol) in CH_2Cl_2 (25 cm^3) was added to complex **1** (0.54 g, 1.3 mmol) in CH_2Cl_2 (30 cm^3) and the mixture was stirred for 2 h. The solution was filtered, the solvent removed and the residue allowed to stand under petroleum ether (20 cm^3) overnight giving the complex as a noncrystalline orange solid. Yield: 0.75 g, 97%. $C_{32}H_{38}Cl_2N_2O_2Ti$: calcd. C 63.6, H 6.3, N 4.6; found C 63.5, H 6.2, N 4.9. ^1H NMR: δ = 1.30 (s, 18 H, CMe_3), 2.39 (s, 6 H, Me-dmbipy), 7.23 and 7.27 [2d, (AB quartet),$^3J_{H,H}$ = 8.8 Hz, 8 H, *o*,-*m*-H], 7.27 (d, obsc., H^2-dmbipy), 7.93 (br. s, 2 H, H^4-dmbipy), 8.96 (d,$^3J_{H,H}$ 5.6 Hz, 2 H, H^1-dmbipy) ppm. ^{13}C NMR: δ = 21.5 (Me-dmbipy), 31.4 (CMe_3), 34.3 (C), 118.5 (*o*-C), 122.5 (C^2-dmbipy), 125.8 (*m*-C), 126.9 (C^4-dmbipy), 145.5 (*p*-C), 148.7 (C^1-dmbipy), 150.4 (C^3 or C^5-dmbipy), 152.4 (C^5 or C^3-dmbipy), 164.8 (*ipso*-C) ppm.

$[TiCl_2(OC_6H_2Me_3\text{-}2,4,6)_2]$ (3): 2,4,6-Trimethylphenol (4.31 g, 31.6 mmol) in toluene (50 cm^3) was added to $TiCl_4$ (3.0 g, 15.8 mmol) in toluene (50 cm^3) and the mixture was refluxed vigorously until the production of HCl gas ceased (10 h). The solution was cooled, filtered and the solvent removed to give the complex as a noncrystalline deep red solid. Yield: 5.97 g, 97%. $C_{18}H_{22}Cl_2O_2Ti$: calcd. C 55.6, H 6.1, Cl 18.2; found C 55.6, H 6.1, Cl 18.8. Cryoscopic mol. mass: found 395.4; required: 389.1. ^1H NMR: δ = 2.22 (s, 6 H, *p*-Me), 2.29 (s, 12 H, *o*-Me), 6.75 (s, 4 H, *m*-H) ppm. ^{13}C NMR: δ = 16.8 (*o*-Me), 20.8 (*p*-Me), 127.3 (*o*-C), 128.6 (*m*-C), 134.1 (*p*-C),166.4 (*ipso*-C) ppm.

$[TiCl_2(OC_6H_2Me_3\text{-}2,4,6)_2(dmbipy)]$ (4): Dmbipy (0.33 g, 1.79 mmol) in CH_2Cl_2 (30 cm^3) was added to complex **3** (0.69 g, 1.78 mmol) in CH_2Cl_2 (30 cm^3) and the mixture was stirred for 3 h. The solution was filtered, the solvent removed and the residue allowed to stand under petroleum ether (20 cm^3) overnight giving the complex as a noncrystalline orange solid. Yield: 1.02 g, 100%. $C_{30}H_{34}Cl_2N_2O_2Ti$: calcd. C 62.8, H 6.4, N 4.9; found C 62.4, H 6.4, N 4.8. ^1H NMR: δ = 2.23 (s, 6 H, *p*-Me), 2.38 (s, 6 H, Me-dmbipy), 2.51 (s, 12 H, *o*-Me), 6.75 (s, 4 H, *m*-H), 7.22 (d, $^3J_{H,H}$ 5.5 Hz, 2 H, H^2- dmbipy), 7.90 (br. s, 2 H, H^4-dmbipy), 8.99 (d, $^3J_{H,H}$ 5.5 Hz, 2 H, H^1-dmbipy) ppm. ^{13}C NMR: δ = 18.1 (*o*-Me), 20.6 (*p*-Me), 21.4 (Me-dmbipy), 122.6 (C^2-dmbipy), 126.5 (C^4-dmbipy), 128.9 (*m*-C), 129.3 (*o*-C), 131.6 (*p*-C), 148.6 (C^1-dmbipy), 150.4 (C^3 or C^5-dmbipy),151.9 (C^5 or C^3-dmbipy), 164.5 (*ipso*-C) ppm.

$[TiCl_2(OC_6H_3iPr_2\text{-}2,6)_2]$ (5): 2,6-Diisopropylphenol (3.76 g, 21.1 mmol) in toluene (50 cm^3) was added to $TiCl_4$ (2.0 g, 10.5 mmol) in toluene (50 cm^3) and the mixture was refluxed vigorously until the production of HCl gas ceased (13 h). The solution was cooled, filtered and the solvent removed to give an oil which failed to solidify over time. Yield: 4.96 g. The product gave an identical NMR spectra to a literature complex.[19]

$[TiCl_2(OC_6H_3iPr_2\text{-}2,6)_2(dmbipy)]$ (6): Dmbipy (0.31 g, 1.79 mmol) in CH_2Cl_2 (30 cm^3) was added to complex **5** (0.8 g, 1.79 mmol) in CH_2Cl_2 (30 cm^3) and the mixture was stirred for 3 h. The solution was filtered, the solvent removed and the residue allowed to stand under diethyl ether (50 cm^3) overnight giving the complex as a noncrystalline deep red solid. Yield: 1.03 g, 88%. $C_{36}H_{46}Cl_2N_2O_2Ti$: calcd. C 65.8, H 7.1, N 4.3; found C 65.9, H 7.0, N 4.8. ^1H NMR: δ = 1.10 (d, $^3J_{H,H}$ = 6.7 Hz, 24 H, CMe_2), 2.43 (s, 6 H, Me-dmbipy), 4.20 (sept, $^3J_{H,H}$ = 6.7 Hz, 4 H, CH), 7.07 (m, 6 H, *m*,*p*-H), 7.25 (d, $^3J_{H,H}$ = 5.4 Hz, 2 H, H^2-dmbipy), 7.92 (br. s, 2 H, H^4-dmbipy), 8.89 (d, $^3J_{H,H}$ = 5.4 Hz, 2 H, H^1-dmbipy) ppm. ^{13}C NMR: δ = 21.6 (Me-dmbipy), 24.5 (CMe_2), 26.1 (CH), 122.7 (C^2-dmbipy), 122.9 (*p*-C), 123.6 (*m*-C), 126.4 (C^4-dmbipy), 140.2 (*o*-C), 148.5 (C^1-dmbipy), 150.4 (C^3 or C^5-dmbipy), 151.8 (C^5 or C^3-dmbipy), 162.6 (*ipso*-C) ppm. The complex is slightly soluble in diethyl ether.

 © 2005 Wiley-VCH Verlag GmbH & Co. KGaA, Weinheim

[$TiCl_2(OC_6H_3Me_2$-2,4)$_2$] (8): 2,4-Dimethylphenol (5.15 g, 42.2 mmol) in toluene (50 cm^3) was added to $TiCl_4$ (4.0 g, 21.1 mmol) in toluene (50 cm^3) and the mixture was refluxed vigorously until the production of HCl gas ceased (10 h). The solution was cooled, filtered and the solvent removed to give the complex as a noncrystalline deep red solid. Yield: 7.28 g, 96%. $C_{16}H_{18}Cl_2O_2Ti$: calcd. C 54.6, H 5.2, Cl 19.0; found C 54.6, H 5.4, Cl 19.4. Cryoscopic mol. mass: found 376.5; required: 360.0. ^{1}H NMR: δ = 2.23 (s, 6 H, Me), 2.25 (s, 6 H, Me), 6.82 (m, 4 H, *m*-H), 6.98 (d, $^3J_{H,H}$ = 7.2 Hz, 2 H *o*-H) ppm. ^{13}C NMR: δ = 16.5 (Me), 20.8 (Me), 119.3 (*o*-CH), 126.4 (*p*-C), 127.0 and 131.0 (*m*-CH), 134.2 (*o*-C), 165.2 (*ipso*-C) ppm.

[$TiCl_2(OC_6H_3$Me-2,4$)_2$(dmbipy)] (9): Dmbipy (0.25 g, 1.36 mmol) in CH_2Cl_2 (20 cm^3) was added to complex **7** (0.49 g, 1.78 mmol) in CH_2Cl_2 (20 cm^3) and the mixture was stirred for 2 h. The solution was filtered, the solvent removed and the residue allowed to stand under petroleum ether (20 cm^3) overnight giving the complex as a noncrystalline orange solid. Yield: 0.69 g, 93%. $C_{28}H_{30}Cl_2N_2O_2Ti$: calcd. C 61.8, H 5.6, N 5.1; found C 61.4, H 5.9, N 4.9. ^{1}H NMR: δ = 2.27 (s, 6 H, Me), 2.42 (s, 6 H, Me), 2.43 (s, 6 H, Me-dmbipy), 6.74 (d, $^3J_{H,H}$ = 8.1 Hz, $^4J_{H,H}$ = 1.2, 2 H, *m*-H), 6.85 (br. s, 2 H, *m*-H), 7.23 (d, $^3J_{H,H}$ = 5.5 Hz, 2 H, H^2-dmbipy), 7.46 (d, $^3J_{H,H}$ = 8.1 Hz, 2 H, *o*-H), 7.92 (br. s, 2 H, H^4-dmbipy), 8.88 (d, $^3J_{H,H}$ = 5.5 Hz, 2 H, H^1-dmbipy) ppm. ^{13}C NMR: δ = 17.0 (Me), 20.8 (Me), 21.5 (Me-dmbipy), 119.7 (*o*-CH), 122.5 (C^2-dmbipy), 126.9 (C^4-dmbipy), 127.0 (*m*-C), 127.2 (*p*-C), 130.8 (*m*-C), 131.9 (*o*-C), 148.5 (C^1-dmbipy), 150.4 (C^3 or C^5-dmbipy),152.2 (C^5 or C^3-dmbipy), 164.3 (*ipso*-C) ppm.

[$TiCl_2(OC_6H_3\{CMe_3\}_2$-2,4$)_2$] (10) and [$TiCl(OC_6H_3\{CMe_3\}_2$-2,4$)_3$]. Procedure A: 2,4-Di-*tert*-butylphenol (6.53 g, 31.6 mmol) in toluene (60 cm^3) was added to $TiCl_4$ (3.0 g, 15.8 mmol) in toluene (50 cm^3) and the mixture was refluxed vigorously until the production of HCl gas ceased (12 h). The solution was cooled, filtered and the solvent removed to give an oil which solidified on standing overnight. NMR spectroscopy showed the product consisted of complex **10** [^{1}H NMR: δ = 1.33 (s, 18 H, CMe_3), 1.52 (s, 18 H, CMe_3), 7.14–7.25 (m, 4 H, *o*,*m*-H), 7.34 (d, $^4J_{H,H}$ 2.1 Hz, 2 H, *m*-H) ppm. ^{13}C NMR: δ = 30.3 (CMe_3), 31.4 (CMe_3), 34.7 (C), 35.1 (C), 123.3 (*o*-CH), 123.4 (*m*-CH), 124.2 (*m*-CH), 135.8 (*p*-C), 148.0 (*o*-C), 165.7 (*ipso*-C) ppm], and [$TiCl(OC_6H_3\{CMe_3\}_3$-2,4$)_3$], which was crystallised from the mixture by dissolving the reaction product in petroleum ether (100 cm^3), reducing the volume to ca. 50 cm^3 while keeping the solution hot, then allowing it to stand and cool. [$C_{42}H_{63}ClO_3Ti$: calcd. C 72.1, H 9.1; found C 72.7, H 9.4].

Procedure B: A solution of *n*-butyllithium (13.2 cm^3, 1.6 mol·L^{-1}) in hexane was added dropwise to a solution of 2,4-di-*tert*-butylphenol (4.35 g, 21.1 mmol) in benzene (50 cm^3) chilled with ice-water. The cooling bath was removed and the mixture stirred for 1 h. The solution and precipitated solid was added slowly to $TiCl_4$ (2.0 g, 10.5 mmol) in benzene (50 cm^3) via a cannula and the mixture stirred overnight. The mixture was allowed to stand for 24 hours to settle the precipitated LiCl, the solution was filtered and the solvent removed to give a red solid which was shown to be a mixture of complex **10** and [$TiCl(OC_6H_3\{CMe_3\}_3$-2,4$)_3$] by NMR spectroscopy. Crystallisation of the mixture as for procedure A, gave [$TiCl(OC_6H_3\{CMe_3\}_3$-2,4$)_3$] [$C_{42}H_{63}ClO_3Ti$: calcd. C 72.1, H 9.1; found C 71.1, H 9.9] which had identical NMR spectra with the sample prepared under procedure A.

[$TiCl_2(OC_6H_3CMe_3$-2-Me-6$)_2$] (11): 2-*tert*-Butyl-6-methylphenol (5.2 g, 31.7 mmol) in toluene (40 cm^3) was added to $TiCl_4$ (3.0 g, 15.8 mmol) in toluene (30 cm^3) and the mixture was refluxed vigorously until the production of HCl gas ceased (18 h). The solution was cooled, filtered from a small amount of solid and the solvent removed to give the complex as an oil which turned into a noncrystalline orange-red solid on standing. Yield: 6.80 g, 96%. $C_{22}H_{30}Cl_2O_2Ti$: calcd. C 59.3, H 6.8, Cl 15.9; found C 59.3, H 6.7, Cl 15.8. Cryoscopic mol. mass: found 454.4; required: 445.3. ^{1}H NMR: δ = 1.52 (s, 18 H, CMe_3), 2.29 (s, 6 H, Me), 6.93 (t, $^3J_{H,H}$ = 7.6 Hz, 2 H, *p*-H), 7.00 (d, $^3J_{H,H}$ = 7.6, $^4J_{H,H}$ = 1.2 Hz, 2 H, *m*-H), 7.17 (d, $^3J_{H,H}$ = 7.6, $^4J_{H,H}$ = 1.2 Hz, 2 H, *m*-H) ppm. ^{13}C NMR: δ = 18.5 (Me), 30.3 (CMe_3), 35.0 (C), 124.6 (*m*-C), 124.7 (*m*-C), 129.1 (*p*-C), 131.1 [*o*-C(methyl)], 137.7 [*o*-C(*tert*-butyl)], 169.3 (*ipso*-C) ppm.

[$TiCl_2(OC_6H_3CMe_3$-2-Me-6$)_2$(dmbipy)] (12): Dmbipy (0.32 g, 1.75 mmol) in CH_2Cl_2 (25 cm^3) was added to complex **11** (0.78 g, 1.75 mmol) in CH_2Cl_2 (30 cm^3) and the mixture was stirred for 3 h. The solution was filtered, the solvent removed and the residue allowed to stand under petroleum ether (20 cm^3) overnight giving the complex as a noncrystalline orange solid. Yield: 0.60 g, 55%. $C_{34}H_{42}Cl_2N_2O_2Ti$: calcd. C 64.9, H 6.7, N 4.5; found C 64.5, H 7.0, N 4.5. ^{1}H NMR: δ = 1.48 (s, 18 H, CMe_3), 2.46 (s, 6 H, Me-dmbipy), 2.76 (s, 6 H, Me-phenoxo), 6.84 (t, $^3J_{H,H}$ = 7.4 Hz, 2 H, *p*-H), 6.99 (bd, 2 H, *m*-H), 7.17 (bd, 2 H, *m*-H), 7.22 (d, $^3J_{H,H}$ 5.5 Hz, 2 H, H^2-dmbipy), 7.93 (br. s, 2 H, H^4-dmbipy), 8.84 (d, $^3J_{H,H}$ 5.5 Hz, 2 H, H^1-dmbipy) ppm. ^{13}C NMR: δ = 21.5 (Me-dmbipy), 21.8 (Me), 31.7 (CMe_3), 35.6 (C), 122.1(CH), 124.5 (CH), 129.8 (CH), 133.0 [*o*-C(methyl)], 140.8 [*o*-C(*tert*-butyl)], 148.6 (C^1-dmbipy), 150.6 (C^3 or C^5-dmbipy), 151.5 (C^5 or C^3-dmbipy), 166.4 (*ipso*-C) ppm. The complex is slightly soluble in petroleum ether.

[$TiCl_2(OC_6H_4$Ph-2$)_2$] (13): 2-Phenylphenol (5.38 g, 31.6 mmol) in CH_2Cl_2 (60 cm^3) was added to $TiCl_4$ (3.0 g, 15.8 mmol) in CH_2Cl_2 (40 cm^3) and the mixture was refluxed vigorously until the production of HCl gas ceased (12 h). The solution was cooled, filtered and the solvent removed to give the complex as an oil which turned into a noncrystalline deep red solid on standing for several days. Yield: 7.21 g, 100%. $C_{24}H_{18}Cl_2O_2Ti$: calcd. C 63.1, H 4.0, Cl 15.5; found C 63.4, H 4.1, Cl 15.5. Cryoscopic mol. mass: found 471.3; required: 457.2. ^{1}H NMR: δ = 6.91–7.49 (m, 18 H, aromatic-H's) ppm. ^{13}C NMR: δ = 115.9, 120.3, 124.3, 127.5, 128.4, 128.5, 129.0, 129.3, 130.1, 137.0 (*o*-C), 161.9 (*ipso*-C) ppm.

[$TiCl_2(OC_{10}H_9)_2$] (14): 1-Napthol (4.56 g, 31.6 mmol) in toluene (60 cm^3) was added to $TiCl_4$ (3.0 g, 15.8 mmol) in toluene (30 cm^3) and the mixture was refluxed vigorously until the production of HCl gas ceased (12 h). The solution was cooled, filtered and the solvent removed to give the complex as a noncrystalline solid. Yield: 6.8 g, 100%. $C_{20}H_{14}Cl_2O_2Ti$: calcd. C 61.3, H 3.9, Cl 16.4; found C 61.4, H 4.1, Cl 15.9. Cryoscopic mol. mass: found 426.9; required: 405.0. The ^{1}H NMR spectrum shows the product contains a small amount of toluene which is difficult to remove by pumping.

Theoretical: Density functional (DFT) calculations were carried out on the model compound [$TiCl_2(OC_6H_5)_2$] and its possible dimeric structures using a hybrid Becke three parameter function together with the Lee–Yang–Parr correlation function (B3LYP).[25,26] For H, C and O a Dunning/Huzinaga valence double-zeta set was used.[27] For Ti and Cl we applied the pseudopotential approximation using the Hay–Wadt parametrization together with valence double-zeta basis.[28] This resulted in 934 basis functions contracted to 368 for the dimeric species. The geometries were fully optimized until the gradients were below 10^{-5} a.u. which took several months of supercomputer time on a 16-processor SGI. The structures are shown in Figure 2 and Figure 4. All calculations were performed with a parallel version of Gaussian98[29] The bonding situation has

 © 2005 Wiley-VCH Verlag GmbH & Co. KGaA, Weinheim

been examined using the natural bond orbital (NBO) partitioning of Weinhold and Reed.[21]

X-ray Crystallography: Data were collected with a Siemens Bruker CCD instrument with graphite-monochromated Mo-K_α radiation (λ = 0.71073 Å) at T = 203(2) K. Crystal decay was monitored by repeating the initial frames at the end of the data collection and analysing the duplicate reflections. This was negligible. Unit cell parameters were obtained by a least-squares fit of all data with $I > 10\ \sigma(I)$. Data were corrected for Lorentz, polarisation and absorption effects.[30] The structures were solved by direct methods and refined on all F^2 by the full-matrix least-squares technique. All non-hydrogen atoms were allowed to assume anisotropic thermal motion. Hydrogen atoms were in calculated positions (C–H, 0.94 Å for phenyl ring H and 0.97 Å for *tert*-butyl H) and refined with a riding model with U_{iso} = 0.08. Programs used were SHELXS[31] for structure solution and SHELXL[32] for refinement. Diagrams were prepared with ORTEP-3 for WINDOWS®.[33]

Crystal Data: [$C_{20}H_{26}Cl_2O_2Ti$], M = 417.21, monoclinic, space group $P\ 2_1/c$, a = 11.265(2), b = 18.603(3), c = 11.491(2) Å, β = 116.59(3)°, V = 2153.4(6) Å^3, Z = 4, $D_{calcd.}$ = 1.287 mg m^3, μ (Mo-K_α) = 0.655 mm^{-1}, crystal size 0.23 × 0.22 × 0.14 mm, ω scans, $\theta_{max.}$ = 28.19°, F(000) = 872, 12833 reflections measured, 4783 unique ($R_{int.}$ = 0.0381), $I_{min.}/I_{max.}$ = 0.8639/0.9139, R_1 = 0.0547 [$I > 2\sigma(I)$], wR_2 = 0.1210 (all data).

CCDC-249718 contains the supplementary crystallographic data for this paper. These data can be obtained free of charge from The Cambridge Crystallographic Data Centre via www.ccdc.cam.ac.uk/data_request/cif.

[1] V. C. Gibson, *Angew. Chem. Int. Ed. Engl.* **1994**, *33*, 1565.
[2] M. G. Thorn, J. E. Hill, S. A. Waratuke, E. S. Johnson. P. E. Fanwick, I. P. Rothwell, *J. Am. Chem. Soc.* **1997**, *119*, 8630.
[3] L. G. Quan, J. K. Cha, *Tetrahedron Lett.* **2001**, *42*, 8567.
[4] a) B. P. Santora, P. S. White, M. R. Gagne, *Organometallics* **1999**, *18*, 2557; b) B. P. Santora, A. O. Larsen, M. R. Gagne, *Organometallics* **1998**, *17*, 3138; c) O. V. Ozerov, F. T. Ladipo, B. O. Patrick, *J. Am. Chem. Soc.* **1999**, *121*, 7941.
[5] S. Fokken, T. P. Spanniol, J. Okuda, F. G. Sernetz, R. Mulhaupt, *Organometallics* **1997**, *16*, 4240.
[6] D. C. Bradley, R. C. Mehotra, *Metal Alkoxides*, Academic Press, New York, **1978**.
[7] A. O. Larsen, P. S. White, M. R. Gagne, *Inorg. Chem.* **1999**, *38*, 4824.
[8] A. W. Duff, R. A. Kamarudin, M. F. Lappert, R. J. Norton, *J. Chem. Soc. Dalton Trans.* **1986**, 489.
[9] S. A. Waratuke, M. G. Thorn, P. L. Fanwick, A. P. Rothwell, I. P. Rothwell, *J. Am. Chem. Soc.* **1999**, *121*, 9111.
[10] a) J. Okuda, S. Fokken, H.-C.Kang, W. Massa, *Chem. Ber.* **1995**, *128*, 221; b) S. L. Latesky, J. Keddington, A. K. McMullen, I. P. Rothwell, J. C. Huffman, *Inorg. Chem.* **1985**, *24*, 995; c) R. A. Jones, J. G. Hefner, T. C. Wright, *Polyhedron* **1984**, *3*, 1121.
[11] K. Waterpaugh, C. N. Caughlan, *Inorg. Chem.* **1966**, *5*, 1782.
[12] M. J. Frazer, Z. Goffer, *J. Inorg. Nucl. Chem.* **1966**, 28, 2410.
[13] A. Flamini, D. Cole-Hamilton, G. Wilkinson, *J. Chem. Soc. Dalton Trans.* **1978**, 454.
[14] A. Shah, A. Singh, R. C. Mehrotra, *Polyhedron* **1986**, 5, 1285.
[15] A. J. Nielson, P. Schwerdtfeger, J. M. Waters, *J. Chem. Soc. Dalton Trans.* **2000**, 529.
[16] British Titan Products Co. Ltd., French Patent Number: 1377130, 1964.
[17] a) H. Yasuda, Y. Nakayama, K. Takei, A. Nakamura, Y. Kai, N. Kanehisa, *J. Organomet. Chem.* **1994**, 473, 105; b) N. Kanehisa, Y. Kai, N. Kasai, H. Yasuda, Y. Nakayama, K. Takei, A. Nakamura, *Chem. Lett.* **1990**, 2167.
[18] M. Ouchi, M. Kamigaito, M. Sawamoto, *Macromolecules* **1999**, 32, 6407.
[19] H. Noeth, M. Schmidt, *Organometallics* **1995**, 14, 4601.
[20] a) A. Bel, W. Clegg, P. W. Dyer, M. R. Elsegood, V. C. Gibson, E. L. Marshall,. *Chem. Soc. Chem. Commun.* **1994**, 224; b) P. Barrie, T. A. Goffey, G. D. Forster, G. Hogarth, *J. Chem. Soc. Dalton Trans.* **1999**, 4519.
[21] NBO version 3.1, E. D. Glendening, A. E. Reed, J. E. Carpenter, F. Weinhold.
[22] N. J. Long, *Metallocenes – An Introduction to Sandwich complexes*, Blackwell Science, Oxford, **1998**.
[23] J. C. Green, M. L. H. Green, J. T. Thomas, P. C. Konidaris, G. H. Maunder, P. Mountford, *J. Chem. Soc. Chem. Commun.* **1992**, 1361.
[24] I. P. Rothwell, *Acc. Chem. Res.* **1988**, 21, 153.
[25] A. D. Becke, *Phys. Rev. A.* **1988**, 38, 3098.
[26] C. Lee, W.Yang, R. G. Parr, *Phys. Rev. B.* **1988**, 37, 785.
[27] T. H. Dunning, P. J. Hay, in: *Modern Theoretical Chemistry* (Ed.: H. F.Schaefer III), Plenum, New York, **1976**, p. 1–28.
[28] W. R. Wadt, P. J. Hay, *J. Chem. Phys.* **1985**, 82, 284.
[29] *Gaussian 98* (Revision A.1), M. J. Frisch, G. W. Trucks, H. B. Schlegel, G. E. Scuseria, M. A. Robb, J. R. Cheeseman, V. G. Zakrzewski, J. A. Montgomery, R. E. Stratman, J. C. Burant, S. Dapprich, J. M. Millam, A. D. Daniels, K. N. Kudin, M. C. Strain, O. Farkas, J. Tomasi, V. Barone, M. Cossi, R. Cammi, B. Mennucci, C. Pomelli, C. Adamo, S. Clifford, J. Ochterski, G. A. Petersson, P. Y. Ayala, Q. Cui, K. Morokuma, D. K. Malick, A. D. Rabuck, K. Raghavachari, J. B. Foresman, J. Cioslowski, J. V. Ortiz, B. B. Stefanov, G. Liu, A. Liashenko, P. Piskorz, I. Komaromi, R. Gomperts, R. L. Martin, D. J. Fox, T. Keith, M. A. Al-Laham, C. Y. Peng, A. Nanayakkara, C. Gonzalez, M. Challacombe, P. M. W. Gill, B. G. Johnson, W. Chen, M. W. Wong, J. L. Andres, M. Head-Gordon, E. S. Replogle, J. A. Pople, Gaussian, Inc., Pittsburgh PA, **1998**.
[30] R. H. Blessing, *Acta Crystallogr. Sect. A* **1995**, 51, 33.
[31] G. M. Sheldrick, *Acta Crystallogr. Sec*t. *A* **1990**, 46, 467.
[32] G. M. Sheldrick, Program for the refinement of Crystal Structures, University of Göttingen, Germany, **1997**.
[33] L. J. Farrugia, ORTEP 3 for Windows, Version 1.06, University of Glasgow, Scotland, U.K.

Received: September 16, 2004

 © 2005 Wiley-VCH Verlag GmbH & Co. KGaA, Weinheim

Nitrosyl Ruthenium Diolato Complexes[‡]

Michael Barth,[a] Xaver Kästele,[a] and Peter Klüfers*[a]

Keywords: Ruthenium / Nitrosyl / Diols / Carbohydrate complexes

[*mer*-(dien)(NO)Ru(AnErytH$_{-2}$)]BPh_4·2H_2O (**1**), [*mer*-(dien)(NO)Ru(*R*,*R*-ChxdH$_{-2}$)]BPh_4 (**2**), [*mer*-(dien)(NO)Ru(EthdH$_{-2}$)]BPh_4 (**3**), and [*mer*-(dien)(NO)Ru(Me-β-D-Rib*f*2,3H$_{-2}$)]BPh_4·5.5H_2O (**4**) have been synthesized in the form of light pink crystals by the reaction of [*mer*-(dien)(NO)$RuCl_2$]X with the respective diol in aqueous sodium hydroxide solution (dien = diethylenetriamine, AnEryt = anhydroerythritol, Chxd = cyclohexane-1,2-diol, Ethd = ethanediol, Rib = ribose; X = BPh_4 or PF_6). The nitrosyl ligand exhibits a strong *trans* influence which causes the *trans*-bonded oxygen atom of the diolato ligand to form a shorter bond with the Ru centre. Mean values are 2.038 for *cis* and 1.946 Å for *trans* *O*-binding. Back donation is strongly supported by the diolato ligand resulting in low energies for the N–O stretch which can be observed as low as 1805 cm^{-1}. *trans*-Oxygen atoms do not act as hydrogen-bond acceptors in any of the cases.
(© Wiley-VCH Verlag GmbH & Co. KGaA, 69451 Weinheim, Germany, 2005)

Introduction

Ruthenium and its compounds are a class of particularly significant catalytically active materials. Carbohydrates on the other hand provide a biogenic, renewable feedstock which, however, is burdened with the problem of "overfunctionalisation". This term emphasises the fact that it is not merely the number but the similarity of the functional groups which causes problems with regioselectivity. Problems of this kind are typically solved in chemistry by means of catalysis. Bearing in mind the aims of the currently topical green chemistry, which promotes both catalytic reactions and the use of renewable resources, it is surprising that there is no structural information on the interaction of ruthenium centres and carbohydrates. This statement holds not only for monosaccharides but also for simple diols which provide the basic functional group of carbohydrates for metal chelation. This paper reports the synthesis and structural characterisation of the first diolato-ruthenium complexes in both the solid-state and solution. As starting materials, we used aqueous solutions of *trans*-dichloro-*mer*-diethylenetriamine-nitrosyl ruthenium(III) salts[1] which contain a nitrosyl ligand linearly bonded to the ruthenium centre thus forming the well-known, tricationic $\{RuNO\}^6$ fragment (for the Enemark–Feltham notation cf. ref.[2]). In the context of the hormonal action of nitrous oxide, the chemistry[3] of $\{RuNO\}^6$-type complexes has recently attracted interest in its own right due to the physiological activity of these species.[4,5]

[‡] Polyol Metal Complexes, 46. Part 45 see: S. Herdin, G. Kettenbach, P. Klüfers, *Z. Naturforsch. Teil B* **2004**, *59*, 134–139.

[a] Department Chemie der Ludwigs-Maximilians-Universität München,
Butenandtstraße 5–13, 81377 München, Germany
Fax: +49-89-2180-77407
E-mail: kluef@cup.uni-muenchen.de

Results and Discussion

Synthesis of Crystalline [*mer*-(dien)(NO)Ru(DiolH$_{-2}$)] Tetraphenylborates

[*mer*-(dien)(NO)$RuCl_2$]BPh_4 reacts with anhydroerythritol (*cis*-oxolane-3,4-diol, AnEryt) in aqueous alkaline solution over the course of 2 h at 70 °C to yield the tetraphenylborate salt of the complex cation [*mer*-(dien)(NO)Ru(AnErytH$_{-2}$)]$^+$ without concomitant removal of the chloro ligands by special reagents such as silver oxide (method 1 in the Experimental Section). The application of slightly harsher reaction conditions allowed the synthesis of the same product to be initiated directly from nitrosyl-ruthenium chloride, diethylenetriamine and anhydroerythritol (method 2 in the Experimental Section). Method 1 achieved completion as judged by NMR spectroscopy. The precipitate was of a colour similar to the crystals. Method 2, however, results in a more or less brown precipitate which clearly contains by-products. Structural analyses using light pink crystals of the products from both methods revealed the formula [*mer*-(dien)(NO)Ru(AnErytH$_{-2}$)]BPh_4·2H_2O (**1**). Complexes of less acidic diols have been prepared with (*R*,*R*)-cyclohexane-1,2-diol [(*R*,*R*)-Chxd] and ethane-1,2-diol (Ethd). Both diols are less reactive than oxolanediol in terms of the diol remaining uncoordinated after the reaction with the ruthenium starting material in an approximately equimolar ratio according to method 1. Hence, about half of the cyclohexanediol and about one fifth of the ethanediol react in this experimental setup. Crystallisation achieved according to the procedures given in the Experimental Section yielded solvent-free crystals containing the attempted diolato complexes with the formulae [*mer*-(dien)(NO)Ru(*R*,*R*-ChxdH$_{-2}$)]BPh_4 (**2**) and [*mer*-(dien)-(NO)Ru(EthdH$_{-2}$)]BPh_4 (**3**). Attempts to include a carbo-

 DOI: 10.1002/ejic.200300925 © 2005 Wiley-VCH Verlag GmbH & Co. KGaA, Weinheim

hydrate derivative were successful for methyl-β-D-ribofuranoside which contains the anhydroerythritol core (Scheme 1). Here, red crystals of [*mer*-(dien)(NO)Ru(Me-β-D-Rib*f*2,3H$_{-2}$)]BPh_4·5.5H_2O (**4**) were obtained by applying method 2.

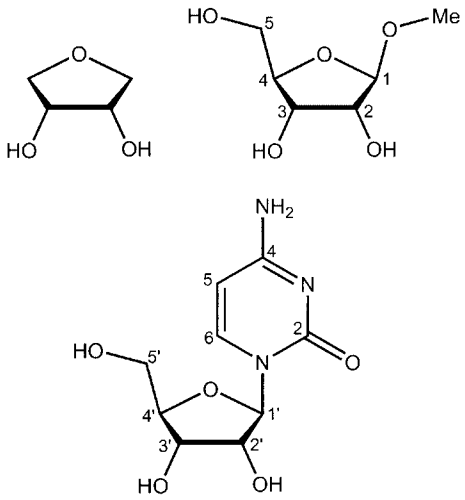

Scheme 1.

The Diolato-{RuNO}^{6} Moiety

The structures of the four complex cations (**1**: Figure 1, **2**: Figure 2, **3**: Figure 3, **4**: Figures 4 and 5) reveal dianionic diolato(2–) ligands bonded to an octahedrally coordinated ruthenium centre. Isomerisation occurred during the course of the reaction: in the starting complex, one nitrogen atom of the dien ligand is *trans* to the nitrosyl group, whereas in the product, all three nitrogen atoms of the *mer*-dien ligand are bonded *cis* to the NO.

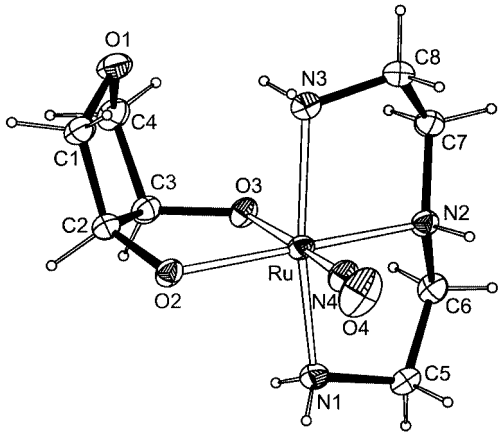

Figure 1. The structure of the [(*mer*-dien)(NO)Ru(AnErytH$_{-2}$)]$^+$ cation in **1**. Distances [Å] and angles [°]: from Ru to: N4 1.746(2), O3 1.940(2), O2 2.046(2), N2 2.070(2), N1 2.108(2), N3 2.112(2); O1–C1 1.443(3), O1–C4 1.443(3), O2–C2 1.416(3), O3–C3 1.432(3), C1–C2 1.540(3), C2–C3 1.542(4), C3–C4 1.518(4); O3–Ru–O2 81.80(7), C2–O2–Ru 112.13(14), C3–O3–Ru 117.92(14), O4–N4–Ru 171.0(2); O2–C2–C3–O3 –22.1(3).

Diolate–RuNO bonding is governed by the *trans*-influence of the nitrosyl ligand. Mean values for significant

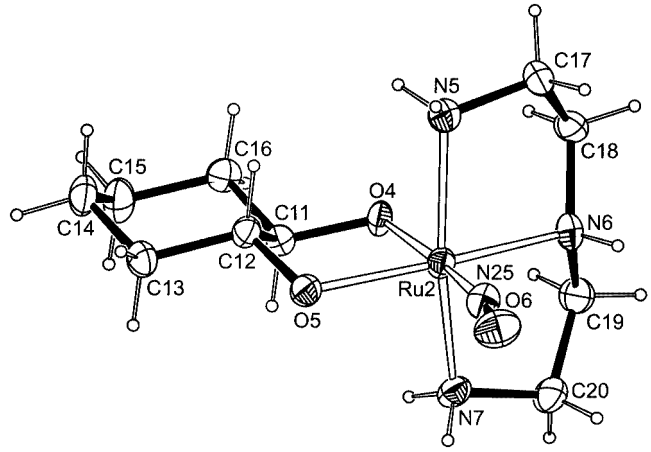

Figure 2. The structure of one of two symmetry-independent [*mer*-(dien)(NO)Ru(*R*,*R*-ChxdH$_{-2}$)]$^+$ cations in **2**. Distances [Å] and angles [°]: from Ru1 to: N4 1.752(5), O2 1.946(4), O1 2.046(4), N2 2.070(4), N3 2.086(5), N1 2.108(5); O1–C1 1.424(6), O2–C2 1.425(5), O3–N4 1.177(6), C1–C2 1.492(6); from Ru2 to: N25 1.725(5), O4 1.955(4), O5 2.041(4), N6 2.090(4), N7 2.091(5), N5 2.126(5); O4–C11 1.439(5), O5–C12 1.426(6), O6–N25 1.161(6), C11–C12 1.516(6); O2–Ru1–O1 82.51(15), C1–O1–Ru1 110.1(3), C2–O2–Ru1 110.4(3), O3–N4–Ru1 169.3(4), O4–Ru2–O5 83.76(15), C11–O4–Ru2 111.4(3), C12–O5–Ru2 106.2(3), O6–N25–Ru2 169.5(5); O1–C1–C2–O2 –49.6(4), O4–C11–C12–O5 –53.4(4).

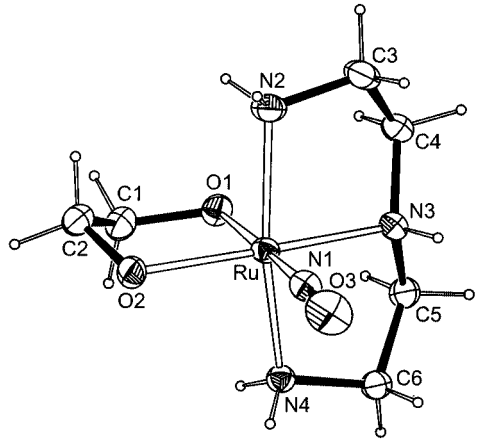

Figure 3. The structure of the [(*mer*-dien)(NO)Ru(EthdH$_{-2}$)]$^+$ cation in **3**. Distances [Å] and angles [°]: from Ru to: N1 1.743(3), O1 1.945(2), O2 2.029(2), N3 2.086(3), N4 2.090(3), N2 2.127(3); O2–C2 1.404(4), O1–C1 1.427(4), O3–N1 1.157(4), C1–C2 1.511(5); O1–Ru–O2 82.50(10), C2–O2–Ru 109.1(2), C1–O1–Ru 113.7(2), O3–N1–Ru 176.8(3); O1–C1–C2–O2 –45.4(4).

parameters have been listed in Table 1. There are some features common to **1**–**4**: (1) the Ru–O(*trans*) distance is always markedly shortened compared with the Ru–O(*cis*) distance, (2) the Ru–O(*trans*)–C angle is always more obtuse than the Ru–O(*cis*)–C angle and, most remarkably, considering the usual features of polyolato-metal structures, (3) the O(*trans*) centre does not act as a hydrogen-bond acceptor in any of the structures. On the other hand, O(*cis*) is a hydrogen-bond acceptor, as is usual.

The energies for the N–O stretching vibration are rather low, the minimum being 1805 cm^{-1} for **2** (cf. 1889 cm^{-1} for the starting material complex [*mer*-(dien)(NO)RuCl_2]BPh_4

 © 2005 Wiley-VCH Verlag GmbH & Co. KGaA, Weinheim

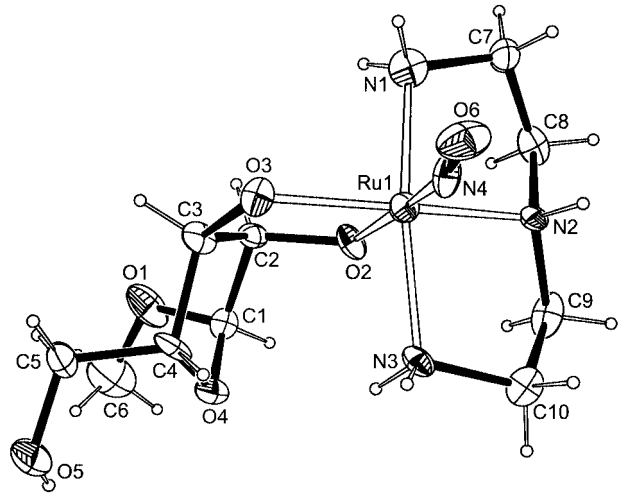

Figure 4. The structure of the O2(*trans*) isomer of the [(*mer*-dien)(NO)Ru(Me-d-Rib*f*2,3H$_{-2}$)]$^+$ cation in **4**. Distances [Å] and angles [°]: from Ru1 to: N4 1.740(9), O2 1.961(6), N2 2.052(8), O3 2.054(6), N1 2.098(9), N3 2.113(8); N4–O6 1.170(10); O2–Ru1–O3 82.2(3), O6–N4–Ru1 168.6(7), C3–O3–Ru1 113.4(6), C2–O2–Ru1 116.8(5); O2–C2–C3–O3 29.1(11).

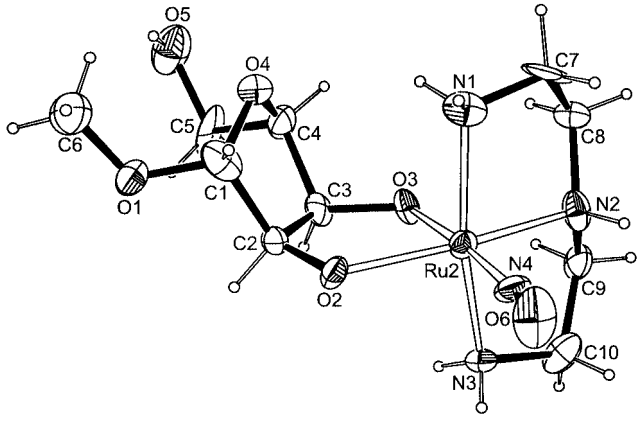

Figure 5. The structure of the O3(*trans*) isomer of the [(*mer*-dien)(NO)Ru(Me-d-Rib*f*2,3H$_{-2}$)]$^+$ cation in **4**. Distances [Å] and angles [°] (add the digit "1" to the labels of the C, N, and O atoms to extract more values from the Crystallographic Information File) from Ru2 to: N4 1.759(9), O3 1.914(6), O2 2.065(6), N2 2.067(8), N3 2.100(9), N1 2.107(8); N4–O6 1.151(10); O3–Ru2–O2 82.6(3), O6–N4–Ru2 169.9(8), C3–O3–Ru2 118.6(6), C2–O2–Ru2 112.7(6); O2–C2–C3–O3 –8.5(12).

with a *trans*-Cl–Ru–NO moiety). Such low values may be expected for *trans* ligands which effectively support electron density donation into the NO π* orbital. Hence, it is not surprising that both the geometric and spectroscopic parameters of **1**–**4** resemble three closely related methoxo and ethoxo complexes which have been reported very recently by Nagoa et al.[6,7] Using pyridine-2-carboxylate (pyca) groups as coligands, these authors reported structural and spectroscopic data for *cis*-[6] and *trans*-[Ru(NO)(OMe)(pyca)$_2$],[7] *cis* and *trans* referring to the orientation of the NO group and the methoxo ligand. These data have been added to Table 1 for comparison. In addition, IR data have been reported on the ethoxo homologue[6] which shares, with our diolates, a low value for the NO stretch of 1815 cm^{-1}. It should be noted that the rules derived by Nagoa et al. regarding the stability of isomers at the {RuNO}^{6} centre are supported by our data. According to these rules, isomers with one of the dien-nitrogen atoms *trans* to the nitrosyl group should be less stable than the species which have been isolated. The number of isomers is thus limited. Due to the equivalence of the hydroxy groups of the parent diols of **1**–**3**, only one isomer can be expected for a diolato complex. In fact, only one ^{13}C signal can be observed for each carbon atom which is part of a ruthenium complex in each of the respective reaction mixtures.

NMR Spectroscopy

One of the reasons for starting the investigation of ruthenium-carbohydrate interactions with {RuNO}^{6} complexes is because of their diamagnetism which enables monitoring of the progress of polyolate binding to the ruthenium centre by NMR spectroscopy. ^{13}C NMR spectra of solutions of **1**–**4** in fact show a marked "coordination-induced shift" (CIS) – a typical down-field shift of the signals of the diol carbon atoms which bear metal-binding oxygens. In addition, the kinetic inertness of the starting material and the product ruthenium complexes is the reason why the signals of metal-bonded and nonbonded diols occur separately in the spectra. This includes the NMR behaviour of possible coordination isomers which, however, are missing for **1**–**3** due to the reasons discussed in the previous paragraph. CIS values are best taken from the spectra of the aqueous reaction mixtures since they contain both the signals of the complex and the free diol (DMSO spectra of the pure products, which are given in the Experimental Section, do not

Table 1. Mean Ru–O distances [Å], Ru–O–C angles [°] and wave numbers ṽ [cm^{-1}] of the N–O stretching vibrations in **1**–**4** and in two isomers of [Ru(NO)(OMe)(pyca)$_2$] (**8**; pyca = pyridine-2-carboxylate).[6,7] *Cis* and *trans* refer to the configuration of NO and the respective diol or methoxo O atom.

	1	**2**	**3**	**4**	**8**
ṽ(NO)	1825	1805	1823	1819, 1838[a]	1838[b]
Ru–O(*trans*)	1.940	1.951	1.945	1.938	1.964[b]
Ru–O(*cis*)	2.046	2.044	2.029	2.060	2.040[c]
Ru–O(*trans*)–C	117.9	110.9	113.7	117.7	123.6[b]
Ru–O(*cis*)–C	112.1	108.2	109.1	113.1	116.2[c]

[a] Cf. Figure 7. [b] Values for the *trans* isomer according to ref.[7] [c] Values for the *cis* isomer according to ref.[6]

 © 2005 Wiley-VCH Verlag GmbH & Co. KGaA, Weinheim

Table 2. ^{13}C NMR spectra of the crude reaction mixtures from which crystals of **4** were isolated (100.5 MHz, 25 °C). Atom numbering is defined in Scheme 1. $\Delta\delta$ values indicating a coordination-induced shift (CIS) are printed **boldface**.

		C1	C2	C3	C4	C5	C6
major isomer	δ/ppm	109.5	88.6	87.0	83.7	63.6	54.3
	$\Delta\delta$/ppm	2.0	**14.8**	**16.7**	1.1	1.3	0.0
minor isomer	δ/ppm	109.0	88.1	86.6	84.6	62.8	54.2
	$\Delta\delta$/ppm	1.5	**14.3**	**16.3**	2.0	0.5	–0.1
Me-β-D-Rib*f*	δ/ppm	107.5	73.8	70.3	82.6	62.3	54.3

Table 3. ^{13}C NMR spectra of the crude reaction mixtures of [*mer*-(dien)(NO)RuCl$_2$]PF$_6$ and cytidine at pH 12.5 (100.5 MHz, 25 °C). Atom numbering is defined in Scheme 1. $\Delta\delta$ values indicating a coordination-induced shift (CIS) are printed **boldface**.

		C1′	C2′	C3′	C4′	C5′	C2	C4	C5	C6
major isomer	δ/ppm	96.2	87.9	85.3	86.7	61.4	165.4	157.4	95.6	140.0
	$\Delta\delta$/ppm	6.6	**14.5**	**16.5**	3.5	1.1	–0.2	0.5	0.0	–1.0
minor isomer	δ/ppm	95.7	90.1	84.8	86.9	60.7	165.4	157.4	95.6	140.0
	$\Delta\delta$/ppm	6.1	**16.7**	**16.0**	3.7	0.4	–0.2	0.5	0.0	–1.0
Cytidine	δ/ppm	89.6	73.4	68.8	83.2	60.3	165.6	156.9	95.6	141.0

show the free diol signals. Hence, a less realistic reference state must be defined). CIS values range from ca. 8 to 15 ppm for **1**–**3** (**1**: 15.0, 13.7 for diol carbons; 3.4, 3.1 for carbons adjacent to the coordinating diol; **2**: 11.6, 9.1 and 1.3, 1.1 in addition to 0.3, 0.2 for the carbons most distant from Ru; **3**: 9.9, 8.1 ppm). For **4** and the related diol cytidine, the coordination induced shifts are slightly larger (Table 2 and Table 3). It is likely that a connection could be made between the differences in the diol CIS values (**1**: 1.3, **2**: 2.5, **3**: 1.7, **4**: 1.9, 2.0; cytidine: 0.7, 2.0) and *cis* and *trans* bonding to NO. However, no sound assignment is possible on the basis of the present data.

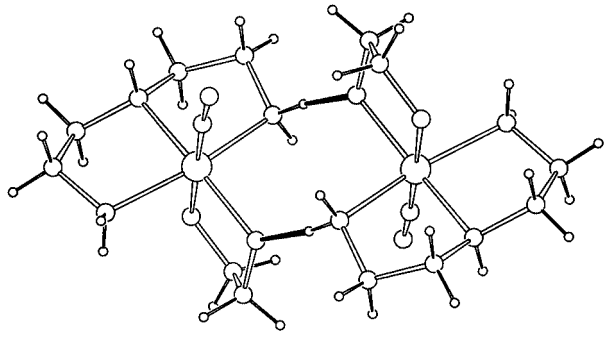

Figure 6. The C_i-symmetric dimer in crystals of **3**. The metric parameters of the hydrogen bond are: N4–H741 0.92, H···O2^{i} 1.76, N4···O2^{i} 2.672(3) Å, N4–H–O2^{i} 170°; symmetry code: ^{i} 1 – *x*, –*y*, –*z*. Similar, but C_1-symmetric dimers are present in the chiral crystals of **2** with the parameters: N3–H732 0.90, H···O5 1.84, N3···O5 2.729(6) Å, N3–H–O5 171°; N7–H771 0.90, H···O1 1.89, N7···O1 2.772(6) Å, N7–H–O1 165°.

Hydrogen Bonds

The individual crystal structures have some special features. Although crystallised from aqueous solution, crystals of **2** and **3** are anhydrous. Hence the N–H functions of the dien ligand are the only possible hydrogen-bond donors. In both structures, only one hydrogen bond is established towards each O(*cis*) acceptor but these bonds are unusually short when compared with N–H···O bonds usually found in polyolato-metal complexes – the shortest one having been observed in **3**: N···O2(*cis*) is 2.672(3) Å. Also, in both structures, two complex cations are linked by two such bonds to form a hydrogen-bonded dimer – a centrosymmetric dimer in **3** (Figure 6) and a similarly assembled dimer of the two symmetrically independent cations of the asymmetrical unit in crystals of the chiral complex **2**.

While there are dimers embedded in an assembly of the large tetraphenylborate counterions in **2** and **3**, the O(*cis*) atoms in **1** and **4** are hydrogen-bonded to water donors and, concomitantly, the complex cations form a structure with the counterions without having close contacts with one another. The structure determination for **1**, which was of a higher quality than that of **4**, reveals typical hydrogen-bonding parameters for the furanoidic ligand with the exception of the lack of such bonds towards the *trans*-oxygen (Table 4). It should be noted that the presence of additional hydrogen-bond acceptors (**1**) or donors and acceptors (**4**) is clearly not the reason for the presence or absence of water molecules in the crystals and the assembly of dimers and vice versa. Using *cis*-cyclopentane-1,2-diol (*cis*-Cptd), which parallels ethanediol and cyclohexanediol in being a simple diol without further functionality, a preliminary structure determination on centrosymmetric triclinic crystals of low quality revealed a hydrated product [*mer*-(dien)(NO)Ru(*cis*-CptdH$_{-2}$)]BPh$_4$·3H$_2$O (**5**). The structure of the complex cation follows the rules presented above. As in **1** and **4**, individual cations and not dimers are embedded in separated counterion surroundings.

Isomers in the Case of Glycoside and Nucleoside Ligation

As mentioned, the hydroxy groups of the diol functions of anhydroerythritol, (*R*,*R*)-cyclohexane-1,2-diol and ethane-1,2-diol are equivalent. Hence no isomers are formed upon rotating the diol functions at the ruthenium centre. The riboside ligand is different in this respect and two iso-

 © 2005 Wiley-VCH Verlag GmbH & Co. KGaA, Weinheim

Table 4. Hydrogen bonds in **1** with distances [Å] and angles [°]. Note that O3 does not act as an acceptor (symmetry codes: [i]*x*, *y* – 1, *z*; [ii] 1 – *x*, –*y*, 1 – *z*; [iii] 1 – *x*, –1 – *y*, 1 – *z*).

D	H	A	D–H	H···A	D···A	D–H···A
O91	H911	O92[i]	0.89(4)	1.89(4)	2.769(3)	172(4)
O91	H912	O1	0.77(5)	2.19(5)	2.942(3)	165(4)
O92	H921	O2	0.80(4)	2.01(4)	2.777(3)	160(3)
O92	H922	O2[ii]	0.81(3)	1.92(3)	2.728(3)	171(3)
N1	H711	O92	0.86(3)	2.46(3)	3.115(3)	133(2)
N3	H731	O1	0.89(3)	2.30(3)	3.099(3)	150(2)
N3	H732	O91[iii]	0.85(3)	2.04(3)	2.874(3)	168(3)

mers can be expected – one in which O2 is the *trans*-oxygen and the other in which O3 occupies that position. Indeed, both isomers are present in crystals of **4**. Formation of the crystals was somewhat unusual. After a brown slurry had precipitated, crystals of **4** grew within this slurry over the course of three days, leaving part of the slurry unchanged. NMR spectra of the redissolved crystals showed the expected number of signals which is twice the number of carbon atoms of the riboside. NMR spectra of the brown residue obtained by washing, filtering and redissolving the slurry in dimethyl sulfoxide, clearly consist of only one half of the signals of the crystalline material. Obviously, the two isomers are not formed in equal amounts during the course of the reaction as expected but there is a main species. Crystallisation proceeds to the point where all of the minor species is spent, leaving the remaining major species in its finely divided state.

Due to the difference in back donation, parameters connected with the {RuNO}^{6} moiety should reflect whether O2 or the slightly more basic O3 atom is *trans* to the ruthenium centre. A measure of this difference is the energy of the N–O stretch. Actually, Figure 7 shows the absorption to be slightly split. Lorentz curve-fitting yields peak values of 1819 and 1838 cm^{-1}. Though the existence of two isomers has been demonstrated from X-ray work as well as NMR and IR spectroscopy, assignment of the spectroscopic data to an individual structure remains uncertain. If higher back donation is assigned to the more basic O3, the main species in the reaction mixture should, hence, be the O3(*trans*) isomer. It should be noted that the quality of the structure analysis did not produce sufficiently sound values for the bond lengths to contribute meaningfully to this study (cf. Experimental Section).

The related nucleosides react differently with the ruthenium starting material. No substantial shift in the ribose signals was observed for uridine and guanosine which bind to ruthenium through the uracil and guanidine residues, respectively. Note that both nucleosides can provide deprotonated amide functions which are obviously stronger ligands for ruthenium than a diolate. With cytidine, however, the ^{13}C NMR spectra closely resemble those of the methyl-β-D-ribofuranoside complexes (cf. the formulae in Scheme 1). The ratio of the major and minor isomers depends on the synthetic procedure chosen. When prepared as described in the Experimental Section by means of microwave heating, there is a distinct difference in the two isomers. Hence, assignment of the signals to one of the isomers is unambiguous. All attempts to crystallise one or both of the isomers have proved unsuccessful so far. The procedure given yielded small needles or platelets both of which were too weakly diffracting for structural analysis.

Conclusions

The {RuNO}^{6} moiety is a well-suited metal fragment for diolate binding. The diolato ligand markedly strengthens back-donation to the nitrosyl ligand. Hence, the energy values for the N–O stretching vibration slightly above 1800 cm^{-1} are at the lower end of those reported in the literature. The applied synthetic methods are suitable for the preparation of complexes of simple diols, nucleosides and other glycosides which are stable under more strongly alkaline conditions and at elevated temperatures. Work is in progress to prepare compounds of this type at conditions which are mild enough such that ruthenium complexes of monosaccharides can also be synthesized.

Experimental Section

trans-Dichloro-*mer*-diethylenetriamine-nitrosyl ruthenium(III) tetraphenylborate (**6**) and *trans*-dichloro-*mer*-diethylenetriamine-

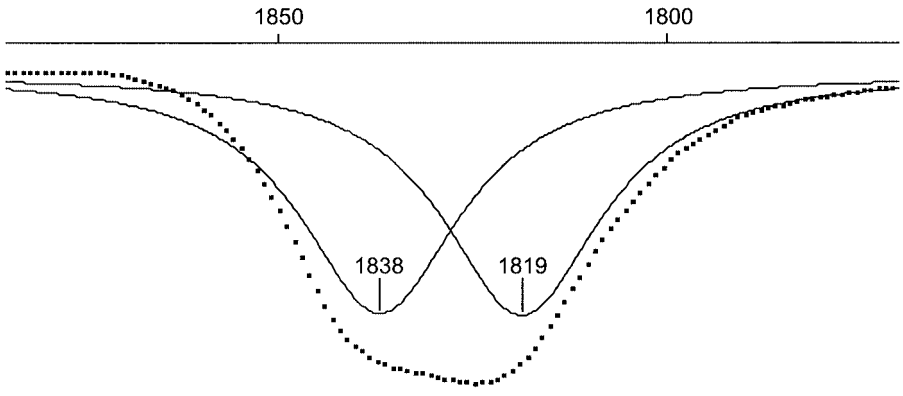

Figure 7. The baseline-corrected region of the N–O stretching vibration taken from crystalline samples of **4**. The numbers given are ṽ values in cm^{-1}.

 © 2005 Wiley-VCH Verlag GmbH & Co. KGaA, Weinheim

nitrosyl ruthenium(III) hexafluorophosphate (**7**) were prepared according to the literature.[1] The results reported appear to be independent of the supplier of the diols, diethylenetriamine and the salts which provide the counterions. It should be noted, however, that the appearance of $Ru(NO)Cl_3 \cdot H_2O$ differs from one supplier to the other. For **1**, we used $Ru(NO)Cl_3 \cdot H_2O$ from Strem and anhydrous $Ru(NO)Cl_3$ from ABCR. For **4**, $Ru(NO)Cl_3 \cdot H_2O$ from Chempur was used.

For the reactions with cytidine a CEM Discover microwave oven was used.

$^{13}C\{^1H\}$ spectra were recorded using 1 mL of the appropriate filtered aqueous reaction mixture in a 5 mm tube. Reference signals of the free diols were subsequently recorded after addition of the respective diol to the measured reaction mixture. Equipment used: ^{13}C NMR spectroscopy: Jeol EX-400. Mass spectrometry: Jeol JMS-700 (ionisation method: FAB^+). IR spectroscopy: Nicolet 520-FTIR.

The equipment used for the structure determinations was an Enraf Nonius KappaCCD diffractometer in the case of **2**–**4** (rotating anode, 4.125 kW source power, Mo-K_α radiation, graphite monochromator) and a Stoe IPDS instrument (sealed tube, 2.75 kW source power, Mo-K_α radiation, graphite monochromator) for **1**. Crystallographic data are summarised in Table 5.

CCDC-226508 (for **1**), 226509 (for **2**), 226510 (for **3**) and 226511 (for **4**) contain the supplementary crystallographic data for this paper. These data can be obtained free of charge from The Cambridge Crystallographic Data Centre via www.ccdc.cam.ac.uk/data_request/cif.

In the structure determination of **3**, a high residual density of 3.4 e Å^{-1} was calculated at a distance of 1.3 Å from Ru. The reason for this high value remains unclear and the next density was as low as 0.6 e Å^{-1}. The structure determination using a crystal of **4** was complicated by a considerable degree of pseudo-symmetry. Though being built up from a chiral motif, most atoms of the unit-cell keep to a centrosymmetric arrangement. Hence, most of the structure can be described in space group $P\bar{1}$ (instead of $P1$). The origin of the pseudosymmetry of the crystals is the pseudosymmetry of the methyl-β-D-ribofuranoside ligand. Taking the methoxy residue at C1 and the hydroxymethyl substituent at C4 as equivalent (Scheme 1), the riboside exhibits C_s symmetry. It is not usual for this pseudosymmetry to find itself expressed in a crystal structure since a hydroxymethyl residue, being a hydrogen-bond donor, is clearly different from the more hydrophobic methoxy group. However, in the structure of **4**, this rare case is realised and it interferes with the structure refinement.

***mer*-Diethylenetriamine-{*cis*-oxolane-2,3-diolato(2–)}-nitrosyl Ruthenium(III) Tetraphenylborate Dihydrate (1). Method 1:** Compound **6** (667 mg, 1.068 mmol) was dissolved in hot water (350 mL) with vigorous stirring. The pH value was adjusted to 12 by addition of 2 M sodium hydroxide. After addition of anhydroerythritol (111 mg, 1.068 mmol), the solution was heated to 70 °C for 2 h. Upon cooling, an orange-pink precipitate formed which was filtered off, washed with some water and dried under vacuum to yield ca.

Table 5. Crystallographic data.

	1	**2**	**3**	**4**
empirical formula	$C_{32}H_{43}BN_4O_6Ru$	$C_{34}H_{43}BN_4O_3Ru$	$C_{30}H_{37}BN_4O_3Ru$	$C_{34}H_{54}BN_4O_{11.5}Ru$
M_r [g mol^{-1}]	691.59	667.61	613.52	814.69
crystal size [mm]	0.29 × 0.19 × 0.15	0.16 × 0.12 × 0.08	0.32 × 0.18 × 0.16	0.35 × 0.18 × 0.15
T [K]	200(2)	293(2)	200(2)	200
diffractometer	Stoe IPDS	KappaCCD	KappaCCD	KappaCCD
crystal system	triclinic	monoclinic	monoclinic	triclinic
space group	$P\bar{1}$	$P2_1$	$P2_1/n$	$P1$
a [Å]	9.2991(8)	11.59660(10)	12.50320(10)	10.6371(2)
b [Å]	10.4514(8)	12.68100(10)	17.6215(2)	11.4939(2)
c [Å]	17.3793(16)	22.8485(2)	12.9580(2)	17.0986(5)
α [°]	86.332(10)	90	90	73.2656(9)
β [°]	79.131(11)	102.1646(4)	92.4843(6)	89.3241(10)
γ [°]	72.835(10)	90	90	72.5096(9)
V [Å^3]	1584.8(2)	3284.57(5)	2852.29(6)	1903.01(8)
Z	2	4	4	2
calcd. density [g cm^{-3}]	1.44930(18)	1.35008(2)	1.42873(3)	1.42180(6)
μ [mm^{-1}]	0.545	0.516	0.588	0.456
absorption correction	numerical	numerical	numerical	none
transmission factor range	0.9242–0.9543	0.9925–0.9975	0.8163–0.9209	–
refls. measured	27826	51865	35849	21490
R_{int}	0.0583	0.0626	0.0425	0.0507
mean $\sigma(I)/I$	0.0586	0.0679	0.0263	0.0748
θ range	3.15–27.51	3.52–27.52	3.20–26.00	3.58–24.00
observed refls.	5915	11321	4936	9594
x,y (weighting Scheme)	0.0114, 0.9645	0.0274, 1.2099	0.0588, 6.2238	0.0345, 1.2526
Flack parameter	–	–0.04(3)	–	–0.02(3)
refls in refinement	7241	14614	5586	11425
parameters	530	775	353	995
restraints	0	1	0	36
$R(F_{obs})$	0.0364	0.0409	0.0432	0.0440
$R_w(F^2)$	0.0739	0.0895	0.1178	0.0986
S	1.042	1.052	1.035	1.022
shift/error$_{max}$	0.001	0.002	0.001	0.001
max. electron density [e Å^{-3}]	0.325	0.531	3.374	0.618
min. electron density [e Å^{-3}]	–0.627	–0.565	–0.565	–0.403

 © 2005 Wiley-VCH Verlag GmbH & Co. KGaA, Weinheim

200 mg of a pink solid. Dissolving the solid in as small an amount of methanol as possible followed by slow evaporation of the solvent gave light pink crystals of **1**. Compound **1** is slightly soluble in water and ethanol and very soluble in methanol. $C_{32}H_{43}BN_4O_6Ru$ (691.59): calcd. C 55.6, H 6.3, B 1.56, N 8.1, Ru 14.6; found C 56.9, H 6.3, B 1.50, N 8.1, Ru 14.9. ^{13}C NMR (100 MHz, [D_6] DMSO): δ = 164.7–163.2 (4 signals, phenyl, C_{ipso}), 136.1 (phenyl, C_{ortho}), 125.9 (phenyl, C_{meta}), 122.1 (phenyl, C_{para}), 88.1, 87.8 (diol, 2H, CH), 77.1, 75.5 (diol, 2H, CH_2), 50.8, 50.4, 50.2, 49.8 (dien, 4H, CH_2) ppm. MS (FAB^+): *m*/*z* (%) = 337 (15) $[M + H]^+$, 336 (8) $[M]^+$. IR (KBr): $\tilde{\nu}$ = 1825 (vs, N–O), 1579 (vw), 1480 (w), 1453 (w), 1427 (w), 1119 (w), 1052 (sh), 1035 (m), 739 (st), 710 (st), 612 (m) cm^{-1}.

Method 2: Anhydrous nitrosyl-ruthenium(III) chloride (445 mg, 1.87 mmol) or the equivalent amount of nitrosyl-ruthenium(III) chloride monohydrate was dissolved in water (20 mL). The pH value was adjusted to 11 by addition of 2 M sodium hydroxide. A solution of diethylenetriamine (193 mg, 1.87 mmol) and anhydroerythritol (195 mg, 1.87 mmol) in water (5 mL) was added dropwise. The pH value was readjusted to 11 by addition of either 0.1 M hydrochloric acid or 0.1 M sodium hydroxide and the solution was then heated to reflux for 3 h. Excess sodium tetraphenylborate was then added to the hot solution. A pink to light-brown precipitate formed which was filtered off, washed with cold water and recrystallised from methanol to yield light pink crystals of **1**. Both methods yield ca. 10% of the crystalline product.

***mer*-Diethylenetriamine-{*R*,*R*-cyclohexane-1,2-diolato(2–)}-nitrosyl Ruthenium(III) Tetraphenylborate (2):** Compound **6** (580 mg, 0.929 mmol) was dissolved in water (300 mL). The pH value was adjusted to 13 with 2 M sodium hydroxide and (*R*,*R*)-cyclohexane-1,2-diol (324 mg, 2.79 mmol) was added. The resultant solution was heated to reflux at 80 °C for 2 h. After standing overnight, a mixture of yellow-pink crystals of **2** and colourless crystals of unreacted starting material were formed. Compound **2** is poorly soluble in water but freely soluble in methanol. $C_{34}H_{43}BN_4O_3Ru$ (667.61): calcd. C 61.2, H 6.5, B 1.62, N 8.4, Ru 15.1; found C 60.9, H 6.4, B 1.51, N 8.3, Ru 15.0. ^{13}C NMR (100 MHz, [D_6]DMSO): δ = 164.7–163.2 (4 signals, phenyl, C_{ipso}), 136.1 (phenyl, C_{ortho}), 125.9 (phenyl, C_{meta}), 122.1 (phenyl, C_{para}), 89.0, 88.5 (diol, 2 CH), 50.8, 50.4, 50.2, 49.8 (dien, 4 CH_2), 35.6, 34.9 (diol, 2 CH_2), 23.1 (diol, 2 isochronous CH_2); signals of the free diol in water: δ = 73.9 (2 CH; C1, C2), 31.5 (2 CH_2; C3, C6), 22.7 (2 CH_2; C4, C5) ppm. MS (FAB^+): *m*/*z* (%) = 349 (65) $[M + H]^+$, 348 (37) $[M]^+$. IR (KBr): $\tilde{\nu}$ = 1805 (vs, N–O), 1579 (m), 1568 (sh), 1480 (m), 1455 (m), 1427 (m), 1089 (m), 1071(m), 1034 (m), 739 (st), 709 (st), 641 (st), 610 (st) cm^{-1}.

***mer*-Diethylenetriamine-{1,2-ethanediolato(2–)}-nitrosyl Ruthenium(III) Tetraphenylborate (3):** Compound **7** (97 mg, 0.216 mmol) was dissolved in water (10 mL). 1,2-Ethanediol (11 mg, 0.216 mmol) was added, the pH value adjusted to 12.5 by addition of 2 M sodium hydroxide and the reaction mixture heated to 70 °C for 2 h. The cooled solution was then carefully layered with sodium tetraphenylborate solution (5 mL) which had been saturated at room temperature. Reddish-brown prisms of **3** crystallised overnight at the boundary between the layers. Solution behaviour resembles that of **2**. $C_{30}H_{37}BN_4O_3Ru$ (613.52): calcd. C 58.7, H 6.1, B 1.76, N 9.1, Ru 16.5; found C 58.7, H 6.1, B 1.56, N 8.9, Ru 16.3. ^{13}C NMR (100 MHz, H_2O): δ = 72.4, 74.2 (diol, 2 CH_2), 50.7, 50.5, 50.1, 49.8 (dien, 4 CH_2); signal of the free diol in the same solution: δ = 64.3 ppm. MS (FAB^+): *m*/*z* (%) = 293 (19) $[M + H]^+$, 292 (17) $[M]^+$. IR (KBr): $\tilde{\nu}$ = 1823 (vs, N–O), 1578 (w), 1453 (w), 1427 (w), 1073 (m), 1054 (m), 1033 (m), 749 (sh), 736 (st), 710 (st), 614 (m) cm^{-1}.

***mer*-Diethylenetriamine-{methyl-β-D-ribofuranosid-2,3-ato(2–)}-nitrosyl Ruthenium(III) Tetraphenylborate 5.5-Hydrate (4):** $Ru(NO)Cl_3 \cdot H_2O$ (0.256 g, 1.00 mmol) was suspended in water (10 mL) and diethylenediamine (0.103 g, 1.00 mmol) in water (2 mL) was added. A red solution formed immediately. Methyl-β-D-ribofuranoside (0.164 g, 1.00 mmol) dissolved in water (3 mL) was added followed by the dropwise addition of NaOH (1.5 mL, 2 M, pH ≈ 11.5). The reddish-brown solution was heated to 100 °C for 3 h (about half of the free glycoside was left in the reaction mixtures containing a 1:1 molar ratio of the ruthenium starting material and the furanoside; however, in terms of NMR spectra, no more product forms after prolonged reaction times). After cooling, sodium tetraphenylborate (0.342 g, 1.00 mmol) in water (15 mL) was added and a brown slurry precipitated. Over the course of 3 d, red crystals of **4** formed which were separated from the slurry by flotation (16% yield). Compound **4** is insoluble in water, ether and dichloromethane but dissolves in DMSO to yield a light-red solution. ^{13}C NMR (100 MHz, [D_6]DMSO): major isomer: δ = 111.3 (C1), 91.4 (C2), 89.7 (C3), 88.9 (C4), 65.1 (C5), 54.6 (C6); minor isomer: 112.3 (C1), 92.9 (C2), 88.8 (C3), 88.3 (C4), 64.0 (C5), 54.9 (C6); the signals of the phenyl residues of the counterion coincide for both isomers, the dien signals coincide partly: 164.7–163.2 (4 signals, phenyl, C_{ipso}), 136.1 (phenyl, C_{ortho}), 125.9 (phenyl, C_{meta}), 122.1 (phenyl, C_{para}); 50.9, 50.7, 50.5, 50.2, 49.9, 49.7 (dien, 4 CH_2 of 2 isomers) ppm.

Reaction of Cytidine with [*mer*-(dien)(NO)$RuCl_2$]PF_6: [*mer*-(dien)(NO)$RuCl_2$]PF_6 (52 mg, 0.116 mmol) was dissolved in sodium hydroxide (2 mL, 0.1 M, pH = 12.5). After addition of cytidine (56 mg, 0.232 mmol) the solution was heated in a microwave oven (10 min, 100 °C, 200 W with cooling). ^{13}C NMR spectroscopy indicated that about half of the nucleoside was bonded to ruthenium. Of this half, a major and a minor isomer are present in a ratio of about 2:1.

Acknowledgments

This work was supported by the Fonds der Chemischen Industrie.

[1] R. Asanuma, H. Tomizawa, A. Urushiyama, E. Miki, K. Mizumachi, T. Ishimori, *Bull. Chem. Soc. Jpn.* **1994**, *67*, 1274–1280.
[2] J. H. Enemark, R. D. Feltham, *Coord. Chem. Rev.* **1974**, *13*, 339–406.
[3] T. W. Hayton, P. Legzdins, W. B. Sharp, *Chem. Rev.* **2002**, *102*, 935–991.
[4] E. Tfouni, M. Krieger, B. R. McGarvey, D. W. Franco, *Coord. Chem. Rev.* **2003**, *236*, 57–69.
[5] P. G. Wang, M. Xian, X. Tang, X. Wu, Z. Wen, T. Cai, A. J. Janczuk, *Chem. Rev.* **2002**, *102*, 1091–1134.
[6] T. Hirano, T. Oi, H. Nagao, K. Morokuma, *Inorg. Chem.* **2003**, *42*, 6575–6583.
[7] T. Hirano, M. Kuroda, N. Takeda, M. Hayashi, M. Mukaida, T. Oi, H. Nagao, *Dalton Trans.* **2002**, 2158–2162.

Received: December 11, 2003

 © 2005 Wiley-VCH Verlag GmbH & Co. KGaA, Weinheim

Adducts of Cyclotriphosphorus Complexes with Cyclopentadienyl Ruthenium Fragments: Synthesis, Solid-State Structure and Solution Behaviour

Pierluigi Barbaro,[b] Massimo Di Vaira,[a] Maurizio Peruzzini,[b] Stefano Seniori Costantini,[a] and Piero Stoppioni*[a]

Keywords: Cyclotriphosphorus / Ruthenium / Cyclopentadienyl / Monodentate P ligands

Treatment of the cyclo-P_3 complexes [(triphos)M(η^3-P_3)]-[triphos = 1,1,1-tris(diphenylphosphanylmethyl)ethane; M = Co (**1**), Rh (**2**)] with stoichiometric amounts of [CpRu-$(CH_3CN)_2(PR_3)$]PF_6 [R = Ph (**3**), Me (**4**), Cy (**5**)] in CH_2Cl_2 in the presence of CH_3CN yields the bimetallic adducts [{(triphos)M}($\mu,\eta^{3:1}$-P_3){CpRu(CH_3CN)(PR_3)}]PF_6 [M = Co; R = Ph (**6**), Me (**7**), Cy (**8**); M = Rh; R = Ph, (**9**), Me (**10**), Cy (**11**)]. The rhodium derivatives **9** and **11**, upon treatment with one equivalent of PMe_3, form the complexes [{(triphos)Rh}($\mu,\eta^{3:1}$-P_3){CpRu(PMe_3)(PR_3}]PF_6 [R = Ph (**12**), Cy (**13**)]. On standing in CH_2Cl_2, the rhodium complexes **9** and **10** lose acetonitrile to yield compounds with the formula [{(triphos)Rh}($\mu,\eta^{3:1,1'}$-P_3){CpRu(PR_3)}]PF_6 [R = Ph (**14**), Me (**15**)]. All the compounds have been characterised by elemental analyses and, in solution, by ^{31}P and ^1H NMR spectroscopy. The $^{31}P\{^1H\}$ EXSY NMR spectroscopic data at different temperatures of **11** and **14** have highlighted the occurrence of independent dynamic processes that exchange both the triphos and the cyclo-P_3 phosphorus nuclei. An X-ray structural investigation carried out on **6** has confirmed the occurrence of the $\mu,\eta^{3:1}$-ligating behaviour of the cyclo-P_3 ligand.

(© Wiley-VCH Verlag GmbH & Co. KGaA, 69451 Weinheim, Germany, 2005)

Introduction

"Naked" group 15 ligands stabilised by transition-metal moieties exhibit lone pair electrons, owing to which they are generally endowed with reactivity toward metal fragments with Lewis acid character. Many compounds have been described that result from the addition of metal moieties, mainly carbonyl or cyclopentadienyl carbonyl metal fragments, to the above metal-supported main group atom ligands. The added moieties, depending on their ligating properties, may bind in η^1-, η^2- or η^3 fashion to the main group units to afford bi-, tri- and tetrametallic complexes.[1–5] The solution structures of these multimetallic adducts may usually be assigned by in-depth ^{31}P NMR spectroscopic studies. These NMR studies have often revealed the occurrence of a dynamic behaviour consisting of (i) skeleton rearrangements of multinuclear cluster compounds,[6–12] (ii) relative rotation of parts of the molecule about symmetry- or pseudosymmetry axes,[13–16] and (iii) scrambling of coordinated fragments.[17,18] In our laboratories the reactivity of a series of neutral[19–21] and cationic[22–25] complexes has been investigated, in which a cyclic triatomic E_3 or E_2X (E = P, As; X = S, Se) group isη^3 bound to a metal atom of the cobalt or of the nickel group and is supported by the tripodal tridentate 1,1,1-tris(diphenylphosphanylmethyl)ethane (triphos) ligand (Scheme 1).[26,27]

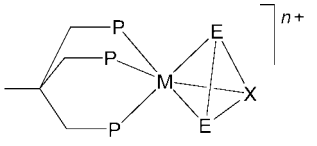

n = 0 M = Co, Rh, Ir; E = X = P

n = 1 M = Ni, Pd, Pt; E = X = P

n = 1 M = Co; E = P, As; X = S, Se

Scheme 1.

The neutral compounds [(triphos)M(η^3-P_3)] (M = Co, Rh) easily add coordinatively unsaturated metal fragments, such as $M(CO)_5$ (M = Cr, W) or $CpMn(CO)_2$, to yield bi-, tri- and tetrametallic adducts in which the geometry of the P_3 ring is only slightly modified from that in the parent compounds.[19,21,28–31] In contrast, the cationic [(triphos)-M(η^3-E_2X)]$^+$ species (M = Ni; E = X = P. M = Co; E = P, As; X = S, Se) do not add carbonyl fragments, but readily insert the 14e $M(PPh_3)_2$ (M = Pd, Pt) carbene-like moieties into an E–E or E–X bond of the triatomic ring.[31–33] Interestingly, all of these polymetallic compounds exhibit dynamic behaviour at room temperature. Recent studies on a series of complexes resulting from the addition of one me-

[a] Dipartimento di Chimica, Università di Firenze, via della Lastruccia, 3, 50019 Sesto Fiorentino, Firenze, Italy
[b] ICCOM-CNR, via Madonna del Piano snc, 50019 Sesto Fiorentino, Firenze, Italy

tal-carbonyl fragment to [(triphos)M(η^3-P_3)] (M = Co, Rh) have definitely shown that two fluxional processes occur in solution, i.e. the scrambling of the metal-carbonyl moiety over the P_3 cyclic system and the relative rotation of the P_3 and {(triphos)M} moieties about their common C_3 axis.[34] Variable-temperature NMR analysis has also established that the rhodium derivatives have a higher rotational barrier than the cobalt derivatives.[34] The scrambling process over cyclo-P_3, which has been blocked at low temperature for both cobalt and rhodium derivatives, has a higher barrier with respect to the {(triphos)M} rotation. Indeed, the latter process has been blocked on the NMR time scale only for the rhodium adduct [{(triphos)Rh}($\mu,\eta^{3:1}$-P_3){$W(CO)_4$-PPh_3}], which is formed with the sterically demanding $W(CO)_4(PPh_3)$ fragment sitting as an end-on ligand on the cyclotriphosphorus unit.[34]

In this work we have investigated the reactivity of [(triphos)M(η^3-P_3)] [M = Co (**1**), Rh(**2**)] toward the [$CpRu(CH_3CN)_2(PR_3)$]PF_6 [R = Ph (**3**), Me (**4**), Cy (**5**)] complexes. These species contain two acetonitrile molecules that can be selectively replaced to generate the 16e [$CpRu(CH_3CN)(PR_3)$]$^+$ and 14e [$CpRu(PR_3)$]$^+$ fragments, respectively.[35] The 16e moieties appear to be particularly suitable, upon reaction with **1** and **2**, to provide further information on the factors affecting the scrambling process of the metal fragment, as they are more sterically hindered than the carbonyl moieties previously employed and, furthermore, their steric demand may be varied by changing the phosphane substituents. Moreover, the lability of the second acetonitrile molecule may further extend the reactivity of the P_3 ring, already activated by the initial end-on coordination of the ruthenium fragment.

Results and Discussion

The dinuclear compounds with the formula [{(triphos)M}($\mu,\eta^{3:1}$-P_3){$CpRu(CH_3CN)(PR_3)$}]PF_6 [M = Co; R = Ph (**6**), Me (**7**), Cy (**8**); M = Rh; R = Ph, (**9**), Me (**10**), Cy (**11**)] are obtained in a straightforward manner by adding a stoichiometric amount of the appropriate [$CpRu(CH_3CN)_2(PR_3)$]PF_6 complex to [(triphos)M(η^3-P_3)] [M = Co (**1**), Rh (**2**)] dissolved in CH_2Cl_2 in the presence of CH_3CN (see the Experimental Section). The complexes **6–11** can be regarded as the mono adducts of the cyclo-P_3 unit in **1** or **2** with 16e [$CpRu(CH_3CN)(PR_3)$]$^+$ (R = Ph, Me, Cy) fragments that readily result from the removal of one labile acetonitrile molecule from [$CpRu(CH_3CN)_2(PR_3)$]PF_6 (Scheme 2). The concentration of CH_3CN is crucial for obtaining **6–11** in both high yield and purity. Actually, **1** and **2** do not react with the ruthenium complexes under conditions of high CH_3CN concentration, which hamper the substitution of the coordinating molecule that occurs through a dissociative pathway.[35] The complexes **6–11** may be handled in air for a limited time; they are soluble in polar organic solvents and their solutions are stable in an inert atmosphere. Solutions of **6–11**, in both $(CH_3)_2CO$ or $CHCl_3$, decompose when heated to 40–50 °C, yielding a mixture of compounds, which could not be characterised.

X-ray Structure Analysis

The structure of **6**, determined by X-ray crystal analysis, consists of [{(triphos)Co}($\mu,\eta^{3:1}$-P_3){$CpRu(CH_3CN)(PPh_3)$}]$^+$ cations (Figure 1), PF_6^- anions, and toluene solvate molecules in a 1:1:2 ratio. Selected values of bond

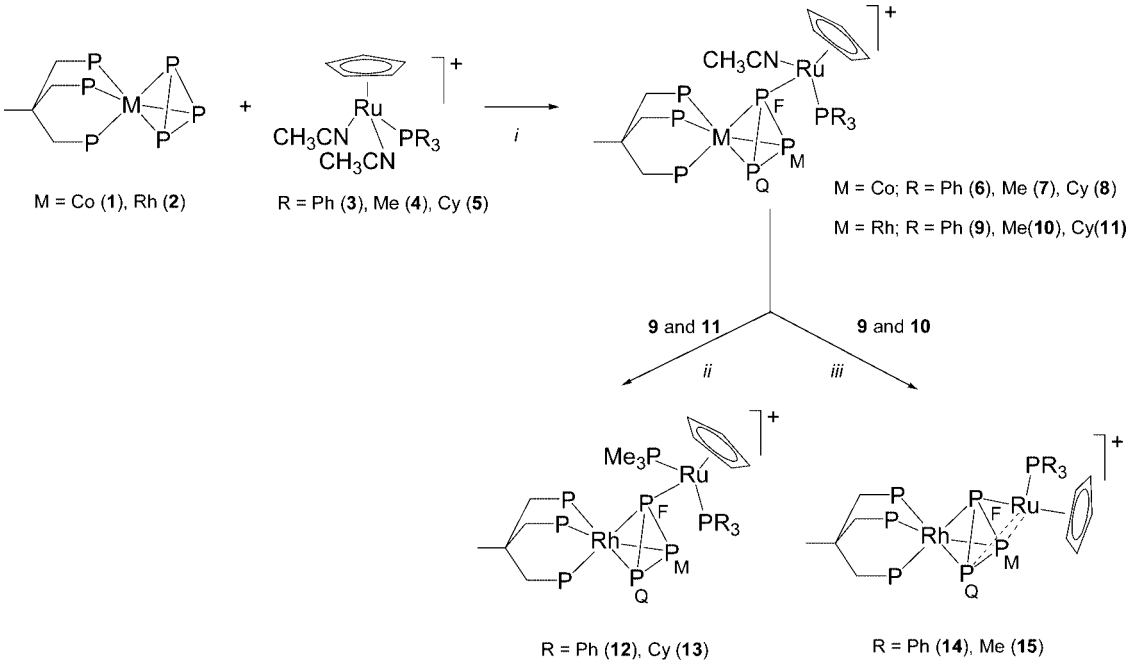

Scheme 2. *i*) CH_3CN, CH_2Cl_2, toluene; *ii*) CH_2Cl_2, PMe_3, toluene; *iii*) CH_2Cl_2, toluene.

 © 2005 Wiley-VCH Verlag GmbH & Co. KGaA, Weinheim

lengths and angles are given in Table 1. In the dimetal cation, the {CpRu(CH_3CN)(PPh_3)} moiety forms through its metal atom an end-on monoadduct on a phosphorus atom of the CoP_3 core. Such a pseudotetrahedral core exhibits some deviations from the regular geometry of the parent compound **1**, consisting of (i) a moderately shorter Co–P bond formed by the bridging phosphorus atom [P(5)] between the two metal atoms, with respect to the other two Co–P bonds, and (ii) slightly shorter P–P bonds formed by the same P(5) atom than the third P–P bond in the P_3 unit. Consistent deviations from regularity have been detected for metal carbonyl monoadducts of **1** and **2**[34] and similar, although more pronounced, deviations have been found for a methyl adduct.[36] Rationalizations for these trends have already been proposed.[13,34]

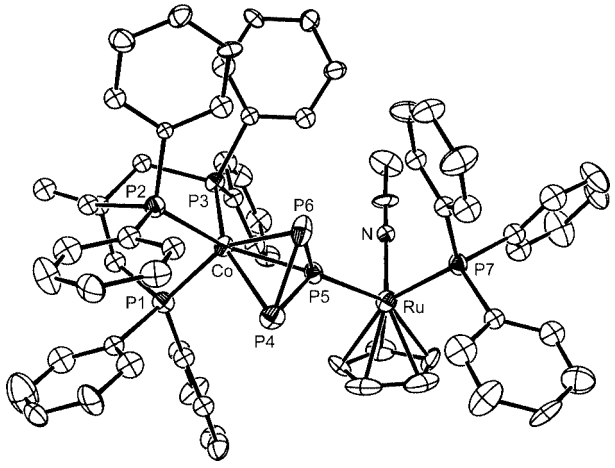

Figure 1. A view of the [{(triphos)Co}(μ,$\eta^{3:1}$-P_3)-{CpRu(CH_3CN)(PPh_3)}]$^+$ cation in the structure of **6**; displacement ellipsoids traced at the 20 % probability level. H atoms are not shown and labels for the carbon atoms are omitted for clarity.

Table 1. Selected bond lengths [Å] and bond angles [°] for **6**.

Bond lengths			
Co–P(1)	2.178(5)	P(4)–P(6)	2.142(6)
Co–P(2)	2.200(5)	P(5)–P(6)	2.100(5)
Co–P(3)	2.209(5)	Ru–P(5)	2.353(4)
Co–P(4)	2.316(5)	Ru–N	2.025(12)
Co–P(5)	2.273(5)	Ru–P(7)	2.325(4)
Co–P(6)	2.333(5)	Ru–Ct[a]	1.849
P(4)–P(5)	2.117(6)		
Bond angles			
P(1)–Co–P(2)	90.4(2)	P(5)–Ru–P(7)	95.5(2)
P(1)–Co–P(3)	96.1(2)	P(5)–Ru–N	94.6(3)
P(2)–Co–P(3)	90.6(2)	P(7)–Ru–N	88.9(3)
P(4)–Co–P(5)	54.9(2)	N–Ru–Ct[a]	124.8
P(4)–Co–P(6)	54.9(2)	P(5)–Ru–Ct[a]	120.2
P(5)–Co–P(6)	54.2(2)	P(7)–Ru–Ct[a]	124.3
Co–P(5)–Ru	156.9(2)		

[a] Distance and angles formed by the centroid (Ct) of the Cp ring. The Ru–C(Cp) distances are in the range 2.195–2.224 Å.

The ruthenium atom forms a slightly longer bond to the P_3 phosphorus atom than to the phosphane donor atom (Table 1). These two P atoms and the CH_3CN nitrogen atom substantially span a face of an octahedron around the ruthenium atom; the opposite side of the coordination sphere is occupied by the cyclopentadienyl ligand. A similar coordination geometry, although in this case the nitrogen atom of a second CH_3CN ligand replaces the P_3 phosphorus atom, has recently been found for a ruthenium derivative, in which the Ru–P(phosphane) and Ru–C(Cp) mean distances are marginally shorter than the present ones and both Ru–N distances are longer by 0.05 Å.[37]

NMR Properties of the Compounds

The room temperature $^{31}P\{^1H\}$ NMR spectra of the compounds **6–11** recorded in CD_2Cl_2 show resonances that fall into two quite distinct regions: a group of signals at low field (50–2 ppm) is assigned to the phosphorus atoms of triphos and of the phosphane bound to ruthenium (see Experimental Section), while a second group of high-field shifted signals (from –150 to –304 ppm) is assigned to the "naked" P atoms from the cyclo-P_3 ligand. Table 2 presents the NMR spectroscopic data for the latter resonances, and the relevant labelling scheme is shown in Scheme 2. The intensity ratios of the signals agree with the proposed formulae. The resonance for the triphos phosphorus atoms exhibits chemical shifts that are similar to those of the parent [(triphos)M(η^3-P_3)] [M = Co (**1**) and Rh (**2**)][22] compounds and of other end-on carbonyl adducts.[13,34] The phosphorus atom of the PR_3 ligand yields a doublet due to coupling with P_F; both the chemical shift and the coupling constant of the phosphane ligand are in the range observed for [CpRu(PR_3)(PR_3')(L)] complexes.[38] This could indirectly suggest that the donor/acceptor properties of the "naked" phosphorus atoms in the "ligand" [(triphos)M(η^3-P_3)] should be similar to those of the phosphanes. Signals due to the P atoms of the cyclo-P_3 unit are split into three distinct multiplets in the high-field region with integral ratios of 1:1:1. Irrespective of the compound, the signal at lower field appears as a triplet, while the other two, occurring at higher field, consist each of a doublet of doublets, with small differences in their chemical shifts. The overall high-field shifts of the P atoms involved in the cyclo-P_3 ring clearly suggest that this unit has undergone only minor modifications upon coordination to the ruthenium fragment. Indeed, severe rearrangements of the cyclic unit, such as cleavage of one of its P–P bonds, significantly affect the chemical shifts, which move to low field with respect to the signal of the parent compound.[32] The multiplicities of the resonances under discussion allow the safe assignment of the low-field triplet to P_F, which is slightly deshielded by coordination to the ruthenium fragment. Consequently, the two high-field resonances may be safely assigned to the two phosphorus atoms P_M and P_Q that are not coordinated to ruthenium. Such an assignment is strongly supported by the analogous shifts observed in the low-temperature ^{31}P NMR spectra of the monoadducts of [(triphos)M(η^3-P_3)] with metal carbonyl fragments.[34] It is worth noting that while the resonance of the end-on Ru-coordinated P_F atom undergoes a low-field shift with respect to that observed for the parent [(triphos)-

Table 2. $^{31}P\{^1H\}$ NMR spectroscopic data at room temperature for the "naked" P atoms of the compounds **6–15**.

Compound[a]	Chemical shift, δ [ppm]			Coupling constant, J [Hz]	
	P_F	P_M or P_Q	P_Q or P_M	$^1J(P_F\text{-}P_M) = {}^1J(P_F\text{-}P_Q)$	$^1J(P_M\text{-}P_Q)$
6	–175.7 (tbr)	–290.8 (ddbr)	–301.5 (ddbr)	320.0	264.0
7	–164.6 (tbr)	–291.8 (ddbr)	–306.8 (ddbr)	320.0	256.0
8	–187.9 (tbr)	–283.6 (ddbr)	–296.0 (ddbr)	321.0	260.0
9	–164.4 (tm)	–284.9 (ddm)	–297.8 (ddm)	337.0	265.0
10	–159.7 (tm)	–288.7 (ddm)	–303.6 (ddm)	338.0	257.0
11	–173.2 (tm)	–278.5 (ddm)	–293.7 (ddm)	335.0	258.0
12	–179.1 (tm)	–269.9 (ddm)	–274.4 (ddm)	340.0	256.0
13	–180.0 (tm)	–267.5 (ddm)	–274.9 (ddm)	330.0	259.0
14	–164.7 (tbr)	–259.1 (ddbr)	–270.9 (ddbr)	303.0	252.0
15	–151.5 (tbr)	–276.7 (dbr)	–276.7 (dbr)	320.0	0

[a] The NMR spectra were recorded in CD_2Cl_2 with a Varian Gemini g300bb spectrometer. Key: d = doublet, t = triplet, m = multiplet, br = broad. The cyclo-P_3 in the parent compounds [(triphos)M(P_3)] yields a broad singlet (δ = –276.2 ppm) for M = Co (**1**) and a doubled quartet [δ = –261.0, ^1J(P–Rh) 13, $^2J(P\text{–}P_{triphos})$ 12 Hz] for M = Rh (**2**).

M(η^3-P_3)] compound, the P_M and P_Q resonances move high field, suggesting an increase of local electron density upon coordination of the ruthenium moiety to the cobalt or rhodium cyclo-P_3 starting material. The inequivalence of P_M and P_Q, that is observed for all of the complexes irrespective of the phosphane substituent, may be ascribed to the chirality of the $[CpRu(CH_3CN)(PR_3)]^+$ fragment, although different environments of the two P atoms are likely to result also from the effects of steric repulsions between the phenyl ends of the {(triphos)M} moiety and the ruthenium fragment. The ^1J coupling constants between P_F, P_M, and P_Q lie in the range spanned by other end-on adducts of cyclo-P_3.[34] Both the triphos and "naked" P atom signals of the cobalt derivatives **6–8** are broadened by the cobalt quadrupole, so that only the largest ^1J coupling constants between the unsubstituted P atoms may be detected. The rhodium complexes **9–11** exhibit broad signals for the triphos P atoms, but sharp patterns for the "naked" phosporus nuclei. Such data point to the occurrence at room temperature of a dynamic process, on the NMR time scale, that involves motion of the triphos ligand with respect to a fixed frame formed by the "naked P" atoms. On the other hand, no dynamic process involving the scrambling motion of the Ru-metal moiety over the P_3 cyclic system is observed at room temperature for **6–11**, irrespective of large differences in the steric requirements of the PR_3 phosphanes employed. This is in contrast with the behaviour of the metal carbonyls previously investigated,[34] which exhibited dynamic behaviour at room temperature, and this suggests that such differences may be influenced by electronic factors, rather than by steric ones. The decomposition of the complexes upon warming their solutions prevented a through investigation of possible dynamic processes involving the Ru-metal moiety and the P_3 cyclic system at higher temperatures. However, the dynamic behaviour of **11** has been carefully investigated at various temperatures by means of ^1H, $^{31}P\{^1H\}$ and 2D $^{31}P\{^1H\}$ EXSY spectroscopic analyses. Sections of selected variable-temperature $^{31}P\{^1H\}$ spectra are shown in Figure 2.

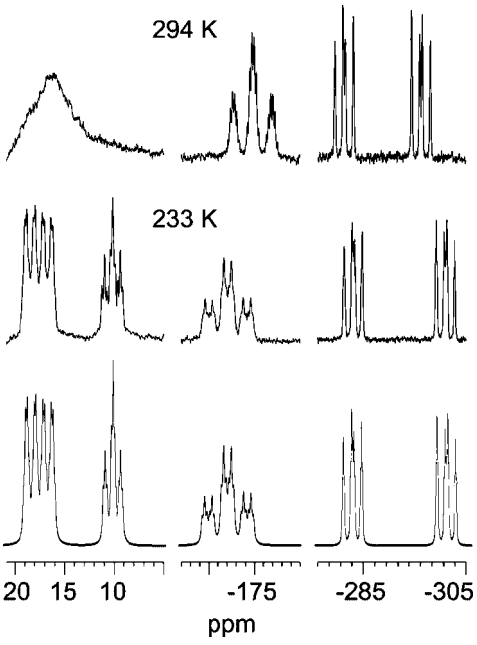

Figure 2. Sections of the $^{31}P\{^1H\}$ NMR spectra of **11** (CD_2Cl_2, 161.95 MHz). Top, experimental spectrum at 294 K; middle, experimental spectrum at 233 K; bottom, simulated spectrum at 233 K. The resonances due to the PCy_3 phosphorus are omitted for clarity.

The rate of the exchange of triphos donor atoms is lowered on cooling the solution. In particular, at 233 K, the triphos phosphorus atoms exhibit separated multiplets centred at 18.45, 16.75 and 10.18 ppm, with coupling constants that range from 29.5 to 130.0 Hz (data obtained by computer simulation) (Table 3). The $^{31}P\{^1H\}$ EXSY spectra recorded at 294 and 248 K are reported in Figure 3. Indeed, two distinct sets of exchange peaks are observed, showing that **11** attains an overall slow motional regime in the above temperature range.[39] A set of exchange peaks is detected at temperatures higher than 260 K, and is relative to the high-field signals due to P_3 (Figure 3, top); the other set, that can be observed below the coalescence point, connects the resonances of the triphos phosphorus atoms (Figure 3, bottom).

This exchange pattern is consistent with the existence of two distinct dynamic processes that have different activation energies; the energy for the process for the P_3 exchange is higher than that for the other one. Such dynamic behaviour

 © 2005 Wiley-VCH Verlag GmbH & Co. KGaA, Weinheim

Table 3. $^{31}P\{^{1}H\}$ NMR spectroscopic data of compound **11**[a].

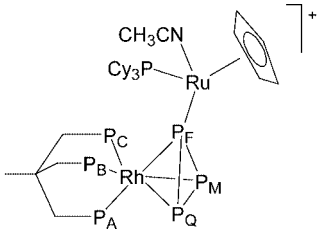

Nucleus	δ [ppm]	Coupling constants J_{PP} [Hz]						J_{PRh} [Hz]
		P_B	P_C	P_F	P_M	P_Q	PCy_3	
P_A	10.18	33.2	29.5	130.0	0.0	0.0	0.0	130.2
P_B	16.75		29.5	0.0	31.0	0.0	0.0	134.3
P_C	18.45			0.0	0.0	29.5	0.0	138.5
P_F	–172.11				336.3	343.8	42.7	43.0
P_M	–282.16					257.2	0.0	32.2
P_Q	–300.78						0.0	30.5
PCy_3	44.46							0.0

[a] In CD_2Cl_2, 161.95 MHz, 233 K. Data by computer simulation.

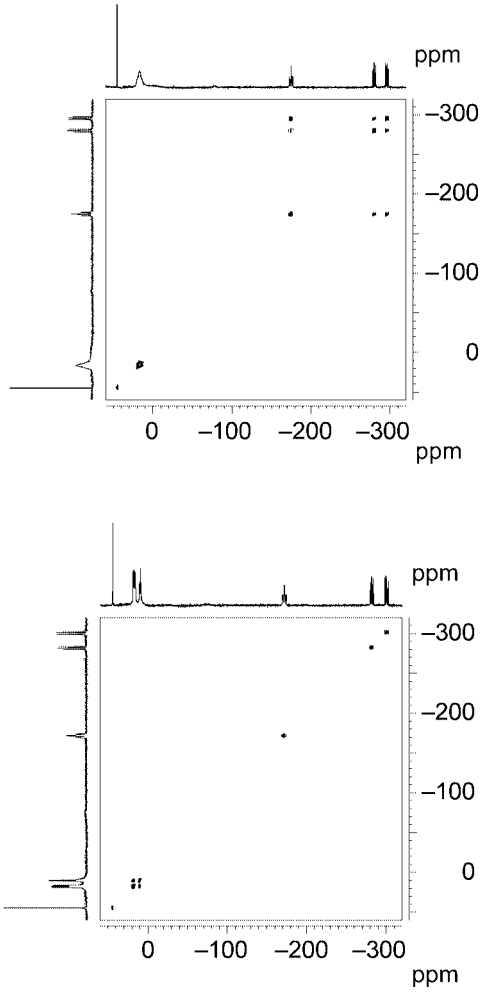

Figure 3. $^{31}P\{^{1}H\}$ EXSY spectra of **11** (CD_2Cl_2, 161.95 MHz, τ_m 0.1 s). Top, spectrum at 294 K; bottom, spectrum at 248 K.

may be accounted for by referring to two types of motion: (i) rotation of the P_3 unit with respect to the other parts of the structure (this motion, shown in Scheme 3 (*i*), involves scrambling of the Ru moiety over the cyclic system and yields the exchange peaks in the 294 K spectrum in Figure 3); and (ii) relative rotation of the {(triphos)M} moiety and the rest of the structure [Scheme 3 (*ii*)] that accounts for the exchange peaks in the EXSY spectrum at 248 K in Figure 3. The two processes are simultaneous and partly related, which makes it impossible, in view of the complex eight-nuclei spin system, to perform any reliable analysis addressing the thermodynamics of each exchange process.

The reactivity of the rhodium derivatives **9–11** has been further investigated, as the fine structure exhibited by the resonances of the "naked" atoms in the ^{31}P NMR spectra may provide more information on the solution behaviour of these dimetallic derivatives. Treatment of **9** and **11** in CH_2Cl_2 with a stoichiometric amount of PMe_3 yields the complexes $[\{(triphos)Rh\}(\mu,\eta^{3:1}\text{-}P_3)\{CpRu(PMe_3)(PR_3)\}]_6$ [R = Ph (**12**), Cy (**13**)] (Scheme 2), which form through replacement of CH_3CN by PMe_3 in the ruthenium coordination sphere. When twice as large an amount of PMe_3 is used, $[(triphos)Rh(\eta^3\text{-}P_3)]$ (**2**) and $[CpRu(PMe_3)_2(PR_3)]PF_6$ (R = Ph, Cy) are formed, which suggests an intrinsic weakness of the cyclo-P_3 coordination to the [CpRu(L)(L′)] unit. The ^{31}P NMR spectra of **12** and **13** (see the Experimental Section and Table 2) exhibit resonances for triphos, PR_3, P_F, P_M, and P_Q with similar features to those observed for **9** and **11**, besides the expected additional resonance for the PMe_3 phosphorus atom that occurs at about 2 ppm as a pseudo triplet; such multiplicity is due to fortuitous coincidence of the coupling constant to both PR_3 (R = Ph, Cy) and P_F. Interestingly, the triphos resonances, which in the parent compounds **9** and **11** appear as a broad signal, occur as a doublet of narrower multiplets, such that the

 © 2005 Wiley-VCH Verlag GmbH & Co. KGaA, Weinheim

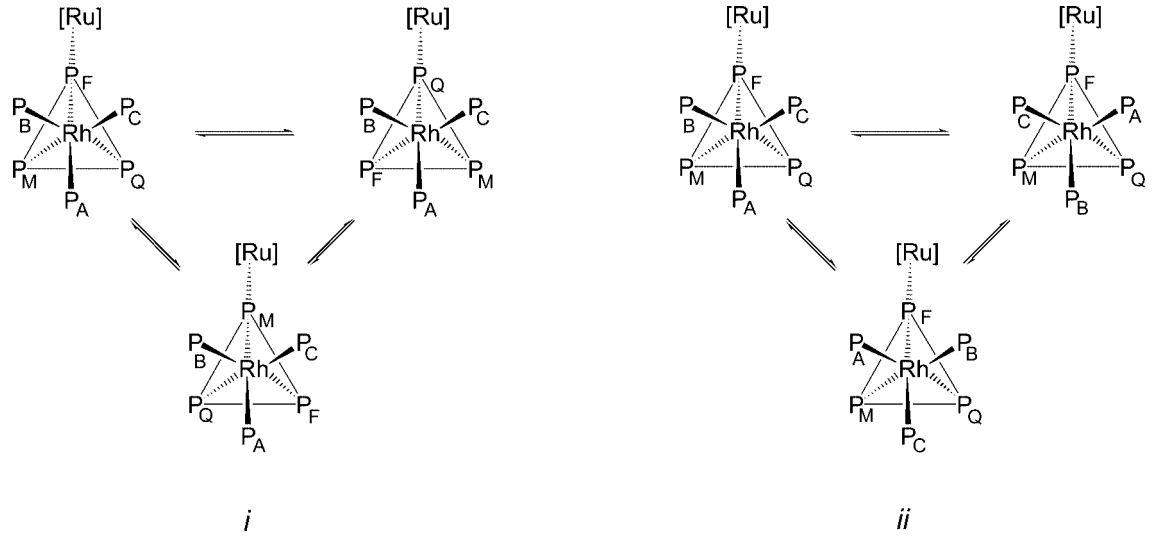

Scheme 3.

$^1J(P_{triphos}–Rh)$ is observed, see Experimental Section. Such a result points to a higher barrier for the type of motion shown in Scheme 3 (*ii*) for **12** and **13** than for **9** and **11**. This in turn may be attributed to the increased steric demand of the ruthenium fragment after replacement of the acetonitrile ligand by trimethylphosphane.

In the absence of acetonitrile, CH_2Cl_2 solutions **9** and **10** are not stable, but slowly transform to compounds with the general formula [(triphos)Rh(P_3){CpRu(PR_3)}]PF_6 [R = Ph (**14**) and Me (**15**)], by releasing the coordinated CH_3CN molecule (Scheme 2). Complexes **14** and **15** have been isolated as brown microcrystals but, in spite of repeated attempts, suitable crystals for X-ray investigations have not been obtained, so their solution structure is proposed on the basis of ^{31}P NMR spectroscopic data. The ^{31}P NMR spectra at room temperature of **14** and **15** (see Experimental Section and Table 2) exhibit resonances for triphos, PR_3, and P_F with similar shifts to those observed for **9** and **10**; the triphos and PR_3 signals are broad; those assigned to P_M and P_Q, on the other hand, appear at significantly lower field than in the parent compounds; the P_F, P_M and P_Q signals still appear as triplets and doublet of doublets, respectively, but their components are broad and only the large ^1J(P–P) coupling constants may be detected. Such data suggest that the dimetal cations in **9** and **10** have undergone minor modifications on the loss of the acetonitrile molecule to yield **14** and **15**, and that the 14e {CpRu(PR_3)} fragment interacts with the P_M and P_Q phosphorus atoms of the P_3 unit. Furthermore, the data are consistent with the rotational motion of the {(triphos)Rh} moiety and, on account of the broad resonances exhibited by the PR_3, P_F, P_M, and P_Q atoms, they point to a further process involving the CpRu(PR_3)P_3 side of the dimetal cation. A type of motion that might account for the latter aspects would be that of the ruthenium fragment, tightly bound to a P_3 phosphorus atom, that shifts between the positions of the other two, and therefore yields a dynamic $\mu,\eta^{3:1,1'}$-P_3 unit. The behaviour of **14** has been investigated at different temperatures by $^{31}P\{^1H\}$ and 2D $^{31}P\{^1H\}$ EXSY spectroscopic data. The $^{31}P\{^1H\}$ spectra show that the rates of exchange decrease on cooling, but even at the lowest reached temperature (230 K), the limiting form is not attained. The $^{31}P\{^1H\}$ EXSY spectra at 294 K and 248 K do not show cross peaks connecting either the triphos or the P_3 phosphorus atoms. These data seem to indicate that the dynamic processes occur with lower barriers than for **9** and **10**. Such a finding is consistent with the suggested geometry in solution; in fact, the ruthenium fragment, on interacting with P_M and P_Q, is expected to move slightly toward the centre of the P_3 unit, thereby releasing some steric repulsions within the cation, which are present in **9** and **10**.

Experimental Section

All reactions and manipulations were performed under dry oxygen-free argon. The solvents were purified according to standard procedures.[40] The ^1H and $^{31}P\{^1H\}$ NMR spectra at room temperature were measured on a Varian Gemini g300bb spectrometer, equipped with a variable-temperature unit, operating at 300 MHz (^1H) and 121.46 MHz (^{31}P). The variable-temperature and EXSY experiments were carried out on a Bruker Avance DRX-400 spectrometer equipped with a variable-temperature control unit accurate to ±0.1 °C and operating at 161.95 and 400.13 MHz. Chemical shifts are relative to tetramethylsilane (^1H) and to H_3PO_4 85 % (^{31}P) as external standards at δ = 0.00 ppm, with downfield values taken as positive; coupling constants are in Hertz. J(P–P) and J(P–Rh) coupling constants of **11** at low temperature were obtained by computer simulation using the gNMR program.[41] 2D NMR spectra were recorded on degassed nonspinning samples using pulse sequences suitable for phase-sensitive representations with TPPI. The 2D $^{31}P\{^1H\}$ EXSY spectra were recorded using a modified NOESY sequence with ^1H decoupling during acquisition: 400 increments of size 3 K (with 400 scans each) covering the full range in both dimensions were collected with a relaxation delay of 0.25 s and mixing times of 50, 100 and 500 ms.[42,43] Analytical data for carbon, hydrogen, nitrogen, and phosphorus were obtained from the Microanalytical Laboratory of the Department of Chemistry of the University of Firenze. The complexes [(triphos)M(η^3-P_3)] (M

 © 2005 Wiley-VCH Verlag GmbH & Co. KGaA, Weinheim

= Co (**1**), Rh (**2**) and $[CpRu(CH_3CN)_2(PR_3)]PF_6$ [PR_3 = PPh_3 (**3**), PMe_3 (**4**) and PCy_3 (**5**)] were synthesized according to literature methods.[19,20,38] The ^1H NMR spectroscopic data of the dinuclear adducts **6–15** and the $^{31}P\{^1H\}$ resonances of the phosphane ligands (triphos and PR_3) are reported in this section. The uninformative ^1H signals of the aromatic protons of triphos and of the PPh_3 derivatives, occurring in the expected region (7.6–6.9 ppm), are not reported. The labelling used for the different phosphorus nuclei is defined in Scheme 2. The PF_6^- anion yields a septet centred at –143.2 [^1J(P–F) 712 Hz] in all the compounds.

Syntheses

[{(triphos)Co}(μ,η$^{3:1}$-P$_3$){CpRu(CH$_3$CN)(PPh$_3$)}]PF$_6$ (6): To a yellowish orange solution of [(triphos)Co(η^3-P$_3$)] (**1**) [132 mg, 0.17 mmol] in CH_2Cl_2 (40 mL) was added at room temperature whilst stirring one equivalent of $[CpRu(CH_3CN)_2(PPh_3)]PF_6$ (**3**) in CH_2Cl_2 (10 mL). The resulting solution was stirred for 3 h at room temperature, and during this time the colour changed to brown-red. Acetonitrile (1 mL) and toluene (10 mL) were then slowly added to yield reddish brown crystals by slowly evaporating the resulting solution at room temperature. Yield: 201 mg (85 %). $C_{66}H_{62}CoF_6NP_8Ru$ (1390.9): calcd. C 57.0, H 4.5, N 1.0 %; found C 57.1, H 4.8, N 0.9 %. ^1H NMR (CD_2Cl_2, 298 K): δ = 4.14 (s, C_5H_5, 5 H), 2.40 (br., CH_2P, 6 H), 2.20 (br. s, CH_3CN, 3 H), 1.37 (br. s, CH_3C, 3 H) ppm. $^{31}P\{^1H\}$ NMR (CD_2Cl_2, 298 K): δ = 50.2 [d, PPh_3, ^2J(PPh_3–P_F) 36.5, 1P], 34.2 (br., $P_{triphos}$, 3P) ppm.

The compounds [{(triphos)M}(μ,η$^{3:1}$-P$_3$){CpRu(CH$_3$CN)(PR$_3$)}]PF_6 [M = Co; R = Me (**7**), Cy (**8**); M = Rh; R = Ph (**9**), Me (**10**), Cy (**11**)] were prepared by the same procedure as for **6** by adding the equimolar amount of $[CpRu(CH_3CN)_2(PR_3)]PF_6$ [R = Ph (**3**), Me (**4**), Cy (**5**)] to a CH_2Cl_2 solution of [(triphos)M(η^3-P$_3$)] [M = Co (**1**), Rh(**2**)].

[{(triphos)Co}(μ,η$^{3:1}$-P$_3$){CpRu(CH$_3$CN)(PMe$_3$)}]PF$_6$ (7): Yield: 123 mg (60 %). $C_{51}H_{56}CoF_6NP_8Ru$ (1204.7): calcd. C 50.8, H 4.7, N 1.2 %; found C 50.7, H 4.8, N 1.0 %. ^1H NMR (CD_2Cl_2, 298 K): δ = 4.27 (s, C_5H_5, 5 H), 2.37 (br., CH_2P, 6 H), 2.17 (s, CH_3CN, 3 H), 1.65 (d, CH_3P, ^2J(H-P) 9.6, 9 H), 1.39 (s, CH_3C, 3 H) ppm. $^{31}P\{^1H\}$ NMR (CD_2Cl_2, 298 K): δ = 32.7 (br., $P_{triphos}$, 3P), 10.0 [d, PMe_3, ^2J(PMe_3–P_F) 46.0, 1P] ppm.

[{(triphos)Co}(μ,η$^{3:1}$-P$_3$){CpRu(CH$_3$CN)(PCy$_3$)}]PF$_6$ (8): Yield: 204 mg (85 %). $C_{66}H_{80}CoF_6NP_8Ru$ (1409.1): calcd. C 56.2, H 5.7, N 1.0 %; found C 56.1, H 5.8, N 0.8 %. ^1H NMR (CD_2Cl_2, 298 K): δ = 4.27 (s, C_5H_5, 5 H), 2.40–1.40 (br. m, C_6H_{11}, CH_2P, CH_3CN, CH_3C, 45 H) ppm. $^{31}P\{^1H\}$ NMR (CD_2Cl_2, 298 K): δ = 42.2 [d, PCy_3, ^2J(PCy_3–P_F) 39.0, 1P], 32.9 (br., $P_{triphos}$, 3P) ppm.

[{(triphos)Rh}(μ,η$^{3:1}$-P$_3$){CpRu(CH$_3$CN)(PPh$_3$)}]PF$_6$ (9): Yield: 207 mg (85 %). $C_{66}H_{62}F_6NP_8RhRu$ (1434.9): calcd. C 55.2, H 4.3, N 1.0 %; found C 55.1, H 4.5, N 0.9 %. ^1H NMR (CD_2Cl_2, 298 K): δ = 4.20 (s, C_5H_5, 5 H), 2.47 (br., CH_2P, 6 H), 2.20 (s, CH_3CN, 3 H), 1.31 (s, CH_3C, 3 H) ppm. $^{31}P\{^1H\}$ NMR (CD_2Cl_2, 298 K): δ = 51.0 [d, PPh_3, ^2J(PPh_3–P_F) 44.5, 1P], 16.9 (br., $P_{triphos}$, 3P) ppm.

[{(triphos)Rh}(μ,η$^{3:1}$-P$_3$){CpRu(CH$_3$CN)(PMe$_3$)}]PF$_6$ (10): Yield: 138 mg (65 %). $C_{51}H_{56}F_6NP_8RhRu$ (1248.7): calcd. C 49.0, H 4.5, N 1.1; found C 49.3, H 4.6, N 1.0 %. ^1H NMR (CD_2Cl_2, 298 K): δ = 4.42 (s, C_5H_5, 5 H), 2.48 (br., CH_2P, 6 H), 2.21 (s, CH_3CN, 3 H), 1.67 (d, CH_3P, ^2J(H-P) = 9.6, 9 H), 1.52 (s, CH_3C, 3 H) ppm. $^{31}P\{^1H\}$ NMR (CD_2Cl_2, 298 K): δ = 16.8 (br., $P_{triphos}$, 3P), 9.8 [d, PMe_3, ^2J(PMe_3–P_F) 49.5, 1P] ppm.

[{(triphos)Rh}(μ,η$^{3:1}$-P$_3$){CpRu(CH$_3$CN)(PCy$_3$)}]PF$_6$ (11): Yield: 210 mg (85 %). $C_{66}H_{80}F_6NP_8RhRu$ (1453.0): calcd. C 54.5, H 5.5, N 1.0, P 17.0 %; found C 54.3, H 5.7, N 0.8, P 16.8 %. ^1H NMR (CD_2Cl_2, 298 K): δ = 4.23 (s, C_5H_5, 5 H), 2.40–1.4 (br. m, C_6H_{11}, CH_2P, CH_3CN, CH_3C) ppm. $^{31}P\{^1H\}$ NMR (CD_2Cl_2, 298 K): δ = 44.4 [d, PCy_3, ^2J(PCy_3–P_F) 44.5, 1P], 16.0 (br., $P_{triphos}$, 3P) ppm.

[{(triphos)Rh}(μ,η$^{3:1}$-P$_3$){CpRu(PMe$_3$)(PPh$_3$)}]PF$_6$ (12): To an orange solution of [{(triphos)Rh}(μ,η$^{3:1}$-P$_3$){CpRu(CH$_3$CN)-(PPh$_3$)}]PF_6 (**9**) [143 mg, 0.10 mmol] in CH_2Cl_2 (20 mL) was added at room temperature whilst stirring an equimolar amount of neat PMe_3. The resulting solution was stirred for 2 h; toluene (15 mL) was then slowly added; reddish-orange crystals were obtained by slowly evaporating the resulting solution at room temperature. Yield: 200 mg (80 %). $C_{67}H_{68}F_6P_9RhRu$ (1469.9): calcd. C 54.7, H 4.7 %; found C 54.5, H 4.6 %. ^1H NMR (CD_2Cl_2, 298 K): δ = 4.34 (s, C_5H_5, 5 H), 2.41 (br., CH_2P, 6 H), 1.52 (s, CH_3C, 3 H), 1.31 [d, CH_3P, ^2J(H–P) = 9.3, 9 H] ppm. $^{31}P\{^1H\}$ NMR (CD_2Cl_2, 298 K): δ = 50.2 [dd, PPh_3, ^2J(PPh_3–PMe_3) 41.5, ^2J(PPh_3–P_F) 36.5, 1P], 16.5 [br. d, $P_{triphos}$, ^1J($P_{triphos}$–Rh) 130.5, 3P], 2.2 [t, PMe_3, ^2J(PMe_3–P_F) 42.0, 1P] ppm.

[{(triphos)Rh}(μ,η$^{3:1}$-P$_3$){CpRu(PMe$_3$)(PCy$_3$)}]PF$_6$ (13): Complex **13** was prepared as described above for **12** by using **11** instead of **9**. Yield: 202 mg (80 %). $C_{67}H_{86}F_6P_9RhRu$ (1488.1): calcd. C 54.1, H 5.8 %; found C 54.2, H 5.9 %. ^1H NMR (CD_2Cl_2, 298 K): δ = 4.32 (s, C_5H_5, 5 H), 2.40–1.30 (br. m, C_6H_{11}, CH_2P, CH_3C, 42 H), 1.25 [d, CH_3P, ^2J(H–P) 8.7, 9 H] ppm. $^{31}P\{^1H\}$ NMR (CD_2Cl_2, 298 K): δ = 46.0 [t, PCy_3, ^2J(PCy_3–PMe_3) = ^2J(PCy_3–P_F) 39.0, 1P], 15.0 [br. d, $P_{triphos}$, ^1J($P_{triphos}$–Rh) 120.0, 3P], 2.1 [t, PMe_3, ^2J(PMe_3–P_F) 40.0, 1P] ppm.

[{(triphos)Rh}(μ,η$^{3:1,1'}$-P$_3$){CpRu(PPh$_3$)}]PF$_6$ (14): [(triphos)Rh(η^3-P$_3$)] (**2**) and $[CpRu(CH_3CN)_2(PPh_3)]PF_6$ (**3**) were reacted as described for **9** avoiding the subsequent addition of acetonitrile. Brown microcrystals were obtained by adding only toluene, and slowly concentrating the resulting solution. Yield: 154 mg (65 %). $C_{64}H_{59}F_6P_8RhRu$ (1393.8): calcd. C 55.1, H 4.3, P 17.8 %; found C 55.2, H 4.4, P 17.6 %. ^1H NMR (CD_2Cl_2, 298 K): δ = 4.02 (s, C_5H_5, 5 H), 2.37 (br., CH_2P, 6 H), 1.53 (s, CH_3C, 3 H) ppm. $^{31}P\{^1H\}$ NMR (CD_2Cl_2, 298 K): δ = 48.4 (br. s, PPh_3, 1P), 15.5 [dq, $P_{triphos}$, ^1J($P_{triphos}$–Rh) 132.0, ^2J($P_{triphos}$–$P_{cyclo\text{-}P3}$) 21.0, 3P] ppm.

[{(triphos)Rh}(μ,η$^{3:1,1'}$-P$_3$){CpRu(PMe$_3$)}]PF$_6$ (15): Brown microcrystals of **15** were obtained as described above for **14** by reacting [(triphos)Rh(η^3-P$_3$)] (**2**) and $[CpRu(CH_3CN)_2(PMe_3)]PF_6$ (**4**) in a 1:1 ratio in CH_2Cl_2. Yield: 123 mg (60 %). $C_{49}H_{53}F_6P_8RhRu$ (1207.6): calcd. C 48.7, H 4.4, P 20.5 %; found C 48.9, H 4.4, P 20.2 %. ^1H NMR (CD_2Cl_2, 298 K): δ = 4.15 (s, C_5H_5, 5 H), 2.37 (br., CH_2P, 6 H), 1.53 (s, CH_3C, 3 H), 1.50 [d, CH_3P, ^2J(H–P) 9.3] ppm. $^{31}P\{^1H\}$ NMR (CD_2Cl_2, 298 K): δ = 16.2 [dm, $P_{triphos}$, ^1J($P_{triphos}$–Rh) 127.0, 3P], 8.0 (m, PMe_3, 1P) ppm.

Crystal Structure Determination

Obtaining crystals suitable for X-ray analyses on these compounds proved to be difficult; a data set could only be collected with a very small crystal of **6**, grown from a diluted CH_2Cl_2/CH_3CN/C_7H_8 solution, which gave relatively low-angle reflections. Data were collected at room temperature with a Bruker CCD diffractometer, equipped with Göbel mirrors and mounted on a rotating-anode generator, using Cu-K_α radiation (λ = 1.5418 Å). Cell constants were obtained by least-squares refinement of the setting angles of 791 reflections in the range $7° < 2\theta < 55°$. Crystallographic data and details on the structure determination and refinement procedure are summarised in Table 4. Although limited absorption effects were expected, in view of the small size of the crystal, a correction for absorption was applied with SADABS,[44] in an attempt to reduce the effects of absorption by the glass fibre, which caused

 © 2005 Wiley-VCH Verlag GmbH & Co. KGaA, Weinheim

high R_{int} values. The structure was solved by direct methods with SIR-97[45] and was extended and refined on F^2 with SHELXL-97.[46] In addition to the ions forming the unit formula of **6**, two solvate toluene molecules were located in the asymmetric unit. In the final sets of the refinement cycles, the metal, P and F atoms, as well as the three outermost C atoms of each phenyl ring − those of the cyclopentadiene ligand and of the two solvent molecules − were refined anisotropically, with soft isotropic restraints on temperature factors of the C atom. The phenyl, cyclopentadiene, and toluene rings were refined as rigid groups, and a constraint was also applied on the C–CH_3 distance of one toluene molecule. Hydrogen atoms were in calculated positions, riding on the respective carrier atom, with $U_H = 1.2U_C^{eq}$ ($U_H = 1.5U_C^{eq}$ for methyl hydrogens). A small damping factor was applied. Features in the final difference synthesis were low and devoid of chemical meaning. Computer programs used included PARST[47] for geometry calculations, and ORTEP[48,49] for graphics.

Table 4. Crystal data and structure refinement parameters for **6**.

Empirical formula	$C_{80}H_{78}CoF_6NP_8Ru$
Formula weight	1575.19
Crystal system	orthorhombic
Space group	*Pcab* (no. 61)
a [Å]	22.138(4)
b [Å]	22.955(5)
c [Å]	30.038(7)
V [Å^3]	15265(6)
Z	8
$D_{calcd.}$ [g cm^{-3}]	1.371
μ [mm^{-1}]	5.364
Transmission factors range	0.549–1.000
Crystal size [mm]	0.05 × 0.08 × 0.40
F(000)	6480
θ range [°]	2.94–37.56
Index ranges	$-17 \le h \le 17$, $-18 \le k \le 17$, $-23 \le l \le 23$
Reflections collected	33678
Independent reflections	3873 [$R_{int} = 0.322$]
Independent observed reflections	1507 [$I > 2\sigma(I)$]
Restraints/Parameters	313/572
Final *R* indices [$I > 2\sigma(I)$]	$R_1 = 0.056$, $wR_2 = 0.071$
R indices (all data)	$R_1 = 0.199$, $wR_2 = 0.093$
Goodness of fit on F^2 (all data)	0.806
Largest diff. peak and hole [e·Å^{-3}]	0.316 to –0.250

CCDC-244899 contains the supplementary crystallographic data for this paper. These data can be obtained free of charge from The Cambridge Crystallographic Data Centre via www.ccdc.cam.ac.uk/data_request/cif.

Acknowledgments

We acknowledge financial support by the Ministero dell'Università e della Ricerca Scientifica e Tecnologica (Rome) and by the European Commission through the program INTAS (00–00018). Thanks are also expressed to THERMPHOS International, Vlissingen, NL for supporting this research.

[1] M. Di Vaira, P. Stoppioni, *Coord. Chem. Rev.* **1992**, *120*, 259–279.
[2] J. Wachter, *Angew. Chem. Int. Ed. Engl.* **1998**, *37*, 751–768.
[3] O. J. Scherer, *Acc. Chem. Res.* **1999**, *32*, 751–762.
[4] M. P. Ehses, A. Romerosa, M. Peruzzini, *Top. Curr. Chem.* **2002**, *220*, 107–140.
[5] B. P. Johnson, G. Balazs, M. Scheer, *Top. Curr. Chem.* **2004**, *232*, 1–23.
[6] O. J. Scherer, G. Berg, G. Wolmershäuser, *Chem. Ber.* **1995**, *128*, 635–639.
[7] A. Barth, G. Huttner, M. Fritz, L. Zsolnai, *Angew. Chem. Int. Ed. Engl.* **1990**, *29*, 929–931.
[8] O. J. Scherer, J. Braun, P. Walther, G. Wolmershäuser, *Chem. Ber.* **1992**, *125*, 2661–2665.
[9] O. J. Scherer, T. Mohr, G. Wolmershäuser, *J. Organomet. Chem.* **1997**, *529*, 379–385.
[10] O. J. Scherer, G. Schwarz, G. Wolmershäuser, *Z. Anorg. Allg. Chem.* **1996**, *622*, 951–957.
[11] G. Friedrich, O. J. Scherer, G. Wolmershäuser, *Z. Anorg. Allg. Chem.* **1996**, *622*, 1478–1486.
[12] O. J. Scherer, G. Berg, G. Wolmershäuser, *Chem. Ber.* **1996**, *129*, 53–58.
[13] M. Di Vaira, M. P. Ehses, M. Peruzzini, P. Stoppioni, *J. Organomet. Chem.* **2000**, *593–594*, 127–134.
[14] O. J. Scherer, B. Werner, G. Heckmann, G. Wolmershäuser, *Angew. Chem. Int. Ed. Engl.* **1991**, *30*, 553–555.
[15] O. J. Scherer, J. Schwalb, G. Wolmershäuser, *New J. Chem.* **1989**, *13*, 399–402.
[16] O. J. Scherer, R. Winter, G. Wolmershäuser, *Z. Anorg. Allg. Chem.* **1993**, *619*, 827–835.
[17] M. Scheer, E. Leiner, P. Kramkowski, M. Schiffer, G. Baum, *Chem. Eur. J.* **1998**, *4*, 1917–1923.
[18] J. E. Davies, M. J. Mays, P. R. Raithby, G. P. Shields, P. K. Tompkin, A. D. Woods, *J. Chem. Soc. Dalton Trans.* **2000**, 1925–1930.
[19] C. A. Ghilardi, S. Midollini, A. Orlandini, L. Sacconi, *Inorg. Chem.* **1980**, *19*, 301–306.
[20] C. Bianchini, C. Mealli, A. Meli, L. Sacconi, *Inorg. Chim. Acta* **1979**, *37*, L543–L544.
[21] C. Mealli, S. Midollini, S. Moneti, L. Sacconi, *Cryst. Struct. Commun.* **1980**, *9*, 1017–1022.
[22] M. Di Vaira, L. Sacconi, P. Stoppioni, *J. Organomet. Chem.* **1983**, *250*, 183–195.
[23] M. Di Vaira, M. Peruzzini, P. Stoppioni, *J. Chem. Soc. Dalton Trans.* **1984**, 359–364.
[24] M. Di Vaira, P. Innocenti, S. Moneti, M. Peruzzini, P. Stoppioni, *Inorg. Chim. Acta* **1984**, *83*, 161–165.
[25] M. Di Vaira, M. Peruzzini, P. Stoppioni, *Polyhedron* **1986**, *5*, 945–950.
[26] M. Di Vaira, L. Sacconi, *Angew. Chem. Int. Ed. Engl.* **1982**, *21*, 330–342.
[27] M. Di Vaira, P. Stoppioni, M. Peruzzini, *Polyhedron* **1987**, *6*, 351–382.
[28] S. Midollini, A. Orlandini, L. Sacconi, *Angew. Chem. Int. Ed. Engl.* **1979**, *18*, 81–82.
[29] M. Di Vaira, D. Rovai, P. Stoppioni, *Polyhedron* **1990**, *9*, 2477–2481.
[30] M. Di Vaira, M. Peruzzini, P. Stoppioni, *J. Chem. Soc. Dalton Trans.* **1990**, 109–113.
[31] M. Di Vaira, P. Stoppioni, *Polyhedron* **1994**, *13*, 3045–3051.
[32] M. Di Vaira, S. Moneti, M. Peruzzini, P. Stoppioni, *J. Organomet. Chem.* **1984**, *266*, C8–C10.
[33] M. Di Vaira, P. Stoppioni, M. Peruzzini, *Acta Crystallogr. Sect. C* **1987**, *43*, 1284–1287.
[34] M. Di Vaira, M. P. Ehses, P. Stoppioni, M. Peruzzini, *Inorg. Chem.* **2000**, *39*, 2199–2205.
[35] W. Luginbühl, P. Zbinden, P. A. Pittet, T. Armbruster, H. B. Bürgi, A. E. Merbach, A. Ludi, *Inorg. Chem.* **1991**, *30*, 2350–2355.
[36] G. Capozzi, L. Chiti, M. Di Vaira, M. Peruzzini, P. Stoppioni, *J. Chem. Soc. Chem. Commun.* **1986**, 1799–1800.
[37] M. Di Vaira, S. Seniori Costantini, F. Mani, M. Peruzzini, P. Stoppioni, *J. Organomet. Chem.* **2004**, *689*, 1757–1762.

 © 2005 Wiley-VCH Verlag GmbH & Co. KGaA, Weinheim

[38] E. Rüba, W. Simanko, K. Mauthner, K. M. Soldouzi, C. Slugovc, K. Mereiter, R. Schmid, K. Kirchner, *Organometallics* **1999**, *18*, 3843–3850.
[39] A. Bax, *Two-dimensional Nuclear Magnetic Resonances in Liquids*, Delft University Press, Dordrecht, The Netherlands, **1982**.
[40] D. D. Perrin, W. L. F. Armarego, *Purification of Laboratory Chemicals*, 3rd ed., Pergamon, New York, **1988**.
[41] P. H. M. Budzelaar, *gNMR V4.0*, Cherwell Scientific Publishing, Copyright **1995**–**1997** Ivory soft.
[42] V. Sklenar, H. Miyashiro, G. Zon, H. T. Miles, A. Bax, *FEBS Lett.* **1986**, *208*, 94–98.
[43] J. Jeener, B. H. Meier, P. Bachmann, R. R. Ernst, *J. Chem. Phys.* **1979**, *71*, 4546–4553.
[44] G. M. Sheldrick, *SADABS, Program for Empirical Absorption Corrections*, University of Göttingen, Göttingen, Germany, **1986**.
[45] A. Altomare, M. C. Burla, M. Camalli, G. L. Cascarano, C. Giacovazzo, A. Guagliardi, A. G. Moliterni, G. Polidori, R. Spagna, *J. Appl. Crystallogr.* **1999**, *32*, 115–119.
[46] G. M. Sheldrick, *Shelxl 97, Program for Crystal Structure Refinement*, University of Göttingen, Göttingen, Germany, **1997**.
[47] PARST : M. Nardelli, *J. Appl. Crystallogr.* **1995**, *28*, 659.
[48] C. K. Johnson, ORTEP, Report ORNL–5138, Oak Ridge National Laboratory, Oak Ridge, TN.
[49] L. J. Farrugia, *J. Appl. Crystallogr.* **1999**, *32*, 837–838.
Received: October 8, 2004

 © 2005 Wiley-VCH Verlag GmbH & Co. KGaA, Weinheim

Binding of Oxovanadium(IV) to Dipeptides Containing Histidine and Cysteine Residues

Eugenio Garribba,*[a] Elzbieta Lodyga-Chruscinska,[b] Giovanni Micera,*[a] Angelo Panzanelli,[a] and Daniele Sanna[c]

Keywords: Vanadium / Peptides / Bioinorganic chemistry / EPR spectroscopy / Coordination modes / Bond theory

The complexation of the oxovanadium(IV) ion with five dipeptides containing L-histidine or L-cysteine (GlyHis, HisHis, HisGly, CysGly, GlyCys) was studied. L-histidinamide ($HisNH_2$) was assumed as a model system for dipeptides with L-histidine in the N-terminal position. The study was performed in aqueous solution through the combined application of potentiometric and spectroscopic (electronic absorption and EPR) techniques. The results indicate that simple dipeptides lacking a strong anchoring group can form mono- and bischelated complexes with the $V^{IV}O$ ion if a suitable "donor" is present in the chain. The ligands behave like amino acids in the acidic and neutral pH range, inhibit the precipitation of hydroxides and suppress the formation of hydrolytic species if at least a fivefold molar excess of ligand is used. In alkaline media all the ligands, except CysGly, promote the deprotonation and N-coordination of the amide group. CysGly forms a bischelated complex with a [2 × (NH_2, S^-)] donor set. The contribution of the deprotonated amide group to the ^{51}V hyperfine coupling constant, A_z, as a function of the total equatorial charge of oxovanadium(IV) ion, is discussed. The results have general validity and are useful to predict the geometry and donor set of complexes involving the bonding of the $V^{IV}O$ ion to the deprotonated amide group.

(© Wiley-VCH Verlag GmbH & Co. KGaA, 69451 Weinheim, Germany, 2005)

Introduction

Vanadium is an important element for higher animals and essential for certain organisms including tunicates, some fungi and bacteria.[1] It elicits a number of physiological responses in human organism, e.g. the inhibition of ATPases,[2] phosphotyrosine phosphatase[3] and so forth. One of the most relevant properties of vanadium is its insulin-mimetic activity.[4] To clarify its biological role, it is of primary importance to understand the mechanisms of reaction (ligand-exchange and redox processes) and complexation of vanadium in organisms and to find the target biomolecules. Among the biomolecules present in intra- and extra-cellular fluids, proteins have a special importance because of their high amount in the cellular environment and their possible interaction with metal ions through a number of active sites. For instance, glutathione plays an important role in the processes of reduction of vanadium(V) to oxovanadium(IV) and in the following complexation reactions.[5a,5b]

Detailed studies on synthetic models of the interaction of vanadium with proteins can contribute greatly to our knowledge of its biological activity. Oligopeptides are among the models most closely related to proteins. These ligands can interact with metal ions through various donor groups: terminal amino and carboxylate groups, intermediate peptide groups and side-chain donor groups, e.g. imidazole-N or thiolate-S. Usually, these groups are not strong enough to keep metal ions in solution at the physiological pH. However, they can play the role of "anchoring group" and promote the deprotonation of the amide bond and its coordination in the $-N^-$ form. Various metal ions exhibit this ability, e.g. Pt^{II}, Pd^{II}, Cu^{II}, Ni^{II} and, in some cases, Zn^{II} and Co^{II}.[6]

Recently, the role of anchoring donor groups was studied with $V^{IV}O$ and it was found that their effectiveness in promoting peptide amide deprotonation and coordination follows the order: phenolate-O^- < alcoholate-O^- < thiolate-S^- < carboxylate-COO^- < NH_2.[7]

The interaction with oligopeptides in the physiological pH range, through the coordination of a deprotonated peptide group, was first proved to involve vanadium(V).[8] The amide coordination of a few synthetic ligands to $V^{IV}O$ ion was observed in the solid state too.[9] Costa Pessoa and coworkers suggested the deprotonation and coordination of $V^{IV}O$ by glycine/alanine dipeptides in aqueous solution.[10a,10b] However, the first unambiguous proof for $V^{IV}O$-amide deprotonation and coordination, favoured by

[a] Department of Chemistry, University of Sassari,
Via Vienna 2, I-07100 Sassari, Italy
Fax: +39-079-212069
E-mail: garribba@uniss.it; micera@uniss.it
[b] Institute of General Food Chemistry, Technical University of Lodz,
ul. Stefanowskiego 4/10, PL-90924 Lodz, Poland
[c] Istituto C. N. R. di Chimica Biomolecolare,
Trav. La Crucca 3, 07040 Li Punti, Sassari, Italy

an anchoring donor like the "hard" phenolate group, was obtained with salicylglycine.[11]

The solution speciation and the characterisation of the $V^{IV}O$ complexes of five dipeptides (GlyHis, HisGly, HisHis, GlyCys and CysGly) are reported in this work. Their structures are displayed in Scheme 1. A model system for the dipeptides with L-histidine in the N-terminal position, L-histidinamide ($HisNH_2$), has been included. Though in aqueous solution terminal $–NH_2$ is not a particularly good anchoring donor for the $V^{IV}O$ ion,[7] additional donors, like the imidazole nitrogen and the thiolate sulfur atoms, favour the binding of the ligands.

Results

L-Histidinamide ($HisNH_2$)

The aromatic nitrogen of imidazole is a major binding site of metalloenzymes. The imidazole nitrogen of L-histidine can compete with the amino acid site and significantly enhance the stability of the complexes. Therefore, imidazole side chains play a relevant role in complex formation. However, the effect depends critically on the position of the histidyl residue.

To model peptides with histidine in the N-terminal position, we examined L-histidinamide. The potentiometric titrations of the ligand (H_2L^{2+}, Table 1 and Scheme 1) indicate two deprotonation steps with pK_a of 5.39 ($–N_{im}H^+$) and 7.49 ($–NH_3^+$). The values are in good agreement with those of the literature. For instance, Michailidis and Martin reported values of 5.85 and 7.78 at 0.5 M ionic strength.[12] $HisNH_2$ forms mono- and biscomplexes with the $V^{IV}O$ ion (Table 1). The concentration distribution curves of the $V^{IV}O$ complexes as a function of pH are depicted in Figure 1.

The detection of a series of $V^{IV}O$ complexes at a ligand-to-metal molar ratio (L/M) as low as 7 is in contrast to the findings for other simple amino acids systems. For instance, L/M values of 77 are needed with glycine.[13a,13b] This substantiates a stronger binding mode, due e.g. to a tridentate behaviour for $HisNH_2$ with the involvement of the imidazole nitrogen in metal coordination. The speciation process was inferred by a pH-potentiometric titration of the metal-ligand system (see Experimental Section). Complex formation starts with a VOL species, which predominates at pH 4–5. The biscomplexes VOL_2H and VOL_2 are major

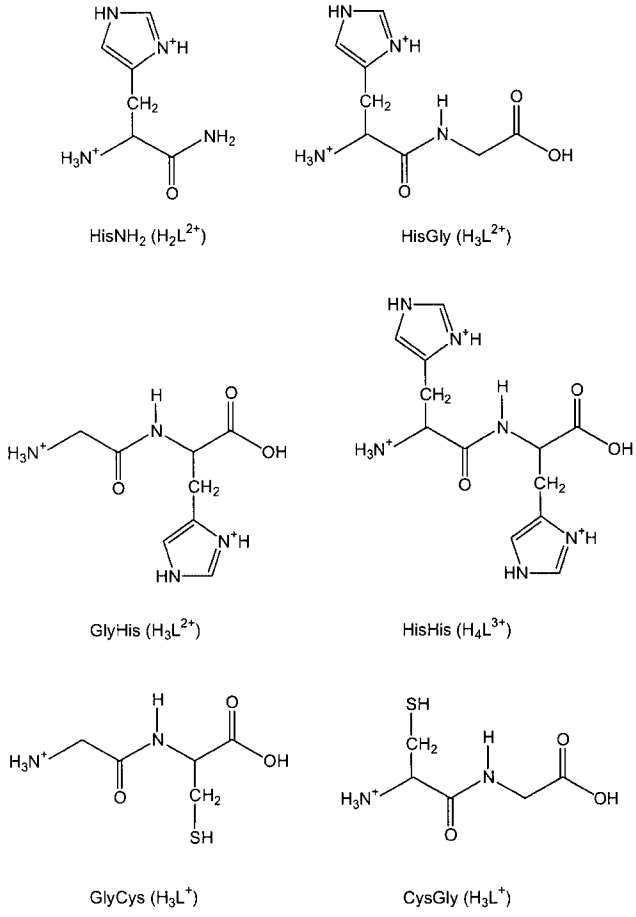

Scheme 1. Structures of the ligands in the fully protonated forms.

Table 1. Protonation constants (log K) and oxovanadium(IV) (log β_{pqr}) stability constants for the studied ligands and complexes at 25.0 ± 0.1 °C and I = 0.20 mol dm^{-3} (KCl).

Log K / log β_{pqr}	$HisNH_2$	HisGly	HisHis	GlyHis	GlyCys	CysGly
–COOH		2.82	2.61	2.51	2.73	3.13
$–N_{im1}H^+$	5.39	5.94	5.68	6.78	–	–
$–N_{im2}H^+$	–	–	6.85	–	–	–
$–NH_3^+$	7.49	7.69	7.79	8.24	8.04	6.94
–SH	–	–	–	–	9.48	9.37
$VOLH_3$			23.67(4)			
$VOLH_2$			20.82(1)	18.00(3)	21.29(2)	
VOLH			16.57(3)			
VOL	7.15(2)	7.00(5)				9.31(2)
VOL_2H_4					41.09(3)	
VOL_2H_3				31.89(3)	36.84(1)	
VOL_2H_2			28.97(3)	27.16(2)	32.14(2)	
VOL_2H	17.48(2)	17.91(4)	22.47(2)	22.10(3)	26.84(2)	
VOL_2	11.42(1)	12.00(4)	15.53(2)	15.56(3)	19.57(3)	16.60(2)
VOL_2H_{-1}	4.22(4)	4.74(4)	7.48(2)	7.04(3)	11.70(4)	
$VOLH_{-2}$					–1.60(3)	

 © 2005 Wiley-VCH Verlag GmbH & Co. KGaA, Weinheim

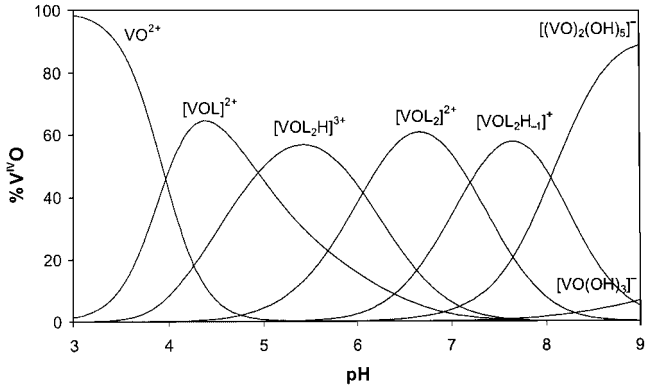

Figure 1. Species distribution for the $V^{IV}O$-$HisNH_2$ system at a metal-to-ligand molar ratio of 1:7 and a $V^{IV}O$ concentration of 1 mM.

species in the pH range 5–7. The log K values for VOL and VOL_2 formation are 7.15 and 4.27, respectively. The "basicity-adjusted" stability constants for the reactions $VO^{2+} + HL^+ \rightarrow [VOL]^{2+} + H^+$ and $[VOL]^{2+} + HL^+ \rightarrow [VOL_2]^{2+} + H^+$ are –0.34 and –3.22, which are greater by about three orders and one order of magnitude, respectively, than those of $V^{IV}O$ complexes of simple amino acids (cf. –3.05 and –4.25 for glycine [14]).

The findings substantiate the involvement of the imidazole nitrogen atom in the coordination of vanadium in VOL. The ligand presumably adopts an equatorial-axial-equatorial (*eq-ax-eq*) binding mode (the two external donor atoms are in the equatorial and the third in the axial position) and this increases the stability of the species. At a pH higher than 5, according to the potentiometric and spectroscopic measurements, a second ligand replaces two water molecules and forms first VOL_2H and then VOL_2. Only two positions of the equatorial plane are available for the second ligand. The pK_a of 6.06 for the VOL_2H to VOL_2 deprotonation, which is very close to that of the free ligand, suggests that the aromatic nitrogen atom of the second ligand molecule does not participate in the coordination. Finally, VOL_2 loses a proton with pK_a = 7.20 to form VOL_2H_{-1} before the start of the processes leading to $[(VO)_2(OH)_5]^-$ and $[VO(OH)_3]^-$. The formation of these hydrolytic species characteristic of $V^{IV}O$ is supported by the potentiometric titrations and by the progressive disappearance of the EPR signal at pH > 8.

The EPR parameters are: g_z = 1.946, A_z = 169×10^{-4} cm^{-1} for VOL, and g_z = 1.950, A_z = 164×10^{-4} cm^{-1} for both VOL_2H and VOL_2 (Table 2). The data are similar to those of the mono- and bischelated complexes of $V^{IV}O$ with L-histidine methyl ester (HisOMe),[15] g_z = 1.946, A_z = 170×10^{-4} cm^{-1} and g_z = 1.950, A_z = 164×10^{-4} cm^{-1}, respectively. Moreover, we compared the EPR spectra with those of the $V^{IV}O$/L-glycine methyl ester (GlyOMe) system at L/M = 500. The stepwise formation of the two species was observed with g_z = 1.946, A_z =

Table 2. EPR parameters and donor sets for oxovanadium(IV) complexes.

Ligand	Complex	g_z	A_z[a]	Donor set
$HisNH_2$	VOL	1.946	169	(NH_2, CO, N_{im}^{ax})
	VOL_2H	1.950	164	[(NH_2, CO, N_{im}^{ax}); (NH_2, CO)]
	VOL_2	1.950	164	[(NH_2, CO, N_{im}^{ax}); (NH_2, CO)]
	VOL_2H_{-1}	1.956	160	[(NH_2, CO, N_{im}^{ax}); (NH_2, CO^-)]
HisGly	VOL	1.946	168	(NH_2, CO, N_{im}^{ax})
	VOL_2H	1.951	165	[(NH_2, CO, N_{im}^{ax}); (NH_2, CO)]
	VOL_2	1.951	165	[(NH_2, CO, N_{im}^{ax}); (NH_2, CO)]
	VOL_2H_{-1}	1.955	160	[(NH_2, CO, COO^-); (CO, NH_2^{ax})]
HisHis	$VOLH_3$	1.934	178	(COO^-)
	$VOLH_2$	1.947	169	(NH_2, CO, N_{im}^{ax})
	VOLH	1.947	169	(NH_2, CO, N_{im}^{ax})
	VOL_2H_2	1.950	164	[(NH_2, CO, N_{im}^{ax}); (NH_2, CO)]
	VOL_2H	1.950	164	[(NH_2, CO, N_{im}^{ax}); (NH_2, CO)]
	VOL_2	1.950	164	[(NH_2, CO, N_{im}^{ax}); (NH_2, CO)]
	VOL_2H_{-1}	1.957	157	[(NH_2, N^-, N_{im}); (CO, NH_2^{ax})]
GlyHis	$VOLH_2$	1.935	177	(COO^-, CO)
	VOL_2H_3	1.938	172	[2×(COO^-, CO)]
	VOL_2H_2	1.943	166	[(NH_2, CO); (COO^-, CO)]
	VOL_2H	1.958	161	[(NH_2, N^-, COO^-); (CO, COO^{-ax})]
	VOL_2	1.959	157	[(NH_2, N^-, N_{im}); (CO, COO^{-ax})]
	VOL_2H_{-1}	1.959	157	[(NH_2, N^-, N_{im}); (CO, NH_2^{ax})]
GlyCys	$VOLH_2$	1.935	176	(COO^-, CO)
	VOL_2H_4	1.940	172	[2×(COO^-, CO)]
	VOL_2H_3	[b]	[b]	[(NH_2, CO); (COO^-, CO)]
	VOL_2H_2	1.950	164	[2×(NH_2, CO)]
	VOL_2H	1.953	160	[(S^-, COO^-); (NH_2, CO)]
	VOL_2	1.959	155	[2×(S^-, COO^-)]
	VOL_2H_{-1}	1.968	144	[(NH_2, N^-, S^-); (S^-, COO^{-ax})]
	$VOLH_{-2}$	1.956	152	[(NH_2, N^-, S^-); OH^-]
CysGly	VOL	1.951	162	(NH_2, S^-)
	VOL_2	1.966	145	[2×(NH_2, S^-)]

[a] A_z measured in 10^{-4} cm^{-1} units. [b] Parameters not measurable because of the low concentration of the species.

 © 2005 Wiley-VCH Verlag GmbH & Co. KGaA, Weinheim

168×10^{-4} cm^{-1} and g_z = 1.951, A_z = 163×10^{-4} cm^{-1}, respectively. They were identified as VOL and VOL_2 with (NH_2, CO) and [2×(NH_2, CO)] coordination modes, respectively. The features suggest that in the monochelated complex, $HisNH_2$ coordinates the metal ion through amino nitrogen and carbonyl oxygen donors in the equatorial plane and the imidazole nitrogen atom in the apical position, which enhances the stability of the species. The resulting donor set is (NH_2, CO, N_{im}^{ax}). The presence of an imidazole nitrogen atom in the axial position does not significantly affect the A_z value, according to the "Chasteen additivity rule", which assumes that only equatorial donors contribute to the parallel hyperfine ^{51}V constant.[16] The second ligand is bound through the (NH_2, CO) donor set: the resulting coordination mode is [(NH_2, CO, N_{im}^{ax}); (NH_2, CO)], as reported in Table 2. The structure is indicated as '**a**' in Scheme 2 with R = H. This scheme explains the rather high stability of the monochelated complex involving a tridentate ligand, compared with the bischelated species (in which a molecule is tridentate and another bidentate).

Potentiometric and spectroscopic studies on the $V^{IV}O$/L-histidine system in aqueous solution indicate that the VOL and VOL_2 species are formed with (NH_2, COO^-, N_{im}^{ax}) and [(NH_2, COO^-, N_{im}^{ax}); (NH_2, COO^-)] donor sets, respectively. The EPR parameters are g_z = 1.945, A_z = 170×10^{-4} cm^{-1} and g_z = 1.944, A_z = 163×10^{-4} cm^{-1}, respectively.[17a,17b]

At pH values higher than 6.5–7, a VOL_2H_{-1} species of $HisNH_2$ is detected by EPR spectroscopy with g_z = 1.956,

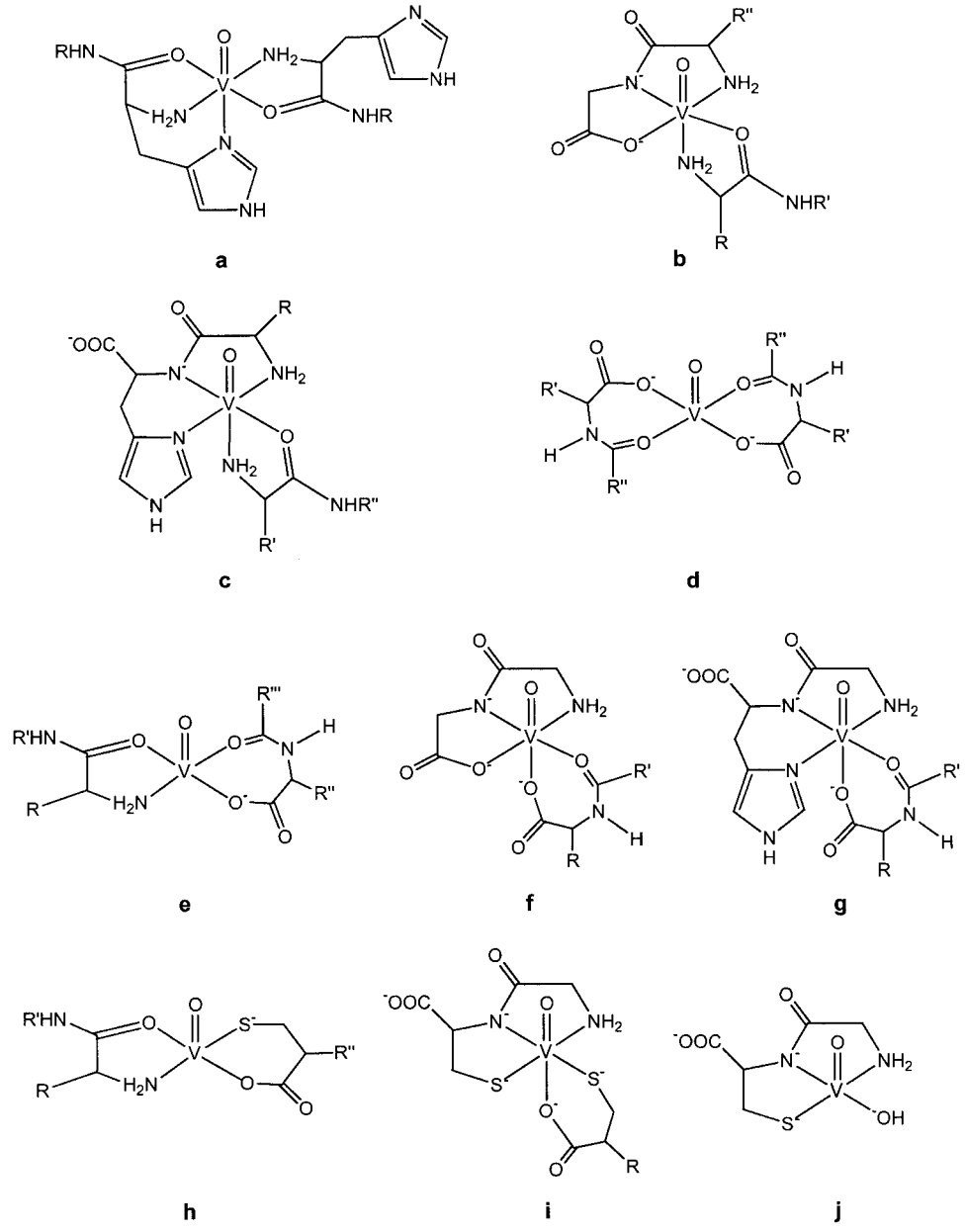

Scheme 2. Structures of the oxovanadium(IV) complexes.

 © 2005 Wiley-VCH Verlag GmbH & Co. KGaA, Weinheim

$A_z = 160 \times 10^{-4}$ cm^{-1}. In this pH range, potentiometry indicates a deprotonation with a pK_a of 7.20. We can exclude the deprotonation of an equatorial water molecule because all the five coordination sites are occupied by ligand molecules, one bound in *eq-ax-eq* mode and another in *eq-eq* mode. The spectral parameters do not support a complexation scheme similar to that of L-histidine, which forms a mixed species with a [(NH_2, COO^-, N_{im}^{ax}); (NH_2, N_{im})] donor set and $g_z = 1.955$, $A_z = 157 \times 10^{-4}$ cm^{-1}. Therefore, the deprotonation can be ascribed to the amide group, whereas donor sets [(NH_2, CO^-, N_{im}^{ax}); (NH_2, CO)] or [(NH_2, N^-, N_{im}^{ax}); (NH_2, CO)] are equally probable for the complex. Only an X-ray determination could solve the ambiguity. Attempts to obtain single crystals of the complex are in progress. However, the coordination of the amide group through a deprotonated nitrogen atom is most likely if a second chelated ring can be closed, as it happens with dipeptides.[6]

Pecoraro and coworkers demonstrated that the $V^{IV}O$ coordination of a ligand with a terminal amide group, e.g. H_2ada = *N*-(carbamoylmethyl)iminodiacetic acid, takes place through the carbonyl oxygen atom of the deprotonated amide group.[18] This is not surprising if the preference of the $V^{IV}O$ ion for oxygen rather than nitrogen donors is considered. Moreover, Kabanos et al. showed that a dipeptide like Hpycan [Hpycan = *N*-(2-nitrophenyl)pyridine-2-carboxamide] coordinates the VO^{2+} ion in a bidentate mode by adopting the (N_{py}, CO_{amide}) rather than the (N_{py}, N_{amide}) donor set.[19] Analogous results were obtained with vanadium(V).[20] Therefore, we can assume that the first coordination mode is more likely.

Glycyl-L-Histidine (GlyHis), L-Histidylglycine (HisGly), and L-Histidyl-L-histidine (HisHis)

The complex formation of dipeptides containing L-histidine depends on the "hardness" of the metal ion.[6] In N-terminal histidyl peptides, the amino and imidazole nitrogen atoms can give rise to a stable six-membered chelated ring. Histamine-like complexes are formed with "soft" ions, like Cu^{2+}. Histamine-like coordination is less favoured with $V^{IV}O$; suitable donors, possibly oxygen atoms, should be involved in anchoring the metal ion.

In simple dipeptides lacking strong anchoring groups in the N-terminal position, the carboxylate group in the C-terminal position and the amide carbonyl group can interact with $V^{IV}O$ at acidic pH values to form a seven-membered (COO^-, CO) chelated ring.[7,21] This favours the deprotonation and coordination of the amide group at higher pH values.

For HisGly (H_3L^{2+}, Table 1 and Scheme 1), three pK_a values were measured: 2.82 (–COOH), 5.94 ($-N_{im}H^+$) and 7.69 ($-NH_3^+$), which are comparable to those reported by Sóvágó et al.[22] The $V^{IV}O$ complexation scheme is very similar to that of $HisNH_2$ and involves the formation of VOL, VOL_2H and VOL_2 below pH 7 (Figure 2). In the pH range 4–7, EPR spectroscopy shows two species with $g_z = 1.946$, $A_z = 168 \times 10^{-4}$ cm^{-1} and $g_z = 1.951$, $A_z = 165 \times 10^{-4}$ cm^{-1}, values comparable with those measured for $HisNH_2$. This confirms that VOL has a (NH_2, CO, N_{im}^{ax}) coordination (**I** in Figure 3) and VOL_2H, a [(NH_2, CO,N_{im}^{ax}); (NH_2, CO)] donor set (**IIa** in Figure 3 and **a** in Scheme 2). The imidazole nitrogen atom of the second ligand molecule is still protonated in VOL_2H. The proton dissociation yielding VOL_2 (**IIb** in Figure 3) takes place with a pK_a value of 5.91, which is in excellent agreement with the value of the free ligand. In this case too, the deprotonation does not affect the coordination sphere of the vanadium atom. The "basicity-adjusted" stability constants for mono-and bischelated species are –0.69 and –2.69, respectively, which means that the monochelated complex is a little less stable and the bischelated species a little more stable than the corresponding species of $HisNH_2$.

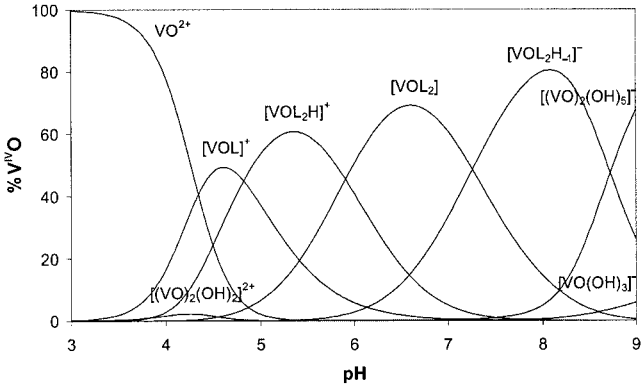

Figure 2. Species distribution for the $V^{IV}O$-HisGly system at a metal-to-ligand molar ratio of 1:10 and a $V^{IV}O$ concentration of 1 mM.

VOL_2 undergoes deprotonation with a pK_a of 7.26 to form a VOL_2H_{-1} species characterised by $g_z = 1.955$, $A_z = 160 \times 10^{-4}$ cm^{-1} (**III** in Figure 3). Also in this case the deprotonation can be attributed to the ligand and we can assign it to the peptide group. However, in contrast with $HisNH_2$, the coordination of a deprotonated nitrogen atom makes the closure of a second chelated ring possible through a bond between the terminal carboxylate group and vanadium. It is commonly accepted that a simple dipeptide coordinates with all the three donor atoms in the equatorial position of a metal ion.[6] Thus, the second molecule of HisGly must change its arrangement from *eq-eq* to *eq-ax*. Since histamine-like coordination is not favoured with the $V^{IV}O$ ion,[17b] we expect that the fourth and fifth coordination sites are occupied by the carbonyl oxygen atom and the amine nitrogen of the N-terminal part, respectively. Therefore, both the donor sets [(NH_2, N^-, COO^-); (CO, NH_2^{ax})] or [(NH_2, N^-, COO^-); (NH_2, CO^{ax})] are acceptable. The following discussion will demonstrate that the first structure, indicated as '**b**' in Scheme 2, is more suitable (vide infra).

HisHis (H_4L^{3+}, Table 1 and Scheme 1) shows four deprotonation steps in the pH range 2–10 with pK_a of 2.61 (–COOH), 5.68 ($-N_{im1}H^+$), 6.85 ($-N_{im2}H^+$) and 7.79 ($-NH_3^+$).[23] The complexation scheme is very similar to

 © 2005 Wiley-VCH Verlag GmbH & Co. KGaA, Weinheim

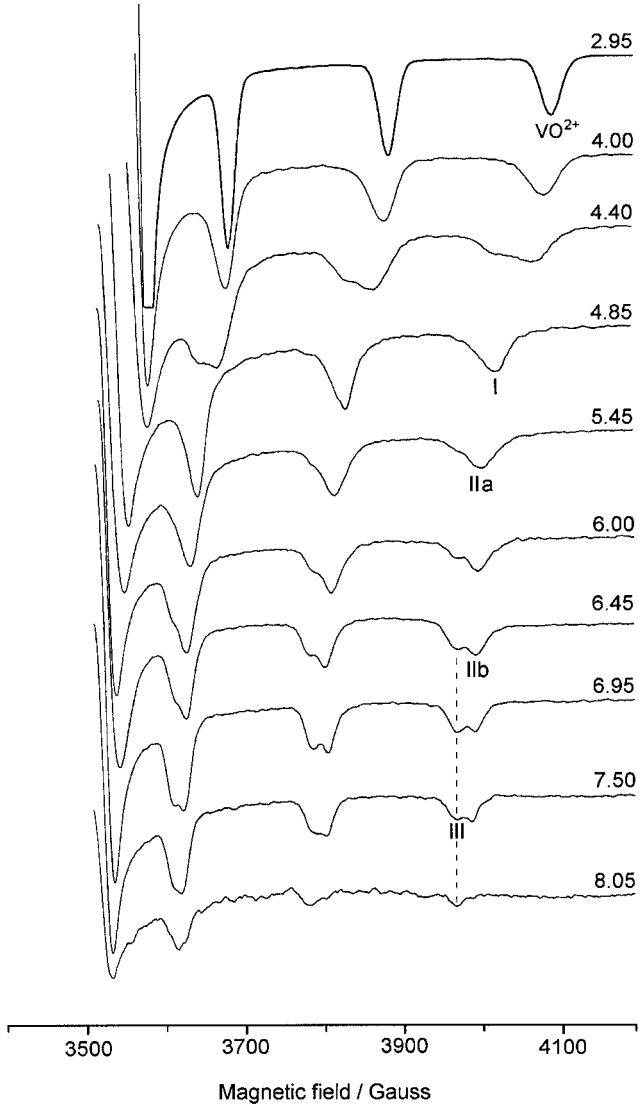

Figure 3. High-field region of the X-Band EPR spectra recorded at 140 K as a function of pH on aqueous solutions of $V^{IV}O$ and HisGly at a metal-to-ligand to molar ratio of 1:10 and a $V^{IV}O$ concentration of 4 mM. The dotted line indicates the high-field resonance of the complex with the deprotonated amide group.

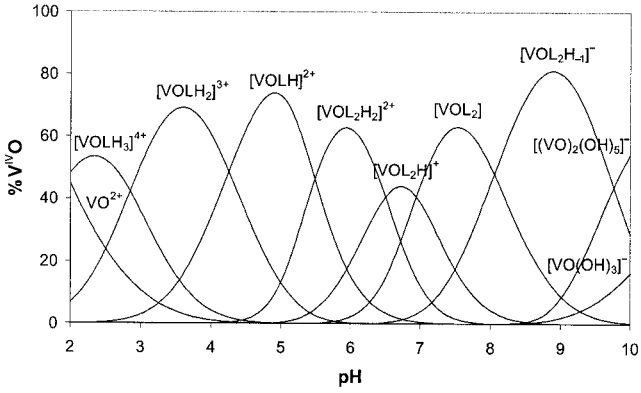

Figure 4. Species distribution for the $V^{IV}O$-HisHis system at a metal-to-ligand molar ratio of 1:3 and a $V^{IV}O$ concentration of 1 mM.

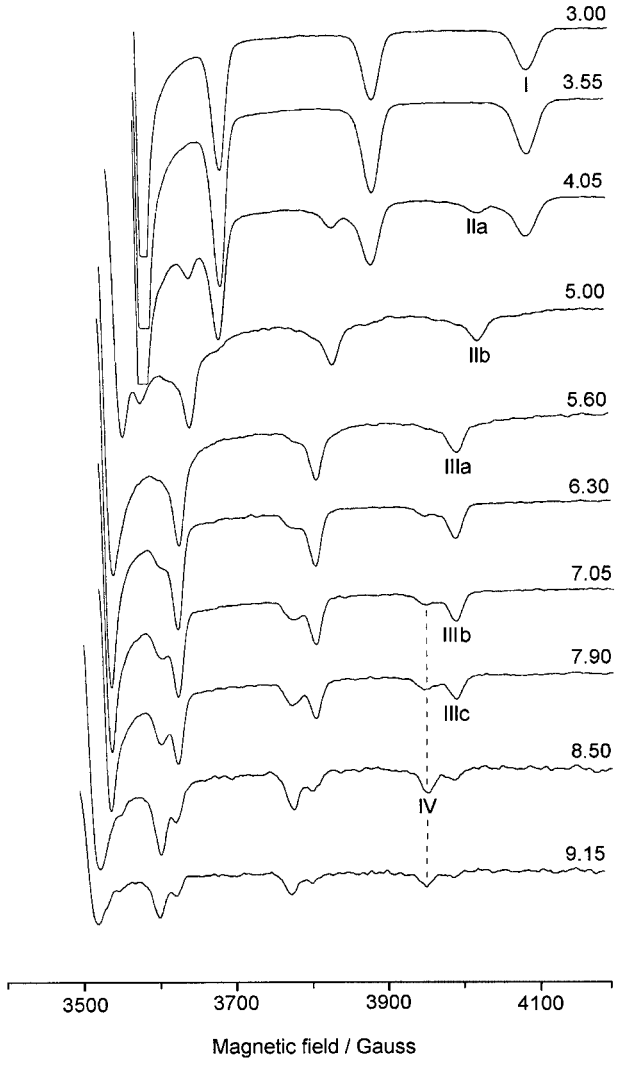

Figure 5. High-field region of the X-Band EPR spectra recorded at 140 K as a function of pH on aqueous solutions of $V^{IV}O$ and HisHis at a metal-to-ligand to molar ratio of 1:3 and a $V^{IV}O$ concentration of 4 mM. The dotted line indicates the high-field resonance of the complex with the deprotonated amide group.

that of $HisNH_2$ and HisGly if the presence of the imidazole ring on the C-terminal part of the dipeptide is taken into account. The distribution curves for this system are shown in Figure 4 and the EPR spectra in Figure 5.The complexation process starts to give $VOLH_3$ through the coordination of the weak carboxylate group (the stronger donor groups, i.e. the two imidazole and the amine nitrogen atoms, are still protonated). EPR and electronic absorption spectra are distinctive of this coordination mode. Indeed, the formation of carboxylate complexes does not change the EPR parameters very significantly (Table 2) relative to the aqua ion, $g_z = 1.934$, $A_z = 178 \times 10^{-4}$ cm^{-1} (**I**, Figure 5). As usual, in the absorption spectra, only a minor shift of the d-d band around 770 nm is observed, accompanied by a better resolution of the shoulder around 640 nm.

 © 2005 Wiley-VCH Verlag GmbH & Co. KGaA, Weinheim

$VOLH_2$ and VOLH (**IIa** and **IIb** in Figure 5) exhibit $g_z = 1.947$, $A_z = 169 \times 10^{-4}$ cm^{-1} indicative of a (NH_2, CO, N_{im}^{ax}) coordination of HisHis; they have two and one imidazole rings still protonated, respectively. Analogously, VOL_2H_2 (**IIIa** in Figure 5 and **a** in Scheme 2) shows the [(NH_2, CO, N_{im}^{ax}); (NH_2, CO)] donor set displayed by $HisNH_2$ and HisGly, and keeps two imidazole residues protonated. The findings are confirmed by EPR ($g_z = 1.950$, $A_z = 164 \times 10^{-4}$ cm^{-1}). The deprotonation of the imidazole groups takes place in distinct steps with pK_a values of 6.50 and 6.94, similar to those of the free ligand, to afford VOL_2H and VOL_2 (**IIIb** and **IIIc** in Figure 5). The "basicity-adjusted" stability constant for the formation of VOL_2H_2 complex through the reaction $[VOLH]^{2+} + LH_2^+ \rightarrow [VOL_2H_2]^{2+} + H^+$ is –2.24, which is comparable to that of the complex of HisGly.

At a pH above 6.5, VOL_2H_{-1} (**IV** in Figure 5 and **c** in Scheme 2) is formed from VOL_2 with a pK_a of 8.05. The species is distinguished by $g_z = 1.957$, $A_z = 157 \times 10^{-4}$ cm^{-1}. The higher g_z and lower A_z values, in comparison with the analogous complex of HisGly, suggest that the imidazole nitrogen atom at the C-terminal part takes part in the coordination to the VO^{2+} ion rather than the weaker carboxylate group. Also for this complex as well as for HisGly, two different donor sets, [(NH_2, N^-, N_{im}); (CO, NH_2^{ax})] or [(NH_2, N^-, N_{im}); (NH_2, CO^{ax})], could be proposed; the first one with the carbonyl group in equatorial position is most probable (vide infra).

GlyHis (H_3L^{2+}, Table 1 and Scheme 1) shows three pK_a values in the titratable pH range: 2.45 (–COOH), 6.85 ($-N_{im}H^+$) and 8.33 ($-NH_3^+$).[22] If histidine is in the C-terminal position of a dipeptide, the complexation scheme is completely different to that of $HisNH_2$, HisGly and HisHis. The species distribution curve, shown in Figure 6 for a molar ligand excess of 10, shows the species $VOLH_2$ and VOL_2H_3 in the pH range 2–5. The $VOLH_2$ complex exhibits $g_z = 1.935$, $A_z = 177 \times 10^{-4}$ cm^{-1}. In less acidic solution, the EPR components shift continuously until pH 5 is reached, with a change of A_z from 178×10^{-4} to 173×10^{-4} cm^{-1}, which supports the coordination of a carboxylate group to the $V^{IV}O$ ion. Similar changes were observed with carboxylic[13b] and amino acids[13a] at high ligand excess, also suggesting COO^- and/or (COO^-; COO^-) coordination. The stability constants of these complexes are somewhat higher than expected for pure carboxylate coordination[24] and indicate the binding of extra donors, presumably the amide carbonyl. A (NH_2, CO) donor set can be excluded because the EPR parameters expected for this coordination mode are $g_z = 1.946$, $A_z = 168 \times 10^{-4}$ cm^{-1} (vide supra). Moreover, the exclusive coordination of a monodentate histidine residue in the N-terminal position can be ruled out because in such a case L/M ratios as high as 500 are necessary to suppress the hydrolysis of the vanadyl ion. This suggests that (COO^-, CO) is the coordination set. In $VOLH_2$, the amino and imidazole nitrogen atoms are still protonated. VOL_2H_3 is characterised by $g_z = 1.938$, $A_z = 172 \times 10^{-4}$ cm^{-1} and can be described as a bischelated complex of the [2×(COO^-, CO)] type, see '**d**' in Scheme 2 and Table 2. The amine and imidazole nitrogen atoms in one ligand are still protonated, whilst in another ligand, only the amino nitrogen atom is protonated. The attributions and the EPR parameters are in agreement with recent contributions,[21,25–27] which report EPR hyperfine coupling constants in the range 175–179×10^{-4} cm^{-1} for monochelated and 171–174×10^{-4} cm^{-1} for bischelated species.

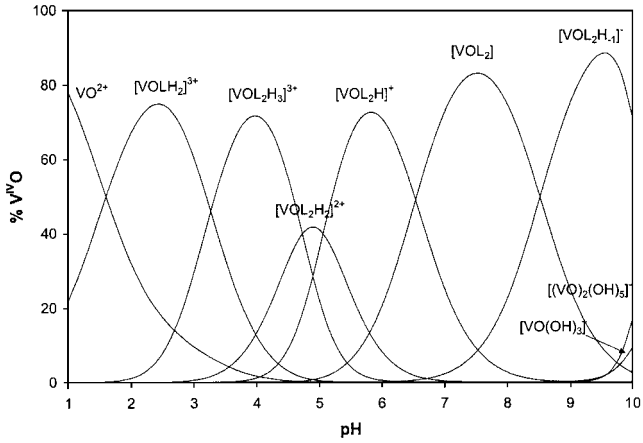

Figure 6. Species distribution for the $V^{IV}O$-GlyHis system at a metal-to-ligand molar ratio of 1:10 and a $V^{IV}O$ concentration of 1 mM.

Upon deprotonation of the first amino group, the dipeptide switches its coordination mode from (COO^-, CO) to (NH_2, CO) and forms a minor VOL_2H_2 species with a [(NH_2, CO); (COO^-, CO)] mixed donor set (**e** in Scheme 2). The EPR parameters ($g_z = 1.943$, $A_z = 166 \times 10^{-4}$ cm^{-1}), intermediate between those of [2×(COO^-, CO)] and [2×(NH_2, CO)], support the coordination mode, whereas potentiometry indicates the presence of this species at around pH 5 (Figure 6).

The coordination of a ligand molecule through (NH_2, CO) hinders hydrolysis and favours the subsequent deprotonation of the amide group to form a VOL_2H species with donor set [(NH_2, N^-, COO^-); (CO, COO^{-ax})], **f** in Scheme 2, which exhibits $g_z = 1.958$, $A_z = 161 \times 10^{-4}$ cm^{-1}. The imidazole and amino groups of the second ligand are still protonated. They undergo deprotonation with pK_a 6.54 and 8.52, respectively; these are both a little higher than for the free ligand. Two new species VOL_2 and VOL_2H_{-1} are formed, and differ only with respect to the protonation of an amino group. Since the same EPR parameters ($g_z = 1.959$, $A_z = 157 \times 10^{-4}$ cm^{-1}) are measured, we suggest a [(NH_2, N^-, N_{im}); (CO, COO^{-ax})] donor set for VOL_2 (**g** in Scheme 2) and [(NH_2, N^-, N_{im}); (CO, NH_2^{ax})] for VOL_2H_{-1} (**c** in Scheme 2). In both species, a carbonyl oxygen atom of the second ligand occupies the equatorial position (vide infra). The coincidence of the hyperfine coupling constants for HisHis and GlyHis complexes supports our conclusion.

Glycyl-L-cysteine (GlyCys), L-Cysteinylglycine (CysGly)

The "soft" deprotonated thiol group of cysteine is very effective as a metal-binding site for transition-metal ions.[6]

 © 2005 Wiley-VCH Verlag GmbH & Co. KGaA, Weinheim

Also in this case, the complexation processes depend on the position of the residue in the peptide and on the "hardness" of the metal ion.[6]

With GlyCys the soft Ni^{2+} and Pd^{2+} ions promote the coordination of the deprotonated amide.[28,29] Instead, Co^{2+}, Zn^{2+} and Cd^{2+}[30,31] prefer the coordination of thiol and carboxylate groups in bischelated complexes with various protonated forms because of the presence of the free terminal amino group.

In the case of CysGly a stable cysteine-like (NH_2, S^-) coordination is favourable for a number of metal ions (e.g. Ni^{2+}, Pd^{2+}, Co^{2+}, Zn^{2+} and Cd^{2+}).[28–31] This means that the N-terminal cysteine residue prevents amide deprotonation, and biscomplexes $[MA_2]^{2-}$ are observed.

GlyCys (H_3L^+, Table 1 and Scheme 1) shows three pK_a values in the measured pH range: 2.73 (–COOH), 8.04 ($-NH_3^+$) and 9.48 (–SH).[30] The speciation scheme of GlyCys is more complex than for other systems. The species distribution curves depicted in Figure 7 indicate that at pH 2–4.5 $VOLH_2$ and VOL_2H_4 (**I** and **II** in Figure 8) are formed in strongly overlapping processes. Their EPR parameters are g_z = 1.935, $A_z = 176\times10^{-4}$ cm^{-1} and g_z = 1.940, $A_z = 172\times10^{-4}$ cm^{-1}, very similar to those of $VOLH_2$ and VOL_2H_3 of GlyHis and of $[VO\text{-}(mpg)]^+$ and $[VO\text{-}(mpg)_2]$, where H_2mpg is 2-mercaptopropionylglycine.[21] As for GlyHis, the features support (COO^-, CO) and [2×(COO^-, CO)] coordination modes (**d** in Scheme 2). In both complexes, the amino and thiol groups in each ligand are protonated.

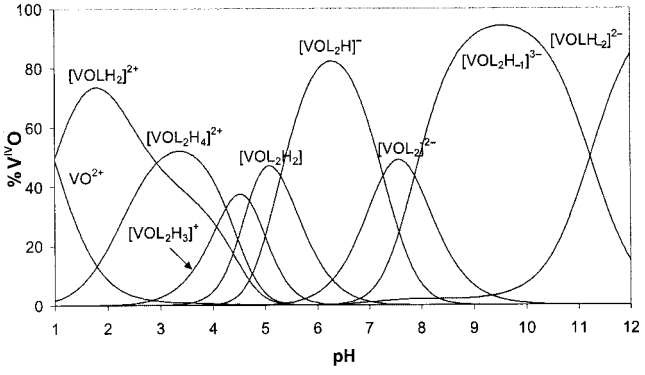

Figure 7. Species distribution for the $V^{IV}O$-GlyCys system at a metal-to-ligand molar ratio of 1:10 and a $V^{IV}O$ concentration of 1 mM.

A two-step deprotonation of the amino groups gives rise to VOL_2H_3 and VOL_2H_2 (**III** and **IV** in Figure 8) at pH 5–6. As suggested by EPR and pH-potentiometry, the first is a minor complex and it is, therefore, a rather hard task to accurately measure the spectral parameters. However, a mixed coordination [(NH_2, CO); (COO^-, CO)] could be proposed (**e** in Scheme 2). The second complex exhibits g_z = 1.950, $A_z = 164\times10^{-4}$ cm^{-1}, indicative of a [2×(NH_2, CO)] coordination.

With increasing pH the first –SH group deprotonates and VOL_2H_2 is replaced by VOL_2H (**V** in Figure 8 and **h** in Scheme 2), presumably a complex with a mixed donor set

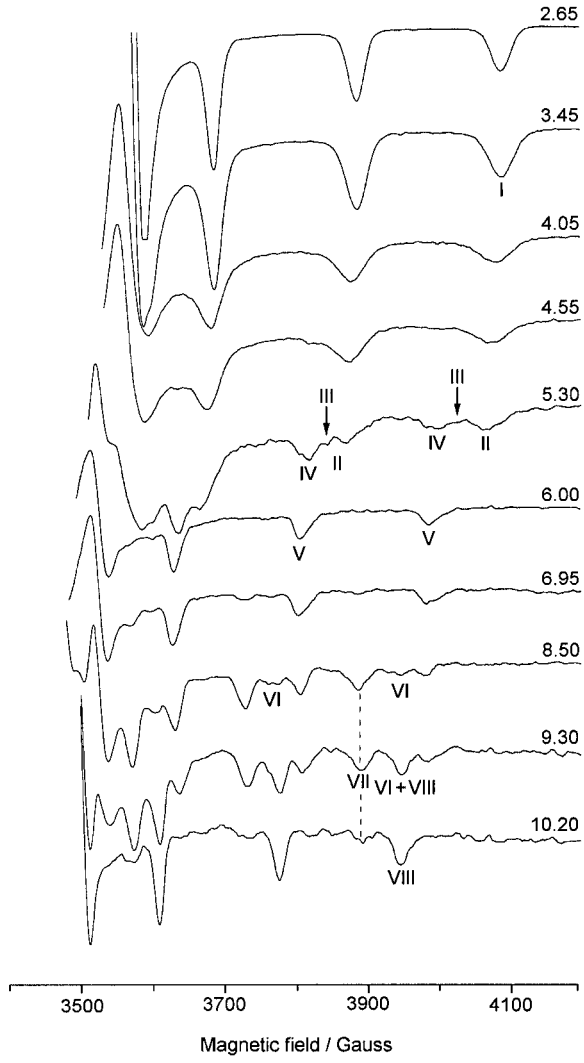

Figure 8. High-field region of the X-Band EPR spectra recorded at 140 K as a function of pH on aqueous solutions of $V^{IV}O$ and GlyCys at metal-to-ligand to molar ratio of 1:10 and a $V^{IV}O$ concentration of 4 mM. The dotted line indicates the high-field resonance of the complex with the deprotonated amide group.

[(S^-, COO^-); (NH_2, CO)]. The conclusion is supported by the EPR parameters, g_z = 1.953, $A_z = 160\times10^{-4}$ cm^{-1}, which are intermediate between those of the [2×(NH_2, CO)] and [2×(S^-, COO^-)] donor sets (g_z = 1.959, $A_z = 155\times10^{-4}$ cm^{-1} for N-acetyl-L-cysteine and g_z = 1.960, $A_z = 154\times10^{-4}$ cm^{-1} for 3-mercaptopropionic acid).[13b] The deprotonation of the thiol group of the second ligand yields VOL_2 (**VI** in Figure 8) with g_z = 1.956, $A_z = 155\times10^{-4}$ cm^{-1} and a [2× (S^-, COO^-)] coordination set.[13b]

At pH values higher than 8, VOL_2 is transformed into VOL_2H_{-1} (**VII** in Figure 8 and **i** in Scheme 2) with a pK_a of 8.43. The EPR parameters are g_z = 1.968, $A_z = 144\times10^{-4}$ cm^{-1}. To this species we attribute a coordination mode of the [(NH_2, N^-, S^-); (S^-, COO^{-ax})] type, according to the assignments for 2-mercaptopropionylglycine.[21]

Finally, at pH >10, a $VOLH_{-2}$ species (**VIII** in Figure 8 and **j** in Scheme 2) exhibits EPR parameters, g_z = 1.956, $A_z = 152\times10^{-4}$ cm^{-1}, which are very similar to those of VOL_2.

 © 2005 Wiley-VCH Verlag GmbH & Co. KGaA, Weinheim

A species with donor set [2×(S⁻, COO⁻)] likely undergoes hydrolysis at pH >9.[13b] Thus, around pH 9, the two species **VI** and **VIII** with similar spectral parameters coexist, whereas only $VOLH_{-2}$ remains in solution at higher pH values. As suggested by potentiometry, most probably this is a hydrolytic species with donor set [(NH_2, N^-, S^-); OH^-], similar to that formed by 2-mercaptopropionylglycine with [(COO^-, N^-, S^-); OH^-] coordination.[21] The difference in the A_z value, 154×10^{-4} cm^{-1} versus 152×10^{-4} cm^{-1} (this work), is attributable to the replacement of a carboxylate by an amino group.

For CysGly (H_3L^+, Table 1 and Scheme 1), three pK_a values were observed by Sóvágó et al.: 3.13 (–COOH), 6.94 (–NH_3^+) and 9.37 (–SH).[30] The complexation behaviour is rather simple because the (NH_2, S^-) donor set can form very stable mono- and bischelated complexes. Besides the aqua ion $[VO(H_2O)_5]^{2+}$, we observe a VOL species around pH 5 with g_z = 1.951, $A_z = 162\times10^{-4}$ cm^{-1}, and another species VOL_2 above pH 6.0 with g_z = 1.966, $A_z = 145\times10^{-4}$ cm^{-1}. The EPR parameters of VOL_2 are very similar to those of the bischelated complexes of cysteamine (g_z = 1.973, $A_z = 144\times10^{-4}$ cm^{-1}) and L-cysteine (g_z = 1.967, $A_z = 144\times10^{-4}$ cm^{-1}) for which a [2×(NH_2, S^-)] donor set was proposed.[13b] To the best of our knowledge, a coordination mode (NH_2, S^-) was never observed: we expect EPR parameters intermediate between those of $[VO(H_2O)_5]^{2+}$ (g_z = 1.933, $A_z = 180\times10^{-4}$ cm^{-1}) and VOL_2. The spectra are consistent with that expected.

The "basicity-adjusted" stability constants for the mono- and bischelated species VOL and VOL_2 in the reactions $VO^{2+} + HL^- \rightarrow [VOL] + H^+$ and $[VOL] + HL^- \rightarrow [VOL_2]^{2-} + H^+$ are –0.06 and –2.08; these are significantly greater than the corresponding complexes of HisGly. This confirms that L-cysteyl is a more efficient anchoring residue than L-histidyl and can hinder the subsequent deprotonation of the amide group (Figure 9).

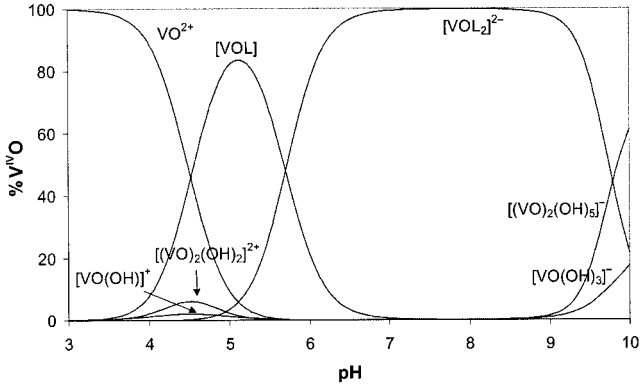

Figure 9. Species distribution for the $V^{IV}O$-CysGly system at a metal-to-ligand molar ratio of 1:10 and a $V^{IV}O$ concentration of 1 mM.

The results for the $V^{IV}O$ complexes of GlyCys and CysGly are similar to those for the Cu^{II} complexes of L-histidyl peptides. In the latter case, amide deprotonation and binding were prevented by an N-terminal side chain and promoted by a C-terminal side chain.[6]

Discussion

Chasteen introduced an "additivity rule" to estimate the parallel ^{51}V hyperfine constant of $V^{IV}O$ complexes, based on the contribution to A_z from each of the four equatorial donor groups.[16] The rule provides a valid criterion for the identification of equatorial donor atoms. Data for amine, carboxylate, alcoholate, phenolate, aromatic nitrogen, hydroxo ion and aliphatic and aromatic thiolate groups were listed by Chasteen (Table 3).[16] Kabanos et al. used values of 44.2 and 43.2×10^{-4} cm^{-1} for Cl^- and SCN^-, respectively.[32] Based on the model $[VO(oxalato)_2]^{2-}$ complex,[33] Kiss and Costa Pessoa changed the COO^- contribution from 42.7 to 41.8×10^{-4} cm^{-1} (Table 3).[21] The mean value for a neutral oxygen atom belonging to an amide CO group is 43.5×10^{-4} cm^{-1}.[18]

Table 3. Contribution of various groups to ^{51}V hyperfine coupling constants A_z.

Donor group	A_z expected[a]	Reference
H_2O	45.6	[16]
COO^-	41.8	[21]
CO	43.5	[18]
OH^-	38.7	[16]
Ar-O^-	38.9	[16]
R–O^-	35.3	[16]
Ar–S^-	35.3	[16]
R–S^-	31.9	[16]
NH_2	40.1	[16]
N(imino)	41.6	this work
N(aromatic)	40.7	[16]
Cl^-	44.2	[32]
SCN^-	43.2	[32]

[a] A_z measured in 10^{-4} cm^{-1} units.

Chasteen did not include the imino nitrogen atom, which, as noticed by Cavaco et al., is certainly different from an aromatic nitrogen atom, e.g. those of 2,2′-bipyridine.[34] On the basis of the EPR parameters of [VO(*N*-salicylidene-glycinato)(bipy)] and [VO(*N*-salicylidene-L-alaninato)(bipy)] Cavaco et al. calculated a value in the range $41.5–43.5\times10^{-4}$ cm^{-1}.[34] From the analysis of the hyperfine coupling constants of twenty three compounds,[34–35] we obtained a more accurate value of $A_z(N_{imino})$; A_z values in the range $38.1–43.7\times10^{-4}$ cm^{-1} were found,[36] with a mean value of 41.6×10^{-4} cm^{-1}, which is in good agreement with those reported by Costa Pessoa.[34,35d] The values used in this work are summarised in Table 3.

With respect to the amide contribution A_z(amide), the values, in the range $29–43\times10^{-4}$ cm^{-1},[37] are sensitive to the balance of the coordination sphere. The A_z(amide) value decreases with increasing donation of electron density from the ligands to the metal ion (Table 4). Tasiopoulos et al. listed the amide contribution for 15 $V^{IV}O$ compounds characterised by X-ray diffraction.[37] They found that A_z(amide) is affected by the charge of the other equatorial donor atoms. If the total charge of the donor atoms in the equatorial plane (TEC) is –2, –3 or 4 (including the –1 charge of the deprotonated peptide nitrogen), the mean A_z(amide) value is 32.2, 36.5 and 40.3×10^{-4} cm^{-1}, respectively.

 © 2005 Wiley-VCH Verlag GmbH & Co. KGaA, Weinheim

Table 4. Contribution of deprotonated amide group to A_z value for oxovanadium(IV) complexes as a function of the equatorial donor set.

Charge	Ligand[a]	Equatorial donor set	g_z	A_z[b]	A_z(amide)[b]	Reference
–4	SalGly	O_{ar}^-, N^-, COO^-; OH^-	1.951	163	43.6	[11]
–4	H_2mpg	COO^-, N^-, RS^-; RS^-	1.968	146.0	40.4	[21]
–4	H_2mpg	COO^-, N^-, RS^-; OH^-	1.960	154.0	41.6	[21]
–4	SalGly-L-Ala	O_{ar}^-, N^-, N^-, COO^-	1.958	159	39.2	[27]
–4	GSH	N^-, RS^-, N^-, COO^-	1.959	154	40.2	[37]
–4	H_4m_2pc	COO^-, N^-, RS^-, RS^-	1.959	149.3	43.7	[37]
–4	H_4m_3pc	COO^-, N^-, RS^-, RS^-	1.959	148.4	42.8	[37]
–4	H_4hybeb	O_{ar}^-, N^-, N^-, O_{ar}^-	1.960	156.2	39.2	[38]
–4	H_4hymeb	RO^-, N^-, N^-, RO^-	1.964	145	37.2	[44]
–3	H_2mpg/phen	COO^-, RS^-, N^-; N_{ar}	1.957	151.1	36.7	[9]
–3	SalGly	O_{ar}^-, N^-, COO^-; H_2O	1.949	165	38.7	[11]
–3	H_2mpg	COO^-, N^-, RS^-; H_2O	1.959	157.0	37.7	[21]
–3	H_2Sal-RGlyGly	O_{ar}^-, N^-, COO^-; H_2O	1.953	164	37.7	[26]
–3	H_2Sal-RGlyGly	O_{ar}^-, NH, N^-; OH^-	1.955	158	40.3	[26]
–3	H_2Sal-RGlyGlyGly	O_{ar}^-, NH, N^-; OH^-	1.960	157	39.3	[26]
–3	SalGly-L-Ala	O_{ar}^-, N^-, CO, COO^-	1.945	165	40.8	[27]
–3	H_3hypyb	N_{ar}, N^-, N^-, O_{ar}^-	1.960	156.1	38.3	[38]
–3	SalenGlyGly	O_{ar}^-, N_{imino}, N^-; COO^-	1.950	160	37.7	[39]
–2	Gly-L-Ala	NH_2, N^-, COO^-; H_2O	1.955	161.7	34.2	[10b]
–2	L-AlaGly	NH_2, N^-, COO^-; H_2O	1.953	160.1	32.6	[10b]
–2	L-Ala-L-Ala	NH_2, N^-, COO^-; H_2O	1.955	161.5	34.0	[10b]
–2	GlyGly	NH_2, N^-, COO^-; H_2O	1.958	161.8	34.3	[10b]
–2	H_2capcah / Cl^-	N_{ar}, N^-, NH; Cl^-	1.946	164.5	39.5	[32]
–2	H_2capcah/SCN^-	N_{ar}, N^-, NH; SCN^-	1.946	160.0	36.0	[32]
–2	GlyGly/ phen	NH_2, N^-, COO^-; N_{ar}	1.952	160.0	37.4	[37]
–2	Gly-L-Ala/phen	NH_2, N^-, COO^-; N_{ar}	1.952	158.6	36.0	[37]
–2	H_2thipca	N_{ar}, N^-, N_{imino}, RS^-	1.965	150.6	33.0	[38]
–2	Gly-L-Val/phen	NH_2, N^-, COO^-; N_{ar}	1.951	159.1	36.5	[40]
–2	Gly-L-Leu/phen	NH_2, N^-, COO^-; N_{ar}	1.952	159.2	36.6	[40]
–2	Gly-L-Asp	NH_2, N^-, COO^-; H_2O	1.953	160.7	33.2	[41]
–2	L-AspGly	NH_2, N^-, COO^-; H_2O	1.950	165.0	37.5	[41]
–2	Gly-L-Phe/phen	NH_2, N^-, COO^-; N_{ar}	1.951	159.0	36.4	[42]
–2	Gly-L-Tyr/phen	NH_2, N^-, COO^-; N_{ar}	1.952	160.0	37.4	[42]
–2	H_2pycac	N_{ar}, N^-, NH, RO^-	1.956	151.4	35.3	[43]
–2	H_2pycbac	N_{ar}, N^-, NH, RO^-	1.957	152.4	36.3	[43]
–2	H_2bpb	N_{ar}, N^-, N^-, N_{ar}	1.955	145	31.8	[44]
–2	H_2phepca	N_{ar}, N^-, N_{imino}, O_{ar}^-	1.961	154	32.8	[44]

[a] SalGly = Salicylglycine; H_2mpg = 2-mercaptopropionylglycine; SalGly-L-Ala = Salicylglycyl-L-alanine; GSH = glutathione; H_4m_2pc = *N*-(2-*m*ercaptopropionyl)cysteine; H_4m_3pc = *N*-(3-*m*ercaptopropionyl)cysteine; H_4hybeb = 1,2-bis(2-hydroxybenzamido)benzene; H_4hymeb = 1,2-bis(2-hydroxy-2-methylpropanamido)benzene; H_2Sal-RGlyGly = *N*-salicylglycylglycine; H_2Sal-RGlyGlyGly = *N*-salicylglycylglycylglycine; H_3hypyb = 1-(2-hydroxybenzamido)-2-(2-pyridinecarboxamido)benzene; SalenGlyGly = *N*-salicylideneglycylglycine; phen = 1,10-phenanthroline; H_2capcah = *N*-{2-[(2-pyridylmethyl)amino]phenyl}pyridine-2-carboxamide; H_2thipca = *N*-[2-((2-thiophenoylmethylene)amino)phenyl]pyridine-2-carboxamide; H_2pycac = *N*-[2-(4-oxopent-2-en-2-ylamino)phenyl]pyridine-2-carboxamide; H_2pycbac = *N*-[2-(4-phenyloxobut-2-en-2-ylamino)phenyl]pyridine-2-carboxamide; H_2bpb = 1,2-bis(2-carboxamidopyridyl)benzene; H_2phepca = [*N*-(salicylideneamine)phenyl]pyridine-2-carboxamide. [b] A_z measured in 10^{-4} cm^{-1} units.

Unfortunately, they analysed only two data for the –3 charge and four for –4 charge, whereas no data for the –1 charge were available.

We included further four solid-state compounds and 18 complexes characterised in solution. Therefore, we have taken into account a total of 37 compounds, nine with a –4 charge, nine with –3, and finally, 19 with a –2 charge.[9,10b,11,21,26,27,32,37–44]

Among 25 $V^{IV}O$ structures involving the coordination of a deprotonated amide group found with a search in the Cambridge Structural Database,[45] we excluded only the octahedral complexes *trans*-[VOX(capca)], where Hcapca is *N*-{2-[(2-pyridylmethylene)amino]phenyl}pyridine-2-carboxamide and X^- (Cl^-, SCN^-, CH_3COO^- and $PhCOO^-$) is an axial ligand,[46] because the authors noticed an anomalous reduction of A_z of about 10% due to the effect of X^-.

On the whole, an evaluation of the contribution of a deprotonated amide group to the hyperfine constant along the *z* axis confirms the results of Kabanos and Deligiannakis.[37] However, the mean values for TEC = –2, –3 and –4 are slightly different: 35.5, 38.3 and 40.9×10^{-4} cm^{-1} in this work versus 32.2, 36.5 and 40.3×10^{-4} cm^{-1}, respectively. As shown in Figure 10, a linear relationship is observed with a correlation coefficient of 0.99. Based on these results, we can obtain the contribution of the amide group with a –1 charge by extrapolation. The calculated value is 32.7×10^{-4} cm^{-1}.

The rather low contribution for an amide group in complexes with TEC = –1 could partially explain the anomalous reduction of the parallel hyperfine coupling constant observed by Kabanos and coworkers and mentioned above.[46] They reported A_z values of $144–148\times10^{-4}$ cm^{-1}

 © 2005 Wiley-VCH Verlag GmbH & Co. KGaA, Weinheim

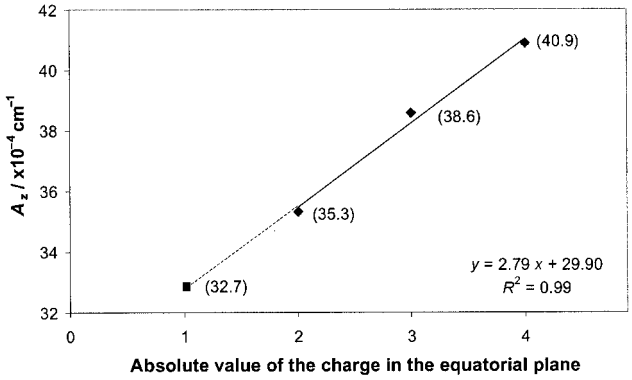

Figure 10. Contribution of a deprotonated amide group to A_z as a function of the absolute value of the charge in the equatorial plane for oxovanadium(IV) complexes.

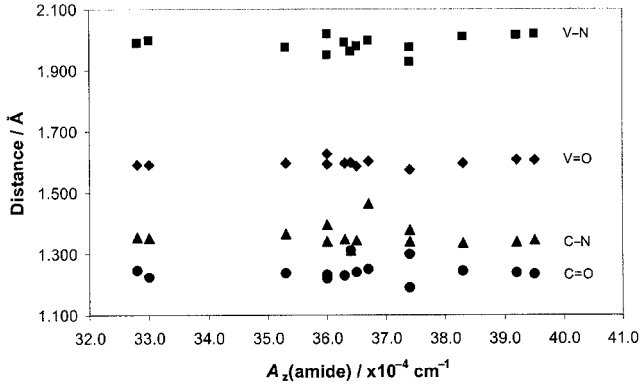

Figure 11. Lengths of V–N, V=O, C–N and C=O bonds as a function of the contribution of the deprotonated amide group to A_z for oxovanadium(IV) complexes. All the solid structures present in literature, for which EPR parameters are reported,[9,32,37,38,40,42–44] were examined.

for the complexes [VOX(capca)], where X^- is Cl^-, SCN^-, CH_3COO^- or $PhCOO^-$ and occupies the axial position, relative to 161×10^{-4} cm^{-1} predicted by Chasteen's rule for (N_{ar}, N_{imino}, N^-, N_{ar}) coordination. With the contribution proposed here for this type of complexes we calculate a value of 155.9×10^{-4} cm^{-1}, which is significantly closer to the experimental one.

The wide range of the A_z(amide) contribution was explained [37,44] by assuming two limit resonance structures for an amide group coordinated through the nitrogen atom: one "amide-like", with the nitrogen atom negatively charged and a double bond between the carbon and oxygen atoms of the carbonyl group (**a** in Scheme 3), and another "imine-like", with the carbonyl oxygen atom negatively charged and a double bond between the carbon and nitrogen atoms (**b** in Scheme 3). The predominance of one of these structures depends on the electronic density of the metal ion: particularly, the importance of the **a** form should increase with decreasing the density (and hence TEC value).

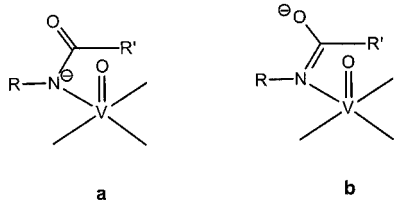

Scheme 3. Limit resonance structures for a deprotonated amide group bound to oxovanadium(IV) species: (a) "amide-like" and (b) "imine-like" form.

If this suggestion is correct, one might expect that the C–N bond is longer and the V–N and C=O bonds are shorter as the "amide-like" form becomes prevalent. In the meantime, the contribution of the deprotonated amide group to A_z should be reduced. A comparison of V–N, C–N and C=O bond lengths, shown in Figure 11, does not reveal any apparent correlation. Therefore, the cause for the difference in the contribution of a deprotonated amide group to A_z must be another one.

The hyperfine coupling constant for ^{51}V can be expressed in the following form:[47]

$$A_z = P_d\left[\beta^2\left(-\kappa - \frac{4}{7}\right) + (g_z - 2.0023) + \frac{3}{14}(g_x - 2.0023) + \frac{3}{14}(g_y - 2.0023)\right]$$

In the above equation $P_d = g_N\beta_N g\beta\langle r^{-3}\rangle$ is the dipolar interaction between the unpaired electron and the ^{51}V nucleus, and is determined by the spatial distribution of the d electron.[47] κ is the Fermi contact term, a measure of the unpaired s-electron spin density at the nucleus, and is influenced by the polarisation of the inner s electrons upon interaction with the unpaired electron. The β^2 factor is, to a good approximation, the population of the ground state d orbital containing the unpaired spin; for $V^{IV}O$ species with C_{2v} symmetry or higher, it measures the population of the d_{xy} orbital. A value of 1 for β^2 indicates that the unpaired electron is localised exclusively on the vanadium d orbital and that there is no delocalisation onto the ligands. On the other hand, values of $\beta^2 < 1$ indicate that a $(1 - \beta^2)$ fraction of the spin density is delocalised onto the ligands.

Since the κ term is considered constant for vanadyl complexes,[48] a reduction in the A_z value could be connected to a decrease of P_d or β^2 or both. According to Kabanos et al.,[32] a reduced P_d value implies a larger $\langle r^{-3}\rangle$ value, which means a radial expansion of the $3d_{xy}$ orbital and a reduced electron density on the metal. This reduced electron density is expected to decrease the V=O bond strength.[49] From Figure 11 it can be observed that no correlation between the A_z(amide) values and the length of V=O bond in vanadyl unit is tenable. Thus, this mechanism can be excluded. This confirms that P_d can also be assumed constant for compounds with similar donor sets, as stated by Pecoraro.[48]

Pecoraro et al. proposed that the overlap of the π orbitals of the ligand with the d_{xy} vanadium atomic orbital would increase the covalence of the metal–ligand bond and produce a decrease in the β^2 value.[48] However, this hypothesis too can be ruled out because the π orbitals of the dipeptides

 © 2005 Wiley-VCH Verlag GmbH & Co. KGaA, Weinheim

Table 5. Coordination modes of $V^{IV}O$ complexes with a deprotonated amide group on the basis of the EPR data.

Ligand	Complex	g_z	A_z exptl.[a]	A_z calcd.[a]	Donor set	Structure[b]
GlyHis	VOL_2H	1.958	160.7	160.7	[(NH_2, N^-, COO^-); (CO, COO^{-ax})]	f
GlyHis	VOL_2	1.959	157.4	157.0	[(NH_2, N^-, N_{im}); (CO, COO^{-ax})]	g
GlyHis	VOL_2H_{-1}	1.959	157.4	157.0	[(NH_2, N^-, N_{im}); (CO, NH_2^{ax})]	c
HisGly	VOL_2H_{-1}	1.955	159.9	160.7	[(NH_2, N^-, COO^-); (CO, NH_2^{ax})]	b
HisHis	VOL_2H_{-1}	1.957	156.7	157.0	[(NH_2, N^-, N_{im}); (CO, NH_2^{ax})]	c
GlyCys	VOL_2H_{-1}	1.968	143.6	142.5	[(NH_2, N^-, S^-); (S^-, COO^{-ax})]	i
GlyCys	$VOLH_{-2}$	1.956	152.3	149.3	[(NH_2, N^-, S^-); OH^-]	j

[a] A_z measured in 10^{-4} cm^{-1} units. [b] See Scheme 2.

and d_{xy} of vanadium are not in a favourable position to overlap with each other.

The only mechanism that may reduce the A_z value is a strong covalent bond between the deprotonated nitrogen atom and the $V^{IV}O$ ion. We suggest that if the TEC of amidate complexes is –4, i.e. the electronic density around the vanadium atom is high, the V–N bond exhibits a minor amount of covalent character and remains close to the ionic limit: this means higher β^2 and A_z values. On the other hand, if the TEC of the complex is –1, the V–N bond is more covalent, and this results in the reduction in the electron density at the d_{xy} nonbonding orbital of vanadium, and therefore a decrease in the β^2 and A_z values is observed.

According to Kabanos and Pecoraro,[32,48] we assume $P_d = 125 \times 10^{-4}$ cm^{-1} and $\kappa = 0.85$. Values of β^2 of approximately 0.92 for TEC = –4, 0.86 for TEC = –3, 0.80 for TEC = –2 and 0.74 for TEC = –1 are thus obtained.

Based on the A_z contribution of the amide group calculated in the previous discussion, we can attempt to find the donor set and the geometry for the $V^{IV}O$ species that involves this group. The first obvious observation is that the experimental coupling constants for the VOL_2H_{-1} species formed by two dipeptides with L-histidine in the C-terminal position show similar A_z values (about 157×10^{-4} cm^{-1}), whilst for HisGly, VOL_2H_{-1} exhibits a value of about 160×10^{-4} cm^{-1}. This substantiates the involvement of the imidazole nitrogen atom in metal coordination. Instead, the very low value of A_z for GlyCys suggests the participation of S^- in the bonding. Therefore, three equatorial positions are filled by HisGly, GlyHis, HisHis and GlyCys through (NH_2, N^-, COO^-), (NH_2, N^-, N_{im}), (NH_2, N^-, N_{im}), and (NH_2, N^-, S^-), respectively. The last two remaining sites of the coordination sphere of the $V^{IV}O$ ion are completed, according to the data in Table 5, by the (CO, NH_2) donor set which acts as a moderately strong donor towards the $V^{IV}O$ ion. The comparison of the experimental with calculated values supports that the CO group is in the equatorial position and the amino group is in the axial position.

The structures of the complexes formed upon deprotonation of the amide group are marked with **b**, **c**, **f**, **g**, **i** and **j** in Scheme 2.

Conclusions

Simple dipeptides coordinate the $V^{IV}O$ ion without the assistance of strong "anchoring" groups. The ligands coordinate the metal ion with (NH_2, CO) or (COO^-, CO) donor sets in the acidic and neutral pH range, and avoid the precipitation of the hydroxide if at least a fivefold excess of ligand is used. The presence of L-histidine in the N-terminal position enhances the strength of the (NH_2, CO) donor set. In the alkaline pH range, all the ligands, except CysGly, promote the deprotonation of the amide group. The effect of additional donors, e.g. imidazole and thiolate, can be seen also in species containing deprotonated amide groups. The donor sets (NH_2, N^-, N_{im}) and (NH_2, N^-, S^-) are stronger than the simple (NH_2, N^-, COO^-) donor set.

The composition of the complexes of GlyCys and CysGly depends on the location of the thiolato group. In GlyCys the coordination mode is (NH_2, N^-, S^-) and the C-terminal carboxylate does not take part in complexation. On the other hand, N-terminal cysteine peptides can form a stable five-membered chelated ring with the participation of the amino group, which gives rise to stable bischelated complexes without amide binding.

According to Kabanos and Cornman[37,44] the total charge on the equatorial plane of vanadium(IV) affects the bond type of the deprotonated amide group and determines the contribution of the nitrogen atom to the ^{51}V hyperfine coupling constant. We have demonstrated that the reduction of A_z(amide) observed when the TEC changes from –4 to –1 does not depend on the "shift" of "imine-like" to "amide-like" coordination. Instead, it is attributable to an increase in the covalence of the V–N bond accompanied by a decrease in the electron density at vanadium. Thus, it could be misleading to take into account a mean value for the contribution of the deprotonated amide groups without considering the effect of the total equatorial charge.

A direct application of these theoretical results allows the prediction of the geometry and donor set of the compounds involving the coordination of the amide group examined in this study.

Experimental Section

Chemicals: The ligands were Aldrich products of puriss. quality. Their purity and concentration were determined by the Gran method.[50] VO^{2+} solutions were prepared following literature methods.[51] The concentration of the metal ion was determined by $KMnO_4$ titration and that of H^+ by a potentiometric titration using the appropriate Gran function. The ionic strength was adjusted to 0.1 M with KNO_3. The temperature was 25.0 ± 0.1 °C.

 © 2005 Wiley-VCH Verlag GmbH & Co. KGaA, Weinheim

Potentiometric Measurements: The protonation constants for the ligands and the stability constants for the $V^{IV}O$ complexes were determined by pH-potentiometric titrations of 2.0 mL samples. The ligand-to-metal molar ratio was in the range 1:1–5:1. The VO^{2+} concentration was 0.001 M. Titrations were performed by adding 0.1 M NaOH with a calibrated syringe under purified argon. The pH values were recorded with a combination glass electrode (Russel CMAWL/S7) calibrated for hydrogen concentration by the method of Irving et al.[52] The reproducibility of the titration points included in the evaluation was within 0.005 pH units in the whole pH range examined (2–12). As usual, the stability of the complexes is reported as the logarithm of the overall formation constant $\beta_{pqr} = [M_pH_qL_r]/[M]^p[H]^q[L]^r$, where M stands for the metal ion, H is the proton, and L is the deprotonated form of the ligand in the absence of metal coordination and was calculated with the aid of the SUPERQUAD program.[53] Standard deviations were calculated by assuming random errors. The conventional notation has been used. Negative indices for protons indicate either the proton dissociation of groups which do not deprotonate in the absence of coordination of the metal ion, or hydroxo ligands. Hydroxo complexes of VO^{2+} were taken into account in the calculations. The following species were assumed: $[VO(OH)]^+$ ($\log \beta_{1-1} = -5.94$), $[(VO)_2(OH)_2]^{2+}$ ($\log \beta_{2-2} = -6.95$), and the stability constants were calculated from the data of Henry et al.[54] and corrected for the different ionic strengths by use of the Davies equation,[55] $[VO(OH)_3]^-$ ($\log \beta_{1-3} = -18.0$) and $[(VO)_2(OH)_5]^-$ ($\log \beta_{2-5} = -22.0$).[56]

Spectroscopic and Analytical Measurements: Anisotropic EPR spectra were recorded on aqueous solutions with an X-band (9.15 GHz) Varian E-9 spectrometer in the temperature range 120–140 K. As usual for low temperature measurements, a few drops of DMSO were added to the samples to ensure good glass formation. The spectra were simulated with the computer program Bruker WinEPR SimFonia. Electronic spectra were recorded with a Beckman Acta MIV spectrophotometer.

[1] D. Rehder, in *Metal Ions in Biological Systems* (Eds.: A. Sigel, H. Sigel), Marcel Dekker, New York, **1995**, vol. 31, p. 1–43.
[2] B. R. Nechay, *Annu. Rev. Pharmacol. Toxicol.* **1984**, *24*, 501–524.
[3] G. Swarup, K. V. Speeg, S. Cohen, D. L. Garbers, *J. Biol. Chem.* **1982**, *257*, 7298–7301.
[4] D. Rehder, J. Costa Pessoa, C. F. G. C. Geraldes, M. M. C. A. Castro, T. Kabanos, T. Kiss, B. Meier, G. Micera, L. Pettersson, M. Rangel, A. Salifoglou, I. Turel, D. Wang, *J. Biol. Inorg. Chem.* **2002**, *7*, 384–396.
[5] a) M. Garner, J. Reglinski, W. E. Smith, J. McMurray, I. Abdullah, R. Wilson, *J. Biol. Inorg. Chem.* **1997**, *2*, 235–241; b) D. C. Crans, M. Mahroof-Tahir, A. D. Keramidas, *Mol. Cell. Biochem.* **1995**, *153*, 17–24.
[6] I. Sóvágó, in *Biocoordination Chemistry* (Ed.: K. Burger.), Ellis Horwood, New York, **1990**, ch. 4, 135–184.
[7] T. Kiss, T. Jakusch, J. Costa Pessoa, I. Tomaz, *Coord. Chem. Rev.* **2003**, *237*, 123–133.
[8] V. M. Fritzsche, V. Vergopoulos, D. Rehder, *Inorg. Chim. Acta* **1993**, *211*, 11–16.
[9] A. J. Tasopoulos, A. T. Vlahos, A. D. Keramidas, T. A. Kabanos, Y. G. Deligiannakis, C. P. Raptopoulou, A. Terzis, *Angew. Chem. Int. Ed. Engl.* **1996**, *35*, 2531–2533.
[10] a) J. Costa Pessoa, S. M. Luz, R. Duarte, J. J. G. Moura, R. D. Gillard, *Polyhedron* **1993**, *12*, 2857–2867; b) J. Costa Pessoa, S. M. Luz, R. D. Gillard, *J. Chem. Soc. Dalton Trans.* **1997**, 569–576.
[11] T. Kiss, K. Petrohan, P. Buglyó, D. Sanna, G. Micera, J. Costa Pessoa, C. Madeira, *Inorg. Chem.* **1998**, *37*, 6389–6391.
[12] M. S. Michailidis, R. B. Martin, *J. Am. Chem. Soc.* **1969**, *91*, 4683–4689.
[13] a) J. Costa Pessoa, L. F. Vilas Boas, R. D. Gillard, R. J. Lancashire, *Polyhedron* **1988**, *7*, 1245–1262; b) A. Dessì, G. Micera, D. Sanna, *J. Inorg. Biochem.* **1993**, *52*, 275–286.
[14] I. Fábián, I. Nagypál, *Inorg. Chim. Acta* **1982**, *62*, 193–199.
[15] E. Garribba, G. Micera, D. Sanna, unpublished results.
[16] N. D. Chasteen, in *Biological Magnetic Resonance* (Eds.: L. J. Berliner, J. Reuben), Plenum Press, New York, **1981**, vol. 3, p. 53–119.
[17] a) L. D. Pettit, J. L. M. Swash, *J. Chem. Soc. Dalton Trans.* **1976**, 588–594; b) D. Sanna, G. Micera, M. G. Molinu, *J. Chem. Research (S)* **1996**, 42–43.
[18] B. J. Hamstra, A. P. L. Houseman, G. J. Colpas, J. W. Kampf, R. LoBrutto, W. D. Frasch, V. L. Pecoraro, *Inorg. Chem.* **1997**, *36*, 4866–4874.
[19] T. A. Kabanos, A. D. Keramidas, A. Papaioannou, A Terzis, *Inorg. Chem.* **1994**, *33*, 845–846.
[20] A. D. Keramidas, S. M. Miller, O. P. Anderson, D. C. Crans, *J. Am. Chem. Soc.* **1997**, *119*, 8901–8915.
[21] T. Jakusch, P. Buglyó, A. I. Tomaz, J. Costa Pessoa, T. Kiss, *Inorg. Chim. Acta* **2002**, *339*, 119–128.
[22] I. Sóvágó, E. Farkas, A. Gergely, *J. Chem. Soc. Dalton Trans.* **1982**, 2159–2163.
[23] C. E. Livera, L. D. Pettit, M. Bataille, B. Perly, H. Koszlowski, B. Radomska, *J. Chem. Soc. Dalton Trans.* **1987**, 661–666.
[24] A. Lorenzotti, D. Lorenzotti, A. Cingolani, P. DiBernardo, *Inorg. Chim. Acta* **1981**, *52*, 149–152.
[25] J. Costa Pessoa, I. Tomaz, T. Kiss, P. Buglyó, *J. Inorg. Biochem.* **2001**, *84*, 259–270.
[26] J. Costa Pessoa, I. Correia, T. Kiss, T. Jakusch, M. M. C. A. Castro, C. F. G. C. Geraldes, *J. Chem. Soc. Dalton Trans.* **2002**, 4440–4450.
[27] T. Jakusch, A. Dörnyei, I. Correia, L. M. Rodriguez, G. K. Tóth, T. Kiss, J. Costa Pessoa, S. Marcão, *Eur. J. Inorg. Chem.* **2003**, 2113–2122.
[28] H. Kozlowski, B. Decock-Le Révérend, D. Ficheux, C. Loucheux, I. Sóvágó, *J. Inorg. Biochem.* **1987**, *29*, 187–197.
[29] K. Cherifi, B. Decock-Le Révérend, K. Várnagy, T. Kiss, I. Sóvágó, H. Kozlowski, *J. Inorg. Biochem.* **1990**, *38*, 69–80.
[30] I. Sóvágó, T. Kiss, K. Várnagy, B. Decock-Le Révérend, *Polyhedron* **1988**, *7*, 1089–1093.
[31] H. Kozlowski, I. Sóvágó, J. Spychala, J. Urbanska, K. Várnagy, A. Kiss, K. Cherifi, *Polyhedron* **1990**, *9*, 831–837.
[32] E. J. Tolis, V. I. Teberekidis, C. P. Raptopoulou, A. Terzis, M. Sigalas, Y. Deligiannakis, T. A. Kabanos, *Chem. Eur. J.* **2001**, *7*, 2698–2710.
[33] P. Buglyó, E. Kiss, I. Fàbiàn, T. Kiss, D. Sanna, E. Garribba, G. Micera, *Inorg. Chim. Acta* **2000**, *306*, 174–183.
[34] I. Cavaco, J. Costa Pessoa, D. Costa, M. T. Duarte, R. D. Gillard, P. Matias, *J. Chem. Soc. Dalton Trans.* **1994**, 149–157.
[35] a) K. P. Callahan, P. J. Durand, *Inorg. Chem.* **1980**, *19*, 3211–3217; b) J. A. Bonadies, C. J. Carrano, *J. Am. Chem. Soc.* **1986**, *108*, 4088–4095; c) J. C. Dutton, G. D. Fallon, K. S. Murray, *Inorg. Chem.* **1988**, *27*, 34–38; d) I. Cavaco, J. Costa Pessoa, M. T. Duarte, R. T. Henriques, P. M. Matias, R. D. Gillard, *J. Chem. Soc. Dalton Trans.* **1996**, 1989–1996; e) C. R. Cornman, K. M. Geisre-Bush, S. R. Rowley, P. D. Boyle, *Inorg. Chem.* **1997**, *36*, 6401–6408.
[36] A_z is 43.7 for [VO(*N*-salicylidene-L-alaninato)(H_2O)] and 42.4×10^{-4} cm^{-1} for [VO(*N*-salicylidene-L-alaninato)(bipy)];[34] 40.8 for [VO(salen)] and 43.4×10^{-4} cm^{-1} for [VO(acen)];[35a] 40.8×10^{-4} cm^{-1} for [VO(salen)];[35b] 42.1 for [VO(tsalen)], 38.1 for VO(tsaltn)], 40.6 for [VO(tsalphen)] and 40.6×10^{-4} cm^{-1} for VO(tsal-4,5-Me_2phen)];[35c] 42.7 for [VO(*N*-salicylidene-L-methioninato)(H_2O)], 40.2 for [VO(*N*-salicylidene-L-methioninato)(bipy)], 41.7 for [VO(*N*-salicylidene-L-valinato)(H_2O)], 41.8 for [VO(*N*-salicylidene-L-valinato)(bipy)], 41.6 for [VO(*N*-salicylidene-L-phenylalaninato)(H_2O)], 41.1 for [VO(*N*-salicylidene-L-phenylalaninato)(bipy)], 43.0 for [VO(*N*-salicylidene-L-isoleucinato)(H_2O)], 42.6 for [VO(*N*-(2-oxido-1-naphthylmethylene-L-valinato))(H_2O)] and 41.9×10^{-4} cm^{-1} for [(*N*-(2-oxido-

 © 2005 Wiley-VCH Verlag GmbH & Co. KGaA, Weinheim

1-naphthylmethylene-L-valinato))(bipy)];[35d] 41.8 for [VO(*N*,*N*′-ethylenebis-*o*-(*tert*-butyl-*p*-methylsalicylaldiminato))$_2$], 42.0 for [VO(*N*,*N*′-propanediylbis-*o*-(*tert*-butyl-*p*-methylsalicylaldiminato))$_2$], 41.8 for [VO(N-methylsalicylaldiminato)$_2$], 41.6 for [VO(*N*-methyl-*o*-*tert*-butyl-*p*-methylsalicylaldiminato)$_2$], 41.6 for [VO(*N*-isopropyl-*o*-methylsalicylaldiminato)$_2$] and 39.8×10^{-4} cm^{-1} for [VO(*N*-methyl-*o*-(*tert*-butyl-*p*-methylsalicylaldiminato))$_2$].[35e]

[37] A. J. Tasiopoulos, A. N. Troganis, A. Evangelou, C. P. Raptopoulou, A. Terzis, Y. Deligiannakis, T. A. Kabanos, *Chem. Eur. J.* **1999**, *5*, 910–921.

[38] A. D. Keramidas, A. P. Papaioannou, A. Vlahos, T. A. Kabanos, G. Bonas, A. Makriyannis, C. P. Raptopoulou, A. Terzis, *Inorg. Chem.* **1996**, *35*, 357–367.

[39] I. Cavaco, J. Costa Pessoa, S. M. Luz,, M. T. Duarte, P. M. Matias, R. T. Henriques, R. D. Gillard, *Polyhedron* **1995**, *14*, 429–439.

[40] A. J. Tasiopoulos, E. J. Tolis, J. M. Tsangaris, A. Evangelou, J. D. Woollins, A. M. Z. Slawin, J. Costa Pessoa, I. Correia, T. A. Kabanos, *J. Biol. Inorg. Chem.* **2002**, *7*, 363–374.

[41] J. Costa Pessoa, T. Gajda, R. D. Gillard, T. Kiss, S. M. Luz, J. J. G. Moura, I. Tomaz, J. P. Telo, I. Török, *J. Chem. Soc. Dalton Trans.* **1998**, 3587–3600.

[42] A. J. Tasiopoulos, Y. G. Deligiannakis, J. D. Woollins, A. M. Z. Slawin, T. A. Kabanos, *J. Chem. Soc. Chem. Commun.* **1998**, 569–570.

[43] G. R. Hanson, T. A. Kabanos, A. D. Keramidas, D. Mentzafos, A. Terzis, *Inorg. Chem.* **1992**, *31*, 2587–2594.

[44] C. R. Cornman, E. P. Zovinka, Y. D. Boyajina, K. M. Geisre-Bush, P. D. Boyle, P. Singh, *Inorg. Chem.* **1995**, *34*, 4213–4219.

[45] F. H. Allen, O. Kennard, 3D Search and Research Using the Cambridge Structural Database, *Chemical Design Automation News* **1993**, *8*, pp. 1 and 31–37.

[46] E. J. Tolis, K. D. Soulti, C. P. Raptopoulou, A. Terzis, Y. Deligiannakis, T. A. Kabanos, *J. Chem. Soc. Chem. Commun.* **2000**, 601–602.

[47] B. R. McGarvey, *J. Phys. Chem.* **1967**, *71*, 51–67.

[48] T. S. Smith II, C. A. Roof, J. W. Kampf, P. G. Rasmussen, V. L. Pecoraro, *J. Am. Chem. Soc.* **2000**, *122*, 767–775.

[49] J. Selbin, *Coord. Chem. Rev.* **1966**, *1*, 293–314.

[50] G. Gran, *Acta Chem. Scand.* **1950**, *4*, 559–577.

[51] I. Nagypál, I. Fábián, *Inorg. Chim. Acta* **1982**, *61*, 109–113.

[52] H. Irving, M. G. Miles, L. D. Pettit, *Anal. Chim. Acta* **1967**, *38*, 475–481.

[53] P. Gans, A. Vacca, A. Sabatini, *J. Chem. Soc. Dalton Trans.* **1985**, 1195–1200.

[54] R. P. Henry, P. C. H. Mitchell, J. E. Prue, *J. Chem. Soc. Dalton Trans.* **1973**, 1156–1159.

[55] C. W. Davies, *J. Chem. Soc.* **1938**, 2093–2098.

[56] A. Komura, M. Hayashi, H. Imanaga, *Bull. Chem. Soc. Jpn.* **1977**, *50*, 2927–2931.

Received: July 2, 2004

 © 2005 Wiley-VCH Verlag GmbH & Co. KGaA, Weinheim

Trinuclear Oxo-Centered Iron and Iron/Nickel Clusters – Ligand-Controlled Homo/Hetero Valency[‡]

Rolf W. Saalfrank,*[a] Andreas Scheurer,[a] Klaus Pokorny,[a] Harald Maid,[a] Uwe Reimann,[a] Frank Hampel,[a] Frank W. Heinemann,[b] Volker Schünemann,[c] and Alfred X. Trautwein[d]

Keywords: Trinuclear complexes / Iron / Nickel / Mixed-valent complexes / Heteronuclear complexes

Cleavage of the all-iron(III) μ_2-O^{2-}-linked dimer $[Fe^{III}_3O(L)_2(OAc)_4]_2O$ (**3**) with lithium chloride yields $[Fe^{III}_3O(L)_2(OAc)_4]Cl$ (**4**) and with sodium benzoate, in combination with complete acetate-to-benzoate coligand exchange, gives $[Fe^{III}_3O(L)_2(OBz)_4]OBz$ (**5**). Reduction of the all-Fe^{III} complex **5** [Fe/L/OBz = 3:2:(4+1)] with sodium iodide affords the homonuclear mixed-valent cluster $[Fe^{II}Fe^{III}_2O(L)_3(OBz)_3]$ (**6**) (Fe/L/OBz = 1:1:1) and requires fundamental coligand-to-ligand exchange. Likewise, when the all-Fe^{III} dimer $[Fe^{III}_3O(L)_2(OAc)_4]_2O$ (**3**) (Fe/L/OAc = 3:2:4) is cleaved with nickel acetate, the mixed-valent heteronuclear complex $[Ni^{II}Fe^{III}_2O(L)_3(OAc)_3]$ (**7**) (M/L/OAc = 1:1:1) is formed.
(© Wiley-VCH Verlag GmbH & Co. KGaA, 69451 Weinheim, Germany, 2005)

Introduction

Recently, we reported that the reaction of *N*-(5-methylthiazol-2-yl)thiazole-2-carboxamide HL (**1**) with fresh iron(II) acetate in fluorobenzene under aerobic conditions yields the deeply violet μ_3-O^{2-}-centered mixed-valent complex $[Fe^{II}Fe^{III}_2O(L)_3(OAc)_3]$ (**2**), whereas aged $Fe(OAc)_2$ in chloroform under aerobic conditions leads to homovalent dimer $[Fe^{III}_3O(L)_2(OAc)_4]_2O$ (**3**) (Scheme 1).[1–4] Most notably, the metal/ligand/coligand ratio (Fe/L/OAc) in mixed-valent **2** is 1:1:1, whereas the ratio in homo-valent **3** is 3:2:4.

Results and Discussion

All-Iron(III) Complexes

Herein we describe the cleavage of the μ_2-O^{2-}-linked dimer $[Fe^{III}_3O(L)_2(OAc)_4]_2O$ (**3**) in chloroform with lithium chloride or sodium benzoate to give $[Fe^{III}_3O(L)_2(OAc)_4]Cl$ (**4**) or $[Fe^{III}_3O(L)_2(OBz)_4]OBz$ (**5**) (Scheme 2). The cleavage of **3** with benzoate ions to give **5** obviously proceeds with complete acetate-to-benzoate coligand exchange.

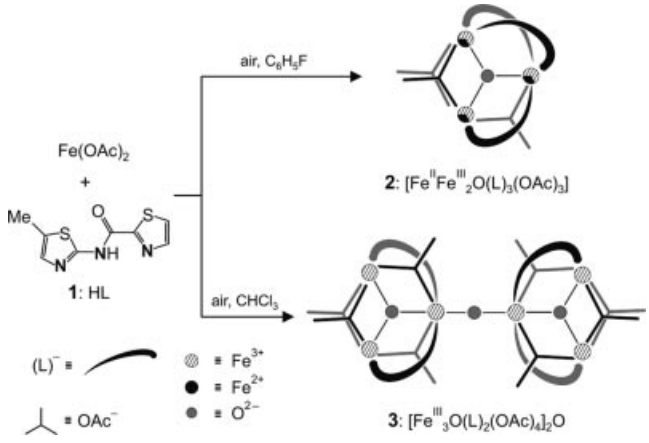

Scheme 1. Synthesis of heteroleptic **2** and **3**. In **2**, the mixed valency and its statistical distribution is highlighted by differently marked segments.

The all-iron(III) character of **4** and **5** was confirmed by Mössbauer spectra of their powder samples recorded at 77 K. The spectra exhibit quadrupolar doublets and isomeric shifts consistent with high-spin iron(III) (**4**: ΔE_Q = 0.77 mm s^{-1}, δ = 0.48 mm s^{-1}, and Γ = 0.36 mm s^{-1}; **5**: ΔE_Q = 0.77 mm s^{-1}, δ = 0.51 mm s^{-1}, and Γ = 0.45 mm s^{-1}). The Mössbauer spectrum of **5** is displayed in Figure 1 as an example.

The structure of **4** was unequivocally determined by single-crystal X-ray analysis.[5–7] According to these data, heteroleptic $[Fe^{III}_3O(L)_2(OAc)_4]Cl$ (**4**) is made up of two ditopic, tridentate ligands $(L)^-$ and four bridging acetate coligands, fixing the three Fe^{III} ions in the corners of a triangle with a μ_3-O^{2-} ion in the center. Fe1/2 are linked by

[‡] Chelate Complexes, 30. Part 29: Ref.[1]
[a] Institut für Organische Chemie der Universität Erlangen-Nürnberg,
Henkestrasse 42, 91054 Erlangen, Germany
Fax: +49-9131-852-1165
E-mail: saalfrank@chemie.uni-erlangen.de
[b] Institut für Anorganische Chemie der Universität Erlangen-Nürnberg,
91058 Erlangen, Germany
[c] Fachbereich Physik, Technische Universität Kaiserslautern,
67663 Kaiserslautern, Germany
[d] Institut für Physik der Medizinischen Universität Lübeck,
23538 Lübeck, Germany
[‡] Chelate Complexes, 30. Part 29: Ref.[1]

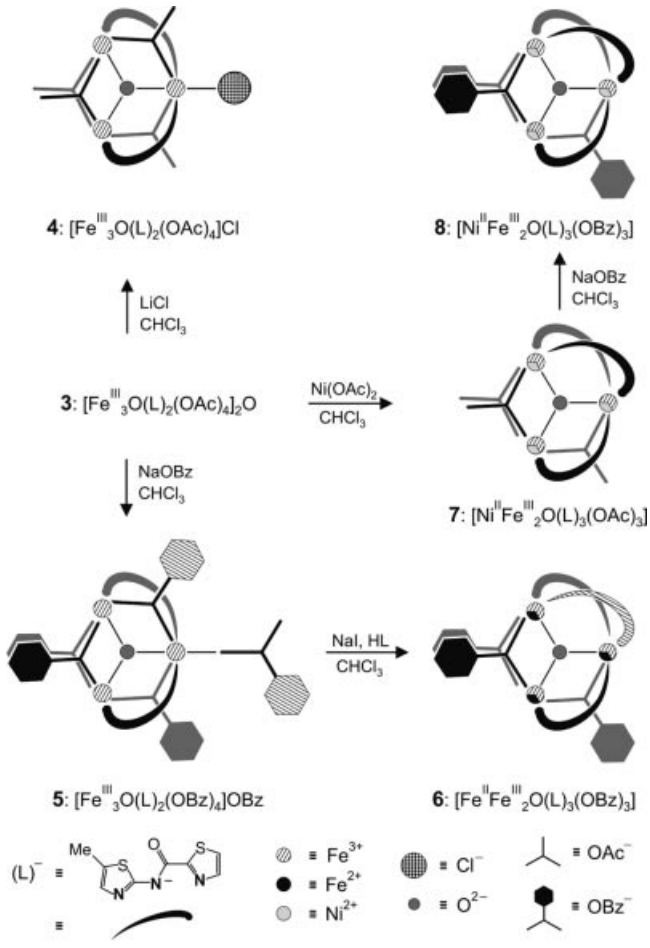

Scheme 2. Synthesis of **4**–**8**. In **5** the monodentate and bidentate $(OBz)^-$ coligands substituted in **6** by ditopic, tridentate $(L)^-$ are highlighted (diagonal). In **6**–**8**, the mixed valency and its statistical distribution are emphasised by differently marked segments.

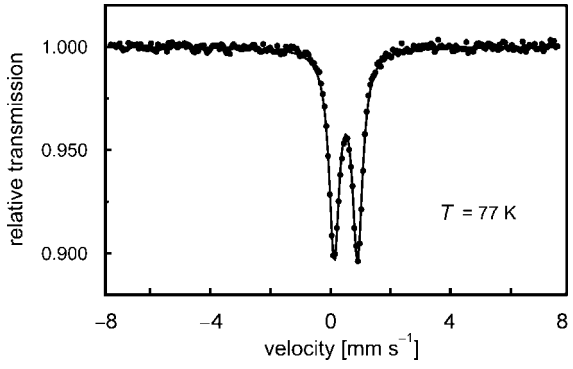

Figure 1. Mössbauer spectrum of **5**.

one ligand $(L)^-$ head-to-tail and Fe2/3 by one ligand $(L)^-$ tail-to-head. Furthermore, Fe1/2 and Fe2/3 are linked by one μ_2-$(OAc)^-$ bridge, each, and Fe1/3 by two μ_2-$(OAc)^-$ bridges. As a consequence, in the all-iron(III) compound **4**, Fe1 and Fe3 are identically octahedrally coordinated. The extra coordination site at Fe2 is occupied by a chloride ion, leading to charge compensation (Figure 2). As with **4**, complexes **2**–**10** were obtained as racemic mixtures.

Since we were not successful in growing single crystals suitable for an X-ray analysis of $[Fe^{III}_3O(L)_2(OBz)_4]OBz$ (**5**), we prepared $[Fe^{III}_3O(L)_2(OBzBr)_4]OBzBr$ (**9**). The all-iron(III) complex **9** was synthesised from iron(II) acetate with an excess of sodium 4-bromobenzoate and *N*-(5-methylthiazol-2-yl)thiazole-2-carboxamide HL (**1**) in chloroform under aerobic conditions, and separated from mixed-valent $[Fe^{II}Fe^{III}_2O(L)_3(OBzBr)_3]$ (**10**) by fractionising crystallization (Scheme 3). According to the X-ray analysis, **9** is isostructural with $[Fe^{III}_3O(L)_2(OAc)_4]Cl$ (**4**) with one μ_1-$(OBzBr)^-$ coligand bound to Fe, necessary for coordination and charge compensation (**9**: $\Delta E_Q = 0.81\ mm\,s^{-1}$, $\delta = 0.48\ mm\,s^{-1}$, and $\Gamma = 0.35\ mm\,s^{-1}$).[6–8]

Mixed-Valent Homonuclear and Mixed-Valent Heteronuclear Complexes

The reversible cyclic voltammograms of redox-active $[Fe^{II}Fe^{III}_2O(L)_3(OAc)_3]$ (**2**) and $[Fe^{II}Fe^{III}_2O(L)_3(OBz)_3]$ (**6**) displayed basically two processes attributable to the reduction of **2** and **6** from $Fe^{II}Fe^{III}_2$ to $Fe^{II}_2Fe^{III}$ and oxidation to the all-Fe^{III} species.[1] The number of electrons transferred at different potentials during this process was determined in acetonitrile vs. Fc/Fc^+ and turned out to be one for the reduction of all-Fe^{III} to $Fe^{II}Fe^{III}_2$ and one for the second reduction to $Fe^{II}_2Fe^{III}$. Further reduction of $Fe^{II}_2Fe^{III}$ to the all-Fe^{II} species is irreversible. Consequently, the cyclic voltammograms of redox-active $[Ni^{II}Fe^{III}_2O(L)_3(OAc)_3]$ (**7**) and $[Ni^{II}Fe^{III}_3O(L)_3(OBz)_3]$ (**8**) represent the reduction of $Ni^{II}Fe^{III}_2$ to $Ni^{II}Fe^{II}Fe^{III}$ and reoxidation to $Ni^{II}Fe^{III}_2$.[1] As determined in acetonitrile vs. Fc/Fc^+, one electron is transferred during this redox process. Further reduction of $Ni^{II}Fe^{II}Fe^{III}$ to the $Ni^{II}Fe^{II}_2$ species is irreversible.

Reduction of the all-iron(III) complex $[Fe^{III}_3O(L)_2(OBz)_4]$-OBz (**5**) in chloroform with 5 equiv. of sodium iodide[9] yields homonuclear mixed-valent cluster $[Fe^{II}Fe^{III}_2O(L)_3(OBz)_3]$ (**6**) (Scheme 2). Worth noting is that reduction of **5** does not simply occur by a one-electron reduction, but rather affords fundamental coligand-to-ligand exchange to give **6**. In order to generate **6** (Fe/L/OBz = 1:1:1), the mono- and bidentate $(OBz)^-$ coligands in **5** [Fe/L/OBz = 3:2:(4+1)] have to be substituted by the ditopic, tridentate ligand $(L)^-$ (Scheme 2). Furthermore, these findings coherently explain the irreversibility of the cyclic voltammograms of **4**, **5**, and **9**.

Likewise, when the all-iron(III) dimer $[Fe^{III}_3O(L)_2(OAc)_4]_2O$ (**3**) (Fe/L/OAc = 3:2:4) is cleaved with nickel acetate in chloroform, the mixed-valent heteronuclear $[Ni^{II}Fe^{III}_2O(L)_3(OAc)_3]$ (**7**) (M/L/OAc = 1:1:1) is formed. This again is a complex reaction and requires the exchange of Fe^{III}-to-Ni^{II} and of $(OAc)^-$ coligand-to-$(L)^-$. Since it was not possible to grow single crystals of acetate **7** suitable for X-ray structure determination, $[Ni^{II}Fe^{III}_2O(L)_3(OBz)_3]$ (**8**) was generated from **7** by exchange of the $(OAc)^-$ coligands with $(OBz)^-$ ions (Scheme 2).

The chelate complexes **6**–**8** are also accessible starting from complex **2**.[1] For example, **6** and **7** were prepared from

 © 2005 Wiley-VCH Verlag GmbH & Co. KGaA, Weinheim

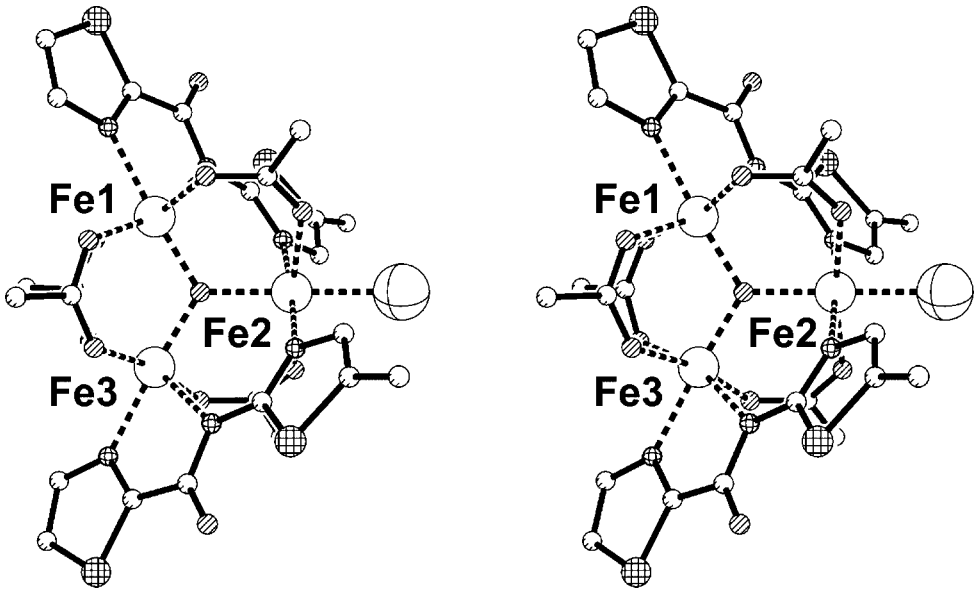

Figure 2. Molecular structure of **4** in the crystal (stereoview, PLUTON presentation, with the numbering of the iron ions, only one stereoisomer shown). H atoms omitted for clarity. C: shaded; N: net; O: diagonal; S: mesh; Fe: void; Cl: cross. Selected bond lengths [Å] and angles [°]: Fe1–μ_3-O 1.87, Fe2–μ_3-O 1.95; Fe1–μ_3-O–Fe2 121.1, Fe1–μ_3-O–Fe3 117.7.

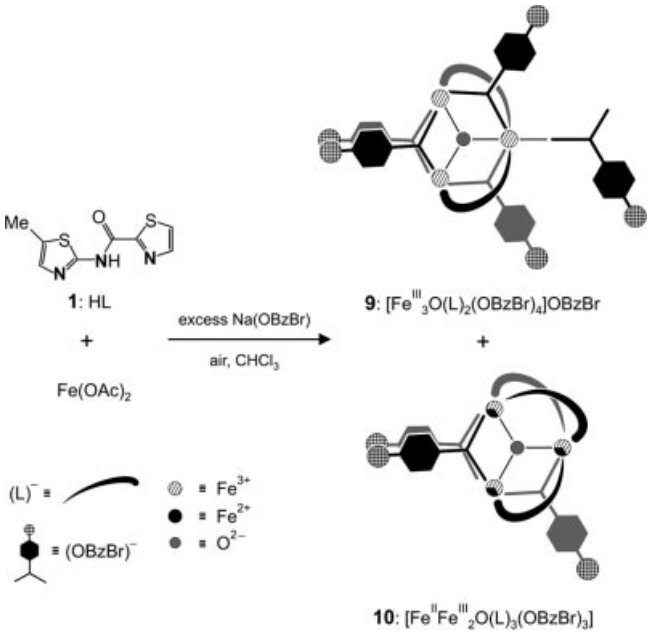

Scheme 3. Synthesis of all-iron(III) complex **9** and mixed-valent species **10**. In **10**, the mixed valency is marked by segments.

mixed-valent homonuclear $[Fe^{II}Fe^{III}_2O(L)_3(OAc)_3]$ (**2**) by mere exchange of the $(OAc)^-$ coligands by $(OBz)^-$ ions and by Fe^{II}-to-Ni^{II} exchange, respectively.

Conclusions

In summary, we have presented the cleavage of dimer **3** into **4**, **5**, and **7** and the interconversion of **5** into **6** and **7** into **8**. Most interestingly, in mixed-valent homonuclear **2** and **6** and in mixed-valent heteronuclear **7** and **8** the metal/ligand/coligand ratio M/L/co-L is 1:1:1, whereas, in homovalent **3**–**5** the ratio is 3:2:4. This result indicates ligand-controlled stabilization of the all-Fe^{III} and mixed-valent species.

Experimental Section

General Methods: IR spectra were recorded from $CHBr_3$ triturations with a Bruker IFS 25 spectrometer. FAB-MS spectra were recorded with a Micromass ZAB-Spec spectrometer. Elemental analyses were performed with an EA 1110 CHNS-Microautomat. The microanalytical data for **4**–**9** deviate from theory due to varying crystal solvents and are not recorded here.

Materials: All reagents and solvents employed were commercially available high-grade purity materials (Fluka, Aldrich), used as supplied without further purification. Ligand HL (**1**) was prepared according to ref.[2] Sodium 4-bromobenzoate was generated by reaction of 4-bromobenzoic acid (1.1 equiv.) with NaH (1.0 equiv.) in dry THF. The precipitate was filtered off, washed with THF and dried in vacuo.

General Procedure: The metal salt (LiCl, NaOBz, $Ni(OAc)_2$, NaI) was added, in one portion, to a solution of complexes **3** or **5** in chloroform. The initially pale violet suspension was stirred at 20 °C for 48 h. After removal of the excess metal salt by filtration through a pad of Celite, the remaining solution was concentrated to dryness.

Compound $[Fe^{III}_3O(L)_2(OAc)_4]Cl$ (4): 3 (131 mg, 0.075 mmol), anhydrous lithium chloride (509 mg, 12 mmol), and chloroform (60 mL). Yield: 110 mg (81%) dark-violet crystals from $CHCl_3$ by vapor diffusion of diethyl ether; m.p. >250 °C (decomp.). IR ($CHBr_3$): $\tilde{\nu}$ = 3137, 3109, 2995, 2923, 1615, 1575, 1556, 1505 cm^{-1}. FAB-MS (*m*-NBA): *m*/*z* (%) = 902 (6) $[M]^+$, 868 (100) $[M - Cl]^+$, 809 (59) $[M - Cl - OAc]^+$, 750 (22) $[M - Cl - 2\ OAc]^+$, 691 (11) $[M - Cl - 3\ OAc]^+$, 644 (33) $[M - Cl - L]^+$, 585 (32) $[M - Cl - OAc - L]^+$, 526 (25) $[M - Cl - 2\ OAc - L]^+$, 470 (21) $[M - Cl - 2\ OAc - L - Fe]^+$, 411 (21) $[M - Cl - 3\ OAc - L - Fe]^+$, 352 (16) $[M - Cl - 4\ OAc - L - Fe]^+$.

 © 2005 Wiley-VCH Verlag GmbH & Co. KGaA, Weinheim

Compound $[Fe^{III}_3O(L)_2(OBz)_4]OBz$ (5): 3 (175 mg, 0.1 mmol), sodium benzoate (2.30 g, 16 mmol), and chloroform (80 mL). Yield: 178 mg (72%) dark-violet microcrystalline solid from $CHCl_3$ by vapor diffusion of diethyl ether; m.p. >250 °C (decomp.). IR ($CHBr_3$): $\tilde{\nu}$ = 3127, 3111, 2922, 1615, 1596, 1557, 1539, 1504 cm^{-1}. FAB-MS (*m*-NBA): *m*/*z* (%) = 1237 (3) $[M]^+$, 1116 (91) $[M – OBz]^+$, 1013 (32) $[M – L]^+$, 995 (100) $[M – 2\ OBz]^+$, 892 (60) $[M – OBz – L]^+$, 874 (41) $[M – 3\ OBz]^+$, 771 (73) $[M – 2\ OBz – L]^+$, 650 (76) $[M – 3\ OBz – L]^+$, 529 (35) $[M – 4\ OBz – L]^+$.

Compound $[Fe^{II}Fe^{III}_2O(L)_3(OBz)_3]$ (6): 5 (247 mg, 0.2 mmol), **1** (45 mg, 0.2 mmol), sodium iodide (50 mg, 0.33 mmol), and chloroform (50 mL). Yield: 129 mg (53%) dark-violet crystals from $CHCl_3$ by vapor diffusion of diethyl ether. For analytical data see ref.[1]

Compound $[Ni^{II}Fe^{III}_2O(L)_3(OAc)_3]$ (7): 3 (123 mg, 0.07 mmol), nickel acetate tetrahydrate (174 mg, 0.7 mmol), and chloroform (30 mL). Yield: 68 mg (47%) brown precipitate from $CHCl_3$/*n*-pentane (5 mL/30 mL; once repeated). For analytical data see ref.[1]

Compound $[Ni^{II}Fe^{III}_2O(L)_3(OBz)_3]$ (8): 7 (52 mg, 0.05 mmol), sodium benzoate (432 mg, 3 mmol), and chloroform (10 mL). Yield: 42 mg (68%) brown crystals from $CHCl_3$ by vapor diffusion of diethyl ether. For analytical data see ref.[1]

Compounds $[Fe^{III}_3O(L)_2(OBzBr)_4]OBzBr$ (9), $[Fe^{II}Fe^{III}_2O(L)_3(OBzBr)_3]$ (10): A suspension of iron(II) acetate (348 mg, 2 mmol) and sodium 4-bromobenzoate (6.70 g, 30 mmol) in chloroform (300 mL) was stirred under nitrogen for 2 h. After addition of HL (**1**) (534 mg, 2.4 mmol), the pale violet reaction mixture was stirred in air for a further 48 h. After removal of the excess metal salt by filtration through a pad of Celite, and concentration to dryness, the mixture of **9** and **10** (ratio of ca. 6:1) was purified by fractionizing crystallization from CH_2Cl_2/ether, yielding dark-violet crystals of **9**. Yield: 348 mg (32%); m.p. >250 °C (decomp.). IR ($CHBr_3$): $\tilde{\nu}$ = 3107, 2920, 1589, 1554, 1504, 1411 cm^{-1}. FAB-MS (*m*-NBA): *m*/*z* (%) = 1656 (2) $[M + Na]^+$, 1431 (80) $[M – OBzBr]^+$, 1408 (14) $[M – L]^+$, 1232 (100) $[M – 2\ OBzBr]^+$, 1207 (39) $[M – L – OBzBr]^+$, 1032 (51) $[M – 3\ OBzBr]^+$, 1008 (49) $[M – L – 2\ OBzBr]^+$, 831 (23) $[M – 4\ OBzBr]^+$, 808 (63) $[M – L – 3\ OBzBr]^+$, 752 (24) $[M – Fe – L – 3\ OBzBr]^+$. Complex **10** was characterized by FAB-MS and was not further purified: FAB-MS (*m*-NBA): *m*/*z* (%) = 1458 (65) $[M + H]^+$, 1256 (100) $[M – OBzBr]^+$, 1058 (31) $[M – OBzBr]^+$.

Acknowledgments

This work was supported by the Deutsche Forschungsgemeinschaft SA 276/26-1, SFB 583, GK 312, SPP 1137, the Bayerisches Langzeitprogramm "Neue Werkstoffe" and the Fonds der Chemischen Industrie. The generous allocation of X-ray facilities by Professor D. Sellmann, Institut für Anorganische Chemie, Universität Erlangen-Nürnberg, cyclovoltammetric measurements by Professor J. Daub and Dr. Ch. Trieflinger, Institut für Organische Chemie, Universität, Regensburg, and Mössbauer measurements by Dipl.-Phys. L. Böttger, Institut für Physik der Medizinischen Universität Lübeck, are also gratefully acknowledged.

[1] R. W. Saalfrank, A. Scheurer, U. Reimann, F. Hampel, C. Trieflinger, M. Büschel, J. Daub, A. X. Trautwein, V. Schünemann, V. Coropceanu, *Chem. Eur. J.*, submitted.

[2] R. W. Saalfrank, U. Reimann, M. Göritz, F. Hampel, A. Scheurer, F. W. Heinemann, M. Büschel, J. Daub, V. Schünemann, A. X. Trautwein, *Chem. Eur. J.* **2002**, *8*, 3614–3619.

[3] Fresh $Fe(OAc)_2$ (Supplier Aldrich 51,793-3; 99.995%); aged $Fe(OAc)_2$ (kept under nitrogen in a Schlenk tube for 6–9 months with occasional opening). We suspect that aging of $Fe(OAc)_2$ leads to the formation of oligonuclear iron species. This assumption is supported by the fact that reaction of ten-membered iron wheel $[Fe^{III}_{10}(OAc)_{10}(OMe)_{20}]$ with HL (**1**) yields a mixture of $[Fe^{II}Fe^{III}_2O(L)_3(OAc)_3]$ (**2**), and $[Fe^{III}_3O(L)_2(OAc)_4]_2O$ (**3**, main product). The Fe^{II} ions in **2** are generated by reduction of Fe^{III} by methanol. We generated $[Fe^{III}_{10}(OAc)_{10}(OMe)_{20}]$ in ≥80% yield simply by stirring $Fe(OAc)_2$ or $FeCl_2$ together with NaOAc in air at 20 °C in methanol for 10 h. The X-ray crystallographic data matched those reported in ref.[10]

[4] For further iron acetate complexes, see: a) C. T. Dziobkowski, J. T. Wrobleski, D. B. Brown, *Inorg. Chem.* **1981**, *20*, 671–678; b) C. J. Harding, R. K. Henderson, A. K. Powell, *Angew. Chem.* **1993**, *105*, 583–585, *Angew. Chem. Int. Ed.* **1993**, *32*, 570–572; c) C. A. Christmas, H.-L. Tsai, L. Pardi, J. M. Kesselman, P. K. Gantzel, R. K. Chadha, D. Gatteschi, D. F. Harvey, D. N. Hendrickson, *J. Am. Chem. Soc.* **1993**, *115*, 12483–12490; d) I. Shweky, L. E. Pence, G. C. Papaefthymiou, R. Sessoli, J. W. Yun, A. Bino, S. J. Lippard, *J. Am. Chem. Soc.* **1997**, *119*, 1037–1042; e) S. J. Lippard, *Angew. Chem.* **1988**, *100*, 353–371; *Angew. Chem. Int. Ed. Engl.* **1988**, *27*, 344–361.

[5] Crystal data for $[Fe^{III}_3O(L)_2(OAc)_4]Cl$ (**4**): $C_{24}H_{24}ClFe_3N_6O_{11}S_4{\cdot}3CHCl_3{\cdot}(C_2H_5)_2O$, M = 1335.96; crystal dimensions 0.30 × 0.10 × 0.10 mm; monoclinic, space group $C2/c$, a = 17.961(4) Å, b = 15.158(3) Å, c = 19.875(4) Å, β = 99.57(3)°, V = 5336(2) $Å^3$; Z = 4; $F(000)$ = 1828, $\rho_{calcd.}$ = 1.663 g/cm^3; Nonius KappaCCD diffractometer, Mo-K_α radiation (λ = 0.71073 Å); T = 173(2) K; graphite monochromator; θ range 2.30° < θ < 27.47°; section of the reciprocal lattice: $-23 \le h \le 23$, $-18 \le k \le 19$, $-25 \le l \le 25$; of 11363 measured reflections, 6097 were independent and 4434 with $I > 2\sigma(I)$; linear absorption coefficient 1.053 mm^{-1}. The structure was solved by direct methods using SHELXS-97 and refinement with all data (309 parameters) by full-matrix least squares on F^2 using SHELXL97; all non-hydrogen atoms were refined anisotropically; $R1$ = 0.0541 for $I > 2\sigma(I)$ and $wR2$ = 0.1651 (all data); largest peak (0.748 e $Å^{-3}$) and hole (–1.226 e $Å^{-3}$).[6,7]

[6] a) G. M. Sheldrick, C. Krüger, P. Goddard, *Crystallographic Computing 3*, Oxford University Press, Oxford **1985**, p. 175; b) G. M. Sheldrick, *SHELXL-97, Program for Crystal Structure Refinement*, University of Göttingen **1997**.

[7] CCDC-213507 (**4**), -250374 (**9**), and -213506 $[Fe^{III}_3O(L)_3(OBz)_3]I_3$[9] contain the supplementary crystallographic data for this paper. These data can be obtained free of charge from The Cambridge Crystallographic Data Centre via www.ccdc.cam.ac.uk/data_request/cif.

[8] Crystal data for $[Fe^{III}_3O(L)_2(OBzBr)_4]OBzBr$ (**9**): $C_{51}H_{32}Br_5Fe_3N_6O_{13}S_4{\cdot}2.5CH_2Cl_2$, M = 1844.48; crystal dimensions 0.25 × 0.20 × 0.20 mm; monoclinic, space group $P2_1/c$, a = 19.506(4) Å, b = 16.882(3) Å, c = 21.112(4) Å, β = 105.74(3)°, V = 6691(2) $Å^3$; Z = 4; $F(000)$= 3624, $\rho_{calcd.}$ = 1.831 g/cm^3; Nonius KappaCCD diffractometer, Mo-K_α radiation (λ = 0.71073 Å); T = 173(2) K; graphite monochromator; θ range 2.89° < θ < 25.05°; section of the reciprocal lattice: $-23 \le h \le 23$, $-18 \le k \le 20$, $-25 \le l \le 25$; of 21421 measured reflections, 11780 were independent and 8118 with $I > 2\sigma(I)$; linear absorption coefficient 4.015 mm^{-1}. The structure was solved by direct methods using SHELXS-97 and refinement with all data (842 parameters) by full-matrix least squares on F^2 using SHELXL97; all non-hydrogen atoms were refined anisotropically; $R1$ = 0.0983 for $I > 2\sigma(I)$ and $wR2$ = 0.2856 (all data); largest peak (2.954 e $Å^{-3}$) and hole (–1.966 e $Å^{-3}$).[6,7]

[9] When **5** was treated with a fortyfold excess of sodium iodide in the presence of air after workup some crystals of all-iron(III) complex $[Fe^{III}_3O(L)_3(OBz)_3]I_3$ were isolated.[7] Crystal data for $[Fe^{III}_3O(L)_3(OBz)_3]I_3$: $C_{45}H_{33}Fe_3I_3N_9O_{10}S_6{\cdot}3CHCl_3$, M = 1958.52; crystal dimensions 0.38 × 0.15 × 0.06 mm; triclinic, space group $P\bar{1}$, a = 14.2184(3) Å, b = 16.2989(3) Å, c = 16.6062(5) Å, α = 97.223(2)°, β = 106.855(2)°, γ = 110.318(2)°,

 © 2005 Wiley-VCH Verlag GmbH & Co. KGaA, Weinheim

V = 3342.2(2) Å^3; Z = 2; F(000)= 1906, $\rho_{calcd.}$ = 1.946 g/cm^3; Nonius KappaCCD diffractometer, Mo-K_α radiation (λ = 0.71073 Å); T = 100(2) K; graphite monochromator; θ range 3.31° < θ < 27.00°; section of the reciprocal lattice: –18 ≤ h ≤ 18, –20 ≤ k ≤ 20, –21 ≤ l ≤ 21; of 61686 measured reflections, 14561 were independent and 9683 with $I > 2\sigma(I)$; linear absorption coefficient 2.635 mm^{-1}. A numerical absorption correction has been performed[11] (T_{min} = 0.744, T_{max} = 0.916). The structure was solved by direct methods and refined with all data (822 parameters) by full-matrix least squares on F^2 using SHELXLTL NT 5.10.[12] With the exception of C301 (representing the minor component of a disordered $CHCl_3$ solvate molecule) all non-hydrogen atoms were refined anisotropically; $R1$ = 0.0574 for $I > 2\sigma(I)$ and $wR2$ = 0.1613 (all data); largest peak (2.653 e Å^{-3}) and hole (–2.052 e Å^{-3}).[6,7] All significant residual electron density maxima can be found in close proximity of either the I_3 anion positions or the disordered solvate molecule.

[10] C. Benelli, S. Parsons, G. A. Solan, R. E. P. Winpenny, *Angew. Chem.* **1996**, *108*, 1967–1970; *Angew. Chem. Int. Ed. Engl.* **1996**, *35*, 1825–1828.
[11] P. Coppens, *Crystallographic Computing*, Munksgaard, Copenhagen, **1970**, p. 255.
[12] *SHELXTL NT 5.10*, Bruker AXS, Inc., Madison WI, USA, **1998**.

Received: September 30, 2004

 © 2005 Wiley-VCH Verlag GmbH & Co. KGaA, Weinheim

New Tris(thioimidazolyl)borate Ligands and Some Zinc Complexes Thereof

Mohamed M. Ibrahim,[a] Mouhai Shu,[a] and Heinrich Vahrenkamp*[a]

Keywords: Alcohol ligands / Alkoxide ligands / S ligands / Tripodal ligands / Zinc

In order to improve the encapsulation of metal ions coordinated by tris(thioimidazolyl)borate ligands, four new such ligands with *o*-substituted phenyl substituents were synthesised as well as ones with *p*-tolyl and cyclohexyl substituents. In order to provide a basis for their bioinorganic zinc complex chemistry, they were converted to some zinc-halide, -carboxylate, -nitrate, -phenolate and -benzylate complexes. They form zinc-perchlorate complexes which are productive starting materials for the attachment of alcohols and alkoxides at zinc, thereby yielding new structural models for the zinc enzyme alcohol dehydrogenase.

(© Wiley-VCH Verlag GmbH & Co. KGaA, 69451 Weinheim, Germany, 2005)

Introduction

Among the zinc enzymes the alcohol dehydrogenases[1] and the thiolate alkylating enzymes[2] have an unusually (cysteine-)sulfur-rich ligand environment of the zinc ion. We[3,4] and others[5–9] have tried to model the structure and function of these enzymes by applying tripodal scorpionate[10] ligands bearing one to three sulfur donors. During these studies Parkin's[5,8,11,12] and our own research group[3,13] have found that the sulfur-rich environment of the tris(thioimidazolyl)borate ligands (Tti^R) enables the attachment of quite unusual and biologically relevant co-ligands X at the zinc ion in an S_3ZnX environment.

During these studies it also became evident that the substituted tris(thioimidazolyl)borates (Tti^R) have one disadvantage in comparison to the widely used tris(pyrazolyl)borates (Tp^R). While the R substituents at the 3-positions of the pyrazolylborates provide an ideal encapsulation of the metal ions bound to the three pyrazole nitrogens due to their orientation, the corresponding R substituents at the 1-nitrogens of the thioimidazolylborates are less efficient in this respect because they point away from the core of the ligands. As encapsulation of the metals is a key feature in the development of ligands for a viable bioinorganic model complex chemistry, there arose the necessity to use Tti^R ligands with sterically more demanding substituents R.

The Tti ligands, which should bear as much potential as the Tp ligands, were introduced by Reglinski in 1996.[14] Remarkably little metal complex chemistry has been done with them in the eight years since, either by Reglinski himself[15–20] or by other research groups.[3,5,8,11–16,21–25] So far only methyl,[14] *tert*-butyl,[3] benzyl,[22] phenyl,[5] *p*-tolyl,[22] mesityl[5] and *p*-cumenyl substituents[3] have been attached at the N^1 nitrogens of the thioimidazolyl moieties, of which only *tert*-butyl and mesityl can be considered as sterically demanding.

Having enjoyed the bioinorganic zinc chemistry of the Tp^R ligands for many years,[26] we trusted the zinc chemistry of the Tti^R ligands to be equally fertile. We therefore set out to lay a basis for it by obtaining Tti^R ligands with improved encapsulation abilities. In order to achieve this we chose *o*-substituted phenyl groups as the substituents R. We prepared two ligands with one *o*-substituent each (**L1**, **L2**), two with two *o*-substituents each (**L3**, **L4**), and we also de-

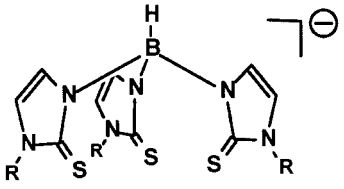

Tti^R

$K[Tti^R]$

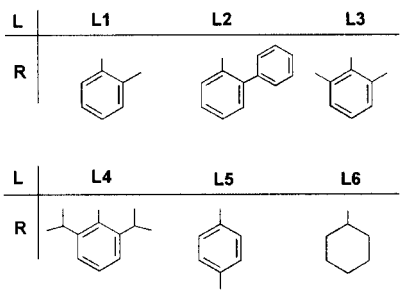

[a] Institut für Anorganische und Analytische Chemie der Universität Freiburg,
Albertstr. 21, 79104 Freiburg, Germany
Fax: +49-761-203-6001
E-mail: vahrenka@uni-freiburg.de

 © 2005 Wiley-VCH Verlag GmbH & Co. KGaA, Weinheim **DOI: 10.1002/ejic.200400994**

scribe a variation of the synthesis of *p*-substituted **L5**[22] and the synthesis of cyclohexyl-substituted **L6**. This paper reports the ligand syntheses, some simple zinc complexes, and some alcohol and alkoxide derivatives relevant to the zinc enzyme alcohol dehydrogenase.

Results and Discussion

Ligand Synthesis

While the preparation of tris(pyrazolyl)borates requires high-temperature reactions between KBH_4 and the pyrazoles in a melt, the thioimidazoles react with KBH_4 under milder conditions, typically in boiling toluene. This made the synthesis of ligands **L1**–**L6** an easy, high-yield process, the most time-consuming part of which is actually the two-step synthesis of the substituted thioimidazoles, whose overall yields rarely exceed 50%.

Except for **L2** (ca. 60%) the potassium salts of the ligands **L** were obtained in yields of around 90%. K[**L1**] and K[**L5**] were obtained analytically pure from the reaction solution, K[**L2**] needed a chromatographic purification, and the other K[**L**] complexes were crystallised from methanol. Their characteristic spectral features are the weak ν(BH) band at around 2500 cm^{-1} and a pair of doublets due to the two imidazole protons in the ^1H NMR spectra.

Complexes of Simple Anions

It was already known[3,5,11] that zinc in the sulfur-rich ligand environment of the tris(thioimidazolyl)borate ligands is complemented favourably by oxygen-containing coligands and by the halides. This was verified here for ligands **L1**, **L3** and **L5** in combination with zinc and simple anionic coligands. In order to obtain complexes **1**–**9** the potassium salts of **L** were either treated directly with $ZnCl_2$, ZnI_2, $Zn(NO_3)_2$ or $Zn(CH_3COO)_2$, or they were reacted first with zinc perchlorate and then with the deprotonated forms of thioacetic acid or *p*-nitrothiophenol. The latter was included with the anionic ligands due to its typical UV/Vis absorption, which we intend to exploit for kinetic studies of the alkylation of Zn–OR species in comparison to Zn–SR species.[8,27] Products **1**–**9** were isolated in very good yields as colourless (**1**–**5**) or yellow (**6**–**9**) powders. Except for **1**, **2** and **3** the characteristic ^1H NMR features of the anionic coligands complement the typical spectral characteristics (see above) of their ligands **L**.

L3•Zn-Cl	**L3**•Zn-I	**L3**•Zn-ONO_2
1	**2**	**3**
L1•Zn-$OCOCH_3$	**L3**•Zn-$OCOCH_3$	**L3**•Zn-$SCOCH_3$
4	**5**	**6**
L1•Zn-$OC_6H_4NO_2$	**L3**•Zn-$OC_6H_4NO_2$	**L5**•Zn-$OC_6H_4NO_2$
7	**8**	**9**

The structure determinations of **1**, **3**, **4**, **5** and **9** confirmed the identities of the ligands, the characteristic structural features of the **L**·Zn units and the coligand attachment. Figure 1 displays the complete molecule of **1** as an example; Table 1 lists the important bonding features. There is a quite uniform array of the four donors around the zinc ions. The attachment of the tripod ligands **L** nicely defines a tetrahedral geometry with remarkably constant bond lengths and angles. The coligands' donor atoms (Cl and O), however, are never positioned correctly on the trigonal axis of the complexes, as defined by the B–Zn line. Table 1 displays this in terms of the X–Zn···B angles. These deviate most from 180° in the case of the nitrate and acetate complexes **3**, **4** and **5**, thus reflecting the semi-bidentate nature of their coligands. As a consequence, the X–Zn–S angles in all complexes described in this paper show a considerable spread, typically between 100° and 120°.

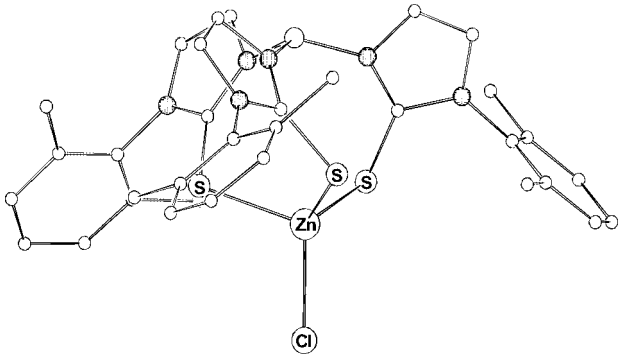

Figure 1. Molecular structure of **1**.

Table 1. Bond lengths [Å] and angles [°] around the zinc ions in complexes **1**, **3**, **4**, **5**, and **9**.

	X	Zn–X	Zn–S(av)	S–Zn–S(av)	X–Zn···B
1	Cl	2.252(2)	2.34(1)	108(2)	175
3	O	2.007(6)	2.33(1)	109(2)	171
4	O	2.005(11)	2.37(1)	107(1)	161
5	O	1.954(5)	2.34(2)	108(1)	172
9	O	1.926(5)	2.33(1)	106(3)	174

The voluminous nature of the tripod ligands **L** somewhat obscures their essential bonding characteristics. Therefore, two views of molecular fragments were chosen to make them visible. One of them is the view along the B···Zn axis (Figure 2), which shows the chiral, screw-like array of the three thioimidazolyl moieties between the boron and zinc atoms that is the most characteristic feature distinguishing the tris(thioimidazolyl)borates from the tris(pyrazolyl)borates. The other is the orientation of the external aromatic substituents (Figure 3). Following the trigonal symmetry of the **L**·Zn units, all three of them are always tilted in the same direction with respect to the thioimidazole rings. The amount of this tilting varies within each complex and between complexes. It places the "down" parts of the aromatic rings in the vicinity of the zinc-bound coligands, thereby providing the encapsulation of the Zn–X units, though in a much less efficient way than in related tris(pyrazolyl)borates. Yet, as Figure 3 shows, the best way to improve this encapsulation should be the attachment of *ortho*-substitu-

 © 2005 Wiley-VCH Verlag GmbH & Co. KGaA, Weinheim

ents at the aromatic rings, which, due to the tilting, are most likely to be located in the vicinity of the Zn–X units.

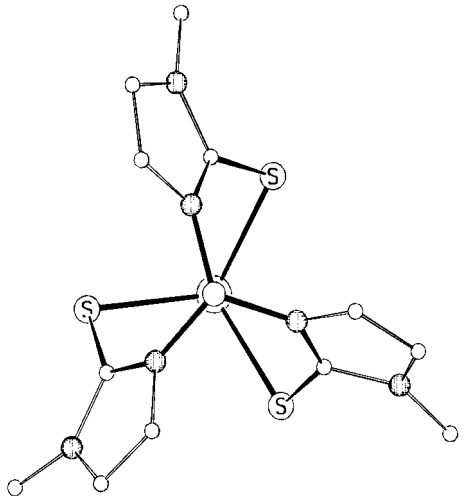

Figure 2. A view of complex **1** down the B···Zn line (aromatic substituents omitted for clarity).

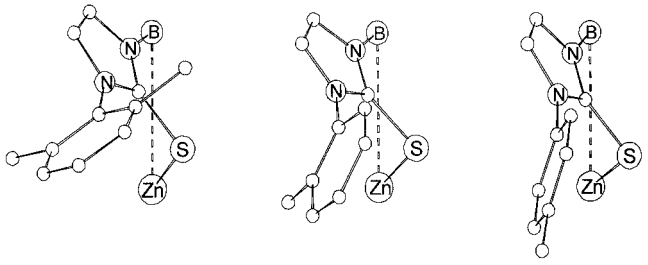

Figure 3. One substituted thioimidazolyl fragment each of complexes **1**, **4** and **21**, viewed perpendicular to the B···Zn line.

Perchlorate Complexes

Quite a number of the complexes described in this paper were prepared by combining a ligand **L** with zinc perchlorate first. This implies that in the intermediate species either perchlorate or the solvent used is coordinated to zinc. Probing this we realized that the **L**·Zn-perchlorate complexes are easily formed and that they can be used as precursors of **L**·Zn complexes with other unusual coligands X. The solvent of choice for this purpose is methanol, which obviously binds less well to zinc than perchlorate. Accordingly, complexes **10**–**14** were obtained from K[**L**] and $Zn(ClO_4)_2$ in methanol.

L1•Zn-$OClO_3$ **10** **L2**•Zn-$OClO_3$ **11** **L3**•Zn-$OClO_3$ **12**

L4•Zn-$OClO_3$ **13** **L6**•Zn-$OClO_3$ **14**

The characteristic feature of **10**–**14**, apart from the weak ν(BH) band, is the very strong perchlorate band in the infrared spectra in the region of 1090 cm^{-1}. The existence of a Zn–$OClO_3$ connection has already been proved by us by the structure determination of tris(*N*-*tert*-butylthioimidazolyl)boratozinc perchlorate.[3] The ease of isolation of **10**–**14** has made it clear now that these complexes are much less labile than originally assumed.

Alkoxide Complexes

In our previous studies of zinc complexes of tris(thioimidazolyl)borate ligands, which were aimed predominantly at modelling alcohol dehydrogenase,[3] alkoxide complexes had evaded us. We now found that they are accessible with the new ligands **L**. In trying to make mononuclear **L**·Zn–OR complexes we learnt that these are still inaccessible with aliphatic alkoxides or with benzylate, but the more electronegative *p*-nitrobenzylate and *p*-(trifluoromethyl)benzylate could be introduced as terminal ligands in complexes **15** and **16**. The procedure which led to them is the reverse of the procedure used for all other complexes: zinc perchlorate and the benzylate are combined first, and only after that is the tripod **L3** attached.

L3•Zn-$OCH_2C_6H_4NO_2$ **15** **L3**•Zn-$OCH_2C_6H_4CF_3$ **16**

The mononuclear nature of **15** and **16** is evident from their solubility in non-polar solvents and from their ^1H NMR spectra, which correspond for the **L3**·Zn unit to those of the other mononuclear **L3**·Zn complexes. In addition the ^1H and ^{19}F NMR spectroscopic data confirm the presence of the benzylate ligands. Unfortunately, complexes **15** and **16** did not yield crystals suitable for a structure determination.

Aliphatic alkoxides could be incorporated using the standard procedure, i.e. first making the intermediate **L**·Zn perchlorate complex and then treating it with the alkoxide. Methoxide, ethoxide and trifluoroethoxide could be combined with **L3**·Zn, but the structure determinations showed that the resulting complexes **17**–**19** are dinuclear and contain bridging alkoxide ligands. The ionic nature of **17**–**19** is reflected by their solubility only in polar solvents. Their ^1H NMR spectra show small but significant shifts compared to those of the mononuclear **L3**·Zn complexes.

[**L3**•Zn-OR-Zn**L3**]ClO_4

17: R = CH_3, **18**: R = C_2H_5, **19**: R = CH_2CF_3

Figure 4 shows the structure of **17** as an example; that of **18** is very similar. In both **17** and **18** the alkoxide bridge is nicely symmetrical with two virtually identical Zn–O distances and Zn–O–C angles each (see Table 2). The Zn–O bond lengths (near 1.95 Å) resemble those for the **L**·Zn nitrophenolates (see above and ref.[3]). We could not find a structurally characterised dizinc complex with a single unsupported alkoxide bridge in the literature, but there are some related complexes with single hydroxide bridges.[28–32] Their Zn–O bond lengths (1.87–2.00 Å) and Zn–O–Zn angles (132–141°) closely resemble those of **17** and **18**. With

 © 2005 Wiley-VCH Verlag GmbH & Co. KGaA, Weinheim

respect to the **L3**·Zn units, specifically the displacement of the bridging oxygen off the B···Zn line, complexes **17** and **18** are completely analogous to the other **L**·Zn–X complexes reported here.

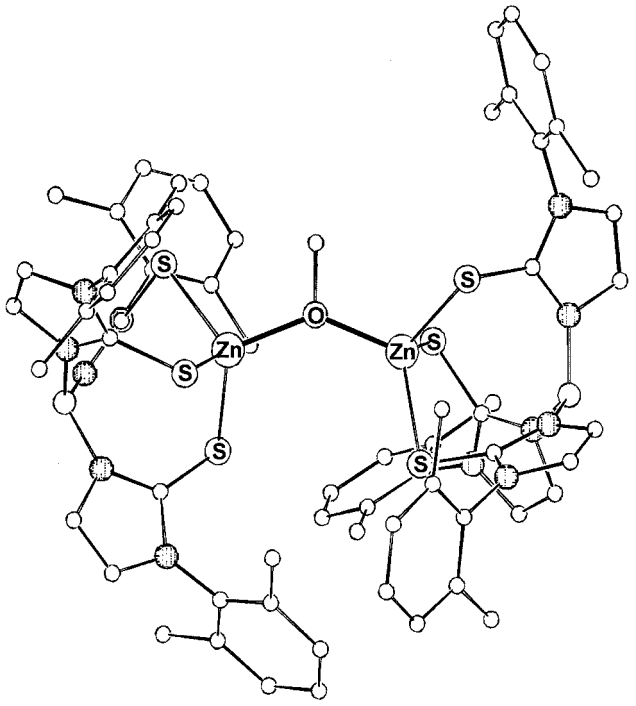

Figure 4. Structure of the dinuclear cation of **17**. See Table 2 for details.

Table 2. Relevant distances [Å] and angles [°] araound the zinc ions in the alkoxide-bridged complexes.

	17	**18**
Zn–O	1.957(5)/1.941(5)	1.959(3)/1.967(3)
Zn···Zn	3.63	3.64
Zn–S(av)	2.35 ± 2	2.36 ± 2
Zn–O–Zn	137.0(3)	136.0(2)
S–Zn–S(av)	108.5 ± 1	107.5 ± 1
O–Zn–S	105–118	107–118
Zn–O–C	109.8(7)/110.2(7)	110.7(3)/111.7(3)

Complexes with Alcohol and Aldehyde Ligands

We have already shown[3] that the electron-rich nature of the **L**·Zn unit and its favourable combination with oxygen donors allows the attachment of ethanol as a coligand. We could now show that with the ligands **L** used in this paper even the weaker oxygen donor 2-propanol can be attached. The 2-propanol complexes **20** and **21** crystallised when **L3** or **L5** were combined with zinc perchlorate in 2-propanol.

[**L3**•Zn(*i*-C_3H_7OH)]ClO_4 **20**

[**L5**•Zn(*i*-C_3H_7OH)]ClO_4 **21**

Complex **21** was chosen for a structure determination (see Figure 5). There are two formula units of **21** in the asymmetric unit. In one of them the 2-propanol ligand is linked through a hydrogen bond (2.67 Å) to another 2-propanol molecule, and in the other it is linked by a hydrogen bond (2.84 Å) to a perchlorate anion. This attachment of an external hydrogen-bond acceptor seems to be a common feature of all zinc–alcohol complexes with tripodal ligands.[3–5] Likewise, the Zn–O bond lengths in both complex units of **21** (av. 1.98 Å) lie within the small range of such bond lengths observed before (1.97–2.01 Å),[3–5] and they are nearly identical to the one in the pentafluorobenzyl alcohol adduct of alcohol dehydrogenase (ADH).[33] This adds complex **21** to the list of structural models of ADH.

The idea of modelling ADH was also the reason for attaching the two functional phenols salicylic alcohol and salicylic aldehyde as phenolates to the **L3**·Zn unit. The *o*-hydroxymethylphenolate complex **22** and the *o*-formylphenolate complex **23** were obtained by treating the deprotonated phenols first with zinc perchlorate and then with K[**L3**]. It was hoped that the chelate effect would enable a coordination of the alcoholic function in **22** and the aldehydic function in **23** to zinc, thereby generating a pair of complexes that mimic the binding of substrate and product in the active centre of ADH, as we had achieved before with $Zn(SR)_2$ systems.[34]

L3•Zn-OC_6H_4-*o*-CH_2OH **22**

L3•Zn-OC_6H_4-*o*-CHO **23**

While the spectroscopic data of **22** are inconclusive, those of **23** indicate coordination of the aldehyde oxygen to zinc: both the ν(CO) IR band (1671 → 1659 cm^{-1}) and the ^1H NMR formyl signal (δ = 9.99 → 11.03 ppm) undergo shifts in the expected direction relative to those of formylphenolate. The structure determination of **23**, however, disproved this assumption. As Figure 6 shows, the formyl oxygen is

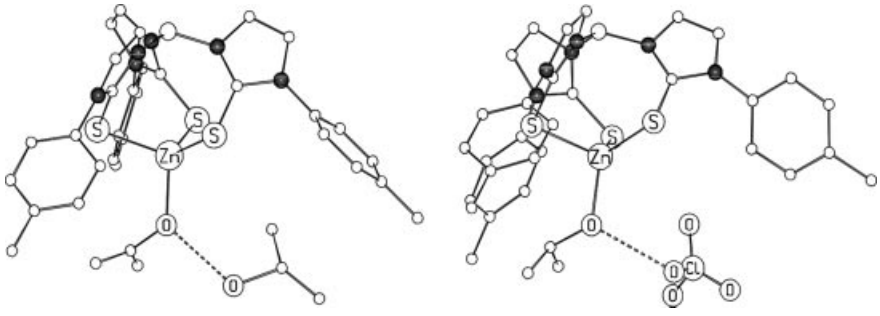

Figure 5. The two crystallographically independent complex cations of **21**. Left (linked to a molecule of 2-propanol): Zn–O 1.979(4), Zn–S 2.307(2), 2.317(2) and 2.332(2) Å. Right (linked to a perchlorate anion): Zn–O 1.984(4), Zn–S 2.309(2), 2.315(2) and 2.332(2) Å.

 © 2005 Wiley-VCH Verlag GmbH & Co. KGaA, Weinheim

oriented away from the zinc ion, thus making **23** a normal phenolate complex comparable to **7**–**9**. Based on this observation, and on the similar non-coordination of the hydroxymethyl group in **24** (see below), it must be concluded that the hydroxymethyl function in **22** is also not coordinated to zinc.

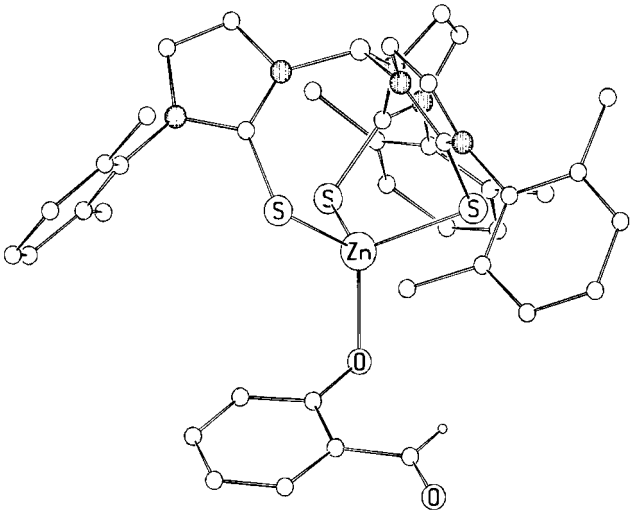

Figure 6. Molecular structure of complex **23**. Zn–O 1.937(2), Zn–S 2.338(1), 2.363(1), and 2.319(1) Å.

The same reasoning as above, together with the knowledge that the **L**·Zn units, unlike the TpZn units, easily bind uncharged nitrogen ligands,[3,5,12,13] led us to the application of 1-methyl-2-hydroxymethylimidazole. It was hoped that the coordination of both its 3-nitrogen and the hydroxymethyl oxygen to zinc would be favoured by the formation of a five-membered chelate ring. The desired complex **24** was formed by treating the intermediate **L5**·Zn perchlorate with the imidazole.

[**L5**•Zn(1-methyl-2-hydroxymethylimidazole)]ClO_4

24

The structure determination of **24** again eliminated the assumption of Zn–OH coordination. Just as observed for $Zn(SR)_2$ complexes of 1-methyl-2-hydroxymethylimidazole and 1-methyl-2-formylimidazole,[34] only the imidazole nitrogen is coordinated to zinc. As Figure 7 shows, complex **24** is essentially an imidazole adduct of [**L5**·Zn]$^+$ with a nicely symmetrical arrangement of the NS_3donor set.

Conclusions

This paper has about doubled the number of available tris(thioimidazolyl)borate ligands and underlined their suitability for a biomimetic zinc complex chemistry. Although they still lack the major advantage of the tris(pyrazolyl)borates, i.e. the ease of encapsulating the metal ion by properly placed substituents, an approach seems to be emerging to achieve this. As the structural dispositions exemplified by Figures 2 and 3 show, voluminous substituents at the *ortho*-positions of phenyl rings at the thioimidazole's N3 nitro-

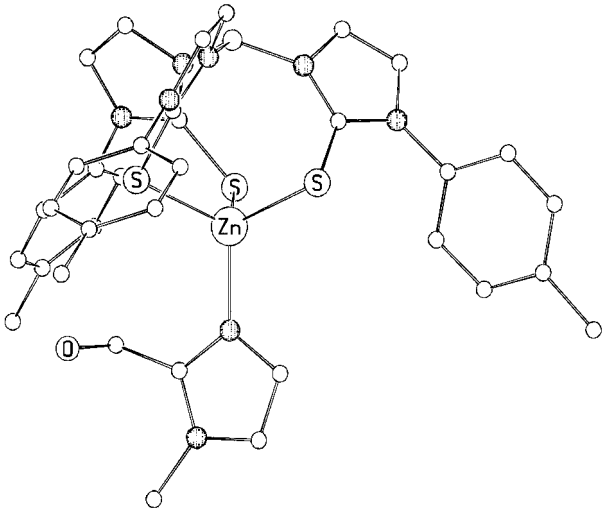

Figure 7. Structure of the complex cation of **24**. Zn–N 1.991(4), Zn–S 2.315(2), 2.325(2), and 2.333(2) Å. S–Zn–S 105.6–109.8(1)°, S–Zn–N 108.0–113.1(1)°.

gens should be oriented towards the neighbourhood of the metal ions and thereby create the desired cavity for them.

We have already observed[3] that the very soft environment of the zinc ion provided by these S_3 tripods results in a reluctance of zinc to bind a fourth soft donor, for instance an alkanethiolate. Conversely, hard oxygen donors are bound very well, as exemplified here by acetate, nitrate and *p*-nitrophenolate. Particularly noteworthy in this respect is the ease of formation of perchlorate complexes, which promise to be good starting materials for further labile **L**·Zn complexes of ligands **L1**–**L6**.

The latter was exemplified by the formation of the 2-propanol complexes **20** and **21**. Thus, 2-propanol is preferred over perchlorate as a donor here. In contrast, methanol is not, as all the perchlorate complexes described here were prepared in methanol. There seems to be a delicate balance of stabilities which is controlled by the substituents on the thioimidazole rings: with R = mesityl Parkin isolated a methanol complex,[5] with R = *tert*-butyl we obtained an ethanol complex,[3] and now with R = 2,6-xylyl and *p*-tolyl the 2-propanol complexes were obtained. We consider it likely that equilibrium mixtures of alcohol and perchlorate complexes exist in solution.

With respect to the modelling of alcohol dehydrogenase some new insights are provided by this work too. One of them is the accessibility of the alcohol complexes. Another is the accessibility of alkoxide complexes. Although the latter could only be obtained with a singly bridging alkoxide for methanol and ethanol, they resulted as monomers with terminal alkoxide ligands for *para*-substituted benzyl alcohol. As before[3] our attempts failed to induce alcohol or aldehyde coordination by the chelate effect: the hydroxymethyl and formyl side-arms of the coligands in complexes **22**–**24** remain uncoordinated. Nevertheless, complexes **20/21** and **15/16** represent the first chemical reproduction of the enzymatic situation where first the alcohol and then the alkoxide are bound to the same **L**·Zn unit.

 © 2005 Wiley-VCH Verlag GmbH & Co. KGaA, Weinheim

Experimental Section

For general working and measuring procedures, see ref.[35] All procedures for the ligand synthesis were performed under an inert gas. The isolation procedures described below yielded the new complexes spectroscopically pure. Samples for elemental analyses were recrystallised from methanol and/or dichloromethane. All *N*-substituted mercaptoimidazoles were prepared from bromoacetaldehyde diethylacetal, the amine RNH_2 and HSCN according to the established procedure.[36,37] They were characterised by ^{1}H NMR spectroscopy in $CDCl_3$ as follows:

R = *o*-tolyl: δ = 2.21 (s, 3 H, Me), 6.72 (d, *J* = 2.3 Hz, 1 H, Im), 6.84 (d, *J* = 2.3 Hz, 1 H, Im), 7.26–7.44 (m, 4 H, Ph), 10.94 (br. s, 1 H, NH) ppm.

R = *o*-biphenylyl: δ = 6.40 (d, *J* = 2.1 Hz, 1 H, Im), 6.62 (d, *J* = 2.1 Hz, 1 H, Im), 7.29–7.43 (m, 4 H, Ph), 7.45–7.65 (m, 5 H, Ar), 12.15 (s, 1 H, NH) ppm.

R = 2,6-xylyl: δ = 2.12 (s, 6 H, Me), 6.72 (d, *J* = 2.2 Hz, 1 H, Im), 6.98 (d, *J* = 2.2 Hz, 1 H, Im), 7.20 [d, *J* = 6.4 Hz, 2 H, Ph(3,5)], 7.29 [t, *J* = 5.6 Hz,, 1 H, Ph(4)], 12.34 (s, 1 H, NH) ppm.

R = 2,6-di(isopropyl)phenyl: δ = 1.12 (d, *J* = 6.9 Hz, 6 H, Me), 1.30 (d, *J* = 6.9 Hz, 6 H, Me), 2.61 (m, *J* = 6.7 Hz, 2 H, CH), 6.64 (d, *J* = 2.2 Hz, 1 H, Im), 6.85 (d, *J* = 2.2 Hz, 1 H, Im), 7.28 [d, *J* = 7.8 Hz, 2 H, Ph(3,5)], 7.43 [t, *J* = 7.3 Hz, 1 H, Ph(4)], 12.20 (s, 1 H, NH) ppm.

R = *p*-tolyl: 2.41 (s, 3 H, Me), 6.80 (d, *J* = 1.6 Hz, 1 H, Im), 6.84 (d, *J* = 1.6 Hz, 1 H, Im), 7.28 (m, 2 H, Ph), 7.45 (m, 2 H, Ph) ppm.

R = cyclohexyl: δ = 1.17–1.56 [p, *J* = 9.8 Hz, 4 H, CH_2(3,5-cyclohexyl)], 1.73–1.85 [q, *J* = 10.8 Hz, 4 H, CH_2(2,6-cyclohexyl)], 1.91 [m, 2 H, CH_2(4-cyclohexyl)], 4.66 (m, *J* = 4.00 Hz, 1 H, CH), 6.71 (d, *J* = 2.3 Hz, 1 H, Im), 6.73 (d, *J* = 2.3 Hz, 1 H, Im), 10.75 (s, 1 H, NH) ppm.

Ligand Synthesis. General Procedure: The *N*-substituted thioimidazole and KBH_4 were ground very finely. Toluene (100 mL) was added and the mixture refluxed for one week. After cooling to room temperature the precipitate was filtered off, washed with toluene and dried in vacuo.

L1: From 11.4 g (60.0 mmol) of *N*-(*o*-tolyl)thioimidazole and 1.08 g (20.0 mmol) of KBH_4. The precipitate was analytically pure. Yield 11.5 g (93%) of **L1** as a colourless powder, m.p. 200 °C (dec.). $C_{30}H_{28}BKN_6S_3$ (618.70): calcd. C 58.24, H 4.56, N 13.58, S 15.55; found C 59.10, H 5.08, N 13.87, S 15.80. ^{1}H NMR ($CDCl_3$): δ = 2.10 (s, 9 H, Me), 6.47 (d, *J* = 2.2 Hz, 3 H, Im), 6.70 (d, *J* = 2.2 Hz, 3 H, Im), 7.29 (m, 12 H, Ph) ppm. IR (KBr): $\tilde{\nu}$ = 2520 w (BH) cm^{-1}.

L2: From 4.92 g (19.50 mmol) of *N*-(*o*-biphenylyl)thioimidazole and 0.35 g (6.50 mmol) of KBH_4. Purification of the ligand required column chromatography over silica gel with methanol/dichloromethane (1:10). Yield 3.26 g (62%) of **L2** as a colourless powder, m.p. 215 °C (dec.). $C_{45}H_{34}BKN_6S_3$ (804.91): calcd. C 67.15, H 4.26, N 10.44, S 11.95; found C 64.73, H 4.49, N 10.02, S 11.73. ^{1}H NMR ($CDCl_3$): δ = 5.77 (d, *J* = 2.0 Hz, 3 H, Im), 6.37 (d, *J* = 2.0 Hz, 3 H, Im), 7.09–7.20 (m, 12 H, Ph), 7.31–7.46 (m, 15 H, Ar) ppm. IR (KBr): $\tilde{\nu}$ = 2482 w (BH) cm^{-1}.

L3: From 4.80 g (23.5 mmol) of *N*-(2,6-xylyl)thioimidazole and 0.42 g (7.8 mmol) of KBH_4. Recrystallisation from methanol yielded 4.57 g (88%) of **L3** as a colourless powder, m.p. 220 °C (dec.). $C_{33}H_{34}BKN_6S_3{\cdot}H_2O$ (660.78 + 18.01): calcd. C 58.39, H 5.35, N 12.38, S 14.17; found C 57.87, H 5.38, N 12.25, S 14.00. ^{1}H NMR ($CDCl_3$): δ = 2.08 (s, 18 H, Me), 6.59 (d, *J* = 2.2 Hz, 3 H, Im), 6.63 (d, *J* = 2.2 Hz, 3 H, Im), 7.15 [d, *J* = 7.4 Hz, 6 H, Ph(3,5)], 7.26 [t, *J* = 6.3 Hz,, 3 H, Ph(4)] ppm. IR (KBr): $\tilde{\nu}$ = 2555 w (BH) cm^{-1}.

L4: From 8.38 g (32.2 mmol) of *N*-(2,6-diisopropylphenyl)thioimidazole and 0.58 g (10.7 mmol) of KBH_4. Recrystallisation from methanol yielded 7.45 g (84%) of **L4** as a colourless powder, m.p. 255 °C (dec.). $C_{45}H_{58}BKN_6S_3$ (829.10): calcd. C 65.19, H 7.05, N 10.14, S 11.60; found C 65.22, H 7.41, N 9.46, S 10.81. ^{1}H NMR ($CDCl_3$): δ = 1.12 (d, *J* = 6.8 Hz, 18 H, Me), 1.30 (d, *J* = 6.8 Hz, 18 H, Me), 2.58 (m, *J* = 6.7 Hz, 6 H, CH), 6.64 (d, *J* = 2.29 Hz, 3 H, Im), 6.85 (d, *J* = 2.3 Hz, 3 H, Im), 7.28 [d, *J* = 7.8 Hz, 6 H, Ph(3,5)], 7.46 [m, 3 H, Ph(4)] ppm. IR (KBr): $\tilde{\nu}$ = 2533 w (BH) cm^{-1}.

L5: From 9.12 g (0.48 mmol) of *N*-(*p*-tolyl)thioimidazole and 0.86 g (0.16 mmol) of KBH_4. The precipitate was analytically pure. Yield 8.61 g (87%) of **L5** as a colourless powder, m.p. 215 °C (dec.). $C_{30}H_{28}BKN_6S_3$ (618.70): calcd. C 58.24, H 4.56, N 13.58, S 15.55; found C 57.55, H 4.80, N 13.57, S 15.37. ^{1}H NMR (CD_3OD): δ = 2.38 (s, 9 H, Me), 6.70 (d, *J* = 2.2 Hz, 3 H, Im), 6.98 (d, *J* = 2.2 Hz, 3 H, Im), 7.26 (d, *J* = 8.2 Hz, 6 H, Ph), 7.45 (d, *J* = 8.2 Hz, 6 H, Ph) ppm. IR (KBr): $\tilde{\nu}$ = 2495 w (BH) cm^{-1}.

L6: From 7.25 g (40.0 mmol) of *N*-cyclohexylthioimidazole and 0.72 g (13.3 mmol) of KBH_4. Recrystallisation from methanol yielded 7.15 g (91%) of **L6** as a colourless powder, m.p. 220 °C (dec.). $C_{27}H_{37}BKN_6S_3{\cdot}2H_2O$ (591.74 + 36.03): calcd. C 51.65, H 6.58, N 13.39, S 15.32; found C 51.74, H 6.98, N 13.35, S 15.39. ^{1}H NMR (CD_3OD): δ = δ = 1.27–1.49 [p, *J* = 12.3, 12 H, CH_2(3,5-cyclohexyl)], 1.49–1.78 [q, *J* = 5.3, 12 H, CH_2(2,6-cyclohexyl)], 1.86 [m, 6 H, CH_2(4-cyclohexyl)], 4.64 (m, *J* = 3.5 Hz, 3 H, CH-cyclohexyl), 6.31 (d, *J* = 2.2 Hz, 3 H, Im), 6.79 (d, *J* = 2.2 Hz, 3 H, Im) ppm. IR (KBr): $\tilde{\nu}$ = 2514 w (BH) cm^{-1}.

Simple Zinc Complexes

1: A solution of 264 mg (0.40 mmol) of **L3** in 10 mL of absolute methanol was added dropwise with stirring to a solution of 55 mg (0.40 mmol) of anhydrous $ZnCl_2$ in 10 mL of absolute methanol. After stirring for 4 h the volume of the solution was reduced to 10 mL in vacuo. The precipitate was filtered off and the filtrate evaporated to dryness. The residue was taken up in 10 mL of dichloromethane, filtered and the solvents evaporated to dryness again, to give 276 mg (96%) of **1** as a colourless powder, m.p. 265 °C (dec.). $C_{33}H_{34}BClN_6S_3Zn$ (722.52): calcd. C 54.86, H 4.74, N 11.63, S 13.31, Zn 9.05; found C 54.07, H 4.97, N 11.29, S 12.89, Zn 8.76. ^{1}H NMR ($CDCl_3$): δ = 1.99 (s, 9 H, Me), 2.10 (s, 9 H, Me), 6.83 (d, *J* = 2.0 Hz, 3 H, Im), 7.08 (d, *J* = 2.0 Hz, 3 H, Im), 7.11 [d, *J* = 4.6 Hz, 6 H, Ph(3,5)], 7.26 [t, *J* = 3.8 Hz, 3 H, Ph(4)] ppm. IR (KBr): $\tilde{\nu}$ = 2438 w (BH) cm^{-1}.

2: Like **1** from 200 mg (0.30 mmol) of **L3** and 97 mg (0.30 mmol) of ZnI_2. Yield 232 mg (94%) of **2** as a colourless powder, m.p. 300 °C (dec.). $C_{33}H_{34}BIN_6S_3Zn$ (813.97): calcd. C 48.69, H 4.21, N 10.32, S 11.82, Zn 8.03; found C 47.77, H, 4.27, N 10.09, S 11.64, Zn 7.91. ^{1}H NMR ($CDCl_3$): δ = 1.99 (s, 9 H, Me), 2.08 (s, 9 H, Me), 6.84 (d, *J* = 2.1 Hz, 3 H, Im), 7.14 (d, *J* = 2.1 Hz, 3 H, Im), 7.16 [d, *J* = 7.6 Hz, 6 H, Ph(3,5)], 7.25 [t, *J* = 7.5 Hz, 3 H, Ph(4)] ppm. IR (KBr): = $\tilde{\nu}$ = 2437 w (BH) cm^{-1}.

3: Like **1** from 200 mg (0.30 mmol) of **L3** and 80 mg (0.30 mmol) of $Zn(NO_3)_2{\cdot}4H_2O$. Yield 194 mg (85%) of **3** as a colourless powder, m.p. 235 °C (dec.). $C_{33}H_{34}BN_7O_3S_3Zn$ (749.08): calcd. C 52.91, H 4.57, N 13.09, S 12.84, Zn 8.72; found C 52.53, H 4.70, N 12.96, S 12.63, Zn 8.58. ^{1}H NMR ($CDCl_3$): δ = 1.95 (s, 9 H, Me), 2.17 (s, 9 H, Me), 6.86 (d, *J* = 2.1 Hz, 3 H, Im), 7.09 (d, *J* = 2.1 Hz, 3

 © 2005 Wiley-VCH Verlag GmbH & Co. KGaA, Weinheim

H, Im), 7.14 [d, J = 7.2 Hz, 6 H, Ph(3,5)], 7.25 [t, J = 7.4 Hz, 3 H, Ph(4)] ppm. IR (KBr): $\tilde{\nu}$ = 2426 w (BH) cm^{-1}.

4: Like **1** from 206 mg (0.33 mmol) of **L1** and 62 mg (0.34 mmol) of $Zn(CH_3COO)_2{\cdot}2H_2O$. Yield 156 mg (67%) of **4** as a colourless crystals, m.p. 265 °C (dec.). $C_{32}H_{31}BN_6O_2S_3Zn$ (704.03): calcd. C 54.59, H 4.4, N 11.94, S 13.66, Zn 9.29; found C 54.48, H 4.34, N 12.00, S 13.59, Zn 9.14. ^1H NMR ($CDCl_3$): δ = 1.76 [s, 3 H, Me(acetate)], 2.1 (s, 9 H, Me), 6.96 (d, J = 2.0 Hz, 3 H, Im), 7.16 (d, J = 2.0 Hz, 3 H, Im), 7.28 (m, 12 H, Ph) ppm. IR (KBr): $\tilde{\nu}$ = 2412 w (BH) cm^{-1}.

5: Like **1** from 264 mg (0.40 mmol) of **L3** and 88 mg (0.40 mmol) of $Zn(CH_3COO)_2{\cdot}2H_2O$. Yield 250 mg (84%) of **4** as a colourless powder, m.p. 235 °C (dec.). $C_{35}H_{37}BN_6O_2S_3Zn$ (746.12): calcd. C 56.34, H 5.00, N 11.27, S 12.89, Zn 8.76; found C 55.40, H 5.30, N 11.85, S 11.85, Zn 8.73. ^1H NMR ($CDCl_3$): δ = 1.82 [s, 3 H, Me(acetate)], 1.99 (s, 9 H, Me), 2.17 (s, 9 H, Me), 6.82 (d, J = 2.2 Hz, 3 H, Im), 7.11 (d, J = 2.2 Hz, 3 H, Im), 7.17 [d, J = 7.6 Hz, 6 H, Ph(3,5)], 7.22 [t, J = 7.4 Hz, 3 H, Ph(4)] ppm. IR (KBr): $\tilde{\nu}$ = 2412 w (BH), 1598 s ($OCOCH_3$) cm^{-1}.

6: A solution of 200 mg (0.30 mmol) of **L3** in 10 mL of methanol was added dropwise with stirring to a solution of 112 mg (0.30 mmol) of $Zn(ClO_4)_2{\cdot}6H_2O$ in 10 mL of methanol. After stirring for 2 h the resulting $KClO_4$ was filtered off. In a separate flask a solution of 33 mg (0.30 mmol) of CH_3COSH was deprotonated with 0.30 mmol of a 0.5 M solution of sodium methoxide in methanol. The two solutions were combined and stirred for 15 h. Then, all volatiles were removed in vacuo, the residue taken up in 15 mL of dichloromethane and filtered again. The filtrate was evaporated to dryness to give 161 mg (70%) of **6** as a yellow powder, m.p. 225 °C (dec.). $C_{35}H_{37}BN_6OS_4Zn$ (762.19): calcd. C 55.19, H 4.89, N 11.03, S 16.83, Zn 8.58; found C 54.76, H 4.96, N 10.87, S 15.72, Zn 8.46. ^1H NMR ($CDCl_3$): δ = 1.75 [s, 3 H, Me(thioacetate)], 1.92 (s, 9 H, Me), 2.04 (s, 9 H, Me), 6.74 (d, J = 2.1 Hz, 3 H, Im), 7.02 (d, J = 2.1 Hz, 3 H, Im), 7.03 [d, J = 7.6 Hz, 6 H, Ph(3,5)], 7.18 [t, J = 7.4 Hz, 3 H, Ph(4)] ppm. IR (KBr): $\tilde{\nu}$ = 2430 w (BH) cm^{-1}.

7: Like **6** from 200 mg (0.32 mmol) of **L1** and 45 mg (0.32 mmol) of *p*-nitrophenol. Yield 197 mg (78%) of **7** as a yellow powder, m.p. 225 °C (dec.). $C_{36}H_{32}BN_7O_3S_3Zn$ (783.09): calcd. C 55.22, H 4.12, N 12.52, S 12.88, Zn 8.35; found C 54.92, H 4.11, N 12.47, S 12.59, Zn 8.56. ^1H NMR ($CDCl_3$): δ = 2.11 (s, 9 H, Me), 6.44 [d, J = 9.1 Hz, 2 H, nitro(2,6)], 6.97 (d, J = 2.2 Hz, 3 H, Im), 7.16 (d, J = 2.2 Hz, 3 H, Im), 7.29–7.42 (m, 12 H, Ph), 7.81 [d, J = 9.1 Hz, 2 H, nitro(3,5)] ppm. IR (KBr): $\tilde{\nu}$ = 2442 w (BH).

8: Like **6** from 213 mg (0.32 mmol) of **L3** and 45 mg (0.32 mmol) of *p*-nitrophenol. Yield 236 mg (89%) of **8** as a yellow powder, m.p. 200 °C (dec.). $C_{39}H_{38}BN_7O_3S_3Zn$ (825.17): calcd. C 56.77, H 4.64, N 11.88, S 11.66, Zn 7.92; found C 55.41, H 4.65, N 12.68, S 11.38, Zn 7.74. ^1H NMR ($CDCl_3$): δ = 2.02 (s, 18 H, Me), 6.51 [d, J = 8.9 Hz, 2 H, nitro(2,6)], 6.89 (d, J = 2.2 Hz, 3 H, Im), 7.13 [d, J = 7.2 Hz, 6 H, Ph(3,5)], 7.17 (d, J = 2.2 Hz, 3 H, Im), 7.27 [t, J = 7.4 Hz, 3 H, Ph(4)], 7.83 [d, J = 8.9 Hz, 2 H, nitro(3,5)] ppm. IR (KBr): $\tilde{\nu}$ = 2440 w (BH).

9: Like **6** from 206 mg (0.38 mmol) of **L5** and 54 mg (0.38 mmol) of *p*-nitrophenol. Yield 193 mg (73%) of **9** as a yellow powder, m.p. 205 °C (dec.). $C_{36}H_{34}BN_7O_3S_3Zn$ (785.11): calcd. C 55.07, H 4.36, N 12.49, S 12.25, Zn 8.33; found C 54.84, H 4.27, N 12.59, S 11.83, Zn 8.22. ^1H NMR ($CDCl_3$): δ = 2.40 (s, 9 H, Me), 6.36 [d, J = 9.3 Hz, 2 H, nitro(2,6)], 7.04 (d, J = 2.2 Hz, 3 H, Im), 7.11 (d, J = 2.2 Hz, 3 H, Im), 7.22 (s, 12 H, Ph), 7.66 [d, J = 9.3 Hz, 2 H, nitro(3,5)] ppm. IR (KBr): $\tilde{\nu}$ = 2345 w (BH) cm^{-1}.

Perchlorate Complexes

10: A solution of 45 mg (0.07 mmol) of **L1** in 5 mL of methanol was slowly added dropwise with stirring into a solution of 27 mg (0.07 mmol) of $Zn(ClO_4)_2{\cdot}6H_2O$ in 5 mL of methanol. After stirring for 2 h the solvent was removed in vacuo. The residue was picked up in 10 mL of dichloromethane and filtered. Evaporation to dryness gave 44 mg (81%) of **10** as a colourless powder, m.p. 220 °C (dec.). $C_{30}H_{28}BClN_6O_4S_3Zn$ (744.44): calcd. C 48.40, H 3.79, N 11.29, S 12.92, Zn 8.78; found C 48.42, H 4.12, N 10.96, S 12.48, Zn 8.48. ^1H NMR ($CDCl_3$): δ = 2.13 (s, 9 H, Me), 6.96 (br, 3 H, Im), 7.16 (br, 3 H, Im), 7.22–7.37 (m, 12 H, Ph) ppm. IR (KBr): $\tilde{\nu}$ = 2448 w (BH), 1105vs. (ClO_4) cm^{-1}.

11: Like **10** from 310 mg (0.38 mmol) of **L2** and 143 mg (0.38 mmol) of $Zn(ClO_4)_2{\cdot}6H_2O$. Yield 245 mg (68%) of **11** as a colourless powder, m.p. 230 °C (dec.). $C_{45}H_{34}BClN_6O_4S_3Zn$ (930.65): calcd. C 58.08, H 3.68, N 9.03, S 10.34, Zn 7.03; found C 56.67, H 4.07, N 8.74, S 10.16, Zn 6.91. ^1H NMR ($CDCl_3$): δ = 6.63 (br, 3 H, Im), 6.78 (br, 3 H, Im), 6.98–7.16 (m, 12 H, Ph), 7.32–7.41 (m, 15 H, Ar) ppm. IR (KBr): $\tilde{\nu}$ = 2437 w (BH), 1090 s (ClO_4^-) cm^{-1}.

12: Like **10** from 264 mg (0.40 mmol) of **L3** and 149 mg (0.40 mmol) of $Zn(ClO_4)_2{\cdot}6H_2O$. Yield 257 mg (82%) of **12** as a colourless powder, m.p. 245 °C (dec.). $C_{33}H_{34}BClN_6O_4S_3Zn$ (786.52): calcd. C 50.39, H 4.36, N 10.69, S 12.23, Zn 8.31; found C 49.27, H 4.51, N 11.12, S 11.79, Zn 8.03. ^1H NMR ($CDCl_3$): δ = 1.98 (s, 9 H, Me), 2.06 (s, 9 H, Me), 6.89 (d, J = 2.1 Hz, 3 H, Im), 7.10 [d, J = 7.4 Hz, 6 H, Ph(3,5)], 7.16 (d, J = 2.1 Hz, 3 H, Im), 7.25 [t, J = 7.4 Hz, 3 H, Ph(4)] ppm. IR (KBr): $\tilde{\nu}$ = 2448 w (BH), 1991 s (ClO_4^-) cm^{-1}.

13: Like **10** from 200 mg (0.24 mmol) of **L4** and 90 mg (0.24 mmol) of $Zn(ClO_4)_2{\cdot}6H_2O$. Yield 193 mg (84%) of **13** as a colourless powder, m.p. 230 °C (dec.). $C_{45}H_{58}BClN_6O_4S_3Zn$ (954.84): calcd. C 56.61, H 6.12, N 8.80, S 10.07, Zn 6.85; found C 56.29, H 6.48, N 8.73, S 10.04, Zn 6.82. ^1H NMR ($CDCl_3$): δ = 0.82 (d, J = 6.6 Hz, 3 H, Me), 0.98 (d, J = 6.6 Hz, 9 H, Me), 1.16 (d, J = 6.6 Hz, 24 H, Me), 2.28 (m, J = 6.7 Hz, 3 H, CH), 2.58 (m, J = 6.7 Hz, 3 H, CH), 6.90 (d, J = 1.6 Hz, 3 H, Im), 7.21 [d, J = 7.6 Hz, 6 H, Ph(3,5)], 7.25 (d, J = 1.6 Hz, 3 H, Im), 7.45 [m, 3 H, Ph(4)] ppm. IR (KBr): $\tilde{\nu}$ = 2449 w (BH), 1102 s (ClO_4^-) cm^{-1}.

14: Like **10** from 178 mg (0.30 mmol) of **L6** and 112 mg (0.30 mmol) of $Zn(ClO_4)_2{\cdot}6H_2O$. Yield 182 mg (84%) of **14** as a colourless powder, m.p. 230 °C (dec.). $C_{27}H_{37}BClN_6O_4S_3Zn{\cdot}CHCl_3$ (717.47 + 119.38): calcd. C 40.19, H 4.58, N 10.04, S 11.50, Zn 7.81; found C 41.15, H 5.19, N 10.32, S 11.63, Zn 8.27. ^1H NMR (CD_3OD): δ = 1.17–1.31 [p, J = 10.2 Hz, 12 H, CH_2(3,5-cyclohexyl)], 1.38–1.58 [q, J = 5.3 Hz, 12 H, CH_2(2,6-cyclohexyl)], 1.78 [m, 6 H, CH_2(4-cyclohexyl)], 4.53 (m, J = 3.8 Hz, 3 H, CH), 6.99 (d, J = 1.9 Hz, 3 H, Im), 7.23 (d, J = 1.9 Hz, 3 H, Im) ppm. IR (KBr): $\tilde{\nu}$ = 2435 w (BH), 1091 s (ClO_4^-) cm^{-1}.

Alkoxide Complexes

15: A solution of 46 mg (0.30 mmol) of *p*-nitrobenzyl alcohol in 5 mL of methanol was treated dropwise, with stirring, first with 0.30 mmol of a 0.5 M solution of $NaOCH_3$ in CH_3OH, then with 112 mg (0.30 mmol) of $Zn(ClO_4){\cdot}6H_2O$ in 10 mL of methanol, and finally with 200 mg (0.30 mmol) of **L3** in 10 mL of methanol. After stirring for 12 h the solvent was removed in vacuo, the residue taken up in 20 mL of dichloromethane and filtered. After evaporation to dryness, 205 mg (81%) of **15** was isolated as a yellow powder, m.p. 200 °C (dec.). $C_{40}H_{40}BN_7O_3S_3Zn$ (839.2): calcd. C 57.25, H 4.80, N 11.68, S 11.46, Zn 7.79; found C 57.72, H 5.36, N 11.71, S 11.54, Zn 7.86. ^1H NMR ($CDCl_3$): δ = 1.99 (s, 18 H, Me), 4.84

 © 2005 Wiley-VCH Verlag GmbH & Co. KGaA, Weinheim

(s, 2 H, CH_2), 6.58 (d, J = 2.1 Hz, 1 H, Im), 6.81 (d, J = 2.1 Hz, 3 H, Im), 6.84 (d, J = 2.1 Hz, 2 H, Im), 6.89 [d, J = 6.2 Hz, 6 H, Ph(3,5)], 7.19 [t, J = 7.6 Hz, 3 H, Ph(4)], 7.53 [d, J = 8.7 Hz, 2 H, nitro(2,6)], 8.22 [d, J = 8.7 Hz, 2 H, Nitro(3,5)] ppm. IR (KBr): $\tilde{\nu}$ = 2444 w (BH) cm^{-1}.

16: Like **15** from 53 mg (0.30 mmol) of *p*-(trifluoromethyl)benzyl alcohol, 112 mg (0.30 mmol) of $Zn(ClO_4)_2 \cdot 6H_2O$ and 200 mg (0.30 mmol) of **L3**. Yield 214 mg (82%) of **16** as a colourless powder, m.p. 180 °C. $C_{41}H_{40}BF_3N_6OS_3Zn \cdot 0.25CH_2Cl_2$ (862.20 + 21.23): calcd. C 56.08, H 4.62, N 9.52, S 10.88, Zn 7.40; found C 56.43, H 4.88, N 9.42, S 10.13, Zn 6.89. ^{1}H NMR ($CDCl_3$): δ = 2.00 (s, 18 H, Me), 4.78 (d, J = 2.8 Hz, 2 H, CH_2), 5.29 (s, 0.5 H, CH_2Cl_2), 6.58 (d, J = 2.1 Hz, 1 H, Im), 6.81 (d, J = 2.1 Hz, 3 H, Im), 6.89 (d, J = 2.1 Hz, 2 H, Im), 7.01 [d, J = 6.6 Hz, 6 H, Ph(3,5)], 7.19 [t, J = 7.4 Hz, 3 H, Ph(4)], 7.48 [d, J = 8.2 Hz, 2 H, trifluoromethyl(2,6)], 7.61 [d, J = 8.2 Hz, 2 H, trifluoromethyl(3,5)] ppm. ^{19}F NMR ($CDCl_3$): δ = 61.21 ppm. IR (KBr): $\tilde{\nu}$ = 2441 w (BH) cm^{-1}.

17: A solution of 200 mg (0.30 mmol) of **L3** and 10 mL of methanol was added dropwise with stirring to a solution of 112 mg (0.30 mmol) of $Zn(ClO_4)_2 \cdot 6H_2O$ in 10 mL of methanol. After stirring for 2 h the resulting $KClO_4$ was filtered off. The filtrate was treated with 0.3 mmol of a 0.25 M solution of $NaOCH_3$ in CH_3OH. After stirring for another 8 h the solvent was removed in vacuo, the residue taken up in 20 mL of dichloromethane and filtered. After evaporation to dryness 161 mg (71%) of **17** was isolated as a colourless powder, m.p. 255 °C (dec.). $C_{67}H_{71}B_2ClN_{12}O_5S_6Zn_2$ (1504.63): calcd. C 53.48, H 4.76, N 11.17, S 12.79, Zn 8.69; found C 53.35, H 4.88, N 11.07, S 12.67, Zn 8.61. ^{1}H NMR ($CDCl_3$): δ = 1.58 (s, 18 H, Me), 1.99 (s, 18 H, Me), 2.10 (s, 3 H, OMe), 6.57 (d, J = 2.1 Hz, 3 H, Im), 6.80 (d, J = 2.1 Hz, 6 H, Im), 6.87–7.09 [d, J = 6.8 Hz, 12 H, Ph(3,5)], 7.13 (d, J = 2.1 Hz, 3 H, Im), 7.19 [t, J = 7.5 Hz, 6 H, Ph(4)] ppm. IR (KBr): $\tilde{\nu}$ = 2439 w (BH), 1095 s (ClO_4^-) cm^{-1}.

18: Like **17** (all operations in absolute ethanol) from 200 mg (0.30 mmol) of **L3**, 112 mg (0.30 mmol) of $Zn(ClO_4)_2 \cdot 6H_2O$ and 0.30 mmol of $NaOC_2H_5$. Yield 180 mg (78%) of **18** as a colourless powder, m.p. 250 °C (dec.). $C_{68}H_{73}B_2ClN_{12}O_5S_6Zn_2$ (1518.65): calcd. C 53.78, H 4.84, N 11.07, S 12.67, Zn 8.61; found C 52.86, H 4.80, N 11.14, S 12.87, Zn 8.75. ^{1}H NMR ($CDCl_3$): δ = 1.24 [t, J = 7.0 Hz, 3 H, Me(Ethyl)], 1.58 (s, 18 H, Me), 2.05 (s, 18 H, Me), 3.72 [q, J = 5.2 Hz, CH_2(Ethyl)], 6.82 (d, J = 2.2 Hz 3 H, Im), 6.84 (d, J = 2.2 Hz, 6 H, Im), 6.88–7.10 [d, J = 6.8 Hz, 12 H, Ph(3,5)], 7.14 (d, J = 2.2 Hz, 3 H, Im), 7.20 [t, J = 7.4 Hz, 6 H, Ph(4)] ppm. IR (KBr): $\tilde{\nu}$ = 2417 w (BH), 1096 s (ClO_4^-) cm^{-1}.

19: Like **17** (all operations in absolute ethanol) from 200 mg (0.30 mmol) of **L3**, 112 mg (0.30 mmol) of $Zn(ClO_4)_2 \cdot 6H_2O$ and 0.30 mmol of $NaOCH_2CF_3$. Yield 166 mg (70%) of **19** as a colourless powder, m.p. 260 °C (dec.). $C_{68}H_{70}B_2ClF_3N_{12}O_5S_6Zn_2$ (1572.62): calcd. C 51.94, H 4.49, N 10.69, S 12.23, Zn 8.32; found C 52.23, H 4.93, N 11.61, S 12.85, Zn 8.73. ^{1}H NMR ($CDCl_3$): δ = 1.58 (s, 18 H, Me), 1.99 (s, 18 H, Me), 2.07 (s, 2 H, CH_2), 6.81 (br, 6 H, Im), 6.84 (br, 3 H, Im), 6.87–7.13 [d, J = 7.2 Hz, 12 H, Ph(3,5)], 7.14 (d, J = 2.1 Hz, 3 H, Im), 7.23 [t, J = 6.0 Hz, 6 H, Ph(4)] ppm. ^{19}F NMR ($CDCl_3$): δ = 77.81 ppm. IR (KBr): $\tilde{\nu}$ = 2490 w (BH), 1097 s (ClO_4^-) cm^{-1}.

Complexes with Alcohol and Aldehyde Ligands

20: A solution of 200 mg (0.30 mmol) of **L3** in 10 mL of absolute 2-propanol was added dropwise with stirring to a solution of 112 mg (0.30 mmol) of $Zn(ClO_4)_2 \cdot 6H_2O$ in 10 mL of absolute 2-propanol. After stirring for 4 h the volume of the solution was reduced to 10 mL in vacuo, the precipitate filtered off, and the filtrate evaporated to dryness. The residue was taken up in 10 mL of dichloromethane, filtered, and the filtrate evaporated to dryness again to give 150 mg (62%) of **20** as a colourless powder, m.p. 275 °C (dec.). $C_{36}H_{42}BClN_6O_5S_3Zn$ (846.62): calcd. C 51.07, H 5.00, N 9.93, S 11.36, Zn 7.72; found C 49.28, H 4.95, N 9.89, S 11.34, Zn 7.71. ^{1}H NMR ($CDCl_3$): δ = 1.12 [d, J = 6.2 Hz, 6 H, Me(*i*Pr)], 1.91 (s, 9 H, Me), 1.97 (s, 9 H, Me), 4.02 [m, J = 6.2 Hz, 1 H, CH(*i*Pr)], 6.82 (d, J = 2.0 Hz, 3 H, Im), 7.07 [d, J = 7.6 Hz, 6 H, Ph(3,5)], 7.09 (d, J = 2.0 Hz, 3 H, Im), 7.19 [t, J = 7.4 Hz, 3 H, Ph(4)] ppm. IR (KBr): $\tilde{\nu}$ = 2448 w (BH), 1101 s (ClO_4^-) cm^{-1}.

21: Like **20** from 206 mg (0.33 mmol) of **L5** and 124 mg (0.33 mmol) of $Zn(ClO_4)_2 \cdot 6H_2O$. Yield 149 mg (56%) of **21** as a

Table 3. Crystallographic data.

	1	**3**	**4**	**5**	**9**
Empirical formula	$C_{33}H_{34}BClN_6S_3Zn \cdot CH_3OH$	$C_{33}H_{34}BN_7O_3S_3Zn \cdot CH_3OH$	$C_{32}H_{31}BN_6O_2S_3Zn$	$C_{35}H_{37}BN_6O_2S_3Zn \cdot 3.5CH_3OH$	$C_{36}H_{32}BN_7O_3S_3Zn \cdot 2CH_3CN$
Molecular mass	722.5 + 32.0	749.1 + 32.0	704.0	746.1 + 112.1	783.0 + 82.1
Crystal size [mm]	0.1×0.2×0.3	0.1×0.2×0.3	0.1×0.2×0.2	0.1×0.1×0.2	0.2×0.2×0.4
Space group	$P2_12_12_1$	$P2_12_12_1$	$R3c$	$P\bar{1}$	$P\bar{1}$
Z	4	4	6	2	4
a [Å]	10.646(2)	11.152(3)	12.776(6)	9.531(2)	13.948(3)
b [Å]	11.439(2)	11.666(3)	12.776(6)	14.915(3)	17.548(4)
c [Å]	29.061(5)	28.563(7)	35.782(2)	16.552(3)	17.681(4)
α [°]	90	90	90	73.989(4)	88.006(4)
β [°]	90	90	90	77.480(4)	89.104(4)
γ [°]	90	90	120	81.549(4)	75.700(4)
V [Å^3]	3538.8(11)	3715.8(15)	5058.2(5)	2198.4(8)	4190.9(17)
d(calcd.) [g cm^{-3}]	1.42	1.39	1.39	1.29	1.37
μ(Mo-$K\alpha$) [mm^{-1}]	0.98	0.88	0.95	0.75	0.79
hkl range	h: –13 to 10 k: –13 to 15 l: –39 to 11	h: –15 to 3 k: –13 to 14 l: –28 to 36	h: –16 to 16 k: –16 to 16 l: –46 to 46	h: –12 to 12 k: –20 to 19 l: –22 to 22	h: –18 to 18 k: –23 to 22 l: –23 to 23
Measured reflections	13 471	13 824	14 153	19 701	38 232
Independent reflections	6895	6874	2747	10 181	19 929
Obsd. reflections [$I > 2\sigma(I)$]	4712	3356	1915	3316	8975
Parameters	414	451	137	475	1031
Refined reflections	6895	6874	2747	10 181	19 929
R_1 (obs.refl.)	0.053	0.058	0.058	0.069	0.061
wR_2 (all refl.)	0.143	0.182	0.171	0.211	0.189
Res. electron density [e Å^{-3}]	+0.6/–0.5	+0.7/–0.4	+0.8/–0.5	+0.8/–0.7	+1.3/–0.7

 © 2005 Wiley-VCH Verlag GmbH & Co. KGaA, Weinheim

Table 4. Crystallographic data.

	17	**18**	**21**	**23**	**24**
Empirical formula	$C_{67}H_{71}B_2ClN_{12}S_6Zn_2$·$CH_3OH$	$C_{68}H_{73}B_2ClN_{12}O_5S_6Zn_2$·$2C_2H_5OH$	$C_{33}H_{36}BClN_6O_5S_3Zn$·$0.25CH_2Cl_2$·$0.5\,i$PrOH·$0.5H_2O$	$C_{40}H_{39}BN_6O_2S_3Zn$·CH_3OH	$C_{35}H_{36}BClN_8O_5S_3Zn$·$1.5CH_2Cl_2$
Molecular mass	1504.6 + 32.0	1518.7 + 92.1	804.5 + 21.2 + 24.0 + 9.0	808.2 + 32.0	856.6 + 127.3
Crystal size [mm]	0.1 × 0.2 × 0.2	0.1 × 0.1 × 0.3	0.3 × 0.2 × 0.1	0.1 × 0.2 × 0.3	0.2 × 0.1 × 0.1
Space group	$P2_1/c$	$P2_1/c$	$P\bar{1}$	$P2_1/c$	$P\bar{1}$
Z	8	8	4	1	2
a [Å]	16.405(3)	16.621(3)	11.014(7)	11.989(2)	13.746(3)
b [Å]	19.815(4)	20.171(4)	16.066(10)	10.775(2)	13.996(3)
c [Å]	24.003(5)	23.854(5)	23.450(15)	32.154(6)	15.878(4)
α [°]	90	90	82.184(10)	90	92.615(4)
β [°]	104.640(4)	106.549(3)	82.050(10)	91.637(4)	112.714(4)
γ [°]	90	90	81.099(10)	90	114.316(3)
V [Å^3]	7549(2)	7666(3)	4032.2(4)	4152.0(13)	2490.6(10)
d(calcd.) [g cm^{-3}]	1.35	1.39	1.42	1.34	1.31
μ(Mo-K_α) [mm^{-1}]	0.89	0.88	0.91	0.79	0.88
hkl range	h: –2 to 22 k: –26 to 26 l: –32 to 32	h: –22 to 22 k: –27 to 26 l: –32 to 31	h: –14 to 14 k: –20 to 21 l: –31 to 31	h: –15 to 16 k: –15 to 14 l: –40 to 44	h: –18 to 17 k: –18 to 17 l: –20 to 20
Measured reflections	67 044	68 310	36 905	40 134	22 054
Independent reflections	18 373	18 624	18 966	11 744	11 307
Obsd. reflections [$I > 2\sigma(I)$]	6012	10 317	8940	7069	6239
Parameters	887	900	973	496	595
Refined reflections	18 373	18 624	18 966	11 744	11 307
R_1 (obs.refl.)	0.079	0.064	0.069	0.061	0.077
wR_2 (all refl.)	0.302	0.215	0.235	0.153	0.259
Res. electron density [e Å^{-3}]	+0.9/–0.8	+1.1/–1.1	+1.5/–0.9	+0.8/–0.6	+1.2/–0.7

colourless powder, m.p. 215 °C (dec.). $C_{33}H_{36}BClN_6O_5S_3Zn$ (804.54): calcd. C 49.27, H 4.51, N 10.45, S 11.96, Zn 8.13; found C 49.45, H 4.89, N 9.97, S 11.19, Zn 7.98. ^{1}H NMR ($CDCl_3$): δ = 1.16 [d, J = 6.0 Hz, 6 H, Me(*i*Pr)], 2.38 (s, 6 H, Me), 2.41 (s, 3 H, Me), 4.03 [m, J = 6.0 Hz, 1 H, CH(*i*Pr)], 7.07 (br, 2 H, Im), 7.09 (d, J = 2.2 Hz, 2 H, Im), 7.14 (br, 2 H, Im), 7.22 (m, 12 H, Ph) ppm. IR (KBr): $\tilde{\nu}$ = 2452 w (BH) cm^{-1}.

22: A solution of 37 mg (0.30 mmol) of 2-hydroxybenzyl alcohol in 5 mL of methanol was treated dropwise with stirring first with 0.30 mmol of a 0.25 M solution of $NaOCH_3$ in CH_3OH, then with a solution of 112 mg (0.30 mmol) of $Zn(ClO_4)_2$·$6H_2O$ in 10 mL of methanol, and finally with a solution of 200 mg (0.30 mmol) of **L3**. After stirring for 12 h the solvent was removed in vacuo, the residue taken up in 10 mL of dichloromethane, filtered and the filtrate evaporated to dryness again to give 218 mg (89%) of **22** as a colourless powder, m.p. 180 °C (dec.). $C_{40}H_{41}BN_6O_2S_3Zn$·$0.5CH_2Cl_2$ (810.20 + 42.46): calcd. C 57.05, H 4.96, N 9.86, S 11.28, Zn 7.67; found C 57.52, H 5.11, N 9.19, S 10.54, Zn 8.07. ^{1}H NMR ($CDCl_3$): δ = 1.99 (s, 18 H, Me), 4.48 (m, 1 H, OH), 4.85 (s, 2 H, CH_2), 5.30 (s, 1 H, CH_2Cl_2), 6.82 (d, J = 2.0 Hz, 3 H, Im), 6.86 (d, J = 2.0 Hz, 3 H, Im), 7.03 [d, J = 5.0 Hz, 6 H, Ph(3,5)], 7.13 [m, 2 H, Ph(3,5-phenolate)], 7.16 [t, J = 6.6 Hz, 3 H, Ph(4)], 7.26 [m, 2 H, Ph(4,6-phenolate)] ppm. IR (KBr): $\tilde{\nu}$ = 2442 w (BH) cm^{-1}.

23: Like **22** from 38 mg (0.30 mmol) of salicylic aldehyde, 112 mg (0.30 mmol) of $Zn(ClO_4)_2$·$6H_2O$ and 200 mg (0.30 mmol) of **L3**. Yield 202 mg (83%) of **23** as a colourless powder, m.p. 180 °C (dec.). $C_{40}H_{39}BN_6O_2S_3Zn$ (808.19): calcd. C 59.45, H 4.86, N 10.40, S 11.90, Zn 8.09; found C 58.23, H 4.83, N 10.99, S 11.87, Zn 8.07. ^{1}H NMR ($CDCl_3$): δ = 1.99 (s, 18 H, Me), 6.82 (d, J = 2.0 Hz, 3 H, Im), 6.85 (d, J = 2.0 Hz, 3 H, Im), 7.02 [d, J = 8.0 Hz, 6 H, Ph(3,5)], 7.13 [m, 2 H, Ph(3,5-salicyl)], 7.20 [t, J = 4.8 Hz, 3 H, Ph(4)], 7.54 [m, 2 H, Ph(4,6-salicyl)], 9.91 [s, 1 H, CHO] ppm. IR (KBr): $\tilde{\nu}$ = 2460 w (BH), 1659 m (CO) cm^{-1}.

24: Equimolar amounts of **L5** and $Zn(ClO_4)_2$ were converted into the **L5**·Zn-$OClO_3$ complex as described above for **10**. Then, a solution of 245 mg (0.33 mmol) of this complex in 5 mL of dichloromethane was treated with a solution of 37 mg (0.33 mmol) of 2-(hydroxymethyl)-1-methylimidazole in 5 mL of dichloromethane. After stirring for 6 h the product was precipitated by addition of 30 mL of petroleum ether (60–70). Filtration and recrystallisation from dichloromethane/petroleum ether yielded 150 mg (53%) of **24** as colourless crystals, m.p. 210 °C (dec.). $C_{35}H_{36}BClN_8O_5S_3Zn$ (856.57): calcd. C 49.08, H 4.24, N 13.08, S 11.23, Zn 7.63; found C 48.10, H 4.54, N 13.18, S 10.18, Zn 7.67. ^{1}H NMR ($CDCl_3$): δ = 22.38 (s, 9 H, Me), 3.62 [s, 3 H, Me(imidazole)], 4.46 [s, 2 H, CH_2(imidazole)], 6.67 (s, 1 H, imidazole), 6.87 (s, 1 H, imidazole), 7.10 (d, J = 2.2 Hz, 6 H, Im), 7.16 (d, J = 8.6 Hz, 6 H, Ph), 7.26 (d, J = 8.6 Hz, 6 H, Ph) ppm. IR (KBr): $\tilde{\nu}$ = 2454 w (BH) cm^{-1}.

Structure Determinations:[38] Crystals of **1**, **3**, **4**, **5**, **17** and **23** were obtained by recrystallisation from methanol/dichloromethane mixtures, those of **18** from ethanol/dichloromethane, those of **9** from acetonitrile/dichloromethane, those of **21** by layering a dichloromethane/2-propanol (1:4) solution with petroleum ether, and those of **24** by layering a dichloromethane solution with petroleum ether. Diffraction data were recorded at room temperature (**10**, **12**), at –50 °C (**3**, **5**, **17**, **18**), at –80° (**1**, **23**, **24**) or at –140 °C (**4**) with a Bruker Smart CCD diffractometer. Empirical absorption corrections were applied to all data sets except those of **9** and **17**. The structures were solved by direct methods and refined anisotropically with the SHELX program suite.[39] Hydrogen atoms were included with fixed distances and isotropic temperature factors 1.5-times those of their attached atoms. Parameters were refined against F^2. The R values are defined as $R_1 = \Sigma|F_o - F_c|/\Sigma F_o$ and $wR_2 = \{\Sigma[w(F_o^2 - F_c^2)^2]\Sigma[w(F_o^2)^2]\}^{1/2}$. Drawings were produced with SCHAKAL.[40] Tables 3 and 4 list the crystallographic data.

Acknowledgments

This work was supported by the Deutsche Forschungsgemeinschaft and the Fonds der Chemischen Industrie. We are indebted to Drs. W. Deck and H. Brombacher for their help with the structure determinations.

[1] Y. Pocker, *Met. Ions Biol. Syst.* **1989**, *25*, 335–358.
[2] R. G. Matthews, *Acc. Chem. Res.* **2001**, *34*, 681–689.
[3] M. Tesmer, M. Shu, H. Vahrenkamp, *Inorg. Chem.* **2001**, *40*, 4022–4029.
[4] M. Shu, R. Walz, B. Wu, J. Seebacher, H. Vahrenkamp, *Eur. J. Inorg. Chem.* **2003**, 2502–2511.
[5] C. Kimblin, B. M. Bridgewater, D. G. Churchill, G. Parkin, *Chem. Commun.* **1999**, 2301–2302.
[6] S. J. Chiou, C. G. Riordan, A. L. Rheingold, *Proc. Natl. Acad. Sci. USA* **2003**, *100*, 3695–3700.
[7] M. M. Mazowska-Grzyska, P. C. Jeppson, R. A. Allred, A. M. Arif, L. M. Berreau, *Inorg. Chem.* **2002**, *41*, 4872–4887.
[8] B. M. Bridgewater, T. Fillebeen, R. A. Friesner, G. Parkin, *J. Chem. Soc., Dalton Trans.* **2000**, 4494–4496.
[9] C. R. Warthen, B. S. Hammes, C. J. Carrano, D. C. Crans, *J. Biol. Inorg. Chem.* **2001**, *6*, 82–90.
[10] S. Trofimenko, *Scorpionates*, Imperial College Press, London, **1999**.
[11] B. M. Bridgewater, G. Parkin, *Inorg. Chem. Commun.* **2001**, *4*, 126–129.
[12] A. Docrat, M. M. Morlok, B. M. Bridgewater, D. G. Churchill, G. Parkin, *Polyhedron* **2004**, *23*, 481–488.
[13] M. Tesmer, M. Shu, J. Seebacher, H. Vahrenkamp, unpublished results.
[14] M. Garner, J. Reglinski, I. Cassidy, M. D. Spicer, A. R. Kennedy, *Chem. Commun.* **1996**, 1975–1976.
[15] J. Reglinski, M. D. Spicer, M. Garner, A. R. Kennedy, *J. Am. Chem. Soc.* **1999**, *121*, 2317–2318.
[16] J. Reglinski, M. Garner, I. D. Cassidy, P. A. Slavin, M. D. Spicer, D. R. Armstrong, *J. Chem. Soc., Dalton Trans.* **1999**, 2119–2126.
[17] P. A. Slavin, J. Reglinski, M. D. Spicer, A. R. Kennedy, *J. Chem. Soc., Dalton Trans.* **2000**, 239–240.
[18] C. A. Dodds, M. A. Lehmann, J. F. Ojo, J. Reglinski, M. D. Spicer, *Inorg. Chem.* **2004**, *43*, 4927–4934.
[19] M. Garner, K. Lewinski, A. Pattek-Janczyk, J. Reglinski, B. Sieklucka, M. D. Spicer, M. Szaleniec, *Dalton Trans.* **2003**, 1181–1185.
[20] I. Cassidy, M. Garner, A. R. Kennedy, G. B. S. Potts, J. Reglinski, P. A. Slavin, M. D. Spicer, *Eur. J. Inorg. Chem.* **2002**, 1235–1239.
[21] J. Seebacher, H. Vahrenkamp, *J. Mol. Struct.* **2003**, *656*, 177–181.
[22] S. Bakbak, V. K. Bhatia, C. D. Incarvito, A. L. Rheingold, D. Rabinovich, *Polyhedron* **2001**, *20*, 3343–3348.
[23] J. L. White, J. M. Tanski, D. Rabinovich, *J. Chem. Soc., Dalton Trans.* **2002**, 2987–2991.
[24] C. Santini, G. Gioia Lobbia, C. Pettinari, M. Pellei, G. Valle, S. Calogero, *Inorg. Chem.* **1998**, *37*, 890–900.
[25] C. Santini, M. Pellei, G. Gioia Lobbia, C. Pettinari, A. Drozdov, S. Troyanov, *Inorg. Chim. Acta* **2001**, *325*, 20–26.
[26] H. Vahrenkamp, *Acc. Chem. Res.* **1999**, *32*, 589–596.
[27] U. Brand, M. Rombach, H. Vahrenkamp, *Inorg. Chem.* **2001**, *40*, 6151–6157.
[28] O. Mamula, A. von Zelewsky, T. Bork, H. Stöckli-Evans, A. Neels, G. Bernordinelly, *Chem. Eur. J.* **2000**, *6*, 3575–3585.
[29] H. Adams, R. Bastida, D. D. Fenton, A. Macias, S. E. Spey, V. Valencia, *J. Chem. Soc., Dalton Trans.* **1999**, 4131–4137.
[30] A. Mondal, G. Mostafa, A. Ghosh, N. R. Chaudhuri, W. T. Wong, *Polyhedron* **1998**, *17*, 1217–1223.
[31] R. Alsfasser, H. Vahrenkamp, *Chem. Ber.* **1993**, *126*, 695–701.
[32] B. S. Hammes, X. Luo, M. W. Carrano, C. J. Carrano, *Inorg. Chim. Acta* **2002**, *341*, 33–41.
[33] S. Ramaswamy, H. Eklund, B. V. Plapp, *Biochemistry* **1994**, *33*, 5230–5237.
[34] B. Müller, A. Schneider, M. Tesmer, H. Vahrenkamp, *Inorg. Chem.* **1999**, *38*, 1900–1907.
[35] M. Förster, R. Burth, A. K. Powell, T. Eiche, H. Vahrenkamp, *Chem. Ber.* **1993**, *126*, 2643–2648.
[36] R. G. Jones, E. C. Kornfeld, K. C. McLaughlin, R. C. Anderson, *J. Am. Chem. Soc.* **1949**, *71*, 4000–4002.
[37] J. Kister, G. Assef, G. Mille, J. Metzger, *Can. J. Chem.* **1979**, *57*, 813–821.
[38] CCDC-257210 (for **1**), -257211 (for **3**), -257212 (for **4**), -257213 (for **5**), -257214 (for **9**), -257215 (for **17**), -257216 (for **18**), -257217 (for **21**), -257218 (for **23**) and -257219 (for **24**) contain the supplementary crystallographic data for this paper. These data can be obtained free of charge from The Cambridge Crystallographic Data Centre via www.ccdc.cam.ac.uk/data_request/cif.
[39] *SHELX* program package for the Bruker Smart CCD diffractometer.
[40] E. Keller, *SCHAKAL* for Windows, University of Freiburg, **1999**.

Received: December 01, 2004

 © 2005 Wiley-VCH Verlag GmbH & Co. KGaA, Weinheim

Zinc Thiolate Complexes of (N,N,S)-Tridentate Ligands for the Modeling of Thiolate Alkylating Enzymes

Mian Ji[a] and Heinrich Vahrenkamp*[a]

Keywords: Bioinorganic chemistry / S ligands / Tridentate ligands / Zinc

Zinc thiolate complexes of three tridentate (N,N,S) ligands were prepared as models for the structure and function of thiolate alkylating zinc enzymes. *N*-(2-Mercaptoisobutyl)(2-pyridin-2-yl-methyl)amine (**L^1**) forms isobutylthiolate-bridged dinuclear complexes with ZnN_2S_3 coordination. *N*-(2-Mercaptoisobutyl)(2-pyridin-2-yl-ethyl)amine (**L^2**) yields isobutylthiolate-bridged dinuclear complexes in which the pyridine donor is not coordinated to zinc, resulting in a $ZnNS_3$ coordination. Only *N*-(2-mercaptoisobutyl)(2-pyridin-2-yl-ethyl)methylamine (**L^3**) forms the desired mononuclear complexes with ZnN_2S_2 coordination. The latter react with the alkylating agents CH_3I and $PO(OCH_3)_3$ in a two-step process. In the first step the isobutylthiolate function is methylated and its position in the ligand sphere of zinc is taken by I^- or $OPO(OCH_3)_2^-$, respectively, and in the second step the additional thiolate ligand is methylated and replaced by a second iodide or dimethyl phosphate anion.

(© Wiley-VCH Verlag GmbH & Co. KGaA, 69451 Weinheim, Germany, 2005)

Introduction

In recent years a number of thiolate alkylating enzymes have been identified that contain zinc in their active centers,[1] the most prominent of which is cobalamine-independent methionine synthase.[2] An unusual feature of these enzymes is that they contain zinc in a sulfur-rich ligand environment, which can typically be represented as NS_2ZnX or N_2SZnX, where N and S stand for the side-chains of histidine and cysteine and X is the coordination position of the substrate. It is believed that the thiol substrates, for example homocysteine, are attached to zinc as thioalates prior to alkylation, for example to methionine. An open mechanistic question is whether the alkylation, typically a methylation by methyl tetrahydrofolate, takes place at the zinc-bound or at the free thiolate.

We[3–5] and others[6–11] have attempted to reproduce this biological process with zinc thiolate complexes of various polydentate ligands, using methyl iodide, dimethyl sulfate, or trimethyl phosphate as methylating agents. In most cases the coligands were bidentate chelators or tripodal donors offering only N coordination. In those cases where mechanistic studies were performed it was found that the thiolate is alkylated in the zinc-bound state. Thus, a reasonable approximation to a functional modeling of the enzymes has been achieved, albeit with rather low reaction rates and not in a catalytic fashion.

At this point the major challenges concern a better structural modeling of the enzymes, which may also be a way to achieve higher reactivities of the zinc thiolate model complexes. This requires modeling the protein environment of zinc by tridentate or tripodal ligands with N_2S and NS_2 donor sets, of which N is part of a nitrogen heterocycle representing histidine's imidazole and S is a thiolate sulfur representing cysteine's thiolate. We are not aware of a model study employing such an NS_2 ligand, and so far just one type of such N_2S ligands seems to have been used for thiolate alkylation in zinc complexes.[8,9]

We have reported various tridentate N_2S ligands[12–15] as well as pyrazolylborate-derived NS_2[16] and N_2S tripods.[17] While we have previously focused on modeling hydrolytic enzymes or alcohol dehydrogenase with their zinc complexes, we are at present using their zinc thiolate complexes for studies of thiolate alkylation. This paper reports our results with the tridentate N_2S systems **L^1**–**L^3**. The goal of our study was to find out whether mononuclear tetrahedral **L**·Zn–SR complexes of **L^1**–**L^3** are accessible and how they behave toward alkylating reagents.

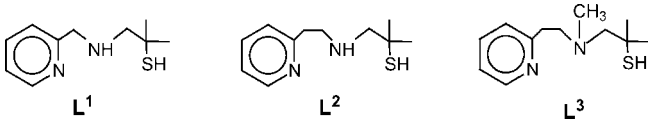

Results and Discussion

All three ligands in their free form are aliphatic thiols and by design are good chelators. They are disubstituted at

[a] Institut für Anorganische und Analytische Chemie der Universität Freiburg,
Albertstr. 21, 79104 Freiburg, Germany
Fax: +49-761-203-6001
E-mail: vahrenka@uni-freiburg.de

the α-carbon of the thiolate function with the purpose of introducing some steric strain in order to reduce their tendency to bridge. Their synthesis consists in the ring opening of 2,2-dimethylthiirane by the corresponding pyridine-substituted aliphatic amine. The two methyl substituents and the CH_2 group of their mercaptoethylamine functions make it easy to identify the complexes of **L¹**–**L³** by ^{1}H NMR spectroscopy. The zinc thiolate complexes of **L¹**–**L³** could be expected to have a ZnN_2S_2 coordination, which in almost all cases − in coordination compounds as well as in zinc-containing proteins − was found to imply mononuclear species with a tetrahedral coordination of zinc.

N-(2-Mercaptoisobutyl)(2-pyridin-2-ylmethyl)amine (L¹)

Ligand **L¹** and some of its zinc complexes have been described previously by us.[14] We observed that the isobutylthiolate function of **L¹** has a high bridging tendency and that the zinc ions in the resulting oligonuclear complexes have coordination numbers of 5 or 6. Yet, except for the thiolate sulfur only hard donor atoms (N and O) are present in these complexes and the N_2S_2 donor composition has not been tested.

This was done now. The thiophenolate complex **1** was generated in a one-step synthesis from deprotonated **L¹**, zinc nitrate, and potassium thiophenolate. The NMR spectroscopic data of **1** are inconclusive in terms of composition and structure in solution, but in the crystalline state **1** was found to be dimeric with a ZnN_2S_3 coordination.

L¹•Zn-SC$_6$H$_5$
1

Figure 1 shows the centrosymmetrical dinuclear molecular units of **1** in which the isobutylthiolate groups function as bridging ligands as observed before.[14] The perfectly planar central Zn_2S_2 unit of the complex is close to being a square. The coordination of the zinc ions is roughly trigonal bipyramidal (85% TBP according to the dihedral angle method of Holmes[18]). This is not so evident from the S1–Zn–N1 angle of 159°, but clearly so from the fact that the axial bonds Zn–S1 and Zn–N1 are considerably longer than their equatorial counterparts Zn–S1′, Zn–S2, and Zn–N2. Complex **1** therefore closely resembles the **L¹**·Zn-acetate complex.[14]

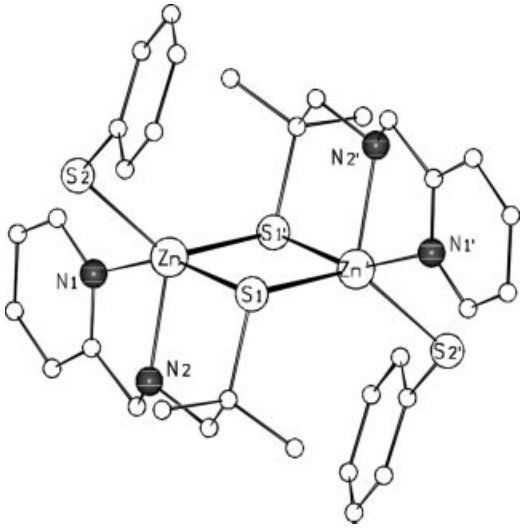

Figure 1. Structure of **1** in the solid state. Relevant bond lengths [Å]: Zn–S1 2.514(2), Zn–S1′ 2.370(2), Zn–S2 2.321(2), Zn–N1 2.305(4), Zn–N2 2.134(4).

One reason for the inaccessibility of tetrahedral zinc complexes with ligand **L¹** seems to be the fact that, upon complexation with **L¹**, two five-membered chelate rings are formed. These enforce two small bond angles and therefore encourage trigonal bipyramidal or octahedral coordination despite the high sulfur content in the ligand sphere of the metal. The investigations with ligand **L¹** were therefore abandoned in favor of those with **L²** and **L³**.

N-(2-Mercaptoisobutyl)(2-pyridin-2-ylethyl)amine (L²)

This ligand has not been described before. We now found that it is easily accessible from 2,2-dimethylthiirane and 2-(2-aminoethyl)pyridine as a colorless liquid with typical ^{1}H NMR resonances for its aliphatic constituents.

While we found it difficult to obtain zinc alkanethiolate complexes of **L²**, aromatic thiolates could easily be incorporated. Again, they resulted from a one-pot synthesis using deprotonated **L²**, $Zn(NO_3)_2$, and the corresponding thiolate. Complexes **2a**–**d** were obtained in reasonable yields as colorless, crystalline materials, except for yellow **2c**.

L²•Zn-SAr

	2a	**2b**	**2c**	**2d**
Ar	C$_6$H$_5$	*p*-CH$_3$C$_6$H$_4$	*p*-NO$_2$C$_6$H$_4$	C$_6$F$_5$

The spectroscopic data of all four complexes **2** are similar enough to justify the statement that they all have a structure like the one that was determined for **2a** (see Figure 2). Again, the complexes crystallize as centrosymmetrical dimers with bridging isobutylthiolate functions.

The unusual feature of this structure is the noncoordination of the pyridine donor of **L²**. Thus, while the expected coordination number 4 is achieved for zinc, this is not due to the lengthening of the ligand arm between the two nitrogen donors but due to the fact that thiolate bridging is preferred over pyridine coordination. Therefore, with three thiolate ligands bound to zinc, anything but a tetrahedral coordination is unlikely, and the $ZnNS_3$ coordination pattern ensues. The coordination geometry of zinc is extremely distorted tetrahedral. The two smallest bond angles (S1–Zn–S1′ and S1–Zn–N2) are enforced by the Zn_2S_2 diamond and the chelate ring, respectively. The opening in the ligand sphere resulting from this then allows the very large S1–

 © 2005 Wiley-VCH Verlag GmbH & Co. KGaA, Weinheim

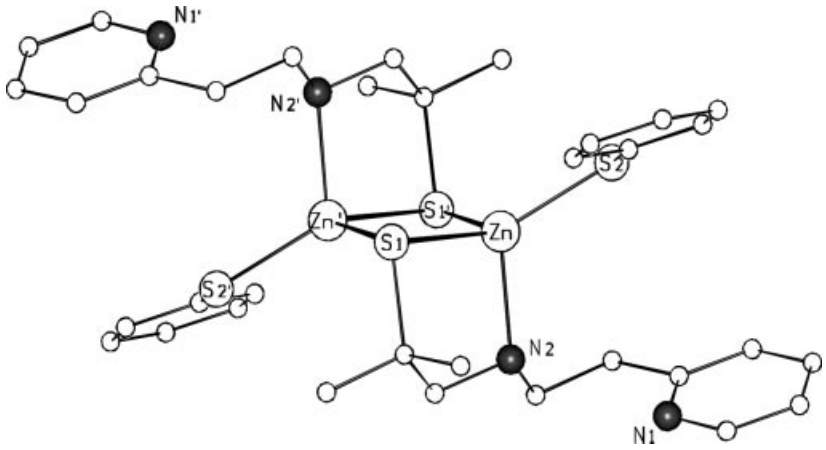

Figure 2. Structure of **2a** in the solid state. Relevant bond lengths [Å] and angles [°]: Zn–S1 2.375(4), Zn–S1′ 2.377(4), Zn–S2 2.254(3), Zn–N2 2.101(5); S1–Zn–S1′ 99.3(1), Zn–S1–Zn′ 80.7(1), S1–Zn–N2 90.1(1), S1–Zn–S2 130.0(1).

Zn–S2 angle. Neither of the structural features of **2a** is unprecedented. A similar dimeric structure with severe bond-angle deviations has been described by Kellogg for an NS_2 chelate ligand,[19] and we have observed the noncoordination of the pyridine arm in the ZnL_2 complex of $\mathbf{L^1}$.[17]

N-(2-Mercaptoisobutyl)(2-pyridin-2-ylethyl)methylamine ($\mathbf{L^3}$)

While ligands $\mathbf{L^1}$ and $\mathbf{L^2}$ yielded zinc complexes that are not suitable for the intended thiolate alkylation studies, ligand $\mathbf{L^3}$, which differs from $\mathbf{L^2}$ only by the methyl group on the central nitrogen atom, did allow the formation of mononuclear tetrahedral **L**·Zn–SR complexes. $\mathbf{L^3}$ was first described by Goldberg et al. and used for zinc chemistry unrelated to thiolate alkylation,[20–22] and these authors had already noted that the larger chelate ring size in relation to that provided by ligands like $\mathbf{L^1}$ favors the formation of four-coordinate complexes.[21] We verified the ability of $\mathbf{L^3}$ to form tetrahedral **L**·Zn–X complexes with soft donors X by preparing $\mathbf{L^3}$·ZnCl from zinc chloride. The molecular structure of $\mathbf{L^3}$·ZnCl (Figure 3) shows that in the mononuclear complexes of these ligands the tetrahedral coordination is also severely distorted due to the small bond angles between the chelate donors and, subsequently, the large bond angle between the two soft donors Cl and S.

$\mathbf{L^3}$•Zn-SR

	3a	**3b**	**3c**
R	CH_2CF_3	$CH_2C_6H_5$	$CH_2C_6H_4Cl$
	3d	**3e**	**3f**
R	C_6H_5	*p*-$NO_2C_6H_4$	C_6F_5

Just like $\mathbf{L^2}$, ligand $\mathbf{L^3}$ did not facilitate access to simple zinc alkanethiolate complexes. However, the trifluoroe-

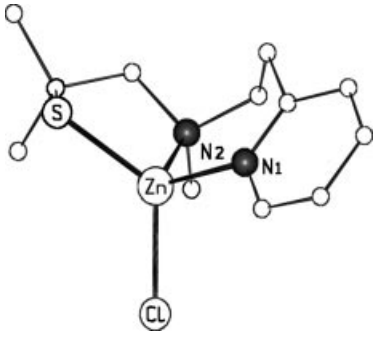

Figure 3. Structure of $\mathbf{L^3}$·Zn–Cl. Relevant bond lengths [Å] and angles [°]: Zn–Cl 2.2354(5), Zn–S 2.2532(5), Zn–N1 2.057(1), Zn–N2 2.108(1); N1–Zn–N2 98.96(5), S–Zn–N2 92.72(4), Cl–Zn–N2 116.38(4), S–Zn–N1 120.09(4), Cl–Zn–N1 101.66(4), Cl–Zn–S 124.55(2).

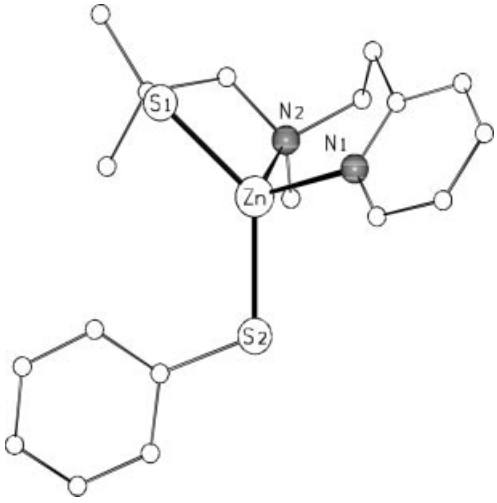

Figure 4. Molecular structure of $\mathbf{L^3}$·Zn–SC_6H_5 (**3d**). Relevant bond lengths [Å] and angles [°]: Zn–N1 2.076(7), Zn–N2 2.149(9), Zn–S1 2.273(3), Zn–S2 2.277(3); N1–Zn–N2 96.9(3), N1–Zn–S1 113.1(2), N1–Zn–S2 102.3(2), N2–Zn–S1 90.8(2), N2–Zn–S2 116.0(2), S1–Zn–S2 132.4(1).

 © 2005 Wiley-VCH Verlag GmbH & Co. KGaA, Weinheim

thanethiolate complex **3a**, the benzylthiolate complexes **3b** and **3c**, as well as the arenethiolate complexes **3d–f** could be synthesized from L^3·ZnBr[21] and the corresponding thiolates. Complexes **3a–f** were isolated in good yields. Except for yellow **3e** they form colorless crystals.

The structures of **3d**, **3e**, and **3f** were determined. They are very similar, making it sufficient to discuss that of **3d**. As Figure 4 shows, the ZnN_2S_2 coordination pattern in the thiolates very much resembles the ZnN_2SCl coordination pattern in the chloride (see Figure 3): the bond angles for the two chelate rings are far below the tetrahedral angle, and the S–Zn–S angle is far above it. Complex **3d** shares these features with our (N_2S-chelate)Zn–SR complex derived from the N_2S-chelate ligand MPPA.[13] The Zn–N and Zn–S distances of the L^3·Zn–SR complexes are in the normal range, comparing well with those both in (N_2S-chelate)[12–14] and in (N_2S-tripod)Zn–SR complexes.[23,24]

The coordination pattern of zinc in complexes **3** is close enough to that in the thiolate alkylating enzymes to justify the investigation of alkylating reactions. They were performed for **3d–f** using methyl iodide and for **3d** using trimethyl phosphate. It was found that both thiolate units attached to zinc are alkylated. However, the alkanethiolate function which is part of ligand L^3 reacts first, according to Equation (1).

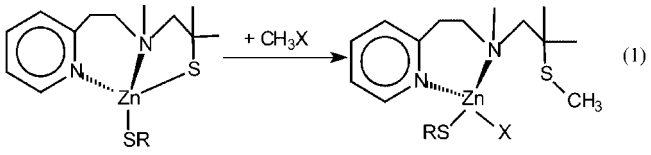

3d: R = C_6H_5
3e: R = $C_6H_4NO_2$
3f: R = C_6F_5

4d: R = C_6H_5, X = I
4e: R = $C_6H_4NO_2$, X = I
4f: R = C_6F_5, X = I
5d: R = C_6H_5, X = $OPO(OMe)_2$

Equimolar amounts of **3d–f** and methyl iodide react smoothly at room temperature in nonpolar solvents. The conversion of ligand L^3 into its methylated form Me-L^3 was evident from the ^{1}H NMR spectra (see Experimental Section), which also indicate by the chemical shifts of the SCH_3 units that in the isolated complexes **4d–f** the thioether functions are not coordinated to zinc, as observed before for a related (N_2S)Zn–SR system and proved by a structure determination.[8] While this could not be proved here by a structure determination it corresponds to the experience that, after alkylation, the sulfur donor is released from zinc and replaced by the anionic constituent of the alkylating agent.[3–5] Actually, the weak donor qualities of thioethers toward zinc, and hence their easy removal from the metal, provide an important part of the driving force for thiolate alkylation by zinc enzymes.[1,2] For complexes **3d–f**, however, the preferred alkylation at the alkanethiolate function corresponds to a partial blocking of ligand L^3, thereby hampering its quality as a model ligand for biomimetic chemistry.

The preference for alkylation at the isobutylthiolate function was not so large as to prevent alkylation at the benzenethiolate function entirely. The NMR spectra of the reaction solutions showed the presence of the aromatic thioethers before the alkylation of the aliphatic thiolate functions was complete. In accord with this the use of a large excess of the alkylating agent brought the reactions to completion according to Equation (2) under the same reaction conditions as for Equation (1).

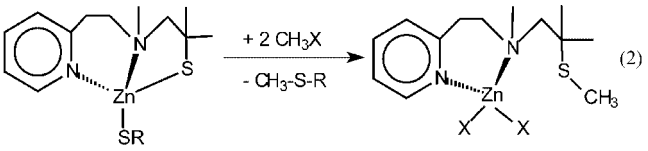

3d: R = C_6H_5
3e: R = $C_6H_4NO_2$
3f: R = C_6F_5

6: X = I
7: X = $OPO(OMe)_2$

The aromatic thioethers ($CH_3SC_6H_5$ from **3d**, $CH_3SC_6H_4$-*p*-NO_2 from **3e**, $CH_3SC_6F_5$ from **3f**) were isolated and identified from their ^{1}H NMR spectra. The product complexes **6** and **7** bearing the partially blocked ligand Me-L^3 offer no special features; they have the conventional ZnN_2Hal_2 and ZnN_2O_2 compositions. The assumption that the thioether function in these complexes is not coordinated to zinc is backed by the fact that there is not a single structure of a complex of ZnN_2Hal_2 coordination known which has any other donor coordinated to zinc.

The alkylation of **3d** with trimethyl phosphate was included in this investigation to test the ability of complexes **3** to model the function of the Ada protein, a zinc enzyme that repairs damaged DNA by transferring alkyl groups from its phosphate units to thiolates.[1,25] Yet, as observed before,[1,5] trimethyl phosphate is so much less reactive than methyl iodide that rather forcing reaction conditions had to be applied for the alkylation process. While the reactions with CH_3I proceeded smoothly in chloroform at room temperature, for the $PO(OMe)_3$ reactions the reagents had to be heated to 80 °C in DMSO for 10–20 days before the formation of **5d** or **7** was complete, and the products could not be isolated pure due to partial decomposition. This supports the notion that alkylations by trimethyl phosphate and by methyl iodide occur by different mechanisms. The facile alkylation by methyl iodide in nonpolar media, and mechanistic evidence from kinetic data,[3–5] support the assumption that it occurs as an intramolecular process at the zinc-bound thiolates. The forcing conditions and the polar environment needed for alkylation by trimethyl phosphate, as well as mechanistic information from related alkylations of $Zn(SR_4)^{2-}$ species by trimethyl phosphate in very polar solvents,[26] make it likely that the thiolates dissociate from zinc before they react.

Conclusions

In our series of investigations on the modeling of thiolate alkylating enzymes by zinc complexes the ligands L^1–L^3

 © 2005 Wiley-VCH Verlag GmbH & Co. KGaA, Weinheim

provide a coordination environment for zinc which more closely than before resembles that in the enzymes. While the studies have shown that **L[1]**–**L[3]** are viable tridentate N_2S donors, they have also made clear that the peculiarities of the coordination chemistry of zinc call for a still better control of the donor arrangement and its functionality around the metal center.

The most striking example of this is the fact that despite their high similarity all three ligands yield zinc thiolate complexes **L**·Zn–SR of completely different structure. Although the ZnN_2S_3 pattern in **1**, the $ZnNS_3$ pattern in **2**, and the ZnN_2S_2 pattern in **3** can subsequently be explained, they came as a surprise; the prevention of thiolate bridging on going from **2** to **3** simply by attaching a methyl group on the remote side of the coordination sphere is particularly noteworthy. Likewise, the preferred alkylation at the aliphatic thiolate function of ligand **L[3]** rather than the aromatic thiolate functions of the "substrates" SAr is explainable by the simple fact that aliphatic thiolates are more nucleophilic than aromatic ones. Yet it was not predictable, as the chelate effect should have resulted in a reduced reactivity of the intact zinc-bound **L[3]**. This sheds light on the delicate balance of stability and reactivity in the thiolate alkylating zinc enzymes, specifically cobalamine-independent methionine syntheses.[1,2] In this enzyme the substrate to be methylated is homocysteine while the protein fixes zinc by two cysteine residues which obviously are not to be methylated. Certainly model chemistry still needs some efforts to reproduce this.

Experimental Section

General: For general working and measuring procedures, see ref.[27] Organic starting materials were obtained commercially. Ligands **L[1]**[14] and **L[3]**[20] were prepared according to the published procedures.

Ligand L[2]: 2-(2-Aminoethyl)pyridine (1.95 g, 16.0 mmol) and 2,2-dimethylthiirane (1.77 g, 20.0 mmol) were refluxed for 30 h in 30 mL of toluene. After cooling to room temp. and filtration the solvent was removed in vacuo and the residue distilled to give 1.08 g (32%) of **L[2]** as a colorless liquid, b.p. 89–90 °C/10^{-1} mbar. $C_{11}H_{18}N_2S$ (210.34): calcd. C 62.81, H 8.63, N 13.32; found C 62.87, H 8.52, N 13.74. IR (film): $\tilde{\nu}$ = 1587 s, 1568 s cm^{-1} (C=N). ^1H NMR ($CDCl_3$): δ = 1.39 (s, 6 H, CH_3), 1.74 (s, 1 H, SH), 2.70 (s, 2 H, CH_2), 2.98–3.18 (m, 4 H, CH_2), 7.13–7.22 (m, 2 H, Ar), 7.64 (m, 1 H, Ar), 8.58 (d, J = 3.8 Hz, 1 H, Ar) ppm.

1: A solution of $Zn(NO_3)_2·6H_2O$ (0.440 g, 1.48 mmol) in 50 mL of methanol was added dropwise, with stirring, within 2 h to a solution of **HL[1]** (0.291 g, 1.48 mmol) and 1.48 mmol of $KOCH_3$ in 50 mL of methanol. Then, a solution of KSC_6H_5 (0.219 g, 1.48 mmol) in 50 mL of methanol was added and the mixture stirred for 15 h. The solvent was removed in vacuo, the residue was taken up in 40 mL of chloroform, and filtered. The solvent was removed in vacuo again and the residue crystallized from chloroform/hexane (1:1) to give 0.35 g (64%) of **1** as off-white crystals, m.p. 198 °C. $C_{16}H_{20}N_2S_2Zn·CHCl_3$ (369.87 + 119.38): calcd. C 41.73, H 4.33, N 5.73, S 13.11; found C 43.15, H 4.58, N 7.30, S 12.60. IR (KBr): $\tilde{\nu}$ = 1604 s, 1575 s cm^{-1} (C=N). ^1H NMR ($CDCl_3$): δ = 1.28 (br. s, 6 H, CH_3), 2.18 (br. s, 1 H, CH_2), 2.78 (br. s, 1 H, CH_2), 3.91 (br. s, 1 H, CH_2), 4.06 (br. s, 1 H, CH_2), 6.76–6.91 (m, 3 H, Ar), 7.14–7.36 (m, 5 H, Ar), 7.71 (m, 1 H, Ar), 8.36 (br. s, 1 H, Ar) ppm.

2a: A solution of $Zn(NO_3)_2·4H_2O$ (0.447 g, 1.71 mmol) in 40 mL of methanol was added dropwise, with stirring, over a period of 1 h to a solution of **HL[2]** (0.360 g, 1.71 mmol) and 1.71 mmol of $NaOCH_3$ in 50 mL of methanol. Then, a solution of KSC_6H_5 (0.254 g, 1.71 mmol) in 40 mL of methanol was added and the mixture stirred for 15 h. The solvent was removed in vacuo and the residue taken up in 30 mL of chloroform and filtered. The solvent was then removed in vacuo again and the product crystallized from chloroform/hexane (1:1) to give 0.312 g (48%) of **2a** as colorless crystals, m.p. 191 °C. IR (KBr): $\tilde{\nu}$ = 1594 s, 1577 s cm^{-1} (C=N). ^1H NMR ($CDCl_3$): δ = 1.09 (br. s, 3 H, CH_3), 1.41 (br. s, 3 H, CH_3), 2.51–3.06 (br. m, 6 H, CH_2), 6.77–6.91 (m, 3 H, Ar), 7.11 (t, J = 7.4 Hz, 2 H, Ph), 7.20–7.29 (m, 2 H, Ar), 7.58 (m, 1 H, Ar), 8.33 (br. s, 1 H, Ar) ppm.

2b: Like **2a** from $Zn(NO_3)_2·4H_2O$ (0.307 g, 1.17 mmol), **HL[2]** (0.247 g, 1.17 mmol), and HSC_6H_4-*p*-CH_3 (0.145 g, 1.17 mmol). Yield 0.246 g (53%) of **2b** as colorless crystals, m.p. 191 °C. $C_{18}H_{24}N_2S_2Zn$ (397.92): calcd. C 54.33, H 6.08, N 7.04, S 16.12; found C 53.94, H 6.01, N 7.34, S 16.00. IR (KBr): $\tilde{\nu}$ = 1594 s, 1567 m cm^{-1} (C=N). ^1H NMR ($CDCl_3$): δ = 1.12 (br. s, 3 H, CH_3), 1.40 (br. s, 3 H, CH_3), 2.11 (s, 3 H, CH_3), 2.42–3.05 (m, 6 H, CH_2), 6.67 (d, J = 7.8 Hz, 2 H, Ar), 7.07–7.17 (m, 4 H, Ar), 7.59 (m, 1 H, Ar), 8.35 (s, 1 H, Ar) ppm.

2c: Like **2a** from $Zn(NO_3)_2·4H_2O$ (0.468 g, 1.79 mmol), **HL[2]** (0.377 g, 1.79 mmol), and HSC_6H_4-*p*-NO_2 (0.346 g, 1.79 mmol). Yield 0.353 g (46%) of **2c** as colorless crystals, m.p. 182 °C. $C_{17}H_{21}N_3O_2S_2Zn$ (428.89): calcd. C 47.61, H 4.93, N 9.80, S 14.95; found C 47.52, H 4.98, N 9.78, S 14.87. IR (KBr): $\tilde{\nu}$ = 1570 s cm^{-1} (C=N). ^1H NMR ($CDCl_3$): δ = 1.28 (s, 3 H, CH_3), 1.44 (s, 3 H, CH_3), 2.54–3.20 (m, 6 H, CH_2), 7.11–7.18 (m, 2 H, Ar), 7.45 (d, J = 8.6 Hz, 2 H, Ar), 7.56–7.73 (m, 3 H, Ar), 8.34 (br. s, 1 H, Ar) ppm.

2d: Like **2a** from $Zn(NO_3)_2·4H_2O$ (0.439 g, 1.68 mmol), **HL[2]** (0.353 g, 1.68 mmol), and HSC_6F_5 (0.336 g, 1.68 mmol). Yield 0.358 g (45%) of **2d** as colorless crystals, m.p. 206 °C. $C_{17}H_{17}F_5N_2S_2Zn$ (473.85): calcd. C 43.09, H 3.62, N 5.91, S 13.53; found C 43.04, H 3.48, N 6.04, S 13.53. IR (KBr): $\tilde{\nu}$ = 1598 s, 1570 s cm^{-1} (C=N). ^1H NMR ($CDCl_3$): δ = 1.29 (br. s, 3 H, CH_3), 1.40 (br. s, 3 H, CH_3), 2.53–3.33 (m, 6 H, CH_2), 4.73 (br. s, 1 H, NH), 7.20–7.27 (m, 2 H, Ar), 7.71 (t, J = 7.6 Hz, 1 H, Ar), 8.49 (d, J = 4.6 Hz, 1 H, Ar) ppm. ^{19}F NMR ($CDCl_3$): δ = –134.0 (s, 2 F), –163.2 (s, 1 F), –165.1 (s, 2 F) ppm.

L[3]·ZnCl: A solution of **HL[3]** (0.122 g, 3.04 mmol) in 15 mL of methanol was treated dropwise with stirring first with NaOH (0.122 g, 3.04 mmol) in 5 mL of methanol and then with $ZnCl_2$ (0.414 g, 3.04 mmol) in 5 mL of methanol. The mixture was stirred for 20 h, filtered, and the filtrate evaporated to dryness. Recrystallization of the residue from methanol yielded 0.374 g (38%) of **L[3]**·ZnCl as colorless crystals, m.p. 203 °C. $C_{12}H_{19}ClN_2S_2Zn$ (324.20): calcd. C 44.46, H 5.91, N 8.64; found C 43.52, H 5.88, N 8.28. IR (KBr): $\tilde{\nu}$ = 1610 s, 1569 s cm^{-1} (C=N). ^1H NMR ($CDCl_3$): δ = 1.42 (s, 3 H, CH_3), 1.60 (s, 3 H, CH_3), 2.55 (d, J = 13.0 Hz, 1 H, CH_2), 2.78 (s, 3 H, NCH_3), 2.87–3.74 (m, 5 H, CH_2), 7.33 (d, J = 7.8 Hz, 1 H, Ar), 7.47 (t, J = 6.5 Hz, 1 H, Ar), 7.88 (m, 1 H, Ar), 8.81 (d, J = 5.0 Hz, 1 H, Ar) ppm.

3a: A solution of $HSCH_2CF_3$ (0.058 g, 0.50 mmol) and 1 mL of a 0.5 M solution of $NaOCH_3$ in methanol (0.50 mmol) in 30 mL of methanol was added dropwise, with stirring, to a solution of

 © 2005 Wiley-VCH Verlag GmbH & Co. KGaA, Weinheim

L^3·ZnBr (0.184 g, 0.50 mmol) in 60 mL of methanol. After stirring overnight the solvent was removed in vacuo. The residue was taken up in 30 mL of chloroform and filtered. After removal of the solvent in vacuo the product was recrystallized from methanol to yield 32 mg (16%) of **3a** as colorless crystals, m.p. 125 °C. $C_{14}H_{21}F_3N_2S_2Zn$ (403.85): calcd. C 41.64, H 5.24, N 6.94, S 15.88; found C 41.68, H 4.56, N 6.45, S 15.44. IR (KBr): $\tilde{\nu}$ = 1608 s, 1571 s cm^{-1} (C=N). ^{1}H NMR ($CDCl_3$): δ = 1.40 (s, 3 H, CH_3), 1.57 (s, 3 H, CH_3), 2.47 (d, J = 13.0 Hz, 1 H, CH_2), 2.77 (s, 3 H, NCH_3), 2.80–3.59 (m, 7 H, CH_2), 7.31 (d, J = 7.8 Hz, 1 H, Ar), 7.45 (t, J = 6.5 Hz, 1 H, Ar), 7.86 (m, 1 H, Ar), 8.87 (d, J = 4.4 Hz, 1 H, Ar) ppm. ^{19}F NMR ($CDCl_3$): δ = –67.29 (s) ppm.

3b: $HSCH_2C_6H_5$ (0.124 g, 1.00 mmol) in 50 mL of methanol was treated with 2.00 mL (1.00 mmol) of a 0.5 M methanol solution of $NaOCH_3$ and then added dropwise, with stirring, to a solution of **L^3·**ZnBr (0.369 g, 1.00 mmol) in 80 mL of methanol. After stirring overnight the solvent was removed in vacuo, the residue taken up in 25 mL of chloroform, and filtered. The filtrate was evaporated to dryness and the product washed with diethyl ether and dried in vacuo. Recrystallization from hexane/chloroform (2:1) yielded 0.239 g (58%) of **3b** as a colorless powder, m.p. 139 °C. $C_{19}H_{26}N_2S_2Zn$ (411.95): calcd. C 55.40, H 6.36, N 6.80, S 15.57; found C 55.14, H 6.20, N 6.67, S 14.74. IR (KBr): $\tilde{\nu}$ = 1607 s, 1568 m cm^{-1} (C=N). ^{1}H NMR ($CDCl_3$): δ = 1.34 (s, 3 H, CH_3), 1.61 (s, 3 H, CH_3), 2.50 (d, J = 13.0 Hz, 1 H, CH_2), 2.67 (s, 3 H, NCH_3), 2.76–3.50 (m, 5 H, CH_2), 3.87 (m, 2 H, CH_2), 7.07–7.28 (m, 6 H, Ar), 7.42 (t, J = 4.2 Hz, 1 H, Ar), 7.76 (m, 1 H, Ar), 8.31 (d, J = 5.4 Hz, 1 H, Ar) ppm.

3c: Like **3b** from $HSCH_2C_6H_4Cl$ (0.159 g, 1.00 mmol), 1.00 mmol of $NaOCH_3$, and **L^3·**ZnBr (0.369 g, 1.00 mmol). Yield 0.331 g (74%) of **3c** as a colorless powder, m.p. 164 °C. $C_{19}H_{25}N_2S_2ClZn$ (446.39): calcd. C 51.12, H 5.84, N 6.28, S 14.37; found C 51.08, H 5.55, N 6.13, S 13.48. IR (KBr): $\tilde{\nu}$ = 1606 s, 1566 s cm^{-1} (C=N). ^{1}H NMR ($CDCl_3$): δ = 1.35 (s, 3 H, CH_3), 1.60 (s, 3 H, CH_3), 2.51 (d, J = 13.0 Hz, 1 H, CH_2), 2.55 (s, 3 H, NCH_3), 2.77–3.48 (m, 5 H, CH_2), 3.84 (m, 2 H, CH_2), 7.16–7.39 (m, 6 H, Ar), 7.79 (m, 1 H, Ar), 8.38 (d, J = 5.2 Hz, 1 H, Ar) ppm.

3d: Like **3b** from HSC_6H_5 (0.115 g, 1.00 mmol), 1.00 mmol of $NaOCH_3$, and **L^3·**ZnBr (0.369 g, 1.00 mmol). Yield 0.224 g (56%) of **3d** as colorless crystals, m.p. 122 °C. $C_{18}H_{24}N_2S_2Zn$ (397.92): calcd. C 54.33, H 6.08, N 7.04, S 16.12; found C 54.30, H 6.29, N 6.99, S 15.43. IR (KBr): $\tilde{\nu}$ = 1608 s, 1578 s cm^{-1} (C=N). ^{1}H NMR ($CDCl_3$): δ = 1.18 (s, 3 H, CH_3), 1.38 (s, 3 H, CH_3), 2.49 (d, J = 13.0 Hz, 1 H, CH_2), 2.66 (s, 3 H, NCH_3), 2.74–3.20 (m, 5 H, CH_2), 6.90–6.95 (m, 3 H, Ar), 7.31–7.44 (m, 4 H, Ar), 7.92 (m, 1 H, Ar), 8.58 (d, J = 5.2 Hz, 1 H, Ar) ppm.

3e: Like **3c** from $HSC_6H_4NO_2$ (0.103 g, 0.66 mmol), 0.66 mmol of $NaOCH_3$, and **L^3·**ZnBr (0.244 g, 0.66 mmol). Yield 0.202 g (69%) of **3e** as yellow crystals, m.p. 81 °C. $C_{18}H_{23}N_3S_2O_2Zn$ (442.92): calcd. C 48.81, H 5.23, N 9.49, S 14.48; found C 48.50, H 5.05, N 9.30, S 14.28. IR (KBr): $\tilde{\nu}$ = 1609 s, 1569 s cm^{-1} (C=N). ^{1}H NMR ($CDCl_3$): δ = 1.34 (s, 3 H, CH_3), 1.47 (s, 3 H, CH_3), 2.54 (d, J = 13.0 Hz, 1 H, CH_2), 2.73 (s, 3 H, NCH_3), 2.80–3.47 (m, 5 H, CH_2), 7.33 (d, J = 7.8 Hz, 1 H, Ar), 7.44 (t, J = 6.5 Hz, 1 H, Ar), 7.73 (d, J = 8.8 Hz, 2 H, Ar), 7.84–7.93 (m, 3 H, Ar), 8.72 (d, J = 1.0 Hz, 1 H, Ar) ppm.

3f: Like **3c** from HSC_6F_5 (0.100 g, 0.50 mmol), 0.50 mmol of $NaOCH_3$, and **L^3·**ZnBr (0.184 g, 0.50 mmol). Yield 0.145 g (59%) of **3f** as colorless crystals, m.p. 110 °C. $C_{18}H_{19}F_5N_2S_2Zn$ (487.88): calcd. C 44.31, H 3.93, N 5.74, S 13.15; found C 44.12, H 3.46, N 5.37, S 11.88. IR (KBr): $\tilde{\nu}$ = 1611 s, 1571 m cm^{-1} (C=N). ^{1}H NMR ($CDCl_3$): δ = 1.26 (s, 3 H, CH_3), 1.57 (s, 3 H, CH_3), 2.53 (d, J = 13.0 Hz, 1 H, CH_2), 2.81 (s, 3 H, NCH_3), 2.85–3.53 (m, 5 H, CH_2), 7.31 (d, J = 7.8 Hz, 1 H, Ar), 7.46 (t, J = 6.3 Hz, 1 H, Ar), 7.80 (t, J = 7.2 Hz, 1 H, Ar), 8.85 (d, J = 5.0 Hz, 1 H, Ar) ppm. ^{19}F NMR ($CDCl_3$): δ = –163.3 (s, 2 F), –161.9 (s, 1 F), –133.9 (s, 2 F) ppm.

4d: A solution of **3d** (0.100 g, 0.25 mmol) in 15 mL of chloroform was treated with methyl iodide (0.036 g, 0.25 mmol). After stirring for 3 d the solvent was removed in vacuo, the residue washed with diethyl ether, and dried in vacuo to give 0.078 g (57%) of **4d** as a colorless powder, m.p. 128 °C. $C_{19}H_{27}IN_2S_2Zn$ (539.86): calcd. C 42.27, H 5.04, N 5.19, S 11.14; found C 39.26, H 5.19, N 5.56, S 12.04. IR (KBr): $\tilde{\nu}$ = 1609 s, 1569 m cm^{-1} (C=N). ^{1}H NMR ($CDCl_3$): δ = 1.26 (s, 3 H, CH_3), 1.38 (s, 3 H, CH_3), 2.03 (s, 3 H, SCH_3), 2.50 (d, J = 9.2 Hz, 1 H, CH_2), 2.81 (s, 3 H, NCH_3), 2.84–3.48 (m, 5 H, CH_2), 6.96–7.00 (m, 3 H, Ar), 7.10–7.44 (m, 4 H, Ar), 7.83 (br. d, J = 6.2 Hz, 1 H, Ar), 8.87 (br. s, 1 H, Ar) ppm.

4e: Like **4d** from **3e** (0.090 g, 0.20 mmol) and methyl iodide (0.029 g, 0.20 mmol). Yield 0.064 g (54%) of **4e** as a yellow powder, m.p. 53 °C. $C_{19}H_{26}IN_3O_2S_2Zn$ (584.86): calcd. C 39.02, H 4.48, N 7.18, S 10.97; found C 39.30, H 4.64, N 7.02, S 10.67. IR (KBr): $\tilde{\nu}$ = 1611 s, 1570 m cm^{-1} (C=N). ^{1}H NMR ($CDCl_3$): δ = 1.34 (s, 3 H, CH_3), 1.44 (s, 3 H, CH_3), 2.06 (s, 3 H, SCH_3), 2.54 (s, 1 H, CH_2), 2.65 (s, 3 H, NCH_3), 2.79–3.18 (m, 5 H, CH_2), 7.28 (d, J = 7.2 Hz, 1 H, Ar), 7.61 (d, J = 8.8 Hz, 2 H, Ar), 7.68–7.84 (m, 2 H, Ar), 8.18 (d, J = 9.0 Hz, 2 H, Ar), 8.66 (br. s, 1 H, Ar) ppm.

4f: Like **4d** from **3f** (0.101 g, 0.21 mmol) and methyl iodide (0.030 g, 0.21 mmol). Yield 0.077 g (58%) of **4f** as a colorless powder, m.p. 58 °C. $C_{19}H_{22}F_5IN_2S_2Zn$ (629.81): calcd. C 36.23, H 3.52, N 4.45, S 10.18; found C 34.78, H 3.27, N 5.13, S 9.72. IR (KBr): $\tilde{\nu}$ = 1610 s, 1571 m cm^{-1} (C=N). ^{1}H NMR ($CDCl_3$): δ = 1.36 (s, 3 H, CH_3), 1.48 (s, 3 H, CH_3), 2.11 (s, 3 H, SCH_3), 2.48 (s, 1 H, CH_2), 2.83 (s, 3 H, NCH_3), 2.95–3.66 (m, 5 H, CH_2), 7.27–7.47 (m, 2 H, Ar), 7.68–7.80 (m, 1 H, Ar), 8.67 (br. s, 1 H, Ar) ppm. ^{19}F NMR ($CDCl_3$): δ = –163.1 (s, 2 F), –161.9 (s, 1 F), –132.9 (s, 2 F) ppm.

5d: A solution of **3d** (0.116 g, 0.29 mmol) and $PO(OMe)_3$ (0.041 g, 0.29 mmol) in 15 mL of DMSO was stirred at 80 °C for two weeks. The solvent was then removed by distillation in vacuo. The residue was washed with diethyl ether and dried in vacuo to give 0.116 g (74%) of **5d** as a slightly yellow wax which could not be purified further and hence was identified only by ^{1}H NMR spectroscopy in $CDCl_3$: δ = 1.40 (br. s, 6 H, CH_3), 1.73 (s, 3 H, SCH_3), 2.55–3.39 (m, 9 H, NCH_3/CH_2), 3.63 (d, J = 11.0 Hz, 6 H, OCH_3), 6.90–7.10 (m, 3 H, Ar), 7.32–7.52 (m, 4 H, Ar), 7.86 (t, J = 7.6 Hz, 1 H, Ar), 8.83 (br. s, 1 H, Ar) ppm. ^{31}P NMR ($CDCl_3$): δ = 0.91 ppm.

Complex 6. a) From 3d: A solution of **3d** (0.120 g, 0.30 mmol) and methyl iodide (0.214 g, 1.50 mmol) in 15 mL of chloroform was stirred for 3 d. The solvent was then removed in vacuo and the residue extracted with two 10-mL portions of diethyl ether. The remaining product was dried in vacuo to give 0.148 g (88%) of **6** as a colorless powder, m.p. 59 °C. $C_{13}H_{22}I_2N_2SZn$ (557.59): calcd. C 28.00, H 3.98, N 5.02, S 5.75; found C 27.48, H 3.97, N 5.53, S 5.27. IR (KBr): $\tilde{\nu}$ = 1610 s, 1570 m cm^{-1} (C=N). ^{1}H NMR ($CDCl_3$): δ = 1.53 (s, 6 H, CH_3), 2.18 (s, 3 H, SCH_3), 2.91 (s, 3 H, NCH_3), 3.18 (br. s, 2 H, CH_2), 3.41–3.52 (m, 4 H, CH_2), 7.41–7.50 (m, 2 H, Ar), 7.90 (m, 1 H, Ar), 8.87 (br. s, 1 H, Ar) ppm.

The diethyl ether phase was evaporated to dryness and the remaining $CH_3SC_6H_5$ identified by ^{1}H NMR ($CDCl_3$): δ = 2.47 (s, 3 H, CH_3), 7.12–7.28 (m, 5 H, Ph) ppm.

b) From 3e: As before from **3e** (0.100 g, 0.23 mmol) and methyl iodide (0.326 g, 2.30 mmol). Yield 0.113 g (88%) of **6**. Identifica-

 © 2005 Wiley-VCH Verlag GmbH & Co. KGaA, Weinheim

Table 1. Crystallographic details.

	1·2 $CHCl_3$	**2a**	**L^3**·ZnCl	**3d**	**3e**	**3f**
Empirical formula	$C_{34}H_{42}Cl_6N_4S_4Zn_2$	$C_{34}H_{44}N_4S_4Zn_2$	$C_{12}H_{19}ClN_2SZn$	$C_{18}H_{24}N_2S_2Zn$	$C_{18}H_{23}N_3O_2S_2Zn$	$C_{18}H_{19}F_5N_2S_2Zn$
Molecular mass	978.49	767.79	324.17	397.88	442.88	487.84
Crystal size (mm)	0.05×0.10×0.10	0.06×0.08×0.4	0.13×0.14×0.35	0.06×0.08×0.15	0.05×0.14×0.20	0.07×0.10×0.22
Space group	$P\bar{1}$	$P\bar{1}$	$P2_1/n$	$P2_12_12_1$	$P2_1/c$	$P2_1/n$
Z	1	1	4	4	4	4
a [Å]	8.801(3)	7.929(2)	8.203(1)	7.645(2)	16.582(3)	10.88(2)
b [Å]	11.201(4)	10.279(2)	14.979(2)	10.716(2)	14.918(3)	17.73(3)
c [Å]	11.656(4)	12.440(2)	11.788(2)	23.273(5)	8.254(2)	11.01(2)
α [°]	102.573(6)	94.38(3)	90	90	90	90
β [°]	91.473(6)	105.75(3)	93.436(2)	90	96.545(4)	98.97(4)
γ [°]	109.623(5)	108.60(3)	90	90	90	90
V [Å³]	1050.3(6)	910(3)	1445.8(4)	1906.6(6)	2028.4(6)	2096(7)
d(calcd.)[g cm^{-3}]	1.55	1.40	1.49	1.39	1.45	1.55
μ(Mo-K_α) [mm^{-1}]	1.75	1.58	2.01	1.51	1.43	1.42
hkl range	h: –11 to 11	h: –10 to 10	h: –10 to 10	h: –7 to 10	h: –20 to 23	h: –14 to 14
	k: –14 to 14	k: –14 to 13	k: –19 to 19	k: –8 to 13	k: –15 to 19	k: –23 to 22
	l: –15 to 15	l: –16 to 15	l: –15 to 15	l: –30 to 9	l: –10 to 10	l: –14 to 14
Measured reflections	9099	8042	12 971	7110	13 303	18 628
Independent reflections	4801	4203	3552	4233	5414	5061
Observed reflections [$I > 2\sigma(I)$]	3070	2211	2944	1918	2492	1628
parameters	221	199	154	208	235	253
Refined reflections	4801	4203	3552	4233	5414	5061
R_1 (obsd.refl.)	0.063	0.038	0.028	0.062	0.049	0.041
wR_2 (all refl.)	0.178	0.078	0.082	0.222	0.130	0.147
Res. electron density [e Å^{-3}]	+1.2/–1.6	+0.9/–1.0	+0.7/–0.6	+0.5/–0.7	+0.5/–0.7	+0.4/–0.6

tion of $CH_3SC_6H_4$-*p*-NO_2 by ^{1}H NMR ($CDCl_3$): δ = 2.47 (s, 3 H, CH_3), 7.19–7.25 (m, 2 H, Ar), 8.03–8.10 (m, 2 H, Ar) ppm.

c) From 3f: As before from **3f** (0.050 g, 0.10 mmol) and methyl iodide (0.142 g, 1.00 mmol). Yield 0.047 g (84%) of **6**. Identification of $CH_3SC_6F_5$ by ^{1}H NMR ($CDCl_3$): δ = 2.47 (CH_3) ppm.

Complex 7: Complex **3d** (0.122 g, 0.31 mmol) and trimethyl phosphate (0.317 g, 1.55 mmol) in 15 mL of DMSO were stirred at 80 °C for two weeks. The solvent was then removed by distillation in vacuo. The residue was extracted with two 10-mL portions of diethyl ether and dried in vacuo to give 0.121 g (71%) of **7** as an impure, waxy material which was identified by ^{1}H NMR ($CDCl_3$): δ = 1.45 (s, 6 H, CH_3), 2.06 (d, J = 2.6 Hz, 3 H, SCH_3), 2.61 (s, 3 H, NCH_3), 2.72–3.05 (m, 4 H, CH_2), 3.32 (s, 2 H, CH_2), 3.64 (d, J = 11.0 Hz, 12 H, OCH_3), 7.15–7.23 (m, 2 H, Ar), 7.46 (t, J = 8.0 Hz, 1 H, Ar), 7.72 (d, J = 6.0 Hz, 1 H, Ar) ppm. ^{31}P NMR ($CDCl_3$): δ = 0.55 ppm.

The diethyl ether phase was evaporated to dryness and the remaining $CH_3SC_6H_5$ identified by ^{1}H NMR spectroscopy as above.

Structure Determinations:[28] Crystals were obtained as described above. Diffraction data were recorded at room temp. for **3d** and **3f** and at 220 K for **1**, **2a**, **3e**, and **L^3**·ZnCl with a Bruker Smart CCD diffractometer. Empirical absorption corrections (SADABS) were applied for **1**, **2a**, and **L^3**·ZnCl. The structures were solved and refined anisotropically with the SHELX program suite.[29] Hydrogen atoms were included with fixed distances and isotropic temperature factors 1.5-times those of their attached atoms. Parameters were refined against F^2. The R values are defined as $R_1 = \Sigma|F_o - F_c|/\Sigma F_o$ and $wR_2 = \{\Sigma[w(F_o^2 - F_c^2)^2]\Sigma[w(F_o^2)^2]\}^{1/2}$. Drawings were produced with SCHAKAL.[30] Table 1 lists the crystallographic data.

Acknowledgments

This work was supported by the Deutsche Forschungsgemeinschaft and the Fonds der Chemischen Industrie. We are indebted to Drs. W. Deck and H. Brombacher for help with the structure determinations and to Mr. B. Benkmil for assistance in the laboratory.

[1] G. Parkin, *Chem. Rev.* **2004**, *104*, 699–767.
[2] R. G. Matthews, *Acc. Chem. Res.* **2001**, *34*, 681–689.
[3] U. Brand, M. Rombach, H. Vahrenkamp, *Chem. Commun.* **1998**, 2717–2718.
[4] U. Brand, M. Rombach, J. Seebacher, H. Vahrenkamp, *Inorg. Chem.* **2001**, *40*, 6151–6157.
[5] J. Seebacher, M. Ji, H. Vahrenkamp, *Eur. J. Inorg. Chem.* **2004**, 409–417.
[6] C. A. Grapperhaus, T. Tuntulani, J. H. Reibenspies, M. Y. Darensbourg, *Inorg. Chem.* **1998**, *37*, 4052–4058.
[7] B. M. Bridgewater, T. Fillebeen, R. A. Friesner, G. Parkin, *J. Chem. Soc., Dalton Trans.* **2000**, 4494–4496.
[8] B. S. Hammes, C. J. Carrano, *Inorg. Chem.* **2001**, *40*, 919–927.
[9] C. R. Warthen, B. S. Hammes, D. C. Crans, C. J. Carrano, *J. Biol. Inorg. Chem.* **2001**, *6*, 82–90.
[10] M. Machuqueiro, T. Darbre, *J. Inorg. Biochem.* **2003**, *94*, 193–196.
[11] S. J. Chiou, J. Innocent, C. G. Riordan, K. C. Lam. L. Liable-Sands, A. L. Rheingold, *Inorg. Chem.* **2000**, *39*, 4347–4353.
[12] U. Brand, H. Vahrenkamp, *Inorg. Chem.* **1995**, *34*, 3285–3293.
[13] U. Brand, H. Vahrenkamp, *Chem. Ber.* **1996**, *129*, 435–440.
[14] U. Brand, H. Vahrenkamp, *Inorg. Chim. Acta* **2000**, *308*, 97–102.
[15] A. Trösch, H. Vahrenkamp, *Z. Anorg. Allg. Chem.* **2001**, *627*, 2523–2527.
[16] M. Shu, R. Walz, B. Wu, J. Seebacher, H. Vahrenkamp, *Eur. J. Inorg. Chem.* **2003**, 2502–2511.
[17] B. Benkmil, M. Ji, H. Vahrenkamp, *Inorg. Chem.* **2004**, *43*, 8212–8214.
[18] R. R. Holmes, *Acc. Chem. Res.* **1979**, *12*, 257–266.
[19] B. Kaptein, L. Wang-Griffin, G. Barf, R. M. Kellogg, *J. Chem. Soc., Chem. Commun.* **1987**, 1457–1459.
[20] S. C. Chang, R. D. Sommer, A. L. Rheingold, D. P. Goldberg, *Chem. Commun.* **2001**, 2396–2397.
[21] S. C. Chang, V. V. Karambelkar, R. C. Di Targiani, D. P. Goldberg, *Inorg. Chem.* **2001**, *40*, 194–195.

[22] S. C. Chang, V. V. Karambelkar, R. D. Sommer, A. L. Rheingold, D. P. Goldberg, *Inorg. Chem.* **2002**, *41*, 239–248.
[23] B. S. Hammes, C. J. Carrano, *Inorg. Chem.* **1999**, *38*, 4593–4600.
[24] B. S. Hammes, C. J. Carrano, *J. Chem. Soc., Dalton Trans.* **2000**, 3304–3309.
[25] L. C. Myers, M. P. Terranova, A. E. Ferentz, G. Wanger, G. L. Verdine, *Science* **1993**, *261*, 1164–1167.
[26] J. J. Wilker, S. Lippard, *Inorg. Chem.* **1997**, *36*, 969–978.
[27] M. Förster, R. Burth, A. K. Powell, T. Eiche, H. Vahrenkamp, *Chem. Ber.* **1993**, *126*, 2643–2648.
[28] CCDC-254409 (for **1**), -254410 (for **2a**), -254411 (for **L3·ZnCl**), -254412 (for **3d**), -25440 254413 (for **3e**), and -254414 (for **3f**) contain the supplementary crystallographic data for this paper. These data can be obtained free of charge from The Cambridge Crystallographic Data Centre via www.ccdc.cam.ac.uk/data_request/cif.
[29] *SHELXTL* program package for the Bruker Smart CCD diffractometer, version 5.1, **2002**.
[30] E. Keller, *SCHAKAL* for Windows, University of Freiburg, **1999**.

Received: November 3, 2004

 © 2005 Wiley-VCH Verlag GmbH & Co. KGaA, Weinheim

EurJIC
European Journal of Inorganic Chemistry

Issue 8/2005

Pages 1409–1620

Papers available ahead of print in Early View at www.interscience.wiley.com

Earliest available Table of Contents:
Automatically, free of charge by e-mail through
www.interscience.wiley.com/alerts

COVER PICTURE

The cover picture shows the absorbance of incident UV light in the bipyridine chromophore of a polypyridyl complex of terbium(3+). Subsequent energy transfer to the metal centre results in a metal-centred emission of VIS light. Topical aspects are presented in the Microreview by A. Døssing on p. 1425ff.

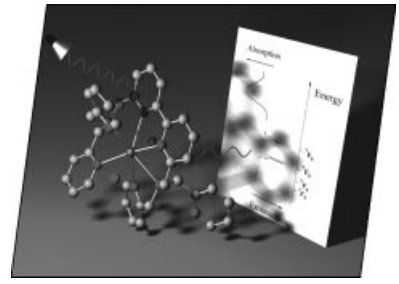

MICROREVIEW

Contents

1425 **A. Døssing***

Luminescence from Lanthanide(3+) Ions in Solution

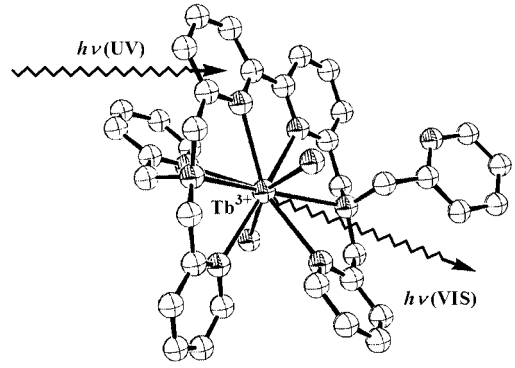

Keywords: Lanthanides / Luminescence / Fluorescent probes

 © 2005 Wiley-VCH Verlag GmbH & Co. KGaA, Weinheim

FULL PAPERS

1435 **H. Yokoyama, K. Yamaguchi,* M. Sugimoto, S. Suzuki**

Cu^{I} and Cu^{II} Complexes Containing Nitrite and Tridentate Aromatic Amine Ligand as Models for the Substrate-Binding Type-2 Cu Site of Nitrite Reductase

Keywords: Bioinorganic chemistry / Copper / N ligands / Tridentate ligands

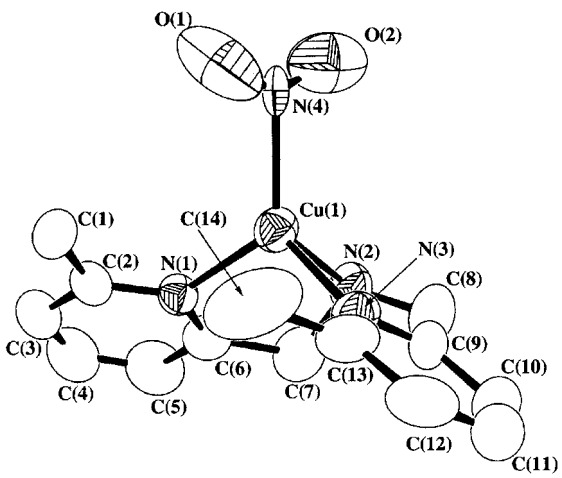

$[Cu^{I}(Me_2bpa)(NO_2)]$

1442 **S. K. Hadjikakou,* C. D. Antoniadis, P. Aslanidis, P. J. Cox, A. C. Tsipis***

An Exploration of the Structural and Bonding Variability in Mixed-Ligand Benzimidazole-2-thione(bromo)(triarylphosphane)dicopper(I) Complexes with Diamond-Shaped $Cu_2(\mu\text{-}X)_2$ Core Structures

Keywords: Bridging ligands / Copper / Density functional calculations / S ligands

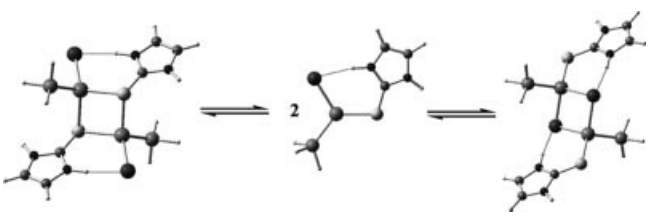

1453 **U. Vogel, K.-C. Schwan, P. Hoemensch, M. Scheer***

Reactivity of Lewis Acid/Base Stabilized Phosphanyl- and Arsanylboranes towards a Platinum(0) Complex

Keywords: Arsenic / Boron / Phosphorus / Reactivity / Platinum

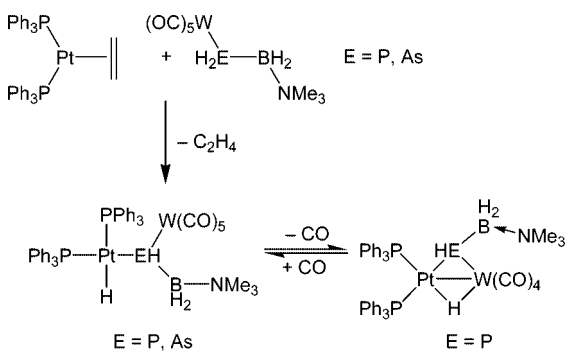

1459 **A. Huber, L. Müller, H. Elias,* R. Klement, M. Valko**

Cobalt(II) Complexes with Substituted Salen-Type Ligands and Their Dioxygen Affinity in *N*,*N*-Dimethylformamide at Various Temperatures

Keywords: Cobalt / Oxygen / Schiff bases / Substituent effects / Thermodynamics

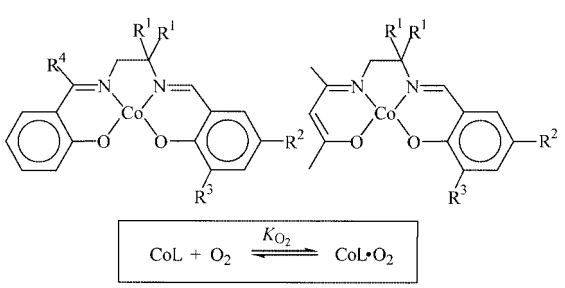

 © 2005 Wiley-VCH Verlag GmbH & Co. KGaA, Weinheim

1468

J. Fresneda, E. de Jesús,* P. Gómez-Sal, C. López Mardomingo

Synthesis of Palladium(II) and Platinum(II) Complexes with Crown Ether Phosphane Ligands: Stille Coupling of Aryl Iodides in Water

Keywords: Aqueous-phase catalysis / Crown compounds / C−C coupling / Palladium / Phosphane ligands

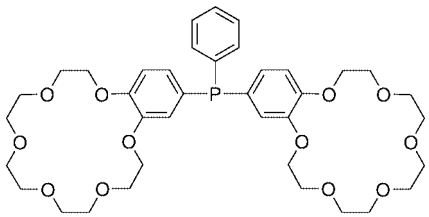

3

1477

P. Kuhn, D. Sémeril, C. Jeunesse, D. Matt,* P. Lutz,* R. Welter

An Efficient Keim-Type Catalyst Based on an Electron-Poor *P,O*-Chelate; Tuning the Selectivity of Ethylene Oligomerisation towards Short α-Olefins

Keywords: Nickel *P,O* complexes / 4-Phosphanylpyrazolonate / Oligomerisation / Phosphorus ylides / Electron-withdrawing ligands / X-ray diffraction

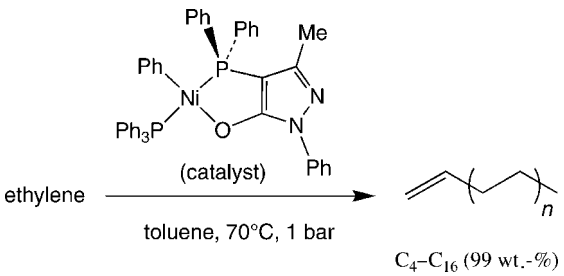

1482

V. Chandrasekhar,* A. Athimoolam, V. Krishnan, R. Azhakar, C. Madhavaiah, S. Verma*

A Copper-Metalated, Hybrid Inorganic−Organic Polymer as an Oxidative Nuclease

Keywords: Chemical nucleases / Phosphazenes / Pendant polymers / Copper complexes / Phosphate ester hydrolysis / Heterogeneous catalysis

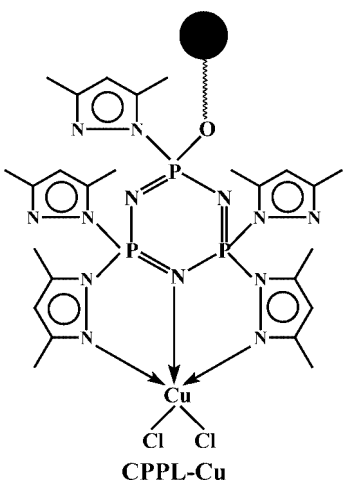

CPPL-Cu

1487

X. Pang, H. Sun, Y. Zhang, Q. Shen,* H. Zhang

Synthesis, Structure, and Luminescent Properties of Guanidinate-Based Terbium Complexes

Keywords: Terbium complex / Guanidinate / Luminescence / Lanthanides

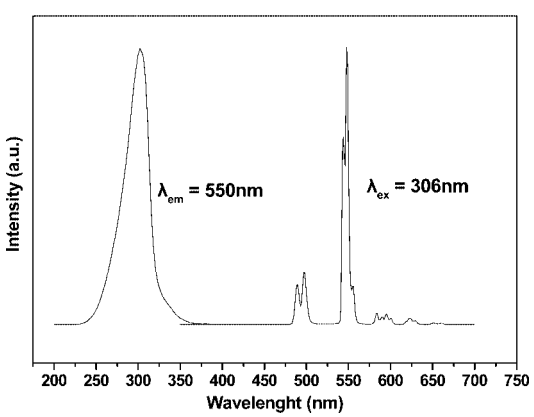

 © 2005 Wiley-VCH Verlag GmbH & Co. KGaA, Weinheim

1492 **A. Barge, M. Botta, U. Casellato, S. Tamburini,* P. A. Vigato**

Selectivity of Asymmetric Macrocyclic Compartmental Lanthanide(III) Complexes towards Alkali and Alkaline-Earth Metal Ions

Keywords: Lanthanides / Schiff bases / Shift reagents / ^{23}Na NMR / Macrocyclic ligands

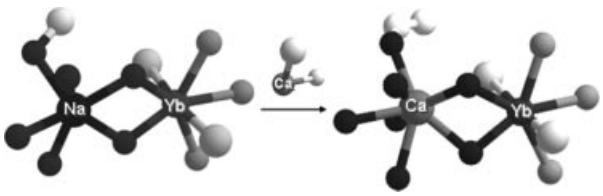

1500 **R. Koner, G.-H. Lee, Y. Wang, H.-H. Wei,* S. Mohanta***

Two New Diphenoxo-Bridged Discrete Dinuclear $Cu^{II}Gd^{III}$ Compounds with Cyclic Diimino Moieties: Syntheses, Structures, and Magnetic Properties

Keywords: Magnetic properties / Compartmental ligands / Gadolinium(III) / Ferromagnetic / Heterometallic complexes

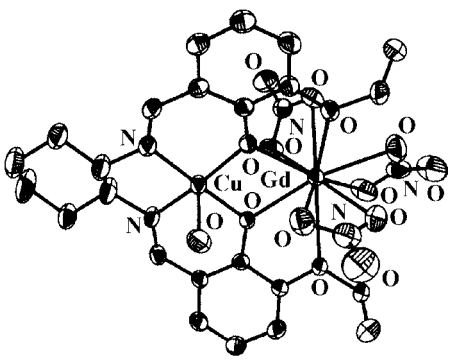

1506 **K. Binnemans,* K. Lodewyckx, B. Donnio, D. Guillon**

Mixed f-d Metallomesogens with an Extended Rigid Core

Keywords: Copper / Lanthanides / Liquid crystals / Metallomesogens / Nickel

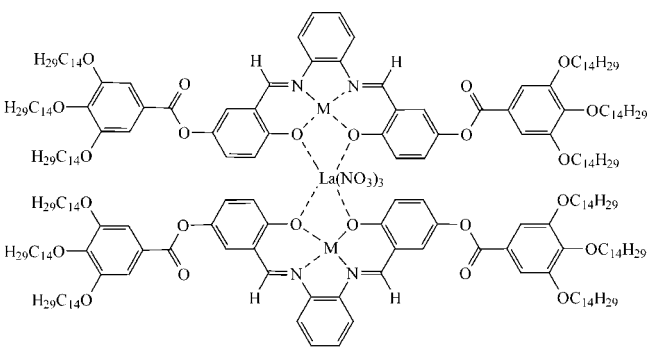

1514 **S. Silver, A. Puranen, R. Sjöholm, T. Repo, R. Leino***

Chiral Indenes and Group-4 Metallocene Dichlorides Containing α- and β-Pinenyl-Derived Ligand Substituents: Synthesis and Catalytic Applications in Polymerization and Carboalumination Reactions

Keywords: Homogeneous catalysis / Indenyl ligands / Metallocenes / Olefin polymerization / Carboalumination

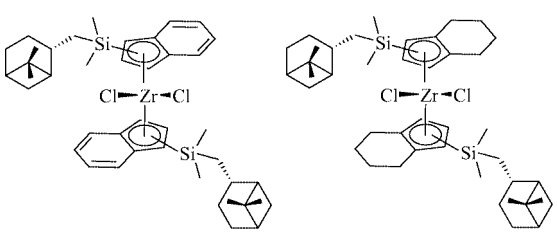

 © 2005 Wiley-VCH Verlag GmbH & Co. KGaA, Weinheim

1530 **J. Klingele (née Hausmann), B. Moubaraki, K. S. Murray, J. F. Boas, S. Brooker***

Dinuclear Copper(II) Complexes of Two Homologous Pyrazine-Based Bis(terdentate) Diamide Ligands

Keywords: N ligands / Copper / Amides / Pyrazine / Hexafluorosilicate

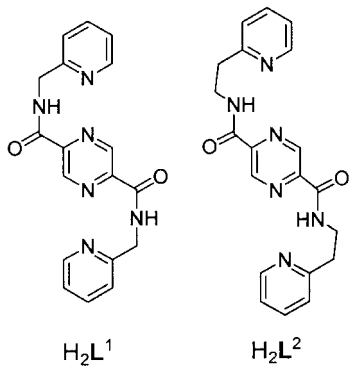

1542 **D. Drewes, E. M. Limanski, B. Krebs***

The First Sandwich-Type Heteropolytungstates Consisting of Trivacant Gallium(III)-Substituted Keggin Fragments

Keywords: Gallium / Heteropolytungstates / Polyoxometalates / Tungsten

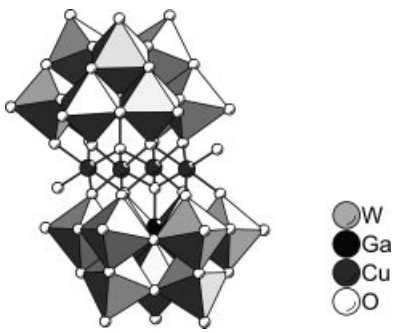

1547 **I. M. Mbomekalle, Y. W. Lu, B. Keita, L. Nadjo,* W. A. Neiwert, K. I. Hardcastle, C. L. Hill,* T. M. Anderson**

Crystallographic Studies of a Molybdenum-Rich Diarsenotungstate and Reaction of Fe^{III} with its Isomerically Pure α_1- and α_2-Monolacunary Derivatives

Keywords: Polyoxometalates / Cyclic voltammetry / Molybdenum / Iron / Tungsten

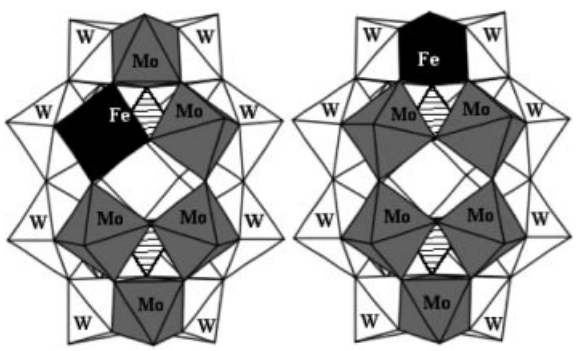

1552 **K. Flogeac, E. Guillon,* M. Aplincourt**

Co-Adsorption of Copper(II) and 3-Amino-1,2,4-triazole at a Water−Natural Macromolecular Compound Interface: Molecular Structure from Adsorption Isotherms Combined with X-ray Absorption Measurements

Keywords: Adsorption / Environmental chemistry / Pesticides / Structure elucidation / Surface chemistry / X-ray absorption spectroscopy

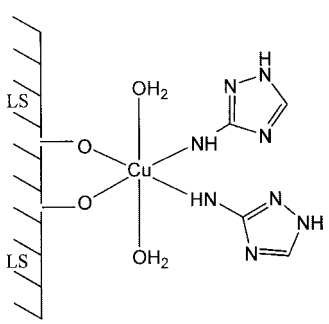

 © 2005 Wiley-VCH Verlag GmbH & Co. KGaA, Weinheim

1559 **M. C. Viola, J. A. Alonso,* J. C. Pedregosa, R. E. Carbonio**

Crystal Structure and Magnetism of the Double Perovskite $Sr_3Fe_2MoO_9$: A Neutron Diffraction Study

Keywords: Double perovskite / Neutron diffraction / Antiferromagnetic ordering

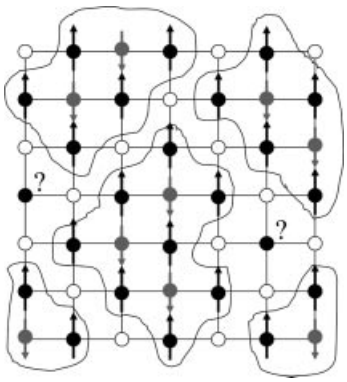

1565 **L. Dubois, D.-F. Xiang, X.-S. Tan, J.-M. Latour**

Kinetic and Thermodynamic Studies of the Disproportionation of Hydrogen Peroxide by Dimanganese(II,II) and -(II,III) Complexes of a Bridging Phenolate Ligand

Keywords: Manganese / Catalase / H_2O_2 disproportionation / Kinetics

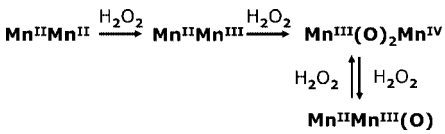

1572 **S. A. Barnett, N. R. Champness,* C. Wilson**

One-Dimensional Chains Formed by First-Row Transition Metal(II) Nitrates and Pyrimidine – Influence of Water Coordination on Structural Reliability

Keywords: Coordination frameworks / Coordination polymer / Crystal structure / Metal nitrates / Pyrimidine

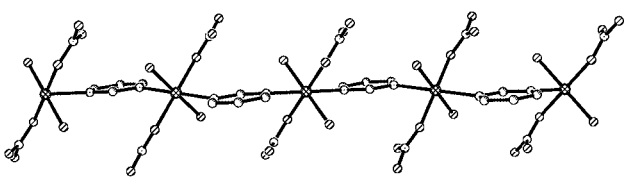

1577 **C. A. S. Barbosa, A. M. D. C. Ferreira, V. R. L. Constantino***

Synthesis and Characterization of Magnesium-Aluminum Layered Double Hydroxides Containing (Tetrasulfonated porphyrin)cobalt

Keywords: Composites / Intercalations / Layered compounds / Organic–inorganic hybrid composites / Porphyrins

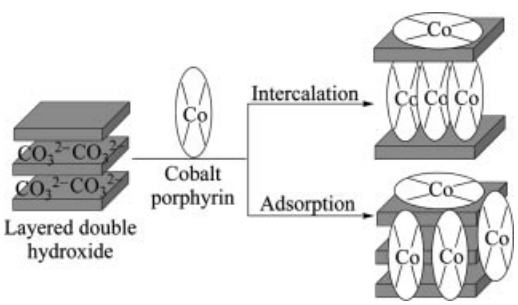

1585 **Y. Jiang, C. Xi,* Y. Liu, J. Niclós-Gutiérrez,* D. Choquesillo-Lazarte**

Intramolecular "CH···π(Metal Chelate Ring) Interactions" as Structural Evidence for Metalloaromaticity in Bis(pyridine-2,6-diimine)Ru^{II} Complexes

Keywords: Metalloaromaticity / Ruthenium / CH···π interaction / Chelates

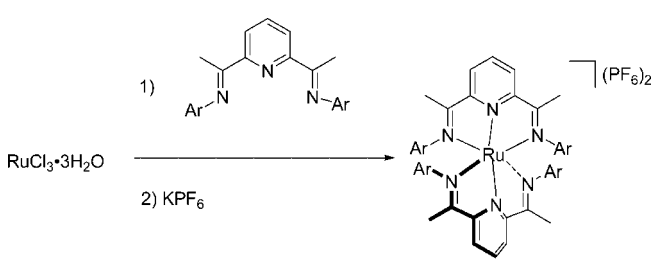

 © 2005 Wiley-VCH Verlag GmbH & Co. KGaA, Weinheim

1589 **C. G. Hartinger,* A. A. Nazarov,* V. B. Arion, G. Giester, M. L. Kuznetsov, M. Galanski, B. K. Keppler***

1,1′-Bis(oxazolin-2-yl)ferrocenes: An Investigation of Their Complexation Behavior toward $[Pd(\eta^3\text{-allyl})Cl]_2$

Keywords: Asymmetric catalysis / Density functional calculations / Mass spectrometry / Metallocenes / Palladium

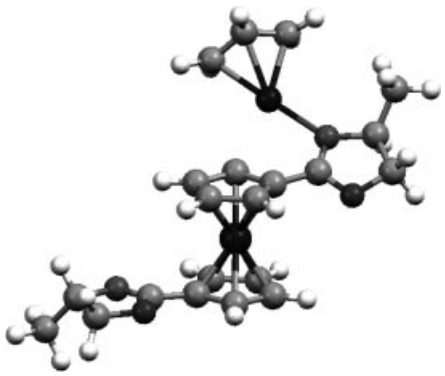

1601 **I. L. Fedushkin, A. A. Skatova, M. Hummert, H. Schumann***

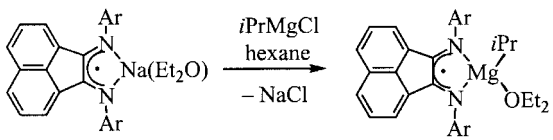

Ar = 2,6-diisopropylphenyl

1

Reductive Isopropyl Radical Elimination from (dpp-bian)Mg-*i*Pr(Et_2O)

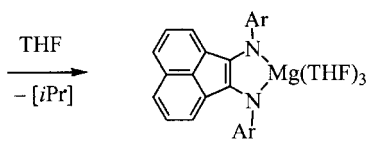

Keywords: Magnesium / N-ligands / Alkyl complexes / Reductive elimination

1609 **J. Shao, E. Steene, B. M. Hoffman,* A. Ghosh***

EPR, ENDOR, and DFT Studies on (β-Octahalo-*meso*-tetraarylporphyrin)copper Complexes: Characterization of the Metal($d_{x^2-y^2}$)−Porphyrin(a_{2u}) Orbital Interaction

Keywords: Copper / Porphyrins / Density functional calculations / ENDOR spectroscopy / EPR spectroscopy

 © 2005 Wiley-VCH Verlag GmbH & Co. KGaA, Weinheim

Luminescence from Lanthanide(3+) Ions in Solution

Anders Døssing*[a]

Keywords: Lanthanides / Luminescence / Fluorescent probes

An overview of recent work dealing with luminescence properties in solution of complexes of the lanthanide(3+) ions Nd^{3+}, Eu^{3+}, Tb^{3+}, Er^{3+} and Yb^{3+} in which an organic chromophore is attached to the metal centre as a sensitizer is given. The various factors that influence the metal-centred luminescence lifetime and intensity are discussed and illustrated with own results and recent literature examples. The VIS emitting metal ions Eu^{3+} and Tb^{3+} require sensitizers that absorb light in the UV or near UV range whereas VIS absorbing sensitizers can be used for the NIR emitting ions Nd^{3+}, Er^{3+} and Yb^{3+}. The latter type of complexes is currently of great interest because of potential applications as luminescent markers in biological systems.

(© Wiley-VCH Verlag GmbH & Co. KGaA, 69451 Weinheim, Germany, 2005)

Introduction

Complexes of the trivalent lanthanide ions (Ln^{3+}) that display a metal-centred luminescence in solution have attracted an increased attention in the recent years owing to their potential use as luminescent tags in biological systems e.g. fluoroimmunoassays.[1] The emission from the excited state Ln^{3+} ions is characterized by narrow emission bands in the NIR to UV range and long emission lifetimes, up to milliseconds, characteristic of the individual metal ion. The energy levels, $^{(2S+1)}L_J$, of selected Ln^{3+} ions are shown in Figure 1.[2] These characteristics are caused by the parity forbidden, and in many cases spin forbidden, nature of the 4f → 4f transitions and the fact that the 4f electrons, being effectively shielded by 5p and 6s electrons, are not involved in chemical bonding.

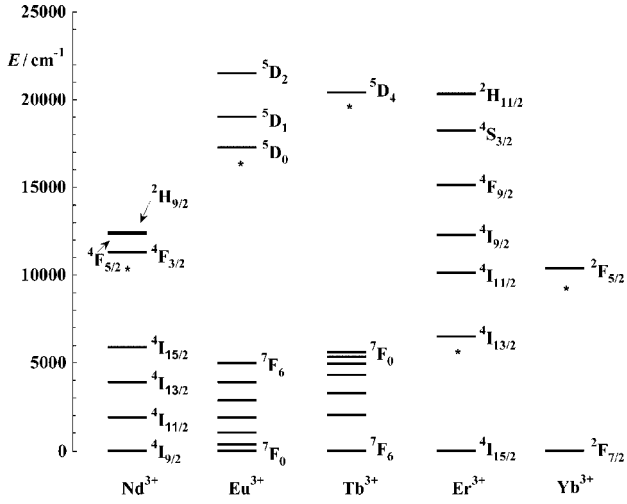

Figure 1. Lower energy levels of selected lanthanide(3+) aqua ions.[2] The luminescent level is marked with an asterisk.

Concerning potential applications of such complexes the parity-forbidden nature of the 4f → 4f transitions is a major draw back. The 4f → 4f transitions have very low molar absorption coefficients ($\varepsilon < 1\ M^{-1}cm^{-1}$), and population of

[a] Department of Chemistry, University of Copenhagen, Universitetsparken 5, 2100 Copenhagen Ø, Denmark
Fax: +45-35320133
E-mail: dossing@kiku.dk

Anders Døssing was born in 1962 in Denmark and received his Ph.D. degree in 1990 from the University of Copenhagen in chemistry under the supervision of Prof. Peter Andersen in the field of hydroxo-bridged, dinuclear chromium(III) complexes. In 1991 he did postdoctoral work in Prof. Peter C. Ford's group at University of California, Santa Barbara where he investigated the photophysical properties of polynuclear copper(I) complexes. In 1992–1994 he worked with Prof. Hans Toftlund at Odense University (Denmark) in the field of lanthanide-polypyridyl complexes. In 1994 he returned to University of Copenhagen as an Assistant Professor and in 1997 he became an Associate Professor.

MICROREVIEWS: This feature introduces the readers to the authors' research through a concise overview of the selected topic. Reference to important work from others in the field is included.

the excited state(s) of the emitting metal ion by direct excitation is consequently inefficient. One way to overcome this problem is to include a highly absorbing chromophore in the ligand coordinated to the metal centre, which is illustrated in the Jablonski diagram in Figure 2. The chromophore absorbs efficiently the excitation energy followed by an energy transfer to the metal centre, and finally a metal-centred, sensitized luminescence occurs. Such a process, where light is harvested by a strongly absorbing chromophore (or sensitizer), is usually referred to as the "antenna effect". The energy transfer from the chromophore to the metal centre in principle can take place either from the singlet excited state S_1 or from the triplet excited state T_1 after an intersystem crossing. It is, however, generally believed that the energy transfer in most cases occurs from T_1 rather than from S_1.[3] Competitive to the intersystem crossing and the subsequent energy transfer is fluorescence, phosphorescence and thermal decay to the ground state S_0. The energy transfer is mediated by two mechanisms. The first is the so-called Förster mechanism,[4] a dipole−dipole mechanism that operates through space with a chromophore–metal distance (r) dependence of r^{-6} and displays a strong dependence on spectral overlap between emission spectrum of the chromophore (T_1) and the absorption spectrum of the metal centre. The selection rule for this mechanism is $\Delta J = 2$, 4, 6. The second is the Dexter mechanism,[5] where energy transfer is mediated through orbitals with ΔJ being 0 or 1 ($0 \leftrightarrow 0$ excluded) and with a distance dependence of e^{-r}. It follows, that the energy difference between T_1 of the chromophore and $^{2S'+1}L'_{J'}$ of the metal centre should not be too large with the energy of T_1 being the higher in energy. On the other hand, a too small energy gap will lead to back energy transfer from $^{2S'+1}L'_{J'}$ to T_1 and possible bimolecular quenching of T_1 by dioxygen (vide infra).

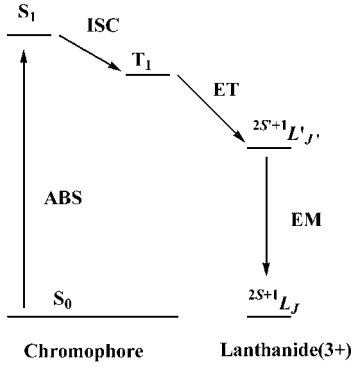

Figure 2. Jablonski diagram illustrating the absorption (ABS) of incident light on the sensitizing chromophore followed by intersystem crossing (ISC) from the singlet (S_1) to the triplet state (T_1) on the chromophore and energy transfer (ET) to the $^{2S'+1}L'_{J'}$ level on the lanthanide(3+) centre from which deactivation to the ground state $^{2S+1}L_J$ by emission of light (EM) occurs.

The metal centre being in the excited state $^{2S'+1}L'_{J'}$ as a result of energy transfer from the chromophore can undergo radiative or nonradiative deactivation to the ground state $^{2S+1}L_J$. The latter is promoted by the high-frequency vibrational modes of coordinated X–H oscillators, such as coordinated water or amine ligands (ν_{OH} = 3300–3500 cm^{-1}, ν_{NH} = 3100–3300 cm^{-1}). The extent of this nonradiative deactivation pathway, which results in luminescence quenching, is inversely proportional to the energy gap between the excited state and the ground state manifold. By inspection of Figure 1 it is seen that the energy gap between $^5D_0$ and $^7F_6$ in Eu^{3+} of 12300 cm^{-1} matches the 2nd vibrational overtone of an O–H oscillator. For Tb^{3+} a gap of 14800 cm^{-1} matches the 3rd overtone, and the vibrational deactivation is therefore less efficient owing to a smaller Frank-Condon overlap between the two wavefunctions. Going to Er^{3+} with an energy gap of only 6500 cm^{-1}, the emission is effectively quenched by coordinated water ligands. The spacing between the vibrational levels in X–D oscillators is smaller than in X–H oscillators and vibrational luminescence quenching is accordingly much less pronounced and can often be neglected. This has been done by Horrocks,[6] who proposed a correlation (1) to estimate the number of coordinated water ligands coordinated to the metal centre, n_{H_2O}, with an alleged uncertainty of 0.5.

$$n_{H_2O} = A\,(k_H - k_D) \quad (1)$$

Here k_H and k_D are the first-order rate constant (in ms^{-1}) for deactivation of the excited state metal in water and D_2O solution, respectively, and A an empirically determined constant being 1.05 ms, 4.2 ms and 0.9 μs for Eu^{3+}, Tb^{3+} and Yb^{3+}, respectively (for Yb^{3+} k_H and k_D should be in units of μs^{-1}). Correlation (1) can be extended to work in methanol solution. The number of coordinated methanol ligands can be estimated by measuring the rate constants in CH_3OH and CD_3OD solution and by use of values of A that are twice the above mentioned, since a methanol ligand only contains one O–H oscillator compared to two in a water ligand. A later and more sophisticated treatment of this subject by Parker[7] has resulted in the modified correlation (2):

$$n_{H_2O} = A'\,(k_H - k_D - B) \quad (2)$$

Here the term B accounts for interaction between the metal centre and outer sphere O–H oscillators. Values for A' in aqueous solution are 1.2 ms, 5 ms and 1.0 μs and for B 0.25 ms^{-1}, 0.06 ms^{-1} and 0.2 μs^{-1} for Eu^{3+}, Tb^{3+} and Yb^{3+}, respectively. The uncertainty of n_{H_2O} in correlation (2) is believed to be smaller than in correlation (1). Attempts to make similar expressions for complexes including other oscillators were made by Parker.[7]

Recently,[8] on the basis of a study of luminescence lifetimes in aqueous solution with 25 Eu^{3+} complexes of ligands not containing any X–H oscillators, Horrocks has proposed correlation (3):

$$n_{H_2O} = 1.11\text{ ms}\,(k_H - k_D - 0.31\text{ ms}^{-1}) \quad (3)$$

 © 2005 Wiley-VCH Verlag GmbH & Co. KGaA, Weinheim

This result in combination with Parkers work[7] that included other X–H oscillators in a series of macrocyclic complexes, gives correlation (4) for Eu^{3+} complexes of ligands containing hydroxo, amine and amide oscillators coordinated to the metal centre:

$$n_{H_2O} = 1.11\ ms\ (k_H - k_D - 0.31\ ms^{-1} + 0.45\ ms^{-1}\ n_{OH} + 0.99\ ms^{-1}\ n_{NH} + 0.075\ ms^{-1}\ n_{O=CNH}) \quad (4)$$

For Nd^{3+} correlation (5) has been proposed by Faulkner[9a]

$$n_{H_2O} = 130\ ns\ (k_H - k_D) - 0.4 \quad (5)$$

with the rate constants in ns^{-1}. Kimura[9b] proposed for Sm^{3+} and Dy^{3+} correlation (6):

$$n_{H_2O} = Ak_H - B \quad (6)$$

with A being $0.026\ ms^{-1}$ and $0.024\ ms^{-1}$ and B being 1.6 and 1.3 for Sm^{3+} and Dy^{3+}, respectively. Obtaining noninteger values of n_{H_2O} by use of the correlations above is not necessarily wrong, since there could be several more or less aquated species coexisting in solution. In summary, a complex that efficiently converts incident light (UV or VIS) to metal-centred, emitted light (VIS or NIR) should fulfil the following conditions: (i) The ligand includes a highly absorbing chromophore, (ii) energy transfer from the ligand-centred excited states is fast and efficient, (iii) X–H oscillators are excluded from the first coordination sphere of the metal, (iv) the complex is thermodynamically stable and kinetically inert. In the following a brief overview of lanthanide complexes that display VIS and NIR luminescence will be given.

VIS Emitters

The most intense emitters in the VIS range among the Ln^{3+} ions are Eu^{3+} and Tb^{3+} with the weaker ones being Sm^{3+} and Dy^{3+}. The energy of the emitting state in Eu^{3+}, $^5D_0$, is ca. 17300 cm^{-1} and in Tb^{3+}, $^5D_4$, is ca. 20500 cm^{-1} as seen in Figure 1. The energy of the triplet state of the sensitizer has, as mentioned above, to be larger and useful sensitizers for Eu^{3+} and Tb^{3+} centred emission should consequently absorb in the UV or near UV range. Heteroaromatic compounds such as bipyridine, phenanthroline, quinoline, terpyridine or benzimidazole have been used in this regard.[10–15] Numerous complexes of the above mentioned compounds have been isolated in the solid state and structurally characterized. However, these compounds coordinate only weakly to the Ln^{3+} ions and the complexes dissociate readily in coordinating solvents such as water or alcohols. This obstacle can be overcomed by incorporating the chromophores as part of larger chelating ligands with podand, macrocyclic or cage type structure. Examples of such ligands are shown in Figure 3 (**1**–**7**). Apart from including the heteroaromatic sensitizers, these ligands more or less exclude solvent molecules from the first coordination sphere, which, as mentioned above, suppresses the nonradiative deactivation pathway.

A widely used ligand structure is based on the cyclic amine 1,4,7,10-tetraazacyclododecane (cyclen) with neutral or anionic donors such as $-CH_2COO^-$ attached as pendant arms to the nitrogen atoms.[16] The ligand DOTA (**8**) forms complexes of very high thermodynamic and kinetic stability. Concerning the influence of the radius of the Ln^{3+} ion on the thermodynamic stability of such complexes, a study by Sherry[17] showed that the Ln^{3+} ions with an ionic radius less than 0.94 Å (Gd^{3+} or later) are more stable. By including UV absorbing sensitizers in the pendant arm(s), sensitized emission from the metal centre has been observed in numerous cases. One interesting example of this was reported by Parker et al.[18] who attached a phenanthridine chromophore to the cyclen unit as seen in **9**. In the Tb^{3+} and Eu^{3+} complexes of **9** a pH and oxygen concentration dependence of the intensity of the metal-centred emission was observed. The pH dependence was explained in terms of protonation equilibria involving the nitrogen atom in the sensitizing phenanthridine chromophore.

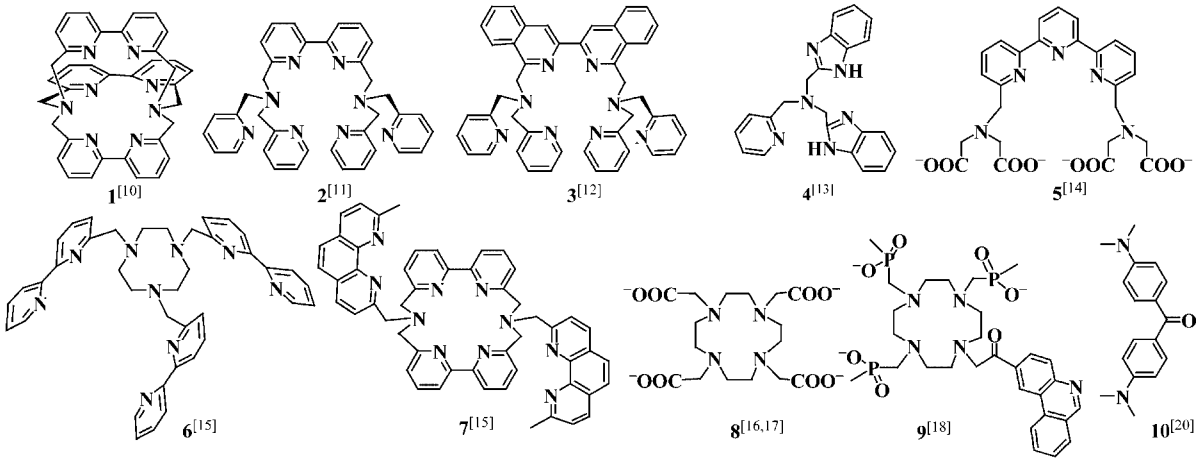

Figure 3. Structure of different ligands.

 © 2005 Wiley-VCH Verlag GmbH & Co. KGaA, Weinheim

In the use of the Eu^{3+} ion as the emitter there is a major draw back resulting from its redox properties. It is well known that the Eu^{3+} ions is the lanthanide ion most readily reduced to the oxidation state 2+ with the standard electrode potential $E^{\circ}_{Eu^{3+}/Eu^{2+}} = -0.35$ V in aqueous solution.[19] The second most readily reduced ion is the Sm^{3+} ion with $E^{\circ}_{Sm^{3+}/Sm^{2+}} = -1.5$ V.[19] In the case of Eu^{3+}, electron transfer from the excited state (S_1) chromophore to the metal centre might then compete with the intersystem crossing (and subsequent energy transfer) with a reduction of the Eu^{3+} to Eu^{2+} as a result. An *rough* estimate of the free energy of the excited-state electron transfer, ΔG°_{el}, can be found by use of correlation (7):

$$\Delta G^{\circ}_{el} = FE^{\circ}_{sens^+/sens} - FE^{\circ}_{Eu^{3+}/Eu^{2+}} - E_{sens*} \quad (7)$$

Here $E^{\circ}_{sens^+/sens}$ is the standard electrode potential for $sens^+$/sens couple, E_{sens*} the energy of the excited state of the sensitizer and F the Faraday constant. A small correction term for charge redistribution has been omitted. As a result of the intramolecular electron transfer, a LMCT excited state will be populated from which a nonradiative deactivation to the ground state is likely to occur. To suppress this deactivation pathway, the sensitizing chromophores should have high values of $E^{\circ}_{sens^+/sens}$, namely, they should be difficult to oxidize. One way achieving that could be done by attaching electron withdrawing substituents to the aromatic rings.

Returning to the energy gap between the sensitizer T_1 state and the acceptor state(s) of the metal centre Latva et al.[14] has systematically studied the emission quantum yield of a large series of Tb^{3+} and Eu^{3+} complexes of heteroaromatic ligands with T_1 energies in the range 18600–27000 cm^{-1}. They found that in the case of Eu^{3+} there was no clear correlation between the T_1 energy and the emission quantum yield. It was concluded that the Eu^{3+} centre is able to accept energy, not only with the $^5D_0$ level but also with the higher ^5D_J levels. In the case of Tb^{3+} there was a clear correlation between the emission quantum yield and the T_1 energy. With an energy gap between the T_1 state and the $^5D_4$ state larger than 1850 cm^{-1} the quantum yields were found in the range 0.12–0.58. Below 1850 cm^{-1}, the quantum yields dropped dramatically to 0.01 or less. One possible explanation for this behaviour is that with small energy gaps, back energy transfer from the metal centre to the sensitizer might occur with a reduction of the emission quantum yield as a result. However, in the case of a small energy gap the energy transfer from the sensitizer T_1 state to dioxygen, which is present in the solution, might compete with the energy transfer to the metal centre efficiently. Again, this resulted in a reduction of the metal-centred emission quantum yield. An example of this phenomenon was observed in the Tb^{3+} complex of the Lehn-cryptand (**1**). Here, the T_1 state of the bipyridine chromophore has an energy of 21600 cm^{-1}. A temperature dependence of the emission quantum yield and a bimolecular quenching of the metal-centred emission by dioxygen was observed[10] with a second-order rate constant $k_q = 3.9 \times 10^6$ $M^{-1}s^{-1}$. This was interpreted in terms of back energy transfer.

The sensitizing chromophores in the ligands **1**–**7** and **9** require irradiation at $\lambda < 400$ nm. A very interesting example of an Eu^{3+} complex that displays a metal-centred luminescence at irradiation wavelengths *above* 400 nm was recently reported by Verhoeven et al.[20] The coordinatively unsaturated tris(β-diketonate) complex [Eu(fod)$_3$] (fod = 6,6,7,7,8,8,8-heptafluoro-2,2-dimethyloctane-3,5-dione) forms in the non-coordinating solvent benzene a 1:1 complex with Michler's ketone [4,4′-bis(dimethylamino)benzophenone, **10**). The compound **10** is a so-called push-pull chromophore, and an intense absorption band at 350 nm ($\varepsilon \approx$ 16000 cm^{-1} M^{-1}) has some charge-transfer character, where electron density is moved from the dimethylamino groups to the carbonyl group. The formation of a bond between the carbonyl oxygen atom on **10** and the Eu^{3+} centre yielding [Eu(fod)$_3$(**10**)] results in a bathochromic shift of this charge-transfer band to 414 nm. Irradiation of such a solution with light gave intense red luminescence at wavelengths up to 450 nm with an emission quantum yield of 0.17 in an aerated solution. From phosphorescence measurements of the complex [Gd(fod)$_3$(**10**)] the triplet energy of coordinated **10** was estimated to be 19600 cm^{-1}, which is only 2300 cm^{-1} above the $^5D_0$ level on Eu^{3+} centre. However, the bond between the carbonyl oxygen and the metal centre is so weak that it is broken in coordinating solvents, which limits the potential applications of this system.

Ln^{3+} complexes of the cage ligand **1** were among the early systems to be investigated.[10] Luminescence lifetime measurements revealed by use of correlation (1) the presence of 2–3 water molecules coordinated to the metal centre in aqueous solution. A later[21] crystal structure determination of the Tb^{3+} complex of **1** showed an open structure (Figure 4) with bond lengths to the bipyridine groups A, B and C being 2.90, 2.55 and 2.74 Å, respectively. Tb^{3+}–bipyridine bond lengths fall typically in the range 2.5–2.6 Å,[22,23] so the cavity size in **1** is obviously too large. Furthermore, a water molecule and a chloride anion are coordinated to the metal centre. This prompted us to investigate Ln^{3+} complexes of the related and more flexible pod-and type ligand **2**.[11] The ligand **2** can be imagined to be the result of hydrogenolysis of the 2,2′ C–C bonds in two of the bipyridine groups. Therefore, the more flexible ligand **2** should enclose the metal centre more efficiently than **1**. Single crystals of the Gd^{3+} complex of **2** were grown from an ethanol solution and the structure is shown in Figure 5.[11a] It is seen that one of the pyridine groups is dangling uncoordinated, and that two chloride anions are coordinated to the metal centre. Therefore, the complex cation should be formulated as $[Gd(\mathbf{2})Cl_2]^+$. Moreover, the complex cation is chiral with the nitrogen atoms N1–N2–N3–N4–N5–N6 forming a helix. The unit cell contains two complex cations of opposite chirality. In collaboration with J. Legendziewicz's group more detailed studies of the luminescence properties of Ln^{3+} complexes of **2** have been done.[11b,11d] From the phosphorescence spectrum of $[Gd(\mathbf{2})Cl_2]^+$ in CH_3OH solution at 77 K the energy of the T_1 state

 © 2005 Wiley-VCH Verlag GmbH & Co. KGaA, Weinheim

in the bipyridine chromophore was found to be 21900 cm^{-1}.[11b] In water or CH_3OH solution the Eu^{3+} and Tb^{3+} complex of **2** displays luminescence on irradiation with UV light. In the case Eu^{3+} the energy of $^5D_0 \rightarrow {}^7F_0$ transition depends on the ligand field, and the presence of more than one peak is therefore indicative of more than one species in the solution. A close scrutiny of the $^5D_0 \rightarrow {}^7F_0$ transition at 77 K in the solid state and in various solvents shows indeed the presence of two components in water and in CH_3OH solution (Figure 6).[11b] In CH_3CN solution and in the solid state the stoichiometry of the complex is likely to be $[Eu(\mathbf{2})Cl_2]^+$, and in water and CH_3OH solution a partly solvatized species, such as $[Eu(\mathbf{2})Cl(CH_3OH)]^{2+}$, is present as well. In agreement with this, luminescence lifetime measurements in CH_3OH and CD_3OD gave in each solvent two luminescence lifetimes τ_1 and τ_2, and by use of correlation (1) it was found that the two species contains 0.0 and 0.6 coordinated CH_3OH molecules, respectively. Investigations of the Tb^{3+} complex of **2** indicated that back energy transfer took place.[11d]

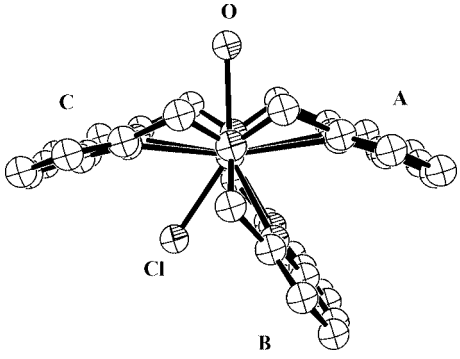

Figure 4. ORTEP drawing of the cation $[Tb(\mathbf{1})(OH_2)Cl]^{2+}$ prepared by Lehn et al.[21] viewed along the axis comprised by the two aliphatic nitrogen atoms. Drawn using coordinates taken from Cambridge Crystallographic Database. Tb–N bond lengths are 2.90 Å (A), 2.55 Å (B) and 2.74 Å (C).

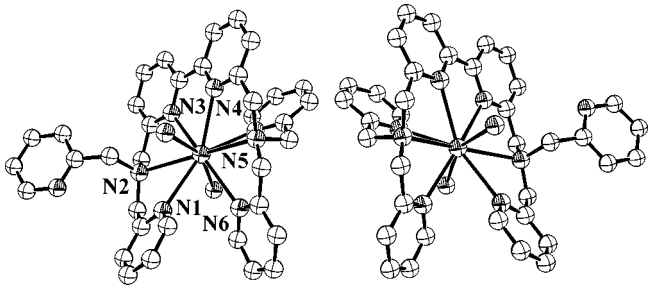

Figure 5. ORTEP drawing of the two complex cations in the unit cell of $[Gd(\mathbf{2})Cl_2]Cl{\cdot}2H_2O{\cdot}\frac{1}{2}EtOH$ prepared by Døssing et al.[11a]

Complexes of La^{3+} are diamagnetic and the structure and dynamics of such complexes in solution can conveniently be studied by use of NMR spectroscopy. The complex $[La(\mathbf{2})]Cl_3{\cdot}4H_2O$ has been studied in CD_3OD and

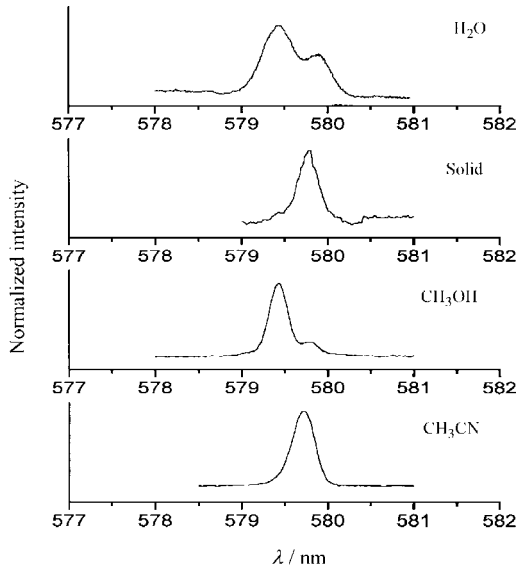

Figure 6. $^5D_0 \rightarrow {}^7F_0$ emission spectra of $[Eu(\mathbf{2})Cl_2]Cl{\cdot}1.5H_2O$ in different solvents at 77 K (λ_{ex} = 320 nm) Redrawn from ref.[11b] with permission from Elsevier.

CD_3CN solution, and the ^1H NMR spectrum in the latter solvent is shown in Figure 7 along with the assignment obtained by help of two-dimensional COSY spectroscopy.[11c] The figure shows that the four pyridine groups exist in two pair-wise equivalent groups and that the bipyridine group is symmetric. The presence of six methylene groups that give rise to the three AX spin systems (α1, α2), (β1, β3) and (β2, β4) of equal intensity shows that the pyridine rings 1 and 3 (and, 2 and 4) are symmetry related, and the complex ion has therefore twofold symmetry. The ^1H NMR spectrum of $[La(\mathbf{2})]Cl_3{\cdot}4H_2O$ in CD_3OD is very similar except for a number of additional low-intensity peaks, which shows the existence of an other species in low concentration. This is not surprising, since this is also the case in Eu^{3+} complexes of **2** in methanol solution (see Figure 6). At higher temperatures the peaks corresponding to the protons in the four pyridine groups are broadened, which indicates that a slow interchange between the two pairs of symmetric pyridine groups takes place. Moreover, the peaks corresponding to the α1 and α1′ protons broadens. No broadening was observed for the peaks corresponding to the protons in the bipyridine group. From the two-dimensional EXSY spectrum showed in Figure 8 the presence of the cross peaks between the four protons in the pyridine groups clearly confirms the interchange. Moreover, cross peaks between primed and unprimed protons in the methylene groups are present. The exchange rates in CD_3CN solution were measured in the temperature range 270–315 K with the first-order rate constant, k, for the interconversion at 300 K being 1.78(5) s^{-1} with $\Delta H^{\ddagger}$ and $\Delta S^{\ddagger}$ being 69(1) $kJ\,mol^{-1}$ and –9(2) $J{\cdot}mol^{-1}{\cdot}K^{-1}$, respectively. In CD_3OD solution the behaviour was similar with $\Delta H^{\ddagger}$ and $\Delta S^{\ddagger}$ being 71(2) $kJ{\cdot}mol^{-1}$ and 4(6) $J{\cdot}mol^{-1}{\cdot}K^{-1}$, respectively. The pseudo-first-order rate constants for substitution of unidentate ligands in the first coordination sphere of the

 © 2005 Wiley-VCH Verlag GmbH & Co. KGaA, Weinheim

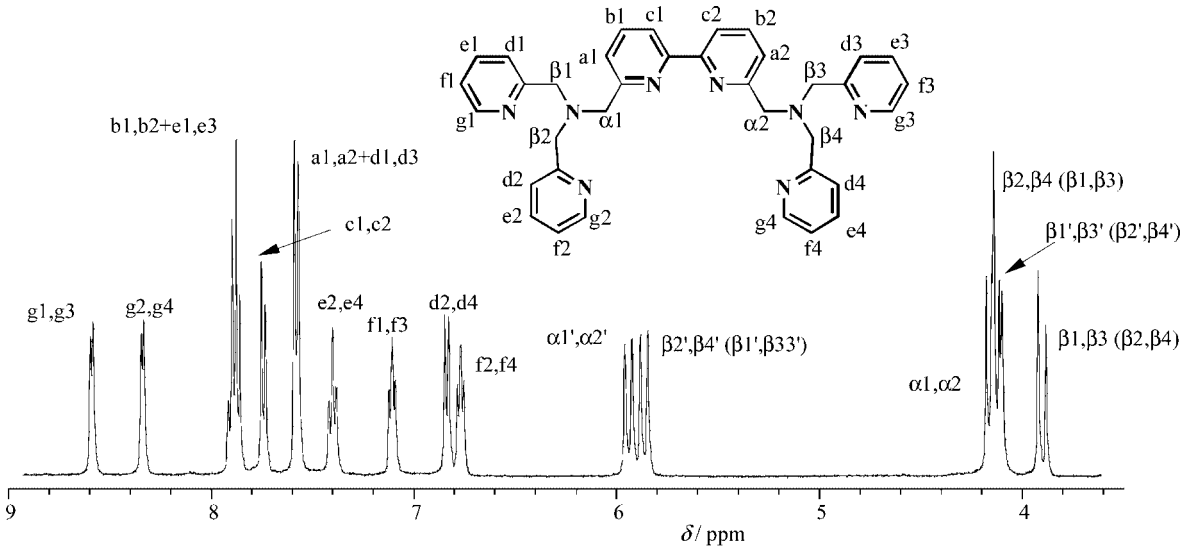

Figure 7. One dimensional ^{1}H NMR spectrum of [La(**2**)]Cl_3·4H_2O in CD_3CN solution at 298 K with assignments. The primed and unprimed methylene protons refer to chemically and magnetically inequivalent protons bound to the same carbon atom. For reasons of clarity the La^{3+} centre has been omitted in the labelling figure.

lanthanide(3+) ions have been found in the range 10^5–10^9 s^{-1},[24] several orders of magnitude higher than the interconversion rate, k. The interconversion process is therefore unlikely to be either an exchange between dangling (uncoordinated) and coordinated pyridine groups or a solvento/chloro ligand exchange but rather a concerted twist. With twofold symmetry the cation could be chiral having a C_2 axis or achiral having a mirror plane. The interconversion is in the first case a conformational change during which the chirality changes and in the second case a mirror-image conformational change through a plane orthogonal to the symmetry plane of the complex. The NMR spectroscopic data did not allow any distinction between the two cases.

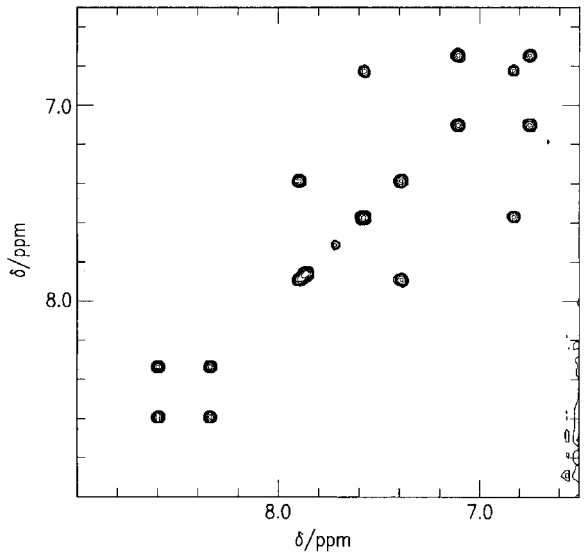

Figure 8. The EXSY spectrum recorded of [La(**2**)]Cl_3·4H_2O in CD_3CN solution at 300 K in the range 6.6–9.0 ppm with an exchange delay of 1.0 s.

One way to clarify if a solution of a luminescent Ln^{3+} complex consists of a racemic mixture of two interconverting enantiomers is by use of circularly polarized (CP) excitation light. A racemic mixture may on excitation with CP light be enantiomerically enriched in the excited state. The metal centre may subsequently display a circularly polarized luminescence (CPL). An excellent review of this technique has been given by J. P. Riehl.[25] The requirement for the detection of a CPL signal is, however, that the rate of the racemization in the excited state (which is probably very close to the racemization rate in the ground state) is slower than the rate of the decay from the metal-centred excited state. In collaboration with J. P. Riehl, Tb^{3+}, Eu^{3+} and Dy^{3+} complexes of **2** have been studied by this technique.[11d] A CPL signal was indeed seen for the $^4F_{9/2} \rightarrow {}^6H_{13/2}$ transition in the Dy^{3+} complex in aqueous solution at room temperature. The $^4F_{9/2}$ excited state lifetime was found to be 10 μs under such conditions. In the cases of Tb^{3+} and Eu^{3+} with the much longer excited state lifetimes in H_2O (1.53 ms and 0.78 ms) no CPL was detected.

In conclusion, CH_3CN solutions of complexes between **2** and Ln^{3+} ions consist of interconverting enantiomers of [Ln(**2**)Cl_2]$^+$ species with **2** being heptadentate as shown in Figure 5 for Ln^{3+} = Eu^{3+}, Gd^{3+}, Tb^{3+} and Dy^{3+} and octadentate in the case of the larger La^{3+} ion. In water and CH_3OH solution solvento ligands partly displace the chloro ligands.

NIR Emitters

The Ln^{3+} ions emitting in the NIR range are Nd^{3+}, Er^{3+}, and Yb^{3+}. For Nd^{3+} the typical emission lines are located around 890 nm ($^4F_{3/2} \rightarrow {}^4I_{9/2}$), 1060 nm ($^4F_{3/2} \rightarrow {}^4I_{11/2}$) and 1350 nm ($^4F_{3/2} \rightarrow {}^4I_{13/2}$), for Er^{3+} around 1540 nm ($^4I_{13/2} \rightarrow {}^4I_{15/2}$) and for Yb^{3+} around 980 nm ($^2F_{5/2} \rightarrow {}^2F_{7/2}$). For

 © 2005 Wiley-VCH Verlag GmbH & Co. KGaA, Weinheim

many reasons luminophores based on the three metal ions have attracted large interest in the recent years. One reason is that this gives the opportunity to use sensitizers that absorb in the VIS range. This gives an advantage in their use as luminescent tags in biological systems compared to tags based on Eu^{3+} and Tb^{3+}, since biological tissue is more transparent to VIS excitation light than UV excitation light, and since cheap light sources such as diode lasers can be used then. Although this review deals with luminescence in solution, in this context it should be mentioned that the Nd^{3+} and Er^{3+} ions complexed by organic groups and doped in polymer waveguides may find use as optical amplifiers of 1300 nm and 1500 nm light, respectively, two standard wavelengths used in telecommunication.[26]

There are some drawbacks in the use of luminophores based on the three above mentioned Ln^{3+} ions. Firstly, the luminescence intensities are low and the luminescence lifetimes are short, typically in the range 10^{-7}–10^{-5} s, which is about 3 orders of magnitude lower than lifetimes in Eu^{3+} and Tb^{3+} complexes. Secondly, the low energy gap between the emitting level and the ground state manifold on the metal centre has the result, that the luminescence is quenched, not only by O–H or N–H oscillators directly bound to the metal centre, but also unbound C–H oscillators nearby, with an r^{-6} distance dependence. The energy gap in Er^{3+} is 6500 cm^{-1} which is resonant with the 1st overtone of the C–H oscillator ($\nu \approx 2950\ cm^{-1}$ in aliphatic groups), but the quenching can be somewhat reduced by deuteration ($\nu_{CD} \approx 2200\ cm^{-1}$). To illustrate this, it was shown by Parker[7] that each CH_2COO^- pendant arm in **8** contributes by 13000 s^{-1} to the first-order deactivation rate constant of the complex $[Yb(\mathbf{8})]^-$, while the contribution in the corresponding Eu^{3+} complex is 45 s^{-1}.

Metal-centred emission from the three above-mentioned lanthanide ions can be sensitized by UV absorbing chromophores such as bipyridine,[9] terpyridine,[27] pyrene[28] (**11**) or dansyl[29] (**12**) (see Figure 9). The accepting energy level(s) on the metal ions Nd^{3+} and Er^{3+} are therefore located higher than the emitting level. However, the most interesting aspects are connected with the use of sensitizers that absorb in the VIS range. Therefore, the following will deal with such ligands.

As light harvesters absorbing in the VIS range, the chromophore fluorescein **13** (Figure 9) has been used extensively. Fluorescein absorbs strongly around 500 nm (depending of the nature of the solvent) with $\varepsilon \approx 80000\ M^{-1}cm^{-1}$ and is widely used as a (green) fluorescent probe in biology.[30]

Reinhoudt et al. described one of the first systems where a Nd^{3+} or Er^{3+} ion is bound to a ligand that is covalently bound to a VIS absorbing organic sensitizer.[31] The metal complexes of **14** in which fluorescein is attached to a calix[4]arene ring (Figure 10) displayed NIR luminescence in CD_3OD and dimethyl sulfoxide (dmso) solution. The luminescence intensity was found to depend on the spacer length with the highest luminescence intensity with the C_3 spacer ($x = 3$). In the case of Er^{3+}, only the fluorescein sensitized the emission whereas in the Nd^{3+} case, also the UV absorbing calix[4]arene moiety was able to sensitize the emission. In another study, a fluorescein chromophore was attached to the chelating ligand diethylenetriaminepentaacetic acid (**15**).[32] This ligand forms 1:1 metal complexes and NIR luminescence of such complexes in aqueous solution was observed. The emission intensity for the Yb^{3+} was found to be much lower than for the Nd^{3+} and Er^{3+} complexes. To explain this we must look at Figure 1, which shows that the two latter ions have several higher lying accepting states above the emitting level and thus a better spectral overlap with the T_1 state (located at 15900 cm^{-1}) of the fluorescein chromophore. The emission was, however, found to be quenched by dissolved molecular dioxygen, and this shows that the energy transfer is rather inefficient. A more efficient energy transfer was observed in metal complexes of **16**,[33] where the binding site of the metal ion is much closer to the sensitizer than in **15**. The attached iminodiacetic acid groups ensures a thermodynamic and kinetic stability of the 1:1 complexes that equals the corresponding EDTA complexes, and NIR emission was observed in aqueous solution. Moreover, the NIR emission is *not* quenched by dissolved dioxygen. The Yb^{3+} complex of **16** is so long-lived (1.91 μs in water), that it is possible to distinguish it from background fluorescence from organic groups in biological systems. Systems with fluorescein (**17**)[34] or its derivatives (**18, 19**)[35] attached to a terphenyl moiety have been studied by Reinhoudt and van Veggel. In the ligands **18** and **19** the two VIS absorbing chromophores (lissamine and Texas Red, respectively) absorb strongly in the near-UV to VIS range with absorption maxima at 568 nm ($\varepsilon = 8.8\times10^4\ M^{-1}cm^{-1}$) and 590 nm ($\varepsilon = 8.5\times10^4\ M^{-1}cm^{-1}$), respectively. They were found to be able to sensitize emission from the Nd^{3+} ion in $[D_6]$dmso solution with luminescence lifetimes close to 2 μs. The triphenylmethane derivative xylenol orange (**20**) is widely used as an indicator for complexometric determination of metal ions. It has been reported that 1:1 complexes with the Ln^{3+} ions were formed, and interestingly, it is able to sensitize emission

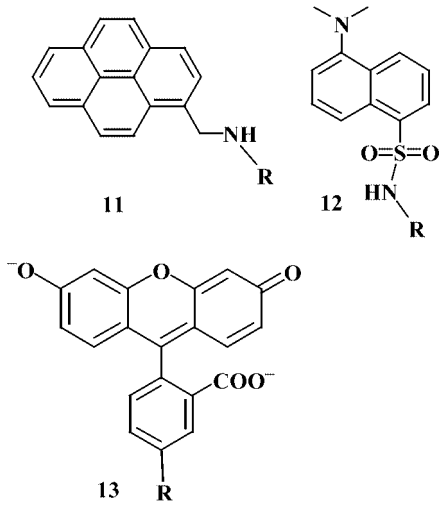

Figure 9. Structure of different chromophores that absorb in the UV range (**11** and **12**) and VIS range (**13**).

 © 2005 Wiley-VCH Verlag GmbH & Co. KGaA, Weinheim

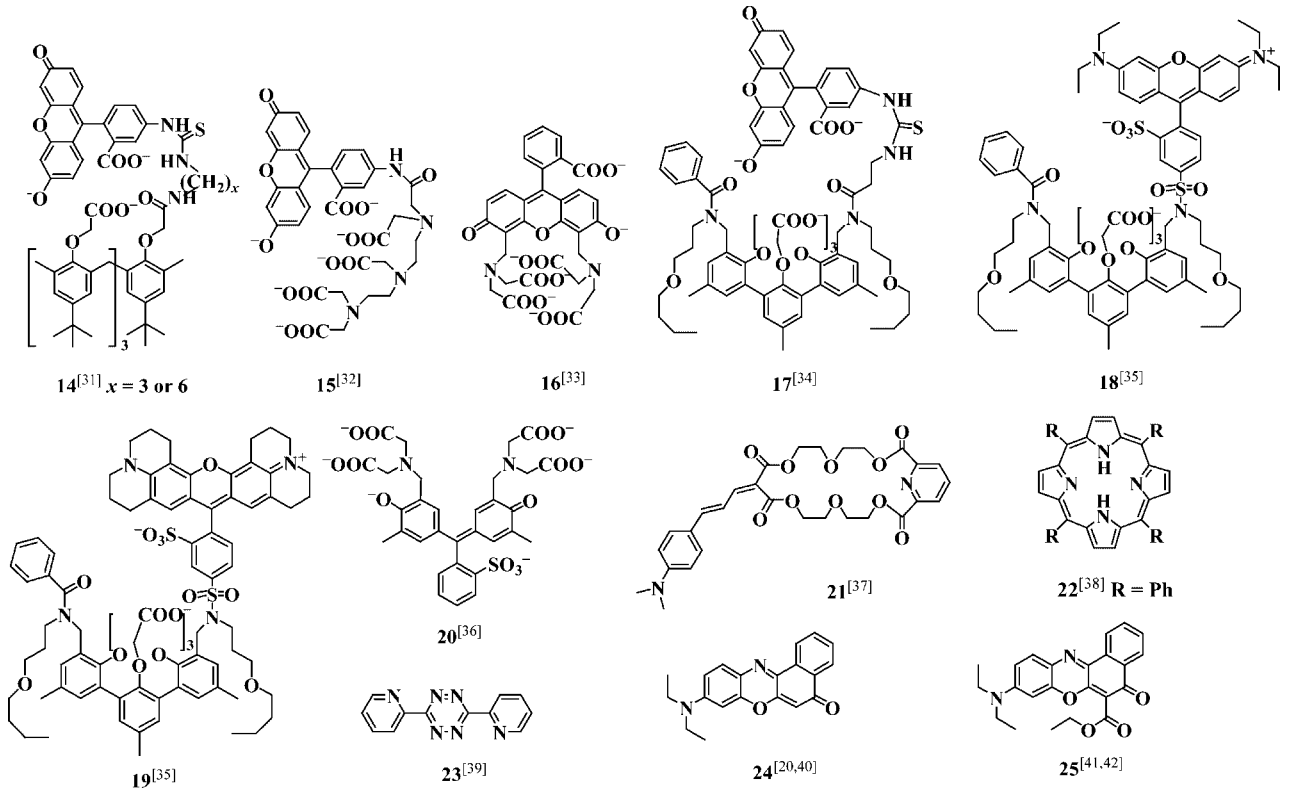

Figure 10. Structure of different VIS absorbing ligands.

from the Nd^{3+} and Yb^{3+} ions.[36] In ligand **21** an oligoene sensitizer is incorporated in a crown ether. The Er^{3+} complex of **21** absorbs VIS light between 400 and 600 nm and displays NIR luminescence in dmso solution.[37] Boncella reported the isolation and structural characterization of tetraphenylporphyrinate, tpp, (**22**, R = Ph) Ln^{3+} complexes capped with multidentate additional ligands such as the tridentate hydridotris(1-pyrazol)borate (tp).[38] The intense Soret bands of the porphyrin group and the low lying T_1 state makes the porphyrin group suitable as sensitizer for the NIR emitting Ln^{3+} ions. The complexes were found to be stable in the solid state in air, but they are sensitive to hydrolysis during which cleavage of the Ln–N bond occurs. The crystal structure of [Yb(tpp)(tp)] is shown in Figure 11, and it is seen that the cavity size of the porphyrin ring is too small for the metal ion to fit in. The ligand field caused the $^2F_{5/2} \rightarrow {}^2F_{7/2}$ transition to be split into multiple bands in the [Yb(tpp)(tp)] complex. The coordinatively unsaturated complex [Ln(tta)$_3$] [Htta = thenoyl(trifluoro)acetone] been found to form complexes with the potentially bis-bidentate bridging imine ligand 3,6-bis(2-pyridyl)tetrazin, bptz (**23**).[39] The crystal structure of a dinuclear complex [{Yb(tta)$_3$}$_2$(μ-bptz)] is shown in Figure 12. The Yb^{3+}, Er^{3+} and Nd^{3+} complexes have an absorption band around 500 nm and exhibit NIR luminescence in CH_2Cl_2 solution.

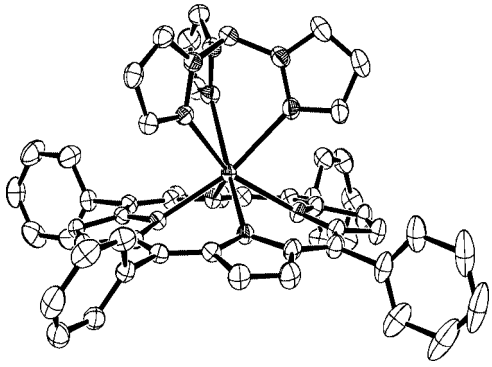

Figure 11. ORTEP drawing of the complex [Yb(tpp)(tp)] prepared by Boncella et al.[38] Drawn using coordinates taken from Cambridge Crystallographic Database. For abbreviations see text.

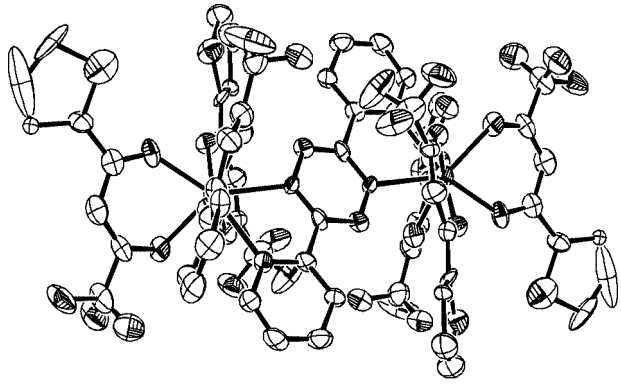

Figure 12. ORTEP drawing of the dinuclear complex [{Yb(tta)$_3$}$_2$(μ-bptz)] prepared by Ward et al.[39] Drawn using coordinates taken from Cambridge Crystallographic Database. For abbreviations see text.

 © 2005 Wiley-VCH Verlag GmbH & Co. KGaA, Weinheim

The compound **24** (Nile Red) is a highly fluorescent laser dye.[40] It is, like **10**, a push-pull chromophore with a strong solvent polarity dependence on the absorption and emission band maxima. The position of the absorption maximum has been found in a wide range moving from 484 nm in pentane to 629 nm in trifluoroacetic acid with values of ε around 35000 $M^{-1}cm^{-1}$,[40a] and the compound has thus been used as a polarity probe in chemical and biophysical environments. This solvatochromic effect has its origin in the fact that the dipole moment in the first excited state is significantly higher than in the ground state.[40b,40c] Verhoeven[20] found that **24** forms a complex (through the carbonyl oxygen atom) in benzene solution with the lewis acids [Ln(fod)$_3$], and that coordinated **24** was able to sensitize NIR emission for Ln = Er or Yb. The complex formation is, however, weak and does not occur in more coordinating solvents. In our laboratory we have tried to circumvent this obstacle by using the derivative of Nile Red **25**. This compound, along with a whole range of other Nile Red derivatives, was first described by Meng and co-workers,[41] and it was conveniently prepared as shown below (Scheme 1).

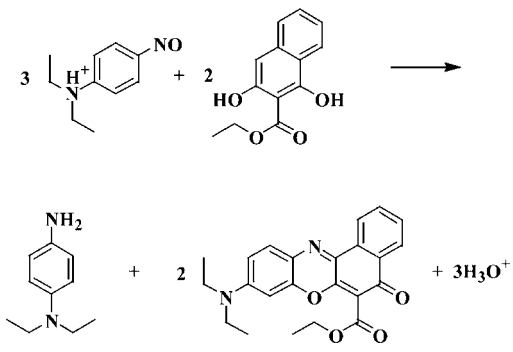

Scheme 1.

The compound **25** is able to form chelate metal complexes as shown in Figure 13 with an increased stability compared to the complexes of **24**. Preliminary experiments[42] showed indeed the complex formation between Ln^{3+} ions and **25** even in coordinating solvents such as CH_3CN or CH_3OH as seen in Figure 14. From an CH_3CN solution of La(OSO$_2$CF$_3$)$_3$ and **25** single crystals of [La(**25**)$_2$(OSO$_2$CF$_3$)$_3$(OH$_2$)$_2$] were grown. A crystal structure determination showed that **25** does coordinate bidentately to the metal centre (Figure 13). The luminescence properties of the Nd^{3+}, Er^{3+}, and Yb^{3+} complexes of **25** are under current investigation.

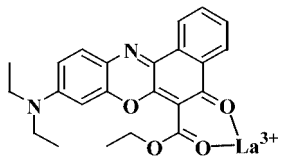

Figure 13. Structure of the [La(**25**)]$^{3+}$ chelate complex.

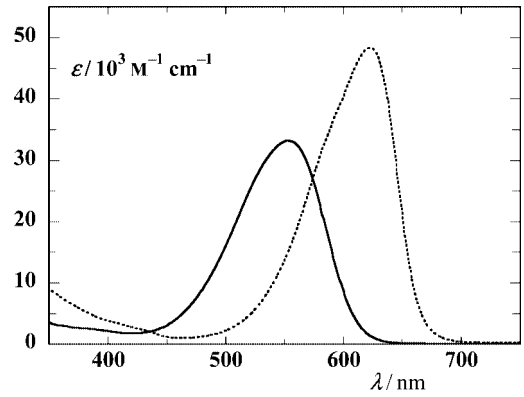

Figure 14. Absorption spectra of 1.05×10^{-5} M **25** (—) and 1.05×10^{-5} M **25**/1.12×10^{-4} M La(CF$_3$SO$_3$)$_3$ (···) in CH_3CN solution at 295 K.

Outlook

Despite the fact that the detection of NIR light requires specialized equipment, it seems very interesting to develop luminescent probes based on the NIR emitting metal ions Nd^{3+}, Er^{3+} and Yb^{3+}. However, the very low overall quantum yields (typically 10^{-4}–10^{-3}) of the metal-centred emission from complexes of the three metal ions in solution has been a disadvantage. The efficiency of the energy transfer from the VIS-absorbing to the metal centre is a bottleneck in that regard, and a better understanding of the mechanism for the energy transfer is needed in order to optimize the ligand design. It is crucial that the ligand enclose the metal centre efficiently so that water molecules are excluded from its first coordination sphere, and that the complex is stable in solution. Moreover, deuteration of the ligand, in proximity to the metal centre, increases the quantum yield significantly. Thus there is much room for improvement of the ligand design, and there are definitely many challenges ahead for synthetic chemists.

[1] a) D. Parker, R. S. Dickins, H. Puschmann, C. Crossland, J. A. K. Howard, *Chem. Rev.* **2002**, *102*, 1977–2010; b) S. Faulkner, J. L. Matthews, *Comprehensive Coordination Chemistry II* (Eds.: J. A. McCleverty, T. J. Meyer), vol. 9, Elsevier, Amsterdam, **2004**, 913–944.
[2] a) W. T. Carnall, P. R. Fields, K. Rajnak, *J. Chem. Phys.* **1968**, *49*, 4424–4442; b) W. T. Carnall, P. R. Fields, K. Rajnak, *J. Chem. Phys.* **1968**, *49*, 4447–4449; c) W. T. Carnall, P. R. Fields, K. Rajnak, *J. Chem. Phys.* **1968**, *49*, 4450–4455.
[3] G. F. de Sá, O. L. Malta, C. de M. Donegá, A. M. Simas, R. L. Longo, P. A. Santa-Cruz, E. F. Da Silva Jr., *Coord. Chem. Rev.* **2000**, *196*, 165–195.
[4] T. Förster, *Faraday Soc.* **1959**, *27*, 7–17.
[5] D. L. Dexter, *J. Chem. Phys.* **1953**, *21*, 836–850.
[6] W. DeWitt Horrocks Jr., D. R. Sudnick, *Acc. Chem. Res.* **1981**, *14*, 384–392.
[7] A. Beeby, I. M. Clarkson, R. S. Dickins, S. Faulkner, D. Parker, L. Royle, A. S. de Sousa, J. A. G. Williams, M. Woods, *J. Chem. Soc. Perkin Trans. 2* **1999**, 493–503.
[8] R. M. Supkowski, W. DeWitt Horrocks Jr., *Inorg. Chim. Acta* **2002**, *340*, 44–48.

 © 2005 Wiley-VCH Verlag GmbH & Co. KGaA, Weinheim

[9] a) S. Faulkner, A. Beeby, M.-C. Carrié, A. Dadabhoy, A. M. Kenwright, P. G. Sammes, *Inorg. Chem. Commun.* **2001**, *4*, 187–190; b) T. Kimura, Y. Kato, *J. Alloys Compd.* **1995**, *225*, 284–287.
[10] B. Alpha, R. Ballardini, V. Balzani. J.-M. Lehn, S. Perathoner, N. Sabbatini, *Photochem. Photobiol.* **1990**, *52*, 299–306.
[11] a) A. Døssing, H. Toftlund, A. Hazell, J. Bourassa, P. C. Ford, *J. Chem. Soc. Dalton Trans.* **1997**, 335–339; b) A. Døssing, J. Sokolnicki, J. P. Riehl, J. Legendziewicz, *J. Alloys Compd.* **2002**, *341*, 150–155; c) A. Døssing, S. M. Kristensen, H. Toftlund, J. A. Wolny, *Acta Chem. Scand.* **1999**, *53*, 575–580; d) P. Gawryszewska, J. Sokolnicki, A. Døssing, J. P. Riehl, J. Legendziewicz , to be published.
[12] A. Døssing, *Acta Chem. Scand.* **1997**, *51*, 981–983.
[13] X.-P Yang, B.-S. Kang, W.-K. Wong, C.-Y. Su, H.-Q. Liu, *Inorg. Chem.* **2003**, *42*, 169–179.
[14] M. Latva, H. Takalo, V.-M. Mukkala, C. Matachescu, J. C. Rodríguez-Ubis, J. Kankare, *J. Lumin.* **1997**, *75*, 149–169.
[15] N. Sabbatini, M. Guardigli, I. Manet, F. Bolletta, R. Ziessel, *Inorg. Chem.* **1994**, *33*, 955–959.
[16] D. Parker, J. A. G. Williams, *J. Chem. Soc. Dalton Trans.* **1996**, 3618–3628 and references cited therein.
[17] W. P. Cacheris, S. K. Nickle, A. D. Sherry, *Inorg. Chem.* **1987**, *26*, 958–960.
[18] D. Parker, P. K. Senanayake, J. A. G. Williams, *J. Chem. Soc. Perkin Trans. 2* **1998**, 2129–2139.
[19] D. A. Johnson, *J. Chem. Soc. Dalton Trans.* **1974**, 1671–1675.
[20] M. H. V. Werts, M. A. Duin, J. W. Hofstraat, J. W. Verhoeven, *Chem. Commun.* **1999**, 799– 800.
[21] I. Bkouche-Waksman, J. Guilhem, C. Pascard, B. Alpha, R. Deschenaux, J.-M. Lehn, *Helv. Chim. Acta* **1991**, *74*, 1163–1170.
[22] G.-F. Liu, Z.-P Qiau, H. Z. Wang, X.-M. Chen, G. Yang, *New J. Chem.* **2002**, *26*, 791–795.
[23] D. S. Moss, S. P. Sinha, *Z. Phys. Chem. (Muenchen Ger.)* **1969**, *63*, 190–192.
[24] S. F. Lincoln, A. E. Merbach, *Advances in Inorganic Chemistry*, Academic Press, New York **1995**, vol. 42, p. 56–64 and references cited therein.
[25] J. P. Riehl, *Encyclopedia of Spectroscopy and Spectrometry* (Eds.: J. C. Lindon, G. E. Trantner, J. L. Holmes), Academic Press, **2000**, 243–249.
[26] L. H. Slooff, A. van Blaaderen, A. Polman, G. A. Hebbink, S. I. Klink, F. C. J. M. van Veggel, D. N. Reinhoudt, J. W. Hofstraat, *J. Appl. Phys.* **2002**, *91*, 3955–3980.
[27] M. Hasegawa, A. Nakao, M. Masui, T. Tamura, D. Suzuki, W. Linert, Y. Fukuda, T. Hoshi, *Chem. Phys.* **2001**, *269*, 323–337.
[28] S. Faulkner, M.-C. Carrié, S. J. A. Pope, J. Squire, A. Beeby, P. G. Sammes, *Dalton Trans.* **2004**, 1405–1409.
[29] V. Vicinelli, P. Ceroni, M. Maestri, V. Balzani, M. Gorka, F. Vögtle, *J. Am. Chem. Soc.* **2002**, *124*, 6461–6468.
[30] M. E. Jolly, C. H. J. Wang, S. J. Ekenberg, M. S. Zeulke, D. M. Kelso, *J. Immunol. Methods* **1984**, *67*, 21–35.
[31] M. P. Oude Wolbers, F. C. J. M. van Veggel, F. G. A. Peters, E. S. E. van Beelen, J. W. Hofstraat, F. A. J. Geurts, D. N. Reinhoudt, *Chem. Eur. J.* **1998**, *4*, 772–780.
[32] M. H. V. Werts, J. W. Hofstraat, F. A. J. Geurts, J. W. Verhoeven, *Chem. Phys. Lett.* **1997**, *276*, 196–201.
[33] M. H. V. Werts, J. W. Verhoeven, J. W. Hofstraat, *J. Chem. Soc. Perkin Trans. 2* **2000**, 433–439.
[34] G. A. Hebbink, L. Grave, L. A. Woldering, D. N. Reinhoudt, F. C. J. M. van Veggel, *J. Phys. Chem. A* **2003**, *107*, 2483–2491.
[35] S. I. Klink, P. Oude Alink, L. Grave, F. G. A. Peters, J. W. Hofstraat, F. Geurts, F. C. J. M. van Veggel, *J. Chem. Soc. Perkin Trans. 2* **2001**, 363–372.
[36] S. B. Meshkova, N. V. Rusakova, D. V. Bolshoi, *Acta Chim. Hung.* **1992**, *129*, 317–323.
[37] F. Meinardi, N. Colombi, S. Destri, W. Porzio, S. Blumstengel, M. Cerminara, R. Tubino, *Synth. Metals* **2003**, *137*, 959–960.
[38] T. J. Foley, B. S. Harrison, A. S. Knefely, K. A. Abboud, J. R. Reynolds, K. S. Schanze, J. M. Boncella, *Inorg. Chem.* **2003**, *42*, 5023–5032.
[39] N. M. Shavaleev, S. J. A. Pope, Z. R. Bell, S. Faulkner, M. D. Ward, *Dalton Trans.* **2003**, 808–814.
[40] a) J. F. Deye, T. A. Berger, A. G. Anderson, *Anal. Chem.* **1990**, *62*, 615–622; b) L. C. Dias Jr., R. Custodio, F. B. T. Pessine, *Chem. Phys. Lett.* **1999**, *302*, 505–510; c) W.-G. Han, T. Q. Liu, F. Himo, A. Toutchkine, D. Bashford, K. M. Hahn, L. Noodleman, *Chem. Phys. Chem.* **2003**, *4*, 1084–1094.
[41] J. Long, Y.-M. Wang, T. Matsuura, J.-B. Meng, *J. Heterocycl. Chem.* **1999**, *36*, 895–899.
[42] A. Døssing, A. M. Frey, article to be published.

Received: December 21, 2004
Published Online: March 7, 2005

 © 2005 Wiley-VCH Verlag GmbH & Co. KGaA, Weinheim

Cu^{I} and Cu^{II} Complexes Containing Nitrite and Tridentate Aromatic Amine Ligand as Models for the Substrate-Binding Type-2 Cu Site of Nitrite Reductase

Hiroshi Yokoyama,[a] Kazuya Yamaguchi,*[a] Manabu Sugimoto,[b] and Shinnichiro Suzuki[a]

Keywords: Bioinorganic chemistry / Copper / N ligands / Tridentate ligands

Cu^{I} and Cu^{II} complexes containing a tridentate aromatic amine compound [bis(6-methyl-2-pyridylmethyl)amine, Me_2bpa] in the absence and presence of nitrite have been prepared as models for the active site of dissimilatory copper-containing nitrite reductase (CuNIR). $[Cu^{II}(Me_2bpa)(H_2O)(ClO_4)]ClO_4$ (**1**), $[Cu^{II}(Me_2bpa)(NO_2)(ClO_4)]$ (**2**), $[Cu^{I}(Me_2bpa)(CH_3CN)]PF_6$ (**3**) and $[Cu^{I}(Me_2bpa)(NO_2)]_2\cdot[(Ph_3P)_2NPF_6]$ (**4**) were prepared. The X-ray crystal structural analyses of **1**, **2**, and **4** reveal that the geometries of the Cu centers are distorted square pyramidal, distorted octahedral, and tetrahedral, respectively. The coordination modes of the nitrite ligands in **2** and **4** depend on the oxidation state of the copper ion: nitrite is coordinated to Cu^{II} and Cu^{I} through two oxygen atoms (*O*,*O*′-coordination mode) and one nitrogen atom (*N*-coordination mode), respectively. A comparison of the absorption spectra of **1** and **2** in acetone solution indicates that the 387-nm absorption band (ε = 780 $M^{-1}cm^{-1}$) of **2** is a charge-transfer transition. The broad absorption band at around 320 nm ($\varepsilon \approx 5000\ M^{-1}cm^{-1}$) of **4** in dichloromethane is also due to a charge-transfer transition. Functional modeling of CuNIR has been accomplished by treating solutions of **4** with acid; the nitrite-binding Cu^{I} complex quantitatively gives the one-electron reduction product,NO. The nitrite reduction of **4** in dichloromethane obeys a second-order rate law, suggesting that the rate-determining step would be protonation of the nitrite ligand of **4**. Electronic structure calculations of the Cu^{I} and Cu^{II} complexes containing Me_2bpa and nitrite by the density functional theory method demonstrate that the net charge of nitrite in $Cu^{I}(Me_2bpa)$(nitro) is larger than that in $Cu^{I}(Me_2bpa)$(nitrito). The mechanism of the nitrite reduction is discussed in comparison with the enzyme reaction mechanism of CuNIR.
(© Wiley-VCH Verlag GmbH & Co. KGaA, 69451 Weinheim, Germany, 2005)

Introduction

The global inorganic nitrogen cycle sustained by bacteria plays an important role in the animal and plant kingdoms. Dinitrogen is introduced into the biosphere by the biological fixation of dinitrogen, and is removed from there into the atmosphere again by denitrification. Denitrification is the dissimilatory reduction of nitrate or nitrite to produce dinitrogen by prokaryotic organisms. Nitrite reductase (NIR), a key enzyme of denitrification, catalyzes the reduction of nitrite to nitrogen monoxide. Cu-containing NIR (CuNIR) is a 110-kDa homotrimer in which a monomer contains one each of type-1 Cu (blue copper) and type-2 Cu (nonblue copper).[1–3] The interatomic distance between the two Cu sites is 12.5 Å. The type-2 Cu site shows a distorted tetrahedral geometry and is bound by three His residues and one solvent water; the active site pocket containing the Cu site lies at the bottom of a 16.5 Å cavity formed at the interface between two adjacent monomers. X-ray crystal structure analyses of nitrite-soaked oxidized NIRs have demonstrated that the substrate is coordinated to type-2 Cu^{II} in an asymmetric bidentate fashion through two oxygen atoms instead of the water ligand,[4–6] and an enzymatic mechanism has been proposed.[7,8] In the very recent X-ray crystal structure of nitrite-soaked oxidized *Alcaligenes faecalis* CuNIR at 1.4 Å resolution, NO_2^- coordinates to the Cu primarily by one O atom, whereas the other O atom interacts more weakly with the metal center.[9] Moreover, the plane defined by the Cu and the two O atoms and the plane defined by the N and the two O atoms form a 75° angle and the NO_2^- binds to the Cu with an almost face-on interaction. Several nitrite adducts of Cu^{II} complexes have been reported as model complexes for the active site of CuNIR.[10–14] Tolman et al. have reported the nitrite-binding copper(I) complexes $L^{iPr_3}Cu(NO_2)$ (L^{iPr_3} = 1,4,7-triisopropyl-1,4,7-triazacyclononane) and $[(L^{iPr_3}Cu)_2(\mu\text{-}NO_2)]^{2+}$ as structural and functional models for the nitrite-binding type-2 Cu site and have discussed a mechanism for NO generation involving these Cu^{I} complexes.[15,16]

[a] Department of Chemistry, Graduate School of Science, Osaka University,
Toyonaka, Osaka 560-0043, Japan
Fax: +81-6-6850-5785
E-mail: kazu@ch.wani.osaka-u.ac.jp
[b] Department of Applied Chemistry and Biochemistry, Graduate School of Science and Technology, Kumamoto University,
Kurokami, Kumamoto 860-8555, Japan
Supporting information for this article is available on the WWW under http://www.eurjic.org or from the author.

We report here the spectral and structural characterization of Cu^{I} and Cu^{II} complexes containing nitrite and a tridentate aromatic amine [bis(6-methyl-2-pyridylmethyl) amine (Me_2bpa)] as a substrate-binding type-2 Cu site model of CuNIR. Moreover, the nitrite reduction mechanism of the Cu^{I} complex is discussed based on the parameters of activation of the transition state. The enzymatic reduction mechanism of nitrite at the type-2 Cu is also proposed in comparison with the present model complexes and the binding mode of nitrite observed in the native and mutant CuNIRs from *Alcaligenes faecalis* S-6 by X-ray crystal structure analysis.[9]

Results and Discussion

Structural and Spectral Aspects of the Cu^{II} Model Complex Containing NO_2^-

The reaction of $[Cu^{II}(Me_2bpa)(H_2O)(ClO_4)]ClO_4$ (**1**) with one equivalent of $NaNO_2$ in H_2O at room temperature gives $[Cu^{II}(Me_2bpa)(NO_2)(ClO_4)]$ (**2**), which was recrystallized from aqueous methanol solution as green crystals. Figure 1 shows the X-ray crystal structures of **1** and **2**.

The geometry of Cu^{II} in **1** is distorted square pyramidal with three nitrogen atoms of the Me_2bpa ligand and one oxygen atom from each of H_2O and ClO_4^-; a 15.0° upside deviation of the O(1) ligating atom of H_2O from the N(1) N(2)N(3) plane of Me_2bpa is observed. The structure of **2** reveals the replacement of the H_2O ligand by nitrite and asymmetric *O*,*O*′-nitrite chelation to the distorted octahedral Cu^{II} ion along with the Me_2bpa and ClO_4^- ligands. The equatorial O(2) coordinating atom deviates from the N(1)N(2)N(3) plane of Me_2bpa by 19.6° and the O(1) ligating atom binds axially to the Cu^{II} ion. The structural studies of nitrite-binding Cu^{II} complexes have shown that nitrite has a variety of coordination modes to a Cu^{II} center (Scheme 1).[17] Complex **2** exhibits two distinct Cu^{II}–$O_{nitrite}$ bond lengths [Cu(1)–O(1) = 2.47(3) Å, Cu(1)–O(2) = 1.98(2) Å] and the coordination mode of NO_2^- (**a** in Scheme 1) is similar to those of the Cu^{II}–NO_2^- model complexes[10–14] and the nitrite-binding type-2 Cu^{II} site in nitrite-soaked NIR at 1.4 Å resolution (Cu–O = 2.29–2.38, 2.04–2.08 Å).[9] The Cu, N(4), and two O(1 and 2) atoms lie in the same plane. The N–O bond lengths [N(4)–O(1) = 1.24(4) Å, N(4)–O(2) = 1.28(4) Å] and the O(1)–N(4)–O(2) angle [115.8(27)°] are similar to those in the free nitrite ion [O–N–O = 114.9(5)° and N–O = 1.240(3) Å].[18]

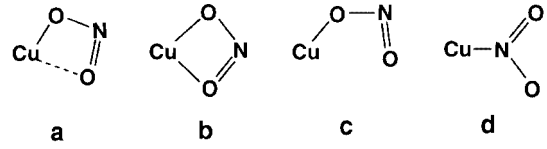

Scheme 1.

The electronic absorption spectrum of **1** in acetone solution (Figure 2) shows one band at 675 nm (ε = 190 $M^{-1}cm^{-1}$), which is assigned to a ligand field transition. Complex **2** exhibits two bands at 378 nm (ε = 780 $M^{-1}cm^{-1}$) and 671 nm (ε = 200 $M^{-1}cm^{-1}$), which are ascribed as a nitrite → Cu^{II} charge transfer (LMCT) and a d-d transition, respectively. The small blue shift of the d-d band from 675 nm to 671 nm is due to the *O*-nitrite coordination of nitrite. Moreover, the 77-K EPR spectra of **1** and **2** in ace-

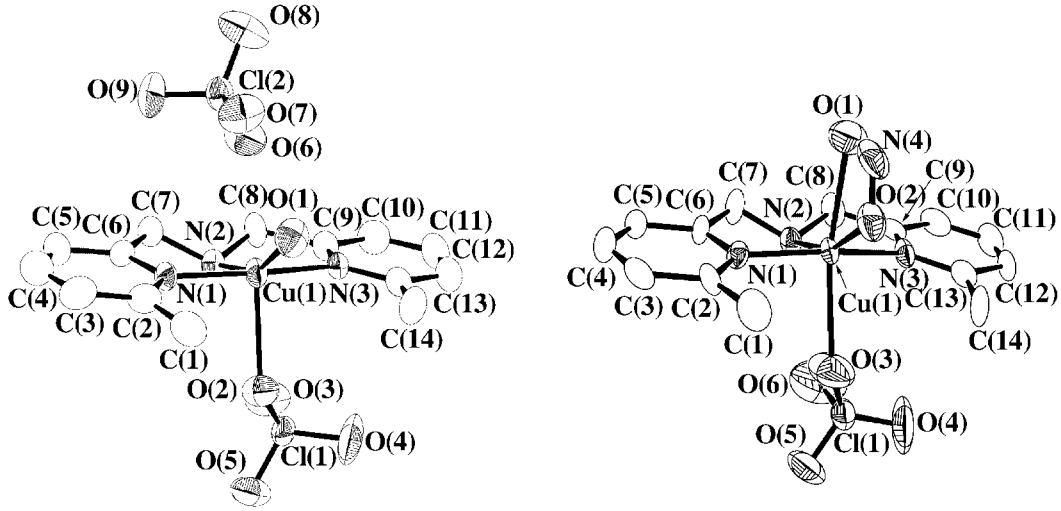

Figure 1. ORTEP plots of **1** (left) and **2** (right) with 50% probability thermal ellipsoids. The hydrogen atoms have been omitted for clarity. Selected distances [Å] and angles [°] for **1** are follows: Cu(1)–O(1) 2.017(7), Cu(1)–O(2) 2.441(7), Cu(1)–N(1) 2.001(6), Cu(1)–N(2) 1.957(7), Cu(1)–N(3) 2.011(6); O(1)–Cu(1)–O(2) 111.6(3), O(1)–Cu(1)–N(1) 93.0(3), O(1)–Cu(1)–N(2) 153.0(3), O(1)–Cu(1)–N(3) 97.4(3), O(2)–Cu(1)–N(1) 90.5(3), O(2)–Cu(1)–N(2) 95.2(3), O(2)–Cu(1)–N(3) 91.7(3), N(1)–Cu(1)–N(2) 83.4(3), N(1)–Cu(1)–N(3) 167.8(3), N(2)–Cu(1)–N(3) 84.4(3). Selected distances [Å] and angles [°] for **2** are follows: Cu(1)–O(1) 2.47(3), Cu(1)–O(2) 1.98(2), Cu(1)–O(3) 2.52(3), Cu(1)–N(1) 2.012(18), Cu(1)–N(2) 1.99(3), Cu(1)–N(3) 2.003(18), O(1)–N(4) 1.20(4), O(2)–N(4) 1.28(4); O(1)–Cu(1)–O(2) 54.9(10), O(1)–Cu(1)–O(3) 159.4(9), O(2)–Cu(1)–N(2) 155.6(10), N(1)–Cu(1)–N(2) 82.8(8), N(2)–Cu(1)–N(3) 82.1(9), N(1)–Cu(1)–O(3) 87.9(8), Cu(1)–O(1)–N(4) 83.7(19), Cu(1)–O(2)–N(4) 105.6(19), O(1)–N(4)–O(2) 115.8(27).

 © 2005 Wiley-VCH Verlag GmbH & Co. KGaA, Weinheim

tone solution reveal the typical axial signals ($g_{\|} > g_{\perp}$) of a tetragonal Cu^{II} chromophore having a $d_{x^2-y^2}$ground state (Figure S1, Supporting Information). The parameters for **2** ($g_{\|}$ = 2.25, $g_{\perp}$ = 2.09, $A_{\|}$ = 16.8 mT) exhibit a slight decrease in the $g_{\|}$ and $A_{\|}$ values with respect to the precursor complex **1** ($g_{\|}$ = 2.27, $g_{\perp}$ = 2.07, $A_{\|}$ = 17.2 mT). The difference between the parameters of these Cu^{II} complexes suggests the weak apical coordination [Cu(1)–O(3)] of nitrite in **2**.

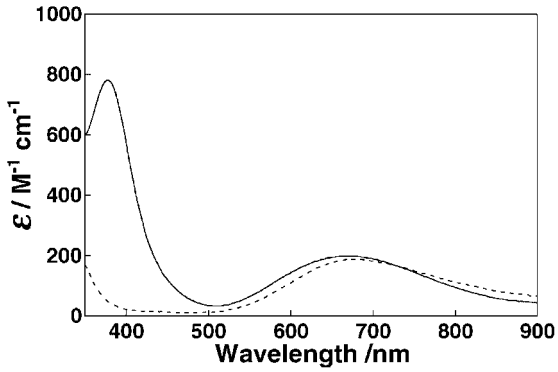

Figure 2. Electronic absorption spectra of **1** (broken line) and **2** (solid line) in acetone at room temperature.

Structural and Spectral Aspects of the Cu^{I} Model Complex Containing NO_2^-

The reduced complex of **1**, the pale-yellow crystalline solid $[Cu^{I}(Me_2bpa)(CH_3CN)]PF_6$ (**3**), was prepared by treatment of $[Cu(CH_3CN)]PF_6$ with Me_2bpa in methanol. The nitrite-binding copper(I) complex, $[Cu(Me_2bpa)(NO_2)]_2\cdot[(Ph_3P)_2NPF_6]$ (**4**) was obtained as a yellow powder from an equimolar mixture of $[Cu(CH_3CN)]PF_6$, Me_2bpa, and $[(Ph_3P)_2N]NO_2$ in acetone under nitrogen. The X-ray crystal structure of **4** (Figure 3) reveals the *N*-nitrite coordination (**d** in Scheme 1) to the Cu^{I} center that adopts a distorted tetrahedral geometry. Although such a binding mode of nitrite in **4** is similar to that of $L^{iPr_3}Cu(NO_2)$, some important structural aspects are different.[15,16] The N–O bond lengths [1.253(5) and 1.238(5) Å] and the O–N–O angle [116.6(4)°] of nitrite in $L^{iPr_3}Cu(NO_2)$[16] are almost the same as those of free nitrite ion,[18] but the nitrite N–O distances [O(1)–N(4) = 1.076(8) Å and O(2)–N(4) = 1.039(8) Å] and the O(1)–N(4)–O(2) angle [133.6(8)°] of **4** are different from the corresponding values of free nitrite. The Cu(1)–N(4) bond length of **4** is 2.053(4) Å, which is longer than the value of 1.903(4) Å in $L^{iPr_3}Cu(NO_2)$.[16] Unfortunately, the large temperature factor of the O-atoms of the nitrite in **4** suggest the rotation/vibration of the NO_2^- ligand and lead to serious errors in the parameters of nitrite bound to Cu^{I} ion.[19] Therefore, it is difficult to discuss the structure of nitrite-binding copper(I) complex in detail on the basis of our present results.

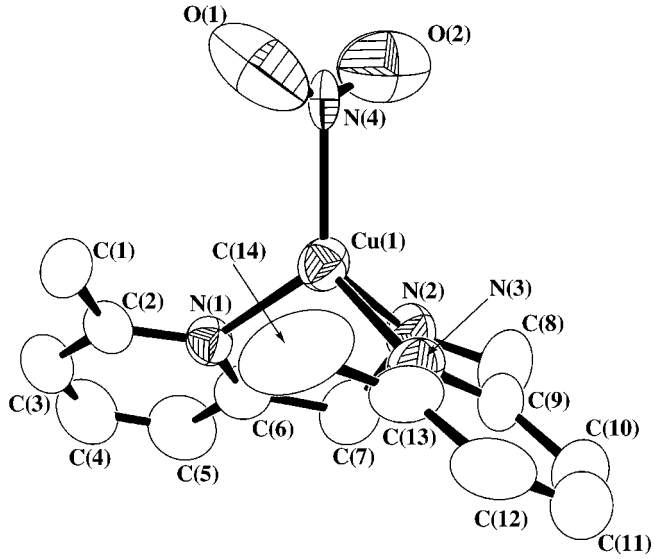

Figure 3. ORTEP plots of the Cu^{I} complex in **4** with 50% probability thermal ellipsoids. The hydrogen atoms and $[(Ph_3P)_2NPF_6]$ have been omitted for clarity. Selected distances [Å] and angles [°] for **4** are follows: Cu(1)–N(1) 2.053(4), Cu(1)–N(2) 2.168(5), Cu(1)–N(3) 2.033(5), Cu(1)–N(4) 2.087(5), O(1)–N(4) 1.076(8), O(2)–N(4) 1.039(8); N(1)–Cu(1)–N(2) 82.4(2), N(1)–Cu(1)–N(3) 111.7(2), N(2)–Cu(1)–N(3) 81.0(2), N(1)–Cu(1)–N(4) 121.9(2), N(2)–Cu(1)–N(4) 118.8(2), N(3)–Cu(1)–N(4) 124.2(2), Cu(1)–N(4)–O(1) 111.5(5) Cu(1)–N(4)–O(2) 114.8(5), O(1)–N(4)–O(2) 133.6(8).

The electronic absorption spectra of **3** and **4** in CH_2Cl_2 are shown in Figure 4. These Cu^{I} complexes have no absorption band in the visible region. Complex **4** exhibits an intense broad band around 320 nm ($\varepsilon \approx 5000\ M^{-1}cm^{-1}$), which is assigned to a $Cu^{I} \rightarrow NO_2^-$ MLCT transition.[10–14] Tolman et al. have reported that $L^{iPr_3}Cu(NO_2)$ exhibits an intense MLCT band at 308 nm (ε = 3800 $M^{-1}cm^{-1}$) in CH_2Cl_2. The shift of the MLCT band could be due to the different electronic structures of **4** and $L^{iPr_3}Cu(NO_2)$.

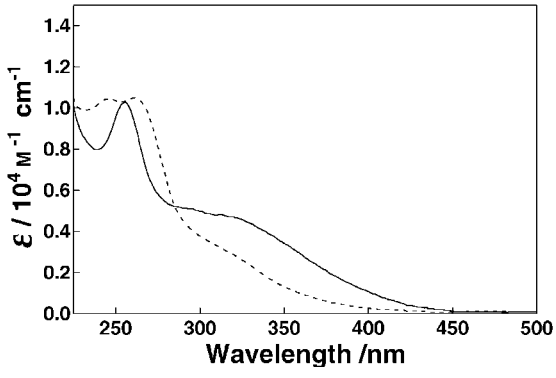

Figure 4. Electronic absorption spectra of **3** (broken line) and **4** (solid line) in CH_2Cl_2 at room temperature.

Nitrite Reductase Reactivity of the Cu^{I} Model Complex Containing NO_2^-

The cyclic voltammogram of **2** in H_2O shows a response with $E_{1/2}$ = –95 mV vs. Ag/AgCl and a peak-to-peak sepa-

 © 2005 Wiley-VCH Verlag GmbH & Co. KGaA, Weinheim

ration, ΔE, of 74 mV in the presence of 500 mM $NaNO_2$ (a in Figure 5). The ΔE value indicates a quasi-reversible electron-transfer process. Addition of acid to the aqueous solution of **2** brings about a strong catalytic current due to the reduction of NO_2^- (b in Figure 5). Thus, **2** serves as an electrocatalyst in the reduction of NO_2^- at pH 5.5.

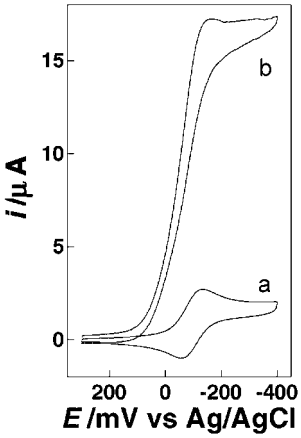

Figure 5. Voltammetric behavior of **2** (a) and after addition of $HClO_4$ (b) in 0.1 M $TBAClO_4$ aqueous solution at 25.0 °C (**2**: 0.5 mM; $NaNO_2$: 500 mM; scan rate: 10 mV s^{-1}).

When four equivalents of trifluoroacetic acid was added to a CH_2Cl_2 solution of **4** at room temperature, the color of the solution was changed from pale yellow to blue and the stoichiometric evolution of NO gas (>95% vs. **4**) was observed by gas chromatography (Figure S2, Supporting Information). No N_2O gas was detected, and [$Cu(Me_2bpa)(OCOCF_3)_2$] was isolated from the reaction mixture. The reaction of **4** with proton was monitored either by recording the transient absorption spectra at one-second intervals or by recording absorption vs. time at a fixed wavelength (320 nm). At 213.0 K, the 320-nm band of **4** was observed to be a sharp peak as shown in Figure 6. Introduction of four equivalents of trifluoroacetic acid to the solution under an Ar atmosphere induced a decrease in the absorbance at 320 nm and a slight increase in the absorbance at about 700 nm. As shown in the inset of Figure 6, the reaction of **4** with proton was found to be first-order both in [**4**] and in [acid] ($v = k_{obs}$[**4**][acid]) at 213.0, 223.0, and 231.8 K. The rate constants (k_{obs}) are listed in Table 1. The activation parameters (Table 2) were estimated from Arrhenius–Eyring plots of the data ($\ln k_{obs} = \ln A - E_a/RT$, $\ln(hk_{obs}/k_BT) = \Delta S^{\neq}/R - \Delta H^{\neq}/RT$; Figure S3, Supporting Information).

The mechanism of nitrite reduction of **4** with proton is illustrated in Scheme 2. The kinetic data of the reaction of **4** with trifluoroacetic acid suggest that the rate-determining step is the first protonation of the nitrite ligand. Since a negative value of $\Delta S^{\neq}$ generally corresponds to the additional loss of freedom of motion by the solvating molecule, the negative $\Delta S^{\neq}$ value (–51 J K^{-1} mol^{-1}) means that protonated **4** will be an active intermediate. The positive $\Delta H^{\neq}$ suggests that **4** is more stable than protonated **4**. The resonance structure of the nitrite ligand in **4** (O=N–O^- ↔ $^-$O–N=O) might contribute to the stability of **4**.

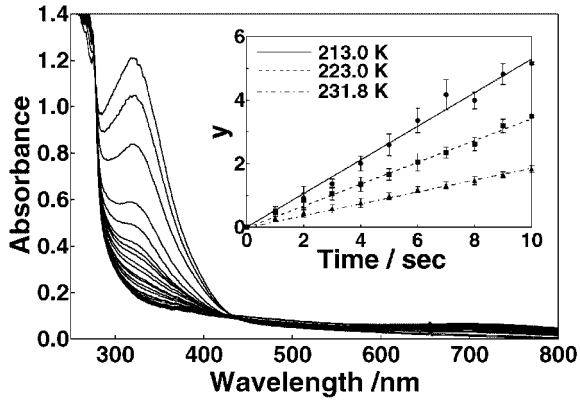

Figure 6. Spectral changes observed during the anaerobic reaction of **4** with trifluoroacetic acid in CH_2Cl_2 at 213.0 K. The subsequent traces, with progressively decreasing absorbance at 320 nm, refer to spectra taken every second Inset: plots of the second-order rate law for the reactions of **4** with CF_3COOH at 213.0, 223.0, and 231.8 K. The *y*-axis is $(1/[\mathbf{4}]_0[acid]_0)\ln([acid]_0[\mathbf{4}]_x/[\mathbf{4}]_0[acid]_x)$.

Table 1. Second-order rate constants for nitrite reduction of **4**.

T [K]	$k_{obsd.}$ [M^{-1} s^{-1}]
231.8	0.53 ± 0.04
223.0	0.34 ± 0.03
213.0	0.18 ± 0.02

Table 2. Activation parameters for nitrite reduction of **4**.

E_a [kJ mol^{-1}]	$\Delta G^{\neq}$ [kJ mol^{-1}]	$\Delta H^{\neq}$ [kJ mol^{-1}]	$\Delta S^{\neq}$ [J K^{-1} mol^{-1}]
23 ± 1	40 ± 2	25 ± 1	–51 ± 3

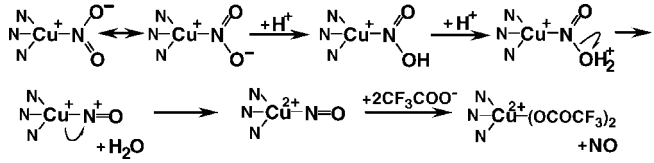

Scheme 2.

Electronic-Structure Calculations of the Cu^I and Cu^{II} Complexes Containing Me_2bpa and Nitrite by the Density Functional Theory (DFT) Method

Electronic-structure calculations of the Cu^I and Cu^{II} complexes containing Me_2bpa and nitrite were carried out with the DFT method using the Gaussian 98 program.[20] The X-ray crystal data of **2** and **4** were employed for initial geometries. The $Cu^{II}(Me_2bpa)$ complex binding nitrite asymmetrically through two oxygen atoms (Cu^{II}–ONO^-, *O,O′*-nitrite coordination) is stabilized by 13.1 kcal mol^{-1} relative to that binding nitrite through one nitrogen atom (Cu^{II}–NO_2^-, *N*-nitrite coordination), while Cu^I–NO_2^- is less stable than Cu^I–ONO^- (1.0 kcal mol^{-1}). Therefore, nitrite is preferentially coordinated to Cu^{II} through two oxygen atoms (Cu^{II}–ONO^-), whereas the Cu^I complex could have two nitrite-binding forms (Cu^I–ONO^- and Cu^I–NO_2^-). These findings are consistent with the experimental data

 © 2005 Wiley-VCH Verlag GmbH & Co. KGaA, Weinheim

that the two L^{iPr_3}-containing Cu^{I} complexes are bridged by nitrite through both nitrogen and oxygen atoms in the dicopper(II) complex $[(L^{iPr_3}Cu)_2(\mu\text{-}NO_2)]PF_6$.[16] The Cu–nitrite bond energies of Cu^{I}–NO_2^- and Cu^{I}–ONO^- were estimated to be 103.2 and 104.2 kcal mol^{-1}, respectively, whereas those of Cu^{II}–NO_2^- and Cu^{II}–ONO^- were calculated to be 200.7 and 213.8 kcal mol^{-1}, respectively. The binding of nitrite to Cu^{II} in both the *N*-nitrite and the *O*,*O*′-nitrite coordination is energetically favored over that of nitrite to Cu^{I} in the two forms. The net charges of the nitrite ligands of Cu^{I}–NO_2^-, Cu^{I}–ONO^-, Cu^{II}–NO_2^- and Cu^{II}–ONO^- were evaluated to be –0.649, –0.562, –0.314, and –0.403, respectively, suggesting that the *N*-coordinated nitrite ligand of Cu^{I}–NO_2^- will be most easily attacked by proton to produce NO and H_2O.

Proposed Mechanism of Nitrite Reductases

According to the crystallographic studies of the nitrite-binding Cu^{II} complexes[10–16] and the nitrite-soaked oxidized CuNIR,[4–6] nitrite preferentially binds to the oxidized type-2 Cu by asymmetric *O*,*O*′-coordination. We have proposed a catalytic mechanism for CuNIR incorporating roles for Asp98 hydrogen-bonded to the substrate and His255 hydrogen-bonded to Asp98 through H_2O, of which both the residues form a hydrogen-bonding network around the type-2 Cu.[8] In an intermediate species during nitrite reduction, one of the two oxygen atoms of nitrite coordinated to type-2 Cu is probably hydrogen-bonded by both the protonated Asp98 and His255 residues. Very recently, Murphy et al. have reported that the nitrite-bound CuNIR crystal structure shows an angular orientation of nitrite bound to the type-2 Cu; the N atom is out of the plane defined by the two O atoms and the Cu atom, which forms a 75° angle with the plane defined by the N and the two O atoms.[9] Therefore, they proposed that electron transfer (ET) from the type-1 Cu reduces the type-2 Cu to trigger a rearrangement of NO_2^- (from *O*,*O*′-coordination to *N*-coordination) to release water and form a Cu^{I}–NO^+ intermediate, that is, the proximity of the N atom of nitrite to the Cu in the substrate-soaked structure will facilitate this rearrangement step. The present studies of the X-ray crystal structure, nitrite reduction kinetics, and electronic-structure calculation of **4** also suggest that nitrite is initially coordinated to the oxidized type-2 Cu by the *O*,*O*′-coordination and then is converted into *N*-coordination by the reduction of the type-1 Cu. As shown in Figure 7, nitrite displaces a water ligand, which leaves a proton on Asp98 and is released as OH^- (I → II). When the type-2 Cu is reduced by an electron from the type-1 Cu, the binding mode of nitrite is changed from *O*,*O*′-coordination to *N*-coordination and the proton of His255, which has an imidazolium group, is donated to the oxygen of *N*-coordinated nitrite (II → III → IV → V). *N*-Coordination of nitrite to the Cu^{I} ion and protonation to the nitrite ligand are supported by the kinetic analysis of **4** and the electronic-structure calculations of **2** and **4**. Finally, the electron transfer from the reduced type-2 Cu to NO_2H would facilitate the N–O bond cleavage to produce NO gas through a Cu^{I}–NO^+ intermediate (V → VI).

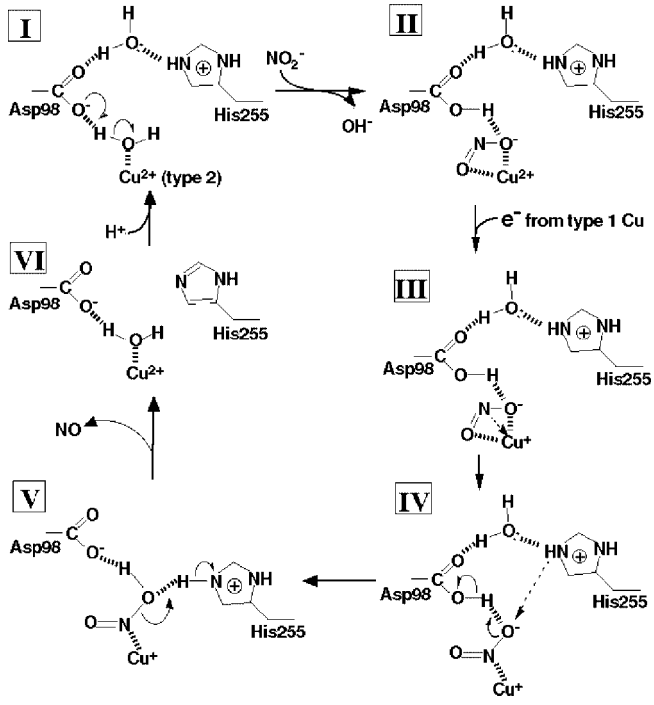

Figure 7. Revized enzymatic reaction mechanism of CuNIR containing type-1 Cu and type-2 Cu (cf. ref.[7]).

Conclusions

Cu^{I} and Cu^{II} complexes containing a tridentate aromatic amine compound (Me_2bpa) and nitrite have been prepared as models for the active site of dissimilatory copper-containing nitrite reductase (CuNIR). The X-ray crystal structural analyses of **2** and **4** reveal that the geometries of the Cu centers are distorted octahedral and tetrahedral, respectively, and the coordination modes of nitrite are *O*,*O*′-coordination and *N*-coordination, respectively. The spectroscopic data of these complexes are consistent with their structural data. The reduction of nitrite by proton donation to **4** gives NO. These findings imply that both structural and functional modeling of CuNIR are achieved with Cu^{I} and Cu^{II} complexes containing the same aromatic amine ligand, Me_2bpa. The kinetic results of the reaction of **4** with acid suggest that the rate-determining step is protonation of the nitrite ligand of **4** and the resultant protonated species is the active intermediate. Moreover, electronic-structure calculations of the Cu^{I} and Cu^{II} complexes containing Me_2bpa and nitrite demonstrate that nitrite is preferentially coordinated to Cu^{II} through two oxygen atoms, but could bind to Cu^{I} by both *O*,*O*′- and *N*-coordination. Since the *N*-coordinated nitrite ligand of **4** will be more easily attacked than the *O*,*O*′-coordinated one by proton, the nitrite reduction of **4** probably occurs through the *N*-coordination of nitrite to Cu^{I}. According to the model complex studies for the active site of CuNIR, we have proposed a revised catalytic mechanism[7] for CuNIR.

 © 2005 Wiley-VCH Verlag GmbH & Co. KGaA, Weinheim

Experimental Section

General Remarks: All reagents used were of the highest grade available. Solvents were dried and distilled under N_2. Bis(6-methyl-2-pyridylmethyl)amine (Me_2bpa),[21] $[Cu(CH_3CN)_4]PF_6$, and $[(Ph_3P)_2N]NO_2$[22] were synthesized according to the published procedures. All air-sensitive reactions were performed by using standard Schlenk and vacuum-line techniques. Electronic absorption spectra were recorded on a Shimadzu UV-2200 spectrophotometer. Low-temperature absorption spectra were obtained with a Shimadzu Multi-Spec 1500 spectrophotometer. X-band EPR spectra were recorded on a JEOL JES-FE1X spectrometer at 77 K. Gas chromatography was performed by using a Shimadzu GC14B analyzer with TCD detector (3-m molecular sieve 13X column, 23.5 mL min^{-1} flow rate, helium carrier gas, and at 50 °C). Cyclic voltammetric analyses were carried out using a Bioanalytical Systems Model CV-50W voltammetric analyzer with a three-electrode system consisting of a Ag/AgCl reference electrode, a gold wire counter electrode, and a glassy carbon working electrode under an Ag atmosphere at 25 °C.

$[Cu^{II}(Me_2bpa)(H_2O)(ClO_4)]ClO_4$ (1): A solution of $Cu(ClO_4)_2 \cdot 6H_2O$ (3.71 g, 10 mmol) in methanol (5 mL) was added to a solution of Me_2bpa (2.27 g, 10 mmol) in methanol (50 mL). The resultant solution was stirred for 1 h and stored for a few days at room temperature to give blue crystals of **1** (4.39 g, 86.5%). $C_{14}H_{19}Cl_2CuN_3O_9$ (507.8): calcd. C 33.11, H 3.78, N 8.28; found C 33.11, H 3.68, N 8.30.

$[Cu^{II}(Me_2bpa)(NO_2)(ClO_4)]$ (2): A solution of $NaNO_2$ (0.069 g, 1 mmol) in H_2O (10 mL) was added to a solution of **1** (0.51 g, 1 mmol) in H_2O (25 mL). The resultant solution was stirred for 1 h at room temperature to give **2** as a green precipitate. The green complex **2** was recrystallized from methanol/H_2O (0.362 g, 83.0%). $C_{14}H_{17}ClCuN_4O_6$ (436.3): calcd. C 38.54, H 3.93, N 12.84; found C 38.37, H 3.95, N 12.83.

$[Cu^{I}(Me_2bpa)(CH_3CN)]PF_6$ (3): $[Cu(CH_3CN)_4]PF_6$ (0.167 g, 0.5 mmol) was added as a solid, under an N_2 atmosphere, to a solution of Me_2bpa (0.114 g, 0.5 mmol) in methanol (5 mL). After stirring at 60 °C for 10 min, the resultant solution was stored at –20 °C. The pale-yellow crystalline solid thus obtained was filtered off, washed with dry diethyl ether, and dried under N_2 (0.196 g, 82.2%). $C_{16}H_{20}CuF_6N_4P$ (476.9): calcd. C 40.29, H 4.24, N 11.75; found C 40.09, H 4.23, N 11.89.

$[Cu^{I}(Me_2bpa)(NO_2)]_2 \cdot [(Ph_3P)_2NPF_6]$ (4): $[Cu(CH_3CN)_4]PF_6$ (0.167 g, 0.5 mmol) was added as a solid, under an N_2 atmosphere, to a solution of Me_2bpa (0.114 g, 0.5 mmol) in acetone (3.5 mL). $[(Ph_3P)_2N]NO_2$ (0.292 g, 0.5 mmol) was then added to the resultant solution, under an N_2 atmosphere. After stirring for 1 h **4** precipitated as a yellow powder (0.301 g, 88.7%). For X-ray analysis, yellow crystals of **4** were obtained from CH_2Cl_2/acetone. $C_{64}H_{64}Cu_2F_6N_9O_4P_3$ (1357.3): calcd. C 56.63, H 4.76, N 9.29; found C 56.64, H 4.90, N 9.41.

Measurement of NO Generated from 3: A solution of **4** (10 mg, 7.5 μmol) in CH_2Cl_2 (0.45 mL) was prepared in a small vial capped with a rubber septum. A degassed solution of CF_3COOH (6 μL) in CH_2Cl_2 (0.05 mL) was then introduced with a syringe at room temperature. The solution changed immediately from yellow to blue. Analysis of the head-space gas by a GC analyzer indicated that NO had been generated (7.3 ± 0.2 μmol).

Kinetics: The kinetic studies of nitrite reduction of **4** in CH_2Cl_2 were carried out by monitoring the intensity decrease of the 320-nm band. The absorbance was detected by a fiber-optics quartz probe (0.2-cm path-length) immersed in a small vessel containing a 5 mL CH_2Cl_2 solution of **4** (3.4 mg, 2.5 μmol) under an Ar atmosphere. The reaction was started with the addition of 100 μL of a CH_2Cl_2 solution containing CF_3COOH (10 μmol), which had been degassed with N_2 beforehand.

X-ray Crystallographic Study of $[Cu^{II}(Me_2bpa)(H_2O)(ClO_4)]ClO_4$ (1) and $[Cu^{II}(Me_2bpa)(NO_2)(ClO_4)]$ (2): The X-ray experiment was carried out on a MAC Science MXC18 diffractometer with graphite-monochromated Mo-K_α radiation (λ = 0.71069 Å). A blue (**1**) or green (**2**) crystal was mounted on a glass capillary. The reflection intensities were monitored by three standard reflections at every 150 measurements, and the decay of intensities was within 2%. The unit-cell parameters used for the refinement were determined by least-square calculations on the setting angles for 22 carefully centered reflections. An absorption correction was applied. Diffraction data were corrected for both Lorentz and polarization effects. The structure was solved by direct methods SIR92[23] using the CRYSTAN-GM program system[24] and refined anisotropically for non-hydrogen atoms by full-matrix least-squares calculations. Each refinement was continued until all shifts were smaller than one-third of the standard deviations of the parameters involved. Atomic scattering factors and anomalous dispersion terms were taken from the literature.[25] All hydrogen atoms were located at their calculated positions. The fundamental crystal data and experimental parameters for structure determination are given in Table 3.

$[Cu^{I}(Me_2bpa)(NO_2)]_2[(Ph_3P)_2NPF_6]$ (4): The X-ray experiment was carried out at –70 °C on a Rigaku Mercury CCD area detector coupled with a Rigaku AFC-7R diffractometer with graphite monochromated Mo-K_α radiation (λ = 0.71069 Å). The pale-yellow crystal was mounted on a glass capillary. The data were corrected for Lorentz and polarization effects, but not for secondary extinction. An empirical absorption correction was applied. The structure was solved by direct methods using the Crystal Structure crystallographic software package[26] and refined anisotropically for non-hydrogen atoms by full-matrix least-squares calculations. Each refinement was continued until all shifts were smaller than one-third of the standard deviations of the parameters involved. Atomic scattering factors and anomalous dispersion terms were taken from the literature.[25] All hydrogen atoms were located at their calculated positions. The maximum and minimum peaks on the final difference Fourier map corresponded to 0.73 and –0.52 e Å^{-3}, respectively. The fundamental crystal data and experimental parameters for structure determination are given in Table 3.

CCDC-251363 (for **1**), -251364, (for **2**) and -251365 (for **4**) contain the supplementary crystallographic data for this paper. These data can be obtained free of charge from The Cambridge Crystallographic Data Centre via www.ccdc.cam.ac.uk/data_request/cif.

Electronic-Structure Calculations: Electronic-structure calculations of the Cu^{I} and Cu^{II} complexes containing Me_2bpa and nitrite were carried out with the DFT method in the Gaussian 98 program.[27] For all molecules, the geometries were fully optimized without any constraints. The three-parameter Becke–Lee–Yang–Parr (B3LYP) functional was adopted as the exchange-correlation functional.[28] The core electrons of Cu were replaced with the effective core potential (ECP) of Hay and Wadt.[29] The basis set for Cu was the split-valence set (LANL2DZ[21]) for the ECP. The Huzinaga–Dunning (9s5p)/[4s2p] and (4s)/[2s] basis sets were used for the first row elements and hydrogen, respectively.[30]

Supporting Information (see also footnote on the first page of this article): Further figures illustrating the ESR spectra of **1** and **2**, the GC chart, and the Arrhenius–Eyring plot for the reaction of **4** with proton are provided.

 © 2005 Wiley-VCH Verlag GmbH & Co. KGaA, Weinheim

Table 3. Crystal data for **1**, **2**, and **4**

	1	**2**	**4**
Formula	$C_{14}H_{19}Cl_2CuN_3O_9$	$C_{14}H_{17}ClCuN_4O_6$	$C_{64}H_{64}Cu_2F_6N_9O_4P_3$
Formula mass	507.80	436.30	1357.27
Color	blue	green	pale yellow
Crystal size [nm]	$0.75\times0.30\times0.30$	$0.45\times0.10\times0.03$	$1.00\times0.50\times0.10$
Crystal system	triclinic	triclinic	monoclinic
Space group	$P1$	$P\bar{1}$	$C2/c$
a [Å]	8.558(5)	8.972(8)	30.72(1)
b [Å]	8.650(7)	12.395(9)	12.950(5)
c [Å]	7.820(5)	8.516(8)	15.596(6)
α [°]	113.18(5)	93.13(7)	-
β [°]	110.95(4)	109.33(7)	96.29(1)
γ [°]	71.86(5)	77.97(6)	–
V [Å^3]	487.1(5)	874.010010(1)	6166.7(3)
Z	1	2	4
$D_{calcd.}$ [g cm^{-3}]	1.731	1.657	1.462
Radiation	Mo-K_α (λ = 0.71073 Å)	Mo-K_α (λ = 0.71073 Å)	Mo-K_α (λ = 0.7107 Å)
μ [cm^{-1}]	14.51	14.435	8.42
F_{000}	259.00	446.00	2800.00
Scan method	θ–2θ	θ–2θ	ω–2θ
$2\theta_{max}$ [°]	52.94	52.86	53.46
No. reflections obsd.	2220	1566	6690
No. reflections used	2205	1454	4312
R[a]	0.069	0.069	0.064
R_w[b]	0.087	0.091	0.097

[a] $R = \Sigma||F_o| - |F_c||/\Sigma|F_o|$. [b] $R_w = [\Sigma w(|F_o| - |F_c|)^2/\Sigma wF_o^2]^{1/2}$; $w = 1/[\sigma^2(F_o) + 0.03F_o^2]$ for **1** and **2**, $w = 1/[\sigma^2(F_o) + 0.005F_o^2]$ for **4**.

Acknowledgments

We thank Prof. Susumu Kitagawa and Dr. Mitsuru Kondo, Kyoto University, and Dr. Tatsuya Kawamoto, Osaka University, for X-ray crystallographic experiments. This work was support by Grants-in-aid for Scientific research (B) (no.11440198 to S. S.) and (C) (no. 12640538 to K. Y.) from the Ministry of Education, Science, Sports and Culture of Japan, to whom we express our thanks.

[1] W. G. Zumft, *Microbiol. Mol. Biol. Rev.* **1997**, *61*, 533–616.
[2] S. Suzuki, K. Kataoka, K. Yamaguchi, T. Inoue, Y. Kai, *Coord. Chem. Rev.* **1999**, *190–192*, 245–265.
[3] S. Suzuki, K. Kataoka, K. Yamaguchi, *Acc. Chem. Res.* **2000**, *33*, 728–735.
[4] E. T. Adman, J. W. Godden, S. Turley, *J. Biol. Chem.* **1995**, *270*, 27 458–27 474.
[5] M. E. P. Murphy, S. Turley, E. T. Adman, *J. Biol. Chem.* **1997**, *272*, 28 455–28 460.
[6] F. E. Dodd, J. V. Beeumen, R. R. Eady, S. S. Hasnain, *J. Mol. Biol.* **1998**, *282*, 369–382.
[7] K. Kataoka, H. Furusawa, K. Takagi, K. Yamaguchi, S. Suzuki, *J. Biochem*. **2000**, 345–350.
[8] M. J. Boulanger, M. Kukimoto, M. Nishiyama, S. Horinouchi, E. P. Murphy, *J. Biol. Chem.* **2000**, *275*, 23957–23964.
[9] E. L. Tocheva, F. I. Rosell, A. G. Mauk, M. E. P. Murphy, *Science* **2004**, *304*, 867–870.
[10] N. Komeda, H. Nagao, Y. Kushi, G. Adachi, M. Suzuki, A. Uehara, K. Tanaka, *Bull. Chem. Soc. Jpn.* **1995**, *68*, 581–589.
[11] L. Casella, O. Carugo, M. Gullotti, S. Doldi, M. Frassoni, *Inorg. Chem.* **1996**, *35*, 1101–1113.
[12] E. Monzani, G. J. Anthony, A. Koolhaas, A. Spandre, E. Leggieri, L. Casella, M. Gullotti, G. Nardin, L. Randaccio, M. Fontani, P. Zanello, J. Reedijk, *J. Biol. Inorg. Chem.* **2000**, *5*, 251–261.
[13] R. T. Stibrany, J. A. Potenza, H. J. Schugar, *Inorg. Chim. Acta* **1996**, *243*, 33–37.
[14] M. Scarpellini, A. Neves, E. E. Castellano, E. F. de Almeida Neves, D. W. Franco, *Polyhedron* **2004**, *23*, 511–518.
[15] J. A. Halfen, S. Mahapatra, M. M. Olmstead, W. B. Tolman, *J. Am. Chem. Soc.* **1994**, *116*, 2173-2174.
[16] J. A. Halfen, S. Mahapatra, E. C. Wilkinson, A. J. Gengenbach, V. G. Young, Jr., L. Que, Jr., W. B. Tolman, *J. Am. Chem. Soc.* **1996**, *118*, 763–776.
[17] R. L. Richards, M. C. Durrant, *J. Chem. Res. (S)* **2002**, 95–98.
[18] M. I. Kay, B. C. Frazer, *Acta Crystallogr.* **1961**, *14*, 56–57.
[19] D. W. J. Cruickshank, *Acta Crystallogr.* **1956**, *9*, 757–756.
[20] M. J. Frisch et al., Gaussian 98, Revision A.6, Gaussian, Inc., Pittsburgh PA, **1998** http://www.gaussian.com.
[21] H. Nagao, N. Komeda, M. Mukaida, M. Suzuki, K. Tanaka, *Inorg. Chem.* **1996**, *35*, 6809–6815.
[22] R. E. Stevens, W. L. Gladfelter, *Inorg. Chem.* **1983**, *22*, 2034–2047.
[23] A. Altomare, G. Cascarano, C. Giacovazzo, A. Guagliardi, *J. Appl. Crystallogr.* **1993**, *26*, 343–350.
[24] A Computer Program for the Solution and Refinement of Crystal Structures for X-ray Diffraction Data, MAC Science Corporation, Yokohama, **1994**.
[25] *International Tables for X-ray Crystallography* (Eds.: J. A. Ibers, W. C. Hamilton), Kynoch Press, Birmingham, **1974**.
[26] *Crystal Structure 2.00*: Crystal Structure Analysis Package, Rigaku and MSC, **2001**.
[28] A. D. Becke, *J. Chem. Phys.* **1993**, *98*, 5648–5652.
[29] P. J. Hay, W. R. Wadt, *J. Chem. Phys.* **1985**, *82*, 299–310.
[30] T. H. Dunning, Jr., P. J. Hay, in *Modern Theoretical Chemistry* (Ed.: H. F. Schaefer), Plenum, New York, **1976**, pp. 1–28.

Received: September 27, 2004

 © 2005 Wiley-VCH Verlag GmbH & Co. KGaA, Weinheim

An Exploration of the Structural and Bonding Variability in Mixed-Ligand Benzimidazole-2-thione(bromo)(triarylphosphane)dicopper(I) Complexes with Diamond-Shaped $Cu_2(\mu\text{-}X)_2$ Core Structures

Sotiris K. Hadjikakou,*[a] Constantinos D. Antoniadis,[a] Paraskevas Aslanidis,[b] Philip J. Cox,[c] and Athanassios C. Tsipis*[a]

Keywords: Bridging ligands / Copper / Density functional calculations / S ligands

Reaction of copper(I) bromide with benz-1,3-imidazole-2-thione ($bzimtH_2$) in the presence of one equivalent of triphenylphosphane (PPh_3), tri-*meta*-tolylphosphane (tmtp) or tri-*para*-tolylphosphane (tptp) in acetonitrile/methanol solvent afforded dinuclear complexes formulated as $[CuBr(bzimtH_2)(PR_3)]_2$. The new complexes were characterized by IR, UV/Vis, and ^1H NMR spectroscopy, while the crystal structures of $[\{CuBr(\mu_2\text{-}S\text{-}bzimtH_2)(PPh_3)\}_2]_{0.78}[\{Cu(\mu_2\text{-}Br)(PPh_3)(bzimtH_2)\}_2]_{0.22}$ (**1**), $[CuBr(\mu_2\text{-}S\text{-}bzimtH_2)(tmtp)]_2$ (**2**) and $[CuBr(\mu_2\text{-}S\text{-}bzimtH_2)(tptp)]_2$ (**3**) were determined by single-crystal X-ray diffraction methods. In complex **1**, with spectator PPh_3 ligands, the unit cell of the crystal consists of two different half-molecules, both corresponding to the formula $[CuBr(bzimtH_2)(PPh_3)]_2$. One of the two molecules (molecule **A**) is a symmetrical dicopper(I) complex in which the exocyclic thione S-atoms serve as bridges between the Cu^I ions. The second one (molecule **B**) is disordered and can be resolved into two separate entities, one μ_2-S dicopper(I) complex, similar to molecule **A** (molecule **B1**), and another one (molecule **B2**) involving μ_2-Br bridges. In contrast, in complexes **2** and **3**, with spectator tmtp and tptp ligands, only the $bzimtH_2$-bridged dicopper complexes are formed. Density functional calculations at the B3LYP level of theory provided a satisfactory description of the structural, bonding, electronic and related properties of all dicopper complexes exhibiting the "diamond-shaped" $Cu_2(\mu\text{-}X)_2$ (X = S or Br) core structures and account well for their structural preferences.

(© Wiley-VCH Verlag GmbH & Co. KGaA, 69451 Weinheim, Germany, 2005)

Introduction

Polynuclear metal–sulfur coordination sites formed by metal ions with a d^{10} configuration constitute the active sites in a super-family of ubiquitous cysteine-rich, low-molecular-weight proteins or polypeptides called metallothioneins.[1,2] Investigations directed to explore the structure and chemistry of metallothioneins in detail are extremely important taking into account that nature makes use of them as multipurpose proteins. Considering that obtaining precise structural information on metallothioneins is a very difficult task, it appears to be appropriate to study the coordination behavior of copper in model complexes reaching from mononuclear to higher nuclearities. All of them might act as structural and spectroscopic models for copper thioneins and might contribute to the understanding of the thionein structure and function. The most useful ligands for modeling cysteine bonding are undoubtedly thiolates. Heterocyclic thiones are an important class of such ligands, and therefore their coordination properties with many transition metals have been studied extensively. Although the coordination chemistry of heterocyclic thiones is characterized by a wealth of coordinating possibilities, studies on their coordination with copper(I) metal centers have revealed that monodentate coordination through the exocyclic thione sulfur atom is the preferred bonding mode of the ligands. Within this class of coordination compounds, the tendency of heterocyclic thiones to bridge metal centers to form oligo- or polymeric species is also well established.[3] In the oligonuclear complexes, which are normally prepared from Cu^I or Cu^{II} salts and thiolates under various reaction conditions in a variety of solvents, the ligands are normally bridging. In the course of our research on the coordination chemistry of copper(I) halides with a variety of thiones and tertiary arylphosphanes we have reported the synthesis and structural studies of symmetrical binuclear species, with the thione ligand coordinated through the exocyclic sulfur atom in a μ_2-S bridging mode.[4–6] However, in many other cases the reaction of copper(I) halides with thione ligands yielded dicopper(I) complexes with a "diamond-shaped" $Cu_2(\mu\text{-}X)_2$ core structure involving the halide as bridging ligands, particularly for the "soft" iodide rather than the "hard" chloride ligand.[4,7]

[a] Section of Inorganic and Analytical Chemistry, Department of Chemistry, University of Ioannina, 45110 Ioannina, Greece
[b] Aristotle University of Thessaloniki, Faculty of Chemistry, Inorganic Chemistry Laboratory, P. O. Box 135, 54124 Thessaloniki, Greece
[c] School of Pharmacy, The Robert Gordon University, Schoolhill, Aberdeen AB10 1FR, Scotland

Thus, the coordination behavior (terminal or bridging) of the thione and halide ligands seems to be determined primarily by the choice of the halide ligand, although the nature of the thione and, to a lesser extent, of the spectator phosphane ligand might also play a significant role. In order to further investigate trends in the formation of these two different types of binuclear copper(I) halide complexes of the general formula $[CuX(thione)(PR_3)]_2$ involving either a double halide or a double thione-sulfur bridge, we report in this work the results of a detailed experimental and quantum chemical (DFT) study of three new, mixed-ligand dinuclear complexes of copper(I) with bromide, benz-1,3-imidazole-2-thione ($bzimtH_2$) and triphenylphosphane (PPh_3), tri-*m*-tolylphosphane (tmtp) or tri-*p*-tolylphosphane (tptp) as ligands pursuing a threefold objective: (i) the examination of the preferred μ_2-S or μ_2-Br bridging mode; (ii) the exploration of the role played by the spectator phosphane ligands, which exert different steric effects while they differ slightly in their basicity; and (iii) the understanding of the role of the bromide ligands, which have a donor capacity on the border between "soft" and "hard", in forming either μ_2-S or μ_2-Br bridges in the dicopper(I) complexes.

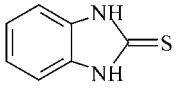

$bzimtH_2$

Results and Discussion

Synthesis

The reaction of equimolar quantities of copper(I) bromide and triphenylphosphane, tri-*m*-tolylphosphane or tri-*p*-tolylphosphane followed by the addition of one equivalent of 1,3-benzimidazole-2-thione ($bzimtH_2$) in dry acetonitrile/methanol solution at 25 °C afforded pale-yellow microcrystalline solids which, on analysis and spectroscopic measurements (IR, ^1H NMR), were found to correspond to the formulae $[\{CuBr(\mu_2\text{-S-}bzimtH_2)(PPh_3)\}_2]_{0.78}[\{Cu(\mu_2\text{-Br})(PPh_3)(bzimtH_2)\}_2]_{0.22}$ (**1**), $[CuBr(\mu_2\text{-S-}bzimtH_2)(tmtp)]_2$ (**2**) and $[CuBr(\mu_2\text{-S-}bzimtH_2)(tptp)]_2$ (**3**). Compounds **1**–**3** are air-stable, diamagnetic, crystalline materials that are soluble in polar solvents such as acetonitrile and dimethyl sulfoxide, slightly soluble in chloroform and dichloromethane, and insoluble in water, diethyl ether and tetrahydrofuran.

The infrared spectra recorded in the range of 4000–250 cm^{-1} show distinct strong vibrational bands due to the phosphane ligand, which remain practically unshifted upon coordination to the metal center. Moreover, the spectra of **1**–**3** contain the usual four "thioamide bands" required by the presence of the heterocyclic thione ligand, as well as the characteristic ν(NH) stretching vibration observed at about 3220 cm^{-1}. The observed shifts of these bands enforced by coordination, in conjunction with the lack of the ν(SH) stretching vibration band, signifies the exclusive S-coordination mode of the 1,3-benzimidazole-2-thione ligand.

The ^1H NMR spectra, recorded in $CDCl_3$, are dominated by the presence of multiplets in the region of δ = 7.45–7.03 ppm attributed to the phenyl protons of the phosphane ligands as well as to the aromatic protons of the thione ligand. The extent of overlapping does not allow resolution between these signals, making assignment of the splitting pattern for the individual thione resonances very difficult. Upon coordination, the methyl protons of the tri-*p*-tolyl- and tri-*m*-tolylphosphane ligands are shifted slightly upfield by 0.09 and 0.08 ppm respectively. Furthermore, the observation of a broad singlet at around δ = 11 ppm due to the proton resonance of the NH groups, and the absence of a signal due to the proton resonance of the SH moiety, strongly suggest that the thione ligand is coordinated to the metal center in its thionato form.

It is well known that deviation from the common four-coordination in copper(I) complexes can be induced by an increase of the bulkiness of the ligands. In this context, according to our previous experience with the use of triarylphosphanes in mixed-ligand Cu^I halide complexes, triphenylphosphane as well as tri-*m*-tolyl- and tri-*p*-tolylphosphane turned out to be relatively small; a coordination number of three could be achieved only for the bulkier tri-*o*-tolylphosphane.[8,9] Similarly, the steric requirements of the neutral heterocyclic thiones used do not affect the coordination number of the complexes, since terminal or bridging S-coordination has been observed but always around a tetrahedrally coordinated copper atom. Thus, on the basis of the chemical composition of the new compounds, we assumed that complexes **1**, **2** and **3** are doubly bridged (μ_2) binuclear complexes. In order to verify our assumption and to confirm the nature of the bridge, we determined the structures of the three complexes by single-crystal X-ray diffraction methods.

Description of the Structures

$[\{CuBr(\mu_2\text{-S-}bzimtH_2)(PPh_3)\}_2]_{0.78}[\{Cu(\mu_2\text{-Br})(PPh_3)(bzimtH_2)\}_2]_{0.22}$ (1)

The unit cell of the crystal consists of two different half-molecules, both corresponding to the formula $[CuBr(bzimtH_2)(PPh_3)]_2$. One of the two molecules (molecule **A**, Figure 1) is a symmetrical dicopper(I) complex in which the thione S-atoms serve as bridges between the Cu^I ions. The second one (molecule **B**, Figure 2) is disordered and can be resolved into two separate entities, one μ_2-S dicopper(I) complex, similar to molecule **A** (molecule **B1**), and another one (molecule **B2**) involving μ_2-Br bridges. The disordered atoms are Br(2), (Br2′), (S2), (S2′), N(4), N(4′), H(4), (H4′), C(26) and (C26′), while the other atoms are considered to overlap. Due to this disorder the hydrogen atoms attached to N(3), C(28) and C(32) in molecule **B** were omitted from the calculations. The six-membered ring C(27)–C(32) has high displacement parameters due to the disorder. Selected bond lengths and angles for **1** are given in Table 1 and ORTEP views showing the atom numbering schemes of molecules **A**, **B1** and **B2** are given in Figures 1

 © 2005 Wiley-VCH Verlag GmbH & Co. KGaA, Weinheim

and 2. Molecule **B1** consists of the atoms Cu(2), Br(2), P(2), S(2), N(3), N(4) and C(26)–C(50) (unprimed, 56% occupancy), while the atoms Cu(2), Br(2′), P(2), S(2′), N(3), N(4′), C(26′), C(27)–C(50) (primed, 44% occupancy) belong to the Br-bridged molecule **B2**. The basic structural unit of molecules **A** and **B1** corresponds to a "diamond-shaped" $Cu_2(\mu\text{-}S)_2$ core formed by the operation of an inversion center. The doubly bridging S atoms and the Cu^I metal centers constitute a strictly planar Cu_2S_2 core in which each copper(I) center displays a distorted tetrahedral environment, with the other two positions of the tetrahedra being occupied by a P donor atom of the PPh_3 ligand and a bromide ligand. The two bromide ligands in *trans* positions stabilize the complex further through the formation of two short, symmetrical, intramolecular hydrogen bonds

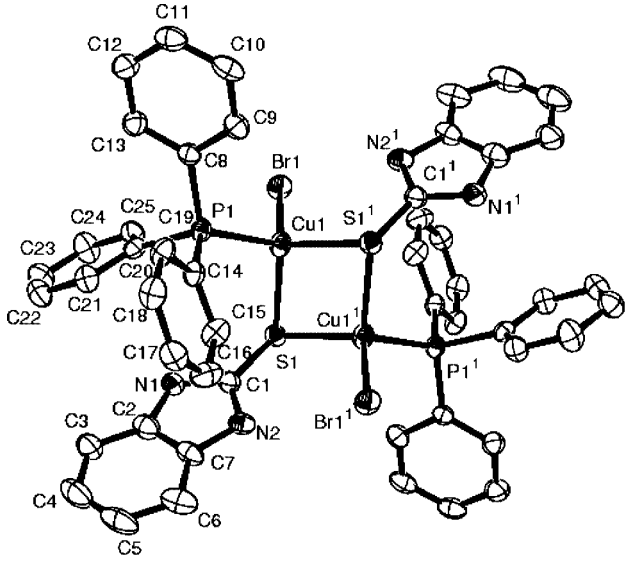

Figure 1. ORTEP view showing the metal environment and the atom labelling scheme in compound **1** (Molecule **A**). Displacement ellipsoids are shown at the 50% probability level.

(Table 1). In general, there are small but definite differences in bond lengths and angles within the central cores of molecules **A** and **B1**. In both structures the bridging sulfur atoms and the two copper atoms form a parallelogram with two short and two longer Cu–S bonds. Although each of these two individual Cu–S distances is not far from the values in other copper(I) complexes with equivalent bonds, the asymmetry in the bridging Cu–S distances is the largest among the thione-S coordinated copper(I) complexes structurally characterized by us so far.

The Cu–P bond lengths in the three individual molecules lie in the range normally found in analogous dicopper(I) complexes with halide or sulfur bridging ligands. In contrast, the significant differences in the corresponding Cu–Br bond lengths are noteworthy. In general terms, the bridging Cu–Br distances are somewhat longer than those found previously in other mixed-ligand dicopper(I) complexes containing bromide, phosphane and heterocyclic thione ligands, but are shorter than those found in $[CuBr(tzdtH)(tmtp)]_2$.[5]

In all three structures the interbond angles around the central copper(I) atoms show remarkable deviations from idealized tetrahedral geometry, with the Br(1)–Cu(1)–S(1) bond angle of 93.89(5)° in molecule **A** representing the most significant distortion. Finally, the S–Cu–S (Br–Cu–Br) and Cu–S–Cu (Cu–Br–Cu) bond angles in the "diamond-shaped" Cu_2S_2 (or Cu_2Br_2) cores are close to the calculated ideal values (109.5 and 70.5°) for a symmetric dimer.

$[CuBr(\mu_2\text{-}S\text{-}bzimtH_2)(tmtp)]_2$ (2) and $[CuBr(\mu_2\text{-}S\text{-}bzimtH_2)(tptp)]_2$ (3)

Selected bond lengths and angles for compounds **2** and **3** are given in Tables 2 and 3 and the molecular structures are displayed in Figures 3 and 4, respectively.

The basic structural unit of both complexes is a dicopper(I) unit with the two copper(I) atoms doubly bridged by two S atoms of the thione ligands to form a strictly planar,

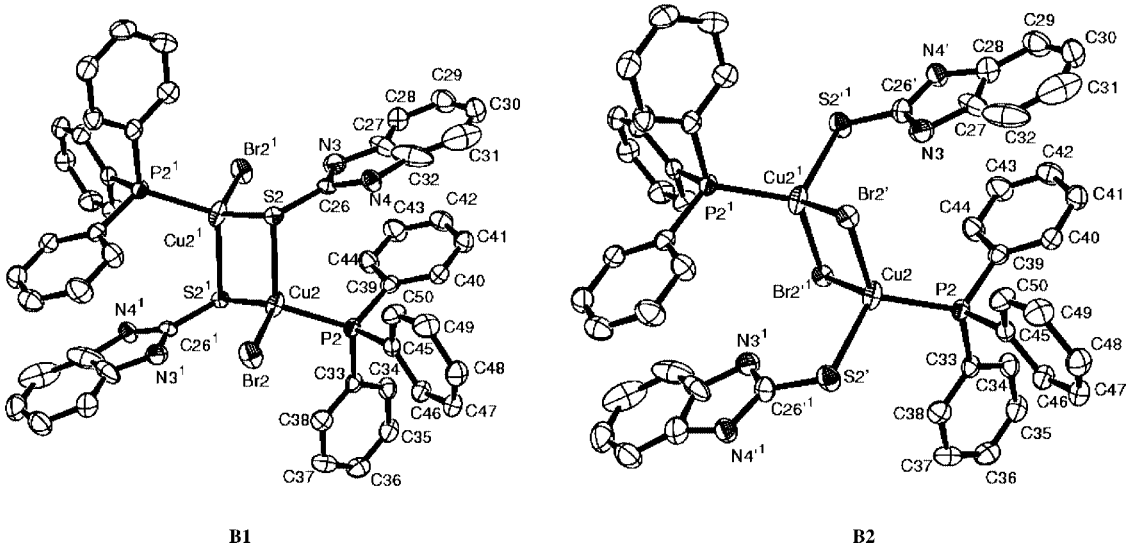

Figure 2. ORTEP views showing the metal environment and the atom labelling scheme in molecules **B1** and **B2**. Displacement ellipsoids are shown at the 50% probability level.

 © 2005 Wiley-VCH Verlag GmbH & Co. KGaA, Weinheim

Table 1. Selected bond lengths [Å] and angles [°] for **1**.[a]

Cu(1)–S(1)#1	2.3385(18)	Cu(2)–Br(2′)	2.453(3)
Cu(1)–Br(1)	2.4586(12)	Cu(2)–S(2′)	2.472(4)
Cu(1)–S(1)	2.5330(19)	Cu(2)–Br(2′)#2	2.508(3)
Cu(1)–Cu(1)#1	2.8973(18)	Cu(2)–S(2)	2.535(5)
S(1)–Cu(1)#1	2.3384(18)	Cu(2)–Cu(2)#2	3.0129(18)
P(1)–C(20)	1.822(6)	Br(2′)–Cu(2)#2	2.508(3)
P(1)–C(8)	1.822(6)	S(2)–Cu(2)#2	2.326(5)
P(1)–C(14)	1.827(6)	P(2)–C(39)	1.830(7)
Cu(2)–P(2)	2.2380(19)	P(2)–C(45)	1.832(6)
Cu(2)–S(2)#2	2.326(5)	P(2)–C(33)	1.833(6)
P(1)–Cu(1)–S(1)#1	114.67(7)	Cu(2)–Br(2′)–Cu(2)#2	74.78(8)
S(1)–Cu(1)–S(1)#1	107.13(6)	Br2′)–Cu(2)–S(2′)	101.82(13)
P(1)–Cu(1)–S(1)	112.41(7)	P(2)–Cu(2)–Br(2′)#2	109.42(8)
Br(1)–Cu(1)–S(1)	93.89(5)	Br(2′)–Cu(2)–Br(2′)#2	105.22(8)
Cu(1)#1–S(1)–Cu(1)	72.87(6)	S(2′)–Cu(2)–Br(2′)#2	110.04(14)
P(2)–Cu(2)–S(2)#2	117.48(13)	P(2)–Cu(2)–S(2)	111.20(13)
P(2)–Cu(2)–Br(2)	105.80(6)	S(2)#2–Cu(2)–S(2)	103.52(16)
S(2)#2–Cu(2)–Br(2)	117.57(13)	Br(2)–Cu(2)–S(2)	99.82(12)
P(2)–Cu(2)–Br(2′)	118.11(9)	Cu(2)#2–S(2)–Cu(2)	75.48(16)
P(2)–Cu(2)–S(2′)	111.77(11)		

[a] Symmetry transformations used to generate equivalent atoms: #1: $-x + 2, -y, -z + 1$.

Table 2. Selected bond lengths [Å] and angles [°] for **2**.[a]

Br(1)–Cu(1)	2.5246(4)	S(1)–C(1)	1.709(3)
Cu(1)–P(1)	2.2552(7)	P(1)–C(20)	1.829(2)
Cu(1)–S(1)	2.3681(7)	P(1)–C(8)	1.833(3)
Cu(1)–S(1)#1	2.4507(7)	P(1)–C(14)	1.836(3)
Cu(1)–Cu(1)#1	2.7504(6)		
P(1)–Cu(1)–S(1)#1	113.35(3)	C(1)–S(1)–Cu(1)#1	107.75(8)
S(1)–Cu(1)–S(1)#1	110.42(2)	Cu(1)–S(1)–Cu(1)#1	69.58(2)
P(1)–Cu(1)–Br(1)	108.82(2)	C(20)–P(1)–C(8)	104.40(11)
S(1)–Cu(1)–Br(1)	112.34(2)	C(20)–P(1)–C(14)	103.96(11)
S(1)#1–Cu(1)–Br(1)	93.81(2)	C(8)–P(1)–C(14)	103.97(11)
P(1)–Cu(1)–Cu(1)#1	136.92(3)	C(20)–P(1)–Cu(1)	111.73(8)
S(1)–Cu(1)–Cu(1)#1	56.621(19)	C(8)–P(1)–Cu(1)	119.95(8)
S(1)#1–Cu(1)–Cu(1)#1	53.797(18)	C(14)–P(1)–Cu(1)	111.36(8)
Br(1)–Cu(1)–Cu(1)#1	107.75(8)		

[a] Symmetry transformations used to generate equivalent atoms: #1: $-x + 2, -y, -z + 1$.

Table 3. Selected bond lengths [Å] and angles [°] for **3**.[a]

Br(1)–Cu(1)	2.4734(3)	S(1)–C(1)	1.706(2)
Cu(1)–P(1)	2.2333(6)	P(1)–C(20)	1.817(2)
Cu(1)–S(1)	2.3535(6)	P(1)–C(8)	1.820(2)
Cu(1)–S(1)#1	2.4053(6)	P(1)–C(14)	1.820(2)
Cu(1)–Cu(1)#1	2.8232(5)		
P(1)–Cu(1)–S(1)	107.22 (2)	C(1)–S(1)–Cu(1)	111.66(8)
P(1)–Cu(1)–S(1)#1	117.37(2)	C(1)–S(1)–Cu(1)#1	105.22 (8)
S(1)–Cu(1)–S(1)#1	107.234(19)	Cu(1)–S(1)–Cu(1)#1	72.766(19)
P(1)–Cu(1)–Br(1)	113.174(19)	C(20)–P(1)–C(8)	101.96(10)
S(1)–Cu(1)–Br(1)	112.187(17)	C(20)–P(1)–C(14)	103.20(10)
S(1)#1–Cu(1)–Br(1)	99.532(17)	C(8)–P(1)–C(14)	103.17(10)
P(1)–Cu(1)–Cu(1)#1	129.67(2)	C(20)–P(1)–Cu(1)	116.30(7)
S(1)–Cu(1)–Cu(1)#1	54.463(17)	C(8)–P(1)–Cu(1)	113.46(7)
S(1)#1–Cu(1)–Cu(1)#1	52.771(16)	C(14)–P(1)–Cu(1)	116.81(7)
Br(1)–Cu(1)–Cu(1)#1	117.124(15)		

[a] Symmetry transformations used to generate equivalent atoms: #1: $-x + 1, -y, -z + 1$.

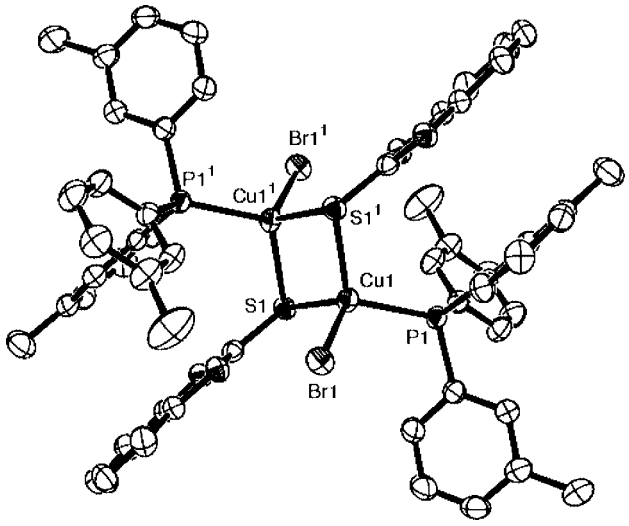

Figure 3. ORTEP view showing the metal environment and the atom labelling scheme in compound **2**. Displacement ellipsoids are shown at the 50% probability level.

four-membered Cu_2S_2 core. The distorted tetrahedral coordination environment around the central copper(I) atoms is completed by one P atom from the phosphane ligand and one bromide ligand. Complex **2** (Figure 3) crystallizes in the monoclinic space group $P2_1/c$ with the unit cell containing two discrete dinuclear species, whereas compound **3** (Figure 4) crystallizes in the triclinic space group $P\bar{1}$. Its structure contains one discrete molecule per unit cell, as well as two CH_3CN, three H_2O and one half CH_3OH lattice molecules; the latter solvate molecules do not interact specifically with the dimer and therefore will not be discussed further.

The Cu–P bond length of 2.2552(7) Å in **2** does not differ significantly from that found in **3** [2.233(6) Å], both values lying in the range normally found for analogous halide- or sulfide-bridged dicopper(I) complexes.[4,7,10] On the other hand, the Cu–Br bonds in **2** and **3** differ remarkably, the latter being shorter by 0.0512 Å. The Cu–Br bond lengths, which are typical for a bromide ligand in the tetrahedral coordination environment of Cu^I complexes, are shorter than those of 2.5693(12) and 2.5369(4) Å found in $[CuBr(dppe)(py2SH)]_2$ [dppe = 1,2-bis(diphenylphosphanyl)ethane][11] and [CuBr(dppb)(pymtH)][12] [dppp = 1,2-bis(diphenylphosphanyl)propane], respectively, but are longer than that found in [CuBr(dppet)(mftztH)].[13] Moreover, both structures exhibit the usual asymmetric $Cu_2(\mu\text{-}S)_2$ core with Cu–S bond lengths in the range found for other dicopper(I) complexes containing bromide, phosphane and heterocyclic thione ligands. Finally, it should be noted that the S–Cu–S and Cu–S–Cu bond angles in the $Cu_2(\mu\text{-}S)_2$

 © 2005 Wiley-VCH Verlag GmbH & Co. KGaA, Weinheim

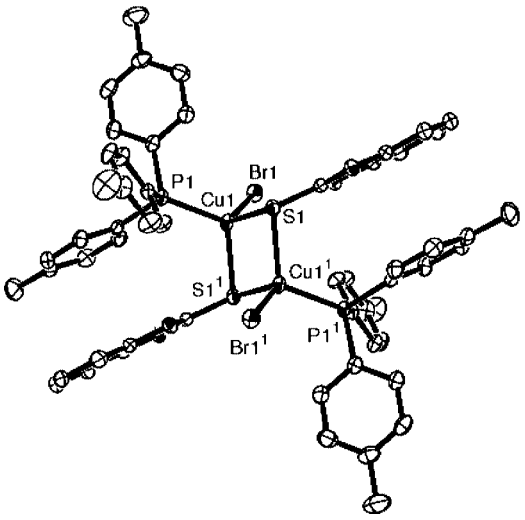

Figure 4. ORTEP view showing the metal environment and the atom labelling scheme in compound **3**. Displacement ellipsoids are shown at the 50% probability level.

core of **2** and **3** closely resemble those of an ideal symmetric dimer.

Electronic Structure Calculations

The structural properties, such as geometrical data, as well as the energetic and spectroscopic properties of the model dicopper complexes $[CuBr(PH_3)(\mu\text{-}S)(imtH_2)]_2$ (**4**) and $[Cu(PH_3)(\mu\text{-}Br)(imtH_2)]_2$ (**5**), which exhibit "diamond-shaped" $Cu_2(\mu\text{-}X)_2$ (X = S or Br) core structures, were examined by electronic structure calculation methods. In order to obtain reliable data it is of outmost importance to find a method/basis set combination that allows the accurate description of the molecules studied herein. In a first attempt, we therefore employed DFT computational techniques at the B3LYP level of theory using a variety of basis sets to reproduce the structure of the $Cu_2(\mu\text{-}X)_2$ (X = S or Br) core of the "real" complexes, the main focus being on the structural parameters of the $Cu_2(\mu\text{-}X)_2$ core in **4** and **5**. The results are compiled in the Supporting Information (Table S1). In all cases the basic structural features of the model compounds **4** and **5** were satisfactorily reproduced by taking into account the different electronic and steric effects of the ligands used to represent the ligands in the "real" complexes. In general terms, the best estimate of the energetic data is that obtained using the larger TZVP and 6-31G(d,p) basis sets. However, more reliable structural data (overall closer to the experiment) were obtained using the DZVP and TZVP rather than the 6-31G(d,p) basis sets. Interestingly, even the smaller SDD basis set performs well with respect to the structural parameters of the model compounds, but could not provide meaningful energetic data. Note that a reliable structure is indispensable for the evaluation of the relative stability of the isomeric species.

Equilibrium Geometries of the Model Compounds

The equilibrium structures of $[CuBr(PH_3)(\mu\text{-}S)(imtH_2)]_2$ (**4**) and $[Cu(PH_3)(\mu\text{-}Br)(imtH_2)]_2$ (**5**) and their monomeric species $[CuBr(PH_3)(imtH_2)]$ (**6**), along with selected structural parameters, computed at the B3LYP/DZVP level of theory are depicted schematically in Figure 5.

Searching the potential energy surface (PES) of the monomeric species $[CuBr(PH_3)(imtH_2)]$ (**6**) we located two stationary points corresponding to two rotamers involving the bromide ligand in a *syn* (**6a**) and *anti* (**6b**) configuration with respect to the imidazole ring. The *syn* rotamer corresponds to the global minimum, while the *anti* one is a local minimum that is 14.7 kcal mol^{-1} higher in energy. The *syn* (**6a**) → *anti* (**6b**) isomerization proceeds across a barrier of 15.1 kcal mol^{-1} through a product-like transition structure $\mathbf{TS_{6a\rightarrow 6b}}$ (Figure 5) with a P–Cu–S–C torsion angle of 57.2°, while the dominant motion of the vibrational mode corresponding to the imaginary frequency (ν_i = 24 cm^{-1}) involves the rotation around the Cu–S bond. Note that the *syn* rotamer is stabilized by the formation of an N–H···Br hydrogen bond. Both rotamers adopt a trigonal planar stereochemistry of C_s symmetry, with the central copper(I) atom and the three donor atoms being coplanar with the imidazole ring. The bending coordination mode of the thione ligand with the Cu^I central atom is noteworthy; the Cu^I–S–C bond angles are 104.3° and 107.6° in the *syn* and *anti* rotamers, respectively. The bending coordination mode of the thione ligand is that expected on the grounds of the bonding interactions between the Cu^I and thione ligand orbitals, which will be discussed later on.

The equilibrium geometries of the dimeric species $[CuBr(PH_3)(\mu\text{-}S)(imtH_2)]_2$ (**4**) and $[CuS(PH_3)(\mu\text{-}Br)(imtH_2)]_2$ (**5**) correspond to a "diamond-shaped" $Cu_2(\mu\text{-}X)_2$ (X = S or Br) core structure where the copper(I) atoms display a distorted tetrahedral coordination environment. The $Cu_2(\mu\text{-}X)_2Cu$ (X = S or Br) parallelogram is perfectly planar with two long and two short asymmetric Cu–X bonds, in line with the available X-ray crystal structure data. The asymmetry in the Cu–X bond lengths of the $Cu_2(\mu\text{-}X)_2Cu$ parallelogram is more pronounced for X = S rather than for X = Br, the difference in the Cu–X bond lengths being 8.4 and 4.5 pm, respectively. The intermetallic Cu···Cu distance is 322.3 and 316.0 pm for the μ_2-S and μ_2-Br dimers, respectively. On the other hand, the X···X distance is equal to 384.9 and 416.2 pm for **4** and **5**, respectively. No cross-ring interactions are possible in either **4** or **5** due to the long Cu···Cu or X···X distances, in agreement with the framework-electron counting (FEC) rule introduced by Alvarez et al.[14] to account for the formation or breaking of transannular bonds in dimetal systems that contain a simple "diamond-shaped" $M_2(\mu\text{-}X)_2$ core structure.

At all levels of theory the μ_2-Br-bridged dimer **5** is predicted to be slightly more stable than the μ_2-S-bridged dimer **4** by 2.5–5.4 kcal mol^{-1}. The computed dimerization energy for **4** and **5** was found to be 18.8 and 21.7 kcal mol^{-1}, respectively, at the B3LYP/TZVP level of theory. The dimerization and relative energies of the model complexes **4** and **5** computed at the B3LYP level of theory using a variety of basis sets are given in detail in the Supporting Information (Table S2). The low computed dimerization energy indicates that **4** and **5** correspond to loose associations of the mono-

 © 2005 Wiley-VCH Verlag GmbH & Co. KGaA, Weinheim

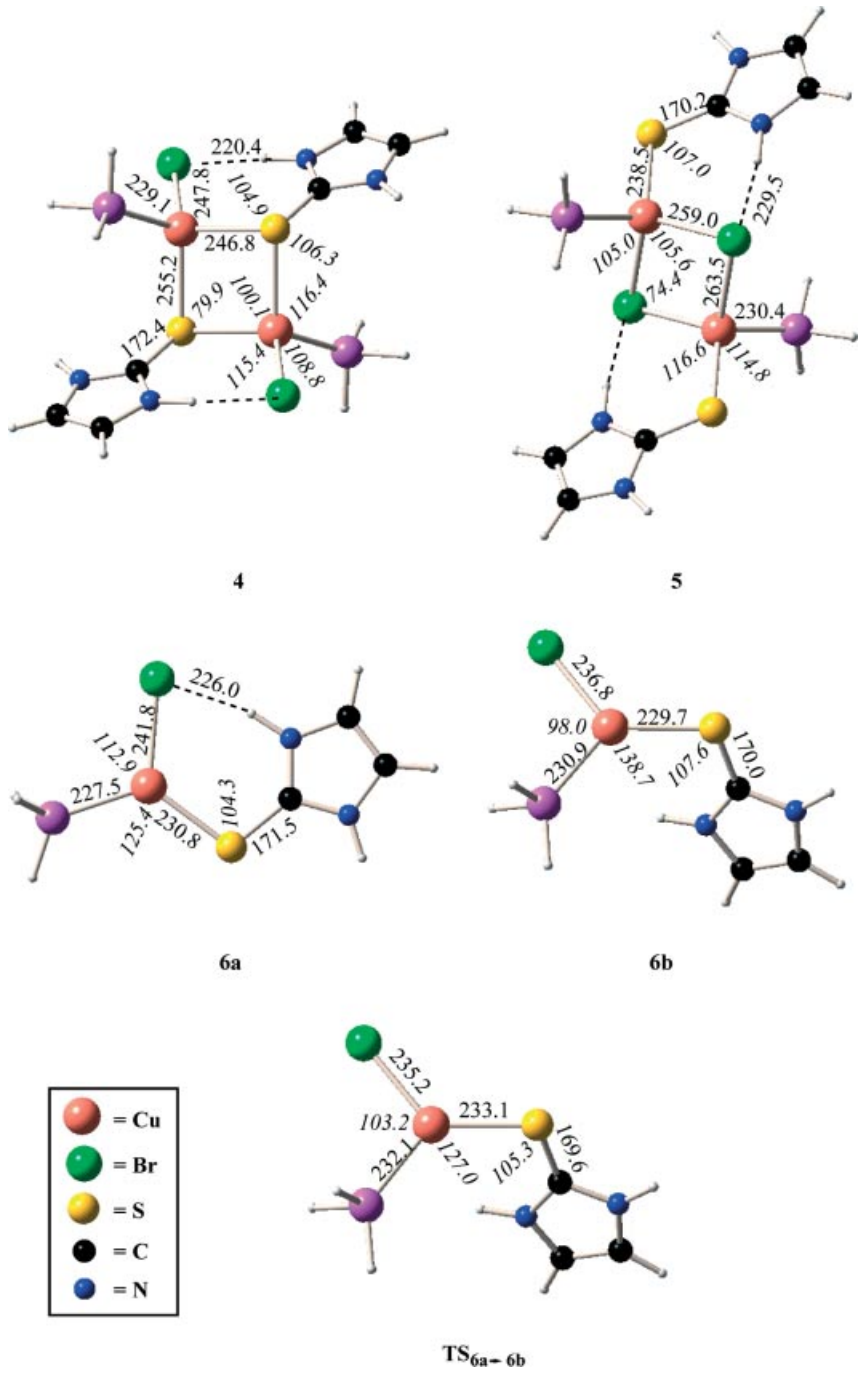

Figure 5. Equilibrium geometries of $[CuBr(PH_3)(\mu\text{-}S)(imtH_2)]_2$ (**4**), $[CuS(PH_3)(\mu\text{-}Br)(imtH_2)]_2$ (**5**) and the monomeric species $[CuBr(PH_3)(imtH_2)]$ in the *syn* (**6a**) and *anti* (**6b**) configurations computed at the B3LYP/DZVP level of theory.

meric species **6a** and strongly suggests that both isomers could be formed during the synthesis. Moreover, because of the low dissociation energy of the dimers they are expected to be in equilibrium with their monomers, therefore the two isomers and their monomeric species could coexist in the solid state, in line with the experiment. The interconversion of the two isomers should follow a dissociative (S_N1) mechanism, as shown in Scheme 1. According to this mechanism the dimer dissociates to the monomer, which then re-associates with a different orientation. The total energies given are those computed at the B3LYP/TZVP level of theory.

Electronic Structure and Bonding Description of the Model Compounds

In order to gain insight into the electronic and bonding properties of the monomer **6** and the dimers **4** and **5** the relevant molecular orbitals (MOs) and the Mulliken population analyses were extracted from the B3LYP/DZVP cal-

 © 2005 Wiley-VCH Verlag GmbH & Co. KGaA, Weinheim

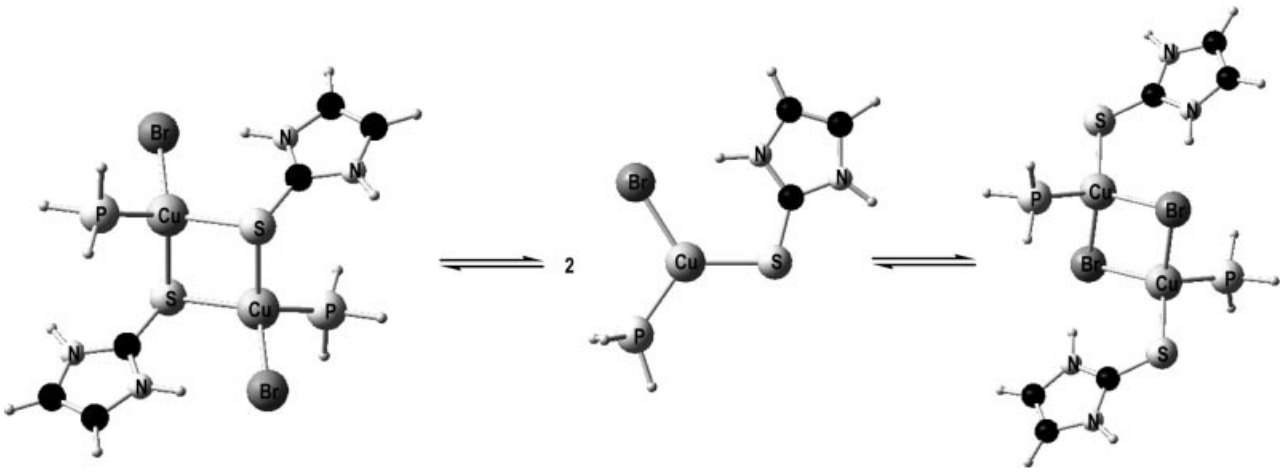

Scheme 1. Mechanism of the **4** → **5** interconversion through a dissociative (S_N1) pathway.

culations. Both the $imtH_2$ and $bzimtH_2$ ligands possess two occupied frontier molecular orbitals (HOMO and HOMO-1) with high sulfur 3p-orbital character (Scheme 2), which are the orbitals primarily involved in the formation of the Cu–S coordination bond. The two π-type MOs were labeled as π_{ip} and π_{op} following the nomenclature previously established by Solomon et al.[15] for phenolate and by Halfen et al.[16] for thiophenolate ligands. The π_{ip} orbital lies in the plane of the imidazole ring, while the π_{op} orbital is perpendicular to this plane. In light of the perfect planarity of the $[CuBr(PH_3)(imtH_2)]$ model compound it is the π_{ip} MO of the thione ligand which participates in the bonding interactions with a vacant metal orbital [a 4s orbital of Cu^I hybridized by mixing with the 4p orbitals in the bent

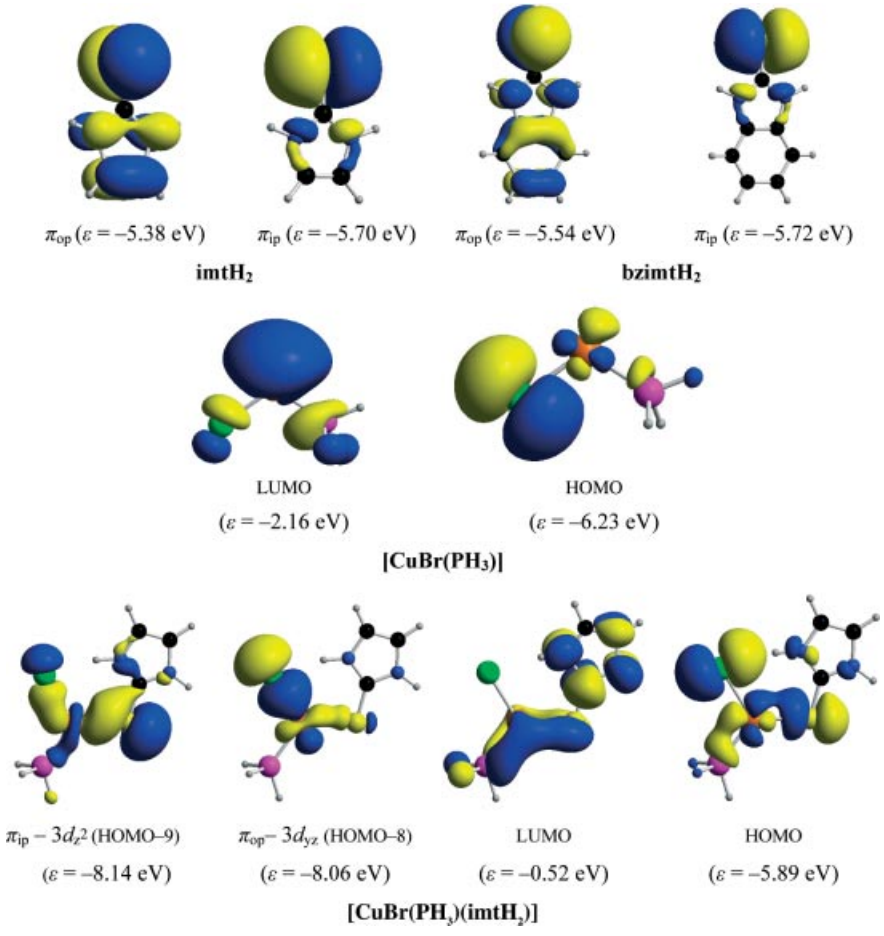

Scheme 2. The most relevant MOs of the $imtH_2$ and $bzimtH_2$ thione ligands and the model $[CuBr(PH_3)]$ and $[CuBr(PH_3)(imtH_2)]$ complexes.

 © 2005 Wiley-VCH Verlag GmbH & Co. KGaA, Weinheim

$CuBr(PH_3)$ fragment, the LUMO in Scheme 2] to form the σ Cu^I–S coordination bond. In order to achieve maximum overlap the π_{ip} MO should point primarily along the Cu^I–S bond, which nicely explains the Cu^I–S–C bending (Cu–S–C bond angle of 104.3°). The π_{op} is perpendicular to the Cu^I–S vector and therefore interacts in a π fashion with a vacant metal orbital.

According to the natural bond orbital (NBO) population analysis the bonding σ(Cu–S) interaction between the Cu and S atoms is constructed from an s NAO (93.29% s-character) on a Cu atom interacting with a p NAO (89.36% p-character) on a sulfur atom, and thus has the form $\sigma(Cu–S) = (0.2868)s_{Cu} + (0.9580)p_S$.

The Mulliken population analysis data given in Table 4 indicate that there is a charge transfer of about 0.14 charge units of electron density from the sulfur donor atom to the central Cu^I atom upon coordination of the thione ligand to the Cu^I metal center of the $[CuBr(PH_3)]$ fragment. This charge transfer increases to 0.20 charge units of electron density upon dimerization of the monomeric species **6**, when sulfur bridges are formed, but remains unchanged when bromide bridges are formed. The charge transfer from sulfur to Cu^I, which is a result of both σ-dative and π-back-bonding interactions, results in the weakening of the C=S bond of the thione ligand, which thus acquires a partial double-bond character that is reflected in the bond overlap population (*bop*) values (Table 4), which correlate well with the charge transferred from S to Cu^I. Moreover, the Cu–S *bop* values indicate that the Cu–S···Cu bridge is not symmetric, while the Cu–S bonds are remarkably weakened upon dimerization.

Based upon the nature of the FMOs of the monomeric species $[CuBr(PH_3)(imtH_2)]$ (**6**; Scheme 2) it can be envisaged that the monomers **6** could be dimerized through favorable HOMO–LUMO interactions that form either weak μ-S or μ-Br bridges. On the other hand, the high HOMO–LUMO energy gap of 5.37 eV illustrates the high stability of the monomer, which should coexist in equilibrium with the dimers. It should be noted that copper is normally monovalent in its thiolate complexes and the coordination is normally trigonal planar, although a number of linearly coordinated examples are known. In oligonuclear complexes, which are normally prepared from Cu^I or Cu^{II} salts and thiolates under various reaction conditions in solvents such as methanol, the ligands are normally bridging. In the series of dinuclear copper thiolates only a few cases are known with a central four-membered Cu_2S_2 unit, probably because of the closed-shell d^{10}···d^{10} Cu···Cu and ligand···ligand repulsions. Examples are $[Cu_2(mimtH)_6]^{2+}$ (mimtH = 1-methylimidazoline-2-thione),[17] the thione complex $[Cu_2\text{-}(SNC_5H_5)_6]Cl_2$,[18] and the thiolate complex $[Cu_2(SC_6H_4\text{-}o\text{-}Me)_2(1,10\text{-phen})_2]$ with phenanthroline as co-ligand.[19]

Single-Point Calculations on the "Real" Complexes

For the single-point calculations, the geometries were based on the corresponding X-ray crystal structures. Moreover, calculations were performed on the monomeric species $[CuBr(PPH_3)(bzimtH_2)]$ (**7**), $[CuBr(tmtp)(bzimtH_2)]$ (**8**) and $[CuBr(tptp)(bzimtH_2)]$ (**9**) resulting from the adiabatic dissociation of the dimers for the dissociation energy to be estimated. The energetic and electronic properties of the "real" complexes and their monomeric species, computed at the B3LYP/DZVP level, are compiled in Table 5.

It can be seen that complex **1A**, which contains μ_2-S bridges, is more stable than its isomeric complex **1B**, which contains μ_2-Br bridges, by about 121 kcal mol^{-1} at the B3LYP/DZVP level. The predicted higher stability of isomer **1A** accounts well for the estimated experimental occupancy of **1A** in the unit cell of the crystal (about 78%). The coexistence of the thermodynamically less stable isomer **1B** in the solid state could be attributed to steric and crystal-packing effects. The dimerization energy of **1A** was predicted to be 52.3 kcal mol^{-1}, thus illustrating that the sulfur bridges are relatively weak. In contrast, the dimerization energy of **1B** was predicted to be only 2.4 kcal mol^{-1}, thus indicating that **1B** corresponds practically to the three-coordinate monomer **7B**. It should be noted that **7B** is stabilized with respect to its isomer **7A** by 35.6 kcal mol^{-1} at the B3LYP/DZVP level. The higher stability of **7B** is also reflected in the higher HOMO–LUMO energy gap (4.37 vs. 3.40 eV). The weak association of the monomer **7B** to form **1B** is also mirrored in the relatively small change of the electron-density distribution introduced by the association of the monomers through the formation of the μ_2-Br bridges.

Finally, complex **2**, which contains the spectator tmtp ligand, is slightly more stable than isomer **3**, which contains

Table 4. Electronic properties of $imtH_2$, $[CuBr(PH_3)(imt)]$, $[CuBr(PH_3)(\mu\text{-}S)(imt)]_2$ and $[CuS(PH_3)(\mu\text{-}Br)(imt)]_2$ model compounds computed at the B3LYP/DZVP level.

	$imtH_2$	$[CuBr(PH_3)(imt)]$	$[CuBr(PH_3)(\mu\text{-}S)(imt)]_2$	$[CuS(PH_3)(\mu\text{-}Br)(imt)]_2$
q_{Cu}		0.04	0.06	0.09
q_S	–0.32	–0.18	–0.12	–0.17
q_{Br}		–0.52	–0.54	–0.46
q_P		–0.05	–0.08	–0.08
bop(Cu1–S)		0.242	0.162	0.181
bop(Cu2–S)			0.102	0.181
bop(Cu1–Br)		0.198	0.160	0.118
bop(Cu2–Br)		0.257	0.160	0.092
bop(Cu–P)		0.128	0.091	0.075
bop(C–S)	0.570	0.393	0.341	0.412

 © 2005 Wiley-VCH Verlag GmbH & Co. KGaA, Weinheim

Table 5. Total electronic energies (Hartrees), dissociation energies (*DE*, kcal mol^{-1}), HOMO and LUMO eigenvalues (eV), and Mulliken net atomic charges of the "real" complexes **1**–**3** and their monomeric species, computed at the B3LYP/DZVP level.

	1A	**1B**	**2**	**3**	**7A**	**7B**	**8**	**9**
E_{tot} (Hartrees)	–12056.27403	–12056.08097	–12292.02752	–12292.01458	–6028.09532	–6028.03856	–6146.00358	–6145.97435
DE	52.3	2.4	12.7	41.3	–	–	–	–
ε_{HOMO} (eV)	–4.94	–4.87	–4.91	–4.81	–5.01	–5.50	–5.35	–4.85
ε_{LUMO} (eV)	–1.32	–0.73	–1.22	–1.22	–1.61	–1.13	–1.36	–1.60
q_{Cu}	–0.23	–0.16	–0.22	–0.29	–0.04	–0.08	–0.08	–0.11
q_S	–0.02	–0.22	–0.01	0.01	–0.14	–0.26	–0.17	–0.10
q_{Br}	–0.56	–0.38	–0.60	–0.59	–0.55	–0.49	–0.60	–0.55
q_P	0.67	0.65	0.64	0.68	0.57	0.59	0.56	0.56

tptp, by about 8.2 kcal mol^{-1}. The same holds also true for the corresponding monomeric species. The monomer **8** is more stable than monomer **9** by about 18.3 kcal mol^{-1} at the B3LYP/DZVP level. The dimerization energies for **8** and **9** were predicted to be 12.8 and 41.3 kcal mol^{-1}, respectively.

Concluding Remarks

We have reported the synthesis of a new series of dinuclear copper(I) complexes formulated as [CuBr-(bzimtH$_2$)(PR$_3$)]$_2$ formed by treatment of copper(I) bromide with benz-1,3-imidazole-2-thione (bzimtH$_2$) in the presence of one equivalent of triphenylphosphane (PPh$_3$), tri-*meta*-tolylphosphane (tmtp) or tri-*para*-tolylphosphane (tptp) in acetonitrile/methanol solvent. The crystal structures of the new complexes [{CuBr(μ_2-S-bzimtH$_2$)(PPh$_3$)}$_2$]$_{0.78}$[{Cu-(μ_2-Br) (PPh$_3$)(bzimtH$_2$)}$_2$]$_{0.22}$ (**1**), [CuBr(μ_2-S-bzimtH$_2$)-(tmtp)]$_2$ (**2**) and [CuBr(μ_2-S-bzimtH$_2$)(tptp)]$_2$ (**3**) have been determined by single-crystal X-ray diffraction methods. Depending on the spectator phosphane ligands either μ_2-S- or μ_2-Br-bridged dimers are formed. In some cases the monomeric three-coordinate Cu^I complexes seem to be stable as well. Thus, for the simple PH$_3$ ligand (a strong σ-donor) both dimeric species are predicted to be formed in equal proportions upon treatment of copper(I) bromide with the thione ligand in the presence of PH$_3$. On the other hand, with the PPh$_3$ ligand (a weaker σ-donor and stronger π-acceptor ligand than PH$_3$) the two isomeric forms involving μ_2-S or μ_2-Br bridges coexist in the solid state, with the former being favored (about 78%). In contrast, with the spectator tmtp and tptp ligands (with comparable electronic effects to those of PPh$_3$, but differing significantly in their steric effects) only the μ_2-S-bridged dicopper complexes are formed. Density functional calculations at the B3LYP level of theory provide a satisfactory description of the bonding, electronic and related properties of the "real" and model dicopper complexes exhibiting the "diamond-shaped" Cu$_2$(μ-X)$_2$ (X = S or Br) core structures and account well for their structural preferences. In all complexes the coordination of the thione ligand is further stabilized by Br···H–N bond formation, which is more pronounced in the μ_2-S bridged dimers. No Cu^I···Cu^I interactions are predicted to occur either in the μ_2-S- or μ_2-Br- bridged dicopper complexes.

Experimental Section

Materials and Instruments: Copper(I) bromide, triphenylphosphane, tri-*m*-tolylphosphane, tri-*p*-tolylphosphane and solvents are commercially available and were used as obtained, while benz-1,3-imidazole-2-thione was recrystallized from hot ethanol prior to use. Elemental analyses for C, H and N were carried out with a Carlo Erba EA MODEL 1108. Melting points were measured in open tubes with a STUART scientific apparatus and are uncorrected. IR spectra in the region of 4000–370 cm^{-1} were obtained in KBr discs while far-IR spectra in the region of 400–50 cm^{-1} were obtained in polyethylene discs, with a Perkin–Elmer Spectrum GX FT-IR spectrometer. ^{1}H NMR spectra were recorded on a Bruker 400 MHFT NMR instrument in CDCl$_3$ solutions with chemical shifts given in ppm relative to internal TMS.

Synthesis of the Complexes 1–3: The appropriate phosphane (0.5 mmol) was added to a suspension of copper(I) bromide (71.7 mg, 0.5 mmol) in 30 mL of dry acetonitrile, and the mixture was stirred for 2 h at ambient temperature during which time a white precipitate of [CuBr(PR$_3$)$_n$]$_m$ [PR$_3$ = triphenylphosphane (PPh$_3$), tri-*p*-tolylphosphane (tptp) or tri-*m*-tolylphosphane (tmtp)] formed. A solution of benz-1,3-imidazole-2-thione (75 mg, 0.5 mmol) in 20 mL of methanol was added dropwise to the reaction mixture whereupon the white precipitate gradually disappeared. After stirring at ambient temperature overnight, the resulting clear solution was filtered off and left to evaporate. The microcrystalline solid that deposited upon standing for several days was filtered off and dried in vacuo.

[{CuBr(μ_2-S-bzimtH$_2$)(PPh$_3$)}$_2$]$_{0.78}$[{Cu(μ_2-Br)(PPh$_3$)(bzimtH$_2$)}$_2$]$_{0.22}$ (1): Pale-yellow crystals; m.p. 235–236 °C. $C_{50}H_{42}Br_2Cu_2N_4P_2S_2$: calcd. C 54.01, H 3.81, N 5.04; found C 53.94, H 3.69, N 5.06. IR: $\tilde{\nu}$ = 3217 m, 3052 s, 2969 m, 2852 m, 1619 s, 1500 vs, 1478 m, 1460 vs, 1434 vs, 1390 m, 1361 s, 1346 s, 1258 m, 1216 m, 1174 vs, 1094 s, 744 vs, 598 s, 520 vs, 497 vs cm^{-1}; far-IR: $\tilde{\nu}$ = 279 w, 219 w, 205 w, 200 w, 192 w, 174 s, 161 s, 151 vs, 146 m, 132 w, 127 w, 121 s, 100 w, 89 w, 80 w, 74 w, 57 w, 38 s cm^{-1}. ^{1}H NMR (CDCl$_3$): δ = 10.92 (s, 2 H, NH), 7.47–7.41 + 7.34–7.22 (m, 15 H, PC$_6$H$_5$ + m, 4 H, CH$_{bzimtH2}$) ppm.

[CuBr(μ_2-S-bzimtH$_2$)(tmtp)]$_2$ (2): Pale-yellow crystals; m.p. 285–288 °C. $C_{56}H_{54}Br_2Cu_2N_4P_2S_2$: calcd. C 56.24, H 4.55, N 4.68; found C 55.93, H 4.48, N 4.62. IR: $\tilde{\nu}$ = 3235 m, 3043 m, 2935 w, 1492 s, 1460 vs, 1360 m, 1341 m, 1167 s, 1103 m, 778 s, 746 vs, 695 vs, 598 s, 548 s; 459 m cm^{-1}; far-IR: $\tilde{\nu}$ = 136 w, 121 w, 96 s, 89 m, 80 w, 73 w, 65 w, 57 m, 37 s cm^{-1}. ^{1}H NMR (CDCl$_3$): δ = 11.03 (s, 2 H, NH), 7.31–7.24 + 7.17–7.13 (m, 12 H, PC$_6$H$_5$ + m, 4 H, CH$_{bzimtH2}$), 2.20 (s, 9 H, CH$_3$-C) ppm.

[CuBr(μ_2-S-bzimtH$_2$)(tptp)]$_2$ (3): Pale-yellow crystals; m.p. 225–227 °C; [($C_{56}H_{54}Cu_2Br_2N_4P_2S_2$)·0.5($CH_3OH$)·2($CH_3CN$)·3($H_2O$)]:

calcd. C 53.08, H 5.14, N 6.35; found C 52.90, H 5.08, N 6.26. IR: 3220 m, 3071 s, 2976 w, 2863 w, 1620 s, 1597 s, 1498 vs, 1465 vs, 1396 s, 1360 s, 1277 m, 1217 m, 1187 vs, 1097 vs, 1018 s, 807 vs, 745 vs, 709 s, 641 s, 630 s, 600 s, 518 vs, 418 vs cm^{-1}; far-IR: $\tilde{\nu}$ = 144 w, 127 w, 113 w, 104 w, 95 s, 81 m, 57 s, 37 s cm^{-1}. ^1H NMR ($CDCl_3$): δ = 11.09 (s, 2H, NH), 7.36–7.31 + 7.27–7.03 (m, 12 H, PC_6H_5 + m, 4 H, $CH_{bzimtH2}$), 2.23 (s, 9 H, CH_3-C) ppm.

X-ray Structural Determinations: Single crystals suitable for crystal structure analysis were obtained by slow evaporation of acetonitrile/methanol solutions of the complexes at room temperature. X-ray diffraction data were collected on a Bruker-Nonius Kappa CCD area-detector diffractometer. The programs DENZO[20] and COLLECT[21] were used in data collection and cell refinement. Details of crystal and structure refinement are shown in Table 6. The structures were solved with SIR97[22] and refined with SHELX-97.[23] Molecular plots were obtained with ORTEP-3.[24]
CCDC-241984 (**1**), -241985 (**2**) and -241986 (**3**) contain the supplementary crystallographic data for this paper. These data can be obtained free of charge from The Cambridge Crystallographic Data Centre via www.ccdc.cam.ac.uk/data_request/cif.

Computational Details: The structural, electronic and energetic properties of all compounds were computed with Becke's three-parameter hybrid functional[25,26] combined with the Lee–Yang–Parr[27] correlation functional (B3LYP level of density functional theory) using several basis sets, such as the SDD basis set, which describes valence electrons with an [8s,7p,6d/6s,5p,3d] valence basis set and Stuttgart–Dresden relativistic ECPs;[28] the larger all-electron double-zeta (DZVP) basis set;[29] the split-valence 6-31G(d) basis set; the LANL2DZ basis set, which describes valence electrons with a [5s,6p,4d/3s,3p,2d] valence basis set and Los Alamos ECPs;[30–32] the LANL2DZ basis set for copper combined with the 6-31G(d) basis for the non-metal atoms. The hybrid B3LYP functional was used since it gives acceptable results for molecular energies and geometries, as well as proton donation, and weak and strong H-bonds.[33–38] No constraints were imposed on the geometry. Full geometry optimization was performed for each structure using Schlegel's analytical gradient method,[39] and the attainment of the energy minimum was verified by calculating the vibrational frequencies that result in an absence of imaginary eigenvalues. All the stationary points were identified for minima (number of imaginary frequencies NIMAG = 0) or transition states (NIMAG = 1). All calculations were performed using the GAUSSIAN 03 series of programs.[40] Moreover, the qualitative concepts and the graphs derived from the Chem3D program suite[41] highlight the basic interactions found from the DFT calculations. Because of the computational cost due to the relatively big size of the compounds under consideration, to obtain a computationally convenient size we used

Table 6. Crystal data and structure refinement for $[\{CuBr(\mu_2\text{-S-bzimtH}_2)(PPh_3)\}_2]_{0.78}[\{Cu(\mu_2\text{-Br})(PPh_3)(bzimtH_2)\}_2]_{0.22}$ (**1**), $[CuBr(\mu_2\text{-S-bzimtH}_2)(tmtp)]_2$ (**2**) and $[CuBr(\mu_2\text{-S-bzimtH}_2)(tptp)]_2$ (**3**).

	1	**2**	**3**
Chemical formula	$C_{50}H_{42}Br_2Cu_2N_4P_2S_2$	$C_{56}H_{54}Br_2Cu_2N_4P_2S_2$	$[C_{28}H_{27}BrCuN_2PS]_2{\cdot}2CH_3CN{\cdot}3H_2O{\cdot}0.5CH_3OH$
Formula weight	1111.84	598.00	1347.56
Temperature	150(2) K	120(2) K	120(2) K
Wavelength	0.71073 Å	0.71073 Å	0.71073 Å
Crystal system	triclinic	monoclinic	triclinic
Space group	$P\bar{1}$	$P2_1/c$	$P\bar{1}$
Unit cell dimensions	a = 12.429(5) Å	a = 13.7360(3) Å	a = 10.3831(3) Å
	b = 13.641(5) Å	b = 15.6560(4) Å	b = 12.0888(3) Å
	c = 14.200(5) Å	c = 12.6520(3) Å	c = 13.4736(4) Å
	α = 94.823(5)°	α = 90°	α = 76.8516(15)°
	β = 90.552(5)°	β = 103.0553(14)°	β = 82.8213(13)°
	γ = 103.806(5)°	γ = 90°	γ = 72.6689(15)°
Volume	2328.6(15) $Å^3$	2650.50(11) $Å^3$	1569.11(8) $Å^3$
Z	2	2	1
Density (calculated)	1.586 $Mg\,m^{-3}$	1.499 $Mg\,m^{-3}$	1.427 $Mg\,m^{-3}$
Absorption coefficient	2.828 mm^{-1}	2.490 mm^{-1}	2.118 mm^{-1}
F_{000}	1120	1216	691
Crystal size	0.10 × 0.10 × 0.05 mm	0.40 × 0.20 × 0.18 mm	0.33 × 0.28 × 0.12 mm
Theta range for data collection	3.02 to 26.41°	3.01 to 27.48°	3.06 to 27.75°
Index ranges	$-15 \le h \le 15$	$-15 \le h \le 17$	$-13 \le h \le 13$
	$-17 \le k \le 17$	$-20 \le k \le 20$	$-15 \le k \le 15$
	$-16 \le l \le 17$	$-16 \le l \le 16$	$-17 \le l \le 17$
Reflections collected	37 573	2 0305	13 558
Independent reflections	9508 [R(int) = 0.0736]	5923 [R(int) = 0.0519]	7196 [R(int) = 0.0350]
Completeness to theta	99.4% (for theta = 26.41°)	97.4% (for theta = 27.48°)	97.1% (for theta = 27.75°)
Max. and min. transmission	0.8715 and 0.7652	0.6628 and 0.4358	0.7852 and 0.5416
Refinement method	Full-matrix least squares on F^2	Full-matrix least squares on F^2	Full-matrix least squares on F^2
Data/restrains/parameters	7518/0/597	5923/0/310	7196/4/379
Goodness-of-fit on F^2 (S)	1.124	1.053	1.043
Final R indices [$I > 2\sigma(I)$]	$R1$ = 0.0675, $wR2$ = 0.1638	$R1$ = 0.0353, $wR2$ = 0.0740	$R1$ = 0.0344, $wR2$ = 0.0786
R indices (all data)	$R1$ = 0.0869, $wR2$ = 0.1722	$R1$ = 0.0475, $wR2$ = 0.0793	$R1$ = 0.0525, $wR2$ = 0.0846
Final weighting scheme	[a]	[b]	[c]
Largest diff. peak and hole	1.585 and –0.834 e $Å^{-3}$	0.334 and –0.464 e $Å^{-3}$	0.367 and –0.522 e $Å^{-3}$

[a] Calcd. $w = 1/[\sigma^2(F_o^2) + (0.0381P)^2 + 18.6558P]$ where $P = (F_o^2 + 2F_c^2)/3$. [b] Calcd. $w = 1/[\sigma^2(F_o^2) + (0.0218P)^2 + 2.0748P]$ where $P = (F_o^2 + 2F_c^2)/3$. [c] Calcd. $w = 1/[\sigma^2(F_o^2) + (0.0416P)^2 + 0.0506P]$ where $P = (F_o^2 + 2F_c^2)/3$.

 © 2005 Wiley-VCH Verlag GmbH & Co. KGaA, Weinheim

models resulting from substitution of the phenyl groups of the spectator phosphane ligands by H atoms, while the benzimidazole-2-thione was replaced by the imidazole-2-thione ($imtH_2$) ligand. The use of such models does not alter the description of the "core" region of the compounds and is ultimately the most efficient and productive route for modeling the electronic structure and related properties of relatively large transition metal coordination compounds. Single point energy calculations on the "real" dicopper(I) complexes were also performed at the B3LYP/LANL2DZ level using the X-ray structural parameters of the two isomeric forms that coexist in the solid state.

[1] P. Gonzalez-Duarte, in *Comprehensive Coordination Chemistry II, Vol. 8* (Eds.: J. A. McLeverty, T. J. Meyer), Elsevier, Amsterdam, **2004**, pp. 213.
[2] G. Henkel, B. Krebs, *Chem. Rev.* **2004**, *104*, 801.
[3] S. E. Raper, *Coord. Chem. Rev.* **1994**, *129*, 91.
[4] S. K. Hadjikakou, P. Aslanidis, P. D. Akrivos, P. Karagiannidis, B. Kojic-Prodic, M. Luic, *Inorg. Chim. Acta* **1992**, *197*, 31.
[5] P. Aslanidis, S. K. Hadjikakou, P. Karagiannidis, B. Kojic-Prodic, M. Luic, *Polyhedron* **1994**, *13*, 3119.
[6] P. Aslanidis, P. J. Cox, S. K. Hadjikakou, C. D. Antoniadis, *Eur. J. Inorg. Chem.* **2002**, 2216.
[7] S. K. Hadjikakou, P. Aslanidis, P. Karagiannidis, A. Hountas, A. Terzis, *Inorg. Chim. Acta* **1991**, *184*, 161.
[8] S. K. Hadjikakou, P. Aslanidis, P. Karagiannidis, A. Hountas, A. Terzis, *Inorg. Chim. Acta* **1991**, *186*, 199.
[9] S. K. Hadjikakou, P. Aslanidis, P. Karagiannidis, A. Aubry, S. Skoulika, *Inorg. Chim. Acta* **1992**, *193*, 129.
[10] P. Karagiannidis, S. K. Hadjikakou, P. Aslanidis, A. Hountas, *Inorg. Chim. Acta* **1990**, *178*, 27.
[11] P. J. Cox, P. Aslanidis, P. Karagiannidis, *Polyhedron* **2000**, *19*, 1615.
[12] P. Aslanidis, P. J. Cox, S. Divanidis, A. C. Tsipis, *Inorg. Chem.* **2002**, *41*, 6875.
[13] P. Aslanidis, P. J. Cox, S. Divanidis, P. Karagiannidis, *Inorg. Chim. Acta* **2004**, *357*, 1063.
[14] S. Alvarez, A. A. Palacios, G. Aullon, *Coord. Chem. Rev.* **1999**, *185–186*, 431 and references cited therein.
[15] M. I. Davis, A. M. Orville, F. Neese, J. M. Zaleski, J. D. Lipscomb, E. I. Solomon, *J. Am. Chem. Soc.* **2002**, *124*, 602.
[16] D. C. Fox, A. T. Fiedler, H. L. Halfen, T. C. Brunold, J. A. Halfen, *J. Am. Chem. Soc.* **2004**, *126*, 7627.
[17] E. S. Raper, J. R. Creighton, D. Robson, J. D. Wilson, W. Clegg, A. Milne, *Inorg. Chim. Acta* **1988**, *143*, 95.
[18] E. C. Constable, P. R. Raithby, *J. Chem. Soc., Dalton Trans.* **1987**, 2281.
[19] R. K. Chadha, R. Kumar, D. G. Tuck, *Can. J. Chem.* **1987**, *65*, 1336.
[20] Z. Otwinowski, W. Minor, in *Methods in Enzymology, Vol. 276, Part A* (Eds.: C. W. Carter, Jr, R. M. Sweet), Academic Press, New York, **1997**, pp. 307.
[21] R. Hooft, *COLLECT Data collection Software*, Nobius B. V., Delft, The Netherlands, **1998**.
[22] A. Altomare, M. C. Burla, M. Camalli, G. L. Cascarano, C. Giacovazzo, A. Guagliardi, A. G. G. Moliterni, G. Polidori, R. Spagna, *J. Appl. Crystallogr.* **1994**, *27*, 435.
[23] G. M. Sheldrick, *SHELXL-97*. Program for crystal structure analysis, Vol. release 97-2, University of Göttingen, Germany, **1997**.
[24] L. J. Farrugia, *J. Appl. Crystallogr.* **1997**, *30*, 565.
[25] A. D. Becke, *J. Chem. Phys.* **1992**, *96*, 215.
[26] A. D. Becke, *J. Chem. Phys.* **1993**, *98*, 5648.
[27] C. Lee, W. Yang, R. G. Parr, *Phys. Rev. B* **1998**, *B37*, 785.
[28] D. Andrae, U. Haussermann, M. Dolg, H. Stoll, H. Preuss, *Theor. Chim. Acta* **1990**, *77*, 123.
[29] N. Golbout, D. R. Salahub, J. Andzelm, E. Winner, *Can. J. Chem.* **1992**, *70*, 560.
[30] P. J. Hay, W. R. Wadt, *J. Chem. Phys.* **1985**, *82*, 299.
[31] P. J. Hay, W. R. Wadt, *J. Chem. Phys.* **1985**, *82*, 284.
[32] P. J. Hay, W. R. Wadt, *J. Chem. Phys.* **1985**, *82*, 270.
[33] J. B. Nicholas, *Top. Catal.* **1997**, *4*, 157.
[34] L. A. Curtis, K. Raghavachari, P. C. Redfern, J. A. Pople, *Chem. Phys. Lett.* **1997**, *270*, 419.
[35] D. M. Smith, B. T. Golding, L. Radom, *J. Am. Chem. Soc.* **1999**, *121*, 9388.
[36] A. K. Chandra, M. T. Nguyen, *Chem. Phys* **1998**, *232*, 299.
[37] J. B. Nicholas, *Top. Catal.* **1999**, *9*, 181.
[38] R. Arnaud, C. Adamo, M. Cossi, A. Millet, Y. Valle, V. Barone, *J. Am. Chem. Soc.* **2000**, *122*, 324.
[39] H. B. Schlegel, *J. Comput. Chem.* **1982**, *3*, 214.
[40] M. J. Frisch, G. W. Trucks, H. B. Schlegel, G. E. Scusseria, M. A. Robb, J. R. Cheeseman, V. G. Zakrzewski, J. A. Montgomery, T. Vreven, K. N. Kudin, J. C. Burant, J. M. Millan, S. S. Iyengar, J. Tomasi, V. Barone, B. Mennucci, M. Cossi, G. Scalmani, N. Rega, G. A. Petersson, H. Nakatsuji, M. Hada, M. Ehara, K. Toyota, F. R., J. Hasegawa, M. Ishida, T. Nakajima, Y. Honda, O. Kitao, H. Nakai, M. Klene, X. Li, J. E. Knox, H. P. Hratchian, J. B. Cross, C. Adamo, J. Jaramillo, R. Gomperts, R. E. Stratmann, O. Yazyev, A. J. Austin, R. Cammi, C. Pomelli, J. W. Ochterski, P. Y. Ayala, K. Morokuma, G. A. Voth, P. Salvador, J. J. Dannenberg, V. G. Zakrzewski, S. Dapprich, A. D. Daniels, M. C. Strain, O. Farkas, D. K. Malick, A. D. Rabuck, K. Raghavachari, J. B. Foresman, J. V. Ortiz, Q. Cui, A. G. Baboul, S. Clifford, J. Cioslowski, B. B. Stefanov, G. Liu, A. Liashenko, P. Piskorz, I. Komaromi, R. L. Martin, D. J. Fox, T. Keith, M. A. Al-Laham, C. Y. Peng, A. Nanayakkara, M. Challacombe, P. M. W. Gill, B. Johnson, W. Chen, M. W. Wong, C. Gonzalez, J. A. Pople, *Gaussian 03, Revision B.02*, Gaussian, Inc., Pittsburgh PA, **2003**.
[41] *ChemOffice 97*, Scientific Computing, Inc., Massachusetts Ave., Suite 41, Cambridge, MA 02139875, USA.

Received October 4, 2004

 © 2005 Wiley-VCH Verlag GmbH & Co. KGaA, Weinheim

Reactivity of Lewis Acid/Base Stabilized Phosphanyl- and Arsanylboranes towards a Platinum(0) Complex

Ulf Vogel,[a] Karl-Christian Schwan,[a] Petra Hoemensch,[a] and Manfred Scheer*[a]

Dedicated to Prof. M. Meisel on the occasion of his 65th birthday

Keywords: Arsenic / Boron / Phosphorus / Reactivity / Platinum

The Lewis acid/base stabilized phosphanylboranes and -arsanes [$(CO)_5W(H_2EBH_2{\cdot}NMe_3)$] (**1a**: E = P; **1b**: E = As) have been shown to react with the platinum(0) complex [$(Ph_3P)_2Pt(C_2H_4)$] under oxidative addition of the E–H bond to the platinum center. The complexes *cis*-[$(Ph_3P)_2Pt(H)(\mu\text{-}EHBH_2{\cdot}NMe_3)W(CO)_5$] (**2a**: E = P; **2b**: E = As) are formed. Complex **2a** is unstable in solution at room temperature and slowly reacts with loss of carbon monoxide to form [$(Ph_3P)_2Pt(\mu\text{-}H)(\mu\text{-}EHBH_2{\cdot}NMe_3)W(CO)_4$] (**3a**: E = P). An analogous complex **3b** (E = As) is formed from **2b** only by refluxing in CH_2Cl_2. The reaction of **2a** to **3a** can be reversed by addition of CO, whereas the arsenic compound **3b** does not show this reactivity pattern. All new compounds have been comprehensively characterized by spectroscopy and X-ray crystallography.

(© Wiley-VCH Verlag GmbH & Co. KGaA, 69451 Weinheim, Germany, 2005)

Introduction

A large number of phosphanylboranes $(R_2BPR'_2)_n$ have been synthesized over the years,[1] whereas only some arsanylboranes $(R_2BAsR'_2)_n$ are known so far.[2] Monomeric compounds of both types have up to now been stabilized exclusively by bulky substituents at the group 13 and group 15 elements. Otherwise an intermolecular oligomerisation occurs by the lone pair of the group 15 element and the acceptor orbital of the boron atom. For the experimentally unobserved parent compounds H_2BPH_2 and H_2BAsH_2 we have recently found a novel method of stabilization by the coordination of a Lewis acid and a Lewis base. Thus, the phosphanyl- and arsanylborane complexes [$(CO)_5W(EH_2BH_2{\cdot}NMe_3)$] (**1a**: E = P; **1b**: E = As) were synthesized by a salt elimination route starting from $Li[(CO)_5WEH_2]$ and $ClBH_2{\cdot}NMe_3$.[3] Herein we report on the reactivity of **1** towards the platinum(0) complex [$(Ph_3P)_2Pt(C_2H_4)$] and the CO elimination/addition reactions of the products.

Results and Discussion

The reaction of [$(CO)_5W(H_2EBH_2{\cdot}NMe_3)$] (**1a**: E = P; **1b**: E = As) with the platinum(0) complex [$(Ph_3P)_2Pt(C_2H_4)$] at ambient temperature results in an initial oxidative addition of the platinum center to the E–H bond of **1**, and the complexes *cis*-[$(Ph_3P)_2Pt(H)(\mu\text{-}EHBH_2{\cdot}NMe_3)W(CO)_5$] (**2a**: E = P; **2b**: E = As) are formed [Equation (1)].

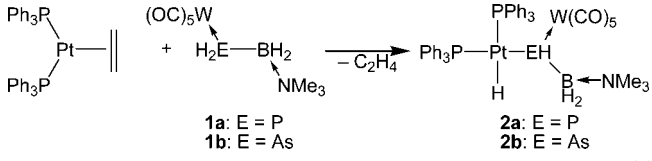

1a: E = P
1b: E = As

2a: E = P
2b: E = As

(1)

For the arsenic substituted compound **2b** the reaction is complete at this stage and **2b** can be isolated as a pure compound. In contrast, even under these conditions **2a** tends to lose 1 equiv. of CO and forms the complex [$(Ph_3P)_2Pt(\mu\text{-}H)(\mu\text{-}PHBH_2{\cdot}NMe_3)W(CO)_4$] (**3a**) bearing a bridging hydrogen ligand. For a full conversion the reaction mixture has to be heated to yield pure **3a** [Equation (2)]. Although pure crystalline **2a** can be isolated from the reaction (1) by fractional crystallization, if it is redissolved it tends to lose CO with formation of complex **3a**.

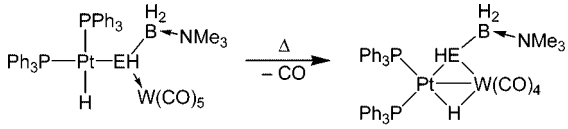

2a: E = P
2b: E = As

3a: E = P
3b: E = As

(2)

[a] Institut für Anorganische Chemie, Universität Regensburg
93040 Regensburg, Germany
Fax: +49-941-943-4439
E-mail: manfred.scheer@chemie.uni-regensburg.de

 DOI: 10.1002/ejic.200400845 © 2005 Wiley-VCH Verlag GmbH & Co. KGaA, Weinheim

Only by heating a CH_2Cl_2 solution of the arsenic complex **2b** the formation of **3b** was detected, and the product could be isolated in pure form. Furthermore, the formation of **3a** from **2a** by loss of carbon monoxide is reversible. On saturation of a solution of **3a** with carbon monoxide, **2a** together with minor amounts of **3a** could be identified by NMR spectroscopy. In contrast, this feature has never been observed for **2b**.

Interestingly, only the diorgano-substituted phosphane complexes of the type $[(CO)_5M(PPh_2H)]$ show a similar reaction behavior of **1** when treated with $[(C_2H_4)Pt(PPh_3)_2]$. Here, initially the complexes *cis*-$[(CO)_5M(\mu\text{-}PPh_2)\text{-}Pt(H)(PPh_3)_2]$ (M = Cr, Mo, W) are formed, which have a strong tendency to lose CO, resulting in the compounds $[(CO)_4M(\mu\text{-}PPh_2)(\mu\text{-}H)Pt(PPh_3)_2]$. For these complexes the initial oxidative addition products could only be identified by NMR spectroscopy.[4] In contrast, the complexes $[(Ph_3P)_2Pt(H)(\mu\text{-}EH_2)W(CO)_5]$ (E = P, As)[5] and $[(Ph_3P)_2\text{-}Pt(H)(\mu\text{-}PRH)M(CO)_5]$ (R = Ph, cyclohexyl; M = Cr, Mo, W),[6] which are structurally more closely related to **2** and are formed in a manner similar to that for **2**, both show no loss of carbon monoxide even at elevated temperatures. Thus, the occurrence of this CO loss does not seem to be caused by steric factors. Furthermore, the complexes $[(Ph_3P)_2Pt(H)(\mu\text{-}EH_2)W(CO)_5]$ (E = P, As)[5] show a *cis*/*trans* isomerization, whereas for **2a** and **2b** only the *cis*-addition products are detected in solution. It is interesting to note that in a related reaction of the phosphane–borane adducts $PhRPH{\cdot}BH_3$ (R = H, Ph) with $Pt(PEt_3)_3$ an oxidative addition of the P–H bond to the platinum center occurs, but in this case the *trans*-substituted complexes $[(Et_3P)_2\text{-}Pt(H)(PPhR{\cdot}BH_3)]$ (R = H, Ph) are formed exclusively.[7]

Complexes **2** are colorless compounds and moderately soluble in CH_2Cl_2 and toluene, whereas complexes **3** are orange crystalline complexes readily soluble in CH_2Cl_2 and toluene. In the vibrational spectra all products show bands for the CO, PH and BH functional groups. The EI mass spectra do not show the molecular ion peaks, but decomposition products including $[(CO)_5W(PPh_3)]$ and $[(CO)_5\text{-}W(H_2EBH_2{\cdot}NMe_3)]$ (E = P, As) can be identified.

In its $^{31}P\{^1H\}$ NMR spectrum **2a** shows a signal at δ = –174.8 ppm ($^1J_{P1,Pt}$ = 1286, $^2J_{P1,P3}$ = 223 Hz) for the P^1 atom of the phosphido group which is only slightly shifted to lower field when compared with free **1a** (δ = –184.2 ppm). The signal is very broad because of the quadrupolar moment of the neighboring boron atom, which is directly bound to the phosphorus atom. Upon recording a $^{31}P\{^{11}B,^1H\}$ NMR spectrum, the coupling to the tungsten atom and to the P^2 atom *cis* to P^1 (see Scheme 1) is also revealed ($^2J_{P1,P2}$ = 11, $^1J_{P1,W}$ = 153 Hz). The P^2 atom shows a pseudo-triplet at δ = 29.4 ppm ($^1J_{P2,Pt}$ = 2099, $^2J_{P2,P1}$ = 11, $^2J_{P2,P3}$ = 14 Hz) and P^3 is detected as a doublet of doublets at δ = 25.9 ppm ($^1J_{P3,Pt}$ = 2199, $^2J_{P3,P2}$ = 14, $^2J_{P3,P1}$ = 223 Hz). This coupling pattern clearly shows the *cis* arrangement of the phosphanidoboranyl ligand relative to the hydrido ligand. The latter ligand is detected in the ^1H NMR spectrum of **2a** as a doublet of doublets of doublets at δ = –4.48 ppm showing platinum satellites. The PH proton appears as a doublet at δ = 2.38 ppm. A signal for the BH_2 protons could not be assigned, as this resonance is too broad to be clearly identified from the background in the spectrum.

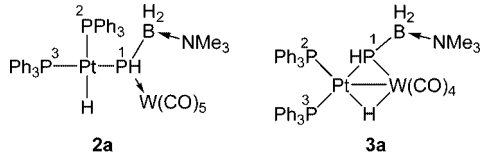

Scheme 1.

Complex **3a** shows a similar $^{31}P\{^1H\}$ NMR spectrum, which is depicted in Figure 1. Here, the P^1 atom shows a broad doublet at δ = –8.7 ppm. Upon additional boron decoupling the signal shows a doublet of doublets bearing platinum satellites. The large downfield shift of the signal compared to **2a** can be explained by the bridging position of the phosphidoboranyl ligand.[8] Also the phosphorus–platinum coupling constant (951 Hz) is much smaller than in **2a** (1286 Hz). A coupling to the tungsten atom is not obvious, but it is presumably hidden under the main signals. Signals for the P^2 and P^3 atoms appear at δ = 15.7 and 19.5 ppm, respectively, and show the same coupling pattern as in **2a**. In its ^1H NMR spectrum **3a** shows a doublet of doublet of doublets with platinum satellites at δ = –7.43 ppm (Figure 1). Due to the small intensity of the hydride signals, the expected tungsten satellites cannot be clearly differentiated from the background noise. The resonance for the PH protons appears as a doublet at δ = 2.60 ppm. As in the case for **2a** the BH_2 signal for **3a** could not be detected.

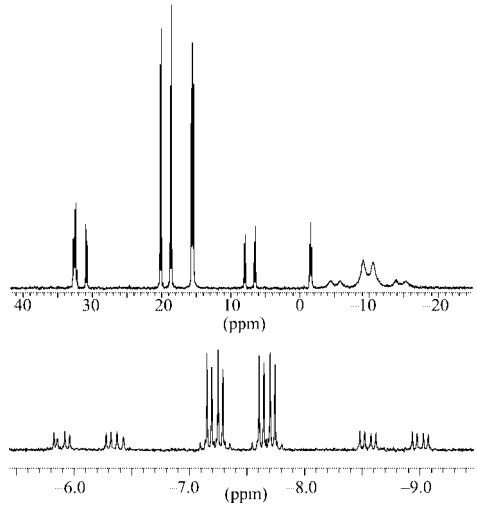

Figure 1. $^{31}P\{^1H\}$ NMR spectrum of **3a** (top). Hydride region of the ^1H NMR spectrum of **3a** (bottom).

The $^{31}P\{^1H\}$ NMR spectrum of compound **2b** (Scheme 2) shows two doublets at δ = 30.7 ppm and 23.6 ppm, both bearing platinum satellites ($^2J_{P1,P2}$ = 13, $^1J_{P1,Pt}$ = 2145Hz, $^1J_{P2,Pt}$ = 2531Hz). In its ^1H NMR spectrum **2b** displays a doublet of doublets at δ = –4.76 ppm with platinum satellites for the hydrido ligand bound to the platinum atom ($^2J_{H,P1}$ = 177, $^2J_{H,P2}$ = 19 Hz). In accord-

 © 2005 Wiley-VCH Verlag GmbH & Co. KGaA, Weinheim

ance with the $^{31}P\{^1H\}$ NMR spectrum this coupling pattern shows the *cis* arrangement of the phosphane ligands around the platinum center. In the ^1H NMR spectrum the protons bound to the arsenic atom give rise to a complex signal centered at δ = –1.27 ppm.

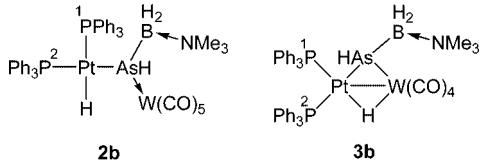

Scheme 2.

In the $^{31}P\{^1H\}$ NMR spectrum complex **3b** (Scheme 2) shows two doublets with platinum satellites at δ = 15.2 ppm and 16.9 ppm ($^2J_{P1,P2}$ = 16, $^1J_{P1,Pt}$ = 2657, $^1J_{P2,Pt}$ = 3433 Hz) for both non-equivalent phosphorus atoms. The ^1H NMR spectrum of **3b** shows the same characteristic signals as that of complex **3a**. The hydrido ligand bound to the platinum atom gives rise to a doublet of doublets with platinum satellites at δ = –6.74 ppm ($^2J_{H,P1}$ = 116, $^2J_{H,P2}$ = 24, $^1J_{H,Pt}$ = 669 Hz). Signals for the nine protons of the trimethylamine group and the 30 protons of the phenyl groups are detected at δ = 1.95 ppm and 6.8–7.6 ppm, respectively.

In order to confirm the proposed structures of **2** and **3** X-ray crystal structure determinations have been performed on all compounds. Single crystals of complex **2** could be obtained from CH_2Cl_2 solutions. Whereas **2b** crystallizes as a dichloromethane solvate, for **2a** no solvent molecule was found in the unit cell. As an example the molecular structure of **2a** is depicted in Figure 2; in Table 1 the bond lengths and angles are compared.

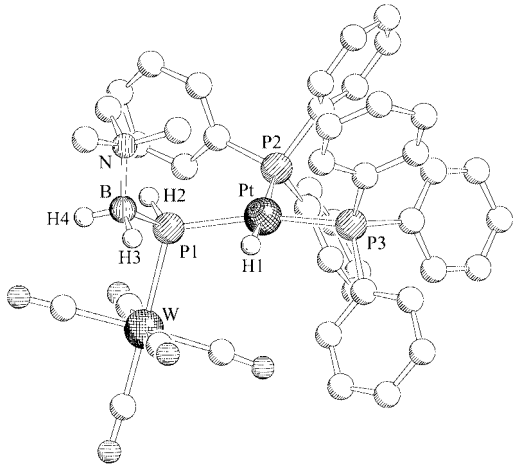

Figure 2. Molecular structure of **2a** in the crystal. Hydrogen atoms at the carbon atoms are omitted for clarity.

The key structural feature of **2** is a central platinum atom which shows an almost perfect planar coordination sphere. Two phenylphosphane ligands are in *cis* arrangement to each other. A hydrido and the phosphanidoboranyl or arsanidoboranyl ligand (**2a** or **2b**) complete the coordination sphere of the 16-electron complexes. The sum of the bond angles around the platinum atom are close to 360° [**2a**: 359.87(5)°; **2b**: 359.01(7)°]. Despite the planar coordination around the platinum atom the bond angles are far from 90° required for a square-planar coordination. All ligands are shifted towards the hydrido ligand to alleviate steric crowding. The Pt–P bond lengths in both compounds are comparable and in a range usually found for such bonds. In comparison to the starting material the B–E [**1a**: 195.5(4); **2a**: 198.1(6): **1b**: 206.7(9): **2b**: 209.4(9) pm] and the E–W bonds [**1a**: 254.2(2); **2a**: 260.5(1); **1b**: 263.5(1); **2b**: 270.15(8) pm] are elongated.[3] The elongation of the E–W bond can be explained by the back-bonding of the E atom to two metal atoms instead of one metal atom as in compound **1**. The same effect can be observed for $[(CO)_5W(\mu\text{-}PH_2)PtH(PPh_3)_2]$ [W–P 260.3(3) pm] in comparison to $[(CO)_5WPH_3]$ [W–P 249.1(2) pm].[5] The change of the electron density at the E atom in **2** and **3** can also explain the elongation of the E–B bond.

Table 1. Comparison of selected bond lengths [pm] and angles [°] in **2a** and **2b**.

Bond lengths[a]	**2a**	**2b**
Pt–E	233.0(2)	243.6(1)
Pt–P_{cis}	233.1(1)	232.1(2)
Pt–P_{trans}	231.0(2)	229.9(2)
E–W	260.5(1)	270.2(1)
E–B	198.1(6)	209.4(9)
B–N	161.8(7)	162(1)
Angles	**2a**	**2b**
E–Pt–P_{cis}	98.29(5)	100.06(5)
E–Pt–P_{trans}	159.71(5)	157.60(5)
P_{cis}–Pt–P_{trans}	101.87(5)	101.35(7)
Pt–E–W	111.20(5)	112.07(3)
Pt–E–B	118.1(3)	116.0(3)
W–E–B	106.1(2)	106.3(3)
E–B–N	116.4(4)	115.2(6)

[a] **2a**: E = P1, P_{cis} = P2, P_{trans} = P3; **2b**: E = As, P_{cis} = P1, P_{trans} = P2.

The compounds **3a** and **3b** are isostructural and crystallize in the triclinic space group $P\bar{1}$ as the dichloromethane solvates. As an example the molecular structure of **3a** is depicted in Figure 3; in Table 2 the bond lengths and angles are compared.

The essential feature of the structures is a $(CO)_4WPt(PPh_3)_2$ moiety which is bridged by a hydrido ligand and a phosphanidoboranyl and an arsanidoboranyl ligand (**3a** or **3b**), respectively. Like in the compounds **2** the platinum atoms show a nearly planar coordination geometry [sum of bond angles **3a**: 357.74(7)°; **3b**: 357.49(7)°]. The long distance between the platinum and the tungsten atom [**3a**: 302.8(1); **3b**: 307.72(9) pm] implies indirect multi-centered bonding through the bridging ligands, rather than a direct metal–metal bond, as was discussed for the structurally related compound $[(CO)_4Cr(\mu\text{-}PPh_2)(\mu\text{-}H)Pt(PEt_3)_2]$.[4b] The E–B distances [**3a**: 197.5(8); **3b** 207.3(8) pm] are comparable to **2a** and **2b**, respectively. In comparison to **2a** and **2b**, respectively, the E–W bond lengths in **3a** and **3b** are significantly reduced [**3a**: 246.0(1); **3b**: 255.57(9) pm] but in a range normally found for similar complexes {$[(CO)_4$-

 © 2005 Wiley-VCH Verlag GmbH & Co. KGaA, Weinheim

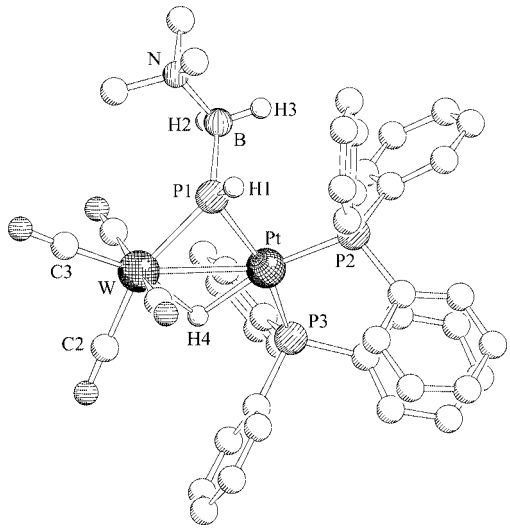

Figure 3. Molecular structure of **3a** in the crystal. Hydrogen atoms at the carbon atoms are omitted for clarity.

Table 2. Comparison of selected bond lengths [pm] and angles [°] of **3a** and **3b**.

Bond lengths[a]	**3a**	**3b**
Pt–E	233.7(2)	245.1(1)
Pt–P_{cis}	228.5(2)	229.0(2)
Pt–P_{trans}	232.3(2)	231.0(2)
Pt–W	302.8(1)	307.7(1)
E–W	246.0(2)	255.6(1)
E–B	197.5(8)	207.3(8)
B–N	162(1)	161(1)
W–C2	199.6(8)	200.6(8)
W–C3	194.9(8)	195.1(8)
Angles	**3a**	**3b**
E–Pt–P_{cis}	95.18(7)	94.89(6)
E–Pt–P_{trans}	159.79(6)	159.50(5)
P_{cis}–Pt–W	144.09(5)	144.90(5)
P_{cis}–Pt–P_{trans}	102.77(7)	103.10(7)
P_{trans}–Pt–W	111.97(5)	110.96(5)
E–Pt–W	52.68(5)	53.63(3)
W–E–B	125.48(5)	125.44(5)
E–B–N	111.04(7)	111.58(6)

[a] **3a**: E = P1, P_{cis} = P2, P_{trans} = P3; **3b**: E = As, P_{cis} = P1, P_{trans} = P2.

$W(\mu\text{-}PPh_2)_2Pt(MeO_2CC{\equiv}CCO_2Me)]$: W–P: 244.3(3) and 243.5(3) pm}.[9]

Conclusions

The results have shown that the Lewis acid/base stabilized phosphanylborane and arsanylborane undergo oxidative addition reactions at a Pt^0 center only at the P–H bond. Initially we had expected that the B–H bond also shows some addition behavior, as it is known for Rh and Ir complexes.[10] However, the boranyl substituent in **1** only functions as an electron-withdrawing substituent at the group 15 atom. Furthermore, in comparison to organo-substituted PH-containing phosphanes, the boranyl-substituted complexes **1** show a similar reaction behaviour toward Pt^0 centers. Oxidative addition of the E–H bond leads to exclusive formation of *cis*-substituted Pt^{II} complexes, which can lose CO to form a complex with a bridging hydrido and pnicogenido substituent, respectively.

Experimental Section

General Remarks: All manipulations were carried out under dinitrogen using standard Schlenk techniques. All solvents were dried using standard procedures and distilled freshly before use. $[(CO)_5W(H_2EBH_2{\cdot}NMe_3)]$ (**1a**: E = P; **1b**: E = As)[3] and $[(Ph_3P)_2Pt(C_2H_4)]$[11] were prepared according to the literature. All NMR spectra were recorded with a Bruker AC 250 with δ referenced to external $SiMe_4$ (^{1}H), $F_3B{\cdot}OEt_2$ (^{11}B) or H_3PO_4 (^{31}P), respectively. IR spectra were measured with a Bruker IFS-28, Raman spectra with a Bruker FRA 106 spectrometer. All mass spectra were recorded with a Varian MATR 711.

***cis*-$[(Ph_3P)_2Pt(H)(\mu\text{-}PHBH_2{\cdot}NMe_3)W(CO)_5]$ (2a):** A mixture of $[W(CO)_5(H_2PBH_2{\cdot}NMe_3)]$ (**1a**) (467 mg, 1.09 mmol) and $[(C_2H_4)Pt(PPh_3)_2]$ (814 mg, 1.09 mmol) was stirred in toluene (20 mL) at room temperature for 14 h. The solution turned to an orange color during this time and a yellow precipitate was formed. The precipitate was separated by filtration and dissolved in a minimum amount of CH_2Cl_2 (ca. 4–5 mL). After 2 d, **2a** was obtained at 4 °C as colorless crystals (if the solution is too concentrated, orange crystals of **3a** crystallize additionally). Yield: 638 mg (51%). $C_{44}H_{43}BNO_5P_3PtW$ (1148.45): calcd. C 46.02, H 3.77, N 1.22; found C 46.23, H 3.87, N 1.14. Raman (solid state) $\tilde{\nu}$ = 3061 (vs), 3006 (w), 2949 (w), 2370 (w), 2295 (w), 2048 (s), 1951 (vs), 1895 (m), 1873 (s), 1518 (s), 1573 (m), 1097 (m), 1029 (m), 1002 (vs), 789 (w), 461 (m), 439 (m), 260 (w), 174 (w), 114 (s) cm^{-1}. ^{1}H NMR (250 MHz, CD_2Cl_2): δ = –4.48 (ddd, $^1J_{Pt,H}$ = 971, $^2J_{P,H}$ = 176, $^2J_{P,H}$ = 33, $^2J_{P,H}$ = 22 Hz, 1 H, HPt), 2.38 (m, $^1J_{P,H} \approx$ 300 Hz, 1 H, PH), 2.49 (s, 9 H, NMe_3), 7.0–7.5 (m, 30 H, PPh_3) ppm. ^{31}P{^{1}H} NMR (101 MHz, CD_2Cl_2): δ = –174.8 (br. d, $^2J_{P,P}$ = 223, $^1J_{Pt,P}$ = 1286 Hz, $PHBH_2$), 25.9 (dd, $^2J_{P,P}$ = 223, $^2J_{P,P}$ = 14, $^1J_{Pt,P}$ = 2199 Hz, PPh_3), 29.4 (t, $^2J_{P,P}$ = 14, $^1J_{Pt,P}$ = 2099 Hz, PPh_3) ppm. ^{31}P{^{11}B,^{1}H} NMR (101 MHz, CD_2Cl_2): δ = –174.8 (dd, $^2J_{P,P}$ = 11 Hz $^2J_{P,P}$ = 223, $^1J_{W,P}$ = 153, $^1J_{Pt,P}$ = 1286 Hz, $PHBH_2$), 25.9 (dd, $^2J_{P,P}$ = 223, $^2J_{P,P}$ = 14, $^1J_{Pt,P}$ = 2199 Hz, PPh_3), 29.4 (t, $^2J_{P,P}$ = 14, $^1J_{Pt,P}$ = 2099 Hz, PPh_3) ppm. EI-MS (170 °C): *m*/*z* (%) = 586 (16) $[W(CO)_5PPh_3]^+$, 558 (4) $[W(CO)_4PPh_3]^+$, 530 (2) $[W(CO)_3PPh_3]^+$, 502 (93) $[W(CO)_2PPh_3]^+$, 474 (1) $[W(CO)PPh_3]^+$, 446 (100) $[WPPh_3]^+$, 429 (22) $[(CO)_5WPH_2BH_2NMe_3]^+$, 401 (11) $[(CO)_4WPH_2BH_2NMe_3]^+$, 373 (14) $[(CO)_3WPH_2BH_2NMe_3]^+$, 370 (50) $[(CO)_5WPH_2BH_2]^+$, 345 (6) $[(CO)_2WPH_2BH_2NMe_3]^+$, 342 (31) $[(CO)_4WPH_2BH_2]^+$, 317 (4) $[(CO)WPH_2BH_2NMe_3]^+$, 314 (15) $[(CO)_3WPH_2BH_2]^+$, 286 (10) $[(CO)_2WPH_2BH_2]^+$, 262 (89) $[PPh_3]^+$.

***cis*-$[(Ph_3P)_2Pt(H)(\mu\text{-}AsHBH_2{\cdot}NMe_3)W(CO)_5]$ (2b):** A mixture of $[W(CO)_5(H_2AsBH_2{\cdot}NMe_3)]$ (**1b**) (75 mg, 0.16 mmol) and $[(C_2H_4)Pt(PPh_3)_2]$ (119 mg, 0.16 mmol) was stirred in toluene (10 mL) at room temperature for 16 h. During this time the orange solution turned to a yellow suspension. The precipitate was separated by filtration and dissolved in a minimum amount of CH_2Cl_2 (3–4 mL). The resulting solution was stored at –25 °C. After 2 d, **2b** was obtained as colorless crystals. Yield: 134 mg (70%). $C_{44}H_{43}AsBNO_5P_2PtW{\cdot}0.5CH_2Cl_2$ (1234.87): calcd. C 43.28, H 3.59, N 1.13; found C 43.43, H 3.32, N 1.28. Raman (solid state) $\tilde{\nu}$ = 3060 (vs), 3006 (w), 2948 (w), 2093 (w), 2046 (s), 1951 (vs), 1874 (s), 1858 (w), 1587 (vs), 1574 (m), 1158 (w), 1096 (m), 1029 (s), 1002 (vs), 465 (m), 439 (m), 259 (w), 205 (w), 175 (w), 110 (s) cm^{-1}. ^{1}H NMR (250 MHz, CD_2Cl_2): δ = –4.95 (dd, $^2J_{P,H}$ = 177,

 © 2005 Wiley-VCH Verlag GmbH & Co. KGaA, Weinheim

$^2J_{P,H}$ = 19, $^1J_{Pt,H}$ = 904 Hz, 1 H, HPt), –1.27 (m, 2 H, AsH_2), 2.48 (s, 9 H, NMe_3), 7.11–7.29 (m, 30 H, PPh_3) ppm. $^{31}P\{^1H\}$ NMR (101 MHz, CD_2Cl_2): δ = 23.6 (d, $^2J_{P,P}$ = 13, $^1J_{Pt,P}$ = 2531 Hz, PPh_3), 30.7 (d, $^2J_{P,P}$ = 13, $^1J_{Pt,P}$ = 2145 Hz, PPh_3) ppm. ^{31}P NMR (101 MHz, CD_2Cl_2): δ = 23.6 (s, 1 P, PPh_3), 30.7 (d, $^2J_{H,P}$ = 177 Hz, PPh_3). EI-MS (200 °C): *m*/*z* (%) = 586 (15) $[(CO)_5WPPh_3]^+$, 558 (16) $[(CO)_4WPPh_3]^+$, 530 (3) $[(CO)_3WPPh_3]^+$, 502 (70) $[(CO)_2WPPh_3]^+$, 446 (67) $[WPPh_3]^+$, 445 (35) $[(CO)_4WAsH_2BH_2{\cdot}NMe_3]^+$, 262 (100) $[PPh_3]^+$.

$[(Ph_3P)_2Pt(\mu\text{-}H)(\mu\text{-}PHBH_2{\cdot}NMe_3)W(CO)_4]$ (3a): A mixture of $[W(CO)_5(H_2PBH_2{\cdot}NMe_3)]$ (**1a**) (467 mg, 1.09 mmol) and $[(C_2H_4)Pt(PPh_3)_2]$ (814 mg, 1.09 mmol) was stirred in toluene (20 mL) at room temperature for 14 h. The solution turned to an orange color during this time and a yellow precipitate was formed. The precipitate was separated by filtration and dissolved in CH_2Cl_2 (10 mL). The resulting solution was heated under reflux for 6 h while a slow stream of nitrogen was passed through the apparatus. Reduction of the solvent to a volume of ca. 2 mL and storage at 4 °C yielded **3a** as orange crystals. Yield: 733 mg (60%). $C_{43}H_{43}BNO_4P_3PtW{\cdot}0.5CH_2Cl_2$ (1162.91): calcd. C 44.93, H 3.81, N 1.20; found C 44.84, H 3.72, N 1.08. Raman (solid state) $\tilde{\nu}$ = 3058 (vs), 3004 (w), 2943 (w), 2392 (w), 2291 (m), 2050 (m), 1987 (m), 1956 (s), 1861 (s), 1821 (w), 1586 (s), 1482 (m, br), 1096 (m), 1028 (m), 1001 (vs), 704 (w), 496 (m), 436 (m), 116 (s) cm^{-1}. ^1H NMR (250 MHz, CD_2Cl_2): δ = –7.43 (ddd, $^1J_{Pt,H}$ = 664, $^2J_{P,H}$ = 113, $^2J_{P,H}$ = 24, $^2J_{P,H}$ = 10 Hz, 1 H, HPt), 2.60 (m, $^1J_{P,H}$ = 287 Hz, 1 H, PH), 2.45 (s, 9 H, NMe_3), 7.0–7.5 (m, 30 H, PPh_3) ppm. $^{31}P\{^1H\}$ NMR (101 MHz, CD_2Cl_2): δ = –8.7 (br. d, $^2J_{P,P}$ = 147, $^1J_{Pt,P}$ = 951 Hz, $PHBH_2$), 15.7 (t, $^2J_{P,P}$ = 17, $^1J_{Pt,P}$ = 3462 Hz, PPh_3), 19.5 (dd, $^2J_{P,P}$ = 147, $^2J_{P,P}$ = 17, $^1J_{Pt,P}$ = 2463 Hz, PPh_3) ppm. $^{31}P\{^{11}B,^1H\}$ NMR (101 MHz, CD_2Cl_2): δ = –8.7 (dd, $^2J_{P,P}$ = 15, $^2J_{P,P}$ = 147, $^1J_{Pt,P}$ = 951 Hz, $PHBH_2$), 15.7 (t, $^2J_{P,P}$ = 17, $^1J_{Pt,P}$ = 3462 Hz, PPh_3), 19.5 (dd, $^2J_{P,P}$ = 147, $^2J_{P,P}$ = 17, $^1J_{Pt,P}$ = 2463 Hz, PPh_3) ppm. EI-MS (90 °C) *m*/*z* = 586 (6) $[W(CO)_5PPh_3]^+$, 558 (8) $[W(CO)_4PPh_3]^+$, 530 (1) $[W(CO)_3PPh_3]^+$, 502 (22) $[W(CO)_2PPh_3]^+$, 474 (1) $[W(CO)PPh_3]^+$, 446 (19) $[WPPh_3]^+$, 429 (19) $[(CO)_5WPH_2BH_2NMe_3]^+$, 401 (6) $[(CO)_4WPH_2BH_2NMe_3]^+$, 373 (6) $[(CO)_3WPH_2BH_2NMe_3]^+$, 370 (16) $[(CO)_5WPH_2BH_2]^+$, 345 (2) $[(CO)_2WPH_2BH_2NMe_3]^+$, 342 (13) $[(CO)_4WPH_2BH_2]^+$, 317 (3) $[(CO)WPH_2BH_2NMe_3]^+$, 314 (6) $[(CO)_3WPH_2BH_2]^+$, 286 (3) $[(CO)_2WPH_2BH_2]^+$, 262 (100) $[PPh_3]^+$.

$[(Ph_3P)_2Pt(\mu\text{-}H)(\mu\text{-}AsHBH_2{\cdot}NMe_3)W(CO)_4]$ (3b): Complex **2b** (70 mg, 0,059 mmol) was dissolved in CH_2Cl_2 (15 mL) and refluxed for 12 h which led to a color change from yellow to orange. Reduction of the volume of the solution to ca. 2 mL and storage at –25 °C yielded **3b** as orange crystals. Yield: 41 mg (60%). $C_{43}H_{43}AsBNO_4P_2PtW{\cdot}0.5CH_2Cl_2$ (1206.86): calcd. C 43.29, H 3.67, N 1.16; found C 43.46, H 3.50, N 1.29. Raman (solid state): $\tilde{\nu}$ = 3054 (vs), 2380 (w), 2294 (w), 2092 (m), 2051 (m), 2031 (s), 1962 (w), 1860(b), 1586 (s), 1185 (w), 1160 (w), 1095 (m), 1028 (m), 1001 (vs), 773 (w), 703 (w), 475 (m), 437 (m), 172 (w), 113 (s) cm^{-1}. ^1H NMR (250 MHz, C_6D_6): δ = –6.74 (dd, $^2J_{P,H}$ = 116, $^2J_{P,H}$ = 24, $^1J_{Pt,H}$ = 669 Hz, 1 H, HPt), 0.32 (s, 1 H, AsH), 1.95 (s, 9 H, NMe_3), 6.8–7.6 (m, 30 H, PPh_3) ppm. $^{31}P\{^1H\}$ NMR (101 MHz, C_6D_6): δ = 15.2 (d, $^2J_{P,P}$ = 16, $^1J_{Pt,P}$ = 3433 Hz, PPh_3), 16.9 (d, $^2J_{P,P}$ = 16, $^1J_{Pt,P}$ = 2657 Hz, PPh_3) ppm. ^{31}P NMR (101 MHz, C_6D_6): δ = 15.2 (d, $^2J_{H,P}$ = 123 Hz, PPh_3), 16.9 (s, PPh_3) ppm. EI-MS (200 °C): *m*/*z* = 586 (20) $[(CO)_5WPPh_3]^+$, 558 (16) $[(CO)_4WPPh_3]^+$, 530 (3) $[(CO)_3WPPh_3]^+$, 502 (70) $[(CO)_2WPPh_3]^+$, 446 (67) $[WPPh_3]^+$, 445 (35) $[(CO)_4WAsH_2BH_2{\cdot}NMe_3]^+$, 262 (100) $[PPh_3]^+$.

X-ray Crystallographic Study: Data were collected with a STOE IPDS area-detector diffractometer using Ag-K_α (λ = 0.56087 Å) radiation. Machine parameters, crystal data and data collection parameters are summarized in Table 3. The structures were solved by direct methods using SHELXS-97,[12a] full-matrix-least-squares

Table 3. Crystallographic data for **2a**,**b** and **3a**,**b**.

	2a	**2b**·0.5CH_2Cl_2	**3a**·0.5CH_2Cl_2	**3b**·0.5CH_2Cl_2
Empirical formula	$C_{44}H_{43}BNO_5P_3PtW$	$C_{44.5}H_{44}AsBClNO_5P_2PtW$	$C_{43.5}H_{44}BClNO_4P_3PtW$	$C_{43.5}H_{44}AsBClNO_4P_2PtW$
M_r	1148.45	1234.87	1162.91	1206.86
T [K]	203(2)	203(2)	203(2)	203(2)
Crystal size	0.20×0.20×0.06	0.18×0.12×0.03	0.20×0.10×0.04	0.25×0.15×0.10
Space group	*Pbcn*	$P2_1/c$	$P\bar{1}$	$P\bar{1}$
Crystal system	orthorhombic	monoclinic	triclinic	triclinic
a [Å]	20.017(4)	14.891(3)	10.661(2)	10.774(2)
b [Å]	24.139(5)	18.897(3)	12.458(3)	12.490(3)
c [Å]	18.389(4)	18.195(3)	18.995(4)	18.976(4)
α [°]	90	90	82.06(3)	81.72(3)
β [°]	90	108.06(3)	76.89(3)	76.18(3)
γ [°]	90	90	71.84(3)	71.67(3)
V [Å^{-3}]	8885(3)	4867.7(15)	2328.5(8)	2347.2(8)
Z	8	4	2	2
d_c [g cm^{-3}]	1.717	1.685	1.659	1.708
μ_c [mm^{-1}]	3.185	3.275	3.066	3.393
2θ range [°]	2.72–41.82	3.40–42.00	3.60–45.00	3.12–44.78
hkl range	$-23 \le h \le 24$	$-19 \le h \le 18$	$-14 \le h \le 14$	$-14 \le h \le 14$
	$-16 \le k \le 29$	$-24 \le k \le 24$	$-16 \le k \le 16$,	$-16 \le k \le 16$
	$-23 \le l \le 23$	$-21 \le l \le 23$	$-25 \le l \le 25$	$-23 \le l \le 24$
Data/restraints/parameters	7960/0/524	10245/0/547	11790/0/528	11591/2/533
No. of unique data	7960 (R_{int} = 0.0501)	10245 (R_{int} = 0.0653)	11790 (R_{int} = 0.0464)	11591 (R_{int} = 0.0519)
Independent reflections [$I > 2\sigma(I)$]	6127	7547	8543	8300
Goodness-of fit on F^2	1.008	1.040	1.022	0.997
R_1[a], wR_2[b] [$I > 2\ \sigma(I)$]	0.0309, 0.0671	0.0415, 0.0953	0.0426, 0.1027	0.0447, 0.1053
R_1[a], wR_2[b] [all data]	0.0492, 0.0731	0.0690, 0.1059	0.0702, 0.1156	0.0724, 0.1176
Largest diff. peak/hole [e·Å^{-3}]	0.611, –0.554	2.015, –0.823	2.238, –1.527	3.172, –1.127

[a] $R = \Sigma||F_o| - |F_c||/\Sigma|F_o|$. [b] $wR_2 = [\Sigma\omega(F_o^2 - F_c^2)^2]/[\Sigma(F_o^2)^2]]^{0.5}$.

 © 2005 Wiley-VCH Verlag GmbH & Co. KGaA, Weinheim

refinement on F^2 in SHELXL-97[12b] with anisotropic displacement for non-H atoms, hydrogen atoms placed in idealized positions and refined isotropically according to the riding model. The H atoms at the heavy atoms were found as residue electron densities and could be freely refined except for the H atom at the As atom in **2b**, which was placed in an idealized position. The use of restraints was necessary for the refinement of **3b** to fix the Cl atoms at the solvent molecule in appropriate distances. CCDC-249065 to -249068 (**2a**,**b** and **3a**,**b**) contain the supplementary crystallographic data for this paper. These data can be obtained free of charge from The Cambridge Crystallographic Data Centre via www.ccdc.cam.ac.uk/data_request/cif.

Acknowledgments

This work was comprehensively supported by the Deutsche Forschungsgemeinschaft and the Fonds der Chemischen Industrie. The authors thank the Degussa and Umicore AG for the gift of precious metal compounds.

[1] For a review see: R. T. Paine, H. Nöth, *Chem. Rev.* **1995**, *95*, 343–379.
[2] Compare: a) M. S. Lube, R. L. Wells, P. S. White, *Main Group Met. Chem.* **1996**, *13*, 733–741; b) M. A. Mardones, A. H. Cowley, L. Contreras, R. A. Jones, C. J. Carrano, *J. Organomet. Chem.* **1993**, *455*, C1–C2; c) M. A. Petrie, M. M. Olmstead, H. Hope, R. A. Bartlett, P. P. Power, *J. Am. Chem. Soc.* **1993**, *115*, 3221–3226; d) R. Goetze, H. Nöth, *Z. Naturforsch.* **1975**, *30B*, 875–882.
[3] U. Vogel, P. Hoemensch, K.-C. Schwan, A. Y. Timoshkin, M. Scheer, *Chem. Eur. J.* **2003**, *9*, 515–519.
[4] a) J. Powell, M. R. Gregg, J. F. Sawyer, *J. Chem. Soc., Chem. Commun.* **1984**, 1149–1150; b) J. Powell, M. R. Gregg, J. F. Sawyer, *Inorg. Chem.* **1989**, *28*, 4451–4460.
[5] U. Vogel, M. Scheer, *Z. Anorg. Allg. Chem.* **2001**, *627*, 1593–1598.
[6] J. Schwald, P. Peringer, *J. Organomet. Chem.* **1987**, *323*, C51–C53.
[7] C. A. Jaska, H. Dorn, A. J. Lough, I. Manners, *Chem. Eur. J.* **2003**, *9*, 271–281.
[8] P. E. Garrou, *Chem. Rev.* **1981**, *81*, 229–266.
[9] E. D. Morrison, A. D. Harley, M. A. Marcelli, G. L. Geoffroy, A. L. Rheingold, W. C. Fultz, *Organometallics* **1984**, *3*, 1407–1413.
[10] For recent reviews see: a) H. Braunschweig, M. Colling, *Coord. Chem. Rev.* **2001**, *223*, 1–51; b) H. Braunschweig, *Angew. Chem.* **1998**, *110*, 1882–1898; *Angew. Chem. Int. Ed. Engl.* **1998**, *37*, 1786–1801; c) G. J. Irvine, M. J. G. Lesley, T. B. Marder, N. C. Norman, C. R. Rice, E. G. Robins, W. R: Roper, G. R. Whittell, L. J. Wright, *Chem. Rev.* **1998**, *98*, 2685–2722.
[11] U. Nagel, *Chem. Ber.* **1982**, *115*, 1998–1999.
[12] a) G. M. Sheldrick, *SHELXS-97*, University of Göttingen, **1997**; b) G. M. Sheldrick, *SHELXL-97*, University of Göttingen, **1997**.

Received: October 7, 2004

 © 2005 Wiley-VCH Verlag GmbH & Co. KGaA, Weinheim

Cobalt(II) Complexes with Substituted Salen-Type Ligands and Their Dioxygen Affinity in *N*,*N*-Dimethylformamide at Various Temperatures

Andreas Huber,[a] Lutz Müller,[a] Horst Elias,*[a] Robert Klement,[b] and Marian Valko[c]

Keywords: Cobalt / Oxygen / Schiff bases / Substituent effects / Thermodynamics

Several unsymmetrically substituted salen-type cobalt(II) Schiff-base complexes CoL [H_2L = 1,6-bis(2-hydroxyphenyl)-3,3-dimethyl-2,5-diaza-1,5-hexadiene (**1**); 1,6-bis(2-hydroxyphenyl)-3,3-dimethyl-2,5-diaza-1,5-heptadiene (**2**); 1-(3-*tert*-butyl-2-hydroxy-5-methylphenyl)-6-(2-hydroxyphenyl)-3,3-dimethyl-2,5-diaza-1,5-heptadiene (**3**); 1-(2-hydroxyphenyl)-6-methyl-2,5-diaza-1,5-nonadien-8-one (**4**); 1-(3-*tert*-butyl-2-hydroxy-5-methylphenyl)-6-methyl-2,5-diaza-1,5-nonadien-8-one (**5**); 1-(2-hydroxyphenyl)-3,3,6-trimethyl-2,5-diaza-1,5-nonadien-8-one (**6**); 1-(3-*tert*-butyl-2-hydroxy-5-methylphenyl)-3,3,6-trimethyl-2,5-diaza-1,5-nonadien-8-one (**7**)] were prepared and characterized by their UV/Vis absorption spectra, magnetic moments, and oxidation potentials. Except for complex **4** (irreversible oxidation with $t_{½} \approx 3$ h), complexes **1**–**3** and **5**–**7** are remarkably resistant against irreversible auto-oxidation in air-saturated *N*,*N*-dimethylformamide (DMF) at ambient temperature. To characterize the Lewis acidity of the cobalt center in **1**–**7**, the equilibrium constant K_{py} was determined for monoadduct formation with pyridine (CoL + py ⇌ CoL·py). An O_2-sensitive optode was used to determine the Henry constant, K_H, for the system O_2/DMF in the temperature range 298–228 K. The formation of 1:1 adducts of complexes **1**–**7** with O_2 in DMF, as characterized by the equilibrium constant K_{O_2}, was followed spectrophotometrically in the temperature range 298–228 K. The parameters ΔH^o, ΔS^o, and K_{O_2} are reported. At 298 K, K_{O_2} ranges from 21.9 M^{-1} (**5**) to 155 M^{-1} (**7**). The overall spectroscopic information, including EPR spectra obtained with frozen solutions of **3** and **7** in O_2-saturated DMF, confirm that the 1:1 adducts CoL·O_2 are cobalt(III) superoxo compounds. The symmetrically substituted salen complex **8** [H_2L = 1,6-bis(3-*tert*-butyl-2-hydroxy-5-methylphenyl)-3,3,4,4-tetramethyl-2,5-diaza-1,5-hexadiene in **8**] is shown to catalyze the oxidation of triphenylphosphane and 2,6-di-*tert*-butylphenol by O_2 in DMF at ambient temperature. The correlation of the data obtained for K_{O_2}, K_{py}, and the oxidation potential $E_{½}$ is discussed.

(© Wiley-VCH Verlag GmbH & Co. KGaA, 69451 Weinheim, Germany, 2005)

Introduction

In 1938 Tsumakis discovered the reversible binding of dioxygen to the cobalt(II) complex Co(salen).[1] Since then there has been a continuous and increasing interest in this complex and its derivatives as well as in other dioxygen-binding Schiff-base cobalt(II) complexes such as Co(acacen) and Cobaloxime. This interest arises from the potential application of these compounds as solids for the storage of dioxygen and for dioxygen-separation processes.[2,3] Furthermore, solutions of these complexes have been widely studied as dioxygen carriers and as catalysts for oxidation processes under mild conditions.[2] Martell and coworkers have prepared a number of derivatives of Co(salen) by introducing substituents in the 3- and/or 5-position of the aromatic rings of the ligand salen and by modifying the CH_2-CH_2 bridge connecting the two nitrogen donor atoms.[3,4] They investigated the formation of dioxygen adducts in systems CoL/O_2/B (CoL = salen-type Co^{II} complex; B = base) in solution at various temperatures and reported the corresponding equilibrium constants K_{O_2} and how they are affected by the nature of the base B coordinated to the cobalt center in the axial position. Busch and coworkers have prepared and studied O_2-binding cobalt(II) complexes with pentadentate salen-type ligands offering a (O∩N)∩N∩(N∩O) set of donor atoms, with the central N atom occupying an axial position at the cobalt center as an internal base.[5]

Co(salen) and Co(acacen) can be classified as four-coordinate chelate Co^{II} complexes with an N_2O_2 set of donor atoms. As shown by the cobaloximes[6] and by Co^{II} complexes with N_4 macrocyclic ligands[7] or with aliphatic N_x and N/O chelate ligands,[8,9] an affinity of the cobalt center for dioxygen is also generated by planar N_4 donor systems. For all the O_2-binding complexes CoL, where L is an N_2O_2- or N_4-type ligand, it is generally found that the interaction

[a] Eduard Zintl-Institut für Anorganische und Physikalische Chemie, Technische Universität Darmstadt,
Petersenstrasse 18, 64287 Darmstadt, Germany
Fax: +49-6151-166040
E-mail: elias@ac.chemie.tu-darmstadt.de
[b] VILA Center, University of Alexander Dubček Trenčín, Študentská 2, 911 50 Trenčín, Slovakia
[c] Faculty of Chemical and Food Technology, Slovak Technical University,
812 37 Bratislava, Slovakia

Supporting information for this article is available on the WWW under http://www.eurjic.org or from the author.

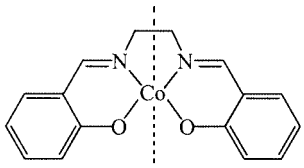

Co(salen) ("Salcomine")

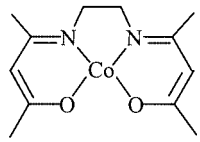

Co(acacen)

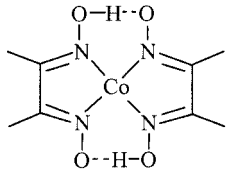

Cobaloxime

of the cobalt with dioxygen is more or less favored by an additional base B (such as pyridine, for example) coordinated in one of the axial positions to form five-coordinate CoL·B.

The ligand salen can be easily modified by the introduction of electron-releasing or electron-withdrawing substituents and sterically demanding groups. The electronic and steric properties of a given set of substituents on modified ligands salen* can drastically effect the electron density at the cobalt in Co(salen*) as well as the accessibility of the axial positions. An aerated solution of Co(salen), for example, is irreversibly auto-oxidized within hours. We found that, in contrast to Co(salen), an aerated solution of the cobalt salen complex **8**, which contains a number of methyl and *tert*-butyl groups (see Scheme 1), is stable for weeks. Nevertheless, complex **8** is a weak catalyst for oxidation reactions with O_2 (see Results and Discussion section).

The ligand salen is "symmetric" in the sense that it consists of two identical halves, as indicated by the dashed line in the structural formula of Co(salen) shown above. This sort of ligand symmetry is also typical for most of the derivatives of Co(salen) reported so far.[3,4] To provide a finer tool for property tuning, we decided to prepare a number of salen-type Co^{II} complexes **1**–**7** with "unsymmetric" ligands and to determine the corresponding equilibrium constants K_{O_2}. Compared to Co(salen), the two halves of the ligands in complexes **1**–**7** are no longer identical.

The present contribution summarizes the results obtained by investigating the effect of the various ligands in complexes **1**–**7** on the dioxygen affinity of the complexes in DMF at various temperatures, as characterized by equilibrium constants K_{O_2} according to Equation (1), on the Lewis acidity of the cobalt center, as characterized by equilibrium constants K_{py} according to Equation (2), and on the oxidation potential, $E_{1/2}$, of complexes **1**–**7**, according to the reaction $Co^{II}L \rightleftharpoons Co^{III}L^+ + e^-$.

$$CoL + O_2 \overset{K_{O_2}}{\rightleftharpoons} CoL{\cdot}O_2 \quad (1)$$

$$CoL + py \overset{K_{py}}{\rightleftharpoons} CoL{\cdot}py \quad (2)$$

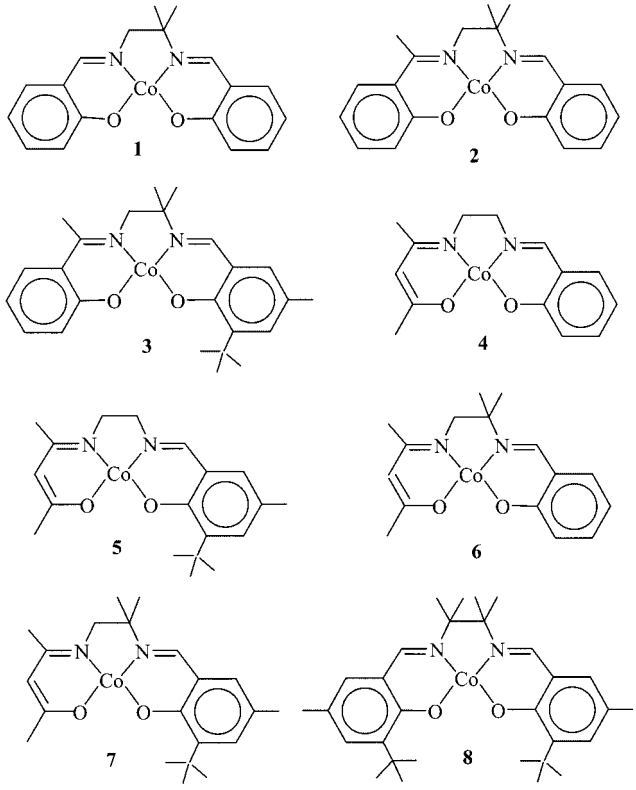

Scheme 1. Structural formulae of the cobalt(II) complexes.

Results and Discussion

Preparation and Properties of the Complexes

Compared to salen and "symmetrically" substituted salen ligands such as the one in complex **8**, the synthesis of "unsymmetric" salen-type ligands is not at all simple. The ligands for the preparation of complexes **2**–**7** were obtained according to an efficient two-step procedure developed earlier.[10] On the basis of the known structure of complexes **3**[10] and **8**[11] one can extrapolate that, in all of the complexes **1**–**8**, the CoN_2O_2 core is nearly planar, with the plane of at least one of the two phenyl rings in **1**–**3** being almost co-planar with the CoN_2O_2 core. The UV/Vis spectra of complexes **1**–**8** are characterized by two intense charge-transfer (CT) bands at approximately 360 nm and 420 nm and by a weak d-d absorption (shoulder) at approximately 500 nm (see Table S1). The absorptivities of complexes **4**–**7** are smaller due to reduced conjugation. The magnetic moments of complexes **1**–**8** at 298 K were found to lie in the range μ_{exp} = 2.31–2.60 μ_B,[11,12] which is typically observed for low-spin d^7 systems of the present type.[13]

Auto-Oxidation of the Complexes in Solution

In air-saturated DMF solution at ambient temperature, the stability of complexes **1**–**8** towards irreversible auto-oxidation can be described by the following order: **8** > **1**–**3** > **5**–**7** > **4**. More specifically, a solution of complex **8** is stable for weeks and the solutions of **1**–**3** are stable for several

 © 2005 Wiley-VCH Verlag GmbH & Co. KGaA, Weinheim

days, whereas those of complexes **5**–**7** change slowly within 24 h (<10%). Complex **4**, the least stable one, undergoes irreversible oxidative decomposition with a $t_{½}$ of about 3 h, which is close to the auto-oxidation rate of the parent complex Co(salen) in air-saturated DMF solution in the absence of bases such as pyridine.[14] One should note, however, that at –40 °C, adduct formation with dioxygen according to Equation (1) was shown to be reversible for all of the complexes **1**–**8**.

Potentials for the Oxidation Step $Co^{II} \rightarrow Co^{III}$

The data obtained for the potential $E_{½}$ in acetonitrile, which describes the quasi-reversible step $Co^{II} \rightarrow Co^{III}$, range from 183 to 274 mV (Table 1). The potential reported for unsubstituted Co(salen) in acetonitrile (258 mV)[15a,15b] lies within this range.

Table 1. Oxidation potentials, $E_{½}$, for complexes **1**–**8** in acetonitrile at 293 K.[a]

Complex	$E_{½}$ [mV][b]	Complex	$E_{½}$ [mV][b]
1	263	**6**	234
2	210	**7**	223
3	183	**8**	274
4	196	Co(salen)	258[c]
5	193	Co(salen)[d]	–33[e]

[a] $E_{½}$ referenced to SCE. [b] The peak separation, $E_p^c - E_p^a$, was in the range 82–144 mV. [c] The value presented is based on $E_{½}$ = –195 mV, as reported for acetonitrile and referenced to Fc/Fc^+ (Fc = ferrocene);[15a] conversion to SCE was achieved according to: $E(SCE) = E(Fc/Fc^+) + 453$ mV.[15b] [d] Solvent DMF. [e] The value presented is based on $E_{½}$ = –466 mV, as reported for DMF and referenced to Fc/Fc^+ (Fc = ferrocene);[15c] conversion to SCE was achieved according to: $E(SCE) = E(Fc/Fc^+) + 433$ mV.[15b]

The qualitative order of stability towards auto-oxidation (**8** > **1**–**3** > **5**–**7** > **4**), as obtained by spectrophotometric monitoring, does not correlate with the parameter $E_{½}$. The most positive oxidation potential (274 mV) is indeed found for the most stable complex **8**, but within the group of complexes **1**–**3**, which show the same sort of stability, the potential drops by 80 mV from 263 mV (**1**) to 183 mV (**3**). Moreover, within the group of complexes **4**–**7** complex **5** is found to be as stable as complexes **6** and **7**, but the potential of **5** (193 mV) is as low as **4** (196 mV), which is the least stable complex. As pointed out above, the instability of **4** resembles that of Co(salen), although the potentials differ by 64 mV.

The lack of a correlation between $E_{½}$ and the observed complex stability is not unexpected. The parameter $E_{½}$ is a measure of the energy needed to abstract an electron from the cobalt. The observed stability towards irreversible auto-oxidation, however, reflects a multi-step process that is probably initiated by docking of the O_2 molecule at the cobalt, followed by electron transfer from the cobalt to O_2, and followed by a further series of reactions that lead finally to the destruction of the complex. All of these steps can be subject to electronic and steric substituent effects in a specific way.

Adduct Formation with Pyridine

The cobalt center in complexes **1**–**8** is weakly Lewis acidic. As an example, Figure 1 shows the spectral changes associated with the stepwise titration of complex **3** with pyridine in toluene. The (A,[py]) data follow the relationship in Equation (6), which describes monoadduct formation according to Equation (2). The occurrence of a sharp isosbestic point indicates that there is no additional diadduct formation. The data obtained for the equilibrium constant K_{py} range from 6.3 M^{-1} for **1** to 0.3 M^{-1} for **7** (Table 2).

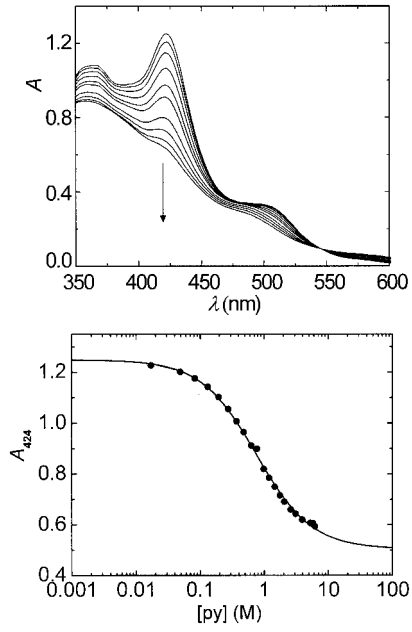

Figure 1. Spectral changes and titration curve describing the stepwise titration of complex **3** with pyridine in toluene at 298 K [solid line obtained by fitting Equation (6) to the (A_{424},[py]) data].

Table 2. Equilibrium constants, K_{py}, for adduct formation of complexes **1**–**8** with pyridine in toluene according to Equation (2) at 298 K.

Complex	K_{py} [M^{-1}]	Complex	K_{py} [M^{-1}]
1	6.3 ± 0.7	**5**	0.50 ± 0.01
2	3.0 ± 0.3	**6**	0.55 ± 0.10
3	1.3 ± 0.1	**7**	0.32 ± 0.01
4	1.3 ± 0.2	**8**	0.47 ± 0.01; 0.06 ± 0.01[a]

[a] The solvent was DMF instead of toluene.

For comparison of the K_{py} data, complexes **1**–**8** should be divided into two groups: in group **A** (complexes **1**–**3** and **8**), the ligand skeleton is that of salen, whereas in group **B** (complexes **4**–**7**) one half of the ligand is based on acetylacetone instead of salicylaldehyde. The fact that $K_{py}(\mathbf{1}) > K_{py}(\mathbf{6})$ reflects clearly that, independent of additional substituent effects, the acetylacetone-containing ligand system of complexes **4**–**7** is a stronger electron donor than that of salen.

In more detail, the analysis of the K_{py} data leads to the following conclusions: (i) the order observed for group **A** complexes, $K_{py}(\mathbf{1}) > K_{py}(\mathbf{2}) > K_{py}(\mathbf{3}) > K_{py}(\mathbf{8})$, reflects the combined electronic and steric effects of an increasing

 © 2005 Wiley-VCH Verlag GmbH & Co. KGaA, Weinheim

number of methyl and *tert*-butyl groups, respectively, which increase the electron density and decrease the accessibility of the cobalt center; (ii) the order observed for group **B** complexes, $K_{py}(\mathbf{4}) > K_{py}(\mathbf{5}) \approx K_{py}(\mathbf{6}) > K_{py}(\mathbf{7})$, is due to the same sort of effects; (iii) the finding that $K_{py}(\mathbf{4}) > K_{py}(\mathbf{6})$ and $K_{py}(\mathbf{5}) > K_{py}(\mathbf{7})$ demonstrates the (probable) steric effect of two methyl groups on the CH_2-$C(CH_3)_2$ bridge of **6** and **7**, which reduce the accessibility of the cobalt; and (iv) the finding that $K_{py}(\mathbf{2}) > K_{py}(\mathbf{3})$, $K_{py}(\mathbf{4}) > K_{py}(\mathbf{5})$, and $K_{py}(\mathbf{6}) > K_{py}(\mathbf{7})$ can be ascribed to the combined electronic and steric substituent effects of the methyl group and *tert*-butyl group, respectively, in the *para*- and *ortho*-position to the phenolic oxygen.

For complex **8**, the addition of pyridine was measured in toluene (K_{py} = 0.47 M^{-1}) as well as in DMF (K_{py} = 0.06 M^{-1}). The apparently lower Lewis acidity in DMF confirms that, in DMF, complexes CoL form CoL(DMF) adducts with the solvent. The base pyridine has to compete for axial coordination according to Equation (3).

$$CoL(DMF) + py \rightleftharpoons CoL(py) + DMF \quad (3)$$

Henry Constant, K_H, for the System O_2/DMF at Various Temperatures

The determination of the temperature dependence of the equilibrium constant K_{O_2} for adduct formation according to Equation (1) requires a knowledge of the Henry constant, K_H, for the temperature range studied. An O_2-sensitive optode was used to determine $[O_2]$, the equilibrium concentration of dioxygen in O_2-saturated DMF at various temperatures (see Experimental Section and Figure S1, Supporting Information). The data obtained for K_H are presented in Table 3.

Table 3. Henry constant, K_H, for the system O_2/*N*,*N*-dimethylformamide in the temperature range 298–223 K.

T [K]	$K_H \times 10^6$ [M Torr^{-1}][a]	T [K]	$K_H \times 10^6$ [M Torr^{-1}][a]
298	6.4	243	7.4
283	6.6	238	7.5
273	6.8	233	7.6
263	7.0	228	7.7
253	7.2		

[a] The error limits for K_H are approximately ±10%.

Equilibrium Constant, K_{O_2}, for Adduct Formation with Dioxygen at Various Temperatures

The Henry constant, K_H, for the system O_2/DMF increases with decreasing temperature (see Table 3) and so does the equilibrium concentration of dioxygen in DMF. As a consequence, adduct formation according to Equation (1) and, correspondingly, the UV/Vis spectra of complexes **1**–**7** in O_2-saturated DMF are shifted towards the dioxygen adducts CoL·O_2. As an example, Figure 2 shows a selection of spectra obtained for the system **1**/O_2/DMF at various temperatures. There are a number of sharp isosbestic points indicating that, in addition to the formation of the 1:1 adduct, there is no further formation of a 1:2 adduct. In line with this, the absorbance data at 406 nm can be well fitted with Equation (8) (see Figure 2, bottom), as derived for monoadduct formation. The fitting procedure finally leads to data for ΔH^o, ΔS^o, and K_{O_2} for complexes **1**–**3** and **5**–**7** (Table 4). The results for complex **4** are missing due to the limited stability of **4** against auto-oxidation.[16]

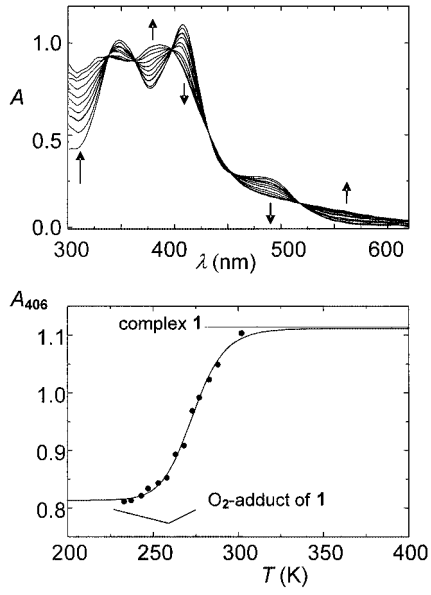

Figure 2. UV/Vis spectra of complex **1** in O_2-saturated *N*,*N*-dimethylformamide at various temperatures (upper diagram; the arrows indicate spectral changes associated with decreasing temperature) and the dependence of the absorbance at 406 nm on the temperature in the range 298–228 K [lower diagram; the fitting curve was obtained by fitting Equation (8) to the (A_{406},T) data].

To have a different experimental method for control, complex **3** in Ar-saturated DMF was titrated with dioxygen at 288 K. The observed spectral changes led to (A_{412},$[O_2]$) data (A_{412} = absorbance at 412 nm) that could be satisfyingly fitted with Equation (9) (see Figure S2, Supporting Information). The equilibrium constant K_{O_2} = 96 ± 9 M^{-1}, as obtained at 15 °C by this titration method (see Table 4), agrees within the limits of error with K_{O_2} = 130 ± 25 M^{-1}, as calculated for 15 °C from the data obtained at various temperatures.

In O_2-saturated DMF, the UV/Vis spectra of complexes **1**–**7** show absorption bands at about 340, 380, and 550 nm (shoulder), even at ambient temperature. These bands can be assigned to M→L charge-transfer processes in the adducts CoL·O_2 and superoxo species $CoL^+ \cdot O_2^-$, respectively (see also EPR data below).[19] In the case of complex **8**, spectral changes associated with the formation of the O_2 adduct were not observed at ambient temperature, but clearly at 223 K.

It follows from Table 4 that complexes **1**–**3** and **5**–**7** do not differ drastically in their dioxygen affinity. At 25 °C, K_{O_2} ranges from 21.9 M^{-1} for **5** to 155 M^{-1} for **7**. The thermo-

 © 2005 Wiley-VCH Verlag GmbH & Co. KGaA, Weinheim

Table 4. Summary of thermodynamic data describing the addition of dioxygen to complexes **1**–**7**, according to Equation (1), in *N*,*N*-dimethylformamide and selected data for 1:1 adducts of cobalt(II) complexes with dioxygen.

Complex	Solvent/base	ΔH° [kJ mol^{-1}]	ΔS° [J K^{-1} mol^{-1}]	K_{O_2} [M^{-1}] at 298 K	$10^4 \times K_{O_2}$ [Torr^{-1}][a] at 298 K	Ref.
1	DMF/–	–65 ± 7	–191 ± 20	24 ± 2	1.56	this work
2	DMF/–	–58 ± 6	–164 ± 22	35 ± 5	2.22	this work
3	DMF/–	–49 ± 5	–131 ± 24	65 ± 12	4.17	this work
3	DMF/–			130 ± 25 (at 15 °C)		this work
3	DMF/–			96 ± 9[b] (at 15 °C)		this work
4	DMF/–	_[c]	_[c]	_[c]	_[c]	this work
5	DMF/–	–51 ± 8	–147 ± 23	22 ± 3	1.40	this work
6	DMF/–	–58 ± 10	–163 ± 10	50 ± 13	3.22	this work
7	DMF/–	–30 ± 5	–58 ± 13	155 ± 33	9.92	this work
Co(salen)	DMSO[d]/–	–67	–281		20[e]	[17]
Co(saltmen)[f]	diglyme[g]/4-Mepy[h]	–25	–168		1.58	[4]
Co(salophen)[i]	diglyme/4-Mepy	–43.2	–197		18.2	[4]
Co(α-CH_3-salen)[j]	diglyme/4-Mepy	–56.1	–230		63.1[k]	[4]
Co(salMeDPT)[l]	acetone/–	–59	–285		0.33	[5]
Co(acacen)	toluene/pyridine	–72.5	–305		5.74[m]	[18]

[a] Calculated according to $K_{O_2}(\text{Torr}^{-1}) = K_{O_2}(\text{M}^{-1}) \times K_H$ (K_H = Henry constant). [b] As determined by stepwise titration with O_2. [c] Due to auto-oxidation of complex **4** at $T \geq 293$ K, the spectroscopic data obtained were not safe enough to determine to K_{O_2} reliably. [d] Dimethyl sulfoxide. [e] Extrapolated from 20 °C to 25 °C with $\Delta H^\circ = -16$ kcal mol^{-1}, taken from ref.[17] [f] The ligand saltmen carries a tetra-methylated $C(CH_3)_2$-$C(CH_3)_2$ bridge instead of the CH_2-CH_2 bridge in Co(salen). [g] Bis(2-methoxyethyl)ether. [h] 4-Methylpyridine. [i] The ligand salophen is the salen analogue resulting from the condensation reaction between salicylaldehyde and 1,2-diaminobenzene instead of 1,2-diaminoethane. [j] The ligand α-CH_3-salen is a salen analogue resulting from the condensation reaction between 1,2-diaminoethane and 2-hydroxyacetophenone instead of salicylaldehyde. [k] Extrapolated from 10 °C to 25 °C with $\Delta H^\circ = -13.4$ kcal mol^{-1}, taken from ref.[4] [l] The ligand salMeDPT is a pentadentate salen derivative resulting from the condensation reaction between salicylaldehyde and bis(2-aminoethyl)methylamine instead of 1,2-diaminoethane. [m] Extrapolated from 0 °C to 25 °C with $\Delta H^\circ = -17.3$ kcal mol^{-1}, taken from ref.[18]

dynamic data indicate that the driving force for dioxygen complex formation is the favorable enthalpy of reaction, corresponding to metal–dioxygen bond formation and, as a consequence, a strengthening of the coordinate bonds between the metal and the ligand donor atoms. As characteristically observed for all oxygenation processes,[4] the entropies of oxygenation are seen to be negative, due to the loss of the translational entropy of the O_2 molecule and the increase in ligand rigidity.

The general expectation is that an increase of the electron density on the cobalt, as introduced by substituents on the ligand, should favor the reaction described by Equation (1) and increase K_{O_2}. Since the methyl and *tert*-butyl groups on the salicylaldehyde unit and the methyl groups on the diamine bridge in complexes **1**–**3** and **5**–**7** can have steric as well as electronic effects, there is no simple prediction concerning their effect on the electron density on the cobalt. The equilibrium constant K_{py}, however, which describes adduct formation with pyridine (see Table 2), is a useful experimental measure of both the electron density on the cobalt and its accessibility. K_{py} should therefore correlate inversely with K_{O_2}. For group **A** complexes **1**–**3**, this correlation is indeed observed with $K_{py}(\mathbf{1}) > K_{py}(\mathbf{2}) > K_{py}(\mathbf{3})$ vs. $K_{O_2}(\mathbf{1}) < K_{O_2}(\mathbf{2}) < K_{O_2}(\mathbf{3})$. In the case of group **B** complexes **5**–**7**, the order $K_{O_2}(\mathbf{5}) < K_{O_2}(\mathbf{6}) < K_{O_2}(\mathbf{7})$ is less well reflected by the finding $K_{py}(\mathbf{5}) \approx K_{py}(\mathbf{6}) > K_{py}(\mathbf{7})$. The inverse correlation between K_{py} and K_{O_2} confirms convincingly that the reaction of the cobalt(II) complexes CoL with O_2 according to Equation (1) is not at all a simple nucleophilic addition reaction. Obviously, electron abstraction and formation of the species $Co^{III}L^+$ is the driving force, with the latter following the electron density on the cobalt, as determined by the ligand L.[20] The order in the oxidation potential, $E_{1/2}(\mathbf{1}) > E_{1/2}(\mathbf{2}) > E_{1/2}(\mathbf{3})$ (Table 1), is paralleled by the reverse order in dioxygen affinity, $K_{O_2}(\mathbf{1}) < K_{O_2}(\mathbf{2}) < K_{O_2}(\mathbf{3})$. This means that the more easily the cobalt(II) is oxidized, the stronger is the interaction with O_2. The corresponding data obtained for group **B** complexes **5**–**7**, however, are not in line with this sort of correlation.

For comparison, Table 4 lists data for pressure-based equilibrium constants $K_{O_2}(\text{Torr}^{-1})$, as reported for a number of "symmetric" salen-type cobalt(II) complexes that form 1:1 adducts with dioxygen. Neglecting possible solvent effects, one learns that the range of dioxygen affinities obtained for complexes **1**–**3** and **5**–**7** [$K_{O_2} \approx (0.1–1) \times 10^{-3}$ Torr^{-1}] covers the K_{O_2} data reported for Co(saltmen),[21] Co(acacen), and Co(salMeDPT).[21] The range of affinities reported for Co(salophen),[21] Co(salen), and Co(α-CH_3-salen)[21] is approximately one order of magnitude higher [$K_{O_2} \approx (2–6) \times 10^{-3}$ Torr^{-1}], but, as a rule, increased affinity means reduced resistance against oxidative attack.

To summarize: (i) compared to Co(salen), the "unsymmetric" salen-type ligands of the present study lead to cobalt(II) complexes with slightly reduced dioxygen affinities, and (ii) the loss in dioxygen affinity is paralleled by an increase in resistance towards irreversible auto-oxidation. Depending on the type of substitution (substituents on the CH_2-CH_2 bridge and/or on the phenyl rings), complexes **1**–**3** and **5**–**7** are O_2-active cobalt(II) compounds with interesting intermediate properties concerning sufficient dioxygen affinity (and possible catalytic activity) on the one hand and

 © 2005 Wiley-VCH Verlag GmbH & Co. KGaA, Weinheim

limited susceptibility to auto-oxidation on the other hand. As an example, in the case of complex **3** the binding constant for O_2 (in DMF) is five times smaller than in the case of Co(salen) (in DMSO). Compared to Co(salen), complex **3** is, however, far more auto-oxidation resistant (at ambient temperature, air-saturated solutions of **3** in DMF are stable for several days). The affinity constant K_{O_2} = 65 M^{-1} for **3** means that, in an O_2-saturated solution of **3** in DMF at 25 °C, not less than 24% of the complex is present in the form of the O_2 adduct.

EPR Spectra of the Dioxygen Adducts of Complexes 3 and 7 in Frozen DMF

We reported earlier that in frozen O_2-saturated solution the O_2 adducts of cobalt(II) complexes with "symmetrically" substituted salen ligands show EPR spectra with well-resolved hyperfine structures.[22] As confirmed by the investigation of complexes **3** and **7**, the "unsymmetrically" substituted cobalt(II) complexes of the present study behave analogously. As an example, Figure 3 shows the experimental and simulated ESR spectrum of the 1:1 dioxygen adduct of complex **3** in O_2-saturated frozen DMF. The EPR data, as obtained by computer simulation, are summarized in Table 5.

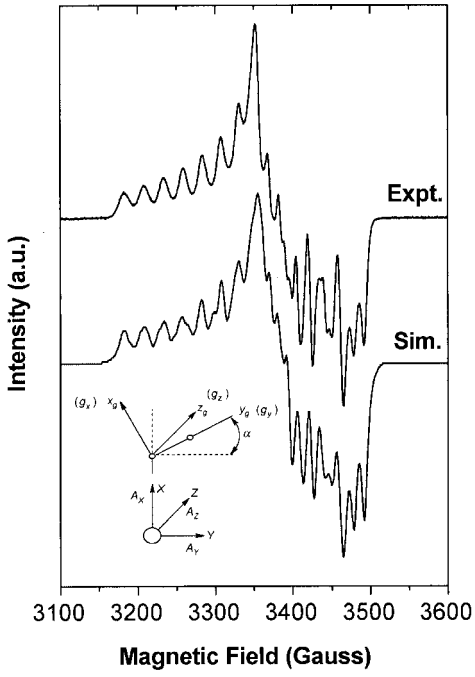

Figure 3. Experimental and simulated X-band ESR spectrum of the dioxygen adduct of complex **3** in O_2-saturated frozen DMF [inset: coordinate system for Zeeman and hyperfine terms of ESR spectra of CoL·O_2 adducts. The principal g axes are x_g, y_g, and z_g, and the principal A axes are X, Y and Z. According to the Smith and Pilbrow notation:[24a] $X(z)$, $Y(y)$ and $Z(x)$, $A_x(Z) = A_Z$, $A_y(Y) = A_Y$, $A_z(X) = A_X$].

As documented earlier, the unpaired electron density in the 1:1 adducts resides mostly on the O_2 moiety.[22] The g-values lie close to the free-electron value and the hyperfine structure arising from the cobalt nucleus (I^{Co} = 7/2) is still present but, compared to CoL Schiff-base complexes in the absence of dioxygen, is strongly reduced in magnitude. The oxygenation of complexes **3** and **7** was found to be complete and the results obtained are in agreement with the general experience that the stability of such 1:1 adducts is enhanced by additional coordination of a base B (in the present system, B = DMF) in the sixth (axial) position *trans* to O_2.

The electronic structure of the O_2 adducts of cobalt(II) complexes is usually discussed in terms of a spin-pairing model, which interprets the cobalt hyperfine structure, observed in the EPR spectra of the adducts, as originating from a direct or indirect (spin-polarization) mechanism.[23] The rather low values of $A_y(Y)$ and $A_x(Z)$ (see Table 5) for the O_2 adducts of complexes **3** and **7** in DMF, which acts as a weak base, and the significant reduction in $A_y(Y)$ and $A_x(Z)$ for the dioxygen adduct of complex **3** in the presence of pyridine, which acts as a strong base, are most probably due to the peculiar balance between the direct and indirect (spin-polarization) contributions to the ^{59}Co hyperfine coupling constants.

In discussing the relationship between g-values and the electronic structure of the O_2 adducts of **3** and **7**, one has to consider the fact (see Table 5) that the g_x and g_z values are close to the free-electron value (2.0023), whereas the data for g_y (along O–O bond) are somewhat greater. This increase in g_y can be rationalized in terms of the energy separation of the dioxygen π*-orbitals.[23,24] According to Equation (4), the size of g_y is controlled by the oxygen spin-orbit coupling parameter, λ, and by the energy separation, Δ, between the π*-dioxygen orbitals. An increase in g_y corresponds to decreasing values of Δ. This points to a lower energy separation of the oxygen π*-orbitals in the O_2 adducts of the CoL(B) complexes, with B being the weak base DMF. The size of Δ could well be related to the strength of the Co–O_2 interaction.[25] An increase in Δ, due to a strong σ-bond interaction between the cobalt d_{z^2} and oxygen π*-orbital leads to an increased strength of the Co–O_2 bond as well. On the other hand, the increased values of g_y observed for the dioxygen adducts of complexes **3** and **7** in DMF (see Table 5) imply lower Δ values. This may in turn suggest a weaker Co–O_2 interaction of these complexes,

Table 5. Evaluated EPR spin-Hamiltonian parameters for the dioxygen adducts of complexes **3** and **7** in O_2-saturated DMF at 77 K.

Complex	g_x[a]	g_y	g_z	$-A_X^{Co}$[a,b]	$-A_Y^{Co}$	$-A_Z^{Co}$	α [°]
3	2.011	2.092	1.985	23	78	36	25
3[c]	2.009	2.079	1.986	26	59	27	26
7	2.009	2.093	1.987	25	86	29	28

[a] The principal axes of the g and A tensors are defined in Figure 3. [b] The hyperfine splitting constants are given in MHz (for conversion to cm^{-1}, divide values by 3×10^4). In the text, the principal components of the A tensor are denoted as follows: $A_x(Z) = A_Z$, $A_y(Y) = A_Y$, $A_z(X) = A_X$. [c] Solvent: DMF containing 5% (v/v) pyridine.

 © 2005 Wiley-VCH Verlag GmbH & Co. KGaA, Weinheim

compared to the O_2 adducts of complexes CoL(B) with a strong base such as pyridine.

$$g_y = 2.0023 + 2\left[\frac{\lambda^2}{\lambda^2 + \Delta^2}\right]^{1/2} \quad (4)$$

Complex 8 as O_2-Activating Catalyst

In O_2-saturated DMF, the symmetrically substituted salen complex **8** is remarkably resistant to irreversible auto-oxidation (see above). At ambient temperature, the UV/Vis spectrum of **8** in O_2-stripped DMF solution does not change upon addition of O_2. At –40 °C, however, reversible adduct formation of **8** with dioxygen according to Equation (1) is observed. This means that, compared to complexes **1**–**7**, the dioxygen affinity of **8** is small. Despite this comparatively limited interaction with dioxygen, complex **8** was found to be a weak catalyst for the O_2-oxidation of triphenylphosphane and 2,6-di-*tert*-butylphenol (DTBP). As shown in Table 6, at ambient temperature 35% of DTBP is oxidized to the corresponding quinone within 24 hours. In the case of PPh_3, 84% of this substrate is oxidized under the same conditions. Although the observed catalytic activity of **8** is very limited, it points to interesting catalytic properties to be expected for complexes **1**–**3** and **5**–**7**. From the point of practical application in catalysis, one is interested in O_2-activating cobalt(II) complexes with intermediate properties concerning the interplay between dioxygen affinity (corresponding to superoxo complex formation) and auto-oxidation rate. Complexes **1**–**3** and **5**–**7** can be suggested as promising candidates.

Table 6. Oxidation of triphenylphosphane (PPh_3) and 2,6-di-*tert*-butylphenol (DTBP) in O_2-saturated *N*,*N*-dimethylformamide according to Equation (10) in the presence of complex **8** as catalyst.

Substrate S	[S] [mM]	[**8**] [mM]	*T* [K]	*t*[a] [h]	Product distribution (%) substrate	oxid. substrate
DTBP	5	0.5	293	24	65	35[b]
PPh_3	10	1	295	5	92	8[c]
PPh_3	10	1	295	24	16	84[c]

[a] Reaction time. [b] 2,6-Di-*tert*-butyl-1,4-benzoquinone. [c] Ph_3PO.

Conclusions

Complexes **1**–**7** are unsymmetrically substituted cobalt(II) complexes of the Co(salen)-type. In solution, all of these complexes behave like Co(salen) in that they interact with dioxygen, according to Equation (1), to form monoadducts with O_2. Due to steric crowding of the ligands, the formation of dinuclear species, as observed for "normal" Co(salen), is obviously suppressed. The spectroscopic information obtained (UV/Vis and EPR) is in line with the interpretation that the monoadducts, $CoL{\cdot}O_2$, are cobalt(III) superoxo compounds.

The resistance against auto-oxidation is ligand-dependent. In air-saturated DMF at ambient temperature, complexes **1**–**3** are stable for several days, **5**–**7** change slowly within one day, and **4** undergoes oxidative decomposition within hours.

The dioxygen affinity of the complexes in DMF, as characterized by the equilibrium constant K_{O_2} for adduct formation with dioxygen, ranges from $K_{O_2} = 21.9\ M^{-1}$ for **5** to $K_{O_2} = 155\ M^{-1}$ for **7** at 298 K. The data obtained for K_{O_2} correlate inversely with the Lewis acidity of the cobalt center, as characterized by the equilibrium constant K_{py} for adduct formation with the base pyridine. As an example, the dioxygen affinity of $K_{O_2} = 65$ for complex **3** means that, in O_2-saturated DMF at 25 °C, not less than 24% of **3** is present in the form of the superoxo species. There is experimental evidence to suggest that the remarkably oxidation-resistant complexes **1**, **2** and **3** in particular are useful catalysts for the oxidation of organic substrates with dioxygen in homogeneous solution under mild conditions.

Experimental Section

Chemicals: The commercially available aldehydes, ketones, and amines needed for ligand synthesis and the salt $Co(AcO)_2{\cdot}4H_2O$ (reagent grade) were used without further purification. Reagent grade *N*,*N*-dimethylformamide (DMF), toluene, and acetonitrile used as solvents for spectrophotometric titrations and CV measurements were stored under Ar.

Ligands: The salen-type ligands used for the preparation of complexes **1**,[26] **3**,[10] and **8**[11] were synthesized according to the literature. The ligands for complexes **2** and **4**–**7** were obtained by a two-step procedure, as developed for the preparation of the "unsymmetric" ligand of complex **3**.[10] In the first step, the corresponding ketone (2′-hydroxyacetophenone or 2,4-pentanedione) was treated with the corresponding diamine (1,2-diamino-2-methylpropane or 1,2-diaminoethane) in a 1:1 ratio to form a tridentate mono Schiff base. In the second step, the mono Schiff base was finally turned into the tetradentate salen-type ligand H_2L by reaction with salicylaldehyde or 3-*tert*-butyl-5-methylsalicylaldehyde. More details concerning the application of this two-step procedure to the preparation of the ligands for complexes **2** and **4**–**7** can be found in the literature.[12]

Complexes: Complex **8** was prepared and characterized as described earlier.[11] To avoid oxidation, the preparation of complexes **1**–**7** according to Equation (5) was carried out under Ar.

$$H_2L + Co(AcO)_2 \rightleftharpoons CoL + 2\ AcOH \quad (5)$$

General Procedure: A solution of 2 mmol of $Co(AcO)_2{\cdot}4H_2O$ in 25 mL of ethanol was added dropwise to a warm solution of 2 mmol of the ligand H_2L in 20–30 mL of ethanol whilst stirring. The red solution was refluxed for 30 min. Upon cooling, the red or red-orange cobalt complex precipitated. Recrystallization was carried out from ethanol (yield: 60–95%).

2: $C_{19}H_{20}CoN_2O_2$ (367.31): calcd. C 62.13, H 5.49, N 7.63; found C 61.89, H 5.52, N 7.58.

 © 2005 Wiley-VCH Verlag GmbH & Co. KGaA, Weinheim

3: $C_{24}H_{30}CoN_2O_2$ (437.44): calcd. C 65.90, H 6.91, N 6.40; found C 65.82, H 7.09, N 6.44.

4: $C_{14}H_{16}CoN_2O_2$ (303.22): calcd. C 55.46, H 5.32, N 9.24; found C 55.06, H 5.34, N 9.04.

5: $C_{19}H_{26}CoN_2O_2$ (373.36): calcd. C 61.12, H 7.02, N 7.50; found C 61.07, H 7.26, N 7.48.

7: $C_{21}H_{30}CoN_2O_2$ (401.42): calcd. C 62.84, H 7.53, N 6.98; found C 62.87, H 7.62, N 7.00.

The identity of complexes **1** and **6** was based on the purity of the ligands applied (CHN, ^{1}H NMR) and on the spectroscopic properties of the complexes (IR, UV/Vis). The visible absorption data of complexes **1**–**8** are presented in Table S1.

Instrumentation: UV/Vis spectra: diode array spectrophotometer (HP, type 8451A). Cyclic voltammetry: CV setup as described earlier.[11] Determination of dioxygen dissolved in DMF: optode (= dioxygen sensor), based on fluorescence quenching.[27] EPR spectra: Bruker SRC 200 D spectrometer, operating at X-band, with variable-temperature unit. An Ar-filled glove box was used for the preparation of O_2-stripped solutions.

Stability of the Complexes in Solution: The stability of complexes **1**–**8** in solution in air-saturated DMF was followed by monitoring the change of the UV/Vis spectra with time at ambient temperature.

Determination of Equilibrium Constant K_{py}: The stepwise titration of freshly prepared solutions of complexes **1**–**8** in toluene (Ar-saturated) with pyridine (Ar-saturated) according to Equation (2) was followed spectrophotometrically at 298 K in the range λ = 350–600 nm. Least-squares fitting of Equation (6) to the (A,[py]) data led to the equilibrium constant K_{py} (A = absorbance).

$$A = (A_o + A_\infty K_{py}\,[py])/(1 + K_{py}\,[py]) \quad (6)$$

The parameters A_o and A_∞ refer to the absorbance of the complexes CoL and CoL·py, respectively, at the initial concentration of CoL, $[CoL]_o$.

Cyclic Voltammetry: The measurements were carried out in O_2-stripped (Ar) acetonitrile (0.1 M $[Bu_4N]ClO_4$) at 293 K with [complex] = 1 mM. The scan rate was 100 mV s^{-1}.

EPR Spectroscopy: Solutions of **3** and **7** in DMF (1 mM) were filled into cylindrical quartz tubes and then purged with O_2 or Ar at ambient temperature before cooling to 77 K. The reversibility of dioxygen binding was checked by warming up the oxygenated frozen solutions, purging with Ar, and repeating the low-temperature measurement.

Henry Constant, K_H, for the System O_2/DMF at Various Temperatures: An O_2-sensitive optode[27] was used to determine $[O_2]$ in O_2-saturated DMF in the temperature range 298–228 K at atmospheric pressure. Calibration of the optode was achieved by determining its signal at 228 K in O_2-saturated DMF ($[O_2]_{rel}$ = 100%) and O_2-stripped (Ar) DMF ($[O_2]_{rel}$ = 0%), respectively. As shown in Figure 1S, $[O_2]_{rel}$ increases linearly with T^{-1}. On the basis of $[O_2] = 4.8 \times 10^{-3}$ M, as reported for O_2-saturated DMF at 298 K,[28] the data shown in Figure S1 lead to Equation (7).

$$[O_2] = 1.42 \times 10^{-3} + 1.01 \cdot T^{-1}\ (M) \quad (7)$$

This equation gives the equilibrium concentration of dissolved dioxygen, $[O_2]$, for O_2-saturated DMF at any temperature in the range 298–228 K. The Henry constant, K_H, follows from $[O_2]$ according to $K_H = [O_2]/p_{O_2}$ (in the present system, $p_{O_2} = 760 - p_{DMF}$; p_{DMF} = vapor pressure of DMF in Torr units).

Determination of Equilibrium Constant K_{O_2} for Adduct Formation with Dioxygen at Various Temperatures: A reaction vessel containing 70 mL of the freshly prepared solution of the complex CoL in Ar-saturated DMF ([CoL] ≈ 10^{-4} M) was placed into a thermostat/cryostat for temperature control. The experimental setup allowed us to saturate the solution with either O_2 or Ar. Spectra of the solution (λ = 300–650 nm) were recorded with a specially designed quartz cell (1 cm path length), immersed in the solution. The cell was equipped with flexible quartz fiber cables for connection to a diode array spectrophotometer. For each CoL/O_2 system, spectra were recorded stepwise at 8–12 temperatures in the range T = 310–230 K. In the first step, the solution was thermostatted at a given temperature in the range 25–35 °C and equilibrated with O_2 for 5 min. After that, the first spectrum was recorded. In the next step, the temperature was lowered by approximately 10 °C and the procedure of thermostatting and equilibrating with O_2 for 5 min was repeated to take the second spectrum. To guarantee O_2-equilibration, there was a continuous flow of O_2 through the solution during all steps. Least-squares fitting of Equation (8) to the observed (A,T) data[29] led to the parameters $m = -\Delta H^o/R$, $b = \Delta S^o/R$, A_{CoL}, and A_{add}. The equilibrium constant K_{O_2} was calculated according to van't Hoff.

$$A = \{(A_{CoL} + A_{add}\,[O_2]\exp(mT^{-1} + b)\}/\{(1 + [O_2]\exp(mT^{-1} + b)\} \quad (8)$$

where A_{CoL} and A_{add} refer to the absorbance of the complex CoL and of its dioxygen adduct, CoL·O_2, respectively, at the initial concentration of CoL, $[CoL]_o$.

The reversibility of adduct formation according to Equation (1) was confirmed by repeatedly running the cycle Ar-saturation/O_2-saturation at a given temperature and recording the corresponding spectra. For a given complex CoL, these experiments led to identical spectra for the O_2-saturated solution and for the Ar-saturated solution.

Determination of Equilibrium Constant K_{O_2} by Titration with Dioxygen: In an alternative approach, K_{O_2} at 288 K was determined by stepwise titration of a freshly prepared solution of complex **3** in Ar-saturated DMF with O_2. The titration was carried out in a spherical reaction vessel equipped with an inlet and with a glass tube, the end of which was sealed with a quartz cell fitting into the cell holder of the spectrophotometer. In an Ar-operated glove box, the solution of CoL in Ar-saturated DMF was filled into the reaction vessel. After that, the inlet was sealed with a septum through which twenty portions of O_2 were successively added with a gastight syringe. After each addition, the system was equilibrated at 288 K and a spectrum was recorded. Least-squares fitting of Equation (9) to the observed (A,$[O_2]$) data led to the equilibrium constant K_{O_2}. The data for $[O_2]$ were obtained from the partial pressure of O_2, p_{O_2}, and the Henry constant, K_H, according to $[O_2] = K_H \cdot p_{O_2}$.

$$A = (A_{CoL} + A_{add}\,K_{O_2}\,[O_2])/(1 + K_{O_2}\,[O_2]) \quad (9)$$

Analytical Procedure for Monitoring the Catalytic O_2-Oxidation of Substrates: The oxidation of substrates S according to Equation (10), as catalyzed by **8**, was studied with S = triphenylphosphane and 2,6-di-*tert*-butylphenol. The formation of the oxidation products, $(Ph_3)PO$ and 2,6-di-*tert*-butyl-1,4-benzoquinone, was

 © 2005 Wiley-VCH Verlag GmbH & Co. KGaA, Weinheim

monitored by ^{31}P NMR and ^{1}H NMR spectroscopy, respectively.[14]

$$S + O_2 \xrightarrow{CoL} S\ (oxid.) \qquad (10)$$

Supporting Information Available (see also footnote on the first page of this article): Table S1, provides visible absorption data of complexes **1**–**8**. Figure S1 presents the calibration curve for the relative concentration of O_2 in DMF at various temperatures, and Figure S2 presents a plot of the (A_{412},[O_2]) data obtained by spectrophotometric monitoring of the titration of complex **3** with O_2 in DMF.

Acknowledgments

Sponsorship of this work by the Deutsche Forschungsgemeinschaft and Verband der Chemischen Industrie e.V. is gratefully acknowledged. The cooperation between Darmstadt and Bratislava was supported within the framework of the program "Scientific and Technological Cooperation", as established between Germany and the Slovak Republic. The EPR laboratory in the Faculty of Chemical and Food Technology, STU Bratislava, is funded by VEGA 1/2450/05.The authors thank Prof. E.-G. Jäger (Universität Jena) for valuable suggestions concerning the manuscript, Dr. M. Rudolph (Universität Jena) for the possibility to do some CV measurements in his laboratory, and Prof. Dr. B. Speiser (Universität Tübingen) for important information concerning the electrochemical data.

[1] T. Tsumakis, *Bull. Chem. Soc. Jpn.* **1938**, *13*, 252.
[2] a) A. E. Martell, D. T. Sawyer, *Oxygen Complexes and Oxygen Activation by Transition Metals*, Plenum Press, New York, **1988**; b) D. H. R. Barton, A. E. Martell, D. T. Sawyer, *The Activation of Dioxygen and Homogeneous Catalytic Oxidation*, Plenum Press, New York, **1993**; c) L. I. Simándi, in *Advances in Catalytic Activation of Dioxygen by Metal Complexes* (Eds.: L. I. Simándi, T. M. Simándi), Kluwer Academic Publishers **2003**, *26*, 265.
[3] D. Chen, A. E. Martell, *Inorg. Chem.* **1987**, *26*, 1026.
[4] D. Chen, A. E. Martell, Y. Sun, *Inorg. Chem.* **1989**, *28*, 2647.
[5] E. V. Rybak-Akimova, W. Otto, P. Deardorf, R. Roesner, D. H. Busch, *Inorg. Chem.* **1997**, *36*, 2746.
[6] L. I. Simándi, T. M. Simándi, Z. May, G. Besenyei, *Coord. Chem. Rev.* **2003**, *245*, 85.
[7] a) E.-G. Jäger, in *Chemistry at the Beginning of the Third Millenium* (Eds.: L. Fabbrizzi, A. Poggi), Springer-Verlag, Berlin Heidelberg New York, **2000**, p 103; b) E.-G. Jäger, J. Knaudt, K. Schuhmann, A. Guba, in *Peroxide Chemistry − Mechanistic and Preparative Aspects of Oxygen Transfer* (Ed.: W. Adam), Wiley-VCH, Weinheim, **2000**, p 249.
[8] a) C. Comuzzi, A. Melchior, P. Polese, R. Portanova, M. Tolazzi, *Eur. J. Inorg. Chem.* **2002**, 2194; b) C. Comuzzi, A. Melchior, P. Polese, R. Portanova, M. Tolazzi, *Eur. J. Inorg. Chem.* **2003**, 1948.
[9] a) C. Comuzzi, A. Melchior, P. Polese, R. Portanova, M. Tolazzi, *Inorg. Chem.* **2003**, *42*, 8214; b) · S. del Piero, A. Melchior, P. Polese, R. Portanova, M. Tolazzi, *Dalton Trans.* **2004**, *9*, 1358.
[10] A. Böttcher, H. Elias, B. Eisenmann, E. Hilms, A. Huber, R. Kniep, C. Röhr, M. Zehnder, M. Neuburger, J. Springborg, *Z. Naturforsch., Teil B* **1994**, *49*, 1089.
[11] A. Böttcher, H. Elias, E.-G. Jäger, H. Langfelderova, M. Mazur, L. Müller, H. Paulus, P. Pelikan, M. Rudolph, M. Valko, *Inorg. Chem.* **1993**, *32*, 4131.
[12] A. Huber, Dr.-Ing. Dissertation, Technische Hochschule Darmstadt, **1997.**
[13] N. N. Greenwood, A. Earnshaw, *Chemie der Elemente*, VCH, Weinheim, **1988**.
[14] L. Müller, Dr.-Ing. Dissertation, Technische Hochschule Darmstadt, **1996**.
[15] a) E. Eichhorn, Dr. rer. nat.-Dissertation, Universität Tübingen, **1995**; b) Private communication by Prof. Dr. Bernd Speiser, Institut für Organische Chemie, Universität Tübingen; c) A. Nishinaga, K. Tajima, B. Speiser, E. Eichhorn, A. Rieker, H. Ohya-Nishiguchi, K. Ishizu, *Chem. Lett.* **1991**, 1403.
[16] The spectral changes observed during the equilibration of complex **4** with O_2 were clearly affected by partial auto-oxidation of the complex, especially at temperatures above 293 K, and did not allow a reliable determination of K_{O_2}. One can estimate, though, that the dioxygen affinity of complex **4** corresponds to an equilibrium constant $K_{O_2} \geq 200\ M^{-1}$ at 298 K.
[17] E.-I. Ochiai, *Inorg. Nucl. Chem.* **1973**, *35*, 1727.
[18] M. J. Carter, D. P. Rilemma, F. Basolo, *J. Am. Chem. Soc.* **1974**, *96*, 393.
[19] a) A. B. P. Lever, H. B. Gray, *Acc. Chem. Res.* **1978**, *11*, 343; b) V. M. Miskowski, *Inorg. Chem.* **1975**, *14*, 2318; c) T. Freedman, G. Yoshida, T. M. Loehr, *J. Chem. Soc., Chem. Commun.* **1974**, 1016; d) Y. Sasaki, J. Fujita, K. Saito, *Bull. Chem. Soc. Jpn.* **1953**, *26*, 72.
[20] For a detailed thermodynamic description of the reaction described by Equation (1) one has to consider the following scheme: $Co^{II}L(DMF) \rightleftharpoons Co^{III}L(DMF)^+ + e^-$ (step 1), $O_2 + e^- \rightleftharpoons O_2^-$ (step 2), $Co^{III}L(DMF)^+ + O_2^- \rightleftharpoons \{Co^{III}L(DMF)^+\}\text{-}\{O_2^-\}$ (step 3). Obviously, the overall reaction, CoL(DMF) + $O_2 \rightleftharpoons$ CoL(DMF)·O_2, is governed by step 1.
[21] The nature of this modified salen ligand is described in Table 4.
[22] M. Valko, R. Klement, P. Pelikán, R. Boca, L. Dlhán, A. Böttcher, H. Elias, L. Müller, *J. Phys. Chem.* **1995**, *99*, 137.
[23] Both mechanisms, i.e. the direct delocalization of the unpaired spin density into the cobalt 3d orbitals (inducing positive spin density on the cobalt orbitals) as well as the indirect spin-polarization of the 3d orbitals (inducing negative spin density on the cobalt orbitals), contribute to the cobalt anisotropic hyperfine structure. Since the two mechanisms put spin of opposite sign in the d orbitals, the contribution to the ^{59}Co hyperfine splitting constant stemming from the direct mechanism may cancel the one from the indirect mechanism or vice versa. For more details see: a) T. D. Smith, J. R. Pilbrow, *Coord. Chem. Rev.* **1981**, *39*, 295; b) T. D. Smith, I. M. Ruzic, S. Tirant, J. R. Pilbrow, *J. Chem. Soc., Dalton Trans.* **1982**, 363.
[24] a) W. Känzig, M. H. Cohen, *Phys Rev. Lett.* **1959**, *3*, 509; b) H. R. Zeller, W. Känzig, *Helv. Phys. Acta* **1967**, *40*, 845.
[25] a) S. Fukuzumi, K. Ohkubo, *Chem. Eur. J.* **2000**, *6*, 4532; b) S. Fukuzumi, H. Ohtsu, K. Ohkubo, S. Itoh, H. Imahori, *Coord. Chem. Rev.* **2002**, *226*, 71.
[26] R. Warmuth, H. Elias, *Inorg. Chem.* **1991**, *30*, 5027.
[27] T. Scheper, F. Plötz, C. Müller, B. Hitzmann, *Trends Biotechnol.* **1994**, *12*, 42.
[28] D. T. Sawyer, G. Chiericato, C. T. Angelis, E. J. Nanni, T. Tsuchiya, *Anal. Chem.* **1982**, *54*, 1720.
[29] The data for the absorbance *A* were corrected for the temperature dependence of the density of the solvent DMF.

Received: October 21, 2005

 © 2005 Wiley-VCH Verlag GmbH & Co. KGaA, Weinheim

Synthesis of Palladium(II) and Platinum(II) Complexes with Crown Ether Phosphane Ligands: Stille Coupling of Aryl Iodides in Water

Jorge Fresneda,[b] Ernesto de Jesús,*[a] Pilar Gómez-Sal,[a] and Carmen López Mardomingo[b]

Keywords: Aqueous-phase catalysis / Crown compounds / C–C coupling / Palladium / Phosphane ligands

The crown ether phosphanes $PAr^{\star}Ph_2$ (**1**) and $PAr^{\star}{}_2R$ [$Ar^{\star}$ = 3,4-(18-crown-6)-phenyl; R = Me (**2**); R = Ph (**3**)], prepared from PCl_2R and $Ar^{\star}Li$, have been studied. The syntheses and characterization of their oxides (**4**–**6**), and their BH_3 (**7**–**9**), $PdCl_2$ (**10**–**12**), and $PtCl_2$ (**13**–**15**) complexes are reported. The molecular structure of the borane complex $PAr^{\star}{}_2Ph{\cdot}BH_3$ (**9**) has been determined by X-ray structural analysis. Spectroscopic data suggest that phosphanes **1**–**3** have similar electronic properties and steric requirements to the corresponding phenylphosphane ligands PPh_2Me and PPh_3. Crown ether methylphosphane **2** and its complexes are remarkably water soluble, but **1** and **3** are only slightly soluble. Palladium(II) complexes **14** and **15** have been tested as catalysts in the Stille coupling of phenyltrichlorostannanes and aryl iodides in water.

(© Wiley-VCH Verlag GmbH & Co. KGaA, 69451 Weinheim, Germany, 2005)

Introduction

The synthesis and study of metal complexes for aqueous-phase homogeneous catalysis is currently an active research area in organometallic chemistry.[1] Aryl- and alkyl-substituted tertiary phosphanes are among the most common ligands present in transition-metal catalysts, but they are hydrophobic and lack water solubility. Hydrophilicity can be introduced into a phosphane by making use of polar substituents, usually anionic or cationic functions, such as sulfonate or ammonium groups.[2,3] Water solubility has also been achieved with nonionic phosphanes, for example with hydroxyalkyl or polyether substituents but, in general, nonionic phosphanes have attracted less attention than ionic phosphanes. Since the first report by Shaw et al. in 1978,[4] several examples of hybrid crown ether phosphane ligands have appeared in the literature.[5–11] Okano and coworkers have reported the synthesis of mono[3,4-(crown)-phenyl]diphenylphosphane ligands $PAr^{*}Ph_2$ with crown heterocycles of different sizes.[6] The water solubility of these phosphanes is low but the crown cavity acts as an extractant and phase-transfer agent for biphasic catalysis.[5,6,12,13] Crown ether phosphanes contain a secondary site for coordination that can play an important role in catalytic processes.[9,10,14] Here, we report the synthesis of bis[3,4-(18-crown-6)-phenyl] analogs of methyldiphenyl- and triphenylphosphane and the preparation of their $PdCl_2$ and $PtCl_2$ complexes. The palladium complexes are tested as catalysts in Stille carbon–carbon couplings[15,16] in an aqueous medium.[17]

[a] Departamento de Química Inorgánica, Universidad de Alcalá, Campus Universitario, 28871 Alcalá de Henares (Madrid), Spain
Fax: +34-91-885-4683
E-mail: ernesto.dejesus@uah.es
[b] Departamento de Química Orgánica, Universidad de Alcalá, Campus Universitario, 28871 Alcalá de Henares (Madrid), Spain

Results and Discussion

Synthesis and Characterization of Crown Ether Phosphanes and Their Complexes

The synthesis of phosphanes $PAr^{*}{}_nR_{3-n}$ [Ar* = 3,4-(18-crown-6)-phenyl, R = Me, *n* = 2 (**2**); R = Ph, *n* = 2 (**3**)] is based on the lithiation of bromo-3,4-(18-crown-6)-benzene and the subsequent reaction of the lithium crown-aryl LiAr* with the corresponding chlorophosphane PCl_nR_{3-n} (Scheme 1), according to the procedure reported previously for the synthesis of $PAr^{*}Ph_2$ (**1**).[6] The main drawback of this procedure lies in the thermal instability[4] of LiAr*, which requires keeping the temperature carefully below the decomposition point (–90 °C) until the reaction with the chlorophosphane is completed, and to use a low concentration of reactants to avoid the formation of a slush at this temperature.[9] In our hands, moderate to high yields (60–90%) were obtained only when the temperature was maintained below –90 °C for at least one hour before and one hour after the addition of the chlorophosphane. The main impurities contaminating the crude product are 1,2-(18-crown-6)-benzene and butylphosphanes derived from unreacted *n*BuLi and chlorophosphanes. In the case of **3**, these are readily removed by crystallization from ethanol/methanol (9:1). In contrast, all our efforts to purify methylphos-

phane **2** by crystallization failed because of its high solubility in water and polar organic media (see below). Moreover, only the oxide **5** was collected from chromatography columns of silica gel or alumina even if an inert atmosphere and deoxygenated solvents were employed. Although triarylphosphanes are more stable, both **1** and **3** were transformed quantitatively into their oxides **4** or **6** when stirred under an air atmosphere for three days at room temperature.

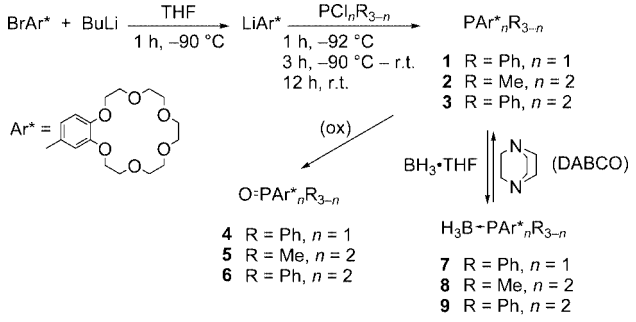

Scheme 1.

The formation of borane adducts is a classical method for the protection of phosphanes against oxidation during purification or synthetic steps (the borane group also plays an activation role in the latter).[18] For the synthesis of the borane complexes **7**–**9**, an equimolar solution of BH_3·THF was treated with the purified phosphanes (only for **1** and **3**) or, alternatively, added directly to the crude product obtained during their preparation. In both cases pure samples of **7**–**9** were obtained in high yields as white, air-stable solids after crystallization from ethanol/methanol. The deprotected phosphanes **1**–**3** were recovered from their borane adducts **7**–**9** by decomplexation with an excess of the diamine ligand 1,4-diazabicyclo[2.2.2]octane (DABCO). A mixture of phosphane, DABCO, and DABCO·BH_3 composed the crude product, from which the phosphanes **1** and **3** were easily separated by crystallization. Again, the properties of **2** complicated the purification of this phosphane, although almost pure samples could be obtained by repeated washings with hexane and long high-vacuum treatments. In practice, we limited the purification step to a short high-vacuum treatment until complete sublimation of the DABCO. Samples thus obtained consisted of a 1.6:1 mixture of phosphane **2** and DABCO·BH_3 and were appropriate for the synthesis of the complexes described here. A clear difference was observed in the complexation/decomplexation process between triarylphosphanes **1** and **3** and methylphosphane **2**. Complexation of the former with BH_3·THF is slower (at room temperature, 24 h for **1** and **3**, and 4 h for **2**) but decomplexation seems to be easier (4 h at 40 °C and 1.2 equiv. of DABCO for **1** and **3**, 5 h at THF reflux and 3.5 equiv. of DABCO for **2**). The enhanced strength of the P–B bond in the more electron-rich phosphane **2** is presumably responsible for these observations. It has been pointed out that BH_3 decomplexation by amine exchange can be an inefficient process for electron-rich, sterically hindered phosphanes.[19]

The platinum (**10**–**12**) and palladium (**13**–**15**) complexes $[MCl_2(PAr^*_nR_{3-n})_2]_2$ were prepared by the displacement of the labile ligand in $[MCl_2(COD)]$ or $[MCl_2(PhCN)_2]$ (Scheme 2). Palladium complex **13** has already been reported[5,6] and is described here only for comparative purposes. The platinum complexes are white solids containing only the *cis* isomers, whereas the palladium ones are yellow and were obtained as *cis*-*trans* mixtures. The *cis*-*trans* ratios obtained (*cis* amount: traces for **13**, 60% for **14**, and 30% for **15**) are independent of the starting material, $[PdCl_2(COD)]$ or $[PdCl_2(PhCN)_2]$. The *cis* and *trans* isomers of **15** were separated on the basis of their different solubility in toluene. The assigned stereochemistry is in agreement with the following experimental data and observations: (*a*) the order of the $^2J(^{31}P\text{-}^{31}P)$ coupling constant, estimated from second-order analysis of the ^1H NMR methyl resonance of PAr^*_2Me complexes,[20] and the ring ^{13}C signals (see below); (*b*) the number of ν(M–X) IR absorptions, two (A_1 + B_1) for *cis*, but one (B_{1u}) for *trans*; (*c*) in square-planar $[MCl_2(PR_3)_2]$ complexes, it has been observed that lower field phosphorus chemical shifts correspond to *cis* and higher field chemical shifts to *trans* isomers in Pd^{II} complexes, whereas the reverse is true for Pt^{II}; (*d*) the estimated phosphorus chemical shift value employing the reported[21] empirical correlation between the chemical shifts of free and coordinated phosphanes; estimated/experimental values are δ = 34.7/33.0 (*cis*-**13**), 23.3/24.1 (*trans*-**13**), 18.4/19.7 (*cis*-**14**), 9.0/7.7 (*trans*-**14**), 35.1/33.4 (*cis*-**15**), and 23.7/23.8 ppm (*trans*-**15**); (*e*) for Pt complexes, yellow colors are typical of *trans* isomers whereas *cis* isomers are usually white;[22] the $^1J(^{31}P\text{-}^{195}Pt)$ value is typically in the range of 2200–2500 Hz for *trans* and 3500–3700 Hz for *cis*-$[PtCl_2(PR_3)_2]$ complexes (3641–3673 Hz for *cis* **10**–**12**).[23]

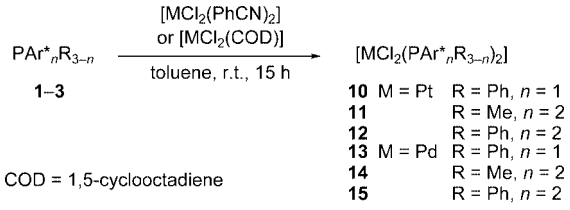

Scheme 2.

Spectroscopic and analytical data for compounds **2**–**15** are given in the Experimental Section. For the assignment of ^1H and ^{13}C NMR signals and the determination of coupling constants, we applied a combination of selective and broadband ($\{^1H\}$ and $\{^{31}P\}$) decoupling techniques together with the simulation of second-order spectra. The ^{31}P nuclei of the crown ether aryl derivatives **2**–**15** resonate almost at the same position as their parent phenyl analogs (PPh_2Me and PPh_3). For example, the ^{31}P NMR chemical shifts for the pair PAr^*_2Me (**2**)/PPh_2Me are as follows (in $CDCl_3$): δ = –25.6/–28 ppm for the free phosphane,[24] δ = 0.9/–1.2 ppm for the *cis* platinum complex,[25] and δ = 7.7/7.8 ppm for the *trans* palladium complex.[26] Therefore, the steric requirements and electronic properties imposed by the Ar* group to the phosphane ligand are possibly very

 © 2005 Wiley-VCH Verlag GmbH & Co. KGaA, Weinheim

similar to those of a Ph group. In fact, Storhoff et al.[11] have evaluated the donor/acceptor characteristics of several crown ether containing phosphanes, including **1**, from the A_1 ν(CO) bands for $[Ni(CO)_3L]$ complexes.[27] They reported that the PPh_2Ar^* complex absorbs 0.6 cm^{-1} lower than the PPh_3 analog, thus indicating that the donor ability of crown ether phosphane **1** is apparently only slightly greater than that of triphenylphosphane. The steric bulk of phosphanes is typically expressed in terms of cone angles, usually the Tolman cone angle, θ_{Tol}, originally derived from space-filling models,[28] or the Musco cone angle, θ_{Mus}, derived from phosphane X-ray diffraction data.[29] The estimation of these angles from the ^{31}P NMR spectroscopic data of *trans*-$[PdCl_2(PR_3)_2]$ complexes is possible because an empirical linear relationship has been demonstrated between the ^{31}P chemical shift and θ.[30] As remarked above, chemical shifts of crown ether complexes *trans*-$[PdCl_2(PAr^*_{3-n}R_n)_2]$ [δ = 24.1 (**13**), 7.7 (**14**), and 23.8 ppm (**15**)] match almost exactly those of the related non-crown ether *trans*-$[PdCl_2L_2]$ [δ = 24.4 (L = PPh_3),[31] 7.8 ppm (L = PPh_2Me)[26]]. Thus, it is predicted that Ar* phosphanes should have identical cone angles to Ph phosphanes. The estimated[32] values are θ_{Tol} = 131° and 147°, and θ_{Mus} = 126° and 134° for methyldiaryl and triarylphosphanes, respectively (actual values for PPh_2Me and PPh_3 are θ_{Tol} = 136° and 145°,[28] respectively).

The magnitude of the ^{13}C–^{31}P coupling constants is highly dependent on structural parameters, such as the coordination state of the P atom.[33] One-bond coupling constants between *ipso* Ph or Ar* carbon-13 and phosphorus-31 appear in a well-defined range for each type of compound: $^1J(^{13}C\text{-}^{31}P)$ = 9–11 (**2** and **3**), 105–108 (**4**–**6**), 58–63 (**7**–**9**), 68–71 (*cis*, **10**–**12**), 55–65 (*cis*, **13**–**15**), and 45–55 Hz (*trans*, **13**–**15**). The pattern of the ^{13}C NMR signals is a source of information about the magnitude of $^2J(^{31}P\text{-}^{31}P)$ coupling constants and serves to elucidate the *cis*-*trans* stereochemistry of square-planar $[MCl_2(PR_3)_2]$ complexes. The Me, Ar*, or Ph ^{13}C nuclei in **10**–**15** constitute the X part of an AA′X spin system,[34] where A and A′ are, respectively, the nearest and the most distant ^{31}P nuclei, for which five symmetrically disposed spectral lines are expected. If we assume $J(^{13}C\text{-}^{31}P_{A'})$ to be essentially zero, the actual appearance of the ^{13}C resonance lies between two limiting cases depending on the relative values of $J(^{13}C\text{-}^{31}P_A)$ and $^2J(^{31}P_A\text{-}^{31}P_{A'})$:[23] (*a*) a triplet produced by the weakening of the two outer lines (resonances marked as *pseudo triplets* in the Experimental Section), favored by larger $^2J(^{31}P_A\text{-}^{31}P_{A'})$ values; (*b*) lower $^2J(^{31}P_A\text{-}^{31}P_{A'})$ values favor an apparent doublet of doublets (or a doublet in the limiting case) due to the vanishing of the central line (*pseudo dd* or *d* in the experimental section). For *cis*-Pd complex **15**, all the carbons are split into doublets when coupled with ^{31}P, as expected for $^2J(^{31}P_A\text{-}^{31}P_{A'}) \approx 0$. For *cis*-Pt complexes, the carbons coupled to ^{31}P appear as pseudo triplets, except those with the largest $J(^{13}C\text{-}^{31}P_A)$ (*ipso* Ph, *ipso* Ar*, and Me carbons), which are observed as pseudo dd or d [a quantitative analysis of *ipso* Ph and *ipso* Ar* resonances gives an estimation for $^2J(^{31}P_A\text{-}^{31}P_{A'})$ of 10–14 Hz]. Finally, pseudo triplets for *ipso* Ph, *ipso* Ar*, or Me carbons are observed in the *trans* complexes, according to the larger P–P coupling constants. The simulated spectra of the Ar* protons match the experimental ones satisfactorily when P–P couplings of 0 (for *cis*-Pd), approx. 12 Hz (for *cis*-Pt), and >100 Hz (for *trans*-Pd) are considered in the second-order interpretation.

The solubility of catalysts in water is a relevant parameter when considering processes in this media. Triarylphosphanes **1** and **3** are only slightly soluble in water. Within this reduced solubility, the affinity for water increases with the number of crown-ether aryl groups as shown by the measured water/toluene distribution constants (7.4×10^{-3} for **1**, 1.46×10^{-3} for **3**). In contrast, the methylphosphane **2** is exceptionally water soluble. These differences are reflected in their metal complexes; for example, the palladium triarylphosphane complex **10** is poorly soluble in water (0.002 g/100 mL), whereas the palladium methyldiarylphosphane complex **11** has a remarkable solubility (>10 g/100 mL).

Crystal Structure of Borane–Phosphane 9

The molecular structure of borane complex $PAr^*_2Ph{\cdot}BH_3$ (**9**) based on X-ray structural analysis is given in Figure 1. In spite of the presence of two 18-crown-6 ether rings, the bond distances and angles around the phosphorus atom, which are listed in Table 1, are almost equal to those of $Ph_3P{\cdot}BH_3$.[35] For example, the mean P–C_{ipso} and P–B distances and C_{ipso}–P–C_{ipso} and B–P–C_{ipso} bond angles are, respectively, 1.811(4) and 1.917(5) Å, and 106.0(2)° and 112.6(2)° in **9**, compared with 1.818 and 1.917 Å, and 106.3° and 112.6° in $Ph_3P{\cdot}BH_3$. Complex **9** adopts a three-fold rotor conformation, according to the Dance and Scudder nomenclature,[36] with B–P–C_{ipso}–C_{ortho} torsion angles within the range 30.4–41.5° (mean: 36.8°). In contrast, the conformation of $Ph_3P{\cdot}BH_3$ is irregular, with two rotor rings and the other parallel to the P–B bond. The crown ether ring O(1)–O(6) is folded toward a face of the phenyl ring with an angle between crown and phenyl mean planes of 129.3(1)°, whereas the disposition of the crown ether O(7)–O(12) is almost coplanar [angle between mean planes = 172.4(1)°]. With respect to the plane defined by the *ipso* carbon atoms [C(1), C(17), and C(33)], the crown O(1)–O(6) is placed completely within the semispace opposite the P–B bond (*endo* orientation), whereas O(7)–O(12) has an *exo* orientation, with half of the crown atoms situated in each semispace. The crystallographic cone angle calculated[37] for the phosphane PAr^*_2Ph (**3**) in the solid-state structure of complex **9** is very large (175°). However, single crystallographic cone angles of ligands with significant conformational freedom are not relevant in describing steric effects in solution and are only representative of the conformation adopted in the particular structure. In this sense, the conformation adopted by the crown ether groups in the solid structure of **9** (*exo*-*endo*) is better ascribed to crystal-packing forces than to intermolecular interactions; chang-

 © 2005 Wiley-VCH Verlag GmbH & Co. KGaA, Weinheim

ing the conformation to an *endo-endo* disposition reduces the cone angle to 160°. This value is only slightly larger than that of PPh_3 in $Ph_3P{\cdot}BH_3$ (155°).[38]

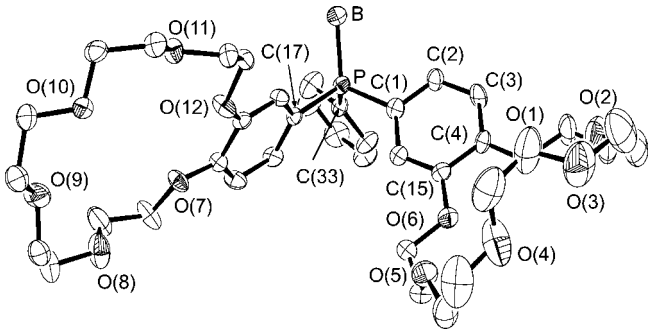

Figure 1. View of the molecular structure of **9** with the atom-numbering scheme.

Table 1. Selected bond distances [Å] and angles [°] for **9**.

P–B	1.917(5)
P–C(1)	1.805(4)
P–C(17)	1.812(4)
P–C(33)	1.817(4)
C(1)–P–B	113.0(2)
C(17)-P–B	112.7(2)
C(33)-P–B	112.3(2)
C(1)–P–C(17)	105.6(2)
C(17)–P–C(33)	106.5(2)
C(33)–P–C(1)	106.2(2)

Palladium-Catalyzed Stille Couplings of Phenyltrichlorostannanes and Aryl Halides in Aqueous Solution

In 1993, Zhang and Daves[39] reported the achievement of Stille coupling reactions in aqueous media that they had been unable to accomplish in nonaqueous solvents. However, reactions carried out in water alone gave very low yields owing to the limited solubility of the reactants. Beletskaya[40] and Collum[41] independently reported successful couplings in water alone, thanks to the application of alkyltrichlorostannanes instead of tetraorganotin compounds; the former are less toxic and expensive, and produce water-soluble anionic alkylhydroxostannates in situ in aqueous alkaline solution. The catalyst employed was $PdCl_2$ with or without the addition of sulfonated water-soluble phosphane ligands such as P(*m*-$C_6H_4SO_3Na)Ph_2$[40] or P(*m*-$C_6H_4SO_3Na)_2Ph$,[41] or, in a recent paper by Wolf, $P(OH)(tBu)_2$.[42]

We chose the coupling of $PhSnCl_3$ and *p*-iodotoluene or *p*-iodoaniline, under the Belestkaya–Collum conditions (Scheme 3), to test the efficiency of the palladium complexes **14** and **15** as aqueous-phase catalysts. [$PdCl_2$(COD)] and [$PdCl_2(PPh_3)_2$] were also tested as a reference. Table 2 summarizes our results. Yields were especially high (>86%) for both crown catalysts **14** or **15**, but the less-soluble catalyst **15** gave quantitative yields whereas those of the highly soluble **14** were a bit lower (may be because of the lower stability of methyldiarylphosphane towards oxidation). Surprisingly, Beletskaya and co-workers[40] reported yields of about 85% when employing 1:2 mixtures of $PdCl_2$ and the monosulfonated phosphane P(*m*-$C_6H_4SO_3Na)Ph_2$. Reactions with [$PdCl_2$(COD)] and [$PdCl_2(PPh_3)_2$] proceed in 62 to 75% yields, normally with decomposition of the catalysts and formation of Pd^0.[43]

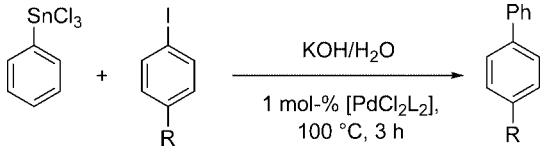

Scheme 3.

Table 2. Yields in reactions of ArI with $PhSnCl_3$ in the presence of palladium complexes **14** and **15** in aqueous alkaline medium.

Aryl iodide	Product	Catalyst[a]	Yield[b]
p-$NH_2C_6H_4I$	*p*-$NH_2C_6H_4$-C_6H_5	[$PdCl_2$(COD)]	62%
p-$NH_2C_6H_4I$	*p*-$NH_2C_6H_4$-C_6H_5	[$PdCl_2(PPh_3)_2$]	75%
p-$NH_2C_6H_4I$	*p*-$NH_2C_6H_4$-C_6H_5	[$PdCl_2(PAr^*_2Me)_2$] (**14**)	95%
p-$NH_2C_6H_4I$	*p*-$NH_2C_6H_4$-C_6H_5	[$PdCl_2(PAr^*_2Ph)_2$] (**15**)	98% [c]
p-$CH_3C_6H_4I$	*p*-$CH_3C_6H_4$-C_6H_5	[$PdCl_2(PPh_3)_2$]	69%
p-$CH_3C_6H_4I$	*p*-$CH_3C_6H_4$-C_6H_5	[$PdCl_2(PAr^*_2Me)_2$] (**14**)	86%
p-$CH_3C_6H_4I$	*p*-$CH_3C_6H_4$-C_6H_5	[$PdCl_2(PAr^*_2Ph)_2$] (**15**)	98% [c]

[a] 1.0 mol-% with respect to the aryl iodide. See Experimental Section for details. [b] Yield of isolated product based on starting ArI. Differences up to 100% were mainly due to unchanged ArI. [c] The reaction proceeded quantitatively and neither starting aryl iodide nor by-products were detected by ^1H NMR spectroscopy or TLC.

Conclusions

We have synthesized the new hybrid phosphane crown ether molecules PAr^*_2Me (**2**) and PAr^*_2Ph (**3**), where Ar* = 3,4-(18-crown-6)-phenyl, and their BH_3, $PtCl_2$, and $PdCl_2$ complexes. Because of the conformational flexibility of the crown ether substituents, the available data suggest that compounds **1–3** are isosteric to the corresponding phenylphosphane ligands (PPh_2Me or PPh_3). If we consider, in addition, the electronic similarity between crown and non-crown ligands, we can conclude that **1–3** are good alternatives to PPh_2Me and PPh_3 when working in aqueous medium. Moreover, the methylphosphane PAr^*_2Me (**2**) furnishes to their complexes a water solubility comparable to those of sulfonated phosphanes. However, solubility is not the only parameter to be considered, as shown by the fact that the only slightly water-soluble phenylphosphane PAr^*_2Ph (**3**) gives the best yields in the Stille coupling reactions in water here studied. Taking into account these preliminary but promising results in catalysis, the work here undertaken is being pursued with the synthesis of new crown ether phosphanes and a more detailed study of Stille and other C–C coupling reactions in water.

Experimental Section

Reagents and General Techniques: All operations were performed under an argon atmosphere by using Schlenk or dry-box tech-

 © 2005 Wiley-VCH Verlag GmbH & Co. KGaA, Weinheim

niques. Solvents were dried and distilled under argon and degassed prior to use, as described elsewhere.[44] Unless otherwise stated, reagents were obtained from commercial sources and used as received. PAr^*Ph_2 (**1**),[6,9] $[PtCl_2(COD)]$, and $[PdCl_2(COD)]$[45] were prepared according to reported procedures. ^1H, ^{13}C, ^{31}P, and ^{11}B NMR spectra were recorded on Varian Unity 300 or 500 Plus spectrometers. Chemical shifts (δ, ppm) are relative to $SiMe_4$ (^1H, ^{13}C), 85% H_3PO_4 (^{31}P), or $F_3B{\cdot}OEt_2$ (^{11}B), and were measured by internal referencing to the deuterated solvent (^{13}C and residual ^1H resonances), or by the substitution method (^{31}P and ^{11}B references). Coupling constants (J) are given in hertz. The ring-numbering system employed in the description of NMR spectroscopic data is given in Figure 2. In ^{13}C NMR, $J_{P\ virtual}$ of *pseudo triplets* (see Results and Discussion) corresponds to $J(^{13}C–^{31}P_A) + J(^{13}C–^{31}P_{A'})$. IR spectra were recorded on a Perkin–Elmer Spectrum 2000 FT-IR spectrometer and data are given in cm^{-1}. The Analytical Services of the Universidad de Alcalá performed the C, H, and N analyses in a Heraeus CHN-O-Rapid microanalyzer, and the MS-ESI+ mass spectra in an Automass Multi, ThermoQuest. MALDI-TOF mass spectra were recorded by the Analytical Services of the Universidad Autónoma de Madrid.

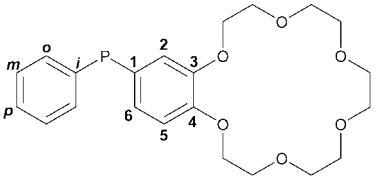

Figure 2. Selected $^{13}C\{^1H\}$ chemical shifts (in ppm) and coupling constants (in Hz) for compounds **2**–**15**, with the ring-labeling scheme employed in the Experimental Section.

PAr^*_2Me (2): The procedure described below for **3** was used for the synthesis of phosphane **2** (0.28 g, 65%) as a colorless oil starting from 4-bromobenzo-3,4-(18-crown-6) (0.500 g, 1.28 mmol), a 1.6 M hexane solution of *n*-butyllithium (0.88 mL, 1.41 mmol), and a 1.0 M solution of dichloromethylphosphane in hexane (0.70 mL, 0.70 mmol). However, this phosphane could not be purified by crystallization as described for **3**, because of its high solubility in water and polar organic media such as methanol or THF. ^1H NMR ($CDCl_3$, 500 MHz): δ = 6.93 [td, J_P = 7.0, J_{H5} = 7.8, J_{H2} = 1.7, 2 H, Ar*(H^6)], 6.87 [dd, J_P = 7.5, 2 H, Ar*(H^2)], 6.82 [dd, J_P = 1.3, 2 H, Ar*(H^5)], 4.12 (m, 4 H, CH_2 crown), 4.07 (m, 4 H, crown), 3.90 (m, 4 H, crown), 3.87 (m, 4 H, crown), 3.74 (m, 8 H, crown), 3.70 (m, 8 H, crown), 3.66 (s, 8 H, crown), 1.51 (d, J_P = 3.3, 3 H, Me) ppm. $^{13}C\{^1H\}$ NMR ($CDCl_3$, 75 MHz): δ = 149.53 [s, Ar*(C^4)], 148.38 [d, J_P = 8.1, Ar*(C^3)], 132.23 [d, J_P = 10.3, Ar*(C^1)], 125.46 [d, J_P = 19.9, Ar*(C^2)], 118.02 [d, J_P = 21.4, Ar*(C^6)], 114.00 [d, J_P = 8.1, Ar*(C^5)], 70.85, 70.78, 70.75, 69.65, 69.61, 69.30, 69.03 (s, CH$_2$ crown), 13.24 (d, $J_{C,P}$ = 8.1, Me) ppm. $^{31}P\{^1H\}$ NMR ($CDCl_3$, 202 MHz): δ = –25.6 ppm.

PAr^*_2Ph (3): In a 100-mL round-bottomed flask equipped with a low-temperature thermometer, a magnetic stirrer, and a dropping funnel, 4-bromobenzo-3,4-(18-crown-6) (0.500 g, 1.28 mmol) was dissolved in freshly distilled THF (60 mL) and cooled in a methanol/liquid nitrogen slush. The temperature was lowered to –95 °C and then a 1.6 M hexane solution of *n*-butyllithium (0.88 mL, 1.41 mmol) was added dropwise to the cooled and stirred solution, keeping the temperature below –92 °C. The stirring was continued for 90 min while the temperature was carefully maintained in the stated range. Then, dichlorophenylphosphane (0.10 mL, 0.73 mmol) dissolved in THF (1 mL) was added gradually to the stirred mixture over a period of 10 min. The temperature was kept below –90 °C over a period of 60 min and then the reaction mixture was allowed to warm up to room temperature in the course of 3 h. Stirring was continued overnight. The solvent was removed in vacuo and the resulting residue was extracted with dichloromethane (3 × 30 mL). The dichloromethane was removed under reduced pressure to provide a colorless oil. Pure **3** (0.390 g, 83%) was obtained by crystallization of the crude from a mixture of absolute ethanol and methanol (9:1). $C_{38}H_{51}O_{12}P$ (730.79): calcd. C 62.46, H 7.03; found C 62.21, H 6.89. ^1H NMR ($CDCl_3$, 500 MHz): δ = 7.28 (m, 3 H, Ph), 7.22 (m, 2 H, Ph), 6.81 (m, 6 H, Ar*), 4.13 (m, 4 H, CH_2 crown), 4.01 (m, 4 H, crown), 3.91 (m, 4 H, crown), 3.83 (m, 4 H, crown), 3.75 (m, 4 H, crown), 3.74–3.68 (m, 12 H, crown), 3.67 (s, 8 H, crown) ppm. $^{13}C\{^1H\}$ NMR ($CDCl_3$, 75 MHz): δ = 149.68 [s, Ar*(C^4)], 148.84 [d, J_P = 9.0, Ar*(C^3)], 138.13 [d, J_P = 10.6, Ar*(C_{ipso})], 133.18 [d, J_P = 18.9, Ph(C_{ortho})], 128.98 [d, J_P = 8.7, Ph(C^1)], 128.38 [s, Ph(C_{para})], 128.33 [d, J_P = 6.7, Ph(C_{meta})], 127.31 [d, J_P = 20.0, Ar*(C^6)], 119.10 [d, J_P = 22.5, Ar*(C^2)], 113.73 [d, J_P = 8.3, Ar*(C^5)], 70.90, 70.79, 70.75, 69.68, 69.57, 69.05, 68.91 (s, CH$_2$ crown) ppm. $^{31}P\{^1H\}$ NMR ($CDCl_3$, 202 MHz): δ = –4.4 ppm.

$P(O)Ar^*Ph_2$ (4): Phosphane PAr^*Ph_2 (**1**) (0.15 g, 0.30 mmol) was dissolved in $CHCl_3$ (10 mL). The solution was stirred at room temperature for 3 d under an air atmosphere. Subsequently, the solvent was evaporated to dryness and the residue crystallized from ethanol at –25 °C to give pure oxide **4** as a white solid (0.13 g, 84%). $C_{28}H_{33}O_7P$ (512.54): calcd. C 65.62, H 6.49; found C 65.71, H 6.42. ^1H NMR ($CDCl_3$, 300 MHz): δ = 7.62 [m, J_P = 11.9, 4 H, Ph(H_{ortho})], 7.50 [m, 2 H, Ph(H_{para})], 7.42 [m, 4 H, Ph(H_{meta})], 7.22 [dd, J_P = 12.1, J_{H6} = 1.8, 1 H, Ar*(H^2)], 7.03 [ddd, J_P = 12.1, J_{H5} = 8.1, 1 H, Ar*(H^6)], 6.86 [dd, J_P = 3.1, 1 H, Ar*(H^5)], 4.16 (m, 2 H, CH_2 crown), 4.08 (m, 2 H, crown), 3.91 (m, 2 H, crown), 3.84 (m, 2 H, crown), 3.77–3.66 (m, 12 H, crown) ppm. $^{13}C\{^1H\}$ NMR ($CDCl_3$, 75 MHz): δ = 152.09 [s, Ar*(C^4)], 148.90 [d, J_P = 14.7, Ar*(C^3)], 132.89 [d, J_P = 104.7, Ph(C_{ipso})], 131.89 [d, J_P = 14.0, Ph(C_{ortho})], 128.41 [d, J_P = 11.8, Ph(C_{meta})], 131.79 [d, J_P = 2.9, Ph(C_{para})], 126.27 [d, J_P = 11.6, Ar*(C^6)], 124.12 [d, J_P = 108.4, Ar*(C^1)], 116.87 [d, J_P = 11.1, Ar*(C^2)], 112.81 [d, J_P = 14.7, Ar*(C^5)], 70.98, 70.94, 70.83, 70.75, 70.68, 69.49, 69.41, 69.23, 68.94 (s, CH$_2$ crown) ppm. $^{31}P\{^1H\}$ NMR ($CDCl_3$, 202 MHz): δ = 30.5 ppm.

$P(O)Ar^*_2Me$ (5) and $P(O)Ar^*_2Ph$ (6): The procedure described above for **4** was used for the synthesis of phosphane oxides **5** (0.084 g, 55%) from **2** (0.150 g, 0.224 mmol), and **6** (0.138 g, 90%) from **3** (0.150 g, 0.205 mmol). The latter was obtained as an oil which was purified by chromatography on a silica gel column using a 1:1 mixture of toluene and ethanol as the mobile phase.

5: $C_{33}H_{49}O_{13}P$ (684.72): calcd. C 57.89, H 7.21; found C 57.95, H 7.08. MS (ESI+): m/z = 707.3 (calcd. for MNa^+: 707.0). ^1H NMR ($CDCl_3$, 500 MHz): δ = 7.19 [dd, J_P = 12.3, J_{H6} = 1.9, 2 H, Ar*(H^2)], 7.13 [ddd, J_P = 12.0, J_{H5} = 8.0, 2 H, Ar*(H^6)], 6.87 [dd, J_P = 2.9, 2 H, Ar*(H^5)], 4.15 (m, 4 H, CH_2 crown), 4.13 (m, 4 H, crown), 3.91 (m, 4 H, crown), 3.89 (m, 4 H, crown), 3.78 (m, 8 H, crown), 3.73 (m, 8 H, crown), 3.65 (s, 8 H, crown), 1.91 (d, J_P = 13.2, 3 H, Me) ppm. $^{13}C\{^1H\}$ NMR ($CDCl_3$, 126 MHz): δ = 151.81 [s, Ar*(C^4)], 148.85 [d, J_P = 14.5, Ar*(C^3)], 125.95 [d, J_P = 106.2, Ar*(C^1)], 124.30 [d, J_P = 10.6, Ar*(C^2)], 115.49 [d, J_P = 11.7, Ar*(C^6)], 112.87 [d, J_P = 15.0, Ar*(C^5)], 70.87, 70.81, 70.75, 70.67, 70.66, 70.60, 69.42, 69.32, 69.15, 68.82 (s, CH$_2$ crown), 16.99 (d, J_P = 75.5, Me) ppm. $^{31}P\{^1H\}$ NMR ($CDCl_3$, 202 MHz): δ = 31.5 ppm.

6: $C_{38}H_{51}O_{13}P$ (746.79): calcd. C 61.12, H 6.88; found C 60.97, H 6.82. ^1H NMR ($CDCl_3$, 300 MHz): δ = 7.60 [m, J_P = 12.1, 2 H,

 © 2005 Wiley-VCH Verlag GmbH & Co. KGaA, Weinheim

Ph(H_{ortho})], 7.50 [m, 1 H, Ph(H_{para})], 7.43 [m, 2 H, Ph(H_{meta})], 7.21 [dd, J_P = 12.5, J_{H6} = 1.7, 2 H, Ar*(H^2)], 7.00 [ddd, J_P = 12.1, J_{H5} = 8.2, 2 H, Ar*(H^6)], 6.86 [dd, J_P = 2.9, 2 H, Ar*(H^5)], 4.13 (m, 4 H, CH_2 crown), 4.01 (m, 4 H, crown), 3.91 (m, 4 H, crown), 3.83 (m, 4 H, crown), 3.75 (m, 4 H, crown), 3.74–3.67 (m, 12 H, crown), 3.66 (s, 8 H, crown) ppm. $^{13}C\{^1H\}$ NMR ($CDCl_3$, 126 MHz): δ = 151.82 [s, Ar*(C^4)], 148.87 [d, J_P = 14.5, Ar*(C^3)], 132.92 [d, J_P = 12.4, Ph(C_{ortho})], 131.52 [d, J_P = 2.6, Ph(C_{para})], 130.01 [d, J_P = 105.6, Ph(C_{ipso})], 128.55 [d, J_P = 11.5, Ph(C_{meta})], 126.68 [d, J_P = 12.0, Ar*(C^6)], 124.02 [d, J_P = 106.9, Ar*(C^1)], 117.52 [d, J_P = 12.1, Ar*(C^2)], 113.03 [d, J_P = 14.3, Ar*(C^5)], 70.93, 70.83, 70.80, 70.67, 70.65, 70.42, 69.45, 69.18, 68.89 (s, CH$_2$ crown) ppm. $^{31}P\{^1H\}$ NMR ($CDCl_3$, 202 MHz): δ = 31.3 ppm.

Ar*Ph$_2$P·BH$_3$ (7): PAr*Ph$_2$ (**1**; 0.11 g, 0.22 mmol) was dissolved in THF (20 mL) and a 1.0 M solution of BH_3·THF in THF (0.22 mL, 0.22 mmol) was added with a syringe. The mixture was stirred at room temperature for 24 h. The solvent was subsequently removed under vacuum to give a white solid. Pure borane complex **7** (0.097 g, 85%) was obtained after crystallization of the crude product from a mixture of absolute ethanol and methanol (18:1) at –25 °C. $C_{28}H_{36}BO_6P$ (510.38): calcd. C 65.89, H 7.11; found C 66.01, H 7.08. MS (ESI+): m/z = 534.0 (calcd. for MNa^+: 533.2), 520.0 (calcd. for MNa^+ – BH_3: 519.2). ^1H NMR ($CDCl_3$, 300 MHz): δ = 7.52 [m, J_P = 10.8, 4 H, Ph(H_{ortho})], 7.47 [m, 2 H, Ph(H_{para})], 7.43 [m, 4 H, Ph(H_{meta})], 7.10 [dd, J_P = 11.4, J_{H6} = 1.8, 1 H, Ar*(H^2)], 7.05 [ddd, J_P = 10.4, J_{H5} = 8.2, 1 H, Ar*(H^6)], 6.87 [dd, J_P = 2.4, 1 H, Ar*(H^5)], 4.15 (m, 2 H, CH_2 crown), 4.05 (m, 2 H, crown), 3.91 (m, 2 H, crown), 3.84 (m, 2 H, crown), 3.74 (m, 2 H, crown), 3.71 (m, 2 H, crown), 3.70 (m, 2 H, crown), 3.68 (m, 2 H, crown), 3.65 (s, 4 H, crown), 1.5–0.6 (very broad, BH_3) ppm. $^{13}C\{^1H\}$ NMR ($CDCl_3$, 126 MHz): δ = 151.64 [d, J_P = 2.2, Ar*(C^4)], 148.98 [d, J_P = 12.8, Ar*(C^3)], 133.03 [d, J_P = 9.5, Ph(C_{ortho})], 132.04 [d, J_P = 2.2, Ph(C_{para})], 129.65 [d, J_P = 57.8, Ph(C_{ipso})], 128.67 [d, J_P = 10.0, Ph(C_{meta})], 127.38 [d, J_P = 9.5, Ar*(C^6)], 120.07 [d, J_P = 62.3, Ar*(C^1)], 118.21 [d, J_P = 12.8, Ar*(C^2)], 113.28 [d, J_P = 12.23, Ar*(C^5)], 70.94, 70.89, 70.80, 70.71, 70.67, 69.45, 69.37, 69.17, 68.88 (s, CH$_2$ crown) ppm. $^{31}P\{^1H\}$ NMR ($CDCl_3$, 202 MHz): δ = 21.5 ppm.

Ar*$_2$MeP·BH$_3$ (8): The procedure described above for **7** was used for the synthesis of borane complex **8** starting from the crude product **2** (0.35 g, 0.52 mmol) and a 1.0 M solution of BH_3·THF in THF (0.52 mL, 0.52 mmol). In this case, the reaction time was reduced to 4 h, and the crude product was recrystallized three times from a mixture of absolute ethanol and methanol (18:1) at –25 °C to provide 0.21 g (60%) of an analytically pure solid which was identified as **8**. $C_{33}H_{52}BO_{12}P$ (682.55): calcd. C 58.07, H 7.68; found C 58.30, H 7.63. MS (ESI+): m/z = 706.0 (calcd. for MNa^+: 705.3). IR (KBr pellets): ν(BH) = 2371 s. ^1H NMR ($CDCl_3$, 500 MHz): δ = 7.19 [dd, J_P = 12.3, J_{H6} = 1.9, 2 H, Ar*(H^2)], 7.13 [ddd, J_P = 12.0, J_{H5} = 8.0, 2 H, Ar*(H^6)], 6.87 [dd, J_P = 2.9, 2 H, Ar*(H^5)], 4.15 (m, 4 H, CH_2 crown), 4.13 (m, 4 H, crown), 3.91 (m, 4 H, crown), 3.89 (m, 4 H, crown), 3.78 (m, 8 H, crown), 3.73 (m, 8 H, crown), 3.65 (s, 8 H, crown), 1.74 (d, J_P = 10.3, 3 H, Me), 1.3–0.5 (very broad, BH_3) ppm. $^{11}B\{^1H\}$ NMR ($CDCl_3$, 160 MHz): δ = –39 ppm. $^{13}C\{^1H\}$ NMR ($CDCl_3$, 126 MHz): δ = 151.52 [s, Ar*(C^4)], 148.97 [d, J_P = 13.3, Ar*(C^3)], 125.52 [d, J_P = 8.9, Ar*(C^6)], 122.20 [d, J_P = 60.5, Ar*(C^1)], 117.25 [d, J_P = 11.8, Ar*(C^2)], 113.55 [d, J_P = 13.3, Ar*(C^5)], 70.91, 70.85, 70.77, 70.68, 69.50, 69.39, 68.94 (s, CH$_2$ crown), 12.5 (d, J_P = 41.3, Me) ppm. $^{31}P\{^1H\}$ NMR ($CDCl_3$, 202 MHz): δ = 10.2 ppm.

Ar*$_2$PhP·BH$_3$ (9): The procedure described above for **7** was used for the synthesis of borane complex **9** (0.308 g, 90%) from **3** (0.250 g, 0.342 mmol). The presence of 1 equiv. of MeOH in the crystalline white solid is suggested by the elemental analyses and confirmed by NMR spectra (resonances of the methanol are omitted in the spectroscopic data below). $C_{38.5}H_{56}BO_{12.5}P$ (760.65, includes 1/2 a molecule of methanol): calcd. C 60.79, H 7.42; found C 60.74, H 7.36. ^1H NMR ($CDCl_3$, 500 MHz): δ = 7.49 [m, J_P = 10.8, 2 H, Ph(H_{ortho})], 7.47 [m, 1 H, Ph(H_{para})], 7.38 [m, 2 H, Ph(H_{meta})], 7.08 [dd, J_P = 11.4, J_{H6} = 1.8, 2 H, Ar*(H^2)], 7.00 [ddd, J_P = 8.6, J_{H5} = 8.4, 2 H, Ar*(H^6)], 6.85 [dd, J_P = 2.6, 2 H, Ar*(H^5)], 4.15 (m, 4 H, CH_2 crown), 4.05 (m, 4 H, crown), 3.91 (m, 4 H, crown), 3.84 (m, 4 H, crown), 3.75 (m, 4 H, crown), 3.74–3.67 (m, 12 H, crown), 3.66 (s, 8 H, crown), 1.5–0.6 (very broad, BH_3) ppm. $^{13}C\{^1H\}$ NMR ($CDCl_3$, 75 MHz): δ = 151.50 [s, Ar*(C^4)], 148.98 [d, J_P = 13.3, Ar*(C^3)], 132.89 [d, J_P = 9.6, Ph(C_{ortho})], 130.95 [d, J_P = 3.0, Ph(C_{para})], 130.11 [d, J_P = 58.2, Ph(C_{ipso})], 128.60 [d, J_P = 10.3, Ph(C_{meta})], 127.17 [d, J_P = 8.9, Ar*(C^6)], 120.57 [d, J_P = 62.7, Ar*(C^1)], 117.97 [d, J_P = 12.5, Ar*(C^2)], 113.17 [d, J_P = 12.5, Ar*(C^5)], 70.90, 70.82, 70.78, 70.69, 70.63, 70.41, 69.36, 69.12, 68.84 (s, CH$_2$ crown) ppm. $^{31}P\{^1H\}$ NMR ($CDCl_3$, 202 MHz): δ = 21.0 ppm.

Decomplexation of Phosphane–Borane Complex 7: This was carried out as described below for complex **9**.

Decomplexation of Phosphane–Borane Complex 8: Complex **8** (0.044 g, 0.065 mmol) and 1,4-diazabicyclo[2.2.2]octane (DABCO) (0.0174, 0.16 mmol) were dissolved in THF (5 mL). The mixture was refluxed at 85 °C for 5 h and then allowed to cool to room temperature. The solvent was removed under reduced pressure and complete decomplexation was evidenced by ^1H NMR spectroscopy. The excess of DABCO was completely eliminated under high vacuum at room temperature and the DABCO·BH_3 formed in the reaction was partially removed in this treatment. The final product was found to be a mixture of phosphane **2** and DABCO·BH_3 (1.6:1, ^1H NMR).

Decomplexation of Phosphane–Borane Complex 9: Complex **9** (0.22 g, 0.30 mmol) and the DABCO ligand (0.040, 0.36 mmol) were dissolved in toluene (20 mL). The mixture was stirred at 40 °C for 4 h. The solvent was removed under reduced pressure and the crude product was identified as a 1:1 mixture of phosphane **3** and complex BH_3·DABCO (^1H NMR), showing that decomplexation was complete. Phosphane **3** (0.20 g, 90%) could be purified by crystallization of the crude mixture with ethanol at –25 °C.

[PtCl$_2$(PAr*Ph$_2$)$_2$] (10): The procedure described below for **12** was used for the synthesis of platinum complex **10** starting from phosphane **1** (0.067 g, 0.13 mmol) and [$PtCl_2$(PhCN)$_2$] (0.028 g, 0.059 mmol). Complex **10** was obtained as a pure white solid containing only the *cis* isomer (0.062 g, 83%). $C_{56}H_{66}Cl_2O_{12}P_2Pt$ (1259.07): calcd. C 53.42, H 5.28; found C 53.11, H 5.31. MS (ESI+): m/z = 1281.0 (calcd. for MNa^+: 1280.3). IR (Nujol): ν(Pt–Cl) = 318, 292. ^1H NMR ($CDCl_3$, 500 MHz): δ = 7.44 [m, 8 H, Ph(H_{ortho})], 7.28 [m, 4 H, Ph(H_{para})], 7.14 [m, 8 H, Ph(H_{meta})], 7.09 [m, J_P = 10.5, J_{H6} = 2.0, 2 H, Ar*(H^2)], 6.93 [m, $J_P \approx$ 8, 2 H, Ar*(H^6)], 6.59 [dd, J_P = 2.2, J_{H5} = 8.3, 2 H, Ar*(H^5)], 4.10 (m, 4 H, CH_2 crown), 3.90 (m, 4 H, crown), 3.76 (m, 8 H, crown), 3.74 (m, 8 H, crown), 3.69 (m, 8 H, crown), 3.66 (s, 8 H, crown) ppm. $^{13}C\{^1H\}$ NMR ($CDCl_3$, 75 MHz): δ = 151.07 [d, J_P = 2.2, Ar*(C^4)], 147.67 [pseudo t, $J_{P\,virtual}$ = 14.4, Ar*(C^3)], 134.44 [pseudo t, $J_{P\,virtual}$ = 9.6, Ph(C_{ortho})], 130.47 [s, Ph(C_{para})], 130.01 [pseudo dd, $J_{apparent}$ = 68.0 and 2.4, Ph(C_{ipso})], 129.01 [pseudo t, $J_{P\,virtual}$ = 9.6, Ar*(C^6)], 127.66 [pseudo t, $J_{P\,virtual}$ = 11.6, Ph(C_{meta})], 120.09 [pseudo dd, $J_{apparent}$ = 68.0 and 1.6, Ar*(C^1)], 120.39 [pseudo t, J_P = 12.6, Ar*(C^2)], 112.03 [pseudo t, J_P = 12.8, Ar*(C^5)], 70.93, 70.90, 70.79, 70.69, 70.58, 69.32, 68.92, 68.79 (s, CH$_2$ crown) ppm.

 © 2005 Wiley-VCH Verlag GmbH & Co. KGaA, Weinheim

$^{31}P\{^1H\}$ NMR ($CDCl_3$, 202 MHz): δ = 15.1 (s with ^{195}Pt satellites, J_{Pt} = 3669 Hz).

[$PtCl_2$(PAr*$_2$Me)$_2$] (11): Phosphane–borane complex **8** (0.044 g, 0.065 mmol) and DABCO (0.0174 g, 0.15 mmol) were refluxed in THF for 5 h. The solvent was removed and the residue was treated with 1 equiv. of [$PtCl_2$(PhCN)$_2$] (0.015 g, 0.032 mmol) in toluene (5 mL). The mixture was stirred at room temperature for 15 h. Subsequently, the solvent was removed in vacuo and the residue washed with hexane. The crude product thus obtained, a mixture of *cis*-**11** and BH_3·DABCO, was chromatographed on a neutral alumina column using a 9:1 mixture of toluene and ethanol as mobile phase. Complex **11** was obtained as a solid and the *cis* isomer (0.032 g, 63%). $C_{66}H_{98}Cl_2O_{24}P_2Pt$ (1603.42): calcd. C 49.44, H 6.16; found C 49.20, H 6.08. MS (MALDI-TOF): *m*/*z* = 1624.4 (calcd. for MNa^+: 1624.48). IR (Nujol): ν(Pt–Cl) = 312, 285. ^1H NMR ($CDCl_3$, 500 MHz,): δ = 7.08 [m, J_P = 12.1, 4 H, Ar*(*H*^{2})], 6.99 [m, $J_P \approx$ 8, 4 H, Ar*(*H*^{6})], 6.71 [dd, J_{H5} = 8.3, J_P = 2.0, 4 H, Ar*(*H*^{5})], 4.12 (m, 8 H, CH_2 crown), 4.00–3.83 (m, 16 H, CH_2 crown), 3.74–3.67 (m, 32 H, CH_2 crown), 3.65 (s, 16 H, CH_2 crown), 1.79 (d, J_P = 10.3, 6 H, Me) ppm. $^{13}C\{^1H\}$ NMR ($CDCl_3$, 126 MHz): δ = 151.35 [s, Ar*(*C*^{4})], 148.46 [pseudo t, $J_{P\ virtual}$ = 13.4, Ar*(*C*^{3})], 126.65 [pseudo t, $J_{P\ virtual}$ = 11.2, Ar*(*C*^{6})], 122.23 [d, J_P = 68.4, Ar*(*C*^{1})], 118.26 [pseudo t, $J_{P\ virtual}$ = 14.4, Ar*(*C*^{2})], 112.81 [pseudo t, $J_{P\ virtual}$ = 14.4, Ar*(*C*^{5})], 70.91, 70.84, 70.79, 70.74, 70.67, 70.62, 69.41, 69.38, 68.90 (s, *C*H_2 crown), 17.71 (d, J_P = 47.8, Me) ppm. $^{31}P\{^1H\}$ NMR ($CDCl_3$, 202 MHz): δ = 0.9 (s with ^{195}Pt satellites, J_{Pt} = 3641 Hz).

[$PtCl_2$(PAr*$_2$Ph)$_2$] (12): Phosphane **3** (0.185 g, 0.25 mmol) and [$PtCl_2$(PhCN)$_2$] (0.060 g, 0.125 mmol) were dissolved in toluene (5 mL). The mixture was stirred at room temperature for 15 h. Then, the solvent was removed in vacuo, the residue washed several times with hexane, and crystallized by addition of absolute methanol to afford **12** as a white solid (0.198 g, 90%). Alternatively, the reaction time was reduced to 1 h when [$PtCl_2$(COD)] (COD = 1,5-cyclooctadiene) was used instead of [$PtCl_2$(PhCN)$_2$]. In both cases, only the *cis* isomer was detected. $C_{76}H_{102}Cl_2O_{24}P_2Pt$ (1727.56): calcd. C 52.84, H 5.95; found C 52.78, H 5.98. IR (Nujol): ν(Pt–Cl) = 317, 290. ^1H NMR ($CDCl_3$, 300 MHz): δ = 7.42 [m, J_P = 9.0, 4 H, Ph(*H*$_{ortho}$)], 7.27 [m, 2 H, Ph(*H*$_{para}$)], 7.15 [m, 4 H, Ph(*H*$_{meta}$)], 7.09 [m, J_P = 12.0, J_{H6} = 1.8, 4 H, Ar*(*H*^{2})], 6.86 [m, J_P = 10.2, 4 H, Ar*(*H*^{6})], 6.57 [dd, J_{H5} = 8.5, J_P = 2.3, 4 H, Ar*(*H*^{5})], 4.11 (m, 8 H, CH_2 crown), 3.90 (m, 8 H, crown), 3.75 (m, 16 H, crown), 3.70 (m, 16 H, crown), 3.67 (m, 16 H, crown), 3.65 (s, 16 H, crown) ppm. $^{13}C\{^1H\}$ NMR ($CDCl_3$, 75 MHz): δ = 151.02 [s, Ar*(*C*^{4})], 147.75 [pseudo t, $J_{P\ virtual}$ = 15.2, Ar*(*C*^{3})], 134.25 [pseudo t, $J_{P\ virtual}$ = 9.4, Ph(*C*$_{ortho}$)], 131.00 [pseudo dd, $J_{apparent}$ = 62.4 and 2.3, Ph(*C*$_{ipso}$)], 130.38 [s, Ph(*C*$_{para}$)], 128.88 [pseudo t, $J_{P\ virtual}$ = 10.6, Ar*(*C*^{6})], 127.62 [pseudo t, J_P = 11.4, Ph(*C*$_{meta}$)], 120.85 [pseudo dd, $J_{apparent}$ = 70.6 and 1.5, Ar*(*C*^{1})], 120.40 [pseudo t, J_P = 13.2, Ar*(*C*^{2})], 112.04 [d, J_P = 13.2, Ar*(*C*^{5})], 70.91, 70.85, 70.79, 70.72, 70.69, 70.56, 69.38, 69.31, 68.97, 68.79 (s, *C*H_2 crown) ppm. $^{31}P\{^1H\}$ NMR ($CDCl_3$, 202 MHz): δ = 14.8 (s with ^{195}Pt satellites, J_{Pt} = 3673 Hz).

[$PdCl_2$(PAr*Ph_2)$_2$] (13): This complex has been previously reported by Okano et al.[6] We employed the same procedure as described above for **12**. The crude product contains traces of the *cis* isomer (δ_P = 33.0 ppm), but after crystallization complex **13** was obtained as a pure yellow solid containing only the *trans* isomer (90%). $C_{56}H_{66}Cl_2O_{12}P_2Pd$ (1170.41): calcd. C 57.47, H 5.68; found C 57.80, H 5.63. MS (ESI+): *m*/*z* = 1193.6 (calcd. for MNa^+: 1192.2). IR (Nujol): ν(Pd–Cl) = 359. ^1H NMR ($CDCl_3$, 300 MHz): δ = 7.62 [m, 8 H, Ph(*H*$_{ortho}$)], 7.45 [td, $J_{P\ virtual}$ = 12.0, J_{H6} = 1.9, 2 H, Ar*(*H*^{2})], 7.40–7.30 [m, 12 H, Ph(*H*$_{meta}$) and Ph(*H*$_{para}$) overlapping], 7.14 [m, $J_{P\ virtual}$ = 10.4, J_{H5} = 8.4, 2 H, Ar*(*H*^{6})], 6.82 [br. d, $J_{P\ virtual} \approx$ 2.0, 2 H, Ar*(*H*^{5})], 4.14 (m, 4 H, CH_2 crown), 4.00 (m, 4 H, crown), 3.91 (m, 4 H, crown), 3.79 (m, 4 H, crown), 3.74 (m, 4 H, crown), 3.70–3.68 (m, 12 H, crown), 3.65 (s, 8 H, crown) ppm. $^{13}C\{^1H\}$ NMR ($CDCl_3$, 75 MHz): δ = 151.03 [s, Ar*(*C*^{4})], 148.16 [pseudo t, $J_{P\ virtual}$ = 14.8, Ar*(*C*^{3})], 134.79 [pseudo t, $J_{P\ virtual}$ = 11.8, Ph(*C*$_{ortho}$)], 130.33 [s, Ph(*C*$_{para}$)], 130.21 [pseudo t, J_P = 50.1, Ph(*C*$_{ipso}$)], 128.94 [pseudo t, $J_{P\ virtual}$ = 11.8, Ar*(*C*^{6})], 127.90 [pseudo t, $J_{P\ virtual}$ = 8.8, Ph(*C*$_{meta}$)], 121.08 [pseudo t, $J_{P\ virtual}$ = 14.8, Ar*(*C*^{2})], 120.80 [pseudo t, $J_{P\ virtual}$ = 53.2, Ar*(*C*^{1})], 112.76 [pseudo t, $J_{P\ virtual}$ = 5.6, Ar*(*C*^{5})], 70.97, 70.83, 70.79, 70.75, 70.66, 69.46, 69.05, 68.84 (s, *C*H_2 crown) ppm. $^{31}P\{^1H\}$ NMR ($CDCl_3$, 202 MHz): δ = 24.1 ppm.

[$PdCl_2$(PAr*$_2$Me)$_2$] (14): The procedure described above for **11** was used for the synthesis of palladium complex **14** starting from **8** (0.064 g, 0.094 mmol), DABCO (0.041 g, 0.37 mmol), and [$PdCl_2$(COD)] (0.012 g, 0.042 mmol). Although complex **14** was formed in greater than 95% yield (^1H NMR evidence) as a pair of *cis*/*trans* isomers (1:0.75), the resultant oil could not be purified by crystallization or chromatography and was used in this form in further catalytic studies. In the NMR spectroscopic data of the unpurified *cis*/*trans* mixture that follows, resonances corresponding to the BH_3·DABCO impurity are omitted, and the *cis*/*trans* ratio has been taken into account in integral values. IR (Nujol): ν(Pd–Cl) = 356 (*trans*), 287, 276 (*cis*). ^1H NMR ($CDCl_3$, 500 MHz,): δ = 7.223 and 7.216 [overlapping m, $J_P \approx$ 10–14, 8 H, Ar*(*H*^{6}) and Ar*(*H*^{2}) *trans* isomer], 7.07 [dd, J_P = 12.4, J_{H6} = 1.9, 4 H, Ar*(*H*^{2}) *cis* isomer], 6.97 [ddd, J_P = 11.8, J_{H5} = 8.3, 4 H, Ar*(*H*^{6}) *cis* isomer], 6.86 [br. d, J_{H6} = 8.4, J_P not observed, 4 H, Ar*(*H*^{5}) *trans* isomer], 6.72 [dd, J_P = 2.6, 4 H, Ar*(*H*^{5}) *cis* isomer], 4.15–3.66 (overlapped m, 80 H, CH_2 crown, *cis* and *trans* isomers), 1.96 (pseudo t, $J_{P\ virtual}$ = 7.1, 6 H, Me *trans* isomer), 1.91 (d, J_P = 11.1, 3 H, Me *cis* isomer) ppm. $^{13}C\{^1H\}$ NMR ($CDCl_3$, 126 MHz): δ = 151.49, 150.93 [s, Ar*(*C*^{4})], 148.65 [d, J_P = 14.3, Ar*(*C*^{3}) *cis* isomer], 148.36 [pseudo t, $J_{P\ virtual}$ = 14.1, Ar*(*C*^{3}) *trans* isomer], 126.8 [m, Ar*(*C*^{6}) *cis* and *trans* overlapping], 123.61 [pseudo t, $J_{P\ virtual}$ = 52.0, Ar*(*C*^{1}) *trans* isomer], 122.78 [d, J_P = 57.5, Ar*(*C*^{1}) *cis* isomer], 118.78 [pseudo t, $J_{P\ virtual}$ = 14.4, Ar*(*C*^{2}) *trans* isomer], 118.22 [d, J_P = 13.8, Ar*(*C*^{2}) *cis* isomer], 113.00 [m, Ar*(*C*^{5}) *cis* and *trans* overlapping], 70.97, 70.95, 70.85, 70.82, 70.76, 70.69, 70.64, 69.48, 69.41, 69.24, 68.91, 68.85 (s, *C*H_2 crown), 18.6 (overlapping d and m, Me) ppm. $^{31}P\{^1H\}$ NMR ($CDCl_3$, 202 MHz): δ = 19.7 (*cis*), 7.7 (*trans*).

[$PdCl_2$(PAr*$_2$Ph)$_2$] (15): The procedure described above for **12** was used for the synthesis of palladium complex **15** starting from phosphane **3** (0.168 g, 0.25 mmol) and [$PdCl_2$(PhCN)$_2$] (0.048 g, 0.125 mmol). A yellow solid was obtained (0.20 g, 98%) that was identified by NMR spectroscopy as a 3:7 mixture of *cis*/*trans* isomers of complex **15**. Both isomers were easily separated because of their different solubility in toluene. The soluble *cis* isomer was extracted in this solvent and subsequently crystallized from methanol whereas the insoluble residue containing the *trans* isomer was crystallized from CH_2Cl_2/toluene. Both were obtained as deep-yellow solids.

***trans*-15:** $C_{76}H_{102}Cl_2O_{24}P_2Pd$ (1638.90): calcd. C 55.70, H 6.27; found C 55.54, H 6.20. IR (Nujol): ν(Pd–Cl) = 356. ^1H NMR ($CDCl_3$, 500 MHz): δ = 7.57 [m, J_P = 12.4, 4 H, Ph(*H*$_{ortho}$)], 7.40–7.30 [m, 10 H, Ph(*H*$_{para}$), Ph(*H*$_{meta}$), and Ar*(*H*^{2}) overlapping], 7.08 [m, J_P = 10.3, J_{H5} = 8.5, J_{H2} = 2.0, 4 H, Ar*(*H*^{6})], 6.80 [br. d, 4 H, Ar*(*H*^{5})], 4.13 (m, 8 H, CH_2 crown), 3.96 (m, 8 H, crown), 3.90 (m, 8 H, crown), 3.79 (m, 8 H, crown), 3.49 (m, 8 H, crown), 3.71–

 © 2005 Wiley-VCH Verlag GmbH & Co. KGaA, Weinheim

3.68 (m, 24 H, crown), 3.67 (s, 16 H, crown) ppm. $^{13}C\{^1H\}$ NMR ($CDCl_3$, 75 MHz): δ = 150.93 [s, Ar*(C^4)], 148.98 [pseudo t, $J_{P\ virtual}$ = 14.8, Ar*(C^3)], 134.59 [pseudo t, $J_{P\ virtual}$ = 11.8, Ph(C_{ortho})], 130.81 [pseudo t, $J_{P\ virtual}$ = 45.4, Ph(C_{ipso})], 130.19 [s, Ph(C_{para})], 128.78 [pseudo t, $J_{P\ virtual}$ = 11.8, Ar*(C^6)], 127.82 [pseudo t, J_P = 10.4, Ph(C_{meta})], 121.25 [pseudo t, $J_{P\ virtual}$ = 53.0, Ar*(C^1)], 120.86 [m, Ar*(C^2), overlapping with Ar*(C^1)], 113.17 [d, J_P = 12.5, Ar*(C^5)], 70.98, 70.94, 70.85, 70.78, 70.65, 69.49, 69.13, 68.85 (s, CH_2 crown) ppm. $^{31}P\{^1H\}$ NMR ($CDCl_3$, 202 MHz): δ = 23.8 ppm.

***cis*-15:** $C_{76}H_{102}Cl_2O_{24}P_2Pd$ (1638.90): calcd. C 55.70, H 6.27; found C 55.78, H 6.19. IR (Nujol): ν(Pd–Cl) = 287, 276. ^1H NMR ($CDCl_3$, 300 MHz): δ = 7.63 [m, J_P = 12.6, 4 H, Ph(H_{ortho})], 7.45 [m, 2 H, Ph(H_{para})], 7.38 [m, 4 H, Ph(H_{meta})], 7.29 [dd, J_P = 13.2, J_{H6} = 1.8, 4 H, Ar*(H^2)], 7.05 [ddd, J_P = 12.1, J_{H5} = 8.4, 4 H, Ar*(H^6)], 6.80 [dd, J_P = 2.5, 4 H, Ar*(H^5)], 4.15 (m, 8 H, CH_2 crown), 4.07 (m, 8 H, crown), 3.92 (m, 8 H, crown), 3.80 (m, 8 H, crown), 3.75 (m, 8 H, crown), 3.71–3.68 (m, 24 H, crown), 3.67 (s, 16 H, crown) ppm. $^{13}C\{^1H\}$ NMR ($CDCl_3$, 75 MHz): δ = 151.89 [d, $J_P \approx$ 1.0, Ar*(C^4)], 148.30 [d, J_P = 15.5, Ar*(C^3)], 134.40 [d, J_P = 11.6, Ph(C_{ortho})], 131.51 [s, Ph(C_{para})], 128.76 [d, J_P = 3.9, Ar*(C^6)], 128.31 [d, J_P = 12.2, Ph(C_{meta})], 128.28 [d, J_P = 54.7, Ph(C_{ipso})], 120.09 [d, J_P = 14.9, Ar*(C^2)], 118.31 [d, J_P = 64.7, Ar*(C^1)], 112.45 [d, J_P = 15.5, Ar*(C^5)], 71.01, 70.95, 70.86, 70.73, 70.71, 70.58, 69.39, 69.34, 69.26, 68.83 (s, CH_2 crown) ppm. $^{31}P\{^1H\}$ NMR ($CDCl_3$, 202 MHz): δ = 33.4 ppm.

Water Solubility of Complexes 10 and 11: The extent of water solubility was assessed by placing a small, accurately weighted quantity of the compound in a vial, followed by slow addition of water, with stirring, from a 50 μL syringe. Solubility measurements were repeated several times to give an average value. Measured solubility in water at 25 °C: 0.002 g/100 mL (**10**) and 10 g/100 mL (**11**).

Distribution Coefficients Between Toluene and Water for Phosphanes 1 and 3: Previously, the UV spectra of phosphanes **1** and **3** were registered in ethanol at several concentrations (from ca. 1×10^{-5} to 1×10^{-4} M). Two absorption bands were observed at λ_{max} = 203 and 261 nm for **1**, and 208 and 283 nm for **3**. Fits of *c* versus *A* plots showed a linear correlation in the entire range of concentrations considered only in the case of the second maximum absorption ($R^2 > 0.999$). Thus, the absorptions at 261 nm (ε = 12100) for **1**, and 283 nm (ε = 13300) for **3** were used as follows in the determination of distribution coefficients. A small, accurately weighted quantity of phosphane (approx. 0.02 mmol) was added to a 1:1 mixture of toluene and water (5 + 5 mL) that was stirred for 20 min at 25 °C. An aliquot of the aqueous solution (2 mL) was removed with a pipette, evaporated to dryness, and dissolved in ethanol (3 mL). The original water-phase concentration was determined by measuring the concentration of phosphane in the ethanol solution by UV spectroscopy, using the *c* versus *A* plots previously obtained. At 25 °C, distribution constants, defined as $[phosphane]_{aq}/[phosphane]_{toluene}$, are 7.4×10^{-3} for **1**, and 1.46×10^{-2} for **3**.

Palladium-Catalyzed Stille Couplings: We used similar conditions to those previously described.[40,41] In a typical experiment, $PhSnCl_3$ (0.31 mL, 1.824 mmol) was dissolved in 2 mL of degassed water. The solution was treated with 5.5 mL of aqueous KOH (1 M) and stirred for several minutes. The *p*-iodoaniline (0.339 g, 1.52 mmol) and the Pd catalyst **14** (0.023 g, 0.0152 mmol) were then added and the mixture was stirred for 3 h at 100 °C under argon. The product was extracted with diethyl ether and dried with sodium sulfate. The solution was filtered off and the solvent removed in vacuo to give a solid. The crude product was analyzed by HPLC-MS and ^1H NMR spectroscopy (95% 4-aminobiphenyl, 5% *p*-iodoaniline) and purified by flash chromatography on silica gel with toluene/ethanol (9:1) to give pure 4-aminobiphenyl (0.244 g, 95%).

X-ray Structure Determinations: White, needle-shaped crystals of **9** were obtained from methanol/ethanol at –25 °C. A summary of crystal data, data collection, and refinement parameters for the structural analysis is given in Table 3. The crystal was glued to a glass fiber and mounted on a Kappa-CCD Bruker–Nonius diffractometer with area detector, and data were collected using graphite monochromated Mo-K_α radiation (λ = 0.71073 Å). Data collection was performed at 200 K, with an exposure time of 24 s per frame (3 sets; 247 frames). Raw data were corrected for Lorenz and polarization effects. The structure was solved by direct methods, completed by subsequent difference Fourier techniques, and refined by full-matrix least-squares on F^2 (SHELXL-97).[46] Anisotropic thermal parameters were used in the last cycles of refinement for the non-hydrogen atoms. Most of the hydrogen atoms were found in the final Fourier map and were refined with isotropic thermal displacement parameters, others were introduced in the last cycle of refinement from geometrical calculations and refined using a riding model. A molecule of methanol with important disorder was located; the hydrogen atoms of the methyl group are not included. All the calculations were made using the WINGX system.[47]

CCDC-253624 contains the supplementary crystallographic data for this paper. These data can be obtained free of charge from The Cambridge Crystallographic Data Centre via www.ccdc.cam.ac.uk/data_request/cif.

Table 3. Crystallographic details for **9**.

Empirical formula	$C_{38}H_{54}BO_{12}P{\cdot}CH_4O$
Habit	needles
Formula mass	776.67
a [Å]	18.7794(19)
b [Å]	8.5756(9)
c [Å]	26.566(4)
β [°]	106.11(1)
λ (Mo-$K\alpha$) [Å]	0.71073
Temp. [K]	200(2)
Space group	monoclinic, $P2_1/n$
Crystal size [mm]	$0.5 \times 0.1 \times 0.1$
V [Å^3]	4110.3(9)
Z	4
$D_{calcd.}$ [g cm^{-3}]	1.226
μ [cm^{-1}]	1.26
θ limits [°]	5.00 to 27.51
Limiting indices	$-24 \le h \le 24$
	$-11 \le k \le 11$
	$-34 \le l \le 23$
Reflections collected	25581
Unique reflections	9222 [R(int) = 0.1577]
Reflections observed with $I > 2\sigma(I)$	4238
Data/restraints/parameters	9222/0/677
R [$I > 2\sigma(I)$]; wR^2 [a]	0.0984; 0.2027
Goodness-of-fit indicator	1.013
Max. peak in final diff. map [e Å^{-3}]	0.578
Min. peak in final diff. map [e Å^{-3}]	–0.390

[a] $R = \Sigma||F_o| - |F_c||/\Sigma|F_o|$; $wR^2 = [\Sigma w(F_o^2 - F_c^2)^2/\Sigma w(F_o^2)^2]^{1/2}$.

Acknowledgments

We gratefully acknowledge financial support from the DGI-Ministerio de Ciencia y Tecnología (Project BQU2001-1160).

 © 2005 Wiley-VCH Verlag GmbH & Co. KGaA, Weinheim

[1] *Aqueous-Phase Organometallic Catalysis: Concepts and Applications* (Eds.: B. Cornils, W. A. Herrmann), VCH, 2nd ed., **2004**.
[2] N. Pinault, D. W. Bruce, *Coord. Chem. Rev.* **2003**, *241*, 1–25.
[3] O. Stelzer, S. Rossenbach, D. Hoff, ref.[1], pp. 100–120.
[4] E. M. Hyde, B. L. Shaw, I. Shepherd, *J. Chem. Soc., Dalton Trans.* **1978**, 1696–1705.
[5] T. Okano, M. Iwahara, T. Suzuki, H. Konishi, J. Kiji, *Chem. Lett.* **1996**, 1467–1470.
[6] T. Okano, M. Iwahara, H. Konishi, J. Kiji, *J. Organomet. Chem.* **1988**, *346*, 267–275.
[7] V. I. Kal'chenko, D. M. Rudkevich, O. A. Aleksyuk, L. N. Markovskii, *Zh. Obshch. Khim.* **1991**, *61*, 2155–2158.
[8] B. S. Muehl, B.-J. Sheu, S. A. Burns, J. E. Fritz, D. A. Tribbett, J. A. Weitgenant, B. N. Storhoff, J. C. Huffman, *J. Coord. Chem.* **1995**, *35*, 359–370.
[9] C. Nataro, H. Baseski, C. M. Thomas, B. J. Wiza, K. M. Rourke, *Polyhedron* **2001**, *20*, 1023–1028.
[10] M. Sawamura, Y. Nakayama, W.-M. Tang, Y. Ito, *J. Org. Chem.* **1996**, *61*, 9090–9096.
[11] L. A. Barg, R. W. Byrn, M. D. Carr, D. H. Nolan, B. N. Storhoff, J. C. Huffman, *Organometallics* **1998**, *17*, 1340–1346.
[12] J. Kiji, T. Okano, *Rev. Heteroatom Chem.* **1994**, *11*, 191–206.
[13] T. Okano, M. Iwahara, J. Kiji, *Synlett* **1998**, 243–244.
[14] V. Berdini, M. Bassetti, G. Mancini, L. Mandolini, D. Monti, *J. Organomet. Chem.* **1998**, *551*, 331–338.
[15] J. K. Stille, *Angew. Chem. Int. Ed. Engl.* **1986**, *25*, 508–524.
[16] P. Espinet, A. M. Echavarren, *Angew. Chem. Int. Ed.* **2004**, *43*, 4704–4734 and references cited therein.
[17] For a review on palladium-catalyzed reactions in aqueous media, see: J. P. Genet, M. Savignac, *J. Organomet. Chem.* **1999**, *576*, 305–317.
[18] B. Mohr, D. M. Lynn, R. H. Grubbs, *Organometallics* **1996**, *15*, 4317–4325 and references cited therein.
[19] H. Brisset, Y. Goudel, P. Pellon, M. L. Corre, *Tetrahedron Lett.* **1993**, *34*, 4523–4526.
[20] J. G. Verkade, *Coord. Chem. Rev.* **1972**, *9*, 1–106.
[21] $\delta_{\text{Coord P}} = \delta_{\text{Free P}} + A\delta_{\text{Free P}} + B$, where for the *trans* and *cis* isomers $A = -0.212$ and $B = 38.6$, and $A = -0.304$ and $B = 26.8$, respectively. A. W. Verstuyft, J. H. Nelson, L. W. Gary, *Inorg. Nucl. Chem. Lett.* **1976**, *12*, 53–58. Parameters for other metal complexes can be found in ref.[26]
[22] F. R. Hartley, *Organomet. Chem. Rev. A* **1970**, *6*, 119–137.
[23] P. S. Pregosin, R. W. Kunz, *^{31}P and ^{13}C NMR of Transition Metal Phosphane Complexes*, Springer-Verlag, Heidelberg, **1979**.
[24] L. Bemi, H. C. Clark, J. A. Davies, C. A. Fyfe, R. E. Wasylishen, *J. Am. Chem. Soc.* **1982**, 438–445.
[25] G. K. Anderson, H. C. Clark, J. A. Davies, *Inorg. Chem.* **1981**, *20*, 3607–3611.
[26] B. E. Mann, C. Masters, B. L. Shaw, R. M. Slade, R. E. Satinbank, *Inorg. Nucl. Chem. Lett.* **1971**, *7*, 881–885.
[27] W. Strohmeir, F. J. Müller, *Chem. Ber.* **1967**, *100*, 2812–2821.
[28] C. A. Tolman, *Chem. Rev.* **1977**, *77*, 313–348.
[29] A. Immirzi, A. Musco, *Inorg. Chim. Acta* **1977**, *25*, L41–L42.
[30] T. Bartik, T. Himmler, *J. Organomet. Chem.* **1985**, *293*, 343–351.
[31] This value (δ =24.4 ppm) has been measured by us and differs from that given in ref.[30] (δ =13.3 ppm). In fact, the value of δ = 24.4 ppm correlates far better with the Tolman angle of 145°.
[32] T. Bartik, B. Bartik, B. E. Hanson, I. Guo, I. Tóth, *Organometallics* **1993**, *12*, 164–170.
[33] L. D. Quin, in *Phosphorous-31 NMR Spectroscopy in Stereochemical Analysis* (Eds.: J. G. Verkade, L. D. Quin), VCH, Deerfield Beach, **1987**, chapter 12.
[34] More rigorously speaking, they form an ABX spin system with $\delta_A \approx \delta_B$, because the ^{13}C nucleus breaks the chemical equivalence of both ^{31}P nuclei.
[35] J. C. Huffman, W. A. Skupinski, K. G. Caulton, *Cryst. Struct. Commun.* **1982**, *11*, 1435–1440.
[36] I. Dance, M. Scudder, *J. Chem. Soc., Dalton Trans.* **2000**, 1579–1585.
[37] E. C. Alyea, S. A. Dias, G. Ferguson, R. J. Restivo, *Inorg. Chem.* **1977**, *16*, 2329–2334.
[38] In a study based on 2388 phosphane complexes, the mean value obtained was 148(5)°, with a range of 129–168°: T. E. Müller, D. M. P. Mingos, *Transition Met. Chem.* **1995**, *20*, 533–539.
[39] H.-C. Zhang, G. D. Daves, Jr., *Organometallics* **1993**, *12*, 1499–1500.
[40] A. I. Roshchin, N. A. Bumagin, I. P. Beletskaya, *Tetrahedron Lett.* **1995**, *36*, 125–128.
[41] R. Rai, K. B. Aubrecht, D. B. Collum, *Tetrahedron Lett.* **1995**, *36*, 3111–3114.
[42] C. Wolf, R. Lerebours, *J. Org. Chem.* **2003**, *68*, 7551–7554.
[43] The formation of Pd^0 complexes and Pd metal precipitation when treating $[PdCl_2(PPh_3)_2]$ complexes with NaOH or KOH has been reported: V. V. Grushin, H. Alper, *Organometallics* **1993**, *12*, 1890–1901.
[44] D. D. Perrin, W. L. F. Armarego, *Purification of Laboratory Chemicals*, 3rd ed., Butterworth-Heinemann Ltd., Oxford, **1988**.
[45] D. Drew, J. R. Doyle, *Inorg. Synth.* **1972**, *13*, 47–55.
[46] G. M. Sheldrick, SHELXL-97, University of Göttingen, Göttingen, Germany, **1997**.
[47] WinGX System: L. J. Farrugia, *J. Appl. Cryst.* **1999**, *32*, 837–838.

Received: October 26, 2005

 © 2005 Wiley-VCH Verlag GmbH & Co. KGaA, Weinheim

An Efficient Keim-Type Catalyst Based on an Electron-Poor *P,O*-Chelate; Tuning the Selectivity of Ethylene Oligomerisation towards Short α-Olefins

Pierre Kuhn,[a] David Sémeril,[a] Catherine Jeunesse,[a] Dominique Matt,*[a] Pierre Lutz,*[b] and Richard Welter[c]

Keywords: Nickel *P,O* complexes / 4-Phosphanylpyrazolonate / Oligomerisation / Phosphorus ylides / Electron-withdrawing ligands / X-ray diffraction

The tertiary phosphane Ph_2P-pzONa, in which the phosphorus atom is substituted by an electron-withdrawing pyrazolonato unit, reacts with *trans*-[NiPhCl(PPh_3)$_2$] to afford quantitatively *trans-P,P′*-[NiPh(Ph_2P-pzO)(PPh_3)] (**4**), the first Keim-type catalyst derived from an amide. In the absence of any cocatalyst, complex **4** converts ethylene in high selectivity and activity into α-olefins. The product distribution is drastically shifted towards lower oligomers when compared to the outcome of the reaction carried out with the conventional SHOP catalyst. Thus, when operating at 1 bar, over 99 wt.-% of the oligomers formed are C_4–C_{16} oligomers. In ethylene-free solvents, **4** was shown to slowly undergo reductive elimination to produce the stabilised phosphorus ylide Ph_3P-pzO (**5**). Both compounds (**4** and **5**) were characterised by single-crystal X-ray diffraction analyses.

(© Wiley-VCH Verlag GmbH & Co. KGaA, 69451 Weinheim, Germany, 2005)

Introduction

Square-planar nickel(II) complexes of the general formula *trans-P,P′*-[NiAr{Ar_2PCH=C(O)R′}(PR_3)] (**1**; R, R′ = aryl, alkyl) have been extensively studied over the last 25 years, mainly because of their ability to oligomerise ethylene into α-olefins under mild conditions.[1–7] The discovery of this catalyst type stretches back to the early seventies, when researchers at SHELL discovered that mixing Ni^0 complexes with phosphorus ylides, e.g. Ph_3PCH=C(O)Ph (**2**), produced highly active oligomerisation catalysts.[8] Later, Keim et al. showed that reaction of **2** with Ni(cod)$_2$ in the presence of PPh_3 resulted in an oxidative addition reaction with cleavage of a P–Ph(ylide) bond and subsequent formation of the phosphanyl-enolato complex [NiPh{Ph_2PCH=C(O)Ph}(PPh_3)] (**1a**), known as Keim's oligomerisation catalyst.[9] Since Keim's pioneering studies, a number of related *P,O*-nickel complexes (*P,O* = 3-electron chelate) have been prepared and studied, but surprisingly little is known about variants in which the *P,O*-chelate behaves as an electron-poor donor, although the complex [NiH{$Ph_2PCH_2C(CF_3)_2O$}PCy_3] was reported to be inactive. Note that several recent publications have focussed on nickel complexes with electron-rich *P,O*-chelates,[10,11] while a few nickel complexes in which the *P,O* ligand behaves as a neutral 4-electron donor have also been studied.[12]

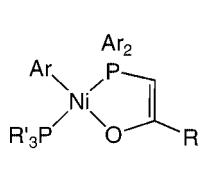

1 R = alkyl, aryl

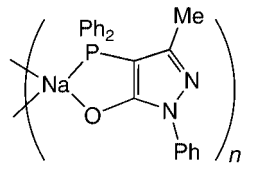

[Na(Ph_2P-pzO)]$_n$ (**3**•Na)

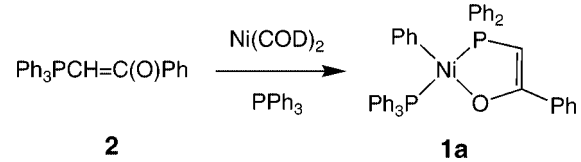

2 **1a**

We now describe the convenient, direct synthesis of the new Keim-type catalyst **4** starting from a P^{III} derivative, namely the sodium pyrazolonato-phosphane Ph_2P-pzONa (**3**•Na).[13] Our investigations show how the presence of the strong electron-withdrawing pyrazolonato ring,[14] known to be stronger than CF_3, drastically drives the product distribution towards shorter olefins. The present study furthers demonstrates that "Keim catalysts" may undergo reductive elimination with formation of a phosphorus ylide. The reported complex **4** is the first example of a Keim-type catalyst derived from an amide.

[a] Université Louis Pasteur, Laboratoire de Chimie Inorganique Moléculaire, UMR 7513 CNRS,
1 rue Blaise Pascal, 67008 Strasbourg Cedex France
E-mail: dmatt@chimie.u-strasbg.fr
[b] Institut Charles Sadron, UPR 22 CNRS,
6 rue Boussingault, 67083 Strasbourg Cedex
[c] DECMET, UMR 7513,
4 rue Blaise Pascal, 67070 Strasbourg Cedex France
Supporting information for this article is available on the WWW under http://www.eurjic.org or from the author.

Results and Discussion

Reaction of [NiPhCl(PPh_3)$_2$] with one equiv. of Ph_2P-pzONa in toluene afforded complex **4** in ca. 90% yield. It is noteworthy that this reaction constitutes a rare case in which a **1a**-analogue was obtained from a phosphanylenolate rather than a phosphorus ylide. The ^{31}P NMR spectrum of **4** displays an AB quartet (δ_A/δ_B = 20.2/–8.6 ppm) with a J(PP′) coupling constant of 280 Hz, typical for *trans*-arranged phosphorus atoms. The phosphorus signal of the P-enolato moiety (δ = –8.6 ppm) is strongly shifted to high field with respect to that of other diphenylphosphanylenolates reported in the literature, thus reflecting the high electron-withdrawing nature of the pyrazolonato ring. The solid-state structure of **4** was elucidated by an X-ray diffraction study (Figure 1), which reveals a significant deviation from the usual square-planar coordination geometry observed in other [NiPh(*PO*)PPh_3] complexes. Thus, while the C(23) and oxygen atoms lie on one side of the mean-squares coordination plane, the two P atoms are turned towards the other side [distances to the plane: C(23) –0.154(1); O –0.160(1); P1 +0.184(1); P2 +0.185(1) Å]. Consistent with the electronic features of the pyrazolonato ring, the Ni–O and the Ni–P(1) bonds [1.955(1) Å and 2.210(1) Å, respectively] are somewhat longer than their counterparts in **1a** (1.914 Å; 2.168 Å). The shortness of the P(1)–C(2) bond [1.770(2) Å] is in keeping with electron delocalisation within the *PO* chelate.

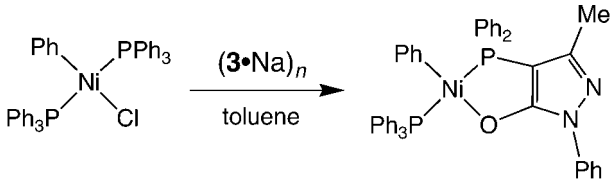

4

Interestingly, we noted that on standing, colourless crystals slowly formed from toluene solutions containing **4**. An X-ray analysis of the product reveals the formation of the phosphorus ylide **5** (Figure 2). Surprisingly, a similar reductive elimination reaction had not been reported for **1a**. A careful reinvestigation of the latter complex showed that, in fact, **1a** undergoes the same slow transformation in toluene, resulting in the formation of $Ph_3PCH{=}C(O)Ph$. Possibly, this transformation is triggered by the presence of trace amounts of air, since we found that bubbling air through a C_6D_6 solution of **4** rapidly produced **5**.

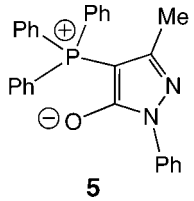

5

Typically for a Keim-type catalyst, complex **4** displays high activity in the low pressure oligomerisation of ethylene without requiring any activating agent to trigger the reaction. Turnover frequencies (TOF) as high as

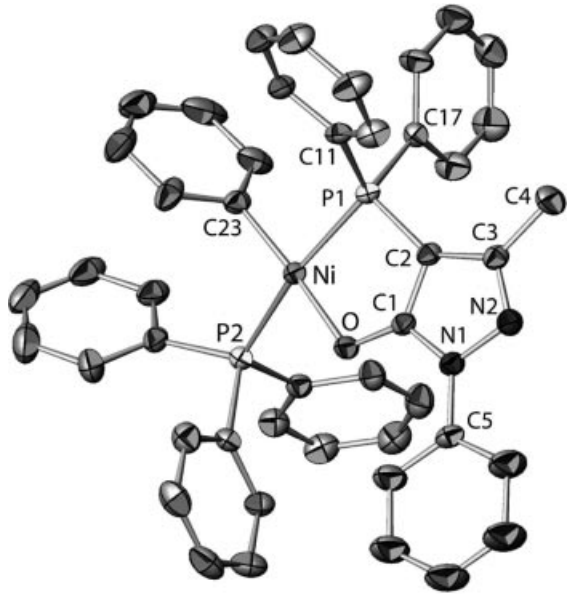

Figure 1. Molecular structure of complex **4**. Important distances [Å] and angles [°]: NiC(23) 1.885(2); NiO 1.955(1); NiP(1) 2.210(1); NiP(2) 2.224(1); P(1)C(2) 1.770(2); P(1)C(17) 1.820(2); P(1)C(11) 1.823(2); OC(1) 1.296(2); C(2)C(1) 1.393(2); C(2)C(3) 1.419(3); N(1)C(1) 1.370(2); N(1)N(2) 1.400(2) P(1)NiP(2) 167.26(2); C(23) NiO 173.83(7).

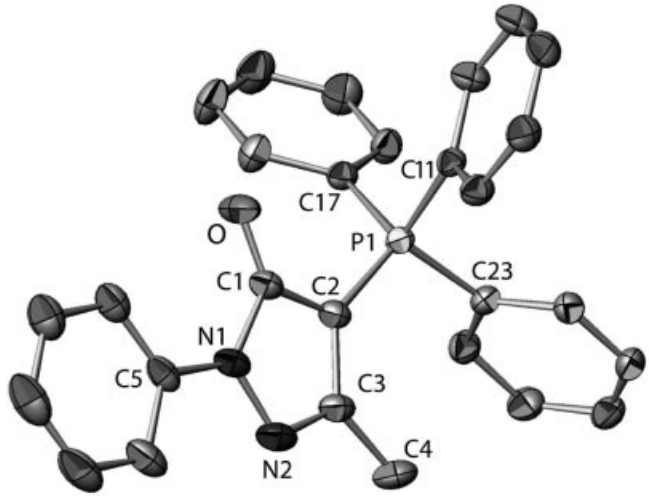

Figure 2. Molecular structure of the phosphorus ylide **5**. Important distances [Å]: P(1)C(2) 1.736(2); P(1)C(23) 1.797(3); P(1)C(17) 1.806(2); P(1)C(11) 1.808(2); OC(1) 1.249(3); C(2)C(1) 1.430(3); C(2)C(3) 1.429(3); N(1)C(1) 1.400(3); N(1)N(2) 1.395(3).

6600 $mol_{ethylene}{\cdot}mol_{Ni}^{-1}{\cdot}h^{-1}$ were observed when operating in toluene at 70 °C under a constant ethylene pressure of 5 bar and a nickel concentration of 0.25 μmol/mL (cf. TOF = 7500 for **1a**) [2 h experiments]. At this pressure, the selectivity in the α-olefins surpassed 95% (Table 1).

The most striking feature of **4** involves the product distribution which considerably shifts towards lower oligomers in comparison with the outcome of Keim's catalyst. Thus, under the conditions outlined above, ca. 72 wt.-% of the oligomers produced after 60 min were C_4–C_{16} olefins; this fraction represents only 15 wt.-% of the total amount of

 © 2005 Wiley-VCH Verlag GmbH & Co. KGaA, Weinheim

Table 1. Ethylene oligomerisation with **1a** and **4**. General conditions: toluene 30 mL, 70 °C, calibrated on heptane.

Ni complex (7.5 μmol)[a]	$P(C_2H_4)$ [bar]	Time [h]	BF_3 [μmol]	TOF [$mol_{ethylene} \cdot mol_{Ni}^{-1} \cdot h^{-1}$]	C_4–C_{16} distribution [wt.-%]
1a	1	2		3400	60.2
1a	5	2		7500	15.3
1a	5	1		15500	15.3
1a[a]	20	1		19900	9.6
1a[a]	20	1	7.5	9400	9.6
4	1	2		1800	98.9
4	5	2		6600	45.2
4	5	1		9700	72.5
4[a]	20	1		6600	25.1
4[a]	20	1	7.5	3800	97.0

[a] Batch experiments, toluene 20 mL, 70 °C.

oligomers produced with **1a** in the same period of time. When applying a constant ethylene pressure of 1 bar, this ratio rose to 99 wt.-% (versus 60% for **1a**). The performances of **4** and **1a** were also compared with those in batch experiments carried out at higher pressures. Thus, when applying an initial pressure of 20 bar ([Ni] = 0.25 μmol/mL), the amount of C_4–C_{16} olefins produced with **4** after 1 h was 25 wt.-% of the total amount of oligomers, versus only 9.6% for **1a**. It must be mentioned here that a SHOP catalyst in which the oxygen atom was involved in hydrogen bonding has been reported to also favour β elimination, hence the formation of shorter oligomers, but not to such an extent.[2] Interestingly, the observed effect can be drastically enhanced by using BF_3 as an additive. For example, in experiments where stoichiometric amounts of BF_3 were used (batch autoclave, $P_{initial}$ = 20 bar, [**4**] = 0.25 μmol/mL), the fraction of C_4–C_{16} olefins obtained after 1 h represented 97% of all oligomers formed. It appears plausible that the BF_3 unit binds to the pyrazole ring, probably through a nitrogen atom,[15] hence increasing the electron deficiency of the nickel atom. Overall, the effect observed by adding BF_3 is reminiscent of the properties of [Ni{$Ph_2PC_6H_4C(O)O$}(Me-2-allyl)],[16] which upon addition of $B(C_6F_5)_3$ shifts ethylene oligomerisation towards the formation of low-weight olefins (butene and hexene).[17]

Finally, we noted that mixing complex **4** with $Ni(cod)_2$ in excess afforded, as expected,[11,18,19] a catalyst which polymerises ethylene. Its activity compares with that of **1a**, but analysis of the polymer reveals that the polyethylene chains are considerably shorter (M_w = 650 g mol^{-1}) than those obtained with **1a** (M_w = 4500 g mol^{-1}) under similar conditions. These findings confirm the remarkable electronic properties of the phosphanyl-pyrazolonato ligand. Further investigations are in progress which aim at the use of electron poor *P,O* chelators that allow the controlled production of industrially relevant α-olefins in the absence of any cocatalyst.

Experimental Section

General: All manipulations were performed in Schlenk-type flasks under dry nitrogen. Solvents were dried by conventional methods and distilled immediately prior to use. $CDCl_3$ was passed down a 5 cm-thick alumina column and stored under nitrogen over molecular sieves (4 Å). IR spectra were measured with a Perkin–Elmer 1605 spectrometer. Routine ^1H and $^{31}P\{^1H\}$ spectra were recorded with FT Bruker instruments (AC-300 or Bruker AM–400). $^{13}C\{^1H\}$ were recorded with an FT Bruker AC-200 spectrometer. ^1H NMR spectra are referenced to residual protiated solvents (δ =7.26 ppm for $CDCl_3$ and 5.32 ppm for CD_2Cl_2); ^{13}C chemical shifts are reported relative to deuterated solvents (δ =77.0 ppm for $CDCl_3$ and 53.8 ppm for CD_2Cl_2); ^{31}P NMR spectroscopic data are given relative to external H_3PO_4. The catalytic solutions were analysed with a Varian 3900 gas chromatograph equipped with a WCOT fused silica column (25 m, 0.32 mm inside diameter, 0.25 mm film thickness). High temperature size exclusion chromatography (HT SEC) measurements were performed at 150 °C with a "PL220" apparatus (Column set HT-MixedB-TCB-01) in 1,2,4-trichlorobenzene (with 0.2% Irganox). Calibration was made with linear PS samples. Ph_2P-pzONa[13] and [NiPhCl-(PPh_3)$_2$][20,21] are reported according to procedures reported in the literature.

[NiPh{Ph_2P-pzO}(PPh_3)] (4): To a stirred suspension of Ph_2P-pzONa (0.766 g, 2.14 mmol) in toluene (30 mL) was added a solution of [NiPhCl(PPh_3)$_2$] (1.491 g, 2.14 mmol) in toluene (40 mL). After stirring for 4 h, the mixture was filtered through Celite in order to remove NaCl. The solution was concentrated to ca. 10 mL. On standing, dark yellow crystals formed overnight. After removal of the supernatant solution, the crystals were washed successively with cold toluene (5 mL) and pentane (10 mL), and then dried in vacuo. Yield: 1.088 g, 60%. Addition of pentane to the mother liquor afforded further amounts of **4** as a yellow powder which increases the yield to 90 %. $C_{46}H_{38}N_2NiOP_2 \cdot C_7H_8$ (M_r = 755.46 + 92.14 = 847.60): calcd. C 75.1, H 5.47, N 3.31; found C 74.6, H 5.39, N 3.34. IR (KBr): 1592.6 (m), 1515.5 (s), 1495.0 (s), 1425.8 s cm^{-1}. ^1H NMR (300 MHz, C_6D_6): δ = 8.25–6.44 (35 H, arom. H), 2.02 (s, 3 H, CH_3) ppm. $^{13}C\{^1H\}$ NMR (75 MHz, $CDCl_3$): δ = 140.76–118.06 (arom. C), 89.83 (d, J(P,C) = 63 Hz, PCH), 14.77 (s, CH_3) ppm. $^{31}P\{^1H\}$ NMR (121 MHz, $CDCl_3$): δ = 20.2 and –8.6 (AB spin system, J(PP′) = 280 Hz).

Ph_3P-pzO (5): [NiPh{Ph_2P-pzO}(PPh_3)] (**4**; 0.100 g, 0.13 mmol) was dissolved in toluene (5 mL). Upon standing in air, crystals of Ph_3P-pzO appeared after 48 h. The supernatant was removed by suction, and the crystals were dried under high vacuum. Yield: 0.056 g, 70%. $C_{28}H_{23}N_2OP$ (M_r = 434.48): calcd. C 77.41, H 5.34, N 6.45; found C 77.49, H 5.38, N, 6.41. $^{31}P\{^1H\}$ NMR (121 MHz, $CDCl_3$): δ = 10.6 ppm (lit.: 12.6[22])

X-ray Crystal Structure Determination of 4·toluene: Single crystals of **4** suitable for X-ray diffraction analysis were obtained from a

 © 2005 Wiley-VCH Verlag GmbH & Co. KGaA, Weinheim

Table 2. Crystallographic data for **4**·toluene and **5**·benzene.

Formula	$C_{46}H_{38}N_2NiOP_2 \cdot C_7H_8$ (**4**·toluene)	$C_{28}H_{23}N_2OP \cdot C_6H_6$ (**5**·benzene)
Formula weight	847.57	512.56
Crystal system	Triclinic	Monoclinic
Space group	$P\bar{1}$	$C2/c$
a [Å]	10.939(1)	29.361(5)
b [Å]	13.283(1)	9.314(1)
c [Å]	16.156(1)	22.758(5)
α [°]	72.29(5)	90
β [°]	75.29(5)	119.06(5)
γ [°]	87.71(5)	90
V [Å^3]	2161.2(3)	5440(3)
Z	2	8
$D_{calcd.}$ [g·cm^{-3}]	1.302	1.252
μ(Mo-K_α) [mm^{-1}]	0.565	0.131
F(000)	888	2160
Crystal Size [mm]	0.08 × 0.10 × 0.13	0.06 × 0.07 × 0.09
Temperature [K]	173(2)	173(2)
Radiation [Å]	Mo-K_α 0.71069	Mo-K_α 0.71069
θ min/max [°]	1.4/30.0	1.6/30.0
Data set	–15/15; –17/18; –22/21	–41/36; 0/13; 0/32
Total, Unique data,	34952, 12654	7963, 7962
R(int)	0.035	0.036
Observed data [$I > 2.0\sigma(I)$]	9904	5436
Number of reflections,	12654	7962
Number of parameters	532	333
R_1, wR_2, S	0.0442, 0.1468, 0.993	0.0781, 0.2297, 1.156
Min. and max. residual density [e·Å^{-3}]	–0.664, 0.453	–0.864, 1.829

concentrated toluene solution of the complex. Data were collected on a Nonius KappaCCD diffractometer (graphite Mo-K_α radiation, λ = 0.71073 Å). The structure was solved by direct methods with the SHELXS-97 program and refined by full-matrix least-squares techniques (SHELXL-97) on F^2.[23] Hydrogen atoms were located by using the geometric method. The crystal data and structural refinement details are listed in Table 2. The compound was found to crystallise with one molecule of toluene (CCDC 242626).

X-ray Crystal Structure Determination of 5·benzene: Single crystals of **5** suitable for X-ray diffraction analysis were obtained from a toluene solution of the complex on standing in air. Data collection and structure solution were as for compound **4**. The compound crystallised with one molecule of benzene. The benzene molecules occupy special positions (–1). CCDC-242627 and CCDC-242626 contain the supplementary crystallographic data for this paper. These data can be obtained free of charge from The Cambridge Crystallographic Data Centre via www.ccdc.cam.ac.uk/data_request/cif.

Catalytic runs

Ethylene oligomerisation: The low pressure catalytic runs (≤5 bar) were carried out in a Büchi miniclave (200 mL) equipped with a Teflon-coated magnetic stirrer. For higher pressures, a stainless steel autoclave was used (100 mL). Both reactors were dried under vacuum at 100 °C for 1 h before use. In a typical procedure, a Schlenk flask was charged with the complex (7.5 μmol) and toluene (10 mL). The resulting solution was injected into the autoclave together with additional toluene (20 mL). The autoclave was then pressurised with ethylene and heated at 70 °C. After completion of the reaction, the autoclave was cooled with an ice bath and depressurized over 1 h. The solution was analysed by GC. Heptane (200 μL) was used as internal reference. For details see Tables S1–S3.

Ethylene Polymerisation: Polymerisations were carried out in a mini-Büchi glass reactor (200 mL), equipped with a Teflon-coated magnetic stirrer and heating (temperature-controlled oil bath), at constant ethylene pressure. The autoclave was heated at 100 °C under vacuum for 1 h before use and purged with ethylene. The reaction temperature refers to the bath temperature.

In a typical run, the reactor was charged at ambient temperature under an ethylene atmosphere, with a solution of catalyst (7.5 μmol) in toluene (15 mL), followed by a solution of Ni(cod)$_2$ (75 μmol) in toluene (15 mL). The autoclave temperature was raised to 70 °C, and pressurised to 5 bar. The reaction was quenched by venting the autoclave, and the reaction mixture was subsequently poured into a stirring solution of methanol (300 mL) and concentrated HCl (10 mL) to precipitate the polymer. The white powder was isolated by filtration, washed with methanol, and dried in vacuo at 50 °C. By using Keim's catalyst (**1a**), 1.80 g of a polymer was obtained and was characterised by M_w = 4500 g·mol^{-1} and M_w/M_n = 1.87 (Catalyst activity: 240 g·mmol$_{cat}^{-1}$·h^{-1}). The polymer (1.51 g) obtained with **4** has the following characteristics: M_w = 650 g·mol^{-1} and M_w/M_n = 1.31 (Activity: 201 g·mmol$_{cat}^{-1}$·h^{-1}).

Supporting Information Available: See also footnote on the first page of this article. Ethylene oligomerisation with the Keim-type complex **1a** (constant pressure) (Table S1). Ethylene oligomerisation with Keim-type complex **4** (constant pressure) (Table S2). Comparison of ethylene oligomerisation with **1a** and **4** in batch experiments (Table S3).

Acknowledgments

P. K. thanks the Ministère de l'Education Nationale et de la Recherche Scientifique for a grant. The authors thank Prof. Dr. R. Müllhaupt and U. Westphal for their help with the HT SEC measurements.

[1] W. Keim, *Angew. Chem. Int. Ed. Engl.* **1990**, *29*, 235–244.
[2] P. Braunstein, Y. Chauvin, S. Mercier, L. Saussine, A. De Cian, J. Fischer, *J. Chem. Soc. Chem. Commun.* **1994**, 2203–2204.
[3] K. Kurtev, A. Tomov, *J. Mol. Catal.* **1994**, *88*, 141–150.
[4] A. L. Monteiro, M. O. de Souza, R. F. de Souza, *Polym. Bull.* **1996**, *36*, 331–336.
[5] G. J. P. Britovsek, V. C. Gibson, D. F. Wass, *Angew. Chem. Int. Ed.* **1999**, *38*, 428–447.
[6] S. D. Ittel, L. K. Johnson, M. Brookhart, *Chem. Rev.* **2000**, *100*, 1169–1204.
[7] V. C. Gibson, S. K. Spitzmesser, *Chem. Rev.* **2003**, *103*, 283–315.
[8] P. W. Glockner, W. Keim, R. F. Mason, U. S. Patent 3.647.914 Shell Oil Co., **1971** [Chem. Abstr. 1971, 75, 88072g].
[9] W. Keim, F. H. Kowaldt, R. Goddard, C. Krüger, *Angew. Chem. Int. Ed. Engl.* **1978**, *17*, 466–467.
[10] K. Hirose, W. Keim, *J. Mol. Catal.* **1992**, *73*, 271–276.
[11] J. Heinicke, M. Koesling, R. Brüll, W. Keim, H. Pritzkow, *Eur. J. Inorg. Chem.* **2000**, 299–305.
[12] J. M. Malinowski, M. Brookhart, *Organometallics* **2003**, *22*, 5324–5335.
[13] D. Matt, N. Sutter-Beydoun, J.-P. Brunette, F. Balegroune, D. Grandjean, *Inorg. Chem.* **1993**, *32*, 3488–3492.
[14] E. C. Okafor, *Spectrochim. Acta Part A* **1987**, *37*, 939.
[15] L. Komorowski, W. Maringgele, A. Meller, K. Niedenzu, J. Serwatowski, *Inorg. Chem.* **1990**, *29*, 3845–3849.
[16] M. C. Bonnet, M. C. Dahan, A. Ecke, W. Keim, R. P. Schultz, I. Tkatchenko, *J. Chem. Soc. Chem. Commun.* **1994**, 615–616.
[17] Z. J. A. Komon, X. Bu, C. G. Bazan, *J. Am. Chem. Soc.* **2000**, *122*, 12379–12380.
[18] U. Klabunde, R. Mulhaupt, T. Herskovitz, A. H. Janowicz, J. Calabrese, S. D. Ittel, *J. Polymer. Sci. Part A Polym. Chem.* **1987**, *25*, 1989–2003.
[19] R. Soula, J. P. Broyer, M. F. Llauro, A. Tomov, R. Spitz, J. Claverie, X. Drujon, J. Malinge, T. Saudemont, *Macromolecules* **2001**, *34*, 2438–2442.
[20] A. Zeller, E. Herdtweck, T. Strassner, *Eur. J. Inorg. Chem.* **2003**, *9*, 1802–1806.
[21] M. Hiodai, T. Kashiwagi, T. Ikeuchi, Y. Uchida, *J. Organomet. Chem.* **1971**, *30*, 279–282.
[22] F. Palacios, A. M. Ochoa de Retana, J. Pagalday, *Tetrahedron* **1999**, *55*, 14451–14458.
[23] G. M. Sheldrick, *SHELX-97, Program for the Refinement of Crystal Structures*, University of Göttingen, Germany, **1997**.
Received: December 10, 2004

 © 2005 Wiley-VCH Verlag GmbH & Co. KGaA, Weinheim

A Copper-Metalated, Hybrid Inorganic–Organic Polymer as an Oxidative Nuclease

Vadapalli Chandrasekhar,*[a] Arunachalampillai Athimoolam,[a] Venkatasubbaiah Krishnan,[a] Ramachandran Azhakar,[a] C. Madhavaiah,[a] and Sandeep Verma*[a]

Dedicated to Professor S. S. Krishnamurthy on the occasion of his 63rd birthday

Keywords: Chemical nucleases / Phosphazenes / Pendant polymers / Copper complexes / Phosphate ester hydrolysis / Heterogeneous catalysis

This study describes nucleolytic activity of a copper-metalated, multisite-coordinating, hybrid polymer **CPPL-Cu** under oxidative conditions. Rapid relaxation of supercoiled plasmid DNA was observed and mechanistic probing by chemical and enzymatic assays revealed involvement of singlet-oxygen-derived reactive species. The heterogeneous nature of the catalyst allowed a facile recycling of the artificial nuclease.
(© Wiley-VCH Verlag GmbH & Co. KGaA, 69451 Weinheim, Germany, 2005)

Introduction

As many phosphate-ester-modifying enzymes depend on metal ions for their catalytic activities, it is not surprising to find that numerous artificial phosphatases and nucleases-containing metal ions have been reported over the past few decades for possible biochemical applications ranging from chemotherapy to synthetic restriction enzymes.[1] These model systems employ a wide range of transition and inner-transition-metal ions coordinated to ligands of natural and synthetic origin. Although enzyme-like substrate recognition, efficiency, and high turnover remain elusive with such systems, they provide incisive insight to the study of the role of metal ions for phosphate ester modification in natural enzymes.[2–5]

Among the many transition-metal ions, copper-based artificial systems have received considerable focus perhaps due to their variable mechanism of reactivity: they can modify natural and non-natural phosphate esters either through an oxidative route or a hydrolytic pathway. The former activity can be attributed to the redox cycling of copper in the presence of exogenously added oxidants or reductants, which leads to in situ formation of reactive species.[6]

[a] Department of Chemistry, Indian Institute of Technology, Kanpur,
Kanpur 208016, India
Fax: +91-512-2590007
+91-512-259-7436
E-mail: vc@iitk.ac.in

Polyphosphazenes, $[N{=}PR_2]_n$, are the most versatile and well-studied family of inorganic polymers.[7] One of the remarkable features of this class of polymers is that individual polymer properties can be readily modulated by a variation of the substituent on the phosphorus center.[8–10] Several applications of these polymers in diverse fields[11–14] are known, including the use of these polymers as matrices for stabilizing gold nanoparticles.[15] A closely related class of hybrid inorganic–organic polymers contains an intact cyclophosphazene ring as a pendant group attached at regular intervals to the backbone of an organic polymer.[16–18] Although much less studied, these polymers also show considerable promise particularly in the design of polymeric ligands.[19–20] We have recently utilized this approach to design new polymeric catalysts, which show applications in phosphate ester hydrolysis[21] or in the Heck arylation reaction.[22] In the following account we report the first application of these hybrid inorganic–organic polymers in DNA cleavage under heterogeneous reaction conditions.

Results and Discussion

A number of inner and outer-transition-metal ions are known for their catalytic assistance towards nucleic acid cleavage, either by a hydrolytic pathway[23–31] or through oxidative damage.[32–35] In particular, copper complexes afford facile nucleic acid oxidative cleavage in the presence of oxidizing and reducing agents,[36–43] in addition to the hydrolytic mechanism.[23,27,29] Most of these artificial phosphatases and nucleases offer homogeneous catalysis, while

only limited applications of heterogeneous catalysts have been reported.[44–52]

We have utilized copper-metalated, pyrazolylcyclotriphosphazene-containing, cross-linked polymeric catalyst CPPL-Cu (Scheme 1) for the oxidative damage to supercoiled plasmid in the presence of oxidizing agents such as magnesium monoperoxyphthalate (MMPP) and oxone. To the best of our knowledge, this is the first instance where an inorganic–organic hybrid polymer, and more specifically, a polyphosphazene-appended polymeric system has been used as a synthetic nuclease. The molecular structure of CPPL-Cu, has been previously established by us.[21] Briefly, the EPR spectrum of CPPL-Cu at 77 K is of the axial type and the parameters obtained viz., $g_{II} = 2.27$, $g_{\perp} = 2.10$, and $A_{II} = 130.5 \times 10^{-4}\ cm^{-1}$, compare very well with that of model compounds $N_3P_3(3,5\text{-}Me_2Pz)_5(O\text{–}C_6H_4\text{–}C_6H_4\text{–}CH{=}CH_2)\cdot CuCl_2$ [$g_{II} = 2.28$, $g_{\perp} = 2.05$, and $A_{II} = 130.5 \times 10^{-4}\ cm^{-1}$] and $N_3P_3(3,5\text{-}Me_2Pz)_5(O\text{–}C_6H_4\text{–}CHO)\cdot CuCl_2$ [$g_{II} = 2.28$, $g_{\perp} = 2.06$, and $A_{II} = 122.0 \times 10^{-4}\ cm^{-1}$].

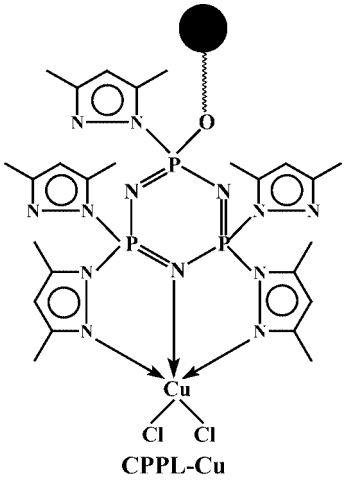

CPPL-Cu

Scheme 1.

The X-ray crystal structure of the model compound $N_3P_3(3,5\text{-}Me_2Pz)_5(O\text{–}C_6H_4\text{–}CHO)\cdot CuCl_2$ has been determined and shows a five-coordinate environment around Cu^{II} containing a cyclophosphazene ring nitrogen atom, two pyrazolyl nitrogen atoms and two chlorine atoms. Further, the diffuse reflectance spectrum of CPPL-Cu shows peaks at 845, 351, 318, 304, and 251 nm. These peak positions are similar to those observed in the solution spectrum of the model compounds. On the basis of this cumulative data, it is suggested that the coordination environment around copper contains two chlorides along with two nongeminal pyrazolyl nitrogens and one cyclophosphazene-ring nitrogen. From the nitrogen analysis it is concluded that every gram of the polymer contains 0.33 g of the cyclophosphazene monomer corresponding to 4.09×10^{-4} moles. From the AAS analysis the amount of copper present per gram of CPPL-Cu was found to be 21.7 mg.[21]

Plasmid (pBR322) modification assisted by the CPPL-Cu complex was studied in the presence of exogenously added co-oxidants MMPP and oxone. Initial experiments were performed using a varying amount of polymer in the presence of MMPP to study the concentration-dependent cleavage of pBR322. These experiments revealed a dependence of polymer concentration on the DNA cleavage (Figure 1). The concentration of catalyst for all subsequent experiments was optimized at 50 μg/20 μL for a 20-min cleavage reaction to set complete relaxation of plasmid DNA.

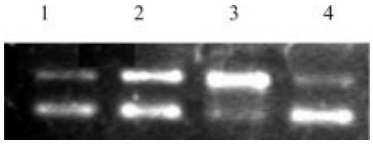

Figure 1. pBR322 cleavage with CPPL-Cu in presence of different amounts of copper polymer [lane 1: DNA + 10 μg of catalyst + MMPP (25 min); lane 2: DNA + 20 μg of polymer + MMPP (25 min); lane 3: DNA + 30 μg of polymer + MMPP (25 min); lane 4: DNA alone].

Both of the peracids effectively activated CPPL-Cu and a complete conversion of supercoiled plasmid DNA, from form I to nicked form II, and linear form III was observed (Figure 2, lanes 6 and 8). Control experiments with unmetalated ligand complex and peracid alone did not produce any detectable strand scission (Figure 2, lanes 2, 3, 5, and 7 respectively). However, the addition of EDTA afforded complete inhibition of plasmid cleavage, thus indicating the crucial role of coordinated copper ions in the cleavage reaction (Figure 2, lane 4).

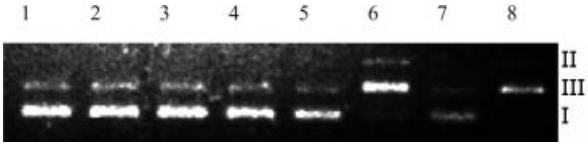

Figure 2. pBR322 cleavage by CPPL-Cu in the presence of MMPP and oxone (lane 1: DNA alone; lane 2: DNA + CPPL; lane 3: DNA + CPPL-Cu; lane 4: DNA + CPPL-Cu + EDTA + MMPP; lane 5; DNA + MMPP; lane 6: DNA + CPPL-Cu + MMPP; lane 7: DNA + oxone; lane 8: DNA + CPPL-Cu + oxone).

The nature of the reactive species responsible for DNA cleavage was probed by performing the reactions in the presence of hydroxyl-radical scavengers such as *tert*-butyl alcohol, dimethyl sulfoxide, and D-mannitol. These reagents partially inhibited the cleavage reaction (Figure 3; lanes 3–5), thus suggesting the possible involvement of reactive radical species in DNA cleavage. The extent of inhibition is limited probably because of the insoluble nature of the catalyst, which may shield the reactive species from freely diffusing out in the solution. Such protection has recently been observed with a trinuclear copper(II) complex where the presence of standard free-radical scavengers failed to reveal any interference against oxidative DNA cleavage.[53] As discussed in the literature, abstraction of C-4′ hydrogen appears to be the most likely mechanism of action for the reactive species so generated, leading to backbone scission.[54]

 © 2005 Wiley-VCH Verlag GmbH & Co. KGaA, Weinheim

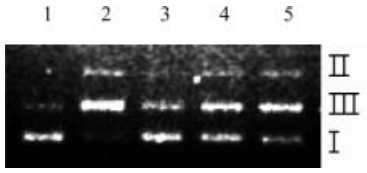

Figure 3. pBR322 cleavage by CPPL-Cu in the presence of radical scavengers (lane 1: DNA alone; lane 2: without the radical scavenger; lane 3: with *t*BuOH; lane 4: with DMSO; lane 5: with D-mannitol).

Enzymatic scavengers such as superoxide dismutase and catalase failed to provide any inhibition of the reaction, thereby suggesting a lack of involvement of the superoxide radical anion and the peroxide species in the cleavage (Figure 4, lanes 3, 4). Curiously, sodium azide afforded almost complete inhibition of plasmid relaxation, and the deployment of anaerobic conditions resulted in partial plasmid modification (Figure 4, lanes 5, 6). Taken together, these observations point towards a possible role of singlet oxygen in DNA modification as sodium azide is an effective quencher of singlet oxygen and some other reactive oxygen species. These results are similar to those of the hydroquinone/Cu^{II} system where the DNA strand cleavage was partially inhibited by HO·scavengers, whereas a greater degree of protection was offered by singlet-oxygen scavengers.[55] This clearly suggests localized generation and attack of singlet oxygen or a related species, because of the possible formation of a copper-peroxide complex, rather than the predominance of HO·in DNA cleavage. A dual mechanism involving hydroxyl radicals and singlet oxygen for DNA cleavage using photoactivated copper-based catalysts has been recently reported by Chakravarty and coworkers.[56]

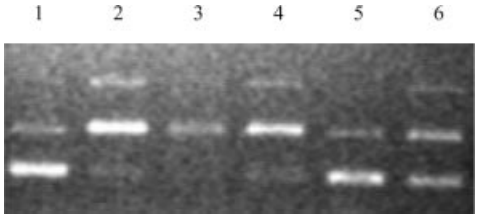

Figure 4. Lane 1: DNA alone; lane 2: DNA + CPPL-Cu + MMPP; lanes 3–5: DNA + CPPL-Cu + MMPP + SOD, catalase, sodium azide, respectively; lane 6: DNA + CPPL-Cu + MMPP under anaerobic conditions.

Growing interest in the development of heterogeneous nucleolytic reagents[44–46,48,51] and their possible application as recyclable catalytic systems has prompted us to explore CPPL-Cu for multiple cleavage reactions. Typically, reaction mixtures were centrifuged after completion of a reaction to leave the catalyst in the form of a pellet. After the removal of the supernatant, the pellet was repeatedly washed with cacodylate buffer (4×100 μL) to ensure complete removal of DNA and then reused for subsequent plasmid modification. Gel electrophoretic tracking was used to detect the complete removal of plasmid and cleaved fragments. CPPL-Cu was recycled for three consecutive reactions and each time a complete conversion of supercoiled form I to linear form III was observed (Figure 5) thus making an emphatic statement about the robust nature of the CPPL-Cu catalytic system.

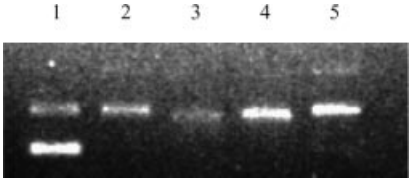

Figure 5. Recycling experiment [lane 1: DNA alone; lane 2: DNA + CPPL-Cu + MMPP (fresh); lane 3: first recycle; lane 4: second recycle; lane 5: third recycle].

We therefore perceive that the role of the cross-linked polymeric matrix is twofold: firstly, stabilization of the coordination complex by providing a suitable hydrophobic environment and secondly, providing an accessible, insoluble embedded metal complex scaffold for participation in the catalytic reactions. The latter property manifests itself in the facile recycling of the catalyst. As this catalyst relaxes plasmid superhelicity, it can also be considered to act as an artificial DNA topoisomerse. Such enzymes catalyze DNA strand scission releasing superhelical stress and religating activities in order to modulate nucleic acid architectures.[57] However, unlike topoisomerases our catalyst has not been optimized for the religation activity and thus, a direct comparison of their respective cleavage/ligation activities will not be meaningful.

Conclusions

In summary, we have demonstrated a novel, effective, and hitherto unreported nucleolytic activity of hybrid polymers with biomolecules, the cleavage of supercoiled plasmid with **CPPL-Cu** by an oxidative mechanism. It was further verified that **CPPL-Cu** is an extremely robust and stable catalyst, and it can be recycled several times over because of the heterogeneous nature of the catalysis. This represents the first application of the cyclophosphazene pendant polymeric system in a biological milieu. It is possible to harness this motif efficiently for the coordination of diverse metal ions to create a set of heterogeneously active catalytic reagents for chemico-biological applications.

Experimental Section

General Remarks: Solvents and other general reagents used in this work were purified according to the standard literature procedures.[58] CPPL and CPPL-Cu were prepared according to the reported procedures.[21] Elemental analyses were carried out with a Carlo–Erba CHNSO 1108 elemental analyzer. The amount of copper present in the polymeric catalyst was determined by atomic absorption spectrometry (AAS) with an Integra XL AAS spectrometer. EPR spectra were recorded with a Varian 109E Line Century Series, X-band spectrometer, at liquid nitrogen temperature. IR spectra of KBr pellets were recorded with a Bruker Vector 22 FTIR spectrophotometer operating from 400 to 4000 cm^{-1}. Ab-

 © 2005 Wiley-VCH Verlag GmbH & Co. KGaA, Weinheim

sorption spectra were recorded with a Shimadzu UV-160 spectrophotometer.

Preparation of CPPL: To a solution of $N_3P_3(3,5\text{-}Me_2Pz)_5(OC_6H_4\text{-}p\text{-}C_6H_4\text{-}p\text{-}CH{=}CH_2)$ (1.0 g, 1.2 mmol) in 1,2-dichloroethane (15 mL) was added 1,4-divinylbenzene (80%, mixture of isomers, 0.4 g, 2.5 mmol) and AIBN (0.03 g, 0.2 mmol). The solution was purged with argon for 45 min and was subsequently heated at 80 °C for 36 h. The cross-linked polymer obtained was filtered and washed with toluene (3 × 20 mL), dichloromethane (3 × 20 mL), methanol (3 × 20 mL), and acetone (3 × 20 mL), and dried thoroughly under vacuum at 40 °C. Yield: 1.04 g. IR (KBr) cm^{-1}: 3397 (s), 2923 (s), 1604 (s), 1573 (s), 1493 (s), 1443 (s), 1412 (s), 1372 (m), 1301 (s), 1218 (vs), 1089 (m), 1023 (m), 967 (m), 902 (m), 824 (m), 796 (m), 711 (w), 597 (m), 525 (m). Found: C 64.98, H 6.2, N 9.32. From the nitrogen analysis it was concluded that every gram of the polymer contained 0.54 g of the cyclophosphazene monomer which corresponded to 6.7×10^{-4} moles.

Preparation of CPPL-Cu: To a solution of anhydrous cupric chloride (0.09 g, 0.7 mmol) in ethanol CPPL (1.0 g, 0.67 mmol of the monomer) was added and stirred for 24 h. The resulting metalated polymer was washed thoroughly with methanol (5 × 20 mL) to remove any unreacted cupric chloride and dried under vacuum at 40 °C. Yield: 1.2 g. IR (KBr) cm^{-1}: 3420 (m), 3020 (m), 2923 (s), 2853 (m), 1649 (w), 1603 (w), 1570 (w), 1492 (m), 1454 (m), 1418 (m), 1374 (w), 1240 (vs), 1187 (vs), 1047 (m), 964 (w), 903 (m), 824 (m), 795 (m), 709 (w), 588 (w), 540 (w). Found: C 55.40, H 5.21, N 6.39. From the nitrogen analysis it was concluded that every gram of the polymer contained 0.33 g of the cyclophosphazene monomer which corresponded to 4.09×10^{-4} moles. From the AAS analysis the amount of copper present per gram of CPPL-Cu was found to be 21.7 mg. EPR (solid, 77 K): $g_{II} = 2.27$; $g_{\perp} = 2.10$; $A_{II} = 130.5 \times 10^{-4}\,cm^{-1}$. Diffuse reflectance UV/Vis [λ_{max}/nm (absorbance)]: λ_{max} = 845 (0.355), 351 (0.294), 318 (0.891), 304 (0.878), 251 (0.920).

pBR322 Cleavage Assay: Plasmid cleavage reactions (20 min) were performed in sodium cacodylate buffer (10 mM, pH 7.5, 20 μL, 30 °C) containing supercoiled plasmid DNA pBR322 (9 ng/μL, New England Biolabs), CPPL-Cu (the concentration of copper was 0.85 mM, if the catalyst was completely soluble in buffer), and an oxidizing agent [magnesium monoperoxyphthalate (100 μM) or oxone (100 μM)]. Individual reactions were quenched by adding the gel loading buffer (5 μL) containing EDTA (100 mM), loaded onto agarose gel (0.7%), containing ethidium bromide (1 μg/mL), and were electrophoresed for 1.5 h (60 mA). Gels were imaged with the Bio-Rad Gel Documentation System 2000. Recycle experiments were performed in a similar fashion except that they were performed for 25 min to ensure complete conversion of the supercoiled form to the relaxed form.

Acknowledgments

We thank DST, India for financial support. A. A., V. K., and C. M. thank the Council of Scientific and Industrial Research, India, for the award of SRF.

[1] J. K. Bashkin, *Curr. Opin. Chem. Biol.* **1999**, *3*, 752.
[2] S. J. Franklin, *Curr. Opin. Chem. Biol.* **2001**, *5*, 201.
[3] E. Kimura, *Curr. Opin. Chem. Biol.* **2000**, *4*, 207.
[4] N. H. Williams, B. Takasaki, M. Wall, J. Chin, *Acc. Chem. Res.* **1999**, *32*, 485.
[5] M. Komiyama, J. Sumaoka, *Curr. Opin. Chem. Biol.* **1998**, *2*, 751.
[6] S. Verma, S. G. Vatsan, C. Madhavaiah, *Nucleic Acids and Molecular Biology* **2003**, *13*, 129 and references cited therein.
[7] J. E. Mark, H. R. Allcock, R. West, *Inorganic Polymers*, Prentice Hall, NJ, **1992**.
[8] H. R. Allcock, M. S. Connolly, J. T. Sisko, S. Al-Shali, *Macromolecules* **1988**, *21*, 323.
[9] R. H. Neilson, P. Wisian-Neilson, *Chem. Rev.* **1988**, *88*, 541.
[10] G. Allen, C. J. Lewis, S. M. Todd, *Polymer* **1970**, *11*, 31.
[11] H. R. Allcock, D. L. Olmeijer, *Macromolecules* **1998**, ***31***, 8036.
[12] I. I. Selvaraj, S. Chaklanobis, V. Chandrasekhar, *J. Electrochem. Soc*. **1995**, *142*, 3434.
[13] R. E Singler, R. A. Willingham, C. Noel, C. Friedrich, L. Bosio, E. Atkins, *Macromolecules* **1991**, *24*, 510.
[14] H. R. Allcock, K. D. Lavin, N. M. Tollefson, T. L. Evans, *Organometallics* **1983**, *2*, 267.
[15] C. H. Walker, J. V. St. John, P. Wisian-Neilson, *J. Am. Chem. Soc.* **2001**, *123*, 3846.
[16] H. R. Allcock, W. R. Laredo, E. C. Kellam, R. V. Morford, *Macromolecules* **2001**, *34*, 787.
[17] E. D. Brown, K. Ramachandran, K. R. Carter, C. W. Allen, *Macromolecules* **2001**, *34*, 2870.
[18] I. I. Selvaraj, V. Chandrasekhar, *Polymer* **1997**, *38*, 3617.
[19] V. Chandrasekhar, A. Athimoolam, K. Vivekanandan, S. Nagendran, *Tetrahedron Lett.* **1999**, *40*, 1185.
[20] V. Chandrasekhar, V. Krishnan, A. Athimoolam, G. T. Senthil Andavan, *Can. J. Chem.* **2002**, *80*, 1415.
[21] V. Chandrasekhar, A. Athimoolam, S. G. Srivatsan, P. Shanmugasundaram, S. Verma, A. Steiner, S. Zacchini, R. Butcher, *Inorg. Chem.* **2002**, *41*, 5162.
[22] V. Chandrasekhar, A. Athimoolam, *Org. Lett.* **2002**, *4*, 2113.
[23] S. R. Korupoju, M. Nagarathinam, P. S. Zacharias, J. Mizuthani, H. Nishihara, *Inorg. Chem.* **2002**, *41*, 4099.
[24] Y. Kitamura, M. Komiyama, *Nucleic Acids Res.* **2002**, *30*, e102.
[25] M. E. Branum, A. K. Tipton, S. Zhu, L. Jr., Que, *J. Am. Chem. Soc.* **2001**, *123*, 1898.
[26] D. K. Chand, P. K. Bharadwaj, H.-J. Schneider, *Tetrahedron* **2001**, *57*, 6727.
[27] R. Ren, P. Yang, W. Zheng, Z. Hua, *Inorg. Chem.* **2000**, *39*, 5454.
[28] A. Sreedhara, J. D. Freed, J. A. Cowan, *J. Am. Chem. Soc.* **2000**, *122*, 8814.
[29] T. Itoh, H. Hisada, T. Sumiya, M. Hosono, Y. Usui, Y. Fiji, *Chem. Commun.* **1997**, 677.
[30] J. Rammo, R. Hettich, A. Roigk, H.-J. Schneider, *J. Chem. Soc. Chem. Commun.* **1996**, 105.
[31] M. Komiyama, *J. Biochem*. **1995**, *118*, 665.
[32] K. J. Humphreys, K. D. Karlin, S. E. Rokita, *J. Am. Chem. Soc.* **2002**, *124*, 8055.
[33] B. C. Gilbert, S. Silvester, P. H. Walton, A. C. Whitwood, *J. Chem. Soc. Perkin Trans. 2* **1999**, 1891.
[34] S. Borah, M. S. Melvin, N. Lindquist, R. A. Manderville, *J. Am. Chem. Soc.* **1998**, *120*, 4557.
[35] S. S. Mandal, N. Vinay Kumar, U. Varshney, S. Bhattacharya, *J. Inorg. Biochem*. **1996**, *63*, 265.
[36] A. Patwardhan, J. A. Cowan, *Chem. Commun.* **2001**, 1490.
[37] Q. Liang, P. C. Dedon, *Chem. Res. Toxicol*. **2001**, *14*, 416.
[38] M. Pitié, B. Donnadieu, B. Meunier, *Inorg. Chem.* **1998**, *37*, 3486.
[39] L. Flowers, S. T. Ohnishi, T. M. Penning, *Biochemistry* **1997**, *36*, 8640.
[40] F. V. Pamatong, C. A. Detmer, J. R. Bocarsly III, *J. Am. Chem. Soc.* **1996**, *118*, 5339.
[41] a) W. A. Prütz, *Biochem. J.* **1994**, *302*, 373; b) D. C. A. John, K. T. Douglas, *Biochem. J.* **1993**, *289*, 463.
[42] M. M. Meijler, O. Zelenko, D. S. Sigman, *J. Am. Chem. Soc.* **1997**, *119*, 1135.
[43] S. Routier, J. L. Bernier, M. J. Waring, P. Colson, C. Houssier, C. Bailly, *J. Org. Chem.* **1996**, *61*, 2326.
[44] C. Madhavaiah, S. Verma, *Chem. Commun.* **2003**, 800.

 © 2005 Wiley-VCH Verlag GmbH & Co. KGaA, Weinheim

[45] S. Verma, S. G. Srivatsan, C. A. Claussen, E. C. Long, *Bioorg. Med. Chem. Lett.* **2003**, *13*, 2501.
[46] C. Madhavaiah, S. G. Srivatsan, S. Verma, *Catal. Commun*. **2003**, *4*, 237.
[47] S. G. Srivatsan, S. Verma, *Chem. Eur. J.* **2002**, *8*, 5184.
[48] K. L. Smith, Z.-F. Tao, S. Hashimoto, C. J. Leitheiser, X. Wu, S. M. Hecht, *Org. Lett.* **2002**, *4*, 1079.
[49] C. M. Hartshorn, A. Singh, E. L. Chang, *J. Mater. Chem.* **2002**, *12*, 602.
[50] B. R. Bodsgard, J. N. Burstyn, *Chem. Commun.* **2001**, 647.
[51] C. S. Jeung, J. B. Song, Y. H. Kim, J. Suh, *Bioorg. Med. Chem. Lett.* **2001**, *11*, 3061.
[52] S. G. Srivatsan, S. Verma, *Chem. Eur. J.* **2001**, *7*, 828.
[53] C. Tu, Y. Shao, N. Gan, Q. Xu, Z. Guo, *Inorg. Chem.* **2004**, *43*, 4761.
[54] T. Oyoshi, H. Sugiyama, *J. Am. Chem. Soc.* **2000**, *122*, 6313.
[55] Y. Li, M. A. Trush, *Carcinogenesis* **1993**, *14*, 1303.
[56] S. Dhar, D. Senapati, P. A. N. Reddy, P. K. Das, A. R. Chakravarty, *Chem. Commun.* **2003**, 2452.
[57] K. D. Corbett, J. M. Berger, *Annu. Rev. Biophys. Biomol. Struct.* **2004**, 33, 95.
[58] A. I. Vogel, Textbook of Practical Organic Chemistry, 5th ed., Longman, London, **1989**.

Received: August 27, 2004

 © 2005 Wiley-VCH Verlag GmbH & Co. KGaA, Weinheim

Synthesis, Structure, and Luminescent Properties of Guanidinate-Based Terbium Complexes

Xingan Pang,[a] Hongmei Sun,[a] Yong Zhang,[a] Qi Shen,*[a,b] and Hongjie Zhang[c]

Keywords: Terbium complex / Guanidinate / Luminescence / Lanthanides

Two guanidinate-based terbium complexes [*i*PrNC(N*i*Pr$_2$)-N*i*Pr]$_m$TbCl$_{3-m}$ [m = 3 (**1**), 2 (**2**)] were synthesized, and the crystal structure of **1** was determined by single-crystal X-ray diffraction. Complexes **1** and **2** were further characterized by elemental analysis, IR, and ^{1}H NMR spectroscopy. In complex **1** the guanidinate ligand coordinates to the terbium atom through the nitrogen atoms in a bidentate chelating coordination mode. As a result of an efficient energy transfer from the guanidinate ligand to the central Tb^{3+}, both **1** and **2** have been found to exhibit strong green emission corresponding to Tb^{3+} $^5D_4$-^7F_J (J = 6, 5, 4, 3) transitions. Among them, the emission $^5D_4$-$^7F_5$ (550 nm) is the most prominent. The lifetimes of the $^5D_4$ Tb^{3+} excited levels of the two complexes were determined to be around 0.90 ms.
(© Wiley-VCH Verlag GmbH & Co. KGaA, 69451 Weinheim, Germany, 2005)

Introduction

The luminescence properties of lanthanide ions (i.e., narrow emission peak, high quantum yield, and long decay time), in particular Tb^{3+} and Eu^{3+}, make them useful in luminescence probes for chemical or biological systems.[1] The strong luminescence of lanthanide complexes depends on the energy-level structure of the ligands and the central metal ions. Therefore, considerable efforts have been made to design and assemble lanthanide complexes with organic ligands such as β-diketones,[2] cryptands,[3] aromatic carboxylic acids,[4] and heterocyclics[5]. Lately, guanidinate anions, $[(RN)_2CNR'_2]^-$, whose steric and electronic effects can be easily modified by the variation of substituents on the N-atoms, have attracted considerable attention in organometallic chemistry,[6] and their application in organolanthanide complexes has led to the synthesis of a series of guanidinate derivatives of lanthanides.[6–14] Moreover, these complexes with guanidinate as the auxiliary ligands have many uses in catalytic chemistry. For example, the guanidinate aryloxy lanthanum complex can act as the catalyst for the ring-opening polymerization of lactide.[10] The guanidinate–methyl complexes of lanthanides are effective initiators not only for the polymerizations of MMA and ε-caprolactone,[11] but also for styrene polymerization.[12] The homoleptic triguanidinate lanthanides can also efficiently initiate the ring-opening polymerization of ε-caprolactone[14] and cyclocarbonate.[15] However, to our best knowledge, the photophysical properties of the guanidinate derivatives of lanthanides still remain unexplored. More recently, our group found that the Tb complex with β-diketiminate as a ligand showed a strong green emission band due to an efficient energy transfer from the β-diketiminate to the central Tb^{3+}.[16] Considering the similar structural characteristics of guanidinate and β-diketiminate, it is interesting to investigate the photoluminescence behavior of the guanidinate complex of lanthanides. Accordingly, two guanidinate complexes of terbium {[*i*PrNC(N*i*Pr$_2$)N*i*Pr]$_m$TbCl$_{3-m}$, m = 3 (**1**), 2 (**2**)} were synthesized and their luminescence spectra were determined. Both of them exhibited strong green emission corresponding to Tb^{3+} $^5D_4$-^7F_J (J = 6, 5, 4, 3) transitions. Herein, we would like to report the results.

[a] Department of Chemistry and Chemical Engineering, Suzhou University,
Suzhou 215006, China
Fax: +86-512-65112371
E-mail: qshen@suda.edu.cn
[b] State Key Laboratory of Organometallic Chemistry, Shanghai Institute of Organic Chemistry, Chinese Academy of Sciences, Shanghai 200032, China
[c] Key Laboratory of Rare Earth Chemistry and Physics, Changchun Institute of Applied Chemistry, Chinese Academy of Sciences,
Changchun 130022, China

Results and Discussion

Synthesis of (*i*PrNC(N*i*Pr$_2$)N*i*Pr)$_m$TbCl$_{3-m}$ [m = 3 (1), 2 (2)]

The complexes **1** and **2** can be easily synthesized by the reaction of freshly-prepared lithium guanidinate with $TbCl_3$. The reaction of $TbCl_3$ with lithium guanidinate in 1:3 and 1:2 mole ratios, respectively, after work up at room temperature, gave the two expected complexes as white crystals [Equation (1)]. The complexes are air- and moisture-sensitive and soluble in THF, diethyl ether, and toluene. The initial characterization of complexes **1** and **2** were supported by elemental analysis and IR spectroscopy. In their IR spectra, no signal of C=N=C near 2110 cm^{-1} was ob-

 DOI: 10.1002/ejic.200400750 © 2005 Wiley-VCH Verlag GmbH & Co. KGaA, Weinheim

served, and a strong absorption at approximately 1640 cm^{-1} assigned to the C=N stretch appeared. The IR data indicated that the electrons within the double bonds of the N–C–N linkage are delocalized in the two complexes

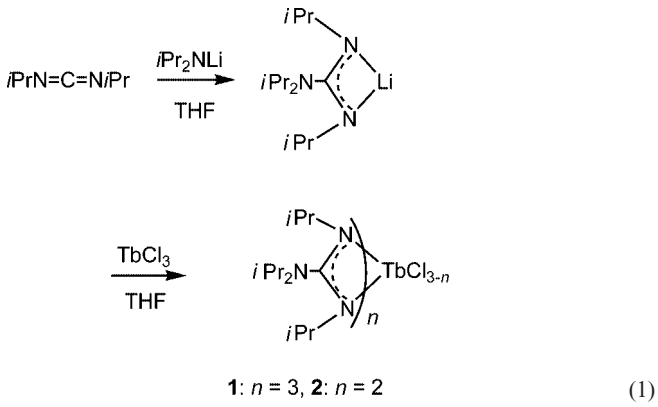

1: n = 3, **2**: n = 2 (1)

Crystal-Structure Analysis of Complex 1

Crystals of complex **1** suitable for X-ray crystallographic analysis were obtained by recrystallization from THF solution at –15 °C. The crystal-structure analyses revealed that complex **1** is a monomer in the solid state. Figure 1 depicts the molecular structure of complex **1**. Selected bond lengths and angles are given in Table 1. The terbium ion in the complex is coordinated to six nitrogen atoms of the three bidentate guanidinate anions and the geometry around the center metal can be best described as a distorted octahedron. The sum of the three angles C(1)–Tb(1)–C(14) [119.36(19)°], C(14)–Tb(1)–C(27) [120.8(2)°], and C(27)–Tb(1)–C(1) [119.87(19)°] equals 360.03°, which indicates that the terbium ion is located in a plane defined by the three central carbon atoms of the guanidinate moieties. All of the C–N bond lengths for the N–C–N moiety of each guanidinate group are intermediate between the C–N and C=N bond lengths. The results indicated the delocalization of the π bond in the N–C–N unit, while the C(1)–N(3), C(14)–N(6), and C(27)–N(9) bond lengths are 1.452(10), 1.411(9), and 1.422(9), respectively; these values fall into the normal C–N single bond-length range. The Tb–N bond lengths range from 2.380 Å to 2.411 Å. The average Tb–N bond length (2.393 Å) is comparable to those for $[(i\mathrm{PrN})_2\mathrm{CN}i\mathrm{Pr}_2]_3\mathrm{Nd}$ (2.464 Å) and $[(\mathrm{CyN})_2\mathrm{CN}i\mathrm{Pr}_2]_3\mathrm{Nd}$ (2.458 Å)[14] when the difference in the ionic radii of Nd and Tb is considered. The angles of the three N–C–N units are slightly different, ranging from 114.0(6)° to 117.2(7)°, which are also comparable to those for $[(i\mathrm{PrN})_2\mathrm{CN}i\mathrm{Pr}_2]_3\mathrm{Nd}$ (115°) and $[(\mathrm{CyN})_2\mathrm{CN}i\mathrm{Pr}_2]_3\mathrm{Nd}$ (114°). The N–Tb–N angle in each TbN_2C moiety is about 56.4°, which is slightly larger than that in the analogous complexes of $[(\mathrm{CyN})_2\mathrm{CN}i\mathrm{Pr}_2]_3\mathrm{Nd}$ (54.5°) and $[(i\mathrm{PrN})_2\mathrm{CN}i\mathrm{Pr}_2]_3\mathrm{Nd}$ (54.2°).

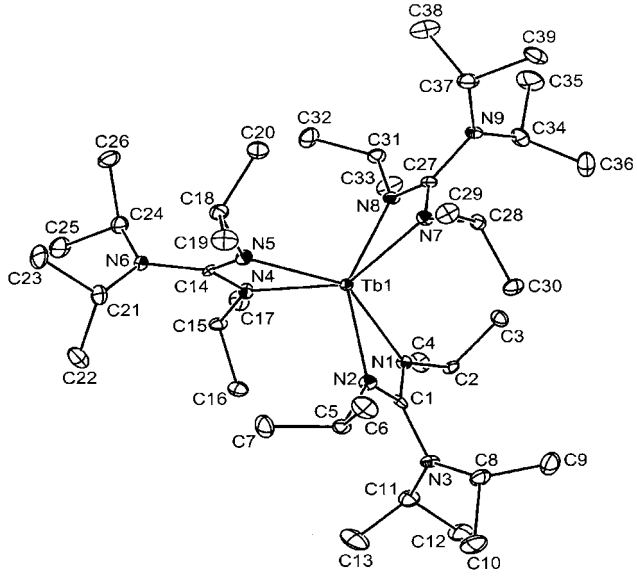

Figure 1. ORTEP diagram of complex **1** (15% thermal ellipsoids).

Table 1. Selected bond lengths [Å] and angles [°] for **1**.

Tb(1)–N(1)	2.382(6)	Tb(1)–N(2)	2.411(6)
Tb(1)–N(4)	2.380(6)	Tb(1)–N(5)	2.392(6)
Tb(1)–N(7)	2.393(6)	Tb(1)–N(8)	2.402(6)
Tb(1)–C(1)	2.803(8)	Tb(1)–C(14)	2.836(7)
Tb(1)–C(27)	2.832(7)	N(1)–C(1)	1.318(9)
N(2)–C(1)	1.333(10)	N(3)–C(1)	1.452(10)
N(4)–C(14)	1.355(10)	N(5)–C(14)	1.343(10)
N(6)–C(14)	1.411(9)	N(7)–C(27)	1.342(9)
N(8)–C(27)	1.335(10)	N(9)–C(27)	1.422(9)
N(1)–Tb(1)–N(2)	56.4(2)	N(4)–Tb(1)–N(5)	56.6(2)
N(7)–Tb(1)–N(8)	56.2(2)	C(1)–Tb(1)–C(27)	119.87(19)
C(1)–Tb(1)–C(14)	119.36(19)	C(27)–Tb(1)–C(14)	120.8(2)
N(1)–C(1)–N(2)	117.2(7)	N(5)–C(14)–N(4)	114.0(6)
N(8)–C(27)–N(7)	115.2(6)		

Photoluminescence Properties of Complexes 1 and 2

Figure 2 shows the excitation spectra of complex **1** in the solid state at room temperature (a), in THF solution at 77 K (b), and of complex **2** in the solid state at room temperature (c). The spectra were monitored by the Tb^{3+} green emission at 550 nm ($^5D_4$-$^7F_5$) and recorded in a range of 200 to 500 nm. The three excitation spectra are very similar and all of them display broad bands: from 230 to 400 nm with a maximum at 345 nm in the solid state at room temperature and at 304 nm in THF at 77 K for complex **1**, and from 250 to 410 nm with a maximum at 355 nm in the solid state for complex **2**. In the excitation spectra of both complexes, determined in the solid state at room temperature (see **a** and **c** in Figure 2), there is a shoulder at 488 nm and a broad band from 200 to 410 nm, which can be attributed to the f-f excitation transition ($^7F_6$-$^5D_4$) within the Tb^{3+} $4f^8$ electron configuration.[17] The wide excitation band observed can be attributed to the π-π* transition of the guanidinate ligand, in accordance with its broad character and strong intensity. Upon excitation into the absorption of the ligand at 345 nm and 350 nm in the solid state at room temperature. for complexes **1** (see **a** in Figure 3) and **2** (see **b** in

 © 2005 Wiley-VCH Verlag GmbH & Co. KGaA, Weinheim

Figure 3), and at 306 nm in the THF solution at 77 K for complex **1** (Figure 4), almost the same emission spectra were obtained. All of the spectra display strong green luminescence with four emission bands at 485, 546, 585, and 624 nm. The broad band from the ligand in the range of 230 to 410 nm was also not observed. These results indicated that an efficient energy transfer from the guanidinate ligand state to the emitting $^5D_4$ level of the Tb^{3+} ion occurs. These bands correspond to the characteristic emission from the $^5D_4$-^7F_J (J = 6, 5, 4, 3) transition of the Tb^{3+} ion. Among them the $^5D_4$-$^7F_5$ transition is the strongest one. The splits of the emission bands corresponding to $^5D_4$-$^7F_6$, $^5D_4$-$^7F_5$, and $^5D_4$-$^7F_4$ are 2, 3, and 4, respectively, which is caused by the crystal field splitting.[18] We can also see that the emission intensity of complex **1** (see **a** in Figure 3) is stronger than that of complex **2** (see **b** in Figure 3), which shows the number of the ligands affects the luminescent intensity of the guanidinate Tb complexes.

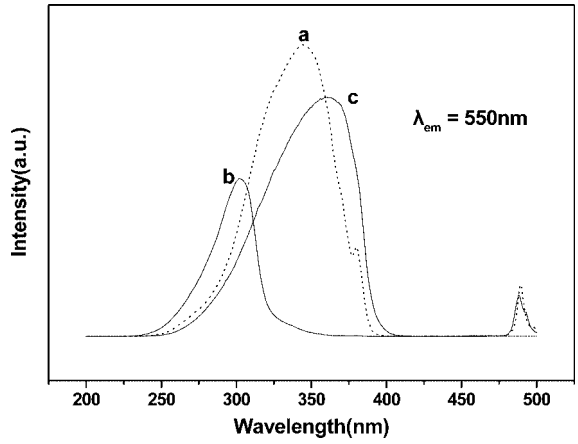

Figure 2. Excitation spectra (a) of complex **1** in the solid state at room temperature; (b) of complex **1** in THF solution at 77 K, and (c) of complex **2** in the solid state at room temperature.

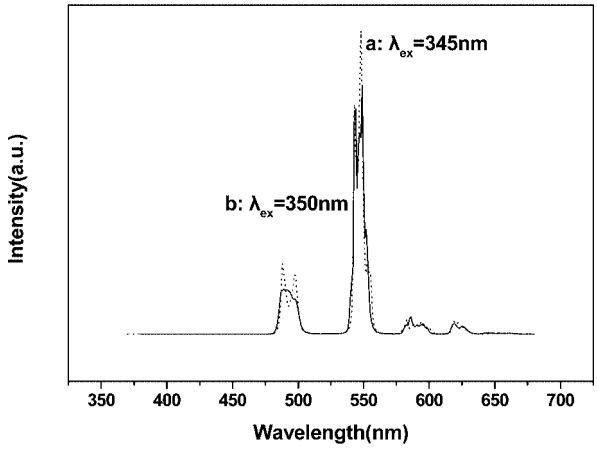

Figure 3. Emission spectra of complexes **1** (a) and **2** (b) in the solid state at room temperature.

The luminescence decay curves of Tb^{3+} ($^5D_4$-$^7F_5$ at 546 nm) in complex **1** were obtained under different excitation wavelengths at room temperature. The decay curves under the excitation wavelengths 546, 485, and 624 nm are

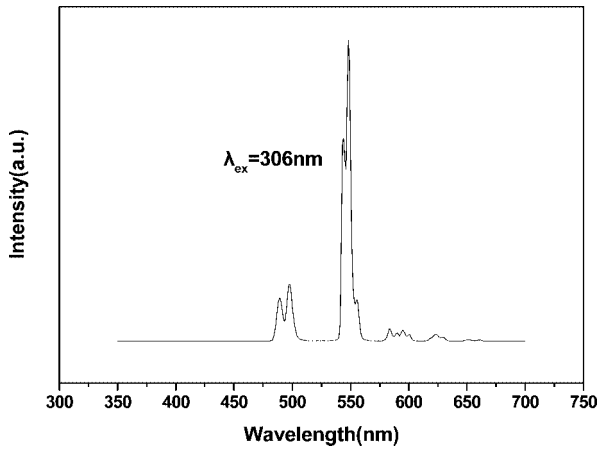

Figure 4. Emission spectrum of complex **1** in THF solution at 77 K.

shown in Figure 5 and Figure 6. It is clear that the luminescence of Tb^{3+} in complex **1** shows simple decay behavior. The decay curves fitted well into a singly exponential function as $I = I_0 \exp(-t/\tau)$ (τ is 1/e lifetime of the rare earth ion), indicating that all the Tb ions occupy the same average local environment. The lifetime of the Tb^{3+} ion (τ) is determined to be 0.91, 0.87, and 0.95 ms for $^5D_4$-$^7F_5$, $^5D_4$-$^7F_6$, and $^5D_4$-$^7F_3$, respectively. This result means that the ligands are efficiently shielding the Tb ion. The lifetime of the $^5D_4$ Tb^{3+} excited level in complex **2** was determined to be 0.86 ms, as shown in Figure 7. This value is very close to that of complex **1**; evidently, the number of ligands in the complex does not influence the lifetime.

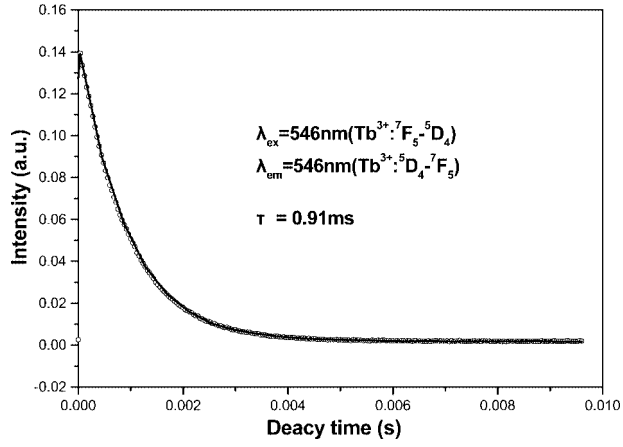

Figure 5. The decay curve for the luminescence of Tb^{3+} in complex **1** under an excitation wavelength of 546 nm.

Conclusions

In summary, bis- and tris-guanidinate terbium complexes can be easily prepared in good yield by the metathesis reaction of lithium guanidinate with anhydrous terbium trichloride at different mole ratios. The structural features of homoleptic terbium guanidinate (**1**) have been determined by X-ray diffraction. Interestingly, both of the two com-

 © 2005 Wiley-VCH Verlag GmbH & Co. KGaA, Weinheim

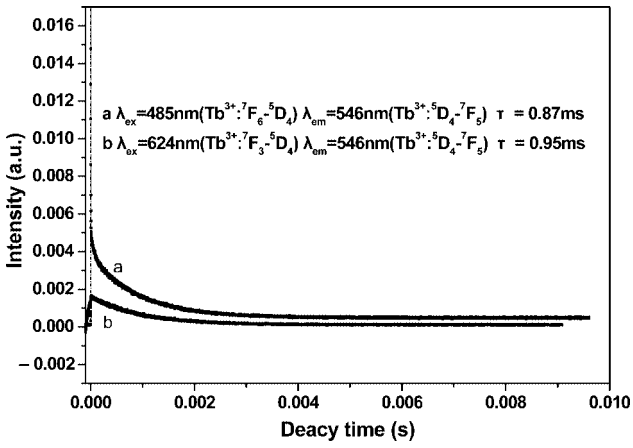

Figure 6. The decay curves for the luminescence of Tb^{3+} in complex **1** under the excitation wavelengths of 485 and 624 nm.

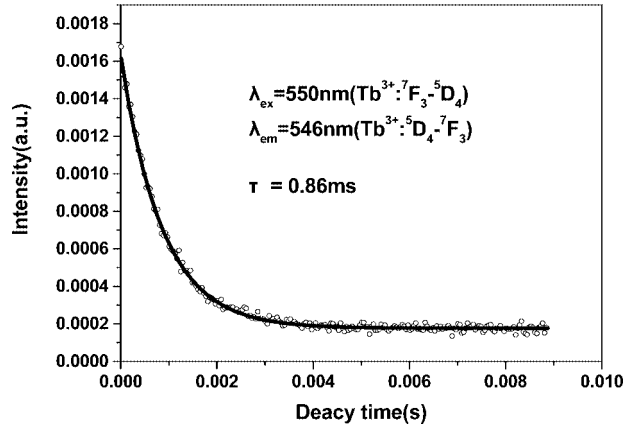

Figure 7. The decay curve for the luminescence of Tb^{3+} in complex **2** under an excitation wavelength of 550 nm.

plexes show rich luminescent properties at room temperature or 77 K. The lifetimes of the $^5D_4$ Tb^{3+} excited levels of the guanidinate complexes were determined to be around 0.90 ms. These results suggest that guanidinate could be used as a novel type of ligand for the synthesis of lanthanide-based luminescent complexes.

Experimental Section

General Procedures: All manipulations were performed under pure Ar with rigorous exclusion of air and moisture by the standard Schlenk techniques. Solvents were distilled from Na/benzophenone ketyl prior to use. Anhydrous $TbCl_3$[19] was prepared according to the literature procedures. *N*,*N*′-diisopropylcarbodiimide was purchased from Aldrich and purified by distillation under reduced pressure. Metal analyses were carried out by complexometric titration. Carbon, hydrogen, and nitrogen analyses were performed by direct combustion with a Carlo–Erba EA-1110 instrument. The IR spectra were recorded with a Magna-IR 550 spectrometer. ^{1}H NMR spectra were measured with a Unity Inova-400 spectrometer. The excitation and emission spectra were obtained with a SPEX FL-2T2 spectrofluorimeter with a 0.8 mm slit and equipped with a 450-W lamp as the excitation source. Luminescence lifetimes were measured with a Lecroy Wave Runner 6100 Digital Oscilloscope (1 GHz) using a 350-nm Ar ion laser (pulse width = 4 ns) as the excitation source (Continuum Sunlite OPO).

Synthesis of [*i*PrNC(*i*Pr$_2$N)N*i*Pr]$_3$Tb (1): A freshly-prepared solution of lithium guanidinate [(*i*PrN)$_2$CN*i*Pr$_2$]Li (2.2 g, 10 mmol) in THF (40 mL) was cannula-transferred into a Schlenk tube (100 mL) containing a solution of $TbCl_3$ (0.88 g, 3.33 mmol) in THF (20 mL) at 0 °C. The reaction mixture was stirred for 20 min at 0 °C and then stirred for 48 h at room temperature. The solvent was removed in vacuo, and the residue was extracted with toluene (45 mL) and LiCl was removed by centrifugation. After the extracts were concentrated and cooled to –15 °C for crystallization, colorless microcrystals were obtained (1.84 g, 66%). ^{1}H NMR (400 MHz, C_6D_6, 25 °C): δ = 2.88–3.76 [m, 12 H, C*H*(CH$_3$)$_2$], 0.68–1.76 [m, 72 H, CH(C*H*$_3$)$_2$] ppm. $C_{39}H_{84}N_9Tb$ (838.07): calcd. C 55.89, H 10.08, N 15.03, Tb 19; found: C 55.77, H 10.12, N 14.98, Tb 19.08. IR [KBr pellet (cm^{-1})]: 2969 (s), 2863 (s), 2709 (m), 2617 (m), 1651 (s), 1450 (s), 1361 (s), 1317 (s), 1210 (s), 1058 (s), 1018 (m), 975 (m), 930 (m), 861 (m), 667 (m), 576 (m) cm^{-1}.

Synthesis of [*i*PrNC(*i*Pr$_2$N)N*i*Pr]$_2$TbCl(THF) (2): Following a procedure similar to the synthesis of **1**, using [(*i*PrN)$_2$CN*i*Pr$_2$]Li (1.74 g, 8 mmol), $TbCl_3$ (1.06 g, 4 mmol), and THF (60 mL), followed by crystallization from THF yielded white crystals (1.72 g, 60%). ^{1}H NMR (400 MHz, C_6D_6, 25 °C): δ = 2.80–3.82 [m, 8 H, C*H*(CH$_3$)$_2$], 0.68–1.80 [m, 48 H, CH(C*H*$_3$)$_2$] ppm. $C_{30}H_{64}N_6ClOTb$ (718.42): calcd. C 50.11, H 8.9, N 11.69, Tb 22.13; found: C 49.98, H 8.86, N 11.98, Tb 22.54. IR [KBr pellet (cm^{-1})]: 2972 (s), 2865 (s), 2612 (s), 2463 (m), 1634 (s), 1473 (s), 1449 (s), 1367 (s), 1322 (s), 1173 (m), 1118 (m), 1014 (m), 922 (m), 866 (m), 809 (m), 722 (m), 661 (s) cm^{-1}.

X-ray Structural Determination of Complex 1: Suitable single crystals of complex **1** were each sealed in a thin-walled glass capillary, and intensity data were collected with a Rigaku Mercury CCD equipped with graphite-monochromated Mo-*Kα* (λ = 0.7107 Å) radiation. Details of the intensity data collection and crystal data are given in Table 2. The crystal structure was solved by direct methods and expanded by Fourier techniques. Atomic coordinates and ther-

Table 2. Details of the crystallographic data collection and refinement for **1**.

Empirical formula	$C_{39}H_{84}N_9Tb$
Molecular mass	838.07
Temperature [K]	298(2)
Wavelength [Å]	0.71070
Size [mm]	0.80 × 0.79 × 0.45
Crystal system	triclinic
Space group	$P\bar{1}$
a [Å]	13.3839(8)
b [Å]	13.3968(9)
c [Å]	18.0812(2)
α [°]	70.27(2)
β [°]	74.38(2)
γ [°]	59.69(2)
V [Å^3]	2614.9(6)
Z [Å^3]	2
$D_{calcd.}$ [g /mL]	1.064
Absorption coefficient (mm^{-1})	1.383
F(000)	892
Theta range for collection [°]	3.06–27.48
Reflection collected	25056
Independent reflections	11382
R [$I > 2\sigma(I)$]	0.1943
Rw	0.1957
Goodness-of-fit on F^2	1.252

 © 2005 Wiley-VCH Verlag GmbH & Co. KGaA, Weinheim

mal parameters were refined by full-matrix least-squares analysis on F^2. All non-hydrogen atoms were refined anisotropically. Hydrogen atoms were all generated geometrically with assigned appropriate isotropic thermal parameters. CCDC-245779 (for **1**) contains the supplementary crystallographic data for this paper. These data can be obtained free of charge from The Cambridge Crystallographic Data Centre via www.ccdc.cam.ac.uk/data_request/cif.

Ackonwledgments

We are indebted to the Chinese National Natural Science Foundation.

[1] G. F. de Sá, O. L. Malta, C. de Mello Donegá, A. M. Simas, R. L. Longo, P. A. Santa-Cruz, E. F. da Silva Jr., *Coord. Chem. Rev.* **2000**, *196*, 165.
[2] H. G. Liu, S. Park, K. Jang, X. S. Feng, C. Kim, H. J. Seoe, Y. I. Lee, *J. Lumin.* **2004**, *106*, 47.
[3] S. Faulkner, A. Beeby, M.-C. Carrié, A. Dadabhoy, A. M. Kenwrignt, P. G. Sammes, *Inorg. Chem. Commun.* **2001**, *4*, 187.
[4] M. C. Yin, C. C. Ai, L. J. Yuan, J. T. Sun, *J. Mol. Struct.* **2004**, *691*, 33.
[5] M. Pietraszkiewicz, J. Karpiuk, O. Pietraszkiewicz, *J. Alloys Compd.* **2000**, *300–301*, 141.
[6] P. J. Bailey, S. Pace, *Coord. Chem. Rev.* **2001**, *214*, 91.
[7] Y. L. Zhou, G. P. A. Yap, D. S. Richeson, *Organometallics* **1998**, *17*, 4387.
[8] Z. Lu, G. P. A. Yap, D. S. Richeson, *Organometallics* **2001**, *20*, 706.
[9] J. Zhang, R. F. Cai, L. H. Weng, X. G. Zhou, *J. Organomet. Chem.* **2003**, *672*, 94.
[10] G. R. Giesbrecht, G. D. Whitener, J. Arnold, *J. Chem. Soc. Dalton Trans.* **2001**, 923.
[11] Y. J. Luo, Y. M. Yao, Q. Shen, K. B. Yu, L. H. Weng, *Eur. J. Inorg. Chem.* **2003**, 318.
[12] Y. J. Luo, Y. M. Yao, Q. Shen, *Macromolecules* **2002**, *35*, 8670.
[13] Y. M. Yao, Y. J. Luo, J. L. Chen, Z. Q. Zhang, Y. Zhang, Q. Shen, *J. Organomet. Chem.* **2003**, *679*, 229.
[14] J. L. Chen, Y. J. Luo, Y. M. Yao, L. Y. Zhou, Y. Zhang, Q. Shen, *J. Organomet. Chem.* **2004**, *689*, 1019.
[15] L. Y. Zhou, Y. M. Yao, Y. Zhang, M. Q. Xue, J. L. Chen, Q. Shen, *Eur. J. Inorg. Chem.* **2004**, 2167.
[16] Z. Q. Zhang, Q. Shen, Y. Zhang, Y. M. Yao, J. Lin, *Inorg. Chem. Commun.* **2004**, *7*, 305.
[17] G. Blasse, B. C. Grabmaier, *Luminescent Materials*, Springer, Berlin, Heidelberg, **1994**.
[18] K. B. Yatsimirski, N. K. Davidenko, *Coord. Chem. Rev.* **1979**, *27*, 223.
[19] M. D. Taylor, C. P. Carter, *J. Inorg. Nucl. Chem.* **1962**, *24*, 387.
Received: September 10, 2004

 © 2005 Wiley-VCH Verlag GmbH & Co. KGaA, Weinheim

Selectivity of Asymmetric Macrocyclic Compartmental Lanthanide(III) Complexes towards Alkali and Alkaline-Earth Metal Ions

Alessandro Barge,[a] Mauro Botta,[b] Umberto Casellato,[c] Sergio Tamburini,*[c] and P. Alessandro Vigato[c]

Keywords: Lanthanides / Schiff bases / Shift reagents / ^{23}Na NMR / Macrocyclic ligands

The asymmetric macrocyclic compartmental ligand H_2L, derived from the [1+1] condensation of 3,3′-(3-oxapentane-1,5-diyldioxy)bis(2-hydroxybenzaldehyde) with 1,5-diamine-3-azamethylpentane, forms the complexes $[LnNa(L)(Cl)_2(CH_3OH)]$ (Ln = La–Nd, Sm–Lu) where the lanthanide(III) ion resides in the N_3O_2 Schiff base coordination site and the sodium ion is located in the O_3O_2 crown-like cavity. The new heterodinuclear complexes $[LnCa(L)(Cl)_2(CH_3OH)(H_2O)]Cl$ (Ln = Tb, Dy, Tm, Yb) were prepared and characterised by single-crystal X-ray diffraction, IR, ^{1}H and ^{13}C NMR spectroscopy and their homogeneity and stoichiometry (Ln:Ca:Cl = 1:1:3 molar ratio) were ascertained by SEM-EDS analysis. The single-crystal X-ray structure of $[YbCa(L)(Cl_2)(EtOH)(H_2O)]\cdot Cl\cdot 2H_2O$ has been determined. The complex is monoclinic, space group $P2_1/c$, with a = 10.033(2), b = 11.702(2), c = 27.796(6) Å and β = 105.51(3)°. The ytterbium ion is seven-coordinate within the N_3O_2 site and is in a pentagonal bipyramidal environment and bonded, in the axial positions, to two chloride ions. The calcium ion is seven-coordinate within the O_3O_2 site and is bonded to the ethyl alcohol oxygen and to one water molecule. The significant contact between the calcium ion and the chloride ions increases the coordination number of the metal ion to eight in a square antiprismatic environment. The selectivity of the etheric site towards alkali and alkaline-earth metal ions has been quantitatively assessed by evaluating, with ^{23}Na NMR spectroscopy, the transmetallation reaction involving the coordinated Na^+ ion in the complexes $[LnNa(L)(Cl)_2(CH_3OH)]$ (Ln = Tb, Dy, Tm and Yb) and Li^+, K^+ and Ca^{2+}. The affinity constants follow the general order $K_{Ca} >> K_{Li} \geq K_K$. Quantitative kinetic analyses were performed on the complex $[TmNa(L)(Cl)_2(CH_3OH)]$ using variable temperature ^{23}Na NMR spectroscopy in CD_3OD. It was ascertained that the exchange rate Na_{bound}/Na_{free} is independent of the presence of increasing amounts of water in the methanolic solution.

(© Wiley-VCH Verlag GmbH & Co. KGaA, 69451 Weinheim, Germany, 2005)

Introduction

In recent years asymmetric compartmental macrocyclic ligands have been designed and extensively studied since they are endowed with two well-defined and different recognition processes at two adjacent sites.[1,2] In these studies, Schiff-base ligands have often been used due to their well known coordinating ability. For the preparation of these systems, appropriate formyl-, keto- or amine-precursors have been condensed under suitable experimental conditions.[3]

Recently we prepared [1+1] cyclic Schiff bases by the condensation of 3,3′-(3-oxapentane-1,5-diyldioxy)bis(2-hydroxybenzaldehyde) or 3,3′-(3,6-dioxaoctane-1,8-diyldioxy)bis(2-hydroxybenzaldehyde) with 1,2-diaminoethane, 1,3-diaminopropane or 1,5-diamine-3-azamethylpentane.[4] These ligands contain one N_2O_2 or N_3O_2 Schiff base site and one O_3O_2 or O_4O_2 crown ether-like site. The N_2O_2 and N_3O_2 sites are particularly suitable for the coordination of transition-metal ions while alkali and alkaline-earth metal ions invariably prefer the O_3O_2 or O_4O_2 sites.[5,6] The 4f-metal(III) ions also prefer the crown ether-like chamber irrespective of the shape and donor atoms of the Schiff base site, as ascertained from X-ray structural determinations.[7,8] However, when this cavity is already filled by an alkali metal ion, the incoming lanthanide(III) ion coordinates to the adjacent chamber if the latter is large enough to accommodate the large 4f-metal ion. This occurs in the N_3O_2 chamber of the above mentioned ligand H_2L, derived from the 1:1 condensation of 3,3′-(3-oxapentane-1,5-diyldioxy)bis(2-hydroxybenzaldehyde) and 1,5-diamine-3-azamethylpentane. Thus, heterodinuclear complexes of the type $[LnNa(L)(Cl)_2(CH_3OH)]$ can be easily prepared.[9] When 1,2-diaminoethane or 1,3-diaminopropane was used, the resultant N_2O_2 site is too small for lanthanide(III) encapsulation although the N_3O_2 group is suitable for such coordination.

[a] Dipartimento di Chimica I. F. M., Università di Torino, Via P. Giuria 7, 10125 Torino, Italy
[b] Dipartimento di Scienze dell'Ambiente e della Vita, Università del Piemonte Orientale "Amedeo Avogadro", Spalto Marengo 33, 15100 Alessandria, Italy
E-mail: mauro.botta@mfn.unipmn.it
[c] Istituto di Chimica Inorganica e delle Superfici-C. N. R., Corso Stati Uniti 4, 35127 Padova, Italy
E-mail: sergio.tamburini@icis.cnr.it

 DOI: 10.1002/ejic.200400812

In these complexes, the lanthanide ion coordinated in the N_3O_2 chamber is able to induce a strong paramagnetic shift (LIS) on the Na^+ ion coordinated in the O_3O_2 site. In the case of the Tb, Dy and Tm complexes, the bound shifts are of the order of several hundred ppm (in methanol) which is more than one order of magnitude higher than the values estimated (in water) for the shift reagents currently available.[10–12,15]

These properties make the heterodinuclear Ln-Na complexes very promising candidates for the development of highly effective shift reagents for metal cations of biological interest. The study of the stability of these complexes in solution and the selectivity of the O_2O_3 chamber towards other alkali or alkaline-earth metal ions thus becomes of paramount importance.

In this work, for the complexes $[LnNa(L)(Cl)_2(CH_3OH)]$, we have investigated the rate of exchange between Na_{bound} and Na_{free} (Ln = Tb, Dy, Tm, Yb) and the transmetallation reaction of Na^+ with K^+, Li^+ and Ca^{2+} (Ln = Tm). Furthermore, the heterodinuclear $[LnCa(L)(Cl)_2(CH_3OH)(H_2O)]Cl$ (Ln = Tb, Dy, Tm, Yb) complexes have been prepared and characterised by single-crystal X-ray diffraction, IR, ^1H and ^{13}C NMR spectroscopy and their homogeneity and stoichiometry ascertained by SEM and EDS analyses.

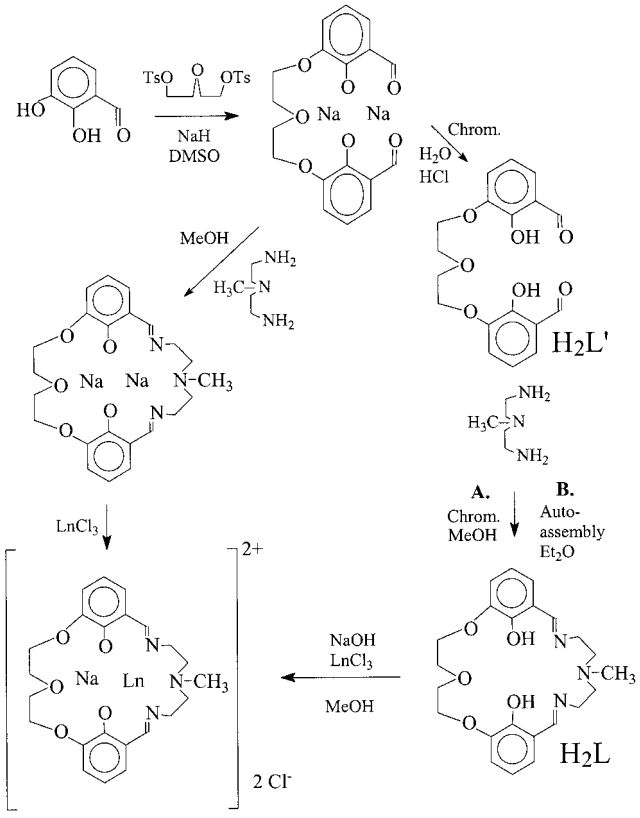

Scheme 1.

Results and Discussion

Preparation and Properties of the Macrocycle H_2L and Related Complexes

The H_2L [1+1] macrocyclic ligand and its homo- and heterodinuclear complexes have been prepared according to Scheme 1.

The diformyl precursor 3,3′-(3-oxapentane-1,5-diyldioxy)bis(2-hydroxybenzaldehyde) H_2L' and its related disodium derivative Na_2L' were prepared as pale yellow air-stable and organic solvent soluble solids by the reaction of the appropriate ditosilate with 2,3-dihydroxybenzaldehyde in anhydrous dimethyl sulfoxide in the presence of NaH. Pure H_2L' was obtained by chromatographic workup on silica gel using $CHCl_3$ as the eluent. The IR spectrum of H_2L' shows a strong ν(C=O) absorption at 1659–1646 cm^{-1}. The ^1H NMR ($CDCl_3$) spectrum consists of a singlet at δ = 9.94 ppm due to CH=O protons, a singlet at δ = 10.96 ppm assignable to the phenolic oxygens and multiplets at δ = 7.15, 4.26 and 3.96 ppm associated with the aromatic and the aliphatic protons of the crown ether chain, respectively. The IR and ^1H NMR spectra of Na_2L' are analogous to those of H_2L'.

The [1+1] macrocyclic ligand H_2L was synthesised by self-condensation of H_2L' with 1,5-diamine-3-azamethylpentane (1:1 molar ratio) in methanol. Alternatively, H_2L can be obtained by the same condensation reaction in the presence of $Ba(ClO_4)_2$ as a templating agent. By following this route, the yellow [1+1] macrocyclic complex $[Ba(H_2L)](ClO_4)_2$ can be demetallated by guanidinium sulphate and the resultant macrocycle H_2L extracted from water with $CHCl_3$. Finally, H_2L can be conveniently prepared in high yield by the condensation of H_2L' and 1,5-diamine-3-azamethylpentane in diethyl ether using the high dilution technique. The latter synthetic route was the chosen method since it gives the macrocyclic ligand in high yield without the need for any further purification. H_2L is a yellow solid and its [1+1] cyclic nature was inferred from the presence of the parent peak $[M - H]^+$ at m/z = 428 in the mass spectrum and by the presence, in the IR spectrum, of a strong ν(C=N) band at 1634 cm^{-1}. The bands attributable to ν(C=O) or ν(NH_2) completely disappeared. Moreover the ^1H NMR spectrum in $CDCl_3$ shows a singlet at δ = 8.19 ppm for the iminic protons, multiplets at δ = 6.75 ppm assignable to the aromatic protons and peaks at δ = 4.20 and 3.95 ppm which can be assigned to the methylenic protons of the crown ether chain. Peaks at δ = 3.63 and 2.78 ppm are due to methylenic protons of the iminic chain and a singlet at δ = 2.32 ppm can be assigned to the methyl group. The ^1H NMR spectrum of Na_2L, obtained from the condensation of the acyclic derivative Na_2L' with $H_2N(CH_2)_2N(CH_3)(CH_2)_2NH_2$, is significantly different from that of H_2L owing to the coordination of the Na^+ ions in the N_3O_2 and O_3O_2 coordination chambers.

By treating Na_2L with the appropriate lanthanide(III) trichloride in methanol in a 1:1 molar ratio, the heterodinuclear complexes $[LnNa(L)(Cl)_2(CH_3OH)]$ were obtained. Alternatively, the macrocycle H_2L can be treated with NaOH and the subsequent addition of $LnCl_3$ yields the same heterodinuclear complexes. The complexes are yellow

 © 2005 Wiley-VCH Verlag GmbH & Co. KGaA, Weinheim

solids which are stable in the solid-state and in solution and yield well formed crystals when recrystallised from alcoholic solutions. The homogeneity of the obtained crystals and the occurrence of the correct Ln/Na/Cl ratio (1:1:2) were checked by electron microscopy and EDS analysis.The IR spectra of $[LnNa(L)(Cl)_2(CH_3OH)]$ show a lower frequency for the ν(C=N) band at 1617–1632 cm^{-1} compared with the free ligand (1634 cm^{-1}). Noticeably, the ν(C=N) resonance lies at 1635–1660 cm^{-1} for the mononuclear complexes $[Ln(H_2L)Cl(H_2O)_4](Cl)_2$ in which the Ln^{3+} ion occupies the O_3O_2 site, with a relevant shift ($\Delta\tilde{\nu}$ = 29–38 cm^{-1}) towards higher wavelengths compared with H_2L. The differences in the C=N stretching frequencies are clearly related to the change in the coordination mode of the lanthanide(III) ion on going from the mononuclear to the heterodinuclear complex.The $[LnCa(L)(Cl)_2(CH_3OH)(H_2O)]Cl$ complexes were prepared by the transmetallation route of $[LnNa(L)(Cl)_2(CH_3OH)]$ with an equimolar quantity of $CaCl_2$ in methanol followed by crystallisation of the resultant powder to eliminate the sodium chloride formed (Scheme 2).

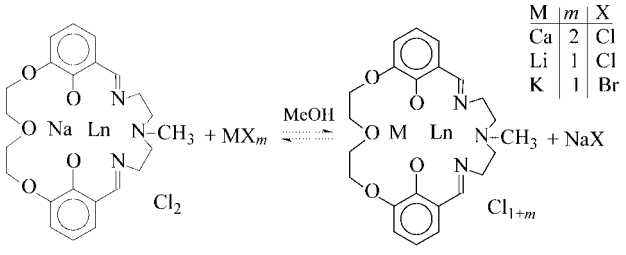

Scheme 2.

The formation of the LnCa(L) complexes was highlighted by elemental analyses as well as IR and NMR spectroscopic measurements and further confirmed by SEM-EDS investigations which indicated the complete disappearance of sodium and the correct Ln:Ca:Cl ratio of 1:1:3. The BSE micrography and the EDX spectra of the complex $[TbCa(L)(Cl)_2(CH_3OH)H_2O]Cl$ are reported in Figure 1.

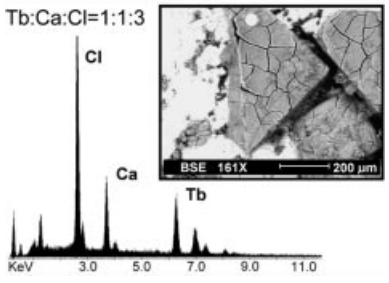

Figure 1. BSE micrography and EDX spectra of the complex $[TbCa(L)(Cl)_2(CH_3OH)H_2O]Cl$.

The ^1H NMR spectra of the paramagnetic calcium complexes closely resemble those of the corresponding sodium complexes. These spectra consist of thirteen resonances spanning a very large chemical shift range. The strict similarity, in terms of chemical shift and bandwidth, between the set of proton resonances for LnCa(L) and LnNa(L) strongly suggests that in both cases the lanthanide ion is coordinated at the N_3O_2 Schiff base site. The IR data also confirm this hypothesis. The ν(C=N) stretching for LnCa(L) is only 2–10 cm^{-1} higher than that of the Ln-Na complex.

Crystal Structure of $[YbCa(L)(Cl)_2(EtOH)(H_2O)]Cl\cdot 2H_2O$

Crystals of $[YbCa(L)(Cl)_2(EtOH)(H_2O)]Cl\cdot 2H_2O$ were obtained by slow diffusion of Et_2O into an ethanol solution of $[YbCa(L)(Cl)_2(CH_3OH)(H_2O)]Cl\cdot H_2O$. ORTEP representations of the complex and its coordination geometries are shown in Figure 2 (see parts a and b).

The macrocyclic ligand accommodates the ytterbium ion in the O_2N_3 chamber and the calcium ion in the O_2O_3 site. The presence of the calcium ion, as already seen with alkaline ions, forces the coordination of the lanthanide at the iminic site although this is generally unfavourable. The heptacoordination around the lanthanide ion is completed by two chloride ions *trans* to each other and the resultant coordination geometry can be described as pentagonal bipyramidal with the two chlorine atoms [Cl(1) and Cl(2)] in the apical positions. Another chlorine atom and two water molecules are not coordinated and are not reported in the figures. The calcium ion, which is heptacoordinated, is bonded to the two phenolic oxygen atoms which act as a bridge to the ytterbium ion, the three etheric oxygen atoms of the ligand as well as one ethanol and one water molecule. A significant contact is also present between the calcium ion and the chlorine atom Cl(2), [Ca···Cl(2) 3.135(6) Å, the sum of ionic radii being 2.80Å] and this increases the coordination number of the calcium ion to eight. The coordination polyhedron can now be described as a square antiprism.

The Yb–O(phenol) distances are 2.205 Å (mean), the Yb–N(iminic) distances are 2.45 Å (mean) and the Yb–N(2) (aminic) distance is 2.49(1) Å. The difference between the two Yb–Cl distances [2.623(4) Å for Cl(1) and 2.639(4) Å for Cl(2)] is due to the interaction of Cl(2) with the calcium ion. The distance between the two metal ions is 3.565(3) Å. The calcium ion is encapsulated into the O_2O_3 ligand site and the Ca–O(phenol) distances are 2.39(1) Å (mean). The Ca–O(ether) distances are longer and vary between 2.48 and 2.56 Å.

A comparison between this complex [YbCa(L)] and the sodium analogue [YbNa(L)] already published[13] indicates remarkable differences in spite of the very similar ionic radii of the two metal ions (0.97 and 0.99 Å for Na^+ and Ca^{2+}, respectively). Clearly, the charge difference plays an important role. The distances involving the ytterbium ion are comparable in the two complexes as well as the contact distances Yb–Na [3.540(2) Å] and Yb–Ca [3.565(3) Å]. The most important structural difference relates to the coordination geometries of the Na^+ and Ca^{2+} ions. In the former the geometry is pentagonal pyramidal whereas for the latter it is square antiprismatic.

Different spatial arrangements of the ligands are present in the two compounds, although both are in a butterfly-like

 © 2005 Wiley-VCH Verlag GmbH & Co. KGaA, Weinheim

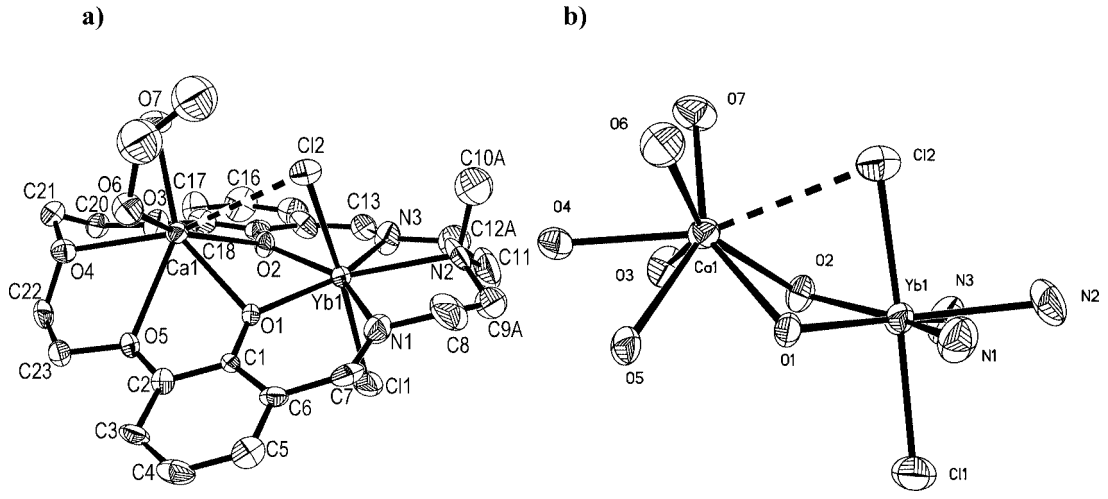

Figure 2. ORTEP representation of (a) the molecular structure of the complex $[YbCa(L)(Cl)_2(EtOH)H_2O]Cl$ and (b) the coordination geometries.

arrangement. The two wings (the two benzene rings) subtend a dihedral angle of 40.7° in the YbNa(L) complex and 32.2° in the YbCa(L) complex. Dissimilar dihedral angles involving the central metals are present and the dihedral angle between Na–O(1)–Yb and Na–O(2)–Yb is 21.1° whereas it increases to 49.3° for the angle between Ca–O(1)–Yb and Ca–O(2)–Yb. A noticeable dissimilarity between the Na–O(etheric) and Ca–O(etheric) bond distances and the torsion angles of the ligand (O–C–C–O and N–C–C–N) is present in the complexes. The conformations of the torsion angles O(3)–C(20)–C(21)–O(4) and O(4)–C(22)–C(23)–O(5) are g^+ and g^- in the Na complex and g^- and g^- in the Ca compound. The conformations of the torsion angles N(1)–C(8)–C(9)–N(2) and N(2)–C(11)–C(12)–N(3) are g^- and g^+ for the Na complex and g^+ and g^- for the Ca complex [because of the presence of disorder, we used the C(9A) and C(12A) atomic positions which show higher population parameters]. The Na–O(etheric) bond distances are 2.38 Å (mean) whereas the corresponding Ca–O(etheric) bond distances are 2.52 Å (mean). The hydrogen bonding networks in the crystal structures of these complexes are remarkable and involve the three chloride anions and all the coordinated and uncoordinated water molecules.

NMR Solution Studies

Selectivity of [LnNa(L)(Cl)$_2$(CH$_3$OH)] towards Li$^+$, K$^+$ and Ca^{2+} Ions

The LnNa(L) complexes appear to be stereochemically rigid on the NMR timescale and their proton spectra are characterised by sharp and well-separated resonances over a wide interval of temperatures.[9] On the other hand, the ^{23}Na NMR spectra show single resonances assignable to the coordinated sodium cation and markedly shifted from the positions of the free ions. Following addition to the methanolic solution of KBr, LiCl or $CaCl_2$, a transmetallation reaction occurs which can be revealed by the appearance, in the ^{1}H NMR spectra, of a second set of resonances closely corresponding to those of the LnNa(L) complex.[9] Alternatively, the course of the reaction can be followed by monitoring the decrease in the intensity of the ^{23}Na NMR peak of the coordinated sodium cations and the concomitant increase of a new resonance due to the free sodium ions (Figure 3). Thus, the replacement of Na^+ by alkali and alkaline-earth metal ions does not modify the structure or the stereochemical rigidity of the complex.

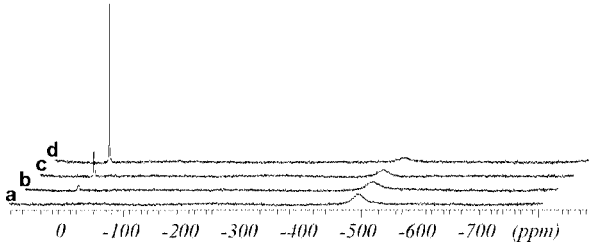

Figure 3. ^{23}Na NMR spectra of $[TbNa(L)(Cl)_2(MeOH)]$ in CD_3OD at 9.4 T and 273 K before (a) and after the addition of equimolar amounts of KBr (b), LiCl (c) and $CaCl_2$ (d).

We have recorded the ^{23}Na NMR spectra of the LnNa(L) complexes (Ln = Tb, Dy, Tm and Yb) in the presence of equimolar amounts of LiCl, KBr and $CaCl_2$ at different temperatures. When LnNa(L) and the lithium, potassium or calcium salts are added together in equimolar amounts, the transmetallation reaction described in Equation (1) assumes a simplified form [Equation (2)] particularly suitable for an NMR study.

$$LnNa(L) + M \leftrightarrow LnM(L) + Na \quad (1)$$

$$K = \frac{[LnM(L)][Na]}{[LnNa(L)][M]} \Rightarrow K = \frac{[Na]^2}{[LnNa(L)]^2} \quad (2)$$

In fact, the equilibrium constant K can be directly assessed by measuring the areas of the ^{23}Na NMR signals

 © 2005 Wiley-VCH Verlag GmbH & Co. KGaA, Weinheim

corresponding to the free and bound sodium cations. For the different lanthanides investigated, we observed different affinities for the complexes towards alkali and alkaline-earth metal ions. Table 1 reports the *K* values for the transmetallation reactions of involving the LnNa(L) complexes (Ln = Tb, Dy, Tm, Yb) with Li^+, K^+ and Ca^{2+}.

Table 1. Equilibrium constants for reaction (1) obtained from ^{23}Na NMR spectroscopic data at 9.4 T and 293 K.

Ln	K_{Li}	K_K	K_{Ca}
Tb	4.3×10^{-2}	1.1×10^{-2} [a]	2.4
Dy	2.7×10^{-2}	3.8×10^{-2} [a]	2.7
Tm	3.2×10^{-1}	7.3×10^{-2}	1.2
Yb	6.4×10^{-2}	1.9×10^{-3}	7.6

[a] Measured at 273 K.

The values of the equilibrium constants follow the general order $K_{Ca} >> K_{Li} \geq K_K$. This behaviour is likely to be related to the ionic radii of the metal ions and the dimension of the O_2O_3 coordination site. Both Na^+ (97 pm) and Ca^{2+} (99 pm) fit rather well into the crown-ether cavity whereas Li^+ (76 pm) and K^+ (138 pm) are either too small or too large. On the other hand, a well defined trend as a function of the ionic radius of the lanthanide ion was not observed. The equilibrium constants for the transmetallation reactions with Li^+ and K^+ are higher for Tm than for the other lanthanide cations, whereas the highest affinity for Ca^{2+} is shown by the Yb complex. Clearly, the affinity of the different Ln^{III} cations towards a given alkali or alkaline-earth metal ion is not simply dictated by the variation of the charge density across the lanthanide series. Although this behaviour cannot easily be rationalised in terms of the available data, it could arise from small structural variations of the complexes which occur on passing from the Tb to the Yb complexes involving primarily the crown-ether site. A powder X-ray diffraction analysis on the Dy complex, obtained from a different solvent, was carried out using a Philips X'Pert system in the range 4–90° (2θ). The resultant diffraction pattern is not analogous with that of the Yb analogue and this is consistent with the differences in the structural details.

The selectivity of the complexes to sodium appears greater than that observed for $TmDOTP^{5-}$ [$DOTP^{8-}$ = tetraazacyclododecane-*N*,*N*′,*N*″,*N*‴-tetrakis(methylphosphonate)], the most effective shift reagent currently available.[14] This latter complex forms very stable 1:1 adducts with Ca^{2+} (and Mg^{2+}) and the ^{23}Na shift is significantly reversed for a $Ca^{2+}/TmDOTP^{5-}$ ratio close to 1. Under similar experimental conditions 48% of the sodium remains bound to the Tm complex in our case (20 °C). On the other hand, the Dy complex with a polyoxa tetraaza macrocyclic tetraacetate ligand shows a higher selectivity for Na^+ than for Ca^{2+} although the paramagnetic shift is much smaller.[15]

Determination of the Na^+ Exchange Rate

The rate of exchange of the Na^+ ion between the coordination site of the complex and the solution is of primary importance for the development of efficient shift reagents for biomedical applications. The exchange rate needs to be sufficiently rapid so as to give rise to an exchange-averaged ^{23}Na NMR signal well shifted from the diamagnetic position and to allow a clear discrimination of the peaks of the Na^+ ions present in two different compartments. The ^{23}Na NMR spectra of the LnNa(L) complexes in methanol can be characterised, at low temperature, by the presence of a broad, highly shifted resonance (–614, –157, +340 and –40 ppm for Tb, Dy, Tm and Yb, respectively, at 253 K and 9.4 Tesla) corresponding to the coordinated Na^+ ion and another narrow peak at 0 ppm corresponding to the free ion.[9,13] The magnitudes of the shifts are very large when compared with common lanthanide-based shift reagents. One possible reason is the presence of a very short Ln–Na distance (ca. 3.5–3.6 Å) which is in contrast to the case of the polyaminocarboxylic complexes in which the ion-paired adducts are characterised by Ln–Na distances of about 4.0 Å and the LnDOTA chelate bearing a crown-ether moiety able to bind sodium where the distance is 5.3 Å.[15] In the complexes discussed here, however, the presence of a contact (through bond) contribution to the shift through the bridging phenolic oxygen atoms cannot be excluded. On the other hand, an accurate evaluation of this contribution is not possible because of the lack of an isostructural trend along the lanthanide series.[12]

The narrow resonance arises from the presence of NaCl which cocrystallises during the recrystallisation of the complexes. By increasing the temperature, the paramagnetically shifted resonance begins to sharpen and shift towards the peak corresponding to the free sodium ions. Exchange-averaged signals can be observed at about 320 K (at ca. +80 and –15 ppm for the Tm and Yb complexes, respectively) which sharpen further upon a further increase in temperature. The lanthanide-based shift reagents currently available produce a shift in the ^{23}Na NMR signal which does not exceed 10 ppm in the compartment in which they distribute.[10–12] These heterodinuclear LnNa(L) complexes are much more effective since they show chemical shifts of hundreds of ppm for the "bound" sodium cation. However, their solubility in water is very poor and, at present, this limits their use for biomedical studies. Clearly, a modification of the ligand is necessary in order to improve the solubility in aqueous media. In this work we have recorded a series of ^{23}Na NMR spectra for the TmNa(L) complex, in the presence of an equimolar amount of NaCl, as a function of temperature and increasing amounts of water. We then calculated the rate of sodium exchange. The complex:NaCl:D_2O molar ratios used were as follows: 1:1:0, 1:1:0.2, 1:1:0.4, 1:1:0.7, 1:1:1.4 and 1:1:2.9. Over a wide range of temperatures, from 263 to 315 K, the resonances due to the coordinated (B) and free (F) Na^+ ions are well separated (large $\Delta\nu_{BF}$) and the system is in the slow exchange regime. These two conditions allows us to assume the validity of the following expression: $1/\tau_B \leq \Delta\nu_{BF}/5$, where $1/\tau_B = k_{ex}$.[16] In this case, the transverse relaxation rate of the resonance of Na_F, calculated from the bandwidth at half-height, $\Delta\nu_F$, can be expressed in terms of Equation (3).[16]

 © 2005 Wiley-VCH Verlag GmbH & Co. KGaA, Weinheim

$$1/T_{2F} = 1/T_{2F}^{ref} + P_B \times k_{ex} \quad (3)$$

where $1/T_{2F}$ and $1/T_{2F}^{ref}$ (given by: $\Delta\nu_F \times \pi$) are the transverse relaxation rates of the free Na^+ ions in the presence and in the absence of chemical exchange, respectively, P_B is the molar fraction of the coordinated sodium ion [P_B = [B]/([B]+[F])] and k_{ex} is the rate constant of the exchange process. A similar expression holds for the transverse relaxation rate of the resonance of Na_B, see Equation (4).

$$1/T_{2B} = 1/T_{2B}^{ref} + P_F \times k_{ex} \quad (4)$$

The temperature dependence of k_{ex} is given by the Arrhenius equation, see Equation (5).

$$k_{ex}^T = k_{ex}^{298} \times T/298.15 \times \exp[\Delta H^{\#}/R \times (1000/298.15 - 1000/T)] \quad (5)$$

where T is the temperature, k_{ex}^T is the exchange rate constant at the temperature T, $\Delta H^{\#}$ (kJ mol^{-1}) is the enthalpy of activation of the exchange process and R is the gas constant. Finally, the temperature dependence of the transverse relaxation rate of the NMR signal in the absence of exchange is given by Equation (6).

$$1/T_2^{ref} = (1/T_2^{ref})^{298} \times \exp[E_a/R \times (1000/T - 1000/298.15)] \quad (6)$$

where E_a represents the activation energy of the process.

With the use of Equations 3–6, we have analysed the temperature dependence of the bandwidth of the ^{23}Na peak of the bound sodium ion for the six different solutions and calculated the rate of chemical exchange. The value of k_{ex} was found to be 600 s^{-1} (at 298 K) for all the solutions investigated and is thus independent of the molar fraction of added water. Thus, the derivatisation of the ligand aimed at increasing the solubility of the complexes in water should not compromise their promising properties as ^{23}Na NMR shift reagents, provided that the chemical modification does not affect the structure and rigidity of the coordination cage.

Conclusions

The transmetallation reactions of the complexes [LnNa(L)(Cl)$_2$(CH$_3$OH)] (Ln = Tb, Dy, Tm and Yb) by Li^+, K^+ and Ca^{2+} ions have been investigated by ^{23}Na NMR spectroscopy in methanolic solutions. The affinities of the macrocyclic complexes towards the alkali and alkaline-earth metal ions are primarily dictated by the match of the ionic radii with the size of the crown-like cavity of the ligand. Interaction of the cation in the O_2O_3 site with the anions may also contribute to the stabilities of the complexes. Large variations were observed in the affinity of a given metal ion for different lanthanide complexes. Small structural changes which may occurs across the lanthanide series seem to have a strong influence on the stabilities of the heterodinuclear complexes. Clearly, further investigations involving a systematic variation of the crown ether cavity are necessary in order to understand the relationship between the selectivity and the structural details of the complexes. The exchange of sodium between the coordination site and the solution is fast enough at physiological temperatures to cause an exchange averaged NMR signal strongly shifted from the diamagnetic position. The rate of exchange is not influenced by the addition of variable amounts of water to the methanolic solution. This property is promising for the development of water soluble derivatives as highly effective shift reagents for cations of biological relevance for diagnostic applications.[11]

Experimental Section

Materials: All solvents, reagents and the lanthanide chlorides, $LnCl_3 \cdot 6H_2O$, were purchased from Aldrich and Fluka and used without further purification.

Physico-Chemical Measurements: Elemental analyses were carried out by using a Fison 1108 analyser. IR spectra were recorded as KBr pellets on a Mattson FTIR spectrometer. The ^1H and ^{13}C NMR spectra for the diamagnetic complexes were recorded on a Bruker AMX300 spectrometer equipped with a broadband multinuclear probe and a variable temperature unit. ^{23}Na spectra were recorded on the same spectrometer on 15–25 m^m solutions of the Ln^{III} complexes (Ln = Tb, Dy, Tm, Yb) in CD_3OD. Typically, 2000 transients were necessary to obtain a satisfactory signal to noise ratio. The data were processed using a line broadening of 20 Hz and a baseline correction. ^{23}Na chemical shifts were measured in relation to the ^{23}Na signal of a 5 M solution of NaCl in CD_3OD. Downfield induced shifts are denoted as positive. The chemical shifts (^{23}Na) and the peak widths were determined by fitting the signals to a Lorenzian line function. All the samples examined were dissolved in deuterated methanol which was also used as an internal reference.

XRD investigations were performed on a Philips X'Pert PW3710 diffractometer using Cu-K_α radiation (40 kV, 30 mA), a high-resolution graphite monochromator, rotating sample holder and a proportional detector. Measurements were carried out in the range 4° $< 2\theta <$ 90° with a step of 0.02°. The morphology, homogeneity and the lanthanide/alkali or alkaline-earth/chlorine ratios of the complexes were investigated using a Philips XL40 model scanning electron microscope equipped with an EDAX DX PRIME X-ray energy dispersive spectrometer.[17] The solvent contents (H_2O or MeOH) were evaluated from thermal analysis curves recorded using Netzsch STA 429 thermoanalytical equipment. The tests were performed under nitrogen (flux rate 250 mL min^{-1}, heating rate 5 °C min^{-1}) and in air under the same conditions. Neutral alumina (Carlo–Erba, Milano, Italy) was used as reference material. All mass spectrometric measurements were performed on a VG ZAB 2F instrument (VG Analytical Ltd.) operating under fast atom bombardment (FAB) conditions (8 keV Xe atoms bombarding a nitrobenzyl alcohol solution of the sample). Also, ESI-MS spectra were recorded using an LQC mass spectrometer (Finnigan) and methanolic solutions of the samples (10^{-5} M).[18]

 © 2005 Wiley-VCH Verlag GmbH & Co. KGaA, Weinheim

Preparation of H_2L' and Na_2L': The diformyl precursor 3,3′-(3-oxapentane-1,5-diyldioxy)bis(2-hydroxybenzaldehyde) (H_2L') and the disodium derivative (Na_2L') were prepared by a modification of the literature procedure.[6,7,19–21]

Preparation of H_2L and $[LnNa(L)(Cl)_2(CH_3OH)]$ (Ln = Y, La, Ce, Nd, Sm, Eu, Gd, Tb, Dy, Ho, Er, Tm, Yb and Lu): The asymmetric [1+1] macrocycle 18-methyl-3,5,8-trioxa-15,18,21-triazacyclo-[21.3.1.1[9,13]]octacosa-1(27),9(28),10,12,14,21,23,25-octaene-27,28-diol (H_2L) and its heterodinuclear complexes $[LnNa(L)(Cl)_2(CH_3OH)]$ were prepared according to a literature procedure.[9]

Preparation of $[LnCa(L)(Cl)_2(CH_3OH)(H_2O)]Cl$ (Ln = Tb, Dy, Yb): $[LnNa(L)(Cl)_2(CH_3OH)]$ (Ln = Tb, Dy, Yb) (1 mmol) in methanol (50 mL) was added to an equimolar methanolic solution (50 mL) of $CaCl_2$. The pale brown solution was stirred for 24 h at room temperature. The mixture was then cleared by filtration and the solvent was evaporated to dryness under reduced pressure. The pale yellow residue was treated with *n*-propanol (30 mL), filtered, dried in vacuo and recrystallised by slow diffusion of diethyl ether into a methanol solution which yielded well-formed yellow crystals suitable for X-ray analysis.

$[TbCa(L)(Cl)_2(CH_3OH)(H_2O)]Cl{\cdot}H_2O$: IR (KBr): $\tilde{\nu}$ = 1631 cm^{-1} (C=N). $C_{24}H_{35}CaCl_3N_3O_8Tb$: calcd. C 36.08, H 4.42, N 5.26; found C 35.82, H 4.71, N 5.02.

$[TmCa(L)(Cl)_2(CH_3OH)(H_2O)]Cl{\cdot}H_2O$: IR (KBr): $\tilde{\nu}$ = 1630 cm^{-1} (C=N). $C_{24}H_{35}CaCl_3N_3O_8Tm$: calcd. C 35.64, H 4.36, N 5.19; found C 35.43, H 4.97, N 4.89.

$[DyCa(L)(Cl)_2(CH_3OH)(H_2O)]Cl\,H_2O$: IR (KBr): $\tilde{\nu}$ = 1630 cm^{-1} (C=N). $C_{24}H_{35}CaCl_3DyN_3O_8$: calcd. C 35.92, H 4.40, N 5.24; found C 35.51, H 4.62, N 4.98.

$[YbCa(L)(Cl)_2(CH_3OH)(H_2O)]Cl{\cdot}H_2O{\cdot}0.5NaCl$: IR (KBr): $\tilde{\nu}$ = 1627 cm^{-1} (C=N). $C_{24}H_{35}CaCl_{3.5}N_3Na_{0.5}O_8Yb$: calcd. C 34.23, H 4.19, N 4.99; found C 34.98, H 4.22, N 4.64.

X-ray: Diffraction data were collected at room temperature on a Philips PW1100 automatic four-circle diffractometer (FEBO System) using graphite monochromated Mo-K_α radiation and the ω-2θ scan method. Lattice parameters were obtained from least-squares refinements of the setting angles of 30 reflections with $9° \leq 2\theta \leq 23°$. No sign of crystal deterioration was revealed by monitoring three standard reflections after every 200 measurements. The structure was solved by standard Patterson methods and subsequently completed by a combination of least-squares techniques and Fourier syntheses with the SHELX program.[22,23] All benzene rings were refined as rigid bodies, the hydrogen atoms were included in idealised positions with fixed C–H distances (C–H = 0.93Å) and isotropic temperature factors fixed to 1.2 times *U*(eq) of the corresponding carbon atom. Table 2 shows a summary of the crystallographic data and structure refinement. The poor quality of the crystals did not give very good data but the data were, however, very useful in understanding the structure and the connectivity of this complex. In particular, serious disorder was found around N2 and for the coordinated ethanol molecule. Two possible positions for C9, C10, C12 and C25 were refined together with the corresponding population parameters. Additional crystallographic data, atomic coordinates, anisotropic thermal parameters and full listings of bond lengths and angles are available as supplementary material from the CCDC. Final geometrical calculations and drawings were carried out with the PARST program[24] and the XP utility of the Siemens package,[25] respectively, running on a DIGITAL ALPHA-AXP 300 computer.

Table 2. Crystal data for $[YbCa(L)(Cl)_2(EtOH)(H_2O)]Cl{\cdot}2H_2O$.

Formula	$C_{25}H_{38}N_3O_9Cl_3CaYb$
F_w	844.0
Crystal system	monoclinic
Space group	$P2_1/c$
a [Å]	10.033(2)
b [Å]	11.702(2)
c [Å]	27.796(6)
β [°]	105.51(3)
Cell volume [$Å^3$]	3145(1)
Z	4
Calcd. density [$g\,cm^{-3}$]	1.783
Absorption μ (mm^{-1}) [Mo-K_α]	3.445
Range of rel. transm. factors[a] [%]	89–100
θ limits [°]	6.9–56
Data collected/unique	4876/4772
Data observed	4521 [$F \geq 3.6\sigma(F)$]
Nr. of param. (observ.per param.)	349/13
R ($\Sigma(\|F_o\| - \|F_c\|) / \Sigma\|F_o\|$)	0.080
R_w $[\Sigma w(\|\|F_o\| - \|F_c\|\|)^2 / \Sigma w(F_o)^2]^{1/2}$	0.18
Highest map residual ($e\,Å^{-3}$)	1.33

[a] Corrections: Lorentz-polarisation and absorption (empirical, ψ scan).

CCDC-249846 contains the supplementary crystallographic data for this paper. These data can be obtained free of charge from The Cambridge Crystallographic Data Centre via www.ccdc.cam.ac.uk/data_request/cif.

Acknowledgments

We thank MIUR-FIRB (project code RBNE019H9K) for financial support.

[1] S. Tamburini, P. A.Vigato, *Coord. Chem. Rev.* in press.
[2] H. Okawa, H. Furutachi, D. E. Fenton, *Coord. Chem. Rev.* **1998**, *174*, 51.
[3] V. Alexander, *Chem. Rev.* **1995**, *95*, 273.
[4] N. Brianese, U. Casellato, S. Tamburini, P. Tomasin, P. A. Vigato, *Inorg. Chim. Acta* **1999**, *263*, 178.
[5] U. Casellato, S. Tamburini, P. Tomasin, P. A. Vigato, *Inorg. Chim. Acta* in press.
[6] A. Caneschi, L. Sorace, U. Casellato, P. Tomasin, S. Tamburini, P. A. Vigato, *Eur. J. Inorg. Chem.* in press.
[7] U. Casellato, S. Tamburini, P. Tomasin, P. A. Vigato, S. Aime, M. Botta, *Inorg. Chem.* **1999**, *38*, 2906.
[8] N. Brianese, U. Casellato, S. Tamburini, P. Tomasin, P. A. Vigato, *Inorg. Chem. Commun.* **1999**, *2*, 149.
[9] M. Botta, U. Casellato, C. Scalco, S. Tamburini, P. Tomasin, P. A. Vigato, S. Aime, A. Barge, *Chem. Eur. J.* **2002**, *8*, 3917.
[10] R. B. Hutchinson, J. I. Shapiro, *Concept Magn. Reson*. **1991**, *3*, 215.
[11] C. S. Springer, Jr., in *NMR Techniques in the Study of Cardiovascular Structure and Function* (Eds.: M. Osbakken, J. Haselgrove), Futura Publishing Co., New York, **1988**, chapter 4.
[12] A. D. Sherry, C. F. G. C. Geraldes, in *Lanthanide Probes in Life, Chemical and Earth Sciences* (Eds.: J.-C. G. Bünzli, G. R. Choppin), Elsevier, Amsterdam, **1989**, chapter 4.
[13] U. Casellato, S. Tamburini, P. Tomasin, P. A. Vigato, S. Aime, A. Barge, M. Botta, *Chem. Commun.* **2000**, 145.
[14] J. Ren, A. D. Sherry, *Inorg. Chim. Acta* **1996**, *246*, 331.
[15] R. M. Sink, D. C. Buster, A. D. Sherry, *Inorg. Chem.* **1990**, *29*, 3645.
[16] J.-J. Delpuech, in *Dynamics of Solutions and Fluids Mixtures by NMR* (Ed.: J.-J. Delpuech), John Wiley & Sons, Chichester, **1995**, chapter 3.

 © 2005 Wiley-VCH Verlag GmbH & Co. KGaA, Weinheim

[17] P. Guerriero, P. A. Vigato, B. Burtet-Fabris, *Inorg. Chim. Acta* **1989**, *164*, 155.
[18] P. P. Morgan, J. M. Beynon, R. M. Bateman, B. M. Green, *Int. J. Mass Spectrom. Ion Phys.* **1978**, *28*, 171.
[19] C. J. van Staveren, J. van Eerden, F. C. J. M. van Veggel, S. Harkema, D. N. Reinhoudt, *J. Am. Chem. Soc.* **1988**, *110*, 4994.
[20] F. C. J. M. van Veggel, M. Bos, S. Harkema, W. Verboom, D. N. Reinhoudt, *Angew. Chem. Int. Ed. Engl.* **1989**, *28*, 746.
[21] F. C. J. M. van Veggel, M. Bos, S. Harkema, H. van de Bovenkamp, W. Verboom, J. Reedijk, D. N. Reinhoudt, *J. Org. Chem.* **1991**, *56*, 22.
[22] *SHELX-86* (Eds.: G. M. Sheldrick, C. Kruger, R. Goddard), *Crystallographic Computing 3*, Oxford University Press, London, **1985**, p. 175.
[23] , *SHELXL-93* G. M. Sheldrick, *Program for Crystal Structure Refinement*, University of Göttingen, Göttingen, Germany, **1993**.
[24] M. Nardelli, *J. Appl. Crystallogr.* **1995**, *28*, 659.
[25] *SHELXTL-PLUS Ver.4.2*, G. M. Sheldrick, Siemens Analytical X-ray Instruments Inc.: Madison, WI, USA, **1991**.

Received: September 28, 2004

 © 2005 Wiley-VCH Verlag GmbH & Co. KGaA, Weinheim

Two New Diphenoxo-Bridged Discrete Dinuclear $Cu^{II}Gd^{III}$ Compounds with Cyclic Diimino Moieties: Syntheses, Structures, and Magnetic Properties

Rajesh Koner,[a] Gene-Hsiang Lee,[b] Yu Wang,[b] Ho-Hsiang Wei,*[c] and Sasankasekhar Mohanta*[a]

Keywords: Magnetic properties / Compartmental ligands / Gadolinium(III) / Ferromagnetic / Heterometallic complexes

Two Schiff base compartmental ligands, H_2L^1 and H_2L^2, derived from the condensation of 3-ethoxysalicylaldehyde with 1,2-diaminocyclohexane and orthophenylenediamine, respectively, have been utilized to isolate two diphenoxo-bridged discrete dinuclear $Cu^{II}Gd^{III}$ complexes, $[Cu^{II}(H_2O)L^1Gd^{III}(NO_3)_3]$ (**3**) and $[Cu^{II}L^2Gd^{III}(NO_3)_3]$ (**4**). This is the first report on the 3d-4f compounds derived from compartmental Schiff base ligands with cyclic diamines. The compounds **3** and **4** crystallize in the triclinic $P\bar{1}$ and orthorhombic *Pna*2(1) space groups, respectively, with the following unit cell parameters – **3**: a = 8.8713(2) Å, b = 12.8399(3) Å, c = 14.0067(3) Å, α = 80.6649(5)°, β = 77.4059(5)°, γ = 76.8879(5)°, and Z = 2; **4**: a = 9.2210(1) Å, b = 16.5407(2) Å, c = 19.9248(4) Å, and Z = 4. Structural analysis reveals that both are discrete dinuclear complexes. In **3**, one water molecule is coordinated to the copper(II) ion to result in a square-pyramidal coordination geometry, while the geometry of the coppe(II) center in **4** is square planar. In both complexes, the gadolinium(III) center has an O_{10} coordination environment. In contrast to expectation, although the N_2O_2 cavity affords a better planar environment for the copper(II) center in **4**, the bridging moiety in complex **3** is more planar than that in **4** or in most of the previously reported examples (the dihedral angle between two CuO_2Gd planes: 2.1° for **3** and 7.1° for **4**). Variable-temperature and variable-field magnetic measurements reveal that the metal centers in both the complexes are ferromagnetically coupled (J values: 6.3 cm^{-1} for **3** and 5.4 cm^{-1} for **4**; $H = -2JS_{Cu}\cdot S_{Gd}$). Interestingly, complex **3** exhibits strongest ferromagnetic interaction among the related compounds.

(© Wiley-VCH Verlag GmbH & Co. KGaA, 69451 Weinheim, Germany, 2005)

Introduction

With the exception of a few examples of carboxylate-bridged dimers,[1] all other reported discrete dinuclear 3d-4f complexes have been derived from Schiff base ligands.[2–19] In these Schiff base compounds, the steric effects imposed by complete encapsulation of the dinuclear core,[2,3] alkyl substituents on the lateral diiminoalkane chain,[4–16] the presence of an apical fifth ligand (1-methyl imidazole, methanol or acetone) coordinated to the square-planar copper(II) center,[6,17] or the distortion of the copper(II) environment from a square plane to tetrahedron have been argued to be the governing factors that stabilize the discrete dinuclear cores.[18]

Costes et al. reported a number of discrete 3d-4f compounds derived from the compartmental Schiff base ligands obtained on condensation of 3-methoxy/ethoxysalicylaldehyde with diaminoalkanes that have alkyl substituents on the lateral alkane chain.[4–16] There is also a recent example in which a discrete $Cu^{II}Gd^{III}$ compound has been synthesized by using the planar diamino chain provided by *S*-methylisothiosemicarbazide.[19] We reported a $Cu^{II}Gd^{III}$ compound derived from *N*,*N*′-ethylenebis(3-ethoxysalicylaldimine) with no alkyl substituent on the lateral chain.[20] In this complex, although the metal ions are well separated, there exists a weak intermolecular antiferromagnetic interaction, probably due to the semicoordination of one nitrate oxygen of one molecule to the copper(II) center of another dinuclear unit. The studies of the reported compounds reveal that although the nature of interaction is ferromagnetic in most cases,[2–20] the ferromagnetic behavior is not intrinsic; it depends on the environment of the metal ions and the structural parameters, and the behavior may also be antiferromagnetic.[14,15] It has also been realized that the dihedral angle between the CuO_2 and LnO_2 planes plays the crucial role in determining the nature and magnitudes of the exchange interactions.[10,17]

Although several acyclic diamines have been used to prepare Schiff base ligands that can stabilize discrete 3d-4f

[a] Department of Chemistry, University of Calcutta,
92 Acharya Prafulla Chandra Ray Road, Kolkata 700009, India
Fax: +91-33-23519755
E-mail: s_mohanta@hotmail.com
[b] Instrumental Center, College of Science, National Taiwan University,
Taipei, Taiwan
[c] Department of Chemistry, Tamkang University,
Tamsui, Taiwan 25137
Fax: +886-2-26209924
E-mail: tkwei@mail.tku.edu.tw

Supporting information for this article is available on the WWW under http://www.eurjic.org or from the author.

complexes, cyclic diamines such as 1,2-diaminocyclohexane or orthophenylenediamine have still not been utilized. By using two compartmental Schiff base ligands, H_2L^1 and H_2L^2, derived from the condensation of 3-ethoxysalicylaldehyde with 1,2-diaminocyclohexane and orthophenylenediamine, respectively, we have isolated two new heteronuclear $Cu^{II}Gd^{III}$ complexes, $[Cu^{II}(H_2O)L^1Gd^{III}(NO_3)_3]$ (**3**) and $[Cu^{II}L^2Gd^{III}(NO_3)_3]$ (**4**) (Scheme 1). We were particularly interested in the designed syntheses of 3d-4f systems that exhibit ferromagnetic interactions of different strengths.

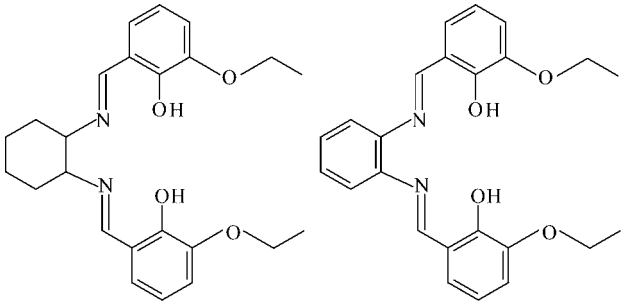

Scheme 1. Chemical structures of H_2L^1 and H_2L^2.

Results and Discussion

Description of the Structures of 3 and 4

The X-ray crystal structures of the two complexes show that both are dinuclear neutral complexes of copper(II) and gadolinium(III). ORTEP representations of **3** and **4** along with atom labels are shown in Figure 1 and Figure 2, respectively. The selected bond lengths and angles are listed in Table 1. In **3**, the cyclohexane moiety exists in a diequatorial *trans* configuration indicating that the condensation takes place with the diequatorial *trans* form of the diamine. The metal centers in both the complexes are doubly bridged by two phenoxo oxygen atoms provided by the ligands. The inner N_2O_2 cavity is occupied by copper(II), while gadolinium(III) occupies the open and larger position of the dinucleating compartmental ligands, $[L^1]^{2-}$ or $[L^2]^{2-}$. Because of the significant difference in size, the bond lengths of copper(II) and gadolinium(III) with bridging phenoxo oxygen atoms are significantly different [**3**: Cu–O(1) = 1.915(2), Cu–O(2) = 1.909(2), Gd–O(1) = 2.380(2), Gd–O(2) = 2.343(2) Å; **4**: Cu–O(1) = 1.884(4), Cu–O(2) = 1.903(5), Gd–O(1) = 2.368(5), Gd–O(2) = 2.419(4) Å].

The gadolinium(III) ion in both compounds has an O_{10} coordination environment. In addition to the phenoxo groups, two ethoxy oxygen atoms coordinate to this metal center. Two oxygen atoms each from the three nitrate groups chelate to gadolinium(III) to complete the decacoordination geometry. There are, as usual, three sets of Gd–O bond lengths.[4–13,18] The shortest and longest bonds involve the linking of the lanthanide with the bridging phenoxo oxygen atoms [**3**: Gd–O(1) = 2.380(2), Gd–O(2) = 2.343(2) Å; **4**: Gd–O(1) = 2.368(5), Gd–O(2) = 2.419(4) Å] and the ethoxy moieties [**3**: Gd–O(3) = 2.712(2), Gd–O(4) = 2.568(2) Å; **4**: Gd–O(3) = 2.544(4), Gd–O(4) = 2.701(4) Å], respectively, while the Gd–O(nitrates) separations [**3**: 2.450(3)–2.554(3) Å; **4**: 2.441(6)–2.551(5) Å] are of intermediate length. The Gd–O (ethoxy, nitrate or phenoxo) bond lengths are almost similar to the bond lengths observed in previously reported examples.[6–15,20]

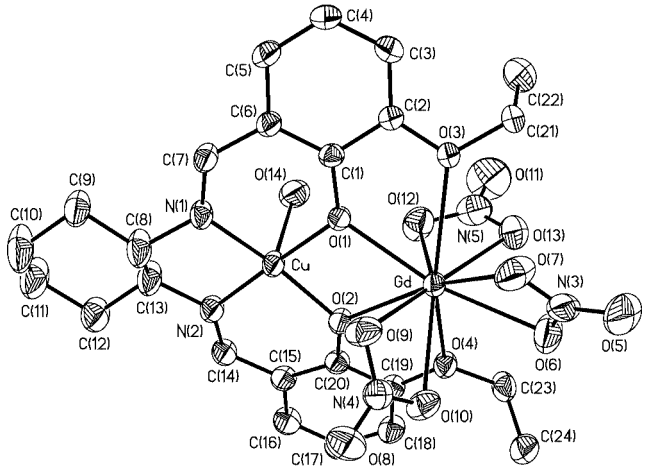

Figure 1. ORTEP representation (40% thermal ellipsoids) of **3** with atom-labeling schemes.

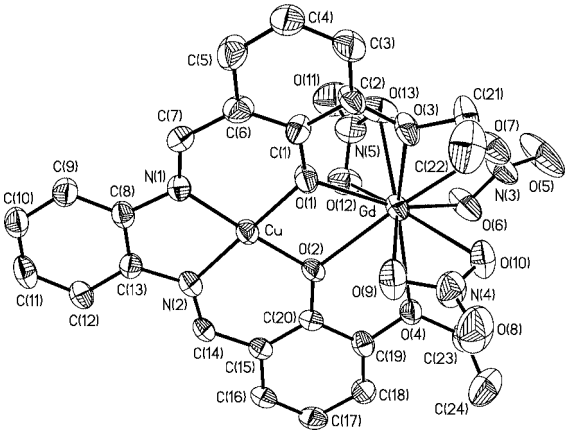

Figure 2. ORTEP representation (40% thermal ellipsoids) of **4** with atom-labeling schemes.

As mentioned before, copper(II) occupies the N_2O_2 cavities of the compartmental ligands in **3** and **4**. The ranges of the *cisoid* [84.23(9)°–96.82(11)°] and *transoid* [178.41(11)° and 168.44(12)°] angles in the N_2O_2 cavity, and the dihedral angles between the CuN(1)N(2) and CuO(1)O(2) planes (δ_1, 11.5°) or the CuN(1)O(1) and CuN(2)O(2) planes (δ_2, 11.7°) indicate that the N_2O_2 moiety affords an approximate square plane to copper(II) in **3**; the donor centers are alternatively above and below the mean N_2O_2 plane by an average of 0.086 Å, while the copper(II) is 0.1 Å below this square plane. In contrast, the N_2O_2 environment in **4** is more planar. Although the range of the *cisoid* angles [83.0(2)°–96.1(2)°] in **4** is similar to that in **3**, the *transoid*

 © 2005 Wiley-VCH Verlag GmbH & Co. KGaA, Weinheim

Table 1. Selected bond lengths [Å] and angles [°] for **3** and **4**.

	3	4
Cu–O(1)	1.915(2)	1.884(4)
Cu–O(2)	1.909(2)	1.903(5)
Cu–N(1)	1.918(3)	1.916(6)
Cu–N(2)	1.922(3)	1.913(5)
Cu–O(14)	2.535(3)	
Gd–O(1)	2.380(2)	2.368(5)
Gd–O(2)	2.343(2)	2.419(4)
Gd–O(3)	2.712(2)	2.544(4)
Gd–O(4)	2.568(2)	2.701(4)
Gd–O(Nitrate)	2.450(3)–2.554(3)	2.441(6)–2.551(5)
Cu–O(1)–Gd	104.18(9)	107.9(2)
Cu–O(2)–Gd	105.77(9)	105.28(18)
O(14)–Cu–O((1)	89.56(10)	
O(14)–Cu–O((2)	94.65(10)	
O(14)–Cu–N((1)	96.82(11)	
O(14)–Cu–N((2)	91.60(12)	
δ[a]	2.1	7.1
δ_1[a]	11.5	1.8
δ_2[a]	11.7	1.9
Cu···Gd[b]	3.401	3.449
Cu···Cu[b]	6.469	6.695
Cu···Gd[b]	7.657	7.192
Gd···Gd[b]	8.871	9.221

[a] δ, δ_1, δ_2 are the dihedral angles between CuO(1)O(2) and GdO(1)O(2), CuN(1)N(2) and CuO(1)O(2), and CuN(1)O(1) and CuN(2)O(2) planes, respectively. [b] Intramolecular interaction. [c] Shortest intermolecular interaction.

angles deviate only by a small degree from 180°. In addition, the dihedral angles δ_1 (1.8°) and δ_2 (1.9°) are close to 0°, which indicates an almost planar copper(II) environment afforded by the hexadentate ligand in **4**; the deviations of the donor centers and the metal ion is 0.01 Å (average). As expected, the copper(II) environment in the N_2O_2 cavity is more planar in **4**. However, interestingly, the planarity of the bridging moieties does not parallel our expectation; the dihedral angles (δ) between the CuO(1)O(2) and GdO(1)O(2) planes in **3** and **4** are 2.1° and 7.1°, respectively. Among the diphenoxo-bridged $M^{II}Ln^{III}$ complexes reported so far, the bridging moiety in one $Cu^{II}Gd^{III}$ complex that has a δ value of 1.7° is more planar than that in **3**.[10] The dihedral angles in other related compounds range from 4.7° to 47.4°.[7–16,20]

In addition to the four donor centers provided by the Schiff base ligand, one water molecule is coordinated to the apical position of the copper(II) center in **3** to result in a square-pyramidal coordination environment. As expected, due to Jahn–Teller distortion, the Cu–O(water) bond length [2.535(3) Å] is much longer than the bond lengths [1.909(2)–1.922(3) Å] of the metal ion with the donor centers in the equatorial plane. The bond angles of the Cu–O(water) axis with the planar Cu–N or Cu–O bonds lie between 89.56(10)° and 96.82(11)° indicating the square-pyramidal geometry of the copper(II) ion in **3**. In contrast, the coordination environment in **4** is square planar.

There exist several types of common intra- and intermolecular hydrogen bonds in both **3** and **4** that result in self-assembled supramolecular structures (one-dimensional for **4** and two-dimensional for **3**; see supporting information for discussion and figures). However, the shortest intermolecular metal···metal distances in **3** (Gd···GdA = 8.871 Å, Cu···GdA = 7.657 Å, Cu···CuC = 6.469 Å; symmetry: A, $x-1, y, z$; C, $1-x, -y, 1-z$) or **4** (Cu···CuA = 6.695 Å, Cu···GdA = 7.192 Å, Gd···GdB = 9.221 Å; symmetry: A, $x-0.5, 0.5-y, z$; B, $x-1, y, z$) are long enough to consider the dinuclear cores in both complexes as discrete.

Magnetic Properties

The variable-temperature (2–300 K) magnetic behavior of **3** and **4** are shown in Figure 3 and Figure 4, respectively, in the form of $\chi_M T$ versus T plots. The $\chi_M T$ values at 300 K for both complexes (8.51 $cm^3 mol^{-1} K$ for **3** and 8.34 $cm^3 mol^{-1} K$ for **4**) are slightly higher than the calculated value (8.25 $cm^3 mol^{-1} K$) for two uncoupled spins with $g = 2$. With a decrease in temperature from 300 K to 85 K, the $\chi_M T$ values slowly increase to reach 8.80 $cm^3 mol^{-1} K$ and 8.55 $cm^3 mol^{-1} K$ for **3** and **4**, respectively. On further lowering of the temperature, $\chi_M T$ increases sharply to 10.31 $cm^3 mol^{-1} K$ at 10 K for **3** and 9.97 $cm^3 mol^{-1} K$ at 2 K

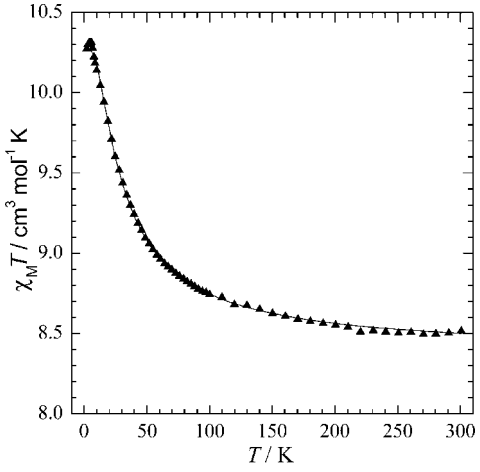

Figure 3. Experimental (triangles) and calculated (solid lines) $\chi_M T$ vs. T plots for $[Cu^{II}(H_2O)L^1Gd^{III}(NO_3)_3]$ (**3**).

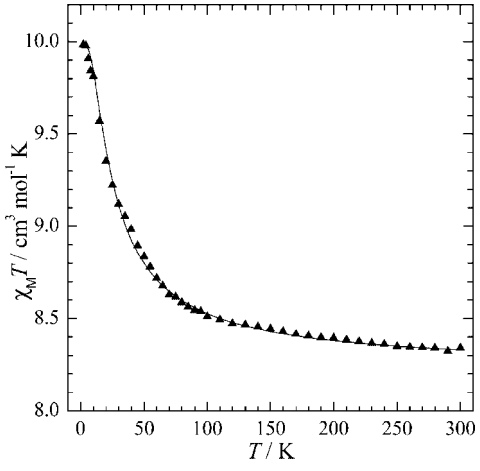

Figure 4. Experimental (triangles) and calculated (solid lines) $\chi_M T$ vs. T plots for $[Cu^{II}L^2Gd^{III}(NO_3)_3]$ (**4**).

 © 2005 Wiley-VCH Verlag GmbH & Co. KGaA, Weinheim

for **4**. Below 10 K, the $\chi_M T$ values of **3** are practically constant. As there is no orbital contribution in the ground state of Gd^{III}, the trends for the magnetic behavior indicate a ferromagnetic interaction between the metal centers in both complexes. The higher value of $\chi_M T$ at 300 K is also consistent with the ferromagnetic interaction between the spin carriers. For **4**, the larger value of $\chi_M T$ at 300 K is also associated with the larger value of g_{Cu} (vide infra).

Using the spin-only HDVV Hamiltonian [$H = -2JS_{Cu}\cdot S_{Gd} + \beta(g_{Cu}\cdot S_{Cu} + g_{Gd}\cdot S_{Gd})H$], the theoretical expression of χ_M for the $Cu^{II}Gd^{III}$ system may be derived as:

$$\chi_M = \frac{4N\beta^2}{k(T-\theta)} \times \frac{7g_3^{\,2} + 15g_4^{\,2}\exp(8J/kT)}{7 + 9\exp(8J/kT)} \quad (1)$$

where g_4 and g_3 are the g values of the pair states $S_T = 4$ and $S_T = 3$, respectively, which, in turn, are related to the local g values as:

$$g_3 = \frac{9g_{Gd} - g_{Cu}}{8}$$

$$g_4 = \frac{7g_{Gd} + g_{Cu}}{8}$$

Least-squares fitting of the experimental data with Equation (1) leads to $J = 6.3\ cm^{-1}$, $g_{Gd} = 2.008$, $g_{Cu} = 2.15$ for **3** and $J = 5.4\ cm^{-1}$, $g_{Gd} = 1.997$, $g_{Cu} = 2.0$ for **4**;[21] the agreement factor defined as $[\sum\{(\chi_M T)_{obs} - (\chi_M T)_{calc}\}^2 / \sum(\chi_M T)_{obs}^2]$ is 1.9×10^{-3} and 2.9×10^{-3} for **3** and **4**, respectively.

The field dependence of magnetization (up to 60000 G for **3** and 55000 G for **4**) at 5 K was measured. In Figure 5 and Figure 6, the magnetization data have been compared with the sum of the Brillouin functions of isolated Gd^{III} and Cu^{II}, as well as with the Brillouin function of the $S_T = 4$ state. The experimental magnetization is always greater than the sum of the noncorrelated spin system and matches well with the calculated values of the $S_T = 4$ state. The analysis confirms the existence of ferromagnetic exchange interactions between Cu^{II} and Gd^{III} in both complexes.

Kahn suggested that because the coupling is dependent on the exchange transfer integral between the 3d orbital of copper(II) and the 4f orbitals of gadolinium(III), the magnitude of J in systems with a CuO_2Gd moiety, like in **3** and **4**, should be a function of the dihedral angle (δ) between the CuO_2 and GdO_2 planes.[17] Later, on analyzing the coupling constants of a limited numbers of structurally characterized diphenoxo-bridged complexes, Costes proposed an exponential relationship, $2J = Ae^{-B\delta}$ ($A = 11.5$, $B = 0.054$).[10] According to this correlation, J should be $5.15\ cm^{-1}$ for **3** ($\delta = 2.1°$) and $3.9\ cm^{-1}$ for **4** ($\delta = 7.1°$). The experimental values of $6.3\ cm^{-1}$ (**3**) and $5.4\ cm^{-1}$ (**4**) are not very different from this hypothesis. For the $Cu^{II}Gd^{III}$ complex with the smallest dihedral angle (1.7°) reported so far, J is $5\ cm^{-1}$.[10] However, compound **4** with a dihedral angle of 2.1° exhibits the strongest ferromagnetic interaction among the reported examples.

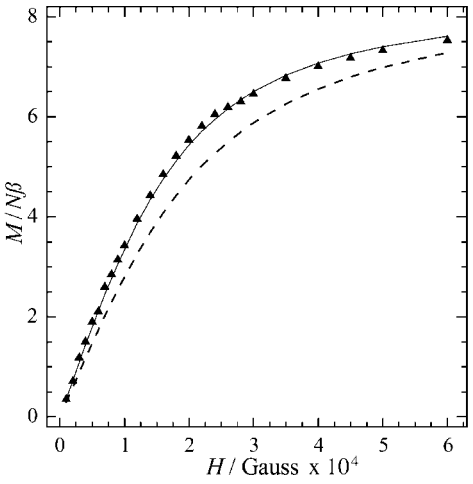

Figure 5. Field dependence of the magnetization at 5 K for $[Cu^{II}(H_2O)L^1Gd^{III}(NO_3)_3]$ (**3**). The solid and dashed lines represent the theoretical magnetization curves for the $S_T = 4$ state and the isolated spin system, respectively.

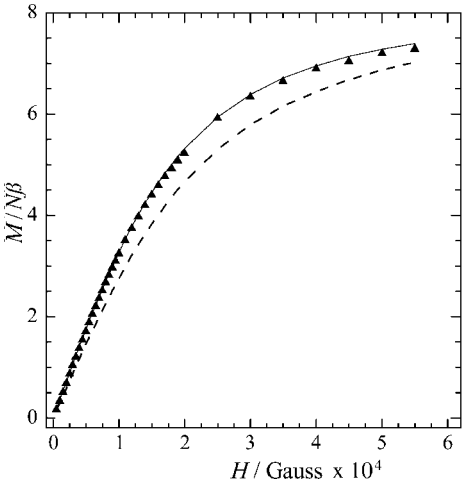

Figure 6. Field dependence of the magnetization at 5 K for $[Cu^{II}L^2Gd^{III}(NO_3)_3]$ (**4**). The solid and dashed lines represent the theoretical magnetization curves for the $S_T = 4$ state and the isolated spin system, respectively.

Conclusions

Two Schiff base compartmental ligands, H_2L^1 and H_2L^2, derived from the condensation of 3-ethoxysalicylaldehyde with 1,2-diaminocyclohexane and orthophenylenediamine, respectively, have been utilized to isolate two diphenoxo-bridged dinuclear $Cu^{II}Gd^{III}$ complexes, $[Cu^{II}(H_2O)L^1Gd^{III}(NO_3)_3]$ (**3**) and $[Cu^{II}L^2Gd^{III}(NO_3)_3]$ (**4**). Cyclic diamines have for the first time been utilized to obtain discrete dinuclear 3d-4f complexes. We expected that **3** would be a discrete $Cu^{II}Gd^{III}$ complex with high δ value that would exhibit a weak ferromagnetic interaction. In contrast, as $[L^2]^{2-}$ should afford a better square plane to copper(II), we expected a more planar bridging moiety in **4** so that this complex would exhibit a stronger ferromagnetic interaction. In contrast to our expectation, although the N_2O_2 cavity affords a better square plane to the copper(II) center in **4**, the

 © 2005 Wiley-VCH Verlag GmbH & Co. KGaA, Weinheim

bridging moiety in complex **3** is more planar than that in **4** or in most of the previously reported examples. Complex **3** exhibits the strongest ferromagnetic interaction (J = 6.3 cm^{-1}; $H = -2JS_{Cu}\cdot S_{Gd}$) among the related compounds reported so far.

Experimental Section

Materials and Physical Methods: All the reagents and solvents were purchased from commercial sources and used as received. Elemental (C, H, N) analyses were performed with a Perkin–Elmer 2400 II analyzer. IR spectra were recorded in the region 400–4000 cm^{-1} on a Perkin–Elmer RXIFT spectrophotometer with samples as KBr disks. Variable-temperature (2–300 K) magnetic susceptibility measurements under a fixed field strength of 0.5 T and the field-dependence magnetization experiments (up to 60000 G for **3** and 55000 G for **4**) at 5 K were carried out with a Quantum Design MPMS SQUID magnetometer. Diamagnetic corrections were estimated from Pascal's constants.

Synthesis of the Complexes

[Cu^{II}L^{1}]·H$_2$O (1): A methanol solution (10 mL) of an equimolar mixture of *cis*- and *trans*-1,2-diaminocyclohexane (0.475 g, 5 mmol) was mixed with a methanol solution (30 mL) of 3-ethoxysalicylaldehyde (1.66 g, 10 mmol), and the mixture was refluxed for 30 min. After cooling to room temperature, an aqueous solution (10 mL) of copper(II) acetate monohydrate (1.0 g, 5 mmol) was added dropwise to the resulting brown solution with stirring. An ash-colored precipitate was separated immediately. After stirring for 1 h, the compound was collected by filtration and air dried. Recrystallization from dimethylformamide resulted in a brown crystalline compound. Yield: 2.1 g (86%). $C_{24}H_{30}N_2O_5Cu$ (490.06): calcd. C 58.82, H 6.17, N 5.71; found C 58.68, H 6.25, N 5.83. IR (cm^{-1}, KBr): ν_{OH}(water), 3541 (m), 3501 (m); ν_{CH}(cyclohexane), 3048 (w), 2985 (w), 2931 (m), 2867 (w); $\nu_{C=N}$, 1623 (s).

[Cu^{II}L^{2}]·H$_2$O (2): This compound was prepared in a similar way to **1**, except with *o*-phenylenediamine instead of 1,2-diaminocyclohexane. Color: brown. Yield: 2.18 g (90%). $C_{24}H_{24}N_2O_5Cu$ (484.01): calcd. C 59.55, H 4.99, N 5.78; found C 59.67, H 4.90, N 5.71. IR (cm^{-1}, KBr): ν_{OH}(water), 3506 (w), 3461 (w); $\nu_{C=N}$, 1606 (s).

[Cu^{II}(H$_2$O)L^{1}Gd^{III}(NO$_3$)$_3$] (3): To a stirred suspension of 1 (0.122 g, 0.25 mmol) in acetone (20 mL) was added a methanol solution (10 mL) of gadolinium(III) nitrate hexahydrate (0.135 g, 0.3 mmol). The color of the solution changed to red. After 20 min of stirring, the solution was filtered to remove the suspended particles and was kept at room temperature for slow evaporation. After a few days, an orange crystalline compound containing diffractable single crystals appeared that was collected by filtration and air dried. Yield: 0.1 g (48%). $C_{24}H_{30}N_5O_{14}CuGd$ (833.32): calcd. C 34.59, H 3.63, N 8.40; found C 34.70, H 3.55, N 8.31. IR (cm^{-1}, KBr): ν_{OH}(water), 3500 (w), 3480 (w); $\nu_{C=N}$, 1632 (s); $\nu_{Nitrate}$, 1393 (s).

[Cu^{II}L^{2}Gd^{III}(NO$_3$)$_3$] (4): This compound was prepared in a similar way to **3**, except with **2** instead of **1**. Color: orange. Yield: 0.14 g (69%). $C_{24}H_{22}N_5O_{13}CuGd$ (809.26): C 35.62, H 2.74, N 8.65; found: C 35.53, H 2.81, N 8.72. IR (cm^{-1}, KBr): $\nu_{C=N}$, 1608 (s); $\nu_{Nitrate}$, 1388 (s).

Crystal Structure Determination: Pertinent crystallographic data of both complexes are summarized in Table 2. Diffraction data for **3** and **4** were collected on a Bruker SMART CCD and a NONIUS Kappa CCD diffractometer, respectively, in the ω–2θ scan mode using graphite monochromated Mo-K_α radiation with λ = 0.71073 Å. The accurate unit cells were obtained by means of least-squares fittings of 25 centered reflections. The intensity data were corrected for Lorentz and polarization effects, and semiempirical absorption corrections were made from ψ-scans. A total of 20780 reflections were collected for **3** in the range 2θ = 3.0–55.0° with $-11 \le h \le 11$, $-16 \le k \le 16$, and $-18 \le l \le 18$, of which 6930 independent reflections (R_{int} = 0.0275) were used for structure determinations. In the case of **4**, among 18891 of the total reflections collected in the 2θ range of 4.92–55.0° with $-11 \le h \le 11$, $-21 \le k \le 21$, and $-25 \le l \le 25$, 6767 were independent (R_{int} = 0.0612). The structures were solved by direct and Fourier methods and refined by full-matrix least-squares methods based on F^2 with the programs SHELXS-97 and SHELXL-97.[22,23] The final least-squares refinements ($R1$) based on $I > 2\sigma(I)$ converged to 0.0255 for **3** and 0.0425 for **4**. CCDC-250133 (**3**) and CCDC-250132 (**4**) contain the supple-

Table 2. Crystallographic data for **3** and **4**.

	3	**4**
Formula	$C_{24}H_{30}N_5O_{14}CuGd$	$C_{24}H_{22}N_5O_{13}CuGd$
Molecular weight	833.32	809.26
Crystal color	orange	orange
Crystal system	triclinic	orthorhombic
Space group	$P\bar{1}$	*Pna*2(1)
a [Å]	8.8713(2)	9.2210(1)
b [Å]	12.8399(3)	16.5407(2)
c [Å]	14.0067(3)	19.9248(4)
α [°]	80.6649(5)	90.00
β [°]	77.4059(5)	90.00
γ [°]	76.8879(5)	90.00
V [Å^3]	1505.77(6)	3038.97(8)
Z	2	4
$D_{calcd.}$ [g cm^{-3}]	1.838	1.769
F(000)	828	1592
μ [cm^{-1}]	2.966	2.934
Crystal size [mm]	0.37 × 0.25 × 0.08	0.15 × 0.07 × 0.02
Temperature [K]	295(2)	295(2)
Final *R* indices [$I > 2\sigma(I)$]	$R1$[a] = 0.0255, w$R2$[b] = 0.0556	$R1$[a] = 0.0425, w$R2$[b] = 0.0820
R indices (all data)	$R1$[a] = 0.0400, w$R2$[b] = 0.0679	$R1$[a] = 0.0804, w$R2$[b] = 0.0979

[a] $R1 = [\Sigma||F_o| - |F_c||/\Sigma|F_o|]$. [b] $wR2 = [\Sigma w(F_o^2 - F_c^2)^2/\Sigma w(F_o^2)^2]^{1/2}$.

 © 2005 Wiley-VCH Verlag GmbH & Co. KGaA, Weinheim

mentary crystallographic data for this paper. These data can be obtained free of charge from The Cambridge Crystallographic Data Centre via www.ccdc.cam.ac.uk/data_request/cif.

Acknowledgments

Financial support from the Department of Science and Technology, Government of India (SR/S1/IC-27/2002) and the National Science Council, Taiwan (NSC93-2113-M032–002) is gratefully acknowledged. SM thanks Dr. Karen J. Hindson, editor of this journal, and the reviewers of the manuscript for their valuable suggestions.

[1] Y.-Y. Yang, Y.-L. Wu, L.-S. Long, X.-M. Chen, *J. Chem. Soc., Dalton Trans.* **1999**, 2005.
[2] S. J. Archibald, A. J. Blake, S. Parsons, M. Schroder, R. E. P. Winpenny, *J. Chem. Soc., Dalton Trans.* **1997**, 173.
[3] Q.-Y. Chen, Q.-H. Luo, Z.-L. Wang, J.-T. Chen, *J. Chem. Soc. Chem. Commun.* **2000**, 1033.
[4] R. E. P. Winpenny, *Chem. Soc. Rev.* **1998**, 447.
[5] M. Sakamoto, K. Manseki, H. Ōkawa, *Coord. Chem. Rev.* **2001**, 219–221, 379.
[6] J.-P. Costes, A. Dupuis, J.-P. Laurent, *Chem. Eur. J.* **1998**, 1616.
[7] J.-P. Costes, F. Dahan, A. Dupuis, J.-P. Laurent, *Inorg. Chem.* **1996**, *35*, 2400.
[8] J.-P. Costes, F. Dahan, A. Dupuis, J.-P. Laurent, *Inorg. Chem.* **1997**, *36*, 3429.
[9] J.-P. Costes, F. Dahan, A. Dupuis, J.-P. Laurent, *Inorg. Chem.* **1997**, *36*, 4284.
[10] J.-P. Costes, F. Dahan, A. Dupuis, *Inorg. Chem.* 2000, *39*, 165.
[11] J.-P. Costes, F. Dahan, A. Dupuis, J.-P. Laurent, *New J. Chem.* **1998**, *22*, 1525.
[12] J.-P. Costes, A. Dupuis, J.-P. Laurent, *Eur. J. Inorg. Chem.* **1998**, 1543.
[13] J.-P. Costes, A. Dupuis, J.-P. Laurent, *J. Chem. Soc., Dalton Trans.* **1998**, 735.
[14] J.-P. Costes, F. Dahan, A. Dupuis, J.-P. Laurent, *Inorg. Chem.* **2000**, *39*, 169.
[15] J.-P. Costes, F. Dahan, B. Donnadieu, J. Garcia-Tojal, J.-P. Laurent, *Eur. J. Inorg. Chem.* **2001**, 363.
[16] G. Novitchi, S. Shova, A. Caneschi, J.-P. Costes, M. Gdaniec, N. Stanica, *J. Chem. Soc., Dalton Trans.* **2004**, 1194.
[17] I. Ramade, O. Kahn, Y. Jeannin, F. Robert, *Inorg. Chem.* **1997**, *36*, 930.
[18] M. Sasaki, K. Manseki, H. Horiuchi, M. Kumagai, M. Sakamoto, H. Nishida, Y. Sakiyama, M. Sakai, Y. Sadaoka, M. Ohba, H. Ōkawa, *J. Chem. Soc., Dalton Trans.* **2000**, 259.
[19] J.-P. Costes, F. Dahan, G. Novitchi, V. Arion, S. Shova, J. Lipkowski, *Eur. J. Inorg. Chem.* **2004**, 1530.
[20] S. Mohanta, H.-H. Lin, C.-J. Lee, H.-H. Wei, *Inorg. Chem. Commun.* **2002**, *5*, 585.
[21] Global minimization takes place with $g = 2.15$. If the value of g is forced to be smaller, the quality of the simulation becomes more and more poor.
[22] G. M. Sheldrick, *SHELXS-97: A Program for Crystal Structure Solution*, University of Göttingen, Germany, **1997**.
[23] G. M. Sheldrick, *SHELXL-97: A Program for Crystal Structure Refinement*, University of Göttingen, Germany, **1997**.

Received: 12 October, 2004

 © 2005 Wiley-VCH Verlag GmbH & Co. KGaA, Weinheim

Mixed f-d Metallomesogens with an Extended Rigid Core

Koen Binnemans,*[a] Katleen Lodewyckx,[a] Bertrand Donnio,[b] and Daniel Guillon[b]

Keywords: Copper / Lanthanides / Liquid crystals / Metallomesogens / Nickel

The liquid-crystalline behaviour of copper(II) and nickel(II) complexes of a mesogenic Schiff-base ligand derived from *N*,*N*′-disalicylidene-1,2-phenylenediamine (salophenH_2) and of the corresponding trinuclear mixed copper(II)/lanthanum(III) and nickel(II)/lanthanum(III) complexes was investigated. High-temperature X-ray diffraction studies revealed that both the parent transition metal complexes and the mixed f-d complexes exhibit a hexagonal columnar phase (Col_h) over an extended temperature range. Complex formation with lanthanum(III) nitrate resulted in an increase of the transition temperatures. The geometrical parameters (lattice parameters and column cross-section) of all the metal complexes are very similar, which indicates that the local organisation in the mesophase is the same despite their structural differences.

(© Wiley-VCH Verlag GmbH & Co. KGaA, 69451 Weinheim, Germany, 2005)

Introduction

Liquid-crystalline metal complexes (metallomesogens) combine the unique properties of both transition metals or rare-earth metals and liquid crystals, and these compounds form an intriguing class of new materials.[1] In this way, it is, for instance, possible to obtain paramagnetic liquid crystals,[2] or redox-active liquid crystals.[3] Nearly all metallic elements of the periodic table have been used to create metallomesogens, but examples of liquid crystals that contain both an f-block metal ion (lanthanide or rare-earth ion) and a d-block metal ion are rare. The first examples of such mixed f-d metallomesogens have been reported recently (Figure 1).[4] A copper(II) complex of a mesogenic 2,2′-*N*,*N*′-bis(salicylidene)ethylenediamine (salen) derivative was used to form adducts with lanthanide(III) nitrates. This work was extended further in the sense that the copper(II) was replaced by nickel(II) (Figure 2), and that the influence of the chain length on the transition temperatures was investigated.[5] In all cases, both the parent transition metal complexes and the f-d complexes exhibit a hexagonal columnar mesophase (Col_h). It should be noticed that salen-type ligands are of interest not only for preparing liquid-crystalline f-d complexes, but also for the design of many types of liquid-crystalline transition metal complexes.[6] The salen-type Schiff-base complexes are important as catalysts.[7]

In this paper we have modified the salen-type ligand that has been used in earlier studies on f-d metallomesogens by replacing 1,2-ethylenediamine as the linking group by 1,2-diaminobenzene. The aim of the work was to investigate the influence of the extension of the rigid part of the core of the ligand on the thermal behaviour of the ligand and metal complexes. Four mesogenic metal complexes were prepared, namely two copper(II) and nickel(II) ones, and two binuclear copper(II)/lanthanum(III) and nickel(II)/lanthanum(III) complexes (Figure 3). Their liquid-crystalline properties were investigated in detail by X-ray diffraction.

Results and Discussion

The synthesis of the *N*,*N*′-disalicylidene-1,2-phenylenediamine (salophenH_2) Schiff-base ligand (H_2L) and of the metal complexes is outlined in Scheme 1. The first step is the synthesis of 3,4,5-tris(tetradecyloxy)benzoic acid by alkoxylation of 3,4,5-trihydroxybenzoic acid ethyl ester (Williamson ether synthesis), followed by formation of the free acid by saponification of the ethyl ester and acidification of the carboxylate salt. The second step is the coupling of 3,4,5-tris(tetradecyloxy)benzoic acid to the 4-position of 2,4-dihydroxybenzaldehyde by an ester bond (with DCC, DMAP). The aldehyde was transformed into the Schiff-base ligand by condensation with 1,2-diaminobenzene in toluene. The water formed during the condensation reaction was removed azeotropically in a Dean–Stark trap. The copper(II) complex CuL and the nickel(II) complex NiL were formed by reaction between the Schiff-base H_2L and copper(II) acetate monohydrate and nickel(II) acetate tetrahydrate, respectively, in a methanol/chloroform mixture.

[a] Katholieke Universiteit Leuven, Department of Chemistry, Celestijnenlaan 200F, 3001 Leuven, Belgium
Fax: +32-16-327-992
E-mail: Koen.Binnemans@chem.kuleuven.ac.be
[b] Institut de Physique et Chimie des Matériaux de Strasbourg – Groupe Matériaux Organiques, UMR 7504 CNRS-Université Louis Pasteur,
B. P. 43, 23 rue du Loess, 67034 Strasbourg, Cedex 2, France

 © 2005 Wiley-VCH Verlag GmbH & Co. KGaA, Weinheim **DOI: 10.1002/ejic.200400880**

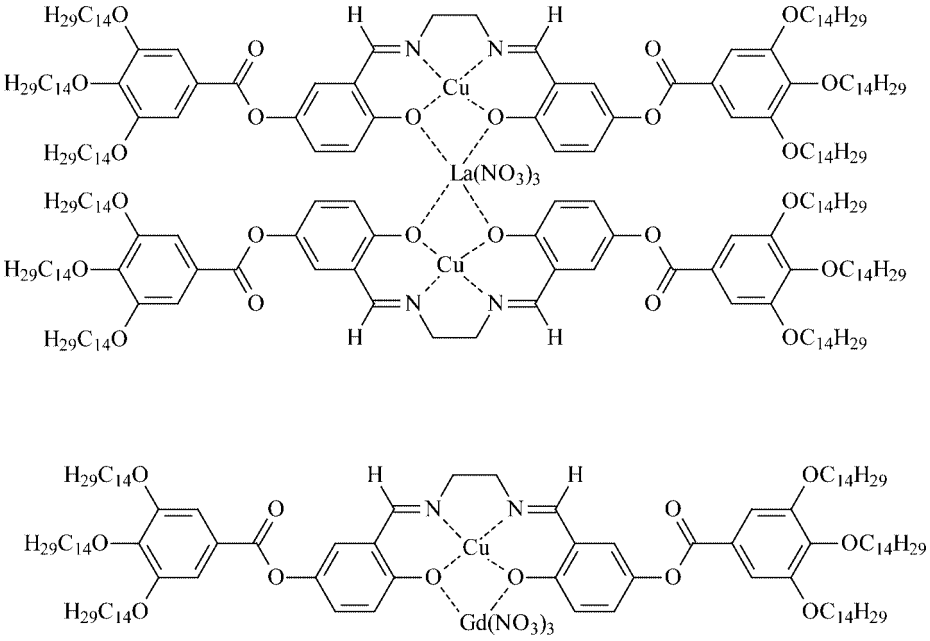

Figure 1. Structure of the first examples of mixed f-d metallomesogens, a trinuclear copper(II)/lanthanum(III) complex and a dinuclear copper(II)/gadolinium(III) complex with a mesogenic 2,2′-*N*,*N*′-bis(salicylidene)ethylene diamine (salen) ligand, reported by Binnemans et al.[4]

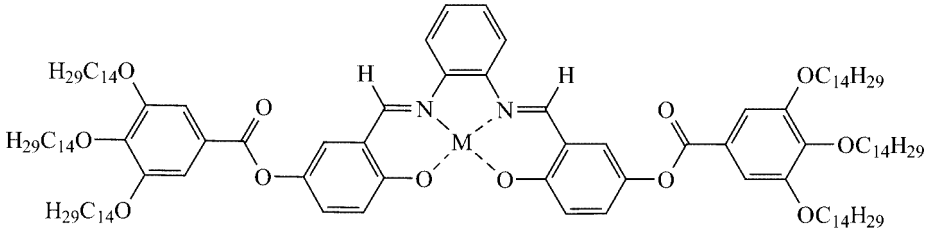

M = Cu, Ni

Figure 2. Structure of the copper(II) complex CuL (M = Cu) and the nickel(II) complex NiL (M = Ni) of the mesogenic *N*,*N*′-disalicylidene-1,2-phenylenediamine (salophenH_2) ligand.

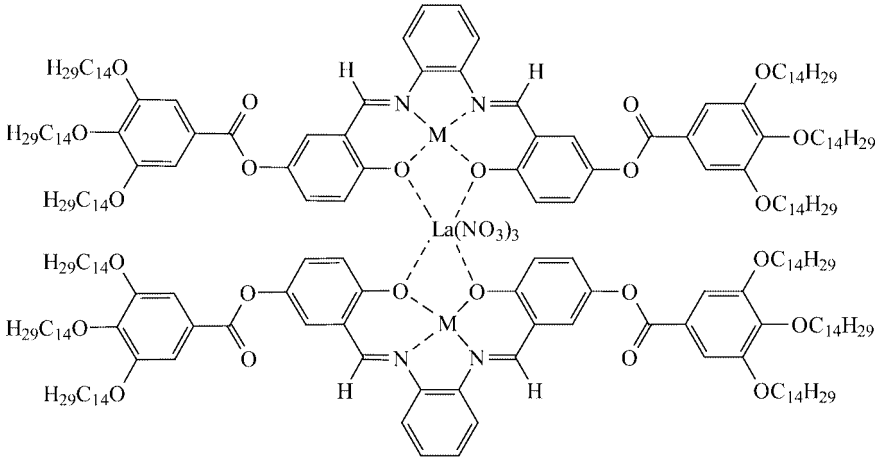

M = Cu, Ni

Figure 3. Structure of the trinuclear copper(II)/lanthanum(III) complex CuLaL (M = Cu) and of the trinuclear nickel(II)/lanthanum(III) complex NiLaL (M = Ni) of the mesogenic *N*,*N*′-disalicylidene-1,2-phenylenediamine (salophenH_2) ligand H_2L described in this study.

 © 2005 Wiley-VCH Verlag GmbH & Co. KGaA, Weinheim

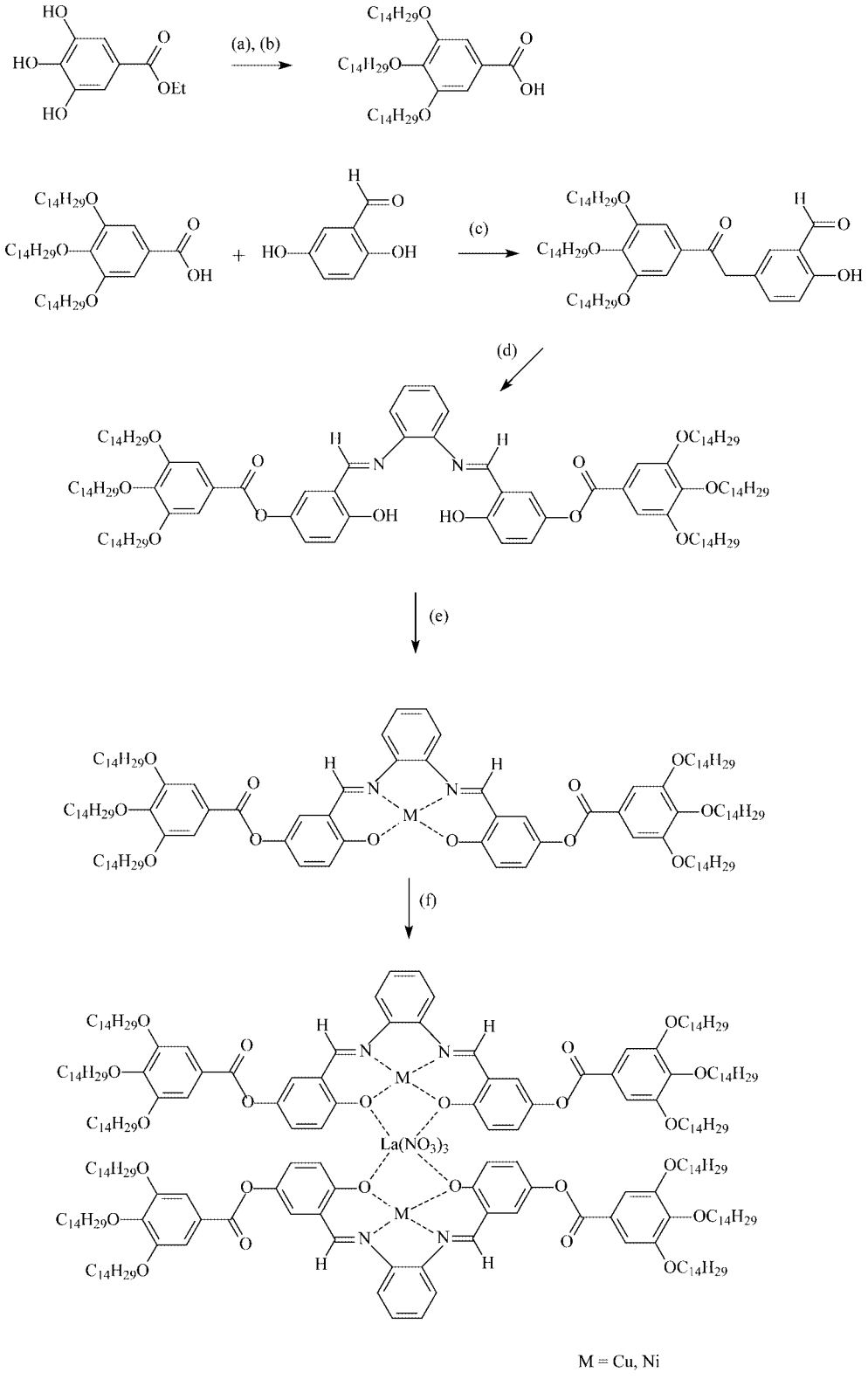

Scheme 1. Synthesis of the Schiff-base ligand H_2L and of the metal complexes. Reagents and conditions: (a) RBr (3 equiv.), K_2CO_3 (6 equiv.), TBAB (phase-transfer catalyst), methyl isobutyl ketone, reflux overnight; (b) NaOH, ethanol, reflux for 4 h; acidification with dilute HCl solution; (c) DCC, DMAP, dichloromethane, 24 h at room temp.; (d) 1,2-diaminobenzene (1/2 equiv.), glacial acetic acid (catalyst), toluene, Dean–Stark trap, 3 h at reflux; (e) $Cu(OOCCH_3)_2{\cdot}H_2O$ (M = Cu) or $Ni(OOCCH_3)_2{\cdot}4H_2O$ (M = Ni) (1 equiv.), methanol/chloroform, reflux overnight; (f) $La(NO_3)_3{\cdot}6H_2O$, acetone, room temp., 24 h.

 © 2005 Wiley-VCH Verlag GmbH & Co. KGaA, Weinheim

The acetate ions act as the base to deprotonate the Schiff-base ligand. The copper(II)/lanthanum(III) complex CuLaL and the nickel(II)/lanthanum(III) complex NiLaL were prepared by reaction between the copper(II) complex CuL or the nickel(II) complex NiL and lanthanum(III) nitrate hexahydrate in acetone. The metal complexes were characterised by infrared spectroscopy and by elemental analysis. Both the copper(II)/lanthanum(III) complex CuLaL and the nickel(II)/lanthanum(III) complex NiLaL were found to be trinuclear species consisting of two transition metal ions [either copper(II) or nickel(II)] and one trivalent lanthanum(III) ion per molecule. The nitrogen content of the lanthanum(III) complexes, as determined by CHN microanalysis, is lower than the calculated value. This discrepancy is due to a systematic error in the CHN microanalysis procedure, and can be attributed to incomplete reduction of the nitrates to dinitrogen gas or to the formation of lanthanum(III) oxonitrides. Although we could not obtain single crystals of our compounds for X-ray structure determination, we can nevertheless deduce some data about the coordination sphere of the lanthanum(III) by referring to the crystal structures published by Kahn et al. for f-d complexes of the salen ligand.[8] The three nitrate ions are coordinated to the lanthanum(III) ion in a bidentate fashion. The coordination number of lanthanum(III) is ten, with six oxygen atoms from the three nitrate groups and four oxygen atoms of the two copper(II) salophen complexes [or nickel(II) salophen complexes]. The coordination polyhedron of lanthanum(III) is irregular and cannot be approximated by a highly symmetric coordination polyhedron. Coordination number 10 is rather unusual for lanthanide complexes, but can in this case be achieved by the small bite angle of the nitrate groups.

The Schiff-base ligand H_2L is not mesomorphic, and it melts directly to an isotropic liquid at 67 °C. All the metal complexes are enantiotropic liquid crystals. The mesophases were studied by polarising optical microscopy (POM), differential scanning calorimetry (DSC) and by high-temperature X-ray diffraction. For the copper and nickel complex, a typical texture of a hexagonal columnar mesophase (Col_h) could be seen by POM upon slow cooling from the isotropic liquid. Only atypical textures were observed for the trinuclear complex CuLaL and for the trinuclear complex NiLaL, so that it was impossible to determine the mesophase unambiguously by POM. Observation of the texture of the copper/lanthanum complex CuLaL was also hampered by the thermal decomposition of the complex in the mesophase before the clearing point was reached. Just above the melting point, the viscosity of the samples is quite high, but the viscosity decreases with increasing temperature. Because no well-resolved DSC curves could be recorded (a problem also encountered in the past for similar complexes),[4] no enthalpy data could be obtained. These problems could be due to the high viscosity of the complexes, and to the low crystallinity of the complexes in the solid phase. The transition temperatures of the complexes were determined by optical microscopy, and the values are given in Table 1.

Table 1. Transition temperatures and mesophase behaviour of the Schiff-base complexes.

Complex	Transition temperatures [°C][a]
CuL	Col_{ho} · 39 · Col_h · 170 · I
NiL	Cr ·40 · Cr′ · 61 · Col_h · 133 · I
CuLaL	Cr ·69 · Col_h · 192 · dec.
NiLaL	Cr · 85 · Col_h · 218 · I

[a] Cr, Cr′: crystalline phases; Col_{ho}: ordered hexagonal columnar phase; Col_h: hexagonal columnar phase; I: isotropic liquid; dec.: decomposition.

Table 2. Characteristic X-ray data of the copper(II) complex CuL.

Temperature [°C]	$d_{measd.}$ [Å]	[*hk*]	$d_{calcd.}$ [Å]	Mesophase and parameters
30	37.3	[10]	37.25	Col_{ho}
	21.4	[11]	21.5	a = 43 Å
	18.7	[20]	18.6	s = 1600 Å^2
	10.3	*h1*		
	4.5	*h2*		
	4.1	*s1*		
50	37.8	[10]	37.8	Col_h
	21.8	[11]	21.8	a = 43.65 Å
	9.8	*h1*		s = 1650 Å^2
	4.5	*h2*		
100	37.05	[10]	36.9	Col_h
	21.35	[11]	21.3	a = 42.6 Å
	18.3	[20]	18.45	s = 1570 Å^2
	9.8	*h1*		
	4.5	*h2*		

Table 3. Characteristic X-ray data of the nickel(II) complex NiL at 100 °C.

$d_{measd.}$ [Å]	[*hk*]	$d_{calcd.}$ [Å]	Mesophase and parameters
36.5	[10]	36.5	Col_h
21.05	[11]	21.1	a = 42.15 Å
9.4	*h1*		s = 1540 Å^2
4.5	*h2*		

Table 4. Characteristic X-ray data of the copper(II)/lanthanum(III) complex CuLaL.

Temperature [°C]	$d_{measd.}$ [Å]	[*hk*]	$d_{calcd.}$ [Å]	Mesophase and parameters
100	36.7	[10]	36.7	Col_h
	21.2	[11]	21.2	a = 42.4 Å
	18.4	[20]	18.35	s = 1560 Å^2
	9.8	*h1*		
	4.5	*h2*		
150	35.7	[10]	35.6	Col_h
	20.5	[11]	20.55	a = 41.1 Å
	17.8	[20]	17.8	s = 1460 Å^2
	13.5	[21]	13.45	
	9.9	*h1*		
	4.5	*h2*		

The mesophase behaviour of the metal complexes was studied in detail by temperature-dependent X-ray measurements. The results of the X-ray measurements are summarised in Tables 2–5. X-ray patterns of the complexes are shown in Figures 4–8. X-ray diffractograms were recorded at 30 °C (Figure 4) and at 50 °C and 100 °C (Figure 5) for

 © 2005 Wiley-VCH Verlag GmbH & Co. KGaA, Weinheim

Table 5. Characteristic X-ray data of the nickel(II)/lanthanum(III) complex NiLaL.

Temperature [°C]	$d_{measd.}$ [Å]	[*hk*]	$d_{calcd.}$ [Å]	Mesophase and parameters
100	36.8	[10]	36.65	Col_h
	21.15	[11]	21.15	a = 42.3 Å
	18.25	[20]	18.3	s = 1550 Å^2
	9.8	*h1*		
	4.5	*h2*		
	3.8	*h3*		
150	35.5	[10]	35.45	Col_h
	20.45	[11]	20.45	a = 40.9 Å
	17.7	[20]	17.7	s = 1450 Å^2
	9.4	*h1*		
	4.5	*h2*		

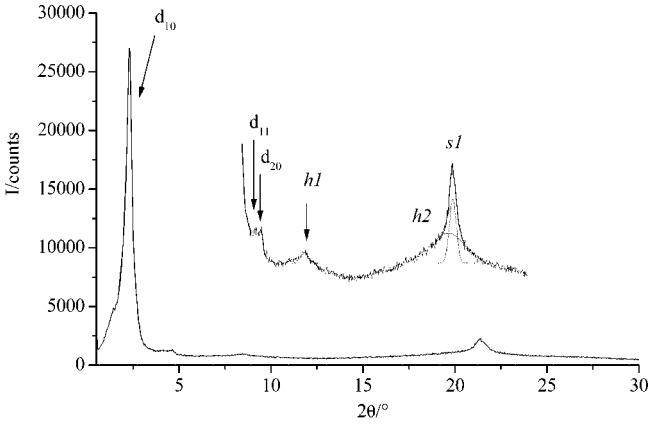

Figure 4. X-ray diffractogram of the copper(II) complex CuL at 30 °C in the Col_{ho} phase.

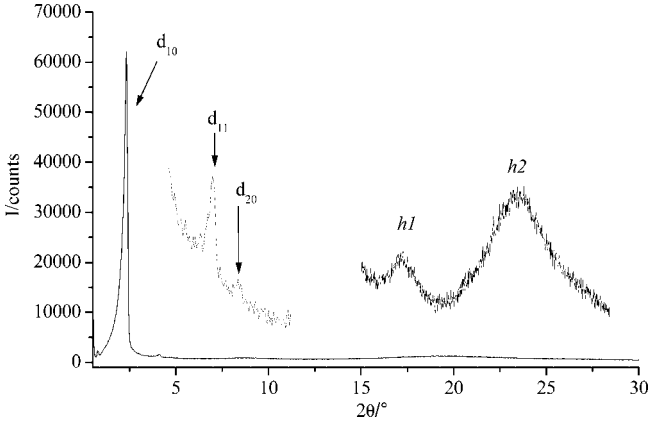

Figure 5. X-ray diffractogram of the copper(II) complex CuL at 100 °C in the Col_h phase.

the mononuclear copper complex CuL (Table 2) and the mononuclear nickel complex NiL (Table 3), and at 100 °C (Figure 6) and 150 °C for the trinuclear copper/lanthanum complex CuLaL (Figure 7, Table 4) and the nickel/lanthanum complex NiLaL (Figure 8, Table 5). All the samples gave similar X-ray patterns when the experiments were performed in the mesomorphic temperature ranges. The X-ray patterns consist of: (a) a diffuse scattering halo (*h2*) in the wide-angle region, corresponding to the liquid-like disorder

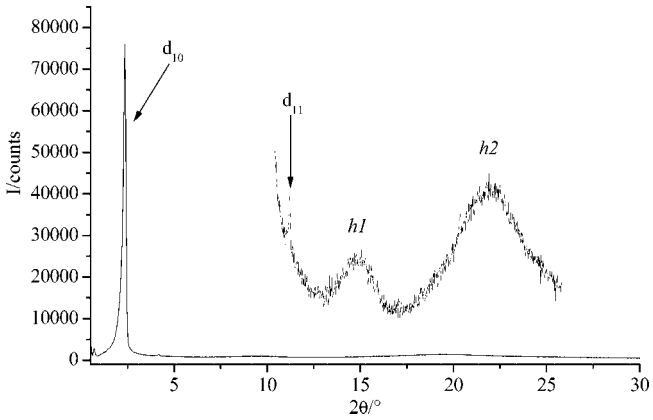

Figure 6. X-ray diffractogram of the nickel(II) complex NiL at 100 °C in the Col_h phase.

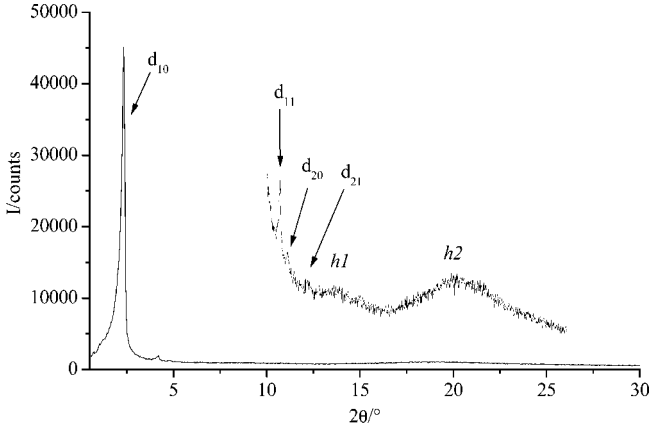

Figure 7. X-ray diffractogram of the copper(II)/lanthanum(III) complex CuLaL at 150 °C in the Col_h phase.

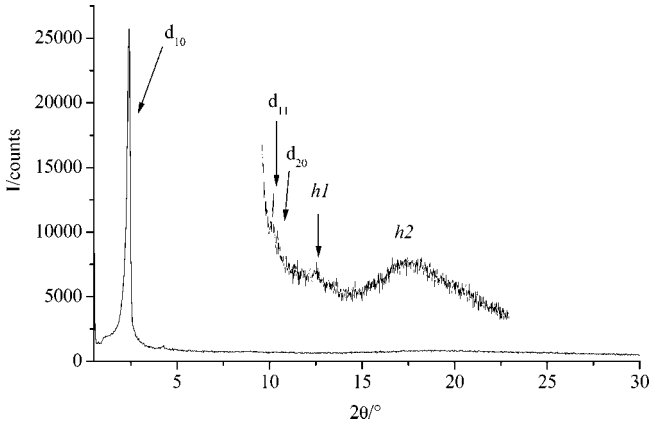

Figure 8. X-ray diffractogram of the nickel(II)/lanthanum(III) complex NiLaL at 150 °C in the Col_h phase.

of the aliphatic chains and rigid parts, at about 4.5 Å, a distance corresponding to <*h*> in Figure 9 and Figure 10; (b) another, slightly less intense diffuse band (*h1*) seen at about 9.4 Å, which could be an indication of a dimeric structure; and (c) three or four sharp, intense reflections in the small-angle region, with the reciprocal spacings in the

 © 2005 Wiley-VCH Verlag GmbH & Co. KGaA, Weinheim

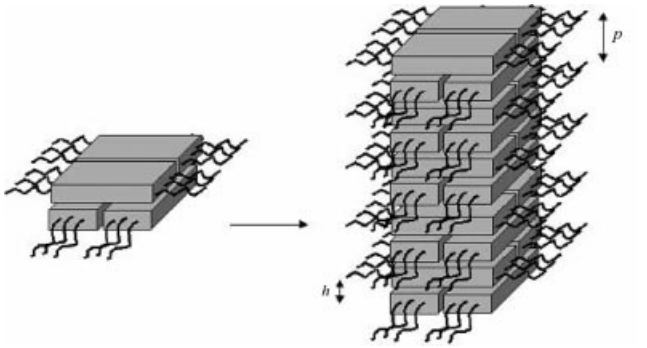

Figure 9. Molecular organisation of the copper(II) complex CuL and the nickel(II) complex NiL within the hexagonal columnar mesophase. The columnar repeat unit is given by $<p>$, and $<h>$ is the average distance between adjacent molten chains.

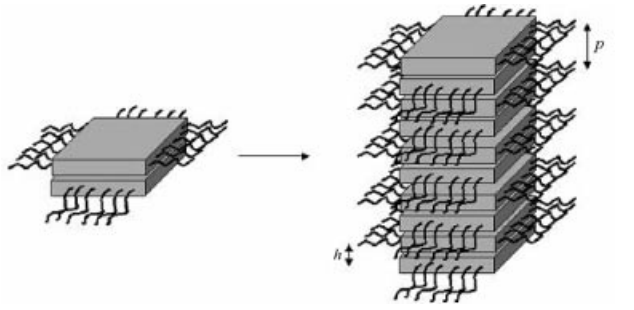

Figure 10. Molecular organisation of the copper(II)/lanthanum(III) complex CuLaL and the nickel(II)/lanthanum(III) complex NiLaL within the columnar mesophase. The columnar repeat unit is given by $<p>$, and $<h>$ is the average distance between adjacent molten chains.

ratio 1, $\sqrt{3}$, $\sqrt{4}$ and $\sqrt{7}$, corresponding to the indexation [*hk*] = [10], [11], [20] and [21], respectively. Such features are characteristic of a two-dimensional hexagonal packing of columns; that is, a hexagonal columnar mesophase (Col_h). The phase is disordered since there is no long-range correlation order within the columns, as evident from the absence of a sharp peak in the wide-angle region which would have corresponded to a more regular stacking along the columnar axis. However, for the copper complex CuL, an ordered columnar mesophase with a hexagonal symmetry (Col_{ho}) was observed below 39 °C. A typical feature in the X-ray diffractogram of this compound is the sharp diffraction peak in the wide-angle region at about 4.1 Å (Figure 4). The corresponding nickel complex NiL is crystalline at temperatures below 61 °C, and undergoes a crystal-to-crystal transition between 35 and 40 °C. The crystalline character of this compound at ambient temperature is evident from the large number of sharp diffraction peaks in the X-ray pattern. For the complexes in the mesophase, the lattice parameter, *a*, and the column cross-section, *s*, were determined from the positions of the small angle diffraction peaks (10), (11), (20) and (21): $a = 2/\sqrt{3}[1/4(d_{10} + \sqrt{3}d_{11} + 2d_{20} + \sqrt{7}d_{21})]$ and $s = 2/\sqrt{3}[1/4(d_{10} + \sqrt{3}d_{11} + 2d_{20} + \sqrt{7}d_{21})]$.[2] The lattice parameters and thus the column cross-sections of all the complexes are very similar. This similarity indicates that the local organisation within the mesophase is the same despite the structural differences. The hexagonal symmetry of the columnar mesophase implies that the hard, columnar core (i.e. the aromatic part) is cylindrical, and that therefore the cross-section is circular. These hard columns are separated from one another by the liquid paraffinic continuum formed by the molten alkyl chains. As far as the copper(II)/lanthanum(III) complex and the nickel(II)/lanthanum(III) complex are concerned, they both have a square-like shape, and it is evident that upon their stacking into an alternated orthogonal fashion (the halo *h1* corresponds to a dimerisation, as shown in Figure 10) and due to the free rotation around the molecular axis, the apparent cross-sections of the columns will appear circular, thus satisfying the geometrical requirements for the formation of the Col_h phase. Moreover, and in agreement with this proposal, we found that the molecular volume considering a density of about 0.95 for each of these two trinuclear compounds corresponds exactly to the volume of one single columnar stratum with a thickness of 4.5–4.6 Å (or to two complexes per portion of column with a thickness of 9.2–9.4 Å). Note also that the molecular dimensions of these two mixed complexes are in good agreement with the lattice parameters of the Col_h phases, and thus they both lie almost flat in the 2D hexagonal lattice. However, due to the lath-like shape of the mononuclear copper and nickel complexes, it is probable that they initially associate into face-to-face dimers (Figure 9) approximating the shape of a large, flat square, which then self-organise into columns as for the trinuclear complexes (Figure 9). Again, considering a density close to unity for both the complexes, it was found that the volume of a portion of column with a thickness of about 4.5 Å can contain two mononuclear complexes, and that the length of the complexes is of the order of the diameter of the columns, *a*. As mentioned above, the presence of the halo *h1* at about 9.4 Å in the X-ray patterns of the mesophases indicates that the repeating unit along the columnar axis $<p>$ is about twice the thickness of the complexes. Thus, the repeating unit is formed by two molecules stacked on top of each other (dimeric structures). A similar behaviour was also observed for the copper complexes and for the copper/lanthanide complexes we reported previously.[4] Structural models for the different metal complexes are shown in Figures 9 and 10. Moreover, a change of the linking group formed by ethylenediamine to a linking group formed by 1,2-diaminobenzene in the Schiff-base ligand has a negligible effect on the column lattice parameters. This is not unexpected due to the presence of the (disordered) alkyl chains in the complexes in the mesophase. For all the complexes, the lattice parameter *a* decreases with increasing temperature.

Conclusions

We have studied the mesophase behaviour of new copper(II), nickel(II), copper(II)/lanthanum(III) and nickel(II)/lanthanum(III) complexes of a mesogenic *N*,*N*′-disalicylidene-1,2-phenylenediamine (salophenH_2) ligand. The cop-

 © 2005 Wiley-VCH Verlag GmbH & Co. KGaA, Weinheim

per(II)/lanthanum(III) and the nickel(II)/lanthanum(III) complexes are trinuclear. All the Schiff-base complexes exhibited a hexagonal columnar mesophase (Col_h). X-ray diffraction measurements on samples in the mesophase indicate that the geometrical parameters (lattice parameter *a* and column cross-section *s*) are largely independent of the type of complex. This indicates that the structure of the mesophase is more or less identical for all the complexes. The metal has an influence on the transition temperatures: higher transition temperatures have been observed, and thus a substantial enhancement of the mesophase stability achieved, for the mixed f-d metallomesogens with respect to the parent transition metal complexes. The replacement of the ethylenediamine linking group present in the first type of mixed f-d metallomesogens by a more rigid 1,2-diaminobenzene linking group has a negligible influence on the mesophase behaviour. This is probably due to the fact that the linking group constitutes only a small part of the total ligand. One could have expected that the enhanced π-π stacking of the aromatic cores would result in higher transition temperatures, but this is not the case. The difference between the copper(II) or nickel(II) ion as the d-block metal is reflected in the thermal stability of the f-d complexes, in the sense that the nickel(II)/lanthanum(III) complex is thermally more stable than the corresponding copper(II)/lanthanum(III) complex. The presence of the rigid linking group is not a sufficient condition to induce a mesophase in the Schiff-base ligand.

Experimental Section

Equipment: The NMR spectra were recorded on a Bruker Avance 300 spectrometer (operating at 300 MHz) and Bruker AMX-400 (operating at 400 MHz), using $CDCl_3$ as solvent and tetramethylsilane (TMS) as internal standard. FTIR spectra were recorded on a Bruker IFS-66 spectrometer, using the KBr pellet method. Elemental analyses were obtained on a CE-Instrument EA-1110 elemental analyzer. The optical textures of the mesophases were observed with an Olympus BX60 polarizing microscope equipped with a LINKAM THMS600 hot stage and a LINKAM TMS93 programmable temperature-controller. DSC traces were recorded with a Mettler–Toledo DSC821e module. The XRD patterns were obtained with two different experimental set-ups, and in all cases the powdered sample was filled in Lindemann capillaries of 1 mm diameter. A linear monochromatic Cu-K_{α_1} beam (λ = 1.5405 Å) obtained with a sealed-tube generator (900 W) and a bent quartz monochromator were used (both generator and monochromator were manufactured by Inel). One set of diffraction patterns was registered with a curved counter Inel CPS 120, for which the sample temperature was controlled to within ±0.05 °C; periodicities up to 60 Å could be measured. The other set of diffraction patterns was registered on an Image Plate detector. The cell parameters were calculated from the position of the reflection at the smallest Bragg angle, which is in all cases the most intense. Periodicities up to 90 Å could be measured, and the sample temperature was controlled to within ±0.3 °C.

Synthesis of 3,4,5-Tris(tetradecyloxy)benzoic Acid: Ethyl 3,4,5-trihydroxybenzoate (19.82 g, 0.1 mol), K_2CO_3 (55.28 g, 0.4 mol), tetrabutylammonium bromide (TBAB, phase-transfer catalyst) (1.61 g, 5 mmol), methyl isobutyl ketone (MIBK; 300 mL) and 1-bromotetradecane (97.05 g, 0.35 mol), were added to a 1 L flask. Subsequently, the reaction mixture was heated to reflux and stirred overnight. The brown mixture was cooled below 100 °C, and water (300 mL) was added. The aqueous layer was separated, and the organic layer was washed with water (300 mL), dilute HCl solution (300 mL, 1.0 M), and water (300 mL) again. The solvent was removed on a rotary evaporator and the crude product was recrystallised from acetone. This product was redissolved in an ethanol solution of NaOH (16 g, 0.4 mol) and refluxed for 4 h. After allowing the solution to cool to room temperature, the reaction mixture was poured into cold water. The solution was acidified with dilute HCl. The precipitate was filtered off, recrystallised from dichloromethane and washed with ethanol. Yield: 57% (42.67 g), m.p. 72 °C. $C_{49}H_{90}O_5$ (749.24): calcd. C 77.52, H 11.95; found C 77.56, H 11.98. ^{1}H NMR ($CDCl_3$, 300 MHz): δ = 0.89 (t, J = 6.3 Hz, 9 H, CH_3), 1.27 (m, 30 H, CH_2), 1.49 (m, 6 H, CH_2CH$_2$CH$_2$O), 1.81 (m, 6 H, CH_2CH$_2$O), 4.03 (t, J = 6.3 Hz, 6 H, CH_2O), 7.33 (s, 2 H, H-aryl) ppm.

Synthesis of 3-Formyl-4-(hydroxyphenyl)-3,4,5-tris(tetradecyloxy)-benzoate: 3,4,5-Tris(tetradecyloxy)benzoic acid (15.16 g, 0.02 mol) and DMAP [4-(dimethylamino)pyridine; 0.24 g, 0.002 mol) were added to a mixture of 2,5-dihydroxybenzaldehyde (2.76 g, 0.02 mol) and *N*,*N*′-dicyclohexylcarbodiimide (DCC; 4.60 g, 0.022 mol) in 600 mL of dichloromethane. The solution was stirred at room temperature for 24 h. The precipitated *N*,*N*′-dicyclohexylurea was filtered off and washed with a saturated $NaHCO_3$ solution (2×400 mL) and water (2×400 mL). The aqueous layers were back-extracted with dichloromethane (200 mL). The combined organic layers were dried with $MgSO_4$ and the solvent was removed on a rotary evaporator. The crude compound was purified by column chromatography (silica, with dichloromethane as the eluent). Yield: 49% (8.60 g), m.p. 70 °C. $C_{56}H_{94}O_7$ (879.34): calcd. C 76.49, H 10.77; found C 76.56, H 10.83. ^{1}H NMR ($CDCl_3$, 300 MHz): δ = 0.89 (t, 9 H, CH_3), 1.27 (m, 30 H, CH_2), 1.50 (m, 6 H, CH_2CH$_2$CH$_2$O), 1.81 (m, 6 H, CH_2CH$_2$O), 4.05 (t, 6 H, CH_2O), 7.06 (d, J_o = 9.15 Hz, 1 H, H-aryl), 7.36 (dd, J_o = 8.91, J_m = 2.84 Hz, 1 H, H-aryl), 7.40 (s, 2 H, H-aryl), 7.44 (d, J_m = 2.58 Hz, 1 H, H-aryl), 9.89 (s, 1 H, CHO), 10.96 (s, 1 H, OH) ppm.

Synthesis of the Schiff-Base Ligand H_2L: 1,2-Diaminobenzene (54 mg, 0.5 mmol) and five drops of glacial acetic acid (as the catalyst) were added to a solution of 3-formyl-4-(hydroxyphenyl)-3,4,5-tris(tetradecyloxy)benzoate (0.88 g, 0.001 mol) in 150 mL of toluene. The mixture was heated for 3 h at reflux, and the water formed by the reaction was removed azeotropically (Dean–Stark trap). After allowing the solution to cool to room temperature, the solvent was removed under reduced pressure. The crude product was purified by recrystallisation from absolute ethanol. Yield: 92% (0.84 g), m.p. 67 °C. $C_{118}H_{192}N_2O_{12}$ (1830.8): calcd. C 77.41, H 10.57, N 1.53; found C 76.94, H 10.57, N 1.54. IR (KBr): $\tilde{\nu}$ = 1626 cm^{-1} (C=N), 1209 (C–O). ^{1}H NMR ($CDCl_3$, 300 MHz): δ = 0.88 (t, 18 H, CH_3), 1.26 (m, 60 H, CH_2), 1.49 (m, 12 H, CH_2CH$_2$CH$_2$O), 1.83 (m, 12 H, CH_2CH$_2$O), 4.05 (m, 16 H, CH_2O, CH_2N), 6.80–7.45 (m, 14 H, H-aryl), 8.59 (s, 2 H, CH=N), 13.01 (s, 2 H, OH) ppm.

Synthesis of the Copper(II) Complex CuL: A hot solution of copper(II) acetate monohydrate, (30 mg, 0.15 mol) in methanol was added dropwise to a hot solution of the Schiff-base ligand H_2L (0.24 g, 0.13 mmol) in chloroform. The reaction mixture was refluxed overnight. After allowing the solution to cool to room temperature, the solvent was removed under reduced pressure. The crude product was crystallised from ethyl acetate, washed with methanol and dried in vacuo. Yield: 92% (0.23 g). IR (KBr): $\tilde{\nu}$ =

 © 2005 Wiley-VCH Verlag GmbH & Co. KGaA, Weinheim

1606 cm^{-1} (C=N), 1203 (C–O). $C_{118}H_{196}CuN_2O_{15}$ (1892.3): calcd. C 72.82, H 10.15, N 1.44; found C 72.88, H 10.24, N 1.49.

Synthesis of the Nickel(II) Complex NiL: A hot solution of nickel(II) acetate tetrahydrate (70 mg, 0.28 mol) in methanol was added dropwise to a hot solution of the Schiff-base ligand H_2L (0.46 g, 0.25 mmol) in chloroform. The reaction mixture was heated at reflux temperature overnight. After allowing the solution to cool to room temperature, the solvent was removed under reduced pressure. The crude product was crystallised from ethyl acetate, washed with methanol and dried in vacuo. Yield: 86% (0.41 g). IR (KBr): $\tilde{\nu}$ = 1606 cm^{-1} (C=N), 1203 (C–O). $C_{118}H_{190}N_2NiO_{12}$ (1887.5): calcd. C 75.09, H 10.15, N 1.48; found C 74.68, H 10.28, N 1.50.

Synthesis of the Copper(II)/Lanthanum(III) Complex CuLaL: A solution of lanthanum(III) nitrate hexahydrate (0.048 g, 0.11 mmol) in acetone was added to a solution of the copper complex CuL (0.189 g, 0.1 mmol) in acetone. The reaction mixture was stirred at room temperature for 24 h. The precipitate was filtered off, washed with cold methanol and dried in vacuo. Yield: 40% (164 mg). IR (KBr): $\tilde{\nu}$ = 1629 cm^{-1} (C=N), 1306 (C–O). $C_{236}H_{380}Cu_2LaN_7O_{33}$ (4105.59): calcd. C 68.98, H 9.33, N 2.39; found C 68.45, H 9.23, N 1.97.

Synthesis of the Nickel(II)/Lanthanum(III) Complex NiLaL: A solution of lanthanum(III) nitrate hexahydrate (0.048 g, 0.11 mmol) in acetone was added to a solution of the nickel complex NiL (0.189 g, 0.1 mmol) in acetone. The reaction mixture was stirred at room temperature for a period of 24 h. The precipitate was filtered off, washed with cold methanol and dried in vacuo. Yield: 46% (187 mg). IR (KBr): $\tilde{\nu}$ = 1627 cm^{-1} (C=N), 1205 (C–O). $C_{236}H_{380}LaN_7Ni_2O_{33}$ (4095.60): calcd. C 69.15, H 9.35, N 2.39; found C 69.23, H 9.36, N 2.06.

Acknowledgments

K. B. thanks the F.W.O.-Flanders (Belgium) for a postdoctoral fellowship. Financial support by the F.W.O.-Flanders (G.0117.03) and by the K. U. Leuven (GOA, 03/03) is gratefully acknowledged. Funding for travel was obtained from a Tournesol project (Project T2004.10).

[1] a) A. M. Giroud-Godquin, P. M. Maitlis, *Angew. Chem. Int. Ed. Engl.* **1991**, *30*, 375–402; b) S. A. Hudson, P. M. Maitlis, *Chem. Rev.* **1993**, *93*, 861–885; c) *Metallomesogens, Synthesis Properties and Applications* (Ed.: J. L. Serrano) Wiley-VCH, Weinheim, **1996**; d) D. W. Bruce, in *Inorganic Materials* (Eds.: D. W. Bruce, D. O'Hare), 2nd edition, Wiley, Chichester, **1996**; chapter 8, p. 429; e) B. Donnio, D. W. Bruce, *Struct. Bonding (Berlin)* **1999**, *95*, 193–247; f) K. Binnemans, C. Görller-Walrand, *Chem. Rev.* **2002**, *102*, 2303–2345; g) B. Donnio, D. Guillon, R. Deschenaux, D. W. Bruce, in *Comprehensive Coordination Chemistry II* (Eds.: J. A. McCleverty, T. J. Meyer), Elsevier, Oxford, **2003**, volume 7 (Eds.: M. Fujita, A. Powell, C. Creutz), chapter 7.9, pp. 357–627.

[2] a) Yu. Galyametdinov, M. A. Athanassopoulou, K. Griesar, O. Kharitonova, E. A. Soto Bustamante, L. Tinchurina, I. Ovchinnikov, I. W. Haase, *Chem. Mater.* **1996**, *8*, 922–926; b) K. Binnemans, Yu. G. Galyametdinov, R. Van Deun, D. W. Bruce, S. R. Collinson, A. P. Polishchuk, I. Bikchantaev, W. Haase, A. V. Prosvirin, L. Tinchurina, I. Litvinov, A. Gubajdullin, A. Rakhmatullin, K. Uytterhoeven, L. Van Meervelt, *J. Am. Chem. Soc.* **2000**, *122*, 4335–4344; c) P. J. Alonso, J. I. Martinez, L. Oriol, M. Pinol, J. L. Serrano, *Adv. Mater.* **1994**, *6*, 663–667; d) J. Barbera, R. Gimenez, M. Marcos, J. L. Serrano, P. J. Alonso, J. I. Martinez, *Chem. Mater.* **2003**, *15*, 958–964.

[3] a) R. Deschenaux, M. Schweissguth, A. M. Levelut, *Chem. Commun.* **1996**, 1275–1276; b) G. H. Walf, R. Benda, F. J. Litterst, U. Stebani, S. Schmidt, G. Lattermann, *Chem. Eur. J.* **1998**, *4*, 93–99; c) B. Donnio, J. M. Seddon, R. Deschenaux, *Organometallics* **2000**, *19*, 3077–3081.

[4] K. Binnemans, K. Lodewyckx, B. Donnio, D. Guillon, *Chem. Eur. J.* **2002**, *8*, 1101–1105.

[5] K. Binnemans, K. Lodewyckx, *Supramol. Chem.* **2003**, *15*, 485–494.

[6] a) R. Paschke, D. Balkow, U. Baumeister, H. Hartung, J. R. Chipperfield, A. B. Blake, P. G. Nelson, G. W. Grey, *Mol. Cryst. Liq. Cryst.* **1990**, *188*, 105–118; b) K. Ohta, Y. Morizumi, T. Fujimoto, I. Yamamoto, K. Miyamura, Y. Gohshi, *Mol. Cryst. Liq. Cryst.* **1992**, *214*, 161–169; c) A. Serrette, P. J. Carroll, T. M. Swager, *J. Am. Chem. Soc.* **1992**, *114*, 1887–1889 (Corrigendum: **1993**, *J. Am. Chem. Soc.* **115**, 11 656); d) R. Paschke, D. Balkow, E. Sinn, *Inorg. Chem.* **2002**, *41*, 1949–1953; e) I. Aiello, M. Ghedini, M. La Deda, D. Pucci, O. Francescangeli, *Eur. J. Inorg. Chem.* **1999**, 1367–1372; f) N. Hoshino, *Coord. Chem. Rev.* **1998**, *174*, 77–108.

[7] P. G. Cozzi, *Chem. Soc. Rev.* **2004**, *33*, 410–421.

[8] M. L. Kahn, T. M. Rajendiran, Y. Jeannin, C. Mathonière, O. Kahn, *C. R. Acad. Sci. Ser. IIc* **2000**, *3*, 131.

Received: October 19, 2004

 © 2005 Wiley-VCH Verlag GmbH & Co. KGaA, Weinheim

Chiral Indenes and Group-4 Metallocene Dichlorides Containing α- and β-Pinenyl-Derived Ligand Substituents: Synthesis and Catalytic Applications in Polymerization and Carboalumination Reactions

Satu Silver,[a] Arto Puranen,[b] Rainer Sjöholm,[a] Timo Repo,[b] and Reko Leino*[a]

Keywords: Homogeneous catalysis / Indenyl ligands / Metallocenes / Olefin polymerization / Carboalumination

The synthesis and characterization of chiral bis(indenyl)zirconium dichlorides containing β-pinenyl-derived ligand substituents is reported. Unbridged metallocene complexes having the {[(1*S*,2*S*,5*S*)-6,6-dimethylbicyclo[3.1.1]hept-2-yl]methyl}dimethylsilyl substituent in both 1- and 2-positions of the indenyl moiety were prepared and isolated in moderate to low yields by reaction of the corresponding indenyllithium salts with $ZrCl_4$ followed by work-up and crystallization procedures. The corresponding tetrahydroindenyl complexes were obtained in excellent yields by catalytic hydrogenation of the indenyl six-membered rings. In a complementary approach, a synthetic route to α-pinenyl-substituted indenyl ligand analogues was briefly evaluated, which however, suffered from low yields. Selected β-pinenyl-substituted indenyl complexes were scanned as catalysts for the dehydropolymerization of phenylsilane upon activation with *n*BuLi, for polymerization of ethylene and propylene upon activation with methylaluminoxane (MAO) as well as for enantioselective carboalumination of 1-octene with triethyl- and trimethylaluminum. The bis(indenyl) complexes catalyzed the carboalumination reaction, albeit only low yields (8–16%) and low enantioselectivities (*ee* = 0.5–10%) were obtained. The 2-substituted bis(indenyl)zirconocene/MAO catalyst system produced atactic low-molecular weight polypropylene with low polymerization activity whereas both 1- and 2-substituted complexes showed high activities in ethylene polymerization producing polyethylenes with high molecular weights ($M_w > 440000$).
(© Wiley-VCH Verlag GmbH & Co. KGaA, 69451 Weinheim, Germany, 2005)

Introduction

Chiral group-4 metallocenes are widely used catalysts or catalyst precursors for the stereoselective polymerization of α-olefins,[1–3] and enantioselective cyclopolymerization of nonconjugated dienes,[4,5] and are employed in various enantioselective organic transformations[6,7] including carbon–carbon,[8–13] carbon–hydrogen[14–18] and carbon–oxygen[19,20] bond formation. Commonly employed chiral precatalysts are the conformationally constrained racemic *ansa*-metallocenes and their resolved single enantiomers,[21] but also unbridged bis(indenyl)metallocenes containing chiral substituents[22–27] have been utilized previously in a number of applications in stereo- and/or enantioselective synthesis.

In a recent communication, we presented a simple route to new chirally substituted indenes by reaction of indenyllithium or 2-indenylmagnesium bromide with a β-pinenyl-derived chlorosilane.[28] As a continuation of the previous work, we report here a detailed study on the utilization of these new chiral ligand precursors for the preparation of new chiral group-4 metallocene complexes as well as a brief evaluation of the chiral metallocenes formed for catalytic applications in olefin polymerization, dehydropolymerization of phenylsilane and enantioselective carboalumination reactions. As a complementary approach, the low-yield synthesis of some α-pinenyl-substituted ligand analogues is briefly described.

Results and Discussion

Ligand Precursor and Metallocene Synthesis

The chiral zirconocene dichloride **2** was prepared by deprotonation of the previously described chiral indene **1**[28] with *n*BuLi followed by reaction with 0.5 equiv. $ZrCl_4$ in toluene (Scheme 1). Subsequent work-up and crystallization from pentane at –20 °C provided pure **2** in 37% isolated yield. Due to the position of the chiral substituent, the π-faces of the indenyl ligand are equivalent (i.e., homotopic) and only one product can be formed upon metallation. Complex **2** was further hydrogenated at 50 bar H_2 in dichloromethane in the presence of PtO_2 catalyst to provide the corresponding chiral tetrahydroindenyl complex **3** in 86% isolated yield. The parent compound **2** is obtained as

[a] Department of Organic Chemistry, Åbo Akademi University, 20500 Åbo, Finland
Fax: +358-2-215-4866
E-mail: reko.leino@abo.fi
[b] Department of Chemistry, Laboratory of Inorganic Chemistry, University of Helsinki,
P. O. Box 55, 00014 University of Helsinki, Finland
Supporting information for this article is available on the WWW under http://www.eurjic.org or from the author.

 © 2005 Wiley-VCH Verlag GmbH & Co. KGaA, Weinheim **DOI: 10.1002/ejic.200400882**

a yellow powder, whereas the hydrogenated congener **3** is a noncrystalline, pale green oil. Apparently, because of the large aliphatic pinenyl substituent, both complexes are remarkably soluble in all common organic solvents including pentane and hexane. Consequently, all our attempts to grow single crystals suitable for X-ray structure determination from either one of the complexes **2** or **3** failed.

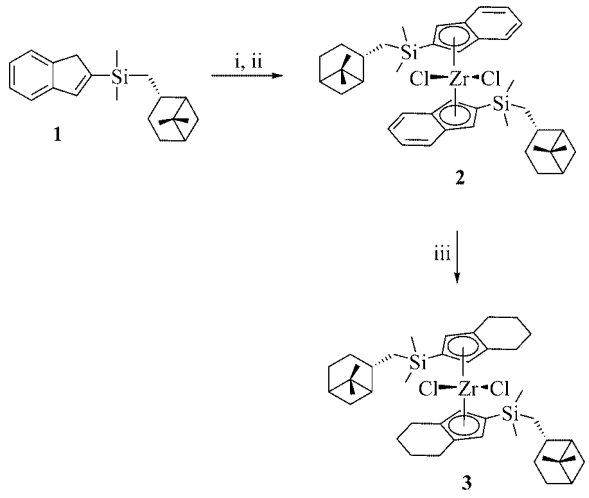

Scheme 1. Synthesis of the chiral metallocenes **2** and **3**. (i) *n*BuLi, Et_2O, 0 °C. (ii) $ZrCl_4$, toluene, 50 °C, 37%. (iii) H_2/50 bar/PtO_2, CH_2Cl_2, 86%.

The change in the position of the chiral substituent from 2- to 1- or 3-indenyl renders the π-faces of the ligand precursor inequivalent [planar chirality: (*pR*) vs. (*pS*)] thus potentially resulting in the formation of three isomeric metallocene complexes [combinations of (*pR*)/(*pR*), (*pS*)/(*pS*) and (*pR*)/(*pS*)] upon metallation with group-4 metal tetrahalides (Figure 1).

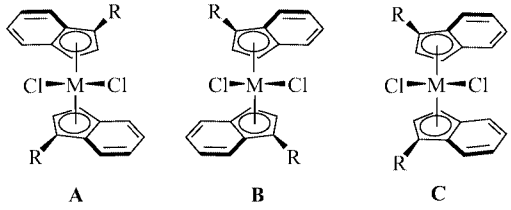

Figure 1. Metallocene diastereomers obtained upon metallation of indenyl ligands with enantiotopic or diastereotopic ligand π-faces [combinations of (*pR*)/(*pR*), (*pS*)/(*pS*) (**A** and **B**) and (*pR*)/(*pS*) (**C**).

If the 1- or 3-indenyl substituent is achiral (*enantiotopic* ligand π-faces), a C_2 symmetric racemic pair of two equienergetic enantiomers (**A** and **B** in Figure 1) is obtained together with a C_s symmetric *meso* form (**C**). A statistical 1:1:2 ratio of the three isomers is observed in most cases. When, as in the present case, the 1- or 3-indenyl substituent is chiral (*diastereotopic* ligand π-faces), a mixture of three diastereomers, two C_2 symmetric "pseudo-racemic" or "racemic-like" complexes (**A** and **B**) and one C_1 symmetric "*meso*-like" diastereomer (**C**), is formed in a ratio depending on the relative energies of the π-face metallation (*pR*) vs. (*pS*) and the mono(indenyl)metallocene trichlorides initially formed.

Thus, when the previously described 1:1 diastereomeric mixture of the chiral 1-substituted indenes (1*R*)-**4a** and (1*S*)-**4b**[28] was deprotonated with *n*BuLi and the resulting chiral indenyl anion lithium salt metallated with 0.5 equiv. of $ZrCl_4$ (Scheme 2), a mixture of the metallocene complexes **5a-c** was obtained in variable ratios depending on the solvent employed in the metallation step, as shown by ^{1}H NMR analyses of the metallocene crude products (Table 1, Figure 2). In all solvents investigated (toluene, Et_2O, THF), the molar ratio between the C_2-symmetric diastereomers (*pR*)(*pR*)-**5a** and (*pS*)(*pS*)-**5b** remained equimolar, consistent with their "pseudo-racemic" character. Formation of the *meso*-like C_1-symmetric diastereomer (*pR*)(*pS*)-**5c** was more favored in the coordinating solvents Et_2O and THF. As observed for the 2-substituted analogue **2**, also complexes **5a**–**c** displayed unusually high solubilities in all common organic solvents rendering their isolation and purification very difficult. The pure, least soluble C_1-symmetric diastereomer (*pR*)(*pS*)-**5c** was, however, obtained in 11% isolated yield as a bright yellow powder from the reaction carried out in Et_2O after subsequent work-up and crystallization from dichloromethane at –20 °C. The *meso*-like diastereomer (*pR*)(*pS*)-**5c** is easily distinguished from the C_2-symmetric diastereomers (*pR*)(*pR*)-**5a** and (*pS*)(*pS*)-**5b** by its ^{1}H and ^{13}C NMR spectra where, unlike in the cases of **5a** and **5b**, separate signal sets are observed for each of the (*pR*)- and (*pS*)-indenyl ligands coordinated to the central metal atom. The corresponding tetrahydroinde-

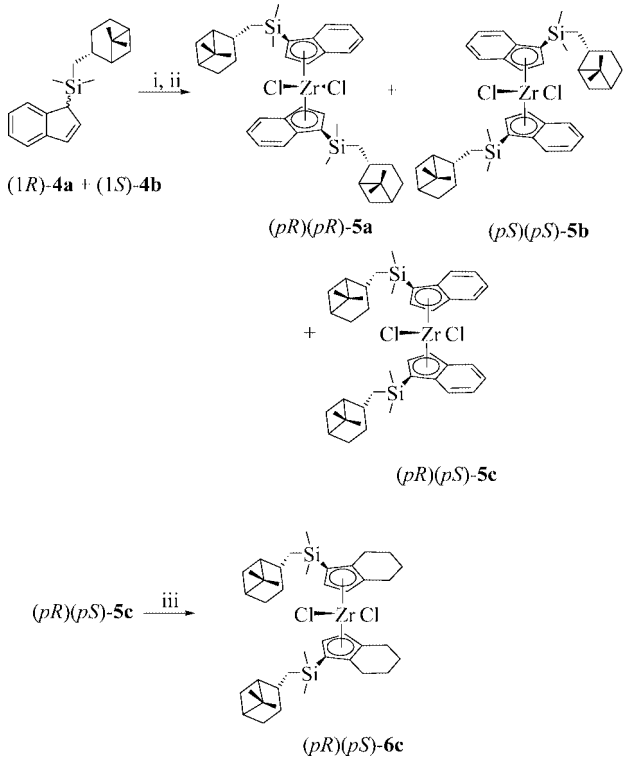

Scheme 2. Synthesis of the chiral metallocenes **5a**–**c** and **6c**. (i) *n*BuLi, Et_2O, 0 °C. (ii) 0.5 $ZrCl_4$, toluene, 50 °C; or 0.5 $ZrCl_4$, Et_2O, room temp.; or 0.5 $ZrCl_4$·2THF, –80 °C. (iii) H_2/50 bar/PtO_2, CH_2Cl_2, 82%.

 © 2005 Wiley-VCH Verlag GmbH & Co. KGaA, Weinheim

nyl analogue (*pR*)(*pS*)-**6c** was then obtained in 82% yield after hydrogenation at 50 bar over PtO_2 catalyst in dichloromethane. Again, despite several attempts, crystals suitable for X-ray structure determination could not be grown from either one of the highly soluble complexes **5c** and **6c**.

Table 1. Relative ratios of the metallocene diastereomers **5a–c** formed in different solvents.

Solvent	*rac*-like **5a**	*rac*-like **5b**	*meso*-like **5c**
Toluene	42.4%	42.4%	15.2%
THF	22.6%	22.6%	54.8%
Et_2O	28.4%	28.4%	43.2%

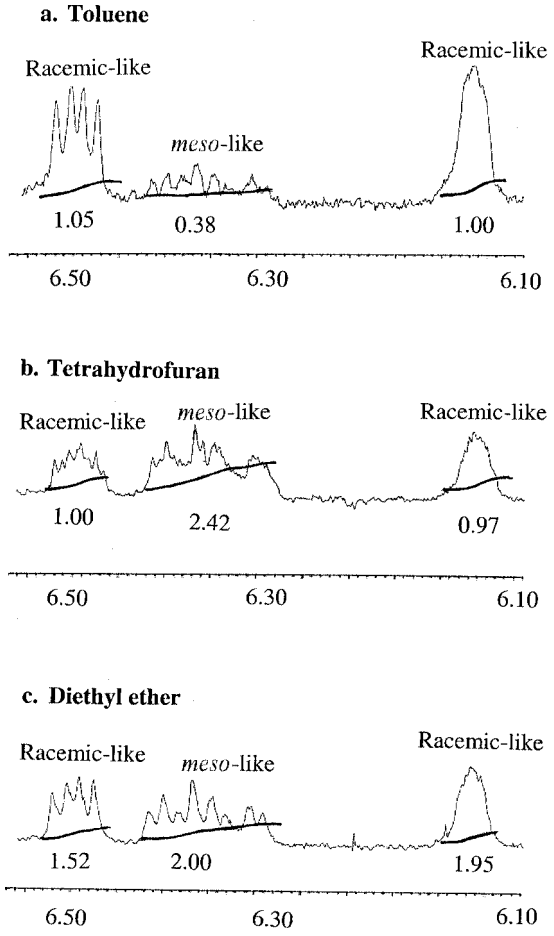

Figure 2. Expansions of the crude product indenyl CH regions of the ^{1}H NMR spectra of complexes **5a–c.**

Unbridged bis(indenyl)zirconocenes with bulky equatorial or σ-ligand substituents may exhibit dynamic behavior in their NMR spectra at subambient temperatures resulting from partially hindered rotation around the Zr–Cp(centroid) axis (Scheme 3).[29] For complexes with achiral ligand substituents the observed interconversion is likely to take place between two C_2 symmetric enantiomeric conformations becoming frozen on the NMR time scale to form a racemic mixture of the interconverting conformational isomers.[30–32] If, however, the ligand substituent is chiral, the interconverting conformational isomers become diastereomeric, one of which could be favored by proper choice of the ligand substitution pattern. Such complexes in turn could prove promising candidates for applications in enantioselective catalysis. In a previous work, Halterman and coworkers demonstrated that for the chiral bis(2-menthyl-4,7-dimethylindenyl)zirconium dichloride one diastereomeric conformation is slightly favored at 223 K (60:40) with a rotational activation barrier of 12.5 ± 0.5 kcal/mol.[25]

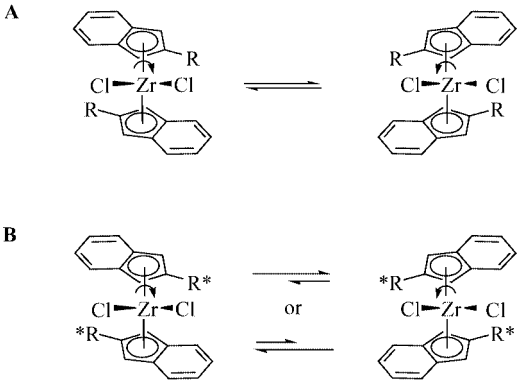

Scheme 3. Conformational equilibration of unbridged bis(indenyl) zirconocenes with (**A**) achiral substituents (enantiomeric conformations), and (**B**) chiral substituents (diastereomeric conformations).

At ambient temperature, the ^{1}H NMR spectra of complexes **2** and **5c** are consistent with unhindered ligand rotation. Upon lowering the monitoring temperature to 213–163 K, complex **2** displays dynamic behavior as indicated by the broadening of the aromatic CH resonances at δ = 5.92 and 5.96 ppm in the five-membered indenyl ring. At the estimated coalescence temperature of 163 K, the signals start to split to the individual resonances resulting from the equilibration of the two C_2 symmetric diastereomeric conformers. However, due to the operational limits of the NMR instrument at such low temperatures, neither the exact point of coalescence nor the associated rotational energy barrier and the eventual predominance of either one of the conformers could be reliably determined.

Next, as an attempt to modify the steric properties of the complex family and as a further extension of the use of the pinenyl group as a chiral indenyl ligand substituent, we prepared the monomethylated analogues of compounds **1** and **4a/b**. Thus, deprotonation of **1** with *n*BuLi and the subsequent reaction of the lithium salt formed with excess methyl iodide provided a diastereomeric mixture of the chiral indenes (1*R*)-**7a** and (1*S*)-**7b** in 74% isolated yield after purification by flash chromatography. Deprotonation of **7a/7b** with *n*BuLi and the subsequent reaction with 0.5 equiv. $ZrCl_4$ formed the expected mixture of the diastereomeric metallocene complexes (*pR*)(*pR*)-**8a**, (*pS*)(*pS*)-**8b** and (*pR*)(*pS*)-**8c** in good yield, as evidenced by ^{1}H NMR analysis of the crude product. All attempts to purify/isolate any of the complexes **8a–c** by fractional crystallization techniques failed due to their extremely high solubilities in all common organic solvents. When, however, the crude product was subjected to flash column chromatography using silanized silica gel[33] under argon, elution with pentane provided a mixture of the pure metallocenes **8a–c** in 53%

 © 2005 Wiley-VCH Verlag GmbH & Co. KGaA, Weinheim

yield (all fractions combined) as a yellow oil. Despite their very similar solubility properties, the diastereomers eluted at slightly different retention times yielding fractions consisting of both **8a/8b** and **8a/8b/8c** in variable ratios. Small differences in the elution properties were observed even between the racemic-like diastereomers **8a** and **8b**, however, due to their high solubilities even in pentane, complete separation was impossible to achieve. Combination of all fractions containing only the racemic-like diastereomers gave an isolated yield of 18% for **8a/8b** obtained as a yellow oil. Crystallization of this mixture from cold pentane (–60 °C) gave 54 mg (3%) of yellow crystals enriched in one of the racemic-like diastereomers in a 53:47 ratio (Scheme 4).

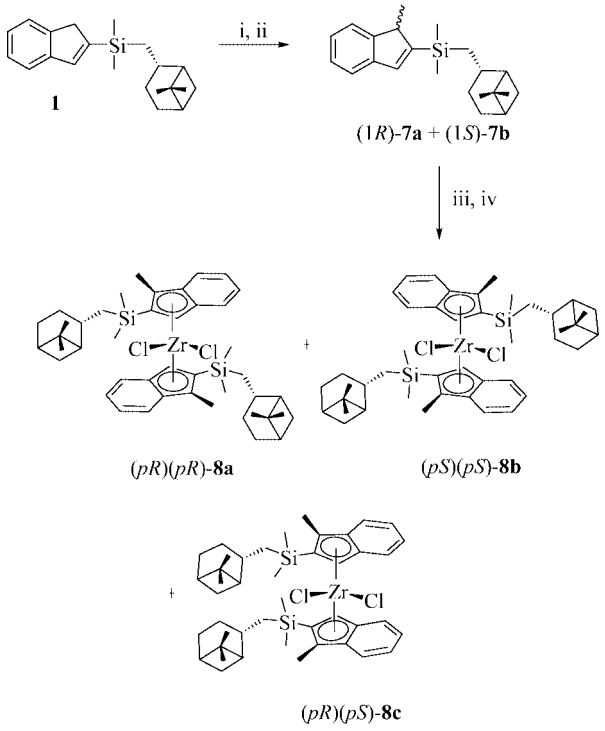

Scheme 4. Synthesis of the chiral indenyl ligand precursor **7a/7b** and the chiral metallocenes **8a**–**c**. (i) *n*BuLi, THF, 0 °C. (ii) MeI, 74%. (iii) *n*BuLi, Et_2O, 0 °C. (iv) 0.5 $ZrCl_4$, 53% (isolated mixture **8a**–**c**), 18% (isolated mixture **8a/8b**).

A diastereomeric mixture of the 3-methyl-substituted chiral indenes (1*R*)-**9a** and (1*S*)-**9b** was in turn obtained in 53% isolated yield by deprotonation of a 1-methylindene/3-methylindene mixture with *n*BuLi followed by quenching with excess chloro{[(1*S*,2*S*,5*S*)-6,6-dimethylbicyclo[3.1.1]-hept-2-yl]methyl}dimethylsilane, work-up and purification by flash chromatography. Deprotonation of **9a/9b** with *n*BuLi and the subsequent reaction with 0.5 equiv. $ZrCl_4$ formed the expected mixture of the diastereomeric metallocene complexes (*pR*)(*pR*)-**10a**, (*pS*)(*pS*)-**10b** and (*pR*)(*pS*)-**10c** in good, approximately 70% yield, as evidenced by ^{1}H NMR analysis of the crude product. All attempts to purify/isolate any of the complexes **10a**–**c** by crystallization failed due to their high solubilities in all common organic solvents. In contrast to complexes **8a**–**c**, the 1-silyl-substituted zirconocenes **10a**–**c** were also unstable under the flash column chromatographic conditions (silanized silica gel under argon atmosphere), yielding ligand precursor as the main decomposition product upon elution with pentane (Scheme 5).

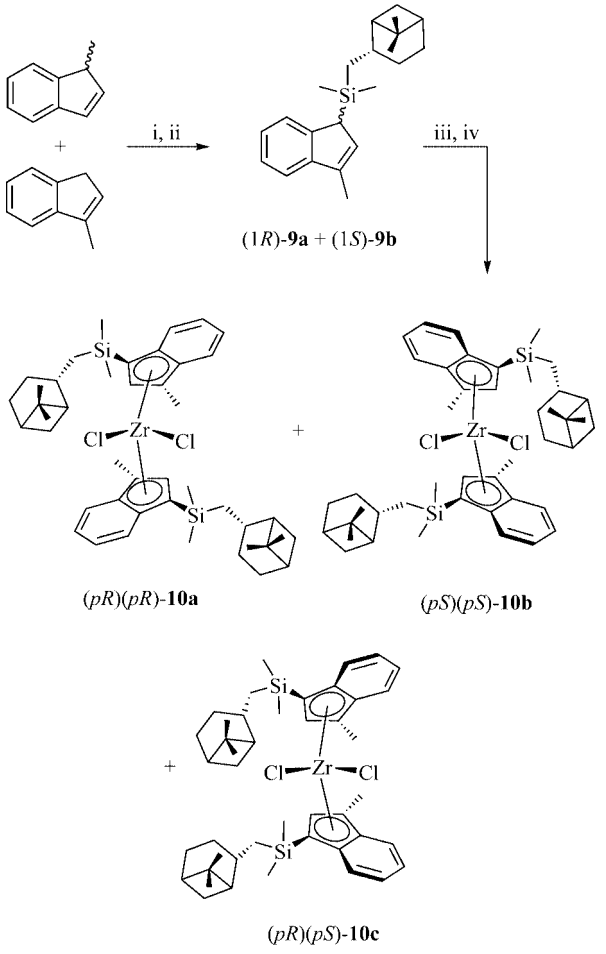

Scheme 5. Synthesis of the chiral indenyl ligand precursor **9a/9b** and the chiral metallocenes **10a**–**c**. (i) *n*BuLi, THF, 0 °C. (ii) Chloro{[(1*S*,2*S*,5*S*)-6,6-dimethylbicyclo[3.1.1]hept-2-yl]methyl}dimethylsilane, 53%. (iii) *n*BuLi, Et_2O, 0 °C. (iv) 0.5 $ZrCl_4$, product not isolated.

In addition, we briefly evaluated the metalation of the ligand percursors **1** and (1*R*)-**4a**/(1*S*)-**4b** with other group-4 metals. Treatment of the from **1** and (1*R*)-**4a**/(1*S*)-**4b** generated lithium salts with 0.5 equiv. $HfCl_4$ in diethyl ether or toluene yielded the desired metallocene complexes in moderate (approximately 30%) yields as shown by ^{1}H NMR analyses of the corresponding crude products. In contrast to their zirconium analogues, these hafnium complexes proved highly unstable resulting in decomposition upon all purification attempts, even when manipulated under strictly inert atmosphere.

From both compounds **1** and (1*R*)-**4a**/(1*S*)-**4b**, a mixture of the trimethylsilyl-substituted derivatives (1*R*)-**11a**/(1*S*)-**11b** and **12** and mixtures of (1*R*)-**15a**/(1*S*)-**15b**/(1*R*)-**16a**/(1*S*)-**16b** were obtained in high yields by quenching the corresponding lithium salts with chlorotrimethylsilane (Scheme 6 resp. Scheme 7). Treatment of these with one

 © 2005 Wiley-VCH Verlag GmbH & Co. KGaA, Weinheim

equivalent of $TiCl_4$ in dichloromethane at –78 °C resulted in competing elimination of both the trimethylsilyl- and the pinenyl-substituted silyl groups providing approximately 1:1 mixtures of the mono(indenyl)titanium trichlorides carrying either a trimethysilyl [(*pR*)-**14a**/(*pS*)-**14b**] or {[(1*S*,2*S*,5*S*)-6,6-dimethylbicyclo[3.1.1]hept-2-yl]methyl}-dimethylsilyl substituent [**13** and (*pR*)-**17a**/(*pS*)-**17b**, respectively]. In the case of the mixture of (1*R*)-**11a**/(1*S*)-**11b** and **12**, conversion of the ligand to mono(indenyl)metallocene appears to be nearly quantitative as evidenced by ^{1}H NMR, whereas in the case of (1*R*)-**15a**/(1*S*)-**15b**/(1*R*)-**16a**/(1*S*)-**16b** the yield of the metallation step is approximately 30%. Due to the similar solubilities of the (trimethylsilylindenyl)-titanium trichloride and the {{[(1*S*,2*S*,5*S*)-6,6-dimethylbicyclo[3.1.1]hept-2-yl]methyl}dimethylsilylindenyl}titanium trichlorides formed, these metallocene mixtures proved inseparable by fractional crystallization techniques.

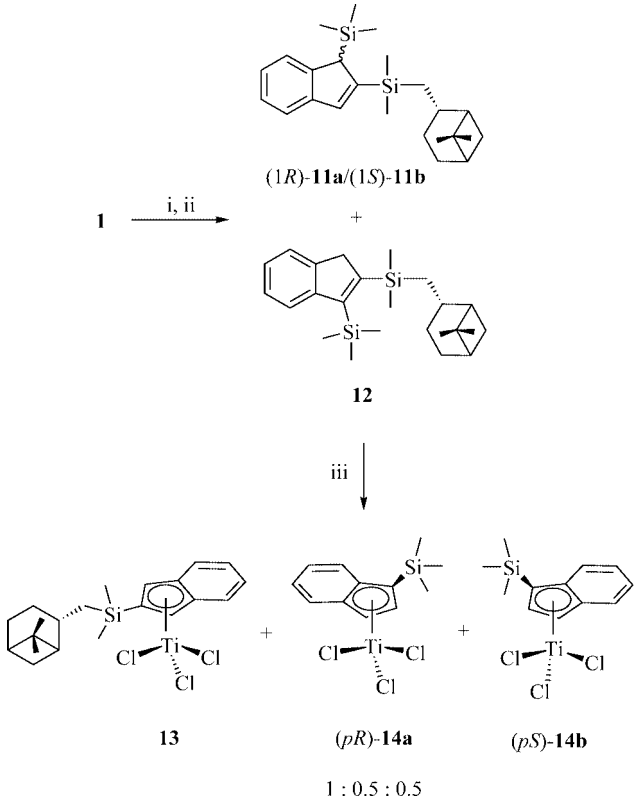

Scheme 6. Attempted synthesis of 2-chirally substituted mono(indenyl)titanium trichlorides. (i) *n*BuLi, THF, 0 °C. (ii) Chlorodimethylsilane, 71%. (iii) $TiCl_4$·CH_2Cl_2, –78 °C, not purified.

When the lithium salts generated from **1** and (1*R*)-**4a**/(1*S*)-**4b** were treated with 0.5 equiv. $FeCl_2$, the desired ferrocenes were formed in approximately 25% and 40% yields, respectively, as evidenced by ^{1}H NMR spectroscopy. Also these compounds proved to have extremely high solubilities in all common organic solvents rendering their purification by crystallization impossible. All attempts to purify the oily crude products by silica gel column chromatography likewise failed due to the apparent high sensitivity of these iron complexes.

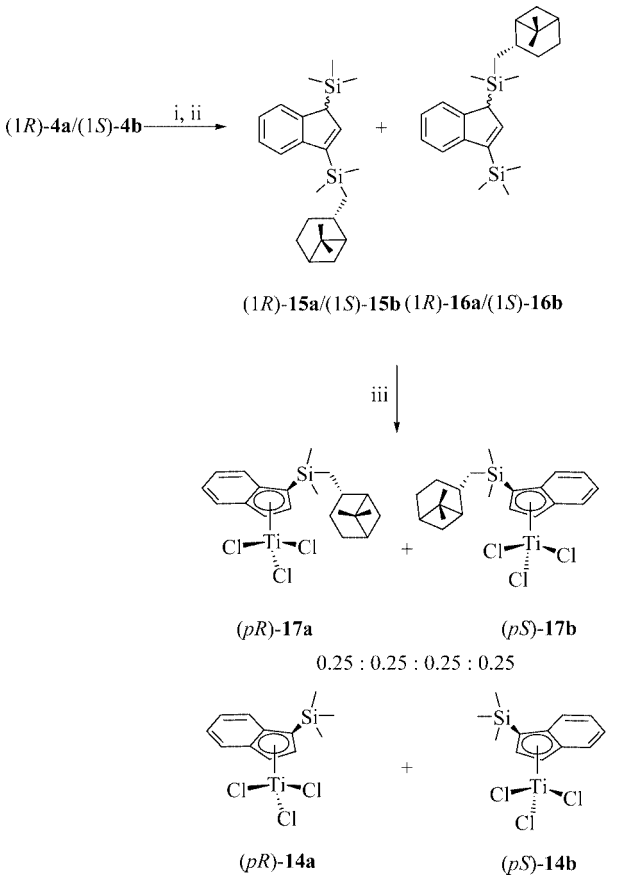

Scheme 7. Attempted synthesis of 1-chirally substituted mono(indenyl)titanium trichlorides. (i) *n*BuLi, THF, 0 °C. (ii) Chlorodimethylsilane, 76%. (iii) $TiCl_4$·CH_2Cl_2, –78 °C, not purified/isolated.

In our previous communication,[28] we also described the preparation of the ethylene-bridged bis(indenyl) ligand analogues of **1** and **4a**/**4b** (compounds **18** and **19**), as well as the 1,3-chirally disubstituted indene analogue **20** (Figure 3). When the dilithium salt of **18** was reacted with $ZrCl_4$ in Et_2O, no metallocene could be detected by ^{1}H NMR or EIMS analysis of the crude product. Reaction of the dilithium salt of **19** with $ZrCl_4$ in THF showed no formation of the desired bis(indenyl)metallocenes. By carrying out the metallation in toluene only traces of zirconium complex diastereomers could be detected together with large amounts of impurities. In Et_2O, however, metallation of **19**-Li_2 with $ZrCl_4$ consumed all of the ligand precursor and formation of zirconocene diastereomers could be proven by both ^{1}H NMR and EIMS analyses, the latter of which gave the observed isotope peak distibutions for [M^+] in matching ratios with the theoretically calculated values. Unfortunately, again apparently due to the very high solubilities of the metallocene complexes formed, all attempts to isolate pure compounds by crystallization from Et_2O, iPr_2O, hexane, THF, toluene and dichloromethane failed.

All our attempts to metallate either the lithium or potassium salt of the 1,3-disubstituted indene **20** with $ZrCl_4$ in Et_2O, toluene and dichloromethane under various reaction conditions failed. In none of the attempts could we observe

 © 2005 Wiley-VCH Verlag GmbH & Co. KGaA, Weinheim

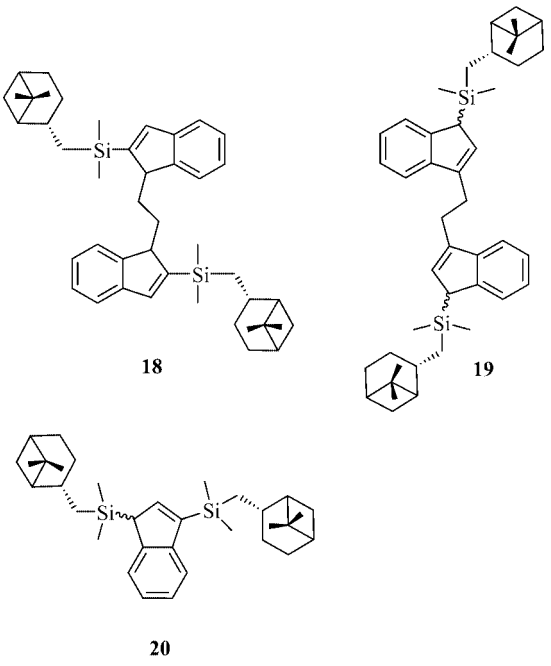

Figure 3. Ethylene-bridged and 1,3-chirally disubstituted ligand precursors **18**–**20**.

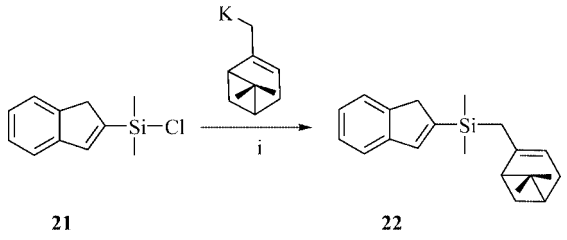

Scheme 8. Synthesis of the 2-chirally substituted indenyl ligand precursor **22**. (i) THF, –72 °C, 3%.

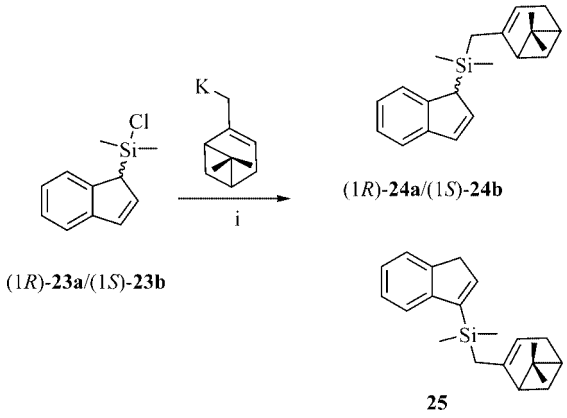

Scheme 9. Synthesis of the 1-chirally substituted indenyl ligand precursors (1*R*)-**24a**/(1*S*)-**24b**/**25**. (i) THF, –72 °C, 21%.

any formation of the desired bis(indenyl)metallocene complex. Considering that the analogous 1,3-bis(trimethylsilyl)-indenyl and other 1,3-bis(trialkyl/arylsilyl)indenyl-derived anions were recently successfully complexed with zirconium and iron in moderately high yields by Chirik and co-workers,[34,35] the observation here is quite surprising and hardly explained by steric factors only. Other examples of both 1,2- and 1,3-trimethylsilyl-substituted bis(indenyl)-iron(II) complexes have also been reported recently.[36]

Finally, in a complementary approach, we investigated the possibility of using α-pinene as the chiral indenyl substituent. By deprotonation of α-pinene with *n*BuLi/*t*BuOK at 50 °C using excess α-pinene[37] and the subsequent reaction of the obtained α-pinenyl potassium salt with 2-(chlorodimethylsilyl)indene[38] **21** or 1-(chlorodimethylsilyl)-indene[39] (1*R*)-**23a**/(1*S*)-**23b**, the corresponding 1- and 2-chirally substituted indenes **22** and (1*R*)-**24a**/(1*S*)-**24b**/**25** were obtained in low (3% and 21%, respectively) yields (Scheme 8 and Scheme 9). The amount of the 3-silyl isomer **25** in the **24a**/**24b**/**25** mixture was estimated to 15% by ^{1}H NMR spectroscopy. All attempts to react α-pinenyl potassium with either 2-indanone or 2-bromoindene failed. Due to the low isolated yields and preparations in small scale, further attempts to utilize the compounds **22** and (1*R*)-**24a**/(1*S*)-**24b**/**25** as ligand precursors for transition metal complexes were not pursued.

Dehydropolymerization of Phenylsilane

Dehydropolymerization of phenylsilane to poly(phenylsilane) with *n*BuLi activated transition-metal catalysts is a well-known reaction.[40,41] Harrod and co-workers reported in 1985 the first effective transition-metal catalyst for silane dehydrocoupling[42] and during the past 20 years a number of metallocene-based catalyst systems have been reported to polymerize phenylsilane.[43–50] Several shortcomings are, however, still to be overcome. Firstly, catalysts producing polyphenylsilanes with narrower polydispersities and with higher molecular weights than the presently existing systems, which seldom yield polymers with M_w's exceeding 5×10^3, would be desirable. Secondly, cleaner reaction mixtures not containing intractable oligo-/polysilane mixtures are required. Finally, the issue of stereocontrol in phenylsilane polymerization remains largely unsolved and only essentially atactic polymers are obtained regardless of chirality/achirality of the initiating catalyst system.

During the course of the present investigation, the chiral metallocenes **2**, **3**, (*pR*)(*pS*)-**5c** and (*pR*)(*pS*)-**6c** were briefly evaluated as catalysts for the dehydropolymerization of phenylsilane using zirconocene dichloride ([Cp_2ZrCl_2]) as reference catalyst (Scheme 10). The polymerization reactions were carried out in neat phenylsilane under argon by activation of 1 mol-% of the metallocene dichloride with 2 mol-% of *n*BuLi. The results are summarized in Table 2.

With the exception of the 1-substituted *meso*-like chiral complex (*pR*)(*pS*)-**5c**, the silane polymerization activities of the pinenyl-substituted systems were significantly lower than obtained with the zirconocene dichloride reference. The 2-substituted bis(indenyl) complex **2** gave polysilane with similar molecular weight to the reference catalyst whereas both 1-substituted complexes **5c** and **6c** and the 2-substituted tetrahydroindenyl analogue **3** produced lower molecular weight polymers. All catalysts investigated pro-

 © 2005 Wiley-VCH Verlag GmbH & Co. KGaA, Weinheim

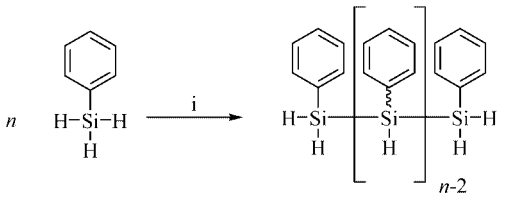

Scheme 10. Zirconocene-catalyzed dehydropolymerization of phenylsilane. (i) 1 mol-% **2**, **3**, (*pR*)(*pS*)-**5c** or (*pR*)(*pS*)-**6c**, 2 mol-% *n*BuLi.

Table 2. Dehydropolymerization of phenylsilane over chiral metallocenes **2**, **3**, (*pR*)(*pS*)-**5c** and (*pR*)(*pS*)-**6c** and the reference catalyst [Cp_2ZrCl_2].

Catalyst[a]	Conv.[b]	*A*[c]	M_w[d]	M_n[d]	MP[d][e]	PDI[d][f]
Cp_2ZrCl_2	98	116.3	715	680	707	1.05
2	97	36.2	705	646	691	1.09
3	46	27.3	n.d.[g]	n.d.[g]	n.d.[g]	n.d.[g]
(*pR*)(*pS*)-**5c**	90	124.9	366[h]	336[h]	274	1.09
(*pR*)(*pS*)-**6c**	25	73.1	n.d.[g]	n.d.[g]	n.d.[g]	n.d.[g]

[a] 1 mol-% of metallocene activated with 2 mol-% *n*BuLi in neat phenylsilane. [b] Conversion in % = (g of polymer)·(g of monomer)$^{-1}$. [c] Activity = (kg of polymer)·(mol of cat.)$^{-1}$·(mol of monomer)$^{-1}$·h^{-1}. [d] Determined by GPC. [e] The place (g/mol) of the top of the molecular mass peak. [f] PDI = M_w/M_n. [g] Not determined. [h] The values reported are indicative only, due to the detection limit (500 g/mol) of the column employed.

duced atactic polysilanes as confirmed by $^{29}Si\{^1H\}$ NMR analysis. As the sole significant difference between zirconocene dichloride and the investigated pinenyl-substituted complexes, it could be shown by ^1H NMR analysis of the polysilanes produced that catalysts **2**, **3**, **5c** and **6c** produced only linear polysilanes whereas mixtures of cyclic and linear poly-/oligomers were obtained with the Cp_2ZrCl_2/*n*BuLi catalyst system. The formation of oligomers and other coupling products was further investigated with GC-MS with compounds detected shown in Figure 4. All by-products **26**–**29** were detected in polymerizations catalyzed by complexes **2** and (*pR*)(*pS*)-**5c**, whereas complex **3** only yielded compounds **26** and **27** and complex **6c** yielded compound **26**. In the reaction catalyzed by the reference catalyst only compounds **26** and **29** were formed.

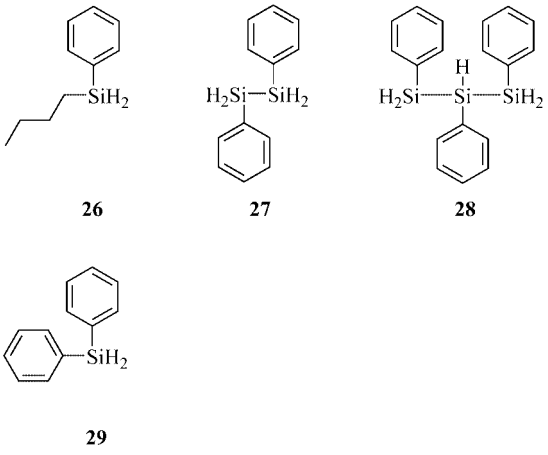

Figure 4. Oligomers/by-products formed in the dehydropolymerization of phenylsilane catalyzed by [Cp_2ZrCl_2], **2**, **3**, **5c** and **6c**/*n*BuLi

Olefin Polymerization

Complexes **2** and (*pR*)(*pS*)-**5c** were activated with methylaluminoxane (MAO) for polymerization of propylene in toluene (T = 50 °C, P = 5.34 bar, [Al]:[Zr] = 2000:1). The results are summarized in Table 3. Under the conditions investigated, the 2-pinenyl-substituted **2**/MAO catalyst system produced only low molecular weight atactic polypropylene (*a*PP) (colorless oil) with low activity, whereas the 1-substituted **5c**/MAO was totally inactive toward propylene intake, most likely due to its greater steric hindrance toward monomer coordination in the vicinity of the metal site induced by placement of the bulky substituents. The experimental pentad distribution for the *a*-PP obtained with **2**/MAO as determined by quantitative ^{13}C NMR with inverse gated ^1H-decoupling is as follows: [*mmmm*] = 5.5%, [*mmmr*] = 8.8%, [*rmmr*] = 5.5%, [*mmrm*] + [*rmrr*] = 25.3%, [*mrmr*] = 16.5%, [*rrrr*] = 8.8%, [*rrrm*] = 11.0% and [*mrrm*] = 7.7%. End group analysis by ^{13}C NMR indicated the presence of *n*-propyl, vinylidene, isobutenyl, *cis*-2-butenyl and *trans*-2-butenyl chain ends (Figure 5).

Table 3. Polymerization of propylene over **2**/MAO and (*pR*)(*pS*)-**5c**/MAO.

Catalyst[a]	*A*[b]	M_w[c]	M_n[c]	M_v[c]	PDI[d]
2/MAO	125	3670	1900	3110	1.93
5c/MAO	–	–	–	–	–

[a] 20 μmol of **2** or (*pR*)(*pS*)-**5c** activated with 40 mmol of MAO (30 vol-% in toluene) in 200 mL dry toluene at T = 50 °C, P = 5.34 bar, [Al]:[Zr] = 2000:1, t = 2 h. [b] Polymerization activity in (kg of PP)·(mol of cat.)$^{-1}$·h^{-1}. [c] By GPC. [d] PDI = M_w/M_n.

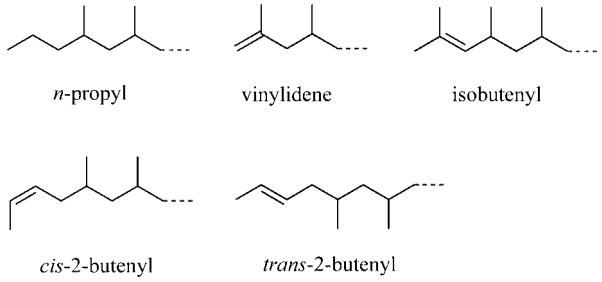

Figure 5. End groups present in the atactic polypropylene produced with **2**/MAO

The MAO-activated bis(indenyl) complexes **2** and (*pR*)(*pS*)-**5c** were further tested in the polymerization of ethylene in toluene (T = 50 °C, P = 3.95 bar, [Al]:[Zr] = 2000:1). In contrast to the propylene polymerization experiments, both catalysts **2**/MAO and **5c**/MAO polymerized ethylene with fairly high activities (2300–2550 kg PE/mol Zr/h) to high molecular weight polyethylene (M_w > 440000), the latter being slightly more active of the two. The polymerization results and characterization data are collected in Table 4 with results of IR-analyses of the poly-

 © 2005 Wiley-VCH Verlag GmbH & Co. KGaA, Weinheim

mer end group composition in Table 5. Both catalysts produced polyethylenes with vinylidene, terminal vinyl and *trans*-vinylene end groups (Figure 6) in slightly different ratios. The fact that the **5c**/MAO catalyst polymerizes ethylene with comparable activity to that of **2**/MAO further suggests that its inactivity toward propylene is most likely of steric origin and a consequence of the orientation of the 1-indenyl substituents over the metal center.

Table 4. Polymerization of ethylene over **2**/MAO and (*pR*)(*pS*)-**5c**/MAO.

Catalyst[a]	A[d]	M_w[e]	M_n[e]	M_v[e]	PDI[f]	T_m[g]
2/MAO[b]	2300	489000	169000	428000	2.9	122–128
5c/MAO[c]	2550	449000	178000	395000	2.5	124–134

[a] 2 μmol of **2** or (*pR*)(*pS*)-**5c** activated with 4 mmol of MAO (30 vol-% in toluene) in 200 mL dry toluene at T = 50 °C, P = 3.95 bar, [Al]:[Zr] = 2000:1. [b] Polymerization time = 0.58 h. [c] Polymerization time = 0.75 h. [d] Polymerization activity in (kg of PE)-(mol of cat.)$^{-1}$ h^{-1}. [e] By GPC. [f] PDI = M_w/M_n. [g] Melting interval in °C by DSC.

Table 5. End group distribution [C=C/1000] in polyethylenes produced by **2**/MAO and (*pR*)(*pS*)-**5c**/MAO.

Catalyst[a]	Vinylidene	Terminal vinyl	*trans*-Vinylene
2/MAO	0.69	1.54	1.11
5c/MAO	0.52	3.85	0.35

[a] By IR.

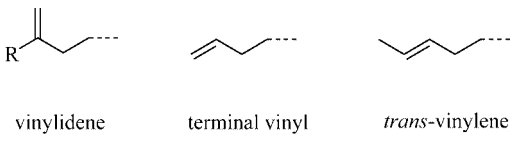

Figure 6. End groups present in polyethylenes produced with **2**/MAO and **5c**/MAO

Carboalumination Reactions

Catalytic asymmetric carboalumination of unactivated terminal alkenes using chiral zirconocene catalysts has considerable synthetic potential as oxidation of the organoaluminum products with molecular oxygen potentially provides access to the corresponding chiral alcohols.[9–13] Recently, this reaction, initially developed by Negishi and coworkers, has been applied successfully e.g., in natural product synthesis via the obtained chiral polypropionate building blocks.[51–53] Of several zirconocene catalysts evaluated previously, high yields and moderate enantioselectivities are almost exclusively obtained by use of the chiral unbridged bis(1-neomenthylindenyl)zirconium dichloride [$(NMI)_2ZrCl_2$], initially developed by Erker and co-workers.[22] Accordingly, we felt motivated to briefly investigate the applicability of the easily prepared chiral zirconocenes **2**, **3**, (*pR*)(*pS*)-**5c** and (*pR*)(*pS*)-**6c** as catalysts for carboalumination reactions. Thus, by reaction of 1-octene with triethylaluminum or trimethylaluminum in the presence of catalytic amounts of the chiral zirconocene complexes **2** and (*pR*)(*pS*)-**5c**, 2-ethyl-1-octanol and 2-methyl-1-octanol were indeed obtained after oxidation with O_2, albeit in disappointingly low yields ranging from 8 to 18% (Scheme 11). Also enantiomeric excesses were low ranging from marginal to 10% as determined by ^{1}H and ^{19}F NMR analysis of the corresponding Mosher esters.[54] By measuring the optical rotations of the enantiomeric product mixtures it could be deduced that the 2-substituted complex **2** produced, in both cases, a slight excess of the (+)-enantiomer of 2-alkyl-1-octanols whereas a slight excess of the (–)-enantiomers was obtained with (*pR*)(*pS*)-**5c**. The hydrogenated congeners **3** and (*pR*)(*pS*)-**6c** proved totally inactive as carboalumination catalysts.

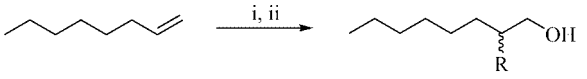

	R = Me		R = Et	
catalyst	**2**	**5c**	**2**	**5c**
yield (%)	8	18	11	16
ee (%)	0.5	3	10	5

Scheme 11. Carboalumination of 1-octene with chiral zirconocene catalysts. (i) Et_3Al or Me_3Al, **2** or (*pR*)(*pS*)-**5c**, dichloromethane. (ii) O_2.

A simplified mechanistic scheme of the carboalumination reaction is displayed in Scheme 12. Based on the previous work by Negishi, Waymouth and others, the NMI_2ZrCl_2 catalyst appears to have an optimal disposal of the chiral ligands coupled with conformational flexibility driving the reaction towards the carboalumination product which in turn can be oxidized to the chiral alcohol. With other catalysts investigated previously, larger amounts of alkene products resulting from hydrometalation/carbometalation and/or hydrogen transfer sequences are often produced. The ligands in **2** and (*pR*)(*pS*)-**5c** are apparently not bulky enough for efficient blocking of the side reactions resulting in low carboalumination yields and selectivities.

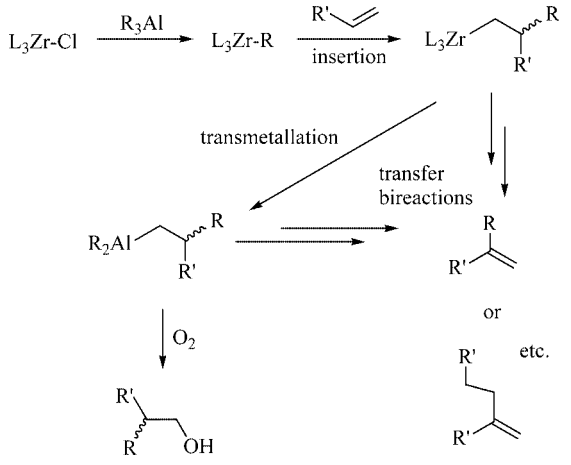

Scheme 12. Simplified mechanism for zirconocene catalyzed carboalumination.

 © 2005 Wiley-VCH Verlag GmbH & Co. KGaA, Weinheim

Nevertheless, some enantiocontrol was obtained with the simple ligand design presented in this work and the results obtained could be considered promising. Unfortunately our attempts to modify the steric properties of these precatalysts by additional methyl substituents were hampered by the difficult (or impossible) isolation and purification of complexes **8a**–**c** and **10a**–**c**. Furher variations in ligand structure are currently in progress.

Summary and Conclusions

In this paper we have reported the synthesis of some new indenes containing a β-pinenyl-derived, chiral substituent and investigated the metallation of these ligand precursors, as well as some previously described ligand analogues,[28] with group-4 metals. Due to the simple accessibility of the ligand precursors and the successful metallations in some of the cases, the route appears attractive for the preparation of new chiral transition metal complexes. The main drawback of the complexes described are the high solubilities of both the ligand precursors and the corresponding metallocenes in nearly all common organic solvents which render their isolation and purification unusually difficult in many cases. The high solubilities in turn are likely a consequence of the high rotational and conformational freedom of the pinenyl part in these molecules.

In addition, we have investigated the catalytic activity of selected metal complexes in polymerization and carboalumination reactions. Metal complexes **2** and (*pR*)(*pS*)-**5c** polymerized ethylene with high activity and polyethylene with high molecular weight was obtained whereas only complex **2** was active in propylene polymerization producing atactic polypropylene with low molecular weight. All of the catalysts investigated produced atactic poly(phenylsilane) with low molecular weight. In catalytic carboalumination reactions, complexes **2** and (*pR*)(*pS*)-**5c** showed to induce some (0.5–10% *ee*) enantioselectivity in the carboalumination of 1-octene with triethyl- and trimethylaluminum whereas their tetrahydroindenyl analogues **3** and (*pR*)(*pS*)-**6c** were not active at all. Nevertheless, we believe that the simple chiral catalyst structures described herein, may prove valuable starting points for further developoment by structural modifications.

Experimental Section

General Comments: All air and moisture sensitive reactions were conducted under argon using standard techniques. Commercially available reagents were used without further purification. Methylindene,[55] α-pinenylpotassium,[37] 2-(chlorodimethylsilyl)indene[38] and 1-(chlorodimethylsilyl)indene[39] were synthesized essentially according to literature procedures. Chloro{[(1*S*,2*S*,5*S*)-6,6-dimethylbicyclo[3.1.1]hept-2-yl]methyl}dimethylsilane was prepared by hydrosilylation of β-pinene with chlorodimethylsilane in the presence of Karstedt's catalyst.[56,57] Diethyl ether and tetrahydrofuran were distilled from sodium/benzophenone ketyl prior to use. Dichloromethane was distilled from calcium hydride and toluene was purified by passage through a series of activated 3-Å molecular sieves and copper catalyst columns. Flash chromatography was performed on silica gel 60 (40–63 μm). Silanized silica gel was prepared according to a literature procedure.[33] NMR spectra were recorded at 298 K with a Bruker Avance 600 (^{1}H NMR 600 MHz, ^{13}C NMR 150.9 MHz), Jeol JNM-A500 (^{1}H NMR 500 MHz, ^{13}C 125.8 MHz), Jeol L-400 (^{1}H NMR 400 MHz, ^{13}C 100.6 MHz, ^{29}Si 79.5 MHz) or Bruker 250 MHz (1H NMR 250 MHz) NMR spectrometer. ^{1}H NMR were referenced against residual ^{1}H-impurities in the solvent and ^{13}C NMR to the solvent signals. In the ^{29}Si NMR experiments TMS was used as external reference. The NMR spectra were recorded in δ values with $CDCl_3$ or CD_2Cl_2 as the solvent. Mass spectra were recorded with a high-resolution mass spectrometer (Fison's ZapSpec). A Hewlett–Packard Series II 5890/Hewlett Packard 5971A Mass selective detector was used in GC-MS analysis. Molecular weights and molecular weight distributions of polysilanes were measured at 30 °C in THF by size exclusion chromatography (GPC) relative to polystyrene standards using a Waters 515 high-pressure liquid chromatography pump, GPC fitted with Styragel columns HR 2, HR 4, and HR 6, a UV detector Waters 2487 and a refractive-index detector Waters 2410. Melting intervals were measured with Perkin–Elmer DSC 7. Polyethylene end group analyses were carried out with a Perkin–Elmer FT-IR spectrometer Spectrum 1000. The optical rotation measurements were made using Perkin–Elmer Polarimeter 241. The molecular weights of the polyethylene and polypropylene samples were determined using a Waters Alliance 2000 GPC equipped with a refractometer, viscometer, and three Waters Styragel HMW columns covering the molecular weight range from 10^2 to 10^8 g/mol. 1,2,4-Trichlorobenzene was used as solvent and the chromatograms were collected at 140 °C. The molecular weights were calculated with the universal calibration based on 11 narrow polystyrene standards.

Bis{2-[(7,7-dimethylnorpinanylmethyl)dimethylsilyl]indenyl}-zirconium Dichloride (2): To 2-[(7,7-dimethylnorpinanylmethyl)dimethylsilyl]indene (**1**) (2.4076 g, 7.8 mmol) in diethyl ether (35 mL) at 0 °C was added *n*BuLi (2.5 M in *n*-hexane, 3.2 mL, 7.8 mmol). The yellow solution was stirred at room temperature for 4 h. The solvent was removed under vacuum leaving a pale yellow foam. Next, $ZrCl_4$ (0.9634 g, 4.1 mmol) was added and the solids were mixed a few minutes before 50 mL of toluene was added. After stirring at 50 °C for 18 h, the suspension was filtered and the filtrate was concentrated under vacuum. The product was crystallized from *n*-pentane at –20 °C yielding 1.1157 g (37%) of pure **2** as a yellow powder. ^{1}H NMR (400 MHz, CD_2Cl_2, 25 °C): δ = 7.81 (m, 4 H, arom. CH in six-membered ring), 7.30 (m, 4 H, arom. CH in six-membered ring), 5.97 (dd, J = 0.92 Hz, 2.14 Hz, 2 H, arom. CH in five-membered ring), 5.94 (dd, J = 0.76 Hz, 2.14 Hz, 2 H, arom. CH in five-membered ring), 1.92 (m, 2 H, aliph. CH in pinenyl ring), 1.87 (m, 2 H, aliph. CH in pinenyl ring), 1.77 (m, 2 H, aliph. CH in pinenyl ring), 1.65 (m, 4 H, aliph. CH_2 in pinenyl ring), 1.55 (m, 2 H, aliph. CH in pinenyl ring), 1.35 (dt, J = 1.32 Hz, 5.57 Hz, 2 H, aliph. CH in pinenyl ring), 1.28 (d, J = 9.92 Hz, 2 H, aliph. CH in pinenyl ring), 1.11 (m, 2 H, aliph. CH in pinenyl ring), 1.06 (s, 6 H, CH_3 in pinenyl ring), 0.69 (s, 6 H, CH_3 in pinenyl ring), 0.53 (dd, J = 7.55 Hz, 14.50 Hz, 2 H, aliph. CH between Si and pinenyl ring), 0.45 (dd, J = 6.56 Hz, 14.50 Hz, 2 H, aliph. CH between Si and pinenyl ring), 0.11 (s, 6 H, CH_3 attached to Si), 0.10 (s, 6 H, CH_3 attached to Si) ppm. ^{13}C NMR (100.6 MHz, CD_2Cl_2, 25 °C): δ = 141.83 (2 C_q), 130.02 (4 C_q), 126.32 (4 arom. CH in six-membered ring), 126.06 (4 arom. CH in six-membered ring), 112.47 (2 arom. CH in five-membered ring), 112.30 (2 arom. CH in five-membered ring), 49.44 (2 aliph. CH in pinenyl ring), 41.30 (2 aliph. CH in pinenyl ring), 39.93 (2 C_q in pinenyl ring), 31.46 (2

 © 2005 Wiley-VCH Verlag GmbH & Co. KGaA, Weinheim

aliph. CH in pinenyl ring), 27.15 (2 CH_3 in pinenyl ring), 26.23 (4 aliph. CH in pinenyl ring), 25.31 (4 aliph. CH in pinenyl ring), 25.10 (2 aliph. CH_2 between Si and pinenyl ring), 23.32 (4 aliph. CH in pinenyl ring), 20.18 (2 CH_3 in pinenyl ring), –1.16 (2 CH_3 attached to Si), –1.47 (2 CH_3 attached to Si) ppm. ^{29}Si NMR (79.5 MHz, CD_2Cl_2, 25 °C): δ = –4.45 (2 Si) ppm. In the EIMS mass spectrum parent ions of composition $C_{42}H_{58}Cl_2Si_2Zr^+$ were observed in the appropriate ratios at *m*/*z* = 778–786. $C_{42}H_{58}Cl_2Si_2Zr$ (781.18): calcd. C 64.57, H 7.48; found C 64.58, H 7.59.

Bis{2-[(7,7-dimethylnorpinanylmethyl)dimethylsilyl]4,5,6,7-tetrahydro-1-indenyl}zirconium Dichloride (3): A suspension of **2** (0.1124 g, 0.1 mmol) and PtO_2 (a catalytic amount) in dichloromethane (50 mL) was hydrogenated in a steel autoclave under 50 bar H_2 for 20 h at room temperature. The catalyst was filtered off and the filtrate was evaporated yielding 0.095 g (86%) of the pure title compound as a pale green oil. ^{1}H NMR (400 MHz, $CDCl_3$, 25 °C): δ = 6.22 (m, 4 H, arom. CH in five-membered ring), 2.78 (m, 4 H, aliph. CH in six-membered ring), 2.59 (m, 4 H, aliph. CH in six-membered ring), 1.86 (m, 10 H, aliph. CH in six-membered ring and in pinenyl ring), 1.62 (m, 10 H, aliph. CH in six-membered ring and in pinenyl ring), 1.45 (m, 2 H, aliph. CH in pinenyl ring), 1.29 (d, *J* = 9.92 Hz, 2 H, aliph. CH in pinenyl ring), 1.14 (m, 2 H, aliph. CH in pinenyl), 1.12 (s, 6 H, CH_3 in pinenyl ring), 0.73 (s, 6 H, CH_3 in pinenyl ring), 0.58 (m, 4 H, CH_2 between Si and pinenyl ring), 0.28 (s, 6 H, CH_3 attached to Si), 0.27 (s, 6 H, CH_3 attached to Si) ppm. ^{13}C NMR (100.6 MHz, $CDCl_3$, 25 °C): δ = 135.15 (2 C_q), 135.02 (2 C_q), 122.26 (2 C_q), 121.09 (2 arom. CH in five-membered ring), 120.81 (2 arom. CH in five-membered ring), 48.85 (2 C, aliph. C in six-membered ring or in pinenyl ring), 40.54 (2 C, aliph. C in six-membered ring or in pinenyl ring), 39.44 (2 C_q in pinenyl ring), 30.97 (2 C, aliph. C in six-membered ring or in pinenyl ring), 26.91 (2 C, aliph. C in six-membered ring or in pinenyl ring), 26.01 (2 C, aliph. C in six-membered ring or in pinenyl ring), 25.59 (2 C, aliph. C in six-membered ring or in pinenyl ring), 25.40 (2 C, aliph. C in six-membered ring or in pinenyl ring), 25.12 (2 C, aliph. C in six-membered ring or in pinenyl ring), 24.71 (2 C, aliph. C in six-membered ring or in pinenyl ring), 22.90 (2 C, aliph. C in six-membered ring or in pinenyl ring), 22.26 (6 C, aliph. C in six-membered ring or in pinenyl ring), 19.94 (2 C, aliph. C in six-membered ring or in pinenyl ring), –0.45 (2 CH_3–Si), –0.88 (2 CH_3–Si) ppm. ^{29}Si NMR (79.5 MHz, $CDCl_3$, 25 °C): δ = –4.71 (2 Si) ppm. In the EIMS mass spectrum parent ions of composition $C_{42}H_{66}Cl_2Si_2Zr^+$ were observed in the appropriate ratios at *m*/*z* = 786–794.

(*pR*)(*pS*)-Bis{1-[(7,7-dimethylnorpinanylmethyl)dimethylsilyl]-indenyl}zirconium Dichlorides (5c): To a diastereomeric mixture of 1-[(7,7-dimethylnorpinanylmethyl)dimethylsilyl]indene (**4a/4b**) (5.5281 g, 17.8 mmol) in diethyl ether (100 mL) at 0 °C was added *n*BuLi (2.5 M in *n*-hexane, 7.2 mL, 18.0 mmol). The yellow solution was stirred at room temperature for 4.5 h. The reaction mixture was cooled to 0 °C and $ZrCl_4$ (2.0870 g, 9.0 mmol) was added. After stirring the suspension at room temperature for 19 h, the solvents were removed under vacuum. The residue was dissolved in dichloromethane, filtered and the filtrate was concentrated. Crystallization from dichloromethane at –20 °C provided 0.7782 g (11%) of the pure (*pR*)(*pS*)-**5c** diastereomer as a yellow powder. ^{1}H NMR (600 MHz, $CDCl_3$, 25 °C): δ = 7.67 (m, 4 H, arom. CH in six-membered ring), 7.25 (m, 4 H, arom. CH in six-membered ring), 6.41 (m, 2 H, arom. CH in five-membered ring), 6.34 (m, 2 H, arom. CH in five-membered ring), 1.94 (m, 4 H, aliph. CH in pinenyl ring), 1.78 (m, 2 H, aliph. CH in pinenyl ring), 1.59 (m, 6 H, aliph. CH in pinenyl ring), 1.44 (m, 2 H, aliph. CH in pinenyl ring), 1.27 (m, 2 H, aliph. CH in pinenyl ring), 1.15 (m, 2 H, aliph. CH in pinenyl ring), 1.07 (s, 6 H, CH_3 in pinenyl ring), 0.76 (m, 4 H, aliph. CH_2 between Si and pinenyl ring), 0.67 (s, 3 H, CH_3 in pinenyl ring), 0.64 (s, 3 H, CH_3 in pinenyl ring), 0.44 (s, 3 H, CH_3 attached to Si), 0.42 (s, 3 H, CH_3 attached to Si), 0.37 (s, 3 H, CH_3 attached to Si), 0.35 (s, 3 H, CH_3 attached to Si) ppm. ^{13}C NMR (150.9 MHz, $CDCl_3$, 25 °C): δ = 145.59 (C_q), 144.37 (C_q), 136.05 (2 C_q), 134.73 (C_q), 134.41 (C_q), 127.35 (2 arom. CH in six-membered ring), 127.31 (2 arom. CH in five-membered ring), 126.42 (arom. CH in six-membered ring), 126.39 (arom. CH in six-membered ring), 126.01 (arom. CH in six-membered ring), 125.96 (arom. CH in six-membered ring), 125.24 (2 arom. CH in six-membered ring), 104.89 (arom. CH in five-membered ring), 104.86 (arom. CH in five-membered ring), 49.16 (aliph. C in pinenyl ring), 49.13 (aliph. C in pinenyl ring), 40.71 (2 aliph. C in pinenyl ring), 39.60 (C_q in pinenyl ring), 39.58 (C_q in pinenyl ring), 31.23 (2 aliph. C in pinenyl ring), 26.98 (CH_3 in pinenyl ring), 26.95 (CH_3 in pinenyl ring), 25.73 (aliph. C in pinenyl ring), 25.68 (aliph. C in pinenyl ring), 25.15 (CH_2 between Si and pinenyl ring), 25.12 (CH_2 between Si and pinenyl ring), 24.88 (2 aliph. C in pinenyl ring), 23.06 (aliph. C in pinenyl ring), 23.05 (aliph. C in pinenyl ring), 20.04 (CH_3 in pinenyl ring), 20.00 (CH_3 in pinenyl ring), 0.06 (CH_3–Si), –0.48 (CH_3–Si), –0.57 (CH_3–Si), –0.81 (CH_3–Si) ppm. ^{29}Si NMR (79.5 MHz, $CDCl_3$, 25 °C): δ = –4.82 (2 Si) ppm. In the EIMS mass spectrum parent ions of composition $C_{42}H_{58}Cl_2Si_2Zr^+$ were observed in the appropriate ratios at *m*/*z* = 778–786. ^{1}H NMR (250 MHz, $CDCl_3$, 25 °C) analysis of the filtrate containing a mixture of diastereomers (*pR*)(*pS*)-bis{1-[dimethyl(7,7-dimethylnorpinanylmethyl)silyl]indenyl}zirconium dichlorides (**5a** and **5b**): δ = 7.73 (m, 4 H, arom. CH in six-membered ring in **5a** and/or **5b**), 7.54 (m, 4 H, arom. CH in six-membered ring in **5a** and/or **5b**), 7.28 (m, 8 H, arom. CH in six-membered ring in **5a** and/or **5b**), 6.49 (m, 4 H, arom. CH in five-membered ring in **5a** and/or **5b**), 6.15 (m, 4 H, arom. CH in five-membered ring in **5a** and/or **5b**), 1.07 (s, 12 H, CH_3 in pinenyl ring in **5a** and/or **5b**), 0.67 (s, 6 H, CH_3 in pinenyl ring in **5a** and/or **5b**), 0.63 (s, 6 H, CH_3 in pinenyl ring in **5a** and/or **5b**), 0.47 (m, 12 H, CH_3 attached to Si in **5a** and/or **5b**), 0.40 (m, 12 H, CH_3 attached to Si in **5a** and/or **5b**), 2.23–0.75 (m, 44 H, aliph. CH in pinenyl substituent in **5a** and **5b**) ppm, signals from the aliph. protons in pinenyl ring in **5a** and **5b** are overlapping with each other and other signals in the region 2.23–0.75 ppm.

{*pR*)(*pS*)-Bis{1-[(7,7-dimethylnorpinanylmethyl)dimethylsilyl]-4,5,6,7-tetrahydro-1-indenyl}zirconium Dichloride (6c): A suspension of **5c** (0.1190 g, 0.2 mmol) and PtO_2 (a catalytic amount) dichloromethane (50 mL) was hydrogenated in a steel autoclave under 50 bar H_2 for 20 h at room temperature. The catalyst was filtered off and the filtrate was evaporated yielding 0.096 g (82%) of pure **6c** as a pale green powder. Recrystallization from dichloromethane at –20 °C yielded 0.037 g (31%) of a pale green solid. ^{1}H NMR (400 MHz, $CDCl_3$, 25 °C): δ = 6.51 (m, 2 H, arom. CH in five-membered ring), 5.58 (m, 2 H, arom. CH in five-membered ring), 3.00 (m, 4 H, aliph. CH in six-membered ring), 2.50 (m, 4 H, aliph. CH in six-membered ring), 1.96 (m, 4 H, aliph. CH in six-membered ring and in pinenyl ring), 1.80 (m, 6 H, aliph. CH in six-membered ring and in pinenyl ring), 1.62 (m, 12 H, aliph. CH in six-membered ring and in pinenyl ring), 1.31 (d, *J* = 10.15 Hz, 1 H, aliph. CH in pinenyl ring), 1.30 (d, *J* = 10.15 Hz, aliph. CH in pinenyl ring), 1.20 (m, 2 H, aliph. CH in pinenyl ring), 1.14 (s, 3 H, CH_3 in pinenyl ring), 1.01 (s, 3 H, CH_3 in pinenyl ring), 0.75 (s, 3 H, CH_3 in pinenyl ring), 0.73 (s, 3 H, CH_3 in pinenyl ring), 0.67 (m, 4 H, CH_2 between Si and pinenyl ring), 0.26 (s, 3 H, CH_3 attached to Si), 0.25 (s, 3 H, CH_3 attached to Si), 0.17 (s, 6 H, CH_3

 © 2005 Wiley-VCH Verlag GmbH & Co. KGaA, Weinheim

attached to Si) ppm. ^{13}C NMR (100.6 MHz, $CDCl_3$, 25 °C): δ = 140.48 (C_q), 140.42 (C_q), 136.24 (C_q), 136.18 (C_q), 118.86 (C_q), 118.68 (C_q), 116.42 (arom. CH), 116.38 (arom. CH), 111.96 (arom. CH), 111.85 (arom. CH), 49.02 (aliph. C in six-membered ring or in pinenyl ring), 48.82 (aliph. C in six-membered ring or in pinenyl ring), 40.60 (aliph. C in six-membered ring or in pinenyl ring), 40.59 (aliph. C in six-membered ring or in pinenyl ring), 39.53 (C_q in pinenyl ring), 39.44 (C_q in pinenyl ring), 31.11 (aliph. C in six-membered ring or in pinenyl ring), 31.01 (aliph. C in six-membered ring or in pinenyl ring), 26.91 (aliph. C in six-membered ring or in pinenyl ring), 26.86 (aliph. C in six-membered ring or in pinenyl ring), 26.10 (aliph. C in six-membered ring or in pinenyl ring), 26.06 (aliph. C in six-membered ring or in pinenyl ring), 25.68 (aliph. C in six-membered ring or in pinenyl ring), 25.61 (aliph. C in six-membered ring or in pinenyl ring), 25.18 (aliph. C in six-membered ring or in pinenyl ring), 25.16 (aliph. C in six-membered ring or in pinenyl ring), 24.76 (aliph. C in six-membered ring or in pinenyl ring), 24.73 (aliph. C in six-membered ring or in pinenyl ring), 24.56 (aliph. C in six-membered ring or in pinenyl ring), 24.54 (aliph. C in six-membered ring or in pinenyl ring), 22.93 (aliph. C in six-membered ring or in pinenyl ring), 22.91 (aliph. C in six-membered ring or in pinenyl ring), 22.64 (2 aliph. C in six-membered ring or in pinenyl ring), 22.26 (aliph. C in six-membered ring or in pinenyl ring), 22.24 (aliph. C in six-membered ring or in pinenyl ring), 19.97 (2 aliph. C in six-membered ring or in pinenyl ring), –0.52 (CH_3–Si), –0.74 (CH_3–Si), –0.99 (CH_3–Si), –1.34 (CH_3–Si) ppm. ^{29}Si NMR (79.5 MHz, $CDCl_3$, 25 °C): δ = –6.37, –6.47 ppm. In the EIMS mass spectrum parent ions of composition $C_{42}H_{66}Cl_2Si_2Zr^+$ were observed in the appropriate ratios at m/z = 786–794.

A Diastereomeric Mixture of (6,6-dimethylbicyclo[3.1.1]hept-2-ylmethyl)dimethyl(1-methyl-1*H*-inden-2-yl)silanes (7a/7b): To **1**[28] (3.4065 g, 11.0 mmol) in tetrahydrofuran (50 mL) at 0 °C was added *n*BuLi (2.5 M in *n*-hexane, 4.5 mL, 11.1 mmol). The orange solution was stirred at room temperature for 3.5 h and to this solution was added dropwise methyl iodide (1.4 mL, 21.9 mmol) at 0 °C. The resulting red reaction mixture was stirred at room temperature for 1.5 h before saturated aqueous NH_4Cl solution (50 mL) was added. The layers formed were separated and the aqueous layer was further extracted with diethyl ether (30 mL). The combined organic layers were dried with Na_2SO_4, filtered and the solvents evaporated to dryness. The crude product was purified with silica gel column chromatography using hexane as eluent providing 2.6259 g (74%) of **7a/7b** (a mixture of two diastereomers) as a colorless oil. ^{1}H NMR (600 MHz, $CDCl_3$, 25 °C): δ = 7.45 (m, 1+1 H, arom. CH), 7.39 (m, 1+1 H, arom. CH), 7.28 (m, 1+1 H, arom. CH), 7.22 (m, 1+1 H, arom. CH), 7.06 (m, 1+1 H, olefinic CH in five-membered ring), 3.59 (m, 1+1 H, aliph. CH in five-membered ring), 2.21 (m, 1+1 H, CH in pinenyl ring), 2.05 (m, 1+1 H, CH in pinenyl ring), 1.88 (m, 1+1 H, CH in pinenyl ring), 1.74 (m, 3+3 H, CH in pinenyl ring), 1.68 (m, 1+1 H, CH in pinenyl ring), 1.42 (m, 1+1 H, CH in pinenyl ring), 1.39 (m, 3+3 H, CH_3 attached to five-membered ring), 1.30 (m, 1+1 H, CH in pinenyl ring), 1.21 (s, 3 H, CH_3 in pinenyl ring), 1.20 (s, 3 H, CH_3 in pinenyl ring), 0.85 (m, 1+1 H, bridging CH between Si and pinenyl ring), 0.84 (s, 3 H, CH_3 in pinenyl ring), 0.83 (s, 3 H, CH_3 in pinenyl ring), 0.75 (m, 1+1 H, bridging CH between Si and pinenyl ring), 0.28 (m, 6+6 H, CH_3 attached to Si) ppm. ^{13}C NMR (150.9 MHz, $CDCl_3$, 25 °C): δ = 155.20 (C_q), 155.14 (C_q), 152.51 (C_q), 152.48 (C_q), 144.36 (2 C_q), 140.01 (olefinic CH in five-membered ring), 140.00 (olefinic CH in five-membered ring), 126.48 (2 arom. CH), 124.98 (2 arom. CH), 122.58 (2 arom. CH), 120.84 (2 arom. CH), 49.51 (CH in pinenyl ring), 49.37 (CH in pinenyl ring), 49.33 (aliph. CH in five-membered ring), 49.32 (aliph. CH in five-membered ring), 40.79 (CH in pinenyl ring), 40.77 (CH in pinenyl ring), 39.69 (2 C_q in pinenyl ring), 31.39 (CH in pinenyl ring), 31.38 (CH in pinenyl ring), 27.07 (2 CH_3 in pinenyl ring), 25.81 (CH_2 in pinenyl ring), 25.69 (CH_2 in pinenyl ring), 24.92 (2 CH_2 in pinenyl ring), 24.35 (bridging CH_2 between Si and pinenyl ring), 24.22 (bridging CH_2 between Si and pinenyl ring), 23.13 (2 CH_2 in pinenyl ring), 20.18 (2 CH_3 in pinenyl ring), 17.24 (CH_3 attached to five-membered ring), 17.20 (CH_3 attached to five-membered ring), –0.78 (CH_3 attached to Si), –1.02 (CH_3 attached to Si), –1.17 (CH_3 attached to Si), –1.38 (CH_3 attached to Si) ppm. ^{29}Si NMR (119.3 MHz, $CDCl_3$, 25 °C): δ = –8.30, –8.43 ppm. EIMS (70 eV) calcd. for $C_{22}H_{32}Si$ 324.2273, found 324.2273.

Bis{2-[(7,7-dimethylnorpinanylmethyl)dimethylsilyl](1-methyl-indenyl}zirconium Dichlorides [(*pR*)(*pR*)-8a, (*pS*)(*pS*)-8b, (*pR*)(*pS*)-8c]: To a mixture of **7a/7b** (1.2887 g, 4.0 mmol) in diethyl ether (30 mL) at 0 °C was added *n*BuLi (2.5 M in *n*-hexane, 1.6 mL, 4.0 mmol). The yellow solution was stirred at room temperature for 4 h. The reaction mixture was cooled to 0 °C and $ZrCl_4$ (0.4626 g, 2.0 mmol) was added. After stirring the suspension at room temperature for 18 h, the solvents were removed under vacuum. The residue was dissolved in dichloromethane, filtered and the filtrate was concentrated. The crude product was purified with silanized silica gel column chromatography under argon using pentane as eluent providing 0.8499 g (53%) of a mixture of **8a**–**c** as a yellow oil. Combination of fractions containing only the racemic-like diastereomers (*pR*)(*pR*)-**8a** and (*pS*)(*pS*)-**8b** yielded 0.2938 g (18%) of a such mixture. When to this mixture was added cold pentane at –60 °C a small sample (0.054 g, 3%) of **8a/8b** was obtained as yellow crystals enriched in one of the racemic-like diastereomers in a 57:43 ratio. ^{1}H NMR (600 MHz, $CDCl_3$, 25 °C): δ = 7.97 (m, 4 H, arom. CH in **8a** and **8b**), 7.59 (m, 4 H, arom. CH in **8a** and **8b**), 7.33 (m, 4 H, arom. CH in **8a** and **8b**), 7.20 (m, 4 H, arom. CH in **8a** and **8b**), 5.14 (m, 2 H, olefinic CH in five-membered ring in **8a** and **8b**), 5.13 (m, 2 H, olefinic CH in five-membered ring in **8a** and **8b**), 2.46 (s, 6 H, CH_3 attached to five-membered ring in **8a** and **8b**), 2.45 (s, 6 H, CH_3 attached to five-membered ring in **8a** and **8b**), 1.87 (m, 4 H, CH in pinenyl ring in **8a** and **8b**), 1.77 (m, 8 H, CH in pinenyl ring in **8a** and **8b**), 1.60 (m, 8 H, CH in pinenyl ring in **8a** and **8b**), 1.49 (m, 4 H, CH in pinenyl ring in **8a** and **8b**), 1.23 (m, 8 H, CH in pinenyl ring in **8a** and **8b**), 1.06 (m, 4 H, CH in pinenyl ring in **8a** and **8b**), 1.01 (s, 6 H, CH_3 attached to pinenyl ring in **8a** or **8b**), 0.99 (s, 6 H, CH_3 attached to pinenyl ring in **8a** or **8b**), 0.64 (s, 6 H, CH_3 attached to pinenyl ring in **8a** or **8b**), 0.63 (s, 6 H, CH_3 attached to pinenyl ring in **8a** or **8b**), 0.43 (m, 4 H, bridging CH_2 between pinenyl ring and Si in **8a** or **8b**), 0.35 (m, 4 H, bridging CH_2 between pinenyl ring and Si in **8a** or **8b**), 0.19 (s, 12 H, CH_3 attached to Si in **8a** or **8b**), –0.08 (s, 6 H, CH_3 attached to Si in **8a** or **8b**), –0.10 (s, 6 H, CH_3 attached to Si in **8a** or **8b**) ppm. ^{13}C NMR (150.9 MHz, $CDCl_3$, 25 °C): δ = 139.13 (2 C_q), 139.08 (2 C_q), 131.65 (2 C_q), 131.64 (2 C_q), 126.15 (4 arom. CH in **8a** and **8b**), 125.74 (2 C_q), 125.72 (2 C_q), 125.04 (4 arom. CH in **8a** and **8b**), 124.79 (4 arom. CH in **8a** and **8b**), 124.52 (4 C_q), 123.96 (2 arom. CH in **8a** and **8b**), 123.93 (2 arom. CH in **8a** and **8b**), 106.70 (4 olefinic CH in five-membered ring in **8a** and **8b**), 48.82 (2 CH in pinenyl ring in **8a** and **8b**), 48.79 (2 CH in pinenyl ring in **8a** and **8b**), 40.71 (2 CH in pinenyl ring in **8a** and **8b**), 40.67 (2 CH in pinenyl ring in **8a** and **8b**), 39.45 (4 C_q in pinenyl ring in **8a** and **8b**), 30.96 (2 CH in pinenyl ring in **8a** and **8b**), 30.87 (2 CH in pinenyl ring in **8a** and **8b**), 26.89 (2 CH_3 attached to pinenyl ring in **8a** or **8b**), 26.83 (2 CH_3 attached to pinenyl ring in **8a** or **8b**), 25.86 (2 CH in pinenyl ring in **8a** and **8b**), 25.80 (2 CH in pinenyl ring in **8a** and **8b**), 25.05 (2 bridging CH_2 between pinenyl ring and

 © 2005 Wiley-VCH Verlag GmbH & Co. KGaA, Weinheim

Si in **8a** or **8b**), 24.96 (2 bridging CH_2 between pinenyl ring and Si in **8a** or **8b**), 24.86 (4 CH in pinenyl ring in **8a** and **8b**), 22.95 (2 CH in pinenyl ring in **8a** and **8b**), 22.92 (2 CH in pinenyl ring in **8a** and **8b**), 20.00 (2 CH_3 attached to pinenyl ring in **8a** or **8b**), 19.95 (2 CH_3 attached to pinenyl ring in **8a** or **8b**), 13.83 (2 CH_3 attached to five-membered ring in **8a** or **8b**), 13.80 (2 CH_3 attached to five-membered ring in **8a** or **8b**), –0.52 (2 CH_3 attached to Si in **8a** or **8b**), –0.86 (2 CH_3 attached to Si in **8a** or **8b**), –1.03 (2 CH_3 attached to Si in **8a** or **8b**), –1.45 (2 CH_3 attached to Si in **8a** or **8b**) ppm. ^{29}Si NMR (119.3 MHz, $CDCl_3$, 25 °C): δ = –4.29 (2 Si in **8a** or **8b**), –4.31 (2 Si in **8a** or **8b**) ppm. In the EIMS mass spectrum parent ions of composition $C_{44}H_{62}Cl_2Si_2Zr^+$ were observed in the appropriate ratios at m/z = 806–814.

A Diastereomeric Mixture of (6,6-Dimethylbicyclo[3.1.1]hept-2-ylmethyl)dimethyl(3-methyl-1*H*-inden-1-yl)silanes (9a/9b): To methylindene[55] (2.1064 g, 16.2 mmol) in tetrahydrofuran (20 mL) at 0 °C was added *n*BuLi (2.5 M in *n*-hexane, 6.6 mL, 16.3 mmol). The brownish green solution was stirred at room temperature for 4 h. The lithium salt was the added dropwise at 0 °C to a solution of the chiral chlorosilane (3.9218 g, 17.0 mmol) in tetrahydrofuran (10 mL). The resulting orange reaction mixture was stirred at room temperature for 2 h before saturated aqueous NH_4Cl solution (50 mL) was added. The layers formed were separated and the aqueous layer was further extracted with diethyl ether (30 mL). The combined organic layers were dried with Na_2SO_4, filtered and the solvents evaporated. The crude product was purified with silica gel column chromatography using hexane as eluent providing 2.7974 g (53%) of **9a/9b** (a mixture of two diastereomers) as a pale yellow oil. ^{1}H NMR (600 MHz, $CDCl_3$, 25 °C): δ = 7.43 (m, 1+1 H, arom. CH), 7.40 (m, 1+1 H, arom. CH), 7.28 (m, 1+1 H, arom. CH), 7.19 (m, 1+1 H, arom. CH), 6.30 (m, 1+1 H, olefinic CH in five-membered ring), 3.38 (m, 1+1 H, aliph. CH in five-membered ring), 2.23 (s, 3+3 H, CH_3 attached to five-membered ring), 2.01 (m, 2+2 H, 2 CH in pinenyl ring), 1.01 (m, 1+1 H, CH in pinenyl ring), 1.73 (m, 2+2 H, 2 CH in pinenyl ring), 1.67 (m, 1+1 H, CH in pinenyl ring), 1.55 (m, 1+1 H, CH in pinenyl ring), 1.32 (m, 2+2 H, 2 CH in pinenyl ring), 1.22 (m, 1+1 H, CH in pinenyl ring), 1.18 (s, 3 H, CH_3 in pinenyl ring), 1.17 (s, 3 H, CH_3 in pinenyl ring), 0.79 (s, 3 H, CH_3 in pinenyl ring), 0.78 (s, 3 H, CH_3 in pinenyl ring), 0.53 (m, 1+1 H, bridging CH between Si and pinenyl ring), 0.45 (m, 1+1 H, bridging CH between Si and pinenyl ring), –0.00 (s, 3 H, CH_3 attached to Si), –0.04 (s, 3 H, CH_3 attached to Si), –0.07 (s, 3 H, CH_3 attached to Si), –0.11 (s, 3 H, CH_3 attached to Si) ppm. ^{13}C NMR (150.9 MHz, $CDCl_3$, 25 °C): δ = 146.23 (2 C_q), 145.38 (2 C_q), 137.03 (2 C_q), 130.97 (2 olefinic CH in five-membered ring), 124.75 (2 arom. CH), 123.66 (2 arom. CH), 122.91 (2 arom. CH), 118.98 (2 arom. CH), 49.45 (CH in pinenyl ring), 49.33 (CH in pinenyl ring), 44.38 (aliph. CH in five-membered ring), 44.36 (aliph. CH in five-membered ring), 40.74 (2 CH in pinenyl ring), 39.66 (2 C_q in pinenyl ring), 31.76 (CH in pinenyl ring), 31.16 (CH in pinenyl ring), 27.06 (2 CH_3 in pinenyl ring), 25.74 (CH_2 in pinenyl ring), 25.62 (CH_2 in pinenyl ring), 24.90 (CH_2 in pinenyl ring), 24.88 (CH_2 in pinenyl ring), 23.08 (2 CH_2 in pinenyl ring), 22.77 (bridging CH_2 between Si and pinenyl ring), 22.70 (bridging CH_2 between Si and pinenyl ring), 20.16 (2 CH_3 in pinenyl ring), 13.09 (2 CH_3 attached to five-membered ring), –2.54 (CH_3 attached to Si), –2.74 (CH_3 attached to Si), –2.80 (CH_3 attached to Si), –3.03 (CH_3 attached to Si) ppm. ^{29}Si NMR (119.3 MHz, $CDCl_3$, 25 °C): δ = –4.13 (2 Si) ppm. EIMS (70 eV) calcd. for $C_{22}H_{32}Si$ 324.2273, found 324.2275.

Bis{3-[(7,7-Dimethylnorpinanylmethyl)dimethylsilyl]-1-methylindenyl}zirconium Dichlorides [(*pR*)(*pR*)-10a, (*pS*)(*pS*)-10b, (*pR*)(*pS*)-10c]: To a mixture of **9a/9b** (0.5294 g, 1.6 mmol) in diethyl ether (10 mL) at 0 °C was added *n*BuLi (2.5 M in *n*-hexane, 660 μL, 1.7 mmol). The pale orange solution was stirred at room temperature for 4 h. The reaction mixture was cooled to 0 °C and $ZrCl_4$ (0.2011 g, 0.9 mmol) was added. After stirring the suspension at room temperature for 20 h, the solvent was removed under vacuum. The residue was dissolved in dichloromethane, filtered and the filtrate was evaporated. The residue was dried in vacuo and the crude product was analyzed with 600 MHz ^{1}H NMR spectroscopy. ^{1}H NMR (600 MHz, $CDCl_3$, 25 °C): δ = 7.71 (m, 4 H, arom. CH in **10a** and/or **10b** and/or **10c**), 7.54 (m, 4 H, arom. CH in **10a** and/or **10b** and/or **10c**), 7.47 (m, 4 H, arom. CH in **10a** and/or **10b** and/or **10c**), 7.38 (m, 2 H, arom. CH in **10a** and/or **10b** and/or **10c**), 7.29 (m, 2 H, arom. CH in **10a** and/or **10b** and/or **10c**), 7.22 (m, 8 H, arom. CH in **10a** and/or **10b** and/or **10c**), 6.41 (m, 2 H, olefinic CH in five-membered ring in **10a** and/or **10b** and/or **10c**), 5.92 (m, 4 H, olefinic CH in five-membered ring in **10a** and/or **10b** and/or **10c**), 2.51 (m, 6 H, CH_3 attached to five-membered ring in **10a** and/or **10b** and/or **10c**), 2.31 (m, 12 H, CH_3 attached to five-membered ring in **10a** and/or **10b** and/or **10c**), 1.10 (m, 18 H, CH_3 in pinenyl ring in **10a** and/or **10b** and/or **10c**), 0.72 (m, 12 H, bridging CH between Si and pinenyl ring in **10a** and/or **10b** and/or **10c**), 0.64 (m, 18 H, CH_3 in pinenyl ring in **10a** and/or **10b** and/or **10c**), 0.38 (m, 36 H, CH_3 attached to Si in **10a** and/or **10b** and/or **10c**), 1.95–1.12 (m, 54 H, aliph. CH in pinenyl ring in **10a** and/or **10b** and/or **10c**), signals from the aliph. protons in pinenyl ring in **10a**, **10b** and **10c** are overlapping with each other and other signals in the region 1.95–1.12 ppm. From the Cp-H (5.92, 6.28 and 6.41 ppm) and Cp-CH_3 signals (2.21, 2.31 and 2.51 ppm) it could be calculated that the amount of the mixture of formed metallocenes was approximately 70%.

Mixture of a Diastereomeric Mixture of 2-[6,6-(Dimethylbicyclo[3.1.1]hept-2-ylmethyl)dimethylsilyl]-1-trimethylsilyl-1*H*-indenes (11a/11b) and 2-[(6,6-dimethylbicyclo[3.1.1]hept-2-ylmethyl)dimethylsilyl]-3-trimethylsilyl-1*H*-indene (12): To **1** (3.3786 g, 10.9 mmol) in tetrahydrofuran (40 mL) at 0 °C was added *n*BuLi (2.5 M in *n*-hexane, 4.4 mL, 11.0 mmol). The orange solution was stirred at room temperature for 3 h and to this solution was added dropwise chlorodimethylsilane (1.4 mL, 10.9 mmol) in tetrahydrofuran (10 mL) at 0 °C. The resulting brownish-orange reaction mixture was stirred at room temperature for 1.5 h before saturated aqueous NH_4Cl solution (50 mL) was added. The layers formed were separated and the aqueous layer was further extracted with diethyl ether (30 mL). The combined organic layers were dried with Na_2SO_4, filtered and the solvents evaporated to dryness. The crude product was purified with silica gel column chromatography using hexane as eluent providing 2.9362 g (71%) of a mixture of **11a/11b** (a mixture of two diastereomers) and **12** as an orange oil. The chemical shifts are largely overlapping both in the ^{1}H NMR and in the ^{13}C NMR spectrum. ^{1}H NMR (600 MHz, $CDCl_3$, 25 °C): δ = 7.53–6.70 (m, 14 H, arom. CH in six-membered ring and olefinic CH in five-membered ring in **11a**, **11b** and **12**), 3.77–3.49 (m, 4 H, aliph. CH in five-membered ring in **11a**, **11b** and **12**), 2.06–1.30 (m, 27 H, aliph. CH in pinenyl ring in **11a**, **11b** and **12**), 1.20 (m, 9 H, CH_3 in pinenyl ring in **11a**, **11b** and **12**), 0.95–0.77 (m, 15 H, CH_3 in pinenyl ring in **11a**, **11b** and **12** and bridging CH between Si and pinenyl ring in **11a**, **11b** and **12**), 0.32 (m, 18 H, CH_3 attached to Si in **11a**, **11b** and **12**), 0.05 (m, 27 H, CH_3 attached to Si in **11a**, **11b** and **12**) ppm. ^{13}C NMR (150.9 MHz, $CDCl_3$, 25 °C): δ = 151.09, 150.95, 149.14, 148.99, 144.83 (10 overlapping C_q in **11a**, **11b** and **12**), 140.26–140.07 and 124.77–120.78 (12 arom. CH in six-membered ring and 2 olefinic CH in five-membered ring in **11a**, **11b** and **12**), 51.21–48.71 (aliph. CH in pinenyl ring in **11a**, **11b** and **12**), 40.77–40.64 (aliph. CH in pinenyl ring in **11a**, **11b** and

 © 2005 Wiley-VCH Verlag GmbH & Co. KGaA, Weinheim

12), 39.68–39.58 (C_q in **11a**, **11b** and **12**), 31.39–30.65 (aliph. CH in pinenyl ring in **11a**, **11b** and **12**), 27.04 (CH_3 in pinenyl ring in **11a**, **11b** and **12**), 24.93–22.79 (aliphtic CH in pinenyl ring in **11a**, **11b** and **12**), 20.17–20.08 (CH_3 in pinenyl ring in **11a**, **11b** and **12**), 0.74 – (–2. 42) (CH_3 attached to Si in **11a**, **11b** and **12**) ppm. EIMS (70 eV) calcd. for $C_{24}H_{38}Si_2$ 382.2512, found 382.2510.

Mixture of [2-({[(1*S*,2*S*5*S*)-6,6-Dimethylbicyclo[3.1.1]hept-2-yl]-methyl}dimethylsilyl)indenyl]titanium Trichloride (13) and [1-(Trimethylsilyl)indenyl]titanium Trichlorides (14a and 14b): To a solution of a mixture of **11a**, **11b** and **12** (0.6153 g, 1.6 mmol) in dichloromethane (4 mL) at –78 °C was added $TiCl_4$·DCM (1.6 mL, 1.6 mmol) in drops. The resulting dark red reaction mixture was gradually warmed to room temperature and after stirring the reaction mixture at room temperature for 19 h the solvent was removed. The reaction product was crystallized from *n*-pentane at –78 °C yielding a 1:1:1 mixture of **13**, **14a** and **14b** as a black solid. ^{1}H NMR (250 MHz, $CDCl_3$, 25 °C): δ = 7.79 (m, 6 H, arom. CH in **13** and/or **14a** and/or **14b**), 7.51 (m, 6 H, arom. CH in **13** and/or **14a** and/or **14b**), 7.37 (6 H, olefinic CH in five-membered ring in **13**, **14a** and **14b**), 2.12 (m, 1 H, aliph. CH in pinenyl ring in **13**), 1.99 (m, 1 H, aliph. CH in pinenyl ring in **13**), 1.84 (m, 1 H, aliph. CH in pinenyl ring in **13**), 1.75 (m, 2 H, aliph. CH in pinenyl ring in **13**), 1.87 (m, 3 H, aliph. CH in pinenyl ring in **13**), 1.33 (m, 1 H, aliph. CH in pinenyl ring in **13**), 1.12 (s, 3 H, CH_3 in pinenyl ring in **13**), 0.85 (m, 2 H, bridging CH_2 between Si and pinenyl ring in **13**), 0.76 (s, 3 H, CH_3 in pinenyl ring in **13**), 0.46 (m, 24 H, CH_3 attached to Si in **13**, **14a** and **14b**).

Mixture of Diastereomeric Mixtures of 3-[(6,6-Dimethylbicyclo[3.1.1]hept-2-ylmethyl)dimethylsilyl]-1-trimethylsilyl-1*H*-indenes (15a/15b) and 1-[(6,6-Dimethylbicyclo[3.1.1]hept-2-ylmethyl)dimethylsilyl]-3-trimethylsilyl-1*H*-indenes (16a/16b): To a diastereomeric mixture of 1-[dimethyl(7,7-dimethylnorpinanylmethyl)silyl]indene (**4a/4b**) (2.9742 g, 9.6 mmol) in tetrahydrofuran (30 mL) at 0 °C was added *n*BuLi (2.5 M in *n*-hexane, 3.9 mL, 9.7 mmol). The orange solution was stirred at room temperature for 3 h and to this solution was added dropwise chlorodimethylsilane (1.3 mL, 9.6 mmol) in tetrahydrofuran (8 mL) at 0 °C. The resulting yellowish-brown reaction mixture was stirred at room temperature for 1.5 h before saturated aqueous NH_4Cl solution (50 mL) was added. The layers formed were separated and the aqueous layer was further extracted with diethyl ether (30 mL). The combined organic layers were dried with Na_2SO_4, filtered and the solvents evaporated to dryness. The crude product was purified with silica gel column chromatography using hexane as eluent providing 2.3547g (76%) of a mixture of the diastereomeric mixtures **15a/15b** and **16a/16b** as an orange oil. The chemical shifts are largely overlapping both in the ^{1}H NMR and in the ^{13}C NMR spectrum. ^{1}H NMR (600 MHz, $CDCl_3$, 25 °C): δ = 7.56–7.18 (m, 16 H, arom. CH in **15a**, **15b**, **16a** and **16b**), 6.93–6.67 (m, 4 H, olefinic CH in five-membered ring in **15a**, **15b**, **16a** and **16b**), 3.62–3.43 (m, aliph. CH in five-membered ring in **15a**, **15b**, **16a** and **16b**), 2.23–1.30 (m, 36 H, aliph. CH in pinenyl ring in **15a**, **15b**, **16a** and **16b**), 1.16 (m, 12 H, CH_3 in pinenyl ring in **15a**, **15b**, **16a** and **16b**), 0.83 (m, 8 H, CH_2 bridging between Si and pinenyl ring in **15a**, **15b**, **16a** and **16b**), 0.78 (m, 12 H, CH_3 in pinenyl ring in **15a**, **15b**, **16a** and **16b**), 0.33 (m, 24 H, CH_3 attached to Si in **15a**, **15b**, **16a** and **16b**), –0.04 (m, 36 H, CH_3 attached to Si in **15a**, **15b**, **16a** and **16b**) ppm. ^{13}C NMR (150.9 MHz, $CDCl_3$, 25 °C): δ = 147.65, 146.58, 141.57 (12 overlapping C_q in **15a**, **15b**, **16a** and **16b**), 145.73–145.58 (4 overlapping olefinic CH in five-membered ring in **15a**, **15b**, **16a** and **16b**), 124.88–121.13 (16 overlapping aromatic CH in **15a**, **15b**, **16a** and **16b**), 49.48–46.44, 40.81–40.74, 31.50–31.14 (16 overlapping aliph. CH in five-membered ring and in pinenyl ring in **15a**, **15b**, **16a** and **16b**), 39.69 (4 C_q in pinenyl ring in **15a**, **15b**, **16a** and **16b**), 27.07 (4 CH_3 in pinenyl ring in **15a**, **15b**, **16a** and **16b**), 25.89–22.56 (12 overlapping CH_2 in pinenyl ring in **15a**, **15b**, **16a** and **16b**), 20.18 (4 CH_3 in pinenyl ring in **15a**, **15b**, **16a** and **16b**), –0.66 – (–3.09) (20 overlapping CH_3 attached to Si in **15a**, **15b**, **16a** and **16b**). EIMS (70 eV) calcd. for $C_{24}H_{38}Si_2$ 382.2512, found 382.2518.

Mixture of {1-{{[(1*S*,2*S*5*S*)-6,6-Dimethylbicyclo[3.1.1]hept-2-yl]-methyl}dimethylsilyl}indenyl}titanium Trichloride (17a and 17b) and [1-(Trimethylsilyl)indenyl]titanium Trichlorides (14a and 14b): To a solution of a mixture of **15a**, **15b**, **16a** and **16b** (0.6045 g, 1.6 mmol) in dichloromethane (4 mL) at –78 °C was added $TiCl_4$·DCM (1.6 mL, 1.6 mmol) in drops. The resulting dark red reaction mixture was gradually warmed into room temperature and after stirring the reaction mixture at room temperature for 19 h the solvent was removed. The crude product was analyzed with ^{1}H NMR (600 MHz, $CDCl_3$, 25 °C): δ = 7.90, 7.82, 7.57, 7.46, 7.38, 7.22 (m, 12 H, overlapping signals from aromatic CH in **17a** and **17b** and olefinic CH in five-membered ring in **17a** and **17b**), 7.82 (m, 4 H, arom. CH in **14a** and **14b**), 7.53 (m, 4 H, arom. CH in **14a** and **14b**), 7.38 (m, 4 H, olefinic CH in five-membered ring in **14a** and **14b**), 2.21–1.24 (m, 18 H, overlapping signals from aliph. CH in pinenyl ring in **17a** and **17b**), 1.18 (s, 3 H, CH_3 in pinenyl ring in **17a** or **17b**), 1.12 (m, 3 H, CH_3 in pinenyl ring in **17a** or **17b**), 0.88 (m, 4 H, bridging CH_2 between Si and pinenyl ring in **17a** or **17b**), 0.82 (s, 3 H, CH_3 in pinenyl ring in **17a** or **17b**), 0.73 (m, 3 H, CH_3 in pinenyl ring in **17a** or **17b**), 0.52 (m, 24 H, CH_3 attached to Si in **17a**, **17b**, **14a** and **14b**), 0.40 (m, 6 H, CH_3 attached to Si in **17a** and **17b**) ppm.

(6,6-Dimethylbicyclo[3.1.1]hept-2-en-2-ylmethyl)-(1*H*-inden-2-yl)dimethylsilane (22): To α-pinene potassium salt (4.4 mmol) in α-pinene (2.1 mL, 13.1 mmol) were added THF (2 mL) and 2-(chlorodimethylsilyl)indene (**21**) (0.9141g, 4.4 mmol) in THF (2 mL) at –72 °C. The resulting brown reaction mixture was taken into room temperature and stirred for 1 h before saturated aqueous NH_4Cl solution (50 mL) was added. The layers formed were separated and the aqueous layer was further extracted with diethyl ether (30 mL). The combined organic layers were dried with Na_2SO_4, filtered and the solvents evaporated. The excess α-pinene was separated from the crude product by distillation under reduced pressure. The residue was further purified with silica gel column chromatography using hexane as eluent providing 0.0378 g (3%) of **22** as a colorless oil. ^{1}H NMR (600 MHz, $CDCl_3$, 25 °C): δ = 7.49 (m, 1 H, arom. CH), 7.41 (m, 1 H, arom. CH), 7.28 (m, 1 H, arom. CH), 7.19 (m, 1 H, arom. CH), 7.12 (m, 1 H, olefinic CH in five-membered ring), 5.06 (m, 1 H, olefinic CH in pinenyl ring), 3.46 (m, 2 H, aliph. CH_2 in pinenyl ring), 2.35 (m, 1 H, aliph. CH in pinenyl ring), 2.22 (m, 2 H, 2 aliph. CH in pinenyl ring), 2.06 (m, 1 H, aliph. CH in pinenyl ring), 1.93 (m, 1 H, aliph. CH in pinenyl ring), 1.77 (d, J = 14.9 Hz, 1 H, aliph. CH between Si and pinenyl ring), 1.61 (d, J = 14.9 Hz, 1 H, aliph. CH between Si and pinenyl ring), 1.25 (s, 3 H, CH_3 in pinenyl ring), 1.18 (d, J = 9.1 Hz, 1 H, aliph. CH in pinenyl ring), 0.88 (s, 3 H, CH_3 in pinenyl ring), 0.24 (s, 3 H, CH_3 attached to Si), 0.23 (s, 3 H, CH_3 attached to Si) ppm. ^{13}C NMR (150.9 MHz, $CDCl_3$, 25 °C): δ = 148.60 (C_q), 146.92 (C_q), 145.76 (C_q), 145.22 (C_q), 141.16 (olefinic CH in five-membered ring), 126.37 (arom. CH), 124.83 (arom. CH), 123.77 (arom. CH), 120.95 (arom. CH), 114.69 (olefinic CH in pinenyl ring), 48.27 (aliph. CH in pinenyl ring), 42.67 (aliph. CH_2 in five-membered ring), 40.68 (aliph. CH in pinenyl ring), 38.07 (C_q), 31.96 (aliph. CH_2 in pinenyl ring), 31.52 (aliph. CH_2 in pinenyl ring), 27.33 (aliph. CH_2 between Si and pinenyl ring), 26.63 (CH_3 in pinenyl), 21.42 (CH_3 in pinenyl), –2.06 (CH_3 attached to Si), –2.23 (CH_3 attached to Si) ppm.

 © 2005 Wiley-VCH Verlag GmbH & Co. KGaA, Weinheim

^{29}Si NMR (119.3 MHz, $CDCl_3$, 25 °C): δ = –9.39 ppm. EIMS (70 eV) calcd. for $C_{21}H_{28}Si$ 308.1960, found 308.1965.

Mixture of a Diastereomeric Mixture of (6,6-Dimethylbicyclo[3.1.1]hept-2-en-2-ylmethyl)-(1*H*-inden-1-yl)dimethylsilanes (24a/24b) and (6,6-Dimethylbicyclo[3.1.1]hept-2-en-2-ylmethyl)-(3*H*-inden-1-yl)dimethylsilane (25): To α-pinene potassium salt (20.6 mmol) in α-pinene (9.8 mL, 62.0 mmol) were added THF (20 mL) and a diastereomeric mixture of 1-(chlorodimethylsilyl)indenes (**23a/23b**) (0.9141g, 4.4 mmol) in THF (40 mL) at –72 °C. The resulting dark brown reaction mixture was taken into room temperature and stirred there for 2 h before saturated aqueous NH_4Cl solution (70 mL) was added. The layers formed were separated and the aqueous layer was further extracted with diethyl ether (50 mL). The combined organic layers were dried with Na_2SO_4, filtered and the solvents evaporated. The residue was purified with silica gel column chromatography using hexane as eluent. The obtained yellow oil still contained some α-pinene, which was separated by distillation under reduced pressure. The yellow residue provided 1.3523 g (21%) of a mixture of diastereomers **24a/24b** and **25**. The amount of the minor product **25** was 15%. ^{1}H NMR (600 MHz, $CDCl_3$, 25 °C): δ = 7.67 (m, 1 H, arom CH in **25**), 7.62 (m, 5 H, arom. CH in **24a**, **24b** and **25**), 7.43 (m, 1 H, arom. CH in **25**), 7.39 (m, 2 H, arom. CH in **24a** and **24b** or 2 arom. CH in **24a** or **24b**), 7.32 (m, 3 H, arom. CH in **24a** and **24b** or 2 arom. CH in **24a** or **24b** and arom. CH in **25**), 7.07 (m, 2 H, olefinic CH in five-membered ring in **24a** and **24b**), 6.90 (m, 1 H, olefinic CH in five-membered ring in **25**), 6.81 (m, 2 H, olefinic CH in five-membered ring in **24a** and **24b**), 5.22 (m, 3 H, olefinic CH in pinenyl ring in **24a**, **24b** and **25**), 3.71 (m, 2 H, aliph. CH in five-membered ring in **24a** and **24b**), 3.54 (m, 2 H, aliph. CH_2 in five-membered ring in **25**), 2.51 (m, 2 H, aliph. CH in pinenyl in **24a** and **24b**), 2.46 (m, 1 H, aliph. CH in pinenyl in **25**), 2.39 (m, 4 H, aliph. CH_2 in pinenyl in **24a** and **24b**), 2.23 (m, 2 H, aliph. CH in pinenyl in **24a** and **24b**), 2.05 (m, 3 H, aliph. CH in pinenyl in **24a** and **24b** and aliph. CH between Si and pinenyl ring in **25**), 1.86 (m, 1 H, aliph. CH between Si and pinenyl ring in **25**), 1.76 (d, J = 13.5 Hz, 1 H, aliph. CH between Si and pinenyl ring in **24a** or **24b**), 1.71 (d, J = 13.5 Hz, 1 H, aliph. CH between Si and pinenyl ring in **24a** or **24b**), 1.59 (d, J = 13.5 Hz, 1 H, aliph. CH between Si and pinenyl ring in **24a** or **24b**), 1.53 (d, J = 13.5 Hz, 1 H, aliph. CH between Si and pinenyl ring in **24a** or **24b**), 1.42 (s, 9 H, CH_3 in pinenyl ring **24a**, **24b** and **25**), 1.35 (m, 4 H, 2 aliph. CH in pinenyl ring in **24a** and **24b**), 1.06 (s, 9 H, CH_3 in pinenyl ring **24a**, **24b** and **25**), 0.49 (s, 6 H, CH_3 attached to Si in **25**), 0.13 (s, 3 H, CH_3 attached to Si in **24a** or **24b**), 0.10 (s, 3 H, CH_3 attached to Si in **24a** or **24b**), 0.04 (s, 3 H, CH_3 attached to Si in **24a** or **24b**), 0.01 (s, 3 H, CH_3 attached to Si in **24a** or **24b**). Almost all signals from the aliph. protons in pinenyl ring (except signal from one CH) in **25** are overlapping with signals from **24a/24b** and the chemical shifts of these overlapping signals are not listed here ppm. ^{13}C NMR (150.9 MHz, $CDCl_3$, 25 °C): δ = 148.11 (C_q in **25**), 145.34 (C_q in **24a** or **24b**), 145.30 (C_q in **24a** or **24b**), 145.11 (C_q in **25**), 144.73 (C_q in **24a** or **24b**), 144.67 (C_q in **24a** or **24b** and olefinic CH in five-membered ring in **25**), 144.60 (C_q in **25**), 144.53 (C_q in **25**), 144.33 (C_q in **24a** or **24b**), 144.27 (C_q in **24a** or **24b**), 135.60 (olefinic CH in five-membered ring in **24a** and **24b**), 129.12 (olefinic CH in five-membered ring in **24a** or **24b**), 129.09 (olefinic CH in five-membered ring in **24a** or **24b**), 126.16 (arom. CH in **25**), 124.92 (arom. CH in **24a** and **24b**), 124.36 (arom. CH in **25**), 123.83 (arom. CH in **25**), 123.77 (arom. CH in **24a** and **24b**), 122.87 (arom. CH in **24a** and **24b**), 122.16 (arom. CH in **25**), 121.17 (arom. CH in **24a** and **24b**), 115.13 (olefinic CH in pinenyl ring in **24a** and **24b**), 114.72 (olefinic CH in pinenyl ring in **25**), 48.25 (aliph. CH in pinenyl ring in **24a** or **24b**), 48.20 (aliph. CH in pinenyl ring in **24a** or **24b**), 45.73 (aliph. CH in five-membered ring in **24a** or **24b**), 45.72 (aliph. CH in five-membered ring in **24a** or **24b**), 40.86 (aliph. CH_2 in five-membered ring in **25**), 40.65 (aliph. CH in pinenyl ring in **24a** or **24b**), 40.63 (aliph. CH in pinenyl ring in **24a** or **24b**), 38.00 (C_q in **24a** and **24b**), 37.97 (C_q in **25**), 31.97 (aliph. CH_2 in pinenyl ring in **24a** or **24b**), 31.94 (aliph. CH_2 in pinenyl ring in **24a** or **24b**), 31.56 (aliph. CH_2 in pinenyl ring in **24a** and **24b**), 26.85 (aliph. CH_2 between Si and pinenyl ring in **25**), 26.61 (CH_3 in pinenyl ring in **24a**, **24b** and **25**), 25.85 (aliph. CH_2 between Si and pinenyl ring in **24a** or **24b**), 25.79 (aliph. CH_2 between Si and pinenyl ring in **24a** or **24b**), 21.41 (CH_3 in pinenyl ring in **24a**, **24b** and **25**), –2.10 (CH_3 attached to Si in **25**), –2.45 (CH_3 attached to Si in **25**), –3.56 (CH_3 attached to Si in **24a** or **24b**), –3.65 (CH_3 attached to Si in **24a** or **24b**), –3.88 (CH_3 attached to Si in **24a** or **24b**), –3.97 (CH_3 attached to Si in **24a** or **24b**). Almost all signals from the aliph. carbons in pinenyl ring (except signal from quaternary carbon) in **25** are overlapping with signals from **24a/24b** and the chemical shifts of these overlapping signals are not listed here ppm. ^{29}Si NMR (119.3 MHz, $CDCl_3$, 25 °C): δ = 3.13 (Si in **24a** or **24b**), 3.09 (Si in **24a** or **24b**), –10.08 (Si in **25**) ppm. EIMS (70 eV) calcd. for $C_{21}H_{28}Si$ 308.1960, found 308.1965.

Dehydropolymerization of Phenylsilane. General Procedure: A tube was charged with 1 mol-% of the metallocene catalyst, evacuated and backfilled with argon. Phenylsilane was added by syringe and the reaction mixture was degassed three times. The catalyst was activated at room temperature by addition of 2 mol-% of *n*BuLi. The reaction mixture was stirred at room temperature for 24 h. The formed viscous solution was dissolved in tetrahydrofuran and filtered through kiselguhr. The filtrate was concentrated in vacuo to leave the polysilane. The polymer obtained was analyzed by GC-MS, ^{1}H NMR, ^{29}Si{^{1}H} NMR and GPC.

Polymerization of Phenylsilane with [Cp_2ZrCl_2]: By applying the general procedure, [Cp_2ZrCl_2] (0.0111 g, 0.04 mmol), *n*BuLi (31 μL, 0.08 mmol) and phenylsilane (480 μL, 3.86 mmol) gave 0.41 g (98%) of polysilane as a yellow, highly viscous oil.

Polymerization of Phenylsilane with 2: By applying the general procedure, **2** (0.0943 g, 0.12 mmol), *n*BuLi (97 μL, 0.24 mmol) and phenylsilane (1.5 mL, 12.1 mmol) gave 1.26 g (97%) of polysilane as a yellow oil.

Polymerization of Phenylsilane with 3: By applying the general procedure, **3** (0.060 g, 0.08 mmol), *n*BuLi (62 μL; 0,16 mmol) and phenylsilane (950 μL, 7.64 mmol) gave 0.38 g (46%) of polysilane as a pale yellow oil.

Polymerization of Phenylsilane with (*pR*)(*pS*)-5c: By applying the general procedure, (*pR*)(*pS*)-**5c** (0.0261 g, 0.03 mmol), *n*BuLi (27 μL, 0.07 mmol) and phenylsilane (420 μL, 3.34 mmol) gave 0.33 g (90%) of polysilane as a yellow oil.

Polymerization of Phenylsilane with (*pR*)(*pS*)-6c: By applying the general procedure, (*pR*)(*pS*)-**6c** (0.0125 g, 0.02 mmol), *n*BuLi (13 μL, 0.03 mmol) and phenylsilane (198 μL, 1.59 mmol) gave 0.04 g (25%) of polysilane as a yellow oil.

Polymerization of Ethylene and Propylene: The olefin polymerization reactions were performed in a steel reactor rinsed with 200 mL of a 0.3% methylaluminoxane (MAO) solution in toluene prior to use. After evacuation of the steel reactor, 200 mL of dry toluene was cannulated in. MAO was added to the reactor by syringe. The system was saturated with the gas (monomer) and after complete saturation and thermal equilibrium of the system (50 °C) the polymerization was started by adding the prepared catalyst solution (in toluene) to the reactor. Gas (monomer) was continuously added

 © 2005 Wiley-VCH Verlag GmbH & Co. KGaA, Weinheim

and the pressure was kept constant during the polymerization reaction and the gas consumption was monitored. The polymerization was quenched by adding the reaction mixture to a dilute hydrochloric acid/methanol mixture. The produced polyethylene, which was insoluble in toluene, was washed with a dilute hydrochloric acid/methanol mixture, filtered, washed further with methanol, filtered and dried at 60 °C overnight. The polypropylene produced was mixed with a dilute hydrochloric acid/methanol mixture and the formed layers were separated and the polypropylene was further washed two times with methanol. The oily polypropylene obtained was dried under vacuum.

Methyl- and Ethyl- Carboalumination of 1-Octene. General Procedure: In a glove box, trimethylaluminum or triethylaluminum was placed in a reaction vessel followed by addition of a catalyst solution in dichloromethane (3 mL) under argon atmosphere. To this mixture was then added 1-octene and the reaction mixture was stirred at room temperature for 19 h. After cooling to 0 °C, oxygen was bubbled through the solution until all volatiles were evaporated. The resulting yellow oil was treated with 15% aqueous NaOH solution and extracted with diethyl ether (40 mL). The organic layer was dried with $NaSO_4$, filtered and the solvents evaporated to dryness. The crude product was purified by silica gel column chromatography (eluent: 1:1 diethyl ether/hexane).

Synthesis of 2-Methyl-1-octanol Using 2 or (*pR*)(*pS*)-5c: By applying the general procedure, 1-octene (157 μL, 1 mmol), trimethylaluminum (96 μL, 1 mmol) and **2** (0.0623 g, 0.08 mmol) or (*pR*)(*pS*)-**5c** (0.0623 g, 0.08 mmol) gave after purification by column chromatography 2-methyl-1-octanol as a colorless oil in 8% (11.7 mg) and 18% (26.2 mg) yields, respectively. ^{1}H NMR (600 MHz, $CDCl_3$, 25 °C): δ = 3.49 (m, 1 H, CH next to OH), 3.40 (m, 1 H, CH next to OH), 2.03 (br. s, 1 H, OH), 1.60 (m, 1 H, CH), 1.38 (m, 2 H, 2 CH), 1.25 (m, 7 H, 3 CH_2 and CH), 1.08 (m, 1 H, CH), 0.90 (d, J = 6.7 Hz, 3 H, CH_3), 0.86 (t, J = 6.9 Hz, 3 H, CH_3) ppm. ^{13}C NMR (150.9 MHz, $CDCl_3$, 25 °C): δ = 68.64 (CH_2–OH), 35.98 (CH), 33.23 (CH_2), 31.96 (CH_2), 29.71 (CH_2), 27.04 (CH_2), 22.88 (CH_2), 16.69 (CH_3), 14.29 (CH_3). EIMS (30eV) calcd. for $C_{19}H_{20}O$ 144.1514, found 144.1499 (reaction using **2**), found 144.1487 (reaction using (*pR*)(*pS*)-**5c**). Enantiomeric excesses were determined from the ^{1}H NMR spectra of the esters formed with (*S*)-(+)-MTPA-Cl using a literature procedure.[54] For the reaction catalyzed by complex **2**: *ee* = 0.5%, $[a]_D^{24}$ = +0.09 (c = 0.0117 g/mL $CHCl_3$). For the reaction catalyzed by (*pR*)(*pS*)-**5c**: *ee* = 3%, $[a]_D^{24}$ = –0.6 (c = 0.0120 g/mL $CHCl_3$).

Synthesis of 2-Ethyl-1-octanol Using 2 or (*pR*)(*pS*)-5c: By applying the general procedure, 1-octene (157 μL, 1 mmol), triethylaluminum (137 μL, 1 mmol) and **2** (0.0623 g, 0.08 mmol) or (*pR*)(*pS*)-**5c** (0.0623 g, 0.08 mmol) gave after purification by column chromatography 2-ethyl-1-octanol as a colorless oil in 11% (16.8 mg) and 16% (26.0 mg) yields, respectively. ^{1}H NMR (600 MHz, $CDCl_3$, 25 °C): δ = 3.54 (m, 2 H, CH_2 next to OH), 1,37 (m, 3 H, CH and CH_2 in ethyl), 1,27 (m, 11 H, 5 CH_2 and OH), 0,88 (m, 6 H, 2 CH_3) ppm. ^{13}C NMR (150.9 MHz, $CDCl_3$, 25 °C): δ = 65.55 (CH_2–OH), 42.24 (CH), 32.03 (CH_2), 30.62 (CH_2), 29.89 (CH_2), 27.02 (CH_2), 23.48 (CH_2 in ethyl), 22.82(CH_2), 14.30 (CH_3 in ethyl), 11.58 (CH_3). EIMS (30eV) calcd. for $C_{10}H_{22}O$ 158.1671, found 158.1639 (reaction using **2**), found 158.1655 (reaction using (*pR*)(*pS*)-**5c**). Enantiomeric excesses were determined from the ^{1}H NMR spectra of the esters formed with (*S*)-(+)-MTPA–Cl using a literature procedure.[54] For the reaction catalyzed by complex **2**: *ee* = 10%, $[a]_D^{24}$ = +0.48 (c = 0.00084 g/mL $CHCl_3$). For the reaction catalyzed by (*pR*)(*pS*)-**5c**: *ee* = 5%, $[a]_D^{24}$ = –0.18 (c = 0.0109 g/mL $CHCl_3$).

Acknowledgments

Financial support from the Neste Research Foundation is gratefully acknowledged. We also thank Mr. Markku Reunanen, Mrs. Päivi Pennanen, Mr. Mattias Roslund, Mr. Esa Kokko and Mr. Mikko Lankinen for their assistance with the ESIMS, EIMS, NMR and GPC-analyses.

[1] L. Resconi, L. Cavallo, A. Fait, F. Piemontesi, *Chem. Rev.* **2000**, *100*, 1253–1346.
[2] G. W. Coates, *Chem. Rev.* **2000**, *100*, 1223–1252.
[3] S. Lin, R. M. Waymouth, *Acc. Chem. Res.* **2002**, *35*, 765–773.
[4] G. W. Coates, R. M. Waymouth, *J. Am. Chem. Soc.* **1991**, *113*, 6270–6271.
[5] G. W. Coates, R. M. Waymouth, *J. Am. Chem. Soc.* **1993**, *115*, 91–98.
[6] A. H. Hoveyda, J. P. Morken, *Angew. Chem. Int. Ed. Engl.* **1996**, *35*, 1263–1284.
[7] A. H. Hoveyda, J. P. Morken, in *Metallocenes – Synthesis Reactivity, Applications* (Eds.: A. Togni, R. L. Halterman), Wiley-VCH, Weinheim, **1998**, vol. 2, chapter 10.
[8] J. P. Morken, M. T. Didiuk, A. H. Hoveyda, *J. Am. Chem. Soc.* **1993**, *115*, 6997–6998.
[9] D. Y. Kondakov, E.-i. Negishi, *J. Am. Chem. Soc.* **1995**, *117*, 10771–10772.
[10] D. Y. Kondakov, E.-i. Negishi, *J. Am. Chem. Soc.* **1996**, *118*, 1577–1578.
[11] K. H. Shaughnessy, R. M. Waymouth, *Organometallics* **1998**, *17*, 5728–5745.
[12] P. Wipf, S. Ribe, *Org. Lett.* **2000**, *2*, 1713–1716.
[13] P. Wipf, S. Ribe, *Org. Lett.* **2001**, *3*, 1503–1505.
[14] R. L. Halterman, K. P. C. Vollhardt, M. E. Welker, D. Bläser, R. Boese, *J. Am. Chem. Soc.* **1987**, *109*, 8105–8107.
[15] R. L. Halterman, Z. Chen, *J. Org. Chem.* **1994**, *59*, 2642–2644.
[16] C. A. Willoughby, S. L. Buchwald, *J. Am. Chem. Soc.* **1994**, *116*, 8952–8965.
[17] M. B. Carter, B. Schiott, A. Gutiérrez, S. L. Buchwald, *J. Am. Chem. Soc.* **1994**, *116*, 11667–11670.
[18] C. A. Willoughby, S. L. Buchwald, *J. Am. Chem. Soc.* **1994**, *116*, 11703–11714.
[19] S. L. Colletti, R. L. Halterman, *Tetrahedron Lett.* **1992**, *33*, 1005–1008.
[20] S. L. Colletti, R. L. Halterman, *J. Organomet. Chem.* **1993**, *455*, 99–106.
[21] F. R. W. P. Wild, M. Wasiucionek, G. Huttner, H. H. Brintzinger, *J. Organomet. Chem.* **1985**, *288*, 63–67.
[22] G. Erker, M. Aulbach, M. Knickmeier, D. Wingbermühle, C. Krüger, M. Nolte, S. Werner, *J. Am. Chem. Soc.* **1993**, *115*, 4590–4601.
[23] G. Erker, M. Aulbach, C. Krüger, S. Werner, *J. Organomet. Chem.* **1993**, *450*, 1–7.
[24] M. Knickmeier, G. Erker, T. Fox, *J. Am. Chem. Soc.* **1996**, *118*, 9623–9630.
[25] R. L. Halterman, D. R. Fahey, E. F. Bailly, D. W. Dockter, O. Stenzel, J. L. Shipman, M. A. Khan, S. Dechert, H. Schumann, *Organometallics* **2000**, *19*, 5464–5470.
[26] H. Schumann, O. Stenzel, S. Dechert, R. L. Halterman, *Organometallics* **2001**, *20*, 1983–1991.
[27] R. L. Halterman, L. D. Crow, *Tetrahedron Lett.* **2003**, *44*, 2907–2909.
[28] S. Silver, E. Johansson, R. Sjöholm, R. Leino, *Tetrahedron Lett.* **2004**, *45*, 249–252.
[29] C. Fritze, M. Knickmeier, G. Erker, F. Zaegel, B. Gautheron, P. Meunier, L. A. Paquette, *Organometallics* **1995**, *14*, 5446–5449.
[30] M. D. Bruce, G. W. Coates, E. Hauptman, R. M. Waymouth, J. W. Ziller, *J. Am. Chem. Soc.* **1997**, *119*, 11174.

 © 2005 Wiley-VCH Verlag GmbH & Co. KGaA, Weinheim

[31] R. Leino, H. J. G. Luttikhedde, A. Lehtonen, R. Sillanpää, A. Penninkangas, J. Strandén, J. Mattinen, J. H. Näsman, *J. Organomet. Chem.* **1998**, *558*, 171–179.
[32] S. Knüppel, J.-L. Fauré, G. Erker, G. Kehr, M. Nissinen, R. Fröhlich, *Organometallics* **2000**, *19*, 1262–1268.
[33] P. Beagley, P. Davies, H. Adams, C. White, *Can. J. Chem.* **2001**, *79*, 731–741.
[34] C. A. Bradley, E. Lobkovsky, J. A. Chirik, *J. Am. Chem. Soc.* **2003**, *125*, 8110–8111.
[35] C. A. Bradley, S. Flores-Torres, E. Lobkovsky, H. D. Abruña, P. J. Chirik, *Organometallics* **2004**, *23*, in press.
[36] G. M. Fern, S. Klaib, O. J. Curnow, H. Lang, *J. Organomet. Chem.* **2004**, *689*, 1139–1144.
[37] L. Brandsma, *Preparative Polar Organometallic Chemistry 2*, Springer-Verlag, Berlin, **1990**, p. 38.
[38] L. Resconi, PCT Int. Appl. (**2000**) WO 2000075151.
[39] T. Weiß, S. Becke, H. Sachse, G. Rheinwald, H. Lang, *Inorg. Chem. Commun.* **2002**, *5*, 159–162.
[40] T. D. Tilley, *Acc. Chem. Res.* **1993**, *26*, 22–29.
[41] M. A. Brook, in *Silicon in Organic, Organometallic and Polymer Chemistry*, John Wiley & Sons, New York, **1999**, pp. 350–351 and references cited therein.
[42] C. Aitken, J. F. Harrod, E. Samuel, *J. Organomet. Chem.* **1985**, *279*, C11–C13.
[43] J. P. Banovetz, K. M. Stein, R. M. Waymouth, *Organometallics* **1991**, *10*, 3430–3432.
[44] T. Imori, T. D. Tilley, *Polyhedron* **1994**, *13*, 2231–2243.
[45] N. Choi, S. Onozawa, T. Sakakura, M. Tanaka, *Organometallics* **1997**, *16*, 2765–2767.
[46] V. K. Dioumaev, K. Rahimian, F. Gauvin, J. F. Harrod, *Organometallics* **1999**, *18*, 2249–2255.
[47] R. M. Shaltout, J. Y. Corey, *Tetrahedron* **1995**, *51*, 4309–4320.
[48] J. L. Huhmann, J. Y. Corey, N. P. Rath, *J. Organomet. Chem.* **1997**, *533*, 61–72.
[49] B. J. Grimmond, J. Y. Corey, *Organometallics* **1999**, *18*, 2223–2229.
[50] B. J. Grimmond, N. P. Rath, J. Y. Corey, *Organometallics* **2000**, *19*, 2975–2984.
[51] S. Huo, E.-i. Negishi, *Org. Lett.* **2001**, *3*, 3253–3256.
[52] M. Magnin-Lachaux, Z. Tan, B. Liang, E.-i. Negishi, *Org. Lett.* **2004**, *6*, 1425–1427.
[53] E.-i. Negishi, Z. Tan, B. Liang, T. Novak, *Proc. Natl. Acad. Sci. USA* **2004**, *101*, 5782–5787.
[54] J. A. Dale, D. L. Dull, H. S. Mosher, *J. Org. Chem.* **1969**, *34*, 2543–2549.
[55] T. E. Ready, J. C. W. Chien, M. D. Rausch, *J. Organomet. Chem.* **1996**, *519*, 21–28.
[56] D. Wang, T. H. Chang, *Tetrahedron Lett.* **1983**, *24*, 1573–1576.
[57] T. Aoki, K. Shinohara, E. Oikawa, *Makromol. Chem. Rapid Commun.* **1992**, *13*, 565–570.

Received: October 19, 2004

 © 2005 Wiley-VCH Verlag GmbH & Co. KGaA, Weinheim

Dinuclear Copper(II) Complexes of Two Homologous Pyrazine-Based Bis(terdentate) Diamide Ligands

Julia Klingele (née Hausmann),[a] Boujemaa Moubaraki,[b] Keith S. Murray,[b] John F. Boas,[c] and Sally Brooker*[a]

Keywords: N ligands / Copper / Amides / Pyrazine / Hexafluorosilicate

The 1:1 reactions of the new bis(terdentate) diamide ligand *N*,*N*′-bis(2-pyridylmethyl)pyrazine-2,5-dicarboxamide ($H_2\mathbf{L^1}$) and its higher homologue *N*,*N*′-bis[2-(2-pyridyl)ethyl]-pyrazine-2,5-dicarboxamide ($H_2\mathbf{L^2}$) with $Cu(BF_4)_2{\cdot}4H_2O$ in the absence of added base have consistently afforded dicopper(II) complexes of the doubly deprotonated ligands $(\mathbf{L^1})^{2-}$ and $(\mathbf{L^2})^{2-}$. The complex $[Cu^{II}_2(\mathbf{L^2})(H_2O)_2(MeCN)_2](BF_4)_2$ (**2a**) has been structurally characterised. Subsequently, reactions employing a correct stoichiometric 2:1 metal-to-ligand ratio in MeCN have afforded bulk samples of the dinuclear complexes. The compounds $[Cu^{II}_2(\mathbf{L^1})(MeCN)_2(H_2O)_2](BF_4)_2{\cdot}H_2O$ (**1a**·H_2O) and $[Cu^{II}_2(\mathbf{L^2})(H_2O)_4(BF_4)_2]{\cdot}2H_2O$ (**2b**·$2H_2O$) have been structurally characterised. While complex **1a**·H_2O of the lower ligand homologue exhibits very weak antiferromagnetic spin coupling ($J = -0.24$ cm^{-1}), complex **2b** of the higher ligand homologue exhibits very weak ferromagnetic spin coupling ($J = +0.67$ cm^{-1}). EPR studies have been carried out on polycrystalline powders and frozen DMF solutions of **1a**·H_2O and **2b**·$2H_2O$. The EPR spectra of the polycrystalline powders indicate the presence of dipolar broadening and weak intermolecular exchange, while those of the frozen DMF solutions are characteristic of dipolar-coupled Cu^{II} pairs within the dinuclear molecules, with no evidence of intra- or intermolecular exchange. The spectral simulations confirm that the binuclear structure and the Cu···Cu distances are retained in frozen solution. Dinuclear SiF_6^{2-} containing compounds, $[Cu^{II}_2(\mathbf{L^1})(H_2O)_4](SiF_6)$ (**1b**) and $\{[Cu^{II}_2(\mathbf{L^1})(H_2O)_2(\mu\text{-}SiF_6)]{\cdot}4H_2O\}_\infty$ (**1c**·$4H_2O$), were obtained serendipitously, in nearly quantitative yield, by the 2:1 reaction of $Cu(BF_4)_2{\cdot}4H_2O$ with $H_2\mathbf{L^1}$ in H_2O. The unexpected SiF_6^{2-} anions were generated in the course of the reaction by partial hydrolysis of the BF_4^- anions employed, thus forming traces of HF which reacted with the glassware.

(© Wiley-VCH Verlag GmbH & Co. KGaA, 69451 Weinheim, Germany, 2005)

Introduction

For the formation of grid-type complexes relatively rigid ligand systems with a repeating linear array of bi- or terdentate binding pockets are necessary.[1] With regard to advanced materials, grid-type complexes containing octahedral rather than tetrahedral metal ions are expected to give rise to a broader range of potentially useful properties. The design of ligands with terdentate rather than bidentate binding pockets is therefore desirable. Grid-type complexes of relatively simple pyrimidine-bridged bis(terdentate) ligands, which exhibit intriguing electronic[2] or magnetic properties,[3] for example, have been reported by Lehn and co-workers. The use of amide-based ligands for the formation of grid-type complexes offers advantages over other systems as amides can usually be synthesised relatively easily. Apart from their ability to coordinate to metal ions, amide groups also reduce the degrees of freedom in a given ligand system.[4]

The two homologous pyrazine-based diamide ligands *N*,*N*′-bis(2-pyridylmethyl)pyrazine-2,5-dicarboxamide ($H_2\mathbf{L^1}$) and *N*,*N*′-bis[2-(2-pyridyl)ethyl]pyrazine-2,5-dicarboxamide ($H_2\mathbf{L^2}$) are relatively rigid, bis(terdentate) chelates with antiparallel coordinate vectors, and in theory they should be able to form [2 × 2] grid-type complexes of octahedral transition metal ions. Indeed, we have recently reported a cobalt(III) [2 × 2] grid-type complex of the doubly deprotonated ligand $(\mathbf{L^2})^{2-}$.[5] Likewise, copper(II)[6] and nickel(II)[7] [2 × 2] grid-type complexes of the ligand *N*,*N*′-bis(2-pyridylmethyl)pyrazine-2,3-dicarboxamide ($H_2\mathbf{L^3}$), which is isomeric to the lower ligand homologue $H_2\mathbf{L^1}$, have been reported recently. However, it has been found that attempts to isolate similar copper(II) [2 × 2] grid-type complexes of either $H_2\mathbf{L^1}$ or $H_2\mathbf{L^2}$, in the presence of base, consistently produced amorphous solids, which analysed as $[CuH\mathbf{L}]^{n+}{}_n$ (1 equivalent of base per ligand strand) and $[Cu_x\mathbf{L}_x]$ (2 equivalents of base per ligand strand) species.[8] These rather intractable solids have not been further characterised. In contrast, in the absence of added base, reactions

[a] Department of Chemistry, University of Otago,
P. O. Box 56, Dunedin, New Zealand
Fax: +64-3-479-7906
E-mail: sbrooker@alkali.otago.ac.nz
[a] School of Chemistry, Building 23, Monash University, Clayton, Victoria 3800, Australia
[a] School of Physics and Materials Engineering, Monash University,
P. O. Box 27, Clayton, Victoria 3800, Australia
Supporting information for this article is available on the WWW under http://www.eurjic.org or from the author.

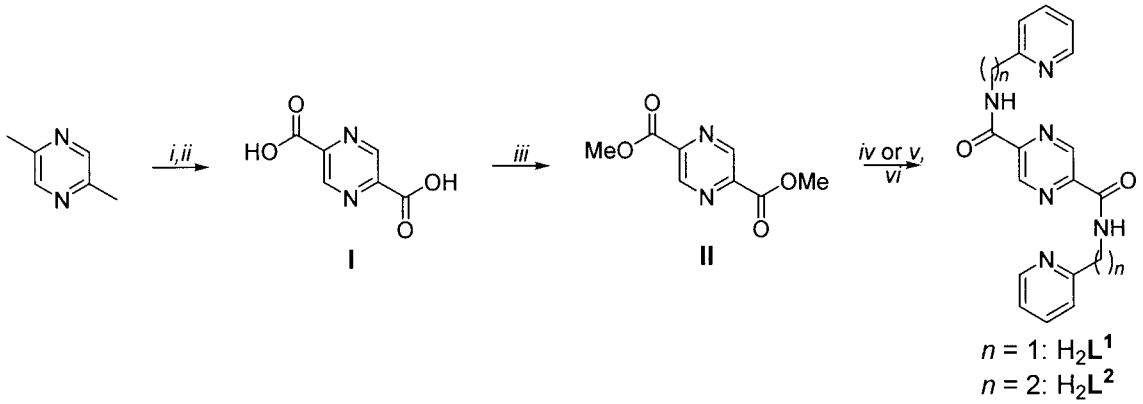

Scheme 1. Synthesis of the ligands $H_2\mathbf{L^1}$ and $H_2\mathbf{L^2}$. Reagents and conditions: (*i*) SeO_2, pyridine/H_2O, (10:1), reflux; (*ii*) H_2O, filtration; (*iii*) $SOCl_2$, MeOH, reflux; (*iv*) 2.2 equiv. 2-(aminomethyl)pyridine, MeOH, 80–90°, open flask; (*v*) 2.2 equiv. 2-(2-aminoethyl)pyridine, MeOH, 80–90°C, open flask; (*vi*) filtration.

of copper(II) with these ligands consistently resulted in the isolation of crystalline samples of dinuclear complexes of a single ligand strand, of the type $[Cu^{II}_2(\mathbf{L^1})(\text{co-ligand})_n]^{2+}$ or $[Cu^{II}_2(\mathbf{L^2})(\text{co-ligand})_n]^{2+}$, which are related to the dinuclear copper(II) complexes obtained by Fleischer and co-workers with the isomeric ligand *N*,*N*′-bis[2-(2-pyridyl)ethyl]pyrazine-2,3-dicarboxamide ($H_2\mathbf{L^4}$).[9,10] In this paper, we report the synthesis of the homologous diamide ligands $H_2\mathbf{L^1}$ and $H_2\mathbf{L^2}$ and describe the X-ray crystal structures of the five dinuclear copper(II) complexes $[Cu^{II}_2(\mathbf{L^1})(MeCN)_2(H_2O)_2]$-$(BF_4)_2\cdot H_2O$ (**1a**·H_2O), $[Cu^{II}_2(\mathbf{L^1})(H_2O)_4](SiF_6)$ (**1b**), $\{[Cu^{II}_2(\mathbf{L^1})(H_2O)_2(\mu\text{-}SiF_6)]\cdot 4H_2O\}_\infty$ (**1c**·$4H_2O$), $[Cu^{II}_2(\mathbf{L^2})(H_2O)_2(MeCN)_2](BF_4)_2$ (**2a**) and $[Cu^{II}_2(\mathbf{L^2})(H_2O)_4(BF_4)_2]\cdot 2H_2O$ (**2b**·$2H_2O$). The magnetic properties and EPR data of **1a**·H_2O and **2b** are also presented.

Results and Discussion

Ligand Syntheses

The ligand precursor, dimethyl pyrazine-2,5-dicarboxylate (**II**),[11,12] was synthesised, by modifying the literature procedure, from commercially available 2,5-dimethylpyrazine in a one-pot two-step procedure (Scheme 1). The first step consisted of the oxidation of the *α*-methyl groups with SeO_2 in aqueous pyridine to afford pyrazine-2,5-dicarboxylic acid (**I**).[11–13] The diacid **I** was not isolated in pure form as the crude product could be esterified with MeOH and $SOCl_2$ yielding analytically pure diester **II** as a crystalline material.

The potentially bis(terdentate) diamide ligands $H_2\mathbf{L^1}$ and $H_2\mathbf{L^2}$ were obtained by reacting the diester **II** with 2-(aminomethyl)pyridine or 2-(2-aminoethyl)pyridine, respectively, in a 1:2.2 molar ratio (Scheme 1). The reactions were carried out in MeOH solutions in open flasks, thus allowing most of the solvent to evaporate. The ligands $H_2\mathbf{L^1}$ and $H_2\mathbf{L^2}$ were obtained by filtration in ca. 80 and 70% yield, respectively, as colourless solids. Both compounds proved to be virtually insoluble in all common solvents at room temperature, but some solubility was observed in $CHCl_3$ and CH_2Cl_2 at room temperature and in MeOH, MeCN and DMF at reflux. However, the poor solubility of these two ligands did not preclude successful complexations being carried out (see below).

Dinuclear Copper(II) Complexes

Complexations of $H_2\mathbf{L^1}$ and $H_2\mathbf{L^2}$ with $Cu(BF_4)_2\cdot 4H_2O$ in a metal-to-ligand ratio of 1:1 in MeCN resulted in the isolation of 2:1 complexes of the doubly deprotonated ligands. Single crystals of $[Cu^{II}_2(\mathbf{L^2})(H_2O)_2(MeCN)_2](BF_4)_2$ (**2a**) suitable for an X-ray crystal structure determination were obtained by the vapour diffusion of Et_2O into the 1:1 MeCN reaction solution (Figure 1, Table 1, Table 2, Table 3 and Table 4).

Complex **2a** features two crystallographically independent but chemically very similar centrosymmetric dinuclear molecules. In each molecule the doubly deprotonated ligand acts as an $(N_3)_2$ bis(terdentate) chelate. Each copper(II) centre is in a distorted N_4O square-pyramidal coordination environment (τ[14] = 0.24, 0.41). The coordination sphere is made up of the equatorially coordinating N_3 terdentate coordination site of the deprotonated amide ligand, an H_2O co-ligand in the remaining equatorial position and a MeCN co-ligand at the apex. As observed in related amide complexes,[6,7,10,15–18] the $Cu–N_{amide}$ distances of **2a** [Cu(1)–N(2) 1.936(2) Å and Cu(2)–N(12) 1.929(2) Å] are shorter than the $Cu–N_{heterocycle}$ distances [$Cu–N_{py}$: Cu(1)–N(3) 2.011(3) Å, Cu(2)–N(13) 1.992(3) Å; $Cu–N_{pz}$: Cu(1)–N(1) 2.027(2) Å, Cu(2)–N(11) 2.021(2) Å]. The canting angles, formed between the mean plane of the pyridine ring and the mean plane of the pyrazine ring, are 33.4(1)° and 39.5(1)° for the two independent molecules Cu(1) and Cu(2), respectively. The intramolecular Cu···Cu distances [Cu(1)···Cu(1A) 6.784(2) Å and Cu(2)···Cu(2B) 6.756(2) Å] across the pyrazine bridge are about 0.1 Å shorter than that found in a related dicopper(II) complex of the chemically related ligand *N*,*N*′-bis(2-pyridylmethyl)pyrazine-2,3-dicarboxamide ($H_2\mathbf{L^3}$).[7] In complex **2a** the independent dinuclear subunits are $O_{water}–H\cdots O_{amide}$ intermolecularly hy-

 © 2005 Wiley-VCH Verlag GmbH & Co. KGaA, Weinheim

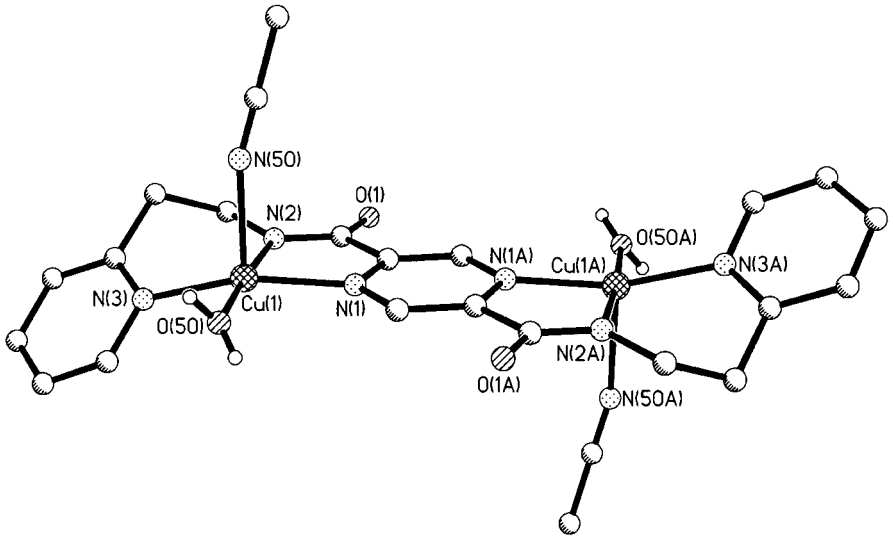

Figure 1. Molecular structure of one of the two independent cations, $[Cu^{II}_2(\mathbf{L^2})(H_2O)_2(MeCN)_2]^{2+}$, of complex **2a**. Hydrogen atoms, except those of the H_2O co-ligands, have been omitted for clarity. Symmetry operation used to generate equivalent atoms: (A) $1 - x$, $2 - y$, $1 - z$.

drogen-bonded, forming a 2D ribbon-like structure [$O_{water}\cdots O_{amide}$ 2.598 Å and 2.595 Å]. Parallel ribbons are connected through O_{water}–H···F–BF_2–F···H–O_{water} hydrogen bonds (Figure S1, Supporting Information; $O_{water}\cdots$F 2.738 Å and 2.801 Å).

As reactions, in the absence of base, employing metal-to-ligand ratios of 1:1 consistently afforded 2:1 products, the complexations of $H_2\mathbf{L^1}$ and $H_2\mathbf{L^2}$ were repeated using 2:1 molar metal-to-ligand ratios to isolate bulk materials (Scheme 2).

Vapour diffusion of Et_2O into the reaction solution containing the lower ligand homologue $H_2\mathbf{L^1}$ and $Cu(BF_4)_2\cdot 4H_2O$ in a 1:2 molar ratio in MeCN afforded the dinuclear compound $[Cu^{II}_2(\mathbf{L^1})(H_2O)_2](BF_4)_2$ (**1**) in 60% yield as a dark turquoise microcrystalline solid (Scheme 2). Single crystals of $[Cu^{II}_2(\mathbf{L^1})(MeCN)_2(H_2O)_2](BF_4)_2\cdot H_2O$ (**1a**·H_2O) (Figure 2, Table 1, Table 2, Table 3 and Table 4) suitable for an X-ray crystal structure determination were obtained by slow evaporation of the reaction solution.

The copper(II) coordination sphere in the centrosymmetric dinuclear complex in **1a**·H_2O is N_4O square-pyramidal, exhibiting only a slight distortion from the perfect geometry ($\tau^{[14]} = 0.06$). As in **2a**, the doubly deprotonated $(N_3)_2$ bis-(terdentate) ligand $(\mathbf{L^1})^{2-}$ in **1a**·H_2O encapsulates each copper(II) ion in an equatorial manner. Again, the copper(II) coordination sphere is completed by a MeCN and an H_2O co-ligand. Compared to complex **2a**, however, these co-ligands have switched their positions, so that in complex **1a**·H_2O the H_2O co-ligand coordinates axially and the MeCN co-ligand coordinates in the equatorial position. Owing to the increase in ligand rigidity due to the methylene instead of the ethylene linkers, the ligand backbone of complex **1a**·H_2O is much flatter than that in **2a**, showing a mean deviation of only 0.048 Å from the mean plane made up of all non-hydrogen atoms of the ligand, and a maximum deviation of only 0.082(4) Å for $C(10)_{(4\text{-}py)}$. The

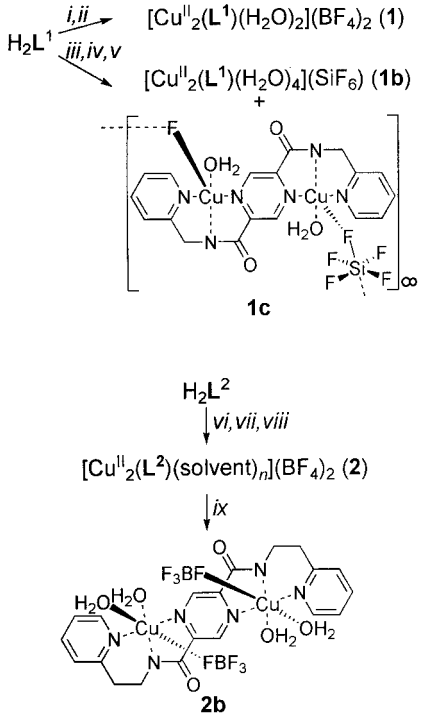

Scheme 2. Synthesis of the complexes **1**, **1b**, **1c**, **2** and **2b**. Reagents and conditions: (*i*) 2 equiv. $Cu(BF_4)_2\cdot 4H_2O$, MeCN, room temp.; (*ii*) Et_2O (vapour diffusion); (*iii*) 2 equiv. $Cu(BF_4)_2\cdot 4H_2O$, H_2O, room temp.; (*iv*) 2 equiv. NEt_3; (*v*) slow evaporation; (*vi*) 2 equiv. $Cu(BF_4)_2\cdot 4H_2O$, MeCN, 60 °C; (vii) room temp., 10 h; (*viii*) filtration; (*ix*) MeCN/EtOH (1:1) (slow evaporation).

Cu···Cu distance of the equivalent copper(II) centres [Cu(1)···Cu(1A) 6.811(3) Å] is slightly longer than that found in complex **2a**. A stair-like chain structure is formed through hydrogen bonding of the axial H_2O co-ligand to the amide oxygen atom of a neighbouring dinuclear subunit [$O_{water}\cdots O_{amide}$ 2.714 Å]. The H_2O co-ligand forms a second

 © 2005 Wiley-VCH Verlag GmbH & Co. KGaA, Weinheim

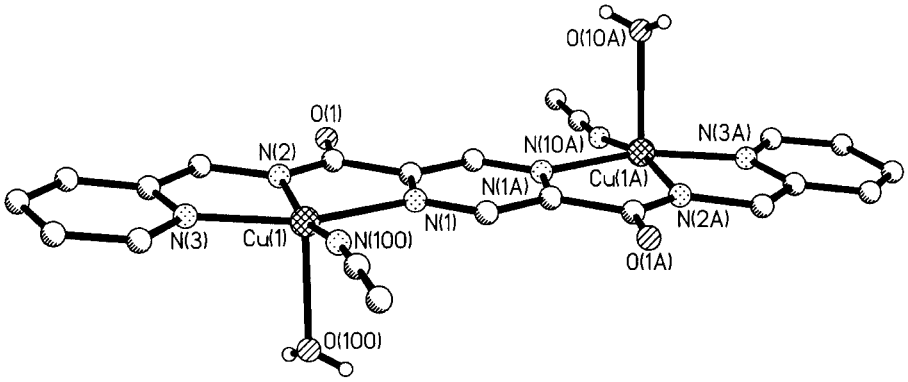

Figure 2. Molecular structure of $[Cu^{II}_2(\mathbf{L^1})(MeCN)_2(H_2O)_2]^{2+}$, the cation of complex **1a**·H_2O. Hydrogen atoms, except those of H_2O co-ligands, have been omitted for clarity. Symmetry operation used to generate equivalent atoms: (A) $2 - x$, $1 - y$, $1 - z$.

Table 1. Crystallographic data for the complexes **1a**·H_2O, **1b**, **1c**·$4H_2O$, **2a** and **2b**·$2H_2O$.

	1a·H_2O	**1b**	**1c**·$4H_2O$	**2a**	**2b**·$2H_2O$
Molecular formula	$C_{22}H_{26}B_2Cu_2F_8N_8O_5$	$C_{18}H_{22}Cu_2F_6N_6O_6Si$	$C_{18}H_{26}Cu_2F_6N_6O_8Si$	$C_{24}H_{28}B_2Cu_2F_8N_8O_4$	$C_{20}H_{30}B_2Cu_2F_8N_6O_8$
M_r [g mol^{-1}]	783.21	687.59	723.62	793.24	783.20
T [K]	150(2)	200(2)	200(2)	168(2)	168(2)
Crystal system	triclinic	monoclinic	triclinic	triclinic	triclinic
Space group	$P\bar{1}$	$C2/c$	$P\bar{1}$	$P\bar{1}$	$P\bar{1}$
a [Å]	8.29650(10)	21.1697(3)	8.00020(10)	9.312(3)	7.898(16)
b [Å]	10.0428(2)	7.55260(10)	8.96160(10)	13.156(4)	8.101(20)
c [Å]	10.1034(2)	15.1687(2)	10.2285(2)	13.802(4)	11.19(3)
α [°]	74.5940(10)	90	71.3330(10)	106.649(4)	84.98(6)
β [°]	69.3420(10)	94.4300(10)	77.7600(10)	101.489(4)	80.11(6)
γ [°]	84.3250(10)	90	69.0230(10)	99.121(4)	85.62(8)
V [Å^3]	759.37(2)	2418.02(6)	644.760(17)	1545.0(8)	701(3)
Z	1	4	1	2	1
$\rho_{calcd.}$ [g cm^{-3}]	1.713	1.889	1.864	1.705	1.855
μ [mm^{-1}]	1.498	1.904	1.796	1.471	1.628
$F(000)$	394	1384	366	800	396
Crystal colour and shape	green block	green block	green block	green block	green block
Crystal size [mm^3]	0.38 × 0.26 × 0.08	0.20 × 0.15 × 0.08	0.40 × 0.20 × 0.08	0.50 × 0.40 × 0.35	0.70 × 0.20 × 0.10
θ range [°]	2.10/25.48	0.96/27.16	2.11/26.42	1.59/26.37	2.53/26.38
Reflections collected	6914	14503	6211	19871	3172
Independent reflections	2803 [R_{int} = 0.0235]	2637 [R_{int} = 0.0380]	2598 [R_{int} = 0.0359]	6216 [R_{int} = 0.0432]	2497 [R_{int} = 0.1674]
Completeness to θ	99.5%	98.0%	98.5%	98.3%	87.4%
Data/restraints/parameters	2803/0/226	2637/0/189	2598/0/205	6216/0/451	2497/0/232
GOF on F^2	1.046	1.072	1.129	1.027	1.108
R indices [$I > 2\sigma(I)$]	R_1 = 0.0464, wR_2 = 0.1210	R_1 = 0.0625, wR_2 = 0.1683	R_1 = 0.0277, wR_2 = 0.0766	R_1 = 0.0426, wR_2 = 0.1127	R_1 = 0.0470, wR_2 = 0.1250
R indices (all data)	R_1 = 0.0507, wR_2 = 0.1244	R_1 = 0.0728, wR_2 = 0.1771	R_1 = 0.0294, wR_2 = 0.0775	R_1 = 0.0538, wR_2 = 0.1194	R_1 = 0.0542, wR_2 = 0.1302
Largest diff. peak/hole [e·A^{-3}]	1.294/–1.364	2.622/–0.858	0.694/–0.524	1.212/–0.758	0.750/–0.728

hydrogen bond, to the BF_4^- anion [$O_{water}\cdots F$ 2.745 Å]. The amide oxygen atom is also involved in another hydrogen bond, to the H_2O solvate molecule [$O_{amide}\cdots O_{solvate}$ 2.907 Å] (Figure S2, Supporting Information).

The 2:1 molar reaction of $Cu(BF_4)_2$·$4H_2O$ with the higher ligand homologue $H_2\mathbf{L^2}$ in MeCN afforded the complex $[Cu^{II}_2(\mathbf{L^2})(solvent)_n](BF_4)_2$ (**2**) in ca. 50% yield in the form of a bottle-green microcrystalline solid, that precipitated from the reaction mixture after several hours of stirring (Scheme 2). Recrystallisation of complex **2** from MeCN/EtOH (1:1) afforded single crystals of $[Cu^{II}_2(\mathbf{L^2})(H_2O)_4(BF_4)_2]$·$2H_2O$ (**2b**·$2H_2O$) suitable for an X-ray crystal structure determination (Figure 3, Table 1, Table 2, Table 3 and Table 4).

The overall molecular structure of the centrosymmetric molecule of complex **2b**·$2H_2O$ is very similar to that of complex **2a**. The major difference is the N_3O_2F distorted octahedral coordination environment about the copper(II) ions in **2b**·$2H_2O$, the two axial positions being elongated and occupied by an H_2O and a BF_4^- co-ligand. The Cu–F_{ax} distance [Cu(1)–F(13B) 2.598(3) Å] is, as expected, somewhat longer than the Cu–O_{ax} distance [Cu(1)–O(60) 2.516(5) Å]. Although BF_4^- ions are commonly regarded as "non-coordinating" a number of structures with coordi-

 © 2005 Wiley-VCH Verlag GmbH & Co. KGaA, Weinheim

Table 2. Selected distances [Å] for the complexes **1a**·H_2O, **1b**, **1c**·4H_2O, **2a** and **2b**·2H_2O.

	1a·H_2O[a]		**1b**[a]		**1c**·4H_2O[a]	
$Cu–N_{am}$	Cu(1)–N(2)	1.906(3)	Cu(1)–N(2)	1.904(4)	Cu(1)–N(2)	1.912(2)
$Cu–N_{py}$	Cu(1)–N(3)	1.999(3)	Cu(1)–N(3)	2.007(5)	Cu(1)–N(3)	2.012(2)
$Cu–N_{pz}$	Cu(1)–N(1)	2.044(3)	Cu(1)–N(1)	2.030(4)	Cu(1)–N(1)	2.052(2)
$Cu–L_{eq}$	Cu(1)–N(100)	1.972(3)	Cu(1)–O(20)	1.949(4)	Cu(1)–O(10)	1.951(2)
$Cu–L_{ax}$	Cu(1)–O(100)	2.201(3)	Cu(1)–O(30)	2.271(5)	Cu(1)–F(1)	2.235(1)
Cu···Cu	Cu(1)···Cu(1A)	6.811(3)	Cu(1)···Cu(1A)	6.775(1)	Cu(1)···Cu(1A) (intra)	6.827(1)
					Cu(1)···Cu(1B) (inter)	7.166(1)
	2a[a]		**2b**·2H_2O[a]			
$Cu–N_{am}$	Cu(1)–N(2)	1.936(2)	Cu(1)–N(2)	1.946(4)		
	Cu(2)–N(12)	1.929(2)				
$Cu–N_{py}$	Cu(1)–N(3)	2.011(3)	Cu(1)–N(3)	1.981(4)		
	Cu(2)–N(13)	1.992(3)				
$Cu–N_{pz}$	Cu(1)–N(1)	2.027(2)	Cu(1)–N(1)	2.021(4)		
	Cu(2)–N(11)	2.021(2)				
$Cu–L_{eq}$	Cu(1)–O(50)	1.972(2)	Cu(1)–O(50)	1.961(4)		
	Cu(2)–O(60)	1.996(2)				
$Cu–L_{ax}$	Cu(1)–N(50)	2.321(3)	Cu(1)–O(60)	2.516(5)		
	Cu(2)–N(60)	2.299(3)	Cu(1)–F(13B)	2.598(3)		
Cu···Cu	Cu(1)···Cu(1A)	6.784(2)	Cu(1)···Cu(1A)	6.764(1)		
	Cu(2)···Cu(2B)	6.756(2)				

[a] Symmetry operations used to generate equivalent atoms: **1a**·H_2O: (A) 2 – *x*, 1 – *y*, 1 – *z*. **1b**: (A) 1 – *x*, 2 – *y*, 1 – *z*. **1c**·4H_2O: (A) –*x*, –*y* – 1, –*z*; (B) –*x*, –*y*, –*z*. **2a**: (A) 1 – *x*, 2 – *y*, 1 – *z*; (B) –*x*, 2 – *y*, –*z*. **2b**·2H_2O: (A) 1 – *x*, 1 – *y*, 1 – *z*; (B) *x* – 1, *y*, *z*.

Table 3. Selected bond angles [°] for the complexes **1a**·H_2O, **1b**, **1c**·4H_2O, **2a** and **2b**·2H_2O.

	1a·H_2O		**1b**		**1c**·4H_2O	
$N_{pz}–Cu–N_{am}$	N(1)–Cu(1)–N(2)	81.1(1)	N(1)–Cu(1)–N(2)	81.6(2)	N(1)–Cu(1)–N(2)	81.27(7)
$N_{pz}–Cu–N_{py}$	N(1)–Cu(1)–N(3)	161.7(1)	N(1)–Cu(1)–N(3)	162.9(2)	N(1)–Cu(1)–N(3)	163.58(7)
$N_{pz}–Cu–L_{eq}$	N(1)–Cu(1)–N(100)	95.9(1)	N(1)–Cu(1)–O(20)	92.0(2)	N(1)–Cu(1)–O(10)	97.53(7)
$N_{pz}–Cu–L_{ax}$	N(1)–Cu(1)–O(100)	94.5(1)	N(1)–Cu(1)–O(30)	96.4(2)	N(1)–Cu(1)–F(1)	87.19(6)
$N_{am}–Cu–N_{py}$	N(2)–Cu(1)–N(3)	81.9(1)	N(2)–Cu(1)–N(3)	82.2(2)	N(2)–Cu(1)–N(3)	82.40(7)
$N_{am}–Cu–L_{eq}$	N(2)–Cu(1)–N(100)	165.2(1)	N(2)–Cu(1)–O(20)	161.0(2)	N(2)–Cu(1)–O(10)	163.68(8)
$N_{am}–Cu–L_{ax}$	N(2)–Cu(1)–O(100)	103.5(1)	N(2)–Cu(1)–O(30)	106.2(2)	N(2)–Cu(1)–F(1)	105.31(6)
$N_{py}–Cu–L_{eq}$	N(3)–Cu(1)–N(100)	99.0(1)	N(3)–Cu(1)–O(20)	101.7(2)	N(3)–Cu(1)–O(10)	97.68(7)
$N_{py}–Cu–L_{qx}$	N(3)–Cu(1)–O(100)	95.8(1)	N(3)–Cu(1)–O(30)	93.4(2)	N(3)–Cu(1)–F(1)	98.75(6)
$L_{eq}–Cu–L_{ax}$	N(100)–Cu(1)–O(100)	95.8(1)	O(20)–Cu(1)–O(30)	92.2(2)	O(10)–Cu(1)–F(1)	90.84(6)
	2a		**2b**·2H_2O[a]			
$N_{pz}–Cu–N_{am}$	N(1)–Cu(1)–N(2)	82.1(1)	N(1)–Cu(1)–N(2)	81.1(2)		
	N(11)–Cu(2)–N(12)	82.3(1)				
$N_{pz}–Cu–N_{py}$	N(1)–Cu(1)–N(3)	161.2(1)	N(1)–Cu(1)–N(3)	173.5(1)		
	N(11)–Cu(2)–N(13)	175.7(1)				
$N_{pz}–Cu–L_{eq}$	N(1)–Cu(1)–O(50)	93.5(1)	N(1)–Cu(1)–O(50)	91.4(2)		
	N(11)–Cu(2)–O(60)	93.7(1)				
$N_{pz}–Cu–L_{ax}$	N(50)–Cu(1)–N(1)	91.4(1)	N(1)–Cu(1)–O(60)	85.5(2)		
	N(60)–Cu(2)–N(11)	84.9(1)	N(1)–Cu(1)–F(13B)	91.6(1)		
$N_{am}–Cu–N_{py}$	N(2)–Cu(1)–N(3)	92.3(1)	N(2)–Cu(1)–N(3)	95.0(2)		
	N(12)–Cu(2)–N(13	94.3(1)				
$N_{am}–Cu–L_{eq}$	N(2)–Cu(1)–O(50)	175.6(1)	N(2)–Cu(1)–O(50)	165.7(1)		
	N(12)–Cu(2)–O(60)	51.4(1)				
$N_{am}–Cu–L_{ax}$	N(2)–Cu(1)–N(50)	92.8(1)	N(2)–Cu(1)–O(60)	102.0(2)		
	N(12)–Cu(2)–N(60)	102.8(1)	N(2)–Cu(1)–F(13B)	91.4(1)		
$N_{py}–Cu–L_{eq}$	N(3)–Cu(1)–O(50)	91.9(1)	N(3)–Cu(1)–O(50)	93.5(2)		
	N(13)–Cu(2)–O(60)	90.5(1)				
$N_{py}–Cu–L_{qx}$	N(3)–Cu(1)–N(50)	106.9(1)	N(3)–Cu(1)–O(60)	90.3(2)		
	N(13)–Cu(2)–N(60)	93.3(1)	N(3)–Cu(1)–F(13B)	93.7(1)		
$L_{eq}–Cu–L_{ax}$	N(50)–Cu(1)–O(50)	87.1(1)	O(50)–Cu(1)–O(60)	89.5(2)		
	O(60)–Cu(2)–N(60)	105.0(1)	O(50)–Cu(1)–F(13B)	76.5(1)		
$L_{ax}–Cu–L_{ax}$			O(60)–Cu(1)–F(13B)	165.7(1)		

[a] Symmetry operations used to generate equivalent atoms: **2b**·2H_2O: (B) *x* – 1, *y*, *z*.

 © 2005 Wiley-VCH Verlag GmbH & Co. KGaA, Weinheim

Table 4. Selected hydrogen bond lengths [Å] for the complexes **1a**·H_2O, **1b**, **1c**·4H_2O, **2a** and **2b**·2H_2O.

	1a·H_2O[a]		**1b**[a]		**1c**·4H_2O[a]	
$O_{amide}\cdots O_{co\text{-}lig.}$	O(1B)···O(100)	2.714	O(1A)···O(20)	2.603(7)	O(1C)···O(10)	2.662
$O_{amide}\cdots O_{solv.}$	O(1)···O(110)	2.907				
$O_{co\text{-}lig.}\cdots O_{solv.}$					O(10)···O(50)	2.571
$O_{co\text{-}lig.}\cdots F_{anion}$	O(100)···F(11)	2.745	O(20)···F(11)	2.760(7)		
			O(20)···F(12)	2.792(7)		
			O(30)···F(11B)	3.169(7)		
			O(30)···F(13C)	3.377(7)		
$O_{solv.}\cdots O_{solv.}$					O(50)···O(60)	2.670
$O_{solv.}\cdots F_{anion}$					O(50)···F(2D)	2.736
					O(60)···F(3E)	2.714
					O(60)···O(1F)	2.845
	2a[a]		**2b**·2H_2O[a]			
$O_{amide}\cdots O_{co\text{-}lig.}$	O(10B)···O(50)	2.598	O(1D)···O(60)	2.828		
	O(1)···O(60)	2.595	O(1E)···O(60)	2.747		
$O_{amide}\cdots O_{solv.}$						
$O_{co\text{-}lig.}\cdots O_{solv.}$						
$O_{co\text{-}lig.}\cdots F_{anion}$	O(50)···F(11)	2.738	O(50)···F(12C)	2.771		
	O(60)···F(12C)	2.801				
$O_{solv.}\cdots O_{solv.}$			O(50)···O(70)	2.620		
			O(60F)···O(70)	2.794		
$O_{solv.}\cdots F_{anion}$			O(70)···(F11)	2.756		

[a] Symmetry operations used to generate equivalent atoms: **1a**·H_2O: (B) $-x+1, -y+1, -z+1$. **1b**: (A) $x, y-1, z$; (B) $1-x, y, 0.5-z$; (C) $-x+1, y+1, -z+0.5$. **1c**·4H_2O: (C) $x+1, y, z$; (D) $-x+1, -y-1, -z$; (E) $x, y-1, z$; (F) $x+1, y-1, z$. **2a**: (B) $x+1, y, z+1$; (C) $x, y, z-1$. **2b**·2H_2O: (C) $-x+2, -y+1, -z+2$; (D) $x+1, y, z$; (E) $x+1, -y+2, -z+1$; (F) $-x+2, -y+1, -z+1$.

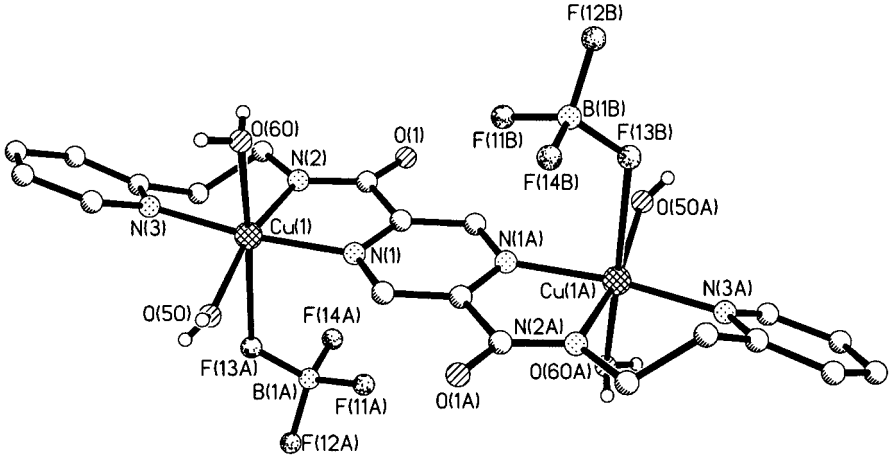

Figure 3. Molecular structure of the complex $[Cu^{II}_2(\mathbf{L^2})(H_2O)_4(BF_4)_2]$ (**2b**·2H_2O). The H_2O solvates and hydrogen atoms, except those of H_2O co-ligands, have been omitted for clarity. Symmetry operations used to generate equivalent atoms: (A) $1-x, 1-y, 1-z$; (B) $x-1, y, z$.

nated BF_4^- ions are known.[19,20] In copper(II) complexes with coordinated BF_4^- ions, Cu–F distances between 2.07 Å[21] and 2.85 Å[22] have been observed, but mostly the distances lie in the range 2.40–2.71 Å. In complex **2b**·2H_2O a 3D network is formed by hydrogen bonds, involving the amide oxygen atoms, both H_2O co-ligands, the BF_4^- co-ligands and the H_2O solvates (Figure S3, Supporting Information).

Dinuclear copper(II) compounds unexpectedly incorporating SiF_6^{2-} as counterions were obtained by reacting $Cu(BF_4)_2$·4H_2O with the lower ligand homologue $H_2\mathbf{L^1}$, in a 2:1 metal-to-ligand ratio, using H_2O as the solvent and a glass vial as the reaction and crystallisation vessel (slow evaporation of the solvent in air). Reactions carried out without base resulted in the isolation of blue-green crystal blocks, along with yellow crystals which, on the basis of elemental and IR analyses, are believed to be $(H_4\mathbf{L^1})$-$(BF_4)_2$. The blue-green crystal blocks were identified as a mixture of the complexes $[Cu^{II}_2(\mathbf{L^1})(H_2O)_4](SiF_6)$ (**1b**) and $\{[Cu^{II}_2(\mathbf{L^1})(H_2O)_2(\mu\text{-}SiF_6)]$·4$H_2O\}_\infty$ (**1c**·4H_2O) by X-ray crystallography (Figure 4 and Figure S4, Supporting information, Table 1, Table 2, Table 3 and Table 4). The formation of the yellow crystals could be prevented by the addition of two equivalents of NEt_3 as a base (Scheme 2), which also resulted in an increased yield (ca. 70–80% yield) of the desired SiF_6^{2-} compounds. The occurrence of SiF_6^{2-}

 © 2005 Wiley-VCH Verlag GmbH & Co. KGaA, Weinheim

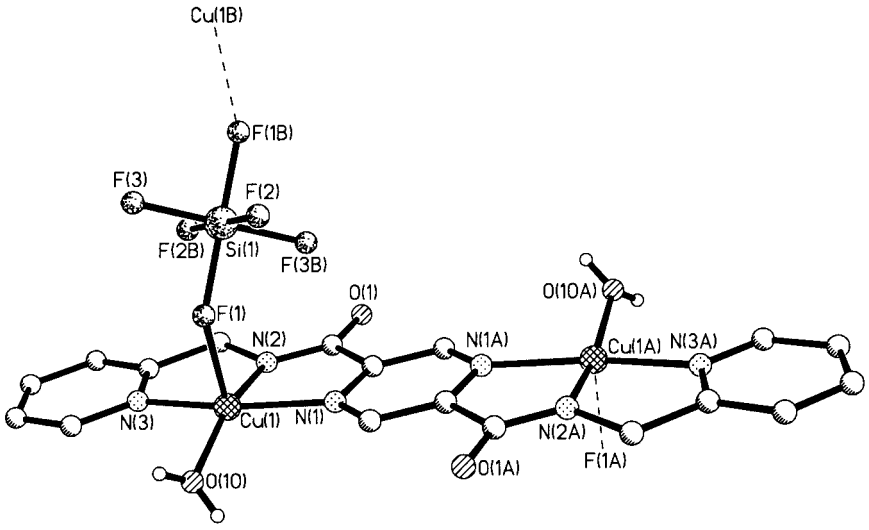

Figure 4. View of the $[Cu^{II}_2(\mathbf{L^1})(H_2O)_2(\mu\text{-}SiF_6)]$ subunit of the polymeric chain structure of the cation of complex **1c**·4 H_2O, emphasising the coordination environment about Cu(1). Hydrogen atoms, except those of H_2O co-ligands, have been omitted for clarity. Symmetry operations used to generate equivalent atoms: (A) $-x, -y - 1, -z$; (B) $-x, -y, -z$.

ions in these compounds, rather than BF_4^- ions, was unexpected but was readily confirmed by the negative ion ESI mass spectrum, which showed a peak at m/z = 123.0 corresponding to the SiF_5^- anion, and the IR spectrum, which showed an intense broad split band (with peaks at 780 and 750 cm^{-1}) typical of the SiF_6^{2-} ion. It has been reported that SiF_6^{2-} anions can arise in compounds originally containing BF_4^- ions as partial hydrolysis of the latter in the presence of moisture can generate traces of HF, which then react with the glassware to form SiF_6^{2-} ions.[23–27]

The molecular structure of the hexafluorosilicate complex **1b** (Figure S4, Supporting Information, Table 1, Table 2, Table 3 and Table 4) is very similar to the structure of the analogous tetrafluoroborate complex **1a**·H_2O. In the centrosymmetric complex **1b** an N_3O_2 distorted square-pyramidal coordination environment about the copper(II) ion is achieved by equatorially and axially coordinated H_2O co-ligands ($\tau_{Cu(1)}$[14] = 0.03). Hydrogen bonding, involving the amide oxygen atom and the equatorial H_2O co-ligand of two neighbouring subunits [$O_{amide}\cdots O_{water}$ 2.603 Å] and both of the H_2O co-ligands with the SiF_6^{2-} anions [$F_{anion}\cdots O_{water}$ 2.760–3.377 Å], is also a feature of this structure.

The related compound **1c**·4 H_2O, obtained from the same reaction mixture, features bridging SiF_6^{2-} co-ligands. The coordination environment about the copper(II) ion is therefore best described as N_3OF square-pyramidal (Figure 4; τ[14] = 0.00).

A polymeric chain structure is formed by the SiF_6^{2-} bridges, which connect two apical positions of two neighbouring dinuclear subunits (Figure 5). The first crystal structure of a chain compound containing bridging SiF_6^{2-} co-ligands, $[Co^{II}(\mathbf{viz})_4(SiF_6)]_\infty$ (**viz** = *N*-vinylimidazole), was reported in 1982 by Reedijk and co-workers.[28] Even now polynuclear compounds with bridging SiF_6^{2-} ions are not very common and all reported compounds incorporate six-coordinate metal ions and mononuclear subunits.[24,29–31] To the best of our knowledge, complex **1c**·4 H_2O is the first polymeric chain compound incorporating square-pyramidal metal ions bridged by SiF_6^{2-} ions and, at the same time, it is the first polymeric compound featuring discrete dinuclear subunits that are bridged by SiF_6^{2-} ions. The Cu–F bond length in complex **1c**·4 H_2O [Cu(1)–F(1) 2.235(1) Å] is around 0.3 Å shorter than in the dimeric complexes $[\{Cu^{II}(H\mathbf{sabh})(H_2O)\}_2(SiF_6)]\cdot 2H_2O$ (H_2**sabh** = salicylaldehyde benzoylhydrazone) (2.522 Å)[32] or $[\{Cu^{II}(H\mathbf{spca})(H_2O)\}_2(SiF_6)]\cdot 2H_2O$ (H_2**spca** = N^3-salicyloylpyridine-2-carboxamidrazone) (2.528 Å),[25] the only crystal structures reported to date that contain square-pyramidal copper(II) ions bridged by the apical positions by SiF_6^{2-} ions. The intermolecular Cu···Cu distance in complex **1c**·4 H_2O is 7.166(1) Å and thus is in between the distances reported for $[\{Cu^{II}(H\mathbf{sabh})(H_2O)\}_2(SiF_6)]\cdot 2H_2O$ (6.04 Å)[32] and $[\{Cu^{II}(H\mathbf{spca})(H_2O)\}_2(SiF_6)]\cdot 2H_2O$ (7.951 Å).[25] The Cu–F–Si angle in complex **1c**·4 H_2O is only 130.45(7)° and is thus smaller than in both $[\{Cu^{II}(H\mathbf{sabh})(H_2O)\}_2(SiF_6)]\cdot 2H_2O$ (144.0°)[32] and $[\{Cu^{II}(H\mathbf{spca})(H_2O)\}_2(SiF_6)]\cdot 2H_2O$ (140.1°)[25] and considerably smaller than in the six-coordinate polymeric chain structures, where the M–F–Si angles range from 152° to 180°.[24,28,33] In complex **1c**·4 H_2O the parallel polymeric strands are interconnected through hydrogen bonds involving the equatorial H_2O co-ligand and the amide oxygen atom [O(10)···O(1C) 2.662 Å]. Furthermore, the two H_2O solvates per asymmetric unit are involved in a network of hydrogen bonds involving all non-coordinated fluorine atoms of the SiF_6^{2-} ligand and the equatorial H_2O co-ligand (Figure 5).

In all of the above structures the Cu–N_{ligand} bond lengths follow the same general trend, specifically Cu–N_{am} < Cu–N_{py} < Cu–N_{pz} (Table 2). Another general, and expected, trend is that in each case on deprotonation and coordination to copper(II) the υ_{CO} band of the free ligand moves to

 © 2005 Wiley-VCH Verlag GmbH & Co. KGaA, Weinheim

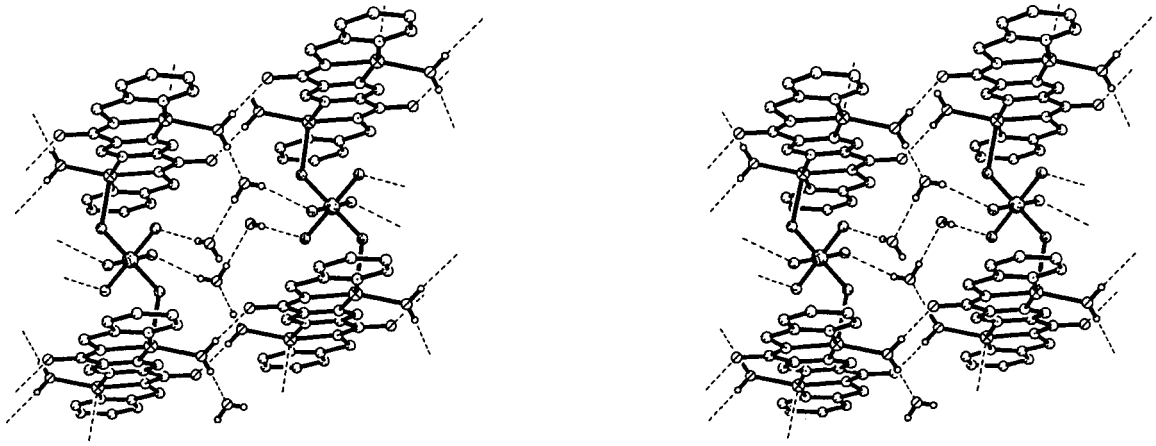

Figure 5. Stereo view of a section of the 3D structure of $\{[Cu^{II}_2(\mathbf{L^1})(H_2O)_2(SiF_6)]\cdot 4H_2O\}_\infty$ (**1c**·4 H_2O). Hydrogen atoms not involved in hydrogen bonds have been omitted for clarity.

lower energy [1681 cm^{-1} for $H_2\mathbf{L^1}$ to 1628–1634 cm^{-1} for the complexes of $(\mathbf{L^1})^{2-}$; 1659 cm^{-1} for $H_2\mathbf{L^2}$ to 1607 cm^{-1} for the complexes of $(\mathbf{L^2})^{2-}$].

Magnetic and EPR Studies

The temperature dependence of the magnetic susceptibility was measured for the two complexes **1a**·H_2O and **2b** over the range 300–4.2 K. The plots of the temperature dependence of μ_{eff} and χ_m are given in the Figures S5–S8 (Supporting Information).

Complex **1a**·H_2O showed Curie-like behaviour at higher temperatures (μ_{eff} = 1.91 μ_B) and only at temperatures below 5 K a small, rapid decrease was observed. Consequently, χ_m increased and no maximum was observed in the plot χ_m vs. *T*. The best fit to the Bleaney–Bowers equation[34] was obtained from the parameters J = –0.24 cm^{-1}, g = 2.2, $TIP = 60\times10^{-6}$ cm^3mol^{-1}. Setting J at zero gave a calculated line that did not reproduce the decrease in μ_{eff} values below 5 K. Calculations of μ_{eff} using the thermodynamic form of susceptibility, applicable to low temperature/high field combinations, rather than the Bleaney–Bowers equation, show that the small decrease is partly, but not wholly, due to Zeeman level depopulation (saturation) effects in the field used (1 T). Nevertheless, the antiferromagnetic coupling interaction was less than that (–7.5 cm^{-1}) of a related dicopper(II) complex of the isomeric ligand *N*,*N*′-bis(2-pyridylmethyl)pyrazine-2,3-dicarboxamide ($H_2\mathbf{L^3}$).[7] In the 2,3-dicarboxamide compound, an internal O···H···O=C hydrogen-bond was present in the $(H\mathbf{L^3})^-$ form of the bridging ligand and the terminal ligands to each copper(II) centre were different to those in **1a**·H_2O. However, the Cu···Cu distances, τ values and *trans-axial* copper(II) geometries were very similar in both cases (vide infra). DFT calculations made on the 2,3-dicarboxamide complex yielded spin densities and spin populations on the pyrazine N-donor atoms compatible with weak antiferromagnetic superexchange coupling of the $Cu^{II}(d_{x^2-y^2})$ orbitals across the pyrazine ring.[7] Thus, while **1a**·H_2O and this 2,3-dicarboxamide analogue are both very weakly antiferromagnetically coupled, there is no clearly identifiable feature which explains this difference in *J* values. For complex **2b** the χ_m values follow Curie behaviour while μ_{eff} is constant at 1.86 μ_B down to 50 K, then increases to 1.92 μ_B at 4 K. Fitting to a dinuclear model gave g = 2.14 and J = +0.67 cm^{-1}. The observed very weak ferromagnetic spin coupling was unexpected, as the main difference between the complexes **2b** and **1a**·H_2O is only the more flexible ethylene containing ligand arm and weak Cu–F coordination in complex **2b**. Furthermore, antiferromagnetic spin coupling has been observed for various copper(II) complexes of the ligands *N*,*N*′-bis(2-pyridylmethyl)pyrazine-2,3-dicarboxamide ($H_2\mathbf{L^3}$)[7] and *N*,*N*′-bis[2-(2-pyridyl)ethyl]pyrazine-2,3-dicarboxamide ($H_2\mathbf{L^4}$),[35] which are isomeric to $H_2\mathbf{L^1}$ and $H_2\mathbf{L^2}$, respectively.

The EPR spectrum of a polycrystalline powder of **1a**·H_2O at 120 K shows a strong resonance near g = 2, with no hyperfine structure being resolved on the parallel feature (Figure S9, Supporting Information). Simulations give $g_\parallel$ = 2.24 and $g_\perp$ = 2.06. An extremely weak resonance of similar shape is observed at $g \approx 4$ (Figure S10, Supporting Information). The spectrum of a polycrystalline powder of **2b**·2 H_2O at both 260 K and 150 K (Figure S11, Supporting Information) shows an asymmetric resonance near g = 2, with the features associated with $g_\parallel$ being unresolved and tailing off to low field. The g-values are estimated as $g_\parallel$ = 2.23 and $g_\perp$ = 2.05. Again, a weak resonance is observed near g = 4 (Figure S12, Supporting Information). None of the polycrystalline powder spectra showed a dependence on temperature between 120 K and 295 K. The appearance of the resonances in the $g \approx 2$ and $g \approx 4$ regions is indicative of the presence of dipolar and weak exchange interactions between the copper(II) ions.[36] The former give rise to spectral broadening while the latter result in exchange narrowing, as is observed here. The effect of the different magnitudes of exchange interaction on the spectra is shown by the collapse of the hyperfine interaction in **1a**·H_2O and the smearing out of the differences in g-value due to a larger exchange interaction in **2b**·2 H_2O.

 © 2005 Wiley-VCH Verlag GmbH & Co. KGaA, Weinheim

The observation of resonances at $g \approx 4$ in the polycrystalline powder systems is additional evidence for interaction between the copper(II) ions. These resonances are not due to Fe^{III} impurities in either the cavity background or in the powders themselves. Although in a three-dimensional extended lattice the $g \approx 4$ resonances are expected to be smeared out unless E_d, $E_{ex} << E_0$,[37] this inequality does not hold in the present case, where the Zeeman energy $E_0 \approx 0.3\ cm^{-1}$, the dipolar coupling energy $E_d \approx 0.01\ cm^{-1}$ and E_{ex} is $-0.24\ cm^{-1}$ for **1a**·H_2O and $+0.67\ cm^{-1}$ for **2b**·2 H_2O. However, this condition is relaxed for low-dimensional magnetic systems. Thus the observation of resonances near $g = 4$ for both complexes implies the existence of low-dimensional intermolecular exchange interactions in the solid state.[37,38]

The EPR spectra of **1a**·H_2O and **2b**·2 H_2O in frozen DMF solution (ca. 1 mM) at 130 K were identical and showed well resolved resonances at $g \approx 2$ and $g \approx 4$ as shown in Figure 6 and Figure 7 respectively. These resonances are typical of those observed for many dinuclear copper(II) complexes in dilute frozen solution[36] and are attributed to the coupling of two copper(II) ions, each with electron spin $S = ½$, by dipole–dipole and exchange interactions to give a triplet state ($S = 1$) and a singlet state ($S = 0$). The resonances in the $g \approx 2$ region are due to the $\Delta M_s = 1$ transitions within the triplet state and those near $g \approx 4$ ("half field") to the "forbidden" or $\Delta M_s = 2$ transitions between the $M_s = \pm 1$ levels of the triplet state.

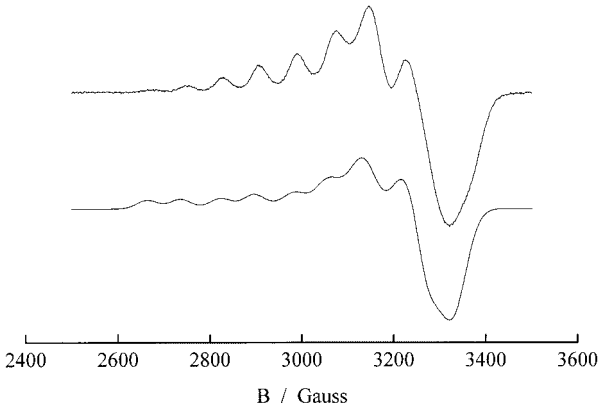

Figure 6. EPR spectrum in the $g = 2$ region of **2b**·2 H_2O in frozen DMF solution at 130 K (approximately 1 mM). Experimental spectrum (top): microwave frequency 9.424 GHz; microwave power 2 mW; 100 kHz modulation amplitude 1 G; receiver gain 2.0×10^4; scan time 167 s; time constant 82 ms. Simulated spectrum (bottom): computed using the parameters referred to in the text.

The spectra can be simulated as shown in Figures 6 and 7 with the following spin Hamiltonian parameters $g_{\|} = 2.290\ (\pm 0.005)$, $g_{\perp} = 2.080\ (\pm 0.005)$, $A_{\|} = 170\ (\pm 5) \times 10^{-4}\ cm^{-1}$, $A_{\perp} = 5\ (\pm 5) \times 10^{-4}\ cm^{-1}$. A $Cu^{II} \cdots Cu^{II}$ distance of 6.9 (± 0.1) Å is obtained with the inter-nuclear vector in the xy plane of the magnetic axes of the copper(II) ions (to within 15°), i.e. perpendicular to the z or symmetry axis of the individual ions. The best fit of experimental and simulated spectra is found with an isotropic exchange interaction $J = 0$. The uncertainties, given in parentheses, represent the range of parameters for which acceptable agreement is found between experimental and simulated spectra. There is no inherent contradiction between the value of $J = 0$ found from the simulation of the frozen solution spectra and the small values of J found by magnetic susceptibility measurements, as the latter may arise from intermolecular interactions in the solid state. Intermolecular exchange is not expected to be significant in dilute frozen solution.

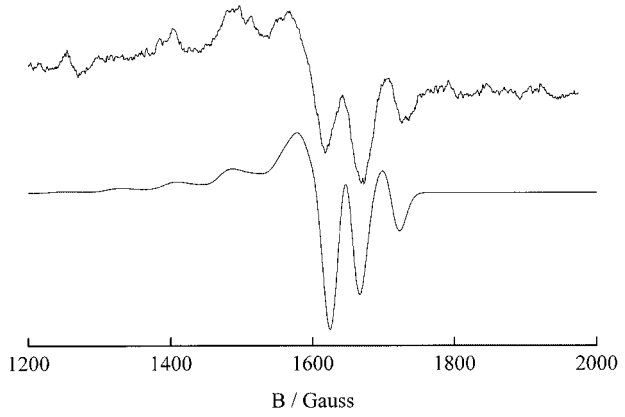

Figure 7. Half-field portion of EPR spectrum of **2b**·2 H_2O in frozen DMF solution at 130 K. Experimental spectrum (top): microwave frequency 9.424 GHz; microwave power 10 mW; 100 kHz modulation amplitude 10 G; receiver gain 5.0×10^5; scan time 84 s; time constant 328 ms; average of 17 scans. Simulated spectrum (bottom): computed using the parameters referred to in the text.

The spin Hamiltonian parameters from the simulation of the frozen solution spectra can be taken as being those of the individual copper(II) ions and give $g_{av} = 2.14$. This value may be compared with the values of g_{av} from the solid-state powder spectra of 2.12 (**1a**·H_2O) and 2.11 (**2b**·2 H_2O) and from magnetic susceptibility of 2.20 (**1a**·H_2O) and 2.14 (**2b**·2 H_2O). The g values of the solid-state powder spectra and those from magnetic susceptibility measurements are subject to significant sources of uncertainty. Nevertheless, the magnetic susceptibility and EPR measurements show that the copper(II) ions retain the $Cu^{II}(d_{x^2-y^2})$ orbital ground state even in solution, consistent with the distorted square pyramidal or octahedral coordination shown by the X-ray crystallographic analysis.

Conclusions

The pyrazine-based bis(terdentate) diamide ligands $H_2\mathbf{L^1}$ and $H_2\mathbf{L^2}$ can be used for the formation of grid-type metal complexes.[5] However, it has been found that on complexation with $Cu(BF_4)_2 \cdot 4H_2O$ both ligands prefer to form dicopper(II) complexes of the type $[Cu^{II}_2(\mathbf{L^1})(\text{co-ligand})_4]^{2+}$ or $[Cu^{II}_2(\mathbf{L^2})(\text{co-ligand})_4]^{2+}$ featuring doubly deprotonated ligands and varying co-ligands. Unlike their isomeric ligands *N*,*N*′-bis(2-pyridylmethyl)pyrazine-2,3-dicarboxamide ($H_2\mathbf{L^3}$)[6] and *N*,*N*′-bis[2-(2-pyridyl)ethyl]pyrazine-2,3-dicarboxamide ($H_2\mathbf{L^4}$),[35] where the addition of base is required to even monodeprotonate the ligand for complexation, no additional base is required to form complexes of

 © 2005 Wiley-VCH Verlag GmbH & Co. KGaA, Weinheim

the doubly deprotonated ligand species $(\mathbf{L^1})^{2-}$ and $(\mathbf{L^2})^{2-}$. All of the complexes described in this paper, except compound **2b**·2 H_2O, feature distorted square-pyramidal coordination spheres for the copper(II) ions. A distorted octahedral coordination sphere with BF_4^- coordination is observed in complex **2b**·2 H_2O. In all cases the central pyrazine ring bridges the metal ions. Very weak antiferromagnetic spin coupling is observed in magnetic studies on complex **1a**·H_2O which features N_4O five-coordinate copper(II) ions, whereas very weak ferromagnetic spin coupling is observed in studies of complex **2b**, which features N_3O_2F six-coordinate copper(II) ions. X-band EPR studies confirm the very weak exchange coupling in the solid state. The frozen solution spectra are interpreted in terms of dipolar coupling with no intramolecular exchange and intra-cluster Cu···Cu separations similar to those obtained by crystallography. Serendipitous formation of SiF_6^{2-} ions, and the almost quantitative crystallisation of the corresponding SiF_6^{2-} compounds **1b** and **1c**·4 H_2O, has been observed when reacting $H_2\mathbf{L^1}$ with $Cu(BF_4)_2$·4 H_2O in H_2O as the solvent and using a glass vial as both the reaction and crystallisation vessel. Complex **1c**·4 H_2O was found to be a rare example of a structure featuring five-coordinate dicopper(II) subunits bridged by SiF_6^{2-} ions.

Experimental Section

General Remarks: Elemental analyses were performed by the Campbell Microanalytical Laboratory at the University of Otago. Melting points were determined with a Gallenkamp melting point apparatus in open-glass capillaries and are uncorrected. ^1H and ^{13}C NMR spectra were recorded with a Varian INOVA-300 or with a Varian INOVA-500 spectrometer at 25 °C. Chemical shifts are given relative to tetramethylsilane (TMS). IR spectra were recorded with a Perkin–Elmer Spectrum BX FT-IR spectrophotometer over the range 4000–400 cm^{-1}. UV/Vis/NIR spectra were recorded with a Varian CARY 500 Scan UV/Vis/NIR spectrophotometer over the range 200–1400 nm. Molar conductivities were measured using 1 mM solutions with a Suntex SC-170 conductivity meter. ESI mass spectra were recorded with a MicroMass LCT spectrometer. For all compounds MeCN was used as the solvent. Magnetic data were recorded over the range 300–4.2 K using a Quantum Design MPMS5 SQUID magnetometer with an applied field of 1 T. Single-crystal X-ray data were collected with a Bruker SMART CCD area detector diffractometer (λ = 0.71073 Å). The structures were solved by direct methods using SHELXS-97[39,40] and refined against F^2 using full-matrix least-squares techniques with SHELXL-97.[41] Continuous wave (CW) EPR spectra were obtained with a Bruker ESP380FT/CW X-band spectrometer at Monash University, using the standard rectangular TE_{012} cavity. Temperatures below room temperature (295 K) down to 120 K were achieved with a Bruker nitrogen flow insert in the cavity. The microwave frequency was measured with an EIP microwave 548A frequency counter and the *g* factors were determined by proton NMR and with reference to the F^+ line in CaO (2.0001 ± 0.0001).[42] Spectrum simulations were performed with either the Bruker SIMFONIA software or (for Figure 6 and Figure 7) with the SOPHE software described by Griffin and co-workers.[43]

Dimethyl Pyrazine-2,5-dicarboxylate (II): A solution of 2,5-dimethylpyrazine (8.11 g, 75.0 mmol) in pyridine/H_2O (10:1) (165 mL) was treated with solid SeO_2 (37.5 g, 337.5 mmol) and the resulting suspension was refluxed for 18 hours. The resulting dark red-brown mixture was evaporated to dryness under reduced pressure. H_2O (250 mL) was added and the solid elemental selenium was filtered off. After evaporation of the red solution to dryness, the resulting dark red brown solid was taken up in MeOH (150 mL), treated with $SOCl_2$ (3.5 mL) and refluxed for 8 hours. The resulting suspension was then filtered whilst hot and the solid was washed with CH_2Cl_2 (5 × 20 mL). The combined organic layers were reduced in volume under reduced pressure (to ca. 100 mL) to give the product in the form of pale yellow-orange feathery crystals. The solid was filtered off and washed with ice-cold MeOH (20 mL) to give 8.98 g (45.8 mmol, 61%) of analytically pure **II**. M.p. 167–168 °C. $C_8H_8N_2O_4$ (196.16): calcd. C 48.98, H 4.11, N 14.28; found C 49.24, H 3.87, N 14.25. TLC (SiO_2, CH_2Cl_2/10% MeOH): R_f = 0.83. ^1H NMR (300 MHz, $CDCl_3$): δ = 9.39 (s, 2 H, pz*H*), 4.07 (s, 6 H, CH_3) ppm. $^{13}C\{^1H\}$ NMR (75 MHz, $CDCl_3$): δ = 163.6 (pz*C*O), 145.6 (*pz*H), 145.3 (*pz*CO), 53.6 (O*C*H_3) ppm. IR (KBr, disk): $\tilde{\nu}$ = 3549, 3472, 3417, 3077, 3015, 2960, 2853, 1720, 1637, 1618, 1472, 1431, 1359, 1279, 1202, 1181, 1144, 1020, 959, 824, 759, 616 495, 466, 425 cm^{-1}.

***N,N′*-Bis(2-pyridylmethyl)pyrazine-2,5-dicarboxamide ($H_2\mathbf{L^1}$):** A suspension of **II** (1.96 g, 10.0 mmol) in MeOH (70 mL) was treated with a solution of 2-(aminomethyl)pyridine (2.38 g, 22.0 mmol) in MeOH (30 mL) and the resulting solution was kept in an open flask at 80–90 °C for 4 hours, allowing most of the solvent to evaporate. Filtration of the resulting suspension gave 2.92 g (8.38 mmol, 84%) of $H_2\mathbf{L^1}$ in the form of an analytically pure colourless powder. M.p. 205–206 °C. $C_{18}H_{16}N_6O_2$ (348.36): calcd. C 62.06, H 4.63, N 24.12; found C 61.94, H 4.66, N 24.30. TLC (SiO_2, CH_2Cl_2/10% MeOH): R_f = 0.60. ^1H NMR (500 MHz, $CDCl_3$): δ = 9.39 (s, 2 H, 2 × pz*H*), 8.88 (t, *J* = 5.0 Hz, 2 H, 2 × N*H*), 8.62 (ddd, $^3J_{6,5}$ = 5.0, $^4J_{6,4}$ = 2.0, $^5J_{6,3}$ = 1.0 Hz, 2 H, 2 × 6-py*H*), 7.69 (dt, $^3J_{4,5}$ = $^3J_{4,3}$ = 7.5, $^4J_{4,6}$ = 2.0 Hz, 2 H, 2 × 4-py*H*), 7.34 (td, $^3J_{3,4}$ = 7.5, $^4J_{3,5}$ = $^5J_{3,6}$ = 1.0 Hz, 2 H, 2 × 3-py*H*), 7.23 (ddd, $^3J_{5,4}$ = 7.5, $^3J_{5,6}$ = 5.0, $^4J_{5,3}$ = 1.0 Hz, 2 H, 2 × 5-py*H*), 4.82 (d, *J* = 5.0 Hz, 4 H, 2 × pyCH_2) ppm. $^{13}C\{^1H\}$ NMR (75 MHz, $CDCl_3$): δ = 162.6 (pz*C*O), 156.0 (2-*py*), 149.5 (6-*py*), 146.4 (*pz*CO), 142.4 (*pz*H), 136.9 (4-*py*), 122.6 (5-*py*), 122.1 (3-*py*), 44.7 (*C*H_2) ppm. IR (KBr, disk): $\tilde{\nu}$ = 3458, 3417, 3338, 2922, 1681, 1572, 1522, 1461, 1434, 1363, 1325, 1208, 1177, 1027, 997, 902, 758, 726, 648, 504, 460 cm^{-1}.

***N,N′*-Bis[2-(2-pyridyl)ethyl]pyrazine-2,5-dicarboxamide ($H_2\mathbf{L^2}$):** This compound was synthesised in an analogous manner to the preparation of $H_2\mathbf{L^1}$, using 2-(2-aminoethyl)pyridine (2.69 g, 22.0 mmol) instead of 2-(aminomethyl)pyridine. Yield: 2.68 g (7.12 mmol, 71%). M.p. 225–227 °C. $C_{20}H_{20}N_6O_2$ (376.42): calcd. C 63.82, H 5.36, N 22.33; found C 63.51, H 5.42, N 22.69. TLC (SiO_2, CH_2Cl_2/10% MeOH): R_f = 0.70. ^1H NMR (500 MHz, $CDCl_3$): δ = 9.28 (s, 2 H, 2 × pz*H*), 8.59 (d, *J* = 5.0 Hz, 2 H, 2 × 6-py*H*), 8.54 (s, 2 H, 2 × N*H*), 7.62 (dt, $^3J_{4,5}$ = $^3J_{4,3}$ = 7.8, $^4J_{4,6}$ = 2.0 Hz, 2 H, 2 × 4-py*H*), 7.20–7.16 (m, 4 H, 2 × 3-py*H* and 2 × 5-py*H*), 3.92 (q, *J* = 6.5 Hz, 4 H, 2 × NHCH_2), 3.13 (t, *J* = 6.5 Hz, 4 H, 2 × pyCH_2) ppm. $^{13}C\{^1H\}$ NMR (75 MHz, $CDCl_3$): δ = 162.5 (pz*C*O), 159.1 (2-*py*), 149.5 (6-*py*), 146.4 (*pz*CO), 142.2 (*pz*H), 136.7 (4-*py*), 123.5 (3-*py*), 121.8 (5-*py*), 38.8 (HN*C*H_2), 37.0 (py*C*H_2) ppm. IR (KBr, disk): $\tilde{\nu}$ = 3369, 3092, 3036, 3013, 1985, 2973, 1659, 1590, 1569, 1535, 1475, 1461, 1441, 1367, 1321, 1286, 1263, 1196, 1169, 1049, 1036, 1017, 993, 951, 884, 857, 763, 745, 654, 633, 614, 512, 494, 472, 449 cm^{-1}.

$[Cu^{II}_2(L^1)(H_2O)_2](BF_4)_2$ (1): A solution of $Cu(BF_4)_2$·4 H_2O (149 mg, 482 μmol) in MeCN (10 mL) was added to a hot (60 °C) solution of $H_2\mathbf{L^1}$ (84.0 mg, 241 μmol) in MeCN (10 mL). The re-

 © 2005 Wiley-VCH Verlag GmbH & Co. KGaA, Weinheim

sulting dark bottle-green solution was left at this temperature for 10 minutes and was then cooled to room temperature. By vapour diffusion of Et_2O into the reaction mixture, 106 mg (155 μmol, 64%) of complex **1** were obtained in the form of a dark turquoise solid. Single crystals of $[Cu^{II}_2(\mathbf{L^1})(MeCN)_2(H_2O)_2](BF_4)_2{\cdot}H_2O$ (**1a**·H_2O) suitable for X-ray analysis were obtained by slow evaporation of the reaction solution, obtained as described above. $[Cu^{II}_2(\mathbf{L^1})(H_2O)_2](BF_4)_2$ ($C_{18}H_{18}B_2N_6O_4F_8Cu_2$) (683.08): calcd. C 31.65, H 2.66, N 12.30; found C 31.86, H 2.23, N 12.30. IR (KBr, disk): $\tilde{\nu}$ = 3424, 3110, 2897, 1634, 1567, 1485, 1449, 1436, 1416, 1361, 1350, 1335, 1288, 1214, 1190, 1167, 1083, 1062, 923, 772, 743, 715, 656, 635, 585, 556, 533, 521, 465, 415 cm^{-1}. ESI-MS (pos, MeCN): *m*/*z* (fragment) = 571.5 ($[Cu^{I}Cu^{II}(\mathbf{L^1})(H_2O)(MeCN)_2]^+$), 531.7 ($[Cu^{I}Cu^{II}(\mathbf{L^1})(H_2O)(MeCN)]^+$), 450.7 ($[Cu^{II}(H\mathbf{L^1})(MeCN)]^+$), 276.9 ($[Cu^{II}_2(\mathbf{L^1})(MeCN)_2]^{2+}$), 237.9 ($[Cu^{I}_2(H_2\mathbf{L^1})]^{2+}$), 225.9 ($[Cu^{II}(H_2\mathbf{L^1})(MeCN)]^{2+}$). UV/Vis/NIR (MeCN): $\lambda_{max.}$ (ε) = 212 (34100), 261 (20500), 349 (4200), 641 nm (204 $M^{-1}cm^{-1}$). Λ_m (MeCN) = 231 $\Omega^{-1}mol^{-1}cm^2$.

$[Cu^{II}_2(\mathbf{L^1})(H_2O)_4](SiF_6)$ (1b) and $\{[Cu^{II}_2(\mathbf{L^1})(H_2O)_2(\mu\text{-}SiF_6)]\cdot 4H_2O\}_\infty$ (1c·4H_2O): Solid $H_2\mathbf{L^1}$ (40.1 mg, 115 μmol) was treated with a solution of $Cu(BF_4)_2{\cdot}4H_2O$ (71.1 mg, 230 μmol) in H_2O (5 mL) and the resulting dark bottle green solution was further treated with a solution of NEt_3 (23.3 mg, 230 μmol) in H_2O (3 mL). The resulting blue-green solution was transferred into a sample vial (SAMCO specimen tubes, soda glass, 75 × 25/26 mm, ISO 9002) and was left to slowly evaporate. After 4 weeks 66 mg (96 μmol, 83%) of huge blue-green crystal blocks were isolated by filtration. The crystal blocks analysed as $[Cu^{II}_2(\mathbf{L^1})](SiF_6){\cdot}4H_2O$. Single crystals suitable for X-ray crystal structure determinations, $[Cu^{II}_2(\mathbf{L^1})(H_2O)_4](SiF_6)$ (**1b**) and $\{[Cu^{II}_2(\mathbf{L^1})(H_2O)_2(\mu\text{-}SiF_6)]\cdot 4H_2O\}_\infty$ (**1c**·4H_2O), were selected from these blocks before filtration. $[Cu^{II}_2(\mathbf{L^1})](SiF_6){\cdot}4H_2O$ ($C_{18}H_{22}N_6O_6F_6SiCu_2$) (687.58): C 31.44, H 3.23, N 12.22; found C 31.45, H 3.23, N 12.08. IR (KBr, disk): $\tilde{\nu}$ = 3442, 3084, 2872, 1628, 1563, 1481, 1449, 1407, 1352, 1289, 1214, 1193, 1163, 1111, 1083, 1060, 1026, 981, 961, 923, 780, 750, 651, 556, 512, 472, 417 cm^{-1}. ESI-MS (pos, MeCN): *m*/*z* (fragment) = 451.1($[Cu^{II}(\mathbf{L^1})(MeCN)_2]^+$), 349.2 ($[H_3\mathbf{L^1}]^+$). ESI-MS (neg, MeCN): *m*/*z* (fragment) = 123.0 ($[SiF_5]^-$).

$[Cu^{II}_2(\mathbf{L^2})(solvent)_n](BF_4)_2$ (2): This compound was synthesised in an analogous manner to the preparation of complex **1**, using $H_2\mathbf{L^2}$ (75.3 mg, 200 μmol) instead of $H_2\mathbf{L^1}$. After 10 hours stirring at room temperature complex **2** could be filtered off as a microcrystalline solid. Yield: 74.2 mg (104 μmol, 52%). Single crystals of $[Cu^{II}_2(\mathbf{L^2})(H_2O)_4(BF_4)_2]{\cdot}2H_2O$ (**2b**·2H_2O) suitable for X-ray crystal structure analysis were obtained by recrystallisation of compound **2** from MeCN/EtOH, 1:1. Single crystals of $[Cu^{II}_2(\mathbf{L^2})(H_2O)_2(MeCN)_2](BF_4)_2$ (**2a**) suitable for X-ray crystal structure analysis were obtained by vapour diffusion of Et_2O into the reaction filtrate of an analogous 1:1 molar reaction of ligand to $Cu(BF_4)_2{\cdot}4H_2O$. $[Cu^{II}_2(\mathbf{L^2})(MeCN)_{0.5}(H_2O)](BF_4)_2$ ($C_{21}H_{21.5}B_2N_{6.5}O_3F_8Cu_2$) (713.65): calcd. C 35.34, H 3.04, N 12.76; found C 34.94, H 3.26, N 13.30. IR (KBr, disk): $\tilde{\nu}$ = 3423, 1607, 1539, 1484, 1445, 1400, 1336, 1307, 1254, 1210, 1083, 1034, 869, 770, 688, 626, 590, 533, 521 cm^{-1}. ESI-MS (pos, MeCN): *m*/*z* (fragment) = 1058.7 ($[(Cu^{II}_2(H\mathbf{L^2})(MeCN)(H_2O)_3]^+$). UV/Vis/NIR (MeCN): $\lambda_{max.}$ (ε) = 261 (26400), 346 (2930), 647 nm (113 $M^{-1}cm^{-1}$). Λ_m (MeCN) = 186 $\Omega^{-1}mol^{-1}cm^2$.

Supporting Information: (See also footnote on the first page of this article) A PDF file (5 pages) with supporting information for this article is available on the WWW under http://www.eurjic.org or from the authors. It contains a view of the extended 3D structures of complexes **2a**, **1a**·H_2O and **2b**·2H_2O (Figures S1–S3), a view of the molecular structure of complex **1b** (Figure S4), the curves for the molar magnetic susceptibilities and effective magnetic moments of complexes **1a** and **2b** over the range 300–4.2 K (Figures S5–S8), the EPR spectra in g = 2 and in low-field regions of powdered samples of **1a**·H_2O and **2b**·2H_2O (Figures S9–S12) and some background information on the effect on EPR spectra of dipole–dipole and exchange interactions. CCDC-252079 (for **1a**·H_2O), -252080 (for **1b**), -252081 (for **1c**·4H_2O), -252082 (for **2a**) and -252083 (for **2b**·2H_2O) contain the supplementary crystallographic data for this paper. These data can be obtained free of charge from The Cambridge Crystallographic Data Centre via www.ccdc.cam.ac.uk/data_request/cif.

Acknowledgments

This work was supported by grants from the University of Otago (Postgraduate Scholarship to J. K. and a Bridging Grant) and the Australian Research Council (Discovery Grant). J. F. B. acknowledges support from the School of Physics and Materials Engineering, Monash University. J. K. thanks Dr. M. H. Klingele (University of Otago) for many helpful discussions. S. B. is grateful to the University of Otago for the granting of sabbatical leave which has facilitated the completion of this manuscript and thanks her host Prof. A. K. Powell (University of Karlsruhe) for helpful discussions and the DFG Research Centre for Functional Nanostructures (CFN) for the award of a visiting Professorship. We thank Prof. W. T. Robinson and Dr. J. Wikaira (University of Canterbury) and Prof. G. Clark, Assoc. Prof. P. D. W. Boyd and T. Groutso (University of Auckland) for the X-ray data collections.

[1] M. Ruben, J. Rojo, R. J. Romero-Salguero, L. H. Uppadine, J.-M. Lehn, *Angew. Chem.* **2004**, *116*, 3728–3747; *Angew. Chem. Int. Ed.* **2004**, *43*, 3644–3662.
[2] M. Ruben, E. Breuning, J.-P. Gisselbrecht, J.-M. Lehn, *Angew. Chem.* **2000**, *112*, 4312–4315; *Angew. Chem. Int. Ed.* **2000**, *39*, 4139–4142.
[3] E. Breuning, M. Ruben, J.-M. Lehn, F. Renz, Y. Garcia, V. Ksenofontov, P. Gütlich, E. Wegelius, K. Rissanen, *Angew. Chem.* **2000**, *112*, 2563–2566; *Angew. Chem. Int. Ed.* **2000**, *39*, 2504–2507.
[4] D. L. Caulder, C. Brückner, R. E. Powers, S. König, T. N. Parac, J. A. Leary, K. N. Raymond, *J. Am. Chem. Soc.* **2001**, *123*, 8923–8938.
[5] J. Hausmann, S. Brooker, *Chem. Commun.* **2004**, 1530–1531.
[6] J. Hausmann, G. B. Jameson, S. Brooker, *Chem. Commun.* **2003**, 2992–2993.
[7] D. S. Cati, J. Ribas, J. Ribas-Ariño, H. Stoeckli-Evans, *Inorg. Chem.* **2004**, *43*, 1021–1030.
[8] J. Hausmann, PhD Thesis, University of Otago (NZ), **2004**.
[9] E. B. Fleischer, M. B. Lawson, *Inorg. Chem.* **1972**, *11*, 2772–2775.
[10] E. B. Fleischer, D. Jeter, R. Florian, *Inorg. Chem.* **1974**, *13*, 1042–1047.
[11] W. J. Schut, H. I. X. Mager, W. Berends, *Recl. Trav. Chim. Pays-Bas* **1961**, *80*, 391–398.
[12] P. E. Spoerri, A. Erickson, *J. Am. Chem. Soc.* **1938**, *60*, 400–402.
[13] T. Sakasai, T. Sakamoto, H. Yamanaka, *Heterocycles* **1979**, *13*, 235–238.
[14] A. W. Addison, T. N. Rao, J. Reedijk, J. van Rijn, G. C. Verschoor, *J. Chem. Soc. Dalton Trans.* **1984**, 1349–1356.
[15] C.-Y. Wu, C.-C. Su, *Polyhedron* **1997**, *16*, 383–392.
[16] C.-Y. Wu, C.-C. Su, *Polyhedron* **1997**, *16*, 2465–2474.

 © 2005 Wiley-VCH Verlag GmbH & Co. KGaA, Weinheim

[17] J. M. Rowland, M. M. Olmstead, P. K. Mascharak, *Inorg. Chem.* **2000**, *39*, 5326–5332.
[18] J. M. Rowland, M. M. Olmstead, P. K. Mascharak, *Inorg. Chem.* **2002**, *41*, 1545–1549.
[19] R. R. Rosenthal, *J. Chem. Educ.* **1973**, *50*, 331–335.
[20] I. Krossing, I. Raabe, *Angew. Chem.* **2004**, *116*, 2116–2142; *Angew. Chem. Int. Ed.* **2004**, *43*, 2066–2090.
[21] J. A. Campo, M. Cano, J. V. Heras, M. C. Lagunas, J. Perles, E. Pinilla, M. R. Torres, *Helv. Chim. Acta* **2002**, *85*, 1079–1095.
[22] C.-C. Su, C.-B. Li, *Polyhedron* **1994**, *13*, 825–834.
[23] R. R. Gagné, M. W. McCool, R. E. Marsh, *Acta Crystallogr. Sect. B* **1980**, 2420–2422.
[24] F. S. Keij, R. A. G. De Graaff, J. G. Haasnoot, J. Reedijk, *Inorg. Chim. Acta* **1989**, *156*, 65–70.
[25] P. J. van Konigsbruggen, J. G. Haasnoot, R. A. G. De Graaff, J. Reedijk, *J. Chem. Soc. Dalton Trans.* **1993**, 483–484.
[26] J. S. Fleming, K. L. V. Mann, S. M. Couchman, J. C. Jeffery, J. A. McCleverty, M. D. Ward, *J. Chem. Soc. Dalton Trans.* **1998**, 2047–2052.
[27] E. Breuning, U. Ziener, J.-M. Lehn, E. Wegelius, K. Rissanen, *Eur. J. Inorg. Chem.* **2001**, 1515–1521.
[28] R. A. J. Driessen, F. B. Hulsbergen, W. J. Vermin, J. Reedijk, *Inorg. Chem.* **1982**, *21*, 3594–3597.
[29] S. Subramanian, M. J. Zaworotko, *Angew. Chem.* **1995**, *107*, 2295–2297; *Angew. Chem. Int. Ed. Engl.* **1995**, *34*, 2127–2129.
[30] S.-i. Noro, R. Kitaura, M. Kondo, S. Kitagawa, T. Ishii, H. Matsuzaka, M. Yamashita, *J. Am. Chem. Soc.* **2002**, *124*, 2568–2583.
[31] S.-i. Noro, S. Kitagawa, M. Kondo, K. Seki, *Angew. Chem.* **2000**, *112*, 2161–2164; *Angew. Chem. Int. Ed.* **2000**, *39*, 2081–2084.
[32] E. W. Ainscough, A. M. Brodie, J. D. Ranford, J. M. Waters, *Inorg. Chim. Acta* **1995**, *236*, 83–88.
[33] M. J. R. Clark, J. E. Fleming, H. Lynton, *Can. J. Chem.* **1969**, *47*, 3859–3861.
[34] B. Bleaney, K. D. Bowers, *Proc. R. Soc. Lond. A* **1952**, *214*, 451–465.
[35] J. Hausmann, S. Brooker, unpublished results.
[36] T. D. Smith, J. R. Pilbrow, *Coord. Chem. Rev.* **1974**, *13*, 173–278. See also: A. Bencini, D. Gatteschi, *Electron Paramagnetic Resonance of Exchange Coupled Systems*, Springer Verlag Berlin, Heidelberg, **1990**, Chapter 3.
[37] A. Lagendijk, D. Schoemaker, *Phys. Rev. B* **1977** *16*, 47–55.
[38] A. Bencini, D. Gatteschi, *Electron Paramagnetic Resonance of Exchange Coupled Systems*, Springer Verlag, Berlin, Heidelberg, **1990**, Chapter 6.
[39] G. M. Sheldrick, *Acta Crystallogr., Sect. A* **1990**, *46*, 467–473.
[40] G. M. Sheldrick, *Methods Enzymol.* **1997**, *276*, 628–641.
[41] G. M. Sheldrick, T. R. Schneider, *Methods Enzymol.* **1997**, *277*, 319–343.
[42] J. E. Wertz, J. W. Orton, P. Auzins, *Disc. Faraday Soc.* **1961**, *31*, 140–150.
[43] M. Griffin, A. Muys, C. J. Noble, D. Wang, C. Eldershaw, K. E. Gates, K. Burrage, G. R. Hanson, *Mol. Phys. Rep.* **1999**, *26*, 60–84.

Received: October 27, 2004

 © 2005 Wiley-VCH Verlag GmbH & Co. KGaA, Weinheim

The First Sandwich-Type Heteropolytungstates Consisting of Trivacant Gallium(III)-Substituted Keggin Fragments

Daniel Drewes,[a] Eva Melanie Limanski,[a] and Bernt Krebs*[a]

Keywords: Gallium / Heteropolytungstates / Polyoxometalates / Tungsten

The new polyoxotungstates $(NH_4)_5Na_9[Cu_4(H_2O)_2(GaW_9O_{34})_2]\cdot 22H_2O$ (**1**) and $(NH_4)_{14}[Zn_4(H_2O)_2(GaW_9O_{34})_2]\cdot 37H_2O$ (**2**) were synthesized in aqueous solution and characterized by IR and Raman spectroscopy, energy dispersive X-ray fluorescence and single-crystal X-ray analysis. Compounds **1** and **2** contain the trivacant α-B-$(GaW_9O_{34})^{11-}$ Keggin fragment, which is structurally characterized for the first time. The lacunary $(GaW_9O_{34})^{11-}$ structure exhibits a centered Ga^{III} atom, which is bound to four oxygen atoms and thus achieves a tetrahedral coordination sphere. The synthesis of **1**–**2** enlarges the class of sandwich-type polyoxoanions and enables the syntheses of a new series of gallium(III)-substituted polyoxotungstates.

(© Wiley-VCH Verlag GmbH & Co. KGaA, 69451 Weinheim, Germany, 2005)

Introduction

Polyoxotungstates and -molybdates[1] have been investigated extensively over the last years. Owing to their unique properties, they attract current attention in view of their potential in medicine, material science, and catalysis.[2,3] Beyond the numerous applications, polyoxoanions exhibit impressing and fascinating large structures.[4] Complex and largely unknown self-assembly reaction mechanisms are responsible for the formation of polyoxometalates and make it difficult to develop a straightforward reaction route for their syntheses. It is therefore an important challenge to synthesize polyoxoanions with novel structural features to provide an insight into building reactions. For the exact description of polyoxometalate structures, single-crystal X-ray structure analysis is the most powerful tool as the standard analytical techniques like IR, UV/Vis and elemental analysis are often insufficient.

Within the class of polyoxotungstates, the Keggin anion $(XW_{12}O_{40})^{(8-x)-}$ (where X is the central atom and x its oxidation state) and its defect fragments are the basis for an enormous number of structurally different polyoxoanions. In our work, we focused on the systematic synthesis of sandwich-type polyoxotungstates containing As, Sb and Bi.[5] Sandwich-type polyoxoanions of the $M_4X_2W_{18}$-type constitute a class of structurally interesting compounds in which two trivacant α-*B*-$(XW_9O_{34})^{n-}$ Keggin fragments (X = P^V, As^V, Si^{IV}, Ge^{IV} etc.) are connected via a belt of four transition metals M. The first anion of this type, $[Co_4(H_2O)_2(PW_9O_{34})_2]^{10-}$, was reported in 1973 by Weakley et al.,[6] and the corresponding nickel-substituted anion was published in 1999.[7] Some analogous structures with As^V were described with M = Zn^{II}, Mn^{II}, Co^{II}, Cu^{II}, Cd^{II}, Ni^{II}.[8,5i] Kortz et al. were able expand the number of polyoxoanions of the $M_4X_2W_{18}$ structure type by synthesizing the first examples of silicotungstates $[M_4(H_2O)_2(SiW_9O_{34})_2]^{12-}$ (M = Mn^{II}, Cu^{II}, Zn^{II}) and germanotungstates $[M_4(H_2O)_2(GeW_9O_{34})_2]^{12-}$ (M = Mn^{II}, Cu^{II}, Zn^{II}, Cd^{II}).[9] Our group reported two novel anions of the $M_4X_2W_{18}$-type in which the transition metal M also can be found in the center of the α-*B*-$(XW_9O_{34})^{n-}$ fragment (M = X = Cu^{II}, Fe^{III}).[10]

The selective incorporation of diverse metals M or X is an important aim in polyoxometalate chemistry and makes it possible to modify the properties of the polyoxoanions. For example, the influence on the magnetic properties of transition metals M[11] or main group metals X[12] has been investigated during the last years as well as the effects on the polyoxoanions' catalytic properties.[5a,13] Most of the known structures contain divalent or trivalent transition metals M. Recently, some main-group substituted anions which contain In^{III} and Sn^{II} have been reported.[5h,5j,14] In this paper, we report for the first time on anions consisting of trivacant $(GaW_9O_{34})^{11-}$ Keggin fragments. Only little research was done to date on polyoxometalates containing gallium as a heteroatom. Ga^{III} is used as heteroatom, e.g. in the monovacant Keggin-type anions $[GaW_{11}Ga(OH)O_{39}]^{7-}$[15] and $[GaW_{11}O_{39}Pb]^{7-}$.[16] A Chinese group reported on polyoxoanions of the general formula $[GaW_9M_3O_{40}]^{n-}$ (with M = Mn^{II}, Co^{II}, Ni^{II}, Fe^{III}, V^V), but these compounds were not investigated by X-ray diffraction studies.[17] In 1982 Zonnevijlle characterized POMs of the general formula α-$XM^{III}(OH_2)W_{11}O_{39}^{n-}$ (X = B, Si, Ge, P,

[a] Westfälische Wilhelms-Universität, Institut für Anorganische und Analytische Chemie,
Corrensstraße 30, 48149 Münster, Germany
Fax: +49-251-83-38 366
E-mail: krebs@uni-muenster.de

 © 2005 Wiley-VCH Verlag GmbH & Co. KGaA, Weinheim **DOI: 10.1002/ejic.200400969**

As; M = Al, Ga, In, Tl) and $X_2M^{III}(OH_2)W_{17}O_{61}^{7-}$ (X = P, As; M = Al, Ga, In, Tl) by elemental analysis, UV/Vis and vibrational spectroscopy.

Results and Discussion

The new polyoxotungstates $(NH_4)_5Na_9[Cu_4(H_2O)_2(GaW_9O_{34})_2]\cdot 22\,H_2O$ (**1**) and $(NH_4)_{14}[Zn_4(H_2O)_2(GaW_9O_{34})_2]\cdot 37\,H_2O$ (**2**) were synthesized in aqueous solution by reaction of WO_4^{2-}, Ga^{3+} and the divalent transition metals Cu^{2+} and Zn^{2+}, respectively. The syntheses of **1** and **2** succeeded using $Ga(NO_3)_3\cdot 9\,H_2O$ as well as Ga_2O_3 as starting material. After adding a 1 M solution of NH_4NO_3 or NH_4Cl, single crystals suitable for X-ray diffraction can be obtained by slow evaporation of the solvent. Although in most cases a stoichiometric molar ratio is the best way to synthesize polyoxoanions, we were only able to get single crystals suitable for X-ray diffraction when using an excess of gallium and tungsten.

Figure 1 shows the $[Cu_4(H_2O)_2(GaW_9O_{34})_2]^{14-}$ anion of **1.** The tetranuclear sandwich clusters $[M_4(H_2O)_2(GaW_9O_{34})_2]^{14-}$ (M = Cu^{II}, Zn^{II}) consist of two analogous α-*B*-$(GaW_9O_{34})^{11-}$ subunits, which are connected by a system of four divalent transition metal atoms. The two trivacant subunits can formally be derived from the Keggin structure by removal of three adjacent edge-sharing WO_6 octahedra. The W–O bond lengths and O–W–O bond angles summarized in Table 1 show typical values and differ only slightly from known structures of the $M_4X_2W_{18}$ type. The center of each lacunary anion is occupied by a Ga^{III} atom that is surrounded by four oxygen atoms. The Ga–O bond are in the range of 1.82(1) and 1.84(1) Å for **1** and 1.84(1) and 1.89(1) Å for **2**. We used bond valence calculations to affirm that a gallium atom is situated in the center of the Keggin fragments and to exclude an occupation of this position by the divalent transition metals. The calculated bond valences for the Ga atoms of 3.1 for **1** and 2.7 for **2** are in good agreement with the formal oxidation state +III of the gallium atoms. Modeling these atoms as copper or zinc atoms, respectively, bond valences of 2.7 for **1** and 2.5 for **2** were calculated which are obviously too high for the divalent metal atoms. The results of the elemental analyses confirm that both compounds contain gallium and copper or zinc, respectively, at a ratio of 2:4. However, we cannot exclude a slight disorder of Ga and Zn in **2** as the Ga–O bond lengths are elongated in comparison to **1**.

The two $(GaW_9O_{34})^{11-}$ Keggin fragments are connected through a $M_4O_{14}(H_2O)_2$ belt (M = Cu^{II}, Zn^{II}). The two crystallographically independent Cu atoms in **1** have a distorted octahedral coordination sphere. For Cu(1), each of the subunits provides three oxygen atoms. Cu(2) is bound to one water molecule, two oxygen atoms of one $(GaW_9O_{34})^{11-}$ subunit and three oxygen atoms of the second $(GaW_9O_{34})^{11-}$ subunit. All Cu–O distances are in the range between 1.92(1) and 2.28(1) Å. The O–Cu–O bond angles summarized in Table 1 show the distortion of the CuO_6 octahedra. In **2**, the Zn^{II} atoms are coordinated in the same way and show also an octahedral coordination sphere. The Zn^{II}–O bond lengths range between 2.00(1) and 2.19(1) Å and show that the ZnO_6 octahedra are less distorted than the CuO_6 octahedra. Figure 2 shows the Cu_4 belt in **1** and its linkage to the Ga^{III} atoms of the $(GaW_9O_{34})^{11-}$ Keggin fragments.

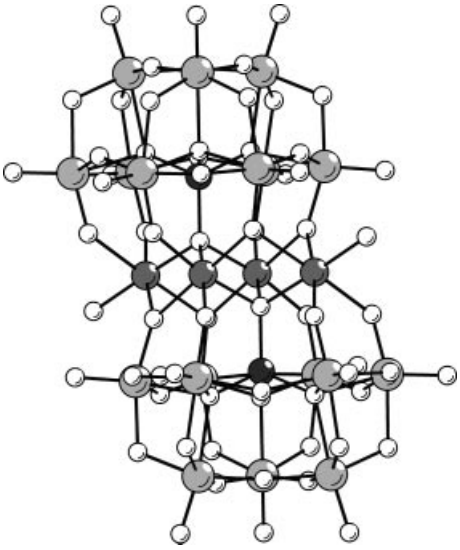

Figure 1. Ball-and-stick representation of the $[Cu_4(H_2O)_2(GaW_9O_{34})_2]^{14-}$ anion in **1**. W light gray, Ga dark gray, Cu middle gray, O white.

Table 1. Selected bond lengths [Å] and angles [°] of **1** and **2** (standard deviations in parentheses). The subscripts indicate the atoms bound to the oxygen atom, t = terminal.

	1 (X = Ga^{III}, M^{II} = Cu^{II})	**2** (X = Ga^{III}, M^{II} = Zn^{II})
W–O_t	1.71(1)–1.76(1)	1.72(1)–1.75(1)
W–O_{W2}	1.88(1)–2.09(1)	1.87(1)–2.06(1)
W–O_{WM}	1.75(1)–1.82(1)	1.76(1)–1.81(1)
W–O_{WM2}	1.82(1)–1.84(1)	1.81(1)–1.83(1)
W–O_{XW3}	2.19(1)–2.31(1)	2.20(1)–2.25(1)
X–O_{XW3}	1.82(1)–1.84(1)	1.88(1)–1.89(1)
X–O_{XM3}	1.83(1)	1.84(1)
M^{II}–O_{WM}	1.92(1)–2.25(1)	2.00(1)–2.16(1)
M^{II}–O_{WM2}	2.06(1)–2.28(1)	2.09(1)–2.19(1)
M^{II}–O_{XM3}	1.98(1)–2.06(1)	2.00(1)–2.01(1)
M^{II}–OH_2	1.99(1)	2.10(1)
O–W–O_{cis}	72.3(5)–105.3(7)	72.3(4)–104.7(5)
O–W–O_{trans}	156.2(5)–173.5(6)	158.8(4)–170.9(4)
O–X–O	105.8(5)–114.3(5)	105.5(4)–113.0(4)
O–M^{II}–O_{cis}	80.7(5)–97.1(6)	81.3(4)–95.7(4)
O–M^{II}–O_{trans}	169.8(5)–177.8(6)	169.9(4)–178.6(4)

The –14 charge of the gallium-substituted polyanions is balanced by nine sodium cations and five ammonium ions in **1** and 14 ammonium ions in **2**. The exact positions of the ammonium ions could not be identified by X-ray diffraction methods as they could not be distinguished from water molecules. However, the results of the elemental analyses are in complete agreement with the formulas of **1** and **2**. In addition, bond valence calculations gave no hints for protonation of the anions.[18]

In both compounds, the anions are linked by an extensive hydrogen bond network. Although the hydrogen atoms

 © 2005 Wiley-VCH Verlag GmbH & Co. KGaA, Weinheim

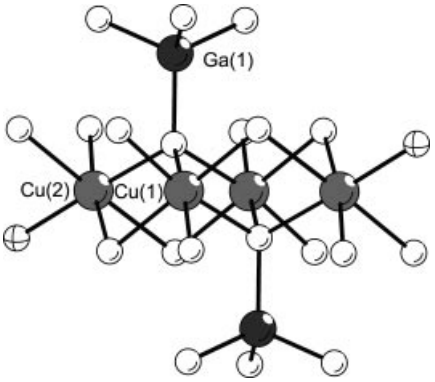

Figure 2. Ball-and-stick representation of the central $Ga_2Cu_4O_{20}(H_2O)_2$ belt in **1.** The color code is the same as in Figure 1, OH white crossed.

have not been located during the refinement, the OW···O and OW···OW distance indicates the linkage of the anions by hydrogen bonds.[18] Even though the anions in **1** and **2** contain transition metals with different chemical characteristics, the metal−metal distances in the $X_2M_4O_{20}(H_2O)_2$ belt show great similarities. The distances given in Table 2 show that these distances differ only slightly in **1** and **2**. In the rhombic M_4O_{16} (M = Cu^{II}, Zn^{II}) fragments, the side lengths of the M_4 unit differ by less than 0.1 Å for both compounds.

Table 2. Metal···metal distances [Å] in **1** and **2** (* = $-x + 1, -y + 1, -z$. ' = $-x + 2, -y + 1, -z + 1$).

	1		**2**
Ga(1)–Cu(1)	3.247(3)	Ga(1)–Zn(1)	3.264(2)
Ga(1)–Cu(2)	3.299(3)	Ga(1)–Zn(2)	3.299(2)
Ga(1)–Cu(1)*	3.327(3)	Ga(1)–Zn(1)′	3.310(3)
Cu(1)–Cu(1)*	3.065(4)	Zn(1)–Zn(1)′	3.032(3)
Cu(1)–Cu(2)	3.076(3)	Zn(1)–Zn(2)	3.102(2)
Cu(1)–Cu(2)*	3.140(3)	Zn(1)–Zn(2)′	3.088(2)

The synthesis of **1** and **2** enables the syntheses of a new series of gallotungstates with the general formula $[M_4(H_2O)_2(GaW_9O_{34})_2]^{n-}$. As the two crystal structures show the synthesis of the $(GaW_9O_{34})^{11-}$ Keggin defect fragments to be reproducible, we think that further anions with M = Co^{II}, Ni^{II}, Mn^{II} or Cd^{II} as heteroatoms can be synthesized.

Conclusions

Two new polyoxotungstates, $(NH_4)_5Na_9[Cu_4(H_2O)_2(GaW_9O_{34})_2]\cdot 22H_2O$ (**1**) and $(NH_4)_{14}[Zn_4(H_2O)_2(GaW_9O_{34})_2]\cdot 37H_2O$ (**2**), were synthesized and characterized by single-crystal X-ray analysis. The present work shows that the class of $M_4X_2W_{18}$ sandwich-type polyoxotungstates can be enlarged by new family of anions with $(GaW_9O_{34})^{9-}$ trivacant lacunary Keggin fragments, which has been synthesized and characterized for the first time. The two exponents of this family with M = Cu^{II} and Zn^{II} establish a new series of tungstates comparable to the known series with X = P^V, As^V, Si^{IV} and Ge^{IV}.

Experimental Section

All starting materials and chemicals were used without further purification.

Preparation of $(NH_4)_5Na_9[Cu_4(H_2O)_2(GaW_9O_{34})_2]\cdot 22H_2O$ (1): $Na_2WO_4\cdot 2H_2O$ (3 g, 9.09 mmol) was dissolved in 20 mL H_2O. The pH value of the solution was adjusted to 7 with concentrated hydrochloric acid. A solution of $Ga(NO_3)_3\cdot 9H_2O$ (0.42 g, 1 mmol) in 2 mL distilled water was added. After stirring the reaction mixture at 70 °C for 15 minutes, a solution of $Cu(CH_3COO)_2\cdot H_2O$ (0.35 g, 1.8 mmol) in 2 mL water was added dropwise. The solution was stirred at 70 °C for one hour. After cooling to room temperature, a greenish residue was removed by filtration and 1 mL of a NH_4NO_3 solution (c = 1 mol/L) was added. Green needles of **1** were obtained on slow evaporation. Yield: 388 mg (16%, based on Cu). IR: $\tilde{\nu}$ (cm^{-1}) = 3477 vs, 1627 s, 1406 m, 931 vs, 882 s, 741 s, 520 w, 455 s. Raman: $\tilde{\nu}$ (cm^{-1}) = 954 s, 780 w, 743 w, 702 w, 628 w 570 w, 512 w, 438 w, 393 w, 327 w, 217 m, 154 m, 106 m. EDX: $Cu_4Ga_2H_{68}N_5Na_9O_{92}W_{18}$ (5505.85): calcd. Cu 4.00, Ga 2.00, W 18.00; found Cu 3.80, Ga 2.15, W 18.00.

Preparation of $(NH_4)_{14}[Zn_4(H_2O)_2(GaW_9O_{34})_2]\cdot 37H_2O$ (2): $Na_2WO_4\cdot 2H_2O$ (4 g, 12.13 mmol) and NaOH (1.0 g, 25 mmol) were dissolved in 50 mL H_2O. A solution of Ga_2O_3 (0.125 g, 0.67 mmol), dissolved in 5 mL of boiling concentrated hydrochloric acid, was added dropwise and the pH was adjusted to 7. The solution was heated to 80 °C and vigorously stirred for two hours. Afterwards, the solution was cooled to room temperature and $Zn(NO_3)_2\cdot 6H_2O$ (446.2 mg, 1.5 mmol), dissolved in 6 mL of water, was added. After 20 minutes, the solution was filtered and 3 mL of a NH_4Cl solution (c = 1 mol/L) was added. Colorless single crystals of **2** were obtained on slow evaporation. Yield: 531 mg (25%, based on Zn). IR: $\tilde{\nu}$ (cm^{-1}) = 3448 vs, br, 2361 w, 2087 w, 1630 s, 1384 m, 925 s, 875 s, 738 s, 451 s. Raman: $\tilde{\nu}$ (cm^{-1}) = 949 s, 900 m, 532 w, 445 w, 351 w, 225 m, 154 m, 107 m. EDX: $Ga_2H_{134}N_{14}O_{107}W_{18}Zn_4$ (5749.40): calcd. Zn 4.00, Ga 2.00, W 18.00; found Zn 4.11, Ga 2.15, W 18.00.

Instrumentation and Analytical Procedures: IR spectra were measured with a Perkin–Elmer 683 spectrometer as KBr pellets. Raman spectra were performed with a Bruker-IFS 113-V-spectrometer. The atomic ratios of the heavy elements were determined by energy dispersive X-ray fluorescence analysis (EDX).

X-ray Crystallography and Data Collection: Diffraction experiments were performed with a STOE IPDS imaging plate system (for **1**) and a Bruker Smart Apex diffractometer with CCD detector (for **2**), both using graphite-monochromated Mo-K_α radiation (λ = 0.71073 Å). Structures were solved by direct methods (for **1**) or Patterson Synthesis (for **2**) with the SHELXS-97[19] and refined with the SHELXL-97 program.[20] No hydrogen atoms were included. Nitrogen atoms of ammonium cations were modeled as oxygen atoms because nitrogen atoms could not be distinguished from oxygen atoms. All metal atoms and oxygen atoms of the anions were refined anisotropically by full-matrix least-squares calculations based on F^2, the crystal water molecules were refined isotropically. The programs SADABS[21] (for **2**) and DECAY[22] (for **1**) were applied as absorption correction. As usual for polyoxometalates, the crystal structures show disorder in the crystal water molecules. Crystallographic data for **1** and **2** are summarized in Table 3.

Further details on the crystal structure investigations may be obtained from the Fachinformationszentrum Karlsruhe, 76344 Eggenstein-Leopoldhafen, Germany; Fax: +49-7247-808-666, E-mail: crysdata@fiz-karlsruhe.de, on quoting the depository number CSD-414617 (for **1**) and CSD-414618 (for **2**).

 © 2005 Wiley-VCH Verlag GmbH & Co. KGaA, Weinheim

Table 3. Crystallographic data for $(NH_4)_5Na_9[Cu_4(H_2O)_2(GaW_9O_{34})_2] \cdot 22\,H_2O$ (**1**) and $(NH_4)_{14}[Zn_4(H_2O)_2(GaW_9O_{34})_2] \cdot 37\,H_2O$ (**2**).

	1	**2**
Formula	$H_{68}Cu_4Ga_2N_5Na_9O_{92}W_{18}$	$H_{134}Ga_2N_{14}O_{107}W_{18}Zn_4$
Formula mass, M [g/mol]	5505.85	5749.40
Crystal color/habit	green needles	colorless needles
Crystal size [mm]	0.9 × 0.1 × 0.1	0.32 × 0.10 × 0.05
Crystal system	orthorhombic	triclinic
Space group	*Pccn*	$P\bar{1}$
a [Å]	21.810(4)	12.401(2)
b [Å]	17.910(4)	13.778(3)
c [Å]	20.360(4)	14.658(3)
α [°]		99.08(3)
β [°]		103.71(3)
γ [°]		102.50(3)
V [Å^3]	7953(3)	2317.0(8)
Z	4	1
$d_{calcd.}$ [g/cm^3]	4.599	4.121
μ [mm^{-1}]	27.805	23.970
T [K]	153(2)	173(2)
Measured reflections	57710	23807
Independent reflections	7781 [R_{int} = 0.1681]	11186 [R_{int} = 0.0603]
Unique refl. [$I > 2\sigma(I)$]	6394	8781
Index range	$-26 \le h \le 26$	$-16 \le h \le 16$
	$-22 \le k \le 22$	$-18 \le k \le 18$
	$-24 \le l \le 25$	$-19 \le l \le 19$
Parameters	356	557
2θ range [°]	$8.52 < 2\theta < 52.08$	$3.94 < 2\theta < 56.08$
R [$I > 2\sigma(I)$]	R_1 = 0.0628[a]	R_1 = 0.0537[a]
	wR_2 = 0.1510[b]	wR_2 = 0.1164[b]
R (all data)	R_1 = 0.0757[a]	R_1 = 0.0732[a]
	wR_2 = 0.1604[b]	wR_2 = 0.1243[b]
Goof on F^2	1.070[c]	1.030[c]
Weighting scheme	a = 0.0874	a = 0.0303
	b = 236.87	b = 32.69
$(\Delta\rho)_{max.}$, [e$^-$Å^3]	2.658	3.406
$(\Delta\rho)_{min.}$, [e$^-$Å^3]	–4.640	–2.941

[a] $R_1 = \Sigma||F_o| - |F_c||/\Sigma|F_o|$. [b] $wR_2 = \{\Sigma[w(F_o^2 - F_c^2)^2]/\Sigma[w(F_o^2)^2]\}^{1/2}$. $w = 1/[\sigma^2(F_o^2) + (aP)^2 + bP]$; with P = (max. $(F_o^2, 0) + 2F_c^2)/3$. [c] Goof = $[(\Sigma w(F_o^2 - F_c^2)^2/(n - p)]^{1/2}$, n = number of reflections, p = parameters used.

Acknowledgments

Support by the Deutsche Forschungsgemeinschaft, the Fonds der Chemischen Industrie, and the Bundesministerium für Bildung und Forschung is gratefully acknowledged. Figure 1 and Figure 2 were generated by Diamond Version 2.1e (copyright Crystal Impact GbR).

[1] a) M. T. Pope, *Heteropoly and Isopoly Oxometalates*, Springer, Berlin, **1983**; b) M. T. Pope, A. Müller (Eds.), *Polyoxometalate Chemistry: From Topology via Self-Assembly to Applications*, Kluwer, Dordrecht, The Netherlands, **2001**.

[2] a) M. T. Pope, A. Müller (Eds.), *Polyoxometalates: from Platonic Solids to Anti-Retroviral Activity*, Kluwer, Dordrecht, The Netherlands, **1994**; b) I. V. Kozhevnikov, *Catalysis by Polyoxometalates*, Wiley, Chichester, **2002**.

[3] a) M. T. Pope, A. Müller, *Angew. Chem.* **1991**, *103*, 56–70; *Angew. Chem. Int. Ed. Engl.* **1991**, *30*, 34–48; b) C. L. Hill, X. Zhang, *Nature* **1995**, *373*, 324–326; c) Y. Inouye, Y. Tokutake, T. Yoshida, A. Yamamoto, T. Yamase, S. Nakamura, *Chem. Pharm. Bull.* **1991**, *39*, 1638–1640; d) C. L. Hill, C. M. Prosser-McCartha, *Coord. Chem. Rev.* **1995**, *143*, 407–455; e) H. Zeng, G. R. Newkome, C. L. Hill, *Angew. Chem.* **2000**, *112*, 1841–1844; *Angew. Chem. Int. Ed.* **2000**, *39*, 1771–1774; f) L. Plault, A. Hauseler, S. Nlate, D. Astruc, J. Ruiz, S. Gatard, R. Neumann, *Angew. Chem.* **2004**, *116*, 2984–2988; *Angew. Chem. Int. Ed.* **2004**, *43*, 2924–2928.

[4] a) K. Wassermann, M. H. Dickman, M. T. Pope, *Angew. Chem.* **1997**, *109*, 1513–1516; *Angew. Chem. Int. Ed. Engl.* **1997**, *36*, 1445–1448; b) A. Müller, E. Krickemeyer, H. Bögge, M. Schmidtmann, F. Peters, *Angew. Chem.* **1998**, *110*, 3567–3571; *Angew. Chem. Int. Ed.* **1998**, *37*, 3360–3363; c) L. Cronin, C. Beugholt, E. Krickemeyer, M. Schmidtmann, H. Bögge, P. Kögerler, T. K. K. Luong, A. Müller, *Angew. Chem.* **2002**, *114*, 2929–2932; *Angew. Chem. Int. Ed.* **2002**, *41*, 2805–2808; d) M. Sadakane, M. H. Dickman, M. T. Pope, *Angew. Chem.* **2000**, *112*, 3036–3038; *Angew. Chem. Int. Ed.* **2000**, *39*, 2914–2916; e) R. C. Howell, F. G. Perez, S. Jain, W. DeWitt Horrocks Jr., A. L. Rheingold, L. C. Francesconi, *Angew. Chem.* **2001**, *113*, 4155–4158; *Angew. Chem. Int. Ed.* **2001**, *40*, 2914–2916; f) P. Mialane, A. Dolbecq, J. Marrot, E. Rivière, F. Sécheresse, *Angew. Chem.* **2003**, *115*, 2324–2327; *Angew. Chem. Int. Ed.* **2003**, *42*, 3523–3526; g) U. Kortz, M. G. Savelieff, B. S. Bassil, M. H. Dickman, *Angew. Chem. Int. Ed.* **2001**, *113*, 3488–3491, *Angew. Chem. Int. Ed. Engl.* **2001**, *40*, 3384–3386; h) U. Kortz, S. S. Hamzeh, N. A. Nasser, *Chem. Eur. J.* **2003**, *9*, 2945–2952.

[5] a) M. Bösing, A. Nöh, I. Loose, B. Krebs, *J. Am. Chem. Soc.* **1998**, *120*, 7252–7259; b) B. Krebs, I. Loose, M. Bösing, A. Nöh, E. Droste, *C. R. Acad. Sci. Ser. IIc* **1998**, 351–360; c) I. Loose, E. Droste, M. Bösing, H. Pohlmann, M. H. Dickman, C. Rosu, M. T. Pope, B. Krebs, *Inorg. Chem.* **1999**, *38*, 2688–2694; d) M. Bösing, I. Loose, H. Pohlmann, B. Krebs, *Chem. Eur. J.* **1997**, *3*, 1232–1237; e) M. Piepenbrink, E. M. Limanski,

 © 2005 Wiley-VCH Verlag GmbH & Co. KGaA, Weinheim

B. Krebs, *Z. Anorg. Allg. Chem.* **2002**, *628*, 1187–1191; f) D. Volkmer, B. Bredenkötter, J. Tellenbröker, P. Kögerler, D. G. Kurth, P. Lehmann, H. Schnablegger, D. Schwahn, M. Piepenbrink, B. Krebs, *J. Am. Chem. Soc.* **2002**, *124*, 10489–10496; g) D. Drewes, E. M. Limanski, M. Piepenbrink, B. Krebs, *Z. Anorg. Allg. Chem.* **2004**, *630*, 58–62; h) E. M. Limanski, D. Drewes, B. Krebs, *Z. Anorg. Allg. Chem.* **2004**, *630*, 523–528; i) D. Drewes, E. M. Limanski, B. Krebs, *Z. Naturforsch.* **2004**, *59b*, 980–984; j) E. Droste, M. Piepenbrink, G. Vollmer, B. Krebs, *C. R. Acad. Sci. Ser. IIc* **2000**, *C3*, 205–210.

[6] T. J. R. Weakley, H. T. Evans Jr., J. S. Showell, G. F. Tourné, C. M. Tourné, *J. Chem. Soc. Chem. Commun.* **1973**, 139–140.

[7] J. M. Clemente-Juan, E. Coronado, J. R. Galán-Mascarós, C. J. Gómez-Garcia, *Inorg. Chem.* **1999**, *38*, 55–63.

[8] a) H. T. Evans, C. M. Tourné, G. F. Tourné, T. J. R. Weakley, *J. Chem. Soc. Dalton Trans.* **1986**, 2699–2705; b) L.-H. Bi, R.-D. Huang, J. Peng, E.-B. Wang, Y.-H. Wang, C.-W. Hu, *J. Chem. Soc. Dalton Trans.* **2001**, 121–129.

[9] a) U. Kortz, S. Isber, M. H. Dickman, D. Ravot, *Inorg. Chem.* **2000**, *39*, 2915–2922; b) U. Kortz, S. Nellutla, A. C. Stowe, N. S. Dalal, U. Rauwald, W. Danquah, D. Ravot, *Inorg. Chem.* **2004**, *43*, 2308–2317.

[10] E. M. Limanski, M. Piepenbrink, E. Droste, K. Burgemeister, B. Krebs, *J. Cluster Sci.* **2002**, *13*, 369–379.

[11] a) N. Casañ-Pastor, J. Bas, E. Coronado, G. Pourroy, L. C. W. Baker, *J. Am. Chem. Soc.* **1992**, *114*, 10380–10383; b) C. J. Cómez-Garcia, E. Coronado, P. Gómez-Romero, N. Casañ-Pastor, *Inorg. Chem.* **1993**, *32*, 3378–3381.

[12] A. C. Stowe, S. Nellutla, N. S. Dalal, U. Kortz, *Eur. J. Inorg. Chem.* **2004**, 3792–3797.

[13] a) R. Neumann, M. Gara, *J. Am. Chem. Soc.* **1995**, *117*, 5066–5074; b) W. Adam, P. L. Alsters, R. Neumann, C. R. Saha-Möller, D. Sloboda-Rozner, R. Zhang, *J. Org. Chem.* **2003**, *68*, 1721–1728, and references cited therein; c) R. Neumann, A. M. Khenkin, *Chem. Commun.* **1998**, 1697–1698.

[14] F. Hussain, M. Reicke, V. Janowski, S. de Silva, J. Futuwi, U. Kortz, *C. R. Chim.* **2005**, doi 10.1016/j.crci.2004.09.017.

[15] F. Zonnevijlle, C. M. Tourné, G. F. Tourné, *Inorg. Chem.* **1982**, *21*, 2742–2750.

[16] G. F. Tourné, C. M. Tourné, A. Schouten, *Acta Crystallogr. Sect. B* **1982**, *38*, 1414–1418.

[17] L.-H. Bi, J. Peng, Y. Chen, J. Lu, L. Qu, *Polyhedron* **1994**, *13*, 2421.

[18] I. D. Brown, D. Altermatt, *Acta Crystallogr. Sect. B* **1985**, *41*, 244–247.

[19] G. M. Sheldrick, *SHELXS-97*, University of Göttingen **1997**.

[20] G. M. Sheldrick, *SHELXL-97*, University of Göttingen **1997**.

[21] SADABS: Area-Detector Absorption Correction, Siemens Industrial Automation, Inc., Madison, WI, **1996**.

[22] Stoe IPDS Software, Version 2.75, Stoe & Cie GmbH, **1996**.

Received: November 22, 2004

 © 2005 Wiley-VCH Verlag GmbH & Co. KGaA, Weinheim

Crystallographic Studies of a Molybdenum-Rich Diarsenotungstate and Reaction of Fe^{III} with Its Isomerically Pure α_1- and α_2-Monolacunary Derivatives

Israel M. Mbomekalle,[a] Yu Wei Lu,[a] Bineta Keita,[a] Louis Nadjo,*[a] Wade A. Neiwert,[b,c] Kenneth I. Hardcastle,[b] Craig L. Hill,*[b] and Travis M. Anderson[b]

Keywords: Polyoxometalates / Cyclic voltammetry / Molybdenum / Iron / Tungsten

An isomerically pure form of the molybdenum-rich polytungstate, $[\alpha_1\text{-}As_2Mo_5W_{12}O_{61}]^{10-}$, was prepared by adding 5 equivalents of Mo^{VI} to $[\alpha\text{-}H_2As_2W_{12}O_{48}]^{12-}$, in the presence of Li^+. The α_2-isomer, $[\alpha_2\text{-}As_2Mo_5W_{12}O_{61}]^{10-}$, was prepared by mild alkaline ($KHCO_3$) degradation of $[\alpha\text{-}As_2Mo_6W_{12}O_{62}]^{6-}$. Both $[\alpha_1\text{-}As_2Mo_5W_{12}O_{61}]^{10-}$ and $[\alpha_2\text{-}As_2Mo_5W_{12}O_{61}]^{10-}$ react with Fe^{III} in aqueous solution to give $[\alpha_1\text{-}As_2(FeOH_2)Mo_5W_{12}O_{61}]^{7-}$ (**1**) and $[\alpha_2\text{-}As_2(FeOH_2)Mo_5W_{12}O_{61}]^{7-}$ (**2**), respectively. The parent complex, $[\alpha\text{-}As_2Mo_6W_{12}O_{62}]^{6-}$, was characterized by X-ray crystallography as a mixed potassium-sodium salt [a = 12.8412(17) Å, b = 14.8145(19) Å, c = 19.913(3) Å, α = 70.058°, β = 81.055(5)°, γ = 64,495°, triclinic, $P\bar{1}$, R_1 = 4.99 % based on 9709 reflections]. All of the complexes were characterized by infrared spectroscopy, cyclic voltammetry, and elemental analyses. ^{183}W NMR studies confirm that **1** and **2** are isomerically pure compounds.

(© Wiley-VCH Verlag GmbH & Co. KGaA, 69451 Weinheim, Germany, 2005)

Introduction

Polyoxometalates (POMs) are a versatile family of molecular metal oxide clusters with applications in catalysis as well as in medicine and material science.[1–4] Interest in the preparation of isomerically pure polytungstate complexes from lacunary (i.e. tungsten-deficient) precursors continues to be at the center of much of this ongoing research. The first coordination complexes derived from the Wells-Dawson anion, $[\alpha\text{-}P_2W_{18}O_{62}]^{6-}$, were prepared using the monotungsten-vacant derivatives, $[\alpha_1\text{-}P_2W_{17}O_{61}]^{10-}$ and $[\alpha_2\text{-}P_2W_{17}O_{61}]^{10-}$.[5] Later, the tri- and hexatungsten-vacant species ($[\alpha\text{-}P_2W_{15}O_{56}]^{12-}$ and $[\alpha\text{-}H_2P_2W_{12}O_{48}]^{12-}$, respectively) were used.[6,7]

Among the various derivatives prepared by metal incorporation into $[\alpha\text{-}P_2W_{15}O_{56}]^{12-}$ and $[\alpha\text{-}H_2P_2W_{12}O_{48}]^{12-}$, those containing Mo^{VI} or simultaneously Mo^{VI} and a first-row transition metal cation are of particular interest for their electrocatalytic properties.[8,9] It is well established that the presence of one or more molybdenum centers in the polytungstate framework can significantly improve the catalytic properties of the complex. For example, electrocatalysis of NO reduction with $[\alpha_2\text{-}P_2MoW_{17}O_{62}]^{6-}$ was observed at a potential which was 0.270 V more positive than that necessary to carry out the same process with $[\alpha\text{-}P_2W_{18}O_{62}]^{6-}$.[10,11]

Substantial changes in the electrochemical properties of the complexes were also observed upon introducing Fe^{III} centers into a mixed-molybdenum-tungsten framework.[12–14] In a pH 2 medium, the Mo^{VI} centers in $[\alpha\text{-}P_2Mo_3W_{15}O_{62}]^{6-}$ are reduced through three diffusion-controlled one-electron waves. In contrast, $[\alpha_2\text{-}P_2(FeOH_2)Mo_2W_{15}O_{61}]^{7-}$ displays a single three-electron wave in a pH 2 medium as a result of pH-induced merging of the molybdenum and iron waves.

As part of an ongoing program designed to prepare new electrocatalysts for multi-electron transfer reactions,[12,15,16] we now report the isomerically pure preparations of the molybdenum-rich polytungstates, $[\alpha_1\text{-}As_2(FeOH_2)Mo_5W_{12}O_{61}]^{7-}$ (**1**) and $[\alpha_2\text{-}As_2(FeOH_2)Mo_5W_{12}O_{61}]^{7-}$ (**2**). These complexes are formed by the reaction of Fe^{III} with the lacunary precursors, $[\alpha_1\text{-}As_2Mo_5W_{12}O_{61}]^{10-}$ and $[\alpha_2\text{-}As_2Mo_5W_{12}O_{61}]^{10-}$, respectively. Both of these species are structurally derived from $[\alpha\text{-}As_2Mo_6W_{12}O_{62}]^{6-}$ (**3**),[17] which is now characterized by X-ray crystallography. The focus of this manuscript will remain exclusively with the As^V species (rather than the complete isomerically pure P^V series) since $[\alpha_1\text{-}P_2(FeOH_2)Mo_5W_{12}O_{61}]^{7-}$ has not yet been prepared and the first several voltammetric waves of the complexes are driven to more positive potentials by the presence of As^V.[18]

[a] Laboratoire de Chimie Physique, UMR 8000, CNRS, Université Paris-Sud,
Bâtiment 420, 91405 Orsay Cedex, France
E-mail: nadjo@lcp.u-psud.fr
[b] Department of Chemistry, Emory University,
Atlanta, Georgia, 30322, USA
[c] Current address: Department of Chemistry, Bethel University,
St. Paul, Minnesota, 55112, USA
Supporting information for this article is available on the WWW under http://www.eurjic.com or from the author.

Results and Discussion

Syntheses: Recently we reported the stereospecific synthesis of $[\alpha\text{-}As_2Mo_6W_{12}O_{62}]^{6-}$ (**3**).[17] Three parameters were identified in order to achieve high yield and high purity. First, the synthesis must be performed in highly acidic media. Second, a 25% molar excess of molybdate (relative to $[\alpha\text{-}H_2As_2W_{12}O_{48}]^{12-}$) must be used in order to prevent the formation of byproducts. Finally, the order of the addition of reactants is important (i.e. solid $K_{12}H_2[\alpha\text{-}As_2W_{12}O_{48}]$ must be slowly added to the molybdate solution in order to keep the Mo concentration as high as possible). Pure complex **3** was the precursor required for the synthesis of $[\alpha_2\text{-}As_2Mo_5W_{12}O_{61}]^{10-}$ (Scheme 1). In contrast, the synthesis of $[\alpha_1\text{-}As_2Mo_5W_{12}O_{61}]^{10-}$ was achieved by adding 5 equivalents of Mo to $[\alpha\text{-}H_2As_2W_{12}O_{48}]^{12-}$, in the presence of Li^+. Syntheses of $[\alpha_1\text{-}As_2(FeOH_2)Mo_5W_{12}O_{61}]^{7-}$ (**1**) and $[\alpha_2\text{-}As_2(FeOH_2)Mo_5W_{12}O_{61}]^{7-}$ (**2**) were straightforward and involved the gentle heating of aqueous mixtures of Fe^{III} and $[\alpha_1\text{-}As_2Mo_5W_{12}O_{61}]^{10-}$ or $[\alpha_2\text{-}As_2Mo_5W_{12}O_{61}]^{10-}$, respectively (Scheme 1). In the case of **1**, excessive heating must be avoided in order to prevent the conversion of **1** to **2** (by "hole migration").[19]

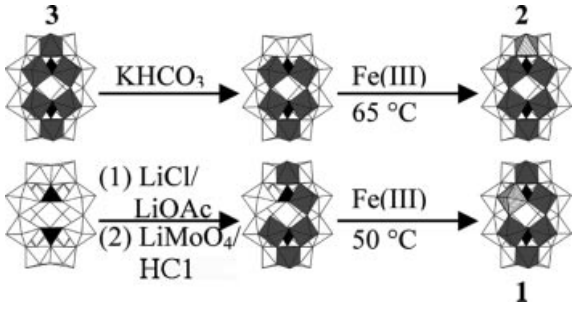

Scheme 1. Synthesis of complexes **1** and **2** from $[\alpha\text{-}H_2As_2W_{12}O_{48}]^{12-}$ and **3**, respectively.

Crystallographic Studies: X-ray quality crystals of $[\alpha\text{-}As_2Mo_6W_{12}O_{62}]^{6-}$ (Scheme 2) were grown by allowing an aqueous solution of the POM (in 1 M NaCl) to slowly evaporate in air over two months. However, over this time period the complex starts to decompose. As a result, the crystals that are obtained are a mixture of 50% $[\alpha\text{-}As_2Mo_6W_{12}O_{62}]^{6-}$ and 50% $[\alpha\text{-}As_2W_{18}O_{62}]^{6-}$. The data show that a contiguous longitudinal strip of six MO_6 (M = metal) sites (one on each cap position and two on each belt position)[20] are 50% MoO_6 and 50% WO_6 (positions 1, 4, 9, 10, 15, and 16 in Scheme 2). The remaining 12 MO_6 sites are 100% WO_6 (two on each cap position and four on each belt position). This assignment is confirmed by elemental analyses which show that the ratio of As:Mo:W is 2:3:15. A thermal ellipsoid plot with 50% probability surfaces is provided in the Supporting Information.

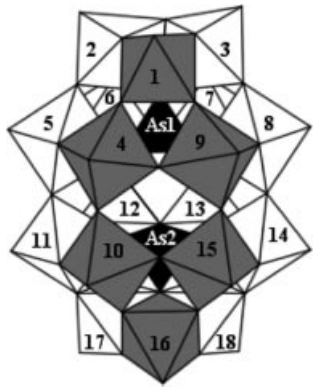

Scheme 2. Numbering scheme for $[\alpha\text{-}As_2Mo_6W_{12}O_{62}]^{6-}$. The MoO_6 octahedra are shown in gray, the WO_6 octahedra are shown in white, and the AsO_4 tetrahedra are shown in black.

Spectroscopic Studies: The infrared spectrum of **3** has a slight shift of the frequencies toward lower wave numbers relative to $[\alpha\text{-}As_2W_{18}O_{62}]^{6-}$ as a result of the weakening of bond force constants imposed by the substitution of Mo^{VI} for W^{VI}.[17] A similar trend is observed for the substitution of Fe^{III} for Mo^{VI} in **1** and **2**. In addition, the incorporation of Fe^{III} into the vacant sites of $[\alpha_1\text{-}As_2Mo_5W_{12}O_{61}]^{10-}$ and $[\alpha_2\text{-}As_2Mo_5W_{12}O_{61}]^{10-}$ partially restores the symmetry in the substituted molecules. The infrared spectra of **1** and **2** are quite similar, but they are clearly distinguishable from their lacunary precursors $[\alpha_1\text{-}As_2Mo_5W_{12}O_{61}]^{10-}$ and $[\alpha_2\text{-}As_2Mo_5W_{12}O_{61}]^{10-}$ (see Supporting Information).

Table 1 gives the ^{183}W NMR chemical shift values for **1**, **2**, and **3** in aqueous buffer solutions. The substitution of a paramagnetic Fe^{III} center into the mixed-molybdenum-tungsten framework of **1** and **2** results in a substantial broadening of the signals for the two most structurally proximal W^{VI} centers such that they are not observed in the spectrum. Previously it was established (primarily by ^{31}P NMR studies) that the presence of paramagnetic metal centers results in dramatic chemical shift changes and/or substantial broadening of signals.[5b] Low solubility and low stability prevented the acquisition of ^{183}W NMR spectroscopic data on the lacunary precursors $[\alpha_1\text{-}As_2Mo_5W_{12}O_{61}]^{10-}$ and $[\alpha_2\text{-}As_2Mo_5W_{12}O_{61}]^{10-}$.

Electrochemical Studies: The electrochemical properties of **3** were previously studied in a pH = 0.33 medium suitable for its stability.[17] The observed pattern consists of three chemically reversible waves featuring three quasi-reversible two-electron processes. The cyclic voltammograms of **1**, **2**, $[\alpha_1\text{-}As_2Mo_5W_{12}O_{61}]^{10-}$, and $[\alpha_2\text{-}As_2Mo_5W_{12}O_{61}]^{10-}$ were

Table 1. ^{183}W NMR chemical shift values (vs. 2 M Na_2WO_4 in D_2O) for complexes **1**, **2**, and **3**.

Compound	^{183}W NMR chemical shifts (ppm)	Reference
1	–89.1 (2 W), –115.0 (2 W), –168.1 (2 W), –183.1 (2 W), –191.3 (2 W)	this work
2	–84.3 (2 W), –103.9 (4 W), –150.2 (4 W)	this work
3	–130.2 (4 W), –138.8 (4 W), –156.6 (4 W)	[17]

 © 2005 Wiley-VCH Verlag GmbH & Co. KGaA, Weinheim

run at a scan rate of 10 mV s^{-1} in a 1 M CH_3COOLi/CH_3COOH (pH = 5) medium. The electrolyte was chosen to ensure the stability of all four of the compounds. Given the fact that the Mo^{VI} and Fe^{III} waves of $[\alpha_2\text{-}P_2(FeOH_2)Mo_2W_{15}O_{61}]^{7-}$ merge in a pH = 2 medium but become increasingly split at higher pH values,[12,13] similar behavior was anticipated for **1** and **2**. Figure 1 compares the cyclic voltammograms of **1** and **2** with those of their lacunary precursors, $[\alpha_1\text{-}As_2Mo_5W_{12}O_{61}]^{10-}$ and $[\alpha_2\text{-}As_2Mo_5W_{12}O_{61}]^{10-}$, respectively. The patterns were restricted to those waves for which derivatization of the electrode surface is not expected. The superposition of the waves highlights their differences, and in analogy with previous work,[12,13,15b,16,17,21,22] facilitates the assignments of the first several waves. In addition, assignment of the waves is further facilitated by the fact that it is well established that the first electron transfer should occur on one of the "belt" atoms.[9b] With these guidelines in mind, each of the first two waves of **1** and $[\alpha_1\text{-}As_2Mo_5W_{12}O_{61}]^{10-}$ moving toward less positive potentials features a one-electron quasi-reversible process, with Mo^{VI} being more easily reduced than the Fe^{III} center. The apparent redox potential of this first wave, estimated as the average between the cathodic and anodic peak potentials, was +0.134 V vs. SCE. In contrast, the first two one-electron redox processes of $[\alpha_2\text{-}As_2Mo_5W_{12}O_{61}]^{10-}$ are almost completely merged, while those of **2** are well separated with an apparent redox potential of +0.096 V (vs. SCE) for the first wave of the latter. Thus electrochemistry establishes clear differences between all four of the POMs in a pH = 5 medium, at least regarding the location of the potential of the first wave and/or the number of electrons consumed on this first wave. Finally, as anticipated, there is a close similarity observed between the present As^V-based POMs and the corresponding P^V-based complex, $[\alpha_2\text{-}P_2(FeOH_2)Mo_5W_{12}O_{61}]^{7-}$.[16]

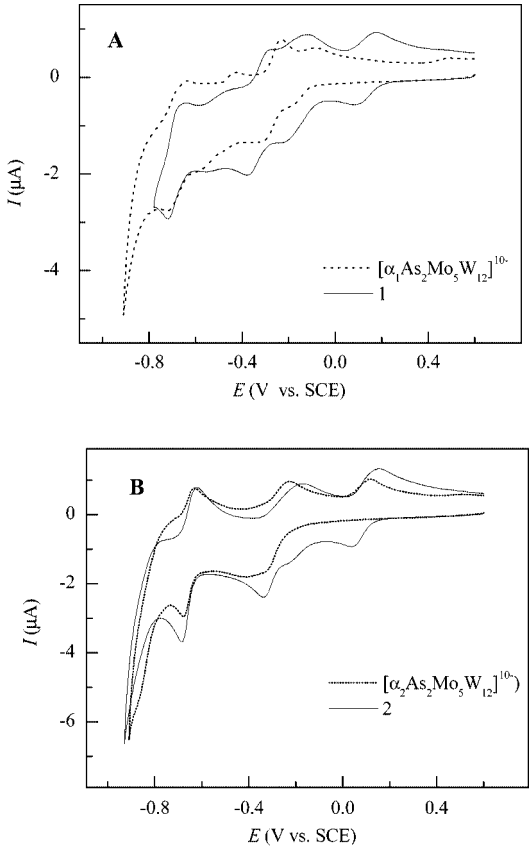

Figure 1. Cyclic voltammograms of 0.2 mM solutions of (**A**) **1** and $[\alpha_1\text{-}As_2Mo_5W_{12}O_{61}]^{10-}$ and (**B**) **2** and $[\alpha_2\text{-}As_2Mo_5W_{12}O_{61}]^{10-}$ in a 1 M CH_3COOLi/CH_3COOH (pH = 5) buffer solution. The working electrode was glassy carbon, the reference electrode was SCE, and the scan rate was 10 mV·s^{-1}.

Conclusions

Molybdenum-rich polytungstates are of proven value in electrocatalysis. However, the preparation of isomerically pure complexes is challenging, in part, due to the high lability of the Mo^{VI} centers. Isomerically pure preparations of $[\alpha_1\text{-}As_2(FeOH_2)Mo_5W_{12}O_{61}]^{7-}$ (**1**) and $[\alpha_2\text{-}As_2(FeOH_2)Mo_5W_{12}O_{61}]^{7-}$ (**2**) were achieved by the reaction of Fe^{III} with the lacunary precursors, $[\alpha_1\text{-}As_2Mo_5W_{12}O_{61}]^{10-}$ and $[\alpha_2\text{-}As_2Mo_5W_{12}O_{61}]^{10-}$, respectively. Both of these species are structurally derived from $[\alpha\text{-}As_2Mo_6W_{12}O_{62}]^{6-}$ (**3**), which is now characterized by X-ray crystallography. The results show that positions 1, 4, 9, 10, 15, and 16 in Scheme 2 are 50% MoO_6 and 50% WO_6. Electrochemical studies reveal that complexes **1** and **2** (and their lacunary precursors) are all clearly distinguishable by cyclic voltammetry.

Experimental Section

General Methods and Materials: $K_6[\alpha\text{-}As_2Mo_6W_{12}O_{62}]\cdot 12H_2O$ and $K_{12}H_2[\alpha\text{-}As_2W_{12}O_{48}]\cdot 23H_2O$ were obtained by published procedures.[17,19,23] Elemental analyses were performed by Kanti Labs (Mississauga, Ontario), and the analysis of W was confirmed by a modified literature method.[24] The water content of the samples was determined by standard methods. Infrared spectra (2% sample in KBr) were recorded with a Perkin–Elmer Spectrum One FT-IR spectrometer. NMR spectra were recorded with a Bruker 400 instrument operating at 16.67 MHz. The ^{183}W chemical shifts were measured with respect to an external 2 M Na_2WO_4 solution in alkaline D_2O.

Synthesis of $K_9Li[\alpha_1\text{-}As_2Mo_5W_{12}O_{61}]\cdot 28H_2O$: A sample of pure α-$K_{12}H_2[As_2W_{12}O_{48}]\cdot 23H_2O$ (12 g; 3 mmol) was dissolved in a solution containing 150 mL of 1 M LiCl and 50 mL of 0.5 M CH_3COOLi (pH ≈ 4.7). This relatively cloudy solution was treated with 15 mL of 1 M $LiMoO_4$ (15 mmol) and 30 mL of 1 M HCl to keep the pH constant (≈ 4.7). The resulting clear, very faintly yellow solution was treated with 60 mL of a saturated KCl solution. The off-white precipitate was filtered (by suction filtration), washed twice with ethyl alcohol and twice with ethyl ether, and dried in air. The amount of pure compound obtained was 13.50 g (yield 96.5% relative to the starting material, α-$K_{12}H_2[As_2W_{12}O_{48}]\cdot 23H_2O$). $K_9Li[\alpha_1\text{-}As_2Mo_5W_{12}O_{61}]\cdot 28H_2O$ (4675): calcd. As 3.19, K 7.45, Mo 9.76, W 46.9; found As 3.21, K 7.52, Mo 10.26, W 47.2. IR (cm^{-1}): $\tilde{\nu}$ = 943.3 (s), 855.3 (w), 823.3 (w), 782.8 (vw), 743.1 (w), 513.7 (vw), 497.9 (w), 419.5 (vw).

Synthesis of $K_{10}[\alpha_2\text{-}As_2Mo_5W_{12}O_{61}]\cdot 21H_2O$: A sample of pure α-$K_6[As_2Mo_6W_{12}O_{62}]\cdot 12H_2O$ (10 g; 2.3 mmol) was dissolved in

 © 2005 Wiley-VCH Verlag GmbH & Co. KGaA, Weinheim

25 mL of de-ionized water. A 22 mL aliquot of 1 M $KHCO_3$ (22 mL; 22 mmol) was then added to the clear solution. A yellow precipitate formed progressively and was left to settle for ca. 45 min, after which it was filtered, washed twice successively with ethyl alcohol and ethyl ether, and dried in air. The amount of pure compound was 10.00 g (yield 94.9% relative to the starting material, α-$K_6[As_2Mo_6W_{12}O_{62}]\cdot 12H_2O$). $K_{10}[\alpha_2\text{-}As_2Mo_5W_{12}O_{61}]\cdot 21H_2O$ (4581): calcd: As 3.31; K 8.61; Mo 10.7, W 48.3; found As 3.27, K 8.54, Mo 10.47, W 48.2. IR (cm^{-1}): $\tilde{\nu}$ = 938.6 (s), 862.5 (s), 818.8 (m), 784.1 (m), 711.0 (s), 519.6 (w), 498.7 (w), 419.1 (w).

Synthesis of $K_7[\alpha_1\text{-}As_2(FeOH_2)Mo_5W_{12}O_{61}]\cdot 22H_2O$: A sample of $Fe(NO_3)_3\cdot 9H_2O$ (0.30 g; 0.75 mmol) was dissolved in 40 mL of deionized water. Then, solid $K_9Li[\alpha_1\text{-}As_2Mo_5W_{12}O_{61}]\cdot 28H_2O$ (3.0 g; 0.64 mmol) was added in small portions. The mixture was heated very gently on a water bath (≈ 50 °C) to enhance solubility. After ca. 20 min, the pale yellow solution was filtered and treated with 5 g of solid KCl. The yellow precipitate that formed was filtered off, washed successively (twice with a saturated KCl solution and twice with ethyl alcohol), and dried in air. The amount of pure compound obtained was 1.70 g (yield 58.2% relative to the starting material, $K_9Li[\alpha_1\text{-}As_2Mo_5W_{12}O_{61}]\cdot 28H_2O$). $K_7[\alpha_1\text{-}As_2(FeOH_2)Mo_5W_{12}O_{61}]\cdot 22H_2O$ (4538): calcd. As 3.26, Fe, 1.25, K 6.12, Mo 10.6, W 48.5, found As 3.29, Fe 1.22, K 6.01, Mo 10.53, W 48.4. IR (cm^{-1}): $\tilde{\nu}$ = 957.0 (s), 882.9 (w), 854.7 (w), 823.3 (w), 762.9 (s), 520.6 (w), 495.7 (w), 420.1 (m).

Synthesis of $K_7[\alpha_2\text{-}As_2(FeOH_2)Mo_5W_{12}O_{61}]\cdot 19H_2O$: A sample of $Fe(NO_3)_3\cdot 9H_2O$ (0.30 g; 0.75 mmol) was dissolved in 40 mL of deionized water. Then, solid $K_{10}[\alpha_2\text{-}As_2Mo_5W_{12}O_{61}]\cdot 21H_2O$ (3.0 g; 0.65 mmol) was added in small portions. The mixture was heated gently on a water bath (≈ 65 °C) to enhance solubility. After ca. 20 min, the pale yellow solution was filtered and treated with 5 g of solid KCl. The yellow precipitate that formed was filtered off, washed successively (twice with a saturated KCl solution and twice with ethyl alcohol), and dried in air. The amount of pure compound obtained was 2.60 g (yield 89.3% relative to the starting material, $K_{10}[\alpha_2\text{-}As_2Mo_5W_{12}O_{61}]\cdot 21H_2O$). $K_7[\alpha_2\text{-}As_2(FeOH_2)Mo_5W_{12}O_{61}]\cdot 19H_2O$ (4484): calcd. K 6.19, As 3.37, Fe 1.32, Mo 10.9, W 50.3, found As 3.37, Fe 1.25; K 6.15, Mo 10.79, W 49.6. IR (cm^{-1}): $\tilde{\nu}$ = 954.1 (s), 882.8 (w), 854.5 (vw), 823.3 (vw), 763.1 (s), 655.3 (w), 522.6 (m), 490.9 (m), 421.7 (s).

Crystallographic Studies of $K_2Na_4[\alpha\text{-}As_2Mo_6W_{12}O_{62}]_{0.5}[\alpha\text{-}As_2W_{18}O_{62}]_{0.5}\cdot 11H_2O$: Single-crystal X-ray crystallographic analysis of $[\alpha\text{-}As_2Mo_6W_{12}O_{62}]^{6-}$ was performed at 173 K with a Bruker D8 SMART APEX CCD sealed tube diffractometer with graphite-monochromated Mo-K_α (0.71073 Å) radiation. Data collection, indexing, and initial cell refinements were performed using SMART software.[25] Frame integration and final cell refinements were performed using SAINT software.[26] Final cell parameters were determined from least-squares refinement on 9709 reflections. Absorption corrections were applied using SADABS.[27] The structure was determined using Direct Methods and difference Fourier techniques. No H atoms associated with the eleven water molecules of $[\alpha\text{-}As_2Mo_6W_{12}O_{62}]^{6-}$ were located in the difference Fourier maps. The final R_1 scattering factor and the anomalous dispersion correction were taken from International Tables for X-ray Crystallography.[28] Structure solution, refinement, and generation of publication materials were performed using SHELXTL V6.12 software. Additional details are provided in Table 2, and may also be obtained from the Fachinformationszentrum Karlsruhe, 76344 Eggenstein-Leopoldshafen, Germany; Fax: +49-7247-808-666, E-mail: crysdata@fiz-karlsruhe.de, on quoting the depository number CSD-414645. Elemental analyses (As, K, Mo, Na and W) on the crystals were performed by Desert Analytics (Tucson, Arizona). $K_2Na_4[\alpha\text{-}As_2Mo_6W_{12}O_{62}]_{0.5}[\alpha\text{-}As_2W_{18}O_{62}]_{0.5}\cdot 11H_2O$ (4556): calcd. As 3.29, K 1.72, Mo 6.32, Na 2.02, OH_2 4.3, W 60.5, found As 3.27, K 1.69, Mo 6.34, Na 2.10, OH_2 4.3, W 59.8.

Table 2. Crystallographic data and structure refinement for $K_2Na_4[\alpha\text{-}As_2Mo_6W_{12}O_{62}]_{0.5}[\alpha\text{-}As_2W_{18}O_{62}]_{0.5}\cdot 11H_2O$.

Empirical formula	$H_{22}As_2K_2Mo_3Na_4O_{73}W_{15}$
Formula mass	4555.75
Space group	$P\bar{1}$
Unit cell [Å, °]	a = 12.8412(17)
	b = 14.8145(19)
	c = 19.913(3)
	α = 70.058(4)
	β = 81.055(5)
	γ = 64.495(4)
V [Å^3]	3213.8(7)
Z	2
Density (calcd.) [g•cm^{-3}]	4.708
Temperature [K]	173(2)
λ [Å]	0.71073
M [cm^{-1}]	2.8588
GOF	1.066
Final R_1[a] [$I > 2\sigma(I)$]	0.0499
Final wR_2[b] [$I > 2\sigma(I)$]	0.1314

[a] $R_1 = \Sigma||F_o| - |F_c||/|F_o|$. [b] $R_2 = \{\Sigma[w(F_o^2 - F_c^2)^2]/\Sigma[w(F_o^2)^2]\}^{0.5}$.

Electrochemical Studies: Cyclic voltammetry studies were performed in a pH 5 acetate (1.0 M CH_3COOLi/CH_3COOH) medium. Solutions were de-aerated with Ar for at least 30 min prior to measurements and kept under positive pressure at all times. The source, mounting, and polishing of the glassy carbon electrodes (GC, Tokai, Japan, 3 mm diameter) have been described in previous work.[21] The electrochemical apparatus was a EG and G 273A under computer control (M270 software). The counter electrode was a platinum gauze of large surface area. All experiments were performed at ambient temperature, and potentials are quoted against a saturated calomel electrode (SCE).

Acknowledgments

This work was supported in part by the University Paris XI and the CNRS (UMR, 8000) and in part by the United States Department of Energy (DOE) (grant number DE-FG02-03ER15461).

[1] M. T. Pope, *Heteropoly and Isopoly Oxometalates*, Springer-Verlag, Berlin, **1983**.
[2] C. L. Hill (Guest Ed.) *Chem. Rev.* **1998**, *98*, 1–389.
[3] M. T. Pope, Polyoxo Anions: Synthesis and Structure, in *Comprehensive Coordination Chemistry II: Transition Metal Groups 3–6* (Ed.: A. G. Wedd), Elsevier Science: New York, **2004**; vol. 4, chapter 4.10, pp. 635–678.
[4] a) R. Neumann, Applications of Polyoxometalates in Homogeneous Catalysis. In *NATO Science Series II: Mathematics, Physics, and Chemistry*; Kluwer Academic Publishers: Dordrecht, **2003**; vol. 98, pp. 327–349; b) I. V. Kozhevnikov, Heterogeneous Catalysis by Heteropoly Compounds, in *NATO Science Series II: Mathematics, Physics, and Chemistry*; Kluwer Academic Publishers: Dordrecht, **2003**; vol. 98, pp. 351–380; c) E. Papaconstantinou, A. Hiskia, Photochemistry and Photocatalysis by Polyoxometalates, in *NATO Science Series II: Mathematics, Physics, and Chemistry*; Kluwer Academic Publishers: Dordrecht, **2003**; vol. 98, pp. 381–416; d) C. L. Hill, Polyoxometalates: Reactivity, in *Comprehensive Coordination Chemistry II: Transition Metal Groups 3–6* (Ed.: A. G. Wedd), Elsevier Science: New York, **2004**; vol. 4, chapter 4.11, pp. 679–759.

[5] Representative work includes: a) S. A. Malik, T. J. R. Weakley, *J. Chem. Soc., A* **1968**, 2647–2650; b) T. L. Jorris, M. Kozik, N. Casan-Pastor, P. J. Domaille, R. G. Finke, W. K. Miller, L. C. W. Baker, *J. Am. Chem. Soc.* **1987**, *109*, 7402–7408; c) R. Contant, in *Inorganic Syntheses* (Ed.: A. P. Ginsberg), John Wiley & Sons: New York, **1990**; vol. 27, pp. 104–111; d) D. K. Lyon, W. K. Miller, T. Novet, P. J. Domaille, E. Evitt, D. C. Johnson, R. G. Finke, *J. Am. Chem. Soc.* **1991**, *113*, 7209–7221, and references cited therein.

[6] Representative work on $[\alpha\text{-}P_2W_{15}O_{56}]^{12-}$ includes: a) R. G. Finke, M. W. Droege, P. J. Domaille, *Inorg. Chem.* **1987**, *26*, 3886–3896; b) T. M. Anderson, X. Zhang, K. I. Hardcastle, C. L. Hill, *Inorg. Chem.* **2002**, *41*, 2477–2488; c) B. J. Hornstein, R. G. Finke, *Inorg. Chem.* **2002**, *41*, 2720–2730.

[7] Representative work on $[\alpha\text{-}H_2P_2W_{12}O_{48}]^{12-}$ includes: a) R. Contant, A. Tézé, *Inorg. Chem.* **1985**, *24*, 4610–4614; b) Ref. [5c]; c) D. A. Judd, Q. Chen, C. F. Campana, C. L. Hill, *J. Am. Chem. Soc.* **1997**, *119*, 5461–5462; d) R. Contant, M. Abbessi, R. Thouvenot, G. Hervé, *Inorg. Chem.* **2004**, *43*, 3597–3604.

[8] M. Sadakane, E. Steckhan, *Chem. Rev.* **1998**, *98*, 219–237.

[9] Representative examples of studies of the electrochemical properties of Mo-substituted polytungstates include: a) B. Keita, L. Nadjo, R. Contant, *J. Electroanal. Chem.* **1998**, *443*, 168–174; b) B. Keita, Y. Jean, B. Levy, L. Nadjo, R. Contant, *New J. Chem.* **2002**, *26*, 1314–1319.

[10] A. Belhouari, B. Keita, L. Nadjo, R. Contant, *New J. Chem.* **1998**, 83–86.

[11] Electrocatalysis with $[\alpha\text{-}P_2Mo_{18}O_{62}]^{6-}$ was observed at a potential which was 0.390 V more positive than the same process with $[\alpha\text{-}P_2W_{18}O_{62}]^{6-}$.

[12] R. Contant, M. Abbessi, J. Canny, A. Belhouari, B. Keita, L. Nadjo, *Inorg. Chem.* **1997**, *36*, 4961–4967.

[13] B. Keita, A. Belhouari, L. Nadjo, R. Contant, *J. Electroanal. Chem.* **1998**, *442*, 49–57.

[14] Examples of Fe-substituted POMs which have useful electrocatalytic properties include: a) J. E. Toth, F. C. Anson, *J. Am. Chem. Soc.* **1989**, *111*, 2444–2451; b) B. Keita, A. Belhouari, L. Nadjo, R. Contant, *J. Electroanal. Chem.* **1995**, *381*, 243–250.

[15] Representative papers include: a) R. Contant, M. Abbessi, J. Canny, B. Keita, A. Belhouari, L. Nadjo, *Eur. J. Inorg. Chem.* **2000**, 567–574; b) B. Keita, Y. W. Lu, L. Nadjo, R. Contant, M. Abbessi, J. Canny, M. Richet, *J. Electroanal. Chem.* **1999**, *477*, 146–157; c) B. Keita, F. Girard, L. Nadjo, R. Contant, J. Canny, M. Richet, *J. Electroanal. Chem.* **1999**, *478*, 76–82.

[16] R. Belghiche, R. Contant, Y. W. Lu, B. Keita, M. Abbessi, L. Nadjo, J. Mahuteau, *Eur. J. Inorg. Chem.* **2002**, 1410–1414.

[17] I. M. Mbomekalle, Y. W. Lu, B. Keita, L. Nadjo, *Inorg. Chem. Commun.* **2004**, *7*, 893–898.

[18] I. M. Mbomekalle, B. Keita, L. Nadjo, P. Berthet, W. A. Neiwert, C. L. Hill, M. D. Ritorto, T. M. Anderson, *Dalton Trans.* **2003**, 2646–2650 and references cited therein.

[19] R. Contant, J. P. Ciabrini, *J. Inorg. Nucl. Chem.* **1981**, *43*, 1525–1528.

[20] a) The same substitution pattern was reported for the structure of $[\alpha\text{-}P_2(NbO_2)_6W_{12}O_{56}]^{12-}$ (see ref. [7c]); b) Six of the 18 metal sites were initially assigned and refined as 100% W, but the thermal parameters were too low to support this assignment. Given the fact that elemental analyses suggested that the ratio of Mo to W in the crystals was 3 to 15, the occupancy of the six sites was set at 50% Mo and 50% W. This change resulted in normal thermal parameters for the six metal sites (i. e. positions 1, 4, 9, 10, 15, and 16 in Scheme 2). The remaining 12 metal sites refined as 100% W with normal thermal parameters. Furthermore, the presence of 50% $[\alpha\text{-}As_2Mo_6W_{12}O_{62}]^{6-}$ and 50% $[\alpha\text{-}As_2W_{18}O_{62}]^{6-}$ in these crystalline samples was confirmed by cyclic voltammetry.

[21] B. Keita, F. Girard, L. Nadjo, R. Contant, R. Belghiche, M. Abbessi, *J. Electroanal. Chem.* **2001**, *508*, 70–80.

[22] B. Keita, E. Abdeljalil, L. Nadjo, B. Avisse, R. Contant, J. Canny, M Richet, *Electrochem. Commun.* **2000**, *2*, 145–149.

[23] R. Contant, R. Thouvenot, *Can. J. Chem.* **1991**, *69*, 1498–1506.

[24] S. Lis, S. But, *J. Alloys Compd.* **2000**, *303–304*, 132–136.

[25] *SMART*, version 5.628; Bruker AXS, Inc.: Madison, WI, **2003**.

[26] *SAINT*, version 6.36A; Bruker AXS, Inc.: Madison, WI, **2002**.

[27] G. Sheldrick, *SADABS*, version 2.10; University of Göttingen: Göttingen, Germany, **2003**.

[28] *International Table for X-ray Crystallography*; Kynoch Academic Publishers: Dordrecht, The Netherlands, **1992**, vol. C.

Received: December 31, 2004

 © 2005 Wiley-VCH Verlag GmbH & Co. KGaA, Weinheim

Co-Adsorption of Copper(II) and 3-Amino-1,2,4-triazole at a Water–Natural Macromolecular Compound Interface: Molecular Structure from Adsorption Isotherms Combined with X-ray Absorption Measurements

Karine Flogeac,[a] Emmanuel Guillon,*[a] and Michel Aplincourt[a]

Keywords: Adsorption / Environmental chemistry / Pesticides / Structure elucidation / Surface chemistry / X-ray absorption spectroscopy

The co-adsorption of Cu^{II} and amitrole at a water–natural macromolecular compound interface was studied by means of batch adsorption experiments, Fourier transform infrared, and X-ray absorption spectroscopy. The binary systems, aqueous amitrole–Cu^{II} complex, and amitrole and Cu^{II} adsorbed on the surface of the solid were studied. The ternary system was investigated over the pH range 2–10 and at varying metal concentrations. The combination of macroscopic and molecular information shows that Cu^{II} and amitrole interact directly at the water–solid interface to form ternary surface complexes. A two-step mechanism is proposed whereby initial formation of a Cu^{II}–amitrole aqueous complex is followed by the sorption of this complex onto the surface. The structure of the ternary complex was elucidated. Copper(II) is bound to the surface in an inner-sphere mode, while two amitrole ligands simultaneously bonded in a monodentate fashion to Cu^{II} to form a six-membered coordination sphere around the metal cation. The copper coordination sphere is completed by two water molecules. This structure and the mechanism proposed are supported by a combination of potentiometric data, IR and UV/visible spectroscopies and XAS measurements.
(© Wiley-VCH Verlag GmbH & Co. KGaA, 69451 Weinheim, Germany, 2005)

Introduction

The monitoring and control of pollutants in the aquatic environment is becoming of increasing concern. Detailed investigations of the interactions between both naturally occurring and anthropogenic species found in the environment have provided information regarding their chemical structure and speciation, and thus the transport, bio-availability and potential toxicity of pollutants.[1–3] In order to fully understand the chemical processes that occur in groundwater, soils and surface waters, it is important to study the role of the solid–water interface as well as the interactions in the aqueous phase. With this aim in mind, this paper investigates ternary surface complexes formed during the adsorption of copper(II) and an organic ligand, 3-amino-1,2,4-triazole (amitrole), onto soil organic matter (SOM). Indeed, there is a lack of mechanistic molecular-level understanding due to the limited knowledge of the speciation and the reactivity of amitrole at the solid–water interface. In this respect, fundamental studies of a simplified model system play an important role since they can provide detailed information about the composition, structure and reactivity of amitrole surface species formed. This information then forms the basis of molecular-level interpretations of observations made on real soils.

It is now widely accepted that SOM, and notably lignin materials, plays a key role in the regulation of metal ions and other pollutants in the environment.[4–7] Lignin is a natural polymer that is produced biologically by random polymerisation processes, which make its study complicated.[8] It is a cross-linked, phenolic polymer built from three basic phenyl propane monomers (*p*-hydroxycinnamyl, coniferyl, and sinapyl alcohols), which are responsible for its chemical heterogeneity. Thus, the solid studied as a model for SOM is a lignocellulosic substrate (LS) extracted from wheat straw by acid/base treatments.

Amitrole is a herbicide that is widely used all over the world. It is used as a systematic herbicide for total weed control in vineyards, orchards, forests, non-crop areas and in aquatic environments such as marshes and drainage ditches.[9] Amitrole is quickly absorbed through the leaves and then migrates into plant tissues to inhibit several biochemical pathways. Moreover, it is often associated with other well-known herbicides such as glyphosate or paraquat. Several studies have been devoted to the adsorption of amitrole in soils but they were essentially focused on quantitative aspects.[10–15] The primary objective of this work is to identify the molecular mechanism(s) of Cu^{II}–amitrole coadsorption on LS. We present new data for the ternary Cu^{II}/amitrole/LS system. Conclusions are drawn based on a comparison of new XAS spectroscopic data and quantita-

[a] GRECI (Groupe de Recherche En Chimie Inorganique), Université de Reims Champagne-Ardenne
BP 1039, 51687 Reims cedex 2 (France)
Fax: +33-3-26913243
E-mail: emmanuel.guillon@univ-reims.fr

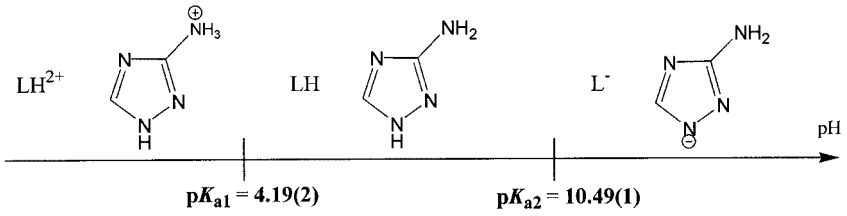

Scheme 1. Different steps of amitrole (LH) deprotonation and their corresponding acidity constants.

tive adsorption data for the three binary systems: aqueous amitrole–Cu^{II}, amitrole–LS and Cu^{II}–LS. We will emphasise how the adsorption characteristics and surface speciation of amitrole are affected by the presence of Cu^{II}, and vice versa. This is the first time that spectroscopic results have been presented for this ternary system, and they allow a good understanding of the molecular mechanism of amitrole retention by SOM in the presence of Cu^{II}.

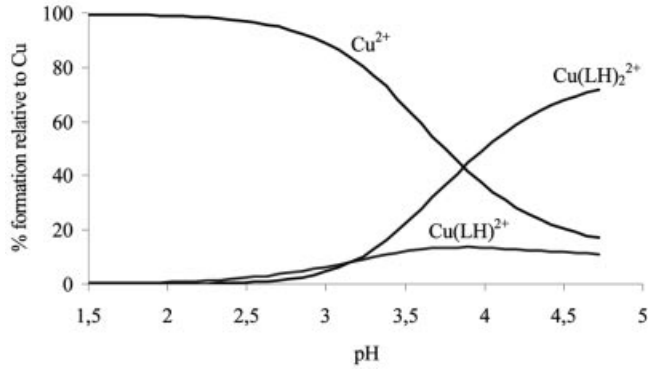

Figure 1. Distribution curves. $C_L = 1.2 \times 10^{-2}$ mol L^{-1}, $C_M = 2.4 \times 10^{-3}$ mol L^{-1}.

Results and Discussion

Binary Systems

The deprotonation reactions of amitrole were studied in KNO_3 (0.1 mol L^{-1}) in the pH range 2–12. The two acidity constants and the deprotonation steps of amitrole are reported in Scheme 1. The constant pK_{a1} corresponds to the deprotonation of the exocyclic nitrogen atom and the constant pK_{a2} to the deprotonation of the endocyclic nitrogen atom. These values are close to the ones obtained by Pichon and Hennion,[16] and Boraei and Mohamed[17] under similar conditions.

The first binary system, Cu^{II}–amitrole, was then studied in aqueous solution by titration with 0.1 mol L^{-1} KOH (ionic strength = 0.1 mol L^{-1}) at variable C_L/C_{Cu} ratios (total ligand to total copper concentration; R). The ligand concentration, C_L, was kept constant (1.2×10^{-2} mol L^{-1}) and the ratio R ranged from 1.08 to 5. The experimental data are shown as distribution curves in Figure 1. It is obvious from this figure that Cu^{II} complexation becomes significant at pH values above 2.5. As formation constant calculations can only be made in a homogeneous medium, the precipitation of a mixed hydroxo-amitrole copper complex since around pH 5 prevents any calculations above this value. Unfortunately, this precipitated complex could not be obtained as a pure compound, but the presence of amitrole was identified by IR spectroscopy. Calculations showed that the best fit between the calculated curves and the experimental data (volume of KOH added, pH) was obtained with two successive complexes having the compositions $Cu(LH)^{2+}$ and $Cu(LH)_2^{2+}$. The logarithmic values of the overall formation constants (log β_n) for these two species are equal to 12.5 and 26.0, respectively. The overall constants $\beta_n = [Cu(LH)_n^{2+}]/[Cu^{2+}][L^-]^n[H^+]^n$ correspond to the general equilibrium $Cu^{2+} + nH^+ + nL^- \rightleftharpoons Cu(LH)_n^{2+}$.

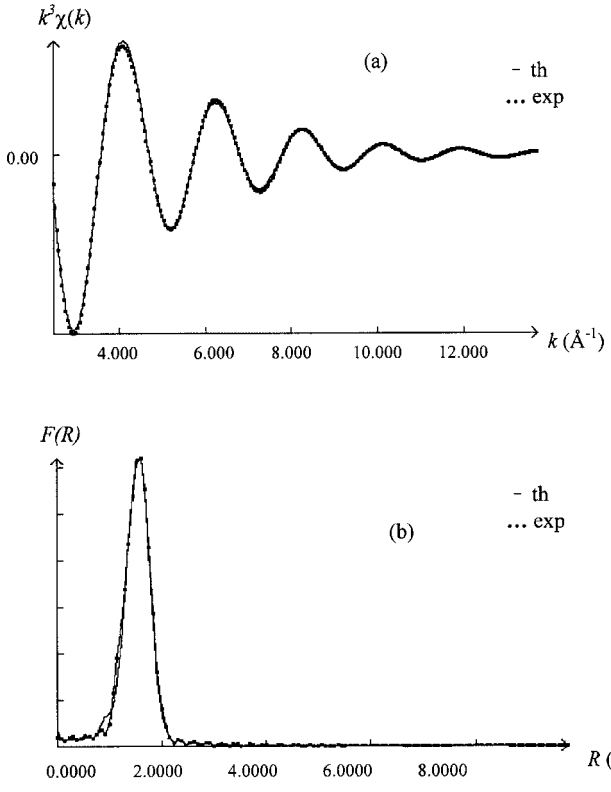

Figure 2. (a) Experimental and fitted first shell (0.96–2.10 Å^{-1}) EXAFS k space spectra of Cu-amitrole solution complex. (b) Fourier transform of the EXAFS signal [$k^3\chi(k)$] at the copper K edge.

The overall stability constants combined with acidity constants lead to the successive complexation constants K_n, which correspond to the equilibrium $Cu^{2+} + n$LH $\rightleftharpoons$ $Cu(LH)_n^{2+}$.

 © 2005 Wiley-VCH Verlag GmbH & Co. KGaA, Weinheim

The logarithmic values of the constants K_n are equal to 2.0 (n = 1) and 3.0 (n = 2). The unexpected variation of these constants ($\log K_1 < \log K_2$) is probably due to a geometric change of the complex or to the Jahn–Teller effect.

In order to obtain structural information about the copper–amitrole complex in solution, UV/visible spectroscopy and XAS experiments were carried out. In the visible region, the absorption spectrum exhibits a broad non-symmetric band centred around 15335 cm^{-1} characteristic of a tetragonal elongated octahedral environment around copper(II) with a CuN_2O_4 chromophore.[18] The structure of the complex in solution was also studied by EXAFS spectroscopy. The first shell was best fit with four oxygen/nitrogen atoms (Figure 2) at an average distance of 2.04 Å from the absorbing copper atom. These four atoms are most likely positioned in the equatorial plane of a Jahn–Teller-distorted, elongated octahedron, similar to the arrangement described for $Cu(OH)_2$.[19] The two axial oxygens of the octahedron are more distant from the copper atom and form weaker bonds, giving rise to higher thermal disorder. These atoms are therefore not expected to contribute significantly to the EXAFS signal. Attempts to fit oxygen at axial positions indeed resulted in high Debye–Waller factors for these atoms (>0.015), and there was no improvement in the fit, compared to including only equatorial oxygen/nitrogen atoms. These EXAFS results combined with those obtained by UV/visible spectroscopy clearly show that the copper in the $Cu(LH)_2^{2+}$ complex is surrounded in the equatorial plane by two nitrogen atoms from amitrole and two water oxygen atoms. The axial position is occupied by two other water molecules. This structure is represented in Scheme 2.

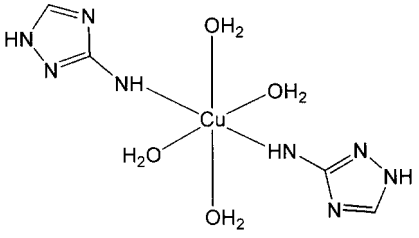

Scheme 2. Molecular structure of $Cu(LH)_2^{2+}$ in solution.

In a second step, we studied the amitrole sorption onto LS as a function of pH. Surprisingly, amitrole was not retained by LS in the pH range 2–12 (Figure 3). This result is unexpected since analogous pesticides are well known to bond to the SOM surface through electrostatic bonds.[20–22] This means that amitrole in a soil with a high content of organic matter such as lignin will be leached towards the surface- and groundwater.

The last binary system is the Cu^{II}–LS system. Copper retention on the solid has been studied previously and the results published in terms of quantitative data[23] and a molecular approach.[24] Briefly, copper is quantitatively sorbed (4.2 mg g^{-1}) at the LS surface. It is surrounded by four oxygen atoms at 1.93 Å and two other ones at 2.41 Å, which corresponds to a tetragonal-distorted octahedral geometry.

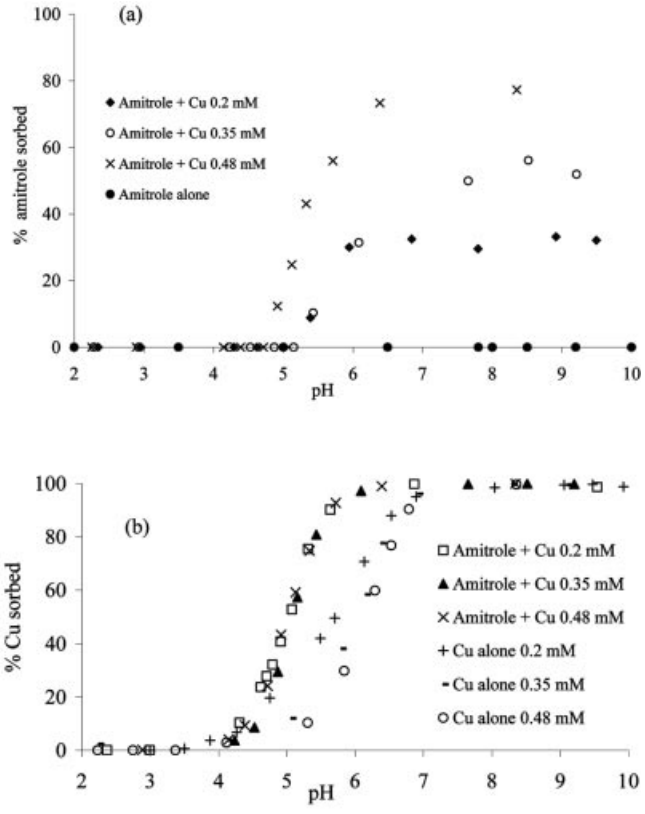

Figure 3. Adsorption of amitrole and Cu^{II} on the LS surface as a function of pH. $C_{amitrole}$ = 0.5 mmol L^{-1}.

Ternary System

The ternary system involving LS, Cu^{II} and amitrole was then studied by means of batch adsorption experiments combined with spectroscopic studies to obtain molecular-level information with the aim of understanding the coadsorption process. Figure 3 shows the adsorption of amitrole, Cu^{II} and both amitrole and Cu^{II} as functions of pH at three different total concentrations of Cu^{II}. The amount of amitrole adsorbed in the presence of Cu^{II} increases proportionally with the introduced copper concentration (Figure 3a). At the same time, all the copper added (three different concentrations) is adsorbed even in the presence of amitrole (Figure 3b). Indeed, in the presence or absence of amitrole, 100% of the copper introduced is sorbed above pH 7. This is in accordance with a mechanism of formation of a ternary complex in two steps: formation of the copper–amitrole complex $Cu(LH)_2^{2+}$ in solution followed by the sorption of this complex onto the LS surface, which leads to the Cu^{II}–amitrole–LS ternary complex, since amitrole alone is not adsorbed onto the LS surface. Moreover, as expected for the three copper concentrations studied, the amount of ligand, copper and copper–amitrole complex adsorbed increases with increasing pH. This enhancement is characteristic of the sorption of a cationic species [$Cu(LH)_2^{2+}$] on a surface, which confirms the mechanism previously proposed for the retention of amitrole in the presence of copper through ternary surface complex formation.

 © 2005 Wiley-VCH Verlag GmbH & Co. KGaA, Weinheim

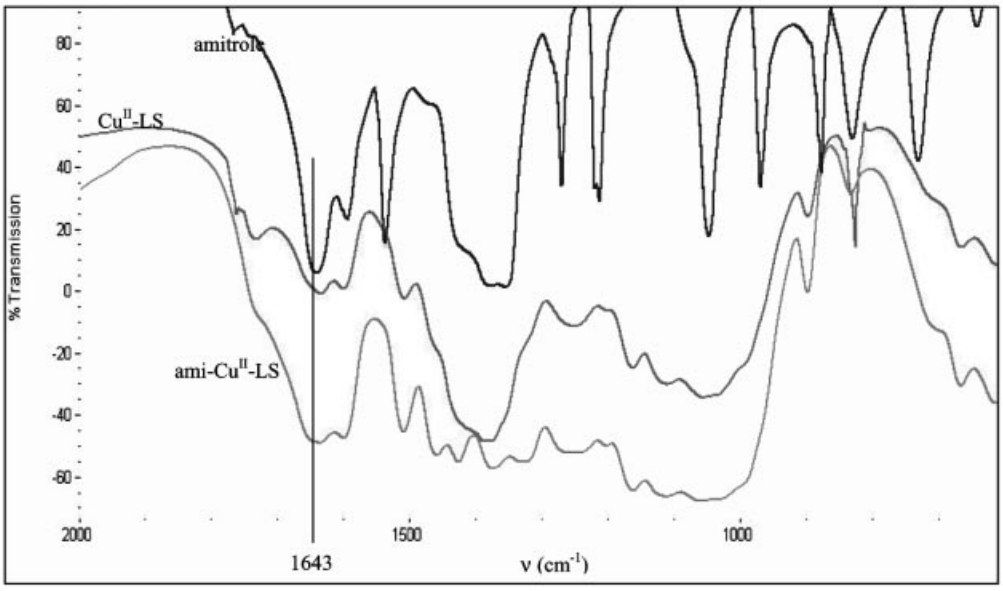

Figure 4. IR spectra of amitrole alone and the Cu^{II}-LS and ami-Cu^{II}-LS systems.

Moreover, the formation of 1:1 [Cu(LH)$^{2+}$] metal/ligand surface complexes cannot be ruled out, since the distribution curves (Figure 1) show the presence of 10% of the Cu(LH)$^{2+}$ species around pH 4–5.

The latter was confirmed by spectroscopic studies, from which structural information were obtained. The IR spectrum of amitrole shows several characteristic absorption bands, in particular the band at 1643 cm^{-1}, which corresponds to the C–N stretching band of the C–NH$_2$ exocyclic group, and the one at 1537 cm^{-1} corresponding to the conjugated ring C=N stretching vibration.[15] The IR spectrum of the Cu^{II}–amitrole–LS sample shows the disappearance of the latter, probably due to the low amitrole concentration on LS. The formation of a ternary complex was confirmed by the presence of a supplementary very weak band characteristic of amitrole at 1643 cm^{-1}, as compared to the Cu^{II}–LS spectra (Figure 4).

XAS experiments were carried out in order to obtain structural information about the ternary surface complex. The *K*-edge XANES spectrum and its first derivative are shown in Figure 5. They are typical of copper(II) complexes with a very weak 1s→3d transition pre-edge feature centred around 8978 eV, which is facilitated by p-d mixing,[25] and an absorption edge centred around 8996 eV. The most important feature of the spectrum at the copper edge is that the low-energy side of the edge exhibits the characteristic shoulder of copper(II) in an elongated tetragonal surrounding.[26] In Figure 5b, in addition to the very weak pre-edge peak, there is a splitting of peaks α and β in the first derivative Cu XANES spectrum. This first derivative can reveal detailed information that is not obvious in this XANES spectrum. The peak α corresponds to the 1s→4p$_{x,y}$ transitions. The second main peak (β) represents the main absorption transition (1s→continuum). The energy gap between the α and β peaks is equal to 6.2 eV. This value gives an estimate of the destabilization of the 4p$_z$ metal orbital (z being the elongation axis). Indeed, it has been suggested that in elongated tetragonal copper(II) complexes, the further the apical site from the metal ion the more displaced this shoulder is towards low energies.[27] The average axial distance around the copper atom was estimated at approximately 2.4 Å by comparison with reference compounds.[24]

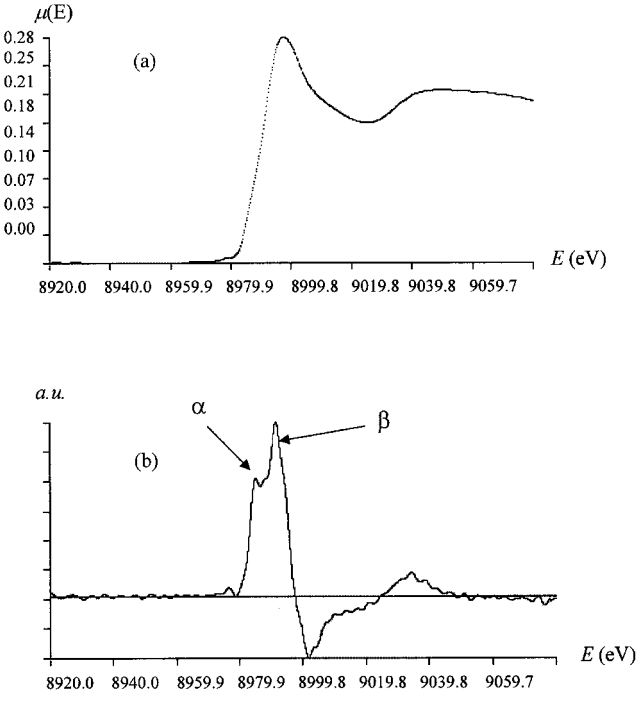

Figure 5. Cu *K*-edge XANES spectrum of the Cu-amitrole-LS ternary complex (a), and its first derivative (b).

 © 2005 Wiley-VCH Verlag GmbH & Co. KGaA, Weinheim

The experimental data and the fitted functions of the ternary system first shell are shown in k space as well as by Fourier transformations in real space in Figure 6. In agreement with the previous results, we found four copper–oxygen/nitrogen average distances of 2.01 Å (σ = 0.001 Å^2) from the adsorbing copper atom. Attempts were made to determine also the two longer axial distances, and two Cu–OH_2 distances equal to 2.36 Å (σ = 0.008 Å^2) were found. These data are consistent with those obtained from the XANES spectrum, i.e. a tetragonally distorted octahedral coordination around copper(II), according to the Jahn–Teller effect. The weak scattering contribution from low-Z elements beyond the first shell to the EXAFS, seen as minor Fourier peaks, prevents a more detailed analysis. However, a structure for the ternary surface complex can be proposed (Scheme 3). In Figure 7, for comparison, the k^3-weighted EXAFS spectra and Fourier transforms are reported for Cu^{II} adsorbed together with amitrole on LS, the $Cu(LH)_2^{2+}$ aqueous complex, and Cu^{II} adsorbed onto LS. Even the EXAFS spectra seem identical, although a faint difference can be observed on the first beating of the sinusoid around 4 Å^{-1}, which is also observed for the Cu^{II}–O/N distances. Indeed, the Cu–O/N distance in the Cu-LS surface complex is equal to 1.93 Å,[24] that in the $Cu(LH)_2^{2+}$ aqueous complex to 2.04 Å, and that in the ternary complex to 2.01 Å. The intermediate value obtained for the ternary complex leads to the proposed structure in which two copper–amitrole and two copper–LS bonds are in the equatorial plan, and two water molecules are in the axial positions. This also rules out a surface precipitation of a mixed hydroxo-amitrole copper complex (see solution chemical study). Moreover, the Fourier transform of the ternary surface complex corresponds to the weighted sum of the Fourier transforms of $Cu(LH)_2^{2+}$ and Cu-LS complexes (Figure 7).

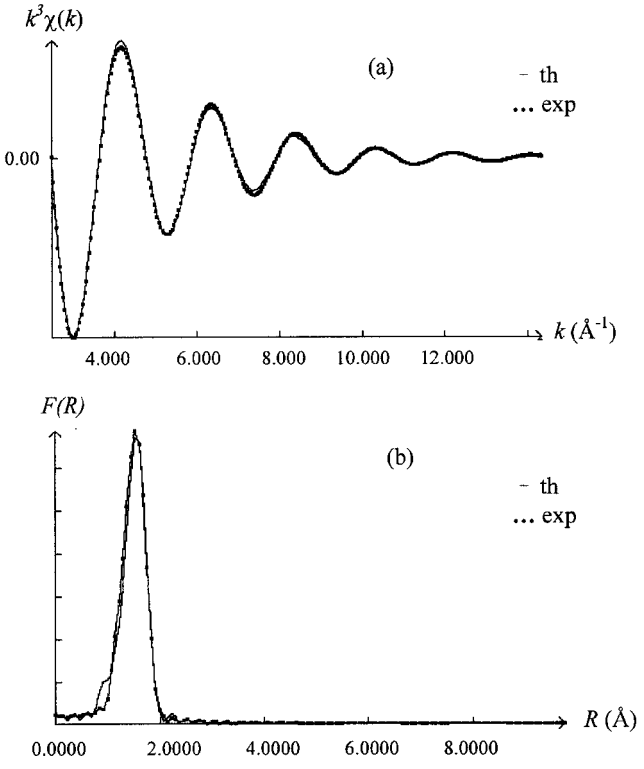

Figure 6. (a) Experimental and fitted first shell (1.16–2.02 Å^{-1}) EXAFS k space spectra of the Cu-amitrole-LS ternary complex. (b) Fourier transform of the EXAFS signal [$k^3\chi(k)$] at the copper K edge.

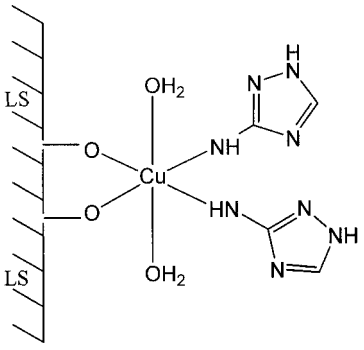

Scheme 3. Proposed structure of the ternary Cu^{II}–amitrole–LS surface complex.

Conclusions

By simultaneously using quantitative and spectroscopic methods we have shown that Cu^{II} and amitrole form ternary complexes on soil organic matter. The retention of amitrole is only possible in the presence of copper. A lack of copper leads to the leaching of the pesticide to surface- and/or groundwater. Potentiometric titrations have underlined the existence of a predominating complex, $Cu(LH)_2$, which was confirmed by IR spectroscopy. Adsorption isotherms and XAS data indicate a molecular structure where copper(II) bonds to the surface in an inner-sphere mode. According to solution studies combined with adsorption and XAS experiments, we have proposed a possible structure for the ternary complex. Two amitrole ligands are probably monodentately bound to Cu^{II} and the copper coordination sphere is completed by two water molecules to form a six-membered coordination sphere around the metal cation (Scheme 3). Finally, it is now obvious that metal ions have a significant influence on the molecular surface speciation of amitrole. The new structure identified is potentially important for elucidating the bio-availability and mechanisms of amitrole degradation in soils. The results obtained in this study are currently being used with modelling software to establish predictive systems for the retention of pesticides in soils in the presence of metallic cations.

Experimental Section

Reagents: All solvents and chemicals from commercial sources were of the highest available purity and were used without further purification. The metal-ion stock solutions were prepared from copper(II) nitrate reagents (Fluka) of the highest purity (>99%). The concentration was determined by EDTA titration {with PAN [1-(2-pyridyl-azo)-2-naphthol] as indicator}. The LS was extracted from

 © 2005 Wiley-VCH Verlag GmbH & Co. KGaA, Weinheim

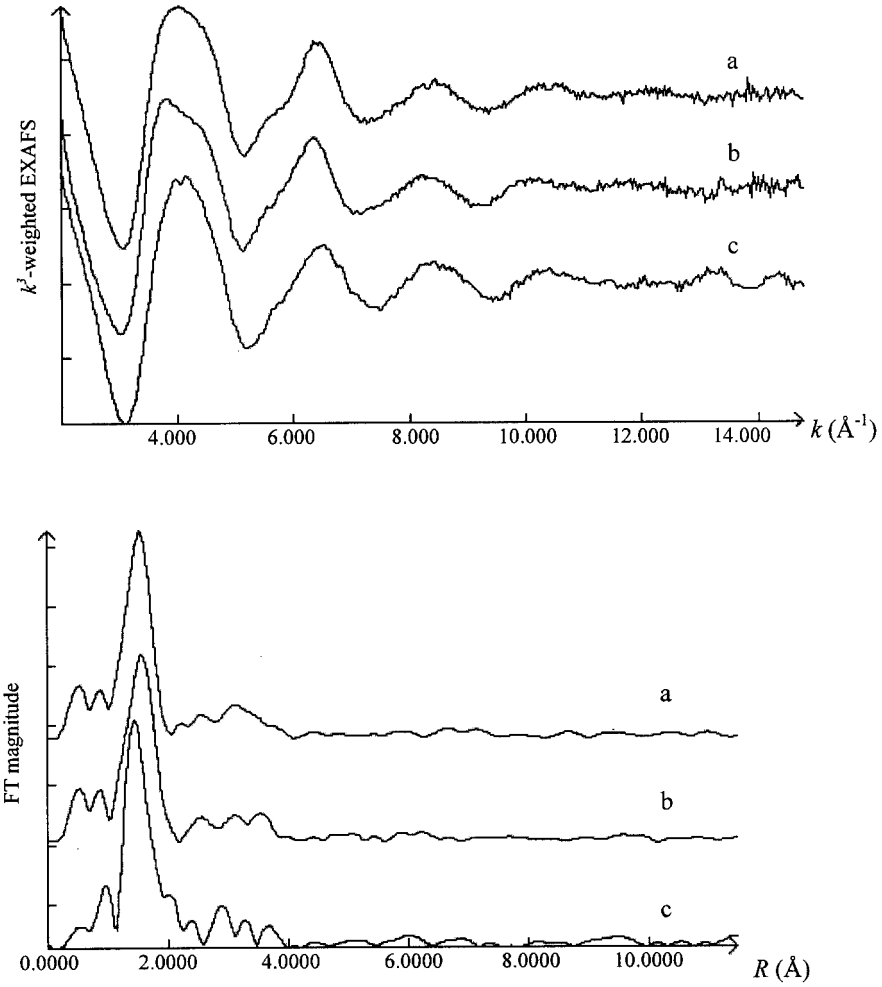

Figure 7. k^3-Weighted EXAFS spectra and Fourier transforms for Cu^{II} adsorbed together with amitrole on LS (a). Included for comparison: k^3-weighted EXAFS spectra and Fourier transforms of (b) $Cu(LH)_2$ (aq.) and (c) Cu^{II} adsorbed on LS.

wheat straw by two successive acid-base treatments,[24] and was fully characterized.[28]

Protometric: Potentiometric titrations were carried out as described previously.[29] Briefly, they were performed with a Metrohm 665 Dosimat and a Metrohm 654 pH-meter. The combined glass electrode was standardized with nitric acid (10^{-2} mol L^{-1}; pH 2.00). All measurements were performed at 20 °C under a nitrogen stream. The curves obtained were fitted with the refining program PROTAF[30] in order to obtain the overall stability constants. The ionic product of water, pK_w, was determined to be 13.78. The concentration of copper(II) varied from 1.09×10^{-2} to 0.24×10^{-2} mol L^{-1}, the concentration of the ligand from 8×10^{-3} to 2×10^{-2} mol L^{-1} and the ratio C_L/C_M from 1.08 to 5. The ionic strength was kept constant (0.1 mol L^{-1}) by addition of potassium nitrate.

Sorption Experiments: Adsorption experiments were conducted as a function of pH using batch experiments at room temperature (293 K). The LS (2 g L^{-1}) was immersed in 15 mL of background electrolyte (0.1 mol L^{-1} KNO_3) solution and stirred with a magnetic stir bar for 24 h, which corresponds to the hydration time of the solid. After this pre-equilibration step, the amitrole (5×10^{-4} mol L^{-1}) was added simultaneously with copper (2×10^{-4}, 3.5×10^{-4} and 4.8×10^{-4} mol L^{-1}), and the pH was incrementally adjusted to a fixed value by dropwise addition of 0.1 mol L^{-1} HNO_3 or 0.1 mol L^{-1} KOH. The final volume was adjusted to 25 mL. The sorption equilibrium (12 h) was predetermined by kinetic experiments in which different contact times from 10 min to 48 h between the sorbents and the solid were applied. When two successive curves were superimposed, the equilibrium time was considered to have been reached. The flasks were then shaken at 293 K for 12 h with an automatic shaker to ensure complete sorption. The experimental pH was taken to be the pH measured after a 12 h reaction time. After filtration through a 0.20 μm polyamide membrane, the supernatants were separated into two fractions. In the first fraction, the solution was acidified and the unsorbed metal-ion concentration was measured with a Varian ICP-AES spectrometer. The amount of copper sorbed was deduced from the initial concentration. The amount of amitrole was determined from the second fraction using the spectrophotometric method described by Sund.[10]

The solid studied by spectroscopic techniques was prepared at pH 5.7 with a copper concentration equal to 2×10^{-4} mol L^{-1} and an amitrole concentration of 5×10^{-4} mol L^{-1}. This pH value was chosen in order to have a maximum copper amount adsorbed and to prevent copper hydroxide precipitation (pH 6.8).

Spectroscopy: The electronic spectra in aqueous solutions were recorded in a 1.00-cm quartz cell with a Perkin–Elmer Lamba-6 UV/Visible spectrophotometer. IR spectra were obtained in pellets with a Nicolet Avatar 320 spectrophotometer.

 © 2005 Wiley-VCH Verlag GmbH & Co. KGaA, Weinheim

EXAFS and XANES Data: The XAS experiments were performed on the XAS 4 beamline of the storage ring DCI (positron energy 1.85 GeV; mean current 300 mA) at LURE (Laboratoire d'Utilisation du Rayonnement Electromagnétique, Paris-Sud University). Data were recorded at the Cu *K* edge (8979 eV) using a channel-cut monochromator Si(111) for EXAFS and Si(311) for XANES. The solids and the aqueous copper(II) solutions were measured at room temperature in the transmission mode with two air-filled ionisation chambers. Internal calibration was made with a copper metal foil and fixed at 8979 eV for the first inflection point. Four scans were summed for the samples. The XANES spectra were recorded step-by-step, every 0.3 eV, with a 2 s accumulation time per point. The spectrum of the 5 μm metallic foil was recorded just before the unknown XANES spectrum to check the energy calibration, thus ensuring an energy accuracy of 0.25 eV. The EXAFS spectra were recorded over 1000 eV, with 2 eV steps, from 8900 to 9900 eV. Data analysis was performed by means of the "EXAFS pour le Mac" package.[31] The $\chi(k)$ functions were extracted from the data with a linear pre-edge background, a combination of polynomials and spline atomic-absorption background, and normalised using the Lengeler–Eisenberg method.[32] The energy threshold, E_0, was taken at the middle of the absorption edge and was corrected for each spectrum in the fitting procedure. The k^3 weighted $\chi(k)$ function was Fourier transformed from k = 2–14 Å^{-1}, by means of a Kaiser–Bessel window with a smoothness parameter equal to 3 (k is the photoelectron wave number). In this work, all Fourier transforms were calculated and presented without phase correction. The peaks corresponding to the first coordination shell were then isolated and back-Fourier transformed into k space to determine the mean coordination number, N, the bond length, R, and the Debye–Waller factor, σ. The resulting EXAFS functions were curve-fitted by calculated model functions using ab initio calculated EXAFS phase $|\varphi_i(k,R_i)|$ and amplitude $|f_i(k,R_i)|$ parameters from FEFF7 code.[33] The errors in the first shell bond lengths (R) were estimated to be ±0.02 Å and coordination numbers (N) were accurate to ±20%.

Acknowledgments

We are grateful to the "Région Champagne-Ardenne" for a grant to K.F. The authors also wish to acknowledge S. Belin (Université Paris Sud, LURE, France) for her help in recording EXAFS and XANES data.

[1] A. Manceau, M. L. Schlegel, M. Musso, V. A. Sole, C. Gauthier, P. E. Petit, F. Trolard, *Geochim. Cosmochim. Acta* **2000**, *64*, 3643–3661.
[2] L. Charlet, A. Manceau, *J. Colloid Interface Sci.* **1992**, *148*, 443–458.
[3] S. E. Fendorf, G. M. Lamble, M. G. Stapleton, M. J. Kelley, D. L. Sparks, *Environ. Sci. Technol.* **1994**, *28*, 284–289.
[4] J. C. Echeverria, M. T. Morera, C. Mazkiaran, J. J. Garrido, *Environ. Pollut.* **1998**, *101*, 275–284.
[5] S. E. Bailey, T. J. Olin, R. M. Bricka, D. D. Adrian, *Water Res.* **1999**, *33*, 2469–2479.
[6] A. Kokorevics, J. Gravitis, E. Chirkova, O. Bikovens, N. Druz, *Cell. Chem. Technol.* **1999**, *33*, 251–266.
[7] P. Merdy, E. Guillon, M. Aplincourt, *New J. Chem.* **2002**, *26*, 1638–1645.
[8] E. Ammälahti, G. Brunow, M. Bordet, D. Robert, I. Kilpeläinen, *J. Agric. Food Chem.* **1998**, *46*, 5113–5117.
[9] R. T. Meister, in *Chemicals Handbook '92* (Meister Publishing Company), Willoughby, OH, USA, **1992**.
[10] K. A. Sund, *J. Agric. Food Chem.* **1956**, *4*, 57–60.
[11] C. D. Ercegovich, D. E. H. Frear, *J. Agric. Food Chem.* **1964**, *12*, 26–29.
[12] J. D. Russell, M. I. Cruz, J. L. White, *J. Agric. Food Chem.* **1968**, *16*, 21–24.
[13] D. C. Nearpass, *Soil Sci.* **1970**, *109*, 77–84.
[14] T. Oesterreich, U. Klaus, M. Volk, B. Neidhart, M. Spiteller, *Chemosphere* **1999**, *38*, 379–392.
[15] E. Morillo, J. L. Pérez-Rodriguez, C. Maqueda, *Clays Clay Miner.* **1991**, *26*, 269–279.
[16] V. Pichon, M. C. Hennion, *Anal. Chim. Acta* **1993**, *284*, 317–326.
[17] A. Boraei, M. C. Mohamed, *Chem. Eng. Data* **2002**, *47*, 987–991.
[18] A. B. P. Lever, in *Inorganic Electronic Spectroscopy*, 2nd ed., Elsevier, Amsterdam, **1984**.
[19] M. Magini, *J. Chem. Phys.* **1981**, *74*, 2523–2529.
[20] N. Senesi, *Sci. Total Environ.* **1992**, *123–124*, 63–76.
[21] M. J. Salloum, B. Chefetz, P. G. Hatcher, *Environ. Sci. Technol.* **2002**, *36*, 1953–1958.
[22] H. R. Schulten, B. Plage, M. Schnitzer, *Naturwissenschaften* **1991**, *78*, 311–312.
[23] P. Merdy, E. Guillon, M. Aplincourt, J. Dumonceau, H. Vezin, *J. Colloid Interface Sci.* **2002**, *245*, 24–31.
[24] E. Guillon, P. Merdy, M. Aplincourt, *Chem. Eur. J.* **2003**, *9*, 4479–4484.
[25] J. E. Hahn, R. A. Scott, K. O. Hodgson, S. Doniach, S. Desjardins, E. I. Solomon, *Chem. Phys. Lett.* **1982**, *88*, 595–598.
[26] N. Kosugi, T. Yokoyama, K. Asakuna, H. Kuroda, *Chem. Phys.* **1984**, *91*, 249–256.
[27] C. Surville-Barland, R. Ruiz, A. Aukauloo, Y. Journaux, I. Castro, B. Cervera, M. Julve, F. Llord, F. Sapina, *Inorg. Chim. Acta* **1998**, *278*, 159–169.
[28] P. Merdy, E. Guillon, J. Dumonceau, M. Aplincourt, *Anal. Chim. Acta* **2002**, *459*, 133–142.
[29] E. Guillon, P. Merdy, M. Aplincourt, J. Dumonceau, H. Vezin, *J. Colloid Interface Sci.* **2001**, *239*, 39–48.
[30] R. Fournaise, C. Petitfaux, *Talanta* **1987**, *34*, 385–395.
[31] A. Michalowicz, EXAFS pour le Mac, Logiciel pour la Chimie, Société Française de Chimie, Paris **1991**, p. 102.
[32] B. Lengeler, P. Eisenberg, *Phys. Rev. B* **1980**, *21*, 4507–4518.
[33] S. I. Zabinsky, J. J. Rehr, A. Ankudinov, R. C. Albers, M. J. Eller, *Phys. Rev. B.* **1995**, *52*, 2995–3009.

Received: September 14, 2004

 © 2005 Wiley-VCH Verlag GmbH & Co. KGaA, Weinheim

Crystal Structure and Magnetism of the Double Perovskite $Sr_3Fe_2MoO_9$: A Neutron Diffraction Study

María C. Viola,[a] José A. Alonso,*[b] José C. Pedregosa,[a] and Raul E. Carbonio[c]

Keywords: Double perovskite / Neutron diffraction / Antiferromagnetic ordering

The $Sr_3Fe_2MoO_9$ double perovskite has been prepared in polycrystalline form by heat treatment, in air, from previously decomposed citrate precursors. This material has been studied by X-ray (XRD), neutron powder diffraction (NPD) and magnetic measurements. At room temperature, the crystal structure is tetragonal, space group *I*4/*m*, with $a = b = 5.5608(2)$ Å, $c = 7.8471(4)$ Å. It is convenient to write the crystallographic formula as $Sr_2Fe(Fe_{1/3}Mo_{2/3})O_6$, according to the usual nomenclature for double perovskites $A_2B'B''O_6$. The structure contains alternating FeO_6 and $(Fe,Mo)O_6$ octahedra, tilted by 3.9° in the basal *ab* plane. Magnetic measurements indicate a weak ferromagnetic behavior below $T_C = 280$ K. Ideally, the $Sr_3Fe_2MoO_9$ double perovskite only contains Fe^{3+} and Mo^{6+} cations, in such a way that superexchange interactions between neighboring Fe^{3+} spins are the only nominal mechanism accounting for the magnetism of this material. Our main finding is that this intrinsically "disordered" sample, containing a random distribution of Fe and Mo at the B′′ positions, exhibits a strong magnetic scattering on the low-angle Bragg positions, originating from naturally occurring groups of Fe^{3+} cations in which strong antiferromagnetic (AFM) Fe–O–Fe superexchange interactions are promoted, similar to those existing in the $LaFeO_3$ perovskite.

(© Wiley-VCH Verlag GmbH & Co. KGaA, 69451 Weinheim, Germany, 2005)

Introduction

In the search for new colossal magnetoresistant materials, some members of the family of double perovskites of composition $A_2B'B''O_6$ (A = alkaline earths; B′, B′′ = transition metals) have been proposed as half-metallic ferromagnets (best described as ferrimagnets), with T_C values well above room temperature, as an alternative to perovskite manganites.[1–5] The revival of interest in this family was triggered by a report on Sr_2FeMoO_6,[1] demonstrating that in the electronic structure only minority spins are present at the Fermi level: this material was shown to exhibit intrinsic tunnelling-type magnetoresistance (TMR) at room temperature.

TMR has also been described for double perovskites containing transition metals other than Mo, such as A_2FeReO_6 (A = Ca, Sr, Ba), which present a half-metallic ground state concomitant with the ferrimagnetic coupling of Fe^{3+} and Re^{5+} ($5d^2$, $S = 2/2$) magnetic moments, and show MR at room temperature. Also, Fe can be replaced by Co, as we have recently shown in Sr_2CoMoO_6,[6] where CMR properties were induced upon chemical reduction, by topotactical removal of oxygen atoms. Both examples illustrate the appealing possibility of searching for new CMR materials within the large family of double perovskite oxides.

The family of materials of the type $A_3B'_2B''O_9$ (A = Ca, Sr, Ba; B′ = transition metal and B′′ = Mo, W, Te or U) has recently attracted our attention. These compounds are also double perovskites whose crystallographic formula could be re-written as $A_2B'(B'_{1/3}B''_{2/3})O_6$. They, thus, display an intrinsic partial disordering over half of the perovskite ($B'_{1/3}B''_{2/3}$) positions. We have prepared different materials with A = Ca, Sr; B′ = Fe and B′′ = Mo, W, Te or U and with X-ray diffraction and Mössbauer spectroscopy we have shown that all the compounds are tetragonal and can be refined in the space group *I*4/*m*.[7] This is the same symmetry and space group found for Sr_2FeMoO_6 or Sr_2CoMoO_6. Additionally, an increase in the disorder of B′′ among the Wyckoff sites 2*a* and 2*b* in the sequence Mo < U < Te < W was found. This degree of disorder is observed as an increase in the width of the Mössbauer lines.[7] The sextuplet displayed in the Mössbauer spectra implies a room-temperature magnetic order for B′′ = U, Te and W. For B′′ = Mo two iron sites are observed as two different doublets, indicative of iron occupying the two different positions (2*a* and 2*b*).

These data have now been complemented with microscopic neutron powder diffraction (NPD) data on $Sr_3Fe_2MoO_9$. In this paper we report on the results of a

[a] Area de Química General e Inorgánica "Dr. Gabino F. Puelles", Departamento de Química, Facultad de Química, Bioquímica y Farmacia, Universidad Nacional de San Luis, Chacabuco y Pedernera, 5700 San Luis, Argentina
[b] Instituto de Ciencia de Materiales de Madrid, C.S.I.C., Cantoblanco, 28049 Madrid, Spain
[c] Instituto de Investigaciones en Físico Química de Córdoba (INFIQC), Departamento de Fisicoquímica, Facultad de Ciencias Químicas, Universidad Nacional de Córdoba, Ciudad Universitaria, 5000 Córdoba, Argentina

high-resolution NPD study, giving a detailed description of the crystal structure as well as its thermal evolution down to 2 K. This study also gives insight on the magnetic structure of this material, which shows an intrinsically high magnetic disordering over the B′′ = Fe/Mo positions. Macroscopic magnetic measurements are also reported and discussed. We show that, in spite of small saturation magnetization exhibited by $Sr_3Fe_2MoO_9$, the magnetic neutron scattering is surprisingly strong for such a magnetically disordered sample. We ascribe the observed scattering to Fe-rich regions, where strong Fe–O–Fe superexchange interactions give rise to the antiferromagnetic (AFM) ordering of the neighboring Fe spins.

Results

$Sr_3Fe_2MoO_9$ was obtained as a black, well-crystallized powder. The XRD pattern is characteristic of a perovskite structure, showing the splitting of certain reflections, characteristic of a tetragonal distortion [for instance, (004) and (220) reflections]. Minor amounts of $SrMoO_4$ were detected from either XRD or NPD data.

Magnetic Data

The magnetic susceptibility vs. temperature curves are displayed in Figure 1. Below 280 K the zero-field-cooled (ZFC) and field-cooled (FC) curves exhibit a distinct evolution. The FC curve shows a progressive increment of the susceptibility as temperature decreases, reminiscent of the spontaneous evolution characteristic of a ferromagnet, although a very small saturation magnetization is reached at low temperatures, of only 0.004 μ_B/f.u. with a measuring field of H = 1000 Oe. The ZFC curve shows a less pronounced susceptibility increment as temperature decreases, and exhibits a broad maximum increment centered at 60 K, suggesting the establishment of a long-range AFM ordering below this temperature. The magnetization vs. magnetic field curves at 2, 100, and 300 K are plotted in Figure 2. Even at the lowest temperature, the magnetization is very far from saturation for the maximum applied field of H = 3 T, reaching a maximum value of 0.15 μ_B/f.u. The hysteretic behavior is characteristic of a weak ferromagnetic system.

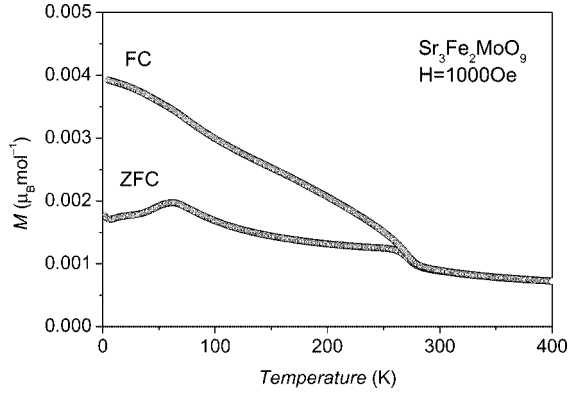

Figure 1. Field-cooled (FC) and zero-field-cooled (ZFC) magnetic susceptibility vs. temperature curves for $Sr_3Fe_2MoO_9$.

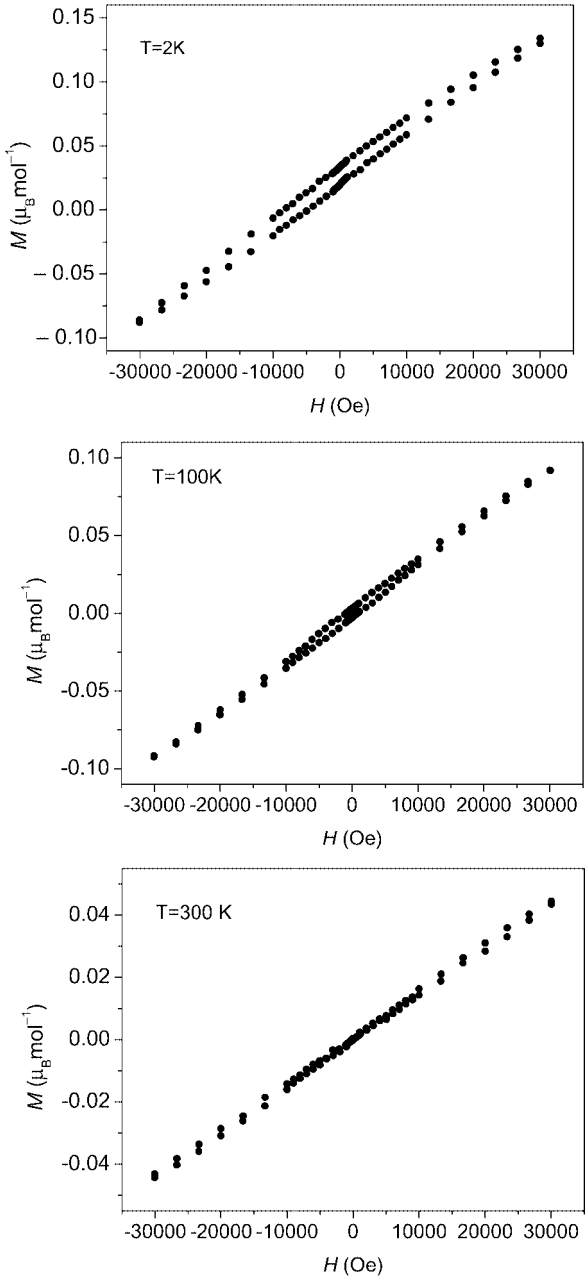

Figure 2. Magnetization vs. magnetic field isotherms (T = 2, 100, and 300 K) for $Sr_3Fe_2MoO_9$.

Structural Refinement

The structural refinement of $Sr_3Fe_2MoO_9$ from room-temperature high-resolution NPD data was performed in the *I*4/*m* space group (No. 87), with unit-cell parameters related to a_0 (ideal cubic perovskite, a_0 = 3.9 Å) as $a = b \approx 2^{1/2} \cdot a_0$ and $c \approx 2a_0$. Sr atoms were located at 4*d* (0,1/2,1/4) positions, Fe/Mo at 2*a* (0,0,0) and Fe at 2*b*(0,0,1/2) sites, and oxygen atoms at 4*e* (0,0,*z*) and 8*h* (*x*,*y*,*z*) positions.

 © 2005 Wiley-VCH Verlag GmbH & Co. KGaA, Weinheim

$SrMoO_4$ was included in the refinement as a second phase, defined[8] in the space group $I4_1/a$ (10.87% of this phase from the scale factors). No *anti*-site disordering was detected, by assuming that some Mo from the 2*a* positions could randomly replace some Fe at the 2*b* positions. In the final refinement, the Fe/Mo occupancy over the 2*a* positions was also allowed to change from the nominal Fe/Mo = 2:1 stoichiometry; no departure from this nominal occupancy was detected within the standard deviations (Table 1). An excellent agreement between observed and calculated NPD profiles was obtained for this model, as illustrated in Figure 3. Table 1 includes the final atomic coordinates and discrepancy factors after the refinement. Table 2 lists the main interatomic distances and angles. A drawing of the structure is shown in Figure 4. The structure contains alternating FeO_6 and $(Fe,Mo)O_6$ octahedra, tilted in *anti*-phase in the basal *ab* plane (along the [001] direction of the pseudocubic cell). This corresponds to the $a^0a^0c^-$ Glazer's notation as derived by Woodward[9] for 1:1 ordering of double perovskites, consistent with space group *I*4/*m*.

Table 1. Positional and thermal parameters for $Sr_2Fe(Fe_{1/3}Mo_{2/3})O_6$ after the Rietveld refinement[a] from NPD data taken at 298 K, space group: *I*4/*m*, $Z = 2$. Unit-cell parameters: $a = b = 5.5608(2)$ Å, $c = 7.8471(4)$ Å, $V = 242.65(2)$ Å^3.

Atom	Wyckoff site	*x*	*y*	*z*	B_{iso} [Å^2]	Occ.
Sr	4*d*	0.0000	0.5000	0.0000	0.97(2)	1.00
Fe	2*a*	0.0000	0.0000	0.0000	0.1(2)	0.33(3)
Mo	2*a*	0.0000	0.0000	0.0000	0.1(2)	0.66(3)
Fe	2*b*	0.0000	0.0000	0.5000	0.9(2)	1.00
O1	4*e*	0.0000	0.0000	0.247(5)	1.3(1)	1.00
O2	8*h*	0.269(3)	0.235(3)	0.0000	1.13(6)	1.00

[a] Discrepancy factors: $R_{Bragg} = 3.48\%$, $R_{wp} = 13.7\%$, $R_{exp} = 4.78\%$, $\chi^2 = 8.21$.

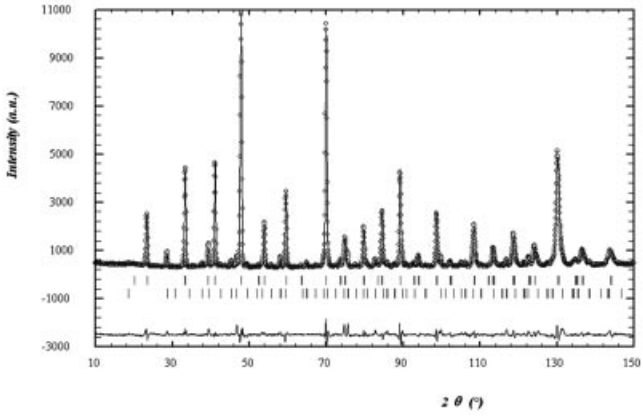

Figure 3. Observed (open circles), calculated (full line) and difference (bottom) NPD Rietveld profiles for $Sr_3Fe_2MoO_9$ at 295 K. The second series of tick marks corresponds to the Bragg reflections of the $SrMoO_4$ impurity phase.

Magnetic Structure

The sequential data collection at D20 from 2 to 262 K showed a strong magnetic contribution to the scattering on

Table 2. Some selected bond lengths [Å] and angles [°] for $Sr_2Fe(Fe_{1/3}Mo_{2/3})O_6$.

Distances	
SrO_{12} icosahedron	
(Sr)–(O1)(x4)	2.7805(4)
(Sr)–(O2)(x4)	2.87(1)
(Sr)–(O2)(x4)	2.69(1)
⟨Sr–O2⟩	2.780(5)
$(Fe/Mo)_{2a}O_6$ octahedron	
$(Fe/Mo)_{2a}$–(O1)(x2)	1.93(4)
$(Fe/Mo)_{2a}$–(O2)(x4)	1.99(2)
$\langle(Fe)_{2b}–O\rangle$	1.97(3)
$Fe_{2b}O_6$ octahedron	
$(Fe)_{2b}$–(O1)(x2)	1.99(2)
$(Fe)_{2b}$–(O2)(x4)	1.93(4)
$\langle(Fe)_{2b}–O\rangle$	1.97(3)
Angles	
$(Fe)_{2b}$–(O1)–$(Fe/Mo)_{2a}$	180.00
$(Fe)_{2b}$–(O2)–$(Fe/Mo)_{2a}$	172.3(6)

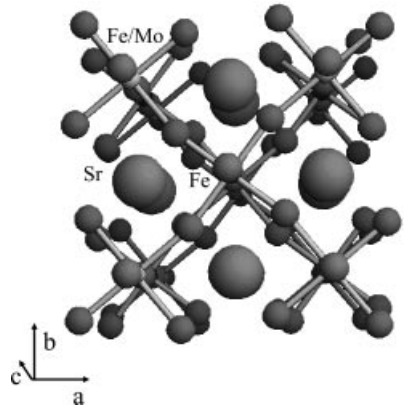

Figure 4. View of the structure of tetragonal $Sr_2Fe(Fe_{1/3}Mo_{2/3})O_6$ approximately along the *c* axis. Large spheres represent Sr; corner-sharing FeO_6 (dark) and $(Fe,Mo)O_6$ octahedra are tilted in *anti*-phase along the *c* axis, in order to optimize Sr–O bond lengths.

allowed Bragg positions ($k = 0$), mainly on the (011) reflection (Figure 5), suggesting a ferro- or ferrimagnetic long-range ordering. This is surprising in this strongly disordered sample, taking into account that the saturation magnetization is very small, of hardly 0.15 μ_B/f.u. with an applied field of 3 T. We would have expected that the structural disordering at the B positions of the perovskite had led to the absence of long-range magnetic ordering between Fe and Mo magnetic moments. As it will be discussed later, we believe that this magnetic scattering originates from Fe-rich patches in which neighboring Fe^{3+} spins exhibit AFM superexchange interactions via Fe–O–Fe paths. We have thus modeled the magnetic structure as a perfect AFM arrangement of Fe spins with alternating directions, occupying all the B positions of a perovskite structure with the same unit-cell and positional parameters as the host $Sr_3Fe_2MoO_9$ perovskite. We have constrained the scale factors of both structural and magnetic models, and refined the magnitude of the Fe magnetic moments. The goodness of the fit is shown in Figure 6, where both structural and magnetic contributions to the scattering have been in-

 © 2005 Wiley-VCH Verlag GmbH & Co. KGaA, Weinheim

cluded. The thermal variation of the magnitude of the ordered Fe magnetic moments is displayed in Figure 7.

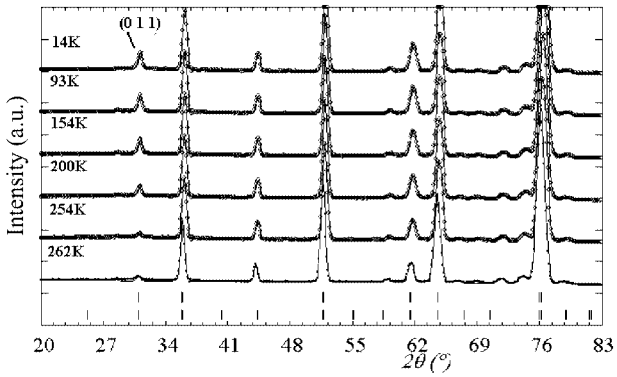

Figure 5. Thermal evolution of the NPD patterns dynamically collected with the high-flux D20 diffractometer, highlighting the appearance at low temperatures of a magnetic contribution to the scattering on the low-angle reflections, especially on the (011) Bragg position.

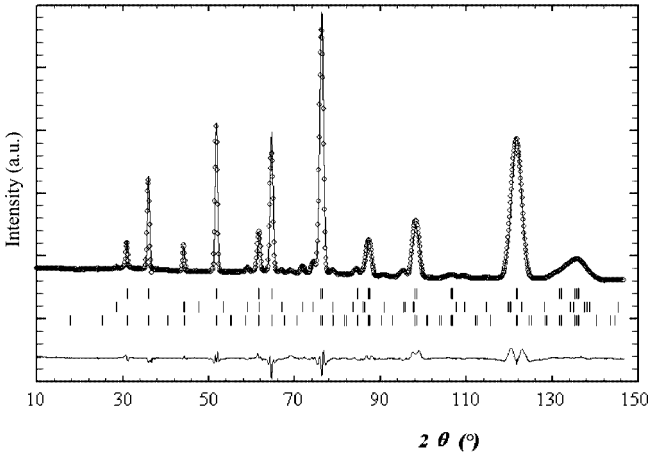

Figure 6. Observed (open circles) and calculated (full line) NPD profiles at 2 K. The three series of allowed Bragg reflections correspond to the crystallographic phase, the $SrMoO_4$ impurity and the magnetic structure for the AFM model described in the text. Unit-cell parameters are $a = b = 5.5346$, $c = 7.8553$ Å; discrepancy factors: $R_{wp} = 3.03\%$, $R_{bragg} = 4.49\%$; $R_{mag} = 11.4\%$.

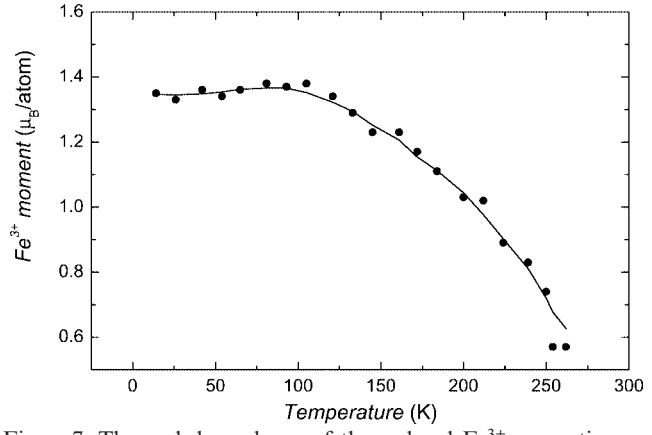

Figure 7. Thermal dependence of the ordered Fe^{3+} magnetic moments sequentially refined from D20 NPD data.

Discussion

Recently, Woodward[9] has described the possible tilting systems for $A_2B'B''O_6$ ordered perovskites, predicting the space groups for each system. When the A cation is large enough, the well-known $(NH_4)_3FeF_6$ structure is adopted by the 1:1 B-site ordered perovskites, such as Ba_2FeMoO_6, which can be described in the cubic space group $Fm\bar{3}m$. For slightly smaller A cations, only a small deformation of the lattice takes place, implying the tilting of the octahedra only along the *c* axis. This tilting means a reduction in symmetry from cubic to tetragonal. The structure of $Sr_3Fe_2MoO_9$, which can ideally be rewritten as $Sr_2Fe(Fe_{1/3}Mo_{2/3})O_6$, is defined in the space group *I*4/*m*, and can be described as the result of a single *anti*-phase octahedral tilting along the *c* axis. Figure 4 illustrates this particular feature. A tilting of 3.9° at room temperature can be derived from the B′–O2–B′′ angle.

The refinement of the occupancy factors of Fe and Mo over the B′′ sites from NPD data indicates a Fe/Mo = 2:1 ratio (within the standard deviations), and no *anti*-site disordering effect was detected, excluding the possibility that some Mo cations could partially replace Fe cations at the 2*b* positions; the actual crystallographic formula is $Sr_2(Fe)_{2b}(Fe_{0.33(3)}Mo_{0.67(3)})_{2a}O_6$. In contrast with Sr_2FeMoO_6, which must be prepared under reducing conditions in order to provide a mixed valence Fe^{3+}–Fe^{2+}/Mo^{5+}–Mo^{6+} state, the present $Sr_3Fe_2MoO_9$ perovskite has been synthesized in air, in such a way that, from the chemical point of view, we should assign a nominal hexavalent oxidation state to the Mo cations, making all Fe cations nominally trivalent. From this point of view, the electronic configuration for this sample would be $Fe^{3+}(3d^5)$–$Mo^{6+}(4d^0)$.

On reinvestigating the example of Sr_2FeMoO_6, electronic band calculations show that the up-spin band, placed below the Fermi level, is mainly occupied by five Fe 3d electrons forming localized spins on the Fe sites. The down-spin band, which has density of states at the Fermi level, is composed mainly of hybridized Mo 4d t_{2g} and Fe 3d t_{2g} states. Thus, the Mo electron which occupies the down-spin band is itinerant and it is shared among Fe and Mo sites.[10–12] The high degree of itinerancy of the Mo electron is responsible for the high conductivity; the superexchange interaction between the localized Fe moment and the partially localized Mo moment accounts for the ferrimagnetic behavior of Sr_2FeMoO_6. Ideally, a perfectly ordered Sr_2FeMoO_6 perovskite should exhibit a saturation magnetization of 4 μ_B/f.u.; in reality, 3.6–3.8 μ_B/f.u. values are obtained due to *anti*-site disordering effects.[13]

In the present $Sr_3Fe_2MoO_9$ material, nominally containing only Fe^{3+} and Mo^{6+}, the lack of an itinerant Mo electron would prevent the magnetic coupling across Fe–O–Mo paths, in such a way that the only possible magnetic superexchange mechanism would take place via Fe–O–Fe paths, in Fe-rich areas of the crystal containing neighboring Fe^{3+} spins. Figure 8 shows a simplified image of the magnetic ordering in this disordered sample; only one layer of B cations is shown for the sake of simplicity. A perfect ferrimag-

 © 2005 Wiley-VCH Verlag GmbH & Co. KGaA, Weinheim

netic coupling between up Fe^{3+} spins at 2*b* sites (black in Figure 8) and down Fe^{3+} spins at 2*a* positions (grey in Figure 8) would ideally give $5\cdot(1 - 1/3) = 2.66\ \mu_B$/f.u., but this would require perfect coherence between Fe-rich patches, as illustrated in Figure 8. Notice that the total absence of coherence between isolated Fe-rich patches would lead, on average, to a null saturation magnetization. In fact, in contrast with Sr_2FeMoO_6, in the double perovskite $Sr_3Fe_2MoO_9$ we observe a strong suppression of the global FM properties although there is a remanent weak FM effect which corresponds to the statistical coherence: for a cubic lattice where B′ = Fe and B′′ is statistically occupied by 1/3 Fe, the long-range magnetic connections through B′–B′′(Fe)–B′ exceed the 31% percolation limit of a simple cubic lattice. The tetragonal distortion observed here does not change these considerations. Only $(2/3)^6 = 9\%$ of the B′ site Fe atoms are not connected to at least one B′′ site Fe^{3+}; these nonconnected atoms are labeled as "?" in Figure 8.

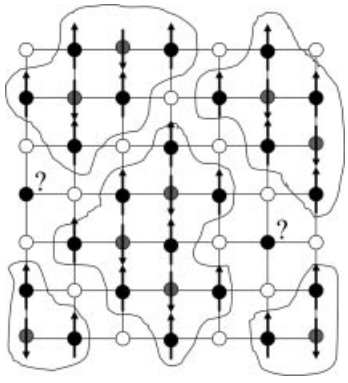

Figure 8. Ideal schematic view of the magnetic coupling in $Sr_2Fe(Fe_{1/3}Mo_{2/3})O_6$. This double perovskite contains Fe at 2*b* positions (black atoms and spins) and randomly distributed Fe (grey atoms and spins) and Mo (white atoms) at 2*a* positions. AFM magnetic coupling is via Fe–O–Fe paths (along the lines). Naturally occurring Fe-rich patches are antiferromagnetically coupled, and there is magnetic coherence between some adjacent patches.

One of the main issues to be addressed in this paper is the origin of the magnetic scattering on the sample showing an important component of intrinsic Fe/Mo disordering. We have been able to accurately fit the magnetic contributions to the neutron scattering by modeling an AFM structure consisting of a perfect arrangement of Fe cations occupying all of the B positions of a perovskite structure with the same unit-cell parameters as the crystallographic $Sr_3Fe_2MoO_9$ phase. The refinement of the magnitude of the magnetic moments on the Fe positions, at 2 K, gives an ordered magnetic moment of 1.4 μ_B, with constrained scale factors for the crystal and magnetic structure. Notice that this is only the average ordered component of the magnetic moment over all the B positions of the perovskite. Our picture thus shows a disordered Fe/Mo pattern in which the Fe–O–Fe superexchange AFM interactions are comparable to those existing in $RFeO_3$ ferrites (R = rare earths). As illustrated in Figure 8, the coupling between near-neighbor Fe–O–Fe cations is always AFM; the important fact is that the coherence between the magnetic ordering of isolated Fe–O–Fe patches is statistically maintained across the solid; the long-range coherence is naturally weaker than that corresponding to a completely ordered compound. Only below temperatures around 30–60 K would the super-superexchange mechanism across Fe–O–Mo–O–Fe paths trigger a complete long-range AFM ordering, as it happens in the antiferromagnet Sr_2FeWO_6 below $T_N = 37$ K.[14] Moreover, we could assign the maximum observed in the ZFC susceptibility curve at 60 K to the onset of these super-superexchange interactions, in addition to the interactions coming from the statistical connections between Fe-rich patches. The thermal variation of the magnetic moment on Fe positions (Figure 7) exhibits an abrupt decay at 250 K, which corresponds to the vanishing of the long-range antiferromagnetic ordering of Fe^{3+} spins, in agreement with the magnetic susceptibility curve.

Conclusions

$Sr_3Fe_2MoO_9$ perovskite is a weak ferromagnet by virtue of the partial long-range coherence established between antiferromagnetically ordered patches of Fe^{3+} spins, composed by some tenths of atoms, naturally arising from the statistical disordering exhibited by this material. The crystal structure, refined from NPD data in the *I*4/*m* space group, contains two kinds of B positions; one of them is fully occupied by Fe^{3+} cations whereas the second one contains a random distribution of Fe^{3+} and Mo^{6+} cations. Below 280 K, the superexchange Fe–O–Fe interactions within naturally occurring Fe-rich patches account for the observed magnetic behavior and the appearance of a significant contribution to the magnetic scattering on the low-angle Bragg reflections. The coherence between isolated Fe-rich patches is statistically provided; only 9% of Fe atoms are magnetically isolated. At lower temperatures, around 60 K, super-superexchange Fe–O–Mo–O–Fe interactions contribute to the long-range AFM ordering of the majority of Fe^{3+} spins. The thermal variation of the ordered Fe^{3+} magnetic moments shows an abrupt decay above 250 K, in agreement with the macroscopic magnetic properties.

Experimental Section

The $Sr_3Fe_2MoO_9$ perovskite was prepared as a black polycrystalline powder from citrate precursors obtained by soft chemistry procedures. Stoichiometric amounts of analytical grade $Sr(NO_3)_2$, $Fe(C_2O_4)\cdot 2H_2O$, and $(NH_4)_6Mo_7O_{24}\cdot 4H_2O$ were dissolved in citric acid. The citrate, nitrate and oxalate solutions were slowly concentrated, leading to organic resins containing a random distribution of the cations involved at an atomic level. These resins were first dried at 120 °C and then slowly decomposed at temperatures up to 600 °C. All the organic materials and nitrates were eliminated in a subsequent treatment at 800 °C in air, for 2 h. This treatment gave rise to highly reactive precursor materials. The resulting black powder was then treated in air at 1000 °C for 24 h and 1150 °C for 48 h.

The initial characterization of the product was carried out by laboratory X-ray diffraction (XRD) measurements (Cu-K_α, λ =

 © 2005 Wiley-VCH Verlag GmbH & Co. KGaA, Weinheim

1.5418 Å). For the structural refinements, a room-temperature NPD pattern was collected with the high-resolution D2B neutron diffractometer (ILL-Grenoble, France). The high-flux mode was used. About 4 g of sample was contained in a vanadium can; the counting time was 3 h. A wavelength of 1.594 Å was selected from a Ge monochromator. The variable-temperature NPD patterns in the range 2–262 K were collected at the D20 high-flux neutron diffractometer (ILL, Grenoble, France), using a wavelength of 2.42 Å, in order to obtain information about the low-temperature magnetic structure and its thermal variation. A standard cryostat was used for the sequential collections. A collimation of 27" was selected. Once cooled to 2 K, the sample was heated at 2 K min^{-1} and the NPD patterns were sequentially collected with counting times of 2 min.

All the patterns were refined by the Rietveld method by using the FULLPROF refinement program.[15] A pseudo-Voigt function was chosen to generate the line shape of the diffraction peaks. The minor $SrMoO_4$ impurity (with scheelite structure) was included as a second crystallographic phase in the refinements. In the final runs, the following parameters were refined: scale factors for the main and impurity phases, background coefficients, zero-point error, unit-cell parameters, pseudo-Voigt corrected for asymmetry parameters, positional coordinates, isotropic thermal factors, *anti*-site disorder for Fe/Mo and occupancy factors for oxygen atoms. The coherent scattering lengths for Sr, Fe, Mo, and O were 7.02, 9.45, 6.72, and 5.803 fm, respectively.

Acknowledgments

We acknowledge the financial support of CICyT for the project MAT2004-0479 and we are grateful to ILL for making all facilities available. J. C. P., M. C. V. and R. E. C. acknowledge the financial support of the Consejo Nacional de Investigaciones Científicas y Técnicas (CONICET PID 4929/96, PIP 380/98 and PIP 02482), the Agencia Nacional de Promoción Científica y Tecnológica (PICT98 06-03041 and PICT99 12-5378), Fundación Antorchas (collaboration project A-13740/1-94), CyT (Universidad Nacional de San Luis – Project 7707) and SECyT-UNC. J. C. P. and R. E. C. are members of CONICET. We acknowledge financial support provided by a CSIC-CONICET collaboration project.

[1] K.-I. Kobayashi, T. Kimura, H. Sawada, K. Terakura, Y. Tokura, *Nature* **1998**, *395*, 677.
[2] B. García-Landa, C. Ritter, M. R. Ibarra, J. Blasco, P. A. Algarabel, R. Mahendiran, J. García, *Solid State Commun.* **1999**, *110*, 435.
[3] A. Maignan, B. Raveau, C. Martin, M. Hervieu, *J. Solid State Chem.* **1999**, *144*, 224.
[4] K.-I. Kobayashi, T. Kimura, Y. Tomioka, H. Sawada, K. Terakura, Y. Tokura, *Phys. Rev. B* **1999**, *59*, 11159.
[5] T. H. Kim, M. Uehara, S.-W. Cheong, S. Lee, *Appl. Phys. Lett.* **1999**, *74*, 1737.
[6] M. C. Viola, M. J. Martínez-Lope, J. A. Alonso, P. Velasco, J. L. Martínez, J. C. Pedregosa, R. E. Carbonio, M. T. Fernández-Díaz, *Chem. Mater.* **2002**, *14*, 812.
[7] M. C. Viola, M. S. Ausburger, R. M. Pinnaca, J. C. Pedregosa, R. E. Carbonio, R. C. Mercader, *J. Solid State Chem.* **2003**, *175*, 252.
[8] E. Guermen, E. Daniels, J. S. King, *J. Chem. Phys.* **1971**, *55*, 1093.
[9] P. M. Woodward, *Acta Crystallogr., Sect. B* **1997**, *53*, 32.
[10] O. Chmaissem, R. Kruk, B. Dabrowski, D. E. Brown, X. Xiong, S. Kolesnik, J. D. Jorgensen, C. W. Kimball, *Phys. Rev. B* **2000**, *62*, 14197.
[11] D. D. Sarma, E. V. Sampathkumaran, S. Ray, R. Nagarajan, S. Majumdar, A. Kumar, G. Nalini, T. N. Guru Row, *Solid State Commun.* **2000**, *114*, 465.
[12] A. S. Ogale, S. B. Ogale, R. Ramesh, T. Venkatessan, *Appl. Phys. Lett.* **1999**, *75*, 537.
[13] Ll. Balcells, J. Navarro, M. Bibes, A. Roig, B. Martínez, J. Fontcuberta, *Appl. Phys. Lett.* **2001**, *78*, 781.
[14] A. K. Azad, S.-G. Eriksson, A. Mellergard, S. A. Ivanov, J. Eriksen, H. Rundlöf, *Mater. Res. Bull.* **2002**, *37*, 1797.
[15] J. Rodríguez-Carvajal, *Physica B (Amsterdam)* **1993**, *192*, 55.
Received: September 8, 2004

 © 2005 Wiley-VCH Verlag GmbH & Co. KGaA, Weinheim

Kinetic and Thermodynamic Studies of the Disproportionation of Hydrogen Peroxide by Dimanganese(II,II) and -(II,III) Complexes of a Bridging Phenolate Ligand[‡]

Lionel Dubois,[a] Dao-Feng Xiang,[a] Xiang-Shi Tan,[a] and Jean-Marc Latour*[a]

Keywords: Manganese / Catalase / H_2O_2 disproportionation / Kinetics

The dimanganese(II,II) complexes $[Mn_2(L)(OAc)_2(CH_3OH)](ClO_4)$ (**1a**) and $[Mn_2(L)(OBz)_2(H_2O)](ClO_4)$ (**1b**) as well as the dimanganese(II,III) complex $[Mn_2(L)(OAc)_2(CH_3OH)](ClO_4)_2$ (**2a**), where HL is the asymmetric phenol ligand 2-[bis(2-pyridylmethyl)aminomethyl]-6-{[(benzyl)(2-pyridylmethyl)amino]methyl}-4-methylphenol, react with hydrogen peroxide in acetonitrile solution. The initial reaction rates and their temperature and acid/base dependencies were investigated by monitoring the dioxygen evolution. These studies revealed a first-order dependence on both the catalyst and H_2O_2 and a strong influence of the carboxylate. Electrospray ionisation mass spectrometry as well as EPR and UV/Vis spectroscopy were used to monitor the reaction catalysed by **2a**. The same bis(μ-oxo)dimanganese(III,IV) and (μ-oxo)dimanganese(II,III) active species as found for **1a** were detected in the catalytic medium. The EPR spectra recorded during the catalase-like reaction revealed the accumulation of the magnetically uncoupled dimanganese(II,III) precursor of the active bis(μ-oxo)dimanganese(III,IV) species which dominates the spectra in the case of **1a**. This difference can be attributed to the different pH conditions generated by the reaction and reflects differences in the initiation phases for the two catalysts. Overall, the kinetic and thermodynamic studies of H_2O_2 disproportionation by these dimanganese complexes are fully consistent with the mechanism deduced from our previous extensive spectroscopic studies.
(© Wiley-VCH Verlag GmbH & Co. KGaA, 69451 Weinheim, Germany, 2005)

Introduction

Although it is a product of aerobic respiration, hydrogen peroxide is potentially toxic since its reduction produces the highly deleterious hydroxyl radical. To prevent formation of HO· and related oxidative stress, cells possess very efficient enzymatic machineries in which the catalase enzymes play an essential role.[1,2] These enzymes eliminate H_2O_2 by means of its disproportionation into harmless dioxygen and water. Most of these enzymes are haemoproteins but a few of them of bacterial origin[3–5] possess a dimanganese active site.[6,7] The two manganese atoms are triply bridged by the carboxylate group of a glutamate and two water-derived ligands, as revealed by the crystallographic studies of the enzymes from *Thermus thermophilus*[8] and *Lactobacillus plantarum*.[9]

Very limited information is available on their mechanism of action. Biochemical[10] and spectroscopic[11] studies have shown that during catalysis, the carboxylate-capped Mn_2O_2 diamond core shuttles between the oxidation states $Mn^{II}Mn^{II}$ and $Mn^{III}Mn^{III}$. However, the fast kinetics of the enzymatic reaction ($k_{cat} \approx 10^5$ s^{-1})[8] and the fact that the oxidised and the reduced forms both react with the same substrate (H_2O_2) have precluded a precise description. As a consequence, most mechanistic proposals have been based on studies of biomimetic compounds.[12–14] The most detailed of these studies were performed on complexes of ligands involving either alkoholates[14,15] or phenolates[13,16] which stabilise the dimanganese unit by providing it with an internal bridge. Depending upon the Mn ligands, all oxidation states of the pair from $Mn^{II}Mn^{II}$ to $Mn^{IV}Mn^{IV}$ have been implicated in the catalysis. In the case of dimanganese complexes of pentadentate bis(aminoalkylimino)phenol ligands, the involvement of oxomanganese(IV) species has been demonstrated by Okawa et al.[16,17] through the observation, in DMF, of a characteristic vibronically split electronic absorption of the $Mn^{IV}(O)$ unit. On the other hand, Nishida et al. provided EPR evidence of the formation of a bis(μ-oxo)dimanganese(III,IV) species in the reaction of hydrogen peroxide with dimanganese complexes of heptadentate hexaaminophenols but did not establish definitely whether this species is a catalytic intermediate or a mere by-product.[18]

As part of our continuing interest in the physical properties and reactivity of dimanganese compounds,[19] we reported the synthesis of the dimanganese(II,II) complexes

[a] Laboratoire de Physicochimie des Métaux en Biologie, Unité Mixte de Rechereche CEA-CNRS-Université Joseph Fourier UMR 5155, Département Réponse et Dynamique Cellulaires, CEA-Grenoble,
38054 Grenoble Cedex 9, France
Fax: +33-43878-3462
E-mail: Jean-Marc.Latour@cea.fr
[‡] Binuclear Manganese Compounds of Potential Biological Significance, 3. Part 2: Ref.[21]

$[Mn_2(L)(OAc)_2(CH_3OH)](ClO_4)$ (**1a**) and $[Mn_2(L)(OBz)_2(H_2O)](ClO_4)$ (**1b**) derived from the asymmetric phenolate ligand 2-{[bis(2-pyridylmethyl)amino]methyl}-6-{[(benzyl)-(2-pyridylmethyl)amino]methyl}-4-methylphenol (HL, Scheme 1).[20] We also showed that the hydrogen peroxide disproportionation induced by these complexes involves two intermediates, namely a (μ-oxo)dimanganese(II,III) species $[Mn_2(L)(OAc)(O)]^+$ and a bis(μ-oxo)dimanganese(III,IV) complex $[Mn_2(L)(OAc)(O)_2]^+$ which were characterised by a combination of electrospray ionisation mass spectrometry (ESI-MS) and EPR spectroscopy.[21] In addition, we described the independent synthesis of the bis(μ-oxo)dimanganese(III,IV) complex and its characterisation by X-ray absorption spectroscopy and we showed that the initial reaction of *tert*-butyl hydroperoxide (and probably H_2O_2 also) with the dimanganese(II,II) complexes is a one-electron oxidation to their dimanganese(II,III) analogue.[21] These results are summarised in Scheme 2.

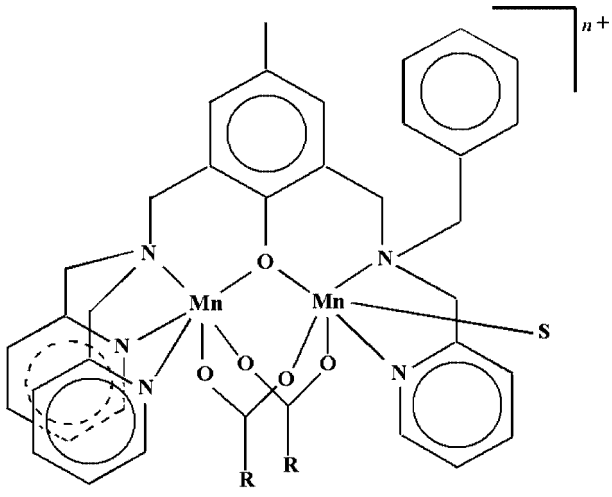

1a: R = Me, **S** = CH_3OH, n = 1
1b: R = Ph, **S** = H_2O, n = 1
2a: R = Me, **S** = H_2O, n = 2

Scheme 1. Complexes used in this study.

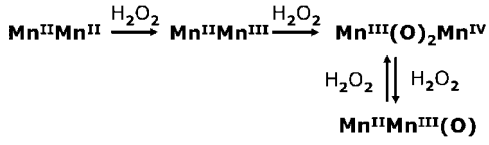

Scheme 2. Overall mechanism of the disproportionation of H_2O_2 by **1a**.

In the present article, we report kinetic and thermodynamic studies of the reaction of H_2O_2 with complexes **1a** and **1b** and the analogous dimanganese(II,III) compound $[Mn_2(L)(OAc)_2(H_2O)](ClO_4)_2$ (**2a**).[20] In addition, spectroscopic monitoring of the reaction of H_2O_2 with **2a** shows that the same intermediates are formed, therefore providing a consistent mechanistic picture for all complexes.

Results

Solvent Influence

Many different solvents were used in previous studies of the catalase-like reaction. In a few cases, solvent effects on the rate of dioxygen evolution were considered but the observed effects were found to depend on the catalyst.[18,23–25] It was also reported that even the mechanism of the reaction can change between DMF and acetonitrile.[18] These observations from the literature prompted us to investigate the solvent influence on the kinetics of dioxygen evolution upon reaction of H_2O_2 with **1a**. Figure 1 illustrates the data obtained at 0 °C in DMF, methanol and acetonitrile. In DMF, the reaction was very slow (0.012 mL min^{-1}) and only a small part (ca. 10%) of hydrogen peroxide was disproportionated. In methanol and acetonitrile, the reaction was faster (1.3 and 1.2 mL min^{-1}, respectively) and H_2O_2 was fully disproportionated. Although the initial rates of reaction are very similar, the reaction in methanol slowed down as it approached completion which is possibly due to the limited stability of the catalyst. For this reason, all subsequent measurements were performed in acetonitrile.

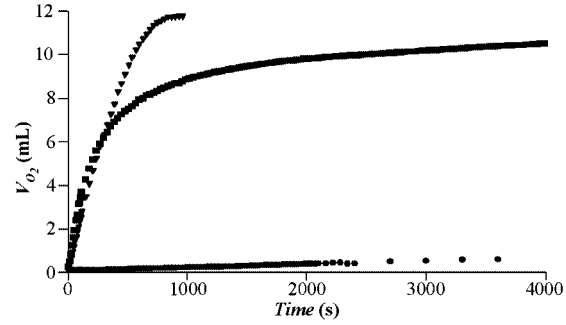

Figure 1. Time dependence of dioxygen evolution upon reaction of **1a** with H_2O_2 in different solvents: methanol (■), acetonitrile (▼) and DMF (●); [**1a**] = 1.0 mM, [H_2O_2] = 460 mM, T = 0 °C.

Comparison of the Catalysts – Stability

The activities of the different catalysts **1a**, **1b** and **2a** were studied under the same conditions as above and the kinetic results are illustrated in Figure 2. The most active catalyst was **2a** with an initial rate of O_2 evolution of 9 mL min^{-1} which can be compared with 1.2 and 0.9 mL min^{-1} for **1a** and **1b**, respectively. In each case, H_2O_2 underwent quantitative disproportionation. At the end of the reaction, the addition of another aliquot of 460 equiv. of hydrogen peroxide gave rise to a new evolution of dioxygen. In the case of **1a**, the rate increased from 1.2 mL min^{-1} for the first H_2O_2 batch to 3.45 mL min^{-1} for the second and 4.5 mL min^{-1} for the third. A sharp decrease in the rate of 2.0 and 0.2 mL min^{-1} was noted for the fourth and the fifth batches, respectively. In the case of **2a**, the rate of O_2 evolution was divided by a factor of 1.8 for the second addition and continued to decrease for the third and the fourth additions where the initial rate became very small (a lag phase was observed in this case).

 © 2005 Wiley-VCH Verlag GmbH & Co. KGaA, Weinheim

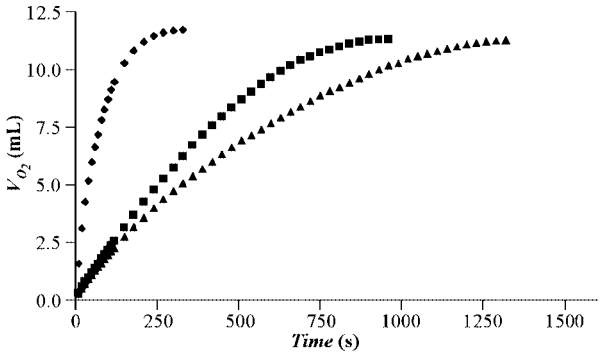

Figure 2. Time dependence of dioxygen evolution upon reaction of H_2O_2 with **1a** (■), **1b** (▼) and **2a** (♦) in acetonitrile; [catalyst] = 1.0 mM, [H_2O_2] = 460 mM, T = 0 °C.

Order of the Reaction

The order of the reaction with respect to the catalyst and hydrogen peroxide was investigated. In the case of **1a**, Figure 3 and Figure 4 show the influence of the complex and hydrogen peroxide concentrations on the reaction rate, respectively. After the initial rate determination, the curve of the Ln(initial rate) = f(concentration) gave a slope of 1.16 (r^2 = 0.998) with respect to the catalyst concentration and 1.12 (r^2 = 0.988) for hydrogen peroxide. It is worth noting that at low H_2O_2 concentrations ([H_2O_2] ≤ 115 mM), an initiation phase was observed over a period of ca. 100 s. In the case of **2a**, the slopes of the curve of the Ln(initial rate) = f(concentration) were 1.17 (r^2 = 0.991) and 0.95 (r^2 = 0.99998) for the catalyst and the hydrogen peroxide concentrations, respectively. Interestingly, no lag phase was detected whatever the H_2O_2 concentration. These results indicate that for **1a** and **2a**, the reaction follows a first-order dependence on both the hydrogen peroxide and the catalyst concentrations.

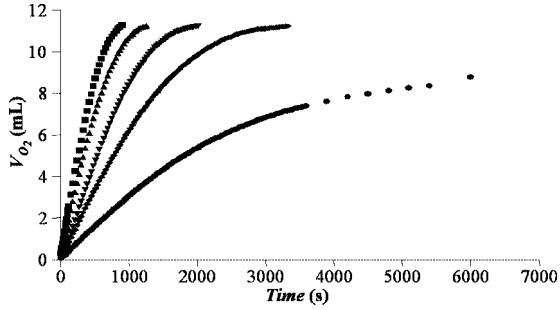

Figure 3. Time dependence of dioxygen evolution upon reaction of H_2O_2 with different concentrations of **1a** in acetonitrile: 1 mM (■), 0.8 mM (▼), 0.6 mM (▲), 0.4 mM (♦), 0.2 mM (●); [H_2O_2] = 460 mM, T = 0 °C.

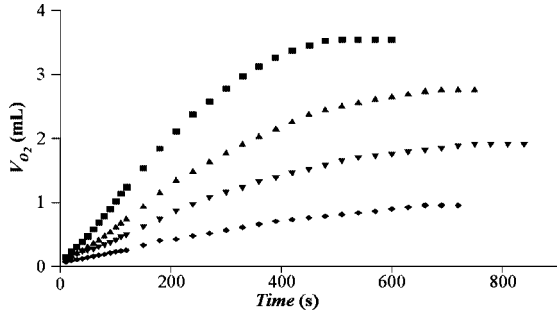

Figure 4. Time dependence of dioxygen evolution upon reaction of **1a** with different concentrations of H_2O_2 in acetonitrile: 115 mM (■), 86 mM (▼), 57 mM (▲), 29 mM (♦); [**1a**] = 1 mM, T = 0 °C.

Temperature Dependence

The determination of the thermodynamic parameters of the catalase-like reaction for the complexes **1a**, **1b** and **2a** was carried out by investigating the rate of dioxygen evolution at different temperatures over the range of –30 °C to +30 °C. After the initial rate determination, the curves Ln(initial rate) = $f(1/T)$ were plotted (Figure 5). For every catalyst, linear regression analysis proved satisfactory thereby indicating that the Arrhenius law is obeyed in all cases. The linear regression analysis provided the activating energy E_a and the preexponential factor k_0 and these parameters are summarised in Table 1. It is noteworthy that the complexes follow a trend in activation energy (**2a** > **1a** > **1b**) which parallels their activities. In other words, the highest activation energy is associated to the most active catalyst (**2a**). This observation contradicts the general view that the higher activity of a catalyst corresponds to a lower activating energy. It follows that the preexponential term k_0 is indeed the dominant factor.

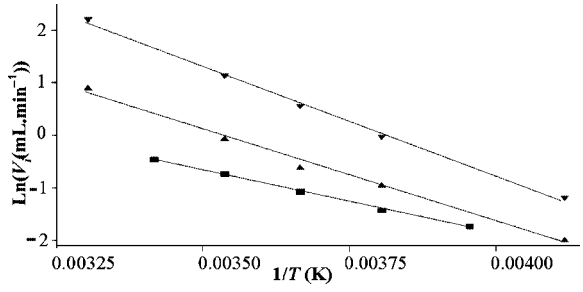

Figure 5. Temperature dependence of the initial rate of the catalase-like reaction in the form of the curve Ln(initial rate) vs. $1/T$ for **1a** (▼), **1b** (■) and **2a** (▲) in acetonitrile; [catalyst] = 1.0 mM, [H_2O_2] = 460 mM.

Table 1.Activation energies and preexponential factors for the reactions of **1a**, **1b** and **2a** with H_2O_2 in acetonitrile.

Catalyst	E_a [kJ mol^{-1}]	ln(k_0)	r^2
2a	35 ± 1	25.2 ± 0.5	0.992
1a	29 ± 1	22.0 ± 0.6	0.997
1b	20.0 ± 0.5	16.2 ± 0.2	0.998

Effect of Acid and Base Addition

In order to further assess the large differences in the abilities of **1a** and **1b** to disproportionate hydrogen peroxide, we decided to study the effect of acid and base addition on

 © 2005 Wiley-VCH Verlag GmbH & Co. KGaA, Weinheim

the reaction rate. Figure 6 shows the effect, on the initial reaction rate in the case of **1a**, upon addition of perchloric acid or triethylamine. Upon addition of triethylamine, the rate increased and this effect reached a maximum at 3 equiv. (per complex) at which point the rate was 3 times higher. A more important effect was observed upon addition of 1 equiv. of perchloric acid and at this concentration the rate of dioxygen evolution was 7 times higher (4.2 mL min^{-1}) than in the absence of perchloric acid. Moreover, it is worth noting that, at this point, the rate is very close to that measured for **2a** (4.5 mL min^{-1} under the same conditions). Further addition of perchloric acid caused a decrease of the initial rate. For **2a**, no change was observed after addition of perchloric acid while addition of base induced its disproportionation into Mn^{II} and $Mn^{III}Mn^{IV}$ species (see below) as shown by EPR spectroscopy.

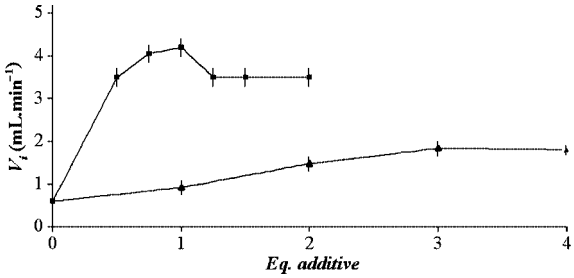

Figure 6. Effect of acid and base addition in the rate of the catalase-like reaction of **1a**: addition of triethylamine (▼), addition of perchloric acid (■).

Spectroscopic Monitoring of Hydrogen Peroxide Disproportionation by 2a

We have previously reported spectroscopic investigations of the mechanism of the reaction of hydrogen peroxide with **1a** and **1b**. We completed this study by monitoring the same reaction for **2a** by combining spectroscopic (UV/Vis, EPR) and mass spectrometric experiments.

UV/Vis Monitoring

When **2a** was treated with hydrogen peroxide in acetonitrile, its characteristic visible spectrum with maxima at 380, 485 and 627 nm[20] disappeared very rapidly (ca. 30 s.) and was replaced by three poorly resolved absorptions at 460, 550 and 630 nm. These absorptions are the signature of a bis(μ-oxo)$Mn^{III}Mn^{IV}$ complex[26] and were similarly observed previously and assigned to the active species in the disproportionation of H_2O_2 by **1a** and **1b**.[21] This spectrum was observed during the whole reaction and tended to disappear at times longer than 5 min.

EPR Monitoring

Figure 7 shows the EPR spectra recorded during the reaction of **2a** with H_2O_2. The initial spectrum (Figure 7a) consists of a large featureless signal between 150 mT and 500 mT with a characteristic poorly resolved 6-line signal superimposed on the central line, as already described.[20] This 6-line signal departs from that of the solvated Mn^{2+} ion and is characteristic of a Mn^{2+} centre bound to the ligand. After addition of H_2O_2 (460 mM, Figure 7b), the signal of **2a** disappeared rapidly (ca. 1 min) and was replaced by a well-resolved 6-line spectrum centred near 350 mT (g = 2). On both the high- and low-field sides of this signal, another weak signal could be detected also with a 16-line pattern which corresponds to a bis(μ-oxo)$Mn^{III}Mn^{IV}$ complex. At longer times (Figure 7c), these two signals decreased in intensity and were replaced by a new poorly resolved 6-line signal at 350 mT (g = 2). After ca. 30 min (Figure 7d), this last signal was the only one observed.

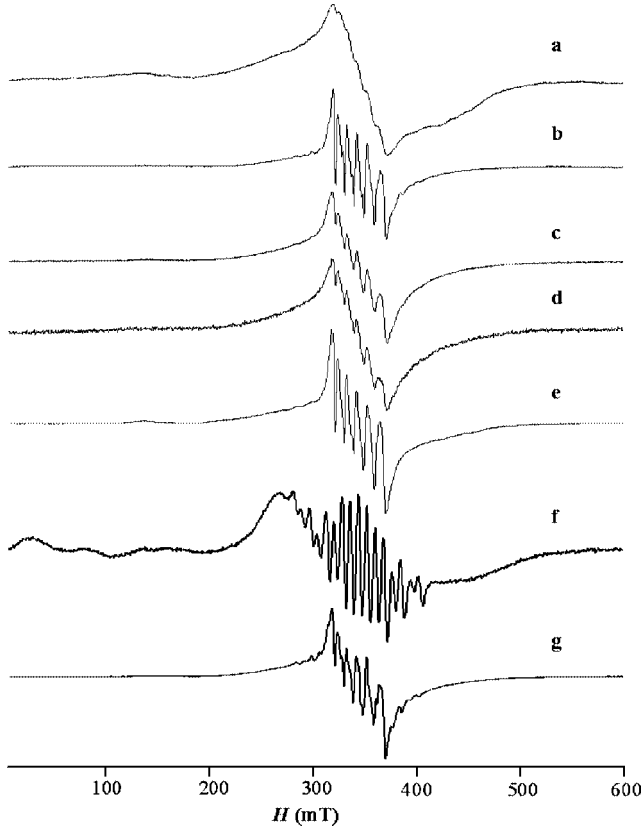

Figure 7. EPR spectra of the reaction of **2a** in acetonitrile with H_2O_2 and after addition of perchloric acid or triethylamine. Spectra a–d: reaction times 0, 1, 8 and 30 min; reaction conditions: [**2a**] = 1 mM, [H_2O_2] = 460 mM, T = –40 °C; spectrum e: **2a** + 1 equiv. perchloric acid; spectrum f: **2a** + 1 equiv. triethylamine; spectrum g: **1a** + 1 equiv. percloric acid + 460 equiv. H_2O_2. Reaction conditions [**1a**] = 1 mM, [H_2O_2] = 460 mM, T = 0 °C.

To further substantiate the effect of addition of acid or base to an acetonitrile solution of **2a**, its EPR spectrum was recorded in the presence of 1 equiv. of perchloric acid (Figure 7e). This spectrum possesses a better resolved 6-line signal centred at 350 mT (g = 2) which is completely different from that of **2a**. This spectrum is very similar to that of **1a** + 1 equiv. of perchloric acid (see Figure 4a in ref.[21]). The spectrum shown in Figure 7f was recorded after addition of 1 equiv. of triethylamine to **2a**. It consists of two signals, one with a 16-line pattern centred at 350 mT (g = 2) corresponding to a bis(μ-oxo)$Mn^{III}Mn^{IV}$ complex. The second one, composed of several transitions between 0 and 5500 G is characteristic of **1a**.[20] These results indicate that

 © 2005 Wiley-VCH Verlag GmbH & Co. KGaA, Weinheim

2a is not stable in a basic medium and disproportionates into **1a** and a bis(μ-oxo)$Mn^{III}Mn^{IV}$ derivative. Spectrum 7 g was recorded during the reaction of **1a** with H_2O_2 after addition of 1 equiv. of perchloric acid. We can notice than this spectrum is very close to that of **2a** without perchloric acid (Figure 7b).

Mass Spectrometry Monitoring

To obtain a better characterisation of the reaction medium during the reaction of **2a** with hydrogen peroxide, it was monitored by ESI-MS. The results obtained are reported in Figure 8. The starting compound **2a** (Figure 8a) appeared in the form of 3 peaks at *m/z* = 854.8, 756.2 and 378.1 which correspond, respectively, to $[Mn^{II}Mn^{III}(\mu\text{-L})(\mu\text{-OAc})_2](ClO_4)]^+$, $[Mn^{II}Mn^{II}(\mu\text{-L})(\mu\text{-OAc})_2]^+$ and $[Mn^{II}Mn^{III}(\mu\text{-L})(\mu\text{-OAc})_2]^{2+}$. The second ion at *m/z* = 756 was formed by reduction of the starting material (or other related species) during the ionisation process and this can be confirmed by its absence in the corresponding EPR spectrum.[20] After addition of hydrogen peroxide (Figure 8b), new peaks appeared at *m/z* = 713.1, 729.2 and 742.3. All these signals were also observed during the reaction of **1a** with hydrogen peroxide[21] and labelling experiments enabled us to assign them to the two intermediates $[Mn^{II}Mn^{III}(\mu\text{-L})(\mu\text{-O})(\mu\text{-OAc})]^+$ and $[Mn^{III}Mn^{IV}(\mu\text{-L})(\mu\text{-O})_2(OAc)]^+$, and the oxidation product $[Mn^{II}Mn^{II}(\mu\text{-L})(\mu\text{-OAc})(\mu\text{-HCOO})]^+$, respectively. After ca. 17 min, the starting compound had been fully consumed as revealed by the spectrum depicted in Figure 8c showing that the peaks of the initial complex had disappeared.

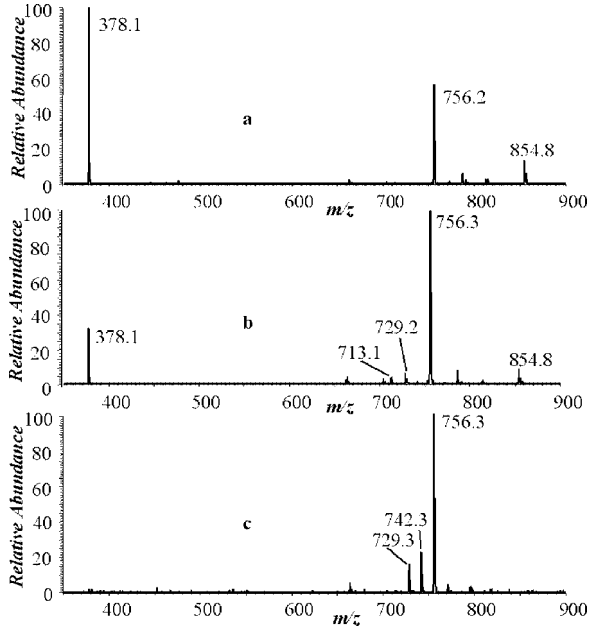

Figure 8. ESI-MS spectra of the reaction of **2a** with H_2O_2 in acetonitrile: spectra a–c: reaction times 0, 1 and 17 min; reaction conditions [**2a**] = 0.6 mM, $[H_2O_2]$ = 460 mM, *T* = –40 °C.

Discussion

Scheme 2 summarises the overall mechanism of H_2O_2 disproportionation by **1a** which emerged from our previous investigations of the reaction by a combination of UV/Vis, EPR, X-ray absorption spectroscopy and ESI mass spectrometry.[21] This mechanism involves an initiation phase in which **1a** is oxidised to the dimanganese(II,III) state with cleavage of the phenoxo bridge. A 6-line EPR signal centred at *g* = 2 is associated with this species. This compound can be viewed as the precursor to the catalytic species since it is further oxidised to the active bis(μ-oxo)dimanganese(III,IV) complex. In the catalase-like reaction, this complex oxidises H_2O_2 and is transformed into the (μ-oxo)dimanganese(II,III) species which is then able to reduce H_2O_2 to water. The present kinetic and thermodynamic studies of dioxygen evolution are fully consistent with this mechanistic scheme. In particular, a lag phase extending over ca. 100 s can be observed at low H_2O_2 concentrations in the case of **1a**. This lag phase more than likely corresponds to the required oxidation process to generate the precursor of the active species. Consistently, no lag phase was observed for **2a** or for **1a** at higher H_2O_2 concentrations. The present kinetic and thermodynamic studies provide a few observations which can valuably improve the understanding of the mechanism.

Firstly, we observed that on the first three successive additions of H_2O_2, the reaction rate of **1a** increased and eventually approached that of **2a**, while the latter did not show such a rate increase. This can be explained if the initiation process is slower than the disproportionation reaction. If this were the case, the disproportionation would start developing before all **1a** had entered the catalytic cycle. Successive additions would therefore bring more of **1a** into the active form. This view is supported by the observation that the less reactive **1b** persists longer than **1a** in the catalytic medium.[21]

Secondly, the kinetic measurements show that the initial rate of the catalase-like reaction is dependent on the nature of the bridging carboxylates. A similar observation was made by Okawa et al.[16,27,28] This result may indicate that at least one of the carboxylate groups remains in the coordination sphere of the active species. This conclusion is perfectly consistent with the results of our previous ESI-MS analyses of **1a** and **1b** which indicated the presence of one carboxylate in both active species.

Thirdly, the thermodynamic analysis of the reaction revealed similar trends (**2a** > **1a** > **1b**) in the activation energies and the preexponential terms. This trend in activation energy is opposite to the reaction efficiency but it is noteworthy that it parallels the bond strengths between the carboxylate ligands and the catalysts. It may then reflect the need to dissociate a carboxylate during the catalysis to make a coordination site available to hydrogen peroxide.

ESI-MS monitoring of the reaction of **2a** with H_2O_2 has shown that the bis(μ-oxo)$Mn^{III}Mn^{IV}$ and the (μ-oxo)Mn^{II}-Mn^{III} intermediates are involved as in the case of **1a**. Nevertheless, the EPR spectra recorded during the course of the reaction were dominated by the 6-line signal of the precursor. It is worth noting that such a species was transiently formed upon reaction of **1a** with H_2O_2.[21] Protonation experiments coupled with EPR spectroscopy showed that the same 6-line EPR spectrum can be obtained upon addition

 © 2005 Wiley-VCH Verlag GmbH & Co. KGaA, Weinheim

of 2 equiv. of $HClO_4$ to **1a** or 1 equiv. to **2a**. This enhanced proton sensitivity of **2a** was attributed to the fact that its Mn^{II}–$O_{phenoxo}$ bond is significantly elongated (2.245 Å) and weakened with respect to the same bonds in **1a** (2.105–2.107 Å)[20] and therefore more susceptible to break in solution. This cleavage of the phenoxide bridge makes the dimanganese unit appear as the individual ions: an EPR-silent Mn^{III} and a mononuclear Mn^{II} with a 6-line signature. The influence of protonation on the reactivity experiments supports this view. Firstly, the rate of the catalase-like reaction of **1a** + 1 equiv. of perchloric acid is very close to that of **2a** without perchloric acid. Secondly, the EPR spectrum recorded during the catalase-like reaction of **1a** + 1 equiv. of perchloric acid and **2a** without perchloric acid are very similar and include a dominating contribution of the precursor (6-line signal at $g \approx 2$) and traces of a bis(μ-oxo)-$Mn^{III}Mn^{IV}$ complex (16-line signal at $g \approx 2$). It appears then that a unique mechanism is likely to be in operation for **1a** and **2a** but the different EPR signatures observed during the catalase-like reaction may reflect different proportions of EPR active species present in solution. Indeed, in the case of **1a**, the EPR spectrum is dominated by the 16-line signal of the active bis(μ-oxo)$Mn^{III}Mn^{IV}$ intermediate and the characteristic EPR signal of **1a** slowly disappears during the reaction. In contrast, in the case of **2a**, the spectrum of the precursor dominates and that of the active bis(μ-oxo)$Mn^{III}Mn^{IV}$ intermediate appears weak. This difference may have its origin in the different proton sensitivities of the starting complexes reinforced by the chemical processes required to form the active bis(μ-oxo)$Mn^{III}Mn^{IV}$ intermediate. Indeed, in the case of **1a**, the reaction requires $^3/_2$ H_2O_2 molecules and generates a single H^+ [Equation (1)].

$$Mn^{II}Mn^{II} + 3/2\ H_2O_2 \rightarrow Mn^{III}Mn^{IV}(\mu\text{-}O)_2 + H_2O + H^+ \quad (1)$$

In contrast, for **2a**, a single H_2O_2 molecule is needed but two H^+ ions are released [Equation (2)].

$$Mn^{II}Mn^{III} + H_2O_2 \rightarrow Mn^{III}Mn^{IV}(\mu\text{-}O)_2 + 2\ H^+ \quad (2)$$

The increased acidity of the medium may be responsible for the higher proportion of the precursor species.

Here we have shown that complexes **1a**, **1b** and **2a** are able to disproportionate 100% of the initial hydrogen peroxide in acetonitrile or methanol solution by means of a first-order reaction with respect to catalyst and hydrogen peroxide. This observation departs from the results of Okawa[13,28] who claimed that the complexes of dissymmetric pentadentate imine/amine-phenolato ligands are able to disproportionate only 65% of the initial hydrogen peroxide, while the symmetric ones disproportionate all the hydrogen peroxide. Nevertheless, the present hexadentate amine ligands and probably also the heptadentate ligand used by Nishida[25] appear flexible enough to accommodate the bis(μ-oxo)dimanganese(III,IV) cores by allowing a phenolate shift which frees some coordination position.[21] Such a situation may not be easily achievable with more conjugated ligands involving imine donors. When the dioxygen evolution rates are compared, our best catalyst (**2a**) is around 9 times more active than the comparable phenolato-bridged complexes described in the literature (after converting initial rates to the same conditions).[13,25] Nevertheless, they appear much less active than the dimanganese(II,II) complexes of tripodal ligands recently reported.[29]

Conclusions

The present kinetic and thermodynamic studies fully support our initial mechanistic investigations of the catalase-like reaction by dimanganese(II,II) complexes. A unique mechanism seems to be operative which is based on shuttling between a (μ-oxo)dimanganese(II,III) and a bis(μ-oxo)dimanganese(III,IV) species. This illustrates the fact that to efficiently disproportionate H_2O_2 the system uses the Mn_2 pairs, the redox potentials of which are the most adapted whatever the initial oxidation states of the Mn ions. The systems differ by the initiation process required to enter the catalytic cycle and the sensitivity to protonation which appears to significantly alter the composition of the medium and the kinetics.

Experimental Section

General: All solvents and reagents were of the highest quality available and were used as received unless noted otherwise. The concentration of the hydrogen peroxide stock solution (30% w/w) was determined monthly by permanganate titration. The ligand HL was prepared according to the literature procedure.[22]

Syntheses: The complexes **1a**, **1b** and **2a** where synthesised according to the procedure described before.[20]

Caution: Perchloric acid and perchlorate salts are potentially dangerous and explosive and must be handled with care and in small quantities.

Spectroscopic Measurements: Electronic absorption spectra were recorded with a Hewlett Packard HP 89090A diode array spectrophotometer. Electrospray ionisation mass spectra were obtained with an LCQ Finnigan Thermoquest ESI source spectrometer with an ion trap and an octupolar analyser. EPR spectra at X band were recorded with an EMX Bruker spectrometer equipped with an Oxford Instruments cryostat ESR900. All spectra presented were recorded with the following set of conditions: T = 10 K, P = 0.2 mW, modulation F = 100 kHz, I = 9 G.

Kinetic Measurements: The rate determinations of the catalase-like reactions were performed by volumetric measurements of the evolved dioxygen. The whole apparatus, constructed from borosilicate glass, was kept at a constant temperature (±0.2 °C) using a thermostatted ethanol circulation bath (Haake FQ-4). In a standard procedure, catalyst solution (2 mL) was placed in the kinetic apparatus. The solution was stirred for 30 min to reach a stable temperature. The chosen volume of hydrogen peroxide stock solution was added and the volume of evolved dioxygen was then measured as a function of time. To compare the kinetics at different temperatures, the volume of the gas was converted to a reference temperature (273 K) using the ideal gas law. The volume was also corrected for the vapour pressure of the solvent at the working temperature using the expression $V_{corr} = V_{mes}*(P_{atm}–P_{vap})/P_{atm}$ where V_{corr} is the corrected volume, V_{mes} the measured volume,

 © 2005 Wiley-VCH Verlag GmbH & Co. KGaA, Weinheim

P_{atm} the atmospheric pressure and P_{vap} the vapour pressure of the solvent at the working temperature. In most cases, the initial rates were obtained by measuring the slopes of the tangents of the curve $v(O_2)$ vs. time at 0 s. When a lag phase was present (i.e. experiments with **1a** at low H_2O_2 concentrations), the largest slope after the initiation phase was used.

[1] B. Halliwell, J. M. C. Gutteridge, *Meth. Enzymol.*, Academic Press, San Diego, **1990**.
[2] E. R. Stadtman, P. B. Berlett, P. B. Chock, *Proc. Natl. Acad. Sci. USA* **1990**, *87*, 384–388.
[3] Y. Kono, I. Fridovich, *J. Biol. Chem.* **1983**, *258*, 6015–6019.
[4] G. S. Allgood, J. J. Perry, *J. Bacteriol.* **1986**, *168*, 563–567.
[5] V. V. Barynin, A. I. Grebenko, *Dokl. Akad. Nauk SSSR* **1986**, *286*, 461–464.
[6] G. C. Dismukes, *Chem. Rev.* **1996**, *96*, 2909–2926.
[7] A. Wu, J. E. Penner-Hahn, V. L. Pecoraro, *Chem. Rev.* **2004**, *104*, 903–938.
[8] S. V. Antonyuk, V. R. Melik-Adamyan, A. N. Popov, V. S. Lamzin, P. D. Hempstead, P. M. Harrison, P. J. Artymyuk, V. V. Barynin, *Crystallogr. Rep.* **2000**, *45*, 105–116.
[9] V. V. Barynin, M. M. Whittaker, S. V. Antonyuk, V. S. Lamzin, P. M. Harrison, P. J. Artymiuk, J. Whittaker, *Structure* **2001**, *9*, 725–738.
[10] S. V. Khangulov, V. V. Barynin, S. V. Antonyuk-Barynina, *Biochim. Biophys. Acta* **1990**, *1020*, 25–33.
[11] G. S. Waldo, J. E. Penner-Hahn, *Biochemistry* **1995**, *34*, 1507–1512.
[12] V. L. Pecoraro, M. J. Baldwin, A. Gelasco, *Chem. Rev.* **1994**, *94*, 807–826.
[13] H. Okawa, H. Sakiyama, *Pure Appl. Chem.* **1995**, *67*, 273–280.
[14] A. E. M. Boelrijk, G. C. Dismukes, *Inorg. Chem.* **2000**, *39*, 3020–3028.
[15] A. Gelasco, S. Bensiek, V. L. Pecoraro, *Inorg. Chem.* **1998**, *37*, 3301–3309.
[16] H. Wada, K. I. Motoda, M. Ohba, H. Sakiyama, N. Matsumoto, H. Okawa, *Bull. Chem. Soc. Jpn.* **1995**, *68*, 1105–1114.
[17] H. Sakiyama, H. Okawa, R. Isobe, *J. Chem. Soc., Chem. Commun.* **1993**, 882–884.
[18] Y. Sasaki, T. Akamatsu, K. Tsuchiya, S. Ohba, M. Sakamoto, Y. Nishida, *Polyhedron* **1998**, *17*, 235–242.
[19] I. Romero, M.-N. Collomb, A. Deronzier, L. Dubois, J.-M. Latour, J. Pécaut, *Inorg. Chem.* **2002**, *41*, 1795–1806.
[20] L. Dubois, D.-F. Xiang, X.-S. Tan, J. Pécaut, P. Jones, S. Baudron, L. Le Pape, J.-M. Latour, C. Baffert, S. Chardon-Noblat, M.-N. Collomb, A. Deronzier, *Inorg Chem.* **2003**, *42*, 750–760.
[21] L. Dubois, R. Caspar, L. Jacquamet, P.-E. Petit, M.-F. Charlot, C. Baffert, M.-N. Collomb, A. Deronzier, J.-M. Latour, *Inorg. Chem.* **2003**, *42*, 4817–4827.
[22] W. Kanda, W. Moneta, M. Bardet, E. Bernard, N. Debaecker, J. Laugier, A. Bousseksou, S. Chardon-Noblat, J. M. Latour, *Angew. Chem. Int. Ed. Engl.* **1995**, *34*, 588–590.
[23] T. Nakamura, K. Niwa, S. Usugi, H. Asada, M. Fujiwara, T. Matsushita, *Polyhedron* **2001**, *20*, 191–201.
[24] C. Palopoli, B. Chansou, J. P. Tuchagues, S. Signorella, *Inorg. Chem.* **2000**, 1458–1462.
[25] Y. Nishida, T. Akamatsu, K. K. Tsuchia, M. Sakamoto, *Polyhedron* **1994**, *13*, 2251–2254.
[26] D. R. Gamelin, M. L. Kirk, T. L. Stemmler, S. Pal, W. H. Armstrong, J. E. Penner-Hahn, E. I. Solomon, *J. Am. Chem. Soc.* **1994**, *116*, 2392–2399.
[27] C. Higuchi, H. Sakiyama, H. Okawa, R. Isobe, D. E. Fenton, *J. Chem. Soc. Dalton Trans.* **1994**, 1097–1103.
[28] C. Higuchi, H. Sakiyama, H. Okawa, D. E. Fenton, *J. Chem. Soc. Dalton Trans.* **1995**, 4015–4020.
[29] M. U. Triller, W.-Y. Hsieh, V. L. Pecoraro, A. Rompel, B. Krebs, *Inorg. Chem.* **2002**, *41*, 5544–5554.

Received: September 24, 2004

 © 2005 Wiley-VCH Verlag GmbH & Co. KGaA, Weinheim

One-Dimensional Chains Formed by First-Row Transition Metal(II) Nitrates and Pyrimidine – Influence of Water Coordination on Structural Reliability

Sarah A. Barnett,[a] Neil R. Champness,*[a] and Claire Wilson[a]

Keywords: Coordination frameworks / Coordination polymer / Crystal structure / Metal nitrates / Pyrimidine

An isostructural family of one-dimensional coordination polymers, $[M(NO_3)_2(pym)(H_2O)_2]_\infty$ [M = Mn (**1**), Co (**2**), Ni (**3**), Zn (**4**); pym = pyrimidine], has been prepared and their phase purity assessed. It is shown that in contrast to other $M(NO_3)_2$–pyrimidine coordination polymers, **1**–**4** show a surprising preference for the structure reported herein rather the wide variety of other possible product architectures. It is also shown that a related complex $[Ni(NO_3)_2(pym)(MeCN)_2]_\infty$ (**5**), in which water ligands observed in **1**–**4** are replaced by MeCN molecules, can also be prepared. However, **5** is highly hygroscopic and readily converts to **3** in the presence of atmospheric water. The implication of the uniformity of structure is discussed in relation to the serendipitous coordination of water molecules to the metal centres.
(© Wiley-VCH Verlag GmbH & Co. KGaA, 69451 Weinheim, Germany, 2005)

Introduction

The construction of coordination frameworks is an extremely topical area of inorganic and materials chemistry.[1] The strong interest in this area arises because the synthetic procedure used to construct these materials allows, in principle, a high degree of design. New materials with tuneable properties have been developed from coordination frameworks over recent years and as synthetic procedures become more advanced so the properties of these materials become more highly evolved.[1] The targeted synthesis of coordination polymers requires an appreciation of not only the variety of possible coordination framework materials that can be prepared, but also an appreciation of which structures are more favourable. An assessment of phase purity of coordination polymers is both valuable from the point of view of material properties, but also gives insight into the structural reliability[2] of a given set of starting building-blocks. We,[3,4] amongst others,[5] have been interested in the use of $M(NO_3)_2$ species as building blocks in coordination polymer construction due to their structural diversity that gives rise to a variety of fascinating coordination framework architectures. We have previously commented on the lack of structural reliability of $M(NO_3)_2$ as a coordination polymer node, and in general they can be viewed as structurally unreliable due to the large number of metal nodes that are generated from such species, but also because of the variety of coordination frameworks that can be generated even when the same $M(NO_3)_2$ node configuration is adopted.[2,3]

Herein, we report a family of isostructural one-dimensional coordination polymers, $[M(NO_3)_2(pym)(H_2O)_2]_\infty$ [M = Mn (**1**), Co (**2**), Ni (**3**), Zn (**4**)], which interestingly form a single phase under the conditions of synthesis used. The serendipitous coordination of water molecules to the metal centres leads to the formation of a hydrogen-bonded array that may contribute to the favourable formation of the observed product.

Results and Discussion

Reaction of $M(NO_3)_2{\cdot}xH_2O$ salts [M = Mn (**1**), Co (**2**), Ni (**3**), Zn (**4**)] dissolved in either MeCN or *i*PrOH with a solution of pyrimidine (pym) in CH_2Cl_2 leads to the formation of insoluble precipitates which are found to have the stoichiometry $[M(NO_3)_2(pym)(H_2O)_2]_\infty$ by elemental analysis. In the case of $Ni(NO_3)_2$ with pym in CH_2Cl_2/MeCN an alternative product $[Ni(NO_3)_2(pym)(MeCN)_2]_\infty$ (**5**) can also be isolated but readily undergoes conversion to **3** in the presence of atmospheric moisture. Single crystals were grown by slow diffusion of the layered solutions of the metal salt and pyrimidine in their respective solvents.

Structural characterisation of **1**–**4** by single-crystal X-ray diffraction showed the formation of one-dimensional coordination polymers with the formula $[M(NO_3)_2(pym)(H_2O)_2]_\infty$. All four compounds are isostructural and crystallize in the space groups *I*2/*a* [non-standard setting of *C*2/*c* (no. 15)]. Each M^{II} centre is pseudo-octahedral and coordinated by two pyrimidine ligands, two η^1-nitrate anions and two water molecules (Figure 1; Table 1). The bridging nature of the pyrimidine ligand results in the formation of a one-dimensional zigzag chain, which is achiral, and runs parallel to the *c* axis (Figure 2).

[a] School of Chemistry, The University of Nottingham, University Park, Nottingham NG7 2RD, U. K.
Fax: +44-115-9513563
E-mail: Neil.Champness@nottingham.ac.uk
Supporting information for this article is available on the WWW under http://www.eurjic.org or from the author.

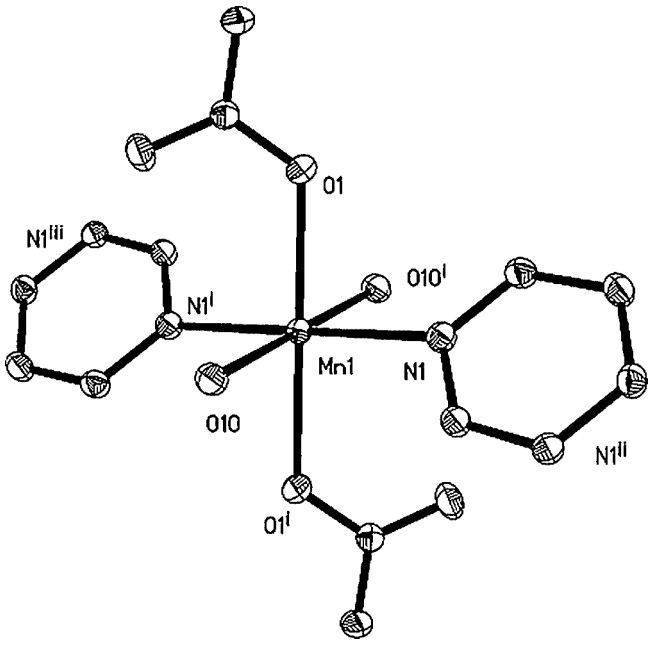

Figure 1. The Mn^{II} coordination environment observed in $[Mn(NO_3)_2(pym)(H_2O)_2]_\infty$ (**1**) showing the numbering scheme used. An analogous numbering scheme was used for compounds **2**–**4**. Displacement ellipsoids drawn at the 50% probability level. Hydrogen atoms are omitted for clarity. Symmetry codes: (i) $-x + 1/2$, $-y + 3/2$, $-z + 1/2$; (ii) $-x + 1/2$, y, $-z$; (iii) x, $-y + 3/2$, $z + 1/2$.

Table 1. Selected bond lengths [Å] and angles [°] for $[M(NO_3)_2(pym)(H_2O)_2]_\infty$ [M = Mn (**1**), Co (**2**), Ni (**3**), Zn (**4**)].

1		**2**	
Mn1–N1	2.2695(11)	Co1–N1	2.1451(13)
Mn1–O1	2.2129(10)	Co1–O1	2.1413(11)
Mn1–O10	2.1742(10)	Co1–O10	2.0773(11)
N1–Mn1–O1	86.00(4)	N1–Co1–O1	86.01(5)
N1–Mn1–O10	87.12(4)	N1–Co1–O10	87.50(5)
O1–Mn1–O10	98.96(4)	O1–Co1–O10	97.85(5)
3		**4**	
Ni1–N1	2.0826(18)	Zn1–N1	2.1318(10)
Ni1–O1	2.0786(16)	Zn1–O1	2.1542(8)
Ni1–O10	2.0624(16)	Zn1–O10	2.1021(8)
N1–Ni1–O1	86.71(7)	N1–Zn1–O1	86.54(3)
N1–Ni1–O10	86.95(7)	N1–Zn1–O10	92.77(4)
O1–Ni1–O10	96.96(7)	O1–Zn1–O10	82.24(3)
5			
Ni1–N1	2.105(3)		
Ni1–O1	2.085(2)		
Ni1–N1S	2.062(3)		
N1–Ni1–O1	89.77(10)		
N1–Ni1–N1S	90.22(11)		
O1–Ni1–N1S	83.22(11)		

In addition to these coordination bonds, however, extensive hydrogen bonding interactions are observed within the structure (Figure 3). These occur between the hydrogen atoms of the coordinated water molecules and the oxygen atoms of the nitrate anions on adjacent chains. Both of the hydrogen atoms of each water molecule participate in a hydrogen bond. However, only one oxygen atom of any given

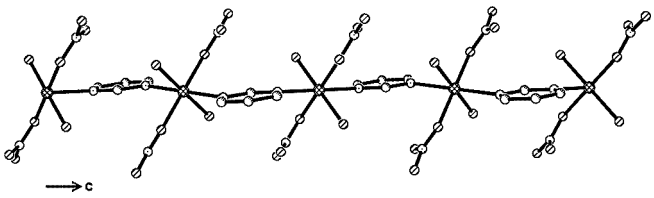

Figure 2. The one-dimensional chain formed by $[Mn(NO_3)_2(pym)(H_2O)_2]_\infty$ (**1**). Compounds **2**–**4** form analogous chains. Mn cross hatch; N dotted; O left hatch.

nitrate anion is involved in hydrogen bonding and, in fact, interacts with two hydrogen atoms from separate, symmetry-equivalent, water molecules. Two crystallographically distinct types of $OH\cdots O(NO_3)$ hydrogen bonds are observed (Table 2); one type links $[M(NO_3)_2(pym)(H_2O)_2]_\infty$ chains parallel to the *a* axis and the second links chains in the direction of the *b* axis. Thus, the hydrogen-bonding interactions form an undulating two-dimensional hydrogen-bonded sheet parallel to the *ab* plane. Each metal node is connected to six adjacent nodes within the sheet using a total of eight hydrogen bonds, utilising all four water hydrogen atoms (two for each H_2O), and both coordinated NO_3^- anions participating in two hydrogen bonds each. These hydrogen-bonded sheets are then crosslinked by the pyrimidine ligands into a three-dimensional network of $3^6.4^{18}.5^3.6$ topology (Figure 4).

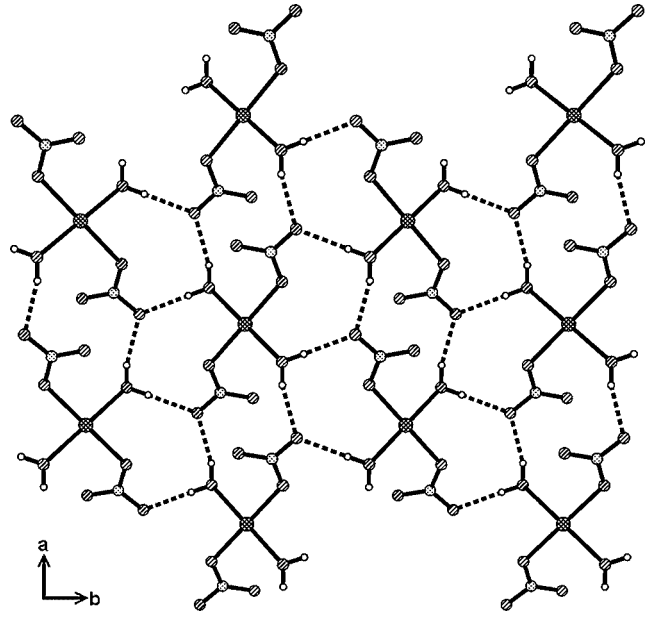

Figure 3. The hydrogen-bonded sheet formed by $[Mn(NO_3)_2(H_2O)_2]$ units viewed in the *ab* plane. $OH\cdots O(NO_3)$ hydrogen bonds indicated by dashed lines. Mn cross hatch; N dotted; O left hatch.

A single-crystal diffraction study of **5** revealed a highly related structure to that observed in **1**–**4**. Thus, each Ni^{II} centre is pseudo-octahedral and coordinated by two pyrimidine ligands, two η^1-nitrate anions and two MeCN molecules replacing the water ligands present in **1**–**4** (Figure 5; Table 1). In the absence of the water ligands no interchain

 © 2005 Wiley-VCH Verlag GmbH & Co. KGaA, Weinheim

Table 2. Bonding interactions observed for $[M(NO_3)_2(pym)(H_2O)_2]_\infty$ **1**–**4**.

Compound		H···O distance [Å]	O···O distance [Å]	O–H···O angle [°]
1	O10–H10A···O2^{i}	1.98(1)	2.792(2)	166(2)
	O10–H10B···O2^{ii}	1.96(1)	2.791(2)	175(2)
2	O10–H10A···O3^{ii}	1.96(1)	2.777(2)	174(2)
	O10–H10B···O3^{iii}	1.99(1)	2.795(2)	163(2)
3	O10–H10A···O2^{ii}	1.95(1)	2.778(2)	176(2)
	O10–H10B···O2^{iii}	2.00(3)	2.811(2)	165(2)
4	O10–H10A···O3^{iv}	1.99(2)	2.800(1)	164(2)
	O10–H10B···O3^{v}	1.95(1)	2.784(1)	176(2)

Symmetry transformations used to generate equivalent atoms: (i) $-x - 1/2, -y + 3/2, -z + 1/2$; (ii) $-x, y + 1/2, -z + 1/2$; (iii) $-x - 1/2, -y + 1/2, -z + 1/2$; (iv) $x, y, z - 1$; (v) $x, -y + 1, -z - 1/2$

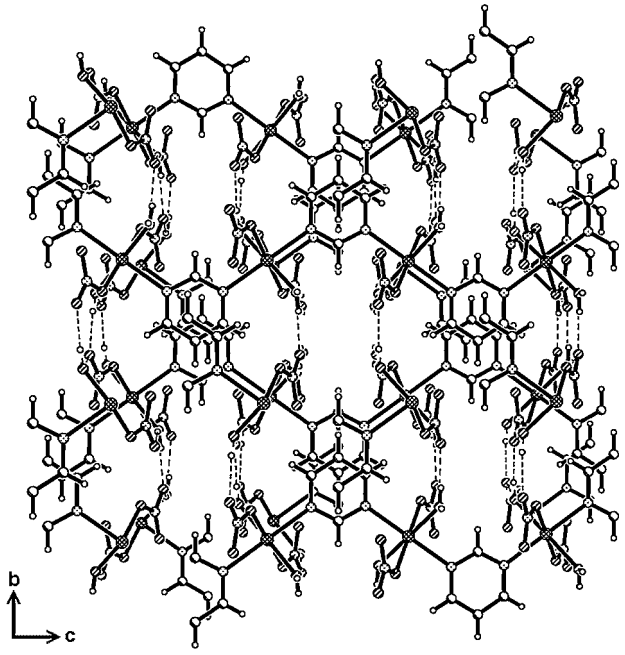

Figure 4. A view of the three-dimensional structure formed by $[Mn(NO_3)_2(pym)(H_2O)_2]_\infty$. Mn cross hatch; N dotted; O left hatch.

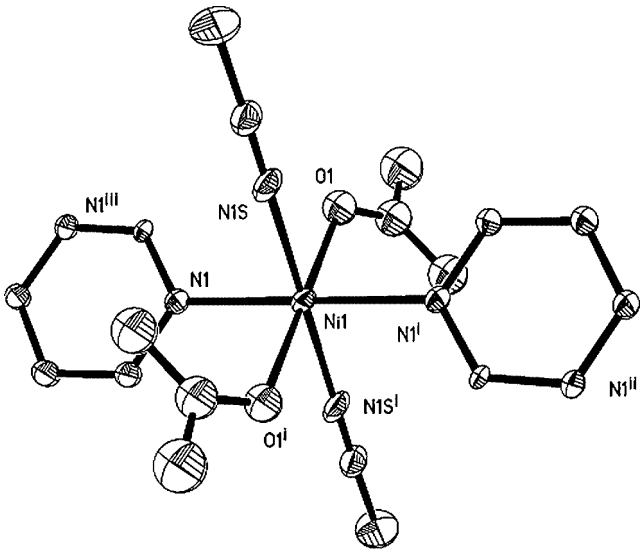

Figure 5. The Ni^{II} coordination environment observed in $\{[Ni(NO_3)_2(pym)(MeCN)_2](MeCN)\}_\infty$ (**5**) showing the numbering scheme used. Displacement ellipsoids drawn at the 50% probability level. Hydrogen atoms are omitted for clarity. Symmetry codes: (i) $-x, -y, 1 - z$; (ii) $x, -y, -1/2 + z$; (iii) $-x, y, 3/2 - z$.

hydrogen bonds are observed and therefore the extended structure observed in **1**–**4** is not present in **5**.

In order that phase purity of these products could be assessed, bulk samples of **1**–**4** were prepared. This is particularly important in the case of metal(II) nitrate bridging N-donor coordination polymers due to the wide variations previously observed in the products of such compounds.[3] Powders were prepared initially by L/M starting ratios of 1:1 in either an $MeCN/CH_2Cl_2$ (**1**, **2**, **4**) or an *i*PrOH/CH_2Cl_2 (**3**) solvent mixture. On comparing the results of X-ray powder diffraction with the calculated powder diffraction patterns using the single-crystal X-ray data, all the samples were confirmed to be pure single phases of the respective complexes (see Figure 6 for example).

The reaction of $Ni(NO_3)_2$ with pym in $MeCN/CH_2Cl_2$ affords crystals of both **3** and **5**. Indeed isolation of samples that contain **5** is difficult as this species proves to be highly hygroscopic, rapidly taking up atmospheric moisture and converting to **3**. All attempts to prepare bulk samples of **5** or to observe its presence in bulk samples of the reaction

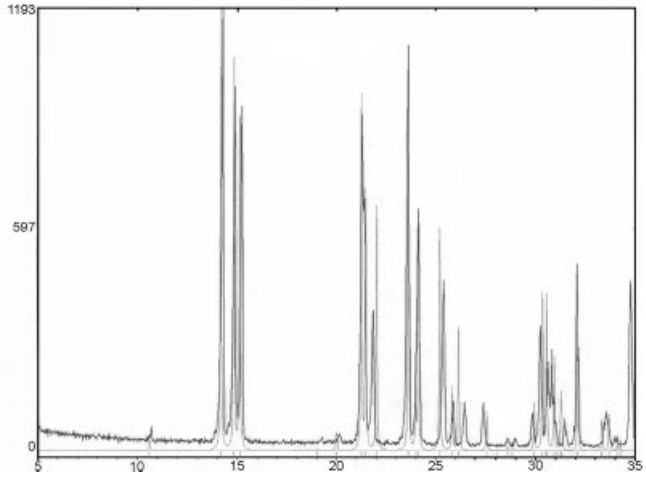

Figure 6. Comparison of the powder diffraction pattern recorded for the bulk product (black line) and that calculated from the single-crystal X-ray diffraction data (grey line) for $[Mn(NO_3)_2(pym)(H_2O)_2]_\infty$ (**1**).

 © 2005 Wiley-VCH Verlag GmbH & Co. KGaA, Weinheim

products were unsuccessful with only identification of pure samples of **3**.

The structure of **1**–**4** observed here has been previously observed in the products of the reactions of other transition metal salts with pyrimidine. Indeed, compounds isostructural with **1**–**4** have previously been observed for $[Cu(NO_3)_2(pym)(H_2O)_2]_\infty$[6] and $[Cd(NO_3)_2(pym)(H_2O)_2]_\infty$.[7] However, it is worth noting that in the case of $Cu(NO_3)_2$ and $Cd(NO_3)_2$ other products with pyrimidine[8,9] are also observed indicating that these metal centres are perhaps less predictable in their behaviour than the transition metal salts reported here. The lack of structural predictability is not particular surprising for either $Cu(NO_3)_2$ or $Cd(NO_3)_2$ considering the Jahn–Teller distortion expected for Cu^{II} and the highly malleable coordination sphere of Cd^{II}.[2,3] Indeed, it is perhaps more surprising that such a uniform, isostructural family of compounds are observed for the system reported here. The uniformity of product clearly reflects the greater stability of this product in comparison to other hypothetical competing structures, but also may be attributed, in part, to the coordination of water molecules to the metal centres in **1**–**4**, which arises due to the use of hydrated $M(NO_3)_2$ starting reagents. The coordination of water molecules to the metal centres has two major effects on the resultant coordination polymer structure. Firstly, by occupying two of the coordination sites of the metal centre the number of pyrimidine ligands that can be coordinated and subsequently bridge metal centres is restricted leading to the formation of the one-dimensional chains that are observed. Secondly, the ability of water to act as a hydrogen-bond donor allows the formation of hydrogen-bonding interactions between adjacent chains undoubtedly strengthening the formation of the observed structure. The relative stability of the structure observed in **1**–**4** is further indicated by the rapid conversion of **5** to **3** by replacement of the MeCN ligands in **5** by water molecules.

In summary, a family of one-dimensional coordination polymers has been prepared and their phase purity assessed. The implications of the uniformity of structure observed have been discussed, and it can be concluded that the preferential formation of the observed products can be attributed, at least in part, to the serendipitous coordination of water molecules to the metal centres.

Experimental Section

General: Infrared spectra were measured as KBr disks with a Nicolet Avatar 380 FT-IR spectrometer over the range 400–4000 cm^{-1}. Microanalyses were performed by the University of Nottingham Chemistry Department microanalytical service with a Perkin–Elmer 240B analyser. Powder X-ray diffraction patterns (PXD) data were collected with a Philips XPERT θ-2θ diffractometer with Cu-K_α radiation. Samples were mounted on flat glass plate sample holders. Ca. 50-min scans were run for each sample to assess phase purity. Short scans were run over the range $5° \leq 2\theta \leq 80°$ with step size $2\theta = 0.02°$ and times per step of 0.65 s. The simulated powder pattern was generated using the PC software packages APD, part of the Philips software package and POWDERCELL,[10] taking the single-crystal structural data for the compound as a model. For details see Supporting information (see footnote on the first page of this article). All chemicals were purchased from Aldrich Chemicals and used without further purification. All single-crystal X-ray experiments were performed with either a Bruker AXS SMART1000 CCD detector diffractometer (**1**–**5**) equipped with an Oxford Cryosystems open flow cryostat[11] [graphite-monochromated Mo-K_α radiation (λ = 0.71073 Å); ω scans] or with an Enraf–Nonius FAST TV Detector diffractometer [graphite-monochromated Mo-K_α radiation (λ = 0.71073 Å)] (**3**). Absorption corrections were applied by a semi-empirical approach (**1**, **2**, **4**, **5**). Other details of crystal data, data collection and processing are given in Table 3. CCDC-258503 (**1**), -258504 (**2**), -258505 (**3**), -258506 (**4**), -258507 (**5**) contain the supplementary crystallographic data for this paper. These data can be obtained free of charge from The Cambridge Crystallographic Data Centre via www.ccdc.cam.ac.uk/data_request/cif. All of the single-crystal structures were solved by direct methods using SHELXS-97[12] and all non-hydrogen atoms were located using subsequent difference-Fourier methods.[13] In all cases, hydrogen atoms were placed in calculated positions and thereafter allowed to ride on their parent atoms, except for water hydrogen atoms which were located from the difference Fourier map. The water hydrogen atoms were refined, with suitable O–H and H···H distance re-

Table 3. Crystallographic data for $[M(NO_3)_2(pym)(H_2O)_2]_\infty$ [M = Mn (**1**), Co (**2**), Ni (**3**), Zn (**4**)] and $\{[Ni(NO_3)_2(pym)(MeCN)_2](MeCN)\}_\infty$ (**5**).

	1	**2**	**3**	**4**	**5**
Empirical formula	$C_4H_8MnN_4O_8$	$C_4H_8CoN_4O_8$	$C_4H_8N_4NiO_8$	$C_4H_8N_4O_8Zn$	$C_{10}H_{13}N_7NiO_6$
M	295.08	299.07	298.85	305.51	385.98
Crystal system	monoclinic	monoclinic	monoclinic	monoclinic	monoclinic
Space group	*I*2/*a*	*I*2/*a*	*I*2/*a*	*I*2/*a*	*C*2/*c*
a [Å]	7.483(3)	7.4070(8)	7.3847(4)	7.4390(6)	21.548(4)
b [Å]	11.702(4)	11.5742(12)	11.4970(5)	11.5804(9)	7.0879(15)
c [Å]	12.105(4)	11.8183(12)	11.6481(4)	11.7508(8)	11.983(2)
B [°]	99.755	99,227(2)	99.125(2)	99.699(4)	117.697(3)
Z	4	4	4	4	4
T [K]	150(2)	150(2)	150(2)	150(2)	150(2)
μ [mm^{-1}]	1.305	1.760	2.032	2.505	1.240
Reflections collected	3011	3179	6117	5083	14462
Unique reflections (R_{int})	1273 (0.017)	1248 (0.022)	1108 (0.065)	1208 (0.018)	1937(0.051)
Final R_1 [$F > 4\sigma(F)$]	0.0192	0.0241	0.0333	0.0172	0.0631
wR_2 (all data)	0.0539	0.0571	0.0715	0.0486	0.1796

 © 2005 Wiley-VCH Verlag GmbH & Co. KGaA, Weinheim

straints. During the refinement of the structure of **5** a region of poorly defined solvent was accounted for using SQUEEZE,[14] which calculated 87 electrons per unit cell, approximating to 4 molecules of MeCN (88 electrons) which were included in the formula. One oxygen atom and the nitrogen atom of the nitrate anion showed disorder and were modelled isotropically over two sites with occupancies 0.6 and 0.4. A large peak of residual electron density remained in a chemically nonsensical position. This may be due to some form of twinning, however, the original data all indexed cleanly using the assigned cell and application of various twin laws did not result in any improvement.

$[Mn(NO_3)_2(pym)H_2O)_2]_\infty$ (1): A solution of $Mn(NO_3)_2{\cdot}xH_2O$ (224 mg, 0.83 mmol) in MeCN (15 cm^3) was added to a solution of pym (67 mg, 0.83 mmol) in CH_2Cl_2 (2 cm^3). The colourless crystals which formed over a 24 h period were filtered off and dried in vacuo. Yield 70% (171 mg). $C_4H_8MnN_4O_8$ (295.1): calcd. C 16.28, H 2.74, N 18.99; found C 16.21, H 2.60, N 18.66. IR (KBr, cm^{-1}): $\tilde{\nu}$ = 3423 w, 3109 w, 3074 w, 1763 w, 1594 s, 1568 w, 1467 s, 1389 s, 1221 m, 1177 m, 1144 w, 1078 s, 1024 m, 825 m, 805 w, 694 s, 656 m. Crystals suitable for single-crystal X-ray diffraction were grown as above.

$[Co(NO_3)_2(pym)(H_2O)_2]_\infty$ (2): A solution of $Co(NO_3)_2{\cdot}6H_2O$ (315 mg, 1.08 mmol) in MeCN (15 cm^3) was added to a solution of pym (87 mg, 1.08 mmol) in CH_2Cl_2 (2 cm^3). The dark pink precipitate was filtered off and dried in vacuo. Yield 87% (281 mg). $C_4H_8CoN_4O_8$ (299.1): calcd. C 16.06, H 2.70, N 18.74; found C 16.08, H 2.60, N 18.62. IR (KBr, cm^{-1}): $\tilde{\nu}$ = 3416 m, 3112 w, 3084 w, 1763 w, 1630 w, 1596 s, 1568 w, 1466 s, 1383 s, 1221 m, 1180 m, 1145 w, 1082 m, 1028 m, 825 m, 802 w, 691 s, 663 m. Single crystals were grown by slow diffusion of layered solutions of $Co(NO_3)_2{\cdot}6H_2O$ in MeCN over pym in CH_2Cl_2.

$[Ni(NO_3)_2(pym)(H_2O)_2]_\infty$ (3): A solution of $Ni(NO_3)_2{\cdot}6H_2O$ (240 mg, 0.83 mmol) in *i*PrOH (15 cm^3) was added to a solution of pym (66 mg, 0.83 mmol) in CH_2Cl_2 (2 cm^3). The light blue precipitate was filtered off and dried in vacuo. Yield 94% (233 mg). $C_4H_8N_4NiO_8$ (298.8): calcd. C 16.08, H 2.70, N 18.75; found C 16.10, H 2.65, N 18.31. IR (KBr, cm^{-1}): $\tilde{\nu}$ = 3405 m, 3118 w, 3091 w, 1767 w, 1636 w, 1597 s, 1570 w, 1467 m, 1386 s, 1221 w, 1182 m, 1145 w, 1085 m, 1048 w, 1031 w, 833 m, 801 w, 692 m, 666 m. Single crystals were grown by slow diffusion of layered solutions of $Ni(NO_3)_2{\cdot}6H_2O$ in *i*PrOH over pym in CH_2Cl_2.

$[Zn(NO_3)_2(pym)(H_2O)_2]_\infty$ (4): A solution of $Zn(NO_3)_2{\cdot}6H_2O$ (133 mg, 0.45 mmol) in MeCN (15 cm^3) was added to a solution of pym (36 mg, 0.45 mmol) in CH_2Cl_2 (2 cm^3). The colourless crystals that formed over a 24 hour period were filtered off and dried in vacuo. Yield 64% (88 mg). $C_4H_8N_4O_8Zn$ (305.5): calcd. C 15.73, H 2.65, N 18.35; found C 15.73, H 2.54, N 18.00. IR (KBr, cm^{-1}): $\tilde{\nu}$ = 3449 w, 3111 w, 1763 w, 1597 s, 1570 w, 1466 m, 1385 s, 1221 w, 1180 w, 1146 w, 1082 m, 1028 w, 825 m, 801 w, 690 s, 661 m. Crystals suitable for single-crystal X-ray diffraction were grown as above.

$[Ni(NO_3)_2(pym)(MeCN)_2]_\infty$ (5): A solution of $Ni(NO_3)_2{\cdot}6H_2O$ (101 mg, 0.35 mmol) in MeCN (10 cm^3) was added to a solution of pym (28 mg, 0.35 mmol) in CH_2Cl_2 (2 cm^3). The light blue precipitate was filtered off and dried in vacuo. Yield ca. 60% (ca. 70 mg). CHN elemental analysis, powder X-ray diffraction and IR spectroscopic studies confirmed that **5** rapidly converted to **3** on exposure to atmospheric moisture. Single crystals were grown by slow diffusion of layered solutions of $Ni(NO_3)_2{\cdot}6H_2O$ in MeCN over pym in CH_2Cl_2. Crystals were rapidly transferred from the reaction solution into drops of oil prior to data collection.

Acknowledgments

We would like to thank the EPSRC for support (S. A. B.). We acknowledge the use of the EPSRC National Service for Crystallography at the University of Southampton.

[1] a) S. Noro, S. Kitagawa, M. Kondo, K. Seki, *Angew. Chem. Int. Ed.* **2000**, *39*, 2082; b) R. Kitaura, S. Kitagawa, Y. Kubota, T. C. Kobayashi, K. Kindo, Y. Mita, A. Matsuo, M. Kobayashi, H. C. Chang, T. C. Ozawa, M. Suzuki, M. Sakata, M. Takata, *Science* **2002**, *298*, 2358; c) O. Kahn, *Acc. Chem. Res. 2000*, *33*, 647; d) O. R. Evans, W. Lin, *Acc. Chem. Res.* **2002**, *35*, 511; e) D. Maspoch, D. Ruiz-Molina, K. Wurst, N. Domingo, M. Cavallini, F. Biscarini, J. Tejada, C. Rovira, J. Veciana, *Nat. Mater.* **2003**, *2*, 190; f) E. Coronado, J. R. Galan-Mascaros, C. J. Gomez-Garcia, V. Laukhin, *Nature* **2000**, *408*, 447.
[2] S. A. Barnett, N. R. Champness, *Heteroatom Chem.* **2002**, *13*, 574.
[3] S. A. Barnett, N. R. Champness, *Coord. Chem. Rev.* **2003**, *246*, 145.
[4] a) S. A. Barnett, A. J. Blake, N. R. Champness, J. E. B. Nicolson, C. Wilson, *J. Chem. Soc., Dalton Trans.* **2001**, 567; b) M. A. Withersby, A. J. Blake, N. R. Champness, P. A. Cooke, P. Hubberstey, W.-S. Li, M. Schroder, *Inorg. Chem.* **1999**, *38*, 2259; c) M. A. Withersby, A. J. Blake, N. R. Champness, P. A. Cooke, P. Hubberstey, M. Schroder, *New J. Chem.* **1999**, *23*, 573; d) M. A. Withersby, A. J. Blake, N. R. Champness, P. A. Cooke, P. Hubberstey, M. Schroder, *J. Am. Chem. Soc.* **2000**, *122*, 4044.
[5] a) Y.-B. Dong, M. D. Smith, R. C. Layland, H.-C. zur Loye, *Chem. Mater.* **2000**, *12*, 1156; b) L. Carlucci, G. Ciani, D. M. Proserpio, *J. Chem. Soc., Dalton Trans.* **1999**, 1799; c) M. Kondo, T. Yoshimoti, K. Seki, H. Matsuzaka, S. Kitagawa, *Angew. Chem. Int. Ed. Engl.* **1997**, *36*, 1725; d) K. Kasai, M. Aoyagi, M. Fujita, *J. Am. Chem. Soc.* **2000**, *122*, 2140.
[6] M. Yasui, Y. Ishikawa, N. Akiyama, T. Ishida, T. Nogami, F. Iwasaki, *Acta Crystallogr., Sect.B* **2001**, *57*, 288.
[7] J. Pickardt, B. Staub, *Z. Naturforsch.* **1997**, *52b*, 1456.
[8] a) I. Riggio, G. A. van Albada, I. Mutikainen, U. Turpeinen, J. Reedijk, *Acta Crystallogr., Sect.C* **2000**, *56*, e380–e381; b) T. Ishida, K. Nakayama, M. Nakagawa, W. Sato, Y. Ishikawa, M. Yasui, F. Iwasaki, T. Nogami, *Synth. Met.* **1997**, *85*, 1655; c) R. Feyerherm, *J. Magn. Magn. Mater.* **2003**, *256*, 328.
[9] S. A. Barnett, A. J. Blake, N. R. Champness, C. Wilson, manuscript in preparation.
[10] G. Nolze, W. Krau, *Powder Diffr.* **1998**, *13*, 256.
[11] J. Cosier, A. M.Glazer, *J. Appl. Crystallogr.* **1986**, *19*, 105.
[12] G. M. Sheldrick, *SHELXS-97*, University of Göttingen, Germany, **1997**.
[13] G. M. Sheldrick, *SHELXL-97*, University of Göttingen, Germany, **1997**.
[14] A. L. Spek, *Acta Crystallogr., Sect. A* **1990**, *46*, C34.

Received: December 16, 2004

 © 2005 Wiley-VCH Verlag GmbH & Co. KGaA, Weinheim

Synthesis and Characterization of Magnesium-Aluminum Layered Double Hydroxides Containing (Tetrasulfonated porphyrin)cobalt

César A. S. Barbosa,[a] Ana Maria D. C. Ferreira,[a] and Vera R. L. Constantino*[a]

Keywords: Composites / Intercalations / Layered compounds / Organic–inorganic hybrid composites / Porphyrins

We report the synthesis and characterization of a magnesium-aluminum layered double hydroxide (LDH) containing [5,10,15,20-tetrakis(4-sulfonatophenyl)porphyrinato]cobalt(II) (CoTPhsP) by two routes: (i) CoTPhsP intercalation by structure reconstruction of the calcined pristine LDH [$Mg_{2.8}Al$-$(CoTPhsP)_{int}$] and (ii) adsorption of the CoTPhsP on the external surfaces of the noncalcined pristine LDH [$Mg_{3.0}Al$-$(CoTPhsP)_{ads}$]. The intercalation and adsorption of CoTPhsP in the LDHs were evaluated using different techniques, such as X-ray diffraction, thermogravimetry, scanning electronic microscopy, and surface area and porosity analysis. Further characterization by electron spin resonance and UV/Vis spectroscopy showed that the CoTPhsP molecules adsorbed and intercalated in the LDHs are present as two predominant species: the complex formed with molecular oxygen (CoTPhsP–O_2) and the corresponding deoxy monomeric species (CoTPhsP). The stability and reactivity of the CoTPhsP immobilized in the LDHs were evaluated in the presence of hydrogen peroxide solution. CoTPhsP in homogeneous conditions is deactivated by molecular aggregation and/or oxidative self-destruction in the presence of H_2O_2. On the other hand, CoTPhsP stability and reactivity were improved when adsorbed and intercalated in the LDHs. $Mg_{3.0}Al(CoTPhsP)_{ads}$ is more active than $Mg_{2.8}Al(CoTPhsP)_{int}$ in the decomposition of hydrogen peroxide to H_2O and O_2. A porosity analysis carried out by N_2 adsorption-desorption experiments for the intercalated material exhibited a type-IV isotherm characteristic of nonmicroporous materials. Hence, the CoTPhsP molecules located in the LDH galleries are not acessible to the H_2O_2, while the metal centers in the $Mg_{3.0}Al(CoTPhsP)_{ads}$ sample are more available, which may explain the enhanced reactivity.
(© Wiley-VCH Verlag GmbH & Co. KGaA, 69451 Weinheim, Germany, 2005)

Introduction

The intercalation of guest species in crystalline layered host matrices is considered to be a versatile synthetic method for the synthesis of nanostructured hybrid materials. The intercalated materials are particularly attractive because different synthetic approaches provide routes to tune the material properties by mediating the chemical composition of the host matrices and the intercalated species.[1,2]

Among two-dimensional matrices, layered double hydroxides (LDHs) have been found to be an interesting system for intercalation of different species.[3,4] The LDH composition is represented by the general formula $[M^{II}_{(1-x)}M^{III}_{x}(OH)_2](A^{n-})_{x/n}\cdot zH_2O$, where A^{n-} is the interlayer anion and M^{II} and M^{III} are di- and trivalent metals, respectively, located in the positively charged brucite-like layers.[5] LDHs with different compositions can be synthesized by varying the nature of M^{II}, M^{III}, and A^{n-}. This versatility has allowed the isolation of LDH materials with varied functionalities, including their use as catalysts,[6] reinforced fillers in organic polymers,[7] ion-exchangers for environmental remediation,[8] and, more recently, as drug[9] and gene carriers.[10]

[a] Instituto de Química, Universidade de São Paulo,
Caixa Postal 26077, CEP 05513-970 São Paulo, SP, Brazil
Fax: +55-11-3815-5579
E-mail: vrlconst@iq.usp.br

Synthetic metalloporphyrins are a well-known class of macrocyclic complexes that have been widely studied as catalysts for organic reactions based on their selective activity in catalyzed oxidations by heme enzymes such as, for example, cytochrome P-450 and peroxidases.[11] However, the reactivity of many synthetic metalloporphyrins is greatly reduced due to their molecular aggregation or oxidative self-destruction in the reaction media. In the presence of hydrogen peroxide these porphyrins are used for catalytic oxidation during important organic conversions due to the formation of a high-valent oxometal–porphyrin active complex.[11] Nevertheless, synthetic metalloporphyrins can lead to the undesired homolytic cleavage of H_2O_2 with generation of hydroxyl radical (Fenton-type reaction), which is a strong, nonselective oxidant of organic substrates and can decompose the metalloporphyrin.[12]

In order to overcome these disadvantages, synthetic metalloporphyrins have been immobilized in different inorganic and organic host networks.[13] In addition to the improved stability and reactivity of the metalloporphyrin catalyst, the immobilization in host matrices has been pointed out as an interesting route for their "heterogenization", facilitating the catalyst separation and recovery from the final reaction mixture.[14]

Sulfonated and carboxylated metalloporphyrins intercalated into LDHs have been prepared by several synthetic

routes, with various M^{2+} and M^{3+} ions and molar ratios in the LDH composition, and also with different transition metals in the porphyrin core.[15–22] Furthermore, nonmetallated anionic porphyrins have also been used to prepare intercalated LDHs.[23–25] These nanostructured hybrid materials have shown interesting properties as catalysts in organic conversions,[15,18,19] sensitizers in photochemical assemblies,[16] and asymmetric charge-carriers for the development of solar-energy conversion devices.[20]

We report in this work the synthesis of magnesium-aluminum LDHs containing [5,10,15,20-tetrakis(4-sulfonatophenyl)porphyrinato]cobalt(II) (CoTPhsP) through two synthetic routes: (i) the structure reconstruction of the calcined $Mg_{3.0}Al(OH)_{8.0}(CO_3)_{0.5}{\cdot}xH_2O$ pristine LDH in the presence of the anionic porphyrin (reconstruction method); (ii) adsorption of the anionic metalloporphyrin onto the external surfaces of the pristine LDH (Figure 1). To the best of our knowledge this is the first report regarding the synthesis and characterization of CoTPhsP adsorbed in a magnesium-aluminum LDH and its successful intercalation into the inorganic matrix by the reconstruction method. The isolated materials were characterized by X-ray diffraction (XRD), surface area and porosity analysis, thermogravimetry (TGA), scanning electronic microscopy (SEM), electron spin resonance (ESR), and infrared (IR) and electronic (UV/Vis) spectroscopy. In addition, the stability and longevity of the immobilized porphyrins (adsorbed and intercalated in the LDHs) were evaluated in the presence of hydrogen peroxide.

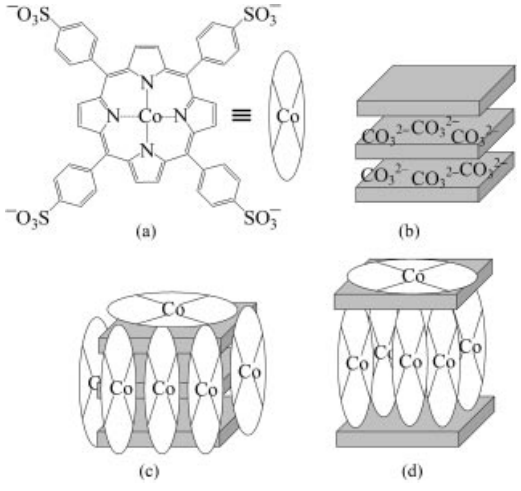

Figure 1. Schematic representation of CoTPhsP (a), $Mg_{3.0}Al\text{-}CO_3$ LDH (b) and idealized immobilization of CoTPhsP in the LDHs through adsorption (carbonate ions located between the layers are omitted for clarity) (c) or intercalation (d).

Results and Discussion

Materials Characterization

A typical XRD pattern was found for $Mg_{3.0}Al\text{-}CO_3$ prepared by coprecipitation (a profile similar to those presented by hydrotalcite-like compounds): sharp and symmetric peaks related to 00*l* reflections and broad and less symmetric peaks related to 0*kl* reflections (Figure 2a). The peaks were indexed in a hexagonal cell with rhombohedral symmetry, where c_0 = 23.4 Å and a_0 = 3.06 Å. From the c_0 parameter, which corresponds to three times the distance between adjacent layers, an interlayer distance of 7.80 Å could be calculated, which is typical for hydrotalcite-like materials containing carbonate anions.[26]

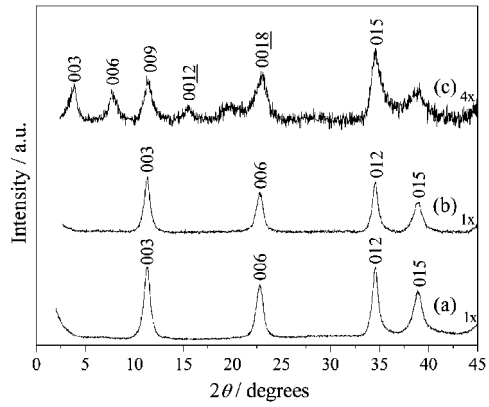

Figure 2. XRD patterns of $Mg_{3.0}Al\text{-}CO_3$ (a), $Mg_{3.0}Al(CoTPhsP)_{ads}$ (b), and $Mg_{2.8}Al(CoTPhsP)_{int}$ (c).

In relation to $Mg_{3.0}Al(CoTPhsP)_{ads}$ which contains the CoTPhsP adsorbed on the LDH external surfaces, the XRD pattern is identical to the $Mg_{3.0}Al\text{-}CO_3$ precursor (Figure 2b). This result shows, as expected, that the anionic porphyrin is not ion-exchanged with carbonate anions in the LDH.

The intercalated material isolated from the synthesis of $Mg_{2.8}Al(CoTPhsP)_{int}$ shows an XRD pattern different from the $Mg_{3.0}Al\text{-}CO_3$ precursor: a lower crystallinity and new peaks observed in the 2θ range 2.5–20° (Figure 2c).

Considering the same crystalline system used to assign the LDH precursor peaks, we find cell dimensions of c_0 = 70.2 Å and a_0 = 3.06 Å. The former corresponds to an interlayer distance of 23.4 Å. By comparing the interlayer distance between $Mg_{3.0}Al\text{-}CO_3$ and $Mg_{2.8}Al(CoTPhsP)_{int}$ one observes that the porphyrin incorporation expands the LDH layers by 15.6 Å. Moreover, by subtracting the LDH layer thickness (4.8 Å) from the interlayer distance, the gallery height of $Mg_{2.8}Al(CoTPhsP)_{int}$ is found to be equal to 18.6 Å, which is similar to the dimensions of the metalloporphyrin molecular plane (ca. 18 × 18 Å).[23] These results indicate that CoTPhsP has been successfully intercalated in a perpendicular orientation to the LDH layers. Such a perpendicular arrangement has been observed for LDHs intercalated with anionic metalloporphyrins[19,20] and nonmetallated anionic porphyrins,[23–25] using different synthetic methods.

Characterization by infrared spectroscopy indicates that CoTPhsP has been intercalated intact into the LDH. The IR spectra (not shown) of both neat and intercalated porphyrin exhibit similar characteristic absorption bands: 854, 885, and 1003 cm^{-1} (C–H pyrrole bending); 1290, 1348, and 1392 cm^{-1} (C–N stretching); 1495 and 1563 cm^{-1} (C–C

 © 2005 Wiley-VCH Verlag GmbH & Co. KGaA, Weinheim

phenyl and pyrrole stretching, respectively); 1038, 1126, and 1186 cm^{-1} (sulfonic groups).[27] In the IR spectra of $Mg_{2.8}Al(CoTPhsP)_{int}$, we noticed some changes in the relative band intensities at 1330–1400 cm^{-1}. In this region, the minor changes are attributed to the carbonate ions present in the LDH interlayer (ν_3 vibrational mode of CO_3^{2-}).[28] The hydroxide anion may also be present in the material, as it is formed in the LDH interlayer when using the reconstitution method[29] during the CoTPhsP intercalation procedure. Hence, it is possible that $Mg_{2.8}Al(CoTPhsP)_{int}$ contains, in addition to the porphyrin, hydroxide anions co-intercalated.

We have reported in a previous work that the intercalation of macrocyclic species in LDHs can lead to composites with an appreciable thermal stability.[30] Moreover, the guest localization in the LDH results in materials with distinct thermal behavior. Similar results were found with the LDH containing intercalated CoTPhsP, according to the thermogravimetric curves of the samples shown in Figure 3.

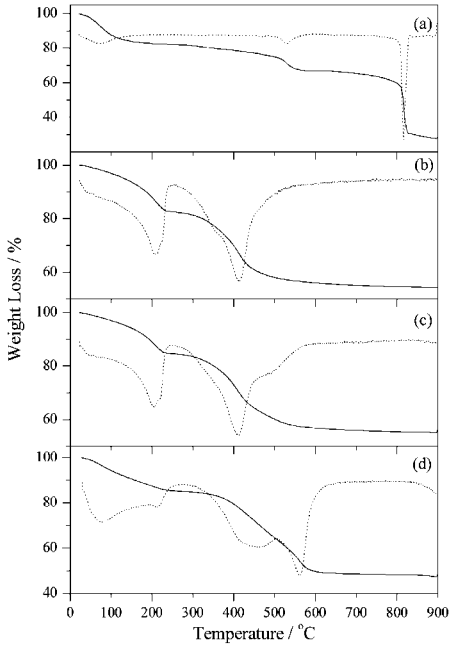

Figure 3. TGA (solid line) and DTG (dotted line) curves for CoTPhsP (sodium salt) (a), $Mg_{3.0}Al\text{-}CO_3$ (b), $Mg_{3.0}Al(CoTPhsP)_{ads}$ (c), and $Mg_{2.8}Al(CoTPhsP)_{int}$ (d).

The TG analysis of CoTPhsP shows a considerable thermal stability of the porphyrin (Figure 3a). A weight loss up to about 200 °C corresponds to the loss of hydration water. The porphyrin decomposition seems to occur in two steps. The first step is observed at about 490 °C and the second one starts at about 625 °C, with the main weight loss occurring at 815 °C. Figure 3b shows the TG curve for the LDH carbonate. The first step of weight loss (up to 210 °C) is ascribed to the water release and the second one (above 300 °C) to the LDH dehydroxylation and decarbonation, as discussed previously.[31]

The thermal behavior of $Mg_{3.0}Al(CoTPhsP)_{ads}$ up to around 600 °C can be interpreted as an overlap of TG curves for neat CoTPhsP and $Mg_{3.0}Al\text{-}CO_3$ (Figure 3c). Nevertheless, the weight loss observed for CoTPhsP above 625 °C is not present in the TG curve of the adsorbed CoTPhsP. The thermal behavior of $Mg_{2.8}Al(CoTPhsP)_{int}$ shows a higher stability towards decomposition of both the LDH matrix and CoTPhsP (Figure 3d). The dehydroxylation and decarbonation events seem to occur at about 330 °C, whereas the $Mg_{3.0}Al\text{-}CO_3$ LDH precursor decomposes at about 300 °C. The weight losses starting at 520 and 850 °C seem to be related to the decomposition of CoTPhsP, which suggests a higher stability than for neat CoTPhsP.

Textural characterization was performed by surface area and porosity measurements. $Mg_{3.0}Al\text{-}CO_3$ shows a surface area of 86 $m^2 g^{-1}$. For $Mg_{2.8}Al(CoTPhsP)_{int}$, the surface area of 34 $m^2 g^{-1}$ indicates that no micropores have been produced in the intercalation product as a substantial increase in the surface area compared to the LDH precursor would be expected if microporosity was present. This assumption was confirmed by N_2 adsorption-desorption isotherms of the sample. $Mg_{2.8}Al(CoTPhsP)_{int}$ exhibits type-IV isotherms (not shown) characteristic of nonmicroporous materials with a hysteresis loop indicating interparticle mesoporosity, according to the IUPAC classification.[32] We have previously observed similar results from the material isolated after intercalation of (phthalocyanine)Cu^{II} tetrasulfonate in the same LDH $Mg_{3.0}Al$ precursor.[30] $Mg_{3.0}Al(CoTPhsP)_{ads}$ shows a surface area of 106 $m^2 g^{-1}$. This increase in the surface area related to the $Mg_{3.0}Al\text{-}CO_3$ does not, however, indicate microporosity in the material. As described before, the interlayer space is occupied by the carbonate ions whereas CoTPhsP molecules are adsorbed on the external surface of the LDH.

Scanning electron micrographs obtained from the samples revealed a different morphology in the LDH after CoTPhsP intercalation by the reconstruction method (Figure 4). The SEM image of $Mg_{3.0}Al\text{-}CO_3$ presents a typical

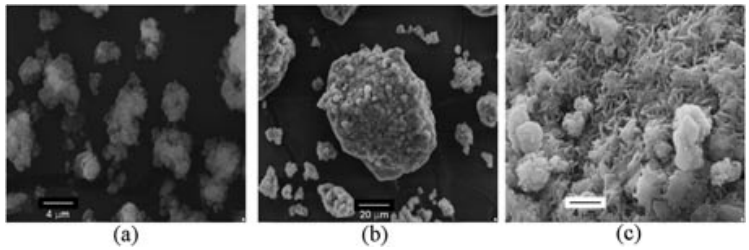

Figure 4. SEM images of $Mg_3Al\text{-}CO_3$ (10 000×) (a) and $Mg_{2.8}Al(CoTPhsP)_{int}$ with different magnifications: 2000× (b) and 10 000× (c).

 © 2005 Wiley-VCH Verlag GmbH & Co. KGaA, Weinheim

morphology expected for synthetic hydrotalcite-like compounds, with round particles of plate-like shapes (Figure 4a).

The adsorption of CoTPhsP on the external surface of the LDH layers results in a higher aggregation of the particles, which present the same morphology as observed for the LDH $Mg_{3.0}Al\text{-}CO_3$ (SEM image not shown). On the other hand, the intercalation of CoTPhsP into the LDH shows a distinct morphology (Figure 4b and Figure 4c). In the SEM images of $Mg_{2.8}Al(CoTPhsP)_{int}$ we observed a new phase with stick-like particles, and also particles with a plate-like shape.

Information about the electronic properties of free and immobilized CoTPhsP in the LDHs was obtained by recording the ESR and UV/Vis spectra of the samples. Figure 5 shows the UV/Vis spectra for CoTPhsP in different solutions.

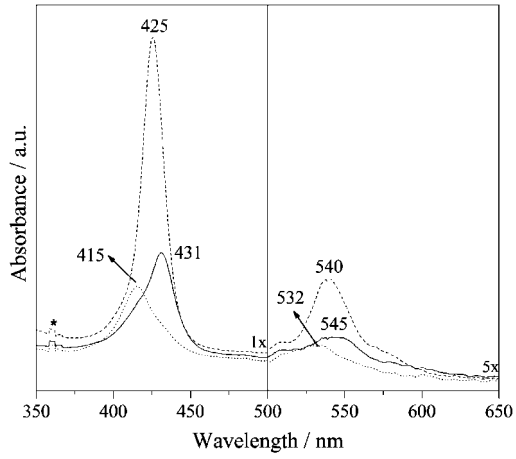

Figure 5. UV/Vis absorption spectra of 2 mmol L^{-1} CoTPhsP in aqueous solution (dashed line), in 90% DMF/10% water solution (solid line), and the latter solution after the addition of sodium dithionite (dotted line). Further details are provided in the text. The feature indicated by an asterisk is an instrument artifact.

The UV/Vis spectrum of CoTPhsP in aqueous solution shows the characteristic bands for metalloporphyrins, dominated by π-π* transitions, located at 425 nm (Soret band) and 540 and 580 nm (Q bands).[33] The presence of *N*,*N*-dimethylformamide (DMF), a coordinating solvent, results in a decrease in the intensity of both Soret and Q bands, accompanied by a small red shift (ca. 5 nm). The ESR spectra for 2 mmol L^{-1} CoTPhsP solutions were recorded for the assignment of the porphyrin species. An aqueous solution of this metalloporphyrin is ESR-silent, as previously reported in the literature.[34] The ESR spectrum of CoTPhsP in 90% DMF/10% water is shown in Figure 6a.

CoTPhsP is a low-spin Co^{II} complex with the single unpaired electron in the d_{z^2} orbital pointing out of the porphyrin plane.[35] This configuration makes the unpaired electron very sensitive to changes in the axial coordination of the metal ion, which makes the ESR technique useful for studying Co^{II}–porphyrins.[34–39] According to the literature,[34,36,39] CoTPhsP in water does not give an ESR signal

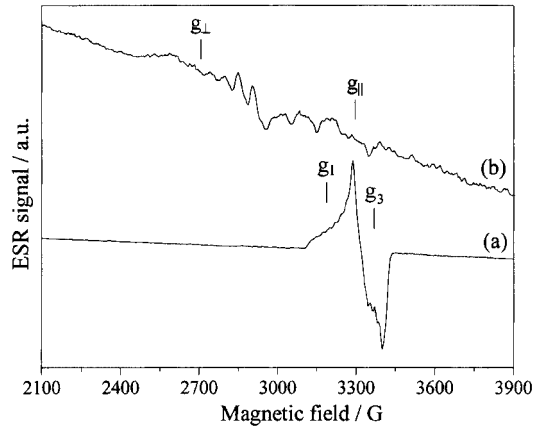

Figure 6. ESR spectra, recorded at 77 K, of 2 mmol L^{-1} CoTPhsP in 90% DMF/10% water solution (a) and after addition of sodium dithionite (b). Further details are provided in the text.

due to aggregation of the metalloporphyrin molecules and/or formation of a diamagnetic μ-peroxo complex with molecular oxygen (CoTPhsP–O_2–CoTPhsP). The addition of DMF causes deaggregation, resulting in a solution containing the monomeric species of the CoTPhsP. The resulting ESR spectra, as reported by de Bolfo et al.,[34] should present a characteristic signal with $g_{\|}$ = 2.040 ($A_{\|}$ = 95×10^{-4} cm^{-1}) and $g_{\perp}$ = 2.410 ($A_{\perp}$ = 43×10^{-4} cm^{-1}). In addition to the CoTPhsP monomeric species, a second ESR signal may be observed due to the complex formed by the metalloporphyrin with molecular oxygen (Co^{II}TPhsP–O_2) with g_1 = 2.088 (A_1 = 22×10^{-4} cm^{-1}), g_2 = 1.998 (A_2 = 8×10^{-4} cm^{-1}), and g_3 = 1.997 (A_3 = 16×10^{-4} cm^{-1}). The CoTPhsP–O_2 complex has also been detected for other cobalt–porphyrins.[35,39] The structure of this complex is also represented by Co^{III}TPhsP–O_2^- (superoxo complex) because the low values of hyperfine coupling in the ESR suggest that the unpaired electron resides primarily on the oxygen molecule.[37]

As shown in Figure 6a, the ESR spectrum for CoTPhsP in 90% DMF/10% water solution shows a signal at around 3300 G with g_1 = 2.090 (A_1 = 21.7×10^{-4} cm^{-1}) and g_3 = 1.997 (A_3 = 15.8×10^{-4} cm^{-1}) (g_2 factor and A_2 unresolved in the spectrum). This signal is attributed to the CoTPhsP–O_2 complex as the *g* factor and hyperfine-coupling values are in agreement with those reported by de Bolfo et al.[34] However, the monomeric ESR signal is not present in the spectrum of the CoTPhsP in solution. According to de Bolfo et al., a solid sample of CoTPhsP stored for a long time in air gives rise to an ESR spectrum showing only the CoTPhsP–O_2 signal, even when this stored sample was dissolved in aqueous solution containing different organic solvents.[34] Indeed, the CoTPhsP sample used in the present study was stored for more than six months without protection from atmospheric air. In an attempt to record the ESR spectra of the monomeric species, oxygen was removed from the 2 mmol L^{-1} CoTPhsP solution in 90% DMF/10% water solution by adding a small amount of sodium dithionite. Indeed, the ESR spectrum (Figure 6b) of this solution

 © 2005 Wiley-VCH Verlag GmbH & Co. KGaA, Weinheim

did not show the CoTPhsP–O_2 signal and a new one appeared, which is related to the monomeric species, with $g_{\|}$ = 2.029 ($A_{\|}$ = 91.2×10^{-4} cm^{-1}) and $g_{\perp}$ = 2.455 ($A_{\perp}$ = 52×10^{-4} cm^{-1}). The UV/Vis spectrum of this deoxygenated CoTPhsP solution shows Soret and Q bands at 415 and 532 nm, respectively, with a blue shift in comparison to the spectrum for the solution containing the CoTPhsP–O_2 complex (Figure 5).

Based on the ESR spectra recorded for free CoTPhsP, we suggest that the UV/Vis absorption bands at 425 and 540 nm for the metalloporphyrin in aqueous solution can be assigned to the CoTPhsP–O_2–CoTPhsP complex, whereas in 90% DMF/10% water solution, the bands at 431 and 545 can be assigned to the CoTPhsP–O_2 complex. The bands observed at 415 and 532 nm, after addition of sodium dithionite to the latter solution, can be attributed to the CoTPhsP monomeric species. In light of these findings, $Mg_{3.0}Al(CoTPhsP)_{ads}$ and $Mg_{2.8}Al(CoTPhsP)_{int}$ were next examined by recording the UV/Vis (Figure 7) and ESR spectra (Figure 8) of these samples.

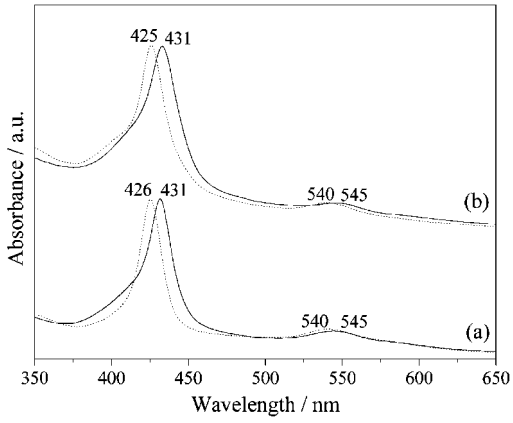

Figure 7. UV/Vis absorption spectra for $Mg_{2.8}Al(CoTPhsP)_{int}$ (a) and $Mg_{3.0}Al(CoTPhsP)_{ads}$ (b) solid samples dispersed in deionized water (dotted line) and 90% DMF/10% water solution (solid line).

The UV/Vis spectra for $Mg_{3.0}Al(CoTPhsP)_{ads}$ and $Mg_{2.8}Al(CoTPhsP)_{int}$ dispersed in deionized water and 90% DMF/10% water solution show a prominent broadening and a shoulder at around 410 nm in relation to neat CoTPhsP in the same solvents (Figure 5), although the Soret and Q band positions remain unchanged. Furthermore, the Soret band peak intensity decreases in relation to the Q band peak. Similar spectral profiles have also been observed in the electronic spectra of sulfonated metalloporphyrins[17,19–21] and nonmetallated sulfonated porphyrins intercalated in different LDHs,[23,24] which were ascribed to the aggregation of the porphyrin.[40,41] However, considering the ESR and UV/Vis spectra recorded for CoTPhsP in deionized water and in DMF/water solutions, we suggest that this broadening and the shoulder around 410 nm for the Soret band in $Mg_{3.0}Al(CoTPhsP)_{ads}$ and $Mg_{2.8}Al(CoTPhsP)_{int}$ are related to the different CoTPhsP species present in the LDHs. The main absorption bands are related to the CoTPhsP–O_2 complex (for dispersion in DMF/water) or the CoTPhsP–O_2–CoTPhsP species (for dispersion in water). The shoulder around 415 nm is due to the presence of monomeric species isolated in $Mg_{3.0}Al(CoTPhsP)_{ads}$ and $Mg_{2.8}Al(CoTPhsP)_{int}$. Indeed, these species were found in the powder ESR spectra for $Mg_{3.0}Al(CoTPhsP)_{ads}$ and $Mg_{2.8}Al(CoTPhsP)_{int}$ (Figure 8).

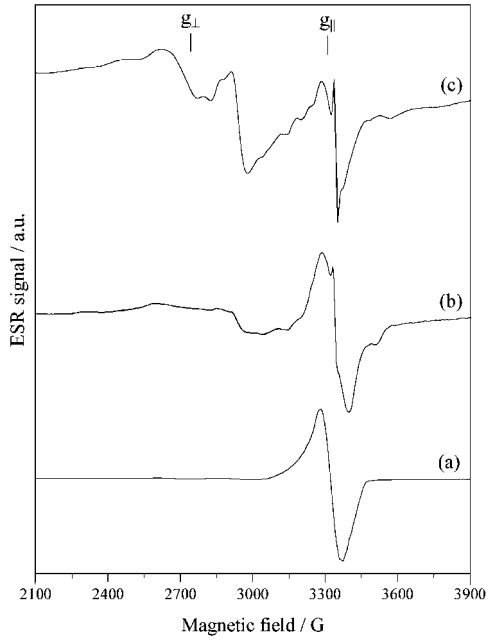

Figure 8. Powder ESR spectra, recorded at 77 K, of CoTPhsP (sodium salt) (a), $Mg_{3.0}Al(CoTPhsP)_{ads}$ (b), and $Mg_{2.8}Al(CoTPhsP)_{int}$ (c).

The ESR spectrum of CoTPhsP immobilized in the LDHs shows a resonance around 3300 G which is similar to that observed for neat CoTPhsP. As discussed before, this ESR signal is characteristic of the CoTPhsP–O_2 complex. Furthermore, a signal related to the monomeric species was also observed. The ESR spectrum of $Mg_{2.8}Al(CoTPhsP)_{int}$ shows a more resolved signal for this species with $g_{\|}$ = 2.043 ($A_{\|}$ = 90.5×10^{-4} cm^{-1}) and $g_{\perp}$ = 2.458 ($A_{\perp}$ = 52.6×10^{-4} cm^{-1}), in good agreement with the values found for CoTPhsP monomeric species in DMF/water solution, as reported by de Bolfo et al.[34] A narrow resonance at $g \approx 2.00$ has also been observed for other cobalt–porphyrins and attributed to a free-radical species[39] or impurities.[34,42] Comparing the relative intensities of the monomeric species and CoTPhsP–O_2 complex signals, $Mg_{2.8}Al(CoTPhsP)_{int}$ contains more CoTPhsP molecules in the monomeric form than the corresponding dioxygen complex. In contrast, the latter species is predominant in $Mg_3Al(CoTPhsP)_{ads}$.

The reactivity of the CoTPhsP complex in solution, intercalated, or adsorbed in the LDH was examined for the decomposition of hydrogen peroxide. Experimental curves of the oxygen released against time are given in Figure 9.

The curve of oxygen evolved obtained at 30 °C and pH = 9.60 (borate-buffered solution) shows a negligible reactivity for $Mg_{3.0}Al$-CO_3 (Figure 9a). The curve for CoTPhsP in homogeneous conditions reveals an oxygen release of 100 μL after 10 min, corresponding to 64% of the H_2O_2 used. Under heterogeneous conditions $Mg_{2.8}Al(CoTPhsP)_{int}$

 © 2005 Wiley-VCH Verlag GmbH & Co. KGaA, Weinheim

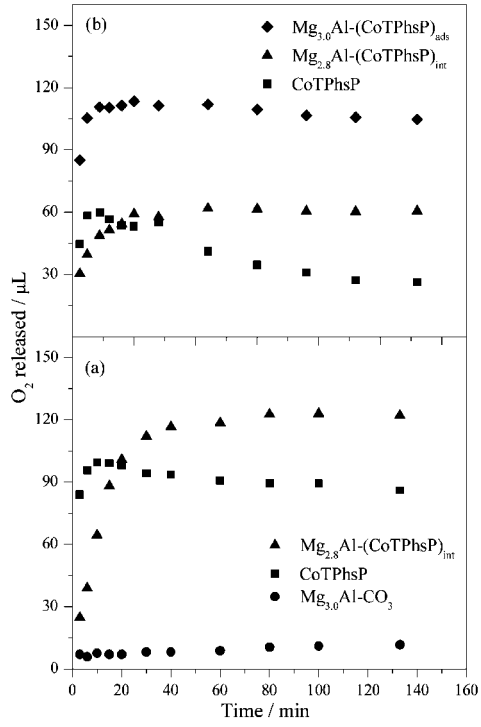

Figure 9. Experimental curves of oxygen released against time for hydrogen peroxide decomposition in the presence of CoTPhsP aqueous solution, $Mg_{3.0}Al$-CO_3, $Mg_{3.0}Al(CoTPhsP)_{ads}$, and $Mg_{2.8}Al(CoTPhsP)_{int}$ at 30 °C and pH = 9.60 (a) and 7.80 (b). Other conditions: 13.8 μmol of H_2O_2 and 3.62 μmol of CoTPhsP (a); 14.7 μmol of H_2O_2 and 7.50 μmol of CoTPhsP (b); final volume of 3.00 mL in borate-buffered solution.

was more active, converting 79% (123 μL) of the H_2O_2. In a second run, we obtained kinetic curves at pH = 7.80 (borate-buffered solution) and 30 °C (Figure 9b). Both CoTPhsP in homogeneous solution and $Mg_{2.8}Al(CoTPhsP)_{int}$ converted about 36% (ca. 60 μL) of the H_2O_2 used. The kinetic curve for $Mg_{3.0}Al(CoTPhsP)_{ads}$ is given in Figure 9b. As can be seen, this sample shows the best activity when compared to CoTPhsP in homogeneous conditions or intercalated into the LDH, converting about 69% (113 μL) of the H_2O_2.

In both pH = 9.60 and 7.80 buffered solution tests, the H_2O_2 decomposition reaction in the first minutes was faster in the presence of CoTPhsP in homogeneous conditions than $Mg_{2.8}Al(CoTPhsP)_{int}$. After this initial time, the CoTPhsP in solution was deactivated whereas the reaction for intercalated CoTPhsP proceeded. Furthermore, and different from $Mg_{2.8}Al(CoTPhsP)_{int}$ behavior, the H_2O_2 decomposition reaction in the presence of $Mg_{3.0}Al(CoTPhsP)_{ads}$ was faster than the CoTPhsP in solution even during the first few minutes of reaction. Finally, one expects a constant value of the released oxygen content after the maximum conversion, indicating the end of the reaction. However, we noticed a depletion of the oxygen evolved in the reaction with the CoTPhsP in homogeneous conditions.

It is well known that natural porphyrins undergo oxidative degradation by peroxides in the *meso* position.[43] The second generation of metalloporphyrin catalysts represented by *meso*-substituted porphyrins is considered less liable to oxidative degradation.[11] Nevertheless, our results indicate that CoTPhsP may be oxidized during the H_2O_2 decomposition reaction. This finding was corroborated by the UV/Vis spectra obtained from the homogeneous catalyst before and after the reaction. The spectrum (not shown) reveals a lower absorption intensity of the Soret band after the reaction. Another possibility for the oxygen depletion is the formation of an inactive μ-oxo complex (CoTPhsP–O–CoTPhsP) in the course of the H_2O_2 decomposition reaction.[11] Considering these paths for CoTPhsP deactivation in the presence of H_2O_2, it is evident that the metalloporphyrin stability is improved when immobilized in the LDHs. In consequence, the CoTPhsP reactivity is further enhanced.

In relation to the different reactivities observed between $Mg_{2.8}Al(CoTPhsP)_{int}$ and $Mg_{3.0}Al(CoTPhsP)_{ads}$, we consider that the CoTPhsP molecules intercalated in the LDH galleries cannot participate in the H_2O_2 decomposition because the intercalation compound is not microporous (N_2 adsorption-desorption isotherm). The active sites should therefore be the CoTPhsP molecules intercalated near the edge sites of the LDH galleries. However, the most important active sites are those located on the external surfaces of the LDH. The CoTPhsP molecules adsorbed on these sites are readily accessible for the H_2O_2 decomposition reaction. We have also observed this enhanced activity for (phthalocyanine)iron(III) tetrasulfonate adsorbed in Mg_xAl-CO_3 LDHs (x = 2, 3, and 4) in the oxidation of catechol.[44] This feature explains the better reactivity observed for $Mg_{3.0}Al(CoTPhsP)_{ads}$, which contains more available active sites than $Mg_{2.8}Al(CoTPhsP)_{int}$. Moreover, the adsorbed CoTPhsP shows a higher specific surface area (106 $m^2 g^{-1}$) than the intercalated material (34 $m^2 g^{-1}$), which further enhances the reactivity of CoTPhsP in the former.

These findings suggest the use of (tetrasulfonated porphyrin)cobalt immobilized in LDHs as heterogeneous catalysts for the conversion of organic substrates, using H_2O_2 as oxidant. This system is capable of decomposing H_2O_2 (catalase route), but oxidation reactions can be performed by stepwise addition of the oxidant to the system, which minimizes the H_2O_2 decomposition.[45] Additionally, peroxidation can be predominant or facilitated in the presence of an oxidizable substrate. The porphyrin immobilization in the LDH prevents rapid catalyst deactivation in the presence of the oxidant and provides easy catalyst recovery and re-use.

Conclusions

CoTPhsP has been successfully intercalated and adsorbed in $Mg_{3.0}Al$-CO_3 LDH. Infrared spectroscopy indicates that the metalloporphyrin structure is intact after its intercalation and adsorption in the LDHs. The intercalation of CoTPhsP into the LDH changes the crystallinity, thermal stability, and morphology of the resultant materials substantially in relation to the LDH-CO_3 precursor. The surface area and porosity analysis suggest that the material

 © 2005 Wiley-VCH Verlag GmbH & Co. KGaA, Weinheim

containing the metalloporphyrin intercalated in LDH has no microporous structure. UV/Vis and electron spin resonance spectroscopy show that the metalloporphyrin immobilized in the LDHs is mainly present in two different forms: the complex formed with molecular oxygen (CoTPhsP–O_2) and the monomeric form (without the dioxygen coordinated).

CoTPhsP is more active and stable in the presence of hydrogen peroxide when the metalloporphyrin is intercalated or adsorbed in the LDHs. The metalloporphyrin adsorbed on the external surfaces of the LDH shows a higher reactivity than the intercalated LDH due to the greater number of active sites available in the former material. Studies involving these materials are underway to test their performance as catalysts for the oxidation of phenols.

Experimental Section

Materials: The reagents $Mg(NO_3)_2{\cdot}6H_2O$, $Al(NO_3)_3{\cdot}9H_2O$, and Na_2CO_3 were obtained from Aldrich. NaOH was obtained from Merck and 35% H_2O_2 (w/w) from Peroxidos do Brasil Ltda. (Tetrasulfonated porphyrin)Co^{II} was supplied by Mid Century. All reagents were used as received.

$Mg_{3.0}Al$-CO_3: The layered precursor containing carbonate ions with an Mg^{2+}/Al^{3+} molar ratio of 3 was prepared by co-precipitation of stoichiometric amounts of Mg^{2+} and Al^{3+} in the presence of CO_3^{2-} at pH = 10.0, as described elsewhere.[30] Chemical analysis confirmed the expected Mg^{2+}/Al^{3+} molar ratio of 3.0 and the water content, measured by TGA, of 3.2 H_2O molecules per Al^{3+} cation, which gives the following composition: $[Mg_{3.0}Al(OH)_{8.0}](CO_3)_{0.5}{\cdot}3.2H_2O$.

$Mg_{2.8}Al(CoTPhsP)_{int}$: The intercalation of CoTPhsP into the LDH was conducted as follows: $Mg_{3.0}Al$-CO_3 (1.0 g, 3.1 mmol) was calcined at 500 °C in air for 4 h; the mixed-metal oxide formed by the thermal decomposition of the LDH was suspended in CoTPhsP solution (130 mL, 4 mmol L^{-1}) using previously decarbonated deionized water, in a Teflon cup. The system was kept in a stainless-steel reactor at 80–85 °C under autogenous pressure for 8 d. The solid was isolated by centrifuging and then washed with decarbonated water until a colorless supernatant was observed. The solid was dried in a desiccator under vacuum with silica gel as drying agent. The following data were found from chemical analysis (C, H, N): C 15.3, H 4.47, N 1.22. Metal analysis indicated Mg^{2+}/Al^{3+} and Co^{2+}/Al^{3+} molar ratios of 2.80 and 0.09, respectively. The water content measured by TGA was equal to 3.2 H_2O molecules per Al^{3+} cation. The intercalated material contains 231 μmol of CoTPhsP per gram of material.

$Mg_{3.0}Al(CoTPhsP)_{ads}$: The CoTPhsP was adsorbed on the external surface of $Mg_{3.0}Al$-CO_3 by suspending it (1.0 g, 3.1 mmol) in CoTPhsP aqueous solution (150 mL, 4 mmol L^{-1}). The suspension was stirred at 80 °C for about 45 h. The sample was washed and dried as described for the intercalated material. Chemical analysis showed that the adsorbed material contains 107 μmol of CoTPhsP per gram of material.

Characterization Techniques: Powder XRD patterns of samples were recorded with a Rigaku diffractometer model Miniflex using Cu-K_α radiation (1.541 Å, 30 kV and 15 mA) and a step of 0.03°.

Specific area data (BET-N_2 method) were determined with a Quantachrome model Quantasorb sorption system after heating the samples at 200 °C under nitrogen gas flow for 2 h. Porosity analysis was determined from N_2 adsorption-desorption isotherms at liquid nitrogen temperature using a Micromeritics Asap 2010 instrument. Samples were heated at 200 °C under vacuum for 2 h before analysis. Scanning electron micrographs were recorded with an LEO 440i instrument using samples sputter-coated with carbon.

Elemental analysis (C, H, N) was performed with a Perkin–Elmer model 2400 analyzer. Magnesium, aluminum and cobalt contents in the LDH samples were determined with a Spectro Analytical Instruments ICP emission spectrometer. Thermogravimetric analysis (TGA) was carried out with a Shimadzu TGA-50 instrument under synthetic air (flow rate = 50 mL min^{-1}) at a heating rate of 10 °C min^{-1} up to 900 °C.

FT-IR spectra of samples in KBr matrix were recorded with a MIDAC model PRS-INT series 192 spectrometer or a Perkin–Elmer model 1750 spectrometer, in the range 4000–400 cm^{-1}. UV/Vis spectra were recorded with a Shimadzu model UV-2401PC spectrophotometer. For spectral acquisition of CoTPhsP solutions at high concentration (> 0.1 mmol L^{-1}), an aliquot of the solution (5 μL) was placed between two 1.25-mm-thick quartz rectangular windows (45 × 12.5 mm) and firmly fastened together in a holder for cells with detachable windows. Solid samples were dispersed in deionized water or water/DMF mixtures and the spectra recorded with the same spectrophotometer equipped with an integration sphere. ESR experiments were conducted with a Bruker ER 200D-SRC instrument, operating at X-band (ca. 9.5 GHz), and using DPPH (α,α-diphenyl-β-picrylhydrazyl) for calibration. Instrumental standard conditions for the measurements were: frequency = 9.48 GHz, microwave power = 20 mW, modulation frequency = 100 kHz, modulation amplitude = 15 G, at liquid nitrogen temperature (77 K).

Reactivity Tests with Hydrogen Peroxide: The reactivity and stability of the CoTPhsP in homogeneous conditions and immobilized in the LDHs towards hydrogen peroxide decomposition were evaluated by monitoring the released molecular dioxygen with a Warburg apparatus from B. Brown, model V-85, at a constant temperature (30 °C). The experiments were carried out at two different pHs in borate-buffered solutions (12.5 mmol L^{-1}). In the first run at pH = 9.60, CoTPhsP (0.30 mL of a 12.5 mmol L^{-1} solution), Mg_3Al-CO_3 (8.1 mg), and $Mg_{2.8}Al(CoTPhsP)_{int}$ (16.9 mg) were added to hydrogen peroxide (2.70 mL of a 5.12 mmol L^{-1} solution). In the second run at pH = 7.80, CoTPhsP (0.30 mL of a 25.0 mmol L^{-1} solution), $Mg_{2.8}Al(CoTPhsP)_{int}$ (34.7 mg) or $Mg_{3.0}Al(CoTPhsP)_{ads}$ (70.3 mg) were added to hydrogen peroxide (2.70 mL of a 5.44 mmol L^{-1} solution). Borate-buffered solution was used to complete the volume to 3.00 mL under the heterogeneous conditions. Each experiment was conducted in duplicate and the amounts of CoTPhsP were the same for both homogeneous and heterogeneous conditions. In order to certify that leaching of CoTPhsP was not taking place under the heterogeneous conditions, at the end of the tests, samples were taken and filtered through 0.22 μm disposable filters (Millipore). UV/Vis spectra of the filtered solutions were registered to check for the presence of free CoTPhsP, which was negative for all runs.

Acknowledgments

The authors are grateful to FAPESP and CNPq (Brazilian agencies) for financial support and fellowships. We also thank Dr. Antonio Carlos V. Coelho (EP-USP) for measuring the N_2 adsorption-desorption isotherms.

 © 2005 Wiley-VCH Verlag GmbH & Co. KGaA, Weinheim

[1] G. Alberti, U. Costantino, in *Solid State Supramolecular Chemistry: Two- and Three-Dimensional Inorganic Networks* (Eds.: G. Alberti, T. Bein), Pergamon, New York, **1996**, vol. 7, p. 1.
[2] J.-H. Choy, *J. Phys. Chem. Solids* **2004**, *65*, 373–383.
[3] F. Trifirò, A. Vaccari, in *Solid State Supramolecular Chemistry: Two- and Three-Dimensional Inorganic Networks* (Eds.: G. Alberti, T. Bein), Pergamon, New York, **1996**, vol. 7, p. 251.
[4] P. S. Braterman, Z. P. Xu, F. Yarberry, in *Handbook of Layered Materials* (Eds.: S. M. Auerback, K. A. Carrado, P. K. Dutta), Marcel Dekker, New York, **2004**, p. 373.
[5] A. de Roy, C. Forano, K. El Malki, J. P. Besse, in *Expanded Clays and Other Microporous Solids* (Eds.: M. L. Occelli, H. E. Robson), Van Nostrand Reinhold, New York, **1992**, vol. 2, p. 108.
[6] B. F. Sels, D. E. de Vos, P. A. Jacobs, *Catal. Rev.* **2001**, *43*, 443–488.
[7] F. Leroux, J. P. Besse, *Chem. Mater.* **2001**, *13*, 3507–3515.
[8] N. K. Lazaridis, A. Hourzemanoglou, K. A. Matis, *Chemosphere* **2002**, *47*, 319–324.
[9] A. I. Khan, D. O'Hare, *J. Mater. Chem.* **2002**, *12*, 3191–3198.
[10] J.-H. Choy, S.-Y. Kwak, J.-S. Park, Y.-J. Jeong, J. Portier, *J. Am. Chem. Soc.* **1999**, *121*, 1399–1400.
[11] B. Meunier, *Chem. Rev.* **1992**, *92*, 1411–1456.
[12] C. Walling, *Acc. Chem. Res.* **1975**, *8*, 125–131.
[13] D. E. de Vos, B. F. Sels, P. A. Jacobs, in *Advances in Catalysis* (Eds.: B. C. Gates, H. Knözinger), Academic Press, New York, **2001**, vol. 46, p.1.
[14] R. A. Sheldon, I. W. C. E. Arends, H. E. B. Lempers, *Catal. Today* **1998**, *41*, 387–407.
[15] L. Barloy, J. P. Lallier, P. Battioni, D. Mansuy, Y. Piffard, M. Tournoux, J. B. Valim, W. Jones, *New J. Chem.* **1992**, *16*, 71–80.
[16] D. S. Robins, P. K. Dutta, *Langmuir* **1996**, *12*, 402–408.
[17] T. Shichi, Z. Tong, S. Hirai, K. Takagi, *Chem. Lett.* **2002**, *31*, 834–835.
[18] M. Halma, F. Wypych, S. M. Drechsel, S. Nakagaki, *J. Porphyrins Phthalocyanines* **2002**, *6*, 502–513.
[19] Z. Tong, T. Shichi, K. Takagi, *Mater. Lett.* **2003**, *57*, 2258–2261.
[20] S. Y. Ryu, M. Yoon, J.-H. Choy, S. H. Hwang, A. Frube, T. Asahi, H. Masuhara, *Bull. Korean Chem. Soc.* **2003**, *24*, 446–452.
[21] Z. Tong, T. Shichi, G. Z. Zhang, K. Takagi, *Res. Chem. Intermed.* **2003**, *29*, 335–341.
[22] F. Wypych, G. A. Bubniak, M. Halma, S. Nakagaki, *J. Colloid Interface Sci.* **2003**, *264*, 203–207.
[23] I. Y. Park, K. Kuroda, C. Kato, *Chem. Lett.* **1989**, *11*, 2057–2058.
[24] S. Bonnet, F. A. de Roy, J. P. Besse, P. Maillard, M. Momenteau, *Chem. Mater.* **1996**, *8*, 1962–1968.
[25] H. Tagaya, A. Ogata, T. Kuwahara, S. Ogata, M. Karasu, J. Kadokawa, K. Chiba, *Microporous Mater.* **1996**, *7*, 151–158.
[26] S. Miyata, *Clays Clay Miner.* **1975**, *23*, 369–375.
[27] T. S. Srivastava, M. Tsutsui, *J. Org. Chem.* **1973**, *38*, 2103-2103.
[28] F. Cavani, F. Trifirò, A. Vaccari, *Catal. Today* **1991**, *11*, 173–301.
[29] S. K. Yun, V. R. L. Constantino, T. J. Pinnavaia, *Microporous Mater.* **1995**, *4*, 21–29.
[30] C. A. S. Barbosa, A. M. D. C. Ferreira, V. R. L. Constantino, A. C. V. Coelho, *J. Incl. Phenom. Macrocycl. Chem.* **2002**, *42*, 15–23.
[31] V. R. L. Constantino, T. J. Pinnavaia, *Inorg. Chem.* **1995**, *34*, 883–892.
[32] K. S. W. Sing, D. H. Everett, R. A. W. Haul, L. Moscou, R. A. Pierotti, J. Rouquérol, T. Siemieniewska, *Pure Appl. Chem.* **1985**, *57*, 603–619.
[33] M. Gouterman, in *The Porphyrins* (Ed.: D. Dolphin), Academic Press, New York, **1979**, vol. 3, p.1.
[34] J. A. de Bolfo, T. D. Smith, J. F. Boas, J. R. Pilbrow, *J. Chem. Soc., Dalton Trans.* **1976**, 1495–1500.
[35] F. A. Walker, *J. Magn. Reson.* **1974**, *15*, 201–218.
[36] F. A. Walker, *J. Am. Chem. Soc.* **1970**, *92*, 4235–4244.
[37] J. Subramanian, in *Porphyrins and Metalloporphyrins* (Ed.: K. M. Smith), Elsevier Scientific. Amsterdam, **1975**, p.555.
[38] I. V. Ruzic, T. D. Smith, J. R. Pilbrow, *J. Chem. Soc., Dalton Trans.* **1981**, 2365–2369.
[39] D. F. Evans, D. Wood, *J. Chem. Soc., Dalton Trans.* **1987**, 3099–3101.
[40] J. A. Shelnutt, M. M. Dobry, J. D. Datterlee, *J. Phys. Chem.* **1984**, *88*, 4980–4987.
[41] W. Xu, H. Guo, D. L. Akins, *J. Phys. Chem. B* **2001**, *105*, 1543–1546.
[42] J. A. Assour, W. K. Kahn, *J. Am. Chem. Soc.* **1965**, *87*, 207–212.
[43] S. B. Brown, H. Hatzikonstantinou, D. G. Herries, *Biochem. J.* **1978**, *174*, 901–907.
[44] C. A. S. Barbosa, P. M. Dias, A. M. D. C. Ferreira, V. R. L. Constantino, *Appl. Clay Sci.* **2005**, *28*, 147–158.
[45] A. Hadasch, A. Sorokin, A. Robion, B. Meunier, *New J. Chem.* **1998**, *22*, 45–51.

Received: October 15, 2004

 © 2005 Wiley-VCH Verlag GmbH & Co. KGaA, Weinheim

Intramolecular "CH···π(Metal Chelate Ring) Interactions" as Structural Evidence for Metalloaromaticity in Bis(pyridine-2,6-diimine)Ru^{II} Complexes

Yan-feng Jiang,[a] Chan-juan Xi,*[a] Yu-zhou Liu,[a] Juan Niclós-Gutiérrez,*[b] and Duane Choquesillo-Lazarte[b]

Keywords: Metalloaromaticity / Ruthenium / CH···π interaction / Chelates

The synthesis and structural characterization of two novel Ru^{II} complexes (**1** and **2)** with tridentate pyridine-2,6-diimine ligands are described. In both compounds, *ortho*-CH bonds from the phenyl or phenyl-like rings produce unexpected CH···π interactions with ruthenium-α,α′-diimine chelate rings. This insight is thought to provide new structural evidence for the metalloaromaticity of the chelate rings in the ruthenium complexes studied. The molecular geometry of complex **1** is remarkably similar to S_4 symmetrical geometry, which is also a consequence of the four CH···π(chelate ring) interactions working cooperatively. In contrast, there are only two pairs of these interactions working in complex **2** because of the steric effects and electronic influences caused by the methyl-group substitutions.
(© Wiley-VCH Verlag GmbH & Co. KGaA, 69451 Weinheim, Germany, 2005)

Introduction

CH···π interactions are the weakest hydrogen bonds that operate between a soft acid CH and a soft or intermediate base π system.[1] It has been recognized that this kind of weaker and softer interaction plays significant roles in various fields of chemistry such as crystal packing,[2] host–guest chemistry,[3] self-assembly,[4] and chiral recognition.[5] As it is nonpolar and effective in water, the CH···π interaction is also especially important in biological systems.[6] In this broad context, the soft base π system, which acts as a CH acceptor, is comprised not only of an organic moiety such as a double bond, a triple bond or a delocalized aromatic ring,[7] but also of a metal−chelate ring of suitable transition-metal complexes that has been reported recently.[8] Zarić and coworkers[8] have reported ample evidence of this phenomenon based on new data as well as on a broad view of structures available in the CSD database. This interesting work represents a remarkable effort towards the definition of structural parameters for the interaction between C–H polar bonds and the whole of a π(metal-chelate ring) system. The concept of "metalloaromaticity" was proposed a long time ago[9] and it is well known that a large variety of transition metal chelate rings feature this metalloaromaticity.[10] Now we report for the first time additional evidence for ruthenium(II) complexes in which the ruthenium−diimine chelate ring could act as a CH acceptor. In this paper we describe the synthesis and structural characterization of ruthenium(II) complexes bearing two 2,6-bis(phenylimine)-pyridine ligands. On the basis of the already known metalloaromaticity of ruthenium-α,α′-diimine chelate rings,[9] we report interesting and novel structural features concerning these 6N-coordinated complexes.

[a] Key Laboratory for Bioorganic Phosphorus Chemistry of the Ministry of Education, Department of Chemistry, Tsinghua University,
Beijing 100084, China
E-mail: cjxi@tsinghua.edu.cn
[b] Department of Inorganic Chemistry, Faculty of Pharmacy, University of Granada,
18071 Granada, Spain
Fax: +86-10-6261-8239
E-mail: jniclos@ugr.es

Results and Discussions

The tridentate 2,6-diimine-pyridine ligand, which was obtained by Schiff base condensation of 2 equiv. of aniline or 2,4-dimethyl-aniline with 2,6-diacetyl-pyridine,[11] reacted with $RuCl_3 \cdot 3H_2O$ in an ethanol/water (1:1) solution under reflux followed by anion exchange, to afford the 2:1 complex $[RuL^1{}_2][PF_6]_2$ (**1**) or $[RuL^2{}_2][PF_6]_2$ (**2**) (Scheme 1).

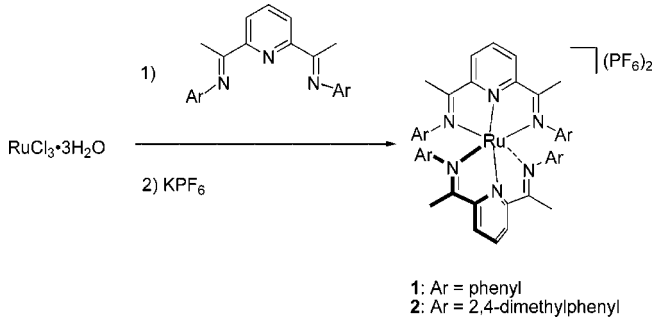

1: Ar = phenyl
2: Ar = 2,4-dimethylphenyl

Scheme 1.

Crystals of complexes **1** and **2** suitable for X-ray structure determination were grown at room temperature by li-

 DOI: 10.1002/ejic.200400864 © 2005 Wiley-VCH Verlag GmbH & Co. KGaA, Weinheim

quid diffusion of Et_2O into CH_3CN solutions. Details of data collection are listed in Table 1. Selected bond lengths and bond angles are listed in Table 2.[12]

Table 1. Crystallographic data for complexes **1** and **2**.

	1	**2**
Empirical formula	$C_{42}H_{40}F_{12}N_6OP_2Ru$	$C_{50}H_{56}F_{12}N_6O_{0.50}P_2Ru$
Formula mass	1035.81	1140.02
Crystal system	triclinic	monoclinic
Space group	$P\bar{1}$	$C2/c$
a [Å]	9.940(2)	27.384(6)
b [Å]	11.438(2)	15.926(3)
c [Å]	22.029(4)	24.620(5)
α [°]	95.60(3)	90.00
β [°]	99.14(3)	98.63(3)
γ [°]	111.07(3)	90.00
V [Å^3]	2274.8(8)	10616(4)
Z	2	8
$D_{calcd.}$ [g cm^{-3}]	1.512	1.427
μ [cm^{-1}]	0.504	0.439
T [K]	293 (2)	293(2)
λ [Å]	0.71073	0.71073
R_1	0.0827	0.0792
wR_2	0.1352	0.2190

Table 2. Selected bond lengths [Å] and angles [°] for complexes **1** and **2**.

	1	**2**
Bond lengths		
Ru–N1	2.099(8)	2.088(6)
Ru–N2	1.960(8)	1.976(5)
Ru–N3	2.062(9)	2.104(5)
Ru–N4	2.060(8)	2.123(5)
Ru–N5	1.962(8)	1.978(5)
Ru–N6	2.058(8)	2.083(5)
Bond angles		
N1–Ru–N2	77.2(3)	77.3(2)
N1–Ru–N3	154.7(3)	153.4(2)
N1–Ru–N4	93.2(3)	90.0(2)
N1–Ru–N5	106.6(3)	95.8(2)
N1–Ru–N6	93.9(3)	96.9(2)
N2–Ru–N3	77.6(4)	77.0(2)
N2–Ru–N4	102.3(3)	112.0(2)
N2–Ru–N5	176.3(4)	168.2(2)
N2–Ru–N6	102.8(3)	94.8(2)
N3–Ru–N4	92.5(3)	93.5(2)
N3–Ru–N5	98.7(4)	110.7(2)
N3–Ru–N6	91.3(3)	91.7(2)
N4–Ru–N5	77.6(4)	77.2(2)
N4–Ru–N6	154.9(3)	153.2(2)
N5–Ru–N6	77.2(4)	76.4(2)

The asymmetric unit of compound **1** consists of a complex cation, two hexafluorophosphate anions, and one non-coordinated water molecule, as shown in Figure 1. The most noteworthy structural feature of complex **1** is that one *ortho*-H from each phenyl ring points towards the center of the corresponding ruthenium-α,α′-diimine chelate ring (Figure 2). Comprehensive analysis was carried out with the program PLATON,[13] and relevant structural parameters, defined as shown in Figure 3, are listed in Table 3. The H-ring centroid (H···Cg) and H···ring plane (H···⊥) distances are in the range of 2.79–3.00 Å and 2.79–2.95 Å, respectively, and the γ angles usually have values below 10°. These data are similar to those (H···Cg distance <3.0 Å and γ <12.5°) reported for CH···π interactions with chelate rings[8] and indicate that CH···π interactions occur between *ortho*-CH bonds and the whole of an electronically delocalized ruthenium chelate ring in complex **1**. The C–H···Cg angles, 125, 102, 103, and 108°, are still below the optimal value (180°) for the strongest CH···π interaction, which may be due to the steric constraints in the molecule. On the basis of the reported metalloaromaticity of benzoquinonediimine ruthenium complex,[10] this kind of CH···π(planar chelate ring) interaction in complex **1** is thought to be a new kind of structural evidence for the metalloaromaticity of such planar chelate rings.

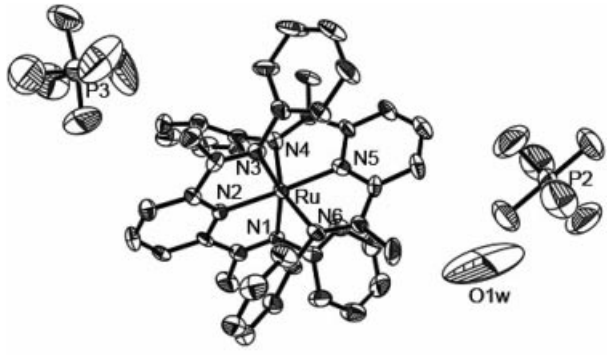

Figure 1. ORTEP drawing of compound **1** with thermal ellipsoids shown at the 30% level; hydrogen atoms were omitted for clarity.

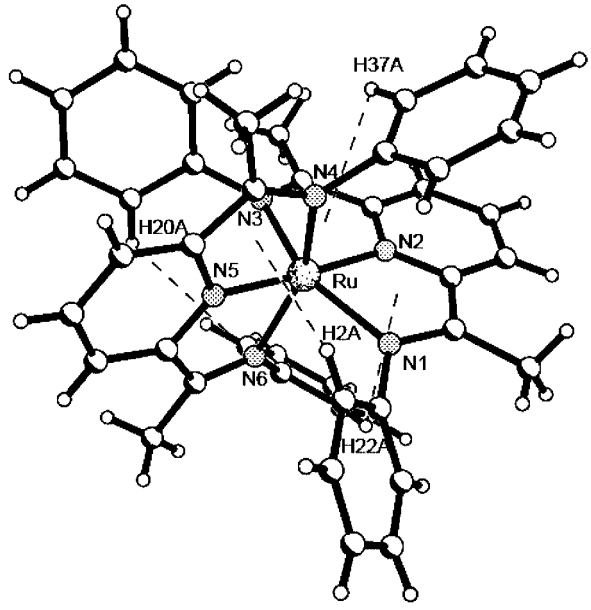

Figure 2. Four pairs of intramolecular "CH···(chelate ring)" interactions [C2H2A−(RuN4N5), C20H20A−(RuN5N6), C22H22A−(RuN1N2), and C37H37A−(RuN2N3)] work cooperatively in complex **1**.

Interestingly, it seemed that complex **1** belonged to a similar S_4 space group, but actually the complex ion $[RuL^1{}_2]^{2+}$ has a crystallographic C_1 symmetry, and the ruthenium atom has a slightly distorted octahedral geometry with *cis* angles at Ru^{II} of 77.2(3), 77.6(4), 92.5(3), 77.6(4), and

 © 2005 Wiley-VCH Verlag GmbH & Co. KGaA, Weinheim

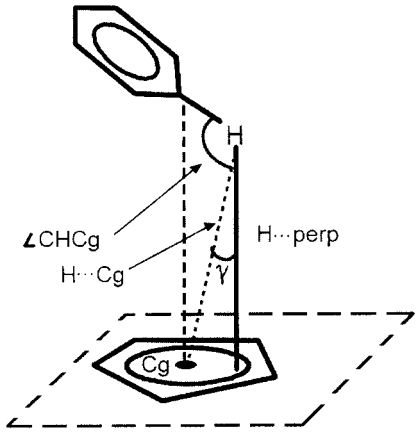

Figure 3. Cg is the centroid of the ruthenium chelate ring; γ is the angle defined by the H···Cg line and perpendicular H···(ring plane) line.

77.2(4)°. Geometry optimization calculations were carried out by the DFT method, and the result at the B3LYP/(LanL2DZ+3-21G*) level[14] proved that the optimized cation $[RuL^1_2]^{2+}$ indeed exhibited an S_4 space group, which may be a consequence of the four pairs of CH···(chelate ring) interactions working cooperatively.

It is also worth mentioning that the average distances of Ru–N(pyridine) bonds [1.961(8) Å] and Ru–N(imine) bonds [2.070(8) Å] in complex **1** are shorter than those reported [1.992(3) Å and 2.140(3) Å, respectively] for the ruthenium complex with a tridentate pyridine-2,6-diimine ligand.[15] It is strongly suggested that the compact and stable structure of **1** is achieved by a cooperation of intramolecular CH···π interactions.[8]

The crystal structure of complex **2** seems to be more complicated and asymmetrical because of the 2- and 4-substituted methyl groups in the phenyl-like rings, as shown in Figure 4. However, the existence of one *ortho*-H per phenyl-like ring in $\mathbf{L^2}$ could enable the formation of intramolecular CH···π interactions similar in nature to those found in complex **1**, but limited to two pairs of CH···(ruthenium-α,α′-diimine chelate ring) interactions, as shown in Figure 5. The difference between complexes **1** and **2** is attributed to the interligand steric repulsions and the electronic effects caused by the additional methyl groups.[1]

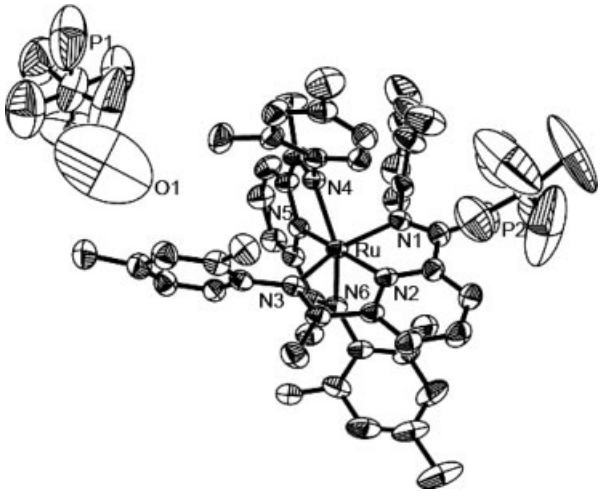

Figure 4. ORTEP drawing of complex **2** with thermal ellipsoids shown at the 30% level; hydrogen atoms were omitted for clarity.

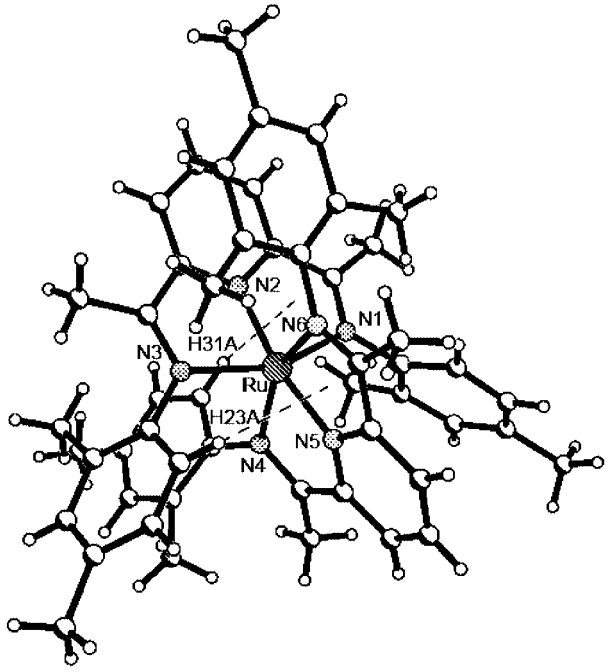

Figure 5. Only two pairs of intramolecular "CH···(chelate ring)" interactions [C23H23A−(RuN5N6) and C31H31A−(RuN1N2)] work cooperatively in complex **2**.

Conclusions

Intramolecular CH···π(chelate ring) interactions between ligand-aryl C–H bonds and ruthenium(II)-α,α′-diimine chelate rings are observed by X-ray crystal structural analysis of complexes **1** and **2**. To the best of our knowledge, this is the first time that these intramolecular CH···π(chelate ring)

Table 3. Intramolecular "CH···π(chelate ring)" interaction parameters for complexes **1** and **2**.

	CH-chelate ring	H···Cg [Å]	H···(ring plane) [Å]	C–H···Cg [°]	Γ [°]
C1	C2H2A−(RuN4N5)	2.79	2.79	125	2.67
	C20H20A−(RuN5N6)	2.97	2.93	102	9.39
	C22H22A−(RuN1N2)	3.00	2.95	103	10.07
	C37H37A−(RuN2N3)	2.92	2.91	108	5.26
C2	C23H23A−RuN5N6	2.89	2.86	126	1.53
	C31H31A−RuN1N2	2.85	2.82	136	6.92

 © 2005 Wiley-VCH Verlag GmbH & Co. KGaA, Weinheim

interactions are used to feature the metalloaromaticity of such Ru^{II}-α,α′-diimine chelate rings.

Experimental Section

General: ^1H, ^{13}C NMR spectra were recorded with a JOEL JNM-ECA300 spectrometer. IR spectra were recorded with an AVATAR FTIR ESP spectrophotometer. ESI-MS spectra were obtained with a Bruker Esquire-LC/MSn spectrometer. Elemental analyses were carried out with a FlashEA1112 microanalyzer. The starting material $RuCl_3·3H_2O$ was purchased from Aldrich; the ligands 2,6-bis{1-(phenylimine)ethyl}pyridine (**L¹**) and 2,6-bis{1-[(2,4-dimethylphenyl)imine]ethyl}pyridine (**L²**) were prepared according to the literature method.[11]

Preparation of $[RuL^1_2][PF_6]_2$: A solution of **L¹** (156 mg, 0.498 mmol) and $RuCl_3·3H_2O$ (50 mg, 0.241 mmol) in ethanol/water (1:1) (20 mL) was refluxed under nitrogen for 24 h until the solution became red or purple. After cooling, the insoluble materials were removed by filtration, and the complex was precipitated by the addition of saturated KPF_6 aqueous solution (5 equiv.). The complex was purified by chromatography on silica gel. It was eluted with CH_3CN/H_2O (25:1). The second fraction afforded $[RuL^1_2][PF_6]_2$ as an orange solid (76 mg, 31%). ESI-MS: *m*/*z* (%) = 364 $\{M - 2PF_6\}^{2+}/2$. $C_{42}H_{38}F_{12}N_6P_2Ru·H_2O$ (M_r = 1035.81): calcd. C 48.70, H 3.89, N 8.11; found C 48.66, H 4.05, N 7.96. ^1H NMR ([D$_3$]acetonitrile): δ = 2.61 (s, 12 H, CH_3), 6.39 (d, ^3J(H,H) = 6.54 Hz, 8 H, aromatic protons), 7.20 (m, 12 H, aromatic protons), 7.92 (t, 2 H, py), 8.11 (d, ^3J(H,H) = 7.92 Hz, 4 H, py). ^{13}C NMR ([D$_3$]acetonitrile): δ = 18, 120, 128, 130, 134, 144, 154, 177. IR (KBr): $\tilde{\nu}$ = 3420 (O–H), 1697 (C=N), 846 cm^{-1} (P–F).

Preparation of $[RuL^2_2][PF_6]_2$: A solution of **L²** (146 mg, 0.395 mmol) and $RuCl_3·3H_2O$ (40 mg, 0.193 mmol) in ethanol/water (1:1) (20 mL) was refluxed under nitrogen for 48 h until the solution became red or purple. After cooling, the insoluble materials were removed by filtration, and the complex was precipitated by the addition of saturated KPF_6 aqueous solution (5 equiv.). The complex was purified by chromatography on silica gel. It was eluted with CH_3CN/H_2O (25:1). The second fraction afforded $[RuL^2_2][PF_6]_2$ as an orange−red solid (34 mg, 16%). ESI-MS: *m*/*z* (%) = 420 $\{M - 2PF_6\}^{2+}/2$. $C_{50}H_{56}F_{12}N_6O_{0.50}P_2Ru$ (M_r = 1140.02): calcd. C 52.68, H 4.95, N 7.37; found C 53.07, H 4.99, N 7.82. ^1H NMR ([D$_3$]acetonitrile): δ = 2.22–2.07 (m, 30 H), 2.65 (s, 6 H), 5.29–5.36 (m, 1 H), 5.77–6.11 (m, 3 H), 6.44 (m, 1 H), 6.57–6.85 (m, 7 H), 7.84–7.94 (m, 2 H), 7.95 (t, 2 H), 8.38–8.41 (m, 2 H). ^{13}C NMR ([D$_3$]acetonitrile): δ = 14, 16, 19, 29, 121, 123, 127, 128, 132, 134, 138, 145, 154, 174, 178. IR (KBr): $\tilde{\nu}$ = 3421 (O–H), 1635 (C=N), 841 cm^{-1} (P–F).

Acknowledgments

We thank the National Natural Science Foundation of China (20172032) (20372041) for supporting this work. We also thank Dr. Biao Wu (Institute of Chemistry, Chinese Academy of Sciences) for his help in the measurement of crystals. We are grateful to Prof. Guoshi Wu (Department of Chemistry, Tsinghua University) for his help in some of the calculations.

[1] a) M. Nishio, *Cryst. Eng. Commun.* **2004**, *6*, 130–158; b) M. Nishio, M. Hirota, Y. Umezawa, *The CH/π Interaction. Evidence, Nature and Consequences*, Wiley-VCH, New York, **1998**; c) H. Suezawa, T. Yoshida, Y. Umezawa, S. Tsuboyama, M. Nishio, *Eur. J. Inorg. Chem.* **2002**, 3148–3155; d) C. Janiak, *J. Chem. Soc. Dalton Trans.* **2000**, 3885–3896.

[2] a) T. Moriuchi, I. Ikeda, T. Hirao, *Organometallics* **1995**, *14*, 3578–3580; b) M. J. Hannon, C. L. Painting, N. W. Alcock, *Chem. Commun.* **1999**, 2023–2024; c) L. R. Hanton, K. Lee, *J. Chem. Soc. Dalton Trans.* **2000**, 1161–1166; d) C.-Y. Su, B. S. Kang, C.-X. Du, Q.-C. Yang, T. C. W. Mak, *Inorg. Chem.* **2000**, *39*, 4843–4849; e) C. D. Abernethy, C. L. B. Macdonald, J. A. C. Clyburne, A. H. Cowley, *Chem. Commun.* **2001**, 61–62; f) Y. Umezawa, S. Tsuboyama, H. Takahashi, J. Uzawa, M. Nishio, *Tetrahedron* **1999**, *55*, 10047–10056; g) M. Matsugi, M. Nojima, Y. Hagimoto, Y. Kita, *Tetrahedron Lett.* **2001**, *42*, 8039–8042; h) M. Kitamura, K. Nakano, T. Miki, M. Okada, R. Noyori, *J. Am. Chem. Soc.* **2001**, *123*, 8939–8950.

[3] a) H. Takahashi, S. Tsuboyama, Y. Umezawa, K. Honda, M. Nishio, *Tetrahedron* **2000**, *56*, 6185–6191; b) S. Re, S. Nagase, *Chem. Commun.* **2004**, *6*, 658–659; c) A. Frontera, C. Garau, D. Quinonero, P. Ballester, A. Costa, P. M. Deya, *Org. Lett.* **2003**, *5*, 1135–1138.

[4] a) S. J. Cantrill, J. A. Preece, J. F. Stoddart, Z.-H. Wang, A. J. P. White, D. J. Williams, *Tetrahedron* **2000**, *56*, 6675–6681; b) A. Arduini, G. Giorgi, A. Pochini, A. Secchi, F. Ugozzoli, *Tetrahedron* **2001**, *57*, 2411–2417.

[5] a) M. Akazome, Y. Ueno, H. Ooiso, K. Ogura, *J. Org. Chem.* **2000**, *65*, 68–76; b) K. Kinbara, Y. Harada, K. Saigo, *J. Chem. Soc. Perkin Trans. 2* **2000**, 1339–1348.

[6] a) K. Burley, G. A. Petsko, *Science* **1985**, *229*, 23–28; b) M. Nishio, Y. Umezawa, M. Hirota, Y. Takeuchi, *Tetrahedron* **1995**, *51*, 8665–8701; c) K. Harata, M. Muraki, *Acta Crystallogr. Sect. D* **1997**, *53*, 650–657; d) M. Nishio, *Bioorg. Med. Chem. Lett.* **1999**, *9*, 221–226.

[7] a) M. C. B. Colbert, J. Lewis, N. J. Long, P. R. Raithby, A. J. P. White, D. J. Williams, *J. Chem. Soc. Dalton Trans.* **1997**, 99–104; b) C. Janiak, *J. Chem. Soc. Dalton Trans.* **2000**, 3885–3896; c) H. Suezawa, T. Yoshida, Y. Umezawa, S. Tsuboyama, M. Nishio, *Eur. J. Inorg. Chem.* **2002**, 3148–3155.

[8] a) G. A. Bogdanović, A. S. Bire, S. D. Zarić, *Eur. J. Inorg. Chem.* **2002**, 1599–1602; b) Z. D. Tomić, V. M. Leovac, S. V. Pokorni, D. Zobel, S. D. Zarić, *Eur. J. Inorg. Chem.* **2003**, 1222–1226; c) S. D. Zarić, *Eur. J. Inorg. Chem.* **2003**, 2197–2209; d) Z. D. Tomić, S. B. Novaković, S. D. Zarić, *Eur. J. Inorg. Chem.* **2004**, 2215–2218; e) V. B. Medaković, M. K. Milčić, G. A. Bogdanović, S. D. Zarić, *J. Inorg. Biochem.* **2004**, *98*, 1867–1873.

[9] M. Calvin, K. Wilson, *J. Am. Chem. Soc.* **1945**, *67*, 2003–2007.

[10] a) H. Masui, *Coord. Chem. Rev.* **2001**, *219*, 957–992; b) A. Castiñeiras, A. G. Sicilia-Zafra, J. M. González-Pérez, D. Choquesillo-Lazarte, J. Niclós-Gutiérrez, *Inorg. Chem.* **2002**, *41*, 6956–6958.

[11] E. C. Alyea, P. H. Merrell, *Synth. React. Inorg. Met.-Org. Chem.* **1974**, *4*, 535–546.

[12] CCDC-247023 (for **1**) and -247022 (for **2**) contain the supplementary crystallographic data for this paper. These data can be obtained free of charge from The Cambridge Crystallographic Data Centre via www.ccdc.cam.ac.uk/data_request/cif.

[13] A. L. Spek, *PLATON: A Multipurpose Crystallographic Tool*, University of Utrecht, The Netherlands, **2001**.

[14] It is notable that the calculated bond lengths and bond angles at the B3LYP/(LanL2DZ+3-21G*) level are in good agreement with the X-ray data (the differences in bond lengths <0.04 Å and bond angles <2°).

[15] a) E. L. Dias, M. Brookhart, P. S. White, *Organometallics* **2000**, *19*, 4995–5004; b) B. Çetinkaya, E. Çetinkaya, M. Brookhart, P. S. White, *J. Mol. Catal. A: Chem.* **1999**, *142*, 101–102.

Received: October 14, 2004

 © 2005 Wiley-VCH Verlag GmbH & Co. KGaA, Weinheim

1,1′-Bis(oxazolin-2-yl)ferrocenes: An Investigation of Their Complexation Behavior toward $[Pd(\eta^3\text{-allyl})Cl]_2$

Christian G. Hartinger,*[a] Alexey A. Nazarov,*[a] Vladimir B. Arion,[a] Gerald Giester,[b] Maxim L. Kuznetsov,[c] Markus Galanski,[a] and Bernhard K. Keppler*[a]

Keywords: Asymmetric catalysis / Density functional calculations / Mass spectrometry / Metallocenes / Palladium

The coordination behavior of several aryl- and alkyl-bis(oxazolinyl)ferrocenes, which were prepared in high yields from ferrocene-1,1′-dicarbonyl dichloride and enantiomerically pure or racemic amino alcohols via the corresponding bis(β-hydroxyamide)s and dimesylates or ditosylates as intermediates, toward $[Pd(\eta^3\text{-allyl})Cl]_2$ was investigated by ESI mass spectrometry. The synthesized compounds were characterized by NMR spectroscopy and elemental analysis and the molecular structures of 1,1′-bis[(*R*)-4-isopropyloxazolin-2-yl]-ferrocene (**6b**), 1,1′-bis[(*S*)-4-isopropyloxazolin-2-yl]ferrocene (**7b**), 1,1′-bis[(*S*)-4-*sec*-butyloxazolin-2-yl]ferrocene (**11b**), 1,1′-bis[(*S*)-4-*tert*-butyloxazolin-2-yl]ferrocene (**12b**), 1,1′-bis[(*R*)-4-phenyloxazolin-2-yl]ferrocene (**13b**), and 1,1′-bis[(*S*)-4-phenyloxazolin-2-yl]ferrocene (**14b**) were determined by single-crystal X-ray diffraction analysis. The coordination behavior studies by ESI-MS show a strong preference for monodentate complex formation. This result is supported by theoretical studies carried out at the B3LYP level of theory. It was found that the latter coordination type of 1,1′-bis[(*S*)-4-methyloxazolin-2-yl]ferrocene (**1b**) to an allylpalladium moiety is kinetically favored over the bidentate one.
(© Wiley-VCH Verlag GmbH & Co. KGaA, 69451 Weinheim, Germany, 2005)

Introduction

Oxazolines are an intensively studied class of compounds. These five-membered heterocycles are found in natural metal chelators,[1–3] show interesting biological properties,[4,5] and also play an important role in synthesis[6–10] as well as have a remarkable range of applicability. Their uses vary widely from organic[6–8] and coordination chemistry,[9,10] via polymer chemistry,[11–13] to antiacaricide as well as antiinsecticidic purposes.[14] Oxazolines are used in a manifold variety of catalytic processes, for example hydrosilylation,[15] transfer hydrogenation,[16] allylic substitution,[17] allylic oxidation,[18] aziridination of olefins,[19] aziridination of imines,[20] cyclopropanation,[21–23] and the Diels–Alder reaction.[24] Furthermore, it should be noted that there is a great interest in oxazolines as they possess interesting properties in asymmetric synthesis when coordinated to transition metals.

Beside the natural occurrence of oxazolines, there are several methods that are useful for constructing the oxazoline or 4,5-dihydrooxazole moiety in the laboratory (for reviews see refs.[6,7,11]): the dehydration and ring formation of some carboxamides, for example hydroxy amides, the reaction between halo carboxamides and strong bases, as well as the addition of oxiranes to nitriles and of amino alcohols to carboxylic acids or imino esters offer a synthetic pathway to build up the required five-membered heterocycle. Lately, coordination-chemistry-driven approaches have moved into the focus of synthetic chemists' interest,[25,26] and the addition of haloalcohol/base or oxirane/chloride systems to Pt^{II}-bound nitrile,[27,28] and reactions between nitriles and amino alcohols catalyzed or mediated by a variety of metal ions, for example Zn^{II}, Cd^{II}, Ni^{II}, Al^{III}, Co^{II}, Cu^{II}, show high potential for the assembly of the oxazoline system.[29–32]

An impressive number of reports and essays show the applicability but also the popularity of ferrocene and its derivatives in many fields of organic, materials, synthetic, and also medicinal chemistry,[33–37] and the use of substituted ferrocenes in metal-catalyzed enantioselective synthesis has been a very important application for more than twenty years. Herein chiral ferrocene derivatives are involved which either bear the center of chirality on a substituent or contain an element of planar chirality.[38]

The combination of the coordinating oxazoline structure, which is easily obtainable (also in an enantiomerically pure form) from reactions involving nonracemic starting materials, such as α-amino alcohols, and ferrocene (with the possibility to introduce planar chirality) has led to the develop-

[a] Institute of Inorganic Chemistry, University of Vienna,
Waehringer Str. 42, 1090 Vienna, Austria
Fax: +43-1-4277-52680
E-mail: bernhard.keppler@univie.ac.at,
christian.hartinger@univie.ac.at
alex.nazarov@univie.ac.at
[b] Institute of Mineralogy and Crystallography, University of Vienna,
Althanstr. 14, 1090 Vienna, Austria
[c] Department of Chemistry, Moscow Pedagogical State University,
Nesvigskiy per. 3, 119021 Moscow, Russian Federation

ment of compounds containing both moieties, i.e., ferrocene and an oxazolinyl moiety.[39–43] This method offers a straightforward way to synthesize chiral ferrocene derivatives which are, due to their distinct structural features, applicable in asymmetric synthesis. Surprisingly, Ahn et al. have reported a lack of catalytic activity for 1,1′-bis[(*S*)-4-*tert*-butyloxazolin-2-yl]ferrocene (**12b**) in the palladium-catalyzed allylic alkylation, while there are many examples of non-metallocene complexes with bisoxazoline ligands that give high enantiomeric excesses and turnover rates.[17,44–48]

Electrospray ionization mass spectrometry (ESI-MS) is the softest desorption/ionization method, and its suitability to determine the coordination behavior of transition metal cations toward ligands has been studied extensively (for examples see refs.[49–52] and for a review see ref.[53]). The desolvation process mainly leads to the presence of ions in the gas phase that are also found in solution.[54] ESI-MS has a number of advantages over other techniques; in particular, it provides information on the characteristic isotopic patterns of compounds (especially metal compounds) and allows low sample consumption and use of many compatible solvents.[49]

In order to clarify the influence of the nature of the substituents on the catalytic potential of 1,1′-bis(oxazolin-2-yl)ferrocenes, several derivatives of the parent compound 1,1′-bis[(*S*)-4-*tert*-butyloxazolin-2-yl]ferrocene (**12b**) were synthesized and tested with respect to their catalytic potential in asymmetric allylic substitution, where the catalytic activity depends strongly on the formation of chelate structures between multidentate ligands and transition metals.[55,56] The coordination behavior of new 1,1′-bis(oxazolin-2-yl)ferrocenes bearing alkyl (**1b**, **7b**, and **12b**) or aryl substituents (**14b**) in the 4-position of the oxazoline ring toward $[Pd(\eta^3\text{-}C_3H_5)Cl]_2$ was studied in detail by ESI-MS. In order to elucidate the energetic preference for the coordination of 1,1′-bis[(*S*)-4-methyloxazolin-2-yl]ferrocene (**1b**) to an allylpalladium moiety, DFT calculations at the B3LYP level of theory were also carried out.

Results and Discussion

Synthesis

The oxazolines bearing alkyl and aryl substituents at the 4- and/or 5-position of the oxazoline residue (see Scheme 1 and Table 1) were synthesized by a condensation reaction of 1,1′-ferrocenedicarbonyl dichloride with the corresponding α-amino alcohols at room temperature, followed by a ring-closing procedure with either methanesulfonyl chloride and triethylamine or *p*-toluenesulfonyl chloride, triethylamine and a catalytic amount of 4-(dimethylamino)pyridine at 0 °C.[41,57–62] The yield for the syntheses of the methyl- and aryl-substituted compounds was higher when using *p*-toluenesulfonyl chloride, and the methyl and diphenyl amides that precipitated during the synthesis were obtained in high purity by filtration. All oxazolines and other amides were isolated by flash column chromatography on silica gel using a mixture of ethyl acetate and *n*-hexane as eluent.

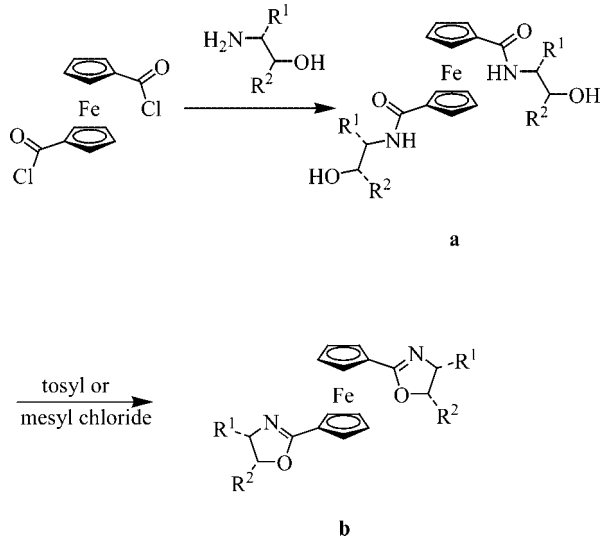

Scheme 1. General scheme for the synthesis of the 1,1′-bis-(oxazolin-2-yl)ferrocenes.

Table 1. List of the synthesized 1,1′-bis(oxazolin-2-yl)ferrocenes.

	Substituents		Tosyl/mesyl chloride	
	R^1	R^2	tosyl	mesyl
1	(*S*)-methyl	H	X	
2	H	(*S*)-methyl	X	
3	(*R*)-ethyl	H		X
4	(*S*)-ethyl	H		X
5	*n*-propyl	H		X
6	(*R*)-isopropyl	H		X
7	(*S*)-isopropyl	H		X
8	*n*-butyl	H		X
9	(*R*)-isobutyl	H		X
10	(*S*)-isobutyl	H		X
11	(*S*)-*sec*-butyl	H		X
12	(*S*)-*tert*-butyl	H		X
13	(*R*)-phenyl	H	X	
14	(*S*)-phenyl	H	X	
15	H	phenyl	X	
16	(*R*)-benzyl	H	X	
17	(*S*)-benzyl	H	X	
18	(*S*)-phenyl	(*R*)-phenyl	X	

NMR spectroscopy was found to be a useful tool to follow the ring-closing process, i.e., the transformation from hydroxy amides to oxazolines. This process is marked in the ^{1}H NMR spectrum by the disappearance of the protons of the hydroxy and amide groups and in the ^{13}C NMR spectrum by a characteristic high-field shift from about δ = 170 to 166 ppm of the CO group, as well as by low-field shifts of the primary (for **2**, **15**, and **18**) or secondary amino alcohol carbon atoms from about δ = 64 ppm to about δ = 73 ppm [with the exception of **8** (from ca. δ = 52 to 73 ppm) and **18** (from ca. δ = 75 to 79 ppm] as well as of the amino alcohol carbon atoms next to the nitrogen from about δ = 50 to about 69 ppm (with the exception of **18**: from approximately δ = 60 to 89 ppm).

 © 2005 Wiley-VCH Verlag GmbH & Co. KGaA, Weinheim

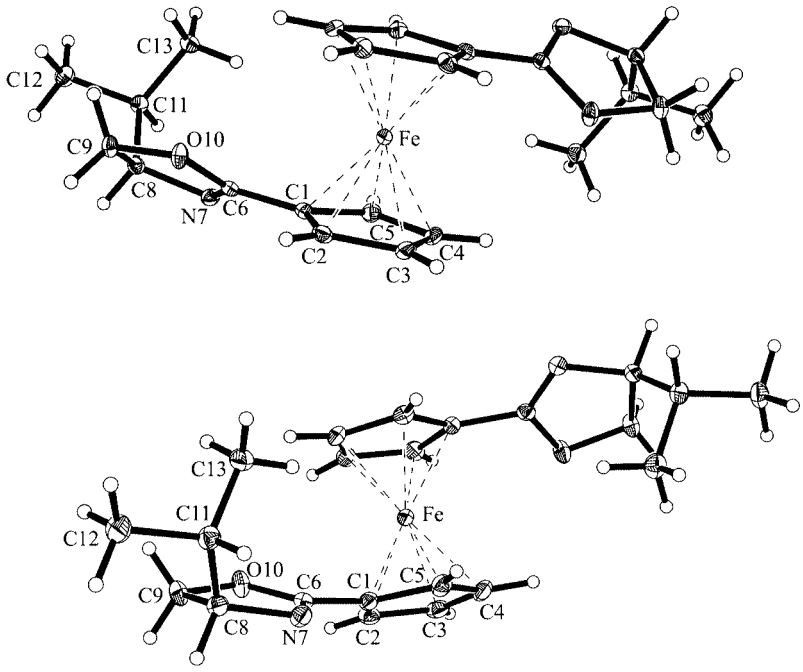

Figure 1. The molecular structure and labeling scheme of 1,1′-bis[(*R*)-4-isopropyloxazolin-2-yl]ferrocene (**6b**; top) and 1,1′-bis[(*S*)-4-isopropyloxazolin-2-yl]ferrocene (**7b**; bottom) with displacement ellipsoids drawn at the 50% probability level.

The syntheses of hydroxy amides as well as of the corresponding oxazolines with (*S*)-isopropyl, (*S*)-*tert*-butyl,[41] and (*S*)-phenyl moieties[39] in the 4-position of the oxazoline moiety have been reported earlier, but no crystal structure data were published. The synthesis of the 1,1′-ferrocenedicarboxamide **6a** has been reported, but no analytical data were presented.[42]

Crystal Structure Analysis

Crystal structure analysis has been performed to elucidate the influence of different substituents, viz., isopropyl, phenyl, *sec*- and *tert*-butyl, at oxazoline rings on the torsional twist angle of the Cp rings around the iron atom.

The results of the X-ray diffraction study of **6b** and **7b**, which crystallized as pure enantiomers in the noncentrosymmetric C_2 space group, are summarized in Figure 1. The asymmetric unit consists of one half of the molecule in **6b** and **7b**. The C8 atom in **6b** and **7b** possesses an (*R*) and (*S*) absolute configuration, respectively. The Cp rings in **6b** and **7b** approach an anticlinal eclipsed arrangement with a torsional twist angle Cp···Fe···Cp of 140.0° and 138.3°, respectively. The Cp rings are almost parallel to each other, the dihedral angles being 2.2° (**6b**) and 2.3° (**7b**). The orientation of the oxazoline ring with respect to the Cp ring can be characterized by the torsion angle C2–C1–C6–O10, which is 28.1° and –28.0° in **6b** and **7b**, respectively. The distribution of the electron density in the 4-isopropyloxazoline fragments in both **6b** and **7b** is very similar (see Table 2). The bond lengths and angles in the ferrocene moiety in both complexes are normal.[39]

Table 2. Selected bond lengths [Å] and angles [°] in **6b**, **7b**, **11b**, and **12b**.

	6b	7b	11b	12b
C1–C6	1.4685(18)	1.468(2)	1.479(8)	1.458(4)
C6–N7	1.2643(18)	1.264(2)	1.259(8)	1.265(3)
C6–O10	1.3641(17)	1.364(2)	1.345(8)	1.361(3)
N7–C8	1.4854(17)	1.487(2)	1.481(8)	1.474(4)
C8–C9	1.5397(19)	1.538(2)	1.520(9)	1.534(4)
C9–O10	1.4586(16)	1.4586(19)	1.455(8)	1.461(3)
C8–C11	1.530(2)	1.525(2)	1.510(8)	1.543(3)
C11–C12	1.5314(19)	1.534(2)	1.466(14)	1.511(4)
C11–C13	1.5312(17)	1.533(2)	1.586(12)	1.517(5)
N7–C8–C9	103.97(11)	103.95(13)	104.8(5)	104.1(2)
N7–C8–C11	110.08(11)	110.03(13)	110.8(6)	111.8(2)
C9–C8–C11	116.23(12)	116.36(15)	116.8(6)	115.5(2)

Like **6b** and **7b**, complex **11b** crystallizes as the (*S*)-enantiomer in the noncentrosymmetric $C222_1$ space group (see Figure 2 top) and the asymmetric unit consists of half the molecule. The Cp rings in **11b** adopt an antiperiplanar (staggered) arrangement with a torsional twist angle Cp···Fe···Cp of 176.5°. The Cp rings are almost parallel to each other, with a dihedral angle of 1.6°. The oxazoline ring is almost parallel to the Cp ring. The torsion angle C2–C1–C6–O10 is 3.2°. Like **11b**, complex **12b** crystallizes as the (*S*)-enantiomer in the noncentrosymmetric $C222_1$ space group (see Figure 2 bottom) and the asymmetric unit consists of half the molecule. The Cp rings in **12b** adopt an antiperiplanar (staggered) arrangement with a torsional twist angle Cp···Fe···Cp of 174.9°. The Cp rings are almost parallel to each other, with a dihedral angle of 0.4°. The oxazoline ring is almost parallel to the Cp ring. The torsion

 © 2005 Wiley-VCH Verlag GmbH & Co. KGaA, Weinheim

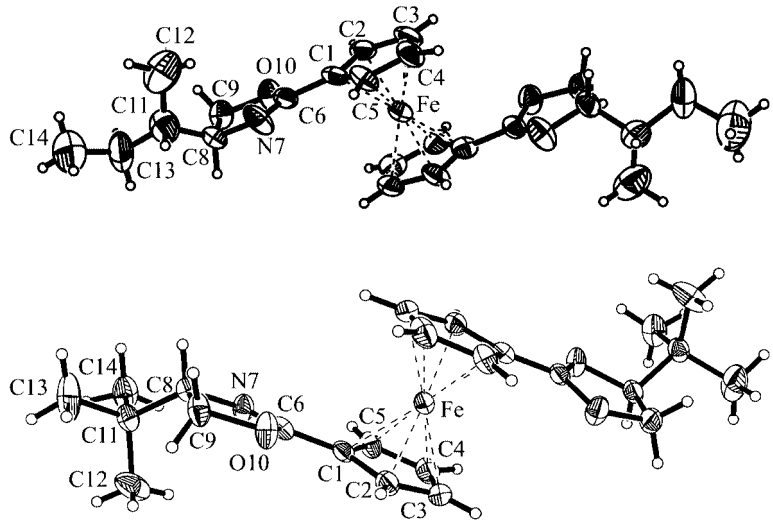

Figure 2. The molecular structure and labeling scheme of 1,1′-bis[(*S*)-4-*sec*-butyloxazolin-2-yl]ferrocene (**11b**; top) and 1,1′-bis[(*S*)-4-*tert*-butyloxazolin-2-yl]ferrocene (**12b**; bottom) with displacement ellipsoids drawn at the 50% probability level.

angle C2–C1–C6–O10 is 8.1°. Selected bond lengths and angles of **11b** and **12b** are given in Table 2.

Figure 3 shows one of the two independent molecules in the crystal structures of **13b** (*R*) and **14b** (*S*). Like in all previous compounds, the ferrocene moiety shows the expected geometry, with no unusual bond lengths or angles. The two Cp rings are almost parallel to each other, with dihedral angles of 4.5° and 2.0° in the two independent molecules of **13b** and 4.4° and 2.0° in **14b**. The Cp···Fe···Cp torsional twist angle is 54.2° and 52.9° for the independent molecules in **13b**, and –54.2° and –53.0° in **14b**, thus indicating a conformation between synclinal staggered (ideal twist angle of 36°) and synclinal eclipsed (ideal twist angle of 72°). As in **12b**, the oxazoline rings are almost parallel to the Cp rings, the torsional angles C2–C1–C6–O10, C18–C17–C22–O26 and C34–C33–C38–O42, C50–C49–C54–O58 being 6.1°, –11.5° and 4.7°, –3.6° in **13b** and –6.6°, 11.4°, –4.2°, 3.3° in **14b** (see Table 3 for selected bond lengths and angles).

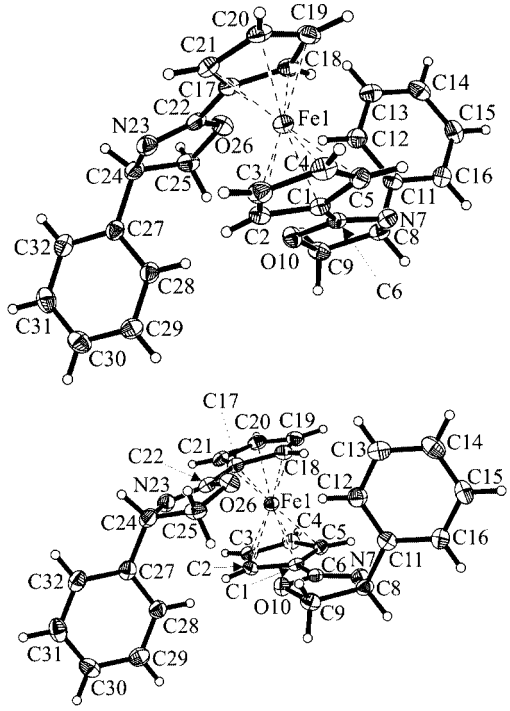

Figure 3. The molecular structure and labeling scheme of 1,1′-bis[(*R*)-4-phenyloxazolin-2-yl]ferrocene (**13b**; top) and 1,1′-bis[(*S*)-4-phenyloxazolin-2-yl]ferrocene (**14b**; bottom) with displacement ellipsoids drawn at the 50% probability level.

Investigation of the Coordination Properties

The application of bisoxazoline-based ligands in palladium-catalyzed allylic alkylation and in many other metal-catalyzed enantioselective reactions is well known.[9,17,44–48] Therefore the results of a study done by Ahn and co-workers, who found no catalytic activity for 1,1′-bis[(*S*)-4-*tert*-butyloxazolin-2-yl]ferrocene (**12b**), is rather surprising, although the ligand does bear a bulky *tert*-butyl group.

The catalytic potential of the ligands applied depends on several structural features, especially the bite angle and the bulkiness of the substituents. In order to study the influence of the substituents nature and of their bulkiness, a series of analogues was synthesized and their catalytic potential in the asymmetric allylic substitution investigated. The experiments were carried out with palladium complexes generated in situ by stirring the corresponding chiral ligand and $[Pd(\eta^3\text{-}C_3H_5)Cl]_2$ under standard conditions, i.e., (*E*)-1,3-diphenylprop-2-enyl acetate as substrate and dimethyl malonate as nucleophile with the *N*,*O*-bis(trimethylsilyl)acetamide base system (BSA-KOAc; see Scheme 2).[63] In agreement with the results of Ahn and co-workers, we did not observe any catalytic activity for any of the synthesized compounds. The variation of the ligand/Pd ratio from 1:1 to a large excess of the Pd compound (up to 10 times excess) did not affect the catalytic activity, and all efforts to isolate a defined Pd complex were unsuccessful.

 © 2005 Wiley-VCH Verlag GmbH & Co. KGaA, Weinheim

Table 3. Selected bond lengths [Å] and angles [°] in **13b** and **14b**.

	13b	**14b**
C1–C6	1.462(3)	1.465(3)
C6–N7	1.269(2)	1.269(3)
C6–O10	1.370(2)	1.367(2)
N7–C8	1.485(2)	1.489(3)
C8–C9	1.542(3)	1.541(3)
C9–O10	1.456(2)	1.455(3)
C8–C11	1.515(3)	1.506(3)
C11–C12	1.396(3)	1.398(3)
C11–C16	1.386(3)	1.394(3)
N7–C8–C9	103.72(14)	103.36(17)
N7–C8–C11	108.53(14)	108.55(17)
C9–C8–C11	115.39(16)	115.73(18)

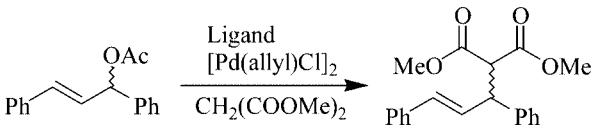

Scheme 2. General scheme for the palladium-catalyzed allylic alkylation.

In order to investigate the reasons for this lack of catalytic activity, the coordination of $[Pd(\eta^3\text{-}C_3H_5)Cl]_2$ toward several 1,1′-bis(oxazolin-2-yl)ferrocenes was studied by ESI-MS in the positive-ion mode (for calculated *m*/*z* ratios of the parent compound and the expected adducts see Table 4). The incubation solution of the Pd complex and the oxazoline ligand was injected directly into the mass spectrometer and the MS measurement parameters were optimized in order to maximize signals corresponding to the mass-to-charge ratio of the ligands (see Table 5).

Table 4. List of the calculated *m*/*z* ratios for the ligands and for the complexes formed with $[Pd(\eta^3\text{-}C_3H_5)Cl]_2$ (measured in positive-ion mode).

	Formula	*m*/*z* ratio
1b	$[C_{18}H_{20}FeN_2O_2 + H]^+$	353
1b + $[Pd(\eta^3\text{-}C_3H_5)Cl]_2$	$[C_{18}H_{20}FeN_2O_2 + Pd(\eta^3\text{-}C_3H_5)]^+$	499
1b + $[Pd(\eta^3\text{-}C_3H_5)Cl]_2$	$[C_{18}H_{20}FeN_2O_2 + PdCl]^+$	495
1b + $[Pd(\eta^3\text{-}C_3H_5)Cl]_2$	$[C_{18}H_{20}FeN_2O_2 + Pd_2(\eta^3\text{-}C_3H_5)_2Cl]^+$	683
7b	$[C_{22}H_{28}FeN_2O_2 + H]^+$	409
7b + $[Pd(\eta^3\text{-}C_3H_5)Cl]_2$	$[C_{22}H_{28}FeN_2O_2 + Pd(\eta^3\text{-}C_3H_5)]^+$	555
7b + $[Pd(\eta^3\text{-}C_3H_5)Cl]_2$	$[C_{22}H_{28}FeN_2O_2 + PdCl]^+$	551
7b + $[Pd(\eta^3\text{-}C_3H_5)Cl]_2$	$[C_{22}H_{28}FeN_2O_2 + Pd_2(\eta^3\text{-}C_3H_5)_2Cl]^+$	739
12b	$[C_{24}H_{32}FeN_2O_2 + H]^+$	437
12b + $[Pd(\eta^3\text{-}C_3H_5)Cl]_2$	$[C_{24}H_{32}FeN_2O_2 + Pd(\eta^3\text{-}C_3H_5)]^+$	583
12b + $[Pd(\eta^3\text{-}C_3H_5)Cl]_2$	$[C_{24}H_{32}FeN_2O_2 + PdCl]^+$	577
12b + $[Pd(\eta^3\text{-}C_3H_5)Cl]_2$	$[C_{24}H_{32}FeN_2O_2 + Pd_2(\eta^3\text{-}C_3H_5)_2Cl]^+$	767
12b + $[Pd(\eta^3\text{-}C_3H_5)Cl]_2$	$[C_{24}H_{32}FeN_2O_2 + Pd_2(\eta^3\text{-}C_3H_5)Cl_2]^+$	761
14b	$[C_{28}H_{24}FeN_2O_2 + H]^+$	477
14b + $[Pd(\eta^3\text{-}C_3H_5)Cl]_2$	$[C_{28}H_{24}FeN_2O_2 + Pd(\eta^3\text{-}C_3H_5)]^+$	623
14b + $[Pd(\eta^3\text{-}C_3H_5)Cl]_2$	$[C_{28}H_{24}FeN_2O_2 + PdCl]^+$	617
14b + $[Pd(\eta^3\text{-}C_3H_5)Cl]_2$	$[C_{28}H_{24}FeN_2O_2 + Pd_2(\eta^3\text{-}C_3H_5)Cl_2]^+$	807

For 1,1′-bis[(*S*)-4-methyloxazolin-2-yl]ferrocene (**1b**), a signal at *m*/*z* = 353 was observed as the most intense peak $[C_{18}H_{20}FeN_2O_2 + H]^+$. Addition of $[Pd(\eta^3\text{-}C_3H_5)Cl]_2$ in 1:1 ligand/Pd molar ratio resulted in the formation of a peak at *m*/*z* = 499 assignable to the mono-palladium complex $[C_{18}H_{20}FeN_2O_2 + Pd(\eta^3\text{-}C_3H_5)]^+$ and a relatively much less abundant one at *m*/*z* = 683 for the bis-palladium one $[C_{18}H_{20}FeN_2O_2 + Pd_2(\eta^3\text{-}C_3H_5)_2Cl]^+$. Increasing the amount of palladium (molar ratio 1:2) in the incubation mixture resulted only in a minor increase of the peak at *m*/*z* = 683; the signal assigned to $[C_{18}H_{20}FeN_2O_2 + Pd(\eta^3\text{-}C_3H_5)]^+$ remained the most intense.

Table 5. Operational MS parameters chosen for investigations on the complexation behavior of **1b**, **7b**, **12b**, and **14b**.

Parameters	Values
HV capillary [V]	4000
Dry gas flow [L min^{-1}]	5
Dry gas temperature [°C]	80
Nebulizer gas [psi]	10
Skimmer 1 [V]	35.7
Capillary exit offset [V]	73.6
Octopole [V]	2.50
Octopole Δ [V]	2.40
Trap drive	30.6
Injection rate [μL min^{-1}]	6
Polarity	positive
Scan range, *m*/*z*	50–1200

Similar investigations were performed for 1,1′-bis[(*S*)-4-isopropyloxazolin-2-yl]ferrocene (**7b**): at a molar ratio of 1:1 the most intense peak was again the ligand coordinated to one Pd^{II} center, which in this case also bears an allyl ligand. At the lower ligand/transition metal molar ratio (1:1) a remarkable amount of $[C_{22}H_{28}FeN_2O_2 + Pd_2(\eta^3\text{-}C_3H_5)_2Cl]^+$ is already detectable in this case. Addition of $[Pd(\eta^3\text{-}C_3H_5)Cl]_2$ to obtain molar ratios of 1:2 and 1:10 influenced the mass spectra by increasing the signal with *m*/*z* = 739, and at a molar ratio of 1:10 there are already peaks with equal relative intensities for the mono-palladium (*m*/*z* = 555) and the bis-palladium conjugates (*m*/*z* = 739; see Figure 4). Additionally, MS/MS experiments of both adducts were done and it was found that the fragmentation of *m*/*z* = 739 leads to a peak for the mono adduct (*m*/*z* = 555).

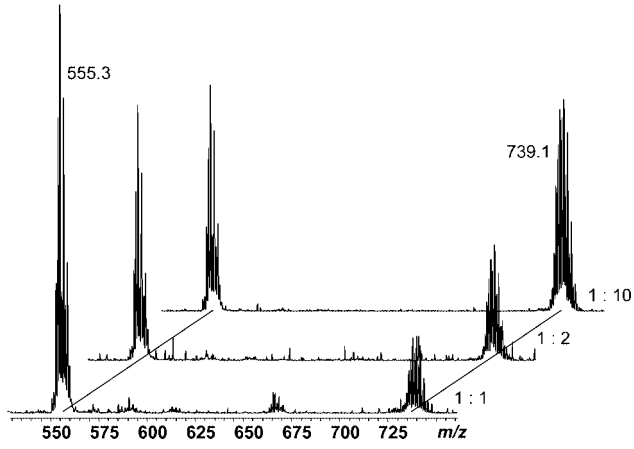

Figure 4. Mass spectrometric investigation of the coordination behavior of 1,1′-bis[(*S*)-4-isopropyloxazolin-2-yl]ferrocene (**7b**) toward $[Pd(allyl)Cl]_2$ at molar ratios of 1:1, 1:2, and 1:10 (ligand/palladium), with peaks found at *m*/*z* = 555 and 739 assignable to the mono- and bis-palladium complexes, respectively.

 © 2005 Wiley-VCH Verlag GmbH & Co. KGaA, Weinheim

Further MS^3 experiments did not result in any assignable signals.

In the case of (*S*)-*tert*-butyloxazoline (**12b**) a major adduct with *m*/*z* = 767 is formed which was assigned to $[C_{24}H_{32}FeN_2O_2 + Pd_2(\eta^3\text{-}C_3H_5)_2Cl]^+$. Additionally, a coordination compound was detected which contains one allyl and two chloro ligands instead of two allyl and one chloro ligand. Note that due to the broad isotope distribution of palladium and chloro ligands an overlapping of the signals with *m*/*z* = 761 and 767 can not be avoided.

The (*S*)-phenyloxazoline **14b** was chosen as representative for the aryloxazolines for the MS experiments. At a molar ratio of 1:1 the monoadduct with $[Pd(\eta^3\text{-}C_3H_5)Cl]_2$ is the most intense peak, while at a 1:2 ratio the dinuclear Pd species is formed. Extension of the reaction times for all the MS experiments did not influence the appearance of the mass spectra. The increase of the peak with two Pd atoms coordinated to the 1,1′-bis(oxazolin-2-yl)ferrocene ligands reveals that there is no stable chelate formed between the two oxazoline rings and the Pd^{II} cation. These results are in good agreement with a report published by Imai et al., who showed by NMR spectroscopy that 1,1′-bis[(*S*)-4-isopropyloxazolin-2-yl]ferrocene (**7b**) functions, independently of the Pd/oxazoline ratio, as a monodentate ligand.[64]

In order to study the experimentally found monodentate coordination of the ferrocene ligand to the allylpalladium moiety instead of the expected chelate formation, quantum-chemical calculations of equilibrium structures of the parent methyl-substituted ligand 1,1′-bis[(*S*)-4-methyloxazolin-2-yl]ferrocene (**1b**) and possible complexes with mono- and bidentate coordination of **1b** to Pd^{II} (**1c** and **1d**, respectively) were carried out at the B3LYP level of theory. The calculated structural parameters of **1b** are in perfect agreement with those found experimentally for **12b**, with a maximum deviation of 0.021 Å for the C8–C9 bond. For the other bonds, the difference between the calculated and experimental bond lengths often appears within the 3σ interval of the X-ray data.

The minima corresponding to both **1c** and **1d** were located (see Figure 5). A comparison of the total energies of these structures shows that the chelate complex **1d** is 19.07 kcal mol^{-1} more stable than complex **1c**. In terms of Gibbs free energy, when the entropic factor is taken into account, the stability of **1d** relative to **1c** decreases slightly but is still significant ($\Delta G = G_{1d} - G_{1c} = -15.83$ kcal mol^{-1}). Consideration of the solvent effects at the CPCM level (for CH_2Cl_2 as a solvent) results in a further, but only moderate, lowering of the energy difference between **1d** and **1c** (by 3.16 kcal mol^{-1}). Thus, the chelate complex displays a significantly higher stability than the monodentate structure despite the possible steric hindrances in the former; the exclusive formation of the monodentate-type complexes must therefore be determined by kinetic factors rather than by thermodynamic ones. Indeed, the formation of chelates is accompanied by the mutual rotation of two Cp cycles and by significant conformational changes in the ligand that should increase the activation energy compared to the formation of **1c** and similar structures.

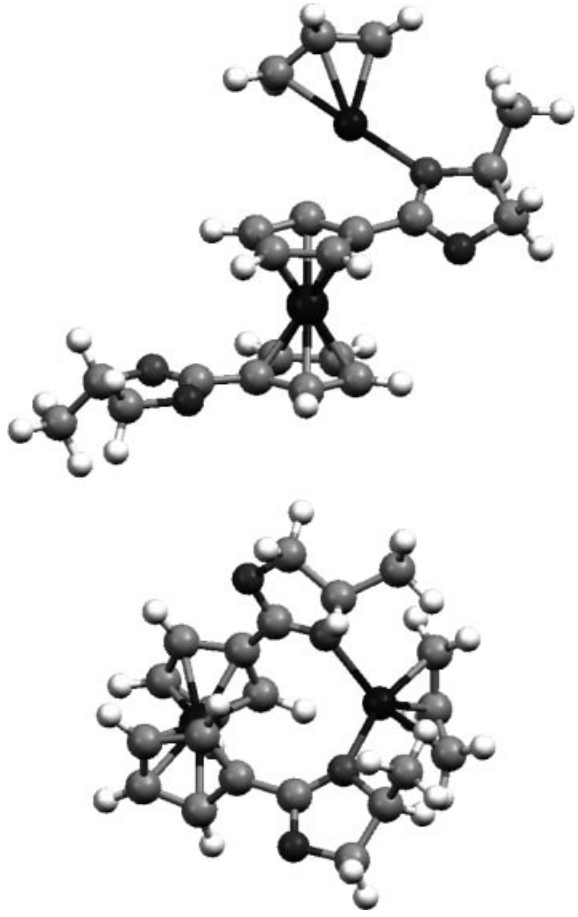

Figure 5. Equilibrium structures of complexes **1c** (top) and **1d** (bottom).

A possible explanation for the preferred monodenticity of the ligands might be the hindrance of rotation of the oxazoline moiety around the C–C axis. Taking into account the crystal structure analyses, the nitrogen atoms are not orientated toward each other and therefore the nitrogen lone-pairs in the solid state point in opposite directions.

Conclusions

Bisoxazolines are known to be excellent ligands in many enantioselective syntheses. A central factor in enantioselective synthesis is the formation of chelate structures by coordination of multidentate ligands to transition metals. The chelation process therefore has a great influence on the success of metal complexes in many catalytic processes.

We have described the synthesis and characterization of a wide variety of differently substituted 1,1′-bis(oxazolin-2-yl)ferrocenes with substituents located in either the 4- or 5-position of the oxazoline rings and being either alkyl or aryl groups. The synthesized compounds were characterized by standard analytical methods (NMR, elemental analysis). Additionally, for compounds **6b**, **7b**, **11b**, **12b**, **13b**, and **14b** the absolute configuration was determined by single-crystal X-ray diffraction analysis.

 © 2005 Wiley-VCH Verlag GmbH & Co. KGaA, Weinheim

The catalytic activity of these compounds was tested in the palladium-catalyzed allylic alkylation. These experiments showed that this type of ligand possesses no activity in the test reaction and that a change of the substituent on the oxazoline ring does not influence this. We suppose that the lack of catalytic activity results from the insufficient coordination properties of the studied 1,1′-bis(oxazolin-2-yl)ferrocenes, i.e., chelate formation with the palladium center, a fact that was enlightened in mass spectrometric studies: the bisoxazolines are not capable of functioning as bidentate ligands. This feature was found to be independent of the type of substituents as well as their positions on the oxazoline ring. Comparing the presented results with the outcome of an NMR study reported by Imai and coworkers it can be assumed that the effect is also independent of the type of palladium complex.

In contrast, DFT calculations for this type of compounds revealed, as expected, that chelating structures are energetically more stable than the equivalent monodentate complexes. Therefore it is suggested that the chelate formation of the ferrocene ligands with an allylpalladium moiety instead of the bidentate one is kinetically controlled.

Experimental Section

General Remarks: All reactions were carried out in dry solvents under argon. The NMR spectra were recorded on a Bruker Avance DPX 400 instrument (Ultrashield™ Magnet) at 400.13 MHz (^{1}H) and 100.63 MHz (^{13}C) at 298 K in [D$_6$]DMSO or $CDCl_3$. Optical rotations were measured with a Perkin–Elmer 341 polarimeter using a 10 cm cell. Melting points were determined with a Büchi B-540 apparatus and are uncorrected. Electrospray ionization mass spectra were recorded on a Bruker esquire$_{3000}$ spectrometer in positive-ion mode (see Table 5 for measurement parameters). The elemental analyses were done by the Laboratory for Elemental Analysis of the Institute of Physical Chemistry, University of Vienna, with a Perkin–Elmer 2400 CHN Elemental Analyzer. Silica gel (Fluka-60 70–230 mesh) was used for column chromatography and silica gel (Polygram® SIL G/UV$_{254}$) for thin layer chromatography.

The full geometry optimization of all structures was carried out in Cartesian coordinates with the Gaussian 98[69] program package at the DFT level of theory. The calculations were performed using Becke's three-parameter hybrid exchange functional[70] in combination with the gradient-corrected correlation functional of Lee et al.[71] (B3LYP). A quasi-relativistic Stuttgart pseudopotential was used for the 28 core-electrons, the appropriate contracted basis set (8s7p6d)/[6s5p3d][72] for the palladium atom, and the 6-31G* basis set[73–76] for other atoms. For the Fe atom, the relativistic Stuttgart pseudopotential describing 10 core-electrons and the appropriate contracted basis set (8s7p6d1f)/[6s5p3d1f][77] was also used in some calculations. Symmetry operations were not applied for all structures. The Hessian matrix was calculated analytically for all equilibrium structures to prove the location of correct minima (no imaginary frequencies were found) and to estimate the thermodynamic functions calculated at 25 °C. Solvent effects were taken into account at the single-point calculations based on the gas-phase equilibrium geometries by using the polarizable continuum model[78] in the CPCM version[79] with CH_2Cl_2 as a solvent.

The *N*-substituted 1,1′-ferrocenedicarboxamides **7a**, **12a**, and **14a**, 1,1′-bis[(*S*)-4-isopropyloxazolin-2-yl]ferrocene (**7b**), 1,1′-bis[(*S*)-4-*tert*-butyloxazolin-2-yl]ferrocene (**12b**), and 1,1′-bis[(*S*)-4-phenyloxazolin-2-yl]ferrocene (**14b**) were prepared following a literature procedure.[39] The synthesized amides were stable for more than one year at room temperature while the oxazolines degraded over time. Therefore they should be stored under argon and in the refrigerator.

***N*,*N*′-Bis[(1*S*)-(2-hydroxy-1-methylethyl)]ferrocene-1,1′-dicarboxamide (1a):** A solution of 1,1′-ferrocenyldicarbonyl dichloride (0.78 g, 2.50 mmol) in CH_2Cl_2 (30 mL) was added slowly at 0 °C to a solution of (*R*)-(–)-2-amino-1-propanol (0.37 g, 5.00 mmol) and triethylamine (0.7 mL, 5.05 mmol) in CH_2Cl_2 (20 mL). The reaction mixture was stirred for 4 h, the formed precipitate was filtered off and washed five times with CH_2Cl_2 (30 mL). This procedure yielded 0.69 g (71%) of pure product after drying in vacuo. $[\alpha]_D^{20}$ = +18 (*c* = 0.25, DMSO); m.p. 200–201 °C decomp. ^{1}H NMR ([D$_6$]DMSO): δ = 7.52 (d, ^3J = 7.6 Hz, 2 H, N*H*), 4.75 (br. s, 4 H, Fc-*H*), 4.29 (br. s, 4 H, Fc-*H*), 3.97 (m, 2 H, NHC*H*), 3.45 (m, 2 H, HOCH_2), 3.38 (m, 2 H, HOCH_2), 1.12 (d, ^3J = 6.5 Hz, 6 H, CH_3) ppm. ^{13}C{^{1}H} NMR: δ = 169.24 (*C*O), 78.83 (Fc-*C*), 72.46 (Fc-*C*), 70.95 (Fc-*C*), 70.65 (Fc-*C*), 65.34 (HO*C*H$_2$), 47.78 (NH*C*H), 18.19 (*C*H$_3$) ppm. $C_{18}H_{24}FeN_2O_4$ (388.2): calcd. C 55.69, H 6.23, N 7.22; found C 55.50, H 6.08, N 6.96.

***N*,*N*′-Bis[(1*S*)-(1-hydroxy-1-methylethyl)]ferrocene-1,1′-dicarboxamide (2a):** Following the same procedure as described for **1a** yielded 0.95 g (98%) of **2a**. $[\alpha]_D^{20}$ = +4 (*c* = 0.25, DMSO); m.p. 122–123 °C decomp. ^{1}H NMR ([D$_6$]DMSO): δ = 7.92 (br. s, 2 H, N*H*), 4.87 (br. s, 2 H, O*H*), 4.77 (br. s, 2 H, Fc-*H*), 4.74 (br. s, 4 H, Fc-*H*), 3.81 (m, 2 H, HOC*H*), 3.15 (m, 2 H, NHCH_2), 3.14 (m, 2 H, NHCH_2), 1.10 (d, ^3J = 6.5 Hz, 6 H, CH_3) ppm. ^{13}C{^{1}H} NMR: δ = 169.66 (*C*O), 78.83 (Fc-*C*), 72.33 (Fc-*C*), 70.74 (Fc-*C*), 70.45 (Fc-*C*), 66.16 (HO*C*H), 47.78 (NH*C*H), 18.19 (*C*H$_3$) ppm. $C_{18}H_{24}FeN_2O_4$ (388.2): calcd. C 55.69, H 6.23, N 7.22; found C 55.41, H 6.44, N 7.15.

***N*,*N*′-Bis[(1*R*)-(1-(hydroxymethyl)propyl]ferrocene-1,1′-dicarboxamide (3a):** A solution of 1,1′-ferrocenyldicarbonyl dichloride (0.78 g, 2.50 mmol) in CH_2Cl_2 (20 mL) was added slowly at 0 °C to a solution of (*R*)-(–)-2-amino-1-butanol (0.45 g, 5.00 mmol) and triethylamine (0.70 mL, 5.05 mmol) in CH_2Cl_2 (20 mL). The reaction mixture was stirred for 4 h and washed with a saturated solution of $NaHCO_3$ and then with brine. The organic phase was dried with Na_2SO_4 and the solvent was removed in vacuo. This procedure yielded 0.68 g (65%) of the title compound **3a** after purification by column chromatography. $[\alpha]_D^{20}$ = –17 (*c* = 0.25, DMSO); m.p. 181–182 °C decomp. ^{1}H NMR ($CDCl_3$): δ = 6.73 (d, ^3J = 6.0 Hz, 2 H, N*H*), 4.70 (br. s, 2 H, Fc-*H*), 4.45 (br. s, 4 H, Fc-*H*), 4.30 (br. s, 2 H, Fc-*H*), 4.26 (br. s, 2 H, O*H*), 3.91 (br. s, 2 H, NHC*H*), 3.83 (br. s, 2 H, HOCH_2), 3.78 (br. s, 2 H, HOCH_2), 1.97 (m, 4 H, CH_2CH$_3$), 1.01 (dd, ^3J = 7.0, 8.5 Hz, 6 H, CH$_2$CH_3) ppm. ^{13}C{^{1}H} NMR: δ = 170.91 (*C*O), 78.28 (Fc-*C*), 72.60 (Fc-*C*), 71.81 (Fc-*C*), 71.34 (Fc-*C*), 69.37 (Fc-*C*), 63.25 (HO*C*H$_2$), 57.51 (NH*C*H), 29.75 (*C*H$_2$CH$_3$), 20.04 (CH$_2$*C*H$_3$) ppm. $C_{20}H_{28}FeN_2O_4$ (416.3): calcd. C 57.70, H 6.78, N 6.73; found C 57.59, H 6.66, N 6.51.

Ferrocene-1,1′-dicarboxamide 4a: Following the same procedure as described for **3a** yielded 0.89 g (86%) of **4a**. $[\alpha]_D^{20}$ = +20 (*c* = 0.25, DMSO); m.p. 181–182 °C decomp. ^{1}H NMR ($CDCl_3$): δ = 6.70 (d, ^3J = 8.5 Hz, 2 H, N*H*), 4.71 (br. s, 2 H, Fc-*H*), 4.49 (br. s, 2 H, Fc-*H*), 4.44 (br. s, 2 H, Fc-*H*), 4.35 (br. s, 2 H, O*H*), 4.33 (br. s, 2 H, Fc-*H*), 4.05 (m, 2 H, NHC*H*), 3.87 (dd, ^3J = 3.0, 11.5 Hz, 2 H, HOCH_2), 3.67 (dd, ^3J = 6.0, 11.5 Hz, 2 H, HOCH_2), 1.65 (m, 4 H, CH_2CH$_3$), 1.00 (dd, *J* = 6.0, 11.5 Hz, 6 H, CH$_2$CH_3) ppm. ^{13}C{^{1}H} NMR: δ = 170.88 (*C*O), 78.28 (Fc-*C*), 71.77 (Fc-*C*), 71.46 (Fc-*C*), 69.87 (Fc-*C*), 64.77 (HO*C*H$_2$), 53.77 (NH*C*H), 24.79 (*C*H$_2$CH$_3$),

 © 2005 Wiley-VCH Verlag GmbH & Co. KGaA, Weinheim

11.19 (CH_2CH_3) ppm. $C_{20}H_{28}FeN_2O_4$ (416.3): calcd. C 57.70, H 6.78, N 6.73; found C 57.63, H 6.83, N 6.68.

Ferrocene-1,1′-dicarboxamide 5a: Following the same procedure as described for **3a** yielded 0.88 g (79%) of **5a**. M.p. 47–48 °C. ^{1}H NMR ($CDCl_3$): δ = 6.77 (d, ^3J = 8.5 Hz, 1 H, N*H*), 6.69 (d, ^3J = 9.0 Hz, 1 H, N*H*), 4.73 (br. s, 2 H, Fc-*H*), 4.55 (br. s, 1 H, Fc-*H*), 4.50 (br. s, 1 H, Fc-*H*), 4.45 (br. s, 1 H, Fc-*H*), 4.41 (br. s, 2 H, Fc-*H*), 4.34 (br. s, 1 H, Fc-*H*), 4.15 (m, 2 H, NHC*H*), 3.87 (dd, ^3J = 3.0, 11.0 Hz, 2 H, HOCH_2), 3.65 (dd, ^3J = 5.0, 11.0 Hz, 2 H, HOCH_2), 1.61–1.52 (m, 4 H, CH_2CH$_2$CH$_3$), 1.47–1.36 (m, 4 H, CH$_2$CH_2CH$_3$), 0.97 (t, ^3J = 8.0 Hz, 3 H, CH$_2$CH$_2$CH_3), 0.94 (t, ^3J = 7.0, 3 H, CH$_2$CH$_2$CH_3) ppm. ^{13}C{^{1}H} NMR: δ = 170.89 (*C*O), 170.86 (*C*O), 78.26 (Fc-*C*), 77.87 (Fc-*C*), 72.43 (Fc-*C*),72.21 (Fc-*C*), 71.81 (Fc-*C*), 71.57 (Fc-*C*), 71.44 (Fc-*C*), 70.11 (Fc-*C*), 69.83 (Fc-*C*), 65.64 (HO*C*H$_2$), 65.23 (HO*C*H$_2$), 52.00 (NH*C*H), 51.95 (NH*C*H), 33.88 (*C*H$_2$CH$_2$CH$_3$) 33.58 (*C*H$_2$CH$_2$CH$_3$), 19.82 (CH$_2$*C*H$_2$CH$_3$), 14.43 (CH$_2$CH$_2$*C*H$_3$), 14.39 (CH$_2$CH$_2$*C*H$_3$) ppm. $C_{22}H_{32}FeN_2O_4$ (444.3): calcd. C 59.47, H 7.26, N 6.30; found C 59.28, H 7.30, N 6.21.

Ferrocene-1,1′-dicarboxamide 6a:[42] Yield: 0.97 g (87%). $[\alpha]_D^{20}$ = –53 (*c* = 0.25, DMSO); m.p. 108–109 °C. ^{1}H NMR ($CDCl_3$): δ = 6.65 (d, ^3J = 9.0 Hz, 2 H, N*H*), 4.72 (br. s, 2 H, Fc-*H*), 4.46 (br. s, 4 H, Fc-*H*), 4.32 (br. s, 2 H, Fc-*H*), 4.16 (br. s, 2 H, O*H*), 3.92 (m, 2 H, NHC*H*), 3.85 (dd, ^3J = 3.0, 11.5 Hz, 2 H, HOCH_2) 3.76 (dd, ^3J = 6.0, 11.5 Hz, 2 H, HOCH_2), 1.97 (m, ^3J = 7.0 Hz, 2 H, C*H*(CH$_3$)$_2$], 1.03 (d, ^3J = 7.0 Hz, 6 H, CH_3), 1.00 (d, ^3J = 7.0 Hz, 6 H, CH_3) ppm. ^{13}C{^{1}H} NMR: δ = 170.84 (*C*O), 78.32 (Fc-*C*), 72.45 (Fc-*C*), 71.79 (Fc-*C*), 71.37 (Fc-*C*), 69.43 (Fc-*C*), 63.30 (HO*C*H$_2$), 57.50 (NH*C*H), 29.80 [*C*H(CH$_3$)$_2$], 20.02 (*C*H$_3$), 19.70 (*C*H$_3$) ppm. $C_{22}H_{32}FeN_2O_4$ (444.3): calcd. C 59.47, H 7.26, N 6.30; found C 59.35, H 7.09, N 6.35.

Ferrocene-1,1′-dicarboxamide 8a: Following the same procedure as described for **3a** yielded 0.73 g (62%) of **8a**. M.p. 39–40 °C. ^{1}H NMR ($CDCl_3$): δ = 6.68 (d, ^3J = 8.0 Hz, 1 H, N*H*), 6.59 (d, ^3J = 8.5 Hz, 1 H, N*H*), 4.75 (br. s, 2 H, Fc-*H*), 4.55 (br. s, 1 H, Fc-*H*), 4.51 (br. s, 1 H, Fc-*H*), 4.46 (br. s, 1 H, Fc-*H*), 4.43 (br. s, 2 H, Fc-*H*), 4.36 (br. s, 1 H, Fc-*H*), 4.14 (m, 2 H, NHC*H*), 3.89 (dd, ^3J = 3.0, 12.0 Hz, 2 H, HOCH_2), 3.65 (dd, ^3J = 5.5, 11.0 Hz, 2 H, HOCH_2), 1.59 [m, 4 H, CH_2(CH$_2$)$_2$CH$_3$], 1.36 [m, 8 H, CH$_2$(CH_2)$_2$CH$_3$], 0.92 [m, 6 H, CH$_2$(CH$_2$)$_2$CH_3]. ^{13}C{^{1}H} NMR: δ = 170.82 (*C*O), 170.78 (*C*O), 78.30 (Fc-*C*), 77.88 (Fc-*C*), 72.51 (Fc-*C*), 72.18 (Fc-*C*), 71.80 (Fc-*C*), 71.53 (Fc-*C*), 71.46 (Fc-*C*), 70.03 (Fc-*C*), 69.82 (Fc-*C*), 65.74 (NH*C*H), 65.29 (NH*C*H), 52.27 (HO*C*H$_2$), 52.19 (HO*C*H$_2$), 31.52 (*C*H$_2$CH$_2$CH$_2$CH$_3$), 31.18 (*C*H$_2$CH$_2$CH$_2$CH$_3$), 28.79 (CH$_2$*C*H$_2$CH$_2$CH$_3$), 23.02 (CH$_2$CH$_2$*C*H$_2$CH$_3$), 22.97 (CH$_2$CH$_2$-*C*H$_2$CH$_3$), 14.45 (CH$_2$CH$_2$CH$_2$*C*H$_3$), 14.41 (CH$_2$CH$_2$CH$_2$*C*H$_3$) ppm. $C_{24}H_{36}FeN_2O_4$ (472.4): calcd. C 61.02, H 7.68, N 5.93; found C 61.15, N 5.93.

Ferrocene-1,1′-dicarboxamide 9a: Following the same procedure as described for **3a** yielded 0.81 g (68%) of **9a**. $[\alpha]_D^{20}$ = –19 (*c* = 0.25, DMSO); m.p. 59–60 °C. ^{1}H NMR ($CDCl_3$): δ = 6.78 (d, ^3J = 8.5 Hz, 2 H, N*H*,), 4.69 (br. s, 2 H, Fc-*H*), 4.45 (br. s, 2 H, Fc-*H*), 4.43 (br. s, 2 H, Fc-*H*), 4.30 (br. s, 2 H, Fc-*H*), 4.25 (m, 2 H, NHC*H*), 3.85 (dd, ^3J = 3.0, 11.0 Hz, 2 H, HOCH_2), 3.61 (dd, ^3J = 5.5, 11.5 Hz, 2 H, HOCH_2), 1.69 [m, 2 H, CH_2CH(CH$_3$)$_2$], 1.57 [m, 2 H, CH_2CH(CH$_3$)$_2$], 1.38 [m, 2 H, CH$_2$C*H*(CH$_3$)$_2$], 0.98 (d, ^3J = 6.6 Hz, 12 H, CH_3) ppm. ^{13}C{^{1}H} NMR: δ = 170.88 (*C*O), 78.14 (Fc-*C*), 72.50 (Fc-*C*), 71.84 (Fc-*C*), 71.42 (Fc-*C*), 69.63 (Fc-*C*), 65.73 (HO*C*H$_2$), 50.34 (NH*C*H), 40.80 [*C*H$_2$CH(CH$_3$)$_2$], 25.46 [CH$_2$*C*H(CH$_3$)$_2$], 23.59 (*C*H$_3$), 22.67 (*C*H$_3$) ppm. $C_{24}H_{36}FeN_2O_4$ (472.4): calcd. C 61.02, H 7.68, N 5.93; found C 60.81, H 7.52, N 5.75.

Ferrocene-1,1′-dicarboxamide 10a: Following the same procedure as described for **3a** yielded 1.14 g (96%) of **10a**. $[\alpha]_D^{20}$ = +18 (*c* = 0.25, DMSO); m.p. 53–54 °C. ^{1}H NMR ($CDCl_3$): δ = 6.70 (d, ^3J = 9.0 Hz, 2 H, N*H*,), 4.69 (br. s, 2 H, Fc-*H*), 4.45 (br. s, 2 H, Fc-*H*), 4.26 (m, 2 H, NHC*H*), 3.87 (dd, ^3J = 3.0, 11.0 Hz, 2 H, HOCH_2), 3.61 (dd, ^3J = 5.5, 11.0 Hz, 2 H, HOCH_2), 1.70 [m, 2 H, CH_2CH(CH$_3$)$_2$], 1.57 [m, 2 H, CH_2CH(CH$_3$)$_2$], 1.38 [m, 2 H, CH$_2$C*H*(CH$_3$)$_2$], 0.98 (d, ^3J = 6.0 Hz, 12 H, CH_3) ppm. ^{13}C{^{1}H} NMR δ = 170.83 (*C*O), 78.16 (Fc-*C*), 72.48 (Fc-*C*), 71.81 (Fc-*C*), 71.42 (Fc-*C*), 69.60 (Fc-*C*), 65.77 (HO*C*H$_2$), 50.35 (NH*C*H), 40.82 [*C*H$_2$CH(CH$_3$)$_2$], 25.46 [CH$_2$*C*H(CH$_3$)$_2$], 23.58 (*C*H$_3$), 22.66 (*C*H$_3$) ppm. $C_{24}H_{36}FeN_2O_4$ (472.4): calcd. C 61.02, H 7.68, N 5.93; found C 60.80, H 7.83, N 5.82.

Ferrocene-1,1′-dicarboxamide 11a: Following the same procedure as described for **3a** yielded 1.08 g (91%) of **11a**. $[\alpha]_D^{20}$ = +23 (*c* = 0.25, DMSO); m.p. 60–61 °C. ^{1}H NMR ($CDCl_3$): δ = 6.66 (d, ^3J = 8.5 Hz, 2 H, N*H*), 4.72 (br. s, 2 H, Fc-*H*), 4.46 (br. s, 4 H, Fc-*H*), 4.32 (br. s, 2 H, Fc-*H*), 3.99 (m, 2 H, NHC*H*), 3.85 (dd, ^3J = 3.0, 11.5 Hz, 2 H, HOCH_2), 3.77 (dd, ^3J = 6.0, 11.5 Hz, 2 H, HOCH_2), 1.78 [m, 2 H, C*H*(CH$_3$)CH$_2$CH$_3$], 1.58 [m, 2 H, CH(CH$_3$) CH_2CH$_3$], 1.24 [m, 2 H, CH(CH$_3$)CH_2CH$_3$], 1.00 (d, ^3J = 6.5 Hz, 6 H, CH_3), 0.95 (t, ^3J = 7.0 Hz, 6 H, CH_3) ppm. ^{13}C{^{1}H} NMR: δ = 170.73 (*C*O), 78.27 (Fc-*C*), 72.49 (Fc-*C*), 71.79 (Fc-*C*), 71.36 (Fc-*C*), 69.36 (Fc-*C*), 63.03 (HO*C*H$_2$), 56.05 (NH*C*H), 36.12 [*C*H(CH$_3$)CH$_2$CH$_3$], 26.21 [CH(CH$_3$)*C*H$_2$CH$_3$], 15.96 (CH$_3$), 11.63 (CH$_3$) ppm. $C_{24}H_{36}FeN_2O_4$ (472.4): calcd. C 61.02, H 7.68, N 5.93; found C 61.12, H 7.70, N 5.83.

Ferrocene-1,1′-dicarboxamide 13a: Following the same procedure as described for **3a** yielded 1.30 g (83%) of **13a**. $[\alpha]_D^{20}$ = –88 (*c* = 0.25, DMSO); m.p. 207–208 °C decomp. ^{1}H NMR ([D$_6$]DMSO): δ = 8.22 (d, ^3J = 7.5 Hz, 2 H, N*H*,), 7.41–7.26 (m, 10 H, Ph-*H*), 5.04 (m, 4 H, NHC*H*, O*H*), 4.91 (br. s, 2 H, Fc-*H*), 4.60 (br. s, 2 H, Fc-*H*), 4.31 (br. s, 2 H, Fc-*H*), 4.26 (br. s, 2 H, Fc-*H*), 3.70.(m, 4 H, HOCH_2) ppm. ^{13}C{^{1}H} NMR: δ = 169.53 (*C*O), 142.36 (Ph-*C*), 128.97 (Ph-*C*), 127.90 (Ph-*C*), 127.73 (Ph-*C*), 78.48 (Fc-*C*), 72.46 (Fc-*C*), 72.25 (Fc-*C*), 71.90 (Fc-*C*), 69.67 (Fc-*C*), 65.23 (HO*C*H$_2$), 56.49 (NH*C*H) ppm. $C_{28}H_{28}FeN_2O_4$ (512.4): calcd. C 65.64, H 5.51, N 5.47; found C 65.52, H 5.41, N 5.25.

Ferrocene-1,1′-dicarboxamide 15a: Following the same procedure as described for **3a** yielded 1.37 g (87%) of **15a**. M.p. 207–208 °C decomp. ^{1}H NMR ([D$_6$]DMSO): δ = 7.96 (m, 2 H, N*H*), 7.42–7.27 (m, 10 H, Ph-*H*), 5.61 (dd, ^3J = 4.5, 9.0 Hz, 2 H, HOC*H*), 4.82 (br. s, 2 H, O*H*), 4.71 (br. s, 4 H, Fc-*H*), 4.29 (br. s, 4 *H*, Fc-*H*), 3.46 (m, 2 H, NHCH_2), 3.26 (m, 2 H, NHCH_2) ppm. ^{13}C{^{1}H} NMR: δ = 169.60 (*C*O), 144.69 (Ph-*C*), 128.94 (Ph-*C*), 127.94 (Ph-*C*), 126.93 (Ph-*C*), 78.52 (Fc-*C*), 72.43 (Fc-*C*), 72.19 (Fc-*C*),70.65 (Fc-*C*), 70.53 (Fc-*C*), 70.43 (HO*C*H), 48.15 (NH*C*H$_2$) ppm. $C_{28}H_{28}FeN_2O_4$ (512.4): calcd. C 65.64, H 5.51, N 5.47; found C 65.34, H 5.69, N 5.31.

Ferrocene-1,1′-dicarboxamide 16a: Following the same procedure as described for **3a** yielded 1.31 g (79%) of **16a**. $[\alpha]_D^{20}$ = +41 (*c* = 0.25, DMSO); m.p. 173–174 °C decomp. ^{1}H NMR ([D$_6$]DMSO): δ = 7.67 (d, ^3J = 8.5, 2 H, N*H*), 7.31 (m, 8 H, Ph-*H*), 7.18 (m, 2 H, Ph-*H*), 4.91 (t, ^3J = 5.5 Hz, 2 H, NHC*H*,), 4.66 (br. s, 2 H, Fc-*H*), 4.32 (br. s, 2 H, Fc-*H*), 4.16 (br. s, 2 H, O*H*), 4.08 (br. s, 2 H, Fc-*H*), 4.05 (br. s, 2 H, Fc-*H*), 3.51 (m, 2 H, HOCH_2), 3.43 (m, 2 H, HOCH_2), 2.99 (m, 2 H, CH_2Ph), 2.76 (m, 2 H, CH_2Ph) ppm. ^{13}C{^{1}H} NMR: δ = 169.33 (*C*O), 140.53 (Ph-*C*), 129.94 (Ph-*C*), 128.99 (Ph-*C*), 126.77 (Ph-*C*), 78.62 (Fc-*C*), 72.37 (Fc-*C*), 72.20 (Fc-*C*), 71.94 (Fc-*C*), 69.12 (Fc-*C*), 64.21 (HO*C*H$_2$), 53.65 (NH*C*H), 37.39 (*C*H$_2$Ph) ppm. $C_{30}H_{32}FeN_2O_4$ (540.4): calcd. C 66.67, H 5.97, N 5.18; found C 66.33, H 5.96, N 5.04.

 © 2005 Wiley-VCH Verlag GmbH & Co. KGaA, Weinheim

Ferrocene-1,1′-dicarboxamide 17a: Following the same procedure as described for **3a** yielded 1.19 g (72%) of **17a**. $[\alpha]_D^{20}$ = –37 (*c* = 0.25, DMSO); m.p. 175–176 °C decomp. ^{1}H NMR ([D$_6$]DMSO): δ = 7.68 (d, ^3J = 8.5 Hz, 2 H, N*H*), 7.31 (m, 8 H, Ph-*H*), 7.18 (m, 2 H, Ph-*H*), 4.92 (t, ^3J = 5.0 Hz, 2 H, NHC*H*), 4.66 (br. s, 2 H, Fc-*H*), 4.32 (br. s, 2 H, Fc-*H*), 4.16 (br. s, 2 H, O*H*), 4.07 (br. s, 2 H, Fc-*H*), 4.04 (br. s, 2 H, Fc-*H*), 3.51(m, 2 H, HOCH_2), 3.42 (m, 2 H, HOCH_2), 2.99 (m, 2 H, CH_2Ph), 2.75 (m, 2 H, CH_2Ph) ppm. ^{13}C{^{1}H} NMR: δ = 169.34 (*C*O), 140.53 (Ph-*C*), 129.94 (Ph-*C*), 128.99 (Ph-*C*), 126.77 (Ph-*C*), 78.62 (Fc-*C*), 72.37 (Fc-*C*), 72.20 (Fc-*C*), 71.94 (Fc-*C*), 69.12 (Fc-*C*), 64.21 (HO*C*H$_2$), 53.65 (NH*C*H), 37.39 (*C*H$_2$Ph) ppm. $C_{30}H_{32}FeN_2O_4$ (540.4): calcd. C 66.67, H 5.97, N 5.18; found C 66.57, H 5.90, N 4.99.

Ferrocene-1,1′-dicarboxamide 18a: Following the same procedure as described for **1a** yielded 1.61 g (79%) of **18a**. $[\alpha]_D^{20}$ = +76 (*c* = 0.25, DMSO); m.p. 277–278 °C decomp. ^{1}H NMR ([D$_6$]DMSO): δ = 8.25 (d, ^3J = 9.0 Hz, 2 H, N*H*), 7.59–7.48 (m, 8 H, Ph-*H*), 7.44–7.02 (m, 12 H, Ph-*H*), 5.44 (br. s, 2 H, O*H*), 5.04 (t, ^3J = 9.0 Hz, 2 H, NHC*H*,), 4.91 (dd, ^3J = 5.5, 8.5 Hz, 2 H, C*H*OH,), 4.35 (br. s, 2 H, Fc-*H*), 4.18 (br. s, 2 H, Fc-*H*), 3.82 (br. s, 2 H, Fc-*H*), 3.78 (br. s, 2 H, Fc-*H*) ppm. ^{13}C{^{1}H} NMR: δ = 168.54 (*C*O), 145.00 (Ph-*C*), 143.07 (Ph-*C*), 129.15 (Ph-*C*), 128.70 (Ph-*C*), 128.55 (Ph-*C*), 128.10 (Ph-*C*), 127.94 (Ph-*C*), 127.57 (Ph-*C*), 78.44 (Fc-*C*), 75.39 (*C*HOH), 72.23 (Fc-*C*), 71.81 (Fc-*C*), 71.07 (Fc-*C*), 69.17 (Fc-*C*), 59.77 (NH*C*H) ppm. $C_{40}H_{36}FeN_2O_4$ (664.6): calcd. C 72.29, H 5.46, N 4.22; found C 72.46, H 5.45, N 4.14.

1,1′-Bis[(*S*)-4-methyloxazolin-2-yl]ferrocene (1b): A solution of *p*-toluenesulfonyl chloride (0.42 g, 2.20 mmol) in CH_2Cl_2 (20 mL) was added dropwise at 0 °C to a solution of **1a** (0.39 g, 1.00 mmol), triethylamine (0.70 mL, 5.00 mmol), and a catalytic amount of 4-(dimethylamino)pyridine in CH_2Cl_2 (50 mL). The reaction mixture was stirred at room temperature for 10 h and then washed with a saturated solution of $NaHCO_3$ and with brine. The water layer was extracted with CH_2Cl_2 and the combined organic phases were dried with Na_2SO_4. Purification by column chromatography gave 0.31 g (88%) of **1b**. $[\alpha]_D^{20}$ = +77 (*c* = 0.25, CH_2Cl_2); m.p. 85–86 °C. ^{1}H NMR ($CDCl_3$): δ = 4.72 (br. s, 4 H, Fc-*H*), 4.41 (t, ^3J = 8.5, 2 H, OCH_2), 4.34 (br. s, 4 H, Fc-*H*), 4.20 (m, 2 H, NC*H*), 3.84 (t, ^3J = 8.0 Hz, 2 H, OCH_2), 1.30 (d, ^3J = 6.6 Hz, 6 H, CH_3) ppm. ^{13}C{^{1}H} NMR: δ = 165.39 (*C*O), 74.15 (OCH$_2$), 72.38 (Fc-*C*), 72.26 (Fc-*C*), 72.01 (Fc-*C*), 71.02 (Fc-*C*), 70.94 (Fc-*C*), 62.26 (NCH), 21.91(*C*H$_3$) ppm. $C_{18}H_{20}FeN_2O_2$ (352.2): calcd. C 61.38, H 5.72, N 7.95; found C 61.36, H 5.80, N 7.76.

1,1′-Bis[(*S*)-5-methyloxazolin-2-yl]ferrocene (2b): Following the same procedure as described for **1b** yielded 0.28 g (79%) of **2b**. $[\alpha]_D^{20}$ = +22 (*c* = 0.25, CH_2Cl_2); m.p. 101–102 °C. ^{1}H NMR ($CDCl_3$): δ = 4.73 (m, 6 H, Fc–*H*, OC*H*), 4.35 (br. s, 2 H, Fc-*H*), 4.32 (br. s, 2 H, Fc-*H*), 3.97 (dd, $^{3,2}J$ = 9.5, 14.0 Hz, 2 H, NCH_2), 3.44 (dd, $^{3,2}J$ = 7.0, 14.0 Hz, 2 H, NCH_2), 1.40 (d, ^3J = 6.5 Hz, 6 H, CH_3) ppm. ^{13}C{^{1}H} NMR: δ = 165.64 (*C*O), 76.20 (O*C*H), 72.42 (Fc-*C*), 72.32 (Fc-*C*), 72.15 (Fc-*C*), 70.78 (Fc-*C*), 70.59 (Fc-*C*), 62.00 (NCH$_2$), 21.62(*C*H$_3$) ppm. $C_{18}H_{20}FeN_2O_2$ (352.2): calcd. C 61.38, H 5.72, N 7.95; found C 61.50, H 5.52, N 7.93.

1,1′-Bis[(*R*)-4-ethyloxazolin-2-yl]ferrocene (3b): Following a similar procedure as described for **1b**, but changing *p*-toluenesulfonyl chloride for methanesulfonyl chloride, yielded 0.29 g (77%) of **3b**. $[\alpha]_D^{20}$ = –63 (*c* = 0.25, CH_2Cl_2); m.p. 75–76 °C. ^{1}H NMR ($CDCl_3$): δ = 4.75 (br. s, 4 H, Fc-*H*), 4.38 (t, ^3J = 9.0 Hz, 2 H, OCH_2,), 4.35 (br. s, 4 H, Fc-*H*), 4.10 (m, 2 H, NC*H*), 3.97 (t, ^3J = 8.0 Hz, 2 H, OCH_2), 1.75 (m, 2 H, CH_2CH$_3$), 1.48 (m, 2 H, CH_2CH$_3$), 0.99 (t, ^3J = 7.5 Hz, 6 H, CH_3) ppm. ^{13}C{^{1}H} NMR: δ = 165.39 (*C*O), 72.37 (Fc-*C*), 72.32 (Fc-*C*), 72.13 (Fc–*C*, OCH$_2$), 71.01 (Fc-*C*), 70.82 (Fc-*C*), 68.27 (NCH), 28.87 (*C*H$_2$), 10.37(*C*H$_3$) ppm. $C_{20}H_{24}FeN_2O_2$ (380.3): calcd. C 63.17, H 6.36, N 7.37; found C 63.28, H 6.36, N 7.45.

1,1′-Bis[(*S*)-4-ethyloxazolin-2-yl]ferrocene (4b): Following the same procedure as described for **3b** yielded 0.30 g (79%) of **4b**. $[\alpha]_D^{20}$ = +52 (*c* = 0.25, CH_2Cl_2); m.p. 72–73 °C. ^{1}H NMR ($CDCl_3$): δ = 4.75 (br. s, 4 H, Fc-*H*), 4.39 (t, ^3J = 8.0 Hz, 2 H, OCH_2,), 4.36 (br. s, 4 H, Fc-*H*), 4.10 (m, 2 H, NC*H*), 3.98 (t, ^3J = 8.0 Hz, 2 H, OCH_2), 1.76 (m, 2 H, CH_2CH$_3$), 1.59 (m, 2 H, CH_2CH$_3$), 1.00 (t, ^3J = 7.5 Hz, 6 H, CH_3) ppm. ^{13}C{^{1}H} NMR: δ = 165.39 (*C*O), 72.37 (Fc-*C*), 72.32 (Fc-*C*), 72.13 (Fc–*C*, OCH$_2$), 71.01 (Fc-*C*), 70.82 (Fc-*C*), 68.30 (NCH), 28.88 (*C*H$_2$), 10.38 (*C*H$_3$) ppm. $C_{20}H_{24}FeN_2O_2$ (380.3): calcd. C 63.17, H 6.36, N 7.37; found C 63.40, H 6.24, N 7.34.

1,1′-Bis(4-propyloxazolin-2-yl)ferrocene (5b): Following the same procedure as described for **3b** yielded 0.18 g (44%) of **5b** as an oil. ^{1}H NMR ($CDCl_3$): δ = 4.74 (br. s, 4 H, Fc-*H*), 4.39 (dd, $^{3,2}J$ = 2.5, 9.0 Hz, 2 H, OCH_2), 4.35 (br. s, 4 H, Fc-*H*), 4.15 (m, 2 H, NC*H*), 3.96 (dd, $^{3,2}J$ = 3.0, 7.5 Hz, 2 H, OCH_2), 1.72 [m, 2 H, (CH_2)$_2$CH$_3$], 1.47 [m, 6 H, (CH_2)$_2$CH$_3$], 0.99 (t, ^3J = 7.0 Hz, 6 H, CH_3) ppm. ^{13}C{^{1}H} NMR: δ = 165.30 (*C*O), 72.60 (OCH$_2$), 72.38 (Fc-*C*), 72.34 (Fc-*C*), 72.32 (Fc-*C*), 72.15 (Fc-*C*), 72.12 (Fc-*C*), 71.01 (Fc-*C*), 70.97 (Fc-*C*), 70.90 (Fc-*C*), 70.84 (Fc-*C*), 66.86 (NCH), 38.49 (*C*H$_2$), 19.51 (*C*H$_2$), 14.55 (*C*H$_3$) ppm. $C_{22}H_{28}FeN_2O_2$ (408.3): calcd. C 64.71, H 6.91, N 6.86; found C 64.54, H 6.83, N 6.83.

1,1′-Bis[(*R*)-4-isopropyloxazolin-2-yl]ferrocene (6b):[42] Yield: 0.37 g (90%). $[\alpha]_D^{20}$ = –83 (*c* = 0.25, CH_2Cl_2); m.p. 64–65 °C. ^{1}H NMR ($CDCl_3$): δ = 4.77 (br. s, 2 H, Fc-*H*), 4.75 (br. s, 2 H, Fc-*H*), 4.36 (br. s, 4 H, Fc-*H*), 4.31 (t, 2 H, OCH_2, J = 9.0), 4.07 (t, ^3J = 9.0 Hz, 2 H, OCH_2), 4.00 (m, 2 H, NC*H*), 1.87 [m, 2 H, C*H*(CH$_3$)$_2$], 1.03 (d, ^3J = 7.0 Hz, 6 H, CH_3,), 0.95 (d, ^3J = 6.5 Hz, 6 H, CH_3) ppm. ^{13}C{^{1}H} NMR: δ = 165.26 (*C*O), 72.84 (NCH), 72.32 (Fc-*C*), 72.27 (Fc-*C*), 70.01 (Fc-*C*), 70.69 (Fc-*C*), 69.91 (OCH$_2$), 32.78 (*C*H), 19.40 (*C*H$_3$), 18.32 (*C*H$_3$) ppm. $C_{22}H_{28}FeN_2O_2$ (408.3): calcd. C 64.71, H 6.91, N 6.86; found C 64.62, H 6.95, N 6.67.

1,1′-Bis(4-butyloxazolin-2-yl)ferrocene (8b): Following the same procedure as described for **3b** yielded 0.34 g (78%) of **8b** as an oil. ^{1}H NMR ($CDCl_3$): δ = 4.76 (br. s, 4 H, Fc-*H*), 4.40 (m, 2 H, OCH_2), 4.36 (br. s, 4 H, Fc-*H*), 4.14 (m, 2 H, OCH_2), 3.96 (m, 2 H, NC*H*), 1.76 [m, 2 H, (CH_2)$_3$CH$_3$], 1.54 [m, 2 H, (CH_2)$_2$CH$_3$], 1.40 [m, 8 H, (CH_2)$_2$CH$_3$], 0.95 (t, ^3J = 7.0 Hz, 6 H, CH_3) ppm. ^{13}C{^{1}H} NMR: δ = 165.31 (*C*O), 72.60 (OCH$_2$), 72.40 (Fc-*C*), 72.37 (Fc-*C*), 72.33 (Fc-*C*), 72.15 (Fc-*C*), 70.98 (Fc-*C*), 70.96 (Fc-*C*), 70.90 (Fc-*C*), 70.84 (Fc-*C*), 67.07 (NCH), 36.00 (*C*H$_2$), 28.41 (*C*H$_2$), 23.16 (*C*H$_2$), 14.44 (*C*H$_3$) ppm. $C_{24}H_{32}FeN_2O_2$ (436.4): calcd. C 66.06, H 7.39, N 6.42; found C 66.00, H 7.27, N 6.36.

1,1′-Bis[(*R*)-4-isobutyloxazolin-2-yl]ferrocene (9b): Following the same procedure as described for **3b** yielded 0.32 g (73%) of **9b** as an oil. $[\alpha]_D^{20}$ = –83 (*c* = 0.25, CH_2Cl_2). ^{1}H NMR ($CDCl_3$): δ = 4.75 (br. s, 4 H, Fc-*H*), 4.43 (t, ^3J = 8.5 Hz, 2 H, OCH_2), 4.36 (br. s, 4 H, Fc-*H*), 4.19 (m, 2 H, NC*H*), 3.92 (t, ^3J = 7.5 Hz, 2 H, OCH_2), 1.77 (m, 2 H, CH_2CH), 1.71 (m, 2 H, CH_2CH), 1.37 (m, 2 H, CH$_2$C*H*), 0.98 (t, ^3J = 6.5 Hz, 12 H, CH_3) ppm. ^{13}C{^{1}H} NMR: δ = 165.28 (*C*O), 73.21 (OCH$_2$), 72.44 (Fc-*C*), 72.33 (Fc-*C*), 72.08 (Fc-*C*), 71.04 (Fc-*C*), 70.92 (Fc-*C*), 65.41 (NCH), 46.04 (*C*H$_2$), 25.87 (*C*H), 23.49 (*C*H$_3$), 23.01 (*C*H$_3$) ppm. $C_{24}H_{32}FeN_2O_2$ (436.4): calcd. C 66.06, H 7.39, N 6.42; found C 66.02, H 7.45, N 6.34.

1,1′-Bis[(*S*)-4-isobutyloxazolin-2-yl]ferrocene (10b): Following the same procedure as described for **3b** yielded 0.36 g (82%) of **10b** as an oil. $[\alpha]_D^{20}$ = –83 (*c* = 0.25, CH_2Cl_2). ^{1}H NMR ($CDCl_3$): δ = 4.73 (br. s, 4 H, Fc-*H*), 4.40 (t, ^3J = 8.5 Hz, 2 H, OCH_2), 4.43 (br. s, 4

 © 2005 Wiley-VCH Verlag GmbH & Co. KGaA, Weinheim

H, Fc-*H*), 4.16 (m, 2 H, NC*H*), 3.90 (t, ^3J = 7.5 Hz, 2 H, OCH_2), 1.77 (m, 2 H, CH_2CH), 1.69 (m, 2 H, CH_2CH), 1.35 (m, 2 H, CH_2C*H*), 0.97 (t, ^3J = 6.0 Hz, 12 H, CH_3) ppm. $^{13}C\{^1H\}$ NMR: δ = 165.10 (*C*O), 73.15 (O*C*H_2), 72.35 (Fc-*C*), 72.26 (Fc-*C*), 72.17 (Fc-*C*), 70.98 (Fc-*C*), 70.86 (Fc-*C*), 65.50 (N*C*H), 46.06 (*C*H_2), 25.86 (*C*H), 23.50 (*C*H_3), 23.00 (*C*H_3) ppm. $C_{24}H_{32}FeN_2O_2$ (436.4): calcd. C 66.06, H 7.39, N 6.42; found C 66.12, H 7.42, N 6.47.

1,1′-Bis[(*S*)-4-*sec*-butyloxazolin-2-yl]ferrocene (11b): Following the same procedure as described for **3b** yielded 0.35 g (80%) of **11b**. $[\alpha]_D^{20}$ = –83 (*c* = 0.25, CH_2Cl_2); m.p. 78–79 °C. ^1H NMR ($CDCl_3$): δ = 4.77 (br. s, 2 H, Fc-*H*), 4.75 (br. s, 2 H, Fc-*H*), 4.36 (br. s, 4 H, Fc-*H*), 4.29 (t, ^3J = 7.5 Hz, 2 H, OCH_2), 4.11 (m, 2 H, NC*H*), 4.08 (m, 2 H, OCH_2), 1.73 (m, 2 H, C*H*), 1.57 (m, 2 H, CH_2), 1.24 (m, 2 H, CH_2), 0.97 (t, ^3J = 7.0 Hz, 6 H, CH_2CH_3), 0.90 (d, ^3J = 6.5 Hz, 6 H, CHCH_3) ppm. $^{13}C\{^1H\}$ NMR: δ = 165.14 (*C*O), 72.32 (Fc-*C*), 71.36 (N*C*H), 70.83 (Fc-*C*), 70.65 (Fc-*C*), 69.29 (O*C*H_2), 39.10 (*C*H), 26.65 (*C*H_2), 14.55 (*C*H_3), 12.17 (*C*H_3) ppm. $C_{24}H_{32}FeN_2O_2$ (436.4): calcd. C 66.06, H 7.39, N 6.42; found C 65.95, H 7.26, N 6.29.

1,1′-Bis[(*R*)-4-phenyloxazolin-2-yl]ferrocene (13b): Following the same procedure as described for **1b** yielded 0.43 g (91%) of **13b**. $[\alpha]_D^{20}$ = +190 (*c* = 0.25, CH_2Cl_2); m.p. 92–93 °C. ^1H NMR ($CDCl_3$): δ = 7.41–7.28 (m, 10 H, Ph-*H*), 5.26 (dd, $^{3,2}J$ = 8.5, 10.0 Hz, 2 H, NC*H*), 4.91 (br. s, 2 H, Fc-*H*), 4.89 (br. s, 2 H, Fc-*H*), 4.73 (dd, $^{3,2}J$ = 8.5, 10.0 Hz, 2 H, OCH_2), 4.47 (m, 4 H, Fc-*H*), 4.22 (t, ^3J = 8.5 Hz, 2 H, OCH_2) ppm. $^{13}C\{^1H\}$ NMR: δ = 166.92 (*C*O), 142.79 (Ph-*C*), 129.18 (Ph-*C*), 128.03 (Ph-*C*), 127.22 (Ph-*C*), 75.08 (O*C*H_2), 72.61(Fc-*C*), 72.46 (Fc-*C*), 71.81 (Fc-*C*), 71.28 (Fc-*C*), 70.50 (N*C*H) ppm. $C_{28}H_{24}FeN_2O_2$ (476.3): calcd. C 70.60, H 5.08, N 5.88; found C 70.45,<ztabr6" pos="x22> H 5.30, N 5.88.

1,1′-Bis(5-phenyloxazolin-2-yl)ferrocene (15b): Following the same procedure as described for **1b** yielded 0.36 g (76%) of **15b** as an oil. ^1H NMR ($CDCl_3$): δ = 7.43–7.32 (m, 10 H, Ph-*H*), 5.58 (m, 2 H, OC*H*), 4.88 (br. s, 2 H, Fc-*H*), 4.86 (br. s, 2 H, Fc-*H*), 4.44 (br. s, 4 H, Fc-*H*), 4.34 (m, 2 H,NCH_2), 3.86 (m, 2 H, NCH_2) ppm. $^{13}C\{^1H\}$ NMR: δ = 161.21 (*C*O), 141.31 (Ph-*C*), 129.21 (Ph-*C*), 128.71 (Ph-*C*), 126.38 (Ph-*C*),126.30 (Ph-*C*), 81.28 (O*C*H), 72.59(Fc-*C*), 72.49 (Fc-*C*), 72.45 (Fc-*C*), 72.32 (Fc-*C*), 72.15 (Fc-*C*), 71.91 (Fc-*C*), 71.33 (Fc-*C*), 70.93 (Fc-*C*), 70.86 (Fc-*C*), 70.59 (Fc-*C*), 63.53 (N*C*H_2) ppm. $C_{28}H_{24}FeN_2O_2$ (476.3): calcd. C 70.60, H 5.08, N 5.88; found C 70.71, H 5.12, N 5.91.

1,1′-Bis[(*R*)-4-benzyloxazolin-2-yl]ferrocene (16b): Following the same procedure as described for **1b** yielded 0.47 g (93%) of **16b** as an oil. $[\alpha]_D^{20}$ = +34 (*c* = 0.25, CH_2Cl_2). ^1H NMR ($CDCl_3$): δ = 7.34 (m, 4 H, Ph-*H*), 7.27 (m, 6 H, Ph-*H*), 4.78 (br. s, 2 H, Fc-*H*), 4.75 (br. s, 2 H, Fc-*H*), 4.45 (m, 2 H, NC*H*), 4.36 (br. s, 2 H, Fc-*H*), 4.34 (br. s, 2 H, Fc-*H*), 4.27(t, ^3J = 8.0 Hz, 2 H, OCH_2), 4.07 (t, ^3J = 8.0 Hz, 2 H, OCH_2), 3.23 (dd, $^{3,2}J$ = 5.0, 13.5 Hz, 2 H, CH_2Ph), 2.72 (dd, $^{3,2}J$ = 9.0, 13.5 Hz, 2 H, CH_2Ph) ppm. $^{13}C\{^1H\}$ NMR: δ = 166.08 (*C*O), 139.55 (Ph-*C*), 129.71 (Ph-*C*), 128.99 (Ph-*C*), 126.93 (Ph-*C*), 72.50 (Fc-*C*), 72.45 (Fc-*C*), 71.89 (O*C*H_2), 71.08 (Fc-*C*), 70.95 (Fc-*C*), 68.85 (Fc-*C*), 68.27 (N*C*H), 42.17 (*C*H_2Ph) ppm. $C_{30}H_{28}FeN_2O_2$ (504.4): calcd. C 71.44, H 5.60, N 5.55; found C 71.31, H 5.89, N 5.74.

1,1′-Bis[(*S*)-4-benzyloxazolin-2-yl]ferrocene (17b): Following the same procedure as described for **1b** yielded 0.40 g (79%) of **17b** as an oil. $[\alpha]_D^{20}$ = +3 (*c* = 0.25, CH_2Cl_2). ^1H NMR ($CDCl_3$): δ = 7.34 (m, 4 H, Ph-*H*), 7.27 (m, 6 H, Ph-*H*), 4.78 (br. s, 2 H, Fc-*H*), 4.76 (br. s, 2 H, Fc-*H*), 4.45 (m, 2 H, NC*H*), 4.36 (br. s, 2 H, Fc-*H*), 4.34 (br. s, 2 H, Fc-*H*), 4.27 (t, ^3J = 9.0 Hz, 2 H, OCH_2), 4.07 (t, ^3J = 9.0 Hz, 2 H, OCH_2), 3.24 (dd, $^{3,2}J$ = 4.5, 13.5 Hz, 2 H, CH_2Ph), 2.73 (dd, $^{3,2}J$ = 9.0, 13.5 Hz, 2 H, CH_2Ph) ppm. $^{13}C\{^1H\}$ NMR: δ = 166.11 (*C*O), 138.43 (Ph-*C*), 129.71 (Ph-*C*), 128.99 (Ph-*C*), 126.93 (Ph-*C*), 72.51 (Fc-*C*), 72.45 (Fc-*C*), 71.90 (O*C*H_2), 71.08 (Fc-*C*), 70.97 (Fc-*C*), 69.84 (Fc-*C*), 68.25 (N*C*H), 42.16 (*C*H_2Ph) ppm. $C_{30}H_{28}FeN_2O_2$ (504.4): calcd. C 71.44, H 5.60, N 5.55; found C 71.24, H 5.52, N 5.65.

1,1′-Bis[(4*R*,5*S*)-4,5-diphenyloxazolin-2-yl]ferrocene (18b): Following the same procedure as described for **1b** yielded 0.13 g (21%) of **18b** as an oil. ^1H NMR ($CDCl_3$): δ = 7.43–7.28 (m, 20 H, Ph-*H*), 5.36 (d, ^3J = 8.0 Hz, 2 H, NC*H*), 5.12 (d, ^3J = 7.5 Hz, 2 H, OC*H*), 5.07 (m, 2 H, Fc-*H*), 5.02 (m, 2 H, Fc-*H*), 4.60 (m, 2 H, Fc-*H*), 4.51 (m, 2 H, Fc-*H*) ppm. $^{13}C\{^1H\}$ NMR: δ = 166.22 (*C*O), 142.36 (Ph-*C*), 140.71 (Ph-*C*), 129.30 (Ph-*C*), 129.26 (Ph-*C*), 128.87 (Ph-*C*), 128.14 (Ph-*C*), 127.23 (Ph-*C*), 126.33 (Ph-*C*), 89.24 (N*C*H), 79.37 (O*C*H), 73.02 (Fc-*C*), 72.62 (Fc-*C*), 71.93 (Fc-*C*), 71.75 (Fc-*C*), 70.80 (Fc-*C*) ppm. $C_{40}H_{32}FeN_2O_2$ (628.5): calcd. C 76.44, H 5.13, N 4.46; found C 76.28, H 5.13, N 4.20.

X-ray diffraction measurements were performed on a Nonius Kappa CCD diffractometer. Single crystals were positioned at 40 mm from the detector and 567 and 495 frames were measured, each for 60 and 40 s over a 1.5° scan for **13b** and **14b**, respectively. The data were processed using the Denzo-SMN software package. Crystal data, data collection parameters, and structure refinement details for **6b**, **7b**, **11b**–**14b** are given in Table 6. The structures were solved by direct methods and refined by full-matrix least-squares techniques. Non-hydrogen atoms were refined with anisotropic displacement parameters. H-atoms were located on difference Fourier

Table 6. Crystallographic data for **6b**, **7b**, **11b**–**14b**.

Compound	**6b**	**7b**	**11b**	**12b**	**13b**	**14b**
Chemical formula	$C_{22}H_{28}FeN_2O_2$	$C_{22}H_{28}FeN_2O_2$	$C_{24}H_{32}FeN_2O_2$	$C_{24}H_{32}FeN_2O_2$	$C_{112}H_{96}Fe_4N_8O_{8.4}$	$C_{112}H_{96}Fe_4N_8O_{8.60}$
Formula mass	408.31	408.31	436.37	436.37	1911.77	1914.97
T [K]	110	110	110	120	120	120
Space group	*C*2	*C*2	$C222_1$	$C222_1$	*C*2	*C*2
a [Å]	20.099(3)	20.092(7)	6.786(6)	6.839(4)	13.637(3)	13.640(2)
b [Å]	6.388(1)	6.387(2)	10.068(1)	10.316(6)	15.431(3)	15.427(3)
c [Å]	7.833(2)	7.872(2)	32.13(4)	30.799(2)	21.698(4)	21.733(3)
β [°]	108.20(1)	108.18(2)			102.03(3)	102.03(2)
V [Å^3]	960.26(4)	959.78(5)	2195.4(7)	2172.9(2)	4465.7(15)	4471.85(13)
Z	2	2	4	4	2	2
$\mu_{calcd.}$ [cm^{-1}]	8.05	8.05	7.09	7.16	7.05	7.04
Flack parameter	0.008(10)	–0.002(12)	0.07(6)	0.03(3)	–0.011(7)	0.001(8)
R_1[a]	0.019	0.023	0.065	0.033	0.0322	0.0463
wR_2[b]	0.0468	0.0552	0.1829	0.0765	0.0643	0.0746

[a] $R_1 = \Sigma||F_o| - |F_c||/\Sigma|F_o|$. [b] $wR_2 = [\Sigma w|F_o^2| - |F_c^2|)^2/\Sigma w|F_o^2|^2]^{1/2}$.

 © 2005 Wiley-VCH Verlag GmbH & Co. KGaA, Weinheim

maps and isotropically refined or calculated. In **13b** and **14b** the positions of the hydrogen atoms at O5 were not determined. Computer programs: structure solution, SHELXS-97,[65] refinement, SHELXL-97,[66] molecular diagrams, ORTEP,[67] scattering factors.[68]

CCDC-240819, -240820, -240821, -240822, -240823, and -240824 (for **6b**, **7b**, **11b**–**14b**, respectively) contain the supplementary crystallographic data for this paper. These data can be obtained free of charge from The Cambridge Crystallographic Data Centre via www.ccdc.cam.ac.uk/data_request/cif.

Acknowledgments

We are grateful for financial support from the FWF (Austrian Science Fund, P12381-CHE) and for technical support and computer time at the Linux-PC clusters Schroedinger I and Schroedinger II of the computer center of the University of Vienna.

[1] R. J. Bergeron, J. S. McManis, J. Dionis, J. R. Garlich, *J. Org. Chem.* **1985**, *50*, 2780–2782.
[2] P. F. Cavanaugh Jr., C. W. Porter, D. Tukalo, O. S. Frankfurt, Z. P. Pavelic, R. J. Bergeron, *Cancer Res.* **1985**, *45*, 4754–4759.
[3] T. Miyasaka, Y. Nagao, E. Fujita, H. Sakurai, K. Ishizu, *J. Chem. Soc., Perkin Trans. 2* **1987**, *11*, 1543–1549.
[4] D. D. Nekrasov, *Khim. Geterosikl. Soedin.* **1996**, *8*, 1011–1025.
[5] C. Camoutsis, *J. Heterocycl. Chem.* **1996**, *33*, 539–557.
[6] J. A. Frump, *Chem. Rev.* **1971**, *71*, 483–506.
[7] S. Robin, G. Rousseau, *Tetrahedron* **1998**, *54*, 13 681–13 736.
[8] G. V. Boyd, *Prog. Heterocycl. Chem.* **1998**, *10*, 209–225.
[9] A. K. Ghosh, P. Mathivanan, J. Cappiello, *Tetrahedron: Asymmetry* **1998**, *9*, 1–45.
[10] M. Gómez, G. Muller, M. Rocamora, *Coord. Chem. Rev.* **1999**, *193–195*, 769–835.
[11] B. M. Culbertson, *Prog. Polym. Sci.* **2002**, *27*, 579–626.
[12] S. Kobayashi, H. Uyama, *J. Polym. Sci., Part A: Polym. Chem.* **2002**, *40*, 192–209.
[13] O. Nuyken, P. Persigehl, R. Weberskirch, *Macromol. Symp.* **2002**, *177*, 163–173.
[14] T. M. Stevenson, V. E. Amoo, G. C. Chiang, E. Keskeny, J. K. Long, B. A. Crouse, P. Sharpe, K. Hillegass, L. Jones, C. Yatsko, *ACS Symp. Ser.* **2002**, *800*, 188–198.
[15] G. Helmchen, A. Krotz, K. T. Ganz, D. Hansen, *Synlett* **1991**, *4*, 257–259.
[16] D. Mueller, G. Umbricht, B. Weber, A. Pfaltz, *Helv. Chim. Acta* **1991**, *74*, 232–240.
[17] P. von Matt, G. C. Lloyd-Jones, A. B. E. Minidis, A. Pfaltz, L. Macko, M. Neuburger, M. Zehnder, H. Rueegger, P. S. Pregosin, *Helv. Chim. Acta* **1995**, *78*, 265–284.
[18] M. B. Andrus, A. B. Argade, X. Chen, M. G. Pamment, *Tetrahedron Lett.* **1995**, *36*, 2945–2948.
[19] D. A. Evans, M. M. Faul, M. T. Bilodeau, B. A. Anderson, D. M. Barnes, *J. Am. Chem. Soc.* **1993**, *115*, 5328–5329.
[20] K. B. Hansen, N. S. Finney, E. N. Jacobsen, *Angew. Chem. Int. Ed. Engl.* **1995**, *34*, 676–678.
[21] R. E. Lowenthal, A. Abiko, S. Masamune, *Tetrahedron Lett.* **1990**, *31*, 6005–6008.
[22] T. G. Gant, M. C. Noe, E. J. Corey, *Tetrahedron Lett.* **1995**, *36*, 8745–8748.
[23] A. V. Bedekar, P. G. Andersson, *Tetrahedron Lett.* **1996**, *37*, 4073–4076.
[24] E. J. Corey, N. Imai, H. Y. Zhang, *J. Am. Chem. Soc.* **1991**, *113*, 728–729.
[25] R. A. Michelin, M. Mozzon, R. Bertani, *Coord. Chem. Rev.* **1996**, *147*, 299–338.
[26] V. Yu. Kukushkin, A. J. L. Pombeiro, *Chem. Rev.* **2002**, *102*, 1771–1802.
[27] R. A. Michelin, U. Belluco, M. Mozzon, P. Berin, R. Bertani, F. Benetollo, G. Bombieri, R. J. Angelici, *Inorg. Chim. Acta* **1994**, *220*, 21–33.
[28] R. A. Michelin, M. Mozzon, P. Berin, R. Bertani, F. Benetollo, G. Bombieri, R. J. Angelici, *Organometallics* **1994**, *13*, 1341–1350.
[29] M. A. Stark, G. Jones, C. J. Richards, *Organometallics* **2000**, *19*, 1282–1291.
[30] P. Segl'a, M. Jamnicky, *Inorg. Chim. Acta* **1993**, *205*, 221–229.
[31] K. M. Button, R. A. Gossage, R. K. R. Phillips, *Synth. Commun.* **2002**, *32*, 363–368.
[32] P. Segl'a, M. Jamnicky, M. Koman, T. Glowiak, *Polyhedron* **1998**, *17*, 2765–2772.
[33] *Ferrocenes* (Eds.: A. Togni, T. Hayashi), Wiley-VCH, Weinheim, **1995**.
[34] *Metallocenes* (Eds.: A. Togni, R. L. Halterman), Wiley-VCH, Weinheim, **1998**.
[35] I. Manners, *Chem. Commun.* **1999**, 857–865.
[36] I. Manners, *Adv. Mater.* **1994**, *6*, 68–71.
[37] P. Koepf-Maier, *Anticancer Res.* **1999**, *19*, 493–504.
[38] M. Sawamura, Y. Ito, *Chem. Rev.* **1992**, *92*, 857–871.
[39] W. Zhang, Y. Adachi, T. Hirao, I. Ikeda, *Tetrahedron: Asymmetry* **1996**, *7*, 451–460.
[40] W. Zhang, T. Hirao, I. Ikeda, *Tetrahedron Lett.* **1996**, *37*, 4545–4548.
[41] J. Park, S. Lee, K. H. Ahn, C.-W. Cho, *Tetrahedron Lett.* **1995**, *36*, 7263–7266.
[42] A. A. Nazarov, Ch. G. Hartinger, T. H. Brehmer, G. Giester, M. Galanski, B. K. Keppler, *Phosphorus, Sulfur Silicon Relat. Elem.* **2001**, *168–169*, 465–468.
[43] S. Lee, J. H. Koh, J. Park, *J. Organomet. Chem.* **2001**, *637–639*, 99–106.
[44] B. M. Trost, M. L. Crawley, *Chem. Rev.* **2003**, *103*, 2921–2944.
[45] O. Hoarau, H. Ait-Haddou, M. Castro, G. G. A. Balavoine, *Tetrahedron: Asymmetry* **1997**, *8*, 3755–3764.
[46] O. Hoarau, H. Ait-Haddou, J.-C. Daran, D. Cramailere, G. G. A. Balavoine, *Organometallics* **1999**, *18*, 4718–4723.
[47] W. Zhang, H. Yoshinaga, Y. Imai, T. Kida, Y. Nakatsuji, I. Ikeda, *Synlett* **2000**, *10*, 1512–1514.
[48] K. H. Ahn, C.-W. Cho, J. Park, S. Lee, *Tetrahedron: Asymmetry* **1997**, *8*, 1179–1185.
[49] S. M. Williams, J. S. Brodbelt, A. P. Marchand, D. Cal, K. Mlinaric-Majerski, *Anal. Chem.* **2002**, *74*, 4423–4433.
[50] S. F. Ralph, M. M. Sheil, L. A. Hick, R. J. Geue, A. M. Sargeson, *J. Chem. Soc., Dalton Trans.* **1996**, *23*, 4417–4424.
[51] Ch. G. Hartinger, A. A. Nazarov, V. Chevchenko, V. B. Arion, M. Galanski, B. K. Keppler, *Dalton Trans.* **2003**, *15*, 3098–3102.
[52] C. Markert, A Pfaltz, *Angew. Chem. Int. Ed.* **2004**, *43*, 2498–2500.
[53] *Electrospray Ionization Mass Spectrometry* (Ed.: R. B. Cole), John Wiley & Sons, New York, **1997**.
[54] R. Dessapt, C. Simonnet-Jegat, A. Mallard, H. Lavanant, J. Marrot, F. Secheresse, *Inorg. Chem.* **2003**, *42*, 6425–6431.
[55] P. W. N. M. Van Leeuwen, P. C. J. Kamer, J. N. H. Reek, *Pure Appl. Chem.* **1999**, *71*, 1443–1452.
[56] D. Rechavi, M. Lemaire, *Chem. Rev.* **2002**, *102*, 3467–3493.
[57] T. Sammakia, H. A. Latham, D. R. Schaad, *J. Org. Chem.* **1995**, *60*, 10–11.
[58] Y. Nishibayashi, K. Segawa, Y. Arikawa, K. Ohe, M. Hidai, S. Uemura, *J. Organomet. Chem.* **1997**, *545–546*, 381–398.
[59] E. Manoury, J. S. Fossey, H. Ait-Haddou, J.-C. Daran, G. G. A. Balavoine, *Organometallics* **2000**, *19*, 3736–3739.
[60] A. Chesney, M. R. Bryce, R. W. J. Chubb, A. S. Batsanov, J. A. K. Howard, *Tetrahedron: Asymmetry* **1997**, *8*, 2337–2346.
[61] C. Bolm, N. Hermanns, M. Kesselgruber, J. P. Hildebrand, *J. Organomet. Chem.* **2001**, *624*, 157–161.
[62] C. Bolm, *Angew. Chem. Int. Ed. Engl.* **1991**, *30*, 542–543.
[63] B. M. Trost, D. J. Murphy, *Organometallics* **1985**, *4*, 1143–1145.

 © 2005 Wiley-VCH Verlag GmbH & Co. KGaA, Weinheim

[64] Y. Imai, W. Zhang, T. Kida, Y. Nakatsuji, I. Ikeda, *Chem. Lett.* **1999**, *3*, 243–244.
[65] G. M. Sheldrick, *SHELXS-97,* University of Göttingen, **1997**.
[66] G. M. Sheldrick, *SHELXL-97,* University of Göttingen, **1997**.
[67] C. K. Johnson, Rep. ORNL-5138, OAK Ridge National Laboratory, OAK Ridge, TN, **1976**.
[68] *International Tables for X-ray Crystallography*, Kluwer Academic Press, Dordrecht, vol. C, Tables 4.2.6.8 and 6.1.1.4, **1992**.
[69] M. J. Frisch, G. W. Trucks, H. B. Schlegel, G. E. Scuseria, M. A. Robb, J. R. Cheeseman, V. G. Zakrzewski, J. A. Montgomery Jr., R. E. Stratmann, J. C. Burant, S. Dapprich, J. M. Millam, A. D. Daniels, K. N. Kudin, M. C. Strain, O. Farkas, J. Tomasi, V. Barone, M. Cossi, R. Cammi, B. Mennucci, C. Pomelli, C. Adamo, S. Clifford, J. Ochterski, G. A. Petersson, P. Y. Ayala, Q. Cui, K. Morokuma, P. Salvador, J. J. Dannenberg, D. K. Malick, A. D. Rabuck, K. Raghavachari, J. B. Foresman, J. Cioslowski, J. V. Ortiz, A. G. Baboul, B. B. Stefanov, G. Liu, A. Liashenko, P. Piskorz, I. Komaromi, R. Gomperts, R. L. Martin, D. J. Fox, T. Keith, M. A. Al-Laham, C. Y. Peng, A. Nanayakkara, M. Challacombe, P. M. W. Gill, B. Johnson, W. Chen, M. W. Wong, J. L. Andres, C. Gonzalez, M. Head-Gordon, E. S. Replogle, J. A. Pople, *Gaussian 98*, revision A.11.1; Gaussian Inc., Pittsburgh PA, **2001**.
[70] A. D. Becke, *J. Chem. Phys.* **1993**, *98*, 5648–5652.
[71] C. Lee, W. Young, R. G. Parr, *Phys. Rev. B* **1988**, *37*, 785–789.
[72] D. Andrae, U. Haeussermann, M. Dolg, H. Stoll, H. Preuss, *Theor. Chim. Acta* **1990**, *77*, 123–141.
[73] R. Ditchfield, W. J. Hehre, J. A. Pople, *J. Chem. Phys.* **1971**, *54*, 724–728.
[74] W. J. Hehre, R. Ditchfield, J. A. Pople, *J. Chem. Phys.* **1972**, *56*, 2257–2261.
[75] P. C. Hariharan, J. A. Pople, *Theoret. Chim. Acta* **1973**, *28*, 213–222.
[76] V. Rassolov, J. A. Pople, M. Ratner, T. L. Windus, *J. Chem. Phys.* **1998**, *109*, 1223–1229.
[77] M. Dolg, U. Wedig, H. Stoll, H. Preuss, *J. Chem. Phys.* **1987**, *86*, 866–872.
[78] J. Tomasi, M. Persico, *Chem. Rev.* **1997**, *94*, 2027–2094.
[79] V. Barone, M. Cossi, *J. Phys. Chem.* **1998**, *102*, 1995–2001.
Received: September 01, 2004

 © 2005 Wiley-VCH Verlag GmbH & Co. KGaA, Weinheim

Reductive Isopropyl Radical Elimination from (dpp-bian)Mg-*i*Pr(Et_2O)

Igor L. Fedushkin*[a] Alexandra A. Skatova,[a] Markus Hummert,[b] and Herbert Schumann*[b]

Dedicated to Prof. Dr. Sergei F. Zhiltsov on the occasion of his 70th birthday

Keywords: Magnesium / N ligands / Alkyl complexes / Reductive elimination

The reaction of (dpp-bian)Na(Et_2O) with one equiv. of *i*PrMgCl in hexane affords (dpp-bian)Mg-*i*Pr(Et_2O) (**1**) whereas (dpp-bian)Mg$(Et_2O)_2$ (**2**) is formed when this reaction is carried out in Et_2O as a result of *isopropyl* radical elimination. Compound **1** which is stable in hexane and Et_2O also decomposes in THF with elimination of *isopropyl* radicals yielding (dpp-bian)Mg$(THF)_2$. The reaction of (dpp-bian)Na_2-$(Et_2O)_3$ with two equiv. of *i*PrMgCl in Et_2O produces **2** and iPr_2Mg, which then interact to give (dpp-bian)$(Mg\text{-}iPr)_2(Et_2O)$ (**3**) when treated with hexane or toluene. Compounds **1**–**3** were characterized by elemental analysis, UV/Vis and NMR spectroscopy, as well as by single-crystal X-ray diffraction.
(© Wiley-VCH Verlag GmbH & Co. KGaA, 69451 Weinheim, Germany, 2005)

Introduction

Grignard compounds[1] are one of the most useful reagents in organic and organometallic chemistry.[2] Several decades after the discovery of these highly reactive species, it has turned out that the substitution of the halogen atom in alkyl- or arylmagnesium halides by other functional groups may strongly affect the reactivity, structure, and solution behavior of such organomagnesium compounds. The first alkylmagnesium amide, *i*PrMgN$Ph_2(Et_2O)_2$ was synthesized in 1967,[3a] and already two years later, X-ray diffraction data of e.g. {$[Me_2N(CH_2)_2MeN]MgMe\}_2$ were published.[3b] Recently, a series of heteroleptic alkyl- and alkynylmagnesium amides have been prepared.[3c] A new period in organomagnesium chemistry started with the use of tris(pyrazolyl)borato[4] and ketiminato ligands[5] which allowed the synthesis of monomeric, low-coordinate magnesiumalkyls.

We have reported on the successful synthesis of main group metal complexes with anionic or radical-anionic species of the 1,2-bis{(2,6-diisopropylphenyl)imino}acenaphthene (dpp-bian) ligand e.g. $\{[M]^+_n[(dpp\text{-}bian)]^{n-}(L)_x\}$ (M = Li, Na; n = 1–4; L = Et_2O, THF)[6a,6b] and $\{[M]^{2+}[(dpp\text{-}bian)]^{2-}(THF)_x\}$ (M = Mg, Ca, Ge).[6c,6d,6e] Up to this time the aryl-bian system was mainly used in transition metal chemistry,[7] but we have demonstrated that the magnesium complex (dpp-bian)Mg$(THF)_3$ is also a powerful reagent in organic synthesis.[6e,8a,8b] Thus, the electron transfer from this complex to Ph_2CO affords the pinacol coupling product, while its reaction with 9-(10H)-anthracenone yields the antryloxymagnesium derivative.[8a]

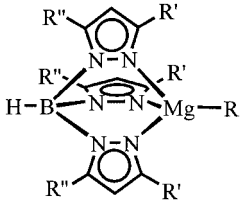

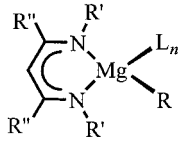

L = coordinating solvent; n = 0 or 1

R = alkyl or aryl; R' and R" = H or alkyl

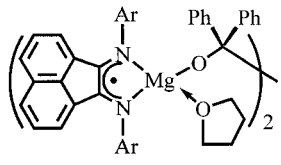

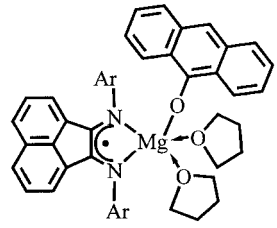

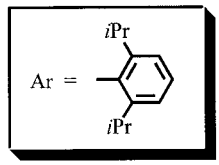

[a] G. A. Razuvaev Institute of Organometallic Chemistry of Russian Academy of Sciences,
Tropinina 49, 603950 Nizhny Novgorod GSP-445, Russia
Fax: +7-8312-661-497
E-mail: igorfed@imoc.sinn.ru
[b] Institut für Chemie der Technischen Universität Berlin,
Straße des 17. Juni 135, 10623 Berlin, Germany
Fax: +49-30-3142-2168
E-mail: schumann@chem.tu-berlin.de

A further interesting type of reaction of (dpp-bian)-$Mg(THF)_3$ is the oxidative addition of acidic substances such as phenylacetylene[8b] or enolizable ketones.[8b]

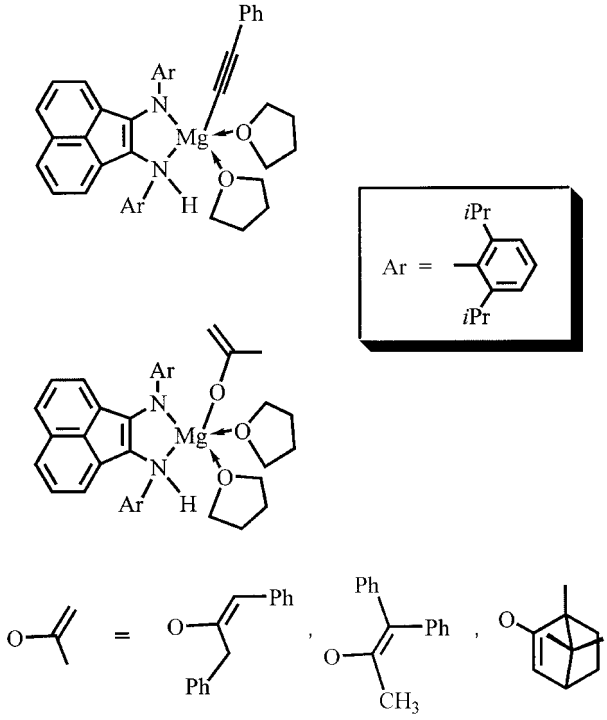

In this paper we report on the solvent induced radical elimination of the *isopropyl* group from (dpp-bian)Mg-*i*Pr-(Et_2O) (**1**) – a process that is possible due to the ability of the dpp-bian radical anion to be further reduced to the dianion.

Results and Discussion

Reaction of *i*PrMgCl with (dpp-bian)$^-$Na$^+$ and (dpp-bian)$^{2-}$Na$^+_2$ in Et_2O and Hexane

Exchange reactions of (dpp-bian)Na(Et_2O) with methyl- and ethylmagnesium bromide or trimethylsilylmethylmagnesium chloride in Et_2O produce cherry-red solutions from which the respective magnesiumalkyls, supported by the dpp-bian ligand, can be isolated as red crystalline substances in high yields.[8d] In contrast, the in situ reaction of (dpp-bian)Na(Et_2O) with one equiv. of *i*PrMgCl in Et_2O affords a green-brown solution from which yellowish-green crystals precipitate. As already indicated by the green color, which signals the presence of dpp-bian dianions, the expected (dpp-bian)Mg-*i*Pr(Et_2O) (**1**) containing (dpp-bian) radical anions is not formed. Accordingly, the isolated product (72% yield) proved to be (dpp-bian)Mg(Et_2O)$_2$ (**2**). The formation of **2** suggests that an intermediate formed in the course of the reaction obviously disproportionates with reduction of the dpp-bian radical anions to dianions and oxidation of the *isopropyl* carbanions to *isopropyl* radicals (Scheme 1). However, we succeeded in the synthesis of (dpp-bian)(Mg-*i*Pr)(Et_2O) (**1**), using hexane instead of Et_2O as the solvent in the reaction of (dpp-bian)Na with *i*PrMgCl. In this case, complex **1** can be isolated in yields up to 40% as blocklike, deep-red crystals along with 30 to 50% of **2** (Scheme 1).

In contrast to our expectations, **1** is stable in Et_2O, which means that an adduct of (dpp-bian)Na with *i*PrMgCl, formed initially in the reaction conducted in Et_2O, will disproportionate with elimination of *i*Pr radicals. But, according to ^{1}H NMR spectroscopic results, **1** disproportionates immediately with elimination of *i*Pr radicals when dissolved in THF.

The above suggested redox reaction and hence the elimination of *isopropyl* radicals should be excluded if the dpp-bian complex used in the reaction with *i*PrMgCl already contains the dpp-bian ligand in the dianionic form. Therefore, we reacted (dpp-bian)Na_2(Et_2O)$_2$ with two equiv. of *i*PrMgCl in Et_2O. The reaction results in an almost quantitative precipitation of **2** and, as a consequence, in the formation of Mg(*i*Pr)$_2$. Evaporation of the solvent from the entire reaction mixture followed by treatment of the remaining green solid components with toluene caused its dissolution at 70 °C yielding a deep-blue solution. Recrystallization of the solid remaining after removal of the toluene in vacuo, from hexane affords deep-blue crystals of (dpp-bian)(Mg-*i*Pr)$_2$(Et_2O) (**3**) with 60% yield (Scheme 2).

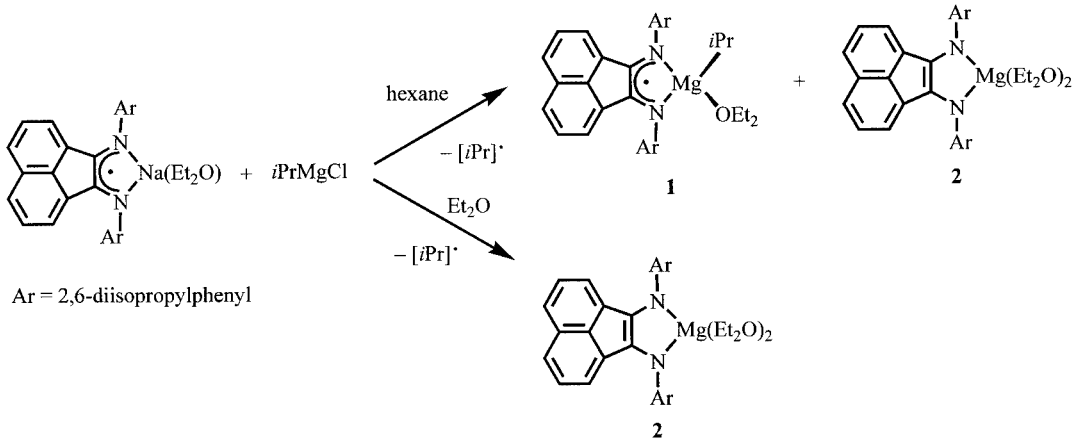

Scheme 1.

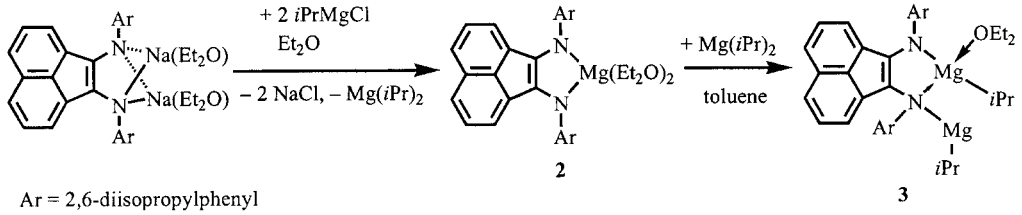

Scheme 2.

Since, according to X-ray crystal structure analysis, complex **3** consists of two *i*PrMg units, asymmetrically coordinated by the dpp-bian dianion, we have proved that the elimination of *i*Pr radicals is very much dependent on whether the coordinating ligand bound to magnesium can be reduced or not. At this point it should be noted, that magnesiumalkyls (alkyl = Me, *i*Pr, *t*Bu) supported by tris(pyrazolyl)borato[4] and ketiminato[5] ligands do not eliminate alkyl radicals because the monoanionic ketiminato and tris(pyrazolyl)borato ligands are not further to reduce.

Molecular Structures of 1, 2, and 3

The molecular structures of **1**, **2**, and **3** are depicted in Figure 1, Figure 2, and Figure 3, respectively. The crystal data collection and structure refinement data of **1**, **2**, and **3** are listed in Table 1, selected bond lengths and bond angles of the molecules are listed in Table 2. X-ray quality crystals were obtained from hexane (**1**) or toluene (**2**, **3**). The molecular structure of (dpp-bian)$Mg(Et_2O)_2$ (**2**) [Mg–N(1) 2.002, Mg–N(2) 2.003 Å] is very close to that of the analogous THF adduct (dpp-bian)$Mg(THF)_2$ [Mg–N(1) 1.994, Mg–N(2) 2.004 Å][6c] and will not be discussed in detail here.

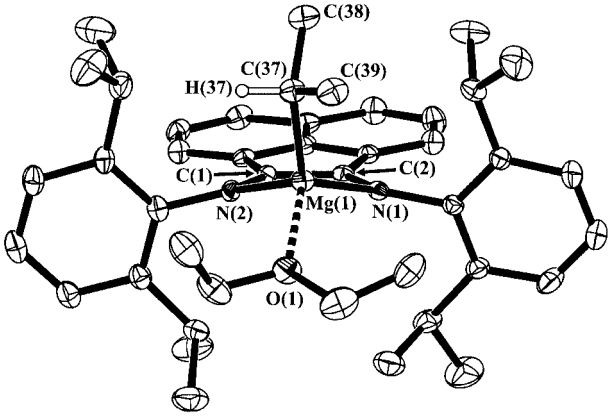

Figure 1. Molecular structure (ORTEP)[9] of **1**. The hydrogen atoms are omitted. Thermal ellipsoids are drawn at 30% probability level.

The unit cell of (dpp-bian)(Mg-*i*Pr)(Et_2O) (**1**) contains two independent molecules, the parameters of which are very much alike. Hence, the molecular structure of only one of them is depicted in Figure 1. Similar to (dpp-bian)$Mg(Et_2O)_2$ (**2**) the magnesium atom in **1** is four-coordinate. The radical anionic character of the dpp-bian ligand in **1** is indicated by the elongated Mg–N distances [Mg(1)–N(1) 2.120, Mg(1)–N(2) 2.103 Å] compared to those in **2** [Mg(1)–N(1) 2.002 and Mg(1)–N(2) 2.003 Å] containing the dianionic dpp-bian ligand. The Mg–O distance in **1** (2.051 Å) only slightly exceeds the Mg–O distances in **2** (2.009 and 2.049 Å). The Mg–C(37) bond length (2.145 Å) in **2** is comparable with the distance between Mg(2) and the methine

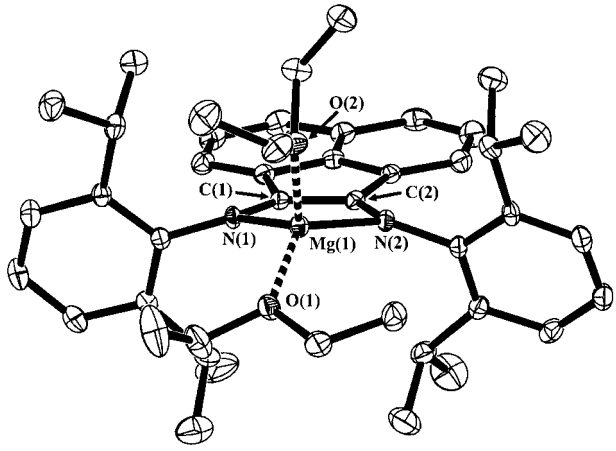

Figure 2. Molecular structure (ORTEP)[9] of **2**. The hydrogen atoms are omitted. Thermal ellipsoids are drawn at 30% probability level.

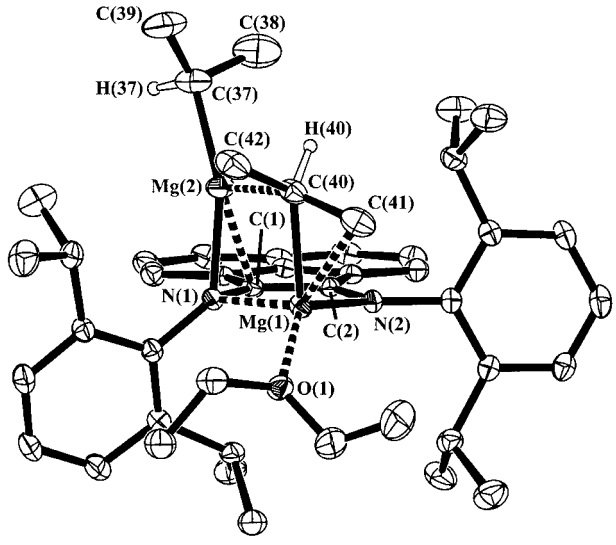

Figure 3. Molecular structure (ORTEP)[9] of **3**. The hydrogen atoms are omitted. Thermal ellipsoids are drawn at 30% probability level.

 © 2005 Wiley-VCH Verlag GmbH & Co. KGaA, Weinheim

carbon atom C(37) of the terminal isopropyl group in **3** (2.129 Å).

In (dpp-bian)(Mg-*i*Pr)$_2$(Et$_2$O) (**3**), the coordinating sites of the two magnesium atoms relative to the dpp-bian ligand are quite different. The Mg(1) atom lies almost perfectly in the plane formed by the diimine fragment, whereas Mg(2) is positioned above this plane. At first sight, the molecular structure of **3** looks like that of a complex of (dpp-bian)-Mg(Et$_2$O)$_2$ (**2**) and *i*Pr$_2$Mg with the magnesium atom of the *i*Pr$_2$Mg unit (Mg(2)) being coordinated by the lone electron pair of N(1). However, the Mg(2)–C(37) bond length (2.129 Å) is much shorter than the Mg(2)–C(40) distance (2.282 Å), which in turn is somewhat longer than the Mg(1)–C(40) bond (2.266 Å). Further, taking into account, that the Mg(1)–N(1) and Mg(1)–N(2) bonds differ in their length (2.101 and 2.030 Å, respectively) and that the Mg(2)–N(1) distance (2.070 Å) is relatively short, it can be concluded that the Mg(1)–N(1) bond is a coordinative bond whereas the Mg(1)–N(2) bond is a covalent amido bond.

Table 2. Selected bond lengths [Å] and angles [°] for complexes **1**, **2**, and **3**.

Compound	**1**	**2**	**3**
C(1)–N(1)	1.331(4)	1.383(4)	1.440(3)
C(1)–C(2)	1.437(5)	1.395(5)	1.406(3)
C(1)–Mg(1)	2.793(4)	2.680(4)	
C(40)–Mg(1)			2.266(3)
C(40)–Mg(2)			2.282(4)
C(41)–Mg(1)			2.534(4)
C(37)–Mg(2)			2.129(3)
C(1)–Mg(2)			2.524(3)
C(2)–N(2)	1.332(4)	1.401(4)	1.368(3)
C(2)–Mg(1)	2.792(4)	2.684(4)	
C(37)–Mg(1)	2.145(4)		
N(1)–Mg(1)	2.120(3)	2.002(3)	2.101(2)
N(1)–Mg(2)			2.070(2)
N(2)–Mg(1)	2.103(3)	2.004(3),	2.030(2)
O(1)–Mg(1)	2.052(3)	2.009(2)	2.007(2)
O(2)–Mg(1)		2.049(3)	
Mg(1)–Mg(2)			2.7524(12)
Mg(1)–C(40)–Mg(2)			74.48(10)
Mg(2)–N(1)–Mg(1)			82.57(8)
O(1)–Mg(1)–N(2)	104.81(12)	128.82(12)	130.17(8)
O(1)–Mg(1)–N(1)	115.94(12)	112.11(11)	108.78(8)
N(1)–Mg(1)–N(2)	81.95(12)	90.27(12)	89.29(9)
N(1)–Mg(1)–O(2)		116.27(12)	
N(2)–Mg(1)–O(2)		113.94(11)	
O(1)–Mg(1)–O(2)		96.93(11)	
O(1)–Mg(1)–C(37)	107.05(14)		
N(2)–Mg(1)–C(37)	118.53(14)		
N(1)–Mg(1)–C(37)	125.26(14)		

UV/Vis and NMR Spectroscopic Studies on Solutions of 1 and 3

The solution behavior of **1** and **3** is quite remarkable. Both compounds are soluble in hexane and toluene and are stable in these solutions for several days. As already mentioned above, compound **1** is also stable in Et$_2$O, but disproportionates in THF while dissolution of **3** in Et$_2$O as well as in THF causes immediate decomposition into (dpp-bian) Mg(Et$_2$O)$_2$ and *i*Pr$_2$Mg.

The electron absorption spectra of solutions of **1** in Et$_2$O and of **3** in hexane and Et$_2$O are presented in Figure 4. The absorption maximum at 520 nm in the UV/Vis spectrum of **1** indicates the presence of dpp-bian radical anions. The absorption maximum at 598 nm in the spectrum of **3** in hexane corresponds to the dianion of dpp-bian, and the

Table 1. Crystal data and structure refinement details for **1**, **2** and **3**

Compound	(dpp-bian)Mg-*i*Pr(Et$_2$O) (**1**)	(dpp-bian)Mg(Et$_2$O)$_2$ (**2**)	(dpp-bian)(Mg-*i*Pr)$_2$(Et$_2$O) (**3**)
Empirical formula	$C_{43}H_{57}MgN_2O$	$C_{51}H_{68}MgN_2O_2$	$C_{46}H_{64}Mg_2N_2O$
Formula mass	624.24	765.38	709.64
Temperature [K]	173(2)	173(2)	173(2)
Crystal system	monoclinic	monoclinic	monoclinic
Space group	$P2_1/n$	$P2_1/n$	$P2_1/n$
Unit-cell dimensions	a = 22.0060(2), b = 17.27160(10), c = 22.2811(2) Å, β = 114.2780(10)°	a = 12.2200(2), b = 19.95660(10), c = 18.6465(2) Å, β = 92.7850(10)°	a = 10.839(1), b = 19.5844(2), c = 19.814(1) Å, β = 93.9550(10)°
Volume [Å^3]	7719.62(11)	4541.94(9)	4195.89(4)
Z	8	4	4
Density (calculated) [g/cm^3]	1.105	1.119	1.123
Absorption coefficient [mm^{-1}]	0.079	0.079	0.093
$F_{(000)}$	2792	1664	1544
Crystal size [mm^3]	0.50×0.30×0.24	0.40×0.28×0.12	0.88×0.30×0.20
θ range for data collection, [°]	1.02 to 25.00	1.50 to 24.00	1.46 to 25.00
Index ranges	$-23 \le h \le 26$, $-20 \le k \le 20$, $-26 \le l \le 26$	$-11 \le h \le 13$, $-21 \le k \le 22$, $-17 \le l \le 21$	$-12 \le h \le 12$, $-23 \le k \le 23$, $-23 \le l \le 15$
Reflections collected	45336	24977	25382
Independent reflections	13575 [R(int) = 0.1492]	7108 [R(int) = 0.1115]	7378 [R(int) = 0.0825]
Max./min. transmission	0.994655/0.650449	0.965465/0.506961	0.980072/0.47254
Data/restraints/parameters	13575/2/872	7108/0/518	7378/4/489
Goodness-of-fit on F^2	0.955	0.999	1.024
Final R indices [$I > 2\sigma(I)$]	$R1$ = 0.0724, $wR2$ = 0.1341	$R1$ = 0.0657, $wR2$ = 0.1307	$R1$ = 0.0598, $wR2$ = 0.1476
R indices (all data)	$R1$ = 0.1821, $wR2$ = 0.1728	$R1$ = 0.1436, $wR2$ = 0.1634	$R1$ = 0.1044, $wR2$ = 0.1661
Largest diff. peak and hole [e/Å^3]	0.300 and –0.310	0.252 and –0.341	0.381 and –0.398

 © 2005 Wiley-VCH Verlag GmbH & Co. KGaA, Weinheim

absorption maximum at 737 nm in the spectrum of **3** in Et_2O indicates the formation of **2** by dismutation of **3** into (dpp-bian)Mg(Et_2O)$_2$ (**2**) and iPr_2Mg. The latter compound is colorless and invisible in the UV/Vis spectrum.

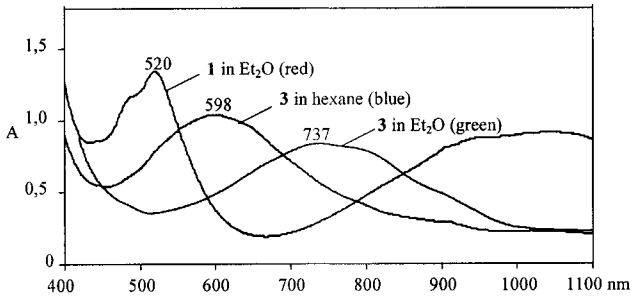

Figure 4. UV/Vis spectra of **1** and **3**.

The ^{1}H NMR spectrum of the blue solution of **3** in [D_8] toluene (Figure 5) reveals six septets, which are assigned to the methine protons of the *i*Pr substituents of the dpp-bian phenyl rings. The integrals of the two septets at δ = 3.69 and 3.54 ppm are five times higher than those of the other four very broad septets at 3.94, 3.80, 3.64 and 3.40 ppm and the overall integral of the six septets is twice as high as that of the multiplet at δ = 0.32 ppm, which is assigned to the methine protons of the isopropyl groups attached to the two magnesium atoms.

We conclude from these facts, that solutions of **3** in [D_8]-toluene contain two kinds of molecules differing in their structure. The major part consists of molecules in which Mg(2) is symmetrically positioned above the center of the metallocycle formed by the atoms C(1)–C(2)–N(1)–N(2)–Mg(1). Therefore, the signals of the two pairs of the *i*Pr methine protons substituting the phenyl rings and being situated above and below the diimine plane are different (3.69 and 3.54 ppm). A similar symmetrical structure has been found for (dpp-bian)(H)MgC≡CPh(THF)$_2$[8b] in THF solution, in which the cation H^+ is delocalized between the two nitrogen atoms. The minor part of the molecules, present in solution, possesses the structure established by crystal structure analysis, thus causing nonequivalence of all four phenyl ring substituting methine protons (3.94, 3.80, 3.64, and 3.40 ppm).

Going from toluene to THF as the solvent causes a dramatic change in the color of solution **3** (blue to green) as well as the appearance of the ^{1}H NMR spectrum (Figure 6).

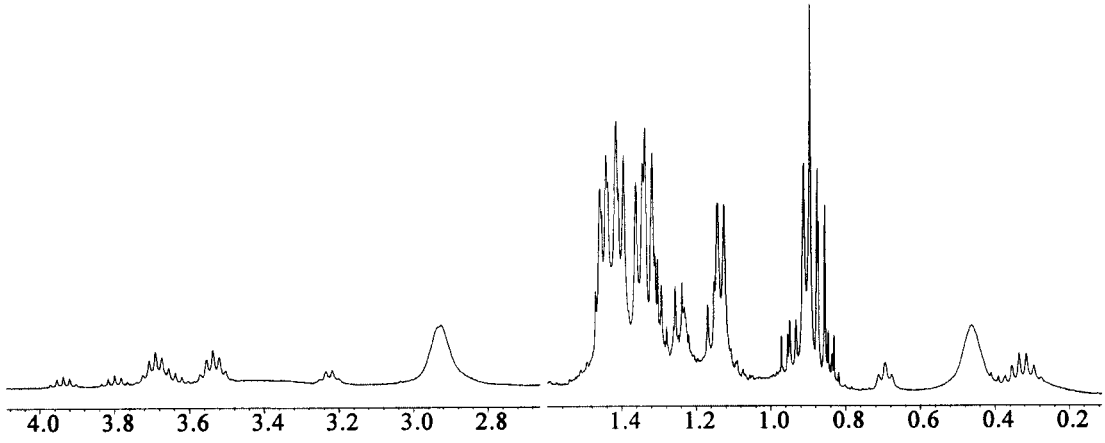

Figure 5. ^{1}H NMR spectrum of **3** in [D_8]toluene (400 MHz, 294 K). The aromatic region is omitted.

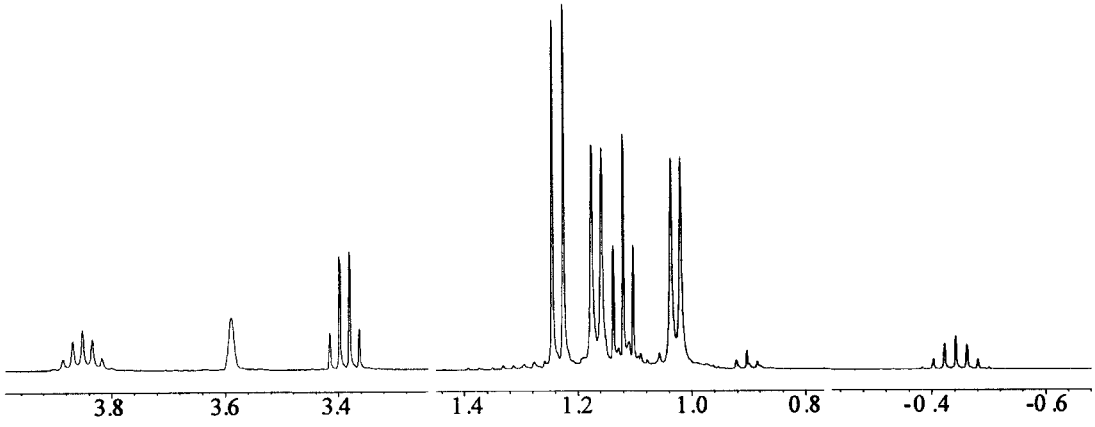

Figure 6. ^{1}H NMR spectrum of **3** in [D_8]THF (400 MHz, 294 K). The aromatic region is omitted.

 © 2005 Wiley-VCH Verlag GmbH & Co. KGaA, Weinheim

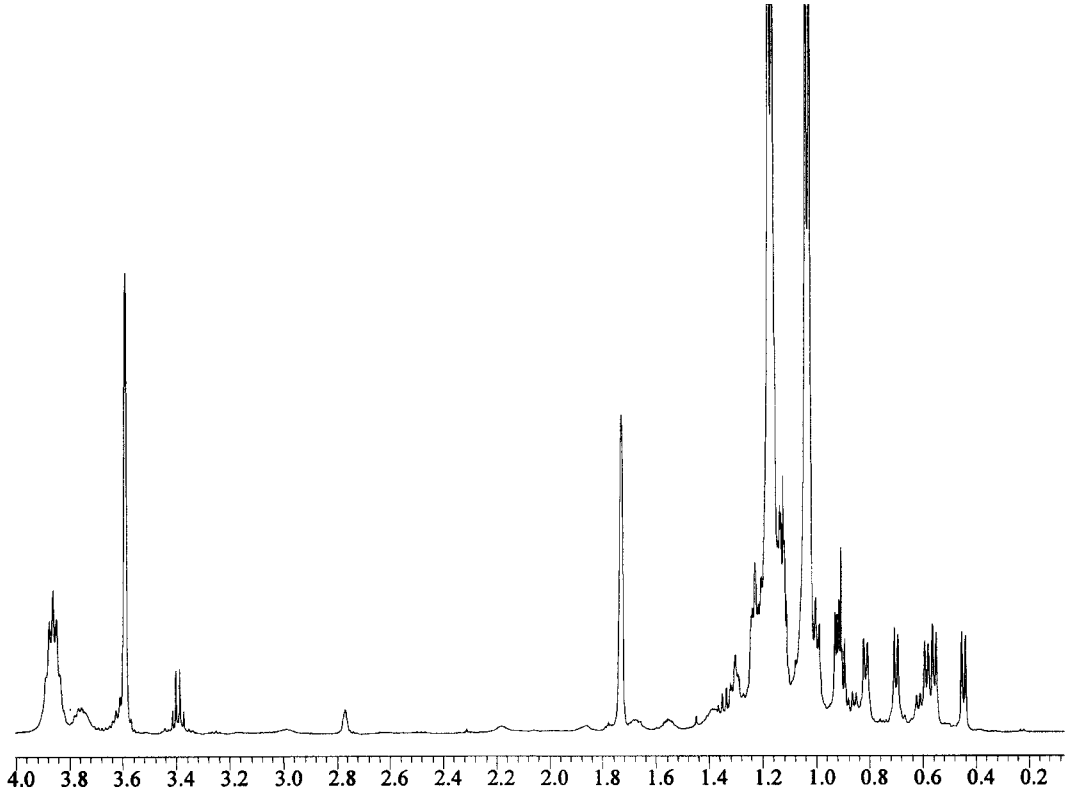

Figure 7. ^{1}H NMR spectrum of **1** in [D_8]THF (500 MHz, 294 K). The aromatic region is omitted.

The spectrum shows only one signal for the methine protons (δ = 3.86 ppm) and two doublets for the methyl protons of the isopropyl substituents of the phenyl rings (1.16 and 1.03 ppm). These signals are assigned to (dpp-bian)Mg(THF)$_3$.[6c] The high field septet at δ = –0.44 ppm and the doublet at δ = 1.23 ppm reflect the presence of *i*Pr$_2$Mg in the solution. Thus, complex **3** being dissolved in THF dissociates into *i*Pr$_2$Mg and (dpp-bian)Mg(THF)$_3$. The ^{1}H NMR spectrum of **1** in [D_{10}]Et_2O is not meaningful because of the paramagnetism of the complex, due to the presence of the dpp-bian radical anion. On dissolution of **1** in [D_8]THF the color of the solution changes within minutes from cherry-red to green and the ^{1}H NMR spectrum indicates the absence of paramagnetic species (Figure 7).

The septet at δ = 3.86 ppm and the doublets at δ = 1.17 and 1.03 ppm prove that diamagnetic (dpp-bian)Mg(THF)$_3$[6c] has been formed as a result of the elimination of *i*Pr radicals. As secondary products of the eliminated isopropyl radicals, the formation of propylene, propane, 2,3-dimethylbutane etc. is to be expected. Though certain amounts of these hydrocarbons are detected in the spectrum, the main reaction of the isopropyl radicals is the attack on THF molecules.

The ^{1}H-^{1}H COSY experiments revealed several cross peaks between pairs of doublets of low intensity (1.0–0.4 ppm) and broadened septets at relatively high fields (2.0–1.4 ppm). Thus, the doublets at 0.95 and 0.42, 0.81 and 0.59, and 0.70 and 0.55 ppm have cross peaks with septets at δ = 1.55, 1.67 and 1.39 ppm, respectively, and we assign these signals to *i*Pr substituted THF molecules. It is supposed that the coordinating strength of *i*Pr substituted THF molecules is somewhat higher than that of unsubstituted THF molecules and that the former will partly take the place of the THF ligands in (dpp-bian)Mg(THF)$_3$. The restricted rotation of the *i*Pr groups of magnesium coordinating *i*PrC_4H_7O ligands makes their methyl groups nonequivalent, thus giving rise to the doublets observed in the range 1.0–0.4 ppm.

Conclusions

The results of our investigations demonstrate that reductive elimination processes can be realized even with complexes of main group metals that are unable to change their oxidation state. This is accomplished when they are supported by the dpp-bian ligand, which may accept or deliver electrons.

Experimental Section

General Remarks: All manipulations were carried out in vacuo or under N_2 using Schlenk techniques. The solvents THF, Et_2O, hex-

 © 2005 Wiley-VCH Verlag GmbH & Co. KGaA, Weinheim

ane and toluene were distilled from sodium/benzophenone prior to use. The deuterated solvents [D_8]THF, and [D_8]toluene (Aldrich) were dried at ambient temperature over sodium/benzophenone and, just prior to use, condensed under vacuum into NMR tubes containing the compounds. The ^1H and ^{13}C NMR spectra were recorded with a Bruker ARX-400 and Bruker ARX-500 spectrometer. The UV/Vis spectra were recorded with a Perkin–Elmer Lambda 25 spectrometer.

(dpp-bian)(Mg-*i*Pr)(Et_2O) (1): A solution of (dpp-bian)Na was prepared by stirring dpp-bian (1.0 g, 2 mmol) and sodium (0.05 g, 2.17 mmol) in Et_2O (50 mL). After the sodium had dissolved completely, the solvent was evaporated in vacuo. Hexane (40 mL) was added to the remaining salt and the suspension that formed was stirred vigorously for 30 min. A 1 M solution of *i*PrMgCl (2.4 mL) in Et_2O was then added with vigorous stirring. Within a few seconds, the powdery (dpp-bian)Na dissolved and a cherry-red solution was formed which was filtered from NaCl and **2** and was then concentrated to 10 mL. Cooling of this solution to 0 °C yielded 0.47 g (37%) of **1** as deep-red crystals. M. p. 136–140 °C (decomp.). $C_{43}H_{57}MgN_2O$ (624.24): calcd. C 80.42, H 8.95; found C 80.33, H 8.96.

(dpp-bian)Mg(Et_2O)$_2$ (2): A 2 M solution of *i*PrMgCl in Et_2O (1.2 mL) was added to a stirred solution of (dpp-bian)Na prepared in situ from dpp-bian (1.0 g, 2 mmol) and sodium (0.05 g, 2.17 mmol) in Et_2O (50 mL). Within a few minutes the solution turned brown-green. The solvent was removed in vacuo and the solid dissolved in hot toluene. Cooling the solution to room temperature caused precipitation of **2** as yellowish-green crystals. Yield 1.1 g (72%) of **2**·(toluene). M. p. > 140 °C (decomp.). ^1H NMR spectrum (400 MHz, [D_8]THF, 20 °C): δ = 6.96 (d, 4 H, CH aromatic, ^3J = 7.3 Hz), 6.84 (t, 2 H, CH aromatic, ^3J = 7.3 Hz), 6.46 (d, 2 H, CH aromatic, ^3J = 6.8 Hz), 6.39 (dd, 2 H, CH aromatic, ^3J = 6.8 Hz), 5.37 (d, 2 H, CH aromatic, ^3J = 6.0 Hz), 3.86 (spt, 4 H, ^3J = 6.6 Hz), 3.34 (q, 8 H, *Et*$_2$*O*), 1.17 (d, 12 H, CH(CH_3)$_2$, ^3J = 6.8 Hz), 1.12 (t, 12 H, *Et*$_2$*O*), 1.03 (d, 12 H, CH(CH_3)$_2$, ^3J = 6.4 Hz). $C_{44}H_{60}MgN_2O_2$·(C_7H_8) (765.4): C 80.03, H 8.95; found C 79.29, H 8.51.

(dpp-bian)(Mg-*i*Pr)$_2$(Et_2O) (3): A 2 M solution of *i*PrMgCl in Et_2O (2.4 mL) was added to a stirred solution of (dpp-bian)Na_2 prepared in situ from dpp-bian (1.0 g, 2 mmol) and sodium (0.1 g, 4.34 mmol) in Et_2O (50 mL). The color of the solution turned green and within seconds yellowish-green **2** precipitated. The solvent was removed in vacuo and the residual solid was treated with 40 mL of toluene. On heating to 70 °C the solid dissolved completely and the solution turned deep blue. The toluene was removed in vacuo and the residue was dissolved in hot hexane (80 mL). From the filtered solution, deep blue almost black crystals of **3** precipitated at 0 °C. Yield 0.85 g (60%). M. p. > 153 °C (decomp.). ^1H NMR spectrum (400 MHz, [D_8]THF, 20 °C): δ = 6.96 (d, 4 H, CH aromatic, ^3J = 7.5 Hz), 6.84 (t, 2 H, CH aromatic, ^3J = 7.5 Hz), 6.44 (d, 2 H, CH aromatic, ^3J = 8.1 Hz), 6.38 (dd, 2 H, CH aromatic, ^3J = 8.1 Hz), 5.36 (d, 2 H, CH aromatic, ^3J = 6.8 Hz), 3.86 (spt, 4 H, ^3J = 6.8 Hz), 3.39 (q, 8 H, *Et*$_2$*O*), 1.23 (d, 12 H, CH(CH_3)$_2$, ^3J = 7.8 Hz, *iPr*$_2$*Mg*), 1.17 (d, 12 H, CH(CH_3)$_2$, ^3J = 7.0 Hz), 1.12 (t, 12 H, *Et*$_2$*O*), 1.03 (d, 12 H, CH(CH_3)$_2$, ^3J = 6.8 Hz), –0.44 (spt, 2 H, ^3J = 7.8 Hz, *iPr*$_2$*Mg*). Anal calcd. (%) for $C_{46}H_{64}Mg_2N_2O$ (709.64): C 77.86, H 9.09; found C 77.25, H 8.97.

X-ray Crystallographic Study of 1–3: The crystal data and details of data collection are given in Table 1. The data for **1**–**3** were collected on a SMART CCD (graphite-monochromated Mo-K_α radiation, ω-scan technique, λ = 0.71073 Å). The structures were solved by direct methods using SHELXS-97[10] and were refined on F^2 using all reflections with SHELXL-97.[11] SADABS[12] was used to perform area-detector scaling and absorption corrections. The geometrical aspects of the structures were analyzed by using the PLATON program.[21] CCDC-250026 (for **1**), -250027 (for **2**) and -250028 (for **3**) contain the supplementary crystallographic data for this paper. These data can be obtained free of charge from The Cambridge Crystallographic Data Centre via www.ccdc.cam.ac.uk/data_request/cif.

Acknowledgments

This work was supported by the Alexander von Humboldt Stiftung (ILF), Russian Foundation for Basic Research (Grant No. 03-03-32246) and the Deutsche Forschungsgemeinschaft.

[1] "Le magnésium en chimie organique": V. O. F. Grignard, *Bull. Soc. Chim. Fr.* **1913**, *13*, 1–37.

[2] a) Ch. Elschenbroich, A. Salzer, *Organometallics*, 2nd ed., Wiley-VCH, Weinheim, **1992**; b) *Handbook of Grignard Reagents* (Eds.: G. S. Silverman, P. E. Rakita), Marcel Dekker: New York, **1996**; c) Grignard Reagents – New Developments (Ed.: H. G. Richey, Jr.), Wiley, Chichester, **2000**; d) P. Knochel, W. Dohle, N. Gommermann, F. F. Kneisel, F. Kopp, T. Korn, I. Sapountzis, V. A. Vu, *Angew. Chem. Int. Ed.* **2003**, *42*, 4302–4320; e) J. F. Garst, M. P. Soriaga, *Coord. Chem. Rev.* **2004**, *248*, 623–652.

[3] a) J. F. Coates, D. J. Ridley, *Biochem. Soc. Trans.* **1967**, 56–59; b) V. R. Magnuson, G. D. Stucky, *Inorg. Chem.* **1969**, *8*, 1427–1433; c) K. C. Yang, C. C. Chang, J. Y. Huang, C. C. Lin, G. H. Lee, Y. Wang, M. Y. Chiang, *J. Organomet. Chem.* **2002**, *648*, 176–187.

[4] a) R. Han, A. Looney, G. Parkin, *J. Am. Chem. Soc.* **1989**, *111*, 7276–7278; b) R. Han, G. Parkin, *J. Am. Chem. Soc.* **1990**, *112*, 3662–3663; c) R. Han, G. Parkin, *Organometallics* **1991**, *10*, 1010–1020; d) R. Han, G. Parkin, *J. Am. Chem. Soc.* **1992**, *114*, 748–757; e) P. Ghosh, G. Parkin, *Inorg. Chem.* **1996**, *35*, 1429–1430; f) M. H. Chisholm, N. W. Eilerts, J. C. Huffman, S. S. Iyer, M. Pacold, K. Phomphari, *J. Am. Chem. Soc.* **2000**, *122*, 11845–11854; g) J. L. Kisko, T. Fillebeen, T. Hascall, G. Parkin, *J. Organomet. Chem.* **2000**, *596*, 22–26.

[5] a) C. F. Caro, P. B. Hitchcock, M. F. Lappert, *J. Chem. Soc. Chem. Commun.* **1999**, 1433–1434; b) V. C. Gibson, J. A. Segal, A. J. P. White, D. J. Williams, *J. Am. Chem. Soc.* **2000**, *122*, 7120–7121; c) P. P. Bailey, S. T. Liddle, C. A. Morrison, S. Parsons, *Angew. Chem. Int. Ed.* **2001**, *40*, 4463–4466; d) M. H. Chisholm, J. C. Huffman, K. Phomphari, *J. Chem. Soc. Dalton Trans.* **2001**, 222–224; e) J. Prust, K. Most, I. Müller, E. Alexopoulos, A. Stasch, I. Usón, H. W. Roesky, *Z. Anorg. Allg. Chem.* **2001**, *627*, 2032–2037; f) P. P. Bailey, R. A. Coxall, C. M. Dick, S. Fabre, S. Parsons, *Organometallics* **2001**, *20*, 798–801; g) A. P. Dove, V. C. Gibson, E. L. Marshall, A. J. P. White, D. J. Williams, *J. Chem. Soc. Chem. Commun.* **2002**, 1208–1209; h) A. P. Dove, V. C. Gibson, P. Hormnirun, E. L. Marshall, J. A. Segal, A. J. P. White, D. J. Williams, *J. Chem. Soc. Dalton Trans.* **2003**, 3088–3097.

[6] a) I. L. Fedushkin, A. A. Skatova, V. A. Chudakova, G. K. Fukin, *Angew. Chem. Int. Ed.* **2003**, *42*, 3294–3298; b) I. L. Fedushkin, A. A. Skatova, V. A. Chudakova, V. K. Cherkasov, G. K. Fukin, M. A. Lopatin, *Eur. J. Inorg. Chem.* **2004**, 388–393; c) I. L. Fedushkin, A. A. Skatova, V. A. Chudakova, G. K. Fukin, S. Dechert, H. Schumann, *Eur. J. Inorg. Chem.* **2003**, 3336–3346; d) I. L. Fedushkin, V. A. Chudakova, A. A. Skatova, N. M. Khvoinova, Yu. A. Kurskii, T. A. Glukhova, G. K. Fukin, S. Dechert, M. Hummert, H. Schumann, *Z. Anorg. Allg. Chem.* **2004**, *630*, 501–507; e) I. L. Fedushkin, A. A. Skatova, A. N. Lukoyanov, V. A. Chudakova, S. Dechert, M. Hummert, H. Schumann, *Russ. Chem. Bull.* in press; f) I. L. Fedushkin, N. M. Khvoinova, A. Yu. Baurin, G. K. Fukin,

 © 2005 Wiley-VCH Verlag GmbH & Co. KGaA, Weinheim

V. K. Cherkasov, M. P. Bubnov, *Inorg. Chem.* **2004**, *43*, 7807–7815; g) I. L. Fedushkin, A. A. Skatova, V. A. Chudakova, N. M. Khvoinova, A. Yu. Baurin, S. Dechert, M. Hummert, H. Schumann, *Organometallics* **2004**, *23* 3714–3718.

[7] a) M. W. van Laren, C. J. Elsevier, *Angew. Chem. Int. Ed.* **1999**, *38*, 3715–3717; b) R. van Belzen, H. Hoffmann, C. J. Elsevier, *Angew. Chem. Int. Ed. Engl.* **1997**, *36*, 1743–1745; c) G. A. Grasa, R. Singh, E. D. Stevens, S. P. Nolan, *J. Organomet. Chem.* **2003**, *687*, 269–279; d) A. Heumann, L. Giordano, A. Tenaglia, *Tetrahedron Letters* **2003**, *44*, 1515–1518; e) A. E. Cherian, E. B. Lobkovsky, G. W. Coates, *Chem. Commun.* **2003**, *20*, 2566–2567; f) M. D. Leatherman, S. A. Svejda, L. K. Johnson, M. Brookhart, *J. Am. Chem. Soc.* **2003**, *125*, 3068–3081; g) J. Kiesewetter, W. Kaminsky, *Chem. Eur. J.* **2003**, *9*, 1750–1758.

[8] a) I. L. Fedushkin, A. A. Skatova, V. K. Cherkasov, V. A. Chudakova, S. Dechert, M. Hummert, H. Schumann, *Chem. Eur. J.* **2003**, *9*, 5778–5783; b) I. L. Fedushkin, N. M. Khvoinova, A. A. Skatova, G. K. Fukin, *Angew. Chem. Int. Ed.* **2003**, *42*, 5223–5226; c) I. L. Fedushkin, A. A. Skatova, G. K. Fukin, M. Hummert, H. Schumann, *Eur. J. Inorg. Chem.*, in press; d) I. L. Fedushkin, A. A. Skatova, G. K. Fukin, M. Hummert, H. Schumann: these results will be published in a following paper.

[9] ORTEP3 for Windows: L. J. Farrugia, *J. Appl. Crystallogr.* **1997**, *30*, 565.

[10] G. M. Sheldrick, SHELXS-97 Program for the Solution of Crystal Structures; University of Göttingen, **1990**.

[11] G. M. Sheldrick, SHELXL-97 Program for the Refinement of Crystal Structures; University of Göttingen, **1997**.

[12] G. M. Sheldrick, SADABS Program for Empirical Absorption Correction of Area Detector Data; University of Göttingen, **1996**.

Received: November 23, 2004

 © 2005 Wiley-VCH Verlag GmbH & Co. KGaA, Weinheim

EPR, ENDOR, and DFT Studies on (β-Octahalo-*meso*-tetraarylporphyrin)copper Complexes: Characterization of the Metal($d_{x^2-y^2}$)−Porphyrin(a_{2u}) Orbital Interaction

Junlong Shao,[a] Erik Steene,[b] Brian M. Hoffman,*[a] and Abhik Ghosh*[b]

Keywords: Copper / Porphyrins / Density functional calculations / ENDOR spectroscopy / EPR spectroscopy

A series of planar (porphyrin)copper(II) complexes and their β-octahalogenated saddled derivatives have been studied by Electron Paramagnetic Resonance (EPR) spectroscopy, Electron Nuclear DOuble Resonance (ENDOR) spectroscopy, and Density Functional Theoretical (DFT) calculations. Both EPR/ENDOR spectroscopy and DFT calculations indicate a decrease in spin density on the central copper(II) ion and on the nitrogen atoms in the saddled compounds relative to the planar complexes. The EPR/ENDOR measurements show that the hyperfine coupling decreases by 12% on the nitrogen atoms and 9% on the copper ion, in going from planar (5,10,15,20-tetraphenylporphyrin)copper (Cu[TPP]) to saddled (2,3,7,8,12,13,17,18-octabromo-5,10,15,20-tetraphenylporphyrin)copper (Cu[Br_8TPP]). Accordingly, saddling results in a decrease in the spin density on the copper ion and on the nitrogen atoms. DFT calculations on Cu[Br_8TPP] yield spin populations of 42.4% on the copper ion, 9.9% on each nitrogen atom and 4.9% on each *meso* carbon atom, relative to DFT spin populations of 62, 10.2 and 0.3% on the copper ion, each nitrogen and each *meso* carbon atom, respectively, for porphinecopper (Cu[P]). These calculations further indicate that the decrease in spin density on the copper ion in the saddled complexes results from a saddling-induced Cu($d_{x^2-y^2}$)−porphyrin(a_{2u}) orbital overlap whereby some of the Cu spin density is delocalized onto the porphyrin ring. The decrease in nitrogen spin population with saddling appears to be a more subtle effect caused by a superposition of two opposing factors. Saddling decreases the overlap between the nitrogen lone pairs and the Cu $d_{x^2-y^2}$ orbital on one hand and enhances the overlap between the copper $d_{x^2-y^2}$ orbital and the porphyrin a_{2u} HOMO on the other.

(© Wiley-VCH Verlag GmbH & Co. KGaA, 69451 Weinheim, Germany, 2004)

Introduction

Nonplanar conformations of porphyrins and related cofactors occur as conserved features of several metalloproteins, and it has been proposed that this nonplanarity is actually of biological importance.[1] Nonplanar deformations such as ruffling and saddling (Figure 1) exert a strong influence on the chemical properties of metalloporphyrins and related molecules; these properties include electrochemical half-wave potentials,[2,3] electronic absorption[4,5] and vibrational spectra,[6−8] energetics of different spin states and electron density distributions as reflected in NMR and EPR spectra,[9−17] DFT calculations,[18] and reactivity toward axial ligands, etc.[9,10,12,13,15,16,18] Many of these effects arise from specific metal(d)−porphyrin(π) orbital interactions that are symmetry-forbidden in planar metalloporphyrins, but which become allowed as a result of nonplanar deformations. For example, ruffling switches on the metal(d_{xy})−porphyrin(a_{2u}) orbital interaction, where the d_{xy} orbital is a "t_{2g}-type" d orbital (in the notation of the O_h point group). Electronic spin density distributions reflecting this orbital interaction have been extensively studied by NMR spectroscopy for ruffled iron(III) porphyrins.[9−12,14,15] Saddling switches on the metal($d_{x^2-y^2}$)−porphyrin(a_{2u}) orbital interaction (as shown

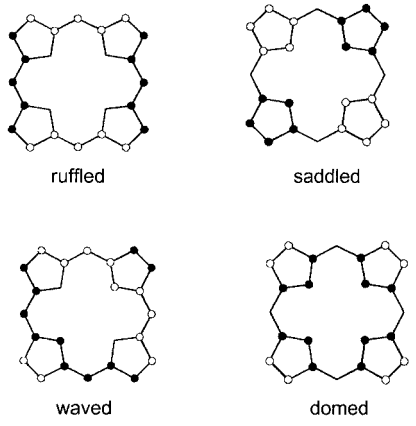

Figure 1. Nonplanar distortions of porphyrins; filled and open circles represent the displacement of the core atoms above and below the porphyrin mean plane

[a] Department of Chemistry, Northwestern University, Evanston, IL 60208, USA
[b] Institute of Chemistry, Faculty of Science, University of Tromsø, 9037 Tromsø, Norway

in Figure 2),[7,19] where the $d_{x^2-y^2}$ orbital is a "e_g-type" d orbital (in the notation of the O_h point group). NMR studies on saddled iron(III) porphyrins have also thrown light on this orbital interaction.[13,16] In this paper, we further[7,19] explore the consequences of the metal-$(d_{x^2-y^2})$−porphyrin(a_{2u}) orbital interaction by EPR and ENDOR spectroscopic studies and density functional theory (DFT) calculations on saddled Cu^{II} porphyrins. The results provide a clear picture of saddling-induced redistribution of unpaired electron density in (porphyrin)Cu^{II} compounds.

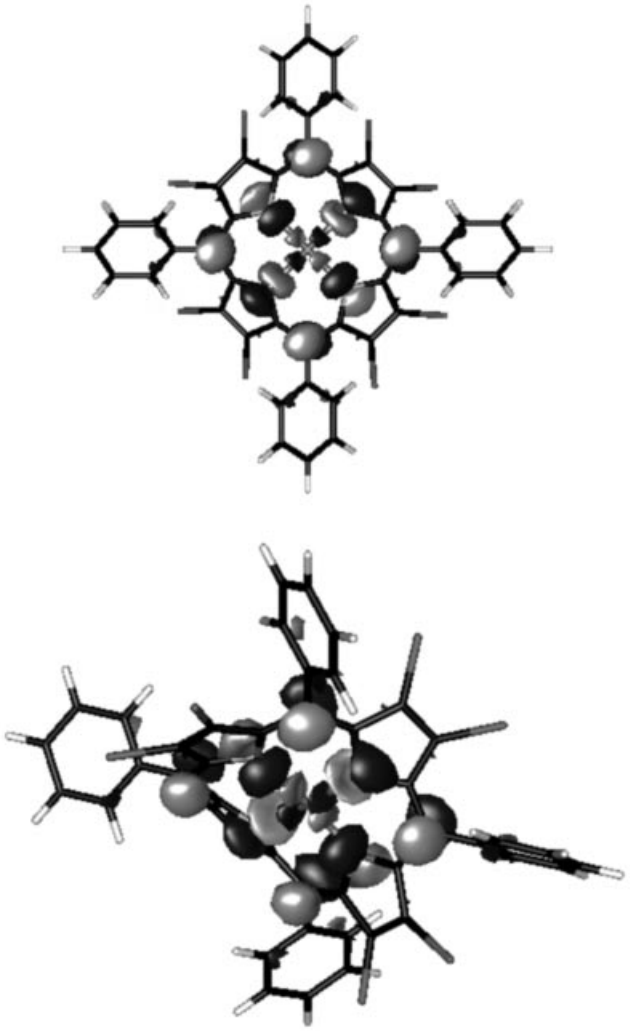

Figure 2. Two views of the singly occupied b_2 (a_{2u}-type) HOMO of Cu[Br_8TPP] (D_{2d})

Investigations of single crystal Cu[TPP] and Ag[TPP] with ^{14}N, ^{1}H, and metal ENDOR spectroscopy by Brown and Hoffman have yielded the complete hyperfine coupling and ^{14}N quadrupolar tensors of the two complexes.[20] Theoretical analyses of the spectra suggested metal spin populations of 0.62 for Cu[TPP] and 0.38 for Ag[TPP]. DFT(PW91/TZP) calculations on Cu^{II} porphine yielded a Cu spin population of 50.7%.[2] In this work, we present EPR and ^{14}N ENDOR measurements on the saddled Cu porphyrin derivatives Cu[Cl_8T(*p*-CF_3-P)P], Cu[Cl_8TPP], Cu[Br_8T(*p*-CF_3-P)P], and Cu[Br_8TPP] (Figure 3), and DFT(PW91/TZP) calculations on Cu[Br_8TPP], Cu[Br_8TPFPP], Cu[Cl_8TPP], and Cu[Cl_8TPFPP] (Figure 4).

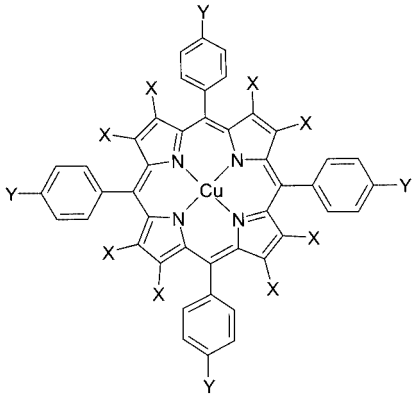

Figure 3. (Porphyrin)copper complexes studied by EPR and ENDOR spectroscopy: Cu[Cl_8T(*p*-CF_3-P)P] X = Cl, Y = CF_3; Cu[Cl_8TPP] X = Cl, Y = H; Cu[Br_8T(*p*-CF_3-P)P] X = Br, Y = CF_3; Cu[Br_8TPP] X = Br, Y = H

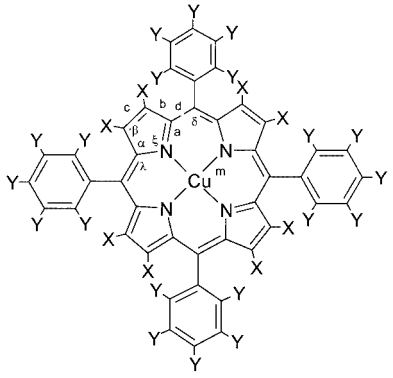

Figure 4. (Porphyrin)copper complexes studied by DFT calculations: Cu[Br_8TPP] X = Br, Y = H; Cu[Br_8TPFPP] X = Br, Y = F; Cu[Cl_8TPP] X = Cl, Y = H; Cu[Cl_8TPFPP] X = Cl, Y = F

Results

The EPR spectra of the (porphyrin)Cu complexes examined here are qualitatively similar to those of other tetragonal planar copper complexes. The $g_{\|}$ peaks partially overlap with the $g_{\perp}$ peaks. The $g_{\|}$, $g_{\perp}$ and $^{Cu}A_{\|}$ values were obtained by EPR simulations with WINEPR SimFornia (version 1.25, Bruker Analytische Messtechnik GmbH) and are listed in Table 1. In the EPR simulations, the nitrogen hyperfine tensors were taken from the ^{14}N ENDOR results. As can be seen from Table 1, the $g_{\|}$ (≈ 2.19) and $g_{\perp}$ (≈ 2.05) values of all the Cu porphyrin complexes examined are identical within experimental error. However, the absolute values of $^{Cu}A_{\|}$ differ significantly among the various compounds studied and decrease in the following order: Cu[T(*p*-CF_3-P)P] ≈ Cu[TPP] > Cu[Cl_8T(*p*-CF_3-P)P] ≈ Cu[Cl_8TPP] > Cu[Br_8T(*p*-CF_3-P)P] ≈ Cu[Br_8TPP]. These

 © 2005 Wiley-VCH Verlag GmbH & Co. KGaA, Weinheim

Table 1. ^{63,65}Cu and ^{14}N hyperfine couplings of (porphyrin)copper complexes[a,b]

	Cu[T(*p*-CF_3-P)P]	Cu[TPP]	Cu[Cl_8T(*p*-CF_3-P)P]	Cu[Cl_8TPP]	Cu[Br_8T(*p*-CF_3-P)P]	Cu[Br_8TPP]
$^{N}A_1$ [MHz]	44.5(2)	44.1(2)	43.2(2)	42.5(2)	40.0(2)	38.7(2)
$^{N}A_2$ [MHz]	42.8(3)	42.8(3)	40.5(5)	40.0(5)	38.5(3)	37.6(3)
$^{N}A_3$ [MHz]	55.0(3)	54.2(3)	53.8(5)	53.0(5)	51.5(3)	50.0(3)
$^{N}A_{iso}$	47.4(2)	47.0(2)	45.8(3)	45.2(3)	43.3(2)	42.1(2)
$^{Cu}A_{\|}$ [MHz]	−618(4)	−615(4)	−591(8)	−591(8)	−588(4)	−585(4)
$g_\perp$	2.04(1)	2.04(1)	2.06(2)	2.06(2)	2.06(1)	2.06(1)
$g_{\|}$	2.17(1)	2.18(1)	2.18(2)	2.21(2)	2.17(1)	2.18(1)

[a] $g_{\|} = 2.19 \pm 0.03$ and $g_\perp = 2.05 \pm 0.02$ for all complexes, within experimental error as obtained by X-band EPR spectroscopy at 77 K. ^{14}N ENDOR were taken at X-band and 4.2 K. [b] Simulations in all cases employed the quadrupole parameters found for Cu[TPP]: $P_1 = -0.3$, $P_2 = -0.6$, and $P_3 = 0.9$.[20]

results are compared with those of other (porphyrin)copper complexes in Table 2.

Table 2. Spin-Hamiltonian parameters of (porphyrin)copper(II) complexes[21]

Complex	Y[a]	X[a]	g	$g_\perp$	$^{Cu}A_{\|}$[b]	ρ_{Cu}[c]	$^{N}A_{iso}$[b]	Ref.
Cu[OEP]	H	CH_2CH_3	2.190	2.035	630	0.64	48	[21]
Cu[TMP]	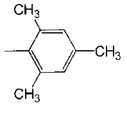	H	2.185	2.031	624	0.64	48	[21]
Cu[TOMePP]	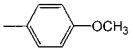	H	2.183	2.031	624	0.61	48	[21]
Cu[TF_5PP]	$-C_6F_5$	H	2.189	2.034	621	0.62	48	[21]
Cu[TCNPP]	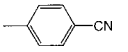	H	2.180	2.034	618	0.60	48	[21]
Cu[TCl_2PP]	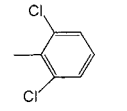	H	2.190	2.036	618	0.62	48	[21]
Cu[T(*p*-CF_3-P)P]	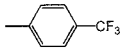	H	2.17	2.04	618	0.60	47.4	this work
Cu[TPP]	$-C_6H_5$	H	2.190	2.045	615	0.62	47.0	[20]
Cu[TMPyP(4)]	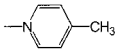	H	2.209	2.054	598	0.63	45.5	[26]
Cu[TMPyP(2)]	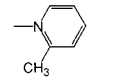	H	2.212	2.055	593	0.63	45.2	[26]
Cu[Cl_8T(*p*-CF_3-P)P]	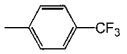	Cl	2.18	2.06	591	0.58	45.8	this work
Cu[Cl_8TPP]	$-C_6H_5$	Cl	2.21	2.06	591	0.63	45.2	this work
Cu[Br_8T(*p*-CF_3-P)P]	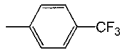	Br	2.17	2.06	588	0.55	43.3	this work
Cu[Br_8TPP]	$-C_6H_5$	Br	2.18	2.06	585	0.57	42.1	this work

[a] X and Y are functional groups marked in Figure 3. [b] Unit is in MHz. [c] Spin density on copper ion calculated with Equation (1).

Figure 5 displays the ^{14}N ENDOR spectra of Cu[TPP] and Cu[Br_8TPP] taken at $g_{\|}$ and $^{Cu}I_{-3/2}$, where only single-crystal-like spectra, derived from the molecules with their symmetry axis parallel to the static magnetic field, were collected for both samples. A significant hyperfine coupling shift (−5.4 MHz or −2.7 MHz peak-to-peak) between Cu[TPP] and Cu[Br_8TPP] was observed. Unlike the well-resolved double ENDOR spectra presented by Schweiger in his review on ENDOR studies of transition metal complexes,[22] the ^{14}N ENDOR spectra of Cu[T(*p*-CF_3-P)P] at both parallel and perpendicular field positions are unresolved, as shown in Figure 6. The well-matched simulation results (obtained with GENSIM, a locally developed software) are also presented in Figure 6. The sharp simulated peaks reveal the positions of the hyperfine couplings ($A_n/2$, $n = 1, 2, 3$), nuclear Zeeman splitting ($2\nu_N$, since $A_n/2 > \nu_N$) and quadrupole splitting ($3P_n$, $n = 1, 2, 3$). The quadrupole splitting was taken from previous work on Cu[TPP] and are assumed to differ only slightly in other complexes. Numerous hyperfine coupling values were attempted in the simulation to best match the simulated and experimental spectra. The $^{N}A_\perp$ at $g_{\|}$ (or $^{N}A_1$) values, unlike the others, were measured directly from the spectra. Unlike the single-crystal-like spectra taken at the parallel field position, there are two components, $^{N}A_2$ (or $^{N}A_\perp$) and $^{N}A_3$ (or $^{N}A_{\|}$), at the perpendicular field position. These originate from the Cu−N vectors perpendicular and parallel to the magnetic field, respectively. The full ^{14}N ENDOR spectra

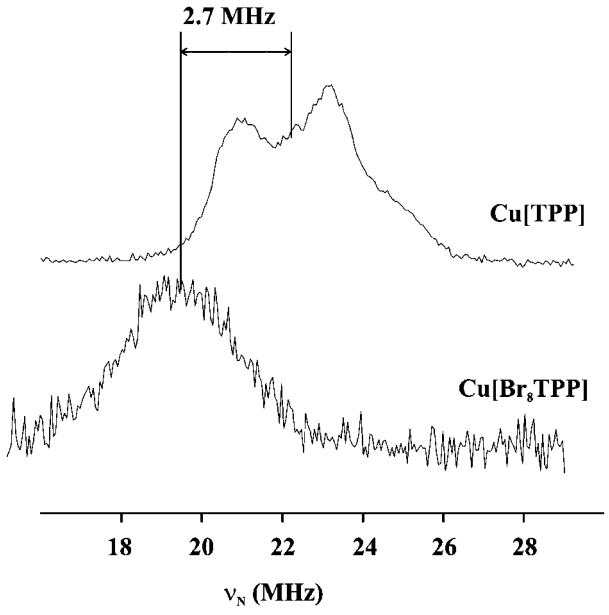

Figure 5. ^{14}N Davies ENDOR spectra of Cu[TPP] and Cu[Br_8TPP] at the parallel field position; the peak center ($A_1/2$) shift is marked between these two (porphyrin)copper complexes; experimental conditions: temperature, 4.2 K; microwave frequency, 9.715 GHz; magnetic field, 0.29 T; microwave pulse length, 32−16−32 ns; τ, 752 ns; RF pulse length, 20 ns; repetition rate, 20 ms; total points of each spectrum, 256; number of shots at each point, 300

 © 2005 Wiley-VCH Verlag GmbH & Co. KGaA, Weinheim

of the various (porphyrin)copper complexes studied at parallel and perpendicular field positions, along with the simulated spectra, are shown in Figures 7 and 8, respectively. The arrows mark the hyperfine splitting peak positions in the spectra and the ^{14}N hyperfine couplings are listed in Table 1. The ^{14}N hyperfine couplings decrease in the same order as $^{Cu}A_{\|}$, namely Cu[T(*p*-CF_3-P)P] ≈ Cu[TPP] > Cu[Cl_8T(*p*-CF_3-P)P] ≈ Cu[Cl_8TPP] > Cu[Br_8T(*p*-CF_3-P)P] ≈ Cu[Br_8TPP]. This sequence is also depicted in the bar graph of Figure 9, which again shows that hyperfine couplings decrease on going from the β-unsubstituted to the β-octachloro and β-octabromo complexes.

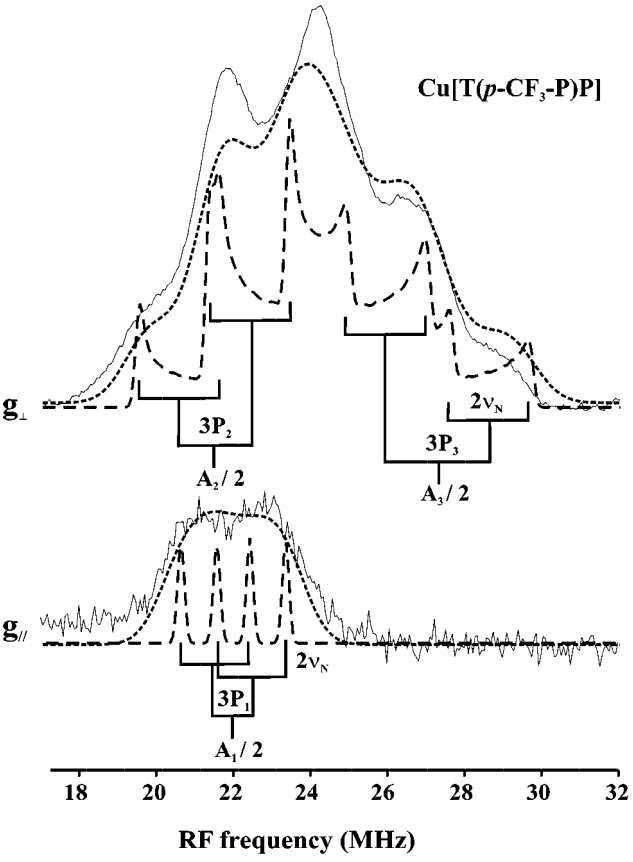

Figure 6. ^{14}N Davies ENDOR spectra of Cu[T(*p*-CF_3-P)P] at both parallel and perpendicular field positions; the solid lines are the experimental spectra, the dotted lines the simulated spectra, and the dashed lines the simulated lines with narrow line width to show the peak positions, which are marked in the graph; the experimental conditions are the same as in Figure 5

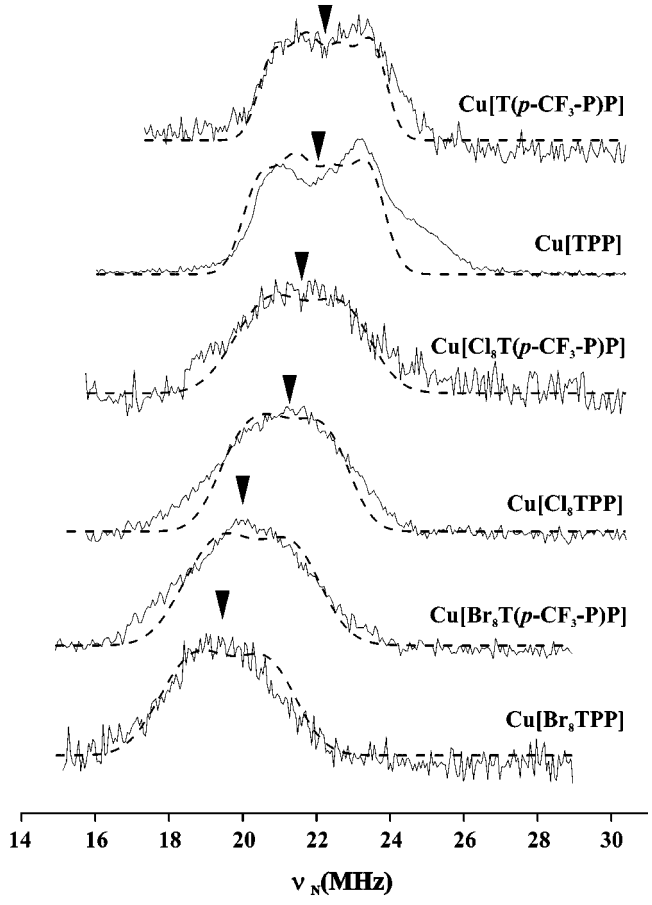

Figure 7. ^{14}N Davies ENDOR spectra of all the complexes at parallel field position; the arrows denote the centers of the hyperfine coupling peaks; the experimental conditions are the same as in Figure 5

Figure 10 shows the X-band (9 GHz, bottom) and K_a-band (35 GHz, top) proton and fluorine ENDOR spectra of Cu[Br_8T(*p*-CF_3-P)P]. With the X-band, the ^{19}F splittings, arising from the trifluoromethyl group, overlap at the low-frequency shoulder of the proton hyperfine coupling profile. With the K_a-band, the hyperfine couplings from the two components are completely separated. Since there are no β-protons on the pyrrole rings in this compound, the proton signals are assigned to phenyl ring protons. This indicates that proton hyperfine couplings originally assigned to pyrrole hydrogen atoms[20] are in fact associated with phenyl hydrogen atoms. Absent selective deuteration or chemical substitution, as done here, the distinction be-

Table 3. Selected optimized geometries [Å, °] and *z*-displacements [Å]

Compound	Distances					Angles					*z*-displacements		
	a	*b*	*c*	*d*	*m*	α	β	ξ	δ	γ	z_α	z_β	z_N
Cu^{II}[Br_8TPP]	1.378	1.449	1.373	1.411	2.023	108.6	107.2	108.1	121.3	122.6	0.449	1.231	0.066
Cu^{II}[Br_8TPFPP]	1.376	1.449	1.372	1.410	2.012	108.6	107.2	108.0	121.8	122.4	0.459	1.217	0.092
Cu^{II}[Cl_8TPP]	1.379	1.450	1.369	1.406	2.032	108.7	107.2	107.9	122.7	124.3	0.344	0.939	0.057
Cu^{II}[Cl_8TPFPP]	1.378	1.450	1.368	1.405	2.027	108.7	107.2	107.8	123.3	124.3	0.334	0.868	0.084

 © 2005 Wiley-VCH Verlag GmbH & Co. KGaA, Weinheim

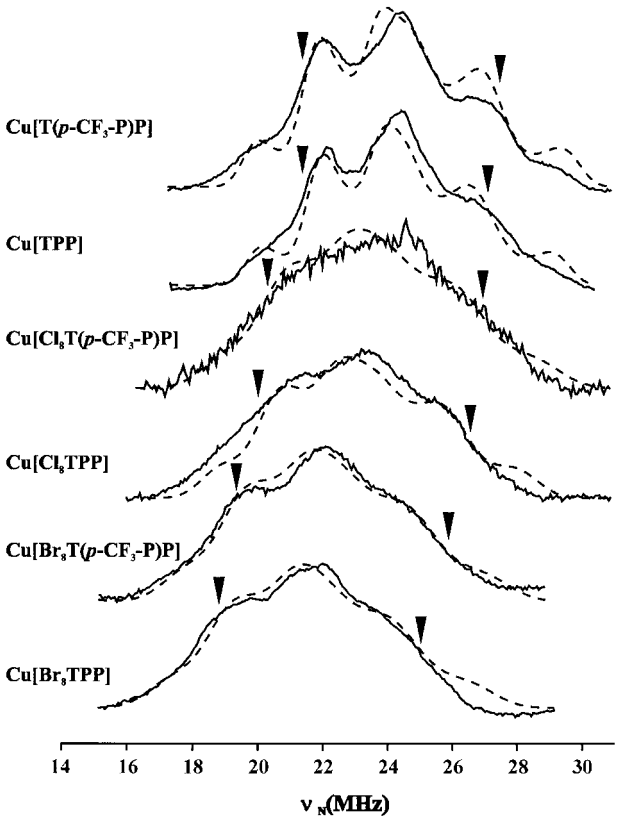

Figure 8. ^{14}N Davies ENDOR spectra of the whole complexes at the perpendicular field position; the arrows denote the centers of the hyperfine coupling peaks; the experimental conditions are the same as in Figure 5

tween these two types of proton at similar distances from Cu is very challenging.

Table 3, in conjunction with Figure 4, shows selected optimized geometry parameters for $Cu^{II}[Br_8TPP]$, $Cu^{II}[Br_8$-TPFPP], $Cu^{II}[Cl_8TPP]$, and $Cu^{II}[Cl_8TPFPP]$. As shown by the out-of-plane *z*-displacement of the β-carbon atoms (z_β), the β-octabrominated complexes are significantly more saddled than the corresponding β-octachlorinated analogues. However, analogous TPP and TPFPP derivatives are comparably saddled. The Cu−N bond lengths are approximately the same (2.01−2.03 Å) in all four molecules. Table 4 shows the calculated atomic spin populations for these four saddled porphyrins, and these data are discussed in the next section.

Table 4. Gross atomic spin populations

Compound	Metal	N_{porph}	C_α	C_β	C_{meso}
$Cu^{II}[Cl_8TPP]$	0.4465	0.1015	−0.0028	0.0039	0.0362
$Cu^{II}[Br_8TPP]$	0.4151	0.0983	−0.0105	0.0034	0.0531
$Cu^{II}[Cl_8TPFPP]$	0.4722	0.1025	−0.0029	0.0043	0.0212
$Cu^{II}[Br_8TPFPP]$	0.4388	0.0998	−0.0076	0.0040	0.0389

Discussion

Isotropic hyperfine coupling arises from the Fermi interaction and is proportional to the spin population on the observed nonmetal nucleus (nitrogen nuclei in this case) [Equation (1)],[23] where g_e is the electron *g* value, $g_{||}$ the par-

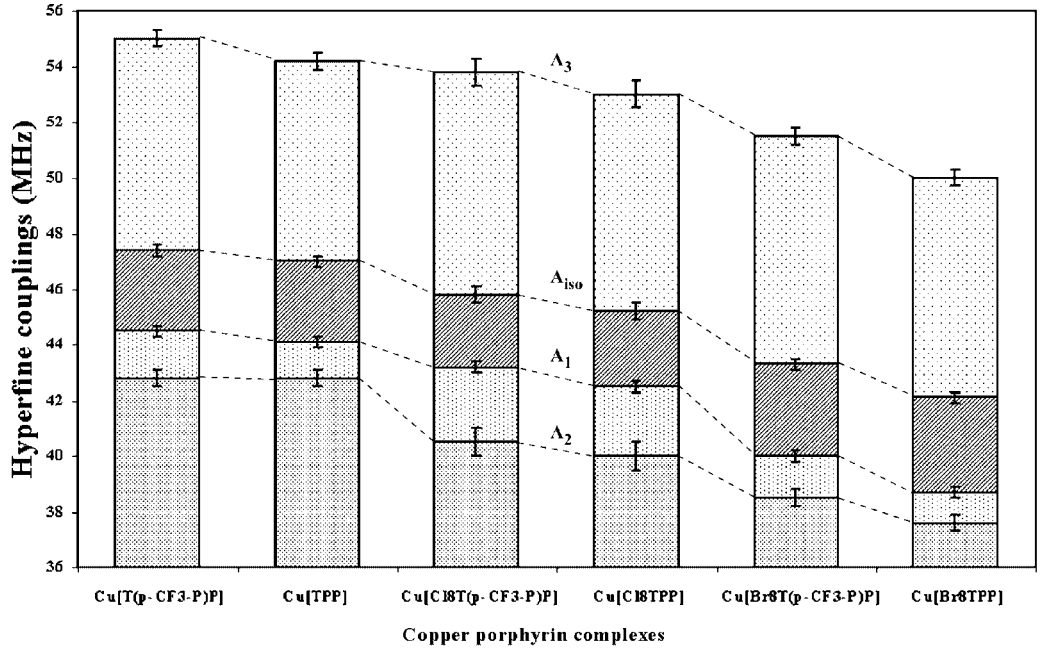

Figure 9. Bar graph of the hyperfine couplings of all (porphyrin)copper complexes

 © 2005 Wiley-VCH Verlag GmbH & Co. KGaA, Weinheim

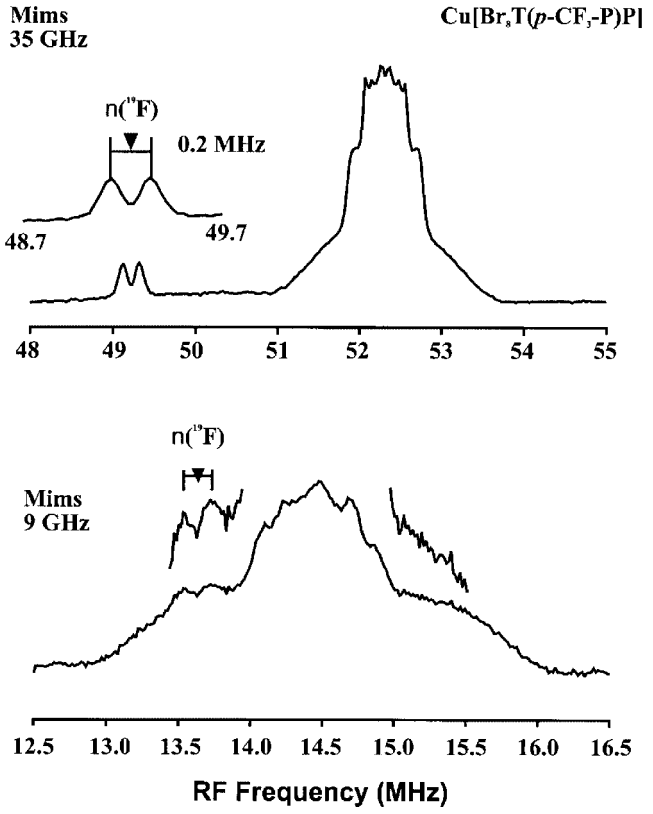

Figure 10. ^{1}H and ^{19}F Mims ENDOR spectra of Cu[Br_8T(*p*-CF_3-P)P] at 9 GHz and 35 GHz at the perpendicular field position; the arrows denote the center of the ^{19}F hyperfine coupling peaks; the experimental conditions at 9 GHz are: temperature, 4.2 K; microwave frequency, 9.720 GHz; magnetic field, 0.34 T; microwave pulse length, 16 ns; τ, 140 ns; RF pulse length, 10 ns; repetition rate, 30 ms; total points of each spectrum, 256; number of shots at each point, 300; the experimental conditions at 35 GHz are: temperature, 2 K; microwave frequency, 35.026 GHz; magnetic field, 1.234 T; microwave pulse length, 48 ns; τ, 300 ns; RF pulse length, 40 ns; repetition rate, 20 ms; total points of each spectrum, 256; number of shots at each point, 80

allel *g* value, $g_\perp$ the perpendicular *g* value, α_1^2 the odd electron populations on the copper ion, ignoring the interactions between copper $d_{x^2-y^2}$ and nitrogen 2s and 2p orbitals.

$$^{Cu}A_\parallel = {}^{Cu}A_1 = P[-\kappa - {}^4/_7\alpha_1{}^2 - {}^3/_7(g_e - g_\perp) - (g_e - g_\parallel)] \quad (1)$$

The parameter *P* is proportional to the radial expectation value of the square of the $d_{x^2-y^2}$ orbital amplitude of the metal, and κ is an empirical constant that describes the inner-shell polarization by the d-shell vacancy and quantifies the isotropic metal hyperfine coupling.[24] By taking $P = 0.037$ and[25] $\kappa = 0.406$ [adjusted value to obtain a spin density of 0.624[20] on the copper ion in Cu[TPP] with Equation (1)], we can empirically estimate the spin populations on all (porphyrin)copper complexes examined. Table 2 summarizes the EPR data for a wide range of (porphyrin)copper complexes, including the empirically estimated copper spin populations. The main conclusions based on Tables 1 and 2 are as follows.

As mentioned above, both the $^{Cu}A_\parallel$ and $^{14}N_{iso}$ hyperfine couplings decrease in the following order: Cu[T(*p*-CF_3-P)P] ≈ Cu[TPP] > Cu[Cl_8T(*p*-CF_3-P)P] ≈ Cu[Cl_8TPP] > Cu[Br_8T(*p*-CF_3-P)P] ≈ Cu[Br_8TPP] (Table 1). In other words, Table 1 indicates that the $^{Cu}A_\parallel$ hyperfine couplings of the saddled complexes are generally considerably lower than those of their planar counterparts and are comparable only to those observed for highly electron-deficient *meso*-tetrakis(pyridiniumyl)porphyrin derivatives, Cu[TMPyP][26] (Table 2). This indicates that the spin populations on the Cu and N atoms decrease with increasing saddling of the macrocycle. The decrease in the Cu spin population is understandable as a simple consequence of the saddling-induced Cu($d_{x^2-y^2}$)−porphyrin(a_{2u}) orbital overlap whereby some of the Cu spin density is delocalized onto the porphyrin ring. However, we believe that the decrease in nitrogen spin population with saddling reflects two opposing factors. On the one hand, saddling inhibits contact between the nitrogen lone-pairs and the Cu $d_{x^2-y^2}$ orbital. On the other hand, saddling encourages and enhances the overlap between the copper $d_{x^2-y^2}$ and the porphyrin a_{2u} HOMO. The combined result of these two factors is a certain decrease in spin population on the nitrogen atoms.

The decrease in spin density on going from the β-unsubstituted to the β-octahalogenated complexes, as measured by the $^{Cu}A_\parallel$ and $^{14}N_{iso}$ hyperfine couplings, is consistent with DFT calculations showing atomic spin populations for Cu^{II}[Br_8TPP]: Cu 42.4, N 9.9 and C_{meso} 4.9%. This can be compared with (porphine)Cu^{II}: Cu 50.7, N 10.8 and C_{meso} 0.2%. The DFT calculations indicate that the loss of spin density on the copper and nitrogen atoms in the saddled complexes is accompanied by an increase in the spin density on C_{meso}. This effect can potentially be explored by EPR and ENDOR analysis of $^{13}C_{meso}$ analogues of the relevant complexes, but such analyses have not yet been completed.

Conclusion

In summary, we have studied a number of (β-octahalo-*meso*-tetraarylporphyrins)copper(II) complexes by using EPR/ENDOR spectroscopy and DFT calculations to better understand the consequences of the saddling-induced metal($d_{x^2-y^2}$)−porphyrin(a_{2u}) orbital overlap on the electron distribution of (porphyrin)copper complexes. Both EPR/ENDOR spectroscopy and DFT calculations show that the spin populations on the central copper ion and on the nitrogen atoms are significantly decreased in these saddled complexes relative to their planar counterparts. The diminished spin density on the copper ion is directly attributable to the saddling-induced Cu($d_{x^2-y^2}$)−porphyrin(a_{2u}) orbital overlap whereby Cu spin density is delocalized onto the porphyrin ring. The decrease in nitrogen spin population with saddling appears to be a more subtle effect caused by a superposition of two opposing factors. Saddling decreases the overlap between the nitrogen lone pairs and the Cu $d_{x^2-y^2}$ orbital on one hand and enhances the

 © 2005 Wiley-VCH Verlag GmbH & Co. KGaA, Weinheim

overlap between the copper $d_{x^2-y^2}$ orbital and the porphyrin a_{2u} HOMO on the other.

Experimental Section

The β-octabrominated (porphyrin)copper complexes studied here have been described previously.[3] The β-octachlorinated (porphyrin)copper complexes were prepared using a slightly modified version of the procedure described by Dolphin and co-workers[27] for β-octachlorination of nickel porphyrins: [tetrakis(*para*-X-phenyl)-porphyrin]Cu^{II} (X = H or CF_3) (0.3 mmol) and *N*-chlorosuccinimide (3.6 mmol, 12 equiv.) were dissolved in *o*-dichlorobenzene and heated to 140 °C. The reaction was monitored by UV/Vis spectroscopy and more *N*-chlorosuccinimide was added during the course of the reaction to ensure complete conversion into the β-octachlorinated product (the Soret absorbance changes from ca. 415 to ca. 436 nm). The total reaction time was approximately 24 h. The resulting crude product was purified by flash chromatography on silica gel with dichloromethane/*n*-hexane (2:1) as eluent and further purified on preparative (20 × 20 cm) TLC plates (silica, 0.5 mm thick) with dichloromethane/*n*-hexane (2:1) as eluent. EPR and ENDOR samples were prepared by dissolving the complexes in a mixed solvent consisting of 40% chloroform (99.9%, Aldrich) and 60% toluene (99.8+%, Aldrich) by volume. The samples were frozen in liquid nitrogen. Powder samples of the complexes were prepared by mixing each complex with NiTPP (which is EPR-silent) in a 1:100 ratio in toluene solution with subsequent evaporation of the toluene. In the case of the rather insoluble Cu[Cl_8T(*p*-CF_3-P)P] complex, a solid sample of this complex was diluted with Ni[Cl_8T(*p*-CF_3-P)P] to generate a powder sample suitable for EPR measurements. In general, the powder samples yielded spectra that were identical to the frozen solution spectra, except that the former exhibited slightly higher resolution. EPR spectra were obtained on a Varian E-4 EPR spectrometer at 77 K. Two home-built X-band and Q-band pulsed ENDOR spectrometers, which have been described elsewhere,[28,29] were used to collect the ENDOR spectra at 4.2 K and 2 K, respectively. DFT calculations on selected saddled (porphyrin)copper complexes (Figure 4) were carried out using Slater-type valence triple-ζ with polarization basis sets, the VWN local functional, Perdew−Wang 1991 gradient corrections, a spin-unrestricted formalism, a fine mesh for numerical integration of matrix elements, full geometry optimizations, and the ADF program system.[30,31]

Acknowledgments

This work was supported by the VISTA program of Statoil and the Norwegian Research Council (E. S. and A. G.) and the NSF (J. S. and B. M. H.). We thank Prof. Joshua Telser, Roosevelt University, for helpful comments on the manuscript.

[1] J. A. Shelnutt, X.-Z. Song, J.-G. Ma, S.-L. Jia, W. Jentzen, C. J. Medforth, *Chem. Soc., Rev.* **1998**, *27*, 31.
[2] F. D'Souza, M. E. Zandler, P. Tagliatesta, Z. P. Ou, J. G. Shao, E. Van Caemelbecke, K. M. Kadish, *Inorg. Chem.* **1998**, *37*, 4567.
[3] A. Ghosh, I. Halvorsen, H. J. Nilsen, E. Steene, T. Wondimagegn, R. Lie, E. van Caemelbecke, N. Guo, Z. Ou, K. M. Kadish, *J. Phys. Chem. B* **2001**, *105*, 8120.
[4] C. M. Drain, S. Gentemann, J. A. Roberts, N. Y. Nelson, C. J. Medforth, S. L. Jia, M. C. Simpson, K. M. Smith, J. Fajer, J. A. Shelnutt, D. Holten, *J. Am. Chem. Soc.* **1998**, *120*, 3781.
[5] S. Gentemann, C. J. Medforth, T. P. Forsyth, D. J. Nurco, K. M. Smith, J. Fajer, D. Holten, *J. Am. Chem. Soc.* **1994**, *116*, 7363.
[6] L. D. Sparks, K. K. Anderson, C. J. Medforth, K. M. Smith, J. A. Shelnutt, *Inorg. Chem.* **1994**, *33*, 2297.
[7] J. A. Shelnutt, C. J. Medforth, M. D. Berber, K. M. Barkigia, K. M. Smith, *J. Am. Chem. Soc.* **1991**, *113*, 4077.
[8] I. Halvorsen, E. Steene, A. Ghosh, *J. Porphyrins Phthalocyanines* **2001**, *5*, 721.
[9] G. Simonneaux, V. Schuenemann, C. Morice, L. Carel, L. Toupet, H. Winkler, A. X. Trautwein, F. A. Walker, *J. Am. Chem. Soc.* **2000**, *122*, 4366.
[10] F. A. Walker, H. Nasri, I. Turowska-Tyrk, K. Mohanrao, C. T. Watson, N. V. Shokhirev, P. G. Debrunner, W. R. Scheidt, *J. Am. Chem. Soc.* **1996**, *118*, 12109.
[11] M. R. Cheesman, F. A. Walker, *J. Am. Chem. Soc.* **1996**, *118*, 7373.
[12] M. K. Safo, G. P. Gupta, C. T. Watson, U. Simonis, F. A. Walker, W. R. Scheidt, *J. Am. Chem. Soc.* **1992**, *114*, 7066.
[13] H. Ogura, L. Yatsunyk, C. J. Medforth, K. M. Smith, K. M. Barkigia, M. W. Renner, D. Melamed, F. A. Walker, *J. Am. Chem. Soc.* **2001**, *123*, 6564.
[14] T. Ikeue, Y. Ohgo, T. Saitoh, M. Nakamura, H. Fujii, M. Yokoyama, *J. Am. Chem. Soc.* **2000**, *122*, 4068.
[15] M. Nakamura, T. Ikeue, H. Fujii, T. Yoshimura, *J. Am. Chem. Soc.* **1997**, *119*, 6284.
[16] T. Ikeue, Y. Ohgo, T. Yamaguchi, M. Takahashi, M. Takeda, M. Nakamura, *Angew. Chem. Int. Ed.* **2001**, *40*, 2617.
[17] M. W. Renner, K. M. Barkigia, Y. Zhang, C. J. Medforth, K. M. Smith, J. Fajer, *J. Am. Chem. Soc.* **1994**, *116*, 8582.
[18] A. Ghosh, E. Gonzalez, T. Vangberg, *J. Phys. Chem. B* **1999**, *103*, 1363.
[19] H. S. Song, C. A. Reed, W. R. Scheidt, *J. Am. Chem. Soc.* **1989**, *111*, 6865.
[20] T. G. Brown, B. M. Hoffman, *Mole. Phys.* **1980**, *39*, 1073.
[21] K. L. Cunningham, K. M. McNett, R. A. Pierce, K. A. Davis, H. H. Harris, D. M. Falck, D. R. McMillin, *Inorg. Chem.* **1997**, *36*, 608.
[22] A. Schweiger, *Angew. Chem. Int. Ed. Engl.* **1991**, *30*, 265−292.
[23] A. H. Maki, B. R. McGarvey, *J. Chem. Phys.* **1958**, *29*, 31.
[24] B. R. McGarvey, *J. Phys. Chem.* **1967**, *71*, 51.
[25] J. M. Assour, *J. Chem. Phys.* **1965**, *43*, 2477.
[26] S. P. Greiner, D. L. Rowlands, R. W. Kreilick, *J. Phys. Chem.* **1992**, *96*, 9132.
[27] D. Dolphin, T. Nakano, T. K. Kirk, T. P. Wijesekera, R. L. Farrell, T. E. Malone, United States Patent, Patent Number 4,892,941, January 9, **1990**.
[28] B. M. Hoffman, V. J. DeRose, J.-L. Ong, C. E. Davoust, *J. Magn. Reson. Ser. A* **1994**, *110*, 52.
[29] C. E. Davoust, P. E. Doan, B. M. Hoffman, *J. Mag. Reson.* **1996**, *119*, 38.
[30] G. T. Velde, F. M. Bickelhaupt, E. J. Baerends, C. F. Guerra, S. J. A. Van Gisbergen, J. G. Snijders, T. Ziegler, *J. Comput. Chem.* **2001**, *22*, 931.
[31] S. J. A. Van Gisbergen, J. G. Snijders, E. J. Baerends, *Comput. Phys. Commun.* **1999**, *118*, 119.

Received May 4, 2004

 © 2005 Wiley-VCH Verlag GmbH & Co. KGaA, Weinheim

SHORT COMMUNICATIONS

1643 **D. Zhang, X. Song, R. Zhang, M. Zhang, F. Liu***

Preparation and Characterization of Ag@TiO_2 Core-Shell Nanoparticles in Water-in-Oil Emulsions

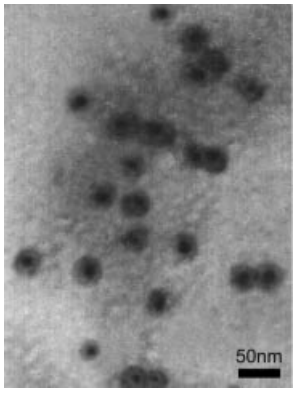

Keywords: Silver / Titanium / Core-shell nanoparticles / Water-in-oil emulsion / Surface photovoltaic spectroscopy

1649 **C. Ma,* Y. Han, R. Zhang, D. Wang**

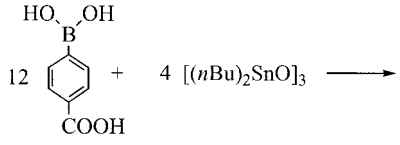

Novel Supramolecular Frameworks Self-Assembled from a Two-Dimensional Polymeric Network: Synthesis and Crystal Structure of a Macrocyclic Organotin(IV) Complex

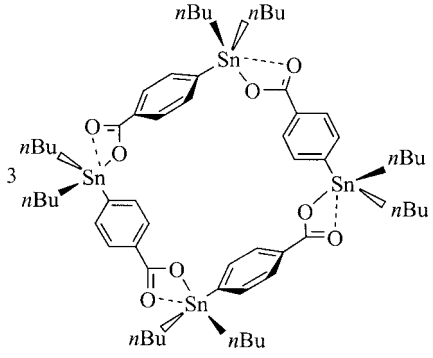

Keywords: Polymers / Self-assembly / Supramolecular chemistry / Tin

1653 **S. V. Krivovichev,* V. Kahlenberg, E. Y. Avdontseva, E. Mersdorf, R. Kaindl**

Self-Assembly of Protonated 1,12-Dodecanediamine Molecules and Strongly Undulated Uranyl Selenate Sheets in the Structure of Amine-Templated Uranyl Selenate: $(H_3O)_2[C_{12}H_{30}N_2]_3[(UO_2)_4(SeO_4)_8](H_2O)_5$

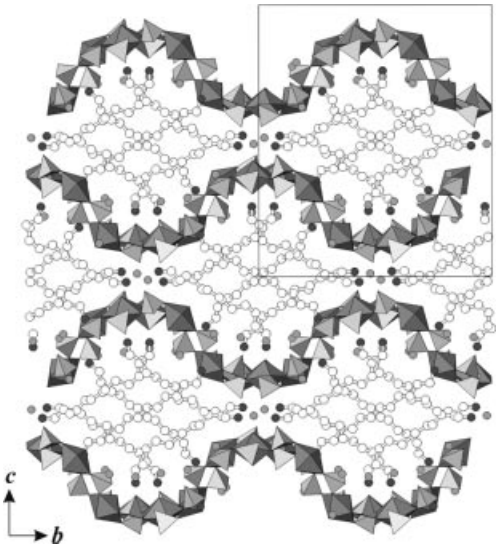

Keywords: Host-guest systems / Layered compounds / Selenium / Self-assembly / Uranium

 © 2005 Wiley-VCH Verlag GmbH & Co. KGaA, Weinheim

1657 **D. Carmona,* J. Ferrer, M. Lorenzo, F. J. Lahoz, I. T. Dobrinovitch, L. A. Oro**

Synthesis and Characterisation of New Iridium Complexes with the (4*S*)-2-[2-(Diphenylphosphanyl)phenyl]-4-isopropyl-1,3-oxazoline Ligand That Catalyse Asymmetric Michael Reactions

Keywords: Iridium / Phosphanyloxazolines / Metal enolates / Michael addition

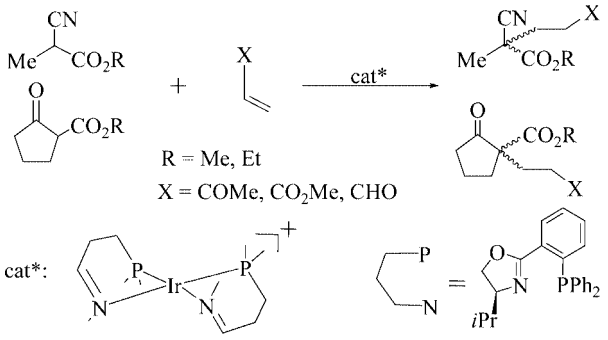

1665 **H.-Y. Wang, G.-X. Jin***

Highly Active Neutral Nickel(II) Complexes Bearing P,N-Chelate Ligands: Synthesis, Characterization and Their Application to Addition Polymerization of Norbornene

Keywords: Nickel / P,N-chelate ligands / Homogeneous catalysts / Polymerization / Polynorbornene

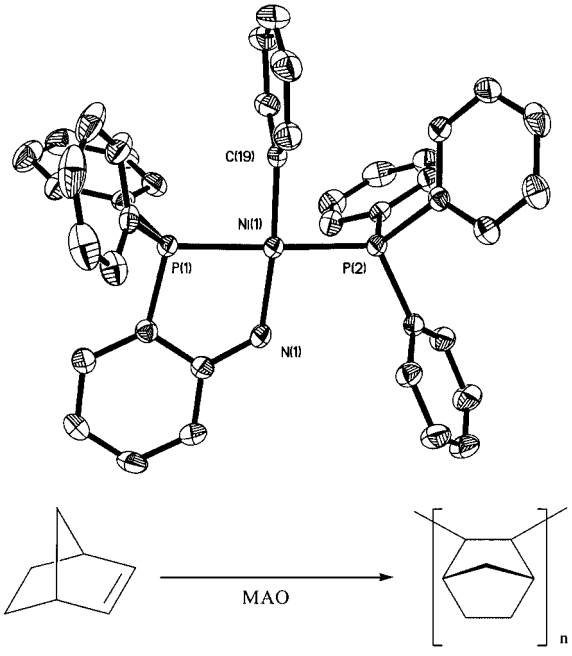

1671 **R. El Mail, M. A. Garralda,* R. Hernández, L. Ibarlucea, E. Pinilla, M. R. Torres, M. Zarandona**

Nortricyclyl- and Norbornenyl-Acylrhodium Complexes from the Reaction of Norbornadiene Rhodium(I) Complexes with *o*-(Diphenylphosphanyl)benzaldehyde

Keywords: Rhodium complexes / Aldehydes / Insertion and rearrangement of norbornadiene / N ligands

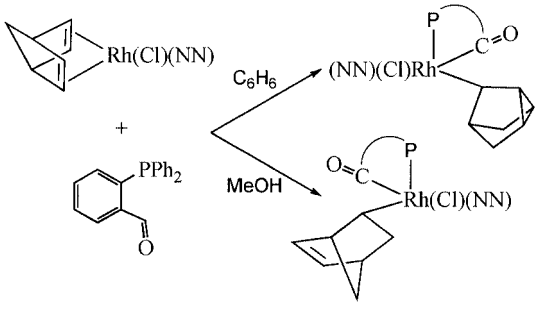

 © 2005 Wiley-VCH Verlag GmbH & Co. KGaA, Weinheim

1678 **Y. Shvedenkov,* M. Bushuev, G. Romanenko, L. Lavrenova, V. Ikorskii, P. Gaponik, S. Larionov**

Magnetic Anisotropy of New Layered Copper(II) Bromide Complexes of 1-Substituted Tetrazoles

Keywords: Copper / Layered compounds / Nitrogen heterocycles / Magnetic properties / Phase transition

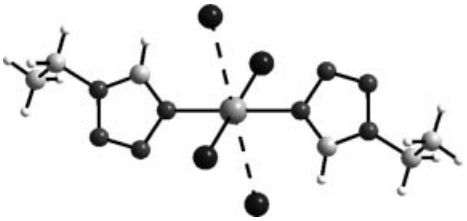

1683 **A. Eichhöfer***

Four New Lead(II) Thiolate Cluster Complexes − Unexpected Products of a Conventional Synthesis

Keywords: Cluster compounds / Lead / Sulfur / UV/Vis spectroscopy

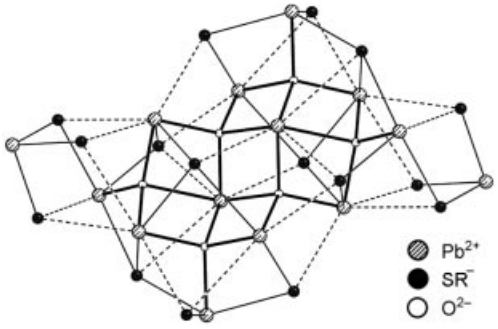

1689 **A. M. Martins,* J. R. Ascenso,* C. G. de Azevedo,* A. R. Dias, M. T. Duarte, H. Ferreira, M. J. Ferreira, R. T. Henriques, M. A. Lemos, L. Li, J. F. da Silva**

Titanium Triamidotriamine Compounds: Syntheses, Structures and Redox Properties

Keywords: Amide ligands / Cyclic voltammetry / N ligands / Titanium

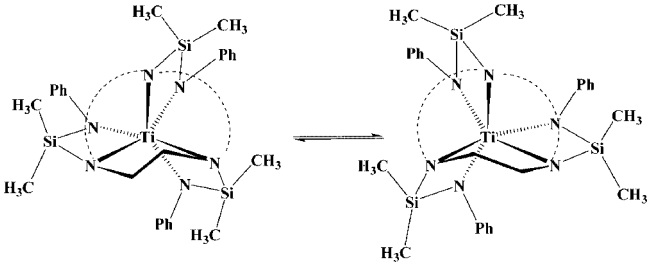

1698 **B. Modec,* J. V. Brenčič**

Novel Methanol-Containing Oxomolybdate(V) Complexes: Synthesis and Structural Characterisation of Intermediates in the Formation of $\{Mo_2O_4\}^{2+}$ Clusters from $[MoOCl_4(H_2O)]^-$ and $[MoOBr_4]^-$ Precursors

Keywords: Cluster compounds / Molybdenum / Polyoxometallates

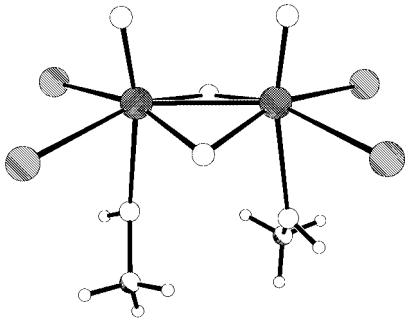

 © 2005 Wiley-VCH Verlag GmbH & Co. KGaA, Weinheim

1710 **M. Laforgia, N. Margiotta, F. Capitelli, V. Bertolasi, G. Natile***

Platinum Complexes with the Novel Ligand Diethyl [(Methylsulfinyl)methyl]phosphonate (SMP): Solid-State Characterization of Potassium Trichloro(SMP)platinum(II) which, in Solution, Gives Dichloro(SMP)platinum(II) and Potassium Chloride

Keywords: Bone tumors / NMR spectroscopy / Phosphonate / Platinum / X-ray crystallography

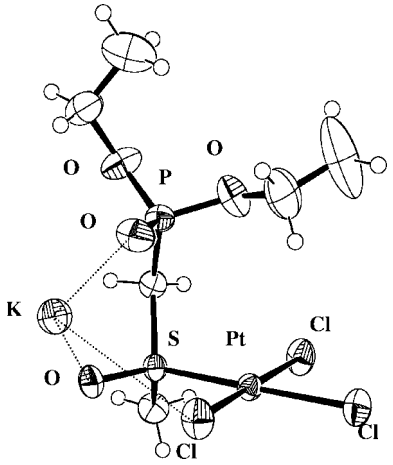

1716 **A. Al-Ajlouni, A. A. Valente, C. D. Nunes, M. Pillinger, A. M. Santos, J. Zhao, C. C. Romão, I. S. Gonçalves,* F. E. Kühn***

Kinetics of Cyclooctene Epoxidation with *tert*-Butyl Hydroperoxide in the Presence of $[MoO_2X_2L]$-Type Catalysts (L = Bidentate Lewis Base)

Keywords: Epoxidation / Homogeneous catalysis / Kinetics / Molybdenum

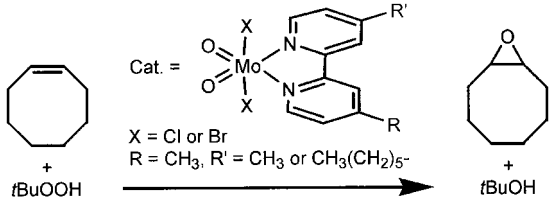

1724 **R. Bielsa, A. Larrea, R. Navarro,* T. Soler, E. P. Urriolabeitia***

Synthesis, Structure, Reactivity, and Catalytic Activity of *C*,*N*- and *C*,*N*,*N*-Orthopalladated Iminophosphoranes

Keywords: C−C Coupling / C−H Activation / Homogeneous catalysis / N ligands / Palladium

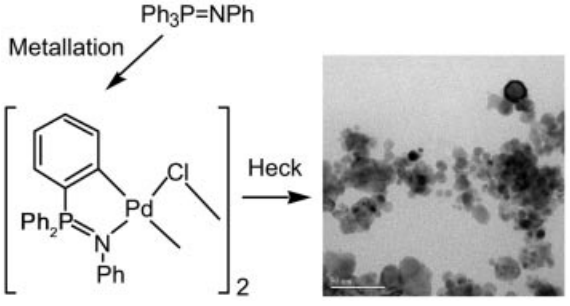

1737 **D. A. Loginov, D. V. Muratov, P. V. Petrovskii, Z. A. Starikova, M. Corsini, F. Laschi, F. de Biani Fabrizi, P. Zanello, A. R. Kudinov***

Reactions of the *B*-Phenylborole Complex $[CpRh(\eta^5\text{-}C_4H_4BPh)]$ with Metalloelectrophiles $[(ring)M]^{2+}$

Keywords: Boron / Electrochemistry / Heterocycles / Rhodium / Sandwich compounds

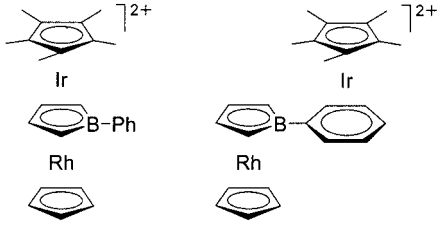

 © 2005 Wiley-VCH Verlag GmbH & Co. KGaA, Weinheim

1747 **O. Exner, S. Böhm***

Acidities of Nitrous and Nitric Acids

Keywords: Ab initio calculations / Isodesmic reaction / Resonance / Acidity

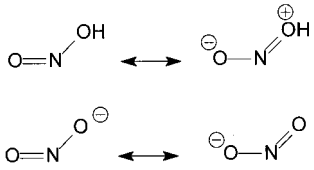

1751 **S. C. Manna, S. Konar, E. Zangrando, M. G. B Drew, J. Ribas,* N. Ray Chaudhuri***

Two New μ-(1,3-Azido)-Bridged Polymers: Alternating Single and Double Bridges in a 1D Nickel(II) Complex and Uniform Bridge in a 2D Copper(II) Complex: Syntheses, Single-Crystal Structures and Magnetic Studies

Keywords: Nickel(II) / Copper(II) / Azide bridges / Crystal structures / Magnetic properties

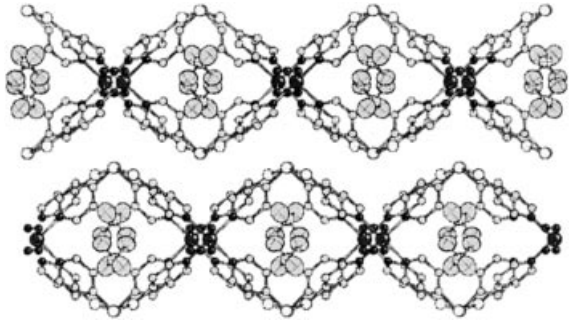

1759 **A. C. Möller, R. Blom, R. H. Heyn,* O. Swang, C.-H. Görbitz, T. Seraidaris**

Synthetic Explorations Towards Sterically Crowded 1,2,3-Substituted Bis(indenyl)zirconium(IV) Dichlorides

Keywords: Metallocenes / Ligand effects / Isomerization / Polymerization / Density functional calculations

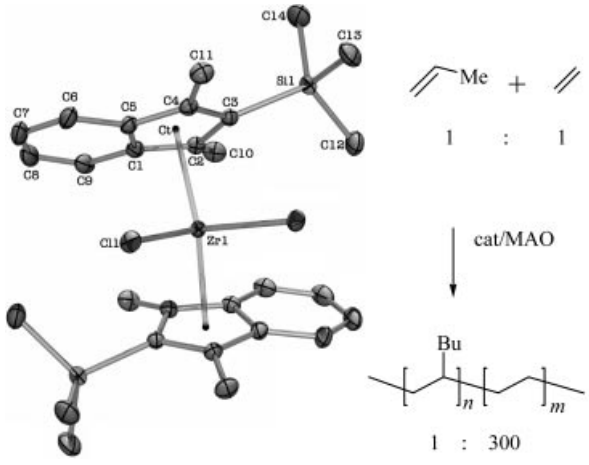

1770 **T. M. Anderson, R. Cao, W. A. Neiwert, K. I. Hardcastle, C. L. Hill,* M. Ammam, B. Keita, L. Nadjo***

Structural and Electrochemical Studies of Dimerization and Rotational Isomerization in Multi-Iron Silicotungstates

Keywords: Polyoxometalates / Cyclic voltammetry / Iron / Tungsten

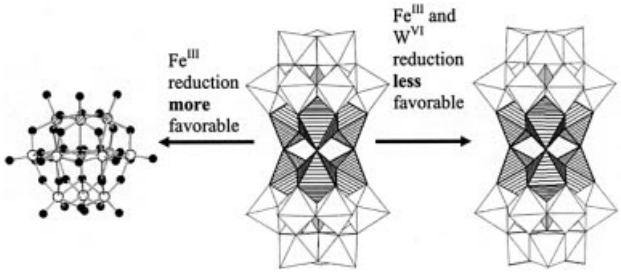

 © 2005 Wiley-VCH Verlag GmbH & Co. KGaA, Weinheim

1776 **A. Burdukov,* Yu. Shvedenkov, N. Pervukhina, V. Reznikov**

New Layered Polymeric Metamagnet Based on Copper(II) Complex with 3-Imidazoline Nitroxide

Keywords: Layered compounds / Copper / Nitroxides / Magnetic properties / Phase transitions

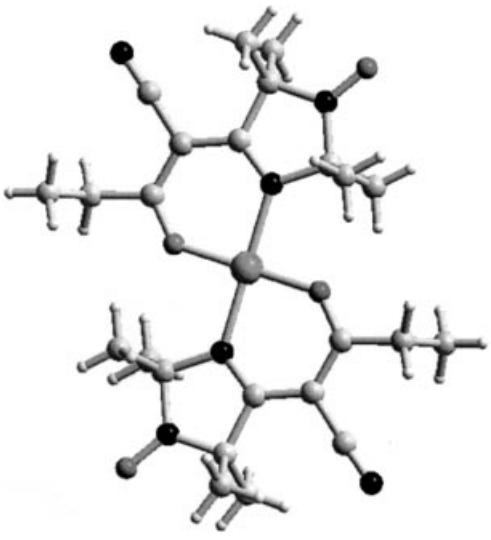

1781 **M. Kucharík, M. Boča,* C. Bessada, H. Fuess**

Do Sodium Oxofluoroaluminates Exist at Room Temperature?

Keywords: Oxofluoroaluminate species / Alumina / Cryolite

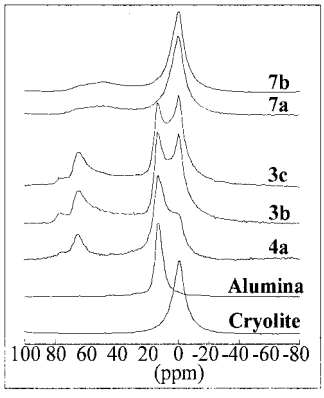

1787 **A. Tomkiewicz, J. Mroziński,* I. Brüdgam, H. Hartl**

Synthesis, Crystal Structure and Magnetic Properties of Heterodimetallic $Re^{IV}Cu^{II}$ Complexes

Keywords: Rhenium(IV) / Chain structures / Copper(II) / Heterometallic complexes

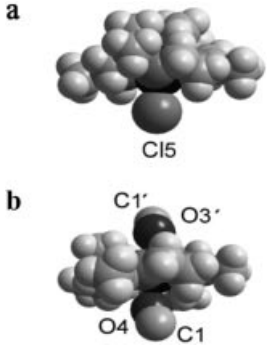

 © 2005 Wiley-VCH Verlag GmbH & Co. KGaA, Weinheim

CORRECTION

1795 **A. Uslu,* S. J. Coles, D. B. Davies, R. J. Eaton, M. B. Hursthouse, A. Kılıç, R. A. Shaw**

Stereoisomerism in Pentaerythritol-Bridged Cyclotriphosphazene Tri-Spiranes: Spiro and Ansa 1,3-Propanediyldioxy Disubstituted Derivatives

Keywords: Cyclotriphosphazene derivatives / Tri-spiranes

 © 2005 Wiley-VCH Verlag GmbH & Co. KGaA, Weinheim

Catalytic Properties and the Role of Copper in Bovine and Lentil Seedling Copper/Quinone-Containing Amine Oxidases: Controversial Opinions

Enzo Agostinelli,*[a,b] Francesca Belli,[a] Laura Dalla Vedova,[a] Silvia Longu,[c] Anna Mura,[c] and Giovanni Floris[c]

Keywords: Cobalt / Cofactors / Copper / Hydrazines / 6-Hydroxydopa / Oxidoreductases

In this microreview, the differences in the catalytic cycle of two copper/quinone-containing amine oxidases, one from lentil seedlings, representative of plant enzymes, and the other from bovine serum, typical of mammalian enzymes, are discussed. Although both enzymes are involved in the control of the levels of mono-, di-, and polyamines, and contain the same organic cofactor, the quinone of 2,4,5-trihydroxyphenylalanine, known as TOPA or TPQ, lentil amine oxidase operates in a different way and with a much higher catalytic activity than the bovine serum enzyme. The role of copper in the two enzymes is also discussed.

(© Wiley-VCH Verlag GmbH & Co. KGaA, 69451 Weinheim, Germany, 2005)

Abbreviations: TPQ or TOPA: quinone of 2,4,5-trihydroxyphenylalanine (6-hydroxydopa quinone). Cu/TPQ-AO: copper/TPQ-containing amine oxidase. LSAO: Cu/TPQ-AO from lentil seedlings. BSAO: Cu/TPQ-AO from bovine serum.

Plant and mammalian plasma amine oxidases [amine:oxygen oxidoreductase (deaminating) (copper containing); EC 1.4.3.6] (Cu/TPQ-AOs) belong to the heterogeneous superfamily of enzymes catalyzing the oxidative deamination of primary amino groups of mono-, di-, and polyamines. Cu/TPQ-AOs share some fundamental structural properties: these enzymes are homodimers, with each subunit containing one tightly bound Cu^{II} ion and one quinone of 2,4,5-trihydroxyphenylalanine (TPQ) as cofactors.[1] These enzymes operate by abstracting two electrons from amines and transferring them to molecular oxygen to form the corresponding aldehyde, ammonia, and hydrogen peroxide. The ping-pong catalytic mechanism of Cu/TPQ-AOs can be divided into two half-reactions: (1) enzyme reduction by substrate at the quinone moiety (TPQ → $TPQH_2$) and (2) its reoxidation by molecular oxygen as shown below:

$$E_{ox} + R\text{-}CH_2\text{-}NH_3^+ \rightarrow E_{red}\text{-}NH_3^+ + R\text{-}CHO \quad (1)$$

$$E_{red}\text{-}NH_3^+ + O_2 + H_2O \rightarrow E_{ox} + NH_4^+ + H_2O_2 \quad (2)$$

Plant amine oxidases are intracellular enzymes, the best known and studied being those from seedlings of lentil (*Lens esculenta*)[2] and pea (*Pisum sativum*),[3] and from the latex of the shrub *Euphorbia characias*.[4] These enzymes prefer short aliphatic diamines, like putrescine (1,4-diaminobutane) and cadaverine (1,5-diaminopentane), as substrates. Plant AOs have an important role in cell growth by regulating the intracellular di- and polyamine levels, while the aldehyde products might have a key role in the biosynthesis of some alkaloids.

Mammalian plasma AOs are extracellular enzymes that are able to metabolize mono-, di-, and polyamines, even though in vitro they are preferentially active towards non-physiological amines like benzylamine. Plasma AOs are generally termed either plasma or serum AOs or benzylamine oxidases. The best known plasma AOs are those from bovine,[5,6] pig,[7] and equine plasma.[8]

In this microreview, a number of controversial questions about the structure and function of AOs are discussed, and

[a] Department of Biochemical Sciences "A. Rossi Fanelli", University of Rome "La Sapienza", Piazzale Aldo Moro 5, 00185 Rome, Italy
Fax: +39-064-440-062
E-mail: enzo.agostinelli@uniroma1.it
[b] IBPM, Istituto di Biologia e Patologia Molecolari – CNR, Piazzale Aldo Moro 5, Rome
[c] Department of Applied Sciences in Biosystems, University of Cagliari, Cagliari, Italy

MICROREVIEWS: This feature introduces the readers to the authors' research through a concise overview of the selected topic. Reference to important work from others in the field is included.

the characteristics of the enzyme from lentil seedlings (LSAO), as representative of plant AOs, are compared with the corresponding features of bovine serum enzyme (BSAO), typical of mammalian proteins.

1. The Organic Cofactor

The first controversial matter involving all Cu/TPQ AOs has been the identification of the organic carbonyl cofactor. For many years, the most likely candidate was considered an unusual covalently bound form of pyridoxal 5-phosphate, but confirmation of such a structure was not forthcoming. In 1984[9,10] two independent reports seemed to have solved this controversial problem by suggesting that pyrroloquinoline quinone might be the active organic cofactor of a variety of eukaryotic proteins, including copper AOs from bovine serum, pig kidney, and from plants. Finally, in 1990 Janes et al. demonstrated that the redox-active cofactor of eukaryotic amine oxidases is the 2,4,5-trihydroxyphenylalanine quinone (6-hydroxydopa; Figure 1).[1]

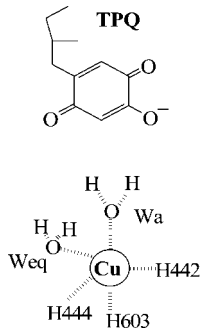

Figure 1. Structure of oxidized form of TPQ and the copper center.

TPQ is derived from the copper-catalyzed oxidation of a post-translationally modified tyrosine residue in the consensus sequence Asn-y-Asp/Glu of the polypeptide chain[11,12] common to plant and mammalian CuAOs analyzed so far.[13] Due to the presence of TPQ, the oxidized form of both LSAO and BSAO has a distinctive pink color and, in addition to the protein absorbance maximum at 278 nm, absorbs in the visible region: BSAO shows the electronic absorption band at 476 nm (ε_{476} = 3800 M^{-1} cm^{-1})[5] whereas

Enzo Agostinelli, Associate Professor of Biochemistry and Molecular Biology, Faculty of Pharmacy, University of Rome "La Sapienza" (Italy). He improved his knowledge on human tumor cell cultures, intracellular microinjection and electroporation in the USA and Canada. He is also studying the nature and functionality of the catalytic site of amine oxidase from bovine serum.

Francesca Belli, Ph.D. student, Faculty of Pharmacy, University of Rome "La Sapienza" (Italy). She is working on the purification and characterization of copper/TPQ bovine amine oxidases and on human tumor cell cultures.

Laura Dalla Vedova, Ph.D. student, Faculty of Pharmacy, University of Rome "La Sapienza" (Italy). She is working on purification and characterization of copper/TPQ bovine amine oxidases and on human tumor cell cultures.

Silvia Longu, Researcher of Biochemistry, Department of Applied Sciences in Biosystems, University of Cagliari (Italy). She is working on purification and characterization of peroxidases and copper/TPQ plant amine oxidases.

Anna Mura, Ph.D. student in Molecular Biology, Department of Applied Sciences in Biosystems, University of Cagliari (Italy). She is working on purification and characterization of copper/TPQ. plant amine oxidases and in plant genes.

Giovanni Floris, Full Professor of Biochemistry and Molecular Biology, Department of Applied Sciences in Biosystems, University of Cagliari (Italy). He is working on purification and characterization of enzymatic proteins, particularly on plant copper/TPQ amine oxidases.

 © 2005 Wiley-VCH Verlag GmbH & Co. KGaA, Weinheim

in LSAO the visible absorption band is centered at 498 nm (ε_{498} = 4100 $M^{-1}cm^{-1}$).[2]

2. The Number of Active Sites

Since all Cu/TPQAOs are homodimers of apparently identical subunits, although the molecular size of the BSAO subunit (85 KDa) is larger than that of LSAO (70 KDa), a problem arose concerning the number of active sites present in native proteins. Thus, a controversial matter on whether one[5,14] or two[15,16] TPQs per dimer are active in AOs from different sources is still debated. The conflicting results obtained on titrating AOs with carbonyl reagents, such as phenylhydrazine, have been rationalized for LSAO.[17] The titration of highly purified samples extrapolated to 1 mol of inhibitor per enzyme subunit indicated the presence of two active quinone moieties per dimer. With carbonyl reagents, such as phenylhydrazine, a stoichiometry of one organic cofactor per protein subunit/mol of inhibitor has been reported for highly purified samples of BSAO,[15] although other research groups, using similar methods, had previously determined a single carbonyl cofactor per dimer.[18,19] Taking into account the results obtained by Janes and Klinman,[15] a spectroscopic study was carefully undertaken on the reaction of BSAO with some inhibitors for determining the stoichiometry of binding.[5] The results showed that BSAO samples having a specific activity comparable to that used by Janes and Klinman react with a stoichiometry of one phenylhydrazine per BSAO dimer. The lower value for the phenylhydrazine/BSAO ratio was mainly attributed to the lower quality of phenylhydrazine being used in the titration, which is reflected by the different molar extinction coefficient of the adduct at 447 nm, corresponding to 41 500 $M^{-1}cm^{-1}$[5] vs. 32 400 $M^{-1}cm^{-1}$.[15] Moreover, reaction of the bovine serum enzyme with other inhibitors like hydrazines and hydrazides[20] led to the proposal of a so-called "half of the sites" reactivity mechanism.[5,21]

3. The Catalytic Cycle Of Cu/TPQ–AOs

Several differences are worth specific mention concerning the catalytic mechanism of LSAO and BSAO.

The Reductive Half-Reaction

As shown in Scheme 1, at least three separate kinetic steps participate in the reductive half cycle: (*i*) the formation of the Michaelis enzyme–substrate complex, (*ii*) the reduction of TPQ together with the oxidation of the bound substrate to yield the enzyme–product complex; (*iii*) the hydrolysis of the enzyme–product complex with the release of the aldehyde and the formation of the aminoquinol derivative.

Formation of the Michaelis Enzyme–Substrate Complex

Step 1: The Substrate Schiff-Base Cu^{II}–Quinone Ketimine

The amine substrate binds to a carbonyl function of TPQ in the resting oxidized enzyme [Cu^{II}–TPQ, (see *a* in Scheme 1; Figure 2)] to form a substrate Schiff base [Cu^{II}–quinone ketimine; (see *b* in Scheme 1)]. Hartmann and coworkers[22] have demonstrated that the reaction of BSAO with benzylamine as substrate under anaerobic conditions generates a detectable relaxation at 340 nm, which was attributed to the quinone ketimine. Thus, the quinone and the quinone ketimine oxidized forms of the enzyme, which both absorb at 476 nm, are spectroscopically distinguishable since only *b* shows a shoulder at 340 nm.

In LSAO, as previously demonstrated,[23] the quinone ketimine intermediate has the same "pink" spectrum as that of the native enzyme

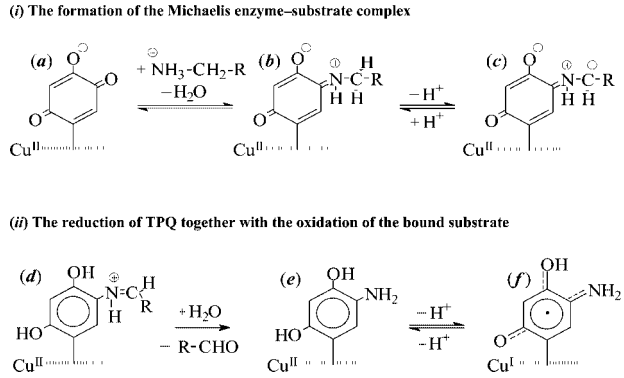

Scheme 1. Catalytic mechanism of Cu–AOs: the reductive half-reaction. (*a*) Resting oxidized enzyme; (*b*) Cu^{II}–quinone ketimine, the substrate Schiff base; (*c*) Cu^{II}–carbanion species; (*d*) Cu^{II}–quinolaldimine, the product Schiff base; (*e*) Cu^{II}–aminoquinol; (*f*) Cu^{I}–semiquinolamine radical.

Step 2: Cu^{II}–Carbanion Species

The oxidation of the amine substrate involves a base-catalyzed hydrogen abstraction from the C bound to nitrogen, leading to the formation of a Cu^{II}–carbanion species (see *c* in Scheme 1). The formation of the carbanion species has been demonstrated, in the case of BSAO, using *para*-substituted benzylamines,[24] and, in LSAO, through the reaction with the electrophilic reagent tetranitromethane to generate the nitroform anion.[25] The active-site base was identified as Asp_{300} in LSAO[26] and Asp_{381} in BSAO.[27]

The Reduction of TPQ Together With the Oxidation of the Bound Substrate

Step 3: The Product Schiff base Cu^{II}–Quinolaldimine

Transformation of the Cu^{II}–carbanion (*c*) into the product Schiff base Cu^{II}–quinolaldimine (see *d* in Scheme 1) involves the transfer of two electrons from the substrate amine to the oxidized form of TPQ, and is associated with the bleaching of the visible absorption band. In LSAO, after addition of the poor substrate *p*-(dimethylamino)benzylamine ($k_{cat} = 2.3 \times 10^{-4}$ s^{-1}) a new intense band centered at 400 nm appears.[2] This band is assigned to the protonated tautomeric form of the quinolaldimine (a "quino"-imine; Figure 3). The quino-imine form was also identified

 © 2005 Wiley-VCH Verlag GmbH & Co. KGaA, Weinheim

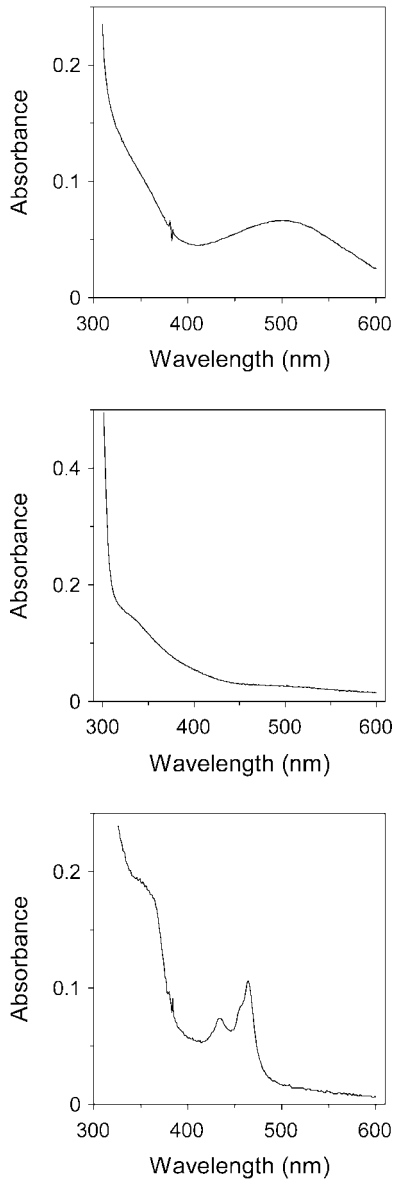

Figure 2. Visible absorption spectrum of LSAO. Top: resting oxidized enzyme; middle: the Cu^{II}–aminoquinol; bottom: Cu^{I}–semiquinolamine radical.

in BSAO[22] due to its broad absorption band at 460 nm. The reason why LSAO and the bovine serum enzyme give a different quino-imine spectrum is not clear.

Step 4: Cu^{II}–Aminoquinol

Oxidation of the bound substrate (followed by hydrolysis) releases the aldehyde product and gives the Cu^{II}–aminoquinol derivative (see *e* in Scheme 1). In both enzymes this species is colorless (Figure 2) and it was impossible to assign a defined difference spectrum attributed to the transformation of quinolaldimine into aminoquinol. In both enzymes the aldehyde is released after hydrolysis of the imine, and ^{15}N-isotope experiments have demonstrated that the amino group from the substrate is still bound to the TPQ ring structure.[28]

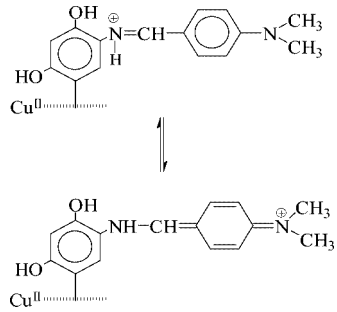

Figure 3. Oxidation of *p*-(dimethylamino)benzylamine by lentil enzyme. The quinolaldimine species is in equilibrium with its tautomeric form, the quino-imine.

Step 5: Cu^{I}–Semiquinolamine Cation Radical Species

This derivative is typical of plant AOs. In lentil enzyme, after the conversion of the TPQ cofactor to the substrate-reduced colorless Cu^{II}–aminoresorcinol, the solution turns yellow immediately as result of the formation of new absorption bands centered at 464, 434, and 360 nm, indicative of a second reduced derivative, the free radical Cu^{I}–semiquinolamine cation species (Scheme 1f; Figure 2).[29] It has been unequivocally demonstrated that copper ion reduction occurs.[2,23] The static spectrum of Cu^{I}–semiquinolamine has been shown to be pH-dependent.[23] The intensities of the absorbances of reduced LSAO observed at pH 7 decrease at both acidic and alkaline pH values, and disappear completely at extreme pH values (pH $<$ 5 or $>$ 10). The titration data have been fitted to an equilibrium between Cu^{I}–semiquinolamine and the bleached Cu^{II}–aminoquinol controlled by two independent ionizable groups with $pK_1 = 5.7$ and $pK_2 = 7.9$:

Cu^{I}–semiquinolamine (pH 7) $\rightleftharpoons$ Cu^{II}–aminoquinol (pH 5 or 10)

The radical species could not be detected below 258 K, and was observed in increasing amounts from 283 to 298 K, the highest temperature investigated.[30] Thus, in LSAO, as in other plant AOs, the Cu^{II}–aminoquinol derivative equilibrates rapidly with the Cu^{I}–semiquinolamine cation radical species by transferring one electron to copper, which in turn is reduced from the cupric to the cuprous state.[31] Even under the most favorable experimental conditions, the population of Cu^{I}–semiquinolamine radical does not exceed 30–40% of the total TPQ, as estimated by ESR spectroscopy.[32]

BSAO does not populate the Cu^{I}–semiquinolamine radical species, but the presence of about 1% of a radical derivative has been demonstrated by Su and Klinman[33] in the mechanism of dioxygen conversion into hydrogen peroxide without the conversion of Cu^{II} to Cu^{I} (see "the oxidative half-reaction" below).

In conclusion, in the reductive half-reaction four steps are quite similar in BSAO and LSAO and, in consideration of the spectroscopic changes described above, in both enzymes the Cu^{II}–quinone ketimine and Cu^{II}–carbanion species are believed to be pink, whereas Cu^{II}–quinolaldimine and Cu^{II}–aminoquinol species are colorless. As described as step five, the yellow Cu^{I}–semiquinolamine cation radical

 © 2005 Wiley-VCH Verlag GmbH & Co. KGaA, Weinheim

species is only present in plant enzymes and represents the biggest difference observed between LSAO and BSAO in the reductive catalytic mechanism.

The Oxidative Half-Reaction

The Oxidative Half-Reaction in BSAO is Very Different to That of LSAO

The Oxidative Half-Reaction in BSAO: Mechanism of Proton-Coupled Electron Transfer to Dioxygen

In an extensive study of the reoxidation of BSAO, an enzyme which does not normally populate the Cu^{I}–semiquinolamine radical, Su and Klinman[33] have reported a detailed analysis of a chemical and kinetic mechanism of dioxygen conversion into hydrogen peroxide that does not require the conversion of Cu^{II} into Cu^{I}. Oxygen initially binds to a non-metal site of the enzyme and the reduced TPQ starts the reaction by transferring one electron to dioxygen to form the superoxide anion. This superoxide may bind to Cu^{II}, thereby facilitating the transfer of a second electron and two protons from the semiquinolamine radical and the release of H_2O_2 (see *g* and *g′* Scheme 2). Thus, during its reoxidation, the reduced BSAO populates a single intermediate species, the reversible oxygen complex $E_{red}O_2$, which has the same absorbance spectrum as E_{red}. The subsequent release of ammonia regenerates the Cu^{II}–quinone species.

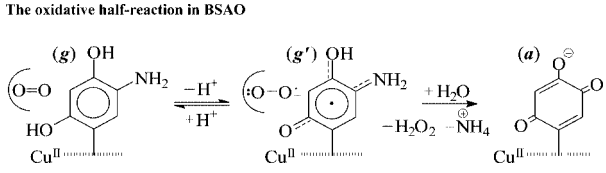

Scheme 2. Catalytic mechanism of BSAO: the oxidative half-reaction. *g, g′*: Cu^{II}–aminoresorcinol–oxygen complex. *a*: Resting oxidized enzyme.

The Oxidative Half-Reaction in LSAO

The Cu^{I}–semiquinolamine cation radical described in "the reductive half-cycle" is the species that reacts rapidly with oxygen.[23,30] This observation has allowed Floris and co-workers[23] to determine the oxidation rate constant of reduced LSAO as a function of the semiquinolamine radical population. Their study demonstrates that both reduced derivatives − the Cu^{I}–semiquinolamine and the Cu^{II}–aminoquinol − are capable of reacting with oxygen, although with widely different rate constants, and that at neutral pH the reaction path involving the semiquinolamine radical intermediate largely predominates. Moreover, under experimental conditions that inhibit the conversion to the radical species, the apparent second-order rate constant for oxidation of LSAO closely approaches that of BSAO, although the stability of the $E_{red}O_2$ complex is much lower in the former enzyme, perhaps because of its faster conversion to the oxidized derivative (E_{ox}). In the same way as BSAO, the subsequent release of ammonia regenerates the Cu^{II}–quinone species.

4. The Role of Copper

The discussion of the oxidative half-reaction implies another controversial matter: the role of copper in the catalytic mechanism of AOs. All Cu/TPQ AOs contain a copper atom in a 1:1 stoichiometric ratio with the organic cofactor. The ESR parameters of copper/TPQ AOs fall in the category of so-called type-2 Cu ESR spectra.[34] The copper ion is coordinated to three hystidine residues and two water molecules (Figure 1) and is located very close to the TPQ cofactor. Copper is essential for the reoxidation of the substrate-reduced enzyme in the presence of oxygen and appears to control the transfer of substrates from a hydrophobic binding site near the protein surface[35] to the deeply buried active site.[3,36]

A Structural Role for Copper

The role of the metal cofactor in the catalytic mechanism of BSAO has partially been solved by studies using both copper-free enzyme[18] and enzymes in which the copper has been replaced with other metals.[37] Copper can be removed from BSAO by treatment with sodium dithionite in the presence of potassium cyanide[18] or benzylamine under anaerobic conditions.[37] The two derivatives contained about 0.22 or 0.70 residual Cu^{II} centers per dimer (corresponding to 10 and 35% residual Cu^{II} per dimer, respectively)[37] depending on the reagent added (potassium cyanide or benzylamine) and were found to be almost totally inactive. The Cu-depleted protein does not react with hydrazine inhibitors and, when reduced by substrate, does not undergo the reoxidation process.[35] After complete removal of copper, the metal binding site of BSAO may accept other metal ions, like Co^{II}, Ni^{II}, and Zn^{II}.[31,38] The addition of cobalt to Cu^{II}-depleted BSAO partially restores the activity of the enzyme (up to 25–40%, corresponding to a k_{cat} value of 0.31–0.49)[18,39] (Table 1), thus confirming that the enzyme does not require the conversion of the cupric copper ion to the cuprous state in the mechanism of dioxygen conversion into H_2O_2. Thus, in BSAO, the metal, whether Cu^{II} or Co^{II}, is not directly involved in amine oxidation, but may have a structural function, as confirmed by the closely similar behavior of Cu^{II} and Co^{II} BSAO derivatives upon deconvolution of their thermal profiles in DSC studies.[38] In these studies, the deconvolution of thermal profiles in native BSAO showed five subpeaks, while the fully-Cu-depleted BSAO required at least six two-state transitions. The thermal profiles of Co^{II}-reconstituted enzyme closely resemble those of the native and Cu^{II}-reconstituted BSAO. The thermograms of both BSAO derivatives can be deconvoluted into five two-state transitions that characterize the native enzyme.[38]

 © 2005 Wiley-VCH Verlag GmbH & Co. KGaA, Weinheim

Table 1. Differences and common features between amine oxidase from bovine serum (BSAO) and lentil seedlings (LSAO).

	BSAO	LSAO
Molecular size subunits (KDa)	85	70
Copper ions (content)	2	2
Number of active sites (TPQ dimer)	2,[15,16] 1[5,14]	2[17]
Absorbance maximum (TPQ oxidized)	476 nm, ε_{476} = 3800 $M^{-1}cm^{-1}$[5]	498 nm, ε_{498} = 4100 $M^{-1}cm^{-1}$[2]
Reduced TPQ aminoquinol	colorless	colorless
Reduced semiquinolamine radical	1% of the total TPQ[33]	30–40% of the total TPQ[29] 464, 434, and 360 nm
Percent activity of Co^{II}-reconstituted enzyme	25–40	7
k_{cat} of native (a) and Co^{II}-substituted (b) enzyme	(a) 1.23,[37,39] (b) 0.31–0.49[37,39]	(a) 155,[44] (b) 11[44]

Reactivity with hydrazine derivatives and assays of the enzymatic activity have shown that in the Co^{II} derivative the TPQ is reactive and the enzyme is catalytically competent. The substitution of copper with cobalt does not greatly impair the enzymatic activity. The Co^{II} derivative has the peculiar effect of decreasing both the k_{cat} and the K_M values.[37,39] Thus, substantially smaller K_M values were obtained for all examined amines than for native BSAO, thus confirming that the catalytic activity of Co^{II}–BSAO is not due to residual (10 or 35%) or spurious copper.[27,37]

Furthermore, the CD spectrum of Co^{II}-reconstituted BSAO shows a band at 540 nm which, like the band at 640 nm of the native protein, is assigned to the metal d–d electronic transition.[19,40] The band at 440 nm, which appears in both spectra, is assigned to a TPQ transition.[40]

Thus, we can conclude that, in BSAO, Cu^{II} does not appear to have the usual redox role.[18,35,41] Rather, it seems to affect the redox potential of TPQ and/or modulate the pK_a of the coordinated water molecule, through which it is bonded to organic cofactor-O_2, thus facilitating the proton transfer to O_2. This makes it possible to identify the bridging water, in the place of Asp385, with the catalytic base with a pK_a of about 8.0 controlling BSAO catalytic activity. Such a function could also, in principle, be carried out by a different metal ion.[27,39]

Involvement of Copper in the Catalytic Cycle

In LSAO, copper can be almost completely removed by treatment with *N*,*N*-diethyldithiocarbamate.[42] The residual copper in the LSAO apoenzyme, measured by atomic absorption spectroscopy, is about 0.2 ± 0.02 residual Cu^{II} atoms per dimer (10% residual Cu^{II} per dimer). Copper-free LSAO is still pink and shows a broad absorption peak in the visible region at 480 nm that is shifted towards shorter wavelengths with respect to the native enzyme, but with similar intensity; apo-LSAO is able to oxidize one equivalent of substrate, although copper removal prevents the formation of the semiquinolamine radical and reoxidation of the enzyme. The oxidation occurs under single turnover conditions and releases one equivalent of aldehyde per enzyme subunit under anaerobic as well as aerobic conditions.[43] Moreover, apo-LSAO reacts with phenylhydrazine in a stoichiometry of two mol of inhibitor per mol of apoenzyme dimer, i.e. in a similar manner as the native enzyme.[42] This suggests that in LSAO copper has not only a structural function, as supposed for BSAO. Through a detailed analysis of fully copper depleted, half reconstituted, or fully reconstituted, and of the Co^{II}-substituted LSAO, Padiglia et al.[44] have shown that copper ions are essential for the fast catalytic rate of lentil enzyme. Although the Co^{II}-substituted enzyme retains some activity, the k_{cat} value for the best substrate (putrescine) is much lower than that of the native enzyme (11 vs. 155), and the formation of the semiquinolamine radical is not proven. Thus, in LSAO, copper is certainly involved in the amine oxidation process, and the formation of the Cu^{I}–semiquinone species is an essential step of the catalytic pathway. Cu^{I}–semiquinolamine radical is the species that reacts preferentially with O_2[2,23,30] and the lower catalytic activity of Co^{II}–LSAO may be ascribed to its slow reoxidation.

5. Concluding Remarks

Amine oxidases, a widespread class of enzymes, are present in all living systems, where they control the level of very active compounds, i.e. mono-, di-, and polyamines. The oxidation of these compounds may generate other biologically active substances, such as aldehydes, ammonia, and hydrogen peroxide. Both copper ions and TPQ are essential for the enzyme function. The findings for the catalytic cycle of BSAO[45] offer an interesting comparison with those reported for plant amine oxidase.[23] The catalytic mechanism for LSAO may be referred to as a "protein–radical enzyme", operating through a free radical located on the cofactor and the reduction of copper from the cupric to the cuprous state. This is in contrast to BSAO, which forms the free radical intermediate only to a minor extent in the course of the reoxidative step without the reduction of copper. Thus, two steps of the catalytic mechanism are significantly slower in BSAO than in LSAO, namely the reoxidation and the proton abstraction occurring in the enzyme substrate complex. The former difference is rationalized as being due to the low to zero concentration of the semiquinolamine-radical intermediate, while the latter is less easily interpreted. Copper, like TPQ, is an essential cofactor and its removal inactivates the enzymes. Moreover, a change in the valence of copper is found only in lentil enzyme, which is much more active than bovine AO by almost two orders of magnitude (k_{cat} LSAO = 155 s^{-1}; k_{cat} BSAO = 1.23 s^{-1}). In conclusion, the presence of two active sites, the formation of the radical species, and the copper reduction might

 © 2005 Wiley-VCH Verlag GmbH & Co. KGaA, Weinheim

be the reason for the higher catalytic activity of LSAO with respect to BSAO (Table 1).

Acknowledgments

Some of the original studies reported here were supported partially by MIUR funds FIRB, COFIN 2002, and PRIN 2003, the University of Rome "La Sapienza", the CNR Target Project on Biotechnology funds, and by the Ministero della Salute (1% Fondo Sanitario Nazionale).

[1] S. M. Janes, D. Mu, D. Wemmer, A. J. Smith, S. Kaur, D. Maltby, A. L. Burlingame, J. P. Klinman, *Science* **1990**, *248*, 981–987.
[2] R. Medda, A. Padiglia, J. Z. Pedersen, G. Rotilio, A. Finazzi Agrò, G. Floris, *Biochemistry* **1995**, *34*, 16 375–16 381.
[3] V. Kumar, D. M. Dooley, H. C. Freeman, J. M. Guss, I. Harvey, M. A. McGuirl, M. C. J. Wilce, V. Zubak, *Structure* **1996**, *4*, 943–955.
[4] A. Padiglia, R. Medda, A. Lorrai, B. Murgia, J. Z. Pedersen, A. Finazzi Agrò, G. Floris, *Plant Physiol.* **1998**, *117*, 5193–5198.
[5] L. Morpurgo, E. Agostinelli, B. Mondovì, L. Avigliano, R. Silvestri, G. Stefancich, M. Artico, *Biochemistry* **1992**, *31*, 2615–2621.
[6] J. P. Klinman, D. Mu, *Annu. Rev. Biochem.* **1994**, *63*, 299–344.
[7] K. D. S. Yadav, P. F. Knowles, *Eur. J. Biochem.* **1981**, *114*, 139–144.
[8] S. R. Carter, M. A. McGuirl, D. E. Brown, D. M. Dooley, *J. Inorg. Biochem.* **1994**, *56*, 127–141.
[9] M. Ameyama, M. Hayashi, K. Matsushita, E. Shinagawa, O. Adachi, *Agric. Biol. Chem.* **1984**, *48*, 561–565.
[10] C. L. Lobenstein-Verbeek, J. A. Jongejan, J. Frank, J. A. Duine, *FEBS Lett.* **1984**, *170*, 305–309.
[11] D. Cai, J. P. Klinman, *J. Biol. Chem.* **1994**, *269*, 32 039–32 042.
[12] R. Matsuzaki, S. Suzuki, K. Yamaguki, T. Fukui, K. Tanizawa, *Biochemistry* **1995**, *34*, 4524–4530.
[13] S. M. Janes, M. M. Palcic, C. H. Scaman, A. J. Smith, D. E. Brown, D. M. Dooley, M. Mure, J. P. Klinman, *Biochemistry* **1992**, *31*, 12 147–12 154.
[14] D. De Biase, E. Agostinelli, G. De Matteis, B. Mondovì, L. Morpurgo, *Eur. J. Biochem.* **1996**, *237*, 93–99.
[15] S. M. Janes, J. P. Klinman, *Biochemistry* **1991**, *30*, 4599–4605.
[16] Z. He, Y. Zou, F. T. Greenaway, *Arch. Biochem. Biophys.* **1995**, *319*, 185–195.
[17] A. Padiglia, R. Medda, G. Floris, *Biochem. Int.* **1992**, *28*, 1097–1107.
[18] S. Suzuki, T. Sakurai, A. Nakahara, T. Manabe, T. Okuyama, *Biochemistry* **1983**, *22*, 1630–1635.
[19] L. Morpurgo, E. Agostinelli, O. Befani, B. Mondovì, *Biochem. J.* **1987**, *248*, 865–870.
[20] L. Morpurgo, O. Befani, S. Sabatini, B. Mondovì, M. Artico, F. Corelli, S. Massa, G. Stefancich, L. Avigliano, *Biochem. J.* **1988**, *256*, 565–570.
[21] M. Bossa, G. O. Morpurgo, L. Morpurgo, *Biochemistry* **1994**, *33*, 4425–4431.
[22] C. Hartmann, P. Brzovic, J. P. Klinman, *Biochemistry* **1993**, *32*, 2234–2241.
[23] R. Medda, A. Padiglia, A. Bellelli, P. Sarti, S. Santanchè, A. Finazzi Agrò, G. Floris, *Biochem. J.* **1998**, *332*, 431–437.
[24] C. Hartmann, J. P. Klinman, *Biochemistry* **1991**, *30*, 4605–4611.
[25] R. Medda, A. Padiglia, J. Z. Pedersen, G. Floris, *Biochem. Biophys. Res. Commun.* **1993**, *196*, 1349–1355.
[26] A. Rossi, M. Petruzzelli, A. Finazzi Agrò, *FEBS Lett.* **1992**, *301*, 253–257.
[27] G. De Matteis, E. Agostinelli, B. Mondovì, L. Morpurgo, *J. Biol. Inorg. Chem.* **1999**, *4*, 348–353.
[28] J. Z. Pedersen, S. El-Sherbini, A. Finazzi Agrò, G. Rotilio, *Biochemistry* **1992**, *31*, 8–12.
[29] A. Finazzi Agrò, A. Rinaldi, G. Floris, G. Rotilio, *FEBS Lett.* **1984**, *176*, 378–380.
[30] R. Medda, A. Padiglia, A. Bellelli, J. Z. Pedersen, A. Finazzi Agrò, G. Floris, *FEBS Lett.* **1999**, *453*, 1–5.
[31] M. Mure, *Acc. Chem. Res.* **2004**, *37*,131–139.
[32] M. Mure, S. A. Mills, J. P. Klinman, *Biochemistry* **2002**, *41*, 9269–9278.
[33] Q. Su, J. P. Klinman, *Biochemistry* **1998**, *37*, 12513–12525.
[34] G. Rotilio, in *Structure and Function of Amine Oxidase* (Ed.: B. Mondovì), CRC Press Inc., Boca Raton, Florida, **1985**, 127–134.
[35] E. Agostinelli, G. De Matteis, A. Sinibaldi, B. Mondovì, L. Morpurgo, *Biochem. J.* **1997**, *324*, 497–501.
[36] M. R. Parsons, M. A. Convery, C. M. Wilmot, K. D. S. Yadav, V. Blakeley, A. S. Corner, S. E. V. Phillips, M. J. McPherson, P. F. Knowles, *Structure* **1995**, *3*, 1171–1184.
[37] E. Agostinelli, G. De Matteis, B. Mondovì, L. Morpurgo, *Biochem. J.* **1998**, *330*, 383–387.
[38] E. Agostinelli, L. Morpurgo, C. Wang, A. Giartosio, B. Mondovì, *Eur. J. Biochem.* **1994**, *222*, 727–732.
[39] L. Morpurgo, E. Agostinelli, B. Mondovì, L. Avigliano, *Biol. Metals* **1990**, *3*, 114–117.
[40] S. Suzuki, T. Sakurai, A. Nakahara, O. Oda, T. Manabe, T. Okuyana, *J. Biochem. (Tokyo)* **1981**, *90*, 905–908.
[41] S. Suzuki, T. Sakurai, A. Nakahara, T. Manabe, T. Okuyama, *Biochemistry* **1986**, *25*, 338–341.
[42] A. Rinaldi, A. Giartosio, G. Floris, R. Medda, A. Finazzi Agrò, *Biochem. Biophys. Res. Commun.* **1984**, *120*, 242–249.
[43] A. Padiglia, R. Medda, A. Lorrai, D. Congiu, J. Z. Pedersen, G. Floris, *Phytochem. Anal.* **1998**, *9*, 223–226.
[44] A. Padiglia, R. Medda, J. Z. Pedersen, A. Finazzi Agrò, A. Lorrai, B. Murgia, G. Floris, *J. Biol. Inorg. Chem.* **1999**, *4*, 608–613.
[45] A. Bellelli, L. Morpurgo, B. Mondovì, E. Agostinelli, *Eur. J. Biochem.* **2000**, *267*, 3264–3269.

Received: December 10, 2004

 © 2005 Wiley-VCH Verlag GmbH & Co. KGaA, Weinheim

Preparation and Characterization of $Ag@TiO_2$ Core-Shell Nanoparticles in Water-in-Oil Emulsions

Dan Zhang,[a] Ximing Song,[b] Rongwei Zhang,[a] Ming Zhang,[a] and Fengqi Liu*[a]

Keywords: Silver / Titanium / Core-shell nanoparticles / Water-in-oil emulsion / Surface photovoltaic spectroscopy

We report a simple route for the effective synthesis of $Ag@TiO_2$ nanoparticles in water-in-oil (w/o) emulsions and provide detailed characterization of the materials with TEM, TG-DTA, IR, XRD, and SPS measurements. Such core-shell hybrid nanoparticles can be fabricated in two simple steps: the formation of the silver core by the reduction of a Tollens reagent with glucose in the water phase, and the hydrolysis of $Ti(OC_4H_9)_4$ at the water/oil interface for the formation of the amorphous TiO_2 shell. The procedure led to the formation of nanocomposites with a crystalline core in a size range from 5 to 15 nm in diameter and an amorphous shell of 6–10 nm thickness in a typical synthesis. The shell was converted to crystalline oxide upon thermal treatment. Surface photovoltaic spectroscopy (SPS) measurements indicate that the materials have potential for application in photoinduced electron storage and photocatalysis.
(© Wiley-VCH Verlag GmbH & Co. KGaA, 69451 Weinheim, Germany, 2005)

Introduction

Core-shell metal nanoparticles with oxide shells have attracted considerable attention owing to their stability under extreme conditions,[1] and their optical and catalytic properties.[2–3] The shells offer protection to the cores as well as introducing new properties to the hybrid structures.[4] An important shell-forming material is TiO_2, which offers wide-ranging properties.[5] A number of methods have been used to prepare the core-shell metal nanoparticles.[1,6–8] Among these methods are citrate reduction,[9] borohydride reduction,[10] sonochemical methods,[11] radiolytic reduction,[12] and metal evaporation-condensation.[13] It was shown that the size, composition, and structure of the resultant particles depended on the preparation conditions.

Water-in-oil (w/o) emulsions are thermodynamically stable with nanosized water droplets that are dispersed in a continuous oil phase and stabilized by surfactant molecules at the water/oil interface. The surfactant-stabilized water pools provide a microenvironment for the preparation of nanoparticles by preventing the excessive aggregation of particles. As a result, the particles obtained in such a medium are generally very fine and monodisperse. Many kinds of nanoparticles have been prepared in w/o emulsions including metals,[14] metal oxides,[15] and organic polymers.[16] However, within the limits of our knowledge, the preparation of core-shell metal nanoparticles with oxide shells in w/o emulsions has not been reported yet. In this paper, we describe an effective method for the preparation of $Ag@TiO_2$ nanoparticles in w/o emulsions and provide detailed characterization of the materials. We shall also touch upon one property we are pursuing currently, namely, surface photovoltaic spectroscopy.

[a] College of Chemistry, Jilin University,
Changchun, 130023, People's Republic of China
Fax: +86-431-8499158
E-mail: fengqiliu@21cn.com
[b] School of Chemical Science and Engineering, Liaoning University
Shenyang, 110036, People's Republic of China
Fax: +86-24-62202380
E-mail: xmsong@lnu.edu.cn
Supporting information for this article is available on the WWW under http://www.eurjic.org or from the author.

Results and Discussion

$Ag@TiO_2$ nanoparticles were fabricated in two simple steps: the formation of the silver core by the reduction of a Tollens reagent with glucose in the water phase of the water-in-oil emulsions, and the hydrolysis of $Ti(OC_4H_9)_4$ (TOB) at the water/oil interface for the formation of the amorphous TiO_2 shell. The water and organic impurities in the as-obtained emulsions containing $Ag@TiO_2$ nanoparticles were removed by vacuum-drying followed by calcination. 0.559 g of $Ag@TiO_2$ nanoparticles were obtained after calcination at 800 °C for 4 h in a typical preparation, and the product yield was approximately 100%.

The transmission electron microscopy (TEM) images and the electron diffraction diagram in Figure 1 clearly illustrate the core-shell structure of $Ag@TiO_2$ nanoparticles with a crystalline core of size 5–15 nm and an amorphous shell of thickness 6–10 nm. The size of the nanoparticles is moderately uniform. There appears some nonuniformity in the shell thickness, but the coverage is complete. In Figure 1 (see B), no diffraction is seen from the amorphous shells at room temperature, but the core manifests bulk fcc patterns. (111), (200), (220), and (311) zone axes are observed.[17]

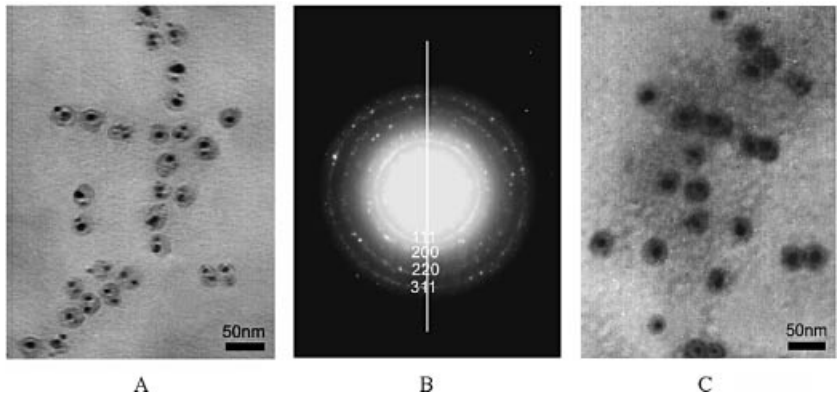

Figure 1. Transmission electron micrographs (A, C) and electron diffraction pattern (B) of $Ag@TiO_2$ nanoparticles. (A) Nanocomposites prepared from 0.59 mmol Ag^+ and 5.9 mmol TOB (wt.-% of Ag: 11.9). (C) Nanocomposites prepared from 0.59 mmol Ag^+ and 7.0 mmol TOB (wt.-% of Ag: 10.2).

The wt.-% of the core component has an influence on the properties of core-shell nanoparticles. In this work, the wt.-% of the Ag component in the nanocomposites could be adjusted by changing the molar ratio of TOB to Ag^+ in the Tollens reagent. From Figure 1 (see A and C), we can conclude that the size of the Ag core does not change and the shell thickness increases with increasing TOB at a fixed amount of Ag^+ in the Tollens reagent, i.e. with the decrease of the relative amount of Ag in the nanocomposites. The variation of the amount of Ag can lead to the formation of nanocomposites with various morphologies. The single-core nanocomposites with various shell thicknesses are the major morphology when the wt.-% of Ag is less than 11.9%, and the multicore nanocomposites are formed when the wt.-% of Ag equals 35.7%, as shown in Figure S2 in the Supporting Information.

The thermal analysis (TG-DTA) curves are shown in Figure 2. The TG curve could be divided into three main stages during the weight loss process of the $Ag@TiO_2$ sample. The first stage was in the range of 100–200 °C, corresponding to desorption or release of solvent and water in the sample. The second stage occurred in the range of 200–500 °C, which resulted mainly from the combustion and decomposition of organic matter, for example Span80, Op10, and butanol, produced from the hydrolysis of TOB. The third loss, less than 4%, was not very obvious in the range 500–700 °C, and was attributed to the dissociation of hydroxyl groups from the surface of TiO_2 nanoparticles. Hydroxyl groups were present in the infrared spectra until the samples were heated to 500 °C. It is well known that there are two types of surface OH groups, terminal Ti–OH and bridge Ti–(OH)–Ti. The dissociation temperatures of these

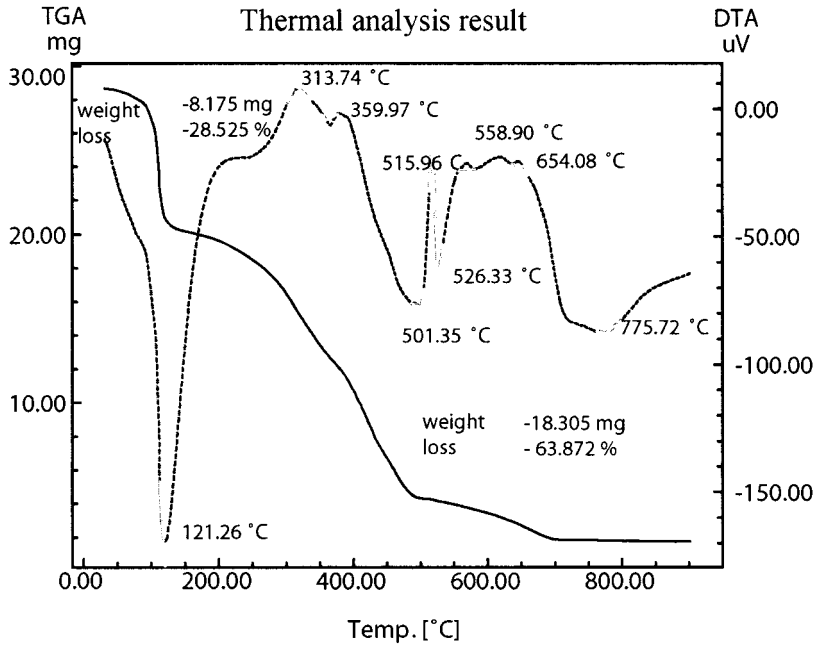

Figure 2. TG-DTA curves of $Ag@TiO_2$ nanoparticles in a typical synthesis.

 © 2005 Wiley-VCH Verlag GmbH & Co. KGaA, Weinheim

surface OH groups differ from each other, and each temperature could also be affected by the chemical surroundings. Thus the decrease in weight appears over a wide temperature range.[18] The DTA curve exhibits a decalescence peak at 121 °C, which corresponds to the desorption or release of solvent and water in the sample . Furthermore, two releasing thermal peaks can be observed at 314 and 360 °C, both corresponding to the combustion and decomposition of the organic matter, and some decalescence and releasing thermal peaks over the range 500–800 °C are also present; they result from the phase transition of TiO_2 from amorphous to anatase (around 500 °C), the dissociation of surface hydroxyl groups (500–700 °C) and the phase transition of TiO_2 from anatase to rutile (around 775 °C). As the oxide cover is solvated with unclear stoichiometry, we did not attempt to analyze the data further.

X-ray powder diffraction (XRD) analysis is usually used for the identification of core-shell structures and crystal phase as well as the estimation of crystallite size.[18] The XRD patterns of TiO_2 and Ag@TiO_2 nanoparticles calcined at 300–800 °C are shown in Figure 3. The peaks at 38°, 44°, 64°, 77° in Figure 3 (see B) are due to the (111), (200), (220), and (311) reflections of the Ag core.[1] Upon thermal treatment to 500 °C for 4 h, an obvious pattern resembling a mixture of anatase and Ag appears (note the peak at 25.3°[19]). The peaks remained almost the same even when the sample was calcined at 700 °C. However, an obvious pattern resembling a mixture of rutile and Ag appeared after calcination at 800 °C for 4 h (note the peak at 27.9°[20]). The phase transformations of the TiO_2 shell from amorphous to anatase and from anatase to rutile occurred with the increase of the calcination temperature, which was in good agreement with the results of TG-DTA. The phase transformation of TiO_2 from anatase, a crystal phase with catalytic activity, to rutile usually occurs at 500–600 °C.[18] However, in our experiments, both TiO_2 and Ag@TiO_2 nanoparticles prepared in the same system of inverse emulsion kept their anatase structure after calcination at 700 °C for 4 h (Figure 3). This observation opens up new possibilities for the application of photocatalysis over a wider temperature range. The effect of preparation methods on the phase-transformation temperature of TiO_2 from anatase to rutile needs further investigation.

The surface photovoltaic spectroscopy (SPS) technique provides a rapid, nondestructive monitor of the surface or interface properties of semiconductors such as TiO_2 and ZnO.[21] The particle size and the surface or interface properties of semiconductors are two important factors affecting the SPS response by influencing the separation efficiency of photoinduced electron–hole pairs.[22] Compared with the bulk or large particles of a semiconductor, the mechanism of SPS generation in a nanosized semiconductor is quite different, and causes the weak SPS signal of a semiconductor nanoparticle.[23] It was found that the smaller the size the weaker the SPS signal of TiO_2 or ZnO nanoparticles.[24] Moreover, the SPS signal of ZnO nanoparticles becomes much weaker when an appropriate amount of nanosized noble metal (Ag or Pd) is deposited on their surface. This

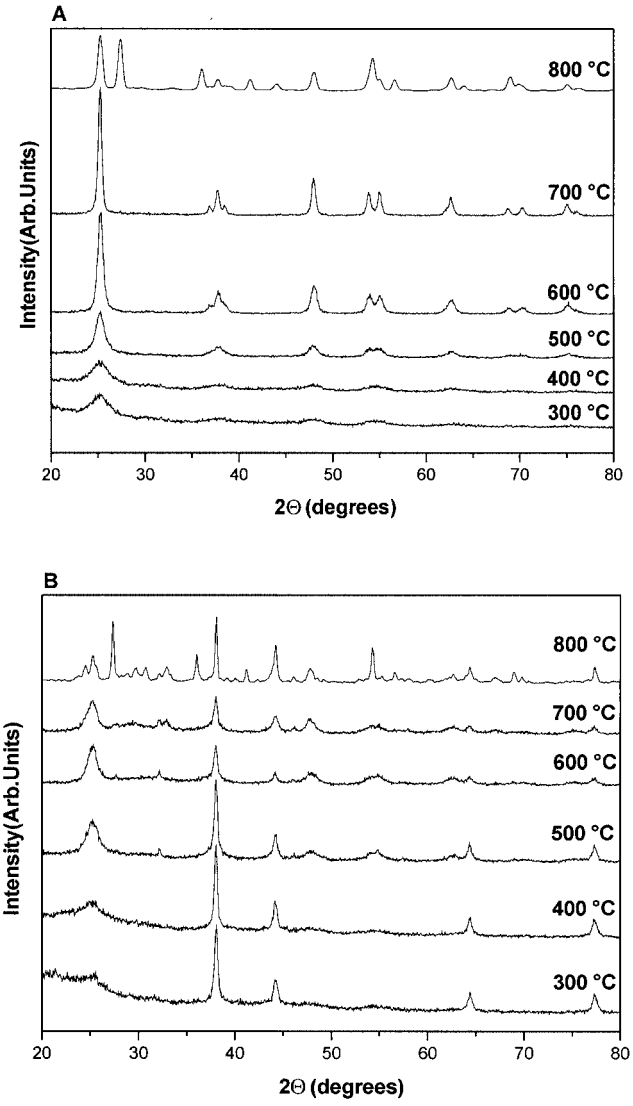

Figure 3. XRD patterns of TiO_2 (A) and Ag@TiO_2 (B) nanoparticles with 11.9% (wt.-%) Ag in a typical synthesis calcined at various temperatures.

may result from the fact that noble metal clusters effectively trap photoinduced electrons.[22]

SPS responses of Ag@TiO_2 and TiO_2 nanoparticles prepared in the same system of inverse emulsion after calcination from 500 °C to 800 °C are shown in Figure 4. The SPS response peaks at 300–400 nm can be attributed to the electron transition from the valence band to the conduction band of TiO_2 ($O_{2p}\rightarrow Ti_{3d}$).[22] The thresholds and surface photovoltages (SPV) obtained from Figure 4 as well as the sizes of the nanoparticles are summarized in Table 1. The red shift of SPS response peaks and the blue shift of thresholds with the increase of calcination temperature may be caused by the quantum size effect.[23] The threshold of Ag@TiO_2 is higher than that of TiO_2 at each calcination temperature (see Table 1) because the Ag core traps photoinduced electrons. The increase in the threshold after the formation of the core-shell structure results in the broadening

 © 2005 Wiley-VCH Verlag GmbH & Co. KGaA, Weinheim

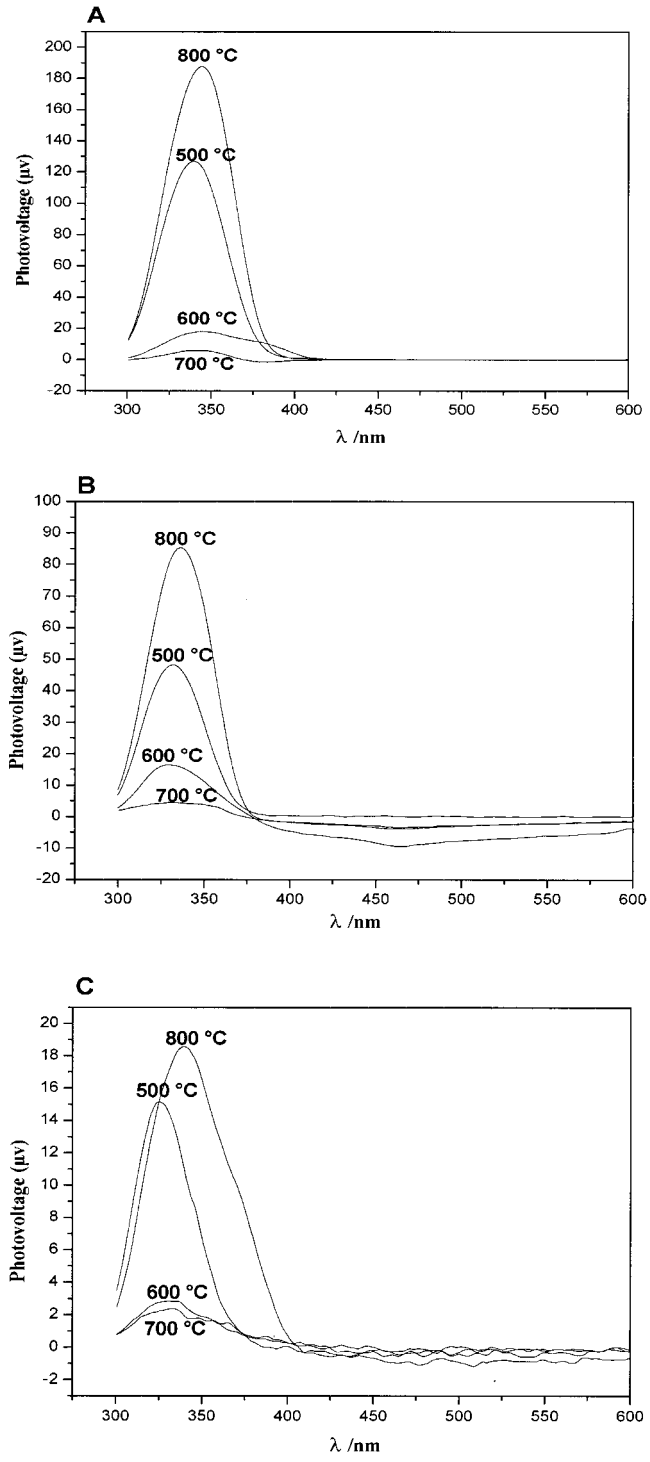

Figure 4. SPS responses of TiO_2 (A) and $Ag@TiO_2$ (B and C) nanoparticles calcined at various temperatures. (B) Nanocomposites prepared from 0.59 mmol Ag^+ and 7.0 mmol TOB (wt.-% of Ag: 10.2). (C) Nanocomposites prepared from 0.59 mmol Ag^+ and 5.9 mmol TOB (wt.-% of Ag: 11.9).

of the bandgap of TiO_2, which improves the separation efficiency of photoinduced carriers.

The SPS response signals of $Ag@TiO_2$ nanoparticles in Figure 4 (see B and C) are much weaker than those of TiO_2 nanoparticles in Figure 4 (see A) at the same calcination temperature, and the red shift of SPS response peaks of $Ag@TiO_2$ nanoparticles in Figure 4 (see C) is much clearer than that of TiO_2 nanoparticles in Figure 4 (see A), both of which are attributed to the effective trapping of photoinduced electrons by the Ag core. Additionally, no SPS signal of a mixture appeared in the SPS spectra when we mixed the same amount of Ag nanoparticles with TiO_2 nanoparticles prepared in the same system of inverse emulsion, because the amount of free Ag nanoparticles was too great.[22,25,26] All these results reveal that Ag nanoparticles were effectively coated with TiO_2 and the presence of the Ag core had an inarguable effect on the SPS signals. On the basis of the SPS responses of $Ag@TiO_2$ nanoparticles with 10.2 and 11.9 wt.-% of Ag, in Figure 4 (see B and C), it is concluded that the SPS response of $Ag@TiO_2$ nanoparticles becomes weaker with an increase in the amount of Ag, because this implies a decrease in the amount of TiO_2 on the surface of the Ag core. In fact, when the wt.-% of Ag in $Ag@TiO_2$ nanoparticles is more than 35.7%, there is no SPS response of $Ag@TiO_2$ nanoparticles at any calcination temperature.

The SPS response signals of $Ag@TiO_2$ and TiO_2 nanoparticles should become stronger with increasing calcination temperature if the size of the nanoparticles had been the only factor influencing SPS response. However, the SPS signals in the range of 500–700 °C for both $Ag@TiO_2$ and TiO_2 nanoparticles in Figure 4 weaken with increasing calcination temperature, which can obviously be attributed to the change of the surface properties of the nanoparticles in this temperature range. TG-DTA and FTIR spectra indicate that the dissociation of hydroxyl groups from the shell surface of $Ag@TiO_2$ nanoparticles takes place in the range of 500–700 °C. The surface hydroxyl groups can play an important role in the photocatalytic actions because the photoinduced holes can attack the surface hydroxyl group and yield a surface-bound OH radical, which efficiently hinders the recombination of electrons and holes.[27] The results of the SPS investigation are in good accordance with those of the TG-DTA and FTIR spectra.

The $Ag@TiO_2$ nanoparticles prepared in w/o emulsions are expected to have a higher photocatalytic activity on the basis of their special SPS responses according to an intrinsic relationship between the SPS response and the photocatalytic activity of TiO_2 or ZnO nanoparticles, i.e. the weaker the SPS signal, the higher the photocatalytic activity.[22] The photocatalytic activity of the $Ag@TiO_2$ nanoparticles is under study.

Conclusions

In summary, we have demonstrated that $Ag@TiO_2$ core-shell nanoparticles could be prepared in water-in-oil emulsions. Such a novel method should be adapted to the preparation of other core-shell metal nanoparticles with oxide shells. The SPS results indicate that $Ag@TiO_2$ nanoparticles

 © 2005 Wiley-VCH Verlag GmbH & Co. KGaA, Weinheim

Table 1. SPS data of TiO_2 and Ag@TiO_2 particles calcined at various temperatures.

Sample[a]	Ag component [wt.-%]	Calcination temperature [°C]	Particle size[b] [nm]	Threshold [eV]	SPV [μV]
A	0	500	45.81	3.05	126.87
A	0	600	52.63	3.01	18.77
A	0	700	68.66	2.99	5.79
A	0	800	115.09	2.92	180.27
B	10.2	500	50.19	3.12	48.25
B	10.2	600	62.45	3.06	16.43
B	10.2	700	70.18	3.02	4.83
B	10.2	800	180.12	2.96	85.28
C	11.9	500	53.42	3.19	15.13
C	11.9	600	66.35	3.10	2.84
C	11.9	700	73.47	3.05	2.37
C	11.9	800	185.31	2.98	18.56

[a] Sample A is TiO_2 nanoparticles. Samples B and C are Ag@TiO_2 nanoparticles corresponding to 10.2 and 11.9 wt.-% of Ag. [b] Obtained from the XRD data by the Scherrer equation: $D = k\lambda/\beta\cos\theta$.

prepared in water-in-oil emulsions have potential applications in photoinduced electron storage and photocatalysis.

Experimental Section

Transmission electron microscopy (TEM) measurements were performed with a Hitachi H-8100 transmission electron microscope. The samples were prepared on carbon-coated copper grids. X-ray diffraction studies were carried out with a Rigaku wide-angle X-ray diffractometer (D/max γA using Cu-K_α radiation at λ = 1.541 Å). The detector was calibrated by using KCl powder as a standard [2θ = 28.345° (200) and 40.507° (220) under Cu-K_α radiation]. IR spectroscopic measurements were performed with a Nicolet Avatar 360 FTIR spectrometer. Surface photovoltaic spectroscopy (SPS) studies were carried out with a home-built apparatus which had a solid junction photovoltaic cell (ITO/sample/ITO) using the light source-monochromator lock-in detection technique. The measurements were performed at room temperature. Thermal analyses (TG-DTA) were carried out with a Rigaku DTG60H thermal analyzer working at a heating rate of 20 °C /min, with α-Al_2O_3 as the reference material.

Two nonionic surfactants, Span80 and Op10, were used for the preparation of w/o emulsions in this work. In a typical preparation procedure of Ag@TiO_2 nanoparticles, in order to obtain an inverse emulsion containing Ag nanoparticles, the water phase [8 mL of 2% (m/v) Tollens reagent (containing 0.59 mmol Ag^+) and 2 mL of an aqueous 10% (m/v) glucose solution] was added to the oil phase (70 mL of toluene containing 13.9 mmol of Span80 and 1.5 mmol of Op10). The mixture was stirred vigorously under nitrogen for 1 h at room temperature. Further stirring with a moderate agitation intensity at 60 °C for 3 h resulted in a brown-black dispersion, which indicated the formation of Ag-nanoparticle colloids. The coating of TiO_2 was carried out as follows: equimolar (5.9 mmol) amounts of $Ti(OC_4H_9)_4$ (TOB) and acetylacetone were mixed under sonication in a standard ultrasound bath for a few minutes and then added to the above dispersion. Acetylacetone was used as a chelating agent to control the hydrolysis and condensation of TOB.[4] The mixture was stirred under nitrogen at 60 °C for 9 h to give a solution containing Ag@TiO_2 nanoparticles, which was used for TEM measurements. The solution was vacuum dried at 60 °C for 72 h to give a viscous residue, which was analyzed by TG-DTA. The viscous residue was calcined at 300–800 °C for 4 h and then characterized by IR, XRD, and SPS measurements.

Acknowledgments

The work was supported by the National Natural Science Foundation of China (20274014).

[1] R. T. Tom, A. S. Nair, N. Singh, M. Aslam, C. L. Nagendra, R. Philip, K. Vijayamohanan, T. Pradeep, *Langmuir* **2003**, *19*, 3439–3445.
[2] A. Ueno, N. Kakuta, K. H. Park, M. F. Finlayson, A. J. Bard, A. Campion, M. A. Fox, S. E. Webber, J. M. White, *J. Phys. Chem.* **1985**, *89*, 3828–3833.
[3] C. Nasr, H. S. Chandini, W. Y. Kim, R. H. Schmehl, P. V. Kamat, *J. Phys. Chem. B* **1997**, *101*, 7480–7487.
[4] I. Pastoriza-Santos, D. S. Koktysh, A. A. Mamedov, M. Giersig, N. A. Kotov, L. M. Liz-Marzan, *Langmuir* **2000**, *16*, 2731–2735.
[5] K. Kalyanasundaram, M. Gratzel, *Optoelectronic Properties of Inorganic Solids* (Eds.: D. M. Roundhill, J. P. Fackler), Plenum Press, New York, **1999**, p. 169.
[6] I. Pastoriza-Santos, L. M. Liz-Marzan, *Langmuir* **1999**, *15*, 948–951.
[7] T. Ung, L. M. Liz-Marzan, P. Mulvaney, *J. Phys. Chem. B* **1999**, *103*, 6770–6773.
[8] L. M. Liz-Marzan, M. Giersig, P. Mulvaney, *Langmuir* **1996**, *12*, 4329–4335.
[9] S. Link, Z. L. Wang, M. A. El-Sayed, *J. Phys. Chem. B* **1999**, *103*, 3529–3533.
[10] L. M. Liz-Marzan, A. P. Philipse, *J. Phys. Chem.* **1995**, *99*, 15120–15128.
[11] Y. Mizukoshi, K. Okitsu, Y. Maeda, T. A. Yamamoto, R. Oshima, Y. Nagata, *J. Phys. Chem. B* **1997**, *101*, 7033–7037.
[12] M. Treguer, C. Cointet, H. Remita, J. Khatouri, M. Mostafavi, J. Amblard, J. Belloni, R. Keyzer, *J. Phys. Chem. B* **1998**, *102*, 4310–4321.
[13] G. C. Papavassiliou, *J. Phys. F: Met. Phys.* **1976**, *6*, L103.
[14] M. Boutonnet, J. Kizling, P. Stenius, G. Maire, *Colloids Surf.* **1982**, *5*, 209–217.
[15] K. Osseo-Asare, F. Arriagada, *J. Colloid Interface Sci.* **1990**, *50*, 321–327.
[16] N. Moumen, M. P. Pileni, R. A. Mackay, *Colloid Surf. A* **1999**, *151*, 409–417.
[17] L. Armelao, R. Bertoncello, E. Cattaruzza, S. Gialanella, S. Gross, G. Mattei, P. Mazzoldi, E. Tondello, *J. Mater. Chem.* **2002**, *12*, 2401–2407.
[18] L. Q. Jing, X. J. Sun, W. M. Cai, Z. L. Xu, Y. G. Du, H. G. Fu, *J. Phys. Chem. Solids* **2003**, *64*, 615–623.
[19] Z. Qinghong, G. Lian, G. Jingkun, B. McKinney, M. Rouse, *Appl. Catal. B* **2000**, *26*, 207–215.

 © 2005 Wiley-VCH Verlag GmbH & Co. KGaA, Weinheim

[20] N. Yoshio, K. Mitsuo, N. Junichi, *J. Phys. Chem. B* **1998**, *102*, 10279–10283.
[21] K. Nauka, T. I. Kamins, *J. Electrochem. Soc.* **1999**, *146*, 292–299.
[22] L. Q. Jing, X. J. Sun, J. Shang, W. M. Cai, Z. L. Xu, Y. G. Du, H. G. Fu, *Sol. Energy Mater. Sol. Cells* **2003**, *79*, 133–151.
[23] X. M. Qian, X. T. Zhang, Y. B. Bai, *J. Nanopart. Res.* **2000**, *2*, 191–198.
[24] L. Q. Jing, Z. L. Xu, *Appl. Surf. Sci.* **2001**, *180*, 308–314.
[25] M. Sadeghi, W. Liu, *J. Phys. Chem.* **1996**, *100*, 19466–19474.
[26] N. J. Renault, *J. Phys. Chem.* **1986**, *90*, 2732–2743.
[27] L. Q. Jing, Y. G. Zhang, Z. L. Xu, *J. Chin. Univ.* **2001**, *22*, 1885–1888.

Received: September 28, 2004

 © 2005 Wiley-VCH Verlag GmbH & Co. KGaA, Weinheim

Novel Supramolecular Frameworks Self-Assembled from a Two-Dimensional Polymeric Network: Synthesis and Crystal Structure of a Macrocyclic Organotin(IV) Complex

Chunlin Ma,*[a,b] Yinfeng Han,[a] and Rufen Zhang,[a] and Daqi Wang[a]

Keywords: Polymers / Self-assembly / Supramolecular chemistry / Tin

The two-dimensional polymer $[n\mathrm{Bu_2Sn(O_2CC_6H_4)}]_4$ has been synthesized by the self-assembly of di-*n*-butyltin oxide and 4-carboxyphenylboronic acid. The X-ray crystal structure shows that the metal ions display a trigonal bipyramidal coordination geometry to bind the endocyclic oxygen atom. Intermolecular π–π stacking interactions between adjacent phenyl groups of the ligand cause the self-assembly into a 1D chain. In this chain one oxygen atom of the carboxylate group binds to one $[n\mathrm{Bu_2Sn(O_2CC_6H_4)}]_4$ unit to give rise to a 2D architecture.
(© Wiley-VCH Verlag GmbH & Co. KGaA, 69451 Weinheim, Germany, 2005)

Introduction

Owing to the enormous variety of intriguing structural topologies and their unexpected properties for potential practical applications,[1–4] the chemistry of novel organotin(IV) polymers based on covalent interactions[5–9] or supramolecular contacts (such as hydrogen bonding and/or π–π stacking interactions)[10–13] has been actively investigated. The vast majority of reported work is based upon the use of polyfunctional organic ligands to bind to the tin ions through self-assembly processes, leading to the formation of compounds with fascinating topologies and physical properties. It has also been shown that the careful selection of appropriate multidentate bridging ligands is helpful not only to tailor effectively the polymer architectures but also to realize various applications. In this field, studies have been focused on benzenecarboxylate ligands, such as benzenetricarboxylic acid. However, much less work has been carried out to investigate organotin polymer boronic acid ligands. In this work, we select 4-carboxyphenylboronic acid as the ligand, on the basis of the following considerations: (i) 4-carboxyphenylboronic acid anions have two different groups, and they may act as linkers to connect metal ions into higher dimensional structures by varied coordination modes; (ii) 4-carboxyphenylboronic acid anions may have different effects in the construction of coordination polymers; (iii) the carboxyl and boronic acid occupy *trans* positions, and thus can act as a good bridging ligand and benefit the molecular self-assembly. Therefore, we selected this ligand with the hope of constructing novel organotin(IV) coordination polymers with fascinating structures and/or characteristic properties. To our surprise, we obtained an unprecedented tetranuclear macrocyclic organotin complex $[n\mathrm{Bu_2Sn(O_2CC_6H_4)}]_4$ by B–C cleavage and the new Sn–C bond formation. To the best of our knowledge, this is the first example where organic linkers are incorporated into one metal–organic polymer by B–C bond cleavage and new Sn–C bond formation. The complex has been characterized by elemental analysis and IR, ^{1}H, and ^{13}C NMR spectroscopy. Furthermore, we have also characterized the complex by X-ray crystallography.

[a] Department of Chemistry, Liaocheng University, Liaocheng 252059, P. R. China
[b] Department of Chemistry, Taishan University, Taian 271021, P. R. China
Fax: +86-538-6715521
E-mail: macl@lctu.edu.cn

Result and Discussion

The synthetic procedure is shown in Scheme 1.

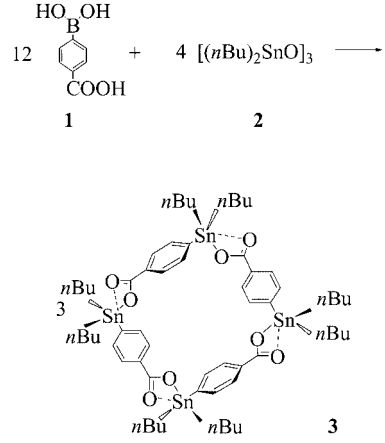

Scheme 1.

The main feature in the IR spectrum is the absence of a band in the region between 2800 and 3320 cm^{-1}, where the

ν(O–H) vibration in the free ligand appears, which indicates metal–ligand bond formation. In organotin carboxylate complexes, the IR spectra can provide useful information concerning the coordination mode of the carboxylate. When the carboxylate group coordinates to the atom in a monodentate manner, the difference between the wavenumbers of the (mode I) asymmetric and symmetric carboxylate stretching bonds, $\Delta\nu$ ($\nu_{asCOO^-} - \nu_{symCOO^-}$), is larger than that observed for ionic compounds. When the ligand chelates (mode II), $\Delta\nu$ is considerably smaller than that for ionic compounds, while for asymmetric bidentate coordination the value is in the range characteristic of monodentate coordination.[14] The characteristic wavenumber difference, $\Delta\nu$, for mode III is larger than that for chelated ions and nearly the same as that observed for ionic compounds (Scheme 2).

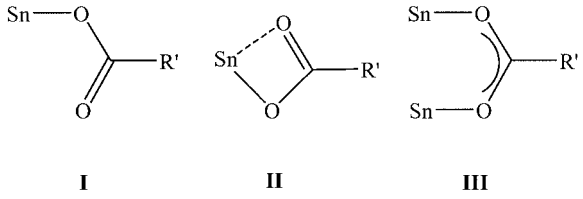

Scheme 2. Different coordination modes of the carboxylate group.

Based on the above results, it was possible to distinguish the coordination mode of the COO^- group. The magnitude of $\Delta\nu$ of about 273 cm^{-1}, compared with that for the corresponding sodium salt, reveals that the carboxylate ligands are monodentate under the conditions employed.[15,16]

The ^1H NMR spectrum of the complex shows that the signal for the OH proton in the spectrum of the ligand is absent in that of the complex, thus indicating the removal of the OH proton and the formation of Sn–O bonds. This consistent with the IR data. The ^{13}C NMR spectroscopic data for the complex are consistent with organotin carboxylate structures. Although at least four different types of carboxylate groups are present, only single resonance are observed for the COO group in the ^{13}C NMR spectrum. This is either due to accidental magnetic equivalence of the carbonyl carbon atoms or the separations between the four peaks of resonance are too small to be resolved.

The molecular structure and a fragment of the crystal lattice are illustrated in Figure 1 and Figure 2, respectively. A crystallographic study of complex **3** shows that the tetranuclear complex is characterized by a 28-membered $C_{20}O_4Sn_4$ macrocyclic ring system with all four oxygen atoms directed into the interior of the cavity and the eight *n*-butyl groups attached to the tin centers approximately perpendicular to the molecular plane (Figure 1). All the tin atoms possess the same ligand environments, with only minor differences in bond lengths and bond angles. For Sn(1), for example, the geometry of the tin atom is distorted tetrahedral and the tin atom forms four primary bonds: two to the butyl groups, one to phenyl, and one to an oxygen atom. Around the tin atom, the angles O(1)–Sn–C(29) [100.9(8)°], C(29)–Sn–C(33) [128.7(9)°], and C(26)–Sn–C(33) [116.4(8)°] are wider while O(1)–Sn–C(26) [93.8(5)°], C(29)–Sn–C(26) [109.1(9)°], and O(1)–Sn–C(33) [98.6(7)°] are narrower than the ideal tetrahedral angle. Also, the weak Sn···O bond [2.906 Å for Sn(1)···O(4′)] between tin and the exocyclic oxygen atoms of adjacent molecules is less than the sum of the van der Waal's radii of tin oxygen atoms (3.68 Å),[17] all of which are similar to those reported in the literature.[18] Therefore, if considering the Sn···O weak interaction, the structural distortion for the tin atom is best described as a trigonal bipyramidal geometry with O(1) and O(4′) atoms occupying the axial sites and an axial-Sn-axial [O(1)–Sn–O(4′)] angle of 175.36°. Sn(1), C(26), C(29), and C(33) are almost completely coplanar with the tin atom. The sum of angles between the tin atom and the equatorial atoms is 354.2°, consistent with the ideal value of 360°.

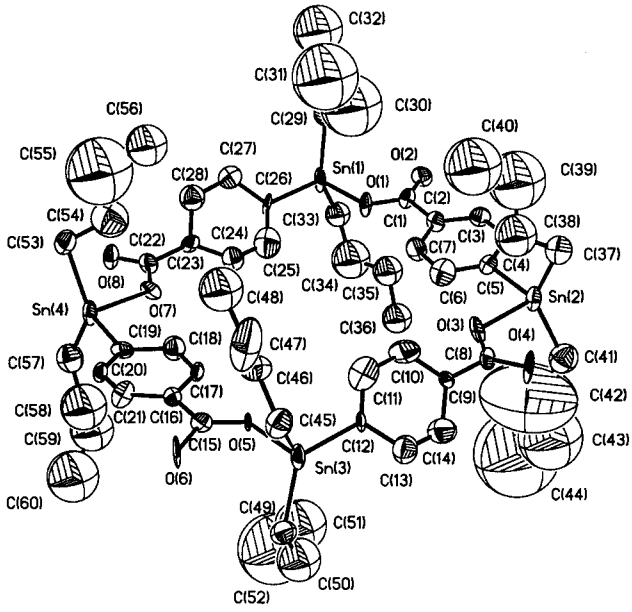

Figure 1. ORTEP plot of the molecular structure of [nBu$_2$Sn-($O_2CC_6H_4$)]$_4$ (**3**). Thermal ellipsoids are drawn with 30% probability. Selected bond lengths [Å] and angles [°]: Sn(1)–O(1) 2.072(10), Sn(1)–C(29) 2.08(2), Sn(1)–C(26) 2.091(15), Sn(1)–C(33) 2.15(2), Sn(1)···O(2) 3.191, Sn(1)···O(4A) 2.905, Sn(2)–O(3) 2.084(11), Sn(2)–C(37) 2.11(3), Sn(2)–C(41) 2.15(3),Sn(2)–C(5) 2.201(19), Sn(2)···O(4) 3.049, Sn(2)···O(6A) 2.769, Sn(3)–O(5) 2.065(10), Sn(3)–C(49) 2.12(2), Sn(3)–C(12) 2.137(15), Sn(3)–C(45) 2.18(2), Sn(3)···O(6) 3.209, Sn(3)···O(8A) 2.898, Sn(4)–O(7) 2.103(12), Sn(4)–C(57) 2.10(3), Sn(4)–C(19) 2.105(18), Sn(4)–C(53) 2.26(2), Sn(4)···O(8) 3.023, Sn(4)···O(2A) 2.751; C(29)–Sn(1)–C(26) 109.1(9), C(49)–Sn(3)–C(12) 116.1(8), C(26)–Sn(1)–C(33) 116.4(8), C(12)–Sn(3)–C(45) 112.9(8), O(1)–C(1)–O(2) 122.1(14), O(5)–C(15)–O(6) 123.1(14), C(37)–Sn(2)–C(41) 133.1(10), C(57)–Sn(4)–C(19) 109.8(9), C(37)–Sn(2)–C(5) 111.5(9), C(57)–Sn(4)–C(53) 135.9(9), C(41)–Sn(2)–C(5) 108.7(10), C(19)–Sn(4)–C(53) 110.0(8), O(3)–C(8)–O(4) 124.1(19), O(7)–C(22)–O(8) 119.8(17).

The size of cavity in this macrocycle can be evaluated from the Sn···Sn and transannular O···O distances, which are 9.181–9.214 Å and 7.219–7.341 Å, respectively, similar to those in di-*n*-butyltin(IV) isophthalate.[19] From the X-ray structure, we found that the tetranuclear macrocyclic rings are linked into a 1D chain through face-to-face π–π stacking and weak Sn···O interactions. In the case of the stacking

 © 2005 Wiley-VCH Verlag GmbH & Co. KGaA, Weinheim

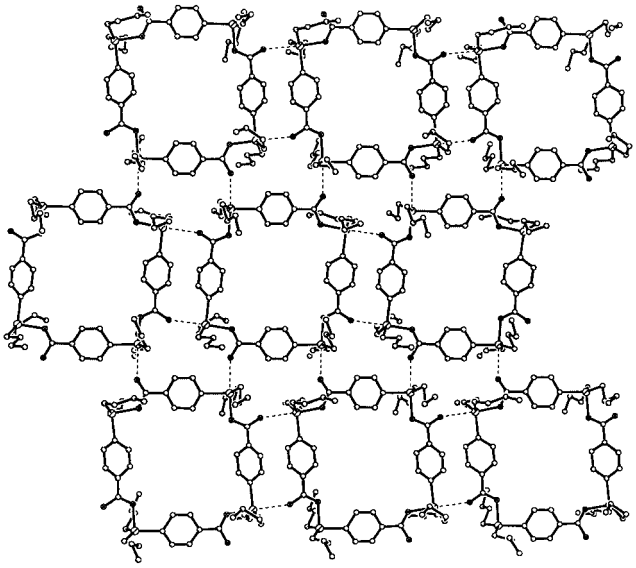

Figure 2. Polymeric network formed through intermolecular Sn···O′ and π–π stacking interactions.

phenyl rings, the centroid–centroid distance is 4.178 Å, which is much shorter than that of the optimized structure for parallel displaced stacking benzene dimer in the gas phase (4.50 Å)[20] and those of other reported stacking aryl groups (4.6 Å[21] and 4.83 Å[22]), thus indicating that the π–π stacking interactions are very strong and it is these interactions that stabilize the 1D chain in the crystal. Therefore, self-assembly occurs through weak Sn···O interactions and helps the molecules form a 2D architecture (Figure 2).

In summary, from the crystal structure described above we can conclude that the B–C cleavage and the new Sn–C bond formation are crucial for the formation of the macrocyclic structure. This discovery may cast light on the reactivity of alkyltin(IV) compounds. That is, we can intentionally design and synthesize alkyltin(IV) compounds to obtain valuable compounds with specific topologies.

Experimental Section

Materials and Measurements: Di-*n*-butyltin oxide and 4-carboxyphenylboronic acid are commercially available, and they were used without further purification. The melting points were obtained with a Kofler micro-melting point apparatus and were uncorrected. IR spectra were recorded on a Nicolet-460 spectrophotometer using KBr discs and sodium chloride optics. ^{1}H, ^{13}C, and ^{119}Sn NMR spectra were recorded on Varian Mercury Plus 400 spectrometer operating at 400, 100.6, and 149.2 MHz, respectively. The spectra were acquired at room temperature (298 K) unless otherwise specified; ^{13}C spectra are broadband proton decoupled. The chemical shifts are reported in ppm with respect to the references (external tetramethylsilane for ^{1}H and ^{13}C NMR, and neat tetramethyltin for ^{119}Sn NMR). Elemental analyses (C,H) were performed with a PE-2400II apparatus.

[*n*Bu$_2$Sn(O$_2$CC$_6$H$_4$)]$_4$ (3): The reaction was carried out under a nitrogen atmosphere. Di-*n*-butyltin oxide (0.497 g, 2 mmol) and 4-carboxyphenylboronic acid (0.332 g, 2 mmol) were added to a solution of dry toluene (50 mL) in a Schlenk flash. Refluxing was continued for 10 h. After filtration the solvent was evaporated in vacuo and the residue crystallized from dichloromethane to give complex **3** as white crystals. Yield: 81%. M.p. 110–112 °C. $C_{60}H_{88}O_8Sn_4$ (1412.18): calcd. C 51.04, H 6.28; found C 51.01, H 6.21. IR (KBr): $\tilde{\nu}$ = 3067, 2960, 2924, 2855, 1634, 1605, 1582, 1448, 1361, 1342, 561, 546, 471 cm^{-1}. ^{1}H NMR ($CDCl_3$): δ = 0.89 (t, CH_3), 1.34–1.72 (m, $^2J_{Sn,H}$ = 75.1 Hz, $CH_2CH_2CH_2$), 7.64 (d, C_6H_4), 8.13 (d, C_6H_4) ppm. ^{13}C NMR ($CDCl_3$): δ = 27.1 (α-CH_2, $^1J_{^{119}Sn,^{13}C}$ = 607 Hz), 28.5 (β-CH_2), 26.3 (γ-CH_2), 13.5 (CH_3), 172.1 (COO) ppm. ^{119}Sn NMR ($CDCl_3$): δ = –57.2 ppm.

X-ray Crystallography. Crystal Data for 3: Monoclinic, $P2_1/n$, a = 14.288(18), b = 28.66(3), c = 19.17(2) Å; β = 110.11(2)°, V = 7371 Å^3, T = 293 K, Z = 4, μ = 1.381 mm^{-1}, 34 071 reflections measured, 11 795 unique (R_{int} = 0.2467) which were used in all calculations. Final R indices were R_1 = 0.0978, wR_2 = 0.1692 [$I > 2\sigma(I)$], R_1 = 0.2967 wR_2 = 0.2391 (all data).
CCDC-225030 contains the supplementary crystallographic data for this paper. These data can be obtained free of charge from The Cambridge Crystallographic Data Centre via www.ccdc.cam.ac.uk/data_request/cif.

Acknowledgments

We thank the National Nature Science Foundation of China (20271025) and the Nature Science Foundation of Shandong Province for financial support.

[1] M. Gielen, *Appl. Organomet. Chem.* **2002**, *16*, 481.
[2] J. P. Ashmore, T. Chivers, K. A. Kerr, J. H. G. Van Roode, *Inorg. Chem.* **1977**. *16*, 191.
[3] J. H. Wengrovius, M. F. Garbauskas, *Organometallics* **1992**, *11*, 1334.
[4] A. Samuel-Lewis, P. J. Smith, J. H. Aupers, D. Hampson, D. C. Povey, *J. Organomet. Chem.* **1992**, *437*, 131.
[5] a) S. Bhandari, C. G. Frost, C. E. Hague, M. F. Mahon, K. C. Molloy, *J. Chem. Soc., Dalton Trans.* **2000**, 663; b) A. Goodger, M. Hill, M. F. Mahon, J. McGinley, K. C. Molloy, *J. Chem. Soc., Dalton Trans.* **1996**, 847; c) M. Hill, M. F. Mahon, K. C. Molloy, *J. Chem. Soc., Dalton Trans.* **1996**, 1857; d) S. Bhandari, M. F. Mahon, J. G. McGinley, K. C. Molloy, C. E. E. Roper, *J. Chem. Soc., Dalton Trans.* **1998**, 3425.
[6] R. Wang, M. Hong, J. Luo, R. Cao, J. Weng, *Eur. J. Inorg. Chem.* **2002**, 2082.
[7] A. Galani, M. A. Demertzis, M. Kubicki, D. Kovala-Demertzi, *Eur. J. Inorg. Chem.* **2003**, 1761.
[8] H. Preut, F. Huber, M. Gielen, *Acta Crystallogr., Sect. C* **1990**, *46*, 2071.
[9] S. W. Ng, *Z. Kristallogr., New Cryst. Struct.* **1998**, *213*, 157.
[10] F. L. Lee, E. J. Gabe, L. E. Khoo, W. H. Leong, G. Eng, F. E. Smith, *Inorg. Chim. Acta* **1989**, *166*, 257.
[11] R. Xiong, J. Zuo, X. You, H. Fun, S. S. S. Raj, *Organometallics* **2000**, *19*, 4183.
[12] F. Huber, B. Mundus-Glowacki, H. Preut, *J. Organomet. Chem.* **1989**, *365*, 111.
[13] a) S. W. Ng, S. S. S. Raj, H. Fun, I. A. Razak, J. M. Hook, *Acta Crystallogr., Sect. C* **2000**, *56*, 966; b) S. W. Ng, J. Holecek, *Acta Crystallogr., Sect. C* **1998**, *54*, 750; c) S. W. Ng, V. G. Kumar, G. Xiao, A. van der Helm, J. Holecek, A. Lycka, *Heteroatom Chem.* **1991**, *2*, 495.
[14] N. W. Alcock, J. Culver, S. M. Roe, *J. Chem. Soc., Dalton Trans.* **1992**, 1477.
[15] G. K. Saudhu, R. Gupta, S. S. Sandhu, R. V. Parish, *Polyhedron* **1985**, *4*, 81.
[16] G. K. Saudhu, R. Gupta, S. S. Sandhu, R. V. Parish, K. Brown, *J. Organomet. Chem.* **1985**, *279*, 373.
[17] A. Bondi, *J. Phys. Chem.* **1964**, *68*, 441.

 © 2005 Wiley-VCH Verlag GmbH & Co. KGaA, Weinheim

[18] V. Chandrasekhar, S. Nagendran, V. Baskar, *Coord. Chem. Rev.* **2002**, *235*, 1.
[19] R. García-Zarracino, J. Ramos-Quiñoes, H. Höpfl, *Inorg. Chem.* **2003**, *42*, 3835.
[20] W. L. Jorgensen, D. L. Severance, *J. Am. Chem. Soc.* **1990**, *112*, 4768.
[21] N. Chikaraishi-Kasuga, K. Onoue, Y. Osawa, S. Nakahama, Y. Ohashi, K. Yamaguchi, *Bull. Chem. Soc. Jpn.* **1997**, *70*, 1961.
[22] J.-Y. Ortholand, A. M. Z. Slawin, N. Spencer, J. F. Stoddart, D. J. Williams, *Angew. Chem. Int. Ed. Engl.* **1989**, *28*, 1394.
Received: December 28, 2004

 © 2005 Wiley-VCH Verlag GmbH & Co. KGaA, Weinheim

Self-Assembly of Protonated 1,12-Dodecanediamine Molecules and Strongly Undulated Uranyl Selenate Sheets in the Structure of Amine-Templated Uranyl Selenate: $(H_3O)_2[C_{12}H_{30}N_2]_3[(UO_2)_4(SeO_4)_8](H_2O)_5$

Sergey V. Krivovichev,*[a] Volker Kahlenberg,[b] Evgeniya Yu. Avdontseva,[a] Edgar Mersdorf,[b] and Reinhard Kaindl[a]

Keywords: Host-guest systems / Layered compounds / Selenium / Self-assembly / Uranium

The amine-templated uranyl selenate $(H_3O)_2[C_{12}H_{30}N_2]_3[(UO_2)_4(SeO_4)_8](H_2O)_5$ (**1**) has been prepared. Its structure [monoclinic, $P2_1/n$, a = 11.3437(7), b = 24.8042(12), c = 29.2496(19) Å, β = 96.701(5)°, V = 8173.8(8) Å^3, Z = 4, R_1 = 0.083] is based upon strongly undulating $[(UO_2)(SeO_4)_2]^{2-}$ sheets consisting of corner-sharing UO_7 bipyramids and SeO_4^{2-} tetrahedra. The undulations of the adjacent sheets have an *anti*-phase character that allows the formation of large eliptical channels that are occupied by rod micelles formed by self-assembly of protonated 1,12-dodecanediamine molecules.

(© Wiley-VCH Verlag GmbH & Co. KGaA, 69451 Weinheim, Germany, 2005)

Introduction

The preparation of new porous uranium-based materials is of interest because of their relevance to radioactive waste disposal, utilization of depleted uranium, catalysis, etc.[1] One of the pathways employed in the synthesis of new compounds is the use of amines as templates.[2] The role of amines as structure-directing agents has been under extensive discussion. There are strong indications that, in some systems, amine molecules may control the formation of new topologies that are not observed in purely inorganic structures, whereas in other systems the role of protonated amine molecules is simply to balance the negative charge of the inorganic part of a structure.[2] We note that in the preparation of uranium-based oxide compounds, short-chain and cyclic amines have mostly been employed, whereas the effect of long-chain amines, especially α,ω-alkyldiamines, is as yet unknown. We report here the synthesis and structure of $(H_3O)_2[C_{12}H_{30}N_2]_3[(UO_2)_4(SeO_4)_8](H_2O)_5$ (**1**), a new uranyl selenate templated by 1,12-dodecanediamine molecules.

Whereas the structural chemistry of uranyl selenites has been intensively investigated over the last few years,[2f,3] uranyl selenates have received much less attention[4] as their synthesis under low-temperature hydrothermal conditions (100–250 °C) rarely results in crystalline selenates, even if selenic acid, H_2SeO_4, is used as a source of selenium. This is caused by the instability of the selenate ion, SeO_4^{2-}, and its easy reduction to selenite, SeO_3^{2-}.[2f,5] To avoid the selenate/selenite reduction, yellow needles of **1** have been prepared by room-temperature evaporation of the solvent from an aqueous solution of uranyl nitrate, selenic acid, and 1,12-dodecanediamine. A semi-quantitative EDX analysis indicated a U/Se ratio of 1:2, and a single-crystal X-ray diffraction experiment allowed the crystal-structure characterization. The results of IR spectroscopic studies were found to be in good agreement with the results of the crystal-structure investigations.

Results and Discussion

The structure of **1** consists of well-defined organic and inorganic substructures (Figure 1). The inorganic substructure contains four symmetrically independent U^{VI} centers that form linear uranyl cations, UO_2^{2+} (U=O distances in the range of 1.732–1.766 Å). These uranyl cations are further coordinated equatorially by five oxygen atoms each to form pentagonal UO_7 bipyramids (U–O 2.326–2.500 Å). There are eight symmetrically independent Se^{VI} cations, each tetrahedrally coordinated by four oxygen atoms (Se–O 1.597–1.671 Å). The bond-valence sums for the U and Se atoms[6] are in the range of 5.89–6.35 valence units (v.u.). The UO_7 bipyramids and SeO_4^{2-} tetrahedra share corners to form the $[(UO_2)(SeO_4)_2]^{2-}$ sheets depicted in Figure 2 (see a). These sheets are parallel to (001) and are strongly undulated along the *c* axis. The undulation vector is parallel to [010] and is equal to *b* (24.804 Å). The undulation amplitude is about 25 Å. The undulations in the adjacent sheets

[a] Department of Crystallography, St. Petersburg State University, University Emb. 7/9, 199034 St. Petersburg, Russia
Fax: +43-512-5072926
E-mail: skrivovi@mail.ru
[b] Institut für Mineralogie und Petrographie, Universität Innsbruck,
Innrain 52, 6020 Innsbruck, Austria
Fax: +43-512-5072926
E-mail: volker.kahlenberg@uibk.ac.at

have an *anti*-phase character which means that large eliptical channels are created along the *a* axis.

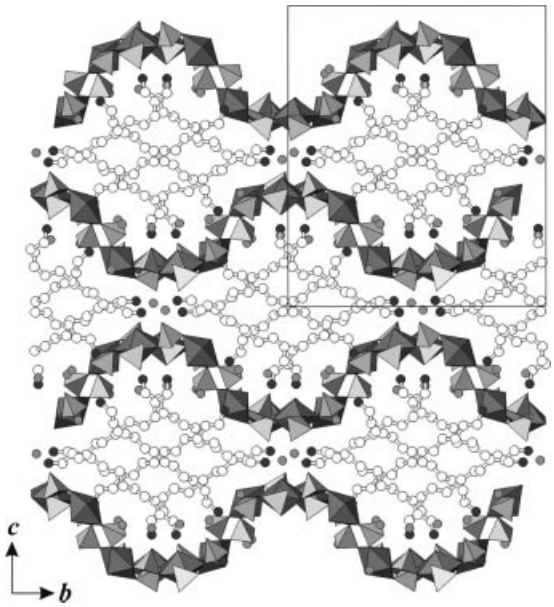

Figure 1. Crystal structure of **1** projected along the *a* axis. $[UO_7]^{8-}$ bipyramids are dark grey, and $[SeO_4]^{2-}$ tetrahedra are light grey. C and N atoms, and H_2O groups are shown as white, dark grey and light grey circles, respectively.

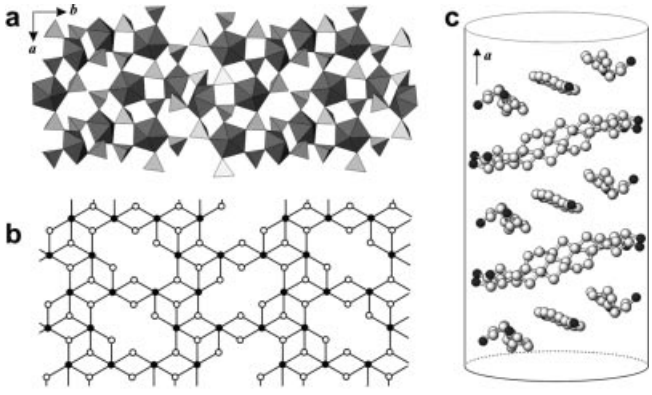

Figure 2. The $[(UO_2)(SeO_4)_2]^{2-}$ sheet in the structure of **1** (a), nodal representation (U and Se polyhedra are symbolized by black and white circles, respectively) (b), and organization of 1,12-dodecanediamine molecules into a rod micelle (c).

The topology of the $[(UO_2)(SeO_4)_2]^{2-}$ sheets is remarkable as it has not been observed previously in any uranium compound. It can be analyzed by means of a nodal representation, which is especially suitable for the description of structures based upon coordination polyhedra of two types.[7] Using this approach, the UO_7 bipyramids and SeO_4 tetrahedra are symbolized by black and white vertices, respectively. The vertices are linked by a line segment if two respective polyhedra share a common oxygen atom. The idealized black-and-white graph of the uranyl selenate sheet observed in **1** is shown in Figure 2 (see b). Although it is new for uranium chemistry, it can be obtained from a more regular (3.6.3.6) graph by eliminating some of its vertices and edges. This topological procedure is common for many sheet topologies observed in uranyl oxo salts.[2c,7]

The organic substructure consists of micelles of protonated 1,12-dodecanediamine molecules oriented parallel to the *a* axis. These micelles occupy the channels created by the packing of the $[(UO_2)(SeO_4)_2]^{2-}$ sheets. The assembly scheme of the 1,12-dodecanediamine chain molecules within the micelle is shown in Figure 2 (see c). The molecules are arranged into sublayers approximately parallel to (–102). The planes of these sublayers are not perpendicular to the micelle axis but form an angle of about 60°. In each layer, there are three parallel oriented $[C_{12}H_{30}N_2]^{2+}$ molecules. The molecules in the adjacent layers are at an angle of 30° relative to each other, which results in the elliptical form of the perpendicular section of the micelle. The lateral dimensions of the micelle are about 20 × 24 Å, i.e. are at the level of nanometers. The interactions between organic and inorganic substructures involve N···O hydrogen bonds to oxygen atoms of uranyl ions and terminal oxygen atoms of selenate tetrahedra. In addition, the structure contains two symmetrically independent H_3O^+ ions and five symmetrically independent H_2O molecules that contribute to the network of hydrogen bonds. The H_3O^+ ions correspond to the O(41) and O(42) sites, which can easily be identified as oxoniums by the analysis of their coordination environment. Both O(41) and O(42) are coordinated to three oxygen atoms located at O···O distances of 2.47–2.64 Å (Table 1). This coordination is a rather flat pyramid that can be inferred from the O···H_3O···O angles of 99.0–123.8°. This coordination geometry is typical for oxonium ions in oxo salt structures and has been observed in the structures of $(H_3O)(HSeO_4)$,[8] $(H_3O)(HSO_4)$,[9] $M(H_3O)(HSO_4)_2$ (M = Na,[10] K,[11] Ag[12]), $(H_3O)Sb_2(SO_4)_2$,[13] $Zr(H_3O)_2(SO_4)_3$,[14] $(H_3O)La(SO_4)_2(H_2O)$,[15] $(H_5O_2)(H_3O)_2Nd(SO_4)_3$,[16] $(H_3O)_2Nd(HSO_4)_3(SO_4)$,[16] etc. There are also several oxonium uranyl selenate hydrates known, although the coordination geometries of the oxonium ions in their structures are not as well-defined as in the structure of **1**. The presence of oxonium in **1** can also be confirmed by the presence of a strong band at 2853 cm^{-1} in the IR spectrum of **1**. This band can be assigned to strong hydrogen bonds corresponding to O···O distances of about 2.5–2.6 Å[17] (compare with the distances given in Table 1).

Protonated long-chain amine molecules are known to form cylindrical micelles in aqueous solutions by a self-assembly process that is governed by competing hydrophobic/hydrophilic interactions.[18] The flexible inorganic complexes present in the reaction mixture could then form around these cylindrical micelles to produce an inorganic structure that reflects the cylindrical form of the micelles. In the case of **1**, the inorganic structure has the form of a strongly undulated sheet, although structures with highly porous uranyl selenate nanotubules have also been observed.[19] This indicates the possibility of preparation of uranium oxo salt mesostructures if larger organic moieties (e.g., block copolymers) are involved in the synthesis procedure. This possibility is favored by the high flexibility of

 © 2005 Wiley-VCH Verlag GmbH & Co. KGaA, Weinheim

Table 1. Selected interatomic distances [Å] for $(H_3O)_2[C_{12}H_{30}N_2]_3[(UO_2)_4(SeO_4)_8](H_2O)_5$ (**1**).

U(1)–O(6)	1.734(12)	U(3)–O(21)	1.733(14)
U(1)–O(3)	1.759(13)	U(3)–O(38)	1.741(13)
U(1)–O(1)	2.362(11)	U(3)–O(10)	2.326(13)
U(1)–O(4)	2.383(13)	U(3)–O(24)	2.331(17)
U(1)–O(25)	2.387(11)	U(3)–O(33)	2.379(13)
U(1)–O(30)	2.395(13)	U(3)–O(11)	2.431(12)
U(1)–O(15)	2.405(12)	U(3)–O(12)	2.468(12)
U(2)–O(27)	1.754(12)	U(4)–O(16)	1.745(12)
U(2)–O(22)	1.766(11)	U(4)–O(2)	1.758(12)
U(2)–O(39)	2.333(12)	U(4)–O(7)	2.367(12)
U(2)–O(17)	2.343(11)	U(4)–O(23)	2.384(11)
U(2)–O(20)	2.379(12)	U(4)–O(26)	2.405(13)
U(2)–O(29)	2.416(11)	U(4)–O(14)	2.423(12)
U(2)–O(18)	2.502(12)	U(4)–O(28)	2.429(11)
Se(1)–O(17)	1.628(11)	Se(5)–O(13)	1.614(13)
Se(1)–O(10)	1.630(13)	Se(5)–O(33)	1.623(13)
Se(1)–O(32)	1.631(12)	Se(5)–O(15)	1.634(12)
Se(1)–O(28)	1.633(11)	Se(5)–O(18)	1.648(12)
Se(2)–O(9)	1.602(13)	Se(6)–O(24)	1.601(17)
Se(2)–O(39)	1.626(12)	Se(6)–O(19)	1.612(14)
Se(2)–O(14)	1.630(12)	Se(6)–O(1)	1.635(12)
Se(2)–O(12)	1.639(12)	Se(6)–O(20)	1.643(12)
Se(3)–O(34)	1.624(13)	Se(7)–O(40)	1.609(15)
Se(3)–O(25)	1.628(11)	Se(7)–O(8)	1.627(16)
Se(3)–O(35)	1.631(14)	Se(7)–O(30)	1.646(13)
Se(3)–O(11)	1.638(12)	Se(7)–O(7)	1.660(12)
Se(4)–O(5)	1.626(12)	Se(8)–O(36)	1.598(17)
Se(4)–O(37)	1.635(13)	Se(8)–O(26)	1.617(13)
Se(4)–O(23)	1.649(11)	Se(8)–O(31)	1.620(18)
Se(4)–O(29)	1.672(11)	Se(8)–O(4)	1.633(13)
$H_3O(41)$–O(5)	2.604(17)	$H_3O(42)$–O(31)	2.44(2)
$H_3O(41)$–O(8)	2.47(2)	$H_3O(42)$–O(34)	2.639(19)
$H_3O(41)$–O(35)	2.554(19)	$H_3O(42)$–O(37)	2.584(19)

the U–O–T links in uranyl compounds with tetrahedral TO_4^{2-} anions (T = S, Cr, Se, Mo).[20] The fabrication of meso- and nanostructures in uranium oxo-systems might be of great interest for the preparation of new functional nanomaterials and their subsequent use in nanotechnology. The latter perspective seems to be a promising direction for the utilization of depleted uranium, thousands tons of which are now stored in countries such as the USA and Russia.

Experimental Section

In a typical synthesis of **1**, 0.028 g of 1,12-dodecanediamine, 0.30 mL of 40% H_2SeO_4, and 0.081 g of $(UO_2)(NO_3)_2{\cdot}6H_2O$, were mixed with 2 mL of distilled H_2O. The mixture was poured into a watch glass and was kept in a fume hood at room temperature. Yellow needles of **1** were formed in approximately 10% yield (0.008 g) in about 3–4 days. The compound was characterized by semi-quantitative electron microprobe analysis. Far-IR and Raman spectra were recorded and the presence of uranyl ions and selenate groups was confirmed. Far-IR (nujol): $\tilde{\nu}$ = 3566 (m), 3486 (s), 3155 (m), 2927 (s), 2853 (s), 1613 (s), 1505 (m), 1470 (w), 1211 (w), 1191 (w), 1150 (w), 1016 (vw), 954 (s), 919 (m), 888 (s), 848 (s), 822 (s), 725 (m) cm^{-1}.

Crystallographic Data for $(H_3O)_2[C_{12}H_{30}N_2]_3[(UO_2)_4(SeO_4)_8](H_2O)_5$: Plate-like crystal ($0.02\times0.04\times0.22\ mm^3$), monoclinic, $P2_1/n$, a = 11.3437(7), b = 24.8042(12), c = 29.2496(19) Å, β = 96.701(5)°, V = 8173.8(8) $Å^3$, Z = 4, ρ_{calc} = 2.405 $g\,cm^{-3}$, $2\theta_{max}$ = 54.28°, λ(Mo-K_α) = 0.71073 Å, ω-scan (1° per image) at φ = 0° (STOE IPDS II), 293 K, 48 038 measured reflections, 17023 independent reflections, 11646 reflections with $|F_o| \geq 4\sigma_F$ (R_{int} = 0.084, R_σ = 0.089), numerical absorption correction (programs X-Shape and X-Red, STOE, Darmstadt, 1998), structure solution by direct methods, full-matrix least-square refinement (263 parameters) on $|F^2|$, no treatment of H atoms [programs SIR-97[21] and SHELXL-97 (G. M. Sheldrick, program for the refinement of crystal structures, Göttingen, **1997**)], R_1 = 0.083, wR_2 = 0.137 for observed reflections, max./min. electron density = 2.703/–1.672.

CCDC-261122 contains the supplementary crystallographic data for this paper. These data can be obtained free of charge from The Cambridge Crystallographic Data via www.ccdc.cam.ac.uk/data_request/cif.

Acknowledgments

This work was financially supported by the Austrian Science Fund (FWF) (project M771-N10). We thank Prof. Dr. Ulrich Griesser for the help with the measurement of the IR spectra.

[1] a) P. C. Burns, M. L. Miller, R. C. Ewing, *Can. Mineral.* **1996**, *34*, 845–880; b) C. L. Cahill, P. C. Burns, *Inorg. Chem.* **2001**, *40*, 1347–1351; c) Y. Li, C. L. Cahill, P. C. Burns, *Chem. Mater.* **2001**, *13*, 4026–4031; d) S. V. Krivovichev, C. L. Cahill, P. C. Burns, *Inorg. Chem.* **2003**, *42*, 2459–1464; e) A. J. Locock, P. C. Burns, *J. Solid State Chem.* **2003**, *175*, 372–379; f) R. E. Sykora, T. E. Albrecht-Schmitt, *Inorg. Chem.* **2003**, *42*, 2179–2181; g) M. B. Doran, C. L. Stuart, A. J. Norquist, D. O'Hare, *Chem. Mater.* **2004**, *16*, 565–566.

[2] a) X. Wang, J. Huang, A. J. Jacobson, *J. Am. Chem. Soc.* **2002**, *124*, 15 190–15 192; b) A. J. Norquist, M. B. Doran, P. M. Thomas, D. O'Hare, *Inorg. Chem.* **2003**, *42*, 5649–5653; c) S. V. Krivovichev, P. C. Burns, *J. Solid State Chem.* **2003**, *170*, 106–117; d) P. M. Almond, T. E. Albrecht-Schmitt, *Inorg. Chem.* **2003**, *42*, 5693–5698.

[3] a) P. M. Almond, S. M. Peper, E. Bakker, T. E. Albrecht-Schmitt, *J. Solid State Chem.* **2002**, *168*, 358–366; b) P. M. Almond, T. E. Albrecht-Schmitt, *Inorg. Chem.* **2002**, *41*, 1177–1183; c) P. M. Almond, T. E. Albrecht-Schmitt, *Inorg. Chem.* **2003**, *42*, 5693–5698.

[4] a) Yu. N. Mikhailov, Yu. E. Gorbunova, O. V. Shishkina, L. B. Serezhkina, V. N. Serezhkin, *Zh. Neorg. Khim.* **2001**, *46*, 1828–1832; b) Yu. N. Mikhailov, Yu. E. Gorbunova, E. E. Baeva, L. B. Serezhkina, V. N. Serezhkin, *Zh. Neorg. Khim.* **2001**, *46*, 2017–2020.

[5] a) D. Udayakumar, M. Dan, C. N. R. Rao, *Eur. J. Inorg. Chem.* **2004**, 1733–1739; b) I. Pasha, A. Choudhury, C. N. R. Rao, *J. Solid State Chem.* **2003**, *174*, 386–391; c) J. N. Behera, A. A. Ayi, C. N. R. Rao, *Chem. Commun.* **2004**, 968–969.

[6] a) P. C. Burns, R. C. Ewing, F. C. Hawthorne, *Can. Mineral.* **1997**, *35*, 1551–1570; b) N. E. Brese, M. O'Keeffe, *Acta Crystallogr., Sect. B* **1991**, *47*, 192–197.

[7] S. V. Krivovichev, *Crystallogr. Rev.* **2004**, *10*, 185–232.

[8] J. O. Lundgren, I. Taesler, *Acta Crystallogr., Sect. B* **1979**, *35*, 2384–2386.

[9] E. Kemnitz, C. Werner, S. I. Troyanov, *Acta Crystallogr., Sect. C* **1996**, *52*, 2665-.

[10] S. I. Troyanov, C. Werner, E. Kemnitz, H. Worzala, *Z. Anorg. Allg. Chem.* **1995**, *621*, 1617–1624.

[11] E. Kemnitz, C. Werner, S. I. Troyanov, H. Worzala, *Z. Anorg. Allg. Chem.* **1994**, *620*, 1921–1924.

[12] A. Stiewe, E. Kemnitz, S. I. Troyanov, *Z. Anorg. Allg. Chem.* **1999**, *625*, 329–335.

 © 2005 Wiley-VCH Verlag GmbH & Co. KGaA, Weinheim

[13] R. Mercier, J. Douglas, P. G. Jones, G. M. Sheldrick, *Acta Crystallogr., Sect. C* **1983**, *39*, 145–147.
[14] S. I. Troyanov, A. Stiewe, E. Kemnitz, *Z. Naturforsch., Teil B* **1996**, *51*, 19–24.
[15] M. S. Wickleder, *Z. Anorg. Allg. Chem.* **2001**, *627*, 1439–1440.
[16] M. S. Wickleder, *Z. Anorg. Allg. Chem.* **1999**, *625*, 474–480.
[17] E. Libowitzky, *Monatsh. Chem.* **1999**, *130*, 1047–1059.
[18] J. S. Beck, J. C. Vartuli, W. J. Roth, M. E. Leonowicz, C. T. Kresge, K. D. Schmitt, C. T.-W. Chu, D. H. Olson, E. W. Sheppard, S. B. McCullen, J. B. Higgins, J. L. Schlenker, *J. Am. Chem. Soc.* **1992**, *114*, 10834–10843.
[19] a) S. V. Krivovichev, V. Kahlenberg, R. Kaindl, E. Mersdorf, I. G. Tananaev, B. F. Myasoedov, *Angew. Chem. Int. Ed.* **2005**, *44*, 1134–1136; b) S. V. Krivovichev, V. Kahlenberg, I. G. Tananaev, R. Kaindl, E. Mersdorf, B. F. Myasoedov, *J. Am. Chem. Soc.* **2005**, *127*, 1072–1073.
[20] S. V. Krivovichev, *Radiochem.* **2004**, *46*, 434–437.
[21] A. Altomare, G. Cascarano, C. Giacovazzo, A. Gualardi, *J. Appl. Crystallogr.* **1993**, *26*, 343–346.

Received: January 19, 2005

 © 2005 Wiley-VCH Verlag GmbH & Co. KGaA, Weinheim

Synthesis and Characterisation of New Iridium Complexes with the (4*S*)-2-[2-(Diphenylphosphanyl)phenyl]-4-isopropyl-1,3-oxazoline Ligand That Catalyse Asymmetric Michael Reactions

Daniel Carmona,*[a] Joaquina Ferrer,[a] Mónica Lorenzo,[a] Fernando J. Lahoz,[a] Isabel T. Dobrinovitch,[a] and Luis A. Oro[a]

Keywords: Iridium / Phosphanyloxazolines / Metal enolates / Michael addition

The chiral iridium compounds [IrCl(COE){(*S*)-PN}] {COE = cyclooctene, PN = (4*S*)-2-[2-(diphenylphosphanyl)phenyl]-4-isopropyl-1,3-oxazoline, (**1**)}, [Ir(acac)ClH{(*S*)-PN}] {Hacac = acetylacetone, (**2**)} and [Ir{(*S*)-PN}$_2$]A {A = Cl (**3a**,**b**); BF_4 (**4a**,**b**); PF_6 (**5a**,**b**)} have been prepared, characterised and employed as catalysts for the asymmetric Michael addition of keto or cyano esters to α,β-unsaturated carbonyl compounds. The X-ray molecular structures of compounds **2** and **5b** are reported. The model catalytic intermediates [IrH(NCCHCO$_2$R){(*S*)-PN}$_2$]Cl {R = Me (**12**), Et (**13**)} have also been isolated and characterised.

(© Wiley-VCH Verlag GmbH & Co. KGaA, 69451 Weinheim, Germany, 2005)

Introduction

The catalytic asymmetric Michael reaction is a powerful and valuable method for the formation of C–C bonds β to a carbonyl group[1] that often allows construction of quaternary carbon centres.[2] Pioneering work was performed by Wynberg et al., who studied the use of chincona alkaloids as catalysts.[3] In 1984, Brunner and Hammer reported the first example of a transition-metal-catalysed asymmetric Michael addition, employing a complex derived from Co(acac) and (*S*,*S*)-1,2-diphenyl-1,2-ethylenediamine.[4] Since then, much attention has been paid to transition-metal-based systems for the asymmetric catalysis of the Michael reaction, and a variety of chiral transition-metal-based catalysts have been developed by several groups.[2b,5–11] Particularly important are the results achieved by Shibasaki et al. with their heterodimetallic catalysts in the Michael reaction of β-dicarbonyls or hydroxyketones with α,β-unsaturated carbonyls.[12] Related heterodimetallic catalysts have been subsequently developed by others.[13] However, although a few platinum-metal-based compounds have been employed as Michael reaction catalysts, the use of iridium derivatives for this reaction is very scarce.[14] On the other hand, most of the metallic catalytic systems are generated in situ by mixing the appropriate metallic precursor and the chiral ligand, and therefore the actual structure of the involved coordination compound(s) is usually unknown.

[a] Departamento de Química Inorgánica, Instituto de Ciencia de Materiales de Aragón, C.S.I.C. – Universidad de Zaragoza, Instituto Universitario de Catálisis Homogénea, Universidad de Zaragoza,
Pedro Cerbuna 12, 50009 Zaragoza, Spain
Fax: +34-76-761187
E-mail: dcarmona@posta.unizar.es

During our studies on phosphanyloxazoline iridium complexes,[15] we realised that the iridium(I) compound [IrCl(COE){(*S*)-PN}] {COE = cyclooctene, PN = (4*S*)-2-[2-(diphenylphosphanyl)phenyl]-4-isopropyl-1,3-oxazoline, (Scheme 1)} (**1**) activated the sp^3 CH methylene bonds of the acetylacetone (Hacac), affording the hydrido(enolato)-iridium(III) [Ir(acac)ClH{(*S*)-PN}] (**2**). The diastereoselective formation of **2** from **1** prompted us to test complex **1** as a catalyst for Michael addition reactions. In this context, Murahashi, Komiya, et al. have reported the formation of the hydrido(enolato)ruthenium(II) complexes, *mer*-[RuH(acac)(PPh$_3$)$_3$] and *mer*-[RuH(NCCHCO$_2$R)(NCCH$_2$CO$_2$R)(PPh$_3$)$_3$], by reacting either the dihydride [RuH$_2$(PPh$_3$)$_4$] or the orthometalated ethylene complex [RuH(PPh$_2$C$_6$H$_4$)(C$_2$H$_4$)(PPh$_3$)$_2$] with Hacac or alkylcyanoacetates, respectively.[16] Notably, it has been shown that a variety of transition-metal α-cyanocarbanion complexes, including the aforementioned, are intermediates in the catalytic Michael reactions of nitriles.[16,17] Furthermore, very recently, Ikayira et al. have isolated and characterised a chiral metal-carbon-bound ruthenium–malonato complex,

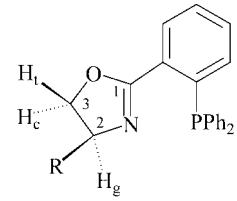

R = *i*Pr, (*S*)-PN;
*i*Bu, (*S*)-PN'

Scheme 1. Phosphanyloxazoline ligands.

 DOI: 10.1002/ejic.200400929 © 2005 Wiley-VCH Verlag GmbH & Co. KGaA, Weinheim

which is the plausible intermediate in the asymmetric Michael reaction of α-substituted acetates with cyclic enones.[18]

Here we report on the synthesis and characterisation of the phosphanyloxazoline iridium complexes **1** and **2**, the related bis(*S*)-PN ligand cationic compounds [Ir{(*S*)-PN}$_2$]A {A = Cl (**3a,b**); BF_4 (**4a,b**); PF_6 (**5a,b**)}, as well as, on their use as catalysts for the Michael addition of cyano or keto esters **6** and **7** to α,β-unsaturated carbonyls **8**–**10** (Scheme 2). The X-ray molecular structures of compounds **2** and **5b** are also included. Furthermore, we also report the preparation and characterisation of the hydrido(enolate)-iridium(III) complexes [IrH(NCCHCO$_2$R){(*S*)-PN}$_2$]Cl {R = Me (**12**), Et (**13**)}, derived from **11a** and **11b**, as possible model intermediates in the catalytic Michael process.

R^1 = Me; R = Me, **6a**; Et, **6b**
R^1 = H; R = Me, **11a**; Et, **11b**

R = Me, **7a**; Et, **7b**

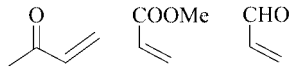

8 **9** **10**

Scheme 2. Catalytic Michael reaction substrates.

Results and Discussion

Treatment of the dimer [Ir(μ-Cl)(COE)$_2$]$_2$[19] with two equivalents of (*S*)-PN, in pentane at –60 °C, afforded [IrCl(COE){(*S*)-PN}] (**1**). Since solutions of **1** in common organic solvents slowly decompose, attempts to obtain an analytically pure sample of this complex failed. However, the spectroscopic data for the generated species, collected at –60 °C, leave no doubt that the proposed formulation for **1** is correct (see Experimental Section).

Complex **1** reacted with acetylacetone, through activation of an sp^3 CH methylene bond, affording the hydrido(enolato)iridium(III) complex [Ir(acac)ClH{(*S*)-PN}] (**2**) stereoselectively. The spectroscopic data indicated the formation of a major isomer (95%) together with trace amounts of some other uncharacterised stereoisomers. The molecular structure of **2** has been determined by a single-crystal X-ray diffraction study (Figure 1). Selected bond parameters are reported in Table 1. Complex **2** has a distorted octahedral coordination environment. The metal centre is coordinated to the two oxygen atoms of an acetylacetonate anion and to the phosphorus and nitrogen atoms of the (*S*)-PN ligand. A chloride anion and a hydride ligand, mutually *trans* (Cl–Ir–H, 169.7°), complete the coordination sphere of the iridium atom. The metal atom is chiral, and the isomer present in the crystal is the *OC*-6–53-*A* diastereomer. The Ir–Cl bond length, 2.512(2) Å, is significantly longer than the mean value observed for terminal chlorides in octahedral Ir complexes, 2.426(7) Å;[20] most probably this fact is a consequence of the high *trans* influence of the hydride that elongates the Ir–Cl bond length to a mean value of 2.500(2) Å when both ligands are situated in a *trans* position relative to each other.[20]

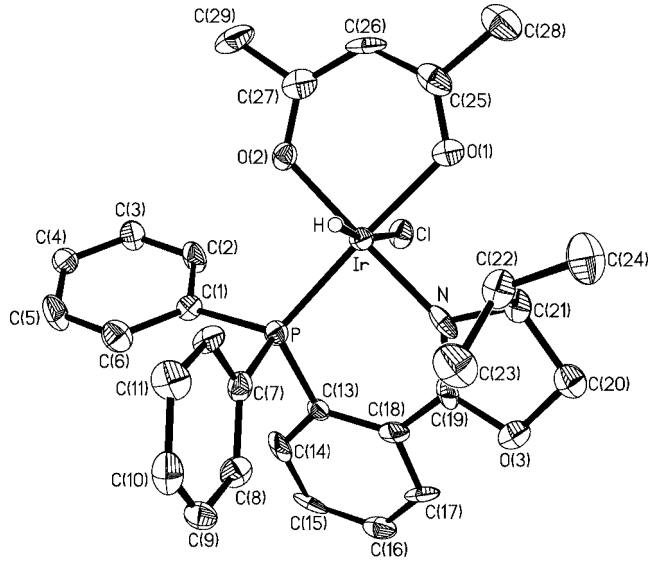

Figure 1. Molecular structure of **2** (organic hydrogen atoms are omitted for clarity).

The highly diastereoselective formation of **2** from **1** prompted us to test complex **1** as a catalyst for Michael addition reactions. A mixture of [Ir(μ-Cl)(COE)$_2$]$_2$ and two equivalents of (*S*)-PN catalysed the addition of the α-cyano propionate **6b** or the β-keto ester **7b** to methyl vinyl ketone with 23 and 26.5% *ee*, respectively. To improve the stereoselectivity, we tried to incorporate one additional (*S*)-PN group to the iridium coordination sphere. Thus, treatment of the dimer [Ir(μ-Cl)(COE)$_2$]$_2$ with 4.5 equivalents of (*S*)-PN, in acetone or dichloromethane, at room temperature, afforded cationic [Ir{(*S*)-PN}$_2$]Cl (**3**) in 75% yield. Complex **3** was isolated as a mixture of two isomers in relative amounts of about 60% (**3a)** and 40% (**3b**). Pure samples of both isomers could be obtained: pure **3b** was obtained when the reaction was carried out in toluene, and complex **3b** isomerised quantitatively to **3a** after refluxing two hours in acetone.

Furthermore, the chloride can be metathetically replaced by the reaction of **3** with $NaBF_4$ or KPF_6, affording the corresponding [Ir{(*S*)-PN}$_2$]A {A = BF_4 (**4a,b**); PF_6 (**5a,b**)} salts.

To obtain further structural information about these complexes, the molecular structure of compound **5b** was determined by X-ray diffractometric methods (Figure 2). Selected bond parameters are reported in Table 1. The cation presents a highly distorted square-planar geometry with relative *trans* arrangement of nitrogen and phosphorus atoms of both (*S*)-PN ligands. Both Ir–P–C–C–C–N six-membered metallacycles adopt an $^1S_2$ screw-boat conformation[21] with a relative *anti* disposition to each other (Figure 3). A similar arrangement has been previously found in

 © 2005 Wiley-VCH Verlag GmbH & Co. KGaA, Weinheim

Table 1. Selected bond lengths [Å] and angles [°] for metal complexes **2** and **5b**.

Complex **2**					
Ir–Cl	2.512(2)		C(13)–C(18)	1.418(10)	
Ir–P	2.197(2)		C(18)–C(19)	1.459(12)	
Ir–N	2.002(7)		N–C(19)	1.289(11)	
Ir–O(1)	2.093(6)		O(1)–C(25)	1.244(11)	
Ir–O(2)	2.009(6)		O(2)–C(27)	1.273(10)	
Ir–H	1.61		C(25)–C(26)	1.407(13)	
P–C(13)	1.815(8)		C(26)–C(27)	1.366(13)	
Cl–Ir–P	97.30(8)		N–Ir–O(2)	177.9(3)	
Cl–Ir–N	91.1(2)		N–Ir–H	95.3	
Cl–Ir–O(1)	88.65(16)		O(1)–Ir–O(2)	91.0(2)	
Cl–Ir–O(2)	87.01(16)		O(1)–Ir–H	83.5	
Cl–Ir–H	169.7		O(2)–Ir–H	86.5	
P–Ir–N	87.89(19)		Ir–P–C(13)	111.0(3)	
P–Ir–O(1)	172.84(16)		Ir–N–C(19)	131.2(6)	
P–Ir–O(2)	93.28(17)		P–C(13)–C(18)	118.1(6)	
P–Ir–H	91.0		C(13)–C(18)–C(19)	124.0(8)	
N–Ir–O(1)	88.0(2)		N–C(19)–C(18)	128.9(8)	
Complex **5b**[a]					
Ir–P(1)	2.2063(14)	2.2103(13)	Ir–N(1)	2.088(4)	2.115(4)
P(1)–C(13)	1.853(5)	1.851(5)	C(18)–C(19)	1.476(8)	1.478(7)
C(13)–C(18)	1.405(7)	1.410(7)	N(1)–C(19)	1.277(7)	1.283(7)
P(1)–Ir–P(51)	101.29(5)		P(51)–Ir–N(1)	167.50(13)	
P(1)–Ir–N(1)	85.05(12)		P(51)–Ir–N(51)	87.07(12)	
P(1)–Ir–N(51)	168.94(13)		N(1)–Ir–N(51)	88.16(16)	
Ir–P(1)–C(13)	108.69(18)	108.22(17)	C(13)–C(18)–C(19)	121.4(5)	123.5(5)
Ir–N–C(19)	130.5(4)	126.6(4)	N–C(19)–C(18)	128.0(5)	128.8(5)
P(1)–C(13)–C(18)	120.8(4)	121.1(4)			

[a] When two values are given in the table, they represent analogous parameters from the two independent (*S*)-PN ligands of complex **5b**.

the related rhodium compound[22] $[Rh\{(S)\text{-}PN\}_2]BF_4$, as well as in the nickel(II) derivative[23] $[Ni\{(S)\text{-}PN'\}_2][O_3SCF_3]_2$, where (*S*)-PN′ represents the *iso*-butyl derivative shown in Scheme 1.

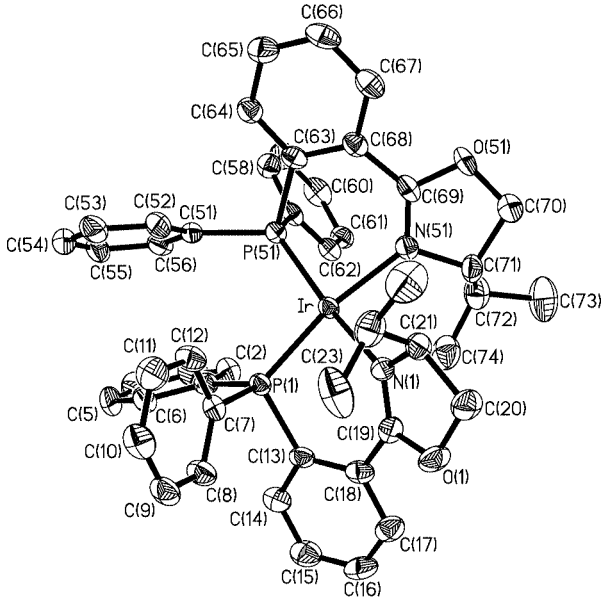

Figure 2. Molecular drawing of the cationic metal complex of **5b** (hydrogen atoms are omitted for clarity).

The NMR spectroscopic data of isomers only differing in the counter-anion are very similar, indicating that they

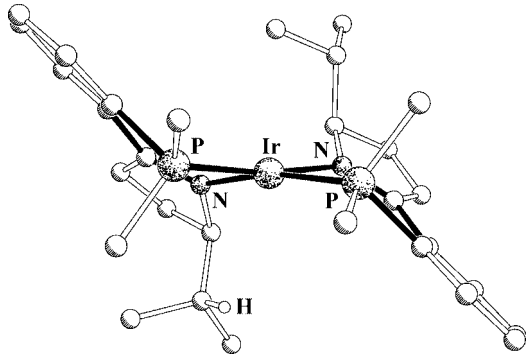

Figure 3. Relative *anti* conformation observed for the metallacycles Ir–P–C–C–C–N in the solid structure of **5b** (view along the pseudo C_2 axis).

should have similar structure. However, while the NMR spectra of **3b-5b** present only one set of signals for the (*S*)-PN ligand, those of **3a-5a** reveal that the two (*S*)-PN ligands are not equivalent. From the molecular structure of **5b**, we propose that, in compounds labelled **b**, the equivalence in solution of the two (*S*)-PN ligands arises from the existence of a C_2 axis, contained in the coordination plane, that bisects the P–Ir–P and N–Ir–N angles (Figure 3). The value of the PP′ coupling constant in **3a**–**5a** is about 15 Hz. Thus, in both types of isomers the phosphorus atoms adopt a *cis* geometry.

Concerning the **3a-5a** isomers, the most notable feature of their ^1H NMR spectra is the shielding of about 1.4 ppm

 © 2005 Wiley-VCH Verlag GmbH & Co. KGaA, Weinheim

of one of the CH isopropyl protons with respect to the other. Inspection of molecular models reveals that one of the CH isopropyl protons lies below the iridium coordination plane pointing to the metal (Figure 3). In fact, this proton is only 3.111(1) Å apart from the iridium in the solid structure of **5b**. From these data, we tentatively propose that the isomerization from **b** to **a** consists of the formation of a C–H···Ir agostic interaction[24] between the iridium atom and one of the CH isopropyl protons.

Preliminary results indicate that compounds **3**–**5** are active catalysts for the Michael addition of cyano or keto esters **6** and **7** to α,β-unsaturated carbonyls **8**–**10** (Scheme 3). Table 2 collects some selected results. Chloride **3b** is a very active catalyst for the Michael additions (entries 1–12), achieving quantitative conversion in most of the cases. However, the *ee* obtained are low. Unsymmetrical chloride **3a** (entries 13–15) is less active but more selective, affording *ee* of up to 39%. Surprisingly, changing the anion to BF_4 or PF_6 strongly decreases the activity (entries 16–22), rendering enantioselectivities ranging from 20 to 30% *ee*.

To obtain mechanistic information about the catalytic system, **3a** or **3b** were treated with excess of ethyl-2-cyanopropionate (**6b**) in catalytic conditions; no conclusive results were obtained, most of the starting substrates remained unaltered. However, when **3a** was reacted with the closely related α-cyanoacetates **11a** or **11b** (Scheme 2), the corresponding hydrido enolate iridium(III) complexes [IrH(NCCHCO$_2$R){(*S*)-PN}$_2$]Cl {R = Me (**12**), Et (**13**)} were diastereoselectively isolated in 85 and 88% yield, respectively. The IR spectra of compounds **12** and **13** show characteristic absorption bands at about 2175 and 2205 cm^{-1} assignable to ν(C≡N) and ν(Ir–H), respectively.

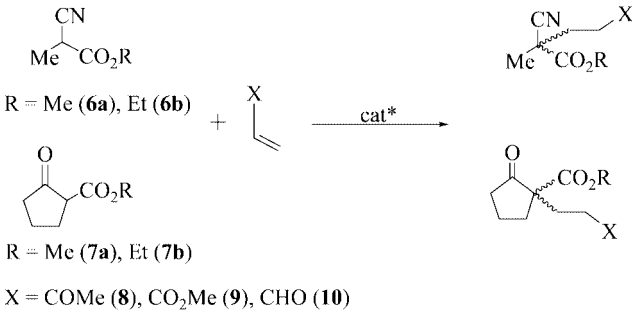

Scheme 3. Catalytic reactions.

An intense band due to ν(C=O) of the enolato ligand appears ca. 1667 cm^{-1}. The ^{1}H NMR spectra show a doublet of doublets at δ = –19.28 ppm (**12**) or –19.23 ppm (**13**) ($^2J_{PH}$ = 13.5, 26.6 Hz) attributed to a hydride ligand coupled to two nonequivalent phosphorus nuclei. Two singlets at δ = 3.57 and 3.18 ppm, assignable to the methyl and methine protons of the enolato ligand, are observed in the spectrum of **12**. For compound **13**, the methyl, methylene and methine protons of the enolato ligand resonate as a triplet at 1.21, a quartet at 4.08 and a singlet at 3.22 ppm, respectively. In both compounds the methine proton has no coupling with the phosphorus nuclei, suggesting that the enolate is N-bonded. The isolation of **12** and **13** from **3a** indicates that most probably, the oxidative addition of the sp^3 CH activated bond of the Michael donors to the iridium(I) complexes **3**–**5** would be the first step in the catalytic path. Interaction of the coordinated enolate with the Michael acceptor followed by adduct elimination would complete the catalytic cycle.

Table 2. Asymmetric Michael reactions using the new iridium compounds **3**–**5** as catalysts.[a]

Entry	Catalyst	Donor	Acceptor	Yield (%)[b]	*ee* (%)
1	[Ir{(*S*)-PN}$_2$]Cl (**3b**)	**6a**	MeCOCH=CH$_2$ (**8**)	100	1.5[c] (*R*)[d]
2		**6a**	COOMeCH=CH$_2$ (**9**)	100	1[c]
3		**6a**	CHOCH=CH$_2$ (**10**)	100	5.5[c]
4		**6b**	MeCOCH=CH$_2$ (**8**)	100	1.3[c] (*R*)[d]
5		**6b**	COOMeCH=CH$_2$ (**9**)	100	15.5[c]
6		**6b**	CHOCH=CH$_2$ (**10**)	100	3.5[c]
7		**7a**	MeCOCH=CH$_2$ (**8**)	66	25[e]
8		**7a**	COOMeCH=CH$_2$ (**9**)	1	10[e]
9		**7a**	CHOCH=CH$_2$ (**10**)	100	22.5[e]
10		**7b**	MeCOCH=CH$_2$ (**8**)	100	8.5[e]
11		**7b**	COOMeCH=CH$_2$ (**9**)	57	2[e]
12		**7b**	CHOCH=CH$_2$ (**10**)	100	2[e]
13	[Ir{(*S*)-PN}$_2$]Cl (**3a**)	**6b**	MeCOCH=CH$_2$ (**8**)	100	39[c] (*R*)[d]
14		**7b**	MeCOCH=CH$_2$ (**8**)	54	20.5[e]
15		**7b**	COOMeCH=CH$_2$ (**9**)	23	2.5[e]
16	[Ir{(*S*)-PN}$_2$]BF_4 (**4b**)	**6b**	MeCOCH=CH$_2$ (**8**)	18	28[c] (*R*)[d]
17		**7b**	MeCOCH=CH$_2$ (**8**)	9.5	24.5[e]
18	[Ir{(*S*)-PN}$_2$]PF_6 (**5b**)	**6b**	MeCOCH=CH$_2$ (**8**)	64	35[c] (*R*)[d]
19		**7b**	MeCOCH=CH$_2$ (**8**)	11	27.5[e]
20	[Ir{(*S*)-PN}$_2$]PF_6 (**5a**)	**7a**	CHOCH=CH$_2$ (**10**)	8	28[e]
21		**7b**	MeCOCH=CH$_2$ (**8**)	10	32[e]
22		**7b**	CHOCH=CH$_2$ (**10**)	90	22[e]

[a] All reactions run at room temperature, using 1 mol-% Ir catalyst, 1 equiv. of donor, 1.5 equiv. of acceptor, in toluene (5 mL). [b] After 22 h of reaction; determined by ^{1}H NMR spectroscopy. [c] Determined by gas chromatography using CP-Chirasil-CB column. [d] Determined by comparison to reported $[\alpha]_D$ data (see ref.[7a]). [e] Determined by gas chromatography using Lipodex-E column.

 © 2005 Wiley-VCH Verlag GmbH & Co. KGaA, Weinheim

In summary, we report the first chiral iridium(I) compounds that are active catalysts for the Michael addition of keto or cyano esters to α,β-unsaturated carbonyl compounds. The enantioselectivity obtained is modest. In fact, few examples of highly enantioselective catalytic Michael addition versions for the synthesis of quaternary stereocentres have been demonstrated to date.[2,11n] However, the catalytic efficiency in these clean quaternary-carbon-centre-forming reactions is promising. Further studies to extend the catalytic reaction to other related metallic systems and substrates are currently under progress in our laboratory.

Experimental Section

General Comments: The compounds described herein were handled with exclusion of air by using standard Schlenk techniques. All solvents were dried by known procedures and distilled under argon prior to use. NMR spectra were recorded with a Varian Gemini 2000 or a Bruker Avance 400 spectrometer. Chemical shifts are expressed in ppm upfield from $SiMe_4$ (^1H, ^{13}C) or 85% H_3PO_4 in D_2O (^{31}P). Coupling constants (*J*) are given in Hertz. For proton and carbon labelling, see Scheme 1. Infrared spectra were recorded with a Perkin–Elmer 783 spectrophotometer. Carbon, hydrogen, and nitrogen analyses were performed with a Perkin–Elmer 240B microanalyser. Molar conductivities were measured in approximately 5×10^{-4} mol dm^{-3} acetone solutions with a Philips PW 9509 digital conductivity meter. Gas chromatographic analyses were performed with a Hewlett–Packard 8590A gas chromatograph equipped with CP-Chirasil-CB or Lipodex-E columns. Optical rotations were measured with a Jasco P-1020 polarimeter. [Ir(μ-Cl)(COE)$_2$]$_2$[19] and (4*S*)-2-[2-(diphenylphosphanyl)phenyl]-4-isopropyl-1,3-oxazoline[25] were prepared according to published procedures. Acetylacetone and compounds **7a**, **7b**, **8**, **9**, **10**, **11a**, and **11b** were purchased from Aldrich Co. Ltd. The α-cyanopropionates **6a** and **6b** were prepared as previously reported.[11f]

Preparation of [IrCl(COE){(*S*)-PN}] (1): (*S*)-PN (83.0 mg, 0.22 mmol) was added to a suspension of [Ir(μ-Cl)(COE)$_2$]$_2$ (100.0 mg, 0.11 mmol) in pentane (10 mL) at –60 °C, under argon. The suspension was stirred for 1 h. During this time, a change of colour from orange to brown took place. The solid formed was filtered off, washed with pentane and vacuum-dried. Yield: 66.0 mg (65%). ^1H NMR (400.13 MHz, $CDCl_3$, –60 °C): δ = 8.8–6.6 (m, 14 H, Ph), 5.93 (m, 1 H, H_g), 4.50 (br., 2 H, CH=CH), 4.34 (m, 2 H, H_c and H_t), 2.81 (m, 1 H, CH *i*Pr), 2.6–0.7 (m, 14 H, COE), 0.83 (d, *J* = 6.0 Hz, 3 H, Me *i*Pr), 0.09 (d, *J* = 6.0 Hz, 3 H, *i*Pr) ppm. ^{13}C NMR (100.61 MHz, $CDCl_3$, –60 °C): δ = 161.88 (C_1), 134.4–123.6 (Ph), 69.06 (C_2), 68.29 (C_3), 64.44 (br., CH=CH), 31.14 (CH *i*Pr), 31.94, 29.97, 26.93, 25.80 (CH_2 COE), 19.36, 13.83 (Me *i*Pr) ppm. $^{31}P\{^1H\}$ NMR (161.97 MHz, $CDCl_3$, –60 °C): δ = 10.1 (s) ppm. IR (Nujol mulls): $\tilde{\nu}$ = 1616 ($\nu_{C=N}$) cm^{-1}.

Preparation of [Ir(acac)ClH{(*S*)-PN}] (2): (*S*)-PN (83.0 mg, 0.22 mmol) was added to a solution of [Ir(μ-Cl)(COE)$_2$]$_2$ (100.0 mg, 0.11 mmol) in acetone (10 mL), under argon. The solution was stirred for 30 min, and then Hacac (0.3 mL) was added. The resulting solution was heated under reflux for 6 h and then concentrated under vacuum. Addition of *n*-hexane led to the precipitation of **2** as a yellow solid, which was filtered off, washed with *n*-hexane, and air-dried. Yield: 134.8 mg (86%). ^1H NMR (300.1 MHz, $CDCl_3$, r.t.): δ = 8.2–6.9 (m, 14 H, Ph), 5.35 (s, 1 H, CH acac), 5.09 (ddd, *J* = 10.2, 5.7, 3.0 Hz, 1 H, H_g), 4.48 (dd, *J* = 10.2, 9.0 Hz, 1 H, H_c), 4.29 (dd, *J* = 9.0, 5.7 Hz, 1 H, H_t), 2.57 (m, 1 H,CH *i*Pr), 1.91 (s, 3 H, Me acac), 1.54 (s, 3 H, Me acac), 0.72 (d, *J* = 7.0 Hz, 3 H, Me *i*Pr), –0.09 (d, *J* = 7.0 Hz, 3 H, Me *i*Pr), –22.86 (d, *J* = 18.5 Hz, 1 H Ir–H) ppm. ^{13}C NMR (75.4 MHz, $CDCl_3$, r.t.): δ = 184.63 (CO acac), 183.81 (CO acac), 161.38 (C_1), 135.4–125.3 (Ph), 101.37 (CH acac), 69.02 (C_2), 66.52 (C_3), 30.93 (CH *i*Pr), 28.42 (Me acac), 26.82 (Me acac), 18.73 (Me *i*Pr), 11.93 (Me *i*Pr) ppm. $^{31}P\{^1H\}$ NMR (121.5 MHz, $CDCl_3$, r.t.): δ = –2.32 (s) ppm. IR (Nujol mulls): $\tilde{\nu}$ = 2216 (ν_{IrH}), 1617 ($\nu_{C=N}$) cm^{-1}. $C_{29}H_{32}ClIrNO_3P$ (701.223): calcd. C 49.74, H 4.61, N 2.00; found C 49.59, H 4.70, N 1.99.

Preparation of [Ir{(*S*)-PN}$_2$]Cl (3a, 3b): (*S*)-PN (187.7 mg, 0.50 mmol) was added to a solution of [Ir(μ-Cl)(COE)$_2$]$_2$ (100.0 mg, 0.11 mmol) in acetone (10 mL), under argon. The solution was refluxed for 2 h and then concentrated under vacuum. Addition of *n*-hexane led to the precipitation of **3a** as a red powder. Yield 185.1 mg (85%). Pure **3b** can also be obtained as a red powder by following the same procedure but using toluene as solvent. Yield 174.1 mg (80%). Compounds **3a** and **3b** had to be stored under argon. **3a:** ^1H NMR (300.1 MHz, CD_2Cl_2, r.t.): δ = 8.2–6.4 (m, 28 H, Ph), 5.25 (m, 1 H, H_g), 4.63 (m, 1 H, $H_{g'}$), 4.54 (m, 1 H, H_t), 4.36 (m, 2 H, $H_{t'}$, $H_{c'}$), 4.23 (m, 1 H, H_c), 2.78 (m, 1 H, CH *i*Pr), 1.42 (m, 1 H, CH *i*Pr′), 0.81 (d, *J* = 6.9 Hz, 3 H, Me *i*Pr′), 0.76 (d, *J* = 7.0 Hz, 3 H, Me *i*Pr), 0.22 (d, *J* = 6.6 Hz, 3 H, Me *i*Pr′), –0.09 (d, *J* = 6.9 Hz, 3 H, Me *i*Pr) ppm. ^{13}C NMR (75.4 MHz, CD_2Cl_2, r.t.): δ = 167.33 (d, *J* = 6.6 Hz), 164.39 (t, *J* = 4.8 Hz) (C_1, $C_{1'}$), 135.5–122.2 (Ph), 77.94, 70.16 (C_2, $C_{2'}$), 69.17, 69.09 (C_3, $C_{3'}$), 30.48, 29.40 (CH *i*Pr), 18.81, 18.34, 12.85, 12.78 (Me *i*Pr) ppm. $^{31}P\{^1H\}$ NMR (121.5 MHz, CD_2Cl_2, r.t.): δ = –11.83 (d, *J* = 14.7 Hz), –13.09 (d) ppm. Molar conductivity (acetone) = 71.9 ohm^{-1} cm^2 mol^{-1}. $C_{48}H_{48}ClIrN_2O_2P_2$ (974.54): calcd. C 59.16, H 4.96, N 2.87; found C 58.64, H 6.44, N 2.58. **3b:** ^1H NMR (300.1 MHz, CD_2Cl_2, r.t.): δ = 8.2–6.4 (m, 28 H, Ph), 4.88 (dd, *J* = 9.6, 9.3 Hz, 1 H, H_c), 4.44 (dd, *J* = 9.6, 3.6 Hz, 1 H, H_t), 4.24 (m, 1 H, H_g), 2.26 (m, 1 H, CH *i*Pr), 0.90 (d, *J* = 6.9 Hz, 3 H, Me *i*Pr), 0.31 (d, *J* = 6.6 Hz, 3 H, Me *i*Pr) ppm. ^{13}C NMR (75.4 MHz, CD_2Cl_2, r.t.): δ = 163.48 (C_1), 135.5–122.2 (Ph), 73.54 (C_2), 69.90 (C_3), 32.36 (CH *i*Pr), 19.90, 15.60 (Me *i*Pr) ppm. $^{31}P\{^1H\}$ NMR (121.5 MHz, CD_2Cl_2, r.t.): δ = 16.20 (s) ppm. $C_{48}H_{48}ClIrN_2O_2P_2$ (974.54): calcd. C 59.16, H 4.96, N 2.87; found C 58.54, H 6.35, N 2.96.

Preparation of [Ir{(*S*)-PN}$_2$]A {A = BF_4 (4a), PF_6 (5a)}: (*S*)-PN (187.7 mg, 0.50 mmol) and $NaBF_4$ or $NaPF_6$ (1 mmol) were added to a solution of [Ir(μ-Cl)(COE)$_2$]$_2$ (100.0 mg, 0.11 mmol) in acetone (10 mL), under argon. The resulting suspension was refluxed for 6 h, and the solvent was evaporated under vacuum. The residue was extracted with CH_2Cl_2 (10 mL) and filtered through a pad of Celite. The resulting solution was concentrated to ca. 1 mL, and the addition of diethyl ether led to the precipitation of a red solid, which was filtered off, washed with the precipitant and vacuum-dried. Yield 167.3 mg (73%) (**4a**) or 188.9 mg (78%) (**5a**). Complexes **4a** and **5a** had to be stored under argon. **4a:** ^1H NMR (300.1 MHz, CD_2Cl_2, r.t.): δ = 8.2–6.4 (m, 28 H, Ph), 5.32 (m, 1 H, H_g), 4.62 (m, 1 H, $H_{g'}$), 4.52 (m, 1 H, H_t), 4.34 (m, 2 H, $H_{t'}$, $H_{c'}$), 4.25 (m, 1 H, H_c), 2.83 (m, 1 H, CH *i*Pr), 1.50 (m, 1 H, CH *i*Pr′), 0.82 (d, *J* = 7.1 Hz, 3 H, Me *i*Pr′), 0.78 (d, *J* = 6.9 Hz, 3 H, Me *i*Pr), 0.23 (d, *J* = 6.4 Hz, 3 H, Me *i*Pr′), 0.07 (d, *J* = 6.9 Hz, 3 H, Me *i*Pr) ppm. ^{13}C NMR (75.4 MHz, CD_2Cl_2, r.t.): δ = 167.43 (d, *J* = 6.5 Hz), 164.49 (t, *J* = 4.8 Hz) (C_1, $C_{1'}$), 134.5–127.2 (Ph), 78.21, 70.25 (C_2, $C_{2'}$), 69.45, 69.26 (C_3, $C_{3'}$), 30.79, 29.74 (CH *i*Pr), 19.13, 18.55, 13.13, 13.13 (Me *i*Pr) ppm. $^{31}P\{^1H\}$ NMR (121.5 MHz, CD_2Cl_2, r.t.): δ = –10.91 (d, *J* = 15.1 Hz), –12.33 (d) ppm. $C_{48}H_{48}BF_4IrN_2O_2P_2$ (1025.89): calcd. C 56.19, H 4.71, N

 © 2005 Wiley-VCH Verlag GmbH & Co. KGaA, Weinheim

2.72; found C 55.63, H 4.07, N 2.11. **5a:** ^{1}H NMR (300.1 MHz, CD_2Cl_2, r.t.): δ = 8.2–6.4 (m, 28 H, Ph), 5.31 (m, 1 H, H_g), 4.60 (m, 1 H, $H_{g'}$), 4.58 (m, 1 H, $H_{t'}$), 4.51 (dd, J = 9.6, 2.2 Hz, 1 H, H_t), 4.31 (m, 1 H, $H_{c'}$), 4.24 (pt, J = 9.0 Hz, 1 H, H_c), 2.81 (m, 1 H, CH *i*Pr), 1.41 (m, 1 H, CH *i*Pr′), 0.81 (d, J = 7.2 Hz, 3 H, Me *i*Pr′), 0.77 (d, J = 6.9 Hz, 3 H, Me *i*Pr), 0.22 (d, J = 6.6 Hz, 3 H, Me *i*Pr′), –0.09 (d, J = 6.9 Hz, 3 H, Me *i*Pr) ppm. ^{13}C NMR (75.4 MHz, CD_2Cl_2, r.t.): δ = 167.43 (d, J = 6.5 Hz), 164.52 (t, J = 4.8 Hz) (C_1, $C_{1'}$), 134.5–127.2 (Ph), 78.07, 70.09 (C_2, $C_{2'}$), 69.26, 69.08 (C_3, $C_{3'}$), 30.55, 29.51 (CH *i*Pr), 18.86, 18.29, 12.84, 12.84 (Me *i*Pr) ppm. ^{31}P{^{1}H} NMR (121.5 MHz, CD_2Cl_2, r.t.): δ = –10.72 (d, J = 14.7 Hz), –12.03 (d) ppm. $C_{48}H_{48}F_6IrN_2O_2P_3$ (1084.049): calcd. C 53.18, H 4.46, N 2.58; found C 52.56, H 4.89, N 2.60.

Preparation of [Ir{(*S*)-PN}$_2$]A {A = BF$_4$ (4b), PF$_6$ (5b)}: Complexes **4b** and **5b** were prepared as described for **4a** or **5a**, but the reactions were carried out at room temperature. Complexes **4b** and **5b** had to be stored under argon. **4b:** ^{1}H NMR (300.1 MHz, CD_2Cl_2, r.t.): δ = 8.0–6.8 (m, 28 H, Ph), 4.48 (pt, J = 9.6 Hz, 1 H, H_c), 4.46 (dd, J = 10.0, 3.7 Hz, 1 H, H_t), 4.28 (m, 1 H, H_g), 2.27 (m, 1 H, CH *i*Pr), 0.90 (d, J = 6.9 Hz, 3 H, Me *i*Pr), 0.30 (d, J = 6.6 Hz, 3 H, Me *i*Pr) ppm. ^{13}C NMR (75.4 MHz, CD_2Cl_2, r.t.): δ = 163.48 (C_1), 135.5–122.2 (Ph), 73.54 (C_2), 69.90 (C_3), 32.36 (CH *i*Pr), 19.90, 15.60 (Me *i*Pr) ppm. ^{31}P{^{1}H} NMR (121.5 MHz, CD_2Cl_2, r.t.): δ = 17.16 (s) ppm. $C_{48}H_{48}BF_4IrN_2O_2P_2$ (1025.89): calcd. C 56.19, H 4.71, N 2.72; found C 55.69, H 4.11, N 2.09. **5b:** ^{1}H NMR (300.1 MHz, CD_2Cl_2, r.t.): δ = 8.2–6.4 (m, 28 H, Ph), 4.48 (pt, J = 9.6 Hz, 1 H, H_c), 4.44 (dd, J = 9.9, 3.7 Hz, 1 H, H_t), 4.20 (m, 1 H, H_g), 2.21 (m, 1 H, CH *i*Pr), 0.90 (d, J = 6.9 Hz, 3 H, Me *i*Pr), 0.30 (d, J = 6.6 Hz, 3 H, Me *i*Pr) ppm. ^{13}C NMR (75.4 MHz, CD_2Cl_2, r.t.): δ = 163.48 (C_1), 135.5–122.2 (Ph), 73.54 (C_2), 69.90 (C_3), 32.36 (CH *i*Pr), 19.90, 15.60 (Me *i*Pr) ppm. ^{31}P{^{1}H} NMR (121.5 MHz, CD_2Cl_2, r.t.): δ = 17.09 (s) ppm. $C_{48}H_{48}F_6IrN_2O_2P_3$ (1084.049): calcd. C 53.18, H 4.46, N 2.58; found C 52.61, H 4.89, N 2.08.

Preparation of [IrH(NCCHCO$_2$R){(*S*)-PN}$_2$]Cl {R = Me (12), Et (13)}: A solution of (*S*)-PN (187.7 mg, 0.50 mmol) in acetone (2 mL) was added to a solution of $[Ir(\mu\text{-}Cl)(COE)_2]_2$ (100.0 mg, 0.11 mmol) in the same solvent (12 mL) at ambient temperature under argon. The solution was stirred for 6 h, and then methyl or ethyl α-cyanoacetate (0.3 mL) was added. The resulting solution was stirred for 22 h and then concentrated to ca. 1 mL. Addition of diethyl ether led to the precipitation of **12** or **13** as a yellow solid, which was filtered off, washed with diethyl ether and air-dried. Yield 197.2 mg (85%) (**12**) or 206.9 mg (88%) (**13**). **12:** ^{1}H NMR (300.1 MHz, $CDCl_3$, r.t.): δ = 8.3–6.6 (m), 5.65 (m, 28 H, Ph), 4.73 (m), 4.64 (m), 4.56 (m), 4.52 (m), 4.32 (m), 4.16 (m, 6 H, H_g, $H_{g'}$, H_c, $H_{c'}$, H_t, $H_{t'}$), 3.57 (s, 3 H, OCH_3), 3.18 (s, 1 H, NCCH), 2.78 (m, 1 H, CH *i*Pr), 2.30 (m, 1 H, CH *i*Pr′), 0.86 (d, J = 6.6 Hz, 3 H, Me *i*Pr′), 0.70 (d, J = 6.9 Hz, 3 H, Me *i*Pr), 0.02 (d, J = 6.6 Hz, 3 H, Me *i*Pr′), –0.40 (d, J = 6.9 Hz, 3 H, Me *i*Pr), –19.28 (dd, J = 26.6, 13.5 Hz, 1 H, Ir-H) ppm. ^{13}C NMR (75.4 MHz, $CDCl_3$, r.t.): δ = 184.77 (CO), 167.46, 164.85 (C_1, $C_{1'}$), 134.9–127.8 (Ph), 73.88, 71.97 (C_2, $C_{2'}$), 69.72, 68.22 (C_3, $C_{3'}$), 51.26 (OCH_3), 50.15 (NC-*C*H), 31.16, 28.99 (CH *i*Pr), 19.56, 18.25, 13.83, 12.70 (Me *i*Pr) ppm. ^{31}P{^{1}H} NMR (121.5 MHz, $CDCl_3$, r.t.): δ = 1.16 (d, J = 14.5 Hz), –13.30 (d) ppm. IR (Nujol): $\tilde{\nu}$ = 2207 sh. (ν_{IrH}), 2177 s (ν_{CN}) cm^{-1}. $C_{52}H_{53}ClIrN_3O_4P_2$ (1073.63): cacld. C 58.17, H 4.97, N 3.91; found C 58.64, H 5.47, N 4.25. **13:** ^{1}H NMR (300.1 MHz, $CDCl_3$, r.t.): δ = 8.3–6.6 (m), 5.68 (m, 28 H, Ph), 4.81 (m), 4.78 (m), 4.62 (m), 4.55 (m), 4.38 (m), 4.22 (m, 6 H, H_g, $H_{g'}$, H_c, $H_{c'}$, H_t, $H_{t'}$), 4.08 (q, J = 6.8 Hz, 2 H, OCH_2CH_3), 3.22 (s, 1 H, NCCH), 2.83 (m, 1 H, CH *i*Pr), 2.36 (m, 1 H, CH *i*Pr′), 1.21 (t, 3 H, OCH_2CH_3), 0.91 (d, J = 6.9 Hz, 3 H, Me *i*Pr′), 0.74 (d, J = 6.9 Hz, 3 H, Me *i*Pr), –0.03 (d, J = 6.9 Hz, 3 H, Me *i*Pr′), –0.36 (d, J = 6.9 Hz, 3 H, Me *i*Pr), –19.23 (dd, J = 26.6, 13.5 Hz, 1 H, Ir-H) ppm. ^{13}C NMR (75.4 MHz, $CDCl_3$, r.t.): δ = 182.92 (CO), 167.40, 164.75 (C_1, $C_{1'}$), 137.3–124.7 (Ph), 73.75, 71.81 (C_2, $C_{2'}$), 69.79, 68.51 (C_3, $C_{3'}$), 58.64 (OCH_2CH_3), 51.04 (NC*C*H), 31.14, 29.01 (CH *i*Pr), 19.51, 18.21 (Me *i*Pr), 14.90 (OCH_2CH_3), 13.90, 12.74 (Me *i*Pr) ppm. ^{31}P{^{1}H} NMR (121.5 MHz, $CDCl_3$, r.t.): δ = 1.18 (d, J = 14.5 Hz), –13.30 (d) ppm. IR(Nujol): $\tilde{\nu}$ = 2206 sh. (ν_{IrH}), 2176 s (ν_{CN}), 1666 s (ν_{CO}) cm^{-1}. $C_{53}H_{55}ClIrN_3O_4P_2$ (1087.65): calcd. C 58.53, H 5.09, N 3.86; found C 57.94, H 4.87, N 3.93.

Catalytic Michael Addition Procedure: The catalyst (0.01 mmol), donor **6** or **7** (1 mmol) and acceptor **8**–**10** (1.5 mmol) were dissolved in toluene (5 mL) under argon at room temperature, and the mixture was stirred for 22 h. After removal of all volatile materials, [D$_8$]toluene (500 μL) was added to the residue. The yield based on the donor was determined by ^{1}H NMR. The crude product was extracted with *n*-hexane, and the extract was purified by chromatography on silica gel. The products were identified by NMR spectroscopy.[7a,11l,26] Enantiomeric excesses were determined by GLC.

X-ray Structure Analyses of Complexes 2 and 5b: Single crystals of both complexes were glued to a glass fiber and mounted on a Bruker SMART APEX (equipped with a CCD area detector) (**2**) or Siemens-Stoe AED-2 diffractometer (**5b**) and examined using graphite-monochromated Mo-K_α radiation (λ = 0.71073 Å). Crystal data for **2** (from 4392 reflections, 2.2 < θ < 23.5°): $C_{29}H_{32}ClIrNO_3P{\cdot}0.5(C_4H_8O)$, tetragonal, space group $P4_12_12$; a = 11.2664(6), c = 46.726(4) Å, V = 5931.1(7) Å^3, Z = 8, D_c = 1.651 Mg m^{-3}, μ(Mo-K_α) = 4.680 mm^{-1}; crystal size 0.13 × 0.12 × 0.07 mm; T = 100.0(2) K, ω scans, max. 2θ = 55.1°; 38251 measured reflections, 6835 unique (R_{int} = 0.0835). Crystal data for **5b** (from 44 reflections, 12.5< θ < 15.0°): $C_{48}H_{48}F_6IrN_2O_2P_3$, M = 1083.99, orthorhombic, space group $P2_12_12_1$; a = 12.9657(10), b = 16.2713(17), c = 21.278(3) Å, V = 4489.1(8) Å^3, Z = 4, D_c = 1.604 Mg m^{-3}, μ(Mo-K_α) = 3.148 mm^{-1}; crystal size 0.23 × 0.20 × 0.19 mm; T = 200.0(2) K, $\theta/2\theta$ scans, max. 2θ = 50.0°; 9769 measured reflections, 7840 unique (R_{int} = 0.0213). Orange crystals of **5b** suitable for X-ray diffraction were grown by slow diffusion of diethyl ether into a solution of the complex in dichloromethane.

Data were integrated with the Bruker SAINT[27] (**2**) and Stoe REDU4 (**5b**) programs. Absorption correction was applied by using the SADABS program[28] (**2**) or the psi-scan approach[29] (**5b**). Structures were solved by direct methods[30] and completed by subsequent difference Fourier techniques. Refinement on F^2 was carried out for both structures by full-matrix least-squares (SHELXL-97).[30] In **2**, half a THF molecule was observed as crystallisation solvent in the structure. All non-hydrogen atoms, including those of the solvent molecule, were refined with anisotropic displacement parameters. The organic hydrogen atoms were included in calculated positions and refined with riding positional and thermal parameters. The hydride ligand was clearly observed in the last cycles of refinement, but it did not support a proper refinement as free isotropic atom. It was incorporated in the refinement with a restrained position and with a fixed displacement parameter. All non-hydrogen atoms in **5b**, except the F atoms in the PF_6^- anion, were refined with anisotropic displacement parameters. The PF_6^- anion was found to be disordered. A model for static disorder was established and the anion was refined with all atoms in two positions; occupancy factors were refined holding the sum of their occupancies equal to one. The hydrogen atoms were included accord-

 © 2005 Wiley-VCH Verlag GmbH & Co. KGaA, Weinheim

ing to their geometry with restrained thermal and positional parameters.

The absolute configuration for both complexes were determined on the basis of the Flack parameter[31] [–0.008(11) for **2** and –0.018(6) for **5b**] and using as internal reference the previously known chirality of the asymmetric carbon atom in the phosphanyloxazoline ligand. Conventional final agreement factors[30] were: R_1 = 0.0506 [for 5588 reflections with $F^2>4\sigma(F^2)$], ωR_2 = 0.0937 and S = 0.968 for all independent reflections of **2**; R_1 = 0.0289 [for 7259 reflections with $F^2>4\sigma(F^2)$], ωR_2 = 0.0651 and S = 1.046 for all independent reflections of **5b**.

CCDC-240695 and CCDC-240696 contain the supplementary crystallographic data for this paper. These data can be obtained free of charge from The Cambridge Crystallographic Data Centre via www.ccdc.cam.ac.uk/data_request/cif.

Acknowledgments

We are grateful to the Dirección General de Investigación for financial support (Project BQU 2003–1096).

[1] a) M. Yamaguchi in *Comprehensive Asymmetric Catalysis* (Eds.: E. N. Jacobsen, A. Pfaltz, H. Yamamoto), Springer, Berlin, **1999**, ch. 31.2, pp. 1121–1139; b) K. Kanai, M. Shibasaki in *Catalytic Asymmetric Synthesis* 2nd ed. (Ed.: I. Ojima), Wiley-VCH, New York, **2000**, pp. 569–592.

[2] a) E. J. Corey, A. Guzmán-Pérez,; *Angew. Chem.* **1998**, *110*, 402–415; *Angew. Chem. Int. Ed.* **1998**, *37*, 388–401; b) J. Christoffers, A. Mann, *Chem. Eur. J.* **2001**, *7*, 1014–1027; c) J. Christoffers, A. Mann, *Angew. Chem. Int. Ed.* **2001**, *40*, 4591–4597; *Angew. Chem.* **2001**, *113*, 4725–4732; d) J. Christoffers, *Chem. Eur. J.* **2003**, *9*, 4862–4867; e) J. Christoffers, A. Baro, *Angew. Chem. Int. Ed.* **2003**, *42*, 1688–1690; *Angew. Chem.* **2003**, *115*, 1726–1728.

[3] a) H. Wynberg, R. Helder, *Tetrahedron Lett.* **1975**, *46*, 4057–4060; b) K. Hermann, H. Wynberg, *J. Org. Chem.* **1979**, *44*, 2238–2244.

[4] H. Brunner, B. Hammer, *Angew. Chem. Int. Ed. Engl.* **1984**, *23*, 312.

[5] a) G. Desimoni, P. Quadrelli, P. P. Righetti, *Tetrahedron* **1990**, *46*, 2927–2934; b) G. Desimoni, G. Dusi, G. Faita, P. Quadrelli, P. P. Righetti, *Tetrahedron* **1995**, *51*, 4131–4144.

[6] a) A. Schionato, S. Paganelli, C. Botteghi, G. Chelucci, *J. Mol. Catal.* **1989**, *50*, 11–18; b) C. Botteghi, A. Schionato, C. Rosini, P. Salvadori, *J. Mol. Catal.* **1990**, *63*, 155–165; c) C. Botteghi, S. Paganelli, A. Schionato, C. Boga, A. Fava, *J. Mol. Catal.* **1991**, *66*, 7–21.

[7] a) M. Sawamura, H. Hamashima, Y. Ito, *J. Am. Chem. Soc.* **1992**, *114*, 8295–8296; b) M. Sawamura, H. Hamashima, Y. Ito, *Tetrahedron* **1994**, *50*, 4439–4454; c) M. Sawamura, H. Hamashima, H. Shinoto, Y. Ito, *Tetrahedron Lett.* **1995**, *36*, 6479–6482; d) M. Sawamura, M. Sudoh, Y. Ito, *J. Am. Chem. Soc.* **1996**, *118*, 3309–3310; e) M. Sawamura, H. Hamashima, Y. Ito, *Bull. Chem. Soc. Jpn.* **2000**, *73*, 2559–2562; f) R. Kuwano, H. Miyazaki, Y. Ito, *J. Organomet. Chem.* **2000**, *603*, 18–29.

[8] N. End, L. Macko, M. Zehnder, A. Pfaltz, *Chem. Eur. J.* **1998**, *4*, 818–824.

[9] a) J. Christoffers, A. Mann, J. Pickardt, *Tetrahedron* **1999**, *55*, 5377–5388; b) J. Christoffers, H. Scharl, *Eur. J. Inorg. Chem.* **2002**, 1505–1508; c) S. Pelzer, T. Kauf, V. van Wüllen, J. Christoffers, *J. Organomet. Chem.* **2003**, *684*, 308–314.

[10] a) D. A. Evans, T. Rovis, M. C. Kozlowski, J. S. Tedrow, *J. Am. Chem. Soc.* **1999**, *121*, 1994–1995; b) D. A. Evans, M. C. Willis, J. N. Johnston, *Org. Lett.* **1999**, *1*, 865–868; c) D. A. Evans, T. Rovis, J. S. Johnson, *Pure Appl. Chem.* **1999**, *71*, 1407–1415; d) D. A. Evans, T. Rovis, M. C. Kozlowski, C. W. Downey, J. S. Tedrow, *J. Am. Chem. Soc.* **2000**, *122*, 9134–9142; e) D. A. Evans, K. A. Scheidt, J. N. Johnston, M. C. Willis, *J. Am. Chem. Soc.* **2001**, *123*, 4480–4491.

[11] a) F. Nonadies, A. Lattanzi, L. R. Orelli, S. Pesci, A. Scettri, *Tetrahedron Lett.* **1993**, *34*, 7649–7650; b) H. Kitajima, K. Ito, T. Katsuki,, *Tetrahedron* **1997**, *53*, 17015–17028; c) K. Inagaki, K. Nozaki, H. Takaya, *Synlett* **1997**, 119–120; d) H.Kitajima, T. Katsuki, *Synlett* **1997**, 568–570; e) M. A. Stark, C. J. Richards, *Tetrahedron Lett.* **1997**, *38*, 5881–5884; f) A. J. Blacker, M. L. Clarke, M. S. Loft, M. F. Mahon, J. M. J. Williams, *Organometallics* **1999**, *18*, 2867–2873; g) J. Ji, D. M. Barnes, J. Zhang, S. A. Fing, S. J. Wittenberger, H. E. Morton, *J. Am. Chem. Soc.* **1999**, *121*, 10215–10216; h) M. A. Stark, G. Jones, C. J. Richards, *Organometallics* **2000**, *19*, 1282–1291; i) S. Kobayashi, C. Ogawa, M. Kawamura, M. Sugiura, *Synlett* **2001**, 983–985; j) M. Nakajima, Y. Yamaguchi, S. Hashimoto, *Chem. Commun.* **2001**, 1596–1597; k) T. Suzuki, T. Torii, *Tetrahedron: Asymmetry* **2001**, *12*, 1077–1081; l) Y. Motoyama, Y. Koga, K. Kobayashi, K. Aoki, H. Nishiyama, *Chem. Eur. J.* **2002**, *8*, 2968–2975; m) J. Zhou, Y. Tang, *J. Am. Chem. Soc.* **2002**, *124*, 9030–9031; n) Y. Hamashima, D. Hotta, M. Sodeoka, *J. Am. Chem. Soc.* **2002**, *124*, 11240–11241; o) K. Itoh, S. Kanemasa, *J. Am. Chem. Soc.* **2002**, *124*, 13394–13395; p) M. Watanabe, K. Murata, T. Ikariya, *J. Am. Chem. Soc.* **2003**, *125*, 7508–7509; q) M. S. Taylor, E. N. Jacobsen, *J. Am. Chem. Soc.* **2003**, *125*, 11204–11205; r) K. Itoh, Y. Oderaotoshi, S. Kanemasa, *Tetrahedron: Asymmetry* **2003**, *14*, 635–639; s) T. Ikariya, H. Wang, M. Watanabe, K. Murata, *J. Organomet. Chem.* **2004**, *689*, 1377–1381.

[12] a) M. Shibasaki, H. Sasai, T. Arai, *Angew. Chem. Int. Ed. Engl.* **1997**, *36*, 1236–1256; *Angew. Chem.* **1997**, *109*, 1290–1310,. and references cited therein; b) K. Yamada, T. Arai, H. Sasai, M. Shibasaki, *J. Org. Chem.* **1998**, *63*, 3666–3672; c) S. Shimizu, K. Ohori, T. Arai, H. Sasai, M. Shibasaki, *J. Org. Chem.* **1998**, *63*, 7547–7551; d) S. Harada, N. Kumagai, T. Kinoshita, S. Matsunaga, M. Shibasaki, *J. Am. Chem. Soc.* **2003**, *125*, 2582–2590; e) K. Majima, R. Takita, A. Okada, T. Ohshima, M. Shibasaki, *J. Am. Chem. Soc.* **2003**, *125*, 15837–15845.

[13] a) G. Manickam, G. Sundararajan, *Tetrahedron: Asymmetry* **1997**, *8*, 2271–2278; b) G. Manickam, G. Sundararajan, *Tetrahedron* **1999**, *55*, 2721–2736; c) B. M. Choudary, N. S. Chowdary, M. L. Kantam, *J. Mol. Catal.* **1999**, *142*, 389–392; d) S. C. Jha, N. N. Joshi, *Tetrahedron: Asymmetry* **2001**, *12*, 2463–2466; e) N. Prabagaran, G. Sundararajan, *Tetrahedron: Asymmetry* **2002**, *13*, 1053–1058; f) S. Velmathi, S Swarnalakshmi, S. Narasimhan, *Tetrahedron: Asymmetry* **2003**, *14*, 113–117.

[14] As far as we know, the reaction of methyl 1-oxo-2-indanecarboxylate with methyl vinyl ketone catalysed by a mixture of $[\{(\eta^5\text{-}C_5Me_5)IrCl\}_2(\mu\text{-}Cl)_2]$ and the chiral diamine (*R*,*R*)-*N*-(4-methylbenzenesulfonyl)-1,2-diphenylethylenediamine is the sole iridium example reported to date (see ref.[11k]).

[15] a) D. Carmona, C. Cativiela, S. Elipe, F. J. Lahoz, M. P. Lamata, M. P. López-Ram de Víu, L. A. Oro C. Vega, F. Viguri, *Chem. Commun.* **1997**, 2351–2352; b) D. Carmona, J. Ferrer, E. Lalaguna, M. Lorenzo, F. J. Lahoz, S. Elipe, L. A. Oro, *Eur. J. Inorg. Chem.* **2002**, 259–263; c) D. Carmona, J. Ferrer, M. Lorenzo, M. Santander, S. Ponz, F. J. Lahoz, J. A. López, L. A. Oro, *Chem. Commun.* **2002**, 870–871; d) D. Carmona, F. J. Lahoz, S. Elipe, L. A. Oro, M. P. Lamata, F. Viguri, F. Sánchez, S. Martínez, C. Cativiela, M. P. López-Ram de Víu, *Organometallics* **2002**, *21*, 5100–5114.

[16] S.-I. Murahashi, T. Naota, H. Taki, M. Mizuno, H. Takaya, S. Komiya, Y. Mizuho, N. Oyasato, M. Hiraoka, M. Hirano, A. Fukuoka, *J. Am. Chem. Soc.* **1995**, *117*, 12436–12451.

[17] a) M. Hirano, M. Hirai, Y. Ito, T. Tsurumaki, A. Baba, A. Fukuoka, S. Komiya, *J. Organomet. Chem.* **1998**, *569*, 3–14; b) M. Hirano, A. Takenaka, Y. Mizuho, M. Hiraoka, S. Komiya, *J. Chem. Soc. Dalton Trans.* **1999**, 3209–3216; c) T. Naota, A. Tannna, S.-I. Murahashi, *J. Am. Chem. Soc.* **2000**, *122*, 2960–

 © 2005 Wiley-VCH Verlag GmbH & Co. KGaA, Weinheim

2961; d) M. Hirano, S. Kiyota, M. Imoto, S. Komiya, *Chem. Commun.* **2000**, 1679–1680; e) T. Naota, A. Tannna, S.-I. Murahashi, *Chem. Commun.* **2001**, 63–64.
[18] a) M. Watanabe, K. Murata, T. Ikayira, *J. Am. Chem. Soc.* **2003**, *125*, 7508–7509; b) T. Ikayira, H. Wang, M. Watanabe, K. Murata, *J. Organomet. Chem.* **2004**, *689*, 1377–1381.
[19] A. Van der Ent, A. L. Onderdelinden, *Inorg. Synth.* **1973**, *14*, 92–93.
[20] F. H. Allen, O. Kennard, R. Taylor, *Acc. Chem. Res.* **1983**, *16*, 146–153.
[21] Puckering parameters for the metallacycles: Ir–P(1)–C(13)–C(18)–C(19)–N(1) ring, φ = 26.1(5), θ = 62.7(4)°, Q = 0.717(3) Å; Ir–P(51)–C(63)–C(68)–C(69)–N(51) ring, φ = 19.4(4), θ = 61.2(4)°, Q = 0.707(3) Å; a) C. Giacovazzo, H. L. Monaco, G. Artioli, D. Viterbo, G. Ferraris, G. Gilli, G. Zanotti, M. Catti, *Fundamentals of Crystallography*, 2nd edn., Oxford University Press, Oxford, **2002**; b) D. Cremer, J. A. Pople, *J. Am. Chem. Soc.* **1975**, *97*, 1354–1358.
[22] F. J. Lahoz, I. T. Dobrinovitch, private communication.
[23] K. L. Bray, C. P. Butts, G. C. Lloyd-Jones, M. J. Murray, *J. Chem. Soc. Dalton Trans.* **1998**, 1421–1422.
[24] L. Brammer, J. M. Charnock, P. L. Goggin, R. J. Goodfellow, A. G. Orpen. T. F. Koetzle, *J. Chem. Soc. Dalton Trans.* **1991**, 1789–1798.
[25] J. V. Allen, G. J. Dawson, C. G. Frost, J. M. J. Williams, *Tetrahedron* **1994**, *50*, 799–808.
[26] J. Christoffers, *J. Chem. Soc. Perkin Trans. 1* **1997**, 3141–3149.
[27] *SAINT*+, Software for CCD diffractometers, v. 6.01; Bruker AXS, Inc., Madison, WI, 2001 and SAINT, version 6.02.
[28] a) R. H. Blessing, *Acta Crystallogr., Sect. A* **1995**, *51*, 33–38; b) SADABS: Area-Detector absorption correction, **1996** Bruker-AXS, Madison, WI (within SAINT+ package, v. 6.01).
[29] A. C. T. North, D. C. Phillips, F. S. Mathews, *Acta Crystallogr., Sect. A* **1968**, *24*, 351–359.
[30] G. M. Sheldrick, *SHELXL-97* Program for Crystal Structure Refinement; University of Göttingen, Göttingen, Germany, 1997.
[31] a) H. D. Flack, *Acta Crystallogr., Sect. A* **1983**, *39*, 876–881; b) G. Bernardinelli, H. D. Flack, *Acta Crystallogr., Sect. A* **1985**, *41*, 500–511.

Received: November 4, 2004
Published Online: March 22, 2005

 © 2005 Wiley-VCH Verlag GmbH & Co. KGaA, Weinheim

Highly Active Neutral Nickel(II) Complexes Bearing P,N-Chelate Ligands: Synthesis, Characterization and Their Application to Addition Polymerization of Norbornene

Hai-Yu Wang[a] and Guo-Xin Jin*[a]

Keywords: Nickel / P,N-chelate ligands / Homogeneous catalysts / Polymerization / Polynorbornene

Neutral nickel(II) complexes [[R–NP]NiPh(PPh_3)](**1**, R = H; **2**, R = CH_3) bearing P,N-chelate ligands ([H–NP] = (2-diphenylphosphanyl)benzenamine $\mathbf{L^1}$; [CH_3–NP] = (2-diphenylphosphanyl) *N*-methylbenzenamine $\mathbf{L^2}$) have been synthesized and characterized. The molecular structure of complex **1** has been confirmed by single-crystal X-ray analyses. After activation with methylaluminoxane (MAO), catalytic precursors **1** and **2** could polymerize norbornene to afford addition-type polynorbornene (PNB) with very high activities (4.43×10^7 g-PNB mol^{-1}-Ni h^{-1}), high molecular weight M_w (3.07×10^6 g mol^{-1}) and moderate molecular weight distribution M_w/M_n. Catalytic activities, polymer yield, M_w and M_w/M_n of PNB have been investigated under various reaction conditions.
(© Wiley-VCH Verlag GmbH & Co. KGaA, 69451 Weinheim, Germany, 2005)

Introduction

Various late transition metal complexes containing chelating ligands act as catalysts for the polymerization and oligomerization of olefins. Early work on the Shell Higher Olefin Process (SHOP)[1] utilized neutral Ni catalysts containing P–O chelates. Subsequent work has investigated, mainly, several classes of ligands: $[O\text{-}P]^-$,[2–6] $[O\text{-}N]^-$,[7–16] $[N\text{-}N]^-$.[17–23] P,N ligands have attracted increasing recent attention because of their bonding versatility with a metal center and the relative ease with which the electronic and steric properties of the donor atoms can be modified.[24–26] Braunstein et al.[27] reported a series of nickel complexes, containing P,N-chelate ligands, and their catalytic ethylene oligomerization behavior. Liang et al.[28] have synthesized several metal complexes supported by bidentate diarylamido phosphane ligands.

Homo-polymer addition of polynorbornenes is of considerable importance because the products have interesting and unique properties, including high chemical resistance, good solubility in organic solvents, good UV resistance, low dielectric constant, high glass-transition temperature, excellent optical transparency, large refractive index, and low birefringence. However, the addition polymerization of norbornene was much less developed than ROMP (ring-opening metathesis polymerization). In 1993, Deming and Novak introduced the first nickel complex for the addition polymerization of norbornene.[29] Several other catalyst systems have also been applied recently to this reaction.[30,31d]

Following our research on neutral nickel complexes,[16,31] we synthesized neutral nickel(II) complexes with a chelating P,N ligands and firstly investigated their catalytic norbornene addition polymerization behaviors. These neutral nickel(II) complexes have very high activities for cyclo-olefin polymerization. This article focuses on the syntheses of neutral nickel(II) complexes **1** and **2** bearing P,N-chelate ligands and the polymerization of norbornene upon activation with methylaluminoxane (MAO). The typical molecular structure of catalytic precursor **1** was characterized by an X-ray crystallographic study. To the best our knowledge, neutral nickel(II) complexes bearing P,N-chelate ligands for the addition polymerization of norbornene have been scarcely investigated.

Results and Discussion

Syntheses of Ligands and Complexes

Syntheses of complexes **1** and **2** are outlined in Scheme 1. (2-Diphenylphosphanyl)benzenamine (ligand $\mathbf{L^1}$) was prepared according to literature methods.[36] Ligand $\mathbf{L^2}$ [(2-diphenylphosphanyl)-*N*-methylbenzenamine] was synthesized by monolithiation of the NH_2 group of ligand $\mathbf{L^1}$ with *n*BuLi (1.0 equiv.), followed by the addition of CH_3I (1.0 equiv.). After workup, $\mathbf{L^2}$ was extracted with hot hexane and obtained after evaporation of solvent as a white solid.

Ligands $\mathbf{L^1}$ and $\mathbf{L^2}$ were treated with *n*BuLi in THF and then treated with *trans*-chloro(phenyl)bis(triphenylphosphane)nickel(II) to give complexes **1** and **2**, respectively. Both complexes were purified by recrystallization from tol-

[a] Laboratory of Molecular Catalysis and Innovative Materials, Department of Chemistry, Fudan University, Shanghai, 200433, China
Fax: +86-21-65641740
E-mail: gxjin@fudan.edu.cn

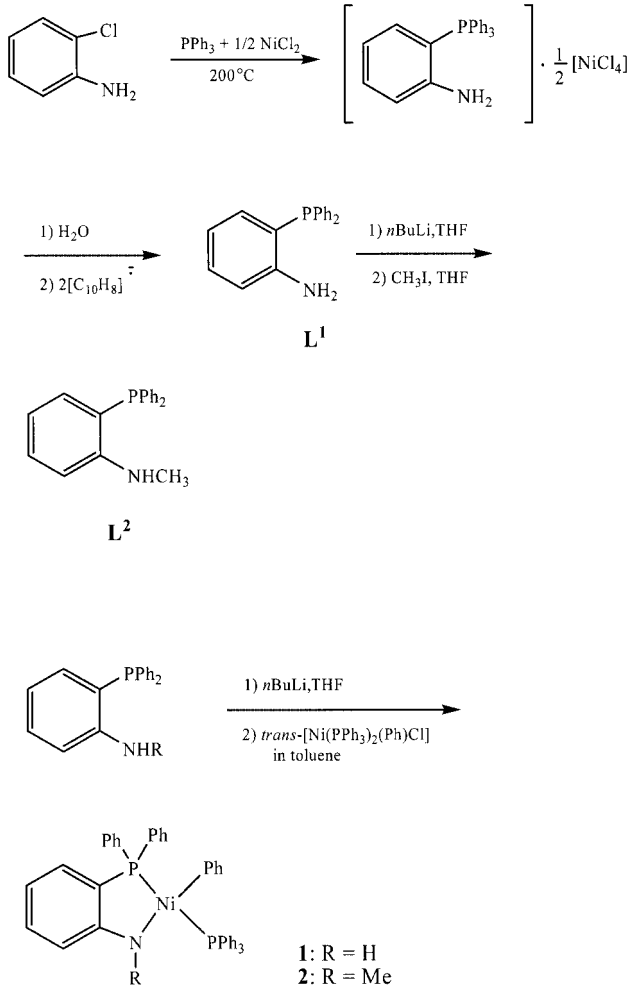

Scheme 1. Syntheses of nickel complexes **1** and **2**.

uene. All compounds were well characterized by ^{1}H NMR, FT-IR as well as elemental analysis.

Single Crystal X-ray Structure Analyses of Complex 1

A single crystal of **1** suitable for X-ray diffraction study was grown from a concentrated CH_2Cl_2 solution at –30 °C. Table 1 summarizes the collection and refinement data of the analyses. Figure 1 shows the ORTEP diagram of **1**. Complex **1** contains a chelating [P,N] ligand, a triphenylphosphane group (PPh_3) and a phenyl group. The bulky diphenylphosphane moiety occupies the position trans to PPh_3, with a nearly linear P(1)–Ni(1)–P(2) angle of 173.97(3)°, and the phenyl group attached to Ni lies trans to N(1), with a C(19)–Ni(1)–N(1) angle of 172.80(10). The *cis* angles at nickel are in the range 84.44–95.83°. Thus, the nickel center lies perfectly on the square plane defined by the four donor atoms. In addition, the metal ion deviates from the [P(1), N(1), P(2) and C(19)] plane by ca. 0.0828 Å.

Table 1. Crystal data and summary of data collection and refinement details for **1**.

Formula	$C_{42}H_{35}NNiP_2$
Formula mass	674.36
Crystal system	monoclinic
Space group	$P2_1/c$
a [Å]	16.011(4)
b [Å]	9.916(2)
c [Å]	21.824(5)
V [Å^3]	3448.2(14)
β [°]	95.634(3)
Z	4
Color	red
Crystal size [mm]	0.20×0.10×0.08
$D_{calcd.}$ [g cm^{-3}]	1.299
μ [mm^{-1}]	0.686
θ limits [°]	1.28/26.01
λ [Å]	Mo-K_α (0.71073)
F(000)	1408
No. of obsd. reflections	6745
No. of parameters refined	415
$R_1[I > 2\sigma(I)]$	0.0379
wR_2(all data)	0.0806
GOF on F^2	0.859

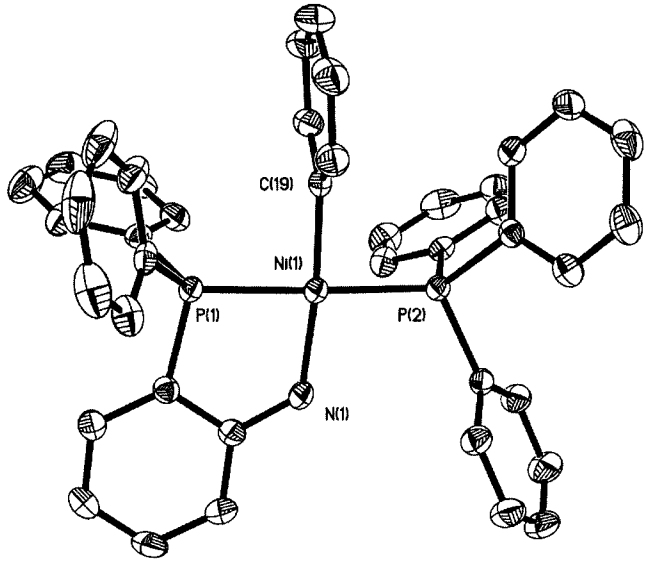

Figure 1. Molecular structure of complex **1.** Selected bond lengths [Å] and angles [°]: Ni(1)–N(1) = 1.892(2), Ni(1)–C(19) = 1.910(2), Ni(1)–P(1) = 2.1670(9), Ni(1)–P(2) = 2.1999(9), P(1)–C(6) = 1.795(3), N(1)–C(1) = 1.366(3) ; N(1)–Ni(1)–C(19) = 172.80(10), N(1)–Ni(1)–P(1) = 84.44(7), C(19)–Ni(1)–P(1) = 89.23(8), N(1)–Ni(1)–P(2) = 95.83(7), C(19)–Ni(1)–P(2) = 90.83(8), P(1)–Ni(1)–P(2) = 173.97(3).

Addition Polymerization of Norbornene

Preliminary experiments indicated that complexes **1**and **2** can not catalyze ethylene polymerization with or without methylaluminoxane (MAO) as co-catalyst at 10 atm of ethylene. However, after activation with MAO, they could catalyze the polymerization of norbornene to afford addition-type polynorbornene (PNB) with high activities (10^7 g-PNB mol^{-1}-Ni h^{-1}), high molecular weight M_w (10^6 g mol^{-1}) and moderate molecular weight distributions M_w/M_n (2.65–3.93). Complexes **1** and **2** themselves and MAO did not

 © 2005 Wiley-VCH Verlag GmbH & Co. KGaA, Weinheim

Table 2. Addition polymerization of norbornene with nickel complexes **1**and **2** activated by methylaluminoxane (MAO).[a]

Entry	Complex	Amount of cocat [equiv.]	Polymer [g]	Activity[b]	M_w[c]	M_w/M_n[c]
1	**1**	500	Trace	–		
2	**1**	1000	1.05	3.14	2.71	3.40
3	**1**	2000	1.13	3.39	2.61	3.20
4	**1**	3000	1.30	3.90	2.57	2.72
5	**1**	4000	1.12	3.36	2.06	2.65
6	**1**	5000	1.06	3.18	2.88	2.32
7	**1**	10000	1.03	3.09	3.07	2.58
8[d]	**1**	–	trace	–		
9	**2**	3000	0.942	2.83	2.46	3.93
10	**2**	4000	0.808	2.42	2.28	3.81
11[d]	**2**	–	trace	–		
12[e]	–	3000	trace	–		

[a] Polymerization conditions: solvent, chlorobenzene; total volume 10 mL; nickel complex (0.2 μmol), norbornene (1.88 g) [norbornene: nickel (molar) = 100 000]; reaction time 10 min; 30 °C. [b] 10^7 g-PNB mol^{-1}-Ni h^{-1}. [c] M_w (10^6 g mol^{-1}) and M_w/M_n determined by GPC. [d] Without co-catalyst MAO. [e] Without nickel complex.

produce polymers under the same conditions (entries 8, 11, 12 in Table 2). In general, the steric structure and bulky group in the nickel complexes slightly influence the catalytic activities. Moreover, the addition mechanism of norbornene, when using neutral nickel complexes, has been hypothesized as the insertion of norbornene into the Ni–C bond.[30i,30l] Thus, the N-methyl group of complex **2** makes the insertion of norbornene into the Ni–C bond more difficult than H of complex **1**, so complex **2** displays lower catalytic activity than complex **1**.

To investigate the reaction parameters affecting addition polymerization of norbornene, the catalytic precursor **1** was studied under different reaction conditions. MAO was essential for the polymerization of norbornene catalyzed by **1** and **2**. It initiates the polymerization of norbornene and probably creates an empty site for insertion of the norbornene monomer. Varying the MAO:complex **1** ratio (expressed here as Al:Ni ratio) had considerable effects on catalytic activity and M_w. The activity of **1** is almost zero for Al:Ni = 500 (entry 1, Table 2), but is up to 10^7 g-PNB mol^{-1}-Ni h^{-1} when Al:Ni > 1000. The catalytic activities of complex **1** increase first and then decrease with increasing Al:Ni ratio; the activity is highest at Al:Ni = 3000. The M_w of polymers also exhibits remarkable changes with Al:Ni, and is lowest at Al:Ni = 4000.

The reaction temperature also affects considerably the catalytic activities and M_w (Table 3). With increasing reaction temperature, the catalytic activities first increase and then decrease – the highest activity is at 30 °C (3.90×10^7 g-PNB mol^{-1}-Ni h^{-1}). In contrast, M_w decreased with increasing temperature while M_w/M_n varied irregularly.

Figure 2 reveals the effects of reaction time on catalytic activities and polymer yields. The yields of PNB gradually increase with increasing reaction time, but the catalytic activities of complex **1** always decrease. After 1 h, the yield is almost up to 90%, but the activity has reduced to 10^6 g-PNB mol^{-1}-Ni h^{-1}.

The concentration of norbornene also exerts a considerable influence on the polymerization reaction (Figure 3). The catalytic activity of complex **1** increases almost linearly with monomer concentration in the range 0.5–2.5 mol L^{-1}, and then remains nearly constant when the concentration exceeds 3.0 mol L^{-1}.

Table 3. Influence of the reaction temperature (T) on activities of complex **1**.

Entry	T[°C]	Polymer [g]	Activity[a]	M_w[b]	M_w/M_n
1	0	0.309	0.927	2.80	3.23
2	30	1.30	3.90	2.57	2.72
3	60	1.08	3.24	1.81	2.67
4	90	0.799	2.40	1.37	2.89

[a] 10^7 g-PNB mol^{-1}-Ni h^{-1}. [b] M_w (10^6 g mol^{-1}). Polymerization conditions: solvent, chlorobenzene; total volume 10 mL, nickel complex (0.2 μmol), norbornene (1.88 g) [norbornene:nickel(molar) = 100000]; MAO (0.35 mL,1.7 M) [Al:Ni = 3000]; reaction time 10 min.

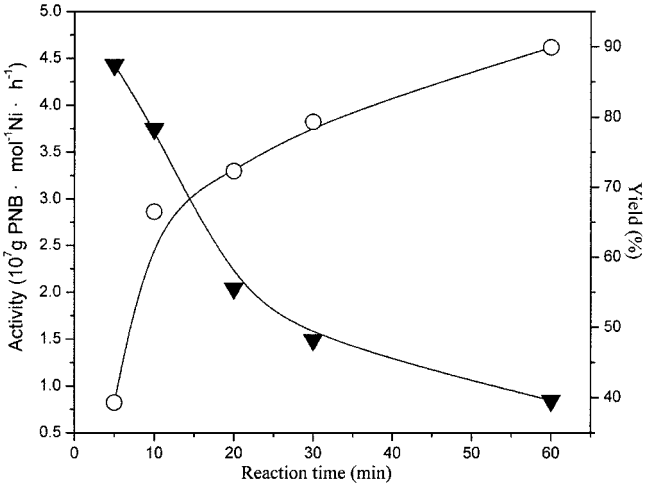

Figure 2. Activity (▲) and yield(○) vs. reaction time; 0.2 μmol complex **1**, norbornene:nickel(molar) = 100 000, Al:Ni = 3000, V_{total} = 10 mL, polymerization at 30 °C.

The crystallinity of the resultant polymers was investigated by XRD. Figure 4 shows the XRD diagram of the obtained PNB. Two broad halos at 2θ of 11 and 18° are present. This pattern is predominantly intrachain, probably corresponding to a short-range order, or to a pseudo-periodicity arrangement of the bicycle units along the chain.

 © 2005 Wiley-VCH Verlag GmbH & Co. KGaA, Weinheim

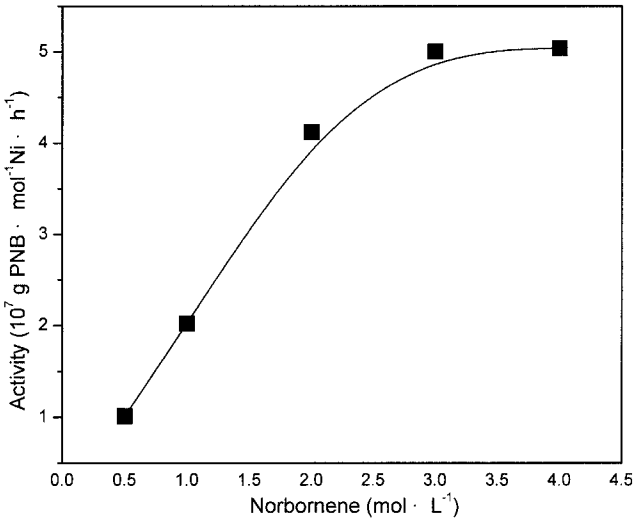

Figure 3. Activity vs. norbornene concentration; 0.2 μmol complex **1**, Al:Ni = 3000, V_{total} = 10 mL, polymerization at 30 °C for 10 min.

This is almost in agreement with reported results.[32,33] No traces of Bragg reflections, characteristic of crystalline regions, are revealed. The PNB is therefore, non-crystalline.

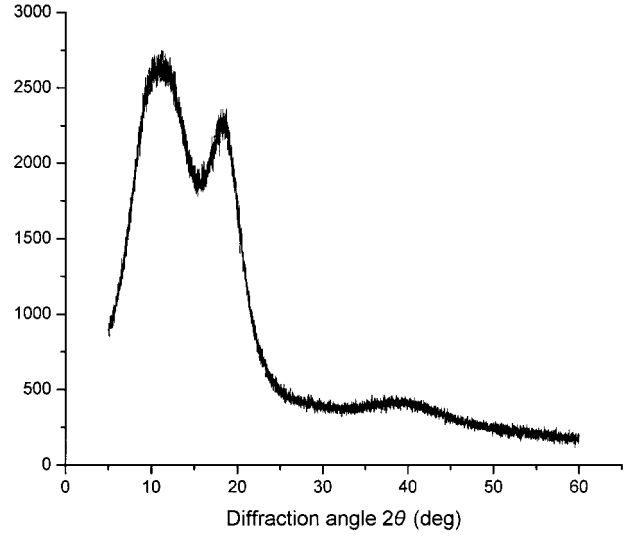

Figure 4. XRD diagram of PNB.

All polymers obtained showed very similar IR and ^{1}H NMR spectra. ^{1}H NMR spectra exhibited no trace of the double bond that is typical for ROMP polynorbornene.[34,30l] PNB resonances appear at 0.9–2.6 (m, maxima at 1.3, 1.5, 1.7, 2.4 ppm). A double bond, which is often seen at 1680–1620 cm^{-1}, was also absent from the IR spectra. The glass transition temperature (T_g) of addition-type homo-polynorbornene has proved difficult to obtain since it is, apparently, close to the temperature at which decomposition tends to set in.[35] Our attempts to determine the T_g of PNB also failed, and DSC studies did not give an endothermic signal upon heating to the decomposition temperature (above 450 °C).

Conclusions

(2-Diphenylphosphanyl)benzenamine (**L^1**) and (2-diphenylphosphanyl)-*N*-methylbenzenamine (**L^2**) were prepared in good yields for the syntheses of neutral nickel(II) complexes **1** and **2**. Complex **1** was characterized by single-crystal X-ray diffraction. Both complexes showed high catalytic activities for the addition polymerization of norbornene after activation with MAO. Catalytic activities of up to 4.43×10^7 g-PNB mol^{-1}-Ni h^{-1} and M_w up to 3.07×10^6 g·mol^{-1} were observed. Activities, polymer yield and M_w can be controlled by varying the reaction parameters. PNBs obtained here are amorphous and soluble in halogenated aromatic hydrocarbons. Therefore, neutral Ni^{ii} complexes with chelating P,N ligands are, perhaps, a promising system for the addition polymerization of norbornene. We are currently working to develop new P-N nickel complexes for the polymerization of norbornene.

Experimental Section

General Remarks: All manipulations of air- and/or water-sensitive compounds were performed under dry nitrogen using standard Schlenk and vacuum-line techniques. Solvents were dried by boiling under reflux with appropriate drying agents and distilled under nitrogen before use. (2-Diphenylphosphanyl)benzenamine[36] and *trans*-[Ni(PPh$_3$)$_2$(Ph)Cl][37] were prepared according to literature procedures. Norbornene (bicyclo[2.2.1]hept-2-ene, Acros) was purified by distillation over sodium and used as a chlorobenzene solution. Methylaluminoxane (MAO) was purchased from Aldrich as 10% weight of a toluene solution and used without further purification. Other commercially available reagents were purchased and used without purification.

^{1}H NMR spectra were recorded with a Varian Unity-400 spectrometer. Elemental analyses were performed on an Elementar vario EL III Analyzer. FT-IR spectra were recorded with a Niclolet-FT-IR-50X spectrometer. NMR spectroscopic data for PNB were obtained at ambient temperature with a Bruker AC 500 spectrometer instruments using [D$_4$]-*o*-chlorobenzene as solvent. Average molecular weight (M_w) and molecular weight distributions (M_w/M_n) of PNB products were determined using a PL GPC-220 gel permeation chromatograph at 150 °C, employing narrow standards calibration, and equipped with three PL gel columns (sets of PL gel 10 m MIXED-B LS). Trichlorobenzene was used as solvent at a flow rate of 1.00 mL min^{-1}. Differential scanning calorimetric (DSC) measurements were performed with a Perkin–Elmer Pyris 1 DSC. The X-ray diffraction (XRD) diagram of the polymer powder was obtained using a Bruker D4 Endeavor X-ray diffractometer with monochromatic radiation at a wavelength of 1.54 Å. Scanning was performed with 2θ ranging from 5 to 60°.

Synthesis of Ligand L^2: A solution of ligand **L^1** (0.555 g, 2.0 mmol) in THF (20 mL) was cooled to –78 °C and *n*BuLi was then added slowly (1.0 equiv., 0.87 mL, 2.3 M, 2.0 mmol). After the solution was stirred for 1 h at –78 °C, CH_3I (1.0 equiv., 0.125 mL, 2.0 mmol) was slowly added at –78 °C. The reaction mixture was then stirred for 2 h at –78 °C and warmed to room temperature overnight. The solution was hydrolyzed with degassed water (5 mL) and extracted with diethyl ether (3 × 3 mL). Finally, the organic phase was separated, dried over degassed $MgSO_4$, and filtered. After evaporation of the diethyl ether, the product was isolated as a white solid (yield 0.456 g, 1.56 mmol, 78%). ^{1}H NMR ($CDCl_3$): δ = 2.82 (s, 3 H, N–

 © 2005 Wiley-VCH Verlag GmbH & Co. KGaA, Weinheim

CH_3), 6.65 (m, 2 H, *m*-H of P), 6.75 (m, 1 H, *p*-H of P), 7.34–7.23 (m, 11 H, Ar–H) ppm.

Synthesis of Complex 1: A solution of ligand $\mathbf{L^1}$ (0.277 g, 1.0 mmol) in THF (15 mL) was cooled to –78 °C, and *n*BuLi was added dropwise (1.0 equiv., 0.48 mL, 2.3 M, 1.0 mmol). This mixture was allowed to warm to room temperature and then stirred for 2 h to afford the lithium salt of $\mathbf{L^1}$. After evaporation of THF under vacuum, the lithium salt of $\mathbf{L^1}$ was dissolved in toluene (10 mL). The resultant solution was slowly channeled into a 50 mL flask with *trans*-[Ni(PPh$_3$)$_2$(Ph)Cl] (0.668 g, 0.96 mmol) in toluene (10 mL) and continuously stirred overnight at room temperature. The resultant reaction mixture was then separated by centrifugation to remove LiCl. After the upper clear dark red solution was concentrated to about 3 mL, hexane (20 mL) was added and complex **1** was obtained as a red-orange solid (yield 0.499 g, 77%). Red single crystals suitable for X-ray were recrystallized from CH_2Cl_2 at –30 °C. $C_{42}H_{35}NP_2Ni$ (674.39): calcd. C 74.80, H 5.23, N 2.08; found C 74.46, H 5.25, N 1.93. ^{1}H NMR ($CDCl_3$): δ = 7.93–7.27 (m, 34 H, Ar–H) ppm.

Synthesis of Complex 2: A dark red powder of complex **2** was obtained in a manner similar to that for complex **1** (yield of 68%, 0.449 g). $C_{43}H_{37}NP_2Ni$ (688.42): calcd. C 75.02, H 5.42, N, 2.03; found C 74.76, H 5.18, N 1.98. ^{1}H NMR ($CDCl_3$): δ = 2.79 (s, 3 H, N–CH_3), 7.91–7.26 (m, 34 H, Ar–H) ppm.

Structure Solution and Refinement for Complex 1: For **1**, a single crystal suitable for X-ray analysis was sealed in a glass capillary, and the intensity data of the single crystal were collected with a CCD-Bruker Smart APEX system. All determinations of the unit cell and intensity data were performed with graphite-monochromated Mo-K_α radiation (λ = 0.71073 Å). All data were collected at room temperature using the ω scan technique. Structures were solved by direct methods, using Fourier techniques, and refined on F^2 by a full-matrix least-squares method. All non-hydrogen atoms were refined anisotropically, and all hydrogen atoms were included but not refined. Crystallographic data are summarized in Table 1.

CCDC-252436 contains the supplementary crystallographic data for this paper. These data can be obtained free of charge from The Cambridge Crystallographic Data Centre via www.ccdc.cam.ac.uk/data_request/cif.

Polymerization of Norbornene: In a typical procedure (entry 4, Table 2), nickel complex **1** (0.2 μmol) in chlorobenzene (1.0 mL), norbornene (1.88 g) in chlorobenzene (3.0 mL) and another 3.0 mL of fresh chlorobenzene were added to a special polymerization bottle (20 mL) with strong stirrer under nitrogen. After keeping the mixture at 30 °C for 10 min, MAO (0.35 mL) was added to the polymerization system via syringe and the reaction was initiated. Ten minutes later, acidic ethanol ($V_{ethanol}$:$V_{concd.HCl}$ = 20:1) was added to terminate the reaction. The PNB produced was isolated by filtration, washed with ethanol and dried at 80 °C for 48 h under vacuum. For all polymerization procedures, the total reaction volume was 10.0 mL (achieved by varying the amount of chlorobenzene when necessary). IR (KBr): $\tilde{\nu}$ = 2950, 2865, 1475, 1453, 1294, 1257, 1220, 1189, 1142, 1105, 937, 890 cm^{-1}. ^{1}H NMR: δ = 0.9–2.6 (m, maxima at 1.3, 1.5, 1.7, 2.4 ppm).

Acknowledgments

Financial support by the National Nature Science Foundation of China for Distinguished Young Scholars (29925101, 20274008) and by the Key Project of Science and Technology of the Education Ministry of China is gratefully acknowledged.

[1] W. Keim, F. H. Kowaldt, R. Goddard, C. Krueger, *Angew. Chem.* **1978**, *90*, 493–493; *Angew. Chem. Int. Ed. Engl.* **1978**, *17*, 466–467.
[2] K. A. O. Starzewski, J. Witte, *Angew. Chem. Int. Ed. Engl.* **1985**, *24*, 599–601.
[3] a) Z. J. A. Komon, X. Bu, G. C. Bazan, *J. Am. Chem. Soc.* **2000**, *122*, 12379–12380; b) Z. J. A. Komon, X. Bu, G. C. Bazan, *J. Am. Chem. Soc.* **2000**, *122*, 1830–1831.
[4] Z. J. A. Komon, G. C. Bazan, C. Fang, X. Bu, *Inorg. Chim. Acta* **2003**, *345*, 95–102.
[5] R. Soula, J. P. Broyer, M. F. Llauro, A. Tomov, R. Spitz, J. Claverie, X. Drujon, J. Malinge, T. Saudemont, *Macromolecules* **2001**, *34*, 2438–2442.
[6] H. A. Kalamarides, S. Iyer, J. Lipian, L. F. Rhodes, *Organometallics* **2000**, *19*, 3983–3990.
[7] C. Wang, S. Friedrich, T. R. Younkin, R. T. Li, R. H. Grubbs, D. A. Bansleben, M. W. Day, *Organometallics* **1998**, *17*, 3149–3151.
[8] T. R. Younkin, E. F. Connor, J. I. Henderson, S. K. Friedrich, R. H. Grubbs, D. A. Bansleben, *Science* **2000**, *287*, 460–462.
[9] F. A. Hicks, M. Brookhart, *Organometallics* **2001**, *20*, 3217–3219.
[10] J. C. Jenkins, M. Brookhart, *Organometallics* **2003**, *22*, 250–256.
[11] F. A. Hicks, J. C. Jenkins, M. Brookhart, *Organometallics* **2003**, *22*, 3533–3545.
[12] F. M. Bauers, S. Mecking, *Angew. Chem. Int. Ed.* **2001**, *40*, 3020–3022.
[13] C. B. Shim, Y. H. Kim, B. Y. Lee, Y. Dong, H. Yun, *Organometallics* **2003**, *22*, 4272–4280.
[14] C. B. Shim, Y. H. Kim, B. Y. Lee, D. M. Shin, Y. K. Chung, *J. Organomet. Chem.* **2003**, *675*, 72–76.
[15] B. Y. Lee, Y. H. Kim, H. J. Shin, C. H. Lee, *Organometallics* **2002**, *21*, 3481–3484.
[16] D. Zhang, G.-X. Jin, *Organometallics* **2003**, *22*, 2851–2584.
[17] B. Domhover, W. Kläui, A. Kermer-Aach, R. Bell, D. Mootz, *Angew. Chem. Int. Ed.* **1998**, *37*, 3050–3052.
[18] H. L. Wiencko, E. Kogut, T. H. Warren, *Inorg. Chim. Acta* **2003**, *345*, 199–208.
[19] R. M. Bellabara, P. T. Gomes, S. I. Pascu, *J. Chem. Soc.*, *Dalton Trans.* **2003**, 4431–4436.
[20] B. Y. Lee, G. C. Bazan, J. Vela, Z. J. A. Komon, X. Bu, *J. Am. Chem. Soc.* **2001**, *123*, 5352–5353.
[21] B. Y. Lee, X. Bu, G. C. Banzan, *Organometallics* **2001**, *20*, 5425–5431.
[22] Y. H. Kim, T. H. Kim, B. Y. Lee, D. Woodmansee, X. Bu, G. C. Bazan, *Organometallics* **2002**, *21*, 3082–3084.
[23] S. J. Diamanti, P. Ghosh, F. Shimizu, G. C. Bazan, *Macromolecules* **2003**, *36*, 9731–9735.
[24] P. Braunstein, F. Naud, *Angew. Chem. Int. Ed.* **2001**, *40*, 680–699.
[25] C. S. Slone, D. A. Weinberger, C. A. Mirkin, *Prog. Inorg. Chem.* **1999**, *48*, 233–250.
[26] G. Helmchen, A. Pfaltz, *Acc. Chem. Res.* **2000**, *33*, 336–345.
[27] a) P. Braunstein, J. Pietsch, Y. Chauvin, S. Mercier, L. Saussine, A. DeCian, J. Fischer, *J. Chem. Soc.*, *Dalton Trans.* **1996**, 3571–3574; b) P. Braunstein, J. Pietsch, Y. Chauvin, A. Decian, J. Fischer, *J. Organomet. Chem.* **1997**, *529*, 387–393; c) J. Pietsch, P. Braunstein, Y. Chauvin, *New J. Chem.* **1998**, *22*, 467–472; d) F. Speiser, P. Braunstein, L. Saussine, R. Welter, *Organometallics* **2004**, *23*, 2613–2624; e) F. Speiser, P. Braunstein, L. Saussine, *Organometallics* **2004**, *23*, 2625–2632; f) F. Speiser, P. Braunstein, L. Saussine, *Organometallics* **2004**, *23*, 2633–2640; g) F. Speiser, P. Braunstein, L. Saussine, R. Welter, *Inorg. Chem.* **2004**, *43*, 1649–1658.
[28] a) L.-C. Liang, W.-Y. Lee, C.-H. Hung, *Inorg. Chem.* **2003**, *42*, 5471–5473; b) L.-C. Liang, M.-H. Huang, C.-H. Hung, *Inorg. Chem.* **2004**, *43*, 2166–2174; c) L.-C. Liang, W.-Y. Lee, C.-H. Yin, *Organometallics* **2004**, *23*, 3538–3547.

 © 2005 Wiley-VCH Verlag GmbH & Co. KGaA, Weinheim

[29] T. J. Deming, B. M. Novak, *Macromolecules* **1993**, *26*, 7089–7091.
[30] a) A. O. Patil, S. Zushma, R. T. Stibrany, S. P. Rucker, L. M. Wheeler, *J. Polym. Sci. Polym. Chem. Ed.* **2003**, *41*, 2095–2106; b) X.-F. Li, Y.-S. Li, *J. Polym. Sci. Polym. Chem. Ed.* **2002**, *40*, 2680–2685; c) H. Yang, Z. Li, W.-H. Sun, *J. Mol. Catal.* **2003**, *206*, 23–28; d) C. Mast, M. Krieger, K. Dehnicke, A. Greiner, *Macromol. Rapid Commun.* **1999**, *20*, 232–235; e) B. Berchtold, V. Lozan, P. G. Lassahn, C. Janiak, *J. Polym. Sci. Polym. Chem. Ed.* **2002**, *40*, 3604–3614; f) W.-H. Sun, H. Yang, Z. Li, Y. Li, *Organometallics* **2003**, *22*, 3678–3683; g) H. Yang, W.-H. Sun, F. Chang, Y. Li, *Appl. Catal. A: General* **2003**, *252*, 261–267; h) V. Lozan, P.-G. Lassahn, C. Zhang, B. Wu, C. Janiak, G. Rheinwald, Z. Lang, *Z. Naturforsch. Teil B* **2003**, *58*, 1152; i) P.-G. Lassahn, V. Lozan, G. A. Timco, P. Christian, C. Janiak, R. E. P. Winpenny, *J. Catal.* **2004**, *222*, 260–267; j) G. M. Benedikt, E. Elce, B. L. Goodall, H. A. Kalamarides, L. H. McIntosh, L. F. Rhodes, K. T. Selvy, C. Andes, K. Oyler, A. Sen, *Macromolecules* **2002**, *35*, 8978–8788; k) D. A. Barnes, G. M. Benedikt, B. L. Goodall, S. S. Huang, H. A. Kalamarides, S. Lenhard, L. H. McIntosh III, K. T. Selvy, R. A. Shick, L. F. Rhodes, *Macromolecules* **2003**, *36*, 2623–2632; l) X. Mi, Z. Ma, N. Cui, L. Wang, Y. Ke, Y. Hu, *J. Appl. Polym. Sci.* **2003**, *88*, 3273–3278; m) P.-G. Lassahn, V. Lozan, B. Wu, A. S. Weller, C. Janiak, *J. Chem. Soc.*, *Dalton Trans.* **2003**, 4437–4450.
[31] a) D. Zhang, G.-X. Jin, N.-H. Hu, *Chem. Commun.* **2002**, *6*, 574–575; b) D. Zhang, G.-X. Jin, N.-H. Hu, *Eur. J. Inorg. Chem.* **2003**, *8*, 1570–1576; c) G.-X. Jin, D. Zhang, *J. Polym. Sci. Polym. Chem. Ed.* **2004**, *42*, 1018–1024; d) D. Zhang, G.-X. Jin, L.-H. Weng, F. Wang, *Organometallics* **2004**, *23*, 3270–3275; e) D. Zhang, G.-X. Jin, *Appl. Catal. A: General* **2004**, *262*, 13–18.
[32] T. F. A. Haselwander, W. Heitz, S. A. Krügel, J. H. Wendorff, *Macromol. Chem. Phys.* **1996**, *197*, 3435–3453.
[33] C. T. Zhao, M. R. Ribeiro, M. N. de Pinho, V. S. Subrahmanyam, C. L. Gil, A. C. de Lima, *Polymer* **2001**, *42*, 2455–2462.
[34] R.-C. Yu, C. Hung, J.-H. Huang, H.-Y. Lee, J.-T. Chen, *Inorg. Chem.* **2002**, *41*, 6450–6455.
[35] a) G. Sartori, F. C. Ciampelli, N. Cameli, *Chim. Ind. (Milan)* **1963**, *45*, 1478; b) P.-G. Lassahn, C. Janiak, J.-S. Oh, *Macromol. Rapid Commun.* **2002**, *23*, 16–20.
[36] M. K. Cooper, J. M. Downes, P. A. Duckworth, *Aust. J. Chem.* **1992**, *45*, 595–609.
[37] a) P. A. Sehun, *Inorg. Synth.* **1972**, *13*, 124; b) M. Hidai, T. Kashiwagi, T. Ikeuchi, Y. Uchida, *J. Organomet. Chem.* **1971**, *30*, 279–282.

Received: October 12, 2004

 © 2005 Wiley-VCH Verlag GmbH & Co. KGaA, Weinheim

Nortricyclyl- and Norbornenyl-Acylrhodium Complexes from the Reaction of Norbornadiene Rhodium(I) Complexes with *o*-(Diphenylphosphanyl)-benzaldehyde

Rachad El Mail,[a] María Angeles Garralda,*[a] Ricardo Hernández,[a] Lourdes Ibarlucea,[a] Elena Pinilla,[b] María Rosario Torres,[b] and Malkoa Zarandona[a]

Keywords: Rhodium complexes / Aldehydes / Insertion and rearrangement of norbornadiene / N ligands

[{Rh(Nbd)Cl}$_2$] (Nbd = norbornadiene) reacts with *o*-(diphenylphosphane)benzaldehyde in benzene solution to give the rhodium(III) complex [Rh(Cl)(C_7H_9){*o*-PPh_2(C_6H_4CO)}]$_n$ (**1**), where C_7H_9 is a nortricyclyl (Ntyl) group. Complex **1** reacts with various bidentate N-donors, such as biacetyldihydrazone, 2,2′-bipyridine, 8-aminoquinoline, 2-(aminomethyl)-pyridine, or pyridine, to afford nortricyclyl [Rh(Cl){*o*-PPh_2(C_6H_4CO)}(Ntyl)(NN)] complexes. The presence of the nortricyclyl group and the structure of the complexes have been confirmed by NMR spectroscopy and, in one case, by single-crystal X-ray diffraction. Nortricyclyl complexes containing bidentate N-donors are also formed by the reaction in benzene of PPh_2(*o*-C_6H_4CHO) with the corresponding [Rh(Cl)(Nbd)(NN)] compounds prepared "in situ". [Rh(Cl)-(Nbd)(bipy)] prepared "in situ" reacts with PPh_2(*o*-C_6H_4CHO) in methanol to give the complex [Rh(Cl){*o*-PPh_2(C_6H_4CO)}(C_7H_9)(bipy)], where C_7H_9 is a norbornenyl (Nbyl) group. This compound has been fully characterized by NMR spectroscopy. A proposal for the selective production of the norbornenyl and the nortricyclyl derivatives is presented.
(© Wiley-VCH Verlag GmbH & Co. KGaA, 69451 Weinheim, Germany, 2005)

Introduction

C–H bond cleavage in aldehydes, promoted by transition metal complexes, is an active area of research.[1] Rhodium and iridium compounds add, oxidatively, aldehyde C–H bonds to afford acylhydride derivatives;[2] such species are involved in catalytic processes such as aldehyde decarbonylation or alkene hydroacylation.[3] *o*-(Diphenylphosphanyl)-benzaldehyde [PPh_2(*o*-C_6H_4CHO)] promotes the chelate-assisted oxidative addition of aldehyde to rhodium(I)[4] iridium(I)[5] platinum(0)[6] or cobalt(I),[7] yielding *cis* acylhydride complexes that contain acylphosphane chelates PPh_2(*o*-C_6H_4CO). Ruthenium and osmium clusters also undergo oxidative addition to afford compounds with bridging acyl and hydride ligands.[8] PPh_2(*o*-C_6H_4CHO) is also a versatile ligand that can coordinate to transition metal atoms: (i) as a monodentate P-donor towards rhodium(I),[9] iridium(III),[10] palladium(II),[11] platinum(II),[12] ruthenium(II),[13] or tungsten(0);[14] (ii) as chelating phosphane-aldehyde ligand with the aldehyde portion bonded through oxygen (σ complex) as in [Ru(η^6-arene)Cl{κ^2-PPh_2(*o*-C_6H_4CHO)}][SbF_6][13] or [Re(Cl)$(CO)_3${κ^2-PPh_2(*o*-C_6H_4CHO)}][15] or through both oxygen and carbon (π complex) as in [Co(C_5Me_5){η^3-PPh_2(*o*-C_6H_4CHO)}][16] or [$W(CO)_2${η^3-PPh_2(*o*-C_6H_4-CHO)}].[14b]

1,5-Cyclooctadiene (Cod) rhodium or iridium complexes react with PPh_2(*o*-C_6H_4CHO) to undergo chelate-assisted oxidative addition, affording different types of complexes. [{Rh(Cod)Cl}$_2$] reacts through diolefin displacement to give a hydride, [Rh(Cl)(H){PPh_2(*o*-C_6H_4CO)}{κ^2-PPh_2(*o*-C_6H_4CHO)}],[17] while the cationic complex [Rh$(Cod)_2$]-ClO_4 affords cyclooctenyl derivative [Rh(η^3-C_8H_{13})-{PPh_2(*o*-C_6H_4CO)}{κ^2-PPh_2(*o*-C_6H_4CHO)}]ClO_4, due to hydride formation being followed by insertion of the diolefin into the Rh–H bond.[18] [{Ir(Cod)Cl}$_2$] gives the 1,5-cyclooctadiene complex [Ir(Cl)(H){PPh_2(*o*-C_6H_4CO)}-(Cod)] – a proposed model intermediate in the hydroacylation of olefins,[5] which reacts with PPh_2(*o*-C_6H_4CHO) to give hydridoirida-β-diketones, most likely via iridium(V) intermediates formed by oxidative addition of aldehyde to Ir^{III} species.[19] Recently, the reaction of [(η^5-C_5Me_5)-M(Cl)(μ-Cl)]$_2$ (M = Rh, Ir) with PPh_2(*o*-C_6H_4CHO) to afford [(η^5-C_5Me_5)M(Cl)(PPh_2(*o*-C_6H_4CO))] with HCl loss has been reported.[20]

We report here on the reactions of norbornadiene-containing rhodium(I) complexes with PPh_2(*o*-C_6H_4CHO).

Results and Discussion

[{Rh(Nbd)Cl}$_2$] (Nbd = norbornadiene) reacts with *o*-(diphenylphosphane)benzaldehyde in benzene solution to

[a] Facultad de Química de San Sebastián, Universidad del País Vasco,
Apdo. 1072, 20080 San Sebastián, Spain
E-mail: qppgahum@sq.ehu.es
[b] Departamento de Química Inorgánica, Laboratorio de Difracción de Rayos X, Facultad de Ciencias Químicas, Universidad Complutense,
28040 Madrid, Spain

 DOI: 10.1002/ejic.200400935 © 2005 Wiley-VCH Verlag GmbH & Co. KGaA, Weinheim

afford a yellow rhodium(III) complex, which according to its elemental analysis corresponds to $[Rh(Cl)(C_7H_9)\{o\text{-}PPh_2(C_6H_4CO)\}]_n$ **1** (see *i* in Scheme 1). Its IR spectrum shows a strong band at 1637 cm^{-1} due to bonded acyl groups. The FAB spectrum shows $[M-Cl]^+$ and $[M-Cl-(C_7H_9)]^+$ peaks for **1** ($n = 3$) at 1525 (47%) and 1432 (20%), respectively, suggesting a trinuclear structure. The four resonances in the 70–74 ppm region of the $^{31}P\{^1H\}$ NMR spectrum are of almost equal intensity as doublets, due to coupling with rhodium ($J_{Rh,P}$ = ca. 200 Hz). The ^1H NMR spectrum also shows four almost equal doublets in the 2.4–2.9 ppm region, complex multiplets in the 1.41–0.22 ppm region and no resonances in the olefinic region. On these spectroscopic grounds, we believe **1** contains a nortricyclyl group formed by the oxidative addition of aldehyde to rhodium to give an acylhydridenorbornadiene complex, followed by hydrogen transfer with a concurrent double bond shift to form the nortricyclyl group. This last type of step has been suggested in the rhodium-catalyzed amination of norbornadiene[21] and, recently, the formation of rhodium(III) complexes containing a nortricyclyl bonded group and using norbornadiene rhodium(I) compounds as starting material has been reported.[22]

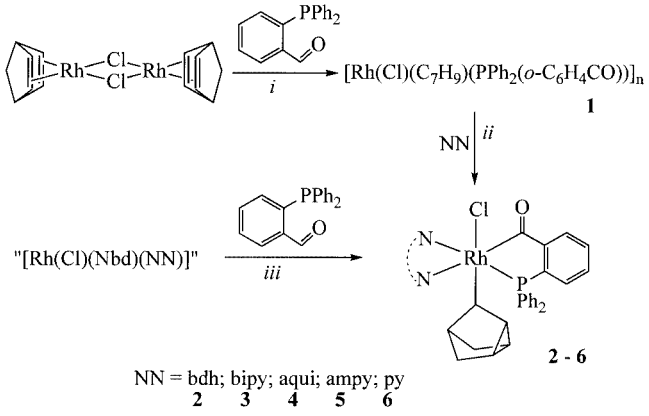

Scheme 1. Formation of nortricyclyl derivatives in benzene.

The complexity of the NMR spectra indicates the presence of several isomers. On raising the temperature to +60 °C, the proton resonances at δ = 2.89, 2.71 and 2.46 ppm, and also three of the four resonances in the $^{31}P\{^1H\}$ NMR spectrum, decrease markedly, while the proton resonance at δ = 2.80 ppm and the doublet at $\delta^{31}P$ 71.52 ppm increase in intensity. These observations, along with the FAB data, suggest that **1** contains a mixture of two trinuclear isomers, one with equivalent phosphorus atoms and equivalent nortricyclyl groups and the other with three inequivalent phosphorus atoms and three inequivalent nortricyclyl groups. At higher temperatures, or longer periods in solution, the complex decomposes and, consequently, we could not obtain either a single isomer or single crystals for X-ray diffraction analysis. The reaction of **1** with several N-donor ligands confirmed the formation of the nortricyclyl (Ntyl) group.

Complex **1** reacts with bidentate N-donors, such as diimines or amino-imines, or with pyridine, to afford nortricyclyl $[Rh(Cl)\{o\text{-}PPh_2(C_6H_4CO)\}(Ntyl)(NN)]$ complexes [NN = biacetyldihydrazone (bdh), **2**; 2,2′-bipyridine (bipy), **3**; 8-aminoquinoline (aqui), **4**; 2-aminomethylpyridine (ampy), **5**; pyridine (py), **6**] (see *ii* in Scheme 1). In all cases, a single complex is obtained, as indicated by NMR spectroscopy. The $^{31}P\{^1H\}$ NMR spectra show only one doublet at low field (68–73 ppm), with $J_{Rh,P}$ of 170–183 Hz, which is consistent with phosphorus atoms trans to nitrogen.[4d] A doublet of doublets in the low-field region of the $^{13}C\{^1H\}$ NMR spectra (ca. 240 ppm) is due to the bonded acyl group, with $J_{Rh,C}$ around 37 Hz and $J_{P,C}$ of ca. 4 Hz. Nortricyclyl group assignments have been made using 2D NMR techniques (Experimental section). The ^1H NMR spectra show a doublet of doublets (1.4–2.4 ppm) for the Ntyl-CH bonded to rhodium, due to coupling with rhodium (ca. 10 Hz) and with a cis phosphorus ($J_{P,H}$ = ca. 2 Hz). Two doublets for each Ntyl-CH_2 group, three triplets due to the Ntyl-cyclopropyl fragment and a broad singlet due to another Ntyl-CH are also observed. $^{13}C\{^1H\}$ NMR spectra show, at ca. 40 ppm, the resonance due to the nortricyclyl carbon atom bonded to rhodium as either a doublet due to rhodium coupling ($J_{Rh,C}$ = ca. 25 Hz) or as a doublet of doublets if additional splitting by a cis phosphorus atom is observed ($J_{P,C}$ = ca. 6 Hz). Complex **2** contains a diimino-coordinated dihydrazone and shows two well-separated resonances for the pendant amino groups at δ = 5.65 and 7.78 ppm, respectively. The low-field resonance is most likely due to hydrogen bond formation. Complexes **4** and **5**, containing bonded amino groups, show the expected displacement of the corresponding amino resonance towards lower field on coordination. Only one isomer is formed, containing the amino group trans to the phosphane. Were the amino group cis to the phosphane, ring current effects originated by its aromatic rings would shift the signals towards higher field.[4d]

An X-ray diffraction study of **2** confirms the presence of the nortricyclyl group and the structure. There appears to be only two previous, recent, structural reports of a nortricyclyl unit bonded to rhodium.[22] The crystal consists of $[Rh(Cl)\{o\text{-}PPh_2(C_6H_4CO)\}(C_7H_9)(H_2NN{=}C(CH_3)C(CH_3){=}NNH_2)]$ neutral molecules and chloroform solvent molecules. Figure 1 shows an ORTEP view of the complex with the atomic numbering scheme, together with selected bond lengths and angles. The rhodium atom is coordinated in a slightly distorted octahedral fashion due to the presence of two bidentate ligands. The maxima deviations of 15.3 and 14.3° correspond to the angles N3–Rh–N2 and C8–Rh–P for the bidentate ligands. The nortricyclyl unit and the chlorine atom occupy axial positions. The equatorial plane, formed by the P, C8, N2 and N3 atoms of the two metallocycles, shows a maximum least-squares deviation of 0.09(1) Å for C8, with the rhodium atom 0.022(1) Å out of this plane. Rh–N2 [2.10(1) Å] trans to phosphorus is slightly shorter than Rh–N3 [2.16(1) Å] trans to acyl, reflecting the stronger trans influence of the acyl ligands. Rh–C1 [2.12(1) Å] is similar to those recently reported in nortricyclylrhodium compounds[22] and longer than Rh–C8 [2.00(1) Å], which is as expected.[4b] The difference between

 © 2005 Wiley-VCH Verlag GmbH & Co. KGaA, Weinheim

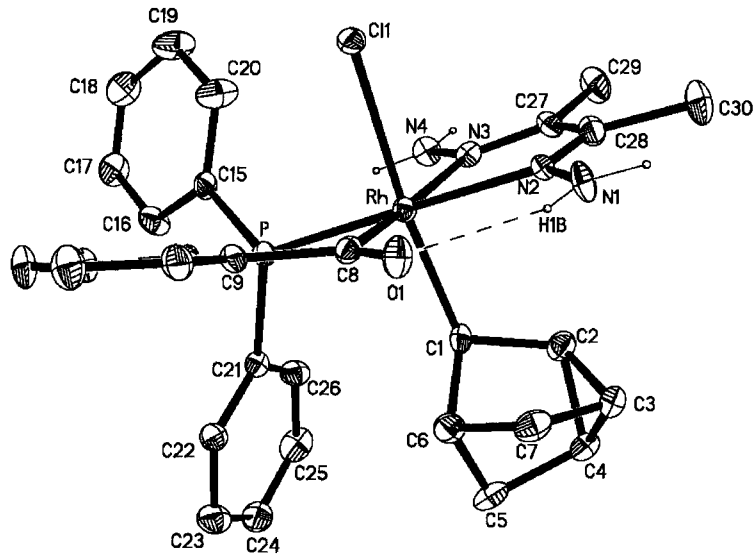

Figure 1. ORTEP view of complex **2**, showing the atomic numbering (30% probability ellipsoids); solvent molecules, some carbon atoms and all hydrogen atoms but four have been omitted for clarity; selected bond lengths [Å] and angles [°]: Rh–C(1) 2.12(2), Rh–C(8), 2.00(2), Rh–N(2) 2.10(1), Rh–N(3) 2.16(1), Rh–P 2.273(3), Rh–Cl(1) 2.525(3), O(1)–C(8) 1.21(1); C(8)–Rh–C(1) 97.8(5), C(8)–Rh–N(2) 97.9(4), C(1)–Rh–N(2) 89.2(4), C(8)–Rh–N(3) 170.7(4), C(1)–Rh–N(3) 87.8(4), N(2)–Rh–N(3) 74.7(4), C(8)–Rh–P(1) 83.2(3), C(1)–Rh–P(1) 90.1(3), N(2)–Rh–P 178.8(3), N(3)–Rh–P 104.3(3), C(8)–Rh–Cl(1) 85.2(3), C(1)–Rh–Cl(1) 174.2(4), N(2)–Rh–Cl(1) 85.5(3), N(3)–Rh–Cl(1) 88.6(3), P(1)–Rh–Cl(1) 95.2(1).

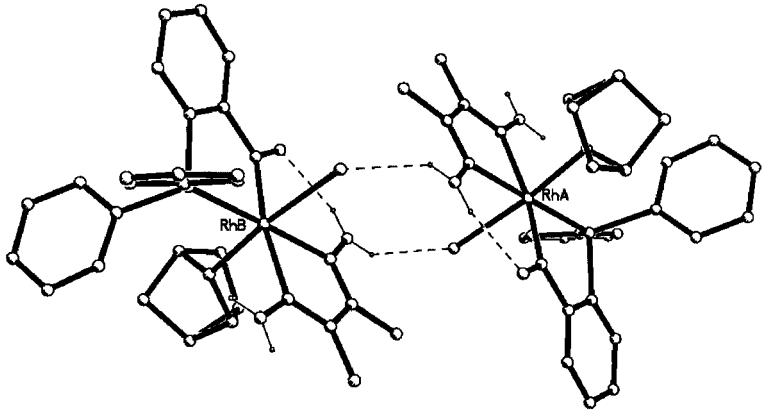

Figure 2. PLUTO view of the "dimer units" showing the hydrogen bonds for **2**.

the Rh–C distances may be viewed as a consequence of the different hybridization, i.e. sp^3 for C1 and sp^2 for C8,[4b,23] and also of C8 being part of a five-membered metallocycle. Complex **2** bears hydrogen bonds through both pendant amino groups of the bdh ligand. One NH_2 group (N1) binds the oxygen atom of the acyl group (O1) intramolecularly (Figure 1) and a solvent molecule through H1B in a bifurcated way. The H1A atom binds to the Cl1′ atom of the centrosymmetric molecule to give dimers (Figure 2). The other NH_2 group (N4) forms hydrogen bonds with two chlorine atoms of two other molecules of solvent. Table 1 lists the hydrogen bond geometry.

Complexes **2**–**5** are also formed, though impure (Experimental section), in the reaction of the corresponding complexes [Rh(Cl)(Nbd)(NN)][24] (NN = bdh, bipy, aqui, ampy), prepared "in situ", with stoichiometric 1:1 amounts of $PPh_2(o\text{-}C_6H_4CHO)$ in benzene (see *iii* in Scheme 1).

Table 1. Hydrogen bond geometry [Å] and angles [°] for [Rh(Cl)-{*o*-$PPh_2(C_6H_4CO)$}$(C_7H_9)(H_2NN{=}C(CH_3)C(CH_3){=}NNH_2)$]·$3\,CHCl_3$ (**2**).[a]

D–H---A	*d*(D–H)	*d*(H---A)	<DHA	*d*(D---A)
N1–H1B---O1	0.860	2.050	142.54	2.78(1)
N1–H1A---Cl1′	0.860	2.549	148.37	3.31(1)
N1–H1B---Cl9′′	0.860	2.846	133.72	3.50(1)
N4–H4A---Cl7′′′	0.860	2.743	145.15	3.48(1)
N4–H4B---Cl5′′′	0.860	2.856	123.46	3.41(1)

[a] (′) Cl1 [$-x$ +1, $-y$ + 1, $-z$]; (′′) [x, y, z – 1]; (′′′) [$-x$ + 1, $-y$ + 1, $-z$ + 1].

Coordinated norbornadiene in transition metal complexes is hydrogenated by both 1,2- and 1,4-addition to give norbornene and nortricyclene, respectively. The products obtained depend markedly on the starting materials and/or reaction conditions.[25]

 © 2005 Wiley-VCH Verlag GmbH & Co. KGaA, Weinheim

When [Rh(Cl)(Nbd)(bipy)], prepared "in situ", is treated with $PPh_2(o\text{-}C_6H_4CHO)$ in methanol, oxidative addition of aldehyde to rhodium followed by insertion of norbornadiene into the Rh–H bond also occurs, but in this case the norbornenyl (Nbyl) derivative [Rh(Cl){o-$PPh_2(C_6H_4CO)$}-Nbyl)(bipy)] (**7**), an isomer of **3**, is obtained [Equation (1)].

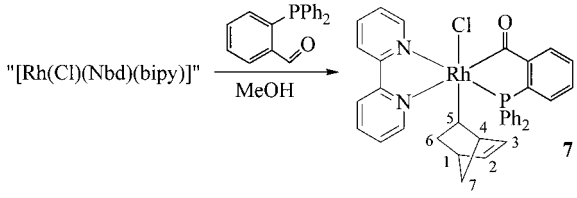

7 (1)

NMR spectroscopy, including 2D experiments, allows complete characterization of complex **7**. The presence of two doublets of doublets at δ = 5.06 and 4.89 ppm in the ^{1}H NMR spectrum, which correlate with two resonances at δ = 134.0 and 134.2 ppm, respectively, in the $^{13}C\{^1H\}$ NMR spectrum, is indicative of a non-coordinated olefin. The norbornenyl-CH group bonded to rhodium shows a multiplet at δ_H = 1.75 ppm and a doublet of doublets at δ^{13}C = 29.9 ppm due to coupling with rhodium and with a cis phosphorus atom. Other ^{1}H and $^{13}C\{^1H\}$ assignments are given in the Experimental section. The spectroscopic features of the acylphosphane chelate in **7** are similar to those in **3**: δ^{13}C=O = 238.5 (dd, $J_{Rh,C}$ = 32.4 Hz, $J_{P,C}$ = 6.0 Hz) ppm and δ^{31}P = 71.1 (d, $J_{Rh,P}$ = 171 Hz) ppm for **7**, and δ^{13}C=O = 235.8 (d, $J_{Rh,C}$ = 38.3 Hz) ppm and δ^{31}P = 72.8 (d, $J_{Rh,P}$ = 176 Hz) ppm for **3** in [D$_6$]DMSO. Therefore, **7** has the structural features shown in Equation (1), with the phosphorus atom and the acyl group trans to nitrogen, as in **3**.

These results show that the solvent plays an important role in the reaction of [Rh(Cl)(Nbd)(bipy)] with $PPh_2(o\text{-}C_6H_4CHO)$. Different paths lead to different isomers (**3** and **7**). Complex **3** remains unchanged in methanol and complex **7** is recovered unaltered from benzene. Scheme 2 presents a proposal for the selective production of the norbornenyl and nortricyclyl derivatives. The rhodium(I) starting material is a saturated species that requires ligand dissociation to undergo oxidative addition. In methanol, dissociation of chlorine to give an unsaturated cationic complex is feasible. Chelate-assisted oxidative addition can then occur with opening of the diolefinic chelate to give a hydride-monoolefin species that can afford the norbornenyl derivative. Related [Rh(Cl)(Cod)(bipy)] undergoes the chelate-assisted oxidative addition of $PPh_2(o\text{-}C_6H_4CHO)$ with diolefin displacement.[4c] Coordination of the norbornadiene as a diolefin is, most likely, a requirement for the hydrogen transfer with concurrent double bond shift to occur. In benzene, dissociation of 2,2′-bipyidine from the neutral pentacoordinate complex may allow the formation of a hydride-diolefin species that affords the nortricyclyl isomer.

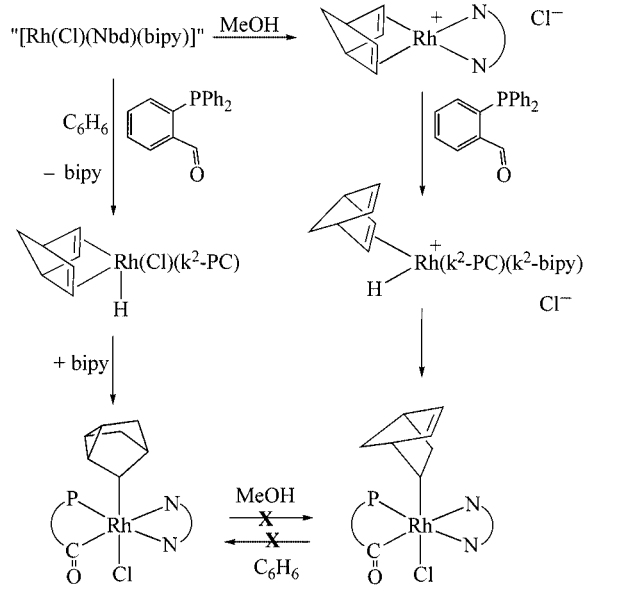

Scheme 2. Proposal for the selective production of nortricyclyl and norbornenyl derivatives.

The reaction of other [Rh(Cl)(Nbd)(NN)] complexes prepared "in situ" (NN = bdh, aqui, ampy; N = py) with $PPh_2(o\text{-}C_6H_4CHO)$ in methanol gave complex mixtures of products. Decomposition products were formed in the reaction of [{Rh(Nbd)Cl}$_2$] with o-(diphenylphosphane)benzaldehyde in methanol.

Conclusions

Norbornadiene rhodium(I) complexes react with o-(diphenylphosphane)benzaldehyde to undergo chelate-assisted oxidative addition followed by hydrogen transfer to norbornadiene, giving acylalkylrhodium(III) derivatives. Nortricyclyl and the norbornenyl isomers have been obtained selectively by using the appropriate solvent. We propose that, in benzene, hydrogen transfer occurs with concurrent double bond shift to form a nortricyclyl group because the norbornadiene is bonded as a diolefin. In an ionising solvent such as methanol, hydrogen transfer to the norbornadiene coordinated as monoolefin can yield a norbornenyl group.

Experimental Section

General Procedures: The metal complexes were prepared at room temperature under nitrogen by standard Schlenk techniques. [{Rh(Nbd)Cl}$_2$][26] and o-(diphenylphosphane)benzaldehyde[27] were prepared according to reported procedures. Microanalyses were carried out with a Leco CHNS-932 microanalyser. IR spectra were recorded with a Nicolet FTIR 740 spectrophotometer in the range 4000–400 cm^{-1} using KBr pellets. NMR spectra were recorded with Bruker Avance DPX 300 or Bruker Avance 500 spectrometers, ^{1}H and $^{13}C\{^1H\}$ (TMS internal standard), $^{31}P\{^1H\}$ (H_3PO_4 external standard) and 2D spectra were measured as $CDCl_3$ or [D$_6$]DMSO solutions. Mass spectra were recorded on a VG Autospec, by liquid secondary ion (LSI) MS, using nitrobenzyl alcohol as matrix and a caesium gun (Universidad de Zaragoza).

 © 2005 Wiley-VCH Verlag GmbH & Co. KGaA, Weinheim

Preparation of [Rh(Cl)(Nortricyclyl){PPh_2(*o*-C_6H_4CO)}]$_n$ (1): A stoichiometric amount of PPh_2(*o*-C_6H_4CHO) (0.12 mmol) was added to a benzene solution of [{Rh(Nbd)Cl}$_2$] (0.06 mmol). Subsequent stirring for 60 min at room temperature gave a yellow solid that was filtered off, washed with benzene and vacuum dried (yield 66%). IR: $\tilde{\nu}$(C=O) = 1637(s) cm^{-1}. ^{1}H NMR ($CDCl_3$): δ = 2.89 (d, $J_{Rh,H}$ = 11.5 Hz), 2.71 (d, $J_{Rh,H}$ = 11.1 Hz), 2.46 (d, $J_{Rh,H}$ = 9.1 Hz) and 2.80 (d, $J_{Rh,H}$ = 9.1 Hz) ppm, HC–Rh. ^{31}P{^{1}H} NMR ($CDCl_3$): δ = 73.1 (d, $J_{Rh,P}$ = 209 Hz), 72.9 (d, $J_{Rh,P}$ = 211 Hz), 71.8 (d, $J_{Rh,P}$ = 203 Hz) and 71.5 (d, $J_{Rh,P}$ = 208 Hz) ppm. FAB MS calcd. for [$C_{26}H_{23}ClOPRh]_3$: 1560; observed 1525 [M–Cl]$^+$, 1432 [M–Cl–(C_7H_9)]$^+$. $C_{26}H_{23}ClOPRh$: calcd. C 59.96, H 4.45; found C 59.66, H 4.29.

Preparation of [Rh(Cl)(Nortricyclyl)(PPh_2(*o*-C_6H_4CO))(NN)] (2–6): A stoichiometric amount of the corresponding bidentate N-ligand (0.06 mmol) or of pyridine (0.12 mmol) was added to a benzene suspension of **1** (0.06 mmol). Subsequent stirring for 60 min at room temperature afforded yellow solids that were filtered off, washed with benzene and vacuum-dried.

Data for 2: Yield 65%. IR: $\tilde{\nu}$ = 3389 (s), 3271 (s), 3138 (s, NH_2), 1600 (s, C=O), 1590 (s, C=N) cm^{-1}. ^{1}H NMR ($CDCl_3$): δ = 7.78, 5.65 (br s, 4 H, NH_2), 2.24, 2.15 (s, 6 H, CH_3), 1.85 (d, J_{gem} = 9.5 Hz, 1 H, Ntyl-CH_2), 1.41 (dd, $J_{Rh,H}$ = 12.8, $J_{P,H}$ = 2.1 Hz, 1 H, HC–Rh), 0.85 (t, $J_{H,H}$ = 4.5 Hz, 1 H, Ntyl-$CH_{cyclopropyl}$), 0.74 (d, J_{gem} = 9.5 Hz, 1 H, Ntyl-CH_2), 0.69 (m, 1 H, Ntyl-CH), 0.54 (d, J_{gem} = 9.1 Hz, 1 H, Ntyl-CH_2), 0.53 (s, 1 H, Ntyl-$CH_{cyclopropyl}$), 0.23 (t, $J_{H,H}$ = 5.2 Hz, 1 H, Ntyl-C*H*$_{cyclopropyl}$–CHRh), –0.08 (d, J_{gem} = 9.1 Hz, 1 H, Ntyl-CH_2) ppm. ^{13}C{^{1}H} NMR ($CDCl_3$): δ = 240.7 (dd, $J_{Rh,C}$ = 33.2, $J_{P,C}$ = 5.9 Hz, 1C, C=O), 149.9, 145.2 (2C, C=N), 39.8 (d, $J_{Rh,C}$ = 22.4 Hz, 1C, HC–Rh), 38.0 (1C, Ntyl-CH), 33.9, 32.0 (2C, Ntyl-CH_2), 17.0 (1C, Ntyl-*C*H$_{cyclopropyl}$–CHRh), 14.5 (1C, CH_3), 12.9 (2C, CH_3 + Ntyl-$CH_{cyclopropyl}$), 11.4 (1C, Ntyl-$CH_{cyclopropyl}$) ppm. ^{31}P{^{1}H} NMR ($CDCl_3$): δ = 71.4 (d, $J_{Rh,P}$ = 172 Hz) ppm. FAB MS: calcd. $C_{30}H_{33}ClN_4OPRh$ 634, *m*/*z* = 599 [M–Cl]$^+$. $C_{30}H_{33}ClN_4OPRh{\cdot}0.3\,C_6H_6$: C 58.01, H 5.33, N 8.51; found: C 57.76, H 5.24, N 7.98%.

Data for 3: Yield 60%. IR: $\tilde{\nu}$ = 1624 (s, C=O) cm^{-1}. ^{1}H NMR ($CDCl_3$): δ = 1.95 (d, J_{gem} = 9.9 Hz, 1 H, Ntyl-CH_2), 1.36 (dd, $J_{Rh,H}$ = 12.0, $J_{P,H}$ = 2.1 Hz, 1 H, HC–Rh), 0.87 (br s, 1 H, Ntyl-CH), 0.65 (d, J_{gem} = 9.9 Hz, 1 H, Ntyl-CH_2), 0.47 (d, J_{gem} = 9.5 Hz, 1 H, Ntyl-CH_2), 0.27 (t, $J_{H,H}$ = 5.4 Hz, 1 H, Ntyl-$CH_{cyclopropyl}$), 0.13 (t, $J_{H,H}$ = 4.9 Hz, 1 H, Ntyl-$CH_{cyclopropyl}$), –0.10 (d, J_{gem} = 9.5 Hz, 1 H, Ntyl-CH_2), –0.49 (t, $J_{H,H}$ = 5.0 Hz, 1 H, Ntyl-C*H*$_{cyclopropyl}$–CHRh) ppm. ^{13}C{^{1}H} NMR ($CDCl_3$): δ = 40.6 (dd, $J_{Rh,C}$ = 26.9, $J_{P,C}$ = 5.2 Hz, 1C, HC–Rh), 38.0 (1C, Ntyl-CH), 34.3, 31.5 (2C, Ntyl-CH_2), 17.8 (1C, Ntyl-*C*H$_{cyclopropyl}$–CHRh), 12.8, 12.2 (2C, Ntyl-$CH_{cyclopropyl}$) ppm. ^{31}P{^{1}H} NMR ($CDCl_3$): δ = 72.8 (d, $J_{Rh,P}$ = 175 Hz) ppm. FAB MS: calcd. $C_{36}H_{31}ClN_2OPRh$ 676; *m*/*z* = 641 [M–Cl]$^+$. $C_{36}H_{31}ClN_2OPRh$: calcd. C 63.87, H 4.62, N 4.14; found: C 63.68, H 4.70, N 3.75.

Data for 4: Yield 30%. IR: $\tilde{\nu}$ = 3257 (m), 3205 (m, NH_2), 1601 (s, C=O) cm^{-1}. ^{1}H NMR ($CDCl_3$): δ = 6.10, 5.72 (m, 2 H, NH_2), 1.86 (dd, $J_{Rh,H}$ = 12.4, $J_{P,H}$ = 2.9 Hz, 1 H, HC–Rh), 1.63 (t, J_{HH} = 5.0 Hz, 1 H, Ntyl-C*H*$_{cyclopropyl}$–CHRh), 1.45 (d, J_{gem} = 10.3 Hz, 1 H, Ntyl-CH_2), 1.17 (t, J_{HH} = 4.7 Hz, 1 H, Ntyl-$CH_{cyclopropyl}$), 0.85 (m, 3 H, Ntyl-CH + Ntyl-CH_2 + Ntyl-$CH_{cyclopropyl}$), 0.76, 0.38 (d, J_{gem} = 9.3 Hz, 2 H, Ntyl-CH_2) ppm. ^{13}C{^{1}H} NMR ($CDCl_3$): δ = 239.36 (dd, $J_{Rh,C}$ = 36.1, $J_{P,C}$ = 4.4 Hz, 1C, C=O), 39.1 (dd, $J_{Rh,C}$ = 25.1, $J_{P,C}$ = 6.6 Hz, 1C, HC–Rh), 37.1 (1C, Ntyl-CH), 34.3, 33.0 (2C, Ntyl-CH_2), 19.1 (1C, Ntyl-*C*H$_{cyclopropyl}$–CHRh), 12.6, 12.3 (2C, Ntyl-$CH_{cyclopropyl}$) ppm. ^{31}P{^{1}H} NMR ($CDCl_3$): δ = 68.5 (d, $J_{Rh,P}$ = 183 Hz) ppm. FAB MS: calcd. $C_{35}H_{31}ClN_2OPRh$ 664; *m*/*z* = 629 [M–Cl]$^+$. $C_{35}H_{31}ClN_2OPRh$: C 63.22, H 4.70, N 4.21; found C 62.96, H 4.76, N 3.85.

Data for 5: Yield 40%. IR: $\tilde{\nu}$ = 3345 (m), 3323 (m), 3261 (m, NH_2), 1603(s, C=O) cm^{-1}. ^{1}H NMR ($CDCl_3$): δ = 5.32 (m, 1 H, ampy-CH_2), 4.64 (br. s, 1 H, NH_2), 4.44 (m, 1 H, ampy-CH_2), 4.32 (br s, 1 H, NH_2), 1.71 (d, $J_{Rh,H}$ = 12.9 Hz, 1 H, HC–Rh), 1.58 (t, J_{HH} = 4.7 Hz, 1 H, Ntyl-C*H*$_{cyclopropyl}$–CHRh), 1.25 (d, J_{gem} = 10.3 Hz, 1 H, Ntyl-CH_2), 1.02 (t, J_{HH} = 4.3 Hz, 1 H, Ntyl-$CH_{cyclopropyl}$), 0.81 (m, 4 H, Ntyl-CH + 2 Ntyl-CH_2 + Ntyl-$CH_{cyclopropyl}$), 0.46 (d, J_{gem} = 9.4 Hz, 1 H, Ntyl-CH_2) ppm. ^{13}C{^{1}H} NMR ($CDCl_3$): δ = 240.7 (dd, $J_{Rh,C}$ = 37.3, $J_{P,C}$ = 4.0 Hz, 1C, C=O), 38.8 (dd, $J_{Rh,C}$ = 25.2, $J_{P,C}$ = 6.9 Hz, 1C, HC–Rh), 37.2 (1C, Ntyl-CH), 34.5, 32.9 (2C, Ntyl-CH_2), 19.2 (1C, Ntyl-*C*H$_{cyclopropyl}$–CHRh), 12.7, 12.5 (2C, Ntyl-$CH_{cyclopropyl}$) ppm. ^{31}P{^{1}H} NMR ($CDCl_3$): δ = 68.3 (d, $J_{Rh,P}$ = 177 Hz) ppm. FAB MS: calcd. $C_{32}H_{31}ClN_2OPRh$ 628; *m*/*z* = 593 [M–Cl]$^+$. $C_{32}H_{31}ClN_2OPRh{\cdot}0.3\,C_6H_6$: C 62.23, H 5.07, N 4.29; found C 62.45, H 5.03, N 4.87.

Data for 6: Yield 55%. IR: $\tilde{\nu}$ = 1609 (s, C=O) cm^{-1}. ^{1}H NMR ($CDCl_3$): δ = 2.45 (dd, $J_{Rh,H}$ = 10.3, $J_{P,H}$ = 3.3 Hz, 1 H, HC–Rh), 1.25 (d, J_{gem} = 9.9 Hz, 1 H, Ntyl-CH_2), 0.78 (br. s, 1 H, Ntyl-CH), 0.67 (d, J_{gem} = 9.9 Hz, 1 H, Ntyl-CH_2), 0.63 (d, J_{gem} = 9.5 Hz, 1 H, Ntyl-CH_2), 0.60 (m, 2 H, Ntyl-$CH_{cyclopropyl}$ + Ntyl-C*H*$_{cyclopropyl}$–CHRh), 0.50 (t, J_{HH} = 4.7 Hz, 1 H, Ntyl-$CH_{cyclopropyl}$), 0.27 (d, J_{gem} = 9.5 Hz, 1 H, Ntyl-CH_2) ppm. ^{13}C{^{1}H} NMR ($CDCl_3$): δ = 240.0 (dd, $J_{Rh,C}$ = 39.1, $J_{P,C}$ = 3.0 Hz, 1C, C=O), 38.1 (dd, $J_{Rh,C}$ = 25.5, $J_{P,C}$ = 6.3 Hz, 1C, HC–Rh), 36.9 (1C, Ntyl-CH), 34.5, 32.6 (2C, Ntyl-CH_2), 19.8 (1C, Ntyl-*C*H$_{cyclopropyl}$–CHRh), 14.2, 12.4 (2C, Ntyl-$CH_{cyclopropyl}$) ppm. ^{31}P{^{1}H} NMR ($CDCl_3$): δ = 72.2 (d, $J_{Rh,P}$ = 183 Hz) ppm. $C_{36}H_{33}ClN_2OPRh$: C 63.68, H 4.90, N 4.13; found C 63.02, H 4.96, N 4.07.

Reaction of "[Rh(Cl)(Nbd)(bdh)]" with PPh_2(*o*-C_6H_4CHO) in Benzene: A stoichiometric amount of bdh (13.7 mg, 0.12 mmol) was added to a benzene solution of [{Rh(Nbd)Cl}$_2$] (27.6 mg, 0.06 mmol), affording a red suspension of [Rh(Cl)(Nbd)(bdh)]. Subsequent addition of PPh_2(*o*-C_6H_4CHO) (34.8 mg, 0.12 mmol) and stirring for 60 min at room temperature gave a yellow solid that was filtered off, washed with benzene and vacuum dried (yield: 62 mg). According to NMR spectra, the solid contains complex **2** as the main product (up to 87%). Small amounts of hydrides (up to 13%), products of diolefin displacement, were also observed.

Preparation of [Rh(Cl)(Norbornenyl)(PPh_2(*o*-C_6H_4CO))(bipy)] (7): A stoichiometric amount of 2,2′-bipyridine (0.12 mmol) and an excess of PPh_2(*o*-C_6H_4CHO) (0.24 mmol) were added to a MeOH suspension of [{Rh(Nbd)Cl}$_2$] (0.06 mmol). Subsequent stirring for 60 min at room temperature gave a yellow solid that was filtered off, washed with methanol and vacuum dried (yield: 46%). IR: $\tilde{\nu}$ = 1624 (s, C=O) cm^{-1}. ^{1}H NMR ([D_6]DMSO): δ = 5.06 (dd, $J_{H3,H2}$ = 5.36, $J_{H1,H2}$ = 2.89 Hz, 1 H, Nbyl-H2), 4.89 (dd, $J_{H4,H3}$ = 2.48 Hz, 1 H, Nbyl-H3), 2.40 (s, 1 H, Nbyl-H4), 1.83 (s, 1 H, Nbyl-H1), 1.75 (m, 1 H, Nbyl-H5), 0.61, 0.15 (d, J_{gem} = 7.23 Hz, 2 H, Nbyl-H7), –0.09, –0.57 (m, 2 H, Nbyl-H6) ppm. ^{13}C{^{1}H} NMR ([D_6]DMSO): δ = 238.5 (dd, $J_{Rh,C}$ = 32.4, $J_{P,C}$ = 6.0 Hz, 1C, C=O), 134.2 (1C, Nbyl-C3), 134.0 (1C, Nbyl-C2), 50.9 (1C, Nbyl-C7), 50.1 (1C, Nbyl-C4), 40.8 (1C, Nbyl-C1), 30.9 (1C, Nbyl-C6), 29.9 (dd, $J_{Rh,C}$ = 28.8, $J_{P,C}$ = 4.4 Hz, 1C, Nbyl-C5) ppm. ^{31}P{^{1}H} NMR ([D_6]DMSO): δ = 71.1 (d, $J_{Rh,P}$ 171 Hz) ppm. FAB MS: calcd. $C_{36}H_{31}ClN_2OPRh$ 676; *m*/*z* (%) = 676 [M]$^+$ (6), 641 [M–Cl]$^+$ (87). $C_{36}H_{31}ClN_2OPRh{\cdot}MeOH$: C 62.68, H 4.98, N 3.95; found C 62.60, H 4.90, N 3.84.

X-ray Crystal Structure Determination of 2: Single crystals of complex **2**, suitable for X-ray diffraction, were successfully grown by allowing slow diffusion of diethyl ether onto chloroform solutions.

 © 2005 Wiley-VCH Verlag GmbH & Co. KGaA, Weinheim

A yellow crystal was epoxy coated and mounted on a Bruker Smart CCD diffractometer using graphite monochromated Mo-K_α radiation (λ = 0.71073 Å) operating at 50 kV and 20 mA. Data were collected over a hemisphere of the reciprocal space by combination of three exposure sets. Each exposure of 10 s covered 0.3 in ω. The first 50 frames were recollected at the end of the data collection to monitor crystal decay after X-ray exposition. Several crystals were tried and the best data collection showed a decay of 18% in the intensities of standard reflections. Fundamental crystal data for the crystal given are summarized in Table 2. The structure was solved by Direct methods and conventional Fourier techniques. Refinement was done by full-matrix least-squares on F^2 (SHELX-97).[28] After three cycles of isotropic refinement of all atoms in the Rh complex, extra electron density was found and was attributed to three molecules of chloroform. All non-hydrogen atoms have been refined anisotropically, except the solvent molecules. All hydrogen atoms were calculated at geometrical positions. It was impossible to locate the hydrogen atoms of the NH_2 groups in a Fourier synthesis. The presence of three $CHCl_3$ molecules of crystallization is probably the source of the problems encountered during the data collection. All these atoms were refined only isotropically and with geometrical restraints and variable common carbon–chlorine distances. Despite these problems, the atoms of the rhodium complex refined well – as can be judged from the reasonable deviation in distances and angles, their thermal parameters and the quality-of-fit indicator. The high values of largest residual peak and hole in the final Fourier difference map and the largest shift/esd ratio were associated with the chlorine atoms of the solvent molecules.

Table 2. Crystal and refinement data for [Rh(Cl)(*o*-$PPh_2(C_6H_4CO)$)$(C_7H_9)(H_2NN{=}C(CH_3)C(CH_3){=}NNH_2)$]·3$CHCl_3$ (**2**).

Empirical formula	$C_{33}H_{36}Cl_{10}N_4OPRh$
Formula mass	993.04
Temperature [K]	293(2)
Wavelength [Å]	0.71073
Crystal system	triclinic
Space group	$P\bar{1}$
a [Å]	11.517(1)
b [Å]	13.481(1)
c [Å]	15.338(1)
α [°]	76.606(2)
β [°]	74.156(2)
γ [°]	73.004(2)
Volume [Å^3]	2160.9(3)
Z	2
Absorption coefficient (mm^{-1})	1.082
Crystal size (mm^3)	0.40 × 0.27 × 0.18
θ range for data collection [°]	1.40 to 28.78
Index ranges	(–15, –18, –20 to 12, 10, 20)
Decay [%]	18
Reflections collected	13935
Independent reflections	9835 [*R*(int.) = 0.0601]
Data/restraints/parameters	9835/9/393
Goodness-of-fit on F^2	1.068
Final *R* indices [$I > 2\sigma(I)$][a]	0.1164 (4539 observed)
wR_2 indices (all data)[b]	0.3785
Largest diff. peak and hole [e Å^{-3}]	2.825 and –1.551

[a] $\Sigma[||F_o| - |F_c||]/\Sigma|F_o|$. [b] $\{\Sigma[w(F_o^2 - F_c^2)^2]/\Sigma[w(F_o^2)^2]\}^{1/2}$.

CCDC-253669 contains the supplementary crystallographic data for this paper. These data can be obtained free of charge from The Cambridge Crystallographic Data Centre via www.ccdc.cam.ac.uk/data_request/cif.

Acknowledgments

Partial financial supports by AECI (Project 119/03/P), Diputación Foral de Guipuzcoa/EU, MCYT (Project BQU2002–0129) and UPV are gratefully acknowledged.

[1] a) T. B. Marder, D. C. Roe, D. Milstein, *Organometallics* **1988**, *7*, 1451–1453; b) E. Gutiérrez-Puebla, A. Monge, M. Paneque, M. L. Poveda, V. Salazar, E. Carmona, *J. Am. Chem. Soc.* **1999**, *121*, 248–249; c) D. M. Tellers, R. G. Bergman, *Organometallics* **2001**, *20*, 4819–4832.
[2] a) D. L. Thorn, *Organometallics* **1982**, *1*, 197–204; b) D. Milstein, *Orgnometallics* **1982**, *1*, 1549–1551; c) D. Milstein, W. C. Fultz, J. C. Calabrese, *J. Am. Chem. Soc.* **1986**, *108*, 1336–1338; d) C. Bianchini, A. Meli, M. Peruzzini, F. Vizza, F. Bachechi, *Organometallics* **1991**, *10*, 820–823; e) J. R. Bleeke, T. Haile, P. R. New, M. Y. Chiang, *Organometallics* **1993**, *12*, 517–528; f) K. Wang, T. J. Emge, A. S. Goldman, C. Li, S. P. Nolan, *Organometallics* **1995**, *14*, 4929–4936; g) R. Goikhman, D. Milstein, *Angew. Chem. Int. Ed.* **2001**, *40*, 1119–1122.
[3] a) D. Milstein, *J. Chem. Soc. Chem. Commun.* **1982**, 1357–1358; b) J. P. Collman, L. S. Hegedeus, J. R. Norton, R. G. Finke, *Principles and Applications of Organotransition Metal Chemistry*, 2nd ed., University Science Books, Mill Valley, **1987**; c) C. H. Jun, J. B. Hong, D. Y. Lee, *Synlett* **1999**, 1–12.
[4] a) C. Bianchini, A. Meli, M. Peruzzini, J. A. Ramirez, A. Vacca, F. Vizza, F. Zanobini, *Organometallics* **1989**, *8*, 337–345; b) R. El Mail, M. A. Garralda, R. Hernández, L. Ibarlucea, E. Pinilla, M. R. Torres, *Organometallics* **2000**, *19*, 5310–5317; c) G. Brockaart, R. El Mail, M. A. Garralda, R. Hernández, L. Ibarlucea, J. I. Santos, *Inorg. Chim. Acta* **2002**, *338*, 249–254; d) M. A. Garralda, R. Hernández, L. Ibarlucea, E. Pinilla, M. R. Torres, M. Zarandona, *Inorg. Chim. Acta* **2004**, *357*, 2818–2826.
[5] T. B. Rauchfuss, *J. Am. Chem. Soc.* **1979**, *101*, 1045–1047.
[6] a) J. J. Koh, W. H. Lee, P. G. Williard, W. M. Risen, *J. Organomet. Chem.* **1985**, *284*, 409–419; b) C. A. Ghilardi, S. Midollini, S. Moneti, A. Orlandini, *J. Chem. Soc.*, *Dalton Trans.* **1988**, 1833–1836.
[7] H. F. Klein, U. Lemke, M. Lemke, A. Brand, *Organometallics* **1998**, *17*, 4196–4201.
[8] a) C. J. Adams, M. I. Bruce, O. Kühl, B. W. Skelton, A. H. White, *J. Organomet. Chem.* **1993**, *445*, C6–C9; b) C. J. Adams, M. I. Bruce, P. A. Duckworth, P. A. Humphrey, O. Kühl, E. R. T. Tiekink, W. R. Cullen, P. Braunstein, S. Coco, B. W. Skelton, A. H. White, *J. Organomet. Chem.* **1994**, *467*, 251–281.
[9] H. Schumann, H. Hemling, V. Ravindar, Y. Badrieh, J. Blum, *J. Organomet. Chem.* **1994**, *469*, 213–219.
[10] a) E. F. Landvatter, T. B. Rauchfuss, *Organometallics* **1982**, *1*, 506–513; b) P. Barbaro, C. Bianchini, C. Mealli, D. Masi, *Acta Crystallogr. Sect. C* **1994**, 1414–1417.
[11] S. E. Watkins, D. C. Craig, S. B. Colbran, *Inorg. Chim. Acta* **2000**, *307*, 134–138.
[12] J. M. Casas, J. Forniés, A. Martín, *J. Chem. Soc.*, *Dalton Trans.* **1997**, 1559–1563.
[13] P. Crochet, M. A. Fernández-Zumel, C. Beauquis, J. Gimeno, *Inorg. Chim. Acta* **2003**, *356*, 114–120.
[14] a) E. W. Ainscough, A. M. Brodie, S. L. Ingham, J. M. Waters, *Inorg. Chim. Acta* **1995**, *234*, 163–167; b) W. Y. Yeh, C. S. Lin, S. M. Peng, G. H. Lee, *Organometallics* **2004**, *23*, 917–920.
[15] X. Chen, F. J. Femia, J. W. Babich, J. Zubieta, *Inorg. Chim. Acta* **2001**, *315*, 147–152.
[16] C. P. Lenges, M. Brookhart, P. S. White, *Angew. Chem. Int. Ed.* **1999**, *38*, 552–555.
[17] R. El Mail, M. A. Garralda, R. Hernández, L. Ibarlucea, *J. Organomet. Chem.* **2002**, *648*, 149–154.
[18] R. El Mail, M. A. Garralda, R. Hernández, L. Ibarlucea, E. Pinilla, M. R. Torres, *Helv. Chim. Acta* **2002**, *85*, 1485–1495.

 © 2005 Wiley-VCH Verlag GmbH & Co. KGaA, Weinheim

[19] M. A. Garralda, R. Hernández, L. Ibarlucea, E. Pinilla, M. R. Torres, *Organometallics* **2003**, *22*, 3600–3603.
[20] M. Nieuwenhuyzen, G. C. Saunders, *Inorg. Chim. Acta* **2004**, *357*, 2870–2874.
[21] H. Trauthwein, A. Tillack, M. Beller, *Chem. Commun.* **1999**, 2029–2030.
[22] a) R. Dorta, L. Konstantinovski, L. J. W. Shimon, Y. Ben-David, D. Milstein, *Eur. J. Inorg. Chem.* **2003**, 70–76; b) J. A. Mata, E. Peris, C. Incarvito, R. H. Crabtree, *Chem. Commun.* **2003**, 184–185.
[23] a) G. R. Clark, T. R. Greene, W. R. Roper, *J. Organomet. Chem.* **1985**, *293*, C25–C28; b) C. Hahn, M. Spiegler, E. Herdtweck, R. Taube, *Eur. J. Inorg. Chem.* **1999**, 435–440.
[24] a) L. Fidalgo, M. A. Garralda, R. Hernández, L. Ibarlucea, *Inorg. Chim. Acta* **1993**, *207*, 121–125; b) G. Zassinovich, G. Mestroni, A. Camus, *J. Organomet. Chem.* **1975**, *91*, 379–388; c) M. A. Garralda, R. Hernández, L. Ibarlucea, M. I. Arriortua, M. K. Urtiaga, *Inorg. Chim. Acta* **1995**, *232*, 9–17.
[25] See for example: a) D. J. Darensbourg, H. H. Nelson, M. A. Murphy, *J. Am. Chem. Soc.* **1977**, *99*, 896–903; b) P. M. Hodges, S. A. Jackson, J. Jacke, M. Poliakoff, J. J. Turner, F. W. Grevels, *J. Am. Chem. Soc.* **1990**, *112*, 1234–1244; c) G. Jia, W. S. Ng, C. P. Lau, *Organometallics* **1998**, *17*, 4538–4540; d) S. H. Liu, S. Y. Yang, S. T. Lo, Z. Xu, W. S. Ng, T. B. Wen, Z. Y. Zhou, Z. Lin, C. P. Lau, G. Jia, *Organometallics* **2001**, *20*, 4161–4169.
[26] E. W. Abel, M. A. Bennett, G. Wilkinson, *J. Chem. Soc., (A)* **1959**, 3178–3182.
[27] J. E. Hoots, T. B. Rauchfuss, D. A. Wrobleski, *Inorg. Synth.* **1982**, *21*, 175–179.
[28] G. M. Sheldrick, *SHELX-97*, University of Göttingen, **1997**.
Received: November 04, 2004

 © 2005 Wiley-VCH Verlag GmbH & Co. KGaA, Weinheim

Magnetic Anisotropy of New Layered Copper(II) Bromide Complexes of 1-Substituted Tetrazoles

Yurii Shvedenkov,*[a] Mark Bushuev,[a] Galina Romanenko,[b] Ludmila Lavrenova,[a] Vladimir Ikorskii,[b] Pavel Gaponik,[c] and Stanislav Larionov[a]

Keywords: Copper / Layered compounds / Nitrogen heterocycles / Magnetic properties / Phase transition

Two new isostructural complexes, dibromobis(1-ethyltetrazole)copper(II) (**1**) and dibromobis(1-hexyltetrazole)copper(II) (**2**), have been synthesised. Each bromine atom in the crystal structure of **1** and **2** is bonded to two copper atoms to give rise to a polymeric corrugated network. The polymeric layers are distinctly separated by tetrazole ligands. Both solids exhibit a phase transition to the ferromagnetic state with Curie temperatures of 8.5 K and 8.9 K for **1** and **2**, respectively, and a strong anisotropy of the magnetic susceptibility below the ordering temperature. The easy magnetisation axis lies along the monoclinic axis, and the hard magnetisation axis is orthogonal to the polymeric layers. Effective anisotropy fields were estimated as (720–3020 Oe).

(© Wiley-VCH Verlag GmbH & Co. KGaA, 69451 Weinheim, Germany, 2005)

Introduction

In the design of new molecular magnets capable of magnetic phase ordering it is necessary to satisfy at least two conditions: the crystal structures of such compounds should be polymeric (2D or 3D), and the formed exchange channels should have sufficient efficiency for the magnetic ordering at experimentally observable temperatures.[1] One of the strategies to obtain such coordination compounds is to use ligands that are potentially capable of realizing a bridging function. Halogen atoms and polynitrogen heterocycles are particularly useful in this respect. It is known that the combination of Cu^{II} salts with heterocyclic azole ligands leads to the formation of mononuclear,[2–5] polynuclear[6–9] and even polymeric[10–15] complexes. For the majority of polymeric complexes one or more of the bridges are *N*,*N*′-didentate divided.[12,16,17] As a result the Cu–Cu distances in these cases are considerably increased. The formation of coordination compounds with a square polymeric lattice of copper atoms and halide ions only is an occasional and specific case for complexes with polynitrogen heterocycle ligands.[18–25] Note that even the use of 1-substituted tetrazoles with furcated substitutes or disubstituted tetrazoles leads to the formation of chain or mononuclear complexes.[10,13,14] From this point of view, 1-substituted tetrazole derivatives with non-furcated substitutes are unique ligands for the design of molecular magnets with a two-dimensional crystal structure.

We have previously reported the formation of layered polymeric structures for a whole series of complexes of Cu^{II} and Co^{II} chlorides with 1-substituted tetrazoles (Rtz, R = ethyl, allyl, vinyl) with the general stoichiometry $[M(Rtz)_2Cl_2]$ (M = Cu^{II}, Co^{II}).[18–23,26] The $[Cu(Rtz)_2Cl_2]$ complexes undergo a ferromagnetic transition at temperatures lower than 10 K and $[Co(alltz)_2Cl_2]$[26] undergoes a phase transition to an antiferromagnetic state with a weak ferromagnetic behaviour at 99.6 K. Recently, complexes $[Cu(teec)_2A_2]$ [teec = 1-(2-chloroethyl)tetrazole; A = Cl^-, Br^-, NO_3^-] have been prepared and studied in detail.[4,25] It was found that $[Cu(teec)_2Cl_2]$ and $[Cu(teec)_2Br_2]$ are soft ferromagnets with T_c = 4.75 K and 8.01 K, respectively.[25] On the other hand, active studies of molecular magnets have stimulated the investigation of the anisotropy of magnetic properties with single crystalline samples. The first study of the magnetic anisotropy of a layered polymeric complex containing a tetrazole derivative was done with $[Co(alltz)_2Cl_2]$.[27]

This work continues our systematic investigation of the synthesis and characterisation of Cu^{II} halide complexes with tetrazoles. We report the preparation, structure and studies of the anisotropy of magnetic properties of a new layered polymer of Cu^{II} bromide with 1-ethyl- and 1-hexyltetrazoles.

Results and Discussion

Single crystals of complexes dibromobis(1-ethyltetrazole)-copper(II) (**1**) and dibromobis(1-hexyltetrazole)copper(II) (**2**)

[a] Nikolaev Institute of Inorganic Chemistry SB RAS,
Lavrent'ev Ave., 3, Novosibirsk, 630090, Russia
Fax: +7-3832-33-1399
E-mail: schved@tomo.nsc.ru
[b] International Tomography Center SB RAS,
Institutskaya Str., 3a, Novosibirsk, 630090, Russia
Fax: +7-3832-33-1399
E-mail: romanenk@tomo.nsc.ru
[c] Instituite of Physico-Chemical Problems, Belarussian State University,
Leningradskaya Str., 14, Minsk, 220050, Belarus
Fax: +7-3832-33-1399
E-mail: gaponik@bsu.by

for both a crystal structure determination and an investigation of the magnetic properties were grown from EtOH solutions under ambient conditions. Note that crystals obtained in a thermostat, while having a nice appearance, appeared to be twins or joints. This may be caused by vibrations originating from the thermostat's operation.

The values of bond lengths and angles of the complexes are listed in Table 1.

In these complexes the copper atom coordinates two tetrazole molecules in the equatorial plane (*trans* to each other) and two bromine atoms to form $[Cu(Rtz)_2Br_2]$ complex fragments (Figure 1).

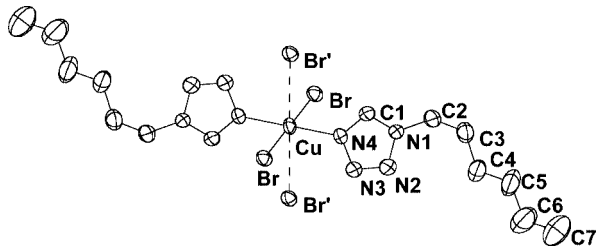

Figure 1. $[Cu(Rtz)_2Br_2]$ molecular structure exemplified by **2**. Hydrogen atoms have been omitted for clarity.

The structures of both complexes are very similar. The environment of the copper atom is a centrosymmetric square bipyramid due to additional bonds to the bromine atoms of neighbouring $\{Cu(Rtz)_2Br_2\}$ fragments. Thus, the bromine atoms form non-symmetric bridges (the Cu–Br–Cu angles are equal to 138.55° and 138.16° for **1** and **2**, respectively) and connect $\{Cu(Rtz)_2Br_2\}$ fragments into layers (Figure 2) parallel to the (100) plane. The tetrazole molecules separate the layers from each other. The tetrazole fragments are practically planar reflecting the π-conjugation in the heterocycle. A comparison of the bond lengths in the tetrazole ring allows us to distinguish between "single" and "double" bonds [N(1)–N(2), N(3)–N(4) and N(2)=N(3)]. The "double" C(1)=N(4) and "single" C(1)–N(1) bond lengths are practically identical in both compounds. The plane of the tetrazole fragment in both complexes does not coincide with the equatorial plane of the tetragonal bipyramid of the copper atom and makes angles of 55.8(1)° and 57.7° for **1** and **2**, respectively.

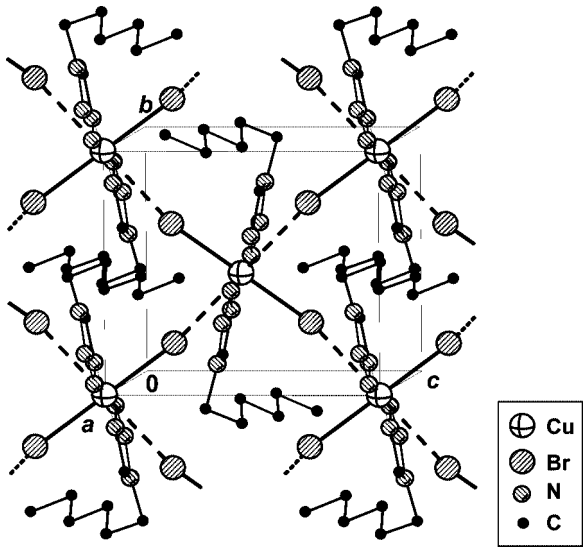

Figure 2. Fragment of $[Cu(Rtz)_2Br_2]$ polymeric layer structure exemplified by **2**. Hydrogen atoms have been omitted for clarity.

The N(1)–C(2) distance is typical for a single bond. The interlayer distance in **2** (19.750 Å) is much greater than in **1** (12.328 Å) because the alkyl groups protrude into the interlayer space. The distances between adjacent Br atoms are close to double the van der Waals radius [Br···Br′ = 3.8702(6) Å in **1** and 3.883(5) Å in **2**].

A comparison of the geometrical characteristics in **1**, **2** and previously reported $[Cu(Rtz)_2Cl_2]$ complexes[21,22,24,26] shows that the Cu–N(4) distances are practically identical for all compounds and are in the range of 1.98–1.99 Å. The lengths of the Cu–Br bonds in the equatorial plane are 2.43–2.45 Å, whereas the lengths of the axial Cu–Br′ bonds are equal to 3.08–3.09 Å. The axial Cu–Cl distances, as a rule, are also approximately 3 Å, and differ from the axial Cu–Br lengths only slightly. The Cu–A–Cu angles, where A = Cl^-, Br^-, are essentially independent of A (136–139°).

The dependencies $\mu_{eff}(T)$ and $1/\chi(T)$ above 10 K, as measured on polycrystalline samples, are presented in Figure 3 and Figure 4. At room temperature, μ_{eff} of complexes **1**, **2** are 1.869 μ_B and 1.884 μ_B, respectively, which correspond to the

Table 1. Relevant bond lengths [Å] and angles [°] in compounds **1** and **2**.

	1	**2**		**1**	**2**
Cu–N(4)	1.990(3)	1.982(3)	Cu–Br–Cu′	138.55(1)	138.16(1)
Cu–Br	2.4302(4)	2.4389(4)	N(4)–Cu–Br	90.12(9)	89.63(8)
Cu–Br′	3.0842(5)	3.0953(4)	N(4)–C(1)–N(1)	109.5(4)	109.0(4)
N(4)–C(1)	1.290(6)	1.304(5)	N(3)–N(4)–C(1)	106.8(4)	106.7(3)
N(3)–N(4)	1.346(5)	1.344(4)	N(3)–N(2)–N(1)	107.0(4)	107.2(3)
N(2)–N(3)	1.285(5)	1.289(4)	N(2)–N(3)–N(4)	109.1(4)	109.4(3)
N(1)–N(2)	1.346(5)	1.343(4)	C(1)–N(1)–N(2)	107.6(4)	107.7(3)
N(1)–C(1)	1.307(6)	1.315(5)	C(1)–N(1)–C(2)	130.5(4)	129.7(4)
N(1)–C(2)	1.472(6)	1.467(5)	N(2)–N(1)–C(2)	122.1(4)	122.6(3)
C(2)–C(3)	1.381(11)	1.487(7)	N(1)–C(2)–C(3)	113.6(7)	113.8(4)
C(3)–C(4)		1.504(7)	C(2)–C(3)–C(4)		116.8(4)
C(4)–C(5)		1.512(8)	C(3)–C(4)–C(5)		113.4(5)
C(5)–C(6)		1.488(10)	C(4)–C(5)–C(6)		114.1(6)
C(6)–C(7)		1.520(14)	C(5)–C(6)–C(7)		110.9(10)

 © 2005 Wiley-VCH Verlag GmbH & Co. KGaA, Weinheim

magnetic moment for $S = 1/2$ with Cu^{II} g-factors equal to 2.158 and 2.175, respectively. At lower temperatures, μ_{eff} increases for compounds **1** and **2** (Figure 3), indicating that ferromagnetic exchange interactions dominate.

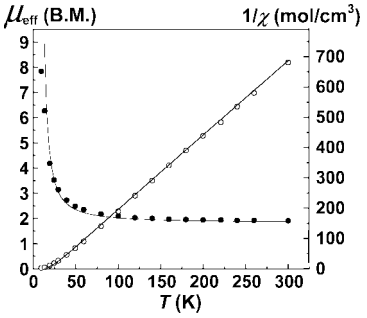

Figure 3. Dependencies $\mu_{eff}(T)$ (●) and $1/\chi(T)$ (○) in the paramagnetic region for **1**. Solid lines are the theoretical approximation.

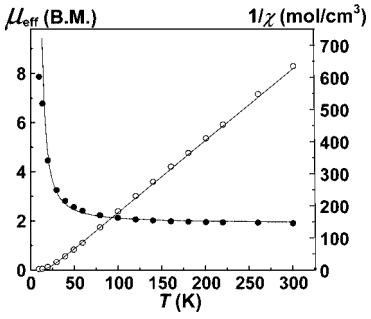

Figure 4. Dependencies $\mu_{eff}(T)$ (●) and $1/\chi(T)$ (○) in the paramagnetic region for **2**. Solid lines are the theoretical approximation.

The magnetic susceptibility follows the Curie–Weiss law [$\chi = C/(T - \theta)$] with the parameters given in Table 2. The values for the exchange parameter (J) between the Cu^{II} ions can be estimated from high-temperature data by series expansion for a two-dimensional Heisenberg model.[28]

Table 2. Magnetochemical parameters of **1** and **2**.

	C [cm^3 mol^{-1} K^{-1}]	θ [K]	J [K]	T_c [K]	H_x [Oe]	H_z [Oe]
1	0.414	19.9	8.77	8.5(3)	2550	720
2	0.409	24.2	9.11	8.9(5)	3020	860

For the high-temperature series expansion the J value is obtained by approximating the experimental dependencies from a known expression for the magnetic susceptibility: $\chi = Ng\beta^2S(S + 1)/3kT(1 + \sum_{n=1}^{10} a_nK^n)$, where $K = 2J/kT$ and a_n is a coefficient for a square-planar lattice. We applied the above formula to the description of $\mu_{eff}(T)$ dependencies of complexes in the temperature interval 10–300 K. The optimal J parameters (Table 2) were calculated this way. The relevant theoretical curves are presented in Figure 3 and 4 as solid lines.

Below 10 K the magnetic properties of **1** and **2** were investigated with single crystalline samples. Figure 5 and Figure 6 show the temperature dependence of the susceptibilities measured in a small magnetic field (1.2 ± 0.5 Oe) and the main curves of magnetisation $\sigma(H)$ at 4.5 K.

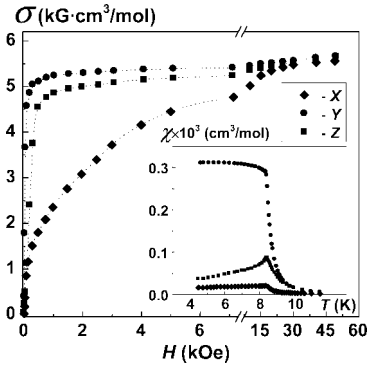

Figure 5. Magnetisation curves (4.5 K) and low field $\chi(T)$ curves in the transition area (insert) for single crystalline **1**.

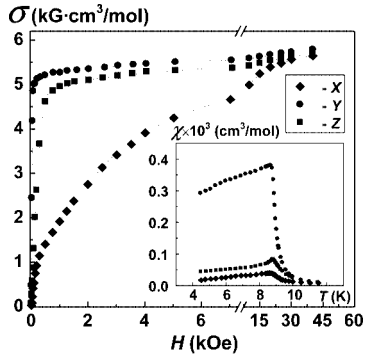

Figure 6. Magnetisation curves (4.5 K) and low field $\chi(T)$ curves in the transition area (insert) for single crystalline **2**.

Both solids exhibit a phase transition to the ferromagnetic state with T_c = 8.5 K and 8.9 K for **1** and **2**, respectively, and a strong anisotropy of the magnetic susceptibility below the ordering temperature (Figure 5 and 6).

By using the known expression $T_c = 4\pi J/\ln(J/J')$[29] (J' is the interlayer interaction) for layered Heisenberg magnets it is possible to estimate the ratio J'/J. For both compounds the ratio J'/J is close to 3×10^{-6} K, which is in good agreement with results for similar systems.

The maximal value of σ at T = 4.5 K is more than 5700 G cm^3 mol^{-1}, which is close to the saturation magnetisation ($Ng\beta S$ = 5585 G cm^3 mol^{-1}) for ferromagnetically coupled spins (S = 1/2) with g = 2. No hysteresis effects were detected for single crystals of **1** and **2** subjected to supermagnetisation. This fact indicates that complexes **1** and **2** behave as soft ferromagnets. The $\chi(T)$ and $\sigma(H)$ curves measured along different directions show essential anisotropy. In both cases, the easy magnetisation axis lies along the y axis, which is the only symmetry axis of the crystals. The hard magnetisation axis coincides with the X direction, which is orthogonal to the polymeric layers. The anisotropy of the magnetic properties

 © 2005 Wiley-VCH Verlag GmbH & Co. KGaA, Weinheim

in the plane of the polymeric layers (*YZ*) is much less than in the perpendicular direction as a consequence of the quasi-two-dimensional magnetic nature of the investigated compounds. Thus, the observed anisotropy in **1** and **2** should be of the "easy plane" type. Anisotropic energies were estimated for the single crystals of **1** and **2**. The free energy of magnetic anisotropy may be represented as $F_i \approx -H_i\sigma_{sat}$, where $i = X, Z$, H_i is the effective anisotropy field and σ_{sat} is the saturation magnetisation.[30] The energy F_i was determined from the experimental magnetisation curves by numerical integration: $F_i = \int_0^{H_{max}} \sigma_y(H)dH - \int_0^{H_{max}} \sigma_i(H)dH$, where H_{max} is the maximum field during the measurements. The calculated effective anisotropy fields for the complexes are presented in Table 2. It is noteworthy that the calculated anisotropy fields of **1** and **2** are approximately three times larger than in layered polymeric CuL_2 complexes of 3-imidazoline nitroxides.[31] This is probably due to the fact that the organic radical is an isotropic paramagnetic centre, therefore in complexes CuL_2 the "effective concentration" of anisotropic magnetic centres is three times lower than in **1** and **2**. On the other hand, the estimated anisotropy fields of the ferrimagnetic compound [Mn(hfac)$_2$(NIT-*i*Pr)] (NIT-*i*Pr = derivative of 2-imidazoline nitroxide) are H_x = 1200 Oe and H_z = 7500 Oe.[32] Such large anisotropy fields for a complex of such a weakly anisotropic ion as Mn^{II} are probably caused by the low-dimensional polymeric chain structure of this compound. Thus, the anisotropy of solids increases not only for complexes with more anisotropic metal ions, but also for solids with lower dimensionality of the crystal structure. For coordination compounds the energy of the anisotropy combined with dipolar interactions contributes greatly to the value of the ordering temperature.[33] From this point of view the increase of anisotropy of a magnetic system can be considered as one of the ways to increase the transition temperature.

Conclusions

The magnetic properties of single crystalline samples of Cu^{II} bromide complexes of 1-substituted tetrazoles have been investigated. In the layered polymer complexes **1** and **2**, we have found a phase transition to the ferromagnetic state at T_c = 8.5 K (**1**) and 8.9 K (**2**) and a strong anisotropy of the magnetic susceptibility below the magnetic ordering temperature.

Experimental Section

General Remarks: All commercially available reagents were used as purchased. 1-Ethyltetrazole (ettz) and 1-hexyltetrazole (htz) were prepared by literature methods.[34] The copper content was determined by complexometric titration, with the samples being mineralized in a 1:1 mixture of concentrated H_2SO_4 and $HClO_4$. Elemental analysis was performed with a Carlo–Erba analyzer.

Dibromobis(1-ethyltetrazole)copper(II) (1) and Dibromobis(1-hexyltetrazole)copper(II) (2): A solution of ettz (0.40 g, 4 mmol) or htz (0.62 g, 4 mmol) in 16 mL of a 1:1 ethanol/hexane mixture was added to a solution of $CuBr_2$ (0.45 g, 2 mol) in 10 mL the same mixture. A brown precipitate formed, which was filtered off, washed with ethanol and dried in air. Yield of **1**: 0.84 g (80%); **2**: 0.62 g (75%).

1: $C_6H_{12}Br_2CuN_8$ (419.56): calcd. C 17.2, H 2.9, Cu 15.1, N 26.7; found C 16.7, H 2.9, Cu 15.4, N 27.1.

2: $C_{14}H_{28}N_8Br_2Cu$ (531.78): calcd. C 31.6, H 5.3, Cu 11.9, N 21.1; found C 31.5, H 5.2, N 20.3, Cu 12.1.

For growing large single crystals the initial solids were dissolved in EtOH at 43 °C. Then, as much solvent as possible was removed with a stream of air with the condition that crystallisation did not occur at room temperature. After that the flasks were stoppered and allowed to stand at ambient temperature. Dark-brown, parallelepiped-shaped single crystals of **1** and **2** with a maximal appearance of up to 3 × 3 × 0.1 mm grew after approximately one month.

X-ray Crystallographic Study: Single crystal data for **1** and **2** were collected on a SMART APEX Bruker AXS automatic diffractometer at ambient temperature using the standard procedure (Mo-K_α radiation). The structures were solved by direct methods. The full-matrix least-squares refinement was performed anisotropically for non-hydrogen atoms and isotropically for hydrogens. Some H-atoms were localised in difference electron density syntheses; the others were generated theoretically. All structure solution and refinement calculations were carried out with SHELXTL software.[35] The crystal data for the compounds and details of experiment, as well as selected bond lengths and angles are given in Table 1 and Table 3.

Table 3. Crystal data and experimental details.

	1	**2**
Formula	$C_6H_{14}Br_2CuN_8$	$C_{14}H_{28}Br_2CuN_8$
T [K]	295	295
Space group	$P2_1/c$	$P2_1/c$
Z	2	2
a [Å]	12.655(2)	20.076(3)
b [Å]	6.915(1)	6.9430(9)
c [Å]	7.668(1)	7.675(1)
β [°]	103.053(2)	100.344(2)
V [Å^3]	653.7(2)	1052.4(2)
D_c [g cm^{-3}]	2.142	1.678
μ [mm^{-1}]	7.776	4.849
I_{hkl} meas./unique	2352/940	4330/1516
R_{int}	0.0218	0.0896
I_{hkl}/N	940/95	1516/172
Goof	0.998	0.845
R_1 [$I > 2\sigma(I)$]	0.0278	0.0338
wR_2	0.0707	0.0750
R_1	0.0309	0.0384
wR_2	0.0726	0.0777

Magnetic Measurements: The magnetochemical experiments were performed with an MPMS-5S ("Quantum Design") SQUID magnetometer at temperatures from 4.5 K to 300 K in a homogeneous external magnetic field of up to 49.5 kOe. Magnetic measurements on single crystals were performed in three mutually orthogonal directions (X, Y, Z). The Y and Z directions were aligned with the crystallographic b and c axes. The molar magnetic susceptibility, χ, of the complexes was calculated by using Pascal's additive scheme including diamagnetic corrections and taking into account the temperature-independent paramagnetism of Cu^{II} ions, which was taken to be 60×10^{-6} cm^3 mol^{-1}. In the paramagnetic region the effective magnetic moment was calculated with the formula $\mu_{eff} = [(3k/N_A\beta^2)\chi T]^{1/2} \approx (8\chi T)^{1/2}$, where k is Boltzmann's constant, N_A is the Avogadro number and β is the Bohr magneton. The magnetic phase transition temperature was determined as the extremum of the derivative of the magnetic susceptibility with respect to temperature $\partial\chi/\partial T$. The magnetisation dependencies $\sigma(H)$ of the single crystals below the transi-

 © 2005 Wiley-VCH Verlag GmbH & Co. KGaA, Weinheim

tion temperature were taken into account for the demagnetisation field of the sample. The real field in the crystal was calculated for each direction by the formula $H_i = H - N_i\sigma_i$, where $i = X, Y, Z$; N is the demagnetisation factor evaluated using the tables for the disk sample.[36]

CCDC-241146 (for **1**) and -241147 (for **2**) contain the supplementary crystallographic data for this paper data can be obtained free of charge from The Cambridge Crystallographic Data Centre via www.ccdc.cam.ac.uk/data_request/cif.

Acknowledgments

The work was supported by CRDF (grant Y1-C-08-12), President of Russia grant (MK-918.2003.03) and Lavrent'ev grant (43). The authors are grateful to Dr. Alexei Burdukov and Dr. Alexander Valishev for their help.

[1] V. I. Ovcharenko, R. Z. Sagdeev, *Russ. Chem. Rev. Int. Ed. Engl.* **1999**, *68*, 345–363.
[2] P. E. M. Wijnands, J. S. Wood, J. Reedijk, W. J. A. Maaskant, *Inorg. Chem.* **1996**, *35*, 1214–1222.
[3] J. G. Haasnoot, *Coord. Chem. Rev.* **2000**, *200*, 131–185.
[4] A. F. Stassen, W. L. Drissen, J. P. Haasnoot, J. Reedijk, *Inorg. Chim. Acta* **2003**, *350*, 57–61.
[5] A. S. Lyakhov, P. N. Gaponik, S. V. Voitekhovich, D. O. Ivashkevich, P. S. Putleva, L. S. Ivashkevich, *Acta Crystallogr., Sect. C* **2001**, *57*, 1374–1376.
[6] W. Clegg, J. R. Nicholson, D. Collison, C. D. Garner, *Acta Crystallogr., Sect. C* **1988**, *44*, 453–461.
[7] F. S. Keij, J. G. Haasnoot, A. J. Oosterling, J. Reedijk, *Inorg. Chim. Acta* **1991**, *181*, 185–193.
[8] C. J. Campbell, W. L. Driessen, J. Reedijk, W. J. Smeets, A. L. Spek, *J. Chem. Soc., Dalton Trans.* **1998**, 2703–2706.
[9] A. V. Virovets, G. A. Bikzhanova, L. G. Lavrenova, *Russ. J. Struct. Chem. Int. Ed. Engl.* **2001**, *42*, 989–994.
[10] A. S. Lyakhov, P. N. Gaponik, M. M. Degtyarik, V. E. Matulis, L. S. Ivashkevich, *Acta Crystallogr., Sect. C* **2003**, *59*, m90–m92.
[11] Y. Garcia, P. J. van Koningsbruggen, G. Bravic, P. Guionneau, A. Chasseau, G. L. Cascarano, J. Moscovici, K. Lambert, A. Michalowicz, O. Kahn, *Inorg. Chem.* **1997**, *36*, 6357–6365.
[12] M. Lagrenee, S. Sueur, J. P. Wignacourt, B. Mernari, A. Boukhari, *J. Chim. Phys. Phys.-Chim. Biol.* **1991**, *88*, 2075–2089.
[13] D. O. Ivashkevich, M. M. Degtyarik, P. N. Gaponik, A. S. Lyakhov, *Acta Crystallogr., Sect. C* **2002**, *58*, m288–m301.
[14] D. O. Ivashkevich, A. S. Lyakhov, M. M. Degtyarik, P. N. Gaponik, *Acta Crystallogr., Sect. E* **2003**, *E59*, m14–m16.
[15] A. V. Virovets, G. A. Bikzhanova, N. V. Podberezskaya, L. G. Lavrenova, *Russ. J. Struct. Chem. Int. Ed. Engl.* **1997**, *38*, 103–109.
[16] S. Decurtins, H. W. Schmalle, P. Schneuwly, L. M. Zheng, J. Ensling, A. Hauser, *Inorg. Chem.* **1995**, *35*, 5501–5506.
[17] G. A. van Albada, R. C. Guijt, J. G. Haasnoot, M. Lutz, A. L. Spek, J. Reedijk, *Eur. J. Inorg. Chem.* **2000**, 121–126.
[18] L. G. Lavrenova, A. N. Bogatikov, L. A. Sheludyakova, V. N. Ikorskii, S. V. Larionov, P. N. Gaponik, *J. Inorg. Chem. USSR Int. Ed. Engl.* **1991**, *36*, 693–698.
[19] L. G. Lavrenova, V. N. Ikorskii, S. V. Larionov, A. N. Bogatikov, P. N. Gaponik, *J. Inorg. Chem. USSR Int. Ed. Engl.* **1993**, *38*, 1416–1417.
[20] A. V. Virovets, I. A. Baydina, V. I. Alekseev, N. V. Podberezskaya, L. G. Lavrenova, *Russ. J. Struct. Chem. Int. Ed. Engl.* **1996**, *37*, 288–294.
[21] A. V. Virovets, N. V. Podberezskaya, L. G. Lavrenova, G. A. Bikzhanova, *Acta Crystallogr., Sect. C* **1995**, *51*, 1084–1087.
[22] L. G. Lavrenova, A. N. Bogatikov, V. N. Ikorskii, L. A. Sheludyakova, E. G. Boguslavskii, P. N. Gaponik, S. V. Larionov, *Russ. J. Inorg. Chem. Int. Ed. Engl.* **1996**, *41*, 406–409.
[23] L. G. Lavrenova, G. A. Bikzhanova, A. N. Bogatikov, V. N. Ikorskii, L. A. Sheludyakova, A. V. Virovets, N. V. Podberezskaya, P. N. Gaponik, S. V. Larionov, *Russ. J. Inorg. Chem. Int. Ed. Engl.* **1996**, *41*, 587–592.
[24] D. O. Ivashkevich, A. S. Lyakhov, P. N. Gaponik, A. N. Bogatikov, A. A. Govorova, *Acta Crystallogr., Sect. C* **2001**, *C57*, m335–m337.
[25] A. F. Stassen, H. Kooijman, A. L. Spec, L. Jos de Jongh, J. P. Haasnoot, J. Reedijik, *Inorg. Chem.* **2002**, *41*, 6468–6473.
[26] Yu. G. Shvedenkov, A. V. Virovets, L. G. Lavrenova, *Russ. Chem. Bull. Int. Ed. Engl.* **2003**, *52*, 1353–1357.
[27] Yu. G. Shvedenkov, V. N. Ikorskii, L. G. Lavrenova, *J. Phys. IV France* **2004**, *114*, 649–650.
[28] R. Navarro, in *Magnetic Properties of Layered Transition Metal Compounds* (Ed.: L. J. De Jongh), Kluwer Academic Publishers, The Netherlands, **1990**, 105–190.
[29] V. L. Pokrovsky, G. V. Uimin, in *Magnetic Properties of Layered Transition Metal Compounds* (Ed.: L. J. De Jongh), Kluwer Academic Publishers, The Netherlands, **1990**, 53–102.
[30] S. V. Vonsovskii, *Magnetism*, Izdatelstvo "Nauka", Moscow, **1971**, p. 476.
[31] Y. Shvedenkov, V. Ikorskii, D. Guschin, E. Fursova, V. Ovcharenko, *Polyhedron* **2001**, *20*, 1207–1213.
[32] A. Caneschi, D. Gatteschi, J.-P. Renard, P. Rey, R. Sessoli, *Inorg. Chem.* **1989**, *28*, 1976–1980.
[33] E. V. Kuzmin, G. A. Petrakovsky, *Izvestiya Vuzov MV I SSO SSSR Fizika* **1988**, *3*, 94–101.
[34] P. N. Gaponik, V. P. Karavai, Yu. V. Grigor'ev, *Chem. Heterocycl. Compd. Int. Ed. Engl.* **1985**, *21*, no. 11, 1255–1258.
[35] *SHELXTL*, version 6.14, Bruker AXS, 8/06/00.
[36] V. I. Chechernikov, *Magnitnie izmereniya* (Ed.: E. I. Kondorskii), Izdatelstvo Moskovskogo Universiteta, **1963**, p. 57.

Received: June 11, 2004

 © 2005 Wiley-VCH Verlag GmbH & Co. KGaA, Weinheim

Four New Lead(II) Thiolate Cluster Complexes – Unexpected Products of a Conventional Synthesis

Andreas Eichhöfer*[a]

Keywords: Cluster compounds / Lead / Sulfur / UV/Vis spectroscopy

The reaction of $Pb(OOCCH_3)_2 \cdot 3H_2O$ with 2.1 equiv. of HS-2,6-$(CH_3)_2C_6H_3$ in ethanol/water is expected to give [Pb{S-2,6-$(CH_3)_2C_6H_3$}$_2$]. However, we obtained an orange powder whose elemental analysis disagrees with that of the expected product and indicates small amounts of oxygen. Layering of concentrated solutions of this orange powder in dry THF with pentane under nitrogen results in the formation of a mixture of three identifiable crystalline compounds, namely [Pb_{10}{S-2,6-$(CH_3)_2C_6H_3$}$_{20}$], [Pb_6S{S-2,6-$(CH_3)_2C_6H_3$}$_{10}(C_4H_8O)_4$] and [Pb_8O_2{S-2,6-$(CH_3)_2C_6H_3$}$_{12}$]. In contrast, fractional crystallization from dilute solutions initially yielded only yellow crystals of [$Pb_{14}O_6${S-2,6-$(CH_3)_2C_6H_3$}$_{16}$]. Further concentration of the supernatant solution yielded, upon layering with pentane, [Pb_6S{S-2,6-$(CH_3)_2C_6H_3$}$_{10}(C_4H_8O)_4$] and [Pb_{10}{S-2,6-$(CH_3)_2C_6H_3$}$_{20}$], which are almost completely separable by controlling the duration of the crystallization step and the amount of condensed pentane. Recrystallization of the crude orange powder under aerobic conditions produces pure [$Pb_{14}O_6${S-2,6-$(CH_3)_2C_6H_3$}$_{16}$] with a yield five times higher than that under nitrogen. This shows that it is sensitive to oxidation by oxygen in solution. The structures of all four complexes have been determined by single-crystal X-ray analysis. The net formed by the six oxygen and twelve lead atoms in the center of [$Pb_{14}O_6${S-2,6-$(CH_3)_2C_6H_3$}$_{16}$] resembles a small piece of a layer of the solid-state structure of red PbO.

(© Wiley-VCH Verlag GmbH & Co. KGaA, 69451 Weinheim, Germany, 2005)

Introduction

Lead chalcogenide nanocrystals (PbS, PbSe, PbTe) have recently attracted interest due to their unique properties.[1–3] Size-quantization effects are strongly pronounced in these materials because of their relatively large exciton Bohr radii. Furthermore, the quantum size effect offers potential photonic applications. Theoretically, PbSe nanocrystals (NCs) are predicted to have absorptive and dispersive nonlinearities 1000 times larger than those of CdSe NCs of the same size.[4] However, in contrast to the recent, distinct growth in the chemistry of transition metal chalcogenide clusters,[5,6] related polynuclear molecules of the heavier main group elements seem to be rather unexplored to date.[7] It is known that the reaction of lead thiolates of the general formula $Pb(SR)_2$ (R = organic group) with stoichiometric amounts of sulfur or selenium yields the corresponding lead chalcogenides.[8] These findings suggest that nonstoichiometric reactions could probably lead to metastable lead chalcogenolato/chalcogenide cluster molecules. Therefore, we became interested in the synthesis of lead thiolate complexes as starting materials for the synthesis of such cluster molecules. In order to avoid known solubility problems of the mostly polymeric lead thiolates[8–10] we followed a recent recommendation of Briand[11] concerning the use of 2,6-dimethylthiophenol, which was reported to yield soluble [Pb{S-2,6-$(CH_3)_2C_6H_3$}$_2$]. However, the direct reaction of $Pb(OOCCH_3)_2 \cdot 3H_2O$ with 2.1 equiv. of HS-2,6-$(CH_3)_2C_6H_3$ at 60 °C obviously leads not only to the expected product [Pb{S-2,6-$(CH_3)_2C_6H_3$}$_2$] but also yields lead thiolate cluster complexes which have sulfur or oxygen atoms incorporated in the cluster framework, the structures of which are reported here.

Results and Discussion

In order to synthesize [Pb{S-2,6-$(CH_3)_2C_6H_3$}$_2$] we used the method of Shaw and Woods developed for the synthesis of [Pb(S-2-$CH_3C_6H_4$)$_2$].[8] The reaction of $Pb(OOCCH_3)_2 \cdot 3H_2O$ with 2.1 equiv. of HS-2,6-$(CH_3)_2C_6H_3$ in aqueous ethanol at 60 °C yielded an orange-red precipitate, which was filtered and dried. The elemental analysis disagrees with the expected product [Pb{S-2,6-$(CH_3)_2C_6H_3$}$_2$] especially with respect to the low amount of sulfur, a fact which has also been observed by Shaw et al. in the related synthesis of some other lead thiolate complexes. Additionally, the presence of small amounts of oxygen is indicated by the analysis. Layering of concentrated solutions of the crude product in dried THF with pentane results in the formation of a mixture of the crystalline compounds **1**–**3**, which could be identified by single-crystal X-ray analysis. In contrast to this, a solution 1/5 as concentrated in dried THF led to the crystallization of small amounts of **4** (12% calculated for

[a] Institut für Nanotechnologie, Forschungszentrum Karlsruhe, Postfach 3640, 76021 Karlsruhe, Germany
Fax: +49-7247-82-6368
E-mail: eichhoefer@int.fzk.de

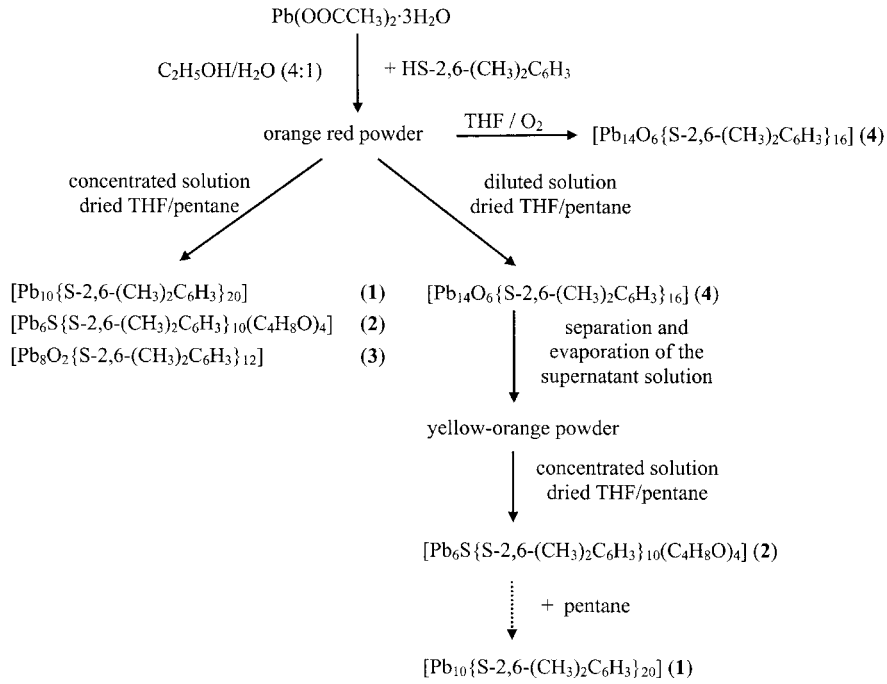

Pb) as the only product. Evaporation of the solvents of the clear supernatant yellow solution in vacuo produced a yellow-orange powder which was redissolved in 10 mL of THF. Layering of this concentrated solution with pentane yielded, firstly, crystals of **2**, followed by crystals of **1**, without any crystals of either **3** or **4**.

Obviously, the oxygen present in the crude orange powder was in this way completely bound by **4** and thus removed from the reaction solution. However, the crystallization of **1** and **2** proceeds in such a way that, initially, orange plate-like crystals of **2** appear, which tend to form solidified droplets of crystalline material after the layering process, while bundles of light-orange needles of **1** start to grow a few days later at higher concentrations of pentane. In this way, **1** and **2** can be nearly completely separated, as shown by powder diffraction patterns and elemental analysis (see below). The yield of **4** could be increased up to 56% by performing the recrystallization under aerobic conditions, which shows that the crude orange powder is sensitive to oxidation by oxygen in solution.

The light-orange, plate-like needles were found to display the desired composition $[Pb\{S\text{-}2,6\text{-}(CH_3)_2C_6H_3\}_2]$. Interestingly, the structure is neither polymeric, as in $[Pb(SC_6H_5)_2]_n$[9] or $[Pb(S\text{-}4\text{-}CH_3C_6H_4)_2]_n$,[10] nor trimeric, as in $[Pb_3(S\text{-}2,6\text{-}i C_3H_7C_6H_3)_6]$,[12] but is found to be oligomeric $[Pb_{10}\{S\text{-}2,6\text{-}(CH_3)_2C_6H_3\}_{20}]$ (**1**). Complex **1** crystallizes in the space group *Pbcn* with the molecule residing on an inversion center (Figure 1). The Pb–S contacts in the range of 255.8–317.5 pm have been assigned as bonds (solid lines), similar to those observed in the lead thiolates mentioned above, while longer contacts have been drawn for all molecules as dashed lines. Contacts to the next molecular unit are larger than 500 pm, which proves the oligomeric character of **1**. The lead atoms exhibit different coordination modes. Pb(2), and Pb(4) are in a distorted tetrahedral geometry comprising three sulfur atoms and the stereochemically active inert electron pair, whilst Pb(3) is bonded to six sulfur atoms in a highly distorted octahedral geometry caused by the additional inert electron pair. Pb(1) and Pb(5) possess complex coordination environments comprised of either five or four sulfur atoms. A comparison of the measured and calculated powder diffraction pattern of **1** (Figure 2) reveals the crystalline purity of the product isolated by fractional crystallization, as mentioned above.

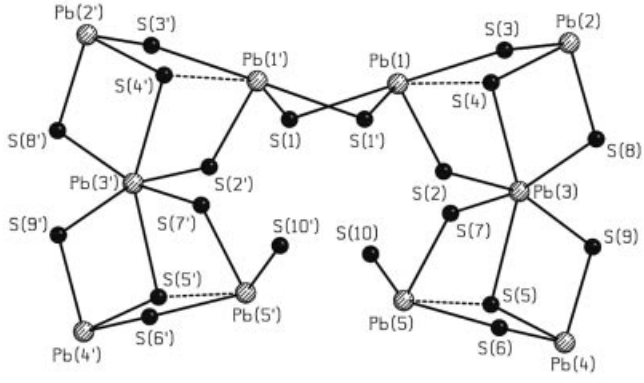

Figure 1. Molecular structure of $[Pb_{10}\{S\text{-}2,6\text{-}(CH_3)_2C_6H_3\}_{20}]$ (**1**). C and H atoms omitted for clarity. Selected bond lengths [pm] (solid lines): Pb(1)–S(2) 265.4(4), Pb(1)–S(1′) 269.1(4), Pb(1)–S(1) 298.1(4), Pb(1)–S(3) 305.9(5), Pb(2)–S(8) 265.8(4), Pb(2)–S(3) 267.9(5), Pb(2)–S(4) 275.4(3), Pb(3)–S(7) 2788(4), Pb(3)–S(2) 280.1(4), Pb(3)–S(4) 293.6(3), Pb(3)–S(5) 303.4(3), Pb(3)–S(8) 313.1(4), Pb(3)–S(9) 317.5(4), Pb(4)–S(9) 263.3(4), Pb(4)–S(5) 272.5(4), Pb(4)–S(6) 275.0(4), Pb(5)–S(10) 255.8(5), Pb(5)–S(7) 266.4(4), Pb(5)–S(6) 278.9(5). Weak contacts [pm] (dashed lines): Pb(5)–S(5) 355.5, Pb(1)–S(4) 362.7. Symmetry transformation for generation of equivalent atoms: $-x, y, -z + 0.5$.

 © 2005 Wiley-VCH Verlag GmbH & Co. KGaA, Weinheim

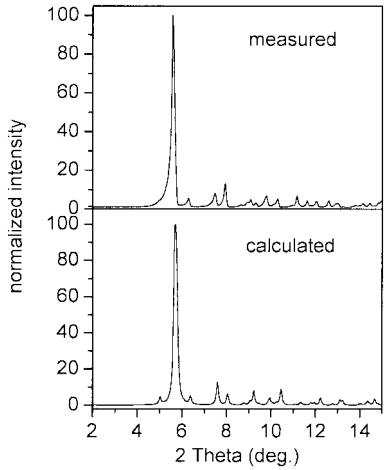

Figure 2. Measured (top) and calculated (bottom) powder diffraction pattern of $[Pb_{10}\{S\text{-}2,6\text{-}(CH_3)_2C_6H_3\}_{20}]$ (**1**).

The orange hexagonally shaped plates that form solidified droplets of crystalline material after the layering process were characterized to be $[Pb_6S\{S\text{-}2,6\text{-}(CH_3)_2C_6H_3\}_{10}(C_4H_8O)_4]$ (**2**). Obviously, part of the precursor thiol undergoes cleavage of the S–Aryl bond under the given experimental conditions. Complex **2** crystallizes in the $P\bar{1}$ space group with the central sulfur atom occupying an inversion center (Figure 3). The six lead atoms form an elongated octahedron whose eight trigonal faces are bridged by sulfur atoms, with Pb–S contacts mapped as bonds ranging from 262.7(2) to 311.3(3) pm. The two "axial" lead atoms [Pb(1) and Pb(1′)] are each additionally bonded to a thiolate ligand, while the equatorial lead atoms [Pb(2), Pb(2′), Pb(3), and Pb(3′)] are weakly coordinated by a THF solvent molecule (Pb–O: 300.2–304.2 pm). This leads to an octahedral coordination geometry for Pb(2), Pb(2′), Pb(3) and Pb(3′) which is distorted by the inert electron pair. Pb(1) and Pb(1′) are bonded to the five nearest sulfur atoms [S(2)–S(5) and symmetry-equivalent atoms] in a distorted square-pyramidal fashion with additional weak coordination by S(1) from the bottom face [Pb(1)–S(1): 350.6 pm]. Again, a comparison of the measured and calculated powder diffraction pattern of **2** (Figure 4) reveals the crystalline purity of the product that was isolated by fractional crystallization, as mentioned above.

Yellow, triclinic-shaped blocks were identified as the mixed lead oxide thiolate cluster complex $[Pb_8O_2\{SC_6H_3(CH_3)_2\}_{12}]$ (**3**). This is even observed when using freshly dried and distilled THF which suggests that Pb–O units are already present in the crude orange powder, a fact which was additionally supported by elemental analysis. The molecular structure of **3** ($\bar{1}$ symmetry), which crystallizes in the $P\bar{1}$ space group, consists of an octanuclear lead thiolate cluster which additionally incorporates two oxygen atoms (Figure 5). The two Pb_3O units are nearly planar [deviation of O(1) from the trigonal plane is 44 pm] with an average of 220.9(2) pm for the Pb–O distances. A similar structural unit is found in the pentanuclear, oxygen-centered lead thiolate cluster $[Pb_5O\{S\text{-}2,4,6\text{-}(CF_3)_3C_6H_2\}_8]\cdot 2C_7H_8$.[13] An additional "PbS-2,6-$(CH_3)_2C_6H_3$" unit is bonded to these two trigonal faces through three thiolate ligands [S(1), S(3), S(4), and equivalent atoms] forming two mixed oxide/thiolate-bridged Pb_4OS_5 cluster units which are linked at their Pb_3O faces by four additional μ_3-thiolate ligands [S(2), S(2′), S(5), and S(5′)]. The Pb–S distances are in the range of 256.2(3)/310.0(3) pm with eight additional weaker and longer contacts between 334.9 pm [Pb(2)–S(5)] and 361.4 pm [Pb(4)–S(4)].

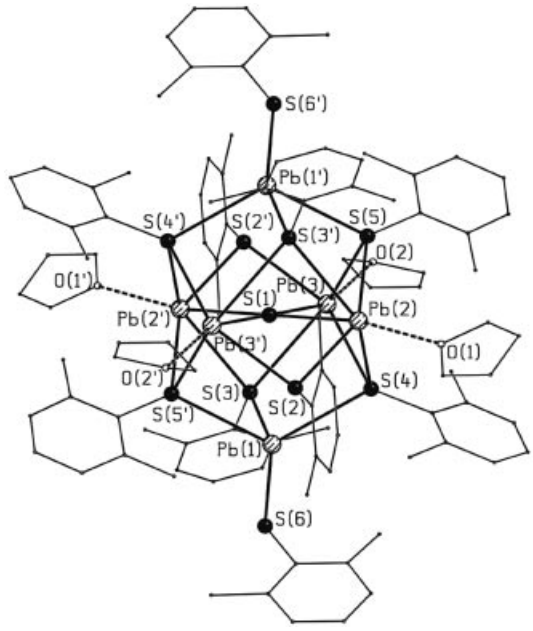

Figure 3. Molecular structure of $[Pb_6S\{S\text{-}2,6\text{-}(CH_3)_2C_6H_3\}_{10}(C_4H_8O)_4]$ (**2**). C and H atoms omitted for clarity. Selected bond lengths [pm] (solid lines): Pb(1)–S(6) 262.7(2), Pb(1)–S(3) 266.4(3), Pb(1)–S(4) 307.6(2), Pb(2)–S(4) 280.6(2), Pb(2)–S(2) 281.8(2), Pb(2)–S(1) 283.5(2), Pb(2)–S(3′) 309.3(2), Pb(2)–S(5) 312.1(2), Pb(3)–S(5) 276.0(2), Pb(3)–S(1) 283.36(8), Pb(3)–S(2′) 284.0(3), Pb(3)–S(4) 311.3(3). Weak contacts [pm] (dashed lines): Pb(1)–S(1) 350.6, Pb(1)–S(2) 353.6, Pb(2)–O(1) 304.1(3), Pb(3)–O(2) 300.2(3). Symmetry transformation for generation of equivalent atoms: $-x + 1, -y + 2, -z + 1$.

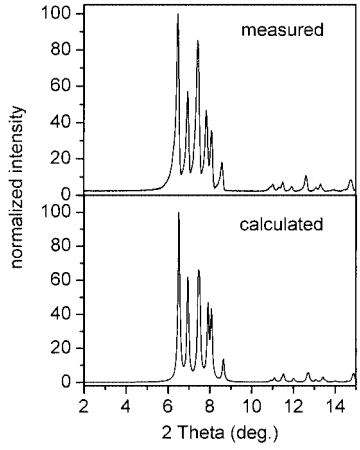

Figure 4. Measured (top) and calculated (bottom) powder diffraction pattern of $[Pb_6S\{S\text{-}2,6\text{-}(CH_3)_2C_6H_3\}_{10}(C_4H_8O)_4]$ (**2**).

 © 2005 Wiley-VCH Verlag GmbH & Co. KGaA, Weinheim

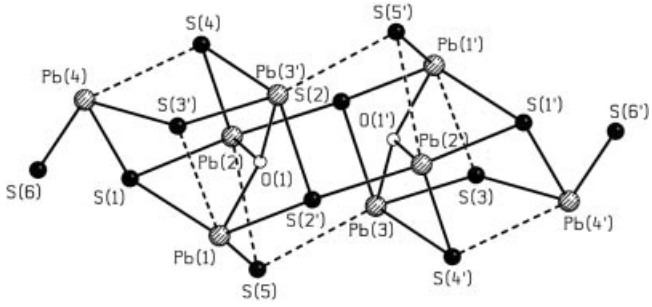

Figure 5. Molecular structure of $[Pb_8O_2\{S\text{-}2,6\text{-}(CH_3)_2C_6H_3\}_{12}]$ (**3**). C and H atoms omitted for clarity. Selected bond lengths [pm] (solid lines): Pb(1)–O(1) 220.5(6), Pb(2)–O(1) 222.4(6) Pb(3)–O(1′) 219.8(7), Pb(1)–S(5) 269.4(3), Pb(1)–S(1) 289.4(3), Pb(2)–S(4) 276.9(3), Pb(2)–S(2) 282.0(3), Pb(2)–S(1) 310.0(3), Pb(3)–S(3) 279.3(3), Pb(3)–S(2) 300.4(4), Pb(3)–S(4′) 302.6(4), Pb(4)–S(6) 256.2(3), Pb(4)–S(3′) 273.8(4), Pb(4)–S(1) 275.8(3). Weak contacts [pm] (dashed lines): Pb(1)–S(3′) 337.5, Pb(2)–S(5) 334.9, Pb(3)–S(5) 342.3, Pb(4)–S(4) 361.4. Symmetry transformation for generation of equivalent atoms: $-x$, $-y + 1$, $-z + 1$.

Small, yellow, needle-like plates of $[Pb_{14}O_6\{SC_6H_3\text{-}(CH_3)_2\}_{16}]$ (**4**) were found to be the only product crystallizing from dilute solutions of the crude orange-red powder in THF. Again, the use of freshly dried and distilled THF suggests that the oxygen can, in principle, only originate from compounds with Pb–O units that are already present in the crude powder. Interestingly, the yield of **4** is considerably increased upon dissolution of the crude powder in THF under aerobic conditions, which suggests that **4** can be seen as a stable oxidation product of the crude orange powder. This is in agreement with the investigations of Edelmann et al., who found $[Pb_5O\{S\text{-}2,4,6\text{-}(CF_3)_3C_6H_2\}_8]\cdot 2C_7H_8$ to be an oxidation product of the lead(II) thiolate $[Pb\{S\text{-}2,4,6\text{-}(CF_3)_3C_6H_2\}_2]$.[13] Complex **4** crystallizes in the $P\bar{1}$ space group and exhibits $\bar{1}$ symmetry (Figure 6). The net formed by the six oxygen [O(1), O(2), O(3), and symmetry-equivalent atoms] and twelve of the lead atoms [Pb(1)–Pb(6) and symmetry-equivalent atoms] resembles a small piece of a layer of the solid-state structure of red PbO, every layer of which is composed of a quadratic packing of oxygen atoms with the lead atoms occupying the quadratic cavities alternately above and below the oxygen planes. The Pb–O distances, with an average of 233.5 pm, are slightly longer in **4** than those in the red form of PbO (230 pm).[14] However, twenty of the contacts lie within a narrow range of 221.5–232.0(10) pm while four distances, namely Pb(2)–O(1′) [242.1(10) pm], Pb(2)–O(2) [269.6(10) pm], and distances to symmetry-equivalent atoms, show significantly larger values. The 16 thiolate ligands additionally bridge the lead atoms in different coordination modes, including the two remaining lead atoms Pb(7) and Pb(7′). The Pb–S bonds have been mapped in Figure 6 and range from 262.7(6) to 315.0(6) pm. A comparison of the measured X-ray powder patterns of a suspension of **4** in the mother liquor with the calculated pattern based on the data from single-crystal X-ray analysis (Figure 7) shows good agreement between the two and thus reveals the crystalline purity of this compound. Small deviations in intensity and reflection position might be due to the fact that the powder measurement was done at room temperature in contrast to 190 K for the single-crystal measurement, and that the needle-like crystals preferably align in the capillary vertical to the beam.

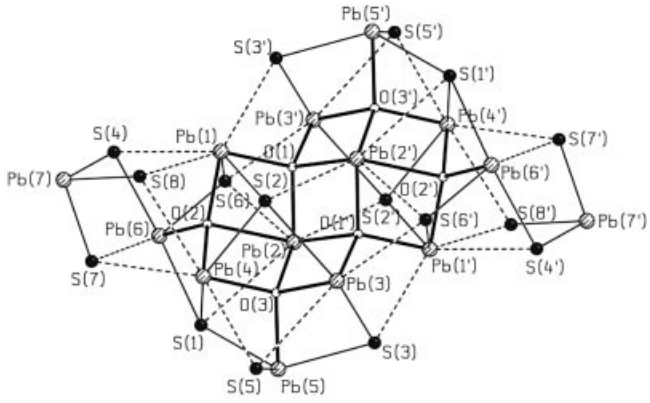

Figure 6. Molecular structure of $[Pb_{14}O_6\{S\text{-}2,6\text{-}(CH_3)_2C_6H_3\}_{16}]$ (**4**). C and H atoms omitted for clarity. Selected bond lengths [pm] (solid lines): Pb(1)–O(2) 225.0(10) Pb(1)–O(1) 231.9(9), Pb(2)–O(1) 227.2(9), Pb(2)–O(3) 238.6(9) Pb(2)–O(1′) 242.1(10) Pb(2)–O(2) 269.6(10), Pb(3)–O(1′) 229.8(8), Pb(3)–O(3) 232.0(10), Pb(1)–S(2) 285.0(4), Pb(4)–O(2) 226.8(9), Pb(4)–O(3) 228.2(9), Pb(5)–O(3) 229.5(9), Pb(6)–O(2) 221.5(10), Pb(3)–S(3) 285.9(5), Pb(4)–S(1) 302.4(5), Pb(4)–S(2) 305.5(4), Pb(5)–S(5) 264.6(5), Pb(5)–S(1) 289.8(6), Pb(5)–S(3) 289.9(6), Pb(6)–S(6) 274.4(5), Pb(6)–S(1) 293.5(5), Pb(6)–S(4) 299.8(5), Pb(7)–S(8) 262.7(6), Pb(7)–S(7) 263.1(6), Pb(7)–S(4) 270.4(6), Pb(7′)–S(8) 263.5(11), Pb(7′)–S(4) 264.1(9). Weak contacts [pm] (dashed lines): Pb(1)–S(4) 334.2, Pb(1)–S(6) 370.1, Pb(1)–S(8) 338.0, Pb(1)–S(3′) 323.2, Pb(2)–S(1) 361.1, Pb(2)–S(6) 333.6, Pb(2)–S(2′) 330.6, Pb(3)–S(5) 349.1, Pb(3)–S(6′) 325.0, Pb(4)–S(5) 331.2, Pb(4)–S(7) 338.6, Pb(4)–S(8) 370.0, Pb(6)–S(7) 322.8. Symmetry transformation for generation of equivalent atoms: $-x + 1$, $-y + 1$, $-z + 1$.

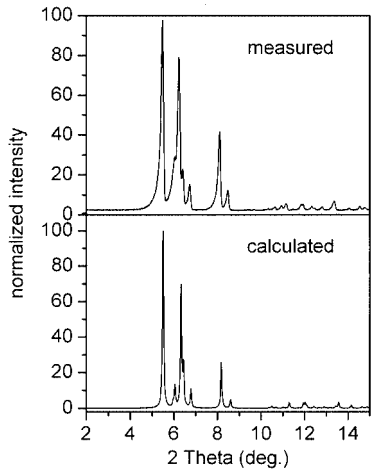

Figure 7. Measured (top) and calculated (bottom) powder diffraction pattern of $[Pb_{14}O_6\{S\text{-}2,6\text{-}(CH_3)_2C_6H_3\}_{16}]$ (**4**).

The UV/Vis spectra of **1**, **2**, and **4** in the solid state (Figure 8, bottom part) show a decrease in wavelength of the absorption onsets on going from **1** to **2** to **4**. Furthermore, the spectra display an almost featureless increase in absorbance down to 220 nm hardly indicating any maxima, of which the small shoulder at 430 nm (2.88 eV) in **4** is the most obvious. The solution spectrum of **4** is similar to that

 © 2005 Wiley-VCH Verlag GmbH & Co. KGaA, Weinheim

of the ground crystalline powders. Starting from higher wavelengths one observes the first absorption maximum in solution as a broad shoulder at around 420 nm (2.95 eV; the extinction coefficient for **4** in THF at 420 nm is 1.63×10^5 M^{-1}cm^{-1}). The following increase in absorbance in the region from 420 nm to 310 nm indicates one further weakly resolved shoulder and shows a last maxima at 256 nm (4.84 eV). The onset of the absorption of **4** in the solid state is thus slightly shifted to higher wavelength, in agreement with findings in other solid-state spectra.[15] In contrast, for **1** the onset of the solution spectrum is shifted by roughly 100 nm compared to the solid-state spectrum, a fact which cannot be simply explained by influences of the different measurement techniques alone. Rather, we assume that oligomeric **1** dissociates in solution into smaller units, probably [Pb{S-2,6-$(CH_3)_2C_6H_3$}$_2$], which displays two absorption maxima at 333 nm (3.72 eV) and 258 nm (4.8 eV) with an extinction coefficient of 5.95×10^5 M^{-1}cm^{-1} at 333 nm. Solutions of **2** in THF decompose immediately after dissolution, as indicated by the formation of a dark precipitate, while the clear supernatant solution displays the same UV/Vis spectrum as measured for **1**. The powder diffraction pattern of the dark precipitate displays weak and broad peaks for cubic PbS[16,17] and weak but sharper ones for cubic elemental lead.[18] This suggests that **2** decomposes in THF to form PbS/Pb and [Pb{S-2,6-$(CH_3)_2C_6H_3$}$_2$].

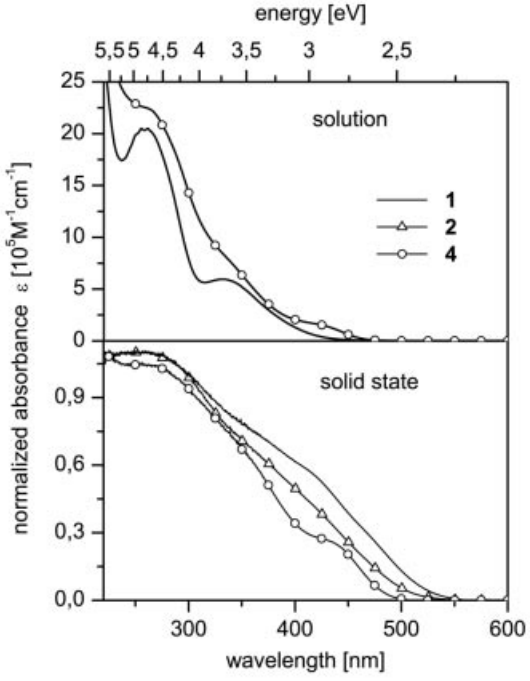

Figure 8. UV/Vis spectra of [Pb_{10}{S-2,6-$(CH_3)_2C_6H_3$}$_{20}$] (**1**), [Pb_6S{S-2,6-$(CH_3)_2C_6H_3$}$_{10}(C_4H_8O)_4$] (**2**), and [$Pb_{14}O_6${S-2,6-$(CH_3)_2C_6H_3$}$_{16}$] (**4**) in solution (THF) and the solid state (mull in nujol between two quartz plates).

These observations are currently part of further investigations where the effect of varying the reaction conditions (temperature, solvent, and stoichiometry) and the arenethiol are being studied. An additional focus will be the investigation of the reaction behavior of metal salts of the neighboring elements − tin, thallium and bismuth − with related thiols with a special focus on the formation of similar metal thiolate cluster complexes.

Experimental Section

General: Standard Schlenk techniques were employed throughout for the recrystallization of the preliminary reaction product using a double manifold vacuum line with high-purity dry nitrogen. All solvents were dried and distilled under nitrogen prior to use. Tetrahydrofuran and diethyl ether were dried with sodium/benzophenone, and pentane with $LiAlH_4$. $Pb(OOCCH_3)_2 \cdot 3H_2O$ (99+%) and 2,6-$(CH_3)_2C_6H_3$-SH (95%) were purchased from Aldrich. UV/Vis absorption spectra of cluster molecules in solution were measured with a Varian Cary 500 spectrophotometer in quartz cuvettes. Solid-state reflection spectra were measured for micron-sized crystalline powders between quartz plates with a Labsphere integrating sphere.

Synthesis: A hot solution (60 °C) of 2,6-$(CH_3)_2C_6H_3$SH (0.37 mL, 2.77 mmol) in 10 mL of ethanol was slowly added to a hot solution (60 °C) of $Pb(OOCCH_3)_2 \cdot 3H_2O$ (0.5 g, 1.32 mmol) in a mixture of 8 mL of C_2H_5OH and 2 mL of H_2O. A yellow precipitate was formed immediately which soon turned orange and finally became red. The reaction solution was heated at 60 °C for a further 30 min and then cooled to room temperature, filtered, washed with ethanol, and dried to give 0.49 g of an orange powder, which contained less sulfur than the expected product [Pb{S-2,6-$(CH_3)_2C_6H_3$}$_2$]. $C_{16}H_{18}PbS_2$ (481.64): calcd. C 39.9, H 3.8, S 13.31; found C 39.5, H 3.4, O 0.3, S 12.1.

1, 2, 3: For recrystallization the dried crude powder (0.49 g) was dissolved in 10 mL of THF and then layered with pentane by slow diffusion by evaporation from a connected flask to give a mixture of crystals of **1**, **2**, and **3**.

4: Pure crystals of **4** were obtained by dissolution of the crude powder (0.49 g) in 50 mL of THF and additional layering of this solution with pentane by slow diffusion by evaporation from a connected flask. (Yield: 0.063 g, 12.9% calculated for Pb). $C_{128}H_{144}O_6Pb_{14}S_{16}$ (5192.3): calcd. C 29.6, H 2.8, S 9.9; found C 29.9, H 2.6, S 10.2. Suitable crystals for X-ray analysis were obtained by careful layering of THF solutions of **4** with Et_2O in a Schlenk tube. The yield of **4** was increased by recrystallization of the crude powder (0.49 g) from 50 mL of THF in air without any layering with pentane. Yield: 0.29 g (56% calculated for Pb).

2: The solvents of the clear supernatant yellow solution from the crystallization of **4** were then removed in vacuo and the dry yellow-orange powder redissolved in 10 mL of THF. Layering of this solution with pentane by slow diffusion by evaporation from a connected flask yielded initially orange plate-like crystals of **2**, which tend to form solidified droplets of crystalline material during the layering process. After 2 d (ca. 6 mL of condensed pentane), the crystals were filtered and washed with pentane to yield 0.135 g (20.9% calculated for Pb) of **2**. $C_{96}H_{122}O_4Pb_6S_{11}$ (2935.9) (**2**·$4C_4H_8O$): calcd. C 39.3, H 4.2, S 12.1; found C 39.6, H 3.9, S 11.5.

1: The filtrate of **2** was again connected to the pentane flask and after 5 d yielded light-orange needles of **1**. Yield: 0.192 g (30.2% calculated for Pb). $C_{160}H_{180}Pb_{10}S_{20}$ (4816.3): calcd. C 39.9, H 3.8, S 13.3; found C 40.2, H 3.8, S 13.1. Continuation of the layering process resulted, at higher concentrations of condensed pentane, in the formation of a pale-yellow precipitate of unknown composition

 © 2005 Wiley-VCH Verlag GmbH & Co. KGaA, Weinheim

Crystallographic Data: Data collection was carried out with a STOE IPDS II diffractometer equipped with a Schneider rotating anode using graphite-monochromated Mo-K_α (λ = 0.71073 Å) radiation at 190 K. The structure solutions and full-matrix least-squares refinements based on F^2 were performed with the SHELX-97 program package.[19] Molecular diagrams were prepared with the program SCHAKAL 97.[20]

1: Light-orange needle-like plates, 0.5 × 0.08 × 0.06 mm, M_r = 4816.14, orthorhombic, space group *Pbcn* (no. 60), a = 31.217(6), b = 21.294(4), c = 30.898(6) Å, V = 20539(7) Å^3, Z = 4, D_c = 1.558 g cm^{-3}, μ(Mo-K_α) = 8.405 mm^{-1} giving a final R_1 value of 0.0672 for 856 parameters and 11 336 unique reflections with $I \geq 2\sigma(I)$ and wR_2 of 0.1830 for all 15 896 reflections (R_{int} = 0.0771).

2: Orange hexagonal plates, 0.24 × 0.18 × 0.02 mm, M_r = 2935.74, triclinic, space group $P\bar{1}$ (no. 2), a = 13.965(3), b = 14.819(3), c = 15.670(3) Å, α = 94.47(3), β = 114.44(3), γ = 115.45°, V = 2533.5(9) Å^3, Z = 1, D_c = 1.924 g cm^{-3}, μ(Mo-K_α) = 10.206 mm^{-1} giving a final R_1 value of 0.0486 for 479 parameters and 8632 unique reflections with $I \geq 2\sigma(I)$ and wR_2 of 0.1424 for all 10 378 reflections (R_{int} = 0.0598).

3: Yellow triclinic blocks, 0.2 × 0.127 × 0.08 mm, M_r = 3480.27, triclinic, space group $P\bar{1}$ (no. 2), a = 14.637(3), b = 15.278(3), c = 15.491(3) Å, α = 97.20(3), β = 108.18(3), γ = 118.38(3)°, V = 2736.0(9) Å^3, Z = 1, D_c = 2.112 g cm^{-3}, μ(Mo-K_α) = 12.536 mm^{-1} giving a final R_1 value of 0.0556 for 552 parameters and 8149 unique reflections with $I \geq 2\sigma(I)$ and wR_2 of 0.1584 for all 10 265 reflections (R_{int} = 0.0602).

4: Yellow plate-like needles, 0.4 × 0.07 × 0.04 mm, M_r = 5192.05, triclinic, space group $P\bar{1}$ (no. 2), a = 15.948(3), b = 17.919(4), c = 18.273(4) Å, α = 109.42(3), β = 100.93(3), γ = 112.51(3)°, V = 4238.1(15) Å^3, Z = 1, D_c = 2.034 g cm^{-3}, μ(Mo-K_α) = 14.083 mm^{-1} giving a final R_1 value of 0.0840 for 428 parameters and 12 414 unique reflections with $I \geq 2\sigma(I)$ and wR_2 of 0.2377 for all 16 723 reflections (R_{int} = 0.0872).

CCDC-246835 (**1**), -246836 (**2**), -246837 (**3**) and -246838 (**4**) contain the supplementary crystallographic data for this paper. These data can be obtained free of charge from The Cambridge Crystallographic Data Centre via www.ccdc.cam.ac.uk/data_request/cif. X-ray powder diffraction patterns (XRD) were measured with a STOE STADI P diffractometer (Cu-K_α radiation, Germanium monochromator, Debye–Scherrer geometry) as a suspension of the crystals in sealed glass capillaries. Theoretical powder diffraction patterns were calculated on the basis of the atom coordinates obtained from single-crystal X-ray analysis by using the program package STOE WinXPOW.[21]

Acknowledgments

This work was supported by the Deutsch-Israelisches Programm (DIP) and the Deutsche Forschungsgemeinschaft (center for functional nanostructures CFN). The author is grateful to Prof. D. Fenske for helpful discussions and for providing excellent working conditions, E. Tröster for her invaluable assistance in the practical work, and Dr. Dale Cave for careful revision of the manuscript.

[1] E. Lifshitz, M. Bashouti, V. Kloper, A. Kigel, M. S. Eisen, S. Berger, *Nano Lett.* **2003**, *3*, 857–862.
[2] B. L. Wehrenberg, C. Wang, P. Guyot-Sionnest, *J. Phys. Chem. B* **2002**, *106*, 10 634–10 640.
[3] H. Du, C. Chen, R. Krishnan, T. D. Krauss, J. M. Harbold, F. W. Wise, M. G. Thomas, J. Silcox, *Nano Lett.* **2002**, *2*, 1321–1324.
[4] A. Olkhovets, R. C. Hsu, A. Lipovskii, F. W. Wise, *Phys. Rev. Lett.* **1998**, *81*, 3539–3542.
[5] S. Dehnen, A. Eichhöfer, D. Fenske, *Eur. J. Inorg. Chem.* **2002**, 279–317.
[6] A. Eichhöfer, P. Deglmann, *Eur. J. Inorg. Chem.* **2004**, 349–355.
[7] M. W. DeGroot, J. F. Corrigan, *J. Chem. Soc., Dalton Trans.* **2000**, 1235–1236.
[8] R. A. Shaw, M. Woods, *J. Chem. Soc. (A)* **1971**, 1569–1571.
[9] A. D. Rae, D. C. Craig, I. G. Dance, M. L. Scudder, P. A. Dean, M. A. Kmetic, N. C. Payne, J. J. Vittal, *Acta Crystallogr., Sect. B* **1997**, *53*, 457–465.
[10] B. Krebs, A. Brömmelhaus, B. Kersting, M. Niehaus, *Eur. J. Solid State, Inorg. Chem.* **1992**, *29*, 167–180 supplement.
[11] S. E. Appleton, G. G. Briand, A. Decken, A. S. Smith, *Dalton Trans.* **2004**, 3515–3520.
[12] P. B. Hitchcock, M. F. Lappert, B. J. Samways, E. L. Weinberg, *J. Chem. Soc., Chem. Commun.* **1983**, 1492–1494.
[13] F. T. Edelmann, J.-K. F. Buijink, S. A. Brooker, R. Herbst-Irmer, U. Kilimann, F. M. Bohnen, *Inorg. Chem.* **2000**, *39*, 6134–6135.
[14] A. F. Holleman, E. Wiberg, *Lehrbuch der Anorganischen Chemie*, 101st ed., Walter de Gruyter, Berlin, New York, **1995**, p. 977.
[15] A. Eichhöfer, O. Hampe, M. Blom, *Eur. J. Inorg. Chem.* **2003**, 1307–1314.
[16] H. E. Swanson, R. K. Fuyat, *National Bureau of Standards Circular* (U.S. Government Printing Office, Washington, D.C.), **1953**, vol. 539, p. 18.
[17] Y. Noda, K. Masumoto, S. Ohba, Y. Saito, K. Toriumi, Y. Iwata, I. Shibuya, *Acta Crystallogr., Sect. C* **1987**, *43*, 1443–1445.
[18] H. E. Swanson, E. Tatge, *National Bureau of Standards Circular* (U.S. Government Printing Office, Washington, D.C.), **1953**, vol. 539, p. 34.
[19] G. M. Sheldrick, *SHELX-97, Program for X-ray crystal structure determination and refinement*, University of Göttingen, Germany, **1997**.
[20] E. Keller, *SCHAKAL 97, A Computer Program for the Graphic Representation of Molecular and Crystallographic Models*, Universität Freiburg, Germany, **1997**.
[21] *STOE, WinXPOW*: STOE & Cie GmbH, Darmstadt, **2000**.

Received: August 6, 2004

 © 2005 Wiley-VCH Verlag GmbH & Co. KGaA, Weinheim

Titanium Triamidotriamine Compounds: Syntheses, Structures and Redox Properties

Ana M. Martins,*[a] José R. Ascenso,*[a] Cristina G. de Azevedo,[a] Alberto R. Dias,[a] M. Teresa Duarte,[a] Humberto Ferreira,[a] M. João Ferreira,[a] Rui T. Henriques,[b] M. Amélia Lemos,[c] Li Li,[a] and João F. da Silva[a]

Keywords: Amide ligands / Cyclic voltammetry / N ligands / Titanium

The preparation of 1,4,7-{NH(2-C_6H_4F)$SiMe_2$}$_3$-1,4,7-triazacyclononane ($H_3N_{3\text{-}F}[9]N_3$) and 1,4,8-{N(H)Ph$SiMe_2$}$_3$-1,4,8-triazacycloundecane ($H_3N_3[11]N_3$), and their sodium derivatives $Na_3N_{3\text{-}F}[9]N_3(THF)_2$ and $Na_3N_3[11]N_3(THF)_2$, is described. The reaction of [$TiCl_3(THF)_3$] with $Na_3N_{3\text{-}F}[9]N_3(THF)_2$ and $Na_3N_3[11]N_3(THF)_2$ leads to [Ti{$N_{3\text{-}F}[9]N_3$}] and [Ti{$N_3[11]N_3$}]. The titanium complexes react readily with I_2 to give the Ti^{IV} derivatives [Ti{$N_{3\text{-}F}[9]N_3$}]I and [Ti{$N_3[11]N_3$}]I. All titanium compounds display distorted trigonal prismatic geometries where the metal is coordinated to the six nitrogen donors. Fluxional processes that convert the conformations of the five- and six-membered metallacycles and the Δ and Λ enantiomers of [Ti{$N_3[11]N_3$}]I have been identified in solution.
(© Wiley-VCH Verlag GmbH & Co. KGaA, 69451 Weinheim, Germany, 2005)

Introduction

The *N*-functionalization of azamacrocycles has been extensively explored as a method to design new ligand frameworks for metal cations. Several substituents and synthetic methodologies have been described and aspects such as structures, stabilities and physical properties have been broadly explored for many compounds. Despite the large number of transition-metal complexes of polyaza macrocyclic ligands bearing functionalized pendant arms reported in the literature,[1–3] the number of compounds displaying amide-tacn fragments as metal donors is much lower.[4–8] In this context we have reported the synthesis of a new six-donor triamidotriamine ligand precursor derived from tacn by introducing three $Si(Me)_2N(H)Ph$ pendant arms on the nitrogen atoms, and the preparation and characterisation of several triamide-tacn metal derivatives.[9,10] The ligand is hexacoordinate in all these complexes, irrespective of the size or oxidation state of the metals used (Ti, lanthanides, U). With the aim of modifying the donor properties of the original set and reduce the ligands' hapticity, with concomitant release of coordination positions at the metal centres, we introduced *ortho*-fluorine substituents in the phenyl rings and increased the macrocyclic framework and replaced tacn with triazacycloundecane (tacu). Although this goal has not been attained, we describe here the syntheses and characterisation of the new ligand precursors together with their sodium, Ti^{III} and Ti^{IV} derivatives. To the best of our knowledge, Ti-tacu complexes have not been reported before. Cyclic voltammetry results are also presented.

[a] Centro de Química Estrutural, Complexo Interdisciplinar, Instituto Superior Técnico,
Av. Rovisco Pais, 1, 1049-001 Lisboa, Portugal
E-mail: ana.martins@ist.utl.pt
[b] Instituto Superior Técnico,
Av. Rovisco Pais, 1, 1049-001 Lisboa, Portugal
[c] Centro de Engenharia Biológica e Química, Instituto Superior Técnico,
Av. Rovisco Pais, 1, 1049-001 Lisboa, Portugal

Results and Discussion

The reaction sequence used to synthesize 1,4,7-[{N(H)-2-C_6H_4F}$SiMe_2$]$_3$-triazacyclononane (**1**, $H_3N_{3\text{-}F}[9]N_3$), 1,4,8-{N(H)Ph$SiMe_2$}$_3$-triazacycloundecane (**2**, $H_3N_3[11]N_3$) and their sodium derivatives $Na_3N_{3\text{-}F}[9]N_3(THF)_2$ (**3**) and $Na_3N_3[11]N_3(THF)_2$ (**4**) is presented in Scheme 1. $H_3N_{3\text{-}F}[9]N_3$ (**1**) and $H_3N_3[11]N_3$ (**2**) were obtained in quantitative yields from the corresponding triazamacrocycle trihydrochloride derivatives.[11,12] $Na_3(THF)_2N_{3\text{-}F}[9]N_3$ (**3**) and $Na_3(THF)_2N_3[11]N_3$ (**4**) were also isolated in quantitative yields from THF from the reaction of **1** and **2** with NaH, respectively.

The characterization data of **1**–**4** are consistent with their formulation as trisubstituted macrocycle derivatives. The NMR spectra of $H_3N_{3\text{-}F}[9]N_3$ and $H_3N_3[11]N_3$ reveal C_{3v} and C_{2v} symmetry, respectively, compatible with fast nitrogen inversion of the macrocyclic amines. On the other hand, in the proton spectra of **3** and **4** the macrocyclic resonances are split into two groups that were identified by NOE difference experiments as the protons pointing towards the $SiMe_2$ pendant arm groups (H_{syn}) and opposite to them (H_{anti}). The differentiation between *syn* and *anti* protons is indicative of the coordination of the macrocyclic amines to the

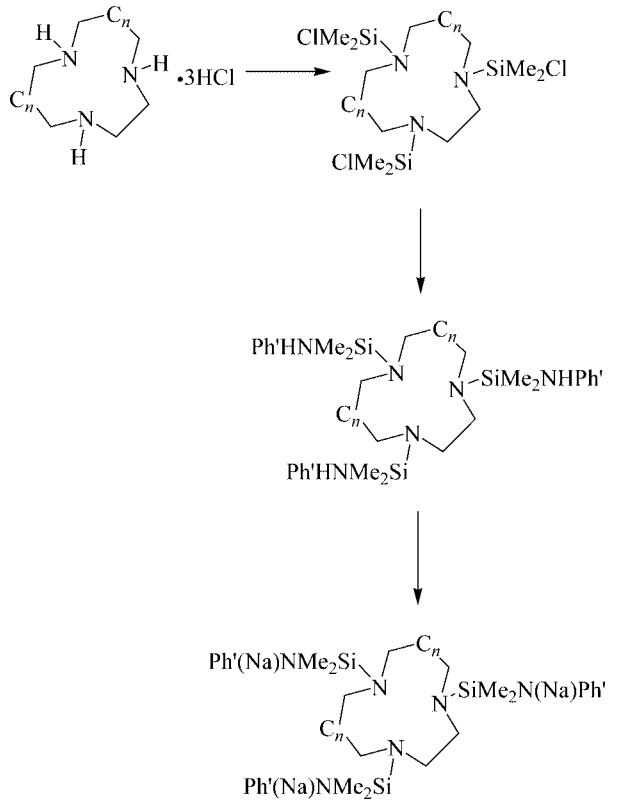

Scheme 1. Syntheses of triazacyclononane and triazacycloundecane ligand precursors. C_n = 0, 1; Ph′ = C_6H_5, *o*-C_6H_4F.

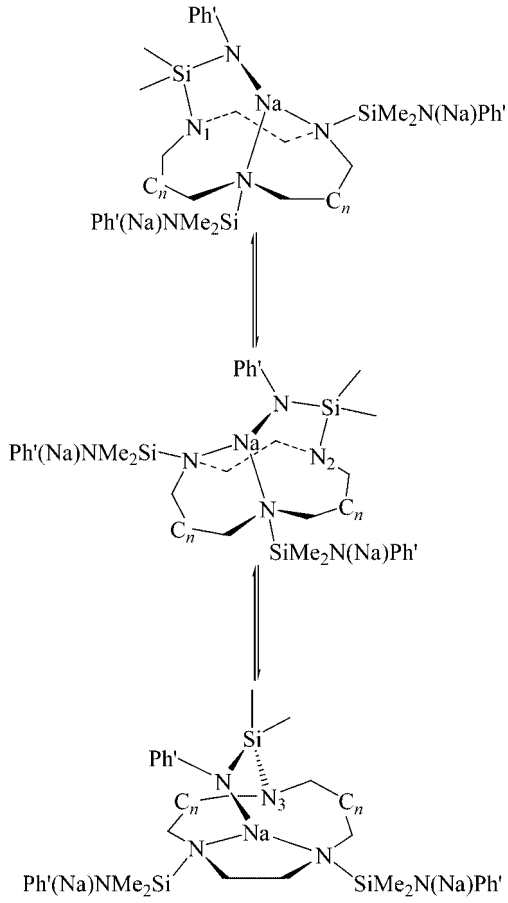

Scheme 2. Fluxional process responsible for the average C_3 and C_s symmetry of **3** and **4**, respectively. C_n = 0, 1; Ph′ = C_6H_5, *o*-C_6H_4F.

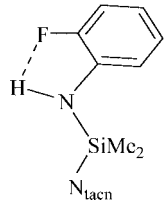

Scheme 3.

sodium cations and attests that, in these conditions, the macrocycle nitrogen inversion is slow on the NMR timescale. Although we have not been able to grow crystals of $Na_3(THF)_2N_{3\text{-}F}[9]N_3$ and $Na_3(THF)_2N_3[11]N_3$ suitable for X-ray structural determination, the similarity between the ^1H and ^{13}C NMR spectra of these compounds and those of $Li_3(THF)_2N_3[9]N_3$ suggests that, in solution, comparable fluxional processes take place.[9] As shown in Scheme 2, the fast exchange between the metals that occupy endocyclic and exocyclic positions creates average C_3 and C_s symmetries for **3** and **4**, respectively. In the case of the tacn derivative **3** this process makes all the pendant arms and macrocyclic carbons equivalent, but for **4**, two sets of resonances owing to the pendant arms (integrating 2:1) and four carbon macrocyclic resonances result. The ^{19}F NMR spectrum of **1** shows a doublet at δ = –57.5 ppm, with coupling constant of 3.9 Hz that results from the coupling with the NH groups through the intramolecular formation of five-membered rings, as represented in Scheme 3.

Treatment of $[TiCl_3(THF)_3]$ with one equivalent of $Na_3(THF)_2N_{3\text{-}F}[9]N_3$ or $Na_3(THF)_2N_3[11]N_3$ in toluene led to the synthesis of $[Ti\{N(2\text{-}FPh)SiMe_2\}_3(tacn)]$ (**5**, $[Ti\{N_{3\text{-}F}[9]N_3\}]$) and $[Ti\{N(Ph)SiMe_2\}_3(tacu)]$ (**6**, $[Ti\{N_3[11]N_3\}]$), respectively (Scheme 4). As expected for paramagnetic compounds, the ^1H NMR spectra of **5** and **6** show broad resonances for all the protons. Large paramagnetic shifts are observed for the macrocyclic protons adjacent to the nitrogens that appear at δ = 5.31 ppm in **5** and δ = 6.27 ppm in **6**. The EPR spectrum of a crystal of **5** at room temperature consists of a symmetrical single line. In solution, at 22 K, a more complex spectrum with g_{av} = 1.953 is obtained, whose hyperfine structure may arise from coupling with fluorine or with ^{47}Ti and ^{49}Ti. The spectral resolution does not allow us to estimate a coupling constant but it is likely that it results from electron coupling to ^{19}F given that coupling to titanium isotopes is rarely observed and has not been detected in the EPR spectrum of the non-fluorinated analogue $[Ti\{N_3[9]N_3\}]$.[9] The solution EPR spectrum of **6** at 298 K shows a symmetrical single line, with g_{av} = 1.944.

Orange crystals of **5** and **6** were grown from toluene solutions at 4 °C. ORTEP illustrations of their molecular structures, as determined by single-crystal X-ray diffraction, are represented in Figure 1 and Figure 2, respectively, and corresponding selected bond length and angles are listed in Table 1 and Table 2.

 © 2005 Wiley-VCH Verlag GmbH & Co. KGaA, Weinheim

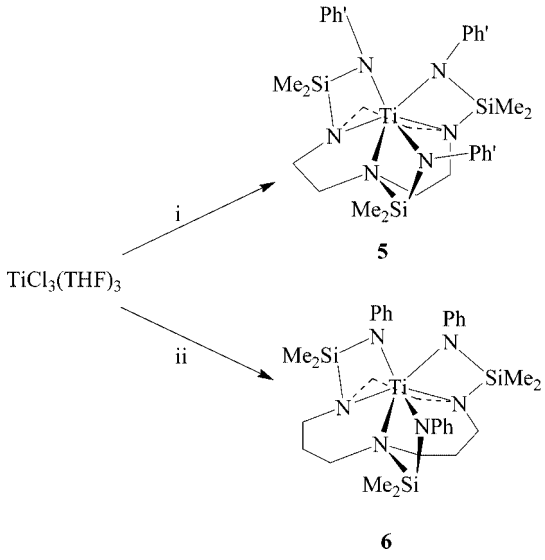

Scheme 4. i) $Na_3N_{3\text{-}F}[9]N_3$, Ph′ = *o*-C_6H_4F; ii) $Na_3N_3[11]N_3$.

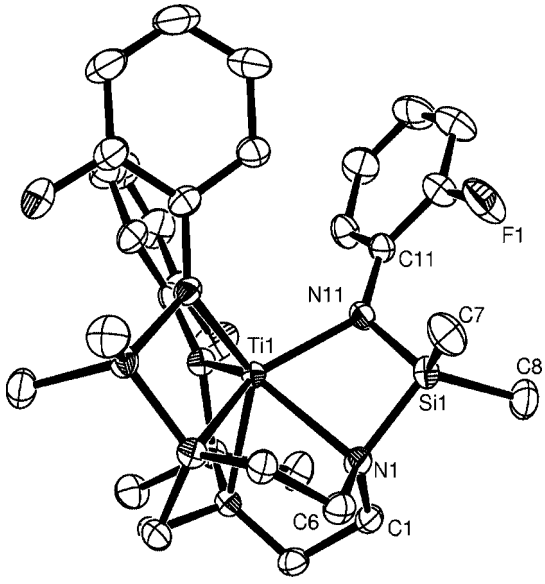

Figure 1. Molecular diagram of compound **5** showing the atomic labelling scheme (ellipsoids at 30% probability level).

In both compounds the metal coordination geometry is best described as distorted trigonal prismatic with three triazamacrocyclic amines and three pendant arm amides bonded to the titanium. Complex **5** crystallizes in the cubic space group $P2_13$ with twist angles between the amide and amine fragments, ϑ, defined by the dihedral angles N_{amino}–cent1–cent2–N_{amido} {N_{amine} and N_{amide} belong to the same pendant arm and cent1 and cent2 are the dummy centroid atoms defined respectively by the three N_{amine} [N(1), N(2), N(3)] and the three N_{amide} atoms [N(11), N(21), N(31)]}[11] of –8.4°, whereas **6** crystallizes in the triclinic space group $P\bar{1}$ with twist angles of –21.1°, –25.8° and –32.2°. The angle between the N(1)–N(2)–N(3) and N(11)–N(21)–N31 planes is 5.5° and the angle cent1–Ti–cent2 is 176.5° for **6** and, obviously, 0° and 180° for **5**. The higher asymmetry reflected by these angles when compared to tacn analogues is

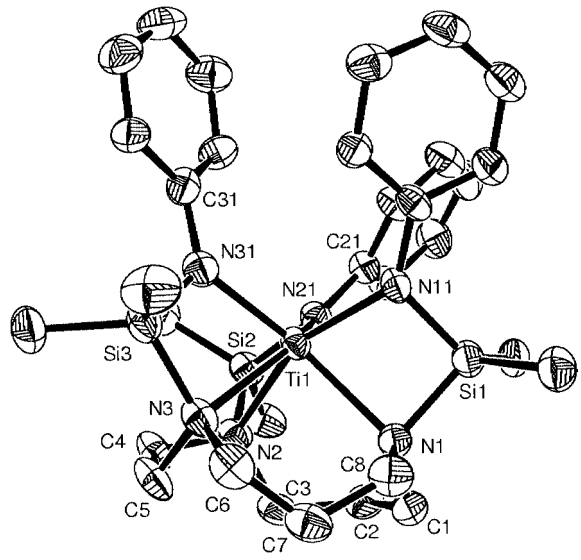

Figure 2. Molecular diagram of compound **6** showing the atomic labelling scheme (ellipsoids at 30% probability level).

a consequence of the different lengths of the tacu methylenic chains.

The distances between the metal and the N_{amine} and N_{amide} planes are 1.65 Å and 0.88 Å in **5** and 1.15 Å and 0.91 Å in **6**, respectively. The longer Ti–N_{tacn} distances compared to Ti–N_{tacu} show the ability of the larger macrocycle chains to adapt to the metal–nitrogen bonding requirements.[14] As it has a larger cavity, the triazacycloundecane ring accommodates the metal cation better than triazacyclononane and thus the metal–amine bonds become shorter. The cooperative effects between the two types of donor fragments is well expressed by the Ti–N_{amide} bond lengths, which follow the opposite trend; that is, the Ti–N_{amide} distances in **5** are shorter than those in **6**. The metal–nitrogen bond length variations are accompanied by different N(i)–Si(i)–N(ij) angles, which are slightly larger in **6** than in **5**. A comparison between the molecular structural parameters of [Ti{$N_{3\text{-}F}[9]N_3$}] and [Ti{$N_3[9]N_3$}] shows that the introduction of the fluorides do not alter the metal···ligand distances significantly, nor the overall coordination geometry. However, the close F···H contacts with the $Si(CH_3)_2$ hydrogens (2.30 Å and 2.73 Å) found in **5** might have induced a more constrained structure than that of [Ti{$N_3[9]N_3$}], thus inducing the crystallization in the cubic space group. Other differences between the two complexes refer to the stereochemical conformation of the TiN-$(CH_2)_2$N metallacycles and to the orientation of the shift between the N_{amido} and N_{amine} planes that is expressed by the twist angles defined above. The configuration of [Ti{$N_3[9]N_3$}] in the solid state was shown to be Δ(λλλ)/Λ(δδδ) whereas that of **5** is Λ(λλλ)/Δ(δδδ).

The two six-membered metallacycles defined by the titanium and the NC_3N chains in **6** display different conformations. The TiN(1)C(8)C(7)C(9)N(3) ring defines a chair conformation while Ti(N1)C(1)C(2)C(3)N(2) has a boat conformation. These arrangements have also been found in [Cu(tacu)Br_2] which is, according to a search performed in

 © 2005 Wiley-VCH Verlag GmbH & Co. KGaA, Weinheim

Table 1. Selected bond lengths [Å] and angles [°] for [Ti{$N_{3\text{-}F}$[9]N_3}] (**5**) and [Ti{$N_{3\text{-}F}$[9]N_3}]I (**7**).

	5	**7**
Ti(1)–N(1)	2.326(3)	2.262(14)
Ti(1)–N(2)	–	2.259(13)
Ti(1)–N(3)	–	2.266(15)
Ti(1)–N(11)	2.078(2)	1.987(13)
Ti(1)–N(21)	–	1.997(13)
Ti(1)–N(31)	–	1.969(12)
N(1)–C(1)	1.490(4)	1.550(18)
Plane[N(1)–N(2)–N(3)]–Ti(1)	1.65(7)	1.60(9)
Plane[N(11)–N(21)–N(31)]–Ti(1)	0.88(7)	0.85(9)
N(1)–Ti(1)–N(11)	70.59(10)	70.1(5)
N(2)–Ti(1)–N(21)	–	72.5(5)
N(3)–Ti(1)–N(31)	–	70.8(5)
N(1)–Ti(1)–N(2)	75.21(10)	75.1(5)
N(2)–Ti(1)–N(3)	–	75.4(5)
N(3)–Ti(1)–N(1)	–	75.8(5)
N(11)–Ti(1)–N(21)	103.45(9)	103.5(5)
N(11)–Ti(1)–N(31)	–	103.0(6)
N(21)–Ti(1)–N(31)	–	104.5(5)
Plane[N(1)–N(2)–N(3)]–Plane[N(11)–N(21)–N(31)]	0	1.6
[N(1)–N(2)–N(3)][a]–Ti(1)–[N(11)–N(21)–N(31)][a]	180	178.1
N(1)–[N(1)–N(2)–N(3)][a]–[N(11)–N(21)–N(31)][a]–N(11)	–8.4	+ 16.3
N(2)–[N(1)–N(2)–N(3)][a]–[N(11)–N(21)–N(31)][a]–N(21)	–	+15.0
N(3)–[N(1)–N(2)–N(3)][a]–[N(11)–N(21)–N(31)][a]–N(31)	–	+ 14.4

[a] Centroid defined by the atoms in brackets.

Table 2. Selected bond lengths [Å] and angles [°] for one of the molecules of [Ti{N_3[11]N_3}] (**6**).

[Ti{N_3[11]N_3}]	
Ti(1)–N(1)	2.340(6)
Ti(1)–N(2)	2.311(5)
Ti(1)–N(3)	2.425(6)
Ti(1)–N(11)	2.074(5)
Ti(1)–N(21)	2.064(6)
Ti(1)–N(31)	2.057(6)
Plane[N(1)–N(2)–N(3)]–Ti(1)	1.48(3)
Plane[N(11)–N(21)–N(31)]–Ti(1)	0.90(3)
N(1)–Ti(1)–N(11)	70.1(2)
N(2)–Ti(1)–N(21)	70.8(2)
N(3)–Ti(1)–N(31)	69.3(2)
N(1)–Ti(1)–N(2)	90.1(2)
N(2)–Ti(1)–N(3)	74.7(2)
N(3)–Ti(1)–N(1)	86.9(2)
N(11)–Ti(1)–N(21)	100.0(2)
N(11)–Ti(1)–N(31)	101.4(2)
N(21)–Ti(1)–N(31)	105.7(2)
Plane[N(1)–N(2)–N(3)]–Plane[N(11)–N(21)–N(31)]	5.5 (3)
[N(1)–N(2)–N(3)][a]–Ti(1)–[N(11)–N(21)–N(31)][a]	176.5(9)
N(1)–[N(1)–N(2)–N(3)][a]–[N(11)–N(21)–N(31)][a]–N(11)	–25.8(10)
N(2)–[N(1)–N(2)–N(3)][a]–[N(11)–N(21)–N(31)][a]–N(21)	–32.2(12)
N(3)–[N(1)–N(2)–N(3)][a]–[N(11)–N(21)–N(31)][a]–N(31)	–21.1(10)

[a] Centroid defined by the atoms in brackets.

CCDC, the only triazacycloundecane complex characterised by X-ray diffraction.[15]

Treatment of **5** and **6** with iodine gave the corresponding Ti^{IV} derivatives [Ti{$N_{3\text{-}F}$[9]N_3}]I (**7**) and [Ti{N_3[11]N_3}]I (**8**). The ^{1}H NMR spectrum of **7** is compatible with an average C_3 symmetry in solution where the macrocyclic protons appear as two sets of resonances attributable to H_{syn} and H_{anti}. The ^{19}F NMR spectrum shows a broad singlet at δ = –41.2 ppm.

The molecular structure of **7** is depicted in Figure 3 and selected bond lengths and angles are reported in Table 1.

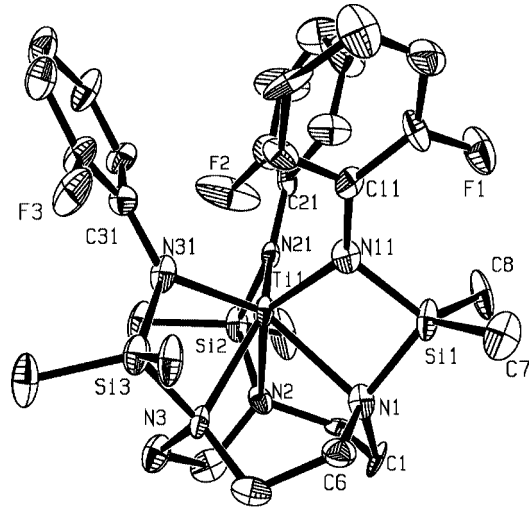

Figure 3. Molecular diagram of the cation of compound **7** showing the atomic labelling scheme (ellipsoids at 30% probability level).

In **7**, the titanium coordination geometry is best described as distorted trigonal prismatic with twist angles, ϑ, of 14.4°, 15.0° and 16.3°. The angle between the N(1)–N(2)–N(3) and N(11)–N(21)–N(31) planes is 1.6° and the angle cent1–Ti–cent2 is 178.1°. The amide nitrogen atoms are planar, with a sum of the angles around them of 359.6° for N(11), 359.8° for N(21) and 360.0° for N(31). The Ti–N_{amine} bond lengths range between 2.259 and 2.266 Å and the Ti–N_{amide} vary from 1.969 to 1.997 Å (see Table 1). Although slightly shorter than the values obtained for the Ti^{III}

 © 2005 Wiley-VCH Verlag GmbH & Co. KGaA, Weinheim

starting material, the metal···nitrogen distances in **7** are close to those found in cations $[Ti\{N_3[9]N_3\}]X$ (X = I, BPh_4), denoting that, once more, the *ortho*-fluorines have no significant influence on the ligand coordination. Similarly to **5**, short F···H distances (2.27–2.38 Å) between the fluoride and the $SiMe_2$ groups of each pendant arm are observed for **7**. The configuration of the five-membered $TiNC_2N$ metallacycles in **7** is the same as for **5** [Λ(λλλ)/Δ(δδδ)].

In CD_2Cl_2, at room temperature, the ^1H NMR spectrum of $[Ti\{N_3[11]N_3\}]I$ (**8**) is consistent with an average C_s symmetry, displaying two sets of aromatic resonances corresponding to the phenyl rings and three singlets for the six CH_3 groups of the bridging dimethylsilyl groups. The C_2-chain methylenic protons lead to different H_{syn} and H_{anti} resonances at δ = 3.39 and 3.68 ppm, respectively, and the C_3-chain protons give rise to four multiplets centred at δ = 2.37 and 2.05 ppm, corresponding to the H_{syn} and H_{anti} protons of the middle of the chain, and at δ = 3.47 and 3.30 ppm corresponding to the H_{syn} and H_{anti} protons adjacent to the nitrogen atoms. This pattern reveals that the three exchange processes available to the molecule at room temperature, namely the trigonal twist of the N_{amine} and N_{amide} planes, which corresponds to the equilibrium between the two possible enantiomers Δ and Λ, the δ/λ interconversion of the five-membered metallacycle and the chair/boat interconversion are fast processes on the NMR timescale (Scheme 5). At –40 °C, the dimethylsilyl protons split into five singlets and the three phenyl rings become non-equivalent, implying that the δ/λ isomerisation is blocked at that temperature. The C_2 macrocyclic protons pattern broadens as a consequence of the splitting into an ABCD system that partially overlaps the C_3 chain resonances. The two other fluxional processes are still operative, as revealed by the equivalence of the two methyl groups of the pendant arm bonded to the nitrogen between the two C_3 macrocyclic chains. At –70 °C these protons also become non-equivalent. Six different methyl resonances and the appearance of a series of interpenetrating multiplets due to non-equivalent macrocyclic protons are indicative that the equilibrium between the two enantiomers is blocked.

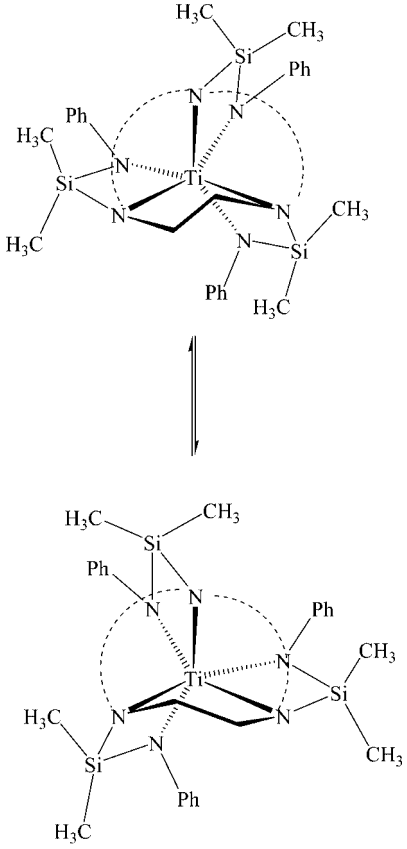

Scheme 5. Exchange processes responsible for the average C_s symmetry of $[Ti\{N_3[11]N_3\}]I$ (**8**).

To evaluate the donor ability of the $N_3[9]N_3$ and $N_{3\text{-}F}[9]N_3$ sets used we performed cyclic voltammetry measurements of complexes $[Ti\{N_{3\text{-}F}[9]N_3\}]$ (**5**), $[Ti\{N_{3\text{-}F}[9]N_3\}]I$ (**7**) and $[Ti\{N_3[9]N_3\}]X$ (X = I, **9**, BPh_4, **10**)[9] in acetonitrile at variable scan rates. The results are listed in Table 3.

Table 3. Electrochemical data for complexes **5**, **7**, **9** and **10**.

Compound[a]	$E^{red}_{1/2}$ [V]	$E^{ox}_{1/2}$ [V]	Solvent
$[Ti\{N_{3\text{-}F}[9]N_3\}]$		–1.59	CH_3CN
$[Ti\{N_{3\text{-}F}[9]N_3\}]I$	–1.58	–0.22	CH_3CN
$[Ti\{N_3[9]N_3\}]\ BPh_4$	–1.71		CH_3CN
	–1.78		CH_2Cl_2
$[Ti\{N_3[9]N_3\}]I$	–1.71	–0.20	CH_3CN

[a] At 25 °C, 6.5×10^{-2} M $(Bu_4N)BPh_4$, 10^{-3} M $FeCp_2$. All potentials were recorded at 200 mV s^{-1}.

The first remark concerns the stability of the different complexes in the medium. Triazacycloundecane derivatives are, in general, less stable than the triazacyclononane-based complexes and this characteristic prevents their study by cyclic voltammetry. The stability of the cations is higher than that of the reduced metal complexes and thus $[Ti\{N_3[9]N_3\}]$ and $[Ti\{N_3[11]N_3\}]$ are not suitable starting materials for CV measurements. Remarkably, $[Ti\{N_{3\text{-}F}[9]N_3\}]$ is much more stable than the other Ti^{III} compounds and, in acetonitrile, a reversible one-electron oxidation at $E^{ox}_{1/2}$ = –1.59 V was detected at a scan rate of 200 mV s^{-1}. Cationic tacn derivatives show reversible one-electron reduction peaks. Figure 4 shows the cyclic voltammogram of $[Ti\{N_3[9]N_3\}]BPh_4$ (**10**) as an example.

The values listed in Table 3 show that the redox potentials for the Ti^{IV}/Ti^{III} couple in complexes **9** and **10** are lower than the values reported for metallocene titanium dichlorides such as $[Cp_2TiCl_2]$, $[Cp^*_2TiCl_2]$ and $[(C_5H_4SiMe_3)_2TiCl_2]$, for which $E^{red}_{1/2}$ values range from –1.295 to –1.621 mV.[16–18] On the other hand, the value of –1.58 mV measured for $E^{red}_{1/2}$ of **7** reflects the additional stability of the LUMO when C_6H_5 is replaced by *o*-C_6H_4F. The similarity between the reduction potential of **7** and that of $[Ti\{O_3[9]N_3\}]PF_6$ ($H_3O_3[9]N_3$ = 1,4,7-tris(5-*tert*-butyl-2-hydroxybenzyl)-1,4,7-triazacyclononane; $E^{red}_{1/2}$ = –1.52 mV) shows that the donor ability of the amide moieties in **7** is comparable to that of the alkoxide fragments in $[Ti\{O_3[9]N_3\}]PF_6$.[17] The voltammograms of **7** and **9** display addition redox

 © 2005 Wiley-VCH Verlag GmbH & Co. KGaA, Weinheim

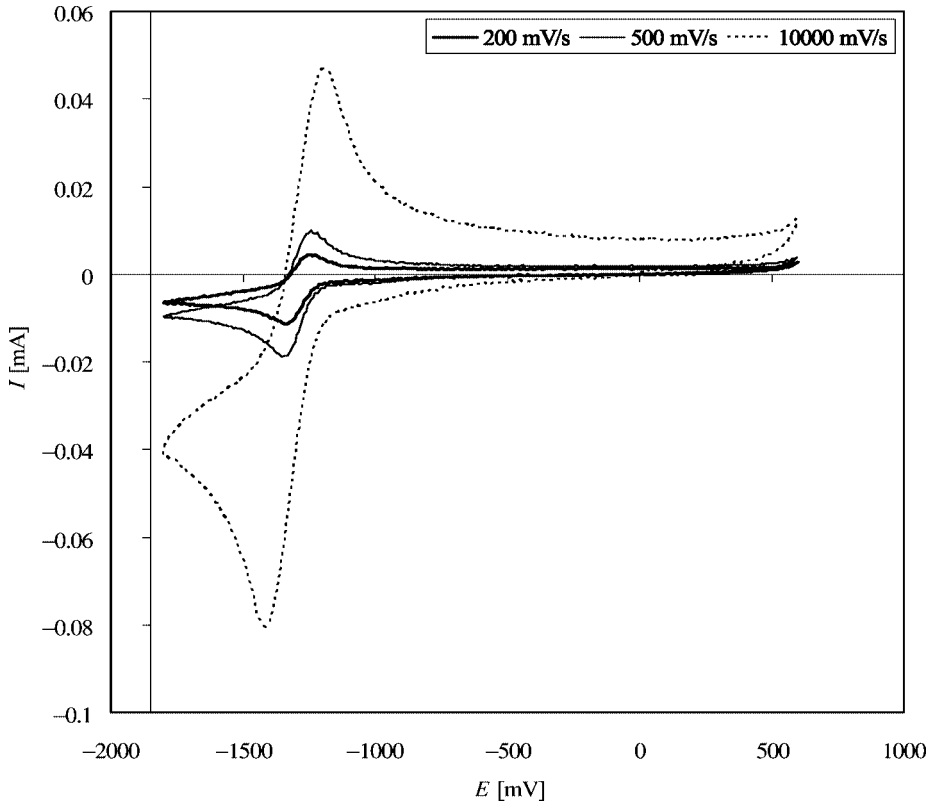

Figure 4. Cyclic voltammogram of [Ti{N_3[9]N_3}]BPh_4 (**10**) in [Bu_4N]BPh_4/CH_3CN, at scan rates of 200 mV s^{-1}, 500 mV s^{-1} and 1000 mV s^{-1}.

peaks at –0.22 V and –0.20 V, respectively, that are due to the I^- counterion.

Experimental Section

General Procedures and Starting Materials: All reactions were conducted under a nitrogen atmosphere. Solvents were pre-dried with 4 Å molecular sieves and refluxed over sodium-benzophenone (diethyl ether, tetrahydrofuran, *n*-hexane and toluene) or calcium hydride (dichloromethane) under an atmosphere of nitrogen, and collected by distillation. Deuterated solvents were dried with molecular sieves and freeze-pump-thaw degassed prior to use. Proton (300 MHz) and carbon (75.419 MHz) NMR spectra were recorded with a Varian Unity 300, at 298 K, unless stated otherwise. The spectra are referenced to internal residual protio-solvent (^1H) or solvent (^{13}C) resonances and reported relative to tetramethylsilane (δ = 0 ppm). Assignments were supported by NOE difference experiments and by ^{13}C-^1H hetero-correlations, as appropriate. EPR spectra were recorded at room temperature with a Bruker 300E spectrometer at X-band frequency ($\nu \approx 9.5$ GHz). Mass spectra were performed at the Laboratoire de Spectrométrie de Masse, Université de Rouen, France. Elemental analyses were obtained from the Laboratório de Análises do IST, Lisbon, Portugal.

Triethylamine, aniline, $SiMe_2Cl_2$, $TiCl_3$ and NaH (60% dispersion in mineral oil) were purchased from Aldrich. NEt_3 and NH_2Ph were pre-dried with molecular sieves, refluxed over calcium hydride, and collected by distillation. $SiMe_2Cl_2$ was purified by removal of residual HCl and then distilled trap-to-trap. NaH was washed with THF prior to use. [$TiCl_3(THF)_3$],[19] tacn·3HCl,[11] tacu·3HCl,[12] and 1,4,7-$(SiMe_2Cl)_3$-tacn[9] were prepared according to described procedures.

Cyclic voltammetric measurements were carried out with a Radiometer DEA 101 Digital Electrochemical Analyser interfaced with an IMT 102 Electrochemical Interface. [Bu_4N][BPh_4] (Fluka, electrochemical grade) was used as supporting electrolyte in CH_2Cl_2 or CH_3CN with a concentration of 6.5×10^{-2} M. All experiments were performed with concentrations of complexes in the range 2–4×10^{-3} M. All potentials are referenced to the ferrocene/ferrocenium couple as internal standard with $E_{1/2}$ = 0.50 V vs. S.C.E. A Pt disc (φ = 1 mm) was used as working electrode. The solvents were distilled immediately before use. All experiments were carried out at 25 °C in the absence of oxygen. Dry nitrogen was bubbled through the solution in the cell before measurements.

1,4,7-[{N(H)(2-C_6H_4F)}$SiMe_2$]$_3$-tacn (1): 2-Fluoraniline (2.1 mL, 21.9 mmol) was added to a suspension of NaH (0.95 g, 39.6 mmol) in THF. The mixture was heated to 60 °C and stirred for 12 h. The excess of NaH was filtered off and washed with 20 mL of THF, at room temperature. The filtrates were added dropwise to a solution of 1,4,7-$(SiMe_2Cl)_3$-tacn (2.74 g, 6.74 mmol) in toluene (80 mL), cooled to –40 °C. The mixture was warmed to room temperature and stirred for 12 h. The solvents were evaporated and the residue was extracted in hexane and filtered. Evaporation to dryness led to a very viscous yellow oil in quantitative yield (4.25 g). ^1H NMR (C_6D_6): δ = 6.94–6.90 (m, 3 H, H_{meta}), 6.88–6.87 (m, 3 H, H_{meta}), 6.85–6.82 (m, 3 H, H_{ortho}), 6.55–6.48 (m, 3 H, H_{para}), 3.77 (d, $J_{H,F}$ = 3.9 Hz, 3 H, N*H*), 2.89 (s, 12 H, NCH_2CH_2N), 0.09 (s, 18 H, CH_3) ppm. $^{13}C\{^1H\}$ NMR (C_6D_6): δ = 153.1 (d, $^1J_{C,F}$ = 236.0 Hz, C_{ortho}), 135.8 (d, $^2J_{C,F}$ = 13.0 Hz, C_{ipso}), 124.8 (d, $^4J_{C,F}$ = 3.5 Hz, C_{meta}), 118.0 (d, $^3J_{C,F}$ = 7.0 Hz, C_{para}), 117.2 (d, $^3J_{C,F}$ = 3.5 Hz,

 © 2005 Wiley-VCH Verlag GmbH & Co. KGaA, Weinheim

C$_{ortho}$), 115.3 (d, $^2J_{C,F}$ = 20.0 Hz, *C*$_{meta}$), 50.5 (N*C*H$_2$*C*H$_2$N), –1.4 (*C*H$_3$) ppm. ^{19}F NMR (C$_6$D$_6$): δ = –57.47 ppm. $C_{30}H_{45}N_6F_3Si_3$ (630.98): calcd. C 57.08, H 7.19, N 13.33; found C 57.06, H 7.20, N 13.20. MS (EI): *m*/*z* = 630 [M]$^+$.

1,4,8-[SiMe$_2$Cl]$_3$-tacu: A suspension of tacu·3HCl (1.06 g, 3.97 mmol) in CH_2Cl_2 (50 mL), cooled to 0 °C, was treated with Et_3N (6,0 mL, 40 mmol). The mixture was stirred during 15 minutes and $SiMe_2Cl_2$ (3.0 mL, 24 mmol) was added. The reaction proceeded overnight at room temperature and a precipitate formed. The volatiles were then evaporated under vacuum and the residue was extracted with hexane and filtered. Evaporation of the hexane led to a white solid in quantitative yield (1.72 g). The reaction was scaled up to 20 mmol of tacu·3HCl. ^{1}H NMR (C$_6$D$_6$): δ = 2.90 (s, 4 H, NC*H*$_2$C*H*$_2$N), 2.83 [t, $^3J_{H,H}$ = 6.9 Hz, 4 H, N(CH$_2$)$_2$C*H*$_2$N(CH$_2$)$_2$N], 2.65 [t, $^3J_{H,H}$ = 6.9 Hz, 4 H, (CH$_2$)$_2$-C*H*$_2$NC*H*$_2$(CH$_2$)$_2$], 1.53 (quint., $^3J_{H,H}$ = 6.9 Hz, 4 H, NCH$_2$C*H*$_2$CH$_2$N), 0.29 (s, 12 H, SiC*H*$_3$), 0.27 (s, 6 H, SiC*H*$_3$) ppm. ^{13}C{^{1}H} NMR (C$_6$D$_6$): δ = 50.4 (N*C*H$_2$*C*H$_2$N), 46.2 [(CH$_2$)$_2$*C*H$_2$-N*C*H$_2$(CH$_2$)$_2$], 45.7 [N(CH$_2$)$_2$*C*H$_2$N(CH$_2$)$_2$N], 30.8 (NCH$_2$*C*H$_2$-CH$_2$N), 2.3 [(CH$_2$)$_3$N{Si(*C*H$_3$)$_2$}(CH$_2$)$_3$], 2.1 [(CH$_2$)$_3$N{Si(*C*H$_3$)$_2$}-(CH$_2$)$_2$] ppm. $C_{14}H_{34}N_3Cl_3Si_3$ (435.06): calcd. C 38.63, H 7.88, N 9.66; found C 38.55, H 7.96, N 9.55. MS (EI): *m*/*z* = 401 [M – Cl]$^+$.

1,4,8-[N(H)(C$_6$H$_5$)SiMe$_2$]$_3$-tacu (2): PhNH$_2$ (6.8 mL, 74 mmol) was added at 0 °C to a suspension of NaH (2.32 g, 93 mmol) in 100 mL of THF. The cooling bath was removed and, once the initial effervescence had stopped, the mixture was warmed at 60 °C for 12 h. The solution was filtered and the residue washed with THF (20 mL). The solution was transferred dropwise, at –40 °C, to a solution of 1,4,8-[ClSiMe$_2$]$_3$-tacu (10.24 g, 23.54 mmol) in 100 mL of toluene. The reaction took place at room temperature during 12 h and the volatiles were then evaporated. The residue was extracted with hexane and filtered off. Evaporation of the solvent led to 14.23 g of **2** (100%). ^{1}H NMR (C$_6$D$_6$): δ = 7.20–7.13 (m, 6 H, *H*$_{meta}$), 6.81–6.73 (m, 3 H, *H*$_{para}$), 6.67 (d, $^3J_{H,H}$ = 8.9 Hz, 4 H, *H*$_{ortho}$), 6.60 (d, $^3J_{H,H}$ = 8.9 Hz, 2 H, *H*$_{ortho}$), 3.15 (s, 2 H, N*H*), 3.12 (s, 1 H, N*H*), 3.02 (s, 4 H, NC*H*$_2$C*H*$_2$N), 2.73 [t, $^3J_{H,H}$ = 6.9 Hz, 4 H, (CH$_2$)$_2$C*H*$_2$NC*H*$_2$(CH$_2$)$_2$], 2.39 [t, $^3J_{H,H}$ = 6.9 Hz, 4 H, N(CH$_2$)$_2$C*H*$_2$N(CH$_2$)$_2$N], 1.63 (quint., $^3J_{H,H}$ = 6.9 Hz, 4 H, NCH$_2$C*H*$_2$CH$_2$N), 0.12 (s, 12 H, SiC*H*$_3$), 0.08 (s, 6 H, SiC*H*$_3$) ppm. ^{13}C{^{1}H} NMR (C$_6$D$_6$): δ = 147.4 (3 C, *C*$_{ipso}$), 129.5 (2 C, C$_{meta}$), 129.4 (4 C, C$_{meta}$), 118.3 (2 C, C$_{para}$), 118.2 (1 C, C$_{para}$), 116.9 (4 C, C$_{ortho}$), 116.8 (2 C, C$_{ortho}$), 50.2 (N*C*H$_2$*C*H$_2$N), 46.7 [(CH$_2$)$_2$*C*H$_2$N*C*H$_2$(CH$_2$)$_2$], 45.3 [N(CH$_2$)$_2$*C*H$_2$N(CH$_2$)$_2$N], 32.0 (NCH$_2$*C*H$_2$CH$_2$N), –1.05 [(CH$_2$)$_3$N{Si(*C*H$_3$)$_2$}(CH$_2$)$_3$], –1.08 [(CH$_2$)$_3$N{Si(*C*H$_3$)$_2$}(CH$_2$)$_2$] ppm. $C_{32}H_{52}N_6Si_3$ (605.06): calcd. C 63.50, H 8.67, N 13.90; found C 63.75, H 8.61, N 13.86. MS (EI): *m*/*z* = 604 [M]$^+$.

[1,4,7-{N(Na)(2-C$_6$H$_4$F)SiMe$_2$}$_3$-tacn]·2THF (3): A solution of 1,4,7-{[N(H)(2-C$_6$H$_4$F)]SiMe$_2$}$_3$-tacn (7.91 g, 12.54 mmol) in THF (25 mL) was added dropwise to a suspension of NaH (1.2 g, 50 mmol) in THF (100 mL). The mixture was then heated at 60 °C for 12 h. The solution was filtered off and the excess of NaH was washed with THF (30 mL). Evaporation of the THF led to a greenish solid in quantitative yield (10.54 g). ^{1}H NMR (C$_6$D$_6$): δ = 6.94 (m, 6 H, *H*$_{ortho}$, *H*$_{meta}$), 6.84 (t, $^3J_{H,H}$ = 6.6 Hz, 3 H, *H*$_{meta}$), 6.24 (m, 3 H, *H*$_{para}$), 3.41 (m, 8 H, OC*H*$_2$, THF), 3.07–2.95 (m, 6 H, C*H*$_2$, *syn*), 2.75–2.63 (m, 6 H, C*H*$_2$, *anti*), 1.30 (m, 8 H, C*H*$_2$, THF), 0.28 (s, 18 H, C*H*$_3$) ppm. ^{13}C{^{1}H} NMR (C$_6$D$_6$): δ = 158.1 (d, $^1J_{C,F}$ = 225.0 Hz, *C*$_{ortho}$), 149.5 (br., *C*$_{ipso}$), 125.1 (*C*$_{meta}$), 124.3 (*C*$_{ortho}$), 114.4 (d, $^2J_{C,F}$ = 24.0 Hz, *C*$_{meta}$), 110.3 (*C*$_{para}$), 67.9 (OCH$_2$, THF), 48.3 (NCH$_2$CH$_2$N), 25.6 (*C*H$_2$, THF), 0.1 (*C*H$_3$) ppm. ^{19}F NMR(C$_6$D$_6$): δ = –63.24 (m) ppm.

1,4,8-[{N(Na)(C$_6$H$_5$)SiMe$_2$}$_3$-tacu]·2THF (4): A solution of 1,4,8-[N(H)(C$_6$H$_5$)SiMe$_2$]$_3$-tacu (7.03 g, 11.62 mmol) in THF (ca. 25 mL) was added to a suspension of NaH (1.00 g, 42 mmol) in 100 mL of THF. The mixture was slowly warmed to 60 °C and stirred at this temperature for 12 h. After cooling to room temperature, the solution was filtered off and the NaH excess was washed with 30 mL of THF that was collected with the filtrate. The solvent was evaporated to dryness and a greenish powder was obtained by scratching the dried material under N_2, at liquid nitrogen temperature. Yield: 8.63 g, quantitative. ^{1}H NMR (C$_6$D$_6$): δ = 7.16 (t, $^3J_{H,H}$ = 7.2 Hz, 2 H, *H*$_{meta}$), 7.07 (t, $^3J_{H,H}$ = 6.9 Hz, 4 H, *H*$_{meta}$), 6.76 (t, $^3J_{H,H}$ = 7.2 Hz, 6 H, *H*$_{ortho}$), 6.58 (t, $^3J_{H,H}$ = 7.2 Hz, 1 H, *H*$_{para}$), 6.47 (t, $^3J_{H,H}$ = 6.9 Hz, 2 H, *H*$_{para}$), 3.27 (m, 8 H, OC*H*$_2$, THF), 2.86 [br. s, 6 H, NC*H*$_{syn}$H$_{anti}$CH$_2$C*H*$_{syn}$H$_{anti}$N(C*H*$_{syn}$H$_{anti}$)$_2$N], 2.56 [br. s, 2 H, N(CH$_{syn}$*H*$_{anti}$)$_2$N], 2.44 (br. s, 4 H, NCH$_{syn}$*H*$_{anti}$CH$_2$CH$_{syn}$-*H*$_{anti}$N), 1.67 (br. s, 2 H, NCH$_2$C*H*$_{syn}$H$_{anti}$CH$_2$N), 1.38 (br. s, 2 H, NCH$_2$CH$_{syn}$*H*$_{anti}$CH$_2$N), 1.24 (m, 8 H, C*H*$_2$, THF), 0.34 (s, 6 H, SiC*H*$_3$), 0.29 (s, 12 H, SiC*H*$_3$) ppm. ^{13}C{^{1}H} NMR (C$_6$D$_6$): δ = 161.1 (1 C, *C*$_{ipso}$), 160.4 (2 C, *C*$_{ipso}$), 130.7 (4 C, *C*$_{meta}$), 130.2 (2 C, *C*$_{meta}$), 122.9 (2 C, *C*$_{ortho}$), 121.8 (4 C, *C*$_{ortho}$), 113.3 (1 C, *C*$_{para}$), 113.2 (2 C, *C*$_{para}$), 67.8 (O*C*H$_2$, THF), 51.4 [(CH$_2$)$_2$*C*H$_2$-N*C*H$_2$(CH$_2$)$_2$], 50.7 [N(CH$_2$)$_2$*C*H$_2$N(CH$_2$)$_2$N], 49.0 [N(*C*H$_2$)$_2$N], 30.0 (NCH$_2$*C*H$_2$CH$_2$N), 25.5 (*C*H$_2$, THF), 1.2 [(CH$_2$)$_3$N{Si-(*C*H$_3$)$_2$}(CH$_2$)$_3$], 0.1 [(CH$_2$)$_3$N{Si(*C*H$_3$)$_2$}(CH$_2$)$_2$] ppm.

[Ti{N(2-C$_6$H$_4$F)SiMe$_2$}$_3$-tacn] (5): A solution of [1,4,7-{N(Na)(2-C$_6$H$_4$F)SiMe$_2$}$_3$-tacn]·2THF (2.30 g, 2.86 mmol) in toluene (10 mL) was rapidly added at –60 °C to a suspension of [TiCl$_3$(THF)$_3$] (1.11 g, 3.00 mmol) in toluene (40 mL). The mixture was allowed to warm to room temperature while being stirred for 12 h. The solution was filtered through a celite layer and the residue was washed with toluene and collected together with the filtrate. The solvents were evaporated under vacuum and the compound was washed at –30 °C with hexane (2 × 5 mL). Yield: 90% (1.69 g). ^{1}H NMR (C$_6$D$_6$): δ = 9.25, 7.98, 6.93 (br., 2-C$_6$*H*$_4$F), 5.30 (br., NC*H*$_2$C*H*$_2$N), 0.61 [br., Si(C*H*$_3$)$_2$] ppm. EPR (10^{-2} M in toluene, 22 K): *g* = 1.953. $C_{30}H_{42}F_3N_6Si_3Ti$ (675.82): calcd. C 53.29, H 6.27, N 12.44; found C 53.20, H 6.36, N 12.43. MS (EI): *m*/*z* = 583 [M$^+$ – C$_6$H$_2$F].

[Ti{N(Ph)SiMe$_2$}$_3$-tacu] (6): A suspension of [TiCl$_3$(THF)$_3$] (1.23 g, 3.31 mmol) in 50 mL of toluene was treated at –60 °C with a solution of 1,4,8-[{N(Na)(C$_6$H$_5$)SiMe$_2$}$_3$-tacu]·2THF (2.36 g, 3.18 mmol) in 10 mL of toluene. The mixture was allowed to reach room temperature and was stirred for a further 12 h. The solution was filtered through a celite layer and the solvent evaporated to dryness. The solid obtained was washed at –30 °C with hexane and dried. Crystals suitable for X-ray diffraction were obtained from toluene at 4 °C. Yield: 80% (1.65 g). EPR (10^{-2} M in toluene, 22 K): *g* = 1.944. $C_{32}H_{49}N_6Si_3Ti$ (649.90): calcd. C 59.11, H 7.60, N 12.94; found C 59.03, H 7.73, N 12.88. MS (EI): *m*/*z* = 649 [M]$^+$.

[Ti{N(2-C$_6$H$_4$F)SiMe$_2$}$_3$-tacn]I (7): A solution of [Ti{N(2-C$_6$H$_4$F)SiMe$_2$}$_3$-tacn] (0.80 g, 1.19 mmol) in 40 mL of toluene, cooled to –60 °C, was treated with I_2 (0.15 g, 0.60 mmol). The solution was allowed to warm to room temperature and was then stirred for 12 h. The solvent was evaporated to dryness and the residue was washed with hexane and dried in vacuo to give **7** as an orange solid in 98% yield (0.93 g). ^{1}H NMR (C$_6$D$_5$Br): δ = 7.37 (br. t, 3 H, *H*$_{meta\text{-}H3}$), 7.30–7.20 (m, 3 H, *H*$_{para}$), 6.95 (t, $^3J_{H,H}$ = 6.6 Hz, 3 H, *H*$_{meta\text{-}H5}$), 5.76 (t, $^3J_{H,H}$ = 7.2 Hz, 3 H, *H*$_{ortho}$), 4.65–4.40 (br. s, C*H*$_{anti}$H$_{syn}$), 3.95–3.75 (m, 6 H, CH$_{anti}$*H*$_{syn}$), 0.72 (s, 18 H, C*H*$_3$) ppm; (CD$_3$CN): δ = 7.09 (ddd, $^3J_{H,F}$ = 11.4, $^3J_{H,H}$ = 8.4, $^4J_{H,H}$ = 1.5 Hz, 3 H, *H*$_{meta\text{-}H3}$), 7.02–6.93 (m, 3 H, *H*$_{para}$), 6.52 (dt, $^3J_{H,H}$ = 7.8, $^5J_{H,F}$ = 1.5 Hz, 3 H, *H*$_{meta\text{-}H5}$), 5.43 (dt, $^3J_{H,H}$

 © 2005 Wiley-VCH Verlag GmbH & Co. KGaA, Weinheim

Table 4. Crystal and refinement data for compounds **5** and **7**.

	5	**7**
Empirical formula	$C_{30}H_{42}F_3N_6Si_3Ti$	$C_{30}H_{42}F_3IN_6Si_3Ti$
Formula mass	675.87	802.77
Temperature	293(2) K	293(2) K
Wavelength	0.71069 Å	0.71069 Å
Crystal system	cubic	orthorhombic
Space group	$P2_13$	$P21cn$
Unit cell dimensions	a = 15.080(2) Å b = 15.0780(16) Å c = 15.0753(16) Å	a = 10.577(5) Å b = 17.772(5) Å c = 18.911(5) Å
Volume	3427.7(7) Å^3	3555(2) Å^3
Z	4	4
Calculated density	1.310 Mg m^{-3}	1.500 Mg m^{-3}
Absorption coefficient	0.401 mm^{-1}	1.256 mm^{-1}
F(000)	1420	1632
Crystal size	prism	parallelepiped
Crystal morphology	0.5×0.3×0.3 mm	0.6×0.4×0.3 mm
Colour	red	red
Theta range for data collection	1.91 to 26.00°	1.57 to 25.97°
Limiting indices	$0 \le h \le 18$ $0 \le k \le 18$ $-18 \le l \le 18$	$0 \le h \le 13$ $0 \le k \le 21$ $0 \le l \le 23$
Reflections collected/unique	7249/2262 [R(int) = 0.0489]	3603/3603 [R(int) = 0.0000]
Completeness to theta	99.7% (θ = 26.00)	97.8% (θ = 25.97)
Refinement method	full-matrix least-squares on F^2	full-matrix least-squares on F^2
Data/restraints/parameters	2262/0/131	3603/1/392
Goodness-of-fit on F^2	1.073	1.074
Final R indices [$I > 2\sigma(I)$]	$R1$ = 0.0400, $wR2$ = 0.0892	$R1$ = 0.0984, $wR2$ = 0.2247
R indices (all data)	$R1$ = 0.0593, $wR2$ = 0.1007	$R1$ = 0.1365, $wR2$ = 0.2663
Absolute structure parameter	0.46(5)	0.08(7)
Largest diff. peak and hole	0.215 and –0.196 e Å^{-3}	3.954 and –2.026 e Å^{-3}

= 7.8, $^4J_{H,F}$ = 7.8, $^4J_{H,H}$ = 2.1 Hz, 3 H, H_{ortho}), 3.63 (s, 12 H, NCH_2CH_2N), 0.42 (s, 18 H, CH_3) ppm. $^{13}C\{^1H\}$ NMR (CD_3CN): δ = 154.8 (d, $^1J_{C,F}$ = 241.0 Hz, C_{ortho}), 140.7 (d, $^2J_{H,F}$ = 13.0 Hz, C_{ipso}), 127.3 (C_{ortho}), 126.3 (d, $^3J_{C,F}$ = 7.3 Hz, C_{para}), 125.5 (d, $^4J_{C,F}$ = 3.7 Hz, C_{meta}), 116.9 (d, $^2J_{C,F}$ = 22 Hz, C_{meta}), 52.4 (NCH_2CH_2N), –0.7 (CH_3) ppm. ^{19}F NMR(CD_3CN): δ = –41.06 (m) ppm. $C_{30}H_{42}F_3IN_6Si_3Ti$ (802.72): calcd. C 44.86, H 5.27, N 10.47; found C 44.68, H 5.27, N 10.37. MS (EI): m/z = 675 [M – I]$^+$.

[Ti{N(Ph)SiMe$_2$}$_3$-tacu]I (8): A solution of [Ti{N(Ph)SiMe$_2$}$_3$-tacu] (3.25 g, 5.0 mmol) in toluene at –60 °C was treated with I_2 (0.69 g, 2.7 mmol). The solution was allowed to warm to room temperature and was then stirred for 12 h. The solvent was removed in vacuo and the residue was washed with hexane (3×5 mL) and dried. The complex was obtained as an orange solid in 96% yield (3.72 g). ^1H NMR (CD_2Cl_2, room temp.): δ = 7.14 (t, $^3J_{H,H}$ = 7.5 Hz, 2 H, H_{meta}), 6.91 (m, 4 H, H_{meta}), 6.68 (m, 3 H, H_{para}), 6.49 (d, $^3J_{H,H}$ = 7.5 Hz, 2 H, H_{ortho}), 6.25 (d, $^3J_{H,H}$ = 7.8 Hz, 4 H, H_{ortho}), 3.68, 3.39 (br., 4 H, NCH_2CH_2N), 3.47, 3.30 (m, 8 H, NCH_2CH_2CH_2N), 2.37, 2.05 (br., m, 4 H, NCH$_2$CH_2CH_2N), 0.70 (s, 6 H, CH_3), 0.46 (s, 6 H, CH_3), 0.21 (br. s, 6 H, CH_3) ppm. ^1H NMR (CD_2Cl_2, –40 °C): δ = 7.10 (m, 2 H, H_{meta}), 6.97–6.84 (m, 4 H, H_{meta}), 6.69–6.23 (m, 3 H, H_{para}), 6.51 (d, $^3J_{H,H}$ = 7.8 Hz, 2 H, H_{ortho}), 6.40 (d, $^3J_{H,H}$ = 7.8 Hz, 2 H, H_{ortho}), 6.23 (d, $^3J_{H,H}$ = 8.1 Hz, 2 H, H_{ortho}), 3.70–3.14 (br. m, 12 H, NCH_2), 2.10, 1.89 (br. m, 4 H, NCH$_2$CH_2CH_2N), 0.83 (s, 3 H, CH_3), 0.75 (s, 3 H, CH_3), 0.43 (s, 6 H, CH_3), 0.21 (s, 3 H, CH_3), 0.12 (s, 3 H, CH_3) ppm. ^1H NMR (CD_2Cl_2, –70 °C): δ = 7.08 (m, 2 H, H_{meta}), 6.94 (m, 2 H, H_{meta}), 6.83 (m, 2 H, H_{meta}), 6.67–6.51 (m, 7 H, H_{para}, H_{ortho}), 6.25 (br. d, 2 H, H_{ortho}), 3.70–3.06 (br. m, 12 H, NCH_2), 2.07, 1.76 (br. m, 4 H, NCH$_2$CH_2CH_2N), 0.95 (s, 3 H, CH_3), 0.78 (s, 3 H, CH_3), 0.44

Table 5. Crystal and refinement data for compound **6**.

	6
Empirical formula	$C_{32}H_{49}N_6Si_3Ti$
Formula mass	649.94
Temperature	293(2) K
Wavelength	1.54180 Å
Crystal system	triclinic
Space group	$P\bar{1}$
Unit cell dimensions	a = 10.497(3) Å b = 18.309(6) Å c = 18.355(3) Å
Volume	3481.6(16) Å^3
Z	2 (2 molecules)
Calculated density	1.240 Mg m^{-3}
Absorption coefficient	3.304 mm^{-1}
F(000)	1388
Crystal morphology	prism
Crystal size	0.6×0.3×0.2 mm
Colour	orange
Theta range for data collection	3.25 to 66.93°
Limiting indices	$-12 \le h \le 0$ $-21 \le k \le 21$ $-21 \le l \le 21$
Reflections collected/unique	13100/12362 [R(int) = 0.0721]
Completeness to theta	99.8% (θ = 66.93)
Refinement method	full-matrix least-squares on F^2
Data/restraints/parameters	12362/0/758
Goodness-of-fit on F^2	0.987
Final R indices [$I > 2\sigma(I)$]	$R1$ = 0.0908, $wR2$ = 0.2300
R indices (all data)	$R1$ = 0.1767, $wR2$ = 0.2726
Largest diff. peak and hole	0.625 and –0.551 e Å^{-3}

 © 2005 Wiley-VCH Verlag GmbH & Co. KGaA, Weinheim

(s, 3 H, CH_3), 0.38 (s, 3 H, CH_3), 0.21 (s, 3 H, CH_3), 0.09 (s, 3 H, CH_3) ppm. $^{13}C\{^1H\}$ NMR (CD_2Cl_2, room temp.): δ = 159.0, 152.8 (C_{ipso}), 129.6, 128.8, 124.1, 122.9, 119.7, 118.6 (C_{Ph}), 52.6, 50.7, 48.3 (NCH_2), 26.7 (NCH$_2$$CH_2$$CH_2$N), 1.8 ($CH_3$), 1.1 ($CH_3$), 0.0 ($CH_3$) ppm. $C_{32}H_{49}IN_6Si_3Ti$ (776.80): calcd. C 49.48, H 6.36, N 10.82; found C 49.18, H 6.27, N 10.39.

X-ray Experimental Details: X-ray data were collected on a MACH3 Nonius diffractometer equipped with Mo-K_α radiation (λ = 0.71069 Å) and a Turbo CAD4 with a rotating anode and Cu-$K_{\alpha1}$ radiation (in the case of compound **7**), at room temperature. Solution and refinement were performed with SIR97[20] and SHELXL[21] included in the WINGX Version 1.64.03b program package.[22] Compound **5** crystallized in the cubic space group $P2_13$, thus only 1/3 of the molecule is present in the asymmetric unit, as the Ti atom is on a 3-fold rotation axis. Compound **6** crystallized in the triclinic centrosymmetric space group $P\bar{1}$ with two similar molecules in the asymmetric unit. Geometrical data are discussed and presented only for one of the molecules. As for compound **7**, a large residual electron density is present near the iodide atom. Several refinements of a possible disorder of I^- (occupying three possible positions with different occupation factors) did not improve the refinement and several satellite residual peaks were kept. The possibility of a disordered I_3^- ion was also attempted but the I–I distances were not acceptable. All non-H atoms were refined anisotropically, and all hydrogen atoms were inserted in idealized positions riding on the parent C atom. All the details concerning data collection and refinement are presented in Table 4 and Table 5. Figures were drawn with ORTEP3.[23]

CCDC-250633 to -250635 (for **5**–**7**, respectively) contain the supplementary crystallographic data for this paper. These data can be obtained free of charge from The Cambridge Crystallographic Data Centre via www.ccdc.cam.ac.uk/data_request/cif.

Acknowledgments

The authors are thankful to the Fundação para a Ciência e a Tecnologia, Portugal for funding this work (research projects POCTI/QUI/39734/2001 and POCTI/QUI/46206/2002).

[1] J. Costamagna, G. Ferraudi, B. Matsuhiro, M. C. Vallette, J. Canales, M. Villagrán, J. Vargas, M. Aguirre, *Coord. Chem. Rev.* **2000**, *196*, 125–164.
[2] J. P. Danks, N. R. Champness, M. Schröder, *Coord. Chem. Rev.* **1998**, *174*, 417–468.
[3] K. P. Wainwright, *Coord. Chem. Rev.* **1997**, *166*, 35–90.
[4] O. Schlager, K. Wieghardt, B. Nuber, *Inorg. Chem.* **1995**, *34*, 6456–6462.
[5] C. M. Cui, G. R. Giesbrecht, J. A. R. Schmidt, J. Arnold, *Inorg. Chim. Acta* **2003**, *351*, 404–408.
[6] J. A. R. Schmidt, G. R. Giesbrecht, C. M. Cui, J. Arnold, *Chem. Commun.* **2003**, 1025–1033.
[7] C. G. J. Tazelaar, S. Bambirra, D. van Leusen, A. Meetsma, B. Hessen, J. H. Teuben, *Organometallics* **2004**, *23*, 936–939.
[8] S. Bambirra, S. J. Boot, D. van Leusen, A. Meetsma, B. Hessen, *Organometallics* **2004**, *23*, 1891–1898.
[9] A. R. Dias, A. M. Martins, J. R. Ascenso, H. Ferreira, M. T. Duarte, R. T. Henriques, *Inorg. Chem.* **2003**, *42*, 2675–2682.
[10] B. Monteiro, D. Roitershtein, H. Ferreira, J. R. Ascenso, A. M. Martins, Â. Domingos, N. Marques, *Inorg. Chem.* **2003**, *42*, 4223–4231.
[11] G. H. Searle, R. J. Geue, *Aust. J. Chem.* **1984**, *37*, 959–962.
[12] T. J. Atkins, J. E. Richman, W. F. Oettle, *Org. Synth.* **1978**, *58*, 652–654.
[13] O. Schlager, K. Wieghardt, H. Grondey, A. Rufinska, B. Nuber, *Inorg. Chem.* **1995**, *34*, 6440–6448.
[14] B. P. Hay, R. D. Hancock, *Coord. Chem. Rev.* **2001**, *212*, 61–78.
[15] E. L. Hegg, S. H. Mortimore, C. L. Cheung, J. E. Huyett, D. R. Powell, J. N. Burstyn, *Inorg. Chem.* **1999**, *38*, 2961–2968.
[16] J. Langmaier, Z. Samec, V. Varga, M. Horáček, K. Mach, *J. Organomet. Chem.* **1999**, *579*, 348–355.
[17] U. Auerbach, T. Weyhermüller, K. Wieghardt, B. Nuber, E. Bill, C. Burzlaff, A. X. Trautwein, *Inorg. Chem.* **1993**, *32*, 508–519.
[18] S. Back, R. A. Gossage, G. Rheinwald, I. del Rio, H. Lang, G. van Koten, *J. Organomet. Chem.* **1999**, *582*, 126–138.
[19] L. E. Manzer, *Inorg. Synth.* **1982**, *21*, 135–137.
[20] Sir97: A new tool for crystal structure determination and refinement: A. Altomare, M. C. Burla, M. Camalli, G. Gascarano, C. Giacovazzo, A. Guagliardi, A. G. G. Moliterni, G. Polidori, R. Spagna, *J. Appl. Crystallogr.* **1999**, *32*, 115–119.
[21] G. M. Sheldrick, *SHELXL, a program for refining crystal structures*, University of Göttingen, Germany, **1997**.
[22] V1.64.03b: L. J. Farrugia, X. Wing, *J. Appl. Crystallogr.* **1999**, *32*, 837–838.
[23] ORTEP3: L. J. Farrugia, *J. Appl. Crystallogr.* **1997**, *30*, 565–566; based on ORTEP-III, v.1.0.3., by C. K. Johnson and M. N. Burnett.

Received: September 28, 2004

 © 2005 Wiley-VCH Verlag GmbH & Co. KGaA, Weinheim

Novel Methanol-Containing Oxomolybdate(v) Complexes: Synthesis and Structural Characterisation of Intermediates in the Formation of $\{Mo_2O_4\}^{2+}$ Clusters from $[MoOCl_4(H_2O)]^-$ and $[MoOBr_4]^-$ Precursors

Barbara Modec*[a] and Jurij V. Brenčič[a]

Keywords: Cluster compounds / Molybdenum / Polyoxometallates

A series of oxomolybdate(v) complexes with methanol was prepared by the reaction of $(PyH)_5[MoOCl_4(H_2O)]_3Cl_2$ (**1**) or $(PyH)[MoOBr_4]$ (PyH^+ = pyridinium cation, $C_5H_5NH^+$) in methanol. $(PyH)_2[MoOCl_4(MeOH)]Cl$ (**2**) is obtained upon substitution of coordinated water for methanol in **1**. Small amounts of weak bases such as pyridine or trifluoroacetate promote further substitution chemistry at the labile sites, followed by dimerisation to the well-known $\{Mo_2O_4\}^{2+}$ core. A dinuclear anion with coordinated methanol can be isolated as its pyridinium salt, $(PyH)_2[Mo_2O_4Cl_4(MeOH)_2]$, in two crystalline modifications, either as a triclinic (**3**) or as an orthorhombic polymorph (**4**). After prolonged reaction times further assembly of dinuclear fragments takes place and tetranuclear $[Mo_4O_8(OMe)_2(MeOH)_2Cl_4]^{2-}$ is formed. The products of the analogous reactions with $(PyH)[MoOBr_4]$ as the starting material depend largely upon the reaction temperature. Dinuclear $(PyH)_2[Mo_2O_4Br_4(MeOH)_2]$ (**5**), which crystallises in an orthorhombic unit cell and whose structure is isotypic to that of **4**, is obtained only if the reaction takes place at low temperature (5 °C); under ambient conditions $(PyH)_2[Mo_4O_8(OMe)_2(MeOH)_2Br_4]$ (**6**) is obtained instead. The tetranuclear anion of **6** consists of a commonly adopted assembly of two $\{Mo_2O_4\}^{2+}$ units. The identity of the products was determined by infrared spectroscopy and X-ray structure analyses.
(© Wiley-VCH Verlag GmbH & Co. KGaA, 69451 Weinheim, Germany, 2005)

Introduction

$\{Mo_2O_4\}^{2+}$ clusters with metal d electrons localised in single metal–metal bonds occupy a prominent position among the polyoxometallates, which continue to be a subject of great interest because of their potential applications ranging from catalysis to medicine.[1] Their basic building blocks, dinuclear $\{Mo_2O_4\}^{2+}$ moieties (Scheme 1) with a well-defined geometry,[2,3] can assemble in many different ways and lead to a variety of metal oxide cores, as illustrated by some recently prepared clusters, i.e., $[(Mo_2O_4)_4(OMe)_6(MeOH)_4Cl_2]$,[4] bimetallic alkoxides $[M_2(Mo_2O_4)_2(O\mathit{i}Pr)_{14}]$ (M = Ta, Nb),[5] $[(Mo_2O_4)_6(\mu_2\text{-}SO_3)_{12}(\mu_3\text{-}SO_3)_4]^{20-}$,[6] $[Na_4(H_2O)_6\{(Mo_2O_4)_{10}(P_2O_7)_{10}(CH_3COO)_8(H_2O)_4\}]^{24-}$,[7] $[(Mo_2O_4)_3(O_3PCH_2PO_3)_3(MoO_4)]^{8-}$,[8] $[Na(H_2O)_2\{(Mo_2O_4)_4(O_3PCH_2PO_3)_4(CO_3)_2\}]^{11-}$,[9] and a series of nano-sized, mixed-valence Mo^V/Mo^{VI} acetate complexes.[10] Theoretical calculations have been performed on some of these species in order to understand the bonding of such complex architectures.[11] Although the $\{Mo_2O_4\}^{2+}$ species were considered at first to be essentially products of inadvertent air oxidation, contemporary research in this field is aimed towards the development of more rational and high-yield synthetic procedures.

[a] Faculty of Chemistry and Chemical Technology, University of Ljubljana,
Aškerčeva 5, 1000 Ljubljana, Slovenia
Fax: +386-1-2419-220
E-mail: barbara.modec@guest.arnes.si

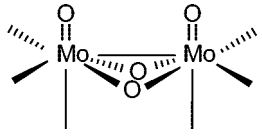

Scheme 1. A basic building unit: $\{Mo_2O_4\}^{2+}$ structural fragment.

We have demonstrated in our previous work that $(PyH)_2[MoOCl_5]$ reacts almost instantaneously in mixtures of methanol and pyridine to form discrete clusters built of two, three, four or six $\{Mo_2O_4\}^{2+}$ subunits.[12] A simple, high-yield preparation method, coupled with the relative stability and the fact that the coordinated chlorides are labile enough under appropriate conditions to allow a facile substitution chemistry, have made $(PyH)_2[MoOCl_5]$ an attractive starting material. Since the widely accepted notion, based on the analytical and spectroscopic data, was that its structure consists of octahedral $[MoOCl_5]^{2-}$ ions,[13] its X-ray structure analysis has not been undertaken until now. The general reaction route leading to $\{Mo_2O_4\}^{2+}$ clusters was proposed to begin with rapid substitution of the chlorides, followed by dimerisation through $Mo(\mu_2\text{-}O)_2Mo$ bridges with concomitant interaction between the two d^1 ions. There are three sites per metal in the $\{Mo_2O_4\}^{2+}$ moiety that are open for coordination of, preferably, oxygen-donor ligands. The multitude of known $\{Mo_2O_4\}^{2+}$ complexes with very diverse mono-, bi- or multidentate ligands suggests that many fulfil the metal's coordination demands.[14]

 © 2005 Wiley-VCH Verlag GmbH & Co. KGaA, Weinheim **DOI: 10.1002/ejic.200400829**

In the absence of ligands in sufficient concentrations, the metal centres attain coordination saturation through the self-assembly of $\{Mo_2O_4\}^{2+}$ units by sharing the initially μ_2-bridging oxo groups. The surface of the clusters thus obtained still possesses sites available for coordination, but their number is greatly reduced compared to the $\{Mo_2O_4\}^{2+}$ subunit. A very important aspect in the process is the formation of methoxide ions and their subsequent incorporation into the cluster, which diminishes its negative charge. Because of the ability of alkoxides to participate in bridging interactions with two or three metal centres, the assembly of $\{Mo_2O_4\}^{2+}$ units in their presence results in a different core structure, as exemplified by the association of two $\{Mo_2O_4\}^{2+}$ units to form a tetranuclear core.[15] The alkoxide was shown to assist in the assembly and either a compact $\{Mo_4O_4(\mu_3\text{-}O)_2(\mu_2\text{-}O)_2(\mu_2\text{-}OR)_2\}^{2+}$ or more rarely $\{Mo_4O_4(\mu_2\text{-}O)_4(\mu_2\text{-}OR)_2\}^{2+}$ core with an open structure were formed. With no alkoxide present, a self-assembly into a cube-like $\{Mo_4O_4(\mu_3\text{-}O)_4\}^{4+}$ core was observed.

The ongoing research in our laboratory has been focused on the isolation and characterisation of the intermediate products in the formation of $\{Mo_2O_4\}^{2+}$ clusters. Knowing their identities would help to elucidate a multi-step reaction pathway from the starting oxohalomolybdate(v) to the final $\{Mo_2O_4\}^{2+}$ clusters. In this context, the reactions of $(PyH)_2[MoOCl_5]$ and $(PyH)[MoOBr_4]$ with pyridine or pyridinium trifluoroacetate in methanol were investigated. Prior to that, however, $(PyH)_2[MoOCl_5]$ was subjected to an X-ray structure analysis.

Results and Discussion

Structural Data

Structure of $(PyH)_5[MoOCl_4(H_2O)]_3Cl_2$ (1)

The X-ray structure analysis of $(PyH)_2[MoOCl_5]$ revealed its true identity as $(PyH)_5[MoOCl_4(H_2O)]_3Cl_2$, whose structure is isotypic with that of $(PyH)_5[MoOBr_4(H_2O)]_3Br_2$.[16] The orthorhombic unit cell contains six $[MoOCl_4(H_2O)]^-$ ions, four non-coordinated chloride ions and ten protonated pyridine molecules as countercations.. There are two crystallographically distinct $[MoOCl_4(H_2O)]^-$ ions (depicted in Figure 1). The one containing Mo(1) lies at the intersection of two mirror planes, with the chloro ligands in the planes and Mo(1), O(11) and O(12) on the twofold axis. Its symmetry is C_{2v}. The other anion has only one crystallographically imposed mirror plane. Mo(2), both oxygen atoms and the two chlorine atoms Cl(21) and Cl(23) lie in this plane. The distorted octahedral environments of Mo(1) and Mo(2) reveal the usual bonding pattern for $[MoOCl_4(H_2O)]^-$ anions:[17] (i) a short Mo=O bond [1.648(4) and 1.650(3) Å], consistent with a multiple bond character, (ii) a water ligand at 2.284(4) and 2.270(3) Å in a position *trans* to the terminal oxo group, and (iii) a displacement of molybdenum from the plane of the four chloro ligands towards the oxo group [0.334(1) Å for Mo(1) and 0.349(1) Å for Mo(2)]. An exhaustive list of structural parameters is given in Table 1.

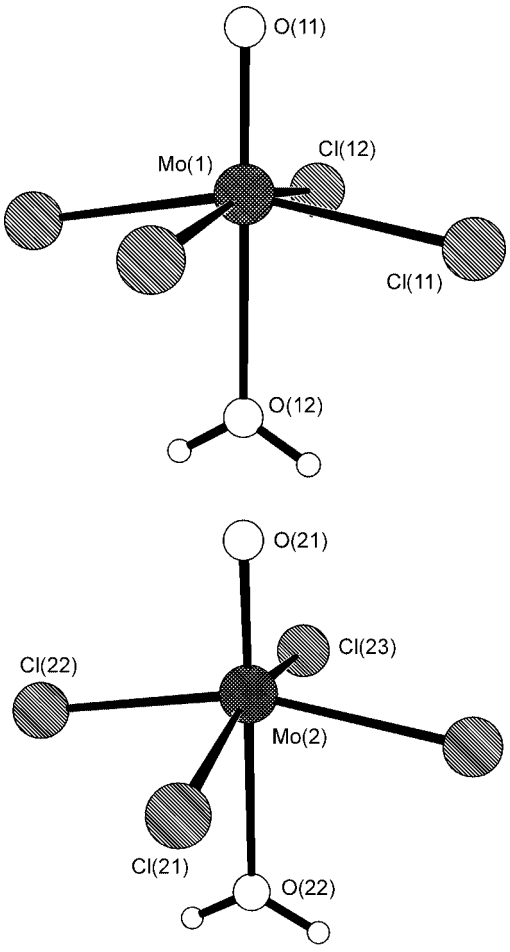

Figure 1. The two crystallographically independent $[MoOCl_4(H_2O)]^-$ ions found in compound **1**. The same drawing scheme pertains to all figures: molybdenum atoms are cross-hatched; chlorine or bromine atoms are lined bottom right to top left; nitrogen atoms are lined bottom left to top right; oxygen atoms are unshaded and carbon atoms shaded, medium-sized spheres and hydrogen atoms are unshaded small-sized spheres.

Table 1. Geometric parameters [Å; °] of the $[MoOCl_4(H_2O)]^-$ ions in **1**.

Mo(1)–O(11)	1.648(4)	Mo(2)–O(21)	1.650(3)
Mo(1)–O(12)	2.284(4)	Mo(2)–O(22)	2.270(3)
Mo(1)–Cl(11)	2.3671(9)	Mo(2)–Cl(21)	2.4065(12)
Mo(1)–Cl(12)	2.3779(12)	Mo(2)–Cl(22)	2.3698(7)
		Mo(2)–Cl(23)	2.3535(11)
O(11)–Mo(1)–Cl(11)	99.76(3)	O(21)–Mo(2)–Cl(21)	95.66(14)
O(11)–Mo(1)–Cl(12)	96.45(4)	O(21)–Mo(2)–Cl(22)	176.96(16)
O(11)–Mo(1)–O(12)	180.0	O(21)–Mo(2)–Cl(23)	99.56(14)
Cl(11)–Mo(1)–Cl(12)	88.909(8)	O(21)–Mo(2)–O(22)	176.96(16)
Cl(11)–Mo(1)–Cl(11)[a]	160.49(6)	Cl(21)–Mo(2)–Cl(22)	89.07(2)
Cl(12)–Mo(1)–Cl(12)[a]	167.10(8)	Cl(22)–Mo(2)–Cl(23)	88.48(2)
Cl(11)–Mo(1)–O(12)	80.24(3)	Cl(21)–Mo(2)–Cl(23)	164.77(5)
Cl(12)–Mo(1)–O(12)	83.55(4)	Cl(22)–Mo(2)–Cl(22)[b]	161.40(4)
		Cl(21)–Mo(2)–O(22)	81.29(10)
		Cl(22)–Mo(2)–O(22)	80.71(2)
		Cl(23)–Mo(2)–O(22)	83.48(10)

[a] Symmetry code: $-x + 1/2, 2 - y, z$. [b] Symmetry code: $x, 2 - y, z$.

A complicated pattern of hydrogen bonds is formed in **1**. Six hydrogen bonds link three $[MoOCl_4(H_2O)]^-$ ions through water ligands to a pair of non-coordinated chloride ions (Figure 2a). Each water molecule is engaged in two

 © 2005 Wiley-VCH Verlag GmbH & Co. KGaA, Weinheim

hydrogen bonds with two chlorides, with lengths of 3.164(3) and 3.129(2) Å. Three pyridinium cations are connected in a similar manner by bifurcated, rather long, hydrogen bonds with a pair of chloride counterions [N(1)···Cl = 3.3299(30) and N(2)···Cl = 3.3876(44) Å; Figure 2b]. Alternation of both types of trimeric assemblies through common chloride ions produces infinite chains which are parallel to the *b* axis (Figure 2c). The environment of each chloride ion in the chain is that of a distorted octahedron consisting of three water molecules and three pyridinium nitrogens.

The $[MoOCl_4(H_2O)]^-$ ion has been structurally characterised in several other compounds.[17] Due to the widespread participation of coordinated water molecules in O–H···Cl or O–H···O(terminal oxo group) hydrogen bonds, pairs of anions or infinite chains are observed in many solid-state structures. The water ligand is bonded in some $[MoOCl_4(H_2O)]^-$ compounds at longer distances. For in-

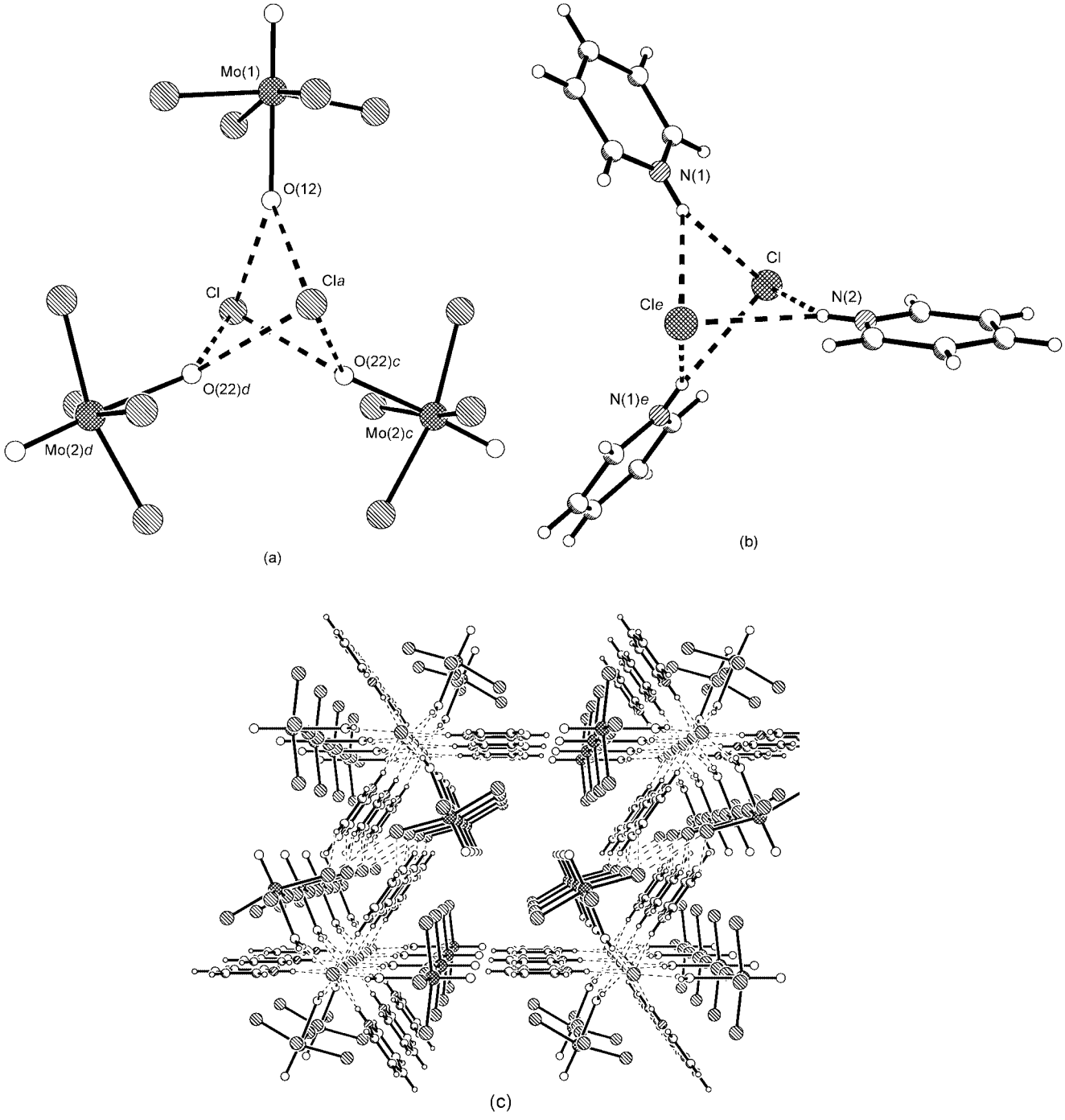

Figure 2. Hydrogen bonds in **1**: (a) three $[MoOCl_4(H_2O)]^-$ ions are linked by a pair of chloride counterions; (b) two chloride ions also link three pyridinium cations. Labels *a*, *c*, *d* and *e* denote symmetry-generated atoms; (c) chains viewed along the *b* axis.

 © 2005 Wiley-VCH Verlag GmbH & Co. KGaA, Weinheim

stance, a distance of 2.393(15) Å is observed in $[As(C_6H_5)_4][MoOCl_4(H_2O)]$.[17c] This lengthening is in agreement with the uniform tendency of Mo=O bonds to weaken bonds *trans* to themselves. Nevertheless, the bond lengths in **1** are still significantly longer than related bonds which are not subject to a *trans* influence, for example 2.148(6) Å determined for $[Mo_4O_8(OH)_2(H_2O)_2(C_4O_4)_2]^{2-}$.[18]

Structure of (PyH)$_2$[MoOCl$_4$(MeOH)]Cl (2)

The asymmetric unit of **2** contains a complex anion with the composition $[MoOCl_4(MeOH)]^-$, as shown in Figure 3, a chloride ion and two protonated pyridine molecules as countercations. The $[MoOCl_4(MeOH)]^-$ ions have pseudo-octahedral coordination spheres characterised by a short Mo=O bond, a methanol ligand in a position *trans* to it and four chloro ligands at 2.3715(6)–2.3817(6) Å. The molybdenum atom is, as expected, displaced away from the least-squares plane of the four chlorine atoms by 0.3212(4) Å towards the oxo group. This necessitates obtuse O=Mo–Cl angles in the range 96.80(6)–98.62(6)°. The molybdenum-to-methanol oxygen bond length is 2.2911(15) Å. Relevant structural parameters of the $[MoOCl_4(MeOH)]^-$ ion are summarised in Table 2. The methanol ligand is also engaged in a relatively short hydrogen-bonding interaction with a chloride counterion Cl(5) [O(2)···Cl(5) = 3.0235(16) Å]. The non-coordinated chloride Cl(5) participates in two more hydrogen bonds. Both are formed with pyridinium nitrogen atoms, the distance to N(1)a is 3.0508(21) Å [(*a*) *x*, *y*, 1 + *z*] and the distance to N(2)b is 3.1384(20) Å [(*b*) –0.5 + *x*, 0.5 – *y*, 0.5 + *z*].

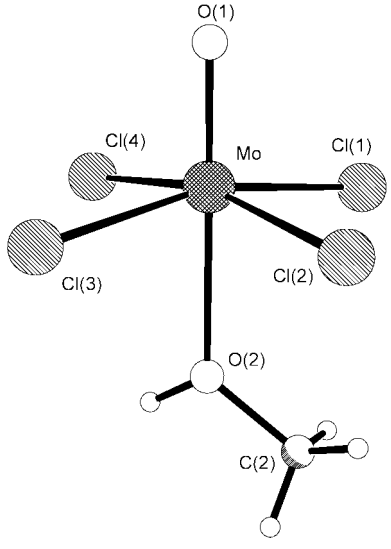

Figure 3. A drawing of the $[MoOCl_4(MeOH)]^-$ unit in **2** with the atom labelling scheme.

Although many $[MoOCl_4L]^-$ compounds with bases, L, such as tetrahydrofuran, dimethylphosphite, dimethylformamide and acetonitrile have been structurally characterised,[19] there were none where L is an alcohol until now. Nevertheless, the existence of the $[MoOCl_4(MeOH)]^-$ ion has been suggested previously in order to explain adequately the electronic spectrum of a methanol solution of $[N(C_4H_9)_4][MoOCl_4]$.[20]

Table 2. Geometric parameters [Å; °] of $[MoOCl_4(MeOH)]^-$ ion in **2**.

Mo–O(1)	1.6581(16)	Mo–Cl(4)	2.3715(6)
Mo–Cl(1)	2.3750(6)	Mo–O(2)	2.2911(15)
Mo–Cl(2)	2.3787(5)	O(2)–C(2)	1.436(3)
Mo–Cl(3)	2.3817(6)		
O(1)–Mo–Cl(1)	97.38(1)	Cl(4)–Mo–Cl(1)	90.22(3)
O(1)–Mo–Cl(2)	98.29(6)	Cl(1)–Mo–Cl(3)	163.98(2)
O(1)–Mo–Cl(3)	98.62(6)	Cl(2)–Mo–Cl(4)	164.91(2)
O(1)–Mo–Cl(4)	96.80(6)	Cl(1)–Mo–O(2)	82.83(5)
O(1)–Mo–O(2)	179.78(8)	Cl(2)–Mo–O(2)	81.80(4)
Cl(1)–Mo–Cl(2)	88.05(2)	Cl(3)–Mo–O(2)	81.17(4)
Cl(2)–Mo–Cl(3)	88.80(2)	Cl(4)–Mo–O(2)	83.11(4)
Cl(3)–Mo–Cl(4)	88.74(2)		

Structure of the Triclinic Modification of (PyH)$_2$[Mo$_2$O$_4$Cl$_4$(MeOH)$_2$] (3)

A perspective view of the $[Mo_2O_4Cl_4(MeOH)_2]^{2-}$ anion is presented in Figure 4, which also shows the atom labelling scheme used. Each anion occupies a general position within the unit cell of a triclinic space group $P\bar{1}$. Associated with each dinuclear anion are two protonated pyridine molecules. A central $\{Mo_2O_4\}^{2+}$ structural core may be recognized with typical geometric parameters.[3] There are two pairs of terminal and bridging oxo ligands with Mo=O and Mo–O(μ_2) distances in the ranges 1.674(4)–1.679(4) and 1.938(8)–1.949(4) Å, respectively. The terminal oxo groups are bent away from each other. The Mo–Mo bond length of 2.5902(6) Å corresponds to a single metal–metal bond. The Mo(μ_2-O)$_2$Mo ring is not planar, but is folded by 146.01(10)° around the vector connecting the bridging oxygen atoms. The puckering of the Mo(μ_2-O)$_2$Mo ring is presumably a means of allowing a close approach of the metal atoms. A pair of chloro ligands and a methanol *trans* to the terminal oxo group complete a distorted octahedral geometry about each metal atom. The molybdenum-to-methanol oxygen bond lengths are, as expected for bonds in this position, relatively long [2.351(4) and 2.372(4) Å]. Pairs of coor-

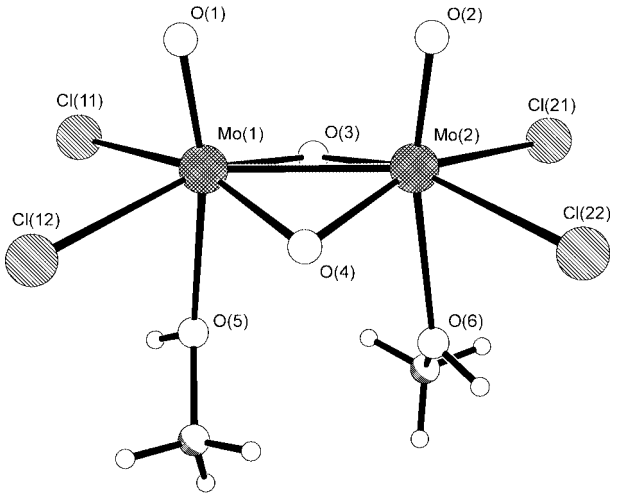

Figure 4. A drawing of the dinuclear $[Mo_2O_4Cl_4(MeOH)_2]^{2-}$ unit in **3** with the atom labelling scheme.

 © 2005 Wiley-VCH Verlag GmbH & Co. KGaA, Weinheim

Table 3. Selected geometric parameters [Å; °] of the $[Mo_2O_4X_4(MeOH)_2]^{2-}$ (X = Cl, Br) ions in **3**, **4** and **5**.

	3	**4**	**5**
Mo=O	1.674(4), 1.679(4)	1.6728(19)	1.670(3)
Mo–O(μ_2)	1.938(8)–1.949(4)	1.9466(16)–1.9470(16)	1.947(3), 1.953(3)
Mo–MeOH	2.351(4), 2.372(4)	2.3591(18)	2.359(3)
Mo–X[a]	2.4419(13)–2.4839(12)	2.4462(6), 2.4765(6)	2.5995(5), 2.6304(5)
Mo–O(μ_2)–Mo	83.56(14), 83.64(14)	83.53(6)	83.01(10)
O(μ_2)–Mo–O(μ_2)	91.60(15), 91.66(15)	91.80(7)	92.19(11)
Mo–Mo	2.5902(6)	2.5934(4)	2.5841(6)
Fold angle[b]	146.01(10)	146.34(5)	145.73(8)

[a] X = Cl for **3** and **4**; X = Br for **5**. [b] As defined in the text.

dinated methanol molecules are oriented with their O–H termini pointing in the opposite directions. Although the entire anion belongs to the asymmetric unit, it comes very close to having C_2 symmetry.

Structures of the Orthorhombic Modifications of $(PyH)_2[Mo_2O_4Cl_4(MeOH)_2]$ (4) and $(PyH)_2[Mo_2O_4Br_4(MeOH)_2]$ (5)

The structures of the orthorhombic modifications of $(PyH)_2[Mo_2O_4X_4(MeOH)_2]$ (X = Cl, Br) are isotypic. Only one half of the anion belongs to the asymmetric unit, the other half being generated by a crystallographic twofold rotation axis, which passes along the Mo=O vectors through the centre of the Mo(μ_2-O)$_2$Mo rhombus. The relevant geometric parameters for the inner coordination spheres for **4** and **5** are given in Table 3. The dimensions of the anion in **4** compare very well with those in **3**.

Comparison of the Structures of Triclinic (3) and Orthorhombic Modification of $(PyH)_2[Mo_2O_4X_4(MeOH)_2]$ [X = Cl (4) and X = Br (5)]

The differences between the two modifications arise in the hydrogen-bonding pattern. The intermolecular hydrogen bonds are formed in both polymorphs between methanol and halo ligands. Two donors of hydrogen bonds in each anion, i.e., a pair of coordinated methanol molecules, are matched with two acceptors, two out of four halo ligands. Therefore each anion forms four hydrogen bonds, in the triclinic modification with two neighbouring anions, while in the orthorhombic modification with four. In the triclinic polymorph one chloro ligand, labelled Cl(11), and the methanol coordinated to the same molybdenum atom of the $\{Mo_2O_4\}^{2+}$ unit form two hydrogen bonds to the methanol and chloro ligand of the closest neighbouring anion (Figure 5), the corresponding O(5)···Cl(11)a distances are 3.176(4) Å [(*a*) 1 – *x*, –*y*, –*z*]. Similarly, Cl(22) and the methanol coordinated to the other molybdenum atom of the dinuclear anion also form two hydrogen bonds with their closest neighbour, the corresponding O(6)···Cl(22)b distances are 3.191(4) Å [(*b*) 2 – *x*, 1 – *y*, 1 – *z*]. A linkage of each anion with two neighbours produces infinite chains that propagate along the unit cell body diagonal. The engagement of two chloro ligands in hydrogen bonds accounts for the variations in the molybdenum-to-chlorine bond lengths: the chloro ligand involved in the hydrogen bond binds to molybdenum at a longer distance, i.e., Mo(1)–Cl(11) = 2.4839(12) Å and Mo(2)–Cl(22) = 2.4779(12) Å vs. Mo(1)–Cl(12) = 2.4419(13) Å and Mo(2)–Cl(21) = 2.4454(13) Å. In the orthorhombic polymorph each anion forms four hydrogen bonds, with lengths of 3.2925(18) Å, to four adjacent anions (Figure 6). Such a connectivity results in infinite layers parallel to the *ab* plane. The engagement of two out of four coordinated chloro ligands in hydrogen bonds is again reflected in the molybdenum-to-chlorine bond lengths, i.e., 2.4765(6) vs. 2.4462(6) Å. By analogy, **5** displays a non-equivalence of the molybdenum-to-bromine bond lengths, 2.6304(5) vs. 2.5995(5) Å.

It can also be observed that the molybdenum-to-chlorine bond lengths in **3** and **4** are similar to those determined for the aqua-ligated ion $[Mo_2O_4Cl_4(H_2O)_2]^{2-}$ [2.453(2) and 2.475(2) Å][21] or the very similar $[Mo_2O_4Cl_3(H_2O)_3]^-$ [2.434(2)–2.450(2) Å],[22] and are longer than in their base-free analogue, $[Mo_2O_4Cl_4]^{2-}$, where the distances are 2.392(6)–2.407(6) Å for the $[As(C_6H_5)_4]^+$ salt[23] or 2.352(4)–2.391(3) Å for $(Ph_3P{=}N{=}PPh_3)(Et_3NH)$-$[Mo_2O_4Cl_4]$.[24] The decrease in the bond lengths in the $[Mo_2O_4Cl_4]^{2-}$ ions with five-coordinate metal atoms is fully in agreement with the reasonable expectation of the increased bond strengths to other ligands when the sixth ligand is absent. The molybdenum-to-bromine bonds in **5** are longer than those determined for $[Mo_4O_8(OEt)_2Br_2Py_4]$ [2.5355(11)–2.5747(10) Å][12a] or mononuclear $(PyH)_5$-$[MoOBr_4(H_2O)]_3Br_2$ [2.498(4)–2.563(4) Å].[16]

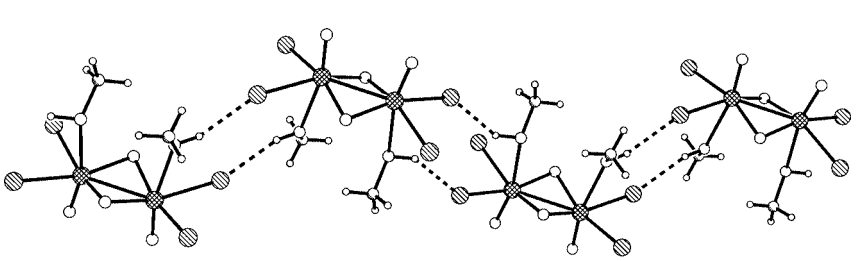

Figure 5. Hydrogen bonds in **3**: pairs of O(methanol)···Cl interactions link dinuclear anions into infinite chains.

 © 2005 Wiley-VCH Verlag GmbH & Co. KGaA, Weinheim

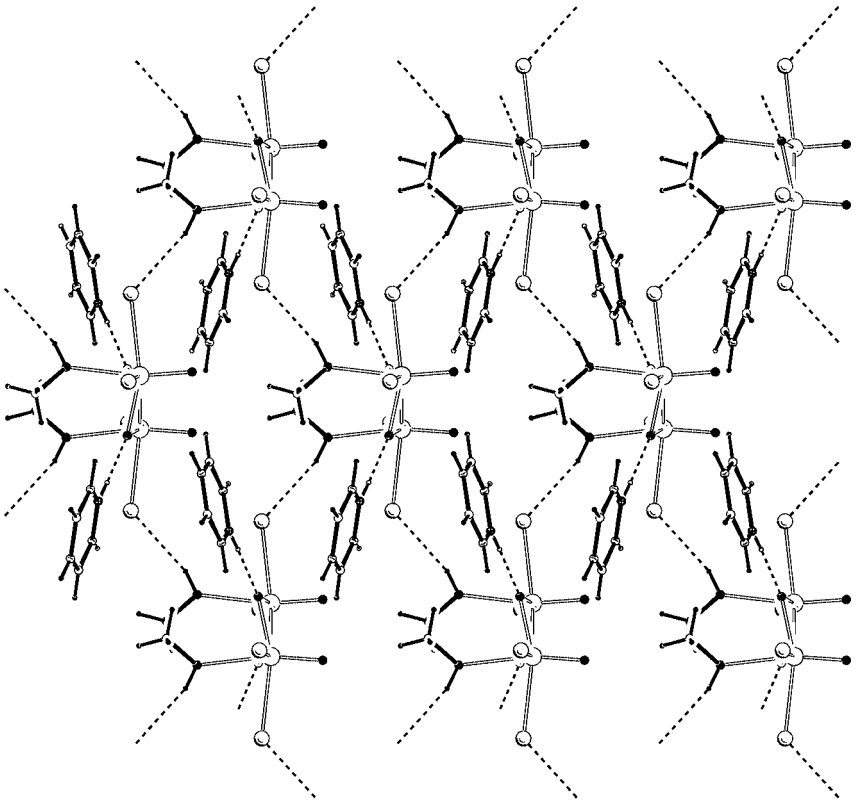

Figure 6. Hydrogen bonds in **4** and **5**: four O(methanol)···X interactions link each anion to four adjacent anions to form infinite layers perpendicular to the *c* axis.

The pyridinium cations are hydrogen bonded to the doubly-bridging oxygen atoms from the anions in both modifications (Figure 7). The corresponding N···O distances are 2.7001(60)–2.7031(62) Å for **3**, 2.6799(27) Å for **4** and 2.7329(45) Å for **5**.

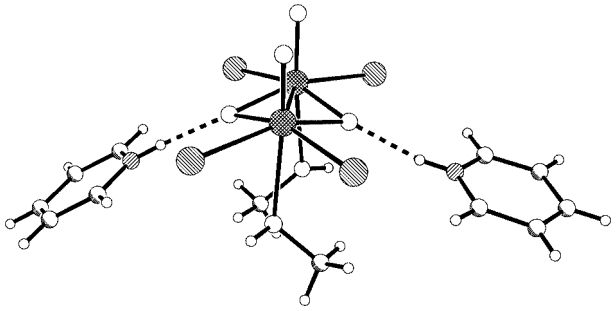

Figure 7. A dinuclear anion in **5** with a pair of hydrogen-bonded pyridinium cations.

Structure of $(PyH)_2[Mo_4O_8(OMe)_2(MeOH)_2Br_4]$ (6)

The structure of compound **6** is similar to its three, already described, analogues $(PyH)_2[Mo_4O_8(OMe)_2(MeOH)_2Cl_4]$ and $(PyH)_2[Mo_4O_8(OEt)_2(EtOH)_2X_4]$ (X = Cl and Br).[12a] It consists of pyridinium cations and tetranuclear anions (Figure 8). Selected geometric parameters are given in Table 4. The centrosymmetric tetranuclear core may be envisioned as two $\{Mo_2O_4\}^{2+}$ units sharing a pair of bridging oxo groups and being linked, in addition, by two methoxide ions (Scheme 2). The six peripheral positions of the $\{Mo_4O_4(\mu_3\text{-}O)_2(\mu_2\text{-}O)_2(\mu_2\text{-}OMe)_2\}^{2+}$ core are occupied by two methanol molecules at 2.2046(28) Å and four bromo ligands, two at shorter distances [2.5709(5) Å] and two at longer distances [2.5923(5) Å]. Methanol is engaged in a hydrogen-bonding interaction with the neighbouring bromo ligand at a distance of 3.2050(30) Å. This hydrogen bond contributes substantially to the stability of **6**. The hydrogen bond accounts for the variations in the molybdenum-to-bromine bond lengths. The pyridinium cations and the anionic clusters are linked, as observed before, through the agency of hydrogen bonds of moderate

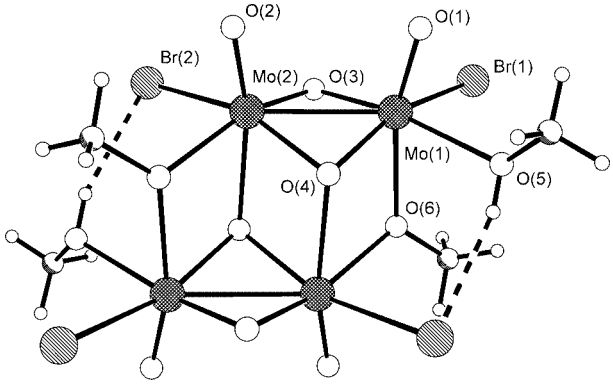

Figure 8. A drawing of the tetranuclear $[Mo_4O_8(OMe)_2(MeOH)_2Br_4]^{2-}$ unit in **6**. Hydrogen bonds between methanol and bromo ligands are drawn as dashed lines.

 © 2005 Wiley-VCH Verlag GmbH & Co. KGaA, Weinheim

strength, localised between the pyridinium nitrogen and the doubly-bridging oxygen from the anion [N(1)···O(3) = 2.7928(47) Å].

Table 4. Relevant geometric parameters [Å; °] of the $[Mo_4O_8(OMe)_2(MeOH)_2Br_4]^{2-}$ ion in **6**.

Mo–Mo	2.5988(4)
Mo=O	1.670(3), 1.679(3)
Mo–O_b[a]	1.932(3)–1.990(3)
Mo–MeOH	2.2046(28)
Mo–Br	2.5709(5), 2.5923(5)
Mo–O_b–Mo	81.77(10), 84.27(11)
O_b–Mo–O_b	93.04(11), 93.65(11)
Fold angle	149.99(14)
O···Br[b]	3.2050(30)

[a] O_b denotes bridging oxo groups in the $\{Mo_2O_4\}^{2+}$ unit: in a tetranuclear core one is formally a μ_2- and the other a μ_3-bridging ligand. [b] An intramolecular hydrogen bond between methanol and the neighbouring bromo ligand.

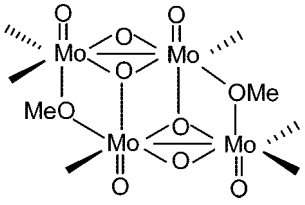

Scheme 2. A tetranuclear $\{Mo_4O_4(\mu_3\text{-}O)_2(\mu_2\text{-}O)_2(\mu_2\text{-}OMe)_2\}^{2+}$ core.

Comments on the Methanol Ligation

Structurally characterised alcohol complexes of molybdenum(V) are relatively rare. Invariably, these are all rather unstable species, in spite of the fact that in most cases the coordinated alcohol is involved in intra- or intermolecular hydrogen-bonding interactions through which some stability is gained. The only structurally characterised mononuclear complex is a very unstable $[MoOCl_3(EtOH)]$ with a square-pyramidal geometry and ethanol *cis* to the strongly bound terminal oxo group.[25] Likewise, the alcohol adopts *cis* positions with respect to the molybdenyl group in a series of dinuclear complexes with the composition $[Mo_2O_4L_2(ROH)_2]$ (L = β′-hydroxy-β-enaminone; R = Me, Et, *i*Pr),[26] tetranuclear $[(Mo_2O_4)_2(OMe)_2(MeOH)_2[HB(pz)_3]_2]$ [$HB(pz)_3^-$ = hydrotris(pyrazolyl)borate],[27] and octanuclear $[(Mo_2O_4)_4(OMe)_6(MeOH)_4Cl_2]$.[4] However, the position of ethanol in $[Mo_2O_2Cl_4(\mu_2\text{-}OEt)_2(\mu_2\text{-}EtOH)]$, where it also serves as a third bridge between metal atoms, is *trans* to both Mo=O groups.[28] The extreme reactivity of the latter complex was further exploited in the preparation of $[Mo_4O_6(OEt)_4(EtOH)_2Cl_4]$[24] and $[Mo_8O_{12}(OH)_6(OEt)_4(EtOH)_4Cl_6]$,[29] which both retain ethanol ligands on their periphery. The methanol ligands in the anions of $(PyH)_2[MoOCl_4(MeOH)]Cl$ (**2**), $(PyH)_2[Mo_2O_4Cl_4(MeOH)_2]$ (**3** and **4**) and $(PyH)_2[Mo_2O_4Br_4(MeOH)_2]$ (**5**) are *trans* to the terminal oxo groups. Owing to the *trans* influence of the latter, the methanol ligand binds at a longer distance. The corresponding bond in **2** is somewhat short taking into account its position. Comparison of the molybdenum-to-alcohol bond lengths in various molybdenum(V) compounds (Table 5) reveals that these can be as long as 2.49 Å or as short as 2.10 Å. The former describes a situation with the alcohol ligand in *trans*, and the latter with the alcohol ligand in the *cis* position with respect to the Mo=O group.

Table 5. Molybdenum-to-alcohol bond lengths [Å] in a series of molybdenum(V) compounds.[a]

	Mo–ROH
2	2.2911(5)
3	2.351(4), 2.372(4)
4	2.3591(18)
5	2.359(3)
6	2.2046(18)
$[Mo_2O_4L_2(MeOH)_2]$[26]	2.199(2), 2.201(2)
$[(Mo_2O_4)_2(OMe)_2(MeOH)_2[HB(pz)_3]_2]$[27]	2.264(3)
$[(Mo_2O_4)_4(OMe)_6(MeOH)_4Cl_2]$[4]	2.084, 2.195[b]
$(PyH)_2[Mo_4O_8(OMe)_2(MeOH)_2Cl_4]$[12a]	2.2070(13)
$(PyH)_2[Mo_4O_8(OEt)_2(EtOH)_2Cl_4]$[12a]	2.2025(19)
$(PyH)_2[Mo_4O_8(OEt)_2(EtOH)_2Br_4]$[12a]	2.2007(22)
$[MoOCl_3(EtOH)]$[25]	2.102(2)
$[Mo_4O_6(OEt)_4(EtOH)_2Cl_4]$[24]	2.144(4)
$[Mo_2O_2Cl_4(\mu_2\text{-}OEt)_2(\mu_2\text{-}EtOH)]$[28]	2.470(6)–2.495(6)

[a] See text for the positions of the alcohol ligands with respect to the Mo=O group. [b] Bond lengths are taken from the CCDC.[30]

Vibrational Spectroscopy

The presence of a terminal metal–oxygen double bond can be correlated with a stretching frequency in the range 1020–940 cm^{-1}.[3,31] The spectrum of $(PyH)_5[MoOCl_4(H_2O)]_3Cl_2$ (**1**) reveals a strong absorption at 982 cm^{-1}. A related compound, the bis(ethylenedithio)tetrathiafulvalene salt of $[MoOCl_4(H_2O)]^-$, displays the Mo=O stretch at 974 cm^{-1}.[17b] The spectra of compounds **2**, **3**, **5** and **6** display several strong bands in the region of 990–950 cm^{-1} which are associated with the Mo=O stretching frequencies.

The alcohol O–H stretching vibration is known to be sensitive to the involvement of the alcohol in hydrogen bonds. As a result, the band is shifted into a lower frequency region, to about 3300 cm^{-1}.[32] The spectrum of $(PyH)_2[Mo_4O_8(OMe)_2(MeOH)_2Br_4]$ (**6**) reveals a weak absorption at 3259 cm^{-1}, which may be attributed to the O–H stretching vibration. A band of medium intensity in a higher frequency region, at 3443 and 3431 cm^{-1}, is displayed in the spectra of $(PyH)_2[Mo_2O_4Cl_4(MeOH)_2]$ (**3**) and $(PyH)_2[Mo_2O_4Br_4(MeOH)_2]$ (**5**), respectively. Similarly, the O–H stretching mode in the spectrum of $[MoOCl_3(EtOH)]$ is also found at 3413 cm^{-1}.[25] Since considerable difficulties were experienced in recording the spectrum of $(PyH)_2[MoOCl_4(MeOH)]Cl$ (**2**), due to its decomposition, no conclusive assignments can be based upon it. Absorptions at 1002 cm^{-1} for **3**, 1003 cm^{-1} for **5** and 1026 cm^{-1} for **6** may be assigned to the C–O stretching vibrations. Their frequencies are consistent with the normally observed range (1075–1000 cm^{-1}).[32] The spectra of all methanol complexes, with **2** included, display a band of medium intensity in a narrow frequency range of 878–851 cm^{-1}. This absorp-

 © 2005 Wiley-VCH Verlag GmbH & Co. KGaA, Weinheim

tion was tentatively ascribed to the methyl rocking vibration.

The Starting Oxohalomolybdates(V)

Although the simple oxohalomolybdates(v), i.e., the six-coordinate, octahedral $[MoOX_5]^{2-}$, $[MoOX_4L]^-$ and five-coordinate, square-pyramidal $[MoOX_4]^-$ (X = F, Cl, Br, I and L = H_2O, THF etc.) have been extensively studied for more than a century,[33] as far as our starting materials, $(PyH)_2[MoOCl_5]$ and $(PyH)[MoOBr_4]$, are concerned, neither their true identities nor their structures were known. The formulation of the former as $(PyH)_2[MoOCl_5]$ was clearly erroneous, as shown by the X-ray structure analysis of **1** which has disclosed that it consists of $[MoOCl_4(H_2O)]^-$ and not $[MoOCl_5]^{2-}$ ions. Since $(PyH)_5[MoOCl_4(H_2O)]_3Cl_2$ (**1**) was isolated from hydrochloric acid, this result is not surprising in view of the previous finding that the species formed on dissolving $(Et_4N)_2[MoOCl_5]$ or $[MoOCl_3]$ in concentrated aqueous hydrochloric acid is $[MoOCl_4(H_2O)]^-$ and not $[MoOCl_5]^{2-}$,[34] as generally supposed.

Contrary to the well-defined geometry of $[MoOX_4L]^-$ ions, there has been considerable ambiguity concerning the structures of the base-free $[MoOX_4]^-$ ions. The metal displays a marked tendency to extend its coordination number to six, for instance by coordinating to water, so the square-pyramidal $[MoOX_4]^-$ ions are unstable in the presence of moisture, unless protected by bulky cations.[35] The sixfold coordination can also be achieved through straight Mo=O···Mo or bent Mo–X···Mo interactions, which result in pair-wise associations or infinite chains. Isopropylideneiminium[36] and trifluoroacetamidinium[37] salts of $[MoOCl_4]^-$ actually exist in the solid state as dimeric $[MoOCl_4]_2^{2-}$ anions where two asymmetric chloro bridges link a pair of molybdenum atoms. In the infinite anionic chains of $[Te_{15}X_4]_n[MoOX_4]_{2n}$ (X = Cl, Br), short, formally Mo=O double bonds with lengths of about 1.63 Å alternate with weaker, longer Mo–O bonds with lengths of around 2.41 Å.[38] On the other hand, the linkage of square-pyramids via asymmetric chloro bridges in $K[MoOCl_4]$ produces infinite zig-zag chains.[39] The presence of the sixth ligand, for instance base L in $[MoOX_4L]^-$, has the effect of altering the strength of the Mo=O bond, and this is reflected in the position of the Mo=O stretching frequency.[40] Consequently, the shift in the Mo=O stretching frequency due to the Mo=O···Mo interaction is even more pronounced. The absorption at 883 cm^{-1} in the infrared spectrum of $(PyH)[MoOBr_4]$ strongly indicates a polymeric chain structure via Mo=O···Mo interactions.[13,41] Support for this also comes from the infrared spectrum of $(PyH)_2[Mo_2O_4Cl_4]\cdot 3H_2O$ whose X-ray structure reveals chains of dinuclear $[Mo_2O_4Cl_4]^{2-}$ ions linked via Mo=O···Mo interactions.[42] The Mo–O stretching band for $(PyH)_2[Mo_2O_4Cl_4]\cdot 3H_2O$ is observed at 888 cm^{-1}.

Synthetic Considerations

The green colour of the solution obtained upon dissolving $(PyH)_5[MoOCl_4(H_2O)]_3Cl_2$ (**1**) in methanol does not suggest a substantial extent of dimerisation. Undisputedly, the first reaction upon dissolving the $[MoOCl_4(H_2O)]^-$ ion in methanol is the substitution of the coordinated water for methanol, which is present in huge excess. The product of this reaction, $[MoOCl_4(MeOH)]^-$, is a labile species, which reacts with atmospheric moisture almost instantaneously. If the solution whose preparation is described in the synthetic procedure for **2** is exposed to air after the addition of diethyl ether, it undergoes a rapid colour change from green to orange. The evaporation of solvents in air produces a substantial amount of orange crystals, which were identified by X-ray diffraction as a triclinic modification of $(PyH)_2[Mo_2O_4Cl_4(MeOH)_2]$ (**3**), within a couple of hours. Overnight evaporation leaves behind a solid residue which consists mainly of large, needle-like crystals of the starting material $(PyH)_5[MoOCl_4(H_2O)]_3Cl_2$ (**1**), and an unidentified, dark blue, amorphous phase. The taking-up of water from the atmosphere by $[MoOCl_4(MeOH)]^-$ and the subsequent deposition of $(PyH)_5[MoOCl_4(H_2O)]_3Cl_2$ (**1**) as the final product, is not surprising. As far as the formation and the fate of the intermediate product, $(PyH)_2[Mo_2O_4Cl_4(MeOH)_2]$ (**3**), are concerned, both are unclear. Bearing in mind that no substantial dimerisation takes place in methanol, it is likely that water from the atmosphere triggers the dimerisation. Since $[Mo_2O_4Cl_4(MeOH)_2]^{2-}$ still possesses labile sites, four chloro and two methanol ligands, further substitution reactions are initiated and accompanied by partial oxidation to the +6 oxidation state, which results in a blue material. Addition of a stoichiometric amount of pyridine or trifluoroacetate to a methanol solution of $[MoOCl_4(H_2O)]^-$ was shown to promote the dimerisation and $(PyH)_2[Mo_2O_4Cl_4(MeOH)_2]$ (**3** and **4**) was isolated. On prolonged reaction times further assembly of $\{Mo_2O_4\}^{2+}$ units into $\{Mo_4O_4(\mu_3\text{-}O)_2(\mu_2\text{-}O)_2(\mu_2\text{-}OMe)_2\}^{2+}$ core (Scheme 2), found in the final product $(PyH)_2[Mo_4O_8(OMe)_2(MeOH)_2Cl_4]$, was observed. The latter process can be avoided by keeping the reaction temperature at 5 °C. Addition of a larger amount of pyridine yields $[Mo_4O_8(OMe)_2Cl_2Py_4]$. Pyridine advances the assembly of dinuclear units and once its concentration is high enough, it coordinates to four out of six terminal positions of the $\{Mo_4O_4(\mu_3\text{-}O)_2(\mu_2\text{-}O)_2(\mu_2\text{-}OMe)_2\}^{2+}$ core.

With the greater lability of the coordinated bromo ligands, the chances of isolating one of the more reactive intermediates are significantly smaller. Rather, the substitution tends to proceed further than in the case of the chloro starting material. Accordingly, the mononuclear $[MoOBr_4(MeOH)]^-$ could not be isolated under analogous conditions to those employed for $[MoOCl_4(MeOH)]^-$. $(PyH)_2[Mo_2O_4Br_4(MeOH)_2]$ (**5**) can only be isolated at 5 °C after the addition of trifluoroacetate to the methanol solution. At room temperature, further assembly of dinuclear subunits takes place with the formation of $(PyH)_2[Mo_4O_8(OMe)_2(MeOH)_2Br_4]$ (**6**) as the final product. The greater reactivity of the bromo-coordinated species is also demonstrated by the reaction where a small amount of pyridine was added to a methanol solution of $(PyH)[MoOBr_4]$, which produced $(PyH)_2[Mo_4O_8(OMe)_2(MeOH)_2Br_4]$ (**6**)

 © 2005 Wiley-VCH Verlag GmbH & Co. KGaA, Weinheim

even at low temperature. $(PyH)_2[Mo_4O_8(OMe)_2(MeOH)_2Br_4]$ (**6**) is the first relatively stable bromo-coordinated species.

Similar compounds to ours have been obtained under strictly anhydrous conditions and temperatures as low as –78 °C from reactions of molybdenum(v) chloride in methanol.[43] The methanolysis of the Mo–Cl bonds was proposed to take place in step with successive formation of Mo=O bonds.[44] The formulae of the products, inferred from the elemental analysis data, are highly reminiscent of our methanol complexes. In particular, this applies to the green product of the reaction of $MoOCl_3$·2MeOH with pyridinium chloride in methanol at –78 °C, formulated as (PyH)[$MoOCl_4$]·MeOH, and the red, crystalline (PyH)[MoO_2Cl_2]·MeOH obtained from the reaction of $MoCl_5$ with pyridine in methanol.[43] The composition of the former resembles that of $(PyH)_2[MoOCl_4(MeOH)]Cl$ (**2**), while the composition of the latter is the same as for $(PyH)_2[Mo_2O_4Cl_4(MeOH)_2]$ (**3**). The lack of spectroscopic data precludes unambiguous conclusions about their true identity, although it can be reasonably expected that both molybdenum(v) chloride and $(PyH)_5[MoOCl_4(H_2O)]_3Cl_2$ (**1**) would react in methanol with the formation of species with, if not exact, at least similar compositions. Irrespective of the starting material, the reactive fragments released in the first stages of the reaction reassemble with the formation of the most stable and least soluble species under the given conditions. In a more recent study of the molybdenum(v) chloride reactions in rigorously dried ethanol, $[MoOCl_3(EtOH)]$, H[$MoOCl_4$]·2EtOH,[25] and $[Mo_2O_2Cl_4(\mu_2\text{-}OEt)_2(\mu_2\text{-}EtOH)]$,[28] were isolated as the very first products, as confirmed by X-ray diffraction analyses. $[Mo_2O_2Cl_4(\mu_2\text{-}OEt)_2(\mu_2\text{-}EtOH)]$, which possesses several good leaving groups, reacts readily to form $[Mo_2O_4Cl_4]^{2-}$ and a series of $\{Mo_2O_2(\mu_2\text{-}O)(\mu_2\text{-}OEt)\}^{3+}$-containing clusters.[24,29] Interestingly, the same structural types are encountered within the $\{Mo_2O_2(\mu_2\text{-}O)(\mu_2\text{-}OEt)\}^{3+}$ clusters as in the larger group of $\{Mo_2O_4\}^{2+}$ clusters. Moreover, hydrogen chloride and chloroethane were found to be side products in the ethanolysis of Mo–Cl bonds. The proposed mechanisms of the formation of Mo–O and Mo–OR bonds cannot be applied to our reaction system as no attempts were made to avoid traces of water. In view of the high susceptibility of $[MoOX_4]^-$ and $[MoOX_4L]^-$ species towards hydrolysis, the role of water inherently present in the used solvents has to be acknowledged. The comparison with the two above-mentioned systems is therefore limited to the nature of the obtained products only.

Conclusions

Facile substitution chemistry of mononuclear $[MoOCl_4(H_2O)]^-$ or polymeric $[MoOBr_4]_n^{n-}$ in methanol solutions has afforded a series of novel molybdenum(v) complexes with coordinated methanol: a mononuclear anion in $(PyH)_2[MoOCl_4(MeOH)]Cl$ (**2**), a dinuclear $\{Mo_2O_4\}^{2+}$-based anion in $(PyH)_2[Mo_2O_4Cl_4(MeOH)_2]$, which crystallises in a triclinic (**3**) and in an orthorhombic (**4**) unit cell, an analogous bromo-coordinated dinuclear anion in $(PyH)_2[Mo_2O_4Br_4(MeOH)_2]$ (**5**) and a tetranuclear anion built of two $\{Mo_2O_4\}^{2+}$ subunits in $(PyH)_2[Mo_4O_8(OMe)_2(MeOH)_2Br_4]$ (**6**). The coordinated methanol molecule invites further investigations as a potentially functional and highly labile group. Such studies are underway.

Experimental Section

General Remarks: Reagents were purchased from Aldrich. No precaution was taken to eliminate traces of moisture present in solvents. The IR spectra were measured on solid samples as Nujol or poly(chlorotrifluoroethylene) mulls using a Perkin–Elmer 2000 series FT-IR spectrometer. Elemental analyses were performed by the Chemistry Department service at the University of Ljubljana. Molybdenum was determined as $PbMoO_4$ and halide by potentiometric titration with a 0.100 M solution of $AgNO_3$.

(PyH)[$MoOBr_4$]: Finely powdered $(NH_4)_2[MoBr_5(H_2O)]$[45] (2.75 g, 5.0 mmol) was added to a mixture of pyridine (0.8 mL) and conc. hydrobromic acid (25 mL). The solution was gently heated at about 80 °C until all solid material had been consumed. Hydrazinum dichloride (0.50 g, 4.76 mmol) was added and the reaction mixture was heated for another five minutes. Meanwhile its colour changed from brown to yellow-red. The obtained solution was left to stand at ambient conditions. The red, block-shaped, crystals that formed overnight were filtered off and washed with hexanes. Yield: 32% (820 mg, 1.6 mmol). IR: $\tilde{\nu}$ = 1627 cm^{-1} (s), 1597 (vs), 1530 (vvs), 1321 (s), 1229 (w), 1195(m), 1164 (m), 1047 (m), 974 (w), 883 (vvs), 747 (m), 731 (vvs), 664 (vvs). $C_5H_6Br_4MoNO$ (511.65): calcd. C 11.74, H 1.18, Br 62.47, Mo 18.75, N 2.74; found C 11.51, H 1.30, Br 62.3, Mo 18.6, N 2.69.

$(PyH)_5[MoOCl_4(H_2O)]_3Cl_2$ (1): This synthetic procedure combines two literature approaches to related compounds.[46] A mixture of conc. hydrochloric acid (12.5 mL) and hydriodic acid (3.5 mL) was added to a 1.0 M solution of molybdenum(VI) oxide in conc. hydrochloric acid (25 mL). The reaction mixture was heated in an open flask until all iodine had been driven off. A mixture of pyridine (6.3 mL) and conc. hydrochloric acid (35 mL) was added, the flask was stoppered and left in an ice bath for two hours. Emerald-green, needle-shaped crystals of **1** were filtered off and washed with hexanes. Yield: 82% (8.80 g, 6.84 mmol). IR: $\tilde{\nu}$ = 3195 cm^{-1} (w), 3146 (w), 3126 (w), 3088 (w), 1631 (m), 1598 (vs), 1525 (vs), 1237 (m), 1196 (m), 1164 (m), 1078 (w), 1047 (m), 1027 (w), 982 (vvs), 905 (m), 749 (vvs), 722 (m), 677 (vvs). $C_{25}H_{36}Cl_{14}Mo_3N_5O_6$ (1286.7): calcd. C 23.34, H 2.82, Cl 38.57, Mo 22.37, N 5.44; found C 23.45, H 2.74, Cl 38.4, Mo 22.3, N 5.37.

$(PyH)_2[MoOCl_4(MeOH)]Cl$ (2): $(PyH)_5[MoOCl_4(H_2O)]_3Cl_2$ (**1**; 400 mg, 0.311 mmol) was dissolved in methanol (4.0 mL). The solution was kept in a stoppered Erlenmeyer flask at ambient conditions overnight. Diethyl ether (8.5 mL) was added dropwise with constant stirring. After the addition of diethyl ether, the colour of the solution changed from yellow-green to light-green. Within one hour large, plate-like crystals of **2** started to grow from the solution. *Note.* The crystals of **2** decompose almost instantaneously when taken out from the mother liquor. IR: $\tilde{\nu}$ = 3207 cm^{-1} (w), 3145 (w), 1632 (m), 1599 (s), 1526 (s), 1322 (m), 1237 (m), 1190 (m), 1164 (m), 1079 (w), 1050 (m), 1056 (m), 1030 (m), 982 (s), 962 (vs), 851 (m), 748 (vs), 729 (vs), 669 (vs), 608 (s).

 © 2005 Wiley-VCH Verlag GmbH & Co. KGaA, Weinheim

Triclinic (3) and Orthorhombic (4) Modifications of $(PyH)_2[Mo_2O_4Cl_4(MeOH)_2]$. Procedure a: $(PyH)_5[MoOCl_4(H_2O)]_3Cl_2$ (**1**; 400 mg, 0.311 mmol) was dissolved in methanol (4.0 mL). Pyridine (1.20 mmol; 2.4 mL of a 0.50 M pyridine solution in methanol) was added to the solution. The colour changed immediately from yellow-green to brown-orange. The Erlenmeyer flask was stoppered and left at ambient conditions for three hours. Orange crystals of **3** could then be filtered off. Yield: 40% (116 mg, 0.187 mmol). IR: $\tilde{\nu}$ = 3611 cm^{-1} (w), 3552 (w), 3443 (m), 3411 (w), 3129 (w), 3107 (w), 3082(w), 3059 (w), 1634 (m), 1615 (m), 1592 (m), 1541 (m), 1484 (vvs), 1253 (m), 1200 (s), 1167 (m), 1103 (m), 1095 (w), 1061 (w), 1051 (w), 1002 (vvs), 986 (vvs), 964 (vvs), 950 (m), 878 (m), 760 (vs), 750 (vvs), 743 (vvs), 735(vvs), 728 (vvs), 681 (vs), 607 (s), 503 (s). *Note.* If the reaction mixture was left at ambient conditions overnight, red, block-like crystals formed. The product revealed an infrared spectrum identical to that described for $(PyH)_2[Mo_4O_8(OMe)_2(MeOH)_2Cl_4]$.[12a] Yield: 41% (91 mg, 0.097 mmol). IR: $\tilde{\nu}$ = 3232 cm^{-1} (m), 3159 (w), 3129 (w), 3105 (w), 3085 (w), 3062 (w), 1635 (vs), 1610 (vvs), 1537 (vvs), 1251 (m), 1201 (s), 1164 (s), 1113 (m), 1032 (vvs), 1002 (vvs), 966 (vvs), 946 (vvs), 878 (w), 755 (vvs), 725 (vvs).

Procedure b: Pyridinium trifluoroacetate (1.20 mmol; 1.0 mL of a 1.20 M solution in acetonitrile) was added to methanol (4.0 mL). $(PyH)_5[MoOCl_4(H_2O)]_3Cl_2$ (**1**; 400 mg, 0.311 mmol) was dissolved in this solution. The orange-brown reaction mixture was left in a closed flask at ambient conditions overnight. A vial containing diethyl ether (2.5 mL) was carefully placed into the flask on the following day. The flask was stoppered and placed in the refrigerator. Orange, rhombic crystals of $(PyH)_2[Mo_2O_4Cl_4(MeOH)_2]$ (triclinic modification **3**) and red, block-shaped crystals of $(PyH)_2[Mo_2O_4Cl_4(MeOH)_2]$ (orthorhombic modification **4**) grew from the solution within 24 hours.

Addition of a Larger Amount of Pyridine to a Methanol Solution of $(PyH)_5[MoOCl_4(H_2O)]_3Cl_2$ (1): $(PyH)_5[MoOCl_4(H_2O)]_3Cl_2$ (**1**; 400 mg, 0.311 mmol) was dissolved in methanol (4.0 mL). After the addition of 12.3 mmol of pyridine (1.0 mL) to the yellow-green solution, its colour changed to brown-orange. The Erlenmeyer flask was stoppered and left at ambient conditions for five hours. A red, crystalline product was filtered off and washed with hexanes. The product revealed an infrared spectrum identical to that described for $[Mo_4O_8(OMe)_2Cl_2Py_4]$.[12f] Yield: 91% (205 mg, 0.213 mmol). IR: $\tilde{\nu}$ = 3391 cm^{-1} (m), 3067 (w), 2788 (m), 1636 (w), 1607 (vvs), 1571 (w), 1540 (w), 1362 (w), 1303 (w), 1246 (w), 1222 (vs), 1164 (m), 1154 (m), 1076 (vvs), 1044 (vvs), 1024 (vvs), 954 (vvs), 933 (vvs), 921 (vvs), 875 (w), 757 (vvs), 744 (vvs).

$(PyH)_2[Mo_2O_4Br_4(MeOH)_2]$ (5): Pyridinium trifluoroacetate (1.20 mmol; 1.0 mL of a 1.20 M solution in acetonitrile) was added to methanol (4.0 mL) in an Erlenmeyer flask. $(PyH)[MoOBr_4]$ (480 mg, 0.94 mmol) was dissolved in this solution. The orange-red solution was immediately placed in the refrigerator (5 °C). Diethyl ether (2.5 mL) was carefully added to the solution on the following day. The reaction mixture was placed back in the refrigerator and after two days a second portion of diethyl ether (4.5 mL) was added. Red, block-shaped crystals of **5** appeared within six hours. *Note.* The crystals are not stable outside the mother liquor. IR: $\tilde{\nu}$ = 3611 cm^{-1} (w), 3563 (w), 3431 (m), 3127 (w), 3101 (w), 3083 (w), 3062 (m), 3059 (w), 2924 (m), 2856 (m), 1625 (vs), 1613 (vs), 1592 (s), 1537 (s), 1483 (vs), 1253 (w), 1200 (m), 1194 (m), 1164 (m), 1093 (w), 1060(m), 1051 (m), 1003 (s), 971 (vvs), 953 (vs), 876 (w), 755 (vs), 718 (vvs), 679 (vs), 606 (s), 490 (s).

$(PyH)_2[Mo_4O_8(OMe)_2(MeOH)_2Br_4]$ (6). Procedure a: The same procedure was used as for the preparation of compound **5**, only the reaction mixture was left to stand at ambient conditions. Pyridinium trifluoroacetate (1.20 mmol; 1.0 mL of a 1.20 M solution in acetonitrile) was added to methanol (4.0 mL) in an Erlenmeyer flask. $(PyH)[MoOBr_4]$ (480 mg, 0.94 mmol) was dissolved in this solution. The flask was stoppered and the orange-red reaction mixture was left to stand at ambient conditions for two days. A vial containing diethyl ether (5.0 mL) was carefully inserted into the flask. The flask was tightly stoppered and left at ambient conditions for two more days. Red, block-shaped crystals of **6** were filtered off and washed with hexanes. Yield: 53% (140 mg, 0.125 mmol).

Procedure b: $(PyH)[MoOBr_4]$ (480 mg, 0.94 mmol) was dissolved in methanol (4.0 mL) and pyridine (1.20 mmol; 2.4 mL of a 0.50 M solution in methanol) was then added. The orange-red solution was left at ambient conditions. A vial with diethyl ether (5.0 mL) was carefully inserted into the Erlenmeyer flask on the following day. Red, block-shaped crystals formed within two days. The product was filtered off and washed with hexanes. Yield: 39% (103 mg, 0.0921 mmol). *Note.* The same product, $(PyH)_2[Mo_4O_8(OMe)_2(MeOH)_2Br_4]$ (**6**), was obtained if the reaction mixture was kept at 5 °C the whole time. IR: $\tilde{\nu}$ = 3259 cm^{-1} (m), 3135 (w), 3132 (w),

Table 6. Crystallographic data for compounds **1**–**6**.

	1	**2**	**3**	**4**	**5**	**6**
Empirical formula	$C_{25}H_{36}Cl_{14}Mo_3N_5O_6$	$C_{11}H_{16}Cl_5MoN_2O_2$	$C_{12}H_{20}Cl_4Mo_2N_2O_6$	$C_{12}H_{20}Cl_4Mo_2N_2O_6$	$C_{12}H_{20}Br_4Mo_2N_2O_6$	$C_{14}H_{26}Br_4Mo_4N_2O_{12}$
Formula mass	1286.7	481.45	621.98	621.98	799.82	1117.77
Crystal system	orthorhombic	monoclinic	triclinic	orthorhombic	orthorhombic	triclinic
Space group	*Pmma*	$P2_1/n$	$P\bar{1}$	*Pcan*	*Pcan*	$P\bar{1}$
T [K]	200(2)	150(2)	150(2)	150(2)	150(2)	150(2)
a [Å]	21.4445(2)	7.35420(10)	8.3525(2)	8.25560(10)	8.32140(10)	9.2712(2)
b [Å]	8.06490(10)	33.3209(4)	9.7414(2)	14.0632(2)	14.4784(3)	9.5517(2)
c [Å]	13.34650(10)	7.88750(10)	14.7231(4)	17.9084(2)	18.3149(4)	9.8151(2)
α [°]	90	90	93.3055(11)	90	90	111.1186(9)
β [°]	90	104.6646(5)	104.1614(11)	90	90	113.3588(9)
γ [°]	90	90	114.5058(12)	90	90	94.5516(11)
V [Å^3]	2308.25(4)	1869.86(4)	1039.57(4)	2079.17(5)	2206.59(7)	718.86(3)
Z	2	4	2	4	4	1
λ [Å]	0.71073	0.71073	0.71073	0.71073	0.71073	0.71073
μ [mm^{-1}]	1.654	1.418	1.750	1.750	8.408	7.318
Collected reflections	5190	7467	7955	4409	4467	5829
Unique reflections, R_{int}	2905, 0.0110	4174, 0.0142	4544, 0.0206	2359, 0.0081	2460, 0.0305	3149, 0.0258
Observed reflections	2512	3974	4370	2257	2200	2871
$R1$ [$I > 2\sigma(I)$]	0.0298	0.0232	0.0416	0.0243	0.0342	0.0287
$wR2$ [all data]	0.0754	0.0789	0.1217	0.0587	0.0873	0.0761

 © 2005 Wiley-VCH Verlag GmbH & Co. KGaA, Weinheim

3103 (w), 3082 (w), 3060 (m), 1635 (s), 1609 (s), 1536 (vs), 1485 (vvs), 1429 (m), 1369 (m), 1250 (m), 1202 (s), 1162 (s), 1106 (m), 1053 (m), 1026 (vvs), 994 (vvs), 965 (vvs), 946 (vvs), 876 (w), 752 (vvs), 724 (vvs), 674 (vvs), 639 (w), 608 (s). $C_{14}H_{26}Br_4Mo_4N_2O_{12}$ (1117.8): calcd. C 15.04, H 2.34, Br 28.60, Mo 34.33, N 2.51; found C 15.12, H 2.42, Br 28.75, Mo 34.2, N 2.45.

X-ray Crystallographic Study: The crystals were mounted on the tip of a glass fibre with a small amount of silicon grease and transferred to a goniometer head. Data were collected with a Nonius Kappa CCD diffractometer. For all compounds, data reduction and integration were performed with the software package DENZO-SMN.[47] Averaging of the symmetry-equivalent reflections largely compensated for the absorption effects. The coordinates of some or all of the non-hydrogen atoms were found by direct methods using the structure solution program SHELXS.[48] The positions of the remaining non-hydrogen atoms were located by use of a combination of least-squares refinement and difference Fourier maps with the SHELXL-97 program.[48] Non-hydrogen atoms were refined with anisotropic displacement parameters. The water hydrogen atoms in **1**, hydroxyl methanol hydrogen atoms in **2**, **3**, **4** and **5** located in the final stages of the refinement from the difference Fourier maps were refined with isotropic displacement parameters. The remaining hydrogen atoms were included in the structure-factor calculations at idealised positions. Cell parameters and refinement results for compounds **1**–**6** are summarised in Table 6. Figures depicting the structures were prepared using SHELXTL[49] and PLATON.[50] CCDC-248502 (for **1**), -248503 (for **2**), -248504 (for **3**), -248505 (for **4**), -248506 (for **5**) and -248507 (for **6**) contain the supplementary crystallographic data for this paper. These data can be obtained free of charge from The Cambridge Crystallographic Data Centre via www.ccdc.cam.ac.uk/data_request/cif.

Acknowledgments

We are grateful to the Slovenian Ministry of Education, Science and Sport for supporting this work through research grant P1-0134. We also thank the same agency for funds to purchase the Nonius Kappa CCD diffractometer.

[1] a) C. L. Hill (Guest editor), *Chem. Rev.* **1998**, *98*, 1–390; b) *Polyoxometallates: From Platonic Solids to Anti-Retroviral Activity* (Eds.: M. T. Pope, A. Müller), Kluwer Academic Publishers, Dordrecht, **1994** and references cited therein.
[2] H. K. Chae, W. G. Klemperer, T. A. Marquart, *Coord. Chem. Rev.* **1993**, *128*, 209–224.
[3] E. I. Stiefel, *Prog. Inorg. Chem.* **1977**, *22*, 1–223.
[4] H. K. Chae, J. Y. Kim, C. Hwang, B. W. Lee, *Chem. Lett.* **2002**, 650–651.
[5] A. Johansson, M. Roman, G. A. Seisenbaeva, L. Kloo, Z. Szabo, V. G. Kessler, *J. Chem. Soc., Dalton Trans.* **2000**, 387–394.
[6] M. J. Manos, J. D. Woollins, A. M. Z. Slawin, T. A. Kabanos, *Angew. Chem. Int. Ed.* **2002**, *41*, 2801–2805.
[7] C. du Peloux, P. Mialane, A. Dolbecq, J. Marrot, F. Secheresse, *Angew. Chem. Int. Ed.* **2002**, *41*, 2808–2810.
[8] E. Dumas, C. Sassoye, K. D. Smith, S. C. Sevov, *Inorg. Chem.* **2002**, *41*, 4029–4032.
[9] C. du Peloux, A. Dolbecq, P. Mialane, J. Marrot, F. Secheresse, *Dalton Trans.* **2004**, 1259–1263.
[10] A. Müller, C. Kuhlmann, H. Bögge, M. Schmidtmann, M. Baumann, E. Krickemeyer, *Eur. J. Inorg. Chem.* **2001**, 2271–2277.
[11] M.-M. Rohmer, M. Benard, *Dalton Trans.* **2003**, 3587–3590.
[12] For a more detailed account see: a) B. Modec, J. V. Brenčič, J. Zubieta, *J. Chem. Soc., Dalton Trans.* **2002**, 1500–1507; b) B. Modec, J. V. Brenčič, *J. Cluster Sci.* **2002**, *13*, 279–302; c) B. Modec, J. V. Brenčič, R. C. Finn, R. S. Rarig, J. Zubieta, *Inorg. Chim. Acta* **2001**, *322*, 113–119; d) B. Modec, J. V. Brenčič, L. Golič, *Polyhedron* **2000**, *19*, 1219–1225; e) B. Modec, J. V. Brenčič, L. Golič, L. M. Daniels, *Polyhedron* **2000**, *19*, 1407–1414; f) B. Modec, J. V. Brenčič, L. Golič, G. Giester, *Inorg. Chim. Acta* **2000**, *307*, 32–40; g) B. Modec, J. V. Brenčič, I. Leban, *Inorg. Chem. Commun.* **1998**, *1*, 161–163.
[13] E. A. Allen, B. J. Brisdon, D. A. Edwards, G. W. A. Fowles, R. G. Williams, *J. Chem. Soc.* **1963**, 4649–4657.
[14] Some of the more recent examples are: a) $[Mo_2O_4(C_4O_4)(R\text{-}Py)_4]$ (R-Py = alkyl-substituted pyridine; $C_4O_4^{2-}$ = squarate anion) [B. Modec, J. V. Brenčič, E. M. Burkholder, J. Zubieta, *Dalton Trans.* **2003**, 4618–4625]; b) $[Mo_2O_4(\eta^2\text{-}C_2O_4)_2Py_2]^{2-}$ and $[\{Mo_2O_4(\eta^2\text{-}C_2O_4)_2\}_2(\mu_4\text{-}C_2O_4)]^{6-}$ [B. Modec, J. V. Brenčič, J. Koller, *Eur. J. Inorg. Chem.* **2004**, 1611–1620]; c) $[Mo_2O_4Cl_2(\eta^2\text{-}NP)_2]$ [NP = 2-pyridyl(diisopropylphosphanyl)-methane] [H.-F. Lang, P. E. Fanwick, R. A. Walton, *Inorg. Chim. Acta* **2002**, *328*, 232–236]; d) $[Mo_2O_4(tpen)]^{2-}$ [tpen = *N*,*N*,*N*′,*N*′-tetrakis(2-pyridylmethyl)ethylenediamine] [R. Hazama, K. Umakoshi, A. Ichimura, S. Ikari, Y. Sasaki, T. Ito, *Bull. Chem. Soc. Jpn.* **1995**, *68*, 456–468].
[15] G. S. Kim, D. A. Keszler, C. W. DeKock, *Inorg. Chem.* **1991**, *30*, 574–577.
[16] A. Bino, F. A. Cotton, *Inorg. Chem.* **1979**, *18*, 2710–2713.
[17] a) A. Bino, F. A. Cotton, *J. Am. Chem. Soc.* **1979**, *101*, 4150–4154; b) C. J. Kepert, M. Kurmoo, M. R. Truter, P. Day, *J. Chem. Soc., Dalton Trans.* **1997**, 607–613; c) C. D. Garner, L. H. Hill, F. E. Mabbs, D. L. McFadden, A. T. McPhail, *J. Chem. Soc., Dalton Trans.* **1977**, 1202–1207; d) S. J. Hibble, S. G. Eversfield, A. M. Chippindale, *Acta Crystallogr., Sect. E* **2002**, *58*, m366–m368 and references cited therein.
[18] L. Lisnard, P. Mialane, A. Dolbecq, J. Marrot, F. Secheresse, *Inorg. Chem. Commun.* **2003**, *6*, 503–505.
[19] Their preparations require strictly anhydrous conditions. See for example: a) S. Chitsaz, E. Iravani, J. Pauls, B. Neumuller, *Z. Naturforsch., Teil B* **2001**, *56*, 759–764; b) M. G. B. Drew, J. D. Wilkins, *J. Chem. Soc., Dalton Trans.* **1975**, 1984–1989; c) D. Fenske, K. Jansen, K. Dehnicke, *Z. Naturforsch., Teil B* **1986**, *41*, 523–526; d) J. Beck, M. Hengstmann, *Z. Anorg. Allg. Chem.* **1998**, *624*, 1943–1950.
[20] O. Piovesana, C. Furlani, *Inorg. Nucl. Chem. Lett.* **1967**, *3*, 535–538.
[21] T. Glowiak, M. Sabat, *J. Cryst. Mol. Struct.* **1975**, *5*, 247–256.
[22] M. I. Khan, Q. Chen, J. Zubieta, *Inorg. Chim. Acta* **1995**, *235*, 135–145.
[23] K. J. Moynihan, P. M. Boorman, J. M. Ball, V. D. Patel, K. A. Kerr, *Acta Crystallogr., Sect. B* **1982**, *38*, 2258–2261.
[24] C. Limberg, A. J. Downs, A. J. Blake, S. Parsons, *Inorg. Chem.* **1996**, *35*, 4439–4448.
[25] C. Limberg, R. Boese, B. Schiemenz, *J. Chem. Soc., Dalton Trans.* **1997**, 1633–1637.
[26] M. Cindrić, V. Vrdoljak, N. Strukan, A. Brbot-Šaranovič, P. Novak, B. Kamenar, *Inorg. Chim. Acta* **2004**, *357*, 931–938.
[27] S. Lincoln, S. A. Koch, *Inorg. Chem.* **1986**, *25*, 1594–1602.
[28] C. Limberg, S. Parsons, A. J. Downs, D. J. Watkin, *J. Chem. Soc., Dalton Trans.* **1994**, 1169–1174.
[29] A. J. Blake, A. J. Downs, C. Limberg, S. Parsons, *J. Chem. Soc., Dalton Trans.* **1995**, 3263–3268.
[30] F. H. Allen, O. Kennard, R. Taylor, *Acc. Chem. Res.* **1983**, *16*, 146–153.
[31] C. G. Barraclough, J. Lewis, R. S. Nyholm, *J. Chem. Soc.* **1959**, 3552–3555.
[32] N. B. Colthup, L. H. Daly, S. E. Wiberley, *Introduction to Infrared and Raman Spectroscopy*, Academic Press, **1964**, pp. 273–274 and 189–190.
[33] a) R. G. James, W. Wardlaw, *J. Chem. Soc.* **1927**, 2145–2156; b) C. D. Garner, J. M. Charnock, in *Comprehensive Coordination*

Chemistry (Eds.: G. Wilkinson, R. D. Gillard, J. A. McCleverty), **1987**, chapter 36.4., pp. 1329–1374.
[34] P. M. Boorman, C. D. Garner, F. E. Mabbs, *J. Chem. Soc., Dalton Trans.* **1975**, 1299–1306.
[35] A. J. Blake, S. Parsons, A. J. Downs, C. Limberg, *Acta Crystallogr., Sect. C* **1995**, *51*, 571–573.
[36] P. Klinzing, A. El-Kholi, U. Müller, K. Dehnicke, K. Findeisen, *Z. Anorg. Allg. Chem.* **1989**, *569*, 83–90.
[37] R. Herbst-Irmer, E. Egert, *Acta Crystallogr., Sect. C* **1992**, *48*, 1843–1844.
[38] J. Beck, M. A. Pell, J. Richter, J. A. Ibers, *Z. Anorg. Allg. Chem.* **1996**, *622*, 473–478.
[39] S. Rabe, U. Müller, *Z. Anorg. Allg. Chem.* **1999**, *625*, 842–844.
[40] J. G. Scane, *Acta Crystallogr.* **1967**, *23*, 85–89.
[41] (PyH)[$MoOBr_4$] crystallises in the shape of relatively large and well-formed, block-like crystals, yet these do not diffract well enough to allow a successful structure solution. Although the infrared spectrum reveals typical absorptions of pyridinium cations, apart from the clearly visible pattern of infinite $[MoOBr_4]_n^{n-}$ chains in the partial structure solution, the remaining residual electron density cannot be associated with pyridinium cations. Cell dimensions for (PyH)[$MoOBr_4$]: $a = b = 8.40$ Å, $c = 4.00$ Å, $\alpha = \beta = \gamma = 90°$, tetragonal (J. V. Brenčič, I. Leban, unpublished results).
[42] R. Mattes, D. Altmeppen, M. Fetzer, *Z. Naturforsch., Teil B* **1976**, *31*, 1356–1359. Similar problems were encountered during the X-ray structure solution as for (PyH)[$MoOBr_4$]: a clearly-visible pattern of anionic $[Mo_2O_4Cl_4]_n^{2n-}$ chains and no pyridinium cations.
[43] a) H. Funk, F. Schmeil, H. Scholz, *Z. Anorg. Allg. Chem.* **1961**, *310*, 86–89; b) H. Funk, M. Hesselbarth, F. Schmeil, *Z. Anorg. Allg. Chem.* **1962**, *318*, 318–322.
[44] N. T. Denisov, N. I. Shuvalova, V. F. Shuvalov, *Zh. Fiz. Khim.* **1971**, *45*, 2796–2799.
[45] R. G. Cavell, J. W. Quail, *Inorg. Chem.* **1983**, *22*, 2597–2599.
[46] a) G. R. Hanson, A. A. Brunette, A. C. McDonell, K. S. Murray, A. G. Wedd, *J. Am. Chem. Soc.* **1981**, *103*, 1953–1959; b) H. K. Saha, M. C. Halder, *J. Inorg. Nucl. Chem.* **1971**, *33*, 705–711.
[47] Z. Otwinowski, W. Minor, *Methods Enzymol.* **1997**, *276*, 307–326.
[48] G. M. Sheldrick, *SHELXS-97* and *SHELXL-97*, University of Göttingen, **1997**.
[49] SHELXTL Version 5.03. Software Package for Crystal Structure Determination, Siemens Analytical X-ray Instrument Division, Madison, WI, **1994**.
[50] A. L. Spek, *J. Appl. Crystallogr.* **2003**, *36*, 7–13.

Received: October 05, 2004

 © 2005 Wiley-VCH Verlag GmbH & Co. KGaA, Weinheim

Platinum Complexes with the Novel Ligand Diethyl [(Methylsulfinyl)-methyl]phosphonate (SMP): Solid-State Characterization of Potassium Trichloro(SMP)platinum(II) which, in Solution, Gives Dichloro(SMP)-platinum(II) and Potassium Chloride

Mariarita Laforgia,[a,b] Nicola Margiotta,[a] Francesco Capitelli,[c] Valerio Bertolasi,[d] and Giovanni Natile*[a,b]

Keywords: Bone tumors / NMR spectroscopy / Phosphonate / Platinum / X-ray crystallography

Phosphonate ligands have been employed in the synthesis of platinum complexes, which are active against bone tumors. The stability of a new compound of this family, $[PtCl_2(SMP)]$ {**1**; SMP = diethyl[(methylsulfinyl)methyl]phosphonate}, has been investigated in water and acetone. The compound is stable in aqueous solution where it undergoes only partial solvolysis that is completely repressed by addition of free chloride ions. However, crystallization of **1** from water/acetone/chloroform (0.2:1:1, v/v/v) containing an equimolar amount of KCl affords a new compound containing monodentate SMP {$K[PtCl_3(SMP\text{-}S)]$, **2**}. Dissolution of **2** in water or acetone restores **1**. The driving force in the formation of **2** appears to be the network of electrostatic interactions between cations and complex anions in the solid state. It is not only the detached P=O oxygen atom, but also the oxygen atom bound to the sulfur atom and a coordinated chloride ligand of the same platinum unit that interact rather strongly with the cation. It is expected that the same reaction (partial detachment of the phosphonate and anchoring of the cation) can take place in hypercalcaemic districts associated to bone tumors.

(© Wiley-VCH Verlag GmbH & Co. KGaA, 69451 Weinheim, Germany, 2005)

Introduction

Platinum(II) complexes are excellent antitumor agents for the treatment of solid tumors, such as testicular, ovarian, and bladder carcinomas; but are much less effective towards other forms of cancer.[1]

We have recently reported on a new class of platinum(II) compounds, which have been designed for the treatment of bone tumors and the hypercalcaemia frequently associated with many cancer diseases.[2] These compounds contain the novel ligand diethyl [(methylsulfinyl)methyl]phosphonate (SMP); the sulfur atom of the sulfoxide and the oxygen atom doubly bonded to the phosphorus atom are the effective donor atoms for the metal ion. Multinuclear NMR spectroscopic data showed that the puckering of the five-membered chelate ring depends upon the configuration at the sulfur atom: δ puckering for the (*S*) configuration of the free ligand.

[a] Dipartimento Farmaco-Chimico, Università degli Studi di Bari, via E. Orabona 4, 70125 Bari, Italy
[b] Consorzio Interuniversitario di Ricerca in Chimica dei Metalli nei Sistemi Biologici, via C. Ulpiani 27, 70125 Bari, Italy
[c] Istituto di Cristallografia (IC-CNR), Via Amendola 122/o, 70126 Bari, Italy
[d] Dipartimento di Chimica e Centro di Strutturistica Diffrattometrica, Università di Ferrara, Via Borsari 46, 44100 Ferrara, Italy
E-mail: natile@farmchim.uniba.it

The use of phosphonate ligands for platinum is not new in the literature. The most representative examples are Keppler's aminobis(phosphonates), which coordinate to the metal ion through a tertiary nitrogen atom and one of the ionized hydroxy groups of the phosphonic acid.[3–6]

Our ligand was designed with the objective of increasing the chemical stability of the platinum compounds while retaining the selective tropism for bone tissue. The chemical stability could be increased by introducing a sulfoxide group with high coordination ability towards platinum ion in the phosphonate molecule. Moreover, in order to increase the lipophilicity of our compounds (a critical parameter for the crossing of the cell membrane), the free acid was converted into the diethyl ester derivative. The use of a phosphonic ester should not preclude the reaction between phosphonate groups and calcium ions of bone tissues, since it is known that phosphonic esters are partially hydrolyzed in vivo by several esterase enzymes present in the biological medium.[7]

Since the newly reported platinum complexes of formula $[PtL_2(SMP\text{-}O,S)]$ (where $L_2 = Cl_2$, dimethyl malonate, ethylenediamine, or 1,2-diaminocyclohexane) were the first in which a phosphonate group was coordinated to a platinum center through the oxygen atom doubly bonded to the phosphorus atom, we wanted to investigate the chemical stability of the Pt–O=P linkage under different experimen-

 DOI: 10.1002/ejic.200400842

tal conditions. Also, the possible hydrolysis of the P–O–Et bonds was considered.

The stability of $[PtCl_2(SMP)]$ (see Scheme 1) in pure water or in water containing 0.1 M chloride ions (a concentration comparable to that of a physiological extracellular medium) was monitored by ^1H, ^{31}P, and ^{195}Pt NMR spectroscopy.

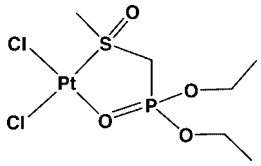

Scheme 1. Shorthand drawing of the complex $[PtCl_2(SMP)]$ (**1**).

The X-ray structure of a crystallized species ($K[PtCl_3(SMP)]$) that is different from that present in solution is also reported.

Results and Discussion

Stability of $[PtCl_2(SMP)]$

Similarly to cisplatin,[8–10] the complex $[PtCl_2(SMP)]$ (**1**) undergoes solvation in aqueous solution. In the starting dichloro complex the methyl group linked to the sulfur atom gives rise to a doublet centered at δ = 3.67 ppm ($^4J_{H,P}$ = 2 Hz) with platinum satellites ($^3J_{H,Pt}$ = 18 Hz).[2] Soon after dissolution, another doublet, slightly shifted to lower field (δ = 3.73 ppm), appears and its intensity increases with time (see Figure 1). This is in agreement with the immediate formation of a monosolvated species obtained by release of the chloride ligand *trans* to the sulfoxide.[11] A second doublet (centered at δ = 3.70 ppm), of very low intensity and overlapping with one ^{195}Pt satellite of the dichloro species can be interpreted as evidence for a second solvato species. Detachment of the second chloride ligand and entering of another water molecule into the coordination sphere of the platinum ion is a possibility; however, because of the asymmetry of the SMP ligand, a second monoaqua species, in which the solvent molecule is *trans* to the phosphonate oxygen atom rather than to the sulfur atom, can be formed. Addition of potassium chloride to the NMR sample leads to regression of the hydrolysis products, as demonstrated by the immediate disappearance of the doublet at lower field.

A parallel investigation by ^{31}P NMR gave similar results. A new phosphorus signal (δ = 15.3 ppm), which appears close to the dominant signal of the starting dichloro species (δ = 15.8 ppm), indicates the formation of an aqua species.

The long-term stability of complex **1** in an aqueous solution containing a 0.1 M chloride concentration was also investigated. No changes in the ^1H, ^{31}P or ^{195}Pt NMR spectra were observed over a period of weeks, except for very weak ^1H and ^{31}P NMR signals belonging to free SMP appearing after three weeks. No intermediate species with monocoordinated SMP or products of the hydrolysis of the ester functions were detected.

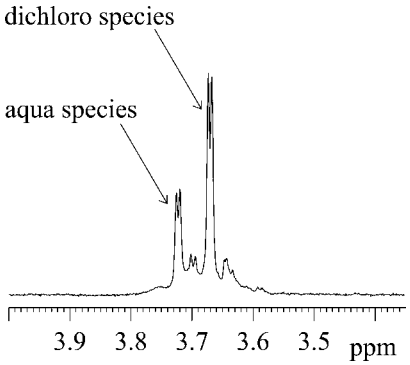

Figure 1. ^1H NMR signals in the region of methyl sulfoxide for complex **1** in aqueous solution, 24 h after dissolution. The signals at δ = 3.70 and 3.64 ppm are essentially ^{195}Pt-coupling satellites ($^3J_{H,Pt}$ = 18 Hz). One ^{195}Pt satellite is also visible for the monoaqua species at δ = 3.76 ppm.

In order to further check the stability of the Pt–O=P bond, we carried out an experiment in which an equimolar amount of potassium chloride was added to a sample of complex **1** in $[D_6]$acetone/D_2O (10:1, v/v; 5 mM concentration). Chloride ions are expected to be more nucleophilic in acetone since they are deprived of their hydration shell. However, no products of partial or complete detachment of the SMP ligand were detected in solution and the ^{31}P and ^{195}Pt NMR spectra still showed the pseudo-triplet (^{31}P) and doublet (^{195}Pt) characteristic of chelated SMP ($^2J_{P,Pt}$ = 90 Hz;[12] see Figure 2). Furthermore the ^1H NMR spectrum remained unchanged.

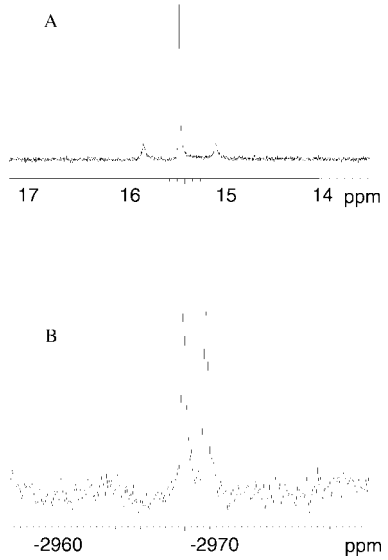

Figure 2. ^{31}P (121.5 MHz; A) and ^{195}Pt (64.3 MHz; B) NMR spectra of complex **1** in $[D_6]$acetone/D_2O solution (10:1, v/v) containing an equimolar amount of KCl.

However, rather unexpectedly, a crystalline orange product, **2**, was obtained by solvent evaporation from a solution of complex **1** and equimolar KCl in water/acetone/chloroform (0.2:1:1, v/v/v). The elemental analysis proved that the composition of the orange crystals corresponds to **1** + KCl. Moreover, the crystals of **2**, redissolved in acetone as well as in water, gave ^1H and ^{31}P NMR spectra perfectly

 © 2005 Wiley-VCH Verlag GmbH & Co. KGaA, Weinheim

overlapping with those of complex **1** containing dicoordinated SMP. Therefore, both the elemental analyses and the NMR experiments confirmed that compound **2** is a product of the co-crystallization of **1** and KCl, and this was in complete agreement with previous observations indicating that complex **1** was perfectly stable in solutions containing free chloride ions. However, the crystal structure revealed that compound **2** is a new species with the formula K[$PtCl_3$(SMP-*S*)]. The details of the anion structure and of the cation/anion crystal packing will be described in a following section.

The [$PtCl_3$(SMP-*S*)]$^-$ anion can be formed from **1** by displacement of the oxygen atom doubly bonded to the phosphorus atom and coordination of a chloride ion. The greater lability of the Pt–O bond with respect to the Pt–S bond, as well as the greater thermodynamic stability of the Cl_3S set of donor atoms with respect to the Cl_2OS set, could both be leading factors in the formation of the [$PtCl_3$(SMP-*S*)]$^-$ anion. However, rather surprisingly, in solution a rapid ring-closure process restores the five-membered chelate and converts **2** back to **1** + KCl.

How can we explain the stability of the form with chelated SMP in a solution containing KCl and the stability of the form with semidetached SMP and coordinated chloride in the solid state? Certainly a key role must be played by the electrostatic interactions between cations and anions in the solid state and these were also elucidated from the X-ray data.

X-ray Structure of K[$PtCl_3$(SMP)]

A view of the molecular structure, together with the atomic numbering scheme, is given in Figure 3. Bond lengths and angles are reported in Table 1.

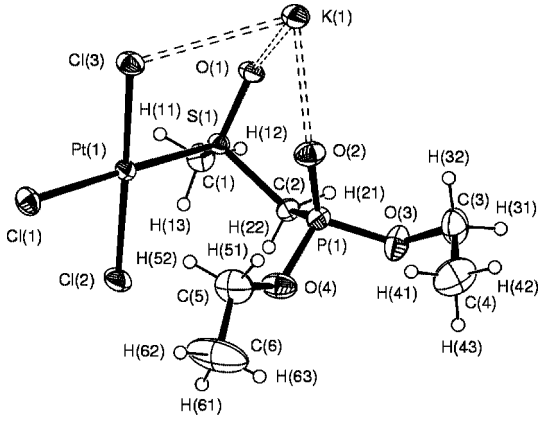

Figure 3. View of the asymmetric unit with the atomic numbering scheme for K[$PtCl_3$(SMP)] (**2**). Thermal ellipsoids enclose 30% probability.

There are no atoms in special positions. The platinum coordination geometry is square planar, with three chlorine atoms and one sulfur atom acting as donors. The four donors are coplanar within 0.06 Å and the platinum atom is displaced by only 0.017 Å from this plane.

Table 1. Bond lengths [Å] and angles [°] for K[$PtCl_3$(SMP)].

Bond lengths		Bond angles	
Pt(1)–S(1)	2.200(1)	Cl(1)–Pt(1)–Cl(2)	88.98(4)
Pt(1)–Cl(1)	2.310(1)	Cl(1)–Pt(1)–Cl(3)	88.01(4)
Pt(1)–Cl(2)	2.307(1)	Cl(1)–Pt(1)–S(1)	178.32(4)
Pt(1)–Cl(3)	2.310(1)	Cl(2)–Pt(1)–Cl(3)	176.58(4)
S(1)–O(1)	1.477(3)	Cl(2)–Pt(1)–S(1)	89.35(4)
S(1)–C(1)	1.777(4)	Cl(3)–Pt(1)–S(1)	93.65(4)
S(1)–C(2)	1.805(4)	Pt(1)–S(1)–O(1)	118.65(12)
P(1)–O(2)	1.464(3)	Pt(1)–S(1)–C(1)	111.62(17)
P(1)–O(3)	1.560(4)	Pt(1)–S(1)–C(2)	110.52(14)
P(1)–O(4)	1.556(3)	O(1)–S(1)–C(1)	107.42(21)
P(1)–C(2)	1.805(4)	O(1)–S(1)–C(2)	107.93(19)
O(3)–C(3)	1.474(6)	C(1)–S(1)–C(2)	98.79(21)
O(4)–C(5)	1.442(7)	O(2)–P(1)–O(3)	116.20(22)
C(3)–C(4)	1.451(9)	O(2)–P(1)–O(4)	114.68(21)
C(5)–C(6)	1.392(9)	O(2)–P(1)–C(2)	114.72(21)
C(1)–H(11)	0.90(6)	O(3)–P(1)–O(4)	105.31(21)
C(1)–H(12)	0.90(9)	O(3)–P(1)–C(2)	99.44(20)
C(1)–H(13)	0.93(6)	O(4)–P(1)–C(2)	104.72(20)
C(2)–H(21)	1.01(5)	P(1)–O(3)–C(3)	121.52(33)
C(2)–H(22)	0.82(5)	P(1)–O(4)–C(5)	124.76(38)
C(3)–H(31)	0.97	S(1)–C(2)–P(1)	113.53(23)
C(3)–H(32)	0.97	O(3)–C(3)–C(4)	110.42(51)
C(4)–H(41)	0.96	O(4)–C(5)–C(6)	113.82(66)
C(4)–H(42)	0.96		
C(4)–H4(3)	0.96		
C(5)–H5(1)	0.97		
C(5)–H5(2)	0.97		
C(6)–H(61)	0.96		
C(6)–H(62)	0.96		
C(6)–H(63)	0.96		

The three Pt–Cl bond lengths are very similar notwithstanding the greater *trans* effect expected for the sulfoxide ligand [2.310(1), 2.307(1), and 2.310(1) Å for Pt(1)–Cl(1), Pt(1)–Cl(2), and Pt(1)–Cl(3), respectively] and are in agreement with previously reported values for anionic [$PtCl_3$(sulfoxide)] complexes.[13–15]

Concerning the bond angles between *cis* ligands, the two Cl–Pt–Cl angles and one of the Cl–Pt–S angles are very close to 90° [Cl(1)–Pt(1)–Cl(2) = 88.98(4)°, Cl(1)–Pt(1)–Cl(3) = 88.01(4)°, Cl(2)–Pt(1)–S(1) = 89.35(4)°], while the second Cl–Pt–S angle is noticeably larger than 90° [Cl(3)–Pt(1)–S(1) = 93.65(4)°]. This is probably due to the steric interaction between Cl(3) and the sulfur-bound O(1). The O(1) atom practically lies on the platinum coordination plane [Cl(2)–Pt(1)–S(1)–O(1) and Cl(3)–Pt(1)–S(1)–O(1) torsion angles of 176.92(14)° and –4.71(15)°, respectively; see Figure 3] and, as a consequence, a repulsive interaction between the oxygen and Cl(3) atoms is expected. The same trend has been observed in analogous compounds with platinum-coordinated sulfoxides.[16–18]

The sulfur center is approximately tetrahedral; the greatest deviation from the ideal value is observed for the Pt(1)–S(1)–O(1) and C(1)–S(1)–C(2) angles [118.65(12)° and 98.79(21)°, respectively].

The phosphorus atom is also approximately tetrahedral with the greatest deviation for the O(3)–P(1)–C(2) angle [99.44(20)°]. The double bond character of P=O is confirmed by the short P(1)–O(2) distance [1.464(3) Å], which should be compared with the distances of the other two P–

 © 2005 Wiley-VCH Verlag GmbH & Co. KGaA, Weinheim

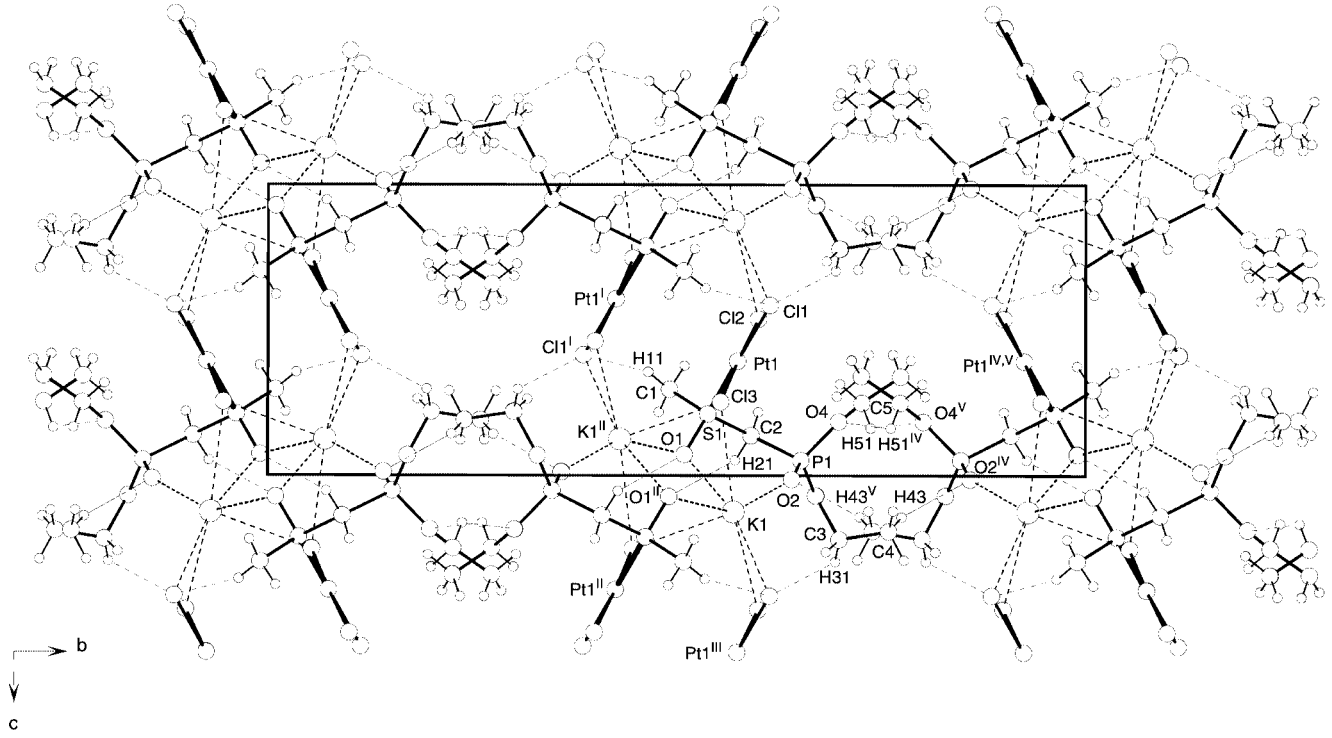

Figure 4. Crystal packing of K[$PtCl_3$(SMP)] (**2**). The numbering of atoms is given only for the fundamental asymmetric unit. The symmetry operations leading to the adjacent asymmetric units (I, II, III, IV, V) are indicated close to the platinum centers. The symmetry operations I, II, III, IV and V are defined as: I = –*x*, –*y*, 1 – *z*; II = 1 – *x*, –*y*, 2 – *z*; III = *x*, *y*, 1 + *z*; IV = 0.5 + *x*, –0.5 – *y*, *z*; V = –0.5 + *x*, –0.5 – *y*, *z*.

O bonds [1.560(4) and 1.556(3) Å for P(1)–O(3) and P(1)–O(4), respectively]. Finally, the S=O bond length of 1.477(3) Å is in good agreement with other reported crystallographic data.[19–21]

Crystal Packing

The three-dimensional network is constructed by pairs of quasi parallel $PtCl_3S$ moieties at a distance of ca. 4.05 Å (Pt1 and Pt1^{I} units in Figure 4). Only the methyl groups of the coordinated sulfoxides protrude in the space between the two coordination planes and the S–Me of each subunit creates an H-bond type interaction with a chlorine atom of the other subunit [C(1)···Cl(1)^{I} = 3.57(1) Å, H(11)···Cl(1)^{I} = 2.73(6) Å, C(1)–H(11)–Cl(1)^{I} = 155(5)°]. Within a pair, the two subunits are also held together by two potassium cations, which interact with Cl(3) and O(1) of one platinum subunit (Pt1) and with Cl(1) and Cl(2) of the second platinum subunit (Pt1^{I}). The same potassium cation also interacts with the Cl(3), O(1) and O(2) atoms of a platinum anion of an adjacent pair (see Pt1^{II} in Figure 4). In this way each potassium cation results trapped in an irregular 7-donor cage formed by four chlorine and three oxygen atoms (the K···Cl and K···O distances are given in the caption to Figure 5).

Adjacent pairs are linked by two K cations (for instance K1 and K1^{II} in Figure 4) and four H-bond type interactions between Cl(1)^{I}, O(1), C(2), and C(3) atoms of one pair and the C(3)^{II}, C(2)^{II}, O(1)^{II}, and Cl(1)^{III} atoms of the adjacent pair, respectively [Cl(1)^{I}···C(3)^{II} = 3.60(1) Å, Cl(1)^{I}···H(31)^{II} = 2.78(0) Å, Cl(1)^{I}–H(31)^{II}–C(3)^{II} = 142(0)°; O(1)···C(2)^{II} = 3.48(1) Å, O(1)···H(21)^{II} = 2.54(4) Å, O(1)–H(21)^{II}–C(2)^{II} = 156(3)°; C(2)···O(1)^{II} = 3.48(1) Å, H(21)···O(1)^{II} = 2.54(4) Å, C(2)–H(21)–O(1)^{II} = 156(3)°; C(3)···Cl(1)^{III} = 3.60(1) Å, H(31)···Cl(1)^{III} = 2.78(0) Å, C(3)–H(31)–Cl(1)^{III} = 142(0)°].

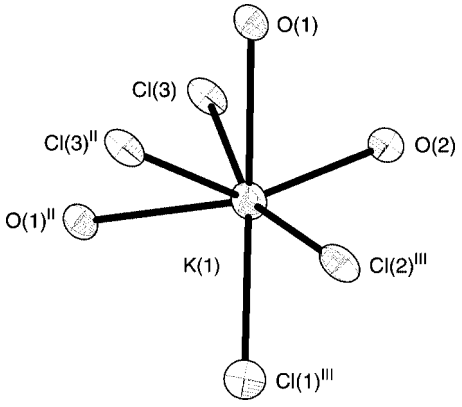

Figure 5. Potassium coordination sphere for K[$PtCl_3$(SMP)]; K···Cl and K···O distances are: K(1)–O(1) 3.048(3), K(1)–O(2) 2.580(3), K(1)–Cl(3) 3.244(2), K(1)–O(1)^{II} 2.980(3), K(1)–Cl(3)^{II} 3.136(2), K(1)–Cl(1)^{III} 3.132(2), K(1)–Cl(2)^{III} 3.280(2) Å. Symmetry: II = 1 – *x*, –*y*, 2 – *z*; III = *x*, *y*, 1 + *z*.

The infinite chains of anion pairs extend along the *c* direction; all the coordination planes of the platinum anions are quasi perpendicular to the *bc* plane (the angle between the mean square platinum plane and the *bc* plane is 82.17°).

 © 2005 Wiley-VCH Verlag GmbH & Co. KGaA, Weinheim

Adjacent chains are held together by hydrophobic interactions between ethyl radicals and H-bond type interactions involving C(5), O(4), O(2), and C(4) atoms of one asymmetric unit and $O(4)^{V}$, $C(5)^{IV}$, $C(4)^{V}$, and $O(2)^{IV}$ atoms of two adjacent units, thus forming a three-dimensional network [C(5)···$O(4)^{V}$ = 3.38(1) Å, H(51)···$O(4)^{V}$ = 2.71(0) Å, C(5)–H(51)–$O(4)^{V}$ = 127(0)°; O(4)···$C(5)^{IV}$ = 3.38(1) Å, O(4)···$H(51)^{IV}$ = 2.71 Å, O(4)– $H(51)^{IV}$–$C(5)^{IV}$ = 127(0)°; O(2)···$C(4)^{V}$ = 3.49(1) Å, O(2)···$H(43)^{V}$ = 2.61(0) Å, O(2)–$H(43)^{V}$–$C(4)^{V}$ = 153(5)°; C(4)···$O(2)^{IV}$ = 3.49(1) Å, H(43)···$O(2)^{IV}$ = 2.61(0) Å, C(4)–H(43)–$O(2)^{IV}$ = 127(0)°].

Conclusions

It has been shown that compound **1** is fairly stable in a water solution containing a chloride ion concentration comparable to that of a physiological medium. Moreover, in the absence of free chloride, only partial solvolysis with release of a chloride ion is observed. However, in the presence of a cation such as K^+ (but the same should apply to any positively charged ion comprising the biologically relevant Ca^{++}), the solution stability of the SMP chelate does not prevent the phosphonate group from leaving the platinum center in order to interact with the cation.

The electrostatic interaction between cations and complex anions in the solid state appears to be the driving force for the formation of **2**. The potassium ion fits perfectly in a cage of seven donors (three oxygen and four chlorine atoms) from three different platinum units.

These findings can be highly relevant to the behavior of this compound in a biological environment. We used the SMP diethyl ester on the ground that in physiological conditions it can undergo enzymatic hydrolysis with the formation of phosphonic acids, which can then interact with calcium cations. However, it has been found that the SMP ligand itself can interact with cations. Not only can the P=O oxygen atom be detached from the platinum atom but the oxygen atom bound to the sulfur atom and even a platinum-bound chlorine ligand are willing to embrace a metal cation. It is expected that the reaction observed in the crystallization of **1** in the presence of KCl can take place in the hypercalcaemic districts associated with bone tumors. In the design of the SMP ligand the sulfoxide functionality was introduced in order to have a good donor atom for platinum, the ability of the sulfur-bound oxygen atom to interact with a cation had not been anticipated and therefore it represents an unexpected fortunate circumstance.

Finally, the very likely hydrolysis of the phosphodiester moiety promoted by esterase enzymes present in the biological medium could further increase the ability of this drug to be captured in calcium-rich districts. It cannot be excluded, however, that the platinum atom can interact with sulfur and nitrogen atoms belonging to the amino acids of such enzymes (methionines and histidines are particularly abundant in these proteins), thereby inhibiting their hydrolytic activity. Biological studies are currently underway.

Experimental Section

General Methods: NMR spectra were recorded with a Bruker AVANCE DPX-WB 300 MHz instrument. ^{1}H chemical shifts were referenced to TMS by using the residual protic peak of the solvent as internal reference (δ = 2.04 ppm for [D_6]acetone and δ = 4.80 ppm for deuterium oxide). ^{31}P chemical shifts were referenced to 85% H_3PO_4. IR spectra were obtained with a Perkin–Elmer Spectrum One Infrared Spectrophotometer using KBr as solid support for pellets. Elemental analyses were performed with a Carlo Erba Elemental Analyzer model 1106 instrument.

Preparation of Complexes: The complex [$PtCl_2$(SMP)] (**1**) was prepared according to the reported procedure.[2]

Preparation of Samples for NMR Experiments: [$PtCl_2$(SMP)] (**1**) (2.5 mg, ca. 0.005 mmol) was dissolved in 1 mL of D_2O or [D_6]acetone and placed in an NMR tube. ^{1}H and ^{31}P NMR experiments were recorded every 3 h for 1 d and every 6 h for the following days.

Crystallization of K[$PtCl_3$(SMP)] (2): [$PtCl_2$(SMP)] (10 mg, 0.02 mmol) and KCl (1.50 mg, 0.02 mmol) were dissolved in a mixture of H_2O/acetone/$CHCl_3$ (0.2:1:1, v/v/v; 2 mL). By spontaneous evaporation of the solvent, orange crystals, which were characterized by elemental analysis, IR spectroscopy, and X-ray crystallography were obtained. $C_6H_{15}Cl_3KO_4PPtS$ (554.75): calcd. C 13.0, H 2.7; found C 13.3, H 2.8. IR: $\tilde{\nu}$ = 2913 ν(C–H), 1253 ν(P=O), 1049 ν(S=O), 1013 ν(P–O–R), 341 ν(Pt–Cl) cm^{-1}.

Crystal Data: $PtC_6H_{15}Cl_3KO_4PS$, monoclinic, space group $P2_1/a$, a = 7.9610(1), b = 23.5720(3), c = 8.6040(1) Å, β = 101.649(1), V = 1581.34(3) $Å^3$, λ = 0.71073 Å, Z = 4, F(000) = 1048, D_c = 2.330 g cm^{-3}, μ(Mo-K_α) = 9.874 mm^{-1}. Yellow/orange prism 0.10 × 0.14 × 0.54 mm. CCDC-252376 contains the supplementary crystallographic data for this paper. These data can be obtained free of charge from The Cambridge Crystallographic Data Centre via www.ccdc.cam.ac.uk/data_request/cif.

Table 2. Crystal data and structure refinement for K[$PtCl_3$(SMP)] (**2**).

Empirical formula	$C_6H_{15}Cl_3KO_4PPtS$
Formula mass	554.75
Crystal family	monoclinic
Space group	$P2_1/a$
T [K]	293(2)
λ [Å]	0.71073
a [Å]	7.9610(1)
b [Å]	23.5720(3)
c [Å]	8.6040(1)
$\alpha = \gamma$ [°]	90
β [°]	101.649(1)
V [$Å^3$]	1581.34(3)
Z	4
$D_{calcd.}$ [g cm^{-3}]	2.330
μ [mm^{-1}]	9.874
F(000)	1048
Crystal size [mm]	0.10 × 0.14 × 0.54
θ range for data coll. [°]	3.46–30.02
Refl. coll./unique	19235/4600 (R_{int} = 0.0573)
Completeness to θ	99.6% (θ = 30.02°)
Data/restr./parameters	4097/0/176
Goodness-of-fit on F^2	1.045
R indices [$I > 2\sigma(I)$]	R = 0.0299, wR = 0.0693
R indices (all data)	R = 0.0360, wR = 0.0713
Larg. diff. peak and hole [e $Å^{-3}$]	0.185 and –0.1984

 © 2005 Wiley-VCH Verlag GmbH & Co. KGaA, Weinheim

Data Collection and Processing: 19235 reflections (4600 unique) were collected in the range $3.46° \leq 2\theta \leq 30.02°$, with a Nonius Kappa CCD diffractometer equipped with a fine-focus sealed-tube graphite-monochromated Mo-K_α radiation. Data were corrected for Lorentz and polarisation effects, and for absorption according to Blessing.[22] Omission of intensities with $I \leq 2\sigma(I_{obs})$ gave 4097 observed reflections, which were employed for the analysis.

Structure Analysis and Refinement: The structure was solved by Direct Methods application (SIR97)[23] and refined by a full-matrix least-squares technique (SHELX-L).[24] Each asymmetric unit contains one independent molecule. All non-hydrogen atoms were refined anisotropically, while hydrogen atoms were localized through Fourier map application, with the exception of H(31), H(32), H(41), H(42), H(43), H(51), H(52), H(61), H(62) and H(63) atoms, which, because of refinement instability, were placed in idealized positions and had a common isotropic thermal parameter [$U_{iso}(H) = 1.2U_{iso}(C)$] assigned. The final cycle of least-squares refinement included 176 parameters {weighting scheme applied: $w^{-1} = [\sigma^2(F_o^2) + (0.0290P)^2 + 3.1142P]$, with $P = [(F_o^2 + 2F_c^2)/3]$}. Final residuals were $R = 0.030$ and $wR = 0.069$, $GoF = 1.045$. Crystal data and structure refinement features are reported in Table 2.

Acknowledgments

The authors thank the University of Bari, the "Ministero dell'Istruzione, Università e Ricerca (MIUR)" (FIRB 2001-RBNE01TTJW_004 within the Postgenoma Strategic Program, and PRIN 2004032118_003), the EC (COST Chemistry projects D20/0001/2000 and D20/0003/01) and Consorzio Interuniversitario di Ricerca in Chimica dei Metalli nei Sistemi Biologici (C.I.R.C.M.S.B.) for financial support.

[1] P. J. Loehrer, L. H. Einhornr, *Ann. Intern. Med.* **1984**, *100*, 704–713.
[2] M. Laforgia, L. Cerasino, N. Margiotta, C. Cardellicchio, M. A. M. Capozzi, F. Naso, G. Natile, *Eur. J. Inorg. Chem.* **2004**, *17*, 3445–3452.
[3] T. Klenner, P. Valenzuela-Paz, F. Amelung, H. Munch, H. Zahn, B. K. Keppler, H. Blum, in: *Metal Complexes in Cancer Chemotherapy* (Ed.: B. K. Keppler), Wiley-VCH, Weinheim, **1993**, p. 85–127.
[4] M. J. Bloemink, J. J. H. Diederen, J. P. Dorenbos, R. J. Heetebrij, B. K. Keppler, J. Reedijk, *Eur. J. Inorg. Chem.* **1999**, 1655–1657.
[5] T. J. Einhauser, M. Galanski, E. Vogel, B. K. Keppler, *Inorg. Chim. Acta* **1997**, *257*, 265–268.
[6] M. J. Bloemink, J. P. Dorenbos, R. J. Heetebrij, B. K. Keppler, J. Reedijk, H. Zahn, *Inorg. Chem.* **1994**, *33*, 1127–1132.
[7] H. Selle, B. E. Chapman, P. W. Kuchel, *Biochem. J.* **1992**, *284*, 61–65.
[8] A. M. Fuertes, C. Alonso, J. M. Pérez, *Chem. Rev.* **2003**, *103*, 645–662.
[9] W. I. Sundquist, S. J. Lippard, *Coord. Chem. Rev.* **1990**, *100*, 293–322.
[10] A. M. J. Fichtinger-Shepman, J. L. Van der Veer, J. H. J. Den Hartog, P. H. M. Lohman, J. Reedijk, *Biochemistry* **1985**, *24*, 707–713.
[11] J. V. Quagliano, L. Schubert, *Chem. Rev.* **1952**, *50*, 201–260.
[12] T. G. Appleton, J. R. Hall, D. W. Neale, *Inorg. Chim. Acta* **1985**, *104*, 19–31.
[13] F. D. Rochon, S. Boutin, P. C. Kong, R. Melanson, *Inorg. Chim. Acta* **1997**, *264*, 89–100.
[14] O. Clement, A. N. Roszak, E. Buncel, *Inorg. Chim. Acta* **1996**, *253*, 53–63.
[15] M. Calligaris, O. Carugo, *Coord. Chem. Rev.* **1996**, *153*, 83–154.
[16] F. D. Rochon, P. C. Kong, R. Melanson, *Inorg. Chem.* **1990**, *29*, 1352–1356.
[17] S. G. de Almeida, J. L. Hubbard, N. Farrell, *Inorg. Chim. Acta* **1992**, *193*, 149–157.
[18] R. Melanson, J. Hubert, F. D. Rochon, *Acta Crystallogr., Sect. B* **1976**, *32*, 1914–1916.
[19] D. P. Bancroft, F. A. Cotton, L. R. Falvello, S. Han, W. Schwotzer, *Inorg. Chim. Acta* **1984**, *87*, 147–153.
[20] P. E. Fanwick, J. L. Huckaby, *Inorg. Chem.* **1982**, *21*, 3067–3071.
[21] F. Capitelli, K. Brouzi, M. Harcharras, A. Ennaciri, A. G. G. Moliterni, V. Bertolasi, *Z. Kristallogr.* **2004**, *219*, 93–98.
[22] R. H. Blessing, *Acta Crystallogr., Sect. A* **1995**, *51*, 33–38.
[23] A. Altomare, M. C. Burla, M. Camalli, G. L. Cascarano, C. Giacovazzo, A. Guagliardi, A. G. Moliterni, G. Polidori, R. Spagna, *J. Appl. Crystallogr.* **1999**, *32*, 115–119.
[24] G. M. Sheldrick, *SHELXL-97, Program for the Refinement of Crystal Structures*, University of Göttingen, Germany, **1997**.
Received: October 7, 2004

 © 2005 Wiley-VCH Verlag GmbH & Co. KGaA, Weinheim

Kinetics of Cyclooctene Epoxidation with *tert*-Butyl Hydroperoxide in the Presence of [MoO_2X_2L]-Type Catalysts (L = Bidentate Lewis Base)

Ahmad Al-Ajlouni,[a] Anabela A. Valente,[b] Carla D. Nunes,[b] Martyn Pillinger,[b] Ana M. Santos,[c,d] Jin Zhao,[c] Carlos C. Romão,[d] Isabel S. Gonçalves,*[b] and Fritz E. Kühn*[c]

Keywords: Epoxidation / Homogeneous catalysis / Kinetics / Molybdenum

Mo^{VI} complexes with the general formula [MoO_2X_2L] [X = Cl, Br; L = 4,4′-dimethyl-2,2′-bipyridine (dmbp) or 4-hexyl-4′-methyl-2,2′-bipyridine (hmbp)] have been prepared and characterized by IR and solution NMR (^1H, ^{13}C, ^{17}O and ^{95}Mo) spectroscopy. The complexes were applied as catalysts in the homogeneous phase for the epoxidation of cyclooctene, with *tert*-butyl hydroperoxide (TBHP) as the oxygen source. The desired epoxide was the only product and turnover frequencies of up to about 9000 h^{-1} could be reached. The catalytic activities increased in the order [MoO_2Br_2(dmbp)] < [MoO_2Br_2(hmbp)] < [MoO_2Cl_2(dmbp)] < [MoO_2Cl_2(hmbp)]. A kinetic model was built up for a homogeneous batch reactor based on a simplified mechanism involving three steps: (i) reversible coordination of TBHP to the starting Mo^{VI} complex to give a Mo^{VI} alkylperoxide; (ii) irreversible oxidation of cyclooctene to cyclooctene oxide by the species formed in step 1, with formation of the starting complex and *tert*-butyl alcohol; (iii) reversible coordination of *tert*-butyl alcohol to the starting complex. This model is consistent with the observed kinetics. The first step in this reaction mechanism was characterized in more detail by studying the kinetics of the reaction of the starting complexes with TBHP in the absence of any reductant by UV/Vis spectroscopy. Rate constants, equilibrium constants, and activation parameters were determined. All $\Delta S^{\ddagger}$ values were negative and therefore support an associative mechanism in which a seven-coordinate intermediate is formed. The results also suggest that the first step is not always the rate-limiting step of cyclooctene epoxidation with these complexes.

(© Wiley-VCH Verlag GmbH & Co. KGaA, 69451 Weinheim, Germany, 2005)

Introduction

Dioxomolybdenum(VI) complexes are important catalysts or catalyst precursors for oxygen-atom transfer reactions in industrial and biological systems.[1] Polymeric compounds of the composition MoO_2X_2 and WO_2X_2 have been known for many years.[2a] With Lewis bases, such as 2,2′-bipyridine, and with donor solvents, such as THF, adducts of the composition [MO_2X_2L] (M = Mo, W) are formed.[2b,2c] A particular interest in complexes of this type arose in the late 1960s when ARCO and Halcon were granted patents on olefin epoxidation catalyzed by Mo^{VI} compounds in the homogeneous phase.[2d,2e] In the following years different mechanisms were suggested to explain the reactivity of these complexes, most notably those by Mimoun et al.[2f] and by Sharpless et al.[2g] The debate has not been settled to date, despite the fact that a lot of information has been derived from NMR studies and catalytic reactivity patterns;[2h] several theoretical and mechanistic studies have also been presented.[2i–2l] It is generally agreed, however, that formation of a Mo^{VI} alkyl peroxide occurs followed by transfer of the distal oxygen atom of the alkyl peroxide rather than an oxo ligand.[2m] It is also becoming clear from the results published during the last decades on Mo^{VI} and W^{VI} complexes that the different catalyst types do not all follow the same mechanism,[2n–2p] as some authors assumed in the early days of this chemistry.[2q,2r]

We have recently published a series of papers focusing on complexes of the type [MO_2X_2L], which are excellent catalyst precursors for olefin epoxidation in the presence of *tert*-butyl hydroperoxide (TBHP).[3] Already in the early 1980s Mimoun et al. assumed that the [MO_2X_2L] complexes are transformed into [$Mo(O_2)_2OL_2$] in the presence of excess H_2O_2,[4] while the reaction of [MoO_2X_2L] with excess TBHP remained unclear. It has to be noted, however, that the industrially applied oxidation agent in the ARCO/Halcon process is TBHP. It is therefore of significant interest to

[a] Department of Applied Chemical Science, Jordan University of Science and Technology,
22110 Irbid, Jordan
[b] Department of Chemistry, CICECO, University of Aveiro,
Campus de Santiago, 3810–193 Aveiro, Portugal
Fax: +351-234-370-084
E-mail: igoncalves@dq.ua.pt
[c] Anorganisch-chemisches Institut der Technischen Universität München,
Lichtenbergstr. 4, 85747 Garching, Germany
E-mail: fritz.kuehn@ch.tum.de
[d] Instituto de Tecnologia Química e Biológica da Universidade Nova de Lisboa,
Quinta do Marquês, EAN, Apt. 127, 2781-901 Oeiras, Portugal

gain a deeper insight into the mechanism of the epoxidation catalysis with $[MoO_2X_2L]$ as the catalyst precursor and TBHP as oxidizing agent. In this paper we present a kinetic model of the epoxidation reaction supported by NMR and UV/Vis spectroscopy, GC/MS, and calculations using the program Kinsim.[5]

Results and Discussion

Preparation and Characterization of the Dioxomolybdenum(VI) Complexes

The dioxomolybdenum(VI) complexes **1**–**4** (Scheme 1) were obtained as pale-yellow, microcrystalline powders in good yields by previously described routes.[3b] In general, the spectroscopic data for these four complexes present no surprises compared with other Lewis-base adducts of bis(halogeno)dioxomolybdenum(VI) prepared using the same method.[3b] Thus, the complexes display their symmetric and asymmetric IR stretching vibrations for the *cis*-dioxo unit in the expected range (905–940 cm^{-1}).[3] ^{17}O NMR solution spectra were obtained for ^{17}O labeled complexes **5**–**8**. The chemical shifts for the dichloro derivatives **5** and **6** are $\delta(^{17}O)$ = 1005 and 993 ppm, respectively, and these are identical within the error range to those of the corresponding dibromo complexes [$\delta(^{17}O)$ = 1003 and 994 ppm]. The related 2,2′-bipyrimidine adducts $[MoO_2X_2(bpym)]$ were also found to exhibit a minimal ^{17}O shift difference between the chloro and bromo derivatives [$\delta(^{17}O)$ = 997 (Cl) and 996 ppm (Br)].[5] For complexes **5** and **6**, and **7** and **8**, the 9–12 ppm ^{17}O NMR shift difference reflects a slightly higher electron density in the complexes containing the unsymmetrical 4-hexyl-4′-methyl-2,2′-bipyridine ligand. ^{95}Mo NMR solution spectra were also recorded for complexes **5**–**8**. The differences in the ^{95}Mo shift between the symmetrical and the unsymmetrical bipyridine ligand is comparatively small, only a few ppm in each case. The chemical shift difference between Cl and Br is about 50 ppm. These results parallel those observed for adducts of the type $[MoO_2X_2L]$ (X = Cl, Br; L = 2,2′-bipyridine, 2,2′-bipyrimidine).[6]

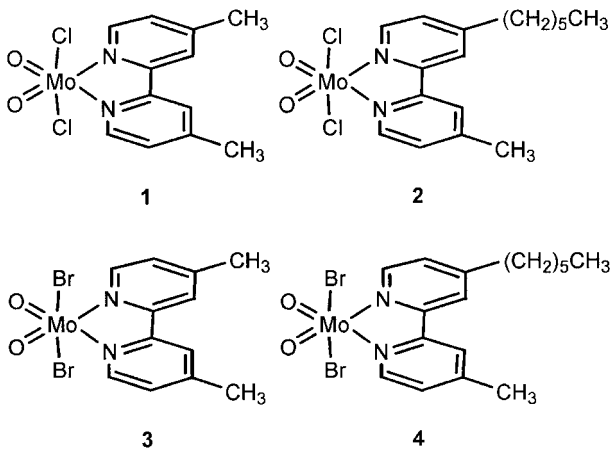

Scheme 1.

Kinetics of Catalytic Olefin Epoxidation With Complexes 1–4

Certain dioxomolybdenum(VI) complexes are able to catalyze the epoxidation of olefins with molecular oxygen as an oxygen source at atmospheric pressure.[7–9] However, preliminary experiments showed that the complexes $[MoO_2Cl_2$(4,4′-dimethyl-2,2′-bipyridine)] (**1**) and $[MoO_2Cl_2$(4-hexyl-4′-methyl-2,2′-bipyridine)] (**2**) are not active for the epoxidation of cyclooctene with molecular oxygen at atmospheric pressure under any of the conditions applied previously in the literature.

The dioxomolybdenum(VI) complexes **1**–**4** are active in the epoxidation of cyclooctene with TBHP as oxidant, at 55 °C, yielding cyclooctene oxide as the only product. The catalytic activity of the complexes depends strongly on the substituent pattern of the donor ligand, in agreement with previous studies on oxomolybdenum complexes.[2p,3d,3e,6,9–11] Cyclooctene conversion is higher in the presence of **2** than **1** (initial activities at a catalyst:substrate ratio of 1:100 are 248 $mol\,mol_{Mo}^{-1}\,h^{-1}$ and 25 $mol\,mol_{Mo}^{-1}\,h^{-1}$, respectively), and the yield of cyclooctene oxide reaches about 97% after 24 h in the case of **2** compared to about 76% for **1** (Figure 1). A similar trend is observed for complexes **3** and **4**. As discussed below, it is possible that the presence of a large organic group on the bipyridine ligand leads to the formation of a more hindered (reactive) oxidizing Mo^{VI} intermediate. The Br catalysts possess lower activity towards cyclooctene epoxidation than the corresponding Cl analogs, in agreement with the results reported in the literature for complexes of this type.[6]

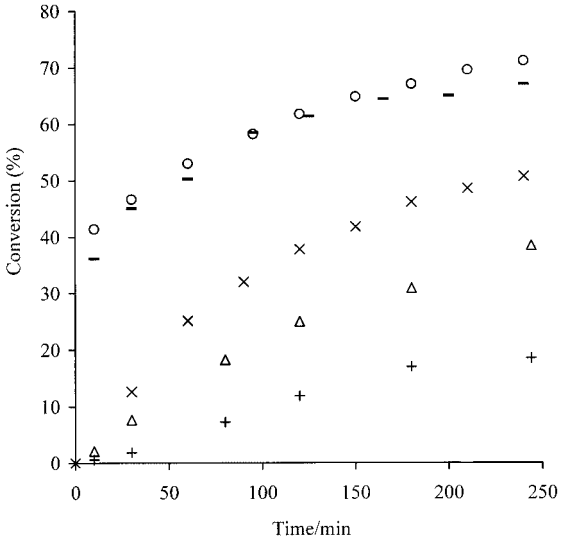

Figure 1. Conversion vs. time profiles for cyclooctene epoxidation using TBHP at 55 °C in the presence of $[MoO_2Cl_2$(4,4′-dimethyl-2,2′-bipyridine)] (**1**; ×), $[MoO_2Cl_2$(4-hexyl-4′-methyl-2,2′-bipyridine)] (**2**; ○), $[MoO_2Br_2$(4,4′-dimethyl-2,2′-bipyridine)] (**3**; +), $[MoO_2Br_2$(4-hexyl-4′-methyl-2,2′-bipyridine)] (**4**; Δ), and a radical scavenger plus **2** (–).

As has already been confirmed with related compounds, such as $[CpMoO_2Cl]$ and derivatives,[12] a catalyst-to-sub-

 © 2005 Wiley-VCH Verlag GmbH & Co. KGaA, Weinheim

strate ratio of 1:100 is far from being optimal. Reducing the catalyst-to-substrate ratio to 1:10 000 leads to the highest turnover frequencies (TOFs). The highest activities have been observed with [MoO_2X_2(4,4′-bis(*tert*-butyl)-2,2′-bipyridine)] and cyclooctene as substrate. The TOF of that system with a 1:10 000:15 000 catalyst:substrate:oxidant ratio is 9360 h^{-1} after five minutes. With compound **2** a TOF of about 8800 h^{-1} is reached under the same reaction conditions. With [$CpMoO_2Cl$] systems TOFs as high as 20 000 h^{-1} can be obtained,[12] while with the very active catalyst methyltrioxorhenium[13] (utilizing H_2O_2 instead of TBHP) TOFs of up to 14 000 have been reported.[13c] Nevertheless, the TOFs reached with some of the [MoO_2X_2L] systems reported here are still impressive and show the potential of these compounds as oxidation catalysts.

In this section a mechanism is proposed based on our experimental results and other studies for similar systems,[14] and a kinetic model is developed for a homogeneous batch reactor. In order to exclude solvent effects on the reaction no additional solvent was used. The fact that complexes **1**–**4** do not oxidize cyclooctene with O_2 at atmospheric pressure makes it unlikely that noncatalytic "olefin autoxidation" operates when the epoxidation is carried out with TBHP, at 55 °C, in air. Furthermore, no induction periods were detected (Figure 1) and without catalyst no conversion was observed (under otherwise identical reaction conditions).

Herrmann et al. have reported that for complexes of the type [MoO_2L_2] (L = pyridyl alcohol) a radical-type mechanism could be involved in olefin epoxidation with elemental oxygen (atmospheric pressure).[9] In the present work, the existence or otherwise of a mechanism involving radical pathways was investigated by carrying out an experiment with complex **2** in the presence of a radical scavenger added at the beginning of the reaction (equimolar amounts of cyclooctene and 2,6-di-*tert*-butyl-4-methylphenol, under identical reaction conditions to those described in the Experimental Section). As shown in Figure 1 the reaction rate was not significantly affected, which suggests that a nonradical reaction mechanism is involved.

According to some authors, the mechanism of molybdenum(VI)-catalyzed epoxidation may be similar to those involving titanium(IV) and vanadium(V).[10,15] The reaction mechanisms suggest that the first step in the epoxidation of an alkene is the coordination of the Lewis basic hydroperoxide to the Lewis acidic metal center by the terminal oxygen, thereby activating the peroxide for oxygen transfer.[2p,6,11,15,16] As expected, in the absence of oxidant no reaction took place. There is a consensus that the nature of the reactive intermediate formed by coordination of TBHP to molybdenum complexes is of the alkylperoxidic type.[4,6,11] We have generalized this to the case of complexes **1**–**4** ([MoL^x], L^x = ligand set) for cyclooctene epoxidation (under the reaction conditions used), in which the oxidizing agent is [$MoL^y(O_2R)$] (R = *tert*-butyl), formed in Equation (1). The incoming TBHP molecule can affect the ligands such that L^x becomes L^y. In a previous study with the complexes [MoO_2X_2(4,4′-dihexyl-2,2′-bipyridine)] (X = Cl, Me) and TBHP we were able to re-isolate the unchanged starting complexes, in quantitative yield, after the catalytic reactions.[6,17] There is no indication that η^2-bisperoxo species of the type [$MoO(O_2)_2L$] are formed and then "recycled" to the starting materials. We can therefore conclude that the Mo–X bonds are not cleaved during the reaction with TBHP and that the catalytically active species exists in an equilibrium with the starting complex in solution.

$$\text{TBHP} + [MoL^x] \underset{k_2}{\overset{k_1}{\rightleftharpoons}} [MoL^y(O_2R)] \quad (1)$$

Many studies have reported that molybdenum(VI) centers favor heterolytic peroxometal pathways (Mo^{VI} alkyl peroxide intermediate), leading to electrophilic attack on the olefinic double bond.[11,18] It has been reported for molybdenum peroxo complexes that oxygen transfer to the olefin takes place irreversibly.[15,16] We will therefore assume that cyclooctene is irreversibly oxidized to cyclooctene oxide (CyO) by [$MoL^y(O_2R)$], with formation of the starting complex [MoL^x] and *tert*-butyl alcohol [TBOH, Equation (2)]. It is known that molybdenum catalysts are active for the conversion of TBHP to TBOH.[10,11,16,19]

$$[MoL^y(O_2R)] + \text{Cy} \xrightarrow{k_3} [MoL^x] + \text{CyO} + \text{TBOH} \quad (2)$$

Molybdenum-catalyzed epoxidations with TBHP can be prone to autoretardation by the co-product TBOH, the extent of which would be related to the equilibrium constants for the formation of catalyst–alkylperoxide and catalyst–alkoxide complexes.[3f,3h,20] Such autoretardation effects would explain the decrease of the observed reaction rate, which is more rapid in the case of the more active complex **2** (Figure 1). When TBOH was added at the beginning of the reaction (equimolar amounts of cyclooctene and TBOH, under identical reaction conditions to those described in the Experimental Section), the initial activity of **2** for cyclooctene epoxidation decreased by about 44%. On the other hand, TBHP efficiency for cyclooctene conversion (determined by iodometric titration at 240 min) was around 95% (TBHP consumed in cyclooctene epoxidation/total conversion of TBHP). It is assumed that TBOH can react reversibly with [MoL^x] to give a complex designated as [$MoL^z(OR)$] [Equation (3)].

$$[MoL^x] + \text{TBOH} \underset{k_5}{\overset{k_4}{\rightleftharpoons}} [MoL^z(OR)] \quad (3)$$

The overall rates of formation of cyclooctene, cyclooctene oxide, TBHP, TBOH, and molybdenum species can be written for the above elementary reactions as follows [Equations (4), (5), (6), (7), (8), (9) and (10)].

 © 2005 Wiley-VCH Verlag GmbH & Co. KGaA, Weinheim

$$r_{Cy} = -k_3[MoL^y(O_2R)][Cy] \quad (4)$$

$$r_{CyO} = k_3[MoL^y(O_2R)][Cy] \quad (5)$$

$$r_{TBHP} = -k_1[TBHP][MoL^x] + k_2[MoL^y(O_2R)] \quad (6)$$

$$r_{TBOH} = k_3[MoL^y(O_2R)][Cy] - k_4[MoL^x][TBOH] + k_5[MoL^z(OR)] \quad (7)$$

$$r_{[MoL^x]} = -k_1[TBHP][MoL^x] + k_2[MoL^y(O_2R)] + k_3[MoL^y(O_2R)][Cy] - k_4[MoL^x][TBOH] + k_5[MoL^z(OR)] \quad (8)$$

$$r_{[MoL^y(O_2R)]} = k_1[TBHP][MoL^x] - k_2[MoL^y(O_2R)] - k_3[MoL^y(O_2R)][Cy] \quad (9)$$

$$r_{[MoL^z(OR)]} = k_4[MoL^x][TBOH] - k_5[MoL^z(OR)] \quad (10)$$

Assuming that $[MoL^x]$, $[MoL^y(O_2R)]$, and $[MoL^z(OR)]$ are the only metal species formed, and that their total concentration at any instant is equal to the initial concentration of complex $[MoLx]_0$, we get [Equation (11)]

$$[MoL^x]_0 = [MoL^x] + [MoL^y(O_2R)] + [MoL^z(OR)] \quad (11)$$

Applying a mole balance to a homogeneous liquid-phase batch reactor (constant-volume reaction process under isothermal operation) the following differential equation can be written with respect to each chemical species [Equation (12)]

$$\frac{d[P]}{dt} = r_p \quad (12)$$

where P is cyclooctene, cyclooctene oxide, TBHP, TBOH, or a molybdenum species. Figure 2 shows the model fitting to data points for the experiments of cyclooctene epoxidation with TBHP in the presence of **1**–**4**. In all cases the predicted kinetic curves fit the experimental data points. The fairly good fitting achieved indicates that the above mechanism of cyclooctene oxidation is consistent with the experimental data and that the assumptions made are valid and reasonable.

UV/Vis Studies of Catalyst Formation

The kinetics of the reaction of $[MoL^x]$ with TBHP in the absence of any reductant was studied by UV/Vis spectroscopy, thereby allowing equilibrium constants and rate constants to be determined for this step.

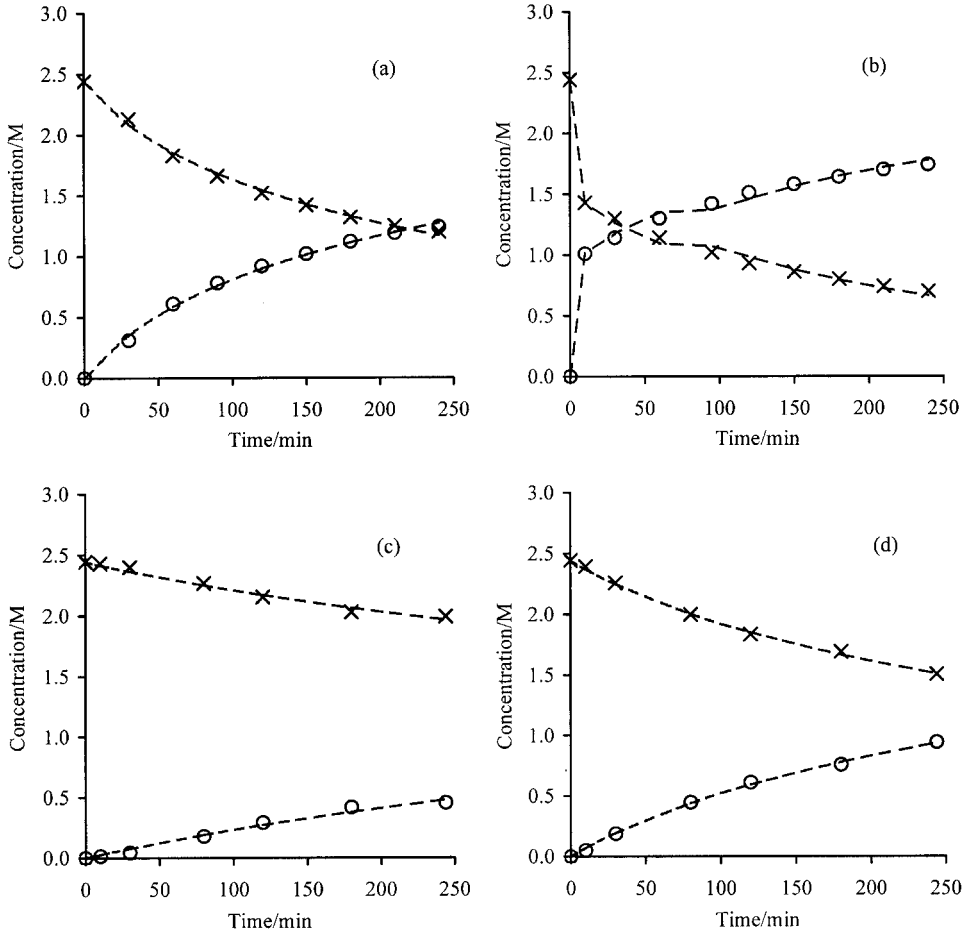

Figure 2. Concentration vs. time profiles of cyclooctene and cyclooctene oxide for (a) **1**, (b) **2**, (c) **3** and (d) **4** determined experimentally (points) and calculated for the proposed model (dashed lines).

 © 2005 Wiley-VCH Verlag GmbH & Co. KGaA, Weinheim

The Equilibrium Constants of Catalyst Formation

The absorbance vs. concentration diagram of solutions of complex **3** and **4** with TBHP is not like a titration curve (see Figure 3 for complex **3**). It continues, however, to build up as more TBHP is added, until finally a plateau is reached. This reaction was assumed to form a 1:1 adduct, $[MoL^y(O_2R)]$, in equilibrium with the original $[MoL^x]$ and TBHP [Equation (1)]. The changes in absorbance (at 300 nm) due to the loss of $[MoL^x]$ and formation of $[MoL^y(O_2R)]$ can be expressed by Equation (13) (assuming a 1.0-cm path-length)

$$Abs = \varepsilon_1[MoL^x] + \varepsilon_2[MoL^y(O_2R)] \quad (13)$$

where ε_1 and ε_2 are the molar absortivities for $[MoL^x]$ and $[MoL^y(O_2R)]$ adducts, respectively. Substituting the equilibrium constant (K_{eq}) for the formation of the $[MoL^y(O_2R)]$ adduct in Equation (13), and using the molar balance $[Mo]_T = [MoL^x] + [MoL^y(O_2R)]$, we obtain Equation (14):

$$\frac{Abs}{[Mo]_T} = \frac{\varepsilon_1 + \varepsilon_2 K_{eq}[TBHP]}{1 + K_{eq}[TBHP]} \quad (14)$$

The data were obtained with a constant initial concentration of MoL^x and over a range of concentrations of TBHP of 5.0–50 mM. The fitting of Equation (14) to the experimental data of absorbance (at equilibrium) as a function of TBHP allowed values for the equilibrium constants to be calculated (Figure 3, Table 1).

The thermodynamic parameters for the reaction of **3** with TBHP to form the catalyst were estimated from the equilibrium constants at 25 °C and 55 °C, determined as 123 ± 19 and 482 ± 34 M^{-1}, respectively (Table 1). The values of ΔG (at 25 °C), ΔH, and ΔS are -12 kJ mol^{-1}, $+28.6$ kJ mol^{-1} and $+136$ J mol^{-1} K^{-1}, respectively, indicating that the formation of the catalyst is an endothermic and spontaneous process. The positive enthalpy value may also indicate that the Mo–OOR bond is weaker than the Mo–X bond. The equilibrium constant for the reaction of **3** with TBHP is seven to eight times greater than that for the reaction of **4** with TBHP. It seems therefore that the presence of the large hexyl substituent (compared with the methyl for **3**) reduces the stability of the catalyst relative to the starting complex. This would explain the observed higher reactivity (lower stability) of the Mo^{VI} oxidizing species bearing a hexyl group towards cyclooctene epoxidation.

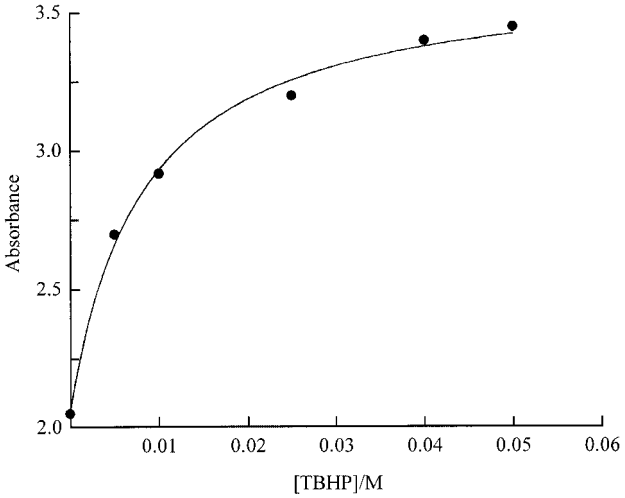

Figure 3. A plot of the absorbance at 300 nm of equilibrium mixtures of TBHP and **3** as a function of [TBHP] at $[Mo]_T = 0.5$ mM in acetonitrile at 25 °C. The solid line is the absorbance calculated from Equation (14) with the values of $K_{eq} = 123$ M^{-1}, $\varepsilon_1 = 4.0 \times 10^3$ M^{-1} cm^{-1} and $\varepsilon_2 = 7.3 \times 10^3$ M^{-1} cm^{-1}.

Kinetic Studies of Catalyst Formation

The rate constants for the reactions of complexes **2**, **3** and **4** with TBHP were determined by initial rate (method I) and pseudo-first-order (method II) methods. In both cases, the complexes were in limiting amount (0.5 mM) and TBHP in large excess (at least 10-fold).

Initial Rate (Method I)

The initial rates (v_i) were calculated from the initial absorbance change (2–5%) of the absorbance-time curves based on Equation (15),

Table 1. The equilibrium constants and the rate constants for the reactions of the Mo^{VI} complexes **2**, **3** and **4** with TBHP.

Complex	K_{eq}	k_1 [L mol^{-1} s^{-1}]	k_2 [10^{-3} s^{-1}]	$\Delta H^{\ddagger}$ [kJ mol^{-1}]	$\Delta S^{\ddagger}$ [J (mol K)$^{-1}$]
2	–[a]	$(1.5 \pm 0.3) \times 10^{-4}$[b]		80 ± 2	-76 ± 32
		$(1.7 \pm 0.4) \times 10^{-3}$[c]			
3	123 ± 19[b]	0.043 ± 0.005[b][d]	0.35[b]	65.7 ± 6.0	-39 ± 5
		0.061 ± 0.008[b][e]	0.50[b]		
	482 ± 34[c]	0.25 ± 0.02[c][d]	0.52[c]		
		0.36 ± 0.06[c][e]	0.75[c]		
4	16 ± 7[b]	0.059 ± 0.008[b][d]	3.7[b]	49.0 ± 4.2	-96 ± 13
		0.067 ± 0.010[b][e]	4.2[b]		
		0.47 ± 0.06[c][d]			
		0.63 ± 0.12[c][e]			

[a] Not determined. [b] At 25 °C. [c] At 55 °C. [d] Obtained by method I. [e] Obtained by method II.

 © 2005 Wiley-VCH Verlag GmbH & Co. KGaA, Weinheim

$$v_i = \frac{\Delta Abs_i}{\Delta t \cdot b \cdot \Delta \varepsilon} \quad (15)$$

where ΔAbs_i is the initial absorbance change observed for the reaction of complex **i** (i = **2**, **3**, **4**) with TBHP in the time interval Δt, $\Delta\varepsilon$ is the difference in the molar absortivities of the starting complex [MoL^x] and the catalyst [$MoL^y(O_2R)$], and b is the light path length. Variation of the initial rate with the initial concentration of TBHP is shown in Figure 4 for complex **3** at 55 °C. The second-order rate constants (k_1, Table 1) were calculated from the slopes based on the rate-law equation $v_i = k_1[MoL^x][TBHP]$, where slope = $k_1[MoL^x]$.

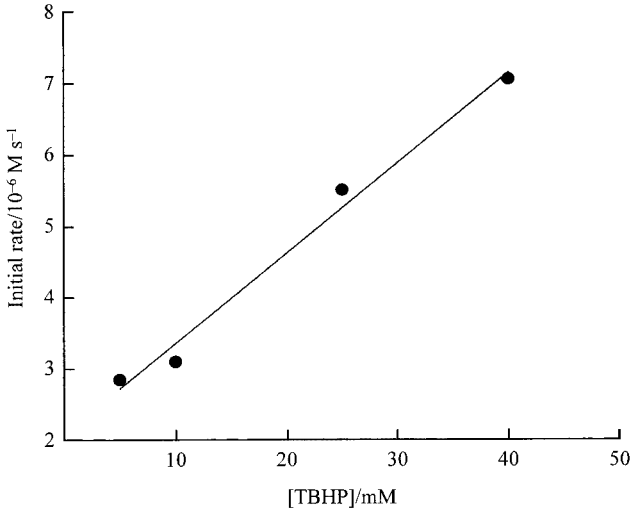

Figure 4. Variation of the initial rate with [TBHP] for the reaction of **3** (0.5 mM) and TBHP in acetonitrile at 55 °C. The solid line represents the calculated data based on a linear fit of the experimental data with slope = $k_1[\mathbf{3}] = 1.25 \times 10^{-4}$ s^{-1}.

Pseudo-First-Order (Method II)

In this method, the pseudo-first-order rate constants (k_ψ) were determined by fitting the last 20–50% of the absorbance vs. time curves to a first-order exponential equation, in a similar fashion to that reported previously.[21] The values of k_ψ vary linearly with [TBHP] in the range 5–25 mM and the slopes give the second-order rate constants (k_1), as shown in Figure 5 for complex **4** at 25 °C. The values of the reverse rate constants k_2 [Equation (1)] were calculated from the values of the second-order rate constants k_1 for the reaction of complexes **2**, **3**, and **4** with TBHP and the equilibrium constants, $k_2 = k_1/K_{eq}$. Methods I and II give similar values of k_1 and k_2 within the range of experimental error (Table 1).

The kinetic results show that the rate of formation of the catalyst, [MoLy(O_2R)], is much faster for the Br complexes than for the Cl ones (Table 1). For example, the rate constant for the formation of the catalysts from the reaction of [MoO_2Br_2(4-hexyl-4′-methyl-2,2′-bipyridine)] (**4**) with

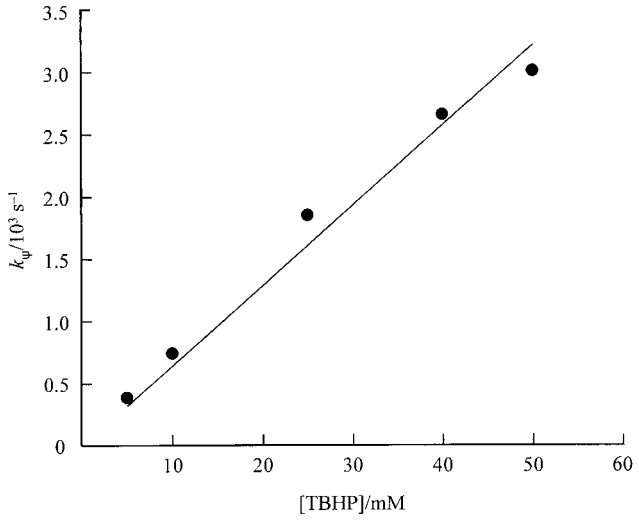

Figure 5. A plot of the pseudo-first-order rate constants as a function of [TBHP] for the reaction of **4** (0.5 mM) with TBHP in acetonitrile at 25 °C.

TBHP is 2–3 orders of magnitude higher than that for the reaction of [MoO_2Cl_2(4-hexyl-4′-methyl-2,2′-bipyridine)] (**2**) with TBHP. These results, taken together with the fact that Br catalysts of this type generally possess lower activity towards epoxidation of an olefin,[6] suggest that the first step (the catalyst formation) is not always the rate-limiting step of cyclooctene epoxidation with these complexes.

Experimental results on the effect of temperature variation in the range 20–60 °C on the catalyst formation from the reaction of complexes **1**–**4** with TBHP showed that the rate increases significantly with increasing temperature. Plots of $\ln(k_1/T)$ vs. $1/T$, where k_1 is the second-order rate constant for the reaction of the Mo complex with TBHP, led to the activation parameters $\Delta H^\ddagger$ and $\Delta S^\ddagger$ (Figure 6,

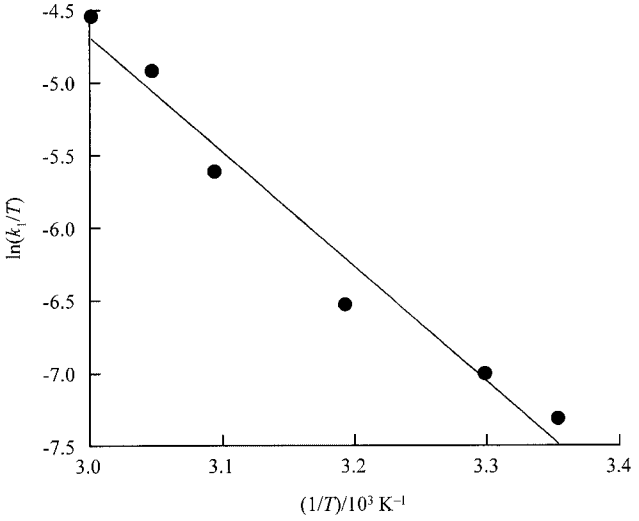

Figure 6. A plot of $\ln(k_1/T)$ vs. $1/T$ for the catalyst formation from the reaction of TBHP with **3** in acetonitrile. The activation parameters were calculated from the slope (–7.9) and the intercept (19.0) based on the equation $\ln(k_1/T) = 23.76 + \Delta S^\ddagger/R - \Delta H^\ddagger/R(1/T)$.

 © 2005 Wiley-VCH Verlag GmbH & Co. KGaA, Weinheim

Table 1). All the $\Delta S^{\ddagger}$ values obtained for the catalyst formation in this study have negative values, thus indicating that the catalyst formation is associated with an entropy decrease. These results support an associative mechanism in which a seven-coordinate intermediate is formed. The trend in the $\Delta H^{\ddagger}$ values confirms the trend in the rate constants for the catalyst formation (k_1 decreases in the order **4** > **3** > **2**). Also, the values of $\Delta H^{\ddagger}$ are of the same order of magnitude as those obtained for similar W complexes.[21] However, in the case of the Mo complexes the values of $\Delta H^{\ddagger}$ are generally lower, which explains the higher activity of Mo catalysts in comparison with the W ones.

Concluding Remarks

Several complexes with the general formula $[MoO_2X_2L]$ (X = Cl, Br) have been synthesized and examined as catalysts for the epoxidation of cyclooctene using TBHP as the oxidant. The kinetics studies support the theory that the first step in the reaction mechanism is associative and involves the reaction of TBHP with the starting complex. It is assumed that the peroxide transfers a hydrogen to one of the Mo=O oxygens and the remaining ROO^- anion binds as a seventh ligand. In contrast to recent findings on tungsten complexes[21] and with theoretical investigations on Mo complexes, the present work indicates that the first step is not always the rate-limiting step. DFT calculations are being carried out in order to probe in more detail various aspects of the reaction mechanism.

Experimental Section

All preparations and manipulations were carried out using standard Schlenk techniques under nitrogen. Solvents were dried by standard procedures (THF, hexane, and diethyl ether over Na/benzophenone ketyl; CH_2Cl_2 and CH_3CN over CaH_2), distilled, and kept under nitrogen over molecular sieves. Microanalyses were performed at the ITQB and the Mikroanalytische Labor of the Technical University of Munich (M. Barth). IR spectra were measured on Mattson Mod 7000 and Perkin–Elmer FTIR spectrometers using KBr pellets. Solution NMR spectra were measured on Bruker CXP 300 (^{1}H, 300 MHz), Bruker Avance DPX-400 (^{1}H: 400 MHz; ^{13}C: 100.28 MHz; ^{95}Mo: 26.07 MHz) and JEOL JNM GX-400 (^{13}C: 100.28 MHz; ^{17}O: 54.14 MHz) spectrometers. 4,4′-Dimethyl-2,2′-bipyridine was purchased from Aldrich and used as received. The compounds 4-hexyl-4′-methyl-2,2′-bipyridine,[22] $[MoO_2X_2]$ (X = Cl, Br)[23] and $[MoO_2X_2(THF)_2]$ (X = Cl, Br)[2b] were prepared according to published procedures with only minor changes.

Synthesis of Complexes 1–4: The complexes $[MoO_2Cl_2(THF)_2]$ (1.37 g, 4.00 mmol) and $[MoO_2Br_2(THF)_2]$ (1.73 g, 4.00 mmol) were each dissolved in CH_2Cl_2 (20 mL) and treated with 1 equiv. of 4,4′-dimethyl-2,2′-bipyridine or 4-hexyl-4′-methyl-2,2′-bipyridine. The resulting turbid solutions were each stirred for a further 1 h. The solvent was removed under vacuum, and the product washed with diethyl ether and dried under vacuum.

$[MoO_2Cl_2$(4,4′-dimethyl-2,2′-bipyridine)] (1): Yield: 1.47 g (96%). Selected IR (KBr): $\tilde{\nu}$ = 1613 cm^{-1} (vs), 1025 (s), 938 (vs) ($Mo{=}O_{asym}$), 907 (vs) ($Mo{=}O_{sym}$), 832 (vs), 517 (s) cm^{-1}. ^{1}H NMR (400 MHz, [D$_6$]DMSO, 20 °C): δ = 3.00 (s, 6 H, CH_3), 8.18 (d, 2 H, py-H), 9.11 (s, 2 H, py-H), 9.68 (d, 2 H, py-H) ppm. ^{95}Mo NMR (DMSO, 20 °C): δ = 205 ppm. $C_{12}H_{12}Cl_2MoN_2O_2$ (383.08): calcd. C 37.62, H 3.16, N 7.31; found C 37.48, H 2.96, N 7.29.

$[MoO_2Cl_2$(4-hexyl-4′-methyl-2,2′-bipyridine)] (2): Yield: 1.65 g (91%). Selected IR (KBr): $\tilde{\nu}$ = 2925 cm^{-1} (s), 1611 (vs), 1417 (s), 1026 (s), 938 (vs) ($Mo{=}O_{asym}$), 913 (vs) ($Mo{=}O_{sym}$) cm^{-1}. ^{1}H NMR (400 MHz, CD_2Cl_2, 20 °C): δ = 0.90 (t, 3 H, CH_3CH$_2$-), 1.33 [m, 6 H, $(CH_2)_3$], 1.75 (m, 2 H, CH_2), 2.60 (s, 3 H, CH_3), 2.86 (m, 2 H, CH_2), 7.54 (d, 2 H, py-H), 8.09 (s, 2 H, py-H), 9.33 (t, 2 H, py-H) ppm. ^{13}C NMR (CD_3Cl, 20 °C): δ = 14.4, 22.15, 22.86, 29.34, 30.49, 31.88, 36.23, 122.68 (py-C), 123.46 (py-C), 127.36 (py-C), 128.10 (py-C), 149.91 (py-C), 151.96 (py-C), 158.26 (py-C) ppm. ^{95}Mo NMR (CD_2Cl_2, 20 °C): δ = 201 ppm. $C_{17}H_{22}Cl_2MoN_2O_2$ (453.21): calcd. C 45.05, H 4.89, N 6.18; found C 45.07, H 4.75, N 6.07.

$[MoO_2Br_2$(4,4′-dimethyl-2,2′-bipyridine)] (3): Yield: 1.47 g (78%). Selected IR (KBr): $\tilde{\nu}$ = 1614 cm^{-1} (vs), 1025 (s), 935 (vs) ($Mo{=}O_{asym}$), 905 (vs) ($Mo{=}O_{sym}$), 830 (s), 517 (s) cm^{-1}. ^{1}H NMR (400 MHz, [D$_6$]DMSO, 20 °C): δ = 2.57 (s, 6 H, CH_3), 7.72 (d, 2 H, py-H), 8.55 (s, 2 H, py-H), 8.73 (d, 2 H, py-H) ppm. ^{95}Mo NMR (DMSO, 20 °C): δ = 254 ppm. $C_{12}H_{12}Br_2MoN_2O_2$ (471.98): calcd. C 30.54, H 2.56, N 5.94; found C 30.42, H 2.40, N 5.77.

$[MoO_2Br_2$(4-hexyl-4′-methyl-2,2′-bipyridine)] (4): Yield: 1.54 g (71%). Selected IR (KBr): $\tilde{\nu}$ = 2925 cm^{-1} (s), 1611 (vs), 1417 (s), 1026 (s), 935 (vs) ($Mo{=}O_{asym}$), 906 (vs) ($Mo{=}O_{sym}$) cm^{-1}. ^{1}H NMR (400 MHz, CD_2Cl_2, 20 °C): δ = 0.83 (t, 3 H, CH_3CH$_2$-), 1.28 [m, 6 H, $(CH_2)_3$], 1.70 (m, 2 H, CH_2), 2.54 (s, 3 H, CH_3), 2.78 (m, 2 H, CH_2), 7.48 (d, 2 H, py-H), 8.02 (d, 2 H, py-H), 9.32 (t, 2 H, py-H) ppm. ^{13}C NMR (CD_3Cl, 20 °C): δ = 14.0, 21.8, 22.5, 29.0, 30.1, 31.5, 35.9, 122.4 (py-C), 123.2 (py-C), 127.0 (py-C), 127.8 (py-C), 149.6 (py-C), 151.9 (py-C), 153.2, 157.9 (py-C) ppm. ^{95}Mo NMR (CD_2Cl_2, 20 °C): δ = 251 ppm. $C_{17}H_{22}Br_2MoN_2O_2$ (542.12): calcd. C 37.66, H 4.09, N 5.17; found C 37.49, H 3.88, N 5.09.

Synthesis of ^{17}O-Labeled Complexes 5–8: The labeled complexes $[Mo^{17}O_2Cl_2(DMF)_2]$ and $[Mo^{17}O_2Br_2(DMF)_2]$ were prepared according to the published procedure using $H_2{}^{17}O$.[4] IR (KBr): $\tilde{\nu}$ = 941 cm^{-1} (s), 928 (vs), 904 (vs), 891 (s), 870 (vs), 860 (s) (Mo=O) cm^{-1}. Recrystallization of $[Mo^{17}O_2X_2(DMF)_2]$ (X = Cl, Br) from THF gave the labeled starting materials $[Mo^{17}O_2Cl_2(THF)_2]$ and $[Mo^{17}O_2Br_2(THF)_2]$, which were subsequently used to prepare the labeled Lewis-base adducts **5**–**8**.

$[Mo^{17}O_2Cl_2$(4,4′-dimethyl-2,2′-bipyridine)] (5): IR (KBr): $\tilde{\nu}$ = 938 cm^{-1} (vs), 924 (s), 908 (vs), 897 (s), 874 (s) (Mo=O) cm^{-1}. ^{17}O NMR (DMSO, 20 °C): δ = 1005 ppm.

$[Mo^{17}O_2Cl_2$(4-hexyl-4′-methyl-2,2′-bipyridine)] (6): IR (KBr): $\tilde{\nu}$ = 937 cm^{-1} (vs), 928 (s), 913 (vs), 903 (s), 889 (m), 871 (s) (Mo=O) cm^{-1}. ^{17}O NMR (CD_2Cl_2, 20 °C): δ = 993 ppm.

$[Mo^{17}O_2Br_2$(4,4′-dimethyl-2,2′-bipyridine)] (7): IR (KBr): $\tilde{\nu}$ = 934 cm^{-1} (s), 922 (s), 904 (vs), 895 (s), 869 (s) (Mo=O) cm^{-1}. ^{17}O NMR (DMSO, 20 °C): δ = 1003 ppm.

$[Mo^{17}O_2Br_2$(4-hexyl-4′-methyl-2,2′-bipyridine)] (8): IR (KBr): $\tilde{\nu}$ = 934 cm^{-1} (vs), 927 (s), 903 (vs), 871 (m) (Mo=O) cm^{-1}. ^{17}O NMR (CD_2Cl_2, 20 °C): δ = 994 ppm.

Catalytic Reactions with Compounds 1–4 as Catalysts: The epoxidation of cyclooctene was carried out at 55 °C, in air, in a batch reactor equipped with a magnetic stirrer. The reactor was loaded with 73 μmol of complex, 7.3 mmol of cyclooctene (1% molar ratio of catalyst/substrate) and 11 mmol of *tert*-butyl hydroperoxide (5.5 M in decane), which was used as oxidant. Samples were with-

 © 2005 Wiley-VCH Verlag GmbH & Co. KGaA, Weinheim

drawn periodically and analyzed with a gas chromatograph (Varian 3800) equipped with a capillary column (SPB-5, 20 m × 0.25 mm × 0.25 μm) and a flame ionization detector. The products were identified by gas chromatography-mass spectrometry (HP, 5890 Series II GC; HP 5970 Series Mass Selective Detector) using He as carrier gas.

UV/Vis Experiments: All kinetic experiments were carried out under pseudo-first-order conditions with excess TBHP in CH_3CN at 25 and 55 °C. The reactions were carried out in quartz cuvettes with a path length of 1 cm. In a typical experiment, TBHP was added to a thermostatted UV cell containing a solution of the catalyst. The catalyst concentration was held constant at 0.5 mM and TBHP concentration was varied in the range 5.0–50 mM. The absorbance changes at 300 nm were recorded with time using a Jasco V-560 spectrophotometer equipped with a Jasco EHC-477S Peltier thermostatted single cell holder. All data analysis was carried out with the KaleidaGraph program.

Acknowledgments

This work was partly funded by the FCT, POCTI, and FEDER (Project POCTI/QUI/37990/2001). The authors are also grateful to DAAD and CRUP (INIDA and Acções Integradas Programme) for financial support. ISG thanks the FCT for a grant (BSAB/372/2003) and AMS is grateful to the Alexander von Humboldt Foundation for a postdoctoral research fellowship. CDN acknowledges grants from the University of Aveiro and the FCT.

[1] a) S. B. Kumar, M. Chaudhury, *J. Chem. Soc., Dalton Trans.* **1991**, 2169–2174; b) P. Palanca, T. Picher, V. Sanz, P. Gómez-Romero, E. Llopis, A. Domenech, A. Cervilla, *J. Chem. Soc., Chem. Commun.* **1990**, 531–533; c) J. P. Wilshire, L. Leon, P. Bosserman, D. T. Sawyer, *J. Am. Chem. Soc.* **1979**, *101*, 3379–3381; d) J. M. Berg, R. H. Holm, *J. Am. Chem. Soc.* **1985**, *107*, 925–932; e) J. P. Caradonna, E. W. Harlan, R. H. Holm, *J. Am. Chem. Soc.* **1986**, *108*, 7856–7858; f) F. J. Feher, K. Rahimian, T. A. Budzichowski, J. W. Ziller, *Organometallics* **1995**, *14*, 3920–3926; g) R. Clarke, M. Gahagan, R. K. Mackie, D. F. Foster, D. J. Cole-Hamilton, M. Nicol, A. W. Montford, *J. Chem. Soc., Dalton Trans.* **1995**, 1221–1226; h) J. R. Backhouse, H. M. Lowe, E. Sinn, S. Suzuki, S. Woodward, *J. Chem. Soc., Dalton Trans.* **1995**, 1489–1495; i) U. Piarulli, D. N. Williams, C. Floriani, G. Gervasio, D. Viterbo, *J. Chem. Soc., Dalton Trans.* **1995**, 3329–3334.

[2] a) A. F. Hollemann, E. Wiberg, *Lehrbuch der Anorganischen Chemie*, Walter de Gruyter, Berlin, New York, **1995**; b) H. L. Krauss, W. Huber, *Chem. Ber.* **1961**, *94*, 2864–2876; c) R. H. Fenn, *J. Chem. Soc. (A)* **1969**, 1764; d) M. N. Sheng, G. J. Zajaczek, ARCO, GB 1.136.923, **1968**; e) J. Kollar, Halcon, US 3.350.422, US 3.351.635, **1967**; f) H. Mimoun, I. Seree de Roch, L. Sajus, *Tetrahedron* **1970**, *26*, 37–50; g) K. B. Sharpless, J. M. Townsend, D. R. Williams, *J. Am. Chem. Soc.* **1972**, *94*, 295–296; h) J. A. Brito, M. Gómez, G. Muller, H. Teruel, J.-C. Clinet, E. Duñach, M. A. Maestro, *Eur. J. Inorg. Chem.* **2004**, 4278–4285, and references cited therein; i) I. V. Yudanov, C. Di Valentin, P. Gisdakis, N. Rösch, *J. Mol. Catal. A: Chem.* **2000**, *158*, 189–197, and references cited therein; j) D. V. Deubel, J. Sundermeyer, G. Frenking, *J. Am. Chem. Soc.* **2000**, *122*, 10 101–10 108; k) D. V. Deubel, J. Sundermeyer, G. Frenking, *Eur. J. Inorg. Chem.* **2001**, 1819–1827; l) D. V. Deubel, J. Sundermeyer, G. Frenking, *Inorg. Chem.* **2000**, *39*, 2314–2320; m) J. M. Mitchell, N. S. Finney, *J. Am. Chem. Soc.* **2001**, *123*, 862–869; n) R. A. Sheldon, in *Applied Homogeneous Catalysis with Organometallic Compounds*, vol. 1 (Eds.: B. Cornils, W. A. Herrmann), Wiley-VCH, Weinheim, New York, **1996**; o) G. Wahl, D. Kleinhenz, A. Schorm, J. Sundermeyer, R. Stohwasser, C. Rummey, G. Bringmann, C. Fickert, W. Kiefer, *Chem. Eur. J.* **1999**, *5*, 3237–3251; p) A. Hroch, G. Gemmecker, W. R. Thiel, *Eur. J. Inorg. Chem.* **2000**, 1107–1114; q) R. A. Sheldon, *Aspects Homog. Catal.* **1981**, *4*, 3; r) M. N. Sheng, J. C. Zajacek, in *Oxidations of Organic Compounds*, vol. 2 (Ed.: F. R. Mayo), *Advances in Chemistry Series* **1968**, *76*, 418.

[3] a) F. E. Kühn, E. Herdtweck, J. J. Haider, W. A. Herrmann, I. S. Gonçalves, A. D. Lopes, C. C. Romão, *J. Organomet. Chem.* **1999**, *583*, 3–10; b) F. E. Kühn, A. D. Lopes, A. M. Santos, E. Herdtweck, J. J. Haider, C. C. Romão, A. G. Santos, *J. Mol. Catal. A: Chem.* **2000**, *151*, 147–160; c) A. D. Lopes. *Ph. D. Thesis*, ITQB/Universidade Nova de Lisboa, **1999**; d) F. E. Kühn, A. M. Santos, A. D. Lopes, I. S. Gonçalves, E. Herdtweck, C. C. Romão, *J. Mol. Catal. A: Chem.* **2000**, *164*, 25–38; e) F. E. Kühn, A. M. Santos, I. S. Gonçalves, C. C. Romão, A. D. Lopes, *Appl. Organomet. Chem.* **2001**, *15*, 43–50; f) F. E. Kühn, A. M. Santos, A. D. Lopes, I. S. Gonçalves, J. E. Rodríguez-Borges, M. Pillinger, C. C. Romão, *J. Organomet. Chem.* **2001**, *621*, 207–217; g) A. M. Santos, F. E. Kühn, K. Bruus-Jensen, I. Lucas, C. C. Romão, E. Herdtweck, *J. Chem. Soc., Dalton Trans.* **2001**, 1332–1337; h) I. S. Gonçalves, C. C. Romão, A. M. Santos, A. D. Lopes, J. E. Rodrígues-Borges, M. Pillinger, P. Ferreira, F. E. Kühn, J. Rocha, *J. Organomet. Chem.* **2001**, *626*, 1–10.

[4] P. Chaumette, H. Mimoun, L. Saussine, J. Fischer, A. Mitschler, *J. Organomet. Chem.* **1983**, *250*, 291–310.

[5] B. A. Barshop, R. F. Wrenn, C. Frieden, *Anal. Biochem.* **1983**, *130*, 134–145.

[6] F. E. Kühn, M. Groarke, É. Bencze, E. Herdtweck, A. Prazeres, A. M. Santos, M. J. Calhorda, C. C. Romão, I. S. Gonçalves, A. D. Lopes, M. Pillinger, *Chem. Eur. J.* **2002**, *8*, 2370–2383.

[7] S. N. Rao, K. N. Munshi, N. N. Rao, *J. Mol. Catal. A: Chem.* **1999**, *145*, 203–210.

[8] S. N. Rao, K. N. Munshi, N. N. Rao, *J. Mol. Catal. A: Chem.* **2000**, *156*, 205–211, and references cited therein.

[9] W. A. Herrmann, G. M. Lobmaier, T. Priermeier, M. R. Mattner, B. Scharbert, *J. Mol. Catal. A: Chem.* **1997**, *117*, 455–469.

[10] W. R. Thiel, T. Priermeier, *Angew. Chem. Int. Ed. Engl.* **1995**, *34*, 1737–1738.

[11] W. R. Thiel, J. Eppinger, *Chem. Eur. J.* **1997**, *3*, 696–705.

[12] M. Abrantes, A. M. Santos, J. Mink, F. E. Kühn, C. C. Romão, *Organometallics* **2003**, *22*, 2112–2118.

[13] a) C. C. Romão, F. E. Kühn, W. A. Herrmann, *Chem. Rev.* **1997**, *97*, 3197–3246; b) W. A. Herrmann, F. E. Kühn, *Acc. Chem. Res.* **1997**, *30*, 169–180; c) M. C. A. van Vliet, I. W. C. E. Arends, R. A. Sheldon, *Chem. Commun.* **1999**, 821–822.

[14] A. A. Valente, J. Moreira, A. D. Lopes, M. Pillinger, C. D. Nunes, C. C. Romão, F. E. Kühn, I. S. Gonçalves, *New J. Chem.* **2004**, *28*, 308–313.

[15] K. A. Jørgensen, *Chem. Rev.* **1989**, *89*, 431–458.

[16] W. R. Thiel, *J. Mol. Catal. A: Chem.* **1997**, *117*, 449–454.

[17] M. Groarke, I. S. Gonçalves, W. A. Herrmann, F. E. Kühn, *J. Organomet. Chem.* **2002**, *649*, 108–112.

[18] R. A. Sheldon, I. W. C. E. Arends, H. E. B. Lempers, in *Supported Reagents and Catalysts in Chemistry* (Eds.: B. K. Hodnett et al.), Royal Society of Chemistry, **1998**, p. 37.

[19] A. O. Chong, K. B. Sharpless, *J. Org. Chem.* **1977**, *42*, 1587–1590.

[20] R. A. Sheldon, J. A. Van Doorn, *J. Catal.* **1973**, *31*, 427–437.

[21] F. E. Kühn, W. M. Xue, A. Al-Ajlouni, A. M. Santos, S. Zang, C. C. Romão, G. Eickerling, E. Herdtweck, *Inorg. Chem.* **2002**, *41*, 4468–4477.

[22] D. K. Ellison, R. T. Iwamoto, *Tetrahedron Lett.* **1983**, *24*, 31–32.

[23] R. Colton, I. B. Tomkins, *Austr. J. Chem.* **1965**, *18*, 447.

Received: October 11, 2004

 © 2005 Wiley-VCH Verlag GmbH & Co. KGaA, Weinheim

Synthesis, Structure, Reactivity, and Catalytic Activity of *C,N*- and *C,N,N*-Orthopalladated Iminophosphoranes

Raquel Bielsa,[a] Angel Larrea,[b] Rafael Navarro,*[a] Tatiana Soler,[a] and Esteban P. Urriolabeitia*[a]

Keywords: C–C Coupling / C–H Activation / Homogeneous catalysis / N ligands / Palladium

The orthopalladated complexes $[Pd(\mu\text{-}Cl)(C_6H_4\text{-}2\text{-}PPh_2{=}NPh\text{-}\kappa\text{-}C,N)]_2$ (**1**) and $[Pd(C_6H_4\text{-}2\text{-}PPh_2{=}N\text{-}C(O)\text{-}2\text{-}NC_5H_4\text{-}\kappa\text{-}C,N,N)Cl]$ (**11**) have been obtained by reaction of $Pd(OAc)_2$ (OAc = acetate) with the iminophosphoranes $Ph_3P{=}NPh$ and $Ph_3P{=}N\text{-}C(O)\text{-}2\text{-}NC_5H_4$, respectively, in the presence of excess LiCl. Complex **11** has been characterised by X-ray diffraction methods. The orthoplatinated derivative $[Pt(C_6H_4\text{-}2\text{-}PPh_2{=}N\text{-}C(O)\text{-}2\text{-}NC_5H_4\text{-}\kappa\text{-}C,N,N)Cl]$ (**12**) can be obtained by reaction of $[PtCl_2(NCPh)_2]$ with $Ph_3P{=}N\text{-}C(O)\text{-}2\text{-}NC_5H_4$ in refluxing 2-methoxyethanol. Complex **1** shows the typical reactivity of *C,N*-orthopalladated complexes, while complex **11** shows that the *C,N,N*-orthometallated ligand is strongly bonded to the Pd atom and cannot be easily displaced. The catalytic activity of the complexes $[Pd(\mu\text{-}Cl)(C_6H_4\text{-}2\text{-}PPh_2{=}NPh\text{-}\kappa\text{-}C,N)]_2$ (**1**), $[Pd(C_6H_4\text{-}2\text{-}PPh_2{=}NPh\text{-}\kappa\text{-}C,N)(Cl)(py)]$ (**4**), $[Pd(C_6H_4\text{-}2\text{-}PPh_2{=}N\text{-}C(O)\text{-}2\text{-}NC_5H_4\text{-}\kappa\text{-}C,N,N)Cl]$ (**11**) and $[Pd(C_6H_4\text{-}2\text{-}PPh_2{=}N\text{-}C(O)\text{-}2\text{-}NC_5H_4\text{-}\kappa\text{-}C,N,N)(NCMe)]ClO_4$ (**13**) in the Mizoroki–Heck (MH) reaction between methyl acrylate and different haloarenes has been examined. All complexes behave as moderate to good catalysts, yielding turnover numbers (TON) up to 526000. Their role as catalysts or precatalysts and the formation of nanoparticles is also discussed.

(© Wiley-VCH Verlag GmbH & Co. KGaA, 69451 Weinheim, Germany, 2005)

Introduction

Iminophosphoranes (phosphane imines) are compounds of general structure $R_3P{=}NR'$ (R, R′ = alkyl, aryl, acyl, etc). They show notable analogies with the phosphorus ylides $R_3P{=}CR'(R'')$,[1] and also have numerous applications in organic chemistry (e.g. the aza-Wittig reaction), either as neutral or as anionic reagents.[1–3] In addition, the bonding properties of these compounds as ligands towards transition metals are still attracting the interest of chemists,[4–28] for several reasons: their ability to form and to stabilize carbene complexes,[5,8] the easy modulation of the electronic and steric properties of different types of catalysts (for instance, in oligo- and polymerisation of ethylene,[4,6,23] hydrogen-transfer processes,[9,10] etc.), their applications in enantioselective synthesis and catalysis (allylic substitution),[25,26] the synthesis of alkaline earth organometallic complexes,[7] and, in general, due to their versatility. In this context, we have recently reported some aspects of the chemistry of the α-stabilized iminophosphoranes $Ph_3P{=}NCN$, $Ph_3P{=}NC(O)CH_2Cl$ and $Ph_3P{=}NC(O)\text{-}2\text{-}NC_5H_4$, which can behave as monodentate, bridging bidentate or chelate bidentate ligands towards Pd^{II} and Pt^{II} complexes using different donor atoms.[29,30]

However, the synthesis of orthometallated aryl complexes derived from iminophosphoranes is still scarcely represented, as well as the properties of the resulting complexes (reactivity, catalytic performance),[31–36] although very recently relevant contributions have appeared in the literature.[37,38]

With the aim of expanding the scope of this type of orthometallated derivatives, and also to gain more insight into their chemical behaviour, we have studied the reactivity of several iminophosphoranes towards Pd^{II} and Pt^{II} metallating reagents. In addition, we have also studied the reactivity of the resulting orthopalladated complexes towards different neutral and anionic ligands. We also report their behaviour as catalysts in specific C–C couplings such as the MH reaction, a field in which the application of orthopalladated complexes is in continuous growth.[39–44]

Results and Discussion

Synthesis of Orthometallated Iminophosphorane Complexes

The reactivity of different iminophosphoranes, such as $Ph_3P{=}NPh$, $Ph_3P{=}NCN$,[45] $Ph_3P{=}NC(O)CH_2Cl$, $Ph_3P{=}NC(O)\text{-}2\text{-}NC_5H_4$[46] and $Ph_3P{=}N{-}N{\equiv}C$[47] towards some standard metallating Pd^{II} and Pt^{II} reagents has been studied. The reaction of $Pd(OAc)_2$ (OAc = acetate) with

[a] Departamento de Química Inorgánica, Instituto de Ciencia de Materiales de Aragón, Universidad de Zaragoza-CSIC, 50009 Zaragoza, Spain
E-mail: esteban@unizar.es
[b] Centro Politécnico Superior, Instituto de Ciencia de Materiales de Aragón, Universidad de Zaragoza-CSIC, 50018 Zaragoza, Spain

Ph_3P=NPh (1:1 molar ratio) in refluxing CH_2Cl_2, followed by evaporation to dryness and treatment of the residue with excess LiCl in MeOH, gives the orthometallated dimer $[Pd(C_6H_4\text{-}2\text{-}PPh_2{=}NPh\text{-}\kappa\text{-}C,N)(\mu\text{-}Cl)]_2$ (**1**) in very good yield (see Scheme 1). It has been previously reported that complexes related to **1**, but with different aryl substituents, can be obtained from the reaction of $Na_2[PdCl_4]$[36] or $Pd(OAc)_2$[37] and the corresponding iminophosphoranes in moderate to good yields (56–97%). The synthesis of **1** has been reported very recently[38] from the reaction of $[o\text{-}C_6H_4\text{-}PPh_2NPh)Li]_2{\cdot}OEt_2$ with $[PdCl_2(COD)]$ (COD = 1,5-cyclooctadiene). However, this process gives a mixture of **1** and the bis-aryl derivative, from which **1** is isolated in very poor yield (14%). As expected, **1** can also be obtained from the reaction of $Li_2[PdCl_4]$ and Ph_3P=NPh, but this reaction gives a mixture of **1** and the N-bonded derivative $[Cl_2Pd\{N(=PPh_3)Ph\}_2]$ from which **1** could not be separated in pure form. Thus, the preparation described here seems to be the most convenient method for the synthesis of **1**. In order to obtain the corresponding Pt^{II} derivative, two different procedures were checked. The first one involves the direct orthometallation of the substrate by reaction with $[PtCl_2(NCPh)_2]$ in refluxing 2-methoxyethanol, a method successfully applied in the synthesis of cycloplatinated complexes derived from phosphonium salts.[48,49] The second one is the reaction of the substrate with the dimer $[Pt(\mu\text{-}Cl)(\eta^3\text{-}2\text{-}MeC_3H_4)]_2$ in refluxing chloroform.[50] However, neither of the two methods gives the expected orthoplatinated dimer: in the first case, complete reduction to black Pt^0 was observed, while in the second case a complex mixture of unidentified products was obtained.

We attempted a similar reaction with the other α-stabilized iminophosphoranes. The reaction of $Pd(OAc)_2$ with Ph_3P=N-C(O)-2-NC_5H_4 and with LiCl, performed under the same experimental conditions as those reported for **1**, gives the orthometallated monomer $[Pd(C_6H_4\text{-}2\text{-}PPh_2{=}N\text{-}C(O)\text{-}2\text{-}NC_5H_4\text{-}\kappa\text{-}C,N,N)(Cl)]$ (**11**) in good yield (see Scheme 2). As described for **1**, the reaction of $Li_2[PdCl_4]$ with Ph_3P=N-C(O)-2-NC_5H_4 gives a mixture of **11** and the coordination product $[Cl_2Pd\{N(=PPh_3)C(O)\text{-}2\text{-}NC_5H_4\}]$, already described by us,[30] and from which **11** could not be cleanly separated. On the other hand, the analogous Pt^{II} complex $[Pt(C_6H_4\text{-}2\text{-}PPh_2{=}N\text{-}C(O)\text{-}2\text{-}NC_5H_4\text{-}\kappa\text{-}C,N,N)(Cl)]$ (**12**) can be easily obtained in moderate yield by reaction of $[PtCl_2(NCPh)_2]$ with Ph_3P=N-C(O)-2-NC_5H_4 (1:1 molar ratio) in refluxing 2-methoxyethanol for 8 h. It is worthwhile to note that the previous reactivity of the iminophosphorane Ph_3P=N-C(O)-2-NC_5H_4 towards different Pd^{II} and Pt^{II} precursors[30] never resulted in a metallated compound. The obvious difference in reactivity with that reported here comes from the reaction conditions: the processes performed at room temperature or at a low reflux temperature (CH_2Cl_2/acetone) give coordination compounds,[30] while those performed in harsh conditions (refluxing 2-methoxyethanol) give the metallated derivatives.

Attempted orthometallation reactions involving the iminophosphoranes $Ph_3P{=}NC{\equiv}N$, $Ph_3P{=}NC(O)CH_2Cl$ and $Ph_3P{=}NN{\equiv}C$ using the methods described above were not successful. In the case of Pd, mixtures of the corresponding *cis*- and *trans*-$[Cl_2Pd(N\text{-ligand})_2]$ derivatives were obtained;[29,30] in the case of platinum only decomposition to black Pt^0 was observed. Due to the lack of reactivity of these iminophosphoranes, they were not further investigated.

Complex **1** has been characterised previously and its structure is shown in Scheme 1.[38] Complexes **11** and **12**

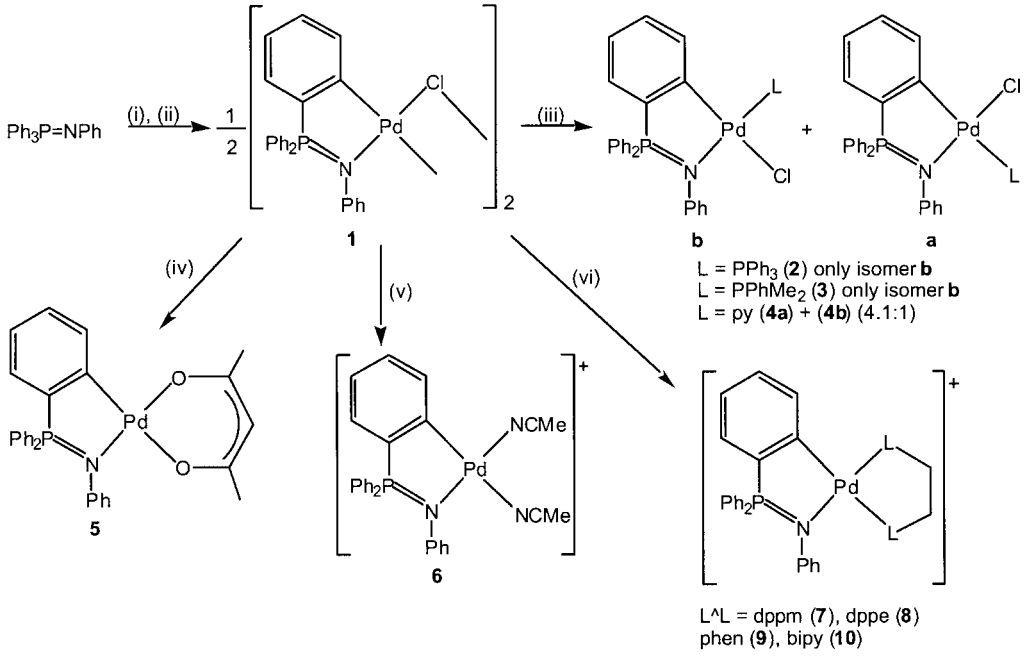

Scheme 1. (i) $Pd(OAc)_2$, reflux, CH_2Cl_2; (ii) LiCl, room temp., MeOH; (iii) L, CH_2Cl_2, room temp.; (iv) Tl(acac), – TlCl, CH_2Cl_2, room temp.; (v) $AgClO_4$, – AgCl, NCMe, room temp.; (vi) $AgClO_4$, – AgCl, L, acetone, room temp.

 © 2005 Wiley-VCH Verlag GmbH & Co. KGaA, Weinheim

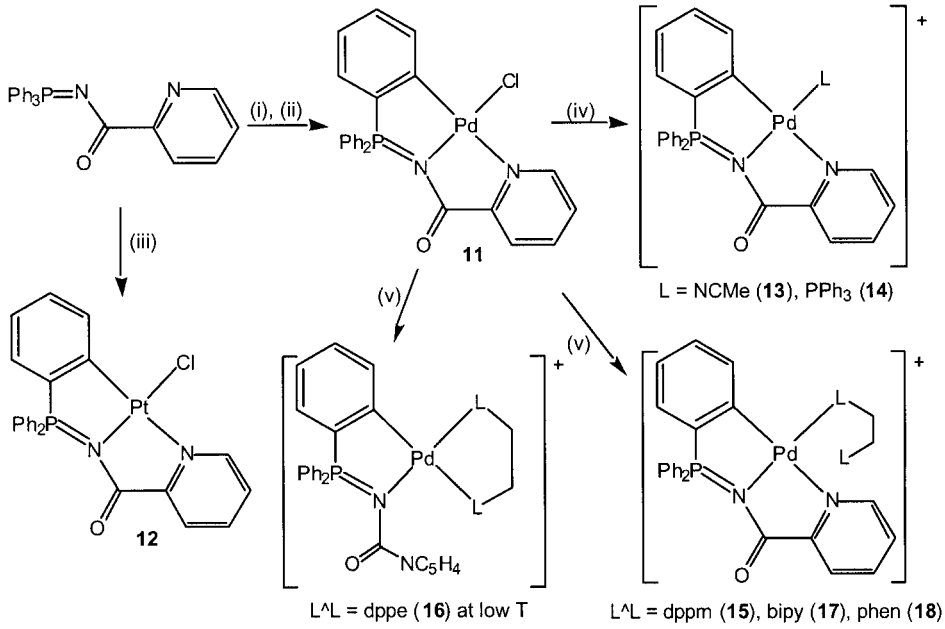

Scheme 2. (i) $Pd(OAc)_2$, reflux, CH_2Cl_2; (ii) LiCl, room temp., MeOH; (iii) $[PtCl_2(NCPh)_2]$, 2-methoxyethanol, reflux; (iv) $AgClO_4$, – AgCl, L, NCMe or acetone, room temp.; v) $AgClO_4$, – AgCl, L, acetone, room temp.

give satisfactory elemental analyses, and their mass spectra show the expected molecular peaks with the correct isotopic distribution. The IR spectra of **11** and **12** show sharp absorptions due to the ν_{CO} stretch at 1644 (**11**) and 1646 (**12**) cm^{-1}, shifted to higher frequencies with respect to the corresponding absorption in the free ligand, and also show two strong bands due to the ν_{PN} stretch at 1332 (**11**) and 1330 (**12**) cm^{-1}, while in the free ligand this absorption appears at 1366 cm^{-1}.[46] These two facts indicate that the iminic N-atom is coordinated to the metal centre.[30] The ^1H NMR spectra of **11** and **12** show similar patterns, and unambiguously reveal the presence of the cyclometallated $[M(C_6H_4\text{-}2\text{-}PPh_2{=}N\text{-})]$ unit. Thus, four different signals assigned to the protons of the C_6H_4 unit can be observed at δ = 7.00, 7.13, 7.28 and 8.10 ppm in complex **11** and at δ = 6.95, 7.05, 7.23 and 8.02 ppm in **12**, with the signal at δ = 8.02 ppm showing ^{195}Pt satellites, as well as signals corresponding to the pyridine group. Moreover, the N-bonding of the pyridine ring can be inferred from the shift to low field of the resonance attributed to the H_α proton (δ = 8.97 ppm in **11**; δ = 9.17 ppm in **12**) with respect to its position in the free ligand (δ = 8.69 ppm),[46] and from the presence, in **12**, of ^{195}Pt satellites for the multiplet at δ = 9.17 ppm ($^3J_{Pt,H} \approx 20$ Hz). These IR and ^1H NMR spectroscopic data are in good agreement with the structure proposed in Scheme 2 for **11** and **12**, in which the orthometallated iminophosphorane acts as a *C*,*N*,*N*-terdentate ligand. The $^{31}P\{^1H\}$ NMR spectra of **11** and **12** show singlet signals at δ = 51.88 ppm in both cases (the signal of **12** shows the expected ^{195}Pt satellites), and these signals are strongly deshielded with respect to their position, not only in the free ligand (δ = 23.89 ppm) but also in the *N*,*N*-bonded complexes ($\delta \approx$ 34 ppm).[30] The position of this resonance is similar to that found in other recently described cyclopalladated derivatives in which the metallated iminophosphorane behaves as a *C*,*N*-chelating group.[37] Finally, the $^{13}C\{^1H\}$ NMR spectrum of **11** shows signals corresponding to the presence of all the expected functional groups, and confirms the structure proposed in Scheme 2. The orthometallated carbon atom C_1-Pd appears at δ = 153.19 ppm.

In summary, the standard methods of C–H bond activation to give orthometallated complexes of Pd^{II} and Pt^{II} can be applied successfully to iminophosphorane ligands to afford cyclopalladated and cycloplatinated complexes. The crystal structure of **11** has been determined by X-ray diffraction methods and provides additional structural information.

X-ray Structure of Complex 11

Crystals of **11** of adequate quality for X-ray purposes were grown by slow vapour diffusion of Et_2O into a CH_2Cl_2 solution of the crude complex at room temperature. A drawing of the organometallic complex is shown in Figure 1. The parameters concerning the data collection and refinement are collected in Table 1, and selected bond lengths and angles are given in Table 2.

The Pd atom is located in a slightly distorted square-planar environment and is surrounded by the metallated carbon atom C(7), the chlorine atom Cl(1) and the two N atoms of the iminophosphorane ligand, the iminic N atom, N(1), and the pyridinic N atom, N(2). Thus, the metallated iminophosphorane behaves as a *C*,*N*,*N*-terdentate ligand, in good agreement with the NMR spectroscopic data, forming two fused, five membered rings. The bite angles of the two chelating moieties are 87.24(9)° [C(7)–Pd(1)–N(1)] and 79.40(8)° [N(1)–Pd(1)–N(2)], and the sum of the bond

 © 2005 Wiley-VCH Verlag GmbH & Co. KGaA, Weinheim

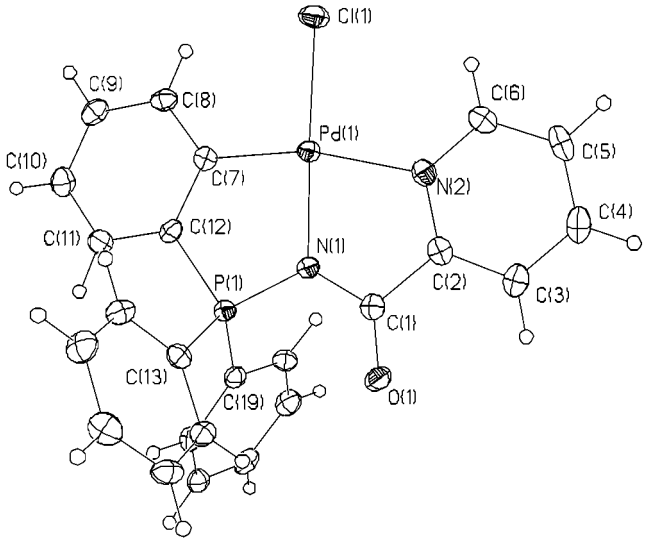

Figure 1. Thermal ellipsoid plot of [Pd(C_6H_4-2-PPh_2=N-C(O)-2-NC_5H_4-κ-C,N,N)Cl] (**11**). Non-hydrogen atoms are drawn at the 50% probability level.

Table 1. Crystal data and structure refinement for complex **11**.

Formula	$C_{24}H_{18}ClN_2OPPd$
Formula mass	523.22
Crystal system	monoclinic
Space group	$P2_1/n$
a [Å]	9.9726(6)
b [Å]	11.4926(7)
c [Å]	18.6220(11)
β [°]	101.033(1)
V [Å^3]	2094.8(2)
Z	4
D_c [Mg m^{-3}]	1.659
μ [mm^{-1}]	1.109
Refl. collected	18137
Unique reflections	4791, R_{int} = 0.0391
Data/restr./param.	4791/0/271
R_1 [$I > 2\sigma(I)$]	0.0300
wR_2 [$I > 2\sigma(I)$]	0.0660
Goodness of fit	1.042
T [K]	100(2)
λ(Mo-K_α) [Å]	0.71073

Table 2. Selected bond lengths [Å] and angles [°] for complex **11**.

Pd(1)–C(7)	1.976(3)	Pd(1)–N(1)	1.997(2)
Pd(1)–N(2)	2.120(2)	Pd(1)–Cl(1)	2.3039(7)
P(1)–N(1)	1.649(2)	P(1)–C(12)	1.777(3)
P(1)–C(13)	1.788(3)	P(1)–C(19)	1.796(3)
C(1)–O(1)	1.227(3)	N(1)–C(1)	1.362(3)
N(2)–C(6)	1.335(3)	N(2)–C(2)	1.347(3)
C(1)–C(2)	1.506(4)	C(7)–C(8)	1.403(3)
C(7)–C(12)	1.416(3)	C(8)–C(9)	1.382(4)
C(9)–C(10)	1.388(4)	C(10)–C(11)	1.383(4)
C(11)–C(12)	1.395(4)		
C(7)–Pd(1)–N(1)	87.24(9)	C(7)–Pd(1)–N(2)	166.54(9)
N(1)–Pd(1)–N(2)	79.40(8)	C(7)–Pd(1)–Cl(1)	96.06(8)
N(1)–Pd(1)–Cl(1)	175.83(6)	N(2)–Pd(1)–Cl(1)	97.35(6)
N(1)–P(1)–C(12)	100.49(11)	C(1)–N(1)–P(1)	122.96(18)
C(1)–N(1)–Pd(1)	118.70(17)	P(1)–N(1)–Pd(1)	117.10(11)
O(1)–C(1)–N(1)	125.2(2)	O(1)–C(1)–C(2)	122.5(2)
N(1)–C(1)–C(2)	112.3(2)		

angles around the Pd(1) atom is 360.05(9)°. The molecule deviates only slightly from planarity: for instance, the maximum deviations found in the best least-square planes defined by [C(7)–C(12)–P(1)–N(1)–Pd(1)] and [Pd(1)–N(1)–C(1)–C(2)–N(2)] are only 0.09 Å and 0.02 Å, respectively. The dihedral angle between these two planes is 4.5°. The Pd(1)–C(7) bond length [1.976(3) Å] is statistically identical or slightly longer than those found in the related complex [Pd{κ^2-*C*,*N*-C_6H_4(PPh_2=NC_6H_4Me-4′)-2}(μ-OAc)]$_2$ [1.964(3) Å and 1.959(3) Å], and is shorter than that found in [Pd{κ^2-*C*,*N*-C_6H_4(PPh_2=NC_6H_4Me-4′)-2}(tmeda)]ClO_4 [2.019(3) Å] (tmeda = *N*,*N*,*N*′,*N*′-tetramethylethylenediamine).[37] The Pd–N(iminic) bond length [Pd(1)–N(1) = 1.997(2) Å] is shorter than those found in the aforementioned related complexes [2.050(2), 2.051(2) and 2.055(2) Å], probably reflecting the low *trans* influence of the chlorine ligand. The Pd–N(pyridine) bond length [Pd–N(2) = 2.120(2) Å] is similar to those found in related arrangements (pyridine *trans* to aryl carbon).[51,52] This distance is longer than those found in related Pd^{II} complexes in which the pyridine fragment is *trans* to an atom with a smaller *trans* influence; for instance, the Pd–N(py) bond length in [Pd($C_6H_4CH_2NMe_2$)(Ph_3PNC(O)-2-NC_5H_4)]ClO_4 is 2.056(3) Å, and in this complex the pyridine is *trans* to the aminic N atom of the NMe_2 group.[30]

The P(1)–N(1) bond length [1.649(2) Å] is longer than those reported in all related complexes. The complex [Pd{κ^2-*C*,*N*-C_6H_4(PPh_2=NC_6H_4Me-4′)-2}(μ-OAc)]$_2$ shows P–N bond length values of 1.605(2) Å and 1.610(2) Å, while that found in [Pd{κ^2-*C*,*N*-C_6H_4(PPh_2=NC_6H_4Me-4′)-2}(tmeda)]ClO_4 is 1.607(3) Å.[37] This clear elongation of the P–N bond in **11** is due to two main facts: the coordination of the N atom and the presence of the carbonyl group, which delocalizes the charge density through the P-N-C-O system. As a comparison, the P–N bond length in [Pd($C_6H_4CH_2NMe_2$)(Ph_3PNC(O)-2-NC_5H_4)]ClO_4 is 1.624(4) Å,[30] and in this complex the iminophosphorane bonds to the palladium through the pyridine N-atom and the carbonyl oxygen, leaving the -N=P fragment uncoordinated. The delocalisation of the charge density is also reflected in the short value of the N(1)–C(1) bond length [1.362(3) Å], which is similar, within experimental error, to that found in Ph_3P=NC(O)Ph [1.353(5) Å].[53,54] Finally, the environment around the P atom is tetrahedral, with P–C bond lengths similar to those found in related complexes.[30,37]

Reactivity of Orthometallated Iminophosphorane Complexes

The reactivity of complexes **1** and **11** was examined in order to check the stability of the metallated chelating (**1**) or pincer (**11**) ligands. The main results are resumed in Scheme 1 and 2, respectively. Thus, the dinuclear complex **1** reacts with neutral monodentate ligands L (L = PPh_3, $PPhMe_2$ or pyridine) to give the corresponding mononuclear derivatives **2**, **3** and **4**, respectively, as a result of the cleavage of the chloride bridging system. The NMR spectra

 © 2005 Wiley-VCH Verlag GmbH & Co. KGaA, Weinheim

of **2** and **3** display a single set of signals in each case, which shows that these complexes are obtained as a single isomer. The $^{31}P\{^1H\}$ NMR spectrum of **2** shows the presence of two doublet signals ($^3J_{P,P}$ = 4.7 Hz), which suggests the *trans* location of the iminic nitrogen and the PPh_3 ligand. The *cis* arrangement of the metallated carbon and the phosphane ligand is in good agreement with the *transphobia* between these ligands.[37,55–57] However, the NMR spectra of complex **4** show the presence of a mixture of isomers **a** and **b** (see Scheme 1) in a molar ratio **4a:4b** of 4.1:1. This fact is worthy of note, since the typical reactivity of *C*,*N*-cyclopalladated halide-bridged dimers towards neutral ligands L (L = phosphanes, pyridines, etc.) always gives a single isomer in which the incoming ligand is coordinated *trans* to the nitrogen atom.[58–60] Moreover, the major isomer **4a** has been characterised as that containing the pyridine ligand *cis* with respect to the iminic nitrogen, that is, to the NPh group. This assignment of structures **4a** and **4b** has been carried out by comparison of the chemical shifts of the H_6 proton of the C_6H_4 group (*ortho* to the metallated position) in the two isomers. Thus, the major isomer **4a** shows the signal corresponding to H_6 at δ = 8.30 ppm, while the minor isomer **4b** shows the corresponding signal at δ = 6.30 ppm. This clear upfield shift can be due to the anisotropic shielding undergone by H_6, which is promoted by the *cis* pyridine ligand in **4b**.[58] In line with this, a mutual anisotropic shielding between the phenyl and pyridine rings in complex **4a** should be possible and, in fact, the chemical shifts of the *ortho* protons of both rings in **4a** are found at higher field than the corresponding ones in **4b** [NPh: δ = 6.79 ppm (**4a**) and δ = 7.13 ppm (**4b**), $\Delta\delta$ = 0.34 ppm; py: δ = 8.52 ppm (**4a**) and δ = 8.90 ppm (**4b**), $\Delta\delta$ = 0.38 ppm]. Obviously, the free rotation of both rings − the pyridine around the Pd–N bond and the phenyl around the N–C bond − gives less-effective shielding (about 0.3–0.4 ppm) than in the case of the fixed orthometallated ring (2 ppm). A similar behaviour is observed in the $^{13}C\{^1H\}$ NMR spectrum of the mixture **4a/4b** (see Experimental Section).

The treatment of **1** with Tl(acac) (acac = acetylacetonate; CH_2Cl_2, 1:2 molar ratio) gives the *O*,*O*′-acac derivative [Pd(C_6H_4-2-PPh_2=NPh)(acac-O,O′)] (**5**), while the reaction of **1** with $AgClO_4$ (1:2 molar ratio) in acetonitrile gives the bis-solvate [Pd(C_6H_4-2-PPh_2=NPh)$(NCMe)_2$]ClO_4 (**6**). The two complexes show correct elemental analyses and mass spectra. Key spectroscopic parameters for **5** are the presence of two strong absorptions attributed to the *O*,*O*′-bonded acac ligand in the IR spectrum (1582, 1515 cm^{-1}) and the presence of the typical signals in the ^1H [δ = 1.74 and 2.06 ppm (CH_3); δ = 5.35 ppm (CH)] and $^{13}C\{^1H\}$ NMR spectra [δ = 27.14 and 27.31 ppm (CH_3); δ = 99.75 ppm (CH); δ = 185.42 and 187.92 ppm (CO)].[61] In the same way, the observation of two absorptions at 2321 and 2291 cm^{-1} in the IR spectrum, and two signals at δ = 2.26 and 2.50 ppm in the ^1H NMR spectrum of **6** suggest the presence of bonded acetonitrile. In these two cases, the presence of the cyclopalladated unit is confirmed through the observation of its characteristic absorptions (IR, ν_{PN}) and resonances in the NMR spectra.

Complex **1** reacts with $AgClO_4$ (1:2 molar ratio) in acetone to give, after filtration of the AgCl, solutions containing the solvated species [Pd(C_6H_4-2-PPh_2=NPh)$(S)_x$]ClO_4 (S = solvent; x = 2). The treatment of these freshly prepared solutions with bidentate ligands L_2 (1:1 molar ratio) gives the cationic complexes [Pd(C_6H_4-2-PPh_2=NPh)(L_2)]ClO_4 [L_2 = $Ph_2PCH_2PPh_2$ (**7**), $Ph_2PCH_2CH_2PPh_2$ (**8**), 1,10-phenanthroline (**9**), 2,2′-bipyridine (**10**)]. We have not observed the displacement of the metallated unit, nor the decoordination of the iminic nitrogen, even if the reactions are performed in presence of an excess of incoming ligand L_2. Compounds **7**–**10** show correct elemental analyses and mass spectra, and their IR spectra show in all cases the presence of a strong absorption in the range 1260–1290 cm^{-1}, assigned to the ν_{PN} stretch, which suggest that the iminic N-atom is bonded to the metal centre. The chelate coordination of the L_2 ligands is clearly inferred from their NMR spectra. The $^{31}P\{^1H\}$ NMR spectrum of **7** shows three signals, one at low field (δ = 48.38 ppm) attributed to the P atom in the metallated ring, and two at high field (δ = –10.60 and –34.16 ppm) characteristic of the *P*,*P*′-chelating dppm.[62] From the analysis of the $^{31}P\{^1H\}$ NMR spectrum of **8** the *P*,*P*′-bonding mode of the dppe is also evident since it shows three low-field signals, one corresponding to the iminophosphorane (δ = 45.31 ppm) and the other two to the dppe ligand (δ = 43.81 and 58.85 ppm).[63] In the case of complex **9** the ^1H NMR spectrum shows, in addition to the signals assigned to the NPh, PPh_2 and C_6H_4 protons, eight sharp peaks attributed to the phen ligand, and this fact clearly reveals the inequivalence of the two halves of the phen ligand due to its *N*,*N*′-bonding to the metal centre. Moreover, the complete attribution of all resonances of the phen ligand can be done unambiguously since one of the *ortho* protons is shifted to high field (δ = 8.00 ppm) with respect to the other (δ = 9.22 ppm) due to the anisotropic shielding exerted by the NPh ring.

In summary, the reactivity of **1** in cleavage reactions with neutral ligands (**2**–**4**) or substitution reactions of the halide bridging system by anionic (**5**) or neutral ligands (**6**–**10**) shows that the five-membered orthometallated iminophosphorane is quite stable, and behaves similarly to other *C*,*N*-orthometallated complexes derived from different amines. However, the reactivity of complex **11**, which contains a *C*,*N*,*N*-terdentate ligand reveals some noteworthy differences.

The reaction of **11** with $AgClO_4$ (1:1 molar ratio) in NCMe gives the solvate derivative [Pd(C_6H_4-2-PPh_2=N-C(O)-2-NC_5H_4-κ-C,N,N)(NCMe)]ClO_4 (**13**). The presence of bonded NCMe is inferred from the observation of an absorption in the IR spectrum at 2328 cm^{-1} (ν_{CN}) and a signal at δ = 2.79 ppm in the ^1H NMR spectrum. A comparison of the spectral parameters of **13** with those of **11** suggests that the metallated iminophosphorane still behaves as a *C*,*N*,*N*-terdentate ligand. The complex [Pd(C_6H_4-2-PPh_2=N-C(O)-2-NC_5H_4-κ-C,N,N)(PPh_3)]ClO_4 (**14**) can be obtained in the same way by treatment of **11** with $AgClO_4$ and PPh_3 (1:1:1 molar ratio) in acetone. The characterisation of **14** is straightforward from its $^{31}P\{^1H\}$ NMR spec-

 © 2005 Wiley-VCH Verlag GmbH & Co. KGaA, Weinheim

trum, which shows the presence of coordinated PPh_3 (δ = 39.34 ppm), and from its ^1H NMR spectrum, which shows all expected signals for the proposed stoichiometry. It is noteworthy that complex **14** is also obtained when the reaction is performed in the presence of an excess of PPh_3 (1:1:2 molar ratio), thus showing that the displacement of the N-bonded pyridine group does not take place under these conditions.

In order to check the strength of the pyridine fragment (usually a ligand easily removable from the metal coordination sphere) and the stability of the terdentate bonding mode κ-C,N,N of the metallated iminophosphorane, we investigated the reactivity of **11** towards several bidentate ligands, which usually act as chelating ligands. Complex **11** does not react with Tl(acac) under the usual experimental conditions (room temperature, 1:1 molar ratio), and unchanged **11** can be recovered at the end of the reaction. However, the reaction of **11** with $AgClO_4$ and $Ph_2PCH_2PPh_2$ (dppm), $Ph_2PCH_2CH_2PPh_2$ (dppe), 1,10-phenanthroline (phen) or 2,2′-bipyridine (bipy) (1:1:1 molar ratio) in acetone gives complexes of stoichiometry $[Pd(C_6H_4\text{-}2\text{-}PPh_2{=}N\text{-}C(O)\text{-}2\text{-}NC_5H_4)(L\text{-}L)]ClO_4$ [L-L = dppm (**15**), dppe (**16**), bipy (**17**), phen (**18**)], in keeping with their elemental analyses and mass spectra. The IR spectra of **15**–**18** show the absorption due to the ν_{PN} stretch in the range 1330–1340 cm^{-1}, thereby suggesting that the Pd–N(imine) bond is still present. The NMR spectra of **15** are temperature independent and show clearly that the metallating ligand is terdentate κ-C,N,N: the $^{31}P\{^1H\}$ NMR spectrum shows three well-defined signals at δ = 49.14 ($N{=}PPh_2$), 27.05 (dppm, $Pd\text{-}PPh_2$) and –24.75 ppm (dppm, free PPh_2). The observation of only one signal at high field (δ = –24.75 ppm) is diagnostic for the presence of monodentate P-dppm.[62] The formation of a four-membered metallacycle (*P*,*P*′-dppm) at the expense of the loss of the more stable five-membered ring by cleavage of the Pd–N(py) bond is probably not an energetically favourable process. In contrast to this, the NMR spectra of **16** are temperature dependent. At room temperature, the $^{31}P\{^1H\}$ NMR spectrum shows only a sharp singlet peak at δ = 47.28 ppm, assigned to the metallated $C_6H_4\text{-}2\text{-}PPh_2{=}N$ unit. On cooling ($CDCl_3$, 233 K) two new signals appear and an AMX spin system is observed. At this temperature, the chemical shift of the iminophosphorane appears at virtually the same position (δ = 47.84 ppm), as a doublet of doublets, and the signals attributed to the dppe ligand appear at δ = 41.38 (dd) and 58.21 ppm (d), clearly showing its *P*,*P*′-chelating mode.[50,63] The cleavage of the Pd–N(py) bond at low temperature is also inferred from the position of the *ortho* proton of the pyridine group, which appears in the ^1H NMR spectrum at δ = 8.72 ppm, that is, shifted to high field with respect to its position in **11**. All these facts suggest that the metallated $C_6H_4\text{-}2\text{-}PPh_2{=}N$ unit behaves statically on the NMR timescale in the range of temperatures measured, while the pyridine and dppe groups are involved into a series of dynamic process of coordination–decoordination, with the two processes being more or less equally favourable at room temperature. This process is stopped at low temperature, with *P*,*P*′-chelation of the dppe ligand.

The ^1H NMR spectra of **17** and **18** are temperature independent from 298 to 213 K (CD_2Cl_2) and show some noteworthy features. The first is the equivalence of the two rings of the bipy or phen ligands, inferred from the presence of a set of only four resonances (see Experimental Section), which do not split on cooling. This equivalence can be explained by assuming that they are bonded to the metal centre through only one nitrogen atom and that there is a rapid exchange of the N-bonded atoms, which can not be stopped at low temperature. This fast exchange can be easily rationalised through either a dissociative mechanism of the Pd–N bond or through a fluxional process, which could be a "single oscillatory motion of the potentially bidentate ligand via a trigonal-bipyramidal transition state". Similar proposals have been reported for related systems.[50,63] Whatever the mechanism, the coordination of the N-N ligands seems to occur in a plane normal to the molecular plane. This fact is clearly reflected in the anisotropic shielding undergone not only by the H_6 proton of the metallated C_6H_4 group (*ortho* to the palladated position), but also by the *ortho* proton of the pyridine fragment (H_α). These two protons appear strongly shifted to high field with respect to their positions in any other derivative. For instance, H_6 (C_6H_4) appears at δ = 6.33 (**17**) or 5.85 ppm (**18**) while in **11** its chemical shift is δ = 8.10 ppm; H_α (py) appears at δ = 7.95 (**17**) or 7.29 ppm (**18**) and at δ = 8.97 ppm in **11**.

In summary, the reactivity of **11** shows that the bonding of the terdentate ligand $[C_6H_4\text{-}2\text{-}PPh_2{=}N\text{-}C(O)\text{-}2\text{-}NC_5H_4\text{-}\kappa\text{-}C,N,N]$ to the Pd atom is remarkably stable. The decoordination of the pyridine fragment is not achieved upon treatment with classical chelating ligands (dppm, phen, bipy) and even in the presence of strongly chelating groups (dppe) only a competitive dynamic process is observed. These facts, together with the stability shown by the *C*,*N*-metallated complexes **1**–**10**, prompted us to study the plausible applications of this type of complex in catalytic processes.

Catalityc Activity of Orthometallated Complexes: Their Role as Precatalysts and the Formation of Nanoparticles in Mizoroki–Heck Processes

Four different complexes were selected in order to check the catalytic activity of orthopalladated iminophosphoranes. Complexes **1** and **4** are representative of complexes with the metallated $Ph_3P{=}NPh$ ligand, one neutral and one cationic, and both of them with available coordination sites. In the same way, **11** and **13** are representative examples of complexes with the metallated $Ph_3P{=}NC(O)$-2-py ligand, and with the same characteristics. The selected catalytic process is the C–C Mizoroki–Heck (MH) coupling between aryl halides and methyl acrylate, due to the exceptional activity shown by C,X-cyclopalladated complexes in this type of reaction (not limited to the MH reaction, but also applied to Suzuki, Stille, etc.),[39–44,50,64–69] and the wide interest in C–C Heck or Heck-type couplings.[70–77]

 © 2005 Wiley-VCH Verlag GmbH & Co. KGaA, Weinheim

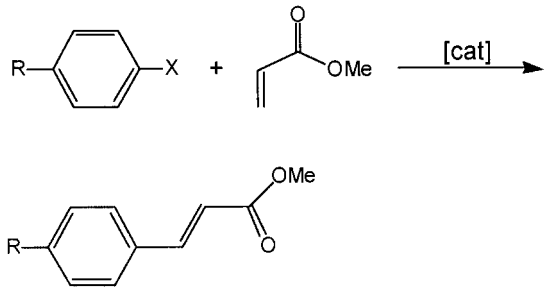

R = H, X = I; R = CHO, X = Br; R = CN, X = Br
[cat] = complex **1**, **4**, **11** or **13**

Conditions:
aryl halide (1.13 mmol); methyl acrylate (1.35 mmol);
DMF (15 mL), NEt_3 (1.13 mmol); reflux 24 h.

Table 3. Catalytic results in the MH reaction performed with catalysts **1**, **4**, **11** and **13**.

Entry	Catalyst	Substrate	Solvent	Yield [%]	TON
1	**1** (1%)	IPh	DMF	92.1	92
2	**1** (0.1%)	IPh	DMF	72.0	720
3	**1** (0.001%)	IPh	DMF	86.0	86000
4	**1** (0.0001%)	IPh	DMF	43.4	434000
5	**4** (1%)	IPh	DMF	64.9	65
6	**4** (0.1%)	IPh	DMF	57.8	578
7	**4** (0.001%)	IPh	DMF	52.0	52000
8	**4** (0.0001%)	IPh	DMF	52.6	526000
9	**11** (1%)	IPh	DMF	80.0	80
10	**11** (0.1%)	IPh	DMF	78.6	786
11	**11** (0.0001%)	IPh	DMF	11.4	114000
12	**13** (1%)	IPh	DMF	72.1	72
13	**13** (0.1%)	IPh	DMF	58.7	587
14	**13** (0.0001%)	IPh	DMF	45.6	456000
15	**1** (1%)	IPh	DMA	27.2	27
16	**4** (1%)	IPh	DMA	42.6	43
17	**11** (1%)	IPh	DMA	20.7	21
18	**13** (1%)	IPh	DMA	6.2	6
19	**1** (1%)	*p*-BrC_6H_4CHO	DMF	8.9	9
20	**4** (1%)	*p*-BrC_6H_4CHO	DMF	47.0	47
21	**11** (1%)	*p*-BrC_6H_4CHO	DMF	14.4	14
22	**13** (1%)	*p*-BrC_6H_4CHO	DMF	15	15
23	**1** (1%)	*p*-BrC_6H_4CN	DMF	5.0	5
24	**4** (1%)	*p*-BrC_6H_4CN	DMF	23.0	23
25	**11** (1%)	*p*-BrC_6H_4CN	DMF	4.1	4
26	**13** (1%)	*p*-BrC_6H_4CN	DMF	11.5	11

All selected complexes behave as moderate to good catalysts (see Experimental Section and Table 3) in the arylation of methyl acrylate to give methyl (*E*)-cinnamate in refluxing DMF (entries 1–14) when phenyl iodide is employed. The best yields are obtained when the amount of catalyst is 10^{-2} (mmol catalyst per mmol aryl halide; entries 1, 5, 9 and 12) but this amount can be as low as 10^{-6} (entries 4, 8, 11 and 14) and still give reasonable yields of isolated products and very high turnover numbers. However, as is evident from Table 3, the yield of isolated cinnamates drops when the concentration of catalyst decreases. The best reaction solvent for this type of process was found to be DMF. In spite of its similarity, very poor yields were obtained when *N*,*N*-dimethylacetamide (DMA) was used (entries 1–4 vs. entries 15–18), and the reaction was completely inhibited in NMP (*N*-methylpyrrolidinone). A comparison of the different catalysts shows that complexes **1** and **4** give better conversions than complexes **11** or **13**, and this fact could be related to the presence of the highly stable terdentate ligand [C_6H_4-2-PPh_2=N-C(O)-2-NC_5H_4-κ-C,N,N] in **11** and **13** (see below). The presence of weakly bonded ligands in **4** or **13** seems also to improve the yields, with respect to **1** or **11**, at low concentrations of catalyst. On the other hand, a comparison of the different substrates shows that the reactivity of deactivated bromoarenes (*p*-BrC_6H_4CN or *p*-BrC_6H_4CHO) is substantially lower for all catalysts than that described for PhI (entries 19–26). Due to these low conversions, no reactions were attempted with activated bromoarenes or with chloroarenes.

As general trends, we have observed that all reactions start after an induction period of approx. 30 min. During this time, the initial yellow or pale-yellow solution becomes dark red but without evidence of formation of palladium black. After the reaction, we attempted the recovery of the catalyst during the workup, but all these attempts were unsuccessful. Moreover, the analysis of the crude of the catalytic reaction, after removal of solvent (DMF) by distillation, by $^{31}P\{^1H\}$ NMR spectroscopy shows only peaks due to O=PPh_3 and other unidentified species; signals due to the initial catalyst were not observed. That is, the orthometallated unit is lost during the catalytic cycle. Interestingly, the resulting dark red solutions obtained at the end of the catalysis are still catalytically active and, after the addition of a second batch of reagents, the catalysis can be reassumed without an induction period. However, the yields drop from the first to the second and following runs, showing the deactivation of the catalytically active species. For instance, in a series of test experiments of four consecutive runs under the conditions described in entry 1 (1% catalyst **1**, PhI, DMF, reflux 24 h for each run) the obtained yields of methyl (*E*)-cinnamate were 90% (1st run), 60% (2nd run), 20% (3rd run) and 0% in the last run.

The observation of an induction period in all catalytic experiments, the evidence of the decomposition of the catalyst by NMR spectroscopy, the obvious impossibility to recover the catalyst after the end of the first run, and the confirmation that the catalysis can be reassumed after the first run strongly suggest that the organometallic derivatives **1**, **4**, **11** or **13** are not the true catalysts, but only the precatalysts. What, therefore, is the nature of the true catalytic species? Recent studies in this area show that, in many cases, the orthopalladated derivatives behave only as palladium reservoirs which, depending on the nature of the metallated unit, produces either low-coordinate Pd^0 species (cyclometallated phosphanes) or palladium nanoparticles (for instance, *C*,*N*-cyclopalladated complexes),[39–41,50,69,78] which are the true catalysts. Since our orthometallated iminophosphoranes can be considered to be closely related to a *C*,*N*-cyclometallated complex, we investigated the plausible formation of nanoparticles of Pd^0 from our catalysts. With this

 © 2005 Wiley-VCH Verlag GmbH & Co. KGaA, Weinheim

purpose, we checked the stability of the complexes under the reaction conditions (DMF, refluxing for 24 h). Thus, complexes **1**, **4**, **11** and **13** were refluxed in DMF for 24 h, and the resulting solutions were analysed by TEM, since this method is one of the best for detecting nanoparticles.[79–81] In all studied cases, the presence of nanoparticles (averaged diameter 10 nm) was evident. Figure 2 shows a TEM image obtained from a solution of complex **4** after thermal treatment. It is worthy of mention that the amount of nanoparticles detected is not the same in all cases. For complexes **1** and **4**, the amount of nanoparticles is substantially higher than that found in solutions of complexes **11** and **13**, after the same thermal treatment. Thus, the simple heating of the complexes in the reaction solvent produces their decomposition and the formation of the nanoparticles, and it is known that nanoparticles of Pd catalyze the MH reaction.[79–81]

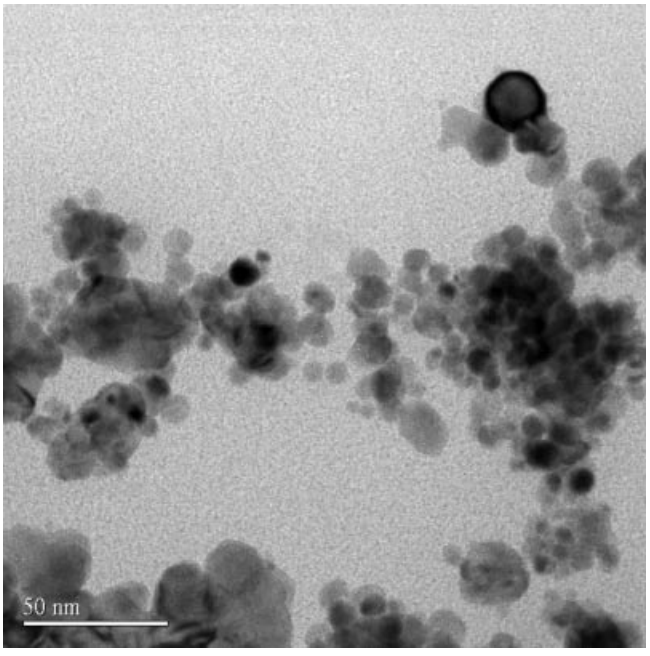

Figure 2. TEM image taken from a solution of complex **4** after 24 h in refluxing DMF.

We then compared the catalytic process described in entry 1 with that performed under the same experimental conditions but using nanoparticles. Monitoring by ^{1}H NMR spectroscopy showed that in the reaction carried out with nanoparticles, generated from **1** as described above, the presence of the reaction product can be detected only 10 min after the start of the reaction (time required to reach reflux temperature), that is, without an induction period, while in the process performed with catalyst **1** (entry 1) the presence of the products of the reaction is not detected until 30 min of additional refluxing. This additional time matches very well with the induction period (change of colour of the solution) observed in all catalytic reactions performed with complexes **1**, **4**, **11** and **13**. The yields obtained in these two processes are very similar (92% with catalyst **1** vs. 98% with nanoparticles). A second test to check the role of the nanoparticles as the catalytically active species is the mercury drop test (poisoning experiments).[78,82–84] The addition of an excess of Hg (with respect to the catalyst) to the process described in entry 1 completely inhibits the reaction and no product, even at trace levels, was detected at the end of the reaction.

In summary, the complexes with orthopalladated iminophosphoranes are precatalysts for the MH arylation of methyl acrylate to give the corresponding (*E*)-cinnamates in moderate to good yields. The true catalytic species are nanoparticles of elemental palladium, whose presence was confirmed by TEM, generated by decomposition of the catalyst.

Conclusions

The orthopalladated complexes [Pd(μ-Cl)(C_6H_4-2-PPh_2=NPh-κ-C,N)]$_2$ (**1**) and [Pd(C_6H_4-2-PPh_2=N-C(O)-2-NC_5H_4-κ-C,N,N)Cl] (**11**) have been obtained by reaction of Pd(OAc)$_2$ with the iminophosphoranes Ph_3P=NPh and Ph_3P=N-C(O)-2-NC_5H_4, respectively, in the presence of excess LiCl. The orthoplatinated derivative [Pt(C_6H_4-2-PPh_2=N-C(O)-2-NC_5H_4-κ-C,N,N)Cl] (**12**) can be obtained by reaction of [$PtCl_2(NCPh)_2$] with Ph_3P=N-C(O)-2-NC_5H_4 in refluxing 2-methoxyethanol. The reactivity of **1** in cleavage reactions with neutral ligands (**2**–**4**) or substitution reactions of the halide-bridging system by anionic (**5**) or neutral ligands (**6**–**10**) shows that the five-membered orthometallated iminophosphorane is quite stable, and behaves similarly to other *C*,*N*-orthometallated complexes derived from different amines. The reactivity of **11** shows that the bonding of the terdentate ligand [C_6H_4-2-PPh_2=N-C(O)-2-NC_5H_4-κ-C,N,N] to the Pd atom is remarkably stable. The decoordination of the pyridine fragment is not achieved with classical chelating ligands (dppm, phen, bipy) and even in the presence of strongly chelating groups (dppe) only a competitive dynamic process is observed. The complexes **1**, **4**, **11** and **13** are precatalysts for the MH arylation of methyl acrylate to give the corresponding (*E*)-cinnamates in moderate to good yields. The true catalytic species are nanoparticles of elemental palladium, whose presence is confirmed by TEM, generated by decomposition of the catalyst.

Experimental Section

CAUTION: *Perchlorate salts of metal complexes with organic ligands are potentially explosive. Only small amounts of these materials should be prepared and handled with great care.*[85]

General Methods: Solvents were dried and distilled under argon using standard procedures. Elemental analyses were performed on a Perkin–Elmer 2400-B microanalyser. Infrared spectra (4000–400 cm^{-1}) were recorded on a Perkin–Elmer Spectrum One FT-IR spectrophotometer from nujol mulls between polyethylene sheets. Mass spectra (positive ion FAB) were recorded from CH_2Cl_2 solutions on a V. G. Autospec spectrometer. ^{1}H, ^{13}C{^{1}H} and ^{31}P{^{1}H} NMR spectra were recorded in $CDCl_3$ or CD_2Cl_2 solutions at room temperature (other temperatures are specified) on Bruker

 © 2005 Wiley-VCH Verlag GmbH & Co. KGaA, Weinheim

ARX-300 or Avance400 spectrometers operating, respectively, at 300.13 MHz (ARX300) and 400.13 MHz (Avance400). The ^1H and $^{13}C\{^1H\}$ NMR spectra were referenced to the residual solvent signal as internal standard and the $^{31}P\{^1H\}$ NMR spectra to external H_3PO_4 (85%). The starting material Ph_3P=NPh is commercially available (Aldrich) and Ph_3P=N-C(O)-2-NC_5H_4 was prepared following published methods.[46]

Complex 1: $Pd(OAc)_2$ (1.000 g, 4.45 mmol) was added to a solution of Ph_3P=NPh (1.572 g, 4.45 mmol) in dry CH_2Cl_2 (20 mL) under argon, and this mixture was refluxed for 1.5 h. The initial orange-brown solution evolved slowly during the reaction time to give a deep orange solution. After cooling, the solvent was removed to dryness, the residue was dissolved in MeOH (20 mL), treated with an excess of anhydrous LiCl (0.755 g, 17.8 mmol) and then stirred at room temperature. After a few seconds complex **1** precipitated as a deep-yellow solid, although stirring was continued for an additional 30 min. After this time **1** was filtered off, washed with MeOH (20 mL) and Et_2O (50 mL) and air dried. Yield: 2.108 g (95.9%). $C_{48}H_{38}Cl_2N_2P_2Pd_2$ (988.50): calcd. C 58.32, H 3.87, N 2.83; found C 58.58, H 3.93, N 2.91. IR: $\tilde{\nu}$ = 1292, 1263 (ν_{PN}) cm^{-1}. NMR spectroscopic data have been reported previously.[38]

Complex 2: PPh_3 (0.041 g, 0.158 mmol) was added to a suspension of **1** (0.078 g, 0.079 mmol) in 5 mL of CH_2Cl_2. The initial orange suspension gradually dissolved and, after 5 min stirring at room temperature, a pale-yellow solution was obtained. The evaporation of this solution and treatment of the oily residue with 20 mL of Et_2O gave **2** as a white solid, which was filtered off, washed with additional Et_2O (10 mL) and air dried. Yield: 0.092 g (77%). $C_{42}H_{34}ClNP_2Pd$ (756.54): calcd. C 66.68, H 4.53, N 1.85; found C 66.51, H 4.47, N 1.85. IR: $\tilde{\nu}$ = 1289 (ν_{PN}) cm^{-1}. MS (FAB+): *m*/*z* (%) = 720 (25) $[M - Cl]^+$. ^1H NMR ($CDCl_3$): δ = 6.46 (tt, $^3J_{H,H}$ = 7.8, $^4J_{H,H}$ = 1.2 Hz, 1 H, C_6H_4), 6.59–6.75 (m, 3 H, C_6H_4), 6.83–6.98 (br. m, 5 H, NPh), 7.18–7.24 (m, 6 H, H^m, PPh_3), 7.27–7.33 (m, 3 H, H^p, PPh_3), 7.48–7.62 [m, 12 H, PPh_3 (6 H^o) + PPh_2 (4 H^m + 2 H^p)], 7.89–7.96 (m, 4 H, H^o, PPh_2) ppm. $^{31}P\{^1H\}$ NMR ($CDCl_3$): δ = 33.46 (d, $^3J_{P,P}$ = 4.7 Hz, 1 P, Pd–PPh_3), 38.69 (d, $^3J_{P,P}$ = 4.7 Hz, 1 P, P=N) ppm.

Complex 3: Complex **3** was prepared following a synthetic procedure similar to that reported for **2**. Thus, **1** (0.200 g, 0.202 mmol) in CH_2Cl_2 (5 mL) was treated with $PPhMe_2$ (57.6 μL, 0.404 mmol) to give **3** as a cream solid. Yield: 0.232 g (90.7%). $C_{32}H_{30}ClNP_2Pd$ (632.4): calcd. C 60.78, H 4.78, N 2.21; found C 60.61, H 4.74, N 1.91. IR: $\tilde{\nu}$ = 1291, 1260 (ν_{PN}) cm^{-1}. MS (FAB+): *m*/*z* (%) = 631 (20) $[M]^+$, 596 (100) $[M - Cl]^+$. ^1H NMR ($CDCl_3$): δ = 1.68 (d, $^2J_{P,H}$ = 10.5 Hz, 6 H, PMe_2), 6.69–6.74 (m, 1 H, C_6H_4), 6.78–6.95 [m, 8 H, C_6H_4 (3 H) + NPh], 7.30–7.38 (m, 3 H, H^m + H^p, PPh), 7.45–7.51 (m, 4 H, H^m, PPh_2), 7.54–7.60 (m, 2 H, H^p, PPh_2), 7.69–7.76 (m, 2 H, H^o, PPh), 7.83–7.89 (m, 4 H, H^o, PPh_2) ppm. $^{31}P\{^1H\}$ NMR ($CDCl_3$): δ = 8.75 (s, 1 P, Pd-$PPhMe_2$), 34.12 (s, 1 P, P=N) ppm.

Complex 4: Complex **4** was prepared following a synthetic procedure similar to that reported for **2**. Thus, **1** (0.200 g, 0.202 mmol) in CH_2Cl_2 (10 mL) was treated with pyridine (65.1 μL, 0.808 mmol) to give **4** as a yellow solid. Yield: 0.198 g (85.3%). Complex **4** was characterised spectroscopically (NMR) as a mixture of the isomers **4a/4b** in a molar ratio of 4.1:1. $C_{29}H_{24}ClN_2PPd$ (573.35): calcd. C 60.75, H 4.22, N 4.89; found C 60.80, H 4.10, N 5.06. IR: $\tilde{\nu}$ = 1589 (py), 1285 (ν_{PN}) cm^{-1}. ^1H NMR ($CDCl_3$) (not all signals for the minor isomer **4b** could be detected due to overlap): δ = 6.30 (dd, $^3J_{H,H}$ = 5.6, $^4J_{H,H}$ = 1.6 Hz, H^6, **4b**), 6.56 (tm, $^3J_{H,H}$ = 7.2, $^4J_{H,H}$ = 1.2 Hz, H^p, NPh, **4a**), 6.65 (t, $^3J_{H,H}$ = 7.2 Hz, H^m, NPh, **4a**), 6.79 (dm, $^3J_{H,H}$ = 7.2, $^4J_{H,H}$ = 1.2 Hz, H^o, NPh, **4a**), 6.86 (ddd, $^3J_{P,H}$ = 10.4, $^3J_{H,H}$ = 7.6, $^4J_{H,H}$ = 1.6 Hz, H^3, C_6H_4, **4a**), 6.94–6.99 (m, H^m, py, **4a**), 7.00–7.04 (m, H^4, C_6H_4, **4a**), 7.13 (dm, $^3J_{H,H}$ = 8.4, $^4J_{H,H}$ = 1.2 Hz, H^o, NPh, **4b**), 7.22 (tt, $^3J_{H,H}$ = 7.2, $^4J_{H,H} \approx {}^5J_{P,H}$ = 1.6 Hz, H^5, C_6H_4, **4a**), 7.31–7.35 (m, H^m, py, **4b**), 7.43 (tt, $^3J_{H,H}$ = 7.6, $^4J_{H,H}$ = 1.6 Hz, H^p, py, **4a**), 7.48–7.55 (m, H^m, PPh_2, **4a** + **4b**), 7.59–7.63 (m, H^p, PPh_2, **4a** + **4b**), 7.74–7.79 (m, H^o, PPh_2, **4a**), 7.88–7.93 (m, H^o, PPh_2, **4b**), 8.30 (ddd, $^3J_{H,H}$ = 7.2, $^4J_{P,H}$ = 1.6, $^4J_{H,H}$ = 1.2 Hz, H^6, C_6H_4, **4a**), 8.52 (dd, $^3J_{H,H}$ = 6.4, $^4J_{H,H}$ = 1.6 Hz, H^o, py, **4a**), 8.90 (dd, $^3J_{H,H}$ = 5.2, $^4J_{H,H}$ = 1.6 Hz, H^o, py, **4b**) ppm. $^{13}C\{^1H\}$ NMR ($CDCl_3$) (not all signals for the minor isomer **4b** could be detected due to overlap): δ = 121.74 (d, $^5J_{P,C}$ = 2.0 Hz, C^p, NPh, **4a**), 123.83 (s, C^m, py, **4a**), 124.04 (d, $^3J_{P,C}$ = 14.1 Hz, C^4, C_6H_4, **4a**), 125.02 (s, C^m, py, **4b**), 127.43 (d, $^3J_{P,C}$ = 9.1 Hz, C^o, NPh, **4a**), 127.72 (s, C^m, NPh, **4a**), 128.24 (d, $^2J_{P,C}$ = 21.1 Hz, C^3, C_6H_4, **4a**), 128.61 (d, $^1J_{P,C}$ = 86.5 Hz, C^{ipso}, PPh_2, **4a**), 128.86 (d, $^3J_{P,C}$ = 11.1 Hz, C^m, PPh_2, **4a**), 128.90 (d, $^3J_{P,C}$ = 11.1 Hz, C^m, PPh_2, **4b**), 130.29 (d, $^4J_{P,C}$ = 3.0 Hz, C^5, C_6H_4, **4b**), 130.38 (d, $^4J_{P,C}$ = 3.1 Hz, C^5, C_6H_4, **4a**), 132.75 (d, $^4J_{P,C}$ = 2.0 Hz, C^p, PPh_2, **4a**), 133.23 (d, $^2J_{P,C}$ = 9.1 Hz, C^o, PPh_2, **4a**), 133.50 (d, $^2J_{P,C}$ = 10.1 Hz, C^o, PPh_2, **4b**), 134.43 (d, $^3J_{P,C}$ = 15.1 Hz, C^6, C_6H_4, **4b**), 136.48 (s, C^p, py, **4a**), 137.35 (s, C^p, py, **4b**), 138.53 (d, $^3J_{P,C}$ = 15.1 Hz, C^6, C_6H_4, **4a**), 140.55 (d, $^1J_{P,C}$ = 139 Hz, C^2, C_6H_4, **4a**), 147.12 (d, $^2J_{P,C}$ = 3.0 Hz, C^{ipso}, NPh, **4a**), 147.19 (d, $^2J_{P,C}$ = 3.0 Hz, C^{ipso}, NPh, **4b**), 151.04 (s, C^o, py, **4a**), 152.27 (d, $^2J_{P,C}$ = 20.1 Hz, C^1, C_6H_4, **4a**), 153.73 (s, C^o, py, **4b**), 156.39 (d, $^2J_{P,C}$ = 20.1 Hz, C^1, C_6H_4, **4b**) ppm. $^{31}P\{^1H\}$ NMR ($CDCl_3$): δ = 44.31 (**4b**), 48.21 (**4a**) ppm.

Complex 5: Tl(acac) (0.123 g, 0.404 mmol) was added to a suspension of **1** (0.200 g, 0.202 mmol) in CH_2Cl_2 (10 mL). The resulting mixture was stirred at room temperature for 1 h, then filtered through Celite. The clear yellow solution was evaporated to dryness and the oily residue treated with cold *n*-hexane (10 mL) to give **5** as a yellow solid. This solid was filtered off and dried in vacuo. Yield: 0.184 g (81.5%). $C_{29}H_{26}NO_2PPd$ (557.91): calcd. C 62.43, H 4.69, N 2.51; found C 62.49, H 4.60, N 2.35. IR: $\tilde{\nu}$ = 1582, 1515 (ν_{CO}), 1287, 1262 (ν_{PN}) cm^{-1}. MS (FAB+): *m*/*z* (%) = 557 (30) $[M]^+$. ^1H NMR (CD_2Cl_2): δ = 1.74 (s, 3 H, Me, acac), 2.06 (s, 3 H, Me, acac), 5.35 (s, 1 H, CH, acac), 6.83 (td, $^3J_{H,H}$ = 7.8, $^4J_{H,H}$ = 1.2 Hz, 1 H, H^p, NPh), 6.95 (dd, $^3J_{H,H}$ = 7.6, $^4J_{H,H}$ = 1.2 Hz, 1 H, H^3, C_6H_4), 6.99 (t, $^3J_{H,H}$ = 7.2 Hz, 2 H, H^m, NPh), 7.05–7.10 [m, 3 H, NPh (H^o) + C_6H_4 (H^4)], 7.27 (tt, $^3J_{H,H}$ = 7.6, $^4J_{H,H} \approx {}^5J_{P,H}$ = 1.6 Hz, 1 H, H^5, C_6H_4), 7.53–7.57 (m, 4 H, H^m, PPh_2), 7.64–7.68 (m, 2 H, H^p, PPh_2), 7.71 (dm, $^3J_{H,H}$ = 8.0 Hz, 1 H, H^6, C_6H_4), 7.82–7.87 (m, 4 H, H^o, PPh_2) ppm. $^{13}C\{^1H\}$ NMR (CD_2Cl_2): δ = 27.14 (s, Me, acac), 27.31 (s, Me, acac), 99.75 (s, CH, acac), 121.39 (s, C^p, NPh), 124.17 (d, $^3J_{P,C}$ = 14 Hz, C^4, C_6H_4), 126.99 (d, $^3J_{P,C}$ = 10 Hz, C^o, NPh), 127.47 (s, C^m, NPh), 127.73 (d, $^2J_{P,C}$ = 22 Hz, C^3, C_6H_4), 128.21 (d, $^1J_{P,C}$ = 85 Hz, C^{ipso}, PPh_2), 128.91 (d, $^3J_{P,C}$ = 11 Hz, C^m, PPh_2), 129.64 (d, $^4J_{P,C}$ = 3 Hz, C^5, C_6H_4), 132.40 (d, $^3J_{P,C}$ = 14 Hz, C^6, C_6H_4), 132.79 (d, $^4J_{P,C}$ = 2 Hz, C^p, PPh_2), 133.22 (d, $^2J_{P,C}$ = 10 Hz, C^o, PPh_2), 140.75 (d, $^1J_{P,C}$ = 139 Hz, C^2, C_6H_4), 146.49 (d, $^2J_{P,C}$ = 3 Hz, C^{ipso}, NPh), 152.99 (d, $^2J_{P,C}$ = 20 Hz, C^1, C_6H_4), 185.42 (s, CO, acac), 187.92 (s, CO, acac) ppm. $^{31}P\{^1H\}$ NMR (CD_2Cl_2): δ = 46.04 ppm.

Complex 6: $AgClO_4$ (0.084 g, 0.405 mmol) was added to a suspension of **1** (0.200 g, 0.202 mmol) in NCMe (15 mL) and the resulting mixture was stirred at room temperature for 30 min with exclusion of light. After this time the grey suspension was filtered through Celite and the resulting pale-yellow solution was evaporated to small volume (approx. 1 mL). Addition of *n*-pentane (10 mL) and continuous stirring gave **6** as a pale-yellow solid, which was filtered off and dried in vacuo. Yield: 0.226 g (87.5%). $C_{28}H_{25}ClN_3O_4PPd$ (640.35): calcd. C 52.52, H 3.93, N 6.56; found C 52.60, H 3.93, N

 © 2005 Wiley-VCH Verlag GmbH & Co. KGaA, Weinheim

6.78. IR: $\tilde{\nu}$ = 2321, 2291 (ν_{CN}), 1287, 1260 (ν_{PN}) cm^{-1}. MS (FAB+): *m*/*z* (%) = 499 (10) [M – ClO_4 – NCMe]$^+$, 458 (25) [M – ClO_4 – 2NCMe]$^+$. ^{1}H NMR ($CDCl_3$): δ = 2.26 (br. s, 3 H, NCMe), 2.50 (s, 3 H, NCMe), 6.85–6.99 [m, 6 H, NPh + C_6H_4 (H^3)], 7.09 (ddt, $^3J_{H,H}$ = 7.2, $^4J_{P,H}$ = 4.8, $^4J_{H,H}$ = 1.5 Hz, 1 H, H^4, C_6H_4), 7.16–7.26 (m, 2 H, H^5 + H^6, C_6H_4), 7.48–7.54 (m, 4 H, H^m, PPh_2), 7.60–7.66 (m, 2 H, H^p, PPh_2), 7.67–7.74 (m, 4 H, H^o, PPh_2) ppm. ^{31}P{^{1}H} NMR ($CDCl_3$): δ = 54.29 ppm.

Complex 7: $AgClO_4$ (0.084 g, 0.405 mmol) was added to a suspension of **1** (0.200 g, 0.202 mmol) in acetone (20 mL) and the resulting mixture was stirred at room temperature for 30 min with exclusion of light. The grey suspension was then filtered through a Celite pad and dppm (0.155 g, 0.404 mmol) was added to the freshly prepared solution of the solvate to give a pale-orange solution. After stirring at room temperature for 4 h, the solvent was evaporated to dryness and the residue treated with Et_2O (10 mL) to give **7** as a pale-orange solid, which was filtered and air dried. Yield: 0.357 g (93.7%). $C_{49}H_{41}ClNO_4P_3Pd$ (942.65): calcd. C 62.43, H 4.38, N 1.48; found C 62.35, H 4.40, N 1.35. IR: $\tilde{\nu}$ = 1263 (ν_{PN}) cm^{-1}. MS (FAB+): *m*/*z* (%) = 842 (100) [M – ClO_4]$^+$. ^{1}H NMR ($CDCl_3$): δ = 4.06 (dd, $^2J_{P,H}$ = 11.1, $^2J_{P,H}$ = 7.8 Hz, 2 H, CH_2), 6.52–6.59 (m, 3 H, NPh), 6.71–6.74 (m, 2 H, NPh), 6.91–6.98 (m, 2 H, C_6H_4), 7.03–7.12 [m, 6 H, C_6H_4 (2 H) + PPh_2], 7.20–7.26 (m, 4 H, PPh_2), 7.35–7.58 (m, 12 H, PPh_2), 7.61–7.76 (m, 10 H, PPh_2) ppm. ^{13}C{^{1}H} NMR ($CDCl_3$): δ = 40.97 (dd, $^1J_{P,C}$ = 28.4, $^1J_{P,C}$ = 21.5 Hz, CH_2), 122.76 (s, C^p, NPh), 125.70 (d, $^3J_{P,C}$ = 13.8 Hz, C^4, C_6H_4), 126.33 (d, $^1J_{P,C}$ = 30.7 Hz, C^{ipso}, PPh_2), 126.49 (d, $^3J_{P,C}$ = 9.5 Hz, C^o, NPh), 127.96 (d, $^1J_{P,C}$ = 30.7 Hz, C^{ipso}, PPh_2), 128.01 (d, $^1J_{P,C}$ = 30.6 Hz, C^{ipso}, PPh_2), 128.40 (s, C^5, C_6H_4), 129.12 (s, C^m, NPh), 129.19 (d, $^3J_{P,C}$ = 10.2 Hz, C^m, PPh_2), 129.20 (d, $^3J_{P,C}$ = 12.1 Hz, C^m, PPh_2), 129.62 (d, $^3J_{P,C}$ = 11.7 Hz, C^m, PPh_2), 131.37 (d, $^4J_{P,C}$ = 1.7 Hz, C^p, PPh_2), 132.60 (s, C^p, PPh_2), 132.69 (d, $^2J_{P,C}$ = 13.2 Hz, C^o, PPh_2), 133.05 (d, $^2J_{P,C}$ = 9.9 Hz, C^o, PPh_2), 133.39 (d, $^4J_{P,C}$ = 2.0 Hz, C^p, PPh_2), 133.75 (d, $^2J_{P,C}$ = 12.8 Hz, C^o, PPh_2), 138.86 (td, $^3J_{P,C}$ = 15.7, $^3J_{P,C}$ = 2.8 Hz, C^6, C_6H_4), 141.92 (d, $^1J_{P,C}$ = 97 Hz, C^2, C_6H_4), 148.85 (s, C^{ipso}, NPh), 160.97 (ddd, $^2J_{P,Ctrans}$ = 135.6, $^2J_{(N)P,C}$ = 23.5, $^2J_{P,Ccis}$ = 10.7 Hz, C^1, C_6H_4) ppm. ^{31}P{^{1}H} NMR ($CDCl_3$): δ = –34.16 (dd, $^2J_{P,P}$ = 68, $^3J_{P,P}$ = 14.5 Hz, 1 P, P *trans* to N), –10.60 (d, $^2J_{P,P}$ = 68 Hz, 1 P, P *trans* to C), 48.38 (d, $^3J_{P,P}$ = 14.5 Hz, 1 P, P=N) ppm.

Complex 8: Complex **8** was prepared following a synthetic procedure similar to that reported for **7**. A solution of **1** (0.200 g, 0.202 mmol) in acetone (20 mL) was treated with $AgClO_4$ (0.084 g, 0.405 mmol) and dppe (0.161 g, 0.404 mmol) to give **8** as a pale-orange solid. Yield: 0.347 g (90%). $C_{50}H_{43}ClNO_4P_3Pd$ (956.67): calcd. C 62.77, H 4.53, N 1.46; found C 62.31, H 4.57, N 1.28. IR: $\tilde{\nu}$ = 1289, 1261 (ν_{PN}) cm^{-1}. MS (FAB+): *m*/*z* (%) = 856 (100) [M – ClO_4]$^+$. ^{1}H NMR ($CDCl_3$): δ = 2.09, 2.16, 2.37, 2.46 (4m, 4 H, CH_2, dppe), 6.42–6.55 (m, 5 H, NPh), 6.79–6.98 (m, 4 H, C_6H_4), 7.14–7.66 (m, 30 H, PPh_2) ppm. ^{31}P{^{1}H} NMR ($CDCl_3$): δ = 43.81 (dd, $^3J_{P,P}$ = 26.2, $^3J_{P,P}$ = 16.0 Hz, 1 P, P *trans* to N), 45.31 (d, $^3J_{P,P}$ = 16.0 Hz, 1 P, P=N), 58.85 (d, $^3J_{P,P}$ = 26.2 Hz, 1 P, P *trans* to C).

Complex 9: Complex **9** was prepared following a synthetic procedure similar to that reported for **7**. A solution of **1** (0.200 g, 0.202 mmol) in acetone (20 mL) was treated with $AgClO_4$ (0.084 g, 0.405 mmol) and 1,10-phenanthroline (0.073 g, 0.404 mmol) to give **9** as a deep-yellow solid. Yield: 0.263 g (88%). $C_{36}H_{27}ClN_3O_4PPd$ (738.46): calcd. C 58.55, H 3.68, N 5.69; found C 58.32, H 3.56, N 5.72. IR: $\tilde{\nu}$ = 1290 (ν_{PN}) cm^{-1}. MS (FAB+): *m*/*z* (%) = 638 (100) [M – ClO_4]$^+$. ^{1}H NMR (CD_2Cl_2): δ = 6.97 (td, $^3J_{H,H}$ = 7.6, $^4J_{H,H}$ = 1.2 Hz, 1 H, H^p, NPh), 7.08 (t, $^3J_{H,H}$ = 7.6 Hz, 2 H, H^m, NPh), 7.18 (br. d, 2 H, H^o, NPh), 7.22 (ddd, $^3J_{P,H}$ = 9.2, $^3J_{H,H}$ = 7.2, $^4J_{H,H}$ = 1.2 Hz, 1 H, H^3, C_6H_4), 7.33 (tdd, $^3J_{H,H}$ = 7.6, $^4J_{P,H}$ = 5.2, $^4J_{H,H}$ = 0.8 Hz, 1 H, H^4, C_6H_4), 7.60–7.62 [m, 5 H, PPh_2 (4 H^m) + C_6H_4 (H^5)], 7.65 (dd, $^3J_{H,H}$ = 8.0, $^3J_{H,H}$ = 4.8 Hz, 1 H, $H^{\beta'}$, phen), 7.69–7.74 (m, 2 H, H^p, PPh_2), 7.75 (br. d, $^3J_{H,H}$ = 8.0 Hz, 1 H, H^6, C_6H_4), 7.76–7.82 (m, 4 H, H^o, PPh_2), 8.00–8.03 (m, 2 H, H^β + $H^{\alpha'}$, phen), 8.12 (s, 2 H, H^δ + $H^{\delta'}$, phen), 8.62 (dd, $^3J_{H,H}$ = 8.0, $^4J_{H,H}$ = 1.2 Hz, 1 H, $H^{\gamma'}$, phen), 8.75 (dd, $^3J_{H,H}$ = 8.4, $^4J_{H,H}$ = 1.6 Hz, 1 H, H^γ, phen), 9.22 (d, $^3J_{H,H}$ = 5.2 Hz, 1 H, H^α, phen) ppm. ^{13}C{^{1}H} NMR (CD_2Cl_2): δ = 122.77 (s, C^p, NPh), 125.26 (s, $C^{\beta'}$, phen), 125.33 (d, $^3J_{P,C}$ = 14.1 Hz, C^4, C_6H_4), 125.69 (s, C^β, phen), 126.64 (d, $^3J_{P,C}$ = 9.1 Hz, C^o, NPh), 126.68 (d, $^1J_{P,C}$ = 91 Hz, C^{ipso}, PPh_2), 127.40, 127.82 (2s, C^δ + $C^{\delta'}$, phen), 128.95 (s, C^m, NPh), 129.34 (d, $^2J_{P,C}$ = 17.1 Hz, C^3, C_6H_4), 129.37 (d, $^3J_{P,C}$ = 12.0 Hz, C^m, PPh_2), 130.11, 130.56 (2C^q, phen), 131.64 (d, $^4J_{P,C}$ = 3.0 Hz, C^5, C_6H_4), 133.36 (d, $^2J_{P,C}$ = 10.6 Hz, C^o, PPh_2), 133.73 (d, $^4J_{P,C}$ = 2.0 Hz, C^p, PPh_2), 135.17 (d, $^3J_{P,C}$ = 14.1 Hz, C^6, C_6H_4), 139.17 (s, C^γ, phen), 139.63 (s, $C^{\gamma'}$, phen), 144.21 (d, $^1J_{P,C}$ = 131 Hz, C^2, C_6H_4), 145.18, 147.14 (2 C^q, phen), 146.45 (d, $^2J_{P,C}$ = 3.0 Hz, C^{ipso}, NPh), 150.06 (s, C^α, phen), 152.15 (s, $C^{\alpha'}$, phen), 160.46 (d, $^2J_{P,C}$ = 18.1 Hz, C^1, C_6H_4) ppm. ^{31}P{^{1}H} NMR (CD_2Cl_2): δ = 45.84 ppm.

Complex 10: Complex **10** was prepared following a synthetic procedure similar to that reported for **7**. A solution of **1** (0.200 g, 0.202 mmol) in acetone (20 mL) was treated with $AgClO_4$ (0.084 g, 0.405 mmol) and 2,2′-bipyridine (0.063 g, 0.404 mmol) to give **10** as a yellow solid. Yield: 0.289 g (100%). $C_{34}H_{27}ClN_3O_4PPd$ (714.43): calcd. C 57.16, H 3.81, N 5.88; found C 57.23, H 3.88, N 5.94. IR: $\tilde{\nu}$ = 1289, 1263 (ν_{PN}) cm^{-1}. MS (FAB+): *m*/*z* (%) = 614 (100) [M – ClO_4]$^+$. ^{1}H NMR ($CDCl_3$): δ = 6.84 (td, NPh, $^3J_{H,H}$ = 7.6, $^4J_{H,H}$ = 1.5 Hz, 1 H, H^p), 6.93 (t, $^3J_{H,H}$ = 8.1 Hz, 2 H, H^m, NPh), 6.95 (d, $^3J_{H,H}$ = 8.1 Hz, 2 H, H^o, NPh), 7.05 (ddd, $^3J_{P,H}$ = 9, $^3J_{H,H}$ = 7.2, $^4J_{H,H}$ = 1.2 Hz, 1 H, C_6H_4, H^3), 7.19 (tdd, $^3J_{H,H}$ = 7.0, $^4J_{P,H}$ = 5.1, $^4J_{H,H}$ = 1.5 Hz, 1 H, C_6H_4, H^4), 7.44 (tt, $^3J_{H,H}$ = 7.2, $^5J_{P,H}$ ≈ $^4J_{H,H}$ = 1.5 Hz, 1 H, C_6H_4, H^5), 7.46–7.66 [m, 15 H, PPh_2 + bipy (4 H, H^β + H^δ) + C_6H_4 (H^6)], 8.07 (br. t, $^3J_{H,H}$ = 6.9 Hz, 1 H, H^γ, bipy), 8.22 (br. t,, $^3J_{H,H}$ = 6.6 Hz 1 H, H^γ, bipy), 8.51 (br. s, 1 H, H^α, bipy), 8.68 (br. d, $^3J_{H,H}$ = 3.9 Hz, 1 H, H^α, bipy) ppm. ^{31}P{^{1}H} NMR ($CDCl_3$): δ = 45.96 ppm.

Complex 11: Ph_3P=NC(O)-2-NC_5H_4 (0.500 g, 1.307 mmol), was added to a solution of $Pd(OAc)_2$ (0.293 g, 1.307 mmol) in 20 mL of dry CH_2Cl_2 and the resulting solution was refluxed for 1 h. At this point, some decomposition was evident. After cooling, the black suspension was treated with charcoal for 30 min and then filtered through a Celite pad. The resulting orange solution was evaporated to dryness and the residue redissolved in MeOH (20 mL). An excess of LiCl (0.222 g, 5.23 mmol) was added to the methanolic solution, which was stirred vigorously at room temperature for 16 h. The yellow precipitate of **11** formed was collected by filtration, washed with MeOH (20 mL) and Et_2O (40 mL) and air dried. Yield: 0.604 g (88.3%). $C_{24}H_{18}ClN_2OPPd$ (523.25): calcd. C 55.09, H 3.47, N 5.35; found C 55.15, H 3.60, N 5.28. IR: $\tilde{\nu}$ = 1644 (ν_{CO}), 1332 (ν_{PN}) cm^{-1}. MS (FAB+): *m*/*z* (%) = 523 (20) [M]$^+$, 487 (100) [M – Cl]$^+$. ^{1}H NMR (CD_2Cl_2): δ = 7.00 (ddd, $^3J_{P,H}$ = 11.1, $^3J_{H,H}$ = 7.8, $^4J_{H,H}$ = 1.5 Hz, 1 H, H^3, C_6H_4), 7.13 (tdd, $^3J_{H,H}$ = 7.8, $^4J_{P,H}$ = 5.1, $^4J_{H,H}$ = 1.2 Hz, 1 H, H^4, C_6H_4), 7.28 (tt, $^3J_{H,H}$ = 7.8, $^4J_{H,H}$ ≈ $^5J_{P,H}$ = 1.5 Hz, 1 H, H^5, C_6H_4), 7.55–7.64 [m, 5 H, PPh_2 (4 H^m) + py (H^β)], 7.69–7.75 (m, 2 H, H^p, PPh_2), 7.87–7.94 [m, 5 H, PPh_2 (4 H^o) + py (H^δ)], 7.98 (td, $^3J_{H,H}$ = 7.5, $^4J_{H,H}$ = 1.5 Hz, 1 H, H^γ, py), 8.10 (ddd, $^3J_{H,H}$ = 8.1, $^4J_{P,H}$ = 2.7, $^4J_{H,H}$ = 1.2 Hz, 1 H, H^6, C_6H_4), 8.97 (ddd, $^3J_{H,H}$ = 5.1, $^4J_{H,H}$ = 1.5, $^5J_{H,H}$ = 0.6 Hz, 1 H, H^α, py) ppm. ^{13}C{^{1}H} NMR (CD_2Cl_2): δ = 124.77 (d, $^1J_{P,C}$ = 90 Hz, C^{ipso}, PPh_2), 125.48 (s, C^3, py), 125.68 (s, C^5, py), 128.84 (s, C^5, C_6H_4), 129.69 (d, $^3J_{P,C}$ = 12.7 Hz, C^m, PPh_2), 130.60 (d, $^2J_{P,C}$ = 22.6 Hz, C^3, C_6H_4), 132.09 (d, $^3J_{P,C}$ = 3.0 Hz, C^4, C_6H_4),

 © 2005 Wiley-VCH Verlag GmbH & Co. KGaA, Weinheim

133.79 (d, $^2J_{P,C}$ = 11.2 Hz, C^o, PPh_2), 134.52 (d, $^4J_{P,C}$ = 2.5 Hz, C^p, PPh_2), 138.48 (d, $^1J_{P,C}$ = 130 Hz, C^2, C_6H_4), 139.11 (d, $^3J_{P,C}$ = 14.5 Hz, C^6, C_6H_4), 139.51 (s, C^4, py), 149.18 (s, C^6, py), 152.98 (s, C^2, py), 153.19 (d, $^2J_{P,C}$ = 8.6 Hz, C^1, C_6H_4), 172.25 (d, $^2J_{P,C}$ = 4.6 Hz, C=O) ppm. $^{31}P\{^1H\}$ NMR (CD_2Cl_2): δ = 51.88 ppm.

Complex 12: A suspension of $[PtCl_2(NCPh)_2]$ (0.200 g, 0.424 mmol) and Ph_3P=NC(O)-2-NC_5H_4 (0.162 g, 0.424 mmol) in 15 mL of 2-methoxyethanol was refluxed for 8 h. During this time the initial suspension dissolved, and a greenish solution (presence of Pt^0) was obtained. After cooling, complex **12** precipitated from the alcoholic medium as a green solid. This solid was filtered and washed with Et_2O (20 mL). The crude solid of **12** was further dissolved in CH_2Cl_2 (40 mL), treated with charcoal and filtered through Celite to give a yellow solution. The evaporation of the solvent to dryness and treatment of the residue with Et_2O (30 mL) gave **12** as a yellow solid. Yield: 0.118 g (45.7%). Complex **12** was recrystallised from CH_2Cl_2/OEt_2 to give yellow needles of **12**·CH_2Cl_2, which were used for analytical and spectroscopic measurements. $C_{24}H_{18}ClN_2OPPt{\cdot}CH_2Cl_2$ (696.87): calcd. C 43.09, H 2.89, N 4.02; found C 42.98, H 2.84, N 4.24. IR: $\tilde{\nu}$ = 1646 (ν_{CO}), 1330 (ν_{PN}) cm^{-1}. MS (FAB+): *m*/*z* (%) = 612 (95) $[M]^+$, 576 (100) $[M - Cl]^+$. ^1H NMR (CD_2Cl_2): δ = 6.95 (ddd, $^3J_{P,H}$ = 11.6, $^3J_{H,H}$ = 6.0, $^4J_{H,H}$ = 1.2 Hz, 1 H, H^3, C_6H_4), 7.05 (tdd, $^3J_{H,H}$ = 7.6, $^4J_{P,H}$ = 5.2, $^4J_{H,H}$ = 1.2 Hz, 1 H, H^4, C_6H_4), 7.23 (tt, $^3J_{H,H}$ = 7.6, $^4J_{H,H} \approx {}^5J_{P,H}$ = 1.6 Hz, 1 H, H^5, C_6H_4), 7.48–7.53 (m, 4 H, H^m, PPh_2), 7.60 (ddd, $^3J_{H,H}$ = 7.2, $^3J_{H,H}$ = 5.2, $^4J_{H,H}$ = 1.2 Hz, 1 H, H$^\beta$, py), 7.62–7.67 (m, 2 H, H^p, PPh_2), 7.78 (dm, $^3J_{H,H}$ = 7.6 Hz, 1 H, H$^\delta$, py), 7.80–7.86 (m, 4 H, H^o, PPh_2), 7.98 (td, $^3J_{H,H}$ = 7.6, $^4J_{H,H}$ = 1.6 Hz, 1 H, H$^\gamma$, py), 8.02 (ddd, $^3J_{H,H}$ = 7.6, $^4J_{P,H}$ = 3.2, $^4J_{H,H}$ = 1.2, $^3J_{Pt,H}$ = 30.4 Hz, 1 H, H^6, C_6H_4), 9.17 (ddd, $^3J_{H,H}$ = 5.2, $^4J_{H,H}$ = 1.6, $^5J_{H,H}$ = 0.4, $^3J_{Pt,H} \approx$ 20 Hz, 1 H, H$^\alpha$, py) ppm. $^{31}P\{^1H\}$ NMR (CD_2Cl_2): δ = 51.88 ($^2J_{Pt,P}$ = 452 Hz) ppm.

Complex 13: $AgClO_4$ (0.040 g, 0.191 mmol) was added to a suspension of **11** (0.100 g, 0.191 mmol) in NCMe (20 mL). The resulting white suspension was stirred at room temperature with exclusion of light for 30 min, then filtered through Celite. The resulting pale-yellow solution was evaporated to small volume (approx. 1 mL). Addition of Et_2O (20 mL) and continuous stirring gave **13** as an off-white solid, which was filtered, washed with additional Et_2O (10 mL) and air dried. Yield: 0.081 g (67.5%). Complex **13** was recrystallised from CH_2Cl_2/OEt_2 to give colourless microcrystals of **13**·2CH_2Cl_2, which were used for analytical and spectroscopic measurements. $C_{26}H_{21}ClN_3O_5PPd{\cdot}2CH_2Cl_2$ (798.17): calcd. C 42.14, H 3.16, N 5.26; found C 41.56, H 3.27, N 5.10. IR: $\tilde{\nu}$ = 2328 (ν_{CN}), 1669 (ν_{CO}), 1323, 1296 (ν_{PN}) cm^{-1}. MS (FAB+): *m*/*z* (%) = 487 (100) $[M - NCMe - ClO_4]^+$. ^1H NMR ($CDCl_3$): δ = 2.79 (s, 3 H, NCMe), 7.04 (ddd, $^3J_{P,H}$ = 10.6, $^3J_{H,H}$ = 7.6, $^4J_{H,H}$ = 1.1 Hz, 1 H, H^3, C_6H_4), 7.23 (tdd, $^3J_{H,H}$ = 7.5, $^4J_{P,H}$ = 5.1, $^4J_{H,H}$ = 1.2 Hz, 1 H, H^4, C_6H_4), 7.37 (tt, $^3J_{H,H}$ = 7.3, $^4J_{H,H} \approx {}^5J_{P,H}$ = 1.7 Hz, 1 H, H^5, C_6H_4), 7.45 (ddd, $^3J_{H,H}$ = 7.6, $^4J_{P,H}$ = 2.2, $^4J_{H,H}$ = 0.8 Hz, 1 H, H^6, C_6H_4), 7.56–7.63 (m, 4 H, H^m, PPh_2), 7.70–7.75 (m, 2 H, H^p, PPh_2), 7.84–7.91 [m, 5 H, PPh_2 (4 H^o) + py (H$^\beta$)], 7.95 (d, $^3J_{H,H}$ = 7.5 Hz, 1 H, H$^\delta$, py), 8.09 (td, $^3J_{H,H}$ = 7.5, $^4J_{H,H}$ = 1.8 Hz, 1 H, H$^\gamma$, py), 8.97 (dd, $^3J_{H,H}$ = 5.4, $^4J_{H,H}$ = 2.2 Hz, 1 H, H$^\alpha$, py) ppm. $^{31}P\{^1H\}$ NMR ($CDCl_3$): δ = 56.71 ppm.

Complex 14: $AgClO_4$ (0.103 g, 0.497 mmol) was added to a suspension of **11** (0.260 g, 0.497 mmol) in acetone (20 mL). The resulting suspension was stirred at room temperature with exclusion of light for 20 min, then filtered through Celite. PPh_3 (0.130 g, 0.497 mmol) was added to this freshly prepared solution and stirring was continued for an additional 30 min. The pale-yellow solution was evaporated to dryness and the oily residue was treated with Et_2O (20 mL). Continuous stirring gave **14** as a white solid, which was filtered, washed with Et_2O (10 mL) and air dried. Yield: 0.321 g (76.0%). Complex **14** was recrystallised from CH_2Cl_2/*n*-hexane to give pale-yellow crystals of **14**·2.5CH_2Cl_2, which were used for analytical and spectroscopic measurements. $C_{42}H_{33}ClN_2O_5P_2Pd{\cdot}2.5CH_2Cl_2$ (1061.9): calcd. C 50.33, H 3.61, N 2.64; found C 49.76, H 3.42, N 2.48. IR: $\tilde{\nu}$ = 1651 (ν_{CO}), 1339 (ν_{PN}) cm^{-1}. MS (FAB+): *m*/*z* (%) = 749 (55%) $[M - ClO_4]^+$. ^1H NMR (CD_2Cl_2): δ = 6.78 (dd, $^3J_{H,H}$ = 5.2, $^4J_{H,H}$ = 0.4 Hz, 1 H, py), 6.85–6.87 (m, 2 H, C_6H_4), 7.13–7.17 [m, 3 H, C_6H_4 (2 H) + py (1 H)], 7.52–7.57 (m, 6 H, H^m, PPh_3), 7.63–7.68 (m, 3 H, H^p, PPh_3), 7.71–7.76 (m, 4 H, H^m, PPh_2), 7.84–7.91 [m, 8 H, PPh_3 (6 H^o) + PPh_2 (2 H^p)], 7.96–8.04 [m, 5 H, PPh_2 (4 H^o) + py (1 H)], 8.07 (dm, $^3J_{H,H}$ = 8.0 Hz, 1 H, py) ppm. $^{31}P\{^1H\}$ NMR ($CDCl_3$): δ = 39.34 (s, 1 P, Pd–PPh_3), 49.18 (s, 1 P, P=N) ppm.

Complex 15: Complex **15** was prepared following a procedure similar to that reported for **14**. A solution of **11** (0.100 g, 0.191 mmol) in acetone (20 mL) was treated with $AgClO_4$ (0.040 g, 0.191 mmol) and dppm (0.073 g, 0.191 mmol) to give **15** as an orange solid. Yield: 0.163 g (87.8%). Complex **15** was crystallised from CH_2Cl_2/OEt_2 to give orange crystals of **15**·CH_2Cl_2, which were used for analytical and spectroscopic measurements. $C_{49}H_{40}ClN_2O_5P_3Pd{\cdot}CH_2Cl_2$ (1056.6): calcd. C 56.84, H 4.00, N 2.65; found C 56.93, H 3.75, N 2.79. IR: $\tilde{\nu}$ = 1650 (ν_{CO}), 1338 (ν_{PN}) cm^{-1}. MS (FAB+): *m*/*z* (%) = 871 (100) $[M - ClO_4]^+$. ^1H NMR ($CDCl_3$): δ = 3.47 (d, $^2J_{P,H}$ = 11.1 Hz, 2 H, CH_2, dppm), 6.84–7.97 (m, 38 H, Ph; extensive overlap of the signals) ppm. $^{31}P\{^1H\}$ NMR ($CDCl_3$): δ = –24.75 (d, $^2J_{P,P}$ = 100 Hz, 1 P, free PPh_2), 27.05 (d, $^2J_{P,P}$ = 100Hz, 1 P, Pd–PPh_2), 49.14 (s, 1 P, P=N) ppm.

Complex 16: Complex **16** was prepared following a procedure similar to that reported for **14**. A solution of **11** (0.100 g, 0.191 mmol) in acetone (20 mL) was treated with $AgClO_4$ (0.040 g, 0.191 mmol) and dppe (0.076 g, 0.191 mmol) to give **16** as a cream solid. Yield: 0.157 g (83.3%). Complex **16** was recrystallised from CH_2Cl_2/*n*-hexane to give pale yellow crystals of **16**·CH_2Cl_2, which were used for analytical and spectroscopic measurements. $C_{50}H_{42}ClN_2O_5P_3Pd{\cdot}CH_2Cl_2$ (1070.6): calcd. C 57.22, H 4.14, N 2.62; found C 57.53, H 4.02, N 2.64. IR: $\tilde{\nu}$ = 1622 (ν_{CO}), 1329 (ν_{PN}) cm^{-1}. MS (FAB+): *m*/*z* (%) = 885 (70) $[M - ClO_4]^+$. Room temperature NMR spectroscopic data: ^1H NMR ($CDCl_3$): δ = 2.22–2.29 (br. s, 4 H, CH_2, dppe), 6.83–7.92 (m, 38 H, aromatics) ppm. $^{31}P\{^1H\}$ NMR ($CDCl_3$): δ = 47.28 (s, P=N) ppm. Low temperature NMR spectroscopic data (233 K): ^1H NMR ($CDCl_3$): δ = 2.31, 2.42, 2.88, 3.01 (4m, 4 H, CH_2, dppe), 6.60 (m, 1 H, C_6H_4), 6.92–7.11 (3m, 3 H, C_6H_4), 7.17–8.12 (m, 33 H, aromatics), 8.72 (dd, $^3J_{H,H}$ = 5.6, $^4J_{H,H}$ = 1.8 Hz, 1 H, H$^\alpha$, py) ppm. $^{31}P\{^1H\}$ NMR ($CDCl_3$): δ = 41.38 (dd, $^3J_{P,P}$ = 27.5, $^3J_{P,P}$ = 13.0 Hz, 1 P, P *trans* to N), 47.84 (dd, $^3J_{P,P}$ = 13.0, $^3J_{P,P}$ = 3.2 Hz, 1 P, P=N), 58.21 (d, $^3J_{P,P}$ = 27.5 Hz, 1 P, P *trans* to C) ppm.

Complex 17: Complex **17** was prepared following a procedure similar to that reported for **14**. A solution of **11** (0.100 g, 0.191 mmol) in acetone (20 mL) was treated with $AgClO_4$ (0.040 g, 0.191 mmol) and 2,2′-bipyridine (0.030 g, 0.191 mmol) to give **17** as a yellow solid. Yield: 0.110 g (77.5%). Complex **17** was crystallised from CH_2Cl_2/*n*-hexane to give yellow crystals of **17**·CH_2Cl_2, which were used for analytical and spectroscopic measurements. $C_{34}H_{26}ClN_4O_5PPd{\cdot}CH_2Cl_2$ (807.13): calcd. C 51.71, H 3.43, N 6.94; found C 51.79, H 2.87, N 7.18. IR: $\tilde{\nu}$ = 1652 (ν_{CO}), 1332 (ν_{PN}) cm^{-1}. MS (FAB+): *m*/*z* (%) = 643 (25) $[M - ClO_4]^+$. ^1H NMR ($CDCl_3$): δ = 6.33 (ddd, $^3J_{H,H}$ = 7.1, $^4J_{P,H}$ = 4.7, $^4J_{H,H}$ = 2.6 Hz, 1 H, H^6, C_6H_4), 6.92–6.99 (m, 1 H, C_6H_4), 7.08–7.12 (m, 2 H, C_6H_4), 7.55 (ddd, $^3J_{H,H}$ = 7.6, $^3J_{H,H}$ = 5.2, $^4J_{H,H}$ = 1.2 Hz, 2 H, H$^\beta$, bipy),

 © 2005 Wiley-VCH Verlag GmbH & Co. KGaA, Weinheim

7.58–7.67 [m, 5 H, PPh_2 (4 H^m) + py (H^β)], 7.71–7.74 (m, 2 H, H^p, PPh_2), 7.76–7.85 (m, 4 H, H^o, PPh_2), 7.87–7.92 (m, 2 H, H^δ + H^γ, py), 7.95 (dd, $^3J_{H,H}$ = 4.0, $^4J_{H,H}$ = 1.5 Hz, 1 H, H^α, py), 8.02 (td, $^3J_{H,H}$ = 7.7, $^4J_{H,H}$ = 1.6 Hz, 2 H, H^γ, bipy), 8.30 (dt, $^3J_{H,H}$ = 7.7, $^4J_{H,H} \approx {}^5J_{H,H}$ = 1 Hz, 2 H, H^δ, bipy), 8.91 (ddd, $^3J_{H,H}$ = 5.2, $^4J_{H,H}$ = 1.6 Hz, 2 H, H^α, bipy) ppm. $^{31}P\{^1H\}$ NMR ($CDCl_3$): δ = 53.96 ppm.

Complex 18: Complex **18** was prepared following a synthetic procedure similar to that reported for **14**. A solution of **11** (0.100 g, 0.191 mmol) in acetone (20 mL) was treated with $AgClO_4$ (0.040 g, 0.191 mmol) and 1,10-phenanthroline (0.034 g, 0.191 mmol) to give **18** as a yellow solid. Yield: 0.100 g (68.2%). $C_{36}H_{26}ClN_4O_5PPd$ (767.45): calcd. C 56.34, H 3.41, N 7.30; found C 56.15, H 3.08, N 7.09. IR: $\tilde{\nu}$ = 1645 (ν_{CO}), 1338 (ν_{PN}) cm^{-1}. MS (FAB+): *m*/*z* (%) = 667 (30) $[M - ClO_4]^+$. ^1H NMR ($CDCl_3$): δ = 5.85 (dd, $^3J_{H,H}$ = 7.8, $^4J_{H,H}$ = 2.4 Hz, 1 H, H^6, C_6H_4), 6.83–6.88 (m, 1 H, C_6H_4), 6.97–7.02 (m, 2 H, C_6H_4), 7.29 (dm, $^3J_{H,H}$ = 4.2, $^4J_{H,H}$ = 0.6 Hz, 1 H, H^α, py), 7.36 (ddd, $^3J_{H,H}$ = 7.5, $^3J_{H,H}$ = 5.1, $^4J_{H,H}$ = 1.5 Hz, 1 H, H^β, py), 7.53–7.58 (m, 1 H, py), 7.63–7.69 (m, 4 H, H^m, PPh_2), 7.75–7.80 (m, 2 H, H^p, PPh_2), 7.88 (dd, $^3J_{H,H}$ = 8.1, $^3J_{H,H}$ = 4.8 Hz, 2 H, H^β, phen), 7.94–8.01 [m, 5 H, PPh_2 (4 H^o) + py (1 H)], 8.10 (s, 2 H, H^δ, phen), 8.61 (dd, $^3J_{H,H}$ = 8.1, $^4J_{H,H}$ = 1.5 Hz, 2 H, H^γ, phen), 9.36 (dd, $^3J_{H,H}$ = 4.8, $^4J_{H,H}$ = 1.8 Hz, 2 H, H^α, phen) ppm. $^{31}P\{^1H\}$ NMR ($CDCl_3$): δ = 53.96 ppm.

Catalytic Mizoroki–Heck Arylations of Methyl Acrylate. General Procedure: Methyl acrylate (1.35 mmol), NEt_3 (1.13 mmol) and the corresponding catalyst (complexes **1**, **4**, **11** or **13**, see amounts in Table 3) were added to a solution of the corresponding aryl halide (1.13 mmol) in dimethylformamide or dimethylacetamide (15 mL). This mixture was refluxed under argon for 24 h. After cooling, water (10 mL) was added. The organic phase was extracted several times with CH_2Cl_2 (3 × 10 mL) and the combined extracts were dried with anhydrous $MgSO_4$. The solvents were distilled off and the residue was extracted with *n*-pentane. Evaporation of the pentane solution to dryness gave the arylation products as white waxy solids or colourless oils (yields are collected in Table 3).

Transmission Electron Microscopy: For the TEM experiments a few drops of a solution of the samples in dichloromethane was deposited onto carbon-coated copper grids. In this way the organic ligands were dissolved whereas the metallic particles remained undissolved and dispersed, thus allowing their observation in the TEM. The observations were carried out with a Jeol 2000FXII microscope (point to point resolution: 2.8 Å) equipped with an Oxford Instruments INCA 200 Energy Dispersive Spectroscopy analyzer and a Gatan MSC-794 CCD camera for recording the images.

Crystallography. Data Collection: Crystals of complex [Pd(C_6H_4-2-PPh_2=N-C(O)-2-NC_5H_4-κ-C,N,N)Cl] (**11**) were grown by slow vapour diffusion of Et_2O into a CH_2Cl_2 solution of the crude complex at room temperature. A crystal of dimensions 0.20 × 0.10 × 0.043 mm was mounted on a quartz fibre in a random orientation and covered with epoxy. Data collection was performed at 100 K on a Bruker Smart Apex CCD diffractometer using graphite-monochromated Mo-K_α radiation (λ = 0.71073 Å). A hemisphere of data was collected based on three ω-scan runs. For each of these runs, frames (606, 435, and 230, respectively) were collected at 0.3° intervals and 10 s per frame. The diffraction frames were integrated using the program SAINT[86] and the integrated intensities were corrected for systematic errors with SADABS.[87]

Structure Solution and Refinement: The structure was solved by Patterson and Fourier methods.[88] All non-hydrogen atoms were refined with anisotropic displacement parameters. The hydrogen atoms were placed at idealised positions and treated as riding atoms. Each hydrogen atom was assigned an isotropic displacement parameter equal to 1.2-times the equivalent isotropic displacement parameter of its parent atom. The structure was refined to F_o^2, and all reflections were used in the least-squares calculations.[89]

CCDC-253369 (for **11**) contains the supplementary crystallographic data for this paper. These data can be obtained free of charge from The Cambridge Crystallographic Data Centre via www.ccdc.cam.ac.uk/data_request/cif.

Acknowledgments

Funding by the Diputación General de Aragón (Spain, Project P061/2001) and Dirección General de Investigación Científica y Técnica (DGICYT) (Spain, Projects BQU2002-0510, BQU2002-00554 and MAT2003-1182) is gratefully acknowledged. R. B. thanks the MECD (Spain) for a predoctoral fellowship and T. S. thanks the MECD (Spain) for a postdoctoral fellowship.

[1] A. W. Johnson, W. C. Kaska, K. A. Ostoja Starzewski, D. A. Dixon, *Ylides and Imines of Phosphorus*, John Wiley & Sons, New York, **1993**, chapter 13 and references cited therein.
[2] A. Steiner, S. Zacchini, P. I. Richards, *Coord. Chem. Rev.* **2002**, *227*, 193.
[3] H. J. Cristau, M. Taillefer, N. Rahier, *J. Organomet. Chem.* **2002**, *646*, 94.
[4] L. P. Spencer, R. Altwer, P. Wei, L. Gelmini, J. Gauld, D. W. Stephan, *Organometallics* **2003**, *22*, 3841.
[5] G. Lin, N. D. Jones, R. A. Gossage, R. McDonald, R. G. Cavell, *Angew. Chem. Int. Ed.* **2003**, *42*, 4054.
[6] H. R. Wu, Y. H. Liu, S. M. Peng, S. T. Liu, *Eur. J. Inorg. Chem.* **2003**, 3152.
[7] M. S. Hill, P. B. Hitchcock, *Chem. Commun.* **2003**, 1758.
[8] W. P. Leung, C. W. So, J. Z. Wang, T. C. W. Mak, *Chem. Commun.* **2003**, 248.
[9] V. Cadierno, P. Crochet, J. Díez, J. García-Alvarez, S. E. García-Garrido, J. Gimeno, *Inorg. Chem.* **2003**, *42*, 3293.
[10] V. Cadierno, P. Crochet, J. Díez, J. García-Alvarez, S. E. García-Garrido, S. García-Granda, J. Gimeno, M. A. Rodríguez, *Dalton Trans.* **2003**, 3240.
[11] M. Alajarín, C. López-Leonardo, P. Llamas-Lorente, D. Bautista, P. G. Jones, *Dalton Trans.* **2003**, 426.
[12] J. D. Masuda, P. Wei, D. W. Stephan, *Dalton Trans.* **2003**, 3500.
[13] V. Cadierno, J. Díez, S. E. García-Garrido, S. García-Granda, J. Gimeno, *J. Chem. Soc., Dalton Trans.* **2002**, 1465.
[14] M. J. Sarsfield, M. Helliwell, D. Collison, *Chem. Commun.* **2002**, 2264.
[15] Y. Matano, H. Nomura, H. Suzuki, *Inorg. Chem.* **2002**, *41*, 1940.
[16] S. Wingerter, M. Pfeiffer, A. Murso, C. Lustig, T. Stey, V. Chandrasekhar, D. Stalke, *J. Am. Chem. Soc.* **2001**, *123*, 1381.
[17] K. Aparna, R. P. Kamalesh Babu, R. McDonald, R. G. Cavell, *Angew. Chem. Int. Ed.* **2001**, *40*, 4400.
[18] G. Aharonian, S. Gambarotta, G. P. A. Yap, *Organometallics* **2001**, *20*, 5008.
[19] M. S. Balakrishna, S. Teipel, A. A. Pinkerton, R. G. Cavell, *Inorg. Chem.* **2001**, *40*, 1802.
[20] M. J. Sarsfield, M. Said, M. Thornton-Pett, L. A. Gerrard, M. Bochmann, *J. Chem. Soc., Dalton Trans.* **2001**, 822.
[21] L. LePichon, D. W. Stephan, *Inorg. Chem.* **2001**, *40*, 3827.
[22] R. P. Kamalesh Babu, R. McDonald, R. G. Cavell, *Organometallics* **2000**, *19*, 3462.
[23] S. Al-Benna, M. J. Sarsfield, M. Thornton-Pett, D. L. Ormsby, P. J. Maddox, P. Brès, M. Bochmann, *J. Chem. Soc., Dalton Trans.* **2000**, 4247.
[24] K. Aparna, R. McDonald, R. G. Cavell, *J. Am. Chem. Soc.* **2000**, *122*, 9314.

 © 2005 Wiley-VCH Verlag GmbH & Co. KGaA, Weinheim

[25] M. Sauthier, J. Forniés-Cámer, L. Toupet, R. Réau, *Organometallics* **2000**, *19*, 553.
[26] Y. K. Kim, S. J. Lee, K. H. Ahn, *J. Org. Chem.* **2000**, *65*, 7807.
[27] R. P. Kamalesh Babu, K. Aparna, R. McDonald, R. G. Cavell, *Inorg. Chem.* **2000**, *39*, 4981.
[28] J. Vicente, A. Arcas, D. Bautista, M. C. Ramírez de Arellano, *Organometallics* **1998**, *17*, 4544.
[29] L. R. Falvello, S. Fernández, M. M. García, R. Navarro, E. P. Urriolabeitia, *J. Chem. Soc., Dalton Trans.* **1998**, 3745.
[30] L. R. Falvello, M. M. García, I. Lázaro, R. Navarro, E. P. Urriolabeitia, *New J. Chem.* **1999**, *23*, 227.
[31] J. García-López, E. Peralta-Pérez, A. Forcén-Acebal, S. García-Granda, F. López-Ortíz, *Chem. Commun.* **2003**, 856.
[32] S. Wingerter, H. Gornitzka, R. Bertermann, S. K. Pandey, J. Rocha, D. Stalke, *Organometallics* **2000**, *19*, 3890.
[33] S. Wingerter, H. Gornitzka, G. Bertrand, D. Stalke, *Eur. J. Inorg. Chem.* **1999**, 173.
[34] M. A. Leeson, B. K. Nicholson, M. R. Olsen, *J. Organomet. Chem.* **1999**, *579*, 243.
[35] A. Steiner, D. Stalke, *Angew. Chem. Int. Ed. Engl.* **1995**, *34*, 1752.
[36] H. Alper, *J. Organomet. Chem.* **1977**, *127*, 385.
[37] J. Vicente, J. A. Abad, R. Clemente, J. López-Serrano, M. C. Ramírez de Arellano, P. G. Jones, D. Bautista, *Organometallics* **2003**, *22*, 4248.
[38] P. Wei, K. T. K. Chan, D. W. Stephan, *Dalton Trans.* **2003**, 3804.
[39] I. P. Beletskaya, A. V. Cheprakov, *Chem. Rev.* **2000**, *100*, 3009.
[40] R. B. Bedford, *Chem. Commun.* **2003**, 1787.
[41] C. Rocaboy, J. A. Gladysz, *New J. Chem.* **2003**, *27*, 39.
[42] S. Gründemann, M. Albretch, J. A. Loch, J. W. Faller, R. H. Crabtree, *Organometallics* **2001**, *20*, 5485.
[43] E. Díez-Barra, J. Guerra, V. Hornillos, S. Merino, J. Tejeda, *Organometallics* **2003**, *22*, 4610.
[44] I. G. Jung, S. U. Son, K. H. Park, K. C. Chung, J. W. Lee, Y. K. Chung, *Organometallics* **2003**, *22*, 4715.
[45] S. Bittner, M. Pomerantz, Y. Assaf, P. Krief, S. Xi, M. K. Witczak, *J. Org. Chem.* **1988**, *53*, 1.
[46] S. Bittner, Y. Assaf, P. Krief, M. Pomerantz, B. T. Ziemnicka, C. G. Smith, *J. Org. Chem.* **1985**, *50*, 1712.
[47] B. Weinberger, W. P. Fehlhammer, *Chem. Ber.* **1985**, *118*, 42.
[48] L. R. Falvello, S. Fernández, C. Larraz, R. Llusar, R. Navarro, E. P. Urriolabeitia, *Organometallics* **2001**, *20*, 1424.
[49] C. Gracia, G. Marco, R. Navarro, P. Romero, T. Soler, E. P. Urriolabeitia, *Organometallics* **2003**, *22*, 4910.
[50] J. Bravo, C. Cativiela, R. Navarro, E. P. Urriolabeitia, *J. Organomet. Chem.* **2002**, *650*, 157.
[51] L. R. Falvello, S. Fernández, R. Navarro, I. Pascual, E. P. Urriolabeitia, *J. Chem. Soc., Dalton Trans.* **1997**, *763*.
[52] J. Spencer, M. Pfeffer, N. Kyritsakas, J. Fischer, *Organometallics* **1995**, *14*, 2214.
[53] I. Bar, J. Bernstein, *Acta Crystallogr., Sect. B* **1980**, *36*, 1962.
[54] F. López-Ortiz, E. Peláez-Arango, F. Palacios, J. Barluenga, S. García-Granda, B. Tejerina, A. García-Fernández, *J. Org. Chem.* **1994**, *59*, 1984. See also references cited in ref. 30.
[55] J. Vicente, J. A. Abad, E. Martínez-Viviente, P. G. Jones, *Organometallics* **2002**, *21*, 4454.
[56] J. Vicente, A. Arcas, D. Bautista, P. G. Jones, *Organometallics* **1997**, *16*, 2127.
[57] J. Vicente, J. A. Abad, A. D. Frankland, M. C. Ramírez de Arellano, *Chem. Eur. J.* **1999**, *5*, 3066.
[58] A. J. Deeming, I. P. Rothwell, M. B. Hursthouse, L. New, *J. Chem. Soc., Dalton Trans.* **1978**, 1490.
[59] A. D. Ryabov, G. M. Kazankov, A. K. Yatsimirsky, L. G. Kuz'mina, D. Y. Burtseva, N. V. Dvortsova, V. A. Polyakov, *Inorg. Chem.* **1992**, *31*, 3083.
[60] F. Maassarani, M. Pfeffer, G. Le Borgne, D. Grandjean, *Organometallics* **1986**, *5*, 1511.
[61] J. Forniés, R. Navarro, M. Tomás, E. P. Urriolabeitia, *Organometallics* **1993**, *12*, 940.
[62] J. Forniés, R. Navarro, E. P. Urriolabeitia, *J. Organomet. Chem.* **1990**, *390*, 257.
[63] C. Cativiela, L. R. Falvello, J. C. Ginés, R. Navarro, E. P. Urriolabeitia, *New J. Chem.* **2001**, *25*, 344.
[64] C. Baleizão, A. Corma, H. García, A. Leyva, *Chem. Commun.* **2003**, 606.
[65] F. R. Roca, C. J. Richards, *Chem. Commun.* **2003**, 3002.
[66] R. B. Bedford, C. S. J. Cazin, S. J. Coles, T. Gelbrich, M. B. Hursthouse, V. J. M. Scordia, *Dalton Trans.* **2003**, 3350.
[67] Q. Yao, E. P. Kinney, C. Zheng, *Org. Lett.* **2004**, *6*, 2997.
[68] Z. Xiong, N. Wang, M. Dai, A. Li, J. Chen, Z. Yang, *Org. Lett.* **2004**, *6*, 3337.
[69] M. R. Eberhard, *Org. Lett.* **2004**, *6*, 2125 and references cited therein.
[70] S. S. Pröckl, W. Kleist, M. A. Gruber, K. Köhler, *Angew. Chem. Int. Ed.* **2004**, *43*, 1881.
[71] N. Tsoureas, A. A. Danopoulos, A. A. D. Tulloch, M. E. Light, *Organometallics* **2003**, *22*, 4750.
[72] C. M. Crawforth, S. Burling, I. J. S. Fairlamb, R. J. K. Taylor, A. C. Whitwood, *Chem. Commun.* **2003**, 2194.
[73] M. Dams, D. E. De Vos, S. Celen, P. A. Jacobs, *Angew. Chem. Int. Ed.* **2003**, *42*, 3512.
[74] S. G. Fiddy, J. Evans, M. A. Newton, T. Neisius, R. P. Tooze, R. Oldman. *Chem. Commun.* **2003**, 2682.
[75] B. Clique, C. H. Fabritius, C. Couturier, N. Monteiro, G. Balme. *Chem. Commun.* **2003**, 272.
[76] J. Evans, L. O'Neill, V. Kambhampati, G. Rayner, S. Turin, A. Genge, A. J. Dent, T. Neisius, *J. Chem. Soc., Dalton Trans.* **2002**, 2207.
[77] I. W. Davies, L. Matty, D. L. Hughes, P. J. Reider, *J. Am. Chem. Soc.* **2001**, *123*, 10 139.
[78] C. Rocaboy, J. A. Gladysz, *Org. Lett.* **2002**, *4*, 1993.
[79] M. T. Reetz, E. Westermann, *Angew. Chem. Int. Ed.* **2000**, *39*, 165.
[80] M. Moreno-Mañas, R. Pleixats, S. Villarroya, *Organometallics* **2001**, *20*, 4524.
[81] J. Le Bars, U. Specht, J. S. Bradley, D. G. Blackmond, *Langmuir* **1999**, *15*, 7621.
[82] D. R. Anton, R. H. Crabtree, *Organometallics* **1983**, *2*, 855.
[83] P. Foley, R. DiCosimo, G. M. Whitesides, *J. Am. Chem. Soc.* **1980**, *102*, 6713.
[84] Y. Na, S. Park, S. B. Han, H. Han, S. Ko, S. Chang, *J. Am. Chem. Soc.* **2004**, *126*, 250.
[85] W. C. Wolsey, *J. Chem. Educ.* **1973**, *50*, A335.
[86] SAINT Version 5.0; Bruker Analytical X-ray Systems, Madison, WI, **1995**.
[87] G. M. Sheldrick, SADABS: Empirical absorption correction program; University of Göttingen, **1996**.
[88] SHELXS-86: G. M. Sheldrick, *Acta Crystallogr., Sect. A* **1990**, *46*, 467.
[89] G. M. Sheldrick, SHELXL-97: FORTRAN program for the refinement of crystal structures from diffraction data; Göttingen University, 1997. Molecular graphics were produced using the commercial package SHELXTL-PLUS, Release 5.05/V; Siemens Analytical X-ray Instruments, Inc.: Madison, WI, **1996**.

Received: October 27, 2004

 © 2005 Wiley-VCH Verlag GmbH & Co. KGaA, Weinheim

Reactions of the *B*-Phenylborole Complex [CpRh(η^5-C_4H_4BPh)] with Metalloelectrophiles [(ring)M]$^{2+}$

Dmitry A. Loginov,[a] Dmitry V. Muratov,[a] Pavel V. Petrovskii,[a] Zoya A. Starikova,[a] Maddalena Corsini,[b] Franco Laschi,[b] Fabrizia de Biani Fabrizi,[b] Piero Zanello,[b] and Alexander R. Kudinov*[a]

Keywords: Boron / Electrochemistry / Heterocycles / Rhodium / Sandwich compounds

Thirty-valence-electron dicationic triple-decker complexes with a bridging borole ligand [CpRh(μ-η^5:η^5-C_4H_4BPh)M(ring)]$^{2+}$ [M(ring) = CoCp* (**3**), IrCp* (**6**), Ru(η-$C_6H_3Me_3$-1,3,5) (**8a**), Ru(η-C_6Me_6) (**8b**)] were obtained by stacking reactions of [CpRh(η^5-C_4H_4BPh)] (**2**) with the corresponding half-sandwich fragments [M(ring)]$^{2+}$. Minor formation of arene-type complexes [CpRh(μ-η^5:η^6-C_4H_4BPh)M(ring)]$^{2+}$ was observed for M(ring) = IrCp* and Ru(arene). On the contrary, the arene-type complex [CpRh(μ-η^5:η^6-C_4H_4BPh)RhCp*]$^{2+}$ (**5**) was isolated as the sole product from the reaction of **2** with the fragment [RhCp*]$^{2+}$; an intermediate formation of the triple-decker complex [CpRh(μ-η^5:η^5-C_4H_4BPh)RhCp*]$^{2+}$ (**4**) in this reaction was detected by ^{1}H NMR spectroscopy. Heating **6** in nitromethane gives the symmetrical triple-decker complex [Cp*Ir(μ-η^5:η^5-C_4H_4BPh)IrCp*]$^{2+}$ (**10**). The cations were isolated as salts with the BF_4^- anion. The structures of **2**, **5**$(BF_4)_2$, **6**$(BF_4)_2$ and **8a**$(BF_4)_2$ were determined by X-ray diffraction. The electrochemical properties of the complexes were also investigated.

(© Wiley-VCH Verlag GmbH & Co. KGaA, 69451 Weinheim, Germany, 2005)

Introduction

The interaction of arenes with 12-valence-electron (VE) metal complex fragments affords arene complexes. For instance, by using dicationic fragments [(ring)M]$^{2+}$ [(ring)M = Cp*Rh, Cp*Ir, (arene)Ru] in the form of their labile solvates with acetone, a great number of arene complexes [(ring)M(arene)]$^{2+}$ has been prepared.[1] A closely related reaction − the electrophilic stacking of sandwich compounds with [(ring)M]$^{n+}$ (n = 1, 2) fragments − has proved to be an effective method for the synthesis of cationic triple-decker complexes.[2] In particular, using this method, complexes with bridging five-electron ligands (cyclopentadienyl[3] and boratabenzene[4]) have been obtained. Herberich et al.[5] have prepared 30 VE triple-decker complexes [(ring)M(μ-η^5:η^5-C_4H_4BPh)CoCp]$^{2+}$ [(ring)M = Cp*Ir and (C_6Me_6)Ru] with a central four-electron borole ligand by reaction of the fragments [(ring)M]$^{2+}$ with the (*B*-phenylborole)cobalt complex [CpCo(η^5-C_4H_4BPh)] (**1**). In a similar reaction with the cyclohexyl-substituted analogue [CpCo(η^5-C_4H_4BCy)] we have synthesized the complexes [(ring)M(μ-η^5:η^5-C_4H_4BCy)CoCp]$^{2+}$ [(ring)M = Cp*Rh, (C_6H_6)Ru, (1,3,5-$C_6H_3Me_3$)Ru; Cy = cyclohexyl].[6]

[a] A. N. Nesmeyanov Institute of Organoelement Compounds, 28 ul. Vavilova, 119991 Moscow, GSP-1, Russian Federation
Fax: +7-095-135-5085
E-mail: arkudinov@ineos.ac.ru
[b] Dipartimento di Chimica, Universitá di Siena, Via Aldo Moro, 53100 Siena, Italy

It is noteworthy that in the case of the phenyl-substituted complexes **1** and [CpRh(η^5-C_4H_4BPh)] (**2**) there are two possible places for attack by the metalloelectrophile: the borole ring or the phenyl substituent. However, for the cobalt complex **1** only electrophilic attack at the borole ligand has been described.[5] Herein we report the reactions of the analogous rhodium complex **2** with dicationic fragments [(ring)M]$^{2+}$ as well as the results of structural and electrochemical study of the products.

Results and Discussion

Stacking Reactions

The electrophilic stacking reaction of **2** with the dicationic fragment [Cp*Co]$^{2+}$ (in the form of its nitromethane solvate)[7] yields the 30 VE triple-decker complex **3** as the sole product, which suggests that the electrophilic attack proceeds exclusively at the borole ring (Scheme 1).[8] The absence of a product formed by attack at the phenyl substituent is in accordance with the known fact that the fragment [Cp*Co]$^{2+}$ does not react with benzene under such conditions.[9]

On the contrary, in the case of a similar reaction with the [Cp*Rh]$^{2+}$ fragment (in the form of its nitromethane or acetone solvate) only the arene-type complex **5** was isolated (Scheme 2). However, it was shown by means of ^{1}H NMR spectroscopy that the starting materials disappear within 5 min in [D_3]nitromethane and the mixture formed contains

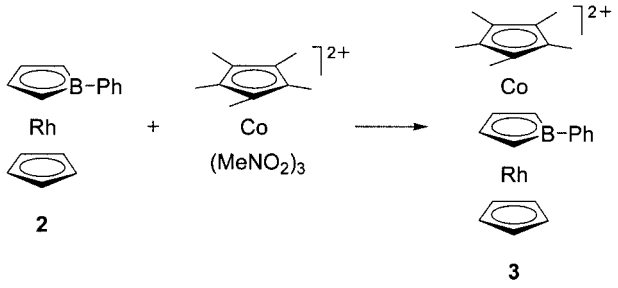

Scheme 1. Formation of the triple-decker complex **3**.

both complex **5** and the triple-decker complex **4** in a ratio of about 1:9. After 4 h the signals of **4** disappear and the intensities of the signals of **5** increase, thus suggesting that **4** is unstable at room temperature and transforms into the arene-type complex **5**. It may be concluded that the initial attack of $[Cp^*Rh]^{2+}$ proceeds at the borole ring with its subsequent transfer to the benzene ring.

The stacking reaction of **2** with the iridium-containing fragment $[Cp^*Ir]^{2+}$, as its $MeNO_2$ solvate, affords the RhIr triple-decker complex **6** which, according to ^1H NMR spectroscopy, contains an admixture of the arene-type complex **7** (ca. 6%) (Scheme 3). In contrast to **4**, both **6** and **7** are stable at room temperature and do not interconvert. Unfortunately, we were unable to purify **6** either by recrystallization or by chromatography. Nevertheless, the content of **7** in the product can be decreased to about 4% by lowing the reaction temperature to –15 °C; this suggests that the electrophilic attack is kinetically controlled. The use of acetone instead of $MeNO_2$ leads to a further decrease of the admixture content (0.8%), apparently due to a slowing of the process caused by the lower reactivity of the acetone solvate. The best purity achieved for the triple-decker **6** was more than 99%. In a similar manner, the reaction of **2** with $[(arene)Ru]^{2+}$ fragments (arene = 1,3,5-$C_6H_3Me_3$, C_6Me_6) yields the RhRu triple-decker complexes **8a**,**b** contaminated with the arene-type complexes **9a**,**b**. The best purity of **8a**,**b** (achieved using acetone as a solvent at –15 °C) was about 97%.

We studied the thermal transformation of the triple-decker complexes **6** and **8a**,**b**, and found that the RhIr complex **6** transforms into the diiridium analogue **10** in refluxing nitromethane, apparently as a result of a symmetrization reaction (Scheme 4);[10] the absence of the corresponding dirhodium complex $[CpRh(\mu\text{-}\eta^5\text{:}\eta^5\text{-}C_4H_4BPh)RhCp]^{2+}$ may be explained by its low stability. However, the reaction is rather slow (according to ^1H NMR spectroscopy the degree of conversion is about 30% after 12 h) and we were unable to obtain complex **10** in pure form. Obviously,

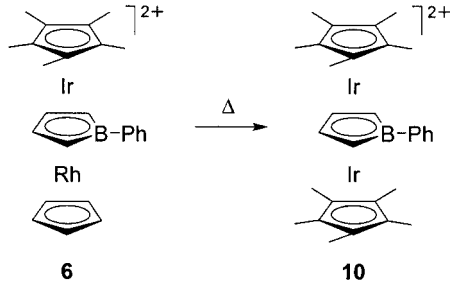

Scheme 4. Thermal transformation of complex **6**.

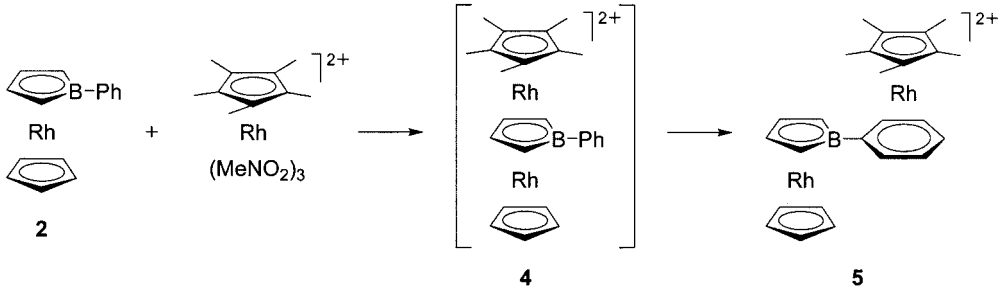

Scheme 2. Formation of the arene-type complex **5**.

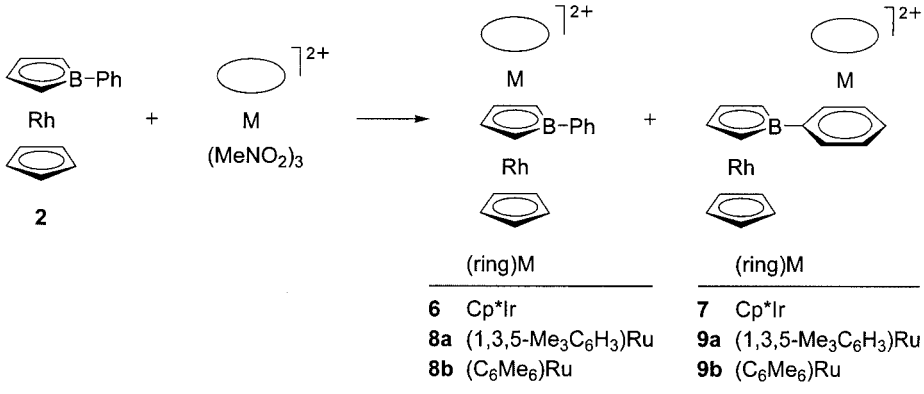

Scheme 3. Reactions of **2** with the fragments $[Cp^*Ir]^{2+}$ and $[(arene)Ru]^{2+}$.

 © 2005 Wiley-VCH Verlag GmbH & Co. KGaA, Weinheim

Table 1. ^1H and ^{11}B NMR spectroscopic data for complexes **2**[21] and **3**–**10**.[a]

	^1H NMR					^{11}B NMR	
	2-/5-H[b]	3-/4-H[b]	RhCp[c]	ML[c]	Ph[b]	C_4H_4B[d]	BF_4^- [c]
2	4.43[e]	5.28[e]	5.17[e]		7.64 (H_o), 7.24 (H_m, H_p)[e]	16.8[f]	
3[g]	5.46	6.57	6.16	1.85 (Cp*)	7.95 (H_o), 7.53 (H_m, H_p)	14.0	–0.1
4[h][i]	5.30	6.24	6.12	1.83 (Cp*)	7.71 (H_o), 7.46 (H_m, H_p)	[j]	[j]
5[g]	4.83	5.62	5.48	2.20 (Cp*)	7.60 (H_o), 7.42 (H_m, H_p)	10.2	–0.2
6[g]	5.55	6.48	6.44	1.97 (Cp*)	7.78 (H_o), 7.46 (H_m), 7.37 (H_p)	10.2	–0.2
7[g][i]	4.79	5.60	5.50	2.32 (Cp*)	[k]	[k]	[k]
8a[g]	5.44	6.43	6.35	6.36 ($C_6H_3Me_3$) 2.21 ($C_6H_3Me_3$)	7.84 (H_o), 7.42 (H_m, H_p)	13.7	–0.1
8b[g]	5.29	6.30	6.24	2.26 (C_6Me_6)	7.78 (H_o), 7.49 (H_m), 7.43 (H_p)	13.0	–0.1
9a[g][i]	4.79	5.57	5.46	6.92 ($C_6H_3Me_3$) 2.44 ($C_6H_3Me_3$)	7.16 (H_o), 6.86 (H_m, H_p)	[k]	[k]
9b[g][i]	4.79	5.62	5.45	2.52 (C_6Me_6)	6.83 (H_m, H_p)	[k]	[k]
10[g][i]	5.15	6.11		1.93 (Cp*)	[l]	[l]	[l]

[a] Chemical shifts in ppm. [b] Multiplets. [c] Singlets. [d] Broad singlets. [e] In $CDCl_3$. [f] In C_2Cl_4. [g] In $(CD_3)_2CO$. [h] In CD_3NO_2. [i] Detected in a mixture with other products. [j] Difficult to measure owing to instability of **4**. [k] Difficult to measure owing to overlap with signals of other products. [l] Difficult to measure due to overlap with signals of the starting compound **6**.

the nucleophilic degradation[3d,11] by solvent molecules is the first stage of this process. In contrast to **6**, the RhRu complexes **8a**,**b** are stable in refluxing nitromethane.

NMR Spectroscopy

The ^1H and ^{11}B NMR spectroscopic data for complexes **3**–**10** are given in Table 1. For the triple-decker complexes **3**, **4**, **6** and **8** the signals of the borole ring protons are strongly shifted downfield ($\Delta\delta$ = 0.7–1.3 ppm) from the corresponding signals for the sandwich compound **2**. For the arene-type complexes **5**, **7** and **9** these signals are shifted in the same direction but to a lesser extent ($\Delta\delta$ = 0.3–0.4 ppm), thus making ^1H NMR spectroscopy sufficiently informative to distinguish between triple-decker and arene-type structures.

In the ^{11}B NMR spectra of the triple-decker complexes **3**, **6** and **8** the signals of the boron atoms of the borole ligand are shifted upfield ($\Delta\delta$ = 2.8–6.6 ppm) from the corresponding signal for **2**. An analogous shift ($\Delta\delta$ = 2.7–5.0 ppm) was observed earlier for the related cobalt-containing triple-decker complexes [(ring)M(μ-η⁵:η⁵-C_4H_4BR)-CoCp]²⁺ (R = Ph, Cy).[5a,6] For the arene-type complex **5** the signal of the borole ring boron atom is also shifted upfield ($\Delta\delta$ = 6.6 ppm), thus suggesting that ^{11}B NMR spectroscopy is not useful for distinguishing between triple-decker and arene-type structure.

X-ray Diffraction Study

Structure of the Sandwich Complex 2

Complex **2** has the expected sandwich structure (Figure 1). Selected bond lengths and angles are given in Table 2. The planes of the Cp and C_4H_4B cycles are approximately parallel; the dihedral angle Cp/C_4H_4B is equal to 2.42°. The Rh–B [2.304(4) Å] and Rh–C(C_4H_4B) [Rh–C 2.122(4)–2.198(4) Å, av. 2.16 Å] bonds are somewhat shorter than the corresponding bonds in [(η⁵-C_4H_4BPh)-$Rh(PPh_3)_2Cl$] [Rh–B 2.400(5) Å; Rh–C 2.137(4)–2.236(4) Å, av. 2.19 Å].[12] This fact is probably connected to stronger back-donation in the case of **2** as a consequence of the strong electron-donor effect of Cp. An analogous shortening of the Rh–B and Rh–C bonds in [(9-SMe_2-7,8-$C_2B_9H_{10}$)RhCp*]⁺ compared with [(9-SMe_2-7,8-$C_2B_9H_{10}$)Rh(dppe)Cl]⁺ (dppe = $Ph_2PCH_2CH_2PPh_2$) has been reported.[13]

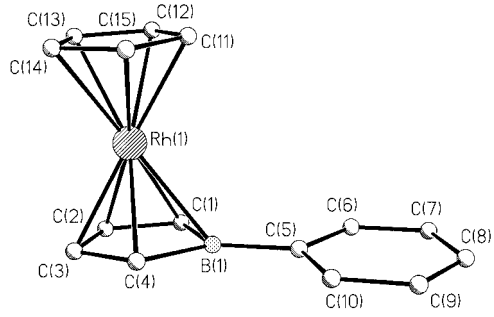

Figure 1. Structure of complex **2**.

Table 2. Selected bond lengths [Å] and angles [°] for complex **2**.

Rh(1)–C(1)	2.198(4)	Rh(1)–C(15)	2.150(5)
Rh(1)–C(2)	2.145(4)	Rh(1)–B(1)	2.304(4)
Rh(1)–C(3)	2.122(4)	C(1)–C(2)	1.425(5)
Rh(1)–C(4)	2.180(4)	C(2)–C(3)	1.445(7)
Rh(1)–C(11)	2.174(4)	C(3)–C(4)	1.418(6)
Rh(1)–C(12)	2.195(4)	B(1)–C(1)	1.543(6)
Rh(1)–C(13)	2.226(4)	B(1)–C(4)	1.547(6)
Rh(1)–C(14)	2.197(5)	B(1)–C(5)	1.562(5)
C(1)–C(2)–C(3)	109.2(4)	C(1)–B(1)–C(4)	101.6(3)
C(2)–C(3)–C(4)	109.9(4)	C(1)–B(1)–C(5)	128.8(4)
C(3)–C(4)–B(1)	109.5(4)	C(4)–B(1)–C(5)	129.5(4)
B(1)–C(1)–C(2)	109.7(4)		

Structures of the Triple-Decker Complexes 6(BF₄)₂ and 8a(BF₄)₂

The structures of complexes **6**$(BF_4)_2$ and **8a**$(BF_4)_2$ contain separated **6** or **8a** cations and BF_4^- anions. The cations

 © 2005 Wiley-VCH Verlag GmbH & Co. KGaA, Weinheim

have triple-decker structures formed by three cyclic frameworks, between which two metal atoms are located (Figure 2). Selected bond lengths and angles are given in Tables 3 and 4. In both cases the planes of the cyclic ligands are almost coplanar (dihedral angles Cp*/C_4H_4B = 0.08° and C_4H_4B/Cp = 1.32° for **6**; $C_6H_3Me_3/C_4H_4B$ = 2.39° and C_4H_4B/Cp = 1.36° for **8a**). It was shown earlier that in the case of triple-decker complexes with bridging boratabenzene and pentaphospholyl ligands all bonds in the triple-decker fragment M(ring)M′ are longer than analogous bonds in related mononuclear sandwich compounds.[4b,11] The same pattern, viz. elongation of all bonds in the fragment M(μ-η^5:η^5-C_4H_4BPh)Rh in comparison with the corresponding bonds in **2**, is observed for **6** and **8a**. For example, the B–C [1.593(11) and 1.617(10) Å, av. 1.605 Å] and C–C [1.478(10), 1.506(10), and 1.488(10) Å, av. 1.491 Å)] bonds in the borole ring of **6** are considerably longer than the corresponding bonds in **2** [B–C 1.543(6) and 1.547(6) Å, av. 1.545 Å; C–C 1.425(5), 1.445(7), and 1.418(6) Å, av. 1.429 Å]. Furthermore, the Rh–C(C_4H_4BPh) bonds in **6** [2.174(7)–2.203(8) Å, av. 2.19 Å] and in **8a** [2.182(4)–2.216(4) Å, av. 2.20 Å] are longer than the corresponding bonds in **2** (av. 2.16 Å). This elongation is apparently connected with a loosening of the bonds upon bifacial coordination of the C_4H_4BPh ligand with two metal atoms as compared with its monofacial coordination with only one metal atom. The elongation of the metal-to-ring distances (Δ) in **6** and **8a** in comparison with **2** could be also expected. However, Δ(Rh···C_4H_4BPh) in **6** (1.778 Å) and **8a** (1.795 Å) is not longer, and is even somewhat shorter, than the corresponding distance in **2** (1.792 Å), which may be connected with a compensation of the expected elongation of Δ by shortening of the metal-to-ring distance as a result of the increase of the ring size.

Table 3. Selected bond lengths [Å] and angles [°] for cation **6** (for one of two independent molecules).

Ir(1)–C(1)	2.215(7)	Rh(1)–C(4)	2.174(7)
Ir(1)–C(2)	2.209(7)	Rh(1)–C(11)	2.148(8)
Ir(1)–C(3)	2.208(7)	Rh(1)–C(12)	2.154(8)
Ir(1)–C(4)	2.232(7)	Rh(1)–C(13)	2.164(8)
Ir(1)–C(16)	2.171(8)	Rh(1)–C(14)	2.173(8)
Ir(1)–C(17)	2.168(7)	Rh(1)–C(15)	2.176(8)
Ir(1)–C(18)	2.185(8)	Rh(1)–B(1)	2.289(8)
Ir(1)–C(19)	2.178(7)	C(1)–C(2)	1.478(10)
Ir(1)–C(20)	2.151(8)	C(2)–C(3)	1.506(10)
Ir(1)–B(1)	2.282(9)	C(3)–C(4)	1.488(10)
Rh(1)–C(1)	2.203(8)	B(1)–C(1)	1.593(11)
Rh(1)–C(2)	2.184(7)	B(1)–C(4)	1.617(10)
Rh(1)–C(3)	2.181(7)	B(1)–C(5)	1.541(11)
C(1)–C(2)–C(3)	108.9(6)	C(1)–B(1)–C(4)	99.8(6)
C(2)–C(3)–C(4)	108.4(6)	C(1)–B(1)–C(5)	131.0(6)
C(3)–C(4)–B(1)	111.0(6)	C(4)–B(1)–C(5)	129.2(7)
B(1)–C(1)–C(2)	111.9(6)		

Table 4. Selected bond lengths [Å] and angles [°] for cation **8a**.

Rh(1)–C(1)	2.216(4)	Ru(1)–C(16)	2.204(4)
Rh(1)–C(2)	2.194(4)	Ru(1)–C(17)	2.226(4)
Rh(1)–C(3)	2.182(4)	Ru(1)–C(18)	2.206(4)
Rh(1)–C(4)	2.207(4)	Ru(1)–C(19)	2.233(4)
Rh(1)–C(11)	2.154(4)	Ru(1)–C(20)	2.200(4)
Rh(1)–C(12)	2.161(4)	Ru(1)–C(21)	2.201(4)
Rh(1)–C(13)	2.182(4)	Ru(1)–B(1)	2.279(4)
Rh(1)–C(14)	2.189(4)	C(1)–C(2)	1.470(6)
Rh(1)–C(15)	2.166(4)	C(2)–C(3)	1.491(6)
Rh(1)–B(1)	2.274(5)	C(3)–C(4)	1.468(6)
Ru(1)–C(1)	2.212(4)	B(1)–C(1)	1.596(6)
Ru(1)–C(2)	2.184(4)	B(1)–C(4)	1.600(6)
Ru(1)–C(3)	2.182(4)	B(1)–C(5)	1.552(6)
Ru(1)–C(4)	2.205(4)		
C(1)–C(2)–C(3)	109.2(4)	C(1)–B(1)–C(4)	100.9(3)
C(2)–C(3)–C(4)	109.5(3)	C(1)–B(1)–C(5)	127.7(4)
C(3)–C(4)–B(1)	110.0(3)	C(4)–B(1)–C(5)	131.3(4)
B(1)–C(1)–C(2)	110.3(3)		

Structure of the Arene-Type Complex 5(BF$_4$)$_2$

The structure of complex **5**$(BF_4)_2$ contains separated cation **5** and BF_4^- anions. The cation **5** consists of two sandwich moieties [CpRh(η^5-C_4H_4B)] and [Cp*Rh(η^6-C_6H_5)] connected to each other by a C–B σ-bond (Figure 3). Selected bond lengths and angles are given in Table 5. The planes of the cyclic ligands in each sandwich moiety are almost coplanar (the dihedral angles Cp/C_4H_4B and Cp*/C_6H_5 are equal to 3.52° and 0.47°, respectively). All bonds in the [CpRh(η^5-C_4H_4B)] moiety are very similar in length to the corresponding bonds in **2**, thus indicating that coor-

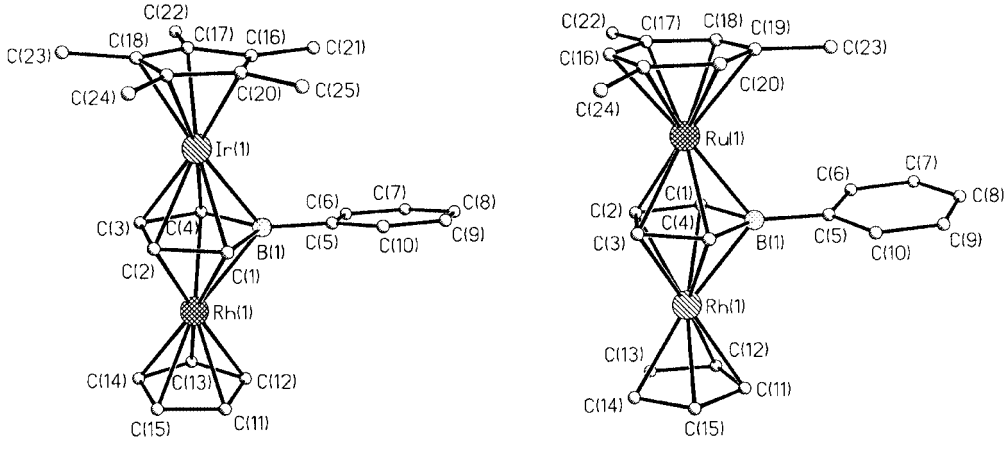

Figure 2. Structures of the triple-decker cations **6** (left) and **8a** (right).

 © 2005 Wiley-VCH Verlag GmbH & Co. KGaA, Weinheim

dination of the metal atom at the phenyl substituent of **2** does not lead to serious changes in the sandwich moiety.

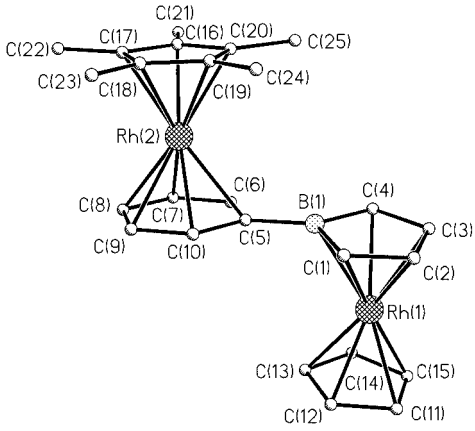

Figure 3. Structure of the arene-type cation **5**.

Table 5. Selected bond lengths [Å] and angles [°] for cation **5**.

Rh(1)–C(1)	2.187(3)	Rh(2)–C(9)	2.259(3)
Rh(1)–C(2)	2.144(3)	Rh(2)–C(10)	2.263(3)
Rh(1)–C(3)	2.159(3)	Rh(2)–C(16)	2.167(3)
Rh(1)–C(4)	2.188(3)	Rh(2)–C(17)	2.169(3)
Rh(1)–C(11)	2.207(4)	Rh(2)–C(18)	2.164(3)
Rh(1)–C(12)	2.188(3)	Rh(2)–C(19)	2.161(3)
Rh(1)–C(13)	2.199(3)	Rh(2)–C(20)	2.171(3)
Rh(1)–C(14)	2.183(3)	C(1)–C(2)	1.422(5)
Rh(1)–C(15)	2.204(3)	C(2)–C(3)	1.441(5)
Rh(1)–B(1)	2.227(4)	C(3)–C(4)	1.432(5)
Rh(2)–C(5)	2.299(3)	B(1)–C(1)	1.533(5)
Rh(2)–C(6)	2.254(3)	B(1)–C(4)	1.545(5)
Rh(2)–C(7)	2.247(3)	B(1)–C(5)	1.561(5)
Rh(2)–C(8)	2.244(3)		
C(1)–C(2)–C(3)	110.1(3)	C(1)–B(1)–C(4)	102.9(3)
C(2)–C(3)–C(4)	109.5(3)	C(1)–B(1)–C(5)	127.5(3)
C(3)–C(4)–B(1)	108.6(3)	C(4)–B(1)–C(5)	129.0(3)
B(1)–C(1)–C(2)	109.0(3)		

Electrochemistry

In principle, the sandwich unit **2** constitutes a poor redox-active component for polynuclear species planned to display intramolecular electronic communication. In fact, in CH_2Cl_2 solution it undergoes an irreversible oxidation at high potential values (controlled potential coulometry consumed 1.5 electrons per molecule, thus indicating that the probable degradation of [**2**]$^+$ leads to redox active by-products). In reality, as we will show, its linking to half-sandwich transition metal units modifies the overall electronic situation such as to improve significantly the electron-transfer ability of the resulting dinuclear species.

As the most representative example, Figure 4 (a) shows the voltammetric picture exhibited by the 30 VE triple-decker CoRh dication [**3**]$^{2+}$.

Two sequential, coulometrically measured one-electron reductions with features of chemical reversibility are displayed, which are interposed by a spurious peak-system, which is assigned to strong adsorption of the reagent.[14] In

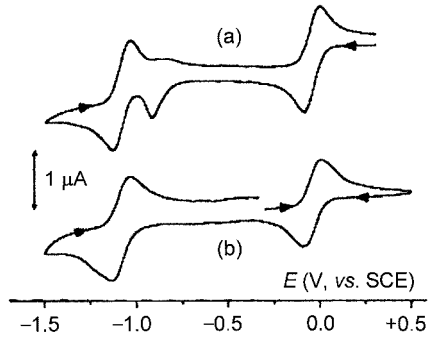

Figure 4. Cyclic voltammetric responses recorded at a platinum electrode in CH_2Cl_2 solution of [**3**]$^{2+}$ (1.0×10^{-3} M): (a) original solution; (b) after exhaustive electrolysis in correspondence of the first reduction. [NBu_4][PF_6] (0.2 M) supporting electrolyte. Scan rate 0.2 V s^{-1}.

fact, as shown in Figure 4 (b), the cyclic voltammetric profile obtained on the exhaustively one-electron-reduced solution (E_w = –0.5 V) no longer exhibits such an anomalous process. More importantly, it can be seen that the response after exhaustive electrolysis is quite complementary to the original one, thus confirming the stability of the corresponding monocation [**3**]$^+$ not only over the short timescale of cyclic voltammetry, but also over the longer time of macroelectrolysis. No traces of oxidation of the parent subunit **2** were detected.

As a matter of fact, analysis of the cyclic voltammograms relevant to the first reduction (due to the above-cited absorption phenomena, mechanical cleaning of the electrode was needed after each scan) with a scan rate varying from 0.02 V s^{-1} to 1.00 V s^{-1} agrees with the occurrence of a simple, chemically and electrochemically reversible, one-electron reduction. In fact: (i) the current ratio i_{pa}/i_{pc} is constantly equal to unity; (ii) the current function $i_{pc} \cdot v^{-1/2}$ is substantially constant; and (iii) the peak-to-peak separation approaches the theoretical value of 59 mV. It should be noted that the electrochemical reversibility indicates that the monocation substantially maintains the geometry of the dication precursor.[14]

In reality, among the dinuclear complexes studied here, the appearance of two consecutive one-electron reductions is essentially limited to [**3**]$^{2+}$, as the other dications (except for [**8a**]$^{2+}$) only display a one-electron reduction, the extent of chemical reversibility of which varies with the nature of the different half-sandwich subunit. As a matter of fact, the i_{pa}/i_{pc} current ratio for the pertinent reduction process is lower than unity in all cases at low scan rate and progressively tends to unity at high scan rates.

Table 6 compiles the formal electrode potentials of the above-cited redox changes, together with the lifetime ($t_{1/2}$) of the different monocations, which, because of the substantial invariance of the responses with concentration, have been assumed to be coupled to a first-order chemical complication.[14]

Apart from the expected roles of the inductive effects of the half-sandwich units added to **2** upon the electrode potentials, the higher stability of the triple-decker mono-

 © 2005 Wiley-VCH Verlag GmbH & Co. KGaA, Weinheim

Table 6. Formal electrode potentials (V, vs. SCE), peak-to-peak separations [mV], current ratios and lifetimes [s] for the electrogenerated products of the redox changes exhibited by the complexes under study in CH_2Cl_2 solution.

Complex	E_p[a][b]	$E°'_{2+/+}$	ΔE_p[b]	i_{pa}/i_{pc}[c]	$t_{1/2\ (monocation)}$	$E°'_{+/0}$	ΔE_p[b]	i_{pa}/i_{pc}[c]
2	+1.12							
$[\mathbf{3}]^{2+}$		–0.04	70	1	stable	–1.08	90	1
$[\mathbf{6}]^{2+}$		–0.31	66	0.7	12			
$[\mathbf{8a}]^{2+}$		–0.26	71	0.8	26	–1.06[a][b]		
$[\mathbf{5}]^{2+}$	+1.65[d]	–0.55	62	0.4[e]	0.06			

[a] Peak-potential value for irreversible processes. [b] Measured at 0.2 V s^{-1}. [c] Measured at 0.05 V s^{-1}. [d] Two-electron process. [e] Measured at 1.0 V s^{-1}.

cations with respect to the extreme lability of the arene-type monocation $[\mathbf{5}]^+$ deserves attention.

Spectroelectrochemistry of the $[3]^{2+}/[3]^+$ Redox Change

UV/Vis spectroelectrochemical measurements on the one-electron reduction of the dication $[\mathbf{3}]^{2+}$ were performed in CH_2Cl_2 solution at 298 K using an OTTLE cell. As Figure 5 shows, the original red dication displays a prominent band at λ_{max} = 320 nm together with a few less-intense transitions at 265, 449 and 520 nm. Upon reduction, the intensity of such bands progressively decreases, except for the transition at 265 nm, which progressively increases with a concomitant blue-shift to 244 nm.

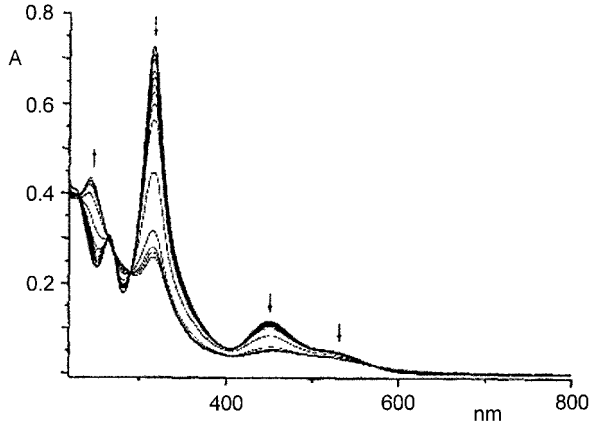

Figure 5. UV/Vis spectra recorded in CH_2Cl_2 solution of $[\mathbf{3}]^{2+}$ (1.0×10^{-3} M) upon one-electron reduction in an OTTLE cell. $[NBu_4][PF_6]$ (0.2 M) supporting electrolyte. E_w = –0.1 V vs. Ag pseudoreference electrode.

The appearance of four isosbestic points, which are due to the mixture of $[\mathbf{3}]^{2+}/[\mathbf{3}]^+$, further supports the chemical reversibility of the electron transfer.

In order to test for a possible assignment of the two lowest energy bands of $[\mathbf{3}]^{2+}$ as metal-to-metal charge transfer (MMCT) absorptions, their solvent dependence concerned with both position and band width was checked. Figure 6 shows the pertinent spectra in tetrahydrofuran, dichloromethane and acetonitrile. In spite of the small blue-shift observed on going from CH_2Cl_2 to the better donor solvents THF and MeCN, the measured half-height band width, $\Delta\nu_{1/2(exp)}$, is too small with respect to the theoretical one, which for a Class II mixed-valent complex is expected to be: $\Delta\nu_{1/2} = [2310(\nu_{max} - \Delta E°)]^{1/2}$, where $\Delta E°$ is the separation of potentials (in cm^{-1}) for the formal redox couples in non-interacting $[CpRh(\eta^5\text{-}C_4H_4BPh)]$ (complex **2**) and $[Cp^*Co(\eta^5\text{-}C_4H_4BPh)]$.[15] In fact, assuming that a MMCT for $[\mathbf{3}]^{2+}$ would involve a Co^{III}-Rh^{III} to Co^{II}-Rh^{IV} transition, a value of $\Delta E°$ = 1.15 V (= 9275 cm^{-1}) may be used, taking into account the $E°'$ measured for the Rh^{III}/Rh^{IV} redox change in $[\mathbf{2}]^+$ (+1.12 V) and approximating the $E°$ of the Co^{II}/Co^{III} redox change in $[Cp^*Co(\eta^5\text{-}C_4H_4BPh)]$ to the formal electrode potential of the first reduction of $[\mathbf{3}]^{2+}$ ($E°'$ = –0.03 V). Accordingly, we obtain $\Delta\nu_{1/2(calc)}$ = 4860 cm^{-1} and $\Delta\nu_{1/2(calc)}$ = 5492 cm^{-1} for the two lowest energy bands in dichloromethane, which is almost two times

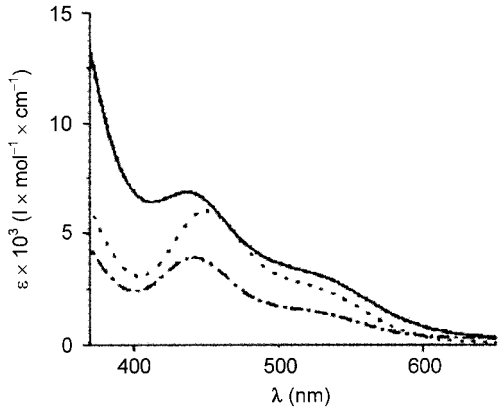

Figure 6. Comparison of the optical spectra of $[\mathbf{3}]^{2+}$ in: MeCN (–), CH_2Cl_2 (·····), THF (·–·–·).

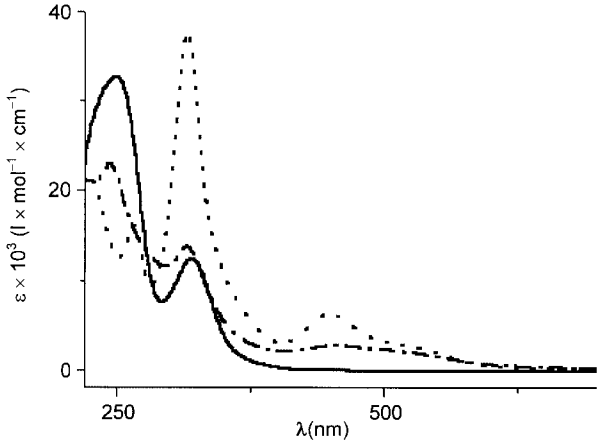

Figure 7. Comparative optical spectra of: (a) **2** (1.4×10^{-3} M)(); (b) $[\mathbf{3}]^{2+}$ (1.0×10^{-3} M) (·····); (c) $[\mathbf{3}]^+$ (1.0×10^{-3} M) (·–·–·). CH_2Cl_2 solution.

 © 2005 Wiley-VCH Verlag GmbH & Co. KGaA, Weinheim

greater than the experimental values $\Delta\nu_{1/2(exp)}$ = 2862 cm^{-1} and $\Delta\nu_{1/2(exp)}$ = 2852 cm^{-1}, respectively. This result therefore rules out the MMCT assignment.

Comparison of the UV/Vis spectra of the triple-deckers [**3**]$^{2+}$ and [**3**]$^{+}$ with the subunit **2** (Figure 7) suggests that the MLCT absorptions at 320 and 244 nm are substantially contributed by the rhodium subunit, whereas the d-d transitions of the Co^{III}/Co^{II} centres in [**3**]$^{2+/+}$ could be responsible for the absorptions at wavelengths higher than 400 nm.

EPR Measurements of the Electrogenerated Monocation [3]$^{+}$

Figure 8 shows the low-temperature X-band EPR spectrum of the electrogenerated 31 VE triple-decker monocation [**3**]$^{+}$ in CH_2Cl_2 solution.

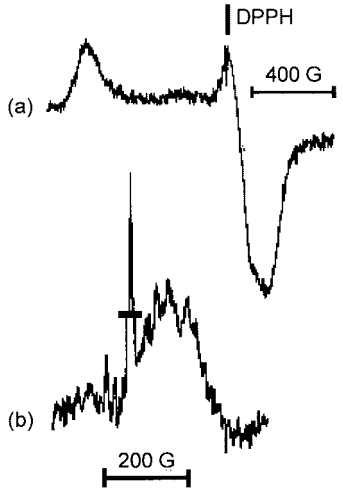

Figure 8. X-band EPR spectrum of [**3**]$^{+}$ in CH_2Cl_2 solution. T = 100 K: (a) first derivative; (b) second derivative.

The broad spectrum shown in Figure 8 (see part a; peak-to-peak separation ca. 1050(5) G) exhibits three rhombic signals with g_i values [g_l = 2.497(8); g_m = 1.971(8); g_h = 1.899(8); $<g>$ = 1/3(g_l + g_m + g_h) = 2.122(8), with l, m and h standing for low-, medium- and high-field, respectively] that are very different from that of a single unpaired electron ($g_{electron}$ = 2.0023). In the second derivative mode, the two partially overlapped high-field signals display resolution of the underlying hpf signals.

A lineshape analysis can be carried out taking into account the anisotropic S = 1/2 Electron Spin Hamiltonian (Zeeman interaction) with resolution of the metallic hyperfine (hpf) signals (IAS interaction).[16]

The second derivative mode is crucial for the understanding of the nature of the metal ion directly involved in the anisotropic IAS interaction. In fact, as shown in Figure 8(see part b), in the high-field region it displays a structured hpf multiplet constituted by almost six well-separated signals of equal intensity [1:1:1:1:1:1; $a_{m,l}$ = 48(8) G], which testifies to the direct coupling of the S = 1/2 unpaired electron with the magnetically active ^{59}Co nucleus [I(^{59}Co) = 7/2; natural abundance = 100%]. The theoretically expected octuplet typical of low-spin Co^{II} centres is not completely resolved as a consequence of both the actual anisotropic linewidth, which affects the overall signals, and the active A-strain effects, which narrow the eight hpf signals to different degrees.[16] The lineshape analysis rules out the assignment of the present high field multiplet to the Rh^{II} subunit in that the expected anisotropic signals should exhibit poorly resolved doublets [I(^{103}Rh) = 1/2; natural abundance = 100%] and the corresponding g_i signals would resonate at different field values.[17]

Moreover, no attribution of the detected multiplet to magnetically coupled ligand ^{1}H nuclei can be proposed as the actual number and the relative intensities of such signals are totally in contrast with the present spectral resolution.

The simulated geometry and the pertinent MO diagram distribution displayed in Figure 9 below confirm the above analysis. In fact, the SOMO of the electrogenerated monocation is mainly constituted by the 3d Co^{II} AOs, with a very minor contribution arising from the Rh^{III} centre and the H and C of the aromatic ligands. On this basis, the intense and narrow signal overlapping the second derivative multiplet is probably due to an organic radical by-product.

Raising the temperature to the glassy-fluid transition (T = 178 K) the large axial spectrum collapses into a broad and unresolved isotropic signal. The lack of Co^{II} hpf resolution in fluid solution is not surprising considering the large Co^{II} λ spin-orbit coupling constant and possible structural anisotropies which fasten the electron spin relaxation rates.[16,18]

At room temperature the spectrum exhibits features compatible with those recorded under glassy conditions [g_{iso} = 2.02(8) and ΔH_{iso} = 470(8) G], although no hpf splittings are detected [likely due to the actual linewidth, (ΔH_{iso}/7 = 67(8) G) $\geq$ a_{iso}(Co)]. These findings suggest that the primary geometry of the monocation is maintained under different experimental conditions. Upon fast refreezing, the previous rhombic signal is partially recovered as a consequence of some chemical lability under not perfectly inert atmosphere.

Molecular Orbital Calculations for [3]$^{2+}$

In order to support the interpretation of the EPR spectrum of the 31 VE triple-decker cation [**3**]$^{+}$, an extended Hückel analysis was carried out. Fragment analyses were performed for a model built by using bond distances and angles taken as the average of the experimental values in analogous complexes.[19] It has been shown previously that the extended Hückel method combined with INDO calculations gives reliable results for μ-borole triple-decker complexes.[20]

This model, and fragments thereof, together with the reference system, are shown at the bottom of Figure 9, which depicts the interaction between the orbitals of the [Cp*Co]$^{2+}$ (shown on the right) and [CpRh(η^5-C_4H_4BPh)] (shown on the left) fragments that generate the [CpRh(μ-η^5:η^5-C_4H_4BPh)CoCp*]$^{2+}$ triple-decker.

 © 2005 Wiley-VCH Verlag GmbH & Co. KGaA, Weinheim

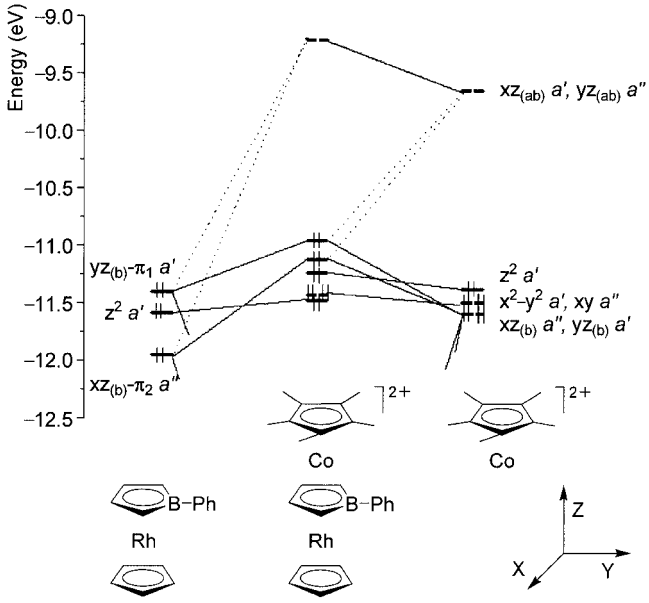

Figure 9. FMO interaction between the frontier orbitals of the $[Cp^*Co]^{2+}$ and $[CpRh(\eta^5\text{-}C_4H_4BPh)]$ fragments to give the $[CpRh(\mu\text{-}\eta^5\text{:}\eta^5\text{-}C_4H_4BPh)CoCp^*]^{2+}$ triple-decker.

The symmetry labels used are those of the C_s point group, which is the lowest symmetry exhibited by the triple-decker model or fragments discussed here, and is imposed by $[CpRh(\mu\text{-}\eta^5\text{:}\eta^5\text{-}C_4H_4BPh)CoCp^*]^{2+}$. The frontier orbital region is characterized by two orthogonal three-orbital-four-electron systems. Indeed, the bonding and antibonding combinations Cp*(π)-Co(d_{xz}) and Cp*(π)-Co(d_{yz}) spawn two degenerate couples of orbitals both having the right a′ and a″ symmetry and the appropriate fit in energy to interact with the bonding set of orbitals Cp(π)-Rh(d_{xz})-C_4H_4BPh(π) and Cp(π)-Rh(d_{yz})-C_4H_4BPh(π). The repulsive interaction between two filled sets of orbitals, which gives rise to the antibonding HOMO and HOMO–1, is therefore stabilised by the interaction with the empty antibonding Cp*(π)-Co(d_{xz}) and Cp*(π)-Co(d_{yz}) orbitals. As a consequence of this interaction, two almost degenerate LUMOs are present, which are antibonding combinations of the fragments $[CpRh(\eta^5\text{-}C_4H_4BPh)]$ and CoCp*, with 33% contribution of Co(d_{xz}) or Co(d_{yz}) and only 4% of Rh(d_{xz}) or Rh(d_{yz}). One of these orbitals is shown in Figure 9, where the major contribution of the cobalt-containing half is evident.

According to these findings, both reduction processes of the 30 VE cation $[\mathbf{3}]^{2+}$ involve mainly the cobalt atom. This is in agreement with the EPR analysis, which also supports a predominant contribution of cobalt in the SOMO of the 31 VE cation $[\mathbf{3}]^{+}$. The absence of oxidation processes for $[\mathbf{3}]^{2+}$ in the experimental window, which is in contrast with the higher energy of its HOMO with respect to **2**, may be explained by the positive charge of this complex, which, on an electrostatic basis, would inhibit any further electron removal.

Conclusions

The electrophilic attack of dicationic fragments $[(ring)M]^{2+}$ has been shown to proceed mainly at the borole ring of the *B*-phenylborole complex **2** to give 30 VE triple-decker complexes $[CpRh(\mu\text{-}\eta^5\text{:}\eta^5\text{-}C_4H_4BPh)M(ring)]^{2+}$. These complexes are stable when (ring)M is Cp*Co, Cp*Ir and (arene)Ru. However, the Cp*Rh analogue **4** transforms into the arene-type complex **5** at room temperature. Comparison of X-ray structural data for complexes **2**, **5**, **6** and **8a** reveals that the coordination of $[(ring)M]^{2+}$ species to the borole ring of **2** leads to elongation of the bonds within this ring, whereas the coordination to the benzene ring does not cause significant changes in the bonds within the borole ring.

The electrochemical data demonstrate the much higher stability of the 31 VE triple-decker monocations $[\mathbf{3}]^{+}$, $[\mathbf{6}]^{+}$ and $[\mathbf{8a}]^{+}$ (formed by one-electron reduction of the corresponding dications) compared with the 31 VE arene-type monocation $[\mathbf{5}]^{+}$. For instance, $[\mathbf{3}]^{+}$ is stable not only over the short times of cyclic voltammetry, but also over the long times of macroelectrolysis. UV/Vis and EPR spectral measurements as well as MO calculations suggest that the reduction process $[\mathbf{3}]^{2+}/[\mathbf{3}]^{+}$ involves mainly the cobalt atom.

Experimental Section

General: The reactions were carried out under an inert atmosphere in dry solvents. The isolation of products was conducted in air. Starting materials **2**,[21] $[Cp^*CoCl_2]_2$,[22] $[Cp^*RhCl_2]_2$,[23] $[Cp^*IrCl_2]_2$,[23] $[(\eta^6\text{-}C_6H_3Me_3\text{-}1,3,5)RuCl_2]_2$[24] and $[(\eta^6\text{-}C_6Me_6)RuCl_2]_2$[25] were prepared as described in the literature. ^1H and $^{11}B\{^1H\}$ NMR spectra were recorded on a Bruker AMX-400 spectrometer (^1H: 400.13; ^{11}B: 128.38 MHz) relative to the residual protons of the solvents (^1H) or $BF_3{\cdot}Et_2O$ (^{11}B, external standard). Materials and apparatus for electrochemistry and joint EPR spectroscopy have been described elsewhere.[26] Unless otherwise specified, potential values are referred to the Saturated Calomel Electrode (SCE). Under the present experimental conditions, the one-electron oxidation of ferrocene occurs at $E^{\circ\prime}$ = +0.39 V. The UV/Vis spectroelectrochemical measurements were carried out using a Perkin–Elmer Lambda 900 UV/Vis spectrophotometer and an OTTLE (optically transparent thin-layer electrode) cell[27] equipped with a Pt minigrid working electrode (32 wires/cm), a Pt minigrid auxiliary electrode, an Ag wire pseudoreference and CaF_2 windows. The electrode potential was controlled during electrolysis by an Amel potentiostat 2059 equipped with an Amel function generator 568. Nitrogen-saturated solutions of the compound under study were used with $[NBu_4][PF_6]$ (0.2 M) as supporting electrolyte. The working potential was fixed at the peak potential of the process under study and the spectra were collected stepwise after each 2 min electrolysis. Extended Hückel calculations were performed using the CACAO98 for Windows programs package.[28] Bond distances and angles of the model molecule were taken as the average of the experimental values. Slater orbital ionization energies were corrected from the default ones by taking H_{ii} from a set of values calculated by DFT theory.[29] The exponentials of the Slater orbitals were taken from the program library.

Synthesis of $3(BF_4)_2$: A mixture of $[Cp^*CoCl_2]_2$ (43 mg, 0.08 mmol) and $AgBF_4{\cdot}3$ dioxane (150 mg, 0.33 mmol) in $MeNO_2$ (1 mL) was

 © 2005 Wiley-VCH Verlag GmbH & Co. KGaA, Weinheim

stirred for 0.5 h at room temperature. The precipitate of AgCl was centrifuged off and the solution obtained was added to **2** (50 mg, 0.16 mmol). The reaction mixture was stirred for 2 h. Diethyl ether (ca. 10 mL) was then added to precipitate **3**$(BF_4)_2$ as a red solid, which was reprecipitated twice from nitromethane by addition of diethyl ether. Yield 50 mg (46%). $C_{25}H_{29}B_3CoF_8Rh$ (675.76): calcd. C 44.44, H 4.33; found C 44.37, H 4.25.

Synthesis of 5$(BF_4)_2$: A mixture of $[Cp^*RhCl_2]_2$ (40 mg, 0.06 mmol) and $AgBF_4$·3 dioxane (120 mg, 0.26 mmol) in $MeNO_2$ or Me_2CO (1 mL) was stirred for 0.5 h at room temperature. The precipitate of AgCl was centrifuged off and the solution obtained was added to **2** (40 mg, 0.13 mmol). The reaction mixture was stirred for 2 h. Diethyl ether (ca. 10 mL) was then added to precipitate **5**$(BF_4)_2$ as a yellow solid, which was reprecipitated twice from acetone by addition of diethyl ether. Yield 65 mg (70%). $C_{25}H_{29}B_3F_8Rh_2$ (719.72): calcd. C 41.72, H 4.06; found C 41.44, H 4.09.

Synthesis of 6$(BF_4)_2$ and 8a,b$(BF_4)_2$: Me_2CO (1 mL) was added to a mixture of $[(ring)MCl_2]_2$ [(ring)M = Cp*Ir, (η^6-$C_6H_3Me_3$-1,3,5)Ru, and (η^6-C_6Me_6)Ru] (0.08 mmol) and $AgBF_4$·3 dioxane (150 mg, 0.33 mmol). The reaction mixture was stirred for ca. 0.5 h and the precipitate of AgCl was centrifuged off. The solution obtained was added to **2** (50 mg, 0.16 mmol) and stirred for 2 h at –15 °C. After warming to room temperature, diethyl ether (ca. 10 mL) was added to precipitate a bright-coloured solid, which was reprecipitated twice from acetone by addition of diethyl ether.

6$(BF_4)_2$: Yellow, yield 84 mg (64%). $C_{25}H_{29}B_3F_8IrRh$ (809.05): calcd. C 37.11, H 3.61; found C 37.05, H 3.67.

8a$(BF_4)_2$: Orange, yield 84 mg (74%). $C_{24}H_{26}B_3F_8RhRu$ (702.86): calcd. C 41.01, H 3.73; found C 40.46, H 3.61.

8b$(BF_4)_2$: Orange, yield 80 mg (67%). $C_{27}H_{32}B_3F_8RhRu$ (744.94): calcd. C 43.53, H 4.33; found C 43.17, H 4.65.

X-ray Crystallographic Study: Crystals of **2** were grown by slow evaporation of its petroleum ether solution. Crystals of **5**$(BF_4)_2$, **6**$(BF_4)_2$ and **8a**$(BF_4)_2$ were obtained by slow interdiffusion of a two-phase system containing diethyl ether and an acetone solution of the complex. The principal crystallographic data, procedures for collecting experimental data, and characteristics of structure refinement are listed in Table 7. Single-crystal X-ray diffraction experiment for **2** was carried out with a Syntex $P2_1$ diffractometer (graphite monochromated Mo-K_α radiation, $\theta/2\theta$ scans technique) at 153 K. Analogous experiments for **5**$(BF_4)_2$, **6**$(BF_4)_2$ and **8a**$(BF_4)_2$ were carried out with a Bruker SMART 1000 CCD area detector, with graphite-monochromated Mo-K_α radiation (λ = 0.71073 Å, ω-

Table 7. Crystal data and structure-refinement parameters for **2**, **5**, **6** and **8a**.

	2	**5**$(BF_4)_2$	**6**$(BF_4)_2$	**8a**$(BF_4)_2$
Empirical formula	$C_{15}H_{14}BRh$	$C_{25}H_{29}B_3F_8Rh_2$	$C_{25}H_{25}B_3F_8IrRh$	$C_{24}H_{26}B_3F_8RhRu$
Formula mass	307.98	719.73	804.99	702.86
Crystal colour, habit	colourless needle	colourless needle	orange plate	red needle
Crystal size [mm]	0.55 × 0.30 × 0.25	0.50 × 0.30 × 0.15	0.45 × 0.20 × 0.05	0.50 × 0.30 × 0.15
Crystal system	orthorhombic	monoclinic	monoclinic	triclinic
Space group	$P2_12_12_1$	$P2_1/n$	$P2_1/c$	$P\bar{1}$
a [Å]	5.927(2)	12.467(4)	16.795(7)	8.716(2)
b [Å]	12.632(4)	10.216(3)	17.947(8)	11.944(3)
c [Å]	16.352(4)	20.841(6)	18.267(8)	13.392(3)
α [°]	90	90	90	92.633(5)
β [°]	90	96.083(6)	91.945(9)	97.688(5)
γ [°]	90	90	90	107.719(4)
V [Å^3]	1224.3(7)	2639.3(12)	5503(4)	1310.7(5)
Z	4	4	8	2
D(calcd.) [g cm^{-3}]	1.671	1.811	1.943	1.781
Diffractometer	Syntex $P2_1$	Bruker SMART 1000 CCD		
Temperature [K]	153	140	120	110
Radiation	Mo-K_α (λ = 0.71073)			
Scan mode	θ–2θ	φ and ω		
$2\theta_{max}$ [°]	60.12	60.12	54.20	56.70
Abs.coeff. μ(Mo-*K*a) [cm^{-1}]	13.65	13.21	54.99	12.75
Absorption correction	multi-scan			
$T_{max.}$ and $T_{min.}$		0.862 and 0.520	0.155 and 0.048	0.928 and 0.594
Completeness [%]	99.1	99.4	99.7	98.9
Structure solution	direct methods			
Refinement method	full-matrix least-squares on F^2			
Collected reflections	2112	21 609	52 556	14 197
Independent reflections	2069 (R_{int} = 0.0190)	7703 (R_{int} = 0.0314)	12 110 (R_{int} = 0.0716)	6692 (R_{int} = 0.0287)
Observed reflections [$I > 2\sigma(I)$]	2024	6258	7994	5305
Abs. structure parameter	–0.05(6)			
Parameters	154	343	685	334
R_1 (on *F* for obsd. reflections)	0.0332	0.0528	0.0442	0.0511
wR_2 (on F^2 for all reflections)	0.0998	0.1333	0.1166	0.1370
Weighting scheme	$w^{-1} = \sigma^2(F_o^2) + (aP)^2 + bP$, $P = 1/3(F_o^2 + 2F_c^2)$			
a	0.1000	0.1000	0.0607	0.0755
b				2.8474
F(000)	616	1424	3072	695
GOOF	0.940	1.038	0.996	1.082
Largest diff. peak and hole [e Å^{-3}]	1.779 and –0.816	5.915 and –1.271	3.369 and –1.811	3.364 and –1.040

 © 2005 Wiley-VCH Verlag GmbH & Co. KGaA, Weinheim

scans with 0.3° steps in ω and 10 s per frame exposure) at 110–140 K. The low temperature of the crystals was maintained with a Cryostream (Oxford Cryosystems) open-flow N_2 gas cryostat. Reflection intensities were integrated by using the SAINT software[30] and the semi-empirical method SADABS.[31] The structures were solved by direct methods and refined by full-matrix least-squares against F^2_{hkl} in an anisotropic (for non-hydrogen atoms) approximation. All hydrogen atoms in the structures were placed in geometrically calculated positions and included in the final refinement using the "riding" model with $U_{iso}(H)$ parameters equal to 1.2 $U_{eq}(C_i)$ or 1.5 $U_{eq}(C_{ii})$, where $U(C_i)$ and $U(C_{ii})$ are the equivalent thermal parameters of the methyne and methyl carbon atoms, respectively, to which the corresponding H atoms are bonded. All calculations were performed on an IBM PC/AT using the SHELXTL software.[32]

CCDC-238739 (for **2**), -238740 [for **5**$(BF_4)_2$], -238741 [for **6**$(BF_4)_2$] and -238742 [for **8a**$(BF_4)_2$] contain the supplementary crystallographic data for this paper. These data can be obtained free of charge from The Cambridge Crystallographic Data Centre via www.ccdc.cam.ac.uk/data_request/cif.

Acknowledgments

This work was supported by the Russian Foundation for Basic Research (Grant No. 03-03-32214), as well as the General Chemistry and Material Science Division of RAS (Grant No 05-07). P. Z. gratefully acknowledges financial support from the Università di Siena (PAR, 2003).

[1] a) C. White, S. J. Thompson, P. M. Maitlis, *J. Chem. Soc., Dalton Trans.* **1977**, 1654–1661 (*Rh and Ir*); b) M. A. Bennett, T. W. Matheson, *J. Organomet. Chem.* **1979**, *175*, 87–93 (*Ru*); c) S. L. Grundy, P. M. Maitlis, *J. Organomet. Chem.* **1984**, *272*, 265–282 (*Ir*); d) D. A. Herebian, C. S. Schmidt, W. S. Sheldrick, C. van Wüllen, *Eur. J. Inorg. Chem.* **1998**, 1991–1998 (*Rh and Ir*); e) C. M. Alvarez, R. J. Angelici, A. Sygula, R. Sygula, P. W. Rabideau, *Organometallics* **2003**, *22*, 624–626 (*Ir*).

[2] A. R. Kudinov, M. I. Rybinskaya, *Izv. Akad. Nauk, Ser. Khim.* **1999**, 1636–1642 [*Russ. Chem. Bull.* **1999**, *48*, 1615–1621 (Engl. Transl.)].

[3] a) H. Werner, A. Salzer, *Synth. Inorg. Met.-Org. Chem.* **1972**, *2*, 239–248; b) A. Salzer, H. Werner, *Angew. Chem. Int. Ed. Engl.* **1972**, *11*, 930–932; c) A. R. Kudinov, M. I. Rybinskaya, Yu. T. Struchkov, A. I. Yanovskii, P. V. Petrovskii, *J. Organomet. Chem.* **1987**, *336*, 187–197; d) G. E. Herberich, U. Englert, F. Marken, P. Hofmann, *Organometallics* **1993**, *12*, 4039–4045; e) G. E. Herberich, U. J. Jansen, *Organometallics* **1995**, *14*, 834–841; f) A. R. Kudinov, A. A. Fil'chikov, P. V. Petrovskii, M. I. Rybinskaya, *Izv. Akad. Nauk, Ser. Khim.* **1999**, 1364–1367 [*Russ. Chem. Bull.* **1999**, *48*, 1352–1355 (Engl. Transl.)].

[4] a) G. E. Herberich, U. Englert, D. Pubanz, *J. Organomet. Chem.* **1993**, *459*, 1–9; b) G. E. Herberich, U. Englert, B. Ganter, C. Lamertz, *Organometallics* **1996**, *15*, 5236–5241; c) A. R. Kudinov, D. A. Loginov, Z. A. Starikova, P. V. Petrovskii, *J. Organomet. Chem.* **2002**, *649*, 136–140.

[5] a) G. E. Herberich, B. J. Dunne, B. Hessner, *Angew. Chem. Int. Ed. Engl.* **1989**, *28*, 737–738; b) G. E. Herberich, U. Büschges, B. A. Dunne, B. Hessner, N. Klaff, D. P. J. Köffer, K. Peters, *J. Organomet. Chem.* **1989**, *372*, 53–60.

[6] A. R. Kudinov, D. A. Loginov, D. V. Muratov, P. V. Petrovskii, *Izv. Akad. Nauk, Ser. Khim.* **2001**, 1267–1268 [*Russ. Chem. Bull.* **2001**, *50*, 1332–1333 (Engl. Transl.)].

[7] All the dicationic fragments were generated as labile solvates $[(ring)M(Solv)_3]^{2+}$ (Solv = $MeNO_2$, Me_2CO) by treatment of $[(ring)MCl_2]_2$ with $AgBF_4$.

[8] All the cationic complexes described here were isolated as salts with the BF_4^- anion (the anions are omitted in the schemes).

[9] G. Fairhurst, C. White, *J. Chem. Soc., Dalton Trans.* **1979**, 1531–1538.

[10] Symmetrization of the FeMn complex [CpFe(μ-η^5:η^5-C_4H_4BPh)Mn$(CO)_3$] has been shown to give a mixture of [CpFe(μ-η^5:η^5-C_4H_4BPh)FeCp] and [$(CO)_3$Mn(μ-η^5:η^5-C_4H_4BPh)Mn$(CO)_3$]: G. E. Herberich, D. P. J. Köffer, K. M. Peters, *Chem. Ber.* **1991**, *124*, 1947–1952.

[11] A. R. Kudinov, D. A. Loginov, Z. A. Starikova, P. V. Petrovskii, M. Corsini, P. Zanello, *Eur. J. Inorg. Chem.* **2002**, 3018–3027, and references cited therein.

[12] G. E. Herberich, W. Boveleth, B. Hessner, M. Hostalek, D. P. J. Köffer, M. Negele, *J. Organomet. Chem.* **1987**, *319*, 311–326.

[13] A. R. Kudinov, D. S. Perekalin, P. V. Petrovskii, K. A. Lyssenko, G. V. Grintselev-Knyazev, Z. A. Starikova, *J. Organomet. Chem.* **2002**, *657*, 115–122.

[14] P. Zanello, *Inorganic Electrochemistry. Theory, Practice and Application*, RS·C, Cambridge, UK, **2003**.

[15] N. Dowling, P. M. Henry, N. A. Lewis, H. Taube, *Inorg. Chem.* **1981**, *20*, 2345–2348.

[16] F. E. Mabbs, D. Collison, *Electron Paramagnetic Resonance of d Transition Metal Complexes*, in *Studies in Inorganic Chemistry*, Vol. 16, Elsevier, New York, **1992**.

[17] a) C. Bianchini, M. Peruzzini, F. Laschi, P. Zanello, *Synthesis Characterization and Chemistry of Rhodium(II) Organometallic Complexes Stabilized by Tripodal Polyphosphine Ligands*, in *Topics in Physical Organometallic Chemistry* (Ed.: M. F. Gielen), Freund Publ. House Ltd, U.K, **1992**, vol. 4, 139–219; b) J. E. Collins, M. P. Castellani, A. L. Rheingold, E. J. Miller, W. E. Geiger, A. L. Rieger, P. H. Rieger, *Organometallics* **1995**, *14*, 1232–1238.

[18] A. Bencini, D. Gatteschi, *ESR Spectra of Metal Complexes of the First Transition Series in Low-Symmetry Environments*, in *Transition Metal Chemistry*, Vol. 8, M. Dekker, New York, **1982**.

[19] The Cambridge Structural Database: version 5.25, November 2003 and VISTA 2.0.

[20] R. Gleiter, I. Hyla-Kryspin, G. E. Herberich, *J. Organomet. Chem.* **1994**, *478*, 95–102.

[21] G. E. Herberich, U. Büschges, B. Hessner, H. Lüthe, *J. Organomet. Chem.* **1986**, *312*, 13–25.

[22] M. J. Macazaga, S. Delgado, R. M. Medina, J. R. Masaguer, *J. Organomet. Chem.* **1984**, *277*, 423–426.

[23] C. White, A. Yates, P. M. Maitlis, *Inorg. Synth.* **1992**, *29*, 228–234.

[24] M. A. Bennett, A. K. Smith, *J. Chem. Soc., Dalton Trans.* **1974**, 233–241.

[25] M. A. Bennett, T.-N. Huang, T. W. Matheson, A. K. Smith, *Inorg. Synth.* **1982**, *21*, 74–78.

[26] P. Zanello, F. Laschi, M. Fontani, C. Mealli, A. Ienco, K. Tang, X. Jin, L. Li, *J. Chem. Soc., Dalton Trans.* **1999**, 965–970.

[27] M. Krejčik, M. Daněk, F. Hartl, *J. Electroanal. Chem.* **1991**, *317*, 179–187.

[28] C. Mealli, D. M. Proserpio, *J. Chem. Educ.* **1990**, *67*, 399.

[29] A. Vela, J. L. Gázquez, *J. Phys. Chem.* **1988**, *92*, 5688–5693.

[30] SMART v. 5.051 and SAINT v. 5.00, Area detector control and integration software, **1998**, Bruker AXS Inc., Madison, WI-53719, USA.

[31] G. M. Sheldrick, *SADABS*, **1997**, Bruker AXS Inc., Madison, WI-53719, USA.

[32] G. M. Sheldrick, *SHELXTL-97*, v. 5.10, Bruker AXS Inc., Madison, WI-53719, USA.

Received: October 27, 2004

 © 2005 Wiley-VCH Verlag GmbH & Co. KGaA, Weinheim

Acidities of Nitrous and Nitric Acids

Otto Exner[a] and Stanislav Böhm*[b]

Keywords: Ab initio calculations / Isodesmic reaction / Resonance / Acidity

The energies of nitrous and nitric acid and their anions were calculated at the MP2(FC)/6-311++G(2d,2p) level. Their acidity was related to the acidity of hydroxylamine derivatives using isodesmic reactions. This procedure reveals that the molecules of HNO_2 and HNO_3 are strongly stabilized (by 119 or 206 kJ·mol^{-1}, respectively) but their anions are stabilized even more (by 282 or 428 kJ·mol^{-1}). The acidity of these acids is thus caused by the low energy of their anions and not by the high energy of the acid molecules, similarly to the case of carboxylic acids. This stability may be partly due to resonance but the contribution of this effect can only be estimated. Correlation of the acidities of various acids with the inductive and polarization parameters led to the following estimate: in the case of nitrous acid 46 % of the acidity enhancement is due to resonance while in the case of nitric acid it is 25 %.
(© Wiley-VCH Verlag GmbH & Co. KGaA, 69451 Weinheim, Germany, 2005)

Introduction

The strong acidity of nitric and nitrous acids – both in the gas phase and in aqueous solution – has been attributed, within the framework of the classic theory of resonance, to resonance in their anions.[1] Description of their structure by resonance formulae is still considered as convenient[2] and used in textbooks; it is a completely analogous explanation to the case of the relatively strong acidity of carboxylic acids. An alternative theory was suggested first for carboxylic acids[3] and then extended to nitrous and nitric acids:[4,5] the origin of the acidity is seen in the charge distribution and in the electrostatic potential of the uncharged molecules of the acids. In the case of carboxylic acids, the problem raised a vivid discussion[6–11] and complete agreement has not yet been reached. In our opinion, the problem can be rationalized (and for the greater part solved) if it is divided into two independent questions:[7,10]
a) Is the acidity of the isolated molecules caused by the low energy of their anions or by the high energy of the acid molecules?
b) Is the acidity dependent on the resonance in the anions (or also in the acid molecules)?

In the case of carboxylic acids, in our opinion the first problem has been solved[10] using the framework of isodesmic reactions.[12,13] Concerning the second problem, several models were advanced estimating the contribution of resonance with a fair agreement to approximately one third of the acidity enhancement.[8–10]

[a] Institute of Organic Chemistry and Biochemistry, Academy of Sciences of the Czech Republic,
16610 Praha 6, Czech Republic
[b] Department of Organic Chemistry, Prague Institute of Chemical Technology,
16628 Praha 6, Czech Republic

In the present article, the above-mentioned approach is applied to the acidity of nitrous and nitric acid. The procedure is not always self-evident since the choice of reference compounds is not as straightforward as for carboxylic acids but, in our opinion, it is just the application of the methods of organic chemistry that may shed light on the problem from a new standpoint. The article will be divided into two sections corresponding to the two questions a) and b). The first part is much more important since the question sub a) can be answered unambiguously. The solution makes use of isodesmic reactions and of the energies calculated by ab initio MO methods.[14] In the second part, only one possible model will be mentioned for estimating the resonance contribution, which is supported by experimental gas-phase acidities. Let us stress that our approach is based either on the experimental energies (mainly the gas-phase acidities) or on the calculated energies that can be related to some experimental values; any reference to fictive or theoretical structures is avoided.

Results and Discussion

Energy of the Anions and of the Acid Molecules

The relatively strong acidity of carboxylic acids has always been evaluated with alcohols as a natural reference.[3,6–11] By the same token, a reference compound for nitrous acid is a hydroxylamine derivative. In the isodesmic and homodesmotic[15] reaction, see Equation (1), the molecule of nitrous acid is constructed from nitrosomethane and *N*,*N*-dimethylhydroxylamine. The reaction energy Δ_1E is a measure of the interaction of the groups N=O and OH in the molecule of nitrous acid. Of course, Equation (1) represents only one possible solution but its merit is that it oper-

 DOI: 10.1002/ejic.200400925 © 2005 Wiley-VCH Verlag GmbH & Co. KGaA, Weinheim

ates exclusively with stable and well-characterized molecules, even when their enthalpies of formation have not been experimentally determined. Introducing the methyl groupsw into Equation (1) has another advantage, that is, molecules of similar polarizability[3,7] are compared. If in Equation (1) hydroxylamine were used instead of *N*,*N*-dimethylhydroxylamine, the results would not be significantly altered.

$$O{=}N{-}CH_3 + (CH_3)_2N{-}OH = O{=}N{-}OH + (CH_3)_2N{-}CH_3 \quad (1)$$

Similarly, the interaction of the two oxygen atoms in the nitrite anion is measured by the reaction energy Δ_2E of the reaction of Equation (2); by this interaction the two oxygen atoms become equivalent.

$$O{=}N{-}CH_3 + (CH_3)_2N{-}O^- = O{=}N{-}O^- + (CH_3)_2N{-}CH_3 \quad (2)$$

An isodesmic reaction generating nitric acid from its component functions would be somewhat complex. On the other hand, one can relate nitric acid to nitrous acid in a simple way by Equation (3).

$$O{=}N{-}OH + (CH_3)_3N{-}O = O{=}N(O){-}OH + (CH_3)_3N \quad (3)$$

The reaction energy Δ_3E represents the difference between the interactions in nitric and nitrous acid; the total interaction in nitric acid is given by $\Delta_1E + \Delta_3E$. Similarly the relation of nitrate and nitrite anions is represented by Equation (4); the total interaction within the nitrate anion is given by $\Delta_2E + \Delta_4E$.

$$O{=}N{-}O^- + (CH_3)_3N{-}O = O{=}N(O){-}O^- + (CH_3)_3N \quad (4)$$

Ab initio calculated energies of the compounds involved in Equations (1) to (4) are listed in Table 1. Few compounds can exist in equilibrium of two conformers, as given in the footnotes to Table 1, but the pertinent energy differences are negligible. Nevertheless, the energies of the isodesmic reactions, Δ_1E to Δ_4E, were always calculated for the equilibrium mixtures of conformers at 298 K (Table 2).

In the qualitative sense, the results are the same for nitrous and nitric acid. The molecule of HNO_2 is strongly stabilized (by more than 100 kJ·mol^{-1}) but the anion NO_2^- is stabilized much more (almost by 300 kJ·mol^{-1}); the difference determines the acidity. For HNO_3 and NO_3^- the values are almost two times greater (200 and 400 kJ·mol^{-1}, respectively). In relation to these figures, any arbitrariness in the isodesmic reactions and imperfections of the theoretical model are of no consequence. Even the conformations of some of the compounds involved are irrelevant from this point of view. Therefore, our results are in contrast to the claim[4,5] that the acidity is due to the initial-state charge distribution.

Table 1. Calculated energies and some bond lengths of nitrous and nitric acid and of reference compounds.

	E a.u.	N=O [Å]	N–O [Å]
HNO_2 *sp*	–205.3335699	1.193[a]	1.397[a]
HNO_2 *ap*	–205.3345614	1.178[a]	1.433[a]
NO_2^-	–204.7851469		1.270
HNO_3 *sp* (planar)	–280.3949067	1.217[b], 1.205[b]	1.413[b]
NO_3^- (planar)	–279.8677848		1.265[c]
$CH_3N{=}O$	–169.4401081	1.224	
$(CH_3)_2NOH$ *ac* [d]	–209.8640456		1.456
$(CH_3)_2NOH$ *sc*	–209.8599901		1.433
$(CH_3)_2NO^-$	–209.2526309		1.408
$(CH_3)_3N{-}O$	–249.0418991		1.368
$(CH_3)_3N$	–174.0148768		

[a] These figures agree with the experimental values[16] with the greatest deviation of 0.008 Å, this is a better agreement than that obtained at the level CCSD(T)/cc-PVQZ(spdf,spd)[17] and much better than at the levels B3LYP/6-311G(d,p)[18] or BH&HLYP/6-311G(d,p)[19]. [b] Agreement with the experimental values[16] within 0.007 Å. [c] Experimental value[20] 1.253(6) Å. [d] The O–H bond eclipsed with the electron lone pair on N.

Correlating our results to experimental values is of vital importance to our approach. For the two conformers of HNO_2, antiperiplanar *ap* and synperiplanar *sp*, we calculated the energy difference of 2.6 kJ·mol^{-1} (the *ap* conformer is more stable); the experimental value[21] is 2.1 kJ·mol^{-1}. The low-level calculations[3] (RHF/3-21+G) gave 3.8 kJ·mol^{-1}. Recent calculations[18] produced satisfactory results only at the MP2/6-311G(3df,2p) or G2M(RCC,MP2) levels while at the QCISD(T)/6-311G(d,p) and lower levels even the order of stability was reversed. The conformational energy is evidently too small and its calculations are sensitive to the level employed. A better idea about the reliability of the calculations can be obtained from the relative acidities of HNO_3 and HNO_2, that is, from Equation (5).

$$HNO_3 + NO_2^- = NO_3^- + HNO_2 \quad (5)$$

Our calculated reaction energy Δ_5E is –57.8 kJ·mol^{-1} (see Table 2) while the experimental Gibbs energy[9] $\Delta_5G°$ is –54.4 kJ·mol^{-1} and the enthalpy[22] $\Delta_5G°$ is –66.6 kJ·mol^{-1}.[23] Calculations at the RHF/3-21+G level yielded[4] –107 kJ·mol^{-1}. This theoretical model was obviously insufficient and further results of this paper[4] can be questioned.[23]

Table 2. Calculated acidities and energies of the isodesmic reactions (kJ·mol^{-1}).

	Formation of the acid	Formation of the anion	Acidity
HNO_2 *ap* [Equations (1) or (2)]	–116.3	–281.7	–165.4
HNO_2 *sp* [Equations (1) or (2)]	–118.9	–281.7	–162.8
HNO_2 equil. mixture	–118.2	–281.7	–163.5
$HNO_3 - HNO_2$ [Equations (3) or (4)]	–88.2	–146.0	–57.8
HNO_3	–206.4	–427.7	–221.3

 © 2005 Wiley-VCH Verlag GmbH & Co. KGaA, Weinheim

Effect of Resonance

When we accept that the strong acidity of both HNO_2 and HNO_3 is due to the low energy of their anions, it does not follow that this low energy is a consequence of resonance. However, resonance may be defined differently and its effect cannot be calculated unambiguously. It is necessary to design a molecule, more or less fictive, without resonance but otherwise similar to the molecule under investigation. In the case of carboxylic acids, several different models were designed and it may be considered as a remarkable agreement that some of them evaluated the effect of resonance to 30–40% of the increased acidity.[8–10] Let us mention here only one model,[10] originated from the fundamental idea of Taft,[9] that relates to stable molecules and is based exclusively on the experimental data. The relative gas-phase acidities of common oxygen acids ROH are defined by Equation (6).

$$R–OH + OH^- = R–O^- + H_2O \quad (6)$$

In the absence of resonance effects, the relative acidity $\Delta_6G°(298)$ can be empirically approximated[9] as a linear function of the inductive constants σ_I and polarizability constants σ_α. For 15 selected R substituents (H, seven alkyl groups, $CH_2C_6H_5$, CH_2OCH_3 and five fluorinated alkyls – mostly organic compounds since derivatives of hydroxylamine are not at our disposal) we obtained Equation (7).

$$\Delta_6G°(298) = 1603(4) – 299.8(73)\sigma_I + 97.9(73)\sigma_\alpha \ (kJ·mol^{-1}) \quad (7)$$

Figure 1 is a graphical representation of this relationship, where experimental[9] $\Delta_6G°(298)$ values were plotted against the right-hand side of Equation (7). The points for HNO_2 and HNO_3 in this graph deviate by the assumed contribution of resonance, 75 or 56 kJ·mol^{-1}, respectively. It follows that resonance should be responsible for 46% or 25%, respectively, of the enhanced acidity. (In the case of HNO_3 this estimate is biased since it starts from the group NO_2 and hence does not include the resonance already involved in this group.) Taking into consideration all the approximations, it seems safe to conclude that resonance is a very important factor in the case of HNO_2 and less important in the case of HNO_3. The explanation of this difference may be found in the so-called crossed conjugation in the anion NO_3^-.

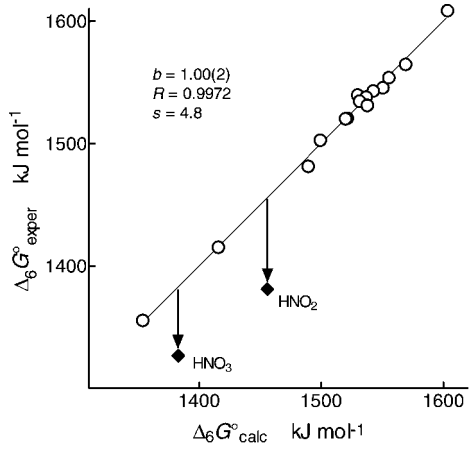

Figure 1. Plot of the experimental gas-phase acidities of the oxygen acids without resonance, Equation (6), vs. their values calculated according to the empirical Equation (7); the points for HNO_2 and HNO_3 deviate due to resonance as shown by the arrows.

In the case of carboxylic acids, a further attempt was made to evaluate separately the effect of resonance in the anion and in the acid molecule.[10] Application of this process to nitrous or nitric acid would require the construction of complex isodesmic reactions involving unstable or nonexisting molecules; their enthalpies of formation should be calculated using high-level models. We have rejected this approach as it is too sophisticated.[25]

In addition to energies, the theory of resonance predicts qualitatively changes of other observable quantities. For our compounds, the effect on the bond lengths should be the most conspicuous: N=O double bonds in HNO_2 and HNO_3 should be lengthened, N–O single bonds shortened. In the anions NO_2^- and NO_3^- the N–O bonds are equal and should be intermediate between single and double bonds. The latter prediction is fulfilled (see Table 1) but the former is not, particularly as the N=O bonds in HNO_2 are not longer than in $CH_3N=O$. Similar results were obtained when testing the resonance theory on amides and carboxylic acids: the single bonds were shortened but the C=O bond was lengthened insignificantly.[27] One must conclude that the resonance formulae are a fairly approximate picture. They can describe some observable quantities surprisingly well but can fail in other cases.

Conclusions

The framework of isodesmic reactions enables us to conclude that the strong acidity of HNO_2 and HNO_3 is caused by the low energy of their anions. The energy of the acid molecules is not particularly high; on the contrary it is also lowered and causes an opposite effect (acid weakening). The energies of the isodesmic reactions are so great that any defect of the model, either in the choice of reference compounds or in the computational procedure, is insignificant. On the other hand, the question of whether the acidity is due to resonance is inexact and can be answered only approximately. Resonance is operating but is less significant than the inductive effect, with HNO_3 maybe less than with HNO_2. In our opinion, this problem is not of particular importance since resonance means always a difference between a real molecule and an artificial formalism. In our opinion it has been merely a tool for identifying the difference between real structures and primitive traditional formulae.

Computational Details

Energies of nitrous and nitric acids, of their anions and of reference compounds were calculated at the levels MP2(FC)6-311++G(2d,2p)//MP2(FC)6-311++G(2d,2p) (Table 1) and B3LYP/6-311++G(2d,2p)//B3LYP/6-311++G(2d,2p)[23] with the

 © 2005 Wiley-VCH Verlag GmbH & Co. KGaA, Weinheim

GAUSSIAN 03 program.[14] All reasonable conformations were taken into consideration and calculations were started from the pertinent near structures. Planarity or any symmetry was never anticipated. All structures were checked by vibrational analysis and behaved as energy minima.

Population of conformers was calculated with the standard approximation that $\Delta G°(298) \approx \Delta E$; with this population the effective ΔE for the equilibrium mixture of conformers for each compound was obtained. The energies of isodesmic reactions, $\Delta_1 E$ to $\Delta_4 E$, were calculated with these effective ΔE values.

Acknowledgments

This work was carried within the framework of the research project Z4 055 905 of the Academy of Sciences of the Czech Republic, and supported by the Ministry of Education of the Czech Republic (Project LN00A032, Center for Complex Molecular Systems and Biomolecules).

[1] a) L. Pauling, *The Chemical Bond*, Cornell University Press, Ithaca, NY, **1967**, p. 164; b) G. W. Wheland, *Resonance in Organic Chemistry*, Wiley, New York, **1955**, p. 156.
[2] *Gmelins Handbook of Inorganic and Organometallic Chemistry*, Supplement B6, Springer-Verlag: Berlin, **1996**, p. 207–208.
[3] M. R. Siggel, T. D. Thomas, *J. Am. Chem. Soc.* **1986**, *108*, 4360–4363.
[4] T. D. Thomas, *Inorg. Chem.* **1988**, *27*, 1695–1696.
[5] K. B. Wiberg, *Inorg. Chem.* **1988**, *27*, 3694–3697.
[6] K. B. Wiberg, J. Ochterski, A. J. Streitwieser, *J. Am. Chem. Soc.* **1996**, *118*, 8291–8299 and previous work cited therein.
[7] O. Exner, *J. Org. Chem.* **1988**, *53*, 1812–1815.
[8] P. R. Rablen, *J. Am. Chem. Soc.* **2000**, *122*, 357–368.
[9] R. W. Taft, I. A. Koppel, R. D. Topsom, F. Anvia, *J. Am. Chem. Soc.* **1990**, *112*, 2047–2052.
[10] O. Exner, P. Čársky, *J. Am. Chem. Soc.* **2001**, *123*, 9564–9570 .and references cited therein.
[11] J. Holt, J. M. Karty, *J. Am. Chem. Soc.* **2003**, *125*, 2797–2803.
[12] A. Pross, L. Radom, R. W. Taft, *J. Org. Chem.* **1980**, *45*, 818–826.
[13] O. Exner, *Org. Reactivity [Tartu]* **1995**, *29*, 1–6.
[14] M. J. Frisch, G. W. Trucks, H. B. Schlegel, G. E. Scuseria, M. A. Robb, J. R. Cheeseman, J. A. Montgomery Jr., T. Vreven, K. N. Kudin, J. C. Burant, J. M. Millam, S. S. Iyengar, J. Tomasi, V. Barone, B. Mennucci, M. Cossi, G. Scalmani, N. Rega, G. A. Petersson, H. Nakatsuji, M. Hada, M. Ehara, K. Toyota, R. Fukuda, J. Hasegawa, M. Ishida, T. Nakajima, Y. Honda, O. Kitao, H. Nakai, M. Klene, X. Li, J. E. Knox, H. P. Hratchian, J. B. Cross, C. Adamo, J. Jaramillo, R. Gomperts, R. E. Stratmann, O. Yazyev, A. J. Austin, R. Cammi, C. Pomelli, J. W. Ochterski, P. Y. Ayala, K. Morokuma, G. A. Voth, P. Salvador, J. J. Dannenberg, V. G. Zakrzewski, S. Dapprich, A. D. Daniels, M. C. Strain, O. Farkas, D. K. Malick, A. D. Rabuck, K. Raghavachari, J. B. Foresman, J. V. Ortiz, Q. Cui, A. G. Baboul, S. Clifford, J. Cioslowski, B. B. Stefanov, G. Liu, A. Liashenko, P. Piskorz, I. Komaromi, R. L. Martin, D. J. Fox, T. Keith, M. A. Al-Laham, C. Y. Peng, A. Nanayakkara, M. Challacombe, P. M. W. Gill, B. Johnson, W. Chen, M. W. Wong, C. Gonzalez, J. A. Pople, *Gaussian 03, Revision B.03*, Gaussian, Inc., Pittsburgh PA, **2003**.
[15] P. George, M. Trachtman, C. W. Bock, A. M. Brett, *J. Chem. Soc. Perkin Trans. 2* **1976**, 1222–1227.
[16] A. P. Cox, M. C. Ellis, C. J. Attfield, A. C. Ferris, *J. Mol. Struct.* **1994**, *320*, 91–106.
[17] F. Richter, M. Hochlaf, P. Rosmus, F. Gatti, H. D. Meyer, *J. Chem. Phys.* **2004**, *120*, 1306–1317.
[18] X. Lu, R. N. Musin, M. C. Lin, *J. Phys. Chem. A* **2000**, *104*, 5141–5148.
[19] Z. F. Xu, M. C. Lin, *Int. J. Chem. Kinet.* **2004**, *36*, 178–187.
[20] I. Howell, G. W. Neilson, P. Chieux, *J. Mol. Struct.* **1991**, *250*, 281–289.
[21] L. H. Jones, R. M. Badger, G. E. Moore, *J. Chem. Phys.* **1951**, *19*, 1599–1604.
[22] *NIST Chemistry WebBook, NIST Standard Reference Database No. 69* (Eds.: W. G. Mallard, P. J. Linstrom), National Institute of Standards and Technology, Gaithersburg MD, **2000**.
[23] In previous work, for instance see ref. [24], we usually got a better fit with the Gibbs energies than with the enthalpies due to less dependability of the latter. In order to test the dependence of our results on the theoretical model we calculated the reaction energy $\Delta_5 E$ still at the level B3LYP/6-311++G(2d,2p)//B3LYP/6-311++G(2d,2p) and obtained –65.4 kJ·mol^{-1}. This theoretical model seems to be somewhat better but note that even the inaccuracy of 10 kJ·mol^{-1} would not change our final results.
[24] J. Roithová, O. Exner, *J. Phys. Org. Chem.* **2001**, *14*, 752–758.
[25] Another approach could be taken by considering the valence bond theory. In the case of carboxylic acids, a reasonable estimate of resonance was obtained, ref. [26], but several possible localized structures were designed with some arbitrariness, even for structures without resonance (ethanol); moreover, the agreement with experimental acidities was very bad. Nevertheless, we agree with a referee that this would be the most important alternative to our approach.
[26] P. C. Hiberty, C. P. Byrman, *J. Am. Chem. Soc.* **1995**, *117*, 9875–9880.
[27] S. Böhm, O. Exner, *Org. Biomol. Chem.* **2003**, *1*, 1176–1180 and references cited therein.

Received: November 03, 2004

 © 2005 Wiley-VCH Verlag GmbH & Co. KGaA, Weinheim

Two New μ-(1,3-Azido)-Bridged Polymers: Alternating Single and Double Bridges in a 1D Nickel(II) Complex and Uniform Bridge in a 2D Copper(II) Complex: Syntheses, Single-Crystal Structures and Magnetic Studies

Subal Chandra Manna,[a] Sanjit Konar,[a] Ennio Zangrando,[b] Michael G. B. Drew,[c] Joan Ribas*[d] and Nirmalendu Ray Chaudhuri*[a]

Keywords: Nickel(II) / Copper(II) / Azide bridges / Crystal structures / Magnetic properties

Two polymeric azido bridged complexes $[Ni_2L_2(N_3)_3]_n(ClO_4)_n$ (**1**) and $[Cu(bpds)_2(N_3)]_n(ClO_4)_n(H_2O)_{2.5n}$ (**2**) [L = Schiff base, obtained from the condensation of pyridine-2-aldehyde with *N*,*N*,2,2-tetramethyl-1,3-propanediamine; bpds = 4,4′-bipyridyl disulfide] have been synthesized and their crystal structures have been determined. Complex **1**, $C_{26}H_{42}ClN_{15}Ni_2O_4$, crystallizes in a triclinic system, space group $P\bar{1}$ with a = 8.089(13), b = 9.392(14), c = 12.267(18) Å, α = 107.28(1), β = 95.95(1), γ = 96.92(1)° and Z = 2; complex **2**, $C_{20}H_{21}ClCuN_7O_{6.5}S_4$, crystallizes in an orthorhombic system, space group *Pnna* with a = 10.839(14), b = 13.208(17), c = 19.75(2) Å and Z = 4. The crystal structure of **1** consists of 1D polymers of nickel(L) units, alternatively connected by single and double bridging μ-(1,3-N_3) ligand with isolated perchlorate anions. Variable temperature magnetic susceptibility data of the complex have been measured and the fitting of magnetic data was carried out applying the Borrás-Almenar formula for such types of alternating one-dimensional S = 1 systems, based on the Hamiltonian $H = -J\Sigma(S_{2i}S_{2i-1} + \alpha S_{2i}S_{2i+1})$. The best-fit parameters obtained are J = –106.7 ±2 cm^{-1}; α = 0.82 ± 0.02; g = 2.21 ± 0.02. Complex **2** is a 2D network of 4,4 topology with the nodes occupied by the Cu^{II} ions, and the edges formed by single azide and double bpds connectors. The perchlorate anions are located between pairs of bpds. The magnetic data have been fitted considering the complex as a pseudo-one-dimensional system, with all copper(II) atoms linked by μ(1,3-azido) bridging ligands at axial positions (long Cu···N_3 distances) since the coupling through long bpds is almost nil. The best-fit parameters obtained with this model are J = –1.21 ± 0.2 cm^{-1}, g = 2.14 ± 0.02.

(© Wiley-VCH Verlag GmbH & Co. KGaA, 69451 Weinheim, Germany, 2005)

Introduction

Azide represents an efficient superexchange pathway for propagating magnetic interaction between paramagnetic centers and along with its versatile coordination modes,[1] it is widely used for preparing magnetic materials of various dimensionality.[2,3] In general, the μ-(1,3-N_3) azide bridge creates an antiferromagnetic interaction while the μ-(1,1-N_3) connection mode shows a ferromagnetic interaction.[4] The M–N–M angle in μ-(1,1-N_3), and the M–N–N angle and the M–N_3–M dihedral angle in μ-(1,3-N_3) are the key factors in tuning the magnetic interaction.[5] It is well-established that the type and the connectivity of the coligand, i.e. monodentate, chelate, chelate-bridge, bridge, etc. (either neutral or ionic), dictate the binding modes of the azide ligand. It is also observed that different coligands of similar denticity with azide, in a particular bridging mode, i.e. μ-(1,1-N_3), μ-(1,3-N_3), etc. can affect the magnetic properties even in a same paramagnetic metal system. In fact the shape and size of coligands control the M–N–M angle in μ-(1,1-N_3), and the M–N–N angle and M–N_3–M dihedral angle in μ-(1,3-N_3).[6] In many cases spacers i.e. 4,4′-bipyridine, pyrazine, 1,2-bis(4-pyridyl)ethane, etc., are used in combination with azide to augment the ease of synthesizing multidimensional coordination polymers, leading to magnetic materials. Recently, the 4,4′-bipyridyl disulfide (bpds) ligand, characterized by the twisted –S–S– bridge, has been employed for the construction of coordination polymers showing topologically interesting assemblies.[7] It is worth noting that in most of the cases the bpds ligand coordinates metals in a double bridged fashion and, thanks to the flexible heterocyclic rings, sometimes stabilizes the structure through strong π–π interactions.[8] A literature survey revealed that molecular architecture obtained from the combination of bpds and azide is scarce.

Moreover, reports of alternate double and single μ-(1,3-N_3) bridges in transition metals is also rarely documented,

[a] Department of Inorganic Chemistry, Indian Association for the Cultivation of Science,
Kolkata 700032, India
E-mail: icnrc@iacs.res.in
[b] Dipartimento di Scienze Chimiche, University of Trieste,
34127 Trieste, Italy
[c] Department of Chemistry, The University of Reading,
Whiteknights, Reading RG6 6AD, UK
[d] Departament de Química Inorgànica, Universitat de Barcelona,
Diagonal, 647, 08028 Barcelona, Spain
E-mail: joan.ribas@qi.ub.es

especially with nickel(II), and up to date only one system, with a triamine as coligand, has been reported.[9] The magnetism in such types of alternate bridging systems appears intriguing owing to the number of variable factors in these compounds.[6] The above facts prompted us to synthesize azide species using bpds as well as the tridentate ligand as a coligand. A Schiff base (L), derived from the condensation of pyridine-2-aldehyde with *N*,*N*,2,2-tetramethyl-1,3-propanediamine, has been chosen in the present work as the tridentate ligand. Previous attempts from our group to synthesize alternate single and double μ-(1,3-N_3) 1D chains of nickel using the mentioned Schiff base afforded 1D polymers comprising only single μ-(1,3-N_3) bridges which exhibited novel metamagnetic behavior.[10] In order to achieve alternating single and double azide bridges we have varied the relative molecular amount of the reagents.

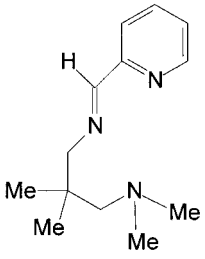

L

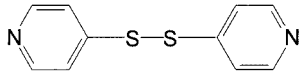

bpds

The present contribution reports the syntheses, crystal structures and variable temperature magnetic behavior of two azido-bridged coordination polymeric networks, namely $[Ni_2L_2(N_3)_3]_n(ClO_4)_n$ (**1**) and $[Cu(bpds)_2(N_3)]_n(ClO_4)_n$-$(H_2O)_{2.5n}$ (**2**). To the best of our knowledge complex **1** is the second example of a μ-(1,3-N_3) alternate single and double bridging Ni^{II} system. Complex **2** is a 2D grid of 4,4 topology with Cu^{II} ions occupying the nodes, where single azide and double bpds connectors take part in the formation of edges. Magnetic properties of complexes **1** and **2** have been interpreted indicating a very strong antiferromagnetic coupling and a weak antiferromagnetic one, respectively.

Results and Discussion

Description of the Structures

Complex 1

Crystal structure determination reveals that complex **1** consists of positively charged 1D polymers, $[Ni_2L_2(N_3)_3]_n^+$ counterbalanced by lattice perchlorate anions. The ORTEP drawing of the metal center with the atom numbering scheme is shown in Figure 1 while selected geometrical parameters are given in Table 1. The nickel(II) center, *meridionally* coordinated by the tridentate Schiff base, completes the distorted octahedral coordination sphere with three end-to-end bridging azide nitrogen atoms, resulting in a

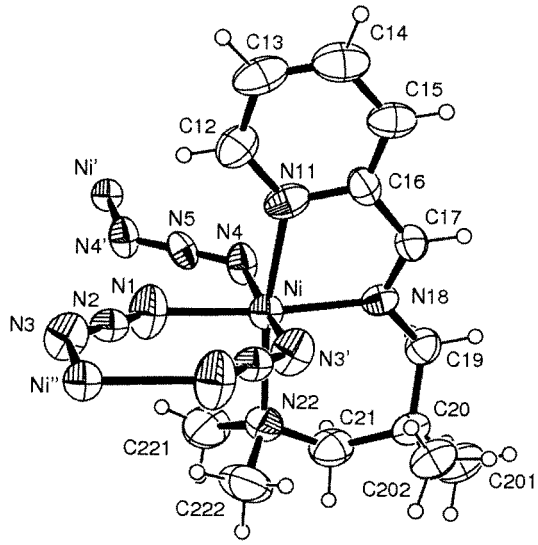

Figure 1. ORTEP plot of complex **1** with atom numbering scheme showing the alternating single and double connecting azide ligands.

Table 1. Selected bond lengths [Å] and angles [°] for complexes **1** and **2**.

Complex **1**[a]			
Ni–N(1)	2.096(7)	Ni–N(18)	2.062(6)
Ni–N(3′)	2.164(6)	Ni–N(22)	2.175(7)
Ni–N(4)	2.127(6)	Ni(′)–Ni	5.875(3)
Ni–N(11)	2.107(7)	Ni–Ni(′′)	5.304(3)
N(1)–Ni–N(3′)	90.2(2)	N(4)–Ni–N(18)	91.52(19)
N(1)–Ni–N(4)	88.8(2)	N(4)–Ni–N(22)	93.1(2)
N(1)–Ni–N(11)	95.0(3)	N(11)–Ni–N(18)	78.6(2)
N(1)–Ni–N(18)	173.5(3)	N(11)–Ni–N(22)	171.1(2)
N(1)–Ni–N(22)	93.5(3)	N(18)–Ni–N(22)	93.0(2)
N(3′)–Ni–N(4)	173.3(2)	N(2)–N(1)–Ni	132.9(5)
N(3′)–Ni–N(11)	83.5(2)	N(2′)–N(3′)–Ni	133.2(5)
N(3′)–Ni–N(18)	88.8(2)	N(5)–N(4)–Ni	122.5(3)
N(3′)–Ni–N(22)	93.5(3)	N(3)–N(2)–N(1)	176.1(7)
N(4)–Ni–N(11)	90.0(2)	N(4)–N(5)–N(4′)	180.0
Complex **2**[b]			
Cu(1)–N(11)	2.055(6)	Cu(1)–N(2)	2.447(7)
Cu(1)–N(22)	2.044(6)	S(17)–S(18)	2.027(4)
N(11′)–Cu–N(11)	89.1(3)	N(22)-Cu–N(22′′)	90.5(3)
N(11)–Cu–N(22)	90.3(2)	N(22)–Cu–N(2′)	90.6(2)
N(11)–Cu–N(22′′)	176.5(2)	N(22)–Cu–N(2)	86.3(2)
N(11)–Cu–N(2)	92.8(2)	N(2)–Cu–N(2′)	175.6(3)
N(11)–Cu–N(2′)	90.3(2)	N(1)–N(2)–Cu(1)	140.2(5)

[a] Symmetry operations: (′) at 1 – *x*, 2 – *y*, 2 – *z*; (′′) 1 – *x*, 1 – *y*, 2 – *z*. [b] Symmetry operations: (′) *x*, –*y* + 3/2, –*z* + 3/2; (′′) *x* – 1, –*y* + 3/2, –*z* + 3/2.

 © 2005 Wiley-VCH Verlag GmbH & Co. KGaA, Weinheim

NiN_6 chromophore. The Schiff base N donors [N(11), N(18), N(22)] and the azide nitrogen atom N(1) define the equatorial plane around each pseudo octahedral nickel ion [Ni–N(1) 2.096(7), Ni–N(11) 2.107(7), Ni–N(18) 2.062(6), Ni–N(22) 2.175(7) Å]. The *trans* axial positions are occupied by the nitrogen atoms from the two different azides (Ni–N(3′) and Ni–N(4) of 2.164 and 2.127(6) Å, respectively) with a N(3′)–Ni–N(4) bond angle of 173.3(2)°. The slight distortion of each Ni^{II} is reflected on the *cisoid* angles [78.6(2)–95.0(8)°]. The equatorial mean plane is slightly tetrahedrally distorted (max deviation of ± 0.02 Å) with the metal displaced by 0.03 Å towards N(4).

The 1D chain developing along axis *b*, is formed by Ni(L) units connected alternatively by single and double bridging μ-(1,3-azide) ligands (Figure 2). The intermetallic separations between the single and double azide bridge are 5.875(3) and 5.304(3) Å, respectively. These values are comparable with those of 5.799 and 5.249 Å found in the closely related alternating system $[Ni_2(\mu\text{-}N_3)_3(dpt)_2](ClO_4)$,[9] where the tridentate amine ligand, dpt is bis(3-aminopropyl)-amine. In contrast, the neutral polymer $[Ni(L)(N_3)_2]_n$[10] with single end-to-end azide junctions, the other N_3 being monocoordinated and pendant from the chain, shows an intermetallic distance of 5.662(1) Å, representing a mean value of the Ni···Ni distances for the present case. The N(2)–N(1)–Ni and N(2)–N(3)–Ni angles exhibited by the coordinated azide nitrogens are comparable, being 132.9(5) and 133.2(5)°, respectively, but somewhat larger than the N(5)–N(4)–Ni of 122.5(3)°. Correspondingly, the azide N(1)–N(2)–N(3) displays an angle of 176.1(7)° and the other [N(4)–N(5)–N(4′)] has a linear arrangement being located on a symmetry center. The pseudo torsion angles Ni–N(1)–N(3)–Ni′′ and Ni–N(4)–N(4′)–Ni′ are 180.0 and 5.3°, respectively.

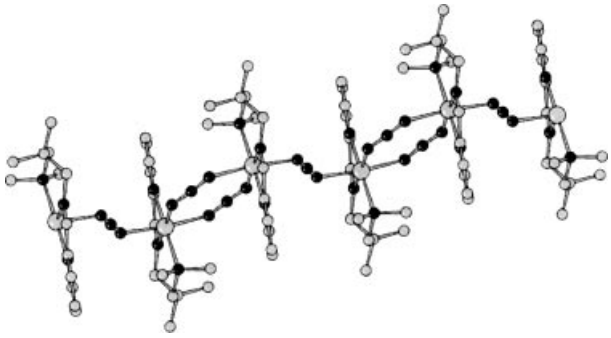

Figure 2. Polymeric structure of complex **1** (inversion centers are located at central nitrogen of the single bridging azide and in the midpoint of the double bridging azide).

Complex 2

The structure determination of **2** reveals that it is comprised of 2D undulated layers of $[Cu(N_3)(bpds)_2]^+_n$, where the charge is counterbalanced by perchlorate (ClO_4^-) anions with disordered water molecules in the crystal lattice. The ORTEP view of the coordination environment with the atom labeling scheme is shown in Figure 3 and a selection of bond lengths and angles is given in Table 1. The copper ion, located on a twofold axis, presents a hexacoordination geometry with four bpds nitrogen donors in the equatorial plane [Cu–N(11) 2.055(6), Cu–N(22) 2.044(6) Å, mean deviations of N donors ± 0.061(4) Å] and two azide nitrogens axially located at significantly longer distances [Cu–N(2), 2.447(7) Å]. The Cu–N(2)–N(1) bond angle presents a rather large value of 140.2(5)°. Taking into account the coordination linkages, the crystal structure can be envisaged as being formed by –Cu–$(bpds)_2$–Cu– polymers of colinear Cu^{II} ions connected by μ-(1,3-N_3) ligands to build a 2D grid of 4,4 topology, with the nodes occupied by the copper ions, and the edges by the single μ-(1,3-N_3) and the double bpds connectors. Figure 4 shows a packing view down axis *c* indicating the perchlorate anions located inside the grid in between the double bpds connectors. The intermetallic distance along the azide is 6.703 Å and through the bpds ligands 10.839 Å (axis *a*). The zigzag arrangement of copper ions, in the –Cu–(N_3)–Cu– array, displays a Cu–Cu–Cu angle of 160.31° and an ideal torsion angle Cu–N–N–Cu of 128.9°.

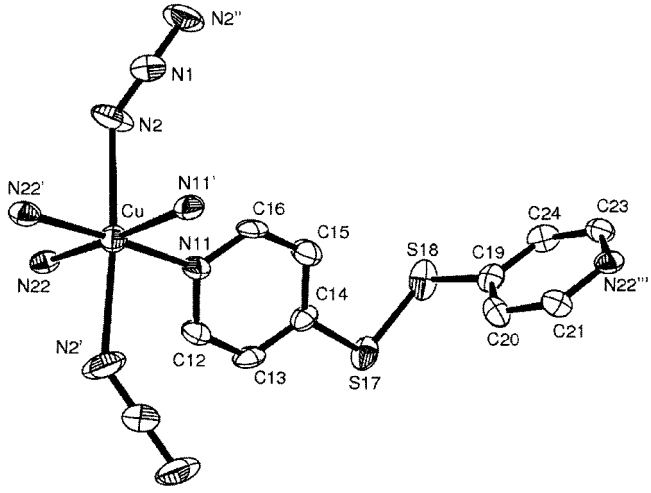

Figure 3. ORTEP plot of complex **2** with atom numbering scheme (symmetry operations: (′) *x*, –*y* + 3/2, –*z* + 3/2; (′′) *x* – 1, –*y* + 3/2, –*z* + 3/2; (′′′) 1 + *x*, *y*, *z*).

The crystal structure evidences a *gauche* conformation for the bpds spacer with a C–S–S–C torsion angle of 92.2(3)°, which is well in the range of 83.8(6)–95.5(8)°, found in a series of coordination polymers containing bpds ligands, in spite of the different coordination metal environment.[7e] However, it is interesting to note that the centrosymmetric space group furnishes both the possible enantiomeric conformers [± 92.2(3)°] for the acyclic disulfide[7c] and each 2D layer, piled parallel to the *ab* plane (Figure 5), contains only one of these.

Magnetic Properties

Complex 1

The magnetic properties of complex **1** in the form of χ_m and $\chi_m T$ (inset) vs. T plots (χ_m is the molar magnetic susceptibility for one Ni^{II} ion) are shown in Figure 6. The

 © 2005 Wiley-VCH Verlag GmbH & Co. KGaA, Weinheim

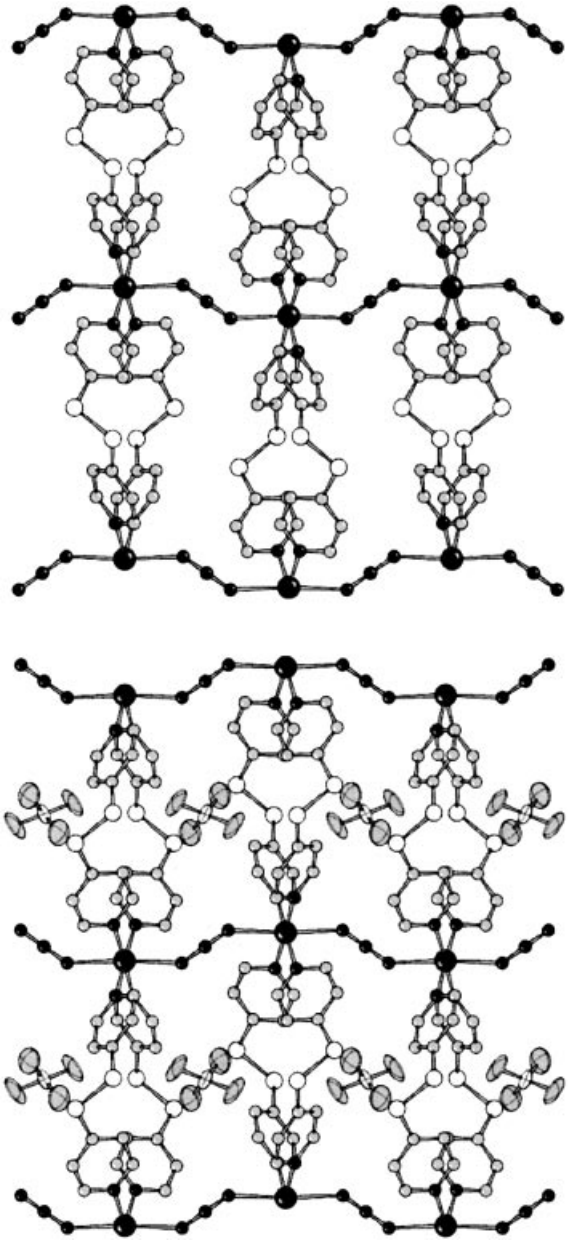

Figure 4. The 2D grid of complex **2** viewed down axis *c* indicating the location of perchlorate anions.

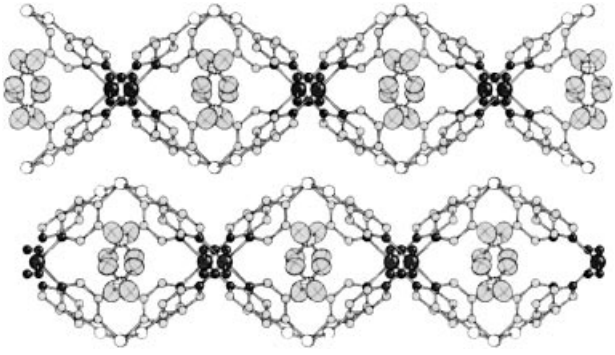

Figure 5. Side view (down axis *b*) of the 2D layers of complex **2** with perchlorate anions indicated as ellipsoids (disordered water molecules not shown).

value of $\chi_m T$ = 0.61 $cm^3 mol^{-1} K$ at 300 K is smaller than the expected value for an isolated Ni^{II} ion with g > 2.00 ($\chi_m T$ close to 1.0 $cm^3 mol^{-1} K$). Starting from room temperature $\chi_m T$ values smoothly decrease down to 0.0 $cm^3 mol^{-1} K$ at 2 K. At room temperature the χ_m value starts at 0.0022 $cm^3 mol^{-1}$ and increases in a uniform manner to a maximum of 0.0023 $cm^3 mol^{-1}$ around 190 K. Then χ_m values decrease to 0.0012 $cm^3 mol^{-1}$ at 25 K and again increase at lower temperature (0.0014 $cm^3 mol^{-1}$ at 2 K). The global feature is characteristic of very strong antiferromagnetic interactions, compensated at low temperature by the presence of small amounts of paramagnetic impurities (usually mononuclear ones following the Curie law) that originate from the increasing of χ_m at low temperatures.

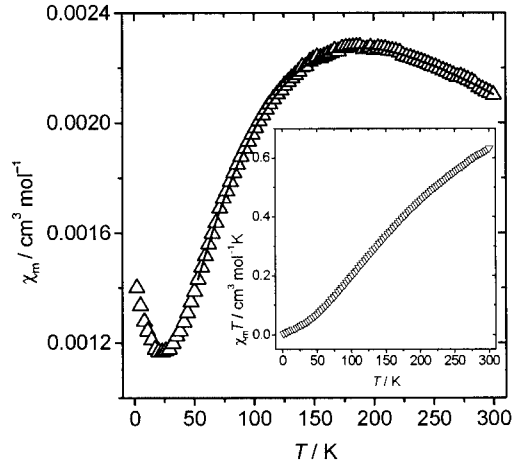

Figure 6. Plot of the χ_m vs. *T* for complex **1** (solid line represents the best-fit calculation; inset: plot of the $\chi_m T$ vs. *T*).

Complex **1** is actually an alternating 1D nickel(II) system with two kinds of alternate azide bridges: single and double end-to-end μ-(1,3-N_3). The fit of the magnetic data has been carried out applying the Borrás–Almenar formula for such types of alternating one-dimensional *S* = 1 systems,[11] based on the Hamiltonian $H = -J\Sigma(S_{2i}S_{21-1} + \alpha S_{2i}S_{2i+1})$. In this Hamiltonian the single-ion anisotropy of Ni^{II} is not included. The work of Borrás–Almenar allows for the employment of two different formulae according to the alternation parameter (α between 0 and 0.5 or between 0.5 and 1). After some preliminary attempts, the best results corresponded to $\alpha > 0.5$. Thus, the formula used in the fit was the following:

$$\chi_m = 0.25g^2/T \cdot (A + Bx + Cx^2):(1 + Dx + Ex^2 + Fx^3)$$

with $A = 1$; $B = 0.5$; $C = 0.1$; $D = 1.13693 + 0.748419\alpha$; $E = 1.650652 - 1.4622193\alpha + 1.668971\alpha^2$; $F = 0.4447955 + 1.162769\alpha$; $x = |J| / kT$.

Considering the shape of the experimental curve at low temperatures (Curie-law impurities) and that the Borrás–Almenar formula is not valid at low temperatures, mainly with a noticeable *J* value, we have removed all the experimental points from 50 to 2 K for the fit. With this condition, the best-fit parameters obtained are $J = -106.7 \pm 2\ cm^{-1}$; $\alpha = 0.82 \pm 0.02$; $g = 2.21 \pm 0.02$ and $R = 1.33 \times 10^{-5}$ (*R* is the agreement factor defined as

 © 2005 Wiley-VCH Verlag GmbH & Co. KGaA, Weinheim

$\Sigma_i[(\chi_m T)_{obs} - (\chi_m T)_{calc}]^2 / \Sigma_i[(\chi_m T)_{obs}]^2$). These results indicate very strong antiferromagnetic coupling through the two kinds of azide bridging ligands. At this point, a question arises: which is which?

To the best of our knowledge only one similar complex has been reported by one of the authors.[9] The calculated J values were $J = -84.6\ cm^{-1}$ (for the double azido bridge) and $J' = -41.4\ cm^{-1}$ (for the single azido bridge). According to reported magneto-structural correlations,[6,9,12] the antiferromagnetic component of J is strongly dependent on the Ni–N–N and the Ni–N–N–N–Ni torsion angles, whereas only slightly from the Ni–N bond, with distances typically in the range, 2.12–2.17 Å.[6,9,12] For the mono-bridged fragment, the maximum coupling is expected for Ni–N–N angles close to 108°, while for greater values, the antiferromagnetic interactions must decrease. An accidentally orthogonal valley, centered at 164°, is found.[6] The values reported in the literature for similar systems range from $J = -100\ cm^{-1}$ (Ni–N–N angle of 120.9°) to $-49\ cm^{-1}$ (Ni–N–N angle of 137.2°). Thus, it seems that the sensitivity to this angle is very important. In complex **1**, the Ni–N–N of 122.52° implies strong antiferromagnetic coupling. Moreover, the Ni–N–N–N–Ni torsion angle is 180°, which allows the maximum AF coupling.[6]

The Ni-$(N_3)_2$-Ni fragment in complex **1** is not comparable to that previously reported.[9,12] In that case, a strong torsion between the two azide bridging ligands was detected, in contrast to parallel azide ligands in complex **1**. Thus, in the present case, the most important factor is only the δ angle, that represents the dihedral angle formed by the $(N_3)_2$ plane and the N–Ni–N plane.[6] For $\delta = 180°$ (0°) the AF coupling is at a maximum, whereas it is strongly reduced as this angle increases. The Ni–N–N is also important in this case. According to literature data, J values occur from $-114.5\ cm^{-1}$ for $\delta = 3.0$ to $-4.6\ cm^{-1}$ for $\delta = 45.0°$.[6] Thus, the small δ angle of 2.66° detected in **1** allows strong AF coupling. It seems to be logical that with the most favorable conditions of the double azide bridges, the J value is greater than that associated with a single azide bridging ligand.[6,9,12] Here these conditions are very favorable: thus the greatest J value may be assigned to the double azide bridging system while the smallest J to the single azide bridging ligand.

Complex 2

Magnetic properties of complex **2** are shown in Figure 7 as $\chi_m T$ vs. T plots (χ_m is the molar magnetic susceptibility for one Cu^{II} ion). The value of $\chi_m T$ at 300 K ($0.43\ cm^3 mol^{-1} K$) is as expected for one magnetically quasi-isolated spin doublet ($g > 2.00$). Starting from room temperature the $\chi_m T$ values smoothly decrease down to 50 K, then quickly to $0.25\ cm^3 mol^{-1} K$ at 2 K. The global feature is characteristic of very weak antiferromagnetic interactions. The reduced molar magnetization at 2 K (Figure 7, inset) also indicates that the antiferromagnetic coupling is very small. The $M/N\beta$ value at 5 T is close to one electron and the experimental curve lies slightly below the Brillouin function, assuming $g = 2.14$ (according to magnetic data and EPR measurements, see below).

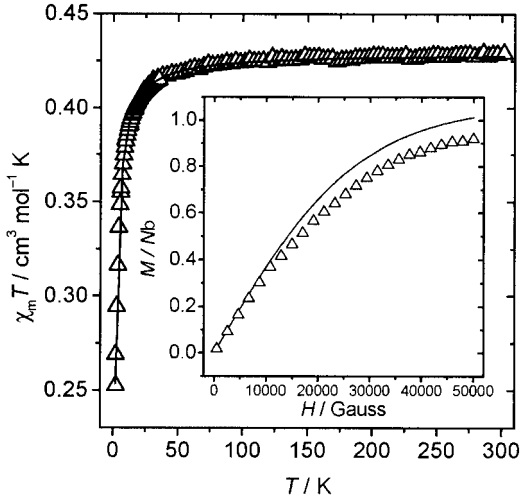

Figure 7. Temperature dependence of $\chi_m T$ vs. T for complex **2** (solid line indicates the best fit); inset: plot of the reduced magnetization ($M/N\beta$) at 2 K (solid line represents the Brillouin formula for the g value calculated from EPR spectra).

Actually complex **2** is a complicated two-dimensional copper(II) network with two kinds of bridging ligands: bpds and μ-(1,3-azide). Taking into consideration the long distances and the number of carbon atoms between adjacent copper(II) ions separated by the bpds, we may consider, from a magnetic point of view, a pseudo-one-dimensional structure. All copper(II) atoms are linked by μ-(1,3-N_3) bridging ligands in apical-apical positions (long-long distances). This gives a uniform $S = 1/2$ system. The fit of the magnetic data has been carried out using the formula given by Bonner and Fisher for this kind of uniform antiferromagnetic $S = 1/2$ chains.[13] The best-fit parameters obtained with this model are $J = -1.21 \pm 0.2\ cm^{-1}$, $g = 2.14 \pm 0.02$ and $R = 2.1 \times 10^{-6}$ (R is the agreement factor defined as $\Sigma_i[(\chi_m T)_{obs} - (\chi_m T)_{calc}]^2 / \Sigma_i[(\chi_m T)_{obs}]^2$. This result indicates very small antiferromagnetic coupling through the μ-(1,3-azide) bridging ligands. The small J value can be interpreted as a consequence of the almost nil overlap between the copper(II) ions through the μ-(1,3-N_3) bridging ligands in the apical(long)-apical(long) coordination mode. Similar features have already been reported for other apical-apical polynuclear azide complexes, such as the dinuclear one reported by Drew et al., where the authors indicated "relatively weak antiferromagnetic interaction" without giving any value of J.[14] Taylor et al.,[15] reported an analogous complex where the lack of significant coupling between copper centers mediated by azide has been rationalized on the basis of the overlap. The major σ pathway for the interaction of two copper ions is via their d_{z^2} orbitals through the azide. The nearly square-pyramidal geometry of the d^9 copper atoms suggests that they have $d_{x^2-y^2}$ ground states:[13] therefore the unpaired electrons are localized in the basal plane and cannot effectively undergo coupling. Finally, one of us reported a similar complex with this kind of azide bridging in combination of bridging oxalate where

 © 2005 Wiley-VCH Verlag GmbH & Co. KGaA, Weinheim

the authors stated that "the coupling parameter corresponding to the apical bridge can reasonably be expected to be very small".[5f] On the other hand, the presence of the bpds bridging ligand which connects the one-dimensional –[μ-(1,3-N_3)Cu]$_n$– polymers can also contribute to the final J value. Thus, although the R value is very good, it must be considered carefully, owing to other possible magnetic interactions.

Let us remember that when the coordination mode is not apical(long)-apical(long) but equatorial(short)-equatorial(short) the coupling is normally strongly antiferromagnetic.[16] However, the most usual coordination mode is neither equatorial(short)-equatorial(short) nor apical(long)-apical(long) but equatorial(short)-apical(long) for the most current five-coordination mode. In this case both weak ferro- or antiferromagnetic coupling can be found, depending mainly on the distortion of the copper(II) ions.

The EPR spectra show the same shape at different temperatures (Figure 8), which is the typical pattern corresponding to an elongated octahedral copper(II) center with $g_{||}$ = 2.28 and $g_{\perp}$ = 2.07 (g_{av} = 2.14), in perfect agreement with the value obtained by magnetic measurements.

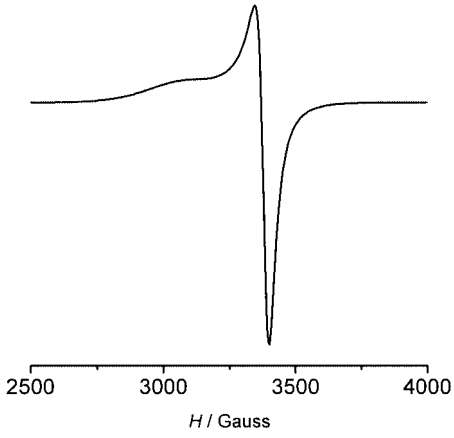

Figure 8. The EPR spectrum of complex **2** at room temperature (same shape was obtained at different temperatures).

Conclusion

We have presented here the syntheses, single-crystal structures and magnetic behaviors of two new azide complexes of nickel(II) (**1**) and copper(II) (**2**) using a Schiff base and 4,4′-bipyridyl disulfide, respectively, as coligands. Complex **1** is a 1D chain of nickel(II) with alternating single and double μ-(1,3-N_3) bridges. Complex **2** is a 2D grid of 4,4 topology comprising single μ-(1,3-N_3) and double bridging 4,4′-bipyridyl disulfide. Magnetic susceptibility data have been fitted using the Borrás–Almenar formula of alternating one-dimensional S = 1 system based on the Hamiltonian $H = -J\Sigma(S_{2i}S_{21-1} + \alpha S_{2i}S_{2i+1})$ for complex **1**. Whereas for complex **2**, susceptibility data were fitted by using the typical formula for a uniform antiferromagnetic S = 1/2 chain. The best-fit parameters for complex **1** indicate very strong antiferromagnetic coupling through the two kinds of azide bridging and for complex **2** reflect very small antiferromagnetic coupling through the μ-(1,3-azide). The magnetic interactions are compared to those of closely related complexes taking into account all the coordination angles involving azide bridging ligands as well as the coordination metal environment.

Experimental Section

Materials: High purity 4,4′-bipyridyl disulfide (Aldrithiol-4; 98%) and *N*,*N*,2,2-tetramethyl-1,3-propanediamine of Aldrich Chemical Co. Inc. were used and all other chemicals were of AR grade.

Physical Measurements: Elemental analyses (carbon, hydrogen and nitrogen) were performed using a Perkin–Elmer 240C elemental analyzer. IR spectra were measured from KBr pellets on a Nicolet 520 FTIR spectrometer. Magnetic measurements were carried out in the "Servei de Magnetoquímica (Universitat de Barcelona)" on polycrystalline samples (20 mg) with a Quantum Design SQUID MPMS-XL magnetometer working in the 2–300 K range. The magnetic field was 0.1 T. The diamagnetic corrections were evaluated from Pascal's constants. EPR spectra were recorded on powder samples at the X-band frequency with a BRUKER 300E automatic spectrometer, varying the temperature between 4–300 K.

Crystallographic Data Collection and Refinement: Data collections of the complexes reported were carried out at 293(2) K on a diffractometer equipped with a Mar-research image plate and Mo-K_α radiation (λ = 0.71073 Å). 95 frames were measured at 2° intervals with a counting time of 2 min, and the crystal positioned at 70 mm from the image plate. The crystallographic data, the condition for the intensity data collection and some features of the structure refinements are listed in Table 2. Data analysis was carried out with the XDS program[17] and the structures were solved by direct methods with the SHELX97 program.[18] An empirical absorption correction was applied using DIFABS.[19] The structures were anisotropically refined on F^2 using the SHELXL program[18] with the contribution of hydrogen atoms at calculated positions. The perchlorate anion of complex **2** was found to be disordered over two positions (refined occupancies of 0.78(2):0.28(2)). Three residuals on the ΔF map of complex **2** were interpreted as disordered water oxygens that account for a total of 1.25 molecules (2.50 per metal unit). All the calculations were performed using the Wingx System Ver. 1.64.5.[20]

Synthesis

Caution! Perchlorate as well as azide salts were used in small quantities and handled with care since explosion may occur.

$[Ni_2L_2(N_3)_3]_n(ClO_4)_n$ (1): The tridentate Schiff base (L) was prepared by refluxing pyridine-2-aldehyde (1 mmol; 0.107 g) and *N*,*N*,2,2-tetramethyl-1,3-propanediamine (1 mmol; 0.130 g) in methanol (10 mL) according to literature method.[21] A methanolic solution (10 mL) of nickel(II) perchlorate hexahydrate (1 mmol; 0.365 g) was added to the hot (ca. 40 °C) methanolic solution (10 mL) of tridentate Schiff-base ligand (1 mmol). The resulting solution was cooled to room temperature. An aqueous solution (5 mL) of sodium azide (1.5 mmol; 0.0975 g) was added dropwise to it with continuous stirring and the resulting reaction mixture was filtered and the filtrate was allowed to evaporate in a refrigerator. Suitable green single crystals for structure determination were obtained from the filtrate after a few days. Yield: 72%. $C_{26}H_{42}ClN_{15}Ni_2O_4$ (781.62): calcd. C 39.91, H, 5.37, N 26.86; found C 39.80, H 5.41, N 26.75. IR (cm^{-1}): 3443 (w), 3378 (w),

 © 2005 Wiley-VCH Verlag GmbH & Co. KGaA, Weinheim

Table 2. Crystal data and refinement details of complexes **1** and **2**.

	1	**2**
Formula	$C_{26}H_{42}ClN_{15}Ni_2O_4$	$C_{20}H_{21}ClCuN_7O_{6.5}S_4$
M_r [g mol^{-1}]	781.62	690.67
Crystal system	triclinic	orthorhombic
Space group	$P\bar{1}$	*Pnna*
a [Å]	8.089(13)	10.839(14)
b [Å]	9.392(14)	13.208(17)
c [Å]	12.267(18)	19.75(2)
α [°]	107.28(1)	90.0
β [°]	95.95(1)	90.0
γ [°]	96.92(1)	90.0
Volume [Å^3]	874(2)	2827(6)
Z	2	4
$D_{calcd.}$ [g cm^{-3}]	1.485	1.623
μ Mo-K_α [mm^{-1}]	1.209	1.213
F(000)	408	1408
θ_{max} [°]	26.10	25.02
Reflect. collected	6707	15554
Unique reflections	3107	2502
*R*int	0.0565	0.0684
Observed $I > 2\sigma(I)$	1879	2254
Parameters	246	188
Goodness of fit (F^2)	1.045	1.261
R_1 [$I > 2\sigma(I)$][a]	0.0702	0.0876
wR_2[a]	0.2091	0.1825
$\Delta\rho$ [e Å^{-3}]	0.574, –0.774	1.273, –0.504

[a] $R_1 = \Sigma \, ||F_o| - |F_c|| \, / \, \Sigma|F_o|$; $wR_2 = \{\Sigma[w(F_o^2 - F_c^2)^2] \, / \, \Sigma[w(F_o^2)^2]\}^{1/2}$.

2964 (m), 2901 (m), 2090 (vs), 2061 (vs), 1598 (m), 1093 (vs), 624 (w).

$[Cu(bpds)_2(N_3)]_n(ClO_4)_n(H_2O)_{2.5n}$ (2): An aqueous solution (10 mL) of copper perchlorate hexahydrate (1 mmol; 0.370 g) was added to a methanolic solution(10 mL) of bpds (2 mmol; 0.440 g). An aqueous solution (10 mL) of sodium azide (1 mmol; 0.065 g) was slowly poured into the resulting greenish solution while stirring. A deep green colored compound separated out. The whole reaction mixture was stirred for 30 min and filtered. The separated solid was washed several times with water-methanol (1:1) and dissolved in a minimum amount of 4(N) ammonia solution resulting in a deep blue solution. Green single crystals suitable for X-ray diffraction quality were obtained after a few days on keeping the solution in a refrigerator. Yield: 75%. $C_{20}H_{21}ClCuN_7O_{6.5}S_4$ (690.67): calcd. C 34.74, H 3.05 N 14.18; found C 34.98, H 3.05, N 14.09. IR: $\tilde{\nu}$ = 3544–3190 (s, v br), 3086 (vw), 2042 (vs), 1591 (vs), 1416 (s), 1099 (vs), 1059 (s), 812 (m), 718 (s), 500 (w)cm^{-1}.

Further details of the crystal structure determination have been deposited with the Cambridge Crystallographic Data Centre as supplementary publication. CCDC-251930 and -251931 for complexes **1** and **2,** respectively, contain the supplementary crystallographic data for this paper. These data can be obtained free of charge from The Cambridge Crystallographic Data Centre via www.ccdc.cam.ac.uk/data_request/cif.

Acknowledgments

N. R. C. thanks the Council of Scientific and Industrial Research, New Delhi and J. R. thanks the Spanish Govt. (BQU2003/00539) for financial support. The authors are grateful to Dr. G. Mostafa for scientific discussions. They are also thankful to EPSRC and the University of Reading for funds for the Image Plate System.

[1] a) *Molecular-Based Magnetic Materials: Theory, Technique and Applications* (Eds.: M. M. Turnbull, T. Sugimoto, L. K. Thomson), ACS Symposium Series 644, American Chemical Society: Washington DC, **1996**; b) S. Sikorav, I. Bkouche-Waksman, O. Kahn, *Inorg. Chem.* **1984**, *23*, 490; c) D. Gatteschi, O. Kahn, J. S. Miller, F. Palacio, *Magnetic Molecular Materials*; NATO ASI, Kluwer: Dordrecht, **1991**; d) J. Ribas, M. Monfort, I. Resino, X. Solans, P. Rabu, F. Maingot, M. Drillon, *Angew. Chem. Int. Ed. Engl.* **1996**, *35*, 2671.

[2] a) J. Ribas, M. Monfort, C. Diaz, C. Bastos, X. Solans, *Inorg. Chem.* **1993**, *32*, 3557; b) J. Ribas, M. Monfort, R. Costa, X. Solans, *Inorg. Chem.* **1993**, *32*, 695; c) M. A. Halcrow, J. C. Huffman, G. Christou, *Angew. Chem. Int. Ed. Engl.* **1995**, *34*, 889; d) A. Escuer, R. Vicente, J. Ribas, M. S. El Fallah, X. Solans, M. Font-Bardia, *Inorg. Chem.* **1994**, *33*, 1842; e) R. Vicente, A. Escuer, J. Ribas, M. S. El Fallah, X. Solans, M. Font-Bardia, *Inorg. Chem.* **1995**, *34*, 1278; f) J. Ribas, M. Monfort, B. K. Ghosh, R. Cortes, X. Solans, M. Font-Bardia, *Inorg. Chem.* **1996**, *35*, 864; g) M. Monfort, J. Ribas, X. Solans, *J. Chem. Soc. Chem. Commun.* **1993**, 350; h) M. Monfort, I. Resino, J. Ribas, H. Stoeckli-Evans, *Angew. Chem. Int. Ed.* **2000**, *39*, 191; i) F. A. Mautner, R. Cortes, L. Lezama, T. Rojo, *Angew. Chem. Int. Ed. Engl.* **1996**, *35*, 96.

[3] a) J. S. Miller, A. J. Epstein, *Angew. Chem. Int. Ed. Engl.* **1994**, *33*, 385; b) A. Caneschi, D. Gatteschi, R. Sessoli, P. Rey, *Acc. Chem. Res.* **1989**, *22*, 392; c) P. S. Mukherjee, T. K. Maji, G. Mostafa, T. Mallah, N. Ray Chaudhuri, *Inorg. Chem.* **2000**, *39*, 5147; d) P. S. Mukherjee, T. K. Maji, G. Mostafa, J. Ribas, M. S. El Fallah, N. Ray Chaudhuri, *Inorg. Chem.* **2001**, *40*, 928; e) P. S. Mukherjee, T. K. Maji, T. Mallah, E. Zangrando, L. Randaccio, N. Ray Chaudhuri, *Inorg. Chim. Acta* **2001**, *315*, 247; f) T. K. Maji, P. S. Mukherjee, S. Konar, G. Mostafa, J. P. Tuchagues, N. Ray Chaudhuri, *Inorg. Chim. Acta* **2001**, *314*, 211; g) D. Gatteschi, *Adv. Mater.* **1994**, *6*, 635.

[4] a) M. I. Arriortua, A. R. Cortes, L. Lezama, T. Rojo, X. Solans, *Inorg. Chim. Acta* **1990**, *174*, 263; b) A. Escuer, R. Vicente, J. Ribas. *J. Magn. Mater.* **1992**, *110*, 181; c) A. Escuer, R. Vicente, J. Ribas, X. Solans. *Inorg. Chem.* **1995**, *34*, 1793.

[5] a) J. Comarmond, P. Plumere, J. M. Lehn, Y. Agnus, R. Louis, R. Weiss, O. Kahn, I. Morgersten-Badarau, *J. Am. Chem. Soc.* **1982**, *104*, 6330; b) O. Khan, S. Sikorav, J. Gouteron, Y. Jeannin, *Inorg. Chem.* **1983**, *22*, 2877; c) S. S. Tandon, L. K. Thompson, M. E. Manuel, J. N. Bridson, *Inorg. Chem.* **1994**, *33*, 5555; d) E. Ruiz, J. Cano, S. Alvarez, P. Alemany, *J. Am. Chem. Soc.* **1998**, *120*, 11122; e) M. A. Aebersold, M. Gillon, O. Plantevin, L. Pardi, O. Kahn, I. Bergeret, V. Seggern, L. Ohrstrom, A. Grand, E. Lelievre-Berna, *J. Am. Chem. Soc.* **1998**, *120*, 5238; f) P. S. Mukherjee, T. K. Maji, G. Mostafa, W. Hibbs, N. Ray Chaudhuri, *New J. Chem.* **2001**, *25*, 760; g) T. K. Maji, P. S. Mukherjee, G. Mostafa, T. Mallah, J. Cano-Boquera, N. Ray Chaudhuri, *Chem. Commun.* **2001**, 1012; h) P. S. Mukherjee, S. Dalai, G. Mostafa, T.-H. Lu, E. Rentschler, N. Ray Chaudhuri, *New J. Chem.* **2001**, *25*, 1203; i) P. S. Mukherjee, T. K. Maji, A. Escuer, R. Vicente, J. Ribas, G. Rosair, F. A. Mautner, N. Ray Chaudhuri, *Eur. J. Inorg. Chem.* **2002**, 943; j) S. Dalai, P. S. Mukherjee, T. Mallah, M. G. B. Drew, N. Ray Chaudhuri, *Inorg. Chem. Commun.* **2002**, *5*, 472; k) S. Konar, E. Zangrando, M. G. B. Drew, T. Mallah, J. Ribas, N. Ray Chaudhuri, *Inorg. Chem.* **2003**, *42*, 5966; l) D. Ghoshal, T. K. Maji, E. Zangrando, T. Mallah, E. Riviére, N. Ray Chaudhuri, *Inorg. Chim. Acta* **2004**, *357*, 1031.

[6] J. Ribas, A. Escuer, M. Monfort, R. Vicente, R. Cortes, L. Lezama, T. Rojo, *Coord. Chem. Rev.* **1999**, *193–195*, 1027.

[7] a) A. J. Blake, N. R. Brooks, N. R. Champness, M. Crew, A. Deveson, D. Fenske, D. H. Gregory, L. R. Hanton, P. Hubberstey, M. Schroder, *Chem. Commun.* **2001**, 1432; b) R. Horikoshi, T. Mochida, H. Moriyama, *Inorg. Chem.* **2001**, *40*, 2430; c) F. M. Tabellion, S. R. Seidel, A. M. Arif, P. J. Stang, *J. Am. Chem. Soc.* **2001**, *123*, 7740; d) M. Hong, W. Su, R.Cao, M.

 © 2005 Wiley-VCH Verlag GmbH & Co. KGaA, Weinheim

Fujita, J. Lu, *Chem. Eur. J.* **2000**, *6*, 427; e) R. Horikoshi, T. Mochida, N. Maki, S. Yamada, H. Moriyama, *J. Chem. Soc. Dalton Trans.* **2002**, *28*.
[8] A. K. Ghosh, D. Ghoshal, T.-H. Lu, G. Mostafa, N. Ray Chaudhuri *Cryst. Growth Des.* **2004**, *4*, 851.
[9] R. Vicente, A. Escuer, J. Ribas, X. Solans, *Inorg. Chem.* **1992**, *31*, 1726.
[10] P. S. Mukherjee, S. Dalai, E. Zangrando, F. Lloret, N. Ray Chaudhuri, *Chem. Commun.* **2001**, 1444.
[11] a) J. J. Borrás-Almenar, Ph. D. Thesis, Valencia, Spain, **1992**; b) J. J. Borrás-Almenar, E. Coronado, J. Curély, R. Georges, *Inorg. Chem.* **1995**, *34*, 2699.
[12] R. Vicente, A. Escuer, *Polyhedron* **1995**, *14*, 2133.
[13] J. C. Bonner, M. E. Fisher, *Phys. Rev. A* **1964**, *135*, 640.
[14] M. G. B. Drew, M. McCann, S. M. Nelson, *J. Chem. Soc. Chem. Commun.* **1979**, 481.
[15] J. H. Satcher, M. W. Droege, T. J. R. Weakley, R. T. Taylor, *Inorg. Chem.* **1995**, *34*, 3317.
[16] a) I. Bkouche-Waksman, M.-L. Boillot, O. Kahn, S. Sikorav, *Inorg. Chem.* **1984**, *23*, 4454; b) P. Chaudhuri, K. Oder, K. Wieghardt, B. Nuber, J. Weiss, *Inorg. Chem.* **1986**, *25*, 2818.
[17] W. Kabsch, *J. Appl. Crystallogr.* **1988**, *21*, 916.
[18] G. M. Sheldrick, *SHELX97, Programs for Crystal Structure Analysis (Release 97–2)*, University of Göttingen, Germany, **1998**.
[19] N. Walker, D. Stuart, *Acta Crystallogr., Sect.* A **1983**, *39*, 158.
[20] L. J. Farrugia, *J. Appl. Crystallogr.* **1999**, *32*, 837.
[21] a) G. Zakrzewski, L. Sacconi, *Inorg. Chem.* **1968**, *7*, 1034; b) P. Bamfield, R. Price, R. G. J. Miller, *J. Chem. Soc. (A)* **1969**, 1447.

Received: November 04, 2004

 © 2005 Wiley-VCH Verlag GmbH & Co. KGaA, Weinheim

Synthetic Explorations Towards Sterically Crowded 1,2,3-Substituted Bis(indenyl)zirconium(IV) Dichlorides

Andreas C. Möller,[a,b] Richard Blom,[a] Richard H. Heyn,*[a] Ole Swang,[a] Carl-Henrik Görbitz,[c] and Tanja Seraidaris[d]

Keywords: Metallocenes / Ligand effects / Isomerization / Polymerization / Density functional calculations

The systematic synthesis of 1,3-dialkyl-substituted 2-silylindenes and their suitability as zirconocene ligands is discussed. Unexpected reactivities rendered a number of substitution patterns unfeasible, especially for alkyl groups other than methyl in 2-(trimethylsilyl)indene derivatives, and essentially for all derivatives of 2-(dimethylsilyl)indene. The syntheses of *rac*/*meso*-bis[1-methyl-2-(trimethylsilyl)indenyl]zirconium(IV) dichloride (**12**) and bis[1,3-dimethyl-2-(trimethylsilyl)indenyl]zirconium(IV) dichloride (**13b**) are described. The solid-state structure of the latter displays strong deformations within the ligand framework and an unusually large $Cp_{centroid}$-Zr–$Cp_{centroid}$ angle. Both, **12**/MAO and **13b**/MAO, displayed ethene and ethene-co-1-hexene polymerization activity. Curiously, **13b**/MAO shows an extraordinary monomer selectivity, which can be rationalized by means of DFT calculations on the active site.
(© Wiley-VCH Verlag GmbH & Co. KGaA, 69451 Weinheim, Germany, 2005)

Introduction

The field of metallocene-catalyzed olefin polymerization has achieved significant improvements on polymer properties. The ligand−tacticity relationship is well understood and, apart from tailor-made stereocontrol, co-monomer incorporation and block length have been emphasized as keys to innovative materials.[1] The detailed polymerization mechanism with all its variations is complicated and the choice of appropriate polymerization conditions to favor one monomer over the other still requires vast and tedious sets of experiments. An outline of the extensive efforts made within this area can be found in the various review articles.[2]

Previous work from our laboratory addressed unbridged zirconocene dichloride with silyl substituents in the 1 or 2 position.[3] Reports on trisubstituted indenyl ligands, i.e. substituents in the 1, 2, and 3 positions, are still quite uncommon. It may be expected that steric congestion in such complexes is significant and that overall polymerization activity may be negatively influenced. In this study, we wish to present our results on a systematic study of 1,3-dialkyl-2-silyl-trisubstituted indene ligands for the synthesis of zirconocene dichlorides.

[a] Department of Hydrocarbon Process Chemistry, SINTEF Materials and Chemistry,
P. O. Box 124, Blindern, 0314 Oslo, Norway
Richard.H.Heyn@sintef.no,
Fax: +47-22 06 73 50
[b] Department of Chemical Engineering, Norwegian University of Science and Technology (NTNU),
7491 Trondheim, Norway
[c] Department of Chemistry, University of Oslo,
P. O. Box 1033 Blindern, 0315 Oslo, Norway
Fax: +47-22 85 54 41
[d] Department of Polymer Technology, Helsinki University of Technology,
P. O. Box 6100, 02015 HUT, Finland

Results and Discussion

Ligand Syntheses

The introduction of alkyl groups in the 1 and 3 position of 2-silylindenes should be feasible in a straight forward manner by simple double alkylation of indenyllithium salts. Deprotonation of 2-(dimethylsilyl)indene (**1a**, 2-DMS-Ind) and 2-(trimethylsilyl)indene (**1b**, 2-TMS-Ind) was achieved by *n*-butyllithium in pentane at room temperature or –90 °C, respectively. In spite of the nonpolar solvent, deprotonation at lower temperatures provided hydride substitution products for **1a**, as observed by Kira et al.[4] Alternatively deprotonation can be achieved with potassium hydride at room temperature.

Methylation of the lithium salt of **1a** with methyl iodide at –40 °C in diethyl ether yielded exclusively 3-Me-2-DMS-Ind (**2a**), while 1-Me-2-TMS-Ind (**2b**) was obtained likewise from 2-TMS-Ind. Repetition of the deprotonation−methylation sequence afforded a 1:4 mixture of the 1,1-dimethyl and 1,3-dimethyl isomers for both, **3a** and **3b**. Deprotonation and washing with pentane provided pure lithium salts of the 1,3-dimethyl-2-silylindenes **3a** and **3b** (Scheme 1). **3a** exhibits diastereotopic methyl resonances of the silyl group in a 1:1 ratio due to the presence of the chiral C(1) atom.

In order to determine whether bulkier alkyl substituents could be placed in the 1,3 positions, studies on the introduction of the *i*Pr group were conducted on **1b**, as the TMS

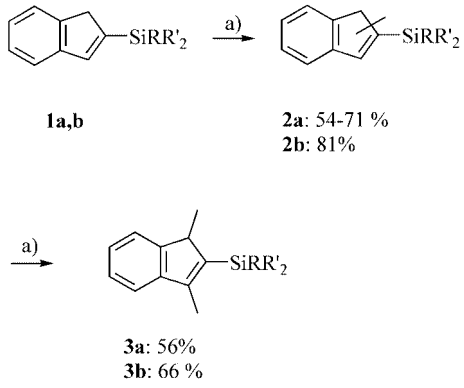

Scheme 1. General route towards 1,3-dialkyl-2-silylindenes. a) *n*BuLi, pentane, room temperature; MeI, diethyl ether, –40 °C. **a:** R = H, R′ = Me. **b:** R = R′ = Me. Yields are reported for the purified lithium salts of **3a** and **3b**, whereas spectroscopic data were obtained on the free ligands.

moiety is less prone to substitution reactions in the presence of lithium organyls. A brief summary of the results is given in Scheme 2. Following the procedure for methylation, exposure of the lithium salt of **1b** to isopropyl iodide sufficed to obtain the 1-*i*Pr isomer **4** in good yield. The proton and carbon NMR spectra of **4** reveal diastereotopic resonances for the *i*Pr methyl groups, and curiously the expected singlet for the trimethylsilyl (TMS) moiety displays two resonance maxima. We interpret these to arise from steric interaction of the *i*Pr and TMS groups. In addition, two different C(1) resonances are found. Deprotonation of **4** with *n*-butyllithium, however, leads to soluble lithium salts, which in a direct second alkylation with isopropyl iodide without prior isolation resulted in a mixture of four isomers, i.e. the mono-alkylated 1 and 3 isomers (3:1 parts) and the dialkylated 1,3 and 1,1 isomers (2:0.1 parts). The slight excess of *n*-butyllithium used in the reaction could be traced by detection of 2-methylhexane (0.3 parts). Deprotonation of **4** with potassium hydride in refluxing THF failed to provide a well-defined, insoluble potassium salt (K[**5**]). Due to the solubility of these salts, washing with pentane was accompanied by a loss of material.

A compelling explanation for these solubilities can be derived from a quenching experiment of Li[**5**] with methyl iodide in THF. GC/MS analysis of the reaction products revealed ten major products, of which one could be identified as 1-*t*Bu-2-TMS-Ind. Apparently Li[**5**] equilibrates between its indenyllithium and alkyllithium derivative, i.e. the lithium migrates from the Cp moiety of the indenyl through the *i*Pr group resulting in a covalent lithium carbon bond. Although satisfactory ^{1}H and ^{13}C NMR spectroscopic data were obtained, K[**5**] appears to be an inhomogeneous, poorly described compound, partially soluble in hydrocarbons. We suspect cation migration is still possible, despite the significantly bigger potassium cation.

Introduction of a *t*Bu group into 2-TMS-Ind may not be expected to be easy. Even in the case of indenyllithium, alkylation with *t*Bu bromide or iodide succeeds only in moderate yields.[5] Aiming for a possibly more demanding, but still more efficient route, we investigated a literature procedure for the synthesis of *t*Bu groups from 6,6-dimethyl(benzo)fulvenes.[6] 6,6-Dimethylbenzofulvene (**6**) is readily available in a one-pot reaction from indene, pyrrolidine and acetone in methanol,[7] and methyllithium is known to react smoothly in a 1,4-addition in diethyl ether to 1-*t*Bu-indenyllithium in a 80% yield. Acidic work-up and distillation afforded 3-*tert*-butylindene (**7**) in a 58% yield. Application of typical activators like TMEDA and $BF_3{\cdot}Et_2O$ does not improve the yield, but running the reaction in pentane in the presence of 10 wt.-% $AlCl_3$ offers the advantage of quantitative conversion, though acidic work-up is required prior to further reactions.

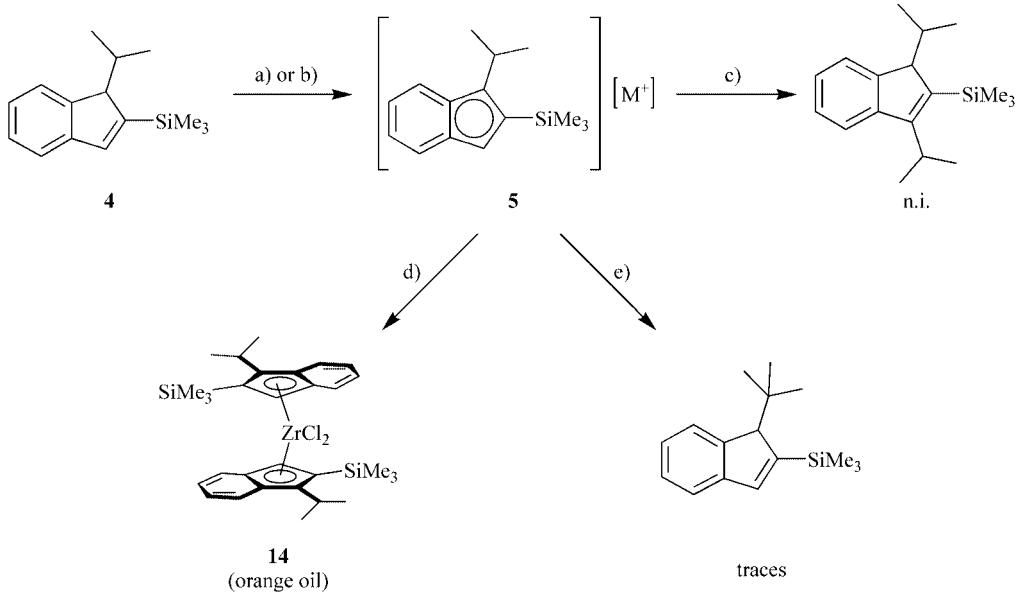

Scheme 2. Reactivity of 1-isopropyl-2-(trimethylsilyl)indene (**4**). a) *n*BuLi, pentane; b) potassium hydride, THF; c) 2-Iodopropane, diethyl ether/THF (n.i. = not isolated); d) $ZrCl_4$, THF, –40 °C; e) MeI, THF.

 © 2005 Wiley-VCH Verlag GmbH & Co. KGaA, Weinheim

Introduction of a second *t*Bu group by the same means is more complicated (Scheme 3). Formation of the 1-*t*Bu-6,6-dimethylbenzofulvene (**8**) does not occur at room temperature, but with an excess of pyrrolidine and refluxing for several days, nearly quantitative conversion is achieved. Addition of methyllithium to **8**, provides 1,3-di-*t*Bu-indene (**9**), albeit in low yield. It may be reasoned that the *t*Bu group raises the energy of the *exo* double bond by its electron releasing character and thus inhibits nucleophilic attack by methyllithium. Disappointingly, we had to find that the synthesis of 2-TMS-6,6-dibenzofulvene starting from **1b** is not possible with the aforementioned procedure. Alternatively we investigated the reaction of the lithium salt of **1b** with acetone and subsequent dehydration with phosphoric acid or acid anhydrides. The first attempt, which employed phosphoric acid, provided the benzofulvene. Reproduction of this reaction was unsuccessful; we are not primarily interested in ill-defined polymers, but could, however, envision the obtained products to be useful for road building purposes.

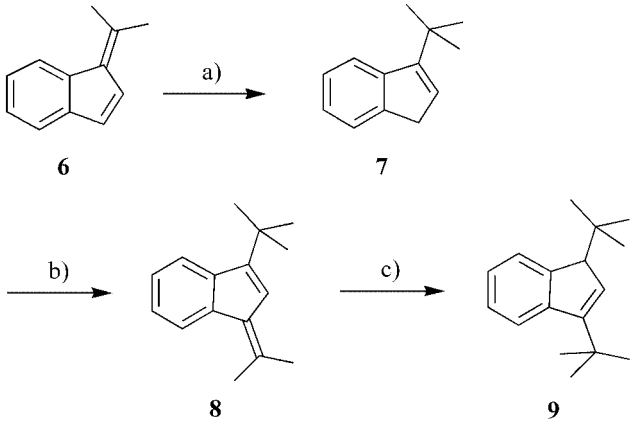

Scheme 3. A selective synthesis of 1,3-di-*t*Bu-indene (**9**). a) MeLi, Et_2O, 0 °C or MeLi, pentane, 5 mol-% $AlCl_3$ / acidic work-up b) $Pyrrolidine_{ex}$, $acetone_{ex}$, MeOH, 48 h reflux; c) MeLi, Et_2O, 6 h reflux.

Zirconocene Syntheses

To facilitate introduction to the coordination sphere of zirconium, **2b**, **3a**–**b** were all converted into their lithium salts **10**, **11a**–**b**, respectively, by exposure to stoichiometric amounts of a organyl lithium in pentane. The observed reactivities mirrored those of the starting material **1a–b**. The syntheses of the zirconium complexes were subsequently attempted by a salt metathesis reaction with zirconium tetrachloride, as illustrated in Scheme 4. For disubstituted ligands, *rac* and *meso* diastereomers may be obtained, whereas trisubstituted ligands exclusively provide enantiomers.

rac/*meso*-Bis[1-methyl-2-(trimethylsilyl)indenyl]zirconium(IV) dichloride (**12**) was obtained as a yellow powder in a respectable 55% yield. The *rac* and *meso* diastereomers were detected by ^1H NMR at a 1:1 ratio, and isolation or enrichment by crystallization at –40 °C failed. The *rac* and

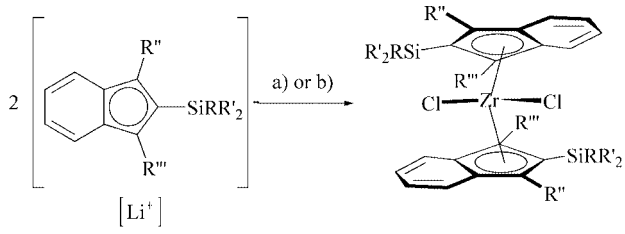

	10	11a	11b	12	13a	13b
R	CH_3	H	CH_3	CH_3	H	CH_3
R′	CH_3	CH_3	CH_3	CH_3	CH_3	CH_3
R″	CH_3	CH_3	CH_3	CH_3	CH_3	CH_3
R‴	H	CH_3	CH_3	H	CH_3	CH_3

Scheme 4. Salt metathesis reaction of the potassium/lithium salts with zirconium tetrachloride to form bis(indenyl)zirconocene dichlorides. a) $ZrCl_4$, Et_2O, 0 °C; b) $ZrCl_4$, THF, –40 °C. When R‴ = H, *rac* and *meso* isomers can be formed of which the latter one is omitted for clarity.

meso diastereomers were assigned according to relative chemical shifts, as published elsewhere.[3]

Reaction of **11a** with zirconium tetrachloride in diethyl ether at 0 °C provided a yellow oil upon filtration through magnesium sulfate and subsequent solvent removal. Crystallization from diethyl ether was only limitedly successful, and we were not able to obtain an analytically pure sample due to the low yield. NMR spectroscopic data suggest, however, formation of bis[1,3-dimethyl-2-(dimethylsilyl)indenyl]zirconium(IV) dichloride (**13a**). Unreacted **11a** could easily be recovered in good yields. A change of solvent from diethyl ether to THF did not improve the reaction and only decomposition products could be obtained.

Metallation of **11b** in diethyl ether succeeded with formation of a yellow precipitate. The solubility of bis[1,3-dimethyl-2-(trimethylsilyl)indenyl]zirconium dichloride (**13b**) in diethyl ether was too limited to allow work-up in this solvent; toluene proved to be suitable. Orange or yellow powders were obtained in a 44% yield upon recrystallization from diethyl ether solution at –40 °C, depending on the crystallinity of the zirconocene. Single crystals grown from diethyl ether solution are bright orange in color.

As it may be anticipated from the observation of inhomegeneity of K[**5**], an orange oil was obtained as its reaction product with zirconium tetrachloride (Scheme 2). Crystallization was unsuccessful, though crystals would form after a few weeks in the drybox. The ductility of the crystals precluded further isolation.

Crystal Structure

An ORTEP[8] view of **13b** is given in Figure 1; selected bond lengths and angles are listed in Table 1. The coordination sphere of the zirconium atom can be described as a distorted tetrahedron. The two indenyl and chloride ligands are related by C_2 symmetry. The dihedral angle φ, which is defined as Si1–C3–C3*–Si1*, is measured to 165.7°, a nearly perfect *anti*-periplanar conformation of the indenyl li-

 © 2005 Wiley-VCH Verlag GmbH & Co. KGaA, Weinheim

gands. As a consequence, the 1,3-methyl groups on the frontside (C11, C11*) almost ideally intersect the Cl1–Zr1–Cl1* angle, which spans 92.8°. The dihedral angle C11–C4–C4*–C11* is – with only 5.7° distortion – close to a perfect *syn*-periplanar orientation of these methyl groups. In contrast, the methyl groups on the backside (C10, C10*) span a dihedral angle (C10–C2–C2*–C10*) of –57.5° and minimize steric interaction by this strongly *syn*-clinal orientation.

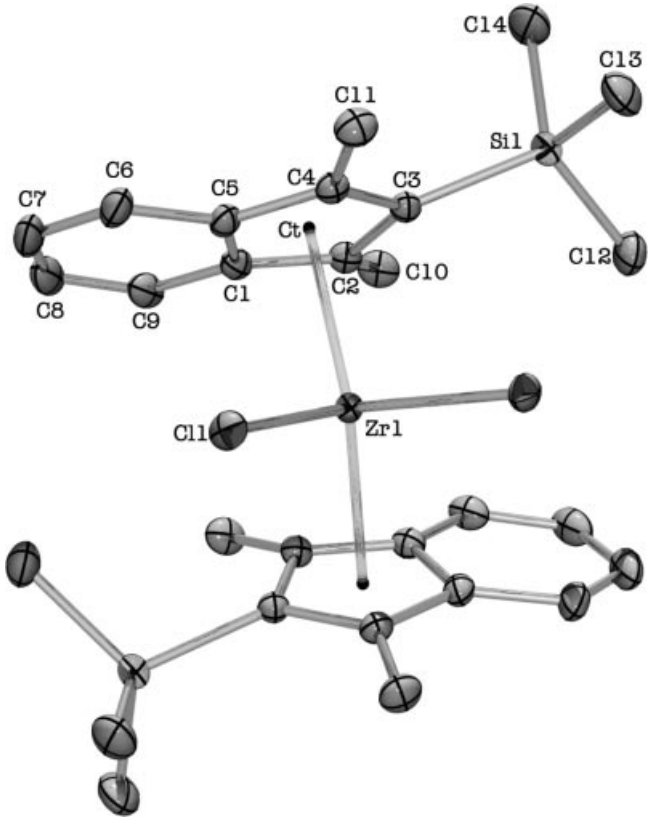

Figure 1. Refined crystallographic structure of bis[1,3-dimethyl-2-(trimethylsilyl)indenyl]zirconium dichloride (**13b**). Hydrogen atoms are omitted for clarity. Thermal ellipsoids are at the 50% probability level.

Table 1. Selected bond lengths [Å] and angles [°] for **13b**.

Bond length/angle [Å / °]	**13b**
Zr1–Cl1	2.4473(3)
Zr1–Ct	2.263
Zr1–C1	2.6188(10)
Zr1–C2	2.5385(10)
Zr1–C3	2.5370(10)
Zr1–C4	2.5320(10)
Zr1–C5	2.6252(9)
Si1–C3	1.8979(10)
Cl1–Zr1–Cl1*	92.843(13)
Ct–Zr1–Ct*	137.40
Ct–C3–Si1	168.84
Ct–C2–C10	167.76
Ct–C4–C11	175.43

The contribution of steric congestion is manifested in the out-of-plane bend angles of the indenyl ligands, which expose a convex surface to the zirconium center. In transversal direction, the frontside methyl groups are bent out of the linear arrangement by 4.6°, whereas the sterically more encumbered methyl groups on the backside are bent out by 12.2° – measured as C11–C4–Ct and C10–C2–Ct, respectively. In longitudinal direction, the curvature climbs from a modest 1.1° within the benzo moiety to 5.2° and 4.2° at the transition from benzo to Cp moiety and within the Cp ring, and finally reaches 19.3° for the transition Cp to silyl moiety. Consequently, the distortion of the tetrahedral symmetry around the zirconium is stronger than usual; the Ct-Zr1–Ct* angle ε measures 137.4°. To the best of our knowledge, this is the largest value ever reported for unbridged bis(indenyl)zirconium dichlorides. The largest values for ε have been reported for *rac*-ferrocenyl-bis(1-indenyl)zirconium dichloride, ferrocenyl-bis[2,3,4,5-tetramethyl-1-Cp]zirconium dichloride[9] and [(1,2,4-tri-(*t*Bu)Cp)(1,2,3,4-tetra-(*i*Pr)Cp)]zirconium dichloride[10] with 129.7, 138.5 and 138.8°, respectively.

Polymerization Characteristics and DF Calculations

In order to establish a rough estimate on the properties of **12** and **13b** as polymerization catalyst precursors in ethene homopolymerizations with MAO as cocatalyst, isobar and isothermal experiments were run at two different catalyst concentrations. Reference experiments were carried out with bis(indenyl)zirconium dichloride/MAO (**RefH**) and bis[2-(trimethylsilyl)indenyl]zirconium dichloride/MAO (**RefTMS**) at concentrations of $c(\mathrm{Zr}) = 1.0 \cdot 10^{-7}$ mol/L and $c(\mathrm{Zr}) = 1.0 \cdot 10^{-6}$ mol/L at Al/Zr ratios of 10000 and 1000, respectively. For **12**/MAO and **13b**/MAO, these conditions were not sufficient for detectable polymerization activity. Rather, **12**/MAO and **13b**/MAO required higher catalyst and MAO concentrations in order to show sufficient activity. A rough comparison of the catalyst's activities and the molecular weights obtained is given in Table 2.

The results for the homopolymerizations suggest a decrease in activity with increasing degree of substitution of the catalysts' ligand framework. We ascribe the significantly lower activities for high catalyst concentrations of **RefH**/MAO and **RefTMS**/MAO to diffusion control in the course of polymerization. The high amount of polymer produced increases the viscosity and hence reduces ethene up-take and agitation of the reaction mixture. Considering the polymer molecular masses, only **12**/MAO displays a notably different value compared to the other catalysts. The higher polydispersity index (PDI) obtained from **12**/MAO may be explained by the presence of the *rac* and *meso* isomer as active sites. The PDI's relative proximity to the value of 2 suggests their polymerization characteristics to be fairly alike.

The comonomer response of the different catalysts cannot be described by a simple consideration of steric congestion. Whereas the unsubstituted **RefH**/MAO displays a positive comonomer response, **RefTMS**/MAO and **12**/MAO suffer from strong deactivation by 80 to 90% relative to the

 © 2005 Wiley-VCH Verlag GmbH & Co. KGaA, Weinheim

Table 2. Polymerization activities of **12**/MAO and **13b**/MAO in ethene and ethene-*co*-1-hexene polymerizations. $c(Zr) = 1.0\cdot10^{-7}$ mol·L^{-1} and $c(Zr) = 1.0\cdot10^{-6}$ mol·L^{-1} at 30 °C in toluene; $c(E) = 0.14$ mol·L^{-1}.

Catalyst HDPE–X_H = 0.0	c(Zr) [mol·L^{-1}]	Activity/ [kg·mol$_{Zr}^{-1}$·mol$_E^{-1}$·h^{-1}]	Al/Zr	M_w [Kg·mol^{-1}]	PDI
RefH	$1.0\cdot10^{-6}$	272000 ± 3500	1000	770	2.7
RefH	$1.0\cdot10^{-7}$	1560000 ± 160000	10000	820	2.0
RefTMS	$1.0\cdot10^{-6}$	327000 ± 52000	1000	625	2.6
RefTMS	$1.0\cdot10^{-7}$	817000 ± 1400	10000	785	2.6
12	$2.0\cdot10^{-7}$	165000 ± 22000	10000	450	3.5
13b	$1.0\cdot10^{-6}$	135000 ± 21000	4000	790	2.6
LLDPE–X_H = 0.6					
RefH	$1.0\cdot10^{-6}$	376000 ± 14000	1000	189	3.0
RefTMS	$1.0\cdot10^{-6}$	53,700 ± 1700	1000	45	16
12	$2.0\cdot10^{-5}$	15900 ± 8800	2000	195	31[a]
13b	$1.0\cdot10^{-6}$	176000	2000	428	2.2

[a] Trimodal distribution observed, M_n = 6.2.

homopolymerization. In contrast, **13b**/MAO displays virtually no response to the comonomer and polymerises with roughly the same rate as before.

The fairly low activity of **13b**/MAO prompts the question of whether or not the catalyst precursor is sufficiently activated by the MAO available during the polymerization. To assess the dependence of **13b**/MAO on the Al/Zr ratio, a series of experiments was run at constant zirconium, ethene, and 1-hexene concentrations, while varying the Al/Zr ratio from approximately 1000 to 19000. The data obtained are listed in Table 3. We suggest that the catalyst activity does not strongly depend on the concentration of MAO or the Al/Zr ratio, though the data point to a slight increase in activity.

Table 3. Polymerization activities of **13b** in ethene-*co*-1-hexene polymerizations as a function of the Al/Zr ratio. $c(Zr) = 1.0\cdot10^{-6}$ mol·L^{-1}, $c(E) = 0.14$ mol·L^{-1}, $X_H = 0.5$ at 30 °C in toluene.

Activity [kg·mol$_{Zr}^{-1}$·mol$_E^{-1}$·h^{-1}]	Al/Zr
6000	950
18600	1900
26100	2800
45400	5700
44000	9500
33000	14200
79100	18900

Another issue of interest is the neutral to positive comonomer response of **13b**/MAO, which does not fit into the trend set by **RefTMS**/MAO and **12**/MAO. A ^{13}C NMR analysis of the copolymer obtained from **13b**/MAO was conducted according to the signal assignments published by Randall[11] and revealed a signal pattern typical for LLDPE polymers. The comonomer content was determined to 0.3 mol-% 1-hexene, which is essentially the detection limit. Assuming that the statistical distribution of the comonomer in the polymer chain is proportional to the equilibrium constant K_{eq} that would describe the population of the active site models **A1** and **A2**, as depicted in Scheme 5, it is possible to calculate the Gibbs energy [Equation (1)] for the enchainment of 1-hexene relative to ethene.

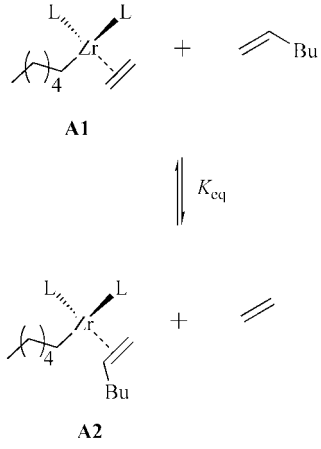

Scheme 5. Simplified representation of the active site with a polymer chain (*n*-hexyl) attached: **A1** with an ethene and **A2** with a 1-hexene ligand. For clarity, the 1,3-dimethyl-2-TMS-indenyl ligands are abbreviated as "L" and charges are omitted.

$$\Delta_r G = -RT\ln(K_{eq}) \quad (1)$$

$$K_{eq} = \frac{x_E x_H}{X_E X_H} \quad (2)$$

At 303.15 K with X_E and X_H = 0.5, and x_E = 0.997 and x_H = 0.003, we obtain $\Delta_r G$ = 11 kJ/mol and estimate the lower and upper limit to 10 and 14 kcal/mol, respectively. This value includes the reaction entropy, which could in general be obtained from an Arrhenius plot. A set of experiments was designed to investigate the dependence of the equilibrium constant K_{eq} on the temperature, as suggested by the van't Hoff equation. The results summarized in Table 4 indicate that there is no detectable relation between the polymerization temperature and catalyst activity or comonomer incorporation. The activity varies unsystematically, and the 1-hexene incorporation is constant. An experimental estimate of the reaction entropy is therefore not available.

 © 2005 Wiley-VCH Verlag GmbH & Co. KGaA, Weinheim

Table 4. Polymerization activities of **13b** in ethene-*co*-1-hexene polymerizations as a function of the reaction temperature. The error indicates the experimental standard deviation; $c(Zr) = 1.0 \cdot 10^{-6}$ mol·L^{-1}, $c(E) = 0.14$ mol·L^{-1}, $X_H = 0.5$ at Al/Zr = 4000 in toluene.

T/°C	Activity [kg·mol$_{Zr}^{-1}$·mol$_E^{-1}$·h^{-1}]	M_w [Kg·mol^{-1}]	PDI	x_H
20	24400 ± 3100	494	11	0.003
30	18900 ± 1900	533	20	0.003
40	29600 ± 2200	391	15	0.003
48	44400 ± 1800	273	2.6	0.003
60	29800 ± 2000	172	6.9	0.003

In order to validate the quality of our estimate of the reaction Gibbs energy, we conducted DF calculations on an active site of **13b** which features a *n*-hexyl ligand and one ethene or 1-hexene unit. For the ethene complex, a pronounced α-agostic interaction of the polymer chain and the zirconium center was found, stretching the C–H bond length to 1.13 Å. The ethene ligand shows slight rehybridization through a HCH bond angle of 116.4° and is symmetrically coordinated at the typical Zr···C distances of 2.72 Å (C1) and 2.85 Å (C2). The 1-hexene complex displays evidence of steric strain already on visual inspection, as the *Z*-side of the 1-hexene ligand is tilted away from the zirconium center by a 16.5° deviation from the perfect orthogonal side-on coordination. This is due to intrusion of the butyl substituent into the space occupied by the methyl groups in the 1 and 3 positions of the indenyl ligands. Consequently, the Zr-olefin distance is increased to 2.78 Å (C1) and 3.32 Å (C2). An α-agostic interaction is not detectable, and there is an insignificant lengthening of the Zr−carbon bond to the polymer chain by 0.03 Å.

The relative energies of both olefin complexes, compared to the energies of the uncoordinated olefins, is a measure of their populations in the equilibrium during the polymerization process (Scheme 5). Since both olefins were present in equal amounts, stoichiometric corrections are not required. For the *rac*-like conformer of the active site the energy difference calculates to 8 kJ/mol, whereas the *meso*-like conformer is somewhat less stable with 13 kJ/mol. A meaningful comparison of product equilibria with stability of starting materials usually requires the knowledge of activation enthaplies. All attempts to calculate the activation enthalpies for the insertion process failed since the optimization of the transition state exclusively led to geometries where the olefin ligands would rotate along the zirconium−olefin bond and result in non-planar geometries. Although we have been able to calculate nonplanar transition states for other systems, the calculations would not converge in the case of **A1** or **A2**. The polydispersity index of 2.2 for the copolymerization suggests that only one active site needs to be considered.

Conclusions

The herein investigated syntheses of sterically demanding 1,2,3-substituted indenyl ligands on the basis of 2-silylindenes are unexpectedly difficult. Apart from hydride substitution problems, which may arise for the DMS moiety, substituents larger than a methyl group are surprisingly prone to hydrogen shift reactions of the deprotonated ligands. This side reaction affects the yield and applicability of the indenyl salts significantly. Introduction of an alkyl moiety without hydrogen shift capability like *t*Bu was precluded by steric strain in the synthesis of a suitable precursor. Further, the DMS-substituted ligand would not afford the desired zirconocene complex. As we have seen in earlier work, the presence of hydrogen on the silyl groups in 2 position does not seem to be favored for the zirconocene synthesis.[3]

In contrast, the syntheses of bis[1-methyl-2-TMS-indenyl]zirconium(IV) dichloride (**12**) and bis[1,3-dimethyl-2-TMS-indenyl]zirconium(IV) dichloride (**13b**) were achieved without undue difficulty, although the separation of the *rac* and *meso* diastereomers of **12** failed. The (basic) polymerization studies presented herein suggest that the activity in ethene polymerizations decreases with an increasing degree of substitution. In contrast to the very moderate activities, the molecular weights are less effected and this may be rationalized by the reduction in available space at the active site. Chain termination by chain transfer requires a β-agostic structure *and* the association of a monomer unit. Chain transfer to MAO requires an intimate interaction with the very same. Both processes are likely to be suppressed by a bulky ligand framework. This effect is even more pronounced for **13b**, which does not show the expected increase in activity with increasing Al/Zr ratio. Such an effect is often observed and poorly understood.

The virtual inertness of **13b** towards 1-hexene as a monomer is an interesting feature, which is to the best of our knowledge unprecedented. The unsuccessful attempts to find the transition state for this process support our idea that the selectivity is governed by steric factors. Nevertheless an interesting agreement between experiment and theory has been found: The calculated energy difference of 8 to 13 kJ/mol for the olefin complexes falls into the same range as the Gibbs energy of 11 kJ/mol, as derived from Boltzmann statistics on the 1-hexene incorporation into the polymer chain. This may indicate that the insertion of the monomer units may be controlled by a single activation barrier, despite our inability to calculate any suitable transition state. Systems like **13b**, employed in a catalyst mixture, are industrially desirable as they show a monomer selectivity which could be used to produce long chain branches in a copolymerization with 1-hexene. The catalyst activity is, however, traded for this selectivity.

Experimental Section

General: Unless otherwise indicated, all procedures were conducted using Schlenk techniques under argon. All solvents were dried from sodium with benzophenone or anthracene (diethyl ether, THF, and toluene) or lithium aluminium hydride (pentane) and distilled prior to use. Acetone (Merck) was dried with anhydrous magnesium sulfate for three days and distilled under argon. When used as a filter agent, magnesium sulfate (Merck) was dried at 140 °C for at least

 © 2005 Wiley-VCH Verlag GmbH & Co. KGaA, Weinheim

two days prior to use. Iodomethane (Fluka) was dried with calcium hydride (Merck, used as received) and distilled under argon. 2-Iodo-propane (Fluka) and methanol p.a. (Merck) were used as received. Aluminum trichloride (resubl. grade, Aldrich Chemicals), pyrrolidine (Fluka), magnesium turnings (Merck and Aldrich Chemicals), *n*-butyllithium (Aldrich Chemicals or Merck), methyllithium (Aldrich Chemicals), *tert*-butyllithium (Aldrich Chemicals), boron trifluoride diethyl etherate (Aldrich Chemicals) and zirconium tetrachloride (Strem, 99.95%+, sublimed grade) were used as received. Column chromatography was conducted on silica gel 60 (0.040–0.063 mm) provided by Merck. Methylalumoxane (MAO) was purchased at Crompton Bergkamen, Germany, as a 10% toluene solution. Prior to use, the MAO solution was filtered through a D4-frit and volatiles removed in vacuo yielding a white solid. Polymerization grade ethene was provided by Borealis Stathelle, Norway. 1-Hexene (Aldrich) was purified before copolymerization by drying over potassium/benzophenone and subsequent distillation in an argon atmosphere. ^{1}H- and ^{13}C NMR spectra acquired with a Varian Gemini 300 MHz instrument were referenced to the residual solvent peaks. Low resolution MS was conducted with a Hewlett–Packard 5973 MSD, coupled with a Hewlett–Packard 6890 GC unit. GC columns used were HP-5, I.D. 0.32 mm, 0.250 µm, 30 m and DB-17, I.D. 0.25 mm, 0.250 µm, 30 m, both manufactured by J&W Scientific. GPC characterizations of the HDPE samples were conducted with a Waters 150CVplus instrument, operating with two HMW 6E and one HMW7, or three HT6E styragel columns (Waters) at 140 °C with trichlorobenzene as elution solvent and a dRI & viscosity detector. Alternatively, weight and number average molecular weights and polydispersity indices were measured at 140 °C with a Waters Alliance 2000 size exclusion chromatography (SEC) instrument equipped with Waters HT3, HT4, HT5 and HT6 columns. 1,2,4-Trichlorobenzene was used as solvent at a flow rate of 1.0 $cm^3 \cdot min^{-1}$. The columns were universally calibrated with narrow molecular weight polystyrene standards. Well-characterized lithium salts which resulted in isolable Zr complexes were not subjected to EA.

2-(Dimethylsilyl)indene (1a) and 2-(Trimethylsilyl)indene (1b): These compounds were prepared according to a published literature procedure.[3]

2-(Dimethylsilyl)-3-methylindene (2a). Potassium Hydride Route: Potassium hydride (432 mg, 10.8 mmol) was dissolved in THF (40 mL) and cooled to –90 °C. 2-(Dimethylsilyl)indene (1.88 g, 10.8 mmol) dissolved in THF (8 mL) was injected into the cold potassium hydride/THF suspension and the reaction mixture was warmed to room temperature while being stirred overnight. Substitution of THF by 20 mL diethyl ether and filtration through a cannula resulted in a clear, yellow-green solution of the 2-(dimethylsilyl)indenylpotassium complex. In a second Schlenk flask equipped with a pressurized addition funnel, methyl iodide (2.0 mL, 32.4 mmol) and diethyl ether (20 mL) were cooled to –40 °C before the potassium complex was added dropwise under isothermal conditions over a period of 30 minutes. The reaction was stirred overnight and warmed to room temperature, to yield a copious white precipitate. Filtration to remove insolubles and acidic quenching was followed by extraction with water (2 × 20 mL). Drying over magnesium sulfate and removal of solvent afforded the product (1.29 g, 6.9 mmol, 64%) at 85% purity. The isomer distribution was 4% 3 isomer, 81% 1 isomer, 8% un- and 7% disubstituted.

***n*-Butyllithium Route:** 2-(Dimethylsilyl)indene (2.04 g, 11.7 mmol) and pentane (50 mL) were placed in a Schlenk flask. *n*-Butyllithium (6.4 mL, 10.3 mmol) was slowly added via syringe. The solution was stirred overnight with waterbath cooling to yield a white precipitate. By filtration with a cannula, washing with pentane (2 × 20 mL) and drying under high vacuum a white powder (1.85 g, 10.3 mmol) was obtained. The 2-(dimethylsilyl)indenyllithium salt was dissolved in 30 mL diethyl ether and placed in an addition funnel mounted on a Schlenk flask charged with methyl iodide (2.9 mL, 46.8 mmol) in diethyl ether (30 mL). Drop-wise addition provided a yellow solution, which was stirred overnight prior to acidic work-up (20 mL 0.1 mol/L hydrochloric acid) in diethyl ether. Phase separation, washing of the organic layer with deionized water followed by drying over magnesium sulfate and removal of solvent at 70 mbar/40 °C afforded a pale yellow liquid (1.56 g, 8.3 mmol, 71%). Impurities were not detectable by GC/MS analysis. ^{1}H NMR (300 MHz, [D$_6$]benzene, 25 °C): δ = 0.19 [d, ^3J = 3.9 Hz, 6 H, SiH(CH_3)$_2$], 2.15 [t, ^5J = 2.1 Hz, 3 H, C(3)-Me], 3.14 [q, ^5J = 2.4 Hz, 2 H, C(1)-H], 4.69 [hept, ^3J = 3.9 Hz, 1 H, SiH(CH$_3$)$_2$], 7.17–7.25 [m, 1 H, C(5)-H], 7.25–7.27 [m, 2 H, C(6,7)-H], 7.32–7.37 [m, 1 H, C(4)-H] ppm. ^{13}C{^{1}H} NMR (75 MHz, [D$_6$]benzene, 25 °C): δ = –3.1 [2 C, SiH(CH_3)$_2$], 13.8 [1 C, C(3)-Me], 42.6 (1 C, C-1), 119.7 (1 C, C-4), 124.0 (1 C, C-7), 125.6 (1 C, C-6), 126.8 (1 C, C-5), 137.2 (1 C, C-3), 147.1 (1 C, C-2), 147.9 (1 C, C-7a), 150.4 (1 C, C-3a) ppm. GC/MS (70 eV): *m*/*z* (%) = 188 (100) [M$^+$], 173 (74) [M$^+$ – CH$_3$], 145 (41) [C$_9$H$_9$Si$^+$], 128 (75) [C$_{10}$H$_8^+$], 115 (15) [C$_9$H$_7^+$], 73 (10) [Si(CH$_3$)$_3^+$], 59 (78) [SiH(CH$_3$)$_2^+$].

1-Methyl-2-(trimethylsilyl)indene (2b): The methylation of **1b** was conducted in a similar manner to **2a**. To a Schlenk flask charged with 2-(trimethylsilyl)indene (3.00 g, 15.0 mmol) dissolved in pentane (40 mL) at room temperature, *n*-butyllithium (19.0 mL, 49.0 mmol) was added through a septum and stirred vigorously. The reaction mixture was stirred overnight and warmed to room temperature to yield a clear, yellow solution. Upon addition of diethyl ether (2.0 mL) and stirring for another ten minutes, the formation of copious precipitate was observed. Solvent volume reduction to approximately 60% and subsequent filtration through a D4-frit provided a white solid, which was washed twice with pentane (10 mL) and dried under vacuum for 1 h. A second Schlenk flask equipped with an addition funnel and charged with methyl iodide (3.0 mL, 48.5 mmol) in diethyl ether (20 mL) was cooled to –40 °C. The lithium salt was dissolved in diethyl ether (30 mL), transferred to the addition funnel of the second Schlenk flask and dropwise added to the methyl iodide solution at –40 °C. After stirring overnight, the reaction was quenched with hydrochloric acid (20 mL, 0.1 mol/L). The organic layer was washed twice with water (20 mL) and dried with magnesium sulfate. Removal of solvent afforded the product (2.45 g, 12.1 mmol, 81%) with a purity of 99%, as determined by GC/MS. ^{1}H NMR (300 MHz, [D$_6$]benzene, 25 °C): δ = 0.24 [s, 9 H, Si(CH_3)$_3$], 1.30 [d, ^3J = 7.4 Hz, 3 H, C(1)-CH$_3$], 3.48 [dq, ^3J = 7.4, ^5J = 1.6 Hz, 1 H, C(1)-H], 6.90 [d, ^5J = 1.6 Hz, 1 H, C(3)-H], 7.28–7.35 [m, 2 H, C(5,6)-H], 7.37–7.43 [m, 2 H, C(4,7)-H] ppm. ^{13}C{^{1}H} NMR (75 MHz, [D$_6$]benzene, 25 °C): δ = –0.2 [3 C, Si(CH_3)$_3$], 17.4 [1 C, C(1)-Me], 49.7 (1 C, C-1), 121.6 (1 C, C-4), 123.2 (1 C, C-7), 125.8 (1 C, C-6), 127.1 (1 C, C-5), 140.9 (1 C, C-3), 145.0 (1 C, C-2), 153.1 (1 C, C-7a), 154.8 (1 C, C-3a) ppm. GC/MS (70 eV): *m*/*z* (%) = 202 (28) [M$^+$], 187 (11) [M$^+$ – CH$_3$], 159 (5) [M$^+$ – C$_3$H$_7$], 145 (6) [M$^+$ – C$_4$H$_9$], 128 (14) [M$^+$ – TMS], 115 (4) [C$_9$H$_7^+$], 73 (100) [TMS$^+$], 59 (7) [SiH(CH$_3$)$_2^+$].

1,3-Dimethyl-2-(dimethylsilyl)indene (3a): The synthesis was carried out in a fashion similar to **2a**. 2-(Dimethylsilyl)-1-methylindene (2.68 g, 14.3 mmol), *n*-butyllithium (8.8 mL, 14.1 mmol) and methyl iodide (3.5 mL, 57.2 mmol) were employed to obtain a yellow liquid (2.65 g). Column chromatography with pentane on silica provided a colorless liquid (1.61 g, 8.0 mmol, 57%), containing

 © 2005 Wiley-VCH Verlag GmbH & Co. KGaA, Weinheim

both the product (70%) and its 1,1 isomer (30%). No further purification was attempted. ^{1}H NMR (300 MHz, [D$_6$]benzene, 25 °C): δ = 0.24 [d, ^3J = 3.9 Hz, 3 H, SiH(CH_3)$_2$], 0.25 [d, ^3J = 3.9 Hz, 3 H, SiH(CH_3)$_2$], 1.21 [d, ^3J = 7.5 Hz, 3 H, C(1)-CH$_3$], 2.12 [d, ^5J = 1.8 Hz, 3 H, C(3)-CH$_3$], 3.36 [dq, ^5J_d = 2.1, ^3J_q = 7.5 Hz, 1 H, C(1)-H], 4.68 [m, ^3J = 3.9 Hz, 1 H, SiH(CH$_3$)$_2$], 7.17–7.24 [m, 2 H, C(5,6)-H], 7.24–7.31 [m, 2 H, C(4,7)-H] ppm. ^{13}C{^{1}H} NMR (75 MHz, [D$_6$]benzene, 25 °C): δ = –2.4 [2 C, SiH(CH_3)$_3$], 17.6 [1 C, C(1)-Me], 25.8 [1 C, C(3)-Me], 49.3 (1 C, C-1), 119.7 (1 C, C-4), 122.9 (1 C, C-7), 126.0 (1 C, C-6), 127.0 (1 C, C-5), 143.5 (1 C, C-3), 146.5 (1 C, C-2), 149.4 (1 C, C-7a), 152.7 (1 C, C-3a) ppm. GC/MS (70 eV): *m/z* (%) = 202 (50) [M$^+$], 187 (33) [M$^+$ – CH$_3$], 159 (19) [C$_{10}$H$_{11}$Si$^+$], 142 (100) [C$_{11}$H$_{10}^+$], 128 (42) [C$_{10}$H$_8^+$], 115 (17) [C$_9$H$_7^+$], 73 (25) [Si(CH$_3$)$_3^+$], 59 (66) [SiH(CH$_3$)$_2^+$].

1,3-Dimethyl-2-(trimethylsilyl)indene (3b): Prior to the addition of *n*-butyllithium (15.0 mL, 37.5 mmol), **2b** (2.45 g, 12.1 mmol) in pentane (30 mL) was placed in a Schlenk flask and cooled to –90 °C. The solution was stirred overnight and warmed to room temperature, affording a suspension with a white precipitate after addition of diethyl ether (1 mL). Reduction of the solvent volume to approximately 60% was followed by a filtration through a D4-frit and washing of the precipitate with pentane (3 × 10 mL). While the white precipitate was dried in vacuo, a second Schlenk flask was equipped with an addition funnel and methyl iodide (2.25 mL, 36.3 mmol) in diethyl ether (20 mL) and cooled to –40 °C. The lithium salt was dissolved in diethyl ether (30 mL) and THF (10 mL), transferred to the addition funnel and dropwise added to the solution at –40 °C. Stirring overnight and acidic work-up provided a pale yellow crude product (2.21 g, 10.2 mmol). Its composition was determined to be ca. 20% of the 1,1 and 80% of the desired 1,3 isomer. No further separation of the isomers was attempted. The spectroscopic data was derived from the hydrolysis of the pure 1,3-dimethyl-2-(trimethylsilyl)indenyllithium. ^{1}H NMR (300 MHz, [D$_6$]benzene, 25 °C): δ = 0.24 [s, 9 H, Si(CH_3)$_3$], 1.20 [d, ^3J = 7.4 Hz, 3 H, C(1)-CH$_3$], 2.08 [d, ^5J = 2.0 Hz, 3 H, C(3)-CH$_3$], 3.48 [qq, ^5J = 2.0, ^3J = 7.4 Hz, 1 H, C(1)-H], 7.19–7.25 [m, 2 H, C(5,6)-H], 7.25–7.31 [m, 2 H, C(4,7)-H] ppm. ^{13}C{^{1}H} NMR (75 MHz, [D$_6$]benzene, 25 °C): δ = 0.9 [3 C, Si(CH_3)$_3$], 18.2 [1 C, C(1)-Me], 26.0 [1 C, C(3)-Me], 49.4 (1 C, C-1), 119.6 (1 C, C-4), 122.9 (1 C, C-7), 125.9 (1 C, C-6), 127.0 (1 C, C-5), 146.0 (1 C, C-3), 146.8 (1 C, C-2), 148.3 (1 C, C-7a), 152.8 (1 C, C-3a) ppm. GC/MS (70 eV): *m/z* (%) = 216 (29) [M$^+$], 201 (12) [M$^+$ – CH$_3$], 141 (11) [M$^+$ – TMS], 128 (11) [M$^+$ – Si(CH$_3$)$_4$], 115 (6) [C$_9$H$_7^+$], 73 (100) [TMS$^+$], 59 (6) [SiH(CH$_3$)$_2^+$].

1-Isopropyl-2-(trimethylsilyl)indene (4): The synthesis was carried out according to the procedure for **2b**. 2-(Trimethylsilyl)indenyllithium (870 mg, 4.5 mmol) and 2-iodopropane (0.5 mL, 5.0 mmol) were reacted to provide a yellow oil (770 mg, 3.3 mmol, 74%). ^{1}H NMR (300 MHz, [D$_6$]benzene, 25 °C): δ = 0.202 [s, 4.5 H, Si-(CH_3)$_3$], 0.204 [s, 4.5 H, Si(CH_3)$_3$], 0.48 [d, ^3J = 6.6 Hz, 3 H, C(1′)-H], 1.21 [d, ^3J = 7.4 Hz, 3 H, C(3′)-H], 2.40 [dqq, ^3J = 3.0, ^3J = 6.9 Hz, 1 H, C(2′)-H], 3.52 [dd, ^4J = 2.4, ^3J = 2.7 Hz, 1 H, C(1)-H], 6.99 [d, ^4J = 1.8 Hz, 1 H, C(3)-H], 7.11 [ddd, ^4J = 1.2, ^3J = 7.2, ^3J = 7.2 Hz, 1 H, C(5)-H], 7.22 [ddm, J = 0.6, ^3J = 7.2, ^3J = 7.2 Hz, 1 H, C(6)-H], 7.30 [dm, J = 0.6, ^3J = 7.5 Hz, 1 H, C(4)-H], 7.45 [d, ^3J = 7.5 Hz, 1 H, C(7)-H] ppm. ^{13}C{^{1}H} NMR (75 MHz, [D$_6$]benzene, 25 °C): δ = –0.2, –0.1 [3 C, Si(CH_3)$_3$], 16.4 (1 C, C-1′), 22.9 (1 C, C-2′), 30.3 (1 C, C-3′), 61.3, 61.4 (1 C, C-1), 121.7 (1 C, C-4), 124.9 (1 C, C-7), 125.4 (1 C, C-6), 127.3 (1 C, C-5), 142.3, 142.4 (1 C, C-3), 146.8 (1 C, C-2), 149.2 (1 C, C-7a), 152.9 (1 C, C-3a). GC/MS (70 eV): *m/z* (%) = 230 (23) [M$^+$], 215 (4) [M$^+$ – CH$_3$], 172 (6) [C$_{11}$H$_{12}$Si$^+$], 156 (16) [C$_{12}$H$_{12}^+$], 141 (7) [C$_{11}$H$_9^+$], 128 (6) [C$_{10}$H$_8^+$], 115 (5) [C$_9$H$_7^+$], 73 (100) [C$_3$H$_9$Si$^+$], 59 (7) [C$_2$H$_7$Si$^+$].

1-Isopropyl-2-(trimethylsilyl)indenyllithium/potassium (5): The preparation of the lithium salt followed a literature procedure.[12] At –90 °C **4** (4.44 g, 19.3 mmol) was reacted with *n*-butyllithium (8.5 mL, 21.3 mmol) in pentane (30 mL). Stirring overnight and warming to room temperature provided an orange solution. A precipitate could be obtained neither by addition of diethyl ether (2 mL) nor by solvent removal. GC/MS analysis after quenching a sample of the reaction with methyl iodide in THF displayed 10 major products, of which 7 could be identified by the fragmentation pattern: **(i)** 1-Methyl-1-isopropyl-2-(trimethylsilyl)indene. GC/MS (70 eV): *m/z* (%) = 244 (32) [M$^+$], 229 (5) [M$^+$ – CH$_3$], 170 (40) [M$^+$ – TMS], 155 (17) [C$_{12}$H$_{11}^+$], 141 (12) [C$_{11}$H$_9^+$], 128 (7), 115 (6) [C$_9$H$_7^+$], 73 (100) [C$_3$H$_9$Si$^+$]; **(ii)** 1-isopropyl-2-(trimethylsilyl) indene (**4**); **(iii)** 3-methyl-1-isopropyl-2-(trimethylsilyl)indene. GC/MS (70 eV): *m/z* (%) = 244 (22) [M$^+$], 229 (6) [M$^+$ – CH$_3$], 201 (12) [M$^+$ – C$_3$H$_7$], 185 (6) [C$_{12}$H$_{14}$Si$^+$], 170 (25) [M$^+$ – C$_3$H$_9$Si], 155 (7) [C$_{12}$H$_{11}^+$], 141 (6) [C$_{11}$H$_9^+$], 128 (6), 73 (100) [C$_3$H$_9$Si$^+$], 59 (8) [C$_2$H$_7$Si$^+$]; **(iv)** 1,3-diisopropyl-2-(trimethylsilyl)indene; **(v)** 1-methyl-3-isopropyl-2-(trimethylsilyl)indene. GC/MS (70 eV): *m/z* (%) = 244 (36) [M$^+$], 229 (8) [M$^+$ – CH$_3$], 170 (54) [M$^+$ – TMS], 155 (14) [C$_{12}$H$_{11}^+$], 141 (9) [C$_{11}$H$_9^+$], 128 (7), 115 (5) [C$_9$H$_7^+$], 73 (100) [C$_3$H$_9$Si$^+$], 59 (7) [C$_2$H$_7$Si$^+$]; **(vi)** 1,1-diisopropyl-2-(trimethylsilyl)indene. GC/MS (70 eV): *m/z* (%) = 272 (19) [M$^+$], 257 (5) [M$^+$ – CH$_3$], 198 (55) [M$^+$ – TMS], 183 (18) [C$_{14}$H$_{15}^+$], 169 (5) [C$_{13}$H$_{13}^+$], 155 (5) [C$_{12}$H$_{11}^+$], 141 (5) [C$_{11}$H$_9^+$], 73 (100) [C$_3$H$_9$Si$^+$], 59 (7) [C$_2$H$_7$Si$^+$]; **(vii)** 3-*tert*-butyl-2-(trimethylsilyl)indene. GC/MS (70 eV): *m/z* (%) = 244 (25) [M$^+$], 229 (69) [M$^+$ – CH$_3$], 214 (100) [M$^+$ – C$_2$H$_6$], 199 (43) [M$^+$ – C$_3$H$_9$], 187 (5) [M$^+$ – C$_4$H$_9$], 169 (5) [C$_{13}$H$_{14}^+$], 155 (13) [C$_{12}$H$_{11}^+$], 141 (6) [C$_{11}$H$_9^+$], 128 (7), 115 (7) [C$_9$H$_7^+$], 73 (7) [C$_3$H$_9$Si$^+$]. Attempted preparation of the potassium salt: Potassium hydride (568 mg, 13.9 mmol) was added to a solution of **4** (2.9 g, 12.6 mmol) in THF (40 mL) at –90 °C. Quantitative reaction was not achieved before refluxing the suspension for several days. Filtration with a cannula, solvent removal, washing with pentane and drying in vacuo afforded a yellow-brown solid (1.8 g, 6.7 mmol, 53%). ^{1}H NMR (300 MHz, [D$_8$]THF, 25 °C): δ = 0.46 [s, 9 H, Si(CH_3)$_3$], 1.68 [d, ^3J = 9.0 Hz, 6 H, C(1′,3′)-H], 3.62 [hept, ^3J = 9.0 Hz, 1 H, C(2′)-H], 6.16 [s, 1 H, C(3)-H], 6.47–6.59 [m, 2 H, C(5,6)-H], 7.39 [m, 1 H, C(4)-H], 7.63–7.71 [m, 1 H, C(7)-H] ppm. ^{13}C{^{1}H} NMR (75 MHz, [D$_8$]THF, 25 °C): δ = 1.9 (3 C), 25.0 (2 C), 32.2, 99.8, 112.5, 112.8, 119.4, 119.8, 121.0, 123.1, 127.6, 132.0 (1 C) ppm.

Attempted Synthesis of 1,3-Diisopropyl-2-(trimethylsilyl)indene: The preparation was attempted by in situ derivatization of Li[**5**] without prior isolation. Following the procedure for the preparation of **3b**, 2-iodopropane (2.1 mL, 21 mmol) was used. After stirring for 6 h and incomplete conversion according to GC/MS analysis, another aliquot of iodopropane was added and reacted overnight. Acidic work-up and GC/MS analysis of the crude product revealed the presence of four components: 1- and 3-isopropyl-2-(trimethylsilyl)-indene, 1,1- and 1,3-diisopropyl-2-(trimethylsilyl)indene. To the crude product dissolved in THF at –40 °C, potassium hydride (791 mg, 19.3 mmol) was added. Stirring overnight afforded a green solution. Solvent removal and extraction with diethyl ether provided a light green precipitate and a dark green filtrate. Washing the light green precipitate with pentane led to partial dissolution of the precipitate. Drying in vacuo provided a light green, pyrophoric powder (3.3 g). We could not isolate a pure fraction of the desired product. GC/MS (70 eV): *m/z* (%) = 228 (24) [M$^+$], 257 (7) [M$^+$ – CH$_3$], 198 (66) [M$^+$ – TMS], 183 [C$_{14}$H$_{15}^+$], 169 (6) [C$_{13}$H$_{14}^+$], 155

 © 2005 Wiley-VCH Verlag GmbH & Co. KGaA, Weinheim

(6) [$C_{12}H_{11}^+$], 141 (6) [$C_{11}H_9^+$], 73 (100) [$C_3H_9Si^+$], 59 (7) [$C_2H_7Si^+$].

Attempted Synthesis of 1-Isopropylidene-2-(trimethylsilyl)indene: To a Schlenk flask charged with dry acetone (0.1 mL, 1.4 mmol) and $BF_3{\cdot}Et_2O$ (0.1 mL, 789 μmol) in diethyl ether (20 mL), 2-(trimethylsilyl)indenyllithium (100 mg, 824 μmol) was added. Formation of a colorless suspension was achieved within one hour. The solvent was replaced by a mixture of pentane and THF (20 mL, 3 mL), prior to addition of orthophosphoric acid (6 mL, 85%). The organic layer turned yellow while stirring overnight. Acidic work-up, washing with deionized water, drying over magnesium sulfate and drying in vacuo provided a yellow oil (100 mg, 284 μmol, 34%). Product: GC/MS (70 eV): *m*/*z* (%) = 228 (31) [M^+], 213 (6) [$M^+ - CH_3$], 197 (13) [$M^+ - C_2H_6$], 155 (6) [$C_{12}H_{11}^+$], 141 (7) [$C_{11}H_9^+$], 128 (5), 115 (6) [$C_9H_7^+$], 73 (100) [$C_3H_9Si^+$]. Hydrated intermediate: GC/MS (70 eV): *m*/*z* (%) = 228 (6) [$M^+ - H_2O$], 201 (14) [$C_{13}H_{17}Si^+$], 187 (43) [$C_{12}H_{14}Si^+$], 173 (12) [$C_{11}H_{12}Si^+$], 157 (6) [$C_{10}H_8Si^+$], 145 (21) [$C_9H_9Si^+$], 128 (11), 115 (12) [$C_9H_7^+$], 73 (100) [$C_3H_9Si^+$], 58 (15) [$C_3H_7O^+$].

6,6-Dimethylbenzofulvene (6): The synthesis followed a literature procedure and does not require Schlenk technique.[7] By stirring indene (5 mL, 42.9 mmol), acetone (3.8 mL, 51.8 mmol) and pyrrolidine (4.3 mL, 51.8 mmol) in methanol (50 mL) for two days and subsequent distillation (0.05Torr), a yellow oil (4.94 g, 31.7 mmol, 74%) was obtained. ^{1}H NMR (300 MHz, [D$_6$]benzene, 25 °C): δ = 1.84 [s, 3 H, C(1′)-CH_3], 1.97 [s, 3 H, C(3′)-CH_3], 6.72 [s, 2 H, C(2,3)-H], 7.17 [m$_c$, 2 H, C(5,6)-H], 7.28 [m$_c$, 1 H, C(4)-H], 7.64 [m$_c$, 1 H, C(7)-H] ppm. ^{13}C{^{1}H} NMR (75 MHz, [D$_6$]benzene, 25 °C): δ = 22.9 (1 C, C-1′), 24.8 (1 C, C-3′), 121.8 (1 C, C-4), 124.3 (1 C, C-7), 125.4 (1 C, C-6), 126.7 (1 C, C-5), 128.2 (1 C, C-3), 129.2 (1 C, C-2), 136.8 (1 C, C-2′), 137.8 (1 C, C-1), 142.7 (1 C, C-7a), 145.0 (1 C, C-3a) ppm. GC/MS (70 eV): *m*/*z* (%) = 156 (93) [M^+], 141 (100) [$M^+ - CH_3$], 128 (21) [$C_{10}H_9^+$], 115 (36) [$C_9H_7^+$].

3-*tert*-Butylindene (7): Following a literature procedure,[6] the product was obtained from reacting **6** (1.51 g, 9.7 mmol) with methyllithium (6.9 mL, 9.7 mmol) at 0 °C in diethyl ether (30 mL). Acidic work-up afforded a colorless liquid (740 mg, 4.3 mmol, 44%). As an alternative, the reaction may be run in pentane in the presence of 10 wt.-% freshly resublimated $AlCl_3$ at room temperature. Addition of methyllithium via syringe provided a white precipitate in quantitative yield within one hour. ^{1}H NMR (300 MHz, [D$_6$]benzene, 25 °C): δ = 1.33 (s, 9 H, *t*Bu), 3.02 [d, ^3J = 2.1 Hz, 2 H, C(1)-H], 5.99 [t, ^3J = 2.1 Hz, 1 H, C(2)-H], 7.12 [ddd, ^4J = 1.8, ^3J = 7.2, ^3J = 7.2 Hz, 1 H, C(5)-H], 7.23 [dd, ^3J = 7.8, ^3J = 7.8 Hz, 1 H, C(6)-H], 7.32 [d, ^3J = 7.5 Hz, 1 H, C(4)-H], 7.59 [d, ^3J = 7.8 Hz, 1 H, C(7)-H] ppm. ^{13}C{^{1}H} NMR (75 MHz, [D$_6$]benzene, 25 °C): δ = 29.9 (3 C, *t*Bu), 33.6 (1 C, *t*Bu), 37.7 (1 C, C-1), 122.8 (1 C, C-2), 124.67 (1 C, C-4), 124.72 (1 C, C-7), 126.35 (1 C, C-6), 126.40 (1 C, C-5), 144.6 (1 C, C-7a), 146.4 (1 C, C-7a), 154.0 (1 C, C-3) ppm. GC/MS (70 eV): *m*/*z* (%) = 172 (78) [M^+], 157 (77) [$M^+ - CH_3$], 142 (78) [$M^+ - C_2H_6$], 128 (29) [$C_{10}H_8^+$], 116 (82) [$C_9H_8^+$], 57 (100) [$C_4H_9^+$].

3-*tert*-Butyl-1-(isopropylidene)indene (8). A Schlenk flask equipped with a condenser was charged with **7** (1.54 g, 8.7 mmol), acetone (1.5 mL, 20.5 mmol), pyrrolidine (1.7 mL, 20.5 mmol), and methanol (30 mL) under air. Reflux of the reaction mixture for three days and removal of all volatiles in vacuo provided a red-brown oil. vacuum distillation provided a yellow liquid boiling at 80 °C$_{0.05\text{Torr}}$ which would solidify at room temperature (1.05 g, 5.0 mmol, 58%). ^{1}H NMR (300 MHz, [D$_6$]benzene, 25 °C): δ = 1.39 (s, 9 H, *t*Bu-H), 1.92 [s, 3 H, C(1′)-CH_3], 2.04 [s, 3 H, C(3′)-CH_3], 6.60 [s, 1 H, C(2)-H], 7.13–7.24 [m, 2 H, C(5,6)-H], 7.60 [m$_c$, 1 H, C(4)-H], 7.72 [m$_c$, 1 H, C(7)-H] ppm. ^{13}C{^{1}H} NMR (75 MHz, [D$_6$]benzene, 25 °C): δ = 23.0 (1 C, C-1′), 24.9 (1 C, C-3′), 30.2 (3 C, *t*Bu-C), 35.6 (1 C, *t*Bu-C), 122.2 (1 C, C-2′), 122.7 (1 C, C-4), 124.4 (1 C, C-7), 124.9 (1 C, C-6), 126.2 (1 C, C-5), 136.3 (1 C, C-2), 138.9 (1 C, C-7a), 139.9 (1 C, C-3a), 143.6 (1 C, C-1), 151.0 (1 C, C-3) ppm. GC/MS (70 eV): *m*/*z* (%) = 212 (29) [M^+], 197 (10) [$M^+ - CH_3$], 182 (5) [$M^+ - C_2H_6$], 165 (15), 156 (100) [$C_{12}H_{12}^+$], 141 (50) [$C_{11}H_9^+$], 128 (13) [$C_{10}H_9^+$], 115 (17) [$C_9H_7^+$], 57 (47) [$C_4H_8^+$].

1,3-Di-(*tert*-butyl)indene (9): The synthesis followed essentially the synthesis of **7**. To an agitated solution of 3-*tert*-butyl-1-(isopropylidene)indene (4.89g, 23.1 mmol) in diethyl ether (30 mL), methyllithium (16.5 mL, 26.4 mmol) was added dropwise at 0 °C. After stirring for 2 h with warming to room temperature, GC/MS analysis of the reaction mixture showed only traces of the product. Addition of more methyllithium (15.0 mL, 24 mmol) and refluxing the reaction for 10 h provided a conversion of 25% (GC/MS). The reaction was poured over a mixture of diluted hydrochloric acid, diethyl ether and crushed ice (300 mL). Adjustment to pH 4 was followed by stirring for 10 minutes and phase separation. The organic layer was washed with deionized water (2 × 100 mL) and dried with magnesium sulfate prior to solvent evaporation. Column chromatography at silica gel (420 g) afforded a colorless liquid (0.652 g, 2.9 mmol, 12%). ^{1}H NMR (300 MHz, [D$_6$]benzene, 25 °C): δ = 0.94 [s, 9 H, C(1)-*t*Bu], 1.34 [s, 9 H, C(3)-*t*Bu], 3.08 [d, ^3J = 2.4 Hz, 1 H, C(1)-H], 6.16 [d, ^3J = 2.1 Hz, 1 H, C(2)-H], 7.10 [ddd, ^4J = 1.8, ^3J = 7.5, ^3J = 7.5 Hz, 1 H, C(5)-H], 7.21 [ddd, ^4J = 1.2, ^3J = 7.8, ^3J = 7.8 Hz, 1 H, C(6)-H], 7.50 [d, ^3J = 7.2 Hz, 1 H, C(4)-H], 7.54 [d, ^3J = 7.5 Hz, 1 H, C(7)-H] ppm. ^{13}C{^{1}H} NMR (75 MHz, [D$_6$]benzene, 25 °C): δ = 23.5 [1 C, C(1)-*C*$(CH_3)_3$], 29.0 [3 C, C(1)-C(*C*$H_3)_3$], 30.0 [3 C, C(3)-C(*C*$H_3)_3$], 32.6 [1 C, C(3)-*C*$(CH_3)_3$], 59.2 (1 C, C-1), 122.8 (1 C, C-4), 124.4 (1 C, C-7), 125.7 (1 C, C-6), 126.6 (1 C, C-5), 130.4 (1 C, C-2), 145.1 (1 C, C-7a), 148.4 (1 C, C-3a), 153.4 (1 C, C-3) ppm. GC/MS (70 eV): *m*/*z* (%) = 228 (41) [M^+], 172 (43) [$M^+ - C_4H_8$], 157 (59) [$C_{12}H_{13}^+$], 141 (31) [$C_{11}H_9^+$], 128 (11) [$C_{10}H_8^+$], 116 (37) [$C_9H_8^+$], 57 (100) [$C_4H_9^+$].

1-Methyl-2-(trimethylsilyl)indenyllithium (10): The deprotonation was carried out in a similar fashion to **2b**. The lithium salt could be isolated as a white powder in quantitative yield.

1,3-Dimethyl-2-(dimethylsilyl)indenyllithium (11a): The deprotonation of the ligand precursors followed a literature procedure.[12] The indene derivative (1.0 equiv.) and *n*-butyllithium (1.0 equiv.) were placed in a Schlenk flask charged with pentane (30 mL). Stirring at room temperature overnight provided little precipitate. Addition of 1 mL diethyl ether lead to the formation of appreciable amounts of precipitate, but filtration via cannula turned out to be difficult due to the formation of a viscous gel. Washing with pentane (2 × 30 mL) and subsequent solvent removal under high-vacuum yielded a light yellow powder (1.07 g, 5.1 mmol, 64%). $C_{13}H_{17}LiSi$ (208.30): calcd. C 74.96, H 8.23; found C 74.40, H 8.16. ^{1}H NMR (300 MHz, [D$_8$]THF, 25 °C): δ = 0.51 [d, ^3J = 3.9 Hz, 6 H, SiH(C$H_3)_2$], 2.65 [s, 6 H, C(1,3)-Me], 4.94 [hept, ^3J = 3.9 Hz, 1 H, SiH(C$H_3)_2$], 6.58 [m$_{AA'XX'}$, 2 H, C(5,6)-H], 7.38 [m$_{AA'XX'}$, 2 H, C(4,7)-H] ppm.

1,3-Dimethyl-2-(trimethylsilyl)indenyllithium (11b): The deprotonation was carried out in a similar fashion to **2b**, but started at –90 °C. Using an isomer mixture of **3b** (2.21 g, 10.2 mmol, 78% purity) and *n*-butyllithium (12.2 mL, 30.6 mmol) in pentane (30 mL) provided a light green powder (1.58 g, 7.1 mmol, 89%) after filtration through a D4-frit, washing with pentane (2 × 10 mL) and solvent removal under high vacuum.

 © 2005 Wiley-VCH Verlag GmbH & Co. KGaA, Weinheim

***rac/meso*-Bis[1-methyl-2-(trimethylsilyl)indenyl]zirconium(IV) Dichloride (12):** To a Schlenk flask equipped with a septum, charged with **10** (714 mg, 3.4 mmol) and zirconium tetrachloride (396 mg, 1.7 mmol) and cooled to 0 °C, diethyl ether (30 mL) was added via syringe. Stirring overnight afforded a suspension of a yellow precipitate. Filtration trough a D4 frit with a layer of magnesium sulfate (3 cm) and washing with diethyl ether until all yellow residue in the Schlenk flask was dissolved, provided a clear, yellow solution. Volume reduction to the formation of precipitate was followed by crystallization at –40 °C. Subsequent crystallizations failed to separate the *rac* and *meso* isomer, which were obtained in a 1:1 ratio (528 mg, 941 μmol, 55%). $C_{26}H_{34}Cl_2Si_2Zr$ (564.86): calcd. C 55.29, H 6.07; found C 55.55, H 6.15. ***rac* Isomer:** ^{1}H NMR (300 MHz, [D$_6$]benzene, 25 °C): δ = 0.32 [s, 18 H, Si(C*H*$_3$)$_3$], 2.29 [s, 6 H, C(1)-CH$_3$], 5.62 [s, 2 H, C(3)-H], 6.84–6.94 [m, 4 H, C(5,6)-H], 7.48–7.56 [m, 2 H, C(4,7)-H] ppm. ***meso* Isomer:** ^{1}H NMR (300 MHz, [D$_6$]benzene, 25 °C): δ = 0.14 [s, 18 H, Si(C*H*$_3$)$_3$], 2.52 [s, 6 H, C(1)-CH$_3$], 5.07 [s, 2 H, C(3)-H], 6.94–7.00 [m, 4 H, C(5,6)-H], 7.10–7.15 [m, 2 H, C(4)-H], 7.25–7.30 [m, 2 H, C(7)-H] ppm. ***rac* and *meso* Isomer:** ^{13}C{^{1}H} NMR (75 MHz, [D$_6$] benzene, 25 °C): δ = 0.7 [6 C, Si(*C*H$_3$)$_3$], 1.1 [6 C, Si(*C*H$_3$)$_3$], 14.1 [2 C, C(1)-CH$_3$], 14.4 [2 C, C(1)-CH$_3$], 106.8 (2 C, C-3), 109.8 (2 C, C-3), 124.7, 124.8, 125.0, 125.1, 125.2, 125.4, 125.6, 125.9, 126.3, 126.6, 127.6, 128.5, 132.3, 133.0, 135.3, 138.8 ppm.

Attempted Synthesis of Bis[1,3-dimethyl-2-(dimethylsilyl)indenyl]zirconium(IV) Dichloride (13a): In a Schlenk flask, **11a** (185 mg, 889 μmol) and zirconium tetrachloride (104 mg, 446 μmol) were reacted in diethyl ether (30 mL) at 0 °C. The initially brown-yellow suspension turned green-yellow while stirring overnight. A clear yellow solution was obtained by filtration through a layer of magnesium sulfate on a D4 frit and washing of the reaction residue with diethyl ether. Volume reduction to 10 mL and refrigeration to –40 °C provided traces of precipitate. The obtained NMR spectroscopic data suggests the formation of the desired product, but reliable analysis including elemental analysis was precluded by the small amount of precipitate obtained. ^{1}H NMR (300 MHz, [D$_6$]benzene, 25 °C): δ = 0.24 [d, ^3J = 3.9 Hz, 12 H, SiH(C*H*$_3$)$_2$], 2.15 [s, 12 H, C(1,3)-CH$_3$], 4.76 [hept, ^3J = 4.2 Hz, 2 H, Si*H*-(CH$_3$)$_2$], 6.80–7.00 [m, 4 H, C(5,6)-H], 7.15–25 [m, 4 H, C(4,7)-H] ppm.

Bis[1,3-dimethyl-2-(trimethylsilyl)indenyl]zirconium(IV) Dichloride (13b): A Schlenk flask with **11b** (1.00 g, 3.4 mmol) and zirconium tetrachloride (0.52 g, 1.69 mmol) was cooled to 0 °C before diethyl ether (30 mL) was added dropwise. The suspension turned dark yellow and formed a yellow precipitate while stirring overnight. Filtration with a cannula and a D4-frit loaded with magnesium sulfate (3 cm) afforded a dark yellow solution. Extraction of the reaction residue and filter cake with diethyl ether and toluene, followed by recrystallization from the respective solvent afforded four crops of a yellow or orange solid (393 mg, 665 μmol, 44%). Single crystals of X-ray quality were grown from a cold saturated diethyl ether solution at –40 °C. $C_{28}H_{38}Cl_2Si_2Zr$ (592.91): calcd. C 56.72, H 6.46; found C 56.75, H 6.48. ^{1}H NMR (300 MHz, [D$_6$]benzene, 25 °C): δ = 0.31 [s, 18 H, Si(C*H*$_3$)$_3$], 2.13 [s, 12 H, C(1,3)-C*H*$_3$], 6.86 [m$_{AA'XX'}$, J_A = 6.5, J_X = 0.8, J = 8.7, J' = 1.0 Hz, 4 H, C(5,6)-H], 7.15–7.19 [m, 4 H, C(4,7)-H] ppm. ^{13}C{^{1}H} NMR (75 MHz, [D$_6$]benzene, 25 °C): δ = 2.0 [6 C, Si(*C*H$_3$)$_3$], 13.8 (4 C, 1,3-*C*H$_3$), 121.0 (4 C, C-1,3), 124.0 (4 C, C-4,7), 124.8 (4 C, C-5,6), 127.7 (4 C, C-3a,7a), 139.9 (2 C, C-2) ppm.

Attempted Synthesis of *rac/meso*-Bis[1-isopropyl-2-(trimethylsilyl)indenyl]zirconium(IV) Dichloride (14): To a Schlenk flask charged with 1-isopropyl-2-(trimethylsilyl)indenylpotassium (**5**) (1.00 g, 3.7 mmol) and zirconium tetrachloride (429 mg, 1.86 mmol), THF (40 mL) was added at –40 °C. Stirring overnight afforded a yellow solution. Solvent change from THF to diethyl ether led to the formation of precipitate. Filtration via cannula and through magnesium sulfate on a D4 frit yielded a brown-yellow oil upon solvent removal. Crystallization occurred after two months of storage in the drybox, though the crystals were too ductile to be isolated. No conclusive NMR spectroscopic data could be obtained for this complex.

Crystal Structure Determination: A yellow platelet with dimensions 0.85 × 0.33 × 0.10 mm was mounted on a glass fiber. Pertinent data for the crystal and solution are collected in Table 5. Reflections were measured with a Siemens SMART 1000 CCD-diffractometer using Mo-K_α radiation. The data collections with SMART[13a] included three sets of exposures with the detector set at 2θ = 26 and crystal-to-detector distance 50 mm. Data integration and cell refinement was carried out by SAINT,[13b] while absorption correction was carried out by SADABS.[13c] SHELXTL[13d] was used for structure solution by direct methods as well as for subsequent full-matrix least-squares refinement on F^2. All atoms except protons were refined anisotropically.

CCDC-253467 contains the supplementary crystallographic data for this paper. These data can be obtained free of charge from The Cambridge Crystallographic Data Centre via www.ccdc.cam.ac.uk/data_request/cif.

Table 5. Crystallographic data, collection and refinement parameters for **13b**.

Parameter	**13b**
Formula	$C_{28}H_{38}Cl_2Si_2Zr$
Mass	592.88
System	orthorhombic
Space group	Fdd2
a [Å]	18.2879(8)
b [Å]	38.1327(17)
c [Å]	8.0947(4)
V [Å^3]	5645.0(4)
Z	8
Radiation	Mo-K_α
λ [Å]	0.71073
T [°C]	–168
$D_{calcd.}$ [g/mL]	1.395
μ (mm^{-1})	0.679
$R(F_0)$	1.91[a]
$R_w(F_O^2)$	4.75[b]
GOF	1.050

[a] Calculated on 5395 reflecions with $I > 2\sigma(I)$. [b] Calculated on all 5687 reflections.

General Polymerization Procedure: Polymerizations were carried out in 100-mL glass reactors equipped with a cooling/heating mantle, an argon/vacuum connection, magnetic stirrer and a septum. Prior to use, the reactors were evacuated at 90 °C for two hours and flushed three times with argon. At 30 °C, the reactors were charged with 50 mL aliquots of freshly distilled toluene, the appropriate amount of solid MAO and subsequently pressurized to a preset pressure of ethene until no further ethene consumption could be registered by the massflow controllers. Polymerization was initiated by injection of the appropriate volume of a toluene solution of the catalyst precursor. Typically, the catalyst precursor solutions had concentrations of $1.0 \cdot 10^{-3}$ mol/L. The reaction was stopped by addition of methanol (5 mL). Work-up of the polymers included extraction of the toluene suspension with methanol/hydrochloric acid (9:1) to remove inorganic residues. Products were fil-

 © 2005 Wiley-VCH Verlag GmbH & Co. KGaA, Weinheim

tered, washed with methanol and dried under high vacuum for two days.

Computational Details: Hybrid DFT calculations were performed with the Gaussian98 package.[14] The B3LYP functional with the 6-31G* basis set was employed for our purposes and proved to be suitable.[15] For Zr, a modified version of the LANL2DZ ECP basis was used.[16] In the original basis set, the 4d shell is described by two contracted functions consisting of three and one primitive Gaussians denoted (31), respectively. To increase flexibility in the d shell we decontracted the set to three functions, consisting of 2, 1, and 1 primitive functions, respectively. For integration, ultrafine grid was employed. All other settings remained default. Due to the high demand for computation time of transition state searches, these were conducted with the Gaussian03 package using the density fitting approximation with auxiliary basis sets as implemented with a pure BP86 functional and a 6-31G* basis set.[17] All calculations were conducted with ultrafine integration grid, while all other parameters remained default.

Acknowledgments

We would like to thank Aud M. Bouzga for assistance with the multi-nuclear NMR experiments. This research was generously supported by the Research Council of Norway through a Dr.-Ing. scholarship (to A. C. M., grant no. 145544/431). Heidi N. Bryntesen's (Borealis Stathelle) generous effort of conducting GPC measurements is very much appreciated.

[1] a) G. W. Coates, R. M. Waymouth, *Science* **1995**, *267*, 217–219; b) W. Kaminsky, *Polym. Mater. Sci. Eng.* **2001**, *84*, 31–32.
[2] a) O. Olabisi, M. Atiqullah, W. Kaminsky, *J. Macromol. Sci. Rev. Macromol. Chem. Phys. C* **1997**, *36*, 519–554; b) H. H. Brintzinger, D. Fischer, R. Mülhaupt, B. Rieger, R. Waymouth, *Angew. Chem.* **1995**, *107*, 1255–1283; *Angew. Chem. Int. Ed.* **1995**, *34*, 1143–1170; c) G. W. Coates, *Chem. Rev.* **2000**, *100*, 1223–1252.
[3] A. C. Möller, R. H. Heyn, R. Blom, O. Swang, C. H. Görbitz, J. Kopf, *Dalton Trans.* **2004**, 1578–1589.
[4] T. Iwamoto, J. Okita, C. Kabuto, M. Kira, *J. Am. Chem. Soc.* **2002**, *124*, 11604–11605.
[5] E. D. Brady, J. S. Overby, M. B. Meredith, A. B. Mussman, M. A. Cohn, T. P. Hanusa, G. T. Yee, M. Pink, *J. Am. Chem. Soc.* **2002**, *124*, 9556–9566.
[6] R. A. Howie, G. P. McQuillan, D. W. Thompson, G. A. Lock, *J. Organomet. Chem.* **1986**, *303*, 213–220.
[7] K. J. Stone, R. D. Little, *J. Org. Chem.* **1984**, *49*, 1849–1853.
[8] ORTEP-3 for Windows: L. J. Farrugia, *J. Appl. Crystallogr.* **1997**, *30*, 565–565.
[9] P. Scott, U. Rief, J. Diebold, H. H. Brintzinger, *Organometallics* **1993**, *12*, 3094–3101.
[10] H. Sitzmann, P. Zhou, G. Wolmershauser, *Chem. Ber.* **1994**, *127*, 3–9.
[11] J. C. Randall, *JMS Rev. Macromol. Chem. Phys.* **1989**, C29(2 & 3), 201–317.
[12] J. S. Merola, R. T. Kacmarcik, *Organometallics* **1989**, *8*, 778–784.
[13] a) Bruker AXS (**1998**). SAINT. Version 6.01 Integration Software; b) Bruker AXS (**1998**). SMART. Version 5.054 Area-Detector Control. Bruker Analytical X-ray Instruments Inc., Madison, Wisconsin, USA; c) Bruker AXS (**2000**). SHELXTL Version 6.10 Bruker Analytical X-ray Systems, Madison, Wisconsin, USA; d) G. M. Sheldrick (**1996**), SADABS, Program for Adsorption Correction, University of Göttingen, Germany.
[14] M. J. Frisch, G. W. Trucks, H. B. Schlegel, G. E. Scuseria, M. A. Robb, J. R. Cheeseman, V. G. Zakrzewski, J. A. Montgomery, Jr., R. E. Stratmann, J. C. Burant, S. Dapprich, J. M. Millam, A. D. Daniels, K. N. Kudin, M. C. Strain, O. Farkas, J. Tomasi, V. Barone, M. Cossi, R. Cammi, B. Mennucci, C. Pomelli, C. Adamo, S. Clifford, J. Ochterski, G. A. Petersson, P. Y. Ayala, Q. Cui, K. Morokuma, P. Salvador, J. J. Dannenberg, D. K. Malick, A. D. Rabuck, K. Raghavachari, J. B. Foresman, J. Cioslowski, J. V. Ortiz, A. G. Baboul, B. B. Stefanov, G. Liu, A. Liashenko, P. Piskorz, I. Komaromi, R. Gomperts, R. L. Martin, D. J. Fox, T. Keith, M. A. Al-Laham, C. Y. Peng, A. Nanayakkara, M. Challacombe, P. M. W. Gill, B. Johnson, W. Chen, M. W. Wong, J. L. Andres, C. Gonzalez, M. Head-Gordon, E. S. Replogle, J. A. Pople, Gaussian 98, Revision A.11, Gaussian, Inc., Pittsburgh PA, **2001**.
[15] a) A. D. Becke, *J. Chem. Phys.* **1993**, *98*, 5648–5652; b) C. Lee, W. Yang, R. G. Parr, *Phys. Rev. B* **1988**, *37*, 785–789.
[16] P. J. Hay, W. R. Wadt, *J. Chem. Phys.* **1985**, *82*, 270–283.
[17] M. J. Frisch, G. W. Trucks, H. B. Schlegel, G. E. Scuseria, M. A. Robb, J. R. Cheeseman, J. A. Montgomery, Jr., T. Vreven, K. N. Kudin, J. C. Burant, J. M. Millam, S. S. Iyengar, J. Tomasi, V. Barone, B. Mennucci, M. Cossi, G. Scalmani, N. Rega, G. A. Petersson, H. Nakatsuji, M. Hada, M. Ehara, K. Toyota, R. Fukuda, J. Hasegawa, M. Ishida, T. Nakajima, Y. Honda, O. Kitao, H. Nakai, M. Klene, X. Li, J. E. Knox, H. P. Hratchian, J. B. Cross, C. Adamo, J. Jaramillo, R. Gomperts, R. E. Stratmann, O. Yazyev, A. J. Austin, R. Cammi, C. Pomelli, J. W. Ochterski, P. Y. Ayala, K. Morokuma, G. A. Voth, P. Salvador, J. J. Dannenberg, V. G. Zakrzewski, S. Dapprich, A. D. Daniels, M. C. Strain, O. Farkas, D. K. Malick, A. D. Rabuck, K. Raghavachari, J. B. Foresman, J. V. Ortiz, Q. Cui, A. G. Baboul, S. Clifford, J. Cioslowski, B. B. Stefanov, G. Liu, A. Liashenko, P. Piskorz, I. Komaromi, R. L. Martin, D. J. Fox, T. Keith, M. A. Al-Laham, C. Y. Peng, A. Nanayakkara, M. Challacombe, P. M. W. Gill, B. Johnson, W. Chen, M. W. Wong, C. Gonzalez, J. A. Pople, Gaussian 03, Revision B.04, Gaussian, Inc., Pittsburgh PA, **2003**.

Received: November 22, 2004

 © 2005 Wiley-VCH Verlag GmbH & Co. KGaA, Weinheim

Structural and Electrochemical Studies of Dimerization and Rotational Isomerization in Multi-Iron Silicotungstates

Travis M. Anderson,[a] Rui Cao,[a] Wade A. Neiwert,[a,c] Kenneth I. Hardcastle,[a] Craig L. Hill,*[a] Malika Ammam,[b] Bineta Keita,[b] and Louis Nadjo*[b]

Keywords: Polyoxometalates / Cyclic voltammetry / Iron / Tungsten

A structural and electrochemical investigation of dimerization and Baker–Figgis (rotational) isomerization in the tri-ferric-substituted silicotungstates has been undertaken because these phenomena are important in a large number of polyoxometalates. A single-crystal X-ray diffraction analysis of $K_4Na_7[(\beta\text{-}SiFe_3W_9(OH)_3O_{34})_2(OH)_3]$ (**β1**) has been carried out [a = 12.9709(7) Å, b = 38.720(2) Å, c = 21.4221(12) Å, orthorhombic, *Pbcm*, R_1 = 8.48 %, based on 13809 independent reflections]. The complex is isostructural with $[(\alpha\text{-}SiFe_3W_9(OH)_3O_{34})_2(OH)_3]^{11-}$ (**α1**) except that the edge-shared W_3O_{13} caps in each $[SiFe_3W_9(OH)_3O_{34}]^{4-}$ unit are rotated by 60°. Electrochemical measurements, performed in a pH 5 acetate buffer, indicate a positive shift in the Fe^{III}-based peak potential (and no change for the W^{VI}-based potential) upon going from **α1** to its monomeric derivative $[(\alpha\text{-}Si(FeOH_2)_3W_9(OH)_3O_{34})]^{4-}$ (**α2**) (–0.484 ± 0.005 V and –0.474 ± 0.005 V, respectively). In contrast, the peak potentials of the Fe^{III}- and W^{VI}-based redox processes of **β1** are both found at more negative values than its rotational isomer **α1**. The absolute values of the reduction peak potential differences are 0.022 V for Fe^{III} and 0.162 V for W^{VI}.

(© Wiley-VCH Verlag GmbH & Co. KGaA, 69451 Weinheim, Germany, 2005)

Introduction

The use of polyoxometalates (POMs) as catalysts constitutes a substantial and rapidly growing literature.[1,2] In particular, d-electron-transition-metal-substituted POMs have attracted much attention as oxidation catalysts because they are thermodynamically stable to oxidative degradation; yet many of the fundamental properties of POMs that impact catalysis and other applications as well, including elemental composition, solubility, redox potentials, charge density, size, and shape, can be systematically altered to a considerable degree. As a result, these compounds combine the stability advantages of heterogeneous catalysts with the selectivity advantages of homogeneous catalysts.

Recently we began a program aimed at the synthesis and characterization of a series of multi-iron heteropolytungstates with the goal of exploring their redox chemistry and catalytic (and electrocatalytic) properties.[3] In general, parameters (such as pH and heteroatom effects) that favor multi-electron-transfer reactions in POMs continue to be a focus on ongoing efforts.[4,5] Previously it was shown in a comparison of the cyclic voltammograms of α_1- and α_2-$[P_2(FeOH_2)W_{17}O_{61}]^{7-}$ that the location of Fe^{III} (cap or belt site) within the heteropolytungstate framework influences the electrochemical properties of the molecules.[6] More recently, we have also shown that the accumulation of multiple edge-sharing Fe^{III} centers in Wells–Dawson-derived sandwich-type complexes leads to more favorable electrocatalytic properties than those observed in monosubstituted complexes such as α_2-$[As(FeOH_2)W_{17}O_{61}]^{7-}$.[7]

This paper focuses on how two different types of common POM structural perturbations influence the electrochemical properties of Fe^{III} redox centers in a series of multi-iron silicotungstates (Figure 1). In one study, two complexes differing only in the rotational arrangement (i.e. Baker–Figgis isomerism)[8] of their edge-shared W_3O_{13} caps, $[(\alpha\text{-}SiFe_3W_9(OH)_3O_{34})_2(OH)_3]^{11-}$ (**α1**) and $[(\beta\text{-}SiFe_3W_9(OH)_3O_{34})_2(OH)_3]^{11-}$ (**β1**), are compared. In the other study, the dimer, **α1**, is compared with its monomeric analogue, $[(\alpha\text{-}Si(FeOH_2)_3W_9(OH)_3O_{34})]^{4-}$ (**α2**).[9] Unlike **α1** and **β1**, complexes **α1** and **α2** have different coordination environments around their Fe^{III} centers. The replacement of a hydroxo ligand in **α1** with an aqua ligand in **α2** results in a 20-nm red shift (from 436 nm to 456 nm) for the Fe^{III}-centered d-d transitions in the electronic spectra of the two complexes.

[a] Department of Chemistry, Emory University, Atlanta, Georgia 30322, USA
E-mail: chill@emory.edu
[b] Laboratoire de Chimie Physique, UMR 8000, CNRS, Université Paris-Sud, Bâtiment 420, 91405 Orsay Cedex, France
E-mail: nadjo@lcp.u-psud.fr
[c] Current address: Department of Chemistry, Bethel University, St. Paul, Minnesota 55112, USA
Supporting information for this article is available on the WWW under http://www.eurjic.org or from the author.

 © 2005 Wiley-VCH Verlag GmbH & Co. KGaA, Weinheim **DOI: 10.1002/ejic.200401061**

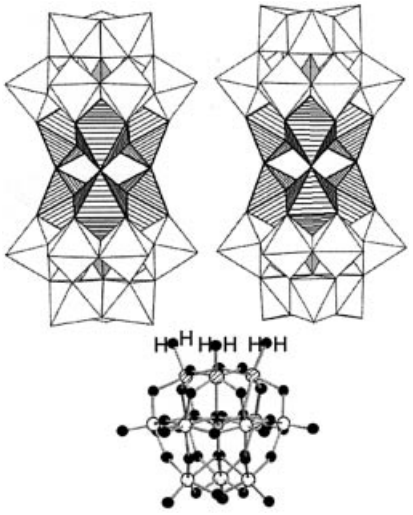

Figure 1. Polyhedral representations of $[(\alpha\text{-}SiFe_3W_9(OH)_3O_{34})_2(OH)_3]^{11-}$ (**α1**, top left) and $[(\beta\text{-}SiFe_3W_9(OH)_3O_{34})_2(OH)_3]^{11-}$ (**β1**, top right), and a ball-and-stick representation of $[(\alpha\text{-}Si(FeOH_2)_3W_9(OH)_3O_{34})]^{4-}$ (**α2**, bottom). White, gray, and striped polyhedra represent WO_6, SiO_4, and FeO_6, respectively (**α1** and **β1**). In **α2**, the W, Fe, Si, and O atoms are shown as white, striped, gray, and black spheres, respectively.

Results and Discussion

Syntheses: The syntheses of $[\alpha\text{-}SiFe_3W_9(OH)_3O_{34}]^{4-}$ (**α2**) and $[\beta\text{-}SiFe_3W_9(OH)_3O_{34}]^{4-}$ (**β2**) were originally reported by Pope.[10] However, mass spectrometry data suggested these complexes contained small to modest amounts of the dimeric species ($[(\alpha\text{-}SiFe_3W_9(OH)_3O_{34})_2(OH)_3]^{11-}$ (**α1**) and $[(\beta\text{-}SiFe_3W_9(OH)_3O_{34})_2(OH)_3]^{11-}$ (**β1**), respectively) as impurities.[10] Recently, we reported a modified procedure that utilizes differences in the acid sensitivities of $Na_7H_3[\alpha\text{-}SiW_9O_{34}]$ and $K_{10}[\alpha\text{-}SiW_9O_{34}]$ to obtain **α1** and **α2**, respectively, in high purity (with 40–70% yield).[9] In this report, an analogous procedure is used to obtain **β1** (i.e. reaction of $Na_9H[\beta\text{-}SiW_9O_{34}]$ with 3 equivalents of Fe^{III} in 0.5 M sodium acetate (pH = 6) yields **β1** in 20% yield).

Solid State Characterization of β1: The X-ray crystallographic studies of **β1** show that two A-type $[\beta\text{-}SiFe_3W_9(OH)_3O_{34}]^{4-}$ units are linked by three Fe-μ-OH–Fe bridges such that the complex has overall ca. D_{3h} symmetry (Figure 1). The complex is isostructural with **α1** except that the edge-shared W_3O_{13} caps in each $[SiFe_3W_9(OH)_3O_{34}]^{4-}$ unit are rotated by 60°. Table 1 gives average bond lengths and angles for the two complexes. Bond valence sum (BVS) calculations for Fe1, Fe2, Fe3, and Fe4 (see Figure S1 in the Supporting Information for the numbering scheme; for supporting information see also the footnote on the first page of this article) give average oxidation states of 2.96, 2.99, 3.06, and 2.99, respectively.[11] BVS calculations (average value = 1.2) also establish that hydroxo bridges are present between the adjacent Fe^{III} centers in each $[SiFe_3W_9(OH)_3O_{34}]^{4-}$ unit.

Table 1. Selected average bond lengths [Å] and bond angles [°] for **α1** and **β1**.

	α1[a]	**β1**
W=O	1.724(8)	1.718(8)
Si–O	1.64(1)	1.63(3)
Fe···Fe	3.713(8)	3.710(11)
W_{belt}–O–W_{cap}	150.4(5)	145.7(8)
Fe1···Fe2···Fe3	61.0(3)	59.1
W1···W2···W3	59.9(3)	60.4

[a] Data from reference[9].

The differential scanning calorimetry curve for **β1** shows one endothermic and two exothermic processes in the region from 20 °C to 600 °C (Figure 2). The endothermic process from 100 °C to 160 °C is attributed to desorption of water molecules of crystallization from the lattice structure. This conclusion is corroborated by thermogravimetric analysis and infrared spectroscopy. The first exothermic process (from 200 °C to 275 °C, indicated by arrows and verified by infrared data) is attributed to the solid-state isomerization (from **β1** to **α1**) of the POM. Infrared spectroscopy shows that there is an 18 cm^{-1} shift in the combination W=O stretching/W–O–W bending mode centered at 883 cm^{-1} in **β1** upon heating the sample to 275 °C. The 18 cm^{-1} shift places this band at 901 cm^{-1}, which is identical to that reported for an authentic sample of **α1** (Figure 3).[9] Finally, there is an exothermic process observed from 550 °C to 600 °C that is attributable to the collapse of the tungsten framework of the POM. This is also corroborated by infrared spectroscopy data, which shows significant changes in the W=O (W–O) stretching and W–O–W bending modes after heating to 550 °C.

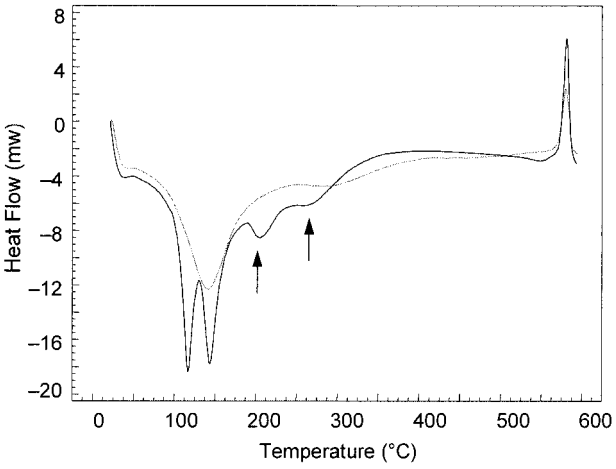

Figure 2. Differential scanning calorimetry data for $K_4Na_7[(\beta\text{-}SiFe_3W_9(OH)_3O_{34})_2(OH)_3]$ (**β1**) (black line) and $K_4Na_7[(\alpha\text{-}SiFe_3W_9(OH)_3O_{34})_2(OH)_3]$ (**α1**) (gray line). The endothermic desorption of solvent water molecules of crystallization from 100 °C to 160 °C in **β1** is nearly resolved into two peaks, whereas the same process in **α1** appears as only one broad peak. The arrows are used to indicate the temperature range of the first exothermic feature based on infrared data. This corresponds to where the solid state rotational isomerization of the W_3O_{13} caps takes place.

Electrochemical Studies: Recently, we reported the detailed electrochemical behavior of the Fe^{III} centers within a

 © 2005 Wiley-VCH Verlag GmbH & Co. KGaA, Weinheim

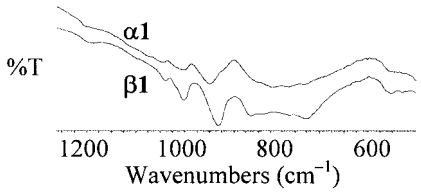

Figure 3. Infrared spectra of **α1** (top) and **β1** (bottom). The spectra are shown in percent transmittance (and labeled as %T on the *y* axis). The band at 883 cm^{-1} in the spectrum of **β1** is shifted by 18 cm^{-1} (to 901 cm^{-1}) in **α1**.

large family of related sandwich-type complexes, including αββα-$[(Fe^{III}OH_2)_2(Fe^{III})_2(X_2W_{15}O_{56})_2]^{12-}$ (X = P^V or As^V).[3a,4,7] In a pH 5 acetate buffer, these compounds show a stepwise reduction of the four edge-sharing Fe^{III} centers. In contrast, the corner-sharing Fe^{III} centers in **α1**, **α2**, and **β1** have a single Fe^{III}-based voltammetric wave in the same pH 5 acetate buffer. In addition, unlike the sandwich-type complexes, **α1**, **α2**, and **β1** also adsorb to different extents onto the surface of the glassy carbon electrode. This behavior was discovered by the observation that there is a steady negative shift in the potentials of the complexes in every other run. This phenomenon is slight for complexes **α1** and **α2**, but it is more pronounced for **β1**. All of the electrochemical data presented in the following paragraphs were obtained with freshly polished glassy carbon electrodes except where noted.

Figure 4 (A) shows the cyclic voltammogram of **α1** in the pH 5 acetate buffer with a scan rate of 10 mV·s^{-1}. The pattern has been restricted to the reduction of the Fe^{III} centers and the first W^{VI} reduction process. The W^{VI}-based wave is electrochemically quasi-reversible and chemically reversible upon reversal of the potential. The Fe^{III}-based wave in this system is observed at E_{pc} = –0.484 ± 0.005 V (vs. SCE). Controlled potential coulometry experiments (with the potential set at –0.550 V vs. SCE) indicate that **α1** consumes 6.08 ± 0.05 electrons per molecule. This is consistent with the simultaneous one-electron reduction of the six Fe^{III} centers. The characteristic blue color of a reduced tungsten-oxygen framework was not observed during this experiment, consistent with the observation that there is a large separation between the Fe^{III}- and the W^{VI}-based redox processes. Finally, it was possible to completely re-oxidize **α1** back to the Fe^{III} state, which confirms and also extends the time dependence of the chemical reversibility and stability of the complex previously observed by cyclic voltammetry.

Figure 4 (B) compares the cyclic voltammograms of **α1** and **α2** under identical conditions (0.2 mM POM in 0.5 M acetate buffer, pH 5; scan rate 10 mV·s^{-1}). The Fe^{III}-based waves of the two complexes have slightly different shapes, with **α2** showing a larger half peak width than **α1** (0.118 vs. 0.080 V for **α2** and **α1**, respectively). The peak potential of **α2** is also at a more positive value than **α1** (–0.474 ± 0.005 V vs. –0.484 ± 0.005 V, respectively). In contrast, the W^{VI}-based waves are superimposable in shape and intensity. Given that the experimental errors for the peak potential

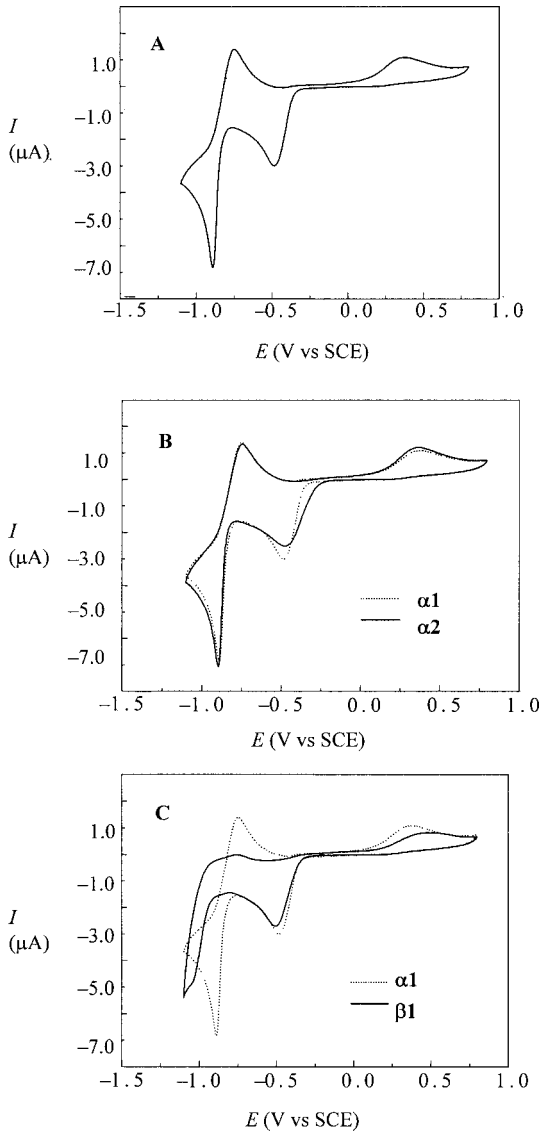

Figure 4. Cyclic voltammograms of **α1**, **α2**, and **β1** in a pH 5 acetate buffer (0.5 M CH_3COONa + CH_3COOH). The pattern has been restricted to the reduction of the Fe^{III} centers and the first W^{VI} reduction process. POM concentration: 0.2 mM; scan rate: 10 mV·s^{-1}; working electrode: glassy carbon; reference electrode: SCE **A:** Cyclic voltammogram of **α1** alone **B:** Cyclic voltammogram of **α1** and **α2** **C:** Cyclic voltammogram of **α1** and **β1**.

measurements of **α2** and **α1** are both ±0.005 V, the difference in the E_{pc} values for the two complexes is quite small. However, the perfect reproducibility of the measurements confirms the order of the peak potentials and suggests their differences are statistically significant. The difference in the peak potentials of **α1** and **α2** could be attributed to the fact that a hydroxo ligand on each Fe^{III} center in **α1** is replaced by an aqua ligand in **α2**. In addition, **α1** has a higher overall negative charge (and slightly higher charge density) than **α2**. Finally, interconversion of the two complexes through protonation equilibria and their co-existence in the same protonation state seems unlikely given the fact that protonation is known to cause the dimer to convert to the monomer.[9]

 © 2005 Wiley-VCH Verlag GmbH & Co. KGaA, Weinheim

Figure 4 (C) compares the cyclic voltammograms of **α1** and its Baker–Figgis rotational isomer, **β1** (0.2 mM POM in 0.5 M acetate buffer, pH 5; scan rate 10 $mV \cdot s^{-1}$). Complex **β1** has a negative shift in its peak potentials for both the Fe^{III} and the W^{VI} redox processes. The absolute values of the reduction peak potential differences are 0.022 V and 0.162 V for Fe^{III} and W^{VI}, respectively. To the best of our knowledge, these observations are unprecedented as all previously characterized β-isomers of the unsubstituted Keggin and Wells–Dawson heteropolytungstates are reduced at potentials that are slightly more positive than their corresponding α-isomers.[12] The Fe^{III}-based waves are chemically reversible for both **α1** and **β1**, but **β1** has more pronounced electrochemical irreversibility than **α1**. In addition, the chemical reversibility of the W^{VI}-based wave of **α1** vanishes completely in **β1**. Finally, a small, reversible process observed between the Fe^{III} and W^{VI} waves of **β1** is tentatively attributed to the formation of a small amount of **α1**.

Differences in the electrochemical properties of **α1** and **β1** must be at least partly attributable to the fact that crystallographic studies show these complexes are truly Baker–Figgis rotational isomers. A correlative reason might be traced to differences in the pK_a values of the various protonateable centers in **α1** and **β1**, the latter complex being the more acidic of the two. To probe this further, exhaustive controlled potential electrolysis of the Fe^{III} centers in **β1** was performed using a glassy carbon plate in pH 5 acetate buffer with the potential set at –0.550 V. The current became negligibly small after the consumption of 5.3 electrons per molecule. Cyclic voltammograms (restricted to the Fe^{III}-based redox process) were run before and after electrolysis. When the same glassy carbon plate was used for the initial voltammogram, electrolysis, and the final voltammogram (for a total of three runs), a desorptive oxidation peak and a composite Fe reduction wave appear. This suggests that adsorption and transformation of **β1** has taken place on the surface of the electrode (see Figure S2 in the Supporting Information). Quantitative re-oxidation of the solution to the Fe^{III} state was not possible, as indicated by controlled potential coulometry data (consumption of 2.5 ± 0.1 electrons per molecule). Figure 5 shows the cyclic voltammogram of **β1** before and after the forward and backward electrolysis using a clean carbon plate electrode. The results show that the Fe-wave has become composite and is now located at a more positive potential. Given the fact that this transformation is not observed for **α1**, these observations collectively suggest that **β1** is less stable than **α1** upon the reduction of the Fe^{III} centers.

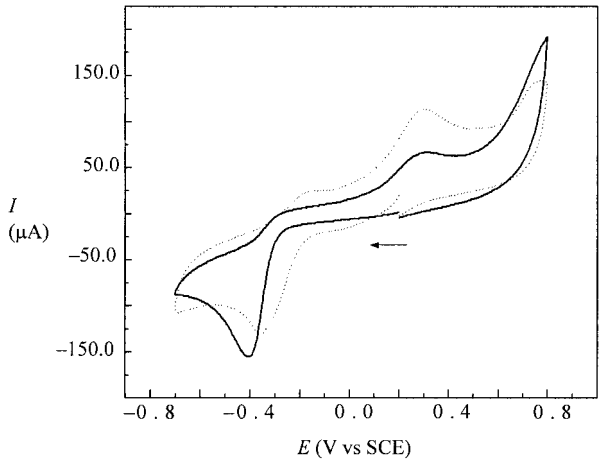

Figure 5. Cyclic voltammograms of **β1** in a pH 5 acetate buffer (0.5 M CH_3COONa + CH_3COOH) before electrolysis of the Fe^{III} centers (solid line) and after exhaustive reduction of the Fe^{III} centers and complete re-oxidation of the resulting solution (dotted line). The pattern has been restricted to the reduction and reoxidation of the Fe^{III} centers only. POM concentration: 0.2 mM; scan rate: 10 $mV \cdot s^{-1}$; working electrode: glassy carbon plate; reference electrode: SCE.

Conclusions

The redox chemistry of three closely related multi-iron silicotungstates have been investigated in order to determine how dimerization and rotational isomerization affects the electrochemical properties of these complexes. In a pH 5 acetate buffer, there is a positive shift in the Fe^{III}-based peak potential upon going from the dimer, $[(\alpha\text{-}Si\text{-}Fe_3W_9(OH)_3O_{34})_2(OH)_3]^{11-}$ (**α1**), to its monomeric derivative $[(\alpha\text{-}Si(FeOH_2)_3W_9(OH)_3O_{34})]^{4-}$ (**α2**). This is due in part to the higher overall charge of the dimer, and it is also partly attributable to differences in the coordination environments of Fe^{III} in the two complexes (i.e. a hydroxo ligand on each Fe^{III} center in **α1** is replaced with an aqua ligand in **α2**, based on BVS calculations on the X-ray crystal structure data). The peak potentials of the Fe^{III}- and W^{VI}-based redox processes of **β1** are both found at more negative values than its rotational isomer **α1**. Exhaustive controlled potential electrolysis studies of the Fe^{III} centers in **β1** collectively suggest that **β1** is less stable than **α1** upon the reduction of the Fe^{III} centers.

Experimental Section

General Methods and Materials: $KNa_3[(\alpha\text{-}Si(FeOH_2)_3W_9(OH)_3O_{34})]$, $K_4Na_7[(\alpha\text{-}SiFe_3W_9(OH)_3O_{34})_2(OH)_3]$, and $Na_9H[\beta\text{-}SiW_9O_{34}]$ were obtained by published procedures[9,13] and purity was confirmed by infrared and UV/Vis spectroscopy and elemental analyses. Elemental analyses of Fe, K, Na, Si, and W were performed by Desert Analytics (Tucson, Arizona). Infrared spectra (2% sample in KBr) were recorded with a Nicolet 510 instrument. The electronic absorption spectra were taken with a Perkin–Elmer Lambda 19 UV/Vis spectrophotometer. Average magnetic susceptibilities were measured with a Johnson-Matthey Model MSB-1 magnetic susceptibility balance as neat powders at 24 °C; the balance was calibrated using $Hg[Co(SCN)_4]$ as a standard. Pascal's constants were used to obtain the final diamagnetic corrections. Differential scanning calorimetric and thermogravimetric data were collected with ISI DSC 550 and TGA 1000 instruments, respectively.

Synthesis of $K_4Na_7[(\beta\text{-}SiFe_3W_9(OH)_3O_{34})_2(OH)_3]\cdot 40H_2O$ (β1): A 0.87 g (2.2 mmol) sample of $Fe(NO_3)_3\cdot 9H_2O$ was dissolved in 30 mL of 0.5 M sodium acetate in an 150 mL beaker. A 2.0 g (0.72 mmol) sample of $Na_9H[\beta\text{-}SiW_9O_{34}]\cdot 18H_2O$[13] was slowly added to the Fe^{III} solution with vigorous stirring. The final pH of

 © 2005 Wiley-VCH Verlag GmbH & Co. KGaA, Weinheim

the solution is ca. 6. Any insoluble material that was present was removed by filtration with Celite, and a solution of 0.5 g of KCl dissolved in 5 mL of H_2O was added to the resulting filtrate. Light green, diffraction quality crystals formed at 10 °C in the resulting filtrate after approximately five days (0.43 g, yield 20%). IR (2% KBr pellet, 1200–500 cm^{-1}): $\tilde{\nu}$ = 1129 (w), 991 (w), 960 (m), 883 (s), 811 (w), 770 (w), 724 (m), and 523 (w). Electronic spectroscopic data (400–700 nm, in H_2O): λ (ε, M^{-1} cm^{-1}) = 436 nm (200). Magnetic susceptibility: μ_{eff} = 7.7 μ_B/mol at 295 K. $H_{89}Fe_6K_4Na_7O_{117}Si_2W_{18}$ (5979.5): calcd. Fe 5.60, K 2.62, Na 2.69, OH_2 12.0, Si 0.94, W 55.3; found Fe 5.65, K 2.61, Na 2.64, OH_2 12.0, Si 0.94, W 54.9.

Crystallographic Studies of β1: Single-crystal X-ray crystallographic analysis of **β1** was performed at 100 K with a Bruker D8 SMART APEX CCD sealed tube diffractometer with graphite-monochromated Mo-K_α (0.71073 Å) radiation. Data collection, indexing, and initial cell refinements were carried out using SMART software.[14] Frame integration and final cell refinements were carried out using SAINT software.[15] Final cell parameters were determined from least-squares refinement on 7765 reflections. Absorption corrections were applied using SADABS.[16] The structure was determined using Direct Methods and difference Fourier techniques. No H atoms associated with the water molecules of **β1** were located in the difference Fourier maps. The final R_1 scattering factor and the anomalous dispersion correction were taken from International Tables for X-ray Crystallography.[17] Structure solution, refinement, and generation of publication materials were performed using SHELXTL V6.12 software. Additional details are provided in Table 2, and may also be obtained from the FIZ Karlsruhe, 76344 Eggenstein-Leopoldshafen, Germany, on quoting the depository number CSD-414457.

Table 2. Crystallographic data and structure refinement for **β1**.

Empirical formula	$H_{90.6}Fe_6K_4Na_7O_{117.8}Si_2W_{18}$
Formula mass	5994.04
Space group	Pbcm
Unit cell	a = 12.9709(7) Å
	b = 38.720(2) Å
	c = 21.4221(12) Å
Volume	10758.9(10) $Å^3$
Z	4
Density (calcd.)	3.701 $g\,cm^{-3}$
Temperature	100(2) K
λ	0.71073 Å
μ	2.0272 cm^{-1}
GOF	1.382
Final R_1[a] [$I > 2\sigma(I)$]	0.0848
Final wR_2[b] [$I > 2\sigma(I)$]	0.1674

[a] $R_1 = \Sigma||F_o| - |F_c||/|F_o|$. [b] $wR_2 = \{\Sigma[w(F_o^2 - F_c^2)^2]/\Sigma[w(F_o^2)^2]\}^{0.5}$.

Electrochemical Studies: Cyclic voltammetry studies were performed on 2×10^{-4} M solutions of **α1**, **α2**, or **β1** in a pH 5 acetate (0.5 M CH_3COONa/CH_3COOH) medium, unless otherwise stated. Solutions were de-aerated with Ar for 30 min prior to measurements and kept under positive pressure at all times. The source, mounting, and polishing of the glassy carbon electrodes (GC, Tokai, Japan, 3 mm diameter) have been described in previous work.[18] The counter electrode was a platinum gauze of large surface area. The electrochemical apparatus was a EG and G 273A under computer control (M270 software). All experiments were performed at ambient temperature, and potentials are quoted against a saturated calomel electrode (SCE). Controlled potential coulometry determinations were performed as described for the cyclic voltammetry experiments except that the working electrode used was a 4 cm^2 surface area glassy carbon plate. In addition, after deaeration, Ar was continuously bubbled through the solution to ensure a constant stirring of the mixture. The stability of the complexes in pH 3–7 buffer solutions was evaluated by UV/Vis prior to making any electrochemical measurements. The UV/Vis spectra of 0.016 mM solutions of the POMs are characterized by well-defined charge transfer peaks with a $\lambda_{max.}$ at 259 nm for **α1** and **α2** or 264 nm for **β1**. After 24 h, **α1** shows an 11% decrease in absorbance at pH 4 and is stable between pH 5–7; **β1** is stable between pH 5–7 and shows a 12% decrease in absorbance at pH 4; **α2** is stable at pH 4 and shows a slight shape modification at pH 5.

Supporting Information (see also the footnote on the first page of this article): Figure S1 shows a thermal ellipsoid plot of **β1** with 50% probability surfaces. Figure S2 shows cyclic voltammograms of 0.2 mM solutions of **β1** before and after the exhaustive reduction of the Fe^{III} centers in a pH 5 acetate (0.5 M CH_3COONa/CH_3COOH) buffer.

Acknowledgments

This work was supported by the National Science Foundation (Grant CHE-0236686), CNRS (UMR 8000), and the University Paris-Sud XI.

[1] C. L. Hill, C. M. Prosser-McCartha, *Coord. Chem. Rev.* **1995**, *143*, 407–455.
[2] Recent reviews include: a) R. Neumann, Applications of Polyoxometalates in Homogeneous Catalysis. In *NATO Science Series II: Mathematics, Physics, and Chemistry*; Kluwer Academic Publishers: Dordrecht, **2003**; vol. 98, pp. 327–349; b) I. V. Kozhevnikov, Heterogeneous Catalysis by Heteropoly Compounds. In *NATO Science Series II: Mathematics, Physics, and Chemistry*; Kluwer Academic Publishers: Dordrecht, **2003**; vol. 98, pp. 351–380; c) E. Papaconstantinou, A. Hiskia, Photochemistry and Photocatalysis by Polyoxometalates. In *NATO Science Series II: Mathematics, Physics, and Chemistry*; Kluwer Academic Publishers: Dordrecht, **2003**; vol. 98, pp. 381–416; d) C. L. Hill, Polyoxometalates: Reactivity. In *Comprehensive Coordination Chemistry II: Transition Metal Groups 3–6* (Ed.: A. G. Wedd) Elsevier Science: New York, **2004**; vol. 4, chapter 4.11, pp. 679–759.
[3] Representative work on the synthesis of multi-iron POMs include: a) X. Zhang, Q. Chen, D. C. Duncan, C. Campana, C. L. Hill, *Inorg. Chem.* **1997**, *36*, 4208–4215; b) C. Nozaki, I. Kiyoto, Y. Minai, M. Misono, N. Mizuno, *Inorg. Chem.* **1999**, *38*, 5724–5729; c) X. Zhang, T. M. Anderson, Q. Chen, C. L. Hill, *Inorg. Chem.* **2001**, *40*, 418–419; d) U. Kortz, M. G. Savalieff, B. S. Bassil, B. Keita, L. Nadjo, *Inorg. Chem.* **2002**, *41*, 783–789; e) T. M. Anderson, X. Zhang, K. I. Hardcastle, C. L. Hill, *Inorg. Chem.* **2002**, *41*, 2477–2488; f) I. M. Mbomekalle, B. Keita, L. Nadjo, W. A. Neiwert, L. Zhang, K. I. Hardcastle, C. L. Hill, T. M. Anderson, *Eur. J. Inorg. Chem.* **2003**, 3924–3928.
[4] B. Keita, I. M. Mbomekalle, Y. W. Lu, L. Nadjo, P. Berthet, T. M. Anderson, C. L. Hill, *Eur. J. Inorg. Chem.* **2004**, 3462–3475.
[5] B. Keita, I. M. Mbomekalle, L. Nadjo, T. M. Anderson, C. L. Hill, *Inorg. Chem.* **2004**, *43*, 3257–3263.
[6] R. Contant, M. Abbessi, J. Canny, A. Belhouari, B. Keita, L. Nadjo, *Inorg. Chem.* **1997**, *36*, 4961–4967.
[7] I. M. Mbomekalle, B. Keita, L. Nadjo, P. Berthet, K. I. Hardcastle, C. L. Hill, T. M. Anderson, *Inorg. Chem.* **2003**, *42*, 1163–1169.
[8] L. C. W. Baker, J. S. Figgis, *J. Am. Chem. Soc.* **1970**, *92*, 3794–3797.
[9] T. M. Anderson, W. A. Neiwert, K. I. Hardcastle, C. L. Hill, *Inorg. Chem.* **2004**, *43*, 7353–7358.

 © 2005 Wiley-VCH Verlag GmbH & Co. KGaA, Weinheim

[10] J. Liu, F. Ortéga, P. Sethuraman, D. E. Katsoulis, C. E. Costello, M. T. Pope, *J. Chem. Soc., Dalton Trans.* **1992**, 1901–1906.
[11] I. D. Brown, D. Altermatt, *Acta Crystallogr. Sect. B* **1985**, *41*, 244–247.
[12] a) M. T. Pope, *Heteropoly and Isopoly Oxometalates*; Springer-Verlag: Berlin, **1983**; b) M. Sadakane, E. Steckhan, *Chem. Rev.* **1998**, *98*, 219–237 and references cited therein.
[13] A. Tézé, G. Hervé, in *Inorganic Syntheses* (Ed.: A. P. Ginsberg); John Wiley & Sons: New York, **1990**; vol. 27, pp. 85–96.
[14] *SMART*, version 5.628; Bruker AXS, Inc.: Madison, WI, **2003**.
[15] *SAINT*, version 6.36A; Bruker AXS, Inc.: Madison, WI, **2002**.
[16] G. Sheldrick, *SADABS*, version 2.10; University of Göttingen: Göttingen, Germany, **2003**.
[17] *International Table for X-ray Crystallography*; Kynoch Academic Publishers: Dordrecht, The Netherlands, **1992**, vol. C.
[18] B. Keita, F. Girard, L. Nadjo, R. Contant, R. Belghiche, M. Abbessi, *J. Electroanal. Chem.* **2001**, *508*, 70–80.

Received: December 29, 2004

 © 2005 Wiley-VCH Verlag GmbH & Co. KGaA, Weinheim

New Layered Polymeric Metamagnet Based on Copper(II) Complex with 3-Imidazoline Nitroxide

Alexei Burdukov,*[a] Yurii Shvedenkov,[a] Natalie Pervukhina,[a] and Vladimir Reznikov[b]

Keywords: Layered compounds / Copper / Nitroxides / Magnetic properties / Phase transitions

A new complex, bis[4-(2-oxido-1-butenyl)-2,2,5,5-tetramethylimidazolidine-1-oxyl]copper(II) (CuL^{Et}_2), has been synthesized. The synthesis, characterization, and magnetic properties as well as the crystal structure of CuL^{Et}_2 have been studied. The layered solid of the complex possesses a metamagnetic phase transition at 4.5 K and shows strong anisotropy of magnetic properties below the ordering temperature. The easy magnetization axis lies along the *b* axis. The hard magnetization axis is orthogonal to the polymeric layers. Effective anisotropy fields have been estimated ($H_\perp$ = 1390 Oe, $H_\parallel$ = 420 Oe).

(© Wiley-VCH Verlag GmbH & Co. KGaA, 69451 Weinheim, Germany, 2005)

Introduction

The design of molecular magnets demands the ability to engineer the desired crystal structure and the means to control the efficiency of interactions of a diverse nature between the paramagnetic centers.[1] One of the peculiarities of molecular magnets derived from coordination compounds is considerable local and bulk anisotropy introduced by transition-metal ions. The majority of coordination compounds have low symmetry in the solid phase and their crystal structures have low dimensionality. The energy of anisotropy of such systems depends appreciably on the dimensionality of the crystal structure and on the contribution of dipolar interactions to the onset of magnetic ordering.[2] The importance of the dimensionality is well illustrated by comparison of the chain polymeric (1D) complex $Mn(hfac)_2NIT$-*i*Pr (NIT-*i*Pr = derivative of 2-imidazoline nitroxide)[3] and of layered polymeric (2D) complex CuL_2 (L = derivatives of 3-imidazoline nitroxide),[4] the effective anisotropy field being approximately five times larger for the former. Also, anisotropic interactions of a nonexchange nature lead to the appearance of metamagnetism in coordination compounds such as $[(CH)_3NH]CuCl_3 \cdot 2H_2O$[5] and CuL^{Me}_2.[4]

With this contribution we continue our systematic studies on the magnetic anisotropy of heterospin compounds based on Cu^{II} complexes with enaminoketone derivatives of 3-imidazoline nitroxide.

These compounds provide a unique series of solids possessing similar layered topology but different structural details, thus providing a very good basis for revealing the correlations between structure and magnetic anisotropy. In this work we report the results of the structural and magnetic investigation of the complex CuL^{Et}_2.

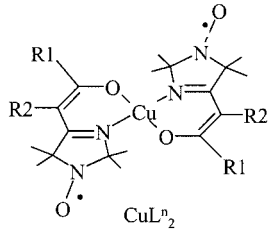

L	R1	R2
L^{Et}	Et	NC
L^{Me}	Me	NC
$L^{C(O)OEt}$	C(O)OEt	H
$L^{C(O)OMe}$	C(O)OMe	H

Results and Discussion

The compound under investigation is built from CuL^{Et}_2 molecules, the copper atom occupying the inversion center [1/2,0,1/2]. The closest coordination environment of copper is formed by two nitrogens N(1) and two oxygens O(1) belonging to the enaminoketone moieties (Figure 1).

The bond lengths and angles within the molecules have the usual values. The axial positions around the copper atom are occupied by two nitroxide oxygens O(2) at a distance of 2.584(3) Å. The Cu–O(2) bond is almost perfectly perpendicular to the coordination square, the deviation being only 0.3°. With a connectivity of four at the copper atom, the molecules arrange into the 4^4 (in Wells notation[6]) chicken-wire nets parallel to the (0,0,1) plane (Figure 2). Within the frame of the *Pbca* space group the neighboring polymeric nets are related with the *c* glide plane with a net-to-net separation of 11.978 Å, as measured between the closest copper atoms. This is somewhat longer than the equivalent separation in CuL^{Me}_2, which is equal to 11.869 Å. This difference in separation between iso-

[a] Nikolaev Institute of Inorganic Chemistry SB RAS,
Lavrent'ev Ave., 3, Novosibirsk 630090, Russia
Fax: +7-3832-344-489
E-mail: alex@cys.che.nsk.su
[b] Vorozhtzov Institute of Organic Chemistry SB RAS,
Lavrent'ev Ave., 7, Novosibirsk 630090, Russia

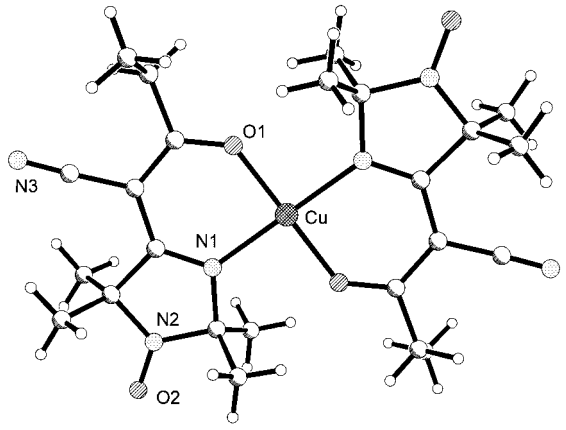

Figure 1. The molecule CuL^{Et}_2.

structural CuL^{Me}_2 and CuL^{Et}_2 is due to the different sizes of the Me and Et substituents which propagate into the interlayer space.

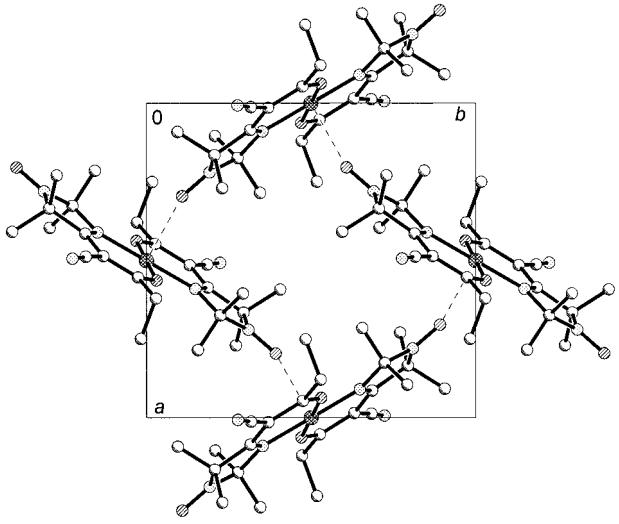

Figure 2. Fragment of the polymeric layered structure of CuL^{Et}_2 projected onto the (001) plane. Hydrogen atoms are omitted for clarity.

Figure 3 illustrates the effective magnetic moment of CuL^{Et}_2 measured along different crystallographic directions above 14 K. In this temperature range, CuL^{Et}_2 behaves as a paramagnet with dominating ferromagnetic exchange interactions between paramagnetic centers. The CuL^{Et}_2 complex possesses two main exchange channels. The first exchange channel is the intramolecular indirect exchange between the nitroxide and copper spins through the heterocycle of the ligand. The other exchange pathway is the direct exchange between the copper(II) ion and the nitroxide group belonging to the adjacent $\{CuL_2\}$ bis-chelate fragment. Both exchange pathways propagate ferromagnetic interactions[7] resulting in the rise of the $\mu_{eff}(T)$ curves with decreasing temperature. The $\mu_{eff}(T)$ curves measured along different directions are quite close (Figure 3). The observed discrepancy in the paramagnetic region is caused by the anisotropy of the copper(II) *g*-factors. An approximation of the experimental data in the 100−300 K temperature interval by the Curie–Weiss equation results in the optimal parameters C_a = 1.22, C_b = 1.24, C_c = 1.15 $cm^3 K mol^{-1}$, and θ_a = 12.6, θ_b = 13.8, θ_c = 11.9 K.

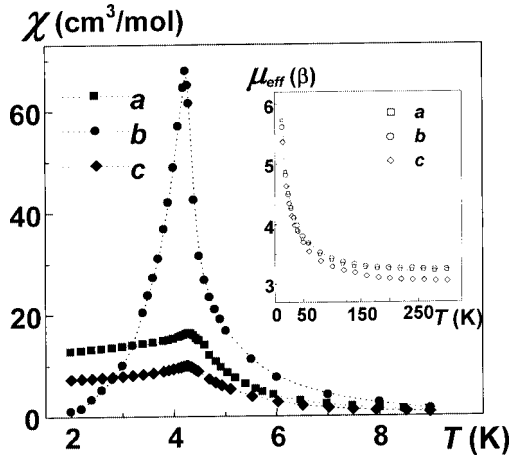

Figure 3. Low field $\chi(T)$ curves in the transition area and $\mu_{eff}(T)$ curves (inset) in the paramagnetic region for a CuL^{Et}_2 single crystal.

The set of constants obtained corresponds to **g**-tensor components along the directions of measurement: g_a = 2.24, g_b = 2.29, g_c = 2.06, which are in good agreement with *g*-factor values known for copper(II) coordination compounds.[8,9] The similarity of the Curie–Weiss parameters suggests that the CuL^{Et}_2 can be considered as an isotropic two-dimensional magnet.[10] On temperature lowering to 10 K, the CuL^{Et}_2 single crystal undergoes a phase transition to the magnetically ordered state. Measurements performed in zero magnetic field (1.2 ± 0.5 Oe) indicate that ordering occurs sharply at 4.5 K. Figure 4 shows the main curves of magnetization, $\sigma(H)$, at 2 K for the single crystal.

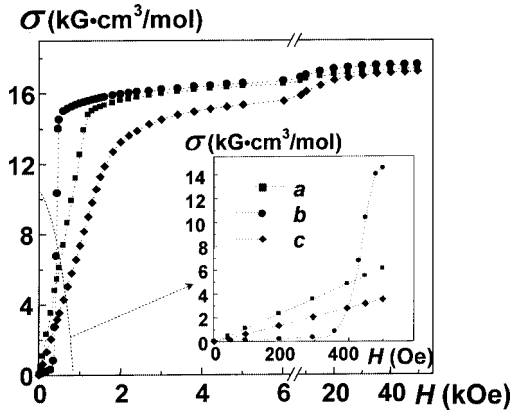

Figure 4. Magnetization curves for a CuL^{Et}_2 single crystal.

Below 400 Oe the magnetization of the CuL^{Et}_2 single crystal measured along unit-cell axes satisfies the equation $\sigma_i(H) = \chi_i H$, where $i = a, b, c$. Thus, a compensated antiferromagnetic structure is formed. At 2 K, the susceptibilities along *a*, *b*, and *c* are 12.515, 0.975, and 7.332 $cm^3 mol^{-1}$), respectively. The susceptibility ratio along different directions unambiguously suggests that $\chi_{||}$ corresponds to the *b* axis, and $\chi_{\perp}$ to the *a* and *c* axes. As follows from the

 © 2005 Wiley-VCH Verlag GmbH & Co. KGaA, Weinheim

magnetization curves, at low fields the antiferromagnetic axis is *b* and the easy magnetization axis is *a*. As the crystal structure of CuL^{Et}_2 is layered polymeric with ferromagnetic exchange interactions dominating inside the layers, it is logical to assume that the antiferromagnetic structure is formed by the magnetic moments of ferromagnetically ordered layers. The interactions leading to the collinear antiferromagnetic structure forming in CuL^{Et}_2 probably have a dipolar nature. For $H > 400$ Oe, the $\sigma(H)$ curves become nonlinear. Magnetization along the *b* axis increases sharply and tends to saturation $Ng\beta S$ for an $S = 3/2$ system. This effect indicates a metamagnetic phase transition in CuL^{Et}_2 with the critical field $H_c = 440$ Oe. The given value of the critical field corresponds to the absolute magnitude of the energy of the interlayer interactions ($3\beta H$) equal to 0.088 K. At high magnetic fields, the $\sigma(H)$ curves measured along different directions diverge because of the *g*-factor anisotropy of the copper(II) ion (Figure 4). No hysteresis effects were detected when CuL^{Et}_2 was subjected to supermagnetization. Thus, the easy magnetization axis coincides with the crystallographic *b* axis. The hard magnetization axis is orthogonal to the polymeric layers. The transition found in CuL^{Et}_2 is characterized by a low critical field, which has the same order of magnitude as that found in coordination compounds {$[(CH)_3NH]CuCl_3 \cdot 2H_2O$[5], CuL^{Me}_2[4]}. This field is 10–30 kOe for classical metamagnets ($MnBr_2$, $FeCl_2$, $CoCl_2$). The anisotropy energies were estimated for the CuL^{Et}_2 single crystal. The free energy of magnetic anisotropy may be represented as $F_i \approx -H_i\sigma_{sat}$, where $i = a, c$; H_i is the effective anisotropy field, and σ_{sat} is saturation magnetization.[11] The energy F_i was determined from the experimental magnetization curves by the numerical integration:

$$F_i = \int_0^{H_{max}} \sigma_b(H)dH - \int_0^{H_{max}} \sigma_i(H)dH$$

where H_{max} is the maximum field during the measurements. For the CuL^{Et}_2 single crystal, the lower bound on the integration domains of the $\sigma(H)$ curves is set by the value of the critical field H_c. The calculated effective anisotropy fields of the complex are $H_\perp = 1390$ Oe (along *c* axis) and $H_{||} = 420$ Oe (along *a* axis). The anisotropy of magnetic properties in a plane of the polymeric layers (*ab*) is much smaller than that in the perpendicular direction as a consequence of the quasi two-dimensional magnetic system. Thus, the anisotropy observed in CuL^{Et}_2 should be attributed to the "easy plane" type.

The single crystals of copper–3-imidazoline nitroxide complexes CuL^{R}_2 have similar structures. Also, their ordering temperatures are very close, indicating the same order of exchange interactions (Table 1).

All four complexes cannot be considered together as they have different symmetries. However, pairwise comparison of CuL^{Et}_2, CuL^{Me}_2 and $CuL^{C(O)OEt}_2$, $CuL^{C(O)OMe}_2$ reveals the decrease of the transition temperature on substitution of the methyl group with ethyl. This substitution also results in some elongation of bonds in the coordination environment of copper as well as the increase of interlayer separations (Table 1). Corresponding evolution is found in the mutual orientation of the {CuL_2} fragments as can be seen from the angles Cu–O (φ1), Cu–N (φ2), and Cu–$O^{(NO)}$ (φ3) between the *b* axis and the relevant bonds (Table 1). The magnetic behavior of the CuL_2 complexes is significantly different in the magnetically ordered phase. Under the transition temperature $CuL^{C(O)OEt}_2$ and $CuL^{C(O)OMe}_2$ are ferromagnets whereas CuL^{Et}_2 and CuL^{Me}_2 behave as metamagnets. At the same time the critical field of the metamagnetic transition for CuL^{Et}_2 is 3.6 times lower than in isostructural CuL^{Me}_2. The increase of the interlayer separation for CuL^{Et}_2 as compared with that of CuL^{Me}_2 correlates with the decrease of H_c. Assuming that metamagnetism originates from dipole interactions only, the $H_c(CuL^{Me}_2)/H_c(CuL^{Et}_2)$ ratio should be proportional to the $R^3(CuL^{Et}_2)/R^3(CuL^{Me}_2)$ ratio, *R* being an effective distance between magnetic dipoles as measured between copper ions belonging to the adjacent polymeric layers. But this supposition does not hold true. For this reason we suppose that the difference in magnetic properties of the CuL_2 complexes originates from the difference in magnetic anisotropy energy. The comparison of the critical fields and the anisotropy fields within the polymeric layers indicates that a large H_c corresponds to a large $H_{||}$, as sketched in Figure 5.

Table 1. Magnetochemical constants and selected structural data for the CuL_2 polymers.

	CuL^{Me}_2	CuL^{Et}_2	$CuL^{C(O)OMe}_2$	$CuL^{C(O)OEt}_2$
Ordering type	metamagnet	metamagnet	ferromagnet	ferromagnet
T_N (or T_c) [K]	4.9	4.5	5	4.2
H_c [Oe]	1600	440	–	–
$H_\perp$ [Oe]	1340	1390	1100	500
$H_{||}$ [Oe]	670	420	300	200
Symmetry	*Pbca*	*Pbca*	$P2_1/c$	$P2_1/c$
Intralayer (Cu–Cu) [Å]	7.780	7.768	7.786	7.919
Interlayer (Cu–Cu) [Å]	11.869	11.978	11.929	11.939
Cu–N [Å]	2.049	2.046	2.061	2.058
Cu–O [Å]	1.902	1.907	1.913	1.994/1.837
Cu–$O^{(NO)}$ [Å]	2.469	2.582	2.513	2.534
(Cu–O–N) [°]	175.8	160.6	157.9	157.53
φ1 [°]	46.7	79.8	72.6	65.5
φ2 [°]	64.2	35.7	59.8	47.9
φ3 [°]	50.2	61.9	29.6	52.9

 © 2005 Wiley-VCH Verlag GmbH & Co. KGaA, Weinheim

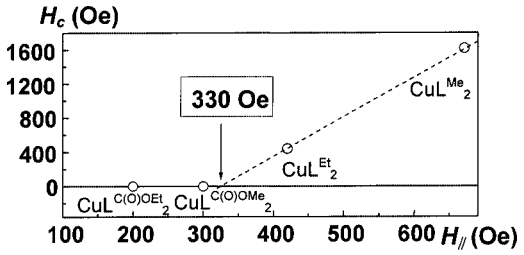

Figure 5. The H_c vs $H_{||}$ plot for the CuL_2 complexes.

The data available are too scarce to deduce the H_c versus $H_{||}$ dependence. However, linear approximation based on CuL^{Me}_2 and CuL^{Et}_2 yields the value 330 Oe for the intercept of $H_{||}$. Following this approximation, the metamagnetic transition does not exist for fields lower than 330 Oe; this conclusion is in agreement with the experimental data. The complexes $CuL^{C(O)OEt}_2$ and $CuL^{C(O)OMe}_2$ fall exactly within this range of the anisotropy field. In contrast to CuL^{Et}_2 and CuL^{Me}_2, the complexes $CuL^{C(O)OEt}_2$ and $CuL^{C(O)OMe}_2$ are monoclinic. Therefore, the free energy of magnetic anisotropy for the latter has a different set of anisotropy constants from that of CuL^{Et}_2 and CuL^{Me}_2. Generally, different values and temperature dependences of anisotropy constants for each type of symmetry can result in the overall stabilization of either the ferromagnetic or the antiferromagnetic ground state.

Conclusion

A novel layered polymeric complex, CuL^{Et}_2, is synthesized and characterized; the complex demonstrates metamagnetic phase transition at 4.5 K. The transition critical field is 440 Oe, corresponding to a magnetic energy of 0.088 K. Below the H_c the antiferromagnetic vector coincides with the b axis, and $\chi_\perp$ with the a and c axes. Above the H_c the easy magnetization axis runs along the crystallographic b direction, the hard magnetization axis being orthogonal to the polymeric layers. The onset of metamagnetic transition and the value of the critical field in the series of CuL_2 complexes are attributed to the difference in magnetic anisotropy energy within the polymeric layers of the complexes.

Experimental Section

General Remarks: All the solvents were used as purchased. The nitroxide HL^{Et} was synthesized according to ref.[12].

Synthesis of CuL^{Et}_2: A mixture of $CuCl_2{\cdot}2H_2O$ (55 mg, 0.32 mmol) and HL^{Et} (150 mg, 0.62 mmol) was dissolved in warm ethanol (15 mL). The solution was filtered and the pH adjusted to 8 with aqueous ammonia. In a span of time varying from hours to days, the solution yielded a light-green precipitate, which was collected, washed with ethanol, and recrystallized from boiling ethanol. Yield 105 mg (65%). M.p. 209−212 °C. Calcd. C 54.0, H 6.2, N 15.7; found C 54.1, H 6.4, N 15.7. The crystals of the complex suitable for an X-ray diffraction study and for magnetic measurements were obtained on slow crystallization of the material from ethanol.

X-ray Crystallographic Study: The X-ray single-crystal data for CuL^{Et}_2 were recorded with an Enraf–Nonius CAD4 four-circle diffractometer. The crystallographic data, conditions used for the intensity data collection, and some features of the structure refinement are listed in Table 2.

Table 2. Crystal data and structure refinement for CuL^{Et}_2.

	CuL^{Et}_2
Empirical formula	$C_{24}H_{34}CuN_6O_4$
Formula mass	534.11
Crystal system	orthorhombic
Space group	*Pbca*
a [Å]	10.732(1)
b [Å]	11.233(1)
c [Å]	21.417(4)
V [Å^3]	2581.9(6)
Z	4
T [K]	293(2)
λ(Mo-K_α) [Å]	0.71069
$d_{calcd.}$ [g cm^{-3}]	1.374
μ(Mo-K_α) [mm^{-1}]	0.887
R_1[a] [$I > 2\sigma(I)$]	0.0285
wR_2[b] [$I > 2\sigma(I)$]	0.0553

[a] $R_1 = \Sigma(|F_o| - |F_c|) / \Sigma|F_o|$. [b] $wR_2 = \{\Sigma[w(F_o^2 - F_c^2)^2] / \Sigma[w(F_o^2)^2]\}^{1/2}$.

Graphite-monochromated Mo-K_α radiation (λ = 0.71069 Å) with the $\theta/2\theta$ technique was used to collect the data set. The accurate unit-cell parameters were determined from automatic centering of 24 reflections, $10° < \theta < 15°$, and refined by least-squares methods. 1726 reflections were collected in the range $1.90° < \theta < 24.96°$; 1064 reflections were assumed to be observed upon applying the condition $I > 2\sigma(I)$. Corrections were applied for Lorentz polarization effects. The structure was solved by direct methods, using the SIR97[13] program, and refined by full-matrix least-squares method with the SHEXL-97[14] package.

Magnetic Measurements: The magnetochemical experiment was run with an MPMS-5S ("Quantum Design") SQUID magnetometer at temperatures from 2 to 300 K in a homogeneous external magnetic field of up to 49.5 kOe. Magnetic measurements on a single crystal were performed along the crystallographic axes a, b, and c. The relation of the crystal appearance to the crystallographic axes was established by X-ray diffraction. The molar magnetic susceptibility χ of the complexes was calculated using Pascal's additive scheme including diamagnetic corrections and taking into account the temperature-independent paramagnetism of Cu^{II} ions, which was taken to be 60×10^{-6} cm^3 mol^{-1}. For the paramagnetic region, the effective magnetic moment was calculated by the formula $\mu_{eff} = [(3k/N_A\beta^2)\chi T]^{1/2} \approx (8\chi T)^{1/2}$, where k is Boltzmann's constant, N_A is the Avogadro number, and β is the Bohr magneton. The magnetic phase transition temperature was determined as the extremum of the derivative of magnetic susceptibility on temperature $\partial\chi/\partial T$. The magnetization dependences $\sigma(H)$ of the CuL^{Et}_2 single crystal in the ferromagnetic state were plotted with allowance for the demagnetization field of the sample. The actual field in the crystal was calculated for each direction by the formula $H_i = H - N_i\sigma_i$, where $i = a$, b, and c; and N is the demagnetization factor evaluated using the tables for a disk sample.[15]

CCDC-243550 and -192277 contain the supplementary crystallographic data for this paper. These data can be obtained free of charge from The Cambridge Crystallographic Data Centre via www.ccdc.cam.ac.uk/data_request/cif.

 © 2005 Wiley-VCH Verlag GmbH & Co. KGaA, Weinheim

Acknowledgments

The work was supported by a CRDF grant(Y1-C-08-12), a President of Russia grant (MK-918.2003.03), and a Lavrent'ev grant (43).

[1] V. I. Ovcharenko, R. Z. Sagdeev, *Russ. Chem. Rev.* **1999**, *68*, 345–363.
[2] E. V. Kuzmin, G. A. Petrakovsky, *Izvestiya Vuzov MV I SSO SSSR, Fizika* **1988**, *3*, 94–101.
[3] A. Caneschi, D. Gatteschi, J. P. Renard, P. Ray, R. Sessoli, *Inorg. Chem.* **1989**, *28*, 1976–1980.
[4] Yu. Shvedenkov, V. Ikorskii, D. Guschin, E. Fursova, V. Ovcharenko, *Polyhedron* **2001**, *20*, 1207–1213.
[5] R. D. Willett, in *Magneto-Structural Correlations in Exchange Coupled Systems* (Eds.: R. D. Willett et al.), D. Reidel Publishing Company, **1985**, pp. 389–420.
[6] A. F. Wells, *Structural Inorganic Chemistry*, Oxford University Press, Oxford, **1986**, p. 313.
[7] V. Ovcharenko, A. Burdukov, R. Musin, *Mol. Cryst. Liq. Cryst.* **1995**, *273*, 89–99.
[8] A. F. Stassen, H. Kooijman, A. L. Spec, L. Jos de Jongh, J. P. Haasnoot, J. Reedijik, *Inorg. Chem.* **2002**, *41*, 6468–6473.
[9] J. J. M. Steijger, E. Frikkee, L. J. De Jongh, W. J. Huiskamp, *Physica B* **1984**, *123B*, 271–283.
[10] R. Navarro, in *Magnetic Properties of Layered Transition Metal Compounds* (Eds.: L. J. De Jongh), Kluwer Academic Publishers, Netherlands, **1990**, pp. 105–184.
[11] S. V. Vonsovskii, in *Magnetism* (Ed.: A. A. Gusev), Izdatelstvo "Nauka", **1971**, p. 476.
[12] V. A. Reznikov, I. Yu. Bagryanskaya, Yu. V. Gatilov, *Russ. Chem. Bull.* **2000**, *49*, 899–905.
[13] A. Altomare, M. C. Burla, M. Camalli, M. Cascarano, C. Giacovazzo, A. Guagliardi, A. G. G. Moliterni, G. Polidori, R. Spagna, *J. Appl. Crystallogr.* **1999**, *32*, 115–119.
[14] G. M. Sheldrick, *SHELX–97, Programs for Crystal Structure Analysis* (*Release 97-2*). University of Göttingen, Germany, **1998**.
[15] V. I. Chechernikov, in *Magnitnie izmereniya* (Ed.: E. I. Kondorskii), Izdatelstvo Moskovskogo Universiteta, **1963**, p. 57.

Received: July 8, 2004

 © 2005 Wiley-VCH Verlag GmbH & Co. KGaA, Weinheim

Do Sodium Oxofluoroaluminates Exist at Room Temperature?

Marián Kucharík,[a] Miroslav Boča,*[a,c] Catherine Bessada,[b] and Hartmut Fuess[c]

Keywords: Oxofluoroaluminate species / Alumina / Cryolite

Alumina dissolution in cryolite melts is currently associated with the formation of oxofluorospecies. Mixtures of Na_3AlF_6 and Al_2O_3 were heated under different conditions of temperature, time and atmosphere. The existence of oxofluorospecies in solidified samples at room temperature was investigated by X-ray diffraction, IR and Magic Angle Spinning NMR spectroscopy. The formation of β-alumina ($NaAl_{11}O_{17}$) was detected depending on the heating conditions, but no oxofluoroaluminate species were found.

(© Wiley-VCH Verlag GmbH & Co. KGaA, 69451 Weinheim, Germany, 2005)

Introduction

During 50 years of structural investigation on cryolite–alumina melts, numerous suggestions on the nature of the possible oxygen-containing species in the melt have been presented.[1] Førland and Ratkje[2] from cryoscopic measurements on the sodium fluoride-rich side in the reciprocal salt system $NaF–AlF_3–Na_2O–Al_2O_3$ suggested the preferred formation of the $Al_2OF_x^{(4-x)}$ (x = 5–8) anion for an ionic ratio of Al^{3+}/O^{2-} greater than five. Based on vapour pressure measurements, Kvande[3] proposed that $Al_2OF_8^{4-}$ is the most important anion for low alumina content in cryolite melts. Sterten[4] developed an ionic structure model for NaF/AlF_3 melts containing alumina. The calculations of anion fractions as a function of the cryolite ratio (*CR*; molar ratio between NaF and AlF_3) suggested that $Al_2OF_6^{2-}$ and $Al_2O_2F_4^{2-}$ are the most frequent species for $1.5 < CR > 3$. For $CR > 5$ the complex anions $Al_2O_2F_4^{2-}$ and $Al_2O_2F_6^{4-}$ were most important. Bache and Ystenes[5] interpreted IR and X-ray diffraction results of quenched mixtures of cryolite and chiolite together with alumina as free of α-Al_2O_3 but consisting of some unspecified oxofluoroaluminates.

The Raman data and thermodynamic measurements of Gilbert et al.[6] and Robert et al.[7] indicate the formation of $Al_2OF_6^{2-}$ or $Al_2OF_8^{4-}$ ions for melts with low Al_2O_3 concentrations. However, at higher Al_2O_3 concentration, $Al_2O_2F_4^{2-}$ anions would be predominant. Daněk et al.[8] directly determined the presence of oxygen on samples from $MF–AlF_3–Al_2O_3$ (M = Li, Na, K) by using a LECO TC–436 Nitrogen/Oxygen analyser. They claim that three anion species are present in $NaF/AlF_3–Al_2O_3$ melts, that is, $Al_2OF_6^{2-}$, $Al_3O_3F_6^{3-}$and $Al_2O_2F_4^{2-}$. At up to 2 mol-% of Al_2O_3 only the $Al_2OF_6^{2-}$ and $Al_3O_3F_6^{3-}$ species are present. At high alumina content, $Al_2O_2F_4^{2-}$ species are abundant. The above assumption was also confirmed by Lacassagne et al.[9] They studied the structure of $NaF/AlF_3–Al_2O_3$ melts by high-temperature NMR spectroscopy for the four nuclei ^{27}Al, ^{23}Na, ^{19}F, and ^{17}O. ^{17}O NMR spectroscopy gave a selective view of the alumina dissolution in molten cryolite, because of its direct signature of the oxofluoride complexes. The variations in the ^{17}O chemical shift were explained by the presence of at least two different oxofluoroaluminate species: $Al_2OF_6^{2-}$ at low alumina content and $Al_2O_2F_4^{2-}$, which becomes the major species for higher amounts of alumina.

If the presence of these oxofluoroaluminate species in the molten state has been demonstrated by spectroscopy, it is difficult to prove their presence in the solidified state. Only Brooker et al.[10] observed Raman spectra with bands that could be assigned to the $Al_2OF_6^{2-}$ anion. Their Raman spectra were obtained from a premelted solid sample containing 5 mol-% Na_2O and 5 mol-% AlF_3 in FLINAK. The bands at 509 cm^{-1} were assigned to the oxide-bridged, totally symmetric stretching mode of $Al_2OF_6^{2-}$. The same bands were observed at 494 cm^{-1} in the molten system with identical composition.

For a better understanding of the spectroscopic signatures of the species formed in the melts, it would be of great interest to succeed in forming stable solid oxofluoroaluminate phases at room temperature.

In order to contribute to the knowledge of oxofluoro–aluminium species, we have studied different solidified mixtures of Na_3AlF_6 and Al_2O_3 by IR spectroscopy, X-ray powder diffraction and multinuclear MAS NMR spec-

[a] Institute of Inorganic Chemistry, Slovak Academy of Sciences, Dúbravská cesta 9, 84536 Bratislava, Slovakia
Fax: +421-(0)2-59410444
E-mail: uachboca@savba.sk
[b] Centre de Recherche sur les Matériaux à Haute Température, CRMHT-CNRS,
1D avenue de la Recherche Scientifique, 45071 Orléans Cedex 2, France
[c] Institute of Materials Science, Darmstadt University of Technology,
Petersenstrasse 23, 64289 Darmstadt, Germany

 DOI: 10.1002/ejic.200400814 © 2005 Wiley-VCH Verlag GmbH & Co. KGaA, Weinheim

troscopy. The combination of these different techniques provides a more precise identification of the different phases formed on cooling.

Results and Discussion

X-ray Powder Diffraction and IR Spectra

Heating under Inert Atmosphere

In the X-ray powder diffraction patterns of the samples **1a** and **1b** only the cryolite phase was clearly detected. The presence of crystalline alumina is not evident. The same conclusion can be reached by considering the IR spectra. No reaction products are therefore present in the mixture, as no reaction seems to take place between cryolite and alumina under inert atmosphere at these experimental conditions.

Heating under Air

X-ray powder diffraction patterns of the samples **2a**, **3a** and **4a** are displayed in Figure 1. After heating for 10 and 20 h only cryolite and α–alumina were detected in **2a** and **3a**. The XRD pattern of sample **4a**, after 50 h of heating, clearly corresponds to $NaAl_{11}O_{17}$. In the case of samples **2b**, **2c**, **3b** and **3c**, a mixture of all components was found (cryolite, α-Al_2O_3, NaF and $NaAl_{11}O_{17}$) while only $NaAl_{11}O_{17}$ was detected in **4b** and **4c**.

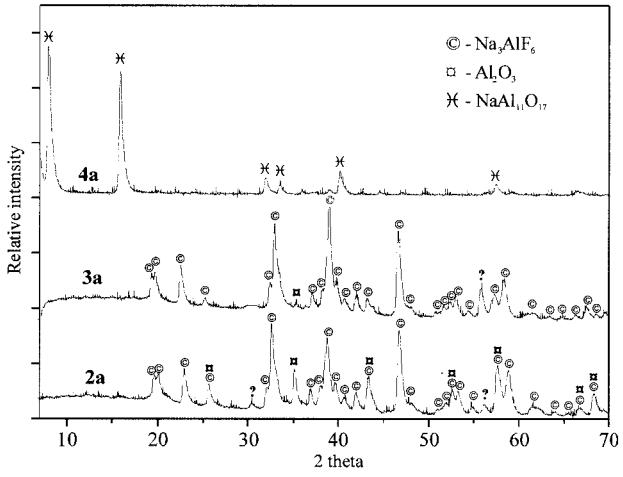

Figure 1. X-ray powder diffraction patterns of the samples **2a**, **3a** and **4a**.

In the IR spectra of all samples (**2b**, **2c**, **3a**, **3b**, **3c**, **4a**, **4b** and **4c**; see Figure 2) cryolite with different concentrations of α–alumina was detected, probably because of the incomplete reaction due to its high concentration. In all samples, except for **2a**, new peaks were detected. The intensities of these new peaks increase with increasing heating time. After 10 and 20 h of heating, peaks at 1135 cm^{-1} and 705 cm^{-1} were observed and after 50 h a peak at 1136 cm^{-1} splits into two peaks at 1148 cm^{-1} and 1121 cm^{-1}. Moreover, two new peaks are also detected at 627 cm^{-1} and at 667 cm^{-1}. The peak at 706 cm^{-1} remains unchanged.[11] These new peaks can be related to the formation of the sodium oxoaluminate $NaAl_{11}O_{17}$. This result will be supported by MAS NMR measurements in the following section.

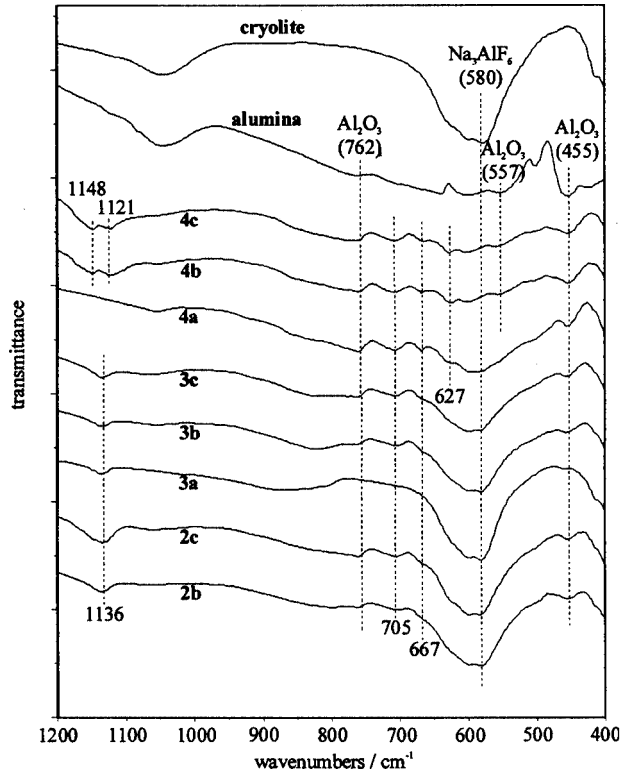

Figure 2. IR spectra of the samples **2b**, **2c**, **3a**, **3b**, **3c**, **4a**, **4b** and **4c**.

Heating in Closed Pt Tubes

The results for this series of experiments (**5a**, **5b**, **5c**, **6a**, **6b**, **6c**, **7a**, **7b**, **7c**, **8** and **9**) are surprisingly identical to those of samples **1a** and **1b**. Crystalline cryolite is detected clearly by both X-ray powder diffraction measurements and by IR spectroscopy while the presence of crystalline alumina is more questionable. No other phases were detected. The only difference can be observed in samples **8** and **9** where α-Al_2O_3 is clearly detected in the X-ray powder diffraction patterns and IR spectra. It means that on spontaneous cooling (samples **8** and **9**) crystalline α-Al_2O_3 can solidify, while for faster cooling (samples **5**–**7**) only crystalline cryolite can be detected without any doubt.

^{27}Al, ^{23}Na and ^{19}F MAS NMR Spectra

^{27}Al MAS NMR Spectra

Aluminium is a quadrupolar nucleus (I = 5/2) and spectra obtained in the solid phase, even at fast MAS conditions, can be very complex.[12] Because of the lines overlapping at 9.4 T, we also report some spectra obtained at higher field (17.6 T) in order to obtain a better resolution. The second order quadrupolar interaction is then minimized and leads to simplified line shapes.

 © 2005 Wiley-VCH Verlag GmbH & Co. KGaA, Weinheim

We have reported a comparison of ^{27}Al MAS spectra obtained at 9.4 T for different mixtures with those of the starting materials: cryolite and α-Al_2O_3 (see Figure 3). The ^{27}Al signature of cryolite is very simple and corresponds to a single $\{AlF_6\}$ site, with a chemical shift at ca. 0 ppm, and very low quadrupolar coupling ($\nu_Q \approx 150$ kHz).[13] For α-alumina, one peak is observed at about 14 ppm corresponding to the $\{AlO_6\}$ environment in the solid state at room temperature. For the mixture of 30 mol-% Al_2O_3 in cryolite heated for 20 h at 1010 °C under air (samples **3b** and **3c**) the spectra are rather complex. In addition to the peaks corresponding to different starting constituents of the mixture, that is, cryolite and α-alumina, we can also detect at least two other signals, with broad quadrupolar line shapes identified by their maxima at $\delta \approx 65$ ppm and at $\delta \approx 75$ ppm.[14] By combining the ^{27}Al MAS spectra obtained at 9.4 T and 17.6 T, we tried to model the NMR spectra more precisely and to determine the different contributions (see Table 2). We can propose some quantitative description of the different phases, in agreement with the XRD conclusions. In addition to the cryolite and α-Al_2O_3 signals, we can evidence typical signatures of transition alumina, with one signal at $\delta = 18$ ppm attributed to six-coordinate aluminium, and a signal at $\delta = 65$ ppm for four-coordinate aluminium (see Table 1).

Two contributions can be assigned to the two structurally non-equivalent tetrahedral $\{AlO_4\}$ environments of the $NaAl_{11}O_{17}$ phase. In the structure of $NaAl_{11}O_{17}$ both octahedral $\{AlO_6\}$ and tetrahedral $\{AlO_4\}$ fragments are clearly resolved.[15]

In order to discuss the broad "amorphous" component, $^{19}F/^{27}Al$ CP MAS coupled with 2D MQ MAS experiments are under progress and will give a more precise view of that complex system.

For the sample **4a**, heated for 50 h, the peak corresponding to alumina remains unchanged and the intensity of the signal of cryolite is rather lowered. Moreover, it was not observed in X-ray powder diffraction patterns, so this confirms its very low contribution. We still detect the very

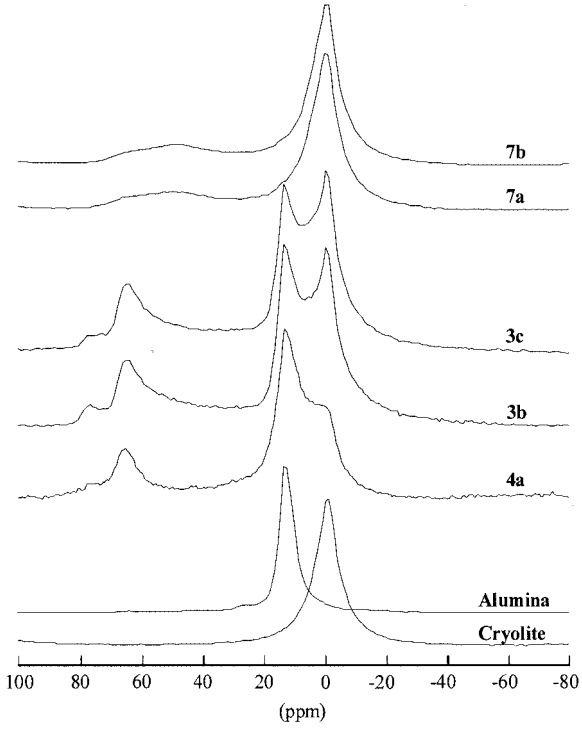

Figure 3. ^{27}Al MAS NMR spectra of the samples **4a**, **3b**, **3c**, **7a** and **7b** in relation with the spectra of the starting materials: cryolite and alumina. The spectra were obtained at 9.4 T with a spinning speed of 32.5 kHz.

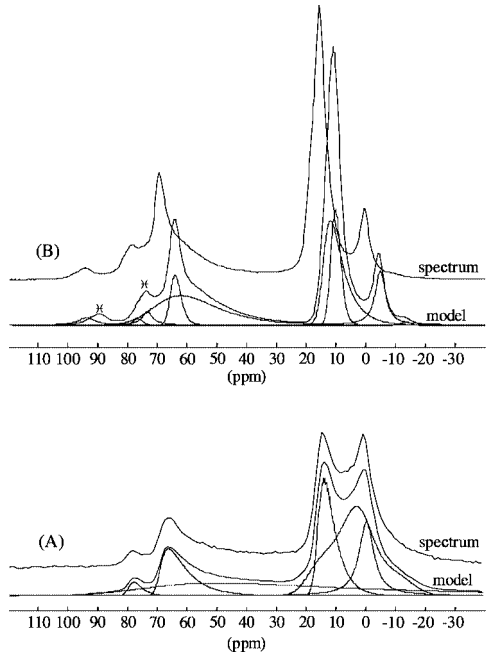

Figure 4. ^{27}Al MAS NMR spectra of the sample **3b** obtained at two different magnetic fields and its decomposition in different contributions.[26] The upper spectrum was obtained at 17.6 T (B) and the lower at 9.4 T (A). The model spectra were computed using the same set of parameters, considering six different sites: three $\{AlO_4\}$, two $\{AlO_6\}$ and one $\{AlF_6\}$. The NMR parameters deduced from the fit are reported in Table 2. The asterisks (*) represent spinning side bands.

Table 1. NMR parameters deduced from the fit[26] of the experimental ^{27}Al MAS spectrum of the sample **3b**. The same set of parameters was used for the fits at 9.4 T and 17.6 T. δ_{iso} is the isotropic chemical shift; ν_Q is the quadrupolar frequency; η is the asymmetry parameter; *I* is the relative intensity.

Sites	AlO_4 sites			AlO_6 sites		AlF_6
δ_{iso} (ppm)	78.5 ± 1.5	68.5 ± 1	77 ± 3	19 ± 0.5	15.5 ± 0.5	–0.5 ± 0.5
ν_Q (kHz)	300 ± 50	480 ± 40	1300 ± 150	700 ± 40	360 ± 40	150 ± 20
η	0.6 ± 0.2	0.6 ± 0.2	0.6 ± 0.2	1 ± 0.2	0.6 ± 0.2	0 ± 0.2
I (%)	1 ± 0.5	9 ± 2	32 ± 2	30 ± 4	15 ± 1	13 ± 1

 © 2005 Wiley-VCH Verlag GmbH & Co. KGaA, Weinheim

broad contribution at around 75 ppm. From the ^{27}Al chemical shift range reported in oxides and fluorides,[16] this high chemical shift cannot be due to the oxofluoro environment for the aluminium atoms in the solidified samples but to the oxide environment (see Figure 4).

^{19}F MAS NMR Spectra

In the ^{19}F MAS NMR spectra we observed unambiguously the signal for cryolite (–190 ppm) and the signal for NaF (–225 ppm)[9] in the samples **3b**, **3c** and **4a**, in agreement with the X-ray powder diffraction and IR spectroscopy results. In the samples **7a** and **7b** only cryolite is present and no other fluoro-species were observed. The ^{19}F chemical shifts-range, reported by Chupas et al.[17] for octahedral aluminium environments with oxygen and fluorine in the first coordination sphere, lies between –115 and –170 ppm. No such signal is detectable in our ^{19}F MAS spectra.

From these experiments we can state the absence of all fluoro-species except for cryolite (see Figure 5).

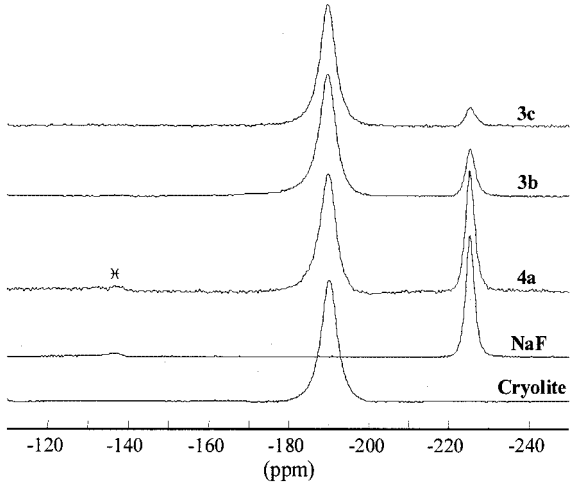

Figure 5. ^{19}F MAS NMR spectra of the samples **4a**, **3b**, **3c**, cryolite and NaF obtained at 9.4 T and at a spinning speed of 32 kHz. The asterisk (*) represents spinning side bands.

^{23}Na MAS NMR Spectra

The signals observed in **3b** and **3c** are superpositions of the cryolite signals ($\delta \approx 1$ ppm and $\delta \approx -11/-14$ ppm) and NaF at $\delta \approx 7$ ppm (see Figure 6).[9] A broad component (clearly visible in the **4a** spectrum) is also observed around –21 ppm. This peak is not easily assigned because of its strong overlap with the other signals, but it can be related to the $NaAl_{11}O_{17}$ phase detected by ^{27}Al NMR spectroscopy. A better resolution could be achieved by a ^{23}Na MQMAS experiment that would provide separation of these different contributions. In the case of samples **7a** and **7b**, again we observed only the signal for cryolite (not reported here).

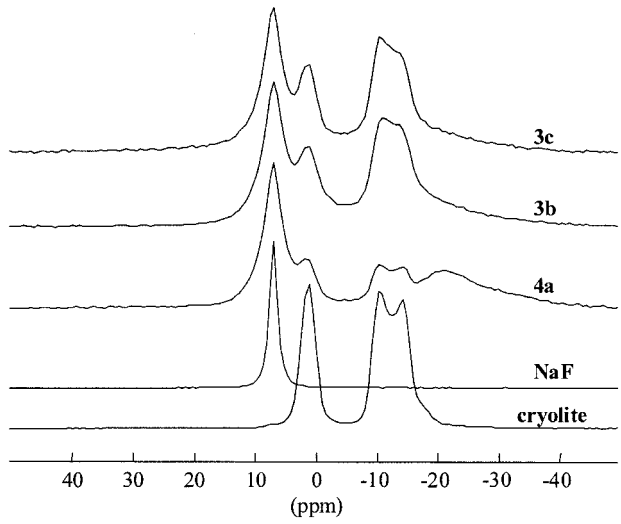

Figure 6. ^{23}Na MAS NMR spectra of the samples **4a**, **3b**, **3c**, cryolite and NaF obtained at 9.4 T and at a spinning speed of 32 kHz.

From different phase diagrams reported for the system Na_3AlF_6–Al_2O_3,[18–20] the eutectic point reported is around 10 wt.-% Al_2O_3 (18.6 mol-%) with an eutectic temperature of 966 °C. Skybakmoen et al.[20] determined the solubility of alumina in molten Na_3AlF_6 by measuring the weight loss of a rotating sinter-corundum disc in the cryolite melt. The results were fitted to [Equation (1)].

$$[Al_2O_3]_{sat} = A\left(\frac{t}{1000}\right)^B \quad (1)$$

where $A = 11.9$, $B = 4.8$ and t is the temperature in °C; the square brackets denote the weight percentage of alumina at saturation (the equation also contains terms for AlF_3, CaF_2, MgF_2 and LiF, which are not included here). According to the above equation, the solubility of alumina in cryolite at 1010 °C is 12.5 wt.-% (22.7 mol-%) Al_2O_3.

In our experiments, we have mainly used a composition of 30 mol-% (17.3 wt.-%) Al_2O_3 in the cryolite melt. At 1010 °C Al_2O_3 is 7.3 mol-% over the solubility limit. During prolonged heating, vapours of $NaAlF_4$ are expected to be formed,[21] as described by [Equation (2)].

$$Na_3AlF_6\ (l) = 2\ NaF\ (l) + NaAlF_4\ (g) \quad (2)$$

and consequently $NaAlF_4$ can decompose during condensation on the top parts of the apparatus according to [Equation (3)].

$$NaAlF_4\ (g) = 1/5\ Na_5Al_3F_{14}\ (s) + 2/5\ AlF_3\ (s) \quad (3)$$

In such a case, the system is enriched in NaF. According to the phase diagram of the system Na_6F_6–Al_2F_6–Al_2O_3–Na_6O_3, given by Foster,[22] the α–alumina in excess is transformed into β-alumina. This process can be expressed by [Equation (4)].

$$2\ NaF\ (l) + (3x + 1)/3\ Al_2O_3\ (s, \alpha) = Na_2O{\cdot}xAl_2O_3\ (s) + 2/3\ AlF_3\ (l) \quad (4)$$

where $x = 11$.

 © 2005 Wiley-VCH Verlag GmbH & Co. KGaA, Weinheim

The above explanations are based on an open system. In the closed system, the results could be explained by the following considerations.

In molten cryolite, it is generally accepted that the ions present are Na^+, F^-, AlF_4^-, AlF_5^{2-} and AlF_6^{3-}. Alumina $[(Al_2O_3)_n]$ dissolves and provides the probable anions AlO_2^- and AlO^+ (the presence of other anions such as $Al_{2n+1}O^-_{3n+2}$ or $Al_{2n+1}O^+_{3n+1}$ cannot be excluded) that would give oxofluoro-anions by reacting in the melt. Even if fluoro- and oxo-anions react in the melt to form oxofluoroaluminates, the cooling rate of ca. 1000 °C/min is not high enough to trap them and may lead to the decomposition of oxofluoroaluminates into cryolite and some amorphous alumina phase (sample **7**). If the cooling rate is even slower (spontaneous cooling), there is enough time to form the crystalline phase of α-alumina (samples **8** and **9**). No reaction seems to take place between cryolite and alumina.

In the case of sample **7**, we observed the NMR signal of cryolite, and no signal for alumina. These results coincide rather well with the observations made by other authors who reported only the cryolite phase from X-ray powder patterns of quenched mixtures of alumina and cryolite.[23,24] An attempt to explain the nature of alumina in quenched cryolite–alumina melts was suggested by Foster.[25] He concluded that alumina dissolves in cryolite to produce one or more species, that is, oxoaluminates or oxofluoroaluminates. He was not able to prove or exclude the presence of oxofluoroaluminate species. Thus he stated that they are only stable in the liquid phase or in insufficient amounts in the mixture below the detection limit of the X-ray diffractometer. According to our investigation, we still cannot decide whether oxofluoroaluminates are stable only in melts but we can exclude their presence in the solidified samples.

Conclusions

The results obtained by X-ray powder diffraction, IR and NMR spectroscopy allow us to give some conclusions about the presence of oxofluoroaluminate species in the solidified mixtures of cryolite and alumina.

Heating 30 mol-% alumina in cryolite under air at 1010 °C for 50 h results in an almost complete reaction of the mixture in $NaAl_{11}O_{17}$ and NaF. The existence of oxofluoroaluminate species can be excluded in the solid phase.

Heating of the alumina–cryolite mixture in hermetically closed Pt tubes at 1500 °C or under an inert atmosphere at 1010 °C and subsequent quenching provides some amorphous alumina phases. No decomposition providing NaF was observed and the presence of oxofluoroaluminates in the solid phase can be excluded.

Heating of the alumina–cryolite mixture in hermetically closed Pt tubes at 1500 °C or under an inert atmosphere at 1010 °C and consequent, spontaneous cooling provides crystalline cryolite with a crystalline alumina phase. No decomposition leading to NaF was observed and the presence of oxofluoroaluminates in the solid phase can be further excluded.

Experimental Section

The chemicals used are hand-picked powdered cryolite from Greenland (m. p. 1009–1011 °C) and powdered Al_2O_3 (Merck, p.a.). The powders were treated in a resistance furnace with a Kanthal coil equipped with a vertical alumina tube and a calibrated Pt–Pt/10Rh thermocouple located close to a platinum crucible.

Heating under Inert Atmosphere: A mixture of Na_3AlF_6 and 30 mol-% Al_2O_3 was heated under nitrogen at 1010 °C for 30 h in the Pt crucible covered with a lid. The nitrogen was bubbled through concentrated sulphuric acid in order to remove water traces. The mixture was then quenched by immersing the platinum crucible with the sample into crushed ice, with a cooling rate of ca. 1000 °C/min. Two samples were collected and powdered. Sample **1a** corresponds to the bottom of the crucible while sample **1b** corresponds to the upper part of the crucible, where the sample condensed and "climbed up" during the experiment (see Figure 6).

Heating under Air: Three mixtures of Na_3AlF_6 and 30 mol-% Al_2O_3 were heated under air at 1010 °C for 10 h (**2**), for 20 h (**3**) and for 50 h (**4**) in the Pt crucible covered with the lid. The mixtures were then treated as in the previous experiment. For each experiment, three samples were collected and powdered: from the bottom of the crucible (**2a**, **3a**, **4a**), from the upper part (**2b**, **3b**, **4b**) and from under the lid (**2c**, **3c**, **4c**) (see Figure 7).

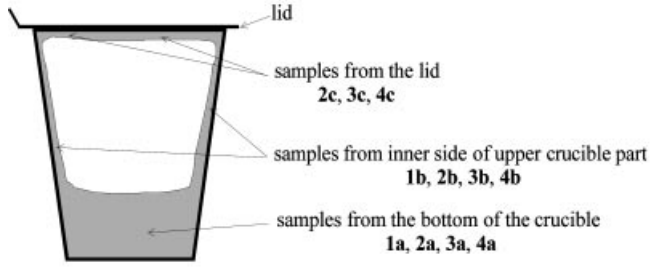

Figure 7. Schematic representation of the position of the investigated samples.

Heating in closed Pt tubes: The mixtures of Na_3AlF_6 and 10 mol-% Al_2O_3 (**5**), 20 mol-% Al_2O_3 (**6**) and 30 mol-% Al_2O_3 (**7**) were heated in the hermetically closed (by welding) Pt tubes at 1500 °C for 15 h and then quenched into ice. The tubes were opened with a saw and the samples collected were powdered. For each composition, three samplings were made from the bottom (**5a**, **6a**, **7a**), the middle (**5b**, **6b**, **7b**) and the top (**5c**, **6c**, **7c**) of the Pt tube.

The mixtures of Na_3AlF_6 and 20 mol-% Al_2O_3, (**8**) and 30 mol-% Al_2O_3, (**9**) were heated in hermetically sealed Pt tubes at 1500 °C for 5 h and left to cool spontaneously by switching off the furnace, which corresponds to a cooling rate of ca. 1.5 °C/min.

Compositions, heating and cooling conditions for the different samples are summarised in Table 2.

X-ray Diffraction Analysis: was carried out using the Philips PW1349/30 diffractometer with Cu-K_α radiation. The X-ray powder diffraction patterns were measured at room temperature in the range 7–70 °C (2θ). Identification of the different phases present in each sample was performed according to the PDF-2 International Centre for Diffraction Data database.

Infrared Spectra: were obtained using an FTIR spectrometer Nicolet Magna 750 equipped with a DTGS detector. The samples were analysed as KBr pellets.

Magic Angle Spinning NMR: experiments have been carried out on a Bruker DSX 400 NMR spectrometer (9.4 T) at operating fre-

 © 2005 Wiley-VCH Verlag GmbH & Co. KGaA, Weinheim

Table 2. Samples description: composition, heating and cooling conditions.

Experiment no.	mol-% Al_2O_3	Heating temperature (°C)	Heating duration (h)	Atmosphere and crucible	Cooling
1	30	1010	30	N_2, Pt crucible with lid	quenching
2	30	1010	10	air, Pt crucible with lid	quenching
3	30	1010	20	air, Pt crucible with lid	quenching
4	30	1010	50	air, Pt crucible with lid	quenching
5	10	1500	15	Pt crucible hermetically closed	quenching
6	20	1500	15	Pt crucible hermetically closed	quenching
7	30	1500	15	Pt crucible hermetically closed	quenching
8	20	1500	5	Pt crucible hermetically closed	slow cooling
9	30	1500	5	Pt crucible hermetically closed	slow cooling

quencies of 104.2 MHz for ^{27}Al, 105.8 MHz for ^{23}Na and 376.3 MHz for ^{19}F. ^{27}Al, ^{23}Na and ^{19}F chemical shifts are referenced to 1 M aqueous solutions of $Al(NO_3)_3$, NaCl and $CFCl_3$, respectively, at room temperature.

^{27}Al and ^{23}Na have nuclear spins of 5/2 and 3/2, respectively, and are thus quadrupolar. In solid state MAS spectra, even in high resolution conditions, line broadening and shifts caused by the second order quadrupolar effect can lead to important overlap of lines, therefore, separation of different peaks becomes difficult and sometimes inaccurate. These quadrupolar effects depend on the quadrupolar interactions and the external magnetic field strength. In order to better understand the ^{27}Al MAS spectra obtained at 9.4 T, we have performed the same experiments at 17.6 T on a Bruker Avance 750 spectrometer. The use of a very high field gives better separation of the different lines and allows us to assign each contribution to the different phases in the sample.

The NMR spectra were acquired using high- and very high-speed Bruker MAS probes with rotors of 4 and 2.5 mm in diameter, for spinning rates of 15 and 32 kHz, respectively. The NMR spectra were fitted using a modified version of the Bruker Winfit program.[26] ^{19}F, ^{27}Al, and ^{23}Na MAS spectra were typically acquired with short pulses of 0.5 μs, recycle delay of 2 s and 1 s, respectively, and each spectrum required approximately 128 acquisitions for fluorine and between 6000 and 12000 scans for ^{27}Al and ^{23}Na.

Acknowledgments

This work was financially supported by the Scientific Grant Agency of the Ministry of Education of the Slovak Republic and the Slovak Academy of Sciences (No. 2/1032/21 and No. 2/4071/04), by the Alexander von Humboldt Foundation and by the EEC ARI contract HPRI-CT-1999–00042.

[1] K. Grjotheim, C. Krohn, M. Malinovský, K. Matiašovský, J. Thonstad, *Aluminum Electrolysis. Fundamentals of the Hall – Heroult Process*, 2nd ed., Aluminium Verlag GmbH, Düsseldorf, **1982**.
[2] T. Førland, S. K. Ratkje, *Acta Chem. Scand.* **1973**, *27*, 1883–1890.
[3] H. Kvande, *Electrochim. Acta* **1980**, *25*, 273–240.
[4] A. Sterten, *Electrochim. Acta* **1980**, *25*, 1673–1677.
[5] Ø. Bache, M. Ystenes, *Acta Chem. Scand.* **1989**, *43*, 97–98.
[6] B. Gilbert, E. Robert, E. Tixhon, J. E. Olsen, T. Østvold, *Light Metals* **1995**, 181–194.
[7] E. Robert, J. E. Olsen, V. Daněk, E. Tixhon, T. Østvold, B. Gilbert, *J. Phys. Chem. Sect. B* **1997**, *101*, 9447–9457.
[8] V. Daněk, Ø. T. Gustavsen, T. Østvold, *Can. Metall. Q.* **2000**, *39*, 153–162.
[9] V. Lacassagne, C. Bessada, P. Florian, S. Bouvet, B. Ollivier, J. P. Coutures, D. Massiot, *J. Phys. Chem. Sect. B* **2002**, *106*, 1862–1868.
[10] M. H. Brooker, R. W. Berg, J. H. Von Barner, N. J. Bjerrum, *Inorg. Chem.* **2000**, *39,* 4725–4730.
[11] We are aware of IR spectra of $NaAl_{11}O_{17}$ only in the FAR region, so a direct comparison with our results is not possible; S. Edvardsson, L. Ojamae, J. O. Thomas, *Phys. Condens. Matter.* **1994**, *6*, 1319–1332.
[12] M. E. Smith, E. R. H. Van Eck, *Progr. NMR Spec.* **1999**, *34*, 159–201.
[13] D. R. Spearing, J. F. Stebbins, I. Farnan, *Phys. Chem. Min.* **1994**, *21*, 373–386.
[14] G. Kunath-Fandrei, T. J. Bastow, J. S. Hall, C. Jäger, M. E. Smith, *J. Phys. Chem.* **1995**, *99*, 15138–15141.
[15] N. J. Zhu, F. Guo, Y. Li, S. X. Shen, L. R. Chen, A. C. Li, *Hua Hsueh Hsueh Pao* **1992***, 50*, 527–532.
[16] C. Bessada, V. Lacassagne, D. Massiot, P. Florian, J. P. Coutures, E. Robert, B. Gilbert, *Z. Naturforsch. Teil A* **1999**, *54*, 162–166.
[17] P. J. Chupas, D. R. Corbin, V. N. M. Rao, J. C. Hanson, C. Grey, *J. Phys. Chem. B* **2003**, *107*, 8327–8336.
[18] J. L. Holm, *Tiddsskr. Kjemi. Bergv., Met.* **1966**, *10*, 165–171.
[19] A. Sterten, I. Maeland, *Acta Chem. Scand.* **1985**, *39*, 241–257.
[20] E. Skybakmoen, A. Solheim, A. Sterten, *Met. Mater. Trans. B.* **1997**, *28B*, 81–86.
[21] M. Bruno, O. Herstad, J. L. Holm, *Acta Chem. Scand.* **1998**, *52*, 1399–1401.
[22] P. A. Foster, Jr., *J. Am. Ceram. Soc.* **1975**, *58,* 288–291.
[23] E. Zintl, W. Morawietz, *Z. Anorg. Allgem. Chem.* **1939**, *240*, 145–149.
[24] H. Ginsberg, A. Bohm, *Z. Electrochem.* **1957**, *61*, 313–320.
[25] P. A. Foster, Jr., *J. Electrochem. Soc.* **1959**,*106,* 971–975.
[26] D. Massiot, F. Fayon, M. Capron, I. King, S. Le Calvé, B. J. O. Alonso, B. Durand Bujoli, Z. Gan, G. Hoatson, *Magn. Res. Chem.* **2002**, *40,* 70–76.

Received: September 29, 2004

 © 2005 Wiley-VCH Verlag GmbH & Co. KGaA, Weinheim

Synthesis, Crystal Structure and Magnetic Properties of Heterodimetallic $Re^{IV}Cu^{II}$ Complexes

Alina Tomkiewicz,[a] Jerzy Mroziński,*[a] Irene Brüdgam,[b] and Hans Hartl[b]

Keywords: Rhenium(IV) / Chain structures / Copper(II) / Heterometallic complexes

The two rhenium(IV)-copper(II) heterometallic complexes $[CuL_\beta][ReCl_4(ox)]\cdot DMF$ (**1**) and $[(CuL_\alpha)_2Cl][ReCl_4(ox)]Cl$ (**2**) (L_β = *N-dl*-5,7,7,12,14,14-hexamethyl-1,4,8,11-tetraazacyclotetradeca-4,11-diene and L_α = *N-dl*-5,7,7,12,12,14-hexamethyl-1,4,8,11-tetraazacyclotetradeca-4,14-diene) were synthesized, and the crystal structures of both compounds were determined at 173(2) K. Complex **1** crystallizes in a monoclinic space group $P2_1$, with a = 9.365(2) Å, b = 15.150(2) Å, c = 10.776(1) Å, β = 110.01(1)°, Z = 2, whereas **2** crystallizes in an orthorhombic space group $Pca2_1$ with a = 16.660(5) Å, b = 16.017(5) Å, c = 17.066(5) Å, and Z = 4. The CuL_β macrocycle cation is approximately planar and coordinated from above and below by $[ReCl_4(ox)]^{2-}$ units through the bis(bidentate) oxalato ligands. It features an oxalato-bridged heterometallic Re^{IV}–Cu^{II} zigzag chain, the shortest intrachain metal–metal distances are Re···Cu = 5.568(2) and 5.870(2) Å in the direction of the *b* axis. The crystal structure of **2** consists of dinuclear complex cations $[(CuL_\alpha)_2Cl]^{3+}$ with $[ReCl_4ox]^{2-}$ and isolated Cl^- as counter anions. Cu atoms in CuL_α are only fivefold coordinated in a square pyramidal surrounding, and the cations $(CuL_\alpha)^{2+}$ are connected in pairs by chloride. The intramolecular Cu···Cu separation is 4.885(3) Å, the shortest Re···Cu distance is 7.612(3) Å. The magnetic behavior of **1** and **2** has been investigated over the temperature range 1.7–300 K. Compound **1** behaves like a ferrimagnetic Cu^{II}-Re^{IV} dimetallic, one–dimensional chain with intrachain antiferromagnetic coupling. Compound **2** shows weak antiferromagnetic interactions within the Cu^{II}–Cu^{II} units.
(© Wiley-VCH Verlag GmbH & Co. KGaA, 69451 Weinheim, Germany, 2005)

Introduction

The design and synthesis of multidimensional magnetic materials is a major focus of molecular-based materials research.[1–2] The typical approach relies on the synthesis of materials with direct exchange coupling between metal ions and coordinated open shell ligands. In the last twenty years several compounds of that type containing metal ions of the first-transition-metal series have been characterized. The magnetic properties of related complexes containing second and third series transition elements, which induce larger spin-orbit coupling effects and a greater degree of covalence, are much less known. This is the case for the rhenium(IV) complexes, where the $5d^3$ ion usually forms octahedral compounds. Numerous types of hexachloro-, hexabromo- and hexaiodorhenate complexes have previously been investigated in full detail.[3–6] The study of magnetic properties of mononuclear hexahalogeno complexes revealed the occurrence of an intermolecular antiferromagnetic interaction whose magnitude depends on the size of the organic cation (bulk effect). The exchange of two chloride ions by an oxalato ligand in the rhenium coordination sphere allows for the synthesis of new heterodinuclear Re^{IV}–Cu^{II} complexes. The oxalate dianion is a well-know ligand, which usually adopts a bidentate coordination mode when acting as a bridge between two metals. In fact, the coordination mode of the rhenium(IV) precursor $[ReCl_4ox]^{2-}$ changes with the nature of the other ligands in the coordination sphere of Cu^{II}, and is monodentate in $[Cu(bipy)_2ReCl_4(ox)]$ (forming a long Cu–O axial bond of 2.65 Å) and a very asymmetric bidentate in $[Cu(terpy)_2ReCl_4(ox)(H_2O)]$ (forming one short and one long Cu–O bond, 2.05 and 2.47 Å, respectively).[7] The coupling between Re^{IV} and Cu^{II} can be ferro- or antiferromagnetic but is very weak in all cases because of the long Cu^{II}–O bonds and bite angle of the oxalate ligand. Distortions in the coordination geometry in reported complexes introduce very poor orbital overlap, which makes the interaction weak. Analysis of literature data suggest that a quite strong coupling should be obtained if the ligand is coordinated is a symmetric bidentate way with two short Cu^{II}–O bonds. For this reason, it seemed interesting to examine macrocyclic copper(II) complexes CuL_α and CuL_β (where L_β = *N-dl*-5,7,7,12,14,14-hexamethyl-1,4,8,11-tetraazacyclotetradeca-4,11-diene and L_α = *N-dl*-5,7,7,12,12,14-hexamethyl-1,4,8,11-tetraazacyclotetradeca-4,14-diene) (Scheme 1) in order to obtain heterometallic systems bridged by oxalato groups. The square planar macrocyclic complexes with two vacant coordination

[a] Faculty of Chemistry, University of Wroclaw,
14 F. Joliot - Curie, 50-383 Wroclaw, Poland
Fax: +48-713-757-307
E-mail: jmroz@wchuwr.chem.uni.wroc.pl
[b] Institute of Chemistry/Inorganic and Analytical Chemistry, Freie Universität Berlin,
Fabeckstr. 34-36, 14195 Berlin, Germany

sites at the metal atom play the role of the so-called "building block".[8] In this paper, we present results of investigations of coordinatively unsaturated complexes of copper(II) as well as of simple $[ReCl_4ox]^{2-}$ ions. It is interesting to show how the configuration of the nitrogen donor ligands influences the crystalline structure as well as the magnetic properties.

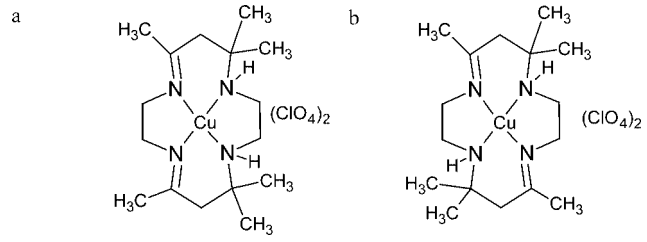

Scheme 1. Schematic view of macrocyclic copper(II) complexes: a) $[CuL_\beta]$, b) $[CuL_\alpha]$.

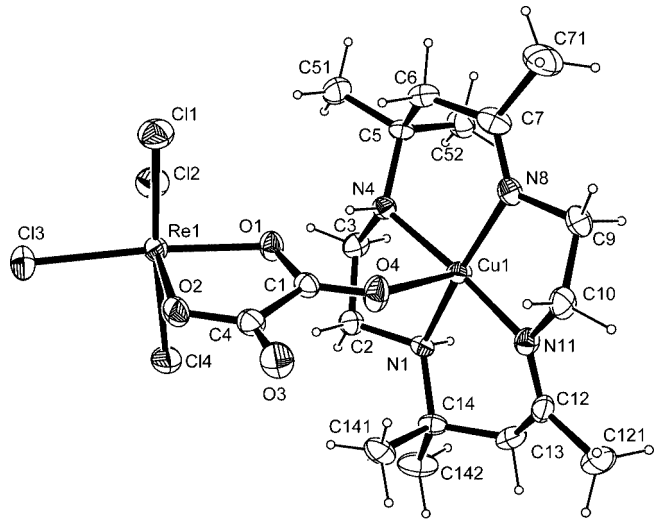

Figure 1. Asymmetric unit of compound **1** (ORTEP plot, 50% probability level).

Results and Discussion

Description of the Structures

[CuLβ][ReCl4(ox)]·DMF (1)

Complex **1** crystallizes in a monoclinic space group $P2_1$ (Table 1). Figure 1 shows an ORTEP plot of the asymmetric unit $[ReCl_4(\mu\text{-ox})CuL_\beta]$ of this compound without the solvent molecule DMF.

In the crystal structure, the $[CuL_\beta]^{2+}$ cations and $[ReCl_4(ox)]^{2-}$ anions are arranged as polymeric chains running parallel to axis *b* (Figure 2). The rhenium atom is coordinated by four chloro and one chelating oxalato ligand.

The two remaining oxygen donor atoms of the tetradentate oxalato ligand are bound to two $[CuL_\beta]^{2+}$ units, widening the nearly planar coordination of Cu^{II} by the four N atoms of the L_β ligand to an elongated octahedron with the oxygen ligands in *trans* position. The bond lengths for Cu1–

Table 1. Crystal data and structure refinement.

Identification Code	$[(CuL\alpha)_2)Cl][ReCl_4(ox)]Cl$	$[CuL_\beta][ReCl_4(ox)]\cdot DMF$
Empirical formula	$C_{34}H_{60}Cl_6Cu_2N_8O_4Re$	$C_{19}H_{35}Cl_4CuN_5O_6Re$
Formula weight	1170.88	821.06
Temperature [K]	173(2)	173(2)
Wavelength [Å]	0.71073	0.71073
Crystal system	orthorhombic	monoclinic
Space group	$Pca2_1$	$P2_1$
a [Å]	16.660(4)	9.3647(14)
b [Å]	16.017(4)	15.1501(13)
c [Å]	17.066(5)	10.7762(9)
β [°]		110.015(8)
Volume [Å^3]	4554(2)	1436.5(3)
Z	4	2
$Density_{calcd.}$ [Mg/m^3]	1.708	1.898
Absorption coefficient [mm^{-1}]	3.974	5.364
Effective transmission min/max	0.689	0.607
F(000)	2348	808
Crystal size [mm]	0.2×0.15×0.1	0.3×0.1×0.06
θ range for data collection [°]	2.13–30.63	2.01–30.56
Index ranges	$-23 \le h \le 23$, $-20 \le k \le 22$, $-24 \le l \le 24$	$-13 \le h \le 13$, $-21 \le k \le 21$, $-15 \le l \le 15$
Reflections collected	53678	17273
Independent reflections	13784 [*R*(int) = 0.0551]	8646 [*R*(int) = 0.0233]
Completeness to θ = 30.63° [%]	99.7	99.8
Refinement method	Full-matrix least-squares on F^2	Full-matrix least-squares on F^2; inversion twin
Data/restraints/parameters	13784/1/517	8646/1/339
Goodness-of-fit on F^2	1.046	0.954
Final *R* indices [$I > 2\sigma(I)$]	*R*1 = 0.0527, *wR*2 = 0.1183	*R*1 = 0.0251, *wR*2 = 0.0468
R indices (all data)	*R*1 = 0.0814, *wR*2 = 0.1310	*R*1 = 0.0309, *wR*2 = 0.0484
Absolute structure parameter	0.016(8)	0.197(4)
Largest diff. peak and hole [e·Å^{-3}]	8.090 and –3.227	1.417 and –0.789

 © 2005 Wiley-VCH Verlag GmbH & Co. KGaA, Weinheim

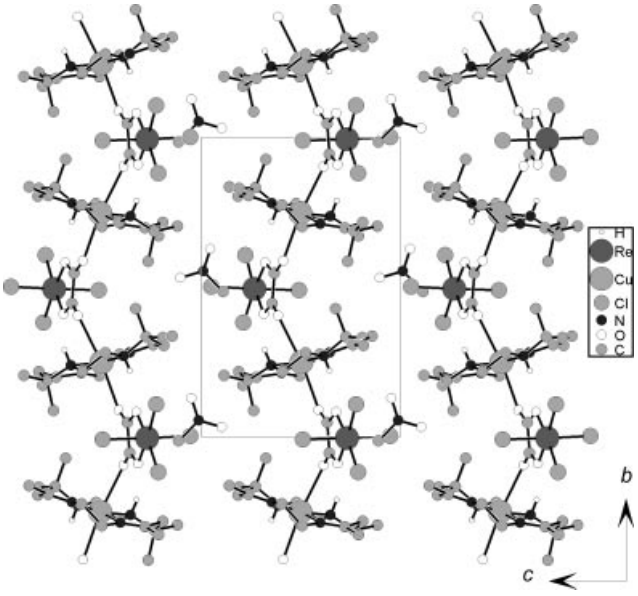

Figure 2. Crystal structure of **1** (view axis *a*; H atoms bound to C have been omitted for clarity).

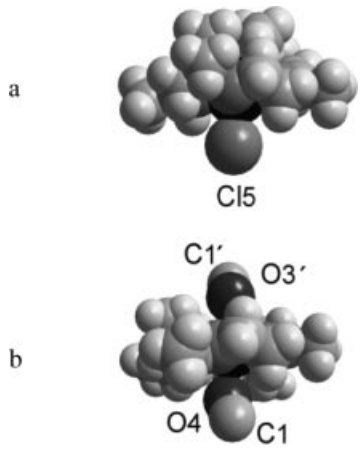

Figure 3. Space-filling model of the Cu surrounding in **2** (a) and **1** (b).

O(3′) and Cu1–O4 are 2.655(4) and 2.58(4) Å, respectively, the O3′–Cu1–O4 angle is 168.1(1)° (Figure 3a). Re^{IV} and Cu^{II} complexes are linked through oxalato bridges resulting in Re···Cu distances of 5.568(2) and 5.870(2) Å and a Cu···Cu interspace distance of 7.550(3) Å within the chains. The shortest interchain Cu···Cu separations are 7.072(4) and 7.596(4) Å.

The ligand L_β in compound **1** is approximately planar with maximum deviations of ±0.48 Å from the least-squares plane defined by the 14 ring atoms and Cu. However, the axial methyl substituents C52 and C141 are placed in *anti* configuration 1.902(4) Å above and 1.711(4) Å below that plane. The Cu^{II} atom in the center of the ligand is thus open for additional coordination from two sides.

The ring members N8 and C7, and N11 and C12 are connected by double bonds; N1 and N4 are protonated. Apart from the C–O and C–C bond lengths of the oxalato ligand, the $[Re(IV)Cl_4ox]^{2-}$ part of the crystal structure shows no apparent structural deviations from those in **2** or in related compounds in the literature.

[(CuL$_\alpha$)$_2$)Cl][ReCl$_4$(ox)]Cl (2)

Complex **2** crystallizes in an orthorhombic space group $Pca2_1$ (Table 1).

The crystal structure consists of dinuclear complex cations $[(CuL_\alpha)_2Cl]^{3+}$ and $[ReCl_4ox]^{2-}$, and isolated Cl^- as counter anions. An ORTEP plot of the asymmetric unit of the compound with the atom labelling is given in Figure 4.

The largest deviations of the 14 ring atoms and the central Cu^{II} from their least-square planes are +0.805(6)/–0.528(6) Å in the first $(Cu^{II}L_\alpha)^+$ complex and +0.514(7)/–0.794(6) Å in the second one with atom labels "a". The ring members N1–C2, N8–C9, N1a–C2a and N8a–C9a are connected by double bonds; N5, N12, N5a and N12a are protonated. The cationic complexes are linked in pairs by a chloride ligand with Cu–Cl bond lengths of 2.156 (2) Å and a Cu1–Cl–Cu1a angle of 152.2(1)°. The varying coordina-

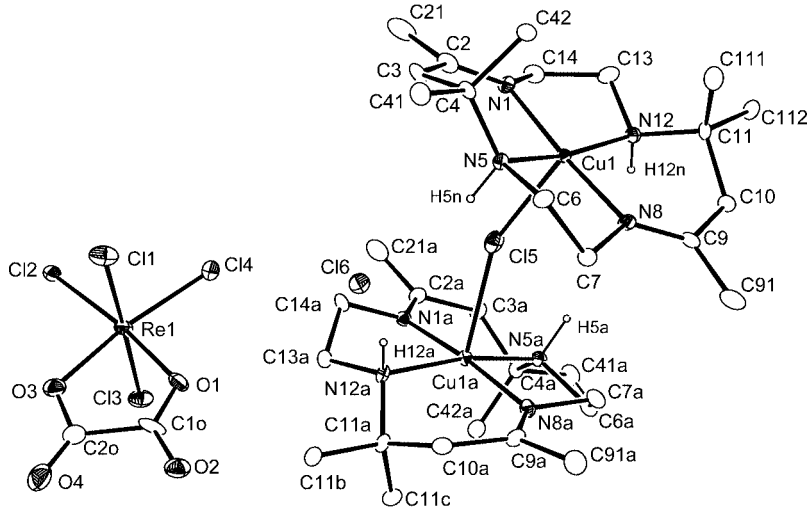

Figure 4. Asymmetric unit of compound **2** (ORTEP plot, 50% probability level; H atoms bound to C have been omitted for clarity).

 © 2005 Wiley-VCH Verlag GmbH & Co. KGaA, Weinheim

tion behavior of Cu^{II} in the investigated compounds **1** and **2** results from the different configurations of the ligands L_α and L_β, respectively. The two axial methyl substituents of each ligand L_α (C42, C111 and C42a, C11c) are arranged in *syn* configuration 2.286(8)/2.353(9) Å above as well as 2.279(9)/2.320(9) Å below the appendant N_4 planes. The cap-shaped ligands enfold the copper atoms Cu1 and Cu1a, which are situated 0.153(3) and 0.143(3) Å out of their respective N_4 planes (Figure 3b). As there is no space for additional coordination on the outside of the cap (Figure 1), the Cu atoms are only fivefold coordinated in a square-pyramidal surrounding. The intramolecular Cu···Cu distance is 4.885(3) Å, and the shortest intermolecular Re···Cu and Re···Re distances are 7.612(3) and 8.581(2) Å, respectively. The $[ReCl_4ox]^{2-}$ anion with a chelating oxalato ligand shows no unusual structural features with respect to bond lengths or angles (Table 2).[9,10] A simplified view of the packing of the ions in the elementary cell is illustrated in Figure 5. The $[(CuL_\alpha)_2Cl]^{3+}$ cations are arranged in layers parallel to *ab* in $c = 0$ and $^1/_2$, the anions $[ReCl_4ox]^{2-}$ and Cl^- in $c = {}^1/_4$ and $^3/_4$, respectively.

Table 2. Selected bond lengths [Å] of **1** and **2**.

$[(CuL\alpha)_2Cl][ReCl_4(ox)]Cl^-$		$[CuL_\beta][ReCl_4(ox)]\cdot DMF$	
Re(1)–Cl(1)	2.344(2)	2.3568(9)	Re(1)–Cl(1)
Re(1)–Cl(4)	2.332(2)	2.322(2)	Re(1)–Cl(3)
Re(1)–Cl(2)	2.337(2)	2.328(2)	Re(1)–Cl(2)
Re(1)–Cl(3)	2.346(2)	2.3497(8)	Re(1)–Cl(4)
Re(1)–O(3)	2.036(6)	2.036(3)	Re(1)–O(2)
Re(1)–O(1)	2.044(5)	2.041(3)	Re(1)–O(1)
Cu(1)–Cl(5)	2.516(2)	2.665(4)	Cu(1)–O(3)
Cu(1A)-Cl(5)	2.517(2)	2.580(4)	Cu(1)–O(4)
Cu(1)–N(8)	1.984(6)	1.974(3)	Cu(1)–N(8)
Cu(1)–N(1)	1.994(6)	1.975(3)	Cu(1)–N(11)
Cu(1)–N(12)	2.015(6)	2.009(3)	Cu(1)–N(1)
Cu(1)–N(5)	2.033(5)	2.011(3)	Cu(1)–N(4)
Cu(1A)–N(8A)	2.517(2)	---	---
Cu(1A)–N(1A)	1.988(5)	---	---
Cu(1A)–N(5A)	1.991(5)	---	---
Cu(1A)-N(12A)	2.009(6)	---	---
O(1)–C(1O)	1.20(1)	1.299(6)	O(1)–C(1)
O(3)–C(2O)	1.32 (1)	1.303(6)	O(2)–C(4)
O(2)–C(1O)	1.24(1)	1.208(6)	O(3)–C(4)
O(4)–C(2O)	1.17(1)	1.212(6)	O(4)–C(1)
C(1O)–C(2O)	1.62(2)	1.550(4)	C(1)–C(4)

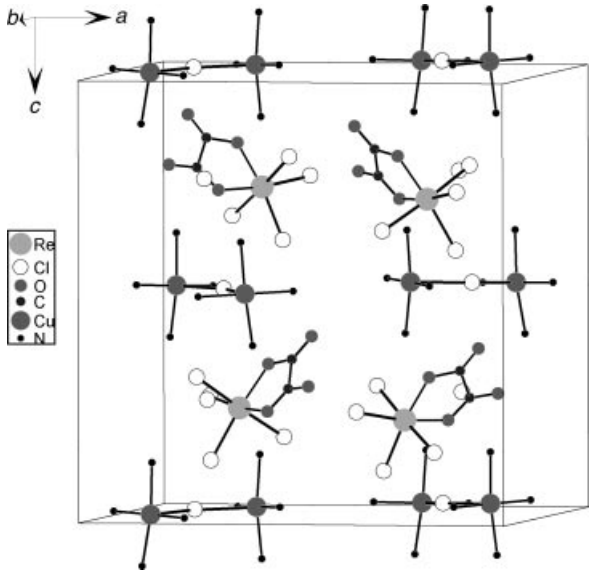

Figure 5. Unit cell of **2** (C and H atoms of the macrocycle have been omitted for clarity).

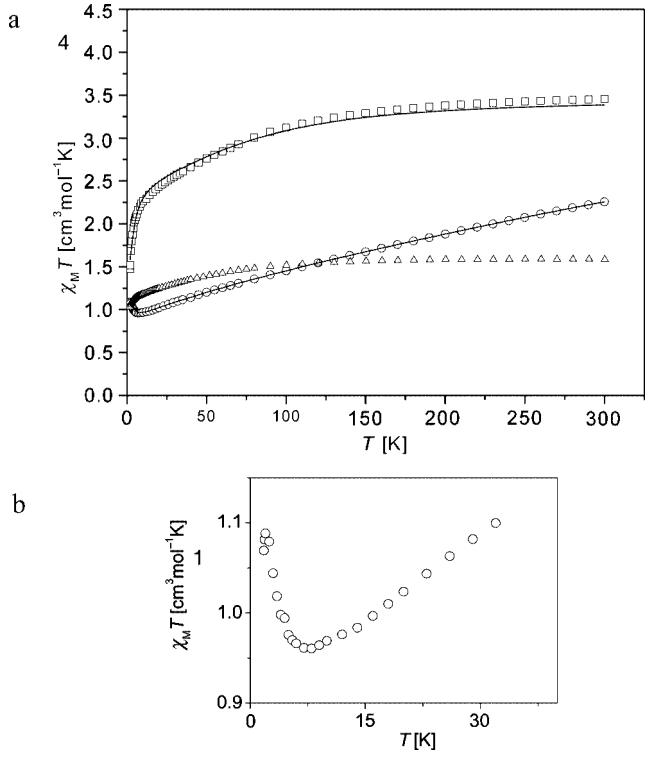

Figure 6. a) Thermal dependence of $\chi_M T$ for: (□) $[CuL_\beta][ReCl_4(ox)]\cdot DMF$ (**1**), (○) $[(Cu_2L_{\alpha 2})Cl][ReCl_4(ox)]Cl$ (**2**), (Δ) $[Bu_4N]_2[ReCl_4(ox)]$. The solid lines are the calculated curves. b) The low-temperature region of $\chi_M T(T)$ for compound **1**.

Magnetic Properties of 1 and 2

The magnetic susceptibility studies for the examined complexes have been performed within the temperature range of 1.7–300 K. The experimental data show the product $\chi_M T$ as a function of temperature (Figure 6a and Figure 6b). The $\chi_M T$ data of $[Bu_4N]_2[ReCl_4ox]$ is also included for comparison.

Complex **1** shows a typical 1D ferrimagnetic behavior. At room temperature, $\chi_M T$ is 2.26 cm^3 mol^{-1} K, a value that is expected for an uncoupled Re^{IV} ($S_{Re} = {}^3/_2$) and Cu^{II} ($S_{Cu} = {}^1/_2$) pair. With decreasing temperature, $\chi_M T$ continuously goes down in value and reaches its minimum (see inset) at 8 K with $\chi_M T = 0.96$ cm^3 mol^{-1} K. The presence of a minimum in the $\chi_M T$ data is consistent with the 1D model, assuming the occurrence of antiferromagnetic exchange interactions between Re^{IV} and Cu^{II} ions.[11] When the temperature is lowered below 8.0 K, $\chi_M T$ increases and reaches a maximum at 2.0 K before rapidly decreasing to between 2.0and 1.80 K. Due to additional exchange interactions between spins of the nearest neighboring chains at these low

 © 2005 Wiley-VCH Verlag GmbH & Co. KGaA, Weinheim

$$H = \sum_i \left\{ \begin{array}{l} -JS^z_{2i-1}S^z_{2i} + g_{\parallel Cu}\beta S^z_{2i-1}H_z + g_{\parallel Re}\beta S^z_{2i}H_z + \\ g_{\perp Cu}\beta\left(S^x_{2i-1}H_x + S^y_{2i-1}H_y\right) + g_{\perp Re}\beta\left(S^x_{2i}H_x + S^y_{2i}H_y\right) + 2D\left[\left(S^z_{2i}\right)^2 - \frac{5}{4}\right] \end{array} \right\} \quad (1)$$

temperatures, the system undergoes a change to 3D antiferromagnetic ordering.[11]

To quantitatively interpret the susceptibility data, we used a one-dimensional model in which the magnetic susceptibility in the high-temperature region of **1** can be described by two contributions: the susceptibility of the $^4A_{2g}$ term of the Re(IV) ions (with zero-field splitting) and that of the $^2T_{2g}$ term of the Cu^{II} ions modified by a factor predicted from the Ising model of the magnetic exchange interactions and different local g values of g_{Cu} and g_{Re}.[1,13,14] The relevant spin Hamiltonian is defined by Equation (1),[12] where the total spins are $S_{2i} = S_{Re}$ and $S_{2i-1} = S_{Cu}$. J is the exchange coupling parameter between the quartet Re^{IV} and doublet Cu^{II} local spins and $2D$ is the energy gap between the ±3/2 and ±1/2 Kramers doublets.

The least-squares fit of the experimental data using this equation was limited to the 8.0–300 K range and leads to $2D = 99.1\ cm^{-1}$, $g_{avRe} = 1.91$, $g_{avCu} = 2.27$ and $J = -3.36\ cm^{-1}$ for **1**. The agreement factor R defined as $R = \Sigma(\chi_{exp}T - \chi_{calc}T)^2/\Sigma(\chi_{exp}T)^2$ is $1.26\cdot10^{-4}$. The calculated curve agrees very well with the magnetic data and illustrates that the J parameter is clearly associated with the exchange pathway involving the oxalato bridge.

The variation of the magnetization M (in B.M. units) versus the magnetic field H at 1.8 K (Figure 7a and Figure 7b), i.e. below magnetic ordering, clearly supports the occurrence of spontaneous magnetic moments in complex **1**. As the magnetic field increases, the M versus H curve is linear up to 1000 G, and then shows a sinusoidal variation before reaching saturation at a value of Ms = 1.51 B.M. perrhenium-copper pair.[13] This value is smaller than that for the tetrabutylammonium compound $[Bu_4N]_2ReCl_4(ox)$, (Ms = 1.60 B.M. per rhenium atom).

The magnetization versus temperature curves (Figure 8) measured at 50 Oe reveal the presence of spontaneous magnetization below the transition temperature T_c = 3.50 K. Spontaneous magnetization appears as the result of switching of the interchain exchange interactions at low temperatures that leads to 3D magnetic ordering of $\{[CuL_\beta]ReCl_4ox\}_n$ ferrimagnetic chains.[13] The magnetic data show the predominance of one-dimensional exchange interactions at $T > 3.50$ K with a crossover to 3D ferrimagnetic ordering at $T \approx 3.50$ K.

Complex **2** exhibits different magnetic properties. The value of $\chi_M T$ at room temperature is $3.96\ cm^3 mol^{-1} K$, which is expected for uncoupled Re^{IV} and Cu^{II}–Cu^{II} units. The $\chi_M T$ value smoothly decreases for a wide temperature range before it rapidly decreases at the lower temperatures [Figure 6]. The slight decrease in $\chi_M T$ can be due to the zero-field splitting effect of Re^{IV} ions and to intramolecular

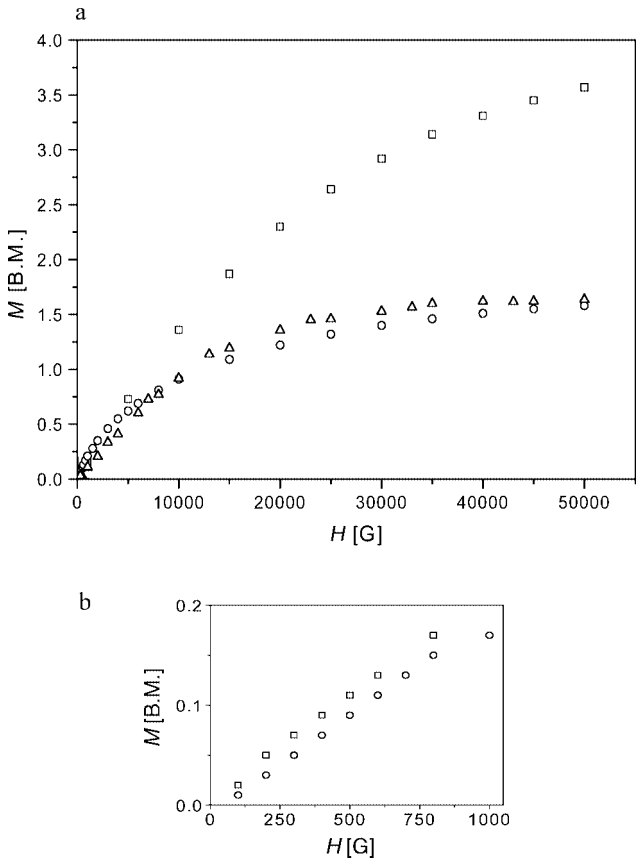

Figure 7. Field dependence of the magnetization for complexes for: (○) $[CuL_\beta][ReCl_4(ox)]\cdot DMF$ (**1**), (□) $[(CuL\alpha)_2Cl][ReCl_4(ox)]Cl$ (**2**), (Δ) $[Bu_4N]_2[ReCl_4(ox)]$.

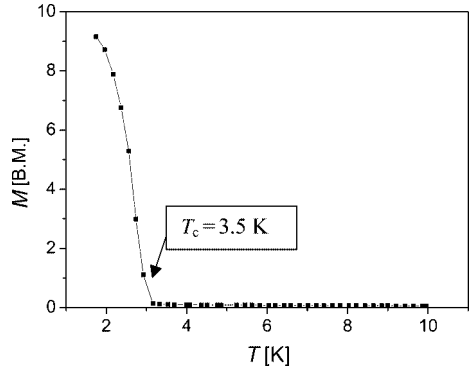

Figure 8. M vs T plots in the low-temperature range and a field of 50 Oe for $[CuL_\beta][ReCl_4(ox)]\cdot DMF$ (**1**).

exchange interactions between Cu^{II}–Cu^{II} ions. The crystal structure of **2** is built up by isolated paramagnetic ions $[(CuL_\alpha)_2Cl]^{3+}$ and $[ReCl_4ox]^{2-}$ and a diamagnetic Cl^- ion,

 © 2005 Wiley-VCH Verlag GmbH & Co. KGaA, Weinheim

so that Wiedemann's equation can be used to interpret the magnetic data. Since the two magnetic ions exist at a ratio of 1:1, the equation [Equation (2)] for molar magnetic susceptibilities of complex **2** can be reduced to the simple form:

$$\chi_{\text{sample}} = \chi_{\text{av}[\text{ReCl}_4\text{ox}]^{2-}} + \chi_{[(\text{CuL}_\alpha)_2\text{Cl}]^{3+}} + \chi_{\text{Cl}^-} \quad (2)$$

where the average magnetic susceptibility of Re^{IV} is equal to $\chi_{av} = \frac{1}{3}\cdot\chi_{II} + \frac{2}{3}\cdot\chi_{\perp}$

The parallel and perpendicular zero-field susceptibilities for $S = 3/2$ (Re^{IV}) with an axial crystal field distortion were described in a previous paper.[9] The magnetic susceptibility of the dinuclear copper unit was specified by the Bleaney–Bowers expression.[14]

A least-squares fit leads to the following set of parameters: $g_{avRe} = 2.30$, $g_{avCu} = 2.21$, $J = -2.81$, $2D = 91.2$ and $R = 5.36\cdot10^{-4}$.

The macrocyclic complex cations CuL_α^{2+} and CuL_β^{2+} used for the synthesis occur in the form of two isomers differing in the configuration of the donor nitrogen atoms. In complex **1** both methyl groups are found in an *anti* configuration, in which the central ion is accessible to the bridging oxalato ligands from both sides. The resulting oxalato bridges in the generated dimetallic zigzag chains are known to mediate magnetic interactions between metal centers. The possible mechanism for the one-dimensional ordering in **1** can be understood through orbital symmetry considerations. The magnitude of the interaction is due to the overlap of the magnetic orbital on either side of the bridge. Tetrahedral distortion of the copper environment is the apparent cause for the four short equatorial bonds to N(4), N(8), N(11), and N(15), which ensure the delocalization of the unpaired electron of the d_{z^2} magnetic orbital within the equatorial plane and disrupt the orthogonality between this orbital and the d_{xy} orbital of Re^{IV} through the oxalato ligand. The oxalato ligand between the Re(1)–Cu(1) pair causes poor overlap resulting in weak antiferromagnetic coupling $J = -3.36\ cm^{-1}$. It deserves to be noted that the $2D$ value for complex **1** is greater than that for $[Bu_4N]_2ReCl_4(ox)$ ($53\ cm^{-1}$).[9] These relatively large values of the $2D$ parameter for third-row transition-metal ions would account for the large value of the spin-orbit parameter ($\lambda \approx 1100\ cm^{-1}$ for the Re^{IV} single ion).

The differences in the crystalline structure of complex **2** compared to complex **1** has a significant influence on its magnetic properties.The partial conversion of the macrocyclic ring conformation in **2** is accompanied by a change of the methyl groups from *anti*- to *syn* conformation. As a consequence the methyl groups block one of the axial sites at the CuL_α^{2+} ion causing the availability of only one vacant site at the central copper(II) ion. This macrocycle ion with a Cu^{II} magnetic center is linked by a chloride bridge to another Cu^{II} unit. Halide bridges have been observed in other copper complexes, but most of these have at least two bridges with angular Cu–halogen–Cu bonds. The Cu–Cl bond distance in the present structure (2.156 Å) is shorter than the average of the bridging Cu–Cl bond distances: 2.514 Å in $[Co(en)_3]_2[Cu_2Cl_8]Cl_2\cdot2H_2O$,[15] 2.501 Å in [Cu(tet b)Cl]ClO_4, and 2.507 Å in $[Cu(L^1)Cl(CuCl_3)]$ (L^1 = 12-methyl-12-nitro-1,4,7,10-tetra-azacyclotridecane).[16] For dinuclear copper(II) compounds with bridging chloride ions, antiferromagnetic exchange interactions have been observed, and the singlet–triplet splitting ($2J$) varies linearly with φ, the bridging Cu–Cl–Cu angle. It should be noted that in the last reported compound $[Cu(L^1)Cl(CuCl_3)]$, which has the same square-based pyramid coordination geometry as complex **2**, there is no antiferromagnetic spin coupling. The magnetic susceptibility from 4.25 to 301.6 K follows the Curie low, with a magnetic moment of 1.86 B.M. In complex **2**, because of the very long Cu(1)···Re(1) axial distance, the overlap between the magnetic orbitals in the Re^{IV} and Cu^{II} dimeric units can be neglected, leading to a nonexchange interaction as observed. On the other hand, observed antiferomagnetic interactions can be understood in terms of the nonzero overlap between the copper(II) magnetic $d_{x^2-y^2}$ orbitals.[17–19] Studies of chloride-bridged dimeric systems have shown that the bridging angle Cu–Cl–Cu of 152.2(1)° generates an antiferromagnetic coupling of copper(II) magnetic centers.[19]

Conclusions

Our results show that it is possible to synthesize new Re^{IV}–Cu^{II} heterodimetallic complexes by using $[ReCl_4(ox)]^{2-}$ anions as components that bridge macrocyclic $[Cu^{II}L]^{2+}$ cations. The magnitude of magnetic coupling between Re^{IV} and Cu^{II} in the examined compounds can be tuned by changing the coordination geometry around the copper(II) ions. This coordination depends on the position of the methyl groups around the equatorial nitrogen atoms of the ligands. In the case of the nearly square-planar coordinated $[CuL_\beta]^{2+}$, a 1D ferrimagnetic chain compound was obtained. Each $[ReCl_4(ox)]^{2-}$ ion is bound by two long Cu^{II}–O bonds to two macrocyclic fragments. The magnetic measurements indicate weak antiferromagnetic interactions between the Re^{IV} and Cu^{II} metal ions within the chains. The temperature dependency of magnetization has revealed a transition from a one-dimensional ferrimagnetic system to a three-dimensional magnetically ordered system. In the case of a non-planar coordination sphere around Cu^{II}, the complex cation is open for coordination only on one side. This position is then occupied by a bridging chloro ligand, which connects two Cu^{II} macrocycle units, and the isolated anion $ReCl_4(ox)^{2-}$ is responsible for the charge balance. Strong antiferromagnetic interaction is not expected in the dimetallic Re^{IV}-Cu^{II} macrocyclic compounds **1** and **2** because of poor overlap of the magnetic orbitals. The analysis of these results suggest that a stronger magnetic interaction should be obtained if the rhenium(IV) ions were coordinated by other first-row transition-metal macrocycles.

 © 2005 Wiley-VCH Verlag GmbH & Co. KGaA, Weinheim

Experimental Section

Physical Measurements: Magnetic measurements in the temperature range 1.7–300 K were performed using a Quantum Design SQUID-based MPMSXL-5-type magnetometer. The SQUID magnetometer was calibrated with the palladium rod sample (Materials Research Corporation, measured purity 99.9985%). The superconducting magnet was generally operated at a field strength ranging from 0 to 5 T. Measurements were made at a magnetic field of 0.5 T. Corrections are based on subtracting the sample-holder signal and contribution χ_D estimated from the Pascal constants.

Materials: All materials used in this work were of reagent grade purity and were used as commercially obtained. The compounds $[Bu_4N]_2[ReCl_4(ox)]$, $[CuL_\alpha](ClO_4)_2$, and $[CuL_\beta](ClO_4)_2$ were prepared as previously reported.[8,9]

Synthesis of the Complexes – $[CuL_\beta][ReCl_4(ox)] \cdot DMF$ (1): A solution of $CuL_\beta(ClO_4)_2$ (2.5 mg, 0.075 mmol) in a MeC/eNO_2 (10 mL) (5:1) mixture was added, dropwise, to a solution of $[Bu_4N]_2ReCl_4(ox)$ (6.7 mg, 0.075 mmol) in 10 mL of the same solvent. The mixture was subsequently stirred. After a few days, by slow evaporation a dark-violet crystalline solid was formed from the violet solution. It was filtered and washed using methanol (2 × 20 mL) and diethyl ether. Yield: 5.86 mg (96%). Polyhedral violet single crystals suitable for X-ray diffraction studies were obtained by the slow mixing of solution of both reagents in DMF/MeCN (8:1) at room temperature. IR: bands associated to the oxalato ligand appear at 1718 (m), 1663 (s), 1375 (m), 800 (m) cm^{-1}. $C_{38}H_{70}N_{10}Cl_8O_{12}Cu_2Re_2$ (821.06): calcd. C 28.44, H 4.21, Cl 18.67, N 7.37; found: C 27.51, H 4.36, Cl 19.42, N 6.99. The rhenium and copper content was determined by ICP method: calcd. Cu 7.73, Re 24.51; found Cu 7.05, Re 24.32.

Synthesis of the Complexes – $[(CuL_\alpha)_2Cl][ReCl_4(ox)]Cl$ (2): A solution of $[CuL_\alpha](ClO_4)_2$ (5.0 mg, 0.15 mmol) in methanol (10 mL) was added dropwise to a solution of $[Bu_4N]_2[ReCl_4(ox)]$ (6.7 mg, 0.075 mmol) in 10 mL of the same solvent. The mixture was subsequently stirred. The resulting pink precipitate was filtered off, washed with diethyl ether and dried in air. Yield: 4.01 mg (46%). Pink crystals of **2** suitable for X-ray diffraction studies were obtained by slow evaporation of a MeC/MF (5:1) solution of the previously prepared precipitate. IR: bands associated to the oxalato ligand appear at 1703 (m), 1666 (m), 1377 (s), 801 (m) cm^{-1}. $C_{136}H_{240}N_{32}Cl_{24}O_{16}Cu_8Re_4$ (1170.88): calcd. C 34.75, H 5.50, Cl 18.14, N 9.51; found: C 35.01, H 5.54, Cl 19.65, N 8.99. The rhenium and copper content were determined by ICP method: calcd. Cu 10.85, Re 15.86; found Cu 10.21, Re 15.12. Note: The chloride ligands on the copper(II) dimer are from the tetrachlorooxalato rhenium(IV) complex anions.

X-ray Crystallographic Study: Single crystal X-ray data was collected on a Bruker-XPS-diffractometer (CCD area detector, Mo-K_α radiation, λ = 0.71073 Å, graphite monochromator), empirical absorption correction using symmetry-equivalent reflections (SADABS),[20] structure solution and refinement by SHELXS-97[21] and SHELXL-97[22] in the WINGX system (Table 1) was performed.[23] Most of the hydrogen atoms were located by difference Fourier syntheses. CCDC-237149 and CCDC-237150 contains the supplementary crystallographic data for this paper. These data can be obtained free of charge from The Cambridge Crystallographic Data Centre via www.ccdc.cam.ac.uk/data_request/cif.

Acknowledgments

This work was financially supported by the Polish State Committee for Scientific Research, Grant No. 4 T09A 115 23.

[1] O. Kahn (Ed.), *Magnetism: A Supramolecular Function*, NATO ASI Series C484, Kluwer Academic Publishers, Dordrecht, **1996**.
[2] O. Kahn, *Molecular Magnetism*, VCH, New York, **1993**.
[3] J. Mrozinski, *J. Bull. Acad. Polon.: Chim.* **1978**, *26*, 789.
[4] J. Mrozinski, *J. Bull. Acad. Polon.: Chim.* **1980**, *28*, 559.
[5] A. Tomkiewicz, F. Villain, J. Mrozinski, *J. Mol. Struct.* **2000**, *555*, 383.
[6] J. Mrozinski, A. Tomkiewicz, H. Hartl, I. Brüdgam, F. Villain, *Polish J. Chem.* **2002**, *76*, 285.
[7] R. Chiozzone, R. González, C. Kremer, G. De Munno, D. Armentano, J. Cano, F. Lloret, M. Julve, J. Faus, *Inorg. Chem.* **2001**, *40*, 4242.
[8] J. Mrozinski, R. A. Koliński, B. Jeżowska-Trzebiatowska, *Bull. Acad. Polon.: Chim.* **1974**, *11*, 999.
[9] A. Tomkiewicz, T. J. Bartczak, R. Kruszynski, J. Mrozinski, *J. Mol. Struct.* **2001**, *595*, 225.
[10] H.-D. Bian, J.-L. Tian, Z.-Q.Liu, W. Gu, J.-Y.Xu, S.-P. Yan, D.-Z. Liao, Z.-H. Jiang, P.Cheng, *Z. Anorg. Allg. Chem.* **2004**, *630*, 327.
[11] O. Kahn, Y. Journaux, *Inorganic Materials*, Wiley, **1992**.
[12] R. Chiozzone, R. González, C. Kremer, G. De Munno, J. Cano, F. Lloret, M. Julve, J. Faus, *Inorg. Chem.* **1999**, *38*, 4745.
[13] H. O. Stumpf, Y. Pei, L. Ouahab, F. Le Berre, E. Codjovi, O. Kahn, *Inorg. Chem.* **1993**, *32*, 5687.
[14] B. Bleaney, K. D. Bowers, *Proc. Roy. Soc., Ser. A* **1952**, *214*, 451.
[15] O. Kahn, *Angew. Chem. Int. Ed. Engl.* **1985**, *24*, 834.
[16] A. Garcia, R. Costa, J. Ribas, T. Mallah, Y. Journaux, J. Sletten, X. Solans, V. Rodriguez, *Inorg. Chem.* **1993**, *32*, 3733.
[17] A. R. Bauer, W. R. Robinson, D. W. Margerum, *J. Chem. Soc., Chem. Commun.* **1973**, 289.
[18] P. Comba, N. F. Curtis, G. A. Lawrance, M. A. O'Leary, B. W. Skelton, A. H. White, *J. Chem. Soc., Dalton Trans.* **1988**, 479.
[19] S. G. N. Roundhill, D. M. Roundhill, D. R. Bloomquist, C. Landee, R. D. Willett, D. M. Dooleg, H. B. Gray, *Inorg. Chem.* **1979**, *18*, 831.
[20] Area-Detector Absorption Correction, Siemens Industrial Automation, Inc., Madison, WI, **1996**.
[21] G. M. Sheldrick, *Acta Crystallogr., Sect*. A **1990**, 467.
[22] G. M. Sheldrick, University of Göttingen, Germany, **1997**.
[23] L. J. Farrugia, *J. Appl. Crystallogr.* **1999**, *32*, 837.

Received: May 25, 2004

 © 2005 Wiley-VCH Verlag GmbH & Co. KGaA, Weinheim

Stereoisomerism in Pentaerythritol-Bridged Cyclotriphosphazene Tri-Spiranes: Spiro and Ansa 1,3-Propanediyldioxy Disubstituted Derivatives

Aylin Uslu,*[a] Simon J. Coles,[b] David B. Davies,[c] Robert J. Eaton,[c] Michael B. Hursthouse,[b] Adem Kılıç,[a] and Robert A. Shaw[c]

Keywords: Cyclotriphosphazene derivatives / Trispiranes

In each spirane structure in Figure 1 on p. 1043 of the original article[1] the spiro atom of the left-hand cyclophosphazene ring should be phosphorus rather than nitrogen; the correct Figure 1 is shown below.

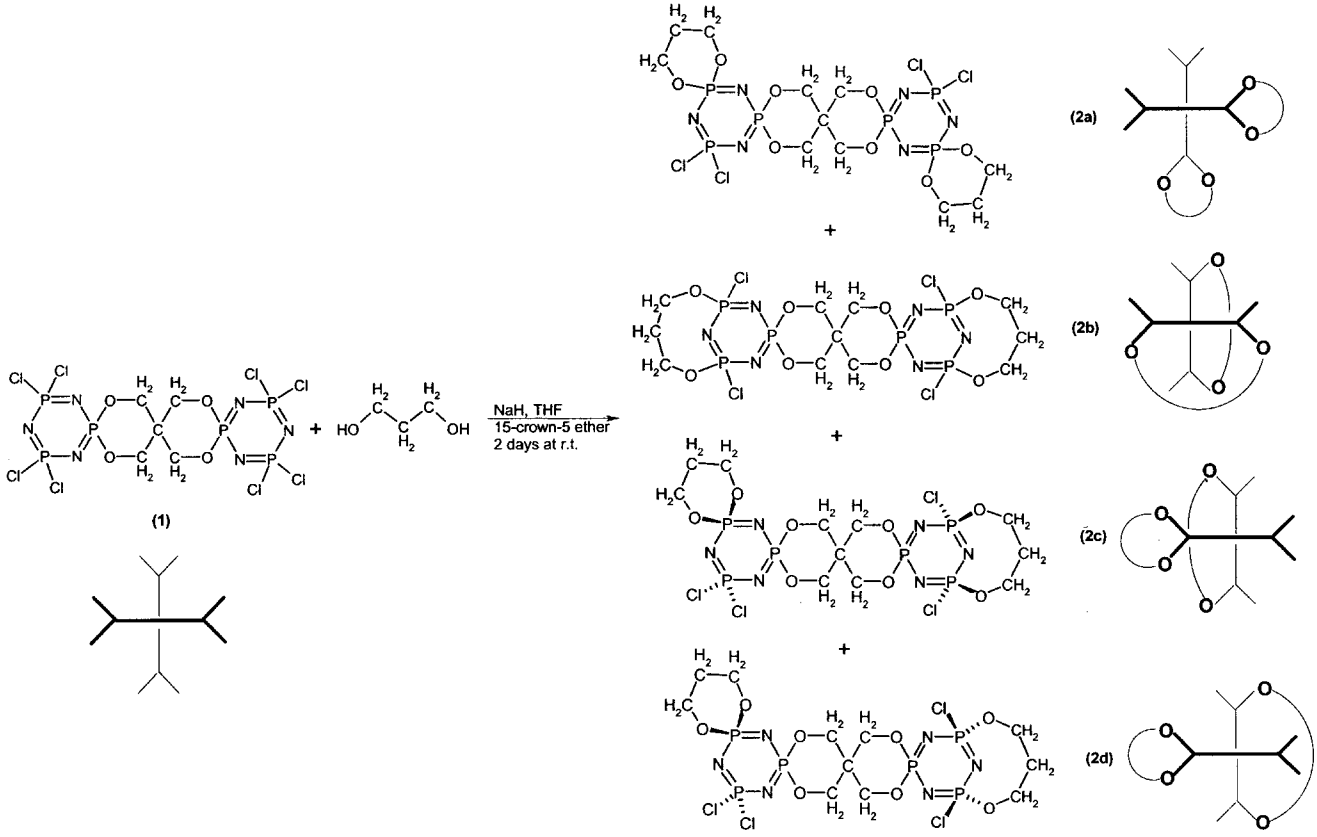

Figure 1. Structures of spirane-bridged unsubstituted, **1**, and disubstituted cyclotriphosphazene derivatives; di-monospiro **2a**, di-monoansa **2b**, and two monospiro-monoansa derivatives (**2c**, *syn*) and (**2d**, *anti*). A diagrammatic representation is also shown for compounds **1** and **2a**−**2d**. For clarity the inner organophosphate rings have been omitted and the outer cyclophosphazene rings, which are orthogonal to each other, are shown in the same projection with the ring to the front in bold type.

[a] Department of Chemistry, Gebze Institute of Technology, Gebze, Kocaeli, Turkey
Fax: +90-262-754-2385
E-mail: aylin@gyte.edu.tr
[b] University of Southampton, Highfield, Southampton SO17 1BG, UK
[c] School of Biological and Chemical Sciences, Birkbeck College (University of London), Malet Street, London WC1E 7HX, UK

[1] A. Uslu, S. J. Coles, D. B. Davies, R. J. Eaton, M. B. Hursthouse, A. Kılıç, R. A. Shaw, *Eur. J. Inorg. Chem.* **2005**, 1042−1047.

Received: March 18, 2005
The Authors

 DOI: 10.1002/ejic.200500235 © 2005 Wiley-VCH Verlag GmbH & Co. KGaA, Weinheim

EurJIC
European Journal of Inorganic Chemistry

Issue 10/2005

Pages 1801–1996

Papers available ahead of print in Early View at www.interscience.wiley.com

Earliest available Table of Contents:
Automatically, free of charge by e-mail through
www.interscience.wiley.com/alerts

COVER PICTURE

The cover picture shows $[Pt(Me_2pipdt)_2][Pt(dtcr)_2]$ (Me_2-pipdt = *N*,*N*′-dimethylpiperazine-2,3-dithione; dtcr = dithiocroconate), an ion-pair CT salt formed by redox-active cationic and anionic platinum–dithiolenes arranged in an infinite, alternate one-dimensional stack. This salt exhibits a strong absorption in the near-infrared region that is assigned to a CT transition from the anion to the cation. NIR CT bands, and semiconducting and photoconducting properties are also observed for similar salts obtained on varying the anion. These properties strongly depend on the degree of electron donation, which in turn depends on the redox potential and on the planarity of the ionic components. Details are discussed in the article by P. Deplano et al. on p. 1829ff. This work has been performed in the framework of European COST action D14-003 "Towards New Molecular Inorganic Conductors".

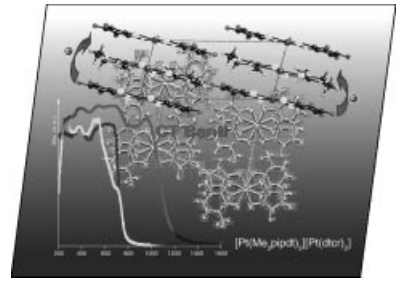

MICROREVIEW

Contents

1815 **N. M. Scott, S. P. Nolan***

Stabilization of Organometallic Species Achieved by the Use of N-Heterocyclic Carbene (NHC) Ligands

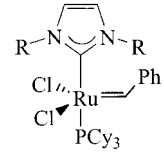

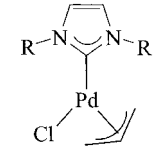

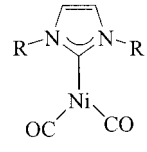

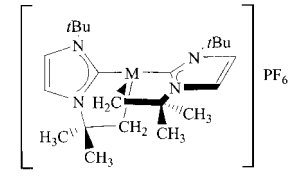

M = Rh, Ir

Keywords: Carbene ligands / Ruthenium / Palladium / Nickel / Rhodium / Iridium

 © 2005 Wiley-VCH Verlag GmbH & Co. KGaA, Weinheim

FULL PAPERS

1829 **P. Deplano,* M. L. Mercuri, L. Marchi, L. Pilia, M. Salidu, A. Serpe, F. Congiu, S. Sanna**

Electro-Conducting Properties of Charge-Transfer Salts Based on Cationic and Anionic Platinum Dithiolenes − Crystal Structure of $[Pt(Me_2pipdt)_2][Pt(dtcr)_2]$

Keywords: Sulfur ligands / Platinum / Charge-transfer / Conducting materials

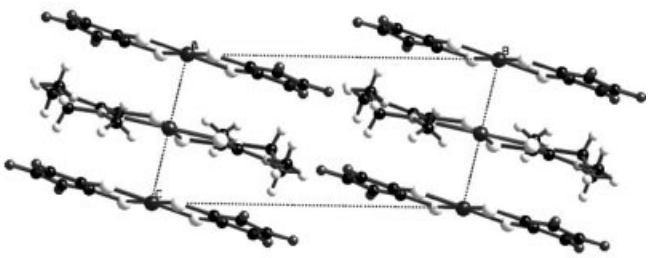

1836 **P. D. Vaz,* P. J. A. Ribeiro-Claro**

The Role of C−H···O Interactions in the Solid and Liquid-Phase Structures of Methyltrioxo Rhenium

Keywords: Rhenium / C−H···O Hydrogen bonds / Ab initio calculations / Raman spectroscopy / Inelastic neutron scattering

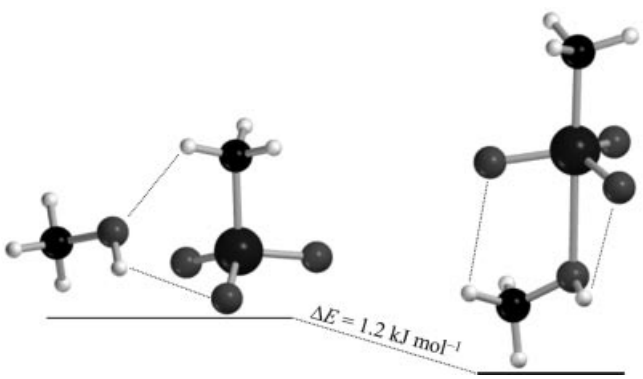

1841 **V. Kalsani, H. Bodenstedt, D. Fenske, M. Schmittel***

Supramolecular Copper Phenanthroline Racks: Structures, Mechanistic Insight and Dynamic Nature

Keywords: Rack / HETPHEN / Self-assembly / Phenanthroline / Dynamics

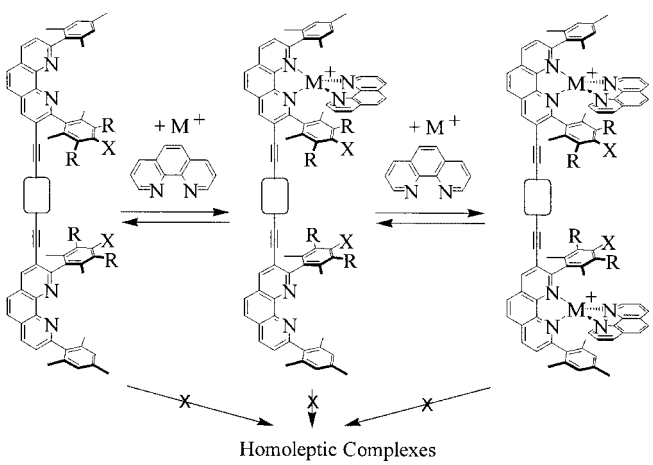

1850 **J.-P. Collin, D. Jouvenot, M. Koizumi, J.-P. Sauvage***

A Ruthenium(II)-Complexed Rotaxane Whose Ring Incorporates a 6,6′-Diphenyl-2,2′-bipyridine: Synthesis and Light-Driven Motions

Keywords: Rotaxanes / Ruthenium / Light-driven motions

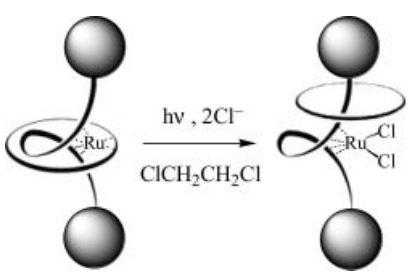

 © 2005 Wiley-VCH Verlag GmbH & Co. KGaA, Weinheim

1856 **X.-J. Liu, J.-K. Feng,* J. Meng, Q.-J. Pan, A.-M. Ren, X. Zhou, H.-X. Zhang**

A Theoretical Investigation of Substituent Effects on the Absorption and Emission Properties of a Series of Terpyridylplatinum(II) Acetylide Complexes

Keywords: Density functional calculations / Electronic structure / N ligands / Platinum

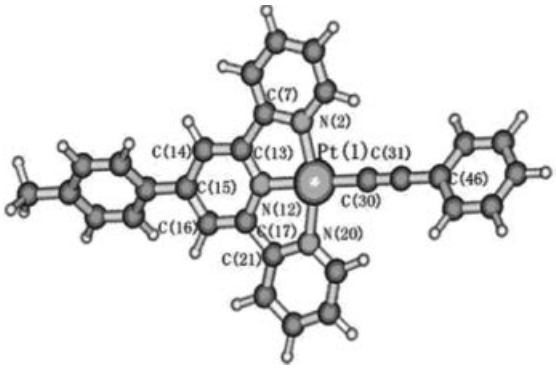

1867 **L. Yang, J.-K. Feng,* A.-M. Ren, M. Zhang, Y.-G. Ma,* X.-D. Liu**

Structures, Electronic States and Electroluminescent Properties of a Series of Cu^{I} Complexes

Keywords: Copper / Density functional calculations / N ligands / Photoluminescence

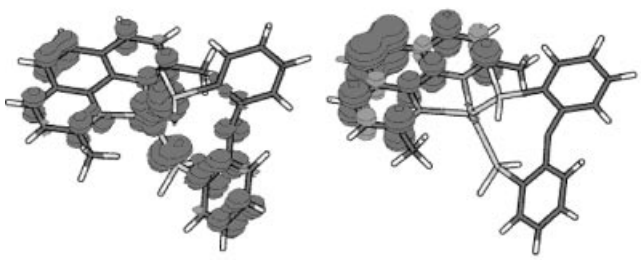

1880 **V. Chandrasekhar,* R. Boomishankar, R. Azhakar, K. Gopal, A. Steiner, S. Zacchini**

N-Bonded Monosilanols: Synthesis and Characterization of $ArN(SiMe_3)SiMe_2Cl$ and $ArN(SiMe_3)SiMe_2OH$ (Ar = C_6H_5, 2,6-$Me_2C_6H_3$, 2,6-*i*$Pr_2C_6H_3$)

Keywords: Monosilanols / *N*-Bonded silanols / Hydrogen bonding / Aminosilanols

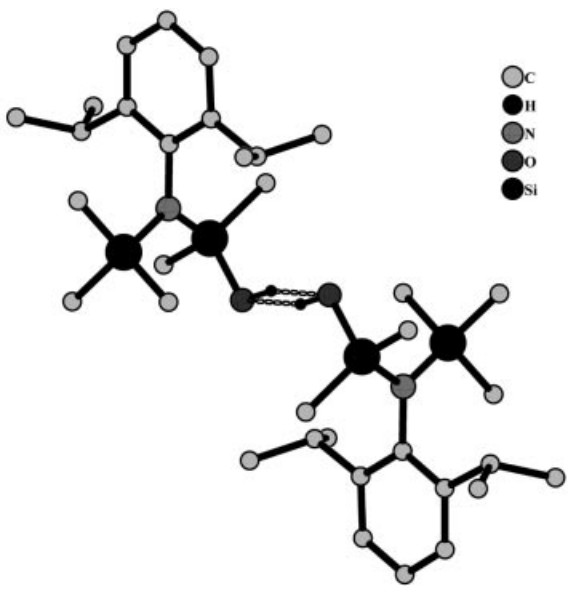

1886 **H.-J. Himmel***

Characterization of Oligomers of AlCl: Al−Cl versus Al−Al Bonding

Keywords: Subvalent compounds / Aluminium / Reaction mechanisms / Matrix isolation / Quantum chemical calculations

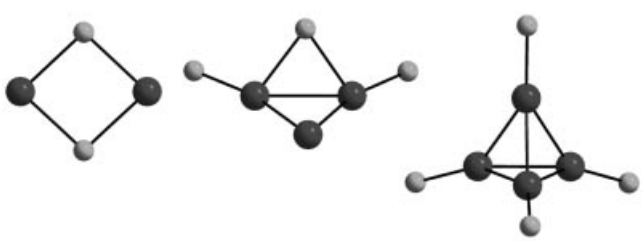

 © 2005 Wiley-VCH Verlag GmbH & Co. KGaA, Weinheim

1895 **H. Nöth,* S. Rojas-Lima, A. Troll**

The Structural Chemistry of *N*-Monolithium Borazines

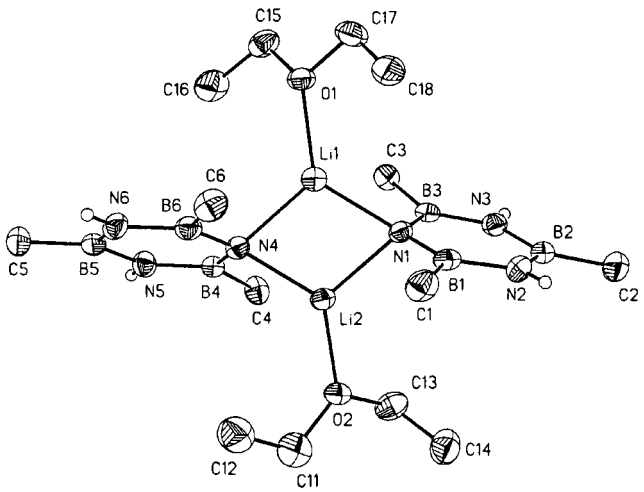

Keywords: Boron / Borazines / Lithiation / N ligands

1907 **J. M. Domínguez-Vera,* J. Suárez-Varela, I. Ben Maimoun, E. Colacio***

Synthesis, Structure, and Properties of μ-Oxo-Bridged Fe^{III}_2 and Heterometallic Azide-Bridged $Fe^{III}_2Cu^{II}$ Complexes of a Picolinamide In-Plane Ligand

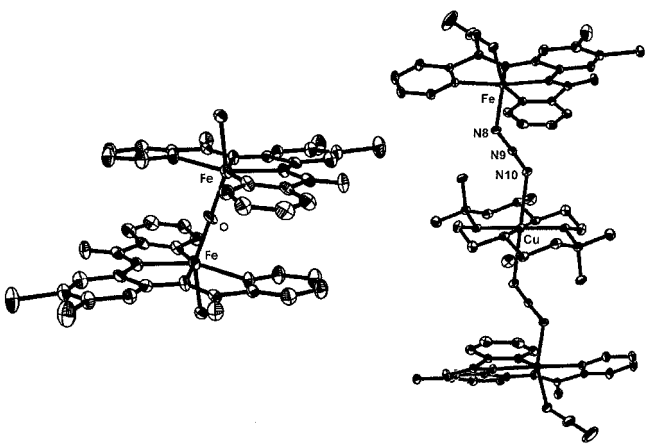

Keywords: Azides / Heterometallic complexes / Iron / Magnetic properties / Oxo ligands

1913 **J.-R. Li, R.-H. Zhang, X.-H. Bu***

Lanthanide Complexes of Disulfoxide Ligands with Varied Configurations: Influence of Lanthanide Contraction on the Structures of the Complexes

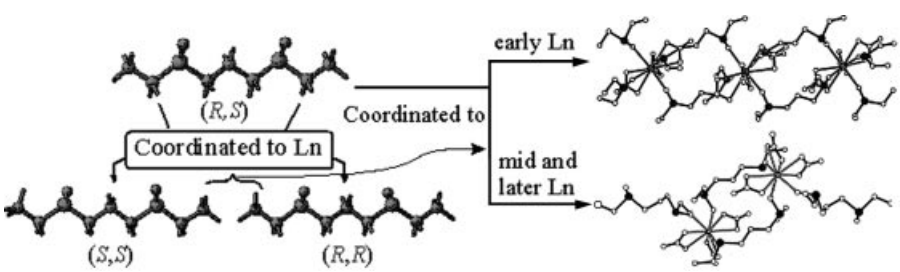

Keywords: Disulfoxides / Lanthanides / Lanthanide contraction / Ligand configuration change / X-ray diffraction

 © 2005 Wiley-VCH Verlag GmbH & Co. KGaA, Weinheim

1919 **G. Zhang, G. Yang,* L. Yang, Q. Chen, J.-S. Ma**

Synthesis, Characterization and Photophysical Properties of Novel Dinuclear Silver(I) and Mononuclear Palladium(II) Complexes with 1,2-Bis[(anthracen-9-ylmethyl)amino]ethane

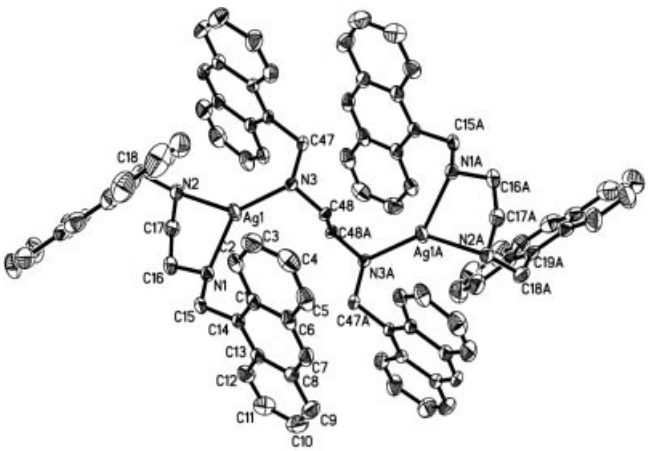

Keywords: N ligands / Palladium / Photophysics / Silver

1927 **Z. Lin, F. Jiang, D. Yuan, L. Chen, Y. Zhou, M. Hong***

The 3D Channel Framework Based on Indium(III)−btec, and Its Ion-Exchange Properties (btec = 1,2,4,5-Benzenetetracarboxylate)

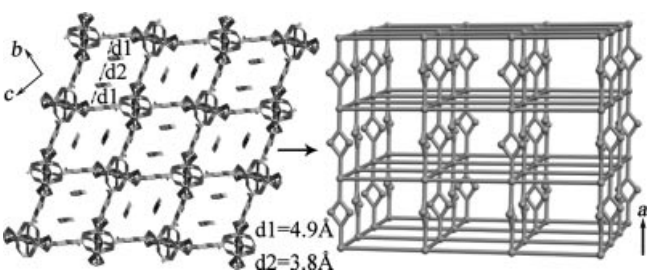

Keywords: Indium / Benzenetetracarboxylate / Crystal structure / Ion exchange / Pyridine derivatives

1932 **H.-W. Lerner,* G. Margraf, L. Kaufmann, J. W. Bats, M. Bolte, M. Wagner**

Syntheses, Reactivity, and X-ray Structure Analyses of the Dimeric Pentaphosphides $[(t\mathrm{Bu_3Si})_3\mathrm{P_5M_2}]_2$ (M = Na, Ag) and the Bicyclo-[2.1.0]pentaphosphane $(t\mathrm{Bu_3Si})_3\mathrm{P_5}$

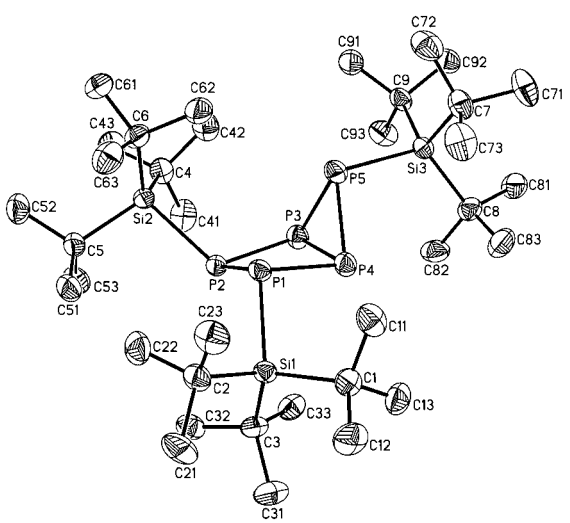

Keywords: Phosphorus / Phosphane / Supersilyl phosphides / Silanide

 © 2005 Wiley-VCH Verlag GmbH & Co. KGaA, Weinheim

1940 **L. Weber,* G. Noveski, U. Lassahn, H.-G. Stammler, B. Neumann**

Synthesis and Structure of the First η^3-1,2-Diphosphaallyl Complexes $[(\eta^5\text{-}C_5H_5)(CO)_2M\{\eta^3\text{-}RPPC(SiMe_3)_2\}]$ (M = Mo, R = *t*Bu, Cy; M = W, R = *t*Bu) from $[(\eta^5\text{-}C_5H_5)(CO)_2M{=}P{=}C(SiMe_3)_2]$ (M = Mo, W) and Inversely Polarized Phosphaalkenes $RP{=}C(NMe_2)_2$ (R = *t*Bu, Cy)

Keywords: Phosphavinylidene complexes / 1,2-Diphosphaallyl complexes / Phosphaalkenes / Molybdenum / Tungsten

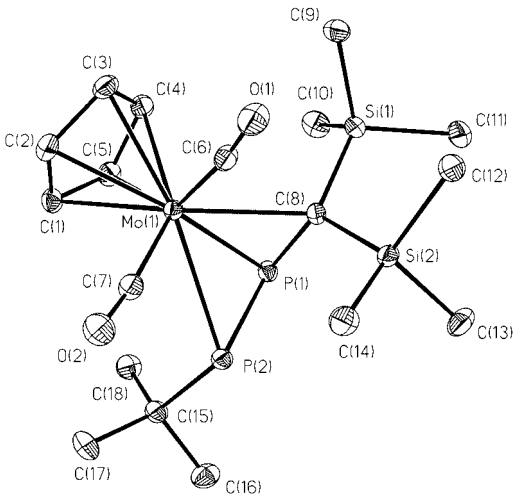

1947 **A.-Q. Wu, G.-H. Guo, C. Yang, F.-K. Zheng, X. Liu, G.-C. Guo,* J.-S. Huang, Z.-C. Dong,* Y. Takano**

Extended Structures and Magnetic Properties of Lanthanide−Copper Complexes with Picolinic Acids as Bridging Ligands

Keywords: Heterometallic complexes / Magnetic properties / Crystal structures / Picolinic acid / Coordination polymers

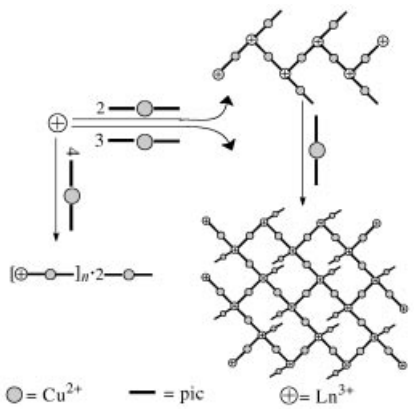

1955 **R. J. Bowen,* M. A. Fernandes, P. W. Gitari, M. Layh,* R. M. Moutloali**

Synthesis and Reactions of Mixed N,P Ligands

Keywords: Cyclic phosphonium salts / Gold phosphane complexes / β-Keto thiophosphane oxide / Keto-enol / Imine-enamide tautomerism

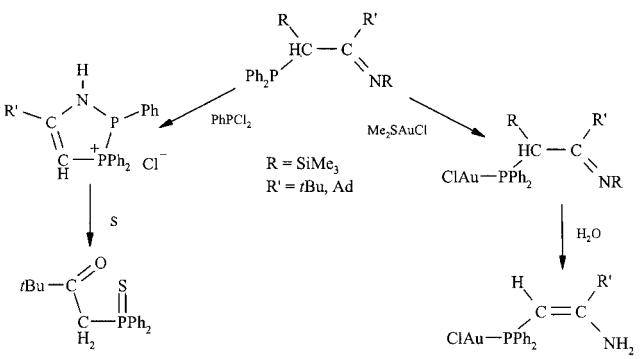

1964 **M. Alexiou, E. Katsoulakou, C. Dendrinou-Samara, C. P. Raptopoulou, V. Psycharis, E. Manessi-Zoupa, S. P. Perlepes,* D. P. Kessissoglou***

Di-2-pyridyl Ketone Oxime in Zinc Chemistry: Inverse 12-Metallacrown-4 Complexes and Cationic Pentanuclear Clusters

Keywords: Cluster compounds / Inverse metallacrowns / Oximato complexes / X-ray crystallography / Zinc

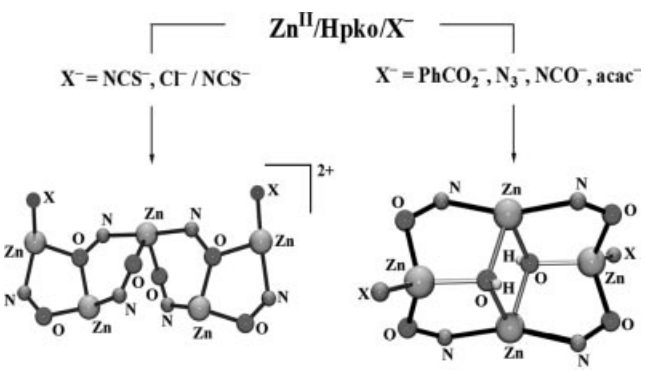

 © 2005 Wiley-VCH Verlag GmbH & Co. KGaA, Weinheim

1979 **I. Krossing,* A. Reisinger**

Perfluorinated Alkoxyaluminate Salts of Cationic Brønsted Acids: Synthesis, Structure, and Characterization of $[H(OEt_2)_2][Al\{OC(CF_3)_3\}_4]$ and $[H(THF)_2][Al\{OC(CF_3)_3\}_4]$

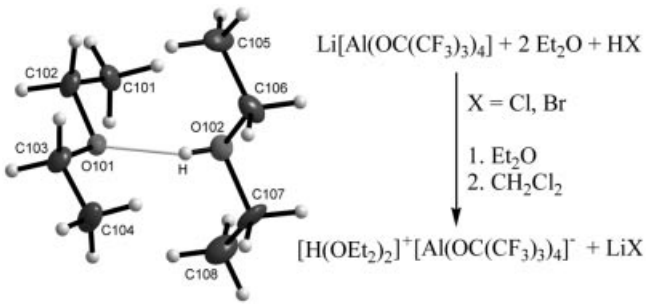

Keywords: Acidity / Aluminum / Brønsted acids / IR spectroscopy / Hydrogen bonds

CORRECTION

1991 **A. Scherer, K. Kollak, A. Lützen, M. Friedemann, D. Haase, W. Saak, R. Beckhaus***

Low-Valent Titanium−Pentafulvene Complexes − Formation of Dinuclear Titanium−Nitrogen Complexes

Keywords: Titanium / Bridging ligands / Nitrogen / Metallocenes / Fulvene ligands

 © 2005 Wiley-VCH Verlag GmbH & Co. KGaA, Weinheim

Stabilization of Organometallic Species Achieved by the Use of N-Heterocyclic Carbene (NHC) Ligands

Natalie M. Scott[a] and Steven P. Nolan*[a]

Keywords: Carbene ligands / Ruthenium / Palladium / Nickel / Rhodium / Iridium

This review describes the stabilization of various coordinatively unsaturated metal centers through the incorporation of N-heterocyclic carbene (NHC) ligands. Such species are more thermally stable compared to the more ubiquitous tertiary phosphane systems. Although NHCs can be considered as phosphane mimics it has become apparent that there are substantial differences between the two ligand families. In general, NHC ligands are much more electron-donating and sterically demanding than bulky phosphane ligands. We also discuss the various thermochemical and infrared studies of metal carbene species that have provided insight into NHC ligands properties, and at last allowed meaningful comparison to tertiary phosphane ligands. While NHCs are generally viewed as strong binding low reactive ligands, in some instances they have been found to be not so innocent and can undergo facile intramolecular C–H activation as well as abnormal ligand binding [C-5(4) vs. C-2]. Here we highlight such reactions with late-transition metal centers that have allowed the isolation of various unsaturated LTM species. These have so far eluded isolation in analogous phosphane-based systems.

(© Wiley-VCH Verlag GmbH & Co. KGaA, 69451 Weinheim, Germany, 2005)

Introductions

Since the first speculation on the existence of transient carbene intermediates in the early 1900s,[1,2] carbenes have evolved from real intermediates whose existence could be demonstrated by kinetic and trapping studies in the 1960s[3–5] to stabilized forms currently being studied in many research groups.[6–8] For the last 6 years we have been interested in the coordination of N-heterocyclic carbenes (NHCs) (imidazol-2-ylidenes, **1**; Scheme 1) to various metal centers and, like many other research groups, have found that NHCs stabilize highly reactive organometallic species.[9–13] Many of these carbene species show high catalytic activity in many metal-mediated organic transformations, e.g. ruthenium-mediated olefin metathesis,[14–19] iridium-catalyzed hydrogenation and hydrogen transfer[20–23] plati-

[a] Chemistry Department, University of New Orleans,
2000 Lakeshore Drive, New Orleans, Louisiana 70148, USA
Fax: +1-504-280-6860
E-mail: snolan@uno.edu

Natalie M. Scott was born in Australia in 1976. She received her B.Sc. (Honors) in chemistry from the Monash University and her Ph.D. from Monash University where she worked with Professor Glen Deacon. She was then awarded a Humboldt postdoctoral fellowship to carry out work with Professor Kempe in Bayreuth where she conducted research in lanthanide chemistry. She then accepted a postdoctoral position at the University of New Orleans where she has carried out late transition metal organometallic synthesis. Her research interests include organometallic chemistry (from early to late transition metals) and homogeneous catalysis.

Steven P. Nolan was born in Quebec City, Canada in 1962. He received his B.Sc. in chemistry from the University of West Florida and his Ph.D. from the University of Miami where he worked under the supervision of Professor Carl D. Hoff. After a postdoctoral stay with Professor Tobin J. Marks at Northwestern University, he joined the Department of Chemistry of the University of New Orleans in 1990. He now holds the rank of University Research Professor of Chemistry. His research interests include organometallic chemistry and homogeneous catalysis.

MICROREVIEWS: This feature introduces the readers to the authors' research through a concise overview of the selected topic. Reference to important work from others in the field is included.

num-catalyzed hydrosilylation,[24] and palladium C–C coupling reactions;[25–28] however, the strong σ-donor nature of the ligands often results in more stable catalysts than analogous phosphane-based systems.

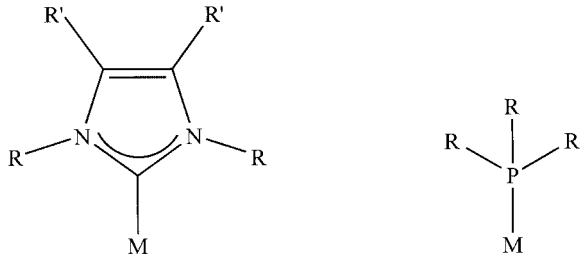

Scheme 1.

A number of studies have suggested that as ligands, nucleophilic carbenes have similar properties to electron rich trialkylphosphanes (strong σ donors with negligible π-accepting ability) (Scheme 1).[17,29–36] Yet phosphane ligands suffer from significant P–C bond degradation at elevated temperatures,[29] while NHCs have been shown to possess greater thermal stability in addition to stronger donating ability.[37] Already, the easily modified NHC ligands are highly acclaimed affording more stable, yet highly reactive, metal catalysts where phosphane analogues have been found less effective or ineffective.[15,24,28,38–44] In addition, they have allowed the stabilization of many reactive organometallic intermediates that have never been fully characterized in analogous phosphane chemistry despite the use of sterically demanding ligands.[45–47] The pioneering studies of Tolman on phosphanes have had a major impact on the development of new and improved phosphane ligands for catalysis,[48] binding studies involving carbene ligands have only just begun to shed light on this ligand class.[36,45,49–53] In this report we describe efforts directed toward the understanding of the NHC ancillary system and their ability to stabilize unsaturated late-transition metal species.

Ruthenium NHC Metathesis Catalysts

The use of more thermally stable NHC-ruthenium catalysts (**1**,[16] **2**[54] Figure 1) in olefin metathesis has resulted in the preparation of new functionalized carbocycles and heterocycles from acyclic diene precursors unattainable using Grubbs catalyst **3**[55–57] or the alkoxy imido molybdenum catalyst **4** developed by Schrock.[58] The differences in reactivity between ruthenium and molybdenum arise from the fact that carbene ruthenium complexes have a greater functional group tolerance and higher moisture and atmospheric oxygen stability relative to those of the extremely sensitive molybdenum system.[59–61]

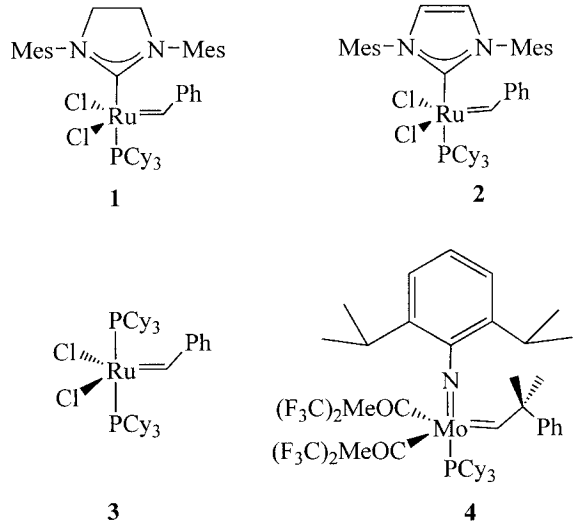

Figure 1. Olefin metathesis catalysts

We have been involved in the catalyst development efforts aimed at improving catalyst activity, functional group tolerance, and versatility for many years. In 1999 we examined electronic and steric properties of bulky NHC ligands with an unsaturated ruthenium complex and compared those results to a PCy_3-containing system.[15,36] The unsaturated tetrameric species $[Cp^*RuCl]_4$ ($Cp^* = \eta^5\text{-}C_5Me_5$)[62] rapidly reacts with sterically demanding phosphanes and various NHC ligands [Equation (1)] in THF to afford deep blue coordinatively unsaturated $[Cp^*Ru(PR_3)Cl]$ (R = cyclohexyl or isopropyl)[63] and [Cp*Ru(NHC)Cl] complexes. The reactions were exothermic and quantitative; facts that allowed for the determination of enthalpies of reaction by anaerobic solution calorimetry. In general, the results showed that the examined NHCs, with the exception of the sterically demanding IAd, are better donors than the best phosphane donor ligands.

$$[Cp^*RuCl]_4 + 4L \xrightarrow[\text{r.t.}]{\text{THF}} Cp^*Ru(L)Cl \qquad (1)$$

L	R		$-\Delta H_{rxn}$ (kcal/mol)	relative BDE (kcal/mol)
	cyclohexyl	ICy:	85.0(0.2)	21.2
	4-methylphenyl	ITol:	75.3(0.4)	18.8
	4-chlorophenyl	IpCl:	74.3(0.3)	18.6
	2,4,6-trimethylphenyl	IMes:	62.6(0.2)	15.6
	adamantyl	IAd:	27.4(0.4)	6.8
PCy_3:			41.9(0.2)	10.5
$PiPr_3$:			37.4(0.3)	9.4

These enthalpy values can be converted into relative bond dissociation enthalpies (BDE) on the basis of a mol of product and clearly indicate that NHCs are better donor ligands than PCy_3 in the [Cp*Ru(L)Cl] system. To further verify the thermochemical results, ligand exchange reactions between $[Cp^*Ru(PCy_3)Cl]$ and IMes or ICy were examined and indeed the formation of free PCy_3 and $[Cp^*Ru(PCy_3)Cl]$ was observed [Equation (2)].

 © 2005 Wiley-VCH Verlag GmbH & Co. KGaA, Weinheim

$$Cp^*Ru(PCy_3)Cl + NHC \xrightarrow[r.t.]{THF} Cp^*Ru(NHC)Cl + PCy_3 \quad (2)$$

NHC = IMes, ICy

The next step in our physicochemical studies was to examine whether this ligand substitution pattern was also valid for a catalytically related system: Ruthenium-based olefin metathesis. This did indeed proved feasible. The better donor ability of the NHC ligands (not including IAd) in supporting activity in metathesis-active ruthenium systems is thought to have a steric and an electronic component.

After our initial studies had been reported, Fürstner and Hermann[64] studied substitution effects on catalytic behavior (Figure 2). They observed that **7** and **8** bearing benzylic residues on the carbene ligands exhibit the lowest activity, whereas high activity was displayed for **5** and **6**. This result is in contrast to the behavior of **1**, in which replacement of PCy_3 by $PiPr_3$ results in a noticeable loss of catalytic activity. As we had observed, complexes bearing only one NHC ligand (**10**, **11**) showed significantly higher activity compared to bis-NHC systems. Mechanistically, since the Ru–NHC is a stronger bond than the Ru–PCy_3 bond, the mixed PR_3/NHC ligand system would proceed by phosphane ligand displacement if a dissociative-type pathway, leading to the active catalyst, is at play.[15,36] Another interesting result is that despite changing halogens in complexes **6** and **9** no difference in catalytic activity was observed. This result contrasts reactivity pattern for **1** where a decrease in activity from chloride to bromide to iodide was observed.[56]

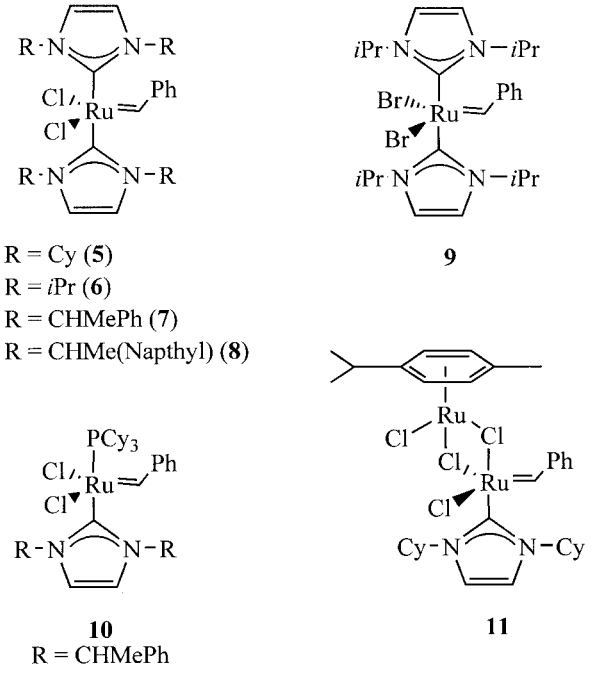

Figure 2. Substitution effects in Ru–NHC metathesis systems

Much work has been and continues to be published in the area of ruthenium-based olefin metathesis since our initial observation of the beneficial use of NHC as supporting ligand. A fundamental understanding of the sterics and electronic properties of the ligands themselves proved invaluable. To say that these results provided a systematic ligand design approach would be incorrect but surely assisted our ligand exploration.

Palladium(0) NHC Complexes

The stability imparted by the NHC ligands to metal centers is further observed in palladium chemistry with the preparation of efficient catalysts that have been shown to possess considerable potential in many C–C bond forming reactions, which have included the Heck reaction,[65–69] the telomerization of alkenes[43,70,71] and the Suzuki–Miyaura cross-coupling reaction.[72–75] These Pd-mediated processes have been shown to proceed through a d^{10}-Pd^0 center. In particular, recent work by Hartwig,[76,77] Cloke[78] and Nolan[79] on reactions involving Ar–X with the precatalyst $[Pd(NHC)_2]$ suggest dissociation of one NHC to generate a PdL fragment, which then undergoes oxidative addition of aryl halide (Scheme 2), a reaction pathway similar to that proposed in analogous phosphane systems.[76,80,81]

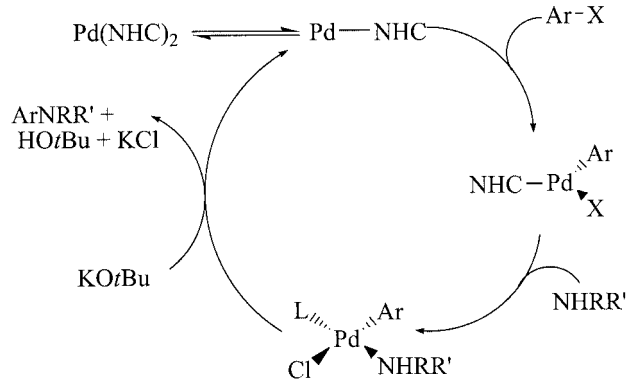

Scheme 2. Proposed mechanism for aryl amination.

While Amatore and Jutand[82] proposed an alternative route for phosphane palladium-catalyzed systems through an anionic three-coordinate complex of the type $[Pd^0L_2Cl]^-$ or $[Pd^0L_2(OAc^-)]$ as the active intermediate, detailed kinetic studies by Cloke suggest that oxidative addition reactions occur via a two-coordinate 14-electron [Pd^0-NHC] complex.[83] Furthermore, the ability of the oxidative addition products $[Pd(ItBu)_2(R\text{-}4\text{-}C_6H_4)Cl]$ (R = Me, CO_2Me, OMe) to reversibly dissociate free carbene according to Scheme 3 was demonstrated. The Pd–NHC dissociation enthalpy value of 25.57 kcal/mol^{-1} for $[Pd(ItBu)_2(Me\text{-}4\text{-}C_6H_4)Cl]$ was determined suggesting that the three-coordinate arylpalladium chloride product was the most likely intermediate in amination reactions.

 © 2005 Wiley-VCH Verlag GmbH & Co. KGaA, Weinheim

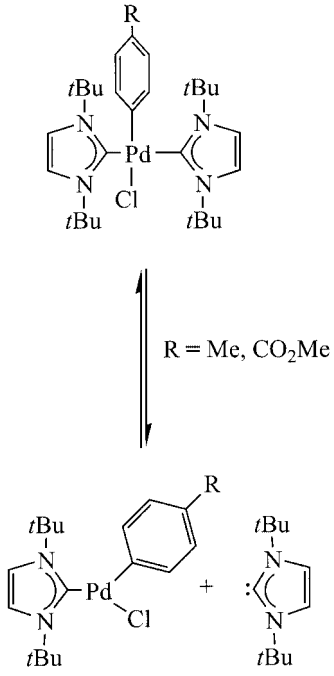

Scheme 3.

Studies by Hermann on the Heck reaction with $[Pd(NHC)_2]$ also suggest the intermediacy of this same Pd–L complex.[66] Hermann noticed short induction periods for Pd^{II} complexes on addition of a reducing agent. However, when Pd^0 was used no induction period was observed suggesting Pd^0 complexes enter in the catalytic cycle faster. Despite an increasing interest in this area over the last 5 years, there are only a few examples of fully characterized Pd^0-carbene complexes.[67,68,70,74,84–86] The isolation of two-coordinate unsaturated NHC Pd^0 complexes was first achieved by Cloke and co-workers.[84] While they prepared a homoleptic $[Pd(I\mathit{t}Bu)_2]$ (I*t*Bu = 1,3-di-*N*-*tert*-butylimidazol-2-ylidene) complex by co-condensation palladium vapor with *N*,*N*′-di-*tert*-butylimidazol-2-ylidene (I*t*Bu). This route was low yielding and limited to NHC ligands that could be sublimed [Equation (3)]. A ligand exchange reaction between $[Pd(PR_3)_2]$ (R = *o*-tolyl) and two equivalents of free NHC afforded $[Pd(NHC)_2]$ in higher yields. Furthermore addition of only one NHC equivalent to $[Pd(PR_3)_2]$ (R = *o*-tolyl) resulted in a mixed $[Pd(PR_3)(NHC)]$ species [Equation (4)]. Alternatively, the synthesis of mixed species can also be generated by mixing the $[Pd(NHC)_2]$ complex with free phosphane $[P(o\text{-tolyl})_3$, $PCy_3]$, suggesting some reversibility is associated with the reaction.[87,88]

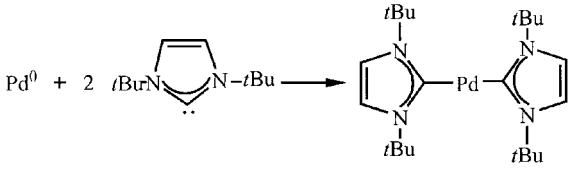

(3)

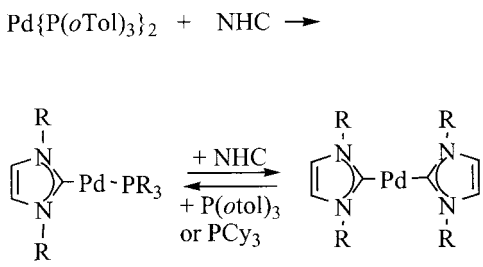

(4)

The derivatives are readily prepared from reaction of [Pd(COD)(alkene)] (COD = cyclooctadiene) with the NHCs [1,3,4,5-tetramethylimidazol-2-ylidene (IMe) and IMes] to afford the complexes $[Pd(IMe)_2(alkene)]$ [alkene = maleic anhydride (MAH) (**12**), tetracyanoethylene (TCNE) (**13**)] (Figure 3).[67] Spectroscopic studies showed significant back-bonding of the olefin on the Pd center suggesting that the carbene ligands are strongly donating. Although **12** and **13** are envisaged as approaching Pd^{II} these complexes readily undergo oxidation reactions typical of Pd^0.

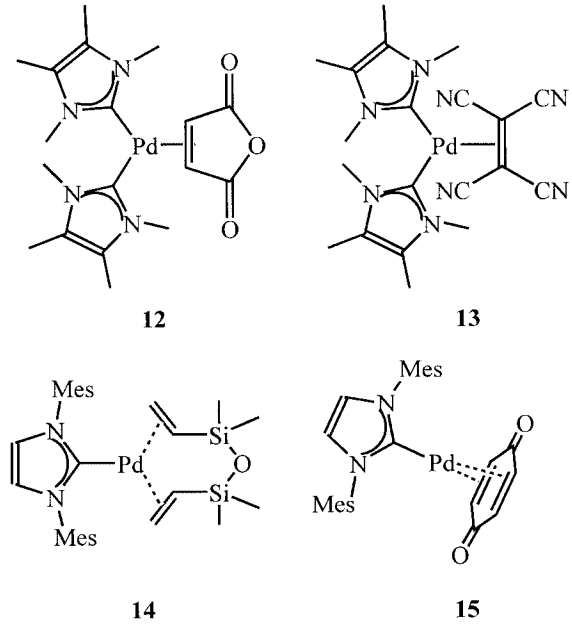

Figure 3. NHC–Pd^0 complexes

Reports of monocarbenepalladium(0) complexes without additional phosphane donors are scarce. Beller et al. recently synthesized a number of monocarbene(diolefin)palladium(0) complexes.[68,69] The addition of IMes to either palladium(0)–diallyl ether complex $[Pd_2(dae)_3]$ (dae = diallyl ether) in 1,1,3,3-tetramethyl-1,3-divinyldisiloxane or [(COD)Pd(quinone)] [quinone = *p*-benzoquinone (BQ), 1,4-naphthoquinone (NQ)] at low temperatures afforded the complexes [(IMes)Pd(dae)] (**14**), [(COD)Pd(BQ)] (**15**) and [(COD)Pd(NQ)] (**16**), respectively. Complexes **14**–**16** showed remarkable productivities and selectivity in a number of telomerization and Heck reactions, again concluding that the active species in carbene Pd-mediated organic transformations appears to be a Pd^0-carbene center.

 © 2005 Wiley-VCH Verlag GmbH & Co. KGaA, Weinheim

Steric Factors of NHC in Palladium(II) Complexes

Recently we reported the synthesis and cross-coupling catalytic reactivity of a family of [(NHC)Pd(allyl)Cl] complexes (Scheme 4).[50] These were synthesized either through addition of two equivalents of free carbene to $[Pd(allyl)Cl]_2$ under inert atmosphere (an adapted procedure from a protocol employed in the preparation of $[(PCy_3)Pd(allyl)Cl]$[89]) or by an in situ liberation of the imidazolium salts, followed by slow addition of $[Pd(allyl)Cl]_2$. The catalytic reactivity of these [(NHC)Pd(allyl)Cl] complexes varied substantially as a function of the identity of the NHC. While electronic differences were ruled out after crystallographic evidence showed little to no difference in the Pd–$C_{carbenic}$ bond lengths, this suggested that steric factors associated with the saturated and unsaturated imidazole backbone and side arm groups on the NHC were involved.

Prompted by this, we undertook a detailed investigation focusing on the steric factors of NHC ligands. The use of the classical "cone angle" steric factor described by Tolman for phosphane ligands[48] cannot be applied to the "fence"- or "fan"-type NHCs. Instead a wing-span model was conceptualized taking into account the wing-span angle (closest carbon substituent on the NHC) to the palladium center. This intial model was recently refined by imposing a sphere of radius (3 Å) centered around the palladium atom and the volume occupied by the ligand determined (Table 1) was then taken as the steric factor associated with any given NHC. Recently, a similar method was used to estimate the steric factor for a series of ruthenium-NHC complexes.[90]

By quantifying the steric demand of each NHC in these complexes, this has allowed a realistic comparison, not only between NHCs but also to tertiary phosphane ligands. The most sterically demanding I*t*Bu, IAd and SIPr ligands resulted in a decreased activity in the studied amination reaction. Furthermore IPr and IMes showed marked differences in reactivity compared to their saturated analoges SIPr and SIMes in spite of having almost identical structures. We associated this difference to the presence of two sp^3 carbon atoms inducing deformation of the dihydroimidazol-2-ylidene ring resulting in supplementary rotation of the aryl moieties around the N–C_{aryl} bond. As a consequence, the Pd center is more sterically protected, thereby presumably facilitating reductive elimination in Scheme 2.

Table 1. Buried volume calculated for [(NHC)Pd(allyl)Cl] complexes.

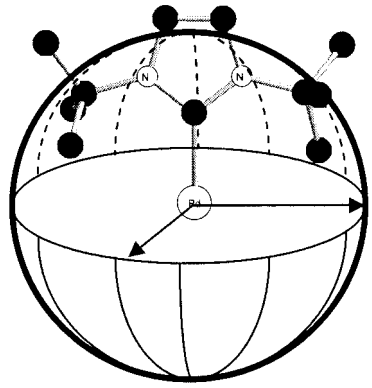

Complex	Buried volume[a] (%)	Buried volume[b] (%)
[(IPr)Pd(allyl)Cl]	26.10	24.99
[(IMes)Pd(allyl)Cl]	26.50	25.87
[(I*t*Bu)Pd(allyl)Cl]	33.37	32.25
[(ICy)Pd(allyl)Cl]	25.17	23.90
[(IAd)Pd(allyl)Cl]	33.56	32.20
[(SIPr)Pd(allyl)Cl]	33.03	32.27
[(SIMes)Pd(allyl)Cl]	27.49	26.91

[a] Calculated buried volume for a fixed distance Pd–$C_{carbenic}$ of 2 Å. [b] Buried volume calculated based on crystallographic distances.

Carbonyl NHC Nickel Complexes

The importance of quantifying steric and electronic effects of ligands have had a major impact in the development of new and improved phosphane ligands for catalysis.[48] In the case of the NHC ligands surprising differences in catalytic activities of the corresponding metal catalysts have already been observed, but could not be rationalized or explained experimentally. Although many spectroscopic studies have indicated the similarities between NHCs and phos-

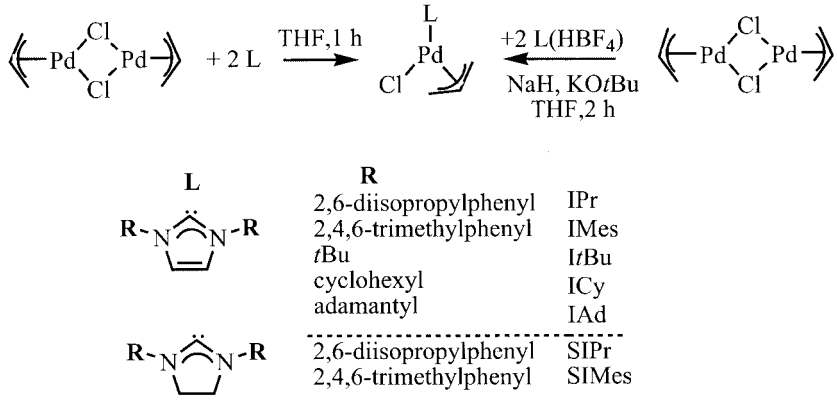

Scheme 4.

 © 2005 Wiley-VCH Verlag GmbH & Co. KGaA, Weinheim

phane, we felt that it was important to experimentally determine properties associated with the most widely used NHCs (depicted in Scheme 5). This would then allow for the direct comparison of NHC and phosphane steric/electronic properties.

The substitution reaction involving [Ni(CO)$_4$] and NHC ligands (IMes, SIMes, IPr, SIPr, ICy) gave rise to the expected, saturated complexes [Ni(CO)$_3$(IMes)], [Ni(CO)$_3$(SIMes)], [Ni(CO)$_3$(IPr)], [Ni(CO)$_3$(SIPr)], [Ni(CO)$_3$(ICy)] (Scheme 5), [Equation (5)].[49] However, the most bulky NHC ligands, I*t*Bu and IAd, led to the isolation of novel, unsaturated three-coordinate carbonyl nickel compounds [Ni(CO)$_2$(I*t*Bu)] and [Ni(CO)$_2$(IAd)].[91]

$$Ni(CO)_4 + NHC \xrightarrow[-CO]{} (NHC)Ni(CO)_3 \text{ or } (NHC)Ni(CO)_2 \quad (5)$$

X-ray characterization was obtained for most of the [Ni(CO)$_3$(NHC)] series and for both [Ni(CO)$_2$(NHC)] complexes (see below for discussion). Ball-and-stick diagrams of [Ni(CO)$_3$(IMes)] and [Ni(CO)$_3$(SIMes)] are presented in Figure 4 and [Ni(CO)$_3$(IPr)] and [Ni(CO)$_3$(SIPr)] in Figure 5. All complexes show the expected tetrahedral geometry around the metal center, with the Ni–C(NHC) bond lengths lying within the range of 1.96–1.98 Å {[(Ni(CO)$_3$(IMes)] 1.971(3) Å; [Ni(CO)$_3$(SIMes)] 1.960(2) Å; [Ni(CO)$_3$(IPr)] 1.979(2) Å; [Ni(CO)$_3$(SIPr)] 1.962(4) Å}. The saturated NHC ligands SIMes and SIPr showed slightly shorter bond lengths than their corresponding analogues containing the unsaturated NHC ligands. However, all the Ni–NHC distances are in good accordance with their exclusive σ donor characteristics.[67,92] As observed in other crystallographic studies on saturated NHC species, the presence of two sp^3 carbon atoms in the heterocyclic ring imidazole backbone, results in torsion angles of 6.4° {for [Ni(CO)$_3$(SIMes)]} and 2.6° {for [Ni(CO)$_3$(SIPr)]}. Surprisingly, the former value is significantly lower than the one for free SIMes (13.4°). The unsaturated NHCs have the aryl substituents disposed at an angle of 90° (+/–10°) with respect to the imidazole backbone plane.

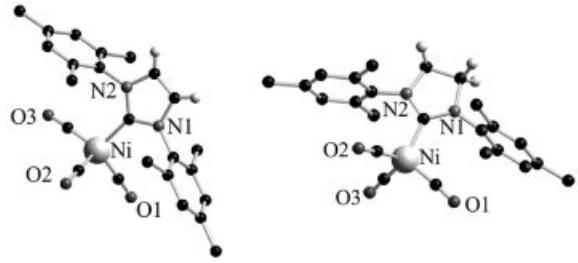

Figure 4. Ball-and-stick representation of [Ni(CO)$_3$(IMes)] (left) and [Ni(CO)$_3$(SIMes)] (right).

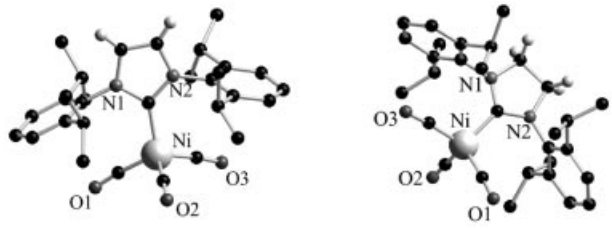

Figure 5. Ball-and-stick representation of [Ni(IPr)(CO)$_3$] (left) and [Ni(SIPr)(CO)$_3$] (right).

The CO infrared frequencies obtained for the [Ni(CO)$_3$(NHC)] complexes confirmed that N-heterocyclic carbenes are better σ donors than tertiary phosphanes (Table 2). Unlike the substantial electronic differences seen in phosphane ligands when moving from ary- to alkyl-substituted P ligands, the overall electronic difference in NHC data was relatively small. Expectably the NHC data showed that ICy was the most basic ligand due to its alkyl substitution. Furthermore, the saturated NHC ligands, SIMes and SIPr, were found to be slightly less electron-donating than their unsaturated analogues IMes and IPr. This supports our recently observed trends in the relative bond disruption enthalpies of ruthenium complexes involving the aforementioned ligands.[90] These experimental results clearly contradict the common assumption that saturated NHC ligands are more electron-donating and that metal complexes incorporating them perform better in catalysis for this reason. Our experimental data suggest that electronic factors are unlikely to play a major role in the differences in catalytic activity, or if this is indeed the case, substantial differences

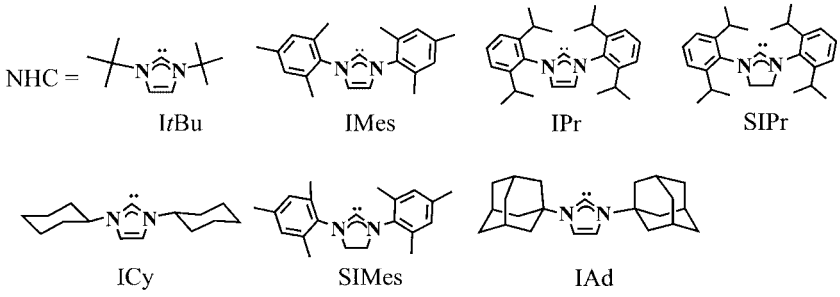

Scheme 5.

 © 2005 Wiley-VCH Verlag GmbH & Co. KGaA, Weinheim

take origin in extremely small electronic differences within the NHC ligand class.

Table 2. CO infrared frequencies in $[Ni(CO)_3(L)]$ complexes.

Complex	ν_{CO} [A_1 (cm^{-1})]; CH_2Cl_2	ν_{CO} [E (cm^{-1})], CH_2Cl_2
$[Ni(CO)_3(IMes)]$	2050.7	1969.8
$[Ni(CO)_3(SIMes)]$	2051.5	1970.6
$[Ni(CO)_3(IPr)]$	2051.5	1970.0
$[Ni(CO)_3(SIPr)]$	2052.2	1971.3
$[Ni(CO)_3(ICy)]$	2049.6	1964.6
$[Ni(CO)_3(PtBu_3)]$[a]	2056.1	1971
$[Ni(CO)_3(PiPr_3)]$[a]	2059.2	1977
$[Ni(CO)_3(PPh_3)]$[a]	2068.9	1990

[a] Taken from ref.[48]

As previously mentioned the most bulky NHC ligands, I*t*Bu and IAd, led to the isolation of novel, unsaturated 16-electron three-coordinate carbonyl nickel compounds $[Ni(CO)_2(ItBu)]$ and $[Ni(CO)_2(IAd)]$ (Figure 6).[91] While carbonyl-free, three-coordinate Ni^0 complexes are not uncommon,[93–95] such unsaturated carbonyl nickel systems are exceedingly rare and the only example known in literature has been isolated as a mixture of $[Ni(CO)_3(L)]$ and $[Ni(CO)_2(L)]$ compounds.[96–102] The closest carbon atom on one of the side-arm R groups in $[Ni(CO)_2(NHC)]$ appears to approach the metal center. However, the distances lie outside the range seen for agostic interactions.[103,104] In fact, within the series of NHCs studied these two ligands are the only ones to contain α-carbon atoms in the side chains that are bound to three additional C atoms. While the aromatic IMes, SIMes, IPr and SIPr as well as ICy can minimize steric interactions with the metal center by orientation of their R-groups perpendicularly to the imidazole plane, such an arrangement cannot be reached for IAd and I*t*Bu.

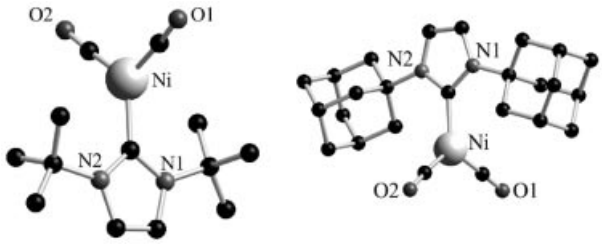

Figure 6. Ball-and-stick representation of $[Ni(CO)_2(ItBu)]$ (left) and $[Ni(CO)_2(IAd)]$ (right). Hydrogen atoms are omitted for clarity.

According to Equation (5), Ni–NHC bond energies could be determined if the reaction was reversible. For saturated complexes $[Ni(CO)_3(NHC)]$ no reactivity was observed, despite applying high CO pressures, showing these complexes to be inert towards displacement of NHC and carbonyl ligands. In contrast, the unsaturated analogues were highly reactive towards ligand substitution and oxidative addition of substrates. Reacting $[Ni(CO)_2(ItBu)]$ and $[Ni(CO)_2(IAd)]$ with 1 atm of CO resulted in the quantitative formation of $[Ni(CO)_4]$,[105] without any formation of $[Ni(CO)_3(NHC)]$ (NHC = I*t*Bu, IAd) complex and thus, allowed the determination of Ni–NHC bond dissociation energies (Table 3).

Table 3. CO and L BDE values, in kcal/mol, in the $[Ni(CO)_2(L)]$ and $[Ni(CO)_3(L)]$ complexes, L = NHC ligand or phosphane, and calculated $\%V_{Bur}$ of the free NHC and PR_3 ligands.

			BDE of L in Ni(CO)$_2$(L)	$\%V_{Bur}$
I*t*Bu	13.3 (15.6)[a]	24.0	44.3	37
SI*t*Bu	10.3 (13.1)[a]	21.8	45.1	38
IAd	7.6 (14.1)[a]	20.4	46.5	37
IMes	28.3 (27.2)[a]	41.1	46.5	26
SIMes	26.8 (26.4)[a]	40.2	47.2	27
IPr	26.7 (27.2)[a]	38.5	45.4	29
SIPr	25.6 (25.8)[a]	38.0	46.1	30
ICy	27.0 (26.1)[a]	39.6	46.3	23
PH_3	30.7	22.7	25.7	17
PPh_3	30.4	26.7	30.0	22
$PtBu_3$	27.4	28.0	34.3	30

[a] Values in brackets obtained with the QM/MM technique.

DFT-calculated BDE values indicated that CO is weakly bound to the SI*t*Bu-, Si*t*Bu- and IAd-based complexes (BDE around 10 kcal/mol). However, CO is much more strongly bound to the IPr, SIPr, ICy, IMes and SIMes complexes (BDE greater than 25 kcal/mol). These results are in good qualitative agreement with the experimental fact that $[Ni(CO)_2(NHC)]$ complexes are observed for NHC = IAd and I*t*Bu, while $[Ni(CO)_3(NHC)]$ complexes are observed for the other NHC ligands. Calculated BDE of the NHC ligands showed a similar pattern, with BDE of NHC ligands in the SI*t*Bu-, Si*t*Bu- and IAd-based $[Ni(CO)_3(NHC)]$ complexes roughly 20 kcal/mol lower than the BDEs of the NHC ligand in the IMes, SIMes, IPr, SIPr and ICy complexes. Furthermore, the calculated BDE of the NHC ligand in $[Ni(CO)_2(ItBu)]$ and $[Ni(CO)_2(IAd)]$ (46.5 and 44.3 kcal/mol, respectively) are in excellent agreement with the experimental values (43 ± 3 and 39 ± 3 kcal/mol, respectively). The BDE values were experimentally tested by treatment of $[Ni(CO)_2(ItBu)]$ with one equivalent of IAd [Equation (6)]. Quantitative formation of $[Ni(CO)_2(IAd)]$ was observed with no detection of the saturated, but sterically disfavored, $[Ni(CO)_2(IAd)(ItBu)]$ species.

$$Ni(ItBu)(CO)_2 + IAd \rightleftharpoons Ni(IAd)(CO)_2 + ItBu \quad (6)$$

In view of the wing-span model seen to describe the steric influence of NHC ligands for palladium (see above), we have now used DFT-optimized geometry studies to extend this model for a greater number of free NHC ligands and again positioned a putative metal atom at 2 Å from the coordinating C atom. The volume as a sphere centered on the metal was measured, buried by overlap with atoms of the various NHC ligands, $\%V_{Bur}$. The volume of this sphere represented the space around the metal atom that must be shared by the different ligands upon coordination. For example bulkier NHC ligands require a larger occupied sphere volume ($\%V_{Bur}$). A list of $\%V_{Bur}$ values is presented in Table 3. The rather different values of $\%V_{Bur}$ between the

 © 2005 Wiley-VCH Verlag GmbH & Co. KGaA, Weinheim

NHC ligands is in qualitative agreement with the different BDEs we calculated.

Unlike data obtained for NHC, the similar carbonyl values for the phosphane-based systems (Table 3) clearly indicated that the steric factor's influence is insignificant in determining the stability of the $[Ni(CO)_3(PR_3)]$ systems. Furthermore, comparison of the BDE of the CO values between the less bulkier NHC systems and the phosphane systems suggest a high stability of the phosphane-based tricarbonyl complexes. The remarkably higher BDE of the NHC–Ni systems vs. the BDE of the PR_3-Ni complexes is in good agreement that NHC ligands bind more tightly to transition metals.

Since the difference between $[Ni(CO)_3(NHC)]$ and $[Ni(CO)_2(NHC)]$ complexes was attributed to steric factors alone, a substitution reaction between $[Ni(CO)_2(NHC)]$ (I*t*Bu, IAd) and two equivalents of smaller NHC ligands, IMes and ICy, afforded the saturated complexes of general composition $[Ni(CO)_2(NHC)_2]$.[53] Other reactions showed that substitution of one carbonyl ligand when reacting $[Ni(CO)_2(NHC)]$ with trifluoropropene was possible and selectively afforded the unsaturated $[Ni(NHC)(CO)(C_3H_3F_3)]$ compound [Equation (7)]. Furthermore both CO ligands were displaced when $[Ni(CO)_2(NHC)]$ was treated with either allyl chloride or allyl bromide [Equation (8)]. The resulting allyl halide complexes of general formula $[NiX(C_3H_5)(NHC)]$ were obtained through oxidative addition of these substrates to the Ni^0 center.[49]

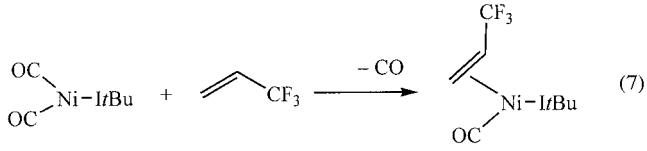

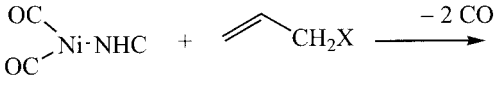

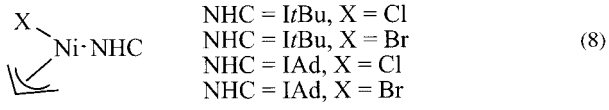

Overall, the performed DFT calculations on the series of $[Ni(L)(CO)_2]$ and $[Ni(L)(CO)_3]$ compounds (L = NHC, PR_3) are supported by experimental results, with the calculations showing that both $[Ni(IAd)(CO)_3]$ and $[Ni(I*t*Bu)(CO)_3]$ are inherently unstable as seen in the BDE values for both the CO and NHC ligands. The lower PR_3–Ni BDE values compared to NHC–Ni are in agreement with the common assumption that NHC ligands bind more tightly to metals. The establishment of a method to quantify the steric factors characterizing NHCs and phosphanes has at last been realized, finally enabling a direct comparison between these ligand classes. The values for the different ligands are measured as buried volume ($\%V_{bur}$). All of these values obtained are in perfect agreement with experimental data, showing that IAd and I*t*Bu are more bulky than $P(tBu)_3$ and other PR_3 and NHC ligands.

NHC Late-Transition Metal (LTM) Carbonyl Complexes

A recent study by Crabtree et al. also confirmed the stronger electron-donor properties of NHC ligands.[52] In lieu of using the synthetic approach of direct complexation of the free NHC to rhodium or iridium centers, a transmetalation reaction from the corresponding silver NHC salt to $[M(COD)Cl]_2$ (M = Rh, Ir) afforded the complexes [(TMIY)Rh(COD)Cl] [TMIY = 1,3-bis(4-tolylmethylimidazolin-2-ylidene], [(TMIY)Ir(COD)Cl] and [(IBu)Ir(COD)Cl] (IBu = 1,3-dibutylimidazolin-2-ylidene) in high yield (Scheme 6). COD was easily displaced from these complexes by CO (1 atm) to give the corresponding dicarbonyl compounds $[(TMIY)RhCl(CO)_2]$ (**18**), $[(TMIY)IrCl(CO)_2]$ (**19**) and $[(IBu)IrCl(CO)_2]$ (**20**) with CO (atm).

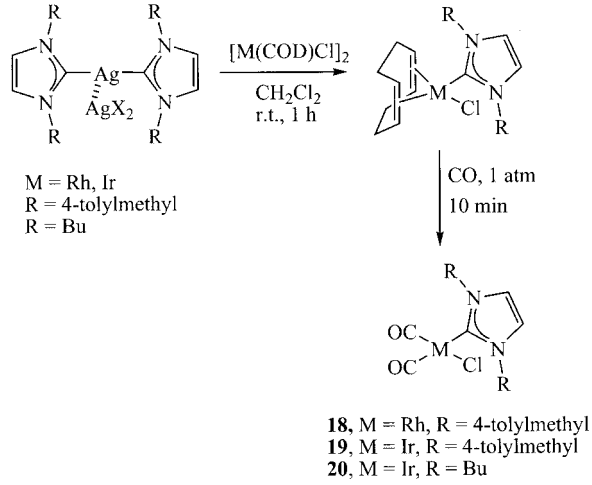

Scheme 6.

A mutually *cis* geometry of the carbonyl groups for complexes **18**–**20** was proposed despite ^{13}C NMR spectroscopy revealing two inequivalent CO carbon atoms. ^1H NMR spectroscopy supported the *cis* geometry with diastereotopic N–CH_2 protons. Low-temperature NMR studies on **18** and **19** showed that the metal–carbon bond had restricted rotation. The activation free energies for metal–carbene bond rotation in **18** and **19** [$\Delta G^{\ddagger}$(kcal·mol) 16.7 and 15.7, respectively] closely agreed to those of Doyle and Lappert[106] on **21** ($\Delta G^{\ddagger}$ = 16 kcal/mol) (Figure 7). Previous studies have strongly indicated that no electronic rotation barrier exists for NHCs. For the sterically crowded systems (**22**,[107] **23**[108] and **24**[109]) no M–C rotation at room temperature was evident. However, studies by Ender and Gielen[110] on **25** and **26** directly supported a steric origin to the rotation barrier, with **25** showing no rotation at room temperature, whereas a lower rotational barrier was observed for **26**.

 © 2005 Wiley-VCH Verlag GmbH & Co. KGaA, Weinheim

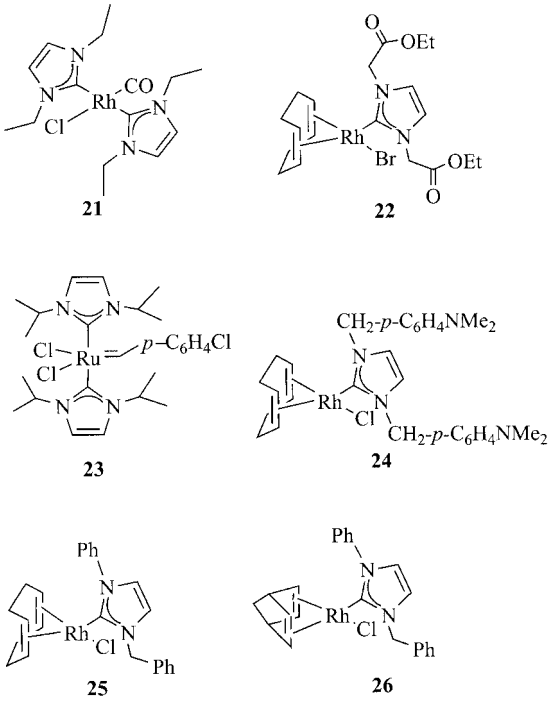

Figure 7. NHC complexes containing a low-energy rotational barrier.

Compounds **19** and **20** were investigated using FT-IR spectroscopy. A plot (Figure 8) of the average ν(CO) values for **19** and **20** together with the ν(CO) data for structurally analogous phosphane compounds $[Ir(PR_3)Cl(CO)_2]$[111,112] were plotted vs. the Tolman electronic parameter (TEP). Also included are the ν(CO) frequencies obtained for the $[Ni(CO)_3(NHC)]$ system described above. The plot shows a good linear correlation on exclusion of phosphite ligands. The IR data indicate that the NHCs listed are more electron donating than even the most basic phosphane ligand. This correlates well to other studies by Crabtree,[113] and with our own studies on $[Ni(CO)_x(NHC)]$ (x = 2,3) systems, in addition to the already discussed calorimetric investigation on ruthenium–NHC compounds.[90] Furthermore, a qualitative comparison of IR data obtained with our rhodium–NHC compound also supports this conclusion.[114]

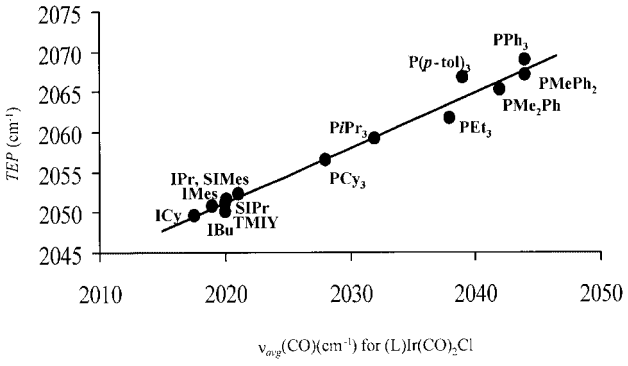

Figure 8. Plot of average ν_{CO} for $LIr(CO)_2Cl$ (L = NHC, PR_3) vs. ν_{CO} for $LNi(CO)_3$, the Tolman electronic parameter (TEP).

Abnormal Binding Modes for NHC Ligands

There have been an increasing number of reports of unexpected late-transition metal products with NHC ligands ranging from unusual binding modes to oxidative addition through C–H bond activation of alkyl side-arm substituents suggesting that these spectator ligands are much less innocent than originally thought. While previous examples in this review show normal metal binding at C-2 (Figure 9, **I**), abnormal C-5(4) (Figure 9, **II**) binding has now been reported.[115–118] The C-5(4) binding mode was previously considered as an unlikely binding possibility because free carbenes isolated by Arduengo et al.[119] always adopted a C-2 binding mode (Figure 9, **III**) with adjacent nitrogen atoms considered as stabilizing both the free carbene (Figure 9, **I**) and the M–C bond.

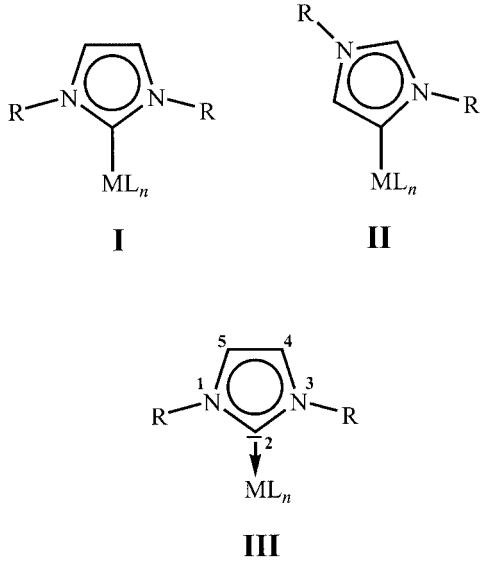

Figure 9. Alternative binding modes of NHC.

Nonclassical carbene formation has been obtained initially from mixing pyridine-substituted imidazolium salts (py-NHC) with $[IrH_5(PPh_3)_2]$ in refluxing C_6H_6. Subsequent loss of H_2 afforded complexes of general composition $[(py\text{-}NHC)IrH_3(PPh_3)_2]$ in moderate yield [Equation (9)].[115] The isolation of these first examples of C-4(5)-bound carbenes was surprising since not only **II** is more stable than **III**, but theoretical and density functional calculations[120] predict that binding at the C-4(5) position can be thermodynamically less favored (23.3 kcal/mol) than C-2 coordination.

In general, it is thought that C-4(5) binding is favored as a result of lower steric congestion around the metal center. Since the C-4(5) binding mode has only been isolated to date using limited variation in the imidazolium salts, the nature of the counterion (X = Br, BF_4, PF_6, SbF_6; R = Me, *i*Pr) was studied and indicated that it has a pronounced effect on the kinetic activity of C-2 vs. C-5(4) binding switching the kinetic product between **27** and **28** [Equation (9)]. The use of bromide afforded almost quantitative yields of C-2-bound iridium(III) NHC product **27**, while SbF_6 re-

 © 2005 Wiley-VCH Verlag GmbH & Co. KGaA, Weinheim

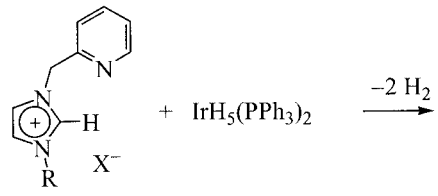

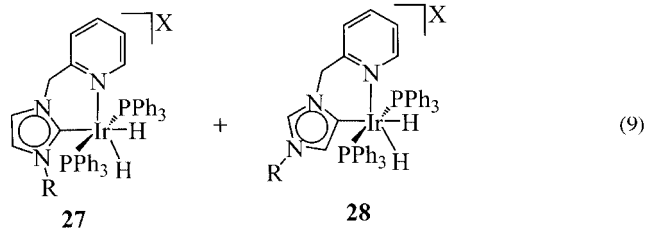

(9)

sulted in the formation of the abnormal C-4(5)-bound **28** as the major product.[121]

Until recently C-4(5) binding was only linked to chelating N-heterocyclic carbenes, and as a result it was reasoned to be mainly due to steric effects.[116] Lebel et al. recently isolated a [(IMes)(IMes′)$PdCl_2$] complex containing both C-2 and C-4(5) NHC ligands in high yield by reaction of palladium(II) acetate and the imidazolium salt IMes·HCl [Equation (10)] under standard reaction conditions (dioxane, 80 °C, 6 h).[118] In comparison, the C-2 ligated [$(IMes)_2PdCl_2$] could be obtained from $PdCl_2$, Cs_2CO_3, and 2 equivalents of IMes·HCl in high yield. However, complex **29** was found to have greater catalytic activity for Suzuki–Miyaura and Heck coupling reactions suggesting that this binding mode results in complexes with enhanced reactivity.

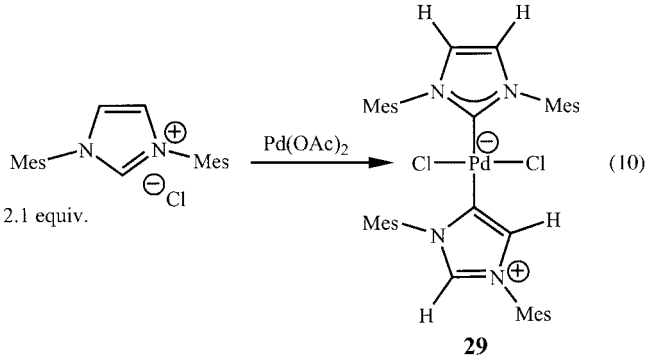

(10)

Recent studies by Crabtree et al.[117] on the electronic and steric properties of this abnormal C-4(5) coordination mode for a series of NHCs (in which the C-2 position has been blocked in one case) have allowed a useful comparison between the abnormal to the normal binding modes. Monodentate abnormal NHC iridium(III) complexes **30** and **31** were synthesized by refluxing their corresponding simple unsymmetrical imidazolium salts, pyridine and [$IrH_5(PPh_3)_2$] in tetrahydrofuran (Figure 10).

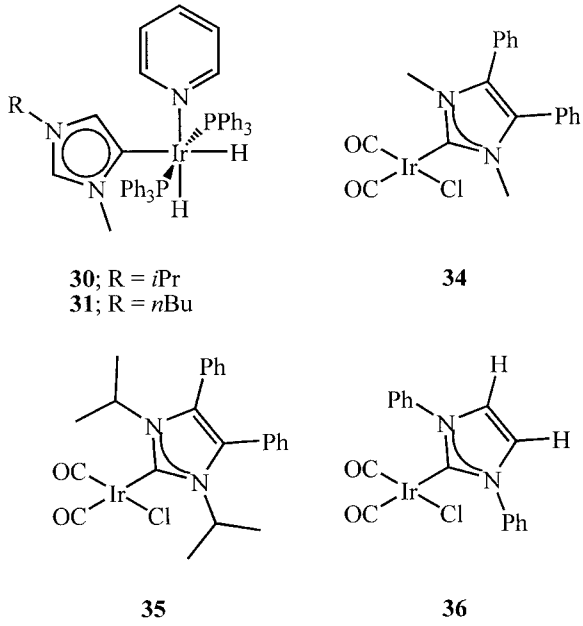

Figure 10. Monodentate abnormal (**30**, **31**) and normal (**34**–**36**) iridium complexes.

A more sophisticated route was developed by blocking the C-2 and C-4(5) positions with a phenyl group [NHC = 1-isopropyl-3-methyl-4,5-diphenylimidazolin-2-ylidene (PMINHC)] to generate the C-4(5) metal complex.[117] A transmetalation reaction between the silver salt of PMINHC and [$(COD)IrCl]_2$ resulted in the C-4(5)-bound complex [(PMINHC)Ir(COD)Cl] (**32**). Reaction of **32** with CO yielded [$(NHC)Ir(CO)_2Cl$] (**33**) (Scheme 7).

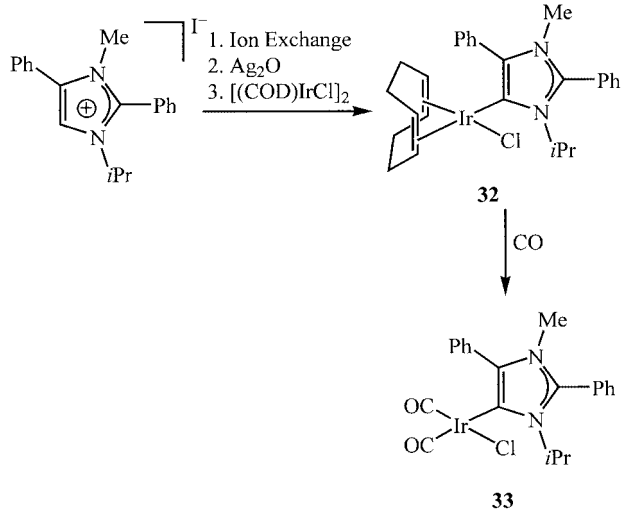

Scheme 7.

A plot of the IR ν(CO) measurements on the abnormal C-4(5)-bound derivative **33** (Figure 11) indicated that the NHC is substantially more electron donating than C-2-bound analogues (**34**–**36**, Figure 12) in addition to ν(CO) data for the [$(NHC)Ni(CO)_3$] system described above.[49] However, more data is clearly warranted to quantify the stronger donor properties of this C-4(5)-bound carbene.

 © 2005 Wiley-VCH Verlag GmbH & Co. KGaA, Weinheim

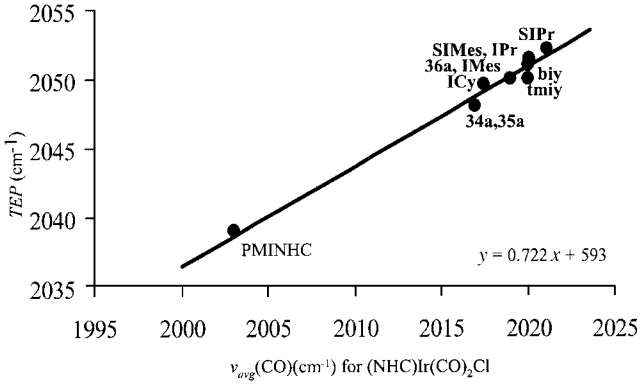

Figure 11. Plot of average ν_{CO} for (NHC)Ir(CO)$_2$Cl vs ν_{CO} for (NHC)Ni(CO)$_3$, the Tolman electronic parameter (TEP).

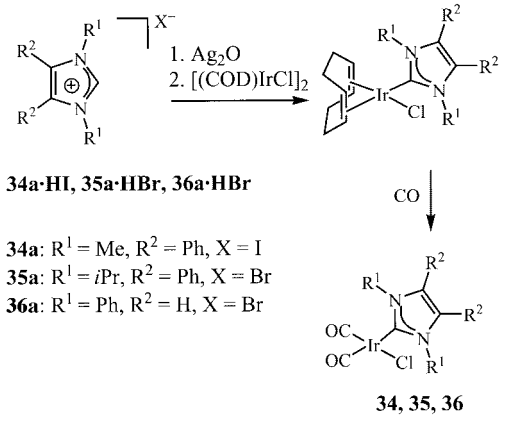

Figure 12. Preparation of (NHC)Ir(I) dicarbonyl complexes.

NHCs with late-transition metals have been found to undergo facile intramolecular C–H bond activation,[114,122–130] and in one example reported by Whittlesey et al. under more forcing conditions C–C bond activation.[131] In all but three of these cases, *N*-substituted phenyl and mesityl groups were present. Herrmann[132] has reported that ICy undergoes C–H bond cleavage by [(Cp*)IrCl$_2$]$_2$ (Cp* = η^5-C$_5$Me$_5$) [β-hydride elimination resulted in the rapid formation of 1-(2-cyclohexenyl)-3-cyclohexylimidazol-2-ylidene (L′) with no direct activation product observed (**IV**)] affording [Cp*(L′)IrH]$^+$(OSO$_2$CF$_3^-$) (**37**) [Equation (11)].

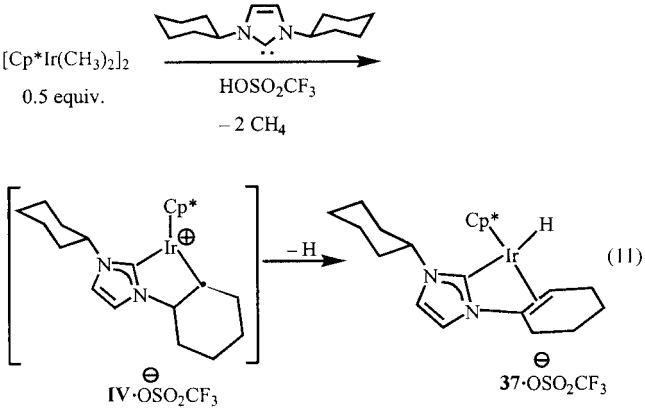

We have very recently described[45] the solvent-selective interaction of I*t*Bu [I*t*Bu = *N*,*N*-di(*tert*-butyl)imidazol-2-ylidene] with [Rh(COE)Cl]$_2$ (COE = *cis*-cyclooctene), which resulted in the isolation of [Rh(COE)(I*t*Bu)Cl] (**38**) as well as two precursors, [Rh(H)Cl(I*t*Bu′)(I*t*Bu)] (**39**) and [Rh(I*t*Bu′)$_2$Cl] (**40**), en route to a unique product by a double cyclometalation process. Analogous reactions with [Ir(COE)Cl]$_2$ led exclusively to the two *en route* precursors [Ir(H)Cl(I*t*Bu′)(I*t*Bu)] (**41**) and [Ir(I*t*Bu′)$_2$Cl] (**42**) with no observation of a [Ir(COE)(I*t*Bu)Cl]$_2$ species using hydrocarbon solvents (Scheme 8).[47] Abstraction of the chloride ion from [M(I*t*Bu′)$_2$Cl] (**40**, **42**) allowed the preparation of the unprecedented "naked" *cis*-divacant four coordinate 14-electron d^6-ML$_4$ Rh^{III} and Ir^{III} complexes of the type [M(I*t*Bu′)$_2$](PF$_6$) [M = Rh (**43**), Ir (**44**)]. These compounds are neither stabilized by agostic interactions, nor by a change in spin state as observed very recently by Caulton et al. for a Ru^{II} compound.[133] Interestingly, the chloride containing 16-electron precursors (**40**, **42**) give complexes that are stabilized by agostic interactions.

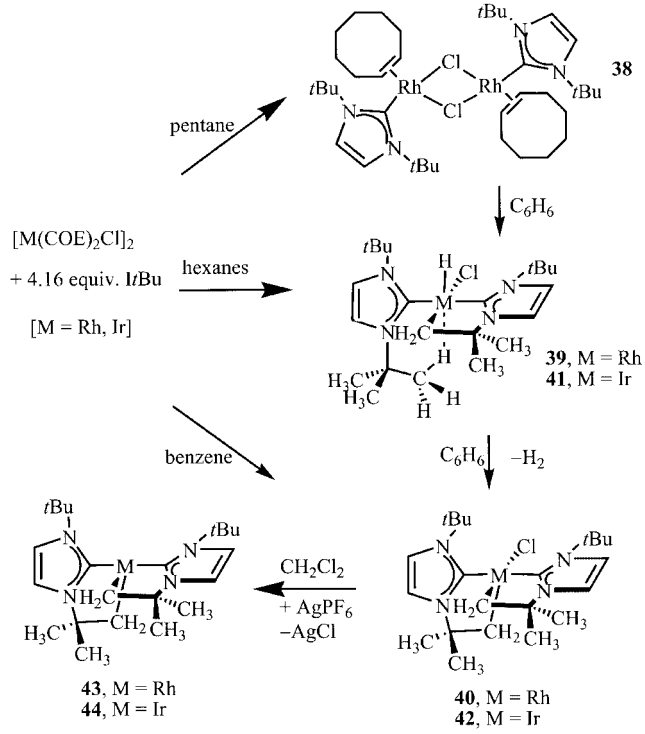

Scheme 8.

Further examination of the coordinatively unsaturated cationic 14-electron complexes [Rh(I*t*Bu′)$_2$]PF$_6$ (**43**) and [Ir(I*t*Bu′)$_2$]PF$_6$ (**44**) and of their neutral 16-electron analogues RhCl(I*t*Bu′)$_2$ (**40**) and IrCl(I*t*Bu′)$_2$ (**42**) by the small linear CO ligand generated the six-coordinate saturated complexes and as a result confirmed the unsaturated nature of the "precursor" complexes **40, 42**–**44** (Scheme 9).

The unusual stability of the unsaturated [M(I*t*Bu′)$_2$Cl] and [M(I*t*Bu′)$_2$](PF$_6$) compounds was attributed to the elec-

 © 2005 Wiley-VCH Verlag GmbH & Co. KGaA, Weinheim

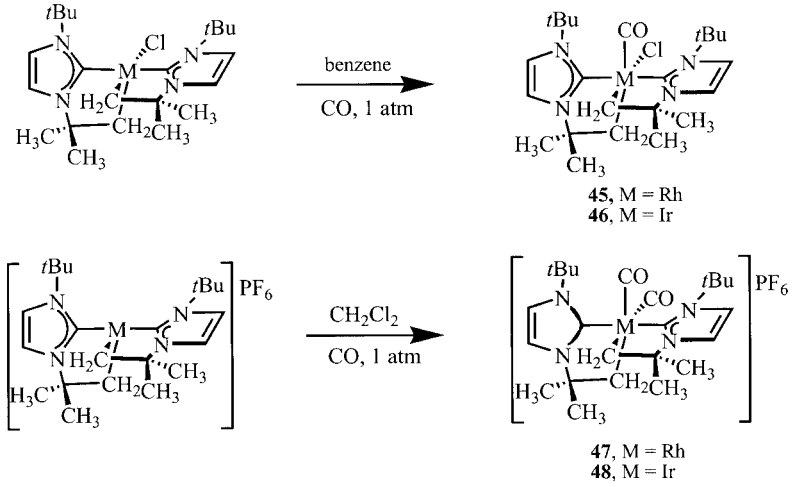

Scheme 9.

tron-donating nature of the all carbon-based NHC ligands surrounding the metals. Detailed DFT studies suggested that not only NHC ligands are simple σ donors but the π orbitals on the NHC ring can be deeply involved in the bonding of the metal. A similar finding was recently published by Meyer,[134] where NHCs were found to accept electron density from electron-rich metals through a d-π* back-donation scheme. Conversely, our study indicates that NHCs can also donate electron density to electron-poor metal atoms through a π-d donation scheme. The stabilization offered through this flexibility might certainly have important implications in catalysis explaining perhaps slower decomposition of catalytically active highly unsaturated species and increased thermal stability in comparison to analogous LTM-PR_3 systems.

Whittlesey and co-workers recently described a rare example of C–H bond activation of an alkyl-substituted N-heterocyclic carbene by thermolysis of $[Ru(IEt_2Me_2)(PPh_3)_2(CO)H_2]$ [IEt_2Me_2 = 1,3-bis(ethyl)-4,5-dimethylimidazol-2-ylidene] (**48**) in the presence of CH_2=$CHSiMe_3$

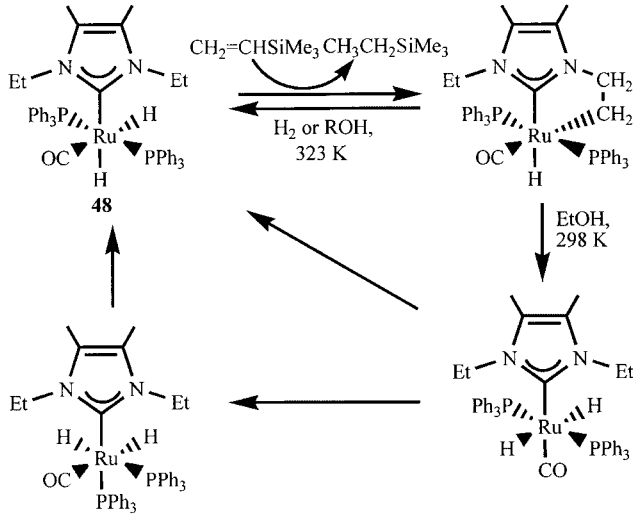

Scheme 10.

(Scheme 10).[135] The process interestingly proved to be reversible by H_2 or alcohols to afford different isomers of the starting dihydride complex.

Conclusions

The unique stabilization of coordinatively unsaturated metal centers by N-heterocyclic carbene ligands has now become well recognized. Many of these complexes have been shown to catalyze a variety of organic transformations through the stabilization of low-valent metal species. It is now evident from thermochemical, structural and infrared studies studies that NHCs are more electron donating and sterically more demanding than the most basic/bulky phosphane ligands. As a result, the stabilization of many reactive intermediates, which have been elusive so far in phosphane chemistry, has helped elucidate the precise effects of the NHC ligand in catalytic systems. Furthermore the versatility of NHCs has only begun to be realized with C-2 vs. abnormal C-4(5) binding modes possible in addition to facile intramolecular C–H activation of the nitrogen substituents with LTM. In this report, we have presented a short illustration of a selected number of important observations dealing with NHCs, it is our belief that this ligand family will continue to surprise.

Acknowledgments

The National Science Foundation is gratefully acknowledged for financial support of this work.

[1] H. Staudinger, O. Kupfer, *Ber. Dtsch. Chem. Ges.* **1912**, *45*, 501.
[2] J. Wallach, *Ber. Dtsch. Chem. Ges.* **1925**, 15, 645.
[3] H. W. Wanzlick, H. J. Kleiner, *Angew. Chem.* **1961**, *73*, 493.
[4] H. W. Wanzlick, H. J. Kleiner, *Angew. Chem. Int. Ed. Engl.* **1962**, *1*, 75–80.
[5] H. W. Wanzlick, F. Esser, H. J. Kleiner, *Chem. Ber.* **1963**, *96*, 1208.
[6] D. Bourissou, O. Guerret, F. P. Gabbaï, G. Bertrand, *Chem. Rev.* **2000**, *100*, 39–91.

 © 2005 Wiley-VCH Verlag GmbH & Co. KGaA, Weinheim

[7] W. A. Herrmann, C. Köcher, *Angew. Chem. Int. Ed. Engl.* **1997**, *36*, 2162–2187.
[8] A. Berndt, *Angew. Chem. Int. Ed. Engl.* **1993**, *32*, 985–1009.
[9] M. Regitz, *Angew. Chem. Int. Ed. Engl.* **1996**, *35*,725–728.
[10] A. J. Arduengo III, R. Krafczyk, *Chem. Ztg.* **1998**, *32*, 6–14.
[11] T. Weskamp, V. P. W. Böcher, W. A. Herrmann, *J. Organomet. Chem.* **2000**, *600*, 12–22.
[12] L. Jafarpour, S. P. Nolan, *Adv. Organomet. Chem.* **2001**, *46*, 181–222.
[13] C. M. Crudden, D. P. Allen, *Coord. Chem. Rev.* **2004**, *248*, 2247–2273.
[14] T. Weskamp, W. C. Schattenmann, M. Spiegler, W. A. Herrmann, *Angew. Chem. Int. Ed.* **1998**, *37*, 2490–2493.
[15] J. Huang, E. D. Stevens, S. P. Nolan, J. L. Petersen, *J. Am. Chem. Soc.* **1999**, *121*, 2674–2678.
[16] M. Scholl, S. Ding, C. W. Lee, R. H. Grubbs, *Org. Lett.* **1999**, *1*, 953–956.
[17] L. Jafarpour, S. P. Nolan, *J. Organomet. Chem.* **2001**, *617*, 17–27.
[18] T. M. Trnka, R. H. Grubbs, *Acc. Chem. Res.* **2001**, *34*, 18–29.
[19] A. Fürstner, *Angew. Chem. Int. Ed.* **2000**, *39*, 3013–3043.
[20] L. D. Vasquez-Serrano, B. T. Owens, J. M. Buriak, *Chem. Commun.* **2002**, 2518–2519.
[21] H. M. Lee, T. Jiang, E. D. Stevens, S. P. Nolan, *Organometallics* **2001**, *20*, 1255–1258.
[22] A. C Hillier,H. M. Lee, E. D. Stevens, S. P. Nolan, *Organometallics* **2001**, *20*, 4246–4252.
[23] L. D.Vasquez-Serrano, B. T. Owens, J. M. Buriak, *Chem. Commun.* **2002**, 2518–2519.
[24] I. E. Markò, S. Stérin, O. Buisine, G. Mignani, P. Branlard, B. Tinant, J.-P. Declerq, *Science* **2002**, *298*, 204–207.
[25] G. A. Grasa, M. S. Viciu, J. Huang, S. P. Nolan, *J. Org. Chem.* **2001**, *66*, 7729–7737.
[26] G. A. Grasa, M. S. Viciu, J. Huang, C. Zhang, M. L. Trudell, S. P. Nolan, *Organometallics* **2002**, *21*, 2866–2873.
[27] M. S. Viciu, R. F. Germaneau, S. P. Nolan, *Org. Lett.* **2002**, *4*, 4053–4056.
[28] O. Navarro, R. A. Kelly III, S. P. Nolan, *J. Am. Chem. Soc.* **2003**, *125*, 16194–16195.
[29] J. P. Collman, L. S. Hedegus, J. R. Norton, R. G. Finke, *Principles and Applications of Organotransition Metal Chemistry*, 2nd ed; University Science: Mill Valley, CA, **1987**.
[30] K. Denk, P. Sirsch, W. A. Herrmann, *J. Organomet. Chem.* **2002**, *649*, 219–224.
[31] L. H. Pignolet (Ed.), *Homogeneous Catalysis with Metal Phosphine Complexes*, Plenum: New York, **1983**.
[32] G. W. Parshall, S. Ittel, *Homogeneous catalysis*; John Wiley & Sons: New York, **1992**.
[33] T. Weskamp, F. J. Kohl, W. Hieringer, D. Gleich, W. A. Herrmann, *Angew. Chem. Int. Ed.* **1999**, *38*, 2416–2419.
[34] J. Huang, L. Jafarpour, A. C. Hillier, E. D. Stevens, S. P. Nolan, *Organometallics* **2001**, *20*, 2878–2882.
[35] A. R. Chianese, X. Li, M. C. Janzen, J. W. Faller, R. H. Crabree, *Organometallics* **2003**, *22*, 1663–1667.
[36] J. Huang, H.-J. Schanz, E. D. Stevens, S. P. Nolan, *Organometallics* **1999**, *18*, 2370–2375.
[37] S. T. Liu, R. Z. Ku, L. Y. Liu, F. M. Kiang, *J. Organomet. Chem.* **1997**, *543*, 249.
[38] D. S. Clyne, J. Jin, E. Genest, J. C. Gallucci, T. V. RajanBabu, *Org. Lett* **2000**, *2*, 1125–1128.
[39] M. T. Powell, D, R. Hou, M. C. Perry, X. H. Cui, K. Burgess, *J. Am. Chem. Soc.* **2001**, *123*, 8878–8879.
[40] M. Albrecht, J. R. Miecznikowski, A. Samuel, J. W. Faller, R. H. Crabtree, *Organometallics* **2002**, *21*, 3596–3604.
[41] I. E. Mehlhofer, T. Stressner, W. A. Herrmann, *Angew. Chem. Int. Ed* **2002**, *41*, 1745–1747.
[42] J. A. Loch, M. Albrecht, E. Peris, J. Mata, J. W. Faller, R. H. Crabtree, *Organometallics* **2002**, *21*, 700–706.
[43] M. S. Vicui, F. K. Zinn, E. D. Stevens, S. P. Nolan, *Organometallics* **2003**, *22*, 3175–3177.
[44] M. Poyatos, E. Mas-Marza, J. A. Mata, M. Sanau, E. Peris, *Eur. J. Inorg. Chem.* **2003**, 1215–1221.
[45] R. Dorta, E. D. Stevens, S. P. Nolan, *J. Am. Chem. Soc.* **2004**, *126*, 5054–5055.
[46] R. Dorta, E. D. Stevens, C. D. Hoff, S. P. Nolan, *J. Am. Chem. Soc.* **2003**, *125*, 10490–10491.
[47] N. M. Scott, R. Dorta, E. D. Stevens, A. Correa, L. Cavallo, S. P. Nolan, *J. Am. Chem. Soc.* **2005**, *127*, 3516–3526.
[48] C. A. Tolman, *Chem. Rev.* **1977**, *77*, 313–324.
[49] R. Dorta, E. D. Stevens, N. M. Scott, C. Costabile, L. Cavallo, C. D. Hoff, S. P. Nolan, *J. Am. Chem. Soc.* **2005**, *127*, in press.
[50] M. S. Viciu, O. Navarro, R. F. Germaneau, R. A. Kelly III, W. Sommer, N. Marion, E. D. Stevens, L. Cavallo, S. P. Nolan, *Organometallics* **2004**, *23*, 1629–1635.
[51] R. A. Diggle, S. A. Macgregor, M. K. Whittlesey, *Organometallics* **2004**, *23*, 1857–1865.
[52] A. R. Chianese, X. Li, M. C. Janzen, J. W. Faller, R. H. Crabtree, *Organometallics* **2003**, *22*, 1663–1667.
[53] P. Mahjoor, N. M. Scott, E. D. Stevens, S. P. Nolan, manuscript in preparation.
[54] L. Jafarpour, S. P. Nolan, *Organometallics* **2000**, *19*, 2055–2057.
[55] P. Schwab, M. B. France, J. W. Ziller, *Angew. Chem. Int. Ed. Engl.* **1995**, *34*, 2039–2041.
[56] P. Schwab, R. H. Grubbs, R. H. Ziller, *J. Am. Chem. Soc.* **1996**, *118*, 100–110.
[57] E. L. Diaz, S. T. Nyugen, R. H. Grubbs, *J. Am. Chem. Soc.* **1997**, *119*, 3887–3897.
[58] R. R. Schrock, J. Murdzeck, G. C. Bazan, J. Robbins, M. DiMare, M. O'Regan, *J. Am. Chem. Soc.* **1990**, *112*, 3875–3886.
[59] A. Briot, M. Bujard, V. Gouverneur, S. P. Nolan, C. Mioskowski, *Org. Lett.* **2000**, *2*, 1517–1519.
[60] L. Jafarour, S. P. Nolan, *Org. Lett.* **2000**, *2*, 4075–4078.
[61] R. Dorta, R. A. Kelly III, S. P. Nolan, *Adv. Synth. Catal.* **2004**, *346*, 917–920.
[62] P. J. Fagan, M. D. Ward, J. V. Caspar, J. C. Calabrese, P. J. Krusic, *J. Am. Chem. Soc.* **1988**, *110*, 2981–2983.
[63] B. K. Campion, R. H. Heyn, T. D. Tilley, *J. Chem. Soc., Chem. Commun.* **1988**, 278–280.
[64] L. Ackermann, A. Fürstner, T. Weskamp, F. J. Kohl, W. A. Herrmann, *Tetrahedron Lett.* **1999**, *40*, 4787–4790.
[65] D. S. McGuiness, M. J. Green, K. J. Cavell, B. W. Skelton, A. H. White, *J. Organomet. Chem.* **1998**, *565*, 165–178.
[66] W. A. Herrmann, M. Elison, J. Fischer, C. Köcher, G. R. J. Artus, *Angew. Chem. Int. Ed. Engl.* **1995**, *34*, 2371–2374.
[67] D. S. McGuiness, K. J. Cavell, B. W. Skelton, A. H. White, *Organometallics* **1999**, *18*, 1596–1605.
[68] K. Selvakumar, A. Zapf, A. Spannerberg, M. Beller, *Chem. Eur. J.* **2002**, *8*, 3901–3906.
[69] K. Selvakumar, A. Zapf, M. Beller, *Org. Lett.* **2002**, *4*, 3031–3033.
[70] R. Jackstell, M. G. Andreu, A. Frisch, K. Selvakumar, A. Zapf, H. Klein, A. Spannenberg, D. Röttger, O. Briel, R. Karch, M. Beller, *Angew. Chem. Int. Ed.* **2002**, *41*, 986–989.
[71] R. Jackstell, A. Frisch, M. Beller, D. Rottger, M. Malaun, B. Bildtein, *J. Mol. Catal. (A)* **2002**, *185*, 105–112.
[72] C. Zhang, J. Huang, M. L. Trudell, S. P. Nolan, *J. Org. Chem.* **1999**, *64*, 3804–3805.
[73] H. Lee, S. P. Nolan, *Org. Lett.* **2000**, *2*, 2053–2055.
[74] C. W. K. Gstöttmayr, V. P. W. Böhm, E. Herdtweck, M. Grosche, W. A. Herrmann, *Angew. Chem. Int. Ed.* **2002**, *41*, 1363–1365.
[75] W. A. Herrmann, C.-P. Reisinger, M. Spiegler, *J. Organomet. Chem.* **1998**, *557*, 93–96.
[76] S. R. Stauffer, S. W. Lee, J. P. Stambuli, S. I. Hauck, J. F. Hartwig, *Org. Lett.* **2000**, *2*, 1423–1426.
[77] S. P. Stambuli, M. Buhl, J. F. Hartwig, *J. Am. Chem. Soc.* **2002**, *124*, 9346–9347.
[78] S. Caddick, F. G. N. Cloke, P. B. Hitchcock, J. Leonard, A. K. de K. Lewis, D. McKerrecher, L. R. Titcomb, *Organometallics* **2002**, *21*, 4318–4319.

 © 2005 Wiley-VCH Verlag GmbH & Co. KGaA, Weinheim

[79] J. Huang, G. Grasa, S. P. Nolan, *Org. Lett.* **1999**, *1*, 1307–1309.
[80] J. F. Hartwig, *Angew. Chem. Int. Ed.* **1998**, *37*, 2046- 2067.
[81] J. Louie, P. F. Hartwig, *Organometallics* **1996**, *15*, 2794–2805.
[82] C. Amatore, A. Jutand, *Acc. Chem. Res.* **2000**, *33*, 314–321.
[83] A. K. de K. Lewis, Caddick, F. G. N. Cloke, N. C. Billingham, P. B. Hitchcock, J. Leonard, *J. Am. Chem. Soc.* **2003**, *125*, 10066–10073.
[84] P. A. Arnold, F. G. N. Cloke, T. Geldbach, P. B. Hitchcock, *Organometallics* **1999**, *18*, 3228–3233.
[85] V. P. W. Böhm, C. W. K. Gstöttmayr, T. Weskamp, W. A. Herrmann, *J. Organomet. Chem.* **2000**, *595*, 186–190.
[86] S. Caddick, F. G. N. Cloke, C. K. B. Clentssmith, P. B. Hitchcock, D. McKerrecher, L. R. Titcomb, M. R. V. Williams, *J. Organomet. Chem.* **2001**, *617–618*, 635–639.
[87] L. R. Titcomb, S. Caddick, F. G. N. Cloke, D. J. Wilson, D. McKerrecher, *Chem. Commun.* **2001**, 1388–1389.
[88] C. W. K. Gstöttmayr, V. P. W. Böhm, E. Herdtweck, M. Grosche, W. A. Herrmann, *Angew. Chem. Int. Ed.* **2002**, *41*, 1363–1365.
[89] G. M. DiRenzo, P. S. White, M. Brookhart, *J. Am. Chem. Soc.* **1996**, *118*, 6225–6234.
[90] A. C. Hillier, W. J. Sommer, B. S. Yong, J. L. Peterson, L. Cavallo, S. P. Nolan, *Organometallics* **2003**, *22*, 4322–4326.
[91] R. Dorta, E. D. Stevens, C. D. Hoff, S. P. Nolan, *J. Am. Chem. Soc.* **2003**, *125*, 10490–10491.
[92] W. A. Herrmann, M. Elison, J. Fischer, C. Kocher, G. R. Artus, *Angew. Chem. Int. Ed. Engl.* **1995**, *34*, 2371–2374.
[93] S. Caddick, F. G. N. Cloke, P. B. Hitchcock, A. K. de K. Lewis, *Angew. Chem. Int. Ed* **2004**, *43*, 5824–5827.
[94] S. Kuhl, R. Schneider, Y. Fort, *Organometallics* **2003**, *22*, 4184–4186.
[95] A. J. Arduengo III, S. F. Gamper, J. C. Calabrese, F. Davidson, *J. Am. Chem. Soc.* **1994**, *116*, 4391–4394.
[96] W. Petz, F.Weller, J. Uddin, G. Frenking, *Organometallics* **1999**, *18*, 619–626.
[97] G. Wilke, *Angew. Chem. Int. Ed. Engl.* **1963**, *2*, 105–108.
[98] B. Bogdanovic, M. Kroener, G. Wilke, *Justus Liebigs Ann. Chem.* **1966**, *699*, 1–23.
[99] L. W. Gosser, C. A. Tolman, *Inorg. Chem.* **1970**, *9*, 2350–2353.
[100] K. Jonas, P. Heimbach, G. Wilke, *Angew. Chem. Int. Ed. Engl. A* **1968**, *7*, 949–950.
[101] B. Gabor, K. Krueger, B. Marczinke, R. Mynott, G. Wilke, *Angew. Chem. Int. Ed. Engl.* **1991**, *30*, 1666–1668.
[102] D. J. Mindiola, G. L. Hillhouse, *J. Am. Chem. Soc.* **2002**, *124*, 9976–9977.
[103] M. Brookhart, M. L. H. Green, L. Wong, *Prog. Inorg. Chem.* **1988**, *36*, 1–124.
[104] R. H. Crabtree, *Angew. Chem. Int. Ed. Engl.* **1993**, *32*, 789–805.
[105] The experimental design of the FTIR cell has previously been described: B. R.Bender, G. J. Kubas, L. H. Jones, B. I. Swanson, J. Eckert, K. B. Capps, C. D. Hoff, *J. Am. Chem. Soc.* **1997**, *119*, 9179–9190.
[106] M. J. Doyle, M. F. Lappert, *J. Chem. Soc.*, *Chem. Commun.* **1974**, 679–680.
[107] W. A. Herrmann, L. J. Goosen, M. J. Spiegler, *J. Organomet. Chem.* **1997**, *547*, 357–366.
[108] T. Weskamp, W. C. Schattenmann, M. Spiegler, W. A. Herrmann, *Angew. Chem. Int. Ed.* **1998**, *37*, 2490–2493.
[109] I. Özdemir, B. Yigit, B. Çetinkaya, D. Ülkü, M. N. Tahir, C. Arici, *J. Organomet. Chem.* **2001**, *633*, 27–32.
[110] D. Enders, H. Gielen, *J. Organomet. Chem.* **2002**, *617/618*, 70–80.
[111] D. E. Morris, H. B. Tinker, U. S. Patent 3948962. **1976**.
[112] W. Z. Chen, M. A. Esteruelas, M. Martin, M. Oliván, L. A. Oro, *J. Organomet. Chem.* **1997**, *534*, 95–103.
[113] L. Perrin, E. Clot, O. Eisenstein, J. Loch, R. H. Crabtree, *Inorg. Chem.* **2001**, *40*, 5806–5811.
[114] J. Huang, E. D. Stevens, S. P. Nolan, *Organometallics* **2000**, *19*, 1194–1197.
[115] S. Gründemann, A. Kovacevic, M. Albrecht, J. W. Faller, R. H. Crabtree, *Chem. Commun.* **2001**, 2274–2275.
[116] S. Gründemann, A. Kovacevic, M. Albrecht, J. W. Faller, R. H. Crabtree, *J. Am. Chem. Soc.* **2002**, *124*, 10473–10481.
[117] A. R. Chianese, A. Kovacevic, B. M. Zeglis, J. W. Faller, R. H. Crabtree, *Organometallics* **2004**. *23*, 2461–2468.
[118] H. Lebel, M. K. Janes, A. B. Charette, S. P. Nolan, *J. Am. Chem. Soc.* **2004**, *126*, 50460–5047.
[119] A. J. Arduengo, R. L. Harlow, M. Kline, *J. Am. Chem. Soc.* **1991**, *113*, 361–363.
[120] G. Sini, O. Eisenstein, R. H. Crabtree, *Inorg. Chem.* **2002**, *41*, 602–604.
[121] A. Kovaceic, S. Gründemann, J. R. Mieczikowski, E. Clot, O. Eisenstein, R. H. Crabtree, *Chem. Commun.* **2002**, 2580–2581.
[122] P. B. Hitchcock, M. F. Lappert, P. L. Pye, *J. Chem. Soc., Chem. Commun.* **1976**, 644–646.
[123] P. B. Hitchcock, M. F. Lappert, P. L. Pye, *J. Chem. Soc., Chem. Commun.* **1977**, 196–198.
[124] P. B. Hitchcock, M. F. Lappert, P. L. Pye, S. Thomas, *J. Chem. Soc., Dalton Trans.* **1979**, 1929–1942.
[125] P. B. Hitchcock, M. F. Lappert, O, Terreros, *J. Organomet. Chem.* **1982**, *239*, C26–C30.
[126] A. A. Danopoulos, S. Winston, M. B. Hursthouse, *J. Chem. Soc. Dalton Trans.* **2002**, 3090–3091.
[127] T. M. Trnka, J. P. Morgan, M. S. Sanford, T. E. Whiheim, M. Scholl, T.-L. Choi, S. Deng, M. W. Day, R. H. Grubbs, *J. Am. Chem. Soc.* **2003**, *125*, 2546–2558.
[128] M. J. Chilvers, R. F. R. Jazzar, M. F. Mahon, M. K. Whittlesey, *Adv. Synth. Catal.* **2003**, *345*, 1111–1114.
[129] D. Guinta, M. Hölischer, C. W. Lehmann, R. Mynott, C. Wirtz, W. Leitner, *Adv. Synth. Catal.* **2003**,*345*, 1139–1145.
[130] K. Adbur-Rashid, T. Fedorkiw, A. J. Lough, R. H. Morris, *Organometallics* **2004**, *23*, 86–94.
[131] R. F. R. Jazzar, S. A. Macgregor, M. F. Mahon, S. Richards, M. K. Whittlesey, *J. Am. Chem. Soc.* **2002**, *124*, 4944–4945.
[132] M. Prinz, M. Grosche, E. Herdtweck, W. A. Herrmann, *Organometallics* **2000**, *19*, 1692–1694.
[133] L. A. Watson, O. V. Ozerov, M. Pink, K. G. Caulton, *J. Am. Chem. Soc.* **2003**, *125*, 8426–8427.
[134] X. Hu, I. Castro-Rodriguez, K. Olsen, K. Meyer, *Organometallics* **2004**, *23*, 755–764.
[135] S. Burling, M. F. Mahon, B. M. Paine, M. K. Whittlesey, J. M. J. Williams, *Organometallics* **2004**, *25*, 4537–4539.

Received: January 11, 2005
Published Online: April 11, 2005

 © 2005 Wiley-VCH Verlag GmbH & Co. KGaA, Weinheim

Electro-Conducting Properties of Charge-Transfer Salts Based on Cationic and Anionic Platinum Dithiolenes − Crystal Structure of $[Pt(Me_2pipdt)_2][Pt(dtcr)_2]$

Paola Deplano,*[a] Maria Laura Mercuri,[a] Luciano Marchiò,[b] Luca Pilia,[a] Marco Salidu,[a] Angela Serpe,[a] Francesco Congiu,[c] and Samuele Sanna[c]

Dedicated to Prof. Emanuele F. Trogu on the occasion of his recent retirement

Keywords: Sulfur ligands / Platinum / Charge-transfer / Conducting materials

The structure/property relationship of the following CT salts, $[M(R_2pipdt)_2][M(mnt)_2]$ (where R_2pipdt = *N*,*N*′-dialkylpiperazine-2,3-dithione; mnt = maleonitrile-2,3-dithiolate), [R = Me, M = Pd (**1a**) and Pt (**2a**); R = Et, M = Pt (**2b**)],which were previously characterised, and $[Pt(R_2pipdt)_2][Pt(dtcr)_2]$ [R = Me, (**3a**); R = Et, (**3b**); dtcr = 4,5-disulfanylcyclopent-4-ene-1,2,3-trionate, known as dithiocroconate] are investigated here. These salts show strong near IR CT bands and semiconducting behaviour. The structural features of **3a** are similar to those found for **2a**: approximately square planar $[Pt(Me_2pipdt)_2]$ dications and regular square planar $[Pt(dtcr)_2]$ dianions form an infinite anion–cation one-dimensional stack along the *c* axis with a Pt···Pt *c*/2 distance of 3.408 (1) Å. In **3a**, a net of weak interactions between the N and O atoms of the cation and of the anion contributes to the alignment of **3a** in the stack. However, these interactions do not overcome the less favourable redox properties of the components, that is, promoting CT interactions with respect to the corresponding mnt salts. The specific electrical conductivity of pressed powder pellets ranges from 10^{-11} to $10^{-5}\ \Omega^{-1}cm^{-1}$ at room temperature, follows the Arrhenius law with activation energies in the range of 0.2–0.6 eV, and is related to the driving force of the electron transfer. Preliminary photoconductivity measurements performed on the two relatively more conducting samples, **2a** and **2b**, show a gain in current during illumination, similarly to that observed in organic–inorganic photoconductor CT salts $C[ML_2]$ (C^{2+} is 2,2′ or 4,4′-bipyridinium or similar derivatives, L^{2-} = dithiolato), which have been extensively investigated by the Kisch group. Crystal data for **3a**: triclinic, $P\bar{1}$; $Z = 2$; $T = 293(2)$ K; $a = 8.683(2)$ Å, $b = 14.009(5)$ Å, $c = 6.815(2)$ Å; $\alpha = 100.58(4)°$, $\beta = 98.99(3)°$, $\gamma = 100.69(3)°$. *R* indices (all data) $R1 = 0.0516$, $wR2 = 0.1412$.
(© Wiley-VCH Verlag GmbH & Co. KGaA, 69451 Weinheim, Germany, 2005)

Introduction

Among several applications in the molecular material field,[1] anionic, square planar d^8 metal bis-dithiolene complexes have been used to prepare ion-pair CT photoconducting salts of the type $\{(C^{2+})[ML_2]^{2-}\}$, (M = Ni, Pd, Pt; L^{2-} = dithiolato) where C^{2+} is a redox-active organic donor such as 4,4′ and 2,2′ bipyridinium derivatives.[2] An extensive investigation on these organic–inorganic CT salts by Kisch's group has led to an understanding of the main factors that affect the structure/property relationship. The supramolecular interaction between the ionic components is reflected by the presence of a strong CT band in the diffuse reflectance spectra of these salts, which exhibit electrical semiconducting behaviour. By applying the "Marcus-Hush model",[3] a linear correlation between thermal and optical electron transition and a linear correlation between the specific electrical conductivity and the free activation energy for the electron transfer is observed. Moreover these CT salts show interesting photoconducting properties. It has been shown that the planarity of the components and their capability to undergo minor structural changes on electron transfer are crucial factors for improving the CT interaction. Thus a rational synthesis of the desired products would allow us to tune the conductivity by a proper selection of the component ions. This prompted us to use metal dithiolenes as the two components of CT salts, extending the investigation from the largely investigated fully organic and organic–inorganic systems to the less common fully inorganic ones.[4] In fact, in d^8 metal dithiolenes the planarity of the central core is maintained by the metal atom which imposes the square planar geometry, while the electronic properties depend on the distribution of the π electrons in the $(C_2S_2)_2M$ core (14 electrons of which four

[a] Dipartimento di Chimica Inorganica ed Analitica, Università di Cagliari,
Cittadella di Monserrato, 09042 Monserrato, Cagliari, Italy
Fax: +39-070-675-4456
E-mail: deplano@unica.it
[b] Dipartimento di Chimica Generale ed Inorganica, Chimica Analitica, Chimica Fisica, Università di Parma,
Parco Area delle Scienze 17A, 43100 Parma, Italy
[c] Dipartimento di Fisica, Università di Cagliari,
Cittadella di Monserrato, 09042 Monserrato, Cagliari, Italy

belong to the metal in the uncharged complex).[5] These species have a rich redox chemistry and the nature of their most accessible status is indicative of the basic *push* or *pull* character of the ligand. The nature of the substituents at the C_2S_2 moieties determines the stabilization of the ML_2 complex with a charge that varies between +2 and –2. The latter limits are due to the fairly isolated frontier MOs (HOMO and LUMO in the uncharged complex), which have π character and can be either empty or populated. In general, C_2S_2 π-donor substituents (*push*) in symmetric complexes raise the energy of both the HOMO and the LUMO so that the former is also preferentially depopulated (cationic complexes). In contrast, π-acceptor substituents (*pull*) lower the energies of the two levels and favour an anionic state of the complex. Thus mnt complexes (mnt = maleonitrile-2,3-dithiolate, *pull* ligand) are most readily synthesized as dianions while the R_2pipdt ones (R_2pipdt = *N*,*N*′-dialkylpiperazine-2,3-dithione, *push* ligand) are synthesized as dications.[6] On the basis of the above, new CT salts $[M(R_2pipdt)_2][M(mnt)_2]$ (M = Pd and Pt) have been recently described.[7,8] In the solid state these salts show features similar to those of $(C)[ML_2]$ compounds, where the acceptors (C) do not deviate too much from planarity.[2] In this paper the dark- and photo-conducting properties of $[M(R_2pipdt)_2][M(mnt)_2]$ {[R = Me, M = Pd (**1a**) and Pt (**2a**); R = Et, M = Pt (**2b**)]}, as well as of the novel salts of $[Pt(R_2pipdt)_2][Pt(dtcr)_2]$ (R = Me, (**3a**); R = Et, (**3b**); dtcr = 4,5-disulfanylcyclopent-4-ene-1,2,3-trionate) are reported; the structural characterization of **3a** is also described. The substitution of mnt by dtcr in **3** was performed in order to investigate the influence of the different redox potentials and of the electron-rich oxo-groups of the anionic component on the properties of these CT salts.

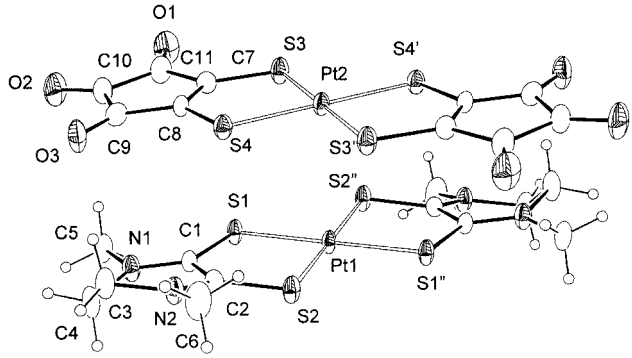

Figure 1. Ortep drawing of $[Pt(Me_2pipdt)_2][Pt(dtcr)_2]$ at the 30% probability level. (′) = –*x*, –*y*, –*z*. (″) = –*x*, –*y*, 1 – *z*.

Table 1. Selected bond lengths [Å] and angles [°] with estimated standard deviations in parentheses for $[Pt(Me_2pipdt)_2][Pt(dtcr)_2]$.

	Cation		
Pt(1)–S(1)	2.289(2)	C(1)–C(2)	1.493(9)
Pt(1)–S(2)	2.287(2)	N(1)–C(1)	1.317(9)
S(1)–C(1)	1.683(6)	N(2)–C(2)	1.311(9)
S(2)–C(2)	1.685(7)		
S(1)–Pt(1)–S(2)	88.48(6)	C(2)–N(2)–C(3)	122.1(6)
C(1)–N(1)–C(5)	123.1(6)	C(6)–N(2)–C(3)	117.1(6)
C(4)–N(1)–C(5)	115.7(7)	C(2)–N(2)–C(6)	120.2(6)
C(1)–N(1)–C(4)	121.0(6)		
	Anion		
Pt(2)–S(3)	2.312(2)	C(7)–C(8)	1.40(1)
Pt(2)–S(4)	2.309(2)	C(11)–O(1)	1.22(1)
S(3)–C(7)	1.696(8)	C(10)–O(2)	1.20(1)
S(4)–C(8)	1.705(7)	C(9)–O(3)	1.24(1)
S(4)–Pt(2)–S(3)	90.23(7)	C(7)–C(8)–C(9)	110.4(7)
C(8)–C(7)–S(3)	123.0(5)	C(9)–C(8)–S(4)	125.6(6)
C(11)–C(7)–S(3)	126.9(6)	C(7)–C(8)–S(4)	123.9(5)
C(8)–C(7)–C(11)	110.1(7)		

Results and Discussion

Preparations and Structures

$[Pt(R_2pipdt)_2][Pt(dtcr)_2]$ [where R = Me (**3a**); R = Et (**3b**)] were obtained by metathesis by treating equimolar amounts of $[Pt(R_2pipdt)_2](BF_4)_2$[7] with $(Bu_4N)_2[Pt(dtcr)_2]$[9] in CH_3CN. Crystals of **3a** suitable for X-ray characterization were grown by using a three-compartment diffusion cell, as described in the Exp. Sect.[10] A molecular drawing of the ionic complex components is depicted in Figure 1, selected bond lengths and angles are reported in Table 1.

In $[Pt(dtcr)_2]^{2-}$ and $[Pt(Me_2pipdt)_2]^{2+}$ the platinum atoms lie on inversion centres and are in a square planar geometry. They are bound by four sulfur atoms from two ligands. The complex cation and the complex anion are alternate and run parallel to the *c* crystallographic axis exhibiting a metal–metal interaction [Pt(1)–Pt(2) = 3.408(1) Å]. Despite the fact that the dtcr ligand can be formally formulated as a dithiolate, its C–S bond lengths are not significantly different from the ones observed for the dithione ligand (Me_2pipdt) in the complex cation (see Table 1). This is ascribed to a negative charge-delocalization on the oxo groups of the ligand (see Scheme 1). In fact, the C(9)–O(3) and C(11)–O(1) bonds are significantly longer than the C(10)–O(2) bond as they are in close proximity to the C(8)–S(4) and C(7)–S(3) groups, respectively, and the Pt–S bond lengths for the complex cation and the complex anion are only slightly different (Table 1). As regards the Me_2pipdt ligand, the thioamide groups are not coplanar {τ[S(1)–C(1)–C(2)–S(2)] = –16.9(8)°} and the C(1)–C(2) bond length [1.493(9) Å] is indicative of a single bond between these two atoms excluding an electron delocalisation between the thioamide moieties.

The ring conformation of the Me_2pipdt ligand {τ[N(1)–C(3)–C(4)–N(2)] = –53.0(9)°} limits the stacking between the cationic and anionic complexes; in fact they are skewed with respect to each other by ca. 45° {τ[S(1)–Pt(1)–Pt(2)–S(4)] = 43.75(7)°}.

A net of weak interactions between the N(1) and O(3) atoms [3.40(1) Å] of the cation and anion contributes to the alignment of $[Pt(Me_2pipdt)_2][Pt(dtcr)_2]$ along the *c* axis. The O(1)–N(2) intermolecular interaction [3.40(1) Å] generates a layer in the [0 1 0] crystallographic plane (Figure 2). To the best of our knowledge structural data on the [Pt-

 © 2005 Wiley-VCH Verlag GmbH & Co. KGaA, Weinheim

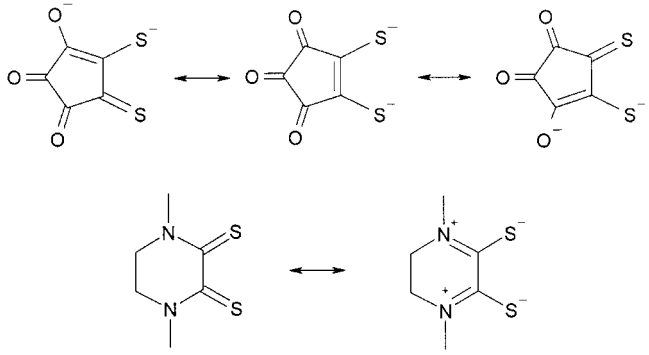

Scheme 1.

$(dtcr)_2]^{2-}$ complex appear here for the first time and are consistent with those found in the crystal structures of $[Bu_4N]_2[ML_2]\cdot I_2$ (where L = 2-dicyanomethylene-4,5-disulfanylcyclopent-4-ene-1,3-dionate; M = Pd, Pt)[9] and of $(Ph_4P)_3[Co(dtcr)_3]\cdot 0.6$ acetone.[11]

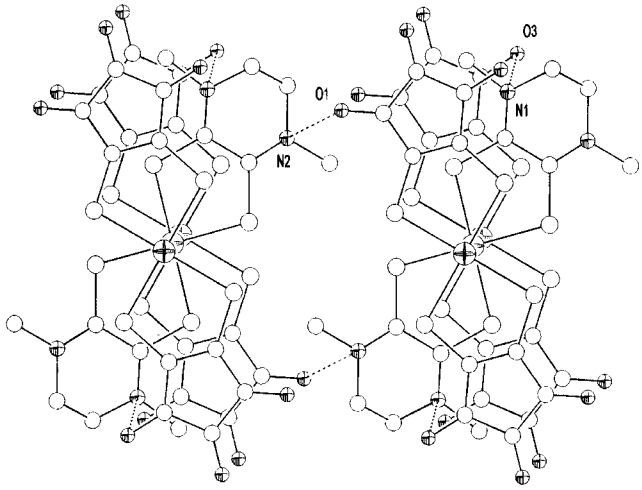

Figure 2. Perspective view of the unit cell content of $[Pt(Me_2pipdt)_2]$-$[Pt(dtcr)_2]$. Projection along the *c* axis.

Electronic Spectral Features

The comparison of the diffuse reflectance (DR) spectra of $[Pt(Me_2pipdt)_2][Pt(dtcr)_2]$ (**3a**) with those of $[Pt(Me_2pipdt)_2](BF_4)_2$ and $(Bu_4N)_2[Pt(dtcr)_2]$ is reported in Figure 3. In the spectrum of **3a**, one adjunctive, strong, long-wavelength absorption appears at 960 nm (930 nm for **3b**). Type **1** $[Pd(Me_2pipdt)_2][Pd(mnt)_2]$ and **2** $[Pt(R_2pipdt)_2]$-$[Pt(mnt)_2]$ (R = Me, Et) salts, where the redox-active planar anions and cations show a similar, alternating stacking, exhibit similarly strong near infrared peaks. These long wavelength absorptions are assigned to intermolecular charge transfer (ICT) transitions from the negatively charged to the positively charged complex.

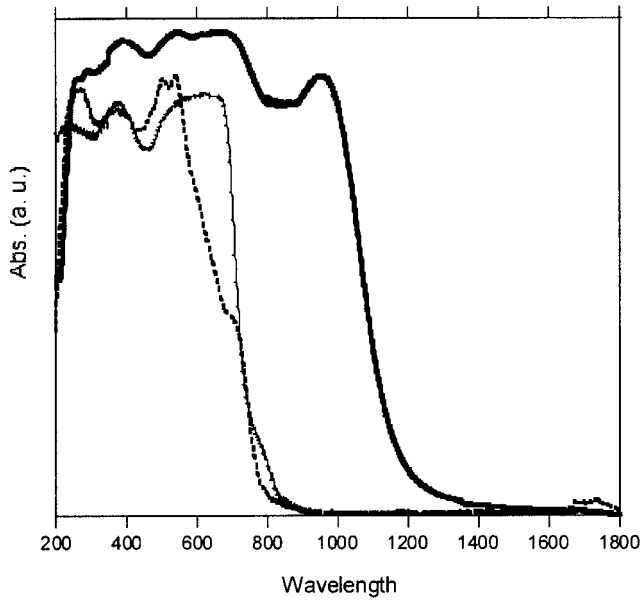

Figure 3. The diffuse reflectance spectra of $[Pt(Me_2pipdt)_2][Pt(dtcr)_2]$ (thick line) and, for comparison, of $[Pt(Me_2pipdt)_2](BF_4)_2$ (dotted line) and $(Bu_4N)_2[Pt(dtcr)_2]$ (thin line). The absorbances are reported in arbitrary units.

Theoretical calculations based on approximate Extended Hückel methods by using the CACAO program[12] have been performed to calculate the frontier orbitals of the cation and of the anions. These orbitals are π-type orbitals, and while a significant contribution of the metal d_{yz} orbital to the HOMOs occurs, the contribution of the metal to the LUMOs is negligible. The transition from the dithiolene metallate donor (HOMO) to the dicationic dithiolene acceptor (LUMO), symmetry allowed, will have charge-transfer character. The nature of the LUMO of the $[M(R_2pipdt)_2]^{2+}$ which is a π* ligand orbital can explain the observed similarity with the behaviour of $C[ML_2]$ Kisch salts (C^{2+} is almost planar, i.e. 2,2′ or 4,4′-bipyridinium derivatives, L^{2-} = dithiolato) where the CT peaks are assigned to a π→π* transition from the same platinum (or nickel) dithiolato donor to a planar organic acceptor based on bipyridinium cations (C^{2+}). The energy of the CT transition is relatable to the driving force of electron transfer from the cation to the anion ($[C]^{2+} + [A]^{2-} \rightarrow [C]^{+} + [A]^{-}$) through the following, modified Hush relation [Equation (1)].

$$E_{IPCT} = \chi + \Delta G_{12} \quad (1)$$

[E_{IPCT} is obtained from the IPCT peak in the reflectance spectra, χ represents the total reorganization energy and ΔG_{IP} is obtained from the components' redox potential difference, $E(C^{2+/+}) - E(A^{-/2-})$]. The redox features of the cation[7,13] and of the anion[9] have been previously reported. The reversible processes of interest here are shown below:

 © 2005 Wiley-VCH Verlag GmbH & Co. KGaA, Weinheim

$$[Pt(R_2pipdt)_2]^{2+} \underset{1e^-}{\overset{E_{1/2}}{\rightleftharpoons}} [Pt(R_2pipdt)_2]^{+}$$

$$[Pt(dtcr)_2]^{-} \underset{1e^-}{\overset{E_{1/2}}{\rightleftharpoons}} [Pt(dtcr)_2]^{2-}$$

Moreover, the free activation enthalpy of thermal electron transfer can be calculated according to Equation (2).

$$\Delta G^* = E^2_{IPCT}/4(E_{IPCT} - \Delta G_{12}) \quad (2)$$

The E_{IPCT}, ΔG_{12}, ΔG^* values, and the reduction potentials related to $[Pt(R_2pipdt)_2][Pt(dtcr)_2]$, as well as data for $[M(R_2pipdt)_2][M(mnt)_2]$, are reported in Table 2. The more positive reduction potential of $[Pt(dtcr)_2]^{-/2-}$ with respect to the corresponding mnt derivative is in agreement with the higher charge delocalisation in the dtcr ligand. Accordingly the position of the CT transition falls at higher energies.

Infrared results are also in agreement with a CT anion–cation description for **3a** and **3b**. The ν(CN) vibration of the ligand of the $[Pt(R_2pipdt)_2]^{2+}$ dication can be used as a probe to evaluate the extent of the charge transfer from the dianion to the dication. This vibration appears as a strong peak near 1550 cm^{-1} in the tetrafluoborate. When the dication accepts charge from the donor (the dianion), a partial population of the LUMO orbital that has CN antibonding character (see Figure 4) is expected. This should produce a shift of ν(CN) to lower frequencies, as observed, although these shifts do not strictly correlate with ΔG_{12}. Differently to what observed in mnt[14] and dmit[15] complexes, where the ν(C=C) of the bond vicinal to sulfur atoms is very sensitive to the charge of the complexes (due to the main C=C bonding contribution to the HOMO in the dianion), no similar ν(C=C) vibration sensitive to the charge is observed in the $[Pt(dtcr)_2]^{2-}$ salts in Table 3. This is related to the different nature of the HOMO (see Figure 4), with no corresponding C=C bonding contribution. Instead an extensive delocalisation involving also the peripheral C=O groups exists.[16] Thus a change in the charge, distributed over the entire complex, has a slight effect on any single vibration, as observed.

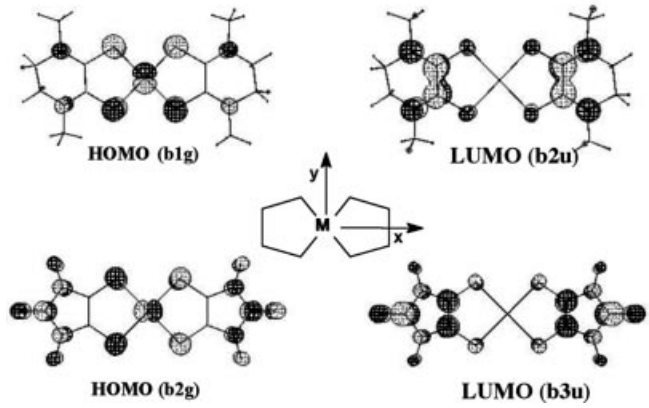

Figure 4. Frontier MOs of $[Pt(Me_2pipdt)_2]^{2+}$ and of $[Pt(dtcr)_2]^{2-}$.

Table 3. Most significant IR peaks. Spectra recorded on KBr pellets.

	ν(C=N) cm^{-1}	ν(C=O) cm^{-1}
$[Pt(R_2pipdt)_2](BF_4)_2$	1550 (R = Me) 1546 (R = Et)	
$(Bu_4N)_2[Pt(dtcr)_2]$		1683, 1668 sh, 1636
$[Pt(Me_2pipdt)_2][Pt(dtcr)_2]$	1541	1684, 1663, 1629
$[Pt(Et_2pipdt)_2][Pt(dtcr)_2]$	1529	1670, 1657, 1639

Conductivity Measurements

The above discussion shows that the structural and optical properties of this new class of ion-pair CT salts, $[M(R_2pipdt)_2][ML_2]$, are similar to those of the organic–inorganic Kisch salts, $C[ML_2]$. The electrical specific conductivity of Kisch salts gave values ranging from 10^{-10} to 10^{-3} $\Omega^{-1}cm^{-1}$ and these values are related to ΔG_{12} and ΔG^*. Moreover these salts exhibit photoconductive properties. In order to find further support in comparing the behaviour of metal-anion-dithiolene/metal-cation-dithiolene and metal-anion-dithiolene/viologen, ion pairs the dark- and photo-conductive properties of these salts were investigated.

Table 2. Reduction potentials of component ions, free reaction and activation enthalpies of the electron transfer between ions and ion-pair charge-transfer band of solid ion pairs.

$[M(R_2pipdt)_2][MA_2]$	E ($C^{2+/+}$) [V][a]	E ($A^{-/2-}$) [V][a]	E_{IPCT} [eV]	ΔG_{12} [V]	ΔG^* [eV]
M = Pt; R = Me; A = mnt (**2a**)	–0.13	+0.21	0.98	+0.34	0.37
M = Pt; R = Et; A = mnt (**2b**)	–0.17	+0.21	1.16	+0.38	0.43
M = Pt; R = Me; A = dtcr (**3a**)	–0.13	+0.40	1.29	+0.53	0.55
M = Pt; R = Et; A = dtcr (**3b**)	–0.17	+0.40	1.33	+0.57	0.58
M = Pd; R = Me; A = mnt (**1a**)	–0.16	+0.46	1.34	+0.62	0.62

[a] The redox potentials are referred to SCE.

 © 2005 Wiley-VCH Verlag GmbH & Co. KGaA, Weinheim

In Figure 5 the DC specific conductivity of pressed powder pellets of samples **1a**, **2a**, **2b** and **3a** are shown. These values range from 10^{-11} to $10^{-5}\ \Omega^{-1}\,cm^{-1}$ and increase with increasing temperature according to the Arrhenius law $\sigma = \sigma_0 \exp(-E_a/k_B T)$ (where σ_0 is the pre-exponential factor, E_a is the activation energy, T is the absolute temperature and k_B is Boltzmann's constant). Due to the very large resistance of compound **3a**, only a limited temperature range could be explored. In general the lowest T for each sample corresponds to the lowest current measurable near the picoammeter limit. The pre-exponential factor, σ_0, calculated from the fit, is approximately $0.2\ \Omega^{-1}\,cm^{-1}$ for all compounds and the activation energies range between 0.2–0.6 eV. The value of the conductivity at room temperature, the large value of the activation energy and the fact that σ_0 is constant indicate that these compounds belong to the class of strongly temperature-activated charge-transfer materials, analogous to the segregated stacks systems whose mobility is temperature independent.[17]

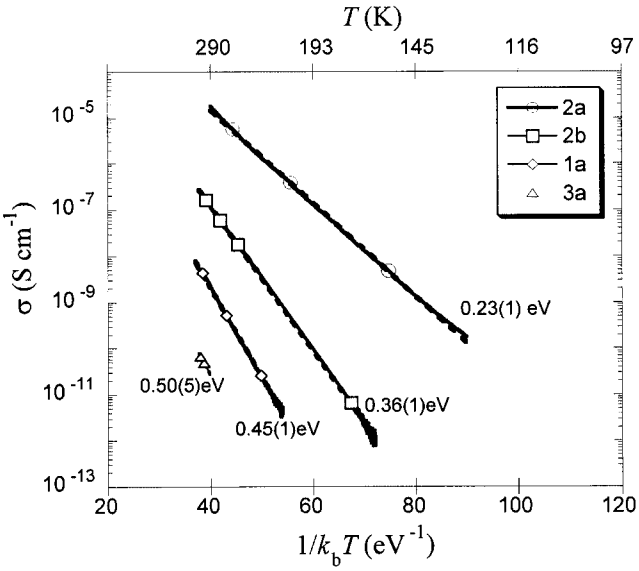

Figure 5. Semilogarithmic plot of the DC conductivity vs. $1/k_bT$, (where k_b = Boltzman costant, T = temperature) for the set of measured compounds. The dotted lines are the best fit of the exponential Arrhenius behaviour. The values of the activation energy E_a are also displayed.

In Figure 6 the σ values at 290 K vs. both the activation energy, E_a, and the free activation enthalpy of electron transfer, ΔG^*, are shown. The data vs. E_a for each compound can be fitted with the equation $\sigma(T_o = 290\ K) = \sigma_0 \exp(-E_a/k_B T_o)$ where σ_0 is approximately $0.2\ \Omega^{-1}\,cm^{-1}$. This behaviour indicates that changes in the conductivity are due only to changes in E_a while the pre-exponential factor σ_0 is approximately the same for all the compounds. For the three Pt salts (**2a**, **2b**, **3a**), where only changes in the nonmetallic sites occur, there is a linear dependence of $\ln\sigma(290K) = a + b\Delta G^*$, with $a \approx 7$ and $b \approx -76$, indicating that for these compounds the transport mechanism within the ion pair is mainly driven by the extent of the charge-transfer interaction, as expected.[18] It is noteworthy that the lnσ(290 K) value for M = Pd (**1a**) does not fall on the same line. Moreover the corresponding lnσ(290 K) vs. ΔG^* dependence for C[ML_2] Kisch salts[18] leads to a linear correlation with different coefficients ($a \approx -3$ and $b \approx -35$). These features suggest that the transport properties and hence the activation energy of CT salts are not simply governed by the activation enthalpy ΔG^*, and some other kind of mechanisms must be involved.

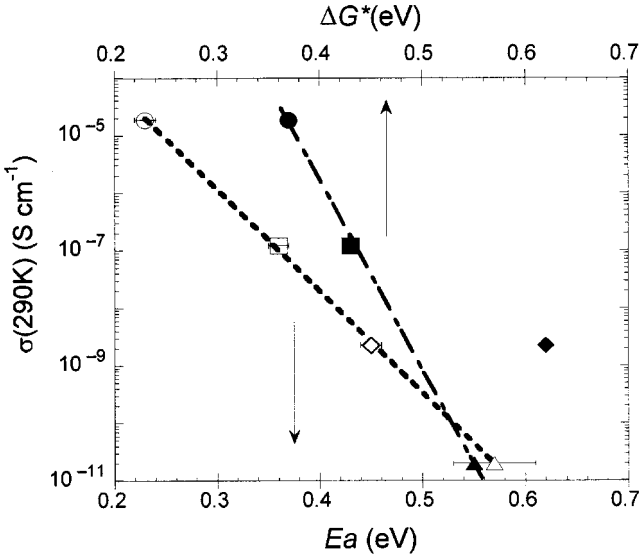

Figure 6. Semilogarithmic plot of the DC conductivity at room temperature vs. the activation energy, E_a, (open symbols) and the free activation enthalpy, ΔG^*, (shaded symbols). The symbols are the same as in Figure 5 (● **2a**, ■ **2b**, ♦ **1a**, ▲ **3a**).

Preliminary photoconductivity measurements have been performed on the two relatively more conducting samples, **2a** and **2b**, by using a lock-in phase, pulsed technique and a halogen lamp (250 W). A low gain in current was observed during illumination. The signal has a decay constant τ of the order of tens of milliseconds and is likely to be related to both the variation of resistance during two different choppered light pulses and to trapping of carriers. The observed photocurrent values I_{ph} ($I_{ph}/I_D \approx 10^{-3}$, where I_D is the dark current) are similar to those reported in Kisch CT salts.[19]

Conclusions

This study has confirmed that cationic and anionic metal-dithiolenes (Pd-Pt) are capable of forming salts that show charge-transfer interactions, responsible for strong NIR CT bands, semiconducting behaviour and photoconducting properties. The properties of these salts are comparable with those of salts formed by dianionic dithiolene metallates with planar organic dications. These properties strongly depend on the amount of electron donation from the donor to the acceptor, which in turn depends on the redox potential and on the planarity of the ionic components of the salt. Since d^8 metal dithiolenes have a rich redox chemistry, which depends on the nature of the substitu-

 © 2005 Wiley-VCH Verlag GmbH & Co. KGaA, Weinheim

ents at the C_2S_2 moieties, and determines the nature of their most accessible status while the metal atom imposes the square planar geometry, they offer a wide range of suitable candidates for forming CT salts.

This study also reports the characterisation of $[Pt(R_2pipdt)_2][Pt(dtcr)_2]$, a new example of ion-pair charge-transfer salts formed by an infinite, mixed, planar anion–cation stack. The presence of peripheral C=O groups in the anion produces a net of weak interactions between the N and O atoms of the cation and of the anion inside the stacks thereby favouring the generation of a layer between them. However, these interactions do not overcome the less favourable redox properties of the components with respect to the corresponding mnt salts, that is, promoting anion–cation CT interactions and related properties.

Experimental Section

General Remarks: Reagents and solvents of reagent grade quality were used as supplied by Aldrich. The ligands and the complexes $[Pt(Me_2pipdt)_2](BF_4)_2]$ and $(Bu_4N)_2[Pt(dtcr)_2]$ were prepared according to references [7] and [9]. Microanalyses were performed on a Carlo–Erba CHNS elemental analyser model EA1108. IR spectra (4000–300 cm^{-1}) were recorded on a Bruker IFS55 FT-IR Spectrometer as KBr pellets. Raman spectra (2200–300 cm^{-1}) on single crystal was carried out at room temperature using a Raman microscope (BX, 40, Olympus) spectrometer (ISA xy 800) equipped with a He-Ne (λ = 632,817, Melles-Criot) laser. A 180° reflective geometry was adopted. The sample was mounted on a glass microscope slide and the scattering peaks were calibrated against an Si standard ($\tilde{\nu}$ = 520 cm^{-1}). The spectrum was collected with a 500 s time constant at a 1 cm^{-1} resolution and was averaged over 5 scans. No sample decomposition was observed during the experiments. Electronic spectra (2000–200 nm) were recorded on a Cary 5 spectrophotometer, equipped with a diffuse reflectance accessory. Diffuse reflectance spectra were run on KBr pellets. For electrical measurements the powder samples were pressed up to 0.4 GPa in rectangular bars of (2 × 1 × 13) mm^3 dimensions. Gold electrodes were sputtered on two point-like regions on the surface of the sample in order to favour the ohmic electrical contacts. The DC current measurements were performed by using a Keithley 485 picoammeter and by applying voltages in the range 0–100 V. The temperature was varied by a closed cycle refrigerator system in the range 100–310 K, regulated at the rate of 1 K/min and measured within an error of 1 K.

$[Pt(Me_2pipdt)_2][Pt(dtcr)_2]$ (3a): The blue CH_3CN solution (15 mL) of $(Bu_4N)_2[Pt(dtcr)_2]$ (72 mg; 0.07 mmol) was slowly added to the warm brown CH_3CN solution (20 mL) of $[Pt(Me_2pipdt)_2](BF_4)_2$ (50 mg; 0.07 mmol) and a quantitative precipitation of brown needle-shaped crystals occurred (yield 72 mg; 95%). Crystals suitable for X-ray characterization were grown using a diffusion cell with three compartments connected through porous glass frits. The solutions of the components were introduced in the terminal compartments, and the crystals were collected in the central compartment filled with CH_3CN. $C_{22}H_{20}N_4O_6Pt_2S_8$ (1083.11): calcd. C 24.40, H 1.86, N 5.17, S 23.68; found: C 24.76, H 1.68, N 5.20, S 22.81. IR (KBr pellets): $\tilde{\nu}$ = 3026 vw, 3000 vw, 2920 vw, 2857 vw, 2123 vw, 1684 vs, 1663 vs, 1629 vs, 1618 vs, 1541 s, 1406 ms, 1387 vs, 1362 sh, 1284 mv, 1265 ms, 1238 sh, 1189 m, 1146 mw, 1097 mw, 1064 w, 1027 mw, 924 w, 902 mw, 804 vw, 781 vw, 668 vw, 598 vw, 545 mw, 480 mw, 428 w cm^{-1}. UV/Vis-NIR (reflectance, KBr pellets) λ = 387, 540, 680, 960 nm.

$[Pt(Et_2pipdt)_2][Pt(dtcr)_2]$ (3b): This compound was prepared as described for **3a** (yield 111 mg; 97%), starting from the CH_3CN solutions of $[Pt(Et_2pipdt)_2](BF_4)_2$ (violet; 77 mg; 0.10 mmol) and $(Bu_4N)_2[Pt(dtcr)_2]$ (blue; 102 mg; 0.10 mmol). $C_{26}H_{28}N_4O_6Pt_2S_8$ (1139.22): calcd. C 27.41, H 2.48, N 4.92, S 22.51; found: C 26.73, H 2.52, N 4.86, S 22.65. IR (KBr pellets): $\tilde{\nu}$ = 2980 vw, 2940 vw, 2385 vw, 2350 vw, 2100 w, 1760 w, 1670 vs, 1657 vs, 1638 vs, 1615 sh, 1529 s, 1452 m, 1393 vs, 1360 vs, 1340 sh, 1278 ms, 1261 ms, 1229 ms, 1199 ms, 1126 ms, 1090 w, 1080 w, 1036 w, 970 m, 940 vw, 918 w, 896 m, 858 w, 801 w, 780 w, 760 w, 625 w, 610 w, 550 mw, 476 ms, 421 m, 355 w, 340 mw, 310 vw, 300 vw cm^{-1}. Raman (on single crystal): 2180 vw, 1702 vs, 1412 m, 1192 vs, 1052 vw, 562 vw, 478 s, 422 w cm^{-1}. UV/Vis-NIR (reflectance, KBr pellets) λ = 390, 544, 730, 930 nm.

Acknowledgments

This work was conducted in the framework of the European COST action D14 "Towards New Molecular Inorganic Conductors". The authors thank Prof. Carlo Muntoni, Dipartimento di Fisica dell'Università di Cagliari, for his support.

[1] a) E. I. Stiefel (Ed.), *Dithiolene Chemistry, Progress in Inorganic Chemistry*, John Wiley & Sons **2004**, vol. 52 (see in particular chapter 8 by C. Faulmann, P. Cassoux); b) A. T. Coomber, D. Beljonne, R. H. Friend, J. K. Brédas, A. Charlton, N. Robertson, A. E. Underhill, M. Kurmoo, P. Day, *Nature* **1996**, *380*, 144; c) N. Robertson, L. Cronin, *Coord. Chem. Rev.* **2002**, *227*, 93–127.

[2] a) I. Nunn, B. Eisen, R. Benedix, H. Kisch, *Inorg. Chem.* **1994**, *33*, 5079–5085; H. Kisch, *Coord. Chem. Rev.* **1997**, *159*, 385–396; H. Kisch, B. Eisen, R. Dinnebier, K. Shankland, W. I. F. David, F. Knoch, *Chem. Eur. J.* **2001**, *7*, 738–748.

[3] a) N. S. Hush, *Progr. Inorg. Chem.* **1967**, *8*, 391–444; b) R. A. Marcus, N. Sutin, *Comments Inorg. Chem.* **1986**, *5*, 119–133.

[4] M. Yamashita, A. Ichikawa, T. Hama, T. Ohishi, T. Manabe, H. Miyamae, D. Yoshida, S. Sugiura, H. Kitagawa, Y. Iwasa, T. Mitani, *Mol. Cryst. Liq. Cryst.* **1996**, *284*, 391–398.

[5] a) Z. S. Herman, R. F. Kirchner, G. H. Loew, U. T. Mueller-Westerhoff, A. Nazal, M. C. Zerner, *Inorg. Chem.* **1982**, *21*, 46–56; b) J. Weber, C. Daul, A. Van Zelewsky, A. Goursot, E. Penigault, *Chem. Phys. Lett.* **1982**, *88*, 78–83; c) C. Lauterbach, J. Fabian, *Eur. J. Inorg. Chem.* **1999**, 1995–2004.

[6] S. Curreli, P. Deplano, C. Faulmann, A. Ienco, C. Mealli, M. L. Mercuri, L. Pilia, G. Pintus, A. Serpe, E. F. Trogu, *Inorg. Chem.* **2004**, *43*, 5069–5079.

[7] F. Bigoli, P. Deplano, M. L. Mercuri, M. A. Pellinghelli, L. Pilia, G. Pintus, A.Serpe, E. F. Trogu, *Inorg. Chem.* **2002**, *41*, 5241–5248.

[8] For M = Ni, $[Ni(R_2pipdt)(mnt)]$ mixed-ligand derivatives, which are potential second order non-linear chromophores showing strong negative solvatochromism and β, have been obtained: F. Bigoli, C.-T. Chen, P. Deplano, M. L. Mercuri, M. A. Pellinghelli, L. Pilia, G. Pintus, E. F. Trogu, *Chem. Commun.* **2001**, 2246–2247.

[9] W. B. Heuer, W. H. Pearson, *J. Chem. Soc., Dalton Trans.* **1996**, 3507–3513.

[10] Single crystal X-ray structure determination of **3a**: The data were collected at T = 293 K on an *Enraf–Nonius CAD4* diffractometer (Cu-$K\alpha$; λ = 1.54184 Å). The structures were solved by direct methods (SIR97, **3a**)[20] and refined with full-matrix least-squares (SHELXL-97),[21] using the Wingx soft-

 © 2005 Wiley-VCH Verlag GmbH & Co. KGaA, Weinheim

ware package.[22] Crystal data of **3a**: violet needle, $0.25 \times 0.12 \times 0.10$ mm, $C_{22}H_{20}N_4O_6Pt_2S_8$, M_r = 1083.08, triclinic, space group $P\bar{1}$, a = 8.683(2) Å, b = 14.009(5) Å, c = 6.815(2) Å, α = 100.58(4)° β = 92.98(2)°, γ = 106.69(2)°, V = 761.1(4) Å^3, Z = 1, μ = 22.477 mm^{-1}, $\rho_{calcd.}$ = 2.363 g cm^{-3}, $R1$ (w$R2$) = 0.0493 (0.1361) {2747 observed [$I > 2\sigma(I)$] for 2316 independent reflections with 197 parameters}. CCDC-253138 contains the supplementary crystallographic data for this paper. These data can be obtained free of charge from The Cambridge Crystallographic Data Centre via www.ccdc.cam.ac.uk/data_request/cif.

[11] W. B. Heuer, W. H. Pearson, *Polyhedron* **1996**, *15*, 2199–2210.

[12] C. Mealli, D. Proserpio, *J. Chem. Educ.* **1990**, *67*, 399–402.

[13] F. Bigoli, P. Deplano, M. L. Mercuri, M. A. Pellinghelli, G. Pintus, A. Serpe, E. F. Trogu, *J. Am. Chem. Soc.* **2001**, *123*, 1788–1789.

[14] a) C. W. Schläpfer, K. Nakamoto, *Inorg. Chem.* **1975**, *14*, 1338; b) J. L. Wootton, J. I. Zink, *J. Phys. Chem.* **1995**, *99*, 7251–7257; c) S. Kutsumizu, N. Kojima, T. Ban, I. Tsujikawa, *Bull. Chem. Soc., Jpn.* **1987**, *60*, 2547–2553.

[15] K. I. Pokhodnya, C. Faulmann, I. Malfant, R. Andreu-Solano, P. Cassoux, A. Mlayah, D. Smirnov, J. Leotin, *Synth. Met.* **1999**, *103*, 2016–2019.

[16] The contributions of the p_z AO are as follows: oxygen (3%), carbon (6%), sulfur (6%) atoms for each ligand and platinum (d_{xz}, 34%) to the HOMO.

[17] J. Simons, J.-J. André, *Molecular Semiconductors* (Eds.: J. M. Lehn, C. W. Rees), Springer-Verlag, Berlin-Heidelberg, **1985**, chapter 6.

[18] H. Kisch, *Comments Inorg. Chem.* **1994**, 113–132.

[19] H. Meier, H. Kish, *J. Phys. Chem.* **1989**, *93*, 7726–7729.

[20] A. Altomare, M. C. Burla, M. Camalli, G. L. Cascarano, C. Giacovazzo, A. Guagliardi, A. G. G. Moliterni, G. Polidori, R. Spagna, *J. Appl. Crystallogr.* **1999**, *32*, 115–119.

[21] G. M. Sheldrick, *SHELX97*. Programs for Crystal Structure Analysis (**1997**) (Release 97-2), University of Göttingen, Germany.

[22] L. J. Farrugia, *J. Appl. Crystallogr.* **1999**, *32*, 837–838.

Received: October 20, 2004
Published Online: April 11, 2005

 © 2005 Wiley-VCH Verlag GmbH & Co. KGaA, Weinheim

The Role of C–H···O Interactions in the Solid and Liquid-Phase Structures of Methyltrioxo Rhenium

Pedro D. Vaz,*[a,b] and Paulo J. A. Ribeiro-Claro[a]

Keywords: Rhenium / C–H···O Hydrogen bonds / Ab initio calculations / Raman spectroscopy / Inelastic neutron scattering

The importance of C–H···O hydrogen bonds involving the less common Re=O acceptor group in the small organometallic methyltrioxorhenium (MTO) is studied by combined vibrational spectroscopy and ab initio calculations. The observed vibrational spectrum is well described by the calculated spectrum of a C–H···O bonded dimer, which accounts for the symmetry decrease and the intermolecular interactions in the solid. Spectral evidence indicates both C–H···O and O–H···O hydrogen bonds are formed in the MTO/methanol solutions. The Re=O stretching mode is sensitive to hydrogen bonding, but the major effects of intermolecular association are observed in the βC–H and νC–H modes of MTO. Ab initio calculations for the MTO/methanol system predict the coexistence of both the Lewis adduct and the hydrogen-bonded complex, with an energy difference of ca. 1.2 kJ·mol^{-1}.

(© Wiley-VCH Verlag GmbH & Co. KGaA, 69451 Weinheim, Germany, 2005)

Introduction

Methyltrioxorhenium (MTO) is a small transition metal organometallic molecule that has been recently studied for its properties in catalysis, mainly as an oxidation catalyst,[1] see Scheme 1.

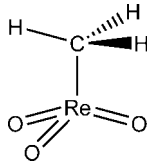

Scheme 1.

The structure of this compound has been previously reported.[2–6] These studies include single crystal neutron diffraction structure determination,[3] as well as several vibrational studies combined with ab initio calculations.[2,4–6] However, some questions concerning the intermolecular interactions in the liquid and solid phases still remain. In a recent work by Gisdakis et al., it was proposed that MTO can associate into dimers through oxo-bridges,[6] where two Re atoms are bound by two Re–O–Re bridges in order to preserve the stoichiometry. Ab initio calculations predicted that the formation of the four proposed geometries would be endothermic, with dimerization energies of between 7.1 kJ·mol^{-1} and 148.4 kJ·mol^{-1}.[6]

In this work, the role of C–H···O interactions in the structure of MTO is studied by vibrational spectroscopy and combined with ab initio calculations. FT-Raman spectra were obtained for the solid phase and as a function of concentration in different solvents. In addition, ab initio calculations were carried out in order to elucidate the structure and energy of possible C–H···O bonded forms and to simulate the corresponding vibrational spectra.

Results and Discussion

Figure 1 presents the fully optimised structure of MTO (a) and of the lowest energy MTO hydrogen-bonded dimer (b).

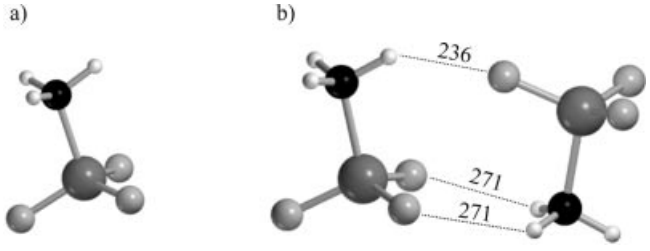

Figure 1. DFT-optimised geometries for a) monomer and b) dimer MTO structures. Distances are in pm.

This MTO dimer – corresponding to a real minimum, i.e. without negative eigenvalues from the frequency calculations – was found to be the most stable configuration among the several MTO dimers tested, and presents three

[a] Departamento de Química, CICECO, Universidade de Aveiro, Campus de Santiago, 3810-193 Aveiro, Portugal
Fax: +351-234-370-084
E-mail: pvaz@dq.ua.pt
[b] Present address: DQB-FCUL, Ed. C8, Campo Grande, 1749-016 Lisboa, Portugal
Fax: +351-217-500-994
E-mail: pmvaz@fc.ul.pt

C–H···O hydrogen bond contacts. The dimerisation energy is –21.8 kJ·mol^{-1} (without corrections) and –15.9 kJ·mol^{-1} (after CP and ZPVE corrections), falling in the expected range for this type of interaction.[7–14] These values show that a C–H···O bonded dimer is clearly more stable than the previously reported dimers based on oxygen bridges.[6] In fact, the dimerisation energy for oxygen bridged dimers, evaluated at the same level of theory, ranges from 7.1 kJ·mol^{-1} to 148.4 kJ·mol^{-1} as mentioned above.

The optimised ab initio geometry for the dimer is in very good agreement with the structure determined by neutron diffraction for the solid,[3] considering the limitations of the "isolated dimer" approach (in the crystal, each molecule has several neighbours), whose structure is represented in Figure 2.

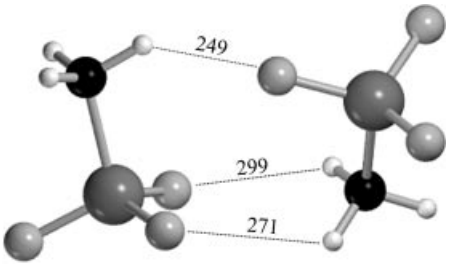

Figure 2. Representation of the interaction motif from the solid structure unit cell of MTO as determined by neutron diffraction.[3] Distances are in pm.

From the three C–H···O hydrogen bond contacts of the calculated geometry, one is clearly favoured by the geometrical orientation (C–H···O angle: 141°) over the other two (C–H···O angle: 128°), which results in a stronger C–H···O contact. The corresponding H···O contact distance (236 pm – ab initio, 249 pm – neutron diffraction) is clearly shorter than the remaining ones (271 pm – ab initio, 299 pm – neutron diffraction). In addition, the bond length of the C–H donor group of the most favoured contact is shorter than the others (ca. 0.1 pm – ab initio, 1.4 pm neutron diffraction). The shortening of the C–H bond length involved in the strongest C–H···O contact (an effect leading to the increase of the corresponding stretching frequency and to the designation of "blue-shifting hydrogen bond") indicates that the behaviour of the C(sp^3)–H···O=Re interaction is similar to that of C(sp^3)–H···O=C.

Figure 3 depicts the comparison between the experimental FT-Raman spectrum and the calculated spectra for both the monomer and the C–H···O bonded dimer. The calculated spectrum for the monomer is clearly oversimplified, as the single molecule model is inadequate to describe the crystal. However, there is an excellent agreement between the calculated and the experimental spectra for the dimer. Although the full description of the solid-state spectra would require a more sophisticated approach, this simple model has the merit of accounting for both the effects of the symmetry reduction and the effects of the most relevant intermolecular contacts. In particular, the magnitude of the splitting of the modes at ca. 750, 950, 1400, and 3000 cm^{-1} is correctly predicted from the fully optimized geometry.

The comparison between the calculated vibrational spectra of the MTO dimer and the experimental vibrational spectra of solid MTO is presented in Table 1 (the full assignment of the vibrational spectra has already been proposed by Parker et al.[5]). The approximate description of the vibrational modes presented in Table 1 assumes that the CH_3ReO_3 molecule is built from two XY_3 independent fragments. In this way, the 18 normal modes are described as 2×3 νXY stretching modes (3 νCH and 3 νReO), 2×5 XY_3 bending modes (3×βCH_3 + 2×CH_3 rocking and 3×βReO_3 + 2×ReO_3 rocking), one interfragment stretching mode (νC–Re) and one interfragment torsional mode (described as τCH_3, since the methyl group is the lighter fragment).

There is an excellent agreement between calculated and experimental assignments, but the results from ab initio calculations with the dimer model suggest a couple of changes relative to the previous vibrational studies.[2,5] The most obvious difference is related to the bands left unassigned previously by Parker at al.[5] (e.g. the bands at 2988, 1364, and 946 cm^{-1}) and not observed in the partial assignment of Mink et al.[2] (e.g. the second component of the 2986–2990 doublet). These bands are now clearly related with modes of the C–H···O bonded dimer. In some cases, the effect of the C–H···O contact yields a noticeable effect on the vibrational mode. For instance, according to ab initio calculations, C–H···O hydrogen bonds in the dimer produce a C–H bond shortening relative to the monomer, with a corresponding blue shift of the νC–H mode. The effect is also observed for the βC–H and γC–H modes, which are calculated at 1377 cm^{-1} and 763 cm^{-1}, respectively, blue-shifted from the predicted fundamentals of the monomer. In this way, the highest wavenumber νC–H, βC–H and γC–H bands have been assigned to the C–H bond engaged in the strongest C–H···O contact.

Another point of interest is the location of the H···O hydrogen bond stretching modes. Ab initio calculations predict the three νH···O modes at 26, 61 and 76 cm^{-1}, the last one being related to the strongest C–H···O bond. In the low wavenumber region, there are several bands observed in the INS spectrum – already assigned to librational and translational modes[5] – and a very weak band in the Raman spectrum at 84 cm^{-1}. On the basis of the proximity of the calculated wavenumber value and weak intensity, we tentatively assign the Raman band at 84 cm^{-1} to the strongest νH···O mode (predicted at 76 cm^{-1} from ab initio calculations). It should be stressed, however, that this is not a conclusive assignment and other bands (e.g. INS bands at 101 cm^{-1} or 50 cm^{-1}) can alternatively be related with this mode (Table 1).

In order to evaluate the relevance of C–H···O interactions in MTO/solvent systems, several solutions of MTO in solvents with acceptor/donor (e.g. CH_3OH, CD_3OD) and weak donor/non-acceptor (e.g. CD_2Cl_2) properties were prepared.

Ab initio calculations of MTO/solvent complexes were also performed, in order to evaluate the possible interactions between MTO and the solvents. As expected, the in-

 © 2005 Wiley-VCH Verlag GmbH & Co. KGaA, Weinheim

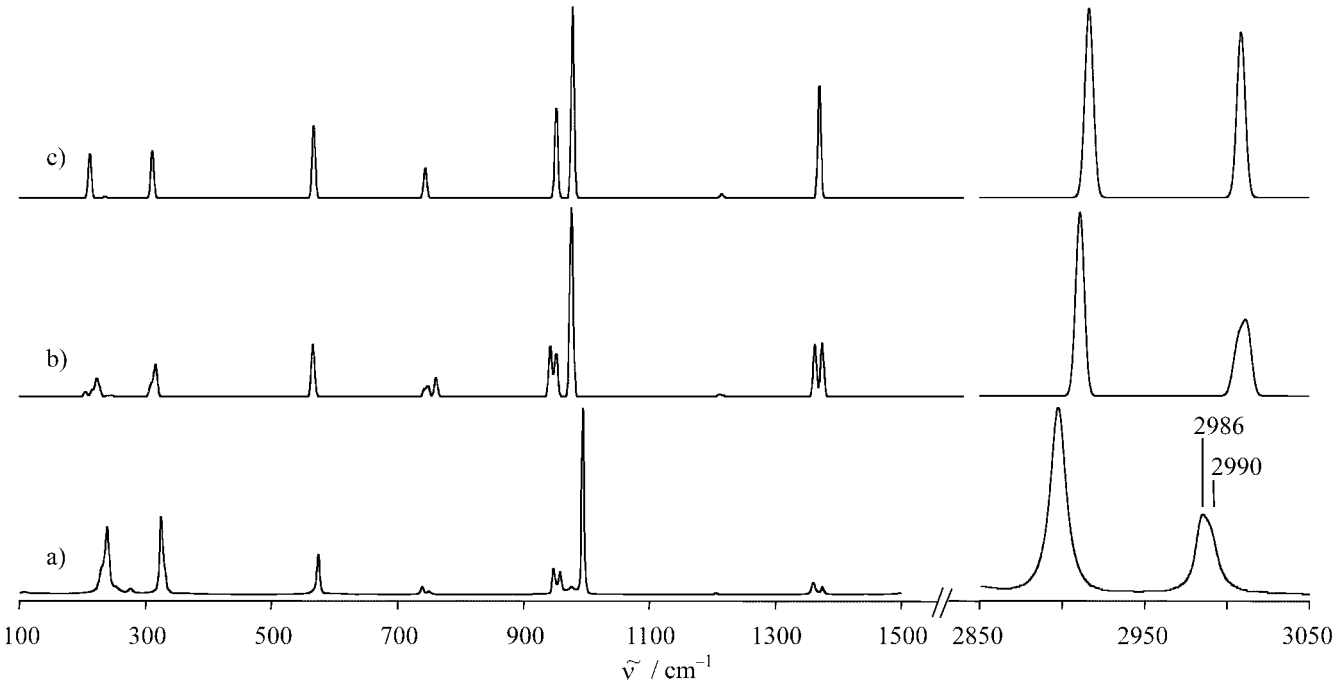

Figure 3. Raman spectra of MTO: a) experimental solid at room temperature, b) ab initio dimer simulation and c) ab initio monomer simulation.

Table 1. Comparison and assignment of the infrared, Raman, INS and ab initio vibrational frequencies ($\tilde{\nu}$/cm^{-1}) of MTO.

IR	Raman	INS[5]	ab initio calc.	Mode	Assignment
2990 (m, sh)	2990 (m, sh)	–	3019	ν_1	νC–H(···O)
2986 (m)	2986 (m)	–	3014	ν_2	νC–H asym
2898 (m)	2898 (s)	–	2921	ν_3	νC–H sym
1373 (w, sh)	1375 (w)	–	1377	ν_4,	βC–H(···O) asym
1359 (m)	1361 (w)	–	1373	ν_5	βC–H asym
1205 (w)	1206 (vw)	–	1217	ν_6	βC–H sym
997 (vs)	995 (vs)	–	982	ν_7	νRe=O sym
959 (vs)	960 (m)	–	954	ν_8	νRe=O asym
948 (vs)	949 (m)	938	944	ν_9	νRe=O asym
–	751 (vw)	–	763	ν_{10}	γC–H(···O) rock
739 (m)	740 (w)	738	747	ν_{11}	γC–H rock
571 (m)	575 (s)	573	570	ν_{12}	νRe–C
–	331 (w, sh)	–	317	ν_{13}	βRe=O sym
322 (m)	325 (vs)	–	313	ν_{14}	βRe=O sym
–	276 (w)	–	237	ν_{15}	βRe=O
–	240 (vs)	241	228	ν_{16}	γRe=O rock
–	231 (sh)	232	213	ν_{17}	γRe=O rock
–	–	199	184	ν_{18}	τCH$_3$
–	107 (w)	109	–	–	–
–	84 (vw)	101, 50	76	–	νH···O

teraction of MTO with CD_2Cl_2 is quite feeble and can be neglected. A different situation arises with methanol. Methanol molecules can interact with MTO either as hydrogen-bond donor or hydrogen-bond acceptor. The formation of a MTO/methanol Lewis acid/base adduct has been described previously by Herrmann et al., on the basis of ^{17}O-NMR spectroscopic data.[15] Figure 4 shows the energy minimized structure for the MTO/methanol hydrogen-bonded complex and for the MTO/methanol Lewis adduct. The hydrogen bonded complex presents a six-membered ring built from O–H···O C–H···O short contacts. In contrast, the adduct geometry only allows a distorted C–H···O contact. A relevant feature of Figure 4 is the small energy difference found between these two forms of MTO/methanol association (ca. 1.2 kJ·mol^{-1} after ZPVE correction), which strongly suggests that both forms can coexist in solution.

Figure 5 shows the Raman spectra of the MTO solutions in the Re=O and C–H stretching regions. These vibrational modes are clearly sensitive to the presence of C–H···O interactions, as well as stronger O–H···O(= Re) hydrogen bonds.

In the νRe=O wavenumber region (920–1020 cm^{-1}), several changes in the band profiles can be observed. Dilution in CD_2Cl_2 produces a shift to higher wavenumbers relative to the solid. This shift can be associated with the interac-

 © 2005 Wiley-VCH Verlag GmbH & Co. KGaA, Weinheim

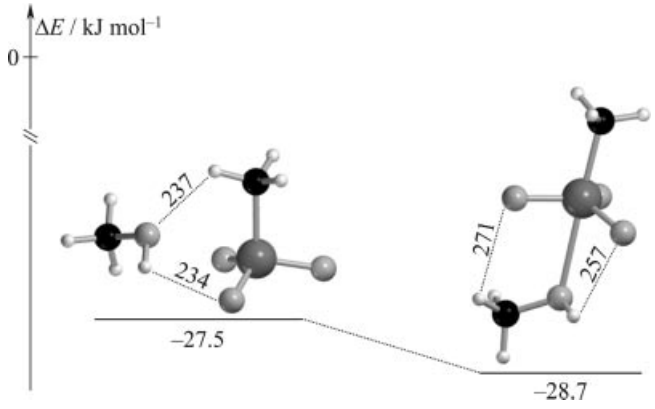

Figure 4. Optimised geometry of the lowest energy MTO/methanol complex based on O–H···O and C–H···O hydrogen bonds, and of the MTO/methanol Lewis adduct. Distances are in pm.

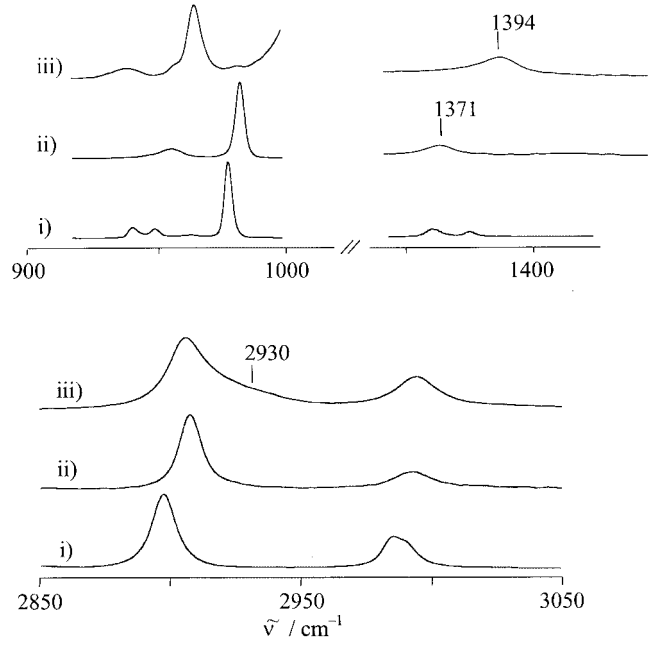

Figure 5. Raman spectra at room temperature of MTO solutions in various solvents in the νRe=O, βC–H and νC–H mode regions: i) pure solid, ii) 5% solution in CD_2Cl_2 and iii) 5% solution in CH_3OH or CD_3OD.

tion-free MTO molecules, as CD_2Cl_2 is not expected to interact with MTO, due to low-polarity of the solvent. Another noticeable effect is the merging of the two νRe=O asymmetric modes into a single broad feature, which is in agreement with the higher symmetry of MTO molecules in solution relative to the solid.

The dilution in methanol yields a large shift towards lower wavenumbers and a marked broadening of the νRe=O band. This large shift can be ascribed to the formation of Lewis adducts and a hydrogen-bonded complex between methanol and MTO, according to ab initio results described above. The presence of four bands in the νRe=O region of methanol solutions is consistent with the coexistence of the adduct and the hydrogen-bonded complex. In fact, the observed spectrum can be qualitatively described by the sum of the calculated spectra for the two species.

The same general behaviour is observed in the βC–H wavenumber region (1350–1450 cm^{-1}). However, the large shift observed from CD_2Cl_2 to methanol solutions can not be explained by bulk solvent effects, such as the change in the dielectric environment,[16] and is consistent with the presence of more specific interactions. According to the ab initio calculations, the MTO methyl group vibrations are virtually insensitive to the formation of the MTO/methanol adduct. On the other hand, C–H···O hydrogen bonds, such as those described in Figure 4, produce wavenumber shifts of the βC–H modes of ca. 23 cm^{-1}, in agreement with the observed value. These hydrogen bonds are expected to occur even for the MTO molecules already engaged in a MTO/methanol adduct (Figure 6). The MTO methyl group can interact through C–H···O hydrogen bonding with three surrounding methanol molecules, and the presence of such interactions can also explain the large asymmetry of the band.

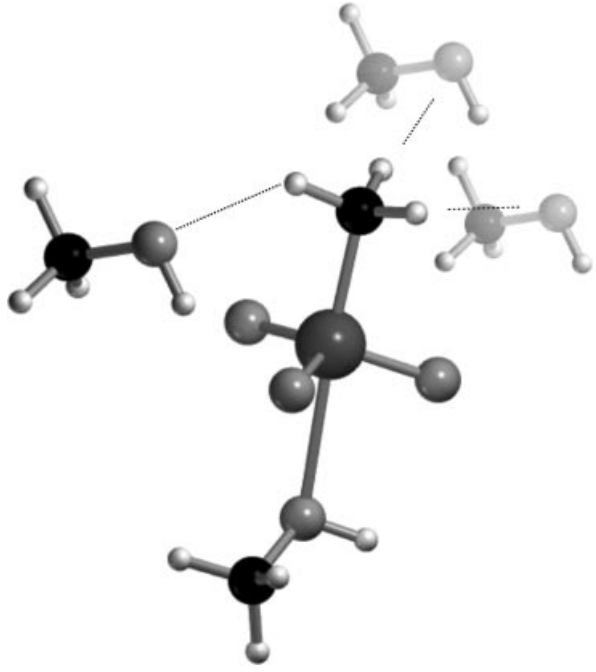

Figure 6. Optimised geometry for the interaction of the MTO/methanol Lewis adduct (O→Re bond length is 264 pm) with a second methanol molecule which is hydrogen bonded (H···O distance is 245 pm). The shadowed methanol molecules represent additional C–H···O contacts assumed to occur in the solution.

In the νC–H wavenumber region (2850–3050 cm^{-1}) some changes are also observed. The dilution in methanol gives rise to a general blue shift of all the νC–H bands. This effect is expected from the bulk solvent effects, due to the change of the dielectric constant.[16] In addition, there is an intensity increase in the higher wavenumber side of the band at 2906 cm^{-1}, leading to a clear band asymmetry. The effect is seen on the symmetric mode and not in the asymmetric ones, which is unexpected for a symmetry-breaking interac-

 © 2005 Wiley-VCH Verlag GmbH & Co. KGaA, Weinheim

tion. Possible explanations are (i) the weakness of the effect (can be hidden due to band broadness) and (ii) the averaging effect of multiple interactions. By comparison with the βC–H region, this band asymmetry can be ascribed to the multiple C–H···O interactions between MTO and methanol solvent molecules. As stated before, C–H···O hydrogen bonds are predicted to result in the blue-shift of the corresponding νC–H modes. Being so, the intensity increase in the 2930 cm^{-1} region may be ascribed to blue-shifting C–H···O hydrogen bonds.

Conclusions

The present work presents evidence of intermolecular interactions through C–H···O hydrogen bonds in solid MTO. The shortening of the C–H bond length involved in the strongest C–H···O hydrogen bond (leading to the blue-shift of the corresponding C–H stretching frequency by ca. 23 cm^{-1}) indicates that the behaviour of the $C(sp^3)$–H···O=Re interaction is similar to that of $C(sp^3)$–H···O=C. To the best of our knowledge, this is the first report of a blue-shifting C–H···O hydrogen bond involving a Re=O acceptor group. Dilution of MTO in the non-polar solvent CD_2Cl_2 yields vibrational features easily interpreted in terms of isolated MTO molecules. On the other hand, with dilution in methanol, the spectral changes are complex and not easily interpreted. The presence of a MTO/methanol Lewis adduct, already described, can account for some of the changes. Nevertheless, a few other changes, such as those observed in the C–H bending and stretching modes of MTO, fit the changes expected from C–H···O hydrogen bonds. The presence of such interactions is also supported by ab initio calculations, which predict a comparable stability for the MTO/methanol Lewis adduct and for the MTO/methanol hydrogen-bonded complex.

Experimental Section

General Remarks: All reagents and solvents were provided by Aldrich Co. and used as received. Raman spectra were recorded on a Jobin–Yvon T64000 spectrometer with a CCD detector, using the 514.5 nm line of an Ar+ laser (Coherent-Inova 90) and on a FT Bruker RFS-100 spectrometer using a Nd:YAG laser (Coherent Compass-1064/500N) with excitation wavelength of 1064 nm, using 2 cm^{-1} resolution. The liquid samples were sealed in Kimax glass capillaires (i.d. 0.8 mm).

Ab initio calculations were performed using the Gaussian 98W program package, rev. A.11.[17] Molecular structures were fully optimised without constraints at the B3LYP with ECP's on the Re atom (short core approximation) and 6-311G(d,p) on all the remaining atoms. The basis set superposition error (BSSE) correction for the dimerisation energies has been estimated by counterpoise calculations using the MASSAGE option of Gaussian 98W. Harmonic vibrational wavenumbers were calculated at the level of theory and scaled by an adequate factor in order to provide the best fit with experimental results.

Acknowledgments

The authors thank the Portuguese Foundation for Science and Technology, FCT, for the financial support (research project POCTI/QUI/35408/99, co-financed by the European Community Fund FEDER). PV thanks FCT for a Ph.D. research grant.

[1] C. C. Romão, F. E. Kühn, W. A. Herrmann, *Chem. Rev.* **1997**, *97*, 3197–3246.
[2] J. Mink, G. Keresztury, A. Stirling, W. A. Herrmann, *Spectrochim. Acta A* **1994**, *50*, 2039–2057.
[3] W. A. Herrmann, W. Scherer, R. W. Fischer, J. Blümel, M. Kleine, W. Mertin, R. Gruehn, J. Mink, H. Boysen, C. C. Wilson, R. M. Ibberson, L. Bachmann, M. Mattner, *J. Am. Chem. Soc.* **1995**, *117*, 3231–3243.
[4] S. Köstlmeier, G. Pacchioni, W. A. Herrmann, N. Rösch, *J. Organomet. Chem.* **1996**, *514*, 111–117.
[5] S. F. Parker, H. Herman, *Spectrochim. Acta A* **2000**, *56*, 1123–1129.
[6] P. Gisdakis, N. Rösch, É. Bencze, J. Mink, I. S. Gonçalves, F. E. Kühn, *Eur. J. Inorg. Chem.* **2001**, 981–991.
[7] X. Li, L. Liu, H. B. Schlegel, *J. Am. Chem. Soc.* **2002**, *124*, 9639–9647.
[8] N. Karger, A. M. Amorim da Costa, P. J. A. Ribeiro-Claro, *J. Phys. Chem. A* **1999**, *103*, 8672–8677.
[9] M. P. M. Marques, A. M. Amorim da Costa, P. J. A. Ribeiro-Claro, *J. Phys. Chem. A* **2001**, *105*, 5292–5297.
[10] P. J. A. Ribeiro-Claro, M. P. M. Marques, A. M. Amado, *ChemPhysChem* **2002**, *3*, 599–606.
[11] P. J. A. Ribeiro-Claro, M. G. B. Drew, V. Felix, *Chem. Phys. Lett.* **2002**, *356*, 318–324.
[12] P. D. Vaz, P. J. A. Ribeiro-Claro, *J. Phys. Chem. A* **2003**, *107*, 6301–6305.
[13] A. Goel, C. N. R. Rao, *J. Chem. Soc. Faraday Trans.* **1971**, 2828–2834.
[14] V. I. Bruskov, V. N. Bushuev, M. S. Okon, N. V. Shulyupina, V. I. Poltev, *Biopolymers* **1989**, *28*, 589–604.
[15] W. A. Herrmann, F. E. Kühn, P. W. Roesky, *J. Organomet. Chem.* **1995**, *485*, 243–251.
[16] P. J. A. Ribeiro-Claro, P. D. Vaz, *Chem. Phys. Lett.* **2004**, *390*, 358–361.
[17] M. J. Frisch, G. W. Trucks, H. B. Schlegel, G. E. Scuseria, M. A. Robb, J. R. Cheeseman, V. G. Zakrzewski, J. A. Montgomery Jr., R. E. Stratmann, J. C. Burant, S. Dapprich, J. M. Millam, A. D. Daniels, K. N. Kudin, M. C. Strain, O. Farkas, J. Tomasi, V. Barone, M. Cossi, R. Cammi, B. Mennucci, C. Pomelli, C. Adamo, S. Clifford, J. Chterski, G. A. Petersson, P. Y. Ayala, Q. Cui, K. Morokuma, D. K. Malick, A. D. Rabuck, K. Raghavachari, J. B. Foresman, J. Cioslowski, J. V. Ortiz, A. G. Baboul, B. B. Stefanov, G. Liu, A. Liashenko, P. Piskorz, I. Komaromi, R. Gomperts, R. L. Martin, D. J. Fox, T. Keith, M. A. Al-Laham, C. Y. Peng, A. Nanayakkara, C. Gonzalez, M. Challacombe, P. M. W. Gill, B. Johnson, W. Chen, M. W. Wong, J. L. Andres, C. Gonzalez, M. Head-Gordon, E. S. Replogle, J. A. Pople, *Gaussian 98*, *Revision A.11*, Gaussian, Inc., Pittsburgh, PA, **1998**.

Received: September 28, 2004

 © 2005 Wiley-VCH Verlag GmbH & Co. KGaA, Weinheim

Supramolecular Copper Phenanthroline Racks: Structures, Mechanistic Insight and Dynamic Nature

Venkateshwarlu Kalsani,[a] Heinrich Bodenstedt,[a] Dieter Fenske,[b] and Michael Schmittel*[a]

Keywords: Rack / HETPHEN / Self-assembly / Phenanthroline / Dynamics

Herein, we describe the preparation of several dynamic multicomponent supramolecular racks based on copper phenanthroline complexes using the HETPHEN concept (**het**eroleptic bis**phen**anthroline complexes). This approach employs bulky aryl substituents at the bisimine coordination sites to control the coordination equilibrium. The racks were characterised by spectroscopic methods, both in solution (^{1}H NMR, ESI-MS, UV/Vis, vapour pressure osmometry) and in the solid state (X-ray). Ligand exchange studies established the reversible nature of the aggregates, the details of which are vital for the development of higher level multicomponent structures. In this regard, the present rack assemblies contrast to the large multitude of known rack motifs that are almost exclusively built using kinetically inert coordination building blocks.

(© Wiley-VCH Verlag GmbH & Co. KGaA, 69451 Weinheim, Germany, 2005)

Introduction

Metallo-rack structures have a high standing in the burgeoning field of supramolecular chemistry due to their spatially well-defined linear array of metal ions that is attractive for many purposes, such as photoactive and electroactive nanowires.[1] Therefore, facile and quantitative access to rack aggregates is the goal of current research efforts.[1] Racks, however, by their very nature are multi-component structures that are most conveniently assembled under kinetic control, cf. the use of kinetically stable ruthenium coordination complexes,[1b,1c,1e–1g] even at the price of moderate yields. Preparation of rack structures under thermodynamic control is much more a challenge since in a dynamic multitopic aggregation scenario the requested heteroleptic combinations have to compete with homoleptic ones.[1d] Rewardingly, dynamic aggregation should allow for self-repair thus securing the most stable complex in very high yields if sufficient thermodynamic bias is installed.[2] Once the proof of principle is established one is set up to construe dynamic aggregates at surfaces that should be very useful for sensory purposes.[3]

At present, only one strategy is known to construct *dynamic* multicomponent rack structures (Scheme 1; strategy A).[4] Accordingly, ring constraints are utilised to prevent the formation of the homoleptic combination of one of the ligands, e. g. of an endotopic macrocyclic ligand. In combination with another rigid ligand the arrested ligand can combine to a heteroleptic rack-pseudorotaxane motif following the maximum site occupancy principle.[1d] A much easier way to *dynamic* multicomponent racks, however, should emerge from the HETPHEN[5] approach (strategy B). We have recently utilised the HETPHEN concept to establish **het**eroleptic bis**phen**anthroline copper complexes as building blocks for large nanostructures.[6] In our approach, heteroleptic aggregation is driven by steric and electronic factors which do not require an endotopic macrocycle. Instead, steric stoppers are required at the 2,9-positions of one of the bisimine coordination sites to prevent any homoleptic combination with itself. Therefore, in combination with another bisimine ligand only hetero combinations will result. This opens a much more facile way to heteroleptic dynamic aggregation than in previous reports.[7]

We have recently disclosed some preliminary results on dynamic rack structures in the context of our work on supramolecular nanogrids.[8] Herein, we now detail the potential of the HETPHEN[9] concept as a general strategy for the construction of multicomponent dynamic racks, provide structural insight into products and intermediates, and interrogate the dynamic nature of these unique assemblies.

Results and Discussion

Following the HETPHEN concept two approaches can be explored to prepare dynamic rack-type aggregates (Scheme 2). In both approaches one set of the ligand has to be instructed with the steric stoppers. In **approach I**, the linear bisphenanthroline is loaded with sterically bulky aryl

[a] Center of Micro- and Nanochemistry and Engineering, Organische Chemie I, Universität Siegen,
Adolf-Reichwein-Str., 57068 Siegen, Germany
Fax: +49-271-740-3270
[b] Institut für Anorganische Chemie, Universität Karlsruhe,
Engesserstr. 3045, 76128 Karlsruhe, Germany

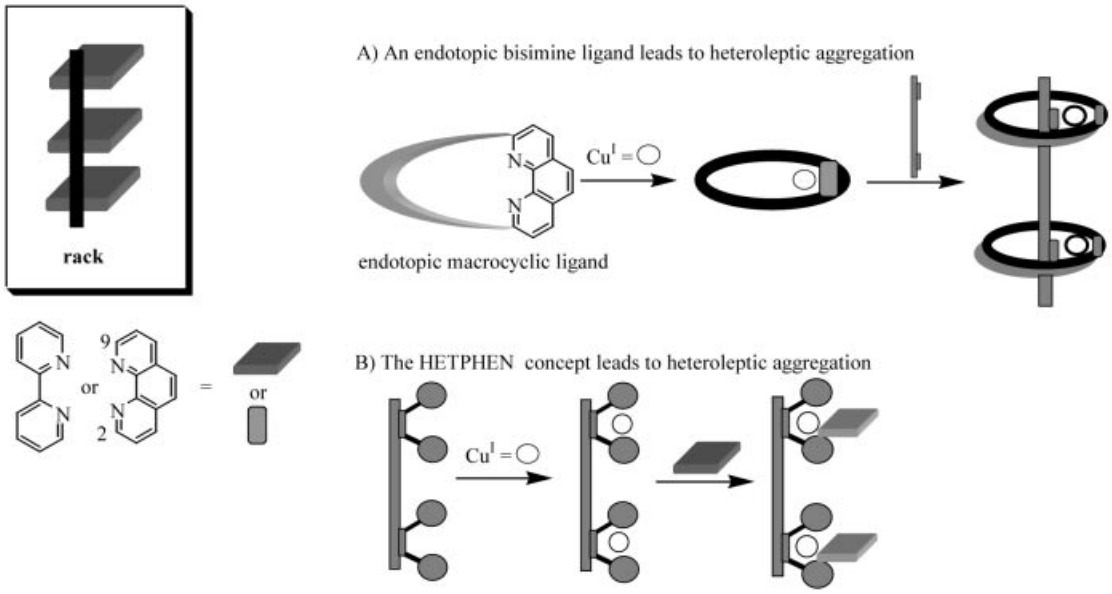

Scheme 1. Strategies to prepare dynamic rack-type motifs.[1d]

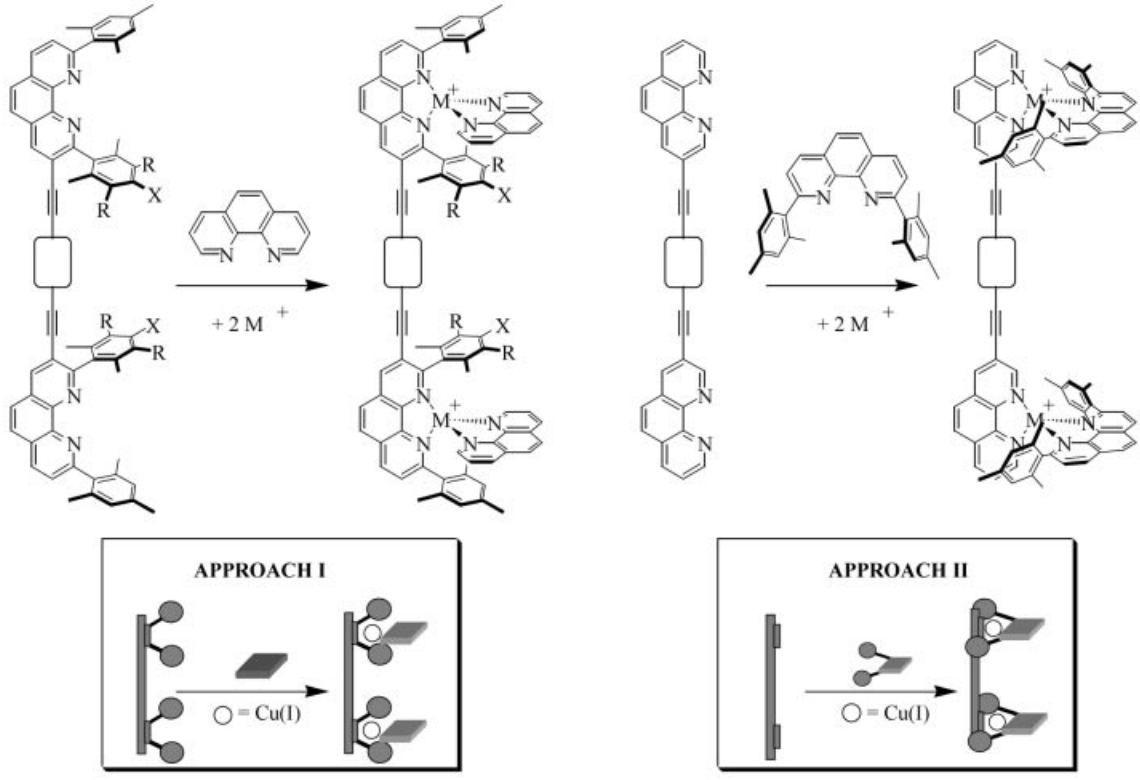

Scheme 2. Two different approaches for constructing dynamic multitopic *rack*-type motifs along the HETPHEN concept (in the bottom: a pictorial cartoon representation of the two approaches).

groups at the 2,9-positions of each phenanthroline site. In contrast, **approach II** makes use of monophenanthrolines that are equipped with the steric stoppers, while the linear bisphenanthroline is devoid of them.

The linear bisphenanthrolines **1a**,[10] **1b**[10] and **2**,[11] as well as the monophenanthrolines **3a**, **3b**,[13] **4a**,[6c] **4b**[12] and **4c**[13] were chosen for this study. Assembly of **1,2** with **3,4** in presence of metal ions of tetrahedral coordination geometry, such as copper(I) or silver(I) ions, is expected to yield the desired dynamic multicomponent racks.

To illustrate the need for control in the formation of dynamic rack assemblies using a coordination approach bisphenanthroline **1a** was treated with **3a** in the presence of $[Cu(MeCN)_4]PF_6$. The desired rack was obtained only as a

 © 2005 Wiley-VCH Verlag GmbH & Co. KGaA, Weinheim

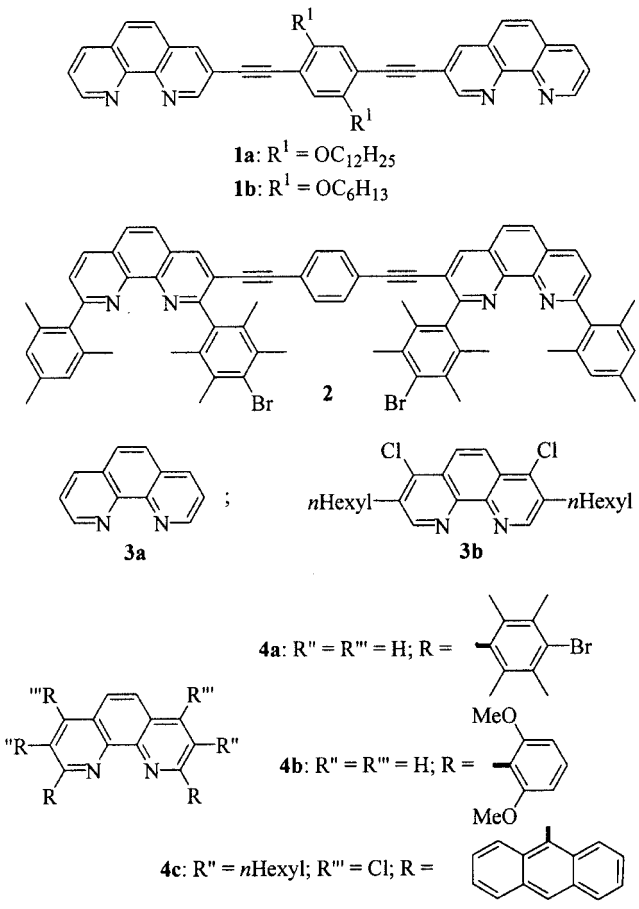

minor component as evidenced by ESI-MS and ^{1}H NMR spectroscopy. Rather, a complex mixture formed showing signals corresponding to the triangular-grid and signals corresponding to the homoleptic complex of **3a** as depicted in Scheme 3. ^{1}H NMR showed various sets of signals which arise from the resulting different aggregates. It is clear from the above experiment that cooperativity[7] can not be used solely to build dynamic heteroleptic aggregates.

Approach I

As discussed above, approach I uses a bisphenanthroline that has steric stoppers (as in ligand **2**) in combination with any phenanthroline with no steric stoppers at 2,9-positions (i.e. **3a**–**3b**). The combination of these two building blocks and Cu^I salt should result in heteroleptic racks.[8] Indeed, upon addition of $[Cu(MeCN)_4]PF_6$ to a dichloromethane solution of **2** and **3** the rack structures **R1,R2** were exclusively furnished as demonstrated by ^{1}H NMR, ^{13}C NMR, ESI-MS, and elemental analysis.

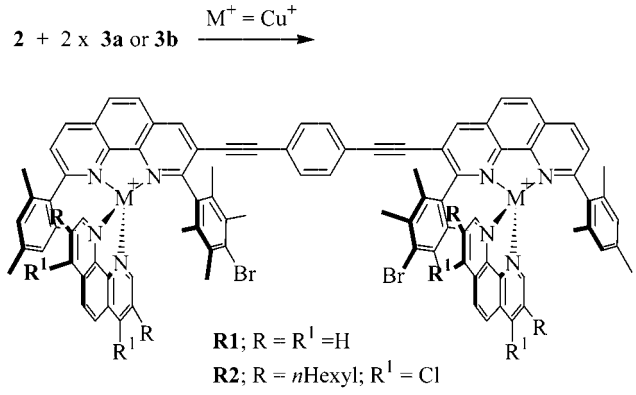

Mechanistic Tests on the Formation of $[Cu_2(2)]^{2+}$. Rack **R1** $[Cu_2(\mathbf{2})(\mathbf{3a})_2]^{2+}$ was selected as a model system and its formation systematically investigated using a variety of spectroscopic techniques (by, ^{1}H NMR, ESI-MS and spectrophotometric titrations). Treatment of ligand **2** with 2 equiv. of $[Cu(MeCN)_4]PF_6$ resulted in a yellow solution, the analysis of which by UV/Vis (absence of a MLCT band at 430–550 nm of a $[Cu(phenanthroline)_2]^+$ complex), ESI-MS and ^{1}H NMR suggested the formation of $[Cu_2(\mathbf{2})(MeCN)_2]^{2+}$ as the sole species. As expected, ligand **2** acts as a **HETPHEN** ligand that is not able to self-assemble to a homoleptic grid.

Progressive addition of $[Cu(MeCN)_4]PF_6$ to **2** (in dichloromethane) provided valuable information about the intermediates as they could be readily detected by ESI-MS, ^{1}H NMR, and UV/Vis spectroscopy. In the ^{1}H NMR spectrum, for example, the mesityl protons Mes-*H* can be used as a diagnostic marker to assign the composition of the intermediate species present in the equilibrium. Addition of Cu^I salt to **2** in dichloromethane resulted in two new sets of signals, one of which built up at the initial stage of the titration and disappeared as the titration proceeded. The first set of signals, formed during addition of the first equiv. of Cu^I salt, was assigned to $[Cu(\mathbf{2})(MeCN)]^+$. After addition of 2 equiv. of Cu^I salt a single set of signals resulted which could be readily assigned to $[Cu_2(\mathbf{2})(MeCN)_2]^{2+}$. Im-

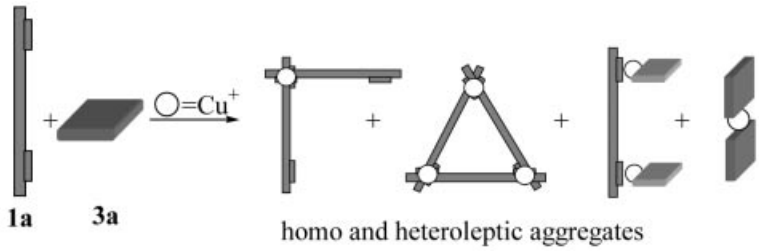

Scheme 3. Cartoon representation of the self-assembly of linear bisphenanthrolines and monophenanthrolines that are not instructed along the HETPHEN concept.

 © 2005 Wiley-VCH Verlag GmbH & Co. KGaA, Weinheim

portantly, during the whole process no signals were detectable at 5–6 ppm, which is considered to be a characteristic range for mesityl protons of a $[Cu(phenanthroline)_2]^+$ complex.[9] ESI-MS titration results further supported the above assignments.

The UV/Vis titration revealed the absence of a band at ca. 500 nm, indicating that formation of a $[Cu(phenanthroline)_2]^+$ complex with its characteristic MLCT had not occurred. These results indicate that in line with the behaviour of monophenanthroline analogs[9] ligand **2** has been successfully instructed not to assemble with itself.

Most convincingly the structure of $[Cu_2(\mathbf{2})(MeCN)_2]^{2+}$ was supported by a single crystal structure analysis (Figure 1). It is worthwhile to note that, though the present system is a simple one, the solid state characterisation of such an intermediate in a coordination equilibrium is quite unique. $[Cu_2(\mathbf{2})(MeCN)_2]^{2+}$ has neither a *syn* or *anti* conformation with regard to the two phenanthroline binding sites. Instead, the two sites comprise a dihedral angle of ca. 122 deg. Each copper(I) center is coordinated to one phenanthroline and a single acetonitrile molecule. The average Cu–N_{phen} bond length is 204 ± 3 pm, while the Cu–N_{MeCN} distance is much shorter with 186 pm (Table 1). In conclusion, the solid-state structure along with the ^{1}H NMR, ESI-MS and UV/Vis studies proves unequivocally that the HETPHEN concept allows to control the coordination equilibrium of specially designed phenanthroline ligands and to prevent formation of any bishomoleptic complex formation.

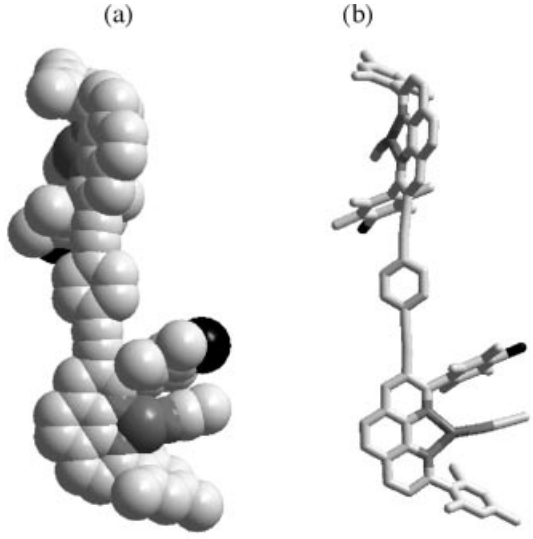

Figure 1. a) Space filling and b) stick representation of the crystal structure of $[Cu_2(\mathbf{2})(MeCN)_2]^{2+}$.

Mechanistic Tests on Formation of $[Cu_2(2)(3a)_2]^{2+}$. Upon addition of a second phenanthroline, such as **3a** or **3b**, to the intermediate $[Cu_2(\mathbf{2})(MeCN)_2]^{2+}$ in dichloromethane, the racks **R1** or **R2** were afforded in basically quantitative yield as evidenced by ^{1}H-NMR and ESI-MS. For example, in case of **R1** ESI-MS showed the presence of one single species at m/z = 814.5 which corresponds to $\mathbf{R1}^{2+}$. Equally, the ^{1}H-NMR illustrated the presence of a single symmetric species (Figure 2). The distinct high field shifts for the mesitylene protons (6.76 to 5.89 ppm) of **2** clearly indicated the formation of a bisheteroleptic complex.

Table 1. Selected Bond Lengths [Å] and Angles [°] for $[Cu_2(\mathbf{2})(MeCN)_2]^{2+}$.

Bond	Length [Å]	Angle	Angle [°]
N1–Cu1	2.016(17)	N1–Cu1–N5	146.14(1)
N2–Cu1	2.050(9)	N2–Cu1–N5	130.10(1)
N5–Cu1	1.856(18)	N2–Cu1–N1	82.91(2)
N3–Cu2	2.071(7)	N3–Cu2–N6	131.88(1)
N4–Cu2	2.017(21)	N4–Cu2–N6	142.61(2)
N6–Cu2	1.861(20)	N3–Cu2–N4	82.54(2)

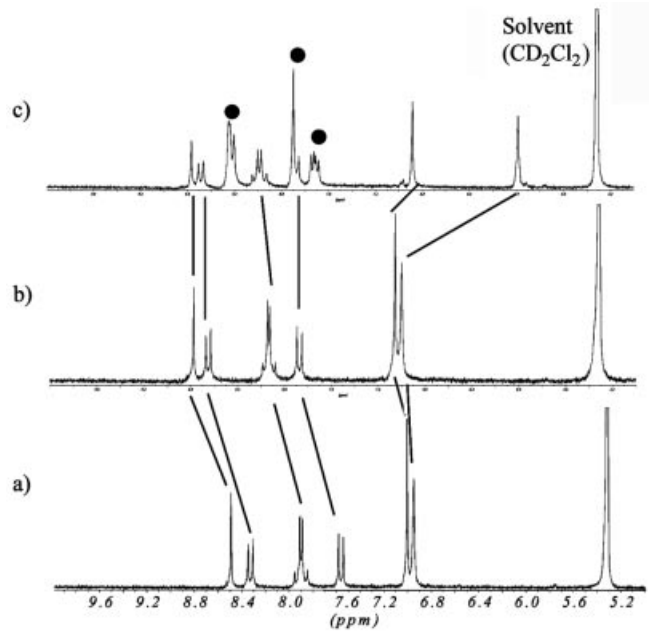

Figure 2. ^{1}H NMR changes in the aromatic region of **2** upon complexation with **3a**. a) free **2**; b) $[Cu_2(\mathbf{2})(MeCN)_2]^{2+}$; c) $[Cu_2(\mathbf{2})(\mathbf{3a})_2]^{2+}$. Signals in Figure **c** being marked by filled spheres belong to phenanthroline (**3a**) protons.

For further understanding, a titration was performed, in which **3a** was added to a dichloromethane solution of $[Cu_2(\mathbf{2})(MeCN)_2]^{2+}$ leading to pronounced changes in the ^{1}H NMR spectra. With the titration proceeding, two different sets of signals evolved for the mesityl protons that were readily assigned to $[Cu(\mathbf{2})(\mathbf{3a})]^+$ and $[Cu_2(\mathbf{2})(\mathbf{3a})_2]^{2+}$ using parallel ESI-MS results. While ESI-MS and ^{1}H NMR titrations proposed a qualitative picture of the mechanism of the self-assembly process, a UV/Vis titration was undertaken to determine the binding constants. It was performed by titrating **2** ($1.2\,10^{-6}$ M) and **3a** ($2.4\,10^{-6}$ M) with aliquot amounts of Cu^I solution in 20 additions (total 4 equiv. of Cu^+). Figure 3 displays the UV/Vis changes upon Cu^I salt addition showing the emerging MLCT transition at ca. 490 nm that is responsible for the red color. As shown in Scheme 4 a two step pathway seems most reasonable for the rack assembly process: it starts out with the formation of $[Cu(\mathbf{2})(\mathbf{3a})]^+$ taking up one more ligand **3a** and Cu^I to furnish the $[Cu_2(\mathbf{2})(\mathbf{3a})_2]^{2+}$ complex. The structure of

 © 2005 Wiley-VCH Verlag GmbH & Co. KGaA, Weinheim

$[Cu_2(\mathbf{2})(\mathbf{3a})_2]^{2+}$ was confirmed by its single crystal analysis.[8] Upon fitting this model with UV/Vis data using the SPECFIT program[14] binding constants could readily be extracted for complexes $[Cu(\mathbf{2})(\mathbf{3a})]^+$ (log K_{111} = 11.6) and $[Cu_2(\mathbf{2})(\mathbf{3a})_2]^{2+}$ (log β_{212} = 23.1). Models that did not fit were rejected.

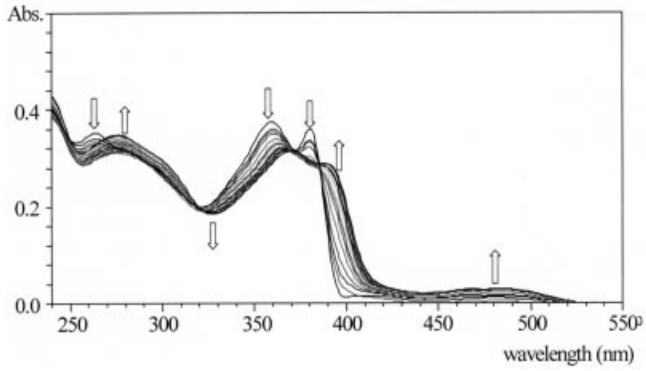

Figure 3. Spectrophotometric titration of **2** and 1,10-phenanthroline (**3a**) by aliquot amounts of Cu^I salt in 20 additions. Solvent: dichloromethane. T = 25(1) °C. [**2**] = 1.20×10^{-6} M and [**3a**] = 2.40×10^{-6} M.

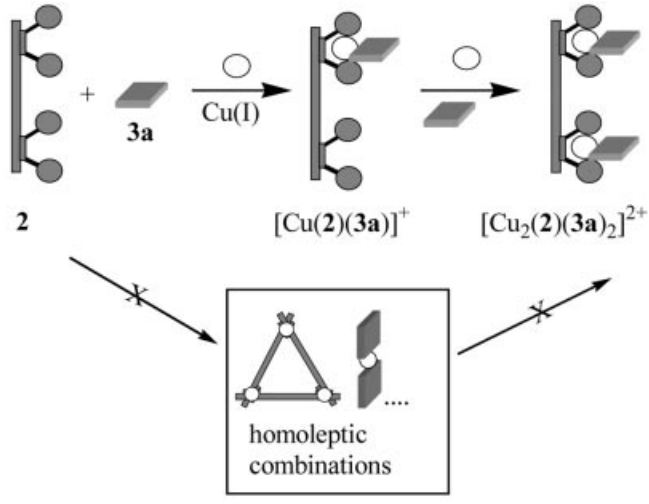

Scheme 4. Self-assembly path for **R1**.

Approach II

As suggested above, rack motifs should also be accessible by approach II. **4a**–**c** were designed according to the HETPHEN strategy, i.e. the 2,9-positions of all monophenanthrolines were loaded with steric stoppers while bisphenanthroline **1a** and **1b** were devoid of this element. Notably, racks **R3**–**R5** were readily afforded upon reacting **1a** with **4a**–**c** in presence of $[Cu(MeCN)_4]PF_6$ (Scheme 5). Similarly, **R6** was obtained by reacting **1b**, **4a** and Cu^I salt in dichloromethane (1:2:2 equiv.). All spectroscopic data was consistent with the proposed composition (see experimental section).

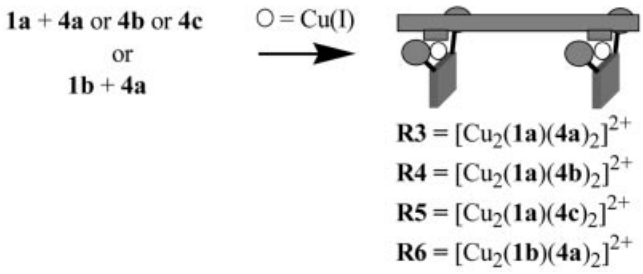

Scheme 5.

Apart from conventional characterisation techniques (^{1}H NMR, ESI-MS, UV/Vis, and elemental analysis), vapour pressure osmometry (VPO) was applied to characterise **R3** as one of the aggregates. VPO is a very useful method to analyse self assembled systems even if they are dynamic;[15] unfortunately, this technique has not been utilised frequently. For **R3** VPO provided a molar mass of 2417 Da, which is in excellent agreement (–2%) with the mass obtained from ESI-MS (2473). The characterisation of even larger dynamic structures by VPO is currently under investigation in our laboratory.

The structure of **R6** was solved by single-crystal X-ray analysis. The stick representation of the solid-state structure of **R6** is depicted in Figure 4. Unlike a previous structure[8] this rack has some deviation from prefect *transoid* conformation. Each copper(I) centre exhibits a pseudotetrahedral coordination geometry (N1–Cu1–N4 108.4°, N2–Cu1–N3 125.0°, N5–Cu2–N8 123.1°, N6–Cu2–N7 120.1°) and finds itself encapsulated by two bromoduryl rings of the bisphenanthroline (Table 2). The duryl groups of **4a** and the phen-

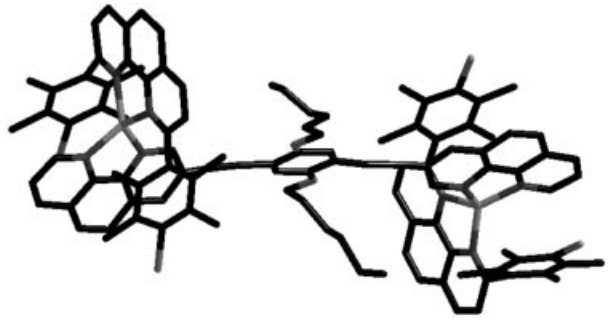

Figure 4. Single crystal structure of **R6**; stick representation.

Table 2. Selected bond lengths [Å] and angles [°] for **R6**.

Bond	Length [Å]	Angle	Angle (in degrees)
Cu1–N4	1.998	N4–Cu1–N2	131.9(4)
Cu1–N3	2.038	N4–Cu1–N3	81.5(4)
Cu1–N2	2.063	N2–Cu1–N3	125.0(4)
Cu1–N1	2.092	N4–Cu1–N1	108.0(4)
N2–Cu1–N1	81.0(5)		
N3–Cu1–N1	135.0(4)		
Cu2–N8	2.062	N7–Cu2–N8	80.0(5)
Cu2–N7	2.006	N7–Cu2–N6	119.5(4)
Cu2–N5	2.029	N8–Cu2–N6	127.5(4)
Cu2–N6	2.069	N7–Cu2–N5	129.0(4)
		N8–Cu2–N5	123.0(4)
		N6–Cu2–N5	82.5(4)

 © 2005 Wiley-VCH Verlag GmbH & Co. KGaA, Weinheim

anthroline plane of the second ligand **1b** are oriented face-to-face separated by 3.5 Å, suggesting π-stacking.

Dynamic Nature of Rack Motifs

The dynamic nature of the rack motifs was tested by an exchange experiment.[16] Specifically, we monitored the ligand exchange between **R3** and **R4** by using ESI-MS, with ligand **1a** being common in both **R3** and **R4** (Scheme 6). ^{1}H NMR experiments on the **R3** + **R4** ⇋ **R7** equilibration could not be performed due to signal overlap. However, the present example was studied by ESI-MS furnishing sensible insight into the dynamics of such aggregates. Such investigations are very informative when NMR application is limited.

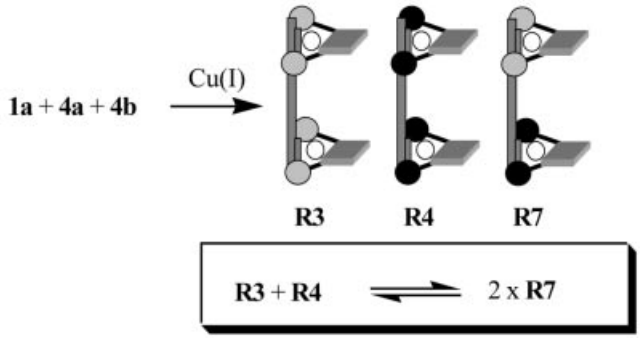

Scheme 6. Cartoon representation of ligand exchange equilibrium in solution after mixing **R3** and **R4**.

R3 and **R4** in dry dichloromethane were reacted in a 1:1 stoichiometric ratio. The ligand exchange process was observed readily (within ca. 5 min) by ESI-MS exhibiting signals corresponding to a mixture of the three racks **R3**, **R4** and **R7** in a %-ratio of 55, 55 and 100, respectively. This ratio did not change after longer times, indicating that equilibrium had been established at room temp. within less than 5 min (Figure 5). Analgous results were obtained when the racks were generated in one pot by reacting **1a**, **4a** and **4b** in presence of Cu^{I} salt. Isotopic distributions of **R3**, **R4** and **R7** were in excellent agreement with the calculated ones.

The composition was further confirmed by collisional fragmentation experiments. At higher voltages and temperature the ESI-MS is dominated by [Cu(**4a** or **4b**)(**1a**)]$^+$

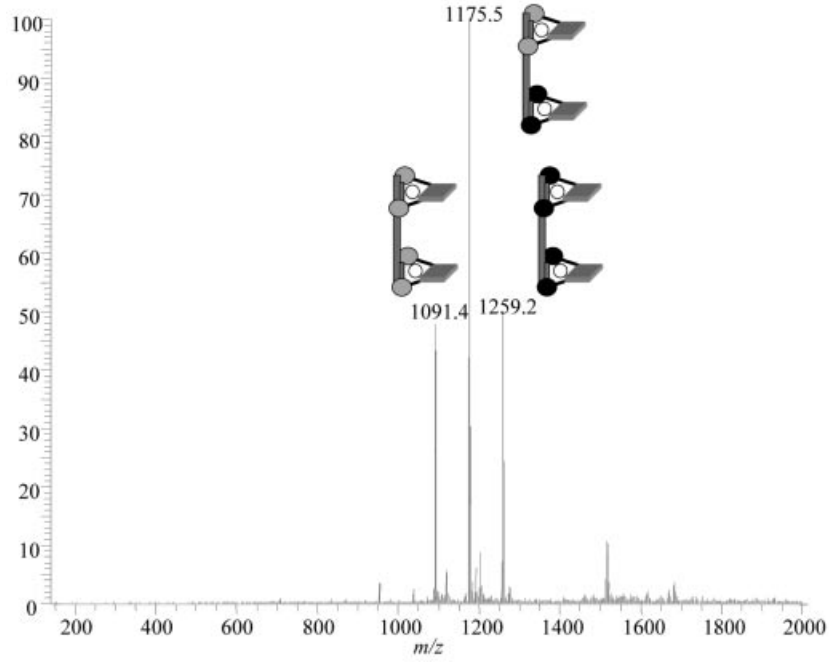

Figure 5. ESI-MS of the reaction mixture obtained when **1a**, **4a**, **4b** are treated with Cu^{I} salt in dichloromethane.

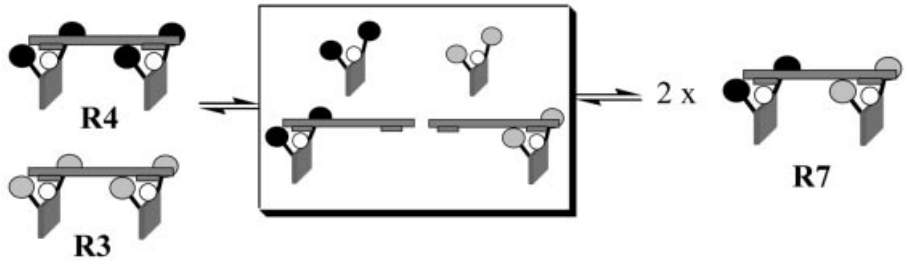

Scheme 7. Mechanism of the dynamic ligand exchange in the interconversion of racks.

 © 2005 Wiley-VCH Verlag GmbH & Co. KGaA, Weinheim

and [Cu(**4a** or **4b**)]$^+$ as fragments. It is interesting to note that a similar behaviour was observed for all rack structures, i.e. it is always the sterically loaded ligand that is bound to the metal ion in fragmentation processes. Presumably due to cation-π interactions between Cu^+ and 2,9-aryl groups complexes [Cu(**4a** or **4b**)]$^+$ are more stable than other combinations. These findings were corroborated through collisional fragmentation experiments of **R3**, **R4** and **R7**. For example, fragmentation of **R4** produced signals corresponding to the [Cu(**4b**)(**1a**)]$^+$ and [Cu(**4b**)]$^+$ species. If we translate these ESI-MS results onto the equilibration process in solution then it is reasonable to assume that in the dynamic ligand exchange any dissociation occurs with the metal ions attached to the sterically shielded HETPHEN ligands (Scheme 7).

Conclusions

In summary, the HETPHEN concept proves its value for the clean preparation of racks **R1**–**R6** from various bisphenanthrolines and monophenanthrolines in presence of Cu^+. X-ray and solution spectroscopic data, including ESI-MS, UV/Vis titrations and vapour pressure osmometry, disclose a clear picture of the self-assembly pathway and the products. Accordingly, ligands shielded along the HETPHEN concept (**2** and **4**) bind strongly to the copper ions but are instructed not to undergo self-association to homoleptic complexes. In combination with unshielded ligands **1** and **3** racks **R1**–**R6** are formed in a stepwise manner. Racks **R1**–**R6** are dynamic in nature as demonstrated in exchange processes at room temperature. Since Cu^I-based bisphenanthroline complexes are potential photoactive devices,[17] the present results should open an easy venue to diverse functional aggregates. Studies are in progress to install multi-functionalities into these rack motifs and to study their properties as a function of the dynamic behaviour.

Experimental Section

Ligands, **1a**,[11] **1b**,[11] **2**,[11] **3b**,[13] **4a**,[6c] **4b**[12] and **4c**[13] were prepared according to known procedures. ^{1}H NMR and ^{13}C NMR were measured on a Bruker AC 200 (200 MHz) or Bruker AC 400 (400 MHz). All ^{1}H NMR measurements were carried at room temperature in [D_2]dichloromethane. ESI-MS spectra were measured on a LCQ Deca Thermo Quest. Typically, each time 25 scans were accumulated for one spectrum. UV/Vis spectra were recorded on a Tidas II spectrophotometer using dichloromethane as the solvent.

Spectrophotometric titrations: Equilibrium constants of the complexes were determined in dichloromethane. Ligands 2 and 3a were titrated with aliquot amounts of a stock solution of copper(I) tetrakisacetonitrile hexafluorophosphate. All stock solutions were prepared by careful weighing (microgram scale) on an analytical balance. Absorption spectra were recorded at 25.0±(0.1) °C. Since the formation is instantaneous as evidenced by proton NMR, ESI-MS analysis and visible colour changes, the solutions were immediately analysed spectroscopically to avoid problems with the volatile solvent. The wavelength region from 240 nm to 600 nm was taken into account. Two equivalents (total) of metal salt in dichloromethane solution were added in 20 portions. The entire data sets comprising absorbances measured with one nanometer resolution were decomposed in their principal components by factor analysis. Subsequently, formation constants and their standard deviations were calculated by using the SPECFIT[14] program. Binding constants were determined from two independent titrations.

Vapor-Pressure Osmometry: The instrument (EuroOsmo 7000) was operated at 27 °C, dry dichloromethane was used as solvent. Calibration was performed by using tetrabutylammonium hexafluorophosphate as standard.

General Procedure for the Preparation of Racks R1–R6: Racks **R1**–**6** were prepared by mixing **1** (or **2**) and **3** (or **4**) with [Cu(MeCN)$_4$]PF_6 (1:2:2 equiv., respectively) in dichloromethane. The resulting dark red compound was analysed without any further purification by ESI-MS, ^{1}H NMR, COSY, ^{13}C NMR, IR and elemental analysis.

[Cu_2(2)(3a)$_2$](PF_6)$_2$ (R1): M.p. > 300 °C. ^{1}H NMR (CD_2Cl_2, 400 MHz): δ = 8.81 (s, 2 H, phen), 8.73 (d, J = 8.1 Hz, 2 H, phen), 8.40–8.50 (m, 8 H, phen), 8.23 (dd, 4 H, J = 8.1, J = 4.0 Hz, phen), 7.94 (s, 4 H, phen), 7.92 (d, J = 8.1 Hz, 2 H, phen), 7.75 (m, 4 H, phen), 6.93 (s, 4 H, phenyl), 6.03 (s, 4 H, mes), 1.81 (s, 12 H, CH_3), 1.59 (s, 12 H, CH_3), 1.57 (s, 18 H, CH_3). ^{13}C NMR (CD_2Cl_2, 100 MHz): δ = 161.3, 159.9, 148.1, 144.3, 143.2, 142.9, 139.9, 139.1, 138.2, 138.1, 136.9, 135.0, 134.1, 133.6, 132.5, 131.9, 129.2, 129.1, 128.7, 128.1, 127.9, 127.6, 127.3, 125.1, 122.9, 122.5, 117.5, 117.1 (arom.); 96.7, 87.7 (ethynyl); 20.6, 20.3 (2C), 18.5 (aliph.). IR (KBr): $\tilde{\nu}$ = 3411, 3057, 2919, 2209 (νC≡C), 1718, 1655, 1636, 1509, 1438, 1381, 1083, 856, 729, 550. ESI-MS: calcd. for $C_{96}H_{76}Br_2Cu_2N_8^{2+}$ [M^{2+}]: *m*/*z* 814.3, found: *m*/*z* 814.5. $C_{96}H_{76}Br_2Cu_2N_8{\times}2\,PF_6{\times}2\,H_2O$ (1954.54): C 58.99, H 4.13, N 5.73; found: C 58.95, H 4.01, N 5.84.

[Cu_2(2)(3b)$_2$](PF_6)$_2$ (R2): M.p. > 300 °C. ^{1}H NMR (CD_2Cl_2, 200 MHz): δ = 8.78 (s, 2 H, phen), 8.74 (d, 2 H, J = 8.4 Hz, phen), 8.20–8.36 (m, 10 H, phen), 7.91 (d, 2 H, J = 7.9 Hz, phen), 7.53 (s, 2 H, phen), 6.84 (s, 4 H, phenyl), 6.15 (s, 4 H, mes), 2.91–3.01 (m, 8 H, hexyl), 1.83 (s, 12 H, benzyl), 1.56 –1.65(m, 30 H, benzyl), 1.33 (s, 32 H, aliph.), 0.86 (s, 12 H, aliph.). ^{13}C NMR (CD_2Cl_2, 100 MHz): δ = 161.0, 159.9, 149.2, 144.1, 142.7, 142.3, 142.1, 140.5, 139.7, 138.6, 138.4, 138.1, 138.0, 137.7, 134.9, 133.4, 132.3, 131.8, 129.9, 129.1, 128.8, 128.1, 127.6, 127.3, 126.8, 124.4, 122.8, 122.5 (arom.); 96.7, 87.5 (ethynyl); 32.1, 31.8, 30.0, 29.4, 22.9, 20.6, 20.3, 20.1, 18.4, 14.2 (aliph.). IR (KBr): $\tilde{\nu}$ = 3439, 2926, 2857, 2212 (νC≡C), 1617, 1571, 1492, 1459, 1421, 1371, 1084, 842, 727, 635, 558. ESI-MS: calcd. for $C_{120}H_{120}Br_2Cl_2Cu_2N_8^{2+}$ [M^{2+}]: *m*/*z* 1051.5, found: *m*/*z* 1052.3. $C_{120}H_{124}Br_2Cl_4Cu_2N_8O_2{\times}2\,PF_6{\times}2\,H_2O$ (2428.96): C 59.34, H 5.15, N 4.61; found: C 59.13, H 4.95, N 4.51.

[Cu_2(1a)(4a)$_2$](PF_6)$_2$ (R3): M.p. > 300 °C. ^{1}H NMR (CD_2Cl_2, 200 MHz): δ = 8.51 (d, J = 8.6 Hz, 4 H, phen), 8.43 (m, 8 H, phen), 7.99 (s, 4 H, phen), 7.91 (m, 8 H, phen), 7.75 (dd, J = 8.9, J = 4.9 Hz, 2 H, phen), 7.06 (s, 2 H, phenyl), 4.01 (t, J = 5.5 Hz, 4 H, -OCH_2-), 1.70 (m, 40 H, benzyl), 1.53 (s, 14 H, benzyl and aliph.), 1.17–1.22 (m, 34 H, aliph.), 0.86 (t, J = 5.5 Hz, 6 H, aliph.). ^{13}C NMR (CD_2Cl_2, 100 MHz): δ = 160.1, 154.2, 149.3, 148.6, 145.1, 143.3, 142.1, 141.7, 138.9, 138.4, 136.3, 134.1, 133.6, 133.1, 130.4, 129.7, 129.1, 127.5, 126.8, 126.4, 123.4, 123.1, 118.5, 113.1 (arom.); 93.5, 91.4 (ethynyl); 33.4, 29.7 (2C), 30.1 (2C), 30.9 (2C), 26.5, 23.4, 21.1 (2C), 20.4, 19.1 (2C), 14.5 (aliph.). IR (KBr): $\tilde{\nu}$ = 3444, 2852, 2208 (νC≡C), 1618, 1579, 1498, 1459, 1426, 1388, 1221, 1164,

 © 2005 Wiley-VCH Verlag GmbH & Co. KGaA, Weinheim

1018, 936, 872, 843, 724, 632, 558. ESI-MS: calcd. for $C_{122}H_{126}Br_4Cu_2N_8O_2^{2+}$ [M^{2+}]: *m/z* 1091.5, found: *m/z* 1090.7. $C_{122}H_{128}Br_4Cu_2N_8O_3\times2PF_6\times H_2O$ (2491.01): C 58.82, H 5.18, N 4.50; found: C 58.62, H 5.29, N 4.34.

[Cu_2(1a)(4b)$_2$](PF_6)$_2$ (R4): M.p. > 300 °C. ^{1}H NMR (CD_2Cl_2, 200 MHz): δ = 8.62 (s, 2 H, phen), 8.58 (s, 4 H, phen), 8.39–8.8.51 (m, 6 H, phen), 8.15 (s, 4 H, phen), 7.18–7.96 (m, 8 H, phen), 7.70 (dd, *J* = 8.9, *J* = 4.1 Hz, 2 H, phen), 7.01 (s, 2 H, phenyl), 6.45 (t, 4 H, *J* = 8.4 Hz, phenyl), 5.71 (m, 8 H, phenyl), 3.95 (t, *J* = 6.7 Hz, 4 H, -OCH_2-), 3.30 (s, 12 H, methoxy), 3.26 (s, 12 H, methoxy), 1.70–1.77 (m, 4 H, aliph.), 1.15–140 (m, 36 H, aliph.), 0.86 (t, *J* = 5.9 Hz, 6 H, aliph.). ^{13}C NMR (CD_2Cl_2, 100 MHz): δ = 160.4, 159.3, 148.6, 143.5, 141.7, 141.5, 139.9, 139.2, 138.1, 137.9, 137.4, 137.1, 134.3, 132.8, 131.7, 131.2, 128.5, 128.2, 127.5, 127.0, 126.2, 123.8, 122.2, 121.9 (arom.); 96.1, 86.9 (ethynyl); 31.5, 31.3, 29.6, 29.4, 28. 8, 22.3, 20.1, 19.7, 19.6, 18.2, 18.0, 17.9, 13.6 (aliph.). IR (KBr): $\tilde{\nu}$ = 3443, 2924, 2851, 2208 (νC≡C), 1589, 1499, 1433, 1253, 1222, 1112, 1023, 841, 777, 723, 558. ESI-MS: calcd. for $C_{114}H_{114}N_8O_{10}Cu_2^{2+}$ [M^{2+}]: *m/z* 941.5, found: *m/z* 941.2. $C_{114}H_{118}Cu_2N_8O_{12}\times2PF_6\times2H_2O$ (2209.22): C 61.98, H 5.38, N 5.07; found: C 61.85, H 4.35, N 5.04.

[Cu_2(1a)(4c)$_2$](PF_6)$_2$ (R5): M.p. > 300 °C. ^{1}H NMR (CD_2Cl_2, 200 MHz): δ = 8.80 (s, 4 H, phen), 7.93 (s, 2 H, phen), 7.83 (d, 2 H, *J* = 7.9 Hz, phen), 7.61 (dd, *J* = 8.8, *J* = 4.1 Hz, 4 H, phen), 6.85–7.22 (m, 40 H, phen and anthracene), 6.64 (m, 4 H, phen and phenyl), 4.19 (t, *J* = 6.4 Hz, 8 H, -OCH_2-), 2.78 (m, 8 H, aliph. and benzyl), 1.24–1.63 (m, 50 H, benzyl), 0.76–0.93 (m, 24 H, aliph.), 0.49 (t, *J* = 5.9 Hz, 12 H, aliph.). ^{13}C NMR (CD_2Cl_2, 100 MHz): δ = 158.4, 158.4, 154.5, 155.2, 149.1, 147.3, 143.7, 143.1, 141.6, 140.9, 140.4, 139.6, 138.4, 136.6, 135.1, 133.5, 130.4, 129.4, 128.3, 127.4, 126.8, 125.9, 125.3, 124.9, 121.3, 117.5, 114.3, 103.9 (arom.); 91.9, 84.5 (ethynyl); 32.4, 32.3 (2C), 31.1 (2C), 30.1 (2C), 29.2 (2C), 26.5, 23.1 (2C), 22.3 (2C), 14.5, 14.3, 13.8 (2C) (aliph.). IR (KBr): $\tilde{\nu}$ = 3461, 3053, 2923, 2853, 2209 (νC≡C), 1622, 1604, 1545, 1498, 1461, 1366, 1345, 1276, 1220, 1106, 1014, 958, 841, 791, 736, 723, 557, 532. ESI-MS: calcd. for $C_{162}H_{158}Cl_4Cu_2N_8O_2^{2+}$ [M^{2+}]: *m/z* 1258.9, found: *m/z* 1257.9. $C_{162}H_{164}Cl_4Cu_2N_8O_5\times2PF_6\times3H_2O$ (2861.92): C 67.99, H 5.78, N 3.92; found: C 67.54, H 5.32, N 3.85.

[Cu_2(1b)(4a)$_2$](PF_6)$_2$ (R6): M.p. > 300 °C. ^{1}H NMR (CD_2Cl_2, 400 MHz): δ = 8.75 (d, *J* = 8.08, 4 H, phen), 8.43–8.52 (m, 8 H, phen), 8.25 (s, 4 H, phen), 7.91 (m, 8 H, phen), 7.75 (q, *J* = 4.8 Hz, 2 H, phen), 7.08 (s, 2 H, phenyl), 4.02 (t, *J* = 6.3 Hz, 4 H, -OCH_2-), 2.40 (s, 3 H, benzyl), 1. 95 (s, 3 H, benzyl), 1.77 (s, 16 H, aliph.), 1.65 (s, 12 H, benzyl), 1.53 (s, 12 H, benzyl), 1.45 (s, 6 H, benzyl), 1.41 (m, 6 H, benzyl), 1.20 (m, 6 H, benzyl), 0.71 (t, *J* = 7.08 Hz, 6 H, aliph.). ^{13}C NMR (CD_2Cl_2, 100 MHz): δ = 159.1, 154.3, 149.0, 148.1, 144.6, 142.4, 141.2, 140.7, 138.7, 138.1, 135.2, 134.6, 133.1, 132.9, 132.5, 129.7, 128.8, 128.1, 127.1, 126.4, 125.2, 121.5, 116.1, 113.2 (arom.); 92.4, 91.1 (ethynyl); 31.2, 29.4, 25.4, 22.1, 21.6, 20.9, 19.6, 14.1 (aliph.). IR (KBr): $\tilde{\nu}$ = 3394, 2921, 2301 (νC≡C), 1736, 1618, 1495, 1427, 1426, 1368, 1018, 956, 842, 724, 633, 557. ESI-MS: calcd. for $C_{110}H_{102}Br_4Cu_2N_8O_2^{2+}$ [M^{2+}]: *m/z* 1007.3, found: *m/z* 1006.2; X-ray structure see Figure 4.

Crystal Structure Determinations: Crystals were obtained by slow diffusion of toluene into a solution of the complexes in dichloromethane. Due to the poor quality of the crystals the crystal data are not excellent. Solvent molecules are severely disordered. The measurements were carried out with a STOE-IPDS2 diffractometer with graphite-monochromatised Mo-*Kα* radiation. Table 3 summarises the crystal data, data collection, and refinement parameters. All calculations were performed with the SHELXS-97 package.

Table 3. X-ray experimental data for [Cu_2(**2**)$(MeCN)_2\times2PF_6$] and [Cu_2(**1b**)(**4a**)$\times2PF_6$].

Formula	[Cu_2(**2**)$(MeCN)_2\times2PF_6$]	[Cu_2(**1b**)(**4a**)$_2\times2PF_6$]
	$C_{76}H_{66}Br_2Cu_2F_{12}N_6P_2$	$C_{110}H_{102}Br_4Cu_2F_{12}N_8O_2P_2$
M_w	1640.21	2304.68
Crystal system	monoclinic	triclinic
Space group	*P*1 21/c 1 (no. 14)	*P*–1 (no. 2)
a [A°]	21.297(4)	13.0625(80)
b [A°]	22.658(5)	21.250(15)
c [A°]	17.044(3)	23.75(2)
α [°]	90.00	113.00(3)
β [°]	104.29(3)	95.00(3)
γ [°]	90.00	94.00(3)
V [A^3]	7970(3)	6006.46(800)
Z	4	2
Color	yellow	red
Crystal shape	needle	needle
Crystal dimensions	0.3×0.15×0.1	0.3×0.15×0.1
$D_{calcd.}$ [$g\,cm^{-3}$]	1.367	1.274
F(000)	3656	2656
Radiation	Mo-*Kα*, graphite-monochromated	Mo-*Kα*, graphite-monochromated
Device type	IPDS2 STOE	IPDS2 STOE
Reflections collected	44882	43551
R(int.)	0.0543	0.1144
Independent reflections	20487	22023
Data/parameters	20487/900	22023/1285
GOF on F^2	1.564	1.234
Rreflections threshold expression	$>2\sigma(I)$	$>2\sigma(I)$
hkl limits (max./min.)	–23/29, –26/31, –23/21	–16/16, –26/26, –29/29
Final *R* indices [$I > 2\sigma(I)$]	R_1 = 0.0919, $_wR_2$ = 0.2404	R_1 = 0.1281, $_wR_2$ = 0.2960
R indices (all data)	R_1 = 0.1259, $_wR_2$ = 0.2558	R_1 = 0.2317, $_wR_2$ = 0.3352

 © 2005 Wiley-VCH Verlag GmbH & Co. KGaA, Weinheim

Acknowledgments

We would like to express our gratitude to the Deutsche Forschungsgemeinschaft (Schm 647/12-1 and -/13-1) and the Fonds der Chemischen Industrie for financial support.

[1] a) H. Sleiman, P. Baxter, J.-M. Lehn, K. Rissanen, *J. Chem. Soc. Chem. Commun.* **1995**, 715–716; b) G. S. Hanan, C. R. Arana, J.-M. Lehn, G. Baum, D. Fenske, *Angew. Chem. Int. Ed. Engl.* **1995**, *34*, 1122–1124; c) G. S. Hanan, C. R. Arana, J.-M. Lehn, G. Baum, D. Fenske, *Chem. Eur. J.* **1996**, *2*, 1292–1302; d) H. Sleiman, P. N. W. Baxter, J.-M. Lehn, K. Airola, K. Rissanen, *Inorg. Chem.* **1997**, *36*, 4734–4742; e) D. Brown, R. Zong, R. P. Thummel, *Eur. J. Inorg. Chem.* **2004**, 3269–3272; f) M. Benaglia, F. Ponzini, C. R. Woods, J. S. Siegel, *Org. Lett.* **2001**, *3*, 967–969; g) P. Ceroni, A. Credi, V. Balzani, S. Campagna, G. S. Hanan, C. R. Arana, J.-M. Lehn, *Eur. J. Inorg. Chem.* **1999**, 1409–1414.

[2] M. Schmittel, V. Kalsani, *Top. Curr. Chem.* **2004**, *245*, 1–53.

[3] a) U. Drechsler, B. Erdogan, V. M. Rotello, *Chem. Eur. J.* **2004**, *10*, 5570–5579; b) P. H. Kwan, M. J. MacLachlan, T. M. Swager, *J. Am. Chem. Soc.* **2004**, *126*, 8638–8639.

[4] a) C. O. Dietrich-Buchecker, J. P. Sauvage, J. P. Kintzinger, *Tetrahedron Lett.* **1983**, *24*, 5095–5098; b) U. Velten, M. Rehahn, *Chem. Commun.* **1996**, 2639–2640; c) S. S. Zhu, P. J. Carroll, T. M. Swager, *J. Am. Chem. Soc.* **1996**, *118*, 8713–8714.

[5] The HETPHEN (**het**eroleptic bis**phen**anthroline) approach is based on steric and electronic effects originating from bulky aryl substituents at the bisimine coordination sites to control the coordination equilibrium both kinetically and thermodynamically.

[6] a) V. Kalsani, H. Ammon, F. Jäckel, J. P. Rabe, M. Schmittel, *Chem. Eur. J.* **2004**, *10*, 5481–5492; b) M. Schmittel, V. Kalsani, L. Kienle, *Chem. Commun.* **2004**, 1534–1535; c) M. Schmittel, A. Ganz, D. Fenske, *Org. Lett.* **2002**, *4*, 2289–2292; d) M. Schmittel, H. Ammon, V. Kalsani, A. Wiegrefe, C. Michel, *Chem. Commun.* **2002**, 2566–2567.

[7] a) A. Marquis-Rigault, A. Dupont-Gervais, P. N. W. Baxter, A. Van Dorsselaer, J.-M. Lehn, *Inorg. Chem.* **1996**, *35*, 2307–2310; b) P. N. W. Baxter, J.-M. Lehn, B. O. Kneisel, G. Baum, D. Fenske, *Chem. Eur. J.* **1999**, *5*, 113–120; c) A. M. Garcia, D. M. Bassani, J.-M. Lehn, G. Baum, D. Fenske, *Chem. Eur. J.* **1999**, *5*, 1234–1238; d) P. N. W. Baxter, J.-M. Lehn, B. O. Kneisel, D. Fenske, *Angew. Chem. Int. Ed. Engl.* **1997**, *36*, 1978–1981.

[8] M. Schmittel, V. Kalsani, D. Fenske, A. Wiegrefe, *Chem. Commun.* **2004**, 490–491.

[9] a) M. Schmittel, A. Ganz, *Chem. Commun.* **1997**, 999–1000; b) M. Schmittel, U. Lüning, M. Meder, A. Ganz, C. Michel, M. Herderich, *Heterocycl. Commun*. 1997, **3**, 493–494.

[10] M. Schmittel, V. Kalsani, unpublished results.

[11] M. Schmittel, C. Michel, A. Wiegrefe, V. Kalsani, *Synthesis* **2001**, 1561–1567.

[12] U. Lüning, M. Müller, *Chem. Ber.* **1990**, *123*, 643–645.

[13] M. Schmittel, C. Michel, S. X. Liu, D. Schildbach, D. Fenske, *Eur. J. Inorg. Chem.* **2002**, 1155–1166.

[14] a) H. Gampp, M. Maeder, C. J. Meyer, A. D. Zuberbühler, *Talanta* **1985**, *32*, 95–101; b) F. J. C. Rossotti, H. S. Rossotti, R. J. Whewell, *J. Inorg. Nucl. Chem.* **1971**, *33*, 2051–2065; c) H. Gampp, M. Maeder, C. J. Meyer, A. D. Zuberbühler, *Talanta* **1985**, *32*, 257–264; d) H. Gampp, M. Maeder, C. J. Meyer, A. D. Zuberbühler, *Talanta* **1986**, *33*, 943–951.

[15] I. Higler, L. Grave, E. Breuning, W. Verboom, F. D. Jong, T. M. Fyles, D. N. Reinhoudt, *Eur. J. Org. Chem.* **2000**, 1727–1734.

[16] a) P. N. W. Baxter, *Comprehensive, supramolecular chemistry* (Eds.: J. L. Atwood, J. E. D. Davies, D. D. MacNicol, F. Vögtle, J.-M. Lehn), Pergamon, Oxford, **1996**, vol. 9, chapter *5*, 165–211; b) L. J. Charbonnière, A. F. Williams, U. Frey, A. E. Merbach, P. Kamalaprija, O. Schaad, *J. Am. Chem. Soc.* **1997**, *119*, 2488–2496; c) B. Olenyuk, A. Fechtenkotter, P. J. Stang, *J. Chem. Soc. Dalton Trans.* **1998**, *11*, 1707–1728; d) S. Leininger, B. Olenyuk, P. J. Stang, *Chem. Rev.* **2000**, *100*, 853–907; e) C. Addicott, N. Das, P. J. Stang, *Inorg. Chem.* **2004**, *43*, 5335–5338; f) F. Würthner, A. Sautter, D. Schmid, P. J. A. Weber, *Chem. Eur. J.* **2001**, *7*, 894–902; g) S. Hiraoka, Y. Kubota, M. Fujita, *Chem. Commun.* **2000**, 1509–1510.

[17] N. Armaroli, *Chem. Soc. Rev.* **2001**, *30*, 113–124.

Received: October 25, 2004

 © 2005 Wiley-VCH Verlag GmbH & Co. KGaA, Weinheim

A Ruthenium(II)-Complexed Rotaxane Whose Ring Incorporates a 6,6′-Diphenyl-2,2′-bipyridine: Synthesis and Light-Driven Motions

Jean-Paul Collin,[a] Damien Jouvenot,[a] Masatoshi Koizumi,[b] and Jean-Pierre Sauvage*[a]

Keywords: Rotaxanes / Ruthenium / Light-driven motions

By incorporating a 6,6′-diphenyl-2,2′-bipyridine (dpbipy) fragment in a ring, *endo* coordination of a ruthenium(II) center is performed selectively and almost quantitatively. The threaded system, containing a helical fragment, could be fully characterized. When the terminal functions of the rod-shaped helical complex threaded through the macrocycle are phenol groups, the complete rotaxane is prepared by the classical Williamson stoppering reaction in moderate yield. Light-induced motions of the unstoppered system (pseudo-rotaxane) and the real rotaxane have been studied. Under visible light irradiation, quantitative decoordination of the dpbipy-containing ring is observed, leading to the separate fragments (ring and helical thread) or to a new rotaxane (uncoordinated ring threaded by the dumbbell).
(© Wiley-VCH Verlag GmbH & Co. KGaA, 69451 Weinheim, Germany, 2005)

Introduction

The use of transition metals as templates to construct various interlocking and knotted topologies has been exploited by various groups in the course of the last few decades.[1–5] On the basis of related strategies, rotaxanes have also been prepared efficiently.[6,7] In the field of molecular machines and motors[8] light-driven machines are particularly promising.[9] In addition, several systems have been proposed which contain an electroactive transition-metal complex as the key component.[10] A related class of molecules is based on photoinduced electron transfer from the metal-to-ligand charge transfer excited state of a transition-metal complex [copper(I) or ruthenium(II)] to afford a new redox state, which will subsequently rearrange.[11] A very distinct family of dynamic molecular systems takes advantage of the dissociative character of ligand-field states in $Ru(diimine)_3^{2+}$ complexes.[12] In these compounds, one part of the system is set in motion by photochemically expelling a given chelate, the reverse motion being performed simply by heating the product of the photochemical reaction so as to regenerate the original state.

Results and Discussion

We have recently reported the synthesis of a [2]rotaxane constructed around a $Ru(diimine)_3^{2+}$ core.[13] The ring was a derivative of 6,6′-dimethyl-2,2′-bipyridine (dmbipy), and, in the course of the threading reaction, we noticed that both *exo*- and *endo*-coordination to the ruthenium(II) center of the rod-like fragment take place, as schematically represented in Scheme 1.

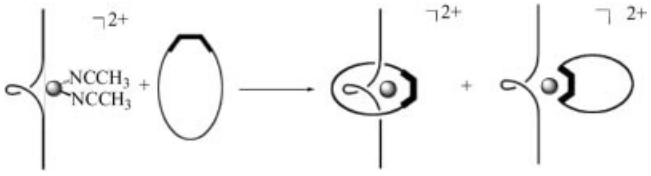

Scheme 1.

In order to circumvent this synthetic difficulty, we replaced the dmbipy motif by a 6,6′-diphenyl-2,2′-bipyridine chelate (dpbipy), which provides the system with greatly improved geometrical control. According to CPK models, exo coordination of a dpbipy-incorporating ring is virtually impossible, except with very large rings. As reported in this paper, this approach proved successful, and the desired rotaxane could be prepared in good yield, without formation of *exo*-coordinated species. In addition, the photochemical behavior of the compound and of its nonstoppered analogue has been investigated. In particular, it was shown that the ring is efficiently decoordinated from the ruthenium(II) center under visible light irradiation.

Synthesis of a Pseudo-Rotaxane

Preliminarily, we investigated the threading reaction leading to a pseudo-rotaxane, both ends of the helical rod-shaped fragment bearing inert $-OCH_3$ groups. As depicted in Figure 1, the starting ruthenium(II) complex $\mathbf{1}^{2+}$ [13] and

[a] Laboratoire de Chimie Organo-Minérale, UMR 7513 du CNRS, Université Louis Pasteur, Faculté de Chimie,
4, rue Blaise Pascal, 67070 Strasbourg Cedex, France
E-mail: sauvage@chimie.u-strasbg.fr
[b] Present address: Graduate School of Pharmaceutical Sciences, The University of Tokyo, ERATO, Japan Science and Technology Agency (JST),
Hongo, Bunkyo-ku, Tokyo 113–0033, Japan

 © 2005 Wiley-VCH Verlag GmbH & Co. KGaA, Weinheim **DOI: 10.1002/ejic.200401008**

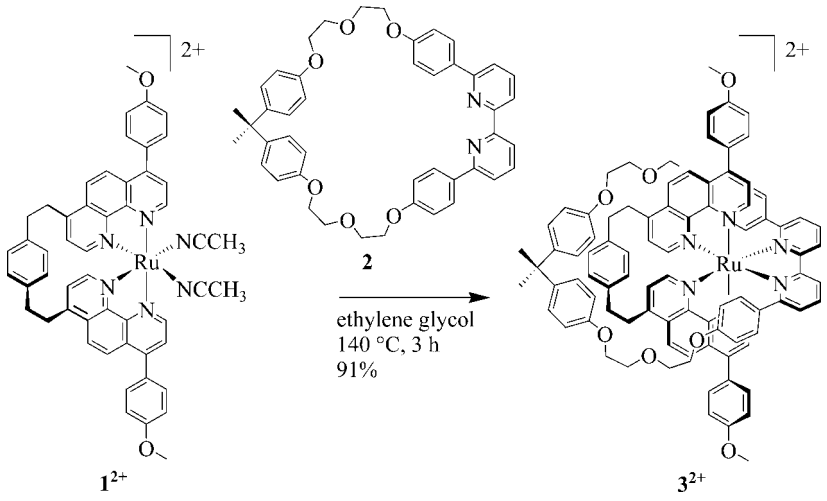

Figure 1. Synthesis of the threaded complex 3^{2+}.

ring **2**[14] reacted under relatively harsh conditions to afford the threaded complex 3^{2+} in good yield (91%) after chromatography (silica). Compound **2** is a 37-membered ring whose synthesis was recently described.[13] The presence of a dpbipy chelate and a bis(phenol) A unit ensures a certain rigidity to the ring, prohibiting swinging of the bis(phenol) A fragment "behind" the bipy chelate. Complex 1^{2+} is a ruthenium(II) complex that contains a helical bis(phenanthroline) organic fragment[13] (Figure 1).

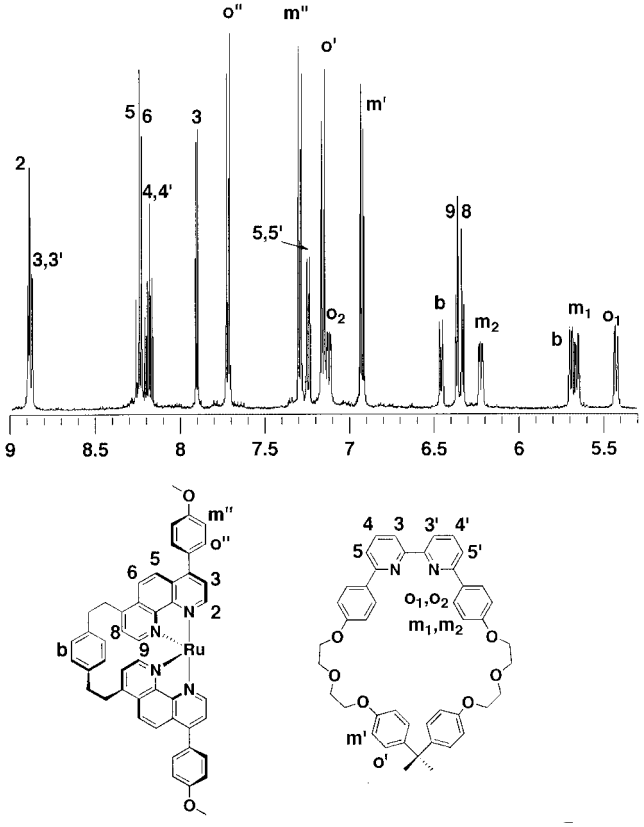

Figure 2. Aromatic region of the ^{1}H NMR spectrum of 3^{2+} in CD_3COCD_3, and proton indexation of the two parts of the molecule (thread and ring).

Complex $\mathbf{3[PF_6]_2}$ is a red complex, which can be recrystallized from an acetone/diethyl ether mixture. As expected, 3^{2+} is the *endo*-coordinated compound, with no contamination by a hypothetical *exo* isomer. ^{1}H NMR spectroscopy turned out to be particularly informative in this respect. The ^{1}H NMR spectrum of 3^{2+} is represented in Figure 2.

The assignment of the various H atoms (indicated on the drawing of the molecular fragments of 3^{2+}) could be done easily by analogy with related systems.[13,14] The most remarkable features of the spectrum are:

(i) The number of signals corresponding exactly to the expected number for a single and *symmetrical* complex ("upper" and "lower" parts of the screwlike fragment identical) and their sharpness.

(ii) The presence of four very well resolved signals for the protons of the two phenyl rings borne by the 2,2′-bipyridine fragment of the ring (o_1, o_2, m_1, m_2). Clearly, the "upper" part and the "lower" part of these phenyl rings are different and they do not interchange, at least at room temperature, as represented in a schematic fashion in the drawing of Figure 2.

Preparation of the Rotaxane

The complete rotaxane was prepared from **2** and 4^{2+}, the phenolic analogue of 1^{2+}, whose synthesis was previously reported.[13] The reaction is represented in Figure 3.

The "threading" step of 4^{2+} through ring **2** afforded the pre-rotaxane 5^{2+} in 82% yield. It was carried out in ethylene glycol at 140 °C. A high-purity sample was obtained by crystallization in acetone/diethyl ether. The "stoppering" reaction was performed using large tetraaryl-methane derivatives of the Gibbson type.[15] The precursor **6** was prepared as previously reported.[16] It reacted with $\mathbf{5[PF_6]_2}$ in DMF, at 60 °C, in the presence of a large excess of K_2CO_3 under argon. After work up and chromatography on silica the real rotaxane 7^{2+} was obtained as a red solid, in 56% yield. The compound can be crystallized in acetone/hexane.

 © 2005 Wiley-VCH Verlag GmbH & Co. KGaA, Weinheim

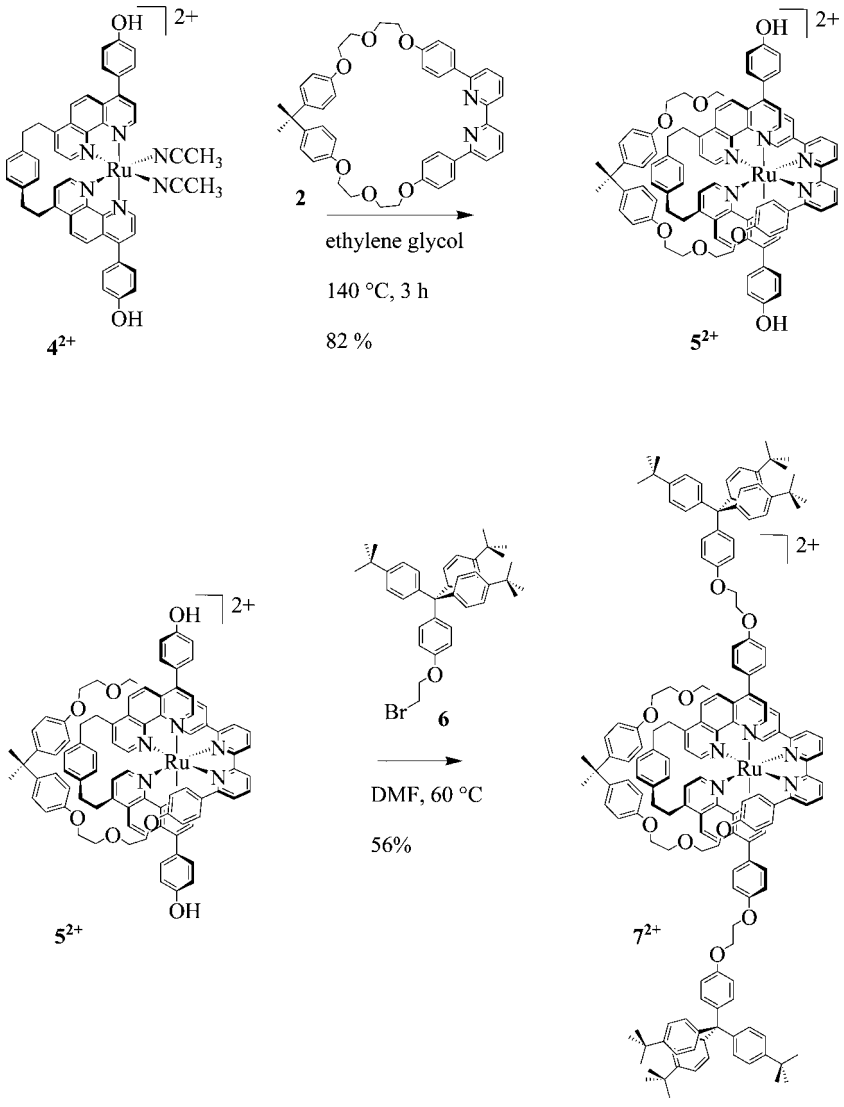

Figure 3. Sequence of reactions leading to the rotaxane 7^{2+}.

In the aromatic region, the ^{1}H NMR spectrum of $\mathbf{7^{2+}}$ is more or less identical to the superimposition of the spectra of $\mathbf{3^{2+}}$ and **6**. The "rope jump" phenomenon observed for pseudo-rotaxanes containing a larger and more flexible ring than in the present case, as already observed,[13,16] is not operative in $\mathbf{7^{2+}}$.

Light-Driven Molecular Motions in the Pseudo-Rotaxane 3^{2+} and in the Rotaxane 7^{2+}

In a first step, the photochemical behavior of complex $\mathbf{3^{2+}}$ was studied. By irradiating a solution of $\mathbf{3[PF_6]_2}$ in 1,2-dichloroethane, using a pass band filter centered around 470 nm and in the presence of a large excess of Cl^-, a clean photochemical reaction takes place. The reaction is schematically represented in Figure 4.

The photoinduced "unthreading" reaction was monitored by UV/Vis spectroscopy. The series of visible spectra, characteristic of metal-to-ligand charge transfer (MLCT) bands, is given in Figure 5.

From a band centered at 465 nm, typical of a Ru(diimine)$_3^{2+}$ complex,[17] a new spectrum is obtained by irradiation, which corresponds to a $RuCl_2$(diimine)$_2$ complex (λ_{max} = 562 nm). As expected, the MLCT band for the photochemical product is strongly bathochromically shifted from that of the tris(diimine) complex. The presence of a clean isosbectic point at 485 nm tends to indicate that the photochemical reaction is selective and quantitative. This has been confirmed by ^{1}H NMR spectroscopy and by thin-layer chromatography (silica; eluent: $CH_3CN/H_2O/KNO_3$, 100:10:1). Complex **8** is the only photochemical product detected and the starting complex $\mathbf{7^{2+}}$ has completely disappeared.

Similar experiments have been performed with the rotaxane. The reaction is represented in a schematic fashion in Figure 6.

The photochemical decoordination of the ring in $\mathbf{7^{2+}}$ is also selective and clean. Here again, in an analogous way as with $\mathbf{3^{2+}}$, an isosbectic point is observed at 486 nm. Thin-layer chromatography turned out to be particularly useful

 © 2005 Wiley-VCH Verlag GmbH & Co. KGaA, Weinheim

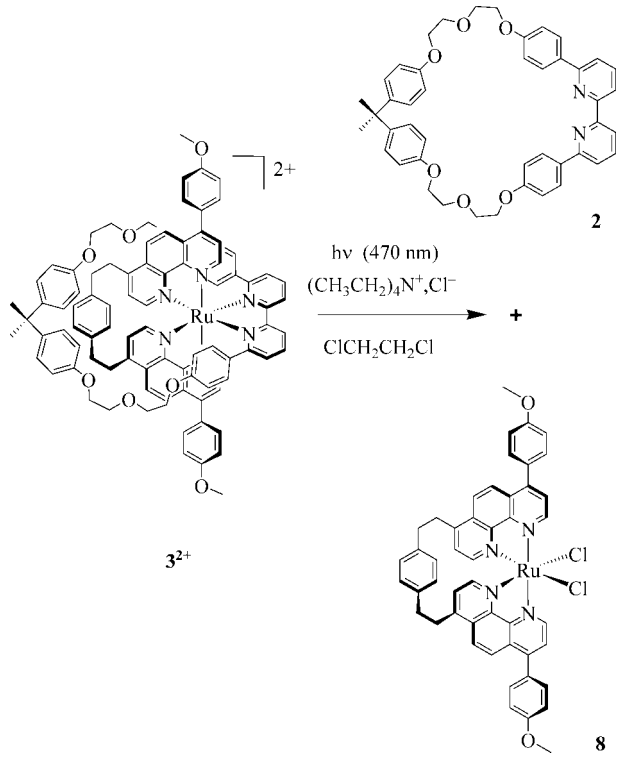

Figure 4. Photochemical expulsion of the macrocycle **2** from the threaded ruthenium complex $\mathbf{3}^{2+}$ in the presence of chloride anions.

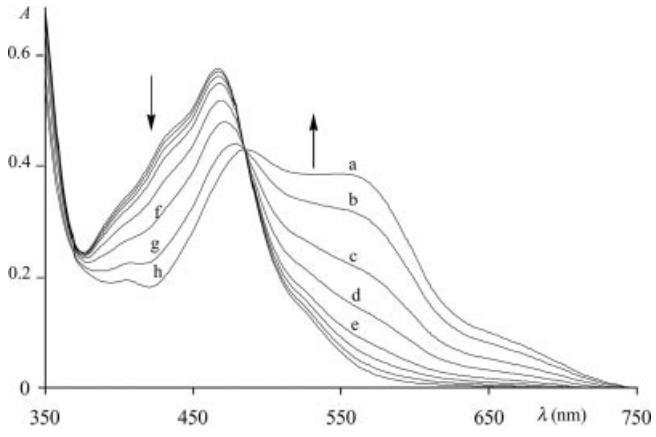

Figure 5. Absorption spectra (visible region) of a solution containing $\mathbf{7}^{2+}$ and $NEt_4^+Cl^-$ in $ClCH_2CH_2Cl$ before, during, and after irradiation. Spectra were recorded at t = 0 s (a), 15 s (b), 40 s (c), 90 s (d), 200 s (e), 400 s (f), 900 s (g), 2400 s (h).

to monitor the reaction. It showed that **7[PF$_6$]$_2$** is gradually converted to a single purple complex, **9**, under irradiation (470 nm). Importantly, traces of the free ring **2** could not be detected, demonstrating that both forms of the rotaxane, $\mathbf{7}^{2+}$ and **9**, do not undergo unthreading, even to a minor extent; The thermal recoordination reaction of **8**, leading back to $\mathbf{7}^{2+}$, is presently under investigation. Unfortunately, preliminary data seem to indicate that this reaction is not as clean and selective as in the case of a related catenane[10] nor as the presently described threading reaction of $\mathbf{1}^{2+}$ through **2**.

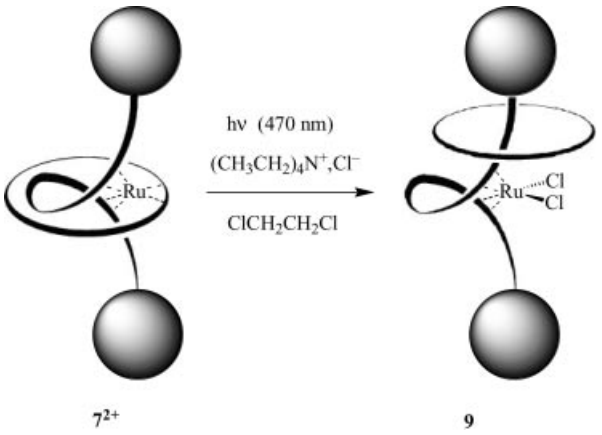

Figure 6. Schematic representation of the photochemical reaction leading to the disconnected rotaxane **9**.

Conclusions

The present report shows that a rotaxane and its non-stoppered analogue could be selectively prepared, the formation of *exo*-coordinated species being completely avoided. The size of the ring is important in controlling the course of the coordination reaction. In the present case, the 37-membered ring is large enough to accommodate the thick helical fragment by which it is threaded. However, it is neither so large nor flexible as to permit unthreading of the rotaxane dumbbell from the ring, once a decoordinated compound such as **9** has been formed.

Preliminary photochemical experiments demonstrated that clean and selective light-induced motions take place, the ring being decomplexed from the ruthenium(II) center. The thermal backward reaction is presently under investigation.

Experimental Section

General Methods: Oxygen- or moisture-sensitive reactions were performed in oven-dried glassware attached to a vacuum line with Schlenk techniques. Dry solvents were distilled from suitable desiccants under argon. Compounds **2** and **6** as well as complex **5[PF$_6$]$_2$** were prepared according to literature procedures.[13,16] All other chemicals were purchased from commercial sources and used without further purification. Column chromatography was carried out on silica gel 60 [Merck, 40–63 (fine) or 63–200 mesh]. Thin-layer chromatography (TLC) was performed on glass plates coated with silica gel 60 F254 (Merck). ^{1}H NMR spectra were recorded with either Bruker AVANCE 300 (300 MHz) or Bruker AVANCE 400 (400 MHz) spectrometers with the deuterated solvent as the lock and residual solvent as the internal reference. Electron-spray ionization mass spectra (ESI-MS) were recorded with a Bruker MicroTOF instrument. UV/Vis spectra (absorption spectroscopy) were recorded with a Kontron Instruments UVIKON 860 spectrometer at room temperature. All solutions were degassed and then saturated with oxygen-free argon. Light irradiation experiments: 3 mL of a sample solution of the complex (c = 10–5 M) were put in a closed UV-visible glass cell. The sample was irradiated with the beam of a 250 W slide projector, filtered by a water filter and focused on the cell. The evolution of the absorption spectrum of the solution was followed with respect to irradiation time.

 © 2005 Wiley-VCH Verlag GmbH & Co. KGaA, Weinheim

3[PF$_6$]$_2$: A suspension of **2** (15.0 mg, 0.0212 mmol) and **1[PF$_6$]$_2$** (16.0 mg, 0.0135 mmol) in degassed ethylene glycol (5 mL) was heated at 140 °C for 2 h under argon. The orange suspension turned into a red solution. After cooling to room temperature, a saturated aqueous solution of KPF_6 (10 mL) was added. The orange precipitate was then filtered and washed with water. The crude product was purified by column chromatography on silica gel [eluent: acetone/H_2O/saturated aqueous KNO_3 (100:0:0 to 100:5:0.5)] affording **3[PF$_6$]$_2$** (22.2 mg, 0.0123 mmol) in 91% yield. Crystallization from acetone/diethyl ether afforded a highly pure sample of **3[PF$_6$]$_2$** (8.9 mg, 0.0051 mmol) in 38% yield. ^{1}H NMR (500 MHz, $(CD_3)_2CO$, 25 °C): δ = 5.43 (d, 2 H, ^3J = 8.6 Hz, H^{o1}), 5.66 (d, 2 H, ^3J = 8.6 Hz, H^{m1}), 5.69 (d, 2 H, ^3J = 9.8 Hz, H^b), 6.23 (d, 2 H, ^3J = 8.5 Hz, H^{m2}), 6.33 (d, 2 H, ^3J = 5.8 Hz, H^8), 6.37 (d, 2 H, ^3J = 5.6 Hz, H^9), 6.46 (d, 2 H, ^3J = 8.6 Hz, H^b), 6.93 (d, 4 H, ^3J = 8.9 Hz, H$^{m'}$), 7.13 (d, 2 H, ^3J = 8.6 Hz, H^{o2}), 7.16 (d, 4 H, ^3J = 9.0 Hz, H$^{o'}$), 7.25 (d, 2 H, ^3J = 7.6 Hz, H$^{5,5'}$), 7.30 (d, 4 H, ^3J = 8.8 Hz, H$^{m''}$), 7.73 (d, 4 H, ^3J = 8.8 Hz, H$^{o''}$), 7.91 (d, 2 H, ^3J = 5.6 Hz, H^3), 8.19 (dd, 2 H, J = 7.6 and 7.9 Hz, H$^{4,4'}$), 8.23 (d, 2 H, ^3J = 9.5 Hz, H^6), 8.26 (d, 2 H, ^3J = 9.4 Hz, H^5), 8.89 (d, 2 H, ^3J = 6.8 Hz, H$^{3,3'}$), 8.90 (d, 2 H, ^3J = 5.2 Hz, H^2) ppm. ESI-MS: m/z = 829.08 ([M – 2 PF_6]/2); calcd. for $C_{93}H_{82}F_6N_6O_8PRu/2$ 829.24.

5[PF$_6$]$_2$: A suspension of **2** (39.4 mg, 0.056 mmol) and **4[PF$_6$]$_2$** (42.5 mg, 0.037 mmol) in degassed ethylene glycol (10 mL) was heated at 140 °C for 2 h under argon. The orange suspension turned into a red solution. After cooling to room temperature, a saturated aqueous solution of KPF_6 (30 mL) was added. The orange precipitate was then filtered and washed with water. The crude product was purified 3 times by column chromatography on silica gel [eluent: acetone/H_2O/saturated aqueous KNO_3 (100:0:0 to 100:10:1)] affording **5[PF$_6$]$_2$** (54.0 mg, 0.03 mmol) in 82% yield. Crystallization from acetone/diethyl ether afforded pure **5[PF$_6$]$_2$** (7.7 mg, 0.0044 mmol) in 12% yield. ^{1}H NMR (300 MHz, $(CD_3)_2CO$, 25 °C): δ = 5.45 (d, 2 H, ^3J = 8.3 Hz, H^{o1}), 5.72 (m, 4 H, H^{m1}, H^b), 6.25 (d, 2 H, ^3J = 8.5 Hz, H^{m2}), 6.36 (d, 2 H, ^3J = 5.6 Hz, H^8), 6.40 (d, 2 H, ^3J = 5.5 Hz, H^9), 6.48 (d, 2 H, ^3J = 7.9 Hz, H^b), 6.96 (d, 4 H, ^3J = 8.8 Hz, H$^{m'}$), 7.22 (m, 12 H, H^{o2}, H$^{o'}$, H$^{5,5'}$, H$^{m''}$), 7.66 (d, 4 H, ^3J = 8.6 Hz, H$^{o''}$), 7.92 (d, 2 H, ^3J = 5.6 Hz, H^3), 8.3 (m, 6 H, H$^{4,4'}$, H^6, H^5), 8.92 (m, 4 H, H$^{3,3'}$, H^2) ppm. ESI-MS: m/z = 1483.65 ([M– 2 PF_6^- – H + e$^-$]); calcd. for $C_{91}H_{77}N_6O_8Ru$ 1483.48.

7[PF$_6$]$_2$: 5[PF$_6$]$_2$ (54.0 mg, 0.03 mmol) and **6** (183.5 mg, 0.3 mmol) were added to a vigorously stirred suspension of K_2CO_3 (42 mg, 0.3 mmol) in DMF (30 mL) under a stream of argon. The mixture was heated to 60 °C and stirred for 42 h. DMF was removed in vacuo and a saturated aqueous solution of KPF_6 (30 mL) was added. The orange precipitate was then filtered and washed with water. The crude product was purified by column chromatography on silica gel [eluent: acetone/H_2O/saturated aqueous KNO_3 (100:0:0 to 100:5:0.5)] affording **7[PF$_6$]$_2$** (39.8 mg, 0.017 mmol) in 56% yield. Crystallization from acetone/*n*-hexane afforded pure **7[PF$_6$]$_2$** (30.7 mg, 0.011 mmol) in 36% yield. ^{1}H NMR (500 MHz, $(CD_3)_2CO$, 25 °C): δ = 5.44 (d, 2 H, ^3J = 8.6 Hz, H^{o1}), 5.67 (d, 2 H, ^3J = 8.3 Hz, H^{m1}), 5.70 (d, ^3J = 8 Hz, 2 H, 6 Hz, H^b), 6.24 (d, 2 H, ^3J = 8.6 Hz, H^{m2}), 6.35 (d, 2 H, ^3J = 5.4 Hz, H^8), 6.38 (d, 2 H, ^3J = 5.4 Hz, H^9), 6.47 (d, 2 H, ^3J = 8.3 Hz, H^b), 6.93 (m, 6 H, H$^{m'}$, H^w), 7.16 (m, 22 H, H^{o2}, H$^{o'}$, H^x, H^y), 7.26 (d, 2 H, ^3J = 7.9 Hz, H$^{5,5'}$), 7.36 (d, 16 H, Hz, H$^{m''}$), 7.74 (d, 4 H, ^3J = 8.6 Hz, H$^{o''}$), 7.93 (d, 2 H, ^3J = 5.4 Hz, H^3), 8.20 (t, 2 H, ^3J = 7.9 Hz, H$^{4,4'}$), 8.23 (d, 2 H, ^3J = 9.4 Hz, H^6), 8.28 (d, 2 H, ^3J = 9.4 Hz, H^5), 8.9 (m, 4 H, H$^{3,3'}$, H^2) ppm. ESI-MS: m/z = 1272.81 ([M – 2 PF_6]/2); calcd. for $C_{169}H_{1706}N_6O_{10}Ru/2$ 1273.1.

Acknowledgments

We thank the CNRS and the European Commission for financial support. We are also grateful to the French Ministry of Education for a fellowship (D. J.). M. K. thanks the JSPS Postdoctoral Fellowship for Research Abroad. We thank also Johnson Matthey Inc. for a loan of $RuCl_3$.

[1] a) C. O. Dietrich-Buchecker, J.-P. Sauvage, *Tetrahedron Lett.* **1983**, *24*, 5095; b) J.-P. Collin, C. Dietrich-Buchecker, C. Hamann, D. Jouvenot, J.-M. Kern, P. Mobian, J.-P. Sauvage, in *From the molecular to the Nanoscale: Synthesis and Structure,* Comprehensive Coordination Chemistry II, vol. 6 (Eds.: M. Fujita, A. Powell), Elsevier, **2003**.

[2] a) C. O. Dietrich-Buchecker, J.-P. Sauvage, *Angew. Chem. Int. Ed. Engl.* **1989**, *28*, 189; b) C. O. Dietrich-Buchecker, J. Guilhem, C. Pascard, J.-P. Sauvage, *Angew. Chem. Int. Ed. Engl.* **1990**, *98*, 1154.

[3] a) D. A. Leigh, P. J. Lusby, S. J. Teat, A. J. Wilson, J. K. Y. Wong, *Angew. Chem.* **2001**, *113,* 1586; *Angew. Chem. Int. Ed.* **2001**, *40,* 1538; b) C. A. Hunter, P. C. Mayers, *Nature* **2001**, *411*, 763; c) L. Hogg, D. A. Leigh, P. J. Lusby, A. Morelli, S. Parsons, J. K. Y. Wong, *Angew. Chem. Int. Ed.* **2004**, *43,* 1217; d) A.-M. Fuller, D. A. Leigh, P. J. Lusby, I. D. H. Oswald, S. Parsons, D. B. Walker, *Angew. Chem. Int. Ed.* **2004**, *43,* 3914.

[4] C. Hamann, J.-M. Kern, J.-P. Sauvage, *Inorg. Chem.* **2003**, *42*, 1877–1883.

[5] K. S. Chichak, S. J. Cantrill, A. R. Pease, S.-H. Chiu, G. W. V. Cave, J. L. Atwood, J. F. Stoddart, *Science* **2004**, *304*, 1308.

[6] a) J.-C. Chambron, A. Harriman, V. Heitz, J.-P. Sauvage, *J. Am. Chem. Soc.* **1993**, *115*, 6109; b) J.-C. Chambron, A. Harriman, V. Heitz, J.-P. Sauvage, *J. Am. Chem. Soc.* **1993**, *115*, 7419; c) J.-C. Chambron, V. Heitz, J.-P. Sauvage, *Bull. Soc. Chim. Fr.* **1995**, *132*, 340; d) M.-J. Blanco, J.-C. Chambron, V. Heitz, J.-P. Sauvage, *Org. Lett.* **2000**, *2*, 3051.

[7] T. J. Kidd, T. J. A. Loontjens, D. A. Leigh, *Angew. Chem. Int. Ed.* **2003**, *42,* 3379.

[8] a) V. Balzani, M. Gimez-Lipez, J. F. Stoddart, *Acc. Chem. Res.* **1998**, *31*, 405; b) J.-P. Collin, C. Dietrich-Buchecker, P. Gaviña, M. C. Jimenez-Molero, J.-P. Sauvage, *Acc. Chem. Res.* **2001**, *34*, 477 (special issue on molecular machines); c) V. Balzani, M. Venturi, A. Credi, *Molecular Devices and Machines: A Journey into the Nanoworld*, Wiley-VCH, Weinheim, **2003**; d) *Molecular Switches* (Ed.: B. L. Feringa), Wiley-VCH, Weinheim, **2001**; e) Molecular Machines and Motors (Ed.: J.-P. Sauvage), Structure and Bonding, vol. 99, Springer, New York, **2001**; f) V. Balzani, A. Credi, F. M. Raymo, J. F. Stoddart, *Angew. Chem. Int. Ed.* **2000**, *112,* 3484.

[9] a) R. Ballardini, V. Balzani, M. T. Gandolfi, L. Prodi, M. Venturi, D. Philp, H. G. Ricketts, J. F. Stoddart, *Angew. Chem. Int. Ed.* **1993**, *32*, 1301; b) A. M. Brower, C. Frochot, F. G. Gatti, D. A. Leigh, L. Mottier, F. Paolucci, S. Roffia, G. W. H. Wurpel, *Science* **2001**, *291*, 2124; c) D. A. Leigh, J. K. Y. Wong, F. Dehez, F. Zerbetto, *Nature* **2003**, *424*, 174.

[10] a) A. Livoreil, C. Dietrich-Buchecker, J.-P. Sauvage, *J. Am. Chem. Soc.* **1994**, *116*, 9399; b) D. J. Cardenas, A. Livoreil, J.-P. Sauvage, *J. Am. Chem. Soc.* **1996**, *118*, 11980; c) L. Raehm, J.-M. Kern, J.-P. Sauvage, *Chem. Eur. J.* 1999, 5, 3310; d) I. Poleschak, J.-M. Kern, J.-P. Sauvage, *Chem. Commun.* **2004**, 474.

[11] a) A. Livoreil, J.-P. Sauvage, N. Armaroli, L. Balzani, V. Flamigni, B. Ventura, *J. Am. Chem. Soc.* **1997**, *119*, 12114; b) N. Armaroli, V. Balzani, J.-P. Collin, P. Gavina, J.-P. Sauvage, B. Ventura, *J. Am. Chem. Soc.* **1999**, *121*, 4397; c) P. R. Ashton, R. Ballardini, V. Balzani, A. Credi, K. R. Dress, E. Ishow, C. J. Kleverlaan, O. Kocian, J. A. Preece, N. Spencer, J. F. Stoddart, M. Venturi, S. Wenger, *Chem. Eur. J.* **2000**, *6*, 3558.

[12] a) A.-C. Laemmel, J.-P. Collin, J.-P. Sauvage, *Eur. J. Inorg. Chem.* **1999**, 383; b) E. Baranoff, J.-P. Collin, J. Furusho, Y.

 © 2005 Wiley-VCH Verlag GmbH & Co. KGaA, Weinheim

Furusho, A.-C. Laemmel, J.-P. Sauvage, *Inorg. Chem.* **2002**, *41*, 1215; c) P. Mobian, J.-M. Kern, J.-P. Sauvage, *Angew. Chem. Int. Ed.* **2004**, *43*, 2392; d) R. Schofield, J.-P. Collin, N. Gruber, J.-P. Sauvage, *Chem. Commun.* **2003**, 188.
[13] D. Pomeranc, D. Jouvenot, J.-C. Chambron, J.-P. Collin, V. Heitz, J.-P. Sauvage, *Chem. Eur. J.* **2003**, *9*, 4247.
[14] J.-P. Collin, D. Jouvenot, M. Koizumi, J.-P. Sauvage, *Inorg. Chem.* Submitted.
[15] H. W. Gibson, S.-H. Lee, P. T. Engen, P. Lecavalier, J. Sze, Y. X. Shen, M. Bhela, *J. Org. Chem.* **1999**, *5*, 3310.
[16] Damien Jouvenot, PhD Thesis, Université Louis Pasteur, Strasbourg, June **2004**.
[17] V. Balzani, A. Credi, M. Venturi, *Coord. Chem. Rev.* **1998**, *171*, 3.

Received: December 08, 2004

 © 2005 Wiley-VCH Verlag GmbH & Co. KGaA, Weinheim

A Theoretical Investigation of Substituent Effects on the Absorption and Emission Properties of a Series of Terpyridylplatinum(II) Acetylide Complexes

Xiao-Juan Liu,[a] Ji-Kang Feng,*[a,c] Jian Meng,[b] Qing-Jiang Pan,[a] Ai-Min Ren,[a] Xin Zhou,[a] and Hong-Xing Zhang[a]

Keywords: Density functional calculations / Electronic structure / N ligands / Platinum

A comprehensive calculational investigation has been carried out on a series of complexes of the type [(terpyridyl-R^1)-Pt(C≡C-R^2)], where terpyridyl-R^1 is a series of substituted 2,2′:6′,2′′-terpyridyl ligands and C≡C-R^2 is a series of substituted acetylide ligands. In one series of complexes (**I**), the energy of the electronic excited state is varied by changing the substituents on the terpyridyl ligand (R^1). In a second series of complexes (**II**), this electronic structure variation is obtained by changing the *para* substituents (R^2) of the acetylide ligand. The effect of varying the substituents on the lowest-energy excited states of the complexes has been assessed by calculating their electronic structures and excitation energies. We anticipated that introduction of electron-withdrawing substituents on the terpyridyl ligand will benefit the LLCT (or MLCT) and prohibit the nonradiative pathways via d-d transitions in these complexes; introduction of electron-donating substituents on the acetylide ligand can also prohibit the nonradiative pathways by increasing the energy gaps between the HOMO–LUMO and d-d transitions. The results also reveal that the lowest-energy excitations of all complexes of series **I** and **IIa–b** complexes are dominated by a π(C≡C)→π*(terp) (LLCT) transition mixed with some energetically dπ(Pt)→terpyridyl (MLCT) transition. However, for the complexes **IIc–IId**, in which phenyl rings are introduced on the acetylide ligand, the lowest-lying absorptions of **IIc** and **IId** are predominately LLCT in character, with less MLCT mixture, due to a lower contribution of the Pt(d) orbital to the HOMO, while for **IIe**, with a stronger donor on the acetylide, the lowest-lying absorption is completely LLCT in character. The absorption and emission calculations using the TDDFT method are based on the optimized geometries obtained at the B3LYP/LanL2DZ and CIS/LanL2DZ levels, respectively.

(© Wiley-VCH Verlag GmbH & Co. KGaA, 69451 Weinheim, Germany, 2005)

Introduction

Transition metal complexes that feature metal-to-ligand charge transfer (MLCT) excited states have fascinated photochemists for four decades.[1–12] This fascination derives from a combination of features exhibited by MLCT excited states, which include visible light absorption, photoluminescence, long lifetimes, and relative inertness toward unimolecular photochemistry.[9] By far the majority of the work that has been carried out on MLCT states has focused on d^6 metal–polypyridine complexes of Ru^{II}, Os^{II}, and Re^{I}.[8,9,13,14] However, recently there has been increasing interest in the properties of d^8 platinum(II) complexes such as [PtL_2(diimine)], where L = halide, nitrile, thiolate, isocyanide, and acetylide.[15–27] These Pt^{II}–diimine complexes feature long-lived excited states that are believed to be based on dπPt→π* diimine MLCT. Terpyridylplatinum(II) complexes have also attracted considerable attention in recent years, mainly because of their interesting spectroscopic behavior[28–33] and useful physical and biological properties.[34,35] Indeed, these complexes have been established as important DNA intercalators[34,36] and protein probes.[37] Their spectroscopic properties and low-energy absorptions generally arise from metal-to-ligand charge transfer (MLCT) transitions. However, the development of the photochemistry of these complexes is limited by their nonemissive or short-lived MLCT excited states in solution at room temperature.[28] This lack of emission originates from low-lying d-d excited states, which provide facile nonradiative deactivation pathways by molecular distortion. For these complexes, the d-d and MLCT excited sates are very close in energy, resulting in fast internal conversion from MLCT to d-d excited states. Many efforts have been performed to obtain emissive terpyridylplatinum(II) complexes with long-lived excited states and high emission quantum yields.[28–33] The main strategy to construct long-lived and emissive terpyridylplatinum(II) complexes involves utilizing substituted terpyridyl ligands with low-lying LUMOs and/or ancillary ligands on acetylide with a large electron-donating ability to raise the HOMO of the metal center, hence resulting in

[a] State Key Laboratory of Theoretical and Computational Chemistry, Institute of Theoretical Chemistry, Jilin University, Changchun 130023, P. R. China
[b] The Key Laboratory of Rare Earth Chemistry and Physics, ChangChun Institute of Applied Chemistry, Chinese Academy of Science, Changchun 130023, P. R. China
[c] The College of Chemistry, Jilin University, Changchun 130023, P. R. China

the reduction of the MLCT excited state energy. As a result, the energy difference between the MLCT and d-d state increases. Yam et al.[33] have synthesized a series of terpyridylplatinum(II) acetylide complexes and studied the absorption and emission properties of these complexes. They found that the emission energies depend on the nature of the acetylide ligands with different substituents on the phenyl ring, i.e., the more electron-withdrawing the group on the phenyl acetylide ligand, the higher the emission energy. This trend is consistent with an assignment of a triplet metal-to-ligand charge transfer (^{3}MLCT) state, probably mixed with some acetylide-to-terpyridine ligand-to-ligand charge transfer (^{3}LLCT) character. Tung et al.[38] have synthesized and investigated a series of 4-tolylterpyridylplatinum(II) acetylide complexes, which show high quantum yield and long lifetime photoluminescence from a triplet metal-to-ligand charge transfer (^{3}MLCT) excited state in fluid solution at room temperature. In their UV/Vis spectra, all the complexes exhibit intense vibronic-structure absorption bands at $\lambda < 350$ nm which come from the ligand-to-ligand (LLCT) transition of terpyridyl and acetylide ligands as well as the charge transfer transition involved in the Pt–C≡CR moieties, while the low-energy absorption bands at 400–500 nm are tentatively assigned to the $d\pi(Pt) \rightarrow \pi^*$(trpy) MLCT transition.

Our aim is to determine to what extent the substituents affect the low-lying electronic transitions of these complexes and thus assess the validity of the generally accepted MLCT assignments of the lowest-energy absorption bands. We hope that our theoretical investigation can provide an important guidance for the design of these metal coordination complexes. Two series of terpyridylplatinum(II) acetylide complexes have been studied. In one series, **Ia**–**Ic**, the substituents (R^1) on the tepyridyl ligand are varied (H, CH_3, and CN) while the structure of the acetylide ligands is held constant as -CH_2OH to investigate the effect of different terpyridyl substituents on the spectra; in the second series, **IIa**–**IIe**, the terpyridyl ligand is held constant (4-tolylterpyridyl) while the *para* substituents (R^2) on the acetylide ligands are varied (CH_2OH, *n*-propyl, C_6H_4Cl-4, C_6H_5, and -$C_6H_5NH_2$) to study the influence of different acetylide substituents. The electronic structures of the complexes were calculated by density functional theory, which was also used to determine the nature of the electronic transitions. The solvent effect was simulated by the polarizable continuum model (PCM).[39]

Results and Discussion

Ground-State Geometry Optimization

The complexes investigated are shown in Scheme 1. To provide the structures to be used for the calculation of the electronic spectra, ground-state geometry optimizations were first performed on the studied complexes. Because of the different substituents R^1 and R^2, the C_{2v} symmetry is broken and the entire molecular point group is reduced to C_1. Taking complex **IId** as an example, the perspective drawing is shown in Figure 1. Selected bond lengths and angles are tabulated in Table 1, along with the available experimental values of the X-ray crystal structure of complex **IId** for comparison.

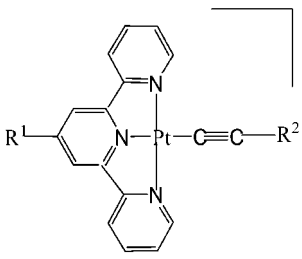

Ia: R^1 = H, R^2 = CH_2OH
Ib: R^1 = CH_3, R^2 = CH_2OH
Ic: R^1 = CN, R^2 = CH_2OH
IIa: R^1 = *p*-tolyl, R^2 = CH_2OH
IIb: R^1 = *p*-tolyl, R^2 = *n*-propyl
IIc: R^1 = *p*-tolyl, R^2 = C_6H_4Cl-4
IId: R^1 = *p*-tolyl, R^2 = C_6H_5
IIe: R^1 = *p*-tolyl, R^2 = $C_6H_4NH_2$-4

Scheme 1. Illustration of the investigated complexes.

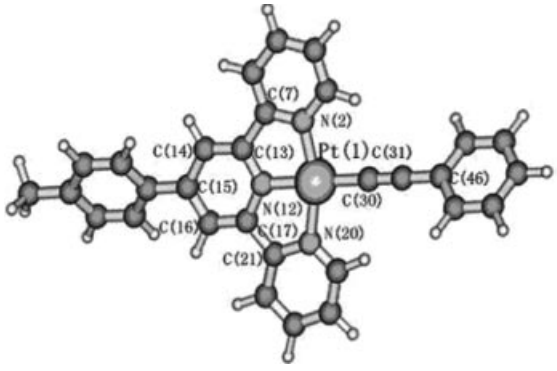

Figure 1. Complex structure and atom-numbering scheme taking complex **IId** as an example.

There is an overall satisfactory agreement between the theoretical and the available experimental data:[33] all the computed distances are within the experimental error (±0.04 Å). Table 1 shows that the variation of the substituents has more influence on the bond angles than on the bond lengths, as the bond lengths are almost unchanged while the bond angles undergo a comparatively large change. In particular, we should note the N(20)–Pt(1)–C(30) and Pt(1)–C(30)–C (31) angles, which show that when CH_2OH is connected to the acetylide ligand the Pt(1)–C(30)–C(31) angle deviates more from 180° (Table 1). This phenomenon is attributed to the weak interaction of CH_2OH with the Pt center. The coordination geometry about platinum is essentially square planar, with the bond length of the platinum to the central nitrogen atom [Pt(1)–N(12) = 1.99 Å] of the terpyridine ligand slightly shorter than to the other two outer nitrogen atoms [Pt(1)–N(2) and Pt(1)–N(20) are 2.05 Å and 2.04 Å, respectively], as required by the steric demands of the terpyridine ligand. These bond lengths are similar to the experimental[33] values of 1.97 Å, 2.01 Å, and 2.03 Å, respectively. Not surprisingly, the N–Pt–N angles [N(2)–Pt(1)–N(12) = 80.3°; N(12)–Pt(1)–N(20) = 80.3°; N(2)–Pt(1)–N(20) = 160.5°] deviate from the idealized values of 90° and 180° as a consequence of the geometric constraints imposed by the terpyridine ligand and the different substituents. The Pt–C bond length is 1.97 Å, which compares well with experimental

 © 2005 Wiley-VCH Verlag GmbH & Co. KGaA, Weinheim

Table 1. Selected calculated bond lengths [Å] and bond angles [°] for all the complexes. The numbers in parentheses are from the X-ray crystal structure of complex **IId**.

Parameter	**Ia**	**Ib**	**Ic**	**IIa**	**IIb**	**IIc**	**IId**	**IIe**
Pt(1)–N(2)	2.05	2.05	2.05	2.05	2.05	2.05	2.05 (2.01)[a]	2.05
Pt(1)–N(12)	1.99	1.99	1.99	1.99	1.99	1.99	1.99 (1.97)	1.98
Pt(1)–N(20)	2.04	2.04	2.04	2.04	2.04	2.04	2.05 (2.03)	2.04
Pt(1)–C(30)	1.96	1.96	1.96	1.96	1.97	1.97	1.97 (1.98)	1.96
C(30)–C(31)	1.23	1.23	1.23	1.23	1.23	1.23	1.24 (1.19)	1.24
C(7)–C(13)	1.48	1.48	1.48	1.48	1.48	1.48	1.48	1.48
C(17)–C(21)	1.48	1.48	1.48	1.48	1.48	1.48	1.48	1.48
N(2)–Pt(1)–N(12)	80.6	80.7	80.7	80.4	80.4	80.2	80.3 (80.6)	80.4
N(12)–Pt(1)–N(20)	80.4	80.3	80.3	80.3	80.4	80.4	80.3 (81.0)	80.3
N(2)–Pt(1)–N(20)	161.2	161.0	161.0	160.8	160.6	160.6	160.5 (161.6)	160.7
N(12)–Pt(1)–C(30)	176.8	177.1	177.2	176.9	179.9	179.9	179.98 (178.8) 179.95	
N(2)–Pt(1)–C(30)	96.2	96.4	96.6	96.5	99.7	99.7	99.7 (99.5)	99.7
N(20)–Pt(1)–C(30)	102.7	102.6	102.5	102.8	99.6	99.7	99.7 (98.9)	99.7
Pt(1)–C(30)–C(31)	168.7	169.2	169.7	169.2	179.6	179.98	179.97 (179.10) 179.98	

[a] From ref.[33]

value of 1.98 Å.[33] The C≡C bond length of 1.22 Å is comparable to the experimental value of 1.19 Å.

Molecular Orbital Analysis

Since the observed differences in the chemical and physical properties of the complexes rely primarily on the changes in the ground-state electronic structure, before dealing with the excited states we will discuss in detail the ground-state electronic structure of these complexes with a special emphasis on the frontier orbital components, HOMO–LUMO energy gaps, and metal–metal transition energies. The calculated frontier orbital energies are tabulated in Table 2 and plotted according to their energy levels in Figure 2. The assignment of the nature of each MO was made on the basis of its components, as shown in Figure 3 and 4, taking complexes **Ib** and **IId** as examples, respectively. Through the contour plots of Figures 3 and 4, we can see that there is a degree of interaction between the π-orbitals of the terpyridyl and acetylide moieties via the Pt dπ-orbitals, and so the substituent effect on both ligands can extend across the Pt center and influence the excitation

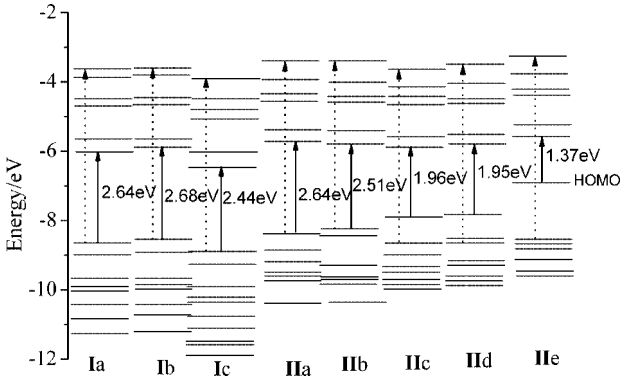

Figure 2. Molecular orbital energy level diagrams summarizing the B3LYP/LanL2DZ results. Solid and dotted arrows represent the energy gaps of HOMO and LUMO orbitals and that of d→d excitations.

nature of the complexes. A complete analysis of the highest occupied and lowest unoccupied molecular orbitals of all the complexes is presented in Table 3, where the orbital character and composition in terms of atomic contributions is presented. Percent contributions were calculated using

Table 2. Energies of the frontier molecular orbitals obtained from the B3LYP/LanL2DZ calculation.

Orbitals	**Ia**	**Ib**	**Ic**	**IIa**	**IIb**	**IIc**	**IId**	**IIe**
LUMO+5	–3.68	–3.58	–3.98	–3.45	–3.41	–3.60	–3.49	–3.27
LUMO+4	–3.94	–3.76	–4.59	–4.00	–4.02	–4.15	–4.06	–3.84
LUMO+3	–4.55	–4.47	–4.84	–4.38	–4.46	–4.58	–4.49	–4.28
LUMO+2	–4.72	–4.64	–5.12	–4.54	–4.53	–4.66	–4.57	–4.35
LUMO+1	–5.70	–5.61	–6.05	–5.42	–5.44	–5.57	–5.48	–5.26
LUMO	–6.03	–5.89	–6.50	–5.77	–5.78	–5.92	–5.83	–5.60
HOMO	–8.67	–8.57	–8.94	–8.41	–8.29	–7.88	–7.78	–6.97
HOMO–1	–9.07	–8.98	–9.34	–8.85	–8.48	–8.69	–8.63	–8.61
HOMO–2	–9.75	–9.68	–9.96	–9.24	–9.24	–8.99	–8.64	–8.68
HOMO–3	–9.93	–9.82	–10.25	–9.58	–9.65	–9.37	–9.26	–8.78
HOMO–4	–10.05	–9.94	–10.36	–9.65	–9.66	–9.49	–9.68	–9.11
HOMO–5	–10.50	–10.41	–10.81	–9.68	–9.79	–9.75	–9.73	–9.49
HOMO–6	–10.88	–10.72	–11.13	–9.81	–10.30	–9.83	–9.74	–9.55
HOMO–7	–11.31	–11.19	–11.52	–10.41	–11.01	–9.93	–9.86	–9.81
Energy gap	2.64	2.68	2.44	2.64	2.51	1.96	1.95	1.37

 © 2005 Wiley-VCH Verlag GmbH & Co. KGaA, Weinheim

Equation (1), where n is the atomic orbital coefficient and $\sum n^2$ is the sum of the squares of all atomic orbital coefficients in a specific molecular orbital.

$$[n^2/\sum n^2] \times 100 = \%\ \text{contribution} \quad (1)$$

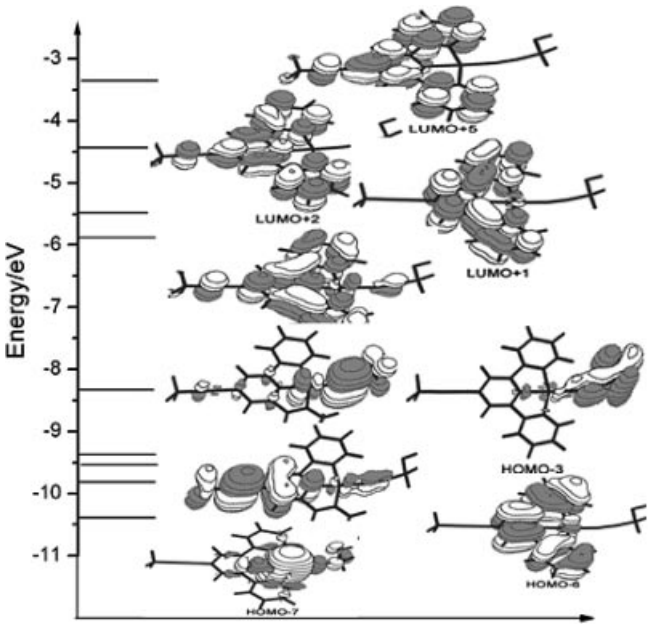

Figure 3. Frontier orbital diagram of complex **Ib** calculated at the B3LYP/LanL2DZ level. The plot on the right is the contour plot for each molecular orbital.

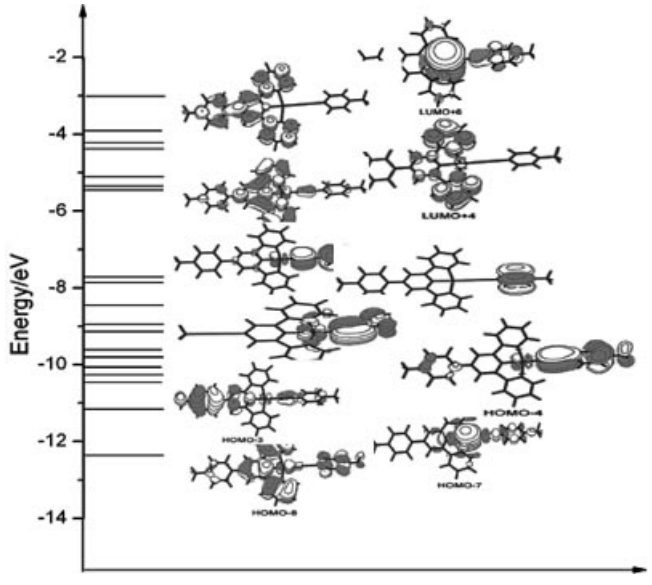

Figure 4. Frontier orbital diagram of complex **IId** calculated at the B3LYP/LanL2DZ level. The plot on the right is the contour plot for each molecular orbital.

Every complex is divided into three parts: the metal, the terpyridyl ligand with the substituent R^1, and the acetylide ligand with R^2. Each part of the percent contributions are the sum of the atomic coefficient squares.

In general, for all the investigated complexes, the first five unoccupied orbitals have the same character as the π*-orbital of the free terpyridyl ligand, although slightly perturbed by a small contribution from the d-orbital of Pt (about 6% for all the investigated complexes), and the LUMO+6 unoccupied orbitals are all composed of both Pt 3s and d_{z^2}orbitals and terpyridyl $2p_z$ orbitals. The low-energy transition character is therefore distinguished by the occupied orbital compositions. For series **I**, the occupied orbital compositions are perturbed by different substituted groups, but the relative ordering and characters are not changed: the HOMO orbitals have predominant -C≡C-R^2 character, mixed with Pt d-orbitals (24%, 37%, and 25% for **Ia**, **Ib** and **Ic**, respectively); the HOMO–3 and HOMO–7 orbitals are Pt- and terpyridyl-localized, respectively, and the HOMO–4 and HOMO–6 orbitals are a combination of Pt d-orbitals and terpyridyl π-orbitals (Table 3). Series **II** complexes can be separated into two groups: **IIa**,**b** (with -CH_2OH and -C_3H_7) in which the alkyl substituents are introduced on the acetylide and **IIc**–**e** in which phenyl rings are introduced on the acetylide. The HOMO orbitals for **IIa** and **IIb** have the same character as series **I** complexes, with predominant contributions from -C≡C-R^2 and some contributions from the Pt d-orbital (27% and 26%, respectively), while for **IIc**–**e** the HOMO orbitals are more –C≡C–R^2 in character due to the lower contributions from the Pt d-orbitals (8%, 10%, and 4% for **IIc**, **IId**, and **IIe**, respectively). In particular, the contribution of the Pt d-orbital to the HOMO (4%) in **IIe** is less than that to the LUMO (6%), so we characterized the HOMO in **IIe** as π(C≡C-R^2). It should be noted that introduction of a phenyl ring with a strong donor will lower the Pt d contribution to the HOMO (such as **IIc** and **IId**) or even change its character (such as **IIe**). According to the analysis of the frontier orbital compositions above, it can be found that the d-d excitations in complexes **Ia**–**c** and **IIa**,**b** occur between the HOMO to LUMO+6 transitions; while in complexes **IIc**–**e** the d-d excitations occur between the HOMO–1 to LUMO+6 transitions (see the dotted arrows in Figure 2).

We also investigated the substituent effects on the electronic orbital energy. Compared with those of complex **Ia**, the HOMO and LUMO molecular orbitals of **Ib** are lifted and the energy gap between the HOMO and LUMO ($\Delta E_{\text{HOMO–LUMO}}$) is increased ($\Delta E_{\text{HOMO–LUMO}}$ is 2.64 eV for **Ia** and 2.68 eV for **Ib**), while the HOMO and LUMO orbitals (especially the LUMO) of complex **Ic** are lowered greatly; the energy gap ($\Delta E_{\text{HOMO–LUMO}}$) decreases to 2.44 eV. According to the analysis above, the introduction of electron-withdrawing substituents on the terpyridyl ligands makes the HOMO→LUMO transition easier by lowering the $\Delta E_{\text{HOMO–LUMO}}$ energy gap, in particular by lowering the LUMOs, which are π* terpyridyl orbitals in this case. For the second series (**IIa**–**IIe**), it can be seen from Table 2 and Figure 2 that, first, compared with those of complexes **I**, the frontier molecular orbitals, especially the HOMOs, are lifted for all the series **II** complexes, and the energy gaps ($\Delta E_{\text{HOMO–LUMO}}$) are decreased further with the increase of the electron-donating ability of the substituents, and second, comparing the frontier orbitals of **IIc**, **IId**, and **IIe**, in which phenyl rings are included in the substituents,

 © 2005 Wiley-VCH Verlag GmbH & Co. KGaA, Weinheim

Table 3. Calculated percentage composition of selected frontier MOs of complexes **Ia**–**IIe**, expressed in terms of component fragments.[a]

MO	Character	Pt	Terpyridyl	Acetylide	MO	Character	Pt	Terpyridyl	Acetylide
	Ia					**IIb**			
90(V)	Pt + terp	36	53	11	118(V)	Pt + terp	40	50	10
89(V)	terp	1	99		117(V)	terp		100	
88(V)	terp	2	98		116(V)	terp	3	97	
87(V)	terp	1	99		115(V)	terp		95	5
86(V)	terp	2	98		114(V)	terp	2	97	1
85(V)	terp	6	92	3	**113(V)**	terp	6	88	6
84(O)	Pt + C≡C–R^2	24	9	67	**112(O)**	Pt + terp	26	13	62
81(O)	Pt	96	3	1	110(O)	terp + R^1		95	5
80(O)	Pt + terp	63	37		107(O)	Pt + terp	64	36	
78(O)	Pt + terp	42	44	14	106(O)	terp	14	86	
77(O)	Pt + terp	22	75	3	102(O)	terp	14	84	2
	Ib					**IIc**			
94(V)	Pt + terp	36	53	10	129(V)	Pt + terp	35	53	11
93(V)	terp	1	96	3	128(V)	terp		100	
92(V)	terp	2	98		127(V)	terp	3	97	
91(V)	terp	2	98		126(V)	terp		100	
90(V)	terp	2	97	1	125(V)	terp	2	98	
89(V)	terp	6	91	3	**124(V)**	terp	6	93	1
88(O)	Pt++C≡C–R^2	37	13	50	**123(O)**	Pt+ C≡C–R^2	8	6	86
85(O)	Pt	97	2	1	122(O)	Pt+ C≡C–R^2	28	9	56
84(O)	Pt + terp	63	37		120(O)	R^1	1	89	10
82(O)	Pt + terp	43	42	15	115(O)	Pt + terp	62	38	
81(O)	terp	11	88	1	114(O)	Pt + terp	19	83	
112(O)	Pt+ C≡C–R^2	24	17	59					
111(O)	Pt + terp	17	80	3					
	Ic					**IId**			
96(V)	Pt + terp	37	53	10	126(V)	Pt + terp	36	54	10
95(V)	terp		100		125(V)	terp		100	
94(V)	terp	2	98		124(V)	terp	3	97	
93(V)	terp	1	98		123(V)	terp		100	
92(V)	terp	2	98		122(V)	terp	2	98	
91(V)	terp	7	90	3	**121(V)**	terp	6	92	
90(O)	Pt + C≡C–R^2	25	10	64	**120(O)**	Pt + C≡C-R^2	10	7	83
88(O)	C≡C–R^2	4	1	95	119(O)	R^2			100
87(O)	Pt	97	2	1	118(O)	Pt + C≡C-R^2	30	10	60
86(O)	Pt + terp	65	35	5	116(O)	Pt + terp	62	38	
85(O)	terp	12	88		114(O)	Pt + C≡C-R^2	21	9	65
84(O)	Pt + terp	27	42	14	113(O)	Pt + terp	62	38	
83(O)	terp	10	80	2	111(O)	Pt + terp + C≡C-R^2	39	35	20
80(O)	terp	17	62	2	109(O)	Pt + terp + C≡C-R^2	14	19	54
	IIa					**IIe**			
114(V)	Pt + terp	35	55	10	130(V)	Pt + terp	36	55	9
113(V)	terp		100		129(V)	terp		100	
112(V)	terp	2	98		128(V)	terp	2	98	
111(V)	terp	1	99		127(V)	terp	100		
110(V)	terp	2	98		126(V)	terp	2	98	
109(V)	terp	6	92	2	**125(V)**	terp	6	87	6
108(O)	Pt + C≡C-R^2	27	12	61	**124(O)**	C≡C-R^2	4	10	86
105(O)	C≡C-R^2	3	4	92	123(O)	Pt + C≡C-R^2	19	14	66
104(O)	R^1	2	97		121(O)	C≡C-R^2			99
102(O)	Pt + terp	62	38		119(O)	R^1		98	
100(O)	Pt + terp	39	46	15	116(O)	Pt + terp	20	80	
					115(O)	Pt + terp + C≡C-R^2	43	32	26
					114(O)	Pt + C≡C-R^2	3	74	23

[a] HOMO and LUMO orbitals are shown in bold.

with those of **IIa** and **IIb**, in which the substituents are only CH_2OH or C_3H_7, the energy gaps ($\Delta E_{HOMO–LUMO}$) are lower for **IIc**, **IId**, and **IIe**, thus indicating that introduction of a phenyl ring will enhance the HOMO→LUMO transition by virtue of the decreasing energy gaps ($\Delta E_{HOMO–LUMO}$). Finally, a comparison of the HOMO levels (see Table 2) and $\Delta E_{HOMO–LUMO}$ (see Table 2 and Figure 2) of complexes **IIa** and **IIb** shows that the donating ability of *n*-propyl is stronger than that of CH_2OH. Furthermore, in complexes **IIc**, **IId**, and **IIe** it is obvious

 © 2005 Wiley-VCH Verlag GmbH & Co. KGaA, Weinheim

that the stronger donor group (NH_2 > H > Cl) on the phenyl rings leads to a greater decrease of the energy gaps ($\Delta E_{HOMO–LUMO}$ is 1.96 eV, 1.95 eV, and 1.37 eV for **IIc**, **IId**, and **IIe**, respectively).

The effect of the substituents on the electronic structures is described more quantitatively in Table 4, which lists the energy gaps of $\Delta E_{HOMO–LUMO}$, the d-d transition ($\Delta E_{d–d}$), and the energy difference between the HOMO–LUMO and the d-d transitions. The values of $\Delta E = \Delta E_{d-d} - \Delta E_{HOMO–LUMO}$ show that introduction of electron-withdrawing (donating) groups on the terpyridyl ligand makes this value larger (smaller) (in the first series this value is 2.35, 2.31, and 2.52 eV for complexes **Ia**, **Ib**, and **Ic**, respectively), and the introduction of electron-donating groups on the acetylide causes this value to increase (in the second series this value is 2.32, 2.37, 3.14, 3.19, and 3.97 eV for complexes **IIa**–**e**, respectively). As a result, with the increase of the energy difference between the HOMO–LUMO and the d-d transitions, the probability of nonradiative deactivation via the d-d state decreases. According to the analysis above, we can anticipate that the introduction of electron-withdrawing substituents on the terpyridyl ligand will benefit the LLCT (or MLCT) and prohibit the nonradiative pathways via d-d transitions in these complexes; the introduction of an electron-donating substituent on the acetylide ligand can also prevent the nonradiative pathways by increasing the energy gap between the HOMO–LUMO and d-d transitions. On the other hand, according to the energy gap law, the lower the energy of the excited state, the shorter the lifetime, so when we try to find effective light-emitting materials, we should consider these competing factors.

Table 4. The energy gaps (eV) of the $d\pi Pt \rightarrow d\pi^*Pt$ transitions ($\Delta E_{d–d}$) and HOMO → LUMO transitions ($\Delta E_{HOMO–LUMO}$), and the energy difference, ΔE, between them.

Complex	$\Delta E_{d–d}$	$\Delta E_{HOMO–LUMO}$	ΔE
Ia	4.99	2.64	2.35
Ib	4.99	2.68	2.31
Ic	4.96	2.44	2.52
IIa	4.96	2.64	2.32
IIb	4.88	2.51	2.37
IIc	5.09	1.96	3.14
IId	5.14	1.95	3.19
IIe	5.34	1.37	3.97

Absorption Properties

The low-energy absorption bands are very solvatochromic. To decrease the difference between calculated and observed transition energies, the effect of the solvent was simulated by the polarizable continuum model included in the Gaussian 98 program. In general, all these complexes show a blue-shift in the polarized solution, and this is in agreement with the recently published experimental data by Che et al.,[40] who pointed out that when the polarity of the solvent increases from benzene to CH_2Cl_2, acetonitrile, and ethanol, the broad low-energy absorption band blue-shifts in energy (a further explanation for this blue-shift is presented later). Taking molecule **IIa** as an example, the calculated absorptions in the gas phase and in dichloromethane solution are comparatively listed in Table 5. It can be seen that the first two absorptions show a comparatively strong solvatochromic effect − the 545 nm and 394 nm absorptions in the gas phase correspond to the 460 nm and 361 nm absorptions in solution, respectively − while the other absorptions show little solvatochromic effect. This phenomenon is in accordance with the experimental results.[28–33,38] The complete absorption spectrum for complex **IIa** is plotted in Figure 5 (in the plot, every absorption with different oscillator strength is selected, *f* is the oscillator strength, and the horizontal axis is the absorption wavelength).

Table 5. Selected calculated TDDFT singlet excitation energies for complex **IIa** in the gas phase and in CH_2Cl_2 solution, together with experimentally observed values.

G98/B3LYP		G98/B3LYP (PCM)		Exp.[a]		Transition designation
λ [nm]	Osc.	λ [nm]	Osc.	λ [nm]	ε [$M^{-1}cm^{-1}$]	
545	0.14	460	0.19	430	7260	LLCT+MLCT
394	0.12	361	0.17	342	19300	LLCT+MLCT
314	0.14	316	0.17	328	18000	LLCT
310	0.15	314	0.25	315	18500	MLCT+IL
269	0.20	272	0.29	274	35900	LLCT
257	0.31	265	0.20			LLCT
254	0.41	247	0.37			LLCT

[a] Taken from ref.[38]

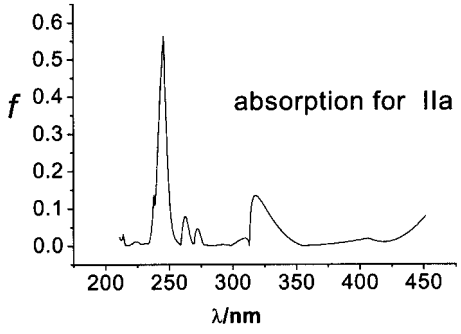

Figure 5. UV/Vis absorption spectrum of **IIa** in dichloromethane solution (*f* is the oscillator strength).

The calculated absorption results in dichloromethane solution from time-dependent DFT calculations (TDDFT) are listed in Table 6. In the first series, complexes **Ia**–**Ic**, introduction of a donor (CH_3 for **Ib**) on the terpyridyl ligands causes the absorptions to be blue-shifted (from 452 nm to 449 nm for the first absorption). This result is in accordance with the electronic-structure calculation results since introduction of an electron-donating group leads to the LUMO being lifted and the energy gap ($\Delta E_{HOMO–LUMO}$) being increased, which causes the absorption to be blue-shifted. This is consistent with the literature,[24] where the blue shift arising from methyl substitution of the bipyridyl ligand is attributable to destabilization of the π* level by electron-donating methyl substituents. The introduction of an electron-withdrawing group (CN) makes the absorption red-shift (from 452 nm to 487 nm for the first absorption). This result is also in accordance with

 © 2005 Wiley-VCH Verlag GmbH & Co. KGaA, Weinheim

the electronic-structure calculations since introduction of electron-withdrawing groups on the terpyridyl ligands leads the LUMO to be lowered and the energy gap ($\Delta E_{HOMO-LUMO}$) to decrease, which results in the red-shift. In the second series of complexes, **IIa**–**IIe**, it can be seen that the stronger the electron-donating nature of the substituents on the acetylide, the more red-shifted the absorptions. This is because the stronger donating substituents on the acetylide raise the molecular HOMO (see Figure 2), and, as a result, the energy gap between the HOMO and LUMO decreases. The first absorption, which is mainly made up of the HOMO→LUMO transition, is red-shifted with an increase of the substituent group donating ability. Interestingly, all our calculated results and conclusions are in accordance with a recently published paper by Che et al.,[33,38] who ascribed the lower-energy band in the absorption spectra to an allowed MLCT transition. This assignment is consistent with the fact that the absorption band is red-shifted by electron-rich acetylide and electron-deficient moieties on diimine (C^N^N)-6-aryl-2,2′-bipyridine.

Table 6. Calculated absorptions (λ, nm) for the complexes in CH_2Cl_2 using the PCM model.

Ia	**Ib**	**Ic**	**IIa**
452 (0.08)	449 (0.09)	487 (0.12)	460 (0.19)/*430*[a]
407 (0.02)	409 (0.02)	426 (0.01)	414 (0.02)/*430*[a]
316 (0.29)	322 (0.03)	330 (0.14)	314 (0.17)/*342*[a]
246 (0.56)	313 (0.19)	253 (0.27)	314 (0.25)/*328*[a]
242 (0.41)	311 (0.12)	250 (0.26)	281 (0.15)/*289*[a]
263 (0.15)	230 (0.37)	247 (0.37)	
247 (0.44)			
241 (0.45)			
IIb	**IIc**	**IId**	**IIe**
480 (0.14)/*441*[a]	492 (0.20)	503 (0.11)/*482*[a]	742 (0.25)
395 (0.12)/*420*[a]	395 (0.12)	427 (0.14)/*433*[a]	399 (0.14)
324 (0.19)/*345*[a]	326 (0.10)	368 (0.12)/*342*[a]	359 (0.11)
309 (0.16)/*317*[a]	309 (0.17)	311 (0.18)/*317*[a]	311 (0.20)
260 (0.36)/*276*[a]	269 (0.31)	272 (0.25)/*289*[a]	286 (0.23)
255 (0.27)	256 (0.57)	260 (0.19)/*266*[a]	279 (0.41)
	252 (0.23)	252 (0.24)	
	245 (0.33)	245 (0.41)	

[a] Taken from ref.[38]

The excited states that arise from transitions between orbitals that are located on different moieties were classified as charge transfer (CT) excited states. Those from π-occupied to π-virtual orbitals located on the same ligand are described as π-π* states (IL), but those from orbitals on different ligands are described as ligand-to-ligand charge transfer (LLCT) states. Metal-to-ligand charge transfer (MLCT) states involve transitions from the metal atom to ligand-centered orbitals. The excited state is platinum centered (MC) if the orbitals involved in the transition are primarily located on the Pt atom.

In order to assign all absorption bands unambiguously, taking complexes **Ib** and **IId** as examples, TDDFT was used to calculate results for both singlet and triplet absorptions, as listed in Table 7. The contour plots for the related orbitals refer to Figure 3 and Figure 4. Commonly, an excited state corresponds to the excitation of an electron from an occupied to a virtual molecular orbital (MO). However, the excited states calculated herein demonstrate that excited-state electronic structures are described in terms of multi-electronic states, wherein a linear combination of several occupied-to-virtual molecular orbital excitations comprises a given optical transition. For simplicity, Table 7 lists only the most significant contributions to each excited state. Where multiple excitations are of comparable importance (i.e., several excitations with coefficients less 50%), each is listed. Assignment of the character of each excited state was based on the components of the occupied and virtual MOs of the dominant excitation(s) for that excited state. The absorptions **Ib** and **IId** are analyzed completely.

For complex **Ib**, it can be seen that the oscillator strengths of the two lowest-energy singlet electronic transitions are weak, which is consistent with the experimental results.[14] The lowest-energy absorption band is assigned to the spin-allowed HOMO→LUMO transition, which can be characterized as a π(C≡C)/d(Pt)→π*(terp) transition and thus as LLCT mixed with MLCT (LLCT/MLCT). The second absorption band (HOMO→LUMO+1) has the same character as the lowest-energy absorption. The third and sixth transitions, which mainly come from the transitions of HOMO–3→LUMO+1 and HOMO–3→LUMO+2, have complete MLCT character due to the predominant metal character of the HOMO–3 orbital. The other absorptions are all characterized as LLCT or IL. Within the calculated range no transitions between mainly platinum-centered orbitals (MC) are found. If they occur, they must therefore be higher in energy than 200 nm, according to our calculated results.

The first triplet excited state is positioned at 2.34 eV, and is therefore lower than the first singlet excited state (2.76 eV). It results from a HOMO to LUMO transition, thus it is featured as LLCT/MLCT. Similarly, the next two excited states are also characterized as LLCT/MLCT. The higher-energy transitions, such as those at 3.23 and 3.44 eV, arising from the transitions of HOMO–4 to the LUMO and HOMO–5 to LUMO, respectively, were assigned as intraligand excited states within the terpyridyl ligand (IL).

In complex **IId**, the first three calculated absorptions are much stronger than those of **Ib**; this is primarily due to the increased strong donating ability of the phenyl ring on the acetylide, which results in facile charge transfer during the excitation. The lowest-energy absorption (503 nm, with an oscillator strength of 0.1065), arising from the HOMO→LUMO transition, is assigned as LLCT/MLCT. Similarly, the 368 and 311 nm absorptions (with oscillator strengths 0.1243 and 0.1825, respectively) result from the HOMO–2→LUMO and HOMO–7→LUMO transitions, respectively, and they were characterized as mixed LLCT and MLCT due to the mixed compositions of HOMO–2 and HOMO–7 (HOMO–2 is made up of 30% Pt d, 10% terpyridyl p, and 60% acetylide p; HOMO–7 is 62% Pt d and s orbitals as well as 38% terpyridyl p orbitals). For the same reasons as for the 251 and 252 nm absorptions, they are also assigned as mixed LLCT and MLCT. The other absorptions (227, 260, and 245 nm) are all assigned as

 © 2005 Wiley-VCH Verlag GmbH & Co. KGaA, Weinheim

Table 7. Selected TDDFT calculated excitation energies and compositions of the lowest-lying singlet and triplet excited states.

State	Composition		ΔE [eV]	λ [nm]	f	Character
Singlet (**Ib**)						
1	HOMO→LUMO	67%	2.76	450	0.0851	LLCT+MLCT
4	HOMO→LUMO+1	69%	3.03	409	0.0199	LLCT+MLCT
8	HOMO–3→LUMO+1	55%	3.85	322	0.0299	MLCT
10	HOMO–4→LUMO	52%	3.96	313	0.1912	ILCT
11	HOMO→LUMO+2	50%	3.98	318	0.1165	LLCT
24	HOMO–3→LUMO+2	51%	4.71	263	0.1524	MLCT
28	HOMO–6→LUMO+1	51%	5.01	247	0.4353	LLCT+ILCT
29	HOMO–7→LUMO	52%	5.14	241	0.4503	ILCT
Triplet (**Ib**)						
1	HOMO→LLUMO	71%	2.34	530		LLCT+MLCT
2	HOMO–2→LUMO	57%	2.90	428		LLCT+MLCT
4	HOMO→LUMO+1	58%	2.95	420		LLCT+MLCT
5	HOMO–2→LUMO+1	63%	3.02	409		LLCT+MLCT
6	HOMO–4→LUMO	71%	3.23	384		ILCT
7	HOMO–5→LUMO	70%	3.44	361		ILCT
Singlet (**IId**)						
1	HOMO→LUMO	68%	2.46	503	0.1065	LLCT+MLCT
2	HOMO–1→LUMO	63%	2.91	427	0.1438	LLCT
7	HOMO–2→LUMO	62%	3.37	368	0.1243	LLCT+MLCT
14	HOMO–7→LUMO	59%	3.98	311	0.1825	ILCT+MLCT
24	HOMO–1→LUMO+4	49%	4.56	272	0.2514	LLCT
	HOMO–6→LUMO+6	39%				
32	HOMO–6→LUMO+2	35%	4.77	260	0.1869	LLCT
	HOMO–4→LUMO+2	41%				
37	HOMO–9→LUMO+1	31%	4.92	252	0.1600	ILCT+MLCT
	HOMO–10→LUMO	28%				
38	HOMO→LUMO+5	29%	4.94	251	0.2257	LLCT+MLCT
	HOMO–2→LUMO+4	35%				
40	HOMO–11→LUMO	26%	5.07	245	0.3307	LLCT
	HOMO–3→LUMO+3	26%				
Triplet (**IId**)						
1	HOMO→LUMO	68%	2.23	555		LLCT+MLCT
2	HOMO–1→LUMO	66%	2.63	472		LLCT
3	HOMO→LUMO+1	65%	2.85	435		LLCT+MLCT
4	HOMO–4→LUMO	59%	2.90	427		ILCT
	HOMO–3→LUMO	34%				
5	HOMO–2→LUMO	67%	2.98	416		LLCT+MLCT
6	HOMO–4→LUMO+1	55%	3.08	403		ILCT
7	HOMO–6→LUMO	70%	3.19	389		LLCT+MLCT

LLCT between the $\pi(C{\equiv}C{-}R^2)$ and π^* (terp) orbitals. Again, within the calculated range no transitions between mainly platinum-centered orbitals (MC) were found. If they occur, they must be higher in energy than 200 nm.

The first triplet excited state is positioned at 2.23 eV, 0.23 eV lower than the first singlet excited state (2.46 eV). It results from a HOMO to LUMO transition, thus it is featured as LLCT/MLCT. Similarly, the third, fifth, and seventh excited states are also characterized as LLCT/MLCT. Other transitions, such as those at 2.63 and 3.08 eV, arise from the transitions of HOMO–1 to the LUMO and HOMO–4 to the LUMO+1, respectively, and were assigned as being due to ligand-to-ligand molecular charge transfer between the acetylide and terpyridyl ligand (LLCT). The 2.90 eV absorption, which comes from the HOMO–4 to LUMO transition, is characterized as IL.

According to the absorption character analysis of complexes **Ib** and **IId**, we can see that, although the transition character of HOMO to LUMO is the same for these two complexes (both are assigned as mixed LLCT/MLCT), the percentage of the MLCT is less in **IId** than that in **Ib**. However, his is not the case for the lowest-energy absorption of **IIe**. It should be noted that the Pt d orbital percentage in the HOMO (only 4%) is less than that of the LUMO (6%), so the lowest-energy transition, which comes from the HOMO to LUMO transition, should be assigned as LLCT.

Optimization of the Excited State

CIS (Configuration Interaction Singlets) has been extensively used to study the properties of excited states.[41–43] We

 © 2005 Wiley-VCH Verlag GmbH & Co. KGaA, Weinheim

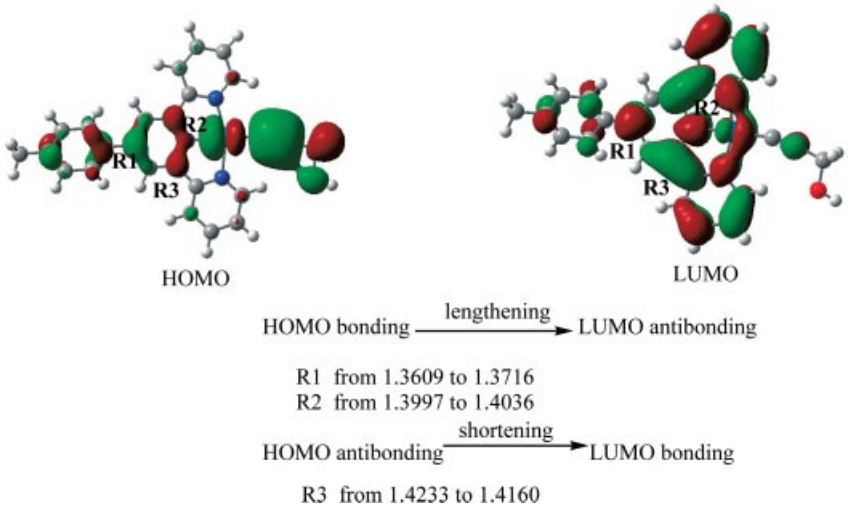

Figure 6. Prediction of the bond length changes between the ground and excited states according to the nodal of the frontier orbitals, taking complex **IIa** as an example (bond lengths in Å).

have examined the lowest triplet state of these complexes by carrying out CIS/LanL2DZ calculations. Comparing the optimized excited-state and ground-state geometries will provide an indication of overall geometry relaxations that occur in the excited state in possible emission processes. Taking complex **IIa** as an example, some of the geometrical parameters (bond lengths) for the optimized ground and excited states are shown in Figure 6. We investigated the geometry relaxations upon excitation by consideration of the nodal patterns of the HOMO and LUMO orbitals. It is considered that if there is no nodal across the bond in the HOMO, while there is a nodal across the same bond in the LUMO, then this bond will be elongated when the complex changes from the ground state to the excited state; in contrast, if there is no nodal across the bond in the LUMO, while there is a nodal across the same bond in the HOMO, then this bond will contract. According to this rule, we investigated the change in the bond lengths in complex **IIa**. The LUMO has nodes across R^1 and R^2, but there are no nodals across them in the HOMO. One would therefore expect elongation of these bonds, and Figure 6 shows that these bonds are in fact considerably longer in the excited state. The HOMO has a node across R^3, and it shows bonding in the LUMO; the data in Figure 6 confirm the anticipated contraction of this bond.

Solvatochromism is closely related to the ground- and excited-state dipole moment. Electronic excitations from HOMO to LUMO involve the displacement of electron charge from the Pt center and the C≡C-R^2 ligands towards the delocalized terpyridyl π*-orbitals. Thus, a reduction of the dipole moment in the excited state is expected, and, as a consequence, the excited state should be less stabilized by polar solvents than the ground state. To testify this assumption, we investigated the dipole moment of the ground and excited states. Taking complex **Ia** as an example, the ground-state dipole moment, μ_g, is –2.36 D and the first triplet excited-state dipole moment, μ_e, is 1.86 D, therefore $\Delta\mu$, the absolute difference between them, is 0.50 D. This dipole moment is in accordance with the assumptions above.

Emission Properties

Based on the optimized excited-state geometries of these complexes, the emission calculation was carried out using the TDDFT method at the B3LYP/LanL2DZ level. The emissions and the calculated Stokes shift are tabulated in Table 8, along with available experimental values for comparison. Obviously, the change tendency with the different substituents of emission is in parallel with those of absorption. The absolute emission value, taking **IId** as an example (693 nm), deviates from the experimental observation of 619 nm. We attribute this deviation to the following reasons: first, the excited-state geometries were obtained using CIS methods, and CIS represents excited states in a general zeroth-order method, just as Hartree–Fock for the ground state of molecular systems, and in CIS theory, the electron correlation effects and higher order excitations are neglected; in addition, the TDDFT approach neglects the spin–orbital coupling, which allows the triplet states to acquire intensity in both absorption and emission and to induce the triplet energies to be shifted. For third row transition metals one estimates the lowest triplet states to be low-

Table 8. Calculated emissions for all the investigated complexes in CH_2Cl_2 solvent, and their Stokes shifts.

Complex	Emission [λ, nm]	
	Calculated	Experiment
Ia	490	
Ib	471	
Ic	498	
IIa	489	552[a]
IIb	495	580[a]
IIc	589	619[a]
IId	693	

[a] Taken from ref.[38]

 © 2005 Wiley-VCH Verlag GmbH & Co. KGaA, Weinheim

ered by 0.2–0.3 eV by interaction with higher states through spin–orbital coupling. However, the tendency of our calculated results changes parallel to the experimental ones, thus indicating that our method is reliable to gain reasonable results.

Conclusions

The ground-state geometries of several terpyridylplatinum(II) acetylide complexes have been calculated at the B3LYP/LanL2DZ level; the calculated geometrical parameters are in good agreement with the X-ray diffraction experiment results. The electronic structures are discussed completely. Introduction of electron-withdrawing groups on the terpyridyl ligand will lower the LUMO, and the introduction of electron-donating groups on the acetylide will raise the HOMO, thus decreasing the energy gap between the HOMO and the LUMO and, at the same time, increasing the energy gap between the lowest excited state and the d-d state, which prevents nonradiative deactivation through the pathways of d-d conversion. The absorptions and emissions for the investigated complexes were calculated at the B3LYP/LanL2DZ level at the optimized ground- and excited-state geometries, respectively. The calculated absorption results are in good agreement with the experimental values. For all the investigated complexes, excluding **IIe**, the lowest-energy absorption has been assigned as an admixture of metal-to-ligand transition to ligand-to-ligand transition (LLCT/MLCT-C≡C(π)/dπ(Pt)→trpy π*) (in **IIe** assigned as LLCT), while the absorptions at higher-energy levels are assigned as ligand-to-ligand charge transfer (LLCT) or IL. Furthermore, different substituents can modulate both the absorptions and emissions − the introduction of an acceptor on terpyridyl and a donor on acetylide induces the absorption and emission to be red-shifted. This result is in accordance with the calculated electronic structure.

The introduction of electron-withdrawing groups on the terpyridyl ligand and electron-donating groups on the acetylide ligand benefits the emission of this series of complex since it decreases the energy gap between the HOMO and the LUMO and increases the energy gap between the d-d transitions.

Computational Methods

Calculations on the electronic ground state of the investigated complexes were carried out using B3LYP density functional theory. B3LYP corresponds to the combination of Becke's three-parameter exchange functional (B3) with the Lee–Yang–Parr for the correlation functional (LYP). A LanL2DZ basis set was used for all the elements, including C, N, O, H, and Pt atoms. A relativistic effective core potential (ECP) on Pt replaced the inner-core electrons, leaving the outer-core [($5s^2$) ($5p^6$)] electrons and the ($5d^8$) valence electrons of Pt. For the C, N, and O atoms only the (1s) orbitals were replaced by effective core potentials; all the other orbital electrons were left as outer-core electrons or valence electrons. The basis sets were taken as Pt (8s6p3d/3s3p2d), C (10s5p/3s2p), N (10s5p/3s2p), O (10s2p/3s2p), and H (4s/2s). The equilibrium ground-state geometries were computed using the B3LYP functional with the LanL2DZ basis set and were fully optimized without symmetry constraints. At the correct ground-state geometry optimizations, time-dependent DFT (TDDFT) calculations using the B3LYP functional were performed to obtain both singlet and triplet absorption spectra. Then, the first triplet excited state (T_1) geometries for all the complexes (except for complex **IIe**) were optimized using an ab initio CIS method with the LanL2DZ basis set. Based on the CIS-optimized excited-state geometries, the luminescent spectra were calculated at the B3LYP/LanL2DZ level. The solvent effect was simulated using the polarizable continuum model (PCM), in which the solvent cavity is seen as a union of interlocking atomic spheres. All the calculations described here were carried out with the Gaussian 98 package.[44]

Acknowledgments

This work was supported by the Major State Basis Research Development Program (no. 2002CB 613406), the National Nature Science Foundation of China (no. 90101026 20173021), and the National Natural Science Foundation of China (no. 20271049 and 20331030).

[1] J. P. Paris, W. W. Brandt, *J. Am. Chem. Soc.* **1959**, *81*, 5001–5002.
[2] J. N. Demas, G. A. Crosby, *J. Mol. Spectrosc.* **1968**, *26*, 72–77.
[3] G. D. Hager, G. A. Crosby, *J. Am. Chem. Soc.* **1975**, *97*, 7031–7037.
[4] G. D. Hager, R. J. Watts, G. A. Crosby, *J. Am. Chem. Soc.* **1975**, *97*, 7037–7042.
[5] K. W. Hipps, G. A. Crosby, *J. Am. Chem. Soc.* **1975**, *97*, 7042–7048.
[6] J. Van Houten, R. J. Watts, *J. Am. Chem. Soc.* **1976**, *98*, 4853–4858.
[7] T. J. Meyer, *Prog. Inorg. Chem.* **1983**, *30*, 389–440.
[8] J. V. Caspar, T. J. Meyer, *J. Phys. Chem.* **1983**, *87*, 952–957.
[9] A. Juris, V. Balzani, F. Barigelletti, S. Campagna, P. Belser, A. von Zelewsky, *Coord, Chem. Rev.* **1988**, *84*, 85–277.
[10] A. T. Yeh, C. V. Shank, J. K. McCusker, *Science* **2000**, *289*, 935–938.
[11] M. Wrighton, D. L. Morse, *J. Am. Chem. Soc.* **1974**, *96*, 998–1003.
[12] A. J. Lees, *Chem. Rev.* **1987**, *87*, 711–743.
[13] J. V. Caspar, E. M. Kober, B. P. Sullivan, T. J. Meyer, *J. Am. Chem. Soc.* **1982**, *104*, 630–631.
[14] L. A. Worl, R. Duesing, P. Chen, L. D. Ciana, T. J. Meyer, *J. Chem. Soc., Dalton Trans.* **1991**, 849–858.
[15] V. M. Miskowski, V. H. Houlding, *Inorg. Chem.* **1989**, *28*, 1529–1533.
[16] H. Kunkely, A. Vogler, *J. Am. Chem. Soc.* **1990**, *112*, 5625–5627.
[17] V. M. Miskowski, V. H. Houlding, C. M. Che, Y. Wang, *Inorg. Chem.* **1993**, *32*, 2518–2524.
[18] C. W. Chan, L. K. Cheng, C. M. Che, *Coord. Chem. Rev.* **1994**, *132*, 87–97.
[19] S. D. Cummings, R. Eisenberg, *J. Am. Chem. Soc.* **1996**, *118*, 1949–1960.
[20] Y. Zhang, K. D. Ley, K. S. Schanze, *Inorg. Chem.* **1996**, *35*, 7102–7110.

 © 2005 Wiley-VCH Verlag GmbH & Co. KGaA, Weinheim

[21] W. B. Connick, H. B. Gray, *J. Am. Chem. Soc.* **1997**, *119*, 11 620–11 627.
[22] W. Paw, S. D. Cummings, M. A. Mansour, W. B. Connick, D. K. Geiger, R. Eisenberg, *Coord. Chem. Rev.* **1998**, *171*, 125–150.
[23] W. B. Connick, D. Geiger, R. Eisenberg, *Inorg. Chem.* **1999**, *38*, 3264–3265.
[24] W. B. Connick, V. M. Miskowski, V. H. Houlding, H. B. Gray, *Inorg. Chem.* **2000**, *39*, 2585–2592.
[25] M. Hissler, W. B. Connick, D. K. Geiger, J. E. McGarrah, D. Lipa, R. J. Lachiocotte, R. Eisenberg, *Inorg. Chem.* **2000**, *39*, 447–457.
[26] M. Hisser, J. E. McGarrah, W. B. Connick, D. K. Geiger, S. D. Cummings, R. Eisenberg, *Coord. Chem. Rev.* **2000**, *208*, 115–137.
[27] C. J. Adams, S. L. James, X. M. Liu, P. R. Raithby, L. J. Yellowlees, *J. Chem. Soc., Dalton Trans.* **2000**, 63–67.
[28] J. F. Michalec, S. A. Bejune, D. G. Cuttell, G. C. Summerton, J. A. Gertenbach, J. S. Field, R. J. Haines, D. R. McMillin, *Inorg. Chem.* **2001**, *40*, 2193–2200.
[29] S. W. Lai, M. C. W. Chan, K. K. Cheung, C. M. Che, *Inorg. Chem.* **1999**, *38*, 4262–4267.
[30] R. Büchner, C. T. Cunningham, J. S. Field, R. J. Haines, D. R. McMillin, G. C. Summerton, *J. Chem. Soc., Dalton Trans.* **1999**, 711–717.
[31] R. Büchner, J. S. Field, R. J. Haines, C. T. Cunningham, D. R. McMillin, *Inorg. Chem.* **1997**, *36*, 3952–3956.
[32] J. F. Michalec, S. A. Bejune, D. R. McMillin, *Inorg. Chem.* **2000**, *39*, 2708–2709.
[33] V. W. W. Yam, R. P. L. Tang, K. M. C. Wong, K. K. Cheung, *Organometallics* **2001**, *20*, 4476–4482.
[34] S. Lippard, *Acc. Chem. Res.* **1978**, *11*, 211–217.
[35] C. S. Peyratout, T. K. Aldridge, D. K. Crites, D. R. McMillin, *Inorg. Chem.* **1995**, *34*, 4484–4489.
[36] G. Arena, L. Monsú Scolaro, R. F. Pasternack, R. Romeo, *Inorg. Chem.* **1995**, *34*, 2994–3002.
[37] E. M. A. Ratilla, H. M. Brothers, N. M. Kostić, *J. Am. Chem. Soc.* **1987**, *109*, 4592–4599.
[38] Q. Z. Yang, L. Z. Wu, L. P. Zhang, C. H. Tung, *Inorg. Chem.* **2002**, *41*, 5653–5655.
[39] C. Amovilli, V. Barone, R. Cammi, E. Cances, M. Cossi, B. Mennucci, C. S. Pomelli, J. Tomasi, *Adv. Quantum Chem.* **1999**, *32*, 227.
[40] W. Lu, B. X. Mi, C. W. Michael, Z. Hui, C. M. Che, N. Y. Zhu, S. T. Lee, *J. Am. Chem. Soc.* **2004**, *126*, 4958–4971.
[41] Q. J. Pan, H. X. Zhang, *J. Chem. Phys.* **2003**, *119*, 4346–4352.
[42] Q. J. Pan, H. X. Zhang, *Eur. J. Inorg. Chem.* **2003**, *23*, 4202–4210.
[43] Q. J. Pan, Zhang, H. X, *Inorg. Chem.* **2004**, *43*, 593–601.
[44] M. J. Frisch, G. W. Trucks, H. B. Schlegel, G. E. Scuseria, M. A. Robb, J. R. Cheeseman, V. G. Zakrzewski, J. A. Montgomery, R. E. Stratmann, J. C. Burant, S. Dapprich, J. M. Millam, A. D. Daniels, K. N. Kudin, M. C. Strain, O. Farkas, J. Tomasi, V. Barone, M. Cossi, R. Cammi, B. Mennucci, C. Pomelli, C. Adamo, S. Clifford, J. Ochterski, G. A. Petersson, P. Y. Ayala, Q. Cui, K. Morokuma, D. K. Malick, A. D. Rabuck, K. Raghavachari, J. B. Foresman, J. Cioslowski, J. V. Ortiz, B. B. Stefanov, G. Liu, A. Liashenko, P. Piskorz, I. Komaromi, R. Gomperts, R. L. Martin, D. J. Fox, T. Keith, M. A. AI-Laham, C. Y. Peng, A. Nanayakkara, C. Gonzalez, M. Challacombe, P. M. W. Gill, B. G. Johnson, W. Chen, M. W. Wong, J. L. Andres, M. Head-Gordon, E. S. Replogle, J. A. Pople, *Gaussian 98*, revision A.9; Gaussian, Inc.: Pittsburgh, PA, **1998**.

Received: June 18, 2004

 © 2005 Wiley-VCH Verlag GmbH & Co. KGaA, Weinheim

Structures, Electronic States and Electroluminescent Properties of a Series of Cu^{I} Complexes

Li Yang,[a] Ji-Kang Feng,*[a,b] Ai-Min Ren,[a] Ming Zhang,[c] Yu-Guang Ma,*[c] and Xiao-Dong Liu[b]

Keywords: Copper / Density functional calculations / N ligands / Photoluminescence

A series of new mixed-ligand copper(I) complexes [Cu(NN)-POP]BF_4, where NN = 1,10-phenanthroline (phen; **1a**), 2,9-dimethyl-phen (DMphen; **1b**), 4,7-diphenyl-phen (DPpehn; **1c**) and 2,2′-bipyridine (bpy; **2a**), have been synthesized. Density functional theory (DFT) was applied to study the ground- and excited-state properties of these copper(I) complexes. The electronic structure variation is obtained by changing the substituted positions on the phenanthroline ligand. A time-dependent-DFT approach (TDDFT) was used to interpret the absorption and emission spectra in this system based on the optimized geometries at the B3LYP/LANL2DZ and CIS/LANL2DZ levels of theory, respectively. The results show that the lowest-energy excitations of all complexes are dominated by $d\pi(Cu)\rightarrow\pi^*$(phen) or bpy (MLCT) excitations. In particular, the lowest triplet state (T_1) corresponds to an excitation from the HOMO to the LUMO in all considered complexes, and emissions occur from T_1, assigned to ^{3}MLCT. Steric effects exerted by the pendent groups at the 2- and 9-positions of the phenanthroline ligands increase the HOMO–LUMO gaps and thus lead to a blue-shift of both absorption and emission spectra and effectively prevent structural relaxation in the MLCT state, which may narrow the energy gap between the excited and ground states and therefore increase nonradiative decay.
(© Wiley-VCH Verlag GmbH & Co. KGaA, 69451 Weinheim, Germany, 2005)

Introduction

The development of practical components for chemical sensors,[1,2] display devices,[3,4] probes of biological systems,[5,6] phototherapy,[7] and solar-energy conversion[8] schemes has fuelled interest in complexes of polypyridine and phenanthroline ligands with transition metals, especially heavy metal ions such as ruthenium(II) or rhenium(I).[9] At the same time, the strongly appealing possibility of using cheap copper(I) complexes for replacing the more expensive compounds based on ruthenium(II) or other metal ions, along with the need for a deeper understanding of the correlation between structural processes and photophysical properties, have pushed a continuous progress in the design of photoluminescent Cu^{I} complexes. However, the emission signals from charge-transfer (CT) excited states of copper(I) complexes are typically weak and short-lived[10–12] because the lowest energy CT state of a d^{10} system involves excitation from a metal–ligand $d\sigma^*$ orbital.[10] An important consequence is that the excited state typically prefers a tetragonally flattened geometry whereas the ground state usually adopts a more tetrahedral-like coordination geometry appropriate for a closed-shell ion.[10,13] Aside from reducing the energy content, the geometric relaxation that occurs in the excited state facilitates relaxation back to the ground state.[14,15] Moreover, donor media also tend to quench the lifetime. Blaskie and McMillin first reported this type of exciplex quenching, and by now, many other studies have confirmed the mechanism. Mixed-ligand systems involving triphenylphosphane initially looked promising because they exhibit long lifetimes in the solid state and frozen solution.[16,17] However, detailed studies of $[Cu(phen)(PPh_3)_2]^+$ (phen = 1,10-phenanthroline) have shown that it is virtually nonemissive in methanol, while $[Cu(dmp)(PPh_3)_2]^+$ (dmp = 2,9-dimethyl-1,10-phenanthroline) has a lifetime of 330 ns in deoxygenated solution.[16] However, even with two bulky triphenylphosphanes and a sterically active dmp ligand in the coordination sphere, temperature-dependent emission studies suggest that photoexcited $[Cu(dmp)(PPh_3)_2]^+$ is still subject to exciplex quenching in methanol.[18] An obvious possibility was that incorporation of a chelating phosphane might suppress ligand dissociation.[19] In this context, a series of new mixed-ligand copper(I) polypyridine and phenanthroline complexes such as $[Cu(NN)(POP)]^+$ [POP = bis-{2-(diphenylphosphanyl)phenyl} ether] that are vastly superior luminophores have been synthesized. It is found that solvent-induced exciplex quenching is relatively

[a] State Key Laboratory of Theoretical and Computational Chemistry, Institute of Theoretical Chemstry, Jilin University, Changchun 130023, P. R. China
Fax: +86-431-894-5942
E-mail: Jikangf@yahoo.com
[b] The college of Chemistry, Jilin University, Changchun 130023, P. R. China
[c] Key Lab for Supramolecular Structure and Materials of the Ministry of Education, Jilin University, Changchun 130023, P. R. China

inefficient for the CT excited state of this POP system. On the other hand, introduction of sterically demanding ligands can impede geometric relaxation as well as solvent attack. Here, steric effects exerted by pendent groups at the 2,9- and different buttressing groups at the 3,7-phenanthroline positions cooperate to effectively block the excited state close to the ground-state geometry. A further approach for blocking structural rearrangements at the excited state is based on the use of aryl groups appended to the phen unit. The metal-to-ligand charge transfer (MLCT) excited states of cuprous diimine compounds are often luminescent and play important roles in photoinduced electron and energy transfer.

Reaction of $[Cu(NCCH_3)_4]BF_4$ with POP and a polypyridine or phenanthroline ligand gives good yields of the copper(I) complexes $[Cu(NN)POP]BF_4$, where NN = 2,2′-bipyridine and substituted bipyridine ligands or phenanthroline and substituted phenanthroline ligands. The emission from $[Cu(NN)(POP)]^+$ is very similar to that reported for the $[Cu(NN)(PPh_3)_2]^+$ system in room temperature DCM solution.[18] Whereas the photophysical properties of $[Cu(NN)(POP)]^+$ systems vary dramatically with the steric requirements of the NN ligand, the steric influence of the alkyl substituents is also evident in the electrochemistry.

In contrast to experimental studies, so far very little theoretical work is available on Cu^I systems. Despite this fact, density functional theory (DFT) has been successful at providing a means to evaluate a variety of ground-state properties with an accuracy close to that of post-HF methods.[20,21] As a consequence, time-dependent density functional theory (TDDFT) has emerged as an accurate method for the calculation of excited state properties of molecules.[22,23] Because of the low computational costs and complexity, TDDFT is applicable to fairly large systems (for recent applications see, for example, refs.[24,25]) for which traditional wavefunction-based methods are not feasible. Only very recently, a DFT study of the Cu^I systems limited to geometry optimization of the molecular structure and the electronic structure, but no excited geometry optimization of the molecular structure and emission spectra, have been performed.[26,27] On the other hand, a theoretical investigation has been performed at the complete DFT level for Ru^{II} complexes such as $[Ru(bpy)_3]^{2+}$ and [Ru(4,4′-COOH-2,2′-bpy)$(NCS)_2$], but there is still no excited state study.[28] In fact, until now the standard method for calculating excited state equilibrium properties of larger molecules is the configuration interaction singles (CIS) method. However, the calculation of excited-state properties typically requires significantly more computational effort than is needed for the ground states and is dramatically constrained by the size of the molecules.

In this paper we report on a series of new copper(I) mixed-ligand complexes, as well as the structures of complexes $[Cu(NN)POP]BF_4$, where NN = 1,10-phenanthroline (phen; **1a**), 2,9-dimethyl-phen (DMphen; **1b**), 4,7-diphenyl-phen (DPpehn; **1c**) and 2,2′-bipyridine (bpy; **2a**; Figure 1). Furthermore, we present a theoretical and experimental investigation of this series of copper(I) mixed-ligand complexes, including DFT calculations of the structural and electronic properties, as well as a TDDFT study of the main features of the near UV/Vis spectra and, more importantly, the excited state and photoluminescence character. The effect of variation of the substituted positions on the lowest-energy excited states of the complexes has been assessed by calculating their electronic structures and excitation energy. We show that with a reasonable computational effort TDDFT well reproduces the spectroscopic properties of the copper(I) mixed-ligand systems, suggesting that this approach could be used to provide insight into the design of new and more-efficient photoluminescent Cu^I complexes.

Results and Discussion

Molecular Structure and X-ray Single-Crystal Diffraction

The molecular structure of the Cu^I complexes was determined by X-ray single-crystal diffraction. The calculated

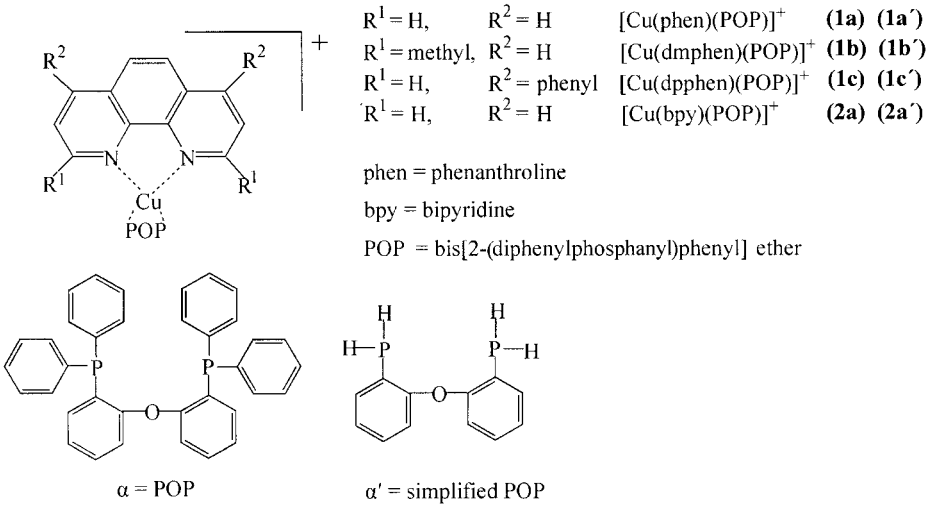

Figure 1. Schematic structures of complexes **1a**–**1c** and **2a** with the POP (α) ligand and **1a′**–**1c′** and **2a′** with the simplified POP ligand (α′).

 © 2005 Wiley-VCH Verlag GmbH & Co. KGaA, Weinheim

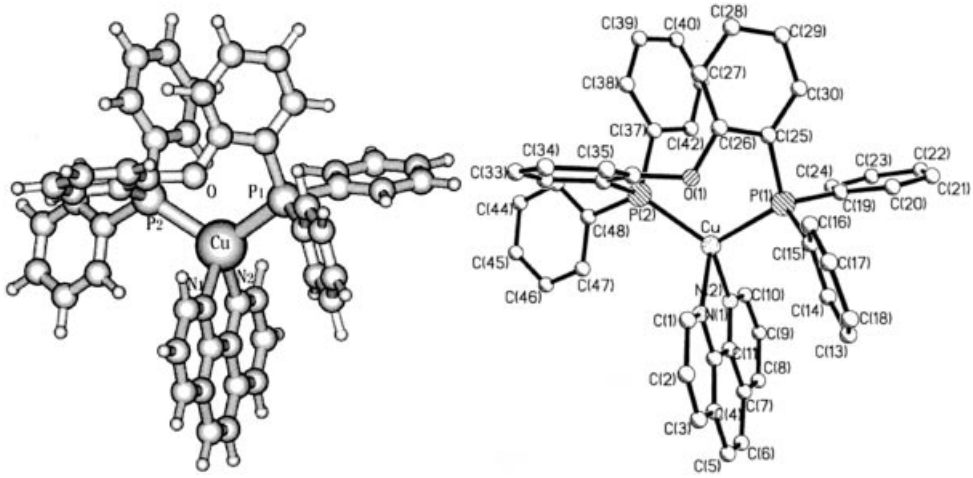

Figure 2. Calculated (left) and crystal (right) structures of complex **1a**.

and crystal structures of complex **1a** are shown in Figure 2, which shows that the calculated structure agrees well with experimental one. Both structures reveal a distorted tetrahedral coordination environment about Cu^{I} with P–Cu–P and N–Cu–N bond angles of 113.52° and 80.88°, respectively. The ether oxygen atom of POP is at a nonbonding distance (>3.1 Å) to the metal center. The resulting eight-membered ···C–C–P–Cu–P–C–C–O··· rings assume a tublike conformation in the solid state, with a dihedral angle between the phenyl rings of 77.9° for complex **1a**. All three $[Cu(NN)(POP)]^{+}$ complexes exhibit similar structures.

The only complex for which a significant intermolecular interaction is present in the solid state is compound **1a**, where the phen ligands of the pairs of symmetry-related cations partially overlay one another (Figure 3). The components of this pair are related to one another through a center of inversion that is located between the phen rings; the closest intermolecular C···C and C···N contacts are in the range 3.59–3.64 Å.

Selected bond lengths and angles for compounds **1a**–**1c** and **2a** are listed in Table 1. The introduction of POP suppresses ligand dissociation and unexpectedly makes the solvent-induced exciplex quenching relatively inefficient for the CT excited state. However, since these POP ligands have little influence on the study of UV/Vis spectra, the excited state, and photoluminescence character, the four phenyls bound to phosphorus but not to oxygen were substituted by hydrogen in order to simplify th calculation, as shown in Figure 1. This simplification has little effect on the molecular structure. In fact, the differences of bond lengths and angles between calculated and experimental structures are within 0.4 Å and 5°, respectively, in all cases. For **1a**, for example, the Cu–N(1) bond length and the N(1)–Cu–N(2) angle differ by 0.04 Å and 0.1°, respectively, from the experimental data; these values are 0.01 Å and 0.8° for **1a**′. The largest difference occurs for P(1)–Cu–P (2), which decreases by nearly 8° compared with the experimental value, although this does not influence the theoretical study of absorption and emission properties. Interestingly, a comparison of the calculated values of simplified structures shows

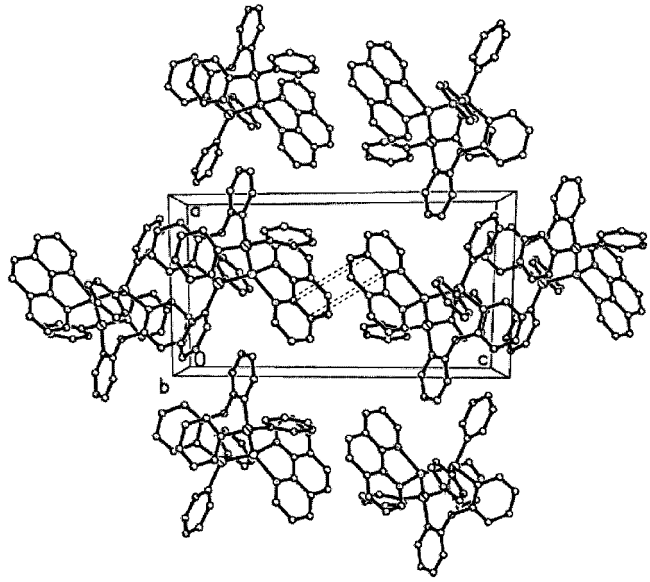

Figure 3. Crystal packing of complex **1a**.

that the Cu–N bond lengths are more strongly influenced than the Cu–P bond lengths by substituents at the 4,6-positions − the latter ones remain nearly equal, whereas the former differ by about 0.02 Å (comparison between **1a**′ and **1c**′). On the contrary, the substituents at the 2,9-positions have less influence on the Cu–N than on the Cu–P bond lengths; the latter differ by about 0.02 Å (comparison between **1a**′ and **1b**′). These structural characteristic should have significant effects on the orbital energy, absorption spectra, and luminescent properties.

A summary of the crystal data for complexes **1a**, **1b**, and **2a** can be found in the Experimental Section. These results indicate that the single crystal has good morphological, structural, and molecular stabilities.

Electronic Structure

Since the observed differences in the chemical and physical properties of the complexes rely primarily on the

 © 2005 Wiley-VCH Verlag GmbH & Co. KGaA, Weinheim

Table 1. Experimental and calculated structure parameters for complexes **1a**–**1c** and **2a**.

	1a				**1b**			**1c**		**2a**	
	Exp.[a]	Exp.[b]	Calcd.[c]	Calcd.[d]	Exp.[a]	Exp.[b]	Calcd.[d]	Calcd.[d]	Exp.[a]	Calcd.[c]	Calcd.[d]
Cu–N(1)	2.078	2.071	2.113	2.102	2.098	2.104	2.102	2.084	2.085	2.102	2.090
Cu–N(2)	2.073	2.064	2.108	2.095	2.075	2.084	2.098	2.089	2.034	2.101	2.079
Cu–P(1)	2.271	2.261	2.402	2.427	2.285	2.273	2.441	2.426	2.245	2.423	2.423
Cu–P(2)	2.235	2.231	2.42	2.414	2.228	2.269	2.421	2.417	2.232	2.402	2.413
Cu···O		3.205	3.164	3.386		3.151	3.444	3.415		3.092	3.347
P(1)–Cu–P(2)	113.52	110.81	114.16	106.46	117.04	116.44	106.58	106.61	111.97	113.47	106.20
N(1)–Cu–N(2)	80.88	80.83	80.97	81.75	81.39	80.88	82.23	81.20	80.13	79.65	80.74
N(1)–Cu–P(1)	103.80		119.38	120.25	108.88		119.28	119.10	123.58	120.06	121.80
N(1)–Cu–P(2)	113.53		116.17	117.89	119.55		115.40	118.42	114.72	111.14	113.74
N(2)–Cu–P(1)	113.50		110.37	114.54	118.84		116.28	114.63	114.73	116.54	121.80
N(2)–Cu–P(2)	124.88		110.18	114.59	105.40		116.11	115.53	109.40	110.64	119.70

[a] Our experimental structure. [b] See ref.[30] [c] Structure with POP. [d] Simplified structure.

changes in the ground-state electronic structure, before dealing with the excited states, we will discuss in detail the ground-state electronic structure of these complexes with a special emphasis on the frontier orbital components and HOMO–LUMO energy gaps. The assignment of the nature of each MO was made on the basis of its composition [see Tables 2 and 3 in which only the most important occupied and virtual (unoccupied) orbitals are listed] and by visual inspection of its three-dimensional representation (see Figures 4 and 5, which show complexes **1a′** and **1b′** as examples, respectively). The atomic orbital contributions for each complex, expressed in percent, are given in Tables 2 and 3. Percent contributions were calculated from Equation (1), where n is the atomic orbital coefficient and $\sum n^2$ is the sum of the squares of all atomic orbital coefficients in a specific molecular orbital.

$$[n^2/\sum n^2] \times 100 = \% \text{ contribution} \quad (1)$$

Every complex is divided into four parts: the metal Cu, pyridine ligand, simplified POP, and different substituents R. Each part of the percent contributions are the sum of the atomic orbital coefficient squares.

In general, for all the investigated complexes, their occupied orbital compositions are perturbed by different substitution positions, but the relative ordering and characters are not changed, as shown in Tables 2 and 3: the two highest occupied orbitals have predominant metal Cu d character (54%, 62%, 53% and 63% in HOMO and 64%, 56%, 59% and 54% in HOMO–1 for **1a′**, **1b′**, **1c′**, and **2a′**, respectively), admixed with some contributions from the phen (bpy) ligand and POP. The HOMO–3 orbital for substituted complexes **1b′** and **1c′** also features roughly metallic antibonding character (60% and 44%, respectively), but for unsubstituted complexes **1a′** and **2a′** the HOMO–3 orbitals are predominantly delocalized on the POP ligand (57% and 65%, respectively), although significant metal contributions (36% and 30%, respectively) remain. Some

Table 2. G03/B3LYP calculated one-electron energy and percentage composition of selected frontier MOs of **1a′** and **1b′** expressed in terms of component fragments.[a]

MO	Energy [eV]	Character **1a′**	phen	Cu	POP	MO	Energy [eV]	Character	phen **1b′**	Cu	POP	Me
115(V)	–2.85	phen	96	1	3	122(V)	–2.84	POP	2	2	94	2
113(V)	–3.00	POP	1	2	97	121(V)	–3.02	POP	2	2	95	1
112(V)	–3.25	POP	2	2	96	119(V)	–3.38	phen	82	2	13	1
111(V)	–3.40	POP	2	2	96	118(V)	–3.41	POP	9	2	88	1
110(V)	–3.64	phen	97	1	2	117(V)	–4.51	phen	97	0	0	3
109(V)	–4.83	phen	99	0	1	**116(V)**	**–4.71**	**phen**	**95**	**2**	**3**	**0**
108(V)	**–4.94**	**phen**	**96**	**2**	**2**	**115(O)**	**–8.58**	**Cu**	**23**	**62**	**14**	**1**
107(O)	**–8.67**	**Cu**	**14**	**54**	**32**	114(O)	–8.64	Cu	15	56	28	1
106(O)	–8.72	Cu	22	64	14	113(O)	–9.00	Cu	11	60	28	1
105(O)	–9.06	POP+Cu	7	36	57	112(O)	–9.12	POP	4	14	82	0
104(O)	–9.13	POP+Cu	6	42	52	110(O)	–9.51	Cu	25	69	5	1
103(O)	–9.57	POP	23	7	70	107(O)	–9.75	POP+phen	37	21	40	2
102(O)	–9.63	Cu	21	72	7	106(O)	–9.76	POP+phen	33	26	39	2
101(O)	–9.65	phen+POP	44	15	41	103(O)	–11.18	phen	89	5	3	3
97(O)	–10.06	phen	86	13	1							
Energy gap (ΔE) = 3.73 eV (HOMO–LUMO)						**Energy gap (ΔE) = 3.87 eV** (HOMO–LUMO)						

[a] HOMO and LUMO orbitals are shown in bold.

 © 2005 Wiley-VCH Verlag GmbH & Co. KGaA, Weinheim

Table 3. G03/B3LYP calculated one-electron energy and percentage composition of selected frontier MOs of **1c′** and **2a′** expressed in terms of composing fragments[a].

MO	Energy [eV]	Character	phen **1c′**	Cu	POP	Me	MO	Energy [eV]	Character **2a′**	phen	Cu	POP
153(V)	–3.04	phen	60	0	2	38	109(V)	–2.74	bpy	94	0	6
152(V)	–3.12	POP	2	2	96	0	108(V)	–2.90	POP	5	5	91
150(V)	–3.42	phen	96	1	3	0	107(V)	–3.06	POP	1	2	97
149(V)	–4.57	phen	91	0	0	9	106(V)	–3.31	POP	1	2	97
148(V)	**–4.66**	**phen**	**88**	**2**	**2**	**8**	105(V)	–3.45	POP	1	2	97
147(O)	**–8.40**	**Cu**	**21**	**53**	**22**	**4**	104(V)	–3.92	bpy	99	0	1
146(O)	–8.42	Cu	24	59	14	3	103(V)	–4.21	bpy	98	1	1
144(O)	–8.94	Cu	18	44	24	14	**102(V)**	**–5.00**	**bpy**	**96**	**2**	**2**
143(O)	–9.00	POP	9	12	67	11	**101(O)**	**–8.67**	**Cu**	**26**	**63**	**11**
142(O)	–9.03	ph	25	11	3	60	100(O)	–8.75	Cu	9	54	37
141(O)	–9.23	ph	3	0	0	97	99(O)	–9.13	POP	5	30	65
140(O)	–9.24	ph	3	0	0	97	98(O)	–9.18	Cu+POP	7	48	46
136(O)	–9.56	phen+ph	52	1	14	34	97(O)	–9.64	POP	4	23	73
135(O)	–9.61	POP	9	17	71	3	96(O)	–9.69	Cu	13	68	19
134(O)	–9.76	POP	1	14	85	0	93(O)	–9.93	phen	81	16	3
Energy gap(ΔE) = 3.74 eV (HOMO–LUMO)							**Energy gap(ΔE) = 3.67 eV** (HOMO–LUMO)					

[a] HOMO and LUMO orbitals are shown in bold.

lower-energy occupied MOs still have significant metal character, but the contributions from phen (bpy) and POP increase. In contrast, the two lowest unoccupied orbitals LUMO and LUMO+1 in each complex are essentially π*-orbitals localized on the phen or bpy moieties (over 90%). LUMO+2 is calculated to have dominant ligand phen or bpy π* character in each complex except for **1b′**, where it is POP-centered (88%). As shown in Tables 2 and 3 higher virtual orbitals are mainly delocalized over the bpy, phen, or POP ligands.

However, comparing **1a′**, **1b′**, and **1c′**, it can be found that there is a greater effect when substituted in the 2,9-phenanthroline positions than in the 4,7-phenanthroline positions. Firstly, the energy gaps (HOMO–LUMO) of **1a′** (3.73 eV) and **1c′** (3.74 eV) are close in energy, and are lower in energy than in **1b′** (3.87 eV). Secondly, the copper d-orbital character in the HOMOs are similar in **1a′** (54%) and **1c′**(53%) and are about 10% lower than that in **1b′** (62%). We interpret this different behavior in terms of structural factors, and suggest that substituents in the 2,9-

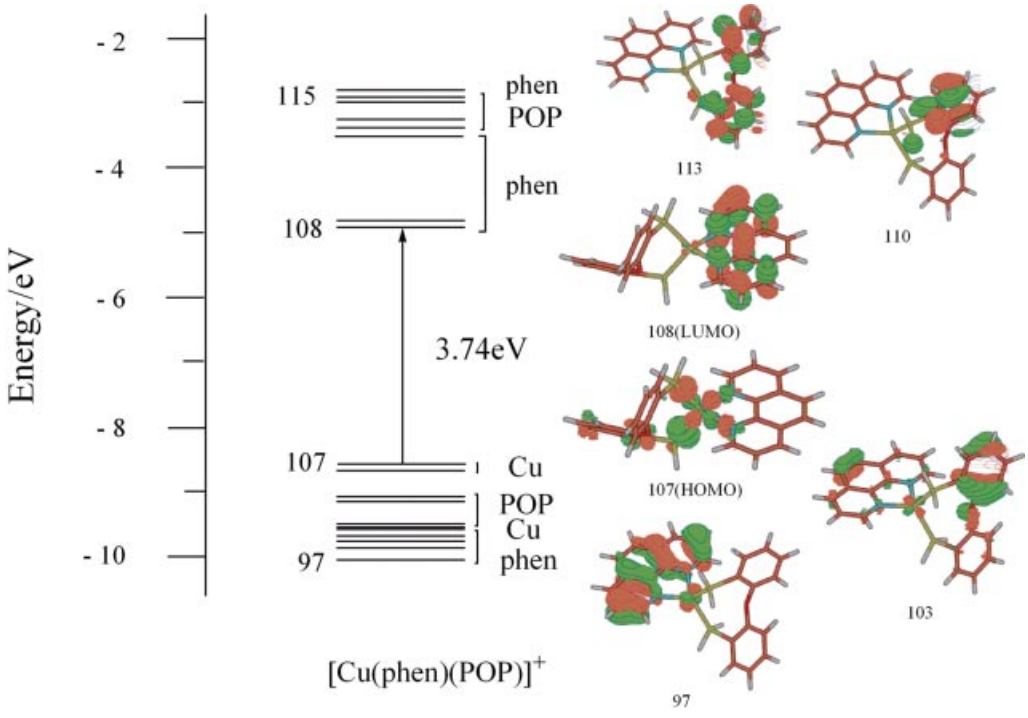

Figure 4. Energy-level diagram of the frontier molecular orbitals together with representative three-dimensional MO plots calculated at the B3LYP/LanL2DZ level for **1a′**. Labels on the right denote the dominant moiety contributing to each molecular orbital. For clarity, only a few of the molecular orbitals are numbered.

 © 2005 Wiley-VCH Verlag GmbH & Co. KGaA, Weinheim

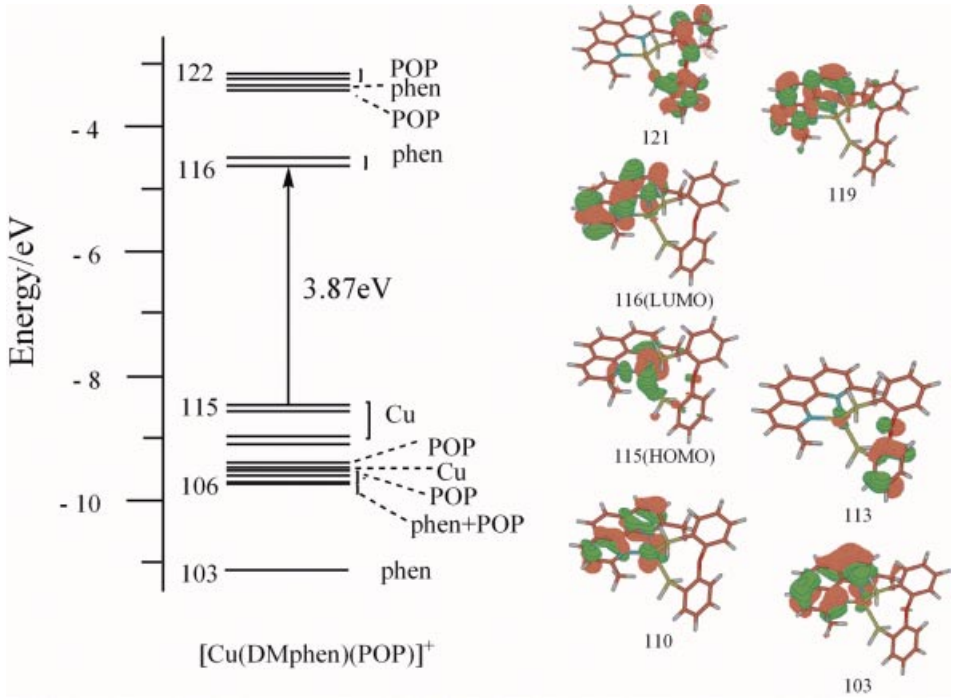

Figure 5. Energy-level diagram of the frontier molecular orbitals together with representative three-dimensional MO plots calculated at the B3LYP/LanL2DZ level for **1b′**. Labels on the left denote the dominant moiety contributing to each molecular orbital. For clarity, only a few of the molecular orbitals are numbered.

phenanthroline positions are optimal to prevent significant ground-state distortions.

The LUMOs of **1a′** and **2a′**, as has already been indicated, are characteristic ofr the two diimines, whereas the valence occupied orbitals exhibit the same character due to the identity of the POP and metal. As from the energetic viewpoint phen and bpy show an almost identical π*-accepting ability (Tables 2 and 3), it is expected that the HOMO–LUMO gap of these complexes will be very similar in energy (differs by 0.06 eV). From the orbital character point of view, the metal's contribution is greater in the latter (about 60%) than in the former (about 50%).

Contour plots of the characteristic occupied and virtual orbitals for molecules **1a′** and **1b′** are depicted in Figures 4 and 5, respectively. In these plots, the metal character is evident in the HOMO, which is an admixture with a phosphorus contribution from POP and a nitrogen contribution from phen (bpy), while the LUMO is delocalized over the phen ligand. Lower-energy occupied orbitals are mainly located on phen and one of POP phenyls, and the higher-energy virtual orbitals are also composed of phen and phenyls of POP.

Cation and Anion Properties

Additional information derived from our calculations provides insight into the interrelationship of structure and electronic behavior, in particular the response of the molecule to the formation of a hole or the addition of an electron. Table 4 contains the ionization potentials (IPs), electron affinities (EAs), and spin density. The vertical IP is obtained by differences in the total self-consistent energies of the cation and the neutral molecule based on the optimized neutral ground-state geometry, as is the EA. In all cases, the energy required to create a hole is about 10 eV and the energy cost to accept an electron is about 3 eV. As shown in Table 4, the cationic spin density for each complex is mainly on the Cu and POP [see Figure 6 (left), which shows **1b′** as an example], which is basically consistent with the orbital character of the HOMO. These all correspond to removal of an electron from the 5d orbital.

Four complexes show relatively weakly bound negative ions, corresponding to the electron affinity. In each complex the unpaired spin density is totally on the phen or bpy ligands [for example, the spin density is mainly on phen in

Table 4. Ionization potentials, electron affinities, and spin densities for the four complexes [eV]. See text for definitions. The IP and EA are vertical values.

		Spin density of cation [%]							Spin density of anion [%]					
	IP [eV]	phen	bpy	Cu	POP	Me	ph	EA [eV]	phen	bpy	Cu	POP	Me	ph
1a′	10.08	10		41	49			2.76	93		2	5		
1b′	9.98	19		33	46	2		3.25	93		1	4	2	
1c′	9.95	23		27	27		23	3.40	93		1	1		7
2a′	10.10		20	41	39			3.47		97	1	2		

 © 2005 Wiley-VCH Verlag GmbH & Co. KGaA, Weinheim

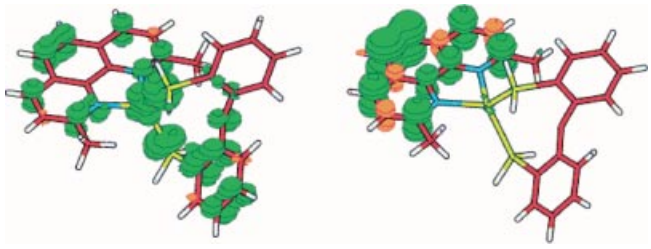

Figure 6. Spin-density surfaces of the cation (left) and the anion (right) for **1b′**.

complex **1b′** as depicted in Figure 6 (right)]. This is consistent with the LUMO being primarily the phen or bpy π*-orbitals.

Absorption Spectra

With the prerequisite ground-state DFT calculation in hand, we proceeded to perform the time-dependent calculation of complexes **1a′** to **2a′** to find the characters and energies of their low-lying singlet and triplet excited states at the TDDFT//B3LYP/LANL2DZ level of theory. Selected low lying singlet and triplet excited states together with their vertical excitation energies and oscillator strengths for **1a′**–**1c′** and **2a′** are displayed in Tables 5, 6, 7, and 8, respectively.

An experimentally used model of an excited state corresponds to the excitation of an electron from an occupied to a virtual MO (i.e., a one-electron picture). However, the excited states calculated herein demonstrate that excited-state electronic structures are best described in terms of multiconfigurations, wherein a linear combination of several occupied-to-virtual MO excitations comprises a given optical transition. Assignment of the character of each excited state was based on the compositions of the occupied and virtual MOs of the dominant configuration(s) for that excited state. Excited states that arise from transitions between orbitals that are located on different moieties were classified as charge transfer (CT) excited states. Those from π-occupied to π-virtual orbitals located on the same ligand were described as π-π* states (IL), but those from orbitals on different ligands were described as ligand-to-ligand charge transfer (LLCT) states. Metal-to-ligand charge transfer (MLCT) states involve transitions from the metal atom to ligand-centered orbitals. For the majority of the excited states under investigation, most of the significant excited states exhibit mixed character as they consist of more than one transition. For example, S_{11} in **1a′** consists of two transitions of 102→109 (45%) and 103→108 (31%). The former transition is from orbital 102, which has mainly metal Cu character, to orbital 109, which is located on phen, and is thus assigned as MLCT, whereas the latter one is from 103(POP) to 108 (phen) and is denoted as LLCT. S_{11} therefore has a mixed character between MLCT and LLCT.

Table 5. Selected TDDFT calculated excitation energies and compositions of the lowest lying singlet and triplet excited states for complex **1a′**.

States	Compositions	ΔE [eV]/$\lambda_{calcd.}$ [nm]	f	$\lambda_{exp.}$ [nm]	Character
		Singlets (**1a′**)			
1	106→108 (55%)	2.81/441	0.0002		MLCT
	107→108 (42%)				MLCT
3	107→108 (53%)	3.19/389	0.1178	391	MLCT
	106→108 (41%)				MLCT
11	102→109 (45%)	4.01/309	0.0148		MLCT
	103→108 (31%)				LLCT
13	102→109 (43%)	4.20/295	0.0134		MLCT
	97→109 (29%)				IL
19	107→110 (50%)	4.45/279	0.0723	269	MLCT
	106→110 (41%)				MLCT
26	107→110 (49%)	4.79/259	0.0518		MLCT
	106→110 (23%)				MLCT
30	105→111 (33%)	4.97/249	0.0582		MLCT + IL
	107→115 (20%)				MLCT
33	107→113 (49%)	5.04/246	0.0391		MLCT
	105→111 (28%)				LLCT + MLCT
		Triplets (**1a′**)			
1	106→108 (55%)	2.64/469	0.0000		MLCT
	107→108 (44%)				MLCT
2	106→108 (55%)	2.81/441	0.0000		MLCT
	107→108 (42%)				MLCT
3	107→108 (53%)	2.82/440	0.0000		MLCT
	106→108 (43%)				MLCT
4	106→109 (41%)	2.87/432	0.0000		MLCT
	101→109 (34%)				LLCT + IL
5	106→109 (56%)	2.99/413	0.0000		MLCT
	107→109 (38%)				MLCT

 © 2005 Wiley-VCH Verlag GmbH & Co. KGaA, Weinheim

Table 6. Selected TDDFT calculated excitation energies and compositions of the lowest lying singlet and triplet excited states for complex **1b′**.

States	Compositions	ΔE [eV]/$\lambda_{calcd.}$ [nm]	f	$\lambda_{exp.}$ [nm]	Character
		Singlets (**1b′**)			
1	115→116(62%)	2.95/420	0.0004		MLCT
3	114→116(60%)	3.32/373	0.1016	383[26]	MLCT
5	114→117(62%)	3.53/352	0.0126		MLCT
14	110→117(49%)	4.37/284	0.0164		MLCT
	115→119 (31%)				MLCT
17	115→118 (63%)	4.53/274	0.0236		MLCT
19	114→119 (41%)	4.60/269	0.0622		MLCT
	107→116 (27%)				LLCT + IL
20	106→116 (41%)	4.61/268	0.0233		LLCT + IL
	107→116 (40%)				LLCT + IL
34	114→121 (49%)	5.00/248	0.0430		MLCT
	112→118 (20%)				IL
		Triplets (**1b′**)			
1	115→116(64%)	2.80/443	0.0000		MLCT
2	111→117(53%)	2.91/426	0.0000		IL
	114→117(35%)				MLCT
3	114→116(62%)	2.96/418	0.0000		MLCT
4	115→117(58%)	3.21/387	0.0000		MLCT
	114→117(31%)				MLCT
5	113→116(62%)	3.38/366	0.0000		MLCT

Table 7. Selected TDDFT calculated excitation energies and compositions of the lowest lying singlet and triplet excited states for complex **1c′**.

States	Compositions	ΔE [eV]/$\lambda_{calcd.}$ [nm]	f	$\lambda_{exp.}$ [nm]	Character
		Singlets (**1c′**)			
1	146→148 (52%)	2.83/438	0.0004		MLCT
	147→148(46%)				MLCT
3	147→148(50%)	3.20/387	0.2139	400	MLCT
	146→148 (44%)				MLCT
4	147→149(50%)	3.30/376	0.0714		MLCT
	146→149 (45%)				MLCT
9	144→149(51%)	3.84/323	0.2594	290	LLCT + MLCT
	143→149 (24%)				
12	142→149(57%)	3.96/313	0.2429		LLCT + MLCT
	143→149 (17%)				
22	136→148(45%)	4.30/288	0.0326		IL
	146→150 (28%)				MLCT
24	136→148(40%)	4.42/281	0.0436		IL
	147→150 (37%)				MLCT
33	147→152(42%)	4.69/265	0.0936		MLCT
	147→153 (24%)				MLCT
		Triplets (**1c′**)			
1	147→148(45%)	2.66/466	0.0000		MLCT
	146→148 (41%)				MLCT
2	147→149(35%)	2.67/464	0.0000		MLCT
	146→148 (32%)				MLCT
3	147→148(49%)	2.76/450	0.0000		MLCT
	146→148 (45%)				MLCT
4	146→148(52%)	2.83/438	0.0000		MLCT
	147→148 (46%)				MLCT
5	146→149(52%)	3.00/414	0.0000		MLCT
	147→149 (45%)				MLCT

Furthermore, from Tables 5–8, it can be seen, as in the case of the energy gaps, that the lowest absorption energies in complexes **1a′** (2.81 eV) and **1c′** (2.83 eV) are similar, and both are lower than that of **1b′** (2.95 eV).

The 35 lowest-energy triplet excited states were also calculated by a similar TDDFT methodology. The first five triplet excited states in each complex are listed in Tables 5–8. MLCT, LLCT, and IL excited states are all observed, but

 © 2005 Wiley-VCH Verlag GmbH & Co. KGaA, Weinheim

Table 8. Selected TDDFT calculated excitation energies and compositions of the lowest lying singlet and triplet excited states for complex **2a′**.

States	Compositions	ΔE [eV]/$\lambda_{calcd.}$ [nm]	f	$\lambda_{exp.}$ [nm]	Character
		Singlets (**2a′**)			
1	101→102(65%)	2.71/458	0.0003		MLCT
2	100→102 (64%)	3.16/393	0.0975	358	MLCT
9	100→103(65%)	3.92/317	0.0501		MLCT
17	96→103 (46%)	4.55/272	0.0829	285	MLCT
	93→102 (37%)				IL
22	99→104 (49%)	4.81/258	0.0224		LLCT + MLCT
	98→104 (42%)				MLCT
24	96→103 (34%)	4.85/255	0.2055		LLCT + MLCT
	93→102 (32%)				IL
26	101→107 (41%)	4.97/249	0.0367		LLCT + IL
	96→104 (31%)				MLCT
31	99→105 (39%)	5.05/246	0.0305		IL
	100→107 (32%)				MLCT + IL
		Triplets (**2a′**)			
1	101→102 (67%)	2.55/487	0.0000		MLCT
2	100→102 (67%)	2.82/439	0.0000		MLCT
3	98→102 (53%)	3.19/388	0.0000		MLCT + LLCT
	99→102 (43%)				MLCT + LLCT
4	93→102 (51%)	3.25/382	0.0000		IL
	96→102 (44%)				MLCT
5	101→103 (37%)	3.56/348	0.0000		MLCT

most of them are mixed-character excited states, as with the singlets. As expected from Hund's rule, transitions to the triplet states tend to be lower in energy than their corresponding singlets. For example, for complex **1a′** the first triplet vertical transition energy is at 2.64 eV, which is lower than that of the first singlet excited state (2.81 eV), although both represent (predominantly) HOMO and HOMO–1→LUMO transitions. The TDDFT results do not provide information on triplet–singlet absorption intensities since spin-orbit coupling effects are not included in current TDDFT approaches, which is why the oscillator strengths are all zero for triplet excited states. Spin-orbit coupling can, however, mix singlet and triplet states, thereby allowing the latter to acquire intensity in both absorption and emission. A second effect is that the triplet energies are shifted by coupling with higher singlet (or other triplet) states. For third row transition metals one[40] can estimate that the lowest triplet states are lowered by about 0.2–0.3 eV due to interactions with higher states through spin-orbital coupling.

Comparison with Experimental Results

Combined with experimental data gathered over time, computed spectra may provide a reference for monitoring the behavior and possible degradation of the organic material in the device. The results of the TDDFT calculations for all considered complexes have been compared with experimental absorption data (see Tables 5–8 and Figure 7). The spectral assignment is based on a comparison of experimental band maxima with calculated energies of transitions with significant oscillator strengths. However, oscillator strengths should be used rather qualitatively to distinguish allowed transitions from forbidden as very weak transitions to other excited states also occur in the relevant energy regions. Moreover, for the S_1 excited state the calculated spin density of positive and negative ions also has significant reference value for transition assignment. In general, the assignment of the character of each excited state was based on the components of the occupied and virtual MOs (see Tables 2 and 3 and Figures 4 and 5) of the dominant excitation(s) for that excited state.

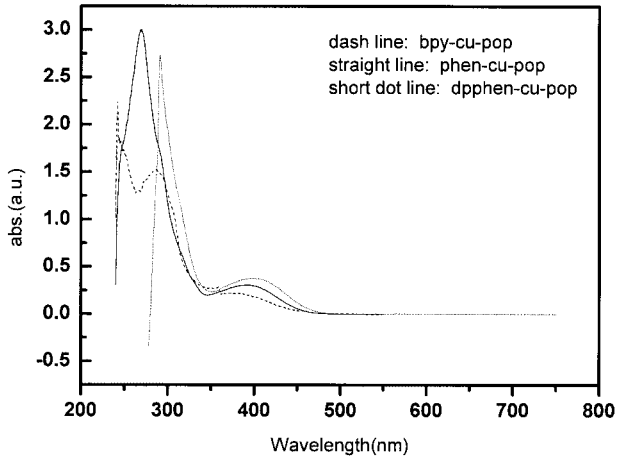

Figure 7. Experimental absorption data of complexes **1a′**, **1c′**, and **2a′** as measured in CH_2Cl_2 solution.

Most of the investigated complexes exhibit two absorption peaks. For complexes **1a′** and **1c′**, the low-energy absorptions are found experimentally at 391 nm and 400 nm,

 © 2005 Wiley-VCH Verlag GmbH & Co. KGaA, Weinheim

both of which are similar to the calculated d(Cu)→π*(phen) (MLCT) excitation arising from S_3 at 389 nm (3.19 eV) and 387 nm (3.20 eV). The other intense calculated absorption peak at 269 nm for **1a′**, arising from singlet state S_{19} at 279 nm (4.45 eV), is assigned as having mainly d(Cu)→π*(phen) (MLCT) character. For **1c′** this peak, which corresponds to excited state S_9, features mixed character between d(Cu)→π*(phen) (MLCT) and π→π* (LLCT), and the latter arises from a transition from the POP ligand (HOMO–4) consisting of the π-orbital of phenyl to ligand phen (LUMO).

For complex **1b′**, the low-energy band at 383 nm occurs in the same region as the singlet state S_3 calculated at 373 nm (3.32 eV), which arises from d(Cu)→π*(phen) (MLCT) consisting of HOMO–1→LUMO.

As with complexes **1a′** and **1c′**, the low-energy absorption peak arising from excited state 2 located at 393 nm (3.16 eV) results from d(Cu)→π*(bpy) (MLCT) and agrees with the experimental value of 383 nm in complex **2a′**. The other absorption band labeled as mixed transition of MLCT and π(bpy)→π*(bpy) (IL) is consistent with the experimental band at 285 nm.

It can be seen from the absorption analysis that substitution at the 3,7-phenanthroline positions has less effect than at the 2,9-phenanthroline positions on the absorption bands. for example, the low-energy bands in complexes **1a′** (389 nm) and **1c′** (387 nm) are similar, and are both at longer wavelength than that in **1b′** (373 nm) due to steric effects exerted by the pendent groups at the 2,9-positions. Different ligands bpy and phen have little influence on the absorption spectra. For example, the low-energy absorption band is found at 389 nm in **1a′** and 393 nm in **2a′**.

The good agreement between theory and experiment suggests that the character of the experimental absorption features can be inferred from our calculations. Specifically, the low-energy edge is largely MLCT in nature, whereas the strongest peaks contain significant contributions from LLCT or IL transitions. In fact, it has been shown before that TDDFT frequently underestimates the transition energies of excitations accompanied by a substantial charge density redistribution.[29–33] For example, TDDFT vacuum calculations of the complexes [Ru(X)(R)$(CO)_2$(diimine)] (X = Cl, Br, I, R = X, Me, $SnPh_3$; diimine = bpy or *N*,*N*′-bis-*i*Pr-1,4-diazabutadiene) have predicted that their low-lying MLCT and LLCT transitions occur at energies well below those of the lowest experimental absorption bands.[31–33] Moreover, this method cannot yet be used to study extended systems as it is not infrequent that the optical properties reach saturation already for quite short chain lengths, whereas the orbital energies still continue to change for longer oligomers. It is known that the exchange-correlation (XC) functionals must decrease with increasing chain length; this trend of variation is in line with the expectation that in more extended systems the electronic repulsion is smaller.[34,35] However, in this study the combined use of DFT//B3LYP/LANL2DZ and TDDFT//B3LYP/LANL2DZ provides a reliable theoretical tool to investigate the properties of $[Cu(NN)^2]^+$ systems.

Lowest Triplet States

Because the calculation of excited-state properties typically requires significantly more computational effort than is needed for the ground states, the lowest triplet states, T_1, of only molecules **1a′**, **1b′**, and **2a′** were fully optimized by carrying out ab initio CIS.[36,37] The optimized structure parameters are shown in Table 9.

Table 9. Calculated bond lengths of the lowest triplet state (T_1) for complexes **1a′**, **1b′**, and **2a′**.

	1a′	**1b′**	**2a′**
Cu–N(1)	2.196	2.195	2.172
Cu–N(2)	2.191	2.202	2.170
Cu–P(1)	2.612	2.598	2.633
Cu–P(2)	2.561	2.625	2.576
Cu···O	3.277	3.431	3.415
P(1)–Cu–P (2)	107.13	105.71	105.01
N(1)–Cu–N(2)	77.23	77.72	77.75
N(1)–Cu–P(1)	114.93	118.54	117.98
N(1)–Cu–P(2)	111.50	117.40	114.15
N(2)–Cu–P(1)	123.52	118.28	118.31
N(2)–Cu–P(2)	119.14	117.97	117.98

A general elongation of all the metal–ligand bond lengths between the excited and ground states is observed. For example, in complex **1a′** the Cu–N bond lengths in the triplet state (2.196 and 2.191 Å) are longer than those in the ground state(2.102 and 2.095 Å) by about 0.1 Å, and the distances between the metal atom and carbon atom (Cu–C) are also longer by about 0.2 Å in the triplet state (2.612 and 2.561 Å) than in the ground state (2.427 and 2.414 Å). As far as the angles are concerned, except for N(1)–Cu–N(2), which decreases from 80° to 77°, the other angles vary by 5°.

Emission Spectra

On the basis of the excited triplet-state geometry TDDFT was employed to calculate the emission spectra. The long-lived decay lifetime obtained experimentally revealed that the photoluminescence of the four complexes is

Table 10. Calculated emissions in thin film for complexes **1a′**, **1b′**, and **2a′**.

Complex	Compositions	ΔE [eV]/$\lambda_{calcd.}$ [nm]	$\lambda^{exp.}$ [nm]	Stokes shifts [nm]		Character
				calcd.	exp.	
1a′	107→108 (70%)	2.19/567	561	178	170	MLCT
1b′	115→117 (68%)	2.23/556	524	183	141	MLCT
2a′	101→102 (70%)	2.18/568	560	175	177	MLCT

 © 2005 Wiley-VCH Verlag GmbH & Co. KGaA, Weinheim

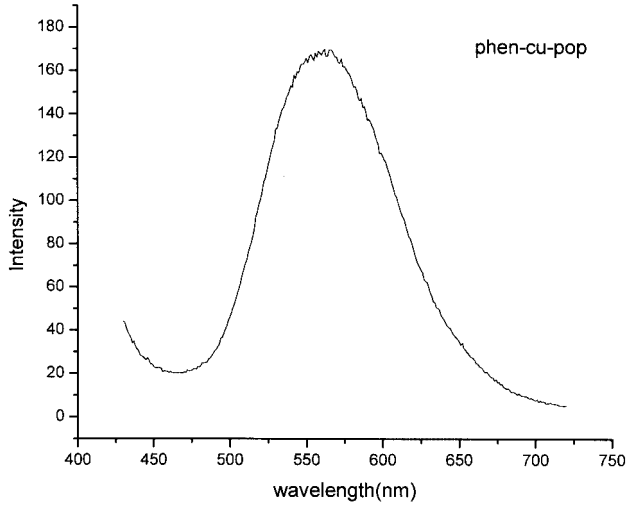

Figure 8. Experimental emission spectra for complex **1a**′ as a thin film.

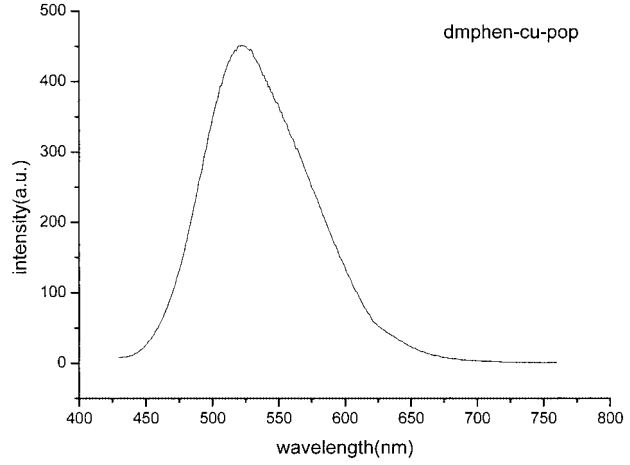

Figure 9. Experimental emission spectra for complex **1b**′ as a thin film.

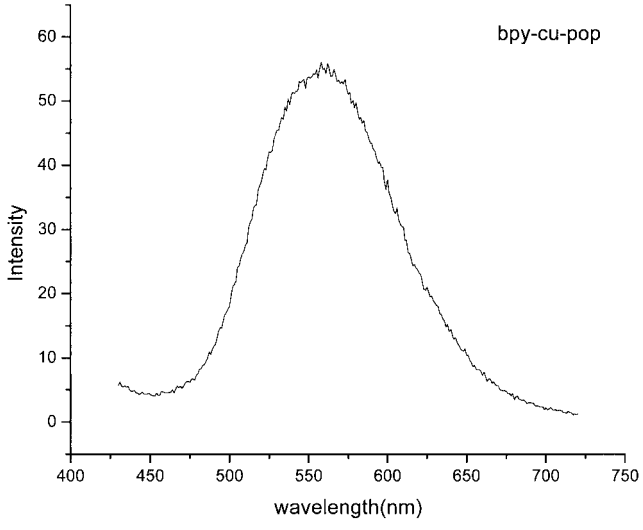

Figure 10. Experimental emission spectra for complex **1c**′ as a thin film.

due to a triplet state transition ($T_1 \rightarrow S_0$) and thus we only optimizes the lowest triplet state (T_1) and calculated the triplet emission spectra. The results of the TDDFT calculations for complexes **1a**′, **1b**′, and **2a**′ are summarized in Table 10, and the experimental emission spectra figures are depicted in Figures 8, 9, and 10 respectively.

The photoluminescence for each complex corresponds to the lowest triplet T_1, which consists of the transition from HOMO to LUMO or LUMO+1, and is thus assigned as having mixed character between MLCT [d(Cu)→π*(phen or bpy)]. The emissions predicted to be at 567, 556, and 568 nm for **1a**′, **1b**′ and **2a**′, respectively, agree well with the experimental values of 561, 524, and 560 nm, and are all assigned to d(Cu)→π*(bpy) (MLCT). It can be seen from these results that all the investigated complexes have large stokes shifts of about 170 nm. Obviously, the change tendency with the different substituted positions of emission is in parallel to that of absorption. In other words, appending groups at 2,9-positions blue-shift the emission spectra due to steric effects.

Conclusions

The ground-state geometries of a series of newly synthesized mixed-ligand, copper(I) polypyridine and phenanthroline complexes such as $[Cu(NN)(POP)]^+$ [POP = bis[2-(diphenylphosphanyl)phenyl] ether] have been calculated at the B3LYP/LANL2DZ level, and the calculated geometrical parameters are in good agreement with the X-ray diffraction experiment results. The electronic structures have been discussed completely. Introduction of groups at the 2,9-positions on the phen ligand lifts the energy gap between the HOMO and the LUMO, and, at the same time, strongly influence the characters of the HOMOs and LUMOs, whereas introduction of groups at the 4,7-positions has little effect on either the energy gap or the character of the frontier orbitals, but makes the orbital characters of the lower occupied and higher unoccupied orbitals change. In addition, there are no pure-metal-character orbitals − the amount of metal 5d character varies from 50% to 70%. Furthermore, substitution at the 2,9-positions makes both the absorption and emission spectra exhibit blue shifts due to steric effects. In all the investigated complexes the lowest-energy absorption and emission are dominant MLCT transitions with some admixture of LLCT transitions. Finally, the results of this work show that careful DFT/TDDFT calculations are capable of accurately describing the spectral features of our investigated complexes, with a quantitative agreement with the experimental data. This suggests that such a theoretical approach may provide useful insights into the design of new and more efficient phosphorescent materials. At the same time, however, it has some drawbacks, especially as it does not consider spin-orbit coupling effects.

Experimental Section

Material and X-ray Diffraction: All complexes, as depicted in Figure 1, were synthesized as described in the literature,[38,39] and then

 © 2005 Wiley-VCH Verlag GmbH & Co. KGaA, Weinheim

Table 11. Crystal data and refinement details for complexes **1a**, **1b**, and **2a**.

	1a	**1b**	**2a**
Empirical formula	$C_{50}H_{39}ClCuF_6N_3O_4P_3$	$C_{60}H_{45}Cu_3F_{18}N_6O_3P_3$	$C_{36}H_{38}CuF_2N_{0.67}O_{0.67}P$
Mol. mass	1003.74	1523.55	623.18
Crystal system	triclinic	triclinic	triclinic
Space group	$P\bar{1}$	$P\bar{1}$	$P\bar{1}$
a [Å]	10.8112(6)	15.1463(2)	11.5938(4)
b [Å]	12.3096(7)	18.4820(3)	12.2320(5)
c [Å]	19.5790(12)	18.6955(5)	16.5078(7)
α [°]	80.5030(19)	108.081(3)	79.251(3)
β [°]	86.899(4)	104.560(2)	81.147(2)
γ [°]	72.278(2)	100.7730(11)	72.379(2)
V [Å^3]	2447.9(2)	4611.34(16)	2180.17(15)
Z	2	4	3
F(000)	1026	3060	978
D(calcd.) [mg m^{-3}]	1.362	2.195	1.424
μ [mm^{-1}]	0.661	1.616	0.848
Temp [K]	293(2)	293(2)	293(2)
λ [Å]	0.71073	0.71069	0.71073
2θ range [°]	1.76–27.48	1.21–27.46	1.26–27.37
Final R indices [$I > 2\sigma(I)$]	$R_1 = 0.0704$	$R_1 = 0.0469$	$R_1 = 0.0506$
	$wR_2 = 0.2331$	$wR_2 = 0.1089$	$wR_2 = 0.1468$
R indices (all data)	$R_1 = 0.0864$	$R_1 = 0.1618$	$R_1 = 0.0676$
	$wR_2 = 0.2470$	$wR_2 = 0.1558$	$wR_2 = 0.1567$
Goodness-of-fit on F^2	1.003	0.605	1.106

purified by vapor diffusion of diethyl ether into an acetonitrile solution. They were all isolated as yellow crystals. Crystal data for **1a**, **1b**, and **2a** are given in Table 11. CCDC-224679 (for **1a**), -224680 (for **1b**) and -224681 (for **2a**) contain the supplementary crystallographic data for this paper. These data can be obtained free of charge from The Cambridge Crystallographic Data Centre via www.ccdc.cam.ac.uk/data_request/cif. [Cu(phen)(POP)]PF_6 was characterized by ^{1}H NMR and, IR spectroscopy, and elemental analysis.

[Cu(phen)(POP)]PF_6: $C_{48}H_{36}CuF_6N_2OP_3$: calcd. C 62.17, H 3.91, N 3.02; found C 62.08, H 3.99, N 2.92.

Instrumentation: The samples for photophysical studies were prepared by spin-coating a mixture of the Cu complex (20 wt.-%) and poly(methyl methacrylate) (80 wt.-%) in dichloromethane onto a glass slide. UV/Vis absorption and PL spectra were recorded on a Perkin–Elmer Lambda 35 UV/Vis spectrophotometer and a Perkin–Elmer LS50B fluorescence spectrophotometer, respectively. The ^{1}H NMR spectra were recorded on an AVANCZ 5000 spectrometer at 298 K, utilizing deuterated chloroform as the solvent and tetramethylsilane (TSM) as the standard. IR spectra were recorded on a Perkin–Elmer spectrophotometer in the 400–4000 cm^{-1} region, using a model RF-5301PC spectrophotometer.

Computational Methods: Calculations on the electronic ground-state of the investigated complexes were carried out at the B3LYP level of density functional theory, which has been proved very useful to calculate molecular orbital distributions for the interpretation of electrochemical and photochemical results for Ru^{II}[40] and square-planar Pt^{II} complexes.[41] B3LYP corresponds to the combination of Becke's three parameter exchange functional (B3) with the Lee–Yang–Parr for the correlation functional (LYP), using the LANL2DZ basis set that includes Dunning/Huzinaga valence double-ξ on the first row and Los Alamos ECP plus DZ on Na–Bi. The excited-state geometries were optimized at the CIS level of theory.[42,43] Time-dependent density functional theory (TDDFT) has recently become a reliable method for calculation of excited-state energies and has proven useful in the assignment of systems as complex as Ru^{II} and Cr^{III} polypyridyl complexes.[42−44] The nature of the low-lying excited states was explored using the time-dependent density functional theory (TDDFT) approach to derive both absorption spectra and emission spectra at the respective ground-state and excite-state geometries, which were compared to existed spectroscopic data. This B3LYP/LANL2DZ level of theory has proven useful for other transition metal systems. McCusker et al. have employed the B3LYP/LanL2DZ level of theory to study the excited-state electronic structures of $[RuL'_2(NCS)_2]^{4-}$ (where L′ = 4,4′-dicarboxylato-2,2′-bipyridine).[42] Adamo and colleagues[45] have presented a combined DFT//B3LYP and TDDFT study to predict the absorption spectra of $[Ru(bpy)(tpy)dmso]^{2+}$ (bpy = 2,2′-bipyridine, tpy = 2,2′:6′,2"-terpyridine; dmso = dimethyl sulfoxide). A double-ζ quality LANL2DZ basis was used for all atoms except oxygen and sulfur, which were described by 6-31G*. The results show good agreement between theory and experiment, with errors within 0.2 eV corresponding to the lowest allowed transition. Hay[46] has well reproduced the low-lying excited electronic states in the Ir^{III} complex $Ir(ppy)_3$ and related complexes using the B3LYP functional. "Double-ζ" quality basis sets were employed for the ligands (6-31G) and the Ir(LANL2DZ). The nature of the excited states, as well as the positive and negative ions with regard to "electron-hole" creation, is relevant to their use in OLED materials. In all computations no constraints were imposed on the geometry. All calculations are performed with the Gaussian 03 program suite. The molecular orbitals were visualized with MOLDEN 3.9.[47] Moreover, the qualitative concepts and the graphs derived from the Chem3D program suite highlight the basic interactions resulting from the DFT calculations.

Acknowledgments

This work was supported by the Major State Basis Research Development Program (no. 2002CB 613406), the National Nature Science Foundation of China (no. 90101026), and the Key Laboratory for Supramolecular Structure and Material of Jilin University.

[1] A. P. de Silva, D. B. Fox, T. S. Moody, S. M. Weir, *Pure Appl. Chem.* **2001**, *73*, 503–511.
[2] C. M. Rudzinski, D. G. Nocera, *Mol. Supramol. Photochem.* **2001**, *7*, 1–3.
[3] C. M. Elliott, F. Pichot, C. J. Bloom, L. S. Rider, *J. Am. Chem. Soc.* **1998**, *120*, 6781–6784.
[4] Y. D. Zhao, A. Richman, C. Storey, N. B. Radford, P. Pantano, *Anal. Chem.* **1999**, *71*, 3887–3893.
[5] K. E. Erkkila, D. T. Odom, J. K. Barton, *Chem. Rev.* **1999**, *99*, 2777–2796.
[6] L. Prodi, F. Bolletta, M. Montaltri, N. Zaccheroni, *Coord. Chem. Rev.* **2000**, *205*, 59–83.
[7] H. Ali, J. E. van Lier, *Chem. Rev.* **1999**, *99*, 2379–2450.
[8] C. A. Bignozzi, R. Argazzi, C. J. Kleverlaan, *Chem. Soc. Rev.* **2000**, *29*, 87–96.
[9] A. Juris, V. Balzani, F. Barigelletti, S. Campagna, P. Belser, A. von Zelewsky, *Coord. Chem. Rev.* **1988**, *84*, 85–98.
[10] D. R. McMillin, K. M. McNett, *Chem. Rev.* **1998**, *98*, 1201–1220.
[11] N. Armaroli, *Chem. Soc. Rev.* **2001**, *30*,113–124.
[12] D. V. Scaltrito, D. W. Thompson, J. A. O'Callaghan, G. J. Meyer, *Coord. Chem. Rev.* **2000**, *208*, 243–266.
[13] Q. S. Zhang, Q. G. Zhou, Y. X. Cheng, L. X. Wang, D. G. Ma, X. B. Jing, *Adv. Mater.* **2004**, *16*, 432–436.
[14] M. K. Eggleston, D. R. McMillin, K. S. Koenig, A. J. Pallenberg, *Inorg. Chem.* **1997**, *36*, 172–173.
[15] C. T. Cunningham, K. L. H. Cunningham, J. F. Michalec, D. R. McMillin, *Inorg. Chem.* **1999**, *38*, 4388–4392.
[16] R. A. Rader, D. McMillin, M. T. Buckner, T. G. Matthews, D. J. Casadonte, R. K. Lengel, S. B. Whittaker, L. M. Darmon, F. E. Lytle, *J. Am. Chem. Soc.* **1981**, *103*, 5906–5912.
[17] P. A. Breddels, P. A. M. Berdowski, G. Blasse, *J. Chem. Soc., Faraday Trans. 2* **1982**, *78*, 595–599.
[18] C. E. A. Palmer, D. R. McMillin, *Inorg. Chem.* **1987**, *26*, 3837–3840.
[19] M. Kranenburg, Y. E. M. van der Burgt, P. C. J. Kamer, P. W. N. M. van Leeuwen, K. Goubitz, J. Fraanje, *Organometallics* **1995**, *14*, 3081–3089.
[20] W. Koch, M. C. Holthausen, *A Chemist's Guide to Density Functional Theory*; Wiley-VCH, Weinheim, Germany, **2000**.
[21] C. Adamo, B. V. di Matteo, *Adv. Quantum Chem.* **1999**, *36*,4–7.
[22] R. Bauernschmitt, R. Ahlrichs, *Chem. Phys. Lett.* **1996**, *256*, 454–464.
[23] F. Furche, *J. Chem. Phys.* **2001**, *114*, 5982–5992.
[24] G. Ricciardi, A. Rosa, E. J. Baerends, *J. Phys. Chem. A* **2001**, *105*, 5242–5454.
[25] F. Furche, R. Ahlrichs, A. Sobanski, F. Vögtle, C. Wachsman, E. Weber, S. Grimme, *J. Am. Chem. Soc.* **2000**, *122*, 1717–1724.
[26] P. Aslanidis, P. J. Cox, S. Divanidis, A. C. Tsipis, *Inorg. Chem.* **2002**, *41*, 6875–6886.
[27] Z. A. Siddique, Y. Yamamoto, T. Ohno, K. Nozaki, *Inorg. Chem.* **2003**, *42*, 6366–6378.
[28] S. Fantacci, F. D. Angelis, A. Selloni, *J. Am. Chem. Soc.* **2003**, *125*, 4381–4387.
[29] O. Gritsenko, E. J. Baerends, *J. Chem. Phys.* **2004**, *121*, 655–661.
[30] A. Dreuw, M. Head-Gordon, *J. Am. Chem. Soc.* **2004**, *126*, 4007–4016.
[31] M. Turki, C. Daniel, S. Záliš, A. Vlèek, Jr., J. van Slageren, D. Stufkens, *J. Am. Chem. Soc.* **2001**, *123*, 11431–11440.
[32] A. Gabrielsson, S. Záliš, P. Matousek, M. Towrie, A. Vlèek, Jr., *Inorg. Chem.* **2004**, *43*, 7380–7388.
[33] S. Záliš, N. Ben Amor, C. Daniel, *Inorg. Chem.* **2004**, *43*, in press.
[34] J. F. Brière, M. Côté, *J. Phys. Chem. B* **2004**, *108*, 3123–3129.
[35] S. Grimme, M. Parac, *ChemPhysChem* **2003**, *4*, 292–295.
[36] H. X. Zhang L. Yang, A. M. Ren, J. K. Feng, X. D. Liu, Y. G. Ma, *Inorg. Chem.* **2004**, *43*, 5961–5972.
[37] L. Yang, A. M. Ren, J. K. Feng, Y. G. Ma, M. Zhang, X. D. Liu, J. C. Shen, H. X. Zhang, *J. Phys. Chem.* **2004**, *108*, 6797–6808.
[38] S. M. Kuang, D. G. Guttell, D. R. McMillin, P. E. Fanwichk, R. A. Walton, *Inorg. Chem.* **2002**, *41*, 3313–3322.
[39] D. G. Cuttell, S. M. Kuang, P. E. Fanwick, D. R. McMillin, D. A. Walton, *J. Am. Chem. Soc.* **2002**, *124*, 6–7.
[40] K. A. Nguyen, J. Kennel, R. Pachter *J. Chem. Phys.* **2002**, *117*, 7128–7136.
[41] S. R. Stoyanov, J. M. Villegas, D. P. Rillema, *Inorg. Chem.* **2003**, *42*, 7852–7860.
[44] J. E. Monat, J. H. Rodriguez, J. K. McCusker, *J. Phys. Chem. A* **2002**, *106*, 7399–7406.
[45] J. H. Rodrigues, D. E. Wheeler, J. K. McCusker, *J. Am. Chem. Soc.* **1998**, *120*, 12051–12068.
[46] K. Zheng, J. Wang, W. Peng, X. Liu, F. Yun, *J. Phys. Chem. A* **2001**, *105*, 10 899–10 905.
[47] H. Ciofini, C. A. Daul, C. Adamo, *J. Phys. Chem. A* **2003**, *107*, 11190–11194.
[48] H. P. Jeffrey, *J. Phys. Chem. A* **2002**, *106*, 1634–1641.
[49] G. Schaftenaar, CAOS/CAMM Center Nijmegen Toernooiveld, Nijmegen, The Netherlands, **1991**.

Received: November 09, 2004

 © 2005 Wiley-VCH Verlag GmbH & Co. KGaA, Weinheim

N-Bonded Monosilanols: Synthesis and Characterization of $ArN(SiMe_3)SiMe_2Cl$ and $ArN(SiMe_3)SiMe_2OH$ (Ar = C_6H_5, 2,6-$Me_2C_6H_3$, 2,6-$iPr_2C_6H_3$)

Vadapalli Chandrasekhar,*[a] Ramamoorthy Boomishankar,[a] Ramachandran Azhakar,[a] Kandasamy Gopal,[a] Alexander Steiner,[b] and Stefano Zacchini[b]

Keywords: Monosilanols / *N*-Bonded silanols / Hydrogen bonding / Aminosilanols

By the use of aniline and the sterically hindered aromatic primary amines, 2,6-$Me_2C_6H_3NH_2$ and 2,6-$iPr_2C_6H_3NH_2$, *N*-bonded monochlorosilanes, $ArN(SiMe_3)SiMe_2Cl$ [Ar = C_6H_5 (**1a**), Ar = 2,6-$Me_2C_6H_3$ (**1b**) and Ar = 2,6-$iPr_2C_6H_3$ (**1c**)] have been prepared by a sequential deprotonation at the nitrogen followed by reaction with silyl chlorides. Hydrolysis of the *N*-bonded monochlorosilanes afforded the *N*-bonded monosilanols $ArN(SiMe_3)SiMe_2OH$ [Ar = C_6H_5 (**2a**), Ar = 2,6-$Me_2C_6H_3$ (**2b**) and Ar = 2,6-$iPr_2C_6H_3$ (**2c**)]. The X-ray crystal structure of **1c** reveals a positional disorder of the Cl and CH_3 substituents on silicon. The X-ray crystal structure of **2c** shows that it is involved in an intermolecular O–H···O hydrogen bonding in the solid state to afford a dimeric structure containing the O_2H_2 ring.
(© Wiley-VCH Verlag GmbH & Co. KGaA, 69451 Weinheim, Germany, 2005)

Introduction

Silanols as compounds containing Si–OH units are attracting considerable interest in recent years because of various reasons. They are excellent precursors for the synthesis of main group and transition metal siloxanes containing the Si–O–M bonds.[1,2] Thus, the reaction of appropriate silanols with suitable metal substrates such as metal halide, hydride, -alkyl, amide or alkoxide leads to the formation of acyclic, cyclic or cage metallasiloxanes.[1,3,4] Often the nature of the synthesized metallasiloxane depends on the type of silanol chosen.[3] A second reason of interest in silanols is their utility to serve as models for silica surfaces particularly in the context of silica-supported transition metal catalysts.[5] More recently, there has also been considerable interest in silanols in organic synthesis.[6a] For example, silanols have been found to be excellent substrates for palladium-catalyzed (and fluoride-, cesium carbonate- or silver oxide-activated) cross-coupling reactions.[6b–6d] The utility of silanols in Mizoroki–Heck-type of coupling reactions has also been demonstrated.[6e] Finally silanols are also gaining importance as bioisosteres with specific interest as transition-state analogues for metalloproteases, aspartic proteases as well as HIV proteases.[7]

Among the various types of silanols that have been reported, monosilanols of the type R_3SiOH, $R_2R'SiOH$ and $RR'R''SiOH$ are the simplest examples as these contain only one Si–OH group per molecule.[8] Although several types of monosilanols are known,[8] there are *none* which contain Si–N bonds. One of the possible reasons for this lacuna is probably the high sensitivity of the Si–N bond towards hydrolysis.[9] On the other hand about 70 to 80% of all silanols are actually synthesized by a hydrolysis reaction of an appropriate Si–X bond (X = F, Cl, Br, I or OR).[8] Recent pioneering efforts of Roesky and coworkers,[10] and our interest in ***N***-bonded silanols[11] has prompted us to assemble *N*-bonded monosilanols. Accordingly, herein, we report the synthesis and spectroscopic characterization of $ArN(SiMe_3)SiMe_2Cl$ [Ar = C_6H_5 (**1a**), 2,6-$Me_2C_6H_3$ (**1b**), 2,6-$iPr_2C_6H_3$ (**1c**)] and $ArN(SiMe_3)SiMe_2OH$ [Ar = C_6H_5 (**2a**), 2,6-$Me_2C_6H_3$ (**2b**), 2,6-$iPr_2C_6H_3$ (**2c**)]. We also report the X-ray structural characterization of **1c** and **2c**.

Results and Discussion

Synthesis and Spectra: Sterically unencumbered as well as hindered aromatic amines (aniline, 2,6-dimethylaniline, 2,6-diisopropylaniline) were used as the starting materials. Sequential deprotonation at nitrogen followed by reaction with silyl halides afforded the *N*-bonded silyl chlorides **1a**, **1b** in excellent yields as distillable oils or as a solid (**1c**) (Scheme 1). In contrast to the situation with corresponding *N*-bonded silicon dichlorides and trichlorides **1b** and **1c** are quite stable to ambient moisture. The compound **1a**, however, is sensitive to ambient moisture and undergoes hydrolysis to the silanol **2a**.

[a] Department of Chemistry, Indian Institute of Technology, Kanpur,
Kanpur 208016, India
Fax: +91-512-2590007-2597436
E-mail: vc@iitk.ac.in
[b] Department of Chemistry, University of Liverpool,
Liverpool, L69 7ZD, U. K.

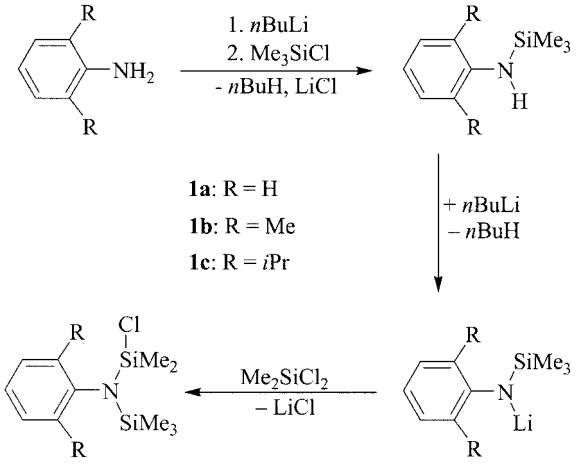

Scheme 1.

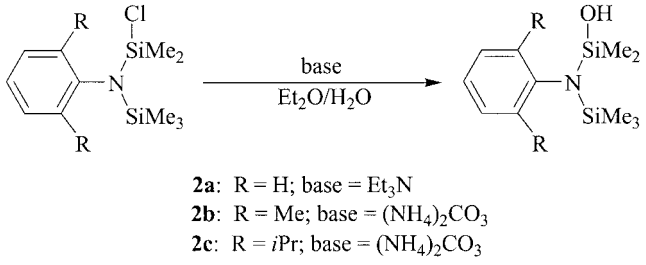

Scheme 2.

Hydrolysis of **1a**, **1b** and **1c** afford the corresponding monosilanols **2a**, **2b** and **2c** (Scheme 2). While hydrolysis of **1a** is effected by the use of triethylamine as the hydrogen chloride scavenger, hydrolysis of **1b** and **1c** require ammonium carbonate. It is important to note that the use of aniline, which is very effective as a mild base for the hydrolysis of *N*-bonded silicon dichlorides and trichlorides, does not result in clean hydrolysis of **1a**, **1b** or **1c**. Although the silanols **2a** and **2b** are isolated as oils, **2c**, which contains the sterically hindered aromatic amine substituent, is a solid. While **2a**, **2b** and **2c** are rare examples of *N*-bonded monosilanols, **2a** represents the first example of *any* silanol (monosilanol, silanediol or silanetriol) where the sterically *unencumbered* aniline is the substituent on silicon.

The new *N*-bonded silyl chlorides and silanols are extremely lipophilic and are soluble in a wide range of organic solvents. The compounds **1a**–**c** and **2a**–**c** have been characterized by mass spectroscopy, elemental analysis, IR spectroscopy and multi-nuclear NMR spectroscopy. The silyl chlorides and the monosilanols show prominent parent ion peaks in their FAB mass spectra. The ^1H NMR spectra of these compounds are consistent with their structures. The ^{29}Si $\{^1H\}$ NMR spectra of the silyl chlorides are characterized by chemical shifts for the $–SiMe_3$ and $–SiMe_2Cl$. While the former resonate between δ = 11.9 and 12.6 ppm the latter are seen at a slightly lower frequency between 7.8 and 8.6 ppm, respectively (Table 1). The $–SiMe_2Cl$ chemical shifts occur at a higher frequency than the corresponding $–SiMeCl_2$ (–1.3 and –1.4 ppm)[11a] and $–SiCl_3$ (–28.2 and –27.9 ppm).[10a] A movement of the ^{29}Si chemical shift to lower frequency occurs upon conversion of $ArSiMe_2Cl$ (**1a**–**1c**) to $ArSiMe_2OH$ (**2a**–**2c**). Thus the latter resonate at –1.7 (**2a**), –1.3 (**2b**) and –0.8 (**2c**) ppm, respectively. These chemical shifts are at a higher frequency in comparison to the corresponding silanediols (–29.4 and –29.6 ppm)[11a] and silanetriols (–66.2 and –65.3 ppm).[10a]

The IR spectra of the silanediols **2a** and **2b** in the solid sate in KBr pellets show broad bands at 3350 and 3416 cm^{-1}, respectively. In **2c** in addition to the peak at 3466 cm^{-1} a sharp peak at 3666 cm^{-1} is also observed. The observation of the latter shows that the formation of the KBr pellet disrupts some of the intermolecular hydrogen bonding in **2c** to give rise to free Si–OH.

X-ray Crystal Structures of 1c and 2c: The X-ray crystal structure of **1c** shows a positional disorder; the Cl and CH_3 groups attached to silicon are disordered over the same sites (Figure 1). Such a positional disorder occurs because of the similar volumes of the Cl and CH_3 groups. This results in the two Si–N distances being the same [1.729(1) Å]. The sum of the bond angles around nitrogen N1 equal 360° reflecting the perfect planarity around nitrogen.

Table 1. ^{29}Si NMR chemical shifts of *N*-bonded silicon chlorides and silanols and related dichlorides, trichlorides, diols and triols.

Compound	δ $NSiMe_3$	δ SiCl	δ $SiCl_2$	δ $SiCl_3$	δ SiOH	δ $Si(OH)_2$	δ $Si(OH)_3$	Ref.
$(C_6H_5)N(SiMe_3)(Me_2SiCl)$	11.9	8.6						this work
$(2,6\text{-}Me_2C_6H_3)N(SiMe_3)(Me_2SiCl)$	12.3	7.8						this work
$(2,6\text{-}iPr_2C_6H_3)N(SiMe_3)(Me_2SiCl)$	12.6	7.8						this work
$(C_6H_5)N(SiMe_3)(Me_2SiOH)$	5.0				–1.7			this work
$(2,6\text{-}Me_2C_6H_3)N(SiMe_3)(Me_2SiOH)$	5.0				–1.3			this work
$(2,6\text{-}iPr_2C_6H_3)N(SiMe_3)(Me_2SiOH)$	5.0				–0.8			this work
$(2,6\text{-}Me_2C_6H_3)N(SiMe_3)(MeSiCl_2)$	10.3		–1.3					[11a]
$(2,6\text{-}iPr_2C_6H_3)N(SiMe_3)(MeSiCl_2)$	10.4		–1.4					[11a]
$(2,6\text{-}Me_2C_6H_3)N(SiMe_3)(MeSi(OH)_2)$	5.7					–29.4		[11a]
$(2,6\text{-}iPr_2C_6H_3)N(SiMe_3)(MeSi(OH)_2)$	5.6					–29.6		[11a]
$(2,6\text{-}Me_2C_6H_3)N(SiMe_3)SiCl_3$	12.5			–28.2				[10a]
$(2\text{-Me-}6\text{-}iPr_2C_6H_3)N(SiMe_3)SiCl_3$	12.2			–27.9				[10a]
$(2,6\text{-}Me_2C_6H_3)N(SiMe_3)Si(OH)_3$	7.7						–66.2	[10a]
$(2\text{-Me-}6\text{-}iPr_2C_6H_3)N(SiMe_3)Si(OH)_3$	7.5						–65.3	[10a]

 © 2005 Wiley-VCH Verlag GmbH & Co. KGaA, Weinheim

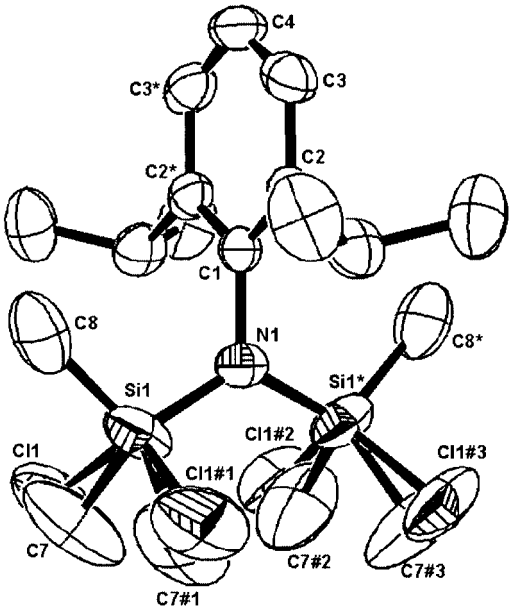

Figure 1. ORTEP diagram of **1c** shown at the 50% probability level. All the hydrogen atoms are omitted for clarity.

The ORTEP diagram of **2c** is shown in Figure 2. Unlike in **1c** two types of Si–N bond lengths are seen viz., Si1–N1, 1.731(1) and Si2–N1, 1.759(1) Å. The longer bond distance is associated with the silicon bearing less electronegative substituents while the shorter distance is associated with *N*-*Si*Me_2OH. The shorter Si1–N1 distance is however, longer than the corresponding distance of 1.7140(18) Å observed in 2,4,6-$Me_3C_6H_2$–N(SiMe_3)SiMe$(OH)_2$. The Si1–O1 distance of 1.648(2) Å is consistent with the trends found in other silanols. This value is shorter than the sum of the covalent radii of silicon and oxygen (1.74 Å). The geometry around nitrogen (N1) is perfectly planar with all the angles around it totaling to 360°.

Intermolecular hydrogen bonding in monosilanols can give rise to different types of arrangements in the solid state, such as a linear dimer,[14a] cyclic dimer,[14b] tetramer,[14c] zigzag polymer[14d] etc. The *N*-bonded monosilanol **2c** shows a cyclic dimer formation (Figure 3) which is quite rare and has been shown before only by the monosilanols containing direct Si–M bonds viz., [(η^5-Cp*)Ru$(CO)_2$]Si(*o*-Tolyl)$_2$-(OH)[14b] and [(η^5-Cp)Fe$(CO)_2]_2$Si(H)(OH).[14e] In the solid state two molecules of **2c** interact with each other and form a planar four-membered O_2H_2 ring. The intermolecular H···O distance is 2.057(1) Å, while the O···O contact is 2.857(2) Å. The O–H···O angle is 158.94(9)°. It is of interest to compare these parameters with those observed earlier. Thus for {(η^5-Cp*)Ru$(CO)_2$}Si(*o*-Tolyl)$_2$(OH) the hydrogen bonding parameters are H···O, 2.172(27) Å. O···O, 2.809(32) Å and O–H···O 134.57(2)°. For {(η^5-Cp)Fe-$(CO)_2\}_2$Si(H)(OH) these values are 2.197 and 2.991 Å and 157.95°.[14b] Thus, the observed hydrogen bonding parame-

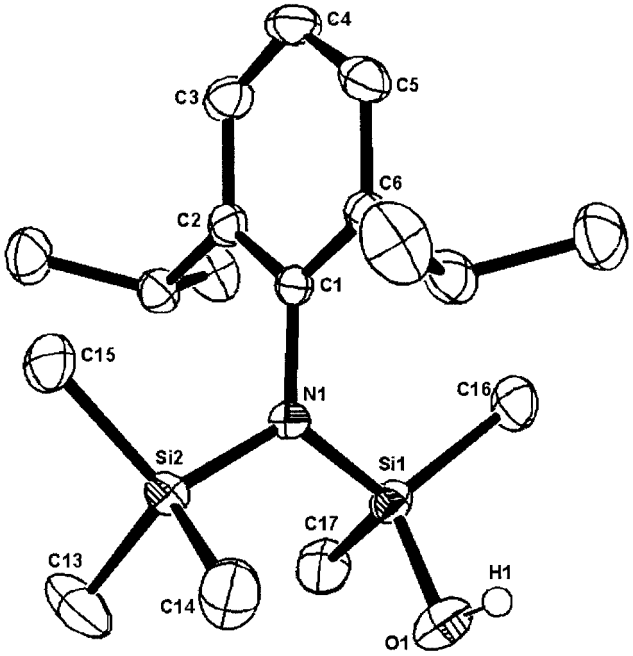

Figure 2. ORTEP diagram of **2c** shown at the 50% probability level. All the hydrogen atoms have been omitted except those of the hydroxy group.

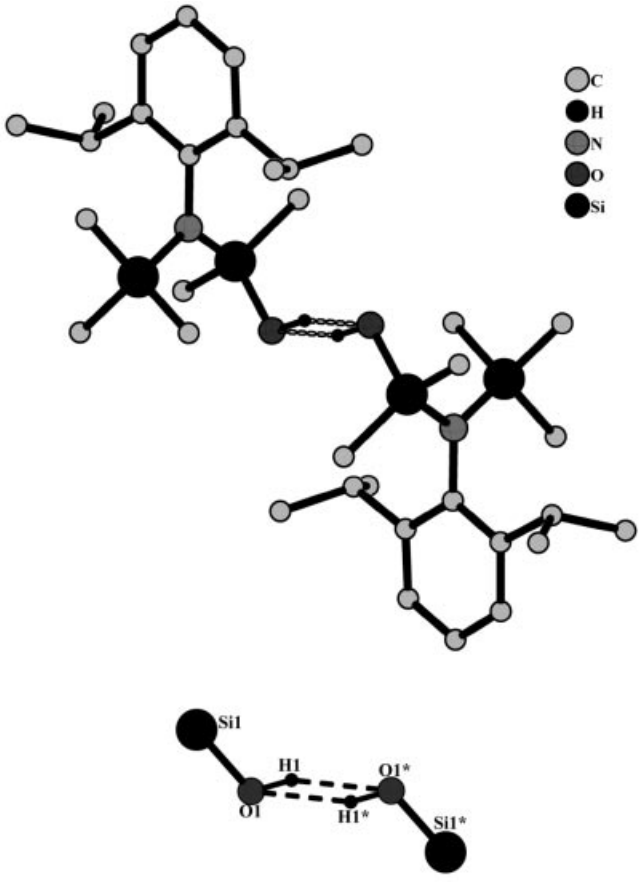

Figure 3. (Top). Formation of a cyclic dimer due to intermolecular hydrogen bonding between two silanol molecules. (Bottom). A perfectly planar arrangement of the four-membered O_2H_2 ring. The metric parameters are: O1–H1, 0.840(1) Å; H1···O1*, 2.057(1) Å; O···O*, 2.857(2) Å; O–H···O*, 158.94(9)°; symmetry, 1 – *x*, 1 – *y*, 2 – *z*.

 © 2005 Wiley-VCH Verlag GmbH & Co. KGaA, Weinheim

ters in **2c** are quite reasonable and indicate the presence of a strong intermolecular hydrogen bonding.

Conclusions

In conclusion we have demonstrated the synthesis of the new examples of *N*-bonded monosilanols. These syntheses were accomplished starting from aromatic amines. A highlight of the synthesis was that for the first time unsubstituted aniline could be utilized to afford an *N*-bonded silanol. X-ray crystal structure of the monosilanol **2c** showed the presence of a hydrogen bonded dimer in the solid-state. All the silanols are extremely lipophilic and air-stable. The utility of these *N*-bonded monosilanols in the assembly of metallasiloxanes is under investigation.

Experimental Section

General Remarks: All manipulations and reactions were carried out under dry nitrogen by employing standard Schlenk techniques. Solvents were dried with sodium benzophenone ketyl and were collected from the still at the time of reaction. 2,6-Dimethylaniline and 2,6-diisopropylaniline (Fluka) were distilled under reduced pressure before use. Chlorotrimethylsilane, dichlorodimethylsilane (Fluka) and *n*-butyllithium (2.5 m solution in hexane) (Aldrich) were used as such without any further purification. Aniline (Spectrochem, India) was stored over CaH_2 and distilled before use. Infrared spectra were recorded in dichloromethane solution as well as neat liquid or as KBr pellets with a FT-IR Bruker-Vector Model. Elemental Analyses were performed with Thermoquest CE instruments CHNS–O, EA/110 model. FAB mass spectra were recorded with a JEOL-SX 102/DA-6000 mass spectrometer/data system using argon/xenon (6 kV, 10 mA) as the FAB gas. The accelerating voltage was 10 kV, and the spectra were recorded at room temperature. EI mass spectra were obtained with a JEOL-d-300 spectrometer. The ^{29}Si $\{^1H\}$, and ^1H NMR spectra were recorded in $CDCl_3$ solutions with a JEOL JNM LAMBDA 400 model spectrometer. Chemical shifts are reported with respect to TMS.

Synthesis: The *N*-bonded monochlorosilanes **1a**, **1b** and **1c** and the corresponding silanols **2a**, **2b**, and **2c** were synthesized by adopting the following general synthetic procedure. The ^{29}Si NMR spectroscopic data for these compounds along with some of the other related compounds are listed in Table 1.

Synthesis of the *N*-Bonded Monochlorosilanes, $ArN(SiMe_3)SiMe_2Cl$ (1a–1c) [Ar = C_6H_5 (1a), R = 2,6-$Me_2C_6H_3$ (1b), 2,6-*i*$Pr_2C_6H_3$ (1c)]: *n*-Butyllithium (75 mmol) was added at a constant rate to a solution of RNH_2 (75 mmol) in diethyl ether (60 mL) at –78 °C. The reaction mixture was stirred at this temperature for 4 h and then brought to ambient temperature. It was then treated with a solution of Me_3SiCl (75 mmol) in diethyl ether (40 mL) at –78 °C and allowed to come to room temperature. The precipitated LiCl was filtered and the filtrate was treated with *n*BuLi (75 mmol) at room temperature. After heating under reflux for 4 h the solution was transferred to a pressure-equalizing funnel and added drop wise to a solution of Me_2SiCl_2 (75 mmol) in diethyl ether (40 mL) and stirred overnight. The precipitated LiCl was filtered and the volatiles from the filtrate were removed in vacuo to give a yellow viscous oily product. Subsequent vacuum distillation afforded the pure silicon chlorides **1a** and **1b** as colorless oily liquids. Compound **1c** was isolated as a solid.

Synthesis of *N*-Bonded Monosilanols. Synthesis of $C_6H_5N(SiMe_3)SiMe_2OH$ (2a): A solution of $C_6H_5N(SiMe_3)SiMe_2Cl$ (**1a**) (12.2 mmol) in Et_2O (50 mL) was added to a well-stirred mixture of Et_2O (50 mL), water (12.2 mmol) and triethylamine (12.2 mmol) at 0 °C over a period of 1 h. It was then allowed to come to room temperature and stirred for 30 h. The precipitated triethylamine hydrochloride was filtered. Removal of solvent from the filtrate in vacuo afforded **2a** as a colorless oil.

Synthesis of 2b and 2c: $RN(SiMe_3)SiMe_2Cl$ (**1b** and **1c**) (12.0 mmol) in diethyl ether (20 mL) was added dropwise through a pressure-equalizing funnel for about 30 min into a rapidly stirred two-phase system consisting of 20 mL of water, 20 mL of diethyl ether and 1.0 g (10.0 mmol) of freshly titrated ammonium carbonate and sodium chloride (7.0 g). The solution was then stirred for another 2 h. The ether layer was separated and the aqueous layer was extracted twice with ether. The combined ether fractions were dried to get crude **2b** and **2c**. The compound **2b** was purified on a neutral alumina column using *n*-hexane/ethyl acetate (90:10) as the eluent to get a pale yellow oil. Compound **2c** was purified by repeated recrystallization from a solution of *n*-hexane.

Characterization Data for Compounds 1a–c and 2a–c

[$C_6H_5N(SiMe_3)SiMe_2Cl$] (1a): Yield 14.7 g (75.9%). B.p. 135 °C/0.08 Torr. $C_{11}H_{20}ClNSi_2$: calcd. C 51.23, H 7.82, N 5.43; found C 51.04, H 7.31, N 5.31. Mass spectrum (EI): *m*/*z* = 258 (41.5) $[M]^+$, (1 Cl isotope pattern). ^1H NMR (400 MHz, $CDCl_3$): δ = 6.85–7.08 (m, 5 H, aromatic), 0.22 [s, 6 H, $Si(CH_3)_2Cl$], 0.00 [s, 9 H, $Si(CH_3)$] ppm.

[2,6-$Me_2C_6H_3N(SiMe_3)SiMe_2Cl$] (1b): Yield 15.2 g (75.9%). B.p. 143 °C/0.08 Torr. $C_{13}H_{24}ClNSi_2$: calcd. C 54.60, H 8.46, N 4.90; found C 54.22, H 8.17, N 4.55. Mass spectrum (FAB): *m*/*z* = 286 (29) $[M^+]$ (1 Cl isotope pattern). ^1H NMR (400 MHz, $CDCl_3$): δ = 6.76–6.84 (m, 3 H, aromatic), 2.13 (s, 6 H, C–CH_3), 0.20 [s, 6 H, $Si(CH_3)_2Cl$], 0.00 [s, 9 H, $Si(CH_3)$] ppm.

[2,6-*i*$Pr_2C_6H_3N(SiMe_3)SiMe_2Cl$] (1c): Yield 16.9 g (66.0%). M.p. 108 °C. $C_{17}H_{32}ClNSi_2$: calcd. C 59.69, H 9.43, N 4.09; found C 59.59, H 8.55, N 3.89. Mass spectrum (FAB): *m*/*z* = 342 (45) $[M^+]$ (1 Cl isotope pattern). ^1H NMR (400 MHz, $CDCl_3$): δ = 6.89–6.96 (m, 3 H, aromatic); 3.30 [septet, ^3J(H,H) = 6.8 Hz 2 H, $HC(CH_3)_2$], 1.03 [d, ^3J(H,H) = 6.84 Hz, 6 H, CH–CH_3], 1.04 [d, ^3J(H,H) = 6.8 Hz, 6 H, CH–CH_3], 0.21 [s, 6 H, $Si(CH_3)_2Cl$], 0.00 [s, 9 H, $Si(CH_3)$] ppm.

[$C_6H_5N(SiMe_3)SiMe_2OH$] (2a): Yield 2.7 g (82.1%). $C_{11}H_{21}NOSi_2$: calcd. C 55.17, H 8.84, N 5.85; found C 54.64, H 8.43, N 5.42. ^1H NMR (400 MHz, $CDCl_3$): δ = 6.81–7.14 (m, 5 H, aromatic), 0.01 [s, 6 H, $OSi(CH_3)$], 0.00 [s, 9 H, $Si(CH_3)$] ppm.

[2,6-$Me_2C_6H_3N(SiMe_3)SiMe_2OH$] (2b): Yield 2.6 g (76.0%). $C_{13}H_{25}NOSi_2$: calcd. C 58.37, H 9.42, N 5.24; found C 58.21, H 9.08, N 5.11. Mass spectrum (FAB): *m*/*z* = 267 (47) $[M]^+$. ^1H NMR (400 MHz, $CDCl_3$): δ = 6.75–6.89 (m, 3 H, aromatic), 2.16 (s, 6 H, C–CH_3), 0.02 [s, 6 H, $OSi(CH_3)_2$], 0.00 [s, 9 H, $Si(CH_3)$] ppm.

[2,6-*i*$Pr_2C_6H_3N(SiMe_3)SiMe_2OH$] (2c): Yield 3.5 g (87.0%). M.p. 108 °C. $C_{17}H_{33}NOSi_2$: calcd. C 63.09, H 10.28, N 4.33; found C 63.19, H 9.52, N 4.18. Mass spectrum (FAB): *m*/*z* = 323 (70) $[M]^+$. ^1H NMR (400 MHz, $CDCl_3$): δ = 6.92–7.13 (m, 3 H, aromatic), 3.35 [m, 2 H, $HC(CH_3)_2$, ^3J(H,H) = 6.84 Hz], 1.07 [d, 6 H, CH–CH_3, ^3J(H,H) = 6.84 Hz], 1.08 [d, ^3J(H,H) = 6.56 Hz, 16 H, CH-(CH_3)], 0.04 [s, 6 H, $OSi(CH_3)$], 0.00 [s, 9 H, $Si(CH_3)$] ppm.

X-ray Crystallography: Crystals of **1c** and **2c** were grown from a solution of *n*-hexane at –20 °C. Colorless block-like crystals suitable for single-crystal X-ray diffraction were loaded with a Bruker

 © 2005 Wiley-VCH Verlag GmbH & Co. KGaA, Weinheim

Table 2. Summary of crystal and structure refinement data for compounds **1c** and **2c**.

Identification code	**1c**	**2c**
Empirical formula	$C_{17}H_{32}ClNSi_2$	$C_{17}H_{33}NOSi_2$
Formula mass	342.07	323.62
Temperature	213(2) K	150(2) K
Wavelength	0.71073 Å	0.71073 Å
Crystal system	orthorhombic	triclinic
Space group	*Cmcm*	$P\bar{1}$
Unit cell dimensions	a = 12.0741(18) Å, α = 90° b = 12.2739(14) Å, β = 90° c = 14.1562(16) Å, γ = 90°	a = 8.4094(5) Å, α = 86.8540(10)° b = 9.6229(6) Å, β = 81.5790(10)° c = 13.0896(8) Å, γ = 71.3230(10)°
Volume	2097.9(5) Å^3	992.61(10) Å^3
Z	4	2
Density (calculated)	1.083 Mg/m^3	1.083 Mg/m^3
Absorption coefficient	0.292 mm^{-1}	0.179 mm^{-1}
F(000)	744	356
Crystal size	0.4×0.3×0.3 mm^3	0.5×0.5×0.4 mm^3
Theta range for data collection	2.37 to 24.34°	1.57 to 28.28°
Index ranges	$-14 \le h \le 13$, $-13 \le k \le 13$, $-16 \le l \le 16$	$-10 \le h \le 11$, $-7 \le k \le 12$, $-16 \le l \le 16$
Reflections collected	6518	6325
Independent reflections	915 [R_{int} = 0.0482]	4384 [R_{int} = 0.0410]
Completeness to θ	96.9% (θ = 24.34°)	89.1% (θ = 28.28°)
Absorption correction	none	none
Refinement method	Full-matrix least-squares on F^2	Full-matrix least-squares on F^2
Data/restraints/parameters	915/1/71	4384/0/200
Goodness-of-fit on F^2	1.100	0.986
Final R indices [$I > 2\sigma(I)$]	R_1 = 0.0399, wR_2 = 0.1091	R_1 = 0.0394, wR_2 = 0.1032
R indices (all data)	R_1 = 0.0482, wR_2 = 0.1130	R_1 = 0.0480, wR_2 = 0.1076
Largest diff. peak and hole	0.214 and –0.216 e·Å^{-3}	0.343 and –0.333 e·Å^{-3}

AXS Smart Apex CCD diffractometer. The details pertaining to the data collection and refinement for **1c** and **2c** are given in Table 2. The structures were solved by direct methods using SHELXS-97 and refined by full-matrix least-squares on F^2 using SHELXL-97.[12,13] The hydrogen atom attached to oxygen atom was located from the difference map and its position was refined. All other hydrogen atoms were included in idealized positions, and a riding model was used. Non-hydrogen atoms were refined with anisotropic displacement parameters. Selected bond lengths and bond angles of **1c** and **2c** are given in Table 3 and Table 4.

Table 3. Selected bond lengths [Å] and angles [°] for **1c**.

Bond lengths			
N1–Si1	1.729(1)	Si1–C8	1.857(4)
Si1–Cl1	2.110(5)	Si1–Cl1#3	2.110(5)
Si1–C7	1.853(8)	N1–C1	1.478(4)
Bond angles			
N1–Si1–C8	108.51(12)	N1–Si1–Cl1	107.76(22)
C8–Si1–Cl1	103.51(21)	Cl1–Si1–Cl#1	124.83(16)
N1–Si1–C7	113.42(33)	C8–Si1–C7	113.19(31)
Cl1#1–Si1–C7#1	15.33(27)	Cl1–Si1–C7	109.86(25)
C7–Si1–C7#1	94.74(34)	C1–N1–Si1	117.46(3)
C1–N1–Si1*	117.46(3)	Si1–N1–Si1*	125.08(5)

Symmetry transformations used to generate equivalent atoms #1, #2 and #3: x, y, $-z + {}^3/_2$

Table 4. Selected bond lengths [Å] and angles [°] for **2c**.

Bond lengths			
Si1–N1	1.731(1)	Si1–C16	1.845(2)
Si2–N1	1.759(1)	Si1–C17	1.859(2)
Si1–O1	1.648(2)	N1–C1	1.448(2)
Bond angles			
Si2–N1–Si1	123.60(7)	N1–Si1–O1	107.07(6)
C1–N1–Si1	119.17(9)	C16–Si1–O1	111.56(8)
C1–Si1–Si2	117.22(10)	C17–Si1–O1	103.86(7)

CCDC-229758 and -229759 contain the supplementary crystallographic data for this paper. These data can be obtained free of charge from The Cambridge Crystallographic Data Centre via www.ccdc.cam.ac.uk/data_request/cif.

Acknowledgments

We are thankful to Department of Science and Technology, New Delhi, India for financial support. AS thanks EPSRC (Engineering and Physical Sciences Research Council), U. K. for financial support.

[1] a) V. Chandrasekhar, R. Boomishankar, S. Nagendran, *Chem. Rev.* **2004**, *104*, 5847; b) R. Murugavel, A. Voigt, M. G. Walawalkar, H. W. Roesky, *Chem. Rev.* **1996**, *96*, 2205.
[2] a) L. King, A. C. Sullivan, *Coord. Chem. Rev.* **1999**, *189*, 19; b) F. J. Feher, T. A. Budzichowski, *Polyhedron* **1995**, *14*, 3239; c) V. Lorenz, A. Fischer, S. Gießmann, J. W. Gilje, Y. Gun′ko, K. Jacob, F. T. Edelmann, *Coord. Chem. Rev.* **2000**, *206–207*, 321.
[3] a) R. Murugavel, V. Chandrasekhar, H. W. Roesky, *Acc. Chem. Res.* **1996**, *29*, 183; b) R. Murugavel, M. Bhattacharjee, H. W. Roesky, *Appl. Organomet. Chem.* **1999**, *13*, 227; c) G. Anantharaman, H. W. Roesky, J. Magull, *Angew. Chem. Int. Ed.* **2002**, *41*, 1226; d) G. Anantharaman, H. W. Roesky, H.-G. Schmidt, M. Noltemeyer, J. Pinkas, *Inorg. Chem.* **2003**, *42*, 970; e) G. Anantharaman, N. D. Reddy, H. W. Roesky, J. Magull, *Organometallics* **2001**, *20*, 5777.
[4] a) K. L. Fujdala, T. D. Tilley, *Chem. Mater.* **2002**, *14*, 1376; b) M. P. Coles, C. G. Lugmair, K. W. Terry, T. D. Tilley, *Chem.*

Mater. **2000**, *12*, 122; c) C. G. Lugmair, K. L. Fujdala, T. D. Tilley, *Chem. Mater.* **2002**, *14*, 888.
[5] a) R. Duchateau, *Chem. Rev.* **2002**, *102*, 3525; b) H. C. L. Abbenhuis, *Chem. Eur. J.* **2000**, *6*, 25.
[6] a) S. E. Denmark, R. F. Sweis, *Acc. Chem. Res.* **2002**, *35*, 835; b) K. Hirabayashi, J. Kawashima, Y. Nishihara, A. Mori, T. Hiyama, *Org. Lett.* **1999**, *1*, 299; c) K. Hirabayashi, A. Mori, J. Kawashima, M. Suguro, Y. Nishihara, T. Hiyama, *J. Org. Chem.* **2000**, *65*, 5342; d) S. E. Denmark, M. H. Ober, *Org. Lett.* **2003**, *5*, 1357; e) K. Hirabayashi, Y. Nishihara, A. Mori, T. Hiyama, *Tetrahedron Lett.* **1998**, *39*, 7893.
[7] a) S. McN. Sieburth, T. Nittoli, A. M. Mutahi, L. Guo, *Angew. Chem. Int. Ed.* **1998**, *37*, 812; b) M. W. Mutahi, T. Nittoli, L. Guo, S. McN. Sieburth, *J. Am. Chem. Soc.* **2002**, *124*, 7363; c) J. Kim, A.Glekas, S. McN. Sieburth, *Bioorg. Med. Chem. Lett.* **2002**, *12*, 3625; d) C.-A. Chen, S. McN. Sieburth, A. Glekas, G. W. Hewitt, G. L. Trainor, S. Erickson-Viitanen, S. S. Garber, B. Cordova, S. Jeffry, R. M. Klabe, *Chem. Biol.* **2001**, *8*, 1161.
[8] P. D. Lickiss, *Adv. Inorg. Chem.* **1995**, *42*, 147.
[9] R. Murugavel, A. Voigt, V. Chandrasekhar, H. W. Roesky, H.-G. Schmidt, M. Noltemeyer, *Chem. Ber.* **1996**, *129*, 391.
[10] a) R. Murugavel, V. Chandrasekhar, A.Voigt, H. W. Roesky, H.-G. Schmidt, M. Noltemeyer, *Organometallics* **1995**, *14*, 5298; b) N. Winkhofer, A. Voigt, H. Dorn, H. W. Roesky, A. Steiner, D. Stalke, A. Reller, *Angew. Chem. Int. Ed. Engl.* **1994**, *33*, 1352.
[11] a) V. Chandrasekhar, S. Nagendran, R. J. Butcher, *Organometallics* **1999**, *18*, 4488; b) V. Chandrasekhar, S. Nagendran, R. Boomishankar, R. J. Butcher, *Inorg. Chem.* **2001**, *40*, 940.
[12] a) G. M. Sheldrick, SHELXL-97, Program for Crystal Structure Analysis (release 97–2), University of Göttingen, Göttingen, Germany, **1998**.
[13] G. M. Sheldrick, SHELXTL, Version 5.03; Siemens Analytical X-ray Division: Madison, WI, **1994**.
[14] a) M. J. MacLachlan, J. Zheng, K. Thieme, A. J. Lough, I. Manners, C. Mordas, R. LeSuer, W. E. Geiger, L. M. Liable-Sands, A. L. Rheingold, *Polyhedron* **2000**, *19*, 275; b) S. Möller, O. Fey, W. Malisch, W. J. Seelbach, *J. Organomet. Chem.* **1996**, *507*, 239; c) J. Beckmann, K. Jurkschat, M. Schürmann, *J. Organomet. Chem.* **2000**, *602*, 170; d) W. Malisch, M. Hofmann, M. Nieger, W. W. Schöller, A. Sundermann, *Eur. J. Inorg. Chem.* **2002**, 3242; e) W. Malisch, M. Vögler, D. Schumacher, M. Nieger, *Organometallics* **2002**, *21*, 2891.

Received: December 10, 2004

 © 2005 Wiley-VCH Verlag GmbH & Co. KGaA, Weinheim

Characterization of Oligomers of AlCl: Al–Cl versus Al–Al Bonding

Hans-Jörg Himmel*[a]

Keywords: Subvalent compounds / Aluminium / Reaction mechanisms / Matrix isolation / Quantum chemical calculations

Oligomers of AlCl have been characterized. By using the matrix isolation technique, the dimer Al_2Cl_2, which exhibits a D_{2h}-symmetric ring structure, was generated in significant quantities and analyzed by its IR and Raman spectra in combination with quantum chemical calculations. The structures of the trimer and tetramer have also been evaluated. A surprising result is that the minimum energy structure of the trimer (C_s symmetry) features direct Al–Al bonds, two terminal Al–Cl bonds, and one bridging Cl atom. A weak, isotopically structured IR band can be assigned to the antisymmetric ν(Al–Cl_t) mode of this trimer (Cl_t denotes a terminal Cl atom). The enthalpy change for each of the oligomerization steps has been calculated. For the dimerization of AlCl to give Al_2Cl_2, the Gibbs energy change was calculated as a function of temperature at different pressures. It turns out that neither the Al_2Cl_2 dimer nor any higher oligomers are present in significant quantities in the gas phase, at least under the conditions of the experiments. The thermodynamic properties show that matrix isolation represents the optimal method of generating and characterizing these species. On the basis of the experimental results the barrier for dimerization of AlCl should be next to zero.
(© Wiley-VCH Verlag GmbH & Co. KGaA, 69451 Weinheim, Germany, 2005)

Introduction

AlCl is an interesting example of a very simple compound featuring Al in the formal oxidation state +1. Several possibilities for generating the molecule have been discussed.[1] These include the reaction of Al with $AlCl_3$, and the reaction of Al with HCl, both requiring high temperatures since AlCl is thermodynamically stable only at high temperatures and disproportionates to Al metal and $AlCl_3$ at lower temperatures. The temperature minimum needed for the generation depends, of course, on the pressure, e.g. under high vacuum (10^{-5} mbar) temperatures around 1250 K or more are needed to generate AlCl in the almost complete absence of $AlCl_3$. The monomer AlCl has already been studied intensively both in the gas phase[2–5] and in inert gas matrices (Figure 1).[6,7] Information about the compound in the solid phase and in solution is, however, sparse.[8]

By using a cocondensation technique and a mixture of solvents, it is possible to obtain metastable solutions of AlCl,[1] which have been used extensively for the preparation of new cluster compounds.[1,9] NMR spectroscopic studies[10] clearly show that the calculated chemical shift of the isolated AlCl molecule (δ = +150 ppm) does not match the position of the NMR signal observed for such solutions (δ = +35 ppm). The calculated NMR spectrum of the tetramer Al_4Cl_4 (δ = +235 ppm) is also not consistent with the experimentally observed spectrum. These results indicate a relatively strong solvent effect, and the AlCl molecules or, more likely, oligomers are coordinated by one or more solvent molecules. However, the exact composition still remains unknown.

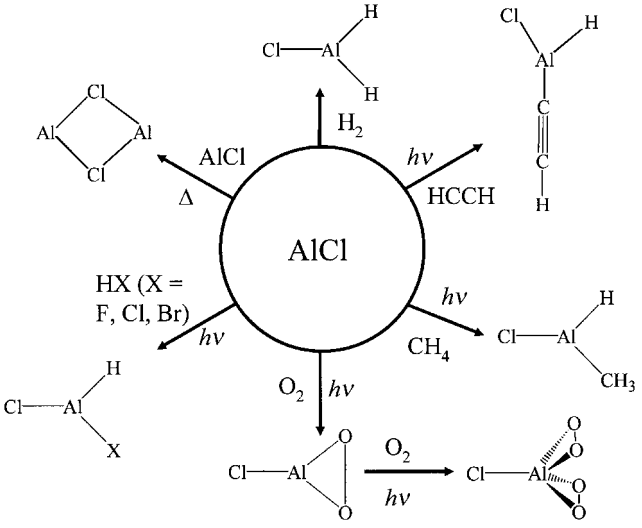

Figure 1. Known reactions of photoactivated AlCl molecules as studied in matrix isolation experiments.

Matrix isolation studies have permitted the reactivity of AlCl monomers to be assessed in some detail. AlCl in its ground electronic state ($^1\Sigma$) is not very reactive. Thus, no spontaneous reaction occurs with O_2 under the conditions of matrix experiments.[11] Only when O atoms are generated is reaction possible, which leads to OAlCl.[12] Photoactivated AlCl reacts, on the other hand, not only with O_2,[11]

[a] Institut für Anorganische Chemie, Universität Karlsruhe, Engesserstr., Geb. 30.45, 76180 Karlsruhe, Germany
Fax: +49-721-608-4854
E-mail: himmel@chemie.uni-karlsruhe.de

 © 2005 Wiley-VCH Verlag GmbH & Co. KGaA, Weinheim DOI: 10.1002/ejic.200401016

but also readily with molecules such as CH_4,[13] H_2,[14] C_2H_2[15] and HX (X = F, Cl or Br).[16] The effect of photolysis has been shown to lead to excitation of an electron from a σ to a π orbital with strong p character localized mainly at the Al atom.[17] The reaction products are all Al^{III} species that are formed exothermally. Figure 1 summarizes the photoactivated reactions and their products which have been studied so far.

The dimer $[AlCl]_2$ had been sighted previously in matrix isolation experiments. Thus, a band at 270 cm^{-1} in the IR spectrum of AlCl that was isolated in an Ar matrix had been assigned to this dimer.[1] However, few details were given, and the fine structure that the band might be expected to show (see the results of this work) was not resolved. Here it will be shown with the aid of higher-resolution IR spectra that this band corresponds to two vibrational modes, each showing the isotopic splitting characteristic of two chemically equivalent Cl atoms in the molecule. In addition, Raman spectra will be reported for the first time, giving clear evidence of one of the $\nu(a_g)$ modes of the dimer. Theoretical studies of $[AlCl]_2$[18] predict a molecule that exhibits a planar, D_{2h}-symmetric structure for its global energy minimum. The experimentally measured frequencies will be used to estimate the bond angles in this ring.

Somewhat surprisingly, no experimental or theoretical information about the trimer Al_3Cl_3 has been available hitherto. Here, the structure of this molecule will be analyzed, and a weak, isotopically structured band in the IR spectrum can tentatively be assigned to it. The tetramer Al_4Cl_4 has been calculated previously,[10,24] and was shown to exhibit a tetrahedral structure with Al–Al and Al–Cl distances of 259.8–263.9 and 209.8–210.9 pm, respectively. Knowledge of the structure and bonding of $[AlCl]_n$ oligomers is desirable in order to anticipate possible structures for solid AlCl. So far, it has proved impossible to characterize the structure of this solid in a more than qualitative way.[8]

Results

IR Spectra

Figure 2a shows the IR spectrum measured for AlCl that was isolated in an Ar matrix. An intense absorption with a doublet pattern occurs at 455.1/449.8 cm^{-1}, as previously assigned to the AlCl monomer. The doublet pattern arises from the presence of the two isotopomers $Al^{35}Cl$ and $Al^{37}Cl$. Two weaker absorptions at high wavenumbers, 462.3 and 459.0 cm^{-1}, also exist. Besides these strong absorptions due to AlCl monomers, the spectrum presents a structured feature at 270 cm^{-1}, which clearly shows several maxima. The structure of the band can be seen in more detail in the higher-resolution spectrum illustrated in Figure 2b.

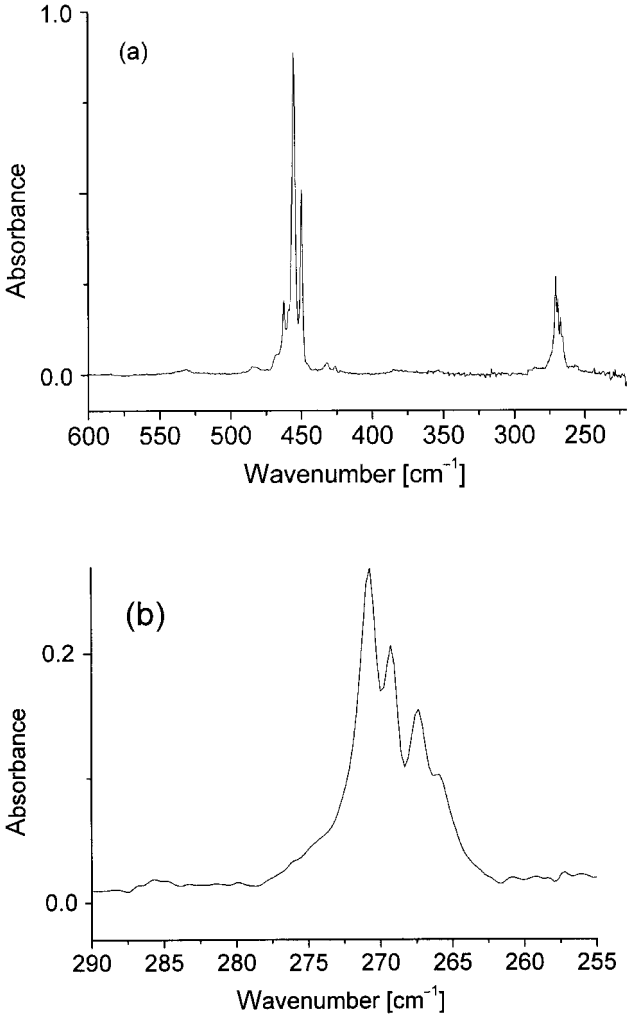

Figure 2. (a) IR spectrum of an Ar matrix containing AlCl vapour. (b) Detailed spectrum of the region around 270 cm^{-1}.

In addition to these intense absorptions, the IR spectrum gives evidence for a weak band, and its maximum is located at 531.3 cm^{-1} (see Figure 3). On the low-energy side of this band, two secondary maxima are visible (at 528.8 and 526.4 cm^{-1}), which are most likely to be due to the presence of different $^{35}Cl/^{37}Cl$ isotopomers.

Raman Spectra

Raman measurements were made to obtain further information. A typical spectrum is displayed in Figure 4a. The ν(Al–Cl) mode of the AlCl monomer near 450 cm^{-1} is clearly visible with the doublet pattern typical for the presence of a single Cl atom in the carrier. Another signal appears with a maximum at 298.6 cm^{-1}. Experiments with varying concentrations of AlCl in the matrix indicate that this signal belongs to the same species as the band near 270 cm^{-1} in the IR experiments.

Discussion

We start this section with a characterization of $[AlCl]_n$ oligomers (n = 1–4) on the basis of the experimental data

 © 2005 Wiley-VCH Verlag GmbH & Co. KGaA, Weinheim

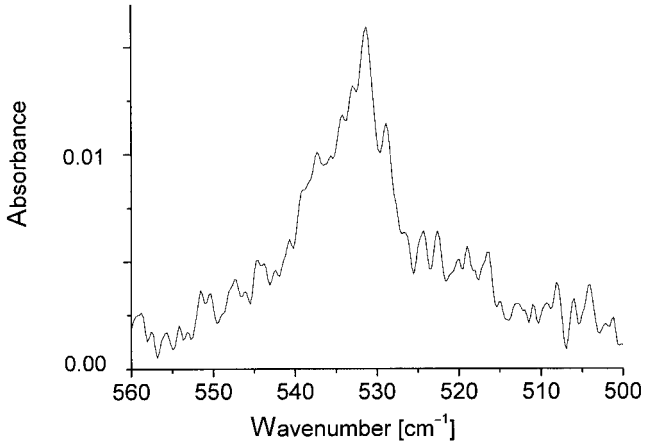

Figure 3. Higher-resolution IR spectrum in the region around 530 cm^{-1}.

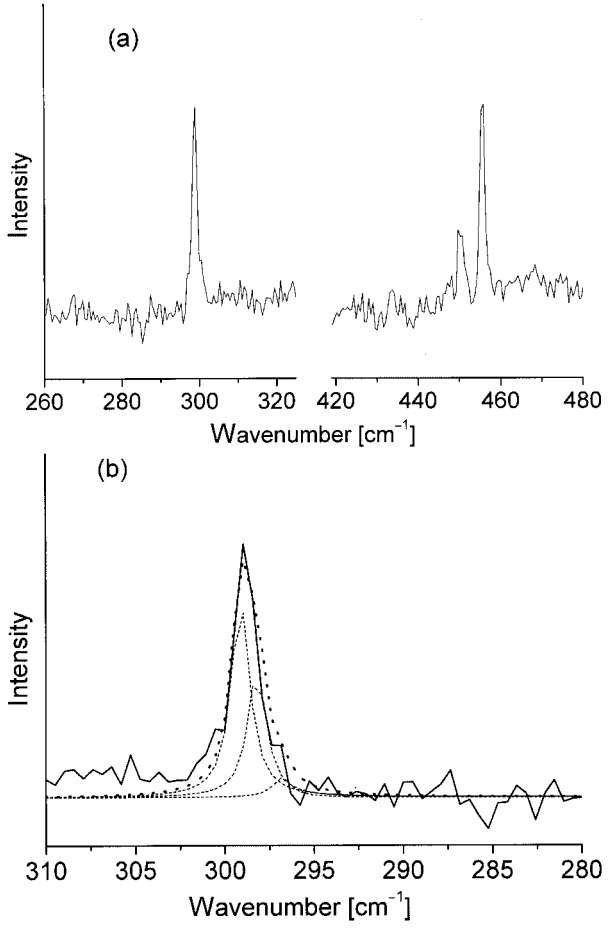

Figure 4. Raman spectra obtained for AlCl isolated in an Ar matrix. (a) In the region of the AlCl monomer and the Al_2Cl_2 dimer. (b) Comparison between the observed signal for the dimer and a fit on the basis of the presence of ^{35}Cl and ^{37}Cl in their natural abundances (see Discussion).

and the results from the quantum chemical calculations. There follows a discussion of the oligomerization process, which considers the enthalpy and Gibbs energy changes for the initial oligomerization reactions.

AlCl

The experimental data indicate that the AlCl monomer is the dominant guest species in the Ar matrices. According to our calculations and with the use of BP/SVP, the Al–Cl distance in the $^1\Sigma$ ground electronic state is 216.4 pm; MP2/TZVPP predicts a value of 215.1 pm. These results are in very good agreement not only with those calculated previously (213–216 pm),[19,20,24] but also with the well-defined experimental estimate (213.0 pm).[2] The IR band at 455.1/449.8 cm^{-1} has already been assigned to the AlCl monomer; the doublet pattern arising from the presence of the two isotopomers $Al^{35}Cl$ and $Al^{37}Cl$. The weaker extra doublet at 462.3/459.0 cm^{-1} also belongs to AlCl, in all probability. This component, shifted by 7.3 cm^{-1} from the main absorption, may well be due to the occupation of a different matrix site. The harmonic wavenumber is predicted to be 476.8 cm^{-1} according to BP/SVP, and 482.1 cm^{-1} according to MP2/TZVPP calculations. The calculated wavenumber is in good agreement with the experimental value of ω_e = 481.30 cm^{-1} for the gaseous molecule.[2,5] The anharmonicity $\omega_e x_e$ was previously determined to be 1.95 cm^{-1}.[5] As expected, a polar molecule like AlCl is subjected to a significant matrix shift (cf. InCl).[21] Analogies between compounds in the two series BF, AlF, AlCl and CO, SiO, SiS have already been discussed in detail.[22]

$[AlCl]_2$

There can be little doubt that the band at around 270 cm^{-1} visible in the IR spectrum can be assigned to an oligomer of AlCl, $[AlCl]_n$. The higher-resolution IR spectrum (see Figure 2a) shows a fine structure within the band which is caused by different isotopomeric forms and allows one to determine, with some confidence, the exact composition of the species. Inspection of the fine structure shows immediately that it cannot be explained by the isotopic pattern of a single mode, but must originate from two different modes with only slightly different wavenumbers. Attempts have been made to simulate the isotopic pattern on the basis of the presence of two Cl atoms in the molecule (with relative natural abundances of 75.8:24.2 for the ^{35}Cl and ^{37}Cl isotopes). In total, six Lorenz-type curves are thus involved in this fit. Figure 5 compares the simulated spectrum with that experimentally observed.

The three Lorentz-type curves of the first mode (which exhibit relative intensities of 57.5:36.7:5.8 reflecting the relative natural abundance of ^{35}Cl and ^{37}Cl) have their maxima at wavenumbers of 270.95, 269.29 and 267.51 cm^{-1}. The three Lorenz curves of the second mode, with the same relative intensities, are located at 267.24, 265.70 and 264.54 cm^{-1}. It can be seen that the simulated spectrum is in good agreement with that observed, a result appearing to confirm the presence of two equivalent Cl atoms in the molecule.

As already mentioned, the experiments give every reason to assume that the signal in the Raman spectrum with its maximum at 298.6 cm^{-1} belongs to the same molecule. Al-

 © 2005 Wiley-VCH Verlag GmbH & Co. KGaA, Weinheim

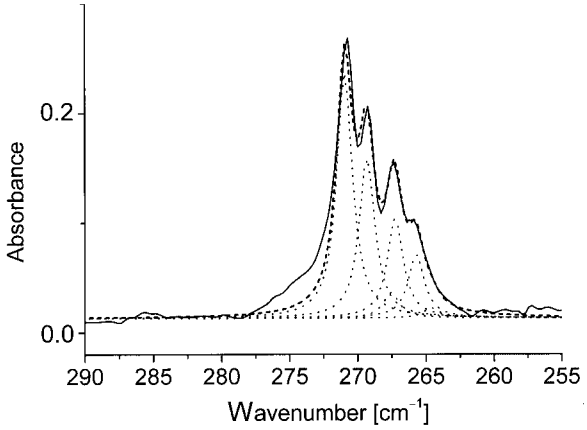

Figure 5. Experimental IR spectrum of $(AlCl)_2$ and fit on the assumption of the presence of two different modes, each with three isotopic components ($^{35}Cl^{35}Cl$, $^{35}Cl^{37}Cl$, and $^{37}Cl^{37}Cl$, in their natural abundances).

though the resolution of the Raman spectra (0.5 cm^{-1}) is unfortunately clearly insufficient to resolve any fine structure of this signal, the profile can be modeled with three Lorenz-type curves. Figure 3b shows the observed signal together with the simulation, again assuming the presence of two chemically equivalent Cl atoms. It can therefore be concluded that this species is most likely to be the dimer Al_2Cl_2.

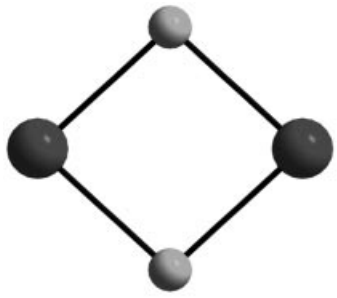

$[AlCl]_2$

Table 1 summarizes the results of quantum chemical calculations on the dimer Al_2Cl_2. According to these calculations, the Al–Cl distance in the dimer is slightly longer than in the AlCl monomer (246.8 versus 216.3 pm). The Cl–Al–Cl and Al–Cl–Al angles are 84.7° and 95.3°, respectively, so that the Al atoms are separated by 364.8 pm. In Table 2, the wavenumbers calculated with BP/SVP are compared with those observed. The general level of agreement is very pleasing. The calculations also give an explanation of why the Raman spectra give evidence for the $\nu_1(a_g)$ mode, but not for the other two modes with *gerade* symmetry.

The Raman intensity calculated for $\nu_1(a_g)$ is more than four times larger than those calculated for $\nu_2(a_g)$ or $\nu_5(b_{3g})$.

It is worth mentioning that the difference in wavenumbers measured between the ν_3 and ν_4 modes of $Al(^{35}Cl)(^{37}Cl)Al$ is not the same as that between the corresponding modes of the $Al(^{35}Cl)_2Al$ and $Al(^{37}Cl)_2Al$ isotopomers. In the case of the ν_3 mode, for example, the $^{35}Cl^{37}Cl$ isotopomer has a wavenumber which is 1.54 cm^{-1} lower than that of the $^{35}Cl^{35}Cl$ isotopomer, but only 1.16 cm^{-1} higher than that of the $^{37}Cl^{37}Cl$ isotopomer. For the ν_4 mode, the situation is reversed, and the difference in wavenumbers from the $^{35}Cl^{37}Cl$ isotopomer is smaller for the $^{35}Cl^{35}Cl$ isotopomer (1.66 cm^{-1}) than for the $^{37}Cl^{37}Cl$ isotopomer (1.78 cm^{-1}). This observation can be explained as a consequence of the symmetry reduction from D_{2h} to C_{2v} in the $^{35}Cl^{37}Cl$ isotopomer. Because of this reduction, the symmetry of the modes changes [$\nu_1(a_g) \rightarrow \nu_1(a_1)$, $\nu_2(a_g) \rightarrow \nu_2(a_1)$, $\nu_3(b_{1u}) \rightarrow \nu_3(b_1)$, $\nu_4(b_{2u}) \rightarrow \nu_4(a_1)$, $\nu_5(b_{3g}) \rightarrow \nu_5(b_1)$, $\nu_6(b_{3u}) \rightarrow \nu_6(b_2)$]. In D_{2h} symmetry, the ν_3 and ν_4 modes belong to two different irreducible representations, b_{1u} and b_{2u}, respectively. There are no other modes with the same symmetry so that neither mode suffers any coupling. In the case of $Al(^{35}Cl)(^{37}Cl)Al$ with C_{2v} symmetry, however, the modes belong to the irreducible representations b_1 and a_1, respectively. The mode ν_5 now also belongs to b_1, and ν_1 and ν_2 belong to a_1. Since the wavenumber calculated for ν_5 (131.6 cm^{-1}) is close to that measured for ν_3 (269.29 cm^{-1}), and that observed for ν_1 (297.7 cm^{-1}) is even closer to that observed for ν_4 (265.70 cm^{-1}), mode coupling is expected to be significant between these two pairs of vibrations. The coupling between ν_3 and ν_5 must lead to an increase in the wavenumber of ν_3 (and a decrease in the wavenumber for ν_5). In the same vein, the coupling between ν_1 and ν_4 must lead to an increase in the wavenumber of ν_1 and a decrease in that of ν_4. This mode coupling is responsible for the wavenumber shifts displayed by the bands caused by $Al(^{35}Cl)(^{37}Cl)Al$, which do not fall midway between the positions of the corresponding modes of $Al(^{35}Cl)(^{35}Cl)Al$ and $Al(^{37}Cl)(^{37}Cl)Al$. The behaviour is thus a good indication that the molecule is, as suggested by the calculations, planar and of high symmetry (D_{2h}).

It should also be mentioned that the angles Cl–Al–Cl and Al–Cl–Al can be estimated purely on the basis of the IR spectra measured for the different isotopomers. In D_{2h} symmetry, the b_{1u} and b_{2u} fundamentals are each unique and do not couple with other modes. The G matrix element for b_{1u}, $G_S(b_{1u})$ (where S denotes G with respect to symmetry coordinates), is as follows:

$$G_S(b_{1u}) = \mu_{Al}(1 + \cos\alpha) + \mu_{Cl}(1 + \cos\alpha) \propto \nu_3^2$$

(α is the Cl–Al–Cl angle and μ_{Al} and μ_{Cl} the inverse masses of Al and Cl, respectively). The corresponding $G_S(b_{2u})$ element is:

$$G_S(b_{2u}) = \mu_{Al}(1 + \cos\alpha) + \mu_{Cl}(1 + \cos\alpha) \propto \nu_4^2$$

This implies that the ratio of ν_4 measured for the two isotopomers $[Al^{35}Cl]_2$ and $[Al^{37}Cl]_2$ is independent of the Cl–Al–Cl angle and should be 1.0120. On the other hand, the corresponding ratio of the ν_3 modes varies with the Cl–Al–Cl angle. The experimental ratios are 1.0129 and 1.0102 for ν_3 and ν_4, respectively. In the event of angles of 90°, the two ratios should be identical. From the experimental data, Cl–Al–Cl and Al–Cl–Al angles of 95° and 85°, respectively, can be calculated. Thus the angles are indeed close to 90° (the error caused by the fit of the experimental curve and the neglect of anharmonicity effects might be about 8°),

 © 2005 Wiley-VCH Verlag GmbH & Co. KGaA, Weinheim

Table 1. Calculated geometric parameters (bond lengths in pm, angles in °), vibrational properties (wavenumbers in cm^{-1}, IR intensities in $km\,mol^{-1}$ given in parentheses, RA intensities relative to the most intense signal in the case of BP/aug-cc-pVTZ) and energy (in hartree) for Al_2Cl_2 (D_{2h} symmetry).

	BP/SVP	MP2/TZVPP	BP/aug-cc-pVTZ
Al–Cl	246.8	243.8	247.2
Al···Al	364.8	361.3	363.0
Cl–Al–Cl	84.7	84.4	85.5
Al–Cl–Al	95.3	95.6	94.5
$\nu_1(a_g)$	298.4 (0)	303.7 (0)	286.8 (IR:0, RA: 100)
$\nu_2(a_g)$	164.0 (0)	176.6 (0)	160.0 (IR: 0, RA:22)
$\nu_3(b_{1u})$	287.1 (311)	292.0 (340)	281.8 (IR: 267, RA: 0)
$\nu_4(b_{2u})$	277.8 (59)	285.2 (84)	265.9 (IR: 76, RA: 0)
$\nu_5(b_{3g})$	132.5 (0)	132.2 (0)	135.3 (IR: 0, RA: 18)
$\nu_6(b_{3u})$	26.4 (0.1)	50.1 (0.1)	34.4 (IR:0.4, RA: 0)
Energy	–1405.08771	–1403.49167	
Energy including ZPVE	–1405.08502	–1403.48885	

Table 2. Comparison between the IR spectroscopic properties observed and calculated for $Al(\mu\text{-}Cl)_2Cl$ in three different isotopic forms [wavenumbers in cm^{-1}, IR intensities (in $km\,mol^{-1}$) given in parenthesis].

	$Al(\mu\text{-}^{35}Cl)_2Al$		$Al(\mu\text{-}^{35}Cl)(\mu\text{-}^{37}Cl)Al$		$Al(\mu\text{-}^{37}Cl)_2Al$	
Assignment[a]	Exp.	Calcd.	Exp.	Calcd.	Exp.	Calcd.
$\nu_1(a_g)$	298.6	298.4 (0)	297.7	297.1 (0.3)	296.3	295.7 (0)
$\nu_2(a_g)$		164.0 (0)		162.5 (0)		160.9 (0)
$\nu_3(b_{1u})$	270.95	287.1 (311)	269.29	285.4 (307)	267.51	283.7 (304)
$\nu_4(b_{2u})$	267.24	277.8 (59)	265.70	276.1 (58)	264.54	274.5 (57)
$\nu_5(b_{3g})$		132.5 (0)		131.6 (0)		130.8 (0)
$\nu_6(b_{3u})$		26.4 (0.1)		26.2 (0.1)		26.0 (0.1)

[a] D_{2h} symmetry. In the case of $Al(\mu\text{-}^{35}Cl)(\mu\text{-}^{37}Cl)Al$, the symmetry is reduced to C_{2v}.

which is in good agreement with the results of the quantum chemical calculations.

$[AlCl]_3$

Calculations on the trimer have not been reported previously. Accordingly, quantum chemical calculations were first carried out for several possible structures. These included a six-membered ring in a planar (**I**) or folded (**II**) structure, and a structure with an Al_3 triangle and three terminal Al–Cl bonds with the Cl atoms either in the plane defined by the three Al atoms (**III**) or outside it (**IV**). Calculations on these four structures were carried out both with BP/SVP and with MP2/TZVPP. It turns out that none of these structures defines the global minimum on the potential energy hypersurface. Surprisingly, such a structure, **V**, features two terminal Al–Cl bonds, a bridging Cl atom, and an Al atom which is bound to two Al atoms, but not to a Cl atom. All five structures as calculated with MP2/TZVPP are shown in Figure 6. Table 3 includes the energies as calculated with BP/SVP and MP2/TZVPP, as well as some salient bond lengths and angles. According to the calculations, structures **I** and **III** do not define minima on the potential energy hypersurface, since the vibrational analysis yields imaginary frequencies. Deviations between the results of BP/SVP and MP2/TZVPP are generally small, the only exception arises in the case of structure **II**. The Al–Cl and Al–Al distances decrease steadily from structure **I** to structure **V**. At the same time, the energy also decreases.

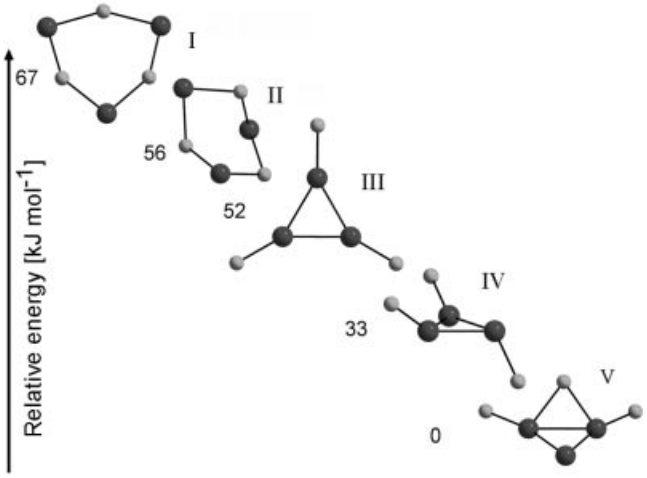

Figure 6. Possible structures of the trimer Al_3Cl_3 and their relative energies as calculated with MP2/TZVPP or BP/SVP.

Table 4 and Table 5 include the wavenumbers calculated for the vibrational modes of cyclic Al_3Cl_3 (structure **II**) and of Al_3Cl_3 in its C_s-symmetric energy minimum form (structure **V**). The mode of **V** which carries most of the IR intensity is located at 533.9 cm^{-1} [$\nu_8(a'')$] according to the calculations, which tallies very closely with the band near 530 cm^{-1} observed in the IR experiments. Although the observed band is weak, it shows evidence of a distinct isotopic pattern. In particular, there are three maxima at 531.3, 528.8 and 526.6 cm^{-1}; the band at 531.3 cm^{-1} carries most

 © 2005 Wiley-VCH Verlag GmbH & Co. KGaA, Weinheim

Table 3. Energies (in hartree), distances (in pm) and angles (in °) as calculated for the different possible structures **I**–**V** of Al_3Cl_3 considered in this work (see Figure 6).

Method	Parameter	**I**[a]	**II**	**III**[a]	**IV**	**V**[b]
BP/SVP	Energy	–2107.63409	–2107.63439	–2107.63695	–2107.64390	–2107.65205
	Al–Cl	246	245–247	215	214–215	213/246 (Cl_b)
	Al···Al	466	454–457	275	268–282	260/280
	Al–Cl–Al	143	135–137			70 (Cl_b)
	Cl–Al–Cl	97	95			109 (Cl_b)
	Al–Al–Al			60	58–64	58–65
MP2/TZVPP	Energy	–2105.23646	–2105.24045	–2105.24199	–2105.24917	–2105.26183
	Al–Cl	244	238–258	212	212–214	211/240 (Cl_b)
	Al···Al	466	372–400	274	267–287	261/278
	Al–Cl–Al	146	100–103			71 (Cl_b)
	Cl–Al–Cl	94	84–91			107 (Cl_b)
	Al–Al–Al			60	58–65	58–65

[a] Structures **I** and **III** define no minima on the potential energy hypersurface since the vibrational analysis yields imaginary frequencies. [b] Cl_b means that the bridging Cl atom is considered.

of the intensity and that at 526.6 cm^{-1} is very weak. If this band indeed belongs to the trimer, it can be assigned to the antisymmetric ν(Al–Cl_t) mode. To simulate the isotopic pattern expected for the minimum energy structure, the wavenumbers for this mode have been calculated for all eight possible isotopomers ($^{35}Cl/^{37}Cl$). Isotopic substitution of the bridging Cl atom has, as anticipated, the smallest effect on the wavenumber of the mode. The $Al_3{}^{35}Cl_2(\mu\text{-}{}^{35}Cl)$ isotopomer has a wavenumber of 535.1 cm^{-1}. The $Al_3{}^{35}Cl_2(\mu\text{-}{}^{37}Cl)$ isotopomer has a corresponding wavenumber also of 535.1 cm^{-1}, and for the two $Al_3{}^{35}Cl^{36}Cl(\mu\text{-}{}^{35}Cl)$ isotopomers, a wavenumber of 532.5 cm^{-1} is found. In the case of two ^{37}Cl atoms and one ^{35}Cl atom in the molecule, a wavenumber of 532.5 cm^{-1} is found if the ^{35}Cl atom occupies a terminal position, while a wavenumber of 530.4 cm^{-1} results if the ^{35}Cl is in the bridging position. Finally, the $Al_3{}^{37}Cl_2(\mu\text{-}{}^{37}Cl)$ isotopomer is calculated to give a wavenumber of 530.4 cm^{-1}. In total, given the half width of the bands, an almost perfect triplet pattern results, which reveals distinct similarities between this and the observed pattern. The position and the isotopic pattern of the observed band is thus consistent with its belonging to the trimer Al_3Cl_3 in its C_s-symmetric energy minimum structure **V**.

In the case of the cyclic Al_3Cl_3 isomer, the mode with the highest wavenumber occurs at ca. 300 cm^{-1} according to the calculations (see Table 4). This implies that such a molecule cannot be responsible for the absorption at ca. 530 cm^{-1} detected in the IR experiment.

An alternative explanation for this band is that it represents the first overtone of the triplet at 267.24/265.70/264.54 cm^{-1} that belongs to Al_2Cl_2. The first overtone should occur at 534.5/531.4/529.1 cm^{-1} in the hypothetical case of zero anharmonicity. However, the wavenumber difference between the three resolved maxima observed within the band near 530 cm^{-1} (2.6 and 2.2 cm^{-1}) is somewhat smaller than that predicted for the overtone (3.1 and 2.3 cm^{-1}). Such an explanation is therefore less plausible. It is possible, on the other hand, that the overtone of the $\nu_3(b_{1u})$ and/or $\nu_4(b_{2u})$ mode of Al_2Cl_2 is responsible for the broader shoulder on the higher-wavenumber side of the band near 530 cm^{-1}. Unfortunately, because of the weak intensity, which also allows detection at very high AlCl concentrations in the matrix, Al_2Cl_2 cannot be distinguished with certainty from Al_3Cl_3 on the basis of intensity changes versus concentration in the matrix.

Table 4. Calculated vibrational properties (wavenumbers in cm^{-1}, IR intensities in $km\,mol^{-1}$ given in parentheses) and energy (in hartree) for cyclic Al_3Cl_3 (**II**).

	BP/SVP	MP2/TZVPP
ν_1	279.0 (310)	311.7 (57)
ν_2	278.0 (277)	296.1 (78)
ν_3	257.2 (7)	272.6 (231)
ν_4	253.7 (22)	248.6 (56)
ν_5	253.0 (17)	195.4 (91)
ν_6	142.8 (0.03)	185.3 (34)
ν_7	136.6 (0.003)	123.3 (2)
ν_8	82.9 (0.2)	98.8 (0.2)
ν_9	82.2 (0.2)	85.6 (11)
ν_{10}	58.2 (0.6)	53.3 (2)
ν_{11}	24.9 (0.03)	46.3 (0.004)
ν_{12}	3.4 (0.03)	39.9 (3)
Energy	–2107.63439	–2105.24045
Energy including ZPVE	–2107.63017	–2105.23599

Table 5. Calculated vibrational properties (wavenumbers in cm^{-1}, IR intensities in $km\,mol^{-1}$ given in parentheses) and energy (in hartree) for Al_3Cl_3 (C_s symmetry, **V**).

	BP/SVP	MP2/TZVPP
ν_1 (a′)	559.9 (79)	581.5 (98)
ν_2 (a′)	337.7 (61)	357.3 (78)
ν_3 (a′)	276.6 (20)	283.9 (23)
ν_4 (a′)	195.8 (2)	214.5 (3)
ν_5 (a′)	94.8 (1)	106.2 (0.3)
ν_6 (a′)	90.3 (1)	100.2 (3)
ν_7 (a′)	41.2 (1)	45.8 (1)
ν_8 (a″)	533.9 (181)	552.5 (223)
ν_9 (a″)	230.8 (8)	246.7 (9)
ν_{10} (a″)	121.0 (2)	149.6 (7)
ν_{11} (a″)	117.3 (1)	119.9 (0.5)
ν_{12} (a″)	92.1 (2)	102.2 (2)
Energy	–2107.65205	–2105.26183
Energy including ZPVE	–2107.64593	–2105.25531

 © 2005 Wiley-VCH Verlag GmbH & Co. KGaA, Weinheim

In comparison with the neutral Al_3R_3 species, there is a higher chance of stabilizing radical anions with the formula $[Al_3R_3]^{\cdot-}$. R should be a sterically demanding group, e.g. $Si(SiMe_3)_3$. Calculations were carried out to determine the possible structures of these species. Figure 7 shows two possible isomers in the case of R = SiH_3, which have been optimized with BP/TZVPP. It turns out that the minimum energy structure again features two terminal Al–Si bonds and a bridging SiH_3 group. Again, the metal atoms form a triangle, and one of the metal atoms is bound directly only to other metal atoms, but not to a silyl group. A structure in which all metal atoms are bound to one silyl group exhibits a slightly higher energy (+10 kJ mol^{-1}). Anions of the form $[Al_3R_4]^-$ are already known, but in those cases, two of the metal atoms are bound to one ligand, and the third metal atom, to two ligands (R = Si*t*Bu$_3$).[23]

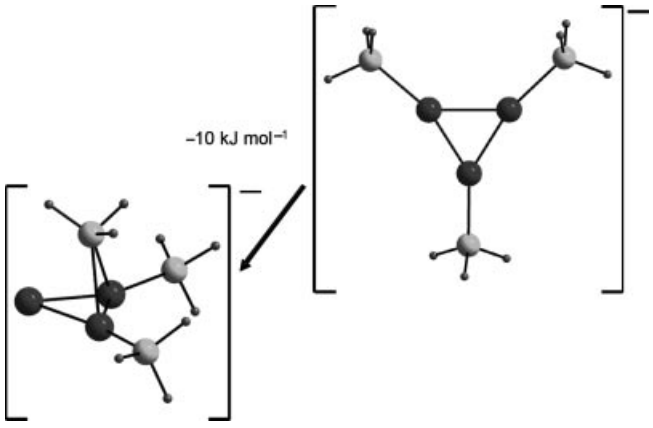

Figure 7. Calculated structures and relative energies for two isomers of $[Al_3(SiH_3)_3]^-$ (BP/TZVPP).

The formal oxidation states of the Al atoms in the minimum energy structure calculated for $(AlCl)_3$ vary. The structure might therefore be described as an intermediate on the way to disproportionation. The results presented herein might be of importance for a better understanding of the disproportionation mechanism.

$[AlCl]_4$

As already mentioned, the structure of the tetramer has already been evaluated before by quantum chemical calculations.[10,24] The molecule exhibits T_d symmetry, with Al–Cl and Al···Al distances (210.9 and 263.9 pm, respectively) that are in good agreement with those calculated previously.[24] Unfortunately, all attempts to gain experimental access to Al_4Cl_4 have so far failed. However, the compound $[AlC_5(CH_3)_5]_4$, featuring also an Al_4 tetrahedron, has been synthesized and structurally characterized.[25] There are also other known representatives of molecules with the overall formula Al_4R_4 [e.g. R = $Si(SiMe_3)_3$[26] or $N(SiMe_3)(2,6\text{-}iPr_2C_6H_3N(SiMe_3)$[27]].

Oligomerization Pathway and Thermodynamic Considerations

The dimerization of AlCl to the cyclic $[AlCl]_2$ dimer is associated with an energy change of –48 kJ mol^{-1} (–46 kJ mol^{-1} including ZPVE corrections) according to calculations with BP/SVP, and of –39 kJ mol^{-1} (–38 kJ mol^{-1} including ZPVE corrections) according to calculations based on MP2/TZVPP.

The question arises of whether the Al_2Cl_2 observed in the IR and Raman spectra is already formed in the gas phase or in the course of a reaction between two AlCl monomers either during or after deposition of the matrix. The relative intensities of the bands belonging to AlCl and to Al_2Cl_2 vary (a) with the rate of HCl which is passed over the aluminum within the Knudsen cell, and (b) with the rate of argon deposition. These findings indicate that most of the Al_2Cl_2 is formed during or after deposition of the matrix and not in the gas phase. However, it is difficult to guarantee exactly identical conditions in the experiments. To answer this question in a more quantitative way, therefore, the intensities of the bands observed in the IR spectrum were first used in combination with the calculated relative intensities to estimate the relative concentration of AlCl and Al_2Cl_2 in the matrix. This gives a ratio AlCl:Al_2Cl_2 of ca. 11:1 in the case of the representative experiment for which the IR spectrum is shown in Figure 2. In the next step, the calculations are used to estimate the equilibrium concentrations of the monomer and dimer in the gas phase. In Figure 8, ΔG for the dimerization reaction is shown as a function of temperature for two different pressures. At a pressure of 10^{-5} mbar and a temperature of 1300 K (conditions typical of a matrix isolation experiment), ΔG is estimated to be +296 kJ mol^{-1}. Accordingly, there is no significant partial pressure of dimer in the gas phase under these conditions. The dimer must therefore be formed almost exclusively either during or after deposition of the matrix. For this pressure, negative ΔG values can be realized only at a temperature below ca. 150 K. In the case of a total pressure of 1 bar, negative ΔG values can be expected up to temperature of ca. 350 K. At these low temperatures, however, AlCl is not stable, since disproportionation to Al and $AlCl_3$ occurs.

The fact that dimerization occurs during or after matrix deposition at very low temperature implies that the activation barrier to this reaction is close to zero. As two electrons in the σ orbital are mainly centered on the Al atom,[17] AlCl resembles silylene, SiH_2. It has been shown that dimerization of SiH_2 (with a $^1A_1$ ground electronic state) along a "least-motion path" to give H_2SiSiH_2 (either in its C_{2h}-energy minimum structure or in the ethylene-like form with D_{2h} symmetry) is symmetry forbidden and opposed by a substantial barrier due to "avoided crossing".[28] On the other hand, dimerization on a "non-least-motion" with low symmetry is possible without a barrier. Although the exact pathway for the dimerization of AlCl has still to be investigated, it is certain that the symmetry has to change during the approach of the two AlCl fragments, and the chances

 © 2005 Wiley-VCH Verlag GmbH & Co. KGaA, Weinheim

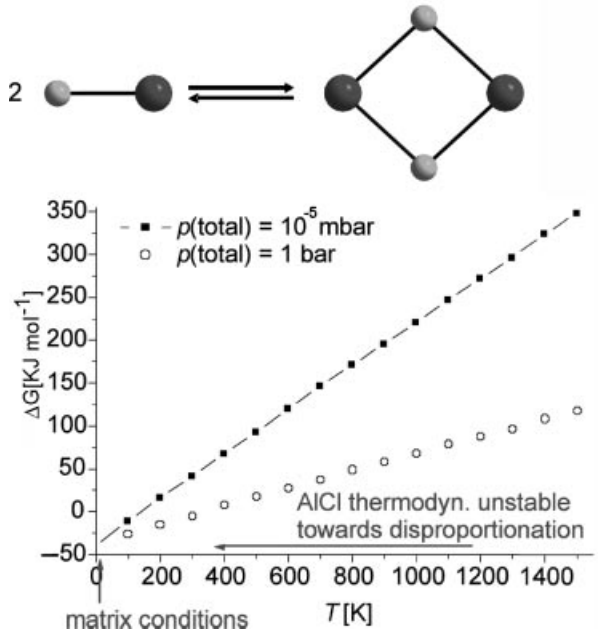

Figure 8. Dependence of ΔG on the temperature at 1 bar and 10^{-5} mbar total pressure for the dimerization of AlCl. Note that AlCl is thermodynamically not stable for temperatures below ca. 1200 K due to disproportionation into Al metal and $AlCl_3$.

of a pathway which includes a symmetry-restricted barrier are reduced. What seems clear, though, is that there is no significant barrier to dimerization.

The reaction of Al_2Cl_2 with another AlCl monomer to give Al_3Cl_3 in its C_s-symmetric energy minimum structure is also calculated to be exothermic. According to BP/SVP, the reaction energy is –78 kJ mol^{-1} without, and –71 kJ mol^{-1} with the inclusion of ZPVE corrections. By using MP2/TZVPP, the values are –84 kJ mol^{-1} without and –77 kJ mol^{-1} with the inclusion of ZPVE corrections. As expected, AlCl is therefore prone to oligomerization. Only at high temperatures do the significant entropy contributions to the Gibbs energy act to reverse this tendency.

Finally, formation of the Al_4Cl_4 tetramer from Al_3Cl_3 and AlCl is associated with an energy change of –218 kJ mol^{-1} (–211 kJ mol^{-1} with ZPVE corrections) at the BP/SVP level, and of –250 kJ mol^{-1} (–243 kJ mol^{-1} with ZPVE corrections) at the MP2/TZVPP level. Overall, the tetramerization energy for AlCl is –358 kJ mol^{-1} at the MP2/TZVPP level and with inclusion of ZPVE corrections. This value is in very good agreement with earlier estimates.[24]

Conclusions

The present studies draw on a combination of experimental and quantum chemical results to explore the oligomerization of AlCl monomers. Dimerization leads to cyclic, D_{2h}-symmetric Al_2Cl_2. This species isolated in an Ar matrix has been characterized in more detail by higher-resolution IR and Raman measurements. An evaluation of the thermodynamics of dimerization shows that the dimer cannot be present in significant amounts in the gas phase. The Gibbs energy change is negative only at low temperatures (but depends critically on the pressure), but at these low temperatures AlCl is thermodynamically unstable toward disproportionation into Al metal and $AlCl_3$. It follows that matrix isolation is the best method for gaining access to the dimer and higher oligomers. An isotopically structured, weak band in the IR spectrum of matrix-isolated AlCl has been assigned to the trimer Al_3Cl_3. This has a surprising structure, consisting of an Al_3 triangle with two terminal Al–Cl bonds and one Al–Cl–Al bridge; one of the Al atoms is directly bound to the other two metal atoms, but not to any of the Cl atoms. Thus, the formal oxidation states of the Al atoms vary. This might shed light on the disproportionation mechanism. Other possible structures have also been calculated, but exhibit a significantly higher energy. Quantum chemical calculations on the tetramer Al_4Cl_4 predict a molecule containing a tetrahedral Al_4 unit, in line with previous theoretical studies.

The results discussed here are of importance for a better understanding of the possible structures of not only solid AlCl but also the solvated species which have been exploited as a starting reagent for the synthesis of cluster compounds.[1] Figure 9 summarizes the oligomerization process and the calculated reaction energies of the relevant steps. It can be seen that the reaction energy is increasingly exothermal for each step.

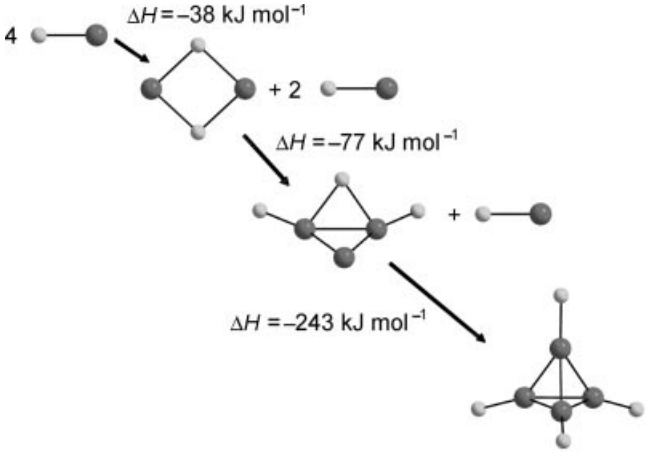

Figure 9. Reaction sequence leading from AlCl monomers via dimers and trimers to the Al_4Cl_4 tetramer. Reaction energies (MP2/TZVPP level, including ZPVE corrections) are given for each of the reactions in this sequence.

Experimental Section

In a resistively heated oven attached to a high vacuum apparatus, HCl was passed over liquid Al at a temperature of 1250 K. The AlCl thus generated was deposited together with excess Ar on a freshly polished Cu block kept at 12 K by means of a closed-cycle refrigerator (Leybold, LB115). Details of the matrix isolation technique can be found elsewhere.[29]

 © 2005 Wiley-VCH Verlag GmbH & Co. KGaA, Weinheim

IR spectra were recorded with a Bruker 113v spectrometer equipped with an MCT detector, a DTGS detector, or a bolometer for measurements in the spectral region 4000–650, 700–200, or 700–30 cm^{-1}, respectively. The spectra were recorded with a resolution of 0.1 cm^{-1}.

Raman spectra were recorded with a Jobin Yvon XY spectrometer equipped with a pre-monochromator with two grids, a spectrograph and a CCD detector (Wright Instruments, England). The spectra were excited with the 514 nm line of an Ar^+ ion laser. The resolution was 0.5 cm^{-1}.

Quantum chemical calculations were carried out with the TURBOMOLE program package.[30] DFT (BP) as well as ab initio (MP2) methods were used in combination with SVP and TZVPP basis sets.

Acknowledgments

Financial support from the *Deutsche Forschungsgemeinschaft* and the *Fonds der Chemischen Industrie* is gratefully acknowledged.

[1] C. Dohmeier, D. Loos, H. Schnöckel, *Angew. Chem. Int. Ed. Engl.* **1996**, *35*, 129.
[2] K. P. Huber, G. Herzberg, *Molecular Spectra and Molecular Structure. IV. Constants of Diatomic Molecules*, van Nostrand Reinhold, New York, **1979**.
[3] A. Fontijn P. M. Futerko, *J. Phys. Chem.* **1993**, *97*, 7222.
[4] D. V. Dearden, R. D. Johnson III, J. W. Hudgens, *J. Chem. Phys.* **1993**, *99*, 7521.
[5] a) D. R. Lide Jr., *J. Chem. Phys.* **1965**, *42*, 1013; b) F. C. Wyse, W. Gordy, *J. Chem. Phys.* **1972**, *56*, 2130.
[6] H. Schnöckel, *Z. Naturforschung B* **1976**, *31*, 1291.
[7] a) H. Schnöckel, *J. Mol. Struct.* **1978**, *50*, 267; b) H. Schnöckel, *J. Mol. Struct.* **1978**, *50*, 275.
[8] M. Tacke, H. Schnöckel, *Inorg. Chem.* **1989**, *28*, 2895.
[9] See, for example: a) A. Schnepf, H. Schnöckel, *Angew. Chem. Int. Ed.* **2002**, *41*, 3533; b) H. Schnöckel, H. Köhnlein, *Polyhedron* **2002**, *21*, 489; c) H. Schnöckel, A. Schnepf, *Adv. Organomet. Chem.* **2001**, *47*, 235; d) G. Linti, H. Schnöckel, *Coord. Chem. Rev.* **2000**, *206–207*, 285.
[10] J. Gauss, U. Schneider, R. Ahlrichs, C. Dohmeier, H. Schnöckel, *J. Am. Chem. Soc.* **1993**, *115*, 2402.
[11] a) J. Bahlo, H.-J. Himmel, H. Schnöckel, *Angew. Chem. Int. Ed.* **2001**, *40*, 4696; b) J. Bahlo, H.-J. Himmel, H. Schnöckel, *Inorg. Chem.* **2002**, *41*, 2678; c) J. Bahlo, H.-J. Himmel, H. Schnöckel, *Inorg. Chem.* **2002**, *41*, 4488.
[12] H. Schnöckel, *J. Mol. Struct.* **1978**, *50*, 267.
[13] H.-J. Himmel, *Eur. J. Inorg. Chem.* **2003**, 4087.
[14] H.-J. Himmel, C. Klaus, *Z. Anorg. Allg. Chem.* **2003**, *629*, 1477.
[15] H.-J. Himmel, *Organometallics* **2003**, *22*, 2679.
[16] H.-J. Himmel, J. Bahlo, M. Haußmann, F. Kurth, G. Stößer, H. Schnöckel, *Inorg. Chem.* **2002**, *41*, 4952.
[17] H.-J. Himmel, *J. Chem. Soc. Dalton Trans.* **2002**, 2678.
[18] a) V. G. Solomonik, *Zhurnal Fizicheskoi Khimii* **1979**, *53*, 552; b) N. C. Baird, *Canadian J. Chem.* **1985**, *63*, 71.
[19] S. Petrie, *J. Phys. Chem. A* **1998**, *102*, 7828.
[20] M. D. Allendorf, C. F. Melius, B. Cosic, A. Fontijn, *J. Phys. Chem. A* **2002**, *106*, 2629.
[21] H.-J. Himmel, A. J. Downs, T. M. Greene, *J. Am. Chem. Soc.* **2000**, *122*, 922.
[22] See, for example: H. Schnöckel, S. Schnunck, T. Mehner, H. S. Plitt, *J. Am. Chem. Soc.* **1989**, *111*, 4578.
[23] N. Wiberg, T. Blank, W. Kaim, B. Schwederski, G. Linti, *Eur. J. Inorg. Chem.* **2000**, *7*, 1475.
[24] R. Ahlrichs, M. Ehrig, H. Horn, *Chem. Phys. Lett.* **1991**, *183*, 227.
[25] C. Dohmeier, C. Robl, M. Tacke, H. Schnöckel, *Angew. Chem. Int. Ed. Engl.* **1991**, *30*, 564.
[26] A. Purath, H. Schnöckel, *J. Organomet. Chem.* **1999**, *579*, 373.
[27] M. Schiefer, N. D. Reddy, H. W. Roesky, D. Vidovic, *Organometallics* **2003**, *22*, 3637.
[28] K. Ohta, E. R. Davidson, K. Morokuma, *J. Am. Chem. Soc.* **1985**, *107*, 3466.
[29] H.-J. Himmel, A. J. Downs, T. M. Greene, *Chem. Rev.* **2002**, *102*, 4191.
[30] a) R. Ahlrichs, M. Bär, M. Häser, H. Horn, C. Kölmel, *Chem. Phys. Lett.* **1989**, *162*, 165; b) K. Eichkorn, O. Treutler, H. Öhm, M. Häser, R. Ahlrichs, *Chem. Phys. Lett.* **1995**, *240*, 283; c) K. Eichkorn, O. Treutler, H. Öhm, M. Häser, R. Ahlrichs, *Chem. Phys. Lett.* **1995**, *242*, 652; d) K. Eichkorn, F. Weigend, O. Treutler, R. Ahlrichs, *Theor. Chem. Acc.* **1997**, *97*, 119; e) F. Weigend, M. Häser, *Theor. Chem. Acc.* **1997**, *97*, 331; f) F. Weigend, M. Häser, H. Patzelt, R. Ahlrichs, *Chem. Phys. Lett.* **1998**, *294*, 143.

Received: December 10, 2004

 © 2005 Wiley-VCH Verlag GmbH & Co. KGaA, Weinheim

The Structural Chemistry of *N*-Monolithium Borazines[‡]

Heinrich Nöth,*[a] Susana Rojas-Lima,[a] and Alexander Troll[a]

Dedicated to Prof. Dr. H. Schmidbaur on the occasion of his 70th birthday

Keywords: Boron / Borazines / Lithiation / N ligands

Trimethylborazine ($Me_3B_3N_3H_3$, **1**) reacts with RLi (R = *n*Bu, *t*Bu) in hexane solution by alkyl group exchange to give a mixture of borazines $Me_{3-n}R_nB_3N_3H_3$. In contrast, deprotonation of **1** to $Me_3B_3N_3H_2Li$ (**2**) occurs upon treatment with MeLi in diethyl ether solution or RLi (R = *n*Bu, *t*Bu) complexed with tetramethylethylenediamine (TMEDA), pentamethyldiethylentriamine (PMDTA), or trimethylhexahydrotriazine (TMTA) in hexane solution, to give solvates of **2**. $[(Me_3B_3N_3H_2)Li(OEt_2)]$ (**2a**), $[(Me_3B_3N_3H_2)Li(tmta)]$ (**2c**), and $[(Me_3B_3N_3H_2Li)_4(tmeda)_3]$ (**2b**) contain dimeric units of **2**. In the case of **2b** two of these dimers are bridged by one tmeda molecule, while the other two are coordinated to a lithium atom of one of its dimeric units, respectively. This molecule therefore contains tri- and tetracoordinated Li atoms. In contrast, $[(Me_3B_3N_3H_2)Li(pmdta)]$ (**2c**) is monomeric. The *N*-lithiation leads to a distortion of the planar B_3N_3 ring system: the B–N bonds at the metallated N atoms are short, the next opposite B–N pair is the longest, followed by a shorter B–N bond involving the B atom in the *para* position. However, all B–N bonds are longer than in the parent compound **1**. Reaction of $tBu_3B_3N_3H_3$ (**3**) with *t*BuLi in the presence of triisopropylhexahydrotriazine (TIPTA) in hexane leads to the salt $[(tipta)_2Li][tBu_4B_3N_3H_3]$ (**4**), while deprotonation occurs with *t*BuLi(tmta) to give monomeric $[(tBu_3B_3N_3H_2)Li(tmta)]$ (**5**) after refluxing the reaction mixture. Similarly, $(Me_2N)_3B_3N_3H_3$ (**6**) can be deprotonated with RLi in the presence of TMTA to give monomeric $[\{(Me_2N)_3B_3N_3H_2\}Li(tmta)]$ (**7b**). The *N*-lithiation has almost no influence on the shielding of the boron nucleus of the borazine nuecleus. Attempts to obtain di- and trilithiated **1** as pure compounds failed: alkyl group exchange and borate formation as well as destruction of the borazine ring were detected by NMR spectroscopy. However, treatment of these reaction mixtures with MeBr gave $Me_3B_3N_3NH_{3-n}Me_n$ (n = 0–3).
(© Wiley-VCH Verlag GmbH & Co. KGaA, 69451 Weinheim, Germany, 2005)

Introduction

Borazines are isoelectronic with benzene and its derivatives.[2] The term "inorganic benzene" has been coined for borazine ($B_3N_3H_6$) because many of its physical properties are similar to those of benzene. However, it is quite clear that the B–N bond polarity is responsible for the inherent chemical differences between the two compounds. For instance, the structure of $[(\eta^6\text{-}C_6Me_6)Cr(CO)_3]$[3] is different to that of $[(\eta^3\text{-}B_3N_3Et_6)Cr(CO)_3]$:[4] while the former shows a planar benzene ring with its MCO bonds pointing to the middle of the C=C bonds of benzene,[3] the borazine complex possesses a puckered six-membered ring where the MCO bond points towards the nitrogen atoms.[4] More recently, DFT calculations by Jemmis et al. have shown that borazine, in spite of its 6π-electron character, is not an aromatic system but is rather antiaromatic,[5] in spite of the fact that the borazine ring and most of its derivatives are planar and possess equal B–N bond lengths. As expected, $B_3N_3H_6$ exhibits two ^1H NMR signals at δ = 5.4 ppm ($^1J_{^{15}N,^1H}$ = 52 Hz) and δ = 4.65 ppm ($^1J_{^{11}B,^1H}$ = 134 Hz).[6] These protons are deshielded relative to those of benzene.

Due to the polarity of the B–N bond, the NH protons of borazines of type $(RB{=}NH)_3$ are acidic. Therefore, it should be easy to deprotonate the NH groups of these borazines. The first deprotonation reactions of borazines were reported by Wagner and Bradford.[7] The resulting *N*-lithioborazines were used to prepare *N*,*B*-borazinylborazines. These *N*-lithioborazines have a synthetic potential similar to aryllithium compounds[8] but, to the best of our knowledge, *N*-lithioborazines have never been isolated, and no structural information is available on these compounds to date. Here we report on the synthesis, characterization and structure determination of several *N*-lithioborazines of type $(R_3B_3N_3H_2)Li$ (R = Me, *t*Bu, Me_2N).

Results

N-Monolithiation of Borazines $(RBNH)_3$

Reactions in Non-Polar Solvents

2,4,6-Trimethylborazine (**1**)[9] is stable up to 450 °C and against photolysis.[10,11] It dissolves in many polar and non-

[‡] Contribution to the Chemistry of Boron, 256. Part 255: Ref.[1]

[a] Department of Chemistry, University of Munich, Butenandtstr. 5–13, 81377 München, E-mail: H.Noeth@lrz.uni-muenchen.de

 DOI: 10.1002/ejic.200400881 © 2005 Wiley-VCH Verlag GmbH & Co. KGaA, Weinheim

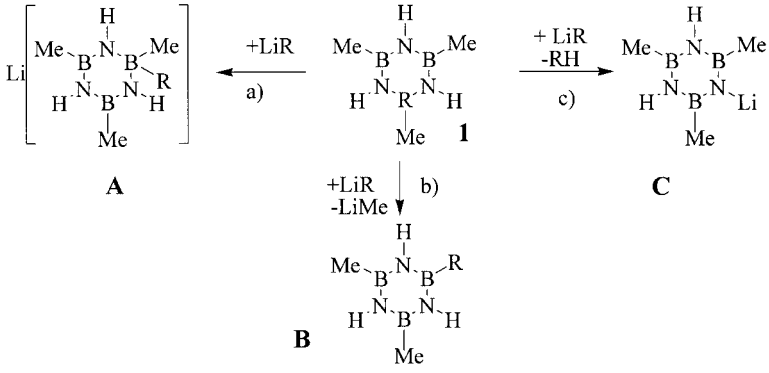

Scheme 1.

polar solvents. Three types of reactions can be expected with RLi compounds: a) addition of RLi across a B–N bond of the borazine derivative, b) exchange of the methyl groups by R of the organometallic compound, c) deprotonation of an NH group (see Scheme 1).

Compounds of type **A** may be precursors for compounds of type **B**, while compound of type **C** are the desired *N*-metallated borazines **2.** In addition, one may also expect ring-opening reactions which may finally lead to *N*-lithioaminoboranes of type R(Me)B–NHLi[12] in the presence of an excess of RLi. Although reactions of 2,4,6-triorganylborazines with *n*BuLi have been described,[8] the formation of *N*-lithioborazines has only been deduced from reaction products obtained with alkyl halides and *B*-haloborazines.[8]

Reaction of **1** with *n*BuLi or *t*BuLi in a 1:1 ration in hexane solution led to products containing tetracoordinate ($\delta_{^{11}B}$ ranging from –2.0 to –4.1 ppm) and tricoordinate boron atoms. Chemical shifts of 38.1 and 36.2 ppm are typical for borazines. A precipitate that formed in these reactions proved to be MeLi (qualitatively checked by gas evolution on hydrolysis). Mass spectrometry of the oily residue obtained from the hexane solutions showed a mixture of all possible *n*-butylmethylborazines $Bu_nMe_{3-n}B_3N_3H_3$ (n = 1, 2, 3). Surprisingly, the 1:1 reaction of *t*BuLi in hexane with **1** also leads to all members of the series $(t\text{Bu})_nMe_{3-n}B_3N_3H_3$ (n = 0, 1,2, 3) with $t\text{BuMe}_2B_3N_3H_3$ the main product ($\delta_{^{11}B}$ = 38.2, 36.0 ppm; ratio 1:2). We were, however, not able to reliably observe B–N cleavage reactions or the *N*-lithiation of **1** in non-polar solvents.

Reactions in the Presence of Auxiliary Bases

It is well known that the reactivity of organolithium compounds is strongly enhanced by polar solvents such as ethers or in non-polar solvents in the presence of donor molecules such as TMEDA because this changes the degree of association of the RLi molecules. Therefore, we studied the reaction of **1** with RLi compounds in diethyl ether solution. In our case both MeLi and *n*BuLi in diethyl ether reacted smoothly with deprotonation of **1** according to Equation (1). The resulting *N*-lithioborazine was isolated as the diethyl ether solvate **2a**. These reactions were quantitative after keeping the reaction mixture under reflux, and yields of up to 85% were obtained.

$$\underset{\mathbf{1}}{2\,Me_3B_3N_3H_3} + 2\,LiR + 2\,OEt_2 \rightarrow \underset{\mathbf{2a}}{Me_3B_3N_3H_2Li{\cdot}OEt_2} + 2\,RH \quad (1)$$

$$4\,Me_3B_3N_3H_3 + 4\,LiBu + 3\,TMEDA \rightarrow \underset{\mathbf{2b}}{(Me_3B_3N_3H_2Li)_4(tmeda)_3} + 4\,BuH \quad (2)$$

$$\underset{\mathbf{2c}}{(Me_3B_3N_3H_2Li)(tmta)} \qquad \underset{\mathbf{2d}}{(Me_3B_3N_3H_2Li)(pmdeta)}$$

$$\underset{\mathbf{3}}{t\text{Bu}_3B_3N_3H_3} + t\text{BuLi} + 2\,TIPTA \rightarrow \underset{\mathbf{4}}{[t\text{Bu}_4B_3N_3H_3]Li(tipta)_2} \quad (3)$$

$$t\text{Bu}_3B_3N_3H_3 + Lit\text{Bu} + TMTA \rightarrow \underset{\mathbf{5}}{t\text{Bu}_3B_3N_3H_2Li(tmta)} + t\text{BuH} \quad (4)$$

N-Lithiation of **1** can also be achieved in hexane upon treatment with *n*BuLi or *t*BuLi in the presence of TMEDA at –78 °C and refluxing the resulting suspension for several days. The precipitate proved to be compound **2b**, as shown in Equation (2). Single crystals of **2b** were obtained from the filtrate. This somewhat unusual stoichiometry is also observed when an excess of TMEDA was employed. When reaction (2) was followed by ^{11}B NMR spectroscopy a signal appeared at δ = 3.6 ppm along with those of the borazine, which indicates that the first step in the reaction is the addition of BuLi to **1** with formation of the borazinate $[(Me_3BuB_3N_3H_3)Li]$ (see Scheme 1). The solvates **2c** and **2d** were obtained from **1** in the presence of trimethylhexahydrotrazine (TMTA) or pentamethyldiethylenetriamine (PMDTA), respectively. All compounds of type **2** are moisture sensitive.

Reaction of $t\text{Bu}_3B_3N_3H_3$ (**3**)[13] with *t*BuLi in hexane at low temperature in the presence of tri(isopropyl)hexahydrotriazine (TIPTA) leads to the salt $[(t\text{Bu}_4B_3N_3H_3)Li(tipta)_2]$ (**4**), as depicted in Equation (3). However, the same reaction in the presence of TMTA yields compound **5** after

 © 2005 Wiley-VCH Verlag GmbH & Co. KGaA, Weinheim

keeping the mixture at reflux. Compound **5** was obtained as single crystals from the solution.

In analogy to the reaction of **1** with *n*BuLi in hexane, we observed an Me_2N/nBu exchange with tris(dimethylamino) borazine (**6**),[14,15] which we prepared from the trichloroborazine $Cl_3B_3N_3H_3$ and Me_3SiNMe_2. However, deprotonation of **6** to **7a** occurred with RLi (R = Me, *n*Bu) in the presence of PMDTA, which on crystallization from CH_2Cl_2 gave compound **8**.[16] Single crystals of **7a** were obtained on crystallizing the precipitate from diethyl ether [see Equation (5) with R = Me]. Compounds **7b** and **7c** were obtained in a similar manner.

$$\underset{\mathbf{6}}{(Me_2N)_3B_3N_3H_3} + LiR + PMDTA \rightarrow \underset{\mathbf{7a}}{(Me_2N)_3B_3N_3H_2Li(pmdta)} + RH \quad (5)$$

$\underset{\mathbf{7b}}{(Me_2N)_3B_3N_3H_2Li(tmta)}$ $\underset{\mathbf{7c}}{(Me_2N)_3B_3N_3H_2Li(tmeda)}$

The *N*-lithiation of the triphenylborazine $Ph_3B_3N_3H_3$ is more complicated than those of the three borazines described in this study. We will report on this shortly.

Multilithiation of 2,4,6-Trimethylborazine

In principle it should be possible to deprotonate **1** not only once but also twice or even three times with RLi compounds. The reaction with MeLi (ratio 1:1) in diethyl ether proceeds quantitatively to give $[(Me_3B_3N_3H_2)Li]$, but all our attempts to isolate pure TMEDA, PMDTA or TMTA complexes of $[(Me_3B_3N_3H)Li_2]$ and $[(Me_3B_3N)Li_3]$ failed. In each case the formation of the tetramethylborate anion was detected in solution by ^{11}B NMR spectroscopy. This indicates that the borazine ring was cleaved to a degree of about 5%.

In order to demonstrate that multilithiation has indeed occurred we treated the solid reaction products with MeBr. After refluxing the mixture and removal of insoluble material (impure LiBr) the filtrate was distilled. A fraction with a boiling point of 85–104 °C (350–500 torr) was obtained for the 1:2 reaction and a fraction with a boiling point of 71–120 °C (300–400 torr) for the 1:3 reaction. NMR spectroscopy and particularly mass spectra showed that the product obtained by distillation contained 2,4,6-$Me_3B_3N_3H_3$, 1,2,4,6-$Me_3B_3N_3H_2Me$, 1,2,3,4,6-$Me_3B_3N_3HMe_2$ and $Me_3B_3N_3Me_3$. This reveals that mono-, di- and tri-lithiation has occurred.

Molecular Structures

Relevant structural parameters of the *N*-monolithioborazine solvates **2a** (Figure 1), **2b** (Figure 2), **2c** (Figure 3), **2d** (Figure 4), **5** (Figure 6), and **7a** (Figure 7) as well as the borazinate **4** (Figure 5) are summarized in Table 1 and Table 2.

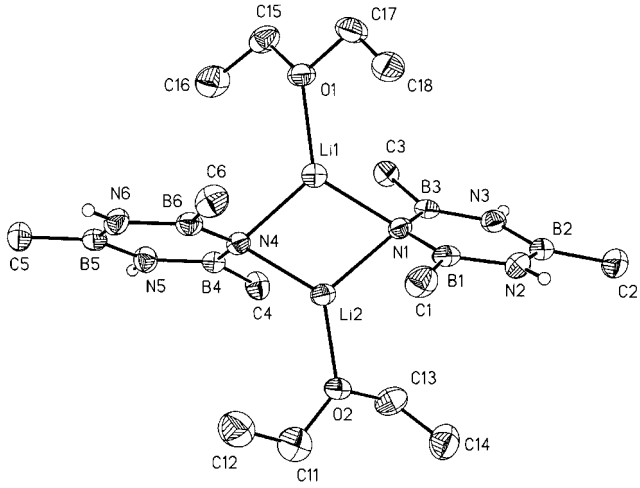

Figure 1. Molecular structure of **2a**. Thermal ellipsoids are shown with 25% probability. Selected atom distances [Å] and bond angles [°] (see also Table 1): Li1–O1 1.985(7), Li2–O2 1.914(7), B1–C1 1.601(6), B2–C2 1.578(6), B3–C3 1.585(6), B4–C4 1.588(5), B5–C5 1.579(6), B6–C6 1.585(6); O1–Li1–N1 128.8(3), O1–Li1–N4 124.3(3), N1–Li1–N4 106.9(3), O2–Li2–N1 121.0(3), O2–Li2–N4 129.4(3)], Li1–N4–Li2 72.4(3), B1–N1–B3 117.4(3), N1–B1–N2 120.2(4), B1–N2–B2 124.2(4), N2–B2–N3 113.4(4), B2–N3–B3 124.2(4), N3–B3–N1 120.4(4), B4–N4–B6 117.9(3), N4–B4–N5 119.0(3), B4–N5–B5 123.8.4(3), N5–B5–N6 114.4(4), B5–N6–B6 124.1(3), N6–B6–N4 119.8(4), N1–B1–C1 122.2(4), C1–B1–N2 117.6(4), C2–B2–N2 123.5(5), C2–B2–N3 123.1(4), C3–B3–N3 117.1(4), C3–B3–N1 125.2(5), Li1–O1–C15 124.9(3), Li1–O1–C17 119.8(3), C15–O1–C17 111.0(4), Li2–O2–C11 129.9(4), Li2–O2–C13 114.2(3), C11–O2–C13 113.4(4). Interplanar angles [°]: Li1N1Li2/B1N1B3 67.7, Li1N1Li2/Li1N4Li2 7.0, Li1N4Li2/B4N4B6 70.6, N4Li1N1/O1C15C17 46.3, C11O2C13/N4Li2N1 55.4. Maximum deviation from the borazine rings: 0.0278 Å for N1 and 0.0183 Å for N4.

All *N*-monolithiated borazines show a significant but systematic distortion of the borazine ring. Most rings remain planar but some of them show slight deviations from planarity. The greatest deviation is found for compound **2d**, where interplanar angles for B1B3N2N3e/-N1B1N3 of 4.5° and B1B3N2N3/N2B2N3 of 2.8° are observed, although these distortions are not highly significant. However, the changes in BN bond lengths for all *N*-monolithioborazines are significant as the BN bonds are no longer equal as found for the borazines **1**[17] and **4**,[18] and, most likely, the BN bonds of $tBu_3B_3N_3H_3$ are also of equal lengths. This change is due to the fact that the N1 ring atom becomes tetra-coordinated due to the dimerization of the $Me_3B_3N_3H_2Li$ units. In general, one can see that the BN bond lengths to the tetracoordinated N atoms are shorter than all other BN ring bonds (see Table 1). In addition, the BN bonds next to the BN bonds at N1, i.e. the pair B1–N2 and B3–N3, are longest while the BN bonds at atom B2 are closer to those of **1** (1.39 Å). However, even these are definitely longer than in the parent borazines, for example **1** with 1.39 Å.[17,18] This bond-length asymmetry also affects, of course, the bond angles, which are 121.0° for N–B–N

 © 2005 Wiley-VCH Verlag GmbH & Co. KGaA, Weinheim

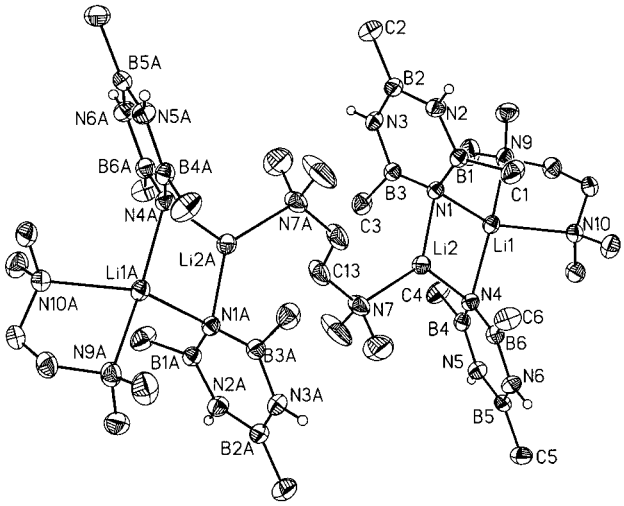

Figure 2. Molecular structure of **2b**. Thermal ellipsoids are shown with 25% probability. Selected atom distances [Å] and bond angles [°] (see also Table 1): Li1–N9 2.366(4), Li1–N10 2.301(4) Li2–N7 2.121(4), Li2–N4 1.990(4), Li2–N1 1.991(5), B1–C1 1.587(4), B2–C2 1.574(4), B3–C3 1.593(4), B4–C4 1.587(4), B5–C5 1.577(4), B6–C6 1.592(4), Li1···Li2 2.487(5); B3–N1–Li2 102.0(2), B3–N1–Li1 118.2(2), Li2–N1–B1 128.7(2), B2–N2–B1 123.5(2), B2–N3–B3 123.3(2), B2–N3B3 123.3(2), N3–B3–N1 120.5(2), N1–Li1–N4 100.5(2), N1–Li1–N9 98.1(2), N1–Li1–N10 146.2(2), N4–Li1–N9 146.8(2), N4–Li1–N10 99.6(2), N4–Li2–C7 140.2(2), N1–Li1–N7 128.5(2).

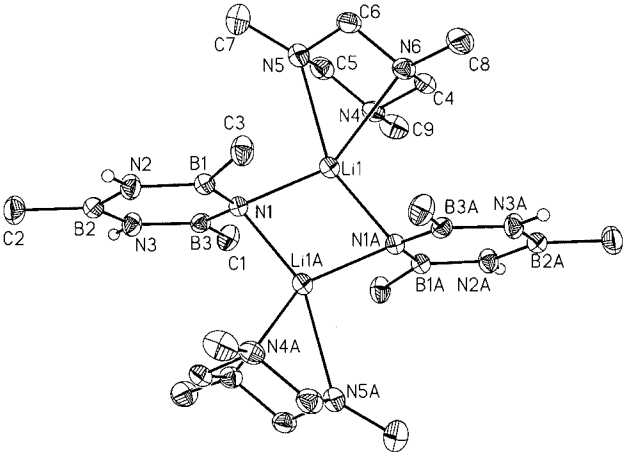

Figure 3. Molecular structure of **2c**. Thermal ellipsoids are shown with 25% probability. Selected atom distances [Å] and bond angles [°] (see also Table 1): Li1–N1 2.049(3), Li1–N1A 2.114(4), Li1–N4 2.199(4), Li1–N5 2.415(4), Li1–N6 2.557(3), Li1···Li1A 2.480(6), B1–C3 1.589(3), B2–C2 1.585(3), B3–C1 1.586(3), C6–N5 1.443(3), N5–C5 1.443(3), C6–N6 1.451(3), N5–C6 1.443(3), N4–C9 1.456(3), N5–C7 1.457(3), N6–C68 1.458(3); N1–Li1–N1A 107.0(1), N1–Li1–N4 128.2(2), N1–Li1–N5 97.5(1), N1–Li1–MN6 147.5(2), Li1–N1–Li1A 73.0(1), Li1–N1–B1 131.5(2), N1–B1–N2 119.8(2), B1–N2–B2 124.1(2), N2–B2–N3 114.8(2), B2–N3–B3 122.7(2), N3–B3–N1 121.1(2), N1–B1–C1 124.2(2), C1–B1–N2 119.8(2), N2–B2–C2 122.5(2), N3–B2–C2 122.8(2), N3–B3–C3 115.3(2), N1–B3–C3 123.6(2), N4–C4–CN5 197.8(2), C4–N5–C5 109.8(2), N5–C5–N6 107.6(2), C5–N6–C4 110.0(2), N6–C6–N4 109.0(2). Interplanar angles [°]: B3–N1–B1/N2–B2–N3 6.0.

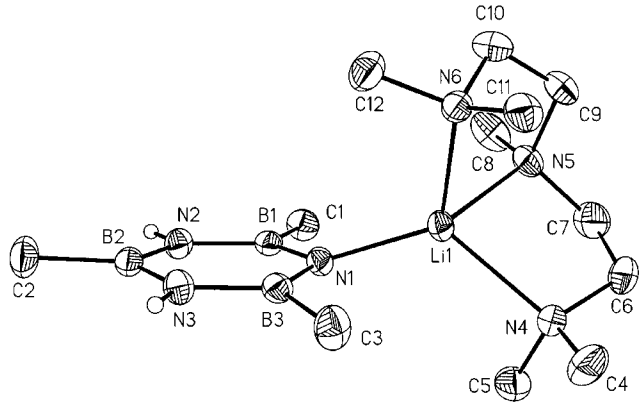

Figure 4. Molecular structure of **2d**. Thermal ellipsoids are depicted with 25% probability. Selected atom distances [Å] and bond angles [°] (see also Table 1): B1–C1 1.602(3), B2–C2 1.589(4), B3–C3 1.589(4), Li1–N1 1.975(4), Li1–N4 2.222(4), Li1–N5 2.203(4), Li1–N6 2.176(4); N1–B1–N2 120.1(2), B1–N2–B2 123.7(2), B2–N3–B3 122.5(2), N3–B3–N1 121.4(2), N1–B1–C1 124.0(2), N2–B1–C1 115.9(2), N3–B2–C2 122.1(2), N2–B2–C2 123.1(2), N3–B3–C3 115.8(2), N1–B3–C3 122.8(2), N1–Li1–N4 123.3(2), N1–Li1–N5 133.0(2), N1–Li1–N6 112.6(2), N4–Li1–N5 82.0(1), N4–Li1–N6 113.4(2), N5–Li1–N6 85.1(1). B2–N1–Li1 157.8. Interplanar angles [°]: Li1N1Li2/B1N1B2N2B3N3 76.7. Max. deviation from borazine plane: –0.0351 Å for N1.

and 119.8° for B–N–B in **1**. For all *N*-monolithioborazines we find a small bond angle at the *para* position B2, centered around 114°, while the B1–N1–B3 bond angles are close to 117°. All other endocyclic bond angles are 120° or up to 4° larger. This distortion leads to a lengthening of the B2–N1 distance across the six-membered ring. Relevant data are given in Table 2. The longest N1···B2 distance is found for the *t*Bu derivative **4** (3.005 Å).

The Li–N1(4) bond lengths are found to cover only a small range, but this bond is particularly short for the monomeric species **2d**, where the N1 atom remains tri-coordinated.

In general, the borazine units in the dimeric species are not orthogonal to the Li_2N_2 rings but neither are they parallel to one another. For instance, the borazine rings in **2a** are twisted against each other by 278.9°, and they form interplanar angles with the Li_2N_2 mean plane of 68.8° and 70.8°, respectively.

Compound **2b** is exceptional insofar as the dimeric *N*-lithioborazine rings contain a tri- and a tetracoordinated Li atom. This is due to the fact that one of the three TMEDA molecules forms a bridge between the two dimeric borazine units, while the other two bind to the remaining Li atoms in a bidentate manner. Consequently, the Li–N bond lengths to these ligands are different, being shorter for the tri-coordinated Li atoms.

Compound **2c** is centrosymmetric. It exhibits longer Li–N bonds both to N1 and the TMTA ligand as the Li atoms are pentacoordinate. Moreover, the TMTA molecule binds asymmetrically to the Li atoms. The borazine ring forms an interplanar angle with the Li_2N_2 plane of 84.8°.

 © 2005 Wiley-VCH Verlag GmbH & Co. KGaA, Weinheim

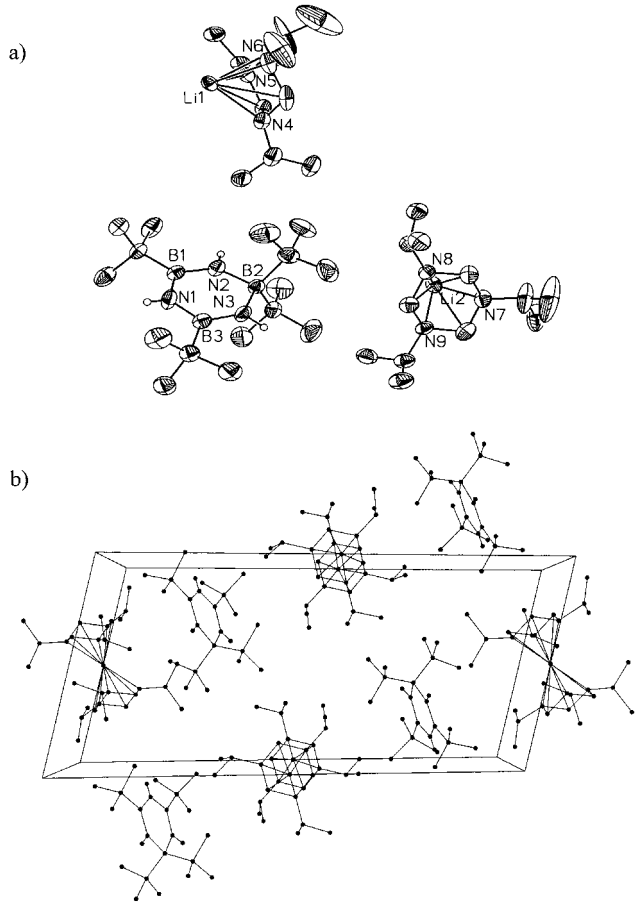

Figure 5. a) The contents of the asymmetric unit and the molecular structure of $[t\mathrm{Bu}_4\mathrm{B}_3\mathrm{N}_3\mathrm{H}_3][\mathrm{Li}(\mathrm{tipta})]$ (**4**). Thermal ellipsoids are shown with 25% probability. Selected atom distances [Å] (see Table 1) and bond angles [°]: N1–B1–N2 115.6(4), B1–N2–B2 129.7(4), N2–N3–B3 128.6(4), N3–B3–N1 116.3(4), N1–B1–C1 119.8(4), N2–B2–C2 107.7(3), N2–B2–C4 109.0(4), N1–B3–C3 119.4(4), C2–B2–C4 117.3(3). b) View of the unit cell down the *a* axis.

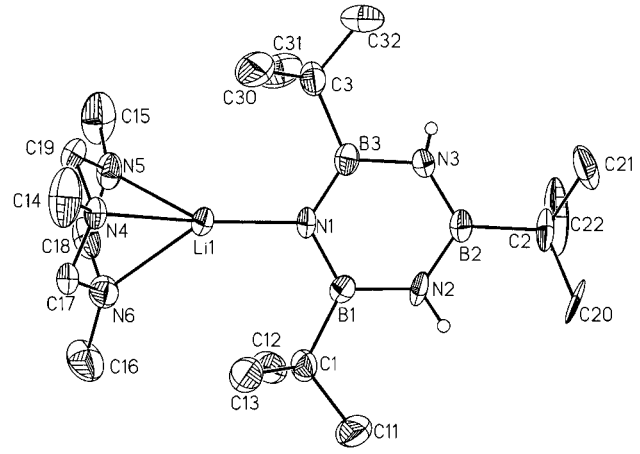

Figure 6. Molecular structure of **5** as found in the asymmetric unit. Thermal ellipsoids are depicted on a 25% probability scale. Selected atom distances [Å] and bond angles [°] (see also Table 1): B1–C1 1.610(7), B2–C3 1.603(8), B3–C3 1.640 (8). Li1–N4 2.224(7), Li1–N5 2.318(8), Li1–N6 2.395(9); N1–B1–N2 118.5(4). B1–N2–B2 124.3(3), B2–N3–B3 124.1(6), N3–B3–N1 120.2(5), N1–Li1–N4 143.1(4), N1–Li1–N5 136.1(4), N1–Li1–N6 143.3(4), N4–Li1–N5 62.4(2), N4–Li1–N6 60.0(2), N5–Li1–N6 61.2(2), N1–B1–C1 124.2(6), N3–B2–C2 124.2(6), N1–B3–C3 123.7(5).

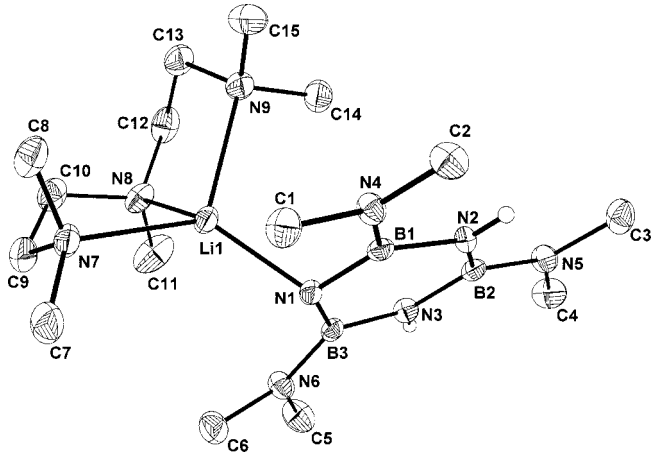

Figure 7. Molecular structure of **7a**. Thermal ellipsoids are depicted on a 25% probability scale. Selected atom distances [Å] and bond angles [°] (see also Table 1): Li1–N1 2.002(4), Li1–N7 2.261(5), Li1–N8 2.217(6), Li1–N9 2.231(6); B1–N1–B3 117.1(3), N1–B1–N2 121.3(2), B1–N2–B2 122.9(3), N2–B2–N3 115.2(3), B2–N3–B3 121.8(3), N3–B3–N1 120.7(3), Li1–N1–B1 112.5(3), Li1–N1–B3 112.5(2), N1–B1–N4 122.2(3), N2–B1–N4 116.7(3), N2–B2–N5 122.2(3), N3–B2–N5 122.4(3), N3–B3–N6 117.3(3), N1–B3–N6 120.0(4), N7–Li1–N8 83.0(2), N7–Li1–N9 113.7(2), N8–Li1–N9 81.2(2). Li1–N1–B2 130.1(3).

In contrast to **2c**, the *t*Bu derivative **5** is a monomer. We attribute this to a steric effect both of the *t*Bu groups and the bulky TIPTA ligand.

The strongest distortion of the borazine ring was observed in **7a**. Atoms B1 and B3 are found below the mean ring-plane. We regard this ring distortion as a consequence of a steric interaction of the Me_2N groups with the PMDTA ligands. The sum of the bond angles at atom N1 in this molecule is 342.5°. This is due to the fact that the Li atom is considerably bent out of the borazine mean-plane as shown by a B2–N1–Li1 angle of 124.4°. It is also worth noting that the exocyclic BN bonds next to atom N1 are longer [1.451 and 1.455(4) Å] than the exocyclic BN bond at atom B2 [1.436(4) Å].

The lithium borazinate **4** differs, of course, in its structure from the *N*-lithioborazines due to the presence of a tetracoordinated boron atom in the ring. The B–N bonds to this boron atom are longer than the other ring BN bonds as the B1–N2 and the N3–B3 bonds are the shortest, but the N2–B2–N3 bond angle is small (105.9°), while the B1–N1–B3 bond angle is wide. Therefore, the charge distribution is strongly influenced whether deprotonation has occurred or carbanion addition.

 © 2005 Wiley-VCH Verlag GmbH & Co. KGaA, Weinheim

Table 1. Selected B_3N_3 ring parameters (bond lengths in angstroms and bond angles in degrees).

	2a	2b	2b	2c	2d	4	5	7a
B1–N1	1.417(6)	1.415(3)	1.421(2)	1.414(3)	1.439(7)	1.419(3)	1.422(6)	1.411(4)
B3–N1	1.415(5)	1.415(3)	1.4204(3)	1.420(3)	1.437(7)	1.408(3)	1.411(7)	1.413(4)
B1–N2	1.438(6)	1.448(3)	1.449(3)	1.459(3)	1.396(6)	1.466(3)	1.449(7)	1.465(4)
B3–N3	1.440(6)	1.448(3)	1.446(3)	1.455(3)	1.394(6)	1.460(3)	1.449(8)	1.469(4)
B2–N2	1.425(6)	1.419(3)	1.421(3)	1.414(3)	1.543(6)	1.410(3)	1.426(8)	1.430(4)
B2–N3	1.415(6)	1.414(3)	1.414(3)	1.412(2)	1.560(6)	1.418(2)	1.376(9)	1.430(4)
B1–N1–B3	117.4(3)	117.5(2)	117.0(2)	117.2(2)	124.7(4)	117.1(2)	118.3(4)	117.1(2)
N2–B2–N3	113.4(4)	114.3(2)	115.3(2)	114.8(2)	105.1(4)	114.8(2)	114.9(5)	115.3(3)

Table 2. Atom distances across the borazine rings and selected bond lengths and angles at Li atoms.

	2a	2b	2c	2d	4	5	7a
Li···Li	2.365	2.487	2.480	–	–	–	–
N1–B2	2.952	2.949	2.954	2.955	3.005	2.931	2.957
N4–B5	2.944	2.960					
Li1–N1	2.009	2.121	2.049	1.975	2.049	1.960	2.002
Li1–N4	2.057	2.162					
Li2–N1	2.026	1.991					
Li2–N4	1.970	1.990					
Li1–N1–B2	156.5	140.5	156.2	157.8	–	175.8	130.1
Li2–N1–B2	136.8	144.1					
Li1–N4–B5	131.1	143.9					
Li2–N4–B5	150.0	141.6					
Li1–N1–Li2	73.7	74.3	73.0	–	–	–	–
Li1–N1–Li2	72.4	73.5	73.0				
N1–Li1–N4	106.9	100.5	107.0				
N1–Li2–N4	108.4	111.7	167.0	–	–	–	–

NMR Spectroscopy

Table 3 contains relevant NMR spectroscopic data of the *N*-monolithioborazines. For all compounds of type **2** the proton resonances of the BMe groups are deshielded relative to **1**, with the exception of **2d**. The protons of the *ortho*-BMe groups are usually more deshielded than those at the *para*-BMe group. The exception for **2d** is due to the fact that this compound is monomeric while **2a**–**c** are dimeric. This also has the consequence that the proton resonances for the NH units are more deshielded in **2d** than in the other solvates of type **2**. Moreover, the shielding of the BMe protons at the *ortho* positions is 0.33 to 0.40 ppm larger than at the *para* position. In the case of mononuclear **2d** the reverse situation is true, i.e. the protons of the *ortho*-BMe groups are more deshielded than those in the *para* position. This suggests that the charge distribution in mononuclear *N*-lithioborazines differs from that of dimeric *N*-lithioborazines.

The ^{13}C resonances of the boron-bonded C atoms could only be observed as broad signals for **2b**–**d**, but not for **2a** and **2e.** It is well known that the large quadrupole moment of boron has a great influence on the relaxation time of the ^{13}C resonance, leading to broad signals, and this may also prevent the observation of the expected ^{13}C NMR signal.

It is somewhat surprising that *N*-lithiation has only a marginal effect on the shielding of the boron nuclei, and there is also no drastic effect on the linewidths of these signals. On the other hand, the ^{7}Li resonances depend in a first approximation on the coordination number of the Li

Table 3. NMR spectroscopic data of *N*-lithioborazines in C_6D_6 solution.

	δ^1H *p*-BMe	δ^1H *o*-BMe	δ^1H NH	$\delta^{13}C$ BMe	$\delta^{11}B$ ($h_{1/2}$; Hz)	$\delta^{7}Li$ ($h_{1/2}$; Hz)
1	0.23		4.37	1.65	36.0	–
2a	0.47 (3 H)	0.59 (6 H)	4.66 (2 H)	n. obs.	35.4 (180)	1.41 (8)
2b	0.46 (3 H)	0.56 (6 H)	4.60 (2H)	2.17	36.2(160)	1.99 (2.35)
2c	0.49 (3 H)	0.63 (6 H)	4.56 (2 H)	1.79	36.2 (190)	2.57 (5)
2d	0.64 (3 H)	0.52 (6 H)	4.79 (2 H)	1.79	36.0 (260)	2.09 (9)
	o-NMe_2	*p*-NMe_2	NH	NMe_2		
6	2.43	2.34	3.07	36.9	26.2 (200)	–
7a	2.98	2.76	3.44	37.0	26.2 (200	1.46 (10)
7b	2.47	2.34	2.95	36.8	26.2 (190)	2.68 (10)
7c	2.44	2.46	2.94	36.4, 36.8	26.1 (170)	1.38 (10)

 © 2005 Wiley-VCH Verlag GmbH & Co. KGaA, Weinheim

atoms. Those which are tricoordinate are at lower frequencies, the tetracoordinate ones are found at around δ = 2 to 2.4 ppm and the pentacoordinate Li atom of **2d** is even more strongly deshielded.

The protons of the Me_2N groups in compound **4a** are deshielded with respect to the parent borazine **4**. Those in compounds **7b** and **7c** are less influenced than those of the monomer **7a**. This suggests that compounds **7b** and **7c** are most likely dimeric with Li_2N_2 bridges. The protons of the NH groups of these latter compounds are slightly shielded compared with the parent molecule, while those of **7a** are deshielded. Compounds **7a** and **7c** show ^{7}Li resonances for tetracoordination at Li, and a higher coordination number is suggested by the stronger deshielding of the Li nucleus in compound **7b**. This could be achieved if the Li atom coordinate in a different way with the borazine N-atoms.

Discussion

The reaction of lithium organyls RLi (R = Me, Bu, *t*Bu) with 2,4,6-trimethylborazine in hexane leads to an exchange of the alkyl groups but not to deprotonation of an NH group of the borazine. This has also been observed for 2,4,6-tris(dimethylamino)borazine, where an Me_2N/R exchange occurs in hexane. However, **1** can be deprotonated at the NH groups in the presence of diethyl ether or an auxiliary nitrogen base such as TMEDA, PMDTA or TMTA. These reactions produce complexes of *N*-monolithioborazines. The characteristic features of these compounds are the small endocyclic ring angles at N1 and B2 while those at N2 and N3 span the range 120–124°. Even more pronounced are the long BN bonds between the *ortho* and *meta* positions of the ring (B1–N2 and N3–B3) while those at B2 and at N1 can be considered to be essentially equal. This shows that the negative charge at the atom N1 obviously weakens the B1–N2 and N3–B3 bonds inductively. Thus, we observe a distortion of the borazine rings, as shown in Scheme 2. In contrast, the $AlBr_3$ adduct of **1** shows the opposite effect, i.e. a widening of the endocyclic bond angles at N1 and B2 and a shortening of the B1–N2 and N3–B3 bonds due to electron withdrawal from the ammonium-type N atom by $AlBr_3$.[19] The small ring angles at atom N1 of the *N*-lithio derivatives of **2**, **5** and **7** can be explained by the VSERP theory of bonding, as the lone pairs of electrons at N1 occupy a larger space. Of course, one has to take the highly polar Li–N interactions into account. Although we have studied the *N*-lithiation of borazines by ab initio methods, we will report on theoretical studies at higher levels of theory in due course.[20]

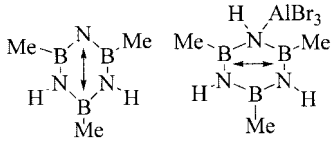

Scheme 2.

It is quite clear that the Li compounds described here can be looked at as formal analogues of aryllithium compounds. For instance. $[LiPh(tmeda)]_2$[21] is structurally akin to compound **2b**, while $[Li(mes)(THF)_2]_2$[22] can be compared with **2a** although the latter has only tricoordinate Li atoms in contrast to the tetracoordinate Li atoms in the mesityl derivative. In this compound the longest C–C bonds are at the carbon atom bonded to Li [C1–C2 = 1.431(2) and C1–C6 = 1.424(2) Å]. Those adjacent to these [C2–C3 = 1.397(2) and C5–C6 = 1.399(2) Å] are shorter, followed by C4–C4 and C4–C5 with 1.393(2) and 1.394(2) Å, respectively. This suggest a different electron distribution in $[Li(mes)(THF)_2]_2$ compared to **2a**. These effects have been addressed H. Bock et al.[23]

However, the bond angles C6–C1–C2 and C3–C4–C5 in $[Li(mes)(THF)_2]_2$ are acute [113.1(1)° and 116.9(1)°] as is also the case for $[LiPh(tmeda)]_2$[24] A similar situation is also observed for tetrameric $[LiPh(OEt_2)]$.[25] There is also a shortening of the C–C bonds on going from the *ipso*-C atom to the *para*-C atom. So, similar to the *N*-lithioborazines described here, a lengthening of the C–C bonds from the *ipso*-C to the *ortho*-C carbon atom seems to be common for aryllithiums, in contrast to the alternating change in the B–N bond lengths in the *N*-lithioborazines.

So far there is no organometallic analogue of $[\{(Me_2NB)_3N_3H_2\}Li(pmdta)]$. We had expected that the Me_2N group may also coordinate to the Li atom, but this is not the case, most likely for two reasons. First, the Me_2N groups form BN π-bonds. This reduces their basicity and, therefore, also their tendency to act as a Lewis base. Secondly, for steric reasons these groups are not able to form chelates as observed in aryllithiums where the phenyl groups carries R_2NCH_2 substituents.[26–28]

The *N*-lithioborazines have proved to be useful reagents for the preparation of a large variety of borazine derivatives which are either not accessible or difficult to prepare by other routes. We will report on these results shortly.

Experimental Section

All experiments were performed by Schlenk techniques employing dry dinitrogen gas or argon as a protective gas. Glassware was heated to 400 °C, filled with dinitrogen gas and allowed to cool. Solvents were dried by conventional methods. NMR: Bruker ACP 200 (^{1}H, ^{7}Li, ^{11}B, ^{13}C), Jeol GSX 270 (^{1}H, ^{7}Li, ^{11}B, ^{29}Si) or Jeol EX 400 (^{1}H, ^{11}B,^{13}C). Standards: C_6D_6, $SiMe_4$, external 1 M aqueous LiCl, $BF_3{\cdot}OEt_2$. IR: Nicolet 520 FT-IR, Nujol hostaflon mulls. Raman: Perkin–Elmer PE 2000, 9324 cm^{-1}, 300 mW. X-ray: Siemens P4 diffractometer equipped with a CCD detector and a LT2 low temperature device. Mo-K_α radiation, graphite monochromator. Commercial chemicals: $BF_3{\cdot}OEt_2$ (BASF), BCl_3 (Elektroschmelzwerk Kempten), Me_3SiCl, $(Me_3Si)_2NH$ (Wacker Chemie), TMEDA, PMDTA, 1,3,5-trimethyl (or isopropyl)hexahydrotriazine (Fluka). Li compounds (Chemetall GmbH).

2,4,6-Trimethylborazine (1):[13] Freshly distilled $(Me_3Si)_2NH$ (250 mL, 1.2 mol, b.p. 134–127 °C) dissolved in CH_2Cl_2 (250 mL) was placed in a one-litre, three-necked flask fitted with a dry ice and an H_2O reflux condenser, a magnetic stirring bar and a pressure equalizer. After cooling to –78 °C $MeBCl_2$ (120.9 g, 1.25 mol) was condensed into the stirred solution within a period of 2 h. During this process a pressure equalizer was placed on top of the dry

 © 2005 Wiley-VCH Verlag GmbH & Co. KGaA, Weinheim

ice reflux condenser, and the water-cooled condenser was closed with a stopcock. Some smoke formation was observed at the beginning of the $MeBCl_2$ addition. The solid that formed was later isolated and characterized as NH_4Cl (3–5% based on $MeBCl_2$). The ^{11}B NMR signals found after that time were at δ = 2.8 ppm [$MeBCl_2$·$HN(SiMe_3)_2$], 36 ppm ($Me_3B_3N_3H_3$), 37.6 ppm [$MeClBN(SiMe_3)_2$], 43.3 $(MeBNH)_2$, 48.9 ppm [$MeB(NHBMe)_n$-$NHSiMe_3$] and 63.0 ppm ($MeBCl_2$) in a ratio of 1:12:4:3:2:1). The solution was then heated to reflux (water-cooled condenser) for 4 to 10 d until the ^{11}B NMR spectrum showed only the signal of **1** at δ = 36 ppm. The ^1H NMR spectrum demonstrated the presence of **1** (δ = 0.23 and 4.37 ppm) and Me_3SiCl (δ = 0.63 ppm, $^2J_{^{29}Si,^1H}$ = 7 Hz) with some minor impurities. The insoluble material was removed from the turbid solution by filtration through a G3 glass frit. Solvent and Me_3SiCl were stripped off in vacuo. The residue solidified within a few hours. Crystallization from hexane provided **1** in 95% yield (46.5 g, 379 mmol), m.p. 36 °C. ***Caution:*** *$MeBCl_2$ ignites in contact with air, therefore precautions have to be taken to avoid contact of the rather volatile boron halide with air. $MeBCl_2$ should be stored in a Schlenk tube equipped with a grease-free stopcock and stored at a temperature below –30 °C.* ^1H NMR (400 MHz, C_6D_6): δ = 0.23 (s, 9 H, C*H3*), 4.37 (br. s, 3 H, NH) ppm. ^{13}C NMR (100 MHz): δ = 1.34 ppm (CH_3). ^{11}B NMR (64 MHz): δ = 36.0 ppm.

Reaction of 1 with *n*BuLi in Hexane (1:1): The borazine **1** (1.15 g, 9.3 mmol) was dissolved in hexane (3.5 mL) and the solution cooled to –30 °C. A solution of *n*BuLi (6.1 mL, 1.6 M in hexane, 9.7 mmol) was slowly added while stirring. A white precipitate formed quickly. No gas evolution was noted. After allowing the suspension to attain ambient temperature it was heated to reflux for 2 h. The solid was then removed by filtration (G3 frit, MeLi, Li_2CH_2). All volatile material was removed in an oil-pump vacuum at 20 °C from 5 mL of the reaction solution and the residue dissolved in 1 mL of C_6D_6. This solution showed ^{11}B NMR signals at δ = 38.1 and 36.2 ppm. The residue obtained from the hexane solution exhibited the following prominent signals in the mass spectrum (correct isotopic pattern) at 70 eV: *m*/*z* (%) = 248 (61) (2,4,6-$Bu_3B_3N_3H_3$), 207 (66) (2,4,6-$Bu_2MeB_3N_3H_3$), 165 (31) (2,4,6-$BuMe_2B_3N_3H_3$), 123 (100) ($Me_3B_3N_3H_3$).

Reaction of 1 with *t*BuLi: Compound **1** (0.97 g, 7. 8 mmol) was dissolved in hexane (35 mL) and the solution cooled to –78 °C. While stirring, a solution of *t*BuLi in hexane (5.0 mL, 1.6 M, 8.0 mmol) diluted with hexane (20 mL) was added *slowly*. After addition of a few drops of the *t*BuLi solution a precipitate formed with no gas evolution. After addition was complete the suspension was allowed to attain room temperature and was then kept for 2 h under reflux. The solid was removed by filtration. The ^{11}B NMR spectrum of the filtrate showed that a Me/*t*Bu exchange had taken place ($\delta_{^{11}B}$ = 38.2, 36.0 ppm in a ratio of 1:2). The mass spectrum of the liquid that remained after evaporation of the solvent proved the presence of $tBu_3B_3N_3H_3$ (*m*/*z* = 248, 11%), $tBu_2MeB_3N_3H_3$ (*m*/*z* = 207, 32%), $tBuMe_2B_3N_3H_3$ (*m*/*z* = 165, 59%), and **1** (*m*/*z* = 123, 100%).

1-Lithio-2,4,6-trimethylborazine Diethyl Ether Adduct (2a): Trimethylborazine (**1**; 0.38 g, 3.1 mmol) was dissolved in diethyl ether (30 mL) and the solution cooled to –78 °C. With stirring, 1.95 mL of an *n*BuLi solution in hexane was added dropwise. This resulted in the formation of a white precipitate. After the suspension had attained room temperature it was heated to reflux until a slightly turbid solution had formed. Then, the very small amount of solid was removed by filtration and all volatile materials removed in vacuo. The oily residue, which was insoluble in pentane, solidified on cooling. It was dissolved in a minimum amount of diethyl ether from which single crystals of **2a** separated on cooling. Yield: 0.55 g (85%), m.p. 105 °C (dec.). ^1H NMR (C_6D_6; see also Table 2): δ = 0.98 (CH_2CH_3, 6 H), 3.17 (OCH_2, 4 H) ppm. ^{13}C NMR: δ = 14.7 (CH_2CH_3), 65.7 (OCH_2) ppm. IR (Nujol): $\tilde{\nu}$ = 3447 w, 3419 m, 2959 m, 1600 w, 1471 st, 1443 st, 1414 st, 1332 st, 1319 st, 1285 st, 1204 m, 1197 m, 1163 m, 1111 m, 1097 m, 1023 w, 886 st, 846 m, 785 m, 776 m, 758 st, 715 m, 587 st, 618 m, 392 m, 324 m. Raman: $\tilde{\nu}$ = 3430 w, 2970 st, 2934 vst, 2900 vst, 2844 m, 1459 m, 1440 m, 1071 w, 852 w, 519 st, 455 w, 340 w, 219 w, 120 m. $C_7H_{19}B_3LiON_3$ (202.63): calcd. C 41.49, H 10.44, N 20.73; found C 42.79, H 10.29, N 19.43.

1-Lithio-2,4,6-trimethylborazine Tetramethylethylenediamine (4/3) Adduct (2b): a) A solution of *n*BuLi in hexane (4.5 mL, 1.6 M, 7.2 mmol) was cooled to –78 °C and TMEDA (1.1 mL, 0.85 g, 7.3 mmol) dissolved in hexane (5 mL) was added with stirring. The precipitate that formed dissolved on warming the suspension to room temperature. This solution was placed into a cooled dropping funnel (–50 °C) and added with stirring to a solution of **1** (0.82 g, 6.7 mmol) in hexane (20 mL) kept at –78 °C. A slight gas evolution was noted and the formation of a suspension. This suspension was then kept at reflux for 4 d until no more gas evolution was observed. Solid material was then removed by filtration and dried in a stream of dinitrogen. Colorless crystals of **2b** separated from the filtrate on cooling to –25 °C. After crystallization from hexane the yield was 1.31 g (91%), m.p. 103–105 °C. ^1H NMR (C_6D_6; see also Table 2): δ = 1.95 (12 H, NMe), 1.97 (4 H, NCH_2) ppm. ^{13}C NMR: δ = 46.2 (NCH_3), 57.4 (NCH_2) ppm. IR (Nujol, Hostaflon): $\tilde{\nu}$ = 3447 w, 3430 m, 2993 m, 2957 st, 2885 m, 2877 m, 2825 st, 2775 st, 2726 w, 2704 w, 1475 vst, 1442 vst, 1414 st, 1370 w, 1358 w, 1331 w, 1286 st, 1249 w, 1217 m, 1179 w, 1158 m, 1130 w, 1110 w, 1100 m, 1074 m, 1034 m, 1024 m, 1008 m, 946 m, 880 st, 848 w, 838 w, 791 m, 715 st, 704 st, 684 w, 583 m, 524 m, 505 m, 458 w, 440 w, 346 m, 299 w, 286 w. Raman: $\tilde{\nu}$ = 3428 m, 2996 st, 2967 vst, 2903 vst, 2829 vst, 2778 st, 1474 st, 1448 m, 1435 m, 1409 w, 1312 w, 1290 w, 1220 w, 1159 w, 1073 w, 1026 w, 938 w, 870 w, 847 w, 793 w, 783 w, 521 st, 461 m, 449 m, 366 w, 121 m. $C_{30}H_{92}B_{12}Li_4N_{18}$ (862.70): calcd. C 41.77, H 10.74, N 29.33; found C 41.43, H 10.80, N 28.34.

b) A hexane solution of *n*BuLi (11.0 mL, 1.6 M, 17.6 mmol) was cooled to –30 °C and a hexane solution of TMEDA (10 mL, 4.2 g, 38 mmol) was added while stirring. The yellow solution was transferred into a dropping funnel and added to a stirred solution of **1** (1.98 g, 16.1 mmol) in hexane (40 mL). The resulting suspension was kept at reflux for 1 d. The solid was removed by filtration and dried (0.7 g of **2b**). It dissolved readily in diethyl ether. Crystals of **2b** were obtained from the diethyl ether solution as well as from the hexane solution on crystallization at –25 °C. Total yield: 3.1 g (90%). These crystals showed the same cell dimensions as those obtained by procedure a).

1-Lithio-2,4,6-trimethylborazine 1,3,5-Trimethylhexahydrotriazine Adduct (2c): Prepared in analogy to procedure a) for **2b**. A solution of *n*BuLi/tmta was prepared from *n*BuLi in hexane (4.90 mmol in 13 mL) and a solution of TMTA (0.63 g, 4.90 mmol) in hexane (5 mL). It was cooled to –50 °C and added to a solution of **1** (580 mg, 4.7 mmol) in hexane (30 mL) kept at –78 °C. The resulting mixture was kept at reflux for 2 d. After filtration crystals of dimeric **2c** separated from the filtrate on storing the solution at –5 °C. Yield: 0.43 g (89%); m.p. 116–119 °C. ^1H NMR (C_6D_6; see also Table 2): δ = 2.06 (9 H, NCH_3), 2.98 (br., 6 H, NCH_2) ppm. ^{13}C NMR: δ = 39.8 (NCH_3), 77.2 (NCH_2) ppm. IR (Nujol): $\tilde{\nu}$ = 3444 w, 3420 m, 2980 m, 1592 w, 1472 st, 1448 vst, 1434 vst, 1386

 © 2005 Wiley-VCH Verlag GmbH & Co. KGaA, Weinheim

st, 1335 m 1282 st, 1276 vst, 1233 w, 1224 m, 1178 w, 1157 st, 1120 vst, 1099 w, 1087 m, 1070 w, 1049 w, 1016 m, 1004 w, 980 w, 940 st, 915 w, 888 m, 786 w, 770 w, 727 m, 716 m, 692 w, 622 w, 580 m, 558 m, 521 w, 477 m, 459 m, 394 w, 336 w, 270 m. Raman: $\tilde{\nu}$ = 2947 vst, 2903 vst, 2798 m, 2580 w, 2144 w, 1470 m, 1451 m, 931 w, 839 w, 471 w. $C_9H_{26}B_3LiN_6$ (215.70): calcd. C 41.94, H 10.17, N 32.61; found C 41.53, H 9.95, N 32.68.

1-Lithio-2,4,6-trimethylborazine Pentamethyldiethylenetriamine Adduct (2d): A solution of MeLi in diethyl ether (6.6 mmol, 1.6 M, 4.5 mL) was cooled to –78 °C. Then, a solution of PMDTA in hexane (2.52 g, 19.6 mmol, 5 mL) was added while stirring. After the mixture had attained room temperature the clear solution was added to a solution of **1** in hexane (0.58 g, 4.7 mmol, 30 mL) at –78 °C. Gas evolution started immediately by adding the MeLi/PMDTA solution with formation of a white solid. The suspension was then kept at reflux for four days. The resulting turbid solution showed a single ^{11}B NMR signal at δ = 36.0 ppm. From the suspension 1.3 g of a solid was isolated which dissolved readily in diethyl ether. Colorless prisms of **2d** separated from this diethyl ether solution on storing at –25 °C. Yield: 1.24 g (62%); m. p. 161 °C (dec.). ^{1}H NMR (C_6D_6; see also Table 2): δ = 2.12 (12 H, NCH_3), 2.19 (3 H, NCH_3), 2.39 (4 H, NCH_2), 2.50 (4 H, NCH_2) ppm. ^{13}C NMR: δ = 42.9 (NCH$_3$), 45.8 [N(CH$_3$)$_2$], 56.6 (CH$_2$); 58.1 (CH$_2$) ppm. IR (Nujol): $\tilde{\nu}$ = 3442 w, 3423 w, 2987 m, 1473 st, 1459 st, 1431 st, 1365 m, 1356 m, 1312 st, 1303 st, 1291 st, 1278 st, 1251 st, 1236 m, 1178 w, 1164 m, 1152 m, 1130 m, 1110 m, 1099 w, 1088 st, 1064 m, 1036 m, 1021 m, 998 w, 985 m, 944 w, 935 m, 899 m, 889 m, 879 m, 839 w, 790 w, 778 m, 763 st, 748 w, 711 st, 675 w, 604 w, 574 m, 521 w, 504 m, 488 w, 460 2 w, 448 w, 431 w, 404 w. Raman: $\tilde{\nu}$ = 2985 st, 2961 vst, 2923 st, 2895 vst, 2836 vst, 2784 st, 1475 m, 1442 m, 1290 w, 1149 w, 1024 w, 945 w, 792 w, 518 w, 465 w. $C_{12}H_{24}B_3LiN_6$ (301.82): calcd. C 47.75, H 11.35, N 27.85; found C 46.68, H 11.11, N 27.52.

Reaction of 1 with MeLi (1:2): Trimethylborazine (**1**; 642 mg, 5.2 mmol) dissolved in diethyl ether (30 mL) was cooled to –78 °C and treated while stirring with a MeLi solution (10.3 mmol in 6.4 mL of diethyl ether). A precipitate formed, and the supernatant solution showed ^{11}B NMR signals at δ = –19.9 (BMe_4^-) and 37.3 ppm in an intensity ratio of 1:6. The suspension was cooled again to –78 °C and treated with a solution of MeBr (1.14 g, 12 mmol) in diethyl ether (5 mL). This mixture was kept at reflux for 2 d. The ether was then removed by distillation. An oily residue remained which was treated with hexane (50 mL) to give a suspension. From this suspension LiBr (0.9 g, 10.4 mmol) was isolated by filtration. The filtrate was distilled. A liquid fraction was obtained using a 30 cm Vigreux column to give 0.52 g of a fraction with a boiling range of 85–104 °C at 350–500 torr. MS (70 eV): *m*/*z* (%) = 165 (61) ($Me_3B_3N_3Me_3$), 151 (95) ($Me_3B_3N_3HMe_2$), 137 (100) ($Me_3B_3N_3H_2Me$), 123 (75) ($Me_3B_3N_3H_3$), 95 (33) ($Me_2B_2N_2HMe$), 81 (35) ($Me_2B_2N_2H_2$), 66 (41) (MeB_2N_2H), 55 (26) (MeBNMe), 41 (38) (MeBNH).

Reaction of 1 with MeLi (1:3): In analogy with the previous experiment a solution of **1** (1.06 g, 8.6 mmol) in diethyl ether (30 mL) was treated with MeLi (26.1 mmol, 16.3 mL of a 1.6 M diethyl ether solution) at –78 °C. The mixture was kept at reflux for 20 h showing ^{11}B NMR signals at δ = –19.9 and 37.3 ppm in a 1:7 ratio. Treatment of the suspension with MeBr (2.56 g, 27 mmol) and work up after refluxing for 2 d gave an oily fraction with a boiling range of 71–102 °C/300–400 torr. MS (70 eV): *m*/*z* (%) = 165 (65) ($Me_3B_3N_3Me_3$), 151 (100) ($Me_3B_3N_3HMe_2$), 137 (93) ($Me_3B_3N_3H_2Me$), 123 (62) ($Me_3B_3N_3H_3$), 95 (37) ($Me_2B_2N_2HMe$), 81 (26) ($Me_2B_2N_2H_2$), 66 (43) MeB_2N_2 H), 55 (57) (MeBNMe), 41 (14) (MeBNH).

Lithium Bis(1,3,5-triisopropylhexahydrotriazine)tetra(*tert*-butyl)borazinate (4): (tBu)$_3$B$_3$N$_3$H$_3$[13] (**3**; 1.45 g, 5.83 mmol) was dissolved in hexane (30 mL), and the solution cooled to –78 °C. Then, a solution of (iPr$_3$NCH$_2$)$_3$ (2.56 g, 12 mmol) and tBuLi (8.5 mL, 1.45 M, 12.3 mmol) in hexane (25 mL) was added slowly dropwise while stirring. Stirring was continued at ambient temperature for 2 h. The slightly turbid solution was filtered, and the filtrate reduced in volume by 1/3. Storing the solution at –25 °C produced a crop of single crystals (yield 1.5 g, 20%); X-ray structure analysis showed them to be compound **4**.

1-Lithio-2,4,6-tri(*tert*-butyl)borazine-1,3,5-trimethylhexahydrotriazine (5): A solution of tBu$_3$B$_3$N$_3$H$_3$ (1.70 g, 6.83 mmol) was dissolved in diethyl ether (20 mL). A solution prepared from a hexane solution of tBuLi (1.45 M, 4.8 mL, 6.96 mmol) diluted with 20 mL of hexane was then added at –30 °C. The mixture was heated to reflux for 24 h to give a turbid solution. After filtration the filtrate was kept at –25 °C. The crystals that formed within a few days were isolated. Yield: 1.65 g (66.6%). These proved to be compound **5** by X-ray structure analysis.

2,4,6-Tris(dimethylamino)borazine (6):[14] A solution of Me_2NSiMe_3 (11.73 g, 100 mmol) in CH_2Cl_2 (50 mL) was slowly added at –78 °C to a solution of $Cl_3B_3N_3H_3$ (6.1 g, 33 mmol) in dichloromethane (300 mL). After the solution had attained room temperature the ^{11}B NMR spectrum showed a quantitative conversion of the chloroborazine to **6**. All volatile material was removed under an oil pump vacuum and the solid residue crystallized twice from CH_2Cl_2 (80 mL each): Yield: 6.9 g (99%); m.p. 112–115 °C.

Reaction of 2,4,6-Tris(dimethylamino)borazine with *tert*-Butyllithium: The borazine **6** (923 mg, 4.4 mmol) was dissolved in hexane (25 mL) and cooled to –78 °C. Then a solution tBuLi in hexane (4.6 mmol, 16.9 mL) was added. The resulting suspension was kept at reflux for 2 d. 5 mL of the supernatant solution was taken as a probe. The solvent was removed in vacuo and the residue dissolved in C_6D_6 for NMR investigation. ^{1}H NMR (C_6D_6): δ = 0.92 (s, $BCMe_3$), 1.03 (s, $BCMe_3$), 1.08 (s, $BCMe_3$), 2.19 (s, NMe_2), 2.43 (s, NMe_2), 2.47 (s, NMe_2), 3.09 (br., NH), 3.22 (br., NH) ppm. ^{13}C NMR: δ = 30.1 (NMe_2), 32.1 (NMe_2), 36.5 (NMe_2), 36.7 (NMe_2), 36.9 (NMe_2), 37.9 ppm (br., BCMe$_3$). ^{11}B NMR: δ = 25.9, 37.9 ppm (2:1). ^{7}Li NMR: δ = 1.29 ppm.

1-Lithio-2,4,6-tris(dimethylamino)borazine Pentamethyldiethylenetriamine Adduct (7a): Compound **6** (1.25 g, 5.9 mmol) was dissolved in hexane (25 mL) and cooled to –78 °C. While stirring, a solution of nBuLi (3.9 mL, 1.6 M, 6.2 mmol) and PMDTA (4.0 mL, 3.32 g, 19.1 mmol) in hexane (24 mL) was added dropwise. The suspension that formed was kept at reflux for 12 h. The solid was separated by filtration. A small amount of **6** crystallized from the filtrate on reduction of the volume of the solution in vacuo. The solid was treated with diethyl ether (2 × 30 mL). Only about 25% dissolved. Crystals of **7a** separated from the diethyl ether solution on concentration and cooling to –25 °C; m.p. 119–121 °C. ^{1}H NMR (C_6D_6; see also Table 2): δ = 2.12 (s, 12 H, 2 NMe_2), 2.19 (s, 3 H, NMe), 2.31 (s, 4 H, NCH_2), 2.39 (s, 4 H, NCH_2) ppm. ^{13}C NMR: δ = 42.9 (NMe), 45.9 (NMe_2), 56.6 (NCH_2), 58.0 (NCH_2) ppm. IR (Nujol, Hostaflon): $\tilde{\nu}$ = 3481 st, 3463 st, 2957 m, 2969 m, 2862 st, 2821 m, 2801 m, 2773 m, 1520 vst, 1474 st, 1431 vst, 1416 m, 1402 m, 1370 st,1352 m, 1328 w, 1303 m, 1263 m, 1198 w, 1152 w, 1100 st, 1043 m, 1032 st, 978 m, 943 w, 897 w, 860 w, 793 m, 717 w, 701 w, 695 st, 662 w, 586 st, 491 w, 464 w, 408 w, 333 w, 311 w. $C_{15}H_{43}B_3LiN_9$ (388.9): calcd. C 46.32, H 11.14, N 32.41; found C 43.41, H 10.29, N 31.98.

1-Lithio-2,4,6-tris(dimethylamino)borazine Tetramethylethylendiamine Adduct (7b): Prepared in analogy to **5**, from a solution of **6**

 © 2005 Wiley-VCH Verlag GmbH & Co. KGaA, Weinheim

(1.22 g, 5.8 mmol) in diethyl ether (25 mL), MeLi (commercial grade containing iodide; 3.8 mL, 1.6 M, 6.1 mmol) and TMEDA (3.0 mL, 20 mmol) diluted with diethyl ether (25 mL). The mixture was stirred for 4 d at room temperature. Half of the diethyl ether was then removed from the solution. Colorless prisms crystallized (105 mg, 2.87 mmol) at –25 °C which proved to be LiI(tmeda)$_2$.[30] After stirring the solution for 4 d and fractional crystallization (by removing solvent) **7b** separated as a microcrystalline powder. Yield: 731 mg (38%). Single crystals formed from the filtrate on standing for several days at –25 °C, m.p. 191–194 °C (dec.). ^{1}H NMR (C_6D_6): δ = 2.09 (s, 12 H, $CNMe_2$), 2.23 (s, 4 H, NCH_2) ppm. ^{13}C NMR: δ = 46.1 ($CNMe_2$), 58.2 (NCH_2) ppm. IR (Nujol, Hostaflon): $\tilde{\nu}$ = 3848 w, 3440 w, 2874 m, 2831 m, 2805 m, 2785 m, 1518 vst, 1492 st, 1431 st, 1415 vst, 1390 vst, 1371 st, 1342 st, 1325 st, 1306 m, 1295 m, 1274 m, 1213 w, 1197 w, 1165 m, 1150 w, 1115, 1099 st, 1063 m, 1055 m, 1044 w, 981 m, 955 st, 871 w, 844 m, 799 m, 727 w, 695 m, 680 w, 636 m, 587 w, 565 w, 520 m, 495 w. $C_{12}H_{36}B_3LiN_8$ (331.85): calcd. C 43.43, H 10.93, N 33.77; found C 41.24, H 10.88, N 32.91.

1-Lithio-2,4,6-tris(dimethylamino)borazine 1,3,5-Trimethylhexahydrotriazine Adduct (7c): A solution of MeLi in diethyl ether (2.8 mL, 4.5 mmol) and 2.8 mL of TMTA (19.8 mmol) was slowly added at –78 °C to a stirred solution of **6** (776 mg, 3.70 mmol) in diethyl ether (25 mL). A precipitate formed and a gas was produced. The suspension was kept for 17 h at reflux. Then the solid (1.05 g) was isolated by filtration. It dissolved completely in diethyl ether (50 mL). After removal of about 1/3 of the solvent the solution was kept at –25 °C where a crystal powder separated. The yield was not determined. Single crystals suitable for X-ray structure determination separated from the filtrate on further standing. ^{1}H NMR (C_6D_6): δ = 2.50 (s, 9 H, CH_2NCH_3), 2.62 (6 H, NCH_2) ppm. ^{13}C NMR: δ = 40.1 (CH_2NCH_3), 77.3 (CH_2N) ppm. IR (Nujol, Hostaflon): $\tilde{\nu}$ = 3480 m, 3405 m, 2970 w, 2926 m, 2865 st, 1520 vst, 1465 st, 1431 vst, 1416 vst, 1494 st, 1367 st, 1363 st, 1314 m, 1302 m, 1275 m, 1263 m, 1247 m, 1196 w, 1157 w, 1100 st, 978 st, 943 w, 915 w, 883 w, 861 w, 825 w, 768 w, 738 w, 716 m, 694 st, 587 br, 491 w, 453 w. $C_{12}H_{35}B_3LiN_9$ (345.85): calcd. C 41.76, H 10.49, N 36.45; found C 39.10, H 10.48, N 36.53.

X-ray Structure Determination: Relevant crystallographic data and information on data collection and structure solution are summarized in Table 4 and Table 5. Single crystals were placed in a poly(fluoro ether) oil (stock point –40 °C) and a suitable specimen selected and mounted on the tip of a glass fiber. An N_2 gas stream was cooled to –80 °C and the crystal, fixed on a goniometer head, was placed in the gas stream. Reflections of 5 sets of 15 frames were used to determine the unit cell with the program SMART.[31] Data collection was performed in the hemisphere mode, and the data reduced by applying the program SAINT.[32] No absorption correction was applied, except for **8**. The structures were solved with either SHELXTL or SHELX 90[33] Non-hydrogen atoms were refined with anisotropic thermal parameters. Most hydrogen atom positions were found from difference Fourier calculation, but in most cases their positions were calculated, and a riding model applied in the refinement with $U_i = 1.2U_{ij}$ of the corresponding C atom. The H position on the N atoms was taken from the difference Fourier map and refined isotropically. Compound **6a** showed

Table 4. Crystallographic data.

	2a	**2b**	**2c**	**2d**
Empirical formula	$C_{14}H_{42}B_6Li_2N_6O_2$	$C_{15}H_{46}B_6Li_2N_9$	$C_9H_{26}B_3LiN_6$	$C_{12}H_{34}B_3LiN_6$
Formula mass	405.28	431.35	257.73	301.82
Crystal size [mm]	0.3×0.3×0.4	0.25×0.3×0.3	0.4×0.5×0.5	0.20×0.32×0.35
Crystal system	triclinic	monoclinic	monoclinic	orthorhombic
Space group	$P\bar{1}$	$P2_1/c$	$P2_1/n$	$P2_12_12_1$
a [Å]	8.719(4)	12.806(4)	8.486(2)	8.945(2)
b [Å]	11.946(7)	10.106(3)	13.140(4)	14.397(4)
c [Å]	14.214(7)	22.238(7)	14.662(5)	15.372(3)
α [°]	82.77(1)	90	90	90
β [°]	73.99(2)	96.01(1)	99.53(1)	90
γ [°]	73.90(2)	90	90	90
V [Å^3]	1365(1)	2862(2)	1612.3(9)	1979.6(8)
Z	2	4	4	4
ρ(calcd.) [Mg m^{-3}]	0.986	1.001	1.062	1.013
μ [mm^{-1}]	0.061	0.059	0.064	0.060
F(000)	440	940	560	664
Index range	$-8 \le h \le 10$	$-14 \le h \le 14$	$-8 \le h \le 8$	$-11 \le h \le 11$
	$-14 \le k \le 14$	$-11 \le k \le 8$	$-14 \le k \le 14$	$-17 \le k \le 17$
	$-16 \le l \le 16$	$-24 \le l \le 24$	$-16 \le l \le 16$	$-17 \le l \le 17$
2θ [°]	49.42	46.50	46.50	57.46
Temperature [K]	183	193(2)	183(3)	193
Reflections collected	6579	11756	6659	11550
Reflections unique	3494	3667	2137	3977
Reflections observed (4σ)	2599	2940	1888	3368
R(int.)	0.0503	0.0334	0.0352	0.0341
No. variables	297	301	186	335
Weighting scheme[a] x/y	0.0942/1.1942	0.0566/1.5741	0.0340/0.7760	0.0929/0.4822
GOOF	1.092	1.078	1.111	1.118
Final R (4σ)	0.0820	0.0587	0.0501	0.0518
Final $wR2$	0.2062	0.1363	0.1111	0.1133
Largest residual peak [e Å^{-3}]	0.284	0.258	0.188	0.144

[a] $w^{-1} = \sigma^2F_o^2 + (xP)^2 + yP$; $P = (F_o^2 + 2F_c^2)/3$.

 © 2005 Wiley-VCH Verlag GmbH & Co. KGaA, Weinheim

Table 5. Crystallographic data.

	4	**5**	**7a**	**8**[16]
Empirical formula	$C_{40}H_{92}B_3LiN_9$	$C_{18}H_{44}B_3LiN_6$	$C_{15}H_{43}B_3LiN_9$	$C_{24}H_{67}B_3Cl_2Li_2N_{12}$
Formula mass	738.60	383.96	388.95	641.11
Crystal size [mm]	0.20×0.20×0.30	0.40×0.60×0.60	0.1×0.3×0.4	0.2×0.2×0.3
Crystal system	triclinic	orthorhombic	monoclinic	monoclinic
Space group	$P\bar{1}$	$Pna2_1$	$P2_1/c$	$P2_1/n$
a [Å]	10.151(1)	11.724(1)	15.233(5)	9.9919(1)
b [Å]	10.878(1)	13.9201(1)	9.815(3)	26.2337(4)
c [Å]	23.331(2)	15.982(2)	16.370(6)	15.4240(2)
α [°]	103.323(2)	90	90	90
β [°]	97.802(2)	90	97.49(1)	99.533(1)
γ [°]	90.360(2)	90	90	90
V [Å^3]	2481.7(4)	2608.3(5)	2426.6(14)	3987.18(9)
Z	2	4	4	4
ρ(calcd.) [Mg m^{-3}]	0.988	0.978	1.065	1.068
μ [mm^{-1}]	0.058	0.057	0.066	0.194
F(000)	826	848	856	1400
Index range	$-12 \le h \le 12$	$-12 \le h \le 12$	$-18 \le h \le 18$	$-11 \le h \le 11$
	$-13 \le k \le 13$	$-13 \le k \le 14$	$-13 \le k \le 8$	$-29 \le k \le 29$
	$-24 \le l \le 29$	$-16 \le l \le 16$	$-21 \le l \le 20$	$-18 \le l \le 18$
2θ [°]	52.74	43.92	58.48	49.42
Temperature [K]	193	193	193	193
Reflections collected	13987	9287	13427	19014
Reflections unique	7268	3049	4621	6425
Reflections observed (4σ)	3405	2628	2544	5053
R(int.)	0.0862	0.0211	0.0591	0.0352
No. variables	505	305	272	463
Weighting scheme[a] x/y	0.1136/0.1876	0.1522/1.0943	0.0621/0.7677	0.0433/3.4600
GOOF	1.044	1.067	1.058	1.079
Final R (4σ)	0.0847	0.0780	0.0714	0.0581
Final $wR2$	0.2009	0.2154	0.1406	0.1276
Largest residual peak [e Å^{-3}]	0.381	0.342	0.203	0.625

[a] $w^{-1} = \sigma^2F_o^2 + (xP)^2 + yP$; $P = (F_o^2 + 2F_c^2)/3$.

a site-disordered pmdta ligand. Free refinement converged at a SOF value close to 0.5. In the final cycles of refinement the SOF was fixed to 0.5. Figure 7 shows only one orientation. Also, the *t*Bu group of compound **4** is site disordered and gave a good fit with SOF = 0.5. Only one orientation is depicted in Figure 6.
CCDC-253312 to -253319 (for **2a**–**d**, **4**, **5**, **7a** and **8**, respectively) contain the supplementary crystallographic data for this paper. These data can be obtained free of charge from The Cambridge Crystallographic Data Centre via www.ccdc.cam.ac.uk/data_request/cif.

Acknowledgments

We thank the University of Munich and Chemetall GmbH for support. We are also indebted to Dr. J. Knizek, Dr. T. Seifert, Dr. H. Schwenk-Kircher and Dr. W. Ponikar for help in data collection and structure solution, to Mr. Peter Mayer for recording many NMR spectra and Mrs. D. Ewald for the MS data.

[1] Contribution to the Chemistry of Boron, 256. For contribution 255 see: K. Knabel, T. M. Klapötke, H. Nöth, I. Schwab, *Eur. J. Inorg. Chem.* 2005, 1099–1108.
[2] E. Wiberg, *Naturwiss.* **1948**, 182–188; E. Wiberg, *Naturwiss.* **1948**, 212–218.
[3] E. O. Fischer, K. Öfele, *Chem. Ber.* **1957**, *90*, 2532–2538.
[4] H. Werner, R. Prinz, E. Deckelmann, *Chem. Ber.* **1969**, *102*, 95–103.
[5] B. Kiran, A. K. Phukan, E. D. Jemmis, *Inorg. Chem.* **2001**, *119*, 3615–3618 and literature cited therein.
[6] G. Beaumelou, M. Pasedeloup, J. P. Laurent, *Org. Magn. Res.* **1973**, *5*, 1588–1590.
[7] R. I. Wagner, J. L. Bradford, *Inorg. Chem.* **1962**, *1*, 93–98, 99–106.
[8] B. Gemünd, PhD Thesis, University of Munich, **2000**.
[9] E. Wiberg, K. Hertwig, A. Bolz, *Z. Anorg. Allg. Chem.* **1948**, *256*, 177–189.
[10] H. S. Turner, *Chem. Ind. (London)* **1958**, 1405–1406.
[11] H. C. Newsom, W. D. English, A. L. McCloskey, W. G. Woods, *J. Am. Chem. Soc.* **1961**, *83*, 4134–4142.
[12] H. Fußstetter, H. Nöth, *Chem. Ber.* **1978**, *111*, 3596–3607.
[13] H. Nöth, *Z. Naturforsch. Teil B* **1961**, *16*, 618–620.
[14] K. Niedenzu, J. W. Dawson, *J. Am. Chem. Soc.* **1959**, *81*, 3561–3564.
[15] V. Gutmann, A. Meller, R. Schlegel, *Monatsh. Chem*. **1963**, *94*, 1071–1091.
[16] A solution of PMDTA (3.11 g, 17.9 mmol) in hexane (5 mL) was added at –78 °C to a stirred solution of *n*LiBu (11.2 mL, 1.6 M, 17.9 mmol). At room temperature the clear solution was placed into a dropping funnel cooled to –50 °C. It was then added to a solution of **6** (3.71 g, 1.7 mmol) in hexane (30 mL). A precipitate formed with some gas evolution. After addition the mixture was kept at reflux for 1 d. The solid was isolated by filtration and CH_2Cl_2 (40 mL) was added to achieve crystallization. At –5 °C crystals, mostly single crystals, separated which proved to be **8**. Yield: 8.8 g (76.7%); m. p. 112–115 °C. ^{1}H NMR (C_6D_6): δ = 2.18 (s, 12 H, 2 NMe_2), 2.29 (s, 3 H, NMe), 2.31 (s, 4 H, NCH_2), 2.43 (s, 18 H, $BNMe_2$), 2.48 (s, 4 H, NCH_2), 3.07 (br., 3 H, NH) ppm. ^{13}C NMR: δ = 36.9 ($BNMe_2$), 44.2 (NMe), 46.0 (NMe_2), 55.3 (CH_2), 57.2 ppm (CH_2). ^{11}B NMR: δ = 26.2 ppm ($h_{1/2}$ = 200 Hz). ^{7}Li NMR: δ = 1.95 ppm. $C_{24}H_{67}B_3Cl_2Li_2N_{12}$ (641.10): calcd. C

 © 2005 Wiley-VCH Verlag GmbH & Co. KGaA, Weinheim

44.96, H 10.53, Cl 11.06, N 26.22; found C 43.94, H 10.40, Cl 11.21, N 25.96. Crystallographic data are listed in Table 5.
[17] K. Anzenhofer, *Mol. Phys.* **1966**, *11*, 425–428.
[18] H. Hess, B. Reiser, *Z. Anorg. Allg. Chem.* **1971**, *91*, 381–388.
[19] K. Anton, H. Fußstetter, H. Nöth, *Chem. Ber.* **1981**, *114*, 2723–2730.
[20] W. Lippert and A. Troll, unpublished results. See also: A. Troll; Ph. D. Thesis, University of Munich, **2000**.
[21] M. A. Beno, H. Hope, M. M. Olmstead, P. P. Power, *Organometallics* **1985**, *4*, 2117–2121.
[22] H. Hope, P. P. Power, *J. Am. Chem. Soc.* **1983**, *105*, 5320–5324.
[23] H. Bock, *Angew. Chem.* **1992**, *104*, 564–595; *Angew. Chem. Int. Ed. Engl.* **1992**, *31*, 560–590.
[24] D. Thoennis, E, Weiss, *Chem. Ber.* **1978**, *111*, 3157–3161.
[25] R. Schlengermann, J. Sieler, S. Jelonek, E. Hey-Hawkins, *Chem. Commun.* **1997**, 197–198.
[26] A. A. H. van de Zeijden, G. van Koten, *Inorg. Chem.* **1986**, *25*, 4723–4727.
[27] A. L. Wayda, R. D. Rogers, *Organometallics* **1985**, *4*, 1440–1446.
[28] S. R. Holl, C. L. Raston, B. W. Skelton, A. H. White, *Inorg. Chem.* **1983**, *22*, 4070–4073.
[29] C. L. Raston, B. W. Skelton, C. R. Whitaker, A. H. White, *J. Chem. Soc., Dalton Trans.* **1988**, 987–990.
[30] C. L. Raston, C. R. Whitaker, A. H. White, *Austr. J. Chem.* **1988**, *41*, 1925–1929. Our crystal structure determination fitted with that reported here.
[31] *SMART*, Siemens Analytical Instruments, Version 4.1, Madison.
[32] *SAINT*, Siemens Analytical Instruments, Version 4.1, Madison.
[33] *SHELX90*, G. W. Sheldrick, University of Göttingen, **1997**; *SHELXTL*, Siemens Analytical Instruments, Version 5.1.

Received: October 19, 2004

 © 2005 Wiley-VCH Verlag GmbH & Co. KGaA, Weinheim

Synthesis, Structure, and Properties of μ-Oxo-Bridged Fe^{III}_2 and Heterometallic Azide-Bridged $Fe^{III}_2Cu^{II}$ Complexes of a Picolinamide In-Plane Ligand

José M. Domínguez-Vera,*[a] José Suárez-Varela,[a] Ikram Ben Maimoun,[b] and Enrique Colacio*[a]

Keywords: Azides / Heterometallic complexes / Iron / Magnetic properties / Oxo ligands

A new μ-oxodiiron(III) complex [{Fe^{III}(bpc)(H_2O)}$_2$O] (**1**) with the bis(picolinamide) N_4 in-plane ligand 4,5-dichloro-1,2-bis-(pyridine-2-carboxamido)benzene (H_2bpc) has been prepared by the reaction of [Fe(bpc)Cl(H_2O)] with a stoichiometric amount of cyanide, and characterized by X-ray structure analysis. The IR and UV/Vis spectroscopic results match well with those expected from the respective previously established spectro-structure correlation. Likewise, the temperature dependence of the magnetic susceptibility shows the existence of a strong antiferromagnetic coupling between the iron(III) centers [$S = 5/2$; with $J = -108.10(3)$ cm^{-1}] that is consistent with the radial and angular overlap Weihe–Güdel model in μ-oxodiiron(III) complexes. Two heterometallic Fe^{III}-$Cu^{II}Fe^{III}$ (**2**) and $Fe^{III}Ni^{II}Fe^{III}$ (**3**) complexes have been prepared from the reaction between [Fe^{III}(bpc)(N_3)$_2$] and [Cu(*meso*-CTH)]$^{2+}$ or [Ni(*meso*-CTH)]$^{2+}$ (CTH = 5,7,7,12,14,14-hexamethyl-1,4,8,11-tetraazacyclotetradecane), respectively. The structure of **2** consists of heterometallic $Fe^{III}Cu^{II}Fe^{III}$ units formed by the simultaneous coordination of two [Fe^{III}-(bpc)(N_3)$_2$] units to the central [Cu(*meso*-CTH)] units through a $\mu_{1,3}$-azide bridging ligand. However, the structure of **3** contains isolated [Fe^{III}(bpc)(N_3)$_2$]$^-$ and [Ni(*meso*-CTH)]$^{2+}$ ions. The treatment of the magnetic data of **2** revealed the existence of a small ferromagnetic interaction between Fe^{III} and Cu^{II} metal ions, with $J_{FeCu} = 3.24(7)$ cm^{-1}. The existence of **2** opens up the possibility of obtaining, in a rational manner, azide-bridged heterometallic complexes starting from the block precursor [Fe^{III}(bpc)(N_3)$_2$]$^-$.
(© Wiley-VCH Verlag GmbH & Co. KGaA, 69451 Weinheim, Germany, 2005)

Introduction

Oxo-bridged diiron complexes have been extensively studied owing to the occurrence of the Fe–O–Fe fragment at the active sites of non-heme iron metalloproteins, such as hemerythrin,[1] ribonucleotide reductase,[2] or methane monooxygensase.[3] The synthetic, spectroscopic, and magnetic study of μ-oxodiiron complexes can provide a reference frame for these biological sites, and with this aim a great number of (μ-oxo)L_2Fe_2 complexes have been structurally characterized and their properties intensively studied.[4] In spite of this, the interest in preparing this kind of complexes remains because minor structural modifications in the L ligand or in the bridging region can generate drastic differences in their reactivity and properties, as is the case at the active site of metalloproteins.

One of the most commonly used strategies to prepare (μ-oxo)L_2Fe_2 complexes has been the hydrolysis, in a basic medium, of an in-plane ligand containing iron(III) complex. The ligand 4,5-dichloro-1,2-bis(pyridine-2-carboxamido)-benzene (H_2bpc) is a good candidate for preparing this kind of diiron(III) complex since it is forced to occupy four in-plane nitrogen coordinative positions around an iron(III) ion. Monodentate ligands such as water, chloride, cyanide, azide, etc. can be bound in axial positions to generate six-coordinate distorted octahedral complexes [Fe^{III}(bpc)X_2] and/or [Fe^{III}(bpc)XY][5,6] (Scheme 1).

In this paper, we report on the synthesis, crystal structure, and magnetic properties of the μ-oxo dimer complex [{Fe^{III}(bpc)(H_2O)}$_2$O] (**1**) and the heterometallic complexes [{Fe^{III}(bpc)(N_3)$_2$}$_2${Cu(*meso*-CTH)}] (**2**) and [{Fe^{III}(bpc)(N_3)$_2$}$_2${Cu(*meso*-CTH)}] (**3**). The former was prepared from the complex [{Fe^{III}(bpc)Cl(H_2O)], whereas **2** and **3** were prepared by the reaction between [Fe^{III}(bpc)-(N_3)$_2$]$^-$ and [Cu(*meso*-CTH)]$^{2+}$ or [Ni(*meso*-CTH)]$^{2+}$ (CTH = 5,7,7,12,14,14-hexamethyl-1,4,8,11-tetraazacyclotetradecane), respectively. The existence of **2** suggests the possibility of preparing, in a rational manner, azide-bridged heterometallic complexes from the precursor [Fe^{III}(bpc)-(N_3)$_2$]$^-$.

[a] Departamento de Química Inorgánica, Facultad de Ciencias, Universidad de Granada,
18071 Granada, Spain
Fax: +34-958-248526
E-mail: ecolacio@ugr.es
[b] Department of Chemistry, Faculty of Sciences M'hannech, University of Tetouan,
Morocco

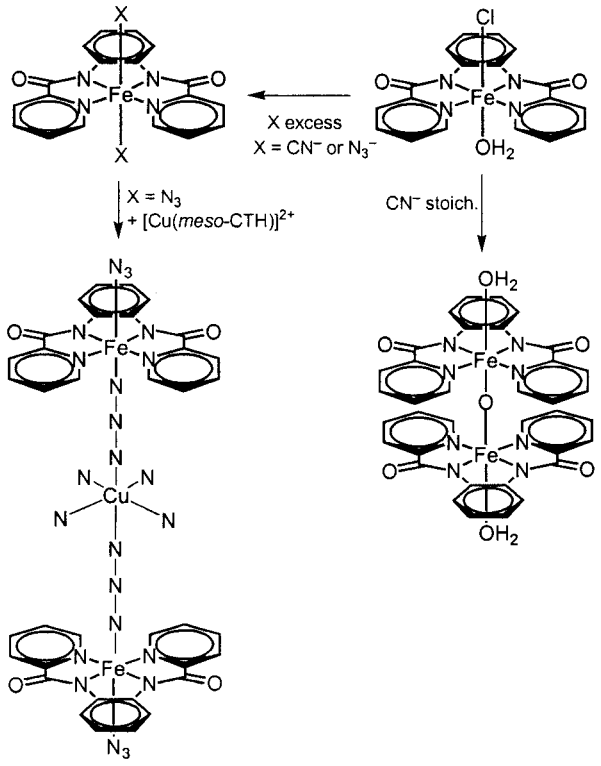

Scheme 1. Schematic preparation of the complexes.

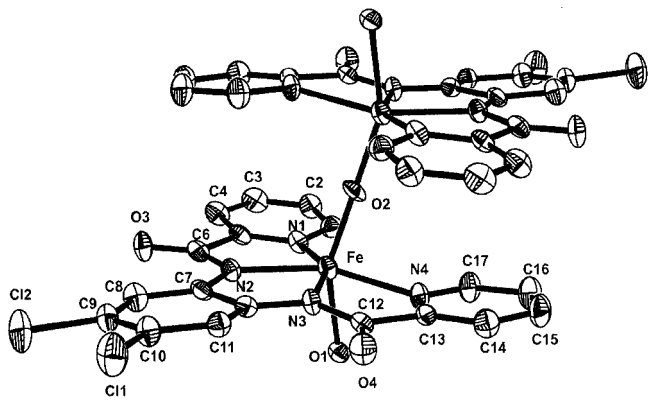

Figure 1. A perspective view of the structure of complex **1**. Hydrogen atoms and lattice water molecules have been omitted for clarity.

Table 1. Selected bond lengths [Å] and angles [°] for complex **1**.

N1–Fe	2.153(5)	N2–Fe	–
N3–Fe	2.086(5)	N4–Fe	–
O1–Fe	2.145(4)	O2–Fe	–
O2–Fe	1.7790(11)		–
Fe–O2–Fe	180.000(1)	O2–Fe–N2	105.29(15)
O2–Fe–N3	110.02(15)	N2–Fe–N3	77.7(2)
O2–Fe–O1	146.77(11)	N2–Fe–O1	99.61(18)
N3–Fe–O1	96.40(17)	O2–Fe–N1	86.09(15)
N2–Fe–N1	75.3(2)	N3–Fe–N1	151.5(2)
O1–Fe–N1	79.27(18)	O2–Fe–N4	87.32(14)
N2–Fe–N4	152.5(2)	N3–Fe–N4	75.0(2)
O1–Fe–N4	80.26(18)	N1–Fe–N4	130.8(2)

Results and Discussion

As previously reported, the complex $[Fe^{III}(bpc)Cl(H_2O)]$ reacts with an excess of cyanide to produce the green complex $[Fe^{III}(bpc)(CN)_2]^-$.[6] However, when we carried out this reaction under stoichiometric conditions we obtained red crystals of the μ-oxodiiron(III) complex $[\{Fe^{III}(bpc)(H_2O)\}_2O]\cdot 3H_2O$ (**1**). This suggests that the role of the cyanide salt in this reaction is as a base rather than as a ligand. In fact, the same complex $[\{Fe^{III}(bpc)(H_2O)\}_2O]$ has previously been obtained using an inorganic base such as $(Bu_4N)(OH)$ instead of cyanide,[7] although its structure was not reported. The molecular structure of **1** is shown in Figure 1, and selected bond lengths and angles are listed in Table 1.

The structure consists of μ-oxo dinuclear molecules in which the two iron atoms have a distorted octahedral geometry, with the four nitrogen atoms of the bis(picolinamidate) ligand in basal positions and two oxygen atoms in axial positions, one belonging to the μ-oxo bridge and another one to a water molecule. The tetradentate behavior of the ligand results in the formation of three five-membered rings around each iron atom. The Fe–N distances involving the pyridine nitrogen atoms N1 (2.154 Å) and N4 (2.167 Å) are significantly longer than those for the amide nitrogen atoms N2 (2.059 Å) and N3 (2.086 Å). Similar bond-length patterns have been observed for other related iron(III) complexes.[8] The central oxygen atom of the Fe–O–Fe fragment lies on an inversion center, with an Fe–O–Fe angle of 180° and an Fe–Fe distance of 3.558 Å, which is typical of a monobridged Fe–O–Fe linear core.[4] The μ-oxo–Fe and Fe–O(water) distances of 1.779 and 2.145 Å are similar to those previously reported for related iron(III) complexes.[9] Within the dimer, essentially planar Fe(bpc) units stack in such a way that the Cl–Cl interactions are minimized, whereas extensive π-π interactions remain in the structure. As a result, the Fe(bpc) fragments are shifted with respect to each other and the angle formed between the μ-oxo oxygen atom O2 and the mean FeN_4 coordination plane increases from 90° to 98°.

The UV/Vis and IR spectroscopic properties of the μ-oxodiiron(III) system have been analyzed in detail, allowing the establishment of nice correlations between structural and spectroscopic data. The UV/Vis spectrum of **1** shows a unique band at 355 nm in the so-called "oxo dimer region", which is consistent with the linearity of the Fe–O–Fe unit found in the present complex.[4] The IR spectrum shows two bands at 837 and 442 cm^{-1}, attributed to the asymmetric and symmetric Fe–O–Fe vibrations, respectively, which usually are in the range 885–725 and 540–380 cm^{-1}.[4] As has been previously established, the location of these two bands depends strongly on the Fe–O–Fe angle: the lower the angle, the less energetic the asymmetric and more energetic the symmetric Fe–O–Fe vibrations observed.[4,10] Therefore, the two bands found for **1** at 837 and 442 cm^{-1} match well with the linearity of the Fe–O–Fe bridge.

As indicated elsewhere, complex **1** can also be obtained from the reaction between $[Fe^{III}(bpc)Cl(H_2O)]$ and cyanide in a 1:1 ratio (Scheme 1). When an excess of cyanide is used, two cyanide ligands coordinate to the iron ion to give the

 © 2005 Wiley-VCH Verlag GmbH & Co. KGaA, Weinheim

complex $[Fe^{III}(bpc)(CN)_2]^-$. Other related $[Fe^{III}(bpc)(X)_2]$ complexes (X = azide, pyridine, etc.) can also be prepared in the presence of an excess of the X ligand (Scheme 1).[5] We explored the possibility of making use of this kind of complex $[Fe^{III}(bpc)(X)_2]$ (X = CN^- or N_3^-) as a precursor of polymetallic complexes in a similar way to that used by Holm[11] and Murray et al.,[12] which is by the coordination of the axial X ligands to metal complexes with empty coordination sites. We observed in the course of this research that the reaction between $[Fe^{III}(bpc)(CN)_2]^-$ and [M(*meso*-CTH)]$(ClO_4)_2$ did not give rise to the expected heterometallic complex but to the μ-oxo dimer **1**. However, from the reaction between Na$[Fe^{III}(bpc)(N_3)_2]$ and [M(*meso*-CTH)]$(ClO_4)_2$ (M = Cu^{II}, Ni^{II}), we succeeded in obtaining the heterometallic complexes [{$Fe^{III}(bpc)(N_3)_2$}$_2${Cu(*meso*-CTH)}] (**2**) and [{$Fe^{III}(bpc)(N_3)_2$}$_2${Ni(*meso*-CTH)}] (**3**), whose structures were solved by X-ray diffraction.

The molecular structure of complex **2** is shown in Figure 2, and selected bond lengths and angles are listed in Table 2.

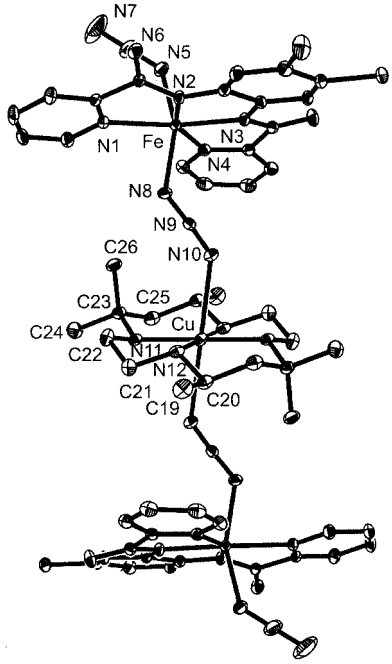

Figure 2. A perspective view of the structure of complex **2**. Hydrogen atoms and the lattice water molecule have been omitted for clarity.

The structure consists of centrosymmetric heterometallic $Fe^{III}Cu^{II}Fe^{III}$ complexes, which are formed by the simultaneous coordination of two $[Fe^{III}(bpc)(N_3)_2]^-$ anions to the central $[Cu(meso\text{-}CTH)]^{2+}$ cation through a single end-to-end azide bridging ligand. The inversion center is located at the Cu^{II} ion and the Fe–Cu distance is 6.43 Å. The ligand environment around the central Cu^{II} ion can be described as a distorted octahedron. The four nitrogen atoms of the CTH ligand are bound in equatorial positions with typical Cu–N distances of about 2 Å, whereas the two azide ligands occupy the axial positions at longer distances of 2.597 Å, giving rise to a *trans* arrangement with a Cu–N10–N9 bond angle of 138.7°. The coordination geometry of the terminal Fe^{III} ions is close to octahedral, with structural parameters in the Fe(bpc) fragment close to those observed in **1** and other related complexes,[5,6] and with Fe–N_{azide} distances of about 2.02 Å. The bond angles Fe–N8–N9 and Fe–N5–N6 are 129.3° and 130.5°. As usual, both the non-bridging and the azide-bridging ligands are practically linear, with values of 176.9(6)° and 174.3(5)°, respectively.

Table 2. Selected bond lengths [Å] and angles [°] for complex **2**.

Cu–N12	2.020(3)	Cu–N11	2.053(2)
N3–Fe	2.050(2)	N4–Fe	–
N1–Fe	2.211(2)	N2–Fe	–
Fe–N5	2.017(3)	Fe–N8	2.028(2)
N12–Cu–N11	94.13(10)	N5–Fe–N8	148.90(12)
N5–Fe–N2	102.43(11)	N8–Fe–N2	102.04(10)
N5–Fe–N3	100.89(11)	N8–Fe–N3	102.75(11)
N2–Fe–N3	77.94(9)	N5–Fe–N4	85.63(10)
N8–Fe–N4	80.83(10)	N2–Fe–N4	153.72(9)
N3–Fe–N4	75.97(9)	N5–Fe–N1	84.57(10)
N8–Fe–N1	83.06(10)	N2–Fe–N1	75.95(9)
N3–Fe–N1	153.88(9)	N4–Fe–N1	130.11(9)
N6–N5–Fe	130.5(3)	N10–N9–N8	–
N9–N8–Fe	129.3(2)	N7–N6–N5	–

However, when we tried to extend this strategy to obtain the heterometallic $Fe^{III}Ni^{II}Fe^{III}$ complex, by treating Na$[Fe^{III}(bpc)(N_3)_2]$ with [Ni(*meso*-CTH)]$(ClO_4)_2$, we obtained the complex [{$Fe^{III}(bpc)(N_3)_2$}$_2${Ni(*meso*-CTH)}], whose structure consists of isolated $[Fe^{III}(bpc)(N_3)_2]^-$ and $[Ni(meso\text{-}CTH)]^{2+}$ ions (Figure 3) with an Ni–N10 distance of 3.453 Å. Selected bond lengths and angles are listed in Table 3. The bond lengths and angles in both ionic units are close to those found in **2** and other analogous compounds

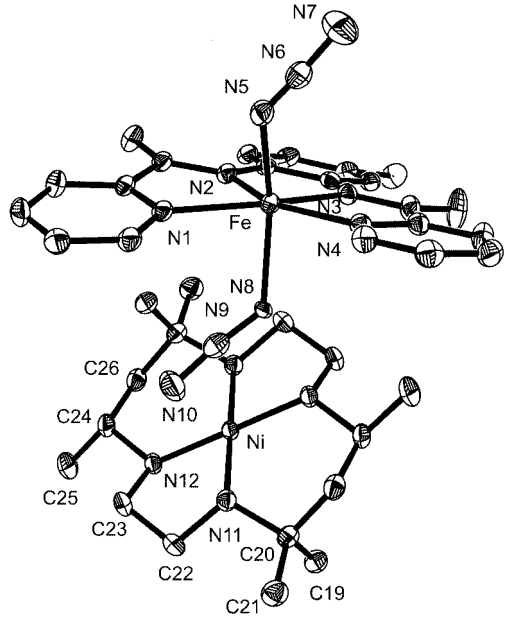

Figure 3. A perspective view of the structure of complex **3**. Hydrogen atoms have been omitted for clarity.

Magnetic Properties

The temperature dependence of χT per Fe for **1** in the range 298–2 K is shown in Figure 4. The χT product de-

 © 2005 Wiley-VCH Verlag GmbH & Co. KGaA, Weinheim

Table 3. Selected bond lengths [Å] and angles [°] for complex **3**.

N1–Fe	2.171(3)	N8–Fe	–
N5–Fe	2.040(4)	N2–Fe	–
N3–Fe	2.055(3)	N4–Fe	–
Ni–N11	1.942(4)	Ni–N12	1.961(3)
N9–N8–Fe	129.9(3)	N8–N9–N10	–
N6–N5–Fe	131.5(4)	N5–N6–N7	–
N5–Fe–N2	98.55(15)	N5–Fe–N3	108.21(15)
N2–Fe–N3	77.21(12)	N5–Fe–N8	149.72(15)
N2–Fe–N8	103.89(13)	N3–Fe–N8	96.50(12)
N5–Fe–N1	82.71(14)	N2–Fe–N1	76.64(12)
N3–Fe–N1	152.90(13)	N8–Fe–N1	82.98(11)
N5–Fe–N4	85.74(14)	N2–Fe–N4	153.37(12)
N3–Fe–N4	76.50(13)	N8–Fe–N4	83.25(12)
N1–Fe–N4	129.96(12)	N11–Ni–N12	93.50(14)

creases with the temperature, as expected for strongly antiferromagnetically coupled $S = 5/2$ pairs. The experimental data were analyzed using the van Vleck equation with $H = -2JS_1 \cdot S_2$ ($S_1 = S_2 = 5/2$). Because the χT plateau value at low temperature is not zero, the existence of a monomer impurity (p) was taken into account, which is a common feature of μ-oxodiiron(III) systems.

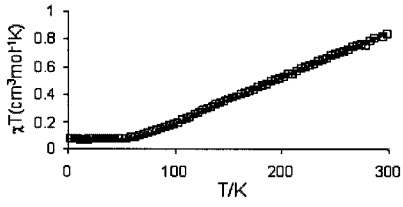

Figure 4. Temperature dependence of $\chi_M T$ for **1**. Solid lines represent the best data fit.

A very good fit of the data was obtained for $J = -108.1$ cm^{-1}, $p = 1.5\%$, and g fixed to 2.00. The J value of –108.1 cm^{-1} compares well with that calculated by using the angular and radial overlap model of Weihe and Gudel ($J = -106.1$ cm^{-1})[13] for μ-oxodiiron(III) complexes. In this model, the Fe–O–Fe angle and the average Fe–O distances are correlated with J. However, by using the empirical correlation obtained by Lippard,[14] which ignores the angular dependence and only includes the Fe–O distance, a J value of –92 cm^{-1} is obtained.

The magnetic susceptibility data for a polycrystalline sample of **2** were measured in the temperature range 2–300 K (Figure 5).

At room temperature, the $\chi_M T$ product (χ_M is the magnetic susceptibility per Fe_2Cu trinuclear molecule) is 8.83 cm^3 mol^{-1} K, which is close to the calculated value of 9.125 for an uncoupled system with two high-spin Fe^{III} ions ($S = 5/2$) and one Cu^{II} ion ($S = 1/2$), assuming an average g value of 2.0. As the temperature is lowered, $\chi_M T$ remains almost constant until about 12 K, then increases very slightly and finally decreases sharply upon cooling to 2 K. If the two iron(III) and the copper(II) ions were magnetically isolated, at low temperature the $\chi_M T$ product should decrease with the temperature in a similar manner as in the mononuclear complex $Bu_4N[Fe(L)(N_3)_2]$. However, as can be observed in Figure 5, the decrease in $\chi_M T$ for $Bu_4N[Fe(L)(N_3)_2]$ begins at higher temperatures, which might suggest the existence of a weak ferromagnetic interaction between the Fe^{III} and Cu^{II} ions in **2** similar to that observed for the closely related complex $[Cu(cyclam)\{Fe(L)(N_3)_2\}_2]$.[15] This fact prompted us to analyze in detail the experimental magnetic data of **2** in order to determine whether or not a weak ferromagnetic interaction exists. Because the sharp decrease in $\chi_M T$ due to local anisotropy of the Fe^{III} ions might mask the increase in $\chi_M T$ caused by a hypothetical ferromagnetic interaction, we removed the contribution of the decrease in $\chi_M T$ for two Fe^{III} ions with a similar coordination environment to that exhibited by the Fe^{III} ions in **2** from the experimental magnetic data. In this regard, we used the magnetic data of the complex $Bu_4N[Fe(L)(N_3)_2]$. As result of this, a different $\chi_M T$ vs. T dependence was obtained. As can be observed in Figure 5, as the temperature is lowered $\chi_M T$ remains almost constant until around 100 K, then increases to reach a maximum with a value of 11.55 cm^3 mol^{-1} K at 3 K. Such a magnetic behavior confirms our hypothesis of the existence of a ferromagnetic coupling between the central Cu^{II} ion and the terminal Fe^{III} ions. The modified data were fitted to the equation for three linearly coupled spins derived from the spin Hamiltonian $H = -J(S_{Fe1} \cdot S_{Cu} + S_{Fe2} \cdot S_{Cu})$. The remote coupling constant, J_{FeFe}, between terminal Fe^{III} ions separated by a distance higher than 12 Å, was assumed to be zero. It was necessary to include a constant, θ, to fit the decrease of $\chi_M T$ at very low temperature. The expression used was $\chi = (C/T - \theta) f(J_{FeCu}, T)$ where $C = Ng^2\mu_B^2/k$ and $f(J_{FeCu}, T)$ is derived from the theoretical equation. The best parameters obtained with this model were $J_{FeCu} = 3.24(7)$ cm^{-1}, $g_{av} = 2.001(1)$, and $\theta = -0.90(2)$. The ferromagnetic coupling observed can be explained in terms of orbital considerations. The magnetic orbital of the copper(II) atom is of the type $d_{x^2-y^2}$ − the x and y axes being defined by the short Cu–N(cyclam) bonds − with a very low spin density on the axial positions (z axis), which are filled by the N atoms of the bridging azide ligands. This leads to a negligible overlap ($J_{AF} \approx 0$) and to a weak ferromagnetic interaction ($J \approx J_F$). The large Cu–N_{azide} distance of 2.597 Å also accounts for the weakness of the magnetic coupling observed. Nevertheless, the value of J should be taken with caution because of the crude procedure followed in its estimation.

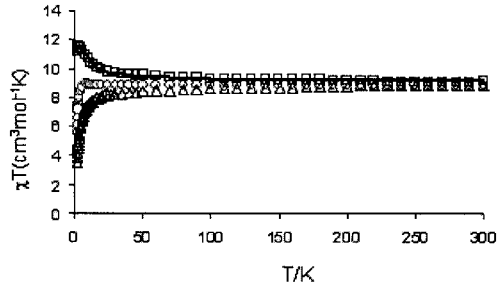

Figure 5. Temperature dependence of $\chi_M T$ for **2** (circles) and $NBu_4[Fe(L)(N_3)_2]$ (triangles). Temperature dependence of of $\chi_M T$ for **2** once the ZFS corresponding to two Fe^{III} ions has been removed (squares). The solid lines represent the best data fit to the theoretical model.

 © 2005 Wiley-VCH Verlag GmbH & Co. KGaA, Weinheim

Experimental Section

Synthesis: The H_2bpc ligand[5] and the complexes $[Fe^{III}(bpc)Cl(H_2O)]\cdot H_2O$, $Na[Fe^{III}(bpc)(N_3)_2]$, $Na[Fe^{III}(bpc)(CN)_2]$,[6] [Cu(*meso*-CTH)]$(ClO_4)_2$. and [Ni(*meso*-CTH)]$(ClO_4)_2$[16] were prepared as previously reported.

Caution: *Perchlorate and cyanide salts are potentially explosive and poisonous, respectively, and should be used in small quantities. Due care must be taken when handling perchlorate and cyanide salts.*

$[\{Fe^{III}(bpc)(H_2O)\}_2O]\cdot 3H_2O$ (1): A methanol suspension (50 mL) of $[Fe^{III}(bpc)Cl(H_2O)]\cdot H_2O$ (0.512 g, 1.0 mmol) containing a stoichiometric amount of NaCN (49 mg) was stirred at room temperature for 1 h. The resultant red solution was kept at room temperature to produce orange crystals, which were filtered and air-dried. Yield: 68%. $C_{36}H_{32}Cl_4Fe_2N_8O_{11}$: calcd. C 42.94, H 3.18, N 11.13; found C 43.02, H 3.28, N 11.19.

$[\{Fe^{III}(bpc)(N_3)_2\}_2\{Cu(meso\text{-}CTH)\}]\cdot 2H_2O$ (2): A methanol suspension (30 mL) of $[Fe(L)Cl(H_2O)]\cdot H_2O$ (41 mg, 0.08 mmol) and NaN_3 (10.4 mg, 0.16 mmol) was stirred until the formation of a clear green solution. The solution was then filtered to remove any insoluble material. A methanol solution (20 mL) of [Cu(cyclam)$(ClO_4)_2$] (22 mg, 0.04 mmol) was slowly added to the filtrate, after which the mixture was stirred for 15 min. Dark-green crystals were obtained from the filtrate by slow concentration at room temperature for 2 d. Yield: 65% based on copper. IR (KBr): ν(N–N–N) = 2073 and 2050 cm^{-1}. $C_{52}H_{60}Cl_4CuFe_2N_{24}O_6$: calcd. C 43.67, H 3.95, N 23.50; found C 43.56, H 4.15, N 23.54.

$[\{Fe^{III}(bpc)(N_3)_2\}_2\{Ni(meso\text{-}CTH)\}]$ (3): This compound was obtained in a similar way as **2** using [Ni(*meso*-CTH)]$(ClO_4)_2$ instead of [Cu(*meso*-CTH)]$(ClO_4)_2$. Yield: 59%. IR (KBr): ν(N–N–N) = 2050 cm^{-1}. $C_{52}H_{56}Cl_4Fe_2N_{24}NiO_4$: calcd. C 44.78, H 4.02, N 24.11; found C 44.87, H 3.91, N 23.96.

Measurements: The IR spectra of powdered samples were recorded with a ThermoNicolet IR200FTIR and the UV/Vis spectra of **1** with a Thermospectronic UV300 spectrophotometer against a reference solution containing appropriate amounts of the ligand bpc. Variable-temperature (1.9–300 K) magnetic susceptibility measurements on polycrystalline samples were carried out with a Quantum Design Squid operating at different magnetic fields. Experimental susceptibilities were corrected for diamagnetism and magnetization of the sample holder.

X-ray Diffraction: The unit-cell parameters were determined and the data collected at room temperature with a Siemens STOE STADI4 four-circle diffractometer. The data were corrected for Lorentz polarization effects and for dispersion, and an empirical absorption correction was applied. The structures were solved by direct methods using SHELXS-97[17] and refined (full-matrix least squares on F^2) with all non-hydrogen atoms refined anisotropically with SHELXL97 and WINGX.[18] All hydrogen atoms were geometrically fixed and allowed to ride on the attached atoms. The crystal and refinement details for compounds **1**–**3** are listed in Table 4. CCDC-253934 to -253936 (**1**–**3**, respectively) contain the supplementary crystallographic data for this paper. These data can be obtained free of charge from The Cambridge Crystallographic Data Centre via www.ccdc.cam.ac.uk/data_request/cif.

Acknowledgments

This work was supported by the Spanish Ministry of Science and Education (Project BQU2001-3221) and the Junta de Andalucia. I. B. M. thanks the Spanish Agency of International Cooperation (AECI) for a predoctoral grant.

[1] R. E. Stenkamp, *Chem. Rev.* **1994**, *94*, 715–726.
[2] J. Stubbe, W. A. Donk, *Chem. Biol.* **1995**, *2*, 793–801.
[3] C. Rosenzweig, P. Nordlund, P. M. Takahara, C. A. Frederick, S. J. Lippard, *Chem. Biol.* **1995**, *2*, 409–418.
[4] D. M. Kurtz, Jr., *Chem. Rev.* **1990**, *90*, 585.
[5] D. J. Barnés, R. L. Chapman, R. S. Vagg, E. C. Watton, *J. Chem. Eng. Data* **1978**, *23*, 349–350.
[6] a) M. Ray, R. Mukherjee, J. F. Richardson, R. M. Buchanan, *J. Chem. Soc., Dalton Trans.* **1993**, 2451–2457; b) S. K. Dutta, U. Beckmann, E. Bill, T. Weyhermüller, K. Wieghardt, *Inorg. Chem.* **2000**, *39*, 3355–3364.
[7] A. K. Patra, R. Mukherkee, *Polyhedron* **1999**, *18*, 1317–1322.
[8] E. Balogh-Hergovich, G. Speier, M. Réglier, M. Giorgi, E. Kuzmann, A. Vértes, *Eur. J. Inorg. Chem.* **2003**, 1735–1740.
[9] P. C. Junk, B. J. McCool, B. Moubaraki, K. S. Murray, L. Spiccia, J. D. Cashion, J. W. Steed, *J. Chem. Soc., Dalton Trans.* **2002**, 1024–1029.
[10] R. E. Norman, R. C. Holz. S. Ménage, C. J. O'Connor, J. H. Zhang, L. Que, Jr., *Inorg. Chem.* **1990**, *29*, 4629–4630.
[11] a) M. J. Scott, R. H. Holm, *J. Am. Chem. Soc.* **1994**, *116*, 11357–67; b) M. J. Scott, C. S. Lee, R. H. Holm, *Inorg. Chem.* **1994**, *33*, 4651–62.

Table 4. Crystal data for complexes **1**–**3**.

	1	**2**	**3**
Empirical formula	$C_{36}H_{32}N_8O_{11}Fe_2Cl_4$	$C_{52}H_{60}N_{24}O_6Fe_2CuCl_4$	$C_{52}H_{56}N_{24}O_4Fe_2NiCl_4$
Formula mass	1006.16	1434.24	1393.42
Crystal system	monoclinic	monoclinic	monoclinic
Space group	$P12_1/n$ (no. 1)	$P12_1/n$ (no. 1)	$P12_1/c$ (no. 1)
a [Å]	12.2156(48)	11.9165(5)	10.0924(7)
b [Å]	9.6771(37)	20.9026(9)	13.8648(9)
c [Å]	17.9909(69)	13.2751(6)	20.7871(13)
α [°]	90	90	90
β [°]	92.173(8)	108.434(1)	96.374(1)
γ [°]	90	90	90
V [$Å^3$]	2125.20(16)	3136.97(11)	2890.74(5)
Z	2	3	2
μ [mm^{-1}]	0.995	1.032	1.072
Goodness-of-fit	0.734	1.132	1.035
Refl. collected/unique	9404/3040	36267/7203	18191/6580
Final R indices	$R_1 = 0.049$	$R_1 = 0.051$	$R_1 = 0.063$
$[I > 2\sigma(I)]$	$wR_2 = 0.081$	$wR_2 = 0.118$	$wR_2 = 0.154$

 © 2005 Wiley-VCH Verlag GmbH & Co. KGaA, Weinheim

[12] R. J. Parker, K. D. Lu, S. R. Batten, B. Moubaraki, K. S. Murray, L. Spiccia, J. D. Cashion, A. D. Rae, A. C. Willis, *J. Chem. Soc., Dalton Trans.* **2002**, 3723–3730.
[13] H. Weihe, H. Gudel, *J. Am. Chem. Soc.* **1997**, *119*, 6539.
[14] S. M. Gorun, S. J. Lippard, *Inorg. Chem.* **1991**, *30*, 1625.
[15] E. Colacio, J.-P. Costes, J. M. Domínguez-Vera, I. B. Maimoun, J. Suárez-Varela, *Chem. Commun.* **2005**, 534–536.
[16] N. F. Curtis, D. A. Swann, T. N. Waters, *J. Chem. Soc., Dalton Trans.* **1973**, 1963.
[17] G. M. Sheldrick, *SHELXLS-97, Program for Solution of Crystal Structure*, University of Göttingen, Germany, **1997**.
[18] a) G. M. Sheldrick, *SHELXL-97, a computer program for refinement of crystal structures*, University of Göttingen, Germany, **1997**; b) L. J. Farrugia, *J. Appl. Crystallogr.* **1999**, *32*, 837.

Received: October 28, 2004

 © 2005 Wiley-VCH Verlag GmbH & Co. KGaA, Weinheim

Lanthanide Complexes of Disulfoxide Ligands with Varied Configurations: Influence of Lanthanide Contraction on the Structures of the Complexes

Jian-Rong Li,[a] Ruo-Hua Zhang,[a] and Xian-He Bu*[a,b]

Keywords: Disulfoxides / Lanthanides / Lanthanide contraction / Ligand configuration change / X-ray diffraction

Four new disulfoxide-Ln^{III} complexes, $[Ln(\mathbf{L})_2(NO_3)_3]_n$ {Ln = La (**1**), $n = n$; Ln = Gd (**2**), Dy (**3**) and Yb (**4**), $n = 2$}, have been prepared by the reaction of $Ln(NO_3)_3{\cdot}nH_2O$ with *meso*-1,3-bis(ethylsulfinyl)propane (*meso*-**L**) in methanol/triethylorthoformate, and their solid-state structures were characterized by IR spectroscopy, elemental analyses and X-ray diffraction. Complex **1** is a 1D double-bridged chain in which the La^{III} ions are ten-coordinate and the **L** ligands adopt both *meso* and *rac* configurations, and a bis-monodentate bridging coordination mode. While complexes **2**–**4** have isostructural dinuclear structures, in which the Ln^{III} ions are nine-coordinate and the ligands show two types of coordination fashions and configurations: bis-monodentate bridging with a *meso*-configuration, and monodentate coordination with a *rac*-configuration. The structural differences between **1** and **2**–**4** indicate the influence of lanthanide contraction on the complex structures. In addition, a change in configuration of the ligand occurs when it reacts with metal ions.
(© Wiley-VCH Verlag GmbH & Co. KGaA, 69451 Weinheim, Germany, 2005)

Introduction

Metal-organic architectures continue to be a subject of intense current interest,[1] because of their fascinating structural diversities and potential applications, such as in functional materials.[2] The rare earth coordination compounds may have interesting luminescence and magnetic properties,[3] and lanthanide cations usually have high coordination numbers and exhibit coordination diversity and flexibility.[4] As is well known, the structures of metal-organic architectures are influenced by many factors, such as the coordination nature of the metal ions and ligands, and reaction conditions etc.[5] Lanthanide contraction is also such a factor that affects the structures of the complexes, and is a significant research topic not only in structural control but also in the theoretical exploration of the electronic configuration of lanthanide elements.[6]

In recent years, we synthesized many metal-organic coordination compounds using flexible disulfoxide ligands,[7] which are a type of ditopic bridging ligands and have many intriguing features, such as a bidentate ditopic nature, and diastereomeric *meso* and *rac* forms. Some successful examples have shown that such ligands are able to generate unusual coordination polymers with unique structures that are governed not only by the spacer lengths and terminal groups of the ligands but also by counter anions and even solvents used in the synthesis.[7] As a continuation of such investigations, we report herein the synthesis and structures of a series of disulfoxide lanthanide complexes, $[Ln(\mathbf{L})_2(NO_3)_3]_n$ {Ln = La (**1**) $n = n$; Ln = Gd (**2**), Dy (**3**) and Yb (**4**), $n = 2$; **L** = 1,3-bis(ethylsulfinyl)propane} (for the *meso* isomer, see Scheme 1). The effect of lanthanide contraction on the structures of the complexes will also be discussed.

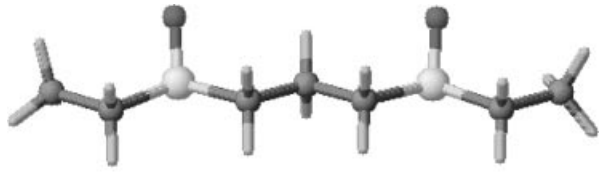

meso-L

Scheme 1.

Results and Discussion

Syntheses and General Characterization

The *meso*-**L** ligand melts in a narrow temperature range of 101–103 °C, which indicates that it is a pure *meso* isomer. Complexes **1**–**4** were prepared by the reactions of *meso*-**L** with $Ln(NO_3)_3{\cdot}nH_2O$ in MeOH at room temperature with the use of triethylorthoformate as a dehydrating reagent. The results of the elemental analysis are consistent with the molecular formula evaluated by X-ray diffraction analyses for **1**–**3**, and complex **4** has a similar composition to that of complexes **2** or **3**. Such complexes are soluble in DMF and DMSO and slightly soluble in CH_3OH and CH_3CN, but almost insoluble in H_2O and acetone. The IR spectrum

[a] Department of Chemistry, Nankai University, Tianjin 300071, P. R. China
Fax: +86-22-23502458
E-mail: buxh@nankai.edu.cn
[b] The State Key Lab of Rare Earth Materials and Chemistry, Peking University, Beijing 100871, P. R. China

of **1** has a $\nu_{S=O}$ band at 986 cm^{-1}; this band occurs at a lower frequency than that of the free ligand (1017 cm^{-1}). The peak at this frequency disappeared in **1** indicating that all the O atoms of the ligands are coordinated to the La^{III} ions.[8] While in the spectra of **2**–**4**, vibration peaks at around 986 and 1010 cm^{-1} were observed, which indicates the partial coordination of the O atoms of the S=O entities. These results are further confirmed by X-ray structural determinations. In addition, the existence of chelating bidentately coordinated nitrate anions in the complexes was also confirmed by their IR spectra.

Structural Descriptions and Discussion

Complexes **1–3** were characterized by X-ray crystallography. The selected bond lengths and angles are listed in Table 1 and Table 2.

The X-ray single crystal structure reveals that complex $[La(\mathbf{L})_2(NO_3)_3]_n$ (**1**) has a 1D, double-bridging chain structure. As shown in Figure 1, the La^{III} center binds to ten O atoms, four from S=O moieties of four distinct **L** ligands and six from three chelating coordinated nitrate anions. The overall geometry is best described as a distorted bi-capped square anti-prism with two O atoms of two distinct nitrate anions in the capped positions. As listed in Table 1, the bond lengths of the La–O bonds that involve the O atoms of the four bis-monodentate **L** ligands are different [2.378(5)–2.656(5) Å with a mean value of 2.522(5) Å], perhaps as a result of steric hindering. The La–O bond lengths of the chelating nitrate anions are in the range 2.579(3)–2.749(4) Å with an average value of 2.667(4) Å, which is longer than that of the disulfoxide ligands. The *cis* bond angles around the La^{III} ion lie in a range from 47.0(2) to 85.1(2)°.

Table 1. Selected bond lengths [Å] and angles [°] for $[La(\mathbf{L})_2(NO_3)_3]_n$ (**1**).[a]

La(1)–O(1)[b]	2.601(5)	La(1)–O(7)	2.602(5)
La(1)–O(2)	2.656(5)	La(1)–O(8)	2.749(4)
La(1)–O(3)	2.378(5)	La(1)–O(9)	2.579(3)
La(1)–O(4)[b]	2.451(3)	La(1)–O(11)	2.705(5)
La(1)–O(6)	2.683(5)	La(1)–O(12)	2.684(3)
O(1)[b]–La(1)–O(2)	76.2(2)	O(3)–La(1)–O(8)	71.2(2)
O(1)[b]–La(1)–O(4)[b]	75.8(2)	O(4)[b]–La(1)–O(9)	73.7(1)
O(1)[b]–La(1)–O(6)	80.9(2)	O(4)[b]–La(1)–O(8)	69.3(2)
O(1)[b]–La(1)–O(9)	72.1(1)	O(6)–La(1)–O(7)	47.0(2)
O(1)[b]–La(1)–O(11)	70.9(1)	O(6)–La(1)–O(9)	70.9(1)
O(2)–La(1)–O(3)	84.2(2)	O(6)–La(1)–O(11)	62.2(2)
O(2)–La(1)–O(4)[b]	76.7(1)	O(6)–La(1)–O(12)	70.4(1)
O(2)–La(1)–O(11)	64.1(2)	O(7)–La(1)–O(8)	65.9(2)
O(2)–La(1)–O(12)	77.9(2)	O(7)–La(1)–O(9)	77.5(2)
O(3)–La(1)–O(4)[b]	85.1(2)	O(7)–La(1)–O(12)	63.9(2)
O(3)–La(1)–O(7)	78.7(2)	O(8)–La(1)–O(9)	46.6(1)
O(3)–La(1)–O(12)	72.2(2)	O(11)–La(1)–O(12)	46.4(1)

[a] Only those related to the higher occupancy part of the disordered atoms are listed. [b] Symmetry code: $x - 1/2, -y - 3/2, z - 1/2$.

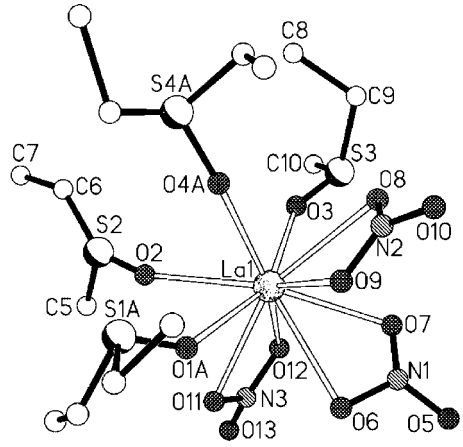

Figure 1. A view of the coordination environment of the La^{III} center in **1** (symmetry code A: $x - 1/2, -y - 3/2, z - 1/2$). The hydrogen atoms and lower occupancy part of the disordered atoms were omitted for clarity).

Table 2. Selected bond lengths [Å] and angles [°] for $[Ln(\mathbf{L})_2(NO_3)_3]_2$ (Ln = Gd, **2**; Dy, **3**).[a]

	2	**3**		**2**	**3**
Ln(1)–O(1)	2.331(2)	2.303(3)	Ln(1)–O(11)	2.505(3)	2.485(3)
Ln(1)–O(2)	2.323(2)	2.298(3)	Ln(1)–O(12)	2.494(2)	2.465(3)
Ln(1)–O(3)	2.306(2)	2.275(3)	S(1)–O(1)	1.515(3)	1.519(3)
Ln(1)–O(5)	2.465(3)	2.437(3)	S(2)–O(2)	1.531(2)	1.528(3)
Ln(1)–O(6)	2.512(2)	2.488(3)	S(3)–O(3)	1.529(2)	1.525(3)
Ln(1)–O(8)	2.522(3)	2.497(3)	S(4)–O(4)	1.472(5)	1.470(5)
Ln(1)–O(9)	2.489(3)	2.443(3)			
O(1)–Ln(1)–O(2)	81.99(8)	81.8(1)	O(3)–Ln(1)–O(8)	73.65(8)	73.2(1)
O(1)–Ln(1)–O(5)	89.72(9)	90.3(1)	O(3)–Ln(1)–O(12)	79.86(8)	80.3(1)
O(1)–Ln(1)–O(6)	76.30(8)	76.3(1)	O(5)–Ln(1)–O(6)	50.79(9)	51.7(1)
O(1)–Ln(1)–O(9)	77.33(8)	77.7(1)	O(5)–Ln(1)–O(11)	74.44(9)	74.1(1)
O(1)–Ln(1)–O(11)	73.38(8)	72.8(1)	O(5)–Ln(1)–O(12)	72.36(9)	72.5(1)
O(2)–Ln(1)–O(3)	82.51(9)	82.3(1)	O(8)–Ln(1)–O(9)	50.75(8)	51.0(1)
O(2)–Ln(1)–O(6)	77.99(8)	77.4(1)	O(8)–Ln(1)–O(12)	74.1(1)	73.9(1)
O(2)–Ln(1)–O(8)	77.44(9)	77.2(1)	O(9)–Ln(1)–O(11)	72.5(1)	72.7(1)
O(2)–Ln(1)–O(9)	80.37(9)	80.7(1)	O(9)–Ln(1)–O(12)	89.40(9)	88.4(1)
O(3)–Ln(1)–O(5)	80.75(9)	80.5(1)	O(11)–Ln(1)–O(12)	50.49(8)	51.1(1)
O(3)–Ln(1)–O(6)	76.23(8)	76.0(1)			

[a] Only those related to the higher occupancy part of the disordered atoms are listed.

 © 2005 Wiley-VCH Verlag GmbH & Co. KGaA, Weinheim

In complex **1**, the ligands **L** act as bis-monodentate bridges to link the adjacent metal centers, and two such ligands link two La^{III} centers to form a 16-membered ring, which expends along the crystallographic *a* direction to form a 1D intercrossed, double-bridging chain (Figure 2). The distance between two metal centers within the ring unit is 8.898 Å. The S atoms of the ligands in **1** are disordered, each of which are refined over two positions with the occupying ratio of 6:4. Based on the higher occupation part, the ligands adopt three kinds of configurations: the *R*,*S*, *R*,*R*, and *S*,*S* forms (Figure 2); the same side chain takes one kind of configuration, either *meso* or *rac*. For the *rac* ligands, the *S*,*S* and *R*,*R* forms are arranged alternatively. The synchronous existence of two kinds of configurations in the complex reveals that the disulfoxide ligand **L** inverts part of its original configuration from *R*,*S* to either the *R*,*R* or the *S*,*S* form. The O coordination adopts a *trans*-*trans* arrangement; the La–O–S–C torsion angles range from 94.0(8) to 174.8(2)° (containing the atoms of the disordered parts). In addition, such 1D chains are parallel to each other in the crystal.

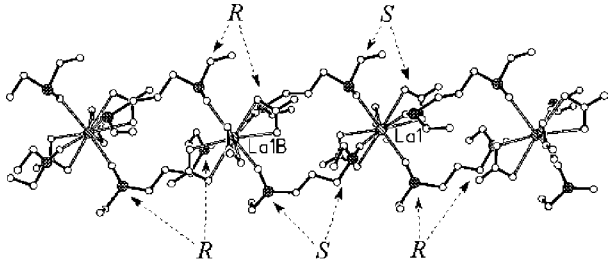

Figure 2. The 1D chain structure of **1** showing the configurations of the S atoms**.** The hydrogen atoms and lower occupancy part of the disordered atoms were omitted for clarity.

Complexes **2** and **3** are isostructural and the structures are composed of neutral dinuclear $[Ln(\mathbf{L})_2(NO_3)_3]_2$ (Ln = Gd, Dy, respectively) entities. The central metal ion is nine-coordinate and binds to three O atoms of distinct **L** ligands and six O atoms of chelating nitrate groups to give a highly disordered, tricapped, trigonal prism configuration (Figure 3). The Ln–O bond lengths involving the S=O and bidentate nitrate groups are in the normal ranges (Table 2), and lie in a more narrow range than those of **1**. The *cis* bond angles around the Ln^{III} ions range from 50.49(8) to 89.72(9)° for **2** and 51.0(1) to 90.3(1)° for **3**, respectively. As shown in Figure 4, in the binuclear entity, the two metal centers are linked by two bis-monodentate bridging ligands to form a twisted 16-membered ring with an Ln···Ln separation of 8.287 Å for **2** and 8.265 Å for **3**. It is interesting to note that the ligands **L** exhibit two kinds of coordination modes: bis-monodentate bridging and monodentate, which is a rare case in disulfoxide complexes.[7c] One of the S atoms of each monodentate disulfoxide is disordered in **2** and **3** (the occupying ratio is 9:1). On the basis of the main part of the disordered entities, the ligands adopt three kinds of configurations, *R*,*S*, *S*,*S*, and *R*,*R* forms (*meso* and *rac*) in **2** and **3**: two monodentate ligands adopt the *R*,*R* and *S*,*S* form, and two bridging ligands adopt the *meso* form. The two S atoms of the bridging ligands around the same metal center adopt the same *S* or *R* configuration, but differ from that of the mono-coordinated one. Thus, as a whole, complexes **2** and **3** are mesomeric. The O=S···S=O quasi-torsion angles between two sulfoxide groups of the ligands are 101.5 and 102.9° for the bridging ligands, and 22.8 and 22.5° for the mono-coordinated ligand in **2** and **3**, respectively. All the O coordinations adopt a *trans*-*trans* arrangement, which is exhibited by the M–O–S–C torsion angles of 109.1–143.4° for **2** and 108.5–144.4° for **3**. In addition, such dinuclear molecules are arranged in an interparallel superposition fashion in the crystal.

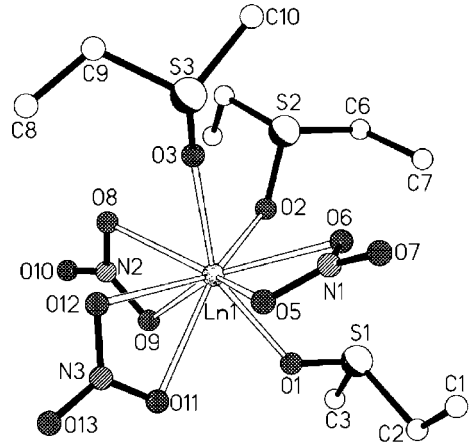

Figure 3. A view of the coordination environment of the Ln^{III} center in **2** and **3**. The hydrogen atoms and lower occupancy part of the disordered atoms were omitted for clarity.

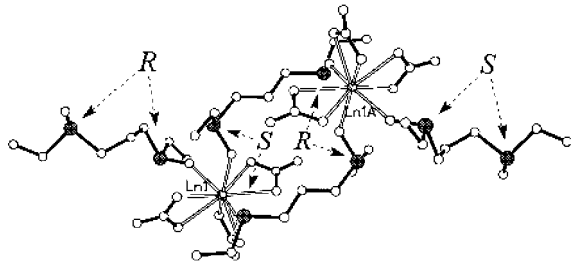

Figure 4. Dinuclear structures of **2** and **3** showing the configurations of the S atoms. The hydrogen atoms and lower occupancy part of the disordered atoms were omitted for clarity.

It should be noted that a partial configuration change of ligand **L** was observed at room temperature from *meso* to *rac* form (Scheme 2) when it reacted with lanthanide nitrate to form complexes with three stereoisomeric forms of the ligands. In some earlier investigations,[7a,9] a configurational change of the sulfoxide entities seems to occur at elevated temperatures (ca. 70–80 °C). This indicates that a metal-assisted configuration change of the disulfoxide compound may happen at room temperature.

 © 2005 Wiley-VCH Verlag GmbH & Co. KGaA, Weinheim

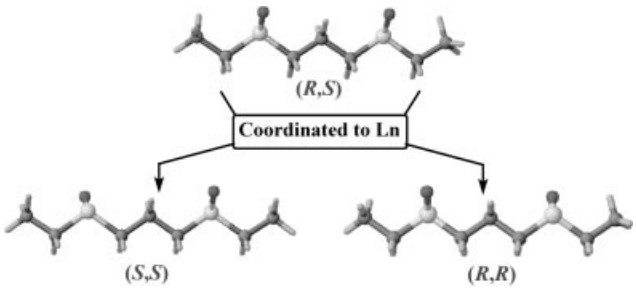

Scheme 2.

The structural differences between **1** and **2** and **3** may be attributed to the difference in the lanthanide ion radii, i.e. lanthanide contraction. In **1**, the La^{III} ion is larger so that it can adopt a ten-coordination mode that can lead to the coordination of four O atoms from the S=O groups. While in **2** and **3**, the radius of Gd^{III} [and Dy^{III}] is smaller than that of La^{III}, so only three sulfoxide O donors take part in the coordination. Thus, **1** has a 1D structure but **2** and **3** are dinuclear.

XRPD Results; Isostructural Determination of 3 and 4

In order to further confirm if **3** and **4** have similar structures, as well as if the crystal structure of **3** is truly representative of its bulk material, X-ray powder diffraction (XRPD) experiments were carried out on the as-synthesized samples. The XRPD experimental patterns of **3** and **4**, and the computer-simulated patterns of **3** are shown in Figure 5. From the simulated and experimental patterns, we can consider that the synthesized bulk material and the as-grown crystals are almost the same for complex **3**, although there are a few unindexed diffraction lines and lines that are slightly broadened relative to those simulated from the single-crystal data. From the similar XRPD experimental patterns of **3** and **4** together with the elemental analysis results and IR spectra, we can conclude that **3** and **4** should have similar structures.

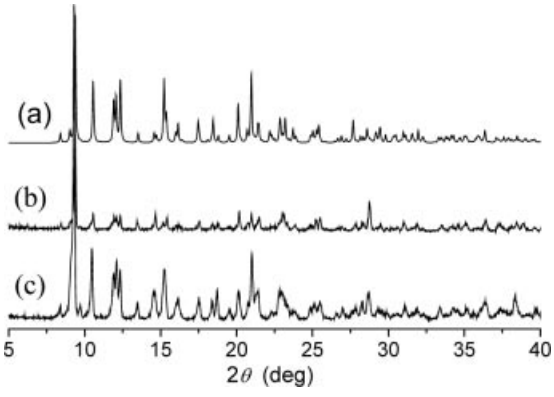

Figure 5. Powder X-ray diffraction patterns of **3** and **4**: (a) the simulated result of **3**, (b) the experimental result of **3,** and (c) the experimental result of **4**.

In addition, a suitable comparison can be made between **4** and a reported Yb^{III} complex, $[Yb(\mathbf{L}')_{1.5}(NO_3)_3]_n$,[7a] with a similar disulfoxide ligand, 1,2-bis(ethylsulfinyl)ethane (**L**′). Although **L**′ has a shorter spacer than **L**, the resulted complex has a 1D single-bridging chain structure. The structural difference may be attributed to the spacer lengths of the ligands.

In summary, a series of new Ln-disulfoxide complexes with 1D or dinuclear structures have been obtained by assembling $Ln(NO_3)_3$ and a flexible disulfoxide ligand. The structural differences between these complexes show the influence of lanthanide contraction on the structures of the complexes. The ligands exhibit different configurations in the complexes, which is interesting for the investigation of disulfoxide metal complexes. In addition, a change in configuration of the ligand at room temperature has been observed when it reacts with Ln^{III} ions.

Experimental Section

Materials and General Methods: All reagents for synthesis and analyses were of analytical grade and used as received. Elemental analyses were performed on a Perkin–Elmer 240C analyzer. IR spectra (KBr pellets) were recorded with a FT-IR 170SX (Nicolet) spectrometer. ^{1}H NMR spectra were measured on a Bruker AC-P500 spectrometer (300 MHz) at 25 °C with tetramethylsilane as the internal reference. Melting point measurements were measured on an X-4 melting point meter.

Synthesis of the Ligand: 1,3-Bis(ethylsulfinyl)propane was synthesized according to a similar method reported previously[10] by oxidizing the bis(thio) precursor 1,3-bis(ethylthio)propane (obtained by the reaction of 1,3-bis(bromo)propane with sodium ethylthiolate). The *meso* isomer was separated from the isomeric mixture products by fractional crystallization from acetone. Yield: 50%. M.p. 101–103 °C. ^{1}H NMR ($CDCl_3$): δ = 2.66–2.78 (m, 8 H, $–CH_2–S–CH_2–$), 2.35 (t, 2 H, $C–CH_2–C$), 1.37 (t, 6 H, $CH_3–$) ppm. IR: 2963 (s), 1427 (m), 1042 (m), 1017 (s), 974 (m), 785 (m), 650 (m) cm^{-1}.

Synthesis of Complexes 1–4: The four complexes were prepared at room temperature according to the following method. A solution of $Ln(NO_3)_3{\cdot}nH_2O$ (0.3 mmol) in methanol (10 mL) was added to a solution of *meso*-**L** (171 mg, 0.6 mmol) in methanol/triethylorthoformate (2:3, 15 mL). The reaction mixture was stirred for about 30 min and filtered to give a colorless solution. Slow solvent evaporation of the resulting solution gave rise to white solid products that contained a few colorless single crystals suitable for X-ray analysis.

$[La(L)_2(NO_3)_3]_n$ (1): Yield: 85 mg, 40%. $C_{14}H_{32}LaN_3O_{13}S_4$ (717.58): calcd. C 23.43, H 4.49, N 5.86; found C 23.11, H 5.02, N 5.65. IR: 2975 (m), 2938 (m), 2506 (w), 1987 (w), 1730 (w), 1631 (w), 1473 (s), 1410 (m), 1384 (s), 1315 (s), 1291(s), 1131 (w), 1027 (s), 986 (s), 967 (s), 816 (m), 780 (w), 736 (m), 627 (w) cm^{-1}.

$[Gd(L)_2(NO_3)_3]_2$ (2): Yield: 97 mg, 44%. $C_{14}H_{32}GdN_3O_{13}S_4$ (735.92): calcd. C 22.85, H 4.38, N 5.71; found C 22.33, H 5.54, N 5.95. IR: 2976 (m), 2940 (m), 2508 (w), 1988 (w), 1732 (w), 1633 (w), 1476 (s), 1410 (m), 1384 (s), 1317 (s), 1296 (s), 1131 (w), 1029 (s), 1009 (m), 986 (s), 968 (s), 817 (m), 779 (w), 739 (m), 629 (w) cm^{-1}.

$[Dy(L)_2(NO_3)_3]_2$ (3): Yield: 104 mg, 47%. $C_{14}H_{32}DyN_3O_{13}S_4$ (741.17): calcd. C 22.69, H 4.35, N 5.67; found C 22.25, H 5.25, N 5.86. IR: 2976 (m), 2941 (m), 2509 (w), 1989 (w), 1733 (w), 1630 (w), 1487 (s), 1410 (m), 1384 (s), 1318 (s), 1299 (s), 1131 (w), 1030

 © 2005 Wiley-VCH Verlag GmbH & Co. KGaA, Weinheim

Table 3. Crystallographic data and structure refinement summary for complexes **1**–**3**.

	$[La(\mathbf{L})_2(NO_3)_3]_n$ (**1**)[a]	$[Gd(\mathbf{L})_2(NO_3)_3]_2$ (**2**)	$[Dy(\mathbf{L})_2(NO_3)_3]_2$ (**3**)
Empirical formula	$C_{14}H_{32}LaN_3O_{13}S_4$	$C_{28}H_{64}Gd_2N_6O_{26}S_8$	$C_{28}H_{64}Dy_2N_6O_{26}S_4$
Formula weight	717.58	735.92	1482.33
Temperature [K]	293(2)	293(2)	293(2)
Crystal system	monoclinic	monoclinic	monoclinic
Space group	*Cc*	$P2_1/n$	$P2_1/n$
a [Å]	18.526(7)	11.800(4)	11.787(4)
b [Å]	10.819(4)	18.281(6)	18.177(6)
c [Å]	16.532(6)	13.182(4)	13.059(4)
β [°]	122.546(5)	99.201(5)	99.393(5)
Volume [Å^3]	2793(2)	2807(2)	2761(2)
Z	4	2	2
Crystal size [mm]	0.26×0.20×0.18	0.26×0.20×0.20	0.28×0.24×0.20
$D_{calcd.}$ [g cm^{-3}]	1.706	1.741	1.783
μ [mm^{-1}]	1.889	2.720	3.071
F(000)	1448	1476	1484
θ range [°]	2.29–26.40	2.07–26.40	2.74–26.43
Reflections measured	6301	15823	15652
Unique reflections	3135	5718	5644
R_{int}	0.0504	0.0464	0.0270
Parameters	376	352	361
Goodness of fit on F^2	1.025	1.016	1.033
R[b]/wR[c]	0.0529/0.1341	0.0453/0.1153	0.0278/0.0650
$\Delta_{max, min}$ [e Å^{-3}]	0.672, –0.652	0.831, –0.893	0.981, –0.579

[a] The "twin" refinement was used [Flack parameter = 0.35(2)]. [b] $R = \Sigma(||F_o| - |F_c||)/\Sigma|F_o|$. [c] $wR = [\Sigma w(|F_o|^2 - |F_c|^2)^2/\Sigma w(F_o^2)]^{1/2}$.

(s), 1011 (m), 986 (s), 968 (s), 817 (m), 779 (w), 741 (m), 630 (w) cm^{-1}.

$[Yb(L)_2(NO_3)_3]_2$ (4): Yield: 88 mg, 39%. $C_{14}H_{32}YbN_3O_{13}S_4$ (751.70): calcd. C 22.37, H 4.29, N 5.59; found C 21.51, H 5.14, N 6.19. IR: 2977 (m), 2941 (m), 2513 (w), 1992 (w), 1735 (w), 1630 (w), 1487 (s), 1409 (m), 1384 (s), 1323 (s), 1299 (s), 1131 (w), 1032 (s), 1010 (s), 990 (s), 969 (s), 816 (m), 778 (w), 745 (m), 630 (w) cm^{-1}.

X-ray Crystallography: Single-crystal X-ray diffraction for **1**–**3** was carried out with a Bruker Smart 1000 diffractometer. Intensities of reflections were measured by using graphite monochromatized Mo-K_α radiation (λ = 0.71073 Å) with ω-φ scan mode at room temperature. Unit cell dimensions were obtained with least-squares refinements, and semi-empirical absorption corrections were applied by using the SADABS program.[11] The structures were solved by direct methods by combining successive difference Fourier syntheses.[12] The final refinement was performed by full-matrix least-squares methods on F^2 with the SHELXL-97 program package.[12] For **1**, the ligand is highly disordered, and some C and S atoms were refined in two different positions (occupation ratio 6:4) and restrained. In **2** and **3**, some S and O atoms were also refined in two different positions with partial occupation factors of 0.9 and 0.1, respectively. Some hydrogen atoms of the ligands in **1**–**3** cannot be added due to the above-mentioned disorder. All added hydrogen atoms were included in calculated positions and refined with fixed thermal parameters riding on the parent atoms. Crystallographic data and experimental details for structural analysis are summarized in Table 3. CCDC-252924–252926 contain the supplementary crystallographic data for **1**–**3**. These data can be obtained free of charge from The Cambridge Crystallographic Data Centre via www.ccdc.cam.ac.uk/data_request/cif.

The X-ray powder diffraction patterns (XRPD) of **3** and **4** were recorded on a Rigaku D/Max-2500 diffractometer, operated at 40 kV and 100 mA, by using a Cu-target tube and a graphite monochromator. Fixed scatter and divergence slits of 1° and a 0.3-mm receiving slit were used. The intensity data were recorded by continuous scan in a $2\theta/\theta$ mode from 3° to 60°, with a step size of 0.02° and a scan speed of 8° min^{-1}. Simulation of the XRPD spectra was carried out by the single-crystal data and diffraction-crystal module of the commercially available Cerius2 program.[13]

Acknowledgments

This work was supported by the National Natural Science Funds for Distinguished Young Scholars (No. 20225101) and NSFC (No. 20373028).

[1] For examples: a) S. Kitagawa, R. Kitaura, S. Noro, *Angew. Chem. Int. Ed.* **2004**, *43*, 2334–2375; b) M. Ruben, J. Rojo, F. J. Romero-Salguero, L. H. Uppadine, J. M. Lehn, *Angew. Chem. Int. Ed.* **2004**, *43*, 3644–3662; c) C. Janiak, *Dalton Trans.* **2003**, 2781–2804; d) S. S. Sun, A. J. Lees, *Coord. Chem. Rev.* **2002**, *230*, 170–191.

[2] For examples: a) S. R. Batten, K. S. Murray, *Coord. Chem. Rev.* **2003**, *246*, 103–130; b) O. R. Evans, W. B. Lin, *Acc. Chem. Res.* **2002**, *35*, 511–522; c) L. H. Gade, *Acc. Chem. Res.* **2002**, *35*, 575–582; d) B. Moulton, M. J. Zaworotko, *Chem. Rev.* **2001**, *101*, 1629–1658; e) M. Edgar, R. Mitchell, A. M. Z. Slawin, P. Lightfoot, P. A. Wright, *Chem. Eur. J.* **2001**, *7*, 5168–5175; f) C. B. Aakeröy, A. M. Beatty, D. S. Leinen, K. R. Lorimer, *Chem. Commun.* **2000**, 935–936.

[3] For examples: a) N. M. Shavaleev, L. P. Moorcraft, S. J. A. Pope, Z. R. Bell, S. Faulkner, M. D. Ward, *Chem. Commun.* **2003**, 1134–1135; b) B. Q. Ma, D. S. Zhang, S. Gao, T. Z. Jin, C. H. Yan, G. X. Xu, *Angew. Chem. Int. Ed.* **2000**, *39*, 3644–3646; c) J. Lengendziewicz, M. Borzechowska, G. Oczko, G. Meyer, *New J. Chem.* **2000**, *24*, 53–59; d) L. Ma, O. R. Evans, B. M. Foxman, W. Lin, *Inorg. Chem.* **1999**, *38*, 5837–5840.

[4] For examples: a) Y. P. Ren, L. S. Long, B. W. Mao, Y. Z. Yuan, R. B. Huang, L. S. Zheng, *Angew. Chem. Int. Ed.* **2003**, *42*, 532–535; b) F. A. A. Paz, J. Klinowski, *Chem. Commun.* **2003**, 1484–1485; c) L. G. Westin, M. Kritikos, A. Caneschi, *Chem. Commun.* **2003**, 1012–1013; d) T. M. Reineke, M. Eddaoudi, D. Moler, M. O'Keefe, O. M. Yaghi, *J. Am. Chem. Soc.* **2000**, *122*, 4843–4844.

 © 2005 Wiley-VCH Verlag GmbH & Co. KGaA, Weinheim

[5] a) J. D. Dunitz, *Chem. Commun.* **2003**, 545–548; b) J. Fan, M. H. Shu, T. Okamura, Y. Z. Li, W. Y. Sun, W. X. Tang, N. Ueyama, *New J. Chem.* **2003**, *27*, 1307–1309.
[6] a) E. A. Quadrelli, *Inorg. Chem.* **2002**, *41*, 167–169; b) L. Pan, X. Y. Huang, J. Li, Y. G. Wu, N. W. Zheng, *Angew. Chem. Int. Ed.* **2000**, *39*, 527–530; c) F. T. Edelmann, V. Lorenz, *Coord. Chem. Rev.* **2000**, *209*, 99–160; d) L. Maron, O. Eisenstein, *J. Phys. Chem. A* **2000**, *104*, 7140–7143.
[7] a) J. R. Li, X. H. Bu, R. H. Zhang, *Inorg. Chem.* **2004**, *43*, 237–244; b) J. R. Li, R. H. Zhang, X. H. Bu, *Cryst. Growth Des.* **2004**, *4*, 219–221; c) J. R. Li, M. Du, X. H. Bu, R. H. Zhang, *J. Solid State Chem.* **2003**, *173*, 20–26; d) X. H. Bu, W. Weng, M. Du, W. Chen, J. R. Li, R. H. Zhang, L. J. Zhao, *Inorg. Chem.* **2002**, *41*, 1007–1010; e) X. H. Bu, W. Weng, J. R. Li, W. Chen, R. H. Zhang, *Inorg. Chem.* **2002**, *41*, 413–415; f) X. H. Bu, W. Chen, S. L. Lu, R. H. Zhang, D. Z. Liao, M. Shionoya, F. Brisse, J. Ribas, *Angew. Chem. Int. Ed.* **2001**, *40*, 3201–3203; g) R. H. Zhang, B. Q. Ma, X. H. Bu, H. G. Wang, X. K. Yao, *Polyhedron* **1997**, *16*, 1123–1127; h) R. H. Zhang, B. Q. Ma, X. H. Bu, H. G. Wang, X. K. Yao, *Polyhedron* **1997**, *16*, 1787–1792.
[8] a) M. Calligaris, *Coord. Chem. Rev.* **2004**, *248*, 351–375; b) H. B. Kagan, B. Ronan, *Rev. Hetero. Chem.* **1992**, *7*, 92–103.
[9] a) J. C. Bao, P. X. Shao, R. J. Wang, H. G. Wang, X.-K. Yao, *Polyhedron* **1995**, *14*, 927–933; b) F. C. Zhu, P. X. Shao, X. K. Yao, R. J. Wang, H. G. Wang, *Inorg. Chim. Acta* **1990**, *171*, 85–88.
[10] R. H. Zhang, Y. L. Zhan, J. T. Chen, *Synth. React. Inorg. Met.-Org. Chem.* **1995**, *25*, 283–292.
[11] G. M. Sheldrick, *SADABS, Siemens Area Detector Absorption Corrected Software*, University of Göttingen, Germany, **1996**.
[12] G. M. Sheldrick, *SHELXTL Version 5.1. Program for Solution and Refinement of Crystal Structures*, University of Göttingen, Germany, **1997**.
[13] *Cerius2*, Molecular Simulation Incorporated, San Diego, CA **2001**.

Received: November 3, 2004

 © 2005 Wiley-VCH Verlag GmbH & Co. KGaA, Weinheim

Synthesis, Characterization and Photophysical Properties of Novel Dinuclear Silver(I) and Mononuclear Palladium(II) Complexes with 1,2-Bis[(anthracen-9-ylmethyl)amino]ethane

Guo-qi Zhang,[a] Guo-qiang Yang,*[a] Lan-ying Yang,[a] Qing-qi Chen,[b] and Jin-Shi Ma[a]

Keywords: N ligands / Palladium / Photophysics / Silver

Silver(I) (**3**) and palladium(II) (**4**) complexes of 1,2-bis-[(anthracen-9-ylmethyl)amino]ethane have been synthesized and structurally characterized. X-ray crystal structure analysis reveals that compound **3** exists as a dinuclear tris(ligand) complex with formula $[Ag_2(\mathbf{2})_3]\cdot 2NO_3$, in which each silver center is three-coordinate to form a slightly distorted planar-trigonal geometry with three nitrogen donors originating from two distinct ligands. Compound **4**, on the other hand, is a mononuclear bis(ligand) complex with formula $[Pd(\mathbf{2})_2]\cdot 2OAc$, in which the palladium center is four-coordinate with four nitrogen donors originating from two distinct ligands to form a square-planar geometry. In crystals of both **3** and **4** strong intermolecular edge-to-face C–H···π packing interactions are observed, which contribute to stabilize the crystalline solid. Studies of the photophysical properties of these compounds (**3**, **4**, and ligand **2**) show apparent fluorescence quenching effect by introduction of metal ions and likely "excimer" emission of anthracene in the crystalline solid.
(© Wiley-VCH Verlag GmbH & Co. KGaA, 69451 Weinheim, Germany, 2005)

Introduction

Multichromophoric supramolecular architectures have been receiving increasing interest in recent years[1,2] because of their potential applications in the areas of biomedicine, molecular recognition, fluorescent sensors, and material sciences.[3–8] Anthryl and pyrenyl polyamine systems have been found to have potential uses in anion recognition, metal ion fluorescent sensors, as well as pH sensors.[9–11] Although a lot of anthryl polyamines and their metal ion complexes have been extensively investigated,[12] complexes of Ag^I and Pd^{II} are still unknown, hence it might be of considerable importance to study the structures of these complexes and correlate the structure and luminescent properties of the resultant Ag^I and Pd^{II} complexes due to the promise of polyamine systems for use as optical chemical sensors.[9] In this paper, we report the synthesis and characterization of 1,2-bis[(anthrancen-9-ylmethyl)amino]ethane (**2**) and its corresponding Ag^I complex **3** and Pd^{II} complex **4**, as well as the results of photophysical investigation on these systems.

Results and Discussion

Synthesis

The Schiff base **1** was synthesized in excellent yield by condensation of ethylenediamine with 2 equiv. of anthracene-9-carbaldehyde in DMF/MeOH at reflux. Upon treating **1** with an excess amount of $NaBH_4$ in CH_2Cl_2/MeOH at room temperature, the corresponding diamine **2** was obtained in good yield (Scheme 1). Both compounds **1** and **2** were fully characterized by combustion analysis, mass spectrometry, and ^1H and ^{13}C NMR spectroscopy.

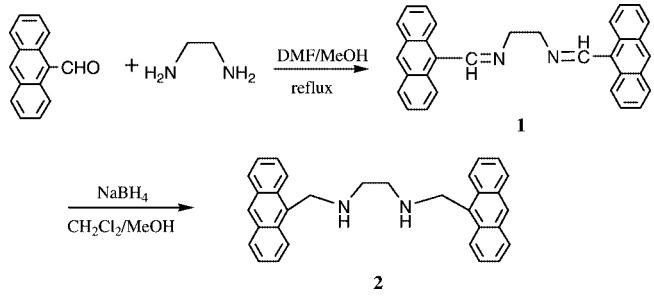

Scheme 1.

Ligand **2** was treated with silver nitrate and palladium acetate in CH_2Cl_2/MeOH (2:1, v/v) to afford the corresponding complexes **3** and **4** in yields of 70% and 64%, respectively. Crystals of **3** and **4** are reasonably stable in the mother liquors in the dark, while they slowly decompose upon exposure to light and air for a long period. Complex **4** was found to have good solubility in most polar solvents such as methanol, ethanol, dichloromethane, chloroform, acetonitrile, THF, DMF, and DMSO, while complex **3** is soluble in dichloromethane, chloroform, acetonitrile, DMF, and DMSO and slightly soluble in THF, methanol, ethanol, acetone etc.

[a] Center for Molecular Science, Institute of Chemistry, Chinese Academy of Sciences,
Beijing 100080, China
Fax: +86-10-8261-7315
E-mail: gqyang@iccas.ac.cn
[b] BioMarin Pharmaceutical, Inc.,
46 Galli Drive, Novato, CA 94949, USA

 DOI: 10.1002/ejic.200400926 © 2005 Wiley-VCH Verlag GmbH & Co. KGaA, Weinheim

Crystal Structure of 3

The silver complex **3** crystallizes in the triclinic system with space group $P\bar{1}$. The unit cell contains two crystallographically independent dinuclear tris(ligand) complexes, three methanol molecules, and four nitrate counterions. An ORTEP drawing of the dinuclear complex cation $[Ag_2(\mathbf{2})_3]^{2+}$ is shown in Figure 1, and selected bond lengths and angles are given in Table 1. The structure consists of two Ag^I centers spanned by three ligands to form a unique dinuclear tris(ligand) complex. Each silver center is three-coordinate and adopts a slightly distorted planar-trigonal geometry with three nitrogen atoms, two of which are from one ligand, and one from the other ligand. Furthermore, two Ag atoms have almost identical coordination environments, with Ag–N bond lengths in the range 2.239(5)–2.474(5) Å. All the bond lengths are among the ranges of those found in analogous Ag^I complexes reported hitherto.[13] Moreover, the N–Ag1(A)–N bond angles of 76.6(2)° for N1(A)–Ag1(A)–N2(A), 141.4(19)° for N1(A)–Ag1(A)–N3(A), and 140.4(2)° for N2(A)–Ag1(A)–N3(A) are identical to the corresponding N–Ag1–N bond angles. In addition, two NO_3^- anions are present in the unit cell as counteranions; the Ag–O bond length is 3.761 Å, which is much longer than that of a normal Ag–O bond.[14] In the crystal of **3**, none of the anthryl moieties show intramolecular or intermolecular face-to-face π···π interactions, although significant intermolecular edge-to-face C–H···π contacts are present, and the shortest distance between an edge ring hydrogen atom and the anthracene ring center of another molecule is 2.833 Å [the angle C–H···M(mid) is 156.9°], which is in the usual range for C–H···π interactions.[15] Two adjacent molecules which show C–H···π interactions are depicted in Figure 2, where it can be seen that the C–H···π interactions serve to stabilize the crystalline solid.

Table 1. Selected bond lengths [Å] and angles [°] for complex **3**.

Ag(1)–N(3)	2.239(5)	Ag(2)–N(5)	2.338(5)
Ag(1)–N(1)	2.296(6)	Ag(2)–N(4)	2.431(6)
Ag(1)–N(2)	2.474(6)	Ag(2)–N(6)	2.234(5)
N(3)–Ag(1)–N(1)	1.44(19)	N(6)–Ag(2)–N(5)	146.19(19)
N(3)–Ag(1)–N(2)	140.4(2)	N(6)–Ag(2)–N(4)	133.94(18)
N(1)–Ag(1)–N(2)	76.6(2)	N(5)–Ag(2)–N(4)	77.6(2)
C(15)–N(1)–C(16)	109.2(6)	C(17)–N(2)–C(18)	114.8(6)
C(15)–N(1)–Ag(1)	117.3(5)	C(17)–N(2)–Ag(1)	100.4(4)
C(16)–N(1)–Ag(1)	109.2(5)	C(18)–N(2)–Ag(1)	128.9(5)
C(47)–N(3)–Ag(1)	117.2(4)	C(48)–N(3)–Ag(1)	114.2(4)

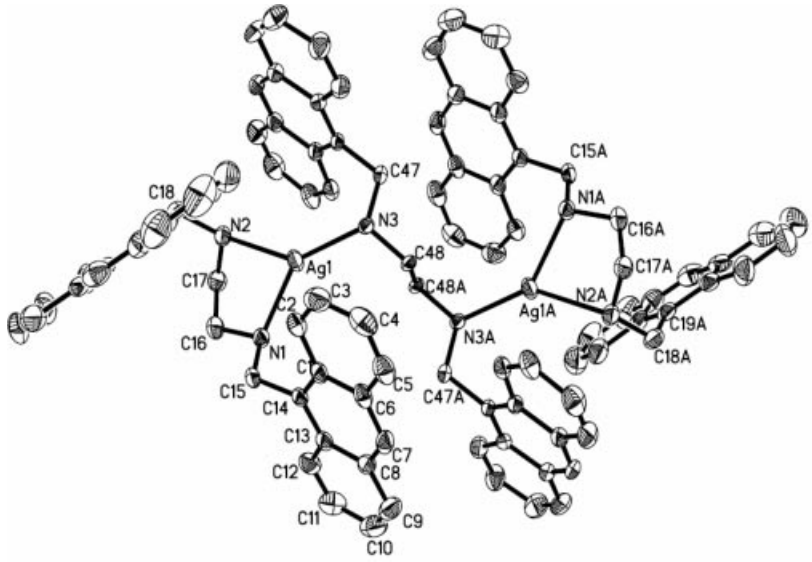

Figure 1. An ORTEP drawing of the complex cation of **3** with thermal ellipsoids at 30% probability. Hydrogen atoms, methanol, and NO_3^- counterions have been omitted for clarity.

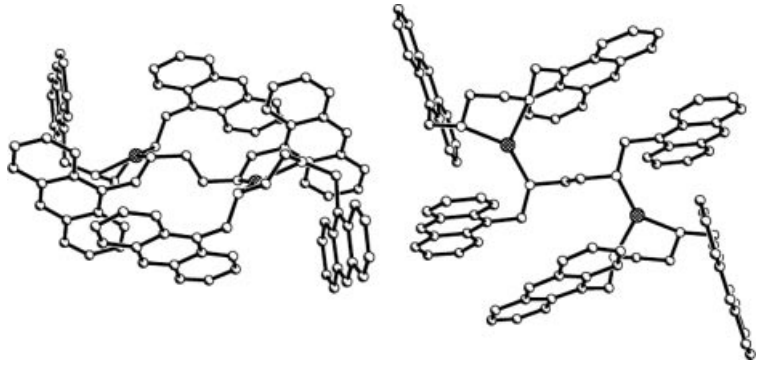

Figure 2. Two adjacent molecules in the crystal packing of **3** showing the intermolecular edge-to-face C–H···π interactions.

 © 2005 Wiley-VCH Verlag GmbH & Co. KGaA, Weinheim

Crystal Structure of 4

The palladium complex **4** also crystallizes in the triclinic system with space group $P\bar{1}$. The unit cell contains seven crystallographically independent methanol molecules and two acetate anions. An ORTEP view of the mononuclear complex cation $[Pd(\mathbf{2})_2]^{2+}$ is shown in Figure 3, and selected bond lengths and angles are given in Table 2. In the crystal, the palladium center is four-coordinate to two distinct ligands to form a slightly distorted square-planar geometry. Due to the steric hindrance of the bulky anthracene group, the Pd–NH bond lengths are found to be 2.061, 2.068, 2.071, and 2.089 Å, respectively, which are slightly longer than those distances found in regular (amino)Pd^{II} (Pd–NH) complexes.[16] Interestingly, in the crystals of **4**, very strong aromatic/aromatic interactions with intermolecular edge-to-face C–H···π packing are observed [the distance between one hydrogen atom from the center ring of one anthryl unit and another molecular anthracene ring center is 2.703 Å, and the angle C–H···M(mid) is 158.1°] in contrast to **3**, which are comparable to previously reported strong C–H···π interactions (Figure 2 and Figure 4).[15]

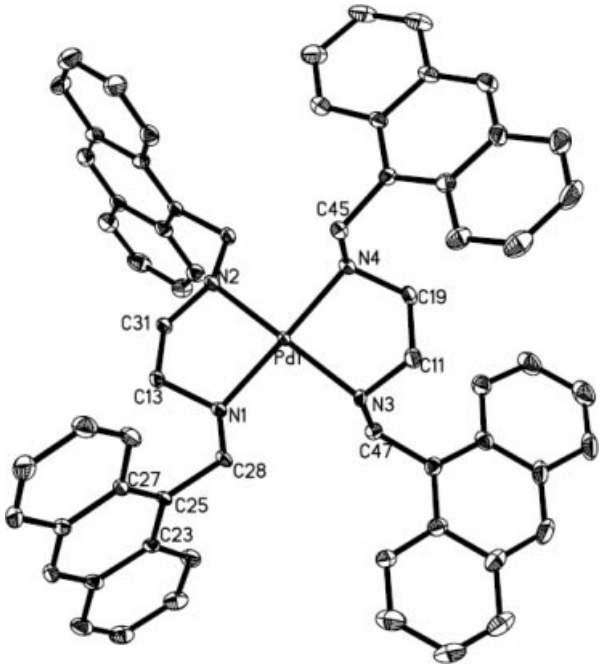

Figure 3. ORTEP view of the complex cation of **4** with thermal ellipsoids at 30% probability. Hydrogen atoms, methanol, and OAc^- counterions have been omitted for clarity.

Table 2. Selected bond lengths [Å] and angles [°] for complex **4**.

Pd–N(3)	2.058(5)	N(2)–C(17)	1.472(8)
Pd–N(2)	2.069(5)	N(2)–C(18)	1.512(8)
Pd–N(4)	2.060(5)	N(3)–C(49)	1.494(8)
Pd–N(1)	2.095(5)	N(3)–C(50)	1.488(7)
N(1)–C(16)	1.468(8)	N(4)–C(48)	1.502(7)
N(1)–C(15)	1.503(7)	N(4)–C(47)	1.495(7)
N(3)–Pd–N(2)	174.65(19)	C(17)–N(2)–C(18)	113.8(5)
N(3)–Pd–N(4)	84.49(19)	C(17)–N(2)–Pd	105.9(4)
N(2)–Pd–N(4)	96.0(2)	C(18)–N(2)–Pd	111.8(4)
N(3)–Pd–N(1)	95.39(19)	C(49)–N(3)–C(50)	113.0(5)
N(2)–Pd–N(1)	84.73(19)	C(49)–N(3)–Pd	106.5(3)
N(4)–Pd–N(1)	173.97(19)	C(50)–N(3)–Pd	113.7(4)
C(16)–N(1)–C(15)	114.5(5)	C(48)–N(4)–C(47)	112.2(4)
C(16)–N(1)–Pd	106.7(4)	C(48)–N(4)–Pd	105.8(3)
C(15)–N(1)–Pd	109.7(3)	C(47)–N(4)–Pd	116.1(4)

Spectroscopic and Photophysical Properties

^{1}H NMR Studies

The ^{1}H NMR spectrum of complex **3** in $CDCl_3$ shows a single set of proton resonances that can be fully assigned, which suggests that it exists as a single species in solution. Compared to the corresponding free ligand, complex **3** shows upfield shifts of 0.55–0.59 ppm for the protons of the CH_2 groups and 0.14–0.38 ppm for the protons of the anthracene rings, probably because of the intermolecular C–H···π interactions resulting from the molecular aggregation in concentrated solution, which is consistent with the case of the crystalline solid. Several attempts to measure the ^{1}H NMR spectrum of pure complex **4** in $CDCl_3$ or CD_3CN gave no satisfactory results for the signals of a single species; the spectrum shows the signals of both free ligand and a small amount of complex, which indicates that complex **4** is not very stable in solution and exists as an

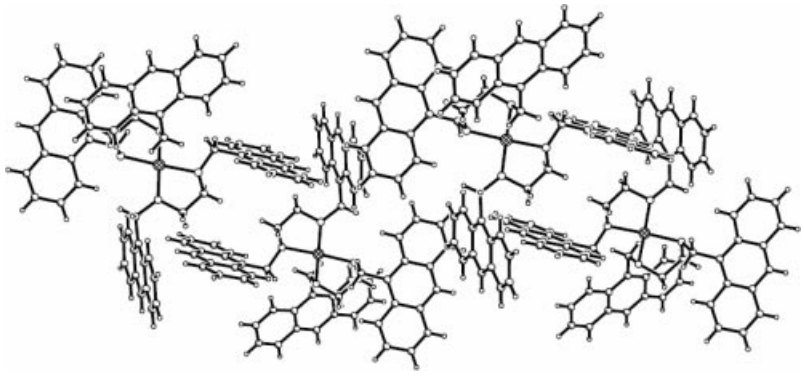

Figure 4. Packing model along the *b* axis in the crystals of complex **4** cations showing the intermolecular edge-to-face C–H···π interactions.

 © 2005 Wiley-VCH Verlag GmbH & Co. KGaA, Weinheim

equilibrium between binding and disassociation due to the low binding constant of palladium ions and ligand **2**. Thus, we cannot measure the steady-state photophysics of **4** in solution, although the solid-state photoluminescence was obtained.

Photophysical Properties of 2 and 3 in Solution

The steady-state absorption and fluorescence emission spectra of **3** were measured and compared with those of the free ligand **2**. The results are reported in Table 3. The electronic absorption spectra of **2** and **3** obtained in acetonitrile at 5 μM concentration display the typical absorptions of the anthracene chromophore in the range 320–400 nm with a very slight (approximately 1–2 nm) bathochromic shift due to the introduction of silver ions (Figure 5). Moreover, in contrast to **2**, the UV/Vis spectrum of **3** shows remarkably strong absorptions at about 300 nm, which are absent in the case of the ligand as well as the silver salt under the same conditions, indicating a strong interaction between the ligand and silver ion (Figure 5).

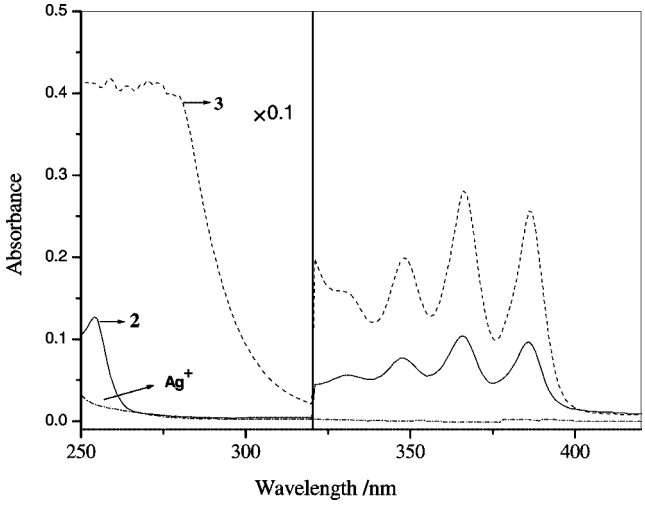

Figure 5. Electronic absorption spectra of ligand **2**, its silver complex **3**, and free Ag^+ ions in acetonitrile at room temperature (conc. 5 μM).

The fluorescence spectra of compounds **2** and **3** were recorded under the same conditions, and are given in Figure 6. The fluorescence excitation spectra were obtained by monitoring the emission at 415 nm. For **3**, except for the typical excitation spectra of the anthracene chromophore, a significantly strong excitation band in the region from 260 to 320 nm, with a maximum absorption at 293 nm, is consistent with the absorption spectra, which indicates that more efficient electronic energy transfer may take place from the metal-centered excited state to the lower energy excited state of the anthracene center.

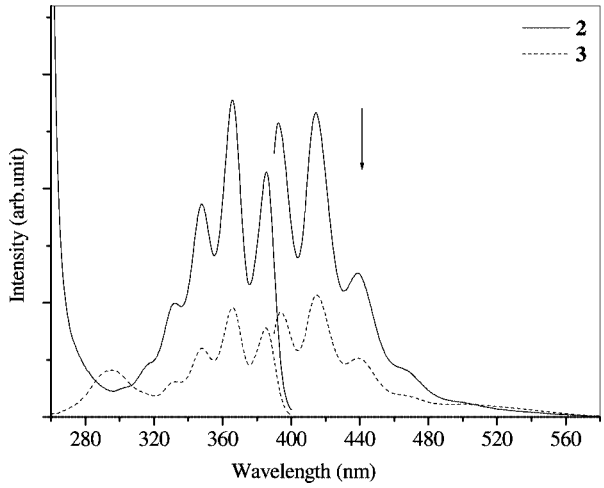

Figure 6. Fluorescence exitation (monitored at 415 nm) and emission spectra (excited at 367 nm) of **2** and **3** in acetonitrile at room temperature (conc. 5 μM).

The fluorescence intensity of the ligand **2** was found to be significantly smaller than the emission of the anthracene moiety due to a photoinduced intramolecular electron transfer (PET) process[17] from the amine lone pairs to the anthracene group, which is in agreement with previously reported anthryl or pyrenyl polyamine systems.[7,18] Upon excitation of the anthracene $S_0 \rightarrow S_1$ transition (λ_{ex} = 367 nm), emission from the anthracene chromophore is evident as a Frank–Condon vibrational process with an origin at 390 nm and a maximum intensity at 415 nm, which is in agreement with the corresponding excitation spectra. Furthermore, complex **3** displays the same quartet emission bands, in spite of the obvious difference of emission intensity. The quantum yields obtained for compounds **2** and **3** are 1.54×10^{-2} and 2.42×10^{-3}, respectively (relative to quinine sulfate in 0.1 N H_2SO_4[19]). The quantum yield of **3** is lower than that of **2**, which is indicative of a chelation-enhanced fluorescence quenching (CHEQ) effect, as reported previously for similar systems.[18] Furthermore, the measurement of fluorescence decay determines the fluorescence

Table 3. Steady-state spectroscopic data for ligand **2** and its complex **3** in CH_3CN.

Compound	Abs λ_{max} [nm]	ε_{max} ($M^{-1}cm^{-1}$]	Emission λ_{max} [nm]	Quantum yield, Φ_f	Decay times[a] τ [ns] (%)[b]	χ^2
2	366	19750	415	1.54×10^{-2}	1.3 (81.5%) 8.5 (18.5%)	1.227
3	367	56160	415	2.42×10^{-3}	1.7 (62.3%) 4.7 (37.7%)	1.193

[a] λ_{ex} = 367 nm, λ_{em} = 415 nm. [b] The percentage was obtained from: for the decay, Fit = $A + B_1 \cdot e^{(-t/\tau 1)} + B_2 \cdot e^{(-t/\tau 2)}$, $\%(\tau_1) = B_1/(B_1 + B_2)$.

 © 2005 Wiley-VCH Verlag GmbH & Co. KGaA, Weinheim

decay behavior of the ligand and complex systems (see Figure 7 for the decay profiles). The fluorescence decays of both **2** and **3** were best fitted to double exponential decay processes.

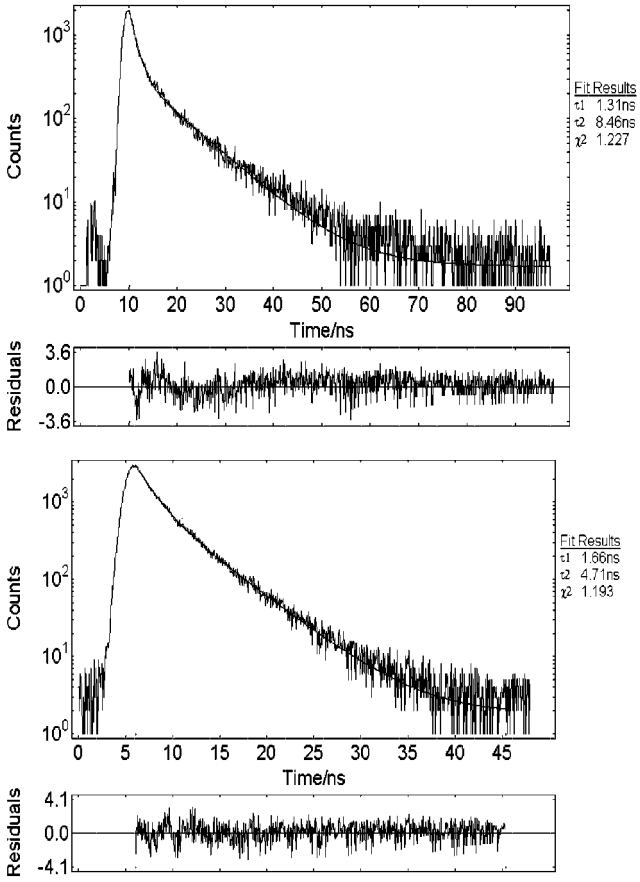

Figure 7. Fluorescence decay profiles of **2** (top) and **3** (bottom) in acetonitrile at an excitation wavelength of 367 nm. Emission monitored at 415 nm.

The transient absorption spectra of ligand **2** and its complex **3** were measured in argon-saturated acetonitrile at room temperature with concentrations of 5×10^{-4} M for **2**, and 2×10^{-4} M for **3**. The excitation wavelength generated by a nanosecond laser was 355 nm. The transient absorption spectrum of ligand **2**, depicted in Figure 8a, can be assigned to the triplet-triplet absorption (T_1-T_n absorption) of anthracene monomer based on the similarity of the spectra obtained in solutions.[20] It is known that the T_1-T_n absorption spectrum has a maximum peak at 423 nm with a molar extinction coefficient value of 64700 $M^{-1}cm^{-1}$ in cyclohexane.[20] In the given anthryldiamine compound, the transient absorption spectrum keeps the characteristic of the triplet-triplet absorption of anthracene monomer with maxima at about 400 nm and 423 nm. It decays without changing its shape and no new absorption band appears as a result of the decay, which suggests that no transient absorption of an intramolecular or intermolecular excimer occurs under these conditions. The transient absorption spectrum of complex **3** is shown in Figure 8b. No distinct absorption band appears at around 400 nm, except for a broad peak between 400 and 460 nm, and the maximum of the T_1-T_n absorption is still at about 423 nm. This may be due to the formation of new triplet species in acetonitrile from the metal-incorporated anthryldiamine **3**, although it maintains partially the characteristic of ligand **2**. In acetonitrile, the lifetime of the triplet species of ligand **2** was estimated to be 20 ± 1 μs based on the fitting to a single exponential decay curve. Obviously, a much faster triplet decay of the ligand occurs than that of triplet-state anthracene alone in solution.[20] The triplet lifetime of **3** was determined as 5.7 ± 0.1 μs with good single exponential decays, which shows that more efficient quenching occurs for the triplet species of the silver complex relative to that of the free ligand.

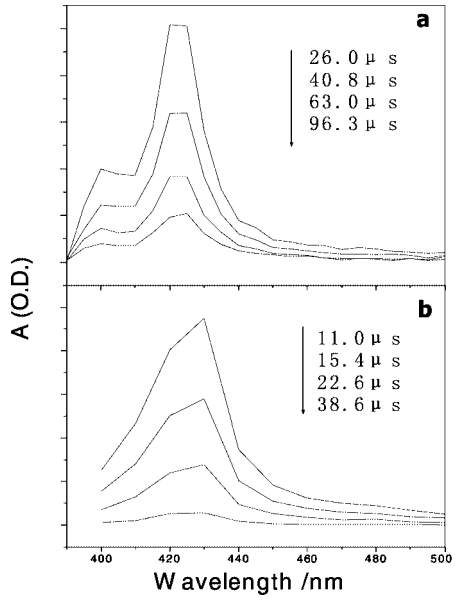

Figure 8. Transient absorption spectra of ligand **2** (a) and its silver complex **3** (b) in Ar-saturated acetonitrile at room temperature.

Photoluminescence in the Solid State

We measured the solid-state photoluminescence of both the ligand and complexes at room temperature. Although we could not measure the photophysical properties of complex **4** in solution due to its instability, the measurement of the solid-state photoluminescence is still helpful for understanding the emission behavior of the complex. More significantly, the solid-state spectra usually exhibit the features of the aggregated state of molecules in combination with the crystal structure in the solid state. Obviously, both the free ligand and complexes are photoluminescent in the solid state (Figure 9) when excited at 366 nm. However, the emission position is remarkably bathochromic relative to that in solution, which may be attributed to the increased intermolecular interaction as a result of closer packing of the molecules in the solid state, and, interestingly, both the ligand and complexes display emission even in the longer wavelength range (>500 nm), which is possibly attributed to an "excimer" emission of anthracene[21,22] reminiscent of the

 © 2005 Wiley-VCH Verlag GmbH & Co. KGaA, Weinheim

structural characterization of the two complexes depicted above. The obviously weak emission of **4** in the solid state may be due to a CHEQ effect similar to the situation of **3** in solution.

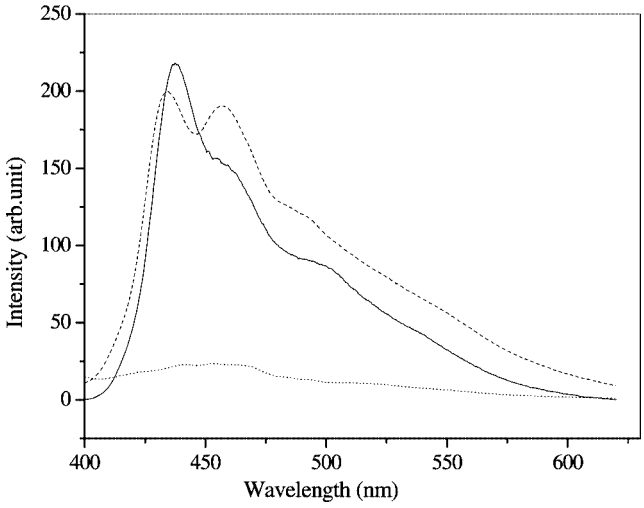

Figure 9. Solid-state photoluminescence spectra of **2** (solid), **3** (dot), and **4** (dash) at room temperature.

Conclusions

In summary, we have synthesized a new anthryldiamine ligand **2** as well as the corresponding silver complex **3** and palladium complex **4**. In the solid state, complex **3** forms a dinuclear tris(ligand) supramolecular architecture, while **4** is a mononuclear bis(ligand) complex. The preferential coordination in these complexes matches the requirements of the steric hindrance of the bulky ligands and the nature of the metal ions. Significantly strong intermolecular edge-to-face C–H···π packing interactions are observed in crystals of both **3** and **4**, which contribute to stabilize the crystalline solid. Complex **3** is very stable while **4** partially disassociates in solution due to its low binding constant. Photophysical studies have shown that the PET process is present in ligand **2** and an efficient CHEQ effect is also observed for its metal complexes. The transient absorption spectra allowed us to determine the absorption features and decay lifetimes of the triplet species of **2** and **3**. The solid-state photoluminescence studies showed the bathochromic emission relative to that in solution and likely "excimer" emission of anthracene in the crystalline solid, thereby indicating the presence of intermolecular interactions, in agreement with the results of ^{1}H NMR studies and the crystal-structure analysis.

Experimental Section

Materials and General Methods: All the reagents were commercially available. Anthracene-9-carbaldehyde, ethylenediamine, sodium borohydride, silver nitrate, and palladium acetate were used without further purification. Solvents for syntheses were purified according to standard methods, while those for spectral measurements were purchased as spectrophotometric grade. Samples for C, H, N analyses were dried under vacuum and the analyses were performed with a Carlo Erba-1106 Instrument. ^{1}H NMR spectra were measured with a Bruker dmx 300 MHz NMR spectrometer at room temperature in $CDCl_3$ with tetramethylsilane as the internal reference. The ESI and MALDI-TOF MS measurements were carried out with a Bruker APEX II instrument. UV/Vis absorption spectra were obtained with a Hitachi UV-3010 absorption spectrophotometer. Steady-state excitation and emission spectra were recorded with a Hitachi F-2500 fluorescence spectrophotometer. Fluorescence lifetime was detected at 415 nm with a fluorescence lifetime analytical spectrometer (Erdinburgh FLS-920) and the samples were excited at 367 nm (maximum absorption wavelength). Time-resolved transient absorption spectra were measured with an Edinburgh LP920 nanosecond flash photolysis instrument.

1,2-Bis[(anthracen-9-ylmethylene)amino]ethane (1): Anthracene-9-carbaldehyde (9.5 g, 46.1 mmol) was dissolved in 120 mL of DMF/MeOH (1:5, v/v), and then heated at reflux. A solution of ethylenediamine (1.6 mL, 23.0 mmol) in 10 mL of methanol was added dropwise to this mixture with vigorous stirring. A yellow precipitate appeared after a few minutes, and the mixture was refluxed for an additional 4 h. Upon cooling, the yellow precipitate was separated by filtration under reduced pressure, then washed with a few drops of DMF and a large volume of methanol. The product was recrystallized from CH_3OH/CH_2Cl_2 to give yellow plates. Yield: 9.2 g (92%), m.p. 229–230°C. ^{1}H NMR (300 MHz, $CDCl_3$, 25°C, TMS): δ = 4.52 (s, 4 H, CH_2), 7.11 (dd, J = 7.8, J = 7.8 Hz, 4 H, anthryl-H), 7.36 (dd, J = 7.8, J = 7.2 Hz, 4 H, anthryl-H), 7.96 (d, J = 8.4 Hz, 4 H, anthryl-H), 8.41 (s, 2 H, anthryl-H), 8.45 (d, J = 7.2 Hz, 4 H, anthryl-H), 9.50 (s, 2 H, imine-H) ppm. ^{13}C NMR (75 Hz, $CDCl_3$): δ = 31.0, 63.1, 125.0, 125.2, 126.5, 128.6, 129.3, 130.0, 131.2, 162.4 ppm. MALDI-TOF-MS: m/z = 436 [M^+]. $C_{32}H_{24}N_2$ (436.2): calcd. C 88.04, H 5.54, N 6.42; found C 87.58, H 5.56, N 6.29.

1,2-Bis[(anthracen-9-ylmethyl)amino]ethane (2): $NaBH_4$ (1.3 g) was dissolved in 10 mL of anhydrous methanol and then added in small portions to a suspension of **1** (1.3 g, 3 mmol) in 150 mL of CH_2Cl_2/MeOH (2:1, v/v) at 50 °C under N_2 over 2 h. The mixture turned gradually to a clear yellowish color and the resulting solution was allowed to react at room temperature overnight. The solvent was then removed under reduced pressure and the residue was treated with excess water. The insoluble materials were then collected by suction, and recrystallized twice from CH_2Cl_2 to give light-yellow needles. Yield: 0.9 g, 68%, m.p. 185–186 °C. ^{1}H NMR (300 MHz, $CDCl_3$, 25°C TMS): δ = 3.07 (s, 4 H, CH_2), 4.72 (s, 4 H, CH_2), 7.44 (m, 8 H, anthryl-H), 8.00 (d, J = 6.0 Hz, 4 H, anthryl-H), 8.29 (d, J = 7.89 Hz, 4 H, anthryl-H), 8.40 (s, 2 H, anthryl-H) ppm. ^{13}C NMR (75 Hz, $CDCl_3$): δ = 45.5, 49.6, 124.0, 124.8, 126.0, 127.1, 129.0, 130.1, 131.4 ppm. MALDI-TOF-MS: m/z = 440 [M^+]. $C_{32}H_{28}N_2 \cdot 1/4H_2O$ (444.7): calcd. C 86.28, H 6.40, N 6.29; found C 86.30, H 6.41, N 6.20.

Ag^I Complex 3: A solution of **2** (132 mg, 0.3 mmol) in CH_2Cl_2 (20 mL) was slowly added to 10 mL of a methanolic solution of $AgNO_3$ (25.5 mg, 0.15 mmol). The resulting colorless solution was stirred at room temperature for 30 min and then filtered. The clear filtrate was allowed to stand in the dark at room temperature, and after about two weeks colorless block-like single crystals suitable for X-ray analysis were collected by filtration. An analytical sample was dried under vacuum to remove the solvents. Yield: 87 mg (70%) based on $AgNO_3$. M.p. 161–162 °C. ^{1}H NMR (300 MHz,

 © 2005 Wiley-VCH Verlag GmbH & Co. KGaA, Weinheim

$CDCl_3$, 25°C TMS): δ = 2.52 (s, 12 H, CH_2), 4.13 (s, 12 H, CH_2), 7.27–7.33 (m, 24 H, anthryl-H), 7.74 (d, J = 8.1 Hz, 12 H, anthryl-H), 7.91 (d, J = 7.89 Hz, 12 H, anthryl-H), 8.08 (s, 6 H, anthryl-H) ppm. MALDI-TOF-MS: m/z = 767.4 [M – 2 NO_3]$^{2+}$. $C_{96}H_{84}Ag_2N_2$·$2NO_3$·CH_3OH (1690.5): calcd. C 68.79, H 5.24, N 6.62; found C 68.91, H 5.24, N, 6.65.

Pd^{II} Complex 4: Complex **4** was prepared by a procedure similar to that of **3**. A solution of **2** (132 mg, 0.3 mmol) in CH_2Cl_2 (20 mL) was slowly added to 10 mL of a methanolic solution of $Pd(OAc)_2$ (33.7 mg, 0.15 mmol). The resulting orange solution was stirred at room temperature for 30 min and then filtered. The clear filtrate was allowed to stand at 5 °C, and after about one week, light-orange, block-like single crystals suitable for X-ray analysis were obtained. An analytical sample was dried under vacuum. Yield: 101 mg, 64%; M.p. 119–121 °C. ESI-MS: m/z = 985.5 [M – 2 OAc – H]$^+$. $C_{64}H_{68}N_4Pd$·2OAc·CH_3OH·H_2O (1154.4): calcd. C 71.71, H 5.93, N 4.85; found C 71.30, H 5.60, N 4.73.

X-ray Crystallography: Crystals suitable for X-ray diffraction studies were obtained by slow evaporation of the solvents from CH_2Cl_2/MeOH solutions. Accurate unit-cell parameters were determined by a least-squares fit of 2θ values measured for 200 strong reflections. Intensity data sets were measured with a Bruker Smart 1000 CCD or Rigaku Raxis Rapid IP diffractometer with Mo-K_α radiation (λ = 0.71073 Å) at room temperature. The intensities were corrected for Lorentz and polarization effects, but no corrections for extinction were made. All structures were solved by direct methods. The non-hydrogen atoms were located in successive difference Fourier syntheses. The final refinement was performed by full-matrix least-squares methods with anisotropic thermal parameters for non-hydrogen atoms on F^2. The hydrogen atoms were added theoretically as riding on the appropriate atoms. Crystallographic data and experimental details for structure analyses are summarized in Table 4. CCDC-230566 (**3**) and -230567 (**4**) contain the supplementary crystallographic data for this paper. These data can be obtained free of charge from The Cambridge Crystallographic Data Centre via www.ccdc.cam.ac.uk/data_request/cif.

Table 4. Crystallographic data for complexes **3** and **4**.

	3	**4**
Empirical formula	$C_{96}H_{84}Ag_2N_8O_6$	$C_{75}H_{83}N_4O_{11}Pd$
Formula mass	1658.46	1322.85
Color	colorless	pale yellow
Crystal system	triclinic	triclinic
Space group	$P\bar{1}$	$P\bar{1}$
T [K]	293(2)	293(2)
λ [Å]	0.71073	0.71073
a [Å]	14.497(7)	12.978(3)
b [Å]	16.595(9)	14.094(3)
c [Å]	17.707(9)	18.590(4)
α [°]	85.859(9)	80.59(3)
β [°]	77.817(8)	84.13(3)
γ [°]	75.575(8)	84.23(3)
V [Å^3]	4032(4)	3324.7(11)
Z	4	2
F(000)	1770	1390
ρ_{calc} [g cm^{-3}]	1.408	1.321
Goodness-of-fit on F^2	1.021	0.998
μ [mm^{-1}]	0.551	0.344
R[a]	0.0625	0.0778
$wR2$[b]	0.1449	0.2066

[a] $R = \Sigma(F_o - F_c)/\Sigma(F_o)$. [b] $wR2 = \Sigma w(F_o^2 - F_c^2)^2/\Sigma w(F_o^2)^2]^{1/2}$.

Acknowledgments

This work was financially supported by NSFC (50221201) and the major state basic research development program (G2000078100) of China.

[1] a) J.-M. Lehn, *Supramolecular Chemistry*, Wiley-VCH, Weinheim, **1995**; b) V. Balzani, F. Scandola, *Supramolecular Photochemistry*, Ellis Horwood, New York, **1991**; c) M. R. Wasielewski, *Chem. Rev.* **1992**, *92*, 435–461; d) K. S. Schanze, D. B. Macqueen, T. A. Perkins, L. A. Cabana, *Coord. Chem. Rev.* **1993**, *122*, 63–89.

[2] J.-E. Sohna, P. Jaumier, F. Fages, *J. Chem. Res. (S)* **1999**, 134–135.

[3] a) S. Boyde, G. F. Strouse, W. E. Jones, T. J. Meryer, *J. Am. Chem. Soc.* **1989**, *111*, 7448–7454; b) S. L. Mecklenburg, K. A. Opperman, P. Chen, T. J. Meryer, *J. Phys. Chem.* **1996**, *100*, 15 145–15 151 and references cited therein.

[4] a) G. J. Wilson, A. Launikonis, W. H. F. Sasse, A. W. H. Mau, *J. Phys. Chem. A* **1997**, *101*, 4860–4866; b) W. E. Ford, M. A. J. Rodgers, *J. Phys. Chem.* **1992**, *96*, 2917–2920.

[5] a) P. Belser, R. Dux, M. Baak, L. De Cola, V. Balzani, *Angew. Chem. Int. Ed. Engl.* **1995**, *34*, 595–598; b) D. R. McDonald, R. J. Crutchley, *Inorg. Chem.* **1994**, *33*, 1899–1906; c) J. Otsuki, N. Okuda, T. Amamiya, K. Araki, M. Seno, *Chem. Commun.* **1997**, 311–312.

[6] B. Bodenant, F. Fages, M. H. Delville, *J. Am. Chem. Soc.* **1998**, *120*, 7511–7519.

[7] R. Martínez-Máñez, F. Sancenón, *Chem. Rev.* **2003**, *103*, 4419–4476 and references cited therein.

[8] M. E. Huston, E. U. Akkaya, A. W. Czarnik, *J. Am. Chem. Soc.* **1989**, *111*, 8735–8737.

[9] a) G. De Santis, L. Fabbrizzi, M. Licchelli, A. Poggi, A. Taglietti, *Angew. Chem. Int. Ed. Engl.* **1996**, *35*, 202–204; b) L. Fabbrizzi, I. Faravelli, G. Francese, M. Licchelli, A. Perotti, A. Taglietti, *Chem. Commun.* **1998**, 971–972; c) L. Fabbrizzi, M. Licchelli, A. Perrotti, A. Poggi, G. Rabaioli, A. Taglietti, *J. Chem. Soc., Perkin Trans. 2* **2001**, 2108–2113; d) L. Fabbrizzi, M. Licchelli, F. Mancin, M. Pizzeghello, G. Rabaioli, A. Taglietti, P. Tecilla, U. Tonellato, *Chem. Eur. J.* **2002**, *8*, 94–101; e) F. Sancenón, A. Benito, J. M. Lloris, R. Martínez-Máñez, T. Pardo, J. Soto, *Helv. Chim. Acta* **2002**, *85*, 1505–1516; f) S. A. Van Arman, A. W. Czarnik, *J. Am. Chem. Soc.* **1990**, *112*, 5376–5377; g) S.-Y. Hong, A. W. Czarnik, *J. Am. Chem. Soc.* **1993**, *115*, 3330–3331.

[10] a) S. A. McFarland, N. S. Finney, *J. Am. Chem. Soc.* **2001**, *123*, 1260–1261; b) J. Kang, M. Choi, J. Y. Kwon, E. Y. Lee, J. Yoon, *J. Org. Chem.* **2002**, *67*, 4384–4386.

[11] a) P. Schwab, M. Levin, J. Michl, *Chem. Rev.* **1999**, *99*, 1863–1934; b) P. V. Bernhardt, E. G. Moore, M. J. Riley, *Inorg. Chem.* **2001**, *40*, 5799–5805; c) P. V. Bernhardt, G. A. Lawrance, T. W. Hambley, *J. Chem. Soc., Dalton Trans.* **1989**, 1059–1066; d) P. V. Bernhardt, E. G. Moore, M. J. Riley, *Inorg. Chem.* **2002**, *41*, 3025–3031; e) F. DeRosa, X. Bu, P. C. Ford, *Inorg. Chem.* **2003**, *42*, 4171–4178; f) M. A. Bernado, F. Pina, E. García-España, J. Latorre, S. V. Luis, J. M. Llinares, J. A. Ramírez, C. Soriano, *Inorg. Chem.* **1998**, *37*, 3935–3942.

[12] a) V. Balzani, M. Juris, M. Venturi, S. Campagna, S. Serrioni, *Chem. Rev.* **1996**, *96*, 759–834; b) J. E. Moser, P. Bonnôte, M. Grätzel, *Coord. Chem. Rev.* **1998**, *171*, 245–250; c) V. Balzani, M. Gómez-López, J. F. Stoddart, *Acc. Chem. Res.* **1998**, *31*, 405–414; d) R. Ballardini, V. Balzani, A. Credi, M. T. Gandolfi, M. Venturi, *Acc. Chem. Res.* **2001**, *34*, 445–455; e) D. Pomeranc, V. Heitz, J.-C. Chambron, J.-P. Sauvage, *J. Am. Chem. Soc.* **2001**, *123*, 12 215–12 221; f) G. Benkö, J. Kallioonen, J. E. I. Korppi-Tommola, A. P. Yartsev, V. Sundström, *J. Am. Chem. Soc.* **2002**, *124*, 489–493.

[13] a) X.-H. Bu, H. Liu, M. Du, K. M.-C. Wong, V. W.-W. Yam, M. Shionoya, *Inorg. Chem.* **2001**, *40*, 4143–4149; b) M. Hong,

 © 2005 Wiley-VCH Verlag GmbH & Co. KGaA, Weinheim

W. Su, R. Cao, M. Fujita, J. Lu, *Chem. Eur. J.* **2000**, *6*, 427–431; c) H. Arii, Y. Saito, Y. Funahashi, T. Ozawa, K. Jitsukawa, H. Masuda, *Eur. J. Inorg. Chem.* **2003**, 2917–2919.
[14] a) M.-L. Tong, X.-M. Chen, B.-H. Ye, L.-N. Ji, *Angew. Chem. Int. Ed.* **1999**, *38*, 2237–2240; b) B. S. Fox, M. K. Beyer, V. E. Bondybey, *J. Am. Chem. Soc.* **2002**, *124*, 13 613–13 623; c) I. Ino, L. P. Wu, M. Munakata, M. Maekawa, Y. Suenaga, T. Kuroda-Sowa, Y. Kitamori, *Inorg. Chem.* **2000**, *39*, 2146–2151.
[15] T. Steiner, *Angew. Chem. Int. Ed.* **2002**, *41*, 48–76 and references cited therein.
[16] a) R. Ahlrichs, M. Ballauff, K. Eichkorn, O. Hanemann, G. Kettenbach, P. Klüfers, *Chem. Eur. J.* **1998**, *4*, 835–844; b) K. Haas, E. M. Ethrenstorfer-Scäfers, K. Polnorn, W. Beck, *Eur. J. Inorg. Chem.* **1999**, 465–469.
[17] A. P. De Silva, R. A. D. D. Rupasinghe, *J. Chem. Soc., Chem. Commun.* **1985**, 1669–1670.
[18] a) J. A. Sclafani, M. T. Maranto, T. M. Sisk, S. A. Van Arman, *Tetrahedron Lett.* **1996**, *37*, 2193–2196; b) J. Yoon, N. E. Ohler, D. H. Vance, W. D. Aumiller, A. W. Czarnik, *Tetrahedron Lett.* **1997**, *38*, 3845–3848; c) F. Pina, M. A. Bernardo, E. Garcia-Espana, *Eur. J. Inorg. Chem.* **2000**, 2143–2157; d) F. Sancenón, A. B. Descalzo, J. M. Lloris, R. Martínez-Máñez, T. Pardo, M. J. Seguí, J. Soto, *Polyhedron* **2002**, *21*, 1397–1404.
[19] J. N. Demas, G. A. Crosby, *J. Phys. Chem.* **1971**, *75*, 991–1024.
[20] a) R. Bensasson, E. Land, *Trans. Faraday Soc.* **1971**, *67*, 1904–1915; b) K. Kikuchi, *Triplet-Triplet Absorption Spectra*, Bunshin Publishing, Tokyo, **1989**.
[21] a) T. Hayashi, N. Mataga, Y. Sakata, S. Misumi, N. Morita, J. Tanaka, *J. Am. Chem. Soc.* **1976**, *98*, 5910–5913; b) J. K. McVey, D. M. Shold, N. C. Yang, *J. Chem. Phys.* **1976**, *65*, 3375–3376; c) W. L. Jorgensen, D. L. Severance, *J. Am. Chem. Soc.* **1990**, *112*, 4768–4774; d) D. A. Evans, K. T. Chapman, D. T. Hung, A. T. Kawaguchi, *Angew. Chem. Int. Ed. Engl.* **1987**, *26*, 1184–1186 and references cited therein.
[22] a) I. Y. Chan, H. Ismail, B. Prass, D. Stehlik, *J. Chem. Phys.* **2002**, *117*, 4419–4427; b) Z. Fei, N. Kocher, C. J. Mohrschladt, H. Ihmels, D. Stalke, *Angew. Chem. Int. Ed.* **2003**, *42*, 783–787.
Received: November 3, 2004

 © 2005 Wiley-VCH Verlag GmbH & Co. KGaA, Weinheim

The 3D Channel Framework Based on Indium(III)–btec, and Its Ion-Exchange Properties (btec = 1,2,4,5-Benzenetetracarboxylate)

Zheng-zhong Lin,[a] Fei-long Jiang,[a] Da-qiang Yuan,[a] Lian Chen,[a] You-fu Zhou,[a] and Mao-chun Hong*[a]

Keywords: Indium / Benzenetetracarboxylate / Crystal structure / Ion exchange / Pyridine derivatives

Hydrothermal reactions of $InCl_3$ with pyromellitic dianhydride and pyridine derivatives produce three coordination polymers: $\{(HL)[In_3(btec)_2(OH)_2]\cdot L\}_n$ [btec = 1,2,4,5-benzenetetracarboxylate, L = 2-picoline (**1**), L = 4-picoline (**2**)] and $\{(Hdpea)[In_3(btec)_2(OH)_2]\}_n$ [dpea = 1,2-bis(4-pyridyl) ethane] (**3**). Single crystal X-ray diffraction and powder X-ray diffraction analyses reveal that compounds **1**–**3** are isostructural and possess the same 3D framework as 1D open channels. Thermal gravimetric studies show that compounds **1**–**3** are stable up to 300 °C. The guests of the protonated pyridine derivatives located at the channels in **1** and **2** can be fully exchanged by Ca^{2+} and Ba^{2+} ions.
(© Wiley-VCH Verlag GmbH & Co. KGaA, 69451 Weinheim, Germany, 2005)

Introduction

The construction of porous structures or open frameworks with new sizes, shapes, and chemical environments that can undergo solvent removal, solvent inclusion, solvent absorption, or ion exchange[1–4] represents one of the most challenging subjects in recent years. In this regard, various carboxylate-containing ligands, including 1,2,4,5-benzenetetracarboxylic acid (H_4btec), have been used in the assembly of such robust frameworks. H_4btec, which exhibits variation in the possible binding mode of the four acid groups and a strong tendency to form large, tightly bound metal cluster aggregates, has been applied as an organic component to construct porous coordination frameworks.[5] Moreover, the rigid conformation of H_4btec endows robustness to the resulting frameworks to make them thermally stable. With the aim of thoroughly investigating the coordination chemistry of H_4btec, we recently began studies on the assembly reactions of H_4btec with indium metal ions. The reason we selected indium(III) is that, in spite of the enormous number of coordination polymers assembled from divalent metal and H_4btec,[6–8] the field of indium(III) with btec ligands remains unexplored. Furthermore, it was postulated that the incorporation of trivalent metal ions might create diverse structures strikingly different from those containing divalent metal ions because of the increased valence charge of the metal centers. The indium ion is liable to hydrolyze, which limits its use in the construction of coordination polymers. However, by adding an appropriate basic reagent to deprotonate H_4btec and carefully controlling the reaction conditions, we have found that indium(III) ions can be used to construct the new frameworks. Herein we report three novel coordination polymers: $\{(HL)[In_3(btec)_2(OH)_2]\cdot L\}_n$ (**1**, L = 2-picoline; **2**, L = 4-picoline), and $\{(Hdpea)[In_3(btec)_2(OH)_2]\}_n$ [**3**, dpea = 1,2-bis(4-pyridyl)ethane]. Complexes **1**–**3** bear the same 3D channel frameworks. The protonated organic guests in complexes **1** and **2** can be fully exchanged by certain inorganic ions. Although a number of compounds based on {M–btc}[3c] or {M–1,4-bdc}[9] (M = metal ions, btc = 1,3,5-benzenetricarboxylate, and 1,4-bdc = 1,4-benzenedicarboxylate) systems are capable of guest exchange, the exchange behavior reported here is rarely found in the coordination polymers based on {M–btec}.

[a] State Key Laboratory of Structural Chemistry, Fujian Institute of Research on the Structure of Matter, Chinese Academy of Sciences, Graduate School of the Chinese Academy of Sciences, Fujian, Fuzhou 350002, China
Fax: +86-591-8371-4946
E-mail: hmc@fjirsm.ac.cn

Results and Discussion

Syntheses and Crystal Structures

The hydrolysis reaction of pyromellitic dianhydride under hydrothermal conditions gives H_4btec, which further aggregates with indium(III) ions to produce compounds **1**–**3**. The in situ method of using pyromellitic dianhydride to synthesize {M–btec} compounds has been reported before.[10] The preparation depends on the pH value of the starting reaction mixture. Pyridine derivatives are added to adjust the pH value and act as templates. So the amount of pyridine derivatives is vital, and the proper pH value ranges between 5 and 6. With a pH value lower than 3 the reaction systems of compounds **1**–**3** produce a byproduct with a 3D structure formulated as $[In_2(H_2btec)_2(OH)_2]_n\cdot 2n\,H_2O$.[11] Thus, to ensure the purity of compounds **1**–**3**, an excessive amount of pyridine derivatives is needed.

As compounds **1**–**3** possess the same framework, compound **2** is selected to represent their structures. There are two kinds of indium coordination environments: the In1 center is bonded to four oxygen atoms from four $btec^{3-}$ ligands, and to two μ_3-OH groups (O9 and its symmetrically equivalent atom) to form a distorted octahedral geometry. Two μ_3-OH groups occupy the axial positions of an octahedron. The In2 center is coordinated to five oxygen atoms from four $btec^{3-}$ ligands, and two μ_3-OH groups to form a pentagonal bipyramidal motif. The two axial positions are occupied by a μ_3-OH group and a carboxylate oxygen atom (Figure 1). The In–O distances range from 2.094(5) to 2.314(5) Å, compatible with those observed in other In^{III}–carboxylate complexes.[12] Bond valence sum (BVS) calculations[13] confirm that all indium ions have an oxidation state of +3. To balance the charge, O9 can be considered to be a μ_3-OH group. This assumption is confirmed by BVS for O9, which gives a result of 1.22. The four carboxylate arms of the btec ligand are all deprotonated, two of them bidentately bind to four indium ions, and the other two adopt the chelating bidentate mode and the monodentate mode (Figure 1). The two μ_3-OH groups bridge indium ions to form an In_4O_{22} tetranuclear cluster in which four indium ions (two In1 and two In2) are in a plane. The two μ_3-OH groups are located at both sides of the plane (Figure 2). If four tetranuclear clusters and eight btec ligands are conceptually viewed as edges, then a subunit similar to a right prism is obtained (Figure 3). Four In1 vertexes are connected by four btec groups to give the rhombic top side of the prism. All btec benzene rings are perpendicular to the top side. The centroids of the four benzene rings connected to the In1 vertexes lie above and below the top side. Above the top side are two neighboring btec benzene rings whose centroids are situated at $x = 0.12608$; the other two btec benzene rings below the top side are located at $x = -0.12608$ (Figure 4). These two positions are related through the centrosymmetric operation. This situation can also be found

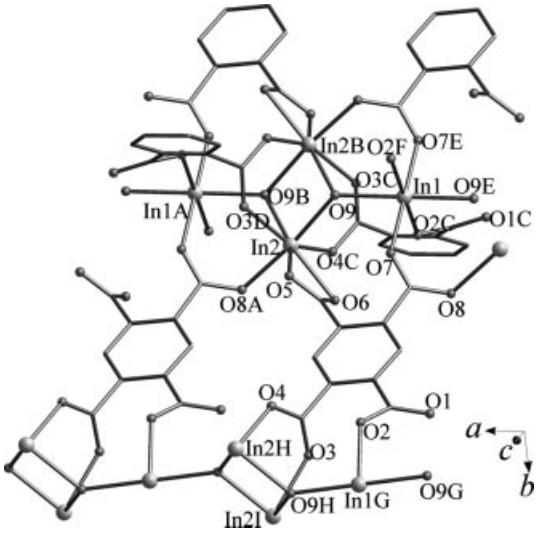

Figure 1. Coordination environment of indium ions in compound **2**. Symmetry code: (A) 1+*x*, *y*, *z*; (B) 1 – *x*, 1 – *y*, –*z*; (C) *x*, 1.5 – *y*, –0.5 + *z*; (D) 1 – *x*, –0.5 + *y*, 0.5 – *z*; (E) –*x*, 1 – *y*, –*z*; (F) –*x*, –0.5 + *y*, 0.5 – *z*; (G) –*x*, 0.5 + *y*, 0.5 – *z*; (H) *x*, 1.5 – *y*, 0.5 + *z*; (I) 1 – *x*, 0.5 + *y*, 0.5 – *z*. For clarity only two carboxylate arms of a part of the btec groups are drawn.

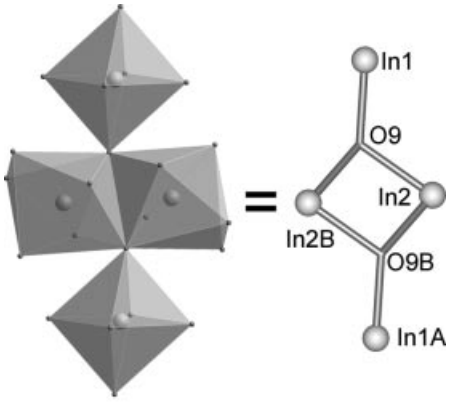

Figure 2. In_4O_{22} tetranuclear cluster and its conceptual representation. In1···In1A= 7.203 Å, In2···In2B = 3.268 Å

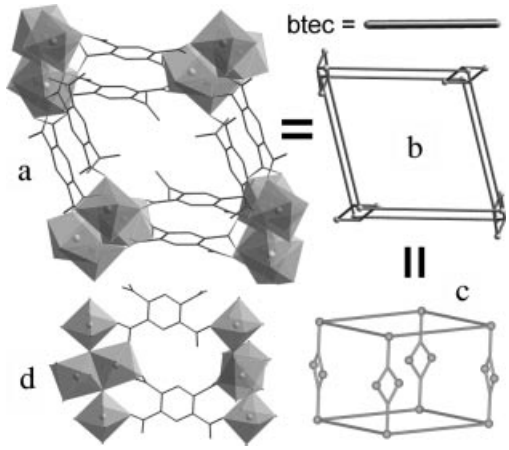

Figure 3. (a) A subunit constructed from four In_4O_{22} tetranuclear clusters and eight btec groups. In the subunit the opposite benzene rings are parallel to each other. It can be seen that the plane defined by four In ions in a tetranuclear clusters is parallel to the plane in the opposite tetranuclear cluster and perpendicular to the plane in the neighboring tetranuclear cluster. (b) The conceptual representation of a right prism for the subunit. (c) Front view of the right prism. (d) The detailed show of one lateral side of the prism.

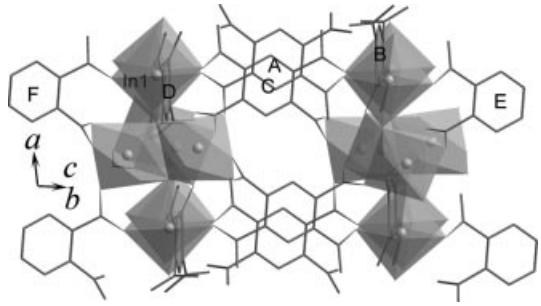

Figure 4. Demonstration of the positions of the btec groups surrounding a prism. Benzene rings A and B are located above the top side and benzene C–F below the top side. For clarity only two carboxylate arms of the lateral btec groups are drawn.

 © 2005 Wiley-VCH Verlag GmbH & Co. KGaA, Weinheim

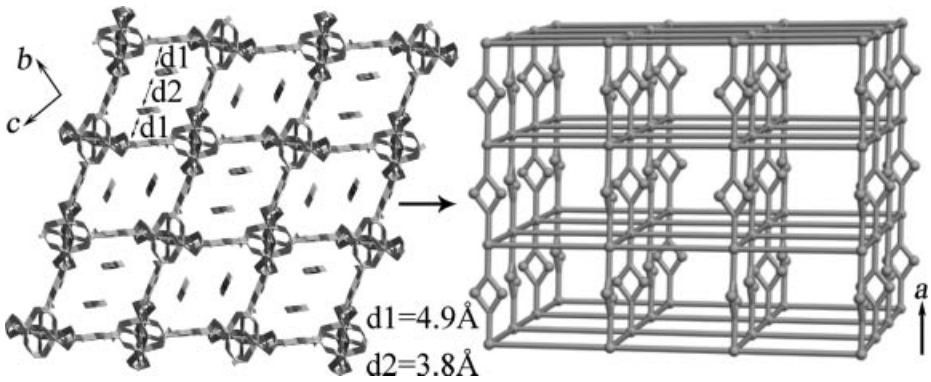

Figure 5. (left) View of a 3-D network in **2** with 1-D channels containing H4pic guests and (right) its conceptual representation (H4pic guests are omitted for clarity; note that the view directions of these two drawings are different).

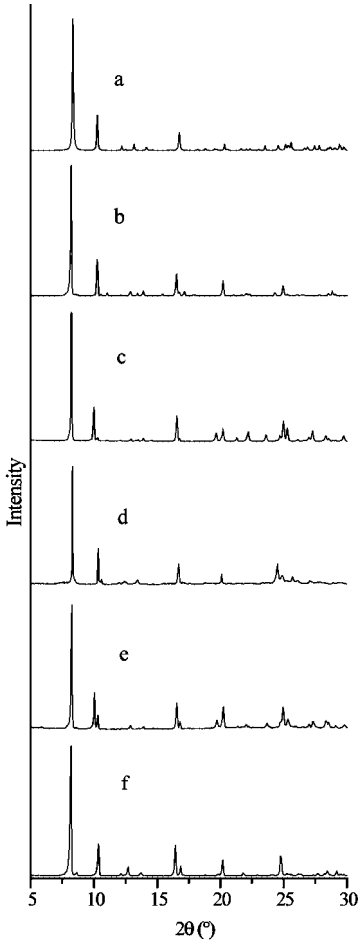

Figure 6. XRPD patterns of compounds **1**–**3**: (a) calculated pattern based on $[In_3(btec)_2(OH)_2]^-$ framework, (b) experimental pattern of **1**, and (c) pattern of the exchanged product of **1** with Ba^{2+}, (d) experimental pattern of **2**, and (e) pattern of the exchanged product of **2** with Ba^{2+}, (f) experimental pattern of **3**.

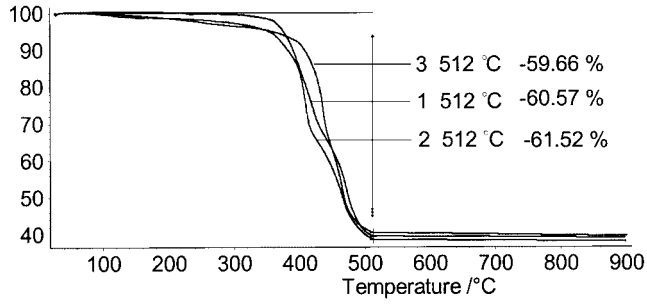

Figure 7. TG curves of **1–3** measured under flowing air.

when arranging the four btec benzene rings connected to the bottom-side In1 vertexes. Prisms are extended along [100], [011], and [0$\bar{1}$1] directions to generate a 3D network (Figure 5) containing the planar layers defined by In1 ions. By sharing In1 vertexes, tetranuclear clusters are extended through the crystallographic *a* axis to give infinite chains which act as pillars to support the planar layer. The shortest contact between the pillars is 5.496 Å (O4···O5). The btec groups reproduced along the [011] axis are alternately arranged above and below the In1 planar layer. This also applies to the btec groups reproduced along the [0$\bar{1}$1] direction. In such an arrangement mode, the btec groups fill in the space between the pillars and therefore prevent the framework from generating channels along the [011] and the [0$\bar{1}$1] directions. The only channel runs through the crystallographic *a* axis with diagonal dimensions as long as 13.425×17.544 Å^2. The organic guests, protonated pyridine derivatives, reside in the channels. The pyridine rings are parallel to each other and the centroid-to-centroid distances are longer than 4.5 Å, indicating no π–π contacts between pyridine rings. However, the centroid-to-centroid distances between pyridine rings and the nearest opposite btec benzene rings are 3.790 Å, indicating strong π–π contact. The nitrogen atoms in pyridine rings have no hydrogen bond interactions with the oxygen atoms in the framework. On the basis of PLATON calculations,[14] the solvent accessible volume constitutes 43.3% of the total crystal volume.

The homogeneities of compounds **1**–**3** are confirmed by X-ray powder diffraction (XRPD) patterns (Figure 6). The fact that the powder patterns obtained experimentally are in good agreement with the calculated patterns indicates that these three compounds are isostructural coordination polymers with the same 3D frameworks.

 © 2005 Wiley-VCH Verlag GmbH & Co. KGaA, Weinheim

Thermal gravimetric (TG) data for compounds **1**–**3** under flowing air are shown in Figure 7. From 360 to 512 °C, compounds **1**–**3** dramatically lose the weight of both organic guests and btec ligands simultaneously. Powder X-ray diffraction for their residues shows that **1**–**3** are finally transformed to In_2O_3 after being heated at 512 °C. The total weight loss of **1**, **2**, and **3** is about 39.43%, 38.48%, and 40.34%, respectively, consistent with the calculated value of In_2O_3 (about 39.1%).

Ion-Exchange Analysis

In a typical ion-exchange experiment, original samples (about 25 mg) of compounds **1**–**3** were each immersed in a solution of $CaCl_2$ and $BaCl_2$ (10 mL, 1.0 M) for one day at 60 °C. The products were filtered, washed with distilled water and then dried in air. After exchange experiments, compounds **1** and **2** became less crystalline, while **3** remained in its crystalline form. Elemental analysis indicates that the guest cations in **1** and **2** can be fully exchanged by Ca^{2+} and Ba^{2+} ions, reflected by the significant decrease in C and N content. Only slight changes in C and N content[15] were observed for the exchanged sample of **3**, indicating that **3** cannot undergo ion exchange. The Hdepa molecule has a larger size than H2pic and H4pic; this inhibits it from moving freely along channels and therefore reduces its exchange ability. The major XRD reflections (Figure 6) of **1** and **2** can also be observed in their sample exchanged with Ba^{2+}, indicating that in both **1** and **2** the $[In_3(btec)_2(OH)_2]^-$ framework remains unchanged after the exchange.

Experimental Section

Preparation: A mixture of $InCl_3{\cdot}4H_2O$ (74.0 mg, 0.25 mmol), pyromellitic dianhydride (55 mg, 0.25 mmol), 2-picoline (typical example: 0.8 mL, 8 mmol), and H_2O (5.0 mL) in a 30-mL Teflon-lined stainless steel vessel was heated at 165 °C for 85 h, and then was cooled to room temperature at a rate of 6 °C·h^{-1}, giving light yellow prism crystals of **1**. The crystals were collected by density difference and washed with *N*,*N*-dimethylformamide (DMF) and water sequentially, giving an isolated yield of 62 mg (70%) based on $InCl_3{\cdot}4H_2O$. Compounds **2** and **3** were prepared in a similar way simply by replacing 2-picoline with 4-picoline (0.8 mL, 8 mmol) or with a mixture of pyridine (0.1 mL, 1.2 mmol) and dpea (368 mg, 2 mmol) and obtained in the yields of 60 mg (68%) and 53 mg (60%), respectively, based on $InCl_3{\cdot}4H_2O$. **1**: $C_{32}H_{21}In_3N_2O_{18}$ (1065.97): calcd. C 36.03, H 1.99, N 2.63; found C 36.22, H 2.12, N 2.66. IR (KBr): $\tilde{\nu}$ = 3503 (br), 3054 (m), 1613 (s), 1589 (vs), 1499 (s), 1411 (s), 1371 (vs), 1317 (m), 1252 (m), 1141 (m), 878 (w), 805 (m), 761 (m) cm^{-1}. **2**: $C_{32}H_{21}In_3N_2O_{18}$ (1065.97): calcd. C 36.03, H 1.99, N 2.63; found C 35.81, H 2.10, N 2.58. IR (KBr): $\tilde{\nu}$ = 3606 (m), 3523 (m), 3221 (m), 3086 (m), 1636 (m), 1595 (vs), 1548 (s), 1505 (m), 1427 (s), 1382 (s), 1337 (s), 1135 (m), 1005 (m), 941 (m), 857 (m), 805 (m), 779 (m), 755 (m) cm^{-1}. **3**: $C_{32}H_{19}In_3N_2O_{18}$ (1063.97): calcd. C 36.12, H 1.80, N 2.63; found C 36.44, H 2.10, N 2.67. IR (KBr): $\tilde{\nu}$ = 3422 (m), 3327 (m), 3129 (m), 1615 (s), 1590 (s), 1552 (sh, vs), 1497 (s), 1402 (s), 1373 (s), 1317 (m), 1140 (m), 932 (m), 878 (m), 815 (m), 761 (m) cm^{-1}.

Crystallographic Studies: Intensity data of **2** and **3**[16] were collected with a Rigaku mercury CCD diffractometer with graphite-monochromated Mo-K_α (λ = 0.71073 Å) radiation by using the ω–2θ scan method at room temperature. The structures were solved by direct methods using SHELXS-97[17a] and were refined on F^2 by the full-matrix least-squares methods SHELXL-97.[17b] Because of a disorder problem, some atoms of the dpea molecule in **3** could not be located. All non-hydrogen atoms were refined anisotropically except for the organic guest molecules. All hydrogen atoms were calculated at the ideal positions and refined isotropically. The crystallographic data, selected bond lengths and angles are summarized in Table 1 and Table 2.

Table 1. Crystallographic data for compounds **2** and **3**.

	2	**3**
Crystal system	monoclinic	monoclinic
Space group	$P2_1/c$	$P21/c$
Empirical formula	$C_{32}H_{21}In_3N_2O_{18}$	$C_{32}H_{19}In_3N_2O_{18}$
Formula mass	1065.97	1063.95
a [Å]	7.203(6)	7.2104(13)
b [Å]	13.43(3)	13.637(2)
c [Å]	17.54(3)	17.379(3)
β [°]	100.76(11)	100.657(7)
V [Å]^3	1666.8(4)	1679.3(5)
Z	2	2
$D_{calcd.}$ [g·cm^{-3}]	2.124	2.104
μ [mm^{-1}]	2.147	2.131
R_1 [$I > 2\sigma(I)$][a]	0.0508	0.0753
wR_2 (all data)[a]	0.1163	0.1784

[a] $R_1 = \Sigma(||F_o| - |F_c||)/\Sigma|F_o|$, and $wR_2 = \{\Sigma w[(F_o^2 - F_c^2)^2]/\Sigma w[(F_o^2)^2]\}^{1/2}$.

Table 2. Selected bond lengths and angles for compounds **2** and **3**.

Bond lengths	[Å]	Angles	[°]
Compound **2**			
In1–O2C[a]	2.094(5)	O2F–In1–O7E	90.8(2)
In1–O7	2.157(5)	O2F–In1–O9	87.5(2)
In1–O9	2.198(4)	O7–In1–O9	86.6(2)
In2–O8A	2.129(5)	O8A–In2–O4C	98.9(2)
In2–O4C	2.174(6)	O8A–In2–O9	172.3(2)
In2–O9	2.203(5)	O4C–In2–O3D	148.9(2)
In2–O3D	2.208(5)	O9–In2–O6	94.5(2)
In2–O6	2.263(5)	O9–In2–O5	90.4(2)
In2–O5	2.275(6)	O4C–In2–O9B	75.9(2)
In2–O9B	2.314(5)	O3D–In2–O6	132.7(2)
Compound **3**			
In1–O2C	2.092(6)	O2F–In1–O7E	90.9(2)
In1–O7	2.147(6)	O2F–In1–O9	87.8(2)
In1–O9	2.196(6)	O7–In1–O9	86.3(2)
In2–O8A	2.125(6)	O8A–In2–O4C	99.0(2)
In2–O4C	2.166(6)	O8A–In2–O9	173.0(2)
In2–O9	2.199(5)	O4C–In2–O3D	149.0(2)
In2–O3D	2.200(6)	O9–In2–O6	94.1(2)
In2–O6	2.264(7)	O9–In2–O5	90.7(2)
In2–O5	2.267(7)	O4C–In2–O9B	75.7(2)
In2–O9B	2.308(6)	O3D–In2–O6	132.7(2)

[a] Symmetry code: A 1 + x, y, z; B 1 – x, 1 – y, –z; C x, 1.5 – y, –0.5 + z; D 1 – x, –0.5 + y, 0.5 – z; E –x, 1 – y, –z; F –x, –0.5 + y, 0.5 – z; G –x, 0.5 + y, 0.5 – z; H x, 1.5 – y, 0.5 + z; I 1 – x, 0.5 + y, 0.5 – z.

 © 2005 Wiley-VCH Verlag GmbH & Co. KGaA, Weinheim

Acknowledgement

This work was supported by grants from the National Nature Science Foundation of China (No. 20231020) and the Nature Science Foundation of Fujian Province.

[1] a) E. Y. Choi, S. Y. Kim, Y. Kim, K. Seff, *Microporous Mesoporous Mater.* **2003**, *62*, 201–210; b) X. M. Zhang, M. L. Tong, H. K. Lee, X. M. Chen, *J. Solid State Chem.* **2001**, *160*, 118–122; c) K. S. Min, M. P. Suh, *J. Am. Chem. Soc.* **2000**, *122*, 6834–6840.

[2] a) K. Biradha, Y. Hongo, M. Fujita, *Angew. Chem. Int. Ed.* **2002**, *41*, 3395–3398; b) E. Y. Lee, M. P. Suh, *Angew. Chem. Int. Ed.* **2004**, *43*, 2798–2801; c) T. J. Prior, M. J. Rosseinsky, *Inorg. Chem.* **2003**, *42*, 1564–1575; d) X. Liu, J. H. Guo, W. J. Zheng, D. Z. Liao, *Chin. J. Struct. Chem.* **2002**, *21*, 347–351.

[3] a) R. Kitaura, K. Fujimoto, S. Noro, M. Kondo, S. Kitagawa, *Angew. Chem. Int. Ed.* **2002**, *41*, 133–135; b) R. Q. Zou, X. H. Bu, R. H. Zhang, *Inorg. Chem.* **2004**, *43*, 5382–5386; c) M. P. Suh, J. W. Ko, H. J. Choi, *J. Am. Chem. Soc.* **2002**, *124*, 10976–10977; d) M. Eddaoudi, J. Kim, N. Rosi, D. Vodak, J. Wachter, M. O'Keeffe, O. M. Yaghi, *Science* **2002**, *295*, 469–472.

[4] a) O. M. Yaghi, G. Li, H. Li, *Nature* **1995**, *378*, 703–706; b) O. M. Yaghi, C. E. Davis, G. Li, H. Li, *J. Am. Chem. Soc.* **1997**, *119*, 2861–2868; c) S. S. Y. Chui, S. M. F. Lo, J. P. H. Charmant, A. G. Orpen, I. D. Williams, *Science* **1999**, *283*, 1148–1150; d) C. J. Kepert, M. J. Rosseinsky, *Chem. Commun.* **1998**, 31–32.

[5] a) H. Kumagai, C. J. Kepert, M. Kurmoo, *Inorg. Chem.* **2002**, *41*, 3410–3422; b) S. O. H. Gutschke, D. J. Price, A. K. Powell, P. T. Wood, *Eur. J. Inorg. Chem.* **2001**, 2739–2741.

[6] a) J. R. Su, K. L. Yin, D. J. Xu, *Chin. J. Struct. Chem.* **2004**, *23*, 399–402; b) J. Kim, B. L. Chen, T. M. Reineke, H. L. Li, M. Eddaoudi, D. B. Moler, M. O'Keeffe, O. M. Yaghi, *J. Am. Chem. Soc.* **2001**, *123*, 8239–8247; c) H. Kumagai, K. W. Chapman, C. J. Kepert, M. Kurmoo, *Polyhedron* **2003**, *22*, 1921–1927.

[7] a) F. D. Rochon, G. Massarweh, *Inorg. Chim. Acta* **2000**, *304*, 190–198; b) F. Jaber, F. Charbonnier, R. Faure, *J. Chem. Crystallogr.* **1997**, *27*, 397–400; c) R. Cao, Q. Shi, D. F. Sun, M. C. Hong, W. H. Bi, Y. J. Zhao, *Inorg. Chem.* **2002**, *41*, 6161–6168.

[8] a) M. Sanselme, J. M. Grenèche, M. Riou-Cavellec, G. Ferey, *Chem. Commun.* **2002**, 2172–2173; b) R. Murugavel, D. Krishnamurthy, M. Sathiyendiran, *J. Chem. Soc., Dalton Trans.* **2002**, 34–39; c) M. L. Hu, D. P. Cheng, J. G. Liu, D. J. Xu, *J. Coord. Chem.* **2001**, *53*, 7–13.

[9] a) M. Eddaoudi, J. Kim, M. O'Keeffe, O. M. Yaghi, *J. Am. Chem. Soc.* **2002**, *124*, 376–377; b) C. Serre, F. Millange, C. Thouvenot, M. Nogues, G. Marsolier, D. Louer, G. Ferey, *J. Am. Chem. Soc.* **2002**, *124*, 13519–13526.

[10] a) D. F. Sun, R. Cao, W. H. Bi, J. B. Weng, M. C. Hong, Y. C. Liang, *Inorg. Chim. Acta* **2004**, *357*, 991–1001; b) C. D. Wu, C. Z. Lu, D. M. Wu, H. H. Zhuang, J. S. Huang, *Inorg. Chem. Commun.* **2001**, *4*, 504–506; c) C. D. Wu, C. Z. Lu, W. B. Yang, S. F. Lu, H. H. Zhang, J. S. Huang, *Eur. J. Inorg. Chem.* **2002**, *4*, 797–800.

[11] Submitted for publication, crystallographic data: monoclinic, space group $P2_1/c$, a = 18.5774(19), b = 7.222, c = 21.4155(15) Å, β = 125.187(6)°, V = 125.187(6) Å^3.

[12] a) N. Audebrand, S. Raite, D. Louer, *Solid State Sci.* **2003**, *5*, 783–794; b) E. Jeanneau, N. Audebrand, D. Louer, *J. Solid State Chem.* **2003**, *173*, 387–394; c) J. Y. Sun, L. H. Weng, Y. M. Zhou, J. X. Chen, Z. X. Chen, Z. C. Liu, D. Y. Zhao, *Angew. Chem. Int. Ed.* **2002**, *41*, 4471–4473.

[13] N. E. Brese, M. O'Keeffe, *Acta Crystallogr., Sect. B.* **1991**, *47*, 192–197.

[14] L. Spek, *A Multipurpose Crystallographic Tool*, Utrecht University, Utrecht, The Netherlands, **1999**.

[15] $\{Ca_{0.5}[In_3(btec)_2(OH)_2]\cdot L\cdot 5H_2O\}_n$: $C_{26}H_{23}Ca_{0.5}In_3NO_{23}$ (1081.7) calcd. C 28.84, H 2.15, N 1.30; found C 29.65, H 2.10, N 1.21. $\{Ba_{0.5}[In_3(btec)_2(OH)_2]\cdot L\cdot 5H_2O\}_n$: $C_{26}H_{23}Ba_{0.5}In_3NO_{23}$ (1130.4) calcd. C 27.60, H 2.06, N 1.24; found C 27.42, H 1.82, N 1.30. $\{Ca_{0.5}[In_3(btec)_2(OH)_2]\cdot L'\cdot 5H_2O\}_n$: $C_{26}H_{23}Ca_{0.5}In_3NO_{23}$ (1081.7) calcd. C 28.84, H 2.35, N 1.30; found C 27.69, H 2.10, N 1.19. $\{Ba_{0.5}[In_3(btec)_2(OH)_2]\cdot L'\cdot 5H_2O\}_n$: $C_{26}H_{23}Ba_{0.5}In_3NO_{23}$ (1130.4) calcd. C 27.60, H 2.06, N 1.24; found C 25.82, H 1.80, N 1.18. L = 2-picoline, L′ = 4-picoline.

[16] The crystallographic data for compound **1** were poor, and an attempt to get high quality crystals of **1** under other conditions was unsuccessful. Thus the crystal data and crystal description of compound **1** are not available.

[17] a) G. M. Sheldrick, *SHELXS97*, *Program for Crystal Structure Solution*. University of Göttingen, Göttingen, Germany, **1997**; b) G. M. Sheldrick, *SHELXL97*, *Program for Crystal Structure Refinement*, University of Göttingen, Göttingen, Germany, **1997**.

Received: November 21, 2004

 © 2005 Wiley-VCH Verlag GmbH & Co. KGaA, Weinheim

Syntheses, Reactivity, and X-ray Structure Analyses of the Dimeric Pentaphosphides $[(t\mathrm{Bu_3Si})_3\mathrm{P_5M_2}]_2$ (M = Na, Ag) and the Bicyclo[2.1.0]pentaphosphane $(t\mathrm{Bu_3Si})_3\mathrm{P_5}$

Hans-Wolfram Lerner,[a]* Günter Margraf,[a] Linda Kaufmann,[a] Jan W. Bats,[b] Michael Bolte,[a] and Matthias Wagner[a]

Keywords: Phosphorus / Phosphane / Supersilyl phosphides / Silanide

The sodium pentaphosphide dimer $[(t\mathrm{Bu_3Si})_3\mathrm{P_5Na_2(THF)}]_2$ has been synthesized in high yield from the reaction of four equivalents of the sodium silanide $t\mathrm{Bu_3SiNa}$ with P_4. X-ray quality crystals of the sodium pentaphosphide dimer $[(t\mathrm{Bu_3Si})_3\mathrm{P_5Na_2(THF)}]_2$ (monoclinic, $P2_1/n$) were grown from benzene. The sodium pentaphosphide $(t\mathrm{Bu_3Si})_3\mathrm{P_5Na_2}$ can be oxidized with one equivalent of TCNE to give the bicyclo[2.1.0]-pentaphosphane $(t\mathrm{Bu_3Si})_3\mathrm{P_5}$; it also reacts with AgOCN to give the silver pentaphosphide $[(t\mathrm{Bu_3Si})_3\mathrm{P_5Ag_2}]_2$ (monoclinic, $P2_1/n$). Crystals of the pentaphosphane $(t\mathrm{Bu_3Si})_3\mathrm{P_5}$ (monoclinic, $P2_1/c$) suitable for X-ray diffraction were obtained from hexane at –25 °C.
(© Wiley-VCH Verlag GmbH & Co. KGaA, 69451 Weinheim, Germany, 2005)

Introduction

The nucleophilic degradation of P_4 with $t\mathrm{Bu_3SiM}$ (M = Li, Na, K) or $t\mathrm{Bu_2PhSiNa}$ in a molar ratio of 1:2 leads to the tetraphosphenediides **1** $[(t\mathrm{Bu_3Si})_2\mathrm{P_4M_2}]$ (M = Li, Na, K) and $[(t\mathrm{Bu_2PhSi})_2\mathrm{P_4Na_2}]$, which dimerize in weakly polar solvents to form the octaphosphides **2** $[(t\mathrm{Bu_3Si})_4\mathrm{P_8M_4}]$ (M = Li, Na, K) and $[(t\mathrm{Bu_2PhSi})_4\mathrm{P_8Na_4}]$ (Scheme 1).[1–4]

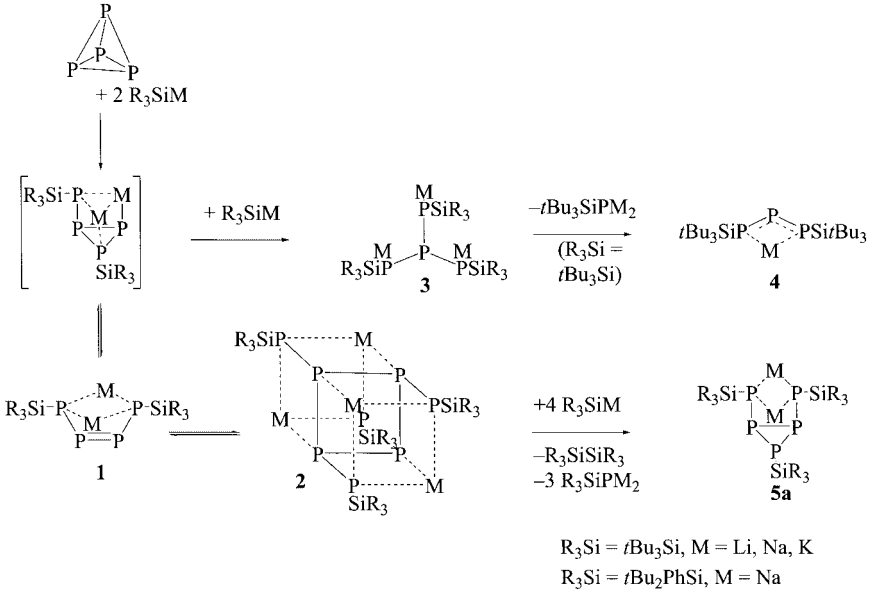

Scheme 1.

Recently we have reported the reaction of P_4 with the silanides $t\mathrm{Bu_3SiM}$ (M = Li, Na) and $t\mathrm{Bu_2PhSiNa}$ in a 1:3 stoichiometry, which leads cleanly to the tetraphosphides **3** $[(t\mathrm{Bu_3Si})_3\mathrm{P_4M_3}]$ (M = Li, Na) and $[(t\mathrm{Bu_2PhSi})_3\mathrm{P_4Na_3}]$, respectively.[5] In contrast, when P_4 was treated with three equivalents of $t\mathrm{Bu_3SiK}$ in tetrahydrofuran, the potassium

[a] Institut für Anorganische Chemie, Johann Wolfgang Goethe-Universität Frankfurt am Main,
Marie-Curie-Straße 11, 60439 Frankfurt am Main, Germany
Fax: +49-69-79829260
E-mail: lerner@chemie.uni-frankfurt.de
[b] Institut für Organische Chemie, Johann Wolfgang Goethe-Universität Frankfurt am Main,
Marie-Curie-Straße 11, 60439 Frankfurt am Main, Germany

tetraphosphenediide $[(t\mathrm{Bu_3Si})_2P_4K_2]$ and the octaphosphide $[(t\mathrm{Bu_3Si})_4P_8K_4]$ were formed as the main products rather than the tetraphosphide $[(t\mathrm{Bu_3Si})_3P_4K_3]$.[4]

Surprisingly, treatment with tri-*tert*-butylsilylpotassium (supersilylpotassium, $t\mathrm{Bu_3SiK}$) slowly transforms the supersilylated potassium tetraphosphenediide $[(t\mathrm{Bu_3Si})_2P_4K_2]$ (**1K$_2$**) and the octaphosphide $[(t\mathrm{Bu_3Si})_4P_8K_4]$ (**2K$_4$**) into the triphosphide $[(t\mathrm{Bu_3Si})_2P_3K]$ (**4K**) and the pentaphosphide $[(t\mathrm{Bu_3Si})_3P_5K_2]$ (**5aK$_2$**), respectively.[4]

The sodium pentaphosphide $[(t\mathrm{Bu_3Si})_3P_5Na_2(THF)_4]$[6] is the first and only structurally characterized derivative of the pentaphosphane **5a** and is a constitutional isomer of the well-known cyclopentaphosphanes of type **5b** (Scheme 2).[7,8] Derivatives of **7a** have been described in a number of recent studies.[9–12] The cation $Br_2P_5^+$ features the structural motif of **7b**.[13,14] The theoretical studies of Böcker and Häser have shown that the bicyclo[2.1.0]pentaphosphane **6** (non-Baudler structure) should be stable.[15]

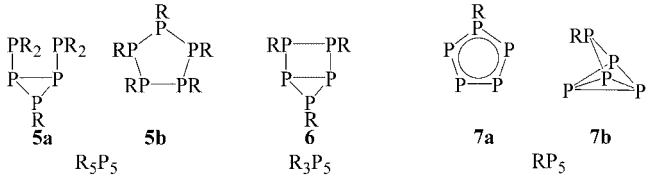

Scheme 2.

In this paper, the synthesis, reactivity and molecular structure of the bicyclo[2.1.0]pentaphosphane $(t\mathrm{Bu_3Si})_3P_5$, the first isolated derivative of the pentaphosphane **6**, is described. We also report here the crystal structures of the dimeric pentaphosphides $[(t\mathrm{Bu_3Si})_3P_5M_2]_2$ (M = Na, Ag).

Results and Discussion

Syntheses

As we noted previously, the sodium pentaphosphide **5aNa$_2$** can be generated by several routes.[6] We have now developed a synthesis by which the sodium pentaphosphide dimer $[(t\mathrm{Bu_3Si})_3P_5Na_2(THF)]_2$ can be produced in large amounts.

The dimeric sodium pentaphosphide **[5aNa$_2$(THF)]$_2$** is accessible by treating P_4 with four equivalents of the sodium silanide $t\mathrm{Bu_3SiNa}$.[16] The first product of this reaction in THF is the sodium tetraphosphenediide $[(t\mathrm{Bu_3Si})_2P_4Na_2]$ (**1Na$_2$**). The ^{31}P NMR spectrum of the resulting THF solution shows signals that can be assigned unambiguously to the sodium tetraphosphenediide **1Na$_2$**. After removing the THF the reaction mixture was treated with heptane and stirred for 12 h. The main product of this procedure was the sodium octaphosphide $[(t\mathrm{Bu_3Si})_4P_8Na_4(THF)_4]$ **[2Na$_4$(THF)$_4$]**, which was characterized by X-ray crystallography. Removal of the heptane and addition of benzene, followed by stirring the resulting reaction mixture for 24 h at ambient temperature, gave the sodium pentaphosphide dimer **[5aNa$_2$(THF)]$_2$** in 77% yield. Superdisilane was produced as a side-product in this reaction, as shown in Equation (1). The dimeric pentaphosphide **[5aNa$_2$(THF)]$_2$** is transformed into the monomeric pentaphosphide **5aNa$_2$** in tetrahydrofuran.

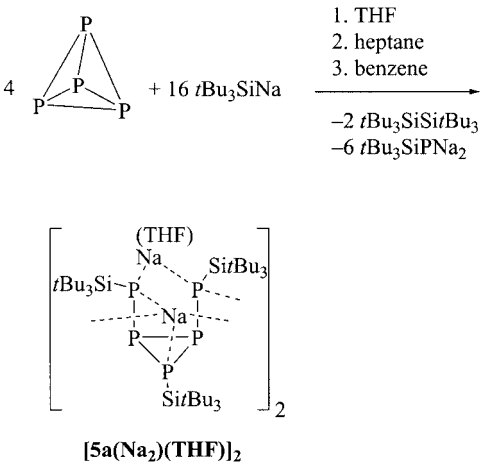

(1)

Interestingly, the pentaphosphide **5aNa$_2$** can be oxidized with TCNE to give the pentaphosphane **6(SitBu$_3$)** in quantitative yield. Treatment of this pentaphosphane with $t\mathrm{Bu_3SiNa}$ leads quantitatively to the pentaphoshide **5aNa$_2$** and the superdisilane $t\mathrm{Bu_3SiSi}t\mathrm{Bu_3}$, as shown in Equation (2). In contrast to the reaction of **5aNa$_2$** with Au$^{\mathrm{I}}$, where a redox process takes place,[17] the pentaphosphide **5aNa$_2$** reacts with AgOCN in a metathesis reaction to give the silver pentaphosphide **[5aAg$_2$]$_2$** in 53% yield [Equation (3)].

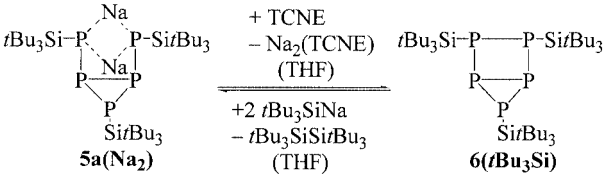

(2)

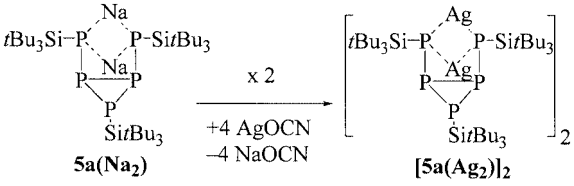

(3)

Surprisingly, the photolysis of **[5aAg$_2$]$_2$** in a mixture of toluene and $[D_6]$benzene at ambient temperature leads to the bicyclo[1.1.0]tetraphosphane **8**[1,3] and the supersilylphosphane **9**[3] in quantitative yield [Equation (4)].

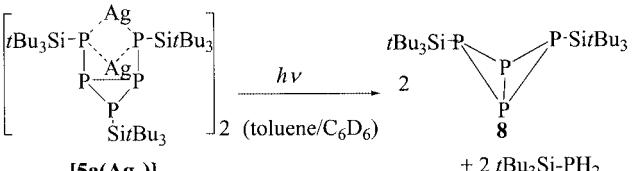

(4)

 © 2005 Wiley-VCH Verlag GmbH & Co. KGaA, Weinheim

Reactivity of $(t\mathrm{Bu_3Si})_3\mathrm{P_5}$

In the thermolysis of the bicyclo[2.1.0]pentaphosphane **6(Si*t*Bu$_3$)** at 120 °C in [D$_6$]benzene the bicyclo[1.1.0]tetraphosphane **8**[1,3] and the deuterated supersilylphosphane **9(D)** were produced quantitatively, as shown in Equation (5). The formation of $t\mathrm{Bu_3SiPD_2}$ in the thermolysis of the bicyclo[2.1.0]pentaphosphane **6(Si*t*Bu$_3$)** can be explained by the reaction of transient supersilylphosphinidene $t\mathrm{Bu_3SiP}$ with [D$_6$]benzene.

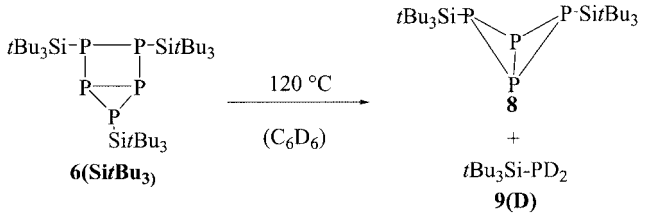

(5)

The bicyclo[2.1.0]pentaphosphane **6(Si*t*Bu$_3$)** is sensitive to oxygen and moisture. It reacts spontaneously with CF_3CO_2H to give the supersilylphosphenium trifluoroacetate $[t\mathrm{Bu_3SiPH_3}][CF_3CO_2]$ and P_4. In this reaction $t\mathrm{Bu_3SiO_2CCF_3}$ is formed as a by-product [Equation (6)].

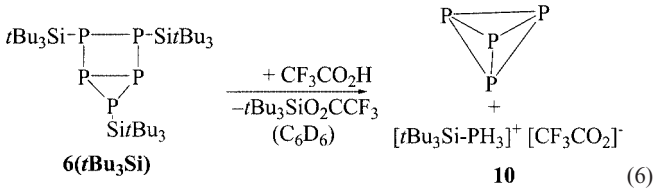

(6)

NMR Spectra

Generally, the NMR spectra of **[5aNa$_2$(THF)]$_2$** resemble those of the monomeric sodium phosphide **5aNa$_2$**.[6] As shown in Figure 2, the signals of all P nuclei of the pentaphosphide dimer **[5aNa$_2$(THF)]$_2$** are broadened, due to Na–P coupling. In contrast, the spectrum of monomeric pentaphosphide **5aNa$_2$** shows only broad signals for P(3) and P(4). The $^{31}P\{^1H\}$NMR spectrum of **5aNa$_2$** features three multiplets with the splitting pattern of an AA′BB′MM′ spin system, as shown in Figure 2.

When **[5a(Na$_2$)(THF)]$_2$** is dissolved in tetrahydrofuran the ^{31}P NMR spectrum becomes like that of **5aNa$_2$**. The $^{31}P\{^1H\}$NMR spectrum of the silver pentaphoshide **[5aAg$_2$]$_2$** resembles that of the dimeric sodium pentaphosphide **[5a(Na$_2$)(THF)]$_2$**. In an earlier report we discussed the NMR spectra of the monomeric pentaphosphide **5aNa$_2$** and the bicyclo[2.1.0]pentaphosphane **6(Si*t*Bu$_3$)** in detail.[6] The $^{31}P\{^1H\}$NMR spectra of the sodium octaphosphide $[(t\mathrm{Bu_3Si})_4P_8Na_4(THF)_4]$ and the DME-complexed sodium octaphosphide $[(t\mathrm{Bu_3Si})_4P_8Na_4(DME)_4]$[1] exhibit the same general features (Figure 1).

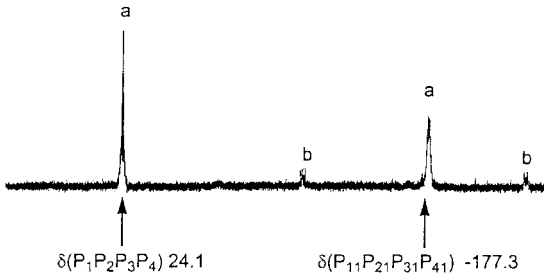

Figure 1. $^{31}P\{^1H\}$NMR spectrum of the reaction solution (after stirring for 12 h in heptane) in C_6D_6 at 161.96 MHz (25 °C, external H_3PO_4). Signal of (a) sodium octaphosphide $[(t\mathrm{Bu_3Si})_4P_8Na_4(THF)_4]$ and (b) dimeric pentaphosphide $[(t\mathrm{Bu_3Si})_3P_5Na_2(THF)]_2$.

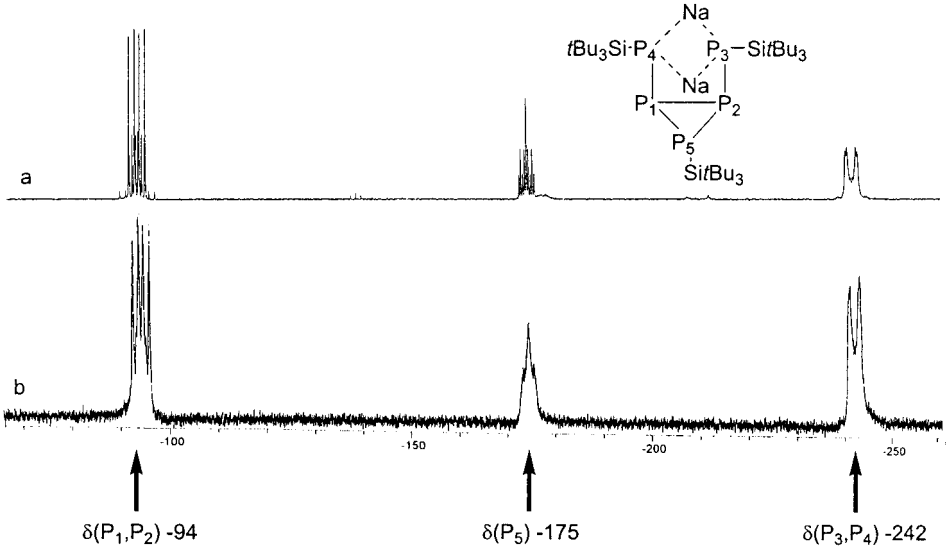

Figure 2. (a) $^{31}P\{^1H\}$NMR spectrum of the monomeric pentaphosphide $[(t\mathrm{Bu_3Si})_3P_5Na_2(THF)_n]$ in [D$_8$]THF at 161.96 MHz (25 °C, external H_3PO_4). (b) $^{31}P\{^1H\}$NMR spectrum of the dimeric pentaphosphide $[(t\mathrm{Bu_3Si})_3P_5Na_2(THF)]_2$ in C_6D_6 at 161.96 MHz (25 °C; external H_3PO_4). Contrary to the signal in the spectrum of the monomeric pentaphosphide, the signal of the P(5) nucleus of the pentaphosphide dimer $[(t\mathrm{Bu_3Si})_3P_5Na_2(THF)]_2$ is broadened due to Na–P coupling. The dimeric pentaphosphide $[(t\mathrm{Bu_3Si})_3P_5Na_2(THF)]_2$ is transformed in tetrahydrofuran into monomeric pentaphosphide $[(t\mathrm{Bu_3Si})_3P_5Na_2(THF)_n]$.

 © 2005 Wiley-VCH Verlag GmbH & Co. KGaA, Weinheim

Structure of the Sodium Octaphosphide $[(t\mathrm{Bu_3Si})_4P_8Na_4(THF)_4]$

Figure 3 shows the molecular structure of the sodium octaphosphide $[(t\mathrm{Bu_3Si})_4P_8Na_4(THF)_4]$ (monoclinic, $P2_1/n$); selected bond lengths and angles are listed in the corresponding figure caption. The structure of $[(t\mathrm{Bu_3Si})_4P_8Na_4(THF)_4]$ shows two symmetrically independent molecules in the unit cell. The central core of $[(t\mathrm{Bu_3Si})_4P_8Na_4(THF)_4]$ possesses the structure of a double cube with four P atoms in the second layer and two P and two Na atoms in the first and third layers. The corners of the first and the third layer in these cubes are alternately occupied by two P and two Na atoms [molecule A: P–Na–P 79.58(16)°, Na–P–Na 86.27(16)°; molecule B: P–Na–P 80.03(19)°, Na–P–Na 84.53(19)°]. A similar structural motif has also been found for $[(t\mathrm{Bu_3Si})_4P_8Na_4(DME)_4]$.[1] Apart from the three P atoms, the Na atom in $[(t\mathrm{Bu_3Si})_4P_8Na_4(THF)_4]$ is coordinated by one molecule of tetrahydrofuran. In contrast to the pentacoordinate Na atoms in $[(t\mathrm{Bu_3Si})_4P_8Na_4(DME)_4]$, the sodium centers of $[(t\mathrm{Bu_3Si})_4P_8Na_4(THF)_4]$ are four-coordinate. The bond lengths and angles of the THF- and DME-solvated sodium octaphosphides $[(t\mathrm{Bu_3Si})_4P_8Na_4(L)_4]$ are quite similar.

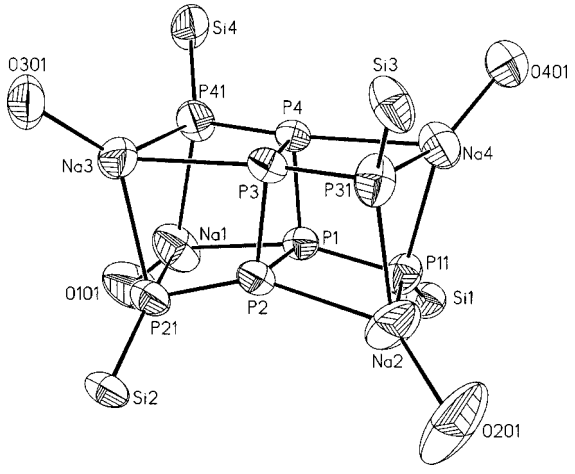

Figure 3. Thermal ellipsoid plot of $[\mathbf{2Na_4(THF_4)}]$ (molecule A), showing the atomic numbering scheme. The displacement ellipsoids are drawn at the 50% probability level. *t*Bu groups have been omitted for clarity. Selected bond lengths [Å] and angles [°]: P–Na 2.843(6) (av.), P–Si 2.210(5) (av.), Na–O 2.243(9) (av.), P(1)–P(11) 2.164(4), P(1)–P(4) 2.251(4), P(1)–P(2) 2.260(4), P(2)–P(21) 2.164(4), P(2)–P(3) 2.271(4), P(3)–P(31) 2.180(4), P(3)–P(4) 2.267(4), P(4)–P(41) 2.184(4), P(2)–P(21) 2.164(4), P(2)–P(3) 2.271(4), P(3)–P(31) 2.180(4), P(3)–P(4) 2.267(4), P(4)–P(41) 2.184(4); P(11)–P(1)–P(4) 108.68(15), P(21)–P(2)–P(3) 110.75(16), P(31)–P(3)–P(2) 95.53(15), P(11)–P(1)–P(2) 102.64(16), P(21)–P(2)–P(1) 102.17(16), P(31)–P(3)–P(4) 103.37(15), P(4)–P(1)–P(2) 89.91(14), P(1)–P(2)–P(3) 89.29(14), P(4)–P(3)–P(2) 89.23(14), P(41)–P(4)–P(1) 96.63(15), P(41)–P(4)–P(3) 102.25(15), P(1)–P(4)–P(3) 89.63(13), P(11)–P(1)–P(4) 108.68(15), P(11)–P(1)–P(2) 102.64(16), P(4)–P(1)–P(2) 89.91(14), P(21)–P(2)–P(1) 102.17(16), P(21)–P(2)–P(3) 110.75(16), P(1)–P(2)–P(3) 89.29(14), P(31)–P(3)–P(4) 103.37(15), P(31)–P(3)–P(2) 95.53(15), P(4)–P(3)–P(2) 89.23(14), P(41)–P(4)–P(1) 96.63(15), P(41)–P(4)–P(3) 102.25(15), P(1)–P(4)–P(3) 89.63(13).

Structure of the Sodium Pentaphosphide Dimer $[(t\mathrm{Bu_3Si})_3P_5Na_2(THF)]_2$

X-ray quality crystals of the sodium pentaphosphide dimer $\mathbf{[5aNa_2(THF)]_2}$ were grown from benzene solution at ambient temperature. It crystallizes in the monoclinic space group $P2_1/n$, and the unit cell contains two formula units. As depicted in Figure 4, the two pentaphosphide dianions $[(t\mathrm{Bu_3Si})_3P_5]^{2-}$ are bridged by two Na cations to form a dimer in the solid state. The sodium pentaphosphide dimer $\mathbf{[5aNa_2(THF)]_2}$ features four P–Na contacts for the two bridging Na atoms and three P–Na contacts for the terminal Na atom. Apart from these three P atoms, the two terminal Na atoms are coordinated by one molecule of tetrahydrofuran. In contrast to the trigonal-planar sodium atom Na(2), the Na(1) center is four-coordinate in $\mathbf{[5aNa_2(THF)]_2}$. The bond lengths and angles of the sodium pentaphosphide dimer $\mathbf{[5aNa_2(THF)]_2}$ are similar to those of the monomeric sodium pentaphosphide $\mathbf{5aNa_2}$ (see caption to Figure 4).

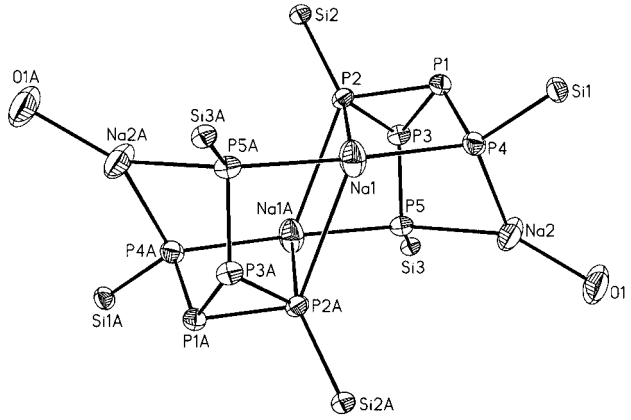

Figure 4. Thermal ellipsoid plot of $\mathbf{[5aNa_2(THF)]_2}$ showing the atom numbering scheme. The displacement ellipsoids are drawn at the 50% probability level. The *t*Bu groups of the pentaphosphide and the CH_2 units of the THF have been omitted for clarity. Selected bond lengths [Å] and angles [°]: P(1)–P(4) 2.1937(16), P(1)–P(3) 2.2393(15), P(1)–P(2) 2.2413(15), P(2)–P(3) 2.2287(15), P(2)–Si(2) 2.3150(15), P(2)–Na(1) 3.051(2), P(2)–Na(1A) 3.385(2), P(3)–P(5) 2.1866(15), P(4)–Si(1) 2.2612(15), P(4)–Na(2) 2.805(2), P(4)–Na(1) 2.846(2), P(5)–Si(3) 2.2648(15), P(5)–Na(2) 2.812(2); P(5)–Na(1A) 2.836(2), Na(1)–P(5A) 2.836(2), Na(1)–P(2A) 3.385(2), P(4)–P(1)–P(3) 111.46(6), P(4)–P(1)–P(2) 104.72(6), P(3)–P(1)–P(2) 59.66(5), P(3)–P(2)–P(1) 60.13(5). Symmetry transformations used to generate equivalent atoms: #1 $-x + 1, -y + 1, -z + 1$.

Structure of the Silver Pentaphosphide Dimer $[(t\mathrm{Bu_3Si})_3P_5Ag_2]_2$

X-ray quality crystals of the silver pentaphosphide dimer $\mathbf{[5aAg_2]_2}$ were grown from a toluene solution at 5 °C. It crystallizes in the monoclinic space group $P2_1/n$. The unit cell contains two formula units and two molecules of tolu-

 © 2005 Wiley-VCH Verlag GmbH & Co. KGaA, Weinheim

ene. As depicted in Figures 5 and 6, the two pentaphosphide dianions $[(t\mathrm{Bu_3Si})_3\mathrm{P_5}]^{2-}$ cap a square-planar four-membered Ag_4 ring that contains a crystallographic inversion center at the midpoint of the molecule. The conformation of the pentaphosphide group is very similar to that of the related group in the crystal structure of **[5aNa$_2$(THF)]$_2$**. Figure 5 shows that the atoms P(1) and P(3) are coordinated to two Ag atoms, while P(2) is coordinated to only one Ag atom. The Ag–P distances range from 2.368(1) to 2.626(1) Å. The shortest Ag···Ag distances are 2.8985(5) and 3.0042(5) Å. The diagonal Ag2···Ag2′ distance of 3.3679(7) Å is slightly longer. The molecule shows nine intramolecular C–H···P contacts with H···P distances of between 2.61 and 2.88 Å. The crystal structure of **[5aAg$_2$]$_2$** features no short intermolecular contacts.

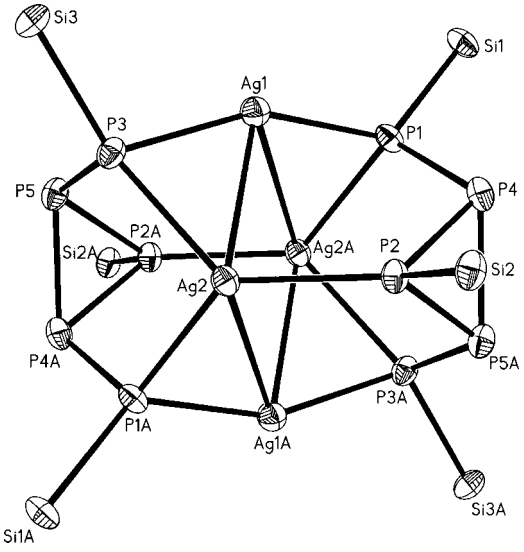

Figure 5. Thermal ellipsoid plot of **[5aAg$_2$]$_2$** showing the atom numbering scheme. The displacement ellipsoids are drawn at the 50% probability level. *t*Bu groups have been omitted for clarity. Selected bond lengths [Å] and angles [°]: Ag(1)–P(1) 2.3678(9), Ag(1)–P(3) 2.3916(9), Ag(1)–Ag(2) 2.8985(5), Ag(1)–Ag(2A) 3.0042(5), Ag(2)–P(1A) 2.5315(9), Ag(2)–P(2) 2.5436(9), Ag(2)–P(3) 2.6258(9), Ag(2)–Ag(1A) 3.0041(5), Ag(2)–Ag(2A) 3.3679(7), P(1)–P(4) 2.1820(13), P(1)–Si(1) 2.2786(12), P(1)–Ag(2A) 2.5315(9), P(3)–P(5) 2.1735(12), P(3)–Si(3) 2.2926(12), P(2)–P(4) 2.2031(12), P(2)–P(5A) 2.2371(12), P(2)–Si(2) 2.3349(12), P(4)–P(5A) 2.2528(13), Si(2)–C(17) 1.933(4), Si(2)–C(13) 1.944(4), Si(2)–C(21) 1.948(4), P(5)–P(2A) 2.2371(12), P(5)–P(4A) 2.2528(13); P(1)–Ag(1)–P(3) 154.41(3), P(1)–Ag(1)–Ag(2) 99.61(2), P(3)–Ag(1)–Ag(2) 58.59(2), P(1)–Ag(1)–Ag(2A) 54.69(2), P(3)–Ag(1)–Ag(2A) 101.94(2), Ag(2)–Ag(1)–Ag(2A) 69.555(14), P(1A)–Ag(2)–P(2) 131.19(3), P(1A)–Ag(2)–P(3) 94.89(3), P(2)–Ag(2)–P(3) 131.31(3), P(1A)–Ag(2)–Ag(1) 124.80(2), P(2)–Ag(2)–Ag(1) 85.07(2), P(3)–Ag(2)–Ag(1) 51.02(2), P(1A)–Ag(2)–Ag(1A) 49.75(2), P(2)–Ag(2)–Ag(1A) 85.80(2), P(3)–Ag(2)–Ag(1A) 125.04(2), Ag(1)–Ag(2)–Ag(1A) 110.447(14), P(1A)–Ag(2)–Ag(2A) 85.11(2), P(2)–Ag(2)–Ag(2A) 81.99(2), P(3)–Ag(2)–Ag(2A) 88.32(2), Ag(1)–Ag(2)–Ag(2A) 56.700(10), Ag(1A)–Ag(2)–Ag(2A) 53.747(10). Symmetry transformations used to generate equivalent atoms: #1 $-x + 1, -y, -z + 2$.

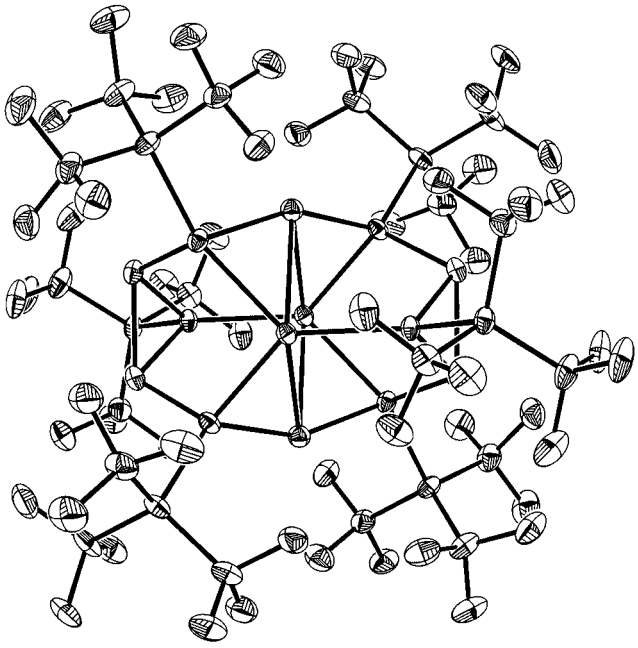

Figure 6. Thermal ellipsoid plot of **[5aAg$_2$]$_2$**. The displacement ellipsoids are drawn at the 50% probability level. The H atoms have been omitted for clarity.

Structure of the Pentaphosphane 6(Si*t*Bu$_3$)

The crystal structure of the bicyclo[2.1.0]pentaphosphane **6(Si*t*Bu$_3$)** is shown in Figures 7 and 8. X-ray quality

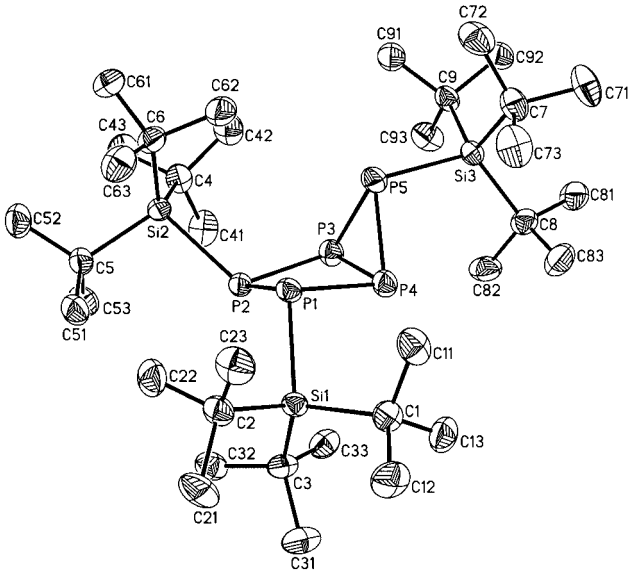

Figure 7. Thermal ellipsoid plot of **6(Si*t*Bu$_3$)** showing the atomic numbering scheme. The displacement ellipsoids are drawn at the 50% probability level. *t*Bu groups have been omitted for clarity. Selected bond lengths [Å] and angles [°]: P(1)–P(4) 2.2410(8), P(1)–P(2) 2.2537(7), P(1)–Si(1) 2.3266(7), P(2)–P(3) 2.2414(8), P(2)–Si(2) 2.3341(8), P(3)–P(5) 2.2184(8), P(3)–P(4) 2.2279(8), P(4)–P(5) 2.1862(8), P(5)–Si(3) 2.3079(8); P(4)–P(1)–P(2) 87.16(3), P(3)–P(2)–P(1) 90.34(3), P(5)–P(3)–P(4) 58.90(2), P(5)–P(3)–P(2) 105.08(3), P(4)–P(3)–P(2) 87.78(3), P(5)–P(4)–P(3) 60.33(2), P(5)–P(4)–P(1) 94.47(3), P(3)–P(4)–P(1) 91.02(3), P(4)–P(5)–P(3) 60.77(2). Symmetry transformations used to generate equivalent atoms: #1 $-x + 2, -y + 2, -z + 1$.

 © 2005 Wiley-VCH Verlag GmbH & Co. KGaA, Weinheim

crystals were grown from hexane at –25 °C. It cocrystallizes with hexane in the monoclinic space group $P2_1/c$. The unit cell contains four formula units. It is interesting to note that $(t\mathrm{Bu_3Si})_3\mathrm{P_5}$ is the first structurally characterized pentaphosphane that features a bicyclus formed by annulated three- and four-membered rings in the solid state. The calculated strain energy of cyclotetraphosphane is lower (27 kcal mol^{-1}) than that of cyclobutane,[9] but only a limited number of compounds are known with a P_4-ring structure.[18–20] Generally, three- and four-membered ring systems of phosphorus are destabilized relative to five-membered ring structures.[7,15] The central core of this bicyclo[2.1.0]pentaphosphane possesses a distorted envelope structure, as shown in Figure 7. The molecular structure of **6(Si*t*Bu$_3$)** features six P–P bonds of around 2.2281(8) Å (av.). These distances are in the range of P–P single bonds. The four-membered ring in **6(Si*t*Bu$_3$)** is not planar, as confirmed by torsion angles of ±14.46(3)° (av.). The supersilyl groups at the P_4-ring are mutually *trans*. No significant variations between the P–Si bonds [2.3229(8) Å av.] are observed.

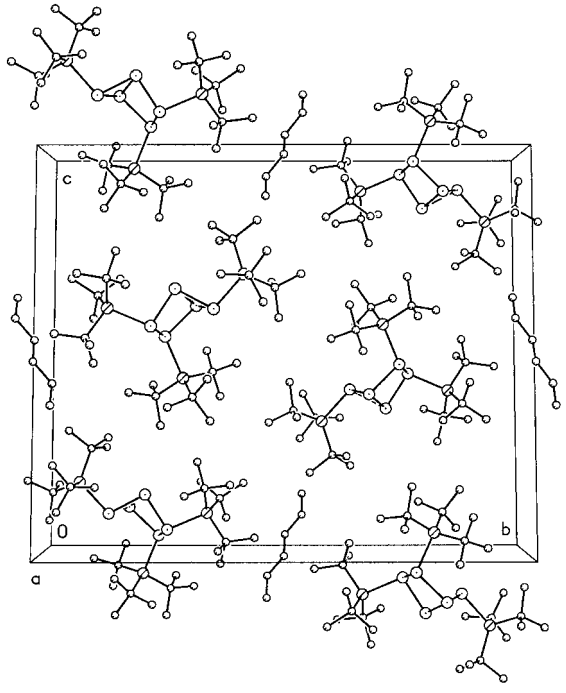

Figure 8. Crystal packing diagram of **6(Si*t*Bu$_3$)**.

Conclusions

In summary, it has been shown that the sodium pentaphosphide dimer **[5aNa$_2$(THF)]$_2$** can be cleanly prepared from $t\mathrm{Bu_3SiNa}$ and white phosphorus. The sodium pentaphosphide **5aNa$_2$** can be oxidized with one equivalent of TCNE to give the bicyclo[2.1.0]pentaphosphane $(t\mathrm{Bu_3Si})_3\mathrm{P_5}$ **[6(Si*t*Bu$_3$)]**. On the other hand, the pentaphosphide **5aNa$_2$** reacts with AgOCN to give the silver phosphide **[5aAg$_2$]$_2$** in 53% yield.

The bicyclo[2.1.0]pentaphosphane **6(Si*t*Bu$_3$)** is sensitive to protonolysis, yielding the supersilylphosphenium cation $[t\mathrm{Bu_3SiPH_3}.]^+$. Thermolysis of this compound in C_6D_6 at 120 °C gives the 1,4-bis(supersilyl)bicyclo[1.1.0]tetraphosphane $(t\mathrm{Bu_3Si})_2\mathrm{P_4}$ and the deuterio supersilylphosphane $t\mathrm{Bu_3SiPD_2}$ quantitatively.

The sodium octaphosphide **2Na$_4$(THF$_4$)**, the pentaphosphide dimers **[5aNa$_2$(THF)]$_2$** and **[5aAg$_2$]$_2$**, and the bicyclo[2.1.0]pentaphosphane **6(Si*t*Bu$_3$)** have been studied by X-ray crystallography. The phosphane **6(Si*t*Bu$_3$)** represents a novel type of pentaphosphane featuring a bicyclus formed by annulated three- and four-membered rings in the solid state.

Experimental Section

General Remarks: All experiments were carried out under dry argon with strict exclusion of air and moisture using standard Schlenk techniques. $t\mathrm{Bu_3SiNa}$[16] was prepared according to literature procedures. All other starting materials were purchased from commercial sources and used without further purification. The solvents (benzene, toluene, tetrahydrofuran) were distilled from sodium/benzophenone prior to use. C_6D_6 was dried over molecular sieves and stored under dry nitrogen.

The NMR spectra were recorded on a Bruker AM 250, a Bruker DPX 250, or a Bruker Avance 400 spectrometer. The ^{29}Si NMR spectra were recorded using the INEPT pulse sequence with empirically optimized parameters for polarization transfer from the *t*Bu substituents.

Synthesis of [(tBu$_3$Si)$_3$P$_5$Na$_2$(THF)]$_2$: A solution of $t\mathrm{Bu_3SiNa}$ (55.2 mmol) in tetrahydrofuran (100 mL) was added to a solution of freshly sublimed P_4 (1.456 g, 11.74 mmol) in 50 mL of tetrahydrofuran at –78 °C and stirred for 4 h. According to the ^{31}P NMR spectrum the tetraphosphide $(t\mathrm{Bu_3Si})_2\mathrm{P_4Na_2}$ was formed as the main product. After all volatile compounds were removed in vacuo the reaction mixture was treated with 50 mL of heptane and stirred for 12 h at ambient temperature. The product of this procedure was the sodium octaphosphide $[(t\mathrm{Bu_3Si})_4\mathrm{P_8Na_4(THF)_4}]$ (by ^{31}P NMR spectroscopy; Figure 1). Crystals of the sodium octaphosphide $[(t\mathrm{Bu_3Si})_4\mathrm{P_8Na_4(THF)_4}]$ suitable for X-ray diffraction were obtained in an NMR tube from [D$_6$]benzene at room temperature. The ^{31}P NMR spectrum of the reaction solution after stirring in heptane for 12 h showed the signal of $[(t\mathrm{Bu_3Si})_4\mathrm{P_8Na_4(THF)_4}]$ (main product 85% P atoms) and the dimeric sodium pentaphosphide $[(t\mathrm{Bu_3Si})_3\mathrm{P_5Na_2(THF)}]_2$ (minor component 15% P atoms; Figure 2). After the heptane was exchanged for benzene and the resulting reaction mixture was stirred again for 24 h at ambient temperature the sodium pentaphosphide dimer $[(t\mathrm{Bu_3Si})_3\mathrm{P_5Na_2(THF)}]_2$ was formed. X-ray quality crystals of $[(t\mathrm{Bu_3Si})_3\mathrm{P_5Na_2(THF)}]_2$ were grown after the reaction mixture had been concentrated in vacuo to a volume of 15 mL and kept at ambient temperature. Yield: 6.306 g (77%).

Selected Data for (tBu$_3$Si)$_2$P$_4$Na$_2$: ^{1}H NMR ([D$_8$]THF, internal TMS): δ = 1.10 (br., 54 H, *t*Bu) ppm. ^{13}C{^{1}H}NMR ([D$_8$]THF, internal TMS): δ = 25.5 (br., *C*Me$_3$), 32.5 (br., C*Me$_3$*) ppm. ^{29}Si{^{1}H}NMR ([D$_8$]THF, external TMS): δ = 22.7 (m, Si*t*Bu$_3$) ppm. ^{31}P{^{1}H}NMR (25 °C; external H_3PO_4): δ = 403.0 (m, $^1J_{P2,P3}$ = –502.6, $^1J_{P1,P2}$ = $^1J_{P3,P4}$ = –432.3, $^2J_{P1,P3}$ = $^2J_{P2,P4}$ = 33.87 Hz, P_2, P_3), –5.1 (m, $^3J_{P1,P4}$ = 184.1, $^1J_{P1,P2}$ = $^1J_{P3,P4}$ = –448.83, $^2J_{P1,P3}$ = $^2J_{P2,P4}$ = –34.7 Hz, P_1, P_4) ppm.

 © 2005 Wiley-VCH Verlag GmbH & Co. KGaA, Weinheim

Selected Data for (tBu$_3$Si)$_4$P$_8$Na$_4$(THF)$_4$: ^{1}H NMR (C_6D_6, internal TMS): δ = 1.30 (br., 108 H, tBu), 1.41 (m, 16 H, CH_2), 3.59 (m, 16 H, OCH_2) ppm. ^{13}C{^{1}H}NMR (C_6D_6, internal TMS): δ = 25.9 (br., *C*Me$_3$), 33.0 (br., C*Me$_3$*), 25.3 (s, *C*H$_2$), 68.0 (s, O*C*H$_2$) ppm. ^{29}Si{^{1}H}NMR (C_6D_6, internal TMS): δ = 19.8 (m, SitBu$_3$) ppm. ^{31}P{^{1}H}NMR (25 °C; external H_3PO_4): δ = 24.1 (m, P_1, P_2, P_3, P_4), –177.3 (m, P_{11}, P_{21}, P_{31}, P_{41}) ppm.

Selected Data for [(tBu$_3$Si)$_3$P$_5$Na$_2$(THF)]$_2$: ^{1}H NMR (C_6D_6, internal TMS): δ = 1.28 (br., 54 H, tBu), 1.26 (br., 27 H, tBu), 1.40 (m, 8 H, CH_2), 3.54 (m, 8 H, OCH_2) ppm. ^{13}C{^{1}H}NMR (C_6D_6, internal TMS): δ = 25.7 (br., *C*Me$_3$), 25.9 (br., *C*Me$_3$), 32.6 (br., C*Me$_3$*), 33.0 (br., C*Me$_3$*), 25.1 (s, *C*H$_2$), 68.0 (s, O*C*H$_2$) ppm. ^{29}Si{^{1}H}NMR (C_6D_6, external TMS): δ = 30.8 (m, 2 SitBu$_3$), 17.8 (m, SitBu$_3$) ppm. ^{31}P{^{1}H}NMR (see Figure 2).

Synthesis of [(tBu$_3$Si)$_3$P$_5$Ag$_2$]$_2$: AgOCN (0.300 g, 2 mmol) was added to a solution of (tBu$_3$Si)$_3$P$_5$Na$_2$ (1 mmol) in 30 mL of tetrahydrofuran at –78 °C and stirred for 12 h. After warming to room temperature the solvent was removed in vacuo. The solid reaction product was extracted into 15 mL of toluene (brown solution). After filtration, [(tBu$_3$Si)$_3$P$_5$Ag$_2$]$_2$ was crystallized from the toluene filtrate at –25 °C. The NMR spectra of the filtrate show small signals which can be assigned to the bicyclo[2.1.0]pentaphosphane (tBu$_3$Si)$_3$P$_5$. Yield: 1.125 g (53%).

Selected Data for [(tBu$_3$Si)$_3$P$_5$Ag$_2$]$_2$: ^{1}H NMR (C_6D_6, internal TMS): δ = 1.38 (br., 27 H, tBu), 1.51 (br., 54 H, tBu) ppm. ^{13}C{^{1}H}NMR (C_6D_6, internal TMS): δ = 25.2 (br., *C*Me$_3$), 25.4 (br., *C*Me$_3$), 32.4 (br., C*Me$_3$*), 32.6 (br., C*Me$_3$*) ppm. ^{29}Si{^{1}H}NMR (C_6D_6, external TMS): δ = 32.2 (m, 2 SitBu$_3$), 18.9 (m, SitBu$_3$) ppm. ^{31}P{^{1}H}NMR (25 °C, C_6D_6, external H_3PO_4): δ = –97.2 (m, P_1, P_3), –160.6 (m, P_2), –252.8 (m, P_4, P_5) ppm.

Synthesis of the Bicyclo[2.1.0]pentaphosphane (tBu$_3$Si)$_3$P$_5$: TCNE (0.855 g, 6.39 mmol) in tetrahydrofuran (20 mL) was added to a solution of (tBu$_3$Si)$_3$P$_5$Na$_2$ (6.28 mmol) in 30 mL tetrahydrofuran at –78 °C and stirred for 5 h. After heating to room temperature the solvent was removed in vacuo. The solid reaction product was extracted into 30 mL of hexane (yellow solution). After filtration, (tBu$_3$Si)$_3$P$_5$ was crystallized from the hexane filtrate at –25 °C. Yield: 3.217 g (62%).

Selected Data for (tBu$_3$Si)$_3$P$_5$: Thermal decomposition of (tBu$_3$Si)$_3$P$_5$: 153 °C. ^{1}H NMR (C_6D_6, internal TMS): δ = 1.30 (br., 54 H, tBu), 1.29 (br., 27 H, tBu) ppm. ^{13}C{^{1}H}NMR (C_6D_6, internal TMS): δ = 26.0 (d, $^2J_{C,P}$ = 6.11 Hz, *C*Me$_3$), 26.5 (d, $^2J_{C,P}$ = 6.09 Hz, *C*Me$_3$), 26.7 (d, $^2J_{C,P}$ = 5.96 Hz, *C*Me$_3$), 31.9 (br., C*Me$_3$*), 31.4 (br., C*Me$_3$*), 32.8 (br., C*Me$_3$*) ppm. ^{29}Si{^{1}H}NMR (C_6D_6, external TMS): δ = 25.8 (m, SitBu$_3$), 24.0 (m, SitBu$_3$). 23.2 (m, SitBu$_3$) ppm. ^{31}P{^{1}H}NMR (25 °C, C_6D_6, external H_3PO_4): δ = –77.9 (m, $^1J_{P1,P5}$ = –154.1, $^1J_{P4,P5}$ = –143.4, $^2J_{P2,P5}$ = 115.5, $^2J_{P3,P5}$ = 44.0 Hz, P_5), –121.8 (m, $^1J_{P1,P3}$ = –115.3, $^1J_{P2,P3}$ = –231.6, $^1J_{P3,P4}$ = –236.7, $^2J_{P3,P5}$ = 44.0 Hz, P_3), –130.6 (m, $^1J_{P3,P4}$ = –236.7, $^1J_{P4,P5}$ = –143.4, $^2J_{P1,P4}$ = 12.0, $^2J_{P2,P4}$ = 13.4 Hz, P_4), –135.9 (m, $^1J_{P1,P2}$ = –193.3, $^1J_{P1,P3}$ = –115.3, $^1J_{P1,P5}$ = –154.1, $^2J_{P1,P4}$ = 12.0 Hz, P_1), –211.1 (m, $^1J_{P1,P2}$ = –193.3, $^1J_{P2,P3}$ = –231.6, $^2J_{P2,P4}$ = 13.4, $^2J_{P2,P5}$ = 115.5 Hz, P_2) ppm. $C_{36}H_{81}P_5Si_3$ (753.16): calcd. C 57.41, H 10.84; found C 55.08, H 9.94. MS-EI: *m*/*z* (%) = 753 (5) $[M]^+$, 554 (100) $[M - Si$$t$$Bu_3]^+$.

Table 1. Crystallographic data and further details of the structure determination of **[2Na$_4$(THF$_4$)]**, **[5aNa$_2$(THF)]$_2$**, **[5aAg$_2$]$_2$**, and **6(SitBu$_3$)**.

	[2Na$_4$(THF$_4$)]	**[5aNa$_2$(THF)]$_2$**	**[5aAg$_2$]$_2$**	**6(SitBu$_3$)**
Empirical formula	$C_{64}H_{140}Na_4O_4P_8Si_4$	$C_{80}H_{178}Na_4O_2P_{10}Si_6$	$C_{86}H_{178}Ag_4P_{10}Si_6$	$C_{39}H_{88}P_5Si_3$
Color	orange	orange	brown	yellow
Formula mass	1425.84	1742.42	2122.00	796.21
Crystal system	monoclinic	monoclinic	monoclinic	monoclinic
Space group	$P2_1/n$	$P2_1/n$	$P2_1/n$	$P2_1/c$
a [Å]	34.116(6)	15.8178(16)	17.834(3)	8.7088(6)
b [Å]	13.758(3)	14.5808(9)	15.224(2)	25.9478(19)
c [Å]	36.576(6)	23.062(2)	20.102(2)	21.8754(15)
α [°]	90	90	90	90
β [°]	91.276(7)	95.367(8)	97.672(11)	97.021(5)
γ [°]	90	90	90	90
V [Å^3], Z	17163(6), 8	5295.6(8), 2	5408.9(12), 2	4906.2(6), 4
$D_{calcd.}$ [Mg/m^3]	1.104	1.093	1.303	1.078
μ(Mo-K_α) [mm^{-1}]	0.277	0.284	0.965	0.284
F(000)	6208	1904	2232	1756
Crystal size [mm^3]	0.25×0.21×0.19	0.31×0.11×0.08	0.40×0.40×0.34	0.47×0.21×0.19
Diffractometer	Stoe-IPDS-II	Stoe-IPDS-II	Siemens Smart CCD	Stoe-IPDS-II
θ-range [deg]	1.58–25.03	3.49–25.36	1.64–30.92	1.88–25.83
Index ranges	–40 ≤ h ≤ 40, –16 ≤ k ≤ 16, –43 ≤ l ≤ 43	–18 ≤ h ≤ 19, –17 ≤ k ≤ 15, –27 ≤ l ≤ 27	–25 ≤ h ≤ 24, –21 ≤ k ≤ 21, –27 ≤ l ≤ 28	–10 ≤ h ≤ 10, –31 ≤ k ≤ 31, –26 ≤ l ≤ 26
No. of reflections collected	229 234	34 209	85 684	41 549
No. of independent reflections	30265	9551	15667	9209
R(int.)	0.3309	0.1348	0.0467	0.0656
Absorption correction	empirical	empirical	empirical	semi-empirical from equivalents
Min./max. transmission	0.934/0.9493	0.9171/0.9776	0.833/1.000	0.8781/0.9480
Data/restraints/parameters	30265/414/1513	9551/0/460	15667/0/428	9209/0/424
Goodness of fit on F^2	1.027	0.797	1.051	0.967
Final R indices [$I > 2\sigma(I)$], R1, $wR2$	0.1312, 0.2789	0.0563, 0.0892	0.0444, 0.1154	0.0320, 0.0666
Largest diff. peak/hole [e Å^{-3}]	0.523/–0.386	0.639/–0.590	3.715/–0.642	0.401/–0.191

 © 2005 Wiley-VCH Verlag GmbH & Co. KGaA, Weinheim

Thermolysis of $(t\mathrm{Bu_3Si})_3P_5$: A solution of $(t\mathrm{Bu_3Si})_3P_5$ (0.050g, 0.066 mmol) in 1 mL of C_6D_6 was heated at 120 °C for 24 h. The NMR spectra (^{1}H, ^{13}C, ^{31}P, ^{29}Si) showed only the signals of the bicyclo[1.1.0]tetraphosphane $(t\mathrm{Bu_3Si})_2P_4$ and the deuterated supersilylphosphane $t\mathrm{Bu_3SiPD_2}$. **$(t\mathrm{Bu_3Si})_2P_4$:** ^{1}H NMR (C_6D_6, internal TMS): δ = 1.21 (br., 6 *t*Bu) ppm. ^{13}C{^{1}H}NMR (C_6D_6, internal TMS): δ = 26.3 (br., *C*Me$_3$), 31.7 (br., C*Me$_3$*) ppm. ^{29}Si{^{1}H}NMR (C_6D_6, external TMS): δ = 16.4 (m, 2 Si*t*Bu$_3$) ppm. ^{31}P{^{1}H}NMR (25 °C, C_6D_6, external H_3PO_4): δ = –139.1 (t, $^1J_{P,P}$ = 100.5 Hz; PSi*t*Bu$_3$), –334.4 (t, $^1J_{P,P}$ = 100.5 Hz) ppm.

$t\mathrm{Bu_3SiPD_2}$: ^{1}H NMR (C_6D_6, internal TMS): δ = 1.11 (d, $^4J_{P,H}$ = 0.46 Hz; 3 *t*Bu) ppm. ^{13}C{^{1}H}NMR (C_6D_6, internal TMS): δ = 22.8 (d, $^2J_{C,P}$ = 6.14 Hz, *C*Me$_3$), δ = 30.9 (d, $^3J_{P,C}$ = 3.0 Hz, C*Me$_3$*) ppm. ^{29}Si{^{1}H}NMR (C_6D_6, external TMS): δ = 24.0 (d, $^1J_{P,Si}$ = 30.72 Hz, Si*t*Bu$_3$) ppm. ^{31}P{^{1}H}NMR (25 °C, C_6D_6, external H_3PO_4): δ = –268.86 (quint, $^1J_{P,D}$ = 29.43 Hz) ppm.

Reaction of $(t\mathrm{Bu_3Si})_3P_5$ with CF_3CO_2H: One drop of CF_3CO_2H was added to a solution of $(t\mathrm{Bu_3Si})_3P_5$ (0.026 g, 0.0340 mmol) in 1 mL of C_6D_6. The NMR spectra (^{1}H, ^{13}C, ^{31}P, ^{29}Si, ^{19}F) showed the signals of supersilylphosphenium trifluoroacetate $[t\mathrm{Bu_3SiPH_3}][CF_3CO_2]$, $t\mathrm{Bu_3SiO_2CCF_3}$, and P_4 as the main products.

$[t\mathrm{Bu_3SiPH_3}][CF_3CO_2]$: ^{1}H NMR ($C_6D_6$, internal TMS): δ = 0.97 (br., 3 *t*Bu) ppm. ^{13}C{^{1}H}NMR (C_6D_6, internal TMS): δ = 22.3 (br., *C*Me$_3$), 30.8 (br., C*Me$_3$*), 115.4 (q, $^1J_{C,F}$ = 284.6 Hz, *C*F$_3$), 159.3 (q, $^2J_{C,F}$ = 84.9 Hz, *C*O$_2$) ppm. ^{29}Si{^{1}H}NMR (C_6D_6, external TMS): δ = 18.3 (d, $^1J_{P,Si}$ = 24.3 Hz, Si*t*Bu$_3$).
$t\mathrm{Bu_3SiO_2CCF_3}$: ^{1}H NMR (C_6D_6, internal TMS): δ = 1.02 (s, 3 *t*Bu) ppm. ^{13}C{^{1}H}NMR (C_6D_6, internal TMS): δ = 23.2 (s, *C*Me$_3$), 29.2 (s, C*Me$_3$*), 114.8 (q, $^1J_{C,F}$ = 285.1 Hz, *C*F$_3$) 159.6 (q, $^2J_{CF}$ = 86.1 Hz, *C*O$_2$) ppm. ^{29}Si{^{1}H}NMR (C_6D_6, external TMS): δ = 22.8 (s, Si*t*Bu$_3$) ppm.

Photolysis of $[(t\mathrm{Bu_3Si})_3P_5Ag_2]_2$: A mixture of crystals of $[(t\mathrm{Bu_3Si})_3P_5Ag_2]_2 \cdot 2(C_6H_8)$ (0.044 g, 0.021 mmol) and 1 mL of C_6D_6 was irradiated at ambient temperature for 24 h. After irradiation the NMR spectra (^{1}H, ^{13}C, ^{31}P, ^{29}Si) of the reaction solution showed only the signals of the bicyclo[1.1.0]tetraphosphane $(t\mathrm{Bu_3Si})_2P_4$ and the supersilylphosphane $t\mathrm{Bu_3SiPH_2}$.

$(t\mathrm{Bu_3Si})_2P_4$: ^{1}H NMR (C_6D_6, internal TMS): δ = 1.21 (br., 6 *t*Bu) ppm. ^{13}C{^{1}H}NMR (C_6D_6, internal TMS): δ = 26.3 (br., *C*Me$_3$), 31.7 (br., C*Me$_3$*) ppm. ^{29}Si{^{1}H}NMR (C_6D_6, external TMS): δ = 16.4 (m, 2 Si*t*Bu$_3$) ppm. ^{31}P{^{1}H}NMR (25 °C, C_6D_6, external H_3PO_4): δ = –139.1 (t, $^1J_{P,P}$ = 100.5 Hz, PSi*t*Bu$_3$), –334.4 (t, $^1J_{P,P}$ = 100.5 Hz) ppm.

$t\mathrm{Bu_3SiPH_2}$: ^{1}H NMR (C_6D_6, internal TMS): δ = 1.09 (d, $^4J_{P,H}$ = 0.49 Hz, 3 *t*Bu) ppm. ^{13}C{^{1}H}NMR (C_6D_6, internal TMS): δ = 23.1 (d, $^2J_{C,P}$ = 5.86 Hz, *C*Me$_3$), 30.7 (d, $^3J_{P,C}$ = 2.44 Hz, C*Me$_3$*) ppm. ^{29}Si{^{1}H}NMR (C_6D_6, external TMS): δ = 24.1 (d, $^1J_{P,P}$ = 33.21 Hz, Si*t*Bu$_3$) ppm. ^{31}P{^{1}H}NMR (25 °C, C_6D_6, external H_3PO_4): δ = –263.82 (t, $^1J_{P,H}$ = 185.43 Hz) ppm.

X-ray Crystallographic Study: Data were collected on a Stoe-IPDS-II diffractometer or Siemens CCD three-circle diffractometer. An empirical absorption correction was performed using MULABS[21] and SADABS.[22] Structure solution was performed by direct methods,[23] and structure refinement by full-matrix least-squares on F^2 with SHELXL-97.[24] Hydrogen atoms were placed at ideal positions and refined with fixed isotropic displacement parameters using a riding model. Further details are given in Table 1.

CCDC-249924 (for **2Na**), -249925 (for **$[5aNa_2(THF)]_2$**), -253618 (for **$[5aAg]_2$**) and -249926 [for **6(Si*t*Bu$_3$)**] contain the supplementary crystallographic data for this paper. These data can be obtained free of charge from The Cambridge Crystallographic Data Center via www.ccdc.cam.ac.uk/data_request/cif.

Acknowledgments

We are grateful to the University of Frankfurt for funding and the Chemetall GmbH for a gift of *tert*-butyllithium. G. M. wishes to thank the "Fonds der Chemischen Industrie" (FCI) and the "Bundesministerium für Bildung und Forschung" (BMBF) for a Ph. D. grant.

[1] N. Wiberg, A. Wörner, K. Karaghiosoff, D. Fenske, *Chem. Ber./Recueil* **1997**, *130*, 135.
[2] N. Wiberg, A. Wörner, H.-W. Lerner, K. Karaghiosoff, D. Fenske, G. Baum, A. Dransfeld, P. von Ragué Schleyer, *Eur. J. Inorg. Chem.* **1998**, 833.
[3] N. Wiberg, *Coord. Chem. Rev.* **1997**, *163*, 217.
[4] H.-W. Lerner, M. Bolte, K. Karaghiosoff, M. Wagner, *Organometallics* **2004**, *23*, 6073.
[5] H.-W. Lerner, M. Wagner, M. Bolte, *Chem. Commun.* **2003**, 990.
[6] N. Wiberg, A. Wörner, H.-W. Lerner, K. Karaghiosoff, H. Nöth, *Z. Naturforsch., Teil B* **1998**, *53*, 1004.
[7] M. Baudler, K. Glinka, *Chem. Rev.* **1993**, *93*, 1623.
[8] H.-G. von Schnering, W. Hönle, *Chem. Rev.* **1988**, *88*, 243.
[9] M. Baudler, *Angew. Chem. Int. Ed. Engl.* **1987**, *26*, 419.
[10] M. Baudler, D. Düster, D. Ouzounis, *Z. Anorg. Allg. Chem.* **1987**, *544*, 87.
[11] M. Detzel, T. Mohr, O. J. Scherer, G. Wolmershäuser, *Angew. Chem. Int. Ed. Engl.* **1994**, *33*, 1110.
[12] E. Urnezius, W. W. Brennessel, C. J. Cramer, J. E. Ellis, P. von Ragué Schleyer, *Science* **2002**, *295*, 832.
[13] I. Krossing, I. Raabe, *Angew. Chem. Int. Ed.* **2001**, *40*, 4406.
[14] M. Gonsior, I. Krossing, L. Müller, I. Raabe, M. Jansen, L. van Wullen, *Chem. Eur. J.* **2002**, *8*, 4475.
[15] S. Böcker, M. Häser, *Z. Anorg. Allg. Chem.* **1995**, *621*, 258.
[16] N. Wiberg, K. Amelunxen, H.-W. Lerner, H. Schuster, H. Nöth, I. Krossing, M. Schmidt-Amelunxen, T. Seifert, *J. Organomet. Chem.* **1997**, *542*, 1.
[17] G. Margraf, I. Sänger, J. W. Bats, M. Wagner, H.-W. Lerner, unpublished results.
[18] M. Baudler, M. Michels, J. Hahn, M. Pieroth, *Angew. Chem. Int. Ed. Engl.* **1985**, *24*, 504.
[19] J. J. Daly, J. Maier, *Nature* **1965**, 208.
[20] R. C. Smith, E. Urnezius, K.-C. Lam, A. Rheingold, J. D. Protasiewicz, *Inorg. Chem.* **2002**, *41*, 5296.
[21] R. H. Blessing, *Acta Crystallogr., Sect. A* **1995**, *51*, 33.
[22] G. M. Sheldrick, SADABS, University of Göttingen, Germany, **2000**.
[23] G. M. Sheldrick, *Acta Crystallogr., Sect. A* **1990**, *46*, 467.
[24] G. M. Sheldrick, *SHELXL-97, A Program for the Refinement of Crystal Structures*, University of Göttingen, Germany, **1997**.
Received: November 22, 2004

 © 2005 Wiley-VCH Verlag GmbH & Co. KGaA, Weinheim

Synthesis and Structure of the First η^3-1,2-Diphosphaallyl Complexes $[(\eta^5\text{-}C_5H_5)(CO)_2M\{\eta^3\text{-}RPPC(SiMe_3)_2\}]$ (M = Mo, R = *t*Bu, Cy; M = W, R = *t*Bu) from $[(\eta^5\text{-}C_5H_5)(CO)_2M{=}P{=}C(SiMe_3)_2]$ (M = Mo, W) and Inversely Polarized Phosphaalkenes $RP{=}C(NMe_2)_2$ (R = *t*Bu, Cy)

Lothar Weber,*[a] Gabriel Noveski,[a] Ulrich Lassahn,[a] Hans-Georg Stammler,[a] and Beate Neumann[a]

Keywords: Phosphavinylidene complexes / 1,2-Diphosphaallyl complexes / Phosphaalkenes / Molybdenum / Tungsten

Reaction of $[(\eta^5\text{-}C_5H_5)(CO)_2M{=}P{=}C(SiMe_3)_2]$ [where M = Mo (**2**), W (**5**)] with the phosphaalkene *t*BuP=C(NMe$_2$)$_2$ (**1a**) afforded the η^3-1,2-diphosphaallyl complexes $[(\eta^5\text{-}C_5H_5)(CO)_2M\{\eta^3\text{-}t\text{BuPPC}(SiMe_3)_2\}]$, [where M = Mo (**3a**); M = W (**6**)]. Similarly, **2** and CyP=C(NMe$_2$)$_2$ (**1b**; where Cy = cyclohexyl) gave rise to the formation of $[(\eta^5\text{-}C_5H_5)(CO)_2Mo\{CyPPC(SiMe_3)_2\}]$ (**3b**) by a phosphinidene transfer process. Small amounts of $[\{\eta^5\text{-}C_5H_5)(CO)_2Mo\}_2\{\eta^2{:}\eta^2\text{-}Cy_3P_5\}]$ (**4**) were formed as a minor product. However, treatment of **2** and **5** with HP=C(NMe$_2$)$_2$ (**1c**) yielded the complexes $[(\eta^5\text{-}C_5H_5)(CO)_2M\{\eta^2\text{-}(Me_3Si)_2CH\text{–}P{=}P\text{–}C(NMe_2)_2\}]$ [where M = Mo (**9**), W (**10**)]. The novel compounds **3a**, **3b**, **9** and **10** were characterized by means of spectroscopy (IR, ^{1}H, ^{13}C{^{1}H}, ^{31}P{^{1}H} NMR, MS). Moreover, the molecular structures of **3a**, **3b**, **4**, **6** and **10** were determined by X-ray diffraction analysis.

(© Wiley-VCH Verlag GmbH & Co. KGaA, 69451 Weinheim, Germany, 2005)

Introduction

Inversely polarized phosphaalkenes R–P=C(NMe$_2$)$_2$ (**I**) with an electron distribution $P^{\delta-}C^{\delta+}$ about the P=C double bond may be described by two canonical formulae (**I** and **I′**).[1] This situation may well be compared with the bonding in phosphorus ylides **II** (see Scheme 1).[2]

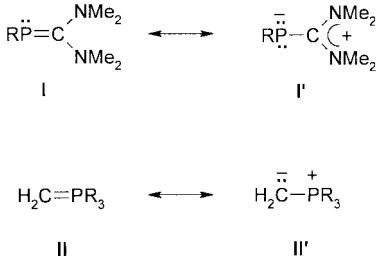

Scheme 1. Mesomeric structures of inversely polarized phosphaalkenes (**I**) and phosphorus ylides (**II**).

The chemical behavior of both classes of compounds (e.g. protonation, alkylation, complexation) can only be rationalized by using the zwitterionic structures **I′** and **II′**. Phosphorus ylides are prominent transfer reagents of alkylidene groups onto electrophilic functionalities (e.g. Wittig reaction). Phosphorus ylides undergo reaction with aryl(alkoxy)carbene complexes of the Fischer type to form enol ethers (see Scheme 2).[3]

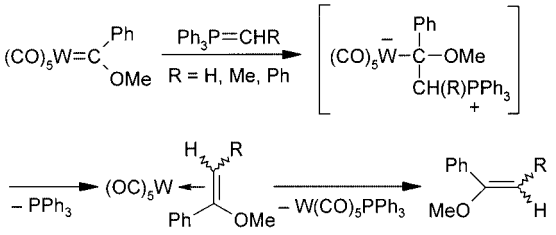

Scheme 2.: Reaction of Fischer carbene complexes with Wittig reagents.

Recently, we discovered that inversely polarized phosphaalkenes R–P=C(NMe$_2$)$_2$ [where R = *t*Bu (**1a**), Me$_3$Si (**1b**)] react with aryl(alkoxy)carbene complexes affording novel phosphaalkene complexes by a formal transfer of the phosphinidene unit onto the carbene ligand (see Scheme 3).[4]

In contrast with this behavior, reaction of the carbene complex **III** (where Aryl = 2-MeOC$_6$H$_4$) with H–P=C(NMe$_2$)$_2$ (**1c**) yielded the phosphaalkene complex **IX** as a mixture of two isomers (see Scheme 4).[4]

In the present contribution we describe the smooth transfer of phosphinidene units from phosphaalkenes **1** to the electrophilic ligand in the phosphavinylidene complexes **2** and **5**.

[a] Fakultät für Chemie der Universität Bielefeld
Universitätsstrasse 25, 33615 Bielefeld, Germany
Fax: +49-521-106-6146
E-mail: lothar.weber@uni-bielefeld.de

 © 2005 Wiley-VCH Verlag GmbH & Co. KGaA, Weinheim **DOI: 10.1002/ejic.200400995**

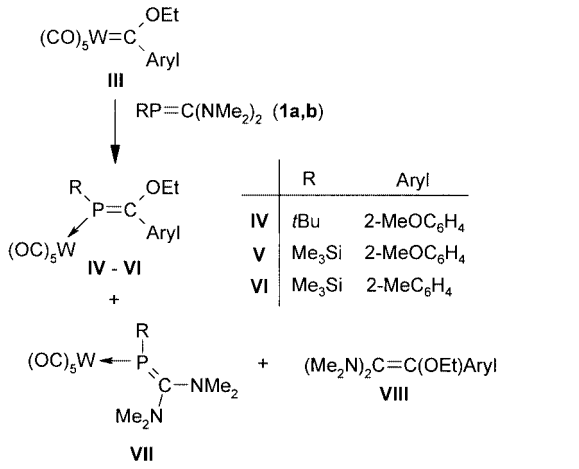

Scheme 3.: Reaction of Fischer carbene complexes with inversely polarized phosphaalkenes.

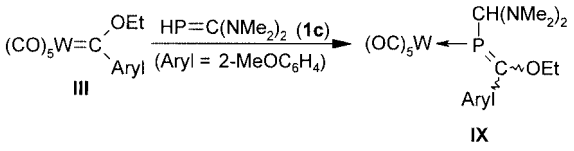

Scheme 4.: Formation of **IX**.

Results and Discussion

Reaction of the phosphavinylidene complex [(η⁵-C_5H_5)$(CO)_2$Mo=P=C$(SiMe_3)_2$] (**2**)[5] with an equimolar amount of phosphaalkene *t*BuP=C$(NMe_2)_2$ (**1a**)[4b] in toluene in the range of –30 °C to room temperature afforded the yellow complex **3a**, which was purified by column chromatography on silica (31% yield). The air- and moisture-sensitive compound is soluble in saturated hydrocarbons, ethereal and aromatic solvents (see Scheme 5). Similarly, compound **2** was converted into the orange product **3b** by treatment with CyP=C$(NMe_2)_2$ (**1b**) (49% yield). Reaction of (η⁵-C_5H_5)$(CO)_2$W=P=C$(SiMe_3)_2$ (**5**) with **1a** under comparable conditions led to the formation of complex **6** (18%yield).

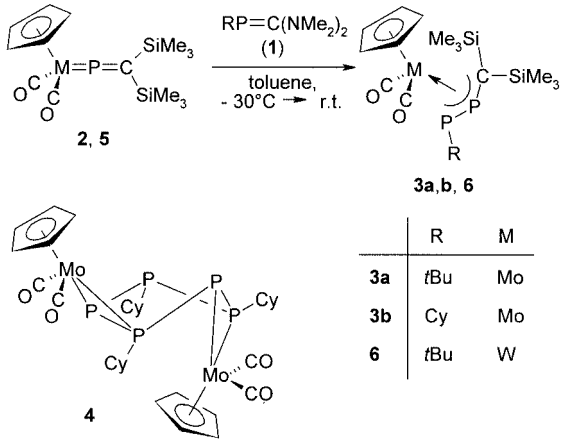

Scheme 5.: Reaction of **2**, **5** with RP=C$(NMe_2)_2$ (R = *t*Bu, Cy).

Purification of **3b** was achieved by column chromatography and crystallization of the crude yellow product from *n*-pentane. A few crystals of the dinuclear complex **4** were obtained from the concentrated mother liquors by cooling. The $^{31}P\{^1H\}$ NMR spectra of **3a**, **3b** and **6** show doublets at δ = 18.1, 2.4 and –10.7 ppm for the terminal phosphorus atoms of the ligand whereas the central ones give rise to doublets at δ = –6.8, –32.9 and –61,6 ppm. The coupling constants $^1J_{PP}$ were determined as 407.0, 382.2 and 378.8 Hz, respectively. Only in the case of **3b**, the $^{13}C\{^1H\}$ NMR spectra displayed a doublet of doublets at δ = 43.8 ($^1J_{PC}$ = 94.4; $^2J_{PC}$ = 6.9 Hz), which we assigned to the carbon atom of the diphosphaallyl ligand. Two discrete doublets for the *ortho*- and *meta*-carbon atoms of the cyclohexyl substituent agree with a centre of chirality at the central P atom. The ^{13}C NMR resonances of the carbonyl ligands were observed as two singlets in **3a** (δ = 234.3, 235.5 ppm), as a doublet and a singlet at δ = 234.1 ($^2J_{PC}$ = 47.1 Hz) and δ = 235.6 ppm in **3b** and as a singlet and a multiplet at δ = 224.4 and 227.7 ppm in **6**. These resonances are shifted to lower field than those for precursors **2** (δ = 230.4 ppm)[5b] and **5** (δ = 218.9 ppm),[5b] indicating the improved donor capacity of the diphosphaallyl ligands. This is also mirrored by the carbonyl stretching frequencies in the IR spectra of **3a**, **3b** and **6**, which are observed as intense bands at $\tilde{\nu}$ = 1943, 1877 (**3a**); 1930, 1859 (**3b**) and 1938, 1851 cm^{-1} (**6**). The corresponding bands in the precursors **2** and **5** appear at $\tilde{\nu}$ = 1944, 1882 cm^{-1} (KBr) and 1952, 1880 cm^{-1} (*n*-hexane).[5b]

Single crystals of **3a** suitable for an X-ray diffraction study were grown from a diethyl ether/pentane mixture (1:9) at –30 °C (see Figure 1). Compound **6** is isostructural to **3a**, and only the latter will be discussed in detail.[21]

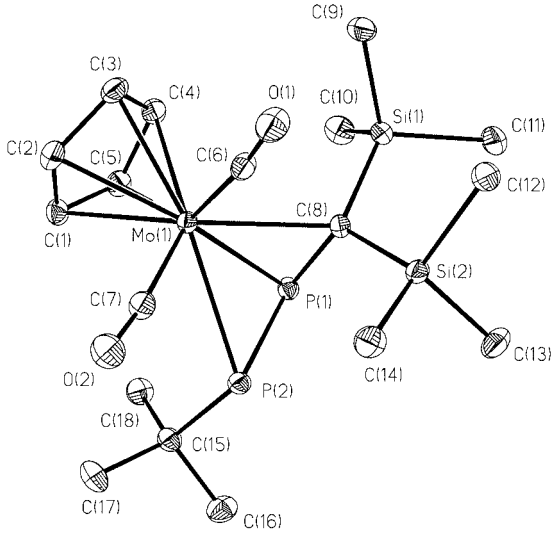

Figure 1. Molecular structure of **3a** in the crystal. Selected bond lengths [Å] and angles [°]: Mo(1)–C(6) 1.9595(12), Mo(1)–C(7) 1.9686(11), Mo(1)–C(8) 2.4372(11), Mo(1)–P(1) 2.4960(3), Mo(1)–P(2) 2.6756(3), P(1)–C(8) 1.7875(12), P(1)–P(2) 2.1234(4), P(2)–C(15) 1.8977(12), C(8)–Si(1) 1.9032(12), C(8)–Si(2) 1.9013(12), C(6)–Mo(1)–C(7) 80.84(5), C(6)–Mo(1)–C(8) 70.91(4), C(7)–Mo(1)–P(2) 64.05(4), C(8)–P(1)–P(2) 97.68(4), P(1)–P(2)–C(15) 103.75(4), P(1)–C(8)–Si(1) 108.09, P(1)–C(8)–Si(2) 123.52(6).

 © 2005 Wiley-VCH Verlag GmbH & Co. KGaA, Weinheim

The analysis displays a molecule with a distorted pianostool geometry [P(2)–Mo(1)–C(7) 64.05(4)°, C(6)–Mo(1)–C(7) 80.84(5)°, C(6)–Mo(1)–C(8) 70.91(4)°] and two nearly linear carbonyl ligands [Mo(1)–C(6)–O(1) 173.84(10)°, Mo(1)–C(7)–O(2) 173.09(11)°]. The most interesting part of the molecule is the 1,2-diphosphaallyl ligand which is unsymmetrically linked to the metal atom in an η^3-fashion via bonds Mo(1)–P(1) [2.4960(3) Å], Mo(1)–P(2) [2.6756(3) Å] and Mo(1)–C(8) [2.4372(11) Å]. The latter bond length significantly exceeds the Mo(1)–C distances displayed by the [C_5H_5Mo] part of the molecule [2.3216(12)–2.3859(12) Å]. In the η^3-1-phosphaallyl complex **7** the observed bond lengths are Mo–C(1) 2.251(3) Å and Mo–C(2) 2.357(3) Å.[6] In complex **7** the Mo–C contact to the central C atom of the phosphaallyl ligand is markedly shorter than the corresponding bond to the terminal C atom. Similarly, in complex **3a** the bond length between the metal and the terminal phosphorus atom of the ligand Mo(1)–P(2) is strongly lengthened [2.6756(3) Å] relative to the Mo(1)–P(1) bond length [2.4960(3) Å]. In complex **7** a metal–phosphorus distance of 2.5343(8) Å was measured.[6] A comparable nonsymmetric ligation of the two phosphorus atoms is present in the "butterfly complex" **8**, featuring two short bonds Mo(1,2)–P(1) [2.466, 2.470 Å] and two longer bonds Mo(1,2)–P(2) [2.542, 2.546 Å].[7]

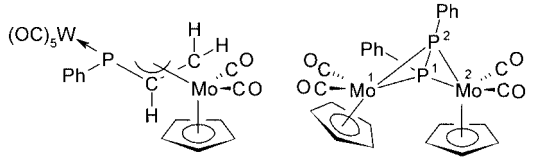

7 **8**

The distance P(1)–P(2) in **3a** [2.1234(4) Å] is intermediate between a double (ca. 2.00 Å)[8] and a single bond (ca. 2.22 Å).[9] In $Cp_2Mo(\eta^2\text{-}P_2H_2)$[10] and **8**, the P–P bond lengths amount to 2.146(3) Å and 2.136 Å, respectively. The bond length P(1)–C(8) in **3a** [1.7875(12) Å] exceeds that of a localized and unsupported P–C double bond (1.65–1.72 Å)[11] but is clearly shorter than a P–C single bond (av. 1.85 Å).[12] In **7** the corresponding bond length was determined as 1.755(3) Å. The η^3-1,2-diphosphaallyl ligand in **3a** is oriented in a fashion in which the terminal atoms P(2) and C(8) are directed towards the two carbonyl ligands. Moreover, the *tert*-butyl substituent at P(2) is located in a *syn* disposition with respect to P(1). The same is found for the atom Si(1). Atoms C(15) and Si(1) are nearly coplanar with the plane defined by the atoms P(2), P(1) and C(8) [torsion angles C(8)–P(1)–P(2)–C(15) = 170.3°; P(2)–P(1)–C(8)–Si(1) = –175.5°]. The substituent $Si(2)Me_3$ at C(8) is directed in an opposite way to the metal atom with a torsion angle P(2)–P(1)–C(8)–Si(2) = 47.1°.

Single crystals of **3b** were grown from pentane at +4 °C (see Figure 2). The analysis shows a molecule, the core of which is comparable to that of **3a** with the cyclohexyl substituent and the group $Si(2)Me_3$ directed towards the central atom P(2) of the η^3-diphosphaallyl ligand. All bond parameters are similar to those in **3a** and do not merit a detailed discussion.

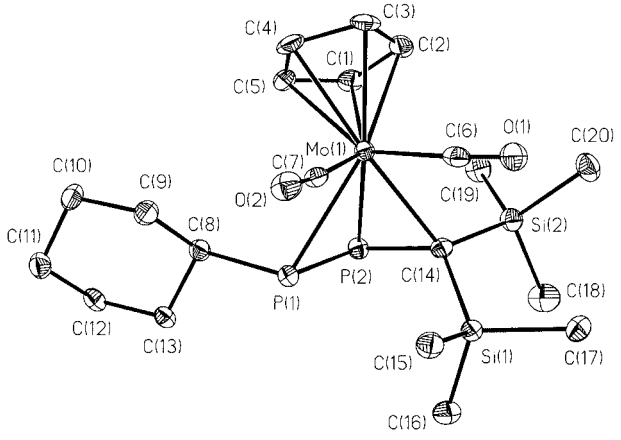

Figure 2. Molecular structure of **3b** in the crystal. Selected bond lengths [Å] and angles [°]: Mo(1)–C(6) 1.964(3), Mo(1)–C(7) 1.954(3), Mo(1)–C(14) 2.428(2), Mo(1)–P(1) 2.6538(6), Mo(1)–P(2) 2.4828(6), P(2)–C(14) 1.784(2), P(1)–C(8) 1.873(2), P(1)–P(2) 2.136(1), C(14)–Si(1) 1.907(2), C(14)–Si(2) 1.907(2); C(6)–Mo(1)–C(7) 79.51(9), C(6)–Mo(1)–C(14) 70.05(8), C(7)–Mo(1)–P(1) 64.63(7), C(14)–P(2)–P(1) 97.95(8), P(2)–P(1)–C(8) 101.18(8), P(2)–C(14)–Si(2) 110.28(12), P(2)–C(14)–Si(1) 120.21(12).

From the view-point of the rules according to Wade and Mingos, **3a** and **3b** display four skeleton atoms with 14 skeleton electrons and thus have to be regarded as *arachno* clusters.

A few crystals of compound **4** were collected from the concentrated *n*-pentane mother liquor at +4 °C (see Figure 3). The complex contains a nearly planar central 2,4,5-tri-cyclohexylcyclopentaphosphane-1,3-diyl ligand, which is

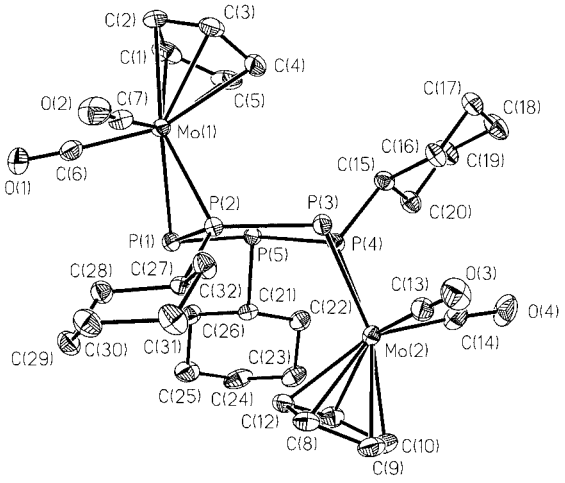

Figure 3. Molecular structure of **4** in the crystal. Selected bond lengths [Å] and angles [°]: Mo(1)–C(6) 1.958(3), Mo(1)–C(7) 1.959(3), Mo(1)–C(1–5) 2.295(2)–2.382(2), Mo(1)–P(1) 2.6204(6), Mo(1)–P(2) 2.4272(6), Mo(2)–C(13) 1.961(3), Mo(2)–C(14) 1.958(2), Mo(2)–C(8–12) 2.344(2)–2.352(2), Mo(2)–P(3) 2.5964(6), Mo(2)–P(4) 2.4480(6), P(1)–P(2) 2.1224(8), P(2)–P(3) 2.1948(8), P(3)–P(4) 2.1281(8), P(4)–P(5) 2.2214(7), P(1)–P(5) 2.2320(8), P(2)–C(27) 1.848(2), P(4)–C(15) 1.860(2), P(5)–C(21), 1.882(2), C(6)–Mo(1)–C(7) 80.67(10), C(6)–Mo(1)–P(1) 77.03(7), C(7)–Mo(1)–P(2) 83.80(7), C(13)–Mo(2)–C(14) 79.48(10), C(13)–Mo(2)–P(3) 71.83(1), C(14)–Mo(2)–P(4) 85.82(7), P(1)–P(2)–P(3) 118.98(3), P(2)–P(3)–P(4) 97.47(3), P(3)–P(4)–P(5) 115.08(3), P(1)–P(5)–P(4) 104.00(3), P(2)–P(1)–P(5) 101.95(3).

 © 2005 Wiley-VCH Verlag GmbH & Co. KGaA, Weinheim

η^2-coordinated to the $Cp(CO)_2Mo(1)$ unit via P(1) and P(2) and to the $Cp(CO)_2Mo(2)$ group via atoms P(3) and P(4). Both metal complex fragments are located on opposite sides of the P_5 ring. The bonds Mo(1)–P(1) [2.6204(6) Å] and Mo(2)–P(3) [2.5964(6) Å] between the metal centers and the tricoordinate P atoms are significantly longer than the bonds between the metal centers and the four-coordinate phosphorus atoms [Mo(1)–P(2) 2.4272(6) Å; Mo(2)–P(4) 2.4480(6) Å]. The longer Mo–P contacts may result from repulsion between the lone pair of electrons at P(1) and P(3) and the electron-rich metal atoms.

Interestingly, the η^2-ligated P–P bonds P(1)–P(2) [2.1224(8) Å] and P(3)–P(4) [2.1281(8) Å] are intermediate between double [2.00 Å][8] and single bonds [2.22 Å],[9] thus indicating some multiple bonding. In contrast to this, the endocyclic bonds P(2)–P(3) [2.1948(8) Å], P(4)–P(5) [2.2214(7) Å] and P(1)–P(5) [2.2320(8) Å] may be considered as single bonds. The cyclohexyl substituents at atoms P(2) and P(5) are directed to the face opposite Mo(1) but sterically approaching the $Mo(2)(CO)_2Cp$ moiety. To the best of our knowledge, this mode of coordination of a P_5 ring is without precedence.

It is conceivable that the formation of complexes **3a**, **3b** and **6** is initiated by a nucleophilic attack of the phosphaalkene by its P atom on the metal centre of precursors **2** or **5** to give adduct **A**. Ring closure and extrusion of $C(NMe_2)_2$ would lead to metallodiphosphiranes **B**. A σ/π-type rearrangement of **B** furnishes the final products **3a**, **3b** and **6** (see Scheme 6). Previously, Mathey et al. observed an equilibrium between a vinylphosphenium tungsten complex and its η^3-phosphaallyl isomer.[6b]

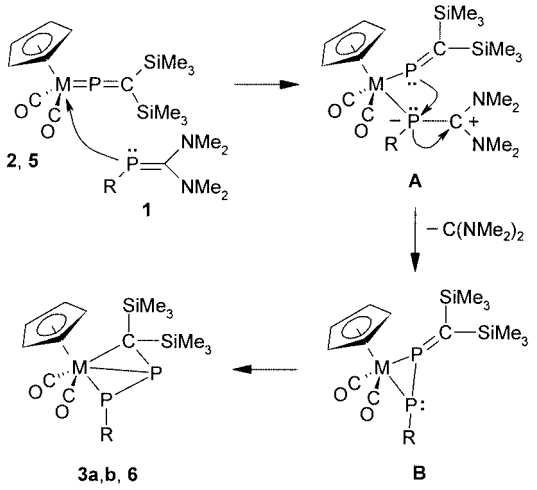

Scheme 6. Proposed mechanism for the formation of **3a**, **3b** and **6**.

Reaction of 2a and 5 with $HP=C(NMe_2)_2$ (1c)

The phosphavinylidene complex **2** was treated with an equimolar amount of phosphaalkene $HP=C(NMe_2)_2$ (**1c**)[13] in diethyl ether in the range of –30 °C to room temperature. Workup by chromatography on a column packed with silica led to the isolation of the light yellow crystalline complex **9** in 21% yield. The corresponding reaction of the tungsten analog $[Cp(CO)_2W=P=C(SiMe_3)_2]$ (**5**) with **1c** was less straightforward and yielded only a few orange crystals of product **10** (see Scheme 7).

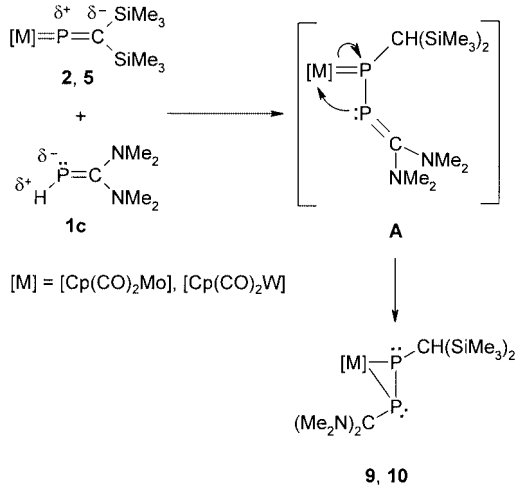

Scheme 7. Formation of **9** and **10**.

The products are very soluble in ethereal and aromatic solvents, whereas they appear to be nearly insoluble in saturated hydrocarbons. Compounds **9** and **10** are dicarbonyl(cyclopentadienyl) complexes featuring the yet unknown diphosphaallyl anion $[(Me_3Si)_2CH–P–P=C(NMe_2)_2]^-$ as an η^2 ligand. The $^{31}P\{^1H\}$ NMR spectra of **9** and **10** displayed AB spin systems at δ = –70 and –75 ppm ($^1J_{AB}$ = 421.9 Hz) and δ = –105.8 ($^1J_{WP}$ = 46.0 Hz) and –114.5 ppm ($^1J_{AB}$ = 400.0 Hz), respectively. In the ^1H NMR spectrum of **9**, the singlets at δ = 0.29, 0.51, 2.49 and 5.06 ppm are attributed to the CH and the Me_3Si groups of the $CH(SiMe_3)_2$ substituent, to the Me_2N unit and the C_5H_5 ligand, respectively. The ^{13}C NMR resonance of the carbonyl ligands of **9** was observed at δ = 203.7 ppm. In comparison with precursor **2** (δ = 230.4 ppm) this resonance is strongly shifted to high field. It is also obvious from the ν(CO) stretching frequencies in **9** ($\tilde{\nu}$ = 1889 s, 1803 cm^{-1}) and **2** (KBr, $\tilde{\nu}$ = 1944 s, 1882 cm^{-1}) that the novel ligand transfers more electron density onto the $[CpMo(CO)_2]$ unit than the phosphavinylidene ligand in **2**. Orange crystals of **10** suitable for X-ray diffraction analysis were grown from diethyl ether at 4 °C. The results of this study are shown in Figure 4, while selected bond lengths and bond angles are given in the caption. The compound consists of a central tungsten atom linked to a cyclopentadienyl ring, two terminal carbonyl ligands, and the η^2-$(Me_3Si)_2CH–P–P=C(NMe_2)_2$ diphosphaallylic ligand; the geometry around the tungsten atom is that of a "four-legged piano-stool" type. The W–P bond lengths [W(1)–P(1) 2.5352(7) Å, W(1)–P(2) 2.5695(7) Å] are not equivalent.

The longer bond is similar to the corresponding distances found in $[W(CO)_5(\mu,\eta^2{:}\eta^1{:}\eta^1)$-$P_2Cl_2\{W(CO)_5\}_2]$, that is, 2.573(4) and 2.582(4) Å.[14] According to structural work by Huttner et al.[15] or Mathey et al.[16] on $[W(CO)_5$-$(\mu,\eta^2{:}\eta^1{:}\eta^1)$-$P_2Ph_2\{W(CO)_5\}_2]$ the W–P bonds of the W–

 © 2005 Wiley-VCH Verlag GmbH & Co. KGaA, Weinheim

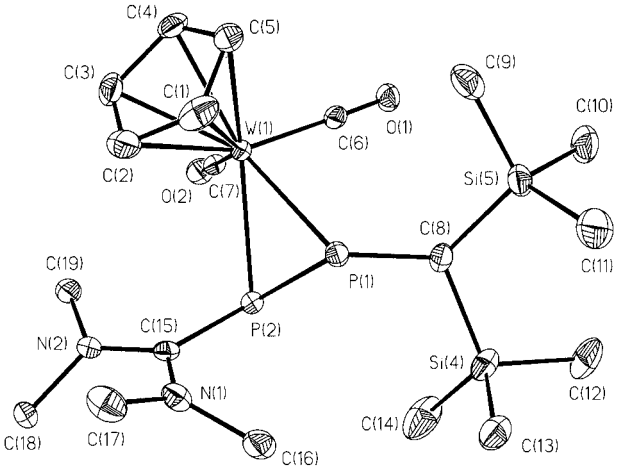

Figure 4. Molecular structure of **10** in the crystal. Selected bond lengths [Å] and angles [°]: W(1)–C(6) 1.946(3), W(1)–C(7) 1.957(3), W(1)–C(1–5) 2.337(3)–2.398(3), W(1)–P(1) 2.5352(7), W(1)–P(2) 2.5695(7), P(1)–P(2) 2.1739(9), P(1)–C(8) 1.889(3), C(8)–Si(4) 1.906(3), C(8)–Si(5) 1.916(3), P(2)–C(15) 1.878(3), N(1)–C(15) 1.342(3), N(2)–C(15) 1.356(3), N(1)–C(16) 1.472(3), N(1)–C(17) 1.477(4), N(2)–C(18) 1.478(3), N(2)–C(19) 1.468(3); C(6)–W(1)–C(7) 77.57(10), C(6)–W(1)–P(1) 84.84(7), C(7)–W(1)–P(2) 77.81(7), C(8)–P(1)–P(2) 107.60(9), P(1)–P(2)–C(15) 102.64(8), P(2)–C(15)–N(1) 123.15(19), P(2)–C(15)–N(2) 119.61(18), N(1)–C(15)–N(2) 117.1(2), C(8)–P(1)–P(2)–C(15) 150.4, P(2)–P(1)–C(8)–Si(4) –72.2, P(2)–P(1)–C(8)–Si(5) 160.0.

η^2-P_2Ph_2 unit are significantly longer [2.604 Å (av)] than in **10**. The elongation of the bond W(1)–P(2) with respect to the bond W(1)–P(1) may be the result of steric repulsion between the C_5H_5 ring and the bis(dimethylamino)carbenium unit. The P–P bond of 2.1739(9) Å is markedly longer than the bonds in complexes $[W(CO)_5(\mu,\eta^2{:}\eta^1{:}\eta^1)$-$P_2Cl_2\{W(CO)_5\}_2]$ [2.1460(6) Å] and $[W(CO)_5(\mu,\eta_2{:}\eta_1{:}\eta_1)$-$P_2Ph_2\{W(CO)_5\}_2]$ [2.140(15) Å[15] and 2.163(3) Å[16]]. It is possible to describe the bonding situation in **9** and **10** as that of a diphosphametallacyclopropane with essentially endocyclic single bonds, well aware of the fact that single bonds in cyclopropane derivatives are usually shorter than C–C bonds in unstrained C–C chains. The bond lengths P(1)–C(8) [1.889(3) Å] and P(2)–C(15) [1.878(3) Å] are as expected for single bonds. Carbon atom C(15) is trigonal planar, the formal positive charge of this carbenium center is stabilized by the planar atoms N(1) and N(2) by π conjugation, which becomes evident by the short C–N contacts [N(1)–C(15) 1.342(3) Å and N(2)–C(15) 1.356(3) Å]. Such a situation is well known from η^1 complexes of inversely polarized phophaalkenes.[1] The substituents at the P(2) unit are in an (*E*) disposition with the carbenium unit directed towards the $M(C_5H_5)$ fragment. The torsion angle C(8)–P(1)–P(2)–C(15) amounts to 150.4°. For a rationalization of the formation of **9** and **10** we postulate the formal addition of the P–H bond of the phosphaalkene **1c** to the P=C double bond of **2** and **5** to yield the intermediate **A**. Coordination of the second P atom to the metal atom with its lone pair gives the observed metalladiphosphiranes (see Scheme 7).

Conclusion

Inversely polarized phosphaalkenes $RP{=}C(NMe_2)_2$ serve as convenient sources of the phosphinidene unit PR, which can be transferred onto carbene ligands to afford η^1-phosphaalkene complexes, as was shown previously. In this paper, this synthetic principle is consistently extended to electrophilic phosphavinylidene complexes, which are cleanly converted into coordination compounds featuring the novel η^3-1,2-diphosphaallylic ligand. It is obvious that the performed synthetic method may easily be generalized with other electrophilic complexes containing vinylidene, phosphinidene, isocyanide and even carbonyl ligands. Moreover, it is tempting to also test this kind of transfer reactions with inversely polarized arsaalkenes.

Experimental Section

General: All manipulations were performed under dry, oxygen-free nitrogen using standard Schlenk techniques. Solvents were vigorously dried with an appropriate drying agent and freshly distilled under N_2 before use. The following compounds were prepared according to literature procedures: $[Cp(CO)_2M{=}P{=}C(SiMe_3)_2]$ M = Mo (**2**); M = W (**5**),[5] *t*BuP=$C(NMe_2)_2$ (**1a**),[4b] HP=$C(NMe_2)_2$ (**1c**);[13] $CyPH(SiMe_3)$,[17] $[(Me_2N)_2CSMe]I$.[18] IR spectra: Bruker FT-IR VECTOR 22. ^{1}H-, ^{13}C- and ^{31}P-NMR spectra: room temp., Bruker AM Avance DRX 500 (^{1}H, 500.13 Hz; ^{13}C, 125.75 MHz; ^{31}P, 202.46 MHz). References: $SiMe_4$ (^{1}H, ^{13}C), 85% H_3PO_4 (^{31}P). MS: Bruker Esquire Ion Trap mass spectrometer. Silica 60 (Merck) was purchased commercially.

CyP=C(NMe$_2$)$_2$ (1b): A solution of cyclohexyltrimethylsilylphosphane (18.8 g, 10.0 mmol) in 100 mL of THF was combined with an equimolar amount of a 1.6 M solution of *n*-butyllithium in *n*-hexane (6.25 mL, 10.0 mmol). The resulting slurry was added dropwise at 20 °C for 2 h to a slurry of *N*,*N*,*N*′,*N*′,*S*-pentamethylthiuronium iodide (27.4 g, 10.0 mmol) in THF (20 mL). Stirring was continued for 15 h. The solvent was removed in vacuo to afford an orange, viscous residue. The latter was triturated with *n*-pentane (150 mL) and filtered. The filter cake was washed with *n*-pentane (2 × 20 mL) and subsequently with diethyl ether until the washings became colorless. The orange-red filtrate was freed from solvents in vacuo at 20 °C. The remaining oil was distilled to give 12.0 g (56%) of **1b** as a yellow oil (b.p. ca. 100 °C at 1.5×10^{-4} bar). ^{1}H NMR (C_6D_6): δ = 1.9 (m, 11 H, C_6H_{11}), 2.56 (s, 12 H, NMe_2) ppm. ^{31}P{^{1}H} NMR (C_6D_6): δ = 57.5 (s) ppm. Because of the sensitivity of the phosphaalkene no reliable elemental analyses were obtained.

[Cp(CO)$_2$Mo{η^3-*t*BuPPC(SiMe$_3$)$_2$}] (3a): A solution of **1a** (0.24 g, 1.28 mmol) in toluene (10 mL) was added dropwise to a well-stirred, chilled solution (–30 °C) of **2** (0.52, 1.29 mmol) in toluene (15 mL). It was slowly warmed to ambient temperature and stirring was continued for 72 h. The reaction mixture was freed from solvent and volatile compounds. The black residue was transferred onto a column (d = 1.5 cm, l = 6 cm) charged with silica. A yellow phase was eluted with 40 mL of a diethyl ether/pentane mixture (1:9). Removal of solvents in vacuo afforded 0.20 g (31%) of orange crystalline **3a**. IR (KBr): $\tilde{\nu}$ = 1943 vs (CO), 1877 vs (CO), 1247 m [$\delta(SiMe_3)$], 847 m [$\rho(SiMe_3)$] cm^{-1}. ^{1}H NMR (C_6D_6): δ = 0.17 (d, $^4J_{PH}$ = 1.3 Hz, $SiMe_3$), 0.47 (d, $^4J_{PH}$ = 1.3 Hz, $SiMe_3$), 1.04 (dd, $^3J_{PH}$ = 10.8, $^4J_{PH}$ = 1.9 Hz, 9 H, *t*Bu), 4.85 (s, 5 H, Cp) ppm. ^{13}C{^{1}H} NMR (C_6D_6): δ = 4.5 (d, $^3J_{PH}$ = 9.8 Hz, $SiCH_3$), 8.8 (d, $^3J_{CP}$ = 11.3 Hz, $SiCH_3$), 32.0 [dd, J_{PC} = 14.4; 8.6 Hz, C(CH_3)$_3$],

 © 2005 Wiley-VCH Verlag GmbH & Co. KGaA, Weinheim

32.6 [d, $^2J_{PC}$ = 47.1 Hz, $C(CH_3)_3$], 90.7 (s, C_5H_5), 234.3 (s, CO), 235.2 (s, CO) ppm. $^{31}P\{^1H\}$ NMR (C_6D_6): δ = 18.1 (d, $^1J_{PP}$ = 407 Hz, P-terminal), –6.8 (d, $^1J_{PP}$ = 407 Hz, P-central) ppm. $C_{18}H_{32}MoO_2P_2Si_2$ (494.50): calcd. C 43.72, H 6.52; found C 43.61, H 6.52.

[Cp(CO)$_2$Mo{η³-CyPPC(SiMe$_3$)$_2$}] (3b) and [{Cp(CO)$_2$Mo}$_2$-η²,η²-{P$_2$(PCy)$_3$}] (4): A solution of CyP=C(NMe$_2$)$_2$ (**1b**) (0.27 g, 1.32 mmol) in toluene (15 mL) was added dropwise at room temp. to a vigorously stirred solution of **2** (0.52 g, 1.32 mmol) in toluene (15 mL). Stirring was continued for 72 h. Solvent and volatile components were removed in vacuo to give a dark-brown solid residue. The latter was chromatographed on a column (l = 6.5 cm, d = 20 cm) filled with silica. An orange-yellow zone was eluted with *n*-pentane to afford 0.30 g (44%) of orange crystalline **3b** after recrystallization. A few orange crystals of compound **4** were isolated from the mother liquor. IR (KBr): $\tilde{\nu}$ = 1930 vs (CO), 1859 vs (CO), 1246 m [δ(SiMe$_3$)], 844 m [ρ(SiMe$_3$)] cm^{-1}. ^{1}H NMR (C_6D_6): δ = 0.18 (s, 9 H, SiMe$_3$), 0.45 (s, 9 H, SiMe$_3$), 0.88–1.90 (m, 11 H, C_6H_{11}), 4.79 (s, 5 H, C_5H_5) ppm. $^{13}C\{^1H\}$ NMR (C_6D_6): δ = 3.90 (d, $^3J_{PC}$ = 9.2 Hz, SiMe$_3$), 8.1 (d, $^3J_{PC}$ = 10.3 Hz, $SiCH_3$), 26.0 (s, C–Cy), 27.1(d, $^1J_{PC}$ = 8.1 Hz, PCH), 32.9 (dd, J_{PC} = 14.4, 5.2 Hz, C–Cy), 37.3 (dd, J_{PC} = 15.5, 2.9 Hz, C–Cy), 42.7 (d, J_{PC} = 13.8 Hz, C–Cy), 43.0 (d, J_{PC} = 13.8 Hz, C–Cy), 43.8 (dd, $^1J_{PC}$ = 95.4, $^2J_{PC}$ = 6.9 Hz, PP*C*), 91.4 (s, C_5H_5), 234.1 (d, $^2J_{PC}$ = 47.1 Hz, CO), 235.6 (s, CO) ppm. $^{31}P\{^1H\}$NMR (C_6D_6): δ = –32.9 (d, $^1J_{PP}$ = 382.2 Hz, P-central), 2.4 (d, $^1J_{PP}$ = 383.2 Hz, P-terminal). $C_{20}H_{34}MoO_2P_2Si_2$ (520.54): calcd. C 46.15, H 6.58; found C 46.13, H 6.53.

[Cp(CO)$_2$W{η³-*t*BuPPC(SiMe$_3$)$_2$}] (6): A solution of **1a** (0.224 g, 1.3 mmol) in toluene (25 mL) was added dropwise at room temp. to a well-stirred solution of **5** (0.65 g, 1.3 mmol) in toluene (25 mL). After stirring for 48 h, solvent and volatile compounds were removed in vacuo. The dark-brown solid residue was chromatographed on silica with pentane, as described before. A yellow zone was eluted with pentane (230 mL). From this elute, compound **6** was isolated as a yellow solid (0.14 g, 18% yield). IR (KBr): $\tilde{\nu}$ = 1938 vs (CO), 1851 vs (CO), 1246 m [δ(SiMe$_3$)], 847 m [ρ(SiMe$_3$)] cm^{-1}. ^{1}H NMR (C_6D_6): δ = 0.16 (d, $^4J_{PH}$ = 1.3 Hz, 9 H, SiMe$_3$), 0.54 (s, 9 H, SiMe$_3$), 1.04 (dd, $^3J_{PH}$ = 10.7, $^4J_{PH}$ = 1.3 Hz, 9 H, *t*Bu), 4.89 (s, 5 H, C_5H_5) ppm. $^{13}C\{^1H\}$ NMR (C_6D_6): δ = 4.2 (d, $^3J_{PC}$ = 9.2 Hz, SiMe$_3$), 9.0 (d, $^3J_{PC}$ = 11.5 Hz, SiMe$_3$), 32.1 (dd, J_{PC} = 14.4, 8.6 Hz, $C(CH_3)_3$), 32.3 (dd, J_{PC} = 49.6, 2.5 Hz, *C*-$(CH_3)_3$), 89.1 (s, C_5H_5), 224.4 (s, CO), 222.7 (m, CO) ppm. $^{31}P\{^1H\}$ NMR (C_6D_6): δ = –10.7 (d, $^1J_{PP}$ = 378.8 Hz, P-terminal), –61.6 (d, $^1J_{PP}$ = 378.8 Hz, P-central) ppm. MS (ESI): m/z = 583 [M + H$^+$], 555 [M – CO + H$^+$], 527 [M – 220 + H$^+$]. $C_{18}H_{32}O_2P_2Si_2W$ (582.41): calcd. C 37.12, H 5.54; found C 37.31, H 5.67.

[Cp(CO)$_2$Mo{η²-(Me$_3$Si)$_2$CH–P=PC(NMe$_2$)$_2$}] (9): A solution of **1c** (0.17 g, 1.31 mmol) in diethyl ether (10 mL) was added dropwise with vigorous stirring to a chilled solution (–30 °C) of **2** (0.53 g, 1.31 mmol) in diethyl ether (15 mL). The brown reaction mixture was warmed to ambient temp. and stirred for 24 h. Solvent and volatile components were removed in vacuo. The black, oily residue was transferred to a column (d = 1.5 cm, l = 6 cm) filled with silica. A yellow phase, eluted with 40 mL of a diethyl ether/*n*-pentane mixture (1:9) was discarded. Subsequently, a burgundy-red phase was eluted with 40 mL of diethyl ether. Removal of solvent led to the isolation of the orange solid **9**. IR (KBr): $\tilde{\nu}$ = 1889 (s, CO), 1803 s (CO), 1260 m [δ(SiMe$_3$)], 840 s [ρ(SiMe$_3$)] cm^{-1}. ^{1}H NMR (C_6D_6): δ = 0.29 (s, ^{1}H, $CHSi_2$), 0.51 (s, 18 H, SiMe$_3$), 2.49 (s, 12 H, NMe$_2$), 5.06 (s, 5 H, C_5H_5) ppm. $^{13}C\{^1H\}$ NMR (C_6D_6): δ = 2.3 (d, $^2J_{CP}$ = 7 Hz, $SiCH_3$), 3.7 (d, $^2J_{CP}$ = 7 Hz, $SiCH_3$), 16.9 (d, $^1J_{CP}$ = 79.3 Hz, $CHSi_2$), 42.5 (br. s, NCH_3), 44.2 (br. s, NCH_3), 91.3 (s, C_5H_5), 203.7 (s, CO) ppm. $^{31}P\{^1H\}$ NMR (C_6D_6): δ = –70.0, –75.0 [AB-spin system, $^1J_{PP}$ = 421 Hz, (Me$_2$N)C*P* and *P*CH(SiMe$_3$)$_2$] ppm. MS (ESI): m/z = 541 [M + H$^+$]. $C_{19}H_{36}MoN_2O_2P_2Si_2$ (538.56): calcd. C 42.37 H 6.74 N 5.06, found C 41.88 H 6.64 N 5.20).

[Cp(CO)$_2$W{η²-(Me$_3$Si)$_2$CH–P=P–C(NMe$_2$)$_2$}] (10): Analogously, equimolar amounts of **1c** (0.17 g, 1.30 mmol) and **5** (0.64 g, 1.30 mmol) were allowed to react in diethyl ether (10 mL). Analogous workup by chromatography and recrystallization from diethyl

Table 1. Crystal data and data-collection parameters.

	3a	**3b**	**4**	**10**
Empirical formula	$C_{18}H_{32}MoO_2P_2Si_2$	$C_{20}H_{34}MoO_2P_2Si_2$	$C_{32}H_{43}Mo_2O_4P_5$	$C_{19}H_{36}N_2O_2P_2Si_2W$
M_r [g mol^{-1}]	494.50	520.53	838.39	626.47
Crystal dimensions [mm]	0.30 × 0.25 × 0.10	0.16 × 0.09 × 0.04	0.15 × 0.13 × 0.04	0.24 × 0.07 × 0.03
Crystal system	monoclinic	monoclinic	monoclinic	monoclinic
Space group	$P2_1/c$	$P2_1/n$	$P2_1/n$	$P2_1/c$
a [Å]	13.7330(1)	7.8680(2)	11.6440(2)	21.437(2)
b [Å]	11.5360(1)	34.6270(5)	10.8760(2)	9.7132(8)
c [Å]	14.7690(1)	9.0300(2)	27.8690(4)	12.8112(17)
β [°]	102.1270(7)	98.5600(7)	98.9550(8)	101.664(10)
V [Å^3]	2287.55(3)	2432.77(9)	3486.31(10)	2612.5(5)
Z	4	4	4	4
$\rho_{calcd.}$ [g cm^{-3}]	1.436	1.421	1.597	1.593
μ [mm^{-1}]	0.827	0.782	0.984	4.652
F(000)	1024	1080	1704	1248
θ [°]	3.33–30.00	3.16–25.00	2.96–27.50	3.09–30.00
No. refl. collected	64677	28194	62827	58131
No. refl. unique	6649	4281	7959	7603
R (int)	0.031	0.050	0.053	0.0563
No. refl. [$I > 2\sigma(I)$]	6054	3656	6421	6213
Refined parameters	235	250	388	263
GOF	1.062	1.040	1.032	1.040
R_F [($I > 2\sigma(I)$]	0.0206	0.0248	0.0280	0.0238
wR_{F2} [$I > 2\sigma(I)$]	0.0520	0.0559	0.0637	0.0501
$\Delta\rho_{max./min.}$ [e Å^{-3}]	0.482/–0.462	0.365/–0.363	0.479/–0.384	0.932/–0.715

 © 2005 Wiley-VCH Verlag GmbH & Co. KGaA, Weinheim

ether led to a few burgundy-red crystals of **10**. ^{1}H NMR (C_6D_6): δ = 0.28 (s, 1 H, $CHSi_2$), 0.51 (s, 18 H, $SiMe_3$), 2.45 (s, 12 H, NMe_2), 5.05 (s, 5 H, Cp) ppm. $^{31}P\{^1H\}$ NMR (C_6D_6): δ = –105.8 [AB spin system, $^1J_{PP}$ = 400, $^1J_{WP}$ = 46 Hz, $PCH(SiMe_3)_2$], –114.5 [AB spin system, $^1J_{PP}$ = 400 Hz, $(MeN)_2CP$] ppm.

X-ray Crystallography: Crystallographic data were collected with a Nonius Kappa CCD diffractometer with Mo-K_α radiation (graphite monochromator, λ = 0.71073 Å) at 100 K. Crystallographic programs used for the structure solution and refinement were from SHELXS-97,[19] SIR-97,[20] and SHELXL-97.[19] The structures were solved by Direct Methods and were refined by using full-matrix least squares on F^2 of all unique reflections with anisotropic thermal parameters for all non-hydrogen atoms. Hydrogen atoms were included at calculated positions with U(H) = 1.2 U_{eq} for CH_2 groups, U(H) = 1.5 U_{eq} for CH_3 groups. Crystal data of the compounds are listed in Table 1.[21]

[1] Review: L. Weber, *Eur. J. Inorg. Chem.* **2000**, 2425–2441.
[2] *Ylides and Imines of Phosphorus* (Ed.: A. W. Johnson), Wiley, New York **1993**.
[3] C. P. Casey, T. J. Burkhardt, *J. Am. Chem. Soc.* **1972**, *94*, 6543–6544.
[4] a) L. Weber, B. Quasdorff, H.-G. Stammler, B. Neumann, *Chem. Eur. J.* **1998**, *4*, 469–475; b) L. Weber, M. Meyer, H.-G. Stammler, B. Neumann, *Chem. Eur. J.* **2001**, *7*, 5401–5408; c) L.Weber, M. Meyer, H.-G Stammler, B. Neumann, *Organometallics* **2003**, *22*, 5063–5068.
[5] a) A. M. Arif, A. H. Cowley, C. M. Nunn, S. Quashie, N. C. Norman, A. G. Orpen, *Organometallics* **1989**, *8*, 1878–1884; b) E. Niecke, H. J. Metternich, M. Nieger, D. Gudat, P. Wenderoth, W. Malisch, C. Hahner, W. Reich, *Chem. Ber.* **1993**, *126*, 1299–1309.
[6] a) C. Hugel–Le Goff, F. Mercier, L. Ricard, F. Mathey, *J. Organomet. Chem.* **1989**, *363*, 325–335; b) F. Mercier, F. Mathey, *Organometallics* **1990**, *9*, 863–864.
[7] D. Fenske, K. Merzweiler, *Angew. Chem.* **1986**, *98*, 357–368; *Angew. Chem. Int. Ed. Engl.* **1986**, *25*, 338.
[8] Review: L. Weber, *Chem. Rev.* **1992**, *92*, 1839–1906.
[9] K. F. Tebbe, *Z. Anorg. Allg. Chem.* **1980**, *468*, 202–212.
[10] E. Camillo, A. Coda, K. Prout, J.-C. Daran, *Acta Crystallogr. Sect. B* **1977**, *33*, 2608–2611.
[11] Review: L. Weber, *Angew. Chem.* **1996**, *108*, 292–310; *Angew. Chem. Int. Ed. Engl.* **1996**, *35*, 271–288.
[12] D. D. C. Corbridge, *The Structural Chemistry of Phosphorus*, Elsevier Scient. Publ. Comp., Amsterdam, **1974**.
[13] M. I. Povolotskii, V. V. Negrebetskii, V. D. Romanenko, V. I. Ivanchenko, T. V. Sarina, L. N. Markovskii, *Zh. Obshch. Khim.* **1990**, *60*, 2238–2244; *Chem. Abstr.* **1991**, *115*, 8934w.
[14] V. Vogel, G. Stößer, M. Scheer, *Angew. Chem.* **2001**, *113*, 1476–1478; *Angew. Chem. Int. Ed. Engl.* **2001**, *40*, 1443–1445.
[15] G. Huttner, J. Borm, L. Zsolnai, *J. Organomet. Chem.* **1986**, *304*, 309–321.
[16] A. Marinetti, C. Charrier, F. Mathey, J. Fischer, *Organometallics* **1985**, *4*, 2134–2138.
[17] G. Becker, O. Mundt, M. Rössler, E. Schneider, *Z. Anorg. Allg. Chem.* **1978**, *443*, 42–52.
[18] H. Lecher, C. Heuck, *Justus Liebigs Ann. Chem.* **1924**, *438*, 179–184.
[19] G. M. Sheldrick, *SHELX-97, program for crystal structure refinement*, University of Göttingen, **1997**.
[20] A. Altomare, M. C. Burla, M. Camalli, B. Carrozzini, G. L. Cascarano, C. Giacovazzo, A. Guagliardi, A. G. G. Moliterni, G. Polidori, R. Rizzi, *J. Appl. Crystallogr.* **1999**, *32*, 115–119.
[21] Further details of the crystal structure investigations are available. CCDC-256916 (**3a**), -255215 (**3b**), -255216 (**4**), -255214 (**6**) and -255217 (**10**) contain the supplementary crystallographic data for this paper. These data can be obtained free of charge from The Cambridge Crystallographic Data Centre via www.ccdc.cam.ac.uk/data_request/cif., together with the names of the authors, and the journal citation.

Received: December 1, 2004

 © 2005 Wiley-VCH Verlag GmbH & Co. KGaA, Weinheim

Extended Structures and Magnetic Properties of Lanthanide–Copper Complexes with Picolinic Acids as Bridging Ligands

A-Qing Wu,[a] Guang-Hua Guo,[a] Chun Yang,[a] Fa-Kun Zheng,[a] Xi Liu,[a] Guo-Cong Guo,*[a] Jin-Shun Huang,[a] Zhen-Chao Dong,*[b] and Yoshihiko Takano[c]

Keywords: Heterometallic complexes / Magnetic properties / Crystal structures / Picolinic acid / Coordination polymers

The first examples of 3d–4f heterometallic complexes containing picolinic acid ligands were synthesized and characterized. Three series of complexes were obtained by the reaction of presynthesized "metallo ligands" $Cu(pic)_2$ and $Ln(ClO_4)_3$ in 2:1, 3:1, and 4:1 mole ratios. Complexes **1**–**3** (denoted as the first series), $[LnCu_2(pic)_4(H_2O)_6](ClO_4)_3{\cdot}H_2O$ (Ln = Sm, Nd, and Pr), are isomorphous and exhibit infinite 1D zigzag chain structures with rare earth ions in tricapped trigonal prismatic coordination. Complexes **4**–**10** (denoted as the second series), $[Ln_2Cu_5(pic)_{10}(H_2O)_8](ClO_4)_6{\cdot}2H_2O$ (Ln = Gd, Nd, Sm, Dy, Eu, Pr, and Yb), are isomorphous too, and exhibit extended 2D layered structures constituted by $Cu(pic)_2$ moieties bridging the zigzag chains. Complex **11** (denoted as the third-type complex), $\{NdCu(pic)_2[CO(NH_2)_2]_4(H_2O)_3\}(ClO_4)_3{\cdot}[Cu(pic)_2]_2$, exhibits another type of nearly linear chain structure with additional $Cu(pic)_2$ moieties trapped in the lattice by hydrogen bonds. Temperature-dependent magnetizations of complexes **2**–**4**, **6**, and **11** indicate that these complexes follow the Curie–Weiss paramagnetic behavior down to 5 K.
(© Wiley-VCH Verlag GmbH & Co. KGaA, 69451 Weinheim, Germany, 2005)

Introduction

Studies on the syntheses, structures and properties of 3d–4f heterometallic complexes are currently of great interest because they are good models for the investigation of the nature of the magnetic interactions between 3d and 4f metal ions in magnetic materials.[1] The main synthetic strategy for 3d–4f complexes is to use bridging ligands to link 3d and 4f paramagnetic building blocks to generate discrete polynuclear or extended topological complexes of high dimensionalities, while the latter may enhance and improve bulk magnetic properties due to the increased number of interacting neighbors.[2] Since the Ln and M (M = transition metal) ions may be connected through bidentate carboxylate groups, efforts have been made to use carboxylate acids and carboxylate-like betaines as ligands. Many such studies focused on discrete polynuclear complexes such as LnM, LnM_2, Ln_2M_2, Ln_2M_4, Ln_2M_8 etc.[3–7] In comparison, multidimensional heterometallic complexes are relatively rare,[8] and the synthesis of the multidimensional 3d–4f complexes is still a great challenge. An effective strategy employed is the use of relatively stable metal complexes containing potential coordinating atoms, that is "metallo ligands", to link rare earth ions to form polymeric networks. This strategy is called stepwise synthesis.[4b,9] In our laboratory, we have synthesized a series of polymeric 3d–4f complexes through the use of carboxylate groups as bridging units.[10] As an extension of this work, picolinic acid (Hpic) was used as a chelating ligand to make the $[COH(NH_2)_2]_2[Cu(pic)_2(ClO_4)_2]$ precursor by reaction with $Cu(ClO_4)_2$;[11] The monomer $Cu(pic)_2$ can be used as a "metallo ligand" to bind lanthanide metal ions for the preparation of complexes containing rare earth and transition metals. We have successfully obtained three novel series of one- and two-dimensional 3d–4f coordination polymers, namely, $[LnCu_2(pic)_4(H_2O)_6](ClO_4)_3{\cdot}H_2O$ [Ln = Sm (**1**), Nd (**2**), and Pr (**3**)] (1D), $[Ln_2Cu_5(pic)_{10}(H_2O)_8](ClO_4)_6{\cdot}2H_2O$ [Ln = Gd (**4**), Nd (**5**), Sm (**6**), Dy (**7**), Eu (**8**), Pr (**9**), and Yb (**10**)] (2D) and $\{NdCu(pic)_2[CO(NH_2)_2]_4(H_2O)_3\}(ClO_4)_3{\cdot}[Cu(pic)_2]_2$ (**11**) (1D). Although picolinic acid ligands were previously used to synthesize a number of metal complexes with transition metals or rare earths alone,[12] to the best of our knowledge, mixed multinuclear or multidimensional 3d–4f heterometallic complexes with picolinic acid ligands have not been reported. Herein, we report the syntheses and structures of **1**–**11**, as well as the magnetic properties of **2**–**4**, **6**, and **11**.

[a] State Key Laboratory of Structural Chemistry, Fujian Institute of Research on the Structure of Matter, Chinese Academy of Sciences,
Fuzhou, Fujian 350002, People's Republic of China
Fax: +86-591-3714946
E-mail: gcguo@ms.fjirsm.ac.cn
[b] Hefei National Laboratory for Physical Sciences at Microscale, University of Science and Technology of China,
96 Jinzhai Road, Hefei, Anhui 230026, People's Republic of China
[c] National Institute for Materials Science,
1-2-1 Sengen, Tsukuba, Ibaraki 305–0047, Japan

Results and Discussion

Syntheses

In order to construct such extended 3d–4f heterometallic structures, an assembly reaction is designed to have the $Cu(pic)_2$ complex acting as a 3d-component precursor and $Ln(ClO_4)_3$ as a 4f-component. The $Cu(pic)_2$ complex with two non-coordinated oxygen atoms of carboxyl groups may function as a "metallo ligand" to the Ln^{III} component. In the course of the investigation, the one-dimensional chain complexes **1**–**3**, $[LnCu_2(pic)_4(H_2O)_6](ClO_4)_3{\cdot}H_2O$, were obtained by the reaction of a 2:1 mole ratio of $Cu(pic)_2$ and $Ln(ClO_4)_3$ in C_2H_5OH/CH_3CN mixed solution at room temperature. Structural analyses indicate that the Ln^{III} atoms in **1**–**3** are surrounded by three $Cu(pic)_2$ moieties in a T-shape fashion to form a zigzag chain structure with large open spaces on the Ln ions (see Figure 1), which suggests that the Ln ions can be further coordinated by more $Cu(pic)_2$ ligands to form higher dimensional structures. On the basis of this idea, the mole ratio of $Cu(pic)_2$ to $Ln(ClO_4)_3$ was increased to 3:1, and seven expected two-dimensional heterometallic isomorphs, $[Ln_2Cu_5(pic)_{10}(H_2O)_8](ClO_4)_6{\cdot}2H_2O$ (**4**–**10**), were successfully obtained. However, we failed to synthesize a three-dimensional heterometallic complex by further increasing the mole ratio to 4:1 with the addition of more carbamide to maintain the pH at 5. Instead, a new structure with a nearly linear one-dimensional chain, $\{NdCu(pic)_2[CO(NH_2)_2]_4(H_2O)_3\}(ClO_4)_3{\cdot}[Cu(pic)_2]_2$ (**11**), showed up with "superfluous" $Cu(pic)_2$ moieties trapped in the lattice. The failure may be related to the large steric effect of $Cu(pic)_2$ ligands and competition coordination of carbamide.

Crystal Structures

The crystal structures of **1**–**11** were determined by single-crystal X-ray diffraction analyses. The crystallographic data are summarized in Table 1 for **1**–**3**, Table 2 for **4**–**6**, Table 3 for **7**–**9**, and Table 4 for **10** and **11**. Complexes **1**–**3** and **4**–**10** are isomorphous, so we chose complexes **1**, **4,** and **11** to

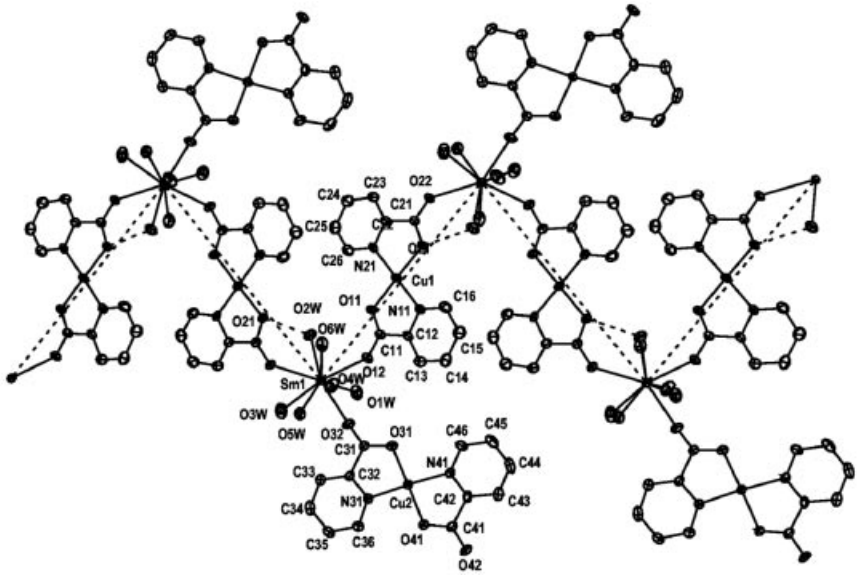

Figure 1. The chain structure of **1** extending along the *b* direction with 35% thermal ellipsoids.

Table 1. Crystal data and structure refinements for complexes **1**–**3**.

Complex $LnCu_2(pic)_4(H_2O)_6$ $(ClO4)_3{\cdot}H_2O$	**1** ($SmCu_2$)	**2** ($NdCu_2$)	**3** ($PrCu_2$)
Formula	$C_{24}H_{30}Cl_3Cu_2N_4O_{27}Sm$	$C_{24}H_{30}Cl_3Cu_2N_4NdO_{27}$	$C_{24}H_{30}Cl_3Cu_2N_4O_{27}Pr$
Fw	1190.30	1184.19	1180.86
Space group	*Pcab*	*Pcab*	*Pcab*
a [Å]	13.690(2)	13.7095(1)	13.7046(3)
b [Å]	14.8425(6)	14.8578(2)	14.8745(1)
c [Å]	39.3740(6)	39.4425(4)	39.4457(7)
V [Å^3]	8000.5(11)	8034.2(2)	8041.0(2)
Z	8	8	8
ρ [g cm^{-3}]	1.973	1.975	1.951
μ [mm^{-1}]	2.635	2.793	2.541
λ [Å]	0.71073	0.71073	0.71073
T [K]	293(2)	293(2)	293(2)
R_1,wR_2 (obs.)	0.0569, 0.1558	0.0583, 0.1323	0.0666, 0.1553
Goodness of fit	1.023	1.037	1.091

 © 2005 Wiley-VCH Verlag GmbH & Co. KGaA, Weinheim

Table 2. Crystal data and structure refinements for complexes **4**–**6**.

Complex $[Ln_2Cu_5(pic)_{10}(H_2O)_8]\cdot 6[ClO_4]\cdot 2H_2O$	Gd_2Cu_5	Nd_2Cu_5	Sm_2Cu_5
Formula	$C_{60}H_{60}Cl_6Cu_5Gd_2N_{10}O_{54}$	$C_{60}H_{60}Cl_6Cu_5N_{10}Nd_2O_{54}$	$C_{60}H_{60}Cl_6Cu_5N_{10}O_{54}Sm_2$
Fw	2630.08	2604.06	2616.28
Space group	$P\bar{1}$	$P\bar{1}$	$P\bar{1}$
a [Å]	8.7129(17)	8.721(2)	8.7205 (1)
b [Å]	14.900(3)	14.9145 (1)	14.9373 (1)
c [Å]	16.791(3)	16.8147(2)	16.8181 (1)
α [°]	81.59(3)	81.563(1)	81.612 (1)
β [°]	86.29(3)	86.260(1)	86.449 (1)
γ [°]	84.59(3)	84.621(1)	84.614 (1)
V [Å^3]	2143.9(7)	2150.84(3)	2155.14(3)
Z	1	1	1
ρ [g cm^{-3}]	2.037	2.010	2.016
μ [mm^{-1}]	3.043	2.699	2.851
λ [Å]	0.71073	0.71073	0.71073
T [K]	293(2)	293(2)	293(2)
R_1, wR_2 (obs.)	0.0408, 0.1106	0.0629, 0.1584	0.0386, 0.0926
Goodness of fit	1.027	1.038	1.040

Table 3. Crystal data and structure refinements for complexes **7**–**9**.

Complex $[Ln_2Cu_5(pic)_{10}(H_2O)_8]\cdot 6[ClO_4]\cdot 2H_2O$	Dy_2Cu_5	Eu_2Cu_5	Pr_2Cu_5
Formula	$C_{60}H_{60}Cl_6Cu_5Dy_2N_{10}O_{54}$	$C_{60}H_{60}Cl_6Cu_5Eu_2N_{10}O_{54}$	$C_{60}H_{60}Cl_6Cu_5N_{10}O_{54}Pr_2$
Fw	2640.58	2619.50	2597.40
Space group	$P\bar{1}$	$P\bar{1}$	$P\bar{1}$
a [Å]	8.71790(10)	8.7140(2)	8.68860(10)
b [Å]	14.9062(3)	14.8939(3)	14.8669(1)
c [Å]	16.8218(3)	16.7935(4)	16.7575(3)
α [°]	81.5480(10)	81.6600(10)	81.5770(10)
β [°]	86.2290(10)	86.3550(10)	86.315(1)
γ [°]	84.4550(10)	84.5680(10)	84.6630(10)
V [Å^3]	2149.19(6)	2144.07(8)	2129.16(5)
Z	1	1	1
ρ [g cm^{-3}]	2.040	2.029	2.037
μ [mm^{-1}]	3.231	2.959	2.652
λ [Å]	0.71073	0.71073	0.71073
T [K]	293(2)	293(2)	293(2)
R_1, wR_2 (obs.)	0.0412, 0.0889	0.0519, 0.0989	0.0650, 0.1499
Goodness of fit	1.062	1.071	1.080

represent the three series for detailed structure discussions. The structural details of the other complexes, **2**, **3**, and **5**–**10**, are deposited with the CCDC.

Table 4. Crystal data and structure refinements for complexes **10** and **11**.

Complex	Yb_2Cu_5	NdCu
Formula	$C_{60}H_{60}Cl_6Cu_5Dy_2N_{10}O_{54}$	$C_{40}H_{46}Cl_3Cu_3N_{14}NdO_{31}$
Fw	2661.66	1660.12
Space group	$P\bar{1}$	$P2_1/c$
a [Å]	8.67570(10)	10.514(2)
b [Å]	14.8466(3)	22.311(5)
c [Å]	16.7580(1)	25.781(5)
α [°]	81.346(1)	90
β [°]	85.909(1)	96.35(3)
γ [°]	84.322(1)	90
V [Å^3]	2119.96(5)	6011(2)
Z	1	4
ρ [g cm^{-3}]	2.085	1.835
μ [mm^{-1}]	3.719	2.133
λ [Å]	0.71073	0.71073
T [K]	293(2)	293(2)
R_1, wR_2 (obs.)	0.0334, 0.0732	0.0614, 0.1709
Goodness of fit	1.064	1.016

$[LnCu_2(pic)_4(H_2O)_6](ClO_4)_3\cdot H_2O$ [Ln = Sm (1), Nd (2), and Pr (3)]

Complex **1** consists of one-dimensional chain $\{[SmCu_2(pic)_4(H_2O)_6]^{3+}\}_\infty$ cations, $[ClO_4]^-$ anions, and lattice water molecules, as shown in Figure 1. The coordination polyhedron of the nine-coordinate Sm atom can be described as a distorted tricapped trigonal prism, which is constructed by three carboxylic oxygen atoms from $Cu(pic)_2$ moieties and six water oxygen atoms. The two trigonal surfaces are both defined by two water O atoms and one carboxylic oxygen atom of one $Cu(pic)_2$ moiety (O2W, O6W and O12 atoms for the top surface, and O3W, O5W and O32 atoms for the bottom surface), while the three capping atoms are occupied by the remaining three coordinated oxygen atoms (O1W, O4W and O22), the Sm^{III} atom deviating from the plane by 0.034(1) Å. The O(cap)-Sm-O(cap) bond angles are 119.41(6) ° for O1W–Sm1–O22, 124.8 ° for O1W–Sm1–O4W, and 115.72(6) ° for O22–Sm–O4W; these are close to 120 ° in a regular triangle. The average Sm–O(prism) bond

 © 2005 Wiley-VCH Verlag GmbH & Co. KGaA, Weinheim

lengths of 2.471(2) Å are shorter than average Sm–O(cap) bond lengths of 2.556(2) Å, as in the case found in Ln complexes.[13,10] The Ln–O bond lengths in **1**–**3** become shorter with increasing atomic number of Ln, because of the lanthanide contraction.

The $Cu(pic)_2$ moieties are nearly coplanar with a maximal deviation of 0.093(4) Å of Cu(2) in the $Cu(2)(pic)_2$ moiety, in which the Cu^{II} atom possesses an approximate centro-symmetric square-planar coordination environment, chelated by two picolinic acid ligands through the nitrogen atoms and carboxylic oxygen atoms of pic ligands. Four donor atoms N_2O_2 of pic ligands form a rectangle with angles close to 90 ° (88.01–92.48 °). The average Cu–N and Cu–O bond lengths are 1.972(3) and 1.940(2) Å, respectively; these lengths are consistent with those found in the $Cu(pic)_2$ complex reported previously.[11]

The Sm^{III} centers act as two-connected nodes and are bridged by two uncoordinated carboxylic O atoms of $Cu(1)(pic)_2$ moieties to form an infinite zigzag 1D chain extending along the *b* direction with the angle Cu1–Sm–Cu1 = 78.474(4) ° and Sm–Cu1–Sm = 174.89(1)° (Figure 1). Simultaneously, there exists a kind of intramolecular hydrogen bond between the atoms O21 and O2W (O2W···O21#A = 2.725(2) Å, symmetry code #A: *x*, –0.5 + *y*, 0.5 – *z*) as shown in Figure 2. The $Cu(2)(pic)_2$ moiety acts as a terminal ligand coordinated to the Sm^{III} ion through one of two uncoordinated carboxylic oxygen atoms. The Sm^{III} and Cu^{II} ions in the chain are nearly coplanar. The shortest intrachain Sm···Cu, Cu···Cu, and Sm···Sm separations are 5.8524(6), 7.4301(3), and 11.7349(5) Å, respectively. The adjacent chains are linked into two-dimensional structure along the *c* direction by intermolecular hydrogen bonds of O1W···O42#B and O5W···O42#B (symmetry code #B: –*x*, 1 – *y*, –*z*) with an average length of 2.837(3) Å, as shown in Figure 2. In each layer, there also exist π–π stacking interactions between the pyridine rings of the terminal coordinated $Cu(2)(pic)_2$ moieties from the adjacent chains with the centroid-centroid distance of 3.766 Å and the dihedral angle of 2.39 °. The lattice water molecules and ClO_4^- anions with hydrogen bonds among them are located between the layers (O7W···O16#C = 3.046 Å; O7W···O33#C = 3.051 Å, symmetry code #C: *x* – 1, *y*, *z*). These lattice molecules form hydrogen bonds with the coordinated water molecules in the layer. These hydrogen bonds bridge the layers to form a three-dimensional framework along the *a* direction. Such π–π stacking and hydrogen bonding interactions lead to the stabilization of the crystal structure.

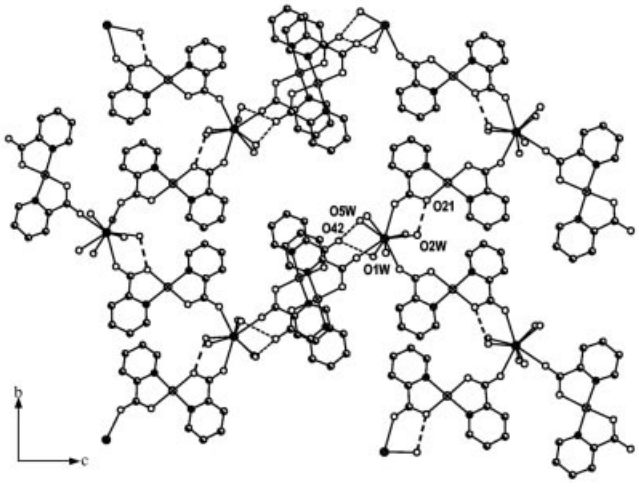

Figure 2. The hydrogen bonding and π–π stacking interactions link the chains into a layer-like structure in **1** along the *c* axis. The intermolecular hydrogen bonds are represented by the thin dashed lines and the intramolecular hydrogen bonds by the thick dashed lines.

[$Ln_2Cu_5(pic)_{10}(H_2O)_8$][$(ClO_4)_6$·$2H_2O$ [Ln = Gd (4), Nd (5), Sm (6), Dy (7), Eu (8), Pr (9) and Yb (10)]

Figure 3 shows the structure of **4** with the asymmetric atoms labeled. The coordination polyhedron of eight-coordinate Gd^{III} can be viewed as a distorted square antiprism, formed by the four carboxylic oxygen atoms from four picolinic acid ligands and four neutral water molecules. One square plane is defined by three water O atoms and one carboxylic oxygen atom of one $Cu(pic)_2$ moiety (O1W, O2W, O3W and O2) with a maximal deviation of 0.059 Å of the O2 atom, while the other square plane is defined by one water O atom and three carboxylic oxygen atoms from three different $Cu(pic)_2$ moieties (O4W, O22, O32, and O42) with a maximal deviation of 0.145 Å of the O22 atom. The O–O–O bond angles in the two square planes range from 81.31 to 98.45 °, they are close to 90 ° for a regular square. The two square planes are nearly parallel with the dihedral angle of 6.63 °. The Gd–O bond lengths are almost identical with a maximal difference of 0.14 Å.

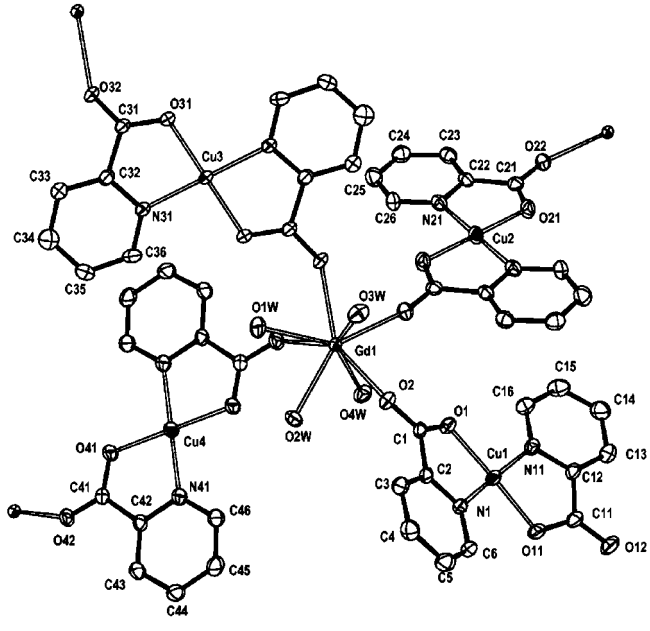

Figure 3. Basic structure unit of **4** with 30% thermal ellipsoids.

There are four $Cu(pic)_2$ units around each Gd^{III}, as shown in Figure 3. The Gd^{III} atoms are linked by the unco-

 © 2005 Wiley-VCH Verlag GmbH & Co. KGaA, Weinheim

ordinated carboxylic O atoms of the $Cu(4)(pic)_2$ and the $Cu(3)(pic)_2$ moieties to form a pseudozigzag chain along the *b* direction. These chains are further bridged by $Cu(2)(pic)_2$ moieties through their two uncoordinated carboxylic O atoms along the *c* direction to form extended two-dimensional layers (Figure 4). The $Cu(1)(pic)_2$ moiety acts as a terminal ligand to Gd^{III} through coordination by one of its two uncoordinated carboxylic oxygen atoms. The closest intralayer separations of Sm···Cu, Cu···Cu, and Sm···Sm are 5.755, 7.45, and 11.510 Å, respectively. The adjacent layers are indirectly connected by hydrogen bonds consisting of coordinated water molecules and oxygen atoms of perchlorate anions or lattice water molecules located between layers, with O···O distances ranging from 2.743(5) to 3.002(6) Å. Simultaneously, the lattice water molecules and oxygen atoms of perchlorate anions form hydrogen bonds among themselves with an O···O distance of 2.933(6) Å.

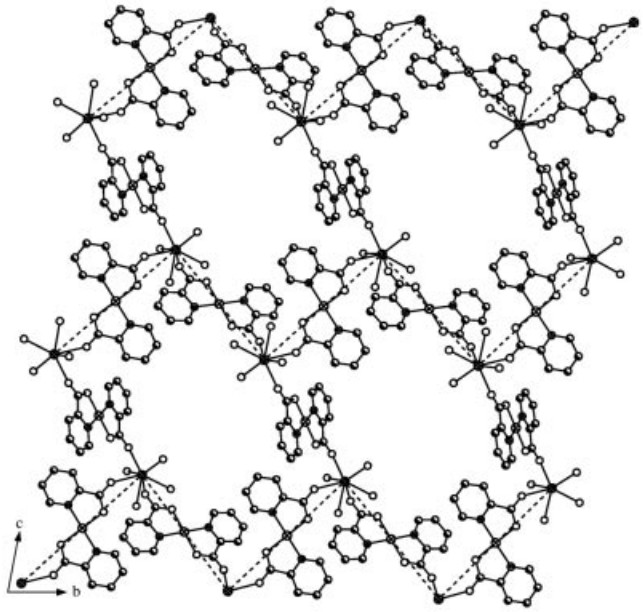

Figure 4. The layer sketch structure of **4** with the zigzag chain represented by dashed lines. Terminal $Cu(1)(pic)_2$ moieties were omitted for clarity.

{NdCu(pic)$_2$[CO(NH$_2$)$_2$]$_4$(H$_2$O)$_3$}(ClO$_4$)$_3$·[Cu(pic)$_2$]$_2$ (11)

Complex **11** consists of $\{NdCu(pic)_2[CO(NH_2)_2]_4(H_2O)_3\}_\infty$ cationic chains, ClO_4^- anions, and two lattice $Cu(pic)_2$ species. The coordination polyhedron of Nd^{III} can be viewed as a slightly distorted square antiprism, formed by two carboxylic oxygen atoms of two $Cu(pic)_2$ moieties (O2, O12), four oxygen atoms of carbamide (O13, O23, O33, O43), and two water oxygen atoms (O1W, O2W). One of the square planes consists of O12, O33, O43, and O2W atoms with a mean deviation of 0.01 Å from the least-squares plane, while O2, O13, O23, and O1W atoms form the other square plane with a mean deviation of 0.004 Å. The two square planes are nearly parallel with a dihedral angle of 5.75 °. The O–O–O bond angles in the two square planes range from 84.34 to 95.123 °. The Nd-O(pic) bond lengths are 2.496 Å for O2 and 2.537 Å for O12, which are longer than those in the reported Nd^{III} complex with the pic ligand (2.400–2.454 Å).[14] The Nd-O(carbamide) bond lengths are nearly identical, spanning a narrow range of 2.381–2.413 Å. The Nd^{III} ions are alternately bridged by $Cu(1)(pic)_2(H_2O)$ moieties through the O2 and O12 carboxylic oxygen atoms of picolinic acid ligands to form a nearly linear chain with a Cu–Nd–Cu angle of 171.32 ° and an Nd–Cu–Nd angle of 171.32 ° extending along the *a* direction, as shown in Figure 5. The closest intrachain Nd···Cu, Cu···Cu, and Nd···Nd separations are 5.326, 10.514, and 10.514 Å, respectively. Unlike the $Cu(pic)_2$ moieties in **1**–**10**, the Cu1 ion in **11** is five-coordinate by the four donor atoms of pic ligands, O1, O12, N1, and N11, and one water molecule (O3W) with a longer distance of 2.413(3) Å due to the Jahn–Tellller effects of the Cu^{II} atom. The O1, O12, N1, and N11 atoms form roughly a planar N_2O_2 with a maximal deviation of 0.145 Å and the copper ion is displaced from this plane toward the axial O3W by 0.183 Å. The average Cu1–O and Cu1–N bond lengths are 1.949 and 1.975 Å, respectively; these are also comparable with the normal value for copper(II) coordinated by pic ligands.[11]

The lattice $Cu(2)(pic)_2$ moieties and ClO_4^- ions are located between the chains. The lattice $Cu(2)(pic)_2$ moieties bridge the adjacent chains to form a double-chain structure through the hydrogen bonds of O21···O1W [2.914(2) Å], O32···O2W [2.738(3) Å] and O22···O3W [2.849(3) Å], while

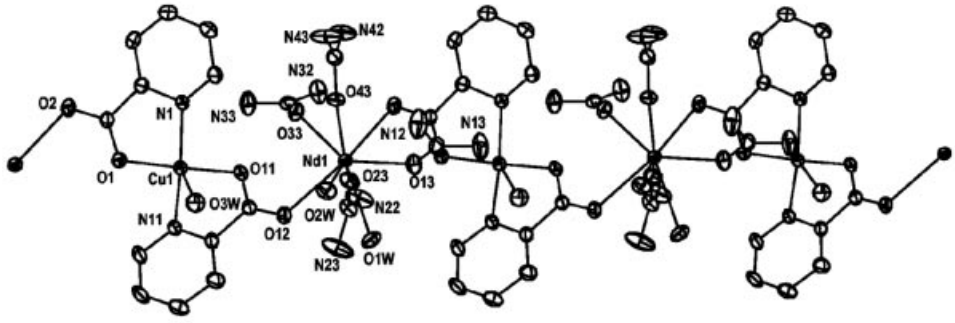

Figure 5. The nearly linear chain structure of **11** with 30% thermal ellipsoids.

 © 2005 Wiley-VCH Verlag GmbH & Co. KGaA, Weinheim

the $Cl(3)O_4^-$ ions are anchored to the chains by hydrogen bonds of O34···O2W (2.797 Å) and O34···O3W (2.986 Å), as shown in Figure 6. In addition, there exist intramolecular hydrogen bonds between the N atom of one of coordinated urea molecules and O3W [N13···O2W = 3.023(3) Å] (Figure 6). The $Cu(3)(pic)_2$ moieties are located at two sides of the double chains.

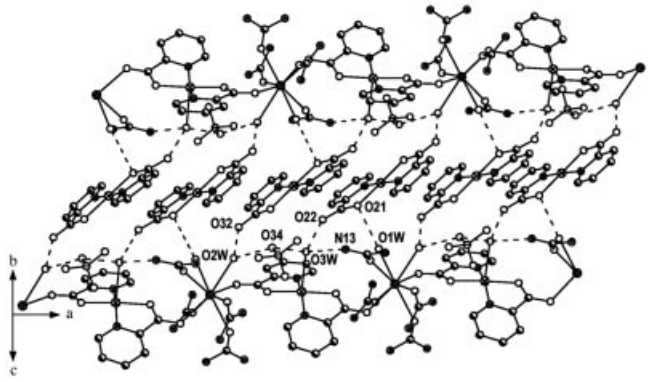

Figure 6. The double chain structure of **11** linked by the hydrogen bonds between lattice $Cu(2)(pic)_2$ moieties and carboxylic O atoms of single chains; the hydrogen bonds are represented by dashed lines.

The relations of mole ratios of different reactants and structures in the three series of complexes are shown in Scheme 1. The layered structures of the second series of complexes may be considered as being composed of the $Cu(pic)_2$ moieties bridging the zigzag chains in a similar manner to that of the first series complex. The Cu–Gd–Cu and Gd–Cu–Gd bond angles of the zigzag chain in **4** are 79.504 and 180.00 °, respectively, which are comparable to those of the first series of complexes [78.474(4) and 174.89(1) °, respectively]. The third series complex is very different from the former two series, in the sense that the $Cu(pic)_2$ moieties bridge lanthanide atoms in a nearly linear chain, with additional $Cu(pic)_2$ moieties serving as lattice molecules located in the lattice.

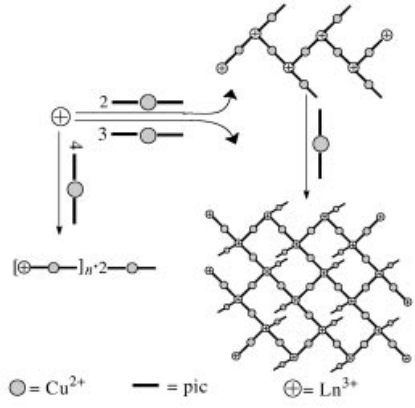

Scheme 1. The relations of mole ratios of different reactants and structures.

Magnetic Properties of Complexes 2–4, 6, and 11

The variable-temperature magnetic susceptibilities for crystalline samples **2**–**4**, **6**, and **11** were measured in the 6–300 K temperature range with an applied field of 1 T. Table 5 shows the non-linear fitting data to $\chi_M = C/(T - \theta) + \chi_0$ above 50 K and the effective magnetic moments, μ_{eff}, of all complexes, in which μ_{eff} is defined as $2.828C^{1/2}\mu_B$, χ_M the molar magnetic susceptibility, C the Curie constant, θ the Weiss constant, and χ_0 the background susceptibility. A Curie–Weiss paramagnetic behavior is observed for all these compounds. The observed effective magnetic moment for each compound is very close to the theoretical value at 293 K, expected for a coupling-free system of isolated Ln^{III} and Cu^{II} ions, which confirms the assignment of oxidation states as judged by the neutrality requirement. As shown in Figure 7, upon cooling, the $\chi_M'T$, where $\chi_M' = \chi_M - \chi_0$, decreases gradually from 300 to 15 K for all complexes. The nature of such antiferromagnetic-like behavior remains to be clarified for 4f–3d compounds, but it may be related to

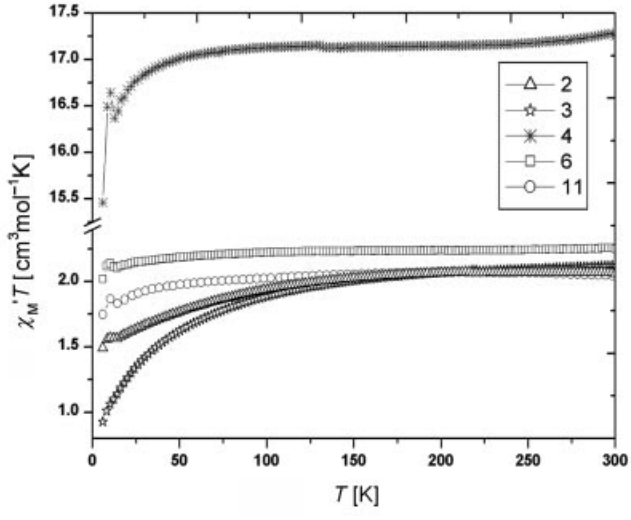

Figure 7. Thermal dependence of $\chi_M'T$ for complexes **2**–**4**, **6** and **11**.

Table 5. Magnetic fitting data of complexes **2**, **3**, **4**, **6**, and **11**.

Complexes	C [cm3 mol–1 K]	θ [K]	χ_0 [cm3 mol^{-1}]	μ_{eff}(exp.) (μ_B)	μ_{eff}(cal.) (μ_B)
$NdCu_2$ (**2**)	2.19(1)	–12.2(3)	$7.7(4)\times10^{-4}$	4.19(1)	4.371
$PrCu_2$ (**3**)	2.27(7)	–20.5(2)	$2(2)\times10^{-5}$	4.27(7)	4.333
Gd_2Cu_5 (**4**)	17.22(1)	–0.58(4)	$7(5)\times10^{-5}$	11.735(3)	11.873
Sm_2Cu_5 (**6**)	2.262(2)	–1.79(3)	$8.2(1)\times10^{-4}$	4.253(2)	4.047
NdCu (**11**)	2.091(7)	–3.0(2)	$5.1(3)\times10^{-4}$	4.261(7)	4.701

 © 2005 Wiley-VCH Verlag GmbH & Co. KGaA, Weinheim

the progressive thermal depopulation of the Ln^{III} Stark components and a possible the Ln^{III}–Cu^{II} interaction.[15] Because of the large separation between the Ln^{III} ions and the well-shielded 4f orbitals by the outer shells of 5s and 5p orbitals as well as relatively low covalence of the lanthanide-to-ligand bonds, the Ln–Ln interactions are expected to be negligibly small. The origin of the small bumps around 15 K for **2**, **4**, **6**, and **11** is still unclear, though the possibility of a systematic error cannot be completely excluded. To date, the understanding of the magnetic interactions containing rare-earth ions in molecular magnets is still a challenge, particularly when the contribution of the first-order orbital momentum is involved. Further experiments are needed for better understanding of the nature of the 4f–3d magnetic interactions in these systems.

Conclusion

In summary, we have demonstrated a facile and controllable approach to 3d–4f heterometallic extended framework complexes. Firstly, we obtain one-dimensional array complexes in a T-shape fashion with a large open space on the other side. The introduction of more $Cu(pic)_2$ precursors into this open space leads to the formation of higher dimensional structures. A series of two-dimensional 3d–4f heterometallic complexes have been obtained in this way by increasing the mole ratio of metal complex precursor to Ln^{III} from 2:1 to 3:1. However, increasing the mole ratio further to 4:1 failed to yield three-dimensional heterometallic complexes, probably because of large steric effects of $Cu(pic)_2$ precursors and the competitive coordination of carbamide. Instead, an unexpected nearly linear heterometallic chain emerged. The present work may provide a useful approach to tuning structural dimensionality and thus magnetic properties through reactant mole ratios.

Experimental Section

Materials and Measurement: All starting reagents, except for $Ln(ClO_4)_3$ and $Cu(ClO_4)_2$, were commercial grade materials and used as received. $Ln(ClO_4)_3$ and $Cu(ClO_4)_2$ were prepared by the reactions of Ln_2O_3 or CuO and perchloric acid in aqueous solution. Elemental analyses (C, H, N) were performed with an Elementar Vario ELIII analyzer. IR spectra were measured on KBr pellets with a Nicolet Magna 750 FTIR spectrometer in the range of 400–4000 cm^{-1}. Magnetic susceptibilities of complexes **2**–**4**, **6**, and **11** were measured by using a Quantum Design SQUID magnetometer in the temperature range 6–300 K at a field of 1 T. The raw data were corrected for the magnetization of the sample holder.

Syntheses: *Caution!* Although we have experienced no problems in handling metal perchlorates, these should be handled with great caution because of the potential for explosion.

Synthesis of the $Cu(pic)_2$ Complex Precursor: The mononuclear precursor $[COH(NH_2)_2]_2[Cu(pic)_2(ClO_4)_2]$ was obtained according to the literature.[11]

Preparations of $[LnCu_2(pic)_4(H_2O)_6](ClO_4)_3\cdot H_2O$ [Ln = Sm (1), Nd (2), and Pr (3)]: A mixture of $Cu(pic)_2$ precursor (0.630 g, 1 mmol) and $Ln(ClO_4)_3$ aqueous solution (0.5 mL, 1 M) was added into C_2H_5OH/CH_3CN (volume ratio 1:1) solution (40 mL), followed by the addition of carbamide to adjust pH = 5, and the solution was stirred thoroughly at room temperature for 12 h and then filtered. The filtrate was concentrated to 20 mL and allowed to stand at room temperature. Deep-blue prismatic crystals were obtained after a few days. Yield: 52.5% (based on Sm) for **1**; 59.3% (based on Nd) for **2**; 62.8% (based on Pr) for **3**. IR (KBr): 1626 (vs), 1598 (vs), 1572 (s), 1481 (w), 1450 (w), 1404 (s), 1386 (m), 1298 (w), 1269 (w), 1144 (vs), 1115 (vs), 1089 (vs), 1053 (m), 1032 (w), 860 (w), 766 (m), 694 (m), 660 (w), 626 (m), 561 (w), 463 (w) cm^{-1} for **1**; 1625 (vs), 1598 (vs), 1569 (vs), 1481 (w), 1450 (w), 1404 (s), 1297 (w), 1269 (w), 1141 (vs), 1113 (vs), 1091 (vs), 1051 (m), 1031 (w), 860 (w), 767 (m), 692 (m), 659 (w), 626 (m), 561 (w), 461 (w) cm^{-1} for **2**. 1629 (vs), 1598 (vs), 1569 (s), 1481 (w), 1450 (w), 1404 (s), 1297 (m), 1268 (w), 1143 (vs), 1114 (vs), 1089 (vs), 1051 (m), 1030 (w), 858 (w), 765 (m), 694 (m), 657 (w), 626 (m), 563 (w), 460 (w) cm^{-1} for **3**. **1**: calcd. C 24.22, H 2.54, N 4.71; found C 24.25, H 2.58, N 4.70. **2**: calcd. C 24.34, H 2.89, N 4.73; found C 24.11, H 2.60, N 4.69. **3**: calcd. C 24.41, H 2.90, N 4.74; found C 24.32, H 2.57, N 4.67.

Preparations of $[Ln_2Cu_5(pic)_{10}(H_2O)_8](ClO_4)_6\cdot 2H_2O$ [Ln = Gd (4), Nd (5), Sm (6), Dy (7), Eu (8), Pr (9) and Yb (10)]: The second series complexes were prepared as mentioned above but the mole ratio of $Cu(pic)_2$ to $Ln(ClO_4)_3$ was changed to 3:1. Deep-blue prismatic crystals were obtained after a few days. Yield: 43.5% (based on Gd) for **4**; 48.3% (based on Nd) for **5**; 41.7% (based on Sm) for **6**; 35.6% (based on Dy) for **7**; 56.9% (based on Eu) for **8**; 42.6% (based on Pr) for **9**; 51.2% (based on Yb) for **10**. IR (KBr): 1631 (vs), 1599 (vs), 1570 (vs), 1481 (m), 1452 (w), 1404 (vs), 1390 (vs), 1352 (m), 1298 (s), 1267 (w), 1242 (w), 1144 (s), 1117 (vs), 1088 (vs), 1053 (s), 1033 (m), 864 (w), 831 (w), 771 (w), 762 (m), 713 (m), 696 (m), 659 (w), 626 (m), 565 (w), 469 (w) cm^{-1} for **4**; 1632 (vs), 1599 (vs), 1570 (vs), 1481 (m), 1452 (w), 1402 (s), 1389 (s), 1352 (m), 1298 (m), 1269 (w), 1242 (w), 1142 (s), 1115 (vs), 1090 (vs), 1051 (s), 1032 (m), 864 (w), 831 (w), 762 (m), 713 (m), 696 (m), 660 (w), 625 (m), 563 (w), 469 (w) cm^{-1} for **5**; 1627 (vs), 1599 (vs), 1570 (vs), 1481 (m), 1452 (w), 1402 (vs), 1389 (s), 1352 (s), 1297 (s), 1269 (m), 1242 (w), 1112 (vs), 1089 (vs), 1051 (s), 1032 (m), 863 (w), 831 (w),773 (m), 762 (m), 711 (m), 696 (m), 657 (w), 624 (m), 561 (w), 470 (w) cm^{-1} for **6**. 1627 (vs), 1602 (vs), 1569 (vs), 1482 (m), 1451 (w), 1402 (s), 1385 (s), 1354 (m), 1299 (m), 1265 (w), 1241 (w), 1143 (vs), 1115 (vs), 1088 (vs), 1052 (s), 1032 (m), 865 (w), 833 (w), 772 (m), 762 (m), 713 (m), 696 (m), 658 (w), 624 (m), 563 (w), 468 (w) cm^{-1} for **7**. 1630 (vs), 1600 (vs), 1570 (vs), 1480 (m), 1455 (w), 1402 (s), 1388 (s), 1354 (m), 1295 (m), 1267 (w), 1240 (w), 1145 (vs), 1110 (vs), 1092 (vs), 1054 (s), 1032 (m), 867 (w), 829 (w), 772 (m), 762 (m), 715 (m), 696 (m), 658 (w), 627 (m), 561 (w), 467 (w) cm^{-1} for **8**. 1633 (vs), 1598 (vs), 1571 (vs), 1481 (m), 1452 (w), 1401 (s), 1390 (s), 1352 (m), 1299 (m), 1269 (w), 1243 (w), 1154 (vs), 1111 (vs), 1091 (vs), 1052 (s), 1033 (m), 864 (w), 831 (w), 773 (m), 762 (m), 713 (m), 697 (m), 659 (w), 623 (m), 562 (w), 469 (w) cm^{-1} for **9**. 1632 (vs), 1601 (vs), 1573 (vs), 1479 (m), 1450 (w), 1410 (s), 1386 (s), 1286 (m), 1267 (w), 1242 (w), 1144 (vs), 1113 (vs), 1086 (vs), 1051 (m), 1032 (w), 862 (w), 837 (w), 762 (m), 694 (m), 650 (w), 625 (m), 561 (w), 463 (w) cm^{-1} for **10**. **4**: calcd. C 27.40, H 2.30, N 5.33; found C 27.35, H 2.31, N 5.31. **5**: calcd. C 27.67, H 2.32, N 5.38; found C 27.64, H 2.35, N 5.35. **6**: calcd. C 27.55, H 2.31, N 5.35; found C 27.53, H 2.34, N 5.30. **7**: calcd. C 27.29, H 2.29, N 5.30; found C 27.30, H 2.25, N 5.34. **8**: calcd. C 27.51, H 2.31, N 5.35; found C 27.52, H 2.30, N 5.29. **9**: calcd. C 27.75, H 2.33, N 5.39; found C 27.67, H 2.30, N 5.33. **10**: calcd. C 27.08, H 2.27, N 5.26; found C 27.15, H 2.30, N 5.23.

 © 2005 Wiley-VCH Verlag GmbH & Co. KGaA, Weinheim

Preparation of $\{NdCu(pic)_2[CO(NH_2)_2]_4(H_2O)_3\}(ClO_4)_3\cdot[Cu(pic)_2]_2$ (11): The procedure of synthesis for the third series complex is similar to that for the first series compounds, but the mole ratio of $Cu(pic)_2$ to $Ln(ClO_4)_3$ is 4:1. Deep-blue prismatic crystals were obtained after a few days. Yield: 46.1% (based on Nd). IR (KBr): 1700 (m), 1660 (s), 1633 (vs), 1604 (vs), 1572 (m), 1480 (m), 1448 (w), 1406 (w), 1371 (s), 1358 (m), 1300 (m), 1290 (w), 1267 (w), 1242 (w), 1146 (s), 1117 (s), 1086 (s), 1049 (m), 1032 (w), 858 (w), 769 (w), 762 (w), 714 (w), 694 (m), 660 (w), 627 (m), 461 (w) cm^{-1}. Calcd. C 28.94, H 2.79, N 11.81; found C 28.89, H 2.77, N 11.78.

X-ray Crystallographic Studies. The crystal structures of the complexes were studied by single-crystal X-ray diffraction analyses. Data collections were performed at 293(2) K with a Siemens SMART CCD diffractometer for **1**–**3**, and **5**–**10** with graphite monochromatic Mo-K_α radiation (λ = 0.71073 Å),[16] with a Rigaku AFC7R diffractometer for **4** with graphite-monochromatic Mo-K_α radiation (λ = 0.71073 Å),[17] and a Rigaku Mercury CCD for **11** with graphite monochromatic Mo-K_α radiation (λ = 0.71073 Å).[18] The structures were solved by direct methods, the positions of the metal atoms were calculated by using the SIEMENS SHELXTL Version 5.0 package of crystallographic software.[19] The remaining non-hydrogen atoms were located by successive different Fourier syntheses. Hydrogen atoms were added according to theoretical models. The structures were refined using full-matrix least-squares refinement on F^2. All non-hydrogen atoms were refined anisotropically. Pertinent crystal data and structure refinement results for the complexes are listed in Table 1 for **1**–**3**, Table 2 for **4**–**6**, Table 3 for **7**–**9**, and Table 4 for **10** and **11**.

CCDC-237564 to -237574 (for **1**–**11**), contain the supplementary crystallographic data for this paper. These data can be obtained free of charge from The Cambridge Crystallographic Data Centre via www.ccdc.cam.ac.uk/data_request/cif.

Acknowledgments

This work was financially supported by the National Natural Science Foundation of China (20001007, 20131020), Natural Sciences Foundation of Fujian Province (2003I031).

[1] a) D. M. J. Doble, C. H. Benison, A. J. Blake, D. Fenske, M. S. Jackson, R. D. Kay, W. S. Li, M. Schröder, *Angew. Chem. Int. Ed.* **1999**, *38*, 1915–1918; b) J. Lisowski, P. Starynowicz, *Inorg. Chem.* **1999**, *38*, 1351–1355; c) J. P. Costes, F. Dahan, A. Dupuis, J. P. Laurent, *Inorg. Chem.* **1997**, *36*, 3429–3433; d) C. Benelli, D. Gatteschi, *Chem. Rev.* **2002**, *102*, 2369–2387; e) G. Li, T. Akitsu, O. Sato, Y. Einaga, *J. Am. Chem. Soc.* **2003**, *125*, 12396–12397; f) H. Z. Kou, B. C. Zhou, S. Gao, R. J. Wang, *Angew. Chem. Int. Ed.* **2003**, *42*, 3288–3291; g) M. Sakamoto, K. Manseki, H. Okawa, *Coord. Chem. Rev.* **2001**, *219–221*, 379–414.

[2] a) H. Z. Kou, S. Gao, J. Zhang, Z. H. Wen, G. Su, R. K. Zheng, X. X. Zhang, *J. Am. Chem. Soc.* **2001**, *123*, 11809–11810; b) B. Q. Ma, S. Gao, G. Su, G. X. Cu, *Angew. Chem. Int. Ed.* **2001**, *40*, 434–437.

[3] T. Kido, Y. Ikuta, Y. Sunatsuki, Y. Ogawa, N. Matsumoto, *Inorg. Chem.* **2003**, *42*, 398–408.

[4] a) A. Bencini, C. Benelli, A. Caneschi, A. Dei, D. Gatteschi, *Inorg. Chem.* **1986**, *25*, 572–575; b) A. Bencini, C. Benelli, A. Caneschi, R. L. Carlin, A. Dei, D. Gatteschi, *J. Am. Chem. Soc.* **1985**, *107*, 8128–8136; c) S. R. Bayly, Z. Xu, B. O. Patrick, S. J. Rettig, M. Pink, R. C. Thompson, C. Orvig, *Inorg. Chem.* **2003**, *42*, 1576–1583.

[5] a) C. Benelli, A. Caneschi, D. Gatteschi, O. Guillou, L. Pardi, *Inorg. Chem.* **1990**, *29*, 1750–1755; b) T. Kido, S. Nagasato, Y. Sunatsuki, N. Matsumoto, *Chem. Commun.* **2000**, 2113-2114.

[6] M. Andruk, L. Ramade, E. Codjovi, O. Guillou, O. Kahn, J. C. Trombe, *J. Am. Chem. Soc.* **1993**, *115*, 1822–1829.

[7] a) R. Georges, O. Kahn, O. Guillou, *Phys. Rev. B* **1994**, *49*, 3235–3242; b) S. Wang, Z. Pang, M. J. Wagner, *Inorg. Chem.* **1992**, *31*, 5381–5388.

[8] a) O. Guillou, O. Kahn, R. L. Oushoorn, *Inorg. Chim. Acta* **1992**, *198–200*, 119–131; b) O. Guillou, P. Bergerat, O. Kahn, E. Bakalbassis, K. Boubekeur, P. Batail, M. Guillot, *Inorg. Chem.* **1992**, *31*, 110–114; c) O. Guillou, R. L. Oushoorn, O. Kahn, K. Boubekeur, P. Batail, *Angew. Chem. Int. Ed. Engl.* **1992**, *31*, 626–628; d) C. Daiguebonne, O. Guillou, M. L. Kahn, O. Kahn, R. L. Oushoorn, K. Boubekeur, *Inorg. Chem.* **2001**, *40*, 176–178; e) Z. He, C. He, E. Q. Gao, Z. M. Wang, X. F. Yang, C. S. Liao, C. H. Yan, *Inorg. Chem.* **2003**, *42*, 2206–2208; f) H. Z. Kou, B. C. Zhou, R. J. Wang, *Inorg. Chem.* **2003**, *42*, 7658–7665; g) B. Zhao, P. Cheng, Y. Dai, C. Cheng, D. Z. Liao, S. P. Yan, Z. H. Jiang, G. L. Wang, *Angew. Chem. Int. Ed.* **2003**, *42,* 934–936.

[9] A. J. Blake, R. O. Gould, P. E. Y. Milne, R. E. P. Winpenny, *J. Chem. Soc. Chem. Commun.* **1992**, 522–524.

[10] a) J. G. Mao, L. Song, X. Y. Huang, J. S. Huang, *Polyhedron* **1997**, *16*, 963–966; b) J. G. Mao, L. Song, J. S. Huang, *J. Chem. Cryst.* **1998**, *28*, 475–479; c) J. G. Mao, J. S. Huang, J. F. Ma, J. Z. Ni, *Transit. Metal Chem.* **1997**, *22,* 277–280; d) Y. Cui, G. Chen, J. Ren, Y. T. Qian, J. S. Huang, *Inorg. Chem.* **2000**, *39*, 4165–4168; e) X. Zhang, Y. Cui, F. K. Zheng, J. S. Huang, *Chem. Lett.* **1999**, 1111–1112.

[11] G. H. Guo, G. C. Guo, G. W. Zhou, M. S. Wang, L. Z. Cai, A. Q. Wu, J. S. Huang, *Chinese J. Inorg. Chem.* **2003***, 19*, 95–98.

[12] a) S. Kiani, A. Tapper, R. J. Staples, P. Stavropoulos, *J. Am. Chem. Soc.* **2000**, *122*, 7503–7517; b) H. J. Eppley, S. M. Aubin, W. E. Streb, J. C. Bollinger, D. N. Hendrickson, G. Christou, *Inorg. Chem.* **1997**, *36*, 109–115; c) D. M. Stearns, W. H. Armstrong, *Inorg. Chem.* **1992**, *31*, 5178–5184; d) J. Kay, J. W. Mcore, M. D. Glick, *Inorg. Chem.* **1972**, *11*, 2818–2827; e) J. F. Ma, N. H. Hu, J. Z. Ni, *Polyhedron* **1996**, *15*, 1797–1799.

[13] Q. D. Liu, S. Gao, J. R. Li, Q. Z. Zhou, K. B. Yu, B. Q. Ma, S. W. Zhang, X. X. Zhang, T. Z.Jin, *Inorg. Chem.* **2000**, *39*, 2488–2492.

[14] P. Starynowicz, *Acta Crystallogr.*, *Sect. C.: Cryst. Struct. Commun.* **1991**, *47*, 294–297.

[15] M. L. Kahn, C. Mathoniere, O. Kahn, *Inorg. Chem.* **1999**, *38*, 3692–3697.

[16] *Siemens SHELXTL™ Version 5 Reference Manual*, Siemens Energy & Automation Inc., Madison, Wisconsin, USA, **1994**.

[17] a) *Rigaku WinAFC*, Rigaku Corporation, **2002**; b) *Rigaku Crystal Structure Version 3.10*, Rigaku Corporation and Rigaku/MSC, **2002**.

[18] *Rigaku CrystalClear 1.35 Software User's Guide for the Rigaku R-Axis, and Mercury and Jupiter CCD Automated X-ray Imaging System*, Rigaku Molecular Structure Corporation, Utah, USA, **2002**.

[19] *Siemens SHELXTL Version 5.0, Reference Manual*, Siemens Analytical X-ray Instruments Inc., Madison, Wisconsin, USA, **1995**.

Received: August 4, 2004

Synthesis and Reactions of Mixed N,P Ligands

Richard J. Bowen,*[a,b] Manuel A. Fernandes,[a] Patricia W. Gitari,[a] Marcus Layh,*[a] and Richard M. Moutloali[a]

Keywords: Cyclic phosphonium salts / Gold phosphane complexes / β-Keto thiophosphane oxide / Keto-enol / Imine-enamide tautomerism

The gold complexes [RN=C(R′)CH(R)PPh$_2$(AuCl)] (**6a**, R′ = *t*Bu; **6b**, R′ = Ad; R = SiMe$_3$) were synthesised from the ketimines RN=C(R′)CH(R)PPh$_2$ (**2a**, R′ = *t*Bu; **2b**, R′ = Ad; R = SiMe$_3$) and Me$_2$SAuCl. The hydrolysis of the complexes to [H$_2$NC(R′)=CHPPh$_2$(AuCl)] (**8a**, R′ = *t*Bu; **8b**, R′ = Ad) in protic solvents was studied and the reaction intermediate [H(R)NC(*t*Bu)=CHPPh$_2$(AuCl)] (**7a**) was isolated. The ketimines were further reacted with PhPCl$_2$ to the cyclic phosphonium salts [Ph$_2$PP(Ph)N(H)C(R′)=CH]X (**3a**, R′ = *t*Bu, X = Cl; **3c**, R′ = Ad, X = Cl; **3d**, R′ = Ad, X = BPh$_4$) and in the case of **3a** oxidised with sulfur to give the ring-opened β-keto thiophosphane oxide Ph$_2$P(S)CH$_2$C(O)*t*Bu (**9**). All compounds were fully characterised by NMR spectroscopy and in the case of **6b**, **8a** and **9** by X-ray crystallography.
(© Wiley-VCH Verlag GmbH & Co. KGaA, 69451 Weinheim, Germany, 2005)

Introduction

While the use of 1-azaallyllithium complexes as ligand transfer agents has received considerable attention,[1] the development of their utility in the context of phosphorus chemistry is in its infancy. In two recent papers,[2,3] it was shown that treatment of the ketimine Me$_3$SiN=C(*t*Bu)-CH(SiMe$_3$)PPh$_2$ (**2a**) with R′′′PCl$_2$ or PCl$_3$ gave the cyclic phosphonium salts [Ph$_2$PP(R′′′)N(H)C(*t*Bu)=CH]Cl **3** (**3a**, R′′′ = Ph; **3b**, R′′′ = Et) and [Ph$_2$PP(Cl)N(R)C(*t*Bu)=CH]-Cl (R = SiMe$_3$) **4**, respectively (Scheme 1). Conversely, treatment of the related ketimine Me$_3$SiN=C(*t*Bu)-CH(SiMe$_3$)$_2$ (**2c**) with PCl$_3$ generated the *trans*-1,3,2,4-diazadiphosphetidine **5** in moderate yield (Scheme 1). The key ketimines **2a** and **2c** were formed by the reactions of the 1-azaallyl RNC(*t*Bu)C(Li)HR (**1a**) with Ph$_2$PCl or CF$_3$SO$_3$R (R = SiMe$_3$), respectively.[2] The successful preparation of compounds such as **1** is dependent on the availability of suitable 1-azaallyl precursors which react preferentially as *C*-centred rather than *N*-centred nucleophiles.[4] For an ambidentate N,C-monoanionic ligand, *C*- over *N*-centred nucleophilicity is often favoured by utilising solvent-free 1-azaallyllithium precursors.[4] The presence of donor solvents such as tetramethylethylenediamine significantly enhances N-nucleophilicity. In preliminary studies, the solvent-free 1-azaallyl, RNC(Ad)C(Li)HR (Ad = adamantyl) (**1b**), was prepared by the reaction of LiCHR$_2$ and AdCN in pentane under ambient conditions.[1] Consequently, it was envisaged that **1b** could be utilised as a *C*-centred nucleophile to prepare adamantyl derivatives of **3**. This present study was stimulated by the emergence of interest in lipophilic cations as a new class of antitumour drugs with the potential to selectively target mitochondria in tumour cells.[5] Several structurally diverse lipophilic cations have demonstrated strong activity by concentrating in mitochondria, for example, rhodamine 123,[6] dequalinium,[7] pyronine Y,[8] ditercalinium,[9] AA-1[10] and MKT-077,[11] the latter having been advanced to phase I clinical trials. Several classes of lipophilic cations have demonstrated that antitumour selectivity is increased as the lipophilic-hydrophilic balance is varied (e.g. bisquaternary ammonium heterocycles,[12] [Au(P-P)$_2$]$^+$, where P-P is a bisphosphane[5,13] and triarylalkylphosphonium salts[14]). Consequently, herein the preparation of lipophilic cations is reported, that is, the cyclic phosphonium salts derived from **1** and chlorophosphane precursors. The chemistry of formation and stability of these compounds is presented with a view of evaluating their potential as a new class of antitumour agent.

[a] Molecular Sciences Institute, School of Chemistry, University of the Witwatersrand,
Private Bag 3, Wits, 2050, Johannesburg, South Africa
[b] Project AuTEK, Mintek,
Private Bag X 3015, Randburg 2125, South Africa

Results and Discussion

Synthesis

In the present study, the solvent-free 1-azaallyllithium, RNC(Ad)C(Li)HR (**1b**) was prepared in high yield by the reaction of LiCHR$_2$ (R = SiMe$_3$) and AdCN (Ad = adamantyl) in hexane at low temperature. This type of reaction has previously been rationalised by insertion of the alkyllithium reagent into the CN bond of the organonitrile to form a lithioaldimine, followed by a 1,3-Me$_3$Si shift to give the 1-azaallyl.[4] Compound **1b**, behaving as a *C*-centred nu-

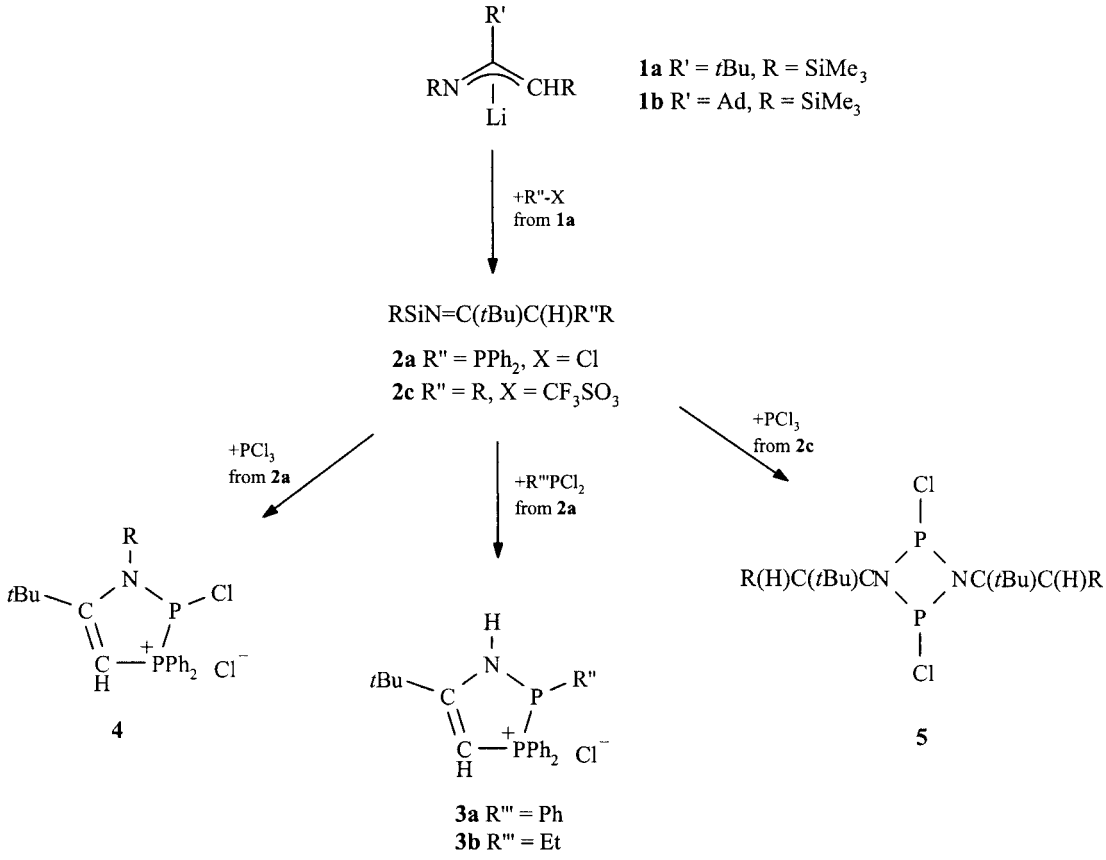

Scheme 1. Reactions of ketimines with phosphorus halides.

cleophile, was reacted with the phosphanyl chloride, Ph_2PCl, to give the novel ketimine $RN=C(Ad)CH(R)PPh_2$ (**2b**) (i, Scheme 2) in a yield comparable to the analogous reaction involving $RNC(tBu)C(Li)HR$ and chlorodiphenylphosphane.[2] The purification of **2b** by distillation was not attempted owing to reports that the corresponding *t*Bu derivative, $RN=C(tBu)CH(R)PPh_2$ (**2a**) isomerised to give the (*Z*)-enamine upon heating under reduced pressure, while subsequent irradiation of the (*Z*)-enamine using a medium-pressure mercury lamp afforded an equilibrium mixture of the *Z* and *E* isomers [Equation (1)].[2] Owing to the stability that a number of transition metals can afford to phosphanes, by σ-donation of the ligand and backbonding from the metal to the vacant d-orbitals of the phosphane, the Au^I complex of **2b** was prepared (ii, Scheme 2). The expected stability and linear two-coordinate geometry of the complex was observed (**6b**), allowing unambiguous assignment of **2b** as a coordinated adduct by NMR and X-ray crystallographic analysis. Similarly, $[Me_3SiN=C(tBu)CH(SiMe_3)PPh_2(AuCl)]$ (**6a**) was prepared in high yield from the reaction of $Me_3SiN=C(tBu)CH(SiMe_3)PPh_2$ (**2a**) and $ClAuSMe_2$ in THF. In both cases, the 1:1 complex was formed irrespective of stoichiometry, and an excess of ligand was typically used to ensure complete complexation. While enhanced thermal stabilities of the ketimines were achieved by coordination of P to Au^I it was found that the $SiMe_3$ group attached to N was readily hydrolysed in the presence of moisture (treatment of **6** with methanol) to give the complexes $[H_2NC(R')=C(H)PPh_2(AuCl)]$ (Scheme 2; **8a**, R′ = *t*Bu; **8b**, R′ = Ad) in high yields. The structure of the *t*Bu derivative was confirmed by crystallographic analysis. The process presumably involves cleavage of the terminal trimethylsilyl group (Scheme 2, iii), followed by a 1,3 trimethylsilyl shift from C to N (Scheme 2, iv) and isomerisation of the ketimine (the sequence of rearrangement iv and isomerisation v may well be reversed or a simultaneous process) to the thermodynamically favoured enamine (Scheme 2, v). The latter intermediate $[H(SiMe_3)NC(R')=CHPPh_2(AuCl)]$ was NMR spectroscopically identified for R′ = *t*Bu (**7a**) as the major product (with **6a** and **8a** as side products) when **6a** was treated with a mixture of diethyl ether and hexane. Hydrolysis of the remaining trimethylsilyl group (Scheme 2, vi) completed a template-assisted synthesis of novel bidentate ligands. For comparison the non-hydrolysable ketimine $Ph_2PCH_2C(Ph)=N(C_6H_3Me_2\text{-}2,6)$[15] was reacted with Me_2SAuCl to synthesise a *N*-aryl analogue of **6**. The gold complex was isolated in good yield (66%) and found to exist in solution as a mixture of four isomers (two tautomers analogous to the ones shown for equilibrium v in Scheme 2 and their respective *Z*/*E* isomers). No decomposition or change in the isomer ratio was observed in acetone solution over a period of two weeks. The described synthesis of **8** represents a new route to mixed P, N donor ligands with C–C backbone. Typically, ligands of this sort are generated by the AIBN-assisted free radical-catalysed[16] (or base-cat-

 © 2005 Wiley-VCH Verlag GmbH & Co. KGaA, Weinheim

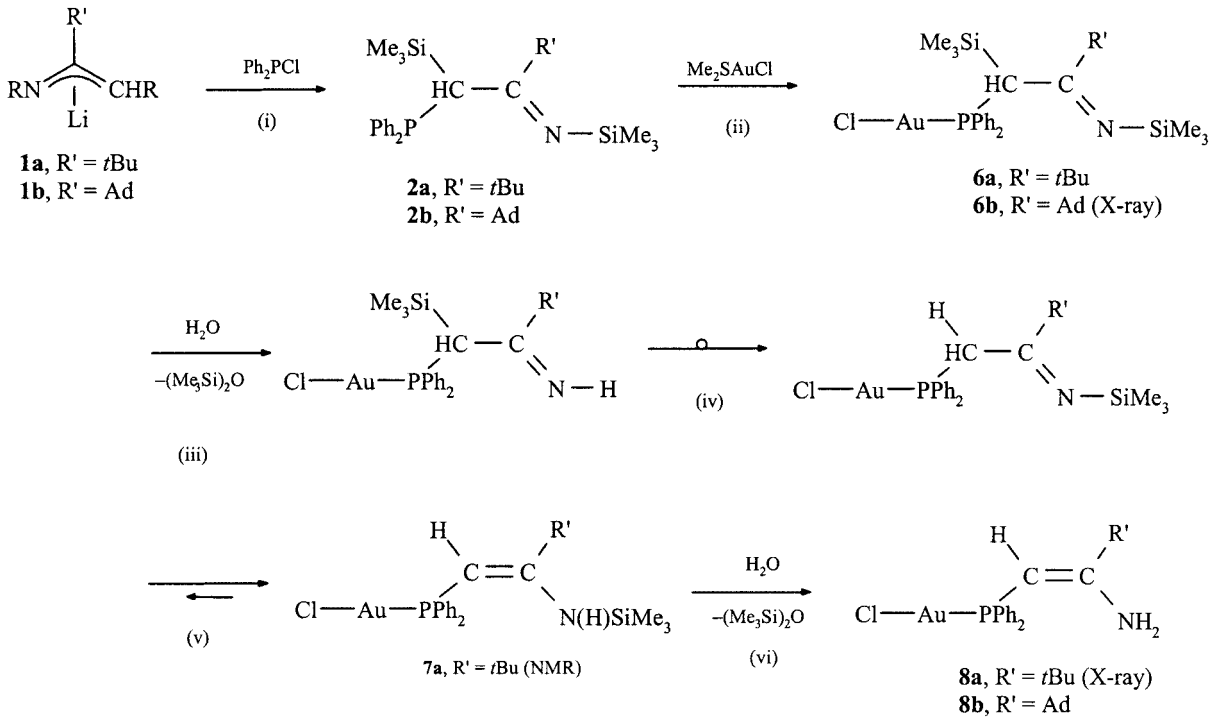

Scheme 2. Synthesis of gold phosphane complexes.

alysed[17]) addition of P–H bonds to vinylamides [e.g. CH_2=C(O)NH_2] or possibly the reaction of N-nucleophiles to ω-chloroalkylphosphanes. The procedure reported here, beginning with *C*-centred nucleophilic attack of a 1-azaallyl on a phosphanyl chloride, followed by template-assisted hydrolysis, not only provides a route to mixed P, N donor ligands, but allows for further alkyl substitution at a single carbon atom.

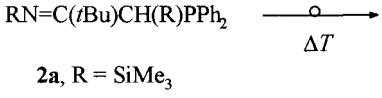

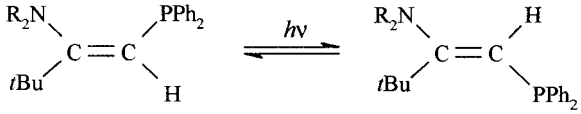

(1)

Since the reaction of Me_3SiN=C(*t*Bu)CH($SiMe_3$)PPh_2 (**2a**) with R′′′PCl_2 proceeded to give the cyclic phosphonium salts [Ph_2PP(R′′′)N(H)C(*t*Bu)=CH]Cl (Scheme 1, R′′′ = Ph, **3a** or Et, **3b**),[2] the Ad-substituted analogue, [Ph_2PP(Ph)N(H)C(Ad)=CH]Cl (**3c**) was prepared by a similar reaction involving Me_3SiN=C(Ad)CH($SiMe_3$)PPh_2 (**2b**) and $PhPCl_2$, albeit in lower yield. In a process that was used to rationalise the formation of the *t*Bu-substituted cyclic phosphonium salts,[2] the formation of [Ph_2PP(Ph)N(H)-C(Ad)=CH]Cl (**3c**) from Me_3SiN=C(Ad)CH($SiMe_3$)PPh_2 (**2b**) is likely to involve, firstly, *N*-centred nucleophilic attack of Me_3SiN=C(Ad)CH($SiMe_3$)PPh_2 at the P atom of $PhPCl_2$, yielding the ketimidophosphorous(III) chloride PhP(Cl)N=C(Ad)CH(R)PPh_2 with concomitant Me_3SiCl elimination. Secondly, cyclisation is invoked by a rearrangement (1,3-$SiMe_3$ shift from C to N) of PhP(Cl)N=C(Ad)-CH(R)PPh_2 into the isomeric enamidophosphorus(III) chloride PhP(Cl)N(R)C(Ad)=C(R)PPh_2 followed by intramolecular nucleophilic displacement of the chloride to give the cyclic phosphonium salt **I**. Hydrolysis completes the conversion to [Ph_2PP(Ph)N(H)C(Ad)=CH]Cl (**3c**). Alternatively, the transformation could proceed through cyclisation of the ketimidophosphorus(III) chloride PhP(Cl)N=C(Ad)-CH(R)PPh_2, to give the cycloketimidophosphonylphosphonium salt [Ph_2PP(Ph)N=C(Ad)CHR]Cl **II**, which subsequently undergoes rearrangement to **I** and hydrolysis to complete the process.

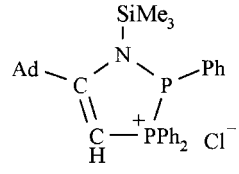

I

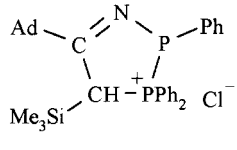

II

Fulfilment of the requirement of stability is necessary before proceeding with biological evaluations. While isolation and characterisation of the cyclic phosphonium salts were possible under inert gas conditions, instability of the five-membered ring (a solution of **3c** in $CDCl_3$ decomposed

 © 2005 Wiley-VCH Verlag GmbH & Co. KGaA, Weinheim

within 24 h completely into two major products on exposure to moist air) necessitated strategies to attempt to induce stability. Consequently, metathesis reactions involving replacement of the chloride with bulkier anions were undertaken. The reaction of $[Ph_2PP(Ph)N(H)C(Ad)=CH]Cl$ (**3c**) with $NaBPh_4$ proceeded almost quantitatively to give $[Ph_2PP(Ph)N(H)C(Ad)=CH]BPh_4$ (**3d**), while the synthesis of related compounds with NO_3^-, $CH_3CO_2^-$, BF_4^- or ClO_4^- as counterion from **3c** and the corresponding silver salts was unsuccessful. ^{31}P NMR analysis of **3d**, however, revealed that the instability under atmospheric conditions was persistent, with decomposition of the five-membered ring being particularly rapid in foetal calf serum (fcs) containing cell-culture medium. Subsequently, in an attempt to acquire an insight into the factors which were responsible for this decomposition, a reaction was undertaken with $[Ph_2PP(Ph)N(H)C(tBu)=CH]Cl$ (**3a**) and one equivalent of sulfur in dichloromethane, since thiol-containing compounds are constituents of fcs and the interaction with sulfur is a reasonable comparison for the observed oxygen- and moisture-facilitated decomposition pathways. Removal of the solvent in vacuo, and recrystallisation of the crude product from propan-1-ol, gave colourless crystals in good yield. Crystallographic analysis of the product revealed that a rare example of a β-keto thiophosphane, i.e. $Ph_2P(S)CH_2C(O)tBu$ (**9**) was obtained. It is plausible that the formation of the β-keto thiophosphane oxide involved initial sulfuration of the quarternary P and concomitant P–P bond scission of the cyclic phosphonium salt $[Ph_2PP(Ph)N(H)C(tBu)=CH]Cl$ to give an intermediary chlorophosphane $Ph_2P(S)CH=C(tBu)N(H)P(Ph)Cl$ (Scheme 3, i). Facile elimination of ClPPhOPr or a related species (Scheme 3, ii), followed by nucleophilic attack of water on the *t*Bu-substituted carbon in a Michael-type addition reaction (the related P^{III} compounds **8** in Scheme 2 are in contrast unreactive) produces a zwitterionic intermediate (Scheme 3, iii) whose negative charge is stabilised by the P=S double bond. Ethene bond reformation is accompanied by the elimination of ammonia (Scheme 3, iv), with enol-keto tautomerism (Scheme 3, v) completing the envisaged reaction pathway involving the formation of $Ph_2P(S)CH_2C(O)tBu$ (**9**) from $[Ph_2PP(Ph)N(H)C(tBu)=CH]Cl$. Reaction of **3c** with oxygen-free water in CH_2Cl_2 resulted in a solid that showed two major signals at δ = 22.5 and 23.3 ppm in the ^{31}P NMR spectrum that were within 1 ppm identical to those found in the above-mentioned decomposition study of **3c** in $CDCl_3$. This implicates the reaction with water as a major reason for the instability of the phosphonium salts. Attempts to isolate the products were unsuccessful and a mass spectrum of the product mixture was inconclusive. The further reaction of **3c** with dry oxygen yielded after removal of the solvent a solid that consisted of a mixture of numerous compounds with unreacted starting material being one of the major components. The mass spectrum of the mixture showed *m*/*z* values consistent with **3c** and an oxygen analogue $[Ph_2P(O)CH_2C(O)Ad]$ of **9**. The persistent instability of the phosphonium salts under atmospheric conditions precluded further biological testing and further development as potential antitumour drugs is at this stage doubtful.

Solid-State Structures of Compounds 6b, 8a and 9

The molecular structures of $[RN=C(Ad)CH(R)PPh_2(AuCl)]$ (**6b**) (R = $SiMe_3$) and $[H_2NC(tBu)=C(H)PPh_2(AuCl)]$ (**8a**) with the atom numbering scheme are shown in Figure 1 and Figure 2, while selected bond lengths are compared in Table 1. Complex **6b** crystallises as a discrete monomer with the Au atom adopting a linear geometry [P–Au–Cl 178.74(9)°]. The Au–P and Au–Cl distances of 2.245(2) and 2.296(2) Å are unexceptional and compare well to those found in related two-coordinate phosphane complexes such as iBu_3PAuCl,[18] Et_3PAuCl,[19] Ph_3PAuCl,[20] $(2\text{-}Pyr)_3PAuCl$[21] or iPr_3PAuCl.[22] The short

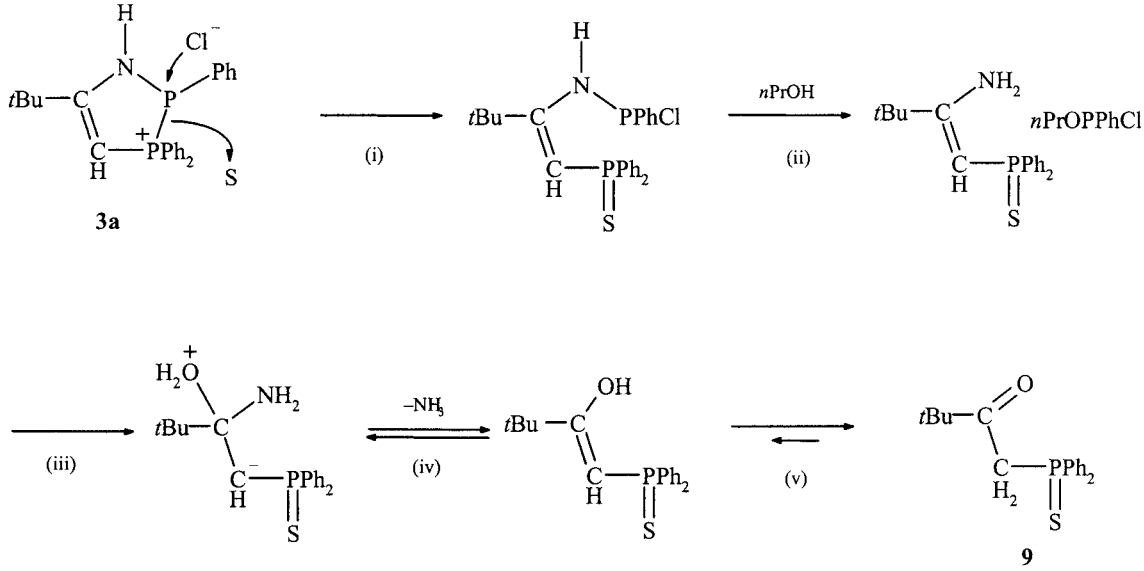

Scheme 3. Possible reaction mechanism for the formation of **9**.

 © 2005 Wiley-VCH Verlag GmbH & Co. KGaA, Weinheim

C2–N [1.266(6) Å] and long C1–C2 [1.558(6) Å] distances are consistent with the alkyl substituent at P being an iminoalkyl. There is considerable steric repulsion between the bulky adamantyl and trimethylsilyl groups attached to the two sp^2 hybridised atoms C2 and N, respectively, as is evident from the deviation of the angles C3–C2–N [123.9(4)°] and C2–*N*–Si3 [151.9(4)°] from the idealised geometry of 120°.

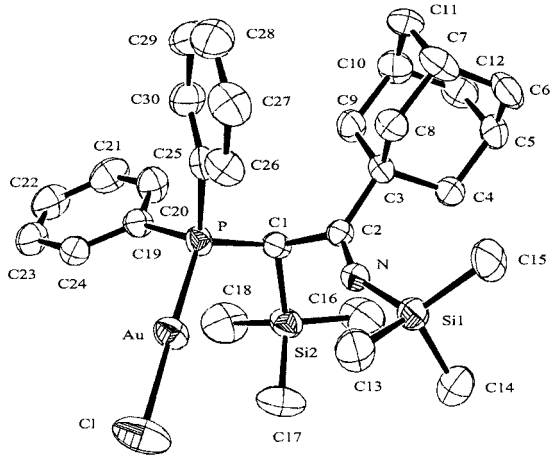

Figure 1. Molecular structure of $ClAuPPh_2CH(SiMe_3)C(Ad)NSiMe_3$ (**6b**). Thermal ellipsoids are drawn at the 50% probability level. H atoms have been omitted for clarity.

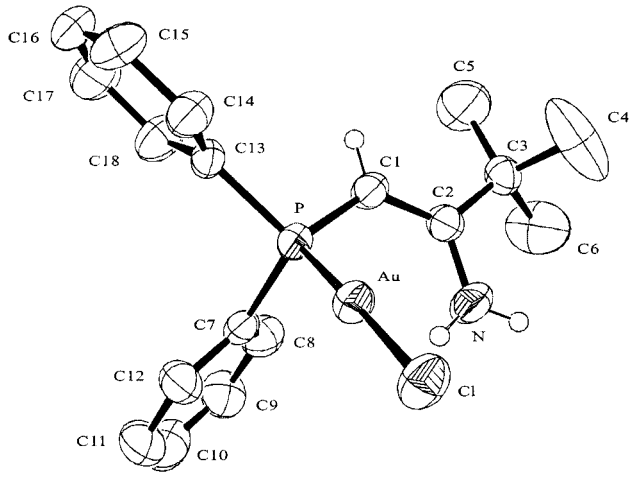

Figure 2. Molecular structure of $ClAuPPh_2CHC(tBu)NH_2$ (**8a**). Thermal ellipsoids are drawn at the 50% probability level. H atoms (except at N, C1) have been omitted for clarity.

Compound **8a** crystallises as a centrosymmetric dimer (Figure 3) as a consequence of conventional hydrogen bonding between the Cl and NH_2 groups of adjacent molecules hereby forming a 14-membered heterocycle $R_2^2(14)$. The Cl···N contacts [3.345(7) Å] are close to the mean value of 3.299(6) Å reported in the literature.[23] The dimers are further weakly hydrogen-bonded by short C–H···Cl interactions (C4–H4···Cl: 2.76 Å, 172°) between the Cl atom and one of the methyl groups of the *t*Bu substituent in the backbone of an adjacent dimer (Figure 3, Table 2). The existence of C–H···Cl (H···A) interactions has been discussed in several recent papers[24] and a C–H···Cl distance of close to 3 Å has been suggested as reasonable.[24a] The closest contact in compound **6b** (C9–H9B···Cl: 2.94 Å, 148°) is in comparison considerably longer. In this context it is noteworthy that the distance between the methyl group (C4) involved in non-classical H-bonding and the central carbon atom of the *t*Bu group (C3) in **8a** [1.54(1) Å] is longer than those to the non-hydrogen-bonded methyl groups [1.52(1), 1.50(1) Å].

Table 1. Selected bond lengths [Å] and angles [°] for compound **6b**, **8a** and **9**.

Bond length/angle	**6b**	**8a**	**9**
Au/S–P	2.245(2)	2.243(2)	1.9563(9)
Au–Cl	2.296(2)	2.295(2)	–
P–C1	1.825(6)	1.777(7)	1.822(2)
P–C[a]	1.838(5)	1.837(7)	1.820(2)
P–C[b]	1.830(6)	1.819(6)	1.821(2)
N/O–C2	1.266(6)	1.369(9)	1.209(3)
C1–C2	1.558(6)	1.361(9)	1.523(3)
P–Au–Cl	178.74(6)	177.24(6)	–

[a] C = carbon C19 (**6b**); carbon C7 (**8a**, **9**). [b] C = carbon C25 (**6b**); carbon C13 (**8a**, **9**).

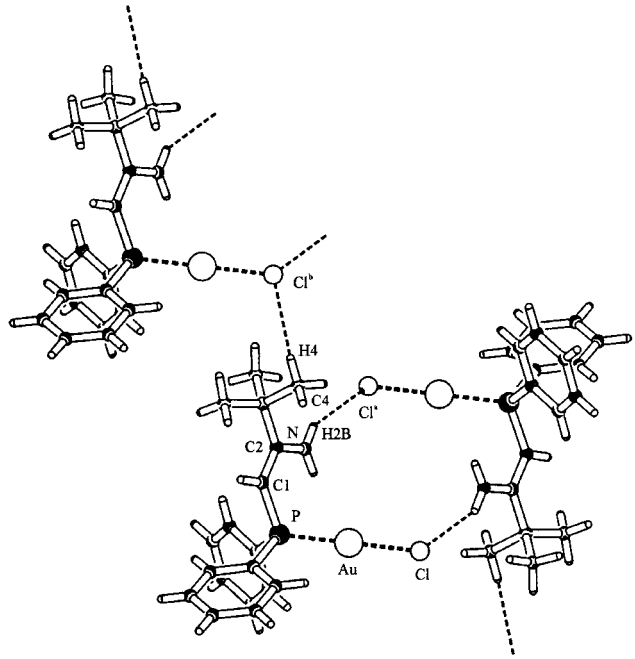

Figure 3. H bonding and intermolecular contacts in compound **8a**. (For symmetry codes see Table 2).

The bond lengths and geometry of the Au atom [Au–P: 2.243(2) Å, Au–Cl: 2.295(2) Å, P–Au–Cl 177.24(6)°] in complex **8a** are similar to those in complex **6b**. The short CN single bond [C1–N 1.369(9) Å] and comparatively long CC double bond [C1–C2 1.361(9) Å] in the phosphane substituent indicate considerable delocalisation within the enamine backbone (*Z* isomer) of the ligand that may extend to some degree to the phosphorus atom (c.f. short P–C1 as compared to long P–Ph distances).

Aurophilic Au···Au contacts[25] that have been found to influence the solid-state structures of gold phosphane com-

 © 2005 Wiley-VCH Verlag GmbH & Co. KGaA, Weinheim

Table 2. Intermolecular contact distances [Å] and angles [°] for compounds **8a** and **9**.

D–H···A	D–H	H···A	D···A	D–H···A
Compound **8a**				
N–H2B···Cl[a]	0.86	2.57	3.345(7)	151
C4–H4···Cl[b]	0.96	2.76	3.717(13)	172
Compound **9**				
C1–H1A···S[c]	0.99	2.80	3.755(2)	163
C15–H15···O[d]	0.95	2.42	3.241(3)	145

[a] Symmetry codes: $-x + 1, -y + 1, -z$. [b] $x, 1 + y, z$. [c] $x, -y, -1/2 + z$. [d] $1/2 + x, -1/2 + y, z$.

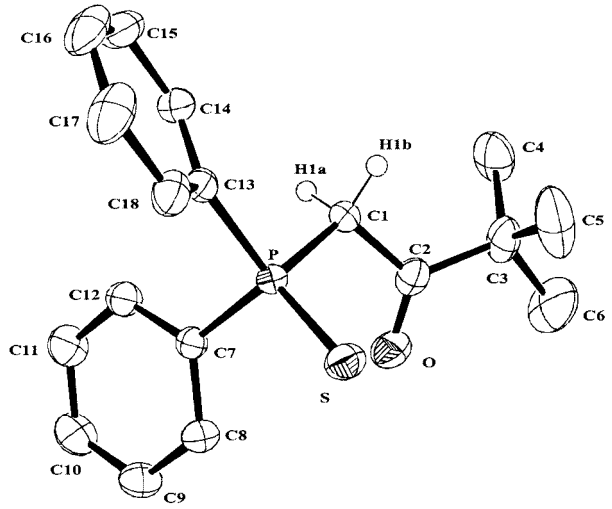

Figure 4. Molecular structure of $Ph_2P(S)CH_2C(O)tBu$ (**9**). Thermal ellipsoids are drawn at the 50% probability level. H atoms (except at C1) have been omitted for clarity.

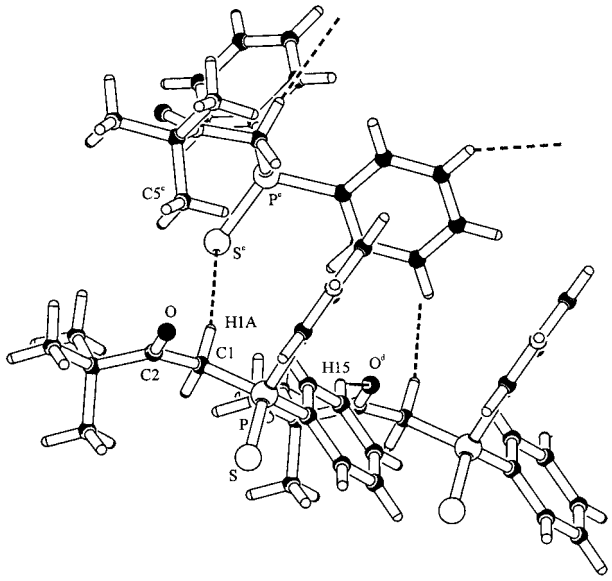

Figure 5. Intermolecular contacts in compound **9**. (For symmetry codes see Table 2).

plexes[26] in the case of less bulky phosphanes are not observed in compound **6b** or **8a**.

The molecular structure of compound **9** and the atom numbering scheme is illustrated in Figure 4. The bond lengths and angles (Table 1) are unexceptional and compare well to the related dimethyl and diphenylphosphane sulfides $Me_2P(S)C(Me)OHC(O)Me$,[27] $Me_2P(S)C(Ph)OHC(O)Ph$[27] and $Ph_2P(S)CHC(O)(CH_2)_4$.[28] The PS and CO groups are not coplanar as indicated by an angle of 71.5(2)° between the two planes formed by the atoms S, P, Cl and C1, C2, O. This facilitates weak intermolecular C–H(Ph)···O and C–H(CH_2)···S interactions (Table 2) between adjacent molecules of **9** (Figure 5). There is also a close contact between C5 and O (C5···O: 3.130 Å).

Experimental Section

All manipulations were carried out under argon, using standard Schlenk techniques. Solvents were distilled from drying agents and degassed. The NMR spectra were recorded in $CDCl_3$, [D_6]acetone and [D_6]DMSO at ambient probe temperature by using the following Bruker instruments: DRX 400 (^{1}H 400.13; ^{31}P 161.9; ^{13}C 100.6 MHz), Avance 300 (^{1}H 300.13; ^{13}C 75.5 MHz) or AC200 (^{1}H 200.13 MHz) and referenced internally to residual solvent resonances (chemical shift data in δ). ^{13}C and ^{31}P NMR spectra were all proton-decoupled. Elemental analyses were determined by the Institute for Soil, Climate and Water, Pretoria, South Africa. The following abbreviations are used throughout the experimental section: s = singlet, br. s = broad singlet, d = doublet, dd = doublet of doublet, m = multiplet, mm = multiple multiplets. Coupling constants (J) are given in Hz.

Synthesis of $Me_3SiNC(Ad)CH(SiMe_3)PPh_2$ (2b): Ph_2PCl (0.38 g, 1.71 mmol) in hexane (15 cm^3) was added dropwise to a magnetically stirred solution (–80 °C) of the 1-azaallyllithium complex **1b** (0.56 g, 1.71 mmol) in hexane (30 cm^3). After stirring for 12 hours, the solution was filtered and the solvent removed in vacuo to give **2b** as a yellow oil (0.73 g, 80%). ^{1}H NMR ($CDCl_3$): δ = –0.04 (s, 9 H, $CSiMe_3$), 0.28 (s, 9 H, $NSiMe_3$), 1.25–1.83 (mm, 15 H, Ad), 3.95 [d, $^2J_{H,P}$ = 6.1 Hz, 1 H, CH] and 7.19–7.74 (mm, 10 H, Ph) ppm. ^{31}P NMR ($CDCl_3$): δ = –2.1 ppm. ^{13}C NMR ($CDCl_3$): δ = 0.4 (s, $CSi\mathit{Me_3}$), 0.5 (s, $NSi\mathit{Me_3}$), 28.6 (s, CH-Ad), 36.5 (s, CH_2-Ad), 31.6 (s, *ipso*-C-Ad), 38.9 [d, $^1J_{C,P}$ = 27.3 Hz, CH], 39.5 (s, CH_2-Ad), 127.7 [d, $^3J_{C,P}$ = 7.1 Hz, *m*-Ph], 128.2 [d, $^3J_{C,P}$ = 7.7 Hz, *m*-Ph], 128.5 (s, *p*-Ph), 129.0 (s, *p*-Ph), 134.3 [d, $^2J_{C,P}$ = 21.8 Hz, *o*-Ph], 134.6 [d, $^2J_{C,P}$ = 19.1 Hz, *o*-Ph], 138.7 [d, $^1J_{C,P}$ = 16.3 Hz, *ipso*-C], 140.3 [d, $^1J_{C,P}$ = 28.5 Hz, *ipso*-C] and 183.1 [d, $^2J_{C,P}$ = 2.2 Hz, CN] ppm.

Synthesis of $Ph_2P^+P(Ph)N(H)C(Ad)CH\ Cl^-$ (3c): $PhPCl_2$ (0.57 g, 3.16 mmol) was added to $Me_3SiN{=}C(Ad)CH(SiMe_3)PPh_2$ (**2b**) (1.60 g, 3.16 mmol). After complete addition, the mixture was heated at 50 °C for 30 min. It liquefied as the $ClSiMe_3$ was given off. The mixture was then dried in vacuo to give a yellow solid (1.43 g, 90%). $C_{27}H_{32}ClNP_2$: calcd. C 69.30, H 6.85, N 2.99; found C 68.52, H 6.87, N 2.47 (the compound incorporates varying amounts of toluene). Pale yellow crystals were obtained from hot toluene (0.40 g, 25%). ^{1}H NMR ($CDCl_3$): δ = 1.71–1.84 (mm, 15 H, Ad), 4.63 [d, $^2J_{H,P}$ = 15.6 Hz, 1 H, NH], 6.90–7.20 (mm, 5 H, Ph), 7.38–7.87 (mm, 10 H, Ph) and 9.99 [dd, $^2J_{H,P}$ = 32.0, $^3J_{H,P}$ = 21.2 Hz, 1 H, CH] ppm. ^{31}P NMR ($CDCl_3$): δ = 13.5 [d, $^1J_{P,P}$ = 239.2 Hz, λ^3P], 41.9 [d, $^1J_{P,P}$ = 239.2 Hz, λ^4P$^+$] ppm. ^{13}C NMR ($CDCl_3$): δ = 28.3 (s, CH-Ad), 36.2 (s, CH_2-Ad), 40.4 [d, $^3J_{C,P}$ =

 © 2005 Wiley-VCH Verlag GmbH & Co. KGaA, Weinheim

11.3 Hz, *ipso*-C-Ad], 41.0 (s, CH_2-Ad), 64.1 [d, $^1J_{C,P}$ = 72.9 Hz, CH], 118.1, [d, $^1J_{C,P}$ = 82.5 Hz, *ipso*-C], 124.2 [dd, $^2J_{C,P}$ = 75.0, $^3J_{C,P}$ = 18.8 Hz, *ipso*-C], 125.2 (s, *ipso*-C), 128.7 (mm of aromatic C atoms) and 186.8 [overlapping dd, $^2J_{C,P}$ = 27.9, $^3J_{C,P}$ = 14.4 Hz, CN] ppm.

Synthesis of $Ph_2P^+P(Ph)N(H)C(Ad)CH\ BPh_4^-$ (3d): $NaBPh_4$ (0.37 g, 1.08 mmol) was added to a magnetically stirred solution of CH_2Cl_2 (20 cm^3) and $Ph_2P^+P(Ph)N(H)C(Ad)CH\ Cl^-$ (**3c**) (0.54 g, 1.07 mmol) at –30 °C. The reaction mixture was stirred for 12 hours and warmed to room temperature giving an off-white solution. It was filtered and the solvent removed in vacuo to give a yellow solid. Various recrystallisation attempts led to the decomposition of the compound. **3d** (crude: 0.76 g, 92%). ^{1}H NMR ($CDCl_3$): δ = 1.57–1.89 (mm, 15 H, Ad), 4.64 [d, 1 H, $^2J_{H,P}$ = 15.3 Hz, NH], 6.00 [dd, $^2J_{H,P}$ = 22.0, $^3J_{H,P}$ = 8.0 Hz, 1 H, CH], 6.84–7.10 (mm, 5 H, Ph) and 7.36–7.64 (mm, 10 H, Ph) ppm. ^{31}P NMR ($CDCl_3$): δ = 10.8 [d, $^1J_{P,P}$ = 241.4 Hz, λ^3P], 43.8 [d, $^1J_{P,P}$ = 241.4 Hz, λ^4P^+] ppm. ^{13}C NMR ($CDCl_3$): δ = 28.0 (s, CH-Ad), 36.0 (s, CH_2-Ad), 39.8 (s, *ipso*-C-Ad), 41.0 (s, CH_2-Ad), 66.4 [d, $^1J_{C,P}$ = 71.4 Hz, CH], 117.3 [d, $^1J_{C,P}$ = 81.0 Hz, *ipso*-C], 121.7 (s, BPh), 122.4 [d, $^1J_{C,P}$ = 32.5 Hz, *ipso*-C], 125.5 (s, BPh), 129.2 [d, $J_{C,P}$ = 5.6 Hz, Ph], 129.5 [d, $J_{C,P}$ = 19.0 Hz, Ph], 130.3 [d, $J_{C,P}$ = 12.6 Hz, Ph], 132.8 [d, $J_{C,P}$ = 10.4 Hz, Ph], 136.3 (s, BPh), 164.2 [q, $^1J_{C,B}$ = 49.3 Hz, *ipso*-C] and 184.8 [d, $^2J_{C,P}$ = 13.0 Hz, CN] ppm.

Synthesis of $ClAuPPh_2CH(SiMe_3)C(tBu)NSiMe_3$ (6a): $ClAuSMe_2$[29] (0.24 g, 0.82 mmol) was added to a solution of $Ph_2PCH(SiMe_3)C(tBu)NSiMe_3$ (**2a**) (0.30 g, 0.85 mmol) in THF (10 cm^3) at 0 °C. The solution was stirred at 0 °C for 10 minutes, warmed to room temperature and stirred for further 15 minutes. The solvent was removed in vacuo to yield a sticky yellow compound (**6a**, 0.45g, 83%). ^{1}H NMR ($CDCl_3$): δ = 0.17 (s, 9 H, $CSiMe_3$), 0.33 (s, 9 H, $NSiMe_3$), 0.88 (s, 9 H, *t*Bu), 4.46 [d, $^2J_{H,P}$ = 15.8 Hz, 1 H, CH] and 7.44 –7.81 (mm, 10 H, Ph) ppm. ^{31}P NMR ($CDCl_3$): δ = 40.7 ppm. ^{13}C NMR ($CDCl_3$): δ = 0.8 [d, $^3J_{C,P}$ = 4.3 Hz, $CSiMe_3$], 3.1 (s, $NSiMe_3$), 29.0 (s, CMe_3), 38.8 [d, $^1J_{C,P}$ = 30.4 Hz, CH], 43.6 (s, *C*Me_3), 128.5 [d, $^2J_{C,P}$ = 11.6 Hz, *o*-Ph], 131.0 [d, $^3J_{C,P}$ = 9.9 Hz, *m*-Ph], 131.8 [d, $^4J_{C,P}$ = 2.4 Hz, , *p*-Ph], 132.8 [d, $^1J_{C,P}$ = 79.0 Hz, *ipso*-C] and 179.4 [d, $^2J_{C,P}$ = 6.0 Hz, CN] ppm.

Synthesis of $ClAuPPh_2CH(SiMe_3)C(Ad)NSiMe_3$ (6b): $ClAuSMe_2$[29] (0.30 g, 1.02 mmol) was added to a solution of $Ph_2PCH(SiMe_3)C(Ad)NSiMe_3$ (**2b**) (0.78 g, 1.54 mmol) in THF (20 cm^3) at 0 °C. The solution was stirred for 15 minutes and the solvent was removed in vacuo to yield a yellow solid. Colourless crystals of **6b** (0.25 g, 33%) were obtained from CH_2Cl_2 at –60 °C. ^{1}H NMR ($CDCl_3$): δ = 0.07 (s, 9 H, $CSiMe_3$), 0.25 (s, 9 H, $NSiMe_3$), 1.26–1.86 (mm, 15 H, adamantyl), 4.37 (d, $^2J_{H,P}$ = 15.9 Hz, 1 H, CH), 7.41–7.43 (mm, 6 H, Ph), 7.71–7.74 (mm, 2 H, Ph) and 7.92–7.98 (mm, 2 H, Ph) ppm. ^{31}P NMR ($CDCl_3$): δ = 40.9 ppm. ^{13}C NMR ($CDCl_3$): δ = 1.0 [d, $^3J_{C,P}$ = 4.0 Hz, $CSiMe_3$], 3.7 (s, $NSiMe_3$), 28.5 (s, CH-Ad), 36.2 (s, CH_2-Ad), 37.6 [d, $^1J_{C,P}$ = 30.2 Hz, CH], 39.6 (s, CH_2-Ad), *ipso*-C-Ad not observed, 128.5 [d, $^3J_{C,P}$ = 11.7 Hz, *m*-Ph], 131.3 [d, $^4J_{C,P}$ = 2.8 Hz, *p*-Ph], 132.3 [d, $^1J_{C,P}$ = 79.9 Hz, *ipso*-C], 134.3 [d, $^2J_{C,P}$ = 14.2 Hz, *o*-Ph] and 179.5 (s, CN) ppm.

Synthesis of $ClAuPPh_2CHC(tBu)N(H)SiMe_3$ (7a): $ClAuPPh_2CH(SiMe_3)C(tBu)NSiMe_3$ (**6a**) was dissolved in a mixture of ether/hexane. A yellow powder of **7a** (0.37 g, 66%) was obtained at –60 °C. ^{1}H NMR ($CDCl_3$): δ = 0.14 (s, 9 H, $SiMe_3$), 1.23 (s, 9 H, *t*Bu), 4.33 [d, $^2J_{H-P}$ = 5.6 Hz, 1 H, CH], 4.81 [br. s, 1 H, NH], 7.42–7.69 (mm, 10 H, Ph) ppm. ^{31}P NMR ($CDCl_3$): δ = 10.6 ppm. ^{13}C NMR ($CDCl_3$): δ = 2.5 (s, $SiMe_3$), 29.8 (s, CMe_3), 38.3 [d, $^3J_{C,P}$ = 8.5 Hz, *C*Me_3], 86.4 [d, $^1J_{C,P}$ = 72.3 Hz, CH], 129.1 [d, $^3J_{C,P}$ = 11.7 Hz, *m*-Ph], 131.2 [d, $^1J_{C,P}$ = 84.5 Hz, *ipso*-C], 131.4 [d, $^4J_{C,P}$ = 2.6 Hz, *p*-Ph], 133.2 [d, $^2J_{C,P}$ = 13.6 Hz, *o*-Ph] and 173.3 (s, CN) ppm.

Synthesis of $ClAuPPh_2C(H)C(tBu)NH_2$ (8a): $ClAuPPh_2CHC(tBu)N(H)SiMe_3$ (**7a**) was dissolved in hot methanol. Colourless crystals of **8a** (0.06 g, 14%) were obtained after slow cooling of the solution at room temperature. $C_{18}H_{22}AuClNP$: calcd. C 41.92, H 4.30, N 2.72; found C 41.20, H 4.33, N 2.70. ^{1}H NMR ($CDCl_3$): δ = 1.23 (s, 9 H, *t*Bu), 4.32 [d, $^2J_{H-P}$ = 8.8 Hz, 1 H, CH], 4.82 (br. s, 2 H, NH_2), 7.44 (6 H, Ph) and 7.57–7.63 (mm, 4 H, Ph) ppm. ^{31}P NMR ($CDCl_3$): δ = 7.1 ppm. ^{13}C NMR ($CDCl_3$): δ = 29.1 (s, CMe_3), 37.2 [d, $^3J_{C,P}$ = 9.8 Hz, *C*Me_3], 72.8 [d, $^1J_{C,P}$ = 71.9 Hz, CH], 129.0 [d, $^3J_{C,P}$ = 11.7 Hz, *m*-Ph], 131.2 [d, $^4J_{C,P}$ = 2.3 Hz, *p*-Ph], 131.9 [s, *ipso*-C], 132.9 [d, $^2J_{C,P}$ = 13.5 Hz], *o*-Phand 168.9 (s, CN) ppm.

Crude **6a** (0.45 g, 0.68 mmol) was dissolved in methanol (20 cm^3) and after a period of 5 minutes a white precipitate started to form. After stirring the reaction mixture for 30 minutes at room temperature the solvent was carefully decanted and the residue dried in vacuo to give 0.31 g (88%) of **8a**.

Synthesis of $ClAuPPh_2C(H)C(Ad)NH_2$ (8b): $ClAuPPh_2CH(SiMe_3)C(Ad)NSiMe_3$ (**6b**) was dissolved in hot methanol. It was cooled slowly and yielded **8b** (0.13 g, 65%) as a pale yellow powder. $C_{24}H_{28}AuClNP$: calcd. C 48.50, H 4.75, N 2.36; found C 48.33, H 4.85, N 2.27. ^{1}H NMR ($CDCl_3$): δ = 1.67–1.83 (mm, 15 H, adamantyl), 4.28 [d, $^2J_{H-P}$ = 9.1 Hz, 1 H, CH], 4.81 (br. s, 2 H, NH_2), 7.42–7.44 (mm, 6 H, Ph) and 7.56–7.64 (mm, 4 H, Ph) ppm. ^{31}P NMR ($CDCl_3$): δ = 7.1 ppm. ^{13}C NMR ($CDCl_3$): δ = 28.4 (s, CH-Ad), 36.5 (s, CH_2-Ad), 38.9 [d, $^3J_{C,P}$ = 9.5 Hz, *ipso*-C, Ad), 40.9 (s, CH_2-Ad), 72.5 [d, $^1J_{C,P}$ = 72.0 Hz, CH], 129.0 [d, $^3J_{C,P}$ = 11.8 Hz, *m*-Ph], 131.2 [d, $^4J_{C,P}$ = 2.5 Hz, *p*-Ph], 132.1 (s, *ipso*-C), 132.9 [d, $^2J_{C,P}$ = 13.4 Hz, *o*-Ph] and 169.1 (s, CN) ppm.

Synthesis of $ClAuPPh_2CH_2C(Ph)N(C_6H_3Me_2$-2,6): $ClAuPPh_2CH_2C(Ph)N(C_6H_3Me_2$-2,6) was obtained from $PPh_2CH_2C(Ph)N(C_6H_3Me_2$-2,6)[15] (0.18 g, 0.44 mmol) and $ClAu(SMe_2)$ (0.11 g, 0.38 mmol) following the same procedure as described for compound **6**. The solvent was removed and the residue recrystallised by layering a toluene solution of the title compound with hexane (approx. ratio 1:4) yielding $ClAuPPh_2CH_2C(Ph)N(C_6H_3Me_2$-2,6) as a colourless powder (0.16 g, 66%). In solution the compound was found to exist as a mixture of two tautomers and their respective *Z*/*E* isomers (the ratio is given in bracket):

$ClAuPPh_2CH_2C(Ph)=N(C_6H_3Me_2$-2,6). Major Isomer (4): ^{1}H NMR ($CDCl_3$): δ = 1.73 (s, 6 H, Me), 3.86 (d, $^2J_{H-P}$ = 13.5 Hz, 2 H, CH) ppm. ^{31}P NMR ($CDCl_3$): δ = 23.8 ppm. ^{13}C NMR ([D_6]acetone) (only CH_2 and CN are assigned): δ = 39.9 [d, $^1J_{C,P}$ = 44 Hz, CH], 165.5 (s, CN) ppm. **Minor Isomer (3):** ^{1}H NMR ($CDCl_3$): δ = 1.88 (s, 6 H, Me), 4.24 (d, $^2J_{H-P}$ = 9.9 Hz, 2 H, CH) ppm. ^{31}P NMR ($CDCl_3$): δ = 25.8 ppm. ^{13}C NMR ([D_6]acetone): not observed.

$ClAuPPh_2CH=C(Ph)N(H)(C_6H_3Me_2$-2,6). Major Isomer (8): ^{1}H NMR ($CDCl_3$): δ = 2.33 (s, 6 H, Me), 4.33 (d, $^2J_{H-P}$ = 5.3 Hz, 1 H, CH), 5.64 (d, $^4J_{H-P}$ = 3.3 Hz, 1 H, NH) ppm. ^{31}P NMR ($CDCl_3$): δ = 17.9 ppm. ^{13}C NMR ([D_6]acetone) (only CH and CN are assigned): δ = 78.9 [d, $^1J_{C,P}$ = 87 Hz, CH], 163.3 (d, $^2J_{C,P}$ = 21 Hz, CN) ppm. **Minor Isomer (1.2):** ^{1}H NMR ($CDCl_3$): δ = 2.11 (s, 6 H, Me), 4.74 (d, $^2J_{H-P}$ = 9.9 Hz, 1 H, CH), 6.55 (br. s, 1 H, NH) ppm. ^{31}P NMR ($CDCl_3$): δ = 8.8 ppm. ^{13}C NMR ([D_6]acetone): not observed. FAB-Mass spectrum: *m*/*z* (%) = 1243 (21) [$(M^+)_2$ – Cl], 639 (20) [M^+], 604 (92) [M^+ – Cl].

 © 2005 Wiley-VCH Verlag GmbH & Co. KGaA, Weinheim

Table 3. Crystal data and refinement for compounds **6b**, **8a** and **9**.

Compound	**6b**	**8a**	**9**
Empirical formula	$C_{30}H_{44}AuClNPSi_2$	$C_{18}H_{22}AuClNP$	$C_{18}H_{21}OPS$
M	738.23	515.75	316.38
T [K]	293(2)	293(2)	173(2) K
Wavelength [Å]	0.71073	0.71073	0.71073
Crystal system	monoclinic	triclinic	monoclinic
Space group	$P21/n$	P-1	Cc
a [Å]	13.630(3)	8.841(6)	16.2497(19)
b [Å]	16.154(3)	10.228(7)	9.8721(11)
c [Å]	14.574(3)	11.224(7)	10.9257(12)
α [°]	90	68.113(11)	90
β [°]	93.783(4)	89.650(12)	98.304(2)
γ [°]	90	86.744(12)	90
V [Å^3]	3201.9(11)	940.1(11)	1734.3(3)
Z	4	2	4
D(calcd.) [Mg/m^3]	1.531	1.822	1.212
μ [mm^{-1}]	4.822	8.047	0.276
F(000)	1480	496	672
Crystal size [mm^3]	0.36 × 0.09 × 0.06	0.26 × 0.22 × 0.04	0.56 × 0.10 × 0.09
Reflections collected	18516	6345	5906
Independent reflections	6273 [R(int.) = 0.074]	4426 [R(int.) = 0.062]	3054 [R(int.) = 0.024]
Data/restraints/parameters	6273/0/332	4426/0/202	3054/2/193
Goodness-of-fit on F^2	0.932	1.032	0.971
Final R indices [$I > 2\sigma(I)$]	R_1 = 0.037, wR_2 = 0.075	R_1 = 0.040, wR_2 = 0.099	R_1 = 0.030, wR_2 = 0.064
R indices (all data)	R_1 = 0.072, wR_2 = 0.084	R_1 = 0.052, wR_2 = 0.105	R_1 = 0.039, wR_2 = 0.067
Extinction coefficient	–	–	0.04(6)
Largest diff. peak and hole [e·Å^{-3}]	1.25 and –0.80	2.34 and –1.24	0.26 and –0.16

Synthesis of $Ph_2P(S)CH_2C(O)tBu$ (9): Sulfur (0.026 g, 0.81 mmol) was added to a magnetically stirred solution of $Ph_2P^+P(Ph)N(H)C(tBu)CH\ Cl^-$ **(3a)** (0.33 g, 0.77 mmol) in CH_2Cl_2 (15 cm^3) at –30 °C. The colourless solution was stirred for 12 hours at room temperature; the solvent was then removed in vacuo to yield a white compound. Colourless crystals of **9** (0.15 g, 61%) were obtained from propanol at –60 °C. Melting point: 210–212 °C. Mass spectrum: m/z = 316 (85) [M$^+$], 259 (15) [M$^+$ – tBu], 231 (65) [Ph_2PSCH_2]. ^{1}H NMR (DMSO): δ = 1.07 (s, 9 H, tBu), 4.32 [d, $^2J_{H-P}$ = 13.1 Hz, 2 H, CH_2], 7.47–7.52 (mm, 6 H, Ph) and 7.88–7.95 (mm, 4 H, Ph) ppm. ^{31}P NMR (DMSO): δ = 38.9 ppm. ^{13}C NMR (DMSO): δ = 25.3 (s, CMe_3), 26.1 [d, $^1J_{C,P}$ = 76.1 Hz, CH_2], 44.4 (s, CMe$_3$), 128.1 [d, $^2J_{C,P}$ = 12.4 Hz, o-Ph], 130.7 [d, $^3J_{C,P}$ = 10.6 Hz, m-Ph], 131.0 [d, $^4J_{C,P}$ = 2.7 Hz, p-Ph], 133.3 [d, $^1J_{C,P}$ = 82.9 Hz, $ipso$-C] and 207.1 [d, $^2J_{C,P}$ = 6.7 Hz, C=O] ppm.

X-ray Crystallography: Intensity data were collected with a Bruker SMART 1K CCD area detector diffractometer with graphite-monochromated Mo-K_α radiation (50 kV, 30 mA). The collection method involved ω-scans of width 0.3°. Data reduction was carried out using the program SAINT+,[30] with face-indexed absorption corrections (compounds **6b** and **8a**) and semi-empirical absorption corrections (compound **9**) carried out using the program XPREP[30] and SADABS,[30] respectively. The crystal structures were solved by direct methods using SHELXTL.[31] Non-hydrogen atoms were first refined isotropically followed by anisotropic refinement by full-matrix least-squares calculation based on F^2 using SHELXTL. Hydrogen atoms were positioned geometrically and allowed to ride on their respective parent atoms. Further crystallographic data are summarised in Table 3. Diagrams and publication material were generated using SHELXTL,[31] PLATON[32] and ORTEP3.[33]

CCDC-244675 to -244677 contain the supplementary crystallographic data for this paper. These data can be obtained free of charge from The Cambridge Crystallographic Data Centre via www.ccdc.cam.ac.uk/data_request/cif.

Acknowledgments

The authors thank CANSA, Mintek (project AuTEK) and the University of the Witwatersrand for financial support.

[1] C. F. Caro, M. F. Lappert, P. Merle, *Coord. Chem. Rev.* **2001**, *219–221*, 605.
[2] P. B. Hitchcock, M. F. Lappert, M. Layh, *J. Organomet. Chem.* **1997**, *529*, 243.
[3] P. B. Hitchcock, M. F. Lappert, M. Layh, *Eur. J. Inorg. Chem.* **1998**, 751.
[4] P. B. Hitchcock, M. F. Lappert, M. Layh, D.-S. Liu, R. Sablong, T. Shun, *J. Chem. Soc., Dalton Trans.* **2000**, 2301.
[5] S. J. Berners-Price, R. J. Bowen, P. Galettis, P. C. Healy, M. J. McKeage, *Coord. Chem. Rev.* **1999**, *185–186*, 823.
[6] L. V. Johnson, M. L. Walsh, L. B. Chen, *Proc. Natl. Acad. Sci. USA* **1980**, *77*, 990.
[7] M. J. Weiss, J. R. Wong, C. S. Ha, R. Bleday, R. R. Salem, G. D. Steele, L. B. Chen, *Proc. Natl. Acad. Sci. USA* **1987**, *84*, 5444.
[8] Z. Darzynkiewicz, J. Kapuscinski, S. P. Carter, F. A. Schmid, M. R. Melamed, *Cancer Res.* **1986**, *46*, 5760.
[9] B. P. Roques, D. Pelaprat, I. Le Guen, G. Porcher, C. Gosse, J. B. Le Pecq, *Biochem. Pharmacol.* **1979**, *28*, 1811.
[10] X. Sun, J. R. Wong, K. Song, J. Hu, K. D. Garlid, L. B. Chen, *Cancer Res.* **1994**, *54*, 1465.
[11] K. Koya, Y. Li, H. Wang, T. Ukai, N. Tatsuta, M. Kawakami, Shishido, L. B. Chen, *Cancer Res.* **1996**, *56*, 538.
[12] W. A. Denny, B. C. Atwell, B. C. Baguely, B. F. Cain, *J. Med. Chem.* **1979**, *22*, 134.

 © 2005 Wiley-VCH Verlag GmbH & Co. KGaA, Weinheim

[13] M. J. McKeage, S. J. Berners-Price, P. Galettis, R. J. Bowen, W. Brouwer, L. Ding, L. Zhuang, B. C. Baguley, *Cancer Chemother. Pharmacol.* **2000**, *46*, 343.
[14] D. C. Rideout, T. Calogeropoulou, J. S. Jaworski, R. J. Dagino, M. R. McCarthy, *Anti-Cancer Drug Des.* **1989**, *4*, 265.
[15] K. S. Coleman, M. L. H. Green, S. I. Pascu, N. H. Rees, A. R. Cowley, L. H. Rees, *J. Chem. Soc., Dalton Trans.* **2001**, 3384.
[16] D. W. Meek, *Homogenous Catalysis with Metal Phosphine Complexes* (Ed.: L. H. Pignolet), **1983**, 257–274.
[17] R. B. King, P. N. Kapoor, *J. Am. Chem. Soc.* **1971**, *93*, 4158.
[18] R. J. Bowen, J. Caddy, M. A. Fernandes, M. Layh, M. A. Mamo, *Polyhedron* **2004**, *23*, 2273.
[19] E. R. T. Tiekink, *Acta Crystallogr., Sect. C* **1989**, *45*, 1233.
[20] N. C. Baenzinger, W. E. Bennet, D. M. Soboroff, *Acta Crystallogr., Sect. B* **1976**, *32*, 962.
[21] C. J. L. Lock, M. A. Turner, *Acta Crystallogr., Sect. C* **1987**, *43*, 2096.
[22] K. Angermaier, E. Zeller, H. Schmidbaur, *J. Organomet. Chem.* **1994**, *472*, 371.
[23] T. Steiner, *Acta Crystallogr., Sect. B* **1998**, *54*, 456.
[24] a) C. B. Aakeröy, T. A. Evans, K. R. Seddon, I. Pálinkó, *New J. Chem.* **1999**, *23*, 145; b) G. R. Desiraju, *Angew. Chem. Int. Ed. Engl.* **1995**, *34*, 2311; c) Y. F. Zefirov, *Crystallogr. Rep.* **1998**, *43*, 283.
[25] P. Pyykkö, *Chem. Rev.* **1997**, *97*, 597.
[26] P. Schwerdtfeger, H. L. Hermann, H. Schmidbaur, *Inorg. Chem.* **2003**, *42*, 1334.
[27] G. Grossmann, K. Krüger, G. Ohms, A. Fischer, P. G. Jones, J. Goerlich, R. Schmutzler, *Inorg. Chem.* **1997**, *36*, 770.
[28] M. Boukraa, T. Jouini, S. Barkallah, A. B. Akacha, H. Zantour, B. Baccar, *Acta Crystallogr., Sect. C* **1995**, *51*, 1851.
[29] a) K. C. Dash, H. Schmidbaur, *Chem. Ber.* **1973**, *106*, 1221; b) T. E. Müller, J. C. Green, D. M. P. Mingos, C. M. McPartlin, C. Wittingham, D. J. Williams, T. M. Woodroffe, *J. Organomet. Chem.* **1998**, *551*, 313.
[30] Bruker, SAINT+. Version 6.02 (includes XPREP and SADABS). Bruker AXS INC., Madison, Wisconsin, USA, **1999**; G. M. Sheldrick, SADABS, University of Göttingen, **1996**.
[31] Bruker, **1999**. SHELXTL, Version 5.1 (includes XS, XL, XP, XSHELL), Bruker AXS INC., Madison, Wisconsin, USA, **1999**.
[32] A. L. Spek, *J. Appl. Crystallogr.* **2003**, *36*, 7.
[33] L. J. Farrugia, *J. Appl. Crystallogr.* **1997**, *30*, 565.

Received: July 14, 2004

 © 2005 Wiley-VCH Verlag GmbH & Co. KGaA, Weinheim

Di-2-pyridyl Ketone Oxime in Zinc Chemistry: Inverse 12-Metallacrown-4 Complexes and Cationic Pentanuclear Clusters

Maria Alexiou,[a] Eugenia Katsoulakou,[b] Catherine Dendrinou-Samara,[a] Catherine P. Raptopoulou,[c] Vassilis Psycharis,[c] Evy Manessi-Zoupa,[b] Spyros P. Perlepes,*[b] and Dimitris P. Kessissoglou*[a]

Keywords: Cluster compounds / Inverse metallacrowns / Oximato complexes / X-ray crystallography / Zinc

The use of di-2-pyridyl ketone oxime (Hpko)/X^- "blends" (X^- = $PhCO_2^-$, N_3^-, NCO^-, $acac^-$, NCS^-) in zinc chemistry yields neutral tetranuclear and cationic pentanuclear clusters. Various synthetic procedures have led to the synthesis of compounds $[Zn_4(OH)_2(O_2CPh)_2(pko)_4]\cdot 3MeCN$ (**1**·3MeCN), $[Zn_4(OH)_2(N_3)_2(pko)_4]\cdot 4DMF$ (**2**·4DMF), $[Zn_4(OH)_2(NCO)_2(pko)_4]\cdot 3DMF\cdot H_2O$ (**3**·3DMF·H_2O), $[Zn_4(OH)_2(acac)_2(pko)_4]\cdot 4CH_2Cl_2$ (**4**·4CH_2Cl_2), $[Zn_5Cl_2(pko)_6][ZnCl(NCS)_3]\cdot 2.5H_2O\cdot 1.5MeOH$ (**5**·2.5H_2O·1.5MeOH) and $[Zn_5(NCS)_2(pko)_6(MeOH)][Zn(NCS)_4]\cdot 2.5H_2O\cdot MeOH$ (**6**·2.5H_2O·MeOH). The structures of the six complexes have been determined by single-crystal X-ray crystallography. The tetranuclear molecules of **1**–**4** lie on a crystallographic inversion centre and have an inverse 12-metallacrown-4 topology. Two triply bridging hydroxides are accommodated in the centre of the metallacrown ring. The pko^- ligands form a propeller configuration that imposes absolute stereoisomerism with Λ and Δ chirality. Two metal ions are in distorted O_2N_4 octahedral environments, whereas the rest are in severely distorted tetrahedral or trigonal bipyramidal environments. The five Zn ions of the cations of **5** and **6** are held together by six pko^- ligands which adopt three different coordination modes; the chloro (**5**) and isothiocyanato (**6**) ligands are terminal. The five Zn ions define two nearly equilateral triangles sharing a common apex, and the novel Zn_5 topology can be described as two "collapsed" 9-metallacrown-3 structures sharing a common Zn apex. Besides the pentanuclear cations, the structures of **5** and **6** contain slightly distorted tetrahedral $[ZnCl(NCS)_3]^{2-}$ and $[Zn(NCS)_4]^{2-}$ ions, respectively, with the isothiocyanato ligands binding the metal ion in a virtually linear fashion.
(© Wiley-VCH Verlag GmbH & Co. KGaA, 69451 Weinheim, Germany, 2005)

Introduction

Metallamacrocycles have gained increasing attention over the past decade due to their potentially unique properties. These molecules have already been used in applications as diverse as catalysis,[1] sensors[2] or as chiral building blocks for two and three-dimensional solids.[3] Metallamacrocycles include complexes such as metallacrowns,[4] metallacrowns containing carbon in the macrocycle,[5] azametallacrowns,[6] anticrowns,[7] metallacrown ethers,[8] metallahelicates,[9] metallacalixarenes,[10] metallacryptates,[11] molecular squares and boxes[1,2,12]and polynuclear alkoxo- or oxometal complexes.[13]

Metallacrowns (MCs),[4] the inorganic structural and functional analogues of crown ethers,[14] are usually formed with transition metal ions and a nitrogen replacing the methylene carbon atoms. MCs exhibit selective recognition of cations and anions, and can display intramolecular magnetic-exchange interactions. The isolation of MCs requires the employment of tri- and tetradentate ligands containing hydroxamate or oximate functionalities to provide a scaffolding within which the desired metal-containing core can be realized. The first MCs were prepared using the triply deprotonated form (shi^{3-}) of salicylhydroxamic acid as ligand.[4,15] This dinucleating agent contains four heteroatoms that are potential metal-binding sites: one metal atom can bind in a five-membered chelate ring formed through the hydroximate group while a second metal atom can bind in a six-membered chelate ring through the iminophenolate group, i.e., shi^{3-} can act as a 2.1111 ligand using Harris notation.[16] This approach yields clusters with M–N–O–M networks linking the ring metal atoms and forms the basis of MCs (Figure 1). The synthesis of MCs is not necessarily restricted to the use of organic ligands with a hydroximate moiety, however. The same M–N–O–M connectivity can be achieved using oximate ligands that can form six- and/or five-membered chelate rings.[4] One example of such a ligand is di-2-pyridyl ketone oxime (Hpko),[17] whose anion (pko^-) can adopt a variety of coordination modes (Figure 1); pko^- is the ligand used in the present study. Even

[a] Department of General and Inorganic Chemistry, Faculty of Chemistry, Aristotle University of Thessaloniki, 54124 Thessaloniki, Greece
E-mail: kessisog@chem.auth.gr
[b] Department of Chemistry, University of Patras, 26504 Patras, Greece
E-mail: perlepes@patreas.upatras.gr
[c] Institute of Materials Science, NCSR "Demokritos", 15310 Aghia Paraskevi Attikis, Greece

 © 2005 Wiley-VCH Verlag GmbH & Co. KGaA, Weinheim **DOI: 10.1002/ejic.200400933**

more interesting are MCs composed of a combination of oximate and hydroximate ligands, e.g., pko^- and shi^{3-}.[4,18]

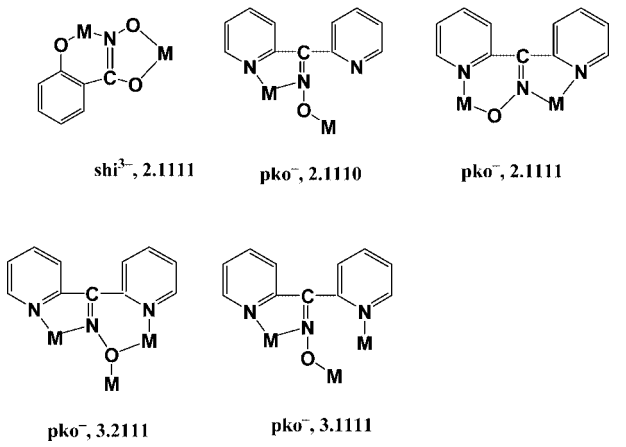

Figure 1. Some of the crystallographically established coordination modes of the ligands shi^{3-} and pko^- discussed in the text, and the Harris notation that describes these modes.

Metallacrown nomenclature is discussed in several key references.[4,18,19] There are now examples of [9-$MC_{M(ox)N(ligand)}$-3],[20] [12-$MC_{M(ox)N(ligand)}$-4],[15,18,19,21] [15-$MC_{M(ox)N(ligand)}$-5][19,22] and [24-$MC_{M(ox)N(ligand)}$-8][17] structural types, as well as fused, dinuclear and mixed-metal MCs.[4,18,19,23] There are nine metals in four oxidation states (II–V) that have been incorporated into the MC ring, while more than 20 metal ions, i.e., lanthanide, actinide, alkali, alkaline earth and transition metal ions have been captured in the central cavity of MCs.

For 12-MC-4 complexes, two structural motifs have been reported: classical or regular[15,18,19,21] and inverse,[24] with most 12-MC-4 compounds belonging to the former type. In the regular motif, there is an N–O–M–N–O–M linkage, i.e., an $[M–N–O]_n$ repeat unit, with the oxygen atoms oriented towards the centre of the cavity and capable of binding cations.[4] In the inverse motif, which has been realized only for Zn[24] and Co,[25] the ring metal ions are oriented towards the centre of the cavity which is now capable of encapsulating anions, whereas the connectivity is transposed to N–O–M–O–N–M.

Our groups have been exploring the chemistry of MCs[17,19,21a,21e,22a,22f,23b,24b,25] and the coordination chemistry of 2-pyridyl oximes,[26,27] the latter not necessarily in relation to the former. There is currently a renewed interest in the coordination chemistry of oximes.[28] Research efforts are driven by a number of considerations, including the solution of pure chemical problems,[29] the development of new oxygen activation catalysts,[30] the application of metal/oxime systems as simple and efficient catalysts for the hydrolysis of organonitriles,[31] the mechanistic study of corrosion inhibition by Acorga P5000 (a modern corrosion inhibitor) on Fe surfaces,[32] and the employment of oximate ligands in the synthesis of homometallic or heterometallic clusters[28a,33,34] and chains[35] with interesting magnetic properties, including single-molecule magnetism[34e] and single-chain magnetism[35] behaviour. For example, the pure chemical interest arises from the ability of the oximate(1–) group (–C=N–O$^-$) to stabilize higher metal oxidation states,[36] such as Ni^{III} or Ni^{IV}, and the fact that the activation of oximes by transition metal centres towards further reactions seems to be an excellent area of modern synthetic chemistry.[28] In contrast to the great number of studies concerning metal complexes of simple oximes and salicylaldoxime,[28,34d,32] little is known about complexes of pyridyl oximes, although this class of compounds could offer unique features in terms of structural characteristics and physical properties.

Di-2-pyridyl ketone oxime (Hpko) occupies a special position amongst the 2-pyridyl oximes. One area to which the ligand pko^- is relevant is the chemistry of MCs (see above). Another attractive aspect of pko^- is its great coordinative flexibility and versatility, characteristics that have led to polynuclear 3d-metal complexes with impressive structures and interesting magnetic properties.[26,27a,27e,37] A last interesting feature is the activation of Hpko by 3d-metal centres, which appears to be a fruitful area of synthetic inorganic chemistry. Examples of this activation are the Mn-assisted transformation of Hpko into the coordinated dianion of the *gem*-diol form of di-2-pyridyl ketone through NO_3^- generation,[27a] and the in-situ transformation of Hpko into the coordinated ligands di-2-pyridylimine, (amino)di-2-pyridylmethyl ethyl ether and (amino)di-2-pyridylmethyl methyl ether upon its reaction with $[V^{III}Cl_3(THF)_3]$ in various solvents.[38]

Zinc(II)/Hpko chemistry has attracted some prior interest. Pecoraro and co-workers have prepared the tetranuclear species $[Zn_4(OH)_2(O_2CMe)_2(pko)_4]$ or $\{(OH)_2$[inv12-$MC_{Zn^{II}N(pko)}$-4]$(O_2CMe)_2\}$[24a] (using the metallacrown nomenclature), which is the archetype of the inverse 12-MC-4 complexes. Some of us have also prepared and studied[24b] $[ZnCl_2(Hpko)]$, $[Zn_4(OH)_2Cl_2(pko)_4]$ or $\{(OH)_2$[inv12-$MC_{Zn^{II}N(pko)}$-4]$Cl_2\}$ and $[Zn_8(shi)_4(pko)_4(MeOH)_2]$; the second of these complexes is also an inverse 12-MC-4 species, while a part of the octanuclear cluster can be described as having a formally anionic [12-$MC_{Zn^{II}N(shi)}$-4]$^{4-}$ core with the 12-membered ring acting as host agent for a dinuclear $Zn_2(pko)_4$ unit and with two of the MC ring Zn^{II} ions creating dinuclear moieties with the remaining metal ions. Using these prior observations as a starting point and seeking to extend the family of the inverse 12-$MC_{Zn^{II}N(pko)}$-4 complexes, to incorporate pseudohalides (N_3^-, NCO^-, SCN^-), carboxylates other than acetates or anionic chelates into the Zn^{II}/pko^- chemistry, and to examine the possibility of creating novel cluster topologies within this chemistry, we report here the successful development of synthetic routes to cationic pentanuclear Zn^{II}/pko^- clusters and to new examples of inverse 12-$MC_{Zn^{II}N(pko)}$-4 compounds featuring N_3^-, NCO^-, SCN^-, $PhCO_2^-$ or $acac^-$ coligands [acac = acetylacetonate(–1) ion].

 © 2005 Wiley-VCH Verlag GmbH & Co. KGaA, Weinheim

Results and Discussion

Synthesis

As stated above, we were interested in extending the very small family of inverse 12-$MC_{Zn^{II}N(pko)}$-4 complexes. In an earlier report, Pecoraro's group reported the preparation of the inverse metallacrown $[Zn_4(OH)_2(O_2CMe)_2(pko)_4]$.[24a] Thus, we decided to seek the benzoate version of this complex. Our main goal was to determine whether the benzoate cluster would have a similar molecular structure. The preparation of compound **1** can be achieved by the 1:1 reaction of $Zn(O_2CPh)_2{\cdot}2H_2O$ with pko^- in MeCN at room temperature [Equation (1)]. Note that both Et_3N and the released $PhCO_2^-$ groups can act as proton acceptors to facilitate formation of OH^- and pko^- ligands.

$$4\ Zn(O_2CPh)_2{\cdot}2H_2O + 4\ Hpko + 4\ Et_3N \xrightarrow{MeCN} [Zn_4(OH)_2(O_2CPh)_2(pko)_4]\ (\mathbf{1}) + 2\ PhCO_2H + 4\ Et_3NHO_2CPh + 6\ H_2O \quad (1)$$

Similar results were obtained in the absence of the external Et_3N base; however, the yield (about 20%) was lower. The formation of **1** in the absence of Et_3N (not reported in the Experimental Section) is summarised by Equation (2).

$$4\ Zn(O_2CPh)_2{\cdot}2H_2O + 4\ Hpko \xrightarrow{MeCN} [Zn_4(OH)_2(O_2CPh)_2(pko)_4]\ (\mathbf{1}) + 6\ PhCO_2H + 6\ H_2O \quad (2)$$

Two years ago we reported[24b] the preparation of the inverse 12-MC-4 $[Zn_4(OH)_2Cl_2(pko)_4]$ from the reaction of $ZnCl_2$ with pko^- or by addition of NaOH to a MeOH/DMF solution of the mononuclear complex $[ZnCl_2(Hpko)]$. We wondered whether pseudohalide analogues of the chloro cluster could be prepared. For example, we could envisage that complexes $[Zn_4(OH)_2X_2(pko)_4]$ (X = N_3^-, SCN^-, OCN^-, ...), with two terminal X^- ligands instead of two terminal chloro ligands, should be stable. Reactions between convenient Zn^{II} sources and a combination of N_3^- or OCN^- and pko^- (ca. 2:1:2) in DMF or DMF/MeOH led to subsequent isolation of pure crystalline complexes **2** and **3** in good yields (ca. 70%) [Equations (3) and (4)]. Single-crystal X-ray crystallography revealed the expected structural similarity between **2** and **3** and the chloro cluster.

$$4\ Zn(NO_3)_2{\cdot}4H_2O + 2\ NaN_3 + 4\ Hpko + 4\ NaOH \xrightarrow{DMF} [Zn_4(OH)_2(N_3)_2(pko)_4]\ (\mathbf{2}) + 6\ NaNO_3 + 2\ HNO_3 + 18\ H_2O \quad (3)$$

$$4\ ZnCl_2 + 2\ NaOCN + 4\ Hpko + 4\ NaOH \xrightarrow{DMF/MeOH} [Zn_4(OH)_2(NCO)_2(pko)_4]\ (\mathbf{3}) + 6\ NaCl + 2\ HCl + 2\ H_2O \quad (4)$$

Two features of the Equations (3) and (4) deserve comments. First, the reaction "solutions" should be filtered before crystallisation to remove a small amount of $NaNO_3$ or NaCl which remains insoluble in DMF. Second, the employment of DMF is beneficial to the syntheses as DMF solvate molecules stabilize the crystal lattices of **2** and **3** and also possibly aid in the "neutralisation" of the produced *dilute* HCl or HNO_3 and, thus, the latter do not decompose the hydroxo clusters.

The next questions we addressed were whether the monodentate ligands $PhCO_2^-$, N_3^-, OCN^- and Cl^- in **1**, **2**, **3** and $[Zn_4(OH)_2Cl_2(pko)_4]$,[24b] respectively, or the *nearly* monodentate $MeCO_2^-$ ligand (in fact the acetato ligand is anisobidentate) in $[Zn_4(OH)_2(O_2CMe)_2(pko)_4]$,[24a] could be replaced by anionic chelates and whether this replacement would preserve the inverse 12-MC-4 structural type. The anionic chelating ligand chosen was the acetylacetonate(–1) ion ($acac^-$). The procedure that leads to pure **4** involves the reaction of $Zn(acac)_2{\cdot}H_2O$ with an almost equimolar amount of Hpko in CH_2Cl_2 under reflux [Equation (5)]. The source of the hydroxo ligands is moisture from the starting materials, and the solvents used for the preparation (CH_2Cl_2) and/or crystallisation (Et_2O) of the complex. Single-crystal X-ray crystallography revealed the existence of an inverse 12-MC-4 motif in **4**. The isolation of the hydroxo cluster **4** from non-polar solvents is strong evidence of the great thermodynamic stability of the $\{Zn_4(\mu_3\text{-}OH)_2(pko)_4\}^{2+}$ unit.

$$4\ Zn(acac)_2{\cdot}H_2O + 4\ Hpko \xrightarrow[T]{CH_2Cl_2} [Zn_4(OH)_2(acac)_2(pko)_4]\ (\mathbf{4}) + 6\ Hacac + 2\ H_2O \quad (5)$$

We initially came across complexes **5** and **6** when we tried to prepare the isothiocyanato analogue of $[Zn_4(OH)_2Cl_2(pko)_4]$, **2** and **3**. These at first glance trivial efforts led to dramatic nuclearity and structural changes. The initial reaction explored was that between $ZnCl_2$, half an equivalent of SCN^- and one equivalent of pko^- (prepared in situ from Hpko and NaOH) in MeOH. The colourless solution obtained gradually turned to pale yellow upon stirring. Concentration of the resulting solution at room temperature gave a mixture of colourless prisms and pale-yellow needles. Their not-too-dissimilar solubility prevented chemical separation; however, the differences in colour and crystal shape allowed manual separation of the two materials. The colourless and pale-yellow crystals were crystallographically identified as complexes $[Zn_5Cl_2(pko)_6][ZnCl(NCS)_3]{\cdot}2.5H_2O{\cdot}1.5MeOH$ (**5**$\cdot 2.5H_2O\cdot 1.5MeOH$) and $[Zn_5(NCS)_2(pko)_6(MeOH)][Zn(NCS)_4]{\cdot}2.5H_2O{\cdot}MeOH$ (**6**$\cdot 2.5H_2O\cdot$MeOH), respectively. Stoichiometric reactions of the formation of **5** and **6** are represented by Equations (6) and (7), respectively.

With the identities of **5** and **6** established, convenient syntheses of pure materials were sought under alternative reaction conditions. Complex **6** has a Zn^{II}/SCN^- ratio of 1:1, whereas the initial reaction solution had a Zn^{II}/SCN^- ratio

 © 2005 Wiley-VCH Verlag GmbH & Co. KGaA, Weinheim

$$6\ ZnCl_2 + 3\ NaSCN + 6\ Hpko + 6\ NaOH \xrightarrow{MeOH} [Zn_5Cl_2(pko)_6][ZnCl(NCS)_3] + 9\ NaCl + 6\ H_2O \quad (6)$$

5

$$6\ ZnCl_2 + 6\ NaSCN + 6\ Hpko + 6\ NaOH + MeOH \xrightarrow{MeOH} [Zn_5(NCS)_2(pko)_6(MeOH)][Zn(NCS)_4] + 12\ NaCl + 6\ H_2O \quad (7)$$

6

of 2:1; thus, attempts to obtain pure **6** were made by decreasing this ratio. Somewhat to our disappointment, the use of $ZnCl_2$/NaSCN ratios of 1:1 or even of 1:2 again gave mixtures of **5** and **6**. It is likely that the reaction solution contains a complicated mixture of several species in equilibrium, with factors such as relative solubility, lattice energy, crystallisation kinetics amongst others determining the identity of the isolated products. Since complex **6** is chloride-free, the next logical step to prepare the pure compound was to exclude Cl^- ions from the reaction mixture. The preparation of pure **6** was achieved by the reaction of a slight excess of $Zn(O_2CMe)_2{\cdot}2H_2O$ with one equivalent of NaSCN and one equivalent of Hpko in MeOH [Equation (8)].

$$6\ Zn(O_2CMe)_2{\cdot}2H_2O + 6\ NaSCN + 6\ Hpko + MeOH \xrightarrow{MeOH} [Zn_5(NCS)_2(pko)_6(MeOH)][Zn(NCS)_4] + 6\ NaO_2CMe + 6\ MeCO_2H + 12\ H_2O \quad (8)$$

6

In seeking to prepare the pure complex **5**, it was logical to carry out reactions employing high $ZnCl_2$/NaSCN ratios. The 3:1:3 and 4:1:4 $ZnCl_2$/NaSCN/pko^- reaction mixtures in MeOH led to precipitation of *almost* pure colourless **5** in good yields (typically higher than 50%). However, careful examination of the crystalline powders from these reactions revealed trace amounts of pale-yellow microcrystals and/or specks which were shown to be complex **6** by IR spectroscopy. Thus, the manual separation of colourless crystals from their above-described mixtures with **6** remains the only source of complex **5** to date for further measurements.

Since complexes **5** and **6** contain different Zn^{II}/SCN^- ratios, it seemed reasonable to suspect that they could be interconverted by treatment of the performed materials with appropriate reagents. The conversion of **5** to **6** can be accomplished quite easily by treatment of the former with an excess of NaSCN in MeOH at 45 °C [Equation (9)]. Addition of a small amount of external H_2O to the reaction mixture is necessary to achieve a clean conversion of **5** to **6**, presumably by keeping the produced NaCl soluble. All efforts to prepare **5** by the reaction of **6** with an excess of NaCl in MeOH or MeOH/H_2O were in vain.

$$[Zn_5Cl_2(pko)_6][ZnCl(NCS)_3] + 3\ NaSCN + MeOH \xrightarrow[45\ ^oC,\ exc.\ NaSCN]{MeOH/H_2O\ (10:1\ v/v)} [Zn_5(NCS)_2(pko)_6(MeOH)][Zn(NCS)_4] + 3\ NaCl \quad (9)$$

5 → **6**

The isolation of **5** and **6** was surprising and, needless to say, unexpected. We suspected that the formation of the pentanuclear clusters might be related to their cationic character. Thus, we tried to prepare such clusters with N_3^- and OCN^- ligands under conditions that favour formation of anionic compounds, i.e., employing bulky non-coordinating counteranions. Synthetic studies of hundreds of ZnX_2/OCN^- or N_3^-/pko^-/Y^- reaction mixtures (X = Cl, NO_3, $MeCO_2$; Y = PF_6, ClO_4, BPh_4) repeatedly led to microcrystalline materials. Analytical data were consistent with the formulation $[Zn_5(OCN)_2(pko)_6]Y_2$ or $[Zn_5(N_3)_2(pko)_6]Y_2$ and IR data indicated the presence of Y^- counterions, but, unfortunately, numerous attempts to obtain crystals suitable for crystallographic studies all were in vain. We were luckier, but at the same time unlucky again, when we employed $acac^-$ (instead of N_3^- or OCN^-) in the above-mentioned reaction mixtures. The reaction, summarised in Equation (10), gave pale-yellow prisms, which were proven to be single crystals.[39] Unfortunately, the crystals were of bad quality and poor diffractors of X-rays and, therefore, we refrain from presenting a full structural analysis here. Nevertheless, single-crystal crystallographic studies clearly revealed the presence of the $[Zn_5(acac)_2(pko)_6]^{2+}$ ion in the product, further emphasising our belief that the pentanuclear clusters are isolable only as cations.

$$5\ Zn(acac)_2{\cdot}H_2O + 6\ Hpko + 3\ NH_4PF_6 \xrightarrow{MeOH} (NH_4)[Zn_5(acac)_2(pko)_6](PF_6)_3 + 6acacH + 2\ NH_4acac + 5\ H_2O \quad (10)$$

Description of Structures

$[Zn_4(OH)_2(O_2CPh)_2(pko)_4]{\cdot}3MeCN$ (1·3MeCN), $[Zn_4(OH)_2(N_3)_2(pko)_4]{\cdot}4DMF$ (2·4DMF), $[Zn_4(OH)_2(NCO)_2(pko)_4]{\cdot}3DMF{\cdot}H_2O$ (3·3DMF·H_2O) and $[Zn_4(OH)_2(acac)_2(pko)_4]{\cdot}4CH_2Cl_2$ (4·4CH_2Cl_2)

Partially labelled plots of the tetranuclear molecules present in compounds **1**·3MeCN, **2**·4DMF, **3**·3DMF·H_2O and **4**·4CH_2Cl_2, are shown in Figures 2, 3, 4, and 5, respectively. Selected interatomic distances and angles are listed in Tables 1, 2, 3, and 4, respectively. The molecular structures of the four complexes are similar in many aspects and, thus, only the structure of the representative complex **1**·3MeCN will be described in detail.

The tetranuclear molecule of **1**·3MeCN lies on a crystallographic inversion centre and has a planar, nearly rhombic arrangement of the metal centres. The two diagonals of the rhombus correspond to the interatomic distances Zn(1)···Zn(1′) and Zn(2)···Zn(2′) which are equal to 5.815(1) and 3.224(1) Å, respectively, the short diagonal being very similar to the sides of the rhombus. Due to the presence of the crystallographic inversion centre, the $\{Zn(2)Zn(2')O(21)O(21')\}^{2+}$ subcore is strictly planar. The metallacrown is characterised as inverse because the Zn ions, rather than the oximate oxygen atoms, are oriented towards the centre of the cavity, while the connectivity is

 © 2005 Wiley-VCH Verlag GmbH & Co. KGaA, Weinheim

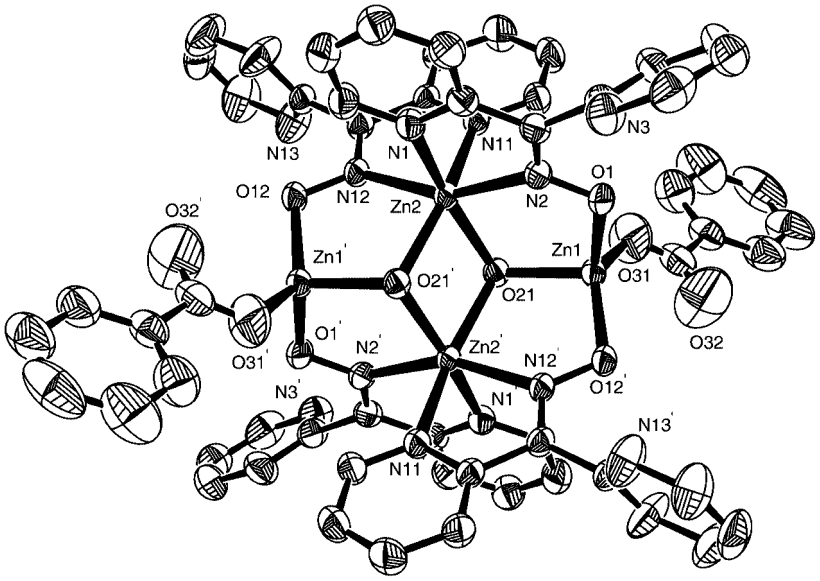

Figure 2. Partially labelled ORTEP plot of the tetranuclear molecule of complex **1**·3MeCN. Primed and unprimed atoms are related by the crystallographic inversion centre. O(21) and O(21′) are the hydroxo oxygen atoms. The connectivity of the inverse metallacrown ring has been highlighted.

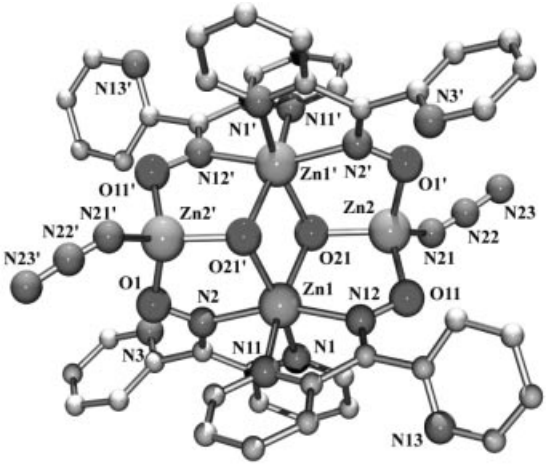

Figure 3. Partially labelled POV-RAY plot of the tetranuclear molecule of complex **2**·4DMF. Other details are as in the caption of Figure 2.

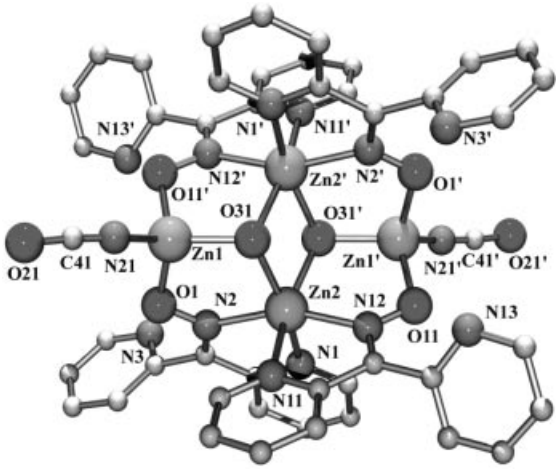

Figure 4. Partially labeled POV-RAY plot of the tetranuclear molecule of complex **3**·3DMF·H_2O. Primed and unprimed atoms are related by the crystallographic inversion centre. O(31) and O(31′) are the hydroxo oxygen atoms. The connectivity of the inverse metallacrown ring has been highlighted.

N–O–Zn–O–N–Zn. The Zn centres are bridged along each side of the rhombus by one μ_3-hydroxide [O(21),O(21′)] and one oximate(–1) group. The pko$^-$ ligands adopt an η^1:η^1:η^1:μ_2 (or 2.1110[16]) coordination mode. The coordination about the hydroxo oxygen atom, O(21), is markedly pyramidal [sum of Zn–O(21)–Zn angles: 319.7°].

The metal ions exhibit two coordination geometries. Zn(2) and Zn(2′) are in distorted O_2N_4 octahedral environments, whereas Zn(1) and Zn(1′) are in severely distorted O_4 tetrahedral environments. Each hydroxo oxygen atom bridges to two octahedral Zn ions and one tetrahedral Zn ion. The octahedral Zn ions are bound to two pko$^-$ moieties by pyridyl nitrogen atoms [N(1), N(11), N(1′), N(11′)] and the oxime nitrogen atoms [N(2), N(12), N(2′), N(12′)] in two five-membered chelating rings. The remaining two coordination sites of the octahedron are filled by the two μ_3-hydroxide ions accommodated in the centre of the MC ring. The ligands form a propeller configuration that imposes absolute stereoisomerism, with Λ chirality at Zn(2) and Δ chirality at Zn(2′). Each tetrahedral Zn ion is bound to one of the bridging hydroxo ligands and to two oximate oxygen atoms, while the fourth site is occupied by an oxygen atom [O(31), O(31′)] from a coordinated benzoate ion. The longer Zn(2)–O bonds [2.085(3), 2.088(4) Å] compared to the Zn(1)–O ones [1.925(5)–1.991(3) Å] are a consequence of the higher coordination number of Zn(2). The angles around Zn(1) [and Zn(1′)] are in the wide 100.9(3)–133.3(2)° range. The benzoate oxygen atom [O(31)] forms a strong bond with Zn(1) [1.925(5) Å]. As is sometimes (but not always) observed for monodentate RCO_2^- groups, there

 © 2005 Wiley-VCH Verlag GmbH & Co. KGaA, Weinheim

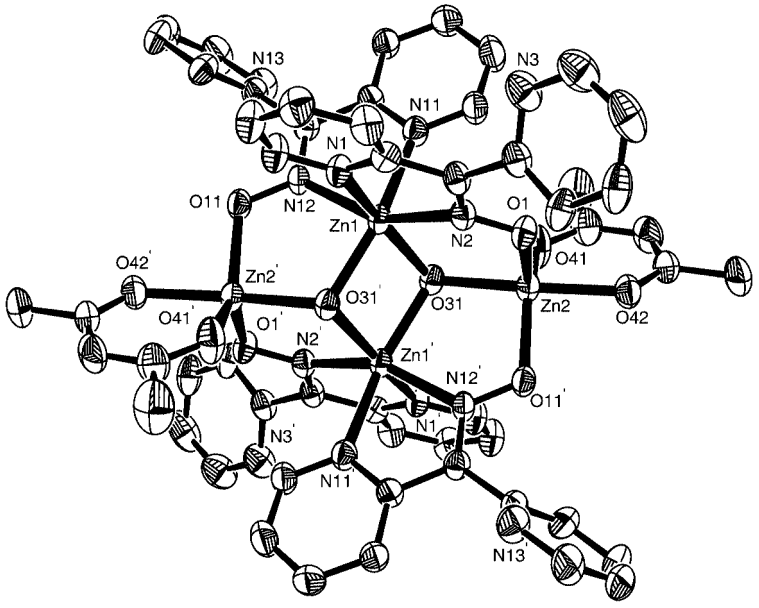

Figure 5. Partially labeled ORTEP plot of the tetranuclear molecule of complex **4**·4CH_2Cl_2. Other details are as in the caption of Figure 4.

Table 1. Selected interatomic distances [Å] and angles [°] for $[Zn_4(OH)_2(O_2CPh)_2(pko)_4]$·3MeCN (**1**·3MeCN).[a]

Zn(1)···Zn(2)	3.334(1)	Zn(1)–O(31)	1.925(5)
Zn(1)···Zn(2′)	3.315(1)	Zn(2)–O(21)	2.088(4)
Zn(1)···Zn(1′)	5.815(1)	Zn(2)–O(21′)	2.085(3)
Zn(2)···Zn(2′)	3.224(1)	Zn(2)–N(1)	2.196(4)
Zn(1)–O(1)	1.974(3)	Zn(2)–N(11)	2.187(3)
Zn(1)–O(12′)	1.951(3)	Zn(2)–N(2)	2.156(3)
Zn(1)–O(21)	1.991(3)	Zn(2)–N(12)	2.158(3)
O(1)–Zn(1)–O(12′)	106.0(1)	N(2)–Zn(2)–N(12)	156.4(1)
O(12′)–Zn(1)–O(31)	133.3(2)	Zn(1)–O(21)–Zn(2)	108.7(2)
O(21)–Zn(1)–O(31)	100.9(3)	Zn(1)–O(21)–Zn(2′)	109.8(1)
O(21)–Zn(2)–N(1)	161.2(1)	Zn(2)–O(21)–Zn(2′)	101.2(2)
O(21′)–Zn(2)–N(11)	158.6(1)		

[a] Primed atoms are related to the unprimed ones by the symmetry transformation $-x + 1, -y, -z + 1$.

Table 2. Selected interatomic distances [Å] and angles [°] for $[Zn_4(OH)_2(N_3)_2(pko)_4]$·4DMF (**2**·4DMF).[a]

Zn(1)···Zn(2)	3.312(1)	Zn(2)–N(21)	1.925(5)
Zn(1)···Zn(2′)	3.301(1)	Zn(1)–O(21)	2.122(3)
Zn(1)···Zn(1′)	3.243(1)	Zn(1)–O(21′)	2.103(3)
Zn(2)···Zn(2′)	5.763(1)	Zn(1)–N(1)	2.171(4)
Zn(2)–O(1′)	1.964(3)	Zn(1)–N(11)	2.194(4)
Zn(2)–O(11)	1.966(3)	Zn(1)–N(2)	2.153(3)
Zn(2)–O(21)	1.953(3)	Zn(1)–N(12)	2.144(3)
O(1′)–Zn(2)–O(11)	102.0(1)	Zn(2)–O(21)–Zn(1)	108.7(2)
O(21)–Zn(2)–N(21)	119.5(2)	Zn(2)–O(21)–Zn(1′)	108.9(2)
O(21)–Zn(1)–N(11)	159.3(1)	Zn(1)–O(21)–Zn(1′)	100.3(1)
O(21′)–Zn(1)–N(1)	159.2(1)	Zn(2)–N(21)–N(22)	134.0(7)
N(2)–Zn(1)–N(1)	160.5(1)	N(21)–N(22)–N(23)	175.8(12)

[a] Primed atoms are related to the unprimed ones by the symmetry transformation $-x, -y, -z + 1$.

Table 3. Selected interatomic distances [Å] and angles [°] for $[Zn_4(OH)_2(NCO)_2(pko)_4]$·3DMF·$H_2O$ (**3**·3DMF·H_2O).[a]

Zn(1)···Zn(2)	3.316(1)	Zn(1)–N(21)	1.918(7)
Zn(1)···Zn(2′)	3.313(1)	Zn(2)–O(31)	2.122(4)
Zn(1)···Zn(1′)	5.788(1)	Zn(2)–O(31′)	2.104(4)
Zn(2)···Zn(2′)	3.233(1)	Zn(2)–N(1)	2.188(6)
Zn(1)–O(1)	1.966(5)	Zn(2)–N(11)	2.163(6)
Zn(1)–O(11′)	1.946(5)	Zn(2)–N(2)	2.130(5)
Zn(1)–O(31)	1.962(4)	Zn(2)–N(12)	2.151(5)
O(1)–Zn(1)–O(11′)	101.6(2)	N(2)–Zn(2)–N(12)	159.9(2)
O(31)–Zn(1)–N(21)	122.2(3)	Zn(1)–O(31)–Zn(2)	108.5(2)
O(31)–Zn(2)–N(1)	160.0(2)	Zn(1)–O(31)–Zn(2′)	109.1(2)
O(31′)–Zn(2)–N(11)	159.6(2)	Zn(2)–O(31)–Zn(2′)	99.8(2)

[a] Primed atoms are related to the unprimed ones by the symmetry transformation $-x + 2, -y + 1, -z$.

Table 4. Selected interatomic distances [Å] and angles [°] for $[Zn_4(OH)_2(acac)_2(pko)_4]$·4$CH_2Cl_2$ (**4**·4CH_2Cl_2).[a]

Zn(1)···Zn(2)	3.433(1)	Zn(2)–O(42)	2.062(5)
Zn(1)···Zn(2′)	3.467(1)	Zn(1)–O(31)	2.066(6)
Zn(1)···Zn(1′)	3.164(1)	Zn(1)–O(31′)	2.051(6)
Zn(2)···Zn(2′)	6.132(1)	Zn(1)–N(1)	2.192(6)
Zn(2)–O(1)	1.983(5)	Zn(1)–N(11)	2.208(6)
Zn(2)–O(11′)	2.005(5)	Zn(1)–N(2)	2.166(6)
Zn(2)–O(31)	2.082(5)	Zn(1)–N(12)	2.163(5)
Zn(2)–O(41)	2.007(6)		
O(1)–Zn(2)–O(31)	97.3(2)	O(31′)–Zn(1)–N(11)	158.2(2)
O(1)–Zn(2)–O(42)	91.3(2)	N(2)–Zn(1)–N(12)	154.0(2)
O(31)–Zn(2)–O(42)	168.3(2)	Zn(2)–O(31)–Zn(1)	111.7(3)
O(41)–Zn(2)–O(42)	87.7(2)	Zn(2)–O(31)–Zn(1′)	114.1(3)
O(31)–Zn(1)–N(1)	159.9(2)	Zn(1)–O(31)–Zn(1′)	100.4(2)

[a] Primed atoms are related to the unprimed ones by the symmetry transformation $-x + 2, -y + 1, -z + 1$.

is evidence for an additional weak interaction between Zn(1) and Zn(1′), and the "free" benzoate oxygen atoms O(32) and O(32′), which generates an asymmetric chelating carboxylate group. Further support for this structural assignment comes from the coordination environment around Zn(1), which is very distorted from tetrahedral geometry; thus, an alternative description for the Zn(1) polyhedron is as an edge-capped tetrahedron.

The separations between neighbouring metal ions in **1** [3.315(1), 3.334(1) Å] are significantly shorter than those

 © 2005 Wiley-VCH Verlag GmbH & Co. KGaA, Weinheim

observed in regular 12-MC-4 complexes [M···M distances are approx. 4.6 Å].[15,18,19,21a] If we consider that, in the inverse 12-MC-4 compounds, the M···M separation is the bite distance, then this separation is longer than the O···O distance in regular MCs (ca. 2.6 Å) which is considered as the bite distance.

Complex **1** is only the second structurally characterised example of a tetranuclear zinc(II) benzoate cluster, the first being $[Zn_4O(O_2CPh)_6]$.[40]

The molecular structures of **2**·4DMF, **3**·3DMF·H_2O and **4**·4CH_2Cl_2 are similar to the structure of **1**·3MeCN except that the two terminal $PhCO_2^-$ ligands of **1** are replaced by two monodentate azido (**2**·4DMF), two monodentate isocyanato (i.e. *N*-bonded, **3**·3DMF·H_2O) or two bidentate chelating acetylacetonate groups (**4**·4CH_2Cl_2). Due to the presence of the purely monodentate N_3^- and NCO^- ligands in **2**·4DMF and **3**·3DMF·H_2O, respectively, instead of the anisobidentate benzoate ligands in **1**·3MeCN, the coordination environments of the tetrahedral Zn ions are less distorted; the angles around these metal ions in **2**·4DMF and **3**·3DMF·H_2O are in the ranges 102.0(1)–119.5(2)° and 101.6(2)–122.2(3)°, respectively [vs. the 100.9(3)–133.3(2)° range observed in **1**·3MeCN]. The presence of the chelating $acac^-$ ligands in **4**·4CH_2Cl_2 creates a truly five-coordination at two metal ions [Zn(2) and Zn(2′) in Figure 5]. The five donor atoms around Zn(2) [and Zn(2′)] do not create a regular polyhedron. Analysis of the shape-determining angles using the approach of Reedijk and coworkers[41] yields a value for the trigonality index, τ, of 0.61 (τ = 0 and 1 for perfect square-pyramidal (spy) and trigonal-bipyramidal (tbp) geometries, respectively). Thus, the geometry about Zn(2) is significantly distorted and can better be described as distorted tbp. With use of this description, the axial sites of Zn(2) are occupied by atoms O(31) and O(42) with atoms O(1), O(11′) and O(41) making up the equatorial plane (Figure 4 and Table 3).

The $Zn–N_{azido}$ [1.925(5) Å] and $Zn–N_{isocyanato}$ [1.918(7) Å] bond lengths in **2**·4DMF and **3**·3DMF·H_2O, respectively, are typical for such terminal bonds in tetrahedral zinc(II) complexes. For comparison, the $Zn–N_{azido}$ bond lengths in $[Zn(N_3)_2(py)_2]$ (py = pyridine)[42] are 1.928(16) and 1.945(17) Å, while the $Zn–N_{isocyanato}$ bond lengths in $[Zn(NCO)_2(4\text{-dmap})_2]$, where 4-dmap is 4-(dimethylamino)pyridine, are 1.909(5) and 1.942(5) Å. The azido and isocyanato ligands are almost linear [N(21)–N(22)–N(23) = 175.8(12)°, N(21)–C(41)–O(21) = 176(2)°]; these ligands are coordinated in a bent (N_3^-) or slightly bent (NCO^-) fashion as indicated by the Zn–N–N [134.0(7)°] and Zn–N–C [160.7(10)°] angles, respectively (Table 4).

The benzoate cluster **1** has a similar structure to its acetate version,[24a] while the molecular structures of the pseudohalide inverse 12-MC-4 complexes **2** and **3** are also very similar to the structure of the halide analogue $[Zn_4(OH)_2Cl_2(pko)_4]$.[24b] Obviously, the replacement of $MeCO_2^-$ by $PhCO_2^-$, and of Cl^- by N_3^- and NCO^- has little structural effect. Rather than discuss similarities, we list in Table 5 comparative structural parameters for the $\{(OH)_2[inv12\text{-}MC_{Zn^{II}N(pko)}\text{-}4]X_2\}$ complexes (X = Cl, N_3, NCO). The remarkable similarity of the molecular structures of the three complexes is clearly evident. The presence of the two five-coordinate Zn anions in **4** {instead of two four-coordinate Zn ions in $[Zn_4(OH)_2Cl_2(pko)_4]$, **2** and **3**} has few slight structural consequences. The $Zn_{five\text{-}coord}–O_{hydroxo}$ [2.082(5) Å] and $Zn_{five\text{-}coord}–O_{oximate}$ [mean value: 1.994(5) Å] bond lengths are longer than the corresponding $Zn_{tetr}–O_{hydroxo}$ and mean $Zn_{tetr}–O_{oximate}$ ones (Table 5), as expected. The $Zn_{five\text{-}coord}\cdots Zn_{five\text{-}coord}$ separation [6.132(1) Å] is longer than the $Zn_{tetr}\cdots Zn_{tetr}$ ones (Table 5), whereas the $Zn_{oct}\cdots Zn_{oct}$ interatomic distance [3.164(1) Å] and the mean $Zn_{oct}–O_{hydroxo}$ bond length [2.059(6) Å] are shorter than the corresponding distances in $\{(OH)_2[inv12\text{-}MC_{Zn^{II}N(pko)}\text{-}4]X_2\}$ (X = Cl, N_3, NCO).

Table 5. Selected, comparative structural data for the halide/pseudohalide inverse 12-MC-4 complexes $[Zn_4(OH)_2Cl_2(pko)_4]$, $[Zn_4(OH)_2(N_3)_2(pko)_4]$ (**2**) and $[Zn_4(OH)_2(NCO)_2(pko)_4]$ (**3**).

Parameter [Å or °]	$[Zn_4(OH)_2Cl_2(pko)_4]$	**2**	**3**
$Zn_{tetr}\cdots Zn_{tetr}$	5.826	5.763	5.788
$Zn_{oct}\cdots Zn_{oct}$	3.231	3.243	3.233
$Zn_{tetr}\cdots Zn_{oct}$[a]	3.326	3.307	3.315
$Zn_{tetr}–O_{hydroxo}$	1.963	1.953	1.962
$Zn_{tetr}–O_{oximate}$[a]	1.960	1.965	1.956
$Zn_{oct}–O_{hydroxo}$[a]	2.118	2.113	2.113
$Zn_{oct}–N_{pyridyl}$[a]	2.178	2.183	2.176
$Zn_{oct}–N_{oximate}$[a]	2.144	2.149	2.141
$Zn_{tetr}–O_{hydroxo}–Zn_{oct}$[a]	109.4	108.8	108.8
$Zn_{oct}–O_{hydroxo}–Zn_{oct}$	99.4	100.3	99.8
$\Sigma(Zn–O_{hydroxo}–Zn)$	318.1	317.9	317.4

[a] Mean value.

$[Zn_5Cl_2(pko)_6][ZnCl(NCS)_3]$·2.5$H_2O$·1.5MeOH (5·2.5$H_2O$·1.5MeOH) and $[Zn_5(NCS)_2(pko)_6(MeOH)][Zn(NCS)_4]$·2.5$H_2O$·MeOH (6·2.5$H_2O$·MeOH)

Fully or partially labelled plots of the cations and anions present in compounds **5**·2.5H_2O·1.5MeOH and **6**·2.5H_2O·MeOH, are shown in Figures 6, 7, 8, and 9. Selected interatomic distances and angles are listed in Tables 6, 7, 8, and 9. The molecular structures of the pentanuclear cations $[Zn_5Cl_2(pko)_6]^{2+}$ and $[Zn_5(NCS)_2(pko)_6(MeOH)]^{2+}$ are similar in many aspects and, thus, only the structure of the chloride-containing cation will be described in detail.

Complex **5**·2.5H_2O·1.5MeOH crystallises in the triclinic space group $P\bar{1}$. Its structure consists of the pentanuclear $[Zn_5Cl_2(pko)_6]^{2+}$ cation, the novel $[ZnCl(NCS)_3]^{2-}$ anion, and solvate H_2O and MeOH molecules; the solvate molecules will not be further discussed. The five Zn ions of the cation are held together by six pko^- ligands which adopt three different coordination modes. Two pko^- ligands adopt the coordination mode 2.1110, two are in the rare 3.1111 fashion, while the rest behave as 3.2111 ligands (see Figure 1). The five metal ions define two nearly equilateral triangles sharing a common apex at Zn(1). The "central" Zn(1) ion is in a distorted $O_2(N_{pyridyl})_2(N_{oximate})_2$ *cis-trans-cis* octahedral environment. Zn(2) and Zn(3) are bound to an $O_2(N_{pyridyl})_2(N_{oximate})$ set of donor atoms, while Zn(4) and Zn(5) are bound to an $O(N_{pyridyl})_2(N_{oximate})Cl$ set. The

 © 2005 Wiley-VCH Verlag GmbH & Co. KGaA, Weinheim

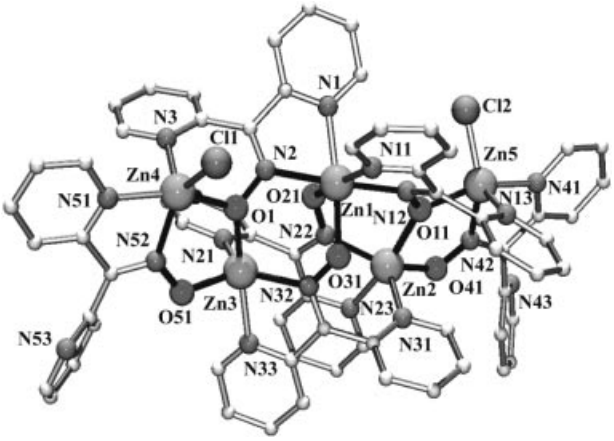

Figure 6. Partially labeled POV-RAY plot of the pentanuclear cation $[Zn_5Cl_2(pko)_6]^{2+}$ of the complex **5**·2.5H_2O·1.5MeOH.

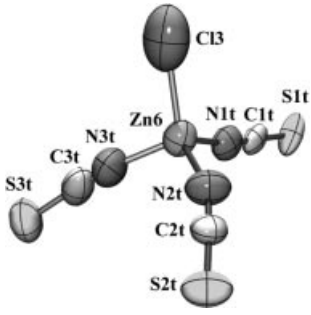

Figure 7. Structure of the anion $[ZnCl(NCS)_3]^{2-}$ of complex **5**·2.5H_2O·1.5MeOH.

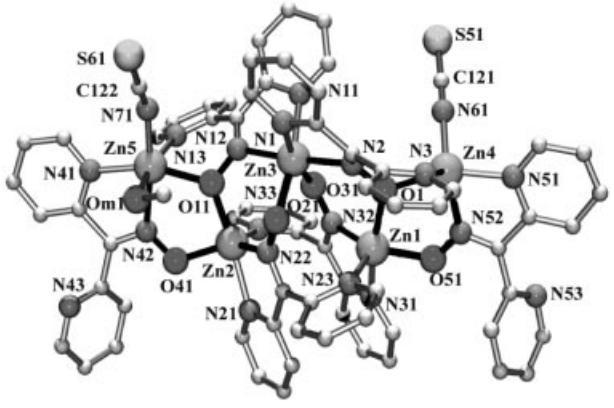

Figure 8. Partially labeled POV-RAY plot of the pentanuclear cation $[Zn_5(NCS)_2(pko)_6(MeOH)]^{2+}$ of complex **6**·2.5H_2O·MeOH.

five donor atoms around Zn(2) and Zn(3) create a very distorted polyhedron. The τ values[41] for Zn(2) and Zn(3) are 0.48 and 0.54, respectively. We prefer to describe the geometry about these metal ions as very distorted tbp. With use of this description, the axial sites of Zn(2) are occupied by atoms O(11) and N(23), while those of Zn(3) by atoms O(1) and N(33). The Zn(4) and Zn(5) coordination geometries are better described as very distorted spy with the 2-pyridyl nitrogenatoms N(3) and N(13) occupying the apical positions for Zn(4) and Zn(5), respectively; The τ values[41] are

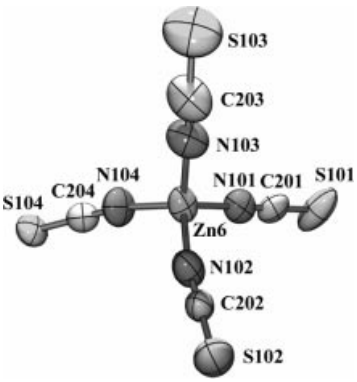

Figure 9. Structure of the anion $[Zn(NCS)_4]^{2-}$ of complex **6**·2.5H_2O·MeOH.

Table 6. Selected interatomic distances [Å] and angles [°] for the cation $[Zn_5Cl_2(pko)_6]^{2+}$ present in complex **5**·2.5H_2O·1.5MeOH.

Zn(1)···Zn(2)	3.767(1)	Zn(2)–N(23)	2.159(7)
Zn(1)···Zn(3)	3.756(1)	Zn(2)–N(31)	2.064(6)
Zn(1)···Zn(4)	4.902(1)	Zn(2)–N(22)	2.073(6)
Zn(1)···Zn(5)	4.896(1)	Zn(3)–O(1)	2.063(5)
Zn(2)···Zn(3)	4.820(1)	Zn(3)–O(51)	1.968(5)
Zn(2)···Zn(4)	7.776(1)	Zn(3)–N(21)	2.091(6)
Zn(2)···Zn(5)	3.627(1)	Zn(3)–N(33)	2.167(7)
Zn(3)···Zn(4)	3.631(1)	Zn(3)–N(32)	2.078(6)
Zn(3)···Zn(5)	7.759(1)	Zn(4)–O(1)	2.089(5)
Zn(4)···Zn(5)	9.785(1)	Zn(4)–N(3)	2.107(7)
Zn(1)–O(21)	2.065(5)	Zn(4)–N(51)	2.089(7)
Zn(1)–O(31)	2.048(5)	Zn(4)–N(52)	2.109(7)
Zn(1)–N(1)	2.152(7)	Zn(4)–Cl(1)	2.232(3)
Zn(1)–N(11)	2.168(7)	Zn(5)–O(11)	2.081(5)
Zn(1)–N(2)	2.138(6)	Zn(5)–N(13)	2.088(7)
Zn(1)–N(12)	2.112(6)	Zn(5)–N(41)	2.078(7)
Zn(2)–O(11)	2.077(6)	Zn(5)–N(42)	2.114(8)
Zn(2)–O(41)	1.973(5)	Zn(5)–Cl(2)	2.169(5)
O(21)–Zn(1)–N(11)	172.2(2)	N(21)–Zn(3)–N(32)	119.7(2)
O(31)–Zn(1)–N(1)	173.4(2)	O(1)–Zn(4)–N(3)	82.7(2)
N(2)–Zn(1)–N(12)	176.6(3)	O(1)–Zn(4)–N(51)	157.9(3)
O(11)–Zn(2)–N(23)	163.9(2)	N(52)–Zn(4)–Cl(1)	137.5(2)
O(41)–Zn(2)–N(23)	88.3(2)	O(11)–Zn(5)–N(41)	159.8(3)
N(31)–Zn(2)–N(22)	119.5(2)	N(13)–Zn(5)–N(41)	100.7(3)
O(1)–Zn(3)–N(21)	95.9(2)	N(42)–Zn(5)–Cl(2)	136.9(2)
O(1)–Zn(3)–N(33)	166.0(2)		

Table 7. Selected bond lengths [Å] and angles [°] for the anion $[ZnCl(NCS)_3]^{2-}$ present in complex **5**·2.5H_2O·1.5MeOH.

Zn(6)–Cl(3)	2.334(10)	Zn(6)–N(2t)	1.933(13)
Zn(6)–N(1t)	1.916(13)	Zn(6)–N(3t)	1.90(2)
Cl(3)–Zn(6)–N(1t)	111.0(4)	N(1t)–Zn(6)–N(2t)	110.7(5)
Cl(3)–Zn(6)–N(2t)	111.0(4)	N(1t)–Zn(6)–N(3t)	111.7(6)
Cl(3)–Zn(6)–N(3t)	106.1(5)	N(2t)–Zn(6)–N(3t)	106.2(6)

0.34 [Zn(4)] and 0.38 [Zn(5)]. The Zn(1)–$N_{pyridyl}$ and Zn(1)–$N_{oximate}$ bonds are slightly longer than the corresponding Zn(2,3,4,5)–N bonds, consistent with the higher coordination number for Zn(1). The novel Zn_5 topology in the cation of **5** could have been described as two 9-MC-3 rings fused at Zn(1) if the Zn(3)–O(1) and Zn(2)–O(11) bonds were absent. In this case, however, the Zn(3) and Zn(2) ions reach across their respective 9-MC-3 rings and bind to the oxime oxygen atoms of the opposite pko^- li-

 © 2005 Wiley-VCH Verlag GmbH & Co. KGaA, Weinheim

Table 8. Selected interatomic distances [Å] and angles [°] for the cation $[Zn_5(NCS)_2(pko)_6]^{2+}$ present in complex **6**·2.5H_2O·MeOH

Zn(1)···Zn(2)	4.793(1)	Zn(2)–N(22)	2.096(4)
Zn(1)···Zn(3)	3.750(1)	Zn(3)–O(21)	2.083(4)
Zn(1)···Zn(4)	3.622(1)	Zn(3)–O(31)	2.038(3)
Zn(1)···Zn(5)	7.710(1)	Zn(3)–N(1)	2.148(4)
Zn(2)···Zn(3)	3.725(1)	Zn(3)–N(11)	2.217(5)
Zn(2)···Zn(4)	7.790(1)	Zn(3)–N(2)	2.166(4)
Zn(2)···Zn(5)	3.587(1)	Zn(3)–N(12)	2.130(4)
Zn(3)···Zn(4)	4.995(1)	Zn(4)–O(1)	2.102(4)
Zn(3)···Zn(5)	4.853(1)	Zn(4)–N(3)	2.091(5)
Zn(4)···Zn(5)	9.829(2)	Zn(4)–N(51)	2.124(5)
Zn(1)–O(1)	2.057(4)	Zn(4)–N(52)	2.089(5)
Zn(1)–O(51)	1.971(4)	Zn(4)–N(61)	1.959(6)
Zn(1)–N(23)	2.064(5)	Zn(5)–O(11)	2.071(4)
Zn(1)–N(31)	2.149(5)	Zn(5)–Om(1)	2.205(4)
Zn(1)–N(32)	2.083(4)	Zn(5)–N(13)	2.183(4)
Zn(2)–O(11)	2.036(4)	Zn(5)–N(41)	2.110(5)
Zn(2)–O(41)	1.986(4)	Zn(5)–N(42)	2.177(5)
Zn(2)–N(21)	2.171(5)	Zn(5)–N(71)	2.020(6)
Zn(2)–N(33)	2.087(4)		
O(1)–Zn(1)–N(31)	162.1(2)	O(1)–Zn(4)–N(51)	158.7(2)
O(51)–Zn(1)–N(32)	134.8(2)	O(1)–Zn(4)–N(61)	96.6(2)
N(23)–Zn(1)–N(31)	101.9(2)	N(3)–Zn(4)–N(51)	99.5(2)
O(11)–Zn(2)–N(21)	166.7(2)	N(3)–Zn(4)–N(52)	113.1(2)
O(41)–Zn(2)–N(22)	131.3(2)	N(3)–Zn(4)–N(61)	114.8(2)
N(21)–Zn(2)–N(33)	92.3(2)	O(11)–Zn(5)–N(41)	157.0(2)
O(21)–Zn(3)–N(11)	170.1(2)	Om(1)–Zn(5)–N(13)	168.5(2)
O(31)–Zn(3)–N(1)	168.9(2)	N(42)–Zn(5)–N(71)	169.0(2)
N(2)–Zn(3)–N(12)	176.0(2)		

Table 9. Selected bond lengths [Å] and angles [°] for the anion $[Zn(NCS)_4]^{2-}$ present in complex **6**·2.5H_2O·MeOH.

Zn(6)–N(101)	1.960(10)	Zn(6)–N(103)	1.925(11)
Zn(6)–N(102)	1.962(9)	Zn(6)–N(104)	1.922(9)
N(101)–Zn(6)–N(102)	109.1(4)	N(102)–Zn(6)–N(103)	105.8(4)
N(101)–Zn(6)–N(103)	109.8(4)	N(102)–Zn(6)–N(104)	109.6(4)
N(101)–Zn(6)–N(104)	111.8(4)	N(103)–Zn(6)–N(104)	110.7(5)

gands. This causes two "collapsed"[4,18] 9-metallacrown-3 structures sharing a common apex at Zn(1). Each "collapsed" structure is essentially a cation-vacant metallacrown.

Besides the pentanuclear cation, the structure contains a novel (from the chemical composition viewpoint) chlorotris(isothiocyanato)zincate(2–) anion (Figure 7). Three NCS^- ions coordinating through their nitrogen atoms and one terminal chloro ligand surround Zn(6). The bond angles about the metal ion are in the range 106.1(5)–111.7(6)°, and show a slight distortion of the ZnN_3Cl tetrahedron. The three isothiocyanate groups bind the zinc ion in a virtually linear fashion, with the C–N–Zn bond angles in the range of 158.2(13)–171.3(11)°.

The molecular structure of the pentanuclear cation of **6**·2.5H_2O·MeOH is similar to the structure of the cation of **5**·2.5H_2O·1.5MeOH except that the two terminal chloro ligands of the latter are replaced by two terminal isothiocyanato ligands in the former and one of the five-coordinate metal ions of **5**·2.5H_2O·1.5MeOH [Zn(5) in Figure 6] has become six-coordinate in **6**·2.5H_2O·MeOH [Zn(5) in Figure 8] through coordination of one terminal MeOH ligand. Again, the five metal ions define two nearly equilateral triangles sharing a common apex [at Zn(3)], the six pko^- ligands adopt three different coordination modes (2.1110, 3.1111, 3.2111, see Figure 1) and the Zn_5 topology can be described as two fused "collapsed" 9-MC-3 rings [in this case the Zn(2) and Zn(1) ions reach across their respective 9-MC-3 rings and bind to the oxime oxygen atoms O(11) and O(1) of the opposite pko^- ligands]. Another slightly different structural feature of **6**·2.5H_2O·MeOH is worthy of comment. In **5**·2.5H_2O·1.5MeOH the two five-coordinate, chloride-bound metal ions [Zn(4) and Zn(5) in Figure 6] have a distorted spy coordination environment, whereas the polyhedron of the unique five-coordinate, isothiocyanate-bound metal ion [Zn(4) in Figure 8] in **6**·2.5H_2O·MeOH is better described as a very distorted trigonal bipyramid (τ = 0.45) with atoms O(1) and N(51) occupying the axial sites. The Zn(4)–$N_{isothiocyanate}$ bond [1.959(6) Å] is shorter than the Zn(5)–$N_{isothiocyanate}$ bond [2.020(6) Å], which is consistent with the lower coordination number for Zn(4) [five vs. six for Zn(5)] (Table 8).

Besides the pentanuclear cation, the structure contains a tetraisothiocyanatozincate(2–) anion (Figure 9). Four NCS^- anions almost equivalently surround Zn(6), coordinating through the nitrogen atoms such that a slightly distorted tetrahedral geometry occurs. The Zn–N bond lengths [1.922(9)–1.962(9) Å] and N–Zn–N bond angles [105.8(4)–111.8(4)°] are typical for complexes containing the $[Zn(NCS)_4]^{2-}$ anion.[45] All the NCS^- groups bind the metal ion in a virtually linear fashion, with the C–N–Zn bond angles in the range 168.4(10)–175.4(9)° (Table 9).

The cations present in compounds **5** and **6** represent the third and fourth, respectively, structurally characterised examples of non-organometallic, pentanuclear Zn^{II} complexes with *O*,*N* ligation (there are several examples with S-, Te- or P-containing ligands). The other two examples are $[\{Zn_2L(O_2CMe)_2\}_2Zn(H_2O)_4]$[46a] and $[Zn_5(poap\text{-}H)_6](ClO_4)_4$,[46b] where L is the trianion of a Schiff base derived from glycine and poap-H the monoanion of an alkoxydiazine polydentate ligand.

A remarkable structural feature of complexes **5** and **6** is the presence of pko^- ligands that adopt three different coordination modes. Since most complexes containing *bridging* pko^- ligands have been reported only recently, we felt it timely to collect all metal complexes of bridging pko^- ligands in Table 10, together with the pko^- coordination modes for convenient comparison. Inspection of Table 10 clearly shows that the 2.1110 ligation mode (Figure 1) is the most common one and that only two previously characterised clusters, namely $[Ni_4(pko)_6(MeOH)_2](OH)(ClO_4)$[26a] and $[Zn_8(shi)_4(pko)_4(MeOH)_2]$,[26b] contain di-2-pyridyl ketone oximate(1–) ligands exhibiting two different coordination modes; thus, the cations of **5** and **6** are unique in exhibiting three different coordination modes of the pko^- ligands.

IR Spectra

The IR spectra of **1**, **2**·4DMF and **4** exhibit a medium band at 3414–3386 cm^{-1} assignable[47a] to $\nu(OH)_{OH^-}$. The

 © 2005 Wiley-VCH Verlag GmbH & Co. KGaA, Weinheim

Table 10. Structurally characterised complexes containing *bridging* pko⁻ ligands.

Complex[a]	Coordination mode[b] of pko⁻	Ref.
$[Ni_4(pko)_6(MeOH)_2]^{2+}$	2.1110, 2.1111	[26a]
$[M_3(pko)_6(CO)_8]$	2.1110	[37]
$[Ru_2(pko)_2(CO)_4]$	2.1110	[37]
$[Os_3(\mu\text{-}H)(pko)(CO)_9]$	2.1110	[37]
$[Mn_{12}O_6(OH)_4(OMe)_2(pko)_{12}]^{4+}$	2.1110	[17]
$[Mn_4(O_2CR)_2X_2(pko)_2\{(py)_2CO_2\}_2]$	2.1110	[27e]
$[Mn_3(OMe)_2Y_2(pko)_4]$	2.1110	[26b,26c]
$Zn_4(OH)_2Cl_2(pko)_4]$	2.1110	[24b]
$[Zn_8(shi)_4(pko)_4(MeOH)_2]$	2.1110, 3.1111	[24b]
$[Mn_4O(3,4\text{-}D)_4(pko)_4]$	2.1110	[26d]
$[Ni_4(NCS)_2(Hshi)_2(pko)_2(DMF)(MeOH)]$	2.1111	[18]
$[Ni_5(O_2CMe)_2(shi)_2(pko)_2]$	3.2111	[18]
$[Ni_{10}(MCPA)_2(shi)_5(pko)_3(MeOH)(H_2O)]$	3.2111	[18,23b]
$[Mn_2Ni_2(O_2CMe)_2(shi)_2(pko)_2(DMF)_5]$	2.1110	[18]
$[Zn_4(OH)_2(O_2CMe)_2(pko)_4]$	2.1110	[24a]
$[Cu_2(pko)_4]$[c]	2.1110	[44]
$[Zn_4(OH)_2Z_2(pko)_4]$	2.1110	this work
$[Zn_5X'_2(pko)_6]^{2+}$	2.1110, 3.2111, 3.1111	this work

[a] Counterions and solvate molecules have been omitted; 3,4-D = the anion of 3,4-dichlorophenoxyacetic acid; Hshi = the dianion of salicylhydroxamic acid; MCPA = the anion of 2-methyl-4-chlorophenoxyacetic acid; $(py)_2CO_2$ = the dianion of the *gem*-diol form of di-2-pyridyl ketone; shi = the trianion of salicylhydroxamic acid; R = Me, Ph; X = Cl, Br; X′ = Cl, NCS; Y = NCS, Cl, NCO; Z = $PhCO_2$, N_3, NCO, acac. [b] Using Harris notation[16] (see also Figure 1). [c] This complex also contains N,N′-chelating, i.e., terminal, pko⁻ ligands.

presence of both hydroxo ligands and water solvate molecules in **3**·3DMF·H_2O is manifested by a broad IR band of medium intensity at about 3400 cm^{-1}.[47b] The ν(OH) band in the spectra of the crystals of **5**·2.5H_2O·1.5MeOH and **6**·2.5H_2O·MeOH appears at 3330 and 3415 cm^{-1}, respectively. The presence of DMF in **2**·4DMF and **3**·3DMF·H_2O is manifested by a strong band at 1672–1665 cm^{-1} and a weak band at around 640 cm^{-1}, assigned to ν(C=O) and δ(OCN), respectively.[48] The absence of shifts of these bands in the complexes, when compared with the corresponding bands in the spectrum of free DMF,[48] confirms that there is no interaction between DMF and the Zn^{II} atoms.

Two bands, one strong at about 1595 cm^{-1} and one of variable intensity at about 1220 cm^{-1}, are common in the spectra of **1**–**6**; these bands are tentatively assigned to the oximate ν(C=N) and ν(N–O) vibrational modes,[24b] respectively, although the higher-wavenumber band may also have an aromatic stretch character.

The strong bands at 1566 and 1366 cm^{-1} in the spectrum of **1** are assigned to the $\nu_{as}(CO_2)$ and $\nu_s(CO_2)$ modes of the benzoate ligands, respectively;[49] the former may also involve a 2-pyridyl stretching character. The difference Δ [$\Delta = \nu_{as}(CO_2) - \nu_s(CO_2)$] is 200 cm^{-1}, more than that for NaO_2CPh (184 cm^{-1}), as expected for monodentate ligation.[49] In the spectrum of **4**, the bands at 1594 and 1518 cm^{-1} certainly involve a $\nu(C{=}C)_{acac^-}$ [coupled with $\nu(C{=}O)_{acac^-}$] character and a $\nu(C{=}O)_{acac^-}$ [coupled with $\nu(C\text{–}C)_{acac^-}$] character, respectively;[50] however, overlap with other modes renders exact assignments difficult. The spectrum of **2**·4DMF exhibits an intense band at 2070 cm^{-1}, assigned to the asymmetric stretching mode of the azido ligands.[50] Similarly, the strong band at 2236 cm^{-1} in the spectrum of **3**·3DMF·H_2O is assigned to the ν_{as}(NCO) [consisting mainly of ν(CN)] vibrational mode of the isocyanato ligands.[50,51] The spectra of the dried samples **5**·2.5H_2O and **6**·2.5H_2O exhibit the ν(CN) mode at 2076 and 2074 cm^{-1}, respectively; These wavenumbers are typical of terminal isothiocyanato groups.[50] The existence of the isothiocyanato ligands at different Zn^{II} coordination environments (tetrahedral, trigonal-bipyramidal, octahedral) in **6** does not lead to two or three ν(CN) bands and, thus, the different environments cannot be differentiated by IR spectroscopy. The expected ν_s(NNN), δ(NNN) [**2**·4DMF], ν_s(NCO) [consisting mainly of ν(CO)], δ(NCO) [**3**·3DMF·H_2O], ν(CS) and δ(NCS) [**5**·2.5H_2O, **6**·2·5H_2O] bands could not be located because they are obscured by pko⁻ absorptions.

Conclusions and Perspectives

The further use of di-2-pyridyl ketone oxime in Zn chemistry has provided access to six new clusters, four tetranuclear and two pentanuclear. Complexes **1**–**4** are valuable additions to the small, but growing, family of inverse metallacrown complexes. The present work also extends the body of results that emphasise the ability of the monoanionic ligand pko⁻ to form new structural types in 3d-metal chemistry. Complexes **5** and **6** are rare examples of pentanuclear zinc complexes with ligands containing N- and/or O-donors. Moreover the "collapsed" double, fused 9-metallacrown-3 structural type observed in these clusters is novel. The structural diversity displayed by the reported complexes stems from the coordinating versatility of pko⁻ and its ability to exhibit two or even three distinct coordination modes in the same compound. The general structure of **5** and **6** is distinctly different from that of **2**, **3** and $[Zn_4(OH)_2Cl_2(pko)_4]$[24b] (these three complexes also have terminal pseudohalide or chloride ligands like **5** and **6**) emphasising the

 © 2005 Wiley-VCH Verlag GmbH & Co. KGaA, Weinheim

dependence of the product identity on the charge of the complex (neutral vs. cationic).

The isothiocyanate analogue of compounds **2** and **3** is not known, at least to date, and it is currently not evident whether the preparation and stability of the neutral $[Zn_4(OH)_2X_2(pko)_4]$ clusters are dependent on the particular nature of the pseudohalide ligand. Work is in progress to clarify this matter, and the use of $SeCN^-$ and $N(CN)_2^-$ is planned. The $PhCO_2^-$, N_3^-, NCO^- and $acac^-$ terminal ligands present in **1**–**4** could have future utility as sites for facile incorporation of other monodentate/bidentate ligands by metathesis, or as a means to access higher-nuclearity neutral or cationic Zn clusters using bis(monodentate)/bis(bidentate) bridging ligands, including aromatic heterocycles and dicarboxylates.

Results at the time of writing reveal that the nature of pko^- makes it a versatile ligand for a variety of objectives/advantages, including μ_3 behaviour, high-nuclearity cluster formation with a variety of 3d-, 4d- and 5d-metals, linking of clusters into polymeric arrays, 3d-4f mixed-metal chemistry and ferromagnetic exchange interactions. Clearly, the use of other polypyridyl oximes offers a potential route to other new clusters, and such studies − already well advanced − will be reported in due course.

Experimental Section

Materials and Physical Measurements: All manipulations were performed under aerobic conditions using materials and most solvents as received. DMF and MeOH were distilled from CaH_2 and Mg, respectively; they were both stored over molecular sieves (3 Å). $Zn(O_2CPh)_2{\cdot}2H_2O$ was prepared by the reaction of $Zn(O_2CMe)_2{\cdot}2H_2O$ with an excess of $PhCO_2H$ in $CHCl_3$ under reflux. C, H and N elemental analyses were performed with Perkin–Elmer 240B and EA 108 Carlo Erba analyzers. Zn was determined for some complexes by atomic absorption with a Perkin–Elmer 1100B spectrophotometer. IR spectra were recorded with Perkin–Elmer PC 16 and 1650 FT-IR spectrometers with samples prepared as KBr pellets.

$[Zn_4(OH)_2(O_2CPh)_2(pko)_4]{\cdot}3MeCN$ (1·3MeCN) or $\{(OH)_2[inv12\text{-}MC_{Zn^{II}N(pko)}\text{-}4](O_2CPh)_2\}{\cdot}3MeCN$: Treatment of a stirred, colourless solution of Hpko (0.120 g, 0.60 mmol) in MeCN (20 mL) with Et_3N (0.100 mL, 0.72 mmol) resulted in a pale-yellow solution. Solid $Zn(O_2CPh)_2{\cdot}2H_2O$ (0.207 g, 0.60 mmol) was slowly added to this solution and it soon dissolved to give an essentially colourless solution. The filtered solution was allowed to slowly concentrate by solvent evaporation at room temperature for a period of 3–4 d. Well-formed colourless cubes appeared which were collected by filtration, washed with ice-cold MeCN (5 mL) and Et_2O (2.5 mL), and dried in air. Yield (based on the oxime): 0.130 g (65%). The dried solid was analysed as MeCN-free **1**. $C_{58}H_{44}N_{12}O_{10}Zn_4$ (1330.7): calcd. C 52.35, H 3.34, N 12.63; found C 52.51, H 3.40, N 12.49. The obtained crystals were good diffractors of X-rays, as long as they were kept in contact with the mother liquor to prevent solvent loss. Selected IR data (KBr pellet): $\tilde{\nu}$ = 3414 cm^{-1} (m, broad), 1596 (s), 1566 (s), 1366 (s) 1214 (m) cm^{-1}.

$[Zn_4(OH)_2(N_3)_2(pko)_4]{\cdot}4DMF$ (2·4DMF) or $\{(OH)_2[inv12\text{-}MC_{Zn^{II}N(pko)}\text{-}4](N_3)_2\}{\cdot}4DMF$: a solution of NaN_3 (0.065 g, 1.00 mmol), Hpko (0.398 g, 2.00 mmol) and NaOH (0.080 g, 2.00 mmol) in DMF (50 mL) was added to a stirred solution of $Zn(NO_3)_2{\cdot}4H_2O$ (0.523 g, 2.00 mmol) in the same solvent (50 mL). The resulting colourless solution was stirred for 1 h, filtered and then allowed to very slowly concentrate at room temperature for a period of 15 d. X-ray quality colourless crystals formed, which were collected by filtration, washed with Et_2O (5 mL) and dried in air. Yield (based on the oxime): 0.51 g (70%). $C_{56}H_{62}N_{22}O_{10}Zn_4$ (1464.8): calcd. C 45.92, H 4.27, N 21.04, Zn 17.85; found C 46.10, H 4.17, N 19.44, Zn 18.80. The crystals of **2**·4DMF were found to be slightly hygroscopic, and they were kept in the mother liquor until a suitable crystal had been found for X-ray crystallography. Selected IR data (KBr pellet): $\tilde{\nu}$ = 3386 cm^{-1} (m, broad), 2070 (s), 1672 (s), 1596 (s), 1218 (s), 640 (w) cm^{-1}.

$[Zn_4(OH)_2(NCO)_2(pko_4]{\cdot}3DMF{\cdot}H_2O$ (3·3DMF·H_2O) or $\{(OH)_2[inv12\text{-}MC_{Zn^{II}N(pko)}\text{-}4](NCO)_2\}{\cdot}3DMF{\cdot}H_2O$: A solution of NaOCN (0.065 g, 1.00 mmol), Hpko (0.398 g, 2.00 mmol) and NaOH (0.080 g, 2.00 mmol) in MeOH (50 mL) was added to a stirred solution of $ZnCl_2$ (0.273 g, 2.00 mmol) in the same solvent (50 mL). The resulting solution was stirred vigorously for about 1 h, filtered and then DMF (50 mL) was added. The new colourless solution obtained was allowed to concentrate by solvent evaporation at room temperature for about 10 d. Well-formed colourless crystals appeared, which were collected by filtration, washed with Et_2O (2 × 3 mL) and dried in air. Yields (based on the oxime) as high as 0.48 g (68%) were obtained. $C_{55}H_{57}N_{17}O_{12}Zn_4$ (1409.65): calcd. C 46.86, H 4.08, N 16.90, Zn 18.55; found C 47.10, H 3.73, N 16.85, Zn 19.06. The crystal selected for X-ray crystallography was kept in contact with the mother liquor to prevent H_2O loss. Selected IR data (KBr pellet): $\tilde{\nu}$ = 3400 cm^{-1} (m, broad), 2236 (s), 1665 (s), 1595 (s), 1216 (s), 638 (w) cm^{-1}.

$[Zn_4(OH)_2(acac)_2(pko)_4]{\cdot}4CH_2Cl_2$ (4·4CH_2Cl_2) or $\{(OH)_2[inv12\text{-}MC_{Zn^{II}N(pko)}\text{-}4](acac)_2\}{\cdot}4CH_2Cl_2$: A solution of Hpko (0.040 g, 0.20 mmol) in CH_2Cl_2 (10 mL) was added dropwise to a colourless slurry of $Zn(acac)_2{\cdot}H_2O$ (0.052 g, 0.18 mmol) in the same solvent (15 mL). No noticeable colour change occurred. The mixture was refluxed under vigorous stirring for 15–20 min, a small quantity of undissolved material was removed by filtration and the filtrate layered with Et_2O (20 mL). Slow mixing gave X-ray quality crystals of **4**·4CH_2Cl_2. The crystals were collected by filtration, washed with cold CH_2Cl_2 (5 mL) and Et_2O (2 × 5 mL) and dried in air. Yield (based on Zn^{II}): 0.036 g (63%). The dried solid was analysed as CH_2Cl_2-free **4**. $C_{54}H_{48}N_{12}O_{10}Zn_4$ (1286.7): calcd. C 50.40, H 3.77, N 13.07; found C 50.53, H 3.71, N 13.00. The obtained crystals were stable as long as they were kept in contact with the mother liquor to prevent CH_2Cl_2 loss. Selected IR data (KBr pellet): $\tilde{\nu}$ = 3378 cm^{-1} (m, broad), 1594 (m), 1518 (s), 1222 (m) cm^{-1}.

$[Zn_5Cl_2(pko)_6][ZnCl(NCS)_3]{\cdot}2.5H_2O{\cdot}1.5MeOH$ (5·2.5H_2O·1.5MeOH) and $[Zn_5(NCS)_2(pko)_6(MeOH)][Zn(NCS)_4]{\cdot}2.5H_2O{\cdot}MeOH$ (6·2.5H_2O·MeOH) as a Mixture: A solution of NaSCN (0.081 g, 1.00 mmol), Hpko (0.398 g, 2.00 mmol) and NaOH (0.080 g, 2.00 mmol) in MeOH (50 mL) was added to a stirred solution of $ZnCl_2$ (0.273 g, 2.00 mmol) also in MeOH (50 mL). The resulting colourless solution was stirred for 1 h and during this time its colour turned to pale yellow. The pale-yellow solution was filtered and allowed to slowly concentrate by solvent evaporation at room temperature. After several days, an approximately 1:3 mixture of colourless prisms and pale-yellow needles formed. The crystals were carefully collected by filtration. The two products were readily separable manually, and the colourless and pale-yellow crystals proved by single-crystal X-ray crystallography to be complexes **5**·2.5H_2O·1.5MeOH and **6**·2.5H_2O·MeOH, respectively. A batch of colourless crystals were used for analyses and IR spectroscopy. The dried (in air) sample was analysed as MeOH-free **5**·2.5H_2O.

 © 2005 Wiley-VCH Verlag GmbH & Co. KGaA, Weinheim

$C_{69}H_{53}Cl_3N_{21}O_{8.5}S_3Zn_6$ (1907.2): calcd. C 43.45, H 2.81, N 15.43; found C 43.67, H 2.77, N 15.36. Selected IR data (KBr pellet): $\tilde{\nu}$ = 3330 cm^{-1} (m, broad), 2076 (s), 1597 (s), 1214 (m) cm^{-1}.

$[Zn_5(NCS)_2(pko)_6(MeOH)][Zn(NCS)_4]\cdot 2.5H_2O\cdot MeOH$ ($6\cdot 2.5H_2O\cdot$ MeOH). Method A: A colourless solution of Hpko (0.060 g, 0.30 mmol) and NaSCN (0.024 g, 0.30 mmol) in MeOH (25 mL) was added to a colourless solution of $Zn(O_2CMe)_2\cdot 2H_2O$ (0.085 g, 0.39 mmol) in the same solvent (10 mL). The resulting pale-yellow solution was stirred for about 10 min and was then allowed to stand undisturbed in a closed flask at room temperature for 2 d. Well-formed pale-yellow crystals appeared, which were collected by filtration, washed with ice-cold MeOH (5 mL) and Et_2O (2 × 5 mL), and dried in air. Yield (based on the oxime): 0.083 g (83%). The crystals, which were kept in contact with the mother liquor to prevent MeOH loss, had identical unit-cell dimensions with those identified as $6\cdot 2.5H_2O\cdot$MeOH in the above-mentioned experiment. The dried solid was analysed as MeOH-free $6\cdot 2.5H_2O$. $C_{73}H_{57}N_{24}O_{9.5}S_6Zn_6$ (2007.2): calcd. C 43.68, H 2.87, N 16.75; found C 44.32, H 2.86, N 16.51. Selected IR data (KBr pellet): $\tilde{\nu}$ = 3415 cm^{-1} (m, broad), 2074 (s), 1596 (s), 1216 (w) cm^{-1}. **Method B:** A suspension of compound $5\cdot 2.5H_2O$ (0.191 g, 0.10 mmol) in warm MeOH/H_2O (40 mL, 10:1, v/v) was treated with an excess of NaSCN (0.041 g, 0.50 mmol). The mixture was stirred overnight at 45 °C, filtered to remove some undissolved starting material, and then allowed to stand undisturbed in closed vials at room temperature. Pale-yellow crystals formed within 12 h, and these were collected by filtration and washed with cold MeOH. Yield (based on $5\cdot 2.5H_2O$): 0.070 g (35%). The product was identified by microanalyses and IR comparison with material from method A.

X-ray Crystallographic Studies: Crystals of $1\cdot$3MeCN, $2\cdot$4DMF, $3\cdot$3DMF$\cdot H_2O$, $4\cdot 4CH_2Cl_2$, $5\cdot 2.5H_2O\cdot 1.5$MeOH and $6\cdot 2.5H_2O\cdot$MeOH were mounted in capillaries filled with drops of mother liquor. Diffraction measurements for $1\cdot$3MeCN, $2\cdot$4DMF, $3\cdot$3DMF$\cdot H_2O$ and $6\cdot 2.5H_2O\cdot$MeOH were carried out with a Crystal Logic Dual Goniometer diffractometer using graphite-monochromated Mo-K_α radiation. The X-ray data sets for $4\cdot 4CH_2Cl_2$ and $5\cdot 2.5H_2O\cdot 1.5$MeOH were collected with a $P2_1$ Nicolet diffractometer upgraded by Crystal Logic using graphite-monochromated Cu-K_a radiation. Complete crystal data and parameters for data collection and refinement are listed in Tables 11 and 12. Unit-cell dimensions were determined and refined by using the angular settings of 25 automatically centred reflections in the ranges $11° < 2\theta < 23°$ (for $1\cdot$3MeCN, $2\cdot$4DMF, $3\cdot$3DMF$\cdot H_2O$ and $6\cdot 2.5H_2O\cdot$MeOH) and $22° < 2\theta < 54°$ (for $4\cdot 4CH_2Cl_2$ and $5\cdot 2.5H_2O\cdot 1.5$MeOH). Intensity data were recorded using the θ-2θ scan method. Three standard reflections monitored every 97 reflections showed less than 3% variation and no decay. Lorentz, polarisation and Ψ-scan absorption (for $3\cdot$3DMF$\cdot H_2O$, $4\cdot 4CH_2Cl_2$, $5\cdot 2.5H_2O\cdot 1.5$MeOH and $6\cdot 2.5H_2O\cdot$MeOH) corrections were applied using the Crystal Logic software package.

The structures were solved by direct methods using SHELXS-86[52a] and refined by full-matrix least-squares techniques on F^2 with SHELX-93[52b] ($1\cdot$3MeCN, $4\cdot 4CH_2Cl_2$ and

Table 11. Crystal data and structure refinement for $[Zn_4(OH)_2(O_2CPh)_2(pko)_4]\cdot$3MeCN ($1\cdot$3MeCN), $[Zn_4(OH)_2(N_3)_2(pko)_4]\cdot$4DMF ($2\cdot$4DMF) and $[Zn_4(OH)_2(NCO)_2(pko_4]\cdot$3DMF$\cdot H_2O$ ($3\cdot$3DMF$\cdot H_2O$).

	$1\cdot$3MeCN	$2\cdot$4DMF	$3\cdot$3DMF$\cdot H_2O$
Empirical formula	$C_{64}H_{35}Zn_4N_{15}O_{10}$	$C_{56}H_{62}Zn_4N_{22}O_{10}$	$C_{55}H_{57}Zn_4N_{17}O_{12}$
Formula mass	1453.70	1464.76	1409.65
Colour and habit	colourless cubes	colourless prisms	colourless prisms
Crystal size [mm]	0.45 × 0.30 × 0.15	0.55 × 0.25 × 0.15	0.25 × 0.20 × 0.15
Crystal system	triclinic	monoclinic	monoclinic
Space group	$P\bar{1}$	$P2_1/c$	$P2_1/c$
a [Å]	12.108(6)	11.905(5)	11.886(5)
b [Å]	11.956(6)	17.660(6)	17.732(9)
c [Å]	13.251(6)	15.833(6)	15.812(7)
α [°]	67.39(2)	90	90
β [°]	83.02(2)	93.14(1)	92.53(1)
γ [°]	73.08(2)	90	90
V [Å^3]	1694(2)	3324(2)	3329(3)
Z	1	2	2
$\rho_{calcd.}$ [g cm^{-3}]	1.425	1.464	1.388
T [°C]	25	25	25
λ(Mo-K_a) [Å]	0.71073	0.71073	0.71073
μ [mm^{-1}]	1.466	1.497	1490
F(000)	742	1504	1444
$2\theta_{max}$ [°]	50.00	50.00	50.02
Index ranges	$-14 \le h \le 14$	$-14 \le h \le 13$	$-14 \le h \le 13$
	$-13 \le k \le 14$	$-21 \le k \le 0$	$0 \le k \le 21$
	$0 \le l \le 15$	$-18 \le l \le 0$	$0 \le l \le 18$
No. of reflections collected	6242	5586	5859
No. of indep. refl./$R_{int.}$	5958/0.0199	5384/0.0186	5584/0.0224
Data with $I > 2\sigma(I)$	4621	4062	4000
Parameters refined	495	465	398
$[\Delta/\sigma]_{max}$	0.023	0.003	0.003
GOF(on F^2)	1.058	1.095	1.083
R_1[a]	0.0486	0.0449	0.0728
wR_2[b]	0.1355	0.1134	0.2038
Residuals [e Å^{-3}]	0.517/–0.525	0.573/–0.545	0.985/–0.785

[a] $R_1 = \Sigma(||F_o| - |F_c||)/\Sigma(|F_o|)$. [b] $wR_2 = \{\Sigma[w(F_o^2 - F_c^2)^2]/\Sigma[w(F_o^2)^2]\}^{1/2}$.

 © 2005 Wiley-VCH Verlag GmbH & Co. KGaA, Weinheim

5·2.5H_2O·1.5MeOH) or SHELX-97[52c] (**2**·4DMF, **3**·3DMF·H_2O and **6**·2.5H_2O·MeOH). For **2**·4DMF almost all hydrogen atoms were located by difference maps and were refined isotropically, whereas for **3**·3DMF·H_2O, **5**·2.5H_2O·1.5MeOH and **6**·2.5H_2O·MeOH all hydrogen atoms were introduced at calculated positions as riding on their parent atoms. For **1**·3MeCN and **4**·4CH_2Cl_2 some hydrogen atoms were located by difference maps and were refined isotropically, and some were introduced at calculated positions as riding on bonded atoms. For example, in **4**·4CH_2Cl_2 all hydrogen atoms were located by difference maps and were refined isotropically, except those of the methyl groups of the $acac^-$ ligand which were introduced at calculated positions as riding on their parent carbon atoms. All non-hydrogen atoms of **4**·4CH_2Cl_2 were refined anisotropically. For the remaining structures, almost all non-hydrogen atoms were refined anisotropically. One of the solvate MeCN molecules of **1**·3MeCN was refined with occupation factor 0.50. For **2**·4DMF, one of the crystallographically independent solvate DMF molecules was refined isotropically; thus, no hydrogen atoms for that molecule were included. For **3**·3DMF·H_2O, one DMF and the H_2O solvate molecules were refined isotropically with occupation factors fixed to 10.5; no hydrogen atoms for these solvate molecules were included in the refinement. All the solvate molecules of **5**·2.5H_2O·1.5MeOH and the H_2O molecules of **6**·2.5H_2O·MeOH were refined isotropically. CCDC-254415 (**1**·3MeCN), -254416 (**2**·4DMF), -254417 (**3**·3DMF·H_2O), -254418 (**4**·4CH_2Cl_2), -254419 (**5**·2.5H_2O·1.5MeOH) and -254420 (**6**·2.5H_2O·MeOH) contain the supplementary crystallographic data for this paper. These data can be obtained free of charge from The Cambridge Crystallographic Data Centre via www.ccdc.cam.ac.uk/data_request/cif.

Acknowledgments

E. K., E. M.-Z. and S. P. P. thank the European Social Fund (ESF), the Operational Program for Educational and Vocational Training II (EPEAEK II) and particularly the Program PYTHAGORAS, for funding the above work. M. A., C. D.-S. and D. P. K. wish to thank The Greek General Secretariat for Research and Technology for the financial support of this research through PENED 2001/1034 Grant.

[1] M. Fujita, J. Y. Kwon, S. Washizu, K. Ogura, *J. Am. Chem. Soc.* **1994**, *116*, 1151–1152.
[2] H. Piotrowski, K. Polborn, G. Hilt, K. Severin, *J. Am. Chem. Soc.* **2001**, *123*, 2699–2700.
[3] a) J. J. Bodwin, V. L. Pecoraro, *Inorg. Chem.* **2000**, *39*, 3434–3435; b) M. Moon, I. Kim, M. S. Lah, *Inorg. Chem.* **2000**, *39*, 2710–2711.
[4] For an excellent review, see: V. L. Pecoraro, A. J. Stemmler, B. R. Gibney, J. J. Bodwin, H. Wang, J. W. Kampf, A. Barwinski, *Prog. Inorg. Chem.* **1997**, *45*, 83–177.
[5] a) A. J. Blake, R. O. Gould, P. E. Y. Milne, R. E. P. Winpenny, *J. Chem. Soc., Chem. Commun.* **1991**, 1453–1455; b) A. J. Blake,

Table 12. Crystal data and structure refinement for $[Zn_4(OH)_2(acac)_2(pko)_4]$·4$CH_2Cl_2$ (**4**·4CH_2Cl_2), $[Zn_5Cl_2(pko)_6][ZnCl(NCS)_3]$·2.5$H_2O$·1.5MeOH (**5**·2.5$H_2O$·1.5MeOH) and $[Zn_5(NCS)_2(pko)_6(MeOH)][Zn(NCS)_4]$·2.5$H_2O$·MeOH (**6**·2.5$H_2O$·MeOH).

	4·4CH_2Cl_2	**5**·2.5H_2O·1.5MeOH	**6**·2.5H_2O·MeOH
Empirical formula	$C_{58}H_{56}Zn_4N_{12}O_{10}Cl_8$	$C_{70.5}H_{59}Zn_6N_{21}O_{10}S_3Cl_3$	$C_{74}H_{61}Zn_6N_{24}O_{10.5}S_6$
Formula mass	1626.22	1955.14	2039.05
Colour and habit	colourless plates	colourless prisms	pale yellow needles
Crystal size [mm]	0.35×0.15×0.08	0.08×0.14×0.30	0.22×0.34×0.70
Crystal system	triclinic	triclinic	monoclinic
Space group	$P\bar{1}$	$P\bar{1}$	$P2_1/n$
a [Å]	12.786(2)	18.552(3)	17.371(6)
b [Å]	13.439(2)	17.569(2)	30.14(1)
c [Å]	12.322(2)	16.493(2)	17.894(6)
α [°]	63.22(1)	105.87(1)	90
β [°]	67.19(1)	104.42(1)	103.65(1)
γ [°]	78.15(1)	105.50(1)	90
V [Å^3]	1741.2(5)	4672.4(11)	9105(5)
Z	1	2	4
$\rho_{calcd.}$ [g cm^{-3}]	1.551	1.390	1.487
T [°C]	25	25	25
λ(Mo-K_a) [Å]			0.71073
λ(Cu-K_a) [Å]	1.54180	1.54180	
μ [mm^{-1}]	4.907	3.614	1.760
F(000)	824	1976	4132
$2\theta_{max}$ [°]	124.90	102.08	45.60
Index ranges	$-13 \le h \le 11$	$-18 \le h \le 17$	$-18 \le h \le 18$
	$-13 \le k \le 14$	$-14 \le k \le 17$	$0 \le k \le 32$
	$0 \le l \le 13$	$0 \le l \le 16$	$-19 \le l \le 0$
No. of reflections collected	4728	10 307	12 767
No. of indep. refl./$R_{int.}$	4499/0.0580	9758/0.0328	12 311/0.0121
Data with $I > 2\sigma(I)$	3372	6712	9178
Parameters refined	488	1025	1098
$[\Delta/\sigma]_{max}$	0.013	0.009	0.013
GOF(on F^2)	1.061	1.052	1.072
R_1[a]	0.0723	0.0665	0.0468
wR_2[b]	0.1991	0.1838	0.1329
Residuals [e Å^{-3}]	1.058/–0.809	0.995/–0.516	0.882/–0.605

[a] $R_1 = \Sigma(||F_o| - |F_c||)/\Sigma(|F_o|)$. [b] $wR_2 = \{\Sigma[w(F_o^2 - F_c^2)^2]/\Sigma[w(F_o^2)^2]\}^{1/2}$.

R. O. Gould, G. M. Grant, P. E. Y. Milne, D. Reed, R. E. P. Winpenny, *Angew. Chem. Int. Ed. Engl.* **1994**, *33*, 195–197.
[6] a) S.-X. Liu, S. Lin, B.-Z. Lin, C.-C. Lin, J.-Q. Huang, *Angew. Chem. Int. Ed.* **2001**, *40*, 1084–1087; b) B. Kwak, H. Rhee, S. Park, M. S. Lah, *Inorg. Chem.* **1998**, *37*, 3599–3602.
[7] a) X. Yang, S. E. Johnson, S. I. Khan, M. F. Hawthorne, *Angew. Chem. Int. Ed. Engl.* **1992**, *31*, 893–896; b) X. Yang, Z. Zheng, C. B. Knobler, M. F. Hawthorne, *J. Am. Chem. Soc.* **1993**, *115*, 193–195; c) X. Yang, C. B. Knobler, Z. Zheng, M. F. Hawthorne, *J. Am. Chem. Soc.* **1994**, *116*, 7142–7159.
[8] a) R. W. Saalfrank, N. Löw, F. Hampel, H.-D. Stachel, *Angew. Chem. Int. Ed. Engl.* **1996**, *35*, 2209–2210; b) R. W. Saalfrank, N. Löw, S. Kareth, V. Seitz, F. Hampel, D. Stalke, M. Teichert, *Angew. Chem. Int. Ed.* **1998**, *37*, 172–175.
[9] a) E. C. Constable, *Prog. Inorg. Chem.* **1994**, *42*, 67–137; b) J. A. Johnson, J. W. Kampf, V. L. Pecoraro, *Angew. Chem. Int. Ed.* **2003**, *42*, 546–549; c) J. W. Steed, J. L. Atwood, *Supramolecular Chemistry*, Wiley, New York, **2000**, pp. 540–548.
[10] H. Rauter, E. C. Hillgeries, A. Erxleben, B. Lippert, *J. Am. Chem. Soc.* **1994**, *116*, 616–624.
[11] C. Dendrinou-Samara, M. Alexiou, C. M. Zaleski, J. W. Kampf, M. L. Kirk, D. P. Kessissoglou, V. L. Pecoraro, *Angew. Chem. Int. Ed.* **2003**, *42*, 3763–3766.
[12] P. J. Stang, K. Chen, *J. Am. Chem. Soc.* **1995**, *117*, 1667–1668.
[13] a) R. W. Saalfrank, I. Bernt, M. M. Chowdhry, F. Hampel, G. B. M. Vaughan, *Chem. Eur. J.* **2001**, *7*, 2765–2769; b) R. W. Saalfrank, C. Deutscher, H. Maid, A. M. Ako, S. Sperner, T. Nakajima, W. Bauer, F. Hampel, B. A. Hess, N. J. R. van Eikema Hommes, R. Puchta, F. W. Heinemann, *Chem. Eur. J.* **2004**, *10*, 1899–1905; c) R. W. Saalfrank, C. Deutscher, S. Sperner, T. Nakajima, A. M. Ako, E. Uller, F. Hampel, F. W. Heinemann, *Inorg. Chem.* **2004**, *43*, 4372–4382; d) A. Caneschi, A. Cornia, S. J. Lippard, *Angew. Chem. Int. Ed. Engl.* **1995**, *34*, 467–469.
[14] a) C. J. Pedersen, *J. Am. Chem. Soc.* **1967**, *89*, 7017–7036; b) C. J. Pedersen, *Angew. Chem. Int. Ed. Engl.* **1988**, *27*, 1021–1027.
[15] M. S. Lah, V. L. Pecoraro, *J. Am. Chem. Soc.* **1989**, *111*, 7258–7259.
[16] R. A. Coxall, S. G. Harris, D. K. Henderson, S. Parsons, P. A. Tasker, R. E. P. Winppeny, *J. Chem. Soc., Dalton Trans.* **2000**, 2349–2356.
[17] C. Dendrinou-Samara, C. M. Zaleski, A. Evagorou, J. W. Kampf, V. L. Pecoraro, D. P. Kessissoglou, *Chem. Commun.* **2003**, 2668–2669.
[18] For example, see: G. Psomas, A. J. Stemmler, C. Dendrinou-Samara, J. J. Bodwin, M. Schneider, M. Alexiou, J. W. Kampf, D. P. Kessissoglou, V. L. Pecoraro, *Inorg. Chem.* **2001**, *40*, 1562–1570.
[19] C. Dendrinou-Samara, G. Psomas, L. Iordanidis, V. Tangoulis, D. P. Kessissoglou, *Chem. Eur. J.* **2001**, *7*, 5041–5051.
[20] B. R. Gibney, A. J. Stemmler, S. Pilotek, J. W. Kampf, V. L. Pecoraro, *Inorg. Chem.* **1993**, *32*, 6008–6015.
[21] a) D. P. Kessissoglou, J. J. Bodwin, J. W. Kampf, C. Dendrinou-Samara, V. L. Pecoraro, *Inorg. Chim. Acta* **2002**, *331*, 73–80; b) J. A. Halfen, J. J. Bodwin, V. L. Pecoraro, *Inorg. Chem.* **1998**, *37*, 5416–5417; c) B. R. Gibney, H. Wang, J. W. Kampf, V. L. Pecoraro, *Inorg. Chem.* **1996**, *35*, 6184–6193; d) A. J. Stemmler, J. W. Kampf, M. L. Kirk, V. L. Pecoraro, *J. Am. Chem. Soc.* **1995**, *117*, 6368–6369; e) B. R. Gibney, D. P. Kessissoglou, J. W. Kampf, V. L. Pecoraro, *Inorg. Chem.* **1994**, *33*, 4840–4849.
[22] a) C. Dendrinou-Samara, L. Alevizopoulou, L. Iordanidis, E. Samaras, D. P. Kessissoglou, *J. Inorg. Biochem.* **2002**, *89*, 89–96; b) A. D. Cutland, J. A. Halfen, J. W. Kampf, V. L. Pecoraro, *J. Am. Chem. Soc.* **2001**, *123*, 6211–6212; c) A. J. Stemmler, J. W. Kampf, M. L. Kirk, B. H. Atasi, V. L. Pecoraro, *Inorg. Chem.* **1999**, *38*, 2807–2817; d) A. J. Stemmler, A. Barwinski, M. J. Baldwin, V. Young, V. L. Pecoraro, *J. Am. Chem. Soc.* **1996**, *118*, 11 962–11 963; e) A. J. Stemmler, J. W. Kampf, V. L. Pecoraro, *Angew. Chem. Int. Ed. Engl.* **1996**, *35*, 2841–2843; f) D. P. Kessissoglou, J. W. Kampf, V. L. Pecoraro, *Polyhedron* **1994**, *13*, 1379–1391.
[23] a) M. S. Lah, B. R. Gibney, D. L. Tierney, J. E. Penner-Hahn, V. L. Pecoraro, *J. Am. Chem. Soc.* **1993**, *115*, 5857–5858; b) G. Psomas, C. Dendrinou-Samara, M. Alexiou, A. Tsohos, C. P. Raptopoulou, A. Terzis, D. P. Kessissoglou, *Inorg. Chem.* **1998**, *37*, 6556–6557.
[24] a) A. J. Stemmler, J. W. Kampf, V. L. Pecoraro, *Inorg. Chem.* **1995**, *34*, 2271–2272; b) M. Alexiou, C. Dendrinou-Samara, C. P. Raptopoulou, A. Terzis, D. P. Kessissoglou, *Inorg. Chem.* **2002**, *41*, 4732–4738; c) J.-L. Song, J.-G. Mao, H.-Y. Zeng, R. K. Kremer, Z.-C. Dong, *Inorg. Chem. Commun.* **2003**, *6*, 891–895.
[25] Th. C. Stamatatos, S. Dionyssopoulou, P. Kyritsis, C. P. Raptopoulou, A. Terzis, R. Vicente, A. Escuer, S. P. Perlepes, *Inorg. Chem.*, in press.
[26] a) M. Alexiou, C. Dendrinou-Samara, C. P. Raptopoulou, A. Terzis, V. Tangoulis, D. P. Kessissoglou, *Eur. J. Inorg. Chem.* **2004**, 3822–3827 ; b) M. Alexiou, C. Dendrinou-Samara, A. Karagianni, S. Biswas, C. M. Zaleski, J. Kampf, D. Yoder, J. E. Penner-Hahn, V. L. Pecoraro, D. P. Kessissoglou, *Inorg. Chem.* **2003**, *42*, 2185–2187; c) M. Alexiou, C. M. Zaleski, C. Dendrinou-Samara, J. Kampf, D. P. Kessissoglou, V. L. Pecoraro, *Z. Anorg. Allg. Chem.* **2003**, *629*, 2348–2355; d) T. Afrati, C. Dendrinou-Samara, C. P. Raptopoulou, A. Terzis, V. Tangoulis, D. P. Kessissoglou, *Angew. Chem. Int. Ed.* **2002**, *41*, 2148–2150.
[27] a) C. J. Milios, P. Kyritsis, C. P. Raptopoulou, A. Terzis, R. Vicente, A. Escuer, S. P. Perlepes, *Dalton Trans.* **2005**, 501–511; b) C. J. Milios, Th. C. Stamatatos, P. Kyritsis, A. Terzis, C. P. Raptopoulou, R. Vicente, A. Escuer, S. P. Perlepes, *Eur. J. Inorg. Chem.* **2004**, 2885–2901; c) C. J. Milios, E. Kefalloniti, C. P. Raptopoulou, A. Terzis, A. Escuer, R. Vicente, S. P. Perlepes, *Polyhedron* **2004**, *23*, 83–95; d) C. J. Milios, E. Kefalloniti, C. P. Raptopoulou, A. Terzis, R. Vicente, N. Lalioti, A. Escuer, S. P. Perlepes, *Chem. Commun.* **2003**, 819–821; e) C. J. Milios, C. P. Raptopoulou, A. Terzis, R. Vicente, A. Escuer, S. P. Perlepes, *Inorg. Chem. Commun.* **2003**, *6*, 1056–1060.
[28] Interesting reviews: a) P. Chaudhuri, *Coord. Chem. Rev.* **2003**, *243*, 143–190; b) V. Yu. Kukushkin, A. J. L. Pombeiro, *Coord. Chem. Rev.* **1999**, *181*, 147–175; c) V. Yu. Kukushkin, D. Tudela, A. J. L. Pombeiro, *Coord. Chem. Rev.* **1996**, *156*, 333–362.
[29] P. Chaudhuri, M. Hess, T. Meyhermüller, E. Bill, H.-J. Haupt, U. Flörke, *Inorg. Chem. Commun.* **1998**, *1*, 39–42.
[30] M. J. Goldcamp, S. E. Robison, J. A. Krause Bauer, M. J. Baldwin, *Inorg. Chem.* **2002**, *41*, 2307–2309.
[31] M. N. Kopylovich, V. Yu. Kukushkin, M. Haukka, J. J. R. Frausto da Silva, A. J. L. Pombeiro, *Inorg. Chem.* **2002**, *41*, 4798–4804.
[32] J. M. Thorpe, R. L. Beddoes, D. Collison, C. D. Garner, M. Helliwell, J. M. Holmes, P. A. Tasker, *Angew. Chem. Int. Ed.* **1999**, *38*, 1119–1121.
[33] J. Lisowski, P. Starynowicz, A. Jezierski, Z. Siatecki, *Polyhedron* **1996**, *15*, 3589–3593.
[34] a) V. V. Pavlishchuk, S. V. Kolotilov, A. W. Addison, M. J. Prushan, D. Schollmeyer, L. K. Thompson, T. Weyhermüller, E. A. Goreshnik, *Dalton Trans.* **2003**, 1587–1595; b) F. Akagi, Y. Michihiro, Y. Nakao, K. Matsumoto, T. Sato, W. Mori, *Inorg. Chim. Acta* **2004**, *357*, 684–688; c) P. Chaaudhuri, M. Hess, E. Rentschler, T. Weyhermüller, U. Flörke, *New J. Chem.* **1998**, *6*, 553–555; d) C. J. Milios, C. P. Raptopoulou, A. Terzis, F. Lloret, R. Vicente, S. P. Perlepes, A. Escuer, *Angew. Chem. Int. Ed.* **2004**, *43*, 210–212; e) H. Miyasaka, T. Nezu, K. Sugimoto, K. Sugiura, M. Yamashita, R. Clérac, *Inorg. Chem.* **2004**, *43*, 5486–5488.
[35] a) R. Clérac, H. Miyasaka, M. Yamashita, C. Coulon, *J. Am. Chem. Soc.* **2002**, *124*, 12 837–12 844; b) H. Miyasaka, R. Clérac, K. Mizushima, K. Sugiura, M. Yamashita, W. Wernsdorfer, C. Coulon, *Inorg. Chem.* **2003**, *42*, 8203–8213.

 © 2005 Wiley-VCH Verlag GmbH & Co. KGaA, Weinheim

[36] a) H.-J. Krüger, G. Peng, R. H. Holm, *Inorg. Chem.* **1991**, *30*, 734–742; b) A. N. Singh, A. Chakravorty, *Inorg. Chem.* **1980**, *19*, 969–971, and references cited therein.
[37] J. A. Cabeza, I. del Rio, V. Rieva, M. Suárez, C. Álvarez-Rúa, S. Garcia-Granda, S. H. Chuang, J. R. Hwu, *Eur. J. Inorg. Chem.* **2003**, 4159–4165.
[38] H. Kumagai, M. Endo, M. Kondo, S. Kawata, S. Kitagawa, *Coord. Chem. Rev.* **2003**, *237*, 197–203.
[39] The full crystallographic formula is $(NH_4)[Zn_5(acac)_2(pko)_6](PF_6)_3{\cdot}H_2O{\cdot}2.6MeOH$. Crystal data: empirical formula $C_{78.6}H_{78.4}Zn_5N_{19}O_{13}P_3F_{18}$, formula mass 2268.56, crystal size $0.10\times0.10\times0.40$ mm, monoclinic, *P*2/*n*, a = 17.903(2), b = 14.875(2), c = 18.745(2) Å, β = 95.33(1)°, V = 4970.2(8) Å^3, Z = 2, $\rho_{calcd.}$ = 1.516 g cm^{-3}, λ(Cu-K_α) = 1.54180 Å, μ = 2.680 mm^{-1}, F(000)= 2298, $2\theta_{max}$ = 103.3°, $-18 \le h \le 0$, $0 \le k \le 15$, $-18 \le l \le 19$.
[40] W. Clegg, D. R. Harbron, C. D. Homan, P. A. Hunt, I. R. Little, B. P. Straughan, *Inorg. Chim. Acta* **1991**, *186*, 51–60.
[41] A. W. Addison, T. N. Rao, J. Reedijk, J. van Rijn, G. C, Verschoor, *J. Chem. Soc., Dalton Trans.* **1984**, 1349–1356.
[42] I. Agrell, *Acta Chem. Scand.* **1970**, *24*, 1247–1261.
[43] P. M. Secondo, J. M. Land, R. G. Baughman, H. L. Collier, *Inorg. Chim. Acta* **2000**, *309*, 13–22.
[44] E. O. Schlemper, J. Stunkel, C. Patterson, *Acta Crystallogr., Sect. C* **1990**, *46*, 1226–1228.
[45] a) H.-J. Chen, L.-Z. Zhang, Z.-G. Cai, G. Yang, X.-M. Chen, *J. Chem. Soc., Dalton Trans.* **2000**, 2463–2466; b) H. Adams, N. A. Bailey, D. Fenton, Q.-Y. He, *J. Chem. Soc., Dalton Trans.* **1996**, 2857–2865; c) Y. Ke-Wu, Y. Yuan-Qi, H. Zhong-Xian, W. Yun-Hua, *Polyhedron* **1996**, *15*, 79–81; d) S. R. Petrusenko, V. N. Kokozay, I. O. Fritsky, *Polyhedron* **1997**, *16*, 267–274.
[46] a) A. Erxleben, J. Hermann, *J. Chem. Soc., Dalton Trans.* **2000**, 569–575; b) C. J. Matthews, L. K. Thompson, S. R. Parsons, Z. Xu, D. O. Miller, S. L. Heath, *Inorg. Chem.* **2001**, *40*, 4448–4454.
[47] a) A. K. Boudalis, N. Lalioti, G. A. Spyroulias, C. P. Raptopoulou, A. Terzis, A. Bousseksou, V. Tangoulis, J. P. Tuchagues, S. P. Perlepes, *Inorg. Chem.* **2002**, *41*, 6474–6487; b) I. Chadjistamatis, A. Terzis, C. P. Raptopoulou, S. P. Perlepes, *Inorg. Chem. Commun.* **2003**, *6*, 1365–1371.
[48] G. S. Papaefstathiou, A, Escuer, M. Font-Bardia, S. P. Perlepes, X. Solans, R. Vicente, *Polyhedron* **2002**, *21*, 2027–2032.
[49] G. B. Deacon, R. J. Phillips, *Coord. Chem. Rev.* **1980**, *33*, 227–250.
[50] K. Nakamoto, *Infrared and Raman Spectra of Inorganic and Coordination Compounds*, 4th ed., Wiley, New York, **1986**, pp. 259–263, 282–290.
[51] R. A. Bailey, S. L. Kozak, T. W. Michelsen, W. N. Mills, *Coord. Chem. Rev.* **1971**, *6*, 407–445.
[52] a) G. M. Sheldrick, *SHELXS-86, Program for the Solution of Crystal Structures*, University of Göttingen, Germany, **1986;** b) G. M. Sheldrick, *SHELXL-93, Program for the Refinement of Crystal Structures*, University of Göttingen, Germany, **1993**; c) G. M. Sheldrick, *SHELXL-97, Crystal Structure Refinement Program*, University of Göttingen, Germany, **1997**.

Received: November 4, 2004

 © 2005 Wiley-VCH Verlag GmbH & Co. KGaA, Weinheim

Perfluorinated Alkoxyaluminate Salts of Cationic Brønsted Acids: Synthesis, Structure, and Characterization of $[H(OEt_2)_2][Al\{OC(CF_3)_3\}_4]$ and $[H(THF)_2][Al\{OC(CF_3)_3\}_4]$

Ingo Krossing*[a,b] and Andreas Reisinger[a,b]

Keywords: Acidity / Aluminum / Brønsted acids / IR spectroscopy / Hydrogen bonds

The strong cationic Brønsted acids $[H(OEt_2)_2][Al\{OC(CF_3)_3\}_4]$ (**1**) and $[H(THF)_2][Al\{OC(CF_3)_3\}_4]$ (**2**) were prepared in up to 95 % yield by reacting stoichiometric amounts of diethyl ether/THF solutions of $Li[Al\{OC(CF_3)_3\}_4]$ and HX (X = Cl, Br), removing the solvent, and extracting the residue with CH_2Cl_2. Compounds **1** and **2** were characterized by multinuclear NMR and IR spectroscopy as well as by their single crystal X-ray structures and additional quantum chemical calculations. The cation in **1** probably contains an unsymmetrical O–H···O hydrogen bond, while in **2** the protic hydrogen atom was not found in the difference Fourier map. From an analysis of all published $[H(OEt_2)_2]^+$ structures, we show that for an unsymmetrical H-bridge further rearrangement of the structure occurs leading to the structural type **III** that may formally be viewed as ethanol coordinating to an ethyl cation. This point of view has hitherto been neglected in the discussion of the nature of short, strong, low-barrier H-bonds, although it needs to be accounted for. Both **1** and **2** are suitable starting materials to introduce the weakly coordinating and chemically very robust $[Al\{OC(CF_3)_3\}_4]^-$ anion by protonolysis.

(© Wiley-VCH Verlag GmbH & Co. KGaA, 69451 Weinheim, Germany, 2005)

Introduction

Salts of protonated ether solvents in superacidic solutions have been known for about 40 years.[1] In 1985 an isolated report of the structure of $[H(OEt_2)_2]_2[Zn_2Cl_6]$ appeared,[2] but in recent years salts of the oxonium acids $[H(OEt_2)_2]^+$ and $[H(THF)_2]^+$ with several weakly coordinating anions (WCAs),[3] such as $[BAr^F{}_4]^-$ [Ar^F = C_6F_5,[4] $C_6H_3(CF_3)_2$],[5,6] $[CHB_{11}R_5X_6]^-$ (R = H, CH_3; X = Cl, Br),[7] $[(F_5C_6)_3B(\mu\text{-}X)B(C_6F_5)_3]^-$ (X = $C_3N_2H_3^-$,[8] NH_2^- [9]) or $[C_6F_4\text{-}1,2\text{-}\{B(C_6F_5)_2\}_2(\mu\text{-}OCH_3)]^-$ [10] have been prepared and characterized by different spectroscopic methods as well as X-ray crystallography. $[H(OEt_2)_2]^+$ salts in particular have emerged as very versatile reagents in organometallic synthesis and catalysis.[4–10,11] However, all the currently known $[H(OEt_2)_2]^+$ salts are hampered by either their low thermal solution stability {i.e. $[H(OEt_2)_2][BAr^F{}_4]$ [Ar^F = $C_6H_3(CF_3)_2$]} or difficulties in obtaining the starting materials due to the need to intermediately prepare explosive C_6F_5Li or the carborane anions. Thus, there is demand for further, easily accessible and in solution thermally stable $[H(OEt_2)_2]^+$ salts.

Recently, we reported the facile preparation of nonoxidizing weakly coordinating anions of type $[Al(OR^F)_4]^-$ [R^F = $CH(CF_3)_2$, $C(CH_3)(CF_3)_2$, $C(CF_3)_3$][12,13] and their use to stabilize weakly bound silver complexes such as $Ag(\eta^2\text{-}P_4)_2^+$ [14] and $Ag(\eta^4\text{-}S_8)_2^+$ [15] as well as highly electrophilic cations like PX_4^+, $P_2X_5^+$, $P_3I_6^+$, and $P_5X_2^+$ (X = Br, I),[16,17] $CS_2Br_3^+$,[18] and CI_3^+.[19] Li^+,[12,13] Ag^+,[12] Tl^+,[20] Cs^+, Ph_3C^+,[21] and NR_4^+ [13,22] salts of these anions are available as starting materials; however, cationic Brønsted acids with the $[Al(OR^F)_4]^-$ anions are still unknown.

Herein we report the synthesis and characterization of $[Al(OR^F)_4]^-$ salts [R^F = $C(CF_3)_3$] of the oxonium acids $[H(OEt_2)_2]^+$ and $[H(THF)_2]^+$. Due to their facile access, the commercial availability of $Li[Al(OR^F)_4]$ (Strem) as well as the weakly coordinating and stable counterion, these compounds are a good alternative to the widely used $[H(OEt_2)_2][BAr^F{}_4]$ salts. Moreover, during the last ten years a considerable experimental and theoretical debate has been going on as to whether a truly symmetrical hydrogen bond exists or not.[7,23] A complete understanding and proof of one of the models has still not been achieved and the nature of these short, strong, low-barrier H-bonds remains somewhat unclear.

[a] Universität Karlsruhe, Institut für Anorganische Chemie, Engesserstr. Geb. 30.45, 76128 Karlsruhe, Germany
[b] Present address: Ecole Polytechnique Fédérale de Lausanne (EPFL), Laboratory of Inorganic and Coordination Chemistry (LCIC), ISIC–BCH, 1015 Lausanne, Switzerland
E-mail: ingo.krossing@epfl.ch
Supporting information for this article is available on the WWW under http://www.eurjic.org or from the author.

Results and Discussion

Synthesis

$LiAl[OC(CF_3)_3]_4$ was prepared by reaction of $LiAlH_4$ with $HOC(CF_3)_3$ in toluene.[12,13] The Li salt was suspended in CH_2Cl_2 and treated with diethyl ether/THF solutions of HX (X = Cl, Br) to produce precipitation of LiX. The products $[H(OEt_2)_2][Al\{OC(CF_3)_3\}_4]$ (**1**) and $[H(THF)_2][Al\{OC(CF_3)_3\}_4]$ (**2**) were isolated after work-up in up to 95% yield [Equation (1)].

$$\begin{array}{l} Li^+[Al(OC(CF_3)_3)_4]^- + 2\,L + HX \\ \qquad\qquad \downarrow\ CH_2Cl_2 \qquad\qquad X = Cl, Br \\ [H(L)_2]^+[Al(OC(CF_3)_3)_4]^- + LiX \qquad L = Et_2O, THF \end{array} \quad (1)$$

Compound **1** was obtained as a white powder by redissolving the residue from the reaction in CH_2Cl_2. This air- and moisture-sensitive powder is stable at room temperature and soluble in several moderately polar organic solvents, such as diethyl ether, diethyl ether/toluene mixtures, chloroform, dichloromethane, and 1,2-dichloroethane. Solutions of **1** in CD_2Cl_2 are stable for at least a week at ambient temperature. Solid **1** is stable for several months at room temperate and may be heated up to 75 °C without alteration (DTA analysis); further heating causes decomposition. In the DTA trace only variations of the gradient at 103 °C (18% weight loss) and 148 °C (further 60% weight loss) can be observed, with no distinct steps. From other DTA traces, and the fact that $LiAl[OC(CF_3)_3]_4$ can be sublimed at about 130–140 °C without decomposition,[12] it seems likely that the decomposition starts with the loss of two diethyl ether molecules (18% obsvd. weight loss vs. theoretical value of 13%). However, it cannot be excluded that $HOC(CF_3)_3$ and one molecule of OEt_2 are ejected first to leave $Et_2O{\cdot}Al[OC(CF_3)_3]_3$ as a nonvolatile residue. The second step between 100 °C and 150 °C results from decomposition of the anion. During that decomposition one equivalent of $HOC(CF_3)_3$ and two equivalents of $F_2COC(CF_3)_2$ are presumably formed, in agreement with a total weight loss of 60% (theory: 60%), to leave the relatively stable $AlF_2(OR)$. Further decomposition and weight loss is slow and spread over 200 °C. The observed weight loss is in agreement with the formation of another equivalent of the epoxide $F_2COC(CF_3)_2$ (exp. 13%; theory 19%). This results in a total weight loss of 91% (theoretical value: 92%) and the formation of nonvolatile AlF_3 at approximately 350 °C. Figure 1 shows a likely route for the thermal decomposition and the differential temperature analysis of **1** between 30 and 350 °C.

The preparation of **2** is less straightforward. After filtration and removal of all volatiles an oily brown residue remained that probably contains THF polymerization products[7] in addition to the product **2**, which is the major component (approx. 80% of the oil, by NMR spectroscopy). Compound **2** crystallized as less-rhombus-shaped crystals in good yield (65%) within two days directly from this oily residue. The crystals were isolated from the oil by decantation followed by several washings with pentane. Crystalline air- and moisture-sensitive **2** is stable at room temperature and soluble in the same solvents as **1** (see above).

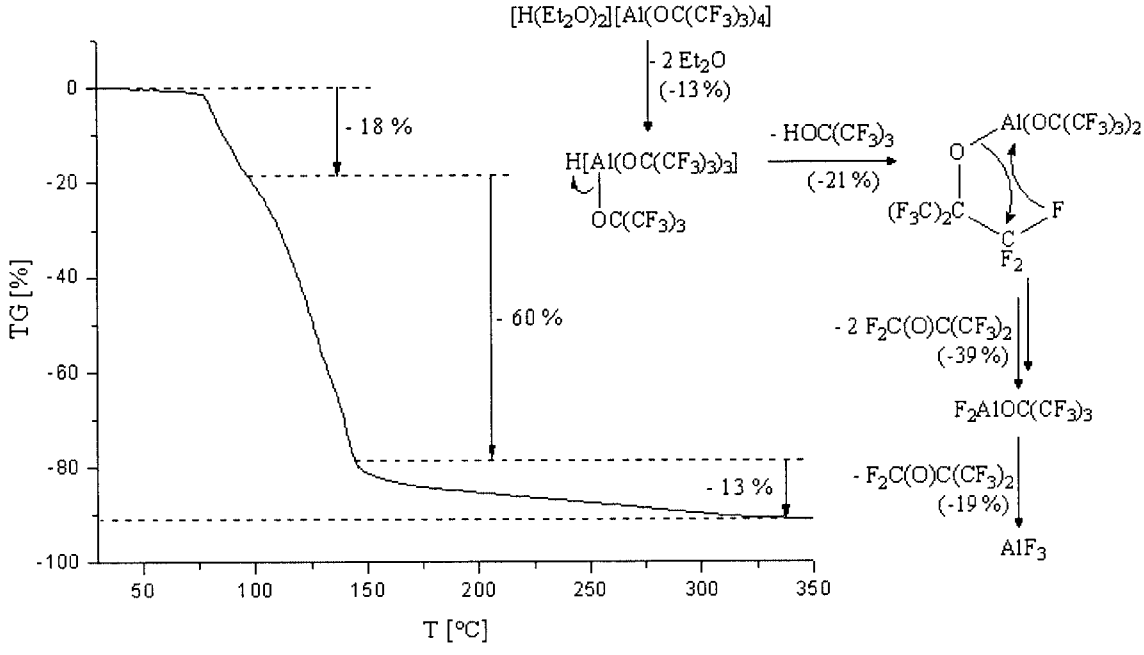

Figure 1. DTA analysis of **1** between 30 and 350 °C (left) and hypothetical route for the decomposition (right).

 © 2005 Wiley-VCH Verlag GmbH & Co. KGaA, Weinheim

Thermodynamics of the Formation of 1

We assessed the driving force for the formation of **1** in more detail. Assuming that the isodesmic reaction (2) takes place in CH_2Cl_2, it is possible to reliably obtain its reaction enthalpy by quantum chemical calculations (see computational details). The part of the anion cancels.

$$[Li(OEt_2)_2]^+_{(solv.)} + [Al(OC(CF_3)_3)_4]^-_{(solv.)} + HBr_{(solv.)}$$

$$\downarrow \quad \Delta G°_{solv.} = -81 \text{ kJ mol}^{-1} \text{ (MP2/TZVPP and BP86/TZVPP)}$$

$$[H(OEt_2)_2]^+_{(solv.)} + [Al(OC(CF_3)_3)_4]^-_{(solv.)} + LiBr_{(s)} \quad (2)$$

As expected for an isodesmic reaction, BP86/TZVPP (DFT) and MP2/TZVPP (ab initio) calculations agree on the same value for $\Delta G°_{solv.}$ of –81 kJ mol^{-1}. However, for the calculations to form an isodesmic reaction, Equation (2) assumes that the rather odd $Li(OEt_2)_2^+$ cation is present in solution. However, the cation $Li(OEt_2)_4^+$ is more likely, as shown by various crystal structures of $Li(L)_4^+$ salts (L = ethereal solvent).[8] Therefore, we assessed reaction (3), which is no longer isodesmic and thus $\Delta G°_{solv.}$ may be less accurate; however, the species presented in (3) are very close to the situation actually taking place in solution.

$$[Li(OEt_2)_4]^+_{(solv.)} + [Al(OC(CF_3)_3)_4]^-_{(solv.)} + HBr_{(solv.)}$$

$$\downarrow \quad \Delta G°_{solv.} = -135 \text{ kJ mol}^{-1} \text{ (BP86/TZVPP)}$$

$$[H(OEt_2)_2]^+_{(solv.)} + [Al(OC(CF_3)_3)_4]^-_{(solv.)} + 2\ OEt_{2(solv.)} + LiBr_{(s)} \quad (3)$$

Again, the part of the anion cancels. Equation (3) is additionally favored by entropy due to the release of two ether molecules. $\Delta G°_{solv.}$ of this reaction is exergonic by –135 kJ mol^{-1} and is thus very favorable, in agreement with the facile preparation of **1**. We assume a similar situation for **2**, although this is not explicitly discussed.

NMR Spectroscopy

Protonated Diethyl Ether Moiety

The ^{19}F and ^{27}Al NMR spectroscopy show one characteristic sharp signal for the intact counterion. In the ^1H NMR spectrum a broad downfield-shifted signal at δ = 18.2 ppm (OH) and signals for the CH_3 and CH_2 protons of the coordinating diethyl ether molecules are observed. The OH signal varies greatly from sample to sample, with values between δ = 14.5 and 18.2 ppm. The integration of the signals shows the constitution as two coordinated diethyl ether molecules per proton, similar to all the earlier synthesized etherates.[4–10] Compared to free diethyl ether,[24] these two signals are slightly shifted downfield (Table 1). The ^{13}C NMR spectrum shows the signals of the anion and two signals which were assigned to the methyl and methylene groups of the cation. In Table 1, the observed ^1H and ^{13}C signals of the cation are collected and compared to different salts of $[H(OEt_2)_2]^+$ as well as the shifts calculated by DFT.

In the article[10] on $[H(OEt_2)_2][C_6F_4\text{-}1,2\text{-}\{B(C_6F_5)_2\}_2(\mu\text{-}OCH_3)]$, the ^{13}C signal at δ = 57.9 ppm was assigned to the methylene group of the cation. Since all the other data of this signal, including the DFT calculations, range from δ = 67.8 to 70.4 ppm it was probably incorrectly assigned. The authors also observed one signal at δ = 69.0 ppm which was assigned to the methoxy group of the anion;[10] however, the collection of chemical shifts in Table 1 clearly indicates that this assignment is erroneous and the shifts must be reversed. i.e. the signal at δ = 69.0 ppm belongs to the CH_2 group of protonated diethyl ether and the signal at δ = 57.9 ppm to the methoxy group of the anion.

^1H and ^{13}C solid-state MAS NMR measurements matched with the solution spectra: in the ^1H NMR spectrum signals are observed at δ = 1.32, 3.90 and 16.6 ppm. Apart from the typical anion signals,[12] the ^{13}C NMR spectrum shows one signal at δ = 12.7 ppm and two signals at δ = 71.1 and 71.6 ppm. None of these signals can be assigned to free diethyl ether since that signal has a chemical shift of δ = 65.2 ppm.[24] This suggests an asymmetric envi-

Table 1. Comparison of the ^1H and ^{13}C chemical shifts of $[H(OEt_2)_2]^+$ salts with different anions and shifts calculated by DFT [BP86/SV(P)].

	$[Al\{OC(CF_3)_3\}_4]$	$[B(C_6F_5)_4]$[4]	$[C_6F_4\text{-}1,2\text{-}[B(C_6F_5)_2]_2(\mu\text{-}OCH_3)]$[10]	$[CHB_{11}R_5X_6]$[7]	(BP86/SV(P))
$\delta_{^1H}(CH_3)$	1.34/1.32[a]	1.42	1.43	0.78	1.2
$\delta_{^1H}(CH_2)$	3.90/3.90[a]	7.55[b]	4.08	3.32	3.5
$\delta_{^1H}(OH)$	18.2/16.6[a]	15.5	16.4	13.8	12.8
$\delta_{^{13}C}(CH_3)$	13.8/12.7[a]	13.9	14.5	–	16.8
$\delta_{^{13}C}(CH_2)$	69.9/71.1–71.7[a]	70.4	69.0	–	75.1

[a] Solution/MAS NMR spectroscopy. [b] Since this value differs from all other experimental and calculated shifts, it is erroneous.

 © 2005 Wiley-VCH Verlag GmbH & Co. KGaA, Weinheim

ronment of the two coordinated ether molecules in the solid state.

Protonated THF

NMR spectroscopy gave the expected sets of signals that match with the DFT calculations and that of the only other reported compound ($[H(THF)_2][CHB_{11}R_5X_6]$, Table 2).[7]

Table 2. Comparison of NMR shifts of $[H(THF)_2]^+$ with two anions and shifts calculated by DFT.

	$[H(THF)_2]$-$[Al\{OC(CF_3)_3\}_4]$	$[H(THF)_2]$-$[CHB_{11}R_5X_6]$[7]	BP86/SV(P)
$\delta_{^1H}(CH_2)$	2.05	1.30	1.9
$\delta_{^1H}(OCH_2)$	3.95	3.60	3.6
$\delta_{^1H}(OH)$	≈ 8, broad (exchange?)	14.80	13.1
$\delta_{^{13}C}(CH_2)$	25.5	–	29.1
$\delta_{^{13}C}(OCH_2)$	70.6	–	73.8

Vibrational Spectroscopy

The IR spectrum of **1**, especially the portion shown in Figure 2, exhibits the typical bands of the perfluorinated aluminate anion in the range between 286 and 1353 cm^{-1}. They can easily be assigned by comparison with other salts of this anion as well as with the calculated vibrational frequencies, as demonstrated in Table 3. The most characteristic anion vibrations are the very strong bands at 727 and 973 cm^{-1} as well as those between 1219 and 1353 cm^{-1}. The fact that the positions of the anion bands remain unchanged relative to the calculated frequencies and the NEt_4^+ salt indicates that there is no coordination of the anion as, for example, occurs with the naked Li^+ or Ag^+ cation. The anion bands of the Raman spectrum of **1** match well with the IR spectrum. The most important differences between the spectra arise from the two strong bands at 744 and 798 cm^{-1} and the absence of the very strong IR bands in the range between 1200 and 1320 cm^{-1}, as can be seen in Table 3.

The remaining bands of the IR spectrum at $\tilde{\nu}$ = 769, 907, 1013, 1063, 1092, 1166, 1366, and 1536 cm^{-1} can now be assigned to vibrations of the cation. Table 4 shows the experimental bands compared to the carboranate anion of Reed,[7] the maxima of the simulated calculated cation spectrum, as well as the experimental[25] and calculated bands of free diethyl ether in the range between 700 and 3000 cm^{-1}. This table also contains an assignment of the calculated bands and the related experimental modes. Compared to the calculated frequencies, the experimental bands match well. The expected bands at 726, 1212, 1312, and around 3000 cm^{-1} are likely overlapped by strong anion or Nujol bands. As already noted earlier, the cation bands are rather broad.[7,23] Similarly to Reed's $[H(OEt_2)_2]$-$[CHB_{11}H_5Cl_6]$ salt, the very strong sharp ν_{as}(C–O–C) band of free Et_2O (1120 cm^{-1}) disappears.[7]

The Raman spectrum of **1** obtained at low temperature shows several bands in the range between 2850 and 3010 cm^{-1} which can be assigned with no doubt to C–H vibrations of the cation. At lower energy two bands at 1467 and 1496 cm^{-1} are in good agreement with the calculated bands at 1450 and 1480 cm^{-1}. Furthermore, there are three bands at 1017, 1082, and 1151 cm^{-1} that may be associated with the IR bands at 1013, 1092, and 1166 cm^{-1}. Finally, the Raman spectrum reveals one band at 472 cm^{-1} which

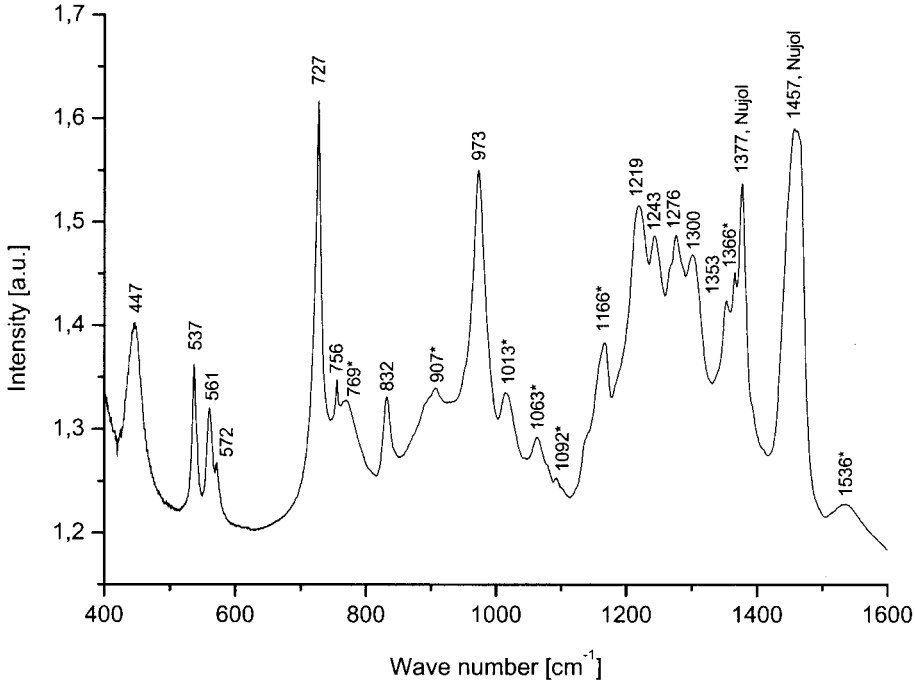

Figure 2. IR spectrum of **1** between 400 and 1600 cm^{-1} (CsI plates, Nujol) with cation bands at $\tilde{\nu}$ = 769, 907, 1013, 1063, 1092, 1166, 1366, and 1536 cm^{-1} (marked with *).

 © 2005 Wiley-VCH Verlag GmbH & Co. KGaA, Weinheim

Table 3. Comparison of the experimental anion bands of **1** and **2** with anion bands of $[NEt_4][Al\{OC(CF_3)_3\}_4]$[22] and calculated frequencies.

$[H(OEt_2)_2][Al\{OC(CF_3)_3\}_4]$ IR	Raman	$[H(THF)_2][Al\{OC(CF_3)_3\}_4]$	$[NEt_4][Al\{OC(CF_3)_3\}_4]$	$[Al\{OC(CF_3)_3\}_4]^-$ (calcd.)
	228 (w)			
286 (mw)	289 (w)	–	286 (mw)	274 (w)
314 (m)	320 (m)	–	316 (m)	302 (w)
329 (w)	332 (m)	–	331 (w)	320 (w)
–	368 (w)	–	367 (mw)	352 (w)
375 (m)	381 (vw)	–	378 (mw)	364 (w)
447 (ms)		446 (ms)	447 (ms)	420 + 436 (mw)
537 (m)	537 (m)	537 (m)	537 (m)	520 (mw)
561 (m)	564 (w)	561 (m)	562 (mw)	546 (mw)
572 (mw)	573 (m)	571 (mw)	571 (w)	556 (w)
727 (vs)		727 (vs)	727 (s)	708 (m)
	744 (s)			
756 (m)		755 (m)	756 (mw)	736 (w)
	798 (s)			
832 (m)	828 (w)	831 (m)	833 (m)	816 (w) + 826 (w)
973 (vs)	975 (w)	973 (vs)	973 (s)	962 (s)
–		–	–	1112 + 1138 (w)
1219 (s)	1216 (vw)	1220 (s)	1217 (vs)	1216 (vs)
1243 (s)	1243 (vw)	1242 (s)	1240 (s)	1230 (vs)
–		–	1254 (s)	–
1276 (s)	1278 (m)	1276 (s)	1277 (vs)	1260 (vs)
1300 (s)	1312 (w)	1300 (s)	1299 (s)	–
1353 (ms)		1353 (ms)	1353 (ms)	1344 (vs)

Table 4. Experimental cation bands of **1** compared to $[H(OEt_2)_2][CHB_{11}H_5Cl_6]$ (**cb**) and calculated frequencies as well as free Et_2O.

Compound **1** (exp.) IR	Raman	**cb**[7] (exp.)	$[H(OEt_2)_2]^+$ (calcd.)[a] Spectrum	Assignment	Et_2O[25] (exp.)	Et_2O (calcd.)
	472 (w)		480 (vw)	O–H–O		
					677	
769 (mw)			774 (w)	O–H–O, C–O	793	810
907 (mw)		925 (vs)	896 + 914 (ms)	C–O, C–C	932	932
1013 (m)	1017 (m)		1006 (m)	C–O, C–C	1025	
1063 (mw)			1064 (m)	O–H–O, C–O	1044	1042
	1082 (w)		1071 (vw)	O–H–O, C–C	1074	1072
1092 (w)						
	1151 (m)		1134 (w)	C–O, C–C	1119	1152
1166 (ms)			1172 (m)	O–O, C–C	1150	1170
[b]			1282 (ms)	C–H	1296	
1366 (m)			1370 (mw)	C–H	1378	1368
[c]			1426 (mw)	O–H–O, C–H		1422
	1467 (m)		1450 (vw)	C–H		
	1496 (w)		1480 (vw)	O–H–O, C–H		
1536 (mw)		1524 (s)	1536 (s)	O–H–O	1547	
[c]	2859 (m)			C–H		
[c]	2894 (m)	2872 (w)		C–H	2777	2838
[c]	2912 (m)	2907 (w)	2968 (mw)	C–H	2807	2852
[c]	2948 (s)	2938 (m)	3046 (w)	C–H	2856	2870
[c]	2961 (s)	2984 (s)	3068 (w)	C–H	2929	2954
[c]	3006 (m)	3000 (m)	3070 (w)	C–H	2972	3044

[a] Only the maxima of the (deposited) simulation are given. [b] Overlapped by strong anion bands. [c] Overlapped by Nujol bands.

matches with the calculated frequency at 480 cm^{-1}. This frequency refers to a vibration of the oxygen atoms of the cation. All cation bands are shown in Table 4 and are compared to several experimental IR bands as well as selected calculated frequencies.

Figure 3 shows a section of the IR spectrum of **2** between 400 and 1500 cm^{-1}. Again, the typical bands of the perfluorinated *tert*-butoxyaluminate anion are clearly visible (Table 3), as discussed above. Similarly, the position of the bands relative to the calculated frequencies and the NEt_4^+ salt indicates a distinct salt structure, which is proved by the solid-state structure (Figure 5).

In Figure 3, the bands at $\tilde{\nu}$ = 603, 775, 894, 918, 1043, 1167, 1365, and 1448 cm^{-1} can be assigned to vibrations of the cation. Table 5 shows the experimental bands compared to the carboranate anion of Reed,[7] the maxima of the simulated calculated cation spectrum, as well as experimental[25] and calculated bands of free THF in a range from

 © 2005 Wiley-VCH Verlag GmbH & Co. KGaA, Weinheim

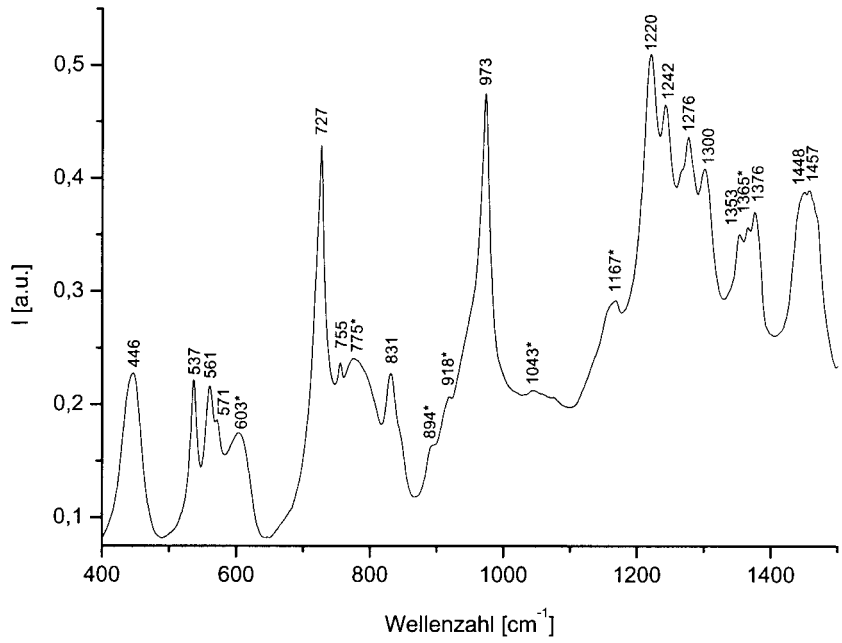

Figure 3. Section of the IR spectrum (CsI, Nujol) of **2** with cation bands at $\tilde{\nu}$ = 603, 775, 894, 918, 1043, 1167, 1365, and 1448 cm^{-1} (*).

Table 5. Experimental cation bands of **2** compared to $[H(THF)_2][CHB_{11}H_5Br_6]$ (**cb**) and calculated frequencies as well as free THF.

Comopound **2** (exp.)	**cb**[7] (exp.)	$[H(THF)_2]^+$ (calcd.)[a]	THF[25] (exp.)	THF (calcd.)
603 (ms)	–	608 (m)	660	630
775 (m)	–	794 (m)		788
	–	826 (w)		852
894 (w)	–	836 (vw)		894
918 (w)	–	904 (w)	920	932
[b]	–	956 (m)		952
1043 (w)	1048 (vs)	986 (w)	1025	1032
–	–	–	1090	1088
[1155 (sh) ?]	–	1136 (m)		1120
[1167 (ms) ?][b]	–	1156 (vw)	1175	1180
[1220 (vs) ?][b]	–	1214 (vs)	1205	1194
–	–	–		1222
[1242 (s) ?][b]	–	1240 (s)	1240	1234
[b]	–	1300 (mw)		
1366 (m)	–	1326 (w)		1322
[b]	–	1346 (w)	1370	1361
[c]	–	1414 (vs)		
1448 (w)	–	1444 (w)	1455	1446
1507 (w, br.)	–	1514 (m)		
1517 (w, br.)	–	1554 (w)		
[c]	2880 (m)		2685	2868
[c]	2909 (m)	2976 (w)		
[c]	2933 (w)	2992 (w)	2860	2986
[c]	2954 (m)	2998 (w)	2975	3018
[c]	2988 (m)	3066 (w)		3044

[a] Only the maxima of the (deposited) simulation are given. [b] Overlapped by strong anion bands. [c] Overlapped by Nujol bands.

700 to 3000 cm^{-1}. Compared to the calculated frequencies, the experimental bands match well; however, the expected bands at 726, 1212, 1312, and around 3000 cm^{-1} are again overlapped by strong anion or Nujol bands.

Solid-State Structures

The solid-state structure of **1** was determined, confirming the NMR spectroscopic data and showing an ionic lattice containing $[H(OEt_2)_2]^+$ and $[Al\{OC(CF_3)_3\}_4]^-$. The molecular structure of one formula unit is shown in Figure 4.

For the anion, typical structural parameters to those reported earlier[12] were found. In contrast to the anion, the structural parameters of the cation show some interesting details: the position of the (O)H atom was found in the difference Fourier map and suggests the presence of an unsymmetrical O–H···O bond with an O–O separation of 242.4 pm (cf. 240 to 245 pm in other $[H(OEt_2)_2]^+$

 © 2005 Wiley-VCH Verlag GmbH & Co. KGaA, Weinheim

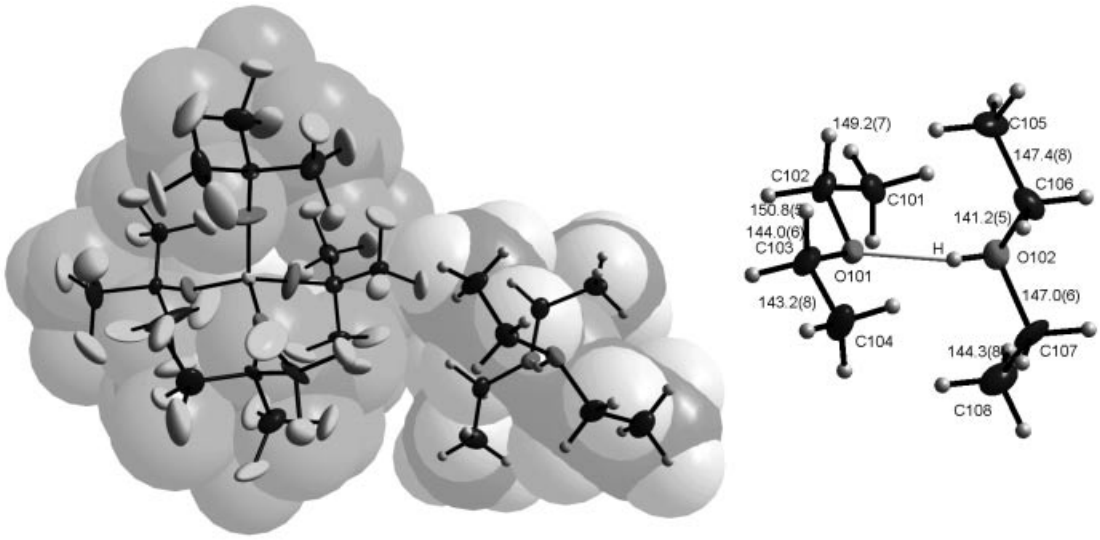

Figure 4. Section of the solid-state structure of **1**. Superposition of a space-filling (light gray) and a thermal ellipsoid model drawn at the 25% probability level.

salts[4,7,10]). No disorder was evident from the structure. The asymmetric coordination also followed from the C–O bond lengths: compared to free solid diethyl ether,[26] which has an average O–C bond length of 142.8 pm the average C–O separations of the diethyl ether molecules are elongated by 5.6 (coordinated ether) and 1.3 pm (protonated ether; Δd = 4.3 pm). This implies that the two diethyl ether molecules in **1** are different and, since the C–O bonds of the coordinated diethyl ether molecules of our oxonium acid are elongated unsymmetrically, the proton is presumably located at one of the two molecules.

The solid-state structure of **2** was also determined by X-ray crystallography. The NMR spectroscopic data could be confirmed as well as the existence of an ionic lattice of $[H(THF)_2]^+$ and $[Al\{OC(CF_3)_3\}_4]^-$. However, the quality of the data does not allow for extensive discussions and the structure is mainly seen as additional evidence for the nature of **2** being a salt of $[H(THF)_2]^+$. The acidic proton was not located in the difference Fourier map and is, therefore, not shown. Figure 5 shows one formula unit of the molecular structure.

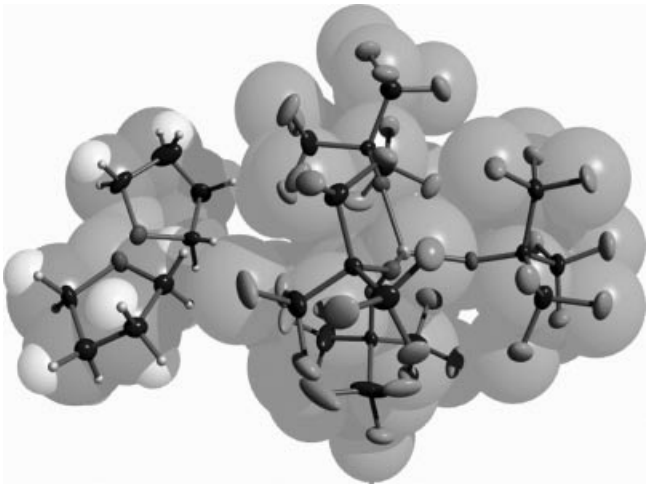

Figure 5. Section of the solid-state structure of **2**. Superposition of a space-filling (pale gray) and a thermal ellipsoid model drawn at 25% probability level.

On the Structure of $[H(OEt_2)_2]^+$

It is clear from first principles as well as the DFT calculations of the structures of $H–OEt_2^+$ vs. symmetric $[H(OEt_2)_2]^+$ in Table 6 that the protonation of the oxygen atom should lead to an elongation of the adjacent C–O bonds. However, if this is true, the acidic proton in **1** is attached to the wrong oxygen atom. Still, a similar unsymmetrical elongation with the apparently wrong oxygen atom protonated also occurs for Jutzi's acid $[H(OEt_2)_2][B(C_6F_5)_4]$ (Δd = 4 pm).[4] A closer analysis shows that the two C–O bond lengths in the nonprotonated diethyl ether molecule are not similar but differ greatly (144.0 vs. 150.8 pm in **1** and 146.6 vs. 154.2 pm in Jutzi's acid). On the other hand, there are two reports of a symmetrically bridged proton in the center of two Et_2O molecules.[2,10] In these cases all four C–O bond lengths are similar and amount to approximately 146 pm. These initial observations suggest that the position of the proton as determined by X-ray diffraction is unreliable and should not be used for the discussion of a symmetrical or unsymmetrical H-bridge. The C–O and C–C bond lengths were determined with much higher accuracy and should, therefore, be used for the comparison. However, although five crystal structures of $[H(OEt_2)_2]^+$ have been published,[2,4,7–9] hitherto nobody has analyzed the structures in detail. Therefore, the structural parameters of all published $[H(OEt_2)_2]^+$ solid-state structures as well as the DFT-calculated parameters of Et_2O, $[HOEt_2]^+$, and symmetrical $[H(OEt_2)_2]^+$ are collected in Table 6.

An analysis of Table 6 underlines the conclusion that the experimentally determined positions of the acidic protons

 © 2005 Wiley-VCH Verlag GmbH & Co. KGaA, Weinheim

Table 6. Comparison of the experimental and BP86/TZVPP calculated structural parameters of OEt_2, $[HOEt_2]^+$ and $[H(OEt_2)_2]^+$ (labeling according to the formula given below. In the asymmetrical case, the two sets of r3 to r6 distances are given).

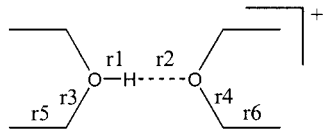

Parameter	OEt_2 (exp./ calcd.)	$[HOEt_2]^+$ (calcd.)	$[H(OEt_2)_2]^+$ (calcd.)	**1**	**A**[2][a]	**B**[8][b]	**C**[7][c]	**D**[4][d]	**E**[10][e]
Type	–	–	sym.	asym.	Sym.	asym.	asym.	asym.	sym.
r1/r2 [pm]	–	98.0	121.9/122.4	(80/170)	(116/124)	(111/134)	(108/154)	(93/152)	(119/121)
r3 [pm]	–	152.7	147.7	141.2/147.0	145.5	144.8/145.6	146.1/150.5	142.9/144.3	f)
r4 [pm]	142.8/142.4	–	147.7	144.0/150.8	146.5	144.1/152.4	144.6/154.4	146.6/154.2	144.6
r5 [pm]	–	149.9	151.1	144.3/147.4	149.0	148.2/147.8	142.1/144.6	138.8/140.7	f)
r6 [pm]	150.6/151.8	–	151.1	143.2/149.2	147.8	126.7/147.6	140.3/149.0	138.7/145.9	144.4

[a] **A** = $[H(OEt_2)_2]_2[Zn_2Cl_6]$. [b] **B** = $[H(OEt_2)_2][(F_5C_6)_3B\text{-}C_3H_2N_2\text{-}B(C_6F_5)_3]$. [c] **C** = $[H(OEt_2)_2][CB_{11}H_6X_6]$. [d] **D** = $[H(OEt_2)_2][B(C_6F_5)_4]$. [e] **E** = $[H(OEt_2)_2][F_4C_6[B(C_6F_5)_2]_2OMe]$. [f] This side of the cation was disordered and, therefore, bond lengths are less accurate and not included.

are unreliable; however, this is common knowledge. More importantly, one realizes from Table 6 that, when concentrating on the C–O and C–C separations, the nature of the H-bridge in $[H(OEt_2)_2]^+$ may not simply be reduced to symmetric (**I**) or asymmetric (**II**) but that in the asymmetric case further rearrangements of the structure occur (**IIIa,b** in Scheme 1).

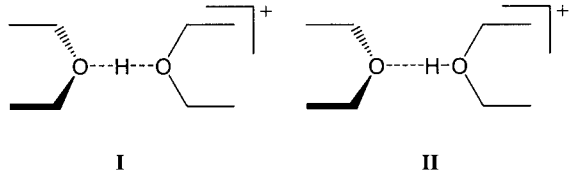

I **II**

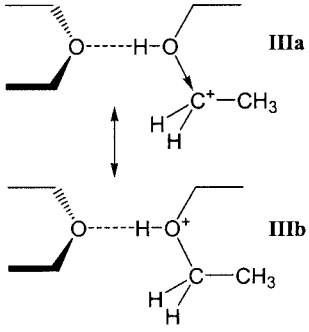

Scheme 1. Possible structures of $[H(OEt_2)_2]^+$.

In structure type **II** the C–O bond lengths of the protonated diethyl ether molecule should be symmetrically elongated. This is obviously not the case (Table 6) and therefore structure **III** is important; resonance form **IIIa**, which formally may be viewed as ethanol coordinated to an ethyl cation, accounts for the unsymmetrical C–O bond lengths of the protonated diethyl ether molecule. From the two symmetric and four asymmetric structures in Table 6 one may therefore extract average structural parameters for **I** and **III**; a schematic representation of the parameters of both forms is given in Scheme 2. A detailed description of the procedure to obtain the average structural data is available as Supporting Information

Symmetrically bridged cation **I**
structures: **A**, **E**

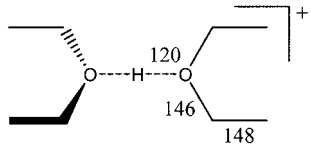

Asymmetric cation **III**
structures: **1**, **B**, **C**, **D**

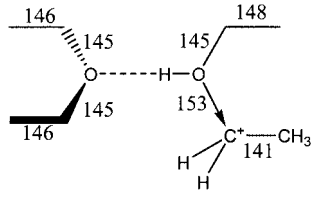

Scheme 2. Average structural parameters of **I** and **III** [pm] extracted from the solid-state structures in Table 6.

The structure of **I** is in very good agreement with that predicted on the basis of the BP86/TZVPP calculations (Table 6). However, regardless of whether one starts with a slightly asymmetric or strongly asymmetric structural type **III** the DFT calculations (gas phase!) always lead to the symmetric structure type **I**. Nevertheless, the average structural parameters of **III** in Scheme 2 are likely and may be compared to related moieties: the short C–C bond length of 141 pm of the formal ethyl cation in **III** may be compared to the BP86/SV(P)-optimized distances of the free ethyl cation (141.2 pm), free ethane (153.1 pm), and the base-stabilized ethyl cations D → $^+CH_2CH_3$ [D = OH_2, d(C–C) = 150.0 pm; D = OMe_2, d(C–C) = 150.7 pm]. The

 © 2005 Wiley-VCH Verlag GmbH & Co. KGaA, Weinheim

formal donor–acceptor C–O bonds in the D → $^{+}CH_2CH_3$ cations are 156.3 pm (H_2O) and 152.9 pm (OMe_2), in good agreement with our estimate of 153 pm in **III**. All other distances are normal. The data in Scheme 2 may not be taken as absolute, however, since libration has not been accounted for and the structures may be affected by a superposition of the asymmetric structures **III** (i.e. the site may partly be occupied as $Et_2O\cdots HO^{+}Et_2$ and partly as $Et_2O^{+}H\cdots OEt_2$; structure **C**, for example, appears to be afflicted by this type of disorder). However, the general trend of the completely asymmetric structural type **III** holds. Further evidence for this assumption comes from the solid state MAS NMR spectrum of **1**: two lines at δ = 71.1 and 71.7 ppm were observed for the OCH_2 groups of the diethyl ether molecules. This again points to an asymmetric coordination in the solid state and supports the formulation of structure **III**. Thus, it appears likely that forms **I** and **III** may be stable in the solid state and the final decision as to which isomer is formed is governed by subtle differences of the anion–cation contacts of the different salts in the solid state. Moreover, it is evident that the discussion of the nature of the short- strong- and low-barrier H-bonds in $[H(OEt_2)_2]^{+}$ may not be reduced to the question of a symmetrical (O···H···O) or asymmetrical (O–H···O) H-bond. If an asymmetrical H-bond is formed, this leads to a further rearrangement of the structure of the $[H(OEt_2)_2]^{+}$ cation, which may be described by the resonance structures **IIIa,b**.

Conclusions

A facile preparation of **1** and **2** as stable salts of the oxonium acids $[H(OEt_2)_2]^{+}$ and $[H(THF_2)_2]^{+}$ has been achieved. Both compounds were fully characterized by experimental and quantum chemical methods; they are strongly Brønsted acidic reagents. Due to the facile preparation, the commercial availability of $Li[Al(OR)_4]$, the good thermal solution stability (especially of **1**), and the weakly coordinating and chemically robust nature of the $[Al(OR)_4]^{-}$ counterion, **1** is an attractive reagent for synthesis, particularly in organometallic chemistry and homogeneous catalysis (for applications of $[H(OEt_2)_2]^{+}$ salts see ref.[4–11]). Interestingly, the solid-state structure of **1** includes an asymmetrically bridging H-atom; symmetric H-bridges have also previously been observed.[10] A symmetric H-bridge is also the minimum structure of the quantum chemical calculations. From an analysis of all published $[H(OEt_2)_2]^{+}$ structures we have shown that if an asymmetric H-bridge is formed, this leads to a further rearrangement of the structure and to the structural type **III** in Scheme 2, which is further supported by solid state MAS NMR spectroscopy. This point has hitherto been neglected in the discussion of the nature of short, strong, low-barrier H-bonds, although it should be taken into account. We conclude that the final decision as to the formation of a symmetrical or an unsymmetrical H-bridge is balanced by subtle differences between the anion–cation contacts of the salts in the solid state. Finally, we have been able to revise some erroneously assigned NMR shifts and give the most complete vibrational characterization of the $[H(OEt_2)_2]^{+}$ and $[H(THF)_2]^{+}$ cations currently available.

Experimental Section

General Procedures: Due to the air- and moisture-sensitivity of most materials all manipulations were undertaken using standard vacuum and Schlenk techniques as well as in a glove box with an argon atmosphere (H_2O and $O_2 < 1$ ppm). All solvents were dried by conventional drying agents and distilled afterwards. The solutions of HX (X = Cl, Br) in Et_2O and THF were prepared by condensing HX from a flask with known volume and pressure. Solution NMR spectra were recorded in CD_2Cl_2 at room temperature on a Bruker AC 250 spectrometer; data are given in ppm relative to the solvent signals, aqueous $AlCl_3$ (^{27}Al) and CF_3Cl (^{19}F). Solid-state NMR spectra were obtained with a Bruker Avance 500 MHz spectrometer. IR spectra were obtained in nujol mull between CsI plates on a Bruker IFS 66 IR spectrometer, Raman spectra were recorded on a Bruker RFS 100/S Raman spectrometer. The differential temperature analysis measurements were performed with a Netzsch STA 429 DSC/DTA unit. About 20 mg of **1** was used for the experiment; preparation of the measurement and weighing were done in a glove box. The DTA curves were recorded at a heating rate of 5 K min^{-1}.

Preparation of $[H(OEt_2)_2][Al\{OC(CF_3)_3\}_4]$ (1): a) $LiAl[OC(CF_3)_3]_4$ (20.02 g, 20.06 mmol) was weighed into a 1-L round-bottomed flask with a glass valve and suspended in a mixture of CH_2Cl_2 (approx. 500 mL) and Et_2O (6.4 mL, 61.7 mmol). The suspension was frozen in liquid nitrogen and HBr (1.746 g, 21.6 mmol) was condensed directly onto the mixture. This mixture was allowed to reach room temperature and stirred overnight; white colloidal LiBr was formed. The LiBr precipitate was filtered off to give a solution of **1** in CH_2Cl_2. After removing all volatiles in vacuo from the filtrate, pure **1** was isolated as a white powder (21.80 g, 94.8%). Larger crystals were obtained by recrystallization of the powder from a mixture of toluene and diethyl ether (10:1).

b) $LiAl[OC(CF_3)_3]_4$ (0.740 g, 0.76 mmol) was suspended in pure diethyl ether (approx. 30 mL) and gaseous HCl (0.030 g, 0.84 mmol) was condensed directly onto the frozen (77 K) mixture. All other manipulations were undertaken according to the description in part a). Yield: 0.766 g (87%). ^{1}H NMR (250 MHz): δ = 1.34 (t, $^{3}J_{H,H}$ = 7.138 Hz, 12 H), 3.90 (br., 8 H), 14.68 (br., 1 H) ppm. $^{13}C\{^{1}H\}$ NMR (63 MHz): δ = 13.8 (s), 69.3 (s), 121.5 (q, $^{1}J_{C,F}$ = 292.2 Hz) ppm. ^{19}F NMR (235 MHz): δ = –75.43 (s) ppm. ^{27}Al NMR (78 MHz): δ = 36 (s). IR (CsI plates, Nujol): $\tilde{\nu}$ = 206 (mw), 286 (mw), 314 (m), 375 (m), 447 (ms), 537 (m), 561 (m), 572 (mw), 727 (vs), 756 (m), 769 (mw), 832 (m), 907 (mw), 973 (vs), 1013 (m), 1063 (mw), 1166 (ms), 1219 (s), 1243 (s), 1276 (s), 1300 (s), 1353 (ms), 1366 (ms), 1377 (s), 1457 (vs), 1536 (mw) cm^{-1}.

Preparation of $[H(THF_2)_2][Al\{OC(CF_3)_3\}_4]$ (2): $LiAl[OC(CF_3)_3]_4$ (0.700 g, 0.719 mmol) was weighed into one side of a two-bulb, frit-plate flask with a glass stem that was closed with two greaseless Young valves, and suspended in CH_2Cl_2 (approx. 30 mL). On the opposite side, HBr (0.95 mL of a 0.834 M solution) dissolved in THF was added with a syringe through a septum. Cooling the suspension to –80 °C caused HBr and THF to condense onto the Li salt. The mixture was allowed to reach ambient temperature and stirred for 48 h to form white colloidal LiBr. After removing all volatiles under vacuum, a dark brown oily residue formed from which **2** precipitated as rhombus-shaped crystals in 65% yield. ^{1}H NMR (250 MHz): δ = 2.05 (m, 8 H), 3.95 (m, 8 H), ca. 8 (broad,

 © 2005 Wiley-VCH Verlag GmbH & Co. KGaA, Weinheim

1 H) ppm. $^{13}C\{^1H\}$ NMR (63 MHz): δ = 25.5 (CH_2), 70.6 (OCH_2), 121.5 (q, $^1J_{C,F}$ = 291.7 Hz) ppm. ^{27}Al NMR (78 MHz): δ = 36 (s) ppm. IR (CsI plates, Nujol): $\tilde{\nu}$ = 446 (ms), 537 (m), 561 (m), 571 (mw), 603 (ms), 727 (vs), 755 (m), 775 (m), 831 (m), 894 (w), 918 (w), 973 (vs), 1043 (w), 1167 (ms), 1220 (s), 1242 (s), 1276 (s), 1300 (s), 1353 (ms), 1365 (ms), 1376 (ms), 1448 (s), 1457 (s), 1626 (w), 2724 (w), 2853 (ms), 2921 (ms), 2957 (ms) cm^{-1}.

X-ray Structure Determination: Suitable crystals of **1** were formed by cooling a solution in toluene containing a small amount of diethyl ether to 5 °C. Crystals of **2** precipitated directly from the oily residue after removal of all volatiles. Data were collected on a Stoe IPDS II diffractometer using Mo-K_α radiation (λ = 0.71073 Å) at 150 K. Single crystals were mounted in perfluoro ether oil on top of a glass fiber and then placed in the cold stream of a low-temperature device so that the oil solidified. Unit-cell parameters were calculated from a least-squares refinement of the setting angles of 5000 reflections collected. The space groups were identified as $P2_1$ (**1**) and $P2_1/c$ (**2**). The structures were solved with the SIR2002 program[27] (**1**) or direct methods in SHELXS[28] (**2**) and successive interpretation of the difference Fourier maps using SHELXL-97. Refinement against F^2 was carried out with SHELXL-97. All non-hydrogen atoms were included anisotropically in the refinement; all hydrogen atoms except the acidic proton in **1** were included isotropically at the calculated positions based on a riding model. The acidic proton in **1** was located in the difference Fourier map and included isotropically in the refinement. The lattice parameters of **1** are very close to being tetragonal (approx. 9, 14, 14 Å; 90, 90, 90°; V = 1950 $Å^3$); in fact, the $[PX_4][Al(OR^F)_4]$ salts (X = Br, I)[17b] crystallize with a very similar truly tetragonal cell (approx. 9, 13.5, 13.5 Å; 90, 90, 90°; V = 1850 $Å^3$; X = I). In the latter structures the Al and P atoms reside on special positions with $\bar{4}$ site symmetry and Z = 2. When a cation with lower symmetry but similar size crystallizes with the symmetric $[Al(OR^F)_4]^-$ anion and the lattice parameters are almost the same, this necessarily leads to twinning, as previously observed when exchanging PX_4^+ for $P_2X_5^+$.[17b] In the case of **1** the $[H(OEt_2)_2]^+$ cation also has less symmetry than PX_4^+, which implies that the symmetry had to be reduced to at least monoclinic. We were able to solve the structure in the space group $P2_1$ and finally solved the twin law (i.e.: TWIN 0 0 1 0 1 0 1 0 0 with BASF 0.43362) that lowered the R_1 value immediately from 15.6% to 4.8%. Relevant data concerning crystallographic data, data collection and refinement details are compiled in Table 7.
CCDC-239426 (for **1**) and -239427 (for **2**) contain the supplementary crystallographic data for this paper. These data can be obtained free of charge from The Cambridge Crystallographic Data Centre via www.ccdc.cam.ac.uk/data_request/cif.

Computational Details: All quantum chemical calculations were carried out with the TURBOMOLE program package.[29] The geometries of $[H(OEt_2)_2]^+$ and $[H(THF_2)_2]^+$ were optimized in C_1 symmetry by DFT calculations using the BP86/SV(P)[30] or BP86/TZVPP[31] basis sets, as well as RI-MP2 methods using the TZVPP basis set.[32] Vibrational frequencies were calculated at the BP86/SV(P) level and used to verify the nature of the obtained minima.[33]

For the estimation of the reaction enthalpies of the formation of compounds **1** and **2**, the oxonium acids as well as a Li cation coordinated by two diethyl ether molecules were calculated by using the same procedure as above. The resulting reaction (2) is isodesmic and inaccuracies arising during the calculation are minimized due to error cancellation. The calculated enthalpies were also corrected for the influences of the Gibbs energy at 298 K (with the semi-empirical PM3 method implemented in Gaussian 98)[34] as well as solvent effects (COSMO model, CH_2Cl_2 solvent with ε_r = 8.93).[35]

Supporting Information: Simulation of IR spectra based on calculations of vibrational frequencies, Raman spectra, IR spectra (200–700 cm^{-1}), tables of optimized atomic coordinates from density functional calculations, tables for the extracted average structural parameters of **I** and **III** in Scheme 2.

Table 7. Summary of crystallographic data collection for **1** and **2**.

	1	**2**
Formula	$C_{24}H_{21}AlF_{36}O_6$	$C_{24}H_{16}AlF_{36}O_6$
Temperature [K]	150	150
Crystal system	monoclinic	monoclinic
Space group	$P2_1$	$P2_1/c$
a [pm]	1405.4	965.39(19)
b [pm]	987.6	1676.3(3)
c [pm]	1406.5	2322.2(5)
β [°]	90.06	98.92(3)
Volume [nm^3]	1.9522	3.7126(13)
Z	2	4
$D_{calcd.}$ [$Mg\,m^{-3}$]	1.899	1.988
Absorption coefficient [mm^{-1}]	0.263	0.276
F(000)	1100	2180
Crystal size [mm^3]	0.8 × 0.5 × 1.0	0.3 × 0.3 × 0.4
θ range for data collection [°]	6.81 to 21.96	6.84 to 24.71
Index ranges	$-14 \le h \le 14$ $-10 \le k \le 10$ $-14 \le l \le 14$	$-11 \le h \le 11$ $-19 \le k \le 12$ $-27 \le l \le 21$
Reflections collected	10 013	11 548
Independent reflections	4620 [R(int.) = 0.0471]	5245 [R(int.) = 0.0950]
Data/restraints/parameters	4620/1/607	5245/93/606
Goodness-of-fit on F^2	1.039	1.095
Final R indices [$I > 2\sigma(I)$]	R_1 = 0.0482, wR_2 = 0.1197	R_1 = 0.1147, wR_2 = 0.2939
R indices (all data)	R_1 = 0.0513, wR_2 = 0.1227	R_1 = 0.1732, wR_2 = 0.3311
Largest diff. peak and hole [$e\,Å^{-3}$]	0.214 and –0.217	0.684 and –0.504

 © 2005 Wiley-VCH Verlag GmbH & Co. KGaA, Weinheim

Acknowledgments

This work was supported by the Deutsche Forschungsgemeinschaft and the Fonds der Chemischen Industrie. We would like to thank Dr. J. Sawatzki of the Bruker demonstration lab for recording the Raman spectrum and Dr. R Witter and Prof. A. Ulrich for recording the MAS NMR spectra. We are grateful to Prof. H. Schnöckel for many useful discussions.

[1] G. A. Olah, A. M. White, D. H. O'Brien, *Chem. Rev.* **1970**, *70*, 561.
[2] S. P. Kolesnikov, I. V. Luyudkovskaya, M. Y. Antipin, Y. T. Strutchkov, O. M. Nefedov, *Bull. Acad. Sci. USSR Div. Chem. Sci. (Engl. Transl.)* **1985**, *34*, 74.
[3] For recent reviews see:a) C. Reed, *Acc. Chem. Res.* **1998**, *31*, 133; b) S. H. Strauss, *Chem. Rev.* **1993**, *93*, 927; c) I. Krossing, I. Raabe, *Angew. Chem.* **2004**, *116*, 2116; d) E. Y.-X. Chen, T. J. Marks, *Chem. Rev.* **2000**, *100*, 1391.
[4] P. Jutzi, C. Müller, A. Stammler, H.-G. Stammler, *Organometallics* **2000**, *19*, 1442.
[5] R. Taube, S. Wache, *J. Organomet. Chem.* **1992**, *428*, 431.
[6] M. Brookhart, B. Grant, A. F. Volpe Jr., *Organometallics* **1992**, *11*, 3920.
[7] D. Stasko, S. P. Hoffmann, K. C. Kim, N. L. Fackler, A. S. Larsen, T. Drovetskaya, F. S. Tham, C. A. Reed, C. E. Rickard, P. D. Boyd, E. S. Stoyanov, *J. Am. Chem. Soc.* **2002**, *124*, 13 869.
[8] D. Vagedes, G. Erker, R. Fröhlich, *J. Organomet. Chem.* **2002**, *641*, 148.
[9] S. J. Lancaster, A. Rodriguez, A. Lara-Sanchez, M. D. Hannant, D. A. Walker, D. H. Hughes, M. Bochmann, *Organometallics* **2002**, *21*, 451.
[10] L. D. Henderson, W. E. Piers, G. J. Irvine, R. McDonald, *Organometallics* **2002**, *21*, 340.
[11] a) L. H. Shultz, M. Brookhart, *Organometallics* **2001**, *20*, 3975; b) L. K. Johnson, C. M. Killian, M. Brookhart, *J. Am. Chem. Soc.* **1995**, *117*, 6414; c) J. Cámpora, J. A. López, P. Palma, P. Valerga, E. Spillner, E. Carmona, *Angew. Chem.* **1999**, *111*, 199; *Angew. Chem. Int. Ed.* **1999**, *38*, 147; d) G. Kehr, R. Roesmann, R. Fröhlich, C. Holst, G. Erker, *Eur. J. Inorg. Chem.* **2001**, 535; e) D. A. Walker, T. J. Woodman, D. L. Hughes, M. Bochmann, *Organometallics* **2001**, *20*, 3772.
[12] I. Krossing, *Chem. Eur. J.* **2001**, *7*, 490.
[13] S. M. Ivanova, B. G. Nolan, Y. Kobayashi, S. M. Miller, O. P. Anderson, S. H. Strauss, *Chem. Eur. J.* **2001**, *7*, 503.
[14] a) I. Krossing, *J. Am. Chem. Soc.* **2001**, *123*, 4603; b) I. Krossing, L. van Wüllen, *Chem. Eur. J.* **2002**, *8*, 700.
[15] T. S. Cameron, A. Decken, I. Dionne, M. Fang, I. Krossing, J. Passmore, *Chem. Eur. J.* **2002**, *8*, 3386.
[16] I. Krossing, *J. Chem. Soc., Dalton Trans.* **2002**, 500.
[17] a) I. Krossing, I. Raabe, *Angew. Chem.* **2001**, *113*, 4544; *Angew. Chem. Int. Ed.***2001**, *40*, 4406; b) M. Gonsior, I. Krossing, L. Müller, I. Raabe, M. Jansen, L. van Wüllen, *Chem. Eur. J.* **2002**, *8*, 4475.
[18] M. Gonsior, I. Krossing, manuscript submitted to *Chem. Eur. J.*
[19] I. Krossing, A. Bihlmeier, I. Raabe, N. Trapp, *Angew. Chem.* **2003**, *115*, 1569–1572; *Angew. Chem. Int. Ed.* **2003**, *42*, 1531.
[20] M. Gonsior, I. Krossing, N. Mitzel, *Z. Anorg. Allg. Chem.* **2002**, *628*, 1821.
[21] I. Krossing, H. Brands, R. Feuerhake, S. Koenig, *J. Fluorine Chem.* **2001**, *112*, 83.
[22] M. Gonsior, I. Krossing, I. Raabe, manuscript in preparation.
[23] Some representative examples: a) C. L. Perrin, *Science* **1994**, *266*, 1665; b) M. E. Tuckerman, D. Marx, M. L. Klein, M. Parinello, *Science* **1997**, *275*, 817; c) J.-C. Jiang, Y.-S. Wang, H.-C. Chang, S. H. Lin, Y. T. Lee, G. Niedner-Schatteburg, H.-C. Chang, *J. Am. Chem. Soc.* **2000**, *122*, 1398; d) G. A. Kumar, M. A. McAllister, *J. Am. Chem. Soc.* **1998**, *120*, 3159.
[24] M. Hesse, H. Meier, B. Zeeh, S*pektroskopische Methoden in der organischen Chemie*, 4th ed., Georg Thieme Verlag, Stuttgart, New York, **1991**.
[25] http://webbook.nist.gov/chemistry.
[26] D. André, R. Fourme, K. Zechmeister, *Acta Crystallogr., Sect. B* **1972**, *28*, 2389.
[27] Sir**2002**.
[28] G. Sheldrick, SHELX software suite, University of Göttingen, Germany.
[29] a) R. Ahlrichs, M. Bär, M. Häser, H. Horn, C. Kölmel, *Chem. Phys. Lett.* **1989**, *162*, 165; b) M. v. Arnim, R. Ahlrichs, *J. Chem. Phys.* **1999**, *111*, 9183.
[30] a) A. D. Becke, *Phys. Rev. A* **1988**, *38*, 3098; b) J. P. Perdew, *Phys. Rev. B* **1986**, *33*, 8822.
[31] K. Eichkorn, F. Weigend, O. Treutler, R. Ahlrichs, *Theor. Chem. Acc.* **1997**, *97*, 119.
[32] a) F. Weigend, M. Häser, *Theor. Chem. Acc.* **1997**, *97*, 331; b) F. Weigend, M. Häser, H. Patzelt, R. Ahlrichs, *Chem. Phys. Lett.* **1998**, *294*, 143.
[33] P. Deglmann, F. Furche, R. Ahlrichs, *Chem. Phys. Lett.* **2002**, *362*, 511.
[34] Gaussian 98, Revision A.11, M. J. Frisch, G. W. Trucks, H. B. Schlegel, G. E. Scuseria, M. A. Robb, J. R. Cheeseman, V. G. Zakrzewski, J. A. Montgomery, Jr., R. E. Stratmann, J. C. Burant, S. Dapprich, J. M. Millam, A. D. Daniels, K. N. Kudin, M. C. Strain, O. Farkas, J. Tomasi, V. Barone, M. Cossi, R. Cammi, B. Mennucci, C. Pomelli, C. Adamo, S. Clifford, J. Ochterski, G. A. Petersson, P. Y. Ayala, Q. Cui, K. Morokuma, P. Salvador, J. J. Dannenberg, D. K. Malick, A. D. Rabuck, K. Raghavachari, J. B. Foresman, J. Cioslowski, J. V. Ortiz, A. G. Baboul, B. B. Stefanov, G. Liu, A. Liashenko, P. Piskorz, I. Komaromi, R. Gomperts, R. L. Martin, D. J. Fox, T. Keith, M. A. Al-Laham, C. Y. Peng, A. Nanayakkara, M. Challacombe, P. M. W. Gill, B. Johnson, W. Chen, M. W. Wong, J. L. Andres, C. Gonzalez, M. Head-Gordon, E. S. Replogle, and J. A. Pople, Gaussian, Inc., Pittsburgh PA, **2001**.
[35] a) A. Klamt, G. Schürmann, *J. Chem. Soc., Perkin Trans. 2* **1993**, 799; b) A. Schäfer, A. Klamt, D. Sattel, J. Lohrenz, F. Eckert, *Phys. Chem. Chem. Phys.* **2000**, *2*, 2187.

Received: May 25, 2004

 © 2005 Wiley-VCH Verlag GmbH & Co. KGaA, Weinheim

Low-Valent Titanium−Pentafulvene Complexes − Formation of Dinuclear Titanium−Nitrogen Complexes

Axel Scherer,[a] Kay Kollak,[a] Arne Lützen,[a] Marion Friedemann,[a] Detlev Haase,[a] Wolfgang Saak,[a] and Rüdiger Beckhaus*[a]

Keywords: Titanium / Bridging ligands / Nitrogen / Metallocenes / Fulvene ligands

In a late stage of production Equation (2) on p. 1006 of the print version[1] was inadvertently replaced by a copy of Equation (3); the electronic version is free of this error. The correct Equation (2) is shown below.

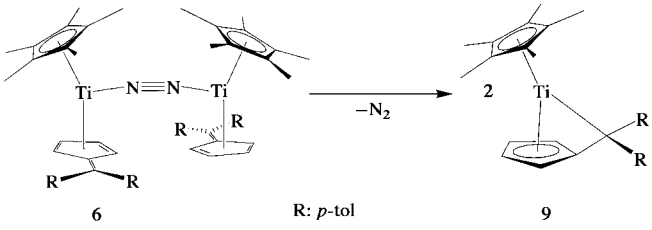

(2)

[1] A. Scherer, K. Kollak, A. Lützen, M. Friedemann, D. Haase, W. Saak, R. Beckhaus, *Eur. J. Inorg. Chem.* **2005**, 1003−1010.

The Editors

[a] Institut für Reine und Angewandte Chemie, Fakultät für Mathematik und Naturwissenschaften, Carl von Ossietzky Universität Oldenburg,
Postfach 2503, 26111 Oldenburg, Germany
Fax: +49-441-798-3581
E-mail: ruediger.beckhaus@uni-oldenburg.de

 DOI: 10.1002/ejic.200500269 © 2005 Wiley-VCH Verlag GmbH & Co. KGaA, Weinheim

EurJIC
European Journal of Inorganic Chemistry

Issue 11/2005

Pages 1997–2264

Papers available ahead of print in Early View at www.interscience.wiley.com

Earliest available Table of Contents:
Automatically, free of charge by e-mail through
www.interscience.wiley.com/alerts

COVER PICTURE

The cover picture shows the reaction of a calix[4]arene methyl ether stabilized nitridomolybdenum complex [MoN(MeCalix)] with $GaCl_3$ to yield the compound [Mo(NGaCl_3)(MeCalix)]. This complex represents the first structurally characterized example of a nitrido-bridged dinuclear compound of a group 6 metal and a group 13 halide [EX_3]. Both metal atoms are unsymmetrically bridged with a short [Mo≡N] and a long [Ga–N] contact. Details on synthesis and structural characterization are discussed in the article by U. Radius et al. on p. 2037ff. In the background there is a view from the University of Karlsruhe (TH) to the adjacent "Hardtwald" on a stormy day photographed by Bernhard Mühr (www.wolkenatlas.de).

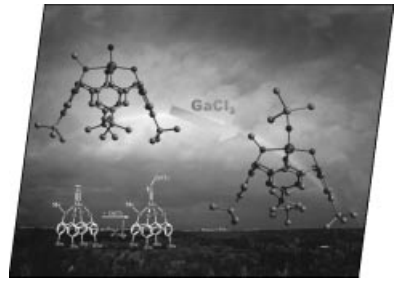

MICROREVIEW

Contents

2015 **J. D. Crowley, B. Bosnich***

Molecular Recognition. Use of Metal-Containing Molecular Clefts for Supramolecular Self-Assembly and Host–Guest Formation

Keywords: Supramolecular / Self-assembly / Host–guest adducts / Molecular cleft receptors / Molecular recognition forces

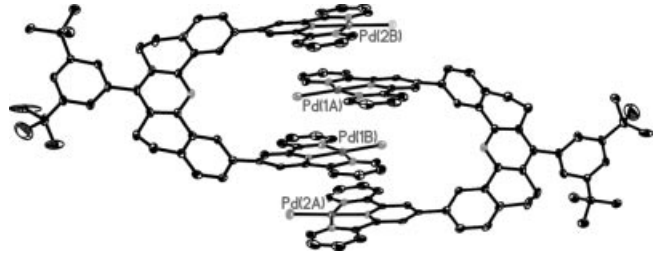

 © 2005 Wiley-VCH Verlag GmbH & Co. KGaA, Weinheim

SHORT COMMUNICATIONS

2027 **G. Giambastiani, W. Oberhauser, C. Bianchini, F. Laschi, L. Sorace, P. Brueggeller, R. Gutmann, A. Orlandini, F. Vizza***

Synthesis and Characterisation of a Novel Copper(II) Azamacrocycle-Phosphonate 3D Polymeric Network

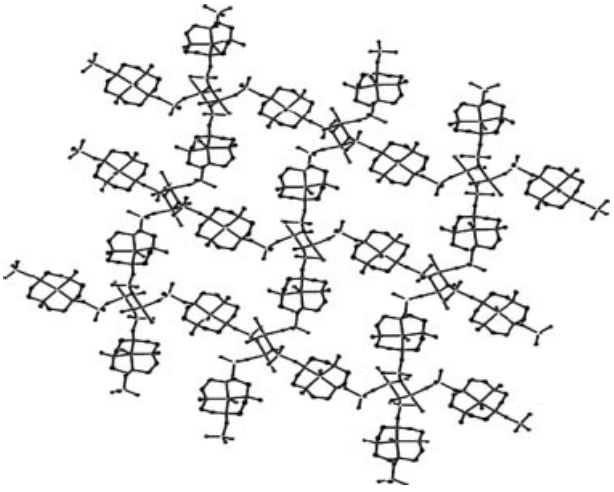

Keywords: Copper / Azamacrocycles / Coordination polymers / Macrocyclic ligands

2032 **S. Nica, A. Pohlmann, W. Plass***

Vanadium(V) Oxoperoxo Complexes with Side Chain Substituted *N*-Salicylidenehydrazides: Modeling Supramolecular Interactions in Vanadium Haloperoxidases

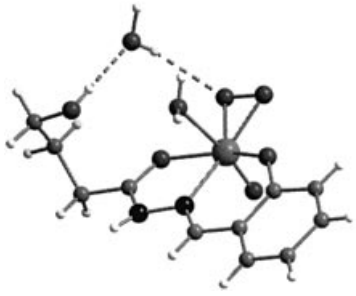

Keywords: Hydrogen bonds / Oxidative bromination / Peroxo ligands / Salicylidenehydrazide ligand / Vanadium

FULL PAPERS

2037 **J. Zeller, S. Büschel, B. K. H. Reiser, F. Begum, U. Radius***

Synthesis, Molecular Structure and Reactivity of a Calix[4]arene Monomethyl Ether Supported Nitridomolybdenum Complex

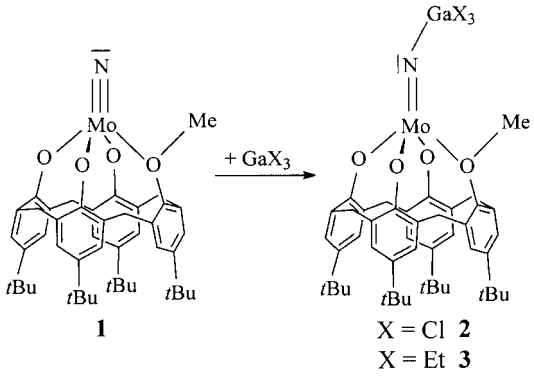

1

X = Cl **2**
X = Et **3**

Keywords: Calixarenes / Density functional calculations / Gallium / Molybdenum / Nitrides

2044 **C. Anda, A. Bencini, E. Berni, S. Ciattini, F. Chuburu, A. Danesi, C. Giorgi,* H. Handel,* M. Le Baccon, P. Paoletti,* R. Tripier, V. Turcry, B. Valtancoli**

Mono- and Dinuclear Cu^{II} and Zn^{II} Complexes of Cyclen-Based Bis(macrocycles) Containing Two Aminoalkyl Pendant Arms of Different Lengths

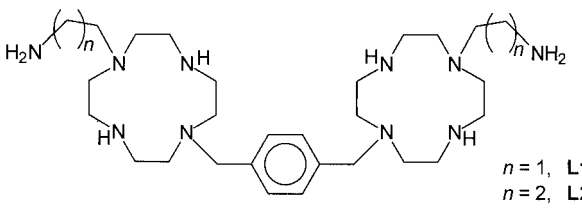

n = 1, **L1**
n = 2, **L2**
n = 3, **L3**

Keywords: Copper / Coordination modes / Macrocyclic ligands / N ligands / Zinc

© 2005 Wiley-VCH Verlag GmbH & Co. KGaA, Weinheim

2054 **Y. Xu, D. Yuan, L. Han, E. Ma, M. Wu, Z. Lin, M. Hong***

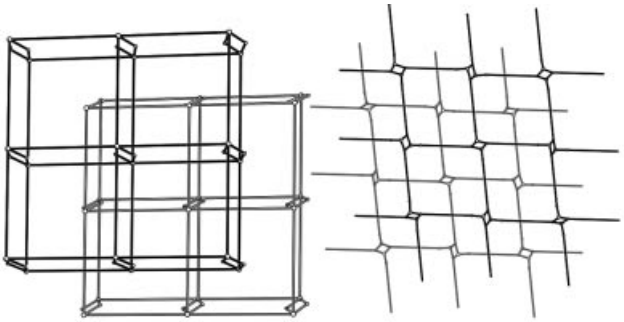

Mono- and Bilayered Lead(II)−bpno Polymers with Unusual Low Energy Emission Properties (bpno = 4,4′-Bipyridine *N*,*N*′-Dioxide)

Keywords: Lead complexes / 4,4′-Bipyridine *N*,*N*′-dioxide / Coordination polymers / Phosphorescence

2060 **G. Li,* S. Pang, Z. Wang, H. Peng, Z. Zhang***

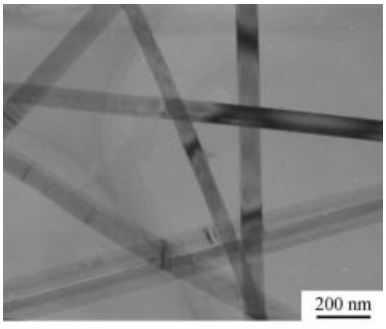

TEM image of $H_2V_3O_8$ nanobelts synthesized at pH 4

Synthesis of $H_2V_3O_8$ Single-Crystal Nanobelts

Keywords: Vanadium / Layered compounds / Nanobelts / Nanostructures

2064 **E. Coronado,* J. R. Galán-Mascarós,* C. J. Gómez-García, E. Martínez-Ferrero, M. Almeida, J. C. Waerenborgh**

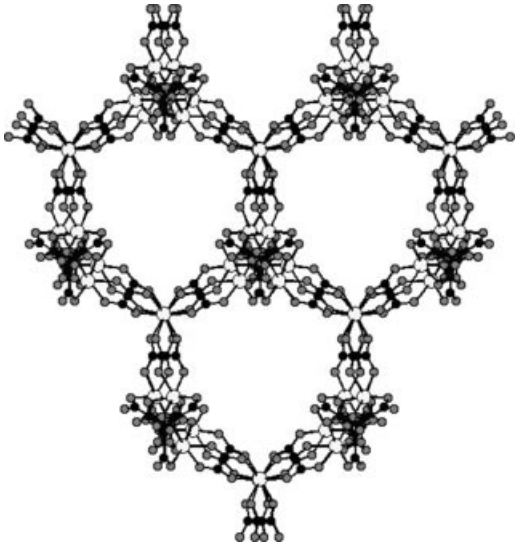

Oxalate-Based 3D Chiral Magnets: The Series $[Z^{II}(bpy)_3][ClO_4][M^{II}Fe^{III}(ox)_3]$ (Z^{II} = Fe, Ru; M^{II} = Mn, Fe; bpy = 2,2′-Bipyridine; ox = Oxalate Dianion)

Keywords: Coordination chemistry / Molecular materials / Magnetic properties / Mössbauer spectroscopy

 © 2005 Wiley-VCH Verlag GmbH & Co. KGaA, Weinheim

2071 **A. M. Kirillov, M. Haukka, M. F. C. Guedes da Silva, A. J. L Pombeiro***

Preparation and Crystal Structures of Benzoylhydrazido- and -diazenidorhenium Complexes with N,O-Ligands and Their Catalytic Activity Towards Peroxidative Oxidation of Cycloalkanes

Keywords: Alkanes / Homogeneous catalysis / N,O ligands / Oxidation / Rhenium

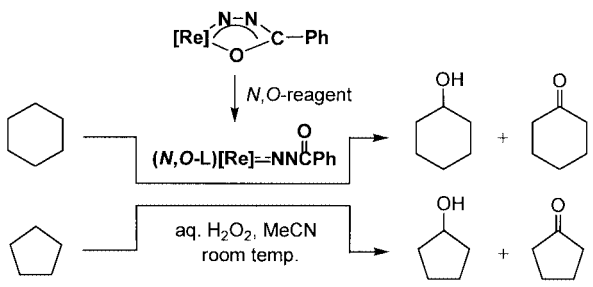

2081 **H. M. El-Kaderi, M. J. Heeg, C. H. Winter***

Synthesis, Structure, and Ligand Redistribution Equilibria of Mixed Ligand Complexes of the Heavier Group 2 Elements Containing Pyrazolato and β-Diketiminato Ligands

Keywords: N ligands / Group 2 elements / Calcium / Strontium / Barium

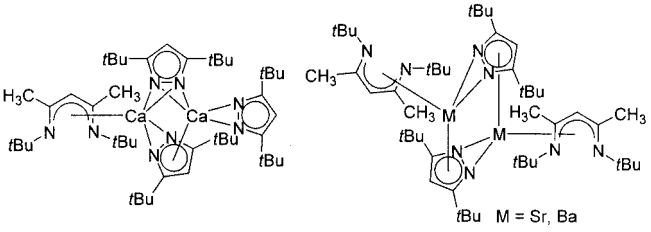

2089 **C. A. Nijhuis, E. Jellema, T. J. J Sciarone, A. Meetsma, P. H. M Budzelaar, B. Hessen***

First-Row Transition Metal Bis(amidinate) Complexes; Planar Four-Coordination of Fe^{II} Enforced by Sterically Demanding Aryl Substituents

Keywords: Transition metals / Solid-state structures / Ligand effects / Amidinate / Density functional calculations

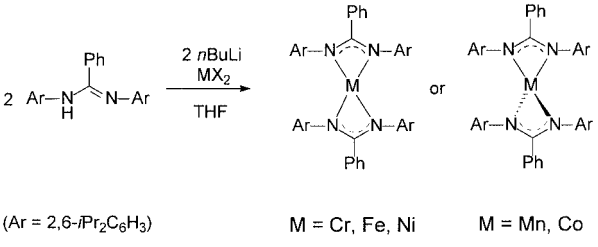

2100 **A. Pärssinen, T. Luhtanen, M. Klinga, T. Pakkanen, M. Leskelä, T. Repo***

Bis(salicylaldiminato)titanium Complexes Containing Bulky Imine Substituents: Synthesis, Characterization and Ethene Polymerization Studies

Keywords: Titanium / Polymerization / Homogeneous catalysis / Molecular modeling / N,O ligands

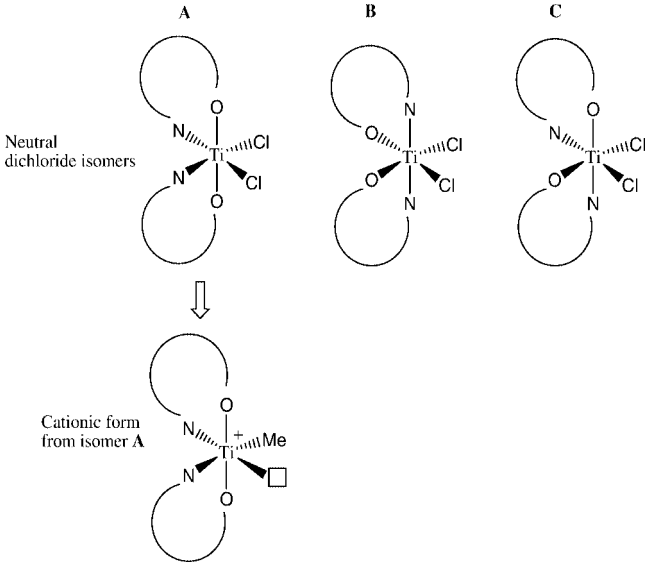

 © 2005 Wiley-VCH Verlag GmbH & Co. KGaA, Weinheim

2110 **P. Baía, J. P. André,* C. G. C. Geraldes, J. A. Martins,* A. E. Merbach, É. Tóth**

Lanthanide(III) Chelates of DTPA Bis(amide) Glycoconjugates: Potential Imaging Agents Targeted at the Asyaloglycoprotein Receptor

Keywords: Chelates / Contrast agents / Lanthanides / Glycoconjugates / Receptors

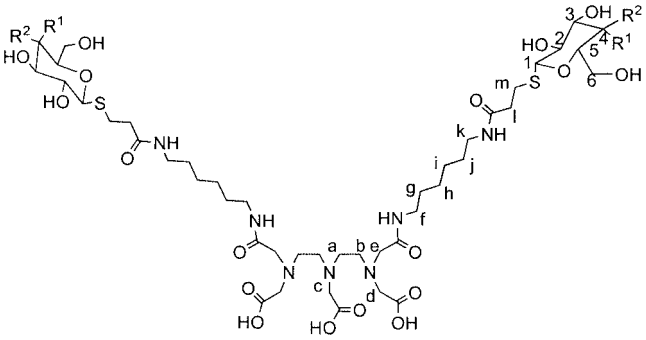

2120 **A. Schnepf***

On the Redox Chemistry of Ge^{I} Bromide

Keywords: Cage compounds / DFT calculations / Germanium / Redox reactions

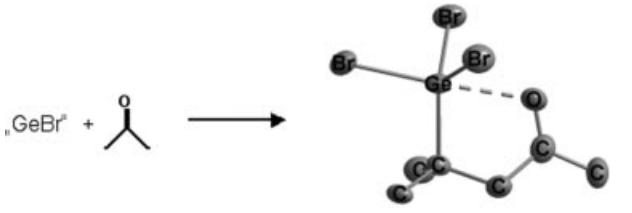

2124 **O. Kirilenko, F. Girgsdies, R. E. Jentoft, T. Ressler***

In Situ XAS and XRD Studies on the Structural Evolution of Ammonium Paratungstate During Thermal Decomposition

Keywords: X-ray diffraction / Tungsten / Oxidation / Decomposition / Structure−activity relationships / Heterogeneous catalysis

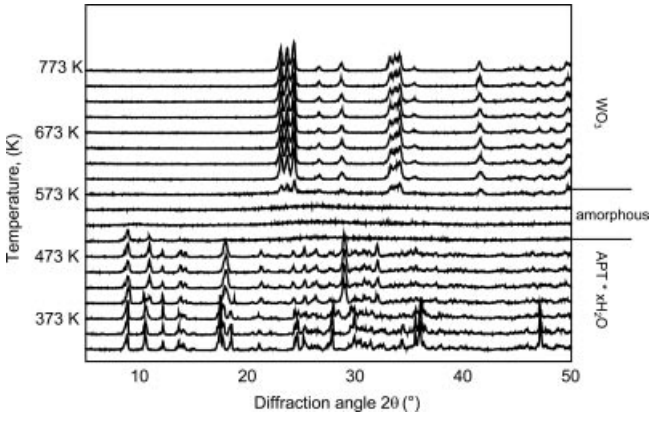

2134 **R. H. R. Castro,* P. Hidalgo, J. A. H. Coaquira, J. Bettini, D. Zanchet, D. Gouvêa**

Surface Segregation in $SnO_2-Fe_2O_3$ Nanopowders and Effects in Mössbauer Spectroscopy

Keywords: Materials science / Nanostructures / Semiconductors / Electron microscopy / Moessbauer spectroscopy

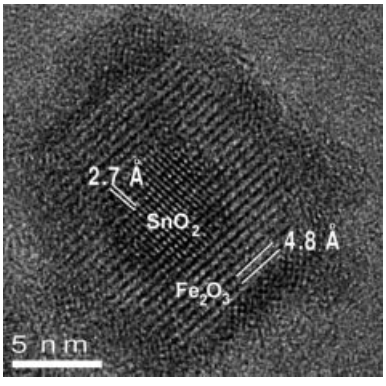

 © 2005 Wiley-VCH Verlag GmbH & Co. KGaA, Weinheim

2139 **M. N. Sokolov*, E. V. Chubarova, R. Hernandez-Molina, M. Clausén, D. Y. Naumov, C. Vicent, R. Llusar, V. P. Fedin**

A New Series of Homologous Cluster Complexes $[Mo_3(M'EPh_3)Q_4Cl_4(H_2O)_5]$ (M′ = Ni, Pd; E = P, As, Sb; Q = S, Se)

Keywords: Molybdenum / Nickel / Palladium / Chalcogenide clusters / Triphenylphosphane and analogs

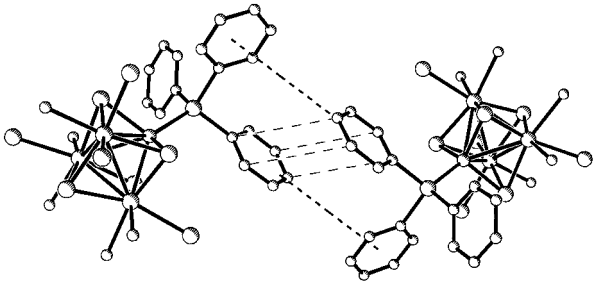

2147 **H. Zhu, J. Chai, H. Fan, H. W. Roesky,* U. N. Nehete, H.-G. Schmidt**

A Rearrangement of Azobenzene upon Interaction with an Aluminum(I) Monomer LAl {L = $HC[(CMe)(NAr)]_2$, Ar = 2,6-iPr$_2$C$_6$H$_3$}

Keywords: Aluminum / Azobenzene / N ligands / Rearrangement

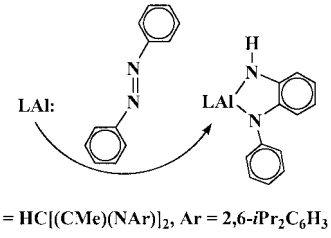

2151 **R. Pietschnig,* S. Spirk, F. Belaj, K. Merz**

Synthesis and Structure of a 2,4-Unsubstituted *cis*/*trans*-1,3-Disilacyclobutane by Dehydrofluorination of a Highly Hindered Fluorosilane

Keywords: Dimerization / Silanes / Silenes / Silicon / Strained molecules

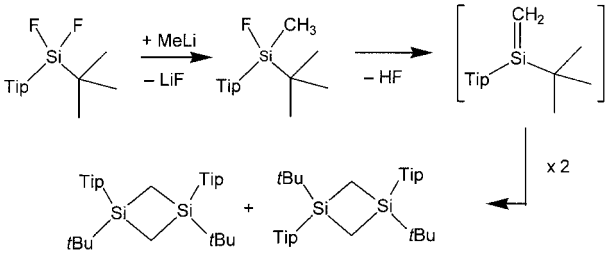

2156 **P. Mahata, S. Natarajan***

Pyridine- and Imidazoledicarboxylates of Zinc: Hydrothermal Synthesis, Structure, and Properties

Keywords: Luminescence / N ligands / Pi interactions / Zinc

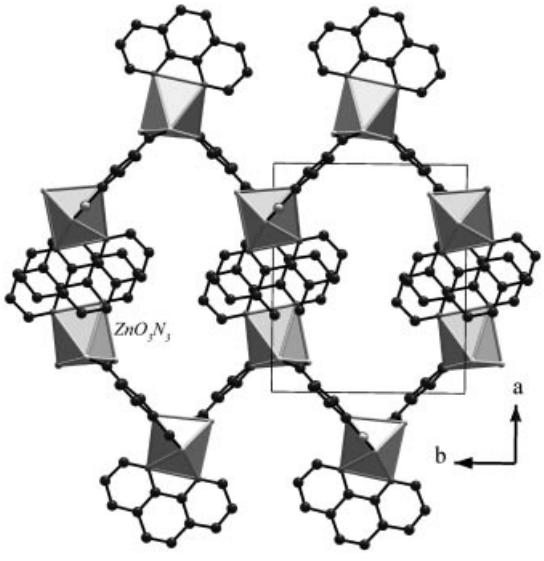

 © 2005 Wiley-VCH Verlag GmbH & Co. KGaA, Weinheim

2164 M. Mariappan,* B. G. Maiya

Effects of Anthracene and Pyrene Units on the Interactions of Novel Polypyridylruthenium(II) Mixed-Ligand Complexes with DNA

Keywords: DNA cleavage / Electrophoresis / Inhibitors / N ligands / Radicals / Ruthenium

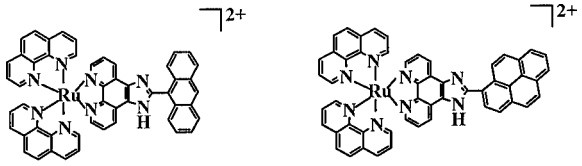

$[Ru(phen)_2(aip)]^{2+}$ $[Ru(phen)_2(pyip)]^{2+}$

2174 J. Yang, J.-F. Ma,* Y.-Y. Liu, S.-L. Li, G.-L. Zheng

Four Novel 3D Copper(II) Coordination Polymers with Different Topologies

Keywords: Coordination polymers / Copper / Self-assembly / Supramolecular chemistry / Topology

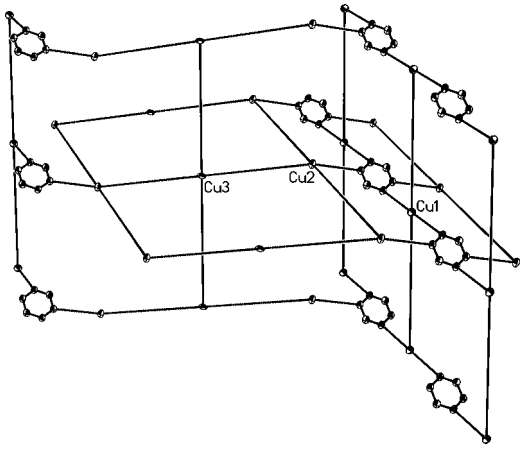

2181 X. He, C.-Z. Lu,* D.-Q. Yuan, S.-M. Chen, J.-T. Chen

Synthesis and Crystal Structures of Four Cyanide-Bridged Coordination Polymers

Keywords: Bridging ligands / Coordination polymers / Copper / Cyanides / Heterometallic complexes

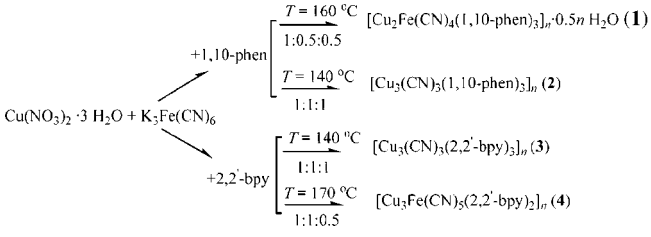

2189 N. Heße, R. Fröhlich, I. Humelnicu, E.-U. Würthwein*

1,3,5-Triazapentadienes as Chelating Ligands: 1,2,4-Triphenyl-1,3,5-triazapentadiene Complexes of Cobalt(II), Nickel(II), Palladium(II), Copper(II) and Zinc(II)

Keywords: Chelates / Ligand design / Triazapentadienes / N ligands / Tautomerism / DFT calculations

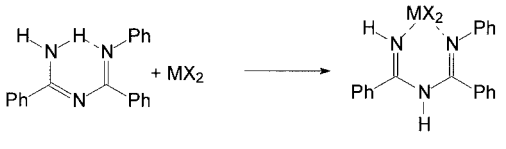

M = Co, Ni, Pd, Cu, Zn X = Cl, NO_3, OTf

 © 2005 Wiley-VCH Verlag GmbH & Co. KGaA, Weinheim

2198 **S. Eringathodi, P. Agnihotri, B. Ganguly, P. Bhatt, P. Sivagnana Subramanian, P. Paul,* P. K. Ghosh***

Towards Understanding of the Selective Precipitation of Alkali Metal Cations in Presence of Dipicrylamine Anion

Keywords: Dipicrylamine / Alkali and alkaline earth metals / Selectivity / Single-crystal X-ray structure / Structure-selectivity correlation

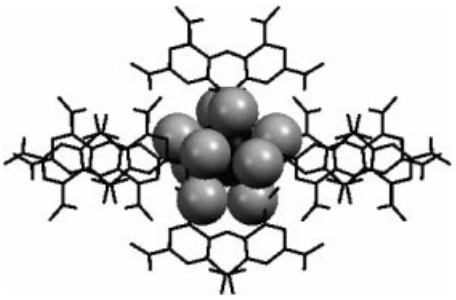

2206 **F. W. Vergeer, M. Lutz, A. L. Spek, M. J. Calhorda, D. J. Stufkens, F. Hartl***

Heterosite Effects in Novel Heteronuclear Clusters $[Os_2Ru(CO)_{11}(PPh_3)]$ and $[Os_2Ru(CO)_{10}$-(2-acetylpyridine-*N*-isopropylimine)]

Keywords: Cluster compounds / Density functional calculations / Time-resolved spectroscopy / Photochemistry / Spectroelectrochemistry

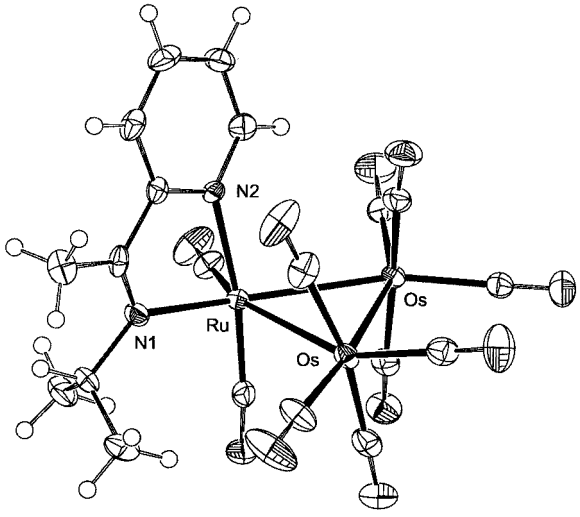

2223 **M. Gressenbuch, V. Lozan, G. Steinfeld, B. Kersting***

Preparation and Characterization of Co^{II}, Ni^{II}, and Zn^{II} Complexes of Sterically Demanding Hexaazamacrocyclic Dithiophenolates

Keywords: Binding pockets / Macrocyclic ligands / Cobalt / Nickel / Zinc

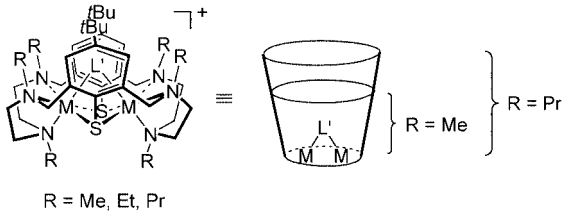

2235 **X.-B. Zhang, D.-Z. Sun, W.-Y. Yin, Y.-J. Chai, M.-S. Zhao***

Crystallographic and Electrochemical Characteristics of $La_{0.7}Mg_{0.3}Ni_{4.5-x}(Al_{0.5}Mo_{0.5})_x$ (x = 0−0.8) Hydrogen Storage Alloys

Keywords: High-rate dischargeability / Low-temperature dischargeability / Exchange current density / Hydrogen diffusion coefficient / Alloys / X-ray diffraction

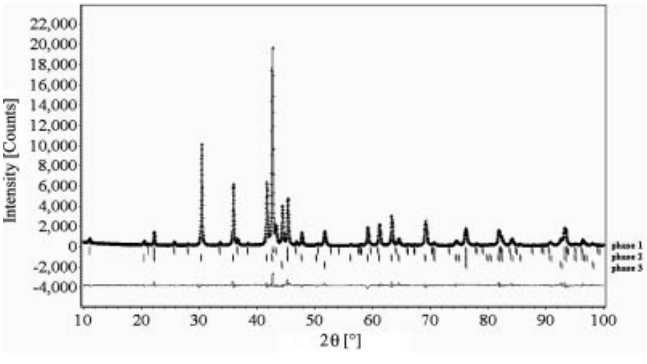

 © 2005 Wiley-VCH Verlag GmbH & Co. KGaA, Weinheim

2242 **A. Rodríguez, A. Sousa-Pedrares, J. A. García-Vázquez, J. Romero, A. Sousa***

Electrochemical Synthesis and Structural Characterisation of Cadmium and Mercury Complexes Containing Pyrimidine-2-thionate Ligands

Keywords: Cadmium / Electrochemistry / Heterocycles / Mercury / S ligands

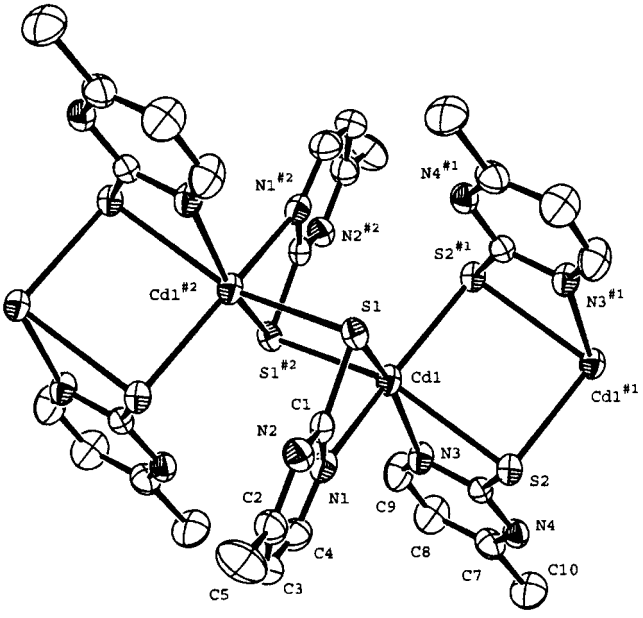

2255 **R. van Gorkum, F. Buda, H. Kooijman, A. L. Spek, E. Bouwman,* J. Reedijk**

Trigonal-Prismatic vs. Octahedral Geometry for Mn^{II} Complexes with Innocent Didentate Ligands: A Subtle Difference as Shown by XRD and DFT on $[Mn(acac)_2(bpy)]$

Keywords: Trigonal prism / Distorted octahedron / Density Functional Theory (DFT) / Manganese(II) / Packing effects

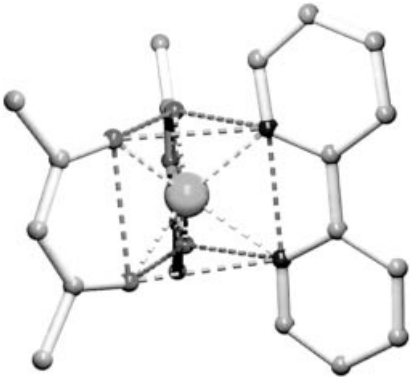

CORRECTION

2262 **S. Steinhauser, U. Heinz, M. Bartholomä, T. Weyhermüller, H. Nick, K. Hegetschweiler***

Complex Formation of ICL670 and Related Ligands with Fe^{III} and Fe^{II}

Keywords: Iron / Ligand design / Chelates / N,O ligands / Redox chemistry

 © 2005 Wiley-VCH Verlag GmbH & Co. KGaA, Weinheim

Molecular Recognition: Use of Metal-Containing Molecular Clefts for Supramolecular Self-Assembly and Host–Guest Formation

James D. Crowley[a] and Brice Bosnich*[a]

Keywords: Supramolecular / Self-assembly / Host–guest adducts / Molecular cleft receptors / Molecular recognition forces

Molecular clefts consisting of a rigid spacer linked to two parallel cofacially disposed terpy-M–X (M = Pd^{2+}, Pt^{2+}) units, which can vary in separation from 6.6 to 7.2 Å, have been used as molecular receptors and for self-assembly with linear and triangular linkers to produce rectangles and trigonal prisms, respectively. Aromatic molecules form multiple host–guest adducts with the molecular cleft receptors and with the rectangles and trigonal prisms. Planar complexes of Pt^{2+} also form host–guest adducts. The forces that control this molecular recognition, namely, π-π interactions, charge-induced dipole interactions, charge-charge forces, weak metal-metal interactions and solvation effects, are discussed and assigned to the various adducts.

(© Wiley-VCH Verlag GmbH & Co. KGaA, 69451 Weinheim, Germany, 2005)

Introduction

Fundamental to the functioning of biological systems are the phenomena of molecular recognition and self-assembly. The former relies on the concerted interaction of weak, noncovalent forces[1] for selectivity. Generally, the adducts that are formed by weak forces are (kinetically) labile but can be very (thermodynamically) stable. Self-assembly in biological systems usually involves the use of weak noncovalent forces for the formation of secondary and tertiary structures rather than for the generation of primary sequences of large molecules. The latter usually rely on kinetically controlled covalent bond formation. However, studies in supramolecular chemistry, have generated large complex structures by self-assembly, usually by deploying covalent (metal) coordinate bonds.[2] The present review focuses on our studies in molecular recognition and self-assembly using the receptors **1**.[3]

[a] Department of Chemistry, The University of Chicago,
5735 S. Ellis Ave, Chicago, IL 60637, USA
Fax: +1-773-702-0805
E-mail: bos5@uchicago.edu

James D. Crowley was born in "windy" Wellington, New Zealand. He obtained his BSc(Hons) in Chemistry in 1997 and an MSc in 1999 from Victoria University of Wellington. He is currently completing his PhD work under the direction of Professor Brice Bosnich at The University of Chicago. His research interests are in self-assembly, molecular recognition and the development of molecular motors and machines.

Brice Bosnich was born in Queensland, Australia. He received his undergraduate degree in the University of Sydney and his Ph.D. in the John Curtin Medical School of the Australian National University, Canberra. He has held posts in University College, London, the University of Toronto and is currently in The University of Chicago. He has worked in the areas of coordination chemistry as well as organometallic chemistry. An underlying theme of his work is the relationship between reactivity and stereochemistry, especially absolute configurations. His current interests are in aspects of supramolecular chemistry, which may be incorporated into the design of molecular switches and motors.

MICROREVIEWS: This feature introduces the readers to the authors' research through a concise overview of the selected topic. Reference to important work from others in the field is included.

 DOI: 10.1002/ejic.200500091 © 2005 Wiley-VCH Verlag GmbH & Co. KGaA, Weinheim

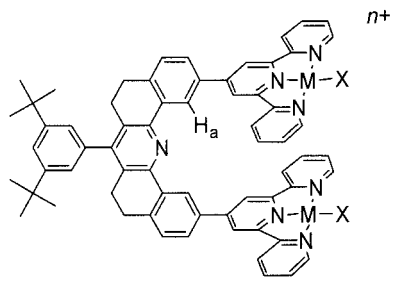

M = Pd^{2+}, Pt^{2+} X = Cl, CH_3CN

1

Receptor **1** incorporates the square-planar metals, Pd^{2+} or Pt^{2+}, and, if X = CH_3CN, this weak ligand is readily displaced. The two terpy-M–X units are parallel to each other and their separation can be modulated by concerted rotation about the spacer while preserving an essentially eclipsed conformation. The terpy-M–X units are charged, are aromatic and, consequently, are expected to incarcerate polarizable aromatic guests, especially those that are negatively charged. The ability of the system to vary the terpy-M–X unit separation allows the receptor to achieve the optimal cleft separation for a particular guest. More complex host structures can be generated from the cleft, **1**, when good leaving groups, X, are present and these clefts are reacted with molecular linkers. Thus linear linkers **2**, or trigonal linkers **3** can provide molecular rectangles **4** or molecular trigonal prisms **5**, respectively.

Self-Assembly: It is well known that Pd^{2+} complexes are more kinetically labile and thermodynamically less stable than the analogous Pt^{2+} complexes. As a consequence the ligands of Pd^{2+} complexes are substituted more readily than analogous ligands of corresponding Pt^{2+} complexes. The relative substitution rates are such that, generally, Pd^{2+} complexes are readily substituted at ambient temperatures whereas Pt^{2+} complexes require higher temperatures to achieve equivalent rates. Thus, whereas the Pd^{2+} complexes have moderate kinetic lability, those of Pt^{2+} are kinetically stable at room temperature.[4] Molecular rectangles **4** can be self-assembled exclusively by mixing the Pd^{2+} molecular cleft, X = CH_3CN, in acetone or acetonitrile with any of the linear linkers **6** to **10**.[5] The isolated yields are essentially quantitative. The Pt^{2+} analogues can also be prepared but require a different route and more forcing conditions. The more flexible linkers **11** react with the Pd^{2+} receptor cleft **1** to give an equilibrium mixture of the desired rectangle and what, by ^1H NMR spectroscopy and electrospray MS,[6] appears to be a macrocycle where a linker joins the two Pd^{2+} atoms of the receptor. Scale molecular models indicate that linkers **7**, **9** and **10** are unlikely to form macrocycles with the receptors. Thus, it appears that molecular rectangles will form exclusively with linear linkers of any practical length provided lengthwise linker rigidity is maintained.

By similar methods the three trigonal linkers **12**, **13** and **14** can be combined with the Pd^{2+} receptor to give quantitative yields of the trigonal prisms, **5**.[7] Because of the insolubility of the trigonal linkers in common solvents, the self-assembly reaction takes several hours with the Pd^{2+} complex. The molecular rectangles **4** and trigonal prisms **5** are distinct from the usual supramolecular structures reported, in that the present structures provide specific binding sites for guests, namely, in the molecular clefts.

Crystal structures of the free ligand[8a] (Figure 1) and that[8b] of the Pd^{2+} receptor, X = Cl, as the PF_6^- salt (Figure 2) are shown. The structures are similar in that pairs of molecules interpenetrate one another; in the case of the free ligand, a terpy unit of one molecule lies between two terpy units of another, and a similar structure is obtained for the terpy-Pd–Cl units of the Pd^{2+} receptor.

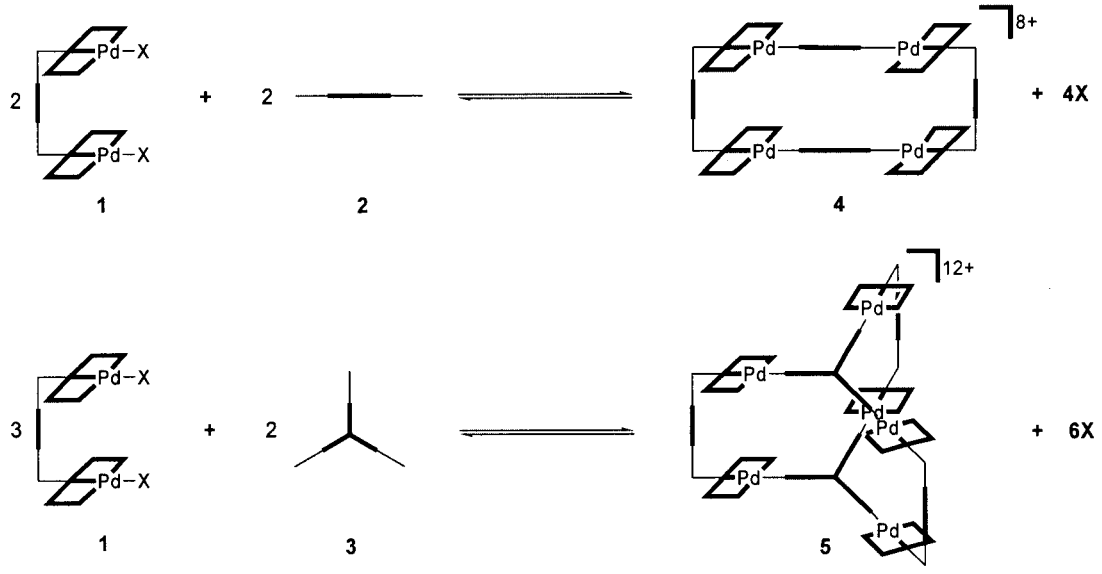

 © 2005 Wiley-VCH Verlag GmbH & Co. KGaA, Weinheim

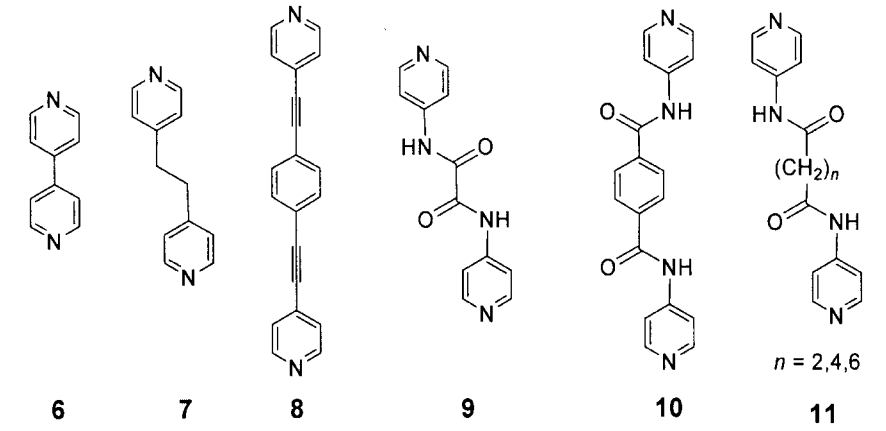

6 **7** **8** **9** **10** **11**

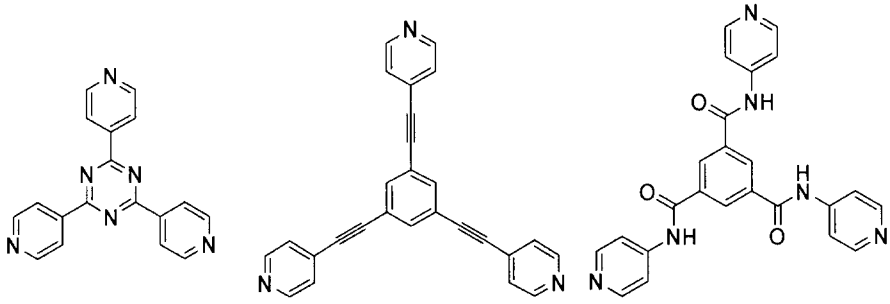

12 **13** **14**

Host–Guest Adducts: The Pd^{2+} or Pt^{2+} receptors **1** (X = Cl or pyridine) form adducts with a variety of guest molecules.[1] Included among these are large aromatic molecules especially those that are electron rich and planar neutral or anionic Pd^{2+} and Pt^{2+} complexes. Although anionic, planar Pd^{2+} and Pt^{2+} complexes, such as [Pd(dipicolinate)Cl]$^-$ and $[Pt(CN)_4]^{2-}$, appear to form red-colored adducts with the receptors **1**. They are invariably insoluble in all common solvents and are very difficult to characterize. Cationic planar complexes such as $[M(terpy)Cl]^+$, (M = Pd^{2+}, Pt^{2+}) do not form adducts with the cationic receptors presumably because of electrostatic repulsion between the positively charged entities. The structure in Figure 2 shows that the cationic terpy-Pd–Cl units can stack on each other in the solid state despite their positive charge. In this case the counterions neutralize the charge repulsion. In solution the receptor shown in Figure 2 shows no evidence of association probably because, as conductivity studies indicate, little or no ion association is present to neutralize the electrostatic repulsion that would ensue upon association.

Host–Guest Adducts with 9-Methylanthracene: Both the Pd^{2+} and Pt^{2+} receptors **1** (X = Cl), form pale yellow solutions, but upon addition of 9-methylanthracene (**15**), (9-MA), the solutions became deep red, indicative of host–guest formation.

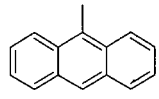

15

Using the ^1H NMR titration mole ratio method (see later),[9] it was found that 1:2 host–guest adducts were formed for both the Pd^{2+} and the Pt^{2+} receptors. The Pd^{2+} receptor has microscopic[10] stability constants[3] of 650 and 100 M^{-1}, which are similar to those for the Pt^{2+} receptor, 800 and 100 M^{-1}, all constants were obtained in CD_3CN solutions at 27 °C. Nuclear Overhauser (^1H ROESY) experiments show[11] that one 9-MA guest resides in the molecular cleft, as expected, but that the other 9-MA molecule lies on the outside faces of the terpy-M–Cl units of the receptors. This solution structure obtains in the solid state for the Pd^{2+} receptor (Figure 3) where pairs of host–guest molecules stack but each receptor carries two 9-MA guests. As will be seen presently, the 9-MA guest always forms a 1:2 host–guest adduct with the molecular cleft, despite the presence of two sterically equivalent outer faces of the

 © 2005 Wiley-VCH Verlag GmbH & Co. KGaA, Weinheim

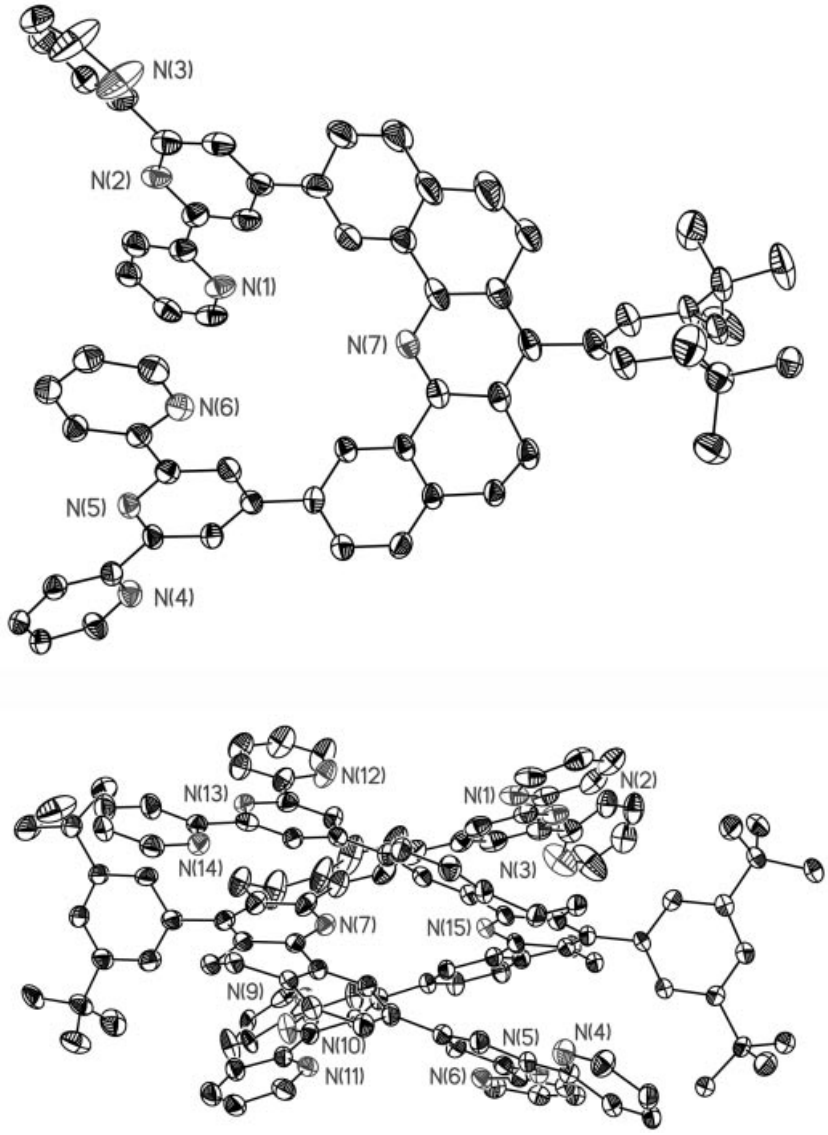

Figure 1. The ORTEP diagram showing a "side" view of the structure that is present in the crystal of the free ligand of **1**. Hydrogen atoms were not located. Thermal ellipsoids are shown at 30% probability. Below, the ORTEP diagram showing the interlocking structure that is present in the crystal of the free ligand of **1**.

terpy-M–X units. However, it is not obvious why 1:3 host–guest adducts are not formed except to suggest that the association of one 9-MA to the outside face of one terpy-M–X unit might lead to electronic polarization of the molecular stack so that the other outer terpy-M–X face is deactivated to association of a 9-MA guest.

The host–guest adducts are very labile. Thus in $(CD_3)_2CO$ solution ^1H NMR spectra indicate that the 9-MA guests are undergoing rapid inter- and intramolecular exchange even at –90 °C. We have addressed the question of the rate of intramolecular exchange as well as the preferred occupancy of the 9-MA guest by studying the two molecules **16** and **17**. The intramolecularly tethered anthracene molecule could lie in the cleft as shown in **16**, or it could lie on the outside face of one of the terpy-Pd–Ligand units. ^1H ROESY spectra show that the anthracene fragment of **16** lies exclusively within the cleft.[11] Hence, we conclude that the larger of the two stability constants for the adducts formed with the receptors **1** and free **15** refers to the case of the guest residing in the cleft, as expected.

At 25 °C in $(CD_3)_2CO$ solution the ^1H NMR spectrum of the system **17** indicates that the two anthracene groups are rapidly exchanging their sites by an intramolecular process.[11] As the temperature is lowered, some of the signals first became broad, and then separate into two signals, a process that was complete at –90 °C. By analyzing this data, it was found that the average residence time (life-time) of the guests in **17** in any site is 1.6×10^{-5} s at 20 °C and 1.3 s at –90 °C. Because of the intramolecular tethering of the guests, their stability within the respective sites is expected

 © 2005 Wiley-VCH Verlag GmbH & Co. KGaA, Weinheim

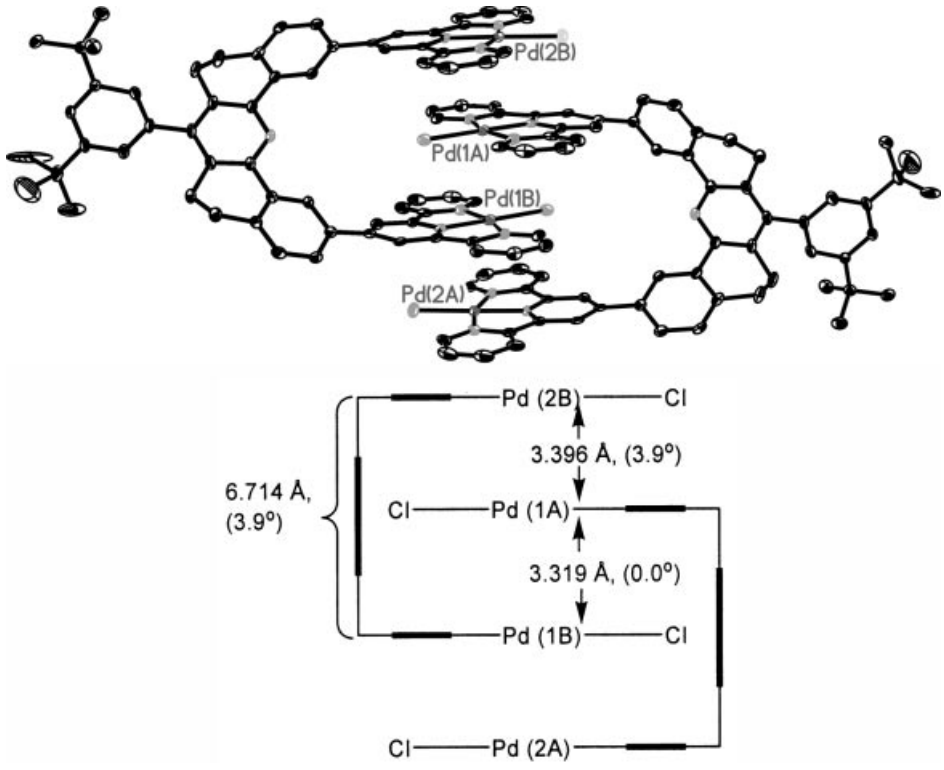

Figure 2. The ORTEP diagram showing a "side" view of the interlocking structure that is present in the crystal of [**1**-Pd^{2+}(X = Cl)]$^{2+}$-$(PF_6)_2$·5CH_3CN. The solvent and counterions have been removed for clarity. Hydrogen atoms were not located. Thermal ellipsoids are shown at 50% probability. Below, a schematic representation of the important structural details from the crystal structure of the receptor, it is noted that the all the terpy-Pd–Cl unit planes are essentially parallel. The interplanar distances are given and the interplanar angles are shown in brackets.

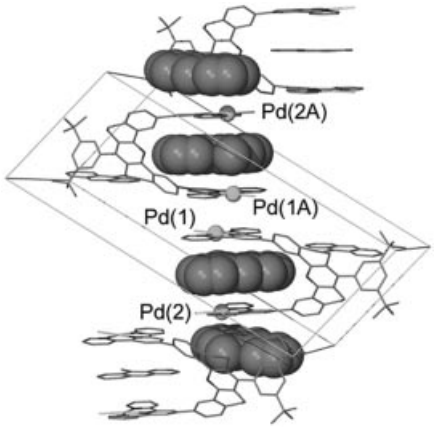

Figure 3. An illustration of the extended crystal structure of [1-Pd^{2+}(X = Cl)]$^{2+}$$(PF_6)_2$·2(9-MA). The box is the unit cell, 9-MA molecules of the stack are shown as space-filling models and the terpy-Pd–Cl units are shown as stick models, as are all other molecules not involved in this stack. Palladium atoms in the stack are shown as spheres.

to be very high, even so, very rapid site exchange occurs. The crystal structure of **17** is shown in Figure 4.

The molecular rectangles **4** derived from **6** and **8**, and the Pd^{2+} receptor form 1:4 9-MA host–guest complexes.[5] This is consistent with two 9-MA molecules residing in the two clefts of the rectangle and with the other two guests residing on the (four) outside faces the terpy-Pd–Ligand units, similar to that observed for the single receptors **1**. This site occupancy is supported by the ^{1}H NMR spectra chemical shifts of requisite protons of the rectangular receptors. The molecular trigonal prisms **5** behave in a similar manner. The Pd^{2+} trigonal prism derived from **12** forms a 1:6 host–guest complex with 9-MA.[7] The larger prism formed by the extended linker **13** gives a 1:7 host–guest adduct with 9-MA. Figure 5 shows ^{1}H NMR titration plots for the host–guest adducts formed by the smaller and larger trigonal prisms with 9-MA. For the smaller prism, the six 9-MA guests reside in the three clefts and on the (six) outer terpy-Pd–Linker unit faces. The seventh 9-MA molecule is assumed to reside between the two phenyl groups of the linker in the larger prism. Molecular models show that the tritopic guest **18** registers almost exactly with the trigonal prism formed with the larger linker **13,** where each of the three anthracene groups occupies a cleft site. Addition of **18** to a solution of the smaller trigonal prism formed from **12** leads to the destruction of the prism presumably because the guest **18** cannot fit strainlessly within this prism. Such decomposition does not occur in [D_7]dimethylformamide (DMF) solutions at 70 °C with the larger prism formed from **13**. In this case a 1:2 host–guest complex is formed, where one guest **18** lies inside of the prism with each an-

 © 2005 Wiley-VCH Verlag GmbH & Co. KGaA, Weinheim

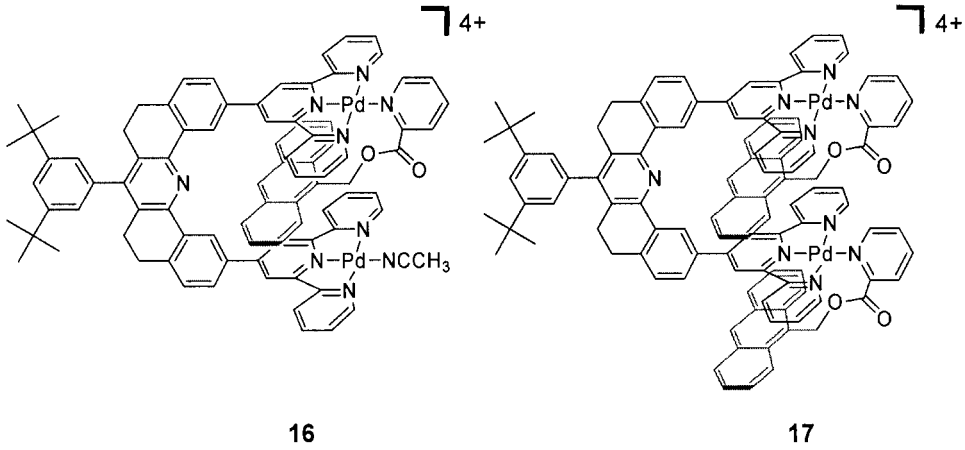

16 17

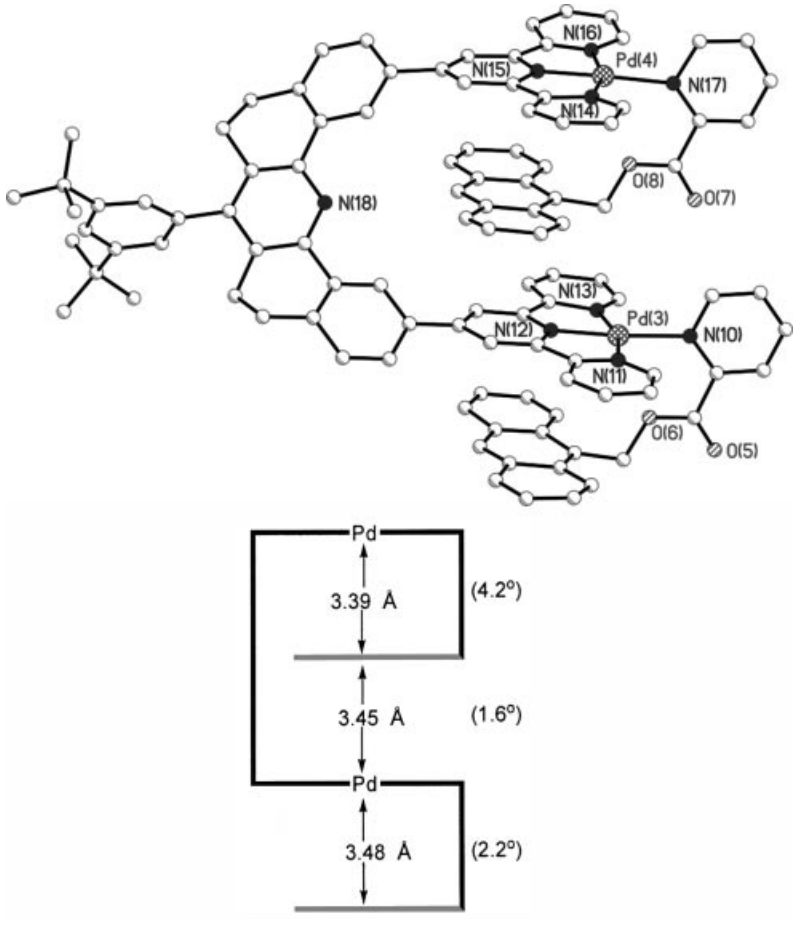

Figure 4. A ball and stick representation of a "side" view for one of the molecules in the unit cell of **17**. Counter ions and solvent molecules have been removed for clarity. Below, a schematic representation of the important structural details from the crystal structure of the **17**. The interplanar distances are given and the interplanar angles are shown in brackets.

thracene group in one of the three clefts, the other guest lies on the "top" and "bottom" faces of the trigonal prism. The host–guest complexes are in rapid intra- and intermolecular exchange.

The host–guest chemistry shown by anthracene derivatives and the molecular clefts **1**, the molecular rectangles **4** and the molecular trigonal prisms **5**, is unexpected in terms of the number of guests that can be incorporated in these

 © 2005 Wiley-VCH Verlag GmbH & Co. KGaA, Weinheim

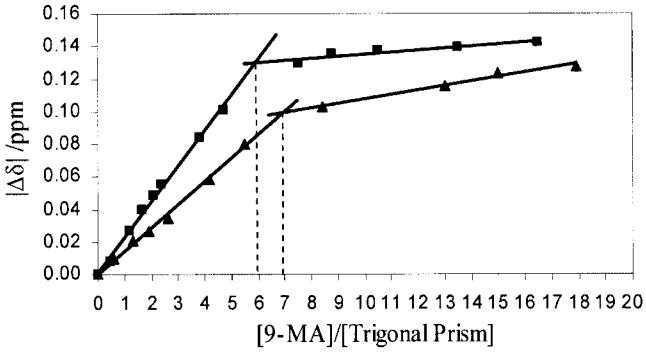

Figure 5. ^{1}H NMR chemical shift difference ($\Delta\delta$) stoichiometry plots for the titration of 9-MA with 4 mM solutions of the trigonal prisms derived from **1** and **12** (■) and **1** and **13** (▲). The experiments were performed at 27 °C in [D_7]DMF. The plot refers to the proton H_a (see, **1**).

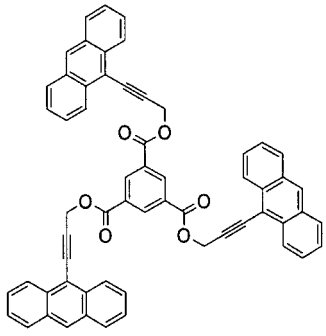

18

receptors. Furthermore, the host–guest chemistry that obtains for the rectangles and trigonal prisms is different from that usually studied where only one single cavity is present. In the present cases, several cavity sites are presented for host–guest formation.

Host–Guest Adducts with Planar Metal Complexes: Magnus' Green Salt[12] $[Pt(NH_3)_4][PtCl_4]$ has long been recognized as the first discovered member of a series of systems containing weak Pt–Pt bonds.[13] Whereas $[Pt(NH_3)_4]^{2+}$ is very pale yellow and $[PtCl_4]^{2-}$ is salmon pink, the green color of Magnus' salt is due to electronic transitions between the states that arise from Pt–Pt bonding.[14] We were interested in determining if weak Pt–Pt (or Pt–Pd) bonds could be used for molecular recognition. The neutral complex **19** was used as a potential guest for both the Pd^{2+} and Pt^{2+} receptors **1** (X = Cl).[13] The guest **19** forms very stable 1:1 adducts with both the Pd^{2+} and Pt^{2+} receptors. At 70 °C in CD_3CN solutions, it was found that the stability constants for the Pd^{2+} and Pt^{2+} receptors are 12000 M^{-1} and 51000 M^{-1}, respectively. ^{1}H NOE spectroscopy of these two adducts shows that the guest **19** lies in the molecular cleft in both cases.[15] The solid-state structure of the **1**-Pt^{2+}·**19** adduct (X = Cl) is shown in Figure 6, where the Pt–Pt distances are 3.303 and 3.262 Å, indicating substantial Pt–Pt interaction.[13] Thus, it is likely that weak metal–metal bonding contributes to host–guest stability.

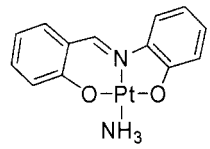

19

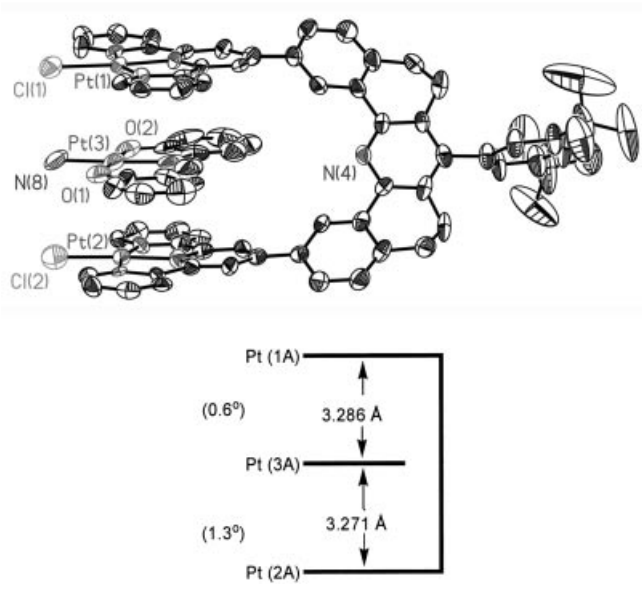

Figure 6. The ORTEP diagram showing a "side" view of the host–guest adduct formed between [**1**-Pt^{2+}(X = Cl)]$^{2+}$(SbF_6)$_2$ and **19**. The solvent and counterions have been removed for clarity. Hydrogen atoms were not located. Thermal ellipsoids are shown at 50% probability. Below, a schematic representation of the important structural details from the crystal structure of the host–guest adduct. The interplanar distances are given and the interplanar angles are shown in brackets.

Solvent Effects: The stability of these adducts depends on the solvent employed. The same host–guest adduct stability constants in [D_7]DMF at 70 °C are an order of magnitude smaller than in CD_3CN solution at 70 °C, namely, 2600 M^{-1} and 4100 M^{-1} for the Pd^{2+} and Pt^{2+} receptors, respectively. Solvent effects in controlling host–guest stability have been considered before.[16] The solvent factors controlling host–guest stability can be delineated by the thermodynamic cycle shown in Scheme 1. The free energy of host–guest formation in solution, $\Delta G_s^{H.G}$, is enhanced by the solvation energy of the host–guest complex, ΔG_{gs}^{H}, and by the intrinsic (gas phase) stability, $\Delta G_g^{H.G}$, but formation is inhibited by the solvation energies of the host, ΔG_{gs}^{H}, and of the guest, ΔG_{gs}^{G}.

Thus, for example, the stability of a host–guest adduct in water will be high when a hydrophobic guest is used. Many of the host–guest complexes reported by Fujita[17] rely on the hydrophobic character of the guests that are incarcerated into water-soluble receptors.

Aside from solvation effects, the stabilities of the host–guest complexes described using 9-MA as a guest are probably controlled by two factors.[1] One is π-π interactions and

 © 2005 Wiley-VCH Verlag GmbH & Co. KGaA, Weinheim

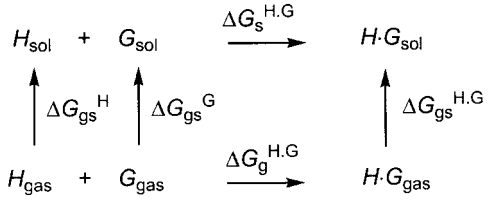

$$-\Delta G_s^{H.G} = -\Delta G_{gs}^{H.G} - \Delta G_g^{H.G} + \Delta G_{gs}^{H} + \Delta G_{gs}^{G}$$

Scheme 1.

the other may involve charge-induced dipole effects, the charge being that carried by the terpy-M–Ligand units. The interplanar separations between the guest in the cleft and the terpy-M–Cl units of the receptor are found to be 3.44 and 3.48 Å (Figure 3), essentially those expected for π-π stacking (3.45 Å).[18] For the case of the 1:1 adduct between the Pt^{2+} receptor and **19,** the separation between the planes of terpy-Pt–Cl units and **19** in the cleft are quite short, 3.286 and 3.271 Å, indicating that the Pt–Pt bonding leads to contraction of the distances from that expected for only π-π stacking.

Electrostatic Interactions: Electrostatic attraction can also be used for host–guest formation.[19] The Pd^{2+} and Pt^{2+}dicationic receptors, **1**, X = Cl, form very insoluble products when their solutions are mixed with solutions of anionic planar complexes, as noted earlier. The potential guest, **20**, however, can be induced to form 1:1 host–guest crystals with **1**, Pd^{2+}, X = Cl and with PF^{-}_{6} as the counterion.[20] The guest, **20**, lies within the cleft and the two terpy-Pd–Cl planes and that of the guest are parallel with separations of 3.21 and 3.29 Å, which are much shorter than those found for π-π interactions. The short spacings appear to be due to electrostatic attraction rather than to metal–metal bonding because the metal–metal distances are 4.0, 4.7 Å, distances much too large for metal–metal bonding.

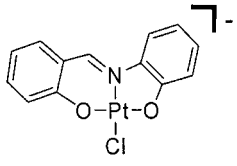

20

The potential guest **21** resembles **19**, but unlike **19** it carries a (free) basic nitrogen atom that can be protonated. Using the Pd^{2+} receptor **1**, X = Cl, in acetonitrile solutions at 70 °C, **21** forms a stable, red 1:1 complex (K = 21000 M^{-1}).[8] Sequential addition of trifluoroacetic acid to an acetonitrile solution of 1:1 host–guest adduct progressively leads to dissociation of the guest, which is accompanied by the loss of the red color. Addition of sufficient base (Et_3N) to such acidified solutions leads to the complete restoration of the adduct (and the red color). The proton-induced dissociation of the guest appears to be controlled by electrostatic repulsion between the cationic receptor and the cationic protonated guest (The nitrogen atom of the spacer is not protonated under the conditions). Thus, electrostatics can be used to control host–guest adduct formation. As noted in our paper,[8] the protonmotive dissociation of the guest can be described in terms of the mechanisms by which molecular motors operate[21,22] although the simple one-stroke process can hardly be described as a motor. However, studies in this area are a prerequisite to designing synthetic molecular motors, machines and switches.

21

We present one final example where electrostatics appears to play a role in host–guest formation but it is of an unconventional kind. Using the two ditopic guests **22** and **23**, and the Pd^{2+} receptor **1** (X = Cl), it was considered possible to form the assembly **24**.[23] The two ditopic guests

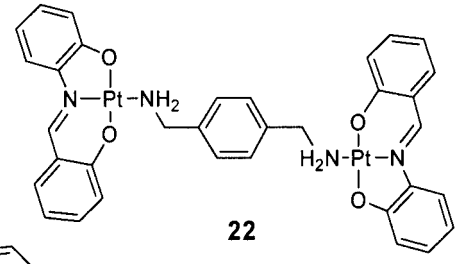

22

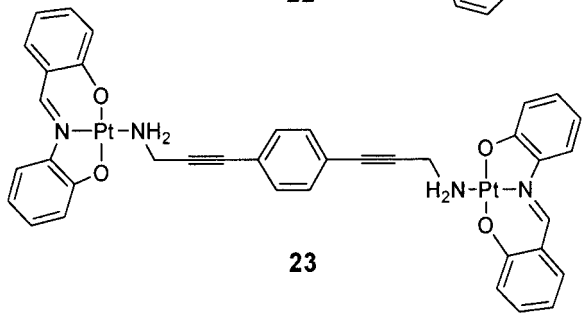

23

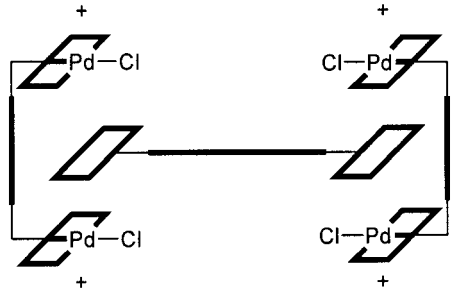

24

 © 2005 Wiley-VCH Verlag GmbH & Co. KGaA, Weinheim

are derivatives of **19** and hence 2:1 host–guest adducts of the kind **24** are expected to form. Molecular models indicate that there are no steric impediments to the formation of the structure **24** with either **22** or **23**, where the closest Pt···Pt distances between receptors are 12.2 and 18.8 Å, respectively. ^{1}H NMR titration of the Pd^{2+} receptor with the two ditopic guests **22** and **23** in [D_7]DMF solutions at 70 °C, shows that **22** forms a 1:1 host–guest adduct (K = 1100 ± 100 M^{-1}) but with the longer guest **23** a 2:1 host–guest complex is formed (K_1 = 1000 ± 100 M^{-1}, K_2 = 400 ± 50 M^{-1}), all Ks are microscopic constants. The negative cooperativity observed with the longer guest **23**, and the extreme case of negative cooperativity seen with the shorter guest **22** suggests that the most likely source of the negative cooperativity is electrostatic repulsion between the two receptor molecules.[23] Approximate electrostatic calculations[23] give results consistent with the host–guest stoichiometries observed.[23]

By the observation of a 1:1 adduct formed between **22** and the Pd^{2+}-based molecular rectangle derived from linker **6** it was demonstrated that the shorter ditopic guest can form adducts with two receptor units. The equilibrium constant was found to be $K^{DMF}_{70\,°C}$ = 1500 ± 200 M^{-1}.

Structure of the Molecular Spacer: The structure of the molecular receptors incorporates important characteristics necessary for the incarceration of the guests in the cleft. As we have noted, the cofacial terpy-M–X units can rotate about the single bonds of the spacer, so that the separation between the terpy-M–X units can be adjusted to optimize the cleft separation for the guest. The result of the concerted rotation of the terpy-M–X unit about the spacer is that the mean molecular plane of the spacer is tilted with respect to the terpy-M–Cl planes. This is illustrated by the "front" view of the structure of the host **1**-Pt^{2+}(X = Cl)$(SbF_6)_2$, with the guest, **19** (Figure 7).

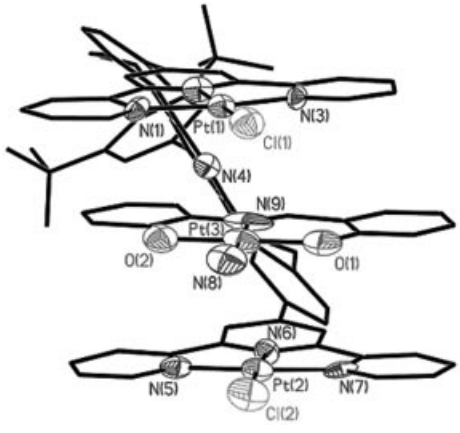

Figure 7. A "front view" of the host–guest complex, [**1**-Pt^{2+}(X = Cl)]$^{2+}$$(SbF_6)_2$:**19**. Note that the mean molecular plane of the spacer is tilted with respect to the terpy-M–Cl and the guest, **19**, planes which are essentially parallel. The tilt of the spacer with respect to the terpy-M–Cl and **19** planes is 42°. Solvent and counterions have been removed for clarity. Thermal ellipsoids are shown at 50% probability.

In addition to terpy-M–X unit rotations, the spacer in all of the crystal structures determined exists in the racemic conformation. The racemic conformation of the spacer causes the M–X vectors of the two terpy-M–X units to twist with respect to each other in a sense dictated by the absolute configuration of the spacer (Figure 7). The rate of interconversion of the puckered spacer from the racemic to the *meso* conformations is likely to be a very rapid process. The large chemical shifts of ^{195}Pt NMR spectra allowed us to determine the rate of this conformational interchange.

Figure 8 shows the temperature variation of the ^{195}Pt NMR in CD_3CN solution of the free Pt^{2+} receptor **1** (X = Cl).[15] At lower temperatures two signals of roughly equal intensities are observed. These are assigned to the racemic and *meso* forms of the spacer. At higher temperature these signals coalesce. Analysis of the spectra indicates that the lifetime of any conformational state at 20 °C is about 5×10^{-4} s, the enthalpy of activation is 2.7 kcal·mol^{-1}, and the statistically adjusted entropy of activation is –34 cal·mol^{-1} K^{-1}. As is evident from the two spectra of the host–guest adduct between **1**, Pt^{2+}, (X = Cl) and **19** shown in Figure 9, rapid conformational interchange also occurs between the racemic and *meso* forms which, at 20 °C, are again approximately in equal proportions. These spectra indicate that the host–guest adduct is supported by both the racemic and *meso* forms of the host which is undergoing

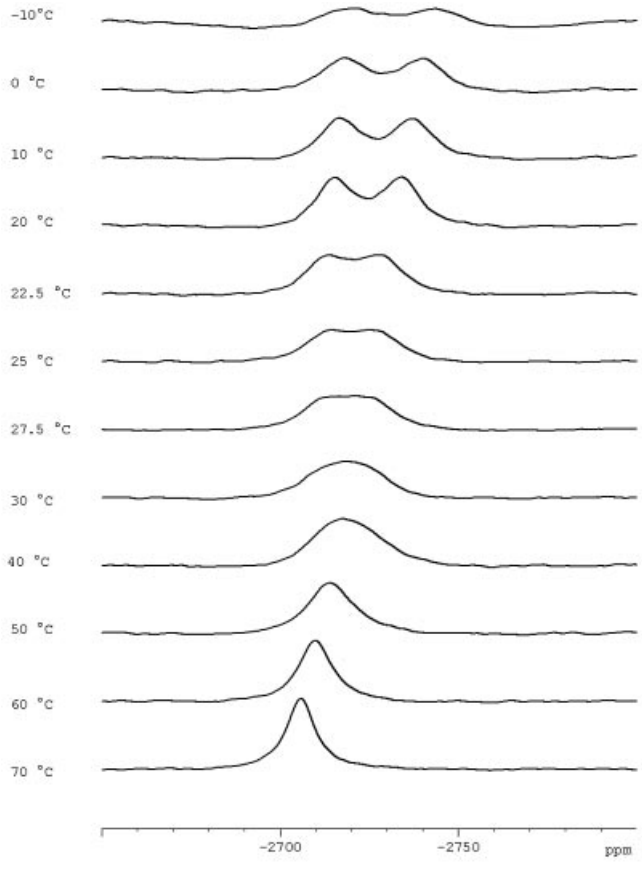

Figure 8. Variable temperature ^{195}Pt NMR spectra of [**1**-Pt^{2+}, (X = Cl)]$^{2+}$$(SbF_6)_2$ in CD_3CN. The chemical shifts (δ scale) are vs. $K_2[PtCl_6]$ in water as an external reference.

 © 2005 Wiley-VCH Verlag GmbH & Co. KGaA, Weinheim

rapid conformation interchange. Thus it is probable that our other host–guest adducts are formed with fluxional receptors.

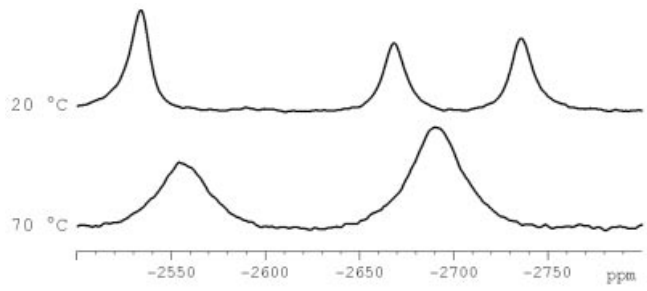

Figure 9. ^{195}Pt NMR spectra of the host–guest adduct formed between [**1**-Pt^{2+} (X = Cl)]$^{2+}$(SbF$_6$)$_2$ and **19** in CD$_3$CN solution (δ scale). No Pt–Pt coupling is observed because of the broadness of the peaks. Three signals are observed for the host–guest adduct at 20 °C; the receptor shows two broad signals at δ = –2669 and –2736 ppm of similar intensities and the incarcerated guest provides a signal at δ = –2534 ppm. Upon raising the temperature to 70 °C, the two receptor signals coalesce to a single peak at δ = –2690 ppm and the guest signal occurs at δ = –2554 ppm.

Conclusions

This brief review of our studies of host–guest formation with the receptors **1**, and the molecular rectangles and trigonal prisms derived from them, serves to illustrate some of the forces that can control molecular recognition. The guest 9-MA (**15**) associates with the molecular clefts by forming 1:2 host–guest adducts so that when the clefts are incorporated in molecular rectangles or trigonal prisms, multiple guest association occurs. The forces that cause these molecular associations are probably π-π interactions, supplemented by charge-induced dipole attractions. A new molecular recognition force, namely weak metal–metal bonding in d^8 complexes, has been shown to add stability to host–guest formation. The strongest of the molecular recognition forces is electrostatic interaction where cationic receptors, such as **1**, do not associate with cationic guests in solution. This has been demonstrated in several ways but perhaps most persuasively by the dissociation of a neutral guest in a cationic cleft after protonation of the guest. Anionic guests form what appear to be strong complexes with the cationic receptors. Electrostatics are responsible for controlling the stoichiometry of ditopic guest interaction with the molecular clefts. An understanding of the forces that control molecular recognition form the basis for designing molecular motors, switches and machines.

Acknowledgments

This work was supported by grants from the Basic Energy Sciences Division of the US Department of Energy.

[1] A. J. Goshe, J. D. Crowley, B. Bosnich, *Helv. Chim. Acta* **2001**, *84*, 2971.
[2] a) S. Leininger, B. Olenyuk, P. J. Stang, *Chem. Rev.* **2000**, *100*, 853; b) M. Fujita, K. Umemoto, M. Yoshizawa, N. Fujita, T. Kusukawa, K. Biradha, K. *Chem. Commun.* **2001**, 509; c) F. Hof, S. L. Craig, C. Nuckolls, J. Rebek, Jr., *Angew. Chem.* **2002**, *114*, 1556; *Angew. Chem. Int. Ed.* **2002**, *41*, 1488; d) S. R. Seidel, P. J. Stang, *Acc. Chem. Res.* **2002**, *35*, 972; e) G. F. Swiegers, T. J. Malefetse, *Chem. Rev.* **2000**, *100*, 3483; f) D. L. Caulder, K. N. Raymond, *Acc. Chem. Res.* **1999**, *32*, 975; g) B. J. Holliday, C. A. Mirkin, *Angew. Chem.* **2001**, *113*, 2076; *Angew. Chem. Int. Ed.* **2001**, *40*, 2022.
[3] R. D. Sommer, A. L. Rheingold, A. J. Goshe, B. Bosnich, *J. Am. Chem. Soc.* **2001**, *123*, 3940.
[4] The exchange rate constants for one CH$_3$CN ligand of the complexes, [Pd(CH$_3$CN)$_4$]$^{2+}$ and [Pt(CH$_3$CN)$_4$]$^{2+}$ in nitromethane solution at room temperature differ by 10^5, where the exchange for the Pd^{2+} complex is fast but is slow for the Pt^{2+} compound. O. F. Wendt, N-F. K. Kaiser, L. I. Elding, *J. Chem. Soc. Dalton Trans.* **1997**, *24*, 4733. This difference in rates allowed us to prepare Pt^{2+} supramolecular assemblies by equilibration at higher temperatures and over longer periods than for the Pd^{2+} analogues. At ambient temperatures the Pt^{2+} assemblies are kinetically stable but the Pd^{2+} analogues are kinetically labile.
[5] a) A. J. Goshe, B. Bosnich, *Synlett* **2001**, 941; b) J. D. Crowley, B. Bosnich, unpublished results, **2004**.
[6] a) C. A. Schalley, T. Muller, P. Linnartz, M. Witt, M. Schafer, A. Lutzen, *Chem. Eur. J.* **2002**, *8*, 3538; b) C. A. Schalley, *Mass Spectrom. Rev.* **2001**, *20*, 253; c) C. A. Schalley, *Int. J. Mass Spectrom.* **2000**, *194*, 11.
[7] J. D. Crowley, A. J. Goshe, B. Bosnich, *Chem. Commun.* **2003**, 2824.
[8] a) A. J. Goshe, PhD Thesis, The University of Chicago, **2003**; b) J. D. Crowley, A. J. Goshe, I. M. Steele, B. Bosnich, *Chem. Eur. J.* **2004**, *10*, 1944.
[9] a) A. S. Meyer, G. H. Ayers, *J. Am. Chem. Soc.* **1957**, *79*, 49; b) H-J. Schneider, *Principles and Methods in Supramolecular Chemistry*, John Wiley & Sons, New York, **2000**; c) H. Tsukube, H. Furuta, A. Odani, Y. Takeda, K. Yoshihiro, Y. Inoue, Y. Liu, H. Sakamoto, K. Kimura, *Comprehensive Supramolecular Chemistry* (Eds.: S. E. D. Davies, J. A. Ripmeester), Permagon, Oxford, UK, **1996**, vol. 8, p. 425.
[10] K. A. Connors, *Binding Constants*, John Wiley & Sons, New York, **1987**.
[11] A. J. Goshe, I. M. Steele, C. Ceccarelli, A. L. Rheingold, B. Bosnich, *Proc. Natl. Acad. Sci. USA* **2002**, *99*, 4823.
[12] G. Magnus, *Pogg. Ann.* **1828**, *14*, 239.
[13] a) J. S. Miller, *Extended Linear Chain Compounds*, Plenum, New York, **1982**–**1983**; vols. 1–3; b) J. R. Miller, *J. Chem. Soc.* **1965**, 713; c) K. Krogmann, *Angew. Chem.* **1969**, *81*, 10; *Angew. Chem. Int. Ed. Engl.* **1969**, *8*, 35; d) V. H. Houlding, V. M. Miskowski, *Coord. Chem. Rev.* **1991**, *111*, 145; e) W. B. Connick, R. E. Marsh, W. P. Schaefer, H. B. Gray, *Inorg. Chem.* **1997**, *36*, 913; f) W. B. Connick, L. M. Henling, R. E. Marsh, H. B. Gray, *Inorg. Chem.* **1996**, *35*, 6261.
[14] a) S. Yamada, R. Tsuchida, *J. Am. Chem. Soc.* **1953**, *75*, 6351; b) S. Yamada, *Bull. Chem. Soc. Japan* **1951**, *24*, 125; c) S. Yamada, *J. Am. Chem. Soc.* **1951**, *73*, 1579; d) S. Yamada, *J. Am. Chem. Soc.* **1951**, *73*, 1182.
[15] A. J. Goshe, I. M. Steele, B. Bosnich, *J. Am. Chem. Soc.* **2003**, *125*, 444.
[16] D. B. Smithrud, S. I. Chao, S. B. Ferguson, D. R. Carcanague, J. D. Evanseck, K. N. Houk, F. Diederich, *Pure Appl. Chem.* **1990**, *62*, 2227.
[17] a) M. Fujita, *Chem. Soc. Rev.* **1998**, *27*, 417; b) J-P. Bourgeois, M. Fujita, *Aust. J. Chem.* **2002**, *55*, 619; c) M. Fujita, *Acc. Chem. Res.* **1999**, *32*, 53; d) M. Fujita, K. Ogura, *Coord. Chem. Rev.* **1996**, *148*, 249.

 © 2005 Wiley-VCH Verlag GmbH & Co. KGaA, Weinheim

[18] a) C. A. Hunter, M. N. Meah, J. K. M. Sanders, *J. Am. Chem. Soc.* **1990**, *112*, 5773; b) C. Janiak, *J. Chem. Soc., Dalton Trans.* **2000**, 3885; c) C. A. Hunter, K. R. Lawson, J. Perkins, C. J. Urch, *J. Chem. Soc. Perkin, Trans. 2* **2001**, 651; d) E. A. Meyer, R. K. Castellano, F. Diederich, *Angew. Chem.* **2003**, *115*, 5116; *Angew. Chem. Int. Ed.* **2003**, *42*, 1210.

[19] a) K. K. Klausmeyer, T. B. Rauchfuss, S. R. Wilson, *Angew. Chem.* **1998**, *110*, 1808; *Angew. Chem. Int. Ed. Engl.* **1998**, *37*, 1694; b) F. P. Schmidtchen, *J. Chem. Soc., Chem. Commun.* **1984**, *16*, 1115; c) M. Fujita, D. Oguro, M. Miyazawa, H Oka, K. Yamaguchi, K. Ogura, *Nature* **1995**, *378*, 469; d) M. Aoyagi, K. Biradha, M. Fujita, *J. Am. Chem. Soc.* **1999**, *121*, 7457; e) T. N. Parac, D. L. Caulder, K. N. Raymond, *J. Am. Chem. Soc.* **1998**, *120*, 8003.

[20] A. J. Goshe, I. M. Steele, B. Bosnich, *Inorg. Chim. Acta* **2004**, *357*, 4544.

[21] a) V. Balzani, M. Venturi, A. Credi, *Molecular Devices and Machines*, Wiley-VCH, Weinheim, **2003**; b) V. Balzani, A. Credi, F. M. Raymo, J. F. Stoddart, *Angew. Chem.* **2000**, *112*, 3484; *Angew. Chem. Int. Ed.* **2000**, *39*, 3349.

[22] G. Oster, H. Wang, *Molecular Motors* (Ed.: M. Schliwa), Wiley-VCH, Weinheim, **2003**, chapter 8, p. 207.

[23] J. D. Crowley, A. J. Goshe, B. Bosnich, *Chem. Commun.* **2003**, 392.

Received: January 28, 2005
Published Online: April 25, 2005

 © 2005 Wiley-VCH Verlag GmbH & Co. KGaA, Weinheim

Synthesis and Characterisation of a Novel Copper(II) Azamacrocycle-Phosphonate 3D Polymeric Network

Giuliano Giambastiani,[a] Werner Oberhauser,[a] Claudio Bianchini,[a] Franco Laschi,[b] Lorenzo Sorace,[c] Peter Brueggeller,[d] Rene Gutmann,[d] Annabella Orlandini,[a] and Francesco Vizza*[a]

Keywords: Copper / Azamacrocycles / Coordination polymers / Macrocyclic ligands

A new azamacrocycle phosphonate in its hydrocloride form (**1**) has been synthesized and characterised by multinuclear NMR spectroscopy and by a single X-ray analysis. The reaction of **1** with Cu^{II} ions gives a polymeric compound (**2**), which exhibits an unprecedented three-dimensional network containing two-dimensional channels filled with guest molecules. The solid-state structure of **2** and its properties have been characterised by means of various analytical methods which include single-crystal X-ray structure analysis, X-ray powder diffraction, thermogravimetric studies as well as magnetic susceptibility and EPR measurements.

(© Wiley-VCH Verlag GmbH & Co. KGaA, 69451 Weinheim, Germany, 2005)

Introduction

Polymeric matrices made up of metal phosphonates and macrocyclic ligands constitute an innovative class of compounds with potential application in catalysis, as sensoring and switching devices, liquid crystals and molecular magnets.[1]

Metal complexes with azacrown ethers, containing phosphonic acids, are often characterised by unusual structures and can also form porous lamellar-structured materials.[2] To the best of our knowledge, no multidimensional network containing channels or cavities assembled by Cu^{II} ions and azamacrocycle phosphonate ligands has been reported in the literature. Indeed, the "macrocyclic effect" exerted by azamacrocycle ligands favours the formation of stable 1:1 adducts, where the nitrogen atoms bind metal ions, such as Co^{II}, Cu^{II} and Ni^{II}. The resulting ML units may be further assembled only in a mono-dimensional chain by hydrogen bonds involving the uncoordinated phosphonate units.[3] In this communication we present the synthesis and characterisation of a new azamacrocycle phosphonate in its HCl-form (**1**), and the synthesis and characterisation of a novel three-dimensional network containing two-dimensional channels assembled by Cu^{II} ions in conjunction with the new macrocycle phosphonate ligand.

Results and Discussion

The new macrocycle 4,10-dimethyl-1,4,7,10-tetraazacyclododecane·-1,7-bis(methanephosphonic acid)·2HCl·3H_2O, Me_2DO2P-4H·2HCl·3H_2O (**1**) was obtained by acid hydrolysis (HCl) of the known ligand 4,10-dimethyl-1,4,7,10-tetraazacyclododecane·-1,7-bis(methanephosphonic acid monoethyl ester)dipotassium salt, $K_2Me_2DO2PME$ (Scheme 1).[4]

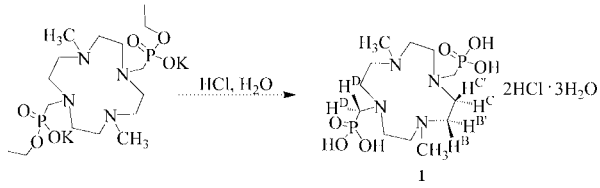

1

Scheme 1.

The X-ray structure of **1** consists of two conformations of the new cationic macrocyclic units $[Me_2DO2P\text{-}6H]^{2+}$, chloride anions and solvent water molecules. An ORTEP plot of **1** is presented in Figure 1.

The phosphonate units and the chloride anions are interlinked by water molecules through hydrogen bonding. The two cationic conformations are very similar, as the methyl and the phosphonate groups are oriented on the same side of the planes defined by the four nitrogen atoms N1–N4 and N5–N8. Furthermore, in both macrocyclic cations the phosphonate groups are doubly protonated. As evidenced

[a] ICCOM-CNR, Area della Ricerca di Firenze,
Via Madonna del Piano, 50019 Sesto Fiorentino (Firenze), Italy
Fax: +39-055-5225203
E-mail: francesco.vizza@iccom.cnr.it
[b] Università di Siena,
Via Aldo Moro 1, Siena, Italy
[c] Dipartimento di Chimica e UdR INSTM, Università di Firenze,
Via della Lastruccia 3, 50019, Sesto Fiorentino (Firenze), Italy
[d] Institut für Allgemeine, Anorganische und Theoretische Chemie der Universität Innsbruck,
Innrain 52a, Innsbruck, Austria
Supporting information for this article is available on the WWW under http://www.eurjic.org or from the author.

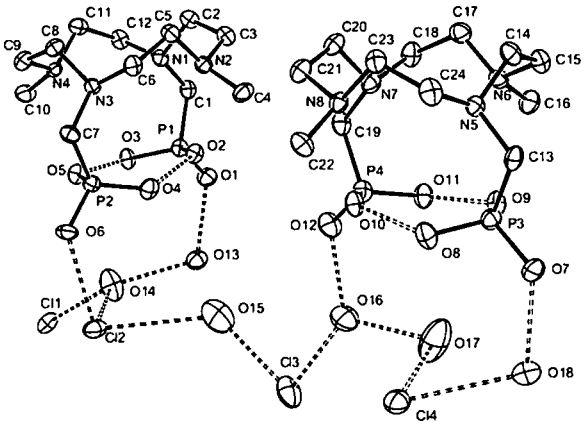

Figure 1. Perspective view of the asymmetric unit of **1**, showing conformer A (left) and conformer B (right) involved in the most important hydrogen-bonding interactions; hydrogen atoms have been omitted for clarity.

by a difference Fourier map, the protonation involves the oxygen atoms O1, O3, O4, O6 of conformer A and the oxygen atoms O7, O8, O11, O12 of conformer B, which is in agreement with the values of the corresponding P–O lengths ranging from 1.530(3) Å to 1.562(2) Å.[5] As expected, the P–O double bonds show bond lengths ranging from 1.489(3) Å to 1.493(3) Å. Both conformers show strong intramolecular hydrogen bonds between P=O and POH units of different phosphonate groups in order to stabilise eight-membered O–H–O–P–O–H–O–P rings. The protonated oxygen atoms O1, O6, O7, and O12 are strongly bonded to water molecules or to chloride anions in order to build up a complex network of hydrogen bonds. In both conformers, the nitrogen atoms bearing the methyl groups are protonated also (the four protons were detected in difference Fourier maps and successfully refined).

^{1}H NMR studies of **1** in D_2O at pH = 1 and room temperature have revealed that the protons of the ethylenic bridge (B, B′ and C, C′) are diastereotopic. This indicates that the system is locked in a rigid conformation on the NMR timescale.

Bright-blue crystals of the polymeric compound $\{[Cu_2Cl_2(Me_2DO2P\text{-}2H)(H_2O)]\cdot(0.5\,C_3H_6O)\cdot(2.5\,H_2O)\}_n$ (**2**) were isolated from the reaction of an equimolar amount of **1** with $Cu(OAc)_2\cdot H_2O$ or $CuCl_2\cdot 2\,H_2O$ in water/acetone at room temperature in the pH range from 1 to 8 (Scheme 2).

When the reaction was carried out in the pH range 9–14, no formation of **2** was observed, which indicates a strong control of both the pH and chloride ligands on the product formation. Indeed, the reaction of the ligand in its potassium salt form (K_4Me_2DO2P) with $Cu(OAc)_2\cdot H_2O$ or with $CuCl_2\cdot 2\,H_2O$ does not yield **2**, yet an undefined compound is produced. It is worth stressing that **2** was obtained even when the ratio between **1** and $Cu(OAc)_2\cdot 2\,H_2O$ or $CuCl_2\cdot 2\,H_2O$ was much greater than the stoichiometric ratio.

The single-crystal X-ray structure analysis of **2** revealed a structural organization that has never been reported for Cu^{II} diphosphonate compounds.[6a] Indeed, **2** adopts a three-dimensional layered structure containing $\{CuClN_4\}$ units and phosphonate O-bridged $\{Cu_2Cl_2O_6\}$ dimers. An ORTEP plot of compound **2** is presented in Figure 2.

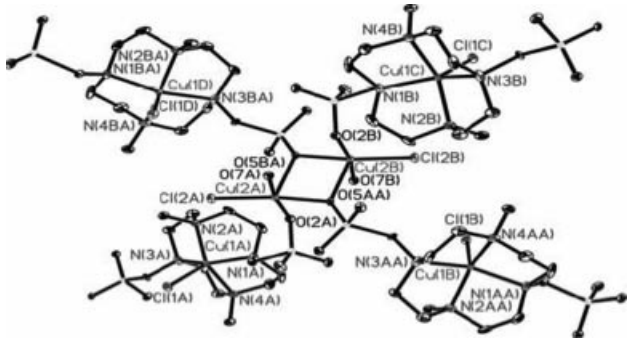

Figure 2. X-ray crystal structure of **2**, showing the connectivity of the centrosymmetric moieties $\{Cu_2Cl_2O_6\}$, projected perpendicular to the *a* axis. Hydrogen atoms and noncoordinating solvent molecules are omitted for clarity.

A three-dimensional porous structure with continuous channels (Figure 3) is apparently formed with no need for a templating agent.[6]

The 12-membered azamacrocycles are tilted towards each other by 35.3°. The methyl and phosphonate groups bound to the nitrogen atoms are all oriented on the same side of the N_4 plane.[7] The Cu^{II} centres of **2** exhibit two different distorted square-pyramidal coordination geometries, which represents an unprecedented structural feature for layered Cu^{II} diphosphonates. The Cu(1A) atom lies 0.546 Å above the N_4 ring, while Cu(2A) deviates by 0.105 Å from the basal plane defined by Cl(2A), O(2A), O(5AA), and O(7A). Typically, the apical Cu(2A)–O(5BA) bond length of 2.241(3) Å is significantly longer than the Cu(2A)–O(5AA) bond length of 1.989(3) Å.[6a,8] The oxygen bridged $\{Cu_2(\mu\text{-}O)_2\}$ dimeric units show a Cu(2A)···Cu(2B) distance of 3.140(1) Å, which is in line with comparable structures.[8a,9] The next larger Cu···Cu distances within the layers are 6.403(1) Å for Cu(1B)···Cu(2B) and

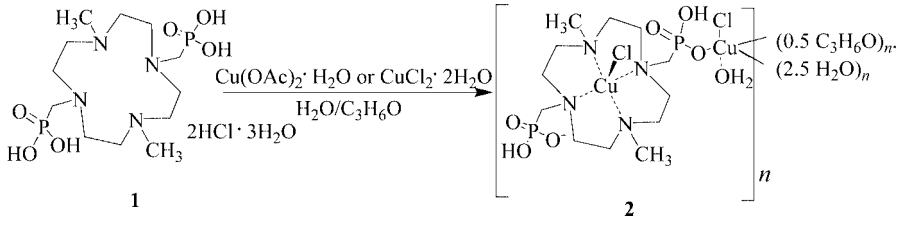

Scheme 2.

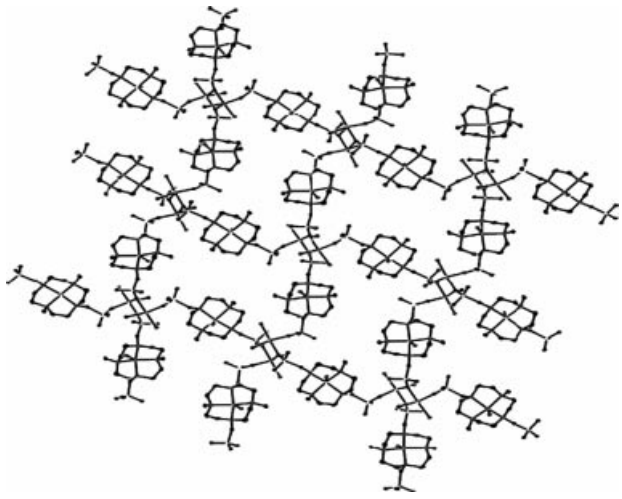

Figure 3. ORTEP plot, showing the propagation of the asymmetric unit in two dimensions, with the projection direction perpendicular to the *a* axis; hydrogen atoms and solvent molecules are omitted for clarity.

6.545(1) Å for Cu(1A)···Cu(2A). The shortest Cu···Cu distance between the layers is 8.277(1) Å. Considering the packing in $\{[Cu_2Cl_2(Me_2DO2P\text{-}2H)(H_2O)]\cdot(0.5\,C_3H_6O)\cdot(2.5\,H_2O)\}_n$ for $n = 2$, four water molecules hold together two adjacent layers by strong hydrogen bonding to two different phosphonate anions. Four O···O contacts in the range 2.54–2.91 Å have been detected. The central disordered water molecule also makes a short contact of 2.83 Å to this chain of hydrogen bonds. Disordered acetone molecules fill up the continuous channels (Figure 4).

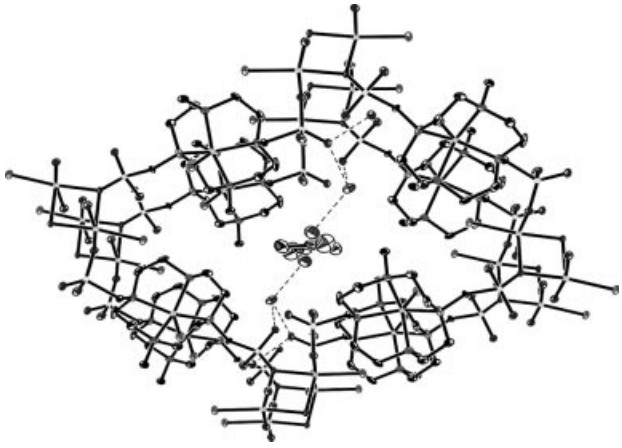

Figure 4. Packing diagram of **2** revealing the continuous channel in the projection plane perpendicular to the *a* axis, occupied by solvent molecules and formed through stacking of macrocyclic moieties. The chain of solvent molecules is indicated with a broken line.

The polymeric compound **2** is soluble in water but insoluble in all common organic solvents. When a sample of **2** is heated in air at 125 °C, its colour becomes bright green, due to the loss of the coordinated water. The crystal morphology does not change even at 160 °C. When the green solid is allowed to cool to room temperature, it again turns dark blue indicating that the coordination of water to the metal centre is restored. The removal of the guest molecules (water, acetone) and its reversible process, which is very important for designing new architectures of porous materials or chemical sensors, was studied by means of a thermogravimetric analysis (TGA) and X-ray powder diffraction (XRPD).

The thermogravimetric analysis of **2**, in the temperature range 36–160 °C, showed a 7% loss of weight, which corresponds to the release of half a molecule of acetone and one molecule of coordinated water per asymmetric unit. Between 160 and 190 °C, a further weight loss of 1.2% was detected, due to the release of the water molecule (half a molecule per formula unit) located in the channel and that shows a short contact of 2.83 Å to the water molecule hydrogen-bonded to two phosphonate units (Figure 4). No chemical decomposition was observed up to 200 °C, yet the bright-green solid lost the original crystal morphology. The X-ray powder diffraction (XRPD) pattern of **2** did not show any change after a dehydration/rehydration cycle conducted by heating of **2** at 160 °C for 10 min and rehydrating at room temperature in a water/acetone (1:10) (v/v) mixture. The sample changed its colour from dark blue to bright green during the heating step, while it turned back to deep blue during cooling and exposure to the water/acetone mixture.

Apparently, the three-dimensional network is sufficiently robust to show reversible coordination of water molecules as well as inclusion of acetone as the guest molecule.

Magnetic susceptibility measurements of **2** showed a Curie–Weiss behaviour down to 5 K. The calculated value of the Curie constant per asymmetric unit, $C = 0.413\ cm^3\,K\,mol^{-1}$ (corresponding to a μ_{eff} value of 1.82 μ_B), indicates that only one Cu^{II} centre, namely that pertaining to the ($CuClN_4$) unit, contributes to the magnetic moment of the system. Consistently, the Cu^{II} centres in the ($Cu_2Cl_2O_6$) units did not display any EPR signal, due to the very intense Cu^{II}–Cu^{II} antiferromagnetic coupling. The observed g values [$g_{\|} = 2.15(3)$, $g_{\perp} = 2.07(1)$], which did not change on cooling, suggest that the signal can be assigned to the $Cu^{II}N_4$ moiety.[10,11]

Conclusions

We synthesized a very rare organic–inorganic Cu^{II} polymer, which represents the first example of a polymeric coordination network obtained by combining an azamacrocycle phosphonate ligand with Cu^{II} ions. Given the hemilability of **1**, the formation of **2** may be seen as a weak-link approach to supramolecular coordination complexes.[12] TGA and XRPD experiments clearly indicate that guest molecules, like water and acetone, can be removed from the three-dimensional network without affecting the solid-state morphology. Intercalation reactions of amines and other organic solvents with the dehydrated compound **2** are being investigated in our laboratories.

 © 2005 Wiley-VCH Verlag GmbH & Co. KGaA, Weinheim

Experimental Section

Elemental analyses were performed with a Carlo–Erba model 1106 elemental analyser. The IR spectroscopic measurements were performed with a FT-IR Spectrum GX instrument. TGA measurements were performed with a TA SDT Q600 apparatus at a heating rate of 2 °C min^{-1} in the range of 30–200 °C. XRPD measurements were performed with a Philips PW 3830 diffractometer (Co, λ = 1.7889 Å) with a voltage of 40 kV and a current of 40 mA. The magnetic susceptibility measurements were carried out in a temperature range from 2 to 300 K at a magnetic field of 1 T with a Cryogenic S600 SQUID magnetometer. The EPR powder spectra were recorded with a Varian E9 spectrometer equipped with a ^{4}He continuous flow cryostat for variable temperature measurements. ^{1}H, ^{13}C, and ^{31}P{^{1}H} NMR spectra were recorded at 200.13, 50.32, and 81.01 MHz, respectively, with a Bruker ACP-200 spectrometer or at 400.13, 100.62, and 161.97 MHz, respectively, with a Bruker Avance DRX-400 spectrometer. Chemical shifts are relative to tetramethylsilane as external reference or were calibrated against solvent resonances. The assignments of the signals resulted from 2D-^{1}H COSY and proton detected ^{1}H-^{13}C correlations using degassed nonspinning samples. 2D-NMR spectra were recorded with a Bruker Avance DRX-400 spectrometer.

1. Synthesis of 4,10-Dimethyl-1,4,7,10-tetraazacyclododecane-1,7-bis(methanephosphonic acid)·2 HCl·3 H_2O [(Me_2DO2P-4H)·2 HCl·3 H_2O, 1]

A solution of 4,10-dimethyl-1,4,7,10-tetraazacyclododecane-1,7-bis(methanephosphonic acid monoethyl ester) dipotassium salt, (K_2Me_2DO2PME) (2.4 g, 4.23 mmol) in HCl (35 mL of a 6 M solution) was stirred at reflux for 3 days in a sealed Schlenk tube. Afterwards, the solvent was concentrated to a small volume (10 mL), and then the slow addition of acetone (5 mL) led to the precipitation of a white crystalline product. The solution was was decanted, and the solid dried under vacuum. The hygroscopic compound was used without further purification and stored under N_2 at room temperature. Yield: 2.1 g (88%). $C_{12}H_{38}Cl_2N_4O_9P_2$ (515.30): calcd. C 27.97, H 7.43; N 10.87; found: C 27.69, H 7.40, N 10.61. ^{1}H NMR (400.13 MHz, D_2O, pH = 1, 25 °C): δ = 3.37 (ddd, $^2J_{B,B'}$ = 14.1, $^3J_{C,B}$ = 3.5, $^3J_{B,\ C'}$ = 7.1 Hz, 4 H, H_B), 3.18 (ddd, $^3J_{B',C}$ = 7.5, $^3J_{B',C'}$ = 2.9 Hz, 4 H, $H_{B'}$), 3.07 (ddd, $^2J_{CC'}$ 14.9 Hz, 4 H, H_C), 2.93 (s, 6 H, CH_3), 2.86 (ddd, 4 H, $H_{C'}$), 2.79 (d, H_D, $^2J_{H,P}$ = 11.07 Hz, 4 H) ppm. ^{13}C{^{1}H} NMR (100.62 MHz, D_2O, pH = 1.0, 25 °C): δ = 54.18(s,C_B), 51.73 (d, ^3J(P,C) = 4.53 Hz, C_c), 52.03 (d, $^1J_{C,P}$ = 108.69 Hz, C_D), 44.12 (s, CH_3) ppm. ^{31}P{^{1}H} NMR (161.97 MHz, D_2O, pH = 1.0, 25 °C): δ = 22.48 ppm. IR features (KBr disk): $\tilde{\nu}$ = 3276 s, 3136 s, 1734 s, 1469 s, 1216 m, 1200–900 s cm^{-1}.

2. Synthesis of {[Cu_2Cl_2(Me_2DO2P-2 H)(H_2O)]·(0.5 C_3H_6O)·(2·5 H_2O)}$_n$ (2)

Method A: Me_2DO2P-4H·2 HCl·3 H_2O (0.3 g, 0.580 mmol) was dissolved in water (10 mL). The reaction mixture was then treated with a solution of $Cu(OAc)_2$·H_2O (0.115 g, 0.58 mmol) in water (5 mL) at room temperature. The resulting blue solution was layered with acetone (15 mL), and on standing, blue crystals separated, which were filtered off and recrystallised from a water/acetone solution (1:1, v/v). Yield: 0.35 g, (44%). $C_{13.5}H_{38}Cl_2Cu_2N_4O_{10}P_2$ (676.40): calcd. C 23.97, H 5.66, N 8.28; found: C 24.02, H 5.80, N 8.59. IR features (KBr disk): $\tilde{\nu}$ = 3412 s (hydrogen bonded water), 3200 s (coordinated water), 2370 m, 2210 w, 2920 s, 2850 s, 1712 s, 1160 s, 1050–915 s cm^{-1}.

Method B: Me_2DO2P-4H·2 HCl·3 H_2O (0.3 g, 0.58 mmol) was dissolved in water (10 mL) and the pH was adjusted to 8 by addition of 1 M KOH. The reaction mixture was then treated with a solution of $CuCl_2$·2 H_2O (0.1 g, 0.58 mmol) in water (5 mL) at room temperature. The resulting blue solution was layered with acetone (15 mL), and on standing, blue crystals separated, which were filtered off and washed with a water/acetone solution (1:1, v/v). Yield: 0.30 g, (38%).

X-ray Crystallographic Studies

X-ray quality crystals of **1** and **2** were obtained from a mixture of water/acetone solution (1:10, v/v) of the respective compounds.

Compound 1: $C_{12}H_{38}Cl_2N_4O_9P_2$, M_r = 515.30, dimensions 0.450 × 0.275 × 0.075 mm, triclinic, space group P-1, a = 14.244(3) Å, b = 15.374(7) Å, c = 11.109(1) Å, α = 97.72(2)°, β = 95.89(1)°, γ = 86.62(3)°, V = 2395.4(12) Å^3, Z = 4, D_c = 1.429 g cm^{-3}, μ(Mo-K_α) = 0.452 mm^{-1}. X-ray data were collected with an Enraf–Nonius CAD4 automatic diffractometer at 293(2) K in the range of 2.01 < Θ < 23.47°. Unit cell parameters were determined by least-squares refinement of the setting angles of 25 carefully centred reflections. The structure was solved by direct methods and refined by full-matrix on F^2, with the WINGX package,[13a] converging at R = 0.0488 [$I > 2\sigma(I)$] with a goodness-of-fit on F^2 of 0.885 for 579 parameters and 7550 reflections, 7046 unique reflections.

Compound 2: $C_{13.5}H_{38}Cl_2Cu_2N_4O_{10}P_2$, M_r = 676.40, dimensions 0.100 × 0.08 × 0.03 mm, monoclinic, space group $P2_1/n$, a = 8.2771(3) Å, b = 20.8384(8) Å, c = 14.9980(4) Å, β = 98.548(2)°, V = 2558.12(2) Å^3, Z = 4, D_c = 1.756 g cm^{-3}, μ(Mo-K_α) = 2.051 mm^{-1}. X-ray data were collected with a Nonius–Kappa CCD diffractometer at 243(2) K in the range of 2.39 < Θ < 26.02°. Cell refinement, data reduction, and the empirical absorption correction were done by Denzo and Scalepack programs.[13b] Unique reflections were used to solve the structure by direct methods with SHELXS-97.[13c] Structure refinement on F^2 by full-matrix least-square methods were carried out with SHELXL-97,[13d] converging at R = 0.030 [$I > 2\sigma(I)$] with a goodness-of-fit on F^2 of 1.014 for 342 parameter and 9687 reflections, 4932 unique reflections.

CCDC-262040 (for **1**) and -242225 (for **2**) contains the supplementary crystallographic data for this paper. These data can be obtained free of charge from The Cambridge Crystallographic Data Centre via www.ccdc.cam.ac.uk/data_request/cif.

Supporting Information: See also footnote on the first page of this article. A thermogravimetric study of compound **2**, a comparison of the XRPD patterns before and after the dehydration/hydration cycle, and magnetic susceptibility as well as EPR measurements of **2** are included.

Acknowledgments

We thank Ente Cassa di Risparmio di Firenze for granting this work through the project Firenze-Hydrolab. P. B. and R. G. thank the Fonds zur Förderung der Wissenschaftlichen Forschung, Austria, for financial support.

[1] a) G. Alberti, U. Costantino, in *Comprehensive Supramolecular Chemistry* (Ed.: J. M. Lehn), Pergamon-Elsevier Science Ltd., London, **1996**; b) A. Clearfield, *Metal Phosphonate Chemistry*, in *Progress in Inorganic Chemistry* (Ed.: K. D. Karlin), John Wiley & Sons, New York, **1998**, 47, 6, 1168.

[2] a) B. Zhang, A. Clearfield, *J. Am. Chem. Soc.* **1997**, *119*, 2751–2752; b) C. V. K. Sharma, A. Clearfield, *J. Am. Chem. Soc.* **2000**, *122*, 1558–1559; c) H. L. Ngo, W. Lin, *J. Am. Chem. Soc.* **2002**, *124*, 14298–14299; d) D. Kong, D. G. Medvedev, A.

 © 2005 Wiley-VCH Verlag GmbH & Co. KGaA, Weinheim

Clearfield, *Inorg. Chem.* **2004**, *43*, 7308–7314; e) D. Kong, A. Clearfield, *Chem. Commun.* **2005**, 1005–1006.
[3] a) I. Lukes, J. Kotec, P. Vojtisek, P. Hermann, *Coord. Chem. Rev.* **2001**, *216–217*, 287–312; b) J. Kotek, P. Hermann, I. Cìsarovà, J. Rohovec, I. Lukes, *Inorg. Chim. Acta* **2001**, *317*, 324–330.
[4] G. Giambastiani, F. Laschi, P. Mariani, A. Vacca, C. Bianchini, F. Vizza, P. Zanello, *Org. Biomol. Chem.* **2003**, *1*, 879–886.
[5] a) I. Làzàr, D. C. Hrncir, W. D. Kim, G. E. Kiefer, A. D. Sherry, *Inorg. Chem.* **1992**, *31*, 4422–4424; b) J. J. Daly, P. J. Wheatley, *J. Chem. Soc. (A)* **1967**, 212; c) S. Midollini, A. Orlandini, A. Vacca, *Inorg. Chem. Commun.* **2004**, *7*, 1113–1116.
[6] a) L. M. Zheng, H. H. Song, C. Y. Duan, X. Q. Xin, *Inorg. Chem.* **1999**, *38*, 5061–5066; b) K. S. Min, M. P. Suh, *Chem. Eur. J.* **2001**, *7*, 303–312; c) H. J. Choi, M. P. Suh, *J. Am. Chem. Soc.* **1998**, *120*, 10622–10628; d) S. Aoki, M. Shiro, T. Koike, E. Kimura, *J. Am. Chem. Soc.* **2000**, *122*, 576–584.
[7] R. L. Webb, M. L. Mino, E. L. Blinn, A. A. Pinkerton, *Inorg. Chem.* **1993**, *32*, 1396–1402.
[8] a) H. H. Song, L. M. Zheng, Y. J. Liu, X. Q. Xin, A. J. Jacobsen, S. Decurtins, *J. Chem. Soc., Dalton Trans.* **2001**, 3274–3278; b) P. Yin, Y. Peng, L. M. Zheng, S. Gao, X. Q. Xin, *Eur. J. Inorg. Chem.* **2003**, 726–730.
[9] S. Koner, S. Saha, T. Mallah, K. I. Okamoto, *Inorg. Chem.* **2004**, *43*, 840–842.
[10] J. R. Pilbrow, *Transition Ion Electron Paramagnetic Resonance*, Clarendon Press, Oxford, **1990**.
[11] K. M. S. Etheredge, S. J. Hwu, *Inorg. Chem.* **1996**, *35*, 5278–5282.
[12] B. J. Holliday, Y. M. Jeon, C. A. Mirkin, C. L. Stern, C. D. Incarvito, L. N. Zakharov, R. D. Sommer, A. L. Rheingold, *Organometallics* **2002**, *21*, 5713–5725.
[13] a) L. J. Farrugia, *J. Appl. Crystallogr.* **1999**, *32*, 837–838; b) Z. Otwinowski, W. Minor, in *Methods Enzymology, Macromolecular Crystallography, Part A* (Eds.: C. W. Carter Jr., R. M. Sweet), Academic Press, New York, **1997**, Vol. 276, 307–326; c) G. M. Sheldrick, *Acta Crystallogr., Sect. A Zeitschrift wurde bereits 1982 stillgelegt!* **1990**, *46*, 467–473; d) G. M. Sheldrick, SHELXL-97, *A Computer Program for Crystal Structure Determination*, University of Göttingen, Germany, **1997**.

Received: February 7, 2005

 © 2005 Wiley-VCH Verlag GmbH & Co. KGaA, Weinheim

Vanadium(V) Oxoperoxo Complexes with Side Chain Substituted *N*-Salicylidenehydrazides: Modeling Supramolecular Interactions in Vanadium Haloperoxidases

Simona Nica,[a] Axel Pohlmann,[a] and Winfried Plass*[a]

Dedicated to Professor Dirk Walther on the occasion of his 65th birthday

Keywords: Hydrogen bonds / Oxidative bromination / Peroxo ligands / Salicylidenehydrazide ligand / Vanadium

The Schiff-base ligand derived from salicylaldehyde and γ-hydroxybutanoic acid hydrazide (H_2Salhyhb) reacts with potassium metavanadate and hydrogen peroxide in a water/methanol solution with a pH value of around two to yield the corresponding vanadium(V) oxoperoxo complex [VO(O_2)-HSalhyhb(H_2O)] (**1**). Complex **1** crystallizes with one molecule of water as **1**·H_2O in the monoclinic space group $P2_1/n$. For the vanadium atom a pentagonal-bipyramidal coordination geometry is observed, with a side-on bonded peroxo ligand in the equatorial plane. The hydroxy side chain of the hydrazide ligand is involved in a hydrogen-bond network with the peroxo ligand at the vanadium atom. This network shows some similarities with the hydrogen-bonding scheme found for the peroxo form of vanadium haloperoxidases. The stoichiometric reaction of **1** with 1,3,5-trimethoxybenzene (TMB) in the presence of tetrabutylammonium bromide leads to the formation of 1-bromo-2,4,6-trimethoxybenzene (Br-TMB), thus mimicking the oxidative halogenation function of the native enzyme. Complex **1** is also capable of oxidizing triphenylphosphane and methylphenylsulfane, yielding a *cis*-dioxovanadium(V) complex and the corresponding phosphane or sulfane oxide, respectively.
(© Wiley-VCH Verlag GmbH & Co. KGaA, 69451 Weinheim, Germany, 2005)

Introduction

Vanadium haloperoxidases (VHPO) are enzymes capable of catalyzing halide oxidation by hydrogen peroxide to give the corresponding hypohalous acid.[1] This oxidized intermediate can halogenate various organic substrates,[2] or react with a second equivalent of hydrogen peroxide to produce singlet oxygen.[3] Moreover, these enzymes can also catalyze the oxidation of organic sulfanes to sulfane oxides.[4] The active site of this class of enzyme consists of a vanadate moiety with proposed trigonal bipyramidal geometry covalently bonded to a histidine residue and held within the protein by strong hydrogen-bonding interactions with several amino acid residues.[5] This active site architecture is also found in certain acid phosphatases,[6] but subtle differences concerning the relative positions of the amino acid residues are apparent,[7] in particular, for those residues that can potentially hydrogen bond with the equatorial oxygen atoms of the vanadate moiety (i.e. lysine, arginine, and serine). Recent theoretical studies and spectroscopic data for vanadium haloperoxidases suggest that the prosthetic group is a doubly protonated $[VO_2(OH)_2]^-$ vanadate moiety.[8]

Spectroscopic and kinetic studies of the native enzyme showed that no change occurs in the redox state of the prosthetic during the catalytic cycle.[9] Thus, it was proposed that the vanadate functions as a Lewis acid catalyst, reacting with hydrogen peroxide first to form a side-on bonded peroxo ligand, which in turn may be activated through hydrogen-bonding interactions with the first shell of amino acids and nearby water molecules.[10] This is proposed to activate the peroxo intermediate by protonation which would increase the electrophilicity of the oxygen atoms of the peroxo group, thus making attack by a halide ion more favorable.[11] This mechanistic feature is also found for the heterolytic cleavage of O–O bonds in heme-based peroxidase enzymes.[12] On the basis of this aspect of the biological function of vanadate in VHPO, the synthesis of structural models with relevant hydrogen-bonding interactions has recently been reported.[13–18]

Renirie et al. spectrophotometrically determined the stability and reactivity of such a peroxo intermediate.[19] The peroxo complex is very stable at a pH value of 8 and exists for a long period of time, but is less stable at a pH value of 5 (the pH for optimum activity for the native enzyme). However, under both conditions, the enzyme is capable of oxidizing chloride ions to hypochloric acid by a pseudo first

[a] Institut für Anorganische und Analytische Chemie,
Friedrich-Schiller-Universität Jena,
Carl-Zeiss-Promenade 10, 07745 Jena, Germany
Fax: +49-3641-948132
E-mail: Sekr.Plass@uni-jena.de

 DOI: 10.1002/ejic.200401060

order reaction. Moreover, mutagenesis studies of vanadium chloroperoxidase proved that the amino acid residues His404, Arg490, Arg360, and Ser402 perform an essential role in haloperoxidase-catalyzed reactions.[20] All of these residues are involved in hydrogen-bonding interactions with the prosthetic group. The proposed bromination of the serine residue during the catalytic turnover has become a matter of debate in recent years.[21] This crucial role could neither be confirmed by site-directed mutagenesis studies,[22] nor by catalytic studies of model systems containing a relevant hydroxy side chain.[17] However, in mutagenesis studies a significant decrease in the enzyme activity could be observed for the chlorination and bromination reactions to about 4 and 20%, respectively.[22] This indicates that the serine residue, although not crucial, plays an important role in affecting the reactivity of the active site.

We recently reported on vanadium(v) complexes derived from the *N*-salicylidene-hydrazide ligand system that exhibit extensive hydrogen bonding.[13–17] Herein we report on the structure and reactivity of the first vanadium(v) oxoperoxo complex with a hydroxy substituted side chain, a basic ligand system that participates in hydrogen-bonding interactions relevant for vanadium haloperoxidases.

Results and Discussion

The new Schiff base ligand derived from 4-hydroxybutanoic acid hydrazide and salicylaldehyde (H_2Salhyhb) reacts with potassium vanadate and hydrogen peroxide in a methanol/water solution at 0 °C in the presence of perchloric acid to afford the orange vanadium(v) oxoperoxo complex [VO(O_2)HSalhyhb·H_2O] (**1**). Due to the acidic reaction conditions the tridentate carbonic acid hydrazide ligand is present in the mono anionic form, and upon coordination it yields the neutral complex **1**. It is worth noting that for vanadium(v) complexes with this kind of ligand system, it has been shown that the N–H proton of the amide group can be reversibly removed, leading to a variable protonation state for this ligand.[14,15,17] Complex **1** dissolves in various organic solvents like alcohols, acetonitrile, and DMF, without undergoing decomposition. The ^{51}V NMR spectrum of **1** recorded in CD_3OD reveals a single resonance in the typical range, i.e. at –551 ppm with a peak width at half height of $\Delta\nu_{1/2}$ = 105 Hz. In [D_6]DMSO complex **1** undergoes fast decomposition as indicated by the appearance of two resonance peaks in the ^{51}V NMR spectrum. The peak at –539 ppm ($\Delta\nu_{1/2}$ = 860 Hz) is attributed to the *cis*-dioxocomplex and the second peak at –572 ppm ($\Delta\nu_{1/2}$ = 1100 Hz) is assigned to the corresponding dimeric *cis*-dioxocomplex; the intensity ratio for the two peaks is approximately 10:1. Both resonances are present immediately after the dissolution of compound **1** in [D_6]DMSO. The molecular structure of complex **1**, as determined by X-ray crystallography, reveals a pentagonal-bipyramidal geometry for the coordination around the vanadium atom, as depicted in Figure 1. The hydrazide ligand coordinates in the mono anionic form, providing an ONO donor set. In the equatorial plane, the vanadium atom is coordinated to atoms O2 and O3 of the side-on bonded peroxo group, and to the donor atoms O4, O5, and N1 of the tridentate hydrazide ligand. The axial positions of the coordination polyhedra are occupied by the oxo group O1 and by the oxygen atom O7 of the coordinated water molecule. The structural parameters given in Figure 1 are consistent with those observed for other vanadium(v) complexes containing hydrazide ligands,[14,15,17,23] and with those reported for vanadium(v) oxoperoxo complexes which generally feature the vanadium atom coordinated to the oxo group in the axial position and the peroxide bound in the equatorial position.[11,18,24] Complex **1** crystallizes with one molecule of water (O8) leading to an extensive hydrogen-bond network in the solid state, as depicted in Figure 2. The first sphere of hydrogen-bonding interactions shown in Figure 2 is located below the plane of the ligand arrangement in a *trans* orientation with respect to the oxo group O1. Consequently, the oxo group O1 and the carbonyl group O5 of the hydrazide ligand are not involved in the hydrogen-bond network, which is in agreement with their relatively low donor ability. Both enantiomers are present in the crystal structure of **1**·H_2O and form hydrogen-bonded chains through the interaction between the protonated hydrazide nitrogen atom, N2, and the peroxo group of a neighboring complex of same enantiomeric form (N2···O2A 280, N2···O3A 305 pm). These two enantiomeric chains form a bilayer that incorporates the hydrogen-bond network shown in Figure 2, and in turn leads to one-dimensional hydrogen-bonded chains parallel to [010] (see Figure 3).

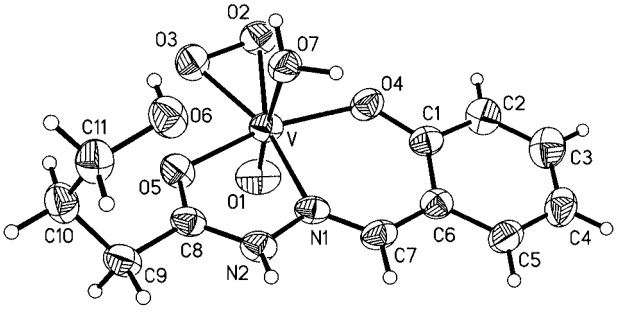

Figure 1. Molecular structure and numbering scheme for **1**. Thermal displacement ellipsoids are drawn at the 50% probability level. Selected bonds lengths [pm] and angles [°]: V–O1 157.8(3), V–O2 189.1(3), V–O3 187.6(3), V–O4 197.6(3), V–O5 207.6(3), V–O7 225.8(3), V–N1 213.2(3), O2–O3 142.9(4); O1–V–O2 103.48(13), O1–V–O3 101.94(14), O1–V–O4 97.52(15), O1–V–O5 94.26(14), O1–V–O7 170.08(13), O2–V–O3 44.57(12), O2–V–O4 79.39(12), O2–V–O5 119.93(12), O2–V–O7 86.31(12), O3–V–O4 123.41(13), O3–V–O5 75.86(12), O3–V–O7 86.08(12), O4–V–O5 154.21(12), O4–V–O7 82.58(11), O5–V–O7 81.95(11), O1–V–N1 94.16(13), O2–V–N1 155.91(12), O3–V–N1 146.81(13), O4–V–N1 82.17(12), O5–V–N1 74.14(12), O7–V–N1 76.01(11).

A situation reminiscent of the role of the active site lysine residue in VHPO[10] is found by considering the hydrogen-bond interaction between the peroxo ligand (O2 and O3) and the acidic N–H group of the hydrazide ligand (N2).[14,15,17] A second type of hydrogen-bond pathway related to the peroxo group originates from the hydroxy side

 © 2005 Wiley-VCH Verlag GmbH & Co. KGaA, Weinheim

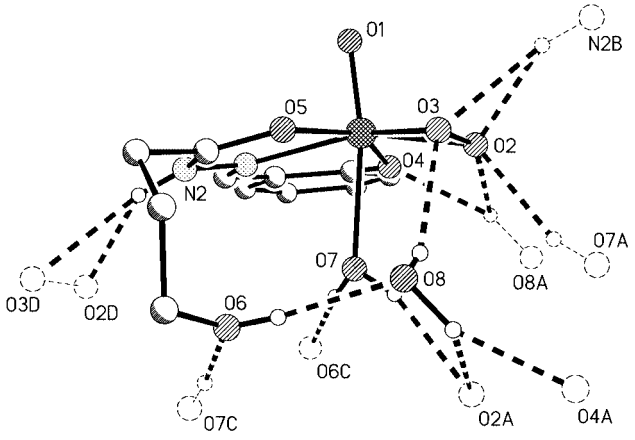

Figure 2. Hydrogen-bond network for complex **1**·H_2O. Only hydrogen atoms bonded to non-carbon atoms are shown, broken lines represent hydrogen bonds, dashed circles and lines represent symmetry equivalent atoms and the bonds between them, respectively (symmetry operators A: 1 – *x*, –*y*, –*z*; B: *x*, *y* – 1, *z*; C: 1 – *x*, 1 – *y*, –*z*; D: *x*, 1 + *y*, *z*). Selected hydrogen bond lengths [pm]: N2···O2D 280.2, N2···O3D 305.2, O6···O8 286.0, O7···O2A 282.7, O7···O6C 271.1, O8···O2A 306.0, O8···O3 299.8, O8···O4A 295.8.

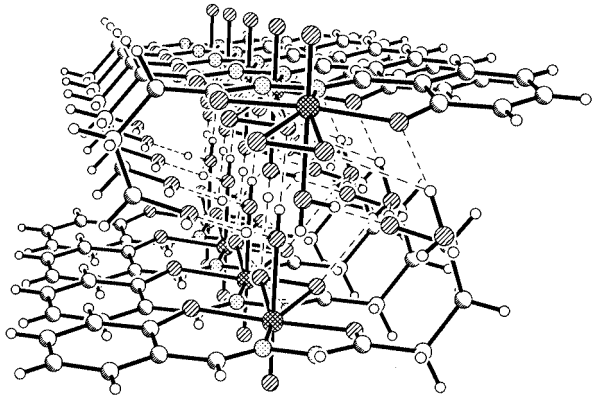

Figure 3. Representation of the hydrogen-bonded bilayer for complex **1**·H_2O, as viewed approximately along the [010] direction.

chain (O6) of the hydrazide ligand system. This side chain is involved in a hydrogen-bonding cascade that includes the water oxygen atom O8 (O6···O8 286 pm); this then leads to an intramolecular interaction with the oxygen atom O3 of the peroxo group (O8···O3 299 pm), and an intermolecular interaction with the peroxo oxygen atom O2 (O8···O2A 306 pm) of a neighboring complex. The latter of these hydrogen bonds is part of a bifurcated interaction between O8 and atoms O2 and O4 (see Figure 2). The hydrogen-bond network is completed by the oxygen atom of the coordinated water molecule, O7, which forms intermolecular contacts with the hydroxy side chain oxygen atom O6 (O6C···O7 271 pm) and with the peroxo oxygen atom O2 (O7···O2A 283 pm) of two different neighboring molecules from opposite enantiomeric chains. The observed hydrogen-bonding interactions are of specific interest due to the presence of the Ser402 residue in the active site of VHPO, in particular, they are of possible relevance to proton transfer reactions.[8]

For VHPO enzymes, a peroxo species has been proposed as an intermediate in the catalytic cycle.[10] Moreover, *cis*-dioxovanadium(V) complexes have been reported as structural and functional models for vanadium haloperoxidases that are capable of catalyzing bromination reactions with hydrogen peroxide in DMF.[25] To probe the haloperoxidase activity of complex **1**, we investigated its ability to catalyze the formation of an oxidizing bromine species. We monitored the formation of the bromo derivatives of 1,3,5-trimethoxybenzene (TMB). TMB is strongly activated towards electrophilic substitution, and can act as a quenching agent. Complex **1** reacts with one equivalent of TMB, in the presence of excess tetra-*n*-butylammonium bromide, and one equivalent of perchloric acid to yield Br-TMB. About 90% of TMB was converted to the corresponding brominated compound in less than 30 min (as monitored by HPLC). It should be noted that in the absence of acid no brominated products could be observed.

Another important reaction catalyzed by VHPO is the oxidation of organic sulfanes to sulfane oxides.[4] Although the mechanism for this reaction is not yet known, it is thought to proceed via a peroxo intermediate. To probe the sulfoxidation reactivity of the reported vanadium(V) oxoperoxo complex, **1** was treated with one equivalent of methylphenylsulfane in a methanol/dichloromethane mixture as solvent. The methylphenylsulfane was oxidized slowly, and about 75% conversion to the corresponding sulfane oxide occurred in about 48 h. It is interesting to note that this is about the same length of time usually observed for a comparable rate of conversion in model systems in which only 1 mol-% of the vanadium catalyst is present.[26] The oxidative capacity of **1** was further tested by investigating its reaction with triphenylphosphane in acetonitrile solution. This reaction was monitored by ^{31}P NMR spectroscopy – the phosphane oxide is readily formed together with the corresponding *cis*-dioxovanadium(V) complex, implying that full conversion of the reactants had occurred.

Conclusions

In this contribution the first example of a vanadium(V) oxoperoxo complex with a hydroxy side chain substituted ligand system is reported. This complex is of interest due to the presence of a serine residue within the active site environment of the prosthetic group. The importance of this residue is exemplified by the vast number of hydrogen-bonding interactions observed, which are involved in pathways relevant to the enzymatic activity. The complex is capable of generating hypobromic acid, which in turn can brominate 1,3,5-trimethoxybenzene as the organic substrate, thus modeling the corresponding enzyme reaction. Moreover, the oxidation of methylphenylsulfane and triphenylphosphane can be preformed by the reported vanadium(V) oxoperoxo complex.

Experimental Section

General Remarks: *N*,*N*-Dimethylformamide was purified and distilled prior to use. All other chemicals and solvents were of analyti-

 © 2005 Wiley-VCH Verlag GmbH & Co. KGaA, Weinheim

cal reagent grade and were used as received. The reaction with triphenylphosphane was carried out under argon using standard Schlenk techniques. Perchloric acid was standardized by potentiometric titration with 1 M NaOH solution utilizing a Mettler Toledo DL 50 titrator. ^{1}H, ^{13}C, and ^{51}V NMR spectra were recorded with Bruker AVANCE 200 and 400 MHz spectrometers. The chemical shift values for ^{51}V are reported relative to $VOCl_3$ as external standard. All NMR spectra were recorded at room temperature. Elemental analyses (C, H, N) were carried out with a Leco CHNS-932 elemental analyzer. Mass spectra were measured with a MAT95XL Finnigan instrument utilizing electron spray ionization and observations were made in the negative mode. IR spectra were recorded with a Bruker IFS55/Equinox spectrometer on samples prepared as KBr pellets. Gas chromatography measurements were performed with a SRI 8610 gas chromatograph using a MXT-1 Restek column. HPLC analyses were performed on a Jasco MD-1515 system equipped with a multiwavelength detector and a Spherisorb ODS-2 column.

Preparation of [VO(O$_2$)HSalhyhb(H$_2$O)]·H$_2$O (1·H$_2$O): KVO_3 (0.69 g, 5 mmol) was dissolved in water (20 mL) and H_2O_2 (0.75 mL of a 30% aqueous solution). A solution of H_2Salhyhb (1.11 g, 5 mmol) in methanol (25 mL) was added dropwise to the KVO_3 solution, which had been cooled to 0 °C, while constantly stirring. The pH of the resulting orange-red solution was adjusted to about 2 with perchloric acid. The solution was stirred at 0 °C for an additional 30 min, and during this time an orange solid precipitated. This was filtered off and washed with cold methanol. The filtrate solution was kept at 5 °C in a closed vessel for about one week. Orange crystals grew, and these were filtered off and dried in vacuo. Yield: 1.38 g (3.9 mmol, 77%). $C_{11}H_{17}N_2O_8V$ (**1**·H_2O) (356.21): calcd. C 37.09, H 4.81, N 7.86; found C 37.73, H 4.71, N 8.09. ^{1}H NMR (400 MHz, CD_3OD): δ = 1.96 (tt, J = 6.8 Hz, 2 H, CH_2CH$_2$OH), 2.52 (t, J = 7.6 Hz, 2 H, CH_2CO), 3.67 (t, J = 6.4 Hz, 2 H, CH_2OH), 4.83 (s, H_2O), 6.91–7.01 (m, 2 H, arom. CH), 7.49–7.58 (m, 2 H, arom. CH), 8.56 (s, 1 H, CH=N) ppm. $^{13}C\{^{1}H\}$ NMR (50 MHz, CD_3OD): δ = 29.0 (*C*H$_2$CO), 30.5 (*C*H$_2$CH$_2$OH), 62.4 (*C*H$_2$OH), 117.7, 121.4, 121.5, 133.4, 133.7 (arom. CH), 153.2 (CH=N), 165.1 (arom. C), 179.7 (C=O) ppm. ^{51}V NMR (105 MHz, CD_3OD): δ = –551 ppm ($\Delta\nu_{1/2}$ = 105 Hz). Selected IR data (KBr): $\tilde{\nu}$ = 978 (V=O), 921 (O–O, peroxo), 765 [asym. V(O)$_2$], 562 [sym. V(O)$_2$] cm^{-1}. ESI-MS (negative mode): m/z = 318.9 [M$^-$, – H, – H_2O].

Bromide Oxidation: The oxidative bromination of 1,3,5-trimethoxybenzene (TMB; 25 mg, 0.15 mmol) with complex **1** (54 mg, 0.15 mmol) in the presence of a 10-fold excess of tetrabutylammonium bromide (0.483 g, 1.5 mmol) and one equivalent perchloric acid, was performed in DMF (30 mL, 5 M in TMB). The reaction (i.e. the formation of Br-TMB) was monitored by HPLC with a Sperisorb ODS-2 column; the solvent system used was a H_2O/CH_3OH (50:50) mixture.

Reaction with Methylphenylsulfane: A solution of complex **1** (19 mg, 0.05 mmol) in a dichloromethane/methanol solution (10 mL of a 7:3 solution) reacted with one equivalent of methylphenylsulfane at room temperature. The reaction (i.e. the formation of methylphenylsulfane oxide) was monitored qualitatively by thin-layer chromatography using an eluent mixture of ethyl acetate/chloroform/methanol (5:10:3), and monitored quantitatively by gas chromatography.

Reaction with Triphenylphosphane: Triphenylphosphane (13 mg, 0.05 mmol) was added to a solution of **1** (19 mg, 0.05 mmol) in acetonitrile (15 mL), and the resulting solution was refluxed for 1 h. Upon cooling to room temperature, a yellow precipitate was formed. This was removed by filtration, and the filtrate solution kept at 5 °C. Additional precipitate formed, which resulted in an overall yield of 9.8 mg (0.03 mmol; 64%) of the *cis*-dioxovanadium(V) complex. ^{51}V NMR (105 MHz, [D$_6$]DMSO): δ = –539 ppm. The formation of triphenylphosphane oxide was monitored by ^{31}P NMR spectroscopy.

X-ray Crystallographic Study for 1·H$_2$O: $C_{11}H_{17}N_2O_8V$, M_r = 356.21 g mol^{-1}, monoclinic, space group $P2_1/n$, a = 1034.3(2), b = 698.86(14), c = 2006.6(4) pm, β = 100.74(3), V = 1425.0(5)·10^6 pm^3, Z = 4, μ(Mo-$K\alpha$) = 0.740 mm^{-1}, 14918 reflections measured with a STOE IPDS imaging plate system at 293 K in the 3.09–29.39° θ range, 3887 unique reflections (R_{int} = 0.1472) were used in the data analysis. The structure was solved by direct methods with SHELXS-97 and subsequently refined against F^2 with SHELXL-97.[27] The refinement converged at $R1$ = 0.0454 for 1467 observed reflections with $I > 2\sigma(I)$, and $wR2$ = 0.0807 for all unique reflections. The goodness-of-fit on F^2 was 0.768. The anisotropic displacement parameters for all non-hydrogen atoms were refined. All hydrogen atoms bonded to carbon atoms were introduced at theoretical positions, and were not refined. The hydrogen atoms bonded to nitrogen and oxygen atoms were located in the difference Fourier map and their isotropic displacement parameters were refined, with the exception of the hydrogen atoms of the free water molecule. The isotropic displacement parameters for these hydrogen atoms were fixed to 1.5 times that of the oxygen atom O8. The largest positive and negative residual Fourier peaks after the refinement were equal to 0.29 and –0.44, respectively. CCDC-258615 contains the supplementary crystallographic data for this paper. These data can be obtained free of charge from The Cambridge Crystallographic Data Centre via www.ccdc.cam.ac.uk/data_request/cif.

Acknowledgments

Support by the Deutsche Forschungsgemeinschaft and the Fonds der Chemischen Industrie is gratefully acknowledged.

[1] a) R. Wever, W. Hemrika, in: *Handbook of Metalloproteins*, vol. 2 (Eds.: A. Messerschmidt, R. Huber, T. Poulos, K. Wieghardt), John Wiley & Sons Ltd., Chichester, **2001**, pp. 1417–1428; b) A. Butler, *Curr. Opin. Chem. Biol.* **1998**, *2*, 279–285.
[2] A. Butler, *Coord. Chem. Rev.* **1999**, *187*, 17–35.
[3] a) R. Renirie, C. Pierlot, J.-M. Aubry, A. F. Hartog, H. E. Schoemaker, P. L. Alsters, R. Wever, *Adv. Synth. Catal.* **2003**, *345*, 849–858; b) R. R. Everett, H. S. Soedjak, A. Butler, *J. Biol. Chem.* **1990**, *265*, 15671–15679.
[4] a) M. Andersson, A. Willetts, S. Allenmark, *J. Org. Chem.* **1997**, *62*, 8455–8458; b) H. B. ten Brink, A. Tuynman, H. L. Dekker, W. Hemrika, Y. Izumi, T. Oshiro, H. E. Schoemaker, R. Wever, *Inorg. Chem.* **1998**, *37*, 6780–6784; c) H. B. ten Brink, H. E. Schoemaker, R. Wever, *Eur. J. Biochem.* **2001**, *268*, 132–138.
[5] a) A. Messerschmidt, R. Wever, *Proc. Natl. Acad. Sci. USA* **1996**, *93*, 392–396; b) M. Weyand, H.-J. Hecht, M. Kiess, M.-F. Liaud, H. Vilter, D. Schomburg, *J. Mol. Biol.* **1999**, *293*, 595–611; c) M. N. Isupov, A. R. Dalby, A. A. Brindley, Y. Izumi, T. Tanabe, G. N. Murshudov, J. A. Littlechild, *J. Mol. Biol.* **2000**, *299*, 1035–1049.
[6] W. Plass, *Angew. Chem.* **1999**, *111*, 960–962; *Angew. Chem. Int. Ed.* **1999**, *38*, 909–912.
[7] K. Ishikawa, Y.Mihara, K. Gondoh, E. Suzuki, Y. Asano, *EMBO J.* **2000**, *19*, 2412–2423.
[8] a) G. Zampella, J. Kravitz, C. Webster, P. Fantucci, M. Hall, H. Carlson, V. Pecoraro, L. Gioia, *Inorg. Chem.* **2004**, *43*, 4127–4136; b) M. Bangesh, W. Plass, *J. Mol. Struct. Theochem.* **2005**, in press.

 © 2005 Wiley-VCH Verlag GmbH & Co. KGaA, Weinheim

[9] E. de Boer, R. Wever, *J. Biol. Chem.* **1988**, *263*, 12326–12332.
[10] A. Messerschmidt, L. Prade, R. Wever, *Biol. Chem.* **1997**, *378*, 309–315.
[11] G. J. Colpas, B. J. Hamstra, J. W. Kampf, V. L. Pecoraro, *J. Am. Chem. Soc.* **1996**, *118*, 3469–3478.
[12] S. Franzen, *J. Am. Chem. Soc.* **2001**, *123*, 12578–12589.
[13] W. Plass, A. Pohlmann, H. P. Yozgatli, *J. Inorg. Biochem.* **2000**, *80*, 181–183.
[14] A. Pohlmann, W. Plass, *J. Inorg. Biochem.* **2001**, *86*, 381.
[15] W. Plass, H. P. Yozgatli, *Z. Anorg. Allg. Chem.* **2003**, *629*, 65–70.
[16] W. Plass, *Coord. Chem. Rev.* **2003**, *237*, 205–212.
[17] A. Pohlmann, S. Nica, T. K. K. Luong, W. Plass, *Inorg. Chem. Commun.* **2005**, *8*, 289–292.
[18] a) C. Kimblin, X. Bu, A. Butler, *Inorg. Chem.* **2002**, *41*, 161–163; b) M. Časný, D. Rehder, *Chem. Commun.* **2001**, 921–922.
[19] R. Renirie, W. Hemrika, S. R. Piersma, R. Wever, *Biochemistry* **2000**, *39*, 1133–1141.
[20] a) W. Hemrika, R. Renirie, S. Macedo-Ribeiro, A. Messerschmidt, R.Wever, *J. Biol. Chem.* **1999**, *274*, 23820–23827; b) S. Macedo-Ribeiro, W. Hemrika, R. Renirie, R. Wever, A. Messerschmidt, *J. Biol. Inorg. Chem.* **1999**, *4*, 209–219.
[21] H. Dau, J. Dittmer, M. Epple, J. Hanss, E. Kiss, D. Rehder, C. Schulzke, H. Vilter, *FEBS Lett.* **1999**, *457*, 237–240.
[22] N. Tanaka, Z. Hasan, R. Wever, *Inorg. Chim. Acta* **2003**, *356*, 288–296.
[23] M. R. Maurya, S. Khurana, C. Schulzke, D. Rehder, *Eur. J. Inorg. Chem.* **2001**, 779–788.
[24] a) M. Sivák, V. Suchá, L. Kuchta, J. Marek, *Polyhedron* **1998**, *18*, 93–99; b) M. Časný, D. Rehder, *Dalton Trans.* **2004**, 839–846.
[25] M. J. Clague, N. L. Keder, A. Butler, *Inorg. Chem.* **1993**, *32*, 4754–4761.
[26] C. Bolm, *Coord. Chem. Rev.* **2003**, *237*, 245–256.
[27] G. Sheldrick, *SHELXS-97* and *SHELXL-97*, University of Göttingen, **1997**.

Received: December 29, 2004
Published Online: May 2, 2005

 © 2005 Wiley-VCH Verlag GmbH & Co. KGaA, Weinheim

Synthesis, Molecular Structure and Reactivity of a Calix[4]arene Monomethyl Ether Supported Nitridomolybdenum Complex

Jürgen Zeller,[a] Susanne Büschel,[a] Benjamin K. H. Reiser,[a] Farida Begum,[b] and Udo Radius[a]*

Keywords: Calixarenes / Density functional calculations / Gallium / Molybdenum / Nitrides

The calix[4]arene monomethyl ether supported nitridomolybdenum complex [MoN(MeCalix)] (**1**) was obtained in high yield from the reaction of [MoN(O*t*Bu)$_3$] and calix[4]arene methyl ether (H_3MeCalix). Contrary to the calix[4]arene dimethyl ether supported dioxomolybdenum complex [MoO_2(*paco*-Me_2Calix)] published earlier, the calix[4]arene ligand in **1** adopts a cone conformation. Complex **1** reacts smoothly with $GaCl_3$ and $GaEt_3$ to yield the compounds [Mo($NGaCl_3$)(MeCalix)] (**2**) and [Mo($NGaEt_3$)(MeCalix)] (**3**), respectively. Complex **2** is the first structurally characterized example of a nitrido-bridged dinuclear compound of a group 6 metal and a group 13 halide (EX_3). The [Mo≡N–$GaCl_3$] unit, in which both metal atoms are unsymmetrically bridged with a short Mo≡N and a long Ga–N contact, shows significant bending at the nitrido bridge. This deviation from a linear alignment is attributed to packing forces.
(© Wiley-VCH Verlag GmbH & Co. KGaA, 69451 Weinheim, Germany, 2005)

Introduction

Calix[*n*]arenes are macrocyclic molecules made of *n* phenol units connected by *ortho* methylene groups.[1–3] Calix[4]arenes (*p*-*tert*-butylcalix[4]arene = H_4Calix) are the simplest and most common compounds of this family, with four phenolic residues in the macrocyclic ring. Because of these four phenoxy groups in the calix[4]arenes, reactions with transition metal complexes can produce metal phenolate complexes with substitution of one to four hydrogen atoms.[4] The fully deprotonated form of the parent calix[4]arene acts as a tetraanionic ligand and almost exclusively assumes the cone conformation in metallacalix[4]arenes, which keeps the set of oxygen donor atoms quasi planar. The charge of the O_4 set can be tuned by etherification or esterification of the lower rim of the calix[4]arene. The Me_2-Calix homologues, in particular, have received much attention in organotransition metal chemistry over the last 10 years, and a rich chemistry has emerged comprising mainly mononuclear group 4 and 5 metals. In these complexes, the $[R_2Calix]^{2-}$ ligands usually provide two negatively charged phenolate oxygen donor atoms and two neutral anisole oxygen donors to a transition metal. If the calix[4]arene ethers coordinate in their elliptically distorted cone conformations, these ligands provide a robust and well-defined O_4 coordination environment, similar to other widely used supporting dianionic ligands such as the O_2,N_2-donor ligands of salen-type Schiff bases or N_4-donor ligands such as porphyrins and dibenzotetraaza[14]annulenes.[5–7] In contrast to these nitrogen-containing ligand systems, the calix[4]arene dialkyl ethers are conformationally flexible.

The coordination form of calix[4]arene alkyl ethers is largely determined by the nature of the ether group, the coordination number of the metal, and the nature of the co-ligands. We have shown that the calix[4]arene ligand in the d^0 transition metal complex [$TiCl_2$(Me_2Calix)] (**A**) adopts an elliptically distorted cone conformation, whereas in the related d^0-transition metal complex [MoO_2(*paco*-Me_2-Calix)] (**B**) the metalated calix[4]arene ligand is coordinated in a partially flattened cone conformation, a form reminiscent of the partial cone (*paco*) conformation of calix[4]arene, in the solid state as well as in solution (see Scheme 1).[8] In compound **B**, the [Mo(Me_2Calix)] complex fragment is further stabilized by two additional oxo ligands, which exhibit a strong *trans* influence, and DFT calculations on models of different isomers of **A** and **B** indicate that this phenomenon is mainly driven by the co-ligands employed in these complexes.

Furthermore, in compounds of the type [Ti(O-4-C_6H_4R)$_2$-(Me_2Calix)] (R = Me or *t*Bu; **C**), both types of coordination behavior have been observed.[9] Bis(phenolate) compounds with *para*-substituted phenolate ligands have been isolated in good to excellent yields from reaction of the imidotitanium complex [Ti(N*t*Bu)(Me_2Calix)] and two equivalents of the corresponding phenol to afford complexes in which the calix[4]arene is coordinated in an elliptically distorted cone conformation. These complexes undergo elimination and/or rearrangement reactions in non-

[a] Institut für Anorganische Chemie der Universität Karlsruhe (TH),
Engesserstr., Geb. 30.45, 76131 Karlsruhe, Germany
E-mail: radius@aoc1.uni-karlsruhe.de
www.ak-radius.de
[b] Department of Chemistry, University of Dhaka,
Dhaka-1000, Bangladesh

 DOI: 10.1002/ejic.200400963 © 2005 Wiley-VCH Verlag GmbH & Co. KGaA, Weinheim

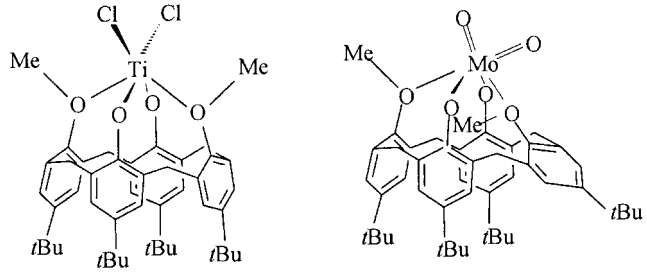

Scheme 1. Coordination of the calix[4]arene ligands in $[TiCl_2(Me_2$-Calix)] (**A**) and $[MoO_2$(*paco*-Me_2Calix)] (**B**).

polar solvents such as pentane or hexane. The metal-containing products of the elimination reactions are dinuclear complexes $[\{Ti(O\text{-}4\text{-}C_6H_4R)(MeCalix)\}_2]$ and the products of the rearrangement reactions are $[Ti(O\text{-}4\text{-}C_6H_4R)_2$(*paco*-$Me_2$Calix)]. In these compounds, one of the methoxy groups is located inside the cavity of the calix[4]arene ligand. DFT calculations on model compounds $[Ti(OC_6H_5)_2$(*cone*-Me_2Calix)] and $[Ti(OC_6H_5)_2$(*paco*-Me_2Calix)] reveal a slight thermodynamic preference for the *paco* isomer. Furthermore, *paco* coordination has only been observed in complexes of the calix[4]arene dimethyl ether in distorted octahedrally coordinated compounds of the type $[MX_2(Me_2$-Calix)].

In titanium complexes of the type [TiX(MeCalix)] (X = Cl, OR, SR, NR_2)[10] the calix[4]arene ligand adopts an elliptically distorted cone conformation in which the Ti–O distances to the anisole oxygen atoms vary in the solid-state structures in a range between 234.2 and 243.8 pm.[11] MP2 calculations on model complexes have revealed that this titanium–anisole oxygen bond is relatively weak, and, particularly in the region between 230 and 280 pm, the potential energy surface is very shallow. Thus, the MeCalix ligand acts in these complexes as a tris(phenolate) ligand with a hemilabile anisole group. Despite the labile anisole ether–titanium bond, isomerization reactions of the calix[4]arene ligand leading to a *paco* coordination have never been observed in these complexes and MP2 calculations have revealed a considerable thermodynamic preference for the cone isomers.

At this point we were interested in extending our studies to calix[4]arene monomethyl ether stabilized complexes of the type [MoX(MeCalix)] (X = ligand with *trans* directing properties), and we wish to report here our first results on the synthesis and molecular structure of the nitridomolybdenum complex [MoN(MeCalix)] and its reaction with Lewis acids of the type GaX_3 (X = Cl, Et).

Results and Discussion

Most of the calix[4]arene-stabilized molybdenum complexes known so far are compounds of the parent *p-tert*-butylcalix[4]arene.[11,12] For calix[4]arene ethers there are, to the best of our knowledge, three complexes available in the literature, $[MoOCl_2(R_2Calix)]$ (R = Me, Et) synthesized by Young et al. starting from $[MoOCl_4]$ and calix[4]arene dialkyl ether,[12j] and a dinuclear complex $[Mo_2(MeCalix)_2]$, prepared in Chisholm's group, in which the metal–metal triple bond is supported by calix[4]arene methyl ethers.[12g] This complex was synthesized by amine or butanol elimination starting from $[Mo_2(NMe_2)_6]$ or $[Mo_2(OtBu)_6]$, respectively, and the calix[4]arene ether. For the preparation of [MoN(MeCalix)] (**1**) we decided to follow a similar strategy and treated $[MoN(OtBu)_3]$[13] with H_3MeCalix in toluene (Scheme 2).

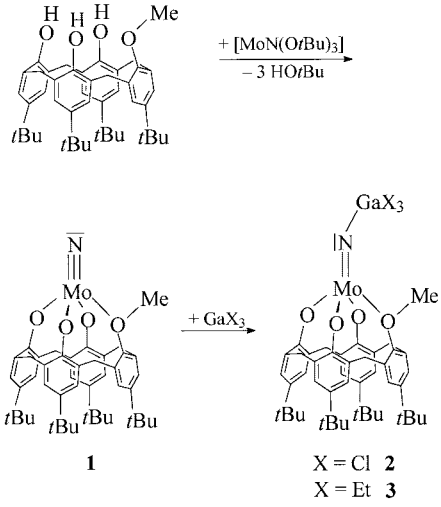

Scheme 2. Synthesis of [MoN(MeCalix)] (**1**) and reaction of **1** with $GaCl_3$ and $GaEt_3$.

This reaction proceeds cleanly with elimination of *tert*-butyl alcohol to afford the calix[4]arene ether-stabilized, neutral nitridomolybdenum(VI) complex **1** in excellent yield. Contrary to the calix[4]arene oxomolybdenum(VI) compound $[MoO(Calix)(H_2O)(PhNO_2)(H_4Calix)]$ reported by Floriani et al.,[12a] the nitrido compound is readily soluble in most organic solvents such as benzene or toluene. Compound **1** is stable with respect to either isomerization of the calix[4]arene ligand or rearrangement to a calix[4]arene-stabilized imidomolybdenum complex [Mo(NMe)(Calix)]. Analytical and spectroscopic data are in accordance with monomeric molecular units in solution as well as in the solid state, in which the calix[4]arene binds in a distorted cone conformation to the molybdenum atom. The ^1H NMR spectrum of **1** reveals a signal pattern typically found for those ligand systems in C_s symmetrical complexes, with three resonances for the *tert*-butyl protons at δ = 0.71, 0.79, and 1.37 ppm in the ratio 1:1:2 and four doublets between δ = 3.10 and 4.71 ppm with coupling constants of 12.4 Hz and 12.7 Hz. Most significantly, the methoxide resonance is detected as a sharp singlet at δ = 4.25 ppm and is not shifted to lower field as usually observed for endohedrally located anisole methyl groups, which are typically found at approximately δ = 0.8 ppm. In the IR spectrum of the complex, an intense absorption is detected in the region of the [Mo≡N] stretch at 1045 cm^{-1}.

 © 2005 Wiley-VCH Verlag GmbH & Co. KGaA, Weinheim

Crystals of **1** suitable for X-ray diffraction were obtained by cooling saturated diethyl ether solutions to –40 °C. The molecular structure of **1** is shown in Figure 1; selected bond lengths and bond angles are given in the figure caption. The structural analysis confirms the proposed mononuclear nature of **1** in the solid state and the cone conformation of the calix[4]arene ligand. In contrast to many solid-state structures of nitrido complexes, in which molecules aggregate through Mo–N···Mo contacts, we observe no intermolecular molybdenum–nitrogen interactions here. The coordination polyhedron at the molybdenum atom is best described as a square pyramid with the calixarene oxygen atoms O(1) to O(4) in the basal plane and the nitrogen atom occupying the apex. The molybdenum atom is displaced out of the calixarene O_4 plane towards the nitrogen atom of the complex, which is indicated by the N–Mo–O angles in a range between 92.4(2)° and 102.7(2)°. The Mo–O distances to the phenoxide entities [191.4(4) pm to 192.5(4) pm] and to the anisole unit [226.3(4) pm] of the calix[4]arene ligand are unexceptional. The Mo–N distance of 163.9(5) pm in **1** is significantly (approximately 8 pm) shorter than Mo–N bonds observed in calix[4]arene imidomolybdenum(VI) complexes[12b,12d] but similar to those found in other mononuclear nitridomolybdenum(VI) complexes such as $[MoN(NtBuPh)_3]$ [165.8(5) pm],[14a] $[MoN(NPh_2)_3]$ [163.4(3) pm],[14b] $[MoN(OtBu)_3]$ [166.1(4) and 167.3(5) pm],[13] $[MoN(Mes)_3]$ [164.9(4) pm],[14c] and $(Ph_4P)[MoNX_4]$ (X = Cl, Br) [163.7(4) and 162.8(15) pm].[14e,f]

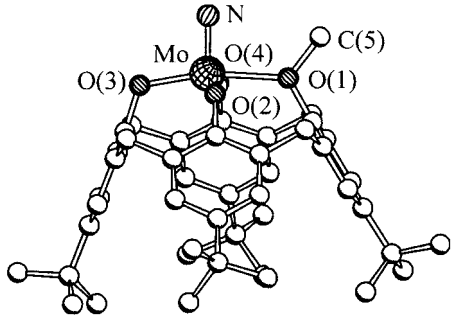

Figure 1. Schakal plot of the molecular structure of the [MoN(MeCalix)] (**1**) unit in **1**·1.5 Et_2O. H atoms and solvent molecules have been omitted for clarity. Selected bond lengths [pm] and angles [°]: Mo–N 163.9(5), Mo–O(1) 226.3(4), Mo–O(2) 191.4(4), Mo–O(3) 192.5(4), Mo–O(4) 192.0(4); N–Mo–O(1) 92.4(2), N–Mo–O(2) 102.8(2), N–Mo–O(3) 100.7(2), N–Mo–O(4) 102.7(2), O(1)–Mo–O(2) 81.29(16), O(1)–Mo–O(3) 166.92(14), O(1)–Mo–O(4) 81.41(15), O(2)–Mo–O(3) 96.21(18), O(2)–Mo–O(4) 149.62(16), O(3)–Mo–O(4) 95.03(17), Mo–O(1)–C(10) 121.7(3), Mo–O(1)–C(5) 124.5(3), Mo–O(2)–C(20) 137.4(4), Mo–O(3)–C(30) 117.6(3), Mo–O(4)–C(40) 138.1(3).

Transition metal nitrido complexes with a terminal nitrido ligand usually show Lewis basic behavior and can thus form nitrido bridges to Lewis acidic species. Compounds that contain a transition metal–nitrogen–main group element linkage have been proven to be a versatile class of compounds that exhibit vastly different chemical behavior depending on the nature of the transition metal and the main group element.[15] The structure of the compounds can range from species that have a linear transition metal–nitrogen–main group element moiety up to molecules where the nitrido linkage is strongly bent. Some compounds are monomeric while others are oligomeric or polymeric. Because of their rich chemistry, nitrido complexes have been the subject of experimental as well as theoretical studies. Whereas the formation and the chemistry of complexes with an $[Re{\equiv}N–EX_3]$ (E = group 13 element) linkage has been rather thoroughly investigated, mainly by the groups of Strähle and Abram,[16] there are few known examples of similar complexes of group 6 metals. With the exception of the complex [*trans*-$Mo(N–BPh_3)(OTf)$(*anti*-Me_8[16]aneS_4)] (Me_8[16]aneS_4 = 3,3,7,7,11,11,15,15-octamethyl-1,5,9,13-tetrathiacyclohexadecane, OTf = SO_3CF_3) published by Yoshida et al.,[17] this type of compound is, to the best of our knowledge, unknown in group 6 chemistry. Therefore we were interested in the adduct formation of complex **1** with group 13 tris(halide) and tris(alkyl) compounds. Calculations published by Frenking and coworkers[18] on model complexes of the type $[Re({\equiv}N–EX_3)(PH_3)_3Cl_2]$ have shown that in the series EH_3 (E = B, Al, Ga) the $[Re{\equiv}N–GaH_3]$ linkage is particularly weakly bonded. The zero-point-corrected dissociation energies at the MP2 level given in this paper are, for the trihydrides, 29.3 kcal mol^{-1} for E = B, 25.3 kcal mol^{-1} for E = Al, and 17.0 kcal mol^{-1} for E = Ga, and in the case of the trichlorides 31.2 kcal mol^{-1} for E = B, 42.6 kcal mol^{-1} for E = Al, and 33.5 kcal mol^{-1} for E = Ga. Because of the lack of known ER_3 and EX_3 adducts of nitridomolybdenum compounds, and the presumably weak interaction with gallium Lewis acids, we decided

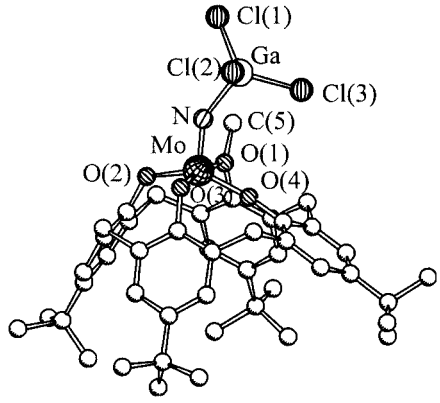

Figure 2. Schakal plot of the molecular structure of the [Mo(N-$GaCl_3$)(MeCalix)] (**2**) unit in **2**·3 C_7H_8. H atoms and solvent molecules have been omitted for clarity. Selected bond lengths [pm] and angles [°]: Mo–N 168.0(5), Mo–O(1) 223.5(4), Mo–O(2) 187.9(4), Mo–O(3) 191.6(3), Mo–O(4) 182.9(4), Ga–N 196.0(5), Ga–Cl(1) 214.1(2), Ga–Cl(2) 213.2(2), Ga–Cl(3) 218.3(3), C(5)–O(1) 146.0(7); Mo–N–Ga 147.2(3), N–Ga–Cl(1) 107.60(14), N–Ga–Cl(2) 104.27(16), N–Ga–Cl(3) 104.11(19), N–Mo–O(1) 91.3(2), N–Mo–O(2) 104.9(2), N–Mo–O(4) 111.2(3), N–Mo–O(3) 98.4(2), O(1)–Mo–O(2) 84.98(15), O(1)–Mo–O(3) 168.97(14), O(1)–Mo–O(4) 79.77(16), O(2)–Mo–O(3) 97.55(16), O(2)–Mo–O(4) 140.9(2), O(3)–Mo–O(4) 91.72(16), Cl(1)–Ga–Cl(2) 113.50(10), Cl(2)–Ga–Cl(3) 115.44(13), Cl(1)–Ga–Cl(3) 110.93(10), Mo–O(1)–C(10) 118.9(3), Mo–O(1)–C(5) 127.5(4), Mo–O(2)–C(20) 130.2(3), Mo–O(3)–C(30) 117.2(3), Mo–O(4)–C(40) 170.7(4).

 © 2005 Wiley-VCH Verlag GmbH & Co. KGaA, Weinheim

to investigate adduct formation of **1** with alkylgallium compounds and gallium halides.

Surprisingly, complex **1** reacts swiftly with $GaCl_3$ and $GaEt_3$ (see Scheme 2). According to NMR investigations, these compounds form the adducts [Mo(N$GaCl_3$)(MeCalix)] (**2**) and [Mo(N$GaEt_3$)(MeCalix)] (**3**) quantitatively without decomposition of the starting material. In the reaction products, the [Mo≡N] stretch does not change very much after coordination of the GaX_3 moieties: we observe these stretching frequencies in the IR spectra at 1046 cm^{-1} (**2**) and 1055 cm^{-1} (**3**). In the NMR spectra of these complexes, the resonances of the calix[4]arene ligands are slightly shifted compared to the resonances found for **1**. In the case of complex **3** the proton and carbon resonances of the $GaEt_3$ group are significantly shifted with respect to the noncoordinated molecule. By way of an example, in the ^1H NMR spectrum they are shifted from δ = 0.56 and 1.28 ppm to δ = 1.02 and 1.74 ppm. To confirm the adduct formation beyond doubt single crystals of the chloride complex **2** were grown from saturated toluene solutions at –40 °C and an X-ray diffraction study was undertaken. The molecular structure of **2** is shown in Figure selected bond lengths and bond angles are given in the figure caption.

Complex **2** crystallizes in the monoclinic space group $P2_1/c$ with three additional toluene molecules in the asymmetric unit. One of these solvent molecules is located inside the calix[4]arene cavity, whereas the others occupy general positions in the lattice. The endohedrally bound toluene molecule does not interact with the metal atom. The molecular structure confirms the composition of **2** as the $GaCl_3$ adduct of [MoN(MeCalix)] (**1**), in which the gallium atom is mounted on the nitrido nitrogen atom of **1**. Although various complexes of group 6 metal nitrido complexes with homoatomic and heteroatomic nitrido bridges [M≡N–M′] to other transition metal complex fragments are known,[19,20] complex **2** is the first structurally characterized example of a dinuclear compound of a group 6 metal complex and a group 13 halide EX_3 (E = B, Al, Ga, In; X = F, Cl, Br) with a central [M≡N–EX_3] nitrido bridge. This nitrido bridge is asymmetric; the molecular structure reveals a short Mo–N bond and a long Ga–N contact. The Mo–N distance of 168.0(5) pm in **2** is approximately 4 pm longer than the Mo–N bond observed in **1**. The Ga–N distance of 196.0(5) pm is similar to other Ga–N distances found in adducts of $GaCl_3$ with nitridorhenium complexes such as [Re(N$GaCl_3$)Cl_2(PMe_2Ph)$_3$] [197(1) pm], [Re(N$GaCl_3$)-Cl(PMe_2Ph)$_3$(NCMe)]$^+$[$GaCl_4$]$^-$ [195.9(4) pm], [Re(N$GaCl_3$)(PMe_2Ph)(Et_2dtc)] [191.6(6) pm; Et_2dtc = diethyldithiocarbamato], or [Re(N$GaCl_3$)Cl(PMe_2Ph)(H_2Et_2tcb)]$^+$-[$GaCl_4$]$^-$ [194.5(3) pm; Et_2tcb = *N*,*N*-diethylcarbamoylbenzamidate].[16b,21] The [Mo–N–Ga] linkage is significantly bent towards O(4) with an angle of 147.2(3)° at the nitrogen atom. The best planes defined by Mo, N, Ga and N, Mo, O(4) intersect each other with an angle of 5.8(6)°. This deviation from linearity is presumably due to packing forces in the lattice, since the distance of one of the chlorine atoms [Cl(1)] to the *tert*-butyl and ring *meta* carbon atoms of the phenolate entities at O(3) and O(4) of the next molecule in the lattice is slightly below 400 pm and would get even closer for an almost linear coordination. Furthermore, the coordination of $GaCl_3$ to [MoN(MeCalix)] (**1**) is accompanied by a distortion of the first coordination sphere at the molybdenum atom. The electron density at the molybdenum atom in **2** is lower than that in complex **1** due to the electron-withdrawing properties of the $GaCl_3$ moiety in the molecule. This is reflected by the shorter Mo–O contacts observed for complex **2** in general. Most significantly, the Mo–O(4) bond length is reduced from 192.0(4) pm in **1** to 182.9(4) pm in **2**, and this phenolate unit of the calixarene ligand coordinates almost linearly to the molybdenum atom [Mo–O(4)–C(40): 170.7(4)°].

The model complex [Mo(N$GaCl_3$)(MeCalix^H)] $\mathbf{2^H}$, in which the *tert*-butyl groups of the calix[4]arene have been replaced by hydrogen atoms to reduce computational effort, optimizes in DFT calculations[22] with a structure with slightly longer Mo–N and Ga–N distances of 169.74 pm (Mo–N) and Ga–N 202.12 pm (Ga–N) compared to the molecular structure of **2**. The calculated Mo–N–Ga angle of 169.74°, however, is closer to linearity than the angle observed in the molecular structure. The distortion of the calix[4]arene ligand in the coordination sphere of the molybdenum atom is also well reproduced in the computations. The zero-point-corrected dissociation energies calculated at the level employed here for the gallium–nitrogen bond in $\mathbf{2^H}$ is 25.8 kcal mol^{-1} and therefore slightly smaller than the dissociation energies computed by Frenking and coworkers for the nitridorhenium system mentioned above (33.5 kcal mol^{-1}) and similar to the dissociation energy calculated for [Cl_3W≡N–$AlCl_3$] (22.06 kcal mol^{-1}) by the same group.[23]

Conclusions

We have shown that [MoN(MeCalix)] (**1**) can be synthesized in high yield in an alcohol elimination reaction starting from [MoN(O*t*Bu)$_3$] and the calix[4]arene H_3MeCalix. Contrary to the dioxomolybdenum complex [MoO_2(*paco*-Me_2Calix)] (**B**) the calixarene ligand in **1** is coordinated in the cone conformation. Complex **1** is stable with respect to either isomerization of the calix[4]arene ligand or rearrangement to a calix[4]arene-stabilized imidomolybdenum complex. The calix[4]arene ether ligand provides enough electron density to the [Mo≡N] moiety in **1** that reactions with $GaCl_3$ and $GaEt_3$ proceed smoothly and afford the complexes [Mo(N$GaCl_3$)(MeCalix)] (**2**) and [Mo(N$GaEt_3$)(MeCalix)] (**3**). Complex **2** is the first structurally characterized nitrido-bridged compound of a group 6 metal complex and a group 13 metal halide [EX_3]. The [M≡N–EX_3] linkage is significantly bent at the nitrido nitrogen atom, which is attributed to packing forces.

Experimental Section

General Remarks: All air/moisture-sensitive manipulations were performed using standard Schlenk-line (N_2) and dry-box (Ar) tech-

 © 2005 Wiley-VCH Verlag GmbH & Co. KGaA, Weinheim

niques. Solvents were pre-dried and refluxed over sodium, potassium, or sodium-potassium alloy (1:3 w/w; benzene, toluene, pentane, hexane, diethyl ether, THF), or P_2O_5 (acetonitrile, dichloromethane) under N_2. Solvents were distilled at atmospheric pressure prior to use. Deuterated solvents were dried with sodium. $GaEt_3$ was obtained from commercial sources and distilled prior to use.

^1H and $^{13}C\{^1H\}$ NMR spectra were recorded on a Bruker AC 250 spectrometer at 298 K. Spectra are referenced internally to residual protonated solvent resonances (^1H; C_6D_6: δ = 7.15 ppm) or solvent (^{13}C; C_6D_6: δ = 128.0 ppm) and are reported relative to tetramethylsilane (δ = 0.00 ppm). Chemical shifts are quoted in δ (ppm) and coupling constants in Hertz. Standard DEPT-135 experiments were recorded to distinguish CH_3- and CH-type carbon atoms from C- or CH_2-type carbon atoms in the ^{13}C NMR spectrum. IR spectra were recorded on a Bruker IFS28 spectrometer as KBr pellets. All data are quoted in wavenumbers (cm^{-1}). Mass spectra were recorded on a Finnigan MAT 900 XLT. All data are quoted as their mass/charge (*m*/*z*) ratios. Elemental analyses were carried out by the analytical laboratory of the Institute of Inorganic Chemistry of the University Karlsruhe (TH). [Mo(N)(O*t*Bu)$_3$][13] and H_3MeCalix[24] were synthesized according to literature procedures.

[MoN(MeCalix)] (1): Toluene (50 mL) was added to a mixture of H_3MeCalix (15.00 g, 22.6 mmol) and [MoN(O*t*Bu)$_3$] (7.44 g, 22.6 mmol). The initially orange-colored solution turned red after a short time and the resulting reaction mixture was stirred for three hours and then filtered through a pad of Celite. The filtrate was evaporated to dryness to afford [MoN(MeCalix)] (**1**) as an orange-red powder. Yield: 16.50 g (21.5 mmol, 95%). Crystals suitable for X-ray diffraction were obtained either from hot saturated toluene solutions or from saturated diethyl ether solutions at –40 °C. $C_{45}H_{55}MoNO_4$ (769.9): calcd. C 70.21, H 7.20, N 1.82; found C 70.48, H 7.30, N 1.84. EI/MS: *m*/*z* (%) = 769 (27) $[M]^+$. IR (KBr): $\tilde{\nu}$ = 1045 cm^{-1} (vs) ν(Mo≡N). ^1H NMR (C_6D_6): δ = 0.71 [s, 9 H, C(CH_3)$_3$], 0.79 [s, 9 H, C(CH_3)$_3$], 1.37 [s, 18 H, C(CH_3)$_3$], 3.10 (d, $^2J_{H,H}$ = 12.7 Hz, 2 H, CH_2), 3.16 (d, $^2J_{H,H}$ = 12.4 Hz, 2 H, CH_2), 4.25 (s, 3 H, OCH_3), 4.35 (d, $^2J_{H,H}$ = 12.4 Hz, 2 H, CH_2), 4.70 (d, $^2J_{H,H}$ = 12.7 Hz, 2 H, CH_2), 6.81 (s, 2 H, Aryl-H_m), 6.88 (s, 2 H, Aryl-H_m), 7.19 (s, 4 H, Aryl-H_m) ppm. $^{13}C\{^1H\}$ NMR (C_6D_6): δ = 30.5, 30.9, 31.9 [C(*C*H$_3$)$_3$], 32.8, 33.4 (*C*H$_2$), 33.7, 33.9, 34.3 [*C*(CH$_3$)$_3$], 76.2 (O*C*H$_3$), 124.4, 125.9, 126.0, 127.0 (Aryl-C_m), 129.5, 129.6, 131.1, 134.7 (Aryl-C_o), 144.7, 146.2, 150.8 (Aryl-C_p), 149.4, 151.6, 156.1 (Aryl-C_i) ppm.

[Mo(NGaCl$_3$)(MeCalix)] (2): [MoN(MeCalix)] (**1**; 0.77 g, 0.99 mmol) was dissolved in toluene (20 mL) and a solution of $GaCl_3$ (0.18 g, 1.01 mmol) in toluene (10 mL) was slowly added at room temperature. The resulting reaction mixture was stirred overnight at room temperature, filtered through a pad of Celite, and the volatile components of the filtrate were removed in vacuo. The resulting solid was suspended in hexane and filtered off to afford **2** as a brown powder Yield: 0.72 mg (0.76 mmol, 77%). Crystals suitable for X-ray diffraction were obtained from saturated toluene solutions at –40 °C. $C_{45}H_{55}Cl_3GaMoNO_4$ (946.0): calcd. C 57.74, H 5.86, N 1.48; found C 58.19, H 5.60, N 1.42. IR (KBr): $\tilde{\nu}$ = 1046 cm^{-1} (vs) ν(Mo≡N). ^1H NMR (C_6D_6): δ = 0.63 [s, 9 H, C(CH_3)$_3$], 0.72 [s, 9 H, C(CH_3)$_3$], 1.33 [s, 18 H, C(CH_3)$_3$], 2.97 (d, $^2J_{H,H}$ = 13.3 Hz, 2 H, CH_2), 3.08 (d, $^2J_{H,H}$ = 12.9 Hz, 2 H, CH_2), 4.07 (d, $^2J_{H,H}$ = 12.9 Hz, 2 H, CH_2), 4.26 (s, 3 H, OCH_3), 4.29 (d, $^2J_{H,H}$ = 13.3 Hz, 2 H, CH_2), 6.72 (s, 2 H, Aryl-H_m), 6.75 (s, 2 H, Aryl-H_m), 7.13 (s, 2 H, Aryl-H_m), 7.14 (s, 2 H, Aryl-H_m) ppm. $^{13}C\{^1H\}$ NMR (C_6D_6): δ = 30.4, 30.7, 31.9 [C(*C*H$_3$)$_3$], 32.6, 33.1 (*C*H$_2$), 33.8, 33.9, 34.6 [*C*(CH$_3$)$_3$], 76.1 (O*C*H$_3$), 125.7, 125.0, 126.0, 126.6 (Aryl-C_m), 129.7, 129.9, 131.9, 133.0 (Aryl-C_o), 149.3, 149.0, 151.0 (Aryl-C_p), 149.1, 151.6, 155.9 (Aryl-C_i) ppm.

[Mo(NGaEt$_3$)(MeCalix)] (3): [MoN(MeCalix)] (**1**; 0.40 g, 0.52 mmol) was dissolved in toluene (20 mL) and a solution of $GaEt_3$ (0.08 g, 0.52 mmol) in toluene (10 mL) was slowly added at room temperature and stirred for an hour. The volatile components of the reaction mixture were removed in vacuo to afford **3** as an orange-brown powder. Yield: 0.48 g (0.51 mmol, 98%). $C_{51}H_{70}GaMoNO_4$ (926.8): calcd. C 66.10, H 7.61, N 1.51; found C 65.98, H 7.39, N 1.41. IR (KBr): $\tilde{\nu}$ = 1055 cm^{-1} (vs) ν(Mo≡N). ^1H NMR (C_6D_6): δ = 0.67 [s, 9 H, C(CH$_3$)$_3$], 0.75 [s, 9 H, C(CH$_3$)$_3$], 1.08 (q, $^3J_{HH}$ = 8.0 Hz, 6 H, GaCH_2R), 1.36 [s, 18 H, C(CH$_3$)$_3$], 1.74 (t, $^3J_{HH}$ = 8.0 Hz, 9 H, GaCH$_2$CH_3), 3.05 (d, $^2J_{H,H}$ = 12.9 Hz, 2 H, CH$_2$), 3.11 (d, $^2J_{H,H}$ = 12.7 Hz, 2 H, CH$_2$), 4.24 (d, $^2J_{H,H}$ = 12.5 Hz, 2 H, CH$_2$), 4.32 (s, 3 H, OCH$_3$), 4.59 (d, $^2J_{H,H}$ = 12.8 Hz, 2 H, CH$_2$), 6.77 (s, 2 H, Aryl-H_m), 6.82 (s, 2 H, Aryl-H_m), 7.15 (s, 4 H, Aryl-H_m) ppm. $^{13}C\{^1H\}$ NMR (C_6D_6): δ = 7.2 (Ga*C*H$_2$CH$_3$), 11.7 (GaCH$_2$*C*H$_3$), 30.5, 30.8, 31.9 [C(*C*H$_3$)$_3$], 32.7, 33.4 (*C*H$_2$), 33.7, 33.9, 34.3 [*C*(CH$_3$)$_3$], 76.0 (O*C*H$_3$), 124.5, 125.9, 126.1, 127.2 (Aryl-C_m), 129.4, 129.5, 130.9, 134.4 (Aryl-C_o), 145.3, 146.8, 149.1 (Aryl-C_p), 150.9, 151.0., 155.8 (Aryl-C_i) ppm.

X-ray Crystallographic Study of [MoN(MeCalix)]·1.5 Et$_2$O and [Mo(NGaCl$_3$)(MeCalix)]·3 C$_7$H$_8$: Crystal data collection and processing parameters are given in Table 1. The crystals were immersed in a film of perfluoropolyether oil on a glass fiber and transferred to a Stoe-STADI 4 (**1**·1.5 Et_2O, Mo-K_α radiation) or Stoe IPDS I diffractometer (**2**·3 C_7H_8, Ag-K_α radiation) equipped with an FTS AirJet low-temperature device. Data were collected at 203 K. The IPDS images were processed with the Stoe IPDS software package and equivalent reflections were merged. Corrections for Lorentz-polarization effects and absorption were performed if necessary and the structures were solved by direct methods. Subsequent difference Fourier syntheses revealed the positions of all other non-hydrogen atoms; hydrogen atoms were included in calculated positions. Extinction corrections were applied as required. Crystallographic calculations were performed with SHELXS-97 and SHELXL-97.[25] For compound **2**·3 C_7H_8 the methyl carbon atoms of two *tert*-butyl groups of the calixarene ligand [C(27) to C(29)] and [C(47) to C(49)] were disordered over two sites and were isotropically refined with occupancy factors of 70 and 30%. The visualization of the molecular structures was performed with the program Schakal 99.[26]

CCDC-256140 (for **1**·1.5 Et_2O) and CCDC-256141 (for **2**·3 C_7H_8) contain the supplementary crystallographic data for this paper.

Table 1. X-ray data collection and processing parameters.

	1·1.5 Et_2O	**2**·3 C_7H_8
Formula	$C_{51}H_{70}MoNO_{5.50}$	$C_{66}H_{79}Cl_3GaMoNO_4$
Formula mass	881.02	1222.31
Crystal system	monoclinic	monoclinic
Space group	*I*2/*a*	$P2_1/c$
a [Å]	24.716(3)	11.3554(6)
b [Å]	13.033(3)	23.4224(12)
c [Å]	30.483(3)	23.7856(14)
β [°]	96.040(3)	94.514(7)
V [Å^3]	9765(3)	6306.6(6)
Z	8	4
μ [mm^{-1}]	0.314	1.053
Total/indep. reflns.	6784/5954	25466/10079
Observed reflns.[a]	4446	7065
Parameters	531	616
Final *R*,[b] wR_2[c][d]	0.0575/0.1260	0.0676/0.1686

[a] Reflections with $I > 2\sigma(I)$. [b] $R = \Sigma||F_o| - |F_c||/\Sigma|F_o|$. [c] $wR_2 = \{\Sigma[w(F_o^2 - F_c^2)^2]/\Sigma[w(F_o^2)^2]\}^{1/2}$. [d] For data with $I > 2\sigma(I)$.

 © 2005 Wiley-VCH Verlag GmbH & Co. KGaA, Weinheim

These data can be obtained free of charge from The Cambridge Crystallographic Data Centre via www.ccdc.cam.ac.uk/data_request/cif.

Acknowledgments

We thank the Fonds der Chemischen Industrie and the Deutsche Forschungsgemeinschaft for financial support. F. B. is thankful for a scholarship from the DAAD for her stay in Germany.

[1] a) *Calixarenes in Action* (Eds.: M. Lucinat, R. Ungaro), Imperial College Press, London **2000**; b) G. J. Lumetta, R. D. Rogers, A. S. Gopalan, *Calixarenes for Separations*, American Chemical Society, Washington D. C. **2000**; c) C. D. Gutsche, *Calixarenes Revisited*, Royal Society of Chemistry, Cambridge **1998**; d) J. Vicens, Z. Asfari, *Calixarenes 50th Anniversary: Commemorative Issue* (Ed.: J. M. Harrowfield), Kluwer Academic Publishers, Dordrecht **1994**; e) *Calixarenes*: *A Versatile Class of Macrocyclic Compounds* (Eds.: J. Vicens, V. Böhmer), Kluwer Academic Publishers, Dordrecht **1991**; f) C. D. Gutsche, *Calixarenes*, Royal Society of Chemistry, Cambridge, **1989**.

[2] a) A. Ikeda, S. Shinkai, *Chem. Rev.* **1997**, *97*, 1713; b) V. Böhmer, *Angew. Chem.* **1995**, *107*, 785; *Angew. Chem. Int. Ed. Engl.* **1995**, *34*, 713; c) C. D. Gutsche, *Aldrichimica Acta* **1995**, *28*, 3; d) S. Shinkai, *Tetrahedron* **1993**, *49*, 8933; e) V. Böhmer, *Liebigs Ann./Recueil* **1997**, 2019; f) A. F. D. De Namor, R. M. Cleverly, M. L. Zapata-Ormachea, *Chem. Rev.* **1998**, *98*, 2485.

[3] a) A. Pochini, R. Ungaro, in *Comprehensive Supramolecular Chemistry* (Ed.: F. Vögtle), vol. 2, Elsevier, Oxford, **1996**, 103; b) Y. K. Agrawal, S. Kunji, S. K. Menon, *Rev. Anal. Chem.* **1998**, *17*, 69; c) M. A. McKervey, F. Arnaud-Neu, M.-J. Schwing-Weill, in *Comprehensive Supramolecular Chemistry* (Ed.: G. Gokel), vol. 1, Pergamon, Oxford, **1996**, p. 537.

[4] a) C. Floriani, R. Floriani-Moro, *Adv. Organomet. Chem.* **2001**, *47*, 167; b) C. Floriani, *Chem. Eur. J.* **1999**, *5*, 19; c) C. Wieser, C. B. Dieleman, D. Matt, *Coord. Chem. Rev.* **1997**, *165*, 93; d) D. M. Roundhill, *Prog. Inorg. Chem.* **1995**, *43*, 533; e) A. J. Petrella, C. L. Raston, *J. Organomet. Chem.* **2004**, *689*, 4125.

[5] a) M. Calligiaris, L. Ranaccio, *Schiff Bases as Acyclic Polydentate Ligands*, in *Comprehensive Coordination Chemistry* (Ed.: G. Wilkinson), vol. 2, Pergamon Press, Exeter, **1987**; b) C. Floriani, *Polyhedron* **1989**, *8*, 1717; c) D. E. Fenton, P. A. Vigato, *Chem. Soc. Rev.* **1988**, *17*, 69; d) J. Costamagna, J. Vargas, R. Latorre, A. Alvarado, G. Mena, *Coord. Chem. Rev.* **1992**, *119*, 67.

[6] a) *Porphyrins and Metalloporphyrins* (Ed.: K. M. Smith), Elsevier, New York, **1975**; b) *The Porphyrins* (Ed.: D. Dolphin), Academic Press, New York, **1977**–**1979**; c) B. D. Berenzin, *Coordination Compounds of Porphyrins and Phthalocyanines*, Wiley, Chichester **1981**; d) T. Mashiko, D. Dolphin, *Porphyrins, Hydroporphyrins, Azaporphyrins, Phthalocyanines, Corroles, Corrines and Related Macrocycles*, in *Comprehensive Coordination Chemistry* (Ed.: G. Wilkinson), vol. 2, Pergamon Press, Exeter, **1987**; e) K. Katylanasundaran, *Photochemistry of Polypyridine and Porphyrin Complexes*, Academic Press, London **1992**; f) *Metalloporphyrins in Catalytic Oxidations* (Ed.: R. A. Sheldon), Marcel Dekker, New York, **1994**; g) *Metal Complexes with Tetrapyrrole Ligands* (Ed.: J. W. Buchler), Springer Verlag, Berlin, **1995**; h) *The Colours of Life: An Introduction to the Chemistry of Porphyrin and Related Compounds* (Ed.: L. R. Milgram), Oxford University Press, Oxford, **1997**; i) H. Brand, J. Arnold, *Coord. Chem. Rev.* **1995**, *140*, 137.

[7] a) L. F. Lindoy, *The Chemistry of Macrocyclic Ligand Complexes*, Cambridge University Press, Cambridge **1989**; b) F. A. Cotton, J. Czuchajowski, *Polyhedron* **1990**, *9*, 2663; c) P. Mountford, *Chem. Soc. Rev.* **1998**, *27*, 105.

[8] U. Radius, *Inorg. Chem.* **2001**, *40*, 6637.

[9] a) U. Radius, *Z. Anorg. Allg. Chem.* **2004**, *630*, 957; b) U. Radius, A. Friedrich, *Z. Anorg. Allg. Chem.* **1999**, *625*, 2154; c) S. R. Dubberly, A. Friedrich, D. A. Willman, P. Mountford, U. Radius, *Chem. Eur. J.* **2003**, *9*, 3634.

[10] A. Friedrich, U. Radius, *Eur. J. Inorg. Chem.* **2004**, 4300.

[11] a) U. Radius, J. Attner, *Eur. J. Inorg. Chem.* **1998**, 299; b) U. Radius, J. Attner, *Eur. J. Inorg. Chem.* **1999**, 2221; c) U. Radius, J. Attner, *Chem. Eur. J.* **2001**, *7*, 783; d) U. Radius, J. Attner, *Eur. J. Inorg. Chem.* **2002**, 161; e) J. Attner, U. Radius, *Z. Anorg. Allg. Chem.* **2002**, *628*, 2345; f) U. Radius, J. Attner, *Inorg. Chem.* **2004** in press.

[12] See for example: a) F. Corazza, C. Floriani, A. Chiesi-Villa, C. Guastini, *J. Chem. Soc., Chem. Commun.* **1990**, 640; b) V. C. Gibson, C. Redshaw, W. Clegg, M. R. J. Elsegood, *J. Chem. Soc., Chem. Commun.* **1995**, 2371; c) J. A. Acho, S. J. Lippard, *Inorg. Chim. Acta* **1995**, *229*, 5; corrigendum: *Inorg. Chim. Acta* **1995**, *233*, 179; d) J. A. Acho, T. Ren, J. W. Yun, S. J. Lippard, *Inorg. Chem.* **1995**, *34*, 5226; e) V. C. Gibson, C. Redshaw, W. Clegg, M. R. J. Elsegood, *Chem. Commun.* **1997**, 1605; f) M. H. Chisholm, K. Folting, W. E. Streib, D.-D. Wu, *Chem. Commun.* **1998**, 379; g) M. H. Chisholm, K. Folting, W. E. Streib, D.-D. Wu, *Inorg. Chem.* **1999**, *38*, 5219; h) V. C. Gibson, C. Redshaw, W. Clegg, M. R. J. Elsegood, *Chem. Commun.* **1998**, 1969; i) C. Redshaw, M. R. J. Elsegood, *Inorg. Chem.* **2000**, *39*, 5164; j) A. J. Millar, J. M. White, C. J. Doonan, C. G. Young, *Inorg. Chem.* **2000**, *39*, 5151; k) G. Guillemot, E. Solari, R. Scopelliti, C. Floriani, *Organometallics* **2001**, *20*, 2446; l) G. Guillemot, E. Solari, R. Scopelliti, C. Floriani, *Organometallics* **2001**, *20*, 2446; m) V. C. Gibson, C. Redshaw, M. R. J. Elsegood, *New J. Chem.* **2002**, *26*, 16; n) F. A. Cotton, L. M. Daniels, C. Lin, C. A. Murillo, *Inorg. Chim. Acta* **2003**, *347*, 1.

[13] D. M.-T. Chan, M. H. Chisholm, K. Folting, J. C. Huffman, N. S. Marchant, *Inorg. Chem.* **1986**, *25*, 4170.

[14] a) C. E. Laplaza, M. J. A. Johnson, J. C. Peters, A. L. Odom, E. Kim, C. C. Cummins, G. N. George, I. J. Pickering, *J. Am. Chem. Soc.* **1996**, *118*, 8623; b) Z. Gebeheyu, F. Weller, B. Neumüller, K. Dehnicke, *Z. Anorg. Allg. Chem.* **1991**, *593*, 99; c) K. G. Coulton, M. H. Chisholm, S. Doherty, K. Folting, *Organometallics* **1995**, *14*, 2585; d) U. Müller, E. Schweda, J. Strähle, *Z. Naturforsch. Teil B* **1983**, *38*, 1299; e) K. Dehnicke, N. Krüger, R. Kujanek, F. Weller, *Z. Kristallogr.* **1980**, *159*, 181.

[15] a) K. Dehnicke, J. Strähle, *Chem. Rev.* **1993**, *93*, 981; b) K. Dehnicke, J. Strähle, *Angew. Chem.* **1992**, *104*, 978–1000; *Angew. Chem. Int. Ed, Angew. Chem. Int. Ed. Engl.* **1992**, *31*, 955–978; c) K. Dehnicke, J. Strähle, *Angew. Chem.* **1981**, *93*, 451–464; *Angew. Chem. Int. Ed. Engl.* **1981**, *20*, 413–426.

[16] See for example: a) J. Strähle, *Z. Anorg. Allg. Chem.* **2003**, *629*, 828 and references cited therein; b) U. Abram, B. Schmidt-Brücken, A. Hagenbach, M. Hecht, R. Kirmse, A. Voigt, *Z. Anorg. Allg. Chem.* **2003**, *629*, 429 and references cited therein.

[17] T. Yoshida, T. Adachi, N. Yabunouchi, T. Ueda, S. Okamoto, *J. Chem. Soc., Chem. Commun.* **1994**, 151.

[18] S. Vyboishchikov, G. Frenking, *Theor. Chem. Acc.* **1999**, *102*, 300.

[19] a) U. Müller, P. Kujanek, K. Dehnicke, *Z. Anorg. Allg. Chem.* **1982**, *495*, 127; b) T. Godemeyer, F. Weller, K. Dehnicke, D. Fenske, *Z. Anorg. Allg. Chem.* **1987**, *554*, 92; c) C. Ergezinger, A. El-Kholi, U. Müller, K. Dehnicke, *Z. Anorg. Allg. Chem.* **1989**, *568*, 55; d) A. Gorge, U. Patt-Siebel, U. Müller, K. Dehnicke, *Z. Naturforsch. B* **1989**, *44*, 903; e) R. Figge, C. Friebel, U. Patt-Siebel, U. Müller, K. Dehnicke, *Z. Naturforsch. B* **1989**, *44*, 1377; f) A. Neuhaus, K. Dehnicke, *Z. Anorg. Allg. Chem.* **1993**, *619*, 775; g) A. Dietrich, B. Neumüller, K. Dehnicke, *Z. Anorg. Allg. Chem.* **1999**, *625*, 1566; h) A. Dietrich, B. Neumüller, K. Dehnicke, *Z. Anorg. Allg. Chem.* **1999**, *625*, 1589; i) E. Gauch, A. Hagenbach, J. Strähle, A. Dietrich, B. Neumüller, K. Dehnicke, *Z. Anorg. Allg. Chem.* **2000**, *626*, 489.

[20] a) M. W. Bishop, J. Chatt, J. R. Dilworth, M. B. Hursthouse, M. Motevalli, *J. Chem. Soc., Chem. Commun.* **1976**, 780; b) G.-S. Kim, C. W. DeKock, *J. Chem. Soc., Chem. Commun.* **1989**,

1166; c) D. L. Hughes, M. Y. Mohammed, C. J. Pickett, *J. Chem. Soc., Dalton Trans.* **1990**, 2013; d) J. D. Lichtenhan, J. W. Ziller, N. M. Doherty, *Inorg. Chem.* **1992**, *31*, 2893; e) W. A. Herrmann, S. Bogdanovic, J. Behm, M. Denk, *J. Organomet. Chem.* **1992**, *430*, C33; f) W. A. Herrmann, S. Bogdanovic, T. Priermeier, R. Poli, J. C. Fettinger, *Angew. Chem.* **1995**, *107*, 63; *Angew. Chem. Int. Ed, Angew. Chem. Int. Ed. Engl.* **1995**, *34*, 112; g) T. P. Pollagi, J. Manna, S. J. Geib, M. D. Hopkins, *Inorg. Chim. Acta* **1996**, *243*, 177; h) P. Legzdins, P. J. Lundmark, S. J. Rettig, *Organometallics* **1996**, *15*, 2988.

[21] a) S. Ritter, R. Hubener, U. Abram, *J. Chem. Soc., Chem. Commun.* **1995**, 2047; b) S. Ritter, U. Abram, *Z. Anorg. Allg. Chem.* **1996**, *622*, 965; c) U. Abram, B. Schmidt-Brücken, S. Ritter, *Polyhedron* **1999**, *18*, 831.

[22] The DFT calculations were carried out with the TURBOMOLE set of programs within the RI-J approximation. Standard SV(P) basis sets and auxiliary basis sets as implemented in the TURBOMOLE package were used for all atoms. Quasi-relativistic pseudo-potentials were used for Mo. All calculations were performed including gradient corrections, Becke's nonlocal correction for exchange, and Perdew's nonlocal correction for correlation to the local density approximation part of the density functional: a) M. Häser, R. Ahlrichs, *J. Comput. Chem.* **1989**, *10*, 104; b) R. Ahlrichs, M. Bär, M. Häser, H. Horn, C. Kölmel, *Chem. Phys. Lett.* **1989**, *162*, 165; c) H. Horn, H. Weiss, M. Häser, M. Ehrig, R. Ahlrichs, *J. Comput. Chem.* **1991**, *12*, 1058; d) O. Treutler, R. Ahlrichs, *J. Chem. Phys.* **1995**, *102*, 346; e) K. Eichkorn, O. Treutler, H. P. Öhm, M. Häser, R. Ahlrichs, *Chem. Phys. Lett.* **1995**, *242*, 652; f) K. Eichkorn, F. Weigend, O. Treutler, R. Ahlrichs, *Theor. Chem. Acc.* **1997**, *97*, 119; g) F. Weigend, M. Häser, H. Patzelt, R. Ahlrichs, *Chem. Phys. Lett.* **1998**, *294*, 143; h) M. v. Arnim, R. Ahlrichs, *J. Chem. Phys.* **1999**, *111*, 9183; i) P. Deglmann, F. Furche, R. Ahlrichs, *Chem. Phys. Lett.* **2002**, *362*, 511; j) P. Deglmann, F. Furche, *J. Chem. Phys.* **2002**, *117*, 9535; k) F. Weigend, *Phys. Chem. Chem. Phys.* **2002**, *4*, 4285; l) A. D. Becke, *Phys. Rev. A* **1988**, *38*, 3098; m) S. H. Vosko, L. Wilk, M. Nusair, *Can. J. Phys.* **1980**, *58*, 1200; n) J. P. Perdew, *Phys. Rev. B* **1986**, *33*, 8822; corrigendum: J. P. Perdew, *Phys. Rev. B* **1986**, *34*, 7406; o) D. Andrae, U. Häußermann, M. Dolg, H. Stoll, H. Preuss, *Theor. Chim. Acta* **1990**, *77*, 123.

[23] P. Spuhler, M. Lein, G. Frenking, *Z. Anorg. Allg. Chem.* **2003**, *626*, 803.

[24] A. Zanotti-Gerosa, E. Solari, L. Giannini, C. Floriani, N. Re, A. Chiesi-Villa, C. Rizzoli, *Inorg. Chim. Acta* **1998**, *270*, 298.

[25] a) G. M. Sheldrick, *SHELXS-97*, *Program for Crystal Structure Solution*, Universität Göttingen, **1997**; b) G. M. Sheldrick, *SHELXL-97*, *Program for Crystal Structure Refinement*, University of Göttingen, **1997**.

[26] E. Keller, *Schakal 99, a Fortran Program for Graphical Representation of Molecular and Crystallographic Models*, University of Freiburg, **1999**.

Received: November 18, 2004
Published Online: April 25, 2005

 © 2005 Wiley-VCH Verlag GmbH & Co. KGaA, Weinheim

Mono- and Dinuclear Cu^{II} and Zn^{II} Complexes of Cyclen-Based Bis(macrocycles) Containing Two Aminoalkyl Pendant Arms of Different Lengths

Carmen Anda,[a] Andrea Bencini,[b] Emanuela Berni,[b] Samuele Ciattini,[b] Françoise Chuburu,[c] Andrea Danesi,[b] Claudia Giorgi*[b] Henri Handel*[c] Michel Le Baccon,[c] Piero Paoletti*[b] Raphaël Tripier,[c] Véronique Turcry,[c] and Barbara Valtancoli[b]

Keywords: Copper / Coordination modes / Macrocyclic ligands / N ligands / Zinc

The basicity and coordination properties towards Cu^{II} and Zn^{II} of the bis(macrocycles) **L1**, **L2** and **L3** have been investigated by means of potentiometric, ^1H NMR and UV/Vis spectroscopic titrations in aqueous solutions. The synthesis of **L1** and **L3** is also described. The three ligands are composed of two [12]aneN$_4$ units separated by a *p*-phenylene spacer and differ in the length of the aminoalkyl pendant arms linked to each macrocyclic unit. **L1**–**L3** form mono- and dinuclear complexes in aqueous solutions; in the dinuclear species each metal ion is coordinated by one of the two identical [12]aneN$_4$ ligand moieties, as shown by the crystal structures of the complexes $[Cu_2\mathbf{L1}]Cl_4\cdot 8H_2O$, $[Zn_2\mathbf{L2}](ClO_4)_4$ and $[Zn_2\mathbf{L3}](ClO_4)_4\cdot H_2O$. In all structures the metal ion is pentacoordinate, and is bound to the four nitrogen donors of the cyclic unit and to the amine group of the side arm. The stability of both the $[ML]^{2+}$ and $[M_2L]^{4+}$ complexes in aqueous solution decreases in the order **L1** > **L2** > **L3**. At the same time, both the $[Cu_2L]^{4+}$ and $[Zn_2L]^{4+}$ complexes show a different ability in proton binding among the three ligands, with the $[M_2\mathbf{L1}]^{4+}$ complexes displaying the highest basicity. These results are explained in terms of the decreasing number of nitrogen donors involved in Cu^{II} or Zn^{II} binding on passing from **L1** to **L3**; in other words, while in the **L1** dinuclear complexes each metal ion is coordinated to the four amine groups of a [12]aneN$_4$ moiety and to the amine group of the side arm, in the **L3** ones the metal cations are bound only to the four donor atoms of a cyclic moiety, the aminobutyl group not being coordinated.
(© Wiley-VCH Verlag GmbH & Co. KGaA, 69451 Weinheim, Germany, 2005)

Introduction

There is a continuing interest in the chemistry of polyazamacrocycles because of their ability to form chelates in aqueous solutions and to act as selective complexing agents for metal cations. Structural factors, such as ligand rigidity and the electron-donor properties of the nitrogen atoms and their disposition, have been shown to play significant roles in determining the binding features of macrocycles toward metal cations.[1–17]

Among polyazamacrocycles, the investigations have been focused on tetraazamacrocycles owing to their proven ability in binding biologically relevant metal ions. For example, cyclen and cyclam and their derivatives have been studied as carriers of metal ions in antitumour and imaging applications.[18–22] Furthermore, metal complexes with these polyazamacrocyclic ligands can behave as metallo-receptors for organic and inorganic anions (similar to thymidine mono- and diphosphate nucleotides).[23,24]

From this point of view the introduction of structural features that impart high selectivity in the recognition of different guests into the molecular framework is one of the goals in the design of synthetic receptors. Aromatic subunits are often introduced into the host molecules. The presence of rigid aromatic systems gives particular coordination properties to the ligands defining distinct preorganized binding sites for the metal ions within the ligand itself. Furthermore, the attachment of an aminoalkyl side arm can strongly effect the coordination properties of the ligand,[25–48] depending on the nature of the donors of the pendant arms.

To gain further insight into the coordination chemistry of cyclen derivatives, we have now synthesised the two homoditopic ligands **L1** and **L3**, which are composed of two [12]aneN$_4$ units separated by a rigid *p*-phenylene spacer; each tetraazamacrocyclic moiety bears an aminoalkyl pendant arm (an aminoethyl pendant arm in the case of **L1** and an aminobutyl one in the case of **L3**).

[a] Department of Inorganic Chemistry, University of Girona, Campus Montilivi s/n 17071 Girona, Spain
[b] Department of Chemistry, University of Florence, via della Lastruccia 3, 50019 Sesto Fiorentino, Florence, Italy
E-mail: claudia.giorgi@unifi.it
[c] Lab. de Chimie, Electrochimie Moléculaires et Chimie Analytique, Université de Bretagne Occidentale, 6, Av. Victor Le Gorgeu (UMR CNRS No 6521), CS 93837, 29238 Brest Cedex 3, France
E-mail: henri.handel@univ-brest.fr

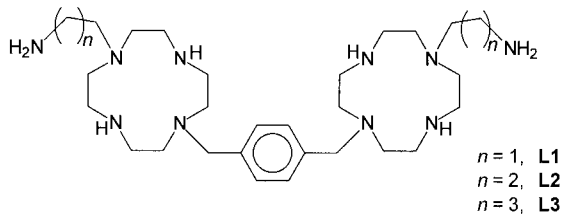

With the aim of making a comparative study of the coordination properties of these homoditopic ligands, the proton binding and Cu^{II} and Zn^{II} complexation with **L1**, **L3** and **L2**,[49] which displays a similar molecular architecture but contains two aminopropyl side arms, were studied in the solid state by X-ray diffraction methods and in aqueous solution by potentiometric and ^1H NMR measurements.

Results and Discussion

Ligand Protonation

The protonation equilibria of **L1**–**L3** were studied by means of potentiometric measurements in 0.1 M Me_4NCl aqueous solution at 298.1 K; the corresponding basicity constants are reported in Table 1.

Table 1. Logarithms of the protonation constants of ligands **L1**, **L2** and **L3** determined by means of potentiometric measurements in 0.1 M Me_4NCl at 298.1 K.

Reaction	log*K*		
	L1	**L2**	**L3**
$LH^+ + H^+ \rightleftharpoons LH_2^{2+}$	9.74(3)[a]	10.07(2)	10.30(2)
$LH_2^{2+} + H^+ \rightleftharpoons LH_3^{3+}$	8.88(5)	9.24(3)	9.54(3)
$LH_3^{3+} + H^+ \rightleftharpoons LH_4^{4+}$	8.39(4)	8.87(2)	9.08(2)
$LH_4^{4+} + H^+ \rightleftharpoons LH_5^{5+}$	7.33(6)	7.69(3)	7.80(4)
$LH_5^{5+} + H^+ \rightleftharpoons LH_6^{6+}$	6.67(6)	7.22(3)	7.40(3)

[a] Values in parentheses are standard deviations in the last significant figure.

Ligands **L1**–**L3** behave as hexaprotic bases, at least in the pH range investigated (2–11). **L1**–**L3** display almost equal basicity constants for the first protonation step (10.07–10.34 log units). Similar high values for the first protonation constant are often found in polyamine macrocycles and are generally attributed to the simultaneous involvement of two or more amine groups in proton binding.[50] The data in Table 1 also show that the first six basicity constants range between about 10 and 7 log units. Further protonation steps are not detectable by potentiometry under our experimental conditions. This behaviour can be rationalised in terms of minimisation of the electrostatic repulsion between the positive charges in the protonated species of polyazamacrocycles. In other words, the first six protons can occupy alternate positions in the macrocycles, separated by a non-protonated amine group and/or by the *p*-phenylene linkage, while three or more protonated nitrogen atoms would necessarily be contiguous in the species with a protonation degree greater than six. For this reason, the $[H_xL]^{x+}$ species with $x > 6$ (L = **L1**, **L2** and **L3**) are not formed, at least in the pH range investigated (2–11).

To shed further light on the basicity properties of these ligands, we carried out ^1H NMR titrations in aqueous solutions. The spectral features of **L1** at pH = 11.0, where the free amine predominates in solution, account for a D_{2h} time-averaged symmetry of the ligand, which is preserved over all the pH range investigated. The pH dependence of the ^1H NMR signals is shown in Figure 1, together with the distribution diagram of the protonated species of **L1**.

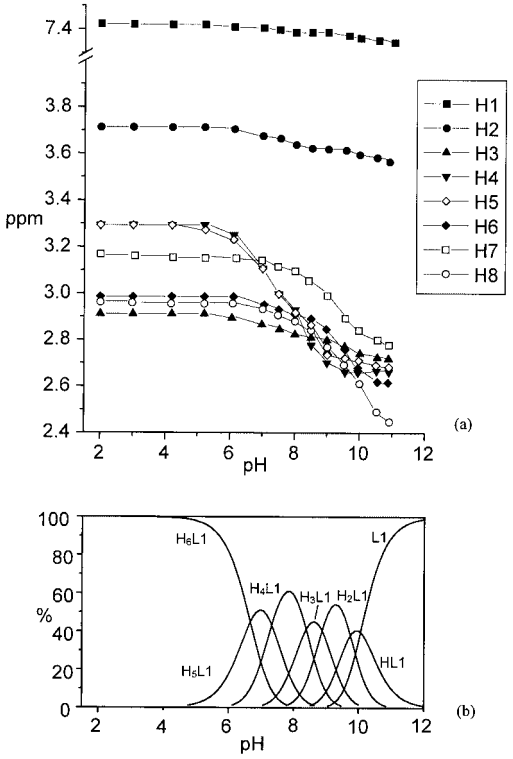

Figure 1. (a) pH dependence of the ^1H NMR signals of **L1**. (b) Distribution diagram of protonated species formed by **L1** as a function of pH (0.1 M Me_4NCl, 298.1 K, [L] = 1×10^{-3} M).

At first glance, Figure 1a shows an overall downfield shift of the resonances of all the methylene groups, with the exception of the signals of H2 and H3, which are adjacent to the tertiary amine group N1, in the pH range 11.0–6.0. This clearly indicates that the tertiary nitrogen atoms N1 are not involved in proton binding over the pH range investigated. A more accurate analysis of the pH dependence of the signals in Figure 1a shows that in the pH range 11.0–9.0, where the first two protons bind to the ligand, the resonance of H8, in the α-position with respect to N4, gives rise to the highest downfield shift (ca. 0.4 ppm), which shows that the first two protonation steps take place on the primary amine groups of the pendant arms. In the same pH range, however, a marked downfield shift (almost 0.3 ppm) is also observed for the H6 and H7 signals, which are adjacent to N3, thereby suggesting the presence of a hydrogen bond between the protonated N4 nitrogen atom and N3 and/or to a partial localisation of the acidic proton on the N3 tertiary nitrogen atom (Scheme 1).

 © 2005 Wiley-VCH Verlag GmbH & Co. KGaA, Weinheim

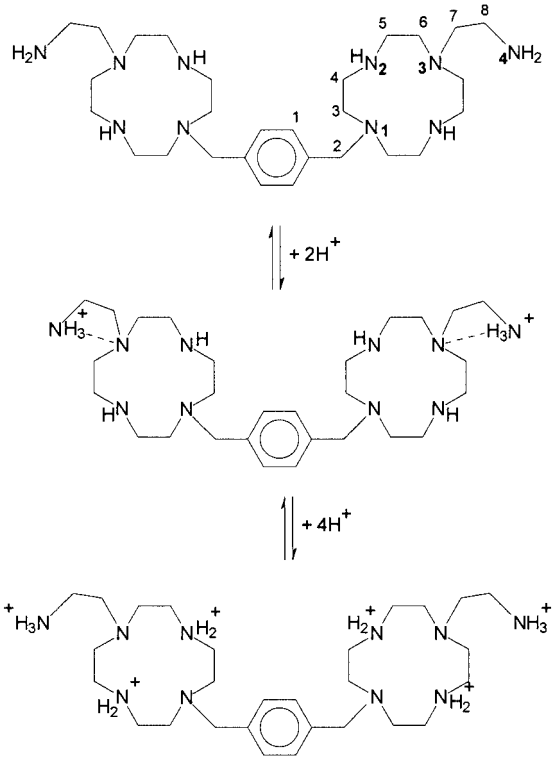

Scheme 1.

The signals of H4 and H5, which are adjacent to the N2 nitrogen atoms, do not shift remarkably (less than 0.1 ppm) up to pH = 9. In the pH range 9–6, however, these signals give rise to a remarkable downfield shift, thus indicating that the further four protonation steps occur on the secondary amine groups of the macrocyclic ring.

Similar protonation patterns, involving initial protonation of the aminoalkyl function and then proton binding to the secondary amine groups of the macrocycle, are also found for **L2** and **L3**.

Metal Coordination

*Crystal Structure of [{Cu_2**L1**}Cl_4]·8H_2O*

The molecular structure consists of centrosymmetric $[Cu_2\mathbf{L1}]^{4+}$ complex cations, chloride anions and water molecules. An ORTEP[51] drawing of the $[Cu_2\mathbf{L1}]^{4+}$ cation is shown in Figure 2, and Table 2 reports selected distances and angles for the coordination environment of the metals.

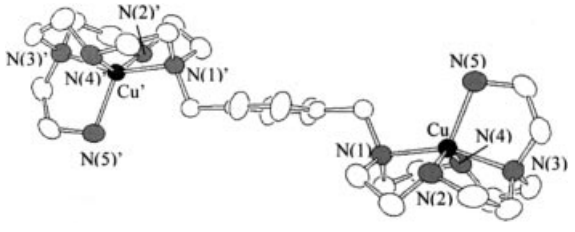

Figure 2. ORTEP drawing of the $[Cu_2\mathbf{L1}]^{4+}$ cation.

Each metal ion is lodged in a cyclic tetraaza moiety and the coordination sphere is completed by the nitrogen atom of the side arm, giving rise to an overall pentacoordination which can best be described as a distorted square pyramid. The axial position is occupied by the N5 nitrogen atom of the side arm, while N1, N2, N3 and N4 define the basal plane [maximum deviation from the mean plane of 0.075(1) Å for N4]. The Cu atom lies 0.512(1) Å above this plane and is shifted toward the apical position, with an angle of 16.65(1)° between the Cu–N5 bond and the normal to the basal plane. The Cu–N bond lengths range between 2.004(6) and 2.127(6) Å (Table 2).

Table 2. Bond lengths [Å] and angles [°] for the metal-ion coordination environments in the $[Cu_2\mathbf{L1}]^{4+}$ cation.

Cu–N1	2.040(6)	N4–Cu–N1	86.1(2)
Cu–N2	2.027(6)	N2–Cu–N1	86.9(2)
Cu–N3	2.049(6)	N4–Cu–N3	86.8(2)
Cu–N4	2.004(6)	N2–Cu–N3	86.0(2)
Cu–N5	2.127(6)	N1–Cu–N3	155.3(3)
		N4–Cu–N5	107.4(2)
		N2–Cu–N5	104.9(3)
		N1–Cu–N5	119.0(2)
		N3–Cu–N5	85.7(2)

Considering the overall conformation of the complex, the ligand presents a rather flat conformation, with the two symmetry-related tetraazamacrocycles lying on two parallel planes and forming an angle of 7.20(1)° with the plane defined by the aromatic unit. In consequence of this flat conformation of the ligand the two Cu^{II} ions lie at a rather long distance [11.447(1) Å].

*Crystal Structures of [{Zn_2**L2**}(ClO_4)$_4$] and [{Zn_2**L3**}(ClO_4)$_4$]·H_2O*

The molecular structures consist of centrosymmetric $[Zn_2L]^{4+}$ (L = **L2** and **L3**) complex cations, perchlorate anions and, in the case of the **L3** complex, water molecules. ORTEP[51] drawings of the $[Zn_2\mathbf{L2}]^{4+}$ and $[Zn_2\mathbf{L3}]^{4+}$ cations are shown in Figure 3a and 3b, respectively, and Table 3 reports selected distances and angles for the metal-ion coordination environments.

The coordination sphere of the Zn^{II} ions is almost equal in the two structures. Each metal ion, in fact, is five-coordinate to the four nitrogen atoms of a cyclic [12]aneN_4 moiety and the nitrogen atom of the side arm. The coordination geometry can be described as a distorted square pyramid; the basal planes are defined by the four amine groups of the [12]aneN_4 units, with maximum deviations from the mean planes being 0.0587(2) Å for N3 (**L2**) and 0.0398(2) Å for N1 (**L3**). The axial positions are occupied by a nitrogen atom of the side arm, with angles of 7.70(1)° (for **L2**) and 4.10(1)° (for **L3**) between the Zn1–N5 bond and the normal to the corresponding basal planes. Finally, the two Zn^{II} cations lie 0.783(2) Å (**L2** complex) and 0.786(2) Å (**L3** complex) above the basal plane, shifted toward the apical position.

The Zn–Zn distances are 11.776(1) and 11.770(1) Å in the Zn^{II} complexes with **L2** and **L3**, respectively.

As far as the overall conformation of the ligand is concerned, it adopts an overall flat conformation in both struc-

 © 2005 Wiley-VCH Verlag GmbH & Co. KGaA, Weinheim

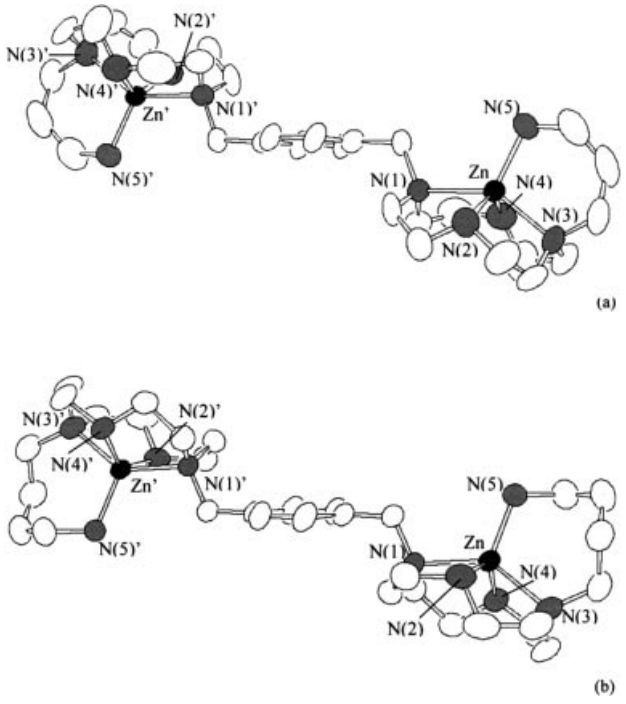

Figure 3. ORTEP drawings of the $[Zn_2\mathbf{L2}]^{4+}$ (a) and $[Zn_2\mathbf{L3}]^{4+}$ (b) cations.

Table 3. Bond lengths [Å] and angles [°] for the metal-ion coordination environments in the $[Zn_2\mathbf{L2}]^{4+}$ and $[Zn_2\mathbf{L3}]^{4+}$ cations.

$[Zn_2\mathbf{L2}]^{4+}$			
Zn1–N1	2.215(8)	N5–Zn1–N2	111.6(4)
Zn1–N2	2.085(9)	N5–Zn1–N4	115.4(4)
Zn1–N3	2.153(9)	N2–Zn1–N4	132.7(4)
Zn1–N4	2.115(1)	N5–Zn1–N3	102.3(4)
Zn1–N5	2.004(9)	N2–Zn1–N3	83.7(5)
		N4–Zn1–N3	82.0(4)
		N5–Zn1–N1	116.5(3)
		N2–Zn1–N1	81.8(4)
		N4–Zn1–N1	82.0(4)
		N3–Zn1–N1	141.2(4)
$[Zn_2\mathbf{L3}]^{4+}$			
Zn1–N1	2.206(4)	N5–Zn1–N4	117.73(18)
Zn1–N2	2.110(4)	N5–Zn1–N2	109.10(17)
Zn1–N3	2.197(5)	N4–Zn1–N2	133.17(17)
Zn1–N4	2.092(5)	N5–Zn1–N3	109.68(18)
Zn1–N5	2.004(4)	N4–Zn1–N3	82.6(2)
		N2–Zn1–N3	82.53(18)
		N5–Zn1–N1	109.76(17)
		N4–Zn1–N1	82.14(18)
		N2–Zn1–N1	81.77(16)
		N3–Zn1–N1	140.43(17)

tures. The two symmetry-related [12]aneN$_4$ units form an angle of 18.83(2)° (**L2** complex) and 22.52(1)° (for **L3** complex) with the plane defined by the aromatic unit. The two zinc ions are lodged within a symmetry-related cyclic unit at each extremity of the ligand, and the nitrogen atoms of the side arms lie *trans* with respect to the plane of the benzene unit.

Cu^{II} and Zn^{II} Coordination in Aqueous Solution

The coordination properties of **L1**–**L3** were studied by means of potentiometric measurements in aqueous solution. Table 4 lists the stability constants of the Cu^{II} and Zn^{II} complexes determined in 0.1 M NMe_4Cl at 298.1 K.

The data in Table 4 clearly outline that all ligands display similar binding features toward Cu^{II} and Zn^{II}, above all a marked ability to form both mono- and dinuclear complexes. Furthermore, the mononuclear $[ML]^{2+}$ complexes show a high tendency to protonate in solution, the three first protonation constants being only slightly lower than the corresponding basicity constants of the free ligands. The rather high values of the equilibrium constants for the protonation of the $[ML]^{2+}$ species can be reasonably ascribed to the protonation of nitrogen atoms not bound to the metal cation in the mononuclear Zn^{II} and Cu^{II} complexes the metal ion is most likely coordinated to a single macrocyclic unit, while the second one is not involved in metal-ion binding and can easily be protonated.

Considering the mononuclear complexes, it was of interest to compare the stability of the present complexes with

Table 4. Stability constants (log K) of the Cu^{II} and Zn^{II} adducts with **L1**, **L2** and **L3**, determined by means of potentiometric measurements in 0.1 M Me_4NCl at 298.1 K.

Reaction	log K					
	L1		**L2**		**L3**	
	Cu	Zn	Cu	Zn	Cu	Zn
$L + M^{2+} \rightleftharpoons ML^{2+}$	20.16(1)	16.45(5)	18.60(2)	14.35(7)	16.09(5)	13.40(5)
$ML^{2+} + H^+ \rightleftharpoons MHL^{3+}$	10.02(2)[a]	9.88(4)	9.55(3)	10.09(8)	10.06(5)	10.16(4)
$MHL^{3+} + H^+ \rightleftharpoons MH_2L^{4+}$	8.53(3)	8.44(4)	9.15(3)	9.16(7)	9.64(7)	9.30(7)
$MH_2L^{4+} + H^+ \rightleftharpoons MH_3L^{5+}$	7.00(3)	6.81(3)	7.76(5)	7.98(6)	8.92(7)	8.49(7)
$MH_3L^{5+} + H^+ \rightleftharpoons MH_4L^{6+}$	3.90(3)	4.32(6)	6.14(5)	5.28(7)	7.60(5)	7.44(6)
$ML^{2+} + OH^- \rightleftharpoons ML(OH)^+$	3.7(1)	4.10(4)	3.41(3)	3.26(8)	2.91(6)	3.26(6)
$ML^{2+} + M^{2+} \rightleftharpoons M_2L^{4+}$	19.77(2)	14.20(3)	17.19(4)	13.18(6)	14.66(6)	10.72(5)
$M_2L^{4+} + H^+ \rightleftharpoons M_2HL^{5+}$	4.28(1)	4.92(3)	6.07(8)	6.26(5)	9.40(6)	8.31(5)
$M_2HL^{5+} + H^+ \rightleftharpoons M_2H_2L^{6+}$			5.73(8)		9.04(6)	
$M_2L^{4+} + OH^- \rightleftharpoons M_2L(OH)^{3+}$			3.0(1)		4.86(4)	3.73(4)
$M_2L(OH)^{3+} + OH^- \rightleftharpoons M_2L(OH)_2^{2+}$						3.44(5)
$M_2L^{4+} + 2OH^- \rightleftharpoons M_2L(OH)_2^{2+}$	5.87(1)			6.11(5)		7.17(5)

[a] Values in parentheses are the standard deviation in the last significant figure.

 © 2005 Wiley-VCH Verlag GmbH & Co. KGaA, Weinheim

that of the corresponding complex with 1,7-dimethyl-1,4,7,10-tetraazacyclododecane (**L4**), which contains two secondary and two tertiary nitrogen donors. The stability of the $[Cu\mathbf{L3}]^{2+}$ complex is somewhat lower than those of $[Cu\mathbf{L4}]^{2+}$ (log K = 16.09 and 17.89 for the equilibrium $Cu^{2+} + L \rightleftharpoons [CuL]^{2+}$, with L = **L3** and **L4**, respectively), while the **L1** complex displays a higher affinity for Cu^{II} than **L4** (log K = 20.16 and 17.89 for the equilibrium $Cu^{2+} + L \rightleftharpoons [CuL]^{2+}$, with L = **L1** and **L4**, respectively). These data suggest that in the $[Cu\mathbf{L3}]^{2+}$ complex the amine group of the side arm is not involved in metal-ion coordination, while in $[Cu\mathbf{L1}]^{2+}$ the amine pendant arm is coordinated to the metal ion. In the case of ligand **L2**, the stability constant of the $[Cu\mathbf{L2}]^{2+}$ complex is intermediate between those observed for the corresponding **L1** and **L3** complexes, suggesting that in $[Cu\mathbf{L2}]^{2+}$ the amine group of the pendant arm is weakly involved in metal-ion coordination.

Considering the formation of the dinuclear complexes, the equilibrium constant for the addition of a second metal ion to the mononuclear $[ML]^{2+}$ complexes is similar to that found for the formation of the corresponding $[ML]^{2+}$ species (for instance, log K = 20.16 for the equilibrium $Cu^{2+} + \mathbf{L1} \rightleftharpoons [Cu\mathbf{L1}]^{2+}$, and log K = 19.77 for the equilibrium $[Cu\mathbf{L1}]^{2+} + Cu^{2+} \rightleftharpoons [Cu_2\mathbf{L1}]^{4+}$). This is in agreement with the involvement of the two identical ligand moieties in the coordination of each metal ion in the dinuclear complexes, as shown by the crystal structures of the dinuclear complexes $[Cu_2\mathbf{L1}]Cl_4 \cdot 8H_2O$, $[Zn_2\mathbf{L2}](ClO_4)_4$ and $[Zn_2\mathbf{L3}](ClO_4)_4 \cdot H_2O$ (see above). This behaviour is clearly depicted by the distribution diagrams of the complexes, as shown in Figure 4 for the system Zn^{II}/**L2**. Both mononuclear and dinuclear complexed species are present in solutions containing the ligand and the metal ion in an equimolecular ratio (Figure 4a). On the other hand, for a 2:1 Zn^{II}/L molar ratio, the formation of monometallic complexes is depressed and only minor percentages of protonated mononuclear complexes are formed at acidic pH (Figure 4b).

The process of Zn^{II} coordination was also monitored by means of ^1H NMR titrations in D_2O at pH = 10, carried out by successive addition of $Zn(ClO_4)_2$ to a ligand solution. Figure 5 displays the ^1H NMR spectra of **L1** in the absence and presence of different amounts of Zn^{II}. Upon adding 0.25 equiv. of Zn^{II} to a solution of **L1**, a different set of signals appears in the ^1H NMR spectrum, together with the resonances of the ligand alone. Although the signals of the ethylenic chains of **L1** are affected by a certain degree of fluxionality in the presence of the metal ion and cannot be confidently attributed, the appearance of a new singlet for the aromatic protons (H1A) and of a doublet for the benzylic hydrogen atoms (H2A) is clearly recognisable, pointing out the formation in solution of a metal complex (**A** species) that is slowly exchanging on the NMR timescale with the free ligand. On addition of further Zn^{II}, the signals of this species are enhanced, while the resonances of L decrease in intensity. With an M^{II}/L molar ratio of 0.5:1, however, a third set of signals (H1B and H2B) appears in the spectrum, due to the formation of a second complexed species (**B** com-

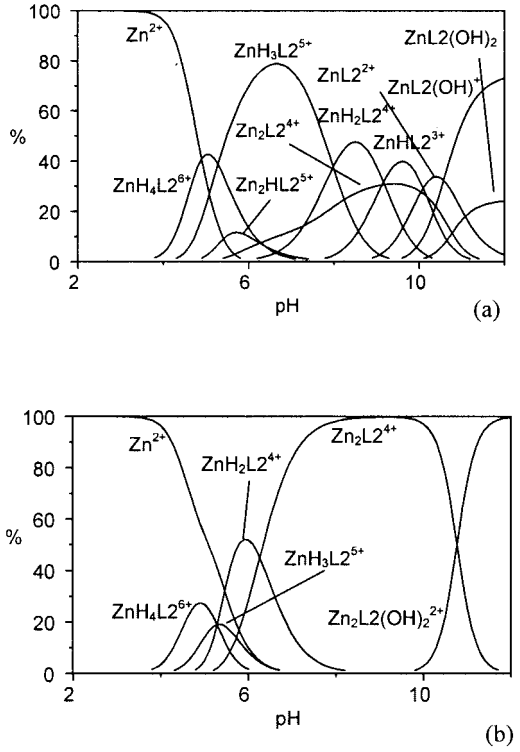

Figure 4. Distribution diagrams of the species for the system Zn^{2+}/**L2** in 1:1 (a) and 2:1 (b) molar ratios ([L] = $[Zn^{2+}] = 1 \times 10^{-3}$ M, 0.1 M Me_4NCl 298.1 K) as a function of pH.

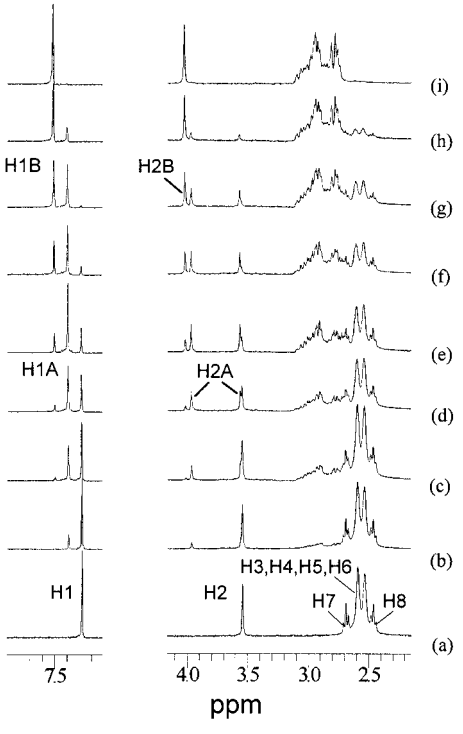

Figure 5. ^1H NMR spectra of **L1** in D_2O in the absence (a) and presence of Zn^{II} in different molar ratios: (b) R = 0.25; (c) R = 0.5; (d) R = 0.75; (e) R = 1.0; (f) R = 1.25; (g) R = 1.5; (h) R = 1.75; (i) R = 2.0; R = $[Zn^{II}]/[\mathbf{L1}]$.

 © 2005 Wiley-VCH Verlag GmbH & Co. KGaA, Weinheim

plex) that is slowly exchanging with the **A** complex on the NMR timescale. When a 1:1 M^{II}/L molar ratio is reached, the predominant species in solution is the **A** complex, most likely the mononuclear Zn^{II} complex. Further additions of Zn^{II} lead to the progressive enhancement of the signals of the **B** complex, accompanied by the disappearance of the signals of the mononuclear complex and of the free ligand. Finally, with a 1:2 **L1**/Zn^{II} molar ratio the $[Zn\mathbf{L1}]^{2+}$ subspectrum disappears and the resulting spectrum can be attributed to a unique dinuclear $[Zn_2\mathbf{L1}]^{4+}$ complex. A similar behaviour is also found for **L2** and **L3**.

A more accurate analysis of the data in Table 4 shows some relevant differences in the coordination properties of the three ligands. First of all, the stability of both the $[ML]^{2+}$ and $[M_2L]^{4+}$ complexes (M = Cu^{II}, Zn^{II}) decreases in the order **L1** > **L2** > **L3** (for instance, log K = 19.77, 17.19 and 14.66 for the equilibrium $Cu^{2+} + [CuL]^{2+} \rightleftharpoons [Cu_2L]^{4+}$ with L = **L1**, **L2** and **L3**, respectively). Second, both the $[Cu_2L]^{4+}$ and $[Zn_2L]^{4+}$ complexes show a different ability in proton binding among the three ligands. The equilibrium constant for the addition of an acidic proton to the $[M_2L]^{4+}$ complexes, in fact, increases in the order **L1** < **L2** < **L3**. In particular, the protonation constants of the $[M_2\mathbf{L1}]^{4+}$ complexes are rather low, less than 5 log units, as expected in the case of protonation of metal-ion-bound amine groups. On the contrary, the protonation constants of the $[M_2\mathbf{L3}]^{4+}$ dinuclear complexes are remarkably high (ca. 9 log units), just slightly lower than the corresponding constants of the "free" ligand, as generally found in the case of nitrogen atoms not involved in metal-ion binding. Finally, the ability of $[M_2L]^{4+}$ complexes to form hydroxylated species decreases from **L3** to **L1** (for instance, log K = 7.17 and 6.11 for the equilibrium $[Zn_2L]^{4+} + 2\ OH^- \rightleftharpoons [Zn_2L(OH)_2]^{2+}$ with L = **L3** and **L2**, respectively, while the $[Zn_2\mathbf{L1}]^{4+}$ complex does not form any hydroxo complex). In polyamine complexes, an increasing tendency to form hydroxo complexes is generally related to a lower number of metal-ion-bound nitrogen donors.

These experimental observations suggest that a decreasing number of nitrogen donors is involved in Cu^{II} or Zn^{II} binding on passing from **L1** to **L3**; in other words, while in the **L1** dinuclear complexes each metal ion is coordinated to the four amine groups of a cyclen moiety and the amine group of the side arm, in the **L3** ones the metal cations are bound only to the four donor atoms of the cyclic moieties. The amine group of the pendant arms seems not to be involved in metal-ion coordination, at least in aqueous solution. In the **L3** complexes a water molecule most likely occupies the apical position in the coordination sphere of both metal ions. In the case of **L2**, the stability constants of the $[M_2\mathbf{L2}]^{4+}$ complexes as well as the equilibrium constants for proton addition to the $[M_2\mathbf{L2}]^{4+}$ species are intermediate between those observed for the corresponding **L1** and **L3** complexes, suggesting that in $[M_2\mathbf{L2}]^{4+}$ the amine groups of the pendant arms are weakly involved in metal-ion coordination.

These hypotheses are confirmed by the UV/Vis spectral features of the dinuclear Cu^{II} complexes. The $[Cu_2L]^{4+}$ complexes display a single band at 610 (ε = 805), 640 (ε = 836) and 693 nm (ε = 888 $cm^{-1}\,mol^{-1}\,L$) for L = **L1**, **L2** and **L3**, respectively (Figure 6). The observed red shift of the absorption maximum on passing from $[Cu_2\mathbf{L1}]^{4+}$ to $[Cu_2\mathbf{L3}]^{4+}$ suggests a decreasing ligand-field splitting at the Cu^{II} centres, in agreement with an increasing number of coordinated nitrogen atoms from the **L3** dinuclear complex to the **L1** one.[52,53]

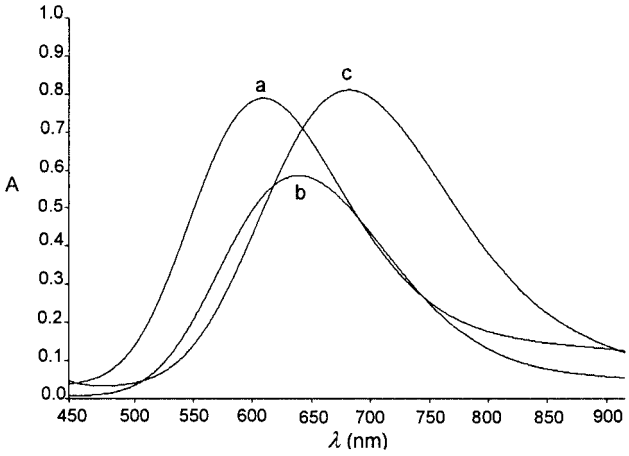

Figure 6. Absorption spectra of $[Cu_2L]^{2+}$: (a) L = **L1**, pH = 8.04; (b) L = **L2**, pH = 8.75; (c) L = **L3**, pH = 10.91 in aqueous solution.

In the case of the dinuclear Zn^{II} complexes, the involvement of the amine group of the pendant arm in metal-ion binding can be determined by analysis of the pH dependence of the ^1H NMR signal of the adjacent methylene group. In the case of $[Zn_2\mathbf{L1}]^{4+}$ and $[Zn_2\mathbf{L2}]^{4+}$ protonation of the complexes gives rise to an upfield shift of this signal (0.2 and 0.15 ppm in the case of the **L1** and **L2** complexes, respectively). This strongly suggests that the formation of protonated complexes implies detachment of the ethyl- or propylamino groups from the metal ion due to protonation of a primary amine function.[54] On the contrary, protonation of the $[Zn_2\mathbf{L3}]^{4+}$ complex is accompanied by a downfield shift of the signal of the methylene group in the α-position with respect to the primary nitrogen atom, as generally observed (see above) in the case of proton binding by amine groups not involved in metal-ion coordination.

The crystal structure of the complex $[Cu_2\mathbf{L1}]Cl_4{\cdot}8H_2O$ shows each metal ion coordinated to the nitrogen atoms of the cyclen unit and to the amine group of a pendant arm, in agreement with the structural hypothesis made on the basis of the solution data. Interestingly, the reflectance spectrum of solid $[Cu_2\mathbf{L1}]Cl_4{\cdot}8H_2O$ shows a single band with λ_{max} = 615 nm, which is very similar to that found for the $[Cu_2\mathbf{L1}]^{4+}$ complex in aqueous solution (λ_{max} = 610 nm), thereby supporting the hypothesis of a similar coordination sphere of the metal ion in the solid state and in solution. In the case of **L3**, however, the crystal structure of $[Zn_2\mathbf{L3}](ClO_4)_4{\cdot}H_2O$ shows that each metal ion is pentacoordinate by the four nitrogen donors of the macrocycle and by the nitrogen donor of the side arm, in contrast to

 © 2005 Wiley-VCH Verlag GmbH & Co. KGaA, Weinheim

the conclusions derived from the solution study. Although no Cu^{II} complex with **L3** was structurally characterised, it is of interest to note that the reflectance spectrum of solid $[Cu_2\mathbf{L3}](ClO_4)_4$ shows a band at 620 nm, which is blue-shifted by 70 nm with respect to that of the $[Cu_2\mathbf{L3}]^{4+}$ complex in solution. This experimental result may suggest a higher number of coordinated nitrogen donors in solid $[Cu_2\mathbf{L3}](ClO_4)_4$. While in the solid state the NH_2 group of the pendant arm is coordinated to the metal ion in a similar fashion to that found in $[Zn_2\mathbf{L3}](ClO_4)_4{\cdot}H_2O$, in the $[Cu_2\mathbf{L3}]^{4+}$ species in solution the alkylamino pendant would most likely not be involved in metal-ion coordination.

In conclusion, in the case of $[M_2\mathbf{L1}]^{4+}$ and $[M_2\mathbf{L2}]^{4+}$ all nitrogen donors are coordinated to the metal ions; the solution data, however, suggest a weaker interaction of the amine group of the pendant arm in the **L2** complex. Protonation of the $[M_2L]^{4+}$ species takes place on the aminoethyl or aminopropyl side arms, with consequent detachment of the primary nitrogen donor from the metal ion. In other words, the coordination sphere of the two metal ions is modulated by the pH of the medium. On the contrary, in the $[M_2\mathbf{L3}]^{4+}$ complexes the butylamino side arms are not involved in metal-ion coordination and facile protonation of the primary nitrogen atoms occurs. This different behaviour can be ascribed to the different length of the chelate ring formed by coordination of the aminoalkyl pendant arm to Cu^{II} or Zn^{II}. In the case of $[M_2\mathbf{L1}]^{4+}$, coordination of the primary nitrogen atom gives rise to a stable five-membered chelate ring, whereas in the $[M_2\mathbf{L3}]^{4+}$ complexes coordination of the NH_2 group would lead to the formation of a less stable seven-membered chelate ring. As a consequence, binding of a water molecule in the apical position of the coordination sphere of the metal ion in the $[M_2\mathbf{L3}]^{4+}$ complexes would be energetically more favoured, and, therefore, the aminoalkyl side arm would not be involved in metal-ion coordination in aqueous solution.

Experimental Section

General Procedures: 3-[7-{4-[{7-(3-Aminopropyl)-1,4,7,10-tetraazacyclododecan-1-yl}methyl]benzyl}-1,4,7,10-tetraazacyclododecan-1-yl]propylamine (**L2**) was prepared as previously reported,[49] recrystallised from an ethanol/water mixture and isolated as **L2**·6HCl·2H_2O. **L1**–**L3** require a suitable protection of two opposite nitrogen atoms of cyclen and, moreover, the control of the two successive steps of N-1 and N-7 alkylations. The bis(aminal) resulting from the reaction of cyclen with aqueous glyoxal proved to be an excellent tool for the synthesis of such dissymmetrical dialkylated macrocyclic adducts.[49,55] The synthetic route used for the synthesis of **L1** and **L3** is depicted in Scheme 2. Cyclen reacts with glyoxal in methanolic solution to give *cis*-decahydro-2a,4a,6a,8a-tetraazacyclopenta[*fg*]acenaphthylene (**1**) quantitatively.[56] The reaction with an electrophilic moiety leads to a stable quaternary ammonium salt; the use of an appropriate solvent in which the solubility of this salt is low prevents further alkylation and allows the control of the monoalkylation of **1**. Salts **2** were found to precipitate in CH_3CN and were subsequently isolated by filtration; salts **3** were obtained in a second step by reaction of the monosalts **2** with 0.5 equiv. of the bis(electrophile) (α,α′-dibromo-*p*-xylene) in DMF, in which salts **2** are partially soluble. Subsequent refluxing of **3** in hydrazine monohydrate according to a previously described procedure[49] afforded ligands **L1**–**L3** in good yields.

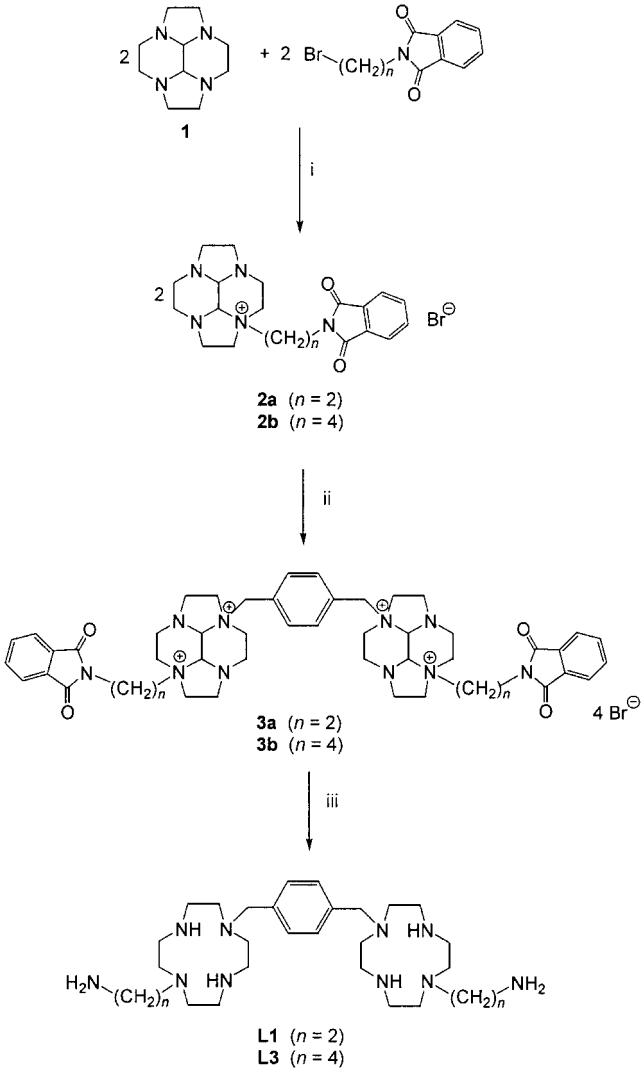

Scheme 2. (i) Stirring in CH_3CN for 2 d at 50°C or at room temp. for **2a** and **2b**, respectively; (ii) α,α′-dibromo-*p*-xylene in DMF at room temp.; (iii) H_2NNH_2, H_2O, reflux overnight.

2a-[3-(1,3-Dioxo-1,3-dihydro-2*H*-isoindol-2-yl)ethyl]decahydro-4a,6a,8a-triaza-2a-azoniacyclopenta[*fg*]acenaphthylene Bromide (2a): A solution of *N*-(bromoethyl)phthalimide (2.9 g, 11 mmol) in dry acetonitrile (5 mL) was added to a stirred solution of **1** (2.0 g, 10 mmol) in 5 mL of dry acetonitrile,. The mixture was stirred at 50 °C for 2 d. The precipitate was collected by filtration, washed with acetonitrile and dried in vacuo to give the monosalt as a white powder. Yield: 1.79 g (40%). ^{13}C NMR (D_2O): δ = 172.3 (CO), 138.0, 133.9, 126.6 (C_{ar}), 87.0, 74.4 (C_{aminal}), 65.1, 60.1, 57.4, 54.1, 51.2, 50.9, 50.7, 50.4, 46.4 (CH_2N), 34.6 ($N^+CH_2CH_2N_{pht}$) ppm. $C_{20}H_{26}BrN_5O_2$ (448.36): calcd. C 53.58, H 5.84, Br 17.82, N 15.62; found C 53.26, H 5.89, Br 17.73, N 15.51.

2a-[3-(1,3-Dioxo-1,3-dihydro-2*H*-isoindol-2-yl)butyl]decahydro-4a,6a,8a-triaza-2a-azoniacyclopenta[*fg*]acenaphthylene bromide (2b): Compound **2b** was obtained from **1** (2.0 g, 10 mmol) and *N*-(bromobutyl)phthalimide (3.2 g, 11 mmol) at room temperature by applying the same procedure as for **2a**. Yield: 4.43 g (93%). ^{13}C

NMR (D_2O): δ = 173.4 (CO), 137.7, 134.0, 126.2 (C_{ar}), 86.6, 74.6 (C_{aminal}), 64.9, 60.6, 59.7, 54.1, 51.3, 51.0, 50.6, 50.5, 46.5 (CH_2N), 39.5 ($N^+CH_2CH_2CH_2CH_2N_{pht}$), 27.7, 22.9 ($N^+CH_2CH_2CH_2CH_2N_{pht}$) ppm. $C_{22}H_{30}BrN_5O_2$ (476.41): calcd. C 55.46, H 6.35, Br 16.77, N 14.70; found C 55.19, H 6.37, Br 16.64, N 14.61.

2a-[4-{[6a-{2-(1,3-Dioxo-1,3-dihydro-2*H*-isoindol-2-yl)ethyl}decahydro-4a,8a-diaza-2a,6a-diazoniacyclo-penta[*fg*]acenaphthylen-2a-yl]methyl}benzyl]-6a-[2-(1,3-dioxo-1,3-dihydro-2*H*-isoindol-2-yl)ethyl]decahydro-4a,8a-diaza-2a,6a-diazoniacyclopenta[*fg*]acenaphthylene Tetrabromide (3a): A solution of α,α′-dibromo-*p*-xylene (0.6 g, 2.38 mmol) in 50 mL of dry DMF was added dropwise to a suspension of **2a** (2.1 g, 4.75 mmol) in 100 mL of dry DMF. The mixture was stirred at room temperature for 2 weeks. The solvent was evaporated, 10 mL of dry acetonitrile was added to the residue and the mixture was stirred for some minutes. The precipitate was collected by filtration, washed with acetonitrile and dried in vacuo. The white crude product was used without further purification. Yield: 2.45 g (89%). ^{13}C NMR (D_2O): δ = 172.4 (CO), 138.3, 136.7, 134.2, 132.4, 126.9 (C_{ar}), 82.1, 80.9 (C_{aminal}), 64.9, 64.3, 63.5, 59.0, 58.2, 57.6, 49.5, 49.0, 45.6 (NCH_2), 34.8 (CH_2N_{pht}) ppm.

2a-[4-{[6a-{2-(1,3-Dioxo-1,3-dihydro-2*H*-isoindol-2-yl)butyl}decahydro-4a,8a-diaza-2a,6a-diazoniacyclopenta[*fg*]acenaphthylen-2a-yl]methyl}benzyl]-6a-[2-(1,3-dioxo-1,3-dihydro-2*H*-isoindol-2-yl)butyl]decahydro-4a,8a-diaza-2a,6a-diazoniacyclopenta[*fg*]acenaphthylene Tetrabromide 3b: Compound **3b** was obtained from α,α′-dibromo-*p*-xylene (0.6 g, 2.38 mmol) and **2b** (2.3 g, 4.75 mmol) by the same procedure as **3a**. The white crude product was used without further purification. Yield: 2.63 g (91%). ^{13}C NMR (D_2O): δ = 173.4 (CO), 137.7, 136.5, 134.1, 132.2, 126.2 (C_{ar}), 81.3, 80.8 (C_{aminal}), 64.5, 64.0, 63.2, 60.2, 58.2, 49.1, 45.5 (NCH_2), 39.6 (CH_2N_{pht}), 27.6, 24.3 ($CH_2CH_2CH_2CH_2$) ppm.

2-[7-{4-[{7-(2-Aminoethyl)-1,4,7,10-tetraazacyclododecan-1-yl}-methyl]benzyl}-1,4,7,10-tetraazacyclododecan-1-yl]ethylamine Hexahydrochloride Dihydrate (L1·6HCl·2H$_2$O): Compound **3a** (2.3 g, 2 mmol) and 6 mL of hydrazine monohydrate were heated at 120 °C overnight. After cooling, the solid was filtered off, dissolved in ethanol and the solvent was evaporated. The resulting oil was dissolved in 10 mL of ethanol and 10 mL of concentrated HCl was added dropwise. The precipitate was filtered off, dissolved in 3 M HCl and the solvent was evaporated. The white solid was recrystallised from an ethanol/water mixture (1:1). Yield: 1.12 g (72%). ^{13}C NMR (D_2O): δ = 137.2, 133.5, 58.7, 52.0, 50.0, 49.7, 45.5, 43.9, 37.2 ppm. $C_{28}H_{66}Cl_6N_{10}O_2$ (787.61): calcd. C 42.70, H 8.45, Cl 27.01, N 17.78; found C 42.45, H 8.53, Cl 26.89, N 17.54.

4-[7-{4-[{7-(4-Aminobutyl)-1,4,7,10-tetraazacyclododecan-1-yl}-methyl]benzyl}-1,4,7,10-tetraazacyclododecan-1-yl]butylamine Hexahydrochloride Dihydrate (L3·6HCl·2H$_2$O): Compound **3b** was treated as above to give a white solid. Yield: 1.48 g (93%). ^{13}C NMR (D_2O): δ = 137.7, 133.4, 58.8, 54.5, 50.0, 49.9, 45.4, 45.3, 42.2, 27.5, 23.0 ppm. $C_{32}H_{74}Cl_6N_{10}O_2$ (843.71): calcd. C 45.55, H 8.84, Cl 25.21, N 16.60; found C 45.81, H 8.87, Cl 25.57, N 16.68.

Synthesis of [{Cu$_2$L1}Cl$_4$]·8H$_2$O: A solution of $Cu(ClO_4)_2·6H_2O$ (14 mg, 0.038 mmol) in water (5 mL) was slowly added to an aqueous solution (10 mL) containing **L1**·6HCl·2H$_2$O (15 mg, 0.019 mmol). The pH was adjusted to 8.0 with 0.01 M NaOH and then $NaClO_4$ (30 mg) was added. Blue crystals of the complex suitable for X-ray analysis were obtained by slow concentration at room temperature. Yield: 11 mg (61%) $C_{28}H_{72}Cl_4Cu_2N_{10}O_8$ (945.85): calcd. C 35.56, H 7.67, N 14.81; found C 35.45, H 7.60, N 14.78.

Caution! Perchlorate salts of organic ligands and their metal complexes are potentially explosive; these compounds must be handled with great care.

Synthesis of [Zn$_2$L2](ClO$_4$)$_4$: Crystals of [{Zn$_2$**L2**}(ClO$_4$)$_4$] suitable for X-ray analysis were obtained by slow concentration, at room temperature, of an aqueous solution containing **L2**·6HCl·2H$_2$O (11 mg, 0.013 mmol) and $Zn(ClO_4)_2$ (10 mg, 0.027 mmol) at pH = 9.0. Yield: 11.72 mg (80%). $C_{30}H_{60}Cl_4N_{10}O_{16}Zn_2$ (1089.4): calcd. C 33.07, H 5.55, N 12.86; found C 33.40, H 5.45, N 12.93.

Synthesis of {[Zn$_2$L3](ClO$_4$)$_4$}·H$_2$O: This complex was synthesised according to the procedure reported for **L2** adjusting the solution pH to 9.3. Yield: 9.45 mg (64%). $C_{32}H_{66}Cl_4N_{10}O_{17}Zn_2$ (1135.5): calcd. C 33.85, H 5.86, N 12.33; found C 33.80, H 5.90, N 12.37.

X-ray Structure Analyses: Analyses on prismatic, blue single crystals of [{Cu$_2$**L1**}Cl$_4$]·8H$_2$O (a), prismatic colourless crystals of [{Zn$_2$**L2**}(ClO$_4$)$_4$] (b) and [{Zn$_2$**L3**}(ClO$_4$)$_4$]·H$_2$O (c) were carried out with CCD SMART 1K (**L1**) and SIEMENS P4 (**L2** and **L3**) diffractometers. A summary of the crystallographic data is given in Table 5. Empirical absorption corrections (SADABS for **L1** and ψ-scan methods for **L2** and **L3**) were applied. No loss of intensity was observed during data collection. Both structures were solved by direct methods with the SIR97 program.[57] Refinements were performed by the full-matrix least-squares method with the SHELXL-97 program.[58] All non-hydrogen atoms were refined anisotropically while hydrogen atoms, except those of the water molecules, were introduced in calculated positions and their coordinates refined according to the linked atom. As is common for perchlorate ligands, in the structure of [{Zn$_2$**L3**}(ClO$_4$)$_4$]·H$_2$O the perchlorate anion Cl1 exhibits disorder (six oxygen peaks, three assigned 33% and three 66% occupancy). CCDC-240959, -240960 and -240961 (**L1**–**L3**, respectively) contain the supplementary crystallographic data for this paper. These data can be obtained free of charge from The Cambridge Crystallographic Data Centre via www.ccdc.cam.ac.uk/data_request/cif.

Potentiometric Measurements: All the pH-metric measurements (pH = –log [H$^+$]) were carried out in degassed 0.1 M Me_4NCl, with CO_2-free solutions, at 298.1 K, with equipment and procedures that have already been described.[59] The combined Ingold 405 S7/120 electrode was calibrated as a hydrogen concentration probe by titrating known amounts of HCl with CO_2-free Me_4NOH solutions and determining the equivalent point by Gran's method,[60,61] which allows the determination of the standard potential, E^o, and the ionic product of water [pK_w = 13.83(1) at 298.1 K in 0.1 M Me_4NCl]. A ligand concentration, [L], of 1×10^{-3} M and metal-ion concentration, [M], from 0.5•[L] to 1.8•[L] were adopted in the complexation experiments. The emf data were treated with the computer program HYPERQUAD[62] which furnished the equilibrium constants reported in Table 1 and Table 4. All titrations were treated either as single sets or as separate entities for each system without significant variation in the values of the determined constants. In the HYPERQUAD[62] program the sum of the weighted square residuals of the observed emf values is minimised. The weights were derived from the estimated errors in emf (0.2 mV) and titrant volume (0.002 mL). The most probable chemical model was selected by using a strategy based on the statistical inferences applied to the variance of the residuals, σ^2. The sample standard deviation should be 1 in the absence of systematic errors and when a corrected weighting scheme is used. However, the agreement is considered good for standard deviation values smaller than 3 ($\sigma^2 < 9$). Values of σ^2 lower than 6 were obtained for all the refined equilibrium models in the present work. If more than one model gave an acceptable σ^2 value the reliability of the proposed specia-

 © 2005 Wiley-VCH Verlag GmbH & Co. KGaA, Weinheim

Table 5. Crystal data and structure refinement for {[Cu_2**L1**]Cl_4}·8H_2O, [Zn_2**L2**]$(ClO_4)_4$ and {[Zn_2**L3**]$(ClO_4)_4$}·H_2O.

	{[Cu_2**L1**]Cl_4}·8H_2O	[Zn_2**L2**]$(ClO_4)_4$	{[Zn_2**L3**]$(ClO_4)_4$}·H_2O
Empirical formula	$C_{28}H_{72}Cl_4Cu_2N_{10}O_8$	$C_{30}H_{60}Cl_4N_{10}O_{16}Zn_2$	$C_{32}H_{66}Cl_4N_{10}O_{17}Zn_2$
Formula weight	945.83	1089.4	1135.5
Crystal system	triclinic	monoclinic	monoclinic
T [K]	298	298	298
λ [Å]	1.54180	1.54180	1.54180
Space group	$P\bar{1}$	$P2_1/n$	$P2_1/n$
a [Å]	8.993(5)	9.180(5)	10.193(5)
b [Å]	9.214(5)	18.05(5)	14.353(5)
c [Å]	14.093(5)	13.58(5)	16.113(5)
α [°]	95.000(5)		
β [°]	91.000(5)	99.00(5)	97.89(5)
γ [°]	111.000(5)		
V [Å^3]	1084.6(9)	2222.5(2)	2335.0(2)
Z	1	2	2
μ [mm^{-1}]	3.929	4.218	4.056
F(000)	484	1132	1180
Reflections collected	4042	3645	4392
Independent reflections	2412	2759	3363
Final R indices [$I > 2\sigma(I)$]: R_1, wR_2[a]	0.0801, 0.2497	0.0842, 0.2084	0.0625, 0.1730
R indices (all data)	0.0858, 0.2566	0.1353, 0.2441	0.0698, 0.1810

[a] $R_1 = \Sigma||F_o| - |F_c||/\Sigma|F_o|$; $wR_2 = [\Sigma w(F_o^2 - F_c^2)^2/\Sigma wF_o^4]^{1/2}$.

tion models was checked by performing F tests at the 0.05 confidence level, using the method reported in ref.[63] and ref.[64] for two different proposed models, A and B. Assuming that the minimum value of the sample variance, σ_A^2, has been reached for the proposed model A, an alternative model B, which supplies a value of the variance σ_B^2, was rejected if $\sigma_B^2/\sigma_A^2 > F$, where σ_A and σ_B are given directly by data treatment with the HYPERQUAD[62] program. The F values were taken from ref.[63] For all the systems investigated this method provided only one acceptable system.

NMR Spectroscopy: 300.0 MHz ^{1}H, 75.46 MHz ^{13}C NMR spectra in D_2O solutions at different pH values were recorded at 298 K with a Varian 300 MHz spectrometer. In the ^{1}H NMR spectra the peak positions are reported relative to HOD at δ = 4.75 ppm. Dioxane was used as reference standard in ^{13}C NMR spectra (δ = 67.4 ppm). ^{1}H-^{1}H and ^{1}H-^{13}C 2D correlation experiments were performed to assign the signals. Small amounts of 0.01 M NaOD or DCl solutions were added to a solution of the three ligands to adjust the pD. The pH was calculated from the measured pD values using the relationship pH = pD – 0.40.[65]

Electronic Spectroscopy: Absorption spectra were recorded with a Perkin–Elmer Lambda 25 spectrophotometer. HCl and NaOH were used to adjust the pH values, which were measured with a Metrohm 713 pH meter.

Acknowledgments

Financial support by the Italian Ministero dell'Università e della Ricerca Scientifica e Tecnologica, within the program COFIN 2002, is acknowledged.

[1] *Chemistry of Heterocyclic Compounds* (Eds.: J. S. Bradshaw, K. E. Krakowiak, R. M. Izatt), vol. 51 (*Aza-crown Macrocycles*), Wiley, New York, **1993**.
[2] R. M. Izatt, K. Pawlak, J. S. Bradshaw, *Chem. Rev.* **1995**, *95*, 2529–2586.
[3] J. M. Lehn, *Supramolecular Chemistry*, VCH, New York, **1995**.
[4] L. F. Lindoy, *Pure Appl. Chem.* **1997**, *69*, 2179–2186.
[5] T. A. Kaden, D. Tschudin, M. Studer, U. Brunner, *Pure Appl. Chem.* **1989**, *61*, 879–883.
[6] A. J. Blake, N. R. Champness, P. Hubberstey, W. S. Li, M. Schröder, M. A. Withersby, *Coord. Chem. Rev.* **1999**, *183*, 117–138.
[7] J. Nelson, V. McKee, G. Morgan, *Progr. Inorg. Chem.* (Ed.: K. D. Karlin), Wiley, New York **1998**, *47*, 167–316.
[8] A. Bencini, A. Bianchi, P. Paoletti, P. Paoli, *Coord. Chem. Rev.* **1992**, *120*, 51–85.
[9] P. Ghosh, P. K. Bharadway, J. Roy, S. Ghosh, *J. Am. Chem. Soc.* **1997**, *119*, 11 903–11 909.
[10] L. Lamarque, C. Miranda, P. Navarro, F. Escartí, E. García-España, J. Latorre, J. A. Ramírez, *Chem. Commun.* **2000**, 1337–1338.
[11] M. Formica, V. Fusi, M. Micheloni, R. Pontellini, P. Romani, *Coord. Chem. Rev.* **1999**, *184*, 347–363.
[12] P. Guerriero, S. Tamburini, P. A. Vigato, *Coord. Chem. Rev.* **1995**, *110*, 17–113.
[13] R. M. Izatt, K. Pawlak, J. S. Bradshaw, R. L. Bruenig, *Chem. Rev.* **1991**, *91*, 1721–2085.
[14] L. Fabbrizzi, M. Licchelli, G. Rabaioli, A. Taglietti, *Coord. Chem. Rev.* **2000**, *205*, 85–108.
[15] L. Fabbrizzi, M. Licchelli, P. Pallavicini, *Acc. Chem. Res.* **1999**, *32*, 846–853.
[16] L. Fabbrizzi, M. Licchelli, A. Taglietti, *Dalton Trans.* **2003**, 3471–3479.
[17] V. Amendola, L. Fabbrizzi, C. Mangano, P. Pallavicini, *Struct. Bonding* **2001**, *99*, 79–115.
[18] R. J. Motekaitis, B. E. Rogers, D. E. Reichert, A. E. Martell, M. J. Welch, *Inorg. Chem.* **1996**, *35*, 3821–3827.
[19] J. M. Connet, C. J. Anderson, L. Guo, S. W Schwarz, K. R. Zinn, B. E. Rogers, B. A. Siegel, G. W. Philpott, M. J. Welch, *Proc. Natl. Acad. Sci. USA* **1996**, *93*, 6814–6818.
[20] Y. H. Jang, M. Blanco, S. Dasgupta, D. A. Keire, J. E. Shively, W. A. Goddard, *J. Am. Chem. Soc.* **1999**, *121*, 6142–6151.
[21] E. Brucher, A. D. Sherry, in the *Chemistry of Contrast Agent in Medical Magnetic Resonance Imaging* (Eds.: A. E. Mercbach, E. Toth), John Wiley, New York, **2001**, ch. 6.
[22] C. S. Cutler, M. Wuest, C. J. Anderson, D. E. Reichert, Y. Sun, A. E. Martell, M. J. Welch, *Nucl. Med. Biol.* **2000**, *27*, 375–380.
[23] S. Aoki, M. Shiro, T. Koike, E. Kimura, *J. Am. Chem. Soc.* **2000**, *122*, 576–584.
[24] S. Aoki, E. Kimura, *J. Am. Chem. Soc.* **2000**, *122*, 4542–4548.
[25] P. V. Bernhardt, G. A. Lawrence, *Coord. Chem. Rev.* **1990**, *104*, 297–343.
[26] K. P. Wainwright, *Coord. Chem. Rev.* **1997**, *166*, 35–90.

 © 2005 Wiley-VCH Verlag GmbH & Co. KGaA, Weinheim

[27] R. I. Haines, *Rev. Inorg. Chem.* **2001**, *21*, 165–205.
[28] K. Eiichi, *S. Afr. J. Chem.* **1997**, *50*, 240.
[29] K. P. Wainwright, *Adv. Inorg. Chem.* **2001**, *52*, 293–334 and references cited therein.
[30] P. Chaudhuri, K. Wieghardt, *Prog. Inorg. Chem.* **1987**, *35*, 329–436.
[31] K. Wieghardt, *Angew. Chem. Int. Ed. Engl.* **1989**, *28*, 1153–1172.
[32] F. N. Penkert, T. Weyhermüller, E. Bill, P. Hildebrandt, S. Lecomte, K. Wieghardt, *J. Am. Chem. Soc.* **2000**, *122*, 9663–9673.
[33] W. B. Tolman, *Acc. Chem. Res.* **1997**, *30*, 227–237.
[34] J. Huskens, A. D. Sherry, *J. Chem. Soc., Dalton Trans.* **1998**, 177–184.
[35] M. Koikawa, K. B. Jemsen, H. Matsushima, T. Tokii, H. Toftlund, *J. Chem. Soc., Dalton Trans.* **1998**, 1085–1086.
[36] A. J. Blake, I. A. Fallis, R. O. Gould, S. Parsons, S. A. Ross, M. Schröder, *J. Chem. Soc., Dalton Trans.* **1996**, 4379–4387.
[37] L. Tei, A. J. Blake, C. Wilson, M. Schröder, *J. Chem. Soc., Dalton Trans.* **2002**, 1247–1249.
[38] D. A. Robson, S. Y. Bylikin, M. Canteul, N. A. H. Male, L. H. Rees, P. Mountford, M. Schroder, *J. Chem. Soc., Dalton Trans.* **2001**, 157–169.
[39] M. Di Vaira, F. Mani, P. Stoppioni, *Inorg. Chim. Acta* **2000**, *303*, 61–69.
[40] M. Di Vaira, F. Mani, P. Stoppioni, *Inorg. Chim. Acta* **1998**, *273*, 151–159.
[41] P. C. McGowan, T. J. Podesta, M. Thornton-Pett, *Inorg. Chem.* **2001**, *40*, 1445–1453.
[42] T. Tanase, H. Inukai, T. Onaka, M. Kato, S. Yano, S. J. Lippard, *Inorg. Chem.* **2001**, *40*, 3943–3953.
[43] A. Warden, B. Graham, M. T. W. Hearn, L. Spiccia, *Org. Lett.* **2001**, *3*, 2855–2858.
[44] A. Hammershoi, A. M. Sargeson, *Inorg. Chem.* **1983**, *22*, 3554–3561.
[45] G. W. Bushnell, D. G. Fortier, A. McAuley, *Inorg. Chem.* **1988**, *27*, 2626–2634.
[46] D. G. Fortier, A. McAuley, *J. Chem. Soc., Dalton Trans.* **1991**, 101–109.
[47] L. Tei, V. Lippolis, A. J. Blake, P. A. Cooke, M. Schröder, *Chem. Commun.* **1998**, 2633–2634.
[48] A. J. Blake, J. P. Danks, W.-S. Li, V. Lippolis, M. Schröder, *J. Chem. Soc., Dalton Trans.* **2000**, 3034–3040.
[49] M. Le Baccon, F. Chuburu, L. Toupet, H. Handel, M. Soibinet, I. Déchamps-Olivier, J. P. Barbier, M. Aplincourt, *New J. Chem.* **2001**, *25*, 1168–1174.
[50] A. Bencini, A. Bianchi, E. Garcia-España, M. Micheloni, J. A. Ramirez, *Coord. Chem. Rev.* **1999**, *188*, 97–156.
[51] C. K. Johnson, M. N. Burnet, *ORTEP-3*, Windows version 1.01 by L. Farrugia, **1997**.
[52] P. Zanello, R. Seeber, A. Cinquantini, G. Mazzocchin, L. Fabbrizzi, *J. Chem. Soc., Dalton Trans.* **1982**, 893–897.
[53] L. Fabbrizzi, P. Paoletti, A. B. P. Lever, *Inorg. Chem.* **1976**, *15*, 1502–1506.
[54] C. Bazzicalupi, A. Bencini, E. Berni, A. Bianchi, L. Borsari, C. Giorgi, B. Valtancoli, C. Lodeiro, J. C. Lima, A. J. Parola, F. Pina, *Dalton Trans.* **2004**, 591–597.
[55] J. Rohovec, R. Gyepes, I. Cisarova, J. Rudovsky, I. Lukes, *Tetrahedron Lett.* **2000**, *41*, 1249–1253.
[56] G. R. Weisman, M. E. Rogers, E. H. Wong, J. P. Jasinski, E. S. Paight, *J. Am. Chem. Soc.* **1990**, *112*, 8604–8065.
[57] A. Altomare, M. C. Burla, M. Camalli, G. L. Cascarano, C. Giacovazzo, A. Guagliardi, A. G. G. Moliterni, G. Polidori, R. Spagna, *J. Appl. Crystallogr.* **1999**, *32*, 115–119.
[58] G. M. Sheldrick, *SHELXL-97*, University of Göttingen, Germany, **1997**.
[59] A. Bianchi, L. Bologni, P. Dapporto, M. Micheloni, P. Paoletti, *Inorg. Chem.* **1984**, *23*, 1201–1205.
[60] G. Gran, *Analyst (London)* **1952**, *77*, 661.
[61] F. J. Rossotti, H. Rossotti, *J. Chem. Educ.* **1965**, *42*, 375–378.
[62] P. Gans, A. Sabatini, A. Vacca, *Talanta* **1996**, *43*, 1739–1753.
[63] W. C. Hamilton, *Statistics in Physical Chemistry*, The Ronald Press Company, New York, USA, **1964**.
[64] L. Bologni, A. Sabatini, A. Vacca, *Inorg. Chim. Acta* **1983**, *69*, 71–75.
[65] A. K. Covington, M. Paabo, R. A. Robinson, R. G. Bates, *Anal. Chem.* **1968**, *40*, 700–706.

Received: October 25, 2004

 © 2005 Wiley-VCH Verlag GmbH & Co. KGaA, Weinheim

Mono- and Bilayered Lead(II)–bpno Polymers with Unusual Low Energy Emission Properties (bpno = 4,4′-Bipyridine *N*,*N*′-Dioxide)

Yanqing Xu,[a] Daqiang Yuan,[a] Lei Han,[a] En Ma,[a] Mingyan Wu,[a] Zhengzhong Lin,[a] and Maochun Hong*[a]

Keywords: Lead complexes / 4,4′-Bipyridine *N*,*N*′-dioxide / Coordination polymers / Phosphorescence

Reaction of 4,4′-bipyridine *N*,*N*′-dioxide (bpno) and lead(II) nitrate with or without dicyanamido ions (dca) in aqueous solution yielded polymeric complexes $\{Pb_2(bpno)_4(dca)_2(NO_3)_2Pb_2(bpno)_4(NO_3)_4\cdot 5H_2O\}_n$ (**1**) and $\{Pb(bpno)(NO_3)_2\cdot H_2O\}_n$ (**2**), respectively. The single-crystal X-ray analyses show that the structures of both complexes consist of dinuclear Pb^{II} units which are bridged through bpno ligands in novel modes to extend their topologies. Compound **1** exhibits a bilayered rhombus grid, while **2** displays a monolayered rhombus grid. The different excitations of solid samples of **1** and **2**, at room temperature, produced intense emission bands which are almost the same in appearance with peak maxima at 616 nm and 617 nm, respectively. Both low-energy emissions were determined to be phosphorescence by their long decay lifetime at room temperature.

(© Wiley-VCH Verlag GmbH & Co. KGaA, 69451 Weinheim, Germany, 2005)

Introduction

The s^2 materials can be important in applications like electroluminescent devices[1] or organic light-emitting diode (OLED) technology etc.,[2] and so have stimulated many scientists' interest. As far as the intrinsic appeal of Pb^{2+} is concerned, the presence of an $6s^2$ outer electron configuration not only leads to interesting topological arrangements,[3] but also plays an important role in the luminescence action of the complex.[4] Consequently, a remarkable amount of studies have been done on the optical properties of lead(II) centers.[5] In 1986 R. Ballardini et al. reported that the Pb(8-quinolinolate)$_2$ chelates exhibit a very weak red intraligand (IL) phosphorescence in addition to a much stronger green IL fluorescence in fluid solution.[6] S. K. Dutta et al. further put forward that Pb^{2+} could act as its own luminescent sensor via the highly luminescent lead halide cluster $Pb_4Br_{11}^{3-}$ due to a delocalized cluster state.[5b] More recent studies by A. Strasser and A. Vogler focused on IL phosphorescence research of the lead(II) β-diketonates at both low temperatures and room temperature.[7] In fact, little attention has been focused on luminescent lead polymers even though there are many interesting structure reports. Taking into account that the presence of lead in coordination polymers will reduce the radiative lifetime of triplets by increased spin-orbit coupling and generate a room-temperature phosphorescence, as is largely related to the application of triplet emitters in OLED technology, we have recently become interested in the phosphorescence properties of lead coordination polymers.

On the other hand, 4,4′-bipyridine *N*,*N*′-dioxide (bpno) possesses a longer bridging spacer and richer coordination modes, compared with 4,4′-bipyridine. As shown in Scheme 1, there are five possible kinds of connection modes for the bpno ligand.[8] The *cis* and *trans* modes have been observed in many compounds.[9] The four-connecting coordination mode (μ-4,4,4′,4′) was newly found in La–bpno.[10] However, the three-connecting mode (μ-4,4,4′) remains unknown. Another ligand, the dicyanamido ion (dca), also exhibits various coordination modes, which makes it a fairly good building block for crystal engineering.[11] By the self-assembly of bpno and/or dca ligands with transition metal ions, coordination frameworks with larger cavities or channels may be expected.[12] Thus, by the reaction of Pb^{2+} and

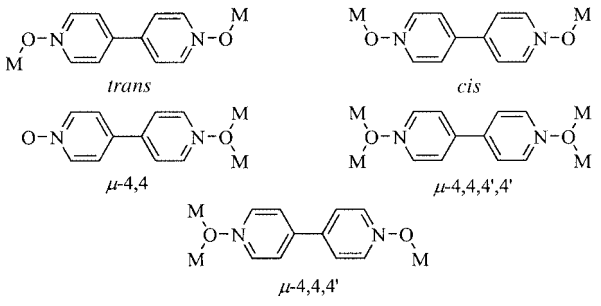

Scheme 1. Schematic illustration showing the coordination modes of bpno.

[a] State Key Laboratory of Structural Chemistry, Fujian Institute of Research on the Structure of Matter, Chinese Academy of Sciences,
Fuzhou, Fujian 350002, China
Fax: +86-591-83714946
E-mail: hmc@ms.fjirsm.ac.cn

Supporting information for this article is available on the WWW under http://www.eurjic.org or from the author.

bpno with or without dca, two novel polymeric complexes, $\{Pb_2(bpno)_4(dca)_2(NO_3)_2Pb_2(bpno)_4(NO_3)_45H_2O\}_n$ (**1**), and $\{Pb(bpno)(NO_3)_2H_2O\}_n$ (**2**) were obtained. Herein, we wish to report their syntheses, crystal structures, TG, IR spectroscopic and luminescent properties. To the best of our knowledge, the three-connecting mode (μ-4,4,4′) has been confirmed for the first time in both compounds.

Results and Discussion

Heating of the mixture of 4,4′-bpno, dca and $Pb(NO_3)\cdot 2H_2O$ in a methanol solution led to yellow prismatic crystals of compound **1**, while heating of the mixture of 4,4′-bpno and $Pb(NO_3)\cdot 2H_2O$ in a methanol solution led to orange prismatic crystals of compound **2**. Single crystal analyses show that both complexes have polymeric structures based on dinuclear Pb^{II} units bridged by bpno ligands.

Crystal Structure of Compound 1

The asymmetric unit of compound **1** consists of two crystallographically independent lead(II) motifs, as well as two and a half free lattice water molecules. As shown in Figure 1a, Pb1 is in an eight-coordinate environment, surrounded only by O atoms, of which five are from bpno ligands, two from a bidentate NO_3^- and one from a monodentate NO_3^- group. Pb1 atoms are linked by the O(3) atoms of the bpno groups, forming a planar four-membered ring Pb(1)–O(3)–Pb(1A)–O(3A) with O–Pb–O bond angles of 62.93° and Pb–O–Pb bond angles of 117.07°. This Pb_2O_2 unit is nearly symmetric with the Pb–O distances being 2.633(9) Å for Pb(1)–O(3) and 2.690(10) Å for Pb(1)–O(3A), respectively. The Pb–(μ-O) bond lengths are comparable to those found in other crystallographically characterized $Pb_2(\mu\text{-}OR)_2$ systems.[3d,13] The distance between the two nonbonded Pb atoms [Pb(1)–Pb(1A)] is about 4.541 Å. The Pb_2O_2 units are bridged by two parallel bpno ligands along the *oa* direction with Pb(1)–O(4F) [2.511(11) Å] and N(3)–O(3) [1.317(14) Å] yielding a double-stranded chain, in which bpno adopts both μ-4,4,4′ and *trans* connection modes. It is noted that bonding in the μ-4,4,4′ mode is exclusive and has been observed in the structure of **1** for the first time. These adjacent chains are further linked through double bpno ligands along the *ob* direction with Pb(1)–O(2D) [2.461(10) Å] and Pb(1)–O(1) [2.647(10) Å] leading to a 2D bilayered coordination network as illustrated in Figure 2a.

The dca ligand is not involved in the Pb1 motif but is in the Pb2 part (Figure 1b). The Pb2 part also adopts an eight-coordination geometry. Because of the existence of the dca ligand, there is only one NO_3^- ion involved in the coordination sphere, which adopts a chelating coordination mode and occupies two coordination points. The dca ligand in this structure bonds to the Pb atom by its amine nitrogen but not the nitrile nitrogen atom. The extended structure is shown in Figure 2b, and no significant differences are observed between the Pb2 and Pb1 grids except that one NO_3^- ion in the Pb1 grid is replaced by dca ligand in the Pb2 grid. The two grids exhibit large open frameworks with the same dimensions 13.465 × 13.465 Å, but unfortunately the two sets of networks cross over in the common stacking form to reduce the dimension of the framework (Figure 3).

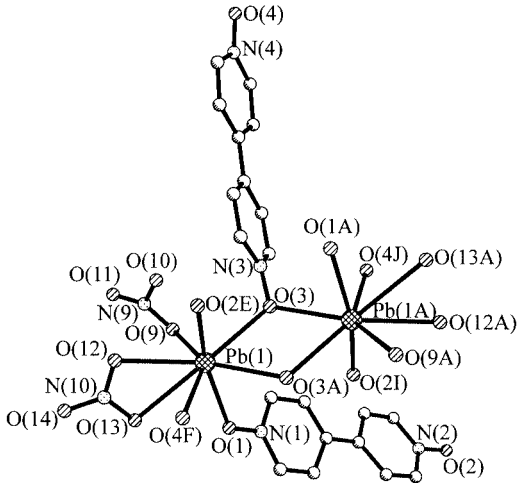

(a) Structure of Pb1 part.

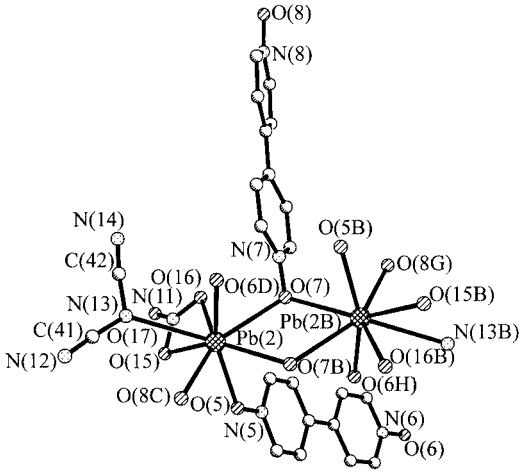

(b) Structure of Pb 2 part.

Figure 1. Coordination environment of two Pb^{II} motifs in compound **1**, hydrogen atoms are omitted. Symmetry code: (a) A: $-x + 2, -y, -z + 1$; B: $-x + 1, -y + 1, -z$; D: $x, y + 1, z$; F: $x - 1, y, z$; I: $-x + 2, -y - 1, -z + 1$; J: $-x + 3, -y, -z + 1$; (b) B: $-x + 1, -y + 1, -z$; C: $x + 1, y, z$; D: $x, y + 1, z$; G: $-x, -y + 1, -z$; H: $-x + 1, -y, -z$.

Crystal Structure of Compound 2

From the structural analysis above, we surmised that the occurrence of two different motifs in **1** might be due to the introduction of the dca ligand into the reaction system. Thus, we were interested in continuing our research without the addition of dca to see if the same structure of the Pb1 grid in **1** could be obtained. However, the result seems to be quite unexpected, and a novel structure of **2** was produced (Figure 4), in which the Pb atom is eight-coordinate with two chelating NO_3^- ions, three bpno ligands, and one water

 © 2005 Wiley-VCH Verlag GmbH & Co. KGaA, Weinheim

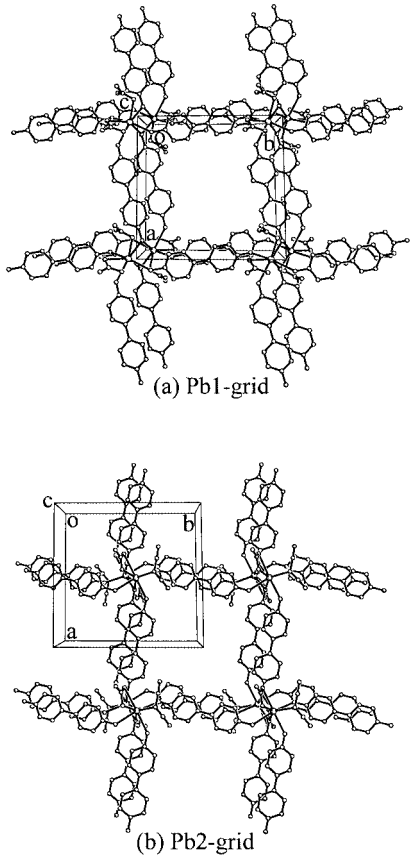

Figure 2. View of the 2D sheet of compound **1**.

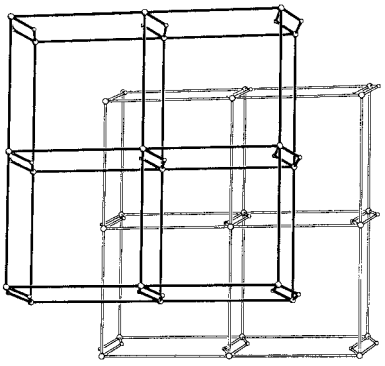

Figure 3. Schematic view of the packed structure in compound **1** ignoring free water molecules.

molecule. Although the $Pb_2(\mu\text{-}4,4,4'\text{-bpno})_2$ unit is again found in this structure, except for the absence of two bpno ligands (contrasted with **1**), the extended structure only leads to a monolayer topology with the dimensions of a rhombus grid 13.814×13.814 Å (Figure 5). All bpno ligands in **2** adopt a μ-4,4,4′ connection mode. As a result of compact stacking in crystallography, the dimension of the open framework is also to be reduced (Figure 6).

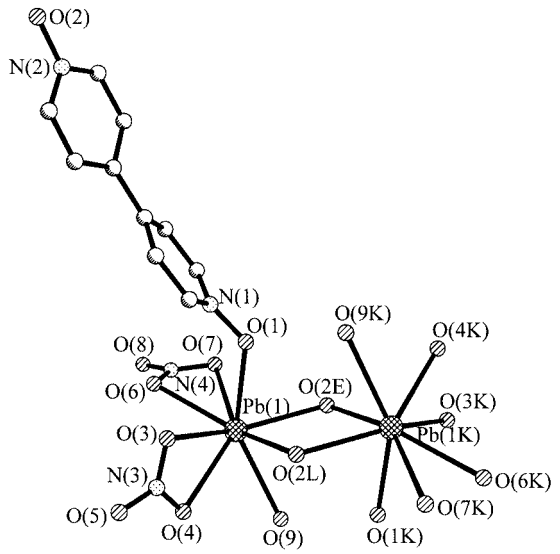

Figure 4. Diagram showing the structure of compound **2**, hydrogen atoms are omitted. Symmetry code: E: $-x$, $y + 1/2$, $-z + 1/2$; L: x, $-y + 1/2$, $z + 1/2$; K: $-x$, $-y+1$, $-z+1$.

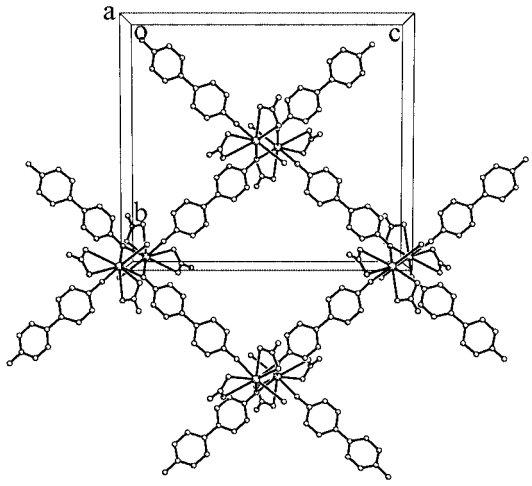

Figure 5. View of the 2D sheet of compound **2**.

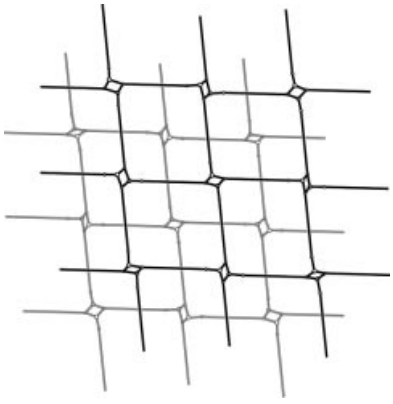

Figure 6. Schematic view of the packed structure in compound **2**.

 © 2005 Wiley-VCH Verlag GmbH & Co. KGaA, Weinheim

IR Spectroscopy

The infrared spectra of solid samples of **1** and **2** are notably different apart from the characteristic bands of the organic ligand. Compound **1** displays absorption peaks at 2257, 2194 and 2144 cm^{-1}, which correspond to $\nu_{sym} + \nu_{asym}(C{\equiv}N)$, $\nu_{sym}(C{\equiv}N)$ and $\nu_{asym}(C{\equiv}N)$ of the dca ligand. The values of the stretching frequencies are relatively lower than those of Na(dca), observed at 2286, 2232 and 2179 cm^{-1}.[14] The shift towards lower frequencies of these peaks reflects the coordination mode of dca through the amide nitrogen atom, which results in decreasing electron density at the cyano groups.[15] A broad absorption band at 3400 cm^{-1} assigned to ν(OH) appears in the spectra, showing the presence of water molecules in both complexes.

Luminescence Properties

Figure 7 shows the emission spectra of **1** and **2** measured at room temperature. The emission spectra of both compounds are dominated by an intense and broad emission band at λ = 616 nm for **1** (λ_{ex} = 388 nm) and λ = 617 nm for **2** (λ_{ex} = 510 nm). The further lifetime measurements at room temperature of each emission maximum gave the results 17.89 μs for **1** and 3.50 μs for **2**. Based on their 10^{-5}–10^{-6} s range lifetime at room temperature, both low-energy emissions could be determined to be phosphorescence, as is consistent with the general idea that the appearance of a room-temperature phosphorescence requires the presence of a heavy metal ion which reduces the radiative lifetime of triplets by increased spin-orbit coupling.[7b] Commonly, the emitting triplets are frequently of the CT (charge transfer) or IL (intraligand) type while LF (ligand field) states are mostly deactivated by radiationless processes.[7b] In order to assign the type of the luminescence, luminescent measurements were taken of both free bpno ligand and bpno complexes. The free bpno ligand in the solid state at room temperature was found to emit at 459 nm under 396 nm radiation (see Figure S1; Supporting Information). But bpno in the *cis* mode (see Scheme 1) was reported to be incapable of activating emission from Eu^{III} in a one-dimensional coordination polymer.[16] We have also reported a mononuclear complex $[Cd(dca)_2(bpno)_2{\cdot}(H_2O)_2]$,[17] in which bpno acts as a terminal ligand. The recent emission measurement on it showed a narrow emissive band at 399 nm (λ_{ex} = 376 nm) (see Figure S2; Supporting Information). From the above measurements, we feel confident to surmise that as an organic fluorophore, the emission action of bpno may vary with the change of the coordination mode and the coordinated metal ion. As a result, increased spin-orbit coupling induced by the heavy-atom effect of lead(II) facilitates intersystem crossing, and the IL phosphorescence is fast enough to successfully compete with radiationless deactivations.[7a] In addition, the $(\mu\text{-}4,4,4'\text{-bpno})_2Pb_2$ dinuclear cluster cannot be neglected in both structures. From the lead halide cluster $Pb_4Br_{11}^{3-}$ it has been reported that the charge transfer states and states delocalized over the bromide-bridged lead ions are important.[5b] Comparably, the emissions in this work may be assigned partly to the delocalized cluster state of the oxygen-bridged lead ions. To the best of our knowledge, such a long lifetime and low-energy luminescence has never been reported for Pb^{2+} coordination polymers. This study suggests that bpno is an appropriate ligand for lead complexes to generate room-temperature phosphorescence, and the results are interesting for finding the long-lived room-temperature phosphorescence relating to Pb^{2+} coordination polymers. We are actively moving towards other related bpno and heavy main group metals with s^2 electron configurations in order to make further progress on the molecule-based functional solids.

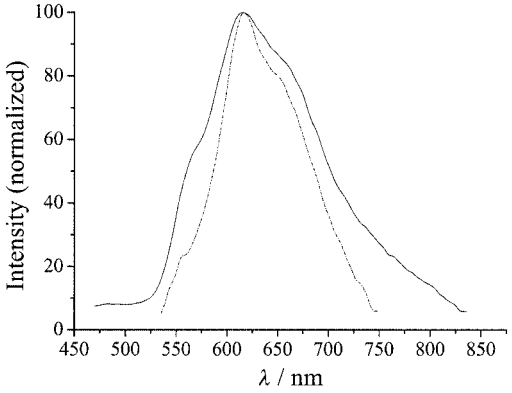

Figure 7. Emission measured for **1** (λ_{ex} = 388 nm) and **2** (λ_{ex} = 510 nm) at room temperature. Solid line for compound **1** and dash-dotted line for **2** and normalized at maximum intensity.

TGA Study

To access the thermal stability of the two compounds, TG analyses were carried out. The TGA diagrams of the crystalline samples showed weight loss in the temperature range 90–165 °C in **1**, corresponding to five free water molecules (3.19%; calculated 3.07%). The anhydrous compound began to decompose at 260 °C. However, the decomposition was still not complete at 800 °C, as could be confirmed by the black color of the residual and the slope of the TGA curves.

For compound **2**, only one coordination aqua ligand exists in the structure. The weight loss was found to be 3.42% in the range of 80–110 °C, which is a little higher than the calculated value of 3.35%. The weight was unchanged until the temperature increased to 309 °C, indicating that the thermal stability of **2** is higher than **1**. Similarly for compound **1**, the decomposition process was incomplete, which was also confirmed by the black color of the residual and the slope of the TGA curves.

Conclusions

In summary, two novel luminescent Pb^{II} coordination polymers with different types of layered grid structures were synthesized. This paper investigated the microscopic features of molecular packing, the luminescent essence and the thermal stability of both compounds. These results are

 © 2005 Wiley-VCH Verlag GmbH & Co. KGaA, Weinheim

interesting not only for confirming new coordination modes of bpno for the first time, but also for finding the long-lived phosphorescence at room temperature emitted from lead coordination polymers, which may have some potential application in OLED technology. Further studies on analogous functional solids will be carried out in the proceeding work.

Experimental Section

General: All chemicals were of reagent-grade quality obtained from commercial sources and used without further purification. Elemental analyses were performed with a German Elementary Varil EL III instrument. IR spectra were recorded in the range 4000–400 cm^{-1} with a Magna 750 FT-IR spectrometer using KBr pellets. TGA analyses were carried out with a Netzsch STA449C unit, at a heating rate of 15 °C min^{-1} under nitrogen from 30 to 800 °C. Fluorescent spectra were measured at room temperature with an Edinburgh FL-FS90 TCSPC system.

Synthesis of 1 and 2: Ligand 4,4′-bpno (0.25 mmol, 0.056 g) and $Pb(NO_3)_2{\cdot}2H_2O$ (0.25 mmol, 0.042 g) were mixed in a methanol (20 mL) solution. Ligand dca (0.50 mmol, 0.045 g) was added to the above solution. The mixture was heated for 15 min with stirring and then filtered. Slow concentration of the filtrate at room temperature led to yellow prismatic crystals of compound **1**. Yield: 0.105 g, 58%. Compound **2** was synthesized by the same procedure as above but without the addition of dca. The resulting solution was allowed to stand at room temperature. Orange prismatic crystals were obtained after 2 d. Yield: 0.088 g, 65%. **1:** $C_{84}H_{74}N_{28}O_{39}Pb_4$ (2928.47): calcd. C 34.40, H 2.55, N 13.38; found C 34.38, H 2.58, N 13.37. IR (KBr): $\tilde{\nu}$ = 3434 (m), 3098 (m), 3064 (m), 3036 (w), 2257 (m), 2194 (m), 2144 (s), 1625 (m), 1545 (m), 1477 (vs), 1384 (vs), 1351 (s), 1240 (s), 1221 (vs), 1184 (vs), 1026 (s), 834 (s), 699 (m), 548 (s), 517 (w), 478 (m) cm^{-1}. **2:** $C_{10}H_{10}N_4O_9Pb$ (537.41): calcd. C 22.30, H 1.87, N 10.41; found C 22.31, H 1.89, N 10.39. IR (KBr): $\tilde{\nu}$ = 3445 (m), 3099 (m), 3074 (m), 3038 (w), 1624 (w), 1545 (m), 1478 (vs), 1380 (vs), 1348 (s), 1243 (s), 1224 (vs), 1183 (vs), 1027 (s), 836 (s), 700 (m), 548 (s), 515 (m), 477 (m) cm^{-1}.

Crystal Structure Characterization: Single crystals of the compounds with approximate dimensions 0.22 mm × 0.19 mm × 0.17 mm for **1** and 0.19 mm × 0.16 mm × 0.15 mm for **2** were coated with epoxy glue and mounted on a glass fiber in a random orientation for data collections. The intensity data were collected with a Smart CCD diffractometer with graphite-monochromated Mo-K_α (λ = 0.71073 Å) radiation at room temperature in the ω-2θ scan mode. An empirical absorption correction was applied to the data using the SADABS program.[18] The structures were solved by direct methods and refined on F^2 by full-matrix least-squares, employing the SHELXTL program.[19] All non-hydrogen atoms were refined with anisotropic thermal parameters. H atoms bonded to C atoms were positioned geometrically (C–H bond fixed at 0.93 Å) and H atoms bonded to O atoms were placed at calculated positions by the HYDROGEN computer program (O–H bond fixed at 0.85 Å),[20] assigned isotropic displacement parameters and allowed to ride on their respective parent atoms. Crystal data and structure refinement parameters are summarized in Table 1. Selected bond lengths and angles are presented in Table 2. CCDC-236662 (**1**) and -236663 (**2**) contain the supplementary crystallographic data for this paper. These data can be obtained free of charge from The Cambridge Crystallographic Data Centre via www.ccdc.cam.ac.uk/data_request/cif.

Table 1. Crystal data and structure refinement for compounds **1** and **2**.

	1	**2**
Empirical formula	$C_{84}H_{74}N_{28}O_{39}Pb_4$	$C_{10}H_{10}N_4O_9Pb$
Formula mass	2928.47	537.41
Space group	$P\bar{1}$	*Pbca*
a [Å]	13.4650(3)	7.8957(5)
b [Å]	13.4669(2)	18.1502(1)
c [Å]	13.7977(3)	20.8299(8)
α [°]	85.4380(10)	90
β [°]	76.2910(10)	90
γ [°]	88.4590(10)	90
V [$Å^3$]	2422.9(1)	2985.1(3)
Z	1	8
ρ(calcd.)[g cm^{-3}]	2.007	2.392
μ [mm^{-1}]	7.034	11.361
Goodness-of-fit on F^2	1.100	1.162
Final *R* indices [$I > 2\sigma(I)$][a]	R_1 = 0.0687, wR_2 = 0.1181	R_1 = 0.0491, wR_2 = 0.1157
R rndices (all data)	R_1 = 0.1127, wR_2 = 0.1389	R_1 = 0.0718, wR_2 = 0.1300

[a] $R_1 = \Sigma(||F_o| - |F_c||)/\Sigma|F_o|$, and $wR_2 = \{\Sigma[w(F_o^2 - F_c^2)^2]/\Sigma[w(F_o^2)^2]\}^{1/2}$ with $w = 1/\sigma^2(F_o^2) + (aP)^2 + bP$, where $P = (F_o^2 + 2F_c^2)/3$.

Table 2. Selected bond lengths [Å] and angles [°] for compounds **1** and **2**.

1[a]			
Pb(1)–O(2D)	2.461(10)	O(3)–Pb(1)–O(3A)	62.9(4)
Pb(1)–O(4F)	2.511(11)	O(12)–Pb(1)–O(13)	45.8(3)
Pb(1)–O(3)	2.633(9)	O(2D)–Pb(1)–O(4F)	80.3(3)
Pb(1)–O(1)	2.647(10)	O(3)–Pb(1)–O(1)	98.8(3)
Pb(1)–O(12)	2.674(11)	O(4F)–Pb(1)–O(3)	137.4(4)
Pb(1)–O(3A)	2.690(10)	O(4F)–Pb(1)–O(1)	92.3(3)
Pb(1)–O(9)	2.754(19)	O(1)–Pb(1)–O(3A)	84.3(3)
Pb(1)–O(13)	2.827(14)	O(4F)–Pb(1)–O(3A)	77.7(4)
Pb(2)–O(5)	2.473(10)	O(7B)–Pb(2)–O(7)	65.4(3)
Pb(2)–O(8C)	2.486(10)	O(16)–Pb(2)–O(15)	43.7(4)
Pb(2)–O(6D)	2.560(10)	O(6D)–Pb(2)–O(7)	80.2(3)
Pb(2)–O(7B)	2.622(10)	O(5)–Pb(2)–O(6D)	157.7(4)
Pb(2)–O(7)	2.643(9)	O(5)–Pb(2)–O(8C)	82.6(3)
Pb(2)–O(16)	2.818(12)	O(7)–Pb(2)–N(13)	132.3(3)
Pb(2)–N(13)	2.824(14)	O(7B)–Pb(2)–N(13)	141.6(4)
Pb(2)–O(15)	2.829(15)	O(8C)–Pb(2)–O(6D)	90.8(3)
2[a]			
Pb(1)–O(1)	2.538(8)	O(2L)–Pb(1)–O(2E)	69.8(3)
Pb(1)–O(2L)	2.541(8)	O(4)–Pb(1)–O(3)	47.8(3)
Pb(1)–O(2E)	2.575(8)	O(6)–Pb(1)–O(7)	46.3(3)
Pb(1)–O(6)	2.638(8)	O(1)–Pb(1)–O(2E)	77.0(3)
Pb(1)–O(4)	2.643(9)	O(1)–Pb(1)–O(2L)	78.3(3)
Pb(1)–O(3)	2.676(11)	O(1)–Pb(1)–O(9)	147.4(3)
Pb(1)–O(9)	2.740(9)	O(2L)–Pb(1)–O(9)	77.0(3)
Pb(1)–O(7)	2.828(10)	O(2E)–Pb(1)–O(9)	74.9(3)

[a] Symmetry transformations used to generate equivalent atoms: A: $-x + 2, -y, -z + 1$; B: $-x + 1, -y + 1, -z$; C: $x + 1, y, z$; D: $x, y + 1, z$; E: $-x, y + 1/2, -z + 1/2$; F: $x - 1, y, z$; L: $x, -y + 1/2, z + 1/2$.

Acknowledgments

We are grateful to the National Natural Science Foundation of China (project 20231020) and the Natural Science Foundation of Fujian Province for financial support.

[1] a) T. Tsuboi, P. Sifsten, *Phys. Rev. B* **1991**, *43*, 1777–1780; b) A. A. Bol, A. Meijerink, *Phys. Stat. Solidi B* **2001**, *1*, 173–177; c) A. A. Bol, A. Meijerink, *Phys. Chem. Chem. Phys.* **2001**, *3*, 2105–2112; d) P. Singh, M. M. Richter, *Inorg. Chim. Acta* **2004**, *357*, 1589–1592.
[2] S. Miyata, H. S. Nalwa (Eds.), *Organic Electroluminescent Materials and Devices*, Gordon and Breach, New York, **1997**.
[3] a) C. S. Weinert, I. A. Guzei, A. L. Rheingold, L. R. Sita, *Organometallics* **1998**, *17*, 498–500; b) M. H. Jack, M. Saeed, A. S. Ali, *Inorg. Chem.* **2004**, *43*, 1810–1812; c) Y. J. Shi, L. H. Li, Y. Z. Li, X. T. Chen, Z. L. Xue, X. Z. You, *Polyhedron* **2003**, *22*, 917–923; d) L. A. Hall, D. J. Williams, S. Menzer, A. J. P. White, *Inorg. Chem.* **1997**, *36*, 3096–3101.
[4] a) S. Deo, H. A. Godwin, *J. Am. Chem. Soc.* **2000**, *122*, 174–175; b) J. Li, Y. Lu, *J. Am. Chem. Soc.* **2000**, *122*, 10466–10467; c) P. C. Ford, A. Vogler, *Acc. Chem. Res.* **1993**, *26*, 220–226; d) H. Y. Duan, X. P. Ai, Z. K. He, *Spectrochim. Acta A* **2003**, *60*, 1447–1451.
[5] a) H. Nikol, A. Vogler, *J. Am. Chem. Soc.* **1991**, *113*, 8988–8990; b) S. K. Dutta, M. W. Perkovic, *Inorg. Chem.* **2002**, *41*, 6938–6940.
[6] R. Ballardini, G. Varani, M. T. Indelli, F. Scandola, *Inorg. Chem.* **1986**, *25*, 3858–3865.
[7] a) A. Strasser, A. Vogler, *J. Photochem. Photobiol. A* **2004**, *165*, 115–118; b) A. Strasser, A. Vogler, *Inorg. Chem. Commun.* **2004**, *7*, 528–530.
[8] B. Q. Ma, H. L. Sun, S. Gao, G. X. Xu, *Inorg. Chem.* **2001**, *40*, 6247–6253.
[9] a) D. L. Long, A. J. Blake, N. R. Champness, C. Wilson, M. Schroder, *Chem. Eur. J.* **2002**, *8*, 2026–2033; b) D. L. Long, A. J. Blake, N. R. Champness, C. Wilson, M. Schroder, *J. Am. Chem. Soc.* **2001**, *123*, 3401–3402; c) S. Tanase, M. Andruh, A. Müller, M. Schmidtmann, C. Mathonière, G. Rombaut, *Chem. Commun.* **2001**, *12*, 1084–1085.
[10] S. L. Ma, W. X. Zhu, G. H. Huang, D. Q. Yuan, X. Yan, *J. Mol. Struc.* **2003**, *646*, 89–94.
[11] a) E. Colacio, F. Lloret, E. Ben Maimoun, R. Kivekäs, R. Sillanpää, J. Suàrez-Varela, *Inorg. Chem.* **2003**, *42*, 2720–2724; b) J. L. Manson, J. Y. Gu, J. A. Schlueter, H. H. Wang, *Inorg. Chem.* **2003**, *42*, 3950–3955; c) J. H. Luo, M. C. Hong, R. H. Wang, R. Cao, Q. Shi, J. B. Weng, *Eur. J. Inorg. Chem.* **2003**, *9*, 1778–1784.
[12] a) B. Q. Ma, S. Gao, H. L. Sun, G. X. Xu, *J. Chem. Soc. Dalton Trans.* **2001**, 130–133; b) A. Nedelcu, Z. Žak, A. M. Madalan, J. Pinkas, M. Andruh, *Polyhedron* **2003**, *22*, 789–794.
[13] a) P. Bhattacharyya, J. Parr, A. M. Z. Slawin, *Inorg. Chem. Commun.* **1999**, *2*, 113–115; b) S. S. Tandon, V. McKee, *J. Chem. Soc. Dalton Trans.* **1989**, *1*, 19–24.
[14] M. Hvastijová, J. Kohout, M. Okruhlica, J. Mrozinski, L. Jäger, *Transition Met. Chem.* **1993**, *18*, 579–582.
[15] S. R. Marshall, C. D. Incarvito, W. W. Shum, A. L. Rheingold, J. S. Miller, *Chem. Commun.* **2002**, *24*, 3006–3007.
[16] C. Seward, S. Wang, *Can. J. Chem.* **2001**, *79*, 1187–1193.
[17] Y. Q. Xu, D. Q. Yuan, Y. Xu, W. H. Bi, Y. F. Zhou, M. C. Hong, *Acta Crystallogr., Sect. E* **2004**. *60*, m713–m714.
[18] G. M. Sheldrick, *SADABS*, *A Program for Empirical Absorption Correction*, University of Göttingen, Germany, **1998**.
[19] G. M. Sheldrick, *SHELXTL*, *Crystallographic Software Package*, version 5.1, Bruker-AXS, Madison, WI, **1998**.
[20] a) M. Nardelli, *J. Appl. Crystallogr.* **1999**, *32*, 563–571; b) L. J. Farrugia, *J. Appl. Crystallogr.* **1999**, *32*, 837–838.

Received: November 1, 2004

 © 2005 Wiley-VCH Verlag GmbH & Co. KGaA, Weinheim

Synthesis of $H_2V_3O_8$ Single-Crystal Nanobelts

Gui-cun Li,*[a,b] Shu-ping Pang,[b] Zhao-bo Wang,[b] Hong-rui Peng,[b] and Zhi-kun Zhang*[a,b]

Keywords: Vanadium / Layered compounds / Nanobelts / Nanostructures

Orthorhombic $H_2V_3O_8$ single-crystal nanobelts with a thickness of less than 30 nm and a length up to several hundreds of micrometers have been synthesized using bulky divanadium pentoxide powders as a precursor. The synthetic process is free of any templates and reducing agents. Divanadium pentoxide undergoes a redox reaction under hydrothermal conditions. The influences of pH, reaction time, and temperature on the morphologies of the resulting products have been investigated. The belt-like $H_2V_3O_8$ with a high surface area may be beneficial to lithium insertion between the V_3O_8 layers for application in batteries.

(© Wiley-VCH Verlag GmbH & Co. KGaA, 69451 Weinheim, Germany, 2005)

Introduction

In recent years, there has been increased interest in synthesizing one-dimensional (1D) nanostructures of vanadium oxides and their derivative compounds, such as nanorod, nanowires, nanotubes, nanobelts, and nanoribbons, because of their diverse physicochemical properties and potential applications including use as cathode materials for lithium batteries,[1] and as electric field-effect transistors.[2,3] Among them, the belt-shaped 1D nanostructures are expected to represent important building blocks for nanodevices.[4,5] Vanadium oxide hydrate ($H_2V_3O_8$), one of the vanadium oxyhydroxides containing V^{5+} and V^{4+} in a ratio of 2 to 1,[6] is of interest because of its layered structure and redox activity. Considerable efforts have been made on the synthesis of 1D nanostructures of vanadium oxide and their derivative compounds. For example, Pinna et al.[7,8] synthesized divanadium pentoxide nanorods and nanowires by a colloidal self-assembly made up of sodium bis(2-ethylhexyl)sulfosuccinate Na(AOT)/isooctane/H_2O. Nesper et al.[9] used neutral surfactant molecules such as primary aliphatic amines, together with vanadium alkoxide precursors to generate redox-active vanadium oxide nanotubes. Yu et al.[10] reported the synthesis of multicomponent $Na_2V_6O_{16}\cdot 3H_2O$ single-crystal nanobelts in the presence of F^- ions, however, without F^- ions or in the presence of other anions such as Cl^-, Br^-, NO_3^-, and SO_4^{2-}, nanobelts could not be obtained. Qian et al.[11] prepared single-crystal $VO_x\cdot nH_2O$ nanoribbons relying on the presence of polyethylene glycol 400, but the values of x and n are uncontrolled. Li et al.[12] reported that metastable vanadium dioxide single-crystal nanobelts were synthesized by hydrothermal synthesis using formic acid as the reducing agent. However, the synthesis of pure $H_2V_3O_8$ 1D nanostructures remains challenging to material scientists. In this paper, we report a low-cost and simple approach for the synthesis of $H_2V_3O_8$ single-crystal nanobelts by hydrothermal processing of bulky divanadium pentoxide (V_2O_5) powders in hydrochloric acid solution without the aid of any templates or reducing agents.

Results and Discussion

XRD patterns of the V_2O_5 precursor and $H_2V_3O_8$ nanobelts are shown in parts A, B of Figure 1, respectively. All the peaks in Figure 1 (see A) can be indexed to the orthorhombic crystalline phase of V_2O_5 in agreement with literature values (JCPDS 89–0612). After hydrothermal treatment, a pure orthorhombic crystalline phase of $H_2V_3O_8$ [space group: *Pnam*] (see B in Figure 1) with calculated lattice contents a = 16.99 Å, b = 9.40 Å, c = 3.64 Å, was obtained, which is consistent with literature values (JCPDS 85–2401). From the structural data, it is expected that the ratio of V^{5+} and V^{4+} in the product is 2 to 1, indicating that V^{5+} is reduced partly to V^{4+}.

Figure 2 shows SEM images of $H_2V_3O_8$ nanobelts synthesized at pH 4. Lower magnification SEM images (see A in Figure 2 and in the Supporting Information Figure 1S) reveal that the precipitates consist of a large quantity of uniform 1D nanostructures with typical lengths in the range of several tens to several hundreds of micrometers. The long fibrillar morphologies can even be seen with the naked eye. A magnified SEM image (B in Figure 2) indicates that the

[a] Fishery College, Ocean University of China, Shandong, Qingdao 266003, P. R. China
[b] Key Laboratory of Nanostructured Materials, Qingdao University of Science and Technology, Shandong, Qingdao 266042, P. R. China
Fax: +86-532-402-2869
E-mail: guicunli@qust.edu.cn
Supporting information for this article is available on the WWW under http://www.eurjic.org or from the author.

 © 2005 Wiley-VCH Verlag GmbH & Co. KGaA, Weinheim DOI: 10.1002/ejic.200400967

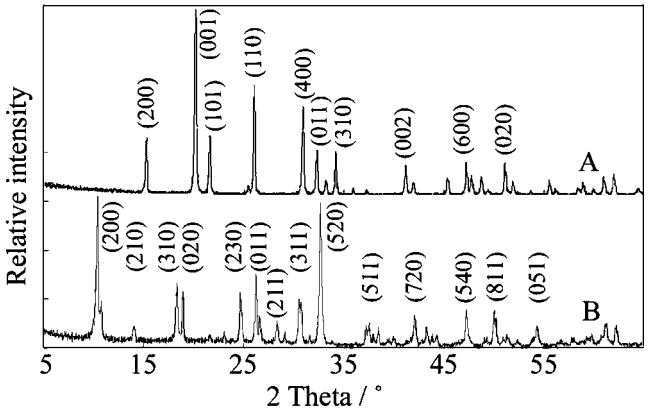

Figure 1. XRD patterns of the initial V_2O_5 precursor (A) and $H_2V_3O_8$ nanobelts synthesized at pH 4 (B).

geometrical shape of the $H_2V_3O_8$ nanostructures is a belt. The ends of these nanobelts are irregular. The typical thickness and width are less than 30 nm and 100–300 nm, respectively. In addition, some nanobelts have terraces of the different $H_2V_3O_8$ layers, indicating that some of the nanobelts stick together. The cleaved $H_2V_3O_8$ layers are clearly visible as indicated by an arrow in Figure 2 (C), so it can be inferred that the belt-like materials may be derived from the cleavage of $H_2V_3O_8$ layers in the reaction process. A typical TEM image of $H_2V_3O_8$ nanobelts is presented in Figure 2 (D). The width is consistent with SEM images (B in Figure 2). The ripple-like strain contrast can also be seen clearly in $H_2V_3O_8$ nanobelts. The selected area electron diffraction (SAED) pattern (E in Figure 2) taken from a single nanobelt indicated that the nanobelts are single crystals and the growth occurs along the [001] direction. The HRTEM image (F in Figure 2) shows the clearly-resolved interplaner distances d_{011} = 0.339 nm and d_{020} = 0.468 nm, which further confirms the growth direction of the nanobelts. The $H_2V_3O_8$ nanobelts are constructed from both VO_6 octahedra and VO_5 trigonal bipyramids. Two VO_6 octahedra are piled up along the *c* axis by sharing edges, which are connected by two-shared VO_5 trigonal bipyramids along the *b* axis, and then a V_3O_8 layer along the *a* axis is formed.[6] The layered structures composed of V_3O_8 layers seem to favor insertion and deinsertion of lithium for application in batteries.[13,14]

The pH value, reaction time, and temperature are important factors for the formation of $H_2V_3O_8$ nanobelts. The width of $H_2V_3O_8$ nanobelts can be controlled by adjusting the pH value. At pH 5, nanobelts with a width of 1 μm are obtained as shown in Figure 3 (A). The nanobelts can be folded without fracture, indicating that their flexibility is very high. At pH 3, the width of the nanobelts in Figure 3 (B) decreased to 90–110 nm. The reaction can proceed without the addition of any hydrochloric acid, but the reaction rate is very slow. It is found that the reaction rate increases when pH values decrease from 7 to 3 possibly because of the formation of various polyvanadate ions at different pH values in aqueous solution. When the reaction is carried out at pH 4 for 6 h, little green product is generated because of

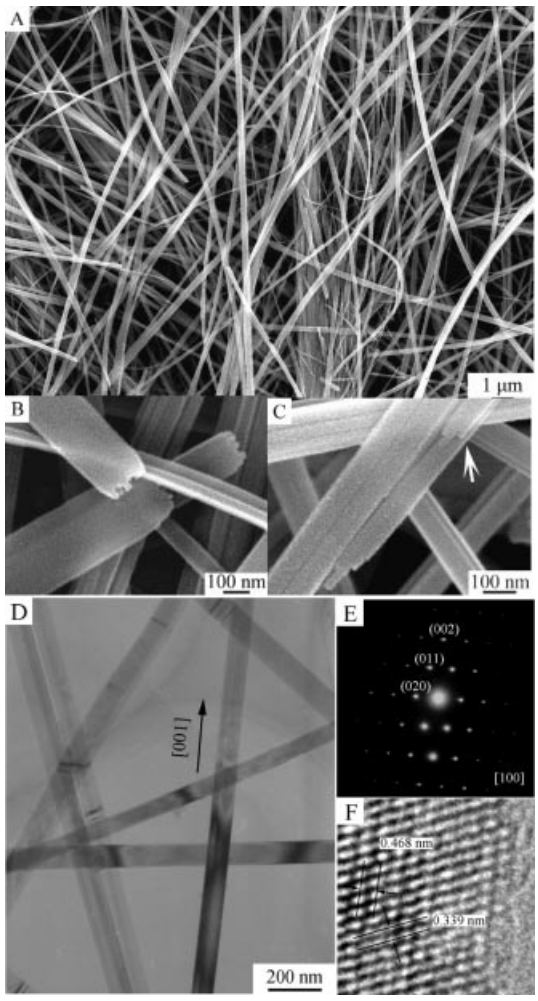

Figure 2. SEM (A, B, and C), TEM (D), and HRTEM (F) images of $H_2V_3O_8$ nanobelts synthesized at pH 4. Figure 2E shows the SAED pattern taken from a single nanobelt.

the inefficient reduction. With an increased reaction time, the color of the product changes from yellow to green. After hydrothermal treatment at pH 4 at 160 °C for 24 h, the reduction is also incomplete, so the nanobelts coexist with particles in the product (see Supporting Information, Figure 2S).

Figure 4 (A, B) present UV/Vis spectra of the initial V_2O_5 precursor and $H_2V_3O_8$ nanobelts synthesized at pH 4, respectively. Part B of Figure 4 shows a broad adsorption peak centered around 850 nm and a weak shoulder around 630 nm, corresponding to the *d–d* electronic transitions of V^{4+} in $H_2V_3O_8$ nanobelts,[15–17] so the product is green. In comparison with Figure 4 (A), the intensity of the adsorption peak of V^{4+} increases greatly, indicating the reduction of V^{5+} to V^{4+} during the course of hydrothermal treatment.

The reaction was carried out in the absence of any reducing agent, so V_2O_5 may undergo a redox reaction under hydrothermal conditions and it is difficult to completely reduce V_2O_5 to VO_2. The basic reaction process for the synthesis of $H_2V_3O_8$ nanobelts may be expressed as follows:

$$6\,V_2O_5 + 4\,H_2O \rightleftharpoons 4\,H_2V_3O_8 + O_2$$

 © 2005 Wiley-VCH Verlag GmbH & Co. KGaA, Weinheim

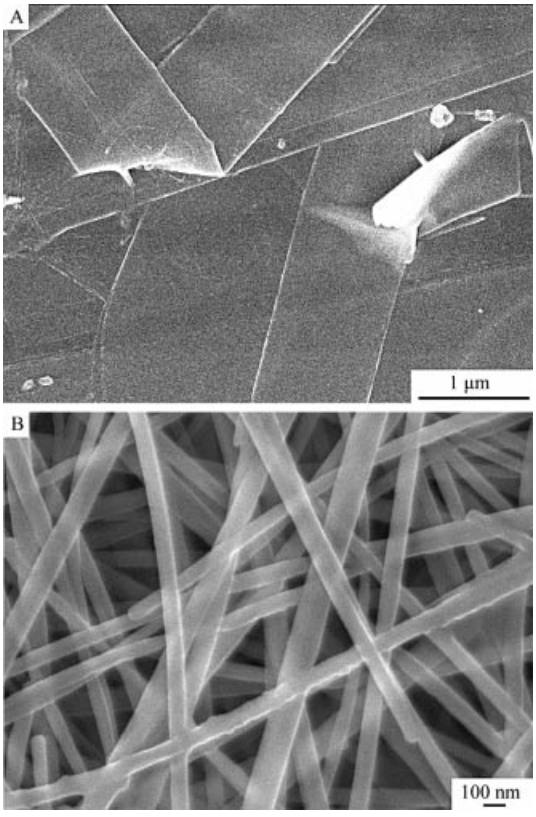

Figure 3. SEM images of $H_2V_3O_8$ nanobelts synthesized with different pH values. (A) at pH 5, (B) at pH 3.

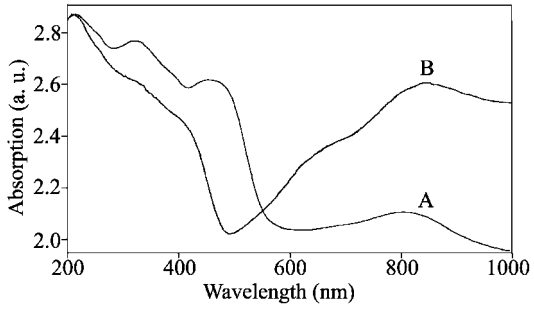

Figure 4. UV/Vis spectra of the initial V_2O_5 precursor (A), and $H_2V_3O_8$ nanobelts synthesized at pH 4 (B).

The redox reaction process is free of any templates and surfactants, so it is supposed that the formation of the belt-like $H_2V_3O_8$ is probably related to the layered structure of $H_2V_3O_8$. V_2O_5 partly dissolves in water to produce various polyvanadate ions at different pH values in aqueous solution, which can undergo a redox reaction to form $H_2V_3O_8$ clusters under hydrothermal conditions. Then, the $H_2V_3O_8$ clusters serve as the sites for the heterogeneous nucleation of the nanobelts, which subsequently crystallize along the [001] direction of $H_2V_3O_8$ single crystals and grow in belt-like structures through a topotactic transformation mechanism.

Conclusions

In conclusion, we have demonstrated a facile route to the synthesis of $H_2V_3O_8$ nanobelts. The synthetic process is free of any templates and reducing agents. The thickness and length of $H_2V_3O_8$ nanobelts are less than 30 nm, and up to several hundreds of micrometers, respectively. The width of $H_2V_3O_8$ nanobelts can be controlled by adjusting the pH values. The belt-like $H_2V_3O_8$ with a high surface area may be beneficial to lithium insertion between the V_3O_8 layers for application in batteries.

Experimental Section

An optimized procedure for the synthesis of $H_2V_3O_8$ single-crystal nanobelts is described as follows: V_2O_5 powder (0.15 g) was dispersed into distilled water (40 mL). Then, an appropriate amount of hydrochloric acid was added dropwise to the orange mixture to adjust pH values in the range of 3–5. The slurry solution was placed in a 50-mL autoclave with a Teflon liner after ultrasonic vibration for 10 min. The autoclave was maintained at 190 °C for 24 h and then air cooled to room temperature. The green precipitate was collected and washed with distilled water and anhydrous alcohol several times, and then dried in vacuo at 60 °C for 10 h. The yield of the $H_2V_3O_8$ nanobelts is estimated to be higher than 90%.

The crystal structures of the initial V_2O_5 precursor and the resulting product were characterized by an X-ray diffractometer (Rigaku D-max-γA XRD with Cu-K_α radiation, λ = 1.54178 Å). The morphologies and sizes of the resulting products were observed by field-emission scanning electron microscopy (FE-SEM, JSM 6700F) and high-resolution transmission electron microscopy (HRTEM, JEOL 2010), respectively. The optical properties of the initial V_2O_5 precursor and the resulting product were determined by UV/Vis spectroscopy (Cary 500 UV/Vis-NIR spectrophotometer).

Supporting Information Available: Figure 1S, lower magnified SEM image of $H_2V_3O_8$ nanobelts synthesized at pH 4 at 190 °C for 24 h. Figure 2S, SEM image of the product obtained at pH 4 at 160 °C for 24 h.

Acknowledgments

This project is partly supported by the National Center for Nanoscience and Technology, P. R. China.

[1] A. Dobley, K. Ngala, S. Yang, P. Y. Zavalij, M. S. Whittingham, *Chem. Mater.* **2001**, *13*, 4382–4386.
[2] G. T. Kim, J. Muster, V. Krstic, J. G. Park, Y. W. Park, S. Roth, M. Burghard, *Appl. Phys. Lett.* **2000**, *76*, 1875–1877.
[3] J. Muster, G. T. Kim, V. Krstić, J. G. Park, Y. W. Park, S. Roth, M. Burghard, *Adv. Mater.* **2000**, *12*, 420–424.
[4] Z. W. Pan, Z. R. Dai, Z. L.Wang, *Science* **2001**, *291*, 1947–1949.
[5] E. Comini, G. Faglia, G. Sberveglieri, Z. W. Pan, Z. L.Wang, *Appl. Phys. Lett.* **2002**, *81*, 1869–1871.
[6] Y. Oka, T. Yao, N. Yamamoto, *J. Solid State Chem.* **1990**, *89*, 372–377.
[7] N. Pinna, U. Wild, J. Urban, R. Schlögl, *Adv. Mater.* **2003**, *15*, 329–331.

 © 2005 Wiley-VCH Verlag GmbH & Co. KGaA, Weinheim

[8] N. Pinna, M. Willinger, K. Weiss, J. Urban, R. Schlögl, *Nano Lett.* **2003**, *3*, 1131–1134.
[9] M. E. Spahr, P. Bitterli, R. Nesper, M. Müller, F. Krumeich, H. U. Nissen, *Angew. Chem., Int. Ed. Engl.* **1998**, *37*, 1263–1265.
[10] J. Yu, J. C. Yu, W. Ho, L. Wu, X. Wang, *J. Am. Chem. Soc.* **2004**, *126*, 3422–3423.
[11] L. Kong, Z. Liu, M. Shao, Q. Xie, W. Yu, Y. Qian, *J. Solid State Chem.* **2004**, *177*, 690–695.
[12] J. Liu, Q. Li, T. Wang, D. Yu, Y. Li, *Angew. Chem., Int. Ed. Engl.* **2004**, *43*, 5048–5052.
[13] V. Legagneur, A. L. G. L. Salle, A. Verbaere, A. Piffard, D. Guyomard, *Electrochim. Acta* **2002**, *47*, 1153–1161.
[14] V. Legagneur, A. L. G. L. Salle, A. Verbaere, A. Piffard, D. Guyomard, *J. Mater. Chem.* **2000**, *10*, 2805–2810.
[15] K. Takahashi, S. J. Limmer, Y. Wang, G. Cao, *J. Phys. Chem. B* **2004**, *108*, 9795–9800.
[16] E. L. Crepaldi, D. Grosso, G. J. A. A. Soler-Illia, P. A. Albouy, H. Amenitsch, C. Sanchez, *Chem. Mater.* **2002**, *14*, 3316–3325.
[17] X. Gao, M. A. Banares, I. E. Wachs, *J. Catal.* **1999**, *188*, 325–331.

Received: November 21, 2004

 © 2005 Wiley-VCH Verlag GmbH & Co. KGaA, Weinheim

Oxalate-Based 3D Chiral Magnets: The Series $[Z^{II}(bpy)_3][ClO_4][M^{II}Fe^{III}(ox)_3]$ (Z^{II} = Fe, Ru; M^{II} = Mn, Fe; bpy = 2,2′-Bipyridine; ox = Oxalate Dianion)

Eugenio Coronado,*[a] José R. Galán-Mascarós,*[a] Carlos J. Gómez-García,[a] Eugenia Martínez-Ferrero,[a] Manuel Almeida,[b] and João C. Waerenborgh[b]

Keywords: Coordination chemistry / Molecular materials / Magnetic properties / Mössbauer spectroscopy

The synthesis, structure, and physical properties of the oxalate-based molecular magnets with the formula $[Z^{II}(bpy)_3][ClO_4][M^{II}Fe^{III}(ox)_3]$ (Z^{II} = Fe, Ru; M^{II} = Mn, Fe; bpy = 2,2′-bipyridine; ox = oxalate dianion) are presented here. All compounds are isostructural and crystallize in the chiral cubic space group $P4_132$, and contain three-dimensional dimetallic networks formed by alternating M^{II} and M^{III} ions that are connected by oxalate anions. These compounds exhibit strong antiferromagnetic interactions that give rise to magnetic ordering as ferrimagnets or weak ferromagnets, with critical temperatures of up to 20 K, which is twice as high as those found for the isostructural magnets based on Cr^{III}, as determined by magnetic measurements and Mössbauer spectroscopy.
(© Wiley-VCH Verlag GmbH & Co. KGaA, 69451 Weinheim, Germany, 2005)

Introduction

Coordination chemistry has yielded many examples of molecule-based magnets. The nature of the ligands, responsible for promoting strong enough magnetic exchange, will be key for the physical properties found in these novel compounds. Most of these magnets are based on coordination polymers with metal centers that are connected by short ligands with a π-extended system such as cyanide,[1] dicyanamide[2–4], oxalate[5–7] and some other organic ligands.[8]

Polynuclear complexes from the oxalato ligand have been shown to be very versatile for the construction of magnetic materials, with one of the key reasons being the synthetic control over the lattice dimensionality. This has been demonstrated with the controlled obtention of dimers,[9] trimers,[10] 1D chains,[11] and extended 2D[5,6] and 3D lattices[12,13] from essentially the same building blocks. Interestingly, some of these coordination polymers are anions that form salts with a variety of molecular cations.

Bulky organic monocations promote the synthesis of compounds with the formula $[A][M^{II}M^{III}(ox)_3]$ ($A = NR_4^+$, PPh_4^+; M^{II} = Mn, Fe, Co, Ni, Cu; M^{III} = Cr, Fe, Ru, Rh),[5,6,14–16] formed by two-dimensional oxalate bridged dimetallic networks. The sign of the magnetic interaction is determined by the nature of the metals – Cr^{III} and Ru^{III} promote ferromagnetic interactions, while Fe^{III} promotes antiferromagnetic interactions. These materials behave as ferromagnets with critical temperatures of up to 15 K, and as ferri- or weak ferromagnets with critical temperatures of up to 44 K. The combination of different trivalent metals in the 2D lattice has given rise to materials with tunable magnetic properties, and large hysteresis loops with coercive fields of over 2 T.[17] On the other hand, insertion of electroactive organometallic or organic molecules in these 2D systems has yielded magnetic multilayers,[18] ferromagnetic metals,[19,20] or photochromic magnets.[21]

Chiral octahedral complexes of the type $[Z(bpy)_3]^{2+}$ (bpy = 2,2′-bipyridine) and analogs favor the formation of the series $[Z^{II}(bpy)_3][ClO_4][M^{II}M^{III}(ox)_3]$ (Z^{II} = Ru, Fe, Co, Ni; M^{II} = Mn, Fe, Co, Ni, Cu; M^{III} = Cr),[12] formed by three-dimensional chiral oxalate-based networks that behave as ferromagnets, but with critical temperatures that are much lower than those of their 2D counterparts. This has been related to the weaker magnetic interactions present in this case, promoted by a different relative orientation of the magnetic orbitals and to larger metal-to-metal distances. Most of these compounds show T_c below 3 K, with a few exceptions that reach up to 6 K.

The added value of these 3D magnets is their chirality, especially as the crystallites are chiral through self-assembly, even starting from a racemic mixture of building blocks. This family constitutes a nice example of chiral magnets, a very sought after combination in recent years[22–24] because of the interest in the investigation of how chirality affects the magnetic properties: it is easy to understand that the imposed anisotropy in such systems will be a key factor that controls the magnetic behavior, but

[a] Instituto de Ciencia Molecular, Universidad de Valencia, Dr. Moliner 50, 46100 Burjasot, Spain
E-mail: eugenio.coronado@uv.es
jose.r.galan@uv.es
[b] Dept. Química, ITN/CFMC-UL, 2686-953 Sacavém, Portugal
Supporting information for this article is available on the WWW under http://www.eurjic.org or from the author.

 © 2005 Wiley-VCH Verlag GmbH & Co. KGaA, Weinheim DOI: 10.1002/ejic.200400977

further, that these systems could also exhibit new physical phenomena, for example, the so-called magnetochiral dichroism.[25]

While the dimetallic 2D magnets have been obtained with a variety of trivalent metals, the analogous 3D systems have only been obtained so far for Cr^{III}. The reason is that the synthetic conditions required for the preparation of the 3D systems are much more exigent. For instance, the presence of alkali metals in solution needs to be avoided, since alkali metals can also form 3D networks with trivalent metals with the general formula $[Z^{II}(bpy)_3][A^IM^{III}(ox)_3]$ (Z^{II} = Ru, Fe, Co, Ni; A^I = Li, Na, K; M^{III} = Cr).[26] These materials have shown interesting electronic properties, such as photoinduced energy transfer, electron transfer,[27] and spin transition in one case, namely $[Co(bpy)_3][LiCr(ox)_3]$,[28,29] but no magnetic ordering since the paramagnetic centers are isolated by diamagnetic alkali neighbors. In addition, more synthetic difficulties need to be overcome, as the trisoxalate complexes are less stable towards ligand substitution. In this work, we present our successful extension of this series to the $[Fe^{III}(ox)_3]^{3-}$building block while searching for increased ordering temperatures for these magnets, as observed in the 2D analogs.

Results and Discussion

Synthesis and Structure

For the synthesis of the desired $[M^{II}M^{III}(ox)_3]^-$ 3D network, the possible formation of the 3D $[A^IM^{III}(ox)_3]^{2-}$ analog, where A^I is an alkali metal or a small cation such as NH_4^+, is one of the main synthetic problems to overcome. Thus, the common $A_3[M^{III}(ox)_3]$ salts cannot be used in this synthesis. Bulky cations cannot be used either, since they template the formation of the corresponding 2D honeycomb networks. To form the 3D $[M^{II}Cr^{III}(ox)_3]^-$ network we already described the use of the silver salt $Ag_3[Cr^{III}(ox)_3]$. The same procedure, however, cannot be used to prepare the $M^{II}Fe^{III}$ derivatives since the $Ag_3[Fe(ox)_3]$ salt is unstable. Thus, we used an analogous procedure, but starting from the slightly more soluble $Tl_3[Fe(ox)_3]$ salt that allows for the precipitation of TlCl, and for the preparation of the desired solution containing the M^{II} and $[Fe(ox)_3]^{3-}$ building blocks exclusively. The mixture of this solution with one containing $[Z^{II}(bpy)_3][ClO_4]_2$ yields a fine powder that must be settled before filtering. Particle sizes are typically uniform and of the order 0.5–3 μm.

Even under these conditions not all possible Z/M^{II} combinations that may be suitable for the formation of oxalate complexes could be obtained, as the $[Fe(ox)_3]^{3-}$ complex is not completely stable in solution when competing with other cations. Because of this reason, the nature of the solvent mixture and temperature are crucial to obtain pure products, and even under such circumstances, some disorder between the alternating positions for trivalent and divalent metals in the network cannot be avoided in some cases, as will be discussed in this paper.

All compounds were structurally characterized by powder X-ray diffraction, which indicates that all compounds are isostructural as the salt $[Ru^{II}(bpy)_3][ClO_4][Mn^{II}Cr^{III}(ox)_3]$ already reported.[12] The structure of these salts consists of 3D oxalate-bridged dimetallic networks that host the cations $[Z^{II}(bpy)_2]^{2+}$ (Figure 1). In the anionic network, the bidentate chelating oxalate ligands connect the metals in an alternating way such that each M^{II} center is surrounded by three M^{III} centers and vice versa, to form 10-unit rings with a (10,3) topology. In a given crystal, all metal centers are of the same chirality, although crystallites of both chiralities are obtained when starting from racemic mixtures of the reagents, as in the compounds prepared for this study. The cations $[Z^{II}(bpy)_3]^{2+}$ of each chiral group template the formation of the corresponding chiral network, and are located in the tunnels left by the polymeric structure. Perchlorate anions fill up the remaining holes in the structure.

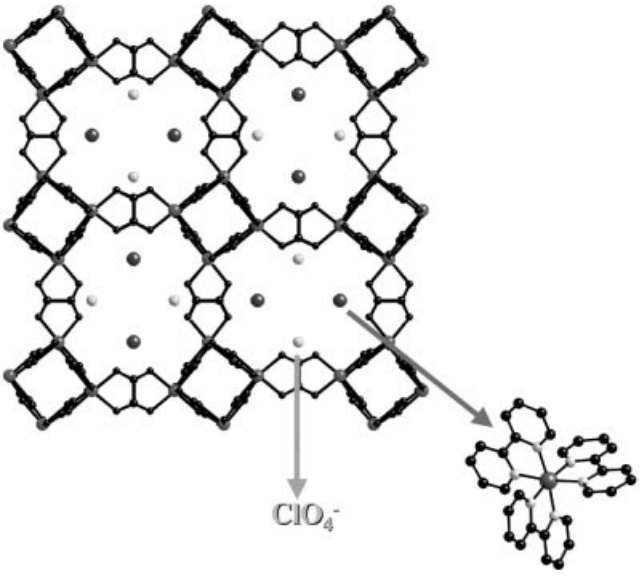

Figure 1. Projection on the *bc* plane of the structure of the family of molecule-based magnets $[Z^{II}(bpy)_3][ClO_4][M^{II}M^{III}(ox)_3]$. Only the Z^{II} ion of the $[Z^{II}(bpy)_3]^{2+}$ cations and the Cl atom of the ClO_4^- anions are drawn in the cavities.

Magnetic Properties

Magnetic susceptibility measurements for the $[Fe^{II}(bpy)_3][ClO_4][M^{II}Fe^{III}(ox)_3]$ derivatives (M^{II} = Mn, Fe) are shown in Figure 2. Both compounds present a clear decrease in the $\chi_m T$ product as the temperature is decreased. This high-temperature regime follows a Curie–Weiss law, and gives Curie constants slightly higher than that expected for spin-only, and large and negative Weiss constants (Table 1), which is indicative of the presence of antiferromagnetic interactions between the metal centers in the network, as is expected for oxalate-bridged dimetallic M^{II}-Fe^{III} compounds. The variation of χ_m with temperature shows a deviation from the regular paramagnetic behavior at low temperatures for both compounds –a jump appears below

 © 2005 Wiley-VCH Verlag GmbH & Co. KGaA, Weinheim

Table 1. Magnetic parameters for the series $[Z^{II}(bpy)_3][ClO_4][M^{II}Fe(ox)_3]$.[a]

Z^{II}	M^{II}	T_c [K]	θ [K]	C [emu K mol^{-1}]	$C_{spin\text{-}only}$ [emu K mol^{-1}]	$H_{coer.}$ [mT]
Fe	Mn	20.0	–58	9.53	8.75	25
Fe	Fe	9.1	–41	7.67	7.375	97
Ru	Mn	17.2	–81	9.46	8.75	30
Ru	Fe	7.9	–46	7.67	7.375	86

[a] T_c, ordering temperature; θ, Weiss constant; C, Curie constant; $H_{coer.}$, coercive field at 2 K.

25 K for Mn^{II} (Figure 2 bottom) and below 12 K for Fe^{II}. After this jump, χ_m does not tend to saturation at very low temperatures in either compound, showing a Curie tail probably because of the presence of small amounts of paramagnetic impurities. These features suggest the appearance of a magnetically ordered regime. This was confirmed by the temperature dependence of the AC magnetic susceptibility (Figure 3), that shows, in both cases, a maximum in χ'_m that corresponds to a peak in χ''_m, with T_c (when χ''_m becomes non zero) at 20.0 K for the Mn derivative and 9.1 K for the Fe derivative. Due to the nature of the short-range interactions in both cases, the Mn^{II} derivative can be considered to be a weak ferromagnet, and the origin for net magnetization comes from canting between the antiferromagnetically aligned $S(Mn^{II}) = S(Fe^{III}) = 5/2$ moments, while the Fe^{II} derivative can be considered to be a ferrimagnet, because of the non total compensation of the antiferromagnetically coupled spins $S(Fe^{III}) = 5/2$ and $S(Fe^{II}) = 2$. In this last compound, a small frequency dependence of the AC peaks is observed, similar to those observed in the analogous 2D network. As in these cases, such a feature can be associated to a disorder in the magnetic 3D network generated by partial substitution of the Fe^{II} centers by Fe^{III}, and vice versa. The field dependence of the magnetization at 2 K for both compounds (Figure 4) shows an almost linear increase, and is far from saturation even at 5 T, confirming the nature of the magnetic ordering. Both compounds show small hysteresis loops at 2 K with coercive fields of 25 (Mn^{II}) and 97 mT (Fe^{II}).

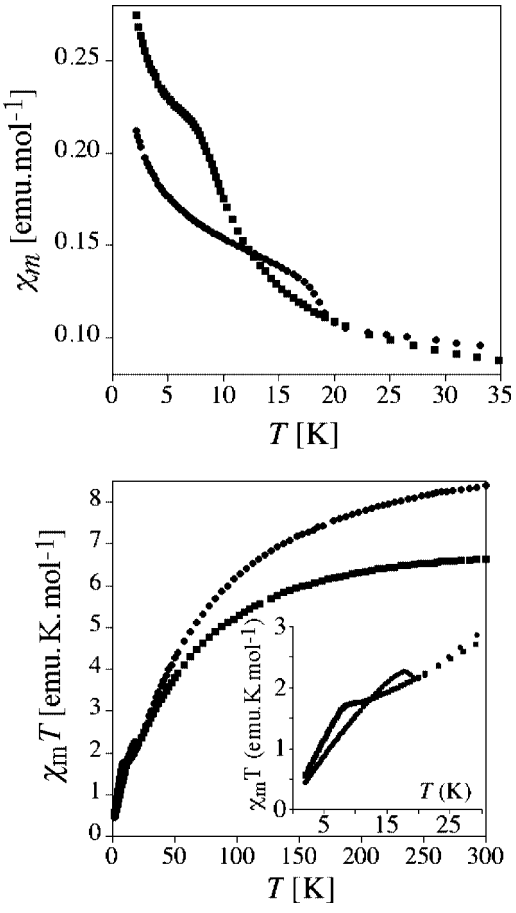

Figure 2. Thermal variation of the magnetic susceptibility χ_m (top) and of the $\chi_m T$ product (bottom) for the salts $[Fe(bpy)_3][ClO_4][M^{II}Fe(ox)_3]$; M^{II} = Mn (circle), Fe (square).

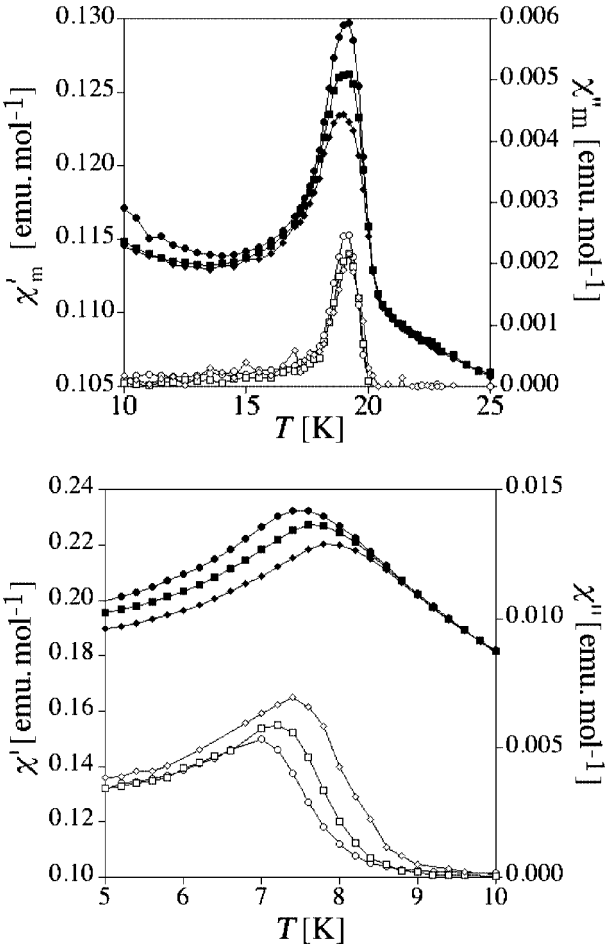

Figure 3. Frequency dependence of the in-phase (filled symbols, χ'_m) and out-of-phase (empty symbols, χ''_m) AC susceptibility of the salts $[Fe(bpy)_3][ClO_4][M^{II}Fe(ox)_3]$ at 1 (circle), 10 (square) and 110 Hz (diamond); M^{II} = Mn (top), Fe (bottom).

 © 2005 Wiley-VCH Verlag GmbH & Co. KGaA, Weinheim

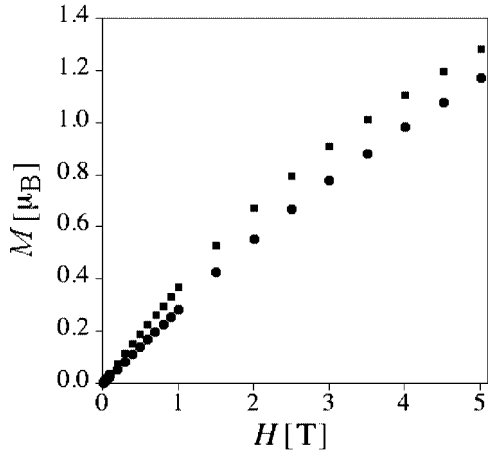

Figure 4. Field dependence of the magnetization at 2 K for the salts $[Fe(bpy)_3][ClO_4][M^{II}Fe(ox)_3]$; M^{II} = Mn (circle), Fe (square).

The $[Ru^{II}(bpy)_3]^{2+}$ derivatives show, as expected, an analogous magnetic behavior, with magnetic parameters very similar to those of the $[Fe^{II}(bpy)_3]^{2+}$ counterparts (see Table 1). The critical temperatures, however, are slightly lower for these derivatives. As mentioned before, this effect of the templating cation on the magnetic properties was also observed in the Cr^{III} derivatives, and works here in the same direction. The AC magnetic susceptibility measurements (Figure 5) show ordering temperatures at 17.2 K for Mn^{II} and 7.9 K for Fe^{II}. The Mn^{II} salt shows a small maximum in χ'_m after the peak, unseen in the rest of materials. This feature has no frequency dependence and no clear origin. As seen before, the Fe^{II} salt shows a small frequency dependence of the peaks. Both compounds show hysteresis loops below T_c, with coercive fields and field dependence of the magnetization at 2 K, which is almost identical to those of their $[Fe^{II}(bpy)_3]^{2+}$ counterparts. The weaker magnetic exchange when going from $[Fe^{II}(bpy)_3]^{2+}$ to $[Ru^{II}(bpy)_3]^{2+}$ has been explained in terms of the different size of the cations, which leads to larger unit cells, and therefore larger intermetallic distances; an effect that obviously influences the magnetic properties.

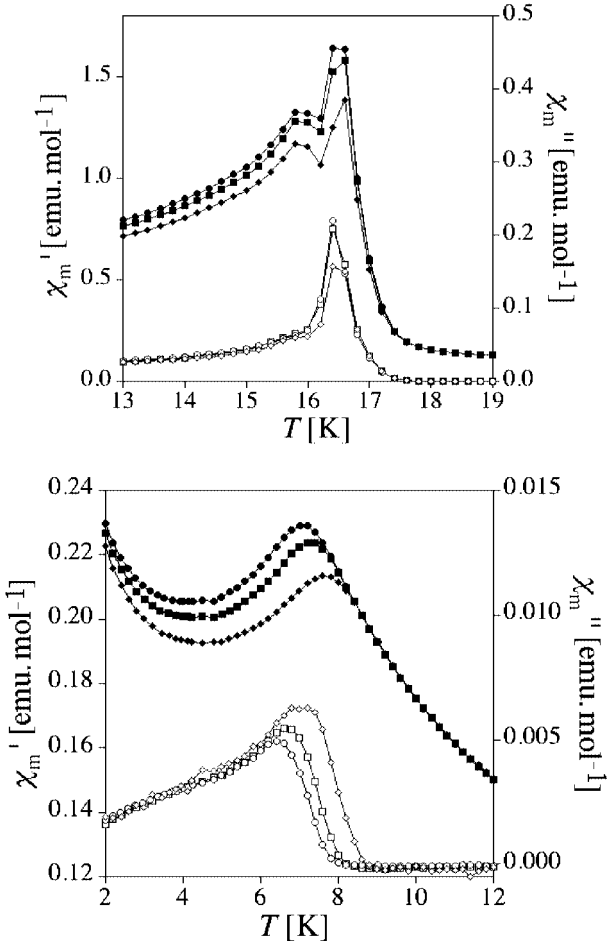

Figure 5. Frequency dependence of the in-phase (filled symbols, χ'_m) and out-of-phase (empty symbols, χ''_m) AC magnetic susceptibility for the salts $[Ru(bpy)_3][ClO_4][M^{II}Fe(ox)_3]$ at 1 (circle), 10 (square) and 332 Hz (diamond); M^{II} = Mn (top), Fe (bottom).

Mössbauer Spectroscopy

Mössbauer spectra of $[Fe(bpy)_3]ClO_4[MnFe(ox)_3]$ were taken at 100 and 6 K (Figure 6). At 100 K, the spectrum consists of three different doublets whose estimated parameters, isomer shift, δ, and quadrupole splitting, Δ, (Table 2), are typical of low-spin (LS) Fe^{II} in a $[Fe(bpy)_3]^{2+}$ complex, of high-spin (HS) Fe^{III} within the anionic oxalate net, and of HS Fe^{II} in the same oxalate net. This HS Fe^{II} is certainly due to impurities in the sample. Incorporation of Fe^{II} into the anionic network was already observed in similar $[Fe(bpy)_3][Mn_2(ox)_3]$ compounds.[32] The spectrum at 6 K (Figure 6) shows a doublet due to LS Fe^{II} in the $[Fe(bpy)_3]^{2+}$ complex (Table 2), a sextet with broad peaks attributed to HS Fe^{III} and a third set of low-intensity peaks. The HS Fe^{III} contribution is a sextet because the relaxation frequency of the corresponding Fe spins strongly decreases between 100 K and 6 K, and becomes significantly lower than the Larmor period of the nuclear moment. This is a strong indication that the $[MnFe(ox)_3]^-$ net is magnetically ordered at 6 K, which is in agreement with the T_c value deduced from magnetization data. It should be noted that LS Fe^{II} in the $[Fe(bpy)_3]^{2+}$ complex remains unaffected by the internal magnetic field.

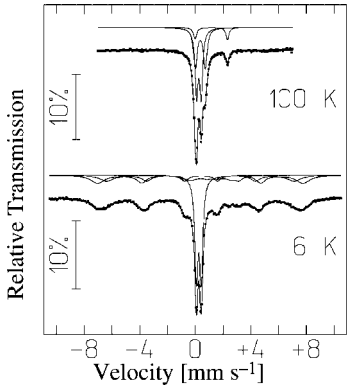

Figure 6. Mössbauer spectra at different temperatures for the salt $[Fe(bpy)_3][ClO_4][MnFe(ox)_3]$.

 © 2005 Wiley-VCH Verlag GmbH & Co. KGaA, Weinheim

Table 2. Estimated parameters from the Mössbauer spectra of $[Fe(bpy)_3][ClO_4][MnFe(ox)_3]$ at different temperatures.[a]

T [K]	Fe site	δ [mm s^{-1}]	Δ, Δ', ε [mm s^{-1}]	B_{hf} [T]	η	Θ [°]	Φ	%
100	$[Fe(bpy)_3]^{2+}$	0.37	0.33	–	–	–	–	51
	$[Fe^{III}(ox)_{3/2}]$	0.46	0.72	–	–	–	–	40
	$[Fe^{II}(ox)_{3/2}]^-$	1.26	2.33	–	–	–	–	9
6	$[Fe(bpy)_3]^{2+}$	0.37	0.35	–	–	–	–	41
	$[Fe^{III}(ox)_{3/2}](1)$	0.50	–0.06	47.6	–	–	–	31
	$[Fe^{III}(ox)_{3/2}](2)$	0.50	0.01	41.6	–	–	–	17
	$[Fe^{II}(ox)_{3/2}]^-$	1.29	–1.69	8.5	1	90	0	11

[a] δ, isomer shift relative to metallic α-Fe at 295 K; Δ, quadrupole splitting in the paramagnetic state; Δ' and ε, quadrupole interaction and quadrupole shift in the magnetically ordered state for Fe^{II} and Fe^{III}, respectively; B_{hf}, magnetic hyperfine field; η, asymmetry parameter; Θ and Φ, angles between B_{hf} and the main axis V_{zz} of the electric field gradient and between B_{hf} and the main axis V_{xx}; %, percentage of the total area corresponding to each subunit. Estimated errors are $\leq$0.02 mm s^{-1} for δ, Δ, Δ' and <0.2 T for B_{hf}. Values of Θ, Φ and η, kept constant during the fitting procedure, are those corresponding to the best final adjustments.

Considering the 100 K spectrum, the third set of low-intensity peaks observed at 6 K is most likely due to the HS Fe^{II} impurities in the oxalate net. These Fe^{II} atoms are also magnetically ordered. However, as previously shown,[14] their contribution cannot be fitted assuming a simple magnetic sextet. In fact, the quadrupole hyperfine interaction cannot be treated as a perturbation of the magnetic hyperfine interaction. The position and relative intensities of the absorption lines of the magnetically ordered HS Fe^{II} atoms therefore have to be calculated by solving the complete Hamiltonian for the hyperfine interactions in both the excited and ground nuclear states of the ^{57}Fe nuclei. In the present work, this calculation was performed following the procedure described by Ruebenbauer and Birchall.[30] The best fit was obtained assuming that the angle between B_{hf} and the main axis of the electric field gradient, V_{zz}, is Θ = 90, and between V_{xx} and B_{hf} is Φ = 0. The final values obtained for the fitted parameters, δ, B_{hf}, the asymmetry parameter η, and $\Delta' = e^2QV_{zz}$ (where e is the electron charge and Q is the ^{57}Fe nuclear quadrupole moment at the 14.4 keV level), are given in Table 2. The estimated parameters obtained are indeed consistent with a HS Fe^{II} atom and similar to those reported for compounds containing $[Fe^{II}(ox)_{3/2}]^-$ units.[14,31] The random substitution of Mn^{II} by these Fe^{II} impurities within the oxalate network gives rise to different environments for the HS Fe^{III} atoms. Differences in the magnetic exchange interactions, which correspond to distinct environments, may be large enough to be observed as a distribution of B_{hf}. This distribution, approximately described by two sextets, whose parameters are summarized in Table 2, explains the broadness of the observed peaks due to the HS Fe^{III} atoms in the oxalate layers and the small frequency dependence of the χ'' peak observed in the AC susceptibility data.

The relative areas estimated for LS Fe^{II} and HS Fe^{III} change significantly between 100 K and 6 K. This fact had already been observed in $[Fe(bpy)_3][M^{II}_2(ox)_3]$ (M = Mn, Fe) compounds that also contained HS Fe^{II} impurities.[32] It may be explained by the different temperature dependence of the Debye–Waller factors for LS Fe^{II} and HS Fe^{III}. Considering that the values of these factors are closer at the lowest temperatures, the relative areas estimated at 6 K are a better approximation to the relative amounts of the different Fe species in the sample. This implies that the HS Fe^{II} impurities that substitute Mn^{II} in the oxalate layers are approximately 10% of the total Fe in the present $[Fe(bpy)_3][ClO_4][MnFe(ox)_3]$ sample; a value similar to those reported for the $[Fe(bpy)_3][M^{II}_2(ox)_3]$ salts.[32]

The Mössbauer spectra of $[Fe(bpy)_3][ClO_4][FeFe(ox)_3]$ at 294 K and 100 K (Figure 7) consist of three doublets attributed to LS Fe^{II} in $[Fe(bpy)_3]^{2+}$, HS Fe^{III} and HS Fe^{II} in the inorganic network (see estimated parameters for $[Fe(bpy)_3][ClO_4][FeFe(ox)_3]$ and $[Fe(bpy)_3][ClO_4][MnFe(ox)_3]$ in Table 2 and Table 3). At 6 K, the spectrum shows that the HS Fe^{III} and HS Fe^{II} atoms in the inorganic network have a slow relaxation, which is consistent with the magnetic ordering of these Fe species and in agreement with the magnetic data. As in the case of $[Fe(bpy)_3][ClO_4[MnFe(ox)_3]$, LS Fe^{II} in $[Fe(bpy)_3]^{2+}$ remains unaffected by the internal

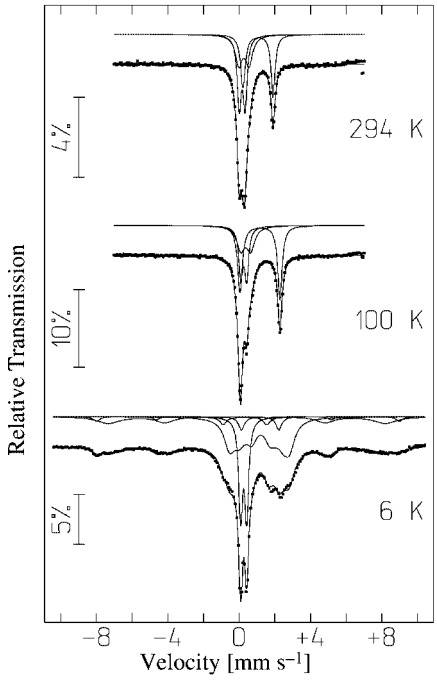

Figure 7. Mössbauer spectra at different temperatures for the salt $[Fe(bpy)_3][ClO_4][FeFe(ox)_3]$.

 © 2005 Wiley-VCH Verlag GmbH & Co. KGaA, Weinheim

Table 3. Estimated parameters from the Mössbauer spectra of $[Fe(bpy)_3][ClO_4][FeFe(ox)_3]$ at different temperatures.[a]

T [K]	Fe site	δ [mm s^{-1}]	Δ, Δ', ε [mm s^{-1}]	B_{hf} [T]	η	Θ [°]	Φ	%
294	$[Fe(bpy)_3]^{2+}$	0.28	0.33	–	–	–	–	38
	$[Fe^{III}(ox)_{3/2}]$	0.38	0.57	–	–	–	–	28
	$[Fe^{II}(ox)_{3/2}]^-$	1.17	1.69	–	–	–	–	34
100	$[Fe(bpy)_3]^{2+}$	0.37	0.33	–	–	–	–	28
	$[Fe^{III}(ox)_{3/2}]$	0.45	0.57	–	–	–	–	26
	$[Fe^{II}(ox)_{3/2}]^-$	1.28	2.24	–	–	–	–	46
6	$[Fe(bpy)_3]^{2+}$	0.37	0.34	–	–	–	–	25
	$[Fe^{III}(ox)_{3/2}](1)$	0.49	0.11	48.1	–	–	–	20
	$[Fe^{III}(ox)_{3/2}](2)$	0.49	0.23	52.6	–	–	–	4
	$[Fe^{II}(ox)_{3/2}]^-(1)$	1.29	1.84	6.2	0.8	90	0	46
	$[Fe^{II}(ox)_{3/2}]^-(2)$	1.29	2.10	–	–	–	–	5

[a] Parameters as defined in Table 2.

magnetic field. The relative areas estimated for HS Fe^{III} and Fe^{II} at 6 K suggest that in $[Fe(bpy)_3][ClO_4][FeFe(ox)_3]$, there is an excess of HS Fe^{II} that could replace HS Fe^{III} in random positions in the oxalate layer. This disorder may be responsible for the observation of a distribution of B_{hf} for HS Fe^{III}, again approximated by two magnetic sextets with large peak widths, as in $[Fe(bpy)_3][ClO_4][MnFe(ox)_3]$. Furthermore, the same disorder may explain why acceptable fits of the 6 K spectrum could only be obtained if a doublet corresponding to paramagnetic HS Fe^{II} was considered in addition to the main magnetically ordered contribution of this Fe species (Table 3). In fact, the disorder resulting from the presence of excess HS Fe^{II} may be associated with the existence of small fractions of these ions that experience rapidly fluctuating B_{hf} even at temperatures lower than T_c (although still close to T_c).

Conclusions

In this paper we have demonstrated that 3D chiral molecular magnets based on dimetallic oxalate complexes can be prepared from the $[Fe(ox)_3]^{3-}$ building block given the right synthetic conditions and with the use of different $[Z^{II}(bpy)_3]^{2+}$ complexes (Z^{II} = Fe, Ru) as templating cations. The salts $[Z^{II}(bpy)_3][ClO_4][M^{II}Fe^{III}(ox)_3]$ (M^{II} = Mn, Fe) are isostructural to the $[Cr(ox)_3]^{3-}$-based ferromagnets and are of identical stoichiometry, while the different sign and strength of the magnetic exchange promoted by the presence of Fe^{III} instead of Cr^{III} yields quite different magnetic properties. As these compounds exhibit strong antiferromagnetic interactions, they behave as ferrimagnets (M^{II} = Fe) or weak ferromagnets (M^{II} = Mn) with critical temperatures in the range 7–20 K, which are much higher than those observed for the analogous ferromagnets, in which the ordering only occurred close to 2 K. This fact must be important in the future studies that investigate the interplay between magnetism and chirality.

Another consideration that needs to be stressed is the effect of the nature of the $[Z^{II}(bpy)_3]$ complex on the magnetic properties. With the same crystal structure, the different sizes of the cations promote an enlargement of the unit cell parameters by 0.2 Å. Such small differences are enough to provoke a change of a few degrees in T_c, as seen in this and other cases. This suggests that hydrostatic pressure should also be able to affect the magnetic properties in these materials. Thus, magnetic measurements under pressure are in progress.

Experimental Section

Synthesis: The complexes $[Z^{II}(bpy)_3]^{2+}$ (Z^{II} = Ru, Fe) were prepared according to literature methods.[33,34] The precursor salt $Tl_3[Fe(ox)_3]\cdot nH_2O$ was prepared by metathesis from the corresponding potassium salt.[35] All other materials and solvents were commercially available and used without further purification.

$[Z^{II}(bpy)_3][ClO_4][M^{II}Fe^{III}(ox)_3]$ (Z^{II} = Fe, Ru; M^{II} = Mn, Fe): $M^{II}Cl_2$ (1.56 mmol) was added in excess to a water solution (10 mL) of $Tl_3[Fe(ox)_3]\cdot nH_2O$ (0.3 g, 0.31 mmol). After stirring for 10 min, a white precipitate of TlCl was removed by filtration. DMF (20 mL) was added to this green solution, which then turned yellow, and this mixture was added dropwise to a DMF (15 mL) solution of $[Z^{II}(bpy)_3][ClO_4]_2$ (0.4 mmol). After stirring for 30 min, the mixture was cooled down to 5 °C overnight. The product was isolated by filtration with use of a vacuum, washed thoroughly with methanol and acetone, and dried at room temperature.

FeMnFe: Yield 61% (183 mg). $C_{36}H_{24}ClFe_2MnN_6O_{16}$ (998.70): calcd. C 43.30, H 2.42, N 8.42; found C 43.18, H 2.30, N 8.35.

FeFeFe: Yield 55% (165 mg). $C_{36}H_{24}ClFe_3N_6O_{16}$ (999.61): calcd. C 43.36, H 2.42, N 8.41; found C 42.95, H 2.11, N 8.10.

RuMnFe: Yield 75% (235 mg). $C_{36}H_{24}ClFeMnN_6O_{16}Ru$ (1043.92): calcd. C 41.42, H 2.32, N, 8.05; found C 41.20, H 2.22, N 7.99.

RuFeFe: Yield 80% (251 mg). $C_{36}H_{24}ClFe_2N_6O_{16}Ru$ (1044.87): calcd. C 41.38, H 2.32, N 8.04; found C 40.93, H 2.12, N 7.80.

Structural Characterization: X-ray powder profiles were collected with a Siemens D-500 X-ray diffractometer (Cu-K_α radiation, λ_α = 1.54184 Å) at 293(2) K. Samples were grounded and mounted on a flat sample plate. Typically, profiles were collected as step scans over a 12 h period in the $2 < 2\theta < 60$ range with a step size of 0.02. The powder diffraction profiles indicate that all compounds are isostructural and show analogous patterns to the simulated profile[36] from the atomic positional parameters of the published crystal structure of $[Ru(bpy)_3][ClO_4][MnCr(ox)_3]$,[12] which has the cubic space group $P4_132$ (see Supporting Information). Indexation

 © 2005 Wiley-VCH Verlag GmbH & Co. KGaA, Weinheim

of the main reflections[37] gave the unit cell parameters shown in Table 4.

Table 4. Crystallographic data for the salts $[Z^{II}(bpy)_3][ClO_4]$-$[M^{II}M^{III}(ox)_3]$.

$Z^{II}M^{II}M^{III}$	a [Å]	V [Å^3]
FeMnFe	15.39(3)	3645(1)
FeFeFe	15.33(2)	3603(1)
RuMnFe	15.48(4)	3709(1)
RuFeFe	15.44(4)	3681(1)

Magnetic Measurements: Magnetic susceptibility measurements were performed on polycrystalline samples with a Quantum Design MPMS-XL-5 susceptometer equipped with a SQUID sensor. The susceptibility data were corrected from the diamagnetic contributions as deduced by using Pascal's constant tables. DC data were collected in the range 2–300 K with an applied field of 0.1 T, and hysteresis loops were collected between –5 and +5 T at 2 K. AC data were collected in the range 2–30 K with an applied alternating field of 0.395 mT at different frequencies in the range 1–997 Hz.

Mössbauer Spectroscopy: ^{57}Fe Mössbauer measurements were recorded in transmission mode with a conventional constant acceleration spectrometer and a 25-mCi ^{57}Co source in Rh matrix. The velocity scale was calibrated by using an α-Fe foil at room temperature. Isomer shift values are given relative to this standard. Spectra were collected with the absorbers between 296 K and 5 K. Low-temperature measurements were obtained with a flow cryostat (temperature stability 0.5 K). The spectra were fitted to Lorentzian lines by using a non-linear least-squares fitting method as described previously.[38]

Acknowledgments

This work was supported by the Ministerio de Ciencia y Tecnología (MCyT projects MAT2001–3507-C02–01 and BQU2002–01091) and by the Generalitat Valenciana (project GV04A-0077). E. M. F. thanks the MCyT for a PhD fellowship.This paper also benefited from COST Action D14.

[1] K. R. Dunbar, R. A. Heintz, *Prog. Inorg. Chem.* **1997**, *45*, 283–391.
[2] M. Kurmoo, C. J. Kepert, *New J. Chem.* **1998**, *22*, 1515–1524.
[3] J. L. Manson, C. R. Kmety, Q. Z. Huang, J. W. Lynn, G. M. Bendele, S. Pagola, P. W. Stephens, L. M. Liable-Sands, A. L. Rheingold, A. J. Epstein, J. S. Miller, *Chem. Mater.* **1998**, *10*, 2552–2560.
[4] a) S. R. Batten, K. S. Murray, *Coord. Chem. Rev.* **2003**, *246*, 103–130; b) S. R. Batten, P. Jensen, B. Moubaraki, K. S. Murray, R. Robson, *Chem. Commun.* **1998**, 430–440.
[5] H. Tamaki, Z. J. Zhong, N. Matsumoto, S. Kida, M. Koikawa, N. Achiwan, Y. Hashimoto, H. Okawa, *J. Am. Chem. Soc.* **1992**, *114*, 6974–6979.
[6] C. Mathonière, C. J. Nuttall, S. G. Carling, P. Day, *Inorg. Chem.* **1996**, *35*, 1201–1206.
[7] R. Pellaux, H. W. Schamalle, R. Hubert, P. Fisher, T. Hauss, B. Ouladiaff, S. Decurtins, *Inorg. Chem.* **1997**, *36*, 2301–2308.
[8] J. R. Galán-Mascarós, K. R. Dunbar, *Angew. Chem. Int. Ed.* **2003**, *42*, 2289–2293.
[9] E. Coronado, J. R. Galán-Mascarós, C. J. Gómez-García, *J. Chem. Soc. Dalton Trans.* **2000**, 205–210.
[10] E. Coronado, J. R. Galán-Mascarós, C. Giménez-Saiz, C. J. Gómez-García, C. Ruíz-Pérez, *Eur. J. Inorg. Chem.* **2003**, 2290–2298.
[11] E. Coronado, J. R. Galán-Mascarós, C. Martí-Gastaldo, manuscript in preparation.
[12] E. Coronado, J. R. Galán-Mascarós, C. J. Gómez-García, J. M. Martínez-Agudo, *Inorg. Chem.* **2001**, *40*, 113–120.
[13] S. Decurtins, H. W. Schmalle, P. Schneuwly, J. Enslin, P. Gütlich, *J. Am. Chem. Soc.* **1994**, *116*, 9521–9528.
[14] E. Coronado, J. R. Galán-Mascarós, C. J. Gómez-García, J. M. Martínez-Agudo, E. Martínez-Ferrero, J. C. Waerenborgh, M. Almeida, *J. Solid State Chem.* **2001**, *159*, 391–402.
[15] J. Larionova, B. Mombelli, J. Sanchiz, O. Kahn, *Inorg. Chem.* **1998**, *37*, 679–684.
[16] E. Coronado, J. R. Galán-Mascarós, C. J. Gómez-García, E. Martínez-Ferrero, S. van Smaalen, *Inorg. Chem.* **2004**, *43*, 4808–4810.
[17] E. Coronado, J. R. Galán-Mascarós, C. J. Gómez-García, J. M. Martínez-Agudo, *Adv. Mater.* **1999**, 558–561.
[18] E. Coronado, J. R. Galán-Mascarós, C. J. Gómez-García, J. Ensling, P. Gütlich, *Chem. Eur. J.* **2000**, *6*, 552–563.
[19] E. Coronado, J. R. Galán-Mascarós, C. J. Gómez-García, V. Laukhin, *Nature* **2000**, *408*, 447–449.
[20] A. Alberola, E. Coronado, J. R. Galán-Mascarós, C. Giménez-Saiz, C. J. Gómez-García, *J. Am. Chem. Soc.* **2003**, *125*, 10774–10775.
[21] S. Bénard, P. Yu, J. P. Audière, E. Rivière, R. Clément, J. Guilhem, L. Tchertanov, K. Nakatani, *J. Am. Chem. Soc.* **2000**, *122*, 9444–9454.
[22] K. Inoue, H, Imai, P. S. Ghalsasi, K. Kikuchi, M. Ohba, H. Okawa, J. V. Yakhmi, *Angew. Chem. Int. Ed.* **2001**, *40*, 4242–4245.
[23] E.-Q. Gao, Y.-F. Yue, S.-Q. Bai, Z. He, C.-H. Yan, *J. Am. Chem. Soc.* **2004**, *126*, 1419–1429.
[24] R. Feyerherm, A. Loose, T. Ishida, T. Nogami, J. Kreitlow, D. Baabe, F. J. Litterst, S. Süllow, H.-H. Klauss, K. Doll, *Phys. Rev. B* **2004**, *69*, 134427.
[25] G. L. J. A. Rikken, E. Raupach, *Nature* **1997**, *390*, 493–494.
[26] S. Decurtins, H. W. Schmalle, P. Schneuwly, H. R. Oswald, *Inorg. Chem.* **1993**, *32*, 1888–1892.
[27] S. Decurtins, H. W. Schmalle, R. Pellaux, P. Schneuwly, A. Hauser, *Inorg. Chem.* **1996**, *35*, 1451–1460.
[28] A. Hauser, H. Riesen, R. Pellaux, S. Decurtins, *Chem. Phys. Lett.* **1996**, *261*, 313–317.
[29] R. Sieber, S. Decurtins, H. Stoeckli-Evans, C. Wilson, D. Yufit, J. A. K. Howard, S. C. Capelli, Hauser, A. *Chem. Eur. J.* **2000**, *6*, 361–368.
[30] K. Ruebenbauer, T. Birchall, *Hyper. Interact.* **1979**, *7*, 125–133.
[31] S. G. Carling, D. Visser, D. Hautot, I. D. Watts, P. Day, J. Ensling, P. Gütlich, G. J. Long, F. Grandjean, *Phys. Rev. B.* **2002**, *66*, 104407–104419.
[32] S. Decurtins, H. W. Schmalle, P. Schneuwly, J. Ensling, P. Gütlich, *J. Am. Chem. Soc.* **1994**, *116*, 9521–9528.
[33] F. H. Burstall, R. S. Nyholm, *J. Chem. Soc.* **1952**, 3570–3579.
[34] S. Anderson, K. R. Seddon, *J. Chem. Res.* **1979**, 75–77.
[35] J. M. Baylar, E. M. Jones, in *Inorganic Synthesis* (Ed.: H. S. Booth), McGraw-Hill, Nueva York, **1939**, vol. 1, p. 35.
[36] *CrystalDiffract 4.0.2* (CrystalMaker software).
[37] *CELSIZ* (Unit Cell Refinement v1.1 XRDUtilities).
[38] J. C. Waerenborgh, M. O. Figueiredo, J. M. P. Cabral, L. C. J. Pereira, *Phys. Chem. Miner.* **1994**, *21*, 460–468.

Received: November 21, 2004

Preparation and Crystal Structures of Benzoylhydrazido- and -diazenidorhenium Complexes with N,O-Ligands and Their Catalytic Activity Towards Peroxidative Oxidation of Cycloalkanes

Alexander M. Kirillov,[a] Matti Haukka,[b] M. Fátima C. Guedes da Silva,[a,c] and Armando J. L. Pombeiro*[a]

Keywords: Alkanes / Homogeneous catalysis / N,O ligands / Oxidation / Rhenium

The η^2-(benzoylhydrazido)rhenium(V) complex [Re{$(OCH_2CH_2)_2N(CH_2CH_2OH)$}{N=NC(O)Ph}$(PPh_3)$] (**2**) and the η^1-(benzoyldiazenido)rhenium(III) compounds [ReCl{$N(CH_2COO)(CH_2CH_2OH)(CH_2CH_2OH)$}{N=NC(O)Ph}$(PPh_3)$] (**3**) and [ReCl(*O*,*N*-L){N=NC(O)Ph}$(PPh_3)_2$] [*O*,*N*-L = N(=O)-CH_2COO (**4**), HN=C(Me)COO (**5**), $C_5H_4N(COO)$ (**6**)], with chelating N,O-ligands (amino alkoxides, amino-, oxyamino-, imino- and pyridinocarboxylates) have been prepared by treatment of [$ReCl_2${N=NC(O)Ph}$(PPh_3)_2$] (**1**) with triethanolamine [$N(CH_2CH_2OH)_3$], *N*,*N*-bis(2-hydroxyethyl)glycine [$N(CH_2CH_2OH)_2(CH_2COOH)$], *N*-hydroxyiminodiacetic acid [$HON(CH_2COOH)_2$], *N*-hydroxy-2,2′-iminodipropionic acid [$HON\{CH(Me)COOH\}_2$] and picolinic acid (NC_5H_4COOH-2), respectively. The N,O-ligands in **4** and **5** result from fragmentation of the *N*-hydroxyiminodicarboxylic acids. All the complexes have been characterized by IR, ^1H and ^{13}C NMR spectroscopy, FAB$^+$-MS, elemental analysis and X-ray diffraction structural analysis, which indicate a π-delocalized chelated benzoylhydrazidorhenium ring in **1** and **2**, and, in the other complexes, an essentially linear η^1-diazenido ligand that is always *trans* to the O-coordinated carboxylate moiety of the N,O-ligand. The complexes act as catalysts (TON values up to about 45) for peroxidative oxidation, by radical mechanisms, of cyclohexane and cyclopentane to the corresponding alcohols and ketones, under mild conditions (room temperature, use of aqueous H_2O_2 and without added acid). This is an unprecedented use of inorganic Re coordination compounds as catalysts in alkane functionalization.
(© Wiley-VCH Verlag GmbH & Co. KGaA, 69451 Weinheim, Germany, 2005)

Introduction

The coordination chemistry of rhenium[1] is a field of current growing interest from various viewpoints, especially for improving fundamental knowledge (e.g. on structural and physicochemical properties and on reactivity) and in topics with an applied character such as the development of diagnostic/radiotherapeutic cancer agents,[2,3] nitrogen fixation (a good number of Re dinitrogen and formally derived organodiazo-type complexes are known)[4–13] and catalysis.[14–24]

For the synthesis of diazenido and dinitrogen complexes with phosphorus-containing coligands, the benzoylhydrazide complex [$ReCl_2${N=NC(O)Ph}$(PPh_3)_2$] (**1**) is a key starting material,[25–28] but its use as a precursor for complexes with N-based coligands is still very rare and is usually limited to amines.[29–31] Hence, one of the aims of this work is to extend the application of complex **1** to the synthesis of benzoyldiazenido complexes with coligands of the latter type.

Another objective of this study is to find catalytic applications of such complexes, thus providing a contribution towards widening the field of catalysis with inorganic coordination compounds of rhenium, which still remains little explored.[32–41] This contrasts with the recently discovered catalytic behaviour of high-valent organorhenium oxides,[14–24] in particular the methyltrioxide [$(Me)ReO_3$], whose catalytic behaviour has been extensively studied for a variety of processes, such as epoxidation and hydroxylation of olefins, oxidation of alkynes, aromatic hydrocarbons, sulfides, amines, silanes, alcohols and ketones, and cyclization reactions.

As the catalytic reaction to be tested, we chose the oxidation of cyclohexane and of cyclopentane to the corresponding alcohols and ketones, as examples with industrial significance within the challenging field of functionalization of alkanes.[42–47] In fact, the cyclohexanol/cyclohexanone mixture is used[42,48–50] for the synthesis of adipic acid, Nylon-6,6′, polyamide-6 and urethane foams and as an acidulant in baking powder and lubricating additives, whereas cyclopentanol and cyclopentanone are used[51–57] in the

[a] Centro de Química Estrutural, Complexo I, Instituto Superior Técnico,
Av. Rovisco Pais, 1049-001 Lisbon, Portugal
Fax: +351-21-8464455
E-mail: pombeiro@ist.utl.pt
[b] University of Joensuu, Department of Chemistry,
P. O. Box 111, 80101, Joensuu, Finland
[c] Universidade Lusófona de Humanidades e Tecnologias,
Campo Grande 376, 1749-024 Lisbon, Portugal
Supporting information for this article is available on the WWW under http://www.eurjic.org or from the author.

preparation of perfumes, dibasic carboxylic acids, dyes and liquid herbicide compositions. We have previously found that the peroxidative oxidation of cyclohexane and cyclopentane to those products is catalyzed by some vanadium(IV) or (V) complexes with N,O-ligands,[58] as well as by heteronuclear iron(III)–chromium(III) hydroxo complexes and hydroxides.[59]

For the current study, as sources of N-ligands we have addressed N,O-types (or related compounds) that we have used for the preparation of vanadium catalysts for alkane functionalization reactions, namely peroxidative hydroxylation, oxygenation and halogenation,[58] and carboxylation.[60] They are the amino alcohol $N(CH_2CH_2OH)_3$, the glycine derivative $N(CH_2CH_2OH)_2(CH_2COOH)$, picolinic acid ($NC_5H_4COOH$-2), *N*-hydroxyiminodiacetic acid [$HON(CH_2COOH)_2$, HIDA] and *N*-hydroxy-2,2′-iminodipropionic acid [$HON\{CH(Me)COOH\}_2$, HIDPA].

Hence, we report herein the synthesis and characterization, including the crystal structures, of a series of new benzoylhydrazido- and -diazenidorhenium complexes with these, or derived, chelating N,O-ligands, as well as their catalytic activity for the peroxidative oxidation under mild conditions (room temperature, aqueous H_2O_2 and without added acid) of cyclohexane and cyclopentane to the corresponding alcohols and ketones, which, to the best of our knowledge, is the first example of such a type of alkane functionalization with Re coordination compounds as catalysts.

Results and Discussion

Synthesis and Spectroscopic Characterization

The reaction of the benzoylhydrazido chelate **1** with various potential N,O-polydentate ligands in refluxing methanol led to the formation of neutral benzoylhydrazido (**2**) and diazenido (**3**–**6**) complexes, in 30–55% yields, as shown in Scheme 1. All complexes were characterized by IR, FAB^+-MS, ^1H and $^{13}C\{^1H\}$ NMR spectroscopy, elemental analysis and single-crystal X-ray diffraction analysis.

In the reaction of **1** with triethanolamine (reaction 1, Scheme 1) the latter, upon deprotonation of two alcohol moieties, provides a dianionic tridentate N,O,O-ligand that replaces one triphenylphosphane and two chloride ligands, with preservation of the chelated benzoylhydrazido fragment in the green product $[Re\{(OCH_2CH_2)_2N(CH_2CH_2OH)\}\{N{=}NC(O)Ph\}(PPh_3)]$ (**2**). *N*,*N*-Bis(2-hydroxyethyl)glycine [bicine, $N(CH_2CH_2OH)_2(CH_2COOH)$] also generates an N,O,O-ligand by deprotonation of the carboxylic acid group. Reduction of the metal to the +3 oxidation state also occurs, the chelated benzoylhydrazido ring opens to form the η^1-NNCOPh diazenido ligand and only one ligated chloride is replaced (besides one of the phosphanes) to afford the greenish-blue complex $[ReCl\{N(CH_2COO)(CH_2CH_2OH)(CH_2COOH)\}\{N{=}NC(O)Ph\}(PPh_3)]$ (**3**) (reaction 2, Scheme 1). In complexes **2** and **3** the N,O,O-ligands contain hydroxyethyl arms, in agreement with the detection, in the IR spectra, of strong and broad bands in the 3500–3200 cm^{-1} range assigned to ν(OH). The IR spectra of **3** and all the other benzoyldiazenido compounds show a strong band in the 1700–1630 cm^{-1} range assigned to ν(C=O), whereas for all the complexes ν(N=N), associated to either η^2- or η^1-NNC(O)Ph, is observed in the 1513–1436 cm^{-1} range.

In their reactions with complex **1**, the *N*-hydroxyiminodicarboxylic acids (HIDA and HIDPA) undergo fragmentation, leading to the formation of the $O{\leftarrow}NCH_2COO^-$ (*N*-oxyaminoacetate) and $HN{=}C(Me)COO^-$ (2-iminopropionate) ligands in the η^1-benzoyldiazenidorhenium(III) products $[ReCl\{N(=O)CH_2COO\}\{N{=}NC(O)Ph\}(PPh_3)_2]$ (**4**)

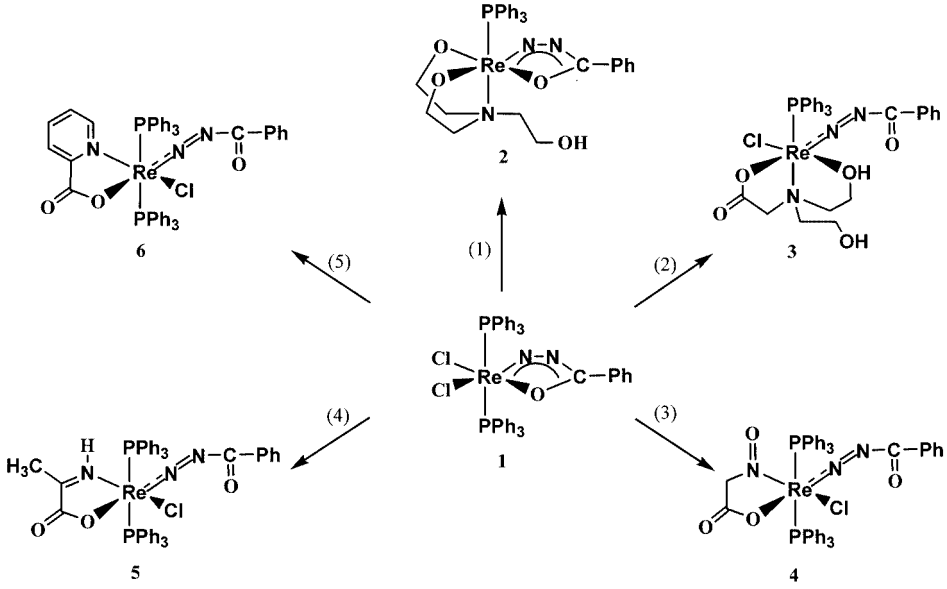

Scheme 1. (1) $N(CH_2CH_2OH)_3$; (2) $N(CH_2CH_2OH)_2(CH_2COOH)$ (bicine); (3) $HON(CH_2COOH)_2$ (HIDA); (4) $HON\{CH(CH_3)COOH\}_2$ (HIDPA); (5) NC_5H_4COOH-2.

 © 2005 Wiley-VCH Verlag GmbH & Co. KGaA, Weinheim

[ν(N=O) = 1626 cm^{-1}] and [ReCl{HN=C(Me)COO}{N=NC(O)Ph}(PPh_3)$_2$] (**5**), respectively (reactions 3 and 4, Scheme 1). HIDPA fragmentations have been rarely characterized, although some examples[61] are provided by the reaction with [PPh_4][$ReOBr_4$], [$ReOCl_3(PPh_3)_2$], [$ReOCl_2$(OEt)(PPh_3)$_2$] or [PPh_4][$MoOCl_4(H_2O)$], leading to the formation of 2-[(1-carboxyethoxy)imino]propionic acid [HOOCC(Me)=N{OCH(Me)COO^-}], 2-iminopropionate [HN=C(Me)COO^-], 2,2′-iminodipropionate [HN{CH(Me)COO^-}$_2$] and 2-oxidoiminopropionic acid [HOOCC(Me)=N→O] ligands, respectively. The 2-iminopropionate ligand in **5** has a precedent in [PPh_4][$ReOBr_3${HN=C(Me)COO}],[61] whereas the *N*-oxyaminoacetate in **4** appears to result from a different type of HIDA fragmentation.

Similar to complexes **4** and **5**, the η^1-benzoyldiazenidorhenium(III) product [ReCl{C_5H_4N(COO)}{N=NC(O)Ph}(PPh_3)$_2$] (**6**) obtained from the reaction of picolinic acid with **1** (reaction 5, Scheme 1) also has an anionic bidentate N,O-ligand, in this case simply corresponding to the basic form of the acid reagent.

The molecular ions were clearly observed with the expected isotopic patterns in the FAB^+-mass spectra of all compounds, except **3**. Other typical peaks correspond to the stepwise fragmentations by loss of Cl, N_2COPh, PPh_3 and N,O-ligand fragments. The ^1H and $^{13}C\{^1H\}$ NMR spectra show resonances at the usual chemical shifts for the coordinated PPh_3, N_2COPh and N,O-ligands.[29–31,62–69] Elemental analyses are also consistent with the proposed formulations, which were authenticated by single-crystal X-ray diffraction studies, as indicated below.

X-ray Crystal Structures

Green single crystals of the starting material **1**·C_6H_6 were grown by slow evaporation at 5 °C of an EtOH/C_6H_6 solution and the crystal structure was solved in order to compare its crystal data with those of the newly obtained complexes. The molecular structure of **1** (Figure 1) consists of discrete mononuclear species of distorted octahedral geometry with *trans* phosphane ligands and the other ligands in equatorial sites. Hence, the chloride ligands are *trans* to the nitrogen and carbonyl oxygen donors of the chelating benzoylhydrazido ligand. The bonding parameters (Table 1) are similar to those of the analogous complex [$ReCl_2${N=NC(O)C_6H_4Cl-4}(PPh_3)$_2$].[70]

All the other complexes also exhibit distorted octahedral coordinations and, for those with two phosphanes (**4**–**6**), these bulky ligands are *trans* to each other, as in complex **1**, in agreement with steric requirements.

In complex **2** (Figure 2), one triethanolamine is deprotonated at two oxygen atoms (O2, O3) and binds the metal through the amino-N and these atoms. The Re–N1, Re–O1, Re–P1 and N1–N2 distances (Table 1) are similar to those of **1**. Within the chelating benzoylhydrazide ligand, the short Re–N1 [1.776(5) and 1.798(3) Å in **1** and **2**, respectively] and N1–N2 [1.309(6) and 1.336(4) Å, respectively]

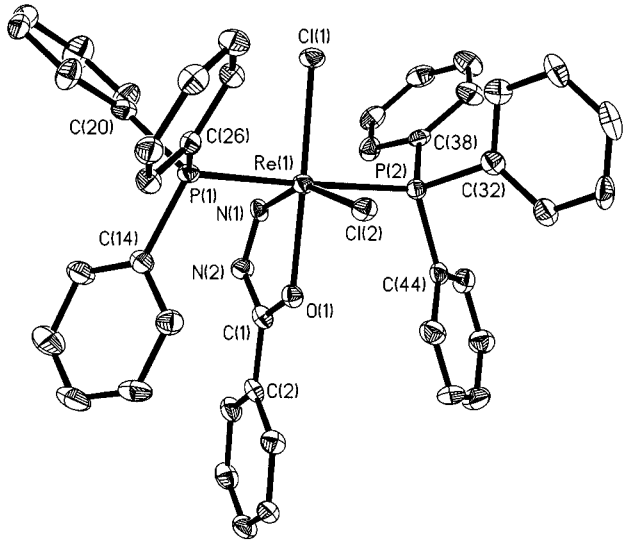

Figure 1. An ORTEP-3 representation of **1**. Hydrogen atoms and solvent molecule have been omitted for clarity.

bond lengths indicate significant multiple bonding character, and therefore a delocalized π-system, which is also in agreement with the Re–N1–N2 angles of 133.4(4)° in **1** and 131.7(3)° in **2**.[70,71] According to a classification of organohydrazido ligands[71] (assuming the convention that all electrons involved in the Re–N bond are donated by the hydrazine precursor), the benzoylhydrazido ligand in the chelates **1** and **2** exhibits features of both a hydrazido(3–) (**a**) and a diazenido(1–) (**b**) species.

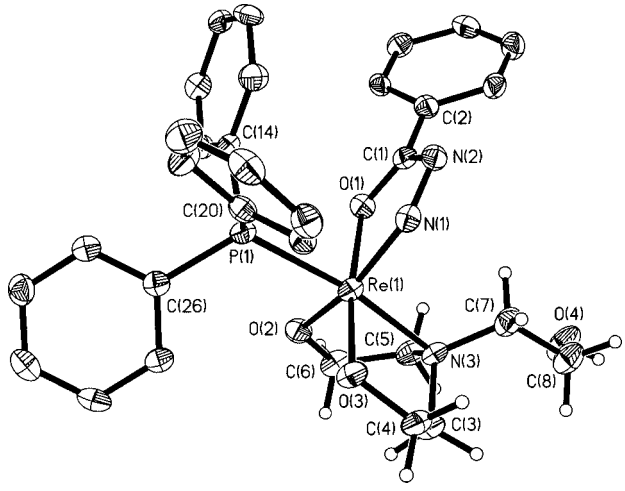

Figure 2. An ORTEP-3 representation of **2**. Ph hydrogen atoms have been omitted for clarity.

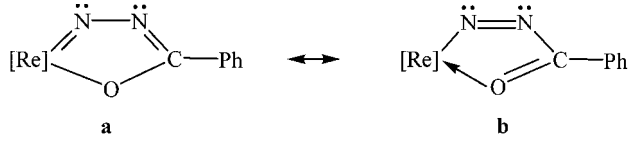

In **2** the Re–O2 and Re–O3 lengths of 1.94–1.97 Å are unexceptional for deprotonated oxygen atoms bonded to a metal centre, and are shorter than Re–O1 [2.170(3) Å]. The

 © 2005 Wiley-VCH Verlag GmbH & Co. KGaA, Weinheim

Table 1. Selected bond lengths [Å] and angles [°] for compounds **1**–**6**.

	1	**2**	**3**	**4**	**5**	**6**
Re–N(1)	1.776(5)	1.798(3)	1.740(3)	1.734(7)	1.735(3)	1.745(6)
N(1)–N(2)	1.309(6)	1.336(4)	1.280(5)	1.264(9)	1.271(5)	1.259(9)
C(1)–N(2)	1.376(7)	1.358(5)	1.381(6)	1.408(11)	1.398(6)	1.396(11)
C(1)–O(1)	1.272(7)	1.279(5)	1.234(5)	1.234(11)	1.228(5)	1.211(11)
C(1)–C(2)	1.470(8)	1.469(6)	1.496(6)	1.476(12)	1.489(6)	1.482(13)
Re–O(1)	2.122(4)	2.170(3)				
Re–N(3)		2.217(3)	2.243(4)	2.078(8)	2.175(3)	2.109(7)
Re–O(2)		1.944(3)	2.119(3)	2.090(6)	2.089(3)	2.067(5)
Re–O(3)		1.974(3)	2.095(3)			
Re–Cl(1)	2.3723(14)		2.3948(10)	2.420(2)	2.4017(10)	2.409(2)
Re–Cl(2)	2.3672(14)					
Re–P(1)	2.4528(15)	2.3798(12)	2.3758(11)	2.475(2)	2.4438(8)	2.4660(16)
Re–P(2)	2.4654(15)			2.487(2)	2.4583(8)	2.4588(16)
C(3)–N(3)		1.497(5)	1.503(6)	1.470(12)	1.417(15)	
C(3)–C(4)		1.502(6)	1.489(7)	1.465(15)	1.577(16)	1.391(15)
C(4)–O(3)		1.434(5)		1.241(11)	1.223(5)	
C(4)–O(2)			1.456(5)	1.295(11)	1.305(5)	
N(3)–O(4)				1.246(14)		
Re–N(1)–N(2)	133.4(4)	131.7(3)	176.0(3)	169.3(6)	177.4(3)	168.3(6)
N(1)–N(2)–C(1)	104.3(5)	105.6(3)	115.7(3)	120.8(7)	115.2(3)	119.3(7)
O(1)–C(1)–N(2)	117.7(5)	119.0(4)	124.3(4)	124.0(8)	123.8(4)	124.1(8)
N(1)–Re–O(1)	71.48(18)	71.72(13)				
N(1)–Re–O(2)		152.65(14)	96.40(14)	176.4(3)	170.42(13)	168.0(2)
N(1)–Re–N(3)		98.67(13)	97.55(15)	99.6(3)	94.55(14)	92.7(3)
N(3)–Re–O(2)		79.51(12)	80.27(13)	77.6(3)	75.91(12)	75.4(2)
Re–N(3)–C(3)		103.9(2)	102.9(3)	113.8(6)	114.1(7)	
Re–O(2)–C(4)			113.1(3)	118.1(6)	121.4(2)	
P(1)–Re–P(2)	174.77(5)			178.11(7)	174.79(8)	175.9(7)
N(3)–Re–P(1)		171.06(9)	174.87(10)	90.1(2)	91.98(10)	89.5(3)
N(3)–Re–Cl(1)			89.25(10)	164.5(2)	164.87(9)	164.68(19)

binding of the triethanolamine ligand involves the chelate rings Re–N3–C3–C4–O3 and Re–N3–C5–C6–O2 with O3–Re–N3 and O2–Re–N3 bite angles of 82.14(12)° and 79.51(12)°, respectively. The Re–N3 bond [2.217(3) Å] is significantly longer than Re–O2 [1.944(3) Å] and Re–O3 [1.974(3) Å], as commonly observed for O,N,O- or N,O-donor ligands,[61,72] and is also longer than the Re–N1 bond [1.798(3) Å], as anticipated for sp^3 hybridization at the N3 site and sp^2 hybridization at N1, and in agreement with the appreciable double-bond character of the latter bond.

In the structures of **3**–**6** (Figures 3, 4, 5 and 6, respectively), the opening of the chelated benzoylhydrazido ring has occurred and the Re–N1–N2 angle of the resulting η^1-diazenido ligand is essentially linear [176.0(3)° in **3**, 169.3(6)° in **4**, 177.4(3)° in **5** and 168.3(6)° in **6**]. The Re–N1, N1–N2 and C1–O1 distances (Table 1) are slightly shorter than those in the η^2-NNC(O)Ph ligand in **1** and **2**, which is indicative of a slight increase of the double-bond character. According to the above classification,[71] the η^1-NNC(O)Ph ligand in compounds **3**–**6** exhibits features of a linear, four-electron donor diazenido(1–) (**c**). In all these complexes, this ligand adopts the position *trans* to the O-coordinated carboxylato group of the chelating N,O-ligand, in preference to being *trans* to any N, Cl or P atoms.

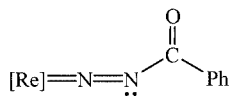

c

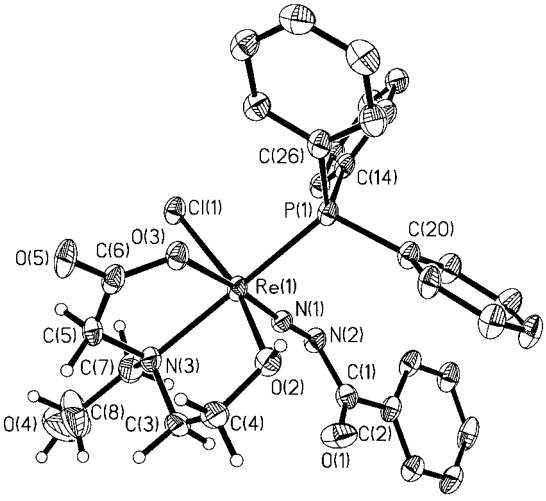

Figure 3. An ORTEP-3 representation of **3**. Ph hydrogen atoms and solvent molecules have been omitted for clarity.

The bicine ligand in **3** involves the chelate rings Re–N3–C3–C4–O2 and Re–N3–C5–C6–O3, with O2–Re–N3 and O3–Re–N3 bite angles of 80.27(13)° 78.84(12)°, respectively. The Re–N3(amine) distance of 2.243(4) Å (Table 1) is comparable with the corresponding one observed for complex **2**, although the Re–O2 and Re–O3 bond lengths of 2.119(3) and 2.095(3) Å are slightly longer than those in **2**.

In the structures of **4**–**6** (Figures 4, 5 and 6, respectively) most of the corresponding bond lengths and angles are sim-

 © 2005 Wiley-VCH Verlag GmbH & Co. KGaA, Weinheim

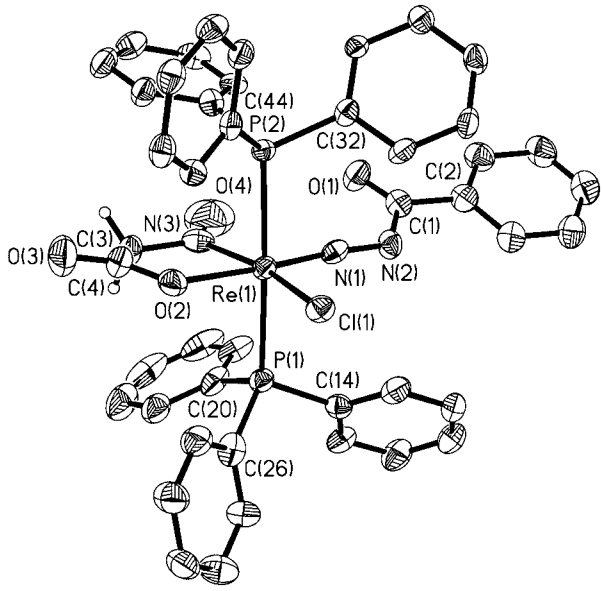

Figure 4. An ORTEP-3 representation of **4**. Ph hydrogen atoms have been omitted for clarity.

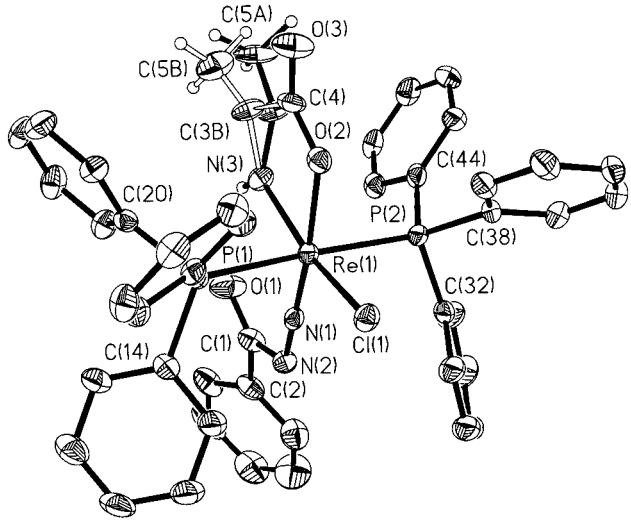

Figure 5. An ORTEP-3 representation of **5**. Ph hydrogen atoms and solvent molecules have been omitted for clarity.

ilar (Table 1). Each N,O-ligand forms a chelate ring with a restricted O–Re–N bite angle, the N3 atom being always *trans* to the chloride and the O2 atom *trans* to the diazenido ligand. The Re–O2 and Re–N3 bond lengths are usually similar to those of other Re complexes.[61,73] Hence, for example, for complex **6** most of the bond lengths are similar to those of related complexes with picolinate or 3-hydroxypicolinate ligands such as $[ReO(Me)(NC_5H_4COO)_2]$, $[ReH(NC_5H_4COO)_2(PPh_3)_2]$, $[ReOI_2\{NC_5H_3(OH\text{-}3)COO\}(PPh_3)]$ and $[ReOCl_3\{NC_5H_3(OH\text{-}3)COO\}]$.[74–77] However, the Re–N3 bond length [2.175(3) Å] in **5** is longer than the Re–O2 distance [2.089(3) Å].

In the $HN{=}C(CH_3)COO^-$ ligand in **5**, the C3–N3 distance of 1.417(15) Å is much longer than the corresponding

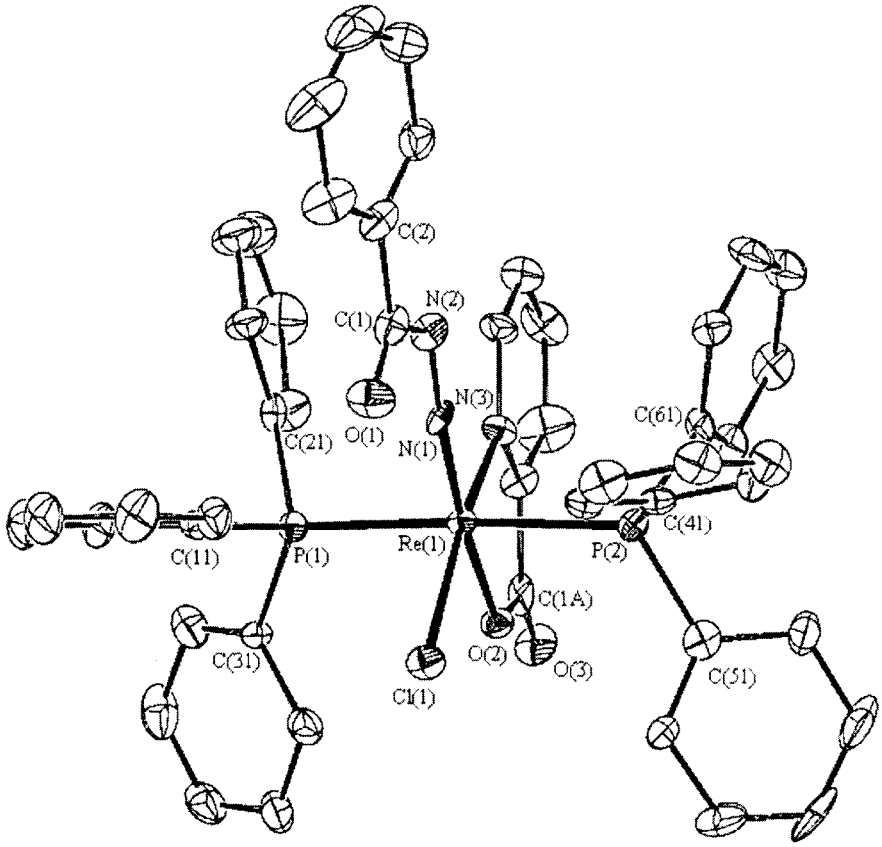

Figure 6. An ORTEP-3 representation of **6**. Hydrogen atoms and solvent molecule have been omitted for clarity.

 © 2005 Wiley-VCH Verlag GmbH & Co. KGaA, Weinheim

C=N bond length in $[PPh_4][ReOBr_3\{HN=C(Me)COO\}]$,[61] even though the X-ray diffraction analysis shows that there is no hydrogen at the C3 atom.

Peroxidative Oxidation of Cyclohexane and Cyclopentane

Acetonitrile solutions of all our complexes **1**–**6** exhibit catalytic activity for the peroxidative oxidation of cyclohexane to the corresponding cyclohexanone and cyclohexanol *at room temperature* (see Scheme 2 and Table 2 for selected data and Table S1 in the Supporting Information). The amount of hydrogen peroxide has a strong effect, and increasing the peroxide-to-catalyst molar ratio within the 2000–32000 range leads to an enhancement of the turnover numbers (TONs); for example, the total TON when using complex **3** as a catalyst increases from 5 to 43 on increasing this ratio from 4000 to 32000 (Figure 7). The highest activity is displayed by complexes **3** and **6**, followed by the chelate **1**, with total TONs of 43, 42 and 39 and turnover frequency (TOF) values of 7.2, 7.0 and 6.5 h^{-1}, respectively, for the latter peroxide-to-catalyst ratio. These values are comparable to those we have achieved (maximum TON of 46)[58] with vanadium catalysts like Amavadine $[V(O,N\text{-}L)]^{2-}$ (*O*,*N*-L = tribasic form of HIDPA) and $[VO\{N(CH_2CH_2O)_3\}]$. The other complexes (**2**, **4** and **5**) are less active for sufficiently high H_2O_2/catalyst ratios, with total TONs (ca. 21–22) that are half of those of the other complexes, for the above peroxide-to-catalyst ratio.

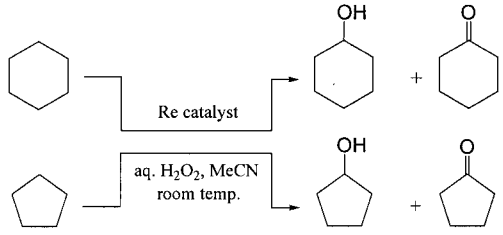

Scheme 2.

Table 2. Peroxidative oxidation of cyclohexane catalyzed by the Re complexes.[a]

Catalyst	Turnover number (TON)[b]			Turnover frequency (TOF)[d]
	Cyclohexanol	Cyclohexanone	Total[c]	
1	24	15	39	6.5
2	13	8	21	3.5
3[e]	27	16	43	7.2
4	14	8	22	3.7
5	13	9	22	3.7
6[f]	25	17	42	7.0

[a] Selected data from Table S1. $n(H_2O_2)/n(C_6H_{12})$ = 2:1, $n(H_2O_2)/n$(Re catalyst) = 32000, molar yield (% relative to substrate) = $6.3 \times TON \times 10^{-3}$, unless stated otherwise. [b] Mol product/mol Re catalyst precursor. [c] Cyclohexanol + cyclohexanone. [d] Mol products/mol Re catalyst precursor per hour. [e] For $n(H_2O_2)/n(C_6H_{12})$ = 16:1 the molar yield is 1.9%. [f] For $n(H_2O_2)/n(C_6H_{12})$ = 16:1 the molar yield is 2.4%.

Higher catalytic activities would be expected upon further increase of the peroxide-to-catalyst ratio (see Figure 7), but this was not tested for safety reasons. All catalysts display a higher selectivity towards the formation of cyclohexanol, in comparison with cyclohexanone, and the average alcohol/ketone molar ratio is within the 1.5–1.8 range.

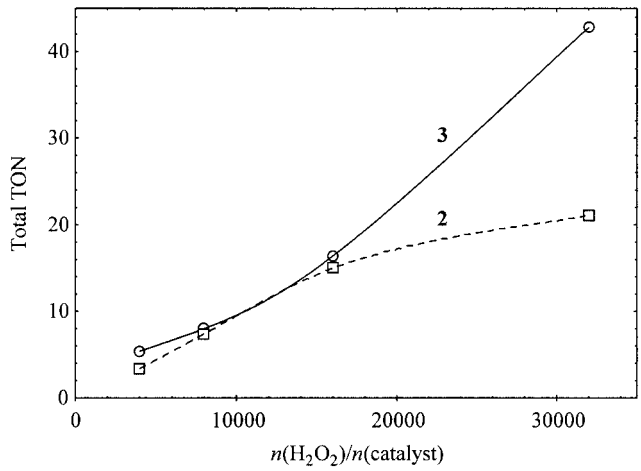

Figure 7. Effect of the oxidant-to-catalyst molar ratio on the total TON values in the oxidation of cyclohexane catalyzed by complexes **2** and **3**.

The Re complexes also catalyze the peroxidative oxidation of cyclopentane to the corresponding cyclopentanol and cyclopentanone, but the catalytic activity (Table S2 in the Supporting Information) is lower than for the oxidation of cyclohexane. The TONs also increase with the amount of hydrogen peroxide. For a peroxide-to-catalyst molar ratio of 32000, the total TON is 13 when using complex **6** as a catalyst, whereas the other complexes exhibit lower TON values (from 3 to 8).

In contrast with the lower activity for cyclopentane than for cyclohexane oxidation, a higher selectivity is observed for the formation of the alcohol, i.e. cyclopentanol, for moderately high peroxide-to-catalyst molar ratios. In fact, cyclopentanol is the only oxidation product detected for all the complexes at $n(H_2O_2)/n$(catalyst) = 16000. However, the formation of cyclopentanone, a more oxidized product, also occurs for complexes **3** and **6** at the higher value of 32000 for the peroxide-to-catalyst molar ratio.

The peroxidative oxidation of cycloalkanes is believed to proceed by a radical mechanism since no traces of cyclohexanol or cyclohexanone are detected when the above reactions that normally lead to the highest TON values are performed in the presence of a radical trap like 2,6-di-*tert*-butyl-4-methylphenol (BHT; 0.5 molar ratio with respect to the alkane). Although we have not yet succeeded in the isolation and full characterization of intermediates, the process conceivably involves[46,47,50,58,78–80] the formation of intermediate peroxo and oxo complexes. It is noteworthy that the oxo-peroxomethylrhenium(VII) complex $[(Me)ReO(O_2)_2]$ is the active species of the known $[(Me)ReO_3]/H_2O_2$ system in olefin and aromatic oxidations.[16] Peroxo-derived radical complexes could abstract an H atom from the alkane (RH) to generate an R˙ radical, which, on reaction with a hydroperoxo or hydroxo complex, could lead to the

 © 2005 Wiley-VCH Verlag GmbH & Co. KGaA, Weinheim

alcohol ROH; further oxidation of the latter would yield the corresponding ketone.

The role of the chelating N,O and diazenido ligands in our systems is still unclear but one can postulate their involvement (e.g. upon decoordination, in the former, of a single N or O atom) in proton-transfer steps among oxo-, peroxo- and hydroxo-Re complexes. Such a role in the promotion of proton transfer from coordinated H_2O_2 to oxo ligands has been proposed[78,79] for some vanadium systems with N,O additives as cocatalysts.

Re-catalyzed alkane oxidations are essentially unexplored. In the only previously published case, the organometallic [(Me)ReO_3]/pyrazine-2-carboxylic acid system was found to be active for the peroxidative oxidation of cyclohexane by anhydrous H_2O_2 in refluxing acetonitrile solution at 80 °C (TON of 126);[80] however, if aqueous 30% H_2O_2 was used almost no oxidation of cyclohexane occurred.[80] Our systems have the advantage of operating under milder conditions, i.e. at room temperature, with aqueous H_2O_2 and without added acid. Nevertheless, in all the cases the yields (based on the alkane), under the experimental conditions used, are still modest (not above 3% for our complexes and even lower (1.5%) for [(Me)ReO_3]), although these are still significant in the field of alkane functionalization under mild or moderate conditions. A maximum yield of 9% was achieved[58] for the same alkane reaction with the above vanadium catalysts.

Conclusions

This work has shown that the benzoylhydrazido chelate [$ReCl_2${NNC(O)Ph}$(PPh_3)_2$] (**1**), which is a recognized key starting material for a diversity of hydrazido, diazenido and even dinitrogen Re complexes with P-based coligands (organophosphanes, -phosphites or -phosphonites), can also provide a convenient entry point for the synthesis of benzoylhydrazido and benzoyldiazenido complexes of Re (in the +5 and the +3 oxidation states) with chelating N,O,O- and N,O-coligands of various types, including amino alkoxides and amino-, oxyamino-, imino- and pyridinocarboxylates. π-Electron delocalization along the hydrazido- and diazenidorhenium moiety has been observed, with the Re–N bond exhibiting some double-bond character. The benzoyldiazenido ligand occupies the *trans* position relative to the O-ligated carboxylato group, preferably to the softer N atom of the N,O- or N,O,O-ligand, an observation that may be of synthetic significance and deserves further exploration.

This study also demonstrates, for the first time, that Re coordination compounds can act as catalysts for alkane hydroxylation and oxygenation, by showing the unprecedented catalytic activity of such a type of complexes, under mild conditions, in the peroxidative oxidation of cycloalkanes to the corresponding alcohols and ketones. The reactions appear to follow a radical mechanism, although complete details have yet to be established. The catalytic activity, although appreciable in the field of mild alkane functionalization, is still modest. Hence, this study provides a contribution towards the development of the still underdeveloped field of catalysis with rhenium inorganic coordination compounds. However, more-effective systems are needed, as well as the extension to other types of alkane-functionalization reactions, points that are currently being addressed in our laboratory.

Experimental Section

General Materials and Procedures: All synthetic work was performed under nitrogen using standard Schlenk techniques. The solvents were dried over appropriate drying agents and degassed by standard methods. Potassium perrhenate (Merck), triphenylphosphane (Aldrich), benzoylhydrazine (Aldrich), triethanolamine (Fluka), *N*,*N*-bis(2-hydroxyethyl)glycine (bicine; Aldrich), picolinic acid (Aldrich), 2,6-di-*tert*-butyl-4-methylphenol (BHT; Aldrich), bromoacetic acid (Merck), hydroxylammonium chloride (Aldrich) and zinc acetate (Aldrich) were obtained from commercial sources and used as received. [*N*-Benzoylhydrazido(3–)-*N*′,*O*]dichlorobis(triphenylphosphane)rhenium(v) [$ReCl_2${NNC(O)Ph}$(PPh_3)_2$] (**1**),[25,26] *N*-hydroxyiminodiacetic acid[81] and *N*-hydroxy-2,2′-iminodipropionic acid[81] were prepared by published methods.

Elemental analyses were carried out by the Microanalytical Service of the Instituto Superior Técnico. Melting points were determined on a Kofler table. Positive-ion FAB mass spectra were obtained on a Trio 2000 instrument by bombarding 3-nitrobenzyl alcohol (NBA) matrices of the samples with 8 keV (ca. 1.18×10^{15} J) Xe atoms. Mass calibration for data system acquisition was achieved with CsI. IR spectra (4000–400 cm^{-1}) were recorded on a Jasco FT/IR-430 instrument as KBr pellets. ^1H and $^{13}C\{^1H\}$ NMR spectra were measured on a Varian UNITY 300 spectrometer at ambient temperature.

[Re{$(OCH_2CH_2)_2N(CH_2CH_2OH)$}{NNC(O)Ph}$(PPh_3)$] (2): An excess of triethanolamine (43 μL, 0.327 mmol) was added to a suspension of **1** (100 mg, 0.109 mmol) in 7.5 mL of MeOH and the reaction mixture was refluxed for about 5 h. The resulting dark-brown clear solution was concentrated under reduced pressure and then treated with 20 mL of Et_2O. The solid (triethanolamine hydrochloride) that separated out from the resulting solution was filtered off and discarded. The filtrate was evaporated under reduced pressure to give a green oil, which was dissolved in 1.5 mL of C_6H_6. The addition of *n*-pentane (20 mL) caused the precipitation of a solid, which was filtered off, washed with *n*-pentane (3 × 10 mL) and dried in vacuo to yield complex **2** as a green solid. Yield: 43 mg (54% based on **1**). Product **2** is soluble in MeOH, Me_2CO, Et_2O and C_6H_6. M.p. 153 °C (dec.). $C_{31}H_{33}N_3O_4PRe$ (728.79): calcd. C 51.02, H 4.56, N 5.76; found C 50.50, H 4.53, N 5.56. FAB$^+$-MS (NBA): *m*/*z* = 730 [M^+ + H], 612 [M^+ – (N_2COPh) + O], 596 [M^+ – (N_2COPh)], 467 [M^+ – PPh_3]. FTIR (KBr): $\tilde{\nu}$ = 3416 and 3311 (s br.) ν(OH), 2960 (m) ν_{as}(CH), 2853 (m) ν_s(CH), 1436 (s) ν(NN), 1355 (s) ν(C–O) cm^{-1}. ^1H NMR ($CDCl_3$): δ = 7.88–7.83 (m, 5 H, Ph), 7.49–7.32 (m, 15 H, PPh_3), 3.66 (t, *J* = 5.4 Hz, 4 H, CH_2-O), 2.69 (t, *J* = 4.8 Hz, 4 H, CH_2-N), 2.37–2.18 (m, 4 H, CH_2CH_2OH) ppm. $^{13}C\{^1H\}$ NMR ($CDCl_3$): δ = 134.2, 134.1, 130.0, 129.7, 128.1 and 128.0 (PPh_3), 132.9, 131.6, 130.6 and 127.6 (Ph), 60.3, 58.1, 59.6 and 56.7 (*C*H_2) ppm; Ph*C*O was not observed. X-ray quality crystals were grown at 5 °C by vapour diffusion of *n*-C_5H_{12} into an Et_2O or an acetone solution of **2**.

[ReCl{$N(CH_2COO)(CH_2CH_2OH)(CH_2CH_2OH)$}{N=NC(O)Ph}$(PPh_3)$] (3): A mixture of **1** (50 mg, 0.055 mmol) and bicine (27 mg, 0.165 mmol) was refluxed in MeOH (10 mL) for about 8 h. The

 © 2005 Wiley-VCH Verlag GmbH & Co. KGaA, Weinheim

resulting dark-brown clear solution was concentrated to 5 mL under reduced pressure and 30 mL of Et_2O was added. The obtained greenish-brown solution was left to stand for 2 d at room temperature. During this time greenish-blue microcrystals of **3** separated out of the solution. They were collected, washed with MeOH (3 × 10 mL) and dried in vacuo. Yield: 21 mg (48% based on **1**). Product **3** is slightly soluble in DMSO and insoluble in C_6H_6, MeOH, Me_2CO, $CHCl_3$ and CH_2Cl_2. M.p. 201 °C (dec.). $C_{31}H_{32}ClN_3O_5PRe$ (779.24): calcd. C 47.78, H 4.14, N 5.39; found C 47.57, H 3.96, N 5.21. FAB$^+$-MS (NBA): *m*/*z* = 744 [M^+ – Cl], 610 [M^+ – Cl – (N_2COPh)], 582 [M^+ – Cl – {$N(CH_2CH_2OH)_2$-(CH_2COO)}]. FTIR (KBr): $\tilde{\nu}$ = 3429 and 3265 (s br.) ν(OH), 2925 (m) ν_{as}(CH), 2854 (m) ν_s(CH), 1631 (s) ν(C=O), 1458 (s) ν(N=N) cm^{-1}. ^{1}H NMR ($CDCl_3$): δ = 7.77–7.33 (m, 20 H, PPh_3 + Ph), 4.25–3.59 and 3.15–2.97 (m, 10 H, CH_2) ppm. ^{13}C{^{1}H} NMR ($CDCl_3$): δ = 179.1 (Ph*C*=O), 167.6 (CH_2*C*=O), 134.1, 133.6, 132.9, 131.6, 130.7, 130.3, 129.3, 128.7 and 128.1 (PPh_3 + Ph), 56.0, 55.6, 54.9, 53.6, and 16.2 (*C*H_2) ppm. X-ray quality crystals of **3**·H_2O were grown by slow evaporation at 5 °C of Et_2O/MeOH or MeOH/Me_2CO solutions.

[ReCl{N(=O)CH_2COO}{N=NC(O)Ph}(PPh_3)$_2$] (4): An excess of HIDA (28 mg, 0.18 mmol) was added to a suspension of **1** (50 mg, 0.055 mmol) in 10 mL of MeOH and the reaction mixture was refluxed for about 7 h. The resulting reddish-yellow clear solution was concentrated under reduced pressure and then treated with 30 mL of Et_2O. The solid that separated out from the resulting solution was filtered off and discarded. The filtrate was evaporated under reduced pressure to give a light-brown oil, which was dissolved in 5 mL of C_6H_6 to form a yellow cloudy solution. Filtration, followed by concentration under reduced pressure, yielded a yellow oil to which 1 mL of benzene was added. The addition of *n*-pentane (20 mL) led to the precipitation of a solid that was filtered off, washed with *n*-pentane (3 × 10 mL) and dried in vacuo to yield complex **4** as a yellow powder. Yield: 19 mg (35% based on **1**). Product **4** is soluble in MeOH, EtOH, Me_2CO, Et_2O, C_6H_6 and $CHCl_3$. M.p. 220 °C (dec.). $C_{45}H_{37}ClN_3O_4P_2Re$ (967.40): calcd. C 55.84, H 3.83, N 4.34; found C 55.73, H 3.77, N 4.07. FAB$^+$-MS (NBA): *m*/*z* = 966 [M^+ – H], 879 [M^+ – ($ONCH_2COO$)], 832 [M^+ – (N_2COPh) – 2H], 746 [M^+ – ($ONCH_2COO$) – (N_2COPh)]. FTIR (KBr): $\tilde{\nu}$ = 2925 (w) ν_{as}(CH), 1700 (s) ν(C=O), 1626 (s) ν(N=O), 1513 (s) ν(N=N) cm^{-1}. ^{1}H NMR ($CDCl_3$): δ = 7.74–7.70 and 7.41–7.43 (m, 30 H, PPh_3), 7.62–7.58 (m, 5 H, Ph), 2.32 (s, 2 H, CH_2) ppm. ^{13}C{^{1}H} NMR ($CDCl_3$): δ = 195.5 (Ph*C*=O), 174.5 (CH_2*C*=O), 134.4, 134.3, 130.4, 128.4 and 128.4 (PPh_3), 133.7, 132.4, 128.8 and 127.9 (Ph), 29.0 (*C*H_2) ppm. X-ray quality crystals were grown by slow evaporation at 5 °C of an EtOH/Me_2CO solution of **4**.

[ReCl{HN=C(Me)COO}{N=NC(O)Ph}(PPh_3)$_2$] (5): Compound **5** was prepared by following the general procedure described for **4**, but using HIDPA instead of HIDA. Yield: 21 mg (40% based on **1**). It is soluble in MeOH, EtOH, Me_2CO, Et_2O, C_6H_6 and $CHCl_3$. M.p. 114 °C (dec.). $C_{46}H_{39}ClN_3O_3P_2Re$ (965.43): calcd. C 57.20, H 4.07, N 4.35; found C 57.50, H 4.29, N 4.09. FAB$^+$-MS (NBA): *m*/*z* = 967 [M^+ + 2H], 932 [M^+ – Cl + 2H], 879 [M^+ – {HN=C(CH_3)COO}], 834 [M^+ – (N_2COPh) + 2H], 799 [M^+ – Cl – (N_2COPh) + 2H], 746 [M^+ – {HN=C(CH_3)COO} – (N_2COPh)], 711 [Re(PPh_3)$_2$]. FTIR (KBr): $\tilde{\nu}$ = 3280 (w) ν(N–H), 1656 (s br.) ν(C=O), 1630 (m) ν(C=N), 1436 (s) ν(N=N) cm^{-1}. ^{1}H NMR ($CDCl_3$): δ = 7.88–7.84 and 7.17 (m, 5 H, Ph), 7.73–7.32 (m, 30 H, PPh_3), 1.46 (s) + 1.43 (s) (3 H, CH_3) ppm; N*H* was not observed. ^{13}C{^{1}H} NMR ($CDCl_3$): δ = 192.4 (Ph*C*=O), 182.2 (N=C(Me) *C*=O), 134.3, 134.0, 132.2, 132.0, 128.6 and 128.5 (PPh_3), 130.5, 128.9, 128.1, 128.0 and 127.4 (Ph), 51.3 (*C*H_3) ppm; *C*=N was not observed. X-ray quality crystals of **5**·2 EtOH were grown by slow evaporation at 5 °C of EtOH/C_6H_6 or EtOH/CH_2Cl_2 solutions.

[ReCl{C_5H_4N(COO)}{N=NC(O)Ph}(PPh_3)$_2$] (6): A mixture of **1** (50 mg, 0.055 mmol) and picolinic acid (21 mg, 0.165 mmol) was refluxed in MeOH (10 mL) for about 12 h. The resulting deep-red cloudy solution was taken to dryness under reduced pressure to give a red residue to which 30 mL of MeOH was added to obtain a suspension of **6**. This was filtered off, washed with MeOH (3 × 15 mL) and dried in vacuo to furnish complex **6** as a red solid. Yield: 30 mg (55% based on **1**). Product **6** is soluble in Me_2CO, Et_2O, C_6H_6, CH_2Cl_2 and $CHCl_3$. M.p. 232 °C (dec.). $C_{49}H_{39}ClN_3O_3P_2Re$ (1001.5): calcd. C 58.73, H 3.93, N 4.20; found C 58.45, H 4.16, N 4.02. FAB$^+$-MS (NBA): *m*/*z* = 1002 [M^+ + H], 966 [M^+ – Cl], 868 [M^+ – (N_2COPh)], 879 [M^+ – (C_5H_4NCOO)], 833 [M^+ – Cl – (N_2COPh)], 746 [M^+ – (C_5H_4NCOO) – (N_2COPh)], 711 [Re(PPh_3)$_2$], 571 [M^+ – Cl – (N_2COPh) – PPh_3], 448 [RePPh_3]. FTIR (KBr): $\tilde{\nu}$ = 1673 and 1638 (s) ν(C=O), 1456 (s) ν(N=N), 1307 (m) ν(C–O) cm^{-1}. ^{1}H NMR ($CDCl_3$): δ = 7.80–7.73 (m, 4 H, Py*H*), 7.59–7.43 (m, 30 H, PPh_3), 6.95–6.85 (m, 5 H, Ph) ppm. ^{13}C{^{1}H} NMR ($CDCl_3$): δ = 134.6, 134.5, 134.2, 133.8, 130.2, 130.0, 128.4, 128.3, 128.0 and 127.8 (Py*C*, PPh_3 and Ph) ppm; *C*=O was not observed. X-ray quality crystals of **6**·Me_2CO were grown by slow evaporation at 5 °C of an acetone solution.

Catalytic Studies: The reaction mixtures were prepared as follows: MeCN (3.00 mL), H_2O_2 (30% in H_2O; 10.00 mmol) and cycloalkane (cyclohexane or cyclopentane; 5.00–0.625 mmol) were added, in this order, to 0.313–5.00 × 10^{-3} mmol of the Re complex **1**–**6** (used either as a solid or as a 0.02 M MeCN solution) in the reaction flask. The reaction mixture was stirred for 6 h at room temperature and normal pressure, then 90 μL of cycloheptanone (as internal standard) and 10.00 mL of diethyl ether (to extract the substrate and the organic products from the reaction mixture) were added. The obtained mixture was stirred for 10 min and then a sample was taken from the organic phase and analyzed by gas chromatography using a FISONS Instruments GC 8000 series gas chromatograph with a DB WAX fused silica capillary column (P/N 123-7032) and the JASCO-BORWIN v.1.50 software. The obtained results for cyclohexane and cyclopentane oxidation are given as Supporting Information (Tables S1 and S2, respectively); selected values are given in Table 2.

Blank experiments were performed for both cycloalkanes with H_2O_2 and confirmed that no product of alkane oxidation was obtained in the absence of metal catalyst.

X-ray Crystal Structure Determinations: Crystals of **1**–**5** were immersed in perfluoropolyether, mounted in a cryo-loops and measured at 100 K. The X-ray diffraction data were collected with a Nonius-Kappa CCD diffractometer (for **1**–**5**) or an Enraf–Nonius MACH3 diffractometer (for **6**), equipped with graphite monochromator and using Mo-K_α radiation. The Denzo-Scalepack program package[82] was used for cell refinements and data reductions for **1**–**5**. All structures were solved by direct methods using the SIR97 or SIR2002 programs[83,84] with the WinGX graphical user interface.[85] An empirical absorption correction was applied to all data (**1**–**5**) using XPREP in the SHELXTL v.6.12 program[86] (T_{min}/T_{max}: 0.21031/0.28346, 0.11746/0.15556, 0.21094/0.26735, 0.12878/0.17642, 0.16825/0.21003 for **1**–**5**, respectively). All structures were refined with the SHELXL-97 program.[87] In the structure of **5** C3 and C5 were refined over two positions with occupancies of 0.57 and 0.43 and the position of the OH hydrogen (H98) was estimated with the CALC-OH program.[88] Other OH, H_2O and NH hydrogens were located from the difference Fourier map. All other hydrogens were placed in idealized positions and constrained to ride on

 © 2005 Wiley-VCH Verlag GmbH & Co. KGaA, Weinheim

Table 3. Crystal data for compounds **1**–**6**.

	1·C_6H_6	**2**	**3**·H_2O	**4**	**5**·2 EtOH	**6**·Me_2CO
Empirical formula	$C_{49}H_{41}Cl_2N_2OP_2Re$	$C_{31}H_{33}N_3O_4PRe$	$C_{31}H_{34}ClN_3O_6PRe$	$C_{45}H_{37}ClN_3O_4P_2Re$	$C_{50}H_{51}ClN_3O_5P_2Re$	$C_{52}H_{45}ClN_3O_4P_2Re$
Molecular mass	992.88	728.77	797.23	967.37	1057.53	1059.50
Temp. (K)	100(2)	100(2)	100(2)	100(2)	100(2)	293(2)
λ [Å]	0.71073	0.71073	0.71073	0.71073	0.71073	0.71069
Crystal system	triclinic	monoclinic	triclinic	monoclinic	monoclinic	orthorhombic
Space group	*P*1	$P2_1/n$	*P*1	$P2_1/n$	$P2_1$	*Pcab*
a [Å]	11.2196(7)	9.783(2)	8.9359(2)	13.8666(6)	11.6355(2)	15.418(2)
b [Å]	11.9274(10)	25.322(5)	11.2862(3)	13.9601(8)	18.0462(5)	19.021(2)
c [Å]	17.6911(12)	11.297(2)	16.0694(5)	20.4390(10)	12.0749(3)	31.593(3)
α [°]	108.027(4)	90	73.7750(10)	90	90	90
β [°]	98.785(4)	91.23(3)	80.903(2)	96.954(3)	112.9970(10)	90
γ [°]	106.011(4)	90	77.423(2)	90	90	90
V [Å^3]	2089.2(3)	2797.9(10)	1510.55(7)	3927.5(3)	2333.94(10)	9265.1(18)
Z	2	4	2	4	2	8
$\rho_{calcd.}$ [Mg m^{-3}]	1.578	1.730	1.753	1.636	1.505	1.519
μ(Mo-K_α) [mm^{-1}]	3.153	4.443	4.213	3.292	2.779	2.799
R_1[a] [$I \geq 2\sigma(I)$]	0.0379	0.0327	0.0268	0.0463	0.0274	0.0459
wR_2[b] [$I \geq 2\sigma(I)$]	0.0765	0.0590	0.0648	0.1010	0.0594	0.0652

[a] $R_1 = \Sigma||F_o| - |F_c||/\Sigma|F_o|$. [b] $wR_2 = [\Sigma\{w(F_o^2 - F_c^2)^2\}/\Sigma\{w(F_o^2)^2\}]^{1/2}$.

their parent atom. The crystallographic data are summarized in Table 3 and selected bond lengths and angles are given in Table 1. CCDC-256902 to –256907 (for **1**·C_6H_6, **2**, **3**·H_2O, **4**, **5**·2 EtOH and **6**·Me_2CO, respectively) contain the supplementary crystallographic data for this paper. These data can be obtained free of charge from The Cambridge Crystallographic Data Centre via www.ccdc.cam.ac.uk/data_request/cif.

Supporting Information: Supplementary tables with the TON values for the peroxidative oxidation of cyclohexane (Table S1) and cyclopentane (Table S2) catalyzed by the Re complexes **1**–**6** (see also footnote on first page of this article).

Acknowledgments

This work was partially supported by the Fundação para a Ciência e a Tecnologia (FCT) and its POCTI programmes (FEDER funded; project POCTI/QUI/43415/2001), Portugal, as well as by a Human Resources and Mobility Marie Curie Research Training Network (AQUACHEM project, CMTN-CT-2003-503864). A.M.K. is grateful to the FCT and the POCTI program for a fellowship (BD/6287/01). The authors also thank Dr. Nadia Bokach for some NMR experiments, Dr. José Armando L. Silva for stimulating discussions, Dr. Maria Cândida Vaz for the direction of the elemental analysis service and Mr. Indalécio Marques for recording the FAB$^+$-mass spectra.

[1] U. Abram, in *Comprehensive Coordination Chemistry* (Eds.: J. A. McCleverty, T. J. Meyer), Elsevier, 2nd ed., **2003**, vol. 5., chapter 5.3, pp. 271–402.
[2] *Technetium, Rhenium and Other Metals in Chemistry and Nuclear Medicine* (Eds.: M. Nicolini, G. Bandoli, U. Mazzi), Raven Press, New York, **2000**, vol. 5.
[3] J. R. Dilworth, S. J. Parrott, *Chem. Soc. Rev.* **1998**, *27*, 43.
[4] A. J. L. Pombeiro, M. F. C. Guedes da Silva, R. A. Michelin, *Coord. Chem. Rev.* **2001**, *218*, 43.
[5] M. D. Fryzuk, S. A. Johnson, *Coord. Chem. Rev.* **2000**, *200–202*, 379.
[6] A. E. Shilov, *Metal Complexes in Biomimetic Chemical Reactions*, CRC Press, New York, **1997**.
[7] D. Sellman, J. Sutter, *Acc. Chem. Res.* **1997**, *30*, 460.
[8] R. L. Richards, *Coord. Chem. Rev.* **1996**, *154*, 83.
[9] G. J. Leigh, *Science* **1995**, *268*, 827.
[10] M. Hidai, Y. Mizobe, *Chem. Rev.* **1995**, *95*, 1115.
[11] G. J. Leigh, *New J. Chem.* **1994**, *18*, 157.
[12] A. J. L. Pombeiro, R. L. Richards, *Coord. Chem. Rev.* **1990**, *104*, 13.
[13] J. Chatt, J. R. Dilworth, R. L. Richards, *Chem. Rev.* **1978**, *78*, 589.
[14] G. S. Owens, J. Arias, M. M. Abu-Omar, *Catal. Today* **2000**, *55*, 317.
[15] F. E. Kuhn, W. A. Herrmann, *Struct. Bonding* **2000**, *97*, 213.
[16] C. C. Romão, F. E. Kuhn, W. A. Herrmann, *Chem. Rev.* **1997**, *97*, 3197.
[17] A. M. Santos, C. C. Romão, F. E. Kuhn, *J. Am. Chem. Soc.* **2003**, *125*, 2414.
[18] R. Bernini, A. Coratti, G. Fabrizi, A. Goggiamani, *Tetrahedron Lett.* **2003**, *44*, 8991.
[19] A. O. Bouh, J. H. Espenson, *J. Mol. Catal. A.* **2003**, *200*, 43.
[20] V. B. Sharma, S. L. Jain, B. Sain, *Tetrahedron Lett.* **2003**, *44*, 3235.
[21] J. Iskra, D. Bonnet-Delpon, J. P. Begue, *Tetrahedron Lett.* **2002**, *43*, 1001.
[22] H. J. Jeon, S. T. Nguyen, *Chem. Commun.* **2001**, 235.
[23] D. W. Lahti, J. H. Espenson, *Inorg. Chem.* **2000**, *39*, 2164.
[24] H. Adolfsson, C. Coperet, J. P. Chiang, A. K. Yudin, *J. Org. Chem.* **2000**, *65*, 8651.
[25] J. Chatt, J. R. Dilworth, G. J. Leigh, V. D. Gupta, *J. Chem. Soc. A* **1971**, 2631.
[26] J. Chatt, W. Hussain, G. J. Leigh, H. M. Ali, C. J. Pickett, D. A. Rankin, *J. Chem. Soc. Dalton Trans.* **1985**, 1131.
[27] M. F. N. N. Carvalho, A. J. L. Pombeiro, *Polyhedron* **1989**, *8*, 1778.
[28] M. F. N. N. Carvalho, A. J. L. Pombeiro, *J. Organomet. Chem.* **1990**, *384*, 121.
[29] A. Lazzaro, G. Vertuani, P. Bergamini, N. Mantovani, A. Marchi, L. Marvelli, R. Rossi, V. Bertolasi, V. Ferretti, *J. Chem. Soc. Dalton Trans.* **2002**, 2843.
[30] S. D. Orth, J. Barrera, M. Sabat, W. D. Harman, *Inorg. Chem.* **1994**, *33*, 3026.
[31] R. M. Chin, J. Barrera, R. H. Dubois, L. E. Helberg, M. Sabat, T. Y. Bartucz, A. J. Lough, R. H. Morris, W. D. Harman, *Inorg. Chem.* **1997**, *36*, 3553.
[32] J. H. Espenson, *Adv. Inorg. Chem.* **2003**, *54*, 157.
[33] J. J. Kennedy-Smith, K. A. Nolin, H. P. Gunterman, F. D. Toste, *J. Am. Chem. Soc.* **2003**, *125*, 4056.
[34] M. M. Abu-Omar, *Chem. Commun.* **2003**, 2102.
[35] J. B. Arterburn, M. Liu, M. C. Perry, *Helv. Chim. Acta* **2002**, *85*, 3225.
[36] J. Arias, C. R. Newlands, M. M. Abu-Omar, *Inorg. Chem.* **2001**, *40*, 2185.
[37] R. Huang, J. H. Espenson, *J. Mol. Catal. A.* **2001**, *168*, 39.

 © 2005 Wiley-VCH Verlag GmbH & Co. KGaA, Weinheim

[38] D. E. Schwarz, J. A. Dopke, T. B. Rauchfuss, S. R. Wilson, *Angew. Chem. Int. Ed.* **2001**, *40*, 2351.
[39] C. Zhang, I. A. Guzei, J. H. Espenson, *Inorg. Chem.* **2001**, *40*, 2437.
[40] J. B. Arterburn, M. C. Perry, S. L. Nelson, B. R. Dible, M. S. Holguin, *J. Am. Chem. Soc.* **1997**, *119*, 9309.
[41] J. B. Arterburn, S. L. Nelson, *J. Org. Chem.* **1996**, *61*, 2260.
[42] C. Jia, T. Kitamura, Y. Fujiwara, *Acc. Chem. Res.* **2001**, *34*, 633.
[43] R. H. Crabtree, *J. Chem. Soc. Dalton Trans.* **2001**, 2437.
[44] A. E. Shilov, G. B. Shul'pin, *Chem. Rev.* **1997**, *97*, 2879.
[45] Y. Fujiwara, K. Takaki, Y. Taniguchi, *Synlett* **1996**, 591.
[46] R. H. Crabtree, *The Organometallic Chemistry of the Transition Metals*, Wiley, New York, **2001**, ch. 12.
[47] *Catalytic Activation and Functionalisation of Light Alkanes* (Eds.: E. D. Derouane, J. Haber, F. Lemos, F. Ramôa Ribeiro, M. Guinet), NATO ASI series, Kluwer Academic Publishers, Dordrecht, **1998**, vol. 44.
[48] U. Schuchardt, D. Cardoso, R. Sercheli, R. Pereira, R. S. da Cruz, M. C. Guerreiro, D. Mandelli, E. V. Spinace, E. L. Pires, *J. Appl. Catal. A* **2001**, *211*, 1.
[49] R. Whyman, *Applied Organometallic Chemistry and Catalysis*, Oxford University Press, Oxford, **2001**.
[50] *The Activation of Dioxygen and Homogeneous Catalytic Oxidation* (Eds.: D. Barton, A. E. Martell, D. T. Sawyer), Plenum Press, New York, **1993**.
[51] H. Fujisawa, Y. Kondou, *World Patent*, WO03011803, **2003**.
[52] M. Yamada, H. Fujisawa, *European Patent*, EP1260572, **2002**.
[53] Du Pont, *GB Patent*, GB697506, **1953**.
[54] Montedison SPA, *GB Patent*, GB864351, **1961**.
[55] Bitzer Diethelm, *GB Patent*, GB1004397, **1965**.
[56] M. J. Huhtala, P. A. W. Harju-Jeanty, *Finland Patent*, FI882317, **1989**.
[57] P. A. W. Harju-Jeanty, *GB Patent*, GB2243551, **1991**.
[58] P. M. Reis, J. A. L. Silva, J. J. R. F. da Silva, A. J. L. Pombeiro, *Chem. Commun.* **2000**, 1845.
[59] M. N. Kopylovich, A. M. Kirillov, A. K. Baev, A. J. L. Pombeiro, *J. Mol. Catal. A.* **2003**, *206*, 163.
[60] P. M. Reis, J. A. L. Silva, A. F. Palavra, J. J. R. F. da Silva, T. Kitamura, Y. Fujiwara, A. J. L. Pombeiro, *Angew. Chem. Int. Ed.* **2003**, *42*, 821.
[61] S. M. Harben, P. D. Smith, R. L. Beddoes, D. Collison, C. D. Garner, *J. Chem. Soc. Dalton Trans.* **1997**, 2777.
[62] Y. H. Chen, Q. T. Liu, Y. H. Deng, H. P. Zhu, C. N. Chen, H. J. Fan, D. Z. Liao, E. Q. Gao, *Inorg. Chem.* **2001**, *40*, 3725.
[63] A. A. Naiini, J. Pinkas, W. Plass, V. G. Young, J. G. Verkade, *Inorg. Chem.* **1994**, *33*, 2137.
[64] E. M. Armstrong, D. Collison, N. Ertok, C. D. Garner, *Talanta* **2000**, *53*, 75.
[65] S. M. Harben, P. D. Smith, M. Helliwell, D. Collison, C. D. Garner, *J. Chem. Soc. Dalton Trans.* **1997**, 4517.
[66] J. Jazwinski, H. Duddeck, *Magn. Reson. Chem.* **2003**, *41*, 921.
[67] X. P. Shan, A. Ellern, J. H. Espenson, *Inorg. Chem.* **2002**, *41*, 7136.
[68] C. Pearson, A. L. Beauchamp, *Can. J. Chem.* **1997**, *75*, 220.
[69] J. O. Dziegielewski, S. Michalik, R. Kruszynski, T. J. Bartczak, J. Kusz, *Polyhedron* **2003**, *22*, 3307.
[70] T. Nicholson, J. Zubieta, *Polyhedron* **1988**, *7*, 171.
[71] M. Hirsch-Kuchma, T. Nicholson, A. Davison, A. G. Jones, *J. Chem. Soc. Dalton Trans.* **1997**, 3189.
[72] M. B. Hursthouse, A. A. S. Jayaweera, A. Quick, *J. Chem. Soc. Dalton Trans.* **1979**, 279.
[73] U. Mazzi, F. Refosco, G. Bandoli, M. Nicolini, *Transition Met. Chem.* **1985**, *10*, 121.
[74] S. M. O. Quintal, H. I. S. Nogueira, V. Felix, M. G. B. Drew, *New J. Chem.* **2000**, *24*, 511.
[75] A. Deloffre, S. Halut, L. Salles, J.-M. Bregeault, J. R. Gregorio, B. Denise, H. Rudler, *J. Chem. Soc. Dalton Trans.* **1999**, 2897.
[76] S. Gatto, T. I. A. Gerber, G. Bondoli, J. Perils, J. G. H. du Preez, *Inorg. Chim. Acta* **1998**, *269*, 235.
[77] P. E. Fanwick, M. Leeaphon, R. A. Walton, *Inorg. Chem.* **1990**, *29*, 676.
[78] G. B. Shul'pin, *J. Mol. Catal. A.* **2002**, *189*, 39.
[79] G. B. Shul'pin, Y. N. Kozlov, G. V. Nizova, G. Suss-Fink, S. Stanislas, A. Kitaygorodskiy, V. S. Kulikova, *J. Chem. Soc. Perkin Trans. 2* **2001**, 1351.
[80] U. Schuchardt, D. Mandelli, G. B. Shul'pin, *Tetrahedron Lett.* **1996**, *37*, 6487.
[81] E. Koch, H. Kneifel, E. Bayer, *Z. Naturforsch. Teil B* **1986**, *41*, 359.
[82] Z. Otwinowski, W. Minor, "Processing of X-ray Diffraction Data Collected in Oscillation Mode", *Methods in Enzymology*, Volume 276, *Macromolecular Crystallography, Part A* (Eds.: C. W. Carter, R. M. Sweet), Academic Press, New York, **1997**, pp. 307–326.
[83] A. Altomare, M. C. Burla, M. Camalli, G. L. Cascarano, C. Giacovazzo, A. Guagliardi, A. G. G. Moliterni, G. Polidori, R. Spagna, *J. Appl. Crystallogr.* **1999**, *32*, 115.
[84] M. C. Burla, M. Camalli, B. Carrozzini, G. L. Cascarano, C. Giacovazzo, G. Polidori, R. Spagna, *J. Appl. Crystallogr.* **2003**, *36*, 1103.
[85] L. J. Farrugia, *J. Appl. Crystallogr.* **1999**, *32*, 837.
[86] G. M. Sheldrick, *SHELXTL v. 6.12*; Bruker Analytical X-ray Systems, Bruker AXS, Inc. Madison, Wisconsin, USA, **2002**.
[87] G. M. Sheldrick, *SHELXL-97*, *Program for Crystal Structure Determination*; University of Göttingen, Germany, **1997**.
[88] M. Nardelli, *J. Appl. Crystallogr.* **1999**, *32*, 563.

Received: November 29, 2004

 © 2005 Wiley-VCH Verlag GmbH & Co. KGaA, Weinheim

Synthesis, Structure, and Ligand Redistribution Equilibria of Mixed Ligand Complexes of the Heavier Group 2 Elements Containing Pyrazolato and β-Diketiminato Ligands

Hani M. El-Kaderi,[a] Mary Jane Heeg,[a] and Charles H. Winter*[a]

Keywords: N ligands / Group 2 elements / Calcium / Strontium / Barium

Treatment of $M[N(SiMe_3)_2]_2(THF)_2$ (M = Ca, Sr, Ba) with various stoichiometries of *N*-*tert*-butyl-4-(*tert*-butylimino)-2-penten-2-amine ($L^{tBu}H$) and 3,5-di-*tert*-butylpyrazole (tBu_2pzH) afforded $[(\eta^2\text{-}tBu_2pz)Ca(\mu\text{-}\eta^5{:}\eta^2\text{-}tBu_2pz)(\mu\text{-}\eta^2{:}\eta^2\text{-}tBu_2pz)Ca(\eta^5\text{-}L^{tBu})]$ (17 %), $[Sr(\mu\text{-}\eta^5{:}\eta^2\text{-}tBu_2pz)(\eta^5\text{-}L^{tBu})]_2$ (50 %), and $[Ba(\mu\text{-}\eta^5{:}\eta^2\text{-}tBu_2pz)(\eta^5\text{-}L^{tBu})]_2$ (66 %) as colorless crystalline solids. The formulations of the new complexes were assigned from spectral and analytical data and by X-ray crystal structure determinations. In the solid state, $[(\eta^2\text{-}tBu_2pz)Ca(\mu\text{-}\eta^5{:}\eta^2\text{-}tBu_2pz)(\mu\text{-}\eta^2{:}\eta^2\text{-}tBu_2pz)Ca(\eta^5\text{-}L^{tBu})]$ exists as a dimer that is held together by $\mu\text{-}\eta^5{:}\eta^2$- and $\mu\text{-}\eta^2{:}\eta^2$-pyrazolato ligands, with a terminal $\eta^2\text{-}tBu_2pz$ ligand on one calcium ion and an $\eta^5\text{-}L^{tBu}$ ligand on the other. The dimeric structures of $[Sr(\mu\text{-}\eta^5{:}\eta^2\text{-}tBu_2pz)(\eta^5\text{-}L^{tBu})]_2$ and $[Ba(\mu\text{-}\eta^5{:}\eta^2\text{-}tBu_2pz)(\eta^5\text{-}L^{tBu})]_2$ are connected by two $\mu\text{-}\eta^5{:}\eta^2$-pyrazolato ligands, and the coordination sphere of each metal ion is capped with an $\eta^5\text{-}L^{tBu}$ ligand. In toluene solution, $[(\eta^2\text{-}tBu_2pz)Ca(\mu\text{-}\eta^5{:}\eta^2\text{-}tBu_2pz)(\mu\text{-}\eta^2{:}\eta^2\text{-}tBu_2pz)Ca(\eta^5\text{-}L^{tBu})]$ exists as an equilibrium mixture of at least four compounds. In toluene solution, $[Sr(\mu\text{-}\eta^5{:}\eta^2\text{-}tBu_2pz)(\eta^5\text{-}L^{tBu})]_2$ exists in equilibrium with $Sr(\eta^5\text{-}L^{tBu})_2$ and $Sr_4(tBu_2pz)_8$. A van't Hoff analysis of this equilibrium between 46 and 104 °C afforded $\Delta H° = 22.2 \pm 0.7$ kcal/mol, $\Delta S° = 43.7 \pm 1.9$ cal/mol·K, and $\Delta G°(298\ K) = 9.2 \pm 0.9$ kcal/mol. $[Ba(\mu\text{-}\eta^5{:}\eta^2\text{-}tBu_2pz)(\eta^5\text{-}L^{tBu})]_2$ exists in toluene solution as a single, pure species between –60 and +80 °C. The overall results suggest that the $\eta^5\text{-}L^{tBu}$ ligand is better at saturating the coordination sphere of the metal ion to which it coordinates than is the tBu_2pz ligand, and is suggested as a more promising ligand for the construction of practical, volatile chemical vapor deposition film growth precursors.

(© Wiley-VCH Verlag GmbH & Co. KGaA, 69451 Weinheim, Germany, 2005)

Introduction

Recent efforts in the coordination chemistry of calcium, strontium, and barium have been driven by applications in polymerization catalysis, organic synthesis, and film growth by chemical vapor deposition (CVD) and related techniques.[1–5] Solid state materials containing the group 2 elements have many significant technological applications, and CVD is commonly used for the growth of thin films of these materials.[1–3] Despite intense investigation, CVD precursors of the heavier group 2 elements remain problematic.[1–3] It has been difficult to identify structures that combine sufficient volatility and thermal stability, due to the high molecular weights, the high coordination numbers, and the low formation constants of complexes containing these elements. The key to future developments in this area must reside with ligand design. To date, the most widely used group 2 CVD precursors have employed substituted cyclopentadienyl[2] or β-diketonato[3] ligands.

Our laboratory has devoted considerable effort to the development of new nitrogen-based pyrazolato[6] and β-diketiminato[7] ligands for the group 2 elements. In particular, we have found that group 2 bis(pyrazolato) complexes form monomers only in the presence of neutral donor ligands, but these complexes decompose prior to sublimation with loss of the neutral ligands to afford oligomeric pyrazolato complexes with very low vapor pressures.[6] We have also recently reported that β-diketiminato ligands with alkyl substituents on the nitrogen atoms bond to group 2 metal centers with π- or η^5-coordination modes, and that these ligands coordinate unexpectedly well to the larger group 2 metal ions.[7] Herein we describe a surprising series of dimeric calcium, strontium, and barium complexes that contain both β-diketiminato and pyrazolato ligands. The β-diketiminato ligands coordinate to the metal centers with a terminal η^5-coordination mode, while the pyrazolato ligands adopt terminal η^2-, $\mu\text{-}\eta^2{:}\eta^2$-, or $\mu\text{-}\eta^5{:}\eta^2$-coordination modes. Documentation of pyrazolato ligand coordination modes has been a central theme of many research reports in recent years,[8] but there have been few reports of heavier group 2 pyrazolato complexes.[6b,9] The results described herein afford unusual examples of pyrazolato ligand coordination to group 2 centers, provide a conceptual method for

[a] Department of Chemistry, Wayne State University, Detroit, Michigan 48202, USA
Fax: +1-313-577-8289
E-mail: chw@chem.wayne.edu

Supporting information for this article is available on the WWW under http://www.eurjic.org or from the author.

reduction of oligomerization in pyrazolato complexes through inclusion of terminal η^5-β-diketiminato ligands, allow direct comparison of the donor characteristics of β-diketiminato and pyrazolato ligands, and suggest new directions for the development of ligands that can be used to manipulate the properties of group 2 complexes. We also describe ligand redistribution equilibria of the new heteroleptic complexes and provide thermodynamic parameters for the $[Sr(\mu\text{-}\eta^5\text{:}\eta^2\text{-}t\text{Bu}_2\text{pz})(\eta^5\text{-L}^{t\text{Bu}})]_2$ equilibria.

Results

Synthetic Chemistry

Treatment of $M[N(SiMe_3)_2]_2(THF)_2$ (M = Ca, Sr, Ba)[10] with various stoichiometries of *N*-*tert*-butyl-4-(*tert*-butylimino)-2-penten-2-amine ($L^{t\text{Bu}}H$)[11] and 3,5-di-*tert*-butylpyrazole ($t\text{Bu}_2\text{pzH}$) as described in Equation (1) afforded $[(\eta^2\text{-}t\text{Bu}_2\text{pz})\text{Ca}(\mu\text{-}\eta^5\text{:}\eta^2\text{-}t\text{Bu}_2\text{pz})(\mu\text{-}\eta^2\text{:}\eta^2\text{-}t\text{Bu}_2\text{pz})\text{Ca}(\eta^5\text{-L}^{t\text{Bu}})]$ (**1**, 17%), $[Sr(\mu\text{-}\eta^5\text{:}\eta^2\text{-}t\text{Bu}_2\text{pz})(\eta^5\text{-L}^{t\text{Bu}})]_2$ (**2**, 50%), and $[Ba(\mu\text{-}\eta^5\text{:}\eta^2\text{-}t\text{Bu}_2\text{pz})(\eta^5\text{-L}^{t\text{Bu}})]_2$ (**3**, 66%) as colorless crystalline solids. Variations in the $L^{t\text{Bu}}H/t\text{Bu}_2\text{pzH}$ stoichiometries away from those required for **1** did not lead to new products, and only **1** crystallized from the reaction mixtures. Interestingly, the highest crystallized yields of **1** were obtained with an $L^{t\text{Bu}}H/t\text{Bu}_2\text{pzH}$ ratio of 2:2 and not 1:3 as required for the stoichiometry of **1**. The order of reagent addition was important in the synthesis of **1**–**3**. If $t\text{Bu}_2\text{pzH}$ was added first, followed by $L^{t\text{Bu}}H$, then complex product mixtures resulted. Complex **1** is soluble in hexane, while **2** and **3** are insoluble in hexane and are moderately soluble in toluene at room temperature. The structural assignments for **1**–**3** were based upon spectral and analytical data as well as X-ray structure determinations. In solution, **1** exists as an equilibrium mixture of at least four species at ambient temperature, while **2** exists as an equilibrium mixture of three species. By contrast, **3** is a single species in solution between –60 and +80 °C. The variable-temperature NMR spectroscopic data for these complexes are described below.

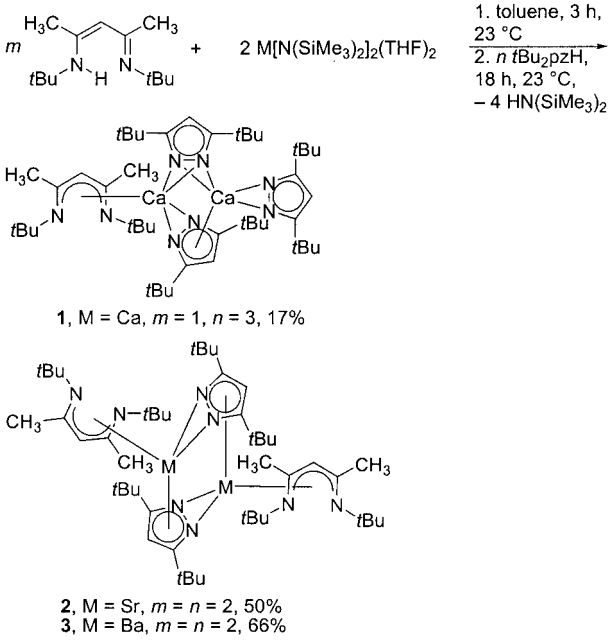

(1)

X-ray Crystal Structure Determinations

The crystal structures of **1**–**3** were determined in order to understand their molecular structures. Perspective views of **1**–**3** are shown in Figures 1, 2 and 3. The crystal data are given in Table 1. Selected bond lengths and angles are presented in Tables 2, 3 and 4.

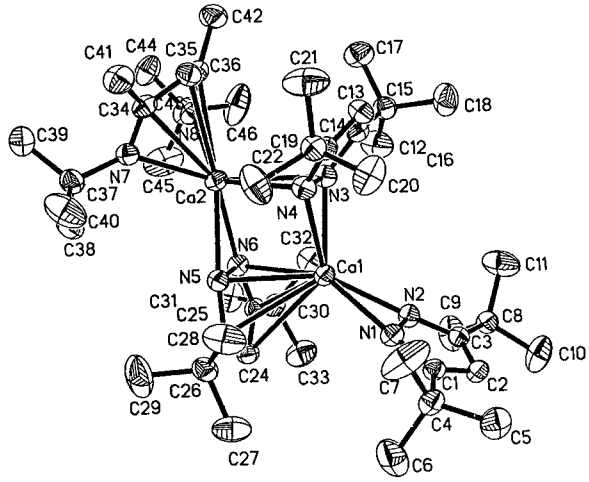

Figure 1. Perspective view of **1** with thermal ellipsoids at the 50% probability level.

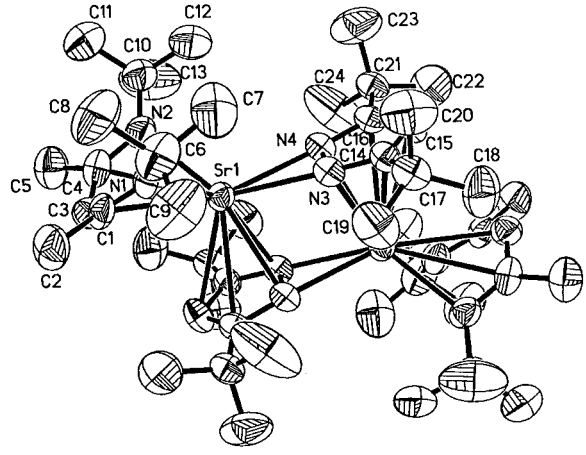

Figure 2. Perspective view of **2** with thermal ellipsoids at the 50% probability level.

In the solid state, **1** can be thought of as $Ca(\eta^5\text{-L}^{t\text{Bu}})(\eta^2\text{-}t\text{Bu}_2\text{pz})$ and $Ca(\eta^2\text{-}t\text{Bu}_2\text{pz})_2$ fragments that dimerize through formation of $\mu\text{-}\eta^5\text{:}\eta^2$- and $\mu\text{-}\eta^2\text{:}\eta^2$-pyrazolato ligands (Figure 1). The $\eta^5\text{-L}^{t\text{Bu}}$ ligand has calcium–nitrogen bond lengths of 2.322(2) and 2.342(2) Å, while the calcium–carbon bond lengths range between 2.741(3) and 2.827(3) Å. These values are slightly shorter than those observed in $Ca(\eta^5\text{-L}^{t\text{Bu}})_2$ (Ca–N 2.342–2.358, Ca–C 2.817–2.901 Å).[7b] The terminal η^2-pyrazolato ligand has cal-

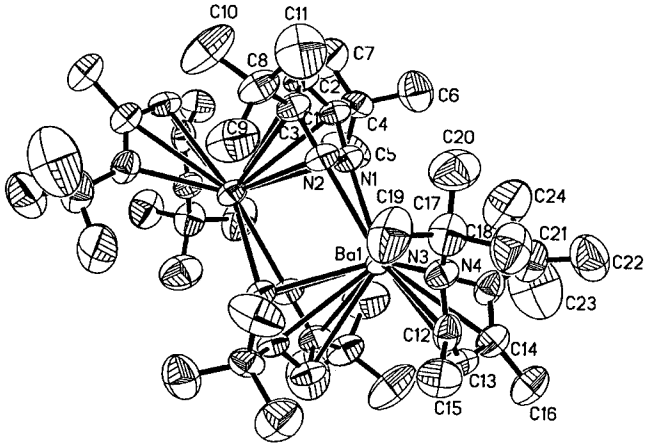

Figure 3. Perspective view of **3** with thermal ellipsoids at the 50% probability level.

Table 1. Summary of crystallographic data for **1**–**3**.

	1	**2**	**3**
Empirical formula	$C_{46}H_{82}Ca_2N_8$	$C_{48}H_{88}N_8Sr_2$	$C_{48}H_{88}Ba_2N_8$
Formula mass	827.36	952.50	1051.94
Temperature [K]	193(2)	295(2)	295(2)
Crystal system	monoclinic	monoclinic	triclinic
Space group	*P*21/*c*	*P*21/*n*	$P\bar{1}$
a [Å]	10.6303(8)	14.609(14)	10.6553(13)
b [Å]	20.8169(15)	12.343(16)	11.4231(15)
c [Å]	22.6456(17)	15.596(18)	12.1090(16)
α [°]	90	90	78.097(2)
β [°]	91.643(2)	101.61(3)	74.841(3)
γ [°]	90	90	83.296(3)
V [Å^{-3}]	5009.2(6)	2755(6)	1388.9(3)
Z	4	2	1
d(calcd.) [g/cm^3]	1.097	1.148	1.258
Absorption coefficient [mm^{-1}]	0.265	1.972	1.445
F(000)	1816	1016	544
Crystal size [mm]	0.30×0.20×0.10	0.20×0.20×0.05	0.12×0.12×0.06
θ range [°]	1.92 to 28.31	1.74 to 28.28	2.30 to 28.32
No. of reflections collected	26303	19680	9890
No. of independent reflections	11683	6410	6393
GOF/F^2	0.998	0.750	0.974
R indices [$I > 2\sigma(I)$]	0.0493	0.0460	0.0637
R indices (all data)	0.1233	0.2021	0.1649
Largest difference peak/hole [e·Å^{-3}]	0.305, –0.339	0.389, –0.599	0.637, –0.833

$R(F) = \Sigma||F_o| - |F_c||/\Sigma|F_o|$; $Rw(F) = [\Sigma w(F_o^2 - F_c^2)^2/\Sigma w(F_o^2)^2]^{1/2}$

Table 2. Selected bond lengths [Å] and angles [°] for **1**.

Ca(1)–N(1) 2.3154(19)	Ca(1)–C(23) 2.832(2)
Ca(1)–N(2) 2.299(2)	Ca(1)–C(24) 2.997(2)
Ca(1)–N(3) 2.438(2)	Ca(1)–C(25) 2.863(2)
Ca(1)–N(4) 2.433(2)	Ca(2)–C(34) 2.773(2)
Ca(1)–N(5) 2.583(2)	Ca(2)–C(35) 2.741(3)
Ca(1)–N(6) 2.5984(19)	Ca(2)–C(36) 2.827(3)
Ca(2)–N(3) 2.642(2)	Ca(1)–Ca(2) 3.5348(7)
Ca(2)–N(4) 2.588(2)	N(1)–Ca(1)–N(2) 35.29(6)
Ca(2)–N(5) 2.480(2)	N(3)–Ca(1)–N(4) 33.74(6)
Ca(2)–N(6) 2.452(2)	N(5)–Ca(1)–N(6) 31.26(6)
Ca(2)–N(7) 2.322(2)	N(5)–Ca(2)–N(6) 32.88(6)
Ca(2)–N(8) 2.342(2)	N(3)–Ca(2)–N(4) 31.35(6)
N(7)–Ca(2)–N(8) 77.87(7)	

Table 3. Selected Bond lengths [Å] and angles [°] for 2.[a]

Sr–N(1) 2.516(5)	Sr–C(15)′ 3.229(5)
Sr–N(2) 2.512(4)	Sr–C(16)′ 3.083(5)
Sr–N(3) 2.618(4)	Sr–Sr′ 4.097(2)
Sr–N(4) 2.614(5)	N(1)–Sr–N(2) 71.95(14)
Sr–N(3)′ 2.897(4)	N(3)–Sr–N(4) 31.15(10)
Sr–N(4)′ 2.855(4)	N(3)′-Sr–N(4)′ 28.26(9)
Sr–C(1) 3.052(6)	N(2)–Sr–N(4) 109.27(17)
Sr–C(3) 3.004(6)	N(1)–Sr–N(4) 127.11(14)
Sr–C(4) 3.025(6)	N(2)–Sr–N(3) 129.79(14)
Sr–C(14)′ 3.148(5)	N(1)–Sr–N(3) 106.43(15)

[a] Primes indicate symmetry-equivalent positions.

Table 4. Selected bond lengths [Å] and angles [°] for **3**.[a]

Ba–N(1) 2.776(6)	Ba–C(3)′ 3.241(8)
Ba–N(2) 2.793(6)	Ba–Ba′ 4.297(2)
Ba–N(3) 2.642(6)	N(1)–Ba–N(2) 28.99(16)
Ba–N(4) 2.633(6)	N(1)–Ba–N(3) 123.49(19)
Ba–N(1)′ 3.004(6)	N(1)–Ba–N(4) 115.4(2)
Ba–N(2)′ 3.036(6)	N(2)–Ba–N(3) 104.98(19)
Ba–C(12) 3.121(8)	N(2)–Ba–N(4) 133.5(2)
Ba–C(13) 3.110(8)	N(3)–Ba–N(4) 67.98(19)
Ba–C(14) 3.176(8)	N(1)′-Ba–N(2)′ 26.67(15)
Ba–C(1)′ 3.189(8)	N(1)′-Ba–N(3) 128.00(18)
Ba–C(2)′ 3.325(8)	N(1)′-Ba–N(4) 144.0(2)

[a] Primes indicate symmetry-equivalent positions

cium–nitrogen bond lengths of 2.315(2) and 2.299(2) Å, which can be compared to the corresponding values in complexes of the formula Ca(η^2-$R_2pz)_2$L (R = Me, *t*Bu;L = neutral donor; Ca–N = 2.311–2.529 Å).[6b] The calcium–nitrogen bond lengths for the μ-η^2:η^2-*t*Bu_2pz ligand are 2.438(2) and 2.433(2) Å for Ca(1) and 2.588(2) and 2.642(2) Å for Ca(2). Thus, the μ-η^2:η^2-*t*Bu_2pz ligand is more strongly bonded to Ca(1), and this metal center is assigned as the Ca(η^2-*t*Bu_2pz)$_2$ fragment. For Ca(2), the calcium–nitrogen bond lengths for the μ-η^5:η^2-*t*Bu_2pz ligand are 2.452(2) and 2.480(2) Å, while for Ca(1) these values are 2.583(2) and 2.598(2) Å. The calcium–carbon bond lengths range from 2.832(2) to 2.997(2) Å. Based upon bond lengths, Ca(2) is more strongly bonded to the pyrazolato ligand containing N(5) and N(6), and thus Ca(2) is assigned as the Ca(η^5-L$^{t\mathrm{Bu}}$)(η^2-*t*Bu_2pz) fragment. The Ca(1)–carbon(pyrazolato) distances are longer than the Ca(2)–C(η^5-L$^{t\mathrm{Bu}}$) distances in **1**, and are comparable to those observed in Ca(η^5-L$^{t\mathrm{Bu}}$)$_2$.[7b] The calcium–carbon bond length in Ca($C_5Me_5)_2$ is 2.64(2) Å.[12] Thus, the η^5-pyrazolato ligand interaction involving Ca(1) within **1** is best described as a π-donor interaction and is different from the terminal η^5-pyrazolato ligand bonding that has been described in several ruthenium complexes.[13]

The overall molecular structures of **2** and **3** are similar, and can be viewed as dimers of two M(η^5-L$^{t\mathrm{Bu}}$)(η^2-*t*Bu_2pz) fragments (Figures 2 and 3). The η^5-L$^{t\mathrm{Bu}}$ ligand in **2** has strontium–nitrogen bond lengths of 2.512(4) and 2.516(5) Å, while the strontium–carbon bond lengths range between 3.004(6) and 3.052(6) Å. The analogous barium–nitrogen distances in **3** are 2.633(6) and 2.642(6) Å, while the barium–carbon distances range between 3.110(8) and 3.176(8) Å. The values are comparable to those of Sr(η^5-

 © 2005 Wiley-VCH Verlag GmbH & Co. KGaA, Weinheim

$L^{tBu})_2$ [Sr–N 2.473(2)–2.517(2) Å, Sr–C 2.928(2)–3.004(2) Å] and Ba(η^5-L^{tBu})$_2$ (Ba–N 2.617–2.680 Å, Ba–C 3.055–3.157 Å).[7b] The metal–carbon distances in **2** and **3** are slightly longer than the metal–carbon distances in Sr[C_5(tBu)$_3H_2$]$_2$(THF) (Sr–$C_{Cp'}$ 2.87 Å avg.)[14] and Ba(C_5Me_5)$_2$ [2.98(1), 2.99(2) Å].[12] The μ-η^5:η^2-tBu$_2$pz ligand in **2** possesses strontium–nitrogen bond lengths of 2.614(5) and 2.618(5) Å for the η^2-interaction, and 2.855(4) and 2.897(4) Å for the η^5-bonded fragment. For **3**, the related values are 2.776(6) and 2.793(6) Å for the η^2-interaction, and 3.004(6) and 3.036(6) Å for the η^5-bonded fragment. The metal–carbon distances associated with the μ-η^5:η^2-tBu$_2$pz ligand range between 3.083(5) and 3.229(5) Å for **2** and 3.189(8)–3.325(8) Å for **3**. These values are similar to or longer than those associated with the η^5-L^{tBu} ligand in **2** and **3** and M(η^5-L^{tBu})$_2$,[7b] and are 5–10% longer than the related distances in Sr[C_5(tBu)$_3H_2$]$_2$(THF) (Sr–$C_{Cp'}$ 2.87 Å avg.)[14] and Ba(C_5Me_5)$_2$ [2.98(1), 2.99(2) Å].[12] Again, the bond lengths associated with the μ-η^5:η^2-tBu$_2$pz ligand suggest that the η^5-interactions are best described as π-donation to satisfy the Lewis acidity of the unsaturated metal centers. The angle between the planes of the β-diketiminato and pyrazolato C_3N_2 cores is 20.8(3)° in **2** and 23.5(3)° in **3**, which can be compared with C_5Me_5(centroid)–metal–C_5Me_5(centroid) angles of 26–33° in the monomeric, base-free metallocenes M(C_5Me_5)$_2$.[12]

Variable-Temperature NMR Behavior of 1–3

Having established the solid-state structures, we next explored the solution structures using NMR spectroscopy. The solution NMR behavior of **1**–**3** differed significantly. Complex **1** exhibited four β-diketiminato ligand β-CH ^{1}H NMR resonances in [D_8]toluene at ambient temperature at δ = 4.60, 4.44, 4.22, and 4.20 ppm, in a ratio of 26:15:12:47. The resonance at δ = 4.22 ppm was identified as the β-CH resonance of Ca(η^5-L^{tBu})$_2$, by comparison with authentic material {also δ = 1.98 (CH_3), 1.34 [C(CH_3)$_3$] ppm}.[7b] Thus, Ca(η^5-L^{tBu})$_2$ is a minor constituent of the solution. A species with resonances consistent with **1** was observed in the ^{1}H NMR spectrum {δ = 6.19, 6.08, 6.04 (tBu$_2$pz β-CH), 4.20 (L^{tBu} β-CH), 1.96 (L^{tBu} CH_3), 1.45, 1.40, 1.28 [L^{tBu} C(CH_3)$_3$]}, and accounted for 47% of the integrated β-CH signals. The remaining two β-diketiminato ligand L^{tBu} β-CH resonances correspond to unknown species, but probably contain mixed pyrazolato/L^{tBu} ligand spheres. The complex Ca$_3$(tBu$_2$Pz)$_6$ has been recently described,[9d] and has tBu$_2$pz β-CH resonances at δ = 6.20, 6.08, and 6.00 ppm and a *tert*-butyl methyl resonance at δ = 1.37 ppm in the ^{1}H NMR in [D_8]toluene at –55 °C. In the ^{1}H NMR spectrum of **1** in [D_8]toluene at –60 °C, tBu$_2$pz β-CH resonances were observed at δ = 6.34, 6.29, 6.23, 6.18, and 6.08 ppm. These resonances do not match those reported for Ca$_3$(tBu$_2$pz)$_6$. It is possible that Ca$_3$(tBu$_2$pz)$_6$ precipitates from [D_8]toluene at –60 °C, and is thus not observed. The presence of **1**, Ca(η^5-L^{tBu})$_2$, and one or two other unidentified species in solutions derived from pure **1** suggest that multiple equilibria are present.

In [D_8]toluene at ambient temperature, **2** exhibited a mixture of two complexes containing β-diketiminato ligands [δ = 4.21, 4.19 (L^{tBu} β-CH) ppm] in a 13:87 ratio. The major species exhibits the resonances expected for **2** {δ = 6.26 (tBu$_2$pz β-CH), 4.19 (L^{tBu} β-CH), 1.99 (L^{tBu} CH_3), 1.47, 1.30 [L^{tBu}, tBu$_2$pz C(CH_3)$_3$]}. The minor species matches the resonances that we have previously reported for Sr(η^5-L^{tBu})$_2$.[7b] The presence of Sr(η^5-L^{tBu})$_2$ suggests the equilibrium depicted in Equation (2), wherein **2** converts partially in [D_8]toluene to Sr(η^5-L^{tBu})$_2$ and the recently reported tetramer Sr$_4$(tBu$_2$pz)$_8$.[9d] The ^{1}H NMR spectrum of **2** at –60 °C in [D_8]toluene revealed 1:1:1 pyrazolato β-CH resonances at δ = 6.35, 6.26, and 6.07 ppm and a *tert*-butyl methyl resonance at δ = 1.44 ppm, after the resonances for Sr(η^5-L^{tBu})$_2$ and **2** had been excluded. For comparison, the ^{1}H NMR spectrum of Sr$_4$(tBu$_2$pz)$_8$ at –60 °C in [D_8]toluene is reported to have pyrazolato β-CH resonances at δ = 6.31, 6.16, and 6.08 ppm and a *tert*-butyl methyl resonance at δ = 1.48 ppm.[9d] Thus, our ^{1}H NMR spectrum at –60 °C supports the presence of Sr$_4$(tBu$_2$pz)$_8$ in the equilibrium mixture. Below 46 °C, the mixture of Sr(η^5-L^{tBu})$_2$ and **2** remained approximately constant, possibly due to a kinetically slow approach to the equilibrium. Above 46 °C, however, the Sr(η^5-L^{tBu})$_2$/**2** ratio increased with temperature (Table 5). Accordingly, we carried out a van't Hoff analysis of the equilibrium depicted in Equation (2). The equilibrium constants shown in Table 2 were determined between 46 and 104 °C by integration of the β-diketonate β-CH resonances of Sr(η^5-L^{tBu})$_2$ and **2**, and then calculating the concentrations of each species. The concentration of Sr$_4$(tBu$_2$pz)$_8$ could not be measured directly between 46 and 104 °C due to very broad signals,[9d] but was calculated at each temperature by assuming a stoichiometry of 1:4 with Sr(η^5-L^{tBu})$_2$. Analysis of the data for the equilibrium depicted in Equation (2) using standard procedures for van't Hoff analyses[15] afforded $\Delta H°$ = 22.2 ± 0.7 kcal/mol, $\Delta S°$ = 43.7 ± 1.9 cal/mol·K, and $\Delta G°$(298 K) = 9.2 ± 0.9 kcal/mol. Consistent with an equilibrium process possessing a positive $\Delta G°$, the equilibrium at 298 K lies strongly toward **2** and is reflected by the small K_{eq} values in Table 2.

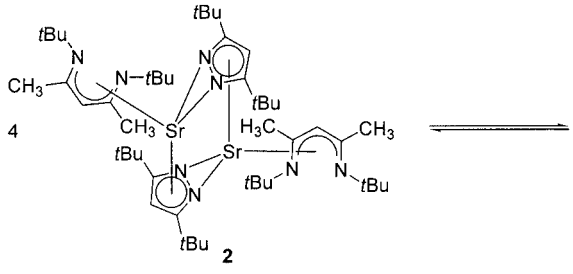

K_{eq} = [Sr(η^5-L^{tBu})$_2$]^4[Sr$_4$(tBu$_2$pz)$_8$]/[**2**]^4 (2)

Table 5. Equilibrium constants for **2** at various temperatures.

T [K]	K_{eq} [M]
319.2	2.17×10^{-6}
323.7	3.20×10^{-6}
328.1	5.26×10^{-6}
332.6	8.60×10^{-6}
337.0	1.39×10^{-5}
341.5	2.54×10^{-5}
345.6	4.52×10^{-5}
350.2	6.66×10^{-5}
354.4	9.74×10^{-5}
358.3	1.19×10^{-4}
363.8	1.41×10^{-4}
368.2	1.93×10^{-4}
372.7	3.29×10^{-4}
377.2	4.40×10^{-4}

In contrast to **1** and **2**, the ^{1}H NMR spectra of **3** between –60 and +80 °C in [D$_8$]toluene revealed a single species with resonances consistent with the solid-state structure. Thus, **3** shows no evidence for equilibria similar to those described for **1** and **2**.

Discussion

The η^5-coordination of the diketiminato ligands is a prominent structural feature of **1**–**3**. We have recently reported that complexes of the formula M(η^5-L$^{t\mathrm{Bu}}$)$_2$ (M = Ca, Sr, Ba) adopt sandwich-like structures with η^5-L$^{t\mathrm{Bu}}$ ligands.[7] In our paper on M(η^5-L$^{t\mathrm{Bu}}$)$_2$,[7b] we analyzed the η^5-L$^{t\mathrm{Bu}}$ bonding in terms of the planes incorporating the atoms MN$_2$ (a), N$_2$(C$_\alpha$)$_2$ (b), and (C$_\alpha$)$_2$C$_\beta$ (c). For M(η^5-L$^{t\mathrm{Bu}}$)$_2$, the a/b angles were between 70 and 72° and the b/c angles were between 25 and 26°, and these metrical parameters were used to support the η^5-coordination mode and differentiate it from the more common η^2-form (which has much smaller a/b and b/c values[7]). The corresponding metrical parameters for **1**–**3** are as follows: **1**: a/b = 74.9° and b/c = 29.4°; **2**: a/b = 70.5° and b/c = 29.0°; **3**: a/b = 70.5° and b/c = 28.7°. These values are close to those of M(η^5-L$^{t\mathrm{Bu}}$)$_2$, and are consistent with similar η^5-bonding of the L$^{t\mathrm{Bu}}$ ligands in **1**–**3**. All of the other heavier group 2 β-diketiminato complexes described to date feature 2,6-diisopropylphenyl,[4d,5,16] 2-methoxyphenyl,[17] or cyclohexyl[18] moieties as the nitrogen substituents. Calcium, strontium, and barium complexes containing the 2,6-diisopropylphenyl-substituted ligand [CH{C(CH$_3$)N(2,6-*i*Pr$_2$C$_6$H$_3$)}$_2$]$^-$ (L$^{\mathrm{Ar}}$) exhibit the η^2-coordination mode, through the nitrogen atoms of L$^{\mathrm{Ar}}$. Use of the *N*-cyclohexyl-substituted diketiminato ligand [CH{C(CH$_3$)N(C$_6$H$_{11}$)}$_2$]$^-$ (L$^{\mathrm{Cy}}$) afforded the dimeric barium complex Ba$_2$(L$^{\mathrm{Cy}}$)$_3$[N(SiMe$_3$)$_2$], which contains η^5-, μ-η^2:η^2:η^5-, and μ-η^2:η^3-β-diketiminato ligands.[18] Adoption of the η^2-coordination mode in complexes containing L$^{\mathrm{Ar}}$ is presumably a steric effect that is driven by the bulky aromatic isopropyl substituents. The various coordination modes of β-diketiminato ligands have been recently reviewed.[19] The η^5-β-diketiminato ligand has been structurally documented in a few main group, lanthanide, and early transition metal complexes, but still remains rare.[7b,18,19] The present results, our previous report on M(η^5-L$^{t\mathrm{Bu}}$)$_2$,[7b] and Ba$_2$(L$^{\mathrm{Cy}}$)$_3$[N(SiMe$_3$)$_2$][18] suggest that the η^5-β-diketiminato coordination mode should be common in the heavier group 2 complexes when alkyl groups or less bulky aromatic rings are present on the nitrogen atoms.

Complex **1** contains terminal η^2-, μ-η^5:η^2-, and μ-η^2:η^2-pyrazolato ligands, while **2** and **3** possess μ-η^5:η^2-pyrazolato ligands. The terminal η^2-coordination mode has been documented in Ca(R$_2$pz)$_2$(L$_n$) (L$_n$ = polydentate oxygen or nitrogen donor),[6b] M(Ph$_2$pz)$_2$(THF)$_4$ (M = Ca, Sr, Ba),[9c] M(Ph$_2$pz)$_2$(DME)$_n$ (M = Ca, Sr, *n* = 2; M = Ba, *n* = 3),[9c] M(Me$_2$pz)$_2$(Me$_2$pzH)$_4$ (M = Ca, Sr),[9c] Ca$_3$(*t*Bu$_2$pz)$_6$,[9d] Sr$_4$(*t*Bu$_2$pz)$_8$,[9d] and Ba$_6$(*t*Bu$_2$pz)$_{12}$.[9d] Terminal η^2-pyrazolato ligands are thus common in the heavier group 2 metal complexes, and are probably driven by achieving maximum electrostatic interactions between the pyrazolato ligand in-plane nitrogen-based orbitals and the group 2 metal ions. One pyrazolato ligand in **1** adopts the μ-η^2:η^2-coordination mode. This coordination mode has been previously observed in Ca$_3$(*t*Bu$_2$pz)$_6$[9d] and in lanthanide complexes such as Ln$_3$(Ph$_2$pz)$_9$ (Ln = La, Nd).[21] The similar ionic radii[22] of Ca$^{\mathrm{II}}$ (1.00 Å), La$^{\mathrm{III}}$ (1.032 Å), and Nd$^{\mathrm{III}}$ (0.983 Å) are most likely the origin of the similar pyrazolato ligand coordination modes. Finally, **1**–**3** contain μ-η^5:η^2-pyrazolato ligands. This coordination mode has been previously observed in the group 2 complexes Ca$_3$(*t*Bu$_2$pz)$_6$,[9d] Sr$_4$(*t*Bu$_2$pz)$_8$,[9d] and Ba$_6$(*t*Bu$_2$pz)$_{12}$,[9d] and in lanthanide complexes such as Ln$_3$(Ph$_2$pz)$_9$ (Ln = La, Nd)[21] and Eu$_4$(*t*Bu$_2$pz)$_8$.[23] Formation of μ-η^5:η^2-pyrazolato ligands appears to arise due to the coordinative unsaturation at the group 2 and lanthanide metal ions, which can be satisfied in the absence of good neutral donor ligands by donation of the out-of-plane π-orbitals of the pyrazolato ligand C$_3$N$_2$ cores to an adjacent metal ion. In **1**–**3**, the μ-η^5:η^2-pyrazolato ligands lead to dimeric species, whereas in the other group 2 and lanthanide complexes, trimers, tetramers, and even hexamers are obtained through formation of μ-η^5:η^2-pyrazolato ligands. It is clear that the good donor capabilities of L$^{t\mathrm{Bu}}$ restrict the degree of oligomerization in **1**–**3**.

The overall structures of **1**–**3** can be compared with those of Ca$_3$(*t*Bu$_2$pz)$_6$,[9d] Sr$_4$(*t*Bu$_2$pz)$_8$,[9d] Ba$_6$(*t*Bu$_2$pz)$_{12}$,[9d] and Eu$_4$(*t*Bu$_2$pz)$_8$.[23] Table 6 compares selected metal–nitrogen bond lengths in **1**–**3** with the related fragments in Ca$_3$(*t*Bu$_2$pz)$_6$,[9d] Sr$_4$(*t*Bu$_2$pz)$_8$,[9d] and Ba$_6$(*t*Bu$_2$pz)$_{12}$.[9d] Remarkably, the Ca$_2$(η^2-*t*Bu$_2$pz)(μ-η^5:η^2-*t*Bu$_2$pz)(μ-η^2:η^2-*t*Bu$_2$pz) fragment in **1** is virtually identical structurally to the coordination sphere of the outer and middle calcium ions in Ca$_3$(*t*Bu$_2$pz)$_6$. Indeed, if an outer Ca(*t*Bu$_2$pz)$_3^-$ fragment in Ca$_3$(*t*Bu$_2$pz)$_6$ is replaced by L$^{t\mathrm{Bu}}$, the molecular structure of **1** is obtained. Such similarity suggests that the Ca$_2$(η^2-*t*Bu$_2$pz)(μ-η^5:η^2-*t*Bu$_2$pz)(μ-η^2:η^2-*t*Bu$_2$pz) fragment is particularly stable. The structural parameters of the M$_2$(μ-η^5:η^2-*t*Bu$_2$pz)$_2$ core fragments in **2** and **3** show a similar high degree of congruence with the inner metal ion M$_2$(μ-η^5:η^2-*t*Bu$_2$pz)$_2$ substructures of Sr$_4$(*t*Bu$_2$pz)$_8$, Ba$_6$(*t*Bu$_2$pz)$_{12}$, and Eu$_4$(*t*Bu$_2$pz)$_8$. In fact, as shown in Table 6, the metal–nitrogen bond lengths of the M$_2$(μ-η^5:η^2-*t*Bu$_2$pz)$_2$ substructures in **2** and Sr$_4$(*t*Bu$_2$pz)$_8$ and **3** and Ba$_6$(*t*Bu$_2$-

 © 2005 Wiley-VCH Verlag GmbH & Co. KGaA, Weinheim

Table 6. Comparison of pyrazolato metal–nitrogen distances in **1**–**3** with those of $Ca_3(tBu_2pz)_6$, $Sr_4(tBu_2pz)_8$, and $Ba_6(tBu_2pz)_{12}$.

Complex	M–N [Å] terminal η^2	M–N [Å] μ-η^2:η^2	M–N [Å] μ-η^5:η^2	M–C [Å] μ-η^5:η^2
1	2.299(2)	2.433(2)	2.452(2)	2.832(2)
	2.315(2)	2.438(2)	2.480(2)	2.997(2)
		2.588(2)	2.583(2) (π)	2.863(2)
		2.642(2)	2.598(2) (π)	
$Ca_3(tBu_2pz)_6$[9d]	2.303(3)	2.447(4)–2.618(4)	2.415(3)–2.455(3)	2.816(5)–2.960(4)
[Ca(1) and Ca(2) only]	2.318(3)		2.577(3)–2.583(3) (π)	
2			2.614(5)	3.083(5)
			2.618(4)	3.229(5)
			2.855(4) (π)	3.148(5)
			2.897(4) (π)	
$Sr_4(tBu_2pz)_8$[9d]			2.453(9)–2.648(6)	3.029(7)–3.381(9)
[Sr(1) and Sr(2) only]			2.730(6)–2.779(6) (π)	
3			2.776(6)	3.189(8)
			2.793(6)	3.325(8)
			3.004(6) (π)	3.241(8)
			3.036(6) (π)	
$Ba_6(tBu_2pz)_{12}$[9d]			2.72(1)–2.84(1)	3.10(1)–3.39(1)
[Ba(1) and Ba(2) only]			2.89(1)–3.06(1) (π)	

$pz)_{12}$ are very similar. Replacement of the outer two $Sr(tBu_2pz)_3^-$ fragments in $Sr_4(tBu_2pz)_8$ by L^{tBu} ligands affords the molecular structure of **2**. In $Ba_6(tBu_2pz)_{12}$, replacement of outer $Ba(tBu_2pz)_3^-$ and $Ba_3(tBu_2pz)_7^-$ fragments by two L^{tBu} ligands affords the molecular structure of **3**. Such close structural similarities suggest that the $M_2(\mu\text{-}\eta^5\text{:}\eta^2\text{-}tBu_2pz)_2$ substructure is particularly stable, and that this unit is likely to be observed in other strontium and barium complexes that contain tBu_2pz ligands. As in **1**, the L^{tBu} ligands in **2** and **3** are sterically saturating and block these complexes from forming higher oligomeric structures.

The redistribution equilibria of **1**–**3** are of relevance to recent reports of lactide polymerization catalysis by unsymmetrical group 2 complexes (LMX) containing β-diketiminato ligands (L).[4e,16,17] In such catalysis, it is presumably the unsymmetrical LMX complex that is the active and desired precatalyst, since X^- possesses the needed nucleophilic properties to initiate catalysis and the steric properties of L are designed to promote stereoselectivity in the polymerizations. By contrast, ML_2 is unlikely to initiate catalysis efficiently and MX_2 may not promote stereoselective polymerization. A recent report by Hill has explored the stability of β-diketiminato complexes of the formula $L^{Ar}M[N(SiMe_3)_2](THF)$ toward ligand redistribution in solution.[16a] Interestingly, $L^{Ar}Ca[N(SiMe_3)_2](THF)$ was found to be inert toward ligand redistribution in [D_8]toluene solution at ambient temperature, while $L^{Ar}Ba[N(SiMe_3)_2](THF)$ was in equilibrium with $Ba(L^{Ar})_2$ and $Ba[N(SiMe_3)_2](THF)_x$ under the same conditions. Thermodynamic parameters were not reported for the latter system. It was proposed that the larger size and lower Lewis acidity of the barium ion makes it more susceptible toward ligand redistribution, compared to $L^{Ar}Ca[N(SiMe_3)_2](THF)$.[16a] The equilibrium trend observed for $L^{Ar}M[N(SiMe_3)_2](THF)$ is the opposite of what we have observed in the present study. Qualitatively, **1** undergoes more ligand redistribution at ambient temperature than **2**, since the percentage of the dimeric starting material present in **1** (47%) is lower than in **2** (87%). Thus, the order of ligand redistribution in solution is **1** > **2** >> **3**. While it was not possible to carry out a van't Hoff analysis on **1**, due to the multiple equilibria, the thermodynamic parameters for **2** provide some insight into the factors that stabilize the heteroleptic structures for **1**–**3**. In view of the positive $\Delta G°$ values for **2** in the temperature range that was studied (46–104 °C), the K_{eq} values are very small and strongly favor the heteroleptic starting material. In **2**, $\Delta H°$ is large (22.2 ± 0.3 kcal/mol), but this value is offset by a large $\Delta S°$ value (43.7 ± 0.3 cal/mol·K), which allows the ΔG° values to decrease and the K_{eq} values to increase with increasing temperature. We have previously proposed that the L^{tBu} ligands in $M(\eta^5\text{-}L^{tBu})_2$ bond most strongly to the barium ion and least strongly to the calcium ion, based upon comparison of the metal–nitrogen and metal–carbon bond lengths with those of Cp^*_2M.[7b] If this proposal holds for **1**–**3**, then the $\Delta H°$ values should increase in the order **1** < **2** < **3**, which follows the qualitative trend in redistribution equilibria. It is also likely that there is an entropic contribution to the equilibria, since the homoleptic pyrazolato complexes adopt the oligomeric structures $Ca_3(tBu_2pz)_6$, $Sr_4(tBu_2pz)_8$, and $Ba_6(tBu_2pz)_{12}$ in the solid state and appear to adopt similar structures in solution.[9d] Thus, the $\Delta S°$ values should decrease in the order **1** > **2** > **3** to reflect the increasing organization required for the oligomeric series. It is likely that the resistance of **3** toward ligand exchange in solution results from a combination of optimum bonding to the L^{tBu} ligands and the entropic penalty associated with the formation of the hexameric product $Ba_6(tBu_2pz)_{12}$. These results suggest that the nature of the ligands has a pronounced effect upon redistribution equilibria of heteroleptic group 2 complexes, and that appropriate choice of ligands can reverse the normal redistribution equilibrium trend of Ca > Sr > Ba.[16a] There are few other equilibrium constant data with which those of **2** can be compared. Cp*CaI(THF)$_2$ is

 © 2005 Wiley-VCH Verlag GmbH & Co. KGaA, Weinheim

reported to dissociate in [D$_8$]THF to afford Cp*$_2$Ca(THF)$_2$ and CaI$_2$(THF)$_2$ with K_{eq} = 4.[24] (C$_5$*i*Pr$_4$H)CaI(OEt$_2$)$_n$ dissociates in diethyl ether to Ca(C$_5$*i*Pr$_4$H)$_2$ and CaI$_2$(OEt$_2$)$_n$ with an estimated K_{eq} of 2.[25] Mixtures of Ba(CH$_2$C$_6$H$_5$)$_2$(THF)$_2$ and Ba(C$_5$Me$_4$SiMe$_2$C$_6$H$_5$)$_2$ favor the heteroleptic complex Ba(C$_5$Me$_4$SiMe$_2$C$_6$H$_5$)(CH$_2$C$_6$H$_5$)(THF) with K_{eq} values that are much greater than one.[26] The complex [Ba(C$_5$H*i*Pr$_4$)(I)(THF)$_2$]$_2$ resists ligand redistribution in tetrahydrofuran, but does scramble ligands in less coordinating solvents such as benzene.[27] Redistribution equilibria are also important for the heavier group 2 Grignard analogs.[28]

With regards to the design of heavier group 2 metal complexes for thin film growth applications, our previous study of M(η^5-L$^{t\mathrm{Bu}}$)$_2$[7b] and the results herein demonstrate that the L$^{t\mathrm{Bu}}$ ligand is very effective at blocking a face of the metal ion to which it coordinates toward further oligomerization. By contrast, the *t*Bu$_2$pz ligand does not provide the same degree of steric saturation as the L$^{t\mathrm{Bu}}$ ligand, which leads to oligomeric complexes containing various pyrazolato ligand coordination modes in the absence of neutral amine or ether donor ligands. While Ca$_3$(*t*Bu$_2$pz)$_6$, Sr$_4$(*t*Bu$_2$pz)$_8$, and Ba$_6$(*t*Bu$_2$pz)$_{12}$ are reported to be volatile,[9d] our experience with Ca(*t*Bu$_2$pz)$_2$(L$_n$)[6b] suggests that the vapor pressures are very low and probably not high enough for practical use in CVD processes employing thermal source delivery. Thus, pyrazolato ligands are not likely to be as promising as other donor ligands in the search for improved volatile group 2 CVD precursors.

Experimental Section

General Considerations: All reactions were performed under argon using either glovebox or Schlenk line techniques. M[N(SiMe$_3$)$_2$]$_2$(THF)$_2$ (M = Ca, Sr, Ba),[10] *N*-*tert*-butyl-4-(*tert*-butylimino)-2-penten-2-amine (L$^{t\mathrm{Bu}}$H),[11] and 3,5-di-*tert*-butylpyrazole[29] were prepared according to reported methods. ^{1}H and ^{13}C{^{1}H} NMR spectra were obtained at 400 and 100 MHz, respectively, in [D$_8$]-toluene. Infrared spectra were obtained using Nujol as the medium. Elemental analyses were performed by Midwest Microlab, Indianapolis, IN. Melting points were obtained with a Haake-Buchler HBI digital melting point apparatus and are uncorrected.

Synthesis of [(η^2-*t*Bu$_2$pz)Ca(μ-η^5:η^2-*t*Bu$_2$pz)(μ-η^2:η^2-*t*Bu$_2$pz)Ca(η^5-L$^{t\mathrm{Bu}}$)] (1): A 100-mL Schlenk flask was charged with Ca[N(SiMe$_3$)$_2$]$_2$(THF)$_2$ (0.420 g, 0.831 mmol) and toluene (30 mL). This solution was treated with L$^{t\mathrm{Bu}}$H (0.175 g, 0.831 mmol) and was stirred at ambient temperature for 3 h. The resultant solution was then treated with *t*Bu$_2$pzH (0.150 g, 0.831 mmol) in small portions and was further stirred for 18 h. The volatile components were removed under reduced pressure and the crude material was extracted with hexane (30 mL). The hexane extract was filtered through a 2-cm pad of Celite on a coarse glass frit to afford a colorless solution. The filtrate was concentrated to a volume of 10 mL and was stored at –30 °C for 24 h to afford **1** as colorless crystals {0.06 g, 17%, based on Ca[N(SiMe$_3$)$_2$]$_2$(THF)$_2$}: m.p. 184–186 °C (dec). IR (Nujol): $\tilde{\nu}$ = 1632 (m), 1500 (m), 1250 (m), 1215 (w), 1188 (w), 1007 (w), 976 (w), 810 (w), 797 (w), 767 (w) cm^{-1}. ^{1}H NMR ([D$_8$]toluene, 23 °C): δ = 1.45, 1.40, 1.34, 1.32, 1.28, 1.13 [pyrazolato and L$^{t\mathrm{Bu}}$ C(C*H*$_3$)$_3$], 1.99, 1.98, 1.96, 1.85 (L$^{t\mathrm{Bu}}$ C*H*$_3$), 4.60, 4.44, 4.22, 4.20 (L$^{t\mathrm{Bu}}$ β-C*H*), 6.22, 6.19, 6.08, 6.04, 5.98 (pyrazolato ring β-C*H*) ppm. C$_{46}$H$_{82}$Ca$_2$N$_8$ (827.36): C 66.78, H 9.99, N 13.54; found C 66.46, H 9.89, N 13.30.

Synthesis of [Sr(μ-η^5:η^2-*t*Bu$_2$pz)(η^5-L$^{t\mathrm{Bu}}$)]$_2$ (2): In a fashion similar to the preparation of **1**, treatment of Sr[N(SiMe$_3$)$_2$]$_2$(THF)$_2$ (0.459 g, 0.831 mmol) with L$^{t\mathrm{Bu}}$H (0.175 g, 0.831 mmol), followed by *t*Bu$_2$pzH (0.150 g, 0.831 mmol) in toluene (30 mL), afforded **2** as colorless crystals upon cooling of a hot toluene solution to –30 °C {0.20 g, 50%, based on Sr[N(SiMe$_3$)$_2$]$_2$(THF)$_2$}: m.p. 245–247 °C. IR (Nujol): $\tilde{\nu}$ = 1250 (m), 1210 (m), 1186 (m), 1025 (w), 994 (w), 797 (w), 768 (w), 757 (w) cm^{-1}. ^{1}H NMR ([D$_8$]toluene, 23 °C): δ = 1.30 [s, 36 H, L$^{t\mathrm{Bu}}$ C(C*H*$_3$)$_3$], 1.47 [s, 36 H, pyrazolato C(C*H*$_3$)$_3$], 1.99 (s, 12 H, C*H*$_3$), 4.19 (s, 2 H, β-C*H*), 6.26 (s, 2 H, pyrazolato ring C*H*) ppm. ^{13}C{^{1}H} NMR ([D$_8$]toluene, 23 °C): δ = 25.21 [s, C(*C*H$_3$)], 31.57 [s, pyrazolato C(*C*H$_3$)$_3$], 32.62 [s, pyrazolato *C*(CH$_3$)$_3$], 33.01 [s, L$^{t\mathrm{Bu}}$ C(*C*H$_3$)$_3$], 54.18 [s, L$^{t\mathrm{Bu}}$ *C*(CH$_3$)$_3$], 92.00 (s, β-*C*H), 102.62 (s, pyrazolato ring *C*H), 160.21 [s, pyrazolato ring *C*C(CH$_3$)$_3$], 164.37 (s, *C*CH$_3$) ppm. C$_{48}$H$_{88}$N$_8$Sr$_2$ (952.50): C 60.53, H 9.31, N 11.76; found C 59.50, H 9.05, N 11.41. In addition to the resonances reported for **2**, 13% of Sr(η^5-L$^{t\mathrm{Bu}}$)$_2$[7b] was also observed in the ^{1}H NMR spectrum at ambient temperature in [D$_8$]toluene, and was identified by comparison of its ^{1}H NMR resonances with those of authentic material.

Synthesis of [Ba(μ-η^5:η^2-*t*Bu$_2$pz)(η^5-L$^{t\mathrm{Bu}}$)]$_2$ (3): In a fashion similar to the preparation of **2**, treatment of Ba[N(SiMe$_3$)$_2$]$_2$(THF)$_2$ (1.00 g, 1.66 mmol) with L$^{t\mathrm{Bu}}$H (0.350 g, 1.66 mmol), followed by *t*Bu$_2$pzH (0.300 g, 1.66 mmol) in toluene (30 mL), afforded **3** as a colorless crystals from toluene (0.580 g, 66%, based on Ba[N(SiMe$_3$)$_2$]$_2$(THF)$_2$): m.p. 289–291 °C. IR (Nujol): $\tilde{\nu}$ = 1247 (w), 1208 (m), 1185 (m), 1042 (w), 1023 (w), 967 (w), 793 (m), 765 (m) cm^{-1}. ^{1}H NMR ([D$_8$]toluene, 23 °C): δ = 1.30 [s, 36 H, L$^{t\mathrm{Bu}}$ C(C*H*$_3$)$_3$], 1.47 [s, 36 H, pyrazolato C(C*H*$_3$)$_3$], 2.00 (s, 12 H, C*H*$_3$), 4.18 (s, 2 H, L$^{t\mathrm{Bu}}$ β-C*H*), 6.27 (s, 2 H, pyrazolato ring C*H*) ppm. ^{13}C{^{1}H} NMR ([D$_8$]toluene, 23 °C): δ = 24.76 [s, C(*C*H$_3$)], 31.63 [s, pyrazolato C(*C*H$_3$)$_3$], 32.31 [s, pyrazolato *C*(CH$_3$)$_3$], 32.88 [s, C(*C*H$_3$)$_3$], 54.27 [s, *C*(CH$_3$)$_3$], 90.41 (s, β-*C*H), 103.25 (s, pyrazolato ring *C*H), 157.86 [s, pyrazolato ring *C*C(CH$_3$)$_3$], 162.68 (s, *C*CH$_3$) ppm. C$_{48}$H$_{88}$Ba$_2$N$_8$ (1051.94): C 54.81, H 8.43, N 10.65; found C 54.88, H 8.47, N 10.38.

X-ray Crystallography: Crystals of **1–3** were grown as described above. Diffraction data were collected with a Bruker P4/CCD diffractometer equipped with Mo radiation and a graphite monochromator at –80 °C (**1**) or at ambient temperature with the crystals mounted in glass capillaries (**2** and **3**). A sphere of data was measured at 10–20 s/frame and 0.2–0.3° between frames. The frame data were indexed and integrated with the manufacturer's SMART, SAINT, and SADABS software.[30] All structures were refined using Sheldrick's SHELX-97 software.[31] In the model for **1**, one of the *tert*-butyl groups was severely disordered and was assigned partial atoms [C(20)–C(22)]. All three structures show typically large thermal parameters in the *tert*-butyl groups. All non-hydrogen atoms were refined anisotropically and the hydrogen atom positions were calculated. Complexes **2** and **3** occupy crystallographic inversion centers. CCDC-260847 (**1**), -260848 (**2**), and -260849 (**3**) contain the supplementary crystallographic data for this paper. These data can be obtained free of charge from The Cambridge Crystallographic Data Centre via www.ccdc.cam.ac.uk/data_request/cif.

van't Hoff Analysis of 2: A 5-mm NMR tube was charged with **2** (0.0150 g, 0.0157 mmol) and [D$_8$]toluene (0.85 mL) and was sealed with a plastic cap. ^{1}H NMR spectra were recorded between 46 and

 © 2005 Wiley-VCH Verlag GmbH & Co. KGaA, Weinheim

104 °C. For analysis of the data, see the text and Supporting Information.

Acknowledgments

We thank the U.S. Army Research Office (grant nos. DAAD19-01-1-0575 and W911NF-04-1-0332) for generous support of this research.

[1] For recent reviews of group 2 complexes and their applications in CVD, see: a) T. P. Hanusa, *Organometallics* **2002**, *21*, 2559–2571; b) J. S. Matthews, W. S. Rees, Jr., *Adv. Inorg. Chem.* **2000**, *50*, 173–192; c) W. A. Wojtczak, P. F. Pfleig, M. J. Hampden-Smith, *Adv. Organomet. Chem.* **1996**, *40*, 215–340; d) D. Schulz, T. J. Marks, *Adv. Mater.* **1994**, *6*, 719–730; e) A. R. Barron, W. S. Rees, Jr., *Adv. Mater. Opt. Electron.* **1993**, *2*, 271–288.

[2] Leading references to group 2 CVD precursors with cyclopentadienyl ligands: a) T. Hatanpää, M. Vehkamäki, I. Mutikainen, J. Kansikas, M. Ritala, M. Leskelä, *J. Chem. Soc., Dalton Trans.* **2004**, 1181–1188; b) M. Vehkamäki, T. Hänninen, M. Ritala, M. Leskelä, T. Sajavaara, E. Rauhala, J. Keinonen, *Chem. Vap. Deposition* **2001**, *7*, 75–80; c) M. Vehkamäki, T. Hänninen, M. Ritala, M. Leskelä, *Electrochem. Solid-State Lett.* **1999**, *2*, 504–506.

[3] Recent selected references to group 2 CVD precursors with β-diketonato and β-ketoiminato ligands: a) A. Kosola, M. Putkonen, L.-S. Johansson, L. Niinistö, *Appl. Surf. Sci.* **2003**, *211*, 102–112; b) V. Sannila, J. Ihanus, M. Ritala, M. Leskelä, *Chem. Vap. Deposition* **1998**, *4*, 227–233; c) A. R. Teren, J. A. Belot, N. L. Edleman, T. J. Marks, B. W. Wessels, *Chem. Vap. Deposition* **2000**, *6*, 175–177; d) D. B. Studebaker, D. A. Neumayer, B. J. Hinds, C. L. Stern, T. J. Marks, *Inorg. Chem.* **2000**, *39*, 3148–3157; e) J. A. Belot, D. A. Neumayer, C. J. Reedy, D. B. Studebaker, B. J. Hinds, C. L. Stern, T. J. Marks, *Chem. Mater.* **1997**, *9*, 1638–1648.

[4] For selected, leading references, see: a) X. He, B. C. Noll, A. Beatty, R. E. Mulvey, K. W. Henderson, *J. Am. Chem. Soc.* **2004**, *126*, 7444–7445; b) S. Harder, S. Müller, E. Hübner, *Organometallics* **2004**, *23*, 178–183; c) M. S. Hill, P. B. Hitchcock, *Chem. Commun.* **2003**, 1758–1759; d) F. Feil, S. Harder, *Macromolecules* **2003**, *36*, 3446–3448; e) M. H. Chisholm, J. Gallucci, K. Phomphrai, *Chem. Commun.* **2003**, 48–49; f) F. Feil, S. Harder, *Eur. J. Inorg. Chem.* **2003**, 3401–3408; g) S. Harder, F. Feil, *Organometallics* **2002**, *21*, 2268–2274; h) S. Harder, F. Feil, A. Weeber, *Organometallics* **2001**, *20*, 1044–1046; i) F. Feil, S. Harder, *Organometallics* **2000**, *19*, 5010–5015.

[5] a) S. Harder, *Angew. Chem. Int. Ed.* **2003**, *42*, 3430–3434; b) S. Harder, *Organometallics* **2002**, *21*, 3782–3787.

[6] a) D. Pfeiffer, M. J. Heeg, C. H. Winter, *Angew. Chem. Int. Ed.* **1998**, *37*, 2517–2519; b) D. Pfeiffer, M. J. Heeg, C. H. Winter, *Inorg. Chem.* **2000**, *39*, 2377–2384.

[7] a) H. M. El-Kaderi, M. J. Heeg, C. H. Winter, *Organometallics* **2004**, *23*, 3488–3495; b) H. M. El-Kaderi, A. Xia, M. J. Heeg, C. H. Winter, *Organometallics* **2004**, *23*, 4995–5002.

[8] For reviews of pyrazolato complexes, see: a) F. Nief, *Eur. J. Inorg. Chem.* **2001**, 891–904; b) J. E. Cosgriff, G. B. Deacon, *Angew. Chem. Int. Ed.* **1998**, *37*, 286–287; c) G. La Monica, G. A. Ardizzoia, *Progr. Inorg. Chem.* **1997**, *46*, 151–238; d) A. P. Sadimenko, S. S. Basson, *Coord. Chem. Rev.* **1996**, *147*, 247–297; e) S. Trofimenko, *Progr. Inorg. Chem.* **1986**, *34*, 115–210; f) S. Trofimenko, *Chem. Rev.* **1972**, *72*, 497–508.

[9] a) A. Steiner, G. T. Lawson, B. Walfort, D. Leusser, D. Stalke, *J. Chem. Soc., Dalton Trans.* **2001**, 219–221; b) A. Steiner, D. Stalke, *Inorg. Chem.* **1995**, *34*, 4846–4853; c) J. Hitzbleck, A. Y. O'Brien, C. M. Forsyth, G. B. Deacon, K. Ruhlandt-Senge, *Chem. Eur. J.* **2004**, *10*, 3315–3323; d) J. Hitzbleck, G. B. Deacon, K. Ruhlandt-Senge, *Angew. Chem. Int. Ed.* **2004**, *43*, 5218–5220.

[10] a) B. A. Vaartstra, J. C. Huffman, W. E. Streib, K. G. Caulton, *Inorg. Chem.* **1991**, *30*, 121–125; b) M. Westerhausen, *Inorg. Chem.* **1991**, *30*, 96–101.

[11] a) N. Kuhn, J. Fahl, S. Fuchs, M. Steimann, G. Henkel, A. H. Maulitz, *Z. Anorg. Allg. Chem.* **1999**, 2108–2114; b) N. Kuhn, H. Lanfermann, P. Schmitz, *Liebigs Ann. Chem.* **1987**, 727–728.

[12] R. A. Williams, T. P. Hanusa, J. C. Huffman, *Organometallics* **1990**, *9*, 1128–1134.

[13] J. R. Perera, M. J. Heeg, H. B. Schlegel, C. H. Winter, *J. Am. Chem. Soc.* **1999**, *121*, 4536–4537.

[14] F. Weber, H. Sitzmann, M. Schultz, C. D. Sofield, R. A. Andersen, *Organometallics* **2002**, *21*, 3139–3146.

[15] For example, see: I. N. Levine, *Physical Chemistry*, 3rd ed., McGraw-Hill, New York, **1988**, pp. 177–180.

[16] a) A. G. Avent, M. R. Crimmin, M. S. Hill, P. B Hitchcock, *Dalton Trans.* **2005**, 278–284; b) M. R. Crimmin, I. J. Casely, M. S. Hill, *J. Am. Chem. Soc.* **2005**, *127*, 2042–2043; c) A. G. Avent, M. R. Crimmin, M. S. Hill, P. B. Hitchcock, *Dalton Trans.* **2004**, 3166–3168; d) M. S. Hill, P. B. Hitchcock, *Chem. Commun.* **2003**, 1758–1759.

[17] M. H. Chisholm, J. C. Galucci, K. Phomphrai, *Inorg. Chem.* **2004**, *43*, 6717–6725.

[18] W. Clegg, S. J. Coles, E. K. Cope, F. S. Mair, *Angew. Chem. Int. Ed.* **1998**, *37*, 796–798.

[19] a) L. Bourget-Merle, M. F. Lappert, J. R. Severn, *Chem. Rev.* **2002**, *102*, 3031–3066.

[20] a) G. B. Nikiforov, H. W. Roesky, D. Vidovic, J. Magull, *J. Mol. Struct.* **2003**, *656*, 155–160; b) P. B. Hitchcock, M. F. Lappert, D.-S. Liu, *J. Chem. Soc., Chem. Commun.* **1994**, 2637–2638; c) M. Rahim, M. J. Taylor, S. Xin, S. Collins, *Organometallics* **1998**, *17*, 1315–1323; d) L. Kakaliou, W. J. Scanlon, B. Qian, S. W. Baek, M. R. Smith III, D. H. Motry, *Inorg. Chem.* **1999**, *38*, 5964–5977; e) R. Vollmerhaus, M. Rahim, R. Tomaszewski, S. Xin, N. J. Taylor, S. Collins, *Organometallics* **2000**, *19*, 2161–2169.

[21] G. B. Deacon, C. M. Forsyth, A. Gitlits, B. W. Skelton, A. H. White, *Dalton Trans.* **2004**, *8*, 1239–1247.

[22] Ionic radii were taken from: N. N. Greenwood, A. Earnshaw, *Chemistry of the Elements*, 2nd ed., Butterworth-Heinemann, Oxford, **1997**, pp. 111, 1233.

[23] G. B. Deacon, A. Gitlits, P. W. Roesky, M. R. Bürgstein, K. C. Lim, B. W. Skelton, A. H. White, *Chem. Eur. J.* **2001**, *7*, 127–138.

[24] M. J. McCormick, S. C. Sockwell, C. E. H. Davis, T. P. Hanusa, J. C. Huffman, *Organometallics* **1989**, *8*, 2044–2049.

[25] D. J. Burkey, E. K. Alexander, T. P. Hanusa, *Organometallics* **1994**, *13*, 2773–2786.

[26] A. Weeber, S. Harder, H. H. Brintzinger, K. Knoll, *Organometallics* **2000**, *19*, 1325–1332.

[27] H. Sitzmann, F. Weber, M. D. Walter, G. Wolmershäuser, *Organometallics* **2003**, *22*, 1931–1936.

[28] a) J. S. Alexander, K. Ruhlandt-Senge, *Eur. J. Inorg. Chem.* **2002**, 2761–2764; b) M. Westerhausen, *Angew. Chem. Int. Ed.* **2001**, *40*, 2975–2977.

[29] J. Elguéro, E. Gonzalez, R. Jacquier, *Bull. Soc. Chim. Fr.* **1968**, 707.

[30] *APEX II*, *SMART*, *SAINT*, and *SADABS* collection and processing programs are distributed by Bruker AXS, Inc., Madison, Wisconsin, USA.

[31] G. Sheldrick, SHELX-97, University of Göttingen, Germany, **1997**.

Received January 26, 2005

 © 2005 Wiley-VCH Verlag GmbH & Co. KGaA, Weinheim

First-Row Transition Metal Bis(amidinate) Complexes; Planar Four-Coordination of Fe^{II} Enforced by Sterically Demanding Aryl Substituents

Christian A. Nijhuis,[a] Erica Jellema,[a] Timo J. J. Sciarone,[a] Auke Meetsma,[a] Peter H. M. Budzelaar,[b] and Bart Hessen*[a]

Keywords: Transition metals / Solid-state structures / Ligand effects / Amidinate / Density functional calculations

The sterically hindered benzamidinate ligand $[PhC(NAr)_2]^-$ (Ar = 2,6-*i*$Pr_2C_6H_3$) has been employed to prepare bis(amidinate) complexes $[\{PhC(NAr)_2\}_2M]$ of the divalent first-row transition metals Cr–Ni (**1**–**5**). For Cr (planar), Mn and Co (tetrahedral) the observed structures follow the electronic preference for the metal ion in its highest spin multiplicity, as determined by DFT calculations. Remarkably, the Fe derivative adopts a distorted planar structure while retaining the high-spin (S = 2) configuration. This rare combination is due to reduced interligand steric interactions in the planar vs. the tetrahedral structure, combined with a relatively small electronic preference of Fe^{II} for the tetrahedral environment. Thus, the simple bidentate ligand *N*,*N*′-diarylbenzamidinate provides a convenient means to make this unusual species accessible for further study.

(© Wiley-VCH Verlag GmbH & Co. KGaA, 69451 Weinheim, Germany, 2005)

Introduction

Amidinate anions, with general formula $[R'NC(R)NR'']^-$, have been employed widely as ligands in transition metal and in main group chemistry.[1,2] Their steric and electronic properties are readily modified through variation of the substituents on the carbon and nitrogen atoms, and they have been employed as ancillary ligands in various catalytic conversions, e.g. oligomerisation[3,4] or polymerisation[5–20] of olefins or of cyclic esters.[21,22] Due to the geometric constraints of the NCN ligand backbone, amidinates have small N–M–N bite angles (typically 63–65°). They have a rich coordination geometry in which both chelating and bridging coordination modes can be achieved. The latter has allowed the synthesis of a range of dinuclear complexes with short metal–metal separations.[23–34] The balance between chelating and bridging coordination is critically governed by the substitution pattern of the amidinate ligand. Steric interactions between the substituents on the carbon and nitrogen atoms influence the orientation of the nitrogen lone pairs. Large substituents on the carbon atom induce a convergent orientation of the lone pairs (favouring chelation), while small substituents lead to a more parallel orientation of the lone pairs (enabling bridging).[34,35]

The substituents on the amidinate nitrogen atoms can be used to tune the steric demand of the ligand, influencing the coordination geometry of the metal centre in bis(amidinate) complexes with chelating amidinate ligands. Thus, Winter et al. have demonstrated that an increase in steric demand of the alkyl substituent R in $[\{MeC(NR_2)\}_2Cr]$ from R = *i*Pr to *t*Bu results in a change from square-planar to tetrahedral coordination of the high-spin Cr^{II} centre.[36] For R = *t*Bu, interligand steric interactions apparently become dominant over an electronic preference for square-planar coordination.[37]

The steric hindrance imparted by alkyl substituents on the amidinate nitrogen atoms has its main effect in the NMN coordination plane. To effect steric shielding above and below this coordination plane, two approaches are possible. Introduction of a terphenyl substituent on the amidinate backbone *carbon* atom provides such shielding (as shown by Arnold et al. in complexes of Li^I, Mg^{II}, Al^{III}, Y^{III} and a series of first-row transition metals),[38–43] but relatively remote from the metal–ligand bonds. Another approach is the use of *ortho*-disubstituted aryl groups on the *nitrogen* atoms. By virtue of the perpendicular orientation of the aryl moieties with respect to the NCN backbone (especially when relatively large substituents on the carbon atom are used), the *ortho* substituents provide steric protection to the sites above and below the coordination plane. The 2,6-(diisopropyl)phenyl group (Ar = 2,6-*i*$Pr_2C_6H_3$) has proven to be very efficient in this respect, and has been used successfully in the development of late transition metal olefin polymerisation catalysts with neutral diimine li-

[a] Dutch Polymer Institute, Center for Catalytic Olefin Polymerisation, Stratingh Institute for Chemistry and Chemical Engineering, University of Groningen,
Nijenborgh 4, 9747 AG Groningen, Netherlands
Fax: +31-50-363-4315
E-mail: hessen@chem.rug.nl
[b] Dutch Polymer Institute, Institute for Molecules and Materials, Metal-Organic Chemistry, Radboud University Nijmegen,
P. O. Box 9010, 6500 GL Nijmegen, Netherlands
Fax: +31-24-355-3450
E-mail: p.budzelaar@science.ru.nl

Supporting information for this article is available on the WWW under http://www.eurjic.org or from the author.

gands[44–47] and in the synthesis of low-coordinate, electron-deficient metal complexes stabilised by β-diketiminates.[48] With amidinate ligands, these substituents have been used only sparingly thus far. The amidines $[RC(NAr)_2]H$ (R = CH_3, 4-MeC_6H_4, 4-$MeOC_6H_4$) were synthesised by Boeré et al., who also reported some initial studies of their Mo^0 coordination chemistry.[49] The amidinates $[tBuC(NAr)_2]^-$, $[4\text{-}MeC_6H_4C(NAr)_2]^-$ and $[PhC(NAr)_2]^-$ have been used as ligands for Al^{III},[50] Ni^{II},[7] group 3 and lanthanide metals.[9,20,22] Due to the positioning of the steric hindrance of these ligands, interesting interligand steric interactions may be anticipated when two of these ligands are attached to (relatively small) first-row transition metals.

Bis(amidinate) complexes of the divalent first-row transition metal ions have been found to adopt either a (distorted) tetrahedral or a (distorted) square-planar geometry. The former is observed for bis(amidinates) complexes of Mn^{II}–Co^{II},[41,51–54] while for bis(amidinate) complexes of Cr^{II} and Ni^{II} both types of geometry have been found to occur.[34,36,41,55–58] In this paper we describe the synthesis and characterisation of the bis(benzamidinate) complexes $[\{PhC(NAr)_2\}M]$ (M = Cr–Ni, Ar = 2,6-$iPr_2C_6H_3$, Figure 1). Interligand interactions between the sterically demanding amidinate ligands are found to enforce a distorted square-planar geometry onto high-spin Fe^{II}, which is exceptional for this ion when bound to two bidentate ligands.

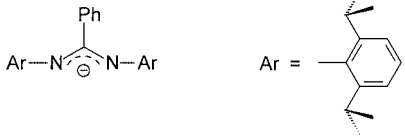

Figure 1. *N*,*N*′-Bis(2,6-diisopropylphenyl)benzamidinate

Results and Discussion

Synthesis

The bis(amidinate) complexes $[\{PhC(NAr)_2\}_2M]$ [M = Cr (**1**), Mn (**2**), Fe (**3**), Co (**4**)] were obtained by reaction of the anhydrous metal chlorides with the lithium amidinate $Li[PhC(NAr)_2]$ (Scheme 1). The latter was generated in situ by deprotonation of the amidine by *n*BuLi in THF. The products were isolated by extraction with hexanes or pentane and crystallisation from the same solvents, affording the air-sensitive, crystalline bis(amidinate) complexes in 48 (**2**) to 91% (**3**) isolated yield. The Ni complex $[\{PhC(NAr)_2\}_2Ni]$ (**5**) was prepared from the lithium amidinate and $[(DME)NiBr_2]$. This complex was obtained in 47% yield after crystallisation from toluene.

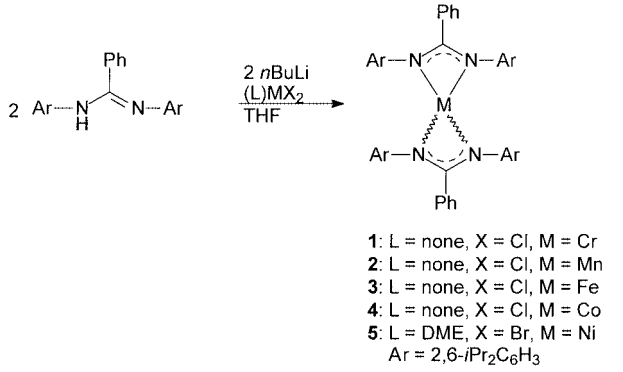

Scheme 1.

The complexes were characterised by elemental analysis, X-ray diffraction, ^1H NMR and IR spectroscopy and solid-state variable-temperature magnetic susceptibility measurements.

Molecular Structures

The molecular structures of the bis(amidinate) complexes were determined by single-crystal X-ray diffraction. Geometric parameters for the structures displayed in Figure 2 are given in Table 1.

All structures show symmetric, chelating coordination of the amidinate ligands with the aryl and phenyl substituents making angles of 61–86° (Ar) and 23–51° (Ph) with the N–M–N coordination planes. The C–N bonds in the amidinate backbones do not differ significantly in length and the nitrogen atoms deviate only slightly from planarity ($\Sigma_{\angle N}$ = 354–360°), suggesting full electron delocalisation in the NCN framework. The bite angle of the ligand is restricted to 64–69° by the geometry of the amidinate backbone.

The Mn and Co complexes **2** and **4** are best described as distorted tetrahedral, in which the NMN coordination planes of the two amidinate ligands are inclined at 74.18(15)° (Mn) and 69.5(4)° (Co), respectively. The average bite angles in the Mn complex (63.59°) are ca. 2° smaller than those in the Co analogue (66.3°) reflecting the smaller ionic radius of the latter metal ion.[59] Consistently, the M–N distances in the Mn^{II} complex are ca. 0.1 Å longer than in the and Co^{II} derivative.

The Cr and Ni complexes **1** and **5** show a distorted planar arrangement of the four coordinating nitrogen atoms. For bis(amidinate) derivatives of Cr^{II}, this coordination geometry is commonly observed,[34,36,57] but planar coordination in Ni^{II} bis(amidinates) is less common, the only example being the complex $[\{PhC(NXyl)(NSiMe_3)\}_2Ni]$ (Xyl = 2,6-$Me_2C_6H_3$) reported recently by Lee et al.[56] The amidinate NMN coordination planes are inclined at 7.73(10)° (Cr) and 4.13(13)° (Ni), respectively. The average bite angles in the Cr complex are approximately 4° smaller than in the Ni complex, consistent with the smaller ionic radius for square planar Ni^{II}.[59] The same trend is observed in the M–N bond lengths, which are significantly shorter for the Ni derivative.

 © 2005 Wiley-VCH Verlag GmbH & Co. KGaA, Weinheim

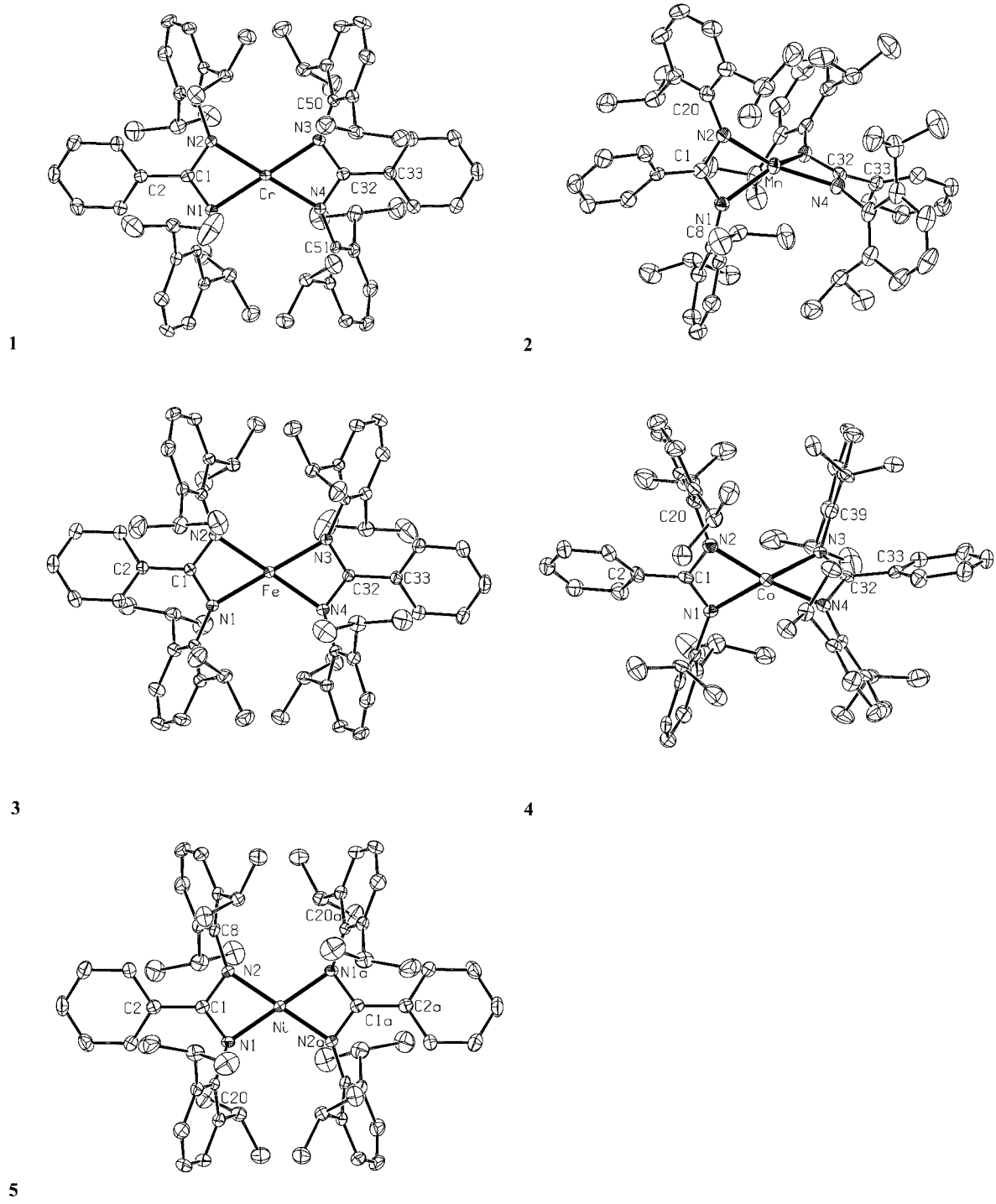

Figure 2. Molecular structures of complexes [{PhC(NAr)$_2$}$_2$M] (**1–5**) (50% ellipsoids). Hydrogen atoms and cocrystallised solvent molecules have been omitted for clarity.

Surprisingly, the Fe complex **3** is also found to adopt a distorted-planar coordination geometry. The angle between the two NMN coordination planes of 12.37(8)° is slightly larger than for the Cr and Ni analogues, but still warrants a description of **3** as a distorted planar structure. The planar coordination geometry in **3** is in sharp contrast to the other homoleptic bis(amidinate) complexes of Fe^{II},[51–54] which are exclusively tetrahedral. Planar structures for Fe^{II} are commonly found with (macrocyclic) tetradentate donor ligands, which are preorganised for this geometry.[60,61] Examples include salen [salen = *N*,*N*′-ethylenebis(salicylideneimine)],[62] calix[4]arene,[63] porphyrins,[64,65] phthalocyanines[66–69] and a number of macrocyclic bis(β-diiminato) ligands.[70–73] Planar coordination of Fe^{II} by two bidentate

 © 2005 Wiley-VCH Verlag GmbH & Co. KGaA, Weinheim

Table 1. Selected bond lengths and angles for bis(amidinate) complexes [{PhC(NAr)$_2$}$_2$M].

Distances [Å]	Cr (**1**)	Mn (**2**)	Fe (**3**)	Co (**4**)	Ni (**5**)[a]
M–N1	2.0577(16)	2.111(3)	2.0662(14)	1.989(7)	1.918(2)
M–N2	2.0546(18)	2.118(3)	2.0532(16)	2.029(6)	1.9288(18)
M–N3	2.0575(16)	2.101(3)	2.0639(12)	1.998(7)	1.918(2)
M–N4	2.0583(18)	2.123(3)	2.0528(16)	2.012(6)	1.9288(18)
N1–C1	1.340(3)	1.343(4)	1.335(2)	1.317(10)	1.344(3)
N2–C1	1.344(2)	1.336(4)	1.338(2)	1.342(12)	1.338(3)
N3–C32	1.343(3)	1.340(4)	1.336(2)	1.322(9)	1.344(3)
N4–C32	1.345(2)	1.323(4)	1.338(2)	1.346(11)	1.338(3)
Angles(°)					
N1–M–N2	64.87(7)	63.55(9)	65.06(6)	66.2(3)	68.63(8)
N1–M–N3	177.08(6)	133.73(10)	174.93(5)	140.4(3)	177.12(8)
N1–M–N4	115.70(7)	125.83(10)	114.72(6)	129.3(3)	111.42(8)
N2–M–N3	114.71(7)	132.3(1)	116.11(5)	123.7(3)	111.42(8)
N2–M–N4	174.69(6)	152.41(10)	171.86(5)	146.8(2)	178.29(9)
N3–M–N4	65.00(7)	63.63(9)	64.90(5)	66.4(3)	68.63(8)
M–N1–C1	92.25(11)	92.00(19)	91.25(10)	92.4(6)	91.88(15)
M–N1–C8	141.74(14)	140.4(2)	142.12(12)	140.2(5)	138.35(16)
C1–N1–C8	123.99(17)	123.2(3)	124.56(15)	124.7(7)	124.0(2)
M–N2–C1	92.27(13)	91.92(19)	91.75(11)	89.9(4)	91.57(14)
M–N2–C20	138.69(13)	141.3(2)	141.81(11)	142.9(6)	139.36(18)
C1–N2–C20	124.91(17)	124.7(3)	124.49(15)	123.9(6)	124.5(2)
M–N3–C32	92.20(11)	91.55(18)	91.59(9)	92.0(5)	91.88(15)
M–N3–C39	140.60(14)	143.2(2)	142.69(11)	137.6(5)	138.35(16)
C32–N3–C39	124.11(17)	121.5(3)	124.50(13)	124.8(7)	124.0(2)
M–N4–C32	92.09(13)	91.08(19)	92.03(11)	90.7(4)	91.57(14)
M–N4–C51	141.20(13)	143.6(2)	140.03(11)	143.1(6)	139.36(18)
C32–N4–C51	123.91(17)	123.7(3)	125.18(15)	124.8(6)	124.5(2)
N1–C1–N2	110.52(17)	112.5(3)	111.93(15)	111.2(7)	107.9(2)
N1–C1–C2	124.97(17)	122.4(3)	124.08(14)	124.5(8)	125.7(2)
N2–C1–C2	124.49(19)	125.2(3)	123.99(16)	124.3(7)	126.4(2)
N3–C32–N4	110.69(17)	113.5(3)	111.42(14)	110.7(7)	107.9(2)
N3–C32–C33	124.66(17)	122.6(3)	124.51(14)	124.8(8)	125.7(2)
N4–C32–C33	124.64(18)	123.8(3)	124.06(15)	124.4(7)	126.4(2)

[a] For ease of comparison, the atoms of the Ni complex (**5**) have been labelled here in analogous fashion to that in the other complexes, in spite of its crystallographic C_2 symmetry (N1_a → N3, N2_a → N4, C1_a → C32 etc.).

ligands is exceptional, although some bis(dithiolato)Fe^{II} dianions have been structurally characterised as distorted square-planar.[74,75]

A prominent feature of the complexes with the planar structure, **1**, **3** and **5**, is that the Ar substituents are all tilted relative to the coordination plane to minimise interligand repulsion by interlocking the *i*Pr substituents. This imparts to these compounds an approximate D_2 symmetry. It is seen by NMR spectroscopy that this behaviour is also present in solution (vide infra).

Magnetic Properties

Except for the diamagnetic Ni derivative **5**, all the bis(amidinate) derivatives reported here are paramagnetic. Variable-temperature magnetic susceptibility measurements were performed on crystalline samples of **1**–**4**. In view of the low symmetry of the complexes, *d*-orbital degeneracy is expected to be largely removed, thus quenching most orbital contributions to the ground state. Normal Curie–Weiss behaviour is therefore anticipated. Indeed, plots of χ^{-1} vs. T in the range 25–300 K (Figure 3) show good linear correlation for the Cr, Mn and Fe complexes with θ = –2.3, –1.3 and 2.5 K, respectively. For the Co derivative **4** a departure from the Curie–Weiss law is seen at elevated temperatures. This behaviour indicates the presence of a temperature-independent paramagnetism (TIP) contribution, which is not unusual for tetrahedral Co^{II}.[76] Over the temperature range of 25–175 K, the susceptibility of **4** can be described by Curie–Weiss behaviour with θ = –5.6 K.

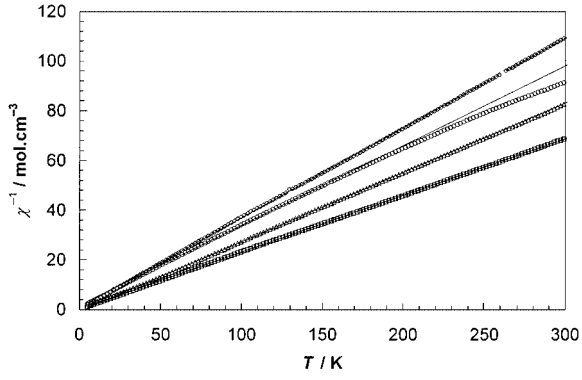

Figure 3. Temperature dependence of reciprocal susceptibility for **1** (diamonds), **2** (squares), **3** (triangles) and **4** (circles). Solid lines represent best fits to Curie–Weiss law.

The room temperature magnetic moments of the complexes **1** (4.7 μ_B), **2** (5.9 μ_B), **3** (5.4 μ_B) and **4** (5.1 μ_B) are

 © 2005 Wiley-VCH Verlag GmbH & Co. KGaA, Weinheim

indicative of maximum spin multiplicity for all four compounds. The observed magnetic moments for **1**, **3** and **4** deviate noticeably from the spin only values [4.90 μ_B for S = 2 (Cr and Fe) or 3.87 μ_B for S = 3/2 (Co)], but are well within the ranges usually observed for high-spin d^4, d^6 and d^7 metals.[77]

The high spin (S = 2) ground state of planar bis(amidinate) **3** contrasts with the more usual observation of an intermediate spin state (S = 1) for Fe^{II} complexes with this geometry,[60,61] and is more common for tetrahedral Fe^{II}.[37,78] The planar Fe^{II} complexes of N_4 macrocycles and dithiolates all exhibit intermediate spin states,[64,66–75] with the planar, but high-spin, salen[62] and calix[4]arene[63] complexes of Fe^{II} constituting the only exceptions.

^{1}H NMR Spectroscopy

The room-temperature ^{1}H NMR spectrum of the diamagnetic Ni complex **5** in [D_6]benzene shows two septuplets for the isopropyl methine protons and four doublets for the isopropyl methyl protons. This is consistent with the approximate D_2 symmetry observed in the solid state in which the aromatic rings are tilted with respect to the N_4Ni coordination plane. This inclination establishes a propeller-like arrangement of the six aromatic rings, thus imparting a screw-sense to the molecule. Apparently, libration of the aryl groups, inverting the screw sense through a D_{2h}-symmetric transition state (Figure 4), is slow on the NMR time scale at ambient temperature. Warming a solution of **5** in [D_8]toluene results in gradual broadening of the isopropyl resonances, but coalescence is not yet reached at 110 °C. Nevertheless, slow chemical exchange of the two isopropyl methine and the two sets of methyl signals is confirmed by positive cross-peaks in the EXSY 2D-spectrum.

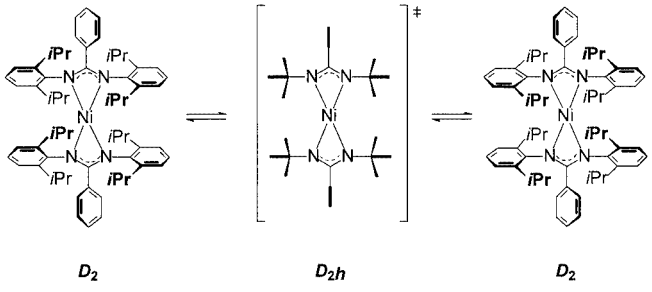

Figure 4. Epimerisation process in [{PhC(NAr)$_2$}$_2$Ni] (**5**).

The rate constant for the interconversion of the enantiomers k = 2.25(38) s^{-1} at 338 K was obtained by plotting the extent of exchange vs. the mixing time.[79] The free energy of activation $\Delta G^{\ddagger}_{338}$ = 80.9(4) kJ·mol^{-1} was calculated from the rate constant k.[80]

In contrast to the Ni complex, the paramagnetic bis(amidinates) **1**–**4** exhibit broad, shifted lines in their ^{1}H NMR spectra in [D_6]benzene. The Cr complex **1** shows resonances in the region +20 to –10 ppm. Severe overlap of the resonances renders the spectrum uninformative. The resonances of the Mn derivative **2** appear in the same spectral region, with even more line-broadening and inherent overlap of resonances. In contrast, the Fe and Co bis(amidinate) complexes display spectra that consist mainly of well-separated, broad singlets. The chemical shifts in the ^{1}H NMR spectrum of the Fe complex **3** span a range from ca. +60 to –30 ppm, displaying 11 lines. For the Co complex **4**, twelve lines are observed from ca. +120 ppm to –140 ppm. Full interpretation of these spectra is complicated, but the number of resonances indicates that the solution structures have symmetries lower than D_{2h} (**3**) and D_{2d} (**4**). This strongly suggests that also for the Fe and the Co derivatives the sterically demanding aryl substituents cause restricted motion of the aryl rings in solution.

Calculations

DFT calculations were used to obtain more insight into the factors that determine the coordination geometry of these complexes. In order to separate electronic from steric contributions, calculations were performed on the model complexes [{HC(NH)$_2$}$_2$M] containing an unsubstituted formamidinate ligand. The system was studied at the B3LYP/SV level using the GAMESS-UK program,[81] using the spin-restricted (S = 0) or spin-unrestricted ($S > 0$) formalism; see Exp. Sect. for details. For every metal, both planar and perpendicular geometries were optimised (constrained to D_{2h} and D_{2d} symmetry, respectively); the spin states assumed for these calculations were the ones found experimentally for the fully substituted system. In Table 2, the geometries calculated to be most stable for the model system are compared to those observed experimentally. The energy differences between the calculated perpendicular and planar geometries are included.

Table 2. Relative energies of tetrahedral vs. planar geometries of [{HC(NH)$_2$}$_2$M] by DFT calculations.

	X-ray [{PhC(NAr)$_2$}$_2$M]	S	B3LYP/SV [{HC(NH)$_2$}$_2$M]	$\Delta E_{\text{tet.–pla}n}$ [kJ·mol^{-1}]
Cr	planar	2	planar	100
Mn	tetrahedral	5/2	tetrahedral	–27.3
Fe	planar	2	tetrahedral	–10.1
Co	tetrahedral	3/2	tetrahedral	–23.2
Ni	planar	0	planar	–[a]

[a] No reasonable orbital occupation for perpendicular S = 0 structure.

For the model complexes, most of the geometries predicted on electronic grounds match the experimental ones, except for Fe (Table 2). However, the calculated energy difference between the two geometries is significantly smaller for Fe than for either Mn or Co. These results for the model system indicate that the observed geometries are determined mainly by the intrinsic electronic preference of the metal. For the special case of Fe, where this preference is calculated to be small, steric factors probably dominate; these seem to favour the planar structure due to a more efficient reduction of interligand repulsion by tilting of the aryl substituents.

 © 2005 Wiley-VCH Verlag GmbH & Co. KGaA, Weinheim

Decrease of Ligand Size

To see whether a slight decrease in ligand steric demand could already cause a reversion of the Fe^{II} bis(amidinate) structure to distorted tetrahedral, the asymmetric amidinate ligand $[PhC(NAr)(NXyl)]^-$ (Ar = 2,6-$iPr_2C_6H_3$, Xyl = 2,6-$Me_2C_6H_3$) was prepared. Reaction of $FeCl_2$ with 2 equiv. of the amidinate lithium salt resulted in formation of *cis*-$[\{PhC(NAr)(NXyl)\}_2Fe]$ (**6**, Scheme 2) that was characterised by single-crystal X-ray diffraction.

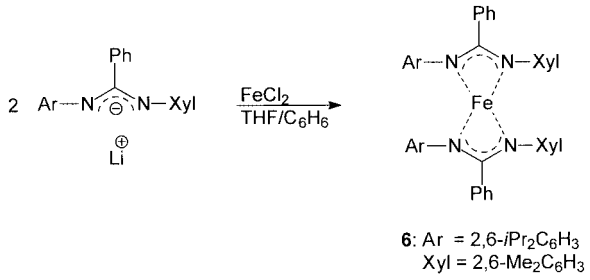

6: Ar = 2,6-$iPr_2C_6H_3$
Xyl = 2,6-$Me_2C_6H_3$

Scheme 2.

The molecular structure of **6** is shown in Figure 5 and selected bond angles and bond lengths are listed in Table 3. It is seen that even with this smaller, asymmetric ligand, the complex still adopts a distorted square-planar geometry. Remarkably, the two 2,6-$iPr_2C_6H_3$ groups are located on the same side of the molecule, with their *i*Pr substituents interlocking in a similar fashion as observed in complex **3**. The NFeN coordination planes in **6** are inclined at an angle of 14.21(6)°, which is only about 2° larger than in **3**. The room-temperature magnetic moment of **6** is 5.6 μ_B, indicative of high-spin Fe^{II}. Despite the difference in steric demand of the substituents, the two Fe–N distances in **6** are essentially equal, but the interligand N–Fe–N angle is noticeably larger on the side with the Ar substituents [125.51(4)°] than on the side with the Xyl substituents [105.97(4)°]. As is the case in the other complexes, the NAr nitrogen atom deviates slightly from planarity ($\Sigma_{\angle N1}$ = 354.64°), whereas the NXyl nitrogen atom is close to perfectly planar ($\Sigma_{\angle N2}$ = 359.03°).

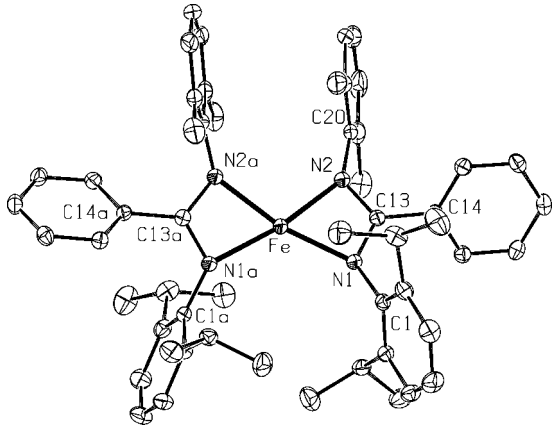

Figure 5. Molecular structure of [{PhC(NAr)(NXyl)}Fe] (**6**) (50% ellipsoids). Hydrogen atoms and cocrystallised benzene molecule have been omitted for clarity.

Table 3. Selected interatomic distances and angles for $[\{Ph(NAr)(NXyl)\}_2Fe]$ (**6**).

Distances [Å]			
Fe–N1	2.0639(10)	N1–C13	1.3408(14)
Fe–N2	2.0697(10)	N2–C13	1.3280(14)
Angles [°]			
N1–Fe–N2	64.82(4)	Fe–N2–C13	91.51(7)
N1–Fe–N1_a	125.51(4)	Fe–N2–C20	140.27(8)
N2–Fe–N2_a	105.97(4)	C13–N2–C20	127.25(10)
N1–Fe–N2_a	167.58(4)	N1–C13–N2	112.23(10)
Fe–N1–C1	140.02(8)	N1–C13–C14	123.71(10)
Fe–N1–C13	91.40(7)	N2–C13–C14	124.06(10)
C1–N1–C13	123.22(9)		

Conclusions

The coordination geometry of the bis(amidinate) complexes of the divalent first-row transition metal ions is governed by a subtle balance between electronic and steric factors. This balance can be tipped by variation of the substituents on the amidinate nitrogen atoms. It was shown by Winter et al. that substituents with steric demand in the amidinate plane (*t*Bu) can force an ion with an electronic preference for a planar geometry (Cr^{II}) to adopt a tetrahedral structure.[36] The work presented here shows that substituents with steric demand above and below the amidinate plane (2,6-$iPr_2C_6H_3$) can force an ion with a mild preference for a tetrahedral geometry (Fe^{II}) to adopt a planar one. Apparently, in this geometry the interligand steric interactions can be more effectively diminished by tilting the aryl rings to allow interlocking of the *i*Pr substituents.

These substituted amidinate ligands provide a simple way to generate rare high-spin (S = 2) Fe^{II} complexes with a planar geometry. It should be interesting to study the reactivity of these species (especially towards oxygen transfer agents) and compare that with the more extensively studied reactivity of planar intermediate spin (S = 1) Fe^{II} systems such as porphyrin and phthalocyanin complexes.

Experimental Section

General Remarks: All manipulations involving air-sensitive compounds were carried out under nitrogen using standard Schlenk and drybox techniques. Diethyl ether and THF (99.9% Aldrich) were percolated through a column of Al_2O_3 and stored under nitrogen. Toluene, hexane and pentane (99.9% Aldrich) were percolated through a column packed with molecular sieves (4 Å) (90 wt-%) and Al_2O_3 (10 wt-%) and stored under nitrogen. Benzene was distilled from Na/K alloy. Deuterated solvents (Aldrich) were dried with Na/K alloy and vacuum-transferred before use. Magnetic susceptibility measurements were performed with a Quantum Design MPMS-7 SQuID magnetometer of the department of Solid State Chemistry at the University of Groningen. NMR spectra were recorded with Varian Inova 500, VXR 300 and Gemini 200 instruments. IR spectra were recorded with a Mattson 4020 Galaxy FT–IR spectrometer. Elemental analyses were performed by the Microanalytical Department at the University of Groningen or by Mikroanalytisches Laboratorium H. Kolbe, Mülheim an der Ruhr,

 © 2005 Wiley-VCH Verlag GmbH & Co. KGaA, Weinheim

Germany. Anhydrous $FeCl_2$[82] and $CoCl_2$[83] and [(DME)$NiBr_2$][84] were prepared according to published procedures. All other chemicals were commercially available products, which were used without further purification.

***N*-(2,6-Diisopropylphenyl)benzanilide:** Benzoyl chloride (39 mL, 0.33 mol) was added to a vigorously stirred mixture of 10% aqueous NaOH (240 mL) and 2,6-diisopropylaniline (57.0 mL, 0.30 mol). After 60 min, the solid was collected on a glass filter and washed several times with water, and once with ethanol. The product was dried in vacuo and isolated as a white powder. Yield: 57.6 g (0.19 mol, 65%). ^{1}H NMR (200 MHz, [D_1]chloroform, room temp.): δ = 7.92 (d, J = 6.6 Hz, 2 H, ArH), 7.58–7.05 (m, 8 H, ArH), 3.15 (sept, J = 6.8 Hz, 2 H, *i*Pr-CH), 1.22 (d, J = 6.8 Hz, 6 H, *i*Pr-CH_3) ppm. IR (KBr): $\tilde{\nu}$ = 3302 cm^{-1} (m), 3293 (m), 3270 (m), 2956 (m), 2923 (s), 2854 (m), 1640 (s), 1580 (w), 1515 (m), 1486 (m), 1463 (m), 1453 (m), 1380 (w), 1361 (w), 1291 (w) cm^{-1}.

***N*-(2,6-Diisopropylphenyl)benzimidoyl Chloride:** A mixture of *N*-(2,6-diisopropylphenyl)benzanilide (57.6 g, 0.19 mol) and thionyl chloride (43.1 mL, 0.58 mol) was refluxed for 1 h. The remainder was distilled using a Kugelrohr apparatus (oven 200 °C, 0.02 Torr), to give the imidoyl chloride as a yellow, slowly solidifying oil. Yield: 51.3 g (0.17 mol, 90%). ^{1}H NMR (300 MHz, [D_1]chloroform, room temp.): δ = 8.26 (d, J = 5.2 Hz, 2 H, ArH), 7.61–7.50 (m, 3 H, ArH), 7.24 (s, 3 H, ArH), 2.88 (sept, J = 4.4 Hz, 2 H, *i*Pr-CH), 1.27 (d, J = 4.4 Hz, 6 H, *i*Pr-CH_3), 1.21 (d, J = 4.4 Hz, 6 H, *i*Pr-CH_3) ppm. IR (KBr): $\tilde{\nu}$ = 2959 (s), 2926 (s), 1665 (s), 1582 (w), 1462 (m), 1451 (m), 1167 (m), 398 (m), 797 (w), 760 (m), 986 (m) cm^{-1}.

***N*,*N*′-Bis(2,6-diisopropylphenyl)benzamidine and *N*-(2,6-Diisopropylphenyl)-*N*′-(2,6-dimethylphenyl)benzamidine:** The amidines were prepared from *N*-(2,6-diisopropylphenyl)benzimidoyl chloride and the appropriate aniline according to a previously reported procedure.[9] Yield and characterisation data for *N*,*N*′-bis(2,6-diisopropylphenyl)benzamidine have been published.[9] Data for *N*-(2,6-diisopropylphenyl)-*N*′-(2,6-dimethylphenyl)benzamidine (obtained as a mixture of isomers): Yield: 7.4 g (19 mmol, 84%). ^{1}H NMR (300 MHz, [D_1]chloroform, room temp.): δ = 7.53–6.70 (m, 11 H, ArH), 5.78, 5.75 (2× s overlapping, 1 H, NH), 3.62–3.11 (4× sept overlapping, 2 H, *i*Pr-CH), 2.42, 2.17, 2.10 (3× s overlapping, 6 H, Xyl-CH_3), 1.42, 1.30, 1.07, 0.97 (4× d, J = 6.6 Hz, 12 H, *i*Pr-CH_3) ppm. ^{13}C NMR (75 MHz, [D_1]chloroform, room temp.): δ = 154.0, 153.5 (N*C*N), 145.8, 144.9, 143.4, 139.2, 137.1, 135.4, 134.6, 134.4, 134.0 (ArC_{ipso}), 129.3, 129.2 (Ar*C*H), 128.8 (ArC_{ipso}), 128.6, 128.4, 128.0, 127.6, 127.5, 126.9, 126.3, 123.5, 123.3, 122.9 (Ar*C*H), 28.4, 28.1 (*i*Pr-*C*H), 24.4, 24.3, 22.8, 21.9 (*i*Pr-*C*H_3), 18.9, 17.6 (Xyl-*C*H_3) ppm. IR (KBr): $\tilde{\nu}$ = 3424 (w, NH), 3354 (m, NH), 3058 (m), 2942 (s), 2915 (s), 1642 (s), 1614 (s), 1588 (s), 1574 (s), 1494 (m), 1435 (s), 1355 (s), 1326 (m), 1301 (w), 1273 (w), 1255 (w), 1220 (w), 1192 (m), 1179 (m), 1162 (w), 1109 (w), 1099 (w), 1077 (w), 1060 (w), 1043 (w), 1026 (w), 923 (w), 898 (w), 835 (w), 806 (w), 775 (s), 742 (w), 697 (s), 616 (w), 600 (w), 577 (w), 543 (w), 516 (w), 507 (w), 487 (w) cm^{-1}. HRMS (EI): calcd. for $C_{27}H_{32}N_2$: 384.2565; found: 384.2571.

Complexes [{PhC(NAr)$_2$}$_2$M] (1–5). General Procedure: [PhC(NAr)$_2$]H (1.0 g, 2.3 mmol) was dissolved in THF (10 mL). *n*BuLi (2.5 M in hexanes, 0.91 mL, 2.3 mmol) was added and the solution was stirred for 30 min. The solution of Li[PhC(NAr)$_2$] thus obtained was added dropwise to a suspension of MCl_2 (1.1 mmol) in THF (10 mL). The mixture was stirred under the conditions mentioned below for the various derivatives. After the reaction, the solvent was pumped off and the residue was freed of any residual THF by suspending it in pentane (10 mL) and subsequent removal of all volatiles in vacuo. The residue was repeatedly extracted with pentane (10 mL, unless mentioned otherwise) until the extracts were colourless. The extract was concentrated and cooled to afford the crystalline bis(amidinate) complex, which was isolated by filtration and dried in vacuo.

[{PhC(NAr)$_2$}$_2$Cr] (1): The general procedure was applied using 0.76 g [PhC(NAr)$_2$]H (1.7 mmol) and 0.11 g $CrCl_2$ (0.86 mmol). The reaction was stirred for 15 h at room temperature. Extraction and crystallisation were carried out using hexanes. The product was obtained as red crystals. Yield: 0.48 g (0.52 mmol, 61%). ^{1}H NMR (300 MHz, [D_6]benzene, room temp.) by deconvolution: δ ($\Delta\nu_{1/2}$) = 15.3 (194), 14.4 (239), 7.0 (140), 5.0 (939), 2.5 (250), 0.9 (5396), –7.6 (205) ppm (Hz); integral ratio 2:2:2:23:1:20:1. $C_{62}H_{78}CrN_4$ (931.32): calcd. C 79.96, H 8.44, N 6.02; found C 79.31, H 8.49, N 5.95.

[{PhC(NAr)$_2$}$_2$Mn] (2): The general procedure was applied for ligand deprotonation using 1.0 g amidine (2.3 mmol). $MnCl_2$ (143 mg, 1.1 mmol) was added as a solid to the Li[PhC(NAr)$_2$] solution. The reaction mixture was stirred for 2 h at room temperature, during which no significant colour change was observed. Off-white crystals were obtained from pentane at –25 °C. Yield: 0.51 g (0.54 mmol, 48%). ^{1}H NMR (300 MHz, [D_6]benzene, room temp.) by deconvolution: δ ($\Delta\nu_{1/2}$) = 15.1 (2761), 14.1 (566), 6.2 (1465), 3.5 (230), –4.2 (784) ppm (Hz); integral ratio 1:2:11:1:6. $C_{62}H_{78}MnN_4$ (934.27): calcd. C 79.71, H 8.42, N 6.00; found C 79.97, H 8.48, N 5.89.

[{PhC(NAr)$_2$}$_2$Fe] (3): The general procedure was applied. The reaction mixture was stirred for 2 h at room temperature, during which the solution turned dark green. Extraction was performed with hexanes. The product was isolated as dark green crystals after recrystallisation from hexanes. Yield: 0.98 g (1.0 mmol, 91%). ^{1}H NMR (300 MHz, [D_6]benzene, room temp.): δ = ($\Delta\nu_{1/2}$, integral) = 57.4 (952, 4 H), 31.9 (74.6, 4 H), 22.2 (74.5, 4 H), 16.8 (61.0, 4 H), 14.8 (158, 12 H), 6.23 (140, 4 H), 3.80 (126, 12 H), –2.05 (54.5, 2 H), –5.19 (89.7, 12 H), –6.18 (64.5, 4 H), –29.2 (274, 12 H) ppm (Hz); one of two expected *i*Pr-CH resonances not observed, possibly due to extreme line-broadening. $C_{62}H_{78}FeN_4$ (935.18): calcd. C 79.63, H 8.41, N 5.99; found C 79.44, H 8.47, N 6.05.

[{PhC(NAr)$_2$}$_2$Co] (4): The general procedure was applied, but in this case no colour change was observed after stirring at room temperature for 30 min. Upon warming the suspension at 50 °C for 30 min, a colour change from green to dark red was observed. The Co complex was obtained as red crystals after recrystallisation of the crude product from hexanes. Yield: 0.70 g (0.74 mmol, 65%). ^{1}H NMR (500 MHz, [D_6]benzene, room temp.): δ ($\Delta\nu_{1/2}$, integral) = 115 (697), 60.9 (140, 4 H), 45.3 (1994), 35.0 (80.9, 2 H), 24.8 (110, 12 H), 21.2 (129, 4 H), 2.77 (119, 4 H), –19.0 (86.6, 4 H), –69.6 (1007), –73.2 (431, 12 H), –84.0 (85.8, 12 H), –138 (2461) ppm (Hz); integration of resonances at δ = 115, 45.3, –69.6 and –138 ppm inaccurate due to extreme broadness. $C_{62}H_{78}CoN_4$ (938.26): calcd. C 79.37, H 8.38, N 5.97; found C 78.60, H 8.42, N 5.88.

[{PhC(NAr)$_2$}$_2$Ni] (5): The general procedure was applied using 0.53 g (1.2 mmol) [PhC(NAr)$_2$]H and [(DME)$NiBr_2$] (0.19 g, 0.6 mmol) as Ni source. The reaction mixture was stirred under reflux conditions for 66 h. The crude product was recrystallised from toluene and the resulting red crystals were washed with diethyl ether. Yield: 0.26 g (0.30 mmol, 47%). ^{1}H NMR (300 MHz, [D_6]benzene, room temp.): δ = 6.87–7.03 (m, 12 H), 6.41–6.64 (m, 10 H), 4.24 (sept, J = 7.0 Hz, 4 H), 3.13 (sept, J = 7.0 Hz, 4 H), 2.31 (d, J = 7.0 Hz, 12 H), 1.55 (d, J = 7.0 Hz, 12 H), 0.60 (d, J = 7.0 Hz, 12 H), 0.49 (d, J = 7.0 Hz, 12 H) ppm. ^{13}C NMR (75 MHz, [D_6]benzene, room temp.): δ = 175.1 (NCN), 144.5, 143.3, 141.5

 © 2005 Wiley-VCH Verlag GmbH & Co. KGaA, Weinheim

(3 × *ipso*-C), 130.8, 130.4 (*ipso*-C), 129.6, 126.8, 125.7, 124.9, 123.6, 29.4, 28.5 (2 × *i*Pr-CH), 24.4, 24.0, 22.3, 21.4 (4 × *i*Pr-CH_3) ppm. $C_{62}H_{78}N_4Ni$ (938.04): calcd. C 79.38, H 8.38, N 5.97; found C 79.37, H 8.29, N 5.88.

[{PhC(NAr)(NXyl)}$_2$Fe] (6): $LiCH_2SiMe_3$ (0.13 g, 1.4 mmol) was added to a stirred solution of *N*-(2,6-diisopropylphenyl)-*N*′-(2,6-dimethylphenyl)benzamidine (0.53 g, 1.4 mmol) in 15 mL 1% THF/C_6H_6 at room temperature. After 15 min, $FeCl_2$ (0.09 g, 0.7 mmol) was added to the yellow solution. The colour of the mixture changed from yellow to green. The reaction mixture was stirred for 2 h after which the solvents were removed in vacuo. Residual THF was removed by suspending the residue in pentane that was subsequently pumped off. The solid was extracted with benzene (40 mL) until the extracts were colourless. The crude product was recrystallised from hot benzene, affording **6**·C_6H_6 as green crystals. Yield: 0.32 mg (0.4 mmol, 50%).^{1}H NMR (300 MHz, [D_6]benzene, room temp.): δ = ($\Delta\nu_{1/2}$, integral): 26.07 (25, 4 H), 25.15 (25, 4 H), 16.55 (18, 4 H), 11.79 (235, 12 H), 4.02 (74, 4 H), 0.46 (43, 12 H), –2.57 (19, 2 H), –5.48 (183, 12 H), –7.24 (22, 2 H), –9.24 (22, 2 H) ppm (Hz). $C_{54}H_{62}FeN_4$·C_6H_6 (901.07): calcd. C 80.0, H 7.6, N 6.2; found C 79.6, H 7.8, N 6.3.

Determination of *k* and $\Delta G^{\ddagger}$ for Epimerisation of 5: ^{1}H 2D EXSY spectra (500 MHz, [D_8]toluene, 338 K) were obtained using the NOESY sequence (d_1–90°–d_2–90°–τ–90°–FID) with an extra gradient during the mixing time τ. The spectral width was 8000 Hz. Mixing times of 0.2, 0.3, 0.4 and 0.5 s were used. The relaxation delay d_1 was 1 s and the increment for the evolution time d_2 was 98 μs. Peak volumes of the isopropyl methine resonances (δ = 4.24 and 3.13 ppm) and their cross-peaks were determined by means of the Gaussian method in the integration program Sparky.[85] The ratio of the peak volumes of the cross-peaks and the diagonal peaks (I_x/I_d) was plotted vs. mixing time τ. The rate constants k for the exchange process was determined by fitting the data to the equation[79]

$$\frac{I_x}{I_d} = \frac{1 - e^{-2k\tau}}{1 + e^{-2k\tau}}$$

The free energy of activation $\Delta G^{\ddagger}$ at 338 K was calculated by substitution of k_{338} according to the relation[80]

$$k = \frac{\kappa k_b T}{h} \cdot e^{-\Delta G^{\ddagger}/RT}$$

Magnetic Measurements: Data were collected on crystalline samples (ca. 25 mg) from 300 to 5 K at a field of 1000 G. Measured magnetic susceptibilities are corrected for diamagnetism using Pascal's constants.[86] Effective magnetic moments are calculated as

$$\mu_{eff.} = 2.828\sqrt{\chi_m T}$$

X-ray Crystallographic Study: Single crystals suitable for X-ray diffraction were obtained by recrystallisation from pentane (**1**), hexanes (**2**, **3**), benzene (**4**, **6**) or diethyl ether (**5**). Some crystals were found to contain cocrystallised solvent molecules (**2**·*n*-hexane, **4**·2C_6H_6 and **6**.C_6H_6). The crystals were mounted on top of a glass fibre, by using inert-atmosphere handling techniques, and aligned on a Bruker[87] SMART APEX CCD diffractometer (Platform with full three-circle goniometer). The diffractometer was equipped with a 4 K CCD detector set 60.0 mm from the crystal. The crystals were cooled using the Bruker KRYOFLEX low-temperature device. Intensity measurements were performed using graphite-monochromated Mo-K_α radiation from a sealed ceramic diffraction tube (SIEMENS). Generator settings were 50 kV/40 mA. SMART[87] was used for preliminary determination of the unit cell constants and data collection control. The intensities of reflections of a hemisphere were collected by a combination of 3 sets of exposures (frames). Each set had a different φ angle for the crystal and each exposure covered a range of 0.3° in ω. A total of 1800 frames were collected with an exposure time of 20.0 s (**1**, **2**, **5**) or 10.0 s (**3**, **4**, **6**) per frame. Data integration and global cell refinement was performed with the program SAINT.[87] The final unit cell was obtained from the *xyz* centroids of 5709 (**1**), 3348 (**2**), 6534 (**3**), 4586 (**4**), 5447 (**5**), 9843 (**6**) reflections after integration. Intensity data were corrected for Lorentz and polarisation effects, scale variation, for decay and absorption: a multi-scan absorption correction was applied, based on the intensities of symmetry-related reflections measured at different angular settings (SADABS),[88] and reduced to F_o^2. The program suite SHELXTL was used for space group determination (XPREP).[87] The unit cells[89] were identified as monoclinic; reduced cell calculations did not indicate any higher metric lattice symmetry.[90] For **4**, The |*E*| distribution statistics were ambiguous about a centrosymmetric/non-centrosymmetric space group.[91] The space groups were derived from the systematic extinctions. Examination of the final atomic coordinates of the structure did not yield extra symmetry elements.[92] The structures of **1**, **2**, **4**, **5** and **6** were solved by Patterson methods and extension of the model was accomplished by direct methods applied to difference structure factors using the program DIRDIF.[93] For **3**, the structure was solved by direct methods with SIR-97.[94,95] The positional and anisotropic displacement parameters for the non-hydrogen atoms were refined. The unit cell of **2** contains a molecule of hexane solvent of which one end is highly disordered. One of the C atoms (C68) was described as occupying two positions with separately refined site occupancy factors. The s.o.f. of the major fraction refined to a value of 0.625(13). Refinement for **4** was complicated by a twinning problem. After introducing a twin matrix as detected by PLATON ([–1 0 0 0 –1 0 0.99 0 1], 180° rotation about the *c** axis), with scale factors for the fractional contributions of the various twin components, the structure refined smoothly. The s.o.f. of the major fraction of the component of the twin model refined to a value of 0.629(3). All hydrogen atoms of **1**, **2**, **5** and **6** (except those belonging to the disordered hexane solvent molecule in **2**) were located from a subsequent difference Fourier synthesis, and their coordinates and isotropic displacement parameters were refined. For **3**, Fourier synthesis resulted in the location of most of the hydrogen atoms. The remaining hydrogen atoms in **3** and all hydrogen atoms in **4** were included in the final refinement riding on their carrier atoms with their positions calculated by using sp^2 or sp^3 hybridisation at the C atom as appropriate with U_{iso} = c × U_{equiv} of their parent atom, where c = 1.2 for the non-methyl hydrogen atoms and c = 1.5 for the methyl hydrogen atoms and where values U_{equiv} are related to the atoms to which the H atoms are bonded. The methyl groups were refined as rigid groups, which were allowed to rotate freely. Neutral atom scattering factors and anomalous dispersion corrections were taken from International Tables for Crystallography.[96] All refinement calculations and graphics were performed with the program packages SHELXL[97] (least-square refinements) and PLATON[98,99] (calculation of geometric data and ORTEP illustrations). No classic hydrogen bonds, no missed symmetry (MISSYM), but potential solvent-accessible

area [voids of 325.2 (**1**), 78.7 (**2**), 372.6 (**3**), 111.2 (**4**) and 296.4 (**5**) Å^3/unit cell] were detected by procedures implemented in PLATON.[98,99] Crystallographic data for **1**–**6** and details of the refinement are listed in Table 4 and Table 5. CCDC-247623 to -247628 contain the supplementary crystallographic data for this paper. These data can be obtained free of charge from The Cambridge Crystallographic Data Centre via www.ccdc.cam.ac.uk/data_request/cif.

Table 4. Crystal, collection and refinement data for complexes **1**–**3**.

	1	**2**	**3**
Empirical formula	$C_{62}H_{78}N_4Cr$	$C_{62}H_{78}MnN_4{\cdot}C_6H_{14}$	$C_{62}H_{78}FeN_4$
Formula mass	931.32	1020.44	935.18
Crystal dimensions [mm]	0.37 × 0.13 × 0.034	0.22 × 0.16 × 0.14	0.40 × 0.40 × 0.08
Colour, habit	red, platelet	pale yellow, block	green, platelet
Crystal system	monoclinic	monoclinic	monoclinic
Space group (no.)[96]	$P2_1/c$ (#14)	$P2_1/c$ (#14)	$P2_1/c$ (#14)
a [Å]	23.795(1)	11.9048(5)	23.846(1)
b [Å]	10.3509(4)	24.826(1)	10.3346(6)
c [Å]	25.189(1)	20.7161(8)	25.211(1)
β [°]	115.714(1)	96.035(1)	115.898(1)
Z	4	4	4
V [Å^3]	5589.7(4)	6088.7(4)	5589.0(5)
$\rho_{calcd.}$ [g/cm^3]	1.107	1.113	1.111
θ range [°]	2.18–26.37	2.14–26.37	2.37–29.80
λ [Å]	0.71073 (Mo-K_α)	0.71073 (Mo-K_α)	0.71073 (Mo-K_α)
T [K]	100(1)	110(1)	105(1)
Data collect. time [h]	13.0	13.6	8.9
No. of measured reflections	43872	48623	43919
No. of unique reflections	11424	12423	14931
μ [cm^{-1}]	2.45	2.59	3.1
No. of parameters	916	983	913
Weighting scheme a, b[a]	0.0559, 0.7843	0.0797, 0.0	0.0842, 1.6145
$R(F)$ for $F_o \geq 4\sigma(F_o)$[b]	0.0483	0.0642	0.0519
$wR(F^2)$[c]	0.1213	0.1719	0.1454
Residual electron density [e Å^{-3}]	–0.27, 0.33(6)	–0.44, 0.56(6)	–0.38, 2.38(7)
GoF[d]	1.017	0.993	1.024

[a] $w = 1/[\sigma^2(F_o^2) + (aP)^2 + bP]$, $P = [\max(F_o^2,0) + 2F_c^2]/3$. [b] $R(F) = \Sigma(||F_o| - |F_c||)/|F_o|$. [c] $wR(F^2) = \{\Sigma[w(F_o^2 - F_c^2)^2]/\Sigma[w(F_o^2)^2]\}^{1/2}$. [d] GoF = $\{\Sigma[w(F_o^2 - F_c^2)^2]/(n - p)\}^{1/2}$, n = # refl., p = # param. refined.

Table 5. Crystal, collection and refinement data for complexes **4**–**6**.

	4	**5**	**6**
Empirical formula	$C_{62}H_{78}CoN_4{\cdot}2C_6H_6$	$C_{62}H_{78}N_4Ni$	$C_{54}H_{62}FeN_4{\cdot}C_6H_6$
Formula mass	1049.49	938.02	901.08
Crystal dimensions [mm]	0.24 × 0.19 × 0.12	0.19 × 0.13 × 0.07	0.55 × 0.42 × 0.21
Colour, habit	red/brown, block	red, block	green, block
Crystal system	monoclinic	monoclinic	monoclinic
Space group (no.)[96]	$P2_1/c$ (#14)	$C2/c$ (#15)	$C2/c$ (#15)
a [Å]	18.028(5)	23.052(2)	8.9541(3)
b [Å]	18.145(5)	10.6550(8)	24.3880(9)
c [Å]	20.797(6)	24.402(2)	23.5938(9)
β [°]	113.146(5)	113.667(1)	99.936(1)
Z	4	4	4
V [Å^3]	6255(3)	5489.5(8)	5075.0(3)
$\rho_{calcd.}$ [g/cm^3]	1.162	1.135	1.179
θ range [°]	2.22–22.21	2.47–28.60	2.42–28.28
λ [Å]	0.71073 (Mo-K_α)	0.71073 (Mo-K_α)	0.71073 (Mo-K_α)
T [K]	110(2)	100(1)	100(1)
Data collect. time [h]	8.0	13.0	8.0
No. of measured reflections	53509	21358	23145
No. of unique reflections	7864	5575	6269
μ [cm^{-1}]	3.19	3.94	3.39
No. of parameters	730	459	430
Weighting scheme a, b[a]	0.0016, 46.8803	0.0304, 5.30	0.0565, 1.690
$R(F)$ for $F_o \geq 4\sigma(F_o)$[b]	0.0938	0.0490	0.0359
$wR(F^2)$[c]	0.2390	0.1041	0.0973
Residual electron density [e/Å^{-3}]	–0.19, 0.24(4)	–0.24, 0.43(6)	–0.25, 0.41(5)
GoF[d]	0.957	1.005	1.083

[a] $w = 1/[\sigma^2(F_o^2) + (aP)^2 + bP]$, $P = [\max(F_o^2,0) + 2F_c^2]/3$. [b] $R(F) = \Sigma(||F_o| - |F_c||)/\Sigma|F_o|$. [c] $wR(F^2) = \{\Sigma[w(F_o^2 - F_c^2)^2]/\Sigma[w(F_o^2)^2]\}^{1/2}$. [d] GoF = $\{\Sigma[w(F_o^2 - F_c^2)^2]/(n - p)\}^{1/2}$, n = # refl., p = # param. refined.

 © 2005 Wiley-VCH Verlag GmbH & Co. KGaA, Weinheim

DFT Calculations: All calculations on the model complexes [{HC(NH)$_2$}$_2$M] were carried out with the GAMESS-UK program.[81] Geometries were optimised at the B3LYP level[100–102] within either D_{2h} or D_{2d} symmetry using the 3-21G basis set[103] on the ligand atoms and LANL2DZ (small-core pseudopotential) on the metal atom.[104–106] Calculations used the spin-restricted (for $S = 0$ states) or spin-unrestricted (for $S > 0$ states) formalism; in the latter case, spin contamination was uniformly found to be negligible.

Supporting Information (see also footnote on the first page of this article): IR data for complexes **1**–**6** and total energies and S^2 values for all calculations mentioned in the text (Table S.1).

Acknowledgments

We thank J. Baas for performing the magnetic susceptibility measurements.

Note Added in Proof (April 15, 2005): A recent paper describes a planar bis(amidinate)magnesium complex with ligands related to those used in this paper: R. T. Boeré, M. L. Cole, P. C. Junk, *New J. Chem.* **2005**, *29*, 128–134.

[1] F. T. Edelmann, *Coord. Chem. Rev.* **1994**, *137*, 403–481.
[2] J. Barker, M. Kilner, *Coord. Chem. Rev.* **1994**, *133*, 219–300.
[3] E. A. C. Brussee, A. Meetsma, B. Hessen, J. H. Teuben, *Chem. Commun.* **2000**, 497–498.
[4] E. A. C. Brussee, A. Meetsma, B. Hessen, J. H. Teuben, *Organometallics* **1998**, *17*, 4090–4095.
[5] C. Averbuj, E. Tish, MS Eisen, *J. Am. Chem. Soc.* **1998**, *120*, 8640–8646.
[6] V. Volkis, M. Shmulinson, C. Averbuj, A. Lisovskii, F. T. Edelmann, MS Eisen, *Organometallics* **1998**, *17*, 3155–3157.
[7] T. Boussie, V. Murphy, J. A. Van Beek, WO 99/05154 to SYMYX Technologies, **1999**.
[8] K. Yokota, US6107232 to Idemitsu Kosan Co., Ltd., **2000**.
[9] S. Bambirra, D. van Leusen, A. Meetsma, J. H. Teuben, *Chem. Commun.* **2003**, 522–523.
[10] M. J. R. Brandsma, E. A. C. Brussee, A. Meetsma, B. Hessen, J. H. Teuben, *Eur. J. Inorg. Chem.* **1998**, 1867–1870.
[11] M. P. Coles, R. F. Jordan, *J. Am. Chem. Soc.* **1997**, *119*, 8125–8126.
[12] J. M. Decker, S. J. Geib, T. Y. Meyer, *Organometallics* **1999**, *18*, 4417–4420.
[13] J. C. Flores, J. C. W. Chien, M. D. Rausch, *Organometallics* **1995**, *14*, 1827–1833.
[14] D. Herskovics-Korine, MS Eisen, *J. Organomet. Chem.* **1995**, *503*, 307–314.
[15] R. J. Keaton, K. C. Jayaratne, D. A. Henningsen, L. A. Koterwas, L. R. Sita, *J. Am. Chem. Soc.* **2001**, *123*, 6197–6198.
[16] K. C. Jayaratne, R. J. Keaton, D. A. Henningsen, L. R. Sita, *J. Am. Chem. Soc.* **2000**, *122*, 10490–10491.
[17] J. Richter, F. T. Edelmann, M. Noltemeyer, H.-G. Schmidt, M. Shmulinson, MS Eisen *J. Mol. Catal. A.* **1998**, *130*, 149–162.
[18] D. Walther, R. Fischer, H. Görls, J. Koch, B. Schweder, *J. Organomet. Chem.* **1996**, *508*, 13–22.
[19] R. Schlund, M. Lux, F. Edelmann, U. Reismann, W. Rohde, US6262198 to BASF Aktiengesellschaft, **2001**.
[20] S. Bambirra, M. W. Bouwkamp, A. Meetsma, B. Hessen, *J. Am. Chem. Soc.* **2004**, *126*, 9182–9183.
[21] B. J. O'Keefe, L. E. Breyfogle, M. A. Hillmyer, W. B. Tolman, *J. Am. Chem. Soc.* **2002**, *124*, 4384–4393.
[22] K. B. Aubrecht, K. Chang, M. A. Hillmyer, W. B. Tolman, *J. Polym. Sci. A: Polym. Chem.* **2001**, *39*, 284–293.
[23] F. A. Cotton, L. M. Daniels, J. H. Matonic, C. A. Murillo, *Inorg. Chim. Acta* **1997**, *256*, 277–282.
[24] F. A. Cotton, N. S. Dalal, C. Y. Liu, C. A. Murillo, J. M. North, X. Wang, *J. Am. Chem. Soc.* **2003**, *125*, 12945–12952.
[25] F. A. Cotton, L. M. Daniels, L. R. Falvello, J. H. Matonic, C. A. Murillo, *Inorg. Chim. Acta* **1997**, *256*, 269–275.
[26] F. A. Cotton, L. M. Daniels, C. A. Murillo, *Angew. Chem. Int. Ed. Engl.* **1992**, *31*, 737–738.
[27] F. A. Cotton, L. M. Daniels, C. A. Murillo, I. Pascual, H.-C. Zhou, *J. Am. Chem. Soc.* **1999**, *121*, 6856–6861.
[28] F. A. Cotton, C. A. Murillo, I. Pascual, *Inorg. Chem.* **1999**, *38*, 2182–2187.
[29] F. A. Cotton, L. M. Daniels, C. A. Murillo, *Inorg. Chem.* **1993**, *32*, 2881–2885.
[30] F. A. Cotton, X. Feng, C. A. Murillo, *Inorg. Chim. Acta* **1997**, *256*, 303–308.
[31] F. A. Cotton, L. M. Daniels, X. Feng, D. J. Maloney, J. H. Matonic, C. A. Murillo, *Inorg. Chim. Acta* **1997**, *256*, 291–301.
[32] F. A. Cotton, L. M. Daniels, D. J. Maloney, J. H. Matonic, C. A. Murillo, *Inorg. Chim. Acta* **1997**, *256*, 283–289.
[33] F. A. Cotton, L. M. Daniels, D. J. Maloney, C. A. Murillo, *Inorg. Chim. Acta* **1996**, *249*, 9- 11.
[34] S. Hao, S. Gambarotta, C. Bensimon, J. J. H. Edema, *Inorg. Chim. Acta* **1993**, *213*, 65–74.
[35] M. P. Coles, D. C. Swenson, R. F. Jordan, V. G. Young Jr., *Organometallics* **1997**, *16*, 5183–5194.
[36] A. R. Sadique, M. J. Heeg, C. H. Winter, *J. Am. Chem. Soc.* **2003**, *125*, 7774–7775.
[37] J. Cirera, P. Alemany, S. Alvarez, *Chem. Eur. J.* **2004**, *10*, 190–207.
[38] J. A. R. Schmidt, J. Arnold, *Chem. Commun.* **1999**, *1999*, 2149–2150.
[39] J. A. R. Schmidt, J. Arnold, *J. Chem. Soc., Dalton Trans.* **2002**, 2890–2899.
[40] J. A. R. Schmidt, J. Arnold, *Organometallics* **2002**, *21*, 2306–2313.
[41] J. A. R. Schmidt, J. Arnold, *J. Chem. Soc., Dalton Trans.* **2002**, 3454–3461.
[42] D. Abeysekera, K. N. Robertson, T. S. Cameron, J. A. C. Clyburne, *Organometallics* **2001**, *20*, 5532–5536.
[43] H. A. Jenkins, D. Abeysekara, D. A. Dickie, J. A. C. Clyburne, *J. Chem. Soc., Dalton Trans.* **2002**, 3919–3922.
[44] L. K. Johnson, C. M. Killian, M. Brookhart, *J. Am. Chem. Soc.* **1995**, *117*, 6414–6415.
[45] B. L. Small, M. Brookhart, A. M. A. Bennett, *J. Am. Chem. Soc.* **1998**, *120*, 4049–4050.
[46] G. J. P. Britovsek, V. C. Gibson, B. S. Kimberley, P. J. Maddox, S. J. McTavish, G. A. Solan, A. J. P. White, D. J. Williams, *Chem. Commun.* **1998**, 849–850.
[47] G. J. P. Britovsek, M. Bruce, V. C. Gibson, B. S. Kimberley, P. J. Maddox, S. Mastroianni, S. J. McTavish, C. Redshaw, G. A. Solan, S. Stromberg, A. J. P. White, D. J. Williams, *J. Am. Chem. Soc.* **1999**, *121*, 8728–8740.
[48] L. Bourget-Merle, M. F. Lappert, J. R. Severn, *Chem. Rev.* **2002**, *102*, 3031–3065.
[49] R. T. Boeré, V. Klassen, G. Wolmershauser, *J. Chem. Soc. Dalton Trans.* **1998**, 4147–4154.
[50] M. P. Coles, D. C. Swenson, R. F. Jordan, V. G. Young Jr., *Organometallics* **1998**, *17*, 4042–4048.
[51] B. S. Lim, A. Rahtu, J.-S. Park, R. G. Gordon, *Inorg. Chem.* **2003**, *42*, 7951–7958.
[52] H. Kawaguchi, T. Matsuo, *Chem. Commun.* **2002**, 958–959.
[53] B. Vendemiati, G. Prini, A. Meetsma, B. Hessen, J. H. Teuben, O. Traverso, *Eur. J. Inorg. Chem.* **2001**, 707–711.
[54] J. R. Hagadorn, J. Arnold, *Inorg. Chem.* **1997**, *36*, 132–133.
[55] D. Walther, P. Gebhardt, R. Fischer, U. Kreher, H. Görls, *Inorg. Chim. Acta* **1998**, *281*, 181–189.
[56] H. K. Lee, T. S. Lam, C.-K. Lam, H.-W. Li, S. M. Fung *New J. Chem.* **2003**, *27*, 1310–1318.
[57] F. A. Cotton, L. M. Daniels, C. A. Murillo, P. Schooler, *J. Chem. Soc., Dalton Trans.* **2000**, 2001–2005.

 © 2005 Wiley-VCH Verlag GmbH & Co. KGaA, Weinheim

[58] J.-K. Buijink, M. Noltemeyer, F. T. Edelmann *Z. Naturforsch.* **1991**, *46b*, 1328–1332.
[59] R. D. Shannon *Acta Crystallogr. A.* **1976**, *32*, 751–767.
[60] P. N. Hawker, M. V. Twigg, "Iron(II) and Lower States", in: *Comprehensive Coordination Chemistry – The synthesis, reactions, properties & applications of coordination compounds*, Pergamon, Oxford, **1987**, p. 1179–1288.
[61] P. N. Hawker, M. V. Twigg, "Iron: Inorganic & Coordination Chemistry", in: *Encyclopedia of Inorganic Chemistry*, John Wiley & Sons, New York, **1994**, p. 1699–1725.
[62] A. Earnshaw, E. A. King, L. F. Larkworthy, *J. Chem. Soc. A* **1968**, 1048–1052.
[63] V. Esposito, E. Solari, C. Floriani, N. Re, C. Rizzoli, A. Chiesi-Villa, *Inorg. Chem.* **2000**, *39*, 2604–2613.
[64] J. P. Collman, J. L. Hoard, N. Kim, G. Lang, C. A. Reed, *J. Am. Chem. Soc.* **1975**, *97*, 2676–2681.
[65] H. Kalish, H. M. Lee, M. M. Olmstead, L. Latos-Grazynski, S. P. Rath, A. L. Balch, *J. Am. Chem. Soc.* **2003**, *125*, 4674–4675.
[66] B. W. Dale, R. J. P. Williams, C. E. Johnson, T. L. Thorp *J. Chem. Phys.* **1968**, *49*, 3441–3442.
[67] A. B. P. Lever, *J. Chem. Soc.* **1965**, 1821 –1829.
[68] B. W. Dale, *Mol. Phys.* **1974**, *28*, 503–511.
[69] C. G. Barraclough, R. L. Martin, S. Mitra, R. C. Sherwood *J. Chem. Phys.* **1970**, *53*, 1643–1648.
[70] T. J. Truex, R. H. Holm, *J. Am. Chem. Soc.* **1972**, *94*, 4529–4538.
[71] V. L. Goedken, Y.-A. Park *J. Chem. Soc. Chem. Commun.* **1975**, 214–215.
[72] S. Koch, R. H. Holm, R. B. Frankel, *J. Am. Chem. Soc.* **1975**, *97*, 6714–6723.
[73] D. P. Riley, J. A. Stone, D. H. Busch, *J. Am. Chem. Soc.* **1977**, *99*, 767–777.
[74] D. Sellmann, T. Becker, F. Knoch, *Chem. Ber.* **1996**, *129*, 509–519.
[75] D. Sellmann, U. Kleine-Kleffmann, L. Zapf, *J. Organomet. Chem.* **1984**, *263*, 321–331.
[76] A. Earnshaw *Introduction to magnetochemistry*, Academic Press Inc. Ltd., London, **1968**.
[77] C. J. O'Connor, "Magnetochemistry – Advances in Theory and Experimentation", in *Progress in Inorganic Cchemistry*, John Wiley & Sons, New York, **1982**, p. 203–283.
[78] R. Poli, *Chem. Rev.* **1996**, *96*, 2135–2204.
[79] R. R. Ernst, G. Bodenhausen, A. Wokaun, *Principles of Nuclear Magnetic Resonance in One and Two Dimensions*, Clarendon Press, Oxford, **1987**, p. 490.
[80] F. A. Carey, R. J. Sundberg, *Advanced Organic Chemistry, Part A: Structure and Mechanisms*, Plenum Press, New York, **1990**, p. 194.
[81] GAMESS-UK is a package of ab initio programs written by M. F. Guest, J. H. Van Lenthe, J. Kendrick, K. Schoffel, P. Sherwood, with contributions from R. D. Amos, R. J. Buenker, H. J. J. Van Dam, M. Dupuis, N. C. Handy, I. H. Hillier, P. J. Knowles, V. Bonacic-Koutecky, W. Von Niessen, R. J. Harrison, A. P. Rendell, V. R. Saunders, A. J. Stone, A. H. De Vries, the package is derived from the original GAMESS code due to M. Dupuis, D. Spangler, J. Wendoloski, NRCC Software Catalog, vol. 1, program no. QG01 (GAMESS), **1980**. DFT module by P. Young under the auspices of EPSRC's Collaborative Computational Project No. 1 (CCP1), **1995–1997**.
[82] P. Kovacic, N. O. Brace, *Inorg. Synth.* **1960**, *6*, 172–173.
[83] G. H. Cady, H. F. Holztclaw, J. Kleinberg, E. G. Rochow, W. C. Schumb, J. D. Scott, *Inorg. Synth.* **1957**, *5*, 153–156.
[84] L. G. L. Ward, *Inorg. Synth.* **1972**, *13*, 162–163.
[85] T. D. Goddard, D. G. Kneller, *SPARKY-V3.106*, University of California, San Francisco, **2003**.
[86] O. Kahn, *Molecular magnetism*; Wiley-VCH, New York, **1993**.
[87] SMART, SAINT, SADABS, XPREP and SHELXTL/NT: Area Detector Control and Integration Software, 2**000**; Smart Apex Software Reference Manuals; Bruker Analytical X-ray Instruments. Inc., Madison, Wisconsin, USA.
[88] G. M. Sheldrick, *SADABS-V2 – Multi-Scan Absorption Correction Program*, University of Göttingen, Göttingen, Germany, **2001**.
[89] A. J. M. Duisenberg *J. Appl. Crystallogr.* **1992**, *25*, 92–96.
[90] A. L. Speok *J. Appl. Crystallogr.* **1988**, *21*, 578–579.
[91] M. R. Snow, E. R. T. Tiekink, *Acta Crystallogr. B* **1988**, *44*, 676–677.
[92] Y. Le Page, *J. Appl. Crystallogr.* **1987**, *20*, 264–269.
[93] P. T. Beurskens, G. Beurskens, R. de Gelder, S. García-Granda, R. O. Gould, R. Israël, J. M. M. Smits, *The DIRDIF-99 Program System*, Crystallography Laboratory, University of Nijmegen, Nijmegen, The Netherlands, **1999**.
[94] A. Altomare, M. C. Burla, M. Camalli, G. L. Cascarano, C. Giacovazzo, A. Guagliardi, A. G. G. Moliterni, G. Polidori, R. Spagna, *J. Appl. Crystallogr.* **1999**, *32*, 115–119.
[95] A. Altomare, M. C. Burla, M. Camalli, G. L. Cascarano, C. Giacovazzo, A. Guagliardi, A. G. G. Moliterni, G. Polidori, R. Spagna, *SIR-97 – A Package for Crystal Structure Solution by Direct Methods and Refinement*, Univ. of Bari, Univ. of Perugia and Univ. of Roma, Italy, **1997**.
[96] *International Tables for Crystallography*, Kluwer Academic Publishers; Dordrecht, The Netherlands, **1992**.
[97] G. M. Sheldrick, *SHELXL-97 – Program for the refinement of crystal structures*, University of Göttingen, Göttingen, Germany, **2003**.
[98] A. L. Spek, *PLATON - Program for the Automated Analysis of Molecular Geometry (A Multipurpose Crystallographic Tool)*, University of Utrecht, Utrecht, The Netherlands, **2002**.
[99] A. L. Spek, *Acta Crystallogr. A* **1990**, *46*, C34–C34.
[100] C. Lee, W. Yang, R. G. Par, *Phys. Rev. B* **1988**, *37*, 785–789.
[101] A. D. Beck, *J. Chem. Phys.* **1993**, *98*, 1372–1377.
[102] A. D. Becke, *J. Chem. Phys.* **1993**, *98*, 5648–5652.
[103] J. S. Binkley, J. A. Pople, W. J. Hehre, *J. Am. Chem. Soc.* **1980**, *102*, 939–947.
[104] P. J. Hay, W. R. Wadt, *J. Chem. Phys.* **1985**, *82*, 270–283.
[105] W. R. Wadt, P. J. Hay, *J. Chem. Phys.* **1985**, *82*, 284–298.
[106] P. J. Hay, W. R. Wadt, *J. Chem. Phys.* **1985**, *82*, 299–310.

Received: January 28, 2005

 © 2005 Wiley-VCH Verlag GmbH & Co. KGaA, Weinheim

Bis(salicylaldiminato)titanium Complexes Containing Bulky Imine Substituents: Synthesis, Characterization and Ethene Polymerization Studies

Antti Pärssinen,[a] Tommi Luhtanen,[b] Martti Klinga,[a] Tapani Pakkanen,[b] Markku Leskelä,[a] and Timo Repo*[a]

Keywords: Titanium / Polymerization / Homogeneous catalysis / Molecular modeling / N,O ligands

A series of titanium complexes bearing two anionic [N, O$^-$] bidentate salicylaldiminato ligands, namely bis[(*N*-salicylidene)anilinato]titanium(IV) dichloride (**1**), bis[(*N*-salicylidene)-2,6-dimethylanilinato]titanium(IV) dichloride (**2**), bis[(*N*-salicylidene)-2,6-di-*i*- propylanilinato]titanium(IV) dichloride (**3**), bis[(*N*-salicylidene)-(1-naphthalenylimino)]titanium(IV) dichloride (**4**), bis[(*N*-salicylidene)-2,6-difluoroanilinato]titanium(IV) dichloride (**5**), and bis[(*N*-3-fluorosalicylidene)-2,6-difluoroanilinato]titanium(IV) dichloride (**6**) have been synthesized with good yields by a two-step procedure. The X-ray structure analysis reveals that in complex **2**, titanium has a distorted octahedral coordination sphere in which the oxygen atoms and the chloride ligands form the basal plane. Both the chloride and the phenoxy moieties have a *cis* orientation and the angle between the chloride ligands is 93.05°. The imine nitrogen atoms complete the octahedral coordination of the Ti center by occupying the axial positions. The newly synthesized (**2** and **4**–**6**) and already known complexes (**1** and **3**) were introduced in detailed ethene-polymerization studies. The activities achieved were low to moderate depending on the size and nature of the imino substituents. The polyethenes (PEs) produced had high molar masses, and the modalities of the molecular weight distributions varyied with polymerization temperature. Based on the results of ab initio calculations and on the experimental data obtained, an explanation for uni- and bimodal polymerization behavior and the differences in catalytic activities are given.

(© Wiley-VCH Verlag GmbH & Co. KGaA, 69451 Weinheim, Germany, 2005)

Introduction

In the middle of the 80s chiral group 4 *ansa*-metallocenes were successfully used for the first time in the homogeneous polymerization of isotactic polypropene with excellent activities when activated with methylaluminoxane (MAO).[1–3] This fundamental observation initiated intensive research activities in academia as well as in the polyolefin industry, and a lot of theoretical and synthetic resources were focused on the development and the understanding of metallocene-catalyzed polymerization reactions.[4,5] At the same time there have also been significant efforts to transfer this know-how to other types of metal complexes that are mainly based on titanium and zirconium. An enormous increase in the number of publications on non-metallocene olefin polymerization catalysis started in the middle of the 90s, and this seems to be an ongoing trend as the research has spread from group 4 metals to nearly all other transition metals. Non-metallocene catalysts and their ethene polymerization properties have been reviewed rather extensively.[6–8]

Fujita and coworkers at Mitsui Chemicals have so far reported the most efficient homogeneous non-metallocene catalysts for ethene polymerization. An activity as high as 80 kg_{PE}/(mmol·bar·h) was achieved for a MAO-activated bis[*N*-(3-*tert*-butylsalicylidene)-2,3,4,5,6-pentafluoroanilinato]zirconium(IV) dichloride catalyst precursor.[9] These types of catalysts are sensitive to the applied substituent pattern on the ligand framework, and depending on the ligand structure, the polymerization activities can vary from 0.1 to 10 kg_{PE}/(mmol·bar·h).[9–12] The structure of the catalyst precursor as well as the polymerization conditions also influence the properties of polyethene. As an augmentation to our earlier studies on non-metallocene polymerization catalysis,[13–15] we report herein a straightforward and efficient synthetic strategy to prepare (salicylaldiminato)-based titanium dichlorides. The ethene polymerization reactions of the newly synthesized (**2** and **4**–**6**) and already known complexes (**1** and **3**) with different aromatic substituents on the imine nitrogen atom were studied in order to evaluate the steric and electronic influences caused by the ligand substituents on the polymerization properties (Scheme 1).

[a] Department of Chemistry, Laboratory of Inorganic Chemistry, P. O. Box 55, 00014 University of Helsinki, Finland
Fax: +358-9-19150198
E-mail: timo.repo@helsinki.fi
[b] Department of Chemistry,University of Joensuu, P. O. Box 111, 80101 Joensuu, Finland

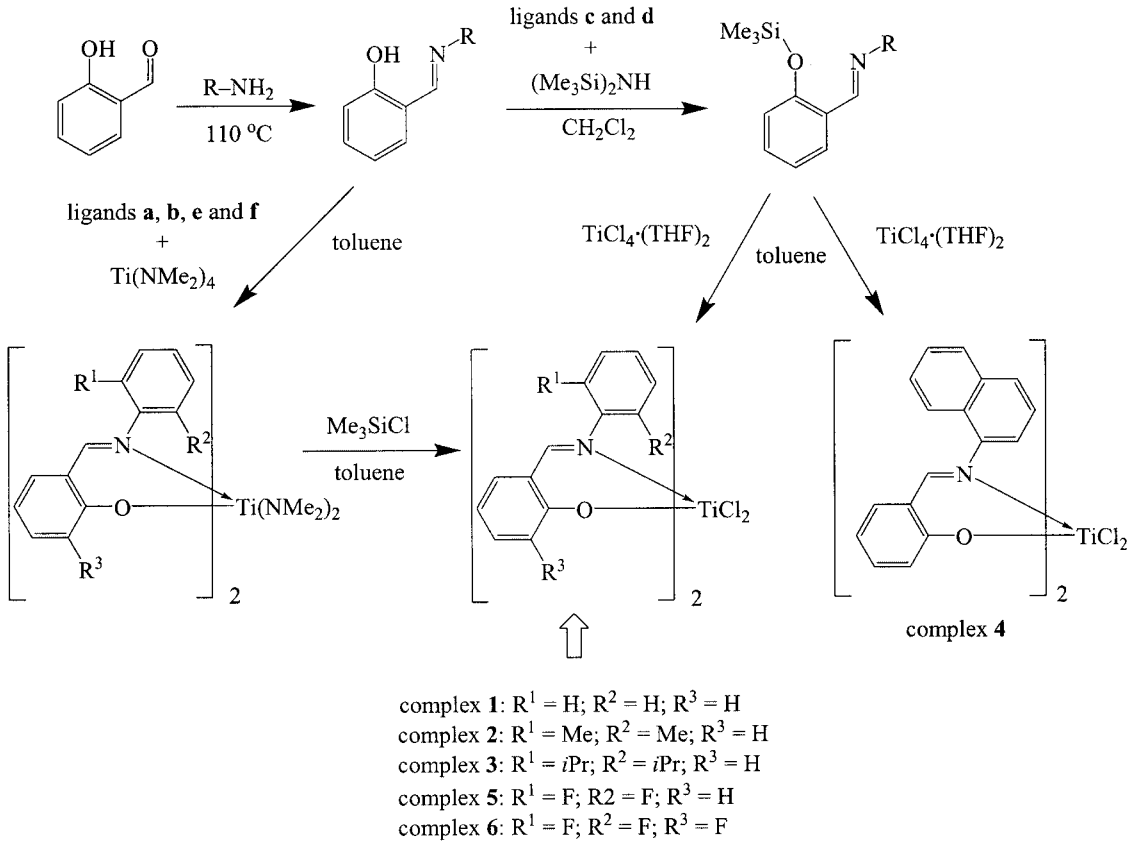

complex **1**: $R^1 = H$; $R^2 = H$; $R^3 = H$
complex **2**: $R^1 = Me$; $R^2 = Me$; $R^3 = H$
complex **3**: $R^1 = i$Pr; $R^2 = i$Pr; $R^3 = H$
complex **5**: $R^1 = F$; R2 = F; $R^3 = H$
complex **6**: $R^1 = F$; $R^2 = F$; $R^3 = F$

Scheme 1. Schematic presentation of the synthesis and the (salicylaldiminato)titanium complexes studied.

Results and Discussion

Synthesis of Ligand Precursors

Ligands containing phenoxy-imino groups are well known and are common in coordination chemistry. In our case, the synthesis of the ligands (**a**–**d**) was performed by the direct reaction between salicylaldehyde and the corresponding aniline by heating the reaction mixture in an oil bath at 110 °C in an open, round-bottomed flask overnight to ensure evaporation of water.[16–18] The novel ligands (**e** and **f**) were synthesized in a similar manner to ligands (**a**–**d**) with two exceptions: the former ligands required a catalytic amount of sulfuric acid to achieve high yields, and the reactions were performed in toluene. The crude products from the reactions with all ligands were isolated in high yields. The color of ligand **d** was dark brown, **e** and **f** were orange, and the others were yellow. According to ^{1}H NMR spectroscopy all these salicylaldimines were pure and no further purifications were required.

Synthesis of Complexes

There are several methods that can be used successfully in the complexation of salicylaldiminato ligands with group 4 metals. *n*BuLi is consistently applied as reagent for ligand deprotonation, and in subsequent complex preparation, metal halides are employed. The yields of the desired bis(salicylaldiminato)titanium dichloride complexes achieved with *n*BuLi varied between (20–80) percent depending on the corresponding ligand.[11] This method produces the insoluble LiCl salt as a side product, and in the case in which the desired metal complex has low solubility, further purification of the product might be complicated as, for example, filtration causes problems. Another interesting complexation method was published by Erker et al., which afforded complexes by direct reaction between $TiCl_4$ and the salicylaldimine ligand in yields of around 60%.[19] The main target in the complex preparation described here was to find a synthesis route that consists of a few high-yield steps and where side products are either volatile or otherwise easily removable. Two improved routes for the preparation of bis(salicylaldiminato)titanium dichlorides from the ligand precursors (**a**–**f**) were developed, and they both fulfill the above-mentioned requirements and are described below.

Method A

The silylation of the phenolic hydroxyl group with a common silylation reagent like trimethylsilyl chloride has been known to be quantitative under mild reaction conditions. Unfortunately, its use with compounds that contain nitrogen can lead to the formation of the undesired intramolecular iminium salt through elimination of HCl. To avoid salt formation, Me_3SiCl was replaced by 1,1,1,3,3,3-hexamethyldisilazane.[20] It is suitable in this context because hexamethyldisilazane residues (bp. 125 °C) as well as

 © 2005 Wiley-VCH Verlag GmbH & Co. KGaA, Weinheim

the by-product 1-trimethylsilylamine (bp. 57 °C) can be easily removed in vacuo after formation of the desired silyl compound.

Complex preparation with silyl-substituted ligand precursors has some limitations. The silylated phenoxy-imine compounds react fast and unselectively with $TiCl_4$. This phenomenon was observed, for example, in the complexation of the silylated ligand precursor **a**. Together with the desired 1:2 complex (L_2TiCl_2), complexes with the stoichiometry $LTiCl_3$ and L_3TiCl were also observed. We assume that the observed unselectivity is due to lack of the steric bulkiness of the aniline substituents; with ligand precursors **(c** and **d)** that have bulky substituents, the complexation proceeded selectively by simple treatment of two molar equivalents of silylated ligand with $TiCl_4{\cdot}(THF)_2$ at –78 °C (Scheme 1).[21] After the reaction, toluene and the by-product trimethylsilylchloride were removed under vacuum, and the corresponding complexes **3** and **4** were isolated with nearly quantitative yields.

Method B

Method B consisted of two steps that were easy to perform as a one-pot reaction. Compounds containing a phenolic hydroxyl proton are susceptible to direct metallation with $Ti(NMe_2)_4$ followed by cleavage of dimethylamine.[22,23] With this method the formation of the bis(salicylaldiminato)$Ti(NMe_2)_2$ complexes was smooth and proceeded with higher selectivity than with method **A**, e.g. complexation of the ligand precursors (**a**, **b**, **e** and **f**) with $Ti(NMe_2)_4$ produced only the desired 1:2 complexes ($L_2Ti(NMe_2)_2$. Despite the low boiling point of the released $(Me)_2NH$, the complete removal of this by-product does not occur even after an extended period under vacuum at 50 °C. This might be due to partial coordination of dimethylamine to the titanium complex. Free rotation of the amine methyl groups is prohibited and therefore in the ^1H NMR spectrum, the signal for the methyl groups are split into two peaks δ = 1.69 and 2.3 ppm.

Titanium amido complexes are known to be less active catalyst precursors in ethene polymerization than their dichloro derivatives,[24] and hence the obtained bis(salicylaldiminato)$Ti(NMe_2)_2$ complexes were converted directly to the corresponding bis(salicylaldiminato)$TiCl_2$ complex with excess chlorotrimethylsilane.[22] The chlorinated complexes formed selectively and quantitatively. The progress of the chlorination reaction can be followed by ^1H NMR spectroscopy. When 75% of the amido groups were converted to chlorides, three different signals from the imine protons can be detected. For example, in the spectrum of complex **1**, one signal can be assigned to L_2TiCl_2 (δ = 8.06 ppm) and two to $L_2TiClNMe_2$ (δ = 7.92 and 8.22 ppm). Further, the signals for the methyl groups in $L_2TiClNMe_2$ appear as two distinct broad signals at δ = 3.6 and 4.0 ppm. When the reaction was continued, signals from the dimethylamido group gradually disappeared, and in the end, only one imine signal at δ = 8.06 ppm remained. After the removal of the coordinated $(Me)_2NH$, the only by-product from the chlorination procedure was soluble Me_3SiNMe_2, which was easy to remove by recrystallization of the bis(salicylaldiminato)$TiCl_2$ complexes. If the coordinated $(Me)_2NH$ was not removed before chlorination was started, it was possible to observe an additional broad signal at δ = 9.0 ppm in the ^1H NMR spectrum, which is evidence for the formation of a salt-like by-product between $(Me)_2NH$ and Me_3SiCl. However, after refluxing and removal of the solvent, only traces of the by-product remained. The isolated yields for all complexes prepared by method **B** were above 90%.

X-ray Studies of Complex 2

Red crystals of complex **2** suitable for X-ray determination were grown at –20 °C from a saturated toluene solution. The solid-state structure is shown in Figure 1, and crystallographic data as well as selected bond lengths and angles are given in Table 1 and Table 2. The titanium center has a distorted octahedral coordination and is located in the plane of the O_2Cl_2 core. The oxygen atoms are oriented *cis* to each other with nearly equidistant bond lengths (Ti–O1 = 1.8432 Å and Ti–O2 = 1.8629 Å). The octahedral coordination of Ti is accomplished by a *trans* orientation of the imine nitrogen atoms with a dihedral angle of 178.69°. Because of the different coordination mode, the Ti–N bonds are significantly longer than the Ti–O bonds (Ti–N1 = 2.21068 Å and Ti–N2 = 2.1949 Å). The chloride ligands

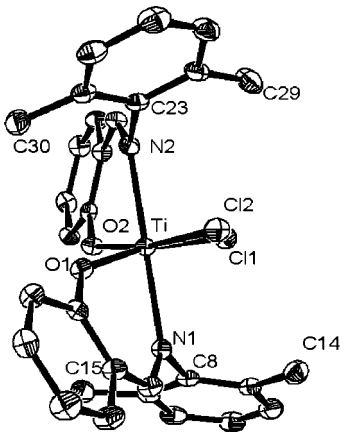

Figure 1. ORTEP plot of **2** with thermal ellipsoids drown at 50% probability level. All hydrogen atoms are omitted for clarity.

Table 1. Selected crystallographic data for complex **2**.[29]

Chemical formula	$C_{30}H_{28}Cl_2N_2O_2Ti$
Formula weight	567.34
Temperature [K]	150(2)
Wavelength [Å]	0.71073
Crystal system	triclinic
Space group	$P\bar{1}$
a [Å]	10.6183
b [Å]	10.7983
c [Å]	13.4618
α [°]	77.596
β [°]	85.990
γ [°]	68.124
Volume [Å^3]	1398.86

 © 2005 Wiley-VCH Verlag GmbH & Co. KGaA, Weinheim

are *cis* oriented and they almost form a right angle (89.90 Å) with equivalent bond lengths (2.33 Å). In general, the bond lengths and angles resemble those reported earlier for bis[(*N*-salicylidene)-2,6-diisopropylanilinato]titanium(IV) dichloride.[19]

Table 2. Selected bond lengths and angles for complex **2**.

Bond lenghts [Å]		Bond angles [°]	
Ti–Cl1	2.333(1)	O2–Ti–N2	81.87(7)
Ti–Cl2	2.332(1)	O1–Ti–N2	98.92(7)
Ti–N1	2.211(2)	O2–Ti–N1	97.02(7)
Ti–N2	2.195(2)	O1–Ti–N1	81.81(7)
Ti–O1	1.843(5)	N2–Ti–Cl2	88.89(5)
Ti–O2	1.863(2)	N1–Ti–Cl2	92.22(5)
O1–C1	1.340(3)	O2–Ti–Cl1	89.62(5)
O2–C16	1.338(3)	O1–Ti–Cl1	170.29(5)
N1–C7	1.300(3)	N2–Ti–Cl1	90.71(5)
N1–C8	1.452(3)	N1–Ti–Cl1	88.59(5)
N2–C22	1.292(3)	Cl–Ti–Cl	89.90(2)
N2–C23	1.456(3)	O–Ti–O	92.98(7)
		N–Ti–N	178.69(7)

Ethene Polymerization

Herein the series of new (**2**, **4**–**6**) and already known (**1** and **3**) bis(salicylaldiminato)$TiCl_2$ complexes with different substituents were introduced in detailed polymerizations after MAO activation to investigate the influence of the ligand structure on the ethene polymerization properties. Because of simple phenyl substitution on the imine nitrogen, **1**/MAO was considered as a reference catalyst. The activity of **1**/MAO, which was 67 $kg_{PE}/(mol_{Ti}\cdot h\cdot bar)$ at (60 °C, 3 bar), rose slowly but constantly with increasing monomer pressure (Table 3). When the pressure was kept constant (5 bar), the activity was enhanced with elevated temperatures and a maximum of 143 $kg_{PE}/(mol_{Ti}\cdot h\cdot bar)$ was achieved at 80 °C. Under harsher polymerization conditions (100 °C, 10 bar), the activity was not significantly better. Irrespective of the applied polymerization conditions, molar masses were between 300–500 kg/mol and the polydispersity (PD) values obtained were narrow. Catalyst **2**/MAO carrying 2,6-methyl-substituted anilines had activities of less than 10 $kg_{PE}/(mol_{Ti}\cdot h\cdot bar)$ under all polymerization conditions, but the molar masses of the polyethenes were twice as high than those obtained with **1**/MAO. All GPC chromatograms represented polymers with unimodal and narrow polydispersities. A subtle tailing toward the low molar mass region was observed only for polymerizations at 80 °C.

The replacement of 2,6-methyl substituents with isopropyl groups further increases the steric congestion aroundthe catalytic active metal center and results in a quite interesting polymerization behavior for **3**/MAO. The polymer produced was clearly bimodal, and the relative ratios between the two molar mass areas varied as a function of temperature. At 40 °C, the distribution curves partly overlapped and therefore the PD value was broad (≈ 14). The average value for the molar mass was around 600 kg/mol. At 60 °C, the catalyst had a distinct bimodal behavior, as two separate curves with narrow distribution were recorded. Molar masses of the separate peaks were 100 and 1000 kg/mol, which is consistent with two active sites. At 80 °C, the molar mass was 350 kg/mol, and the distribution curve was more or less unimodal again with a small shoulder at around 100 kg/mol. Polymerization activities were lower throughout than those with **1**/MAO under similar conditions as they remained below 50 $kg_{PE}/(mol_{Ti}\cdot h\cdot bar)$.

Under the applied polymerization conditions, the activity of naphthyl-substituted **4**/MAO remained below 30 $kg_{PE}/(mol_{Ti}\cdot h\cdot bar)$, and the polymer had a bimodal character. At 40 °C, the distribution curves overlapped, and as a consequence, the observed curve was rather broad and almost flat from the top. This complicated the determination of accurate molar mass values, but the average value for the molar masses was around 800 kg/mol. Polymers prepared at 80 °C have molar masses of 600 kg/mol and a compara-

Table 3. Selected ethene polymerization results with MAO-activated complexes **1**-, **2**- and **3**/MAO ([Al]/[Ti] = 2000) polymerization time 50 min.

Run	Complex	Cat. [μmol]	T_p [°C][a]	p [bar][b]	Activity[c]	M_w [kg/mol]	M_w/M_n	T_m [°C]
1	**1**	20	60	3	67	430	2.6	136
2	**1**	20	40	5	63	340	2.3	140
3	**1**	20	60	5	80	330	2.2	135
4	**1**	20	80	5	143	520	3.5	133
5	**1**	10	60	10	72	370	2.7	141
6	**2**	10	60	3	8	380	6.9	136
7	**2**	5	40	5	6	940	2.4	140
8	**2**	5	60	5	3	740	9.0	135
9	**2**	5	80	5	9	600	7.3	133
10	**2**	10	60	10	5	870	4.3	141
11	**3**	20	60	3	18	710	17.8	133
12	**3**	20	60	5	26	1060	49.5	134
13	**3**	20	60	10	14	750	44	135
14	**3**	20	40	5	21	615	8.9	133
15	**3**	20	80	5	18	600	8.9	133

[a] Polymerization temperature. [b] Monomer pressure. [c] Activity in $(10^3\ g_{PE})/(mol_{Ti}\cdot h\cdot bar)$. [d] Onset melting temperatures of the polyethenes after heating the samples to 230 °C and cooling down again to 30 °C (cooling and heating rate 20 °C/min).

 © 2005 Wiley-VCH Verlag GmbH & Co. KGaA, Weinheim

Table 4. Selected ethene polymerization results with MAO-activated complexes **4**-, **5**- and **6**/MAO ([Al]/[Ti] = 2000) polymerization time 50 min.

Run	Complex	Cat. [μmol]	T_p [°C][a]	p [bar][b]	Activity[c]	M_w [kg/mol]	M_w/M_n	T_m [°C]
16	**4**	20	60	3	19	480	18.2	128
17	**4**	20	60	5	21	600	14.9	136
18	**4**	20	60	10	19	480	79	135
19	**4**	20	40	5	42	615	8.9	134
20	**4**	20	80	5	8	630	7.5	134
21	**5**	20	60	3	20	270	6.8	136
22	**5**	20	60	5	36	590	7.0	136
23	**5**	10	60	10	95	1540	1.5	142
24	**5**	20	40	5	162	910	1.9	142
25	**5**	20	80	5	41	950	6.6	135
26	**5**	10	100	10	265	1090	1.6	144
27	**6**	10	60	3	37	460	3.0	137
28	**6**	10	60	5	72	1990	3.0	143
29	**6**	10	60	10	713	1520	3.8	144
30	**6**	10	40	5	194	690	4.5	143
31	**6**	10	80	5	120	620/30	1.4/1.4	143

[a] Polymerization temperature. [b] Monomer pressure. [c] Activity in (10^3 g_{PE})/(mol_{Ti}·h·bar). [d] Onset melting temperatures of the polyethenes after heating the samples to 230 °C and cooling down again to 30 °C (cooling and heating rate 20 °C/min).

tively unimodal distribution curve. Only a small shoulder was observed around the 100 kg/mol region.

The replacement of aniline with 2,6-difluoroaniline changes the catalyst performance considerably. At 40 °C, the activity of **5**/MAO [165 kg_{PE}/(mol_{Ti}·h·bar)] was significantly higher than **1**/MAO [63 kg_{PE}/(mol_{Ti}·h·bar)], but by increasing the temperature its activity decreased to same level as catalyst **1**/MAO. This, together with the fact that the molar mass distributions were considerably expanded with a bimodal behavior at higher temperatures, might indicate changes in the catalytically active species. Catalyst **5**/MAO showed a rather linear enhancement of its activity with increasing ethene pressure. Actually, the highest activity for **5**/MAO [265 kg_{PE}/(mol_{Ti}·h·bar)] was achieved at 100 °C and 10 bar. At lower ethene pressures, the catalyst tended to produce polymers with bimodal distributions; however, with sufficient monomer concentrations, single-center behavior of the catalyst appeared, and polydispersities of the polymers were below 2.

In general, **6**/MAO had similar trends in the variation of polymerization conditions as **5**/MAO. It was slightly more tolerant against thermal changes since only a bimodal distribution curve was observed at 80 °C. The catalyst **6**/MAO revealed the highest activity, 713 kg_{PE}/(mol_{Ti}·h·bar) and gave polyethene with the highest molar mass (2000 kg/mol) (Table 4, runs 28 and 29). The molar mass distribution of polyethene was less than four and unimodal under all conditions. Only at 80 °C was the PE formed bimodal, and the chromatogram consisted of two overlapping curves with equal areas (Figure 2, Figure 3).

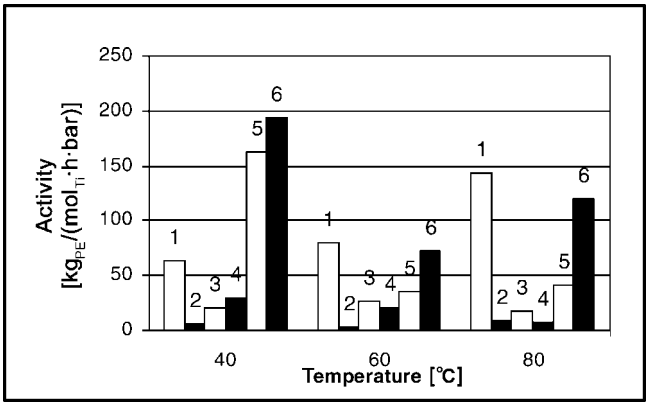

Figure 2. Activities of the catalysts (**1**–**6**)/MAO at different temperatures in ethene polymerization at 5 bar.

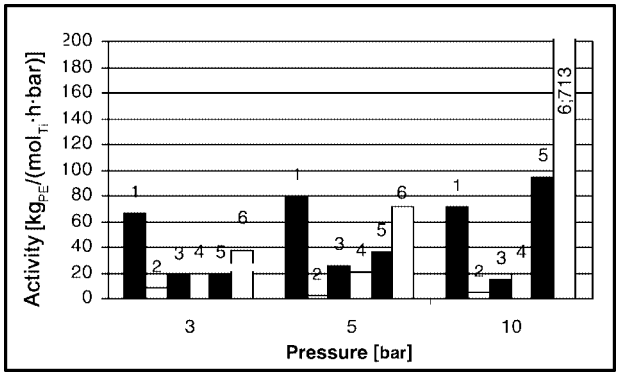

Figure 3. Activities of the catalysts (**1**–**6**)/MAO at different pressures in ethene polymerization at 60 °C.

Correlation Between Complex Structure and Polymerization Behavior

Bis(salicylaldiminato)$TiCl_2$ complexes have three isomers that could be considered as active precatalysts in ethene polymerization as they all have chloride ions in a *cis* position (Figure 4). In two of the possible conformations, the imine nitrogen atoms are in *cis*- and the oxygen atoms, in *trans* positions, or vice versa. In the third conformation both the nitrogen and oxygen atoms occupy the *cis* orientation. The existence of all of these isomers has been experimentally verified by crystal-structure determination.[19,25] The com-

 © 2005 Wiley-VCH Verlag GmbH & Co. KGaA, Weinheim

plexes bearing bulky imino substituents have nitrogen atoms in a *cis* orientation, while complexes having fluorine or hydrogen at the 2,6-positions in the anilino part favor a *trans* orientation.

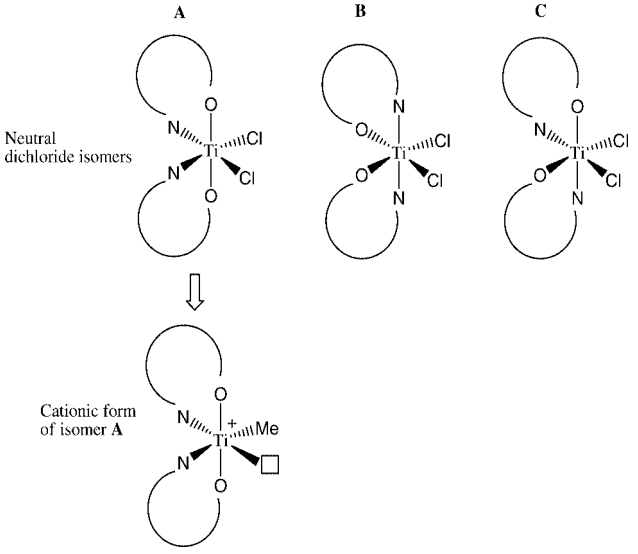

Figure 4. Schematic presentation of the neutral and active isomers in ethene polymerization.

The structures of the complexes calculated with ab initio methods[26,27] and those measured experimentally by X-ray diffraction are indeed in good agreement for complexes **1**–**3**. According to the solid-state structure, in complex **1**, the imine nitrogen atoms are in *cis* positions (Figure 4, A), and this conformer has a significantly lower energy than the isomer in which the nitrogen atoms occupy the axial corners of the octahedra (Figure 4, B). Due to steric interactions, the increasing bulkiness on the aniline moiety raises the energy level of the *cis* isomer, and the *trans* isomer is favored. This is in accordance with the solid-state structures of complexes **2** and **3**. The structural data for the rest of the complexes studied were calculated by theoretical methods only: *trans* isomer for complex **4**, while for **5** and **6**, which both have 2,6-fluoroaniline, the *cis* isomer was the most stable isomer.

In the solid state, complex **1** has the imine nitrogen atoms *cis* to each other, and the angle between the chloride ligands is 97°. In complex **2**, which carryies 2,6-dimethylaniline, the imine moieties are *trans* to each other (179°), and the angle between the chloride ligands is reduced to 89°. When the size of the aniline substituents is increased, the angle between the nitrogen atoms (172°) in **3** becomes smaller, and the angle between chloride ligands increases (94°). By comparing the polymerization activities and the geometries of the complexes, a clear dependence can be observed – the catalyst precursors that prefer the imine nitrogen atoms in the *cis* position, **1**, **5** and **6**, are more active in ethene polymerization than those that have a *trans* configuration. In any event, this observation does not provide answers to the question "what will happen after activation and why does PE have uni- and bimodal distribution curves". Therefore, the stability of the bis(salicylaldiminato)Ti^+–Me species was the subject of further calculations as the stability of the metal cation is one of the crucial parameters which determines polymerization activity of a certain catalytic species (Figure 4).[28]

The energy differences between the dichloro complexes and corresponding monomethyl cation forms were calculated for each isomer. According to the data, the relative stability of the structural isomers is altered after activation, e.g. complex **6** prefers a *cis* orientation but for the cation, the *trans* isomer has the lowest energy (Table 5). This phenomenon complicates the direct comparison of the calculated stability values and the experimental polymerization activities, and raises the question whether the species responsible for the catalytic activity has the same conformation as the corresponding dichloro complex. In fact, elegant ^{15}N NMR spectroscopic studies by Fujita et al. indicate that some of the bis(salicylaldiminato)$ZrCl_2$ complexes possess fluxional behavior, and intramolecular change of the complex geometry can occur.[29]

Table 5. The relative stability energies E_{Rel} in kJ/mol of the dichloro complexes **1**–**6** $E_{Rel}(Cl_2)$ and their cationic forms $E_{Rel}(Ti^+)$ including different isomeric structures. The most stable isomer has been marked. In the calculations the *trans* isomer of each catalyst precursor has been chosen as a point of reference. The stability of Ti^+ was compared with the cationic form of $TiCl_4$.

Complex	$E_{Rel}(Cl_2)$	$E_{Rel}(Ti^+)$	Stability of Ti^+
1-*cis*	**–21**	**0**	–435
1-*ciscis*	–8	0	–448
1-*trans*	0	**0**	**–456**
2-*cis*	40	**0**	**–479**
2-*ciscis*	48	79	–409
2-*trans*	**0**	**0**	–439
3-*cis*	43	**–26**	**–495**
3-*ciscis*	65	0	–491
3-*trans*	**0**	0	–426
4-*cis*	3	**0**	–453
4-*ciscis*	13	**0**	**–463**
4-*trans*	**0**	**0**	–450
5-*cis*	**–7**	15	–440
5-*ciscis*	31	3	**–490**
5-*trans*	0	**0**	–462
6-*cis*	**–17**	10	–437
6-*ciscis*	21	5	**–479**
6-*trans*	0	**0**	–464

Whenever the conformation of the catalyst changes, one of the coordination bonds is released, after which rotation of the ligand can take place. This gives an option that the *cis* or *trans* isomers can be converted directly into the *ciscis* isomer, which is also the required intermediate isomer if ever the exchange between *cis* and *trans* isomer takes place. Taking this possibility into account, the observed activities as well as the multisite behaviors of the complexes can be rationalized.

In the series complexes, **1** prefers a *cis* conformation, and after MAO activation, it produces polyethene with good activity. At low polymerization temperatures, **1**/MAO gives PE with unimodal PD, while at higher temperatures, bimodal behavior is apparent. According to the calculations, all cationic isomers have an equal possibility of occurring,

 © 2005 Wiley-VCH Verlag GmbH & Co. KGaA, Weinheim

while the *trans* geometry gives the most stable active center and it should be the dominant species in the polymerization (Table 5). The neutral and cationic form of **2** prefers the *trans* isomer, and in addition the *ciscis* isomer is located significantly higher in energy and, therefore, the geometry of the catalyst is frozen to the initial *trans* conformer with low stability. This is in accordance with the observed low activity and unimodal behavior of the catalyst. As a neutral complex, **3** favors the *trans* conformer, while in the cationic form the *cis* isomer is more favorable. Because the *ciscis* intermediate is low in energy such a change in the coordination sphere is easily achievable and is reflected in the polymerization behavior of 3/MAO. The interchange of catalyst geometries can be seen as a broad distribution curve at 40 °C, bimodal at 60 °C, but at 100 °C, PE with narrow PD (1.84) is obtained, which implicates the presence of only one type of active center (*cis*). Complex **4** prefers the *cis* form, but after activation all isomers have an equal possibility of occurring – the stability of the *ciscis* isomer is only slightly favorable. Therefore, under certain conditions, **4**/MAO produced PE with trimodal character. Before activation, **5** and **6** adopt a *cis* conformation, but in the cationic form the *trans* isomers are slightly favored. In fact, catalyst **6**/MAO produces PE with a high activity and mainly with a unimodal distribution. Only at 80 °C is the polymer clearly bimodal, which is in accordance with the presence of the higher energy *ciscis* isomer. Due to the lower energy gap between the *trans*- and *ciscis* isomers, **5**/MAO is more prone to produce bimodal PE.

In addition to the stability of the cation, the steric shielding of the catalyst is also one of the crucial factors that determine the activity in polymerization. In the series of catalysts, **3** exhibits the highest calculated stability value but only medium catalytic activity has been detected. This raises the question about the steric shielding of the metal center. In fact, Fujita et al. have also reported the deleterious effects of aniline's alkyl substituents on the catalytic activity and they suggested that the alkyl groups increase the steric congestion around the active site.[12,30] We assume that the low activity of **3** as well as **2** and **4**, combined with low stability of the cation, arises from the same origin. Tuning of the size of the substituent has a significant influence on the average polymerization activity.[31]

Electron-withdrawing fluoro substituents on aniline have been considered as highly desirable as they give catalyst precursors with highest activities. We assume that the coordination between imino-N and Ti weakens, and affords, therefore, rapid intramolecular exchange towards the conformation with the highest stability even at low polymerization temperatures (25 °C and below). When the polymerization temperature is increased (above 60 °C), the catalyst precursor with aniline (**1**) possesses similar or even higher activities than that bearing 2,6-difluoro aniline (**5**).

Conclusions

Bis(salicylaldiminato)$TiCl_2$ complexes are often described as catalyst precursors that are able to produce polyethene with narrow polydispersities, and even a living polymerization of α-olefins has been reported.[11] The series of bis(salicylaldiminato) catalysts described here posses a tunable multisite character with high activity. Similar multisite behavior of bis(salicylaldiminato)$TiCl_2$ catalyst precursors has been reported only for bis[(3-(3,5-dicumyl)salicylidene) anilinato]zirconium(IV) dichloride; depending on polymerization conditions uni-, bi- and trimodal polyethene have been obtained.[29]

Subtle variations in the ligand structure and polymerization conditions can significantly change the polymer properties. What is apparent from this study is the fact that the structure of the catalyst precursor does not predict the polymerization properties of the activated complex. The most important factor is the conformation of the active catalyst. The catalysts studied here are prone to change their coordination sphere after the activation process, and the relative stability energies of the different cation isomers vary with the ligand substituents. The relative stabilities of the different isomers depend on the ligand substituents. Different conformers of the active species can be present at the same time, which is seen by a multimodal behavior in polymerization. The ratio of the active species present in polymerization can be also fine tuned by the reaction temperature. In this series of catalysts, the metal cations with a *trans* conformation possess highest activities. For example, the activity of the catalyst **1**/MAO is three times greater than that of catalysts **3**/MAO and **4**/MAO, for which the most stable isomer is the *cis* isomer. It is reasonable to assume that in the *trans* conformation, the active center is sterically protected by the imino substituents. As a conclusion, the phenomenon described above illustrates the fluxional character of bis(salicylaldiminato)$TiCl_2$ complexes, which depends on the ligand substituents, and is therefore unique for each catalyst.

Experimental Section

All organometallic syntheses were performed under argon using standard Schlenk techniques and dry solvents.

Materials: Toluene, *n*-hexane, and tetrahydrofuran (THF) of HPLC grade were dried and purified by refluxing over sodium and benzophenone, followed by distillation under argon. Dichloromethane (CH_2Cl_2) was dried and purified over CaH_2 by refluxing for 4 h and subsequent distillation. Toluene, *n*-hexane, and THF were stored with sodium flakes under argon. Salicylaldehyde (Fluka), 3-fluorosalicylaldehyde (Aldrich), 3-*tert*-butylsalicylaldehyde (Aldrich), aniline (Aldrich), 2,6-dimethylaniline (Aldrich), 2,6-diisopropylaniline (Aldrich), naphthylamine (Aldrich), 2,6-difluoroaniline (Aldrich), 2,3,4,5,6-pentafluoroaniline (Aldrich), Tetrakis(dimethylamino)titanium (Aldrich), and $TiCl_4$ (Riedel-de Haën) were used as received, methylaluminoxane (MAO, 30 wt.-% solution in toluene) was received from Borealis Polmers Oy.

^1H- and ^{13}C NMR spectra were collected on a Varian Gemini 2000 (200 MHz) spectrometer. Chemical shifts were referenced internally with respect to $CHCl_3$ (δ =7.27 and 77.23 ppm, respectively). Mass spectra (EI) were acquired by a JEOL-SX102 spectrometer. DSC

 © 2005 Wiley-VCH Verlag GmbH & Co. KGaA, Weinheim

measurements (melting point) were performed on a Perkin–Elmer DSC-2, calibrated with indium (temperature scanning 20 °C/min). Scan area was from 25 °C to 232 °C. Mass average molecular weights (M_w), number average molecular weights (M_n), and molecular weight distribution (MWD, M_w/M_n) of the polyethene samples were determined by GPC (Waters Alliance GPCV 2000, high-temperature gel chromatographic device). HMW7, 2*HMWGE and HMW2 Waters Styrogel columns were used for GPC. Measurements were performed in 1,2,4-trichlrobentzene (TCB) at 160 °C relative to polyethene standards, and 2,6-di-*tert*-butyl-4-methylphenol was used as a stabilizer.

Syntheses of the Compounds a–f

***N*-(Salicylidene)aniline (a):** Fully detailed analyses can be found in the literature.[16] Salicylaldehyde (5 ml, 1.146 g/ml, 0.047 mol) and aniline (4.82 mL, 93.13 g/mol, 0.047 mol) were added to a 100-mL round-bottomed flask at room temperature and were warmed to 120 °C. The heated mixture was stirred overnight. The crude product was recrystallized from propanol (8.34 g, 90%). ^{1}H NMR (200 MHz, $CDCl_3$, 29 °C): δ = 6.93–7.08 (m, 2 H, H–Ph) 7.26–8.63 (m, 5 H, H–Ph), 8.63 (s, 1 H, CNH), 13.31 (s, 1 H, OH) ppm.

***N*-(Salicylidene)-2,6-dimethylaniline (b):** Fully detailed analyses can be found in the literature.[17] Compound **b** was prepared by a similar method as described above for **a**. Salicylaldehyde (5 ml, 1.146 g/ml, 0.047 mol) and 2,6-dimethylaniline (5.9 mL, 121.18 g/mol, 0.047 mol) were mixed. The product was isolated as yellow crystals. Yield: 9.53 g, 90%. ^{1}H NMR (200 MHz, $CDCl_3$, 29 °C): δ = 2.24 (s, 6 H, CH_3), 6.95–7.12 (m, 5 H, H–Ph), 7.35–7.48 (m, 2 H, H–Ph), 8.37 (s, 1 H, CNH), 13.13 (s, 1 H, OH) ppm. MS (EI): *m*/*z* = 224–225 with appropriate isotope ratio for [$C_{15}H_{15}NO^+$].

***N*-(Salicylidene)-2,6-diisopropylaniline (c):** Fully detailed analyses can be found in the literature.[17] Compound **c** was prepared by a similar method as described above for **a**. Salicylaldehyde (5 mL, 1.146 g/ml, 0.047 mol) and 2,6-diisopropylaniline (17.7 mL, 177.29 g/mol, 0.047 mol) were mixed. The product was isolated as yellow crystals. Yield: 10.58 g, 80%. ^{1}H NMR (200 MHz, $CDCl_3$, 29 °C): δ = 1.26 (d, 12 H, CH_3), 3.08 (sept, 2 H, CH), 7.05–7.55 (m, 7 H, H–Ar), 8.39 (s, 1 H, CNH), 13.18 (s, 1 H, OH) ppm.

***N*-Naphthylsalicylaldimine (d):** Fully detailed analyses can be found in the literature.[18] Compound **d** was prepared by a similar method as described above for **a**. Salicylaldehyde (5 mL, 1.146 g/ml, 0.047 mol) and naphthylamine (6.73 g, 0.047 mol) were mixed. The product was isolated as a brown powder. Yield: 8.14 g, 70%. ^{1}H NMR (200 MHz, $CDCl_3$, 29 °C): δ = 6.67–6.97 (m, 3 H, H–Ar), 7.12–7.32 (m, 3 H, H–Ar), 7.49–7.53 (m, 2 H, H–Ar), 7.56–7.65 (m, 2 H, H–Ar), 7.95–8.03 (m, 2 H, H–Ar), 8.42 (s, 1 H, CNH) ppm.

***N*-(Salicylidene)-2,6-difluoroaniline (e):** Salicylaldehyde (5 mL, 1.146 g/ml, 0.047 mol) and 2,6-difluoroaniline (5.1 mL, 1.199 g/ml, 0.047 mol) were added to a 100-mL round-bottomed flask at room temperature. To the mixture were added a catalytic amount of concentrated sulfuric acid and toluene (40 mL), and the mixture was warmed to 110 °C. The heated mixture was stirred overnight. The formed imine was dissolved in CH_2Cl_2, dried with solid Na_2SO_4, and the mixture was filtered. The product was isolated as an orange–yellow powder. Yield: 9.86 g, 90%. ^{1}H NMR (200 MHz, $CDCl_3$, 29 °C): δ = 6.93–7.22 (m, 5 H, H–Ar), 7.38 and 7.42 (d, 2 H, H–Ar), 8.88 (s, 1 H, CNH), 12.94 (s, 1 H, OH) ppm. ^{13}C{1H} NMR (50.3 MHz, $CDCl_3$, 29 °C): δ = 107.27 (Ar), 112.05–112.53 (m, 2 H, Ar), 117.76 (Ar), 119.34 (Ar), 126.71 (t, 1 H, Ar), 132.98 (Ar), 134.12 (Ar), 153.64 and 153.75 (d, Ar), 158.65 and 158.79 (d, Ar), 161.63 (Ar), 168.93 (t, Ar) ppm. MS (EI): *m*/*z* = 233–234 with appropriate isotope ratio for [$C_{13}H_9F_2NO^+$].

***N*-(3-Fluorosalicylidene)-2,6-difluoroaniline (f):** Compound **f** was prepared by a similar method as described above for **e**. 3-Fluorosalicylaldehyde (1.0 g, 0.00713 mol) and 2,6-difluoroaniline (0.77 mL, 0.00713 mol) were mixed. The product was isolated as an orange–yellow powder. Yield: 1.61 g, 90%. ^{1}H NMR (200 MHz, $CDCl_3$, 29 °C): δ = 6.84–8.94 (m, 6 H, H–Ar), 8.94 (s, 1 H, CNH), 13.21 (s, 1 H, OH) ppm. MS (EI): *m*/*z* = 250–251 with appropriate isotope ratio for [$C_{13}H_8F_3NO^+$].

Syntheses of the Complexes 1–6

Bis[*N*-(salicylidene)anilinato]titanium(IV) Dichloride (1): Fully detailed analyses of complex **1** can be found in the literature.[19] Compound **a** (2.0 g, 0.010 mol) was dissolved in toluene (60 mL), and cooled to –78 °C, after which it was slowly transferred with a syringe to a precooled solution of toluene (60 mL) and $Ti(NMe_2)_4$ (1.2 mL, 224.21 g/mol, 0.0050 mol). The solution obtained was stirred overnight at room temperature. Quantitative formation of the complex bis(dimethylamino)bis[*N*-salicylidene)anilinato]titanium was observed. ^{1}H NMR (200 MHz, $CDCl_3$, 29 °C): δ = 1.69 (s, 6 H, HN*Me*$_2$), 2.30 (s, 6 H, HN*Me*$_2$), 3.5 (b, 12 H, TiN*Me*$_2$), 4.83 (s, 2 H, *H*NMe_2), 5.89 and 5.93 (d, 2 H, H–Ar), 6.58–7.57 (m, 16 H, H–Ar), 8.49 (s, 2 H, CNH) ppm. MS (EI): *m*/*z* = 528 with appropriate isotope ratio for [$C_{30}H_{32}N_4O_2Ti^+$]. The amount of the solvent was reduced to 40 mL, and trimethylsilylchloride (20× excess, 25 mL, 0.856 g/ml, 0.2 mol) was added at room temperature. The reaction mixture was stirred overnight, followed by 2 h of heating in refluxing toluene and removal of side-product residues at 70 °C in vacuo. The procedure was repeated twice (may be necessary). Traces of unidentified amine compounds were still observed by ^{1}H NMR spectroscopy, otherwise the product was pure according to EA, NMR, MS. Yield: 2.55 g, 98%. ^{1}H NMR (200 MHz, $CDCl_3$, 29 °C): δ = 6.47 and 6.51 (d, 2 H, H–Ar), 6.98–7.34 (m, 16 H, H–Ar), 8.27 (s, 2 H, CNH) ppm. MS (EI): *m*/*z* = 511 with appropriate isotope ratio for [$C_{26}H_{20}Cl_2N_2O_2Ti^+$]. $C_{26}H_{20}Cl_2N_2O_2Ti$: calcd. C 61.08, H 3.94, N 5.48; found C 61.22, H 4.01, N 5.57.

Bis[*N*-(salicylidene)-2,6-dimethylanilinato]titanium(IV) Dichloride (2): Complex **2** was prepared by a similar method as described above for **1**.

Analyses of the quantitative formation of the intermediate product bis(dimethylamino)bis[*N*-salicylidene)-2,6-dimethylanilinato]titanium. ^{1}H NMR (200 MHz, $CDCl_3$, 29 °C): δ = 2.16 (s, 6 H, Ar–CH_3), 2.35 (s, 6 H, Ar–CH_3), 2.56 (s, 6 H, NCH_3), 2.87 (s, 6 H, CH_3, NCH_3), 6.37 and 6.41 (d, 2 H, H–Ar), 6.59 (t, 2 H, H–Ar), 7.00–7.27(m, 10 H, H–Ar), 8.06 (s, 2 H, CNH) ppm. MS (EI): *m*/*z* = 584 with appropriate isotope ratio for [$C_{34}H_{40}N_4O_2Ti^+$].

Analyses of the final product. The product was isolated as yellow crystals. Yield: 2.55 g, 90%. ^{1}H NMR (200 MHz, $CDCl_3$, 29 °C): δ = 2.47 and 2.50 (d, 12 H, Ar–CH_3), 6.76 and 6.80 (d, 2 H, Ar), 6.98–7.17 (m, 8 H, H–Ar), 7.53–7.65 (m, 4 H, H–Ar), 8.38 (s, 2 H, CNH) ppm. ^{13}C{1H} NMR (50.3 MHz, $CDCl_3$, 29 °C): δ = 19.15 (s, Ar–*C*H_3), 19.85 (s, Ar–*C*H_3), 115.48 (Ar), 122.11 (Ar), 124.34 (Ar), 126.95 (Ar), 127.81 (Ar), 129.06 (Ar), 130.11 (Ar), 131.54 (Ar), 134.64 (Ar), 137.04 (Ar), 154.01 (Ar), 164.01 (Ar), 169.58 (Ar) ppm. MS (EI): *m*/*z* = 566 with appropriate isotope ratio for [$C_{30}H_{28}Cl_2N_2O_2Ti$]$^+$.

Bis[*N*-(salicylidene)-2,6-diisopropylanilinato]titanium(IV) Dichloride (3): Fully detailed analyses of the complex **3** can be found in the literature.[19] Compound **c** (3.0 g, 10.6 mmol) was dissolved in dry CH_2Cl_2 (30 mL) in a Schlenk flask, under argon. Hexamethylsilazane (3.0 mL, 0.765 g/ml, 14.22 mmol) was added to the solution with a syringe. The reaction mixture was kept at room temperature

 © 2005 Wiley-VCH Verlag GmbH & Co. KGaA, Weinheim

and was stirred overnight. Evaporation of excesshexamethylsilazane and by-products under vacuum at 50 °C over 5 h purified the product. The silylated *N*-(salicylidene)-2,6-diisopropylaniline was a slightly yellow, viscose liquid. The yield was quantitative (3.15 g). ^{1}H NMR (200 MHz, $CDCl_3$, 29 °C): δ= 0.37 (s, 9 H, SiCH_3), 1.28 (d, 12 H, CH_3), (sept, 2 H, CH), 6.97 (d, 1 H, H–Ar), 7.15–7.33 (m, 4 H, H–Ar), 8.45 (t, 1 H, H–Ar), 8.29 (d, 1 H, H–Ar), 8.62 (s, 1 H, CNH) ppm. The silylated compound **c** (3.55 g, 10.07 mmol) was dissolved in dry THF (60 mL) in a Schlenk flask, and cooled to the freezing point of THF with liquid nitrogen. The same cooling procedure was performed with $TiCl_4$·$(THF)_2$ (2.23 g, 5.04 mmol), which was dissolved on THF (150 mL). Precooled silylated compound **c** was slowly transferred to the titanium solution with syringe under an argon flow. The solution immediately turned to light red. The reaction mixture was stirred overnight, and allowed to come to room temperature. During that time, the color of the mixture turned to deep red. The titanium complex was purified by evaporation of the formed trimethylsilylchloride and THF. Recrystallization was performed from *n*-hexane/THF (7:1). Yield: 2.91 g, 85%. ^{1}H NMR (200 MHz, $CDCl_3$, 29 °C): δ = 1.14 (d, 12 H, CH_3), 1.30 (d, 6 H, CH_3), 1.46 (d, 6 H, CH_3), 1.90 (4 H, THF), 3.62 (sept, 4 H, CH), 3.80 (4 H, THF), 6.78 (d, 2 H, H–Ar), 7.10 (t, 2 H, H–Ar), 7.17 (m, 6 H, H–Ar), 7.48 (m, 4 H, H–Ar), 8.42 (s, 1 H, CNH) ppm. MS (EI): *m*/*z* = 679–684 with appropriate isotope ratio for [$C_{38}H_{44}N_2O_2TiCl_2^+$]. $C_{38}H_{44}N_2O_2TiCl_2$: calcd. C 67.16, H 6.53, N 4.12, Ti 7.05; found C 66.84, H 6.71, N 4.26, Ti 7.17.

Bis[*N*-(naphthylsalicylaldiminato]titanium(IV) Dichloride (4): Complex **4** was prepared by a similar method as described above for **3**. Silylated compound **d** was a slightly yellow, viscous liquid. The yield was quantitative (3.39 g). ^{1}H NMR (200 MHz, $CDCl_3$, 29 °C): δ = 0.33 (s, 9 H, SiCH_3), 6.90–7.20 (m, 3 H, H–Ar), 7.18–7.58 (m, 4 H, H–Ar), 7.77 (d, 1 H, aromatic), 7.85 (m, 1 H, H–Ar), 8.38 (m, 1 H, H–Ar), 8.90 (s, 1 H, CNH) ppm. MS (EI): *m*/*z* = 319–322 with appropriate isotope ratio for [$C_{20}H_{21}NOSi^+$]. The desired titanium complex precipitated out as a powder from an *n*-hexane/THF (5:1) solution. Yield: 2.62 g, 90%. ^{1}H NMR (200 MHz, $CDCl_3$, 29 °C): δ = 1.86 (4 H, THF), 3.76 (4 H, THF), 5.62 (d, 1 H, H–Ar), 6.02 (d, 1 H, H–Ar), 6.20 (d, 1 H, H–Ar), 6.50–8.40 (m, 19 H, H–Ar), 8.70 (s, 2 H, CNH) ppm. ^{13}C{1H} NMR (50.3 MHz, $CDCl_3$, 29 °C): δ = 25.85 (THF), 68.28 (THF), 116.24 (Ar), 116.76 (Ar), 117.52 (Ar), 119.00 (Ar), 119.23 (Ar), 121.56 (Ar), 121.92 (Ar), 122.54 (Ar), 123.56 (Ar), 123.99 (Ar), 125.00 (Ar), 125.24 (Ar), 125.76 (Ar), 126.88 (Ar), 123.99 (Ar), 125.00 (Ar), 125.24 (Ar), 125.76 (Ar), 126.88 (Ar), 127.80 (Ar), 128.44 (Ar), 133.87 (Ar), 134.69 (Ar), 135.02 (Ar), 136.33 (Ar), 137.06 (Ar), 149.60 (Ar), 162.13 (Ar), 162.53 (Ar), 168.47 (Ar), 169.05 (Ar), 169.62 (Ar) ppm. MS (EI): *m*/*z* = 610–615 with appropriate isotope ratio for [$C_{34}H_{24}N_2O_2TiCl_2^+$]. $C_{34}H_{24}N_2O_2TiCl_2$: calcd. C 66.83, H 3.93, N 4.58, Cl 11.62, Ti 7.86; found: C 64.89, H 4.41, N 4.18, Cl 10.14, Ti 8.69.

Bis[*N*-(salicylidene)-2,6-difluoroanilinato]titanium(IV) Dichloride (5): Complex **5** was prepared by a similar method as described above for **1**. Yield: 2.33 g, 80%. ^{1}H NMR (200 MHz, $CDCl_3$, 29 °C): δ = 6.43–6.47 (m, 4 H, H–Ar), 6.97–7.01 (m, 6 H, H–Ar), 7.36–7.40 (m, 4 H, H–Ar), 8.25 (s, 2 H, CNH) ppm. MS (EI): *m*/*z* = 583–586 with appropppriate isotope ratio for [$C_{26}H_{16}Cl_2F_4N_2O_2Ti^+$]. $C_{26}H_{16}Cl_2F_4N_2O_2Ti$: calcd. C 53.55, H 2.77, N 4.80; found C 53.16, H 3.16, N 4.4.

Bis[*N*-(3-fluorosalicylidene)-2,6-difluoroanilinato]titanium(IV) Dichloride (6): Complex **6** was prepared by a similar method as described above for **1**. Yield: 1.11 g, 90%. ^{1}H NMR (200 MHz, $CDCl_3$, 29 °C): δ = 6.30 (b, 2 H, H–Ar), 6.88–7.40 (m, 10 H, H–Ar), 8.30 (s, 2 H, CNH) ppm. MS (EI) *m*/*z* = 619–620 with appropriate isotope ratio for [$C_{26}H_{14}Cl_2F_6N_2O_2Ti^+$]. $C_{26}H_{14}Cl_2F_6N_2O_2Ti$: calcd. C 50.44, H 2.28, N 4.52; found C 49.91, H 2.46, N 4.10.

Polymerization Experiments: Polymerization runs were performed in a Büchi 1.0-dm^3 stainless steel autoclave equipped with a Julabo ATS-3 and Lauda RK 20 temperature controlling unit. Mechanical stirring was applied with a stirring speed of 800 r.p.m. During polymerization, the partial pressure of ethene and the temperature were kept constant. Ethene consumption was measured with a calibrated mass flow meter and monitored online together with the temperature and pressure inside the vessel by using the Genie™ computer program for data acquisition.

Toluene (250 cm^3) and the cocatalyst (MAO) were introduced to the argon-purged reactor. Once the polymerization temperature had been reached, the vessel was charged with ethene to the appropriate pressure. Polymerization was started by injecting 20 cm^3 of the catalyst precursor solution (5–20 μmol solution in toluene) into the reactor. The polymerization was completed by pouring the contents of the vessel into methanol, acidified with a small amount of concentrated hydrochloride acid. The solid polyethene was collected by filtration, washed with methanol, and dried overnight at 70 °C.

X-ray Crystallographic Study: A single crystal of compound **2** was selected for the X-ray measurement and mounted on the glass fibre using the oil-drop method (Kottke & Stalke, 1993). Data were collected at 120(2) K with a Nonius KappaCCD diffractometer. The intensity data were corrected for Lorentz and polarization[32] effects and for absorption by multi-scan method.[33] The structures were solved by direct methods (SHELXS-97).[34] The refinements and graphics were performed by using the SHELXL-97 and SHELXTL/PC program packages, respectively.[35] All non-hydrogen atoms were refined anisotropically. The H atoms were introduced in calculated positions and refined with fixed geometry with respect to their carrier atoms.

X-ray Data for Complex 2: Z, calculated density 2, 1.347 Mg/m^3, absorption coefficient 0.527 mm^{-1}, F(000) 588, crystal size 0.35 × 0.15 × 0.10 mm, θ range for data collection 2.08 to 26°, reflections collected 27130, unique reflections 5489(R_{int} = 0.0925), completeness to θ = 26.00: 99.7%, absorption correction semi empirical from equivalents, max. and min. transmission 0.9492 and 0.8372, refinement method full-matrix least-squares on F^2, data/restraints/parameters 5489/0/339, goodness of fit on F^2 = 1.120, final R indices [$I > 2\sigma(I)$] R_1 = 0.0492, wR_2 = 0.01252, R indices (all data) R_1 = 0.0570, wR_2 = 0.1298, extinction coefficient 0.0098(19), largest diff. peak and hole 0.538 and –0.672 eÅ^{-3} (see also: Table 1, Table 2, and Figure 1).

CCDC-235033 contains the supplementary crystallographic data for this paper. These data can be obtained free of charge from The Cambridge Crystallographic Data Centre via www.ccdc.cam.ac.uk/data_request/cif.

Theoretical Calculations: Geometry optimisations were performed at the HF/3-21G* level, which has been shown to provide reliable structures for group 4 transition-metal complexes, especially for titanium-based complexes. Based on our earlier studies, neither increasing the size of the basis set nor inclusion of electron correlation at the MP2 level has a significant influence on the geometries, but would certainly increase calculation times. Single-point MP2 calculations were performed to confirm the relative stability order of conformations of the studied titanium complexes. At the single-point calculations, basis set 6-31G* for C, H, O and N, and

 © 2005 Wiley-VCH Verlag GmbH & Co. KGaA, Weinheim

equal-level generated basis set for Ti were used. The stability orders, produced by both methods, are generally in good agreement with each other. The geometry minima were confirmed by frequency calculations. All calculations were carried out by the Gaussian 03 program package.[26]

Acknowledgments

We gratefully acknowledge financial support from Borealis Polymers Oy and the Academy of Finland (project no. 204408), Technology Development Centre (TEKES). We are also obliged to Sami Lipponen (GPC), Markku Hyttinen (EA), Jorma Matikainen (MS) and T. Liitiä (NMR). A.P. extends his thanks on K. Axenov, and E. Aitola.

[1] F. Wild, L. Zsolnai, G. Huttner, H. H. Brintzinger, *J. Organomet. Chem.* **1982**, *232*, 233.
[2] J. Ewen, *J. Am. Chem. Soc.* **1984**, *106*, 6355–6364.
[3] W. Kaminsky, K. Külper, H. H. Brintzinger, F. Wild, *Angew. Chem.* **1985**, *97*, 507.
[4] H. H. Brintzinger, D. Fischer, R. Mülhaupt, B. Rieger, R. Waymouth, *Angew. Chem. Int. Ed.* **1995**, *34*, 1143.
[5] G. H. Alt, A. Köppl, *Chem. Rev.* **2000**, *100*, 1205–1221.
[6] G. P. J. Britovsek, V. C. Gibson, F. D. Wass, *Angew. Chem. Int. Ed.* **1999**, *38*, 428–447.
[7] M. Brookhart, S. D. Ittel, L. K. Johnson, *Chem. Rev.* **2000**, *100*, 1169–1203.
[8] V. C. Gibson, S. K. Spitzmesser, *Chem. Rev.* **2003**, *103*, 283–315.
[9] S. Matsui, T. Fujita, *Catalysis Today* **2001**, *66*, 63–73.
[10] J. Tian, P. D. Hustad, G. W. Coates, *J. Am. Chem. Soc.* **2001**, *123*, 5134–5135.
[11] M. Mitani, J.-I. Mohri, Y. Yoshida, J. Saito, S. Ishii, K. Tsuru, S. Matsui, R. Furuyama, T. Nakano, H. Tanaka, S.-I. Kojoh, T. Matsugi, N. Kashiwa, T. Fujita, *J. Am. Chem. Soc.* **2002**, *124*, 3327–3336.
[12] R. Furuyama, J. Saito, S.-I. Ishii, M. Mitani, S. Matsui, Y. Tohi, H. Makio, N. Tanaka, T. Fujita *J. Mol. Cat. A: Chem.* **2003**, *200*, 31–42.
[13] L. Matilainen, M. Klinga, M. Leskelä, *J. Chem. Soc. Dalton Trans.* **1996**, *2*, 219–25.
[14] T. Repo, M. Klinga, P. Pietikäinen, M. Leskelä, *Macromolecules* **1997**, *30*, 171–175.
[15] T. V. Laine, M. Klinga, M. Leskelä, *Eur. J. Inorg. Chem.* **1999**, 959–964.
[16] R. V. Singh, J. P. Tandon, *Monatshefte fuer Chemie* **1980**, *111*, 1391–1397.
[17] M. Goyal, S. Mishra, A. Singh, *Main Group Met. Chem.* **2001**, *24*, 829–834.
[18] L. S. Skorokhod, I. I. Seifullina, S. A. Dzhambek, *Russian Journal of Coordination Chemistry* **2002**, *28*, 643–646.
[19] J. Strauch, T. H. Warren, G. Erker, R. Frölich, P. Saarenketo, *Inorg. Chim. Acta* **2000**, *300–302*, 810–821.
[20] R. Anwander, J. Eppinger, I. Nagl, W. Scherer, M. Tafipolsky, P. Sirsch, *Inorg. Chem.* **2000**, *39*, 4713–4720.
[21] H. Luttikhedde, L. Reko, C.-E. Wilen, E. Laine, R. Sillanpää, J. Näsman, *J. Organomet. Chem.* **1997**, *547*, 129–132.
[22] A. L. McKnight, Md. A. Masood, R. M. Waymouth, *Organometallics* **1997**, *16*, 2879–2885.
[23] I. Westmoreland, I. Munslow, P. O'Shaughnessy, P. Scott, *Organometallics* **2003**, *22*, 2972–2976.
[24] I. Kim, F. R. Jordan, *Macromolecules* **1996**, *29*, 489–491.
[25] J. P. Corden, W. Errington, P. Moore, M. G. H. Wallbridge, *Chem. Comm.* **1999**, 323–324.
[26] M. J. Frisch, G. W. Trucks, H. B. Schlegel, G. E. Scuseria, M. A. Robb, J. R. Cheeseman, J. A. Montgomery, T. Vreven Jr., K. N. Kudin, J. C. Burant, J. M. Millam, S. S. Iyengar, J. Tomasi, V. Barone, B. Mennucci, M. Cossi, G. Scalmani, N. Rega, G. A. Petersson, H. Nakatsuji, M. Hada, M. Ehara, K. Toyota, R. Fukuda, J. Hasegawa, M. Ishida, T. Nakajima, Y. Honda, O. Kitao, H. Nakai, M. Klene, X. Li, J. E. Knox, H. P. Hratchian, J. B. Cross, C. Adamo, J. Jaramillo, R. Gomperts, R. E. Stratmann, O. Yazyev, A. J. Austin, R. Cammi, C. Pomelli, J. W. Ochterski, P. Y. Ayala, K. Morokuma, G. A. Voth, P. Salvador, J. J. Dannenberg, V. G. Zakrzewski, S. Dapprich, A. D. Daniels, M. C. Strain, O. Farkas, D. K. Malick, A. D. Rabuck, K. Raghavachari, J. B. Foresman, J. V. Ortiz, Q. Cui, A. G. Baboul, S. Clifford, J. Cioslowski, B. B. Stefanov, G. Liu, A. Liashenko, P. Piskorz, I. Komaromi, R. L. Martin, D. J. Fox, T. Keith, M. A. Al-Laham, C. Y. Peng, A. Nanayakkara, M. Challacombe, P. M. W. Gill, B. Johnson, W. Chen, M. W. Wong, C. Gonzalez, J. A., Pople, Gaussian, Inc., Pittsburgh PA, **2003**.
[27] M. Linnolahti, T. A. Pakkanen, *Macromolecules* **2000**, *33*, 9205–9214.
[28] S.-I. Ishii, J. Saito, M. Mitani, J.-I. Mohri, N. Matsukawa, Y. Tohi, S. Matsui, N. Kashiwa, T. Fujita, *J. Mol. Cat. A: Chem.* **2002**, *179*, 11–16.
[29] Y. Tohi, H. Makio, S. Matsui, M. Onda, T. Fujita, *Macromolecules* **2003**, *36*, 523–525.
[30] S. Matsui, M. Mitani, J. Saito, Y. Tohi, H. Makio, N. Matsukawa, Y. Takagi, K. Tsuru, M. Nitabaru, T. Nakano, H. Tanaka, N. Kashiwa, T. Fujita, *J. Am. Chem. Soc.* **2001**, *123*, 6847–6856.
[31] S. Matsui, Y. Tohi, M. Mitani, J. Saito, H. Makio, H. Tanaka, M. Nitabaru, T. Nakano, T. Fujita, *Chem. Lett.* **1999**, *10*, 1065.
[32] *TEXSAN, Single Crystal Structure Analysis Software Version 1.6*, Molecular Structure Corporation, 3200 Research Forest Drive, The Woodlands, TX 77381, USA, **1993**.
[33] *XPREP in SHELTL version 5.1*, Bruker AXS, **1998**.
[34] G. M. Sheldrick, *SHELXS-97, Program for Crystal Structure Solution*, University of Göttingen, Germany, **1997**.
[35] G. M. Sheldrick, *SHELXS-97, Program for Crystal Structure Refinement*, University of Göttingen, Germany, **1997**.

Received: September 6, 2004

 © 2005 Wiley-VCH Verlag GmbH & Co. KGaA, Weinheim

Lanthanide(III) Chelates of DTPA Bis(amide) Glycoconjugates: Potential Imaging Agents Targeted at the Asyaloglycoprotein Receptor

Paula Baía,[a] João P. André,*[a] Carlos F. G. C. Geraldes,[b] José A. Martins,*[a] André E. Merbach,[c] and Éva Tóth[c]

Keywords: Chelates / Contrast agents / Lanthanides / Glycoconjugates / Receptors

The synthesis and characterisation of a new class of DTPA bis(amide) linked glycoconjugates of different sugars [lactose (Lac) and galactose (Gal)] and valencies (di and tetra) and their Ln^{III} complexes is reported. The ^1H NMR spectra of the Sm^{III} and Eu^{III} complexes of $DTPAGal_2$, $DTPAGal_4$, and $DTPALac_2$, obtained between 7 and 80 °C, indicate that several of the four possible diastereoisomeric pairs of structures resulting from the chirality of the three bound DTPA nitrogen atoms are present in solution, with different relative populations. The dynamic effects of racemisation of the central nitrogen atom in the NMR spectra show that this process is fast at 60 °C for the Sm^{III} complexes and slow at 7 °C for the Eu^{III} complexes. The in vitro r_1 nuclear magnetic relaxation dispersion (NMRD) of the water protons of the Gd^{III}–DTPA bis(amide) glycoconjugate containing two lactosyl moieties [Gd^{III}–$DTPALac_2$] was studied, yielding the molecular parameters that govern its relaxivity. Its r_1 value, at 25 °C and 20 MHz, is 13 % higher than that reported for Gd^{III} chelates of lower molecular weight DTPA bis(amides), such as DTPA-BMA, consistent with a five times larger τ_R value. The water exchange rate, k_{ex}, and the electron spin relaxation parameters of the Gd^{III}–$DTPALac_2$ complex are within the usual range for similar Gd^{III}–DTPA bis(amide) chelates.

(© Wiley-VCH Verlag GmbH & Co. KGaA, 69451 Weinheim, Germany, 2005)

Introduction

Magnetic resonance imaging (MRI) is one of the fastest growing techniques in medical diagnosis due to the excellent spatial resolution and contrast, in particular for soft tissues. The image contrast is based mainly on the differences of water proton longitudinal ($1/T_1$) and transversal ($1/T_2$) relaxation rates in different tissues. This contrast can be enhanced with the administration, prior to the scan, of paramagnetic contrast agents (CAs), usually Gd^{III} ($4f^7$) complexes,[1,2] which accelerate the proton relaxation processes in the surrounding water through dipolar interactions between the unpaired electron spin of the metal ion and the proton nuclei of the water molecules. The Gd^{III} chelate of DTPA [DTPA = 3,6,9-tris(carboxymethyl)-3,6,9-triazaundecane-1,11-dioic acid)], $[Gd(DTPA)(H_2O)]^{2-}$, was the first contrast agent (CA) used for human MRI, under the name of Magnevist®.[3] Its success stimulated further studies on modifications of its structure, leading, amongst others, to the neutral derivative [Gd(DTPA-BMA)(H_2O)] [Omniscan®; DTPA-BMA = diethylenetriaminepentaacetic acid *N*,*N*′′-bis(methylamide)], in which two carboxylate groups have been converted into amide functions.[4] These, as well as other hydrophilic linear or macrocyclic Gd^{III} chelates of similar dimensions and simplicity, once injected, rapidly diffuse from the intravascular space into the interstitial space, but do not enter the intracellular space. Their rapid renal elimination produces a rapid decrease in tissue Gd concentration.[5]

Although much used, for example in neuropathological conditions, which are often associated with disruption of the blood brain barrier (BBB) or altered capillary permeability, these extracellular fluid (ECF) CAs also have inherent disadvantages due to their lack of biospecificity, low relaxivities, and poor uptake elsewhere in the body. Their rapid diffusion from the vasculature limits their uses as blood pool agents, for example in estimates of blood flow and perfusion. For such applications, several formulations of DTPA conjugates have been tested, both through covalent binding of the Gd^{III} chelate to suitable macromolecules (albumin,[6] dextran,[7] polylysine,[8] dendrimers[9]) or noncovalent binding to HSA (human serum albumin),[10] for example the Gd–DTPA derivative MS-325.[11] The search for new ligands with high tissue and/or organ specificity

[a] Centro de Química, Campus de Gualtar,Universidade do Minho,
4710-057 Braga, Portugal
Fax: +351-253-678-983
E-mail: jandre@quimica.uminho.pt
jmartins@quimica.uminho.pt
[b] Departamento de Bioquímica, Centro de Espectroscopia RMN e Centro de Neurociências e Biologia Celular, Universidade de Coimbra,
Coimbra, Portugal
[c] Laboratoire de Chimie Inorganique et Bioinorganique, École Polytechnique Fédérale de Lausanne
Switzerland

Supporting information for this article is available on the WWW under http://www.eurjic.org or from the author.

started with hepatobiliary CAs, such as Gd^{III} chelates, which are hepatocyte-specific and are excreted through the hepatobiliary system. Amongst these are Gd^{III} chelates of DTPA-derived ligands bearing various lipophilic substituent groups which promote specific carrier-mediated uptake into the hepatocytes, such as benzyloxymethyl in $[Gd(BOPTA)(H_2O)]^{2-}$ [BOPTA = 4-carboxy-5,8,11-tris(carboxymethyl)-1-phenyl-2-oxa-5,8,11-triazatridecan-13-oic acid][12] and ethoxybenzyl in $[Gd(EOB\text{-}DPTA)(H_2O)]^{2-}$ [EOB-DTPA = (*S*)-*N*-{2-[bis(carboxymethyl)amino]-3-(4-ethoxyphenyl)propyl}-*N*-{2-[bis(carboxymethyl)amino]-ethyl}glycine].[13] Liposomes can also be efficient carriers to deliver Gd^{III}-based CAs to the liver and spleen and hence enhance their MRI image contrast. The amphiphilic Gd(DTPA)–stearylamide, for example, is incorporated into the phospholipid lamella of egg lecithin and cholesterol liposomes.[14]

The hepatocyte cells on liver express a tissue-specific lectin (hepatic lectin) that recognizes terminal β-galactosyl residues on desialylated glycoproteins − the asialoglycoprotein receptor (ASGPR).[15] Liver targeting has been successfully achieved through conjugation of pharmaceutical agents to galactose/lactose.[16] Moreover, a multivalence effect has been demonstrated on the liver uptake of glycoconjugates (tetra > tri > di > mono).[17] Several agents that rely on macromolecular bioconjugates and on polymer scaffolds have been described for hepatic imaging through the targeting of the ASGPR.[18–25] These agents have the drawback of being inherently polydisperse and ill characterised.

In a previous paper we reported the synthesis and physicochemical characterisation of a new class of multivalent glycoconjugates − Ln^{III} chelates of the tetraazatetracarboxylate chelator DOTA conjugated to glycodendrimeric moieties [DOTA = 1,4,7,10-tetrakis(carboxymethyl)-

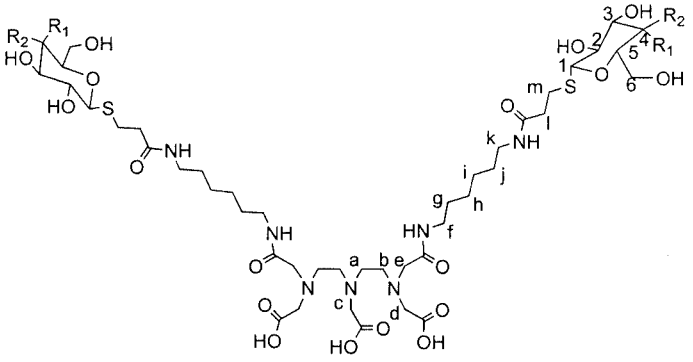

1a R^1 = OH and R^2 = H **DTPA(Gal)$_2$**
1b R^1 =H and R^2 = β–D-galactopyranosyl **DTPA(Lac)$_2$**

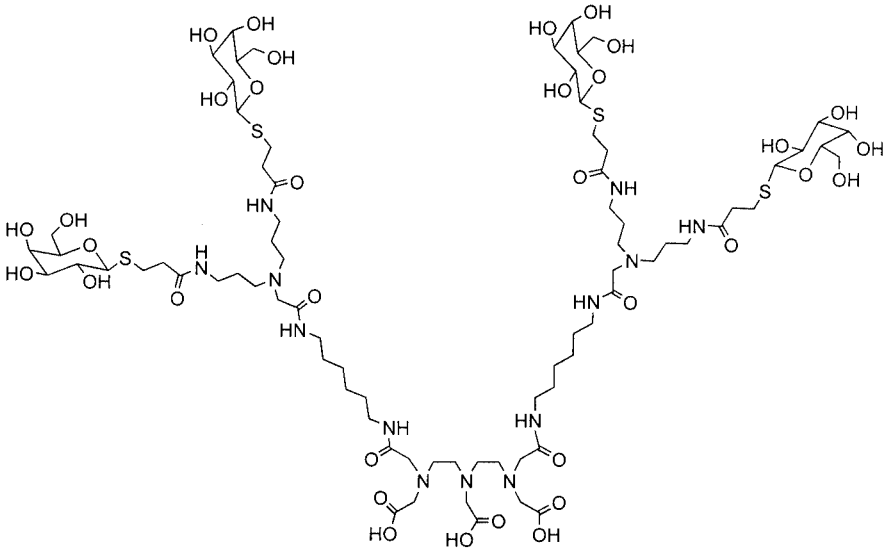

2 DTPA(Gal)$_4$

Figure 1. Structures of the DPTA bis(amide) glycoconjugates (the labelling of the protons for spectral assignments is shown).

 © 2005 Wiley-VCH Verlag GmbH & Co. KGaA, Weinheim

1,4,7,10-tetraazacyclododecane].[26] Previous to our work, only a class of low molecular weight and well-characterised galacto/mannopyranosyl conjugates of DOTA-like chelators had been described for potential MRI and scintigraphic applications.[27] These monovalent Gd^{III}–glycoconjugates are responsive contrast agents activated by galactosidase/mannosidase-mediated hydrolysis.[28] In this paper we report the synthesis and characterisation of (thio)glycoconjugates of the linear chelator DTPA, namely the DTPA bis(amides) **1** and **2** with different terminal sugar residues − galactose (Gal) and lactose (Lac) − and different valences (2 and 4; Figure 1). The thioglycosides are galactosidase-resistant ligands that probe a conformational space and display biological activities very similar to that of their *O*-linked natural counterparts, thus ensuring an increased metabolic stability in vivo.[29] The physicochemical characterisation of some of their Ln^{III} complexes in aqueous solution by ^1H NMR and water ^1H NMRD studies is also described. The proton relaxivity of the Gd^{III} chelates describes the efficiency of the magnetic dipolar coupling between the water proton nuclei and the paramagnetic metal ion, therefore it is a direct measure of the efficacy of the chelate as a CA.

Results and Discussion

Synthesis of the Ligands

The synthesis of the DTPA bis(amides) **1** and **2** (Figure 1) was undertaken through a well-established route consisting of the derivatisation of the commercially available DTPA bis(anhydride) with amine-functionalised blocks. Two different types of amine-functionalised sugar blocks were prepared: a monovalent block **5** (Scheme 1) and a divalent glycodendrimer block **9** (Scheme 2).[26,31] The standard DCC/HOBT coupling procedure was found to be successful for preparing the fully protected amino-functionalised sugar blocks. These compounds were deprotected with TFA/CH_2Cl_2 to afford the terminal amines **6** and **10** as their TFA salts.

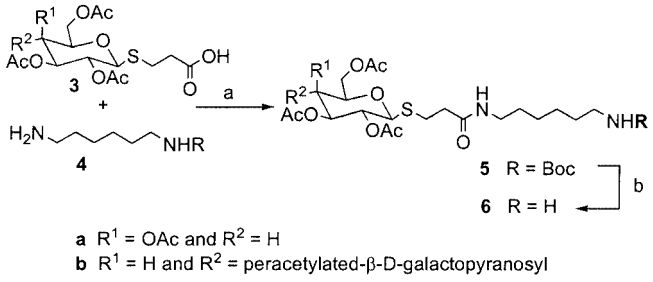

Scheme 1. a) DCC/HBT, DCM; b) TFA/DCM (1:3).

In order to ensure the formation of the required bis(amides), the amino-functionalised blocks **6** and **10** were used in a slight excess, over two mol-equiv. in relation to the DTPA bis(anhydride) block (Scheme 3). The intermediate sugar-protected bis(amides) were carried through and deprotected with KOH in methanol/water to give the final compounds **1** and **2** in reasonable yields.

NMR Studies of the Ln^{III} Glycoconjugates

The ^1H NMR spectra of the 1:1 diamagnetic (La^{III}) and paramagnetic (Sm^{III} and Eu^{III}) complexes with the ligands $DTPAGal_2$, $DTPALac_2$ and $DTPAGal_4$ were obtained in D_2O at pH = 7.5 as a function of temperature (7, 25, 40, 60 and 80 °C; see Figures 2–4 for some typical spectra). The spectra of the La^{III} complexes show many identical resonances to those of the corresponding free ligand at the same pH for the protons of the sugar rings and bridging arms (Figure 2). However, the protons of the DTPA moiety, or next to it, such as CH_2(f), give more complex resonances as a result of ion coordination: a multiplet at δ = 2.92 ppm for CH_2(f), multiplets at δ = 2.95, 2.78, 2.68 and 2.45 ppm for the backbone NCH_2CH_2N protons, and a series of partially

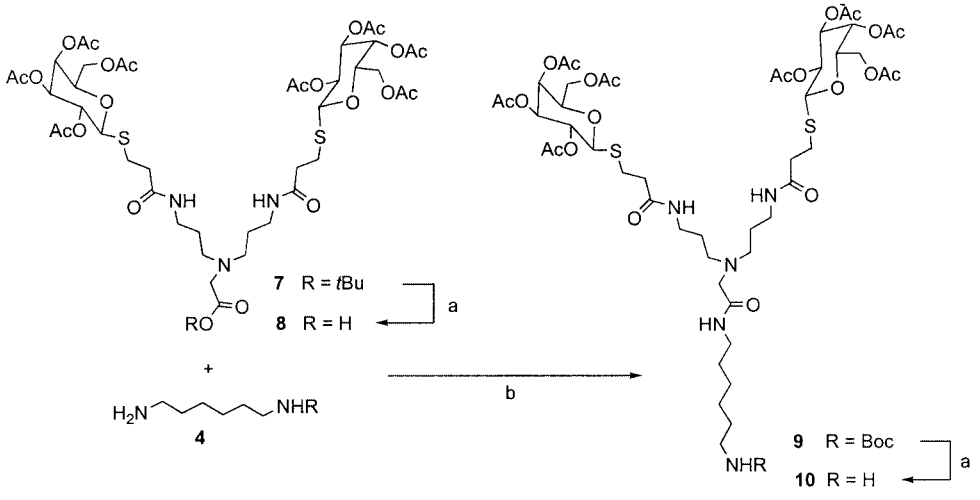

Scheme 2. a) TFA/DCM (1:3); b) i. DIPEA/DCM; ii. DCC/HBT, DCM.

 © 2005 Wiley-VCH Verlag GmbH & Co. KGaA, Weinheim

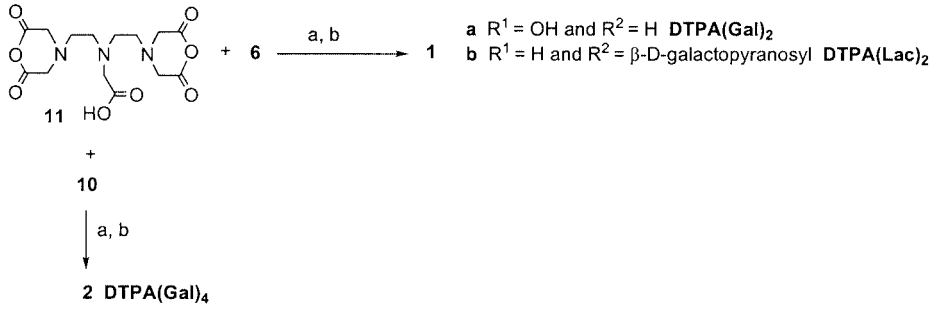

Scheme 3. a) i. DIPEA/DCM; ii. DMF/Py; b) i. KOH/EtOH; ii. Amberlyst 15, elution with NH_3.

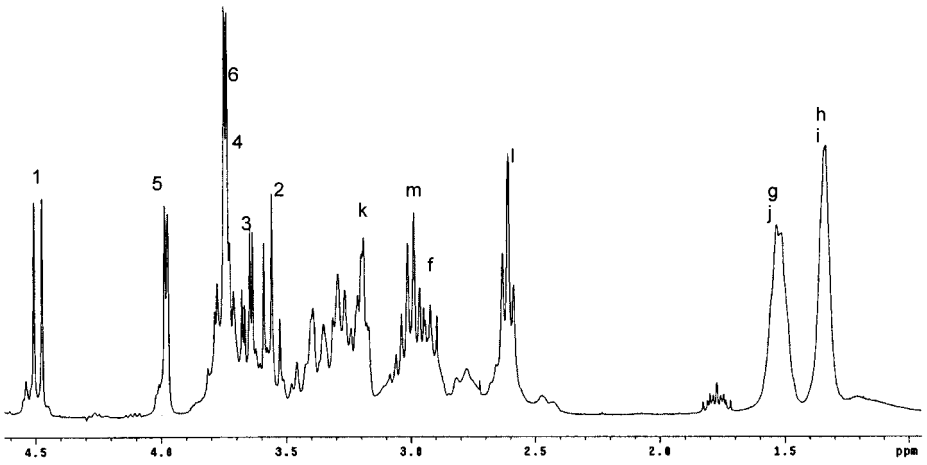

Figure 2. ^{1}H NMR spectrum of La^{III}–DTPAGal$_2$ glycoconjugate in D_2O, pH = 7.0, T = 25 °C.

overlapping AB patterns in the δ = 3.2–3.5 ppm region for the CH_2 protons of the acetate and amide arms, quite similar to what has been described for $[La(DTPA)]^{2-}$ and other La[DTPA bis(amides)].[32–36] For the Sm^{III} and Eu^{III} complexes, the ligand protons far from the paramagnetic centre, at the sugar rings (H-1–H-6) and at bridging arms [CH_2(g–m)], show very small paramagnetic broadenings and their shifts are easily assigned (see Figure 3).[36] The strongly shifted and broadened proton resonances of the side chain CH_2(f) and the CH_2 of the DTPA amide moiety could not be specifically assigned, despite showing some features similar to the corresponding paramagnetic complexes of the parent DTPA and some DTPA bis(amide) ligands.[36–42]

For the Sm^{III} complexes, most of these strongly shifted resonances are too broad to be detected at 25 °C but sharpen at higher temperatures. At 60 °C some appear in the diamagnetic region (δ = 5.8–4.8 and 3.3–0.6 ppm) and seven are shifted to the low frequency δ = 0.1 to –1.4 ppm region (Figure 3). In contrast, in the Eu^{III} complexes the shifted resonances are quite sharp at low temperature (7 °C, see Figure 4): ten resonances are observed in the high-frequency δ = 35–15 ppm region, about eight in the δ = 10–5 ppm region and about twenty in the δ = –3 to –18 ppm region. These are totally broadened when the temperature is increased to 25 °C, but at 60 °C some sharp, less shifted resonances reappear, for example in the δ = 6.2 to –10.2 ppm region (data not shown).

In Ln^{III} complexes of DTPA bis(amides) with non-chiral centres in the side chains, with a cation nine-coordinate by one inner-sphere water molecule and eight ligand donor atoms, all three bound nitrogen atoms are chiral and four diastereoisomeric pairs of enantiomers are possible, leading to a maximum of eight NMR signals for each group of magnetically equivalent protons.[36,40] This type of complex can undergo two distinct isomerisation processes in solution. The racemisation of the terminal N atoms, involving decoordination-inversion-coordination of the N atoms and the neighbouring acetate groups, has a high energy barrier. A lower energy process involves racemisation of the central nitrogen atom by interconversion between the two possible conformations of the ethylene bridges, which results in the magnetic averaging of the two halves of the complex around the central glycinate group of DTPA and reduces by half the number of observed resonances.[36,40] This is the dynamic process observed in the present study, which is fast at 60 °C for the Sm^{III} complexes and slow at 7 °C for the Eu^{III} complexes due to the much larger dipolar shifts induced by Eu^{III} relative to Sm^{III}.

The total number of strongly shifted proton resonances observed for the Sm^{III} and Eu^{III} complexes studied here, although they could not be assigned, leads to the unambiguous conclusion that they occur as more than one isomer in solution. A comparison of the ^{1}H NMR spectra with those of corresponding DTPA complexes[33,39] suggests that

 © 2005 Wiley-VCH Verlag GmbH & Co. KGaA, Weinheim

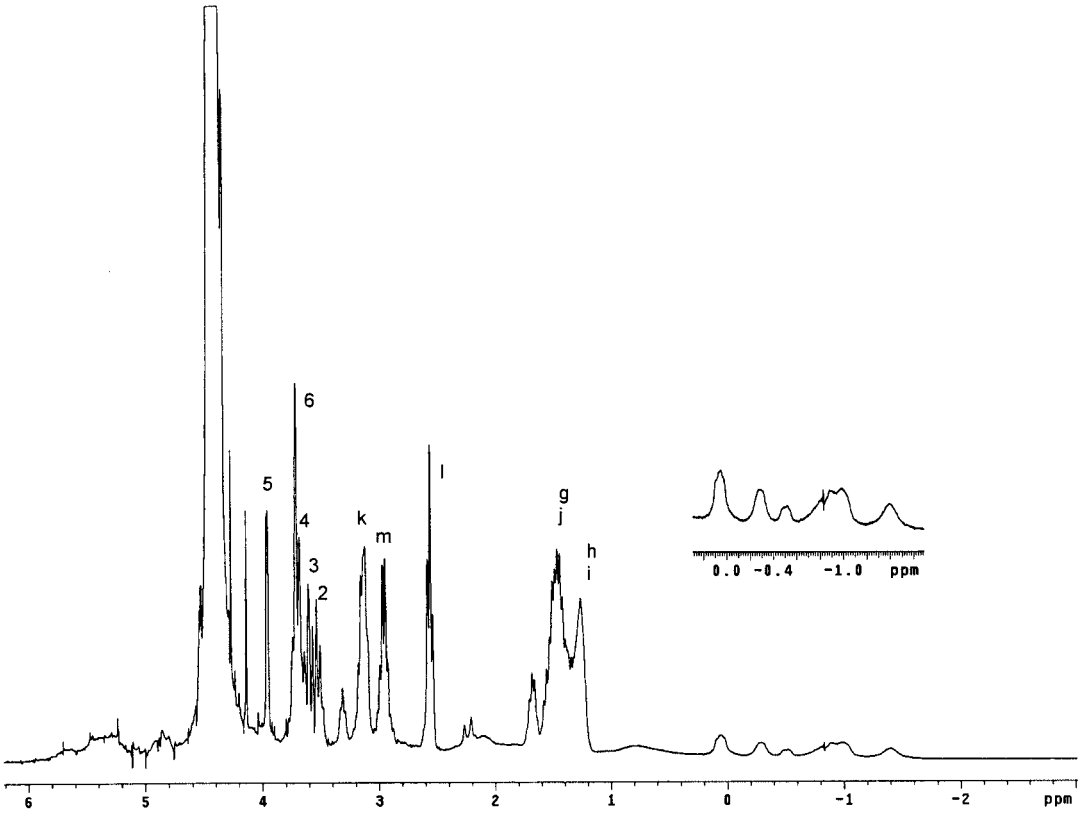

Figure 3. ^{1}H NMR spectrum of Sm^{III}–DTPAGal$_2$ glycoconjugate in D_2O, pH = 7.0, T = 60 °C.

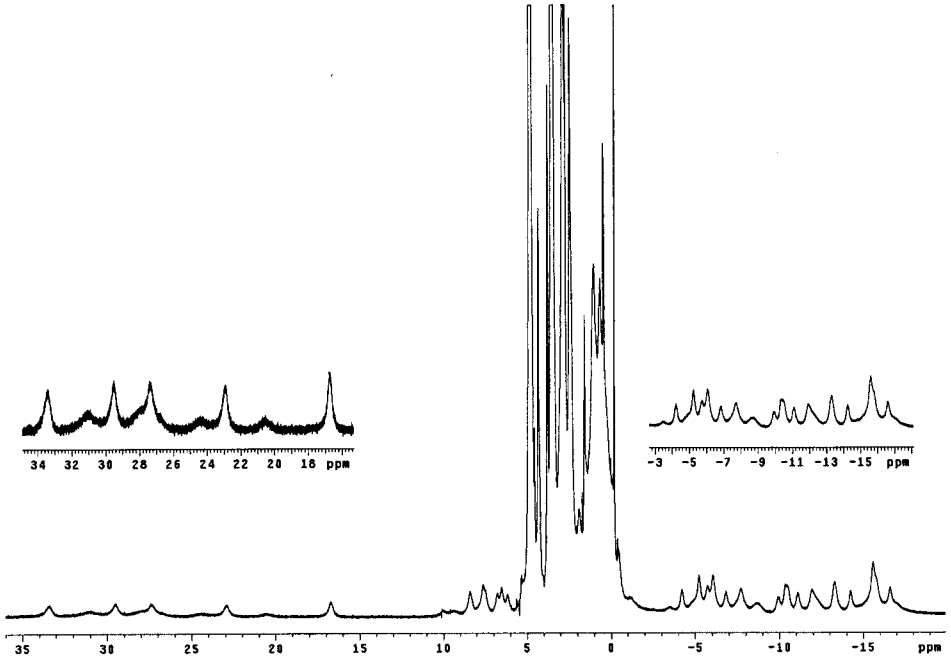

Figure 4. ^{1}H NMR spectrum of Eu^{III}–DTPAGal$_2$ glycoconjugate in D_2O, pH = 7.0, T = 7 °C.

the strongly shifted resonances at low frequencies for the Sm^{III} complex and at high frequencies for the Eu^{III} complex correspond to two CH_2 protons of the DTPA ethylenediamine backbone, which, in the DTPA complexes, have the largest induced dipolar shifts.[36,39] With this assumption, the minimum of seven low-frequency-shifted resonances observed for the Sm^{III} complex at high temperature (Figure 3), resulting from two ethylenic protons, confirms that several of the four possible isomers are present in solution. This is also in agreement with the observation of a mini-

 © 2005 Wiley-VCH Verlag GmbH & Co. KGaA, Weinheim

mum of ten high-frequency-shifted resonances in the Eu^{III} complex at high temperature (out of a maximum of sixteen) for these two ethylenic protons (Figure 4). The Ln^{III} complexes of other DTPA bis(amides), such as DTPA-BPA [BPA = bis(propylamide)] and DTPA-BENGALAA {BENGALAA = *N*,*N*′′-bis[*N*-(aza-D-galacto-5,6,7,8,9-pentahydroxynonyl)carbamoylmethyl]amide},[35,41] show the presence of four diastereoisomeric pairs, while for bis(amides) containing long (C_{14} to C_{18}) aliphatic chains only two pairs have been detected in solution.[42]

Water Proton Relaxation (NMRD) Studies of Gd^{III}-DTPALac$_2$

The efficiency of a contrast agent is given by its proton relaxivity, defined as the paramagnetic enhancement of the longitudinal water proton relaxation rate at a concentration of 1 mM (r_1, in $s^{-1}mM^{-1}$). Proton relaxivity has contributions from interactions of the Gd^{III} ion with the inner-sphere water protons (inner-sphere relaxivity) as well as with the bulk water protons (outer-sphere relaxivity). The inner-sphere term is determined by the exchange rate of the inner-sphere water protons (usually equal to the water exchange rate, k_{ex}), the rotational correlation time of the complex (τ_R) and the longitudinal and transverse electronic relaxation rates of the Gd^{III} ($1/T_{1e}$ and $1/T_{2e}$). The outer-sphere contribution to the overall proton relaxivity depends on the electron spin relaxation rates and the diffusion coefficient for the diffusion of a water proton away from a Gd^{III} chelate (see Supporting Information).[43]

The water proton longitudinal relaxivity of the Gd^{III}–DTPALac$_2$ chelate was measured in aqueous solution at 25 and 60 °C at proton Larmor frequencies between 0.2 and 20 MHz. The NMRD profiles obtained (Figure 5) are typical of low molecular weight Gd^{III} chelates. They were fitted to the usual Solomon–Bloembergen–Morgan relationship that relates the paramagnetic relaxation rates to the microscopic parameters of the Gd^{III} chelates (see equations in Supporting Information). In the analysis of the NMRD profiles we fixed the number of inner-sphere water molecules to one, and the water exchange rate and its activation enthalpy to values that were previously determined for similar DTPA bis(amide) complexes ($k_{ex}^{298} = 0.40 \times 10^6\ s^{-1}$ and $\Delta H^{\ddagger} = 40.0\ kJ\,mol^{-1}$).[43] The diffusion coefficient and its activation energy were also fixed to common values ($D_{GdH}^{298} = 24 \times 10^{-10}\ m^2\,s^{-1}$; $E_{DGdH} = 20\ kJ\,mol^{-1}$), as these two parameters are not particularly dependent on the nature of low molecular weight complexes.[43,44] Thus, in the analysis of the proton relaxivities we fitted the rotational correlation time, τ_R, its activation energy, E_R, and the parameters describing the electron spin relaxation, i.e. the trace of the square of the transient zero-field-splitting (ZFS) tensor, Δ^2, and the correlation time for the modulation of the ZFS, τ_v.[45] The parameters obtained for the Gd^{III}–DTPALac$_2$ conjugate are presented in Table 1 and compared with those available for other relevant small Gd^{III} complexes. The fits of the NMRD profiles obtained are shown in Figure 5.

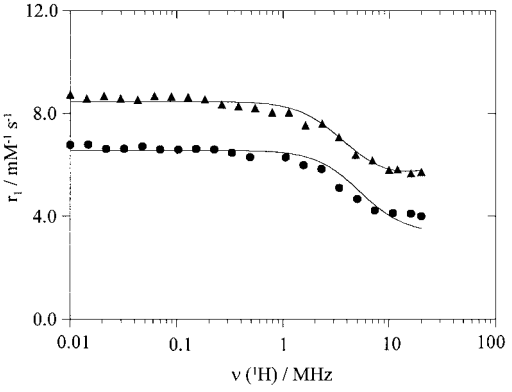

Figure 5. Variable-temperature NMRD profiles for Gd^{III}–DTPALac$_2$; T = 25 °C (triangles); and 60 °C (circles). The lines represent the least-squares fit to the experimental data points as described in the text.

The relaxivity of Gd^{III}–DTPALac$_2$ (mol. wt. = 1569) at 25 °C and 20 MHz is $5.72\ mM^{-1}\,s^{-1}$, which corresponds to an increase of 13% compared to that for the commercial contrast agent Gd^{III}–DTPA-BMA, which is a lower molecular weight DTPA bis(amide) complex (mol. wt. = 574).[44] This relaxivity difference is consistent with the five-fold increase in the rotational correlation time, as it is τ_R that dominates the high-field NMRD values. Another DTPA bis(amide) chelate, Gd^{III}–DTPA-BENGALAA, with an intermediate molecular weight (963), also has an intermediate τ_R value.[41] The temperature dependence of the NMRD profiles clearly shows that the proton relaxivity of these small molecular weight chelates is limited by fast rotation: proton relaxivities increase when the temperature decreases; thus, the rotation slows down. The parameters obtained for the electron spin relaxation of the Gd^{III} complex

Table 1. Parameters obtained from the analysis of the NMRD profiles for Gd^{III}–DTPALac$_2$ in comparison with other Gd^{III} complexes.

	DTPA[44]	DTPA-BMA[44] [bis(amide)]	DTPA-BENGALAA[41] [bis(amide)]	DTPALac$_2$ [bis(amide)]	DOTALac$_2$[26] [mono(amide)]
k_{ex}^{298} [$10^6\ s^{-1}$]	3.3	0.45	0.22	*0.40*[a]	*1.2*[a]
$\Delta H^{\ddagger}$ [$kJ\,mol^{-1}$]	51.6	47.6	42.5	*40.0*[a]	*30.0*[a]
τ_{rH}^{298} [ps]	58	66	265	332 ± 10	306
E_{RH} [$kJ\,mol^{-1}$]	17.3	21.9	19.7	36.3 ± 0.2	29.9
τ_v^{298} [ps]	25	25	16	10 ± 2	33
E_v [$kJ\,mol^{-1}$]	1.6	3.9	5.5	*1*[a]	*1*[a]
Δ^2 [$10^{20}\ s^{-2}$]	0.46	0.41	0.53	0.63 ± 0.02	0.12

[a] Parameters in italics have been fixed in the fit.

 © 2005 Wiley-VCH Verlag GmbH & Co. KGaA, Weinheim

are also within the usual range for similar Gd^{III}–DTPA bis(amide) chelates. Although the simplified model of electron spin relaxation used here is not fully adequate to describe Gd^{III} chelates,[46] the application of the novel theories requires EPR data in a large field range, which is beyond the scope of the present study.

Conclusions

We have devised the synthesis of a new class of hydrophilic glycoconjugate DTPA bisamides. Their dendrimeric architecture is especially suited for the variation of the valence of the glycoconjugates from a reduced number of building blocks in an interactive fashion. The ^1H NMR studies of the Sm^{III} and Eu^{III} chelates of these glycoconjugates in aqueous solution, despite being too complex to be fully assigned, unambiguously show that these complexes occur as more than one of the isomers that result from the chirality of the three bound ligand nitrogen atoms. This is to be compared with the presence of the four possible diastereoisomeric pairs of enantiomers for the Ln^{III} complexes of other DTPA bis(amides) with smaller substituents, such as DTPA-BMA and DTPA-BENGALAA,[35,41] while for bis(amides) containing long, micelle-forming, aliphatic chains, only two pairs have been detected in solution,[42] possibly stabilized by intermolecular interactions.

The NMRD studies of the Gd^{III}–$DTPALac_2$ glycoconjugate chelate are compatible with the presence of one inner-sphere water molecule. The value found for its r_1 relaxivity at 25 °C and 20 MHz is 13% higher than that reported for Gd^{III} chelates of lower molecular weight DTPA bis(amides), such as DTPA-BMA, consistent with a larger τ_R value. The τ_R value of these Gd^{III} chelates is expected to increase linearly with molecular weight, as long as the internal mobility of the side chains does not change significantly, thereby leading to a proportional increase of the 20 MHz relaxivity. This result suggests that the relaxivity of the tetravalent Gd^{III}–$DTPAGal_4$ glycoconjugate (mol. wt. = 2088) would be substantially higher. Their potential to target the ASGPR (studies under way), makes these compounds potentially useful for medical imaging agents using gamma scintigraphy, while they also constitute a promising first step towards the design of ASGPR-targeted MRI contrast agents, which will depend on the optimisation of their relaxivity.

Experimental Section

Materials and Equipment: Chemicals were purchased from Sigma–Aldrich and used without further purification. Solvents used were of reagent grade and were purified by usual methods. Reactions were monitored by TLC on Kieselgel 60 F_{254} (Merck) on aluminium support. Detection was by examination under UV light (254 nm), by adsorption of iodine vapour or by charring with 10% sulfuric acid in ethanol. Flash chromatography was performed on Kieselgel 60 (Merck, mesh 230–400). The relevant fractions from flash chromatography were pooled and concentrated under reduced pressure, at a temperature below 40 °C. FAB mass spectra (positive mode) were recorded with a VG Autospec mass spectrometer with 3-nitrobenzyl alcohol (NBA) as matrix. Electrospray ionisation (ESI) mass spectra were obtained for compounds with molecular weights above 2000. ^1H (1D and 2D) and ^{13}C NMR spectra were recorded with a Varian Unity Plus 300 NMR spectrometer operating at 299.938 MHz and 75.428 MHz, for ^1H and ^{13}C, respectively. Chemical shifts (δ) are given in ppm relative to the $CDCl_3$ solvent (^1H: δ = 7.27 ppm; ^{13}C: δ = 77.36 ppm) as internal standard. For ^1H and ^{13}C NMR spectra recorded in D_2O, chemical shifts (δ) are given in ppm relative to TSP as internal reference (^1H: δ = 0.0 ppm) and *tert*-butyl alcohol as external reference (^{13}C: CH_3 δ = 30.29 ppm). ^{13}C NMR spectra were proton broad-band decoupled using a GARP-1 modulated decoupling scheme. Assignments of the ^1H and ^{13}C NMR spectra were aided by recording two-dimensional DQF-COSY and HMQC spectra. The pD of the D_2O solutions was adjusted with DCl or CO_2-free NaOD and converted to pH values using the isotopic correction pH = pD – 0.4. The pD values were measured with a HANNA pH-meter with a HI1310 combined electrode (HANNA instruments, Italy). The $1/T_1$ nuclear magnetic relaxation dispersion (NMRD) profiles of the water protons at 25 and 60 °C were obtained with a Spinmaster FFC fast cycling NMR relaxometer (Stelar), covering a continuum of magnetic fields from 5×10^{-4} to 0.47 T (corresponding to a proton Larmor frequency range of 0.022–20 MHz). The Gd^{III} concentration was verified by ICP measurement (Perkin–Elmer Instruments, Optim 2000 DV).

Synthesis of Fully Protected Hexanediamine-Functionalised Monovalent Thioglycosides 5a and 5b. Typical Procedure for 5a: A solution of peracetylated (galactosylthio)propionic acid (**3a**;[29a] 0.375 g, 0.859 mmol), 1,6-hexanediamine monoBoc (**4**; 0.169 g, 0.781 mmol) and HBT (1-hydroxybenzotriazol; 0.140 g, 0.940 mmol) in dichloromethane (10 mL) was ice-cooled. A solution of DCC (dicyclohexylcarbodiimide; 0.194 g, 9.40 mmol) in dichloromethane (5 mL) was added dropwise to this solution. After 15 min, the reaction mixture was removed from the ice bath and allowed to reach room temperature. The reaction mixture was further stirred at room temperature overnight. The DCU (dicyclohexylurea) precipitate was removed by filtration and washed with dichloromethane. The filtrate was concentrated under reduced pressure to give a viscous syrup. This material was taken up in ethyl acetate (100 mL) and sequentially washed with $KHSO_4$ (aq. 1 M; 3×50 mL), $NaHCO_3$ (satd. sol.; 3×50 mL) and brine (50 mL). The organic phase was concentrated under reduced pressure to give a white foam. Purification by flash chromatography (CH_2Cl_2/MeOH; 100% CH_2Cl_2 → 50% MeOH) afforded the title compound as a white foam (0.480 g, 97% yield). ^1H NMR (300 MHz, $CDCl_3$): δ = 1.34 (m, 4 H, $NHCH_2CH_2CH_2$), 1.43 (s, 9 H, *t*Bu), 1.50 (m, 4 H, $NHCH_2CH_2$), 1.99, 2.05, 2.06 and 2.16 (s, 12 H, $4\times$OAc), 2.50 (m, 2 H, SCH_2CH_2), 2.88–3.06 (m, 2 H, SCH_2), 3.09 [m, 2 H, $CH_2NHC(O)OtBu$], 3.24 [m, 2 H, $C(O)NHCH_2$], 3.48 (br. m, 1 H), 3.95 (ddd, J = 7.2, 5.7 and 0.9 Hz, 1 H, H-5), 4.11 (dd, J = 11.2 and 5.7 Hz, 1 H, H-6a), 4.19 (dd, J = 11.2 and 7.2 Hz, 1 H, H-6b), 4.54 (d, J = 9.9 Hz, 1 H, H-1), 5.04 (dd, J = 10.2 and 3.3 Hz, 1 H, H-3), 5.23 (app t, J = 9.9 Hz, 1 H, H-2), 5.43 (dd, J = 3.3 and 0.9 Hz, 1 H, H-4), 5.98 (br. t, 1 H, N*H*) ppm. HRMS (FAB^+, NBA): calcd. for $C_{28}H_{47}N_2O_{12}S$ $[M + H]^+$ 635.2844; found 635.2856. **5b:** Starting from peracetylated (lactosylthio)propionic acid (**3b**;[29a] 1.70 g, 2.35 mmol) and 1,6-hexanediamine monoBoc (**4**; 0.507 g, 2.35 mmol), the title compound **5b** was obtained as a white foam (2.01 g, 93%). ^1H NMR (300 MHz, $CDCl_3$): δ = 1.33 (m, 4 H, $NHCH_2CH_2CH_2$), 1.42 (s, 9 H, *t*Bu), 1.70 (m, 4 H, $NHCH_2CH_2$), 1.97, 2.04, 2.05, 2.07, 2.13 and 2.16 (s, 21 H, $7\times$OAc), 2.46 (t, J = 6.6 Hz, 2 H, SCH_2CH_2), 2.81 (m, 1 H,

 © 2005 Wiley-VCH Verlag GmbH & Co. KGaA, Weinheim

SCH_aH_b), 3.03 (m, 1 H, SCH_aH_b), 3.08 [m, 2 H, CH_2NHC(O)-O*t*Bu], 3.21 (m, 2 H, $NHCH_2$), 3.45 (m, 1 H) 3.59 (m, 1 H, H-5), 3.78 (app t J = 9.6 Hz, 1 H, H-4), 3.89 (app t, J = 7.0 Hz, 1 H, H-5′), 4.03–4.16 (m, 3 H), 4.28 (m, 1 H), 4.52 (d, J = 7.8 Hz, 1 H, H-1′), 4.65 (d, J = 10.5 Hz, 1 H, H-1), 4.90 (app t, J = 9.6 Hz, 1 H, H-2), 4.96 (dd, J = 10.2 and 3.3 Hz, 1 H, H-3′), 5.09 (dd, J = 10.5 and 7.8 Hz, 1 H, H-2′), 5.19 (app t, J = 9.3 Hz, 1 H, H-3), 5.34 (d, J = 2.4 Hz, 1 H, H-4′), 6.30 (br. t, 2 H, *NH*CO) ppm. MS (FAB^+, NBA): *m*/*z* (%) = 923 (3) $[M + H]^+$. HRMS (FAB^+, NBA): calcd. for $C_{40}H_{63}N_2O_{20}S$ $[M + H]^+$ 923.3695; found 923.3683.

Synthesis of Fully Protected Amino-Functionalised Divalent 9: A solution of divalent thiogalactoside **7**[26] (0.968 g, 0.895 mmol) was stirred overnight in CH_2Cl_2/TFA (3:1, 10 mL). The solvent was removed under reduced pressure to give a light yellow foam, which was redissolved in dichloromethane (DCM; 10 mL). The solvent was then removed under reduced pressure. This procedure was repeated several times and the material was further dried under vacuum to give the carboxylic acid deprotected compound **8** as a viscous, light-yellow foam. ^{1}H NMR analysis revealed the disappearance of the signal at δ = 1.4 ppm assigned to the *tert*-butyl group. No further purification or characterisation was carried on this material. All the material obtained (we assumed a 100% yield for the deprotection reaction) was dissolved in ice-cooled DCM (10 mL) and titrated (pH paper) to pH = 9–10 with DIPEA (diisopropylethylamine). To this solution was added a solution of 1,6-hexanediamine monoBoc (**4**; 0.230 g, 1.07 mmol) in dichloromethane (5 mL) and HBT (0.140 g, 0.940 mmol). A solution of DCC (0.230 g, 1.10 mmol) in dichloromethane (5 mL) was then added dropwise. After 15 min, the reaction mixture was removed from the ice bath and allowed to reach room temperature. The reaction mixture was further stirred at room temperature overnight. The DCU precipitate was removed by filtration and washed with dichloromethane. The filtrate was concentrated under reduced pressure to give a viscous syrup. This material was taken up in ethyl acetate (150 mL) and sequentially washed with $NaHCO_3$ (satd. sol.; 3 × 100 mL) and brine (100 mL). The organic phase was concentrated under reduced pressure to give a light-yellow foam. Purification by flash chromatography (CH_2Cl_2/MeOH; 100% CH_2Cl_2 → 50% MeOH) afforded the title compound as a white foam (1.01 g, 92% yield). ^{1}H NMR (300 MHz, $CDCl_3$): δ = 1.32 [m, 4 H, C(O)$NHCH_2CH_2CH_2$], 1.43 (s, 9 H, *t*Bu), 1.51 [m, 4 H, C(O)$NHCH_2CH_2$], 1.72 (m, 4 H, NCH_2CH_2), 1.99, 2.05, 2.06 and 2.16 (s, 24 H, 8 × OAc), 2.52 (m, 8 H, overlapping signals from SCH_2CH_2 and NCH_2), 2.88–3.14 [m, 8 H, overlapping signals from SCH_2, NCH_2C(O) (singlet at 3.02) and CH_2NHC(O)O*t*Bu], 3.29 [m, 6 H, $NCH_2CH_2CH_2$ and $NCH_2C(O)NHCH_2$], 3.40–3.56 (m, 1 H), 3.96 (td, J = 6.4 and 0.9 Hz, 2 H, H-5), 4.09 (dd, J = 11.4 and 6.3 Hz, 2 H, H-6a), 4.20 (dd, J = 11.2 and 6.4 Hz, 2 H, H-6b), 4.56 (d, J = 10.2 Hz, 2 H, H-1), 4.74 (br. t, 1 H, N*H*), 5.05 (dd, J = 10.0 and 3.3 Hz, 2 H, H-3), 5.25 (app t, J = 9.9 Hz, 2 H, H-2), 5.44 (dd, J = 3.3 and 0.9 Hz, 2 H, H-4), 6.74 (br. t, 2 H, N*H*), 7.10 (br. t, 2 H) ppm. MS (FAB^+, NBA): *m*/*z* (%) = 1223 (100) $[M - H]^+$. HRMS (FAB^+, NBA): calcd. for $C_{53}H_{86}N_5O_{23}S_2$ $[M + H]^+$ 1224.5155; found 1224.5119.

Synthesis of DTPA Glycoconjugate Bis(amides9 1 and 2. Typical Procedure Illustrated for DTPAGal$_2$ (1a): A solution of fully protected amino-functionalised monovalent thiogalactoside **5a** (0.618 g, 0.973 mmol) was stirred overnight in CH_2Cl_2/TFA (3:1, 10 mL). The solvent was removed under reduced pressure to give a light-yellow foam, which was redissolved in DCM (10 mL); the solvent was then removed under reduced pressure. This procedure was repeated several times and the material was further dried under vacuum to give a viscous, light-yellow foam of **6a**. ^{1}H NMR analysis revealed the disappearance of the signal at δ = 1.47 ppm assigned to the *tert*-butyl group. No further purification or characterisation was carried out on this material. All the material obtained (we assumed a 100% yield for the deprotection reaction) was dissolved in ice-cooled DCM (5 mL) and titrated (pH paper) to pH = 9–10 with DIPEA. This solution was added to a solution of DTPA bis(anhydride) (0.158 g, 0.442 mmol) in DMF (40 mL) and pyridine (1 mL). The reaction mixture was stirred at room temperature overnight and concentrated under reduced pressure to give a colourless oil. This material was carried through without further purification or characterisation. The residue was redissolved in a mixture of ethanol (10 mL) and KOH (aq. sol. 1 M, 10 mL) and stirred at room temperature overnight. The reaction mixture was adjusted to pH ≈ 1 with Amberlyst 15. The resin was transferred into a column, thoroughly washed with water and eluted with aq. 0.5 M NH_3. The relevant fractions were pooled and concentrated under reduced pressure (temperature < 40 °C) to give the fully deprotected glycoconjugate as an off-white solid (0.342 g, 71% yield over two steps). ^{1}H NMR (300 MHz, D_2O, pH = 7.0): δ = 4.48 (d, J = 9.0 Hz, 2 H, H-1), 3.54 (app t, J = 9.0 Hz, 2 H, H-2), 3.64 (dd, J = 9.0 and 3.3 Hz, 2 H, H-3), 3.70 (m, 2 H, H-4), 3.96 (app d, J = 3.3 Hz, 2 H, H-5), 3.73 (m, 4 H, H-6a + H-6b), 1.32 [m, 8 H, C(O)$NHCH_2CH_2CH_2$], 1.51 [m, 8 H, C(O)$NHCH_2CH_2$], 3.20 [m, 8 H, C(O)$NHCH_2$], 2.60 (m, 4 H, SCH_2CH_2), 2.95–3.01 (m, 4 H, SCH_2), 3.24 [s, 4 H, DTPA amide $NCH_2C(O)$], 3.76 (s, 2 H, DTPA central acetate $NCH_2CO_2^-$), 3.40 (s, 4 H, DTPA terminal acetate $NCH_2CO_2^-$), 3.34, 3.08 (two m, 8 H, DTPA skeleton NCH_2) ppm. ^{13}C NMR (75.6 MHz, D_2O): δ = 86.18 (C-1), 69.67 (C-2), 74.05 (C-3), 79.07 (C-4), 68.94 (C-5), 61.30 (C-6), 25.90, 25.83 [C(O)$NHCH_2CH_2CH_2$], 28.29, 28.42 [C(O)$NHCH_2CH_2$], 39.23, 39.54 [C(O)$NHCH_2$], 26.49 (SCH_2), 36.57 (SCH_2CH_2), 58.86 [DTPA amide $NCH_2C(O)$], 54.58 (DTPA central acetate $NCH_2CO_2^-$), 58.95 (DTPA terminal acetate $NCH_2CO_2^-$), 50.59, 52.79 (DTPA skeleton NCH_2), 170.77, 173.02, 174.28, 178.40 [DTPA acetate $NCH_2CO_2^-$ and amide $NCH_2C(O)$, other $CH_2C(O)NH$] ppm. MS (FAB^+, NBA): *m*/*z* (%) = 1091 (23) $[M + H^+]$. HRMS (FAB^+, NBA) calcd. for $C_{44}H_{80}N_7O_{20}S_2$ $[M + H]^+$: 1090.4899; found 1090.4859.

DTPALac$_2$ (1b): Fully protected monovalent thiolactoside **5b** (0.997 g, 1.08 mmol) was deprotected as described for compound **1a**. Reaction with DTPA bis(anhydride) (0.183 g, 0.512 mmol), followed by deprotection and purification afforded glycoconjugate **1b** as an off-white solid (0.345 g, 48% yield over two steps). ^{1}H NMR (300 MHz, D_2O, pH = 7.0): δ = 4.46 (d, J = 7.8 Hz, 2 H, H-1), 3.54 (dd, J = 10.2 and 7.8 Hz, 2 H, H-2), 3.63 (dd, J = 10.2 and 3.3 Hz, 2 H, H-3), 3.66 (m, 2 H, H-4), 3.94 (app d, J = 3.3 Hz, 2 H, H-5), 3.70 (m, 4 H, H-6a + H-6b), 4.58 (d, J = 10.2 Hz, 2 H, H-1′), 3.36 (app t, 2 H, H-2′), 3.64 (app t, 2 H, H-3′), 3.68 (dd, 2 H, H-4′), 3.99 (m, 2 H, H-5′), 3.72 (m, 4 H, H-6a′ + H-6b′; Gal unit: H-1–H-6b; Gluc unit: H-1′–H-6b′), 1.32 [m, 8 H, C(O)-$NHCH_2CH_2CH_2$], 1.52 [m, 8 H, C(O)$NHCH_2CH_2$], 3.20 [m, 8 H, C(O)$NHCH_2$], 2.61 (m, 4 H, SCH_2CH_2), 2.98–3.01 (m, 4 H, SCH_2), 3.23 [s, 4 H, DTPA amide $NCH_2C(O)$], 3.76 (s, 2 H, DTPA central acetate $NCH_2CO_2^-$), 3.38 (s, 4 H, DTPA terminal acetate $NCH_2CO_2^-$), 3.37, 3.08 (8 H, two m, DTPA skeleton NCH_2) ppm. ^{13}C NMR (75.6 MHz, D_2O): δ = 103.08 (C-1), 71.15 (C-2), 78.42 (C-3), 72.71 (C-4), 60.49 (C-5), 75.55 (C-6), 85.59 (C-1′), 72.11 (C-2′), 78.82 (C-3′), 75.92 (C-4′), 68.76 (C-5′), 61.22 (C-6′) (Gal unit: C-1–C-6; Gluc unit: C-1′–C-6′), 25.86, 25.94 [C(O)$NHCH_2CH_2CH_2$], 28.33, 28.47 [C(O)$NHCH_2CH_2$], 39.26, 39.58 [C(O)$NHCH_2$], 26.45 (SCH_2), 36.61 (SCH_2CH_2), 58.86 [DTPA amide $NCH_2C(O)$], 54.33 (DTPA central acetate $NCH_2CO_2^-$), 59.03, 59.11 (DTPA terminal acetate $NCH_2CO_2^-$), 50.53, 52.88

 © 2005 Wiley-VCH Verlag GmbH & Co. KGaA, Weinheim

(DTPA skeleton NCH_2), 170.60, 173.41, 174.24, 178.82 [DTPA acetate $NCH_2CO_2^-$ and amide NCH_2C(O), other CH_2C(O)NH] ppm. HRMS (ESI): calcd. for $C_{56}H_{100}N_7O_{30}S_2$ $[M + H]^+$ 1414.5950; found 1414.5971.

$DTPAGal_4$ (2): Fully protected amino-functionalised divalent thiogalactoside **9** (0.464 g, 0.379 mmol) was deprotected as described for compound **1a**. Reaction with DTPA bis(anhydride) (0.064 g, 0.179 mmol), followed by deprotection and purification afforded glycoconjugate **2** as an off-white solid (0.240 g, 69% yield over two steps). ^{1}H NMR (300 MHz, D_2O, pH = 7.0): δ = 4.46 (d, J = 9.0 Hz, 4 H, H-1), 3.52 (app t, J = 9.0 Hz, 4 H, H-2), 3.64 (dd, J = 9.0 and 3.3 Hz, 4 H, H-3), 3.68 (m, 4 H, H-4), 3.95 (app d, J = 3.3 Hz, 4 H, H-5), 3.71 (m, 8 H, H-6a + H-6b), 1.28 [m, 8 H, C(O)NHCH$_2$CH$_2$*CH$_2$*], 1.49 [m, 8 H, C(O)NHCH$_2$*CH$_2$*], 3.18 [m, 8 H, C(O)NH*CH$_2$*], 3.48 [m, 4 H, N*CH$_2$*C(O)], 2.75 (m, 8 H, N*CH$_2$*), 1.83 (m, 8 H, NCH$_2$*CH$_2$*), 3.20 (m, 8 H, NCH$_2$CH$_2$*CH$_2$*), 2.59 (m, 8 H, SCH$_2$*CH$_2$*), 2.97 (m, 8 H, S*CH$_2$*), 3.20 [s, 4 H, DTPA amide N*CH$_2$*C(O)], 3.71 (s, 2 H, DTPA central acetate N*CH$_2$*CO_2^-), 3.33 (s, 4 H, DTPA terminal acetate N*CH$_2$*CO_2^-), 3.34, 3.18 (two m, 8 H, DTPA skeleton N*CH$_2$*) ppm.^{13}C NMR (75.6 MHz, D_2O): δ = 86.29 (C-1), 69.66 (C-2), 74.09 (C-3), 79.08 (C-4), 68.95 (C-5), 61.41 (C-6), 25.33 [C(O)NHCH$_2$CH$_2$*CH$_2$*], 28.53 [C(O)NHCH$_2$*CH$_2$*], 39.32, 39.18 [C(O)NH*CH$_2$*], 56.57 [N*CH$_2$*C(O)], 52.51 (N*CH$_2$*), 25.38 (NCH$_2$*CH$_2$*), 37.11 (NCH$_2$CH$_2$*CH$_2$*), 26.70 (S*CH$_2$*), 36.52 (SCH$_2$*CH$_2$*), 59.20 [DTPA amide N*CH$_2$*C(O)], 54.50 (DTPA central acetate N*CH$_2$*CO_2^-), 59.11 (DTPA terminal acetate N*CH$_2$*CO_2^-), 50.51, 52.89 (DTPA skeleton N*CH$_2$*), 170.51, 173.40, 174.48, 178.85 [DTPA acetate $NCH_2CO_2^-$ and amide NCH_2C(O) NH, other CH_2C(O)NH] ppm. MS (FAB^+, NBA): *m/z* (%) = 1932 (20) $[M^+]$, 1055 (100). HRMS (FAB^+, NBA): calcd. for $C_{78}H_{142}N_{13}O_{34}S_4$ $[M + H]^+$ 1932.8665; found 1932.8576.

Preparation of Ln^{III} Glycoconjugates for NMR Studies: The Ln^{III} glycoconjugates were prepared by adding a slight excess (1.1 equiv.) of $LnCl_3$ aqueous solution to an aqueous solution of the glycoconjugate. The pH of the solution was slowly adjusted to 5 with KOH (aq.), stirred at 70 °C for 8 h and adjusted to pH = 7 with KOH (aq.). Any precipitate was filtered off. The solution was concentrated and purified by gel filtration with Sephadex G10, eluting with water. The relevant fractions were pooled and freeze-dried to afford the Ln^{III} complexes.

Preparation of Gd^{III}-$DTPALac_2$ for NMRD Measurements: Initially, the $DTPALac_2$ conjugate was left to react with an excess of $Gd(ClO_4)_3$ stock solution and the excess of metal ion was back-titrated with Na_2H_2EDTA solution, allowing the calculation of the exact concentration of glycoconjugate. The Gd^{III} chelate of $DTPALac_2$ was prepared by adding an appropriate quantity of the glycoconjugate to an aqueous solution of gadolinium perchlorate (3–5% glycoconjugate excess). The solution pH was slowly adjusted to 7 with KOH (aq.). The Gd^{III} glycoconjugate solution was freeze-dried and diluted with 25 mM phosphate buffer (pH = 7.4). The absence of free Gd^{III} in the solution was verified by addition of xylenol orange indicator.[30] The Gd^{III} concentration (4.63 mM) was verified by ICP measurement.

Supporting Information (see also the footnote on the first page of this article): Table containing the proton relaxivities of Gd^{III}–$DTPALac_2$, and equations for the determination of the relaxivity parameters.

Acknowledgments

This work was performed within the framework of the EU COST Action D18 "Lanthanide chemistry for diagnosis and therapy". The work was supported by the Foundation of Science and Technology (F.C.T.), Portugal (project POCTI/QUI/47005/2002) and FEDER. É. T. and A. E. M. acknowledge the Swiss National Science Foundation and the Swiss Federal Office for Education and Science for financial support. The authors are grateful to László Burai for his help with the NMRD measurements.

[1] P. Caravan, J. J. Ellison, T. J. McMurry, R. B. Lauffer, *Chem. Rev.* **1999**, *99*, 2293–2352.
[2] É. Tóth, L. Helm, A. E. Merbach, *Top. Curr. Chem.* **2002**, *221*, 61–101.
[3] H. J. Weinmann, R. C. Brasch, W. R. Press, G. E. Wesbey, *Am. J. Roentgenol.* **1984**, *142*, 619–624.
[4] a) A. D. Watson, *J. Alloys Compd.* **1994**, *207/208*, 14–19; b) C. F. G. C. Geraldes, A. M. Urbano, M. C. Alpoim, A. D. Sherry, K.-T. Kuan, R. Rajagopalan, F. Maton, R. N. Muller, *Magn. Reson. Imaging* **1995**, *13*, 401–420.
[5] R. C. Brasch, *Mag. Reson. Med.* **1991**, *22*, 282–287.
[6] K. P. Aicher, J. W. Dupon, D. L. White, S. L. Aukerman, M. E. Moseley, R. J. Juster, W. Rosenau, J. L. Winkelhace, R. C. Brasch, *Cancer Res.* **1990**, *50*, 7376–7381.
[7] S. C. Wang, M. G. Wikstrom, D. L. White, J. Klaveness, E. Holtz, P. Ronved, M. E. Moseley, R. C. Brasch, *Radiology* **1990**, *175*, 483–488.
[8] G. Schuhmann-Giampieri, H. Schmitt-Willich, T. Frenzel, W. R. Press, H. J. Weinmann, *Invest. Radiol.* **1991**, *26*, 969–974.
[9] E. C. Wiener, S. Konda, A. Shadron, M. Brechbiel, O. Gansow, *Invest. Radiol.* **1997**, *32*, 748–754.
[10] S. Aime, M. Fasano, E. Terreno, M. Botta, *Protein-Bound Metal Chelates*, in *The Chemistry of Contrast Agents in Medical Magnetic Resonance Imaging* (Eds.: É. Tóth and A. E. Merbach), Wiley, Chichester, **2001**, p. 193–241.
[11] R. B. Lauffer, D. J. Parmalee, S. U. Dunham, H. S. Ouellet, R. P. Dolan, S. Witte, T. J. McMurry, R. C. Walowitch, *Radiology* **1998**, *207*, 529–538.
[12] F. Cavagna, M. Daprà, F. Maggioni, C. de Haën, E. Felder, *Magn. Reson. Med.* **1991**, *22*, 329–333.
[13] H. Schmitt-Willich, M. Brehm, C. L. J. Ewers, G. Mischl, A. Müller-Farnow, O. Petrov, J. Platzek, B. Radüchel, D. Sülzle, *Inorg. Chem.* **1999**, *38*, 1134–1144.
[14] G. Kabalka, E. Buonocore, K. Hubner, T. Moss, N. Norley, L. Huang, *Radiology* **1987**, *163*, 255–258.
[15] P. H. Weigel, J. H. N. Yik, *Biochim. Biophys. Acta (General Subjects)* **2002**, *1572*, 341–363.
[16] a) G. Gregoriadis, *Lancet* **1981**, *2*, 241–246; b) D. R. Vera, R. Stadalnik, K. Krohn, *J. Nucl. Med.* **1985**, *26*, 1157–1167; c) S. Ishibashi, R. E. Hammer, J. Herz, *J. Biol. Chem.* **1994**, *269*, 27 803–27 806; d) K. A. Deal, M. E. Criste, M. J. Welsh, *Nucl. Med. Biol.* **1998**, *25*, 379–385.
[17] a) Y. C. Lee, R. R. Townsend, M. R. Hardy, J. Lönngren, J. Arnarp, M. Haraldsson, H. Lönn, *J. Biol. Chem.* **1983**, *258*, 199–202; b) R. T. Lee, Y. C. Lee, *Biochem. Biophys. Res. Commun.* **1988**, *155*, 1444–1451; c) E. A. L. Biessen, H. Broxterman, J. H. VanBoom, T. J. VanBerkel, *J. Med. Chem.* **1995**, *38*, 1846–1852.
[18] S. D. Colquhoum, C. A. Conelly, D. R. Vera, *J. Nucl. Med.* **2001**, *42*, 110–116.
[19] K. Miki, K. Kubota, Y. Inoue, D. R. Vera, M. Makuuchi, *J. Nucl. Med.* **2001**, *42*, 733–737.
[20] N. Shuke, H. O. Kizaki, S. Kino, J. Sato, Y. Ishikawa, C. L. Zhao, S. Kineya, N. Watabane, K. Yokoama, T. Aburano, *J. Nucl. Med.* **2003**, *44*, 475–482.
[21] B. K. Schaffer, C. Linker, M. Papisov, E. Tsai, N. Nossiff, T. Shibata, A. Bogdanov, T. J. Brady, R. Weissleder, *Magn. Reson. Imaging* **1993**, *11*, 411–417.
[22] P. Reimer, R. Weissleder, A. S. Lee, S. Buettner, J. Wittenberg, T. J. Brady, *Radiology* **1991**, *178*, 769–774.
[23] P. Reimer, R. Weissleder, T. J. Brady, *Radiology* **1992**, *182*, 1161–1167.

 © 2005 Wiley-VCH Verlag GmbH & Co. KGaA, Weinheim

[24] B. Gallez, V. Lacour, R. Demeure, R. Debuyst, F. Dejehet, J. L. Dekeyser, P. Dumont, *Magn. Reson. Imag.* **1994**, *12*, 61–69.
[25] D. R. Vera, M. H. Buonocore, E. R. Wisner, R. W. Katzberg, R. C. Stadalnik, *Acad. Radiol.* **1995**, *2*, 497–506.
[26] J. P. André, C. F. G. C. Geraldes, J. A. Martins, A. E. Merbach, M. I. M. Prata, A. C. Santos, J. J. P. de Lima, É. Tóth, *Chem. Eur. J.* **2004**, *10*, 5804–5816.
[27] M. M. Alauddin, A. Y. Louie, A. Shahinian, T. J. Meade, P. S. Conti, *Nucl. Med. Biol.* **2003**, *30*, 261 –265.
[28] R. A. Moats, S. E. Fraser, T. J. Meade, *Angew. Chem. Int. Ed. Engl.* **1997**, *36*, 726–728.
[29] a) M. Elofsson, B. Walse, J. Kihlberg, *Tetrahedron Lett.* **1991**, *32*, 7613–7616; b) M. Elofsson, S. Roy, B. Walse, J. Kihlberg, *Carbohydr. Res.* **1993**, *246*, 89–103; c) M. J. Kiefel, R. J. Thomson, M. Radovanovik, M. V. Itzstein, *J. Carbohydr. Chem.* **1999**, *18*, 937–959.
[30] G. Brunisholtz, M. Randin, *Helv. Chim. Acta* **1959**, *42*, 1927–1938.
[31] D. Zanini, R. Roy, *J. Org. Chem.* **1996**, *61*, 7348–7354.
[32] G. R. Choppin, P. A. Baisden, S. A. Khan, *Inorg. Chem.* **1979**, *18*, 1330–1332.
[33] S. Aime, M. Botta, *Inorg. Chim. Acta* **1990**, *177*, 101–105.
[34] E. N. Rizkalla, G. R. Choppin, W. Cacheris, *Inorg. Chem.* **1993**, *32*, 582–586.
[35] C. F. G. C. Geraldes, R. Delgado, A. M. Urbano, J. Costa, F. Janasada, F. Nepveu, *J. Chem. Soc., Dalton Trans.* **1995**, 327–335.
[36] J. A. Peters, E. Z.-Bovens, D. Corsi, C. F. G. C. Geraldes, *Structure and Dynamics of Gadolinium Based Contrast Agents*, in *The Chemistry of Contrast Agents in Medical Magnetic Resonance Imaging* (Eds.: É. Tóth, A. E. Merbach), Wiley, Chichester, **2001**, p. 315–381.
[37] B. M. Alsaadi, F. J. C. Rossotti, R. J. P. Williams, *J. Chem. Soc., Dalton Trans.* **1980**, 2151–2154.
[38] J. A. Peters, *Inorg. Chem.* **1988**, *27*, 4686–4691.
[39] a) B. J. Jenkins, R. B. Lauffer, *J. Magn. Reson.* **1988**, *80*, 328–336; b) B. J. Jenkins, R. B. Lauffer., *Inorg. Chem.* **1988**, *27*, 4730–4738.
[40] C. F. G. C. Geraldes, A. M. Urbano, M. A. Hoefnagel, J. A. Peters, *Inorg. Chem.* **1993**, *32*, 2426–2432.
[41] H. Lammers, F. Maton, D. Pubanz, M. W. van Laren, H. van Bekkum, A. E. Merbach R. N. Muller, J. A. Peters, *Inorg. Chem.* **1997**, *36*, 2527–2538.
[42] K. Kimpe, T. Parac-Vogt, S. Laurent, C. Piérart, L. Vander Elst, R. N. Muller, K. Binnemans, *Eur. J. Inorg. Chem.* **2003**, 3021–3027.
[43] É. Tóth, L. Helm, A. E. Merbach, *Relaxivity of Gadolinium(iii) Complexes: Theory and Mechanism*, in *The Chemistry of Contrast Agents in Medical Magnetic Resonance Imaging* (Eds.: É. Tóth, A. E. Merbach), Wiley, Chichester, **2001**, p. 45–119.
[44] D. H. Powell, O. M. Ni Dhubhghaill, D. Pubanz, L. Helm, Y. S. Lebedev, W. Schlaepfer, A. E. Merbach, *J. Am. Chem. Soc.* **1996**, *118*, 9333–9346.
[45] a) A. D. McLachlan, *Proc. R. Soc. London, A* **1964**, *280*, 271; b) D. H. Powell, A. E. Merbach, G. González, E. Brücher, K. Micskei, M. F. Ottaviani, K. Köhler, A. von Zelewsky, O. Y. Grinberg, Y. S. Lebedev, *Helv. Chim. Acta* **1993**, *76*, 2129–2146.
[46] a) S. Rast, A. Borel, L. Helm, E. Belorizky, P. H. Fries, A. E. Merbach, *J. Am. Chem. Soc.* **2001**, *123*, 2637–2644; b) S. Rast, P. H. Fries, E. Belorizky, A. Borel, L. Helm, A. E. Merbach, *J. Chem. Phys.* **2001**, *115*, 7554–7563.

Received: September 15, 2004

 © 2005 Wiley-VCH Verlag GmbH & Co. KGaA, Weinheim

On the Redox Chemistry of Ge^{I} Bromide

Andreas Schnepf*[a]

Keywords: Cage compounds / DFT calculations / Germanium / Redox reactions

First results on the redox chemistry of Ge^{I} bromide are reported herein. During the attempt to solubilize $Ge^{I}Br$, which is synthesized in preparative scale using a co-condensation technique of the high-temperature molecule $Ge^{I}Br$, a redox reaction with the solvent acetone occurs. During this unexpected redox reaction Ge^{I} is oxidized to Ge^{IV} and acetone is reductively coupled to 1,1-dimethyl-3-oxobutan-1-yl.

(© Wiley-VCH Verlag GmbH & Co. KGaA, 69451 Weinheim, Germany, 2005)

Introduction

$Ge^{I}Br$ is a good starting material for the synthesis of germanium cluster compounds with "naked" germanium atoms,[1] which represent a new class of cluster compounds in germanium chemistry.[2] $Ge^{I}Br$ can be synthesized by a preparative co-condensation technique, in which the high-temperature molecule $Ge^{I}Br$, synthesized at 1600 °C, is condensed together with a solvent at –196 °C.[3] When toluene is used as the solvent during the co-condensation reaction, $Ge^{I}Br$ is isolated as an orange solid. Sadly, this solid $Ge^{I}Br$ is insoluble in inert solvents such as THF, Et_2O, or $C_2H_4Cl_2$ and therefore it cannot be used for the synthesis of molecular cluster compounds of germanium, which is our main goal. To get $Ge^{I}Br$ in a soluble form we performed in the following co-condensation reactions where we used a mixture of toluene and a donor molecule as the solvent. During these experiments, it turned out that donor molecules such as THF, Et_2O, NEt_3, or CH_3CN, which worked quite well in the case of subvalent group 13 halides such as $Ga^{I}Br$ or $Al^{I}Br$,[4] are not capable to solubilize $Ge^{I}Br$, and thus we always obtained the solid $Ge^{I}Br$. However, the use of amines with long alkyl chains such as N*n*Pr_3 or N*n*Bu_3 led to a different result.

When a mixture of toluene/N*n*Pr_3 is used as the solvent during the co-condensation reaction, an emulsion of a dark-red oil in a pale yellow solution is obtained after heating the co-condensate to –78 °C. This means, if either N*n*Pr_3 or N*n*Bu_3 are used as the donor component during the co-condensation reaction, $Ge^{I}Br$ is obtained in the form of a dark-red oil which can be used for subsequent reactions. Using this emulsion as the starting material, we synthesized the cluster compounds $Ge_8[N(SiMe_3)_2]_6$[5] and $\{Ge_9[Si(SiMe_3)_3]_3\}^-$[6] by the reaction with $Li[N(SiMe_3)_2]$ and $Li[Si(SiMe_3)_3]$, respectively.

These reactions are carried out inside the co-condensation apparatus, because isolation of the emulsion leads to a great loss in yield of $Ge^{I}Br$, as the dark-red oil remains almost quantitatively inside the apparatus. Since the performance of these reactions inside the co-condensation apparatus are very complex − e.g. it is difficult to observe and to monitor the reaction process − it is desirable to obtain $Ge^{I}Br$ solutions, which might then be isolated and used outside the apparatus for subsequent reactions. Thus, we expect to obtain better control of the reaction conditions (temperature, stoichiometry etc.) and we will be able to observe the color gradient during the reaction, which, for technical reasons, is not possible inside the co-condensation apparatus. Therefore, we had to find a solvent or a mixture of solvents for the co-condensation reaction which would lead to $Ge^{I}Br$ solutions. Herein we report on the attempt to obtain such $Ge^{I}Br$ solutions.

Results and Discussion

$Ge^{I}Br$ appears to be soluble in acetone, since while cleaning the co-condensation apparatus with acetone, we observed that the remaining $Ge^{I}Br$ gave initially a dark-red solution. Consequently, we conducted a co-condensation experiment of $Ge^{I}Br$ with dry acetone as the solvent. After allowing the temperature of the co-condensate to increase from –196 to –78 °C, a dark-red solution was obtained and no residue remained inside the apparatus. This means that $Ge^{I}Br$ was quantitatively dissolved. Unfortunately, it turned out that $Ge^{I}Br$ is not stable in acetone, as the dark red color of the solution vanishes on warming to room temperature leading to a pale yellow solution. On concentrating this solution, we were able to isolate a product of the reaction in the form of colorless crystals. X-ray crystal structure analysis of these crystals reveals that the compound

[a] Institut für Anorganische Chemie der Universität Karlsruhe (TH),
Engesserstr., Geb. 30.45, 76128 Karlsruhe
Fax: +49-721-608-4854
E-Mail: schnepf@aoc2.uni-karlsruhe.de

$Br_3GeC_6H_{11}O$ (**1**), whose molecular structure is shown in Figure 1, was formed in 30% yield.

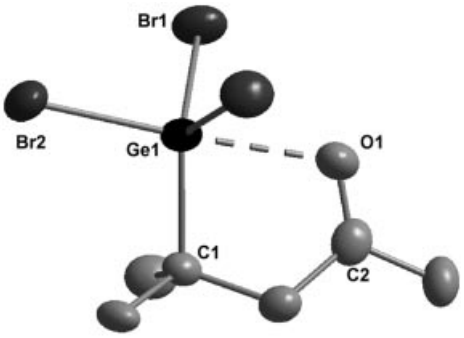

Figure 1. Molecular structure of $C_6H_{11}Br_3GeO$ (**1**) (hydrogen atoms are ommited). Selected bond lengths [pm] and angles (°): Ge1–Br1: 230.6(1), Ge1–Br2: 238.9(1); Ge1–C1: 198.3(8), Ge1–O1: 242.4(1); C2–O1: 120.8(1); Br1–Ge1–C1: 120.4(3); Br2–Ge1–C1: 104.2(1).

Clearly compound **1** contains germanium in the oxidation state +4. The central germanium atom is surrounded tetrahedrally by three bromine atoms and a carbon atom of the organic ligand 1,1-dimethyl-3-oxobutan-1-yl.

The organic ligand in **1** is oriented in such a way that an additional Ge–O contact is formed (dashed bond in Figure 1). Because of this Ge–O contact, the Ge–Br bond length to the oppositely-bound bromine atom is elongated by 9 pm (239 pm) with respect to the other Ge–Br bond lengths (230 pm), which are as long as those found in other $RGeBr_3$ compounds.[7] Therefore, a 4+1 coordination of the Ge atom is found, which leads to a strong distortion of the tetrahedral surrounding of the Ge atom towards a trigonal-bipyramidal surrounding.

The organic ligand in **1** originates from the solvent acetone, as acetone was the only organic compound present during the reaction. The ligand is built up from two molecules of acetone, in which the carbonyl function of one molecule is completely reduced.

This means that $Ge^{I}Br$ reacts with acetone in a redox reaction in which Ge^{I} is oxidized to Ge^{IV} and acetone is reductively coupled to 1,1-dimethyl-3-oxobutan-1-yl in which the former carbonyl carbon atom (formal oxidation state +2) is bonded directly to the germanium atom (formal oxidation state –1). Such a redox reaction is not known for Ge^{II} halides, which indicates that the redox potential of Ge^{II} halides is too small to reduce acetone which has a reduction potential of –2.84 V.[8] As the redox reaction works with Ge^{I} bromide, the minimum redox potential for the oxidation of Ge^{I} bromide in this reaction is –2.84 V and is therefore in the range of the alkali metals (Na = –2.71 V; K = –2.93 V[8]), showing that Ge^{I} bromide is a strong reducing agent.

To get a first insight into the reaction mechanism of this redox reaction, we performed DFT calculations[9] for the initial step of the reaction on the model system GeBr and H_2CO, taking into account the reaction sequence outlined in Scheme 1.[10]

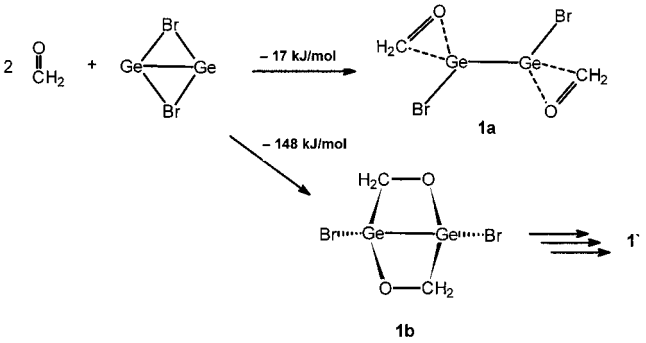

Scheme 1. Possible first step for the model redox reaction of GeBr and H_2CO.

The calculations show that the formation of three-membered Ge–C–O rings (**1a**) is energetically favored by only 17 kJ mol^{-1}, which can therefore be regarded as a weak complex in which H_2CO is only coordinated to the germanium center leading to a small elongation of the C–O bond length to 128 pm, with respect to uncoordinated H_2CO where the C–O bond length is 121 pm. The formation of four-membered C–O–Ge–Ge rings (**1b**) is energetically favored by 148 kJ mol^{-1}, which can therefore be regarded as a possible first product in the redox reaction, where the C–O bond length is now considerably elongated to 139 pm.

The formation of a similar four-membered M_2CO ring is also known for the adsorption of acetone on a (2×1)-reconstructed Si(001) surface, where the surface-lattice structure undergoes a reconstruction in which adjacent silicon dimers pair together and form dimers through a σ bond and a π bond.[11] In this system the carbonyl function reacts with silicon dimers in a similar way to a [2+2] cycloaddition reaction.[12] Such a [2+2] cycloaddition is also possible for the redox reaction discussed here, as the bond between the germanium atoms in BrGeGeBr can formally be seen as a "triple" bond (Br–Ge≡Ge–Br). Therefore, it seems plausible that the first step of the discussed redox reaction is a [2+2] cycloaddition of the carbonyl function to $(GeBr)_2$, which is also suggested by the results of the quantum chemical calculations.

The oxygen atom that originates from this redox reaction is found in a second compound, which can also be isolated in the form of colorless crystals on further concentration of the reaction solution. Crystal structure analysis of these crystals shows that **2** is a cationic germanium oxocluster compound $[Ge_6O_8R_6{\cdot}2H_2O]^{2+}$ (R = $C_6H_{11}O$) which crystallizes together with two $GeBr_3^-$ anions. The molecular structure of **2** is shown in Figure 2.

The Ge–O backbone of **2** consists of a central Ge_4O_4 eight-membered ring in chair conformation. Two planar Ge_3O_3 six-membered rings are condensed on opposite sides of the eight-membered ring. Structurally, **2** can be compared with $Ge_6O_8R_6Cl_2$ (R = *t*Bu) (**3**) which was synthesized by Puff et al. by careful hydrolysis of *t*BuGeCl_3.[13] The major difference between **2** and **3** is the fact that **2** is a cationic species while **3** is neutral. As **2** is a cationic compound, two different Ge sites are found inside the cluster

 © 2005 Wiley-VCH Verlag GmbH & Co. KGaA, Weinheim

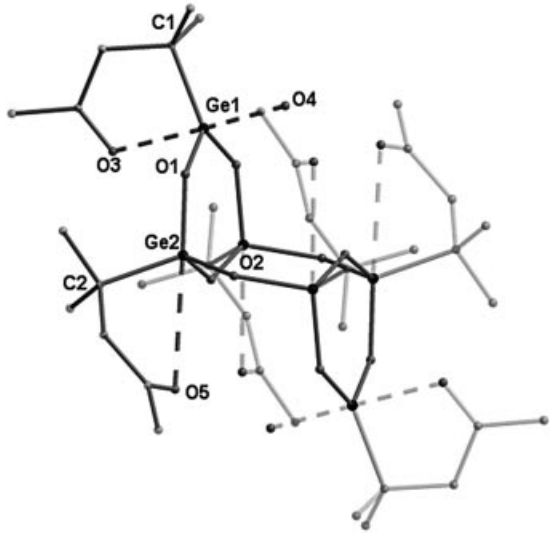

Figure 2. Molecular structure of $[Ge_6O_8(C_6H_{11}O)_6{\cdot}2H_2O]^{2+}$ (**2**) (hydrogen atoms are ommited for clarity and two five-membered GeC_3O rings are highlighted). Selected bond lengths [pm] and angles (°): Ge1–O1: 174.3(3); Ge1–O3: 222.5(3); Ge1–O4: 199.8(3); Ge1–C1: 196.3(4); Ge2–O1: 178.3(3); Ge2–O2: 175.8(3); Ge2–O5: 282.4(4); Ge2–C2: 197.3(4); O1–Ge1–C1: 119.91(18); O3–Ge1–O4: 178.17(13); O1–Ge2–O2: 104.80(13); Ge1–O1–Ge2: 126.51(16).

core. Four germanium atoms are tetrahedrally coordinated by three oxygen atoms (Ge–O: 177 pm) and the carbon atom of the organic ligand (Ge–C: 197 pm). Two germanium atoms have a trigonal-planar geometry and are surrounded (sum of angles: 358.5°) by two oxygen atoms (Ge–O: 174 pm) and a carbon atom of the organic ligand (Ge–C: 196 pm). Additionally, two further germanium oxygen contacts are found: one to the oxygen atom of the keto group of the organic ligand (Ge–O: 222 pm) and one to the oxygen atom of a water molecule (Ge–O: 200 pm). Therefore, the coordination number is 3+2. The reason why **2** is isolated as a cationic species might be the fact that the carbonyl function of the organic ligand is able to stabilize the cationic center, forming a five-membered GeC_3O ring. On the other hand, the presence of the Br^- acceptor $GeBr_2$ is necessary. The formation of a five-membered ring is also found in the case of the tetrahedrally coordinated germanium atoms, although in this case the germanium–oxygen contact between the germanium atom and the oxygen atom of the carbonyl function is much longer (282 pm), but is still significantly shorter than the sum of the van der Waals radii (ca. 310 pm).

Conclusions

The results presented here show that it is possible to get Ge^IBr solutions. Ge^IBr is hereby, as expected, more reactive than the corresponding $Ge^{II}Br_2$ for which no comparable redox reactions are known. In the case of acetone, this reactivity is too high to apply acetone as a solvent. However, this redox capability might be of great interest for redox reactions and C–C coupling reactions in organic chemistry.

In the case of our planned chemistry where we would like to use the disproportionation reaction of Ge^IBr to get to cluster compounds, such a redox reaction has to be ruled out. Therefore, we had to search for other solvents which would be able to solubilize Ge^IBr and which would be stable enough towards reduction to act only as a solvent. Another suitable method might be the introduction of donor molecules to lower the reactivity of the Ge^I halide. These investigations are the subject of current experiments.

Experimental Section

Liquid germanium was treated with HBr under high vacuum at 1550 °C, and the resulting gaseous products (ca. 15 mmol GeBr) were condensed together with acetone (150 mL) at a surface at –196 °C. After the co-condensate was allowed to warm to –78 °C a dark-red solution was obtained. The solution was heated to room temperature. During the heating process the color of the solution changed from dark red to pale yellow. The solution was concentrated and stored at –28 °C, whereby colorless crystals of $Br_3GeC_6H_{11}O$ (**1**) formed (600 mg, 30%). Unfortunately, for technical reasons (hydrolyses or oxidation of the microcrystalline samples) it proved impossible to obtain a satisfactory elemental analysis.

The solution was filtered and further concentrated to yield colorless crystals containing $[Ge_6O_6(C_6H_{11}O)_6{\cdot}2H_2O]^{2+}$ (**2**) (20 mg, 0.6%).

Compound 1: ^{1}H NMR (250 MHz, C_6D_6): δ = 1.03 (s, 6 H, CH_3), 1.42 (s, 3 H, CH_3), 2.90 (s, 2 H, CH_2) ppm. ^{13}C NMR (63 MHz, C_6D_6): δ = 23.9 (CH_3), 30.3 (CH_3), 46.2 (C), 51.7 (CH_2), 205.8 (C=O) ppm.

Crystal Structure Data of $Br_3GeC_6H_{11}O$: M_r = 411.47 g mol^{-1}, monoclinic, $P2(1)$, a = 7.2981(15), b = 12.119(2), c = 20.085(4) Å, β = 97.40(3), V = 1761.6(6) Å^3, Z = 6, $\rho_{calcd.}$ = 2.327 g cm^{-3}, μ_{Mo} = 12.768 mm^{-1}, $2\theta_{max}$ = 52.10°, 13708 measured reflections, 6338 independent reflections [R(int.) = 0.0550], numerical absorption correction (min./max. transmission 0.0402/0.1019), R_1 = 0.0360, wR_2 = 0.0856. Stoe IPDS-diffractometer (Mo-K_α radiation, λ = 0.71073 Å, 200 K).

Crystal Structure Data of $C_{36}H_{70}Br_6Ge_8O_{16}$: M_r = 1819.1 g mol^{-1}, triclinic, P-1, a = 10.5934(16), b = 12.2614(16), c = 13.5835(19) Å, α = 63.462(15), β = 76.452(17), γ = 81.486(17)°, V = 1532.6(4) Å^3, Z = 1, $\rho_{calcd.}$ = 1.971 g cm^{-3}, μ_{Mo} = 7.831 mm^{-1}, $2\theta_{max}$ = 52.10°, 11842 measured reflections, 5509 independent reflections [R(int.) = 0.0594], numerical absorption correction (min./max. transmission 0.0784/0.1378), R_1 = 0.0370, wR_2 = 0.0978. Stoe IPDS-diffractometer (Mo-K_α radiation, λ = 0.71073 Å, 200 K). CCDC-245799 (for **1**) and -245800 (for **2**) contain the supplementary crystallographic data for this paper. These data can be obtained free of charge from The Cambridge Crystallographic Data Centre via www.ccdc.cam.ac.uk/data_request/cif.

Acknowledgments

We gratefully acknowledge the financial support of the Deutsche Forschungsgemeinschaft. We also thank Prof. Schnöckel for helpful discussions.

[1] A. Schnepf, *Phosphorus, Sulfur, Silicon, Relat. Elem.* **2004**, *179*, 695.
[2] A. Schnepf, *Angew. Chem.* **2004**, *116*, 680, *Angew. Chem. Int. Ed.* **2004**, *43*, 664.

 © 2005 Wiley-VCH Verlag GmbH & Co. KGaA, Weinheim

[3] A. Schnepf, R. Köppe, *Z. Anorg. Allg. Chem.* **2002**, 2914.
[4] C. Dohmeier, D. Loos, H. Schnöckel, *Angew. Chem.* **1996**, *108*, 141, *Angew. Chem. Int. Ed.* **1996**, *35*, 129.
[5] A. Schnepf, R. Köppe, *Angew. Chem.* **2003**, *115*, 940, *Angew. Chem. Int. Ed.* **2003**, *42*, 911.
[6] A. Schnepf, *Angew. Chem.* **2003**, *115*, 2728, *Angew. Chem. Int. Ed.* **2003**, *42*, 2624.
[7] a) H. Preut, F. Huber, *Acta Crystallogr., Sect. B* **1979**, *35*, 83; b) G. S. Zaitseva, S. S. Karlov, A. V. Churakov, J. A. K. Howard, E. V. Avtomonov, J. Lorberth, *Z. Anorg. Allg. Chem.* **1997**, *623*, 1144; c) A. A. Korlyukov, N. V. Alekseev, S. P. Knyazev, E. A. Chernyshev, K. V. Pavlov, O. V. Krivolapova, V. V. Shcherbinin, M. Yu. Antipin, K. A. Lyssenko, *Russ. Chem. Bull.* **2001**, *50*, 2203.
[8] D. R. Lide, CRC Handbook of Chemistry and Physics, 76th ed., **1995**, 8–32, CRC, New York.
[9] Quantum chemical calculations were carried out with the RI-DFT version of the Turbomole program package, by employing the Becke–Perdew 86-functional. The basis sets were of SVP quality. Turbomole: O. Treutler, R. Ahlrichs, *J. Chem. Phys.* **1995**, *102*, 346; BP-86 functional: J. P. Perdew, *Phys. Rev. B* **1986**, *33*, 8822; A. D. Becke, *Phys. Rev. A* **1988**, *38*, 3098; RI-DFT: K. Eichkorn, O. Treutler, H. Öhm, M. Häser, R. Ahlrichs, *Chem. Phys. Lett.* **1995**, *240*, 283; SVP: A. Schäfer, H. Horn, R. Ahlrichs, *J. Chem. Phys.* **1992**, *97*, 2571.
[10] As no structural information was available about $Ge^{I}Br$ in solution, we had to assume an initial structure for the calculations. Here we assumed, that the monomeric $Ge^{I}Br$ radical which was trapped in the matrix of solvent molecules during the co-condensation dimerizes first to give Ge_2Br_2. This process is energetically favored by 238 kJ mol^{-1} according to quantum chemical calculations (ref.[9]). This dimer (Ge_2Br_2) is then used as starting point for the calculations.
[11] H. N. Waltenburg, J. T. Yates Jr., *Chem. Rev.* **1995**, *95*, 1589; J. D. Chadi, *Phys. Rev. Lett.* **1987**, *59*, 1961.
[12] C. Hamia, A. Takagi, M. Taniguchi, T. Matsumoto, T. Kawai, *Angew. Chem.* **2004**, *116*, 1373, *Angew. Chem. Int. Ed.* **2004**, *43*, 1349.
[13] H. Puff, K. Braun, S. Franken, T. Riza Kök, W. Schuh, *J. Organomet. Chem.* **1987**, *335*, 167.

Received: October 07, 2004

 © 2005 Wiley-VCH Verlag GmbH & Co. KGaA, Weinheim

In Situ XAS and XRD Studies on the Structural Evolution of Ammonium Paratungstate During Thermal Decomposition

Olga Kirilenko,[a] Frank Girgsdies,[a] Rolf E. Jentoft,[a] and Thorsten Ressler*[a]

Keywords: In situ studies / X-ray absorption spectroscopy / X-ray diffraction / Tungsten / Oxidation / Decomposition / Structure–activity relationships / Heterogeneous catalysis

The bulk structural evolution during the decomposition of ammonium paratungstate (APT) under various oxidizing and reducing gases was elucidated by the complementary techniques, in situ XAS, in situ XRD, and TG/DSC, combined with mass spectrometry. In the temperature range from 300 to 650 K, the decomposition of APT proceeds nearly independently of the gas employed. At higher temperatures, an oxidizing gas results in the formation of crystalline triclinic WO_3 as the majority phase at 773 K, while mildly reducing gases (propene, propene and oxygen, and helium) result in the formation of partially reduced and highly disordered tungsten bronzes. No further reduction is observed under propene or helium, and this indicates a strongly hindered oxygen mobility in the tungsten oxide lattice in the temperature range employed. The decomposition of APT under hydrogen results in the formation of WO_2 and, eventually, tungsten metal. During the thermal treatment of APT, major changes occur at ca. 500 K where a complete structural rearrangement takes place that results in the destruction of the polyoxotungstate ion of APT and the formation of a tungsten oxide bronze. The rather low temperature for the formation of a three-dimensional lattice compared to the thermal treatment of common polyoxomolybdate precursors indicates the lower stability of the precursor and intermediates as ligands are removed. For tungsten to act as a potential structural or electronic promoter in molybdenum oxide based catalysts, tungsten needs to be incorporated in regular molybdenum oxide structures already at a very early stage of the catalyst preparation.

(© Wiley-VCH Verlag GmbH & Co. KGaA, 69451 Weinheim, Germany, 2005)

Introduction

Molybdenum oxide based catalysts are extensively employed for the partial oxidation of light alkanes and alkenes.[1] Binary molybdenum oxides have a limited catalytic applicability, mostly because of their tendency to readily transform into the less active molybdenum trioxide, MoO_3, under the reaction conditions. Thus, it would be desirable to stabilize the active nanostructure of the molybdenum oxides (e.g. Mo_5O_{14}-type structures[2]) with the substitution of some of the molybdenum by additional metal centers such as vanadium, niobium, or tungsten.

Mixed oxide catalysts are commonly prepared by chemically or physically mixing suitable catalyst precursors. In order to prepare and stabilize the appropriate molybdenum oxide phase, the behavior of the catalyst precursors during thermal treatment needs to be elucidated. Previously, we reported on the structural evolution of ammonium heptamolybdate (AHM)[3] and heteropolyoxomolybdates (HPOM)[4] during thermal activation.

Ammonium paratungstate [$(NH_4)_{10}H_2W_{12}O_{42}{\cdot}4H_2O$, APT] is a common precursor for the preparation of Mo/W mixed oxides. Because they are less complex than the industrially employed catalysts, these oxides constitute suitable model systems to reveal structure–activity relationships of mixed oxides under the reaction conditions. Therefore, investigations of the decomposition of APT are required to identify and quantify tungsten oxide phases and their formation under various gases, and to reveal correlations between catalytic activity and the structural evolution of APT.

The thermal decomposition of APT has been investigated by numerous authors who employed a variety of methods.[5–18] Thermal analysis studies[14] combined with in situ Fourier transform infrared (FT-IR) spectroscopy[13] identified WO_3 as the product of decomposition at temperatures above ca. 650 K. The mechanism for thermal decomposition of APT in air has been studied by X-ray diffraction, thermogravimetry, and IR and UV/Vis diffuse reflectance spectroscopy.[15] Ammonium tungsten bronze, $(NH_4)_{0.33}WO_3$, and hexagonal WO_3 were identified in the calcination reaction of APT at 673 K for 2 h under static air. On heating up to 770 K, the tungsten bronze together with hexagonal WO_3 transformed completely into triclinic tungsten trioxide.

In more detail, the decomposition of APT in air has been studied by in situ laser Raman spectroscopy (LRS) combined with thermal gravimetric analysis (TGA), differential

[a] Fritz-Haber-Institut of the MPG, Department of Inorganic Chemistry,
Faradayweg 4–6, 14195 Berlin, Germany
Fax: +49-30-8413-4405
E-mail: ressler@fhi-berlin.mpg.de

 DOI: 10.1002/ejic.200400872

thermal analysis (DTA), and X-ray diffraction (XRD).[16] It was found that the decomposition in air proceeds through three steps in the temperature ranges 300–473 K, 473–623 K and 623–773 K. The formation of WO_3 was detected at temperatures above 623 K. Besides studies in air, the thermal decomposition of APT was also investigated under hydrogen.[17,18] In the temperature range 470–520 K, APT was found to decompose into $(NH_4)_{0.33}WO_3$. This compound is stable in the temperature range 520–840 K, and is reduced to a mixture of WO_2 and tungsten metal at 870 K, while complete reduction to tungsten metal is achieved at about 1000 K. In total, although the decomposition of APT has been investigated before, several questions remain unanswered with regard to the sequence of formation of the intermediates, their characterization, and the dependence of the decomposition pathways on the reaction gases for catalytically relevant gas phases (e.g. propene, and propene and oxygen).

The catalytic properties of tungsten trioxide has been investigated in a variety of reactions.[19–25] The selective oxidation of propene to acrolein has been studied with two series of mixed molybdenum/tungsten oxide catalysts.[24,25] The first series of oxides exhibits the typical WO_3-type structure, which consists of corner-sharing WO_6 units and the general formula $Mo_xW_{1-x}O_3$ (x = 0.4–0.9). The second series, with the general formula $(Mo_xW_{1-x})_nO_{3n-1}$ (x = 0.4–0.9; n = 8–14), comprises crystallographic shear structures. Members of the latter series showed a higher conversion and selectivity than the corresponding members of the first series. Selectivity was found to decrease as the tungsten content increased and as the density of crystallographic shear planes decreased. In situ oxidation of the reduced molybdenum oxide series of catalysts $(Mo_xW_{1-x})_nO_{3n-1}$ resulted in little change in selectivity but a significant decrease in conversion.

In this work, the decomposition of APT was studied with in situ X-ray diffraction (XRD) and in situ X-ray absorption spectroscopy (XAS) to reveal the influence of different treatment parameters on the decomposition process, and to provide a detailed analysis of the short- and long-range structure evolution during the treatments. The decomposition of APT was studied under various oxidative and reductive gases (oxygen, propene and oxygen, helium, propene, and hydrogen), and the structural changes detected are discussed and compared with the mechanism for the decomposition of common polyoxomolybdates.

Results

Characterization of Ammonium Paratungstate

The experimental X-ray diffraction pattern of APT is depicted in Figure 1 together with a simulated pattern and a schematic structural representation. The simulated pattern of APT was obtained by using the corresponding single-crystal structural data of APT [$(NH_4)_{10}H_2W_{12}O_{42}\cdot4H_2O$, ICSD 15237, $P2_1/n$, a = 15.08 Å, b = 14.45 Å, c = 11.00 Å, β = 109.4°]. The refined lattice constants are a = 15.04 Å, b = 14.46 Å, c = 10.95 Å, and β = 109.1°, which are in good agreement with the single-crystal data. The crystallite size calculated from XRD peak-broadening was about 600 nm. No further crystalline phases were detectable in the experimental pattern of APT. Figure 2 shows the experimental and theoretical WL_{III}-edge EXAFS FT[$\chi(k)\cdot k^3$] of APT. The corresponding distances and Debye–Waller factors obtained from the XAFS refinement are given in Table 1. The model of the local structure around the W centers in the polyoxotungstate ion of APT is adequate to simulate the WL_{III} EXAFS spectrum. The good agreement between the theoretical structural data (XRD, XAS, TG) and the experimental data confirms that the ammonium paratungstate tetrahydrate used does indeed correspond to $(NH_4)_{10}H_2W_{12}O_{42}\cdot4H_2O$ (ICSD 15237) and excludes the presence of major impurity phases, either crystalline or amorphous.

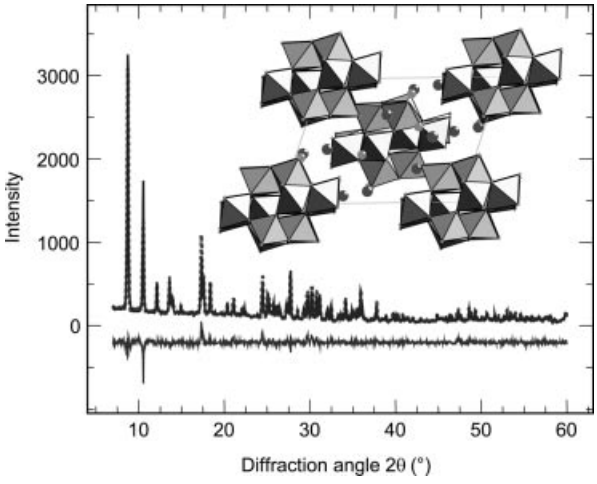

Figure 1. Experimental (dotted) and simulated (solid) X-ray diffraction pattern of ammonium paratungstate (APT), together with a schematic structural representation.

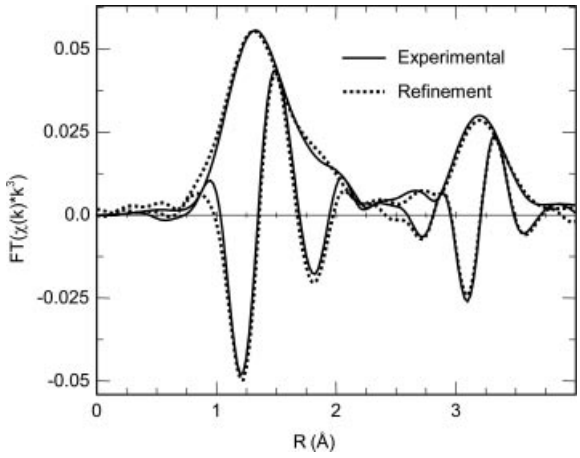

Figure 2. Experimental (dotted) and theoretical (solid) WL_{III} XAFS FT[$\chi(k)\cdot k^3$] of ammonium paratungstate. Structural parameters are given in Table 1.

 © 2005 Wiley-VCH Verlag GmbH & Co. KGaA, Weinheim

Table 1. Structural parameters [type of pairs and number (N) of nearest neighbors at distance R] obtained from a refinement of the ammonium paratungstate model structure (based on ICSD 15237) to the experimental XAFS functions $\chi(k)$ of APT (Figure 2) at the WL_{III} edge (N_{ind} = 23, N_{free} = 14, 12 single scattering paths and 29 multiple scattering paths, R range 0.8–4.4 Å, k range 1.8–13.4 Å^{-1}, E_0 = 7.6 eV, S_0^2 = 0.9).

Type	N	R_{model} [Å]	R [Å]	σ^2 [Å]^2
W–O	1	1.72	1.70	0.0020
W–O	2	1.84	1.83	0.0021
W–O	1	1.92	1.96	0.0021
W–O	1	2.02	2.13	0.0022
W–O	1	2.30	2.26	0.0023
W–W	2	3.33	3.27	0.0035
W–W	2	3.70	3.67	0.0035
W–W	1	3.84	3.84	0.0036

Thermal Decomposition of Ammonium Paratungstate (TG/DSC)

The evolution of the mass loss during thermogravimetric measurements of APT under various gases (helium, 5% hydrogen in helium, 20% oxygen in helium, 10% propene in helium, and 10% propene, and 10% oxygen in helium) is shown in Figure 3. The measurements were conducted at a heating rate of 6 K min^{-1} and a total gas flow of 100 mL min^{-1}. Additionally, the evolution of the MS signals for water (m/z = 18) and ammonia (m/z = 15) measured during the decomposition of APT under 20% oxygen are depicted in Figure 3. The gas-phase product composition is nearly identical for decomposition under oxygen, helium and hydrogen, even during the last step of the decomposition. In addition to the signals for water and ammonia, signals at m/z = 30 and m/z = 44 were also detected. These signals could be assigned to NO and N_2O; however, the intensity of these signals follows the intensity of the signal for ammonia throughout the decomposition, and they may be artifacts formed by the mass spectrometer. Additionally, mass signals m/z = 30 and m/z = 44 were also detected during thermal decomposition of ammonium iodide (NH_4I) in an inert gas, and this corroborates the assumption that these masses cannot be assigned unambiguously to the evolution of NO or NO_2 at particular reaction temperatures during the decomposition of APT.

In the temperature range 300–650 K, the evolution of the mass loss from APT during thermal decomposition is nearly independent of the gas employed. Four decomposition steps at 360, 470, 520, and 680 K can be distinguished in the TG and MS traces measured. The decomposition steps at 470, 520, and 680 K are accompanied by the evolution of water and ammonia, whereas for the decomposition steps at 360 K, only water is detectable in the gas phase. The weight loss after the first decomposition step at 360 K is 1.2% and corresponds to a loss of 2 equiv. of water of crystallization (1.1%). Apparently, the treatment under helium performed prior to the TG/DSC measurements to remove adsorbed water already reduced the number of equiv. of water of crystallization from the initial 4 to 2. The major mass loss of 8.8% at about 520 K is accompanied by the largest signals in the water and ammonia MS traces. The total weight loss after the forth decomposition step at 680 K depends on the gas used and is 9.9% under oxygen, 10.1% under propene and oxygen, 10.4% under helium, 10.5% under propene, and 10.8% under hydrogen. Because the decomposition under oxygen resulted in WO_3, the other weight losses indicate the formation of partially reduced tungsten oxide species under reducing gases. Assuming that the initial material is identical, or alternatively, that the intermediates at 400 K are identical in composition, then the extent of reduction of the tungsten oxide at the end of the decomposition can be calculated. For the hydrogen-containing gas, this partial reduction results in an oxide formula of about $WO_{2.85}$. The difference between a theoretical mass change when decomposing APT to WO_3 of 11.2% and the loss of 9.9% measured here during the decomposition under oxygen is accounted for by the above-mentioned loss of 2 equiv. of water of crystallization before the start of the TG experiments.

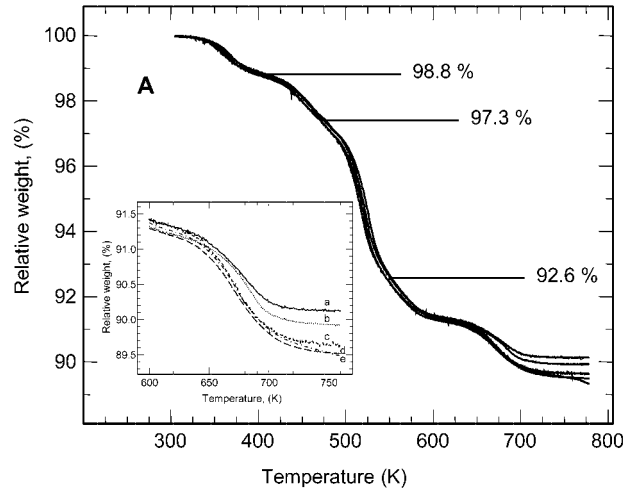

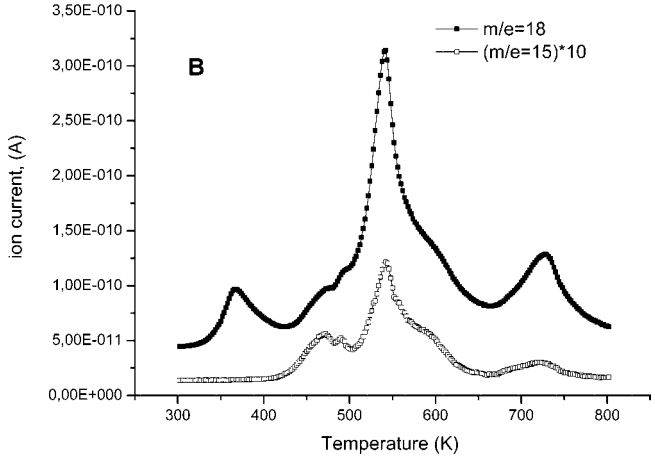

Figure 3. Evolution of relative weight during decomposition of ammonium paratungstate under (a) 20% oxygen in helium, (b) 10% propene and 10% oxygen in helium, (c) helium, (d) 10% propene in helium, and (e) 5% hydrogen in helium (flow rate 100 mL min^{-1}, heating rate 6 K min^{-1}), together with the MS signals for H_2O (m/z = 18) and NH_3 (m/z = 15) measured for the decomposition of APT in 20% oxygen in helium.

 © 2005 Wiley-VCH Verlag GmbH & Co. KGaA, Weinheim

The differential scanning calorimetry traces measured during the decomposition of APT under various gases are depicted in Figure 4. Independent of the gas-phase composition, each of the first three mass losses shows one or more endothermic signals; the strongest endothermic signal accompanies the third decomposition step at about 520 K. The DSC measurements indicate an endothermic decomposition step at 700 K under reducing gases. However, a strong exothermic signal is observed at 700 K during the decomposition of APT under oxygen. Because the gas-phase products are nearly identical for both the oxygen and helium decomposition, the exothermic signal must be due either to a phase change, or to a reaction such as the re-oxidation of a somewhat reduced tungsten oxide, which would give no gas-phase products.

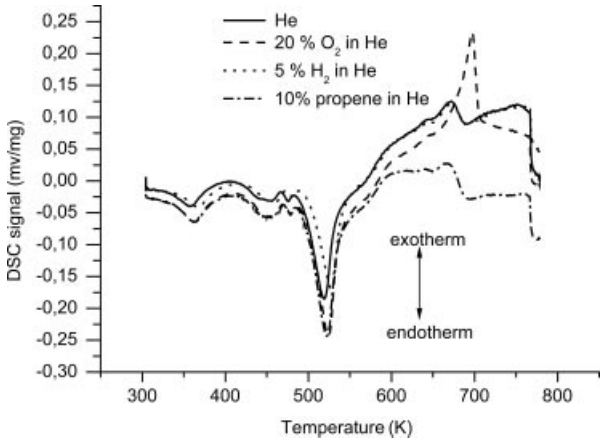

Figure 4. Comparison of the DSC signal measured during decomposition of ammonium paratungstate under helium (solid), 20% oxygen in helium (dashed), 5% hydrogen in helium (dotted), and 10% propene in helium (dash-dotted) (for the corresponding weight loss evolution see Figure 3).

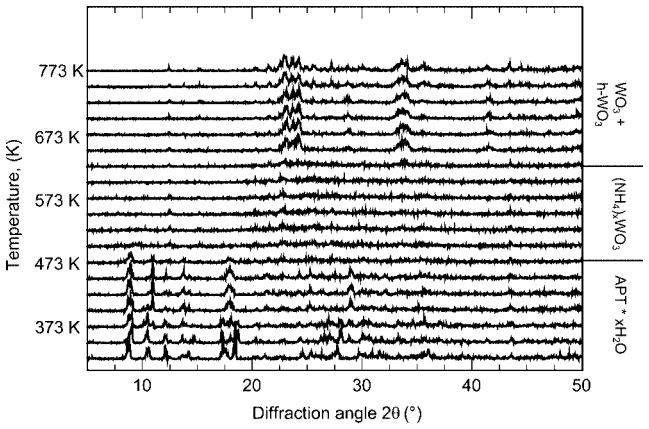

Figure 5. Evolution of X-ray diffraction patterns measured during decomposition of ammonium paratungstate under 20% oxygen in helium in the temperature range 300–770 K (effective heating rate 0.1 K min^{-1}, flow rate 80 mL min^{-1}). Three major stages of the decomposition are indicated.

The WL_{III}-edge XAFS FT[$\chi(k)\cdot k^3$] of APT measured during decomposition under 20% oxygen in helium in the temperature range 300–770 K are shown in Figure 6. Three temperature regions in the evolution of the local structure around the W centers can be distinguished. At 500 K, the initial APT spectrum exhibits changes, particularly, in the region between 2 and 4 Å (not phase-shift-corrected). The decreasing amplitude in this region indicates a significant loss of structural order. Conversely, the increasing amplitude of the first shell at ca. 1.5 Å indicates a decreasing degree of distortion in the first W–O coordination. At ca. 650 K, a decrease in the amplitude of the first shell and distinct changes in the region between 2 and 4 Å can be observed in the experimental FT[$\chi(k)\cdot k^3$], which corresponds to the last step in the decomposition of APT.

Thermal Decomposition of Ammonium Paratungstate (in Situ XRD and XAS)

Decomposition of APT under 20% Oxygen

The evolution of X-ray diffraction patterns measured during decomposition of APT under 20% oxygen in helium in the temperature range 300–770 K is depicted in Figure 5. Three major stages of the decomposition are indicated. The first series of patterns up to ca. 450 K corresponds to APT – a decreasing amount of water of crystallization accounts for the changes in peak intensities and phase composition observed. In the region from 450 K to about 620 K, a pronounced loss of crystallinity is visible from the XRD patterns. The few reflections detectable could not be assigned to any particular tungsten phase on the basis of the ICDD-PDF database. The last step in the structural evolution during decomposition of APT under oxygen at 620 K is accompanied by the occurrence of distinct XRD reflections, which can be assigned to triclinic WO_3 as the majority phase.

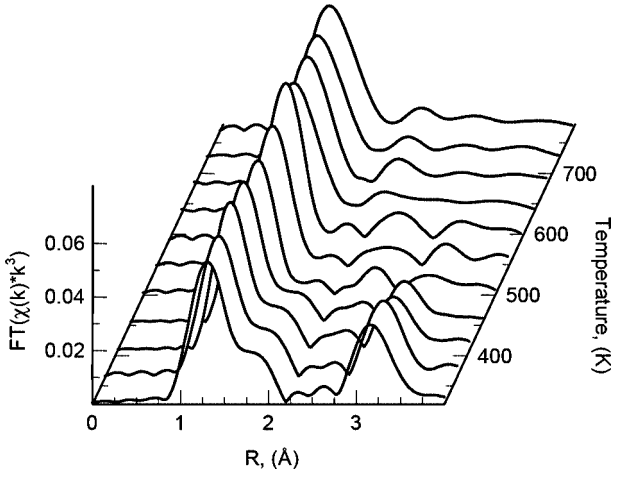

Figure 6. Evolution of WL_{III}-edge XAFS FT[$\chi(k)\cdot k^3$] of ammonium paratungstate during decomposition under 20% oxygen in helium (heating rate 5 K min^{-1}, flow rate 40 mL min^{-1}). Three principle regions can be distinguished: (300–500 K) APT, (500–650 K) $(NH_4)_xWO_3$, (650–770 K) triclinic WO_3.

 © 2005 Wiley-VCH Verlag GmbH & Co. KGaA, Weinheim

Decomposition of APT under Reducing Gases

The evolution of X-ray diffraction patterns measured during the decomposition of APT under 5% hydrogen in helium in the temperature range 300–770 K is depicted in Figure 7. Similar to the decomposition of APT under 20% oxygen, the first series of patterns up to about 450 K corresponds to APT with a decreasing amount of water of crystallization. In the region from 450 K to about 620 K, a complete loss of crystallinity is visible resulting in an X-ray-amorphous phase. At 620 K, the formation of highly disordered hexagonal and triclinic WO_3 and tungsten oxide bronzes $(NH_4)_xWO_3$ is observed. The WO_3 formed exhibits a much lower crystallinity than that obtained during decomposition of APT under oxygen. Eventually, at 770 K under 5% hydrogen, the onset of the reduction of tungsten oxides to tungsten metal is detected in the XRD patterns. The evolution of the WL_{III}-edge FT[$\chi(k)\cdot k^3$] measured during decomposition of APT under the reducing gases studied (i.e. propene, hydrogen, helium, propene and oxygen) is very similar to that of the decomposition under oxygen.

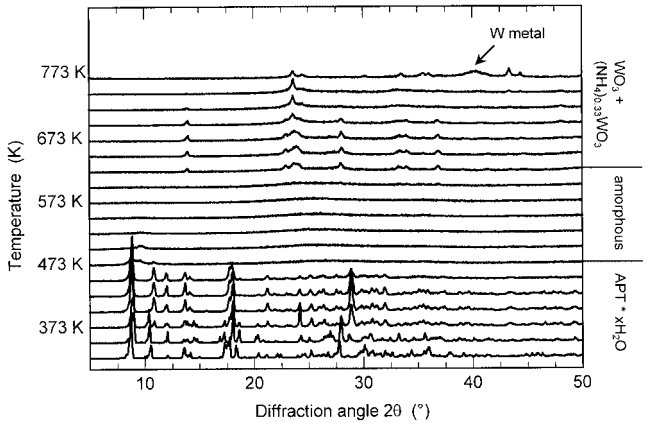

Figure 7. Evolution of X-ray diffraction patterns measured during decomposition of ammonium paratungstate under 5% hydrogen in helium in the temperature range 300–770 K (effective heating rate 0.1 K min^{-1}, flow rate 80 mL min^{-1}). Three major stages of the decomposition are indicated.

Decomposition of APT in Air (Static Conditions)

The evolution of X-ray diffraction patterns measured during the decomposition of APT in static air in the temperature range 300–770 K is shown in Figure 8. Similar to the decomposition of APT under oxygen, three major stages can be distinguished. The first series of patterns up to about 470 K corresponds to APT with a decreasing amount of crystal water. In the region from 470 K to about 550 K, the formation of an X-ray-amorphous phase is detected. Eventually, at 570 K, the formation of well-ordered and phase-pure triclinic WO_3 is observed. The temperature range over which no crystalline phase is detected is smaller in static air than under flowing oxygen and hydrogen, and an increased stability of APT in the temperature region below 470 K and an accelerated formation of crystalline WO_3 at 570 K already are observed. The onset temperature for the decomposition of APT to the amorphous phase is increased by about 25 K, while the formation temperature of WO_3 is lowered by about 25 K.

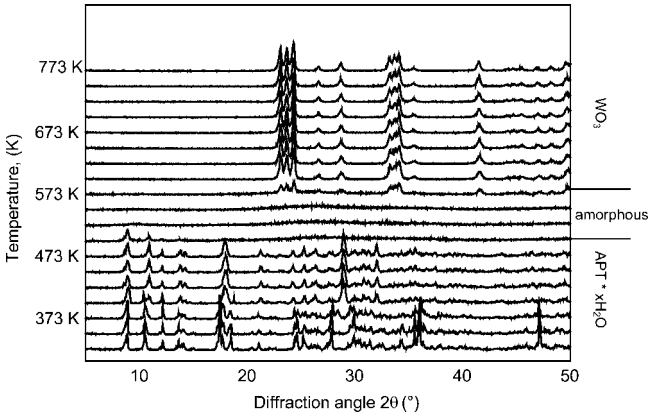

Figure 8. Evolution of X-ray diffraction patterns measured during decomposition of ammonium paratungstate in static air in the temperature range 300–770 K (effective heating rate 0.1 K min^{-1}, flow rate 80 mL min^{-1}). Three major stages of the decomposition are indicated.

Characterization of the Decomposition Intermediates and Products

The XRD pattern of the crystalline product of the decomposition of APT under 20% oxygen in helium can be simulated very well by a mixture of hexagonal and triclinic WO_3 (Figure 9). A Rietveld refinement of the corresponding model structures to the experimental pattern resulted in a phase composition of ca. 90% triclinic WO_3 and ca. 10% hexagonal WO_3, with crystallite sizes of 60 nm and 120 nm, respectively, and lattice constants that are in good agree-

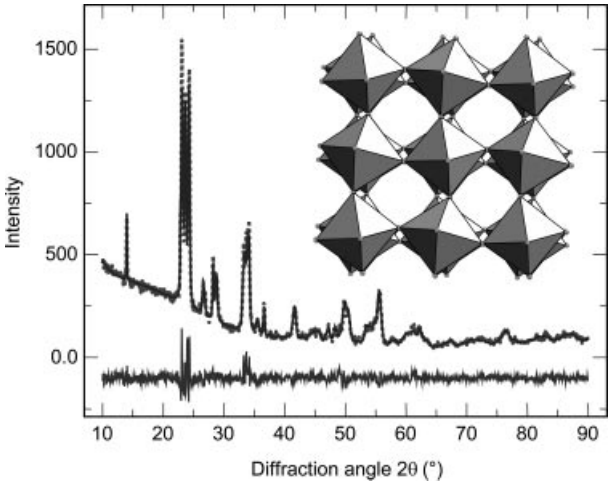

Figure 9. Experimental (dotted) and simulated (solid) X-ray diffraction pattern of the product of the decomposition of ammonium paratungstate under 20% oxygen in helium (300–770 K), together with a schematic structural representation of the corresponding triclinic WO_3 phase.

 © 2005 Wiley-VCH Verlag GmbH & Co. KGaA, Weinheim

ment with the single-crystal data [triclinic WO_3 (ICSD 1620, a = 7.31 Å, b = 7.52 Å, c = 7.68 Å, α = 88.8°, $\beta = \gamma$ = 90.9°) a = 7.34 Å, b = 7.53 Å, c = 7.69 Å, α = 89.6°, $\beta = \gamma$ = 90.5°]. A schematic representation of the structure of triclinic WO_3 is depicted in Figure 9. The nearest-neighbor distances in triclinic WO_3 are given in Table 2. The structure is related to the ReO_3 structure and consists of edge-sharing WO_6 units with W–O distances ranging from 1.8 to 2.2 Å. In comparison with the ReO_3 structure, the WO_6 units in triclinic WO_3 are strongly tilted with respect to each other resulting in a triclinic unit cell.

Table 2. Structural parameters [type of pairs and number (N) of nearest neighbors at distance R] obtained from a refinement of a triclinic WO_3 model structure (based on ICSD 1620) and a hexagonal $(NH_4)_{0.25}WO_3$ model structure (ICSD 23537) to the experimental XAFS functions $\chi(k)$ of the product (at 300 K; Figure 10B) and of an intermediate (at 545 K; Figure 10A) of the decomposition of APT under oxygen at the WL_{III} edge (N_{ind} = 28, N_{free} = 16, 12 single-scattering paths and 29-multiple scattering paths, R range 0.8–4.2 Å, k range 1.7–13.1 $Å^{-1}$, E_0 = 6.2 eV, S_0^2 = 0.9).

Type	N	WO_3			N	$(NH_4)_{0.25}WO_3$		
		Model	Product (300 K)			Model	Intermediate (545 K)	
		R [Å]	R [Å]	σ^2 [$Å^2$]		R [Å]	R [Å]	σ^2 [$Å^2$]
W–O	3	1.78	1.78	0.0014	2	1.88	1.75	0.0040
W–O	1	1.95	1.95	0.0015	2	1.89	1.90	0.0041
W–O	1	2.06	2.07	0.0015	2	1.96	2.13	0.0042
W–O	1	2.21	2.19	0.0016	–	–	–	–
W–W	2	3.71	3.71	0.0060	4	3.70	3.65	0.0084
W–W	3	3.80	3.81	0.0060	2	3.78	3.74	0.0084
W–W	1	3.86	3.90	0.0060	–	–	–	–

A detailed XAFS analysis of the APT decomposition product under oxygen and of a representative intermediate of the decomposition from the amorphous region in the XRD series was performed to elucidate the local structure around the W centers in the two stages of decomposition. The experimental and theoretical WL_{III} FT[$\chi(k)\cdot k^3$] of the intermediate of the thermal decomposition of APT at 523 K and of WO_3 as the product of the decomposition at 773 K are depicted in Figure 10, A and B, respectively. The corresponding structural parameters are given in Table 2. It can be seen that the local structure around the W centers in the product WO_3 is in good agreement with that in the triclinic WO_3 model structure. Similarly, the local structure around the W center in the intermediate of the decomposition at 523 K can also be simulated by the triclinic WO_3 model structure. However, characteristic deviation in the first W–O distances (i.e. absence of neighbors at 2.2 Å) indicates a higher degree of regularity in the WO_6 units of the intermediate phase relative to those of triclinic WO_3. Moreover, the W–W distances obtained are slightly smaller than those determined for triclinic WO_3. It emerges that the local structure around the W centers in the intermediate phase at 523 K can be better explained by assuming a hexagonal tungsten bronze such as $(NH_4)_{0.25}WO_3$ (ICSD 23537). A schematic structural representation of $(NH_4)_{0.25}WO_3$ is depicted in Figure 11.

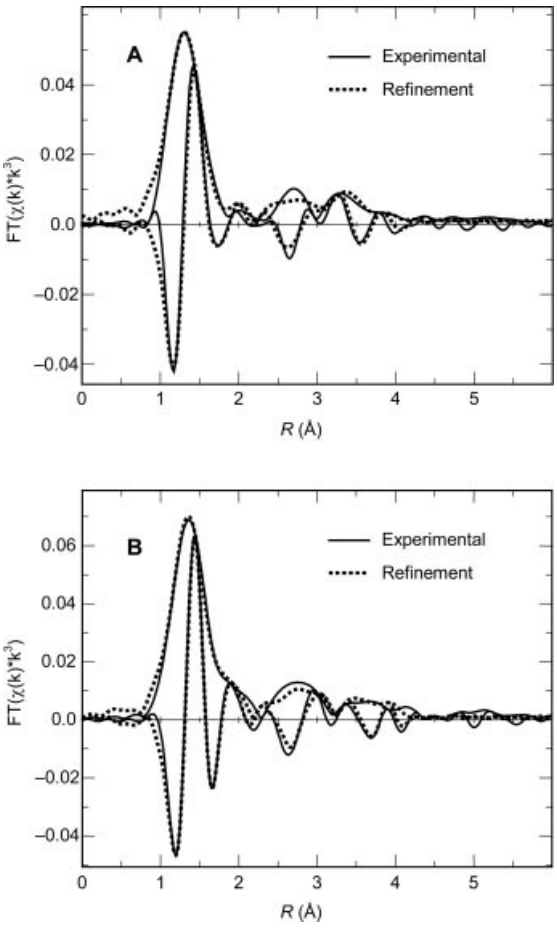

Figure 10. Experimental (dotted) and theoretical (solid) WL_{III} XAFS FT[$\chi(k)\cdot k^3$] of the intermediate of the thermal decomposition of ammonium paratungstate at 523 K (A) and of WO_3 as the product of the decomposition at 773 K (B) measured at 300 K. The corresponding structural parameters are given in Table 2.

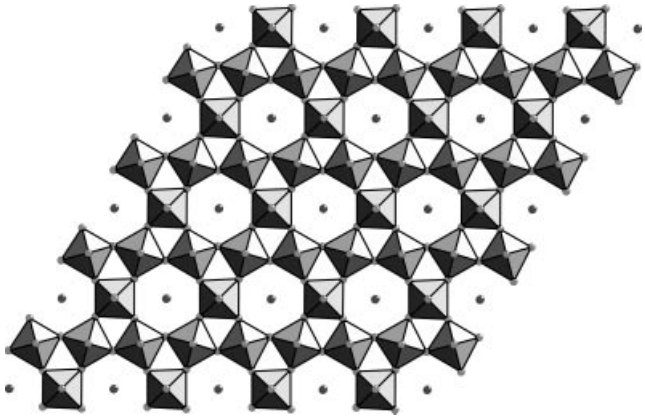

Figure 11. Schematic structural representation of hexagonal $(NH_4)_{0.25}WO_3$ (ICSD 23537).

Discussion

Thermal Decomposition of Ammonium Paratungstate

The thermal analysis data shown in Figures 3 and 4 for the decomposition of APT under the various gases em-

 © 2005 Wiley-VCH Verlag GmbH & Co. KGaA, Weinheim

ployed indicate that up to a temperature of ca. 650 K, the decomposition proceeds largely independently of the gas. This is corroborated by the XRD data presented in Figures 5, 7, and 8, which exhibit a series of patterns corresponding to a loss of water of crystallization up to 470 K, and transformation into a poorly crystalline or amorphous phase that persists up to ca. 650 K. At temperatures above 650 K, the product of decomposition depends on the gas-phase composition. This holds for both the phase composition and the crystallinity of the products obtained.

While under oxidizing gases triclinic WO_3 is formed as the majority phase,[14,18] the decomposition under reducing gases results in the formation of partially reduced tungsten bronzes.[16] However, reduction of WO_{3-x} formed at 650 K under reducing gases (i.e. helium, propene, and hydrogen) to WO_2 or tungsten metal is detected during the decomposition of APT under hydrogen only.[17,26–28] Apparently, propene is not capable of further reducing WO_3 in the temperature range employed. This difference between the reducing powers of hydrogen and propene has already been observed for the reduction of MoO_3 under propene and hydrogen.[29] While hydrogen is capable of entering the lattice of MoO_3 and WO_3, reduction of the oxide by propene requires the facilitated diffusion of oxygen to the surface to react with the propene molecules adsorbed at the surface. On the one hand, this is the case for the reduction of MoO_3 under propene and helium, where oxygen can readily diffuse in the layer structure of orthorhombic MoO_3. On the other hand, diffusion of oxygen appears to be considerably hindered in the ReO_3-type structure of WO_3. Thus, no lattice oxygen is made available at the surface of the WO_{3-x} crystallites formed in the decomposition of APT, and no significant oxidation of propene by lattice oxygen with the corresponding reduction of the WO_3 lattice occurs.

The major mass loss (Figure 3) and thermal DSC event (Figure 4), together with the major structural changes (e.g. Figure 5) during the decomposition of APT proceeds at ca. 520 K. The amorphous or poorly crystalline phase detected by XRD at temperatures above 500 K can be identified by XAS to correspond to a 3D network structure similar to that of triclinic WO_3. While the local coordination of tungsten by the nearest-neighbor oxygen atoms in the intermediate phase at 500 K exhibits a characteristic distortion very similar to that of triclinic WO_3 (and different from that of hexagonal WO_3), the medium-range order appears to be more similar to that of a hexagonal WO_3 structure, $(NH_4)_{0.25}WO_3$. A schematic representation of $(NH_4)_{0.25}WO_3$ is depicted in Figure 11. The rather short W–W distances found in the local structure around the W center in the intermediate at ca. 500 K is characteristic for this hexagonal tungsten oxide. Hence, the major decomposition stage observed at ca. 500 K corresponds to a complete destruction of the polyoxo ions of APT, followed by a restructuring and formation of a three-dimensional network of corner-sharing WO_6 units. During the decomposition in the temperature range 470–650 K prior to the formation of triclinic WO_3, the evolution of FT[$\chi(k)\cdot k^3$] shows that the distortion in the first oxygen coordination sphere decreases resulting in more regular WO_6 units similar to those characteristic of tungsten bronzes. With increasing temperature, the last decomposition stage and formation of triclinic WO_3 at ca. 650 K results in an increased distortion of the WO_6 units characteristic of triclinic WO_3.

Decomposition of APT under Partial Oxidation Reaction Conditions

During the decomposition of APT under propene, and propene and oxygen no significant amounts of oxidation products of propene (i.e. acrolein or carbon dioxide) are detected in the gas phase. As mentioned above, no reduction of WO_3 by propene is detected, indicating no availability of lattice oxygen for propene oxidation. The absence of propene oxidation activity in the temperature range studied is in agreement with a generalized mechanism of propene oxidation, which requires a certain weakening of the metal–oxygen bonds to ensure the presence of characteristic surface defects required for the activation of gas-phase oxygen and propene and the availability of oxygen to the gas-phase reactants.[30,31] The invariance of the WO_3 structure under propene, and propene and oxygen at temperatures above 600 K indicates that the W–O bonds in the more regular WO_6 building units of WO_3, relative to the highly distorted MoO_6 building units of α-MoO_3, are less susceptible of forming non-oxygen-terminated catalytically active surface sites. Conversely, treatment of MoO_3 under propene and oxygen clearly shows that the onset of catalytic activity at ca. 600 K is correlated to the mobility of lattice oxygen at this temperature. The latter is evident from the onset of reduction of MoO_3 under propene at the same temperature. In contrast with the characteristic layer structure of orthorhombic MoO_3, which is capable of accommodating oxygen vacancies by the formation of crystallographic shear defects, the corner-sharing octahedrons in the triclinic WO_3 structure are less flexible, energetically more stable and are thus not capable of permitting an increased amount of oxygen vacancies in the tungsten oxide lattice. Under the decomposition conditions investigated, which encompass those used for the calcination of catalyst precursors in the literature, no catalytically active tungsten oxide bronzes or tungsten oxide shear-structures are obtained. The rather stable ReO_3-like three-dimensional tungsten oxides that already form at temperatures as low as 500 K exhibit no sufficient oxygen mobility and, hence, no partial oxidation activity in the temperature range employed.

Comparison of the Decomposition of APT and Polyoxomolybdates

In previous works, we reported on the characteristic evolution of phases during the decomposition of ammonium heptamolybdate (AHM)[3] and heteropolyoxomolybdate (HPOM)[4] under various reaction gases. In Figure 12 the schematic pathway for the decomposition of APT is compared to those determined for the decomposition of AHM

 © 2005 Wiley-VCH Verlag GmbH & Co. KGaA, Weinheim

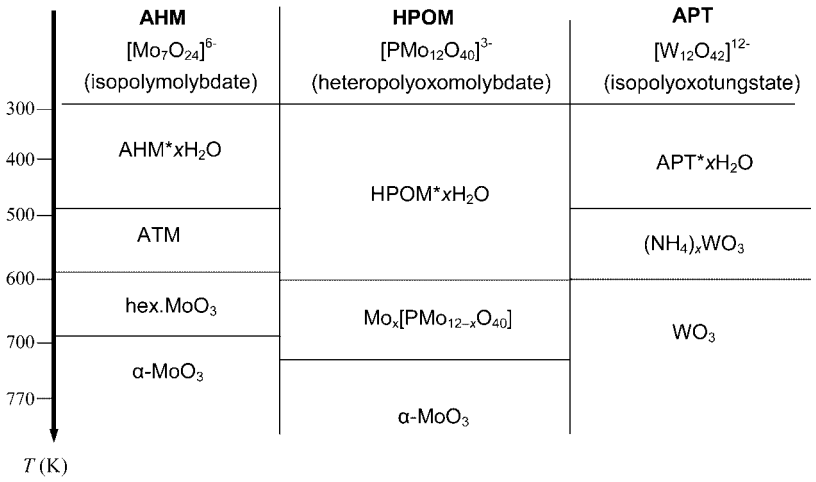

Figure 12. Schematic representation of the structural evolution during decomposition of ammonium heptamolybdate (AHM), a Keggin-type heteropolyoxo molybdate ($[PMo_{12}O_{40}]^{3-}$), and ammonium paratungstate $[(NH_4)_{10}H_2W_{12}O_{42}\cdot 4H_2O]$ under 20% oxygen in helium in the temperature range 300–773 K.).

and HPOM under oxygen. In all three cases, decomposition starts with the loss of water of crystallization, present in varying amounts in the three materials. The decomposition of the relatively small Anderson-type polyoxomolybdate ions of AHM proceeds according to a series of polycondensation steps that result in an increasing dimensionality of the structure of the decomposition intermediates.[3] The X-ray-amorphous phase that forms at ca. 500 K during the decomposition of AHM under flowing reactants could be identified as ammonium tetramolybdate possessing a 1D chain structure. A three-dimensional lattice structure (hexagonal MoO_3) forms at ca. 600 K and is eventually transformed into orthorhombic MoO_3 at ca. 700 K. Evidently, the thermal decomposition of both APT and AHM proceeds through the formation of an ammonium- and water-containing hexagonal phase, which eventually decomposes into mainly triclinic WO_3 and orthorhombic MoO_3, respectively. In contrast to the decomposition of APT, the products obtained from the decomposition of AHM depend strongly on the gas employed.[3]

Heteropolyoxomolybdates of the Keggin type, $[PMo_{12}O_{40}]^{3-}$, exhibit a significantly increased stability compared to APT, with a similar stoichiometry. Partial decomposition and reduction of the Keggin ion starts at about 600 K, which coincides with the formation of a three-dimensional lattice during decomposition of AHM. At 600 K, the HPOM forms a lacunary Keggin ion with one molybdenum center on an extra-Keggin framework position. This arrangement is stable to about 700 K where a complete structural rearrangement and formation of α-MoO_3 is detected. While the extra-Keggin Mo center certainly acts as the first step towards "condensation" of the Keggin ions and formation of the extended MoO_3 structure, no further well-defined intermediates with an increasing degree of condensation are observed. Because the decomposition of HPOM results eventually in the formation of MoO_3 at temperatures above 700 K, the final product composition at 773 K is strongly dependent on the gas used (i.e. MoO_3 under oxidizing gases, MoO_2 under moderately reducing gases, and Mo metal under hydrogen). Thus, two effects result in a pronounced stability of the Keggin-type HPOM relative to APT. First, the stability of the three-dimensional network of edge-sharing WO_6 units in WO_3 favors the decomposition of polyoxotungstate and the formation of WO_3. Second, the Keggin ions of heteropolyoxomolybdates are considerably stabilized by the phosphorus heteroatom. With respect to the preparation of tungsten-containing, mixed-metal oxide, the differences in the decomposition schemes revealed for ammonium paratungstate relative to other common catalyst precursors such as ammonium heptamolybdate and heteropolyoxomolybdates indicate certain prerequisites for suitable preparation routes. Because of the low formation temperature of a stable 3D lattice structure during decomposition of APT, precursor mixtures with APT as a separate phase will most likely result in oxide mixtures containing catalytically less interesting triclinic or hexagonal tungsten oxides. Hence, in order to use the structure-promoting and stabilizing effect of the W centers in mixed molybdenum oxide catalysts, tungsten has to be incorporated into the Mo precursors to ensure the presence of W in the final catalyst.

Conclusions

The bulk structural evolution during the decomposition of APT under various oxidizing and reducing gases was elucidated by the complementary techniques in situ XAS, in situ XRD, and TG/DSC combined with mass spectrometry. In the temperature range 300–650 K, the decomposition of APT proceeds nearly independently of the gas employed. Oxidizing gases result in the formation of crystalline triclinic WO_3 as the majority phase at 773 K, while mildly reducing gases (propene, propene and oxygen, and helium) result in the formation of partially reduced and highly disordered tungsten bronzes. No further reduction is observed

 © 2005 Wiley-VCH Verlag GmbH & Co. KGaA, Weinheim

under propene or helium, indicating strongly hindered oxygen mobility in the tungsten oxide lattice in the temperature range employed. Because of the particular reducing capabilities of hydrogen (i.e. incorporation in the lattice and formation of bronzes), the decomposition of APT under hydrogen results in the formation of WO_2 and, eventually, tungsten metal.

During the thermal treatment of APT major changes occur at ca. 520 K where a complete structural rearrangement takes place which results in the destruction of the polyoxotungstate ion of APT and the formation of a tungsten oxide bronze. This bronze already exhibits a three-dimensional structure consisting of corner-shared WO_6 units with a local structure around the W centers similar to that in triclinic WO_3. The rather low temperature for the formation of a three-dimensional lattice relative to the thermal treatment of common polyoxomolybdate precursors indicates the particular structural stability of the arrangement of corner-sharing WO_6 units in WO_3 and tungsten oxide bronzes. For tungsten to act as a potential structural or electronic promoter in molybdenum oxide based catalysts, tungsten needs to be incorporated in regular molybdenum oxide structures already at a very early stage of the catalyst preparation instead of employing paratungstate-containing phase mixtures.

Experimental Section

Ammonium Paratungstate Tetrahydrate, $(NH_4)_{10}H_2W_{12}O_{42}\cdot 4H_2O$: Ammonium paratungstate tetrahydrate [APT, $(NH_4)_{10}H_2W_{12}O_{42}\cdot 4H_2O$] was used as purchased (Osram). For the investigations described here, a sieved fraction with particles in the size range 100–200 μm was employed (Figure 13).

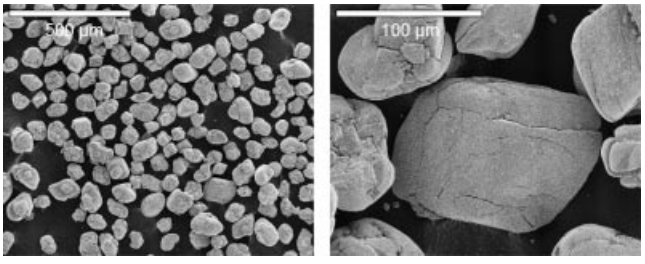

Figure 13. Scanning electron micrographs of a sieved fraction of as-purchased ammonium paratungstate [$(NH_4)_{10}H_2W_{12}O_{42}\cdot 4H_2O$] with particles in the size range 100–200 μm.

X-ray Diffraction (XRD): In situ XRD studies were performed with a STOE Bragg–Brentano diffractometer (Ge secondary monochromator, Cu-K_α radiation) equipped with a Bühler HDK S1 high-temperature cell. The product composition in the gas phase was continuously monitored by using a mass spectrometer in a multiple ion detection mode (Pfeiffer QMS 200). XRD measurements were conducted in the temperature range 323–773 K with an effective heating rate of 0.1 K min^{-1}. Diffraction patterns were recorded every 25 K in a 2θ range of 5–50°. Analysis of experimental diffraction patterns was performed by using the software TOPAS (Bruker AXS) Version 2.1. Crystallite sizes were estimated by using the Scherrer equation. The ICDD-PDF (International center for diffraction data) database and the ICSD (Inorganic crystal structure database) were used for phase analysis and structure refinement.

X-ray Absorption Spectroscopy (XAS): Transmission X-ray absorption spectra were measured in situ with the sample pellet in a flow reactor under a controlled reactant gas.[32] In situ XAS experiments were performed at the WL_{III} edge (10.204 keV) (Hamburger Synchrotronstrahlungslabor, HASYLAB, beamline X1), by using an Si (311) double crystal monochromator. Temperature-programmed decomposition of APT was conducted at temperatures between 293 and 773 K under helium, 5% hydrogen in helium, 20% oxygen in helium, 10% propene in helium, and 10% propene and 10% oxygen in helium. For the in situ XAS measurements, 4 mg of APT was mixed with 30 mg of boron nitride and pressed into pellets of 5 mm in diameter (edge jump $\Delta\mu_x \approx 1.5$ at the WL_{III} edge). The gas-phase composition was continuously monitored by using a mass spectrometer in a multiple ion detection mode (Omnistar, Pfeiffer). Data analysis of XAFS spectra was performed with the software WinXAS 3.0.[33] The spectra were energy-calibrated with respect to a tungsten metal foil reference spectrum. For background subtraction and normalization, first-order polynomials were refined to the pre-edge and EXAFS region. Spectra were converted to k space using an E_0 defined as the first inflection point in the WL_{III} edge. Atomic absorption, μ_o, fitting was performed by using a cubic spline with 7 knots to minimize peaks at low R values (<1 Å) in the Fourier-transformed EXAFS $\chi(k)$. The pseudo radial distribution function FT[$\chi(k)\cdot k^3$] was calculated by Fourier transforming the k^3-weighted experimental $\chi(k)$ function, multiplied by a Bessel window, into the R space. EXAFS data analysis was performed by using theoretical backscattering phases and amplitudes calculated with the ab initio multiple-scattering code FEFF7.[34] Single-scattering and multiple-scattering paths in monoclinic APT, hexagonal $(NH_4)_{0.25}WO_3$ (intermediate), and triclinic WO_3 (decomposition product) were calculated up to 6.0 Å with a lower limit of 8.0% in amplitude with respect to the strongest backscattering path. EXAFS refinements were performed in R space simultaneously to magnitude and imaginary part of a Fourier transformed k^3-weighted and k^1-weighted experimental $\chi(k)$ by using the standard EXAFS formula.[34] Structural parameters that are determined by a least-squares EXAFS refinement of a model structure to the experimental spectra are (i) one overall E_0 shift, (ii) Debye–Waller factors for single-scattering paths, and (iii) distances of single-scattering paths. Coordination numbers (CN) and S_0^2 were kept constant in the refinement.

Thermal Analysis (TG and DSC): Thermal analysis [thermogravimetry (TG) and differential scanning calorimetry (DSC)] was performed with a Netzsch STA 449 C TG/DSC instrument combined with an Omnistar (Pfeiffer) mass spectrometer under pure helium, 5% hydrogen in helium, 20% oxygen in helium, 10% propene in helium, and 10% propene, and 10% oxygen in helium. Measurements were carried out at heating rates of 6 K min^{-1}, and at a total flow of 100 mL min^{-1}.

Scanning Electron Microscopy: Scanning electron microscopy (SEM) was conducted with an S 4000 FEG microscope (Hitachi). The acceleration voltage was set at 10 kV, the objective aperture was 30 mm, and the working distance was 10 mm.

Acknowledgments

The Hamburger Synchrotronstrahlungslabor, HASYLAB, is acknowledged for providing beamtime for this work. G. Weinberg is acknowledged for conducting the SEM measurements. We thank B. Kniep, A. Szizybalski, E. Rödel, J. Osswald, and J. Wienold for

assistance at the beamline and for numerous valuable discussions. The authors are grateful to Prof. R. Schlögl for his continuous support.

[1] A. Bielanski, J. Haber, *Oxygen in Catalysis*, Marcel Dekker, New York, **1991**.
[2] S. Knobl, G. A. Zenkovets, G. N. Kryukova, O. Ovsitser, D. Niemeyer, R. Schlögl, G. Mestl, *J. Catal.* **2003**, *215*, 177–187.
[3] J. Wienold, R. E. Jentoft, T. Ressler, *Eur. J. Inorg. Chem.* **2003**, 1058–1071.
[4] J. Wienold, O. Timpe, T. Ressler, *Chem. Eur. J.* **2003**, *9*, 1–12.
[5] E. Lassner, W. Schubert, *Thermochim. Acta* **2000**, *343*, 139–143.
[6] B. Gerand, G. Nowogrocki, M. Figlarz, *J. Solid State Chem.* **1981**, *38*, 312–320.
[7] M. F. Daniel, B. Desbat, J. C. Lassegues, B. Gerand, M. Figlarz, *J. Solid State Chem.* **1987**, *67*, 235–247.
[8] John W. van Put., G. J. Witkamp, G. M. van Rosmalen, *Hydrometallurgy* **1993**, 187–201.
[9] Y. Zhu, A. Manthiram, *J. Solid State Chem.* **1994**, *110*, 187–189.
[10] J. Pfeifer, E. Badaljan, P. Tekula-Buxbaum, T. Kovacs, O. Geszti, A. L. Toth, H.-J. Lunk, *J. Cryst. Growth* **1996**, *169*, 727–733.
[11] N. E. Fouad, A. K. H. Nohman, M. J. Zaki, *Thermochim. Acta* **1994**, *239*, 137–145.
[12] M. Boulowa, G. Lucazeau, *J. Solid State Chem.* **2002**, *167*, 425–434.
[13] C. Li, H. Zhang, K. L. Wang, Y. F. Miao, Q. Xin, *Appl. Spectrosc.* **1993**, *47*, 56–61.
[14] I. K. Bhatnaga, D. K. Chakraba, A. B. Biswas, *Indian J. Chem.* **1972**, *10*, 1025–1028.
[15] N. E. Fouad, A. K. H. Nohman, M. A. Mohamed., M. J. Zaki, *J. Anal. Appl. Pyrolysis* **2000**, *56*, 23–31.
[16] X. S. Li, B. Z. Zhu, L. Wang, Y. F. Miao, Q. Xin, *Chin. Chem. Lett.* **1995**, *6*, 1085–1086.
[17] N. E. Fouad, A. K. H. Nohman, *Thermochim. Acta* **2000**, *343*, 139–143.
[18] J. Pfeifer, E. G. Badaljan, P. Tekula-Buxbaum, K. Vadasdi, *J. Solid State Chem.* **1993**, *105*, 588–594.
[19] I. Rodriguez-Ramos, A. Guerro-Ruiz, N. Homs, R. de la Piscina, J. L. G. Fierro, *J. Mol. Catal.* **1995**, *95*, 147–156.
[20] D. Hoegaets, B. Sels, D. Fos, F. Verpoort, P. Jacobs, *Catal. Today* **2000**, *60*, 209–218.
[21] M. O'Keeffe, *Fast Ion Transport in Solids – Solid State Batteries and Devices*, Elsevier, New York, **1973**, 233–247.
[22] A. Cimino, F. S. Stone, *Adv. Catal.* **2002**, *47*, 141–306.
[23] S. De Rossi, I. Igughi, M. Schiavello, R. J. D. Tilley, *Z. Phys. Chem. (Muenchen Ger.)* **1976**, *103*, 193–202.
[24] J. Haber, J. Janas, M. Schiavello, R. J. D. Tilley, *J. Catal.* **1983**, *82*, 395–403.
[25] S. Barber, J. Booth, D. R. Pyke, R. Reid, R. J. D. Tilley, *J. Catal.* **1982**, *77*, 180–191.
[26] D. S. Venables, M. E. Brown, *Thermochim. Acta* **1996**, *285*, 361–382.
[27] C. Bigey, L. Hilaire, G. Maire, *J. Catal.* **1999**, *184*, 406–420.
[28] V. Logie, P. Wehrer, A. Katrib, G. Maire, *J. Catal.* **2000**, *189*, 438–448.
[29] T. Ressler, R. E. Jentoft, J. Wienold, T. Neisius, *J. Catal.* **2002**, *210*, 67–83.
[30] P. Mars, D. W. van Krevelen, *Chem. Ing. Sci.* **1954**, *3*, 41–52.
[31] T. Ressler, J. Wienold, R. E. Jentoft, F. Girgsdies, *Eur. J. Inorg. Chem.* **2003**, 301–312.
[32] T. Ressler, R. E. Jentoft, J. Wienold, M. M. Guenter, O. Timpe, *J. Phys. Chem. B* **2000**, *104*, 6360–6370.
[33] T. Ressler, *J. Synchrotron Radiat.* **1998**, *5*, 118–122.
[34] J. J. Rehr, C. H. Booth, F. Bridges, S. I. Zabinsky, *Phys. Rev. B* **1994**, *49*, 12347–12350.

Received: October 15, 2004

 © 2005 Wiley-VCH Verlag GmbH & Co. KGaA, Weinheim

Surface Segregation in SnO_2–Fe_2O_3 Nanopowders and Effects in Mössbauer Spectroscopy

Ricardo H. R. Castro,*[a,b] Pilar Hidalgo,[a] José A. H. Coaquira,[c] Jefferson Bettini,[d] Daniela Zanchet,[d] and Douglas Gouvêa[a]

Keywords: Materials science / Nanostructures / Semiconductors / Electron microscopy / Moessbauer spectroscopy

SnO_2–Fe_2O_3 nanopowders prepared by the polymeric precursor method were studied by combined conventional and high-resolution techniques. The powders treated at 500 °C were analyzed by EDS local probe associated with HRTEM to directly detect surface segregation of Fe ions onto SnO_2 nanoparticles over a broad range of concentrations. The segregation of these ions controls the system microstructure by changing the surface energies and acting as nucleation sites for the formation of a Fe oxide phase (magnetite) at high Fe concentrations. A technologically interesting core–shell-type particle structure, with a magnetic shell and semiconductor core, was observed for the first time. The influence of the segregated Fe ions in Mössbauer spectra is also addressed as a new proposal for the interpretation of the effects of composition changes in both the bulk and at the interface of particles. In this proposal, the two observed sites in Mössbauer spectra would be independently related to bulk-substituted and surface-segregated Fe ions.
(© Wiley-VCH Verlag GmbH & Co. KGaA, 69451 Weinheim, Germany, 2005)

Introduction

In the past few decades the electrical and magnetic properties of oxide systems containing Fe ions have greatly increased commercial interest in such materials for application as gas sensors, catalysts and other devices.[1,2] These properties have been extensively studied for many systems,[1–13] and a number of efforts have been carried out to establish the relationship between the observed properties and structural features of these solids. However, since most of the techniques used are not suitable for detecting surface-segregated atoms,[3,9] the discussions rarely consider this phenomenon as a relevant issue, and its influence on the structure and microstructure are usually disregarded. This could lead to incomplete microstructure characterizations that could have reflected in unreliable conclusions about the related properties. In fact, the presence of atoms at the surface can change the interpretation of several phenomena and open up new perspectives for the development of new devices.

Techniques such as X-ray photoelectron spectroscopy (XPS) have shown that surface segregation of components occurs in a wide range of compositions in a large number of systems and, moreover, these segregated components should play an important role in oxide systems.[12–17] This role should involve not only effects on the final properties of the materials, such as electrical and optical, but also on their microstructure and structure evolution.

Although considered an extensive solid-solution system, and with a number of studies concerning this topic,[18–20] surface segregation has recently been hypothesized in the technologically relevant Fe_2O_3–SnO_2 system.[21,22] The hypothesis firstly emerged from the fact that, despite the similarity between the ionic radii of Fe^{3+} and Sn^{4+}, which should induce the formation of an extensive solid solution, Fe_2O_3 (hematite) possesses a corundum-type structure whereas Sn^{4+} hardly forms this structure type and, therefore, their mutual solubility should be lower than that expected by the radius analysis. Actually, only some indirect evidence, fundamentally based on surface IR spectroscopy and surface charges, has indicated that the lower concentration component of this system, instead of forming a bulk solid solution, could be segregating onto the surface of the particles as a surface solid solution. This conclusion was based on the very pronounced effects of the components in the surface sensitivity measurements even at low concentrations and, moreover, on the lack of apparent peak dislocations or second phases in the XRD patterns.[23]

This paper intends to address the surface segregation in the Fe_2O_3–SnO_2 system by using energy dispersive spectroscopy (EDS), XRD, and HRTEM to clarify the ions' distribution in this system and also consider the microstructure of different compositions. Moreover, since the segrega-

[a] Escola Politecnica, Department of Metalurgical and Materials Engineering, University of São Paulo,
Av. Prof. Mello Moraes 2463, São Paulo, SP 05508-900, Brazil
Fax: +55-11-3091-5238
E-mail: ricardo@cecm.usp.br
[b] Centro Universitário da FEI,
Av. Humberto A. C. Branco, 3973, São Bernardo do Campo, SP 09850-901, Brazil
[c] Instituto de Física, University of São Paulo
CP 33618, São Paulo, SP 05315-970, Brazil
[d] Brazilian Synchrotron Light Laboratory, LNLS,
CP 6192, Campinas, SP 13084-971, Brazil

 © 2005 Wiley-VCH Verlag GmbH & Co. KGaA, Weinheim **DOI: 10.1002/ejic.200400879**

tion of the lower concentration component on the surface of the power can be confirmed by these techniques, this work also readdresses Mössbauer spectroscopy in this system by taking into account the influence of the segregated components. Although this spectroscopy has been the subject of several studies in this system[3,19] and, moreover, this technique has already been independently described to consist of a crystalline contribution and an interface one,[24] surface segregation and its influence on the interface contribution have not been addressed, and even nowadays, Mössbauer studies of the SnO_2–Fe_2O_3 system are still exclusively based on the same solid-solution concepts.[18]

Results and Discussion

Figure 1(a) shows the XRD patterns of SnO_2 powders containing increasing amounts of Fe prepared by a polymeric precursor method.[25,26] Up to 30 mol-% Fe all reflection peaks can be assigned to the SnO_2 tetragonal phase. In 50 and 80 mol-% Fe samples, additional peaks appear in the XRD patterns indicating a second-phase nucleation that could be related to the (220) and (311) reflections of both

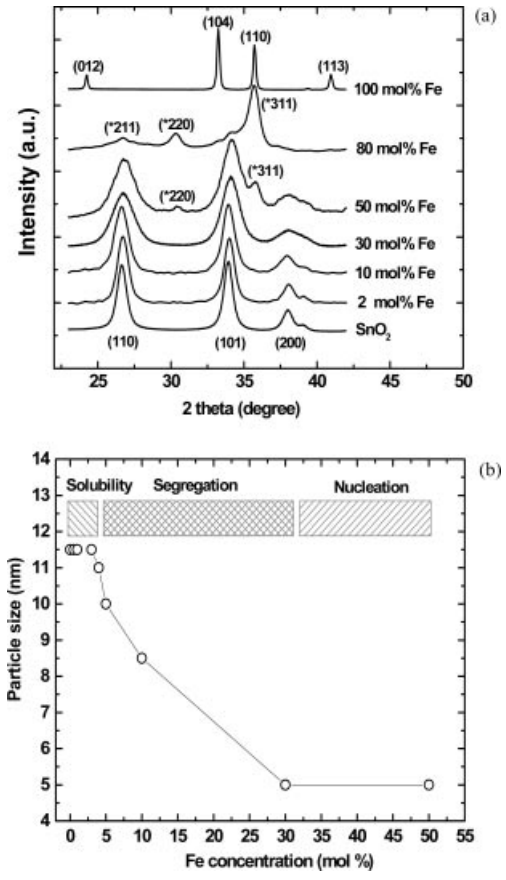

Figure 1. (a) XRD spectra of SnO_2 powders containing different amounts of Fe. The peaks identified by * correspond to the formation of a second phase. (b) SnO_2 particle diameters estimated by the Sherrer method as a function of Fe concentration. Note the three distinct regimes: solubility, segregation, and second-phase nucleation.

magnetite and maghemite phases. The XRD pattern of the 100 mol-% Fe sample corresponds to pure hematite phase.

Since only slight changes can be observed in the diffractograms up to 50 mol-% Fe, one may suggest the solubility and segregation ranges of Fe in the SnO_2 structure to be below 50 mol-% Fe, after which nucleation of the second phase occurs. The solubility range can be determined from the data in Table 1, where the lattice parameters of the SnO_2 phase, extracted from the XRD patterns of 0–10 mol-% Fe samples, are presented. Note that the lattice parameter *a* remains almost constant with increasing Fe concentration, whereas lattice parameter *c* increases with increasing Fe content up to about 4 mol-%. The distortion of the SnO_2 lattice can be attributed to the incorporation of Fe^{3+}, thus suggesting that the solubility limit for this system is around this concentration. A further increase of the Fe content does not significantly change the lattice parameters. Since no crystalline second phases are observed at this stage, both amorphous second phase or the surface segregation of Fe ions can be considered. Based on the literature reports and the HRTEM and EDS data presented below, an amorphous phase can be disregarded. That is to say, after saturation of the lattice by the additive, and above this limit, the segregation of atoms onto the particle surface is supposed to be relatively energetically favorable for the additive. The existence of a solubility limit, however, does not mean that segregation is not occurring before it, but that a smooth transition between both phenomena should exist. This explains why surface-segregation effects are already observed with 2 mol-% Fe but are much more pronounced at about 5 mol-% Fe.[23]

Table 1. Refined values of unit-cell parameters of SnO_2 containing different Fe contents.

Sample	*a* [Å]	*c* [Å]	*c*/*a*
SnO_2[a]	4.7367(1)	3.1855(1)	0.672
SnO_2	4.7406(1)	3.238(4)	0.683
1 mol-% Fe	4.7402(3)	3.263(7)	0.688
2 mol-% Fe	4.7406(2)	3.277(6)	0.691
4 mol-% Fe	4.7401(1)	3.296(7)	0.695
5 mol-% Fe	4.7403(1)	3.291(8)	0.694
10 mol-% Fe	4.7406(5)	3.30(2)	0.696

[a] Data taken from the literature.[27]

The particle size changes as a function of Fe concentration shown in Figure 1(b) reinforce the segregation hypothesis and allow a more precise determination of its occurrence range. The particle diameters were estimated from the XRD peaks by the Sherrer method and confirmed by HRTEM images. Note that below the solubility limit the particle size remains almost constant, suggesting that the inclusion of the additive inside the lattice does not significantly increase the diffusion mechanisms responsible for grain growth. After this point, and between 4 and 30 mol-%, the particle diameters decrease substantially. This is coherent with the proposition of segregation occurrence beyond 4 mol-% Fe, i.e., after the matrix saturation by the additive, an excess of Fe ions segregate onto the particle surfaces, slightly reducing the surface energies and, conse-

 © 2005 Wiley-VCH Verlag GmbH & Co. KGaA, Weinheim

quently, decreasing the final particle sizes, as predicted by the Ostwald ripening model.[22,23,28–30] Since the surface energy is highly dependent on the Fe surface concentration, the particle size of the system decreases as the Fe surface concentration increases until the total coverage of the surface, determined as the segregation limit. Above the segregation limit, the nucleation of a second phase becomes energetically favorable for the additive. This is the case for concentrations higher than about 30 mol-%; in this case the SnO_2 particle diameter remains approximately constant.

A local probe technique (EDS) associated with HRTEM images is a conclusive tool to prove surface segregation and is particularly useful for understanding the second-phase nucleation mechanism. Figure 2(a) shows a 2 mol-% Fe micrograph where only SnO_2 particles, identified by the lattice fringes, have been confirmed (corresponding to the (110) planes). Figure 2(b) shows particles of 30 mol-% Fe for comparison. A decrease in particle sizes is clearly seen, as discussed previously.

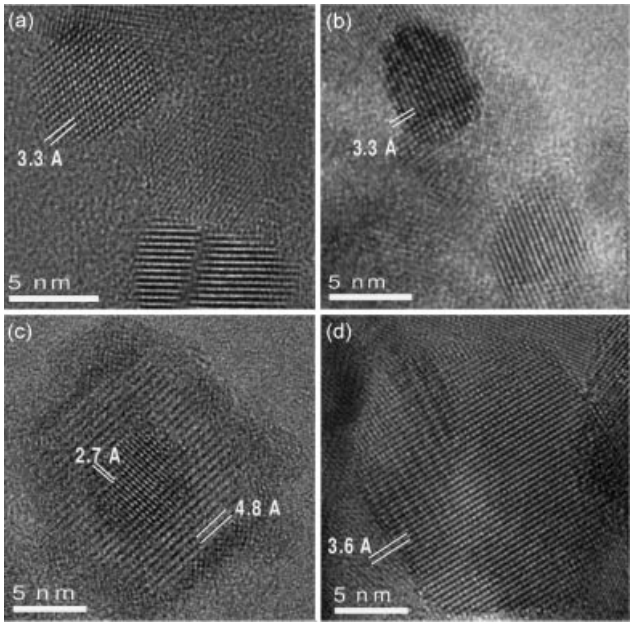

Figure 2. HRTEM images of SnO_2 powders containing: (a) 2, (b) 30, (c) 80, and (d) 100 mol-% Fe. Lattice fringes correspond to (a) and (b) (110) tetragonal SnO_2 planes; (c) core: (101) tetragonal SnO_2 planes, shell: (111) cubic Fe oxide; (d) (110) hematite.

Segregation of Fe onto the surface is, however, only confirmed by EDS measurements when collecting data at the center and at the edge of SnO_2 particles containing different Fe contents (3 nm beam probe). A general EDS was also measured for comparison purposes. Figure 3 compiles the results of the 30 mol-% Fe and demonstrates that there is indeed an excess of Fe ions located on the SnO_2 particle surface. The concentration at the surface is about 1.3-times higher than that computed at the center of this particle. Similar effects are observed in particles containing 10, 50, and 80 mol-% Fe, with different ratios, showing that the segregation occurs in a broad range of compositions. These results are shown in the inset of Figure 3. A relatively high ratio is observed in particles containing 80 mol-% Fe; this is related to the particular second-phase nucleation process, as explained below.

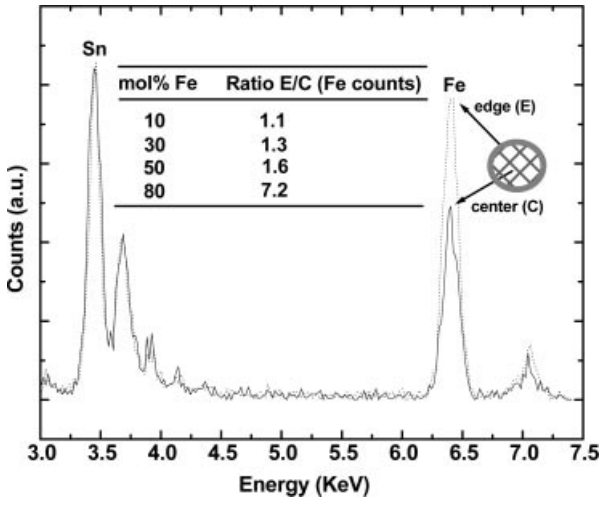

Figure 3. EDS spectra at the center (C) and at the edge (E) of a 30 mol-% Fe particle. Inset: EDS results as a function of Fe concentration, at 6.3 keV. The data is presented as the height peak of the edge-to-center ratio (E/C) after normalization to the Sn peak intensity.

Increasing the Fe content in the SnO_2-based powder saturates the segregation path and induces the second-phase nucleation regime. This was observed by XRD measurements, but the mechanism of the process that takes place and the nature of the new phase could not be conclusively identified. Using HRTEM images both aspects are now better addressed. Figure 2(c) shows an HRTEM image of an 80 mol-% Fe particle, where an interesting core–shell structure can be identified. This result confirms the formation of a second phase and reveals that, in fact, it nucleates on the surface of the SnO_2 particle forming a surface coating. This can be understood based on the segregation of Fe on the surface of SnO_2, where the segregated atoms work as heterogeneous nucleation sites for the new phase growth. Interestingly, since the nucleation occurs on the surface of SnO_2, an epitaxial-type growth may be expected, and a metastable Fe oxide phase other than the thermodynamically stable hematite has been detected. Hematite is the phase formed in the absence of SnO_2 by this synthesis method, as shown by XRD, and confirmed by HRTEM [Figure 2(d); lattice fringes correspond to the (110) planes]. In Figure 2(c), lattice fringes crossing the core–shell structure suggest an epitaxial-type growth. The center of the particle shows the (101) planes of the SnO_2 structure, whereas the shell lattice fringes correspond to either the (111) planar distances of maghemite or magnetite. These results thus explain the high ratio observed for 80 mol-% Fe samples by EDS, indicating that the probe is in fact detecting the Fe_2O_3 surface nucleated phase. The nature of the nucleated phase was further clarified by Mössbauer spectroscopy measurements.

 © 2005 Wiley-VCH Verlag GmbH & Co. KGaA, Weinheim

The segregation regime occurring between solid solution and second phase nucleation appears as a new element in this system evolution, and therefore the Mössbauer spectroscopy results should be revised by considering these three additive incorporation regimes. In fact, Mössbauer spectra have already been described to consist of a crystalline component and an interface one.[23] Therefore, especially when dealing with nanometric particle sizes, characterized by a high specific surface area, one may argue that Mössbauer spectroscopy signals may be strongly affected by the segregated atoms, and neglecting this phenomenon may lead to mistaken conclusions.

Figure 4 shows the Mössbauer spectra at room temperature for 2–100 mol-% Fe samples. For 2, 10, and 30 mol-% Fe, the experimental data have been adjusted using least-squares criteria by considering the presence of two doublets (sites I and II). The obtained parameters are shown in Table 2. In this concentration range, only electric quadrupoles (doublets) are detected, with no indication of magnetic hyperfine structures (sextets). A magnetic interaction does not appear even when the data were colleted at 78 K. This indicates that, if there is any superparamagnetic relaxation, it is occurring at temperatures below 78 K. This class of spin relaxation is expected because of the observed small particle sizes (ca. 5 nm) and is related to the relaxation time of the atom spin (spin–spin or spin–orbital) smaller than the Larmor precession time.[31]

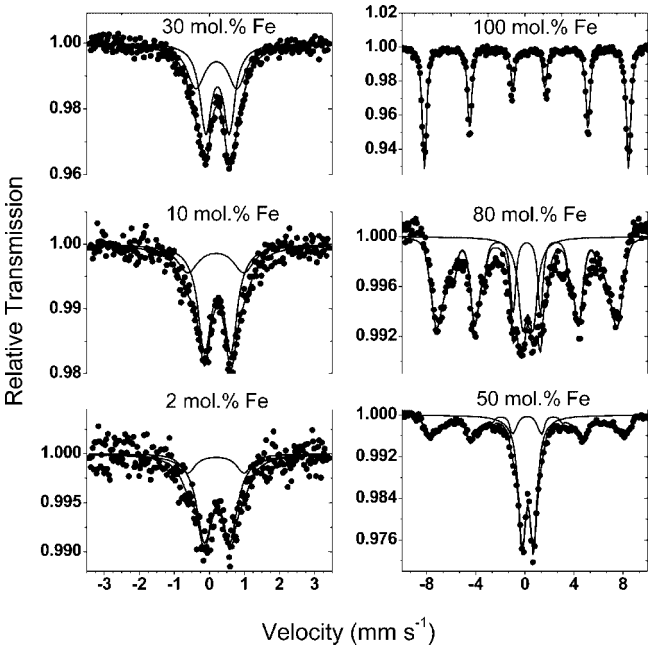

Figure 4. Mössbauer spectra at room temperature for SnO_2 powders containing different contents of Fe.

An important point to note is that the area of site I decreases and that of site II slightly increases with increasing Fe content, as noted in the deconvolution of the peaks. Upon varying the concentration of Fe from 2 to 30 mol-% the area of site I decreases by about 30%. A similar behavior has been observed previously, although no reasonable explanation was given.[19] The phenomenon may be explained by considering the spectra to consist of both interface and bulk contributions. That is to say, each of the observed sites corresponds to a different position of the Fe ions. The Fe atoms located inside the SnO_2 lattice would contribute to the Mössbauer signal in site I and those segregated on the surface would be responsible for the site-II signal. This is coherent with the model described above concerning the solubility and segregation of the low component atom in the system SnO_2–Fe_2O_3. Since the solubility limit is observed at about 4 mol-% for the Fe ion in the SnO_2 lattice, any further increase in the concentration of the additive causes it to segregate on the surface. Such segregated atoms are not well crystallized and give rise to high electric quadrupoles due to local lattice distortions. With increasing Fe content, the surface coating is increased, and the site-II area increases as well.

Such an area increase in the Mössbauer spectra is observed until the second-phase nucleation occurs. Therefore, a nuclear hyperfine magnetic structure is observed for the powder containing 50 mol-% of Fe_2O_3. This hyperfine magnetic structure is the same as that detected in the 80 mol-% Fe_2O_3 sample, but different from that observed for 100 mol-% Fe (hematite). Since the hyperfine parameters of maghemite and magnetite are very similar,[31,32] these data confirm the presence of the new phase but could not be used to clearly identify the phase. Note the presence of the doublet due to Fe ions incorporated in the SnO_2 lattice (site I) when dealing with the samples with 50 and 80 mol-% Fe, which is related to the SnO_2 cores found by the micrograph [Figure 2(c)] saturated by Fe ions. Site II, related to segregated Fe, is not observed in these samples since it has been replaced by the hyperfine magnetic structure grown on the surface.

Table 2. Mössbauer spectroscopy parameters. Isomer shifts are related to metallic Fe. 50 and 80 mol-% samples were fitted with just one doublet and a magnetic sextet; 100 mol-% sample has just the magnetic component as presented in the table. HF means hyperfine field in Tesla [T]. Site I is related to Fe inside SnO_2 lattice. Site II is related to surface-segregated Fe.

	Site I			Site II			Magnetic site			
Fe [mol%]	QS [mm s^{-1}]	IS [mm s^{-1}]	AE [%]	QS [mm s^{-1}]	IS [mm s^{-1}]	AE [%]	QS [mm s^{-1}]	IS [mm s^{-1}]	HF [T]	AE [%]
2	0.731(40)	0.306(10)	81(5)	1.60(17)	0.270(50)	19(5)	–	–	–	–
10	0.751(18)	0.323(6)	70(4)	1.60(12	0.268(26)	30(4)	–	–	–	–
30	0.672(19)	0.317(4)	56(5)	1.17(9)	0.285(10)	44(5)	–	–	–	–
50	0.930(6)	0.351(3)	58(5)	–	–	–	0.012(22)	0.303(12)	43.6(2)	42(5)
80	0.847(29)	0.357(9)	28(5)	–	–	–	0.008(14)	0.267(10)	43.6(2)	72(5)
100	–	–	–	–	–	–	0.194(4)	0.341(2)	51.5(2)	100

 © 2005 Wiley-VCH Verlag GmbH & Co. KGaA, Weinheim

Conclusions

The distribution of the components in SnO_2–Fe_2O_3 nanopowders in different compositions can be understood based on the correlation of XRD with spatial high-resolution characterization tools, such as EDS and HRTEM, thus avoiding the loss of information about segregated components. At lower concentration (<4 mol-%), the Fe ions are preferentially incorporated in the SnO_2 lattice to form a solid solution; at intermediate values (4–30 mol-%) the Fe ions segregate onto the SnO_2 surface, as confirmed by EDS. The segregated atoms have important effects in Mössbauer spectroscopy measurements, suggesting that the spectra are a combination of the independent effects of bulk and interface components. At higher concentrations (>30 mol-%) a second phase is nucleated and corresponds to an unexpected magnetite or maghemite phase. Core–shell-type particles with an SnO_2 core structure and a magnetic shell structure are observed for the first time at high Fe contents.

Experimental Section

SnO_2–Fe_2O_3 nanopowders were prepared based on Pechini's method.[24] The process can be briefly described as follows: (a) The cationic precursors were introduced into a mixture of ethylene glycol (20.6 wt.-%) and citric acid (47.7 wt.-%). $Sn_2(C_6O_7H_4)\cdot H_2O$ (tin citrate, prepared from $SnCl_2\cdot 2H_2O$; Synth P.A.) and $Fe(NO_3)_3\cdot 9H_2O$ (Synth P.A.) were used as the precursors and HNO_3 was added to the system to promote the solubilization of the citrate. The amounts of precursors were calculated to achieve the desired molar concentrations. (b) The prepared solution was heated to 180–200 °C to promote polyesterification, i.e. polymerization between citric acid and ethylene glycol to give rise to a polymer chain with sites available to react with the ions present. These sites randomly react with tin or iron ions. (c) The obtained liquid precursor was thermally treated at 450 °C for 4 h to give a dry carbon-rich powder. After grinding, the powder was treated at 500 °C for 15 h to guarantee total carbon elimination and an energetically stable distribution of the additives and particle size.[22,25,26] XRD measurements were carried out with a Philips X'Pert MPD diffractometer, using Cu-K_α radiation (λ = 1.5406 Å), at room temperature. A step of 0.05° with an exposure time of 5 s per step was used in the measurements. To determine the lattice parameters, however, XRD was carried out using θ = 0.02° with an exposure time of 10 s and using an internal Si standard. Mössbauer spectra were obtained in the transmission geometry and the γ-radiation source was ^{57}Co atoms immersed in an Rh matrix. The radioactive source was mounted in a constant acceleration transductor and the maximum speed was determined by calibrating the system with a metallic Fe sheet; γ-ray detection was carried out with a proportional detector and the electronically amplified signal was sent to a digital analyzer. EDS and HRTEM images were acquired with a JEM 3010 URP microscope operating at 300 keV (0.17 nm resolution). For EDS a 3-nm beam-size was used and the background obtained for the Cu grid was then subtracted.

Acknowledgments

The authors thank CAPES (Coordenação do Aperfeiçoamento de Pessoal de Nível Superior) and FAPESP (Fundação de Amparo à Pesquisa do Estado de São Paulo) processes 96/09604-9, 99/10798-0, and 01/10053-7 for financial support. LME/LNLS is acknowledged for the use of HRTEM. LSI/EPUSP is acknowledged for help with the electrical measurements.

[1] P. Poizot, S. Laruelle, S. Grugeon, L. Dupont, J. M. Tarascon, *Nature* **2000**, *407*, 496–499.
[2] T. Matsumura, N. Sonouama, R. Kanno, M. Takano, *Solid State Ionics* **2003**, *158*, 253–260.
[3] S. Ichiba, T. Yamaguchi, *Chem. Lett.* **1984**, *10*, 1681–1682.
[4] S. Popovic, B. Grzeta, G. Stefanic, I. CzakoNagy, S. J. Music, *J. Alloys Compd.* **1996**, *241*, 10–15.
[5] M. Ristic, S. Popovic, M. Tonkovic, S. J. Music, *J. Macromol. Sci., Chem.* **2000**, *407*, 496.
[6] P. Polzot, *Nature* **2000**, *407*, 496.
[7] G. Stefanic, S. J. Music, S. Popovic, K. Nomura, *J. Mol. Struct.* **1999**, *481*, 627–631.
[8] M. Ristic, I. Nowik, S. Popovic, S. Music, *Croat. Chem. Acta* **2000**, *73*, 525–540.
[9] F. Schneider, K. Melzer, H. Mehner, G. Dehe, *Phys. Status Solidi A* **1977**, *39*, K115–K117.
[10] V. G. Bhide, S. K. Data, *J. Inorg. Nucl. Chem.* **1969**, *31*, 2394.
[11] M. Takano, *J. Solid State Chem.* **1987**, *68*, 153–162.
[12] D. A. Hramov, V. S. Urusivm, *Akad. Izv. Nauk. SSSR Neorg. Mater.* **1983**, *11*, 1880.
[13] F. Berthier, J. Creuze, R. Tetot, B. Legrand, *Phys. Rev. B: Condens. Matter* **2002**, *65*, 195413.
[14] A. V. Ruban, H. L. Skriver, J. K. Norskov, *Phys. Rev. B: Condens. Matter* **1999**, *59*, 15990–16000.
[15] D. Szczuko, J. Werner, S. Oswald, G. Behr, K. Wetzig, *Appl. Surf. Sci.* **2001**, *179*, 301–306.
[16] G. Bozzolo, J. Ferrante, R. D. Noebe, B. Good, F. S. Honecy, P. Abel, *Comp. Mater. Sci.* **1999**, *15*, 169–195.
[17] B. Slater, C. R. A. Catlow, D. H. Gay, D. E. Williams, V. Dusastre, *J. Phys. Chem. B* **1999**, *103*, 10644–10650.
[18] H. Dulli, P. A. Dowben, S. H. Liou, E. W. Plummer, *Phys. Rev. B: Condens. Matter.* **2000**, *62*, 14629–14632.
[19] M. Sorescua, L. Diamandescua, D. Tarabasanu-Mihailab, V. S. Teodorescub, B. H. Howard, *J. Phys. Chem. Solids* **2004**, *65*, 1021–1029.
[20] S. J. Music, S. Popovic, M. Metikoshukovic, V. Gvozdic, *J. Mater. Sci. Lett.* **1991**, *10*, 197–200.
[21] R. Ruck, Y. Dusausoy, C. N. Trung, J. M. Gaite, A. Murciego, *Eur. J. Mineral.* **1989**, *1*, 343–352.
[22] R. H. R. Castro, P. Hidalgo, P. Hidalgo, R. Muccillo, D. Gouvea, *Appl. Surf. Sci.* **2003**, *214*, 172–177.
[23] G. J. Pereira, R. H. R. Castro, D. Gouvea, *Appl. Surf. Sci.* **2002**, *195*, 274–280.
[24] C. H. Shek, G. M. Lin, J. K. L. Lai, *Nanostruct. Mater.* **1999**, *11*, 831–835.
[25] M. Pechini, US patent no. 3330697, **1967**.
[26] D. Gouvea, R. L. Villalobos, J. D. T. Capocchi, *Mater. Sci. Forum* **1999**, *299*, 91–96.
[27] J. Haines, J. M. Léger, *Phys. Rev. B* **1997**, *55*, 11144.
[28] D. Gouvea, J. A. Varela, E. Longo, A. Smith, J. P. Bonnet, *Eur. J. Solid State Inorg. Chem.* **1993**, *30*, 915.
[29] S. H. Overbury, P. A. Bertrand, G. A. Somorjai, *Chem. Rev.* **1975**, *75*, 547–560.
[30] Y.-M. Chiang, D. Birnie, W. D. Kingery, *Physical Ceramics – Principles for Ceramic Science and Engineering*, John Wiley & Sons Inc., New York, **1997**.
[31] V. I. Goldanskii, E. F. Makarov, *Chemical Applications of Mössbauer Spectroscopy*, Academic Press, New York, **1968**.
[32] Q. A. Pankhurst, R. J. Pollard, in *Mössbauer Spectroscopy Applied to Magnetism and Materials Science* (Eds.: J. Long, F. Granjean), Plenum Press, New York, **1993**, vol. 1.

Received: October 19, 2004

A New Series of Homologous Cluster Complexes $[Mo_3(M'EPh_3)Q_4Cl_4(H_2O)_5]$ (M′ = Ni, Pd; E = P, As, Sb; Q = S, Se)

Maxim N. Sokolov,*[a] Elena V. Chubarova,[a] Rita Hernandez-Molina,[b] Maria Clausén,[b] Dmitry Yu. Naumov,[a] Cristian Vicent,[c] Rosa Llusar,[c] and Vladimir P. Fedin[a]

Keywords: Molybdenum / Nickel / Palladium / Chalcogenide clusters / Triphenylphosphane and analogs

Cluster aqua complexes $[Mo_3(M'Cl)S_4(H_2O)_9]^{3+}$ (M′ = Ni, Pd) react with EPh_3 (E = P, As, Sb) in HCl/CH_3OH to give neutral $[Mo_3(M'EPh_3)S_4Cl_4(H_2O)_5]$ (M′ = Pd, E = P (**1**), E = As (**2**), E = Sb (**3**); M′ = Ni, E = P (**4**), E = As (**5**); E = Sb (**6**). $[Mo_3(PdPPh_3)Se_4Cl_4(H_2O)_5]$ (**7**) was also obtained. X-ray crystal structures were determined for **3**, **4** and **5**. The role of supramolecular interactions in crystal packing is discussed. ESI-MS spectra were also studied and were used to follow the coordination of the solvent molecules at Mo sites and to assess relative strength of bonding in the clusters. Thermal properties were studied for **4** and **5**.

(© Wiley-VCH Verlag GmbH & Co. KGaA, 69451 Weinheim, Germany, 2005)

Introduction

The extensive family of cuboidal clusters with a tetrahedral M_4 core, $M_3M'Q_4$ (where M = Mo, W; Q = S, Se; M′ can be one of more than 20 transition or post-transition metals) has attracted interest because it provides a good opportunity to study how the metal-metal bonding and reactivity at metal centres are affected by changes in the nature of M, M′ and Q.[1] The bioinorganic significance of metal sulfide clusters is well known, and it has been put forward that the $Mo_3M'S_4$ (M′ = Co, Ni) clusters in particular can constitute molecular models for the active sites of the industrial heterogeneous Co/MoS_2 or Ni/MoS_2 catalysts.[2] The $Mo_3PdS_4^{4+}$ clusters catalyze nucleophilic addition to alkynes[3] and $[Mo_3NiS_4(H_2O)_{10}]^{4+}$ has proved to be efficient in various heterogeneous catalytic processes.[4,5] Recently it was found that the heterometal in $M_3M'S_4^{4+}$ clusters (M = Mo, W; heterometal (M′) = Ni, Pd) stabilize very labile molecules of $P(OH)_3$, $RP(OH)_2$ (R = H, Ph) and $Ph_2P(OH)$ by coordination at phosphorus[6–8]. Nonlinear optical properties of $[M_3(CuX)Q_4(dmpe)_3X_3]PF_6$ (M = Mo, W; X = Cl, Br; Q = S, Se) were also studied.[9]

A rational synthesis of these clusters is based on an addition of a heterometal in a low oxidation state (or even M'^0) to the trinuclear complexes with the $M_3Q_4^{4+}$ cores. Especially productive are incorporations into the aqua complexes $[M_3Q_4(H_2O)_9]^{4+}$ (M = Mo, W; Q = S, Se),[10] into the complexes with diphosphanes such as $[M_3Q_4(dmpe)_3X_3]^+$,[9,11] and $[M_3S_4Cp'_3]^+$ (Cp′ = methylcyclopentadienyl).[12–14] Dithiophosphates, dithiophosphinates, and dithiocarbamates $[M_3S_4((RO)_2PS_2)_4L]$, $[M_3S_4(R_2PS_2)_4L]$, $[M_3S_4(R_2NCS_2)_4L]$ were used for incorporation of Cu^I (and $d^{10}s^2$-post-transition metal ions).[15] Metal incorporation into the aqua complexes has been most widely used and it was found that even a noble metal, Pd (taken as Pd black), reacts with $[Mo_3Q_4(H_2O)_9]^{4+}$ in HCl to give $[Mo_3(PdCl)Q_4(H_2O)_9]^{3+}$ (Q = S, Se).[16,17] Extensive aqueous solution chemistry of these clusters has been reviewed.[10] The crystallization problems are efficiently dealt with by using *p*-toluenesulfonate as a counterion, and by formation of well-defined supramolecular complexes with cucurbit[6]-uril.[10] However, ligand substitution has not been widely used so far for the isolation of the heterometallic clusters from aqueous solutions. A few examples are transformation of $[Mo_3(PdCl)S_4(H_2O)_9]^{3+}$ into $[Mo_3(PdCl)S_4(tacn)_3]^{3+}$[16] and $[Mo_3(Pd(dppe))S_4(dppe)_3Cl_3]Cl$[18], and of $[Mo_3(NiCl)S_4(H_2O)_9]^{3+}$ into $[Mo_3(NiCl)S_4(dppe)_3]Cl$.[18] Substitution of water ligands by nitrylotriacetate (nta^{3-}) is also possible and was used to prepare $[Mo_3(CuCl)S_4(Hnta)_3]^{2-}$ and $[Mo_3(NiCl)S_4(Hnta)(nta)_2]^{5-}$.[19,20] This scarcity may be attributed to enhanced lability of the cluster cores upon changing the coordination environment, which leads to the loss of the heterometal. Increasing of pH, necessary for complexation of various ligands, may have the same effect, as well as cause undesirable hydrolysis.

Here we report facile synthesis and structural characterization of a family of cluster complexes, $[Mo_3(M'EPh_3)Q_4Cl_4(H_2O)_5]$ (M′ = Ni, Pd; E′ = P, As, Sb; Q = Se), obtained by adding EPh_3 to solutions of $[Mo_3(M'Cl)Q_4(H_2O)_9]^{3+}$ in HCl/CH_3OH mixtures. These products are air-stable, soluble in polar organic solvents and are convenient starting materials for introduction of various ligands into the cluster coordination sphere.

[a] A.V.Nikolayev Institute of Inorganic Chemistry SB RAS, pr. Lavrentyeva 3, 630090 Novosibirsk, Russia
[b] Universidad de La Laguna, 38200 La Laguna, Tenerife, Spain
[c] Universitat Jaume I, 12080, Castellon, Spain

Results and Discussion

Synthesis

Addition of methanolic solutions of EPh_3 (E = P, As, Sb) to the solutions of $[Mo_3(M'Cl)S_4(H_2O)_9]^{3+}$ (M′ = Ni, Pd) in HCl produces characteristic color changes to brown in the case of Pd, and to various shades of blue in the case of Ni. Methanol enhances the ligand solubilities and is essential for the reaction, which does not take place without it. It is worth mentioning that under the employed conditions, no substitution at the Mo atoms takes place. Slow evaporation of methanol from resulting solutions leads to crystallization of the neutral complexes **1–7**. However, the ^{31}P NMR spectroscopic monitoring of the complexation shows that in the reaction solutions of $[Mo_3(PdCl)S_4(H_2O)_9]^{3+}$ + PPh_3 (**1a**), $[Mo_3(PdCl)Se_4(H_2O)_9]^{3+}$ + PPh_3 (**7a**) and $[Mo_3(NiCl)S_4(H_2O)_9]^{3+}$ + PPh_3 (**4a**) three closely spaced singlets are observed in each case: at δ = 31.6, 32.5 and 33.4 ppm for **1a**, 31.3, 32.2 and 33.3 ppm for **7a**, and at δ = 39.7, 40.7 and 41.9 ppm for **4a**. This can be explained by the formation of either different isomers or of several species $[Mo_3(M'PPh_3)S_4(H_2O)_{9-x}Cl_x]^{(4-x)+}$ in solution, that are sufficiently kinetically inert in the NMR time-scale. Note the high-field shift on going from Ni to Pd, just as was observed for corresponding Cp derivatives.[12]

The electronic spectra show little, if any, dependence on the change of EPh_3, but there is a strong hypsochromic shift on going from Ni to Pd. The complexes are air stable, soluble in common organic solvents, and slowly, but completely soluble in water, apparently undergoing a hydrolytic decomposition.

ESI-MS Spectrum of $[Mo_3(M'EPh_3)S_4(H_2O)_5Cl_4]$ (M′ = Ni, Pd; E = P, As, Sb)

Electrospray mass spectrometry (ES-MS) is becoming a valuable tool for the investigation of coordination compounds allowing the study of solution speciation,[21] formation of aggregates,[22,23] or identification of major and minor products in solutions on a microscale,[24] since it allows pre-existing ions to be transferred into the gas phase with minimal fragmentation. Applications to a number of inorganic and organometallic systems have demonstrated the versatility of the technique.[25] In this work we have studied the family of cuboidal cluster complexes $[Mo_3(M'EPh_3))S_4(H_2O)_5Cl_4]$ (M′ = Ni, Pd; E = P, As, Sb) by ESI-MS in the 400–1100 *m*/*z* range in methanol. All compounds **1–7** show similar fragmentation pathways, although the relative intensities of the fragmentation peaks depend on the nature of the incorporated heterometal M′. Figure 1 shows the ESI-MS for compound **5** in methanol at different cone voltages.

The ionisation of these neutral complexes takes place by the loss of one chloride ligand and is accompanied by complete replacement of the coordinated water molecules by methanol except for compound **7** where only a partial substitution is found (see Table 1). A typical pattern is shown in Figure 1 (illustrated here by complex **5**): at low cone voltages a peak corresponding to the $[Mo_3(Ni(AsPh_3))S_4(CH_3OH)_6Cl_3]^+$ ion (*m*/*z* = 1078 a.m.u.) is detected, where the vacant position left by the chloride ion is replaced by methanol keeping the octahedral environment around the molybdenum atoms. Additional peaks due to the sequential loss of methanol molecules are also present, even

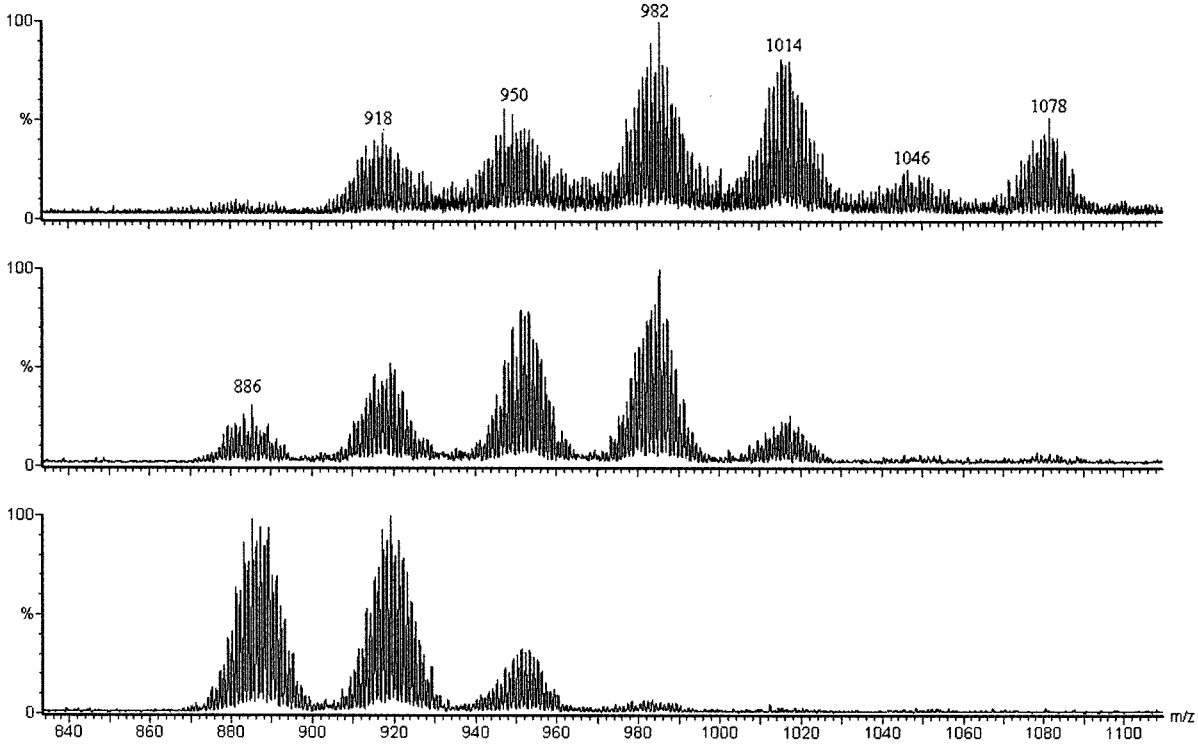

Figure 1. ESI-MS spectra of compound **5** at 10 V (top), 30 V (medium) and 50 V (bottom).

 © 2005 Wiley-VCH Verlag GmbH & Co. KGaA, Weinheim

at 10 V (Figure 1 top). Increasing the cone voltage results in the consecutive losses of methanol molecules (Figure 1, bottom) up to 80 V, where the neutral EPh_3 is also lost. The cluster core $[Mo_3M'S_4]$ does not fragment under these experimental conditions as is also seen for the $[Mo_3Q_4(dmpe)_3Cl_3]^+$, $[Mo_3M'Q_4(dmpe)_3Cl_3]^+$ (Q = S, Se; M′ = Ni, Co) complexes demonstrating robustness of the Mo_3Q_4 and $Mo_3M'Q_4$ cluster units.[11,26–28] Additional experiments using CH_3CN or THF as solvents resulted in substitution of water molecules by acetonitrile in the former case, analogously as described for methanol, whereas no substitution is observed for THF. Thus the qualitative order of substitution of coordinated water molecules in the large excess of another solvent is $CH_3OH \approx CH_3CN >> THF$.

Table 1. Listing of the ions detected upon increasing the cone voltage for compounds **1**–**7**.

	Chemical composition of the ions	Main ion peak (a.m.u.). and intensity at 50 V and 30 V
1	$[Mo_3(PdPPh_3)S_4Cl_3]^+$	891 (100) (87)
	$[Mo_3(PdPPh_3)S_4(MeOH)Cl_3]^+$	923 (72) (100)
	$[Mo_3(PdPPh_3)S_4(MeOH)_2Cl_3]^+$	955 (34) (86)
	$[Mo_3(PdPPh_3)S_4(MeOH)_3Cl_3]^+$	987 (15) (28)
2	$[Mo_3(PdAsPh_3)S_4Cl_3]^+$	934 (100) (51)
	$[Mo_3(PdAsPh_3)S_4(MeOH)Cl_3]^+$	966 (73) (100)
	$[Mo_3(PdAsPh_3)S_4(MeOH)_2Cl_3]^+$	998 (23) (84)
	$[Mo_3(PdAsPh_3)S_4(MeOH)_3Cl_3]^+$	1030 (27)
3	$[Mo_3(PdSbPh_3)S_4Cl_3]^+$	982 (100) (49)
	$[Mo_3(PdSbPh_3)S_4(MeOH)Cl_3]^+$	1014 (59) (100)
	$[Mo_3(PdSbPh_3)S_4(MeOH)_2Cl_3]^+$	1046 (20) (70)
	$[Mo_3(PdSbPh_3)S_4(MeOH)_3Cl_3]^+$	1078 (20)
4	$[Mo_3(NiPPh_3)S_4Cl_3]^+$	843 (84) (16)
	$[Mo_3(NiPPh_3)S_4(MeOH)Cl_3]^+$	875 (100) (41)
	$[Mo_3(NiPPh_3)S_4(MeOH)_2Cl_3]^+$	907 (39) (68)
	$[Mo_3(NiPPh_3)S_4(MeOH)_3Cl_3]^+$	939 (11) (100)
	$[Mo_3(NiPPh_3)S_4(MeOH)_4Cl_3]^+$	971 (6) (25)
5	$[Mo_3(NiAsPh_3)S_4Cl_3]^+$	886 (98) (38)
	$[Mo_3(NiAsPh_3)S_4(MeOH)Cl_3]^+$	918 (100) (54)
	$[Mo_3(NiAsPh_3)S_4(MeOH)_2Cl_3]^+$	950 (35) (95)
	$[Mo_3(NiAsPh_3)S_4(MeOH)_3Cl_3]^+$	982 (5) (100)
	$[Mo_3(NiAsPh_3)S_4(MeOH)_4Cl_3]^+$	1014 (32)
6	$[Mo_3(NiSbPh_3)S_4Cl_3]^+$	934 (76) (40)
	$[Mo_3(NiSbPh_3)S_4(MeOH)Cl_3]^+$	966 (100) (58)
	$[Mo_3(NiSbPh_3)S_4(MeOH)_2Cl_3]^+$	998 (42) (54)
	$[Mo_3(NiSbPh_3)S_4(MeOH)_3Cl_3]^+$	1030 (11) (100)
	$[Mo_3(NiSbPh_3)S_4(MeOH)_4Cl_3]^+$	1062 (5) (52)
7	$[Mo_3(PdPPh_3)Se_4Cl_3]^+$	1078 (100) (98)
	$[Mo_3(PdPPh_3)Se_4(MeOH)Cl_3]^+$	1010 (42) (100)
	$[Mo_3(PdPPh_3)Se_4(MeOH)(H_2O)Cl_3]^+$	1028 (60) (69)

It is well known that the efficiency of the ionization varies with the ion size and in our study only minor changes are expected based on the similar charge and size of the complexes **1**–**7**. Therefore, we assume that the ratios of the apparent intensities of each peak are proportional to the relative abundance of the corresponding species. In order to obtain some insight into the energetics of the molybdenum–solvent bonds, we have analyzed the relative intensity of the different fragments obtained upon increasing the cone voltage from 30 V to 50 V to establish qualitatively how the nature of M′, E and Q affects the binding energy of the $Mo–O_{(MeOH)}$ bond. Table 1 shows the ions detected and the peak intensities at 30 and 50 V for sample solutions in methanol.

Clusters containing nickel (**4**–**6**) all show as base peaks $[Mo_3(NiEPh_3)S_4(MeOH)_3Cl_3]^+$ and $[Mo_3(NiEPh_3)S_4(MeOH)Cl_3]^+$ at 30 and 50 V, respectively, whereas the palladium derivatives **1**–**3,7** show $[Mo_3(PdEPh_3)S_4(MeOH)Cl_3]^+$ at 30 V and $[Mo_3(PdEPh_3)Q_4Cl_3]^+$ at 50 V under identical conditions. These experimental observations clearly show that the binding Mo–MeOH energy is affected by the nature of the heterometal that is incorporated, which then interacts with the molybdenum atoms by direct metal–metal bonding. In particular the Mo–MeOH bond in the palladium derivatives is more prone to rupture than in the nickel analogs. In contrast, no clear tendency is observed upon substitution of either the PPh_3, $AsPh_3$ and $SbPh_3$ nor the chalcogen atom (in the case of the $PdPPh_3$ derivatives **1** and **7**).

Crystal Structures of $[Mo_3(M'EPh_3))S_4(H_2O)_5Cl_4]\cdot n\,H_2O$ (M′ = Ni, Pd; E = P, As, Sb)

The structures of the compounds **3**, **4** and **5** have been determined by single-crystal X-ray diffraction. They all crystallize in the same triclinic space group *P*-1 and share the structural features with previously reported $[Mo_3(PdPPh_3))S_4(H_2O)_5Cl_4]\cdot 3\,H_2O\cdot 0.5\,CH_3OH$ (**1**).[6] Figure 2 shows the structure of the neutral complex $[Mo_3(NiAsPh_3))S_4(H_2O)_5Cl_4]\cdot 3\,H_2O$ (**5**), with the atom numbering Scheme.

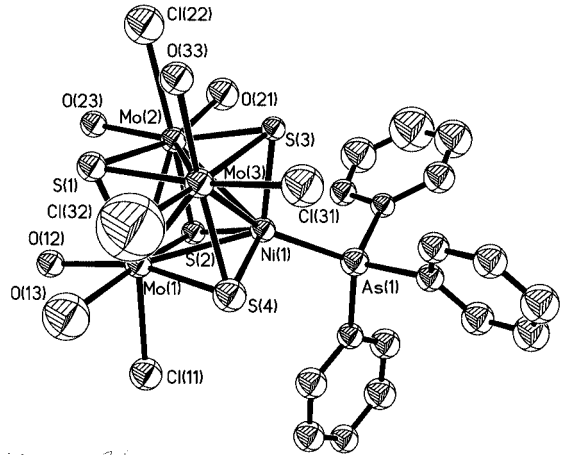

Figure 2. ORTEP representation (50% ellipsoid probability) of the neutral complex **5** with the atom numbering scheme.

The cluster core consists of a slightly distorted tetrahedral arrangement of one nickel/palladium and three molybdenum atoms. Each tetrahedral face is capped by a μ_3-coordinated sulfide ligand thus generating a cubanelike structure. The coordination sphere on one molybdenum atom is completed by one water molecule and two chlorine atoms while the two remaining molybdenum atoms fill their octahedral environment with two water molecules and one chlorine atom. Cl(31) and Cl(11) are *trans* to the unique S(1) atom, while Cl(32) and Cl(22) occupy *cis*-positions. It is re-

 © 2005 Wiley-VCH Verlag GmbH & Co. KGaA, Weinheim

Table 2. Selected averaged bond lengths [Å] for compounds **1**, **3**, **4** and **5**.[a]

	Mo–Mo av.	Mo–M′ av.	M′–E	Ref.
$[Mo_3Pd(PPh_3)S_4Cl_4(H_2O)_5]\cdot 3H_2O$ (**1**)	2.745[4]	2.81[1]	2.292(2)	[6]
$[Mo_3Pd(SbPh_3)S_4Cl_4(H_2O)_5]\cdot 3H_2O$ (**3**)	2.759[2]	2.788[8]	2.528(2)	this work
$[Mo_3Ni(PPh_3)S_4Cl_4(H_2O)_5]\cdot 3H_2O$ (**4**)	2.755[3]	2.68[1]	2.197(9)	this work
$[Mo_3Ni(AsPh_3)S_4Cl_4(H_2O)_5]\cdot 2.5H_2O$ (**5**)	2.763[2]	2.663[9]	2.272(2)	this work
$[(\eta^5\text{-Cp}')_3Mo_3Ni(AsPh_3)S_4][pts]$	2.833[5]	2.699[5]	2.255(1)	[12]
$[(\eta^5\text{-Cp}')_3Mo_3Ni(PPh_3)S_4][pts]$	2.831[4]	2.718[8]	2.160(2)	[13]
$[(\eta^5\text{-Cp}')_3Mo_3Pd(PPh_3)S_4][pts]$	2.836[4]	2.864[8]	2.277(1)	[13]

[a] Averaged values are given in square brackets.

markable that from several possible geometric isomers expected from various ways of occupying nine coordination sites available to four chloride ligands, only one is realised in **1**, **3**, **4** and **5**. This is most probably dictated by packing requirements, which lead to formation of large channels, defined by Cl···H_2O hydrogen bonds (Figure 4, see the discussion below). Three bridging sulfur atoms and the EPh_3 ligand define the tetrahedral environment on the heterometal. The tetrahedral coordination is severely distorted due to a bending of EPh_3 ligands to one side. This distortion is strongest in **3**, where the angles around Pd vary from 103.3(2) to 118.3(4)°. The geometries of the cuboidal units $[Mo_3M'S_4]$ (M′ = Pd, Ni) in the crystal structures determined in this work are similar to those found in other related complexes. Table 2 shows the most relevant bond lengths within the cluster unit together with those of previously reported structures.

The Mo–Mo bond lengths are consistent with single bonds between metal atoms and no significant differences are detected upon changing either the heterometal M′ or the EPh_3 fragment. However an increase of ca. 0.08 Å is observed by replacement of the Mo-bonded ligands, water and chloride, by the Cp′ groups. The Mo–Ni and Mo–Pd bond lengths are slightly shorter on going from P to Sb, but again the largest difference is due to the substitution of the Mo-bonded ligands, the η^5-Cp′ derivatives having the longest Mo–M′ (by ca. 0.04 Å) bonds. The Mo–M′ and M′–E bonds regularly expand on going from nickel to palladium (0.18 Å for complexes **1** and **4)** and from P to Sb as expected, due to the increase in the covalent radii. The same tendency has been described previously for the isostructural family $[M_3(M'EPh_3)S_4(\eta^5\text{-Cp}')][pts]$ (M = Mo, W; M′ = Ni, Pd, Pt; E = P, As).[12,13]

Supramolecular Structure and Thermal Properties

A current challenge of crystal engineering is to control the assembly and orientation of solid-state structures in three dimensions.[29,30] This task is of a great complexity because the ionic/molecular building blocks can adopt a vast number of conformations in the crystal, thus making structural predictions extremely difficult. Covalent interactions or supramolecular connections (such as hydrogen bonds or π–π interactions) have been widely used to prepare coordination polymers and much effort has been devoted to control and predict the assembled motifs.[31–33] In this context it appears that compounds **1**, **3**, **4** and **5** are promising candidates to form supramolecular networks since they contain: a) five strong hydrogen-bond donors (water molecules); b) four strong electronegative atoms (chlorine) which are capable of propagating networks through Cl···Cl or Cl···H_2O interactions;[34] c) an organic part consisting of three phenyl rings which can expand the network by π–π interactions. These three potential sources of interactions, which can play a significant and predictable structure-determining role, can be grouped based on their hydrophilic (points a and b) or hydrophobic (point c) nature. Both functionalities (hydrophilic and hydrophobic) are located at opposite ends of the discrete molecular cluster, thus we can anticipate that the resulting supramolecular network will be expanded by bringing face to face ends of a similar nature.

A detailed analysis of the packing of neutral complexes **1**, **3, 4** and **5** shows that all of them are expanded in the crystalline lattice through π–π interactions (from the organic end) and short Cl···H_2O contacts (both from the outer water ligands and water of crystallization) as will be described below. Regarding the organic part, it is well known that molecules containing PPh_3 ligands and PPh_4^+ cations commonly associate in crystals in different supramolecular patterns such as the sextuple phenyl embrace (SPE).[35,36] The source of the substantial attraction in these motifs is the interaction between phenyl groups where three types of pair-wise phenyl-phenyl configurations are recognized, namely the offset face-to-face **off**, edge-to-face **ef**, vertex-to-face **vf** and intermediate situations between these three configurations. The intermolecular structure of compounds **1**, **3**, **4** and **5** shows centrosymmetrical dimers formed by π–π interactions involving the phenyl rings through one offset face-to-face and two vertex-to-face interactions as depicted in Figure 3, a) for compound **5**.

Following the nomenclature introduced by Dance et al. this supramolecular motif belongs to the parallel quadruple phenyl embrace **PQPE** type. The values of the intercentroid distances between phenyl groups are 4.27 and 6.05 Å for the **off** and **vf** configurations (similar values are observed for complexes **1**,**3** and **4**) which are comparable to those published by Dance in his comprehensive structural report.[36] These dimers are further connected along the three crystallographic axes through weaker additional π–π interactions with **off**, **vf** and **ef** configurations. Even though these secondary interactions are weaker than those of PQPE type, the intercentroid distances between the phenyl

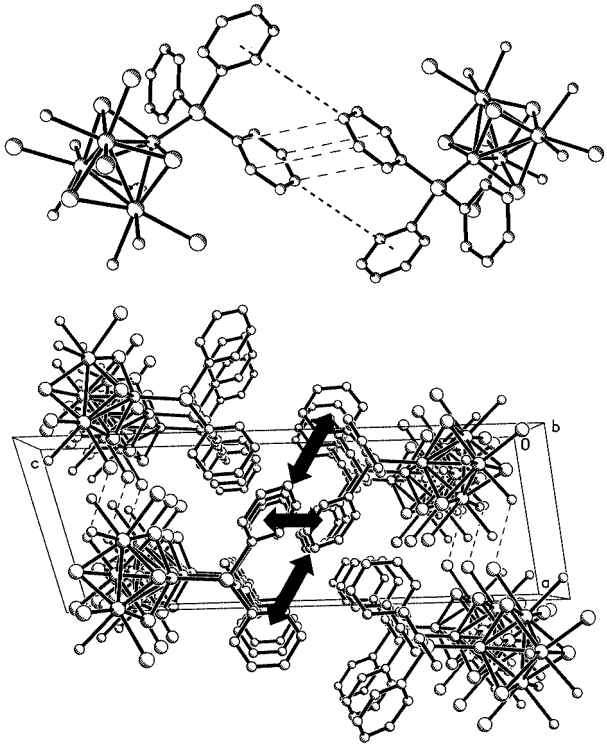

Figure 3. (a) PQPE type configuration of the phenyl rings where dashed lines show the **off** and the **vf** contacts. (b) View across the *ac* plane emphasizing the phenyl ring interactions (PQPE type contacts are shown by black narrows) which lead to the formation of organic columns along the *a* direction.

rings are below 8 Å and also contribute to the stabilization of organic columns as shown in Figure 3, b).

These well-defined π–π interactions force the cluster discrete units to arrange one to each other forming columns, thus applying a key constraint for the accommodation of the remaining molecules in the solid-state structure. As a consequence of this constraint, the remaining molecules are also forced to reproduce this arrangement, and to direct the hydrophilic ends in such a way that additional short contacts between chlorine and water molecules, either of crystallization or coordinated to molybdenum atoms, arise. This arrangement also expands the solid structure through the three dimensions leaving hydrophilic cavities running along *a* and *b* axes. The complementarity of both packing principles leads to a supramolecular 3D network formed by segregated inorganic-organic columns where the water molecules of crystallization are accommodated in the hydrophilic cavities as shown in Figure 4.

Recently, the importance of preparing porous solids where labile terminal ligands are present pointing toward the center of the voids has been outlined. This makes them susceptible to both dissociation and evacuation from the pores, thereby producing periodically unsaturated open-metal sites to allow the study of metal site reactivity.[30,37] In order to evaluate this possibility, TGA-measurements for compounds **4** and **5,** representative of the whole family, were carried out in the 25–200 °C range (Figure 5), coupled with monitoring the peak at m/z = 18 a.m.u. during the

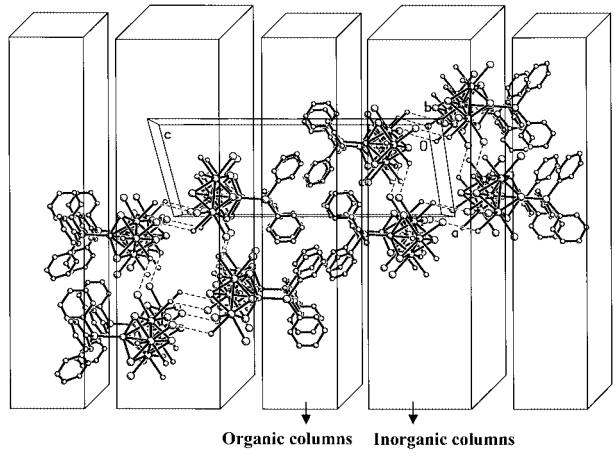

Figure 4. Supramolecular 3D network showing the alternate organic-inorganic columns and the voids left by the inorganic part.

thermal process by mass-spectroscopy. The first weight loss step (3.9% and 4.4% for **4** and **5**, respectively) at 25–80 °C corresponds to the loss of water of crystallization, which closely matches the percentage of water calculated from the X-ray structure determinations (4.6% and 5.3% for compounds **4** and **5**, respectively). The second weight loss of 8.1% and 7.8% (8.5% and 9.2% calculated from the X-ray analysis) for compounds **4** and **5**, respectively, between 100–150 °C is attributed to the loss of water molecules coordinated to molybdenum atoms. Simultaneously, XPD experiments at different temperatures for compound **5** showed a gradual lost of crystallinity from 25 to 250 °C to yield an amorphous solid above 150 °C clearly showing that the 3D network collapses. The low thermal stability of these compounds can be attributed to the evacuation of water molecules belonging to the cluster units, which as mentioned before connect the discrete molecular clusters along the three crystallographic axes and therefore are essential for the support of the 3D network. In this context it would be interesting to study the effect on the thermal stability upon replace-

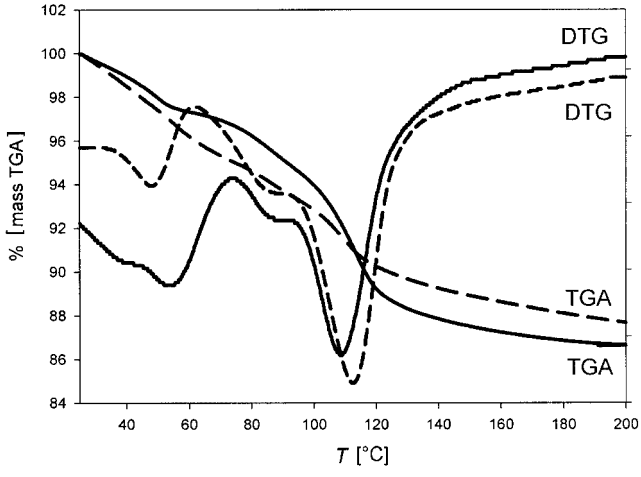

Figure 5. TGA and DTG curves for neutral complexes **4** and **5** (dashed lines) in the 25–200 °C range.

 © 2005 Wiley-VCH Verlag GmbH & Co. KGaA, Weinheim

ment of the chlorine ligands by other monoanionic ligands with the aim to obtain more robust solid-state structures.

Experimental Section

General Procedures

The solutions of $[Mo_3(PdCl)S_4(H_2O)_9]^{3+}$ and $[Mo_3(NiCl)S_4(H_2O)_9]^{3+}$ were prepared by published procedures[16,38] and concentrated by absorption on a cation-exchange Dowex 50W-X2 column, followed by elution with 4 M HCl. Triphenylphosphane (CHEMAPOL) was recrystallized from ethanol. $AsPh_3$ (Aldrich), $SbPh_3$ (Aldrich) and other reagents were used as purchased.

The electronic spectra were recorded with a UV-2201 "Shimadzu" UV/Vis spectrophotometer. The ^{31}P NMR spectra were measured with a Bruker 250 MHz spectrometer using 85% H_3PO_4 as external standard. A Quattro LC (quadrupole-hexapole-quadrupole) mass spectrometer with an orthogonal Z-spray-electrospray interface (Micromass, Manchester, UK) was used. The drying gas, as well as nebulizing gas, was nitrogen at flow rates 400 L/h and 80 L/h, respectively. Sample solutions in methanol (ca.10^{-4} M) were infused via syringe pump directly to the interface at a flow rate of 6 μL/min. The temperature of the source block was set to 120 °C and of the interface to 150 °C. A capillary voltage of 3.5 kV was used in the positive scan mode and the cone voltage varied between +10 and +80 V. The signal intensities were obtained by averaging approximately 40 scans and measuring the intensities of the three most intense peaks within the isotopic pattern of each signal. The chemical composition of each peak was assigned by comparison of the experimental and calculated isotopic patterns using the MassLynx 3.5 program. TGA/SDTA analysis were measured on a Mettler Toledo 851e instrument in the 25–300 °C range at 20 °C/min coupled to a ThermoStar Balzers GSD300T mass spectrometer. XPD pictures were obtained at 25, 100, 200 and 250 °C on a SIEMENS D5000 diffractometer using Cu-K_α radiation.

Preparation of $[Mo_3(PdPPh_3)S_4(H_2O)_5Cl_4]\cdot 0.5\,CH_3OH\cdot 3\,H_2O$ (1): The complex was prepared as described in ref.[6]

Preparation of $[Mo_3(PdAsPh_3)S_4(H_2O)_5Cl_4]$ (2): A solution of $AsPh_3$ (30 mg, 0.09 mmol) in methanol (5 mL) was added to 10 mL of a solution of $[Mo_3(PdCl)S_4(H_2O)_9]^{3+}$ (4 mM, 0.04 mmol) in 2 M HCl. The solution rapidly turned from blue to brown. Keeping it in an open vial for 2 days gave a crop of brown crystals, which were filtered off. Yield quantitative. The compound was kept in a vacuum desiccator over P_4O_{10} to remove all solvent molecules. Electronic spectrum [λ_{max}, nm (ε, $M^{-1}\,cm^{-1}$ in $CHCl_3$)]: 308 (15412), 441(4077), 480 (sh, 3378).

Preparation of $[Mo_3(PdSbPh_3)S_4(H_2O)_5Cl_4]\cdot 3\,H_2O$ (3): In the same manner, brown complex **3** was prepared from 10 mL of a 4 mM solution of $[Mo_3(PdCl)S_4(H_2O)_9]^{3+}$ (0.04 mmol) in 2 M HCl and a solution of $SbPh_3$ (30 mg, 0.08 mmol) in methanol (5 mL) in quantitative yield. The compound was kept in a vacuum desiccator over P_4O_{10} overnight before elemental analysis in order to remove all solvent molecules. For $C_{18}H_{25}Cl_4O_5SbS_4Mo_3Pd$: calcd. C 19.52, H 2.28, S 11.58; found C 19.60, H 2.36, S 11.53. Electronic spectrum [λ_{max}, nm (ε, $M^{-1}cm^{-1}$ in $CHCl_3$)]: 311 (16227), 438 (4776), 473 (sh, 3846).

Preparation of $[Mo_3(NiPPh_3)S_4(H_2O)_5Cl_4]\cdot 3\,H_2O$ (4): A solution of PPh_3 (62 mg, 0.238 mmol) in MeOH (11 mL) was added to a solution of $[Mo_3(NiCl)S_4(H_2O)_9]^{3+}$ (8.5 mL, 14 mM, 0.119 mmol) in 2 M HCl. The reaction mixture was heated while stirring at 40 °C for 30 min. The color slowly changed from olive-green to wine-red. Blue-violet crystals appeared after a few days of slow evaporation. Yield 60%. For $C_{18}H_{25}Cl_4O_5PS_4Mo_3Ni$: calcd. C 20.75, H 3.17, S 12.30, found C 21.16, H 2.96, S 12.40 (after drying). Electronic spectrum [λ_{max}, nm (ε, $M^{-1}cm^{-1}$ in $CHCl_3$)] 316 (15369), 488 (1667), 574 (940).

Preparation of $[Mo_3(NiAsPh_3)S_4(H_2O)_5Cl_4]\cdot 2.5\,H_2O$ (5): A solution of $AsPh_3$ (30 mg, 0.09 mmol) in methanol (5 mL) was added to 10 mL of a solution of $[Mo_3(NiCl)S_4(H_2O)_9]^{3+}$ (4 mM, 0.04 mmol) in 2 M HCl. The color slowly turned from green to purple. Keeping the solution in an open vial for 2 days gave a crop of dark blue crystals, which were filtered off. Yield quantitative. The compound was kept in a vacuum desiccator over P_4O_{10} overnight before elemental analysis to remove all solvent molecules. For $C_{18}H_{25}Cl_4O_5AsS_4Mo_3Ni$: calcd. C 21.34, H 2.49, S 12.66; found, C 21.75, H 2.55, S 12.59. Electronic spectrum [λ_{max}, nm (ε, $M^{-1}cm^{-1}$ in $CHCl_3$)] 313 (13879), 491 (1405), 573 (898).

Preparation of $[Mo_3(NiSbPh_3)S_4(H_2O)_5Cl_4]\cdot 2.5\,H_2O$ (6): Prepared in the same way as **5**. Yield quantitative. Electronic spectrum [λ_{max}, nm (ε, $M^{-1}cm^{-1}$ in $CHCl_3$)] 315 (18315), 491 (1745), 578 (958). For $C_{18}H_{25}Cl_4O_5SbS_4Mo_3Ni$: calcd. C 19.10, H 2.92, S 11.31; found C 19.16, H 2.99, S 12.03.

Preparation of $[Mo_3(PdPPh_3)Se_4(H_2O)_5Cl_4]$ (7): A solution of PPh_3 (70 mg, 0.27 mmol) in methanol (10 mL) was added to 10 mL of a solution of $[Mo_3(PdCl)Se_4(H_2O)_9]^{3+}$ (25 mM, 0.25 mmol) in 4 M HCl.[17] The color of the solution rapidly turned to brown. Excess PPh_3 precipitated and was filtered off. Keeping the solution in an open vial for 2 days gave a crop of brown crystals which were filtered off and thoroughly washed with diethyl ether to remove any PPh_3. Electronic spectrum [λ_{max}, nm (ε, $M^{-1}cm^{-1}$ in $CHCl_3$)] 326 (10659), 473 (3588).

X-ray Crystallography: The data collection on **4** was performed with a Bruker Smart CCD diffractometer using graphite-monochromated Mo-$K\alpha$ radiation (λ = 0.71073 Å) with a nominal crystal-to-detector distance of 40 mm. A hemisphere of data was colleted based on three ω-scan runs (starting ω = –28°) at values φ = 0°, 90° and 180° with the detector at 2θ = 28°. At each of these runs, frames (606, 435 and 230, respectively) were collected at 0.3° intervals and 25 seconds per frame. The diffraction frames were integrated using SAINT, and corrected for absorption with the SADABS package. The data collection for **3** and **5** was performed on a Bruker–Nonius X8APEX CCD diffractometer using graphite-monochromated Mo-$K\alpha$ radiation (λ = 0.71073 Å) with a nominal crystal-to-detector distance of 37.5 mm. The data was colleted based on a full range φ-scan run (739 frames were collected at 0.5° intervals and 30 seconds per frame). The diffraction frames were integrated using the program SAINT package and corrected for absorption with SADABS.[39,40] The crystal parameters and basic information relating to the data collection and structure refinement for the three compounds are summarized in Table 3.

The positions of the heavy atoms were determined by direct methods and successive difference electron density maps using the SHELXTL 5.10 software package were calculated to locate the remaining atoms.[41] Refinement was performed by the full-matrix least-squares method based on F^2. All cluster atoms in compounds **3**, **4** and **5** were refined anisotropically except phenyl carbon atoms in compound **4**. Hydrogen atoms of the phenyl groups and water molecules were refined geometrically except for the water molecules in compound **4** which were not included in the refinement. Although the crystal quality of **4** was poor, the bond length analysis and the packing diagram enabled comparisons to be made.

CCDC-251550, -252539 and -252540 contain the supplementary crystallographic data for this paper (for **3**, **4** and **5**, respectively).

 © 2005 Wiley-VCH Verlag GmbH & Co. KGaA, Weinheim

Table 3. Crystallographic Data for $[Mo_3(PdSbPh_3)S_4Cl_4(H_2O)_6]\cdot 3H_2O$ (**3**), $[Mo_3(NiPPh_3)S_4Cl_4(H_2O)_6]\cdot 3H_2O$ (**4**) and $[Mo_3(NiAsPh_3)S_4Cl_4(H_2O)_6]\cdot 2.5H_2O$ (**5**).

Compound	**3**	**4**	**5**
Empirical formula	$C_{18}H_{31}Cl_4Mo_3O_8PdS_4Sb$	$C_{18}H_{31}PCl_4Mo_3NiO_8S_4$	$C_{18}H_{30}AsCl_4Mo_3NiO_{7.50}S_4$
Formula mass	1161.44	1022.97	1057.91
Crystal system	triclinic	triclinic	triclinic
a [Å]	8.9799(18)	9.263(5)	9.1050(11)
b [Å]	9.2193(18)	9.287(5)	9.2248(11)
c [Å]	24.487(5)	23.121(11)	23.332(3)
α [°]	79.90(3)	92.747(11)	91.274(2)
β [°]	99.58(3)	101.260(12)	100.074(2)
γ [°]	117.21(3)	118.510(10)	117.328(2)
V [Å^3]	1766.4(6)	1691.0(14)	1702.3(4)
T [K]	173(2)	293(2)	293(2)
Space group	$P\bar{1}$	$P\bar{1}$	$P\bar{1}$
Z	2	2	2
μ(Mo-K_α) [mm^{-1}]	2.865	2.283	3.184
Reflections collected	7523	9349	7244
φ range for data collection	2.50 to 23.28	0.91 to 25.00	2.50 to 23.26
Unique reflections/R_{int}	5018 [R(int.) = 0.0516]	5889 [R(int.) = 0.1405]	4795 [R(int.) = 0.0243]
Goodness-of-fit on F^2	0.998	1.429	1.130
R_1[a]/wR_2[b]	R_1 = 0.0696, wR_2 = 0.1566	R_1 = 0.1504, wR_2 = 0.2919	R_1 = 0.0613, wR_2 = 0.1674
R_1[a]/wR_2[b] (all data)	R_1 = 0.1216, wR_2 = 0.1792	R_1 = 0.2725, wR_2 = 0.3309	R_1 = 0.0743, wR_2 = 0.1760
Residual ρ [e A^{-3}]	1.65 and –1.28	2.67 and –2.42	1.97 and –1.01

[a] $R1 = \Sigma||F_o| - |F_c||/\Sigma F_o$. [b] $wR2 = \{\Sigma[w(F_o^2 - F_c^2)^2]/\Sigma[w(F_o^2)^2]\}^{1/2}$.

These data can be obtained free of charge from The Cambridge Crystallographic Data Centre via www.ccdc.cam.ac.uk/data_request/cif.

Acknowledgments

A grant from the Russian Science Support Foundation to M.N.S is gratefully acknowledged. M.N.S is also grateful to the Bancaixa Foundation (Castellón) for an invited professorship grant. The work was supported by INTAS (grant 2356), Generalitat Valenciana (grant GV04B-029) and Russian Foundation for Basic Research (grants 02-03-32604 and 04-03-32159). R.H.M is grateful to the MCYT of Spain for Project BQU2003-09198. Thanks are also extended to the SCIC of the University Jaume I for providing us with the mass spectrometry and X-ray facilities.

[1] M. N. Sokolov, V. P. Fedin, A. G. Sykes, *Comprehensive Coord. Chem. V. 3*, **2003**, 761–823.
[2] M. Brorson, J. D. King, K. Kiriakidou, F. Prestopino, E. Nordlander, In: Metal Clusters, in: *Chemistry* (Eds.: P. Braunstein, L. A. Oro, P. R. Raitby), Wiley-VCH: Weinheim, **1999**, vol. 2, 741–781.
[3] M. Hidai, Sh. Kuwata, Y. Mizobe, *Acc. Chem. Res.* **2000**, *33*, 46.
[4] M. Taniguchi, D. Imamura, H, Ishige, Y. Ishii, T. Murata, M. Hidai, T. Tatsumi, *J. Catal.* **1999**, *187*, 139.
[5] M. Taniguchi, Y. Ishii, T. Murata, T. Tatsumi, M. Hidai, *J. Chem. Soc. Chem. Commun.* **1995**, 2533.
[6] M. N. Sokolov, E. V. Chubarova, A. V. Virovets, R. Llusar, V. P. Fedin, *J. Cluster Science* **2003**, *14*, 227.
[7] M. N. Sokolov, A. V. Virovets, D. N. Dybtsev, E. V. Chubarova, V. P. Fedin, D. Fenske, *Inorg. Chem.* **2001**, *40*, 4816.
[8] M. N. Sokolov, R. Hernandez-Molina, W. Clegg, V. P. Fedin, A. Mederos, *Chem. Commun.* **2003**, 140.
[9] M. Feliz, J. M. Garriga, R. Llusar, S. Uriel, M. G. Humphrey, N. T. Lukas, M. Samoc, B. Luter-Davies, *Inorg. Chem.* **2001**, *40*, 6132.
[10] R. Hernandez-Molina, M. N. Sokolov, A. G. Sykes, *Acc. Chem. Res.* **2001**, *34*, 223.
[11] R. Llusar, S. Uriel, C. Vicent, *J. Chem. Soc. Dalton Trans.* **2001**, 2813.
[12] K. Herbst, P. Zanello, M. Corsini, N. D'Amello, L. Dahlenburg, M. Brorson, *Inorg. Chem.* **2003**, *42*, 974.
[13] K. Herbst, B. Rink, L. Dahlenburg, M. Brorson, *Organometallics* **2001**, *20*, 3655.
[14] K. Herbst, M. Monari, M. Brorson, *Inorg. Chem.* **2001**, *40*, 2979.
[15] R. Llusar, S. Uriel, *Eur. J. Inorg. Chem.* **2003**, 1271.
[16] T. Murata, Y. Mizobe, H. Gao, Y. Ishii, T. Wakabayashi, F. Nakano, T. Tanase, Sh. Yano, M. Hidai, I. Echizen, H. Nanikawa, Sh. Motomura, *J. Am. Chem. Soc.* **1994**, *116*, 3389.
[17] V. P. Fedin, M.-S. Seo, D. M. Saysell, D. N. Dybtsev, M. R. J. Elsegood, W. Clegg, A. G. Sykes, *J. Chem. Soc. Dalton Trans.* **2002**, 138.
[18] D. Masui, Y. Ishii, M. Hidai, *Bull. Chem. Soc. Japan* **2000**, *73*, 931.
[19] H. Akashi, T. Shibahara, *Inorg. Chim. Acta* **2000**, *300–302*, 572.
[20] T. Shibahara, M. Yamasaki, H. Akashi, T. Katayama, *Inorg. Chem.* **1991**, *30*, 2693.
[21] E. Collange, J. A. Garcia, R. Poli, *New J. Chem.* **2002**, *26*, 1249.
[22] P. A. W. Dean, K. Fisher, D. Craig, M. Jennings, O. Ohene-Fianko, M. Scudder, G. Willett, I. Dance, *J. Chem. Soc. Dalton Trans.* **2003**, 1520.
[23] A. Macchioni, A. Romani, C. Zuccaccia, *Organometallics* **2003**, *22*, 1526.
[24] S. W. Audi Fong, W. T. Yap, J. J. Vittal, W. Henderson, T. S. A. Hor, *J. Chem. Soc. Dalton Trans.* **2002**, 1826.
[25] W. Henderson, B. K. Nicholson, L. J. McCaffrey, *Polyhedron* **1998**, *17*, 4291.
[26] M. Feliz, R. Llusar, S. Uriel, C. Vicent, M. G. Humphrey, N. T. Lucas, M. Samoc, B. Luther-Davies, *Inorg. Chim. Acta* **2003**, *349*, 69.
[27] M. Feliz, R. Llusar, S. Uriel, C. Vicent, *unpublished results.*
[28] M. Feliz, R. Llusar, S. Uriel, C. Vicent, E. Coronado, C. J. Gomez-Garcia, *Chem. Eur. J.* **2004** in press.
[29] J. Maddox, *Nature* **1988**, *335*, 201.

 © 2005 Wiley-VCH Verlag GmbH & Co. KGaA, Weinheim

[30] M. Eddaoudi, D. B. Moler, H. Li, B. Chen, B. Reineke, M. O'Keefe, O. M. Yaghi, *Acc. Chem. Res.* **2001**, *34*, 319.
[31] S. Kitagawa, R. Kitaura, S.-I. Noro, *Angew. Chem. Int. Ed.* **2004**, *43*, 2334.
[32] O. R. Evans, W. Lin, *Acc. Chem. Res.* **2002**, *35*, 512.
[33] A. N. Khlobystov, A. J. Klake, Champness, N. R., D. A. Lemenovskii, A. G. Majouga, N. V. Zyk, M. Schröder, *Coord. Chem. Rev.* **2001**, *222*, 155.
[34] G. R. Desiraju, R. Parthasarathy, *J. Am. Chem. Soc.* **1989**, *111*, 8725.
[35] I. Dance, M. L. Scudder, *J. Chem. Soc. Chem. Commun.* **1995**, 1039.
[36] I. Dance, M. Scudder, *Chem. Eur. J.* **1996**, *2*, 485.
[37] O. M. Yaghi, H. Li, C. Davis, D. Richardson, T. L. Groy, *Acc. Chem. Res.* **1998**, *31*, 474.
[38] M. N. Sokolov, R. Hernandez-Molina, D. N. Dybtsev, E. V. Chubarova, S. F. Solodovnikov, N. V. Pervukhina, C. Vicent, R. Llusar, V. Fedin, *Z. Anorg. Allg. Chem.* **2002**, *628*, 2335.
[39] SAINT 6.2, Bruker Analytical X-Ray Systems, Madison, WI, **2001**.
[40] G. M. Sheldrick, SADABS Empirical Absorption Program **1996**.
[41] G. M. Sheldrick, SHELXTL 5.1, Madison, WI., **1997**.
Received: October 24, 2004

 © 2005 Wiley-VCH Verlag GmbH & Co. KGaA, Weinheim

A Rearrangement of Azobenzene upon Interaction with an Aluminum(I) Monomer LAl {L = HC[(CMe)(NAr)]$_2$, Ar = 2,6-*i*Pr$_2$C$_6$H$_3$}

Hongping Zhu,[a] Jianfang Chai,[a] Hongjun Fan,[b] Herbert W. Roesky,*[a] Umesh N. Nehete,[a] Hans-Georg Schmidt,[a] and Mathias Noltemeyer[a]

Keywords: Aluminum / Azobenzene / N ligands / Rearrangement

Reaction of LAl (**1**) or [LAl{η^2-C$_2$(SiMe$_3$)$_2$}] (**2**) {L = HC[(CMe)(NAr)]$_2$, Ar = 2,6-*i*Pr$_2$C$_6$H$_3$} with azobenzene affords a five-membered ring compound [LAl{N(H)-*o*-C$_6$H$_4$N(Ph)}] (**3**). In the formation of **3** a three-membered intermediate [LAl(η^2-N$_2$Ph$_2$)] (**A**) is suggested by a [1 + 2] cycloaddition reaction; **A** is not stable and further rearranges to **3**. DFT calculations on similar compounds with modified L′ {L′ = HC[(CMe)(NPh)]$_2$} show that the complexation energy of the reaction of L′Al with azobenzene to form [L′Al(η^2-N$_2$Ph$_2$)] is about –39 kcal mol^{-1}, and the best estimate of the energy difference between [L′Al(η^2-N$_2$Ph$_2$)] and [L′Al{N(H)-*o*-C$_6$H$_4$N(Ph)}] is –76 kcal mol^{-1}.
(© Wiley-VCH Verlag GmbH & Co. KGaA, 69451 Weinheim, Germany, 2005)

Introduction

The reactions of Group 13 metal(I) tetramers (RM)$_4$ (R = organic group, M = Al, Ga, In) with unsaturated molecules [H$_2$C=C(Me)–C(Me)=CH$_2$, PhC(O)–C(O)Ph, RN=C(H)–C(H)=NR, R = Me, *i*Pr][1–3] allow the trapping of the corresponding monomer RM, and are also an interesting oxidative addition of compounds with unsaturated bonds to low-valent metal centers.[4] This leads to heterocyclic compounds containing novel heavier main-group elements that have potential applications in pharmaceutical, agrochemical, and materials science.[5] We have recently prepared the aluminum(I) monomer LAl {**1**, L = HC[(CMe)(NAr)]$_2$, Ar = 2,6-*i*Pr$_2$C$_6$H$_3$}, which has a singlet carbene character.[6] The reductive coupling reaction of LAlI$_2$ with potassium in the presence of alkynes follows a [1 + 2] cycloaddition pathway to yield the aluminacyclopropene [LAl{η^2-C$_2$(R)(R′)}] (R = R′ = SiMe$_3$, Ph; R = Ph, R′ = SiMe$_3$).[7] A direct coupling reaction between LAl and alkyne (Me$_3$SiC≡CC≡CSiMe$_3$) is subsequently realized to form [LAl{η^2-C$_2$(SiMe$_3$)(C≡CSiMe$_3$)}].[8] In this context, we are interested in the interaction of the Al^I center with compounds containing an N=N double bond. The reaction of **1** or [LAl{η^2-C$_2$(SiMe$_3$)$_2$}] (**2**) with azobenzene unexpectedly resulted in the formation of the five-membered ring complex [LAl{N(H)-*o*-C$_6$H$_4$N(Ph)}] (**3**). Compound **3** contains an N(H)-*o*-C$_6$H$_4$N(Ph) moiety which is formed by an isomerization of azobenzene. Obviously, a rearrangement of azobenzene is occurring upon interaction with LAl.

Results and Discussion

Upon stirring of a toluene solution of **1** and azobenzene at elevated temperature (80 °C) for 5 h, the red color changed to orange. Partial removal of the solvent in vacuo and addition of *n*-hexane led to the crystallization of **3**, at 4 °C, as orange crystals in good yield. An alternative route to **3** was investigated by treating **2** with azobenzene in the temperature range from –50 °C to room temperature. The result indicated that **2** could be used as a good precursor for **1**.

Compound **3** is thermally stable, as indicated by its high melting point (260–261 °C) and its most intense molecular ion peak {*m*/*z* (%) = 626 (100) [M$^+$]} found in the EI mass spectrum. Complex **3** has been fully characterized by spectroscopic, analytical, and X-ray single-crystal measurements.

The molecular structure of **3** is shown in Figure 1. The central Al atom is involved as part of two fused five- (AlN$_2$C$_2$) and six-membered (AlN$_2$C$_3$) rings. The corresponding AlN$_4$ core appears in a distorted tetrahedral geometry. The Al–N bond lengths within the AlN$_2$C$_2$ ring are 1.807(2) Å [Al–N(H)] and 1.847(1) Å [Al–N(Ph)], and are similar to those of the AlN$_4$ ring complex [1.815(2), 1.851(2) Å].[9] The Al–N$_{\beta\text{-diketiminato}}$ bond lengths [1.893(1) and 1.862(1) Å] fall in the range [1.874(1)–1.959(3) Å] observed for other four-coordinate (β-diketiminato)aluminum compounds,[7,10] although one bond is a little shorter than these values. The AlN$_2$C$_2$ ring is nearly planar (Δ = 0.0719 Å) and this planar character can be extended to the

[a] Institut für Anorganische Chemie der Universität Göttingen, Tammannstrasse 4, 37077 Göttingen, Germany
Fax: +49-551-39-3373
E-mail: hroesky@gwdg.de
[b] Labor für Physikalische und Theoretische Chemie, Universität Siegen, 57068 Siegen, Germany

adjacent disubstituted phenyl group (Δ = 0.0816 Å). It is interesting to note that, within the AlN_2C_2 ring, the C(31)–C(36) bond [1.429(2) Å] is longer than the remaining ones of the phenyl ring [1.382(2)–1.393(2) Å]. This obviously contributes to the AlN_2C_2 ring formation. The phenyl groups involved in different structural environments [disubstituted C_6H_4, N(Ph), Ar] exhibit diverse resonances for their aromatic protons in the ^1H NMR spectrum of **3**. An unambiguous assignment of the resonances was not possible. The NH proton resonates at δ = 3.06 (s) ppm and in the IR spectrum the absorption at 3220 cm^{-1} is assignable to ν_{NH}.

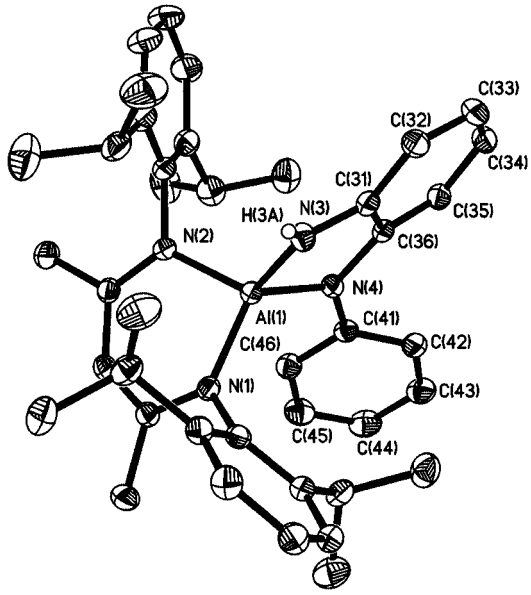

Figure 1. Molecular structure of compound **3**. The hydrogen atoms of the C–H bonds have been omitted for clarity. Selected bond lengths [Å] and angles [°]: Al(1)–N(1) 1.862(1), Al(1)–N(2) 1.893(1), Al(1)–N(3) 1.807(2), Al(1)–N(4) 1.847(1), N(3)–C(31) 1.386(2), C(31)–C(36) 1.429(2), C(36)–N(4) 1.420(2); N(1)–Al(1)–N(2) 97.68(6), N(3)–Al(1)–N(4) 90.39(6), Al(1)–N(3)–C(31) 109.86(10), N(3)–C(31)–C(36) 115.57(14), C(31)–C(36)–N(4) 113.40(10), C(36)–N(4)–Al(4) 108.44(10).

The reaction of **1** with azobenzene may initially proceed through an [LAl(η^2-N_2Ph_2)] (**A**) intermediate, which is formed by a [1 + 2] cycloaddition reaction. **A** is not stable due to the highly strained, metal-containing, three-membered AlN_2 ring, and therefore rearranges by cleaving the N–N bond, with migration of a hydrogen atom from the *ortho* position of one adjacent phenyl ring to yield **3** (Scheme 1). Compounds with similar structures to **A** are known for transition and lanthanide metals, for which different electronic interaction modes (π-bonds and one-electron transfer) have been discussed.[11–13] A three-membered AlN_2 heterocycle bearing an exocyclic N=C double bond at one of the two N atoms has also been reported.[14] Correspondingly, an easy cleavage of the N–N bond and the rearrangement of the adjacent *ortho*-phenyl hydrogen atom of azobenzene have also been observed in the reaction of an FeH-containing active site with azobenzene,[15,16] and in a cyclometalation[17,18] and a substitution[19] reaction.

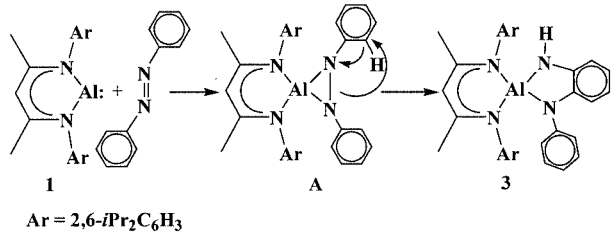

Scheme 1. Proposed formation of **3** from the reaction of **1** and PhNNPh.

A further insight into this proposed mechanism can be gained from theoretical calculations.[20] The computed results show that the complexation energy of the initial reaction of L′Al with azobenzene to form [L′Al(η^2-N_2Ph_2)] {L′ is HC[(CMe)(NPh)]$_2$ for simplicity of calculation} is about –39 kcal mol^{-1}. This indicates a reasonable possibility that **A** is an intermediate in the reaction of **1** with azobenzene. The value of –39 kcal mol^{-1} is even lower than that calculated for the complexation energy of LAl with alkyne (ca. –21 kcal mol^{-1}) using the same method.[10] When [L′Al(η^2-N_2Ph_2)] is further converted into [L′Al{N(H)-*o*-C_6H_4N(Ph)}], a best estimate of the energy difference between these two isomers is –76 kcal mol^{-1}. This suggests an energetically favored stable rearrangement, and is also in agreement with the rearrangement of a three- to a five-membered ring. Furthermore, the D_{298}(Al–η^2-N_2) value is comparable to that of the Al–N bond strength in donor–acceptor $H_3Al{\cdot}NH_3$ species predicted by ab initio studies with a zero-point vibrational energy correction [D_{298}(Al–N) = 26 kcal mol^{-1}].[21] This implies a reasonably strong Al–η^2-N_2 bonding. Therefore, the cleavage of the corresponding N–N bond in the rearrangement of **A** to **3** is highly favored, although no such bond dissociation energy data are available for comparison.[22]

Conclusions

In summary, we have investigated the reaction of aluminum(I) monomer LAl (**1**) with azobenzene. The formation of a five-membered AlN_2C_2 ring containing product **3** is different to the [1 + 2] cycloaddition product formed in the reaction of LAl with alkyne, and indicates an interesting rearrangement of azobenzene via a possible three-membered AlN_2 intermediate (**A**) upon interaction with LAl.

Experimental Section

General: All manipulations were carried out under purified nitrogen using Schlenk techniques. The solvents were dried by standard methods. Chemicals were purchased from Aldrich or Fluka and were used as received. LAl (**1**)[6] and [LAl{η^2-$C_2(SiMe_3)_2$}] (**2**)[7] were prepared as described in the literature. Elemental analyses were performed by the Analytisches Laboratorium des Instituts für Anorganische Chemie der Universität Göttingen. ^1H (300.13 MHz) and ^{13}C (125.76 MHz) NMR spectra were recorded with a Bruker AM 300 spectrometer and IR spectra with a Bio-Rad Digilab FTS-7 spectrometer. EI mass spectra were recorded with a Finnigan

 © 2005 Wiley-VCH Verlag GmbH & Co. KGaA, Weinheim

MAT 8230 or a Varian MAT CH5 instrument. Melting points were measured in sealed glass tubes and are not corrected.

Synthesis of [LAl{N(H)-*o*-C_6H_4N(Ph)}] (3). Method A: A toluene solution (30 mL) of LAl (**1**, 0.22 g, 0.5 mmol) and PhNNPh (0.09 g, 0.5 mmol) was stirred and heated slowly to 80 °C for 5 h. The color of the solution changed from red to orange. The volume of the solution was reduced in vacuo (ca. 10 mL) and *n*-hexane was added (10 mL). Upon keeping this solution at 4 °C for one week, orange X-ray quality crystals of **3** were obtained (0.15 g) and collected. The mother liquor was concentrated again (ca. 4 mL) and *n*-hexane added (8 mL). Another crop of orange crystals (0.10 g) was obtained by keeping the solution at –26 °C for 24 h. Total yield: 0.25 g (81%). M.p. 260–261 °C. ^{1}H NMR (300.13 MHz, C_6D_6, 298 K): δ = 0.90 [d, $^3J_{H,H}$ = 6.8 Hz, 2×3 H, CH(CH_3)$_2$], 0.92 [d, $^3J_{H,H}$ = 6.8 Hz, 2×3 H, CH(CH_3)$_2$], 1.07 [d, $^3J_{H,H}$ = 6.8 Hz, 2×3 H, CH(CH_3)$_2$], 1.23 [d, $^3J_{H,H}$ = 6.8 Hz, 2×3 H, CH(CH_3)$_2$], 1.47 (s, 2×3 H, β-CH_3), 3.05 [sept, $^3J_{H,H}$ = 6.8 Hz, 2×1 H, CH(CH$_3$)$_2$], 3.06 (s, 1 H, NH), 3.14 [sept, $^3J_{H,H}$ = 6.8 Hz, 2×1 H, CH(CH$_3$)$_2$], 5.12 (s, 1 H, γ-CH), 6.31–6.34 (m, 1 H), 6.58–6.66 (m, 2 H), 6.82–6.92 (m, 3 H), 6.94–7.02 (m, 4 H), 7.22–7.30 (m, 4 H), 7.48–7.52 (m, 15 H, Ar-H and Ph-H) ppm. ^{13}C{^{1}H} NMR (125.77 MHz, C_6D_6, 298 K): δ = 23.4, 24.2, 24.5, 24.9, 25.1, 28.3, 29.2 [CH(*C*H$_3$)$_2$, β-*C*H$_3$], 99.2 (γ-*C*), 112.3, 114.0, 115.1, 118.8, 124.0, 125.1, 127.9, 128.2, 129.0, 139.5, 143.1, 143.7, 145.3, 148.8 (Ar-*C*, Ph-*C*), 171.5 (*C*N) ppm. IR (Nujol mull): $\tilde{\nu}$ = 3220 (NH) cm^{-1}. EI-MS: *m*/*z* (%) = 626 (100) [M$^+$]. $C_{41}H_{51}AlN_4$ (626.87): calcd. C 78.56, H 8.20, N 8.14; found C 78.23, H 8.18, N 8.24. **Method B:** A toluene solution (5 mL) of PhNNPh (0.18 g, 1 mmol) was added to a toluene solution (20 mL) of [LAl{η^2-C_2(SiMe$_3$)$_2$}] (**2**; 0.62 g, 1 mmol) at –50 °C. The mixture was allowed to warm to room temperature whilst being stirred. The solution changed from black to orange. After continuing the stirring for 12 h, the solution was concentrated to dryness in vacuo and washed with *n*-hexane (10 mL) to afford an orange crystalline solid, which was characterized as **3** by m.p. and EI mass measurements.

Table 1. Crystallographic data for compound **3**.

	3
Empirical formula	$C_{41}H_{51}AlN_4$
Formula mass	626.84
T [K]	133(2)
Crystal system	triclinic
Space group	$P\bar{1}$
a [Å]	11.704(3)
b [Å]	12.612(2)
c [Å]	12.980(4)
α [°]	86.460(2)
β [°]	77.11(2)
γ [°]	86.40(2)
V [Å^3]	1861.7(7)
Z	2
$\rho_c$alcd. [Mg m^{-3}]	1.118
μ [mm^{-1}]	0.087
F(000)	676
θ range [°]	1.61–24.88
Index ranges	$-13 \le h \le 13$ $-14 \le k \le 14$ $-15 \le l \le 15$
No. of reflections collected	27600
No. of independent reflections (R_{int})	6396 (0.0536)
No. of data/restraints/parameters	6396/0/424
GoF/F^2	1.015
R_1,[a] wR_2[b] [$I > 2\sigma(I)$]	0.0391, 0.0915
R_1,[a] wR_2[b] (all data)	0.0539, 0.0979
Largest diff peak/hole [e Å^{-3}]	0.210/–0.235

[a] $R = \Sigma||F_o| - |F_c||/\Sigma|F_o|$. [b] $wR_2 = [\Sigma w(F_o^2 - F_c^2)^2/\Sigma w(F_o^2)]^{1/2}$.

X-ray Structure Determination and Refinement: The crystallographic data for compound **3** were collected with a Stoe IPDS II array detector system with graphite-monochromated Mo-K_α radiation (λ = 0.71073 Å). The structure was solved by direct methods (SHELXS-96)[23] and refined against F^2 using SHELXL-97.[24] All non-hydrogen atoms were located by difference Fourier synthesis and refined anisotropically; hydrogen atoms were included using the riding model with U_{iso} tied to the U_{iso} of the parent atoms. A summary of cell parameters, data collection, and structure solution and refinement is given in Table 1. CCDC-253931 (**3**) contains the supplementary crystallographic data for this paper. These data can be obtained free of charge from The Cambridge Crystallographic Data Centre via www.ccdc.cam.ac.uk/data_request/cif.

Acknowledgments

This work was supported by the Deutsche Forschungsgemeinschaft, the Fonds der Chemischen Industrie, and the Göttinger Akademie der Wissenschaften.

[1] C. Dohmeier, D. Loos, H. Schnöckel, *Angew. Chem.* **1996**, *108*, 141–161; *Angew. Chem. Int. Ed. Engl.* **1996**, *35*, 129–149.
[2] W. Uhl, S. U. Keimling, S. Pohl, W. Saak, R. Wartchow, *Chem. Ber./Recueil* **1997**, *130*, 1269–1272.
[3] A. H. Cowley, J. D. Gorden, C. D. Abernethy, J. A. C. Clyburne, B. G. Burnett, *J. Chem. Soc., Dalton Trans.* **1998**, 1937–1938.
[4] W. Uhl, *Rev. Inorg. Chem.* **1998**, *18*, 239–282.
[5] E. C. Taylor, *The Chemistry of Heterocyclic Compounds*, John Wiley & Sons, New York, **1993**.
[6] C. Cui, H. W. Roesky, H.-G. Schmidt, M. Noltemeyer, H. Hao, F. Cimpoesu, *Angew. Chem.* **2000**, *112*, 4444–4446; *Angew. Chem. Int. Ed.* **2000**, *39*, 4274–4276.
[7] C. Cui, S. Köpke, R. Herbst-Irmer, H. W. Roesky, M. Noltemeyer, H.-G. Schmidt, B. Wrackmeyer, *J. Am. Chem. Soc.* **2001**, *123*, 9091–9098.
[8] LAl reacts with $Me_3SiC{\equiv}CC{\equiv}CSiMe_3$ to afford [LAl{η^2-C_2(SiMe$_3$)(C≡CSiMe$_3$)}], which contains a three-membered ring: H. Zhu, J. Chai, H. W. Roesky, H.-G. Schmidt, M. Noltemeyer, *Organometallics*, to be submitted.
[9] C. Cui, H. W. Roesky, H.-G. Schmidt, M. Noltemeyer, *Angew. Chem.* **2000**, *112*, 4705–4707; *Angew. Chem. Int. Ed.* **2000**, *39*, 4531–4533.
[10] H. Zhu, J. Chai, Q. Ma, V. Jancik, H. W. Roesky, H. Fan, R. Herbst-Irmer, *J. Am. Chem. Soc.* **2004**, *126*, 10 194–10 195.
[11] R. S. Dickson, J. A. Ibers, S. Otsuka, Y. Tatsuno, *J. Am. Chem. Soc.* **1971**, *93*, 4636–4637.
[12] W. J. Evans, D. K. Drummond, L. R. Chamberlain, R. J. Doedens, S. G. Bott, H. C. Zhang, J. L. Atwood, *J. Am. Chem. Soc.* **1988**, *110*, 4983–4994.
[13] J. Takats, X. W. Zhang, V. W. Day, T. A. Eberspacher, *Organometallics* **1993**, *12*, 4286–4288.
[14] W. Uhl, F. Hannemann, *Eur. J. Inorg. Chem.* **1999**, 201–207.
[15] G. Guillemot, E. Solari, R. Scopelliti, C. Floriani, *Organometallics* **2001**, *20*, 2446–2448.
[16] J. M. Smith, R. J. Lachicotte, P. L. Holland, *J. Am. Chem. Soc.* **2003**, *125*, 15 752–15 753.
[17] A. J. Craty, *Organomet. Chem. Rev., Sect A* **1972**, 191–243, and references cited therein.
[18] a) A. Omenat, M. Ghedini, *J. Chem. Soc., Chem. Commun.* **1994**, 1309–1310; b) S. A. Hudson, P. M. Maitlis, *Chem. Rev.* **1993**, *93*, 861–885; c) M. Ghedini, D.Pucci, A. Crispini, G. Barberio, *Organometallics* **1999**, *18*, 2116–2124.
[19] A. Risaliti, S. Bozzini, A. Stener, *Tetrahedron* **1969**, *25*, 143–148.

 © 2005 Wiley-VCH Verlag GmbH & Co. KGaA, Weinheim

[20] The DFT calculations were performed by analyzing the energy difference of products and reactants in the reaction of L′Al and PhNNPh to form [L′Al(η^2-N_2Ph_2)] and then [L′Al{N(H)-*o*-C_6H_4N(Ph)}], where L′ is HC[(CMe)(NPh)]$_2$ for simplicity of calculation. The corresponding geometries were optimized according to the real structures or related ones at the BP86/TZVP level with RI approximation {L′Al to LAl,[6] PhNNPh in *cis* position, [L′Al(η^2-N_2Ph_2)] to [LAl(η^2-C_2Ph_2)][7] but with an N–N single bond, and [L′Al{N(H)-*o*-C_6H_4N(Ph)}] to [LAl{N(H)-*o*-C_6H_4N(Ph)}]} using the TURBOMOLE 5.5 program: R. Ahlrichs, M. Bär, H.-P. Baron, R. Bauernschmitt, S. Böcker, P. Deglmann, M. Ehrig, K. Eichkorn, S. Elliott, F. Furche, F. Haase, M. Häser, H. Horn, C. Hättig, C. Huber, U. Huniar, M. Katannek, A. Köhn, C. Kölmel, M. Kollwitz, K. May, C. Ochsenfeld, H. Öhm, A. Schäfer, U. Schneider, M. Sie, O. Treutler, B. Unterreiner, M. V. Arnim, F. Weigand, P. Weis, H. Weiss, *TURBOMOLE 5.5*, University of Karlsruhe, Germany, **2002**.

[21] C. M. B. Marsh, T. P. Hamilton, Y. Xie, H. F. Schaefer, *J. Chem. Phys.* **1992**, *96*, 5310–5317.

[22] The N–N bond strength for H_2N–NHPh (D_{298} = 57 ± 2 kcal mol^{-1}) has been reported previously: D. F. McMillen, D. M. Golden, *Annu. Rev. Phys. Chem.* **1982**, *33*, 493–496.

[23] *SHELXS-90, Program for Structure Solution:* G. M. Sheldrick, *Acta Crystallogr. Sect. A* **1990**, *46*, 467–473.

[24] G. M. Sheldrick, *SHELXL-97, Program for Crystal Structure Refinement*; University of Göttingen, Göttingen, Germany, **1997**.

Received: November 02, 2004

 © 2005 Wiley-VCH Verlag GmbH & Co. KGaA, Weinheim

Synthesis and Structure of a 2,4-Unsubstituted *cis*/*trans*-1,3-Disilacyclobutane by Dehydrofluorination of a Highly Hindered Fluorosilane

Rudolf Pietschnig,*[a] Stefan Spirk,[a] Ferdinand Belaj,[a] and Klaus Merz[b]

Keywords: Dimerization / Silanes / Silenes / Silicon / Strained molecules

The preparation, molecular structure, and metalation behavior of a sterically highly congested fluorosilane (*t*BuTipMeSiF) are described. This silane is subjected to dehydrofluorination under thermally mild conditions. A *C*-unsubstituted transient intermediate – either the silene or the corresponding silenoid – is generated in a metalation/elimination sequence at low temperatures, and this intermediate dimerizes to give the corresponding 1,3-disilacyclobutane exclusively, even in the presence of a trapping agent. The significant steric hindrance in the starting fluorosilane and the final 1,3-disilacyclobutane is corroborated by their crystal structures.

(© Wiley-VCH Verlag GmbH & Co. KGaA, 69451 Weinheim, Germany, 2005)

Introduction

Since the preparation of the first stable silenes a broad variety of methods to synthesize such compounds has been developed.[1,2] *C*-Substituted transient and stable silenes can be prepared under especially mild conditions by a metalation/elimination sequence. For this approach, all so-far-known examples carry activating silyl groups at the carbon atom designated for metalation. Besides steric protection of the resulting silene, these substituents also provide an increase of the acidity of the neighboring C–H unit due to the α-silyl effect.[3] Alternatively, α-lithiohalosilanes have also been prepared by conjugate addition of organolithium reagents to halovinylsilanes. Since the first reaction of this type, described by Jones and Lim in 1977,[4,5] many other transient silenes have been synthesized by this route, particularly by Auner and coworkers,[6] but also by some other authors.[7] Despite the use of more and more bulky substituents, all these silenes are unstable at room temperature and lead to dimeric 1,3-disilacyclobutanes (head-to-tail dimerization), except for the stable dimesitylneopentylsilene.[8] Since in these silenes the multiply bonded carbon atom also carries at least one substituent, we were interested in whether the scope of the metalation/elimination technique could be extended to silenes without any activating or protecting groups at the carbon end of the silene unit. In this contribution, we describe the preparation and structure of a sterically crowded fluorosilane which should be a suitable precursor for a *C*-unsubstituted α-lithiofluorosilane. Upon metalation, the corresponding transient silenoid is formed, which subsequently eliminates LiF. The resulting silene is unstable and dimerizes to the corresponding 1,3-disilacyclobutane. The precursor for metalation as well as the resulting *cis*-1,3-disilacyclobutane have been characterized spectroscopically and by X-ray diffraction on single crystals.

[a] Institut für Chemie, Karl-Franzens-Universität Graz, Schubertstraße 1, 8010 Graz, Austria
Fax: +43-316-380-9835
E-mail: rudolf.pietschnig@uni-graz.at
[b] Fakultät für Chemie, Ruhr-Universität Bochum, Universitätsstraße 150, 44780 Bochum, Germany

Results and Discussion

In the reaction of sterically encumbered halosilanes with organolithium compounds direct nucleophilic halide displacement competes with lithiation of activated sites such as the α-position. Therefore, the steric protection of the silicon center in fluorosilanes is crucial to favor metalation over nucleophilic displacement. To accomplish the formation of a silenoid by direct deprotonation of a methyl group adjacent to a fluorosilyl, we synthesized a suitable precursor starting from *t*BuTipSiF_2 (**1**, Tip = 2,4,6-triisopropylphenyl).[9,10] Since no C–H bonds are available in the α-position to the silicon atom in this fluorosilane, we selectively introduced a methyl group as the designated site for further metalation. The methyl group can be introduced in a straightforward manner by treating **1** with methyllithium at low temperature to cleanly afford **2** (Scheme 1). The NMR spectra of **2** show a ^{19}F resonance at δ = –160.5 ppm, and the ^{29}Si signal at δ = 25.0 ppm is split into a doublet with a $^1J_{Si,F}$ coupling constant of 287 Hz (Figure 1). We were able to obtain a crystal structure of **2** which illustrates the steric situation within the molecule (Table 1).

Even though **1** and **2** are isoelectronic, the steric situation around the silicon center appears to be even more congested in **2**. Accordingly, the Si(1)–F(1) bond length increases from 1.595(2) Å in **1**[9] to 1.625(2) Å in **2** and is even longer than in the closely related compound *i*Pr_2TipSiF.[11] Also, the silicon–carbon distances for the *tert*-butyl and the

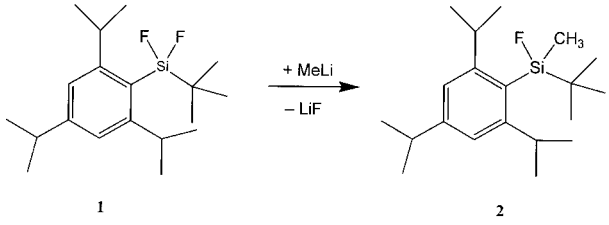

Scheme 1. Synthesis of **2**.

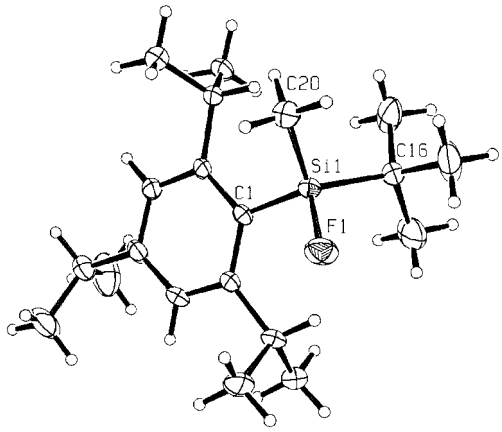

Figure 1. Molecular structure of **2** in the solid state.

Table 1. Selected bond lengths [Å] and angles [°] for **2**.

Si(1)–F(1)	1.625(2)	F(1)–Si(1)–C(20)	101.17(14)
Si(1)–C(20)	1.866(4)	F(1)–Si(1)–C(16)	106.18(14)
Si(1)–C(16)	1.883(3)	F(1)–Si(1)–C(1)	107.42(12)
Si(1)–C(1)	1.892(4)	C(20)–Si(1)–C(16)	111.27(16)
C(16)–Si(1)–C(1)	114.09(15)	C(20)–Si(1)–C(1)	115.36(16)

2,4,6-triisopropylphenyl group in **2** are, at 1.883(3) and 1.892(4) Å, respectively, longer than in **1**, while the bond to the methyl carbon atom is slightly shorter [1.866(4) Å]. Surprisingly, the bond between Si(1) and the aryl carbon atom C(1) is longer than the corresponding Si–C_{alkyl} distances of the molecule. The steric repulsion of the substituents at silicon is also obvious from the angles between the groups adjacent to this atom. Hence, the C–Si–C angles are, at 111.27(16)°, 114.09(15)°, and 115.36(16)°, larger than the corresponding F–Si–C angles [101.17(14)°, 106.18(14)°, and 107.42(12)°].

The sterically congested situation in **2** combined with the absence of activated C–H bonds other than in the methyl group makes this fluorosilane an ideal starting material for the generation of a Li–F silenoid without further substituents on carbon. To achieve metalation of the methyl group, we treated **2** with *tert*-butyllithium at low temperature (–100 °C). No reaction could be detected in apolar solvents such as pentane, even when the mixture was warmed to room temperature. In contrast, the onset of a reaction can be observed by the formation of a precipitate along with a color change on addition of stoichiometric amounts of coordinating reagents such as TMEDA or THF, even at –100 °C. After warming to room temperature, the corresponding 1,3-disilacyclobutane (**5**) was obtained as the final product (Scheme 2).

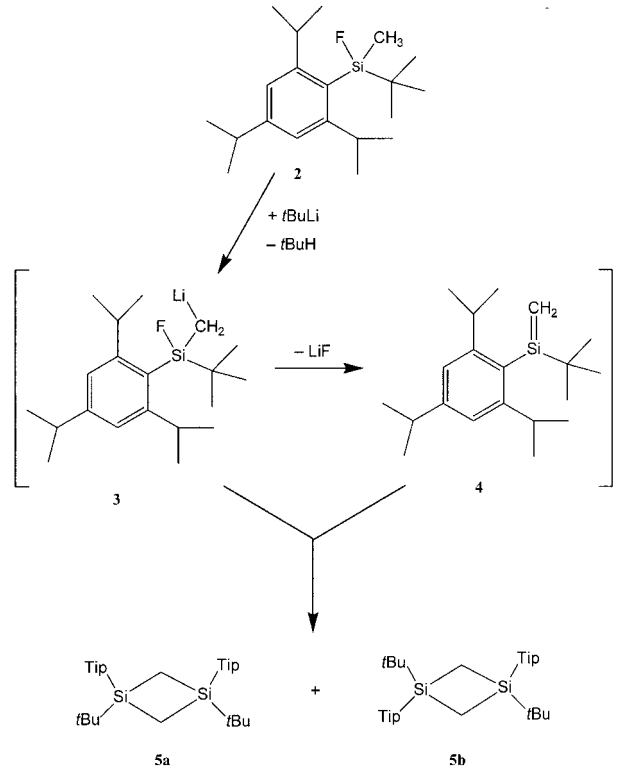

Scheme 2. Metalation of **2** and formation of **5** (Tip = 2,4,6-triisopropylphenyl).

In the ^{29}Si NMR spectrum **5** shows a resonance for each of the two isomers [*cis* (**5a**)/*trans* (**5b**)] which appear very close to each other at δ = 9.2 and 9.3 ppm. The ratio of the isomers is approximately 1:1, which in related cases has been found to be indicative of the formation of the 1,3-disilacyclobutane from intermediate silenes rather than silenoids.[12,13] Upon recrystallization we were able to obtain crystalline samples of the *cis*-isomer of **5** that were suitable for analytical purposes and X-ray diffraction.

The molecular structure of **5** proves the presence of a central 1,3-disilacyclobutane system, where the ring carbon atoms are unsubstituted while the silicon atoms carry sterically demanding 2,4,6-triisopropylphenyl and *tert*-butyl groups (Figure 2). The internal angles of the 1,3-disilacyclobutane ring are all approximately 90°, with smaller values found at the silicon atoms [88.31(10)°, 88.37(10)°, 90.86(10)°, and 91.28(11)°] (Table 2).

The ring-puckering angle [11.79(11)°], which is defined by the dihedral angle of the two Si–Si–C planes of the ring, falls well within the range of such angles in other structurally characterized 1,3-disilacyclobutanes (0–25.5°).[14–17] As a consequence of the steric repulsion of the substituents at the silicon atoms, the Si–C distances within the ring [1.901(2)–1.909(2) Å] are the longest observed so far for 1,3-disilacyclobutanes without substituents at the ring carbon atoms. According to previous studies long Si–C bond lengths in the ring correspond to reduced puckering angles.[18] The steric pressure at the silicon atoms is also

 © 2005 Wiley-VCH Verlag GmbH & Co. KGaA, Weinheim

obvious from the exocyclic Si–C distances, which are significantly longer than standard Si–C bond lengths.[19] Therefore, as expected, the Si–C_{aryl} distances [1.907(2) and 1.909(2) Å] are slightly shorter than the Si–C_{alkyl} distances [1.932(3) and 1.933(3) Å]. The solution NMR spectra corroborate the steric pressure within **5** derived from the static picture of the crystal structure. Hence, in the ^{13}C NMR spectra the CH_3 units of the isopropyl groups in the *ortho* position of the Tip substituent are not equivalent at room temperature. Obviously, the rotation by which they would become equivalent is prevented by the proximity of the *tert*-butyl group. As a consequence of the puckered structure of the disilacyclobutane ring, the dihedral angles between the methylene carbon atoms and the transannular methylene hydrogen atoms differ significantly [C(1)–Si(1)–C(2)–H(21) = 124.6°; C(1)–Si(1)–C(2)–H(22) = –108.1°]. Therefore, in the proton-coupled ^{13}C NMR spectra the coupling of only one of these protons with the carbon atom is observed ($^3J_{C,H}$ = 4.9 Hz) apart from the coupling with the directly bonded chemically inequivalent methylene protons ($^1J_{C,Ha}$ = 117.9, $^1J_{C,Hb}$ = 121.7 Hz).

Although we were unable to directly observe any of the intermediates discussed in the formation of **5**, this process is likely to proceed by the initial formation of silenoid **3**, which could either dimerize to yield **5** directly, or eliminate LiF to form silene **4** which, on dimerization, would yield the same product (**5**). As is known from the literature, the ratio of the *cis*/*trans* isomers of the resulting 1,3-disilacyclobutane can be used as an indicator of which of the above mechanisms is dominant.[12,13] According to these findings, the 1:1 ratio of the isomers found in our experiments should be indicative of the formation of **5** from transient silene **4**. In contrast, the occurrence of a precipitate, along with the color change observed on addition of stoichiometric amounts of THF at low temperature, could be interpreted as a hint for the formation of silenoid **3**. The identity of this precipitate was elucidated with a trapping experiment with a reactive chlorophosphane. On addition of the latter at low temperature the precipitate disappears. However, in the ^{31}P NMR spectra the resonance of the resulting product indicates that the initially formed precipitate is not silenoid **3** but rather an etherate of butyllithium.[20]

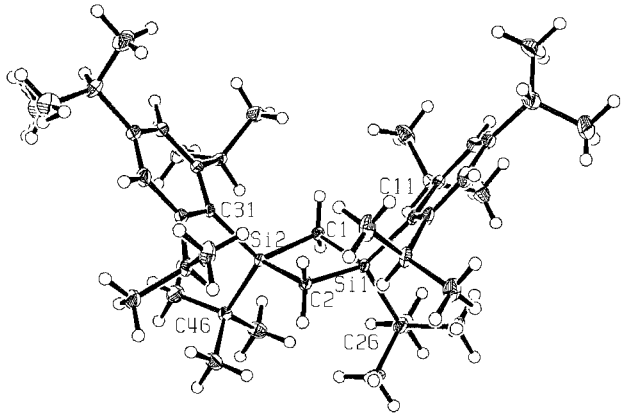

Figure 2. Molecular structure of **5a** in the solid state.

Conclusions

Compound **2** is a sterically hindered fluorosilane that can be metalated selectively in the α-position despite of the absence of activating groups. The resulting Li–F silenoid carries no further substituents at the carbon end of the metalated unit and spontaneously eliminates LiF below room temperature. Due to insufficient steric protection, transient silenoid **3** or silene **4** dimerize to the corresponding 1,3-disilacyclobutane. The ratio of the *cis* and *trans* isomers indicates formation from the silene rather than from the silenoid, although no direct evidence for the silene could be found. The sterically highly congested silenoid precursor **2** and the final product **5** have been fully characterized and their crystal structures determined. From their geometric parameters, as well as from spectroscopic data, the steric hindrance within both molecules is evident. However, to accomplish the stabilization of a C-unsubstituted silene a further increase of the steric congestion at the silicon end of the unsaturated unit will be necessary.

Experimental Section

All chemical experiments were performed under argon using standard Schlenk techniques or a glovebox. Solvents other than $CDCl_3$ were dried with sodium/potassium alloy and stored under argon.

Table 2. Selected bond lengths [Å] and angles [°] for the central Si_2C_2 ring of **5a**.

Si(1)–C(2)	1.903(2)	Si(2)–C(1)	1.909(2)
Si(1)–C(1)	1.909(2)	Si(2)–C(2)	1.901(2)
Si(1)–C(11)	1.909(3)	Si(2)–C(31)	1.907(2)
Si(1)–C(26)	1.933(3)	Si(2)–C(46)	1.932(3)
C(2)–Si(1)–C(1)	88.31(10)	C(2)–Si(2)–C(31)	112.99(11)
C(2)–Si(1)–C(11)	115.51(11)	C(2)–Si(2)–C(1)	88.37(10)
C(1)–Si(1)–C(11)	113.11(11)	C(31)–Si(2)–C(1)	116.95(11)
C(2)–Si(1)–C(26)	113.37(11)	C(2)–Si(2)–C(46)	115.41(11)
C(1)–Si(1)–C(26)	117.28(11)	C(31)–Si(2)–C(46)	108.63(10)
C(11)–Si(1)–C(26)	108.41(11)	C(1)–Si(2)–C(46)	113.58(11)
Si(1)–C(1)–Si(2)	90.86(10)	Si(2)–C(2)–Si(1)	91.28(11)
Si(1)–C(1)–Si(2)–C(2)	8.22(11)	C(2)–Si(1)–C(26)–C(28)	4.0(2)
C(2)–Si(1)–C(11)–C(12)	35.6(2)	C(1)–Si(2)–C(46)–C(48)	11.0(2)
C(1)–Si(2)–C(31)–C(32)	37.9(2)	Si(1)···Si(2)	2.270(2)

 © 2005 Wiley-VCH Verlag GmbH & Co. KGaA, Weinheim

^{1}H, ^{13}C, ^{19}F, and ^{29}Si NMR spectra were recorded on Bruker AMX 360 or Bruker Avance DRX 500 instrument. Mass spectra were measured on a Masslab VG 12-250 by the electron impact ionization technique. Melting points were determined on a Mettler FP 61 in glass capillaries. *tert*-Butyldifluoro(2,4,6-triisopropylphenyl) silane [tBu(2,4,6-iPrC_6H_2)SiF_2] was prepared according to literature procedures.[9,10] Other chemicals were obtained from different chemical suppliers and used as received.

Synthesis of *tert*-Butylfluoro(methyl)(2,4,6-triisopropylphenyl)silane (2): A solution of MeLi (1.6 M in diethyl ether; 8.8 mL, 14 mmol) was added, at –100 °C, to a solution of tBu(2,4,6-iPrC_6H_2)SiF_2 (4.17 g, 12.8 mmol) in diethyl ether (40 mL), while stirring. The mixture was warmed to room temperature; the precipitate that formed at –80 °C redissolved at higher temperatures. Stirring was continued for 16 h, after which the solvent was removed in vacuo. The residue was extracted with hexanes (2 × 30 mL) and the insoluble precipitate (LiF) was separated by filtration. The filtrate was recovered and removal of the solvent in vacuo and recrystallization from chloroform yielded **2** as colorless, deliquescent crystals (4.09 g, 98.9%); m.p. 49.4 °C. ^{1}H NMR ($CDCl_3$, 360 MHz, 25 °C): δ = 7.08 (s, 2 H), 3.23 (sept, $^{3}J_{H,H}$ = 6.6 Hz, 1 H), 2.90 (sept, $^{3}J_{H,H}$ = 7.0 Hz, 2 H), 1.29 (d, $^{3}J_{H,H}$ = 7.0 Hz, 12 H), 1.26 (d, $^{3}J_{H,H}$ = 6.6 Hz, 6 H), 1.08 (s, 9 H), 0.57 (d, $^{3}J_{H,F}$ = 10.3 Hz, 3 H) ppm. ^{13}C NMR ($CDCl_3$, 91 MHz, 25 °C): δ = 156.58 (s), 150.54 (s), 127.04 (d, $^{2}J_{C,F}$ = 11.1 Hz), 121.70 (s), 34.12 (s), 33.84 (s), 26.63 (s), 25.61 (s), 23.74 (s), 20.12 (d, $^{2}J_{C,F}$ = 12.5 Hz), 0.16 (d, $^{2}J_{C,F}$ = 18.7 Hz) ppm. ^{19}F NMR ($CDCl_3$, 471 MHz, 25 °C): δ = –160.5 (q, $^{3}J_{F,H}$ = 9.9 Hz) ppm. ^{29}Si NMR ($CDCl_3$, 72 MHz, 25 °C): δ = 25.0 (d, $^{1}J_{Si,F}$ = 287 Hz) ppm. MS: *m*/*z* (%) = 322.2494 (high resolution: Δ = 0.89 ppm) (8) [M^+], 265.1 (100) [M^+ – tBu], 245.1 (12) [M^+ – tBu– HF], 187.1 (10), 77.0 (19). $C_{20}H_{35}FSi$ (322.58): calcd. C 74.47, H 10.94; found C 74.41, H 11.25.

Synthesis of *cis*/*trans*-1,3-Di-*tert*-butyl-1,3-bis(2,4,6-triisopropylphenyl)-1,3-disilacyclobutane (5): A solution of **2** (0.85 g, 2.6 mmol) in pentane (10 mL) was cooled to –100 °C and 1.7 mL (2.9 mmol) of a solution of tBuLi (1.7 M in pentane) was added while stirring. Upon addition of THF (0.74 mL, 9 mmol) the mixture turned yellow and a precipitate was observed. The temperature was maintained for 2 h and the mixture was then slowly warmed to room temperature. Stirring was continued for 12 h, after which the solution was concentrated under reduced pressure to obtain a sample suitable for the recording of ^{29}Si NMR spectra [^{29}Si NMR (THF/$CDCl_3$, 72 MHz, 25 °C): δ = 9.3, 9.2 ppm]. After complete removal of the solvent in vacuo, the residue was extracted with hexanes (2 × 30 mL) and the insoluble precipitate (LiF) was separated by filtration. The filtrate was recovered and removal of the solvent in vacuo and recrystallization from acetone yielded *cis*-**5** as colorless crystals (0.7 g, 44.0%); m.p. 243 °C (dec.). ^{1}H NMR ($CDCl_3$, 360 MHz, 25 °C): δ = 6.94 (s, 4 H), 3.26 (sept, $^{3}J_{H,H}$ = 7.0 Hz, 4 H), 2.84 (sept, $^{3}J_{H,H}$ = 7.0 Hz, 2 H), 1.25 (d, $^{3}J_{H,H}$ = 7.0 Hz, 24 H), 1.19 (d, $^{3}J_{H,H}$ = 7.0 Hz, 12 H), 1.15 (s, 18 H), 0.44 (s, 4 H) ppm. ^{13}C NMR ($CDCl_3$, 91 MHz, 25 °C): δ = 154.75, 149.18, 133.82 ($^{1}J_{C,Si}$ = 45.8 Hz), 121.57, 34.00, 33.79, 30.59, 25.84, 25.45, 23.75, 17.94 ($^{1}J_{C,Si}$ = 32.6 Hz), 8.12 ($^{1}J_{C,Si}$ = 36.8 Hz) ppm. ^{29}Si NMR ($CDCl_3$, 72 MHz, 25 °C): δ = 9.3 ppm. MS: *m*/*z* (%) = 604.5 (3) [M^+], 547.5 (100) [M^+ – tBu], 302, (25) [M^+/2], 245.1 (15) [M^+/2 – tBu], 57.1 (8) [tBu$^+$]. $C_{40}H_{68}Si_2$ (605.14): calcd. C 79.39, H 11.33; found C 78.85, H 11.70.

Trapping Experiments: The procedure for the synthesis of **5** was followed to the point where a precipitate occurred on addition of the lithiating reagent. After addition of chlorobis(diethylamino)-phosphane as trapping reagent, at –70 °C, we observed no conversion of the starting fluorosilane **2** in the NMR spectra. The trapping reagent, in contrast, was completely converted into *tert*-butylbis(diethylamino)phosphane under these conditions, as is evident from its ^{31}P NMR chemical shift.

Crystallographic Details for 2: A colorless crystal of **2** with dimensions 0.1 × 0.2 × 0.1 mm^3 was coated in paraffin oil, mounted on a glass fiber, and placed under a cold stream of nitrogen. All the measurements were performed using graphite-monochromated Mo-K_α radiation at 213 K. A total of 3201 reflections were collected (θ_{max} = 23°), of which 2238 were unique (R_{int} = 0.0162). Additional experimental details are given in Table 3. The structure was solved by direct methods (SHELXS-97) and refined by full-matrix least-squares techniques against F^2 (SHELXL-97).[21,22] The non-hydrogen atoms were refined with anisotropic displacement parameters without any constraints. For 199 parameters final R indices of R = 0.0539 and $wR2$ = 0.1553 (GOF = 1.102) were obtained.

Table 3. Crystal data and structure refinement for **2** and **5a**.

	2	**5a**
Formula	$C_{20}H_{35}FSi$	$C_{40}H_{68}Si_2$
Formula mass	322.58	605.12
Temperature [K]	213	100
Wavelength	0.71073	0.71069
Crystal system	triclinic	monoclinic
Space group	$P\bar{1}$	$P2_1/n$
a [Å]	9.495(5)	9.771(3)
b [Å]	9.933(5)	18.957(4)
c [Å]	11.976(6)	21.025(4)
α [°]	68.236(15)	90
β [°]	86.175(13)	94.64 (2)
γ [°]	83.452(18)	90
V [Å^3]	1041.8(9)	3882.2(16)
Z	3	4
Density (calcd.) [Mg m^{-3}]	1.028	1.035
μ [mm^{-1}]	0.118	0.116
θ Range for data collection [°]	1.83–22.47	2.61–26.00
Goodness-of-fit on F^2	1.102	1.042
$R1$ (obsd. data)	0.0539	0.0600
wR_2 (all data)	0.1553	0.1401

Crystallographic Details for 5a: A colorless crystal of **5a** with dimensions 0.15 × 0.10 × 0.10 mm^3 was coated in paraffin oil, mounted on a glass fiber, and placed under a cold stream of nitrogen. All the measurements were performed with graphite-monochromated Mo-K_α radiation at 100 K. A total of 8923 reflections were collected (θ_{max} = 26.0°), of which 7606 were unique (R_{int} = 0.0472), with 5689 having $I > 2\sigma(I)$. The structure was solved by direct methods (SHELXS-97) and refined by full-matrix least-squares techniques against F^2 (SHELXL-97).[21,22] One methyl group was disordered over two positions (C41 and C51). The atoms C41 and C51 have site occupation factors of 0.454(18) and 0.546(18), respectively, and were isotropically refined with the constraint of equal bond lengths to C40. All other non-hydrogen atoms were refined with anisotropic displacement parameters without any constraints. The H atoms of the CH_2 groups were refined with common isotropic displacement parameters for the H atoms of the same group and idealized geometry with approximately tetrahedral angles and C–H distances of 0.99 Å. The C atoms of the phenyl rings were refined without any constraints. The H atoms were put at the external bisector of the C–C–C angle at a C–H distance of 0.95 Å and common isotropic displacement parameters were used for the H atoms of the same phenyl group. The H atoms of the tertiary C–H groups were refined with all X–C–H angles equal at

 © 2005 Wiley-VCH Verlag GmbH & Co. KGaA, Weinheim

a C–H distance of 1.00 Å and with common isotropic displacement parameters for the H atoms of the tertiary C–H groups bonded to the same phenyl ring. The H atoms of the methyl groups were refined with common isotropic displacement parameters for the H atoms of the same group and idealized geometry with tetrahedral angles, enabling rotation around the X–C bond, and C–H distances of 0.98 Å. For 419 parameters final R indices of $R = 0.0600$ and $wR_2 = 0.1401$ (GOF = 1.042) were obtained. The largest peak in the difference Fourier map was 0.479 e Å^{-3}. CCDC-254269 (for **2**) and -254270 (for **5a**) contain the supplementary crystallographic data for this paper. These data can be obtained free of charge from The Cambridge Crystallographic Data Centre via www.ccdc.cam.ac.uk/data_request/cif.

Acknowledgments

We acknowledge financial support by the Fonds der Chemischen Industrie (Germany).

[1] A. G. Brook, M. A. Brook, *Adv. Organomet. Chem.* **1996**, *39*, 71.
[2] K. M. Baines, M. S. Samuel, in *Science of Synthesis*, Thieme, Stuttgart, vol. 4, **2002**, p. 125.
[3] M. A. Brook, *Silicon in Organic, Organometallic, and Polymer Chemistry*, Wiley, New York, **2000**.
[4] P. R. Jones, T. F. O. Lim, *J. Am. Chem. Soc.* **1977**, *99*, 2013.
[5] P. R. Jones, T. F. O. Lim, *J. Am. Chem. Soc.* **1977**, *99*, 8447.
[6] T. Müller, W. Ziche, N. Auner, in *Chemistry of Organic Silicon Compounds* (Eds.: Z. Rappoport, Y. Apeloig), Wiley, Chichester, UK, vol. 2(2), **1998**, p. 857.
[7] J. Escudie, C. Couret, H. Ranaivonjatovo, *Coord. Chem. Rev.* **1998**, *178–180*, 565.
[8] G. Delpon-Lacaze, C. de Battisti, C. Couret, *J. Organomet. Chem.* **1996**, *514*, 59.
[9] R. Pietschnig, F. Belaj, *Appl. Organomet. Chem.* **2004**, *18*, 300.
[10] Y. Nakadaira, K. Oharu, H. Sakurai, *J. Organomet. Chem.* **1986**, *309*, 247.
[11] R. Pietschnig, K. Merz, *Appl. Organomet. Chem.* **2005**, *19*, 206.
[12] P. R. Jones, A. H.-B. Cheng, T. E. Albanesi, *Organometallics* **1984**, *3*, 78.
[13] R. T. Conlin, M. P. Bessellieu, P. R. Jones, R. A. Pierce, *Organometallics* **1982**, *1*, 396.
[14] K. M. Baines, A. G. Brook, P. D. Lickiss, J. F. Sawyer, *Organometallics* **1989**, *8*, 709.
[15] J. L. Robison, W. M. Davis, D. Seyferth, *Organometallics* **1991**, *10*, 3385.
[16] J. Braddock-Wilking, M. Y. Chiang, P. P. Gaspar, *Organometallics* **1993**, *12*, 197.
[17] N. P. Toltl, M. Stradiotto, T. L. Morkin, W. J. Leigh, *Organometallics* **1999**, *18*, 5643.
[18] V. G. Avakyan, S. L. Guselnikov, L. E. Gusel'nikov, *J. Organomet. Chem.* **2003**, *686*, 257.
[19] P. Rademacher, *Strukturen organischer Moleküle*, VCH, Weinheim, **1987**.
[20] C. G. Screttas, J. F. Eastham, *J. Am. Chem. Soc.* **1966**, *88*, 5668.
[21] G. M. Sheldrick, *SHELXS-97: Program for the Solution of Crystal Structures*, University of Göttingen, Germany, **1997**.
[22] G. M. Sheldrick, *SHELXL-97: Program for the Refinement of Crystal Structures*, University of Göttingen, Germany, **1997**.

Received: November 03, 2004

 © 2005 Wiley-VCH Verlag GmbH & Co. KGaA, Weinheim

Pyridine- and Imidazoledicarboxylates of Zinc: Hydrothermal Synthesis, Structure, and Properties

Partha Mahata[a] and Srinivasan Natarajan*[a]

Keywords: Luminescence / N ligands / Pi interactions / Zinc

The reaction of hetrocyclic dicarboxylic acids, such as pyridine-2,5-dicarboxylic acid and imidazole-4,5-dicarboxylic acid, under hydrothermal conditions in the presence of an appropriate zinc salt yields three new zinc coordination polymers $^{0}_{\infty}[\{Zn_2(H_2O)_4\}\{C_5H_3N(COO)_2\}_2]$ (**1**), $^{1}_{\infty}[\{Zn(C_{12}H_8N_2)\}\{C_5H_3N(COO)_2\}\cdot 0.5H_2O]$ (**2**), and $^{1}_{\infty}[\{Zn(C_{12}H_8N_2)\}\{C_3HN_2(COO)_2\}]$ (**3**). While **1** forms with a zero-dimensional molecular rectangular box structure, **2** and **3** have zig-zag one-dimensional chain structures. The Zn^{2+} ions are coordinated by both the carboxylate oxygen atoms and also by the nitrogen atoms of the heterocycles. The 1,10-phenanthroline molecules in **2** and **3** act as a secondary ligands and occupy the inter-chain spaces. The moderate hydrogen-bond interaction energy in **1** and the π···π interactions in **2** and **3** appear to play an important role for the structural stability. The structures of **2** and **3** appear to be related, even though they are formed with different carboxylic acids. All three compounds exhibit photoluminescence at room temperature.
(© Wiley-VCH Verlag GmbH & Co. KGaA, 69451 Weinheim, Germany, 2005)

Introduction

Research in the area of metal-organic frameworks (MOFs) exhibiting open structures continues to be interesting due to their many applications, both actual as well as potential.[1] Of the many MOF compounds investigated, those containing benzenecarboxylates constitute an important family[1–10] as they combine the principles of supramolecular chemistry along with favorable π···π interactions that give rise to fascinating crystal structures. The role of hydrogen bonding in metal-coordinated network structures is beginning to gain importance as it results in a large number of coordination polymers. Recently, the scope of the investigations on benzenecarboxylates has been enhanced by the use of heterocyclic carboxylic acids such as pyridine-, pyrazole-, and imidazolecarboxylic acids. These acids can act both as a multiple proton donor and acceptor and can use their carboxylate oxygen and nitrogen atoms, which are highly accessible to metal ions, to form interesting network structures. Thus, Lin and co-workers have employed pyridinecarboxylic acid to prepare a series of Zn^{2+} and Cd^{2+} coordination polymers using a molecular building-block approach.[11–14] Pyrazoledicarboxylates have also given rise to interesting network structures of varying dimensionality.[15–17] Although many polymeric complexes have been prepared employing heterocyclic carboxylates, previously uncharacterized compounds with novel crystal structures often emerge during hydrothermal synthetic conditions. We have combined the advantages of the hydrothermal method of synthesis and multifunctional carboxylic acids in the presence of 1,10-phenanthroline to form a large number of new inorganic coordination polymers.[18,19] In continuation of this theme, we have now synthesized three new Zn coordination polymers, namely $^{0}_{\infty}[\{Zn_2(H_2O)_4\}\{C_5H_3N(COO)_2\}_2]$ (**1**), $^{1}_{\infty}[\{Zn(C_{12}H_8N_2)\}\{C_5H_3N(COO)_2\}\cdot 0.5H_2O]$ (**2**), and $^{1}_{\infty}[\{Zn(C_{12}H_8N_2)\}\{C_3HN_2(COO)_2\}]$ (**3**), by employing pyridine- and imidazoledicarboxylic acids. Compounds **1** and **2** were prepared from pyridine-2,5-dicarboxylic acid, whereas **3** was prepared from imidazole-4,5-dicarboxylic acid. While **1** possesses a zero-dimensional structure with a rectangular molecular-box arrangement, **2** and **3** have one-dimensional structures and all the structures are stabilized by hydrogen-bonding and π···π interactions. In this paper we describe the synthesis, structure, and properties of these compounds.

Results and Discussion

The asymmetric unit of **1** consists of 30 non-hydrogen atoms, of which two zinc atoms are crystallographically independent (Figure 1). Both the Zn^{2+} ions have a distorted square-pyramidal geometry formed by two carboxylate oxygen atoms, two bonded water molecules and a nitrogen atom of the pyridine ring. An average distance of 2.0395 and 2.092 Å for the Zn–O and Zn–N bonds, respectively, results from this connectivity. The O/N–Zn–O/N bond angles are in the range 78.01(2)–156.2(2)°. There are two different pyridine-2,5-dicarboxylate anions present in the structure and all the carboxylate groups have only mono-

[a] Framework Solids Laboratory, Solid State and Structural Chemistry Laboratory, Indian Institute of Science
Bangalore 560012, India
E-mail: snatarajan@sscu.iisc.ernet.in
Supporting information for this article is available on the WWW under http://www.eurjic.org or from the author.

 © 2005 Wiley-VCH Verlag GmbH & Co. KGaA, Weinheim **DOI: 10.1002/ejic.200400937**

dentate connectivity with the Zn^{2+} cations. The bond lengths and angles associated with the pyridine-2,5-dicarboxylate anions are in the range expected for this type of bonding. The terminal Zn–O bonds formed by the oxygen atoms [O(1) and O(4) for Zn(1) and O(6)and O(8) for Zn(2)] are formally water molecules. The two proton positions observed in the difference Fourier map for each of these oxygen atoms also confirm this. Selected bond lengths and angles are listed in Table 1. The connectivity between Zn^{2+} and the pyridine-2,5-dicarboxylate anions gives rise to a zero-dimensional unique molecular box. Each molecular box consists of four Zn^{2+} cations and four carboxylate anions, as shown in Figure 2a. The terminal water molecules and the presence of terminal C–O bonds in **1** gives rise to a large number of significant O–H···O hydrogen bonds. The hydrogen-bond interactions between the molecular box units form an extended two-dimensional structure (Figure 2b and c). Both intra- and intermolecular box hydrogen bonds are observed in **1**; a complete list of these interactions is given in Table 2.

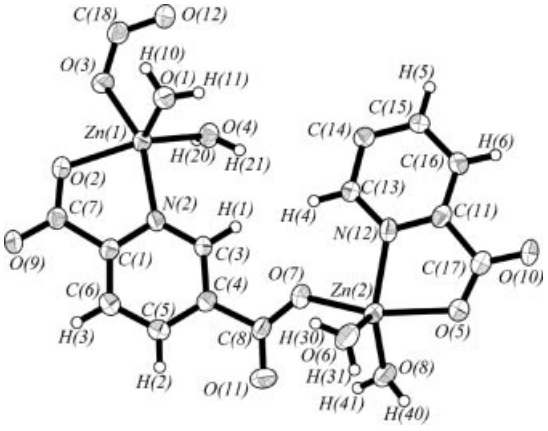

Figure 1. ORTEP drawing of $^{0}_{\infty}[\{Zn_2(H_2O)_4\}\{C_5H_3N(COO)_2\}_2]$ (**1**) showing the asymmetric unit. Thermal ellipsoids are given at 50% probability.

Table 1. Selected bond lengths [Å] and angles [°] in $^{0}_{\infty}[\{Zn_2(H_2O)_4\}\{C_5H_3N(COO)_2\}_2]$ (**1**).

Zn(1)–O(1)	2.012(5)	Zn(2)–O(5)	2.103(5)
Zn(1)–O(2)	2.113(4)	Zn(2)–O(6)	1.983(6)
Zn(1)–O(3)	2.022(5)	Zn(2)–O(7)	2.036(5)
Zn(1)–O(4)	2.039(5)	Zn(2)–O(8)	2.008(5)
Zn(1)–N(2)	2.113(5)	Zn(2)–N(12)	2.070(6)
O(1)–Zn(1)–O(3)	100.1(2)	O(6)–Zn(2)–O(8)	113.4(2)
O(1)–Zn(1)–O(4)	102.5(2)	O(6)–Zn(2)–O(7)	99.6(2)
O(3)–Zn(1)–O(4)	91.1(2)	O(8)–Zn(2)–O(7)	89.6(2)
O(1)–Zn(1)–O(2)	105.7(2)	O(6)–Zn(2)–N(12)	111.0(2)
O(3)–Zn(1)–O(2)	83.05(2)	O(8)–Zn(2)–N(12)	135.5(2)
O(4)–Zn(1)–O(2)	151.7(2)	O(7)–Zn(2)–N(12)	86.8(2)
O(1)–Zn(1)–N(2)	99.7(2)	O(6)–Zn(2)–O(5)	102.8(2)
O(3)–Zn(1)–N(2)	155.9(2)	O(8)–Zn(2)–O(5)	88.6(2)
O(4)–Zn(1)–N(2)	98.0(2)	O(7)–Zn(2)–O(5)	156.2(2)
O(2)–Zn(1)–N(2)	78.44(2)	N(12)–Zn(2)–O(5)	78.01(2)

The asymmetric unit of **2** consists of 28 non-hydrogen atoms, of which only one Zn atom is crystallographically independent (Figure 3). The Zn^{2+} ions have a distorted octahedral geometry formed by three carboxylate oxygen atoms and three nitrogen atoms, two of which belong to the 1,10-phenanthroline ligand. The Zn–O and the Zn–N bonds have average values of 2.162 and 2.145 Å, respectively. The O/N–Zn–O/N bond angles are in the range 58.98(2)–164.70(2)°, thereby indicating the heavy distortion of the Zn^{2+} octahedra (ideal octahedral values are 90° and 180°). The two carboxylate units of the pyridine-2,5-dicarboxylate show differences in their connectivity with respect to the Zn^{2+} ions − one has a monodentate connectivity and the other a bis(didentate) connectivity. The bond lengths and angles associated with the carboxylate group have typical values. Selected bond lengths and angles are listed in Table 3. In **2**, the connectivity between Zn^{2+} and the pyridine-2,5-carboxylate units gives rise to one-dimensional zig-zag chains (Figure 4). The 1,10-phenanthroline molecules act as a ligand to the Zn^{2+} ions and occupy the inter-chain spaces, along with the lattice water, and contribute to the stability of **2** by forming favorable π···π interactions (Figure 4). The presence of these interactions gives rise to a channel-like structure in **2**. Unlike **1**, no significant hydrogen-bond interactions are observed in **2**.

The asymmetric unit of **3** consists of 26 non-hydrogen atoms, of which only one Zn atom is crystallographically independent (Figure 5). The Zn^{2+} ions have a distorted octahedral geometry formed by two carboxylate oxygen atoms and four nitrogen atoms, two of which belong to the 1,10-phenanthroline ligand and the other two to the imidazole ring. The Zn–O and Zn–N bonds have average values of 2.225 Å and 2.151 Å, respectively. The O/N–Zn–O/N bond angles are in the range 74.63(8)–171.54(8)°, thereby indicating distortion of the Zn^{2+} octahedra. Both the carboxylate groups of the imidazole-4,5-dicarboxylate have only monodentate connectivity with Zn^{2+} ions. The bond lengths and angles associated with the imidazole-4,5-dicarboxylate have typical values. Selected bond lengths and angles are given in Table 3. The connectivity between the Zn^{2+} and the imidazole-4,5-carboxylate units gives rise to one-dimensional zig-zag chains (Figure 6). The 1,10-phenanthroline molecules act as a ligand to the Zn^{2+} ions and occupy the inter-chain spaces (Figure 6).

Room-temperature solid-state photoluminescence studies performed on powdered samples are presented in Figure 7. Photoluminescence studies of coordination polymers of the type discussed here have been investigated in great detail during the past few years.[19–28] In our present study, we found that coordination polymers **1**–**3** all exhibit photoluminescence. Compound **1** exhibits a single broad emission band at 430 nm, whilst compounds **2** and **3** exhibit two peaks at about 375 nm and at 390 nm when excited at 337 nm. The emission peak at 430 nm for **1** and at about 375 nm for **2** and **3** can be assigned to the intraligand fluorescent emission, since the acid displays a rather weak emission (λ_{max} = 410 nm). The lifetime, τ, for the emissions are 0.016 and 0.018 ns for **2** and **3**, respectively. This indicates that the luminescence should be assigned to fluorescence. The peak at 390 nm observed for **2** and **3** can be assigned to intraligand emission from the 1,10-phenanthroline ligand.[28] Similar ligand-to-metal charge transfer (LMCT)

 © 2005 Wiley-VCH Verlag GmbH & Co. KGaA, Weinheim

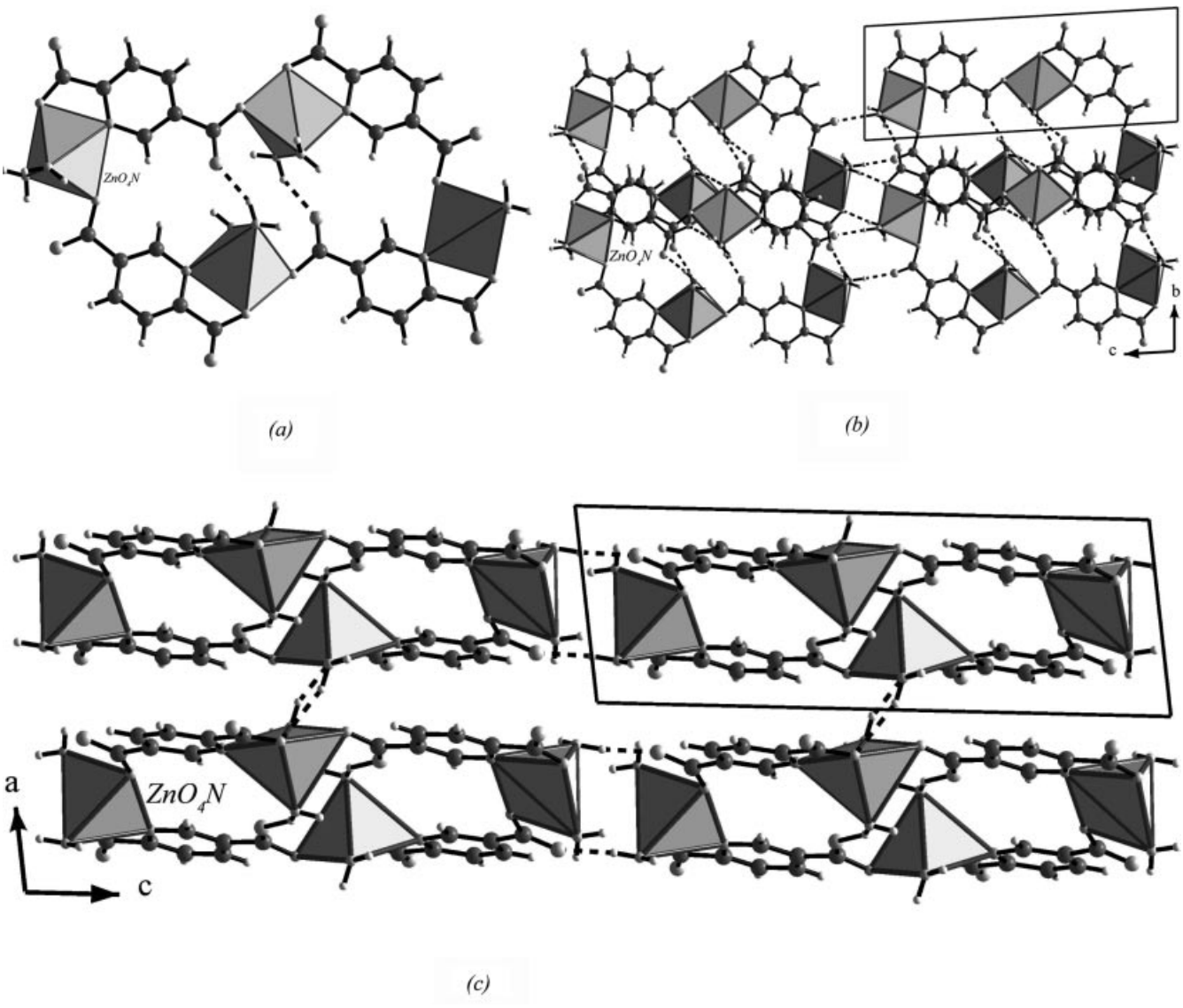

Figure 2. (a) A figure showing the connectivity between the Zn^{2+} ions and the pyridine-2,5-dicarboxylate anions. Note that the connectivity forms a molecular box. Dotted lines represent hydrogen-bond interactions. (b) The connectivity between the molecular box in the *bc* plane. Dotted lines represent hydrogen-bond interactions. (c) The connectivity between the molecular box in the *ac* plane.

Table 2. Selected hydrogen-bond interactions in $^{0}_{\infty}[\{Zn_2(H_2O)_4\}\{C_5H_3N(COO)_2\}_2]$ (**1**).

D–H···A[a]	D–H [Å]	H···A [Å]	D···A [Å]	D–H···A [°]
O(1)–H(10)···O(2)$^{\#1}$	0.85	2.09	2.882(8)	156
O(1)–H(11)···O(12)$^{\#2}$ (intra)	0.85	1.87	2.676(7)	156
O(4)–H(20)···O(2)$^{(\#3}$	0.85	2.13	2.943(8)	159
O(4)–H(21)···O(9)$^{\#4}$	0.85	1.79	2.618(8)	166
O(6)–H(30)···O(10)$^{\#1}$	0.85	1.89	2.726(9)	173
O(6)–H(31)···O(11)$^{\#5}$	0.85	1.81	2.653(8)	171
O(8)–H(40)···O(5)$^{\#6}$	0.85	1.85	2.674(8)	162
O(8)–H(41)···O(10)$^{\#3}$	0.85	2.45	3.202(9)	147

[a] #1: 1 – *x*, –*y*, 1 – *z*; #2: 2 – *x*, 1 – *y*, 1 – *z*; #3: 1 – *x*, 1 – *y*, 1 – *z*; #4: *x*, –1 + *y*, *z*; #5: 1 – *x*, –*y*, –*z*; #6: *x*, –1 + *y*, –1 + *z*.

transitions have been observed in many metal-organic coordination polymers.[19–28] It is known that free 1,10-phenanthroline exhibits weak emission peaks at 425 and 445 nm in the solid state at room temperature (see Supporting Information). The enhancement and the blue shift of the luminescence of the 1,10-phenanthroline ligand compared to that of free 1,10-phenanthroline may, therefore, be attributed to the chelating effect of the 1,10-phenanthroline ligand to the Zn^{2+} ion. This effectively enhances the rigidity of the ligand and reduces the loss of energy by radiationless decay of the intraligand emission of the excited state. Similar blue-shifts involving rigid ligand molecules and coordination polymers have been observed before.[28–30] In addition, fluorescent emission of carboxylate ligands resulting

 © 2005 Wiley-VCH Verlag GmbH & Co. KGaA, Weinheim

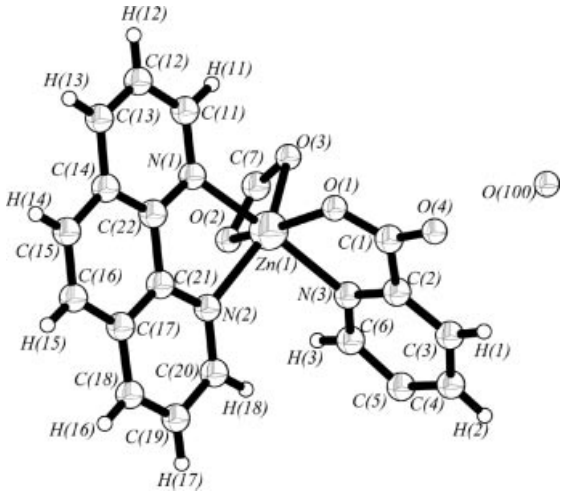

Figure 3. ORTEP drawing of $^1_\infty$[{Zn($C_{12}H_8N_2$)}{$C_5H_3N(COO)_2$}·0.5H_2O] (**2**) showing the asymmetric unit. Thermal ellipsoids are given at 50% probability.

Table 3. Selected bond lengths [Å] and angles [°] in $^1_\infty$[{Zn($C_{12}H_8N_2$)}{$C_5H_3N(COO)_2$}·0.5H_2O] (**2**) and $^1_\infty$[{Zn($C_{12}H_8N_2$)}{$C_3HN_2(COO)_2$}] (**3**).

2		**3**	
Zn(1)–O(1)	2.057(4)	Zn(1)–O(1)	2.2271(19)
Zn(1)–O(2)	2.312(5)	Zn(1)–O(4)	2.222(2)
Zn(1)–O(3)	2.118(4)	Zn(1)–N(1)	2.143(2)
Zn(1)–N(1)	2.151(4)	Zn(1)–N(2)	2.286(2)
Zn(1)–N(2)	2.163(4)	Zn(1)–N(3)	2.073(2)
Zn(1)–N(3)	2.121(4)	Zn(1)–N(4)	2.100(2)
O(1)–Zn(1)–O(3)	103.08(17)	N(3)–Zn(1)–N(4)	103.30(8)
O(1)–Zn(1)–N(3)	79.07(14)	N(3)–Zn(1)–N(1)	158.67(8)
O(3)–Zn(1)–N(3)	98.19(14)	N(4)–Zn(1)–N(1)	96.94(8)
O(1)–Zn(1)–N(1)	90.69(14)	N(3)–Zn(1)–O(4)	98.01(8)
O(3)–Zn(1)–N(1)	95.17(14)	N(4)–Zn(1)–O(4)	78.54(8)
N(3)–Zn(1)–N(1)	164.70(14)	N(1)–Zn(1)–O(4)	92.48(8)
O(1)–Zn(1)–N(2)	104.39(15)	N(3)–Zn(1)–O(1)	79.28(7)
O(3)–Zn(1)–N(2)	151.60(16)	N(4)–Zn(1)–O(1)	92.60(8)
N(3)–Zn(1)–N(2)	93.93(14)	N(1)–Zn(1)–O(1)	93.29(8)
N(1)–Zn(1)–N(2)	77.50(14)	O(4)–Zn(1)–O(1)	169.95(7)
O(1)–Zn(1)–O(2)	158.01(15)	N(3)–Zn(1)–N(2)	84.99(8)
O(3)–Zn(1)–O(2)	58.98(16)	N(4)–Zn(1)–N(2)	171.54(8)
N(3)–Zn(1)–O(2)	90.45(15)	N(1)–Zn(1)–N(2)	74.63(8)
N(1)–Zn(1)–O(2)	102.86(15)	O(4)–Zn(1)–N(2)	102.24(7)
N(2)–Zn(1)–O(2)	95.50(14)	O(1)–Zn(1)–N(2)	87.23(7)

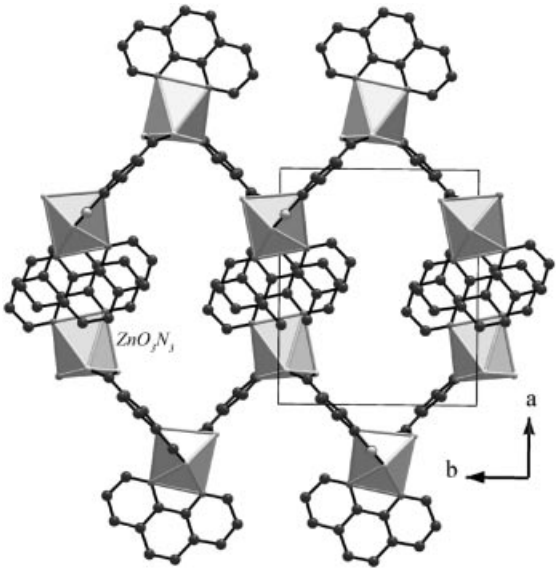

Figure 4. One-dimensional zig-zag chains observed in **2** in the *ab* plane. Note that the 1,10-phenanthroline ligands occupy interchain spaces and interact through π···π interactions (see text).

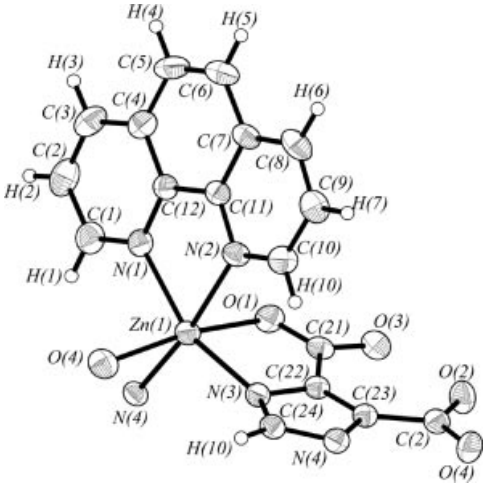

Figure 5. ORTEP drawing of $^1_\infty$[{Zn($C_{12}H_8N_2$)}{$C_3HN_2(COO)_2$}] (**3**) showing the asymmetric unit. Thermal ellipsoids are given at 50% probability.

from the π* → n transition is very weak compared with that of the π* → π transition of the 1,10-phenanthroline ligand. The strongly electron-withdrawing carboxylate group results in a fluorescence quenching, so the carboxylate ligands hardly contribute to the fluorescent emission of the as-synthesized polymers. As can be seen, the main emission bands of **2** and **3** are located almost at the same position, but with differences in the band shapes, which has been attributed to the π* → π transition of the coordinated 1,10-phenanthroline ligand.[28–30] The differences in the band shape might also be due to the minor differences in the structural topologies of the two structures.

The three new compounds were obtained by employing hydrothermal methods. The compounds have zero- and one-dimensional structures. While **1** forms with a zero-dimensional molecular box structure, **2** and **3** are formed with zig-zag one-dimensional chain structures. However, all three compounds are related in a subtle way. While compound **2** is formed by adding 1,10-phenanthroline to the synthesis mixture of **1**, **3** is obtained by replacing pyridine-2,5-dicarboxylic acid with imidazole-4,5-dicarboxylic acid in the synthesis mixture of **2**. The secondary ligand, 1,10-phenanthroline, replaces the terminal water molecules in **1** and, during this process, the coordination environment of the Zn^{2+} ions also changes from distorted square-pyramidal (five-coordinate) to an octahedral one (six-coordinate). In addition, the coordination mode of the pyridine-2,5-dicarboxylate also changes from being a simple monodentate coordination in **1** to a combination of mono- and bis(didentate) in **2**. In **3**, however, the imidazole-4,5-dicarboxylate has

 © 2005 Wiley-VCH Verlag GmbH & Co. KGaA, Weinheim

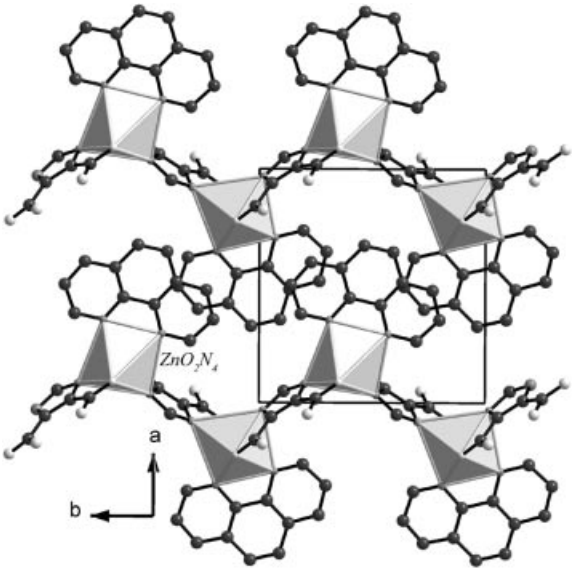

Figure 6. One-dimensional chains observed in **3** in the *ab* plane. Note that the 1,10-phenanthroline ligands occupy the inter-chain spaces and interact through π···π interactions (see text).

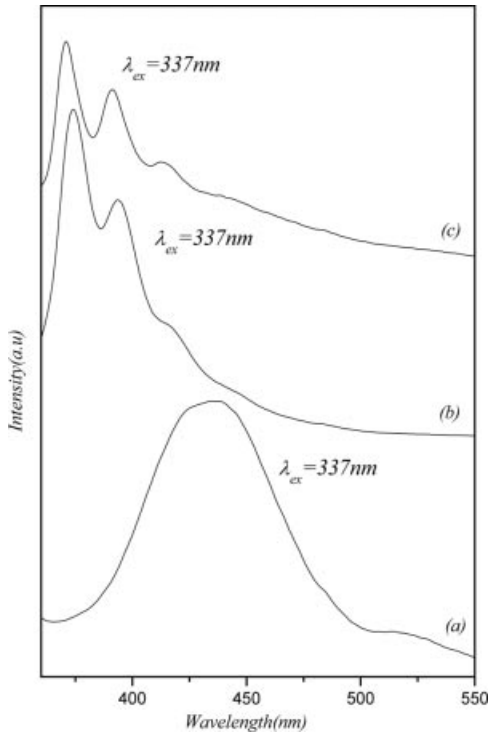

Figure 7. Emission spectra in the solid state at room temperature for (a) **1**, (b) **2**, and (c) **3**.

a simple monodentate connectivity with Zn^{2+} ions. The striking similarities between **2** and **3** can best be seen when viewing the structures down the chain axis. The 1,10-phenanthroline ligands occupy similar positions in both **2** and **3**, thus indicating that the favorable π···π interactions between the ligand molecules play an important role in the formation and stability of these compounds.

The use of heterocyclic carboxylic acids provides both the proton donor as well as the acceptor through the carboxylate oxygen and the ring nitrogen atoms. Both these centers are highly accessible to the participating metal ions during the synthesis for the formation of both monodentate and/or multidentate M–O and M–N bonds. The structural motifs thus formed can then readily participate in hydrogen bonding to give rise to a variety of networks. In the present system of compounds, we observe differences in the connectivity of the carboxylate oxygen atoms but the nitrogen atom, in all cases, participates in bonding with the Zn^{2+} ions. Similar behavior has been observed before.[17] In addition, moderate O–H···O-type hydrogen bonding is observed in **1** that gives rise to extended networks. It is likely that the presence of the rather bulky 1,10-phenanthroline as the secondary ligand in **2** and **3** prevents the formation of any hydrogen-bond interactions and only π···π interactions are observed (Figure 8).

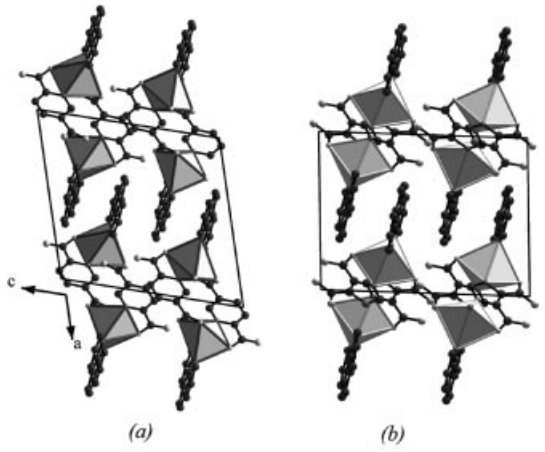

Figure 8. Arrangement of the one-dimensional chains in the *ac* plane for (a) **2** and (b) **3**. Note the similarity between the two structures and the arrangement of the 1,10-phenanthroline ligands.

The role of π···π interactions in the stability of lower dimensional structures in metal-organic coordination polymers has been a topic of much interest.[31,32] In the present compounds π···π interactions involving the 1,10-phenanthroline ligands are observed, especially in **2** and **3**. The centroid–centroid distance (*d*) between the 1,10-phenanthroline rings and their interplanar angles (θ) for **2** and **3** are shown in Figure 9. Favorable π···π interactions between these rings, with d = 3.66 Å and 3.45 Å and θ = 0.8° and 1.93° for **2** and **3**, respectively, are observed. From the interplanar angles (θ), it is clear that the two 1,10-phenanthroline rings are arranged one over the other, but are stacked anti-parallel to each other. This type of anti-parallel arrangement of aromatic rings is commonly observed in systems exhibiting dipolar properties. To understand the role of π···π interactions, we have performed preliminary calculations using the AM1-parameterized Hamiltonian available in the Gaussian program suite.[33,34] AM1 methods, together with a semi-classical dipolar description, have been employed recently to establish the relationship between the stability and geometries of organic molecules.[35]

 © 2005 Wiley-VCH Verlag GmbH & Co. KGaA, Weinheim

From these calculations, the dipole moment of the independent single 1,10-phenanthroline molecules was found to be 2.8 Debye; in **2** and **3**, the dipole moment values for the stacked arrangement were found to be exactly zero. It is likely that the anti-parallel arrangement of the 1,10-phenanthroline molecules reduces the dipole–dipole repulsion and paves the way for π-electron polarizations.

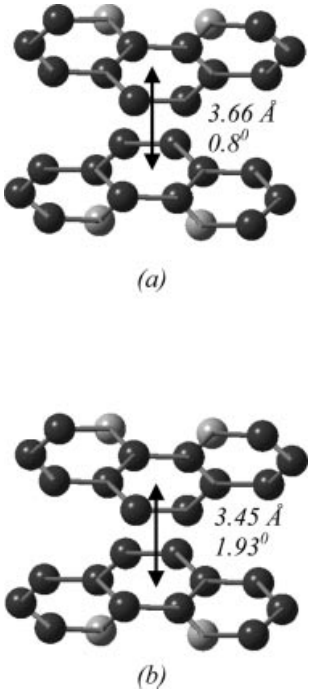

Figure 9. Stacking of the 1,10-phenanthrolines in **2** and **3**. Note that in both the cases the molecules are in an anti-parallel arrangement.

We also evaluated the strength of the π···π interactions in **2** and **3** based on single-point energy calculations, without symmetry constraints, on the basis of the crystal structure geometry. The π···π interaction energies were found to be 7.27 and 7.32 kcal mol^{-1}, respectively, for **2** and **3**. These energies are comparable to the intermediate hydrogen-bond strengths (approx. 10–15 kcal mol^{-1}) in N–H···O and O–H···O hydrogen-bond systems.[36] It should be noted that the carboxylate groups in **1** are stacked exactly one over other, while in **2** and **3** they are in an anti-parallel arrangement (Figure 10). It is likely that the presence of 1,10-phenanthroline ligands and their π···π interactions influence the geometry of the carboxylate groups in **2** and **3**, although all the carboxylate groups are separated by 6–7 Å in the structures. When the separation between the benzene rings is greater, as for instance between the pyridinecarboxylates in **1** and **2** and between the imidazolecarboxylates in **3**, the π···π interactions are negligible. Of the three compounds described in this paper, the moderate hydrogen-bond interaction energy in **1** and the π···π interactions in **2** and **3** appear to play an important role for the observed structural stability. It is likely that the study of similar systems would open up new avenues for our understanding of the nature of π···π interactions and their role in structural stability.

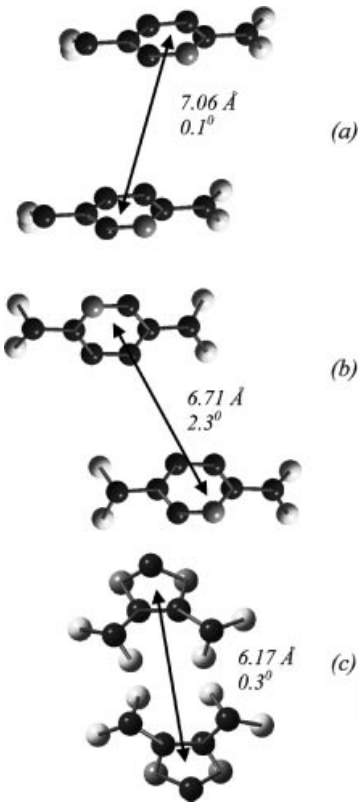

Figure 10. Arrangement of the carboxylate units in (a) **1**, (b) **2**, and (c) **3**.

Experimental Section

General: All three compounds were synthesized by hydrothermal methods. In a typical synthesis of **1**, $ZnSO_4 \cdot 7H_2O$ (0.144 g, 0.5 mmol) was dissolved in 4 mL of 0.125 M NaOH solution. Pyridine-2,5-dicarboxylic acid (H_2PyDC; 0.085 g, 0.5 mmol) and 0.03 mL of triethylamine (Et_3N) were then added, with continuous stirring, and the mixture was homogenized at room temperature for 30 min. The final mixture was sealed in a 7-mL PTFE-lined stainless-steel acid digestion bomb and heated at 150 °C for 5 d. The initial and final pH of the reaction mixture were 4 and 3.5, respectively. The final product contained large quantities of colorless rectangular crystals, which were filtered off, washed with copious quantities of deionized water under vacuum, and dried under ambient conditions. Compound **2** was prepared under identical synthetic conditions but with the addition of 0.1 g of 1,10-phenanthroline to the reaction mixture. For **3**, zinc acetate (0.056 g, 0.25 mmol) was dissolved in 10 mL of water along with imidazole-4,5-dicarboxylic acid (0.085 g, 0.5 mmol), NaOH (0.04 g, 1 mmol), Et_3N (0.03 mL, 0.25 mmol), and 1,10-phenanthroline (0.05 g, 0.25 mmol). The reaction mixture was heated in a 23-mL autoclave at 150 °C for 7 d. The initial and final pH of the reaction mixture were 10 and 6, respectively. The colorless crystals obtained were filtered, washed with water, and dried under ambient conditions. **1:** $C_{14}H_{14}N_2O_{12}Zn_2$ (533.01): calcd. C 31.52, H 2.66, N 5.25; found C 31.4, H 2.53, N 5.1. **2:** $C_{19}H_{12}N_3O_{4.5}Zn$ (419.68): calcd. C 54.33, H 2.85, N 10.01; found C 54.4, H 2.79, N 10.14. **3:** $C_{17}H_9N_4O_4Zn$ (398.65): calcd. C 51.17, H 2.26, N 14.05; found C 51.27, H 2.33, N 13.96. The powder XRD patterns were recorded on crushed single crystals in the 2θ range 5–50° using Cu-K_α radiation (Rich-Seifert, 3000TT). The XRD patterns indicated that the products were new materials; the patterns were entirely consistent with the structures

 © 2005 Wiley-VCH Verlag GmbH & Co. KGaA, Weinheim

Table 4. Crystal data and structure-refinement parameters for $^{0}_{\infty}[\{Zn_2(H_2O)_4\}\{C_5H_3N(COO)_2\}_2]$ (**1**), $^{1}_{\infty}[\{Zn(C_{12}H_8N_2)\}\{C_5H_3N(COO)_2\}\cdot 0.5H_2O]$ (**2**), and $^{1}_{\infty}[\{Zn(C_{12}H_8N_2)\}\{C_3HN_2(COO)_2\}]$ (**3**).

Structure parameter	**1**	**2**	**3**
Empirical formula	$C_{14}H_{14}N_2O_{12}Zn_2$	$C_{19}H_{12}N_3O_{4.5}Zn$	$C_{17}H_9N_4O_4Zn$
Formula mass	533.01	419.68	398.65
Crystal system	triclinic	monoclinic	monoclinic
Space group	$P\bar{1}$ (no. 2)	$P2_1/c$ (no. 14)	$P2_1/c$ (no. 14)
a [Å]	7.0649(2)	12.6890(8)	10.4517(8)
b [Å]	7.3913(2)	10.2007(6)	10.1014(7)
c [Å]	18.477(4)	13.6742(8)	13.7713(10)
α [°]	90.02(2)	90	90
β [°]	96.99(2)	107.014(1)	92.723(1)
γ [°]	115.68(3)	90	90
Volume [Å^3]	861.5(3)	1692.48(18)	1452.29(18)
Z	2	4	4
T [K]	293(2)	293(2)	293(2)
$\rho_{calcd.}$ (g cm^{-3})	2.055	1.643	1.823
μ [mm^{-1}]	2.860	1.487	1.727
θ range [°]	1.11–23.29	1.68–23.25	1.95–23.28
λ (Mo-K_α) [Å]	0.71073	0.71073	0.71073
R indexes [$I > 2\sigma(I)$][a]	$R_1 = 0.0492$, $wR_2 = 0.1294$	$R_1 = 0.0425$, $wR_2 = 0.1372$	$R_1 = 0.0271$, $wR_2 = 0.0709$
R (all data)[a]	$R_1 = 0.0674$, $wR_2 = 0.1521$	$R_1 = 0.0520$, $wR_2 = 0.1428$	$R_1 = 0.0332$, $wR_2 = 0.0740$

[a] $R_1 = \Sigma||F_o| - |F_c||/\Sigma|F_o|$; $wR_2 = \{\Sigma[w(F_o^2 - F_c^2)^2]/\Sigma[w(F_o^2)^2]\}^{1/2}$. $w = 1/[\sigma^2(F_o)^2 + (aP)^2 + bP]$, where $P = [\max.(F_o^2,0) + 2(F_c)^2]/3$ and $a = 0.0460$ and $b = 1.5472$ for **1**, $a = 0.0460$ and $b = 1.5472$ for **2**, and $a = 0.0460$ and $b = 1.5472$ for **3**.

determined by single-crystal X-ray diffraction. Thermogravimetric analysis (TGA) was carried out (Metler-Toledo) under oxygen (flow rate = 50 mL min^{-1}) in the temperature range 25–700 °C (heating rate = 5 °C min^{-1}). The studies showed similar results for the compounds, with one weight loss. The total observed weight losses of 73, 79, and 78.5% for **1**, **2**, and **3**, respectively, correspond well with the loss of the carboxylate and bonded water in **1** (calcd. 70%), carboxylate, lattice water, and 1,10-phenanthroline in **2** (calcd. 79.5%), and carboxylate and 1,10-phenanthroline in **3** (calcd. 80%). The final calcined product was found to be crystalline by powder XRD and corresponded to ZnO (JCPDS: 36-1451). IR spectroscopic studies were carried out in the mid-IR region on KBr pellets (Bruker IFS-66v). The spectra show characteristic sharp lines with almost similar bands. Minor variations between the bands were found between the compounds. **1:** $\tilde{\nu}$ = 3467 (m) (ν_{as}OH), 2889 (w) [ν_s(C–H)$_{aromatic}$], 1633 (m) [ν_s(C=O)], 1605 (w) (δ_sH$_2$O), 1575 (m) (C–C)$_{skeletal}$, 1362 (s) [δ_s(COO)], 1041 (s) [δ(C–N$_{skeletal}$)], 803 (s) [δ(CH$_{aromatic}$)$_{out\text{-}of\text{-}plane}$] cm^{-1}. **2:** $\tilde{\nu}$ = 3475 (m) (ν_{as}OH), 1645 (s) [ν_s(C=O)], 1605 (w) (δ_sH$_2$O), 1351 (s) [δ_s(COO)], 1294 (m) [δ(CH$_{aromatic}$)$_{in\text{-}of\text{-}plane}$], 1036 (s) [$\delta$(C–N$_{skeletal}$)], 848 (s) [$\delta$(CH$_{aromatic}$)$_{out\text{-}of\text{-}plane}$] cm^{-1}. **3:** $\tilde{\nu}$ = 2888 (w) [ν_s(C–H)$_{aromatic}$], 1567 (s) [ν_s(C=O)], 1552 (s) [(C–C)$_{skeletal}$], 1392 (s) [δ_s(COO)], 1299 (s) [δ(CH$_{aromatic}$)$_{in\text{-}of\text{-}plane}$], 1034 (w) [$\delta$(C–N$_{skeletal}$)], 910 (s) [$\delta$(CH$_{aromatic}$)$_{out\text{-}of\text{-}plane}$] cm^{-1}. A suitable single crystal of each compound was carefully selected under a polarizing microscope and glued to a thin glass fiber. Crystal structure determination by X-ray diffraction was performed with a Siemens Smart-CCD diffractometer equipped with a normal focus, 2.4 kW sealed-tube X-ray source (Mo-K_α radiation, λ = 0.71073 Å) operating at 40 kV and 40 mA. An empirical absorption correction was applied using the SADABS program.[37] The structure was solved and refined with the SHELXTL-PLUS suite of programs.[38] All the hydrogen atoms of the carboxylic acids and the bound water molecules were located in the difference Fourier maps. For the final refinement, the hydrogen atoms on the carboxylic acid were placed geometrically and held in the riding mode. Final refinement included atomic positions for all the atoms, anisotropic thermal parameters for all the non-hydrogen atoms, and isotropic thermal parameters for all the hydrogen atoms. Full-matrix least-squares refinement against $|F^2|$ was carried out with the SHELXTL-PLUS[38] suite of programs. Details of the structure solution and final refinement for all three compounds are given in Table 4. CCDC-258001 to -258003 (**1**–**3**) contain the supplementary crystallographic data for this paper. These data can be obtained free of charge from The Cambridge Crystallographic Data Centre via www.ccdc.cam.ac.uk/data_request/cif.

Supporting Information (see footnote on the first page of this article)**:** Experimental and simulated powder XRD patterns, IR and TGA curves.

Acknowledgments

S. N. thanks the Department of Science and Technology (DST), Government of India, for the award of a research grant, and P. M. thanks the Council of Scientific and Industrial Research (CSIR), Government of India, for the award of a research fellowship.

[1] C. N. R. Rao, S. Natarajan, R. Vaidhyanathan, *Angew. Chem.* **2004**, *116*, 1490–1521; *Angew. Chem. Int. Ed.* **2004**, *43*, 1466–1496.
[2] B. Chen, M. Eddaoudi, T. M. Reineke, J. W. Kampf, M. O'Keeffe, O. M. Yaghi, *J. Am. Chem. Soc.* **2000**, *122*, 11 559–11 560.
[3] K. Barthelet, J. Marrot, D. Riou, G. Ferey, *Angew. Chem. Int. Ed.* **2002**, *41*, 281–284.
[4] C. J. Kepert, T. J. Prior, M. J. Rosseinsky, *J. Am. Chem. Soc.* **2000**, *122*, 5158–5168.
[5] J. C. Dai, X. T. Wu, Z. Y. Fu, C. P. Cui, S. H. Hu, W. X. Du, L. M. Wu, H. H. Zhang, R. Q. Sun, *Inorg. Chem.* **2002**, *41*, 1391–1396.
[6] M. Edgar, R. Mitchell, A. M. Z. Slawin, P. Lightfoot, P. A. Wright, *Chem. Eur. J.* **2001**, *7*, 5168–5175.
[7] W. Chen, J. Y. Wang, C. Chen, Q. Yue, H. M. Yuan, J. S. Chen, S. N. Wang, *Inorg. Chem.* **2003**, *42*, 944–948.
[8] R. Murugavel, D. Krishnamurthy, M. Sathiyendiran, *J. Chem. Soc., Dalton Trans.* **2002**, 34–39.
[9] M. Sanselme, J. M. Greneche, M. R. Cavellec, G. Feréy, *Chem. Commun.* **2002**, 2172–2173.

 © 2005 Wiley-VCH Verlag GmbH & Co. KGaA, Weinheim

[10] R. Cao, Q. Shi, D. Sun, M. Hong, W. Bi, Y. Zhao, *Inorg. Chem.* **2002**, *41*, 6161–6168.
[11] W. Lin, O. R. Evans, R. G. Xiong, Z. Wang, *J. Am. Chem. Soc.* **1998**, *120*, 13 272–13 273.
[12] O. R. Evans, R. G. Xiong, Z. Wang, G. K. Wong, W. Lin, *Angew. Chem.* **1999**, *111*, 557–559; *Angew. Chem. Int. Ed.* **1999**, *38*, 536–538.
[13] W. Lin, L. Ma, O. R. Evans, *Chem. Commun.* **2000**, 2263–2264.
[14] P. Ayyappan, O. R. Evans, W. Lin, *Inorg. Chem.* **2001**, *40*, 4627–2632.
[15] L. Pan, X. Y. Huang, J. Li, Y. G. Wu, N. W. Zheng, *Angew. Chem.* **2000**, *112*, 537–540; *Angew. Chem. Int. Ed.* **2000**, *39*, 527–530.
[16] L. Pan, N. Ching, X. Y. Huang, J. Li, *Inorg. Chem.* **2001**, *40*, 1271–1283.
[17] L. Pan, N. Ching, X. Y. Huang, J. Li, *Chem. Eur. J.* **2001**, *7*, 4431–4437.
[18] A. Thirumurugan, S. Natarajan, *Dalton Trans.* **2004**, 2923–2928.
[19] A. Thirumurugan, S. Natarajan, *Solid State Sci.* **2004**, *6*, 599–604.
[20] J. Tao, J. X. Shi, M. L. Tong, X. X. Zhang, X. M. Chen, *Inorg. Chem.* **2001**, *40*, 6328–6330.
[21] Y. Hou, S. Wang, E. Shen, E. Wang, D. Xiao, Y. Li, L. Xu, C. Hu, *Inorg. Chim. Acta* **2004**, *357*, 3155–3161.
[22] Y. B. Chen, J. Zhang, J. K. Cheng, Y. Kang, Z. J. Li, Y. G. Yao, *Inorg. Chem. Commun.* **2004**, *7*, 1139–1141.
[23] G. P. Yong, Z. Y. Wang, Y. Cui, *Eur. J. Inorg. Chem*. **2004**, 4317–4323.
[24] J. F. Ma, J. Yang, S. L. Li, S. Y. Song, *Cryst. Growth Des.* **2005**, 5, 807–812.
[25] X. Shi, G. S. Zhu, Q. R. Fang, G. Wu, G. Tian, R. W. Wang, D. L. Zhang, M. Xue, S. L. Qiu, *Eur. J. Inorg. Chem.* **2004**, 185–191.
[26] J. C. Dai, X. T. Wu, Z. Y. Fu, S. M. Hu, W. X. Du, C. P. Cui, *Chem. Commun.* **2002**, 12–13.
[27] X. M. Quyang, D. J. Liu, T. Okamura, H. W. Bu, W. Y. Sun, W. X. Tang, N. Ueyama, *Dalton Trans.* **2003**, 1836–1845.
[28] X. Shi, G. Zhu, X. Wang, G. Li, Q. Gand, X. Zhao, G. Wu, G. Tian, M. Xue, R. Wang, S. Qiu, *Cryst. Growth Des.* **2004**, *5*, 341–346.
[29] L. Y. Zhang, G. F. Liu, S. L. Zheng, B. H. Ye, X. M. Zhang, X. M. Chen, *Eur. J. Inorg. Chem.* **2003**, 2965–2971 and references cited therein.
[30] X. M. Zhang, M. L Tong, M. L. Gong, X. M. Chen, *Eur. J. Inorg. Chem.* **2003**, 138–142.
[31] C. A. Hunter, J. K. M. Sanders, *J. Am. Chem. Soc.* **1990**, *112*, 5525–5534.
[32] C. A. Hunter, J. Singh, J. K. M. Sanders, *J. Mol. Biol.* **1991**, *218*, 837–846.
[33] M. J. Frisch, G. W. Trucks, H. B. Schlegel, G. E. Scuseria, M. A. Robb, J. R. Cheeseman, J. A. Montgomery, Jr., T. Vreven, K. N. Kudin, J. C. Burant, J. M. Millam, S. S. Iyengar, J. Tomasi, V. Barone, B. Mennucci, M. Cossi, G. Scalmani, N. Rega, G. A. Petersson, H. Nakatsuji, M. Hada, M. Ehara, K. Toyota, R. Fukuda, J. Hasegawa, M. Ishida, T. Nakajima, Y. Honda, O. Kitao, H. Nakai, M. Klene, X. Li, J. E. Knox, H. P. Hratchian, J. B. Cross, C. Adamo, J. Jaramillo, R. Gomperts, R. E. Stratmann, O. Yazyev, A. J. Austin, R. Cammi, C. Pomelli, J. W. Ochterski, P. Y. Ayala, K. Morokuma, G. A. Voth, P. Salvador, J. J. Dannenberg, V. G. Zakrzewski, S. Dapprich, A. D. Daniels, M. C. Strain, O. Farkas, D. K. Malick, A. D. Rabuck, K. Raghavachari, J. B. Foresman, J. V. Ortiz, Q. Cui, A. G. Baboul, S. Clifford, J. Cioslowski, B. B. Stefanov, G. Liu, A. Liashenko, P. Piskorz, I. Komaromi, R. L. Martin, D. J. Fox, T. Keith, M. A. Al-Laham, C. Y. Peng, A. Nanayakkara, M. Challacombe, P. M. W. Gill, B. Johnson, W. Chen, M. W. Wong, C. Gonzalez, J. A. Pople, *Gaussian 03*, Revision B.05, Gaussian, Inc., Pittsburgh, PA, USA, **2003**..
[34] M. J. S. Dewar, E. G. Zoebisch, E. F. Healy, J. J. P. Stewart, *J. Am. Chem. Soc.* **1985**, *107*, 3902–3909.
[35] A. Dutta, S. K. Pati, *J. Chem. Phys.* **2003**, *118*, 8420–8427.
[36] *Hydrogen Bonding: A Theoretical Perspective* (Ed.: S. Scheiner), Oxford University Press, **1997**.
[37] G. M. Sheldrick, *SADABS, Siemens Area Detector Absorption Correction Program*, University of Göttingen, Göttingen, Germany, **1994**.
[38] G. M. Sheldrick, *SHELXTL-PLUS, Program for Crystal Structure Solution and Refinement*, University of Göttingen, Göttingen, Germany, **1997**.

Received: November 8, 2004,

 © 2005 Wiley-VCH Verlag GmbH & Co. KGaA, Weinheim

Effects of Anthracene and Pyrene Units on the Interactions of Novel Polypyridylruthenium(II) Mixed-Ligand Complexes with DNA

Mariappan Mariappan*[a] and Bhaskar G. Maiya[a][†]

Keywords: DNA cleavage / Electrophoresis / Inhibitors / N ligands / Radicals / Ruthenium

2-(9-Anthryl)-1*H*-imidazo[4,5-*f*][1,10]phenanthroline (aip) and [2-(1-pyrenyl)-1*H*-imidazo[4,5-*f*][1,10]phenanthroline (pyip) and their complexes $[Ru(phen)_2(aip)]^{2+}$ (**1**) and $[Ru(phen)_2(pyip)]^{2+}$ (**2**) (phen = 1,10-phenanthroline) have been synthesized and characterized by elemental analysis, UV/Vis, IR and ^1H NMR spectroscopy, FAB-MS and cyclic voltammetry methods. Both **1** and **2** are redox-active and undergo oxidation at 1.43 and 1.47 V (vs. SCE), respectively. Both **1** and **2** show only the ^{3}MLCT emission typical of any polypyridylruthenium(II) complex. These new complexes are seen to be excellent binders of calf-thymus (CT) DNA, as revealed by the results of absorption, luminescence, viscometric titrations, and thermal denaturation studies. These results also indicate that while ruthenium-bound aip and pyip intercalate within the base pairs of the duplex, the phen moieties act only as spectator ligands in each case. Steady-state emission studies carried out in aqueous media with and without DNA reveal that $[Ru(phen)_2(pyip)]^{2+}$ is a better "molecular light switch" for DNA than $[Ru(phen)_2(aip)]^{2+}$. Under an identical set of experimental conditions of light and drug dose, the DNA photocleavage ability of $[Ru(phen)_2(pyip)]^{2+}$ is also higher than that of $[Ru(phen)_2(aip)]^{2+}$. "Inhibitor studies" suggest that the oxygen species are mainly responsible for the DNA photocleavage by these complexes.
(© Wiley-VCH Verlag GmbH & Co. KGaA, 69451 Weinheim, Germany, 2005)

Introduction

Considerable attention is being directed towards the design of DNA-binding and -photocleaving ruthenium(II) complexes in order to develop novel therapeutic agents, chemical probes for nucleic acids, and novel diagnostic agents targeted to double-helical DNA.[1–4] Presently, most attention has centered upon metal complexes that are capable of binding DNA by intercalation.[5–11] Due to their luminescent characteristics and strong DNA-binding affinity, the polypyridylruthenium(II) class of metallointercalators have received particular attention.[12–14] Barton and co-workers have shown that the strong binding of $[Ru(L)_2(dppz)]^{2+}$ complexes (L = 2,2′-bipyridine or 1,10-phenanthroline) to DNA gives rise to the "molecular light-switch effect", where the nearly undetectable emission from the triplet metal-to-ligand charge transfer (MLCT) excited state of $[Ru(L)_2(dppz)]^{2+}$ in water is strongly enhanced due to the intercalation of the planar dppz ligand between the base pairs of DNA.[10,15–17] One important characteristic of these ligands is that they all possess extended π-aromatic structures and are planar, which is crucial for the intercalation of the Ru^{II} complexes containing them. In our efforts to design metal complexes coordinated to ligands having planar, aromatic subunits, we have recently reported a series of complexes containing modified phen/dppz ligands (phen = 1,10-phenanthroline and dppz = dipyrido[3,2-*a*:2′,3′-*c*]-phenazine). These new ligands have been designed so that besides containing the expansively aromatic "dppz" type of structure, they are also endowed with other electroactive subunits that impart special properties for the complexes in the presence of DNA.[18–21]

Some of the complexes containing a non-planar ligand also exhibit interesting properties upon binding to DNA,[22,23] It is well known that the five-membered imidazole ring is a component of the purine bases in DNA. Ji and co-workers have reported a series of imidazole-modified phen/bpy ligands where the imidazole ring is out of the plane of the phen moiety, and also biphenyl derivatives of phen/dppz, all of which help to explain the effect of ligand planarity on the DNA binding strength of the complexes.[24–28] The ancillary ligands of polypyridylruthenium(II) complexes have also been shown to have a significant effect on the spectral properties and the DNA-binding behavior of the complexes.[29–31] All the above studies revealed that modification of the ligands would lead to subtle or substantial changes in the binding modes, location, and affinities, and provide the chance to explore various valuable conformation- or site-specific DNA probes and potential chemotherapeutical agents. Thus, we focused on the construction of novel polypyridyl ligands containing fluorophores such as pyrene and anthracene in their imidazole architecture. This paper deals with the synthesis, characteri-

[a] School of Chemistry, University of Hyderabad
Hyderabad 500 046, India
Fax: +91-40-2301-2460
E-mail: tmmari@yahoo.com
[†] Deceased.

 © 2005 Wiley-VCH Verlag GmbH & Co. KGaA, Weinheim **DOI: 10.1002/ejic.200400952**

zation, DNA binding, and photocleavage studies of the mixed-ligand Ru^{II} complexes $[Ru(phen)_2(aip)]^{2+}$ and $[Ru(phen)_2(pyip)]^{2+}$ containing ligands which have anthracene [viz. 2-(9-anthryl)-1*H*-imidazo[4,5-*f*][1,10]phenanthroline (aip)] or pyrene {viz. [2-(1-pyrenyl)-1*H*-imidazo[4,5-*f*][1,10]phenanthroline (pyip)} fluorophores in their architecture.

Results and Discussion

Synthesis and Characterization

The ligands aip and pyip were prepared by a method similar to that described by Steck and Day.[32] Condensation reactions of 1,10-phenanthroline-5,6-dione and 9-anthraldehyde or 1-pyrenecarboxaldehyde in the presence of ammonium acetate and glacial acetic acid produced aip and pyip, respectively. The corresponding ruthenium(II) complexes were synthesized by treating $[Ru(phen)_2Cl_2]\cdot 2H_2O$ with either aip or pyip (Figure 1). Each synthetic step involved here is straightforward and provides a good-to-moderate yield of the desired product in pure form. These products were characterized by elemental analysis, ^1H NMR, IR, luminescence, and UV/Vis spectroscopy, and MALDI-TOF mass spectrometry. The MALDI-TOF spectra show the base-peak at m/z = 396 for aip and at m/z = 420 for pyip. In the case of the corresponding mixed-ligand Ru^{II} complexes, peaks are seen at m/z = 1003 $[M - PF_6]^+$ and 858 $[M - 2\ PF_6]^+$ for $[Ru(phen)_2(aip)](PF_6)_2$ and similarly at m/z = 1026 $[M - PF_6]^+$ and 883 $[M - 2\ PF_6]^+$ for $[Ru(phen)_2(pyip)](PF_6)_2$, typical of PF_6 salts of polypyridylruthenium(II) complexes.[18–20,33]

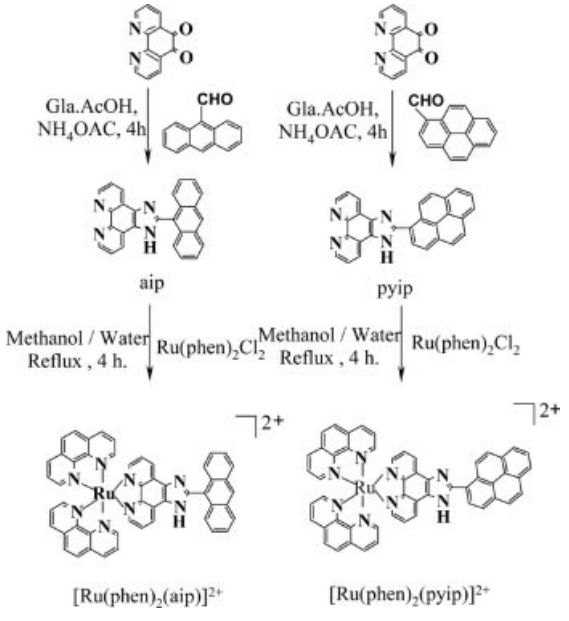

Figure 1. Scheme showing the synthesis of aip and pyip and their mixed-ligand ruthenium(II) complexes.

The ^1H NMR spectra of the two ligands (Figure 2) display a characteristic broad peak at δ = 14.20 (aip) and 13.73 ppm (pyip) for the N–H group of the imidazole ring.[27,28] In each of the two complexes, the signal of the proton on the nitrogen atom of the imidazole ring was not observed. Metal coordination causes electron deficiency in the ligand and, as a result, the imidazole proton becomes active and there is fast proton exchange between the two imidazole nitrogen atoms. Similar observations have been reported earlier.[27,28,34] In both complexes the signals of the *ortho*- and *para*-protons of the phenanthroline fragment of the ligands are shifted downfield and those of the *meta*-protons are shifted upfield compared to the free ligands. However, the proton signals of the anthracene and pyrene fragments of the ligands do not experience much shift compared to the free ligands. The other protons of both the complexes and the ligands give well-defined ^1H NMR spectra, which permit their unambiguous identification and assessment of purity.

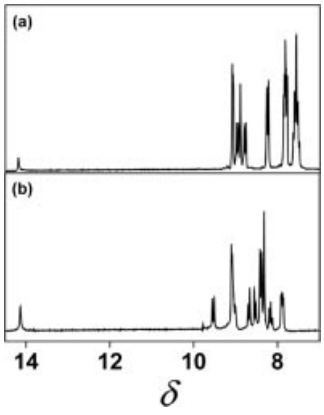

Figure 2. ^1H NMR spectra of (a) aip and (b) pyip in $CDCl_3$/CD_3OD and $[D_6]DMSO$.

The UV/Vis spectra of aip, pyip, and their ruthenium(II) complexes, along with the corresponding reference compounds synthesized during this study, are summarized in Table 1. The UV/Vis and luminescence spectra of both complexes are shown in Figure 3. As can be seen, the spectra of aip and pyip are characterized by low intensity but structured $\pi\rightarrow\pi^*$ transition absorption bands at 383 and 366 nm for aip and at 368 nm for pyip. These bands are ascribed to the anthracene and pyrene chromophores attached to the phenanthroline moiety.[35,36] The high-energy bands (aip: 251 nm; pyip: 234 and 280 nm) are attributed to the $\pi\rightarrow\pi^*$ transitions corresponding to the phenanthroline moiety of the ligands.

The low-energy bands at 452 (ε = 19675 $M^{-1}cm^{-1}$) and 457 nm (ε = 24066 $M^{-1}cm^{-1}$) are assigned as the MLCT $Ru(d\pi)\rightarrow aip/pyip(\pi^*)$ transitions for the complexes $[Ru(phen)_2(aip)]^{2+}$ and $[Ru(phen)_2(pyip)]^{2+}$, respectively, typical of any polypyridylruthenium(II) complex. The λ_{max} values of the MLCT transitions of these new complexes are bathochromically shifted in relation to the MLCT band of $[Ru(phen)_3]^{2+}$ (446 nm), with $[Ru(phen)_2(pyip)]^{2+}$ showing a higher red shift of 5 nm than $[Ru(phen)_2(aip)]^{2+}$ due to the extent of π delocalization of the chromophore. The bands centered at 254 and 264 nm are attributed to an in-

 © 2005 Wiley-VCH Verlag GmbH & Co. KGaA, Weinheim

Table 1. UV/Vis and emission spectroscopic data.[a]

Compound	Absorbance[b] λ_{max} [nm] (log ε) Ligand transitions	MLCT	Emission[c] λ_{max} [nm] (φ)
phen	226 (4.71), 264 (4.55)	–	–
phen-dione	232 (3.82), 260 (3.81), 304 (3.64)	–	–
9-anthraldehyde	261 (4.29), 371 (3.15), 399 (3.16)	–	–
1-pyrenecarboxaldehyde	233 (4.70), 287 (4.57), 362 (4.44), 372 (4.42), 394 (4.33)	–	–
aip	251(4.94), 366 (3.89), 383 (3.88)	–	447, 535 (0.81)
pyip	234 (4.71), 280 (4.52), 368 (4.44)	–	411, 443, 494 (0.63)
$[Ru(phen)_3](PF_6)_2$	223 (4.93), 263 (5.07), 422 (4.25)	446 (4.28)	596 (0.028)
$[Ru(phen)_2(aip)](PF_6)_2$	221 (4.96), 254 (5.22), 385 (4.30)	452 (4.29)	604 (0.005)
$[Ru(phen)_2(pyip)](PF_6)_2$	376 (4.64); 264 (5.08); 225 (5.00)	457 (4.38)	601 (0.0006)

[a] Spectra were recorded in CH_3CN. [b] Error limits: λ_{max}: ±1 nm; log ε: ±10%. [c] Error limits: λ_{em}: ±1 nm; φ: ±10%.

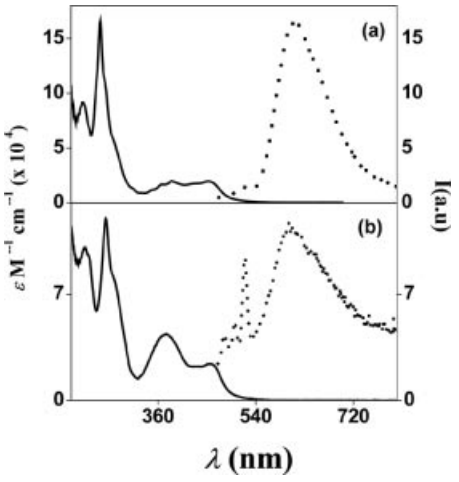

Figure 3. UV/Vis (– – –) and luminescence (·····) spectra of $[Ru(phen)_2(aip)]^{2+}$ (a) and $[Ru(phen)_2(pyip)]^{2+}$ (b) in CH_3CN.

traligand (IL) π→π* transition for $[Ru(phen)_2(aip)]^{2+}$ and $[Ru(phen)_2(pyip)]^{2+}$, respectively.

When aip is excited at 360 nm, the emission maximum appears at 535 nm (φ = 0.81 in CH_3CN). In the case of pyip (excited at 330 nm), the emission maximum appears at 494 nm (φ = 0.63 in CH_3CN). The steady-state and time-resolved absorption and fluorescence spectroscopic properties of aip, which is a bichromophoric molecule, reveal that a rapid and efficient intra-EET process dominates its excited-state relaxation dynamics in solution.[37] $[Ru(phen)_2(aip)]^{2+}$ and $[Ru(phen)_2(pyip)]^{2+}$ show an emission band centered at 604 and 601 nm with quantum yields of 0.005 and 0.0006, respectively in CH_3CN (λ_{exc} = 450 nm; see Figure 3). The origin of the spike at around 520 nm in the emission spectrum (Figure 3b) is due to Raman scattering. Since $[Ru(phen)_2(pyip)]^{2+}$ is weakly fluorescent and the gain of the instrument has to be increased to compensate for the low quantum yield (φ = 0.0006 in CH_3CN), the Raman scatter becomes visible. For highly fluorescent $[Ru(phen)_2(aip)]^{2+}$ (φ = 0. 005 in CH_3CN), the emission spectra overwhelms the Raman peak and thus it is not observed. The spectral shape and the λ_{em} values are quite similar to those of $[Ru(phen)_2(dppz)]^{2+}$, the ^{3}MLCT emission band maximum of which has been reported to be located at 618 nm.[17] The emission quantum yields of the complexes (Table 1) investigated here are lower than that of $[Ru(phen)_3]^{2+}$ (φ = 0.028 in CH_3CN)[38] and the order is $[Ru(phen)_3]^{2+}$ > $[Ru(phen)_2(aip)]^{2+}$ >> $[Ru(phen)_2(pyip)]^{2+}$.

Electrochemistry

During the cathodic scans in the cyclic voltammetric experiments, carried out in DMF containing 0.1 M TBAP, ligands aip and pyip show reversible (i_{pc}/i_{pa} = 0.9–1.0) and diffusion-controlled [$i_{pc}/v^{1/2}$ is constant in the scan-rate (v) range 50–500 mV s^{-1}] one-electron transfer (ΔE_P = 60–70 mV; ΔE_P = 65 ± 3 mV for the Fc^+/Fc couple)[39] responses at –1.48 and –1.46 V (vs. SCE), respectively. These potentials are close to those observed for the one-electron reductions of phen-dione (–1.47 V). The second reduction step appears as either quasi-reversible (i_{pc}/i_{pa} = 0.2–0.7 and ΔE_P = 90–200 mV at a scan rate over the range of 100–500 mV s^{-1}) or totally irreversible responses for aip and pyip at –1.61 and –1.64 V, respectively. The oxidation of pyip occurs at +1.42 V, whereas for aip it occurs at +1.38 V. The oxidation potential shifts more positively for pyip than for aip due to the greater π-delocalized nature of the pyrene moiety in the case of pyip when compared to anthracene in aip.

The cyclic and differential-pulse voltammograms of the two new complexes are compared with that of $[Ru(phen)_3]^{2+}$ in Figure 4. Each complex exhibits well-shaped oxidation and reduction waves in the sweep range from –2.0 to +1.6 V vs. SCE containing 0.1 M TBAP. The complex $[Ru(phen)_2(aip)]^{2+}$ exhibits a well-shaped reversible oxidation wave (+1.43 V) in acetonitrile and three reduction waves –1.29, –1.49, and –1.96 V in DMF. The first two reduction waves are reversible and the last one at –1.96 V is a poorly shaped quasi-reversible wave. For $[Ru(phen)_2(pyip)]^{2+}$, a reversible oxidation wave at +1.47 V in acetonitrile and two reversible reduction waves at –1.21 and –1.43 V in DMF are observed. The redox potential data for all the above compounds as measured by the cyclic and differential-pulse voltammetric method are summarized in Table 2.

 © 2005 Wiley-VCH Verlag GmbH & Co. KGaA, Weinheim

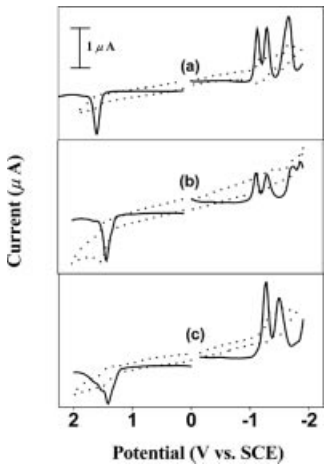

Figure 4. Cyclic (·····) and differential-pulse (−) voltammograms of (a) $[Ru(phen)_3]^{2+}$, (b) $[Ru(phen)_2(aip)]^{2+}$, and (c) $[Ru(phen)_2(pyip)]^{2+}$. CH_3CN and DMF containing 0.1 M TBAP were used as solvents for the anodic and cathodic runs, respectively. Scan rate: 100 mV s^{-1}.

Table 2. Redox potential data.[a]

Compound	Oxidation, $E_{1/2}$ (V vs. SCE)	Reduction, $E_{1/2}$ (V vs. SCE)
phen	–	–1.92[d]
phen-dione	–	–0.45, –1.08[c]
9-anthraldehyde	+1.67[b]	–1.12[d]
pyrene	+1.49[c]	–
1-pyrenecarboxaldehyde	+1.64[b]	–1.27[d]
aip	+1.38[b]	–1.48, –1.61[d]
pyip	+1.42[b]	–1.46, –1.64[d]
$[Ru(phen)_3](PF_6)_2$	+1.37[c]	–1.19, –1.34, –1.69[d]
$[Ru(phen)_2(dppz)](PF_6)_2$	+1.41[c]	–0.82, –1.25, –1.47[d]
$[Ru(phen)_2(aip)](PF_6)_2$	+1.43[c]	–1.29, –1.49, –1.96[d]
$[Ru(phen)_2(pyip)](PF_6)_2$	+1.47[c]	–1.21, –1.43[d]

[a] Obtained from the differential-pulse voltammetric measurements. Error limits: $E_{1/2}$: ±0.03 V. [b] CH_2Cl_2, 0.1 M TBAP. [c] CH_3CN, 0.1 M TBAP. [d] DMF, 0.1 M TBAP.

Oxidation of the complexes involves removal of an electron from the dπ orbital of Ru^{II}, while reduction involves transfer of an electron to the ligand-centered orbitals.[28] As expected, the oxidation potential of $[Ru(phen)_2(pyip)]^{2+}$ is 40 mV more positive than $[Ru(phen)_2(aip)]^{2+}$. The attachment of a pyrene ring (extended hydrophobicity/aromaticity) to the IP (imidazophenanthroline) moiety expands the π delocalization and thus decreases the σ-donor capacity of pyip, which leads to a decrease in the electron density on the Ru^{II} ion and, in turn, stabilizes the metal π (t_{2g}) orbital.[40] As a result, the oxidation potential shifts positively for $[Ru(phen)_2(pyip)]^{2+}$ when compared to $[Ru(phen)_2(aip)]^{2+}$. The first reduction in both the complexes is expected to be centered at aip/pyip because of the availability of the most stable LUMO.[41] The other reductions observed for both complexes are characteristic of the ancillary phen ligands.[42] Thus, in the case of $[Ru(phen)_2(aip)]^{2+}$, reductions at –1.29, –1.49, and –1.96 V are assigned to aip/$aip^{\cdot-}$, $phen_1/phen_1^{\cdot-}$, and $phen_2/phen_2^{\cdot-}$ couples, respectively. For $[Ru(phen)_2(pyip)]^{2+}$, the reductions at –1.21 and –1.43 V are assigned to pyip/$pyip^{\cdot-}$ and $phen_1/phen_1^{\cdot-}$ processes, respectively; the second reduction associated with $phen_2$ could not be observed.

DNA-Binding Experiments

Binding of the chloride salts of the two Ru^{II} complexes synthesized in this study with CT DNA were monitored by absorption, luminescence, thermal denaturation, and viscosity methods, and the results are summarized in this section, which also discusses aspects related to the ability of these complexes to act as "molecular light switches" for DNA.

Absorption Titration

Both $[Ru(phen)_2(aip)]^{2+}$ and $[Ru(phen)_2(pyip)]^{2+}$ were titrated with CT DNA. The change in the spectral profiles during titration is shown in Figure 5a and b. As the DNA concentration is increased, $[Ru(phen)_2(aip)]^{2+}$ and $[Ru(phen)_2(pyip)]^{2+}$ show hypochromicity (39% and 61%,) and isosbestic points (482 and 496 nm), along with bathochromic shifts of 6 and 9 nm, respectively. To compare quantitatively the affinity of the two complexes towards

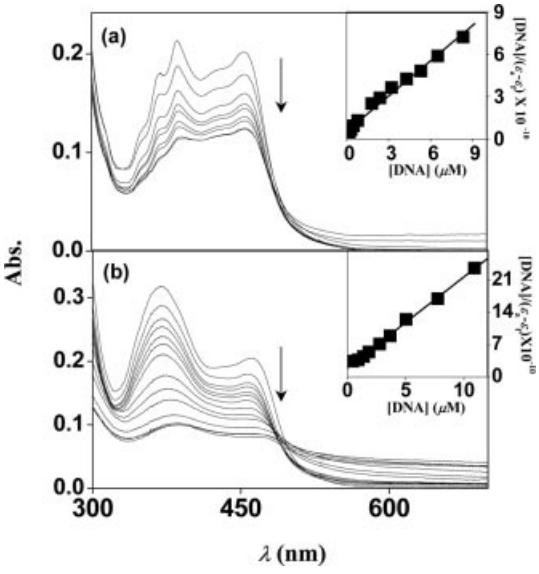

Figure 5. UV/Vis spectra of (a) $[Ru(phen)_2(aip)]^{2+}$ (5 μM) and (b) $[Ru(phen)_2(pyip)]^{2+}$ (5 μM) in the absence (top curve) and presence (subsequent curves) of increasing concentrations (0–100 μM) of CT DNA in buffer A. The inset graph shows a fit of the absorbance data used to obtain the binding constant.[56]

Table 3. Results of absorption titration and thermal melting experiments.[a]

Compound	K_b [M^{-1}]	T_m [°C] (σ_T)
DNA	–	61 (19)
$[Ru(phen)_3]^{2+}$	8.24×10^3	62 (21)
$[Ru(phen)_2(aip)]^{2+}$	1.01×10^6	64 (28)
$[Ru(phen)_2(pyip)]^{2+}$	1.57×10^6	65 (25)
$[Ru(phen)_2(dppz)]^{2+}$	$>10^7$	65 (26)

[a] Error limits: K_b: ±10%; T_m: ±1 °C; σ_T: ±1°.

 © 2005 Wiley-VCH Verlag GmbH & Co. KGaA, Weinheim

DNA, the intrinsic binding-constant values (K_b) were determined by monitoring the absorbance at the MLCT band position and were found to be as high as $1.01 \pm 0.1 \times 10^6$ and $1.57 \pm 0.8 \times 10^6$ M^{-1} for $[Ru(phen)_2(aip)]^{2+}$and $[Ru(phen)_2(pyip)]^{2+}$, respectively (Table 3). The extent of hypochromism commonly parallels the intercalative strength of the ligand and, moreover, a higher planar area, an extended π system, hydrophobicity, and aromaticity lead to deep penetration and hence more stacking within the base-pairs of DNA. Thus, the intercalative strength follows the order $[Ru(phen)_2(dppz)]^{2+} \approx [Ru(ip)_2(dppz)]^{2+} \geq [Ru(phen)_2(pyip)]^{2+} > [Ru(phen)_2(aip)]^{2+} > [Ru(phen)_3]^{2+}$ (ip = imidazo[4,5-*f*][1,10]phenanthroline).[29]

Luminescence Titration

The steady-state emission spectra of 7 μM solutions of $[Ru(phen)_2(aip)]^{2+}$ and $[Ru(phen)_2(pyip)]^{2+}$ in Tris buffer (5 mM Tris, 50 mM NaCl, pH = 7.1) show an increase in the emission intensity with successive addition of CT DNA. In the case of $[Ru(phen)_2(aip)]^{2+}$, the emission maximum at 604 nm due to the ^{3}MLCT [dπ(Ru)→π*(aip)][38] state increases initially at low [DNA nucleotide phosphate]/[Ru] ratio, but reaches a plateau, with an apparent enhancement factor of about 5, at a higher [DNA nucleotide phosphate]/[Ru] ratio of 27. The complex has an appreciable emission in the buffer in the absence of DNA and shows a marginal red-shift of 2 nm on addition of DNA (Figure 6a). The luminescence due to $[Ru(phen)_2(pyip)]^{2+}$ at 601 nm is assigned as a ^{3}MLCT [dπ(Ru)→π*(pyip)] state, and increases steadily with increasing addition of CT DNA, reaching a maximum (approx. 9 times) at a [DNA nucleotide phosphate]/[Ru] ratio of 43 (see Figure 6b). The complex has very weak emission in the aqueous medium in the absence of DNA, but on addition of increasing amounts of DNA the emission intensity increases with a bathochromic shift of about 4 nm. The emission enhancement of both complexes in the presence of DNA is much smaller than that observed for the dppz-based polypyridylruthenium(II) intercalators reported by Barton et al.[10,15,17] The shielding of the nitrogen atoms on the intercalating ligands, especially the imidazole nitrogen atoms, from protonation in the bulk solvent medium causes an emission enhancement, which has been extensively characterized and described as a "molecular light switch".[10,15,17] The mobility of these complexes is restricted at the binding site and so the vibrational modes of relaxation (collision and energy dissipation) decrease on intercalation.[28] The binding constants obtained are reasonably well in agreement with the values from the absorption titration experiment. The binding site sizes (n) for $[Ru(phen)_2(aip)]^{2+}$ and $Ru(phen)_2(pyip)]^{2+}$ are evaluated as 2 and 3.

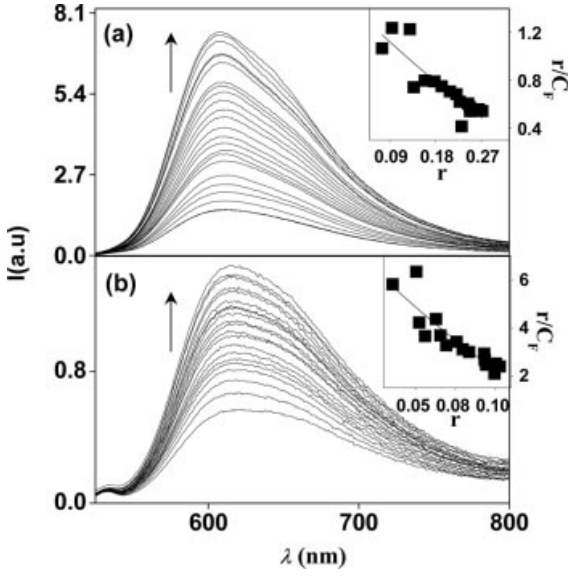

Figure 6. Luminescence spectra of (a) $[Ru(phen)_2(aip)]^{2+}$ (7 μM) and (b) $[Ru(phen)_2(pyip)]^{2+}$ (7 μM) in the absence (bottom curve) and presence (subsequent curves) of increasing concentrations (0–300 μM) of CT DNA in buffer A (λ_{exc} = 450 nm). The inset graph shows a fit of the emission data to Equation (4).

DNA Melting Experiments

Other strong evidence for the intercalation of both the complexes into the helix was obtained from the DNA melting studies. Intercalation of small molecules into the double helix is known to increase the helix melting temperature (T_m), the temperature at which the double helix denatures into single-stranded DNA.[43] The extinction coefficient of DNA bases at 260 nm in the double-helical form is much less than in the single-stranded form; hence, melting of the helix leads to an increase in the absorption[44] at this wavelength. CT DNA was seen to melt at 61 ± 1 °C (2 mM NaCl, 1 mM phosphate) in the absence of any added complex. The T_m of DNA is increased by 4 and 5 °C in the presence of $[Ru(phen)_2(aip)]^{2+}$ and $[Ru(phen)_2(pyip)]^{2+}$ (at [DNA nucleotide phosphate]/[complex] = 25), respectively. The DNA melting curves in the absence and in the presence of both complexes are presented in Figure 7 and the T_m and the σ_T values of CT DNA in the absence and presence of the

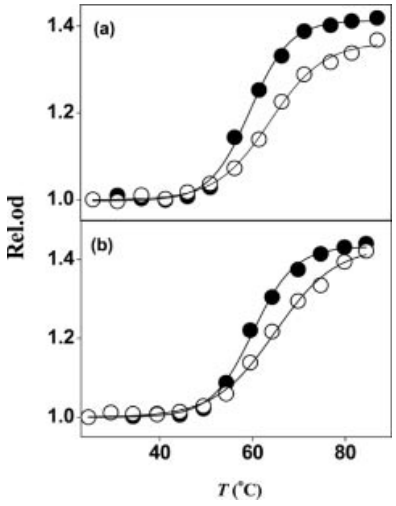

Figure 7. Melting curves for CT DNA in the absence (filled circles) and in the presence (open circles) of $[Ru(phen)_2(aip)]^{2+}$ (a) and $[Ru(phen)_2(pyip)]^{2+}$ (b) in buffer B.

 © 2005 Wiley-VCH Verlag GmbH & Co. KGaA, Weinheim

complexes are tabulated in Table 3. These establish the increased stability of the double helix when $[Ru(phen)_2(aip)]^{2+}$ and $[Ru(phen)_2(pyip)]^{2+}$ bind to DNA. The increases in the melting temperatures are comparable to the values observed with the classical intercalator ethidium and lend strong support for intercalation into the helix.[44,45]

Viscometric Titration

Intercalation of a ligand into DNA is known to cause a significant increase in the viscosity of a DNA solution due to an increase in the separation of the base pairs at the intercalation site and, hence, an increase in the overall DNA molecular length (contour length). In contrast, a ligand that binds in the DNA grooves causes a less-pronounced change (positive or negative) or no change in the viscosity of a DNA solution.[46] The effects of $[Ru(phen)_2(aip)]^{2+}$, $[Ru(phen)_2(pyip)]^{2+}$, ethidium bromide (EtBr), and $[Ru(phen)_3]^{2+}$ on the viscosity of CT DNA solution were studied in order to assess the binding mode of these complexes with DNA. Plots of $(\eta/\eta_o)^{1/3}$ vs. [Drug]/[DNA] are shown in Figure 8. The viscosity of DNA bound with $[Ru(phen)_2(aip)]^{2+}$, $[Ru(phen)_2(pyip)]^{2+}$, and EtBr increases dramatically, thus indicating that both complexes, as well as the classical intercalator EB, intercalate the base pairs of DNA and that $[Ru(phen)_2(pyip)]^{2+}$ has a slightly stronger binding affinity than $[Ru(phen)_2(aip)]^{2+}$**.** However, addition of $[Ru(phen)_3]^{2+}$ has no effect on the DNA viscosity, as reported previously.[46]

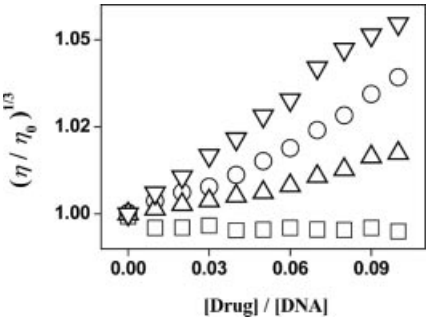

Figure 8. Results of viscometric titrations carried out for CT DNA (300 μM) in the presence of $[Ru(phen)_3]^{2+}$ (squares), $[Ru(phen)_2(aip)]^{2+}$ (triangles, tip up), $[Ru(phen)_2(pyip)]^{2+}$ (open circles) and EB (triangles, tip down) in buffer C.

DNA Photocleavage

When circular plasmid DNA is subjected to electrophoresis relatively fast migration is observed for the supercoiled form (form I), whereas if scission occurs on one strand (nicking), the supercoils will relax to generate a slower moving open circular form (form II). DNA photocleavage experiments were carried out with both the complexes and with $[Ru(phen)_3]^{2+}$ (for comparison). Figure 9 summarizes the results. Control runs in the agarose-gel electrophoresis experiments suggested that untreated pBR 322 DNA does not show any cleavage in the dark, and even upon irradiation with a 450 ± 5 nm light (compare lanes 1 and 2; Figure 9). Lower activity was observed for pBR 322 treated with $[Ru(phen)_2(aip)]^{2+}$, $[Ru(phen)_2(pyip)]^{2+}$, and $[Ru(phen)_3]^{2+}$ in the dark experiments (lanes 3, 5, and 7; Figure 9). After irradiation for 60 min (see lanes 4, 6, and 8; Figure 9) single-strand nicking is observed, and the percentage of conversion from form I to form II was calculated with Equation (5) (see Exp. Sect.). Based on the percentage conversion from form I to form II for these complexes, DNA-nicking efficiencies were seen to roughly follow the trend $[Ru(phen)_2(pyip)]Cl_2$ > $[Ru(phen)_2(aip)]Cl_2$ > $[Ru(phen)_3]Cl_2$. These can be explained on the basis of the binding nature of the intercalating ligands in the complexes due to the extended π-aromatic nature in the case of pyip when compared to aip. The photocleavage efficiencies of these complexes are similar to those of $[Ru(bpy)_2(ip)]^{2+}$ and $[Ru(bpy)_2(pip)]^{2+}$ (ip = imidazo[4,5-*f*][1,10]phenanthroline; pip = 2-phenylimidazo[4,5-*f*][1,10]phenanthroline) reported in the literature.[28]

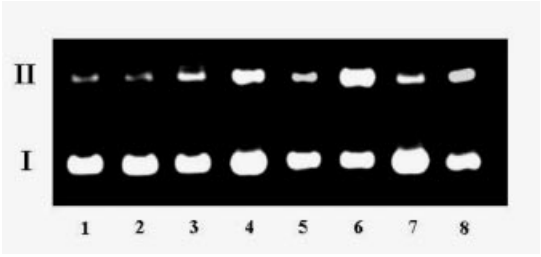

Figure 9. Light-induced nuclease activities of the investigated ruthenium(II) complexes. Dark and light experiments: lanes 1 and 2: untreated pBR 322 (100 μM) in the dark and upon irradiation. Lanes 3, 5, and 7: pBR 322 + $[Ru(phen)_2(aip)]^{2+}$, $[Ru(phen)_2(pyip)]^{2+}$, and $[Ru(phen)_3]^{2+}$ respectively (10 μM) in the dark. Lanes 4, 6, and 8: pBR 322 + $[Ru(phen)_2(aip)]^{2+}$, $[Ru(phen)_2(pyip)]^{2+}$, and $[Ru(phen)_3]^{2+}$, respectively, upon irradiation. λ_{irr} = 450 ± 5 nm (60 min) in each case.

In attempts to unravel the probable DNA photocleavage mechanism of these new complexes, a few control experiments were conducted in the presence of various "inhibitors". Photocleavage by $[Ru(phen)_3]Cl_2$ has been reported[47] to involve a $^1O_2$-based mechanism. In the case of $[Ru(phen)_2(aip)]^{2+}$ (see Figure 10), irradiation for 60 min in the presence of DABCO (lane 5; a $^1O_2$ "quencher") or Tiron (lane 7; a superoxide anion radical quencher) does not affect the photocleavage mechanism. Purging the reaction mixture with N_2 (lane 3) for 15 min to remove O_2 was also found not to inhibit the photocleavage mechanism. Inhibition was seen in the presence of DMSO (lane 4) and manni-

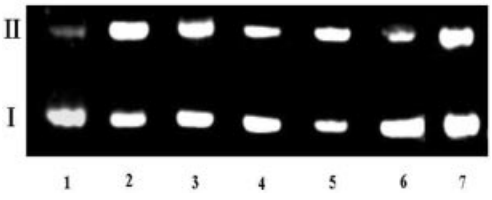

Figure 10. Effect of "inhibitors" on the light-induced nuclease activity of $[Ru(phen)_2(aip)]^{2+}$. Lanes 1 and 2: pBR 322 and $[Ru(phen)_2(aip)]^{2+}$. Lanes 3–7: pBR 322 + $[Ru(phen)_2(aip)]^{2+}$ in the presence of N_2, DMSO (200 mM), DABCO (10 mM), mannitol (100 mM), and Tiron (10 mM), respectively, upon irradiation for 60 min at 450 ± 5 nm in each case.

 © 2005 Wiley-VCH Verlag GmbH & Co. KGaA, Weinheim

tol (lane 6), and mannitol is a better inhibitor than DMSO. Both DMSO and mannitol are scavengers of hydroxyl radicals.

In the case of $[Ru(phen)_2(pyip)]^{2+}$ (Figure 11), moderate activity was still observed in the presence of DABCO (lane 5) and DMSO (lane 4), whereas no effect was observed with N_2 (lane 3) or Tiron (lane 7). However, the activity is inhibited very strongly in the presence of mannitol (lane 6). These results suggest that the reactive oxygen species ·OH and singlet oxygen (to a lesser extent) play a significant role in the cleavage mechanism for $[Ru(phen)_2(pyip)]Cl_2$, whereas for $[Ru(phen)_2(aip)]Cl_2$ only the hydroxyl radical plays a role in the photocleavage mechanism.[48]

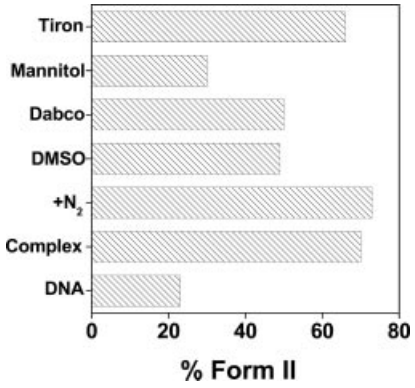

Figure 11. Bar diagram representation of the effect of "inhibitors" on the light-induced nuclease activity of $[Ru(phen)_2(pyip)]^{2+}$. Lanes 1 and 2: pBR 322 and $[Ru(phen)_2(pyip)]^{2+}$. Lanes 3–7: pBR 322 + $[Ru(phen)_2(pyip)]^{2+}$ in the presence of N_2, DMSO (200 mM), DABCO (10 mM), mannitol (100 mM), and Tiron (10 mM), respectively, upon irradiation for 60 min at 450 ± 5 nm in each case.

Conclusions

Two new anthracene/pyrene chromophore-appended polypyridyl ligands (aip and pyip), and their mixed-ligand ruthenium(II) complexes $[Ru(phen)_2(aip)]^{2+}$ and $[Ru(phen)_2(pyip)]^{2+}$, have been synthesized and fully characterized by spectroscopic and electrochemical methods. Studies with DNA have revealed that these complexes bind to DNA, mainly in an intercalative mode, with moderate strengths. The observation that $[Ru(phen)_2(pyip)]^{2+}$ binds DNA more strongly than $[Ru(phen)_2(aip)]^{2+}$ suggests that the increased surface area available for stacking by this complex within the duplex leads to a substantial increase in its intercalative binding affinity. In accordance with this interpretation, $[Ru(phen)_2(pyip)]^{2+}$ is found to be a better "molecular light switch" for DNA than $[Ru(phen)_2(aip)]^{2+}$. The photonuclease activity is also higher for $[Ru(phen)_2(pyip)]^{2+}$ than $[Ru(phen)_2(aip)]^{2+}$ and is comparable to that of $[Ru(bpy)_2(ip)]^{2+}$ and $[Ru(phen)_3]^{2+}$. Moreover, the reactive oxygen species ·OH plays a significant role in the cleavage mechanism of both $[Ru(phen)_2(pyip)]Cl_2$ and $[Ru(phen)_2(aip)]Cl_2$. Studies carried out so far have revealed that modification of phen, especially extension of the planarity of the ligand and attaching aromatic chromophores to it, will increase the strength of interaction of its complexes with DNA.

Experimental Section

Materials: All common chemicals and solvents utilized in this study were obtained in their highest available purity from B.D.H (Mumbai, India). Ruthenium trichloride hydrate, tetrabutylammonium perchlorate (TBAP), and tetrabutylammonium chloride (TBACl) were obtained from Aldrich Chemical Co. (USA). Pyrene, 1-pyrenecarboxaldehyde, 9-anthraldehyde, the deuterated solvents, and the calf-thymus DNA (CT DNA) were also purchased from Aldrich. Agarose (molecular biology grade) and ethidium bromide were purchased from Bio-Rad Laboratories Inc. (USA). Supercoiled pBR 322 DNA (CsCl purified) was obtained from Bangalore Genie (Bangalore, India) and was used as received. All the solvents utilized for spectroscopic and electrochemical work were rigorously purified before use according to standard procedures.[49] Deionized, triply distilled water was used for preparing various buffers. 1,10-phenanthroline-5,6-dione,[50] and $[Ru(phen)_2Cl_2]\cdot 2H_2O$,[51] were synthesized by applying the reported procedures.

2-(9-Anthryl)-1*H*-imidazo[4,5-*f*][1,10]phenanthroline (aip): A mixture of phen-dione (0.53 g, 2.50 mmol), 9-anthraldehyde (0.72 g, 3.50 mmol), ammonium acetate (3.88 g, 50.00 mmol), and glacial acetic acid (15 mL) was refluxed for 4 h and then cooled to room temperature. It was diluted with water and dropwise addition of concentrated aqueous ammonia gave a yellow precipitate, which was collected, washed with water, and dried. The crude product obtained was purified by recrystallization from $CHCl_3$/MeOH (4:1, v/v) and dried. Yield: 0.71 g (72%). $C_{27}H_{16}N_4$ (396.45): calcd. C 81.70, H 4.04, N 14.13; found C 81.63, H 4.11, N 14.19. MALDI-TOF: *m*/*z* = 396 $[M]^+$. IR (KBr): $\tilde{\nu}$ = 3441 (N–H), 1604 (C=N) cm^{-1}. ^1H NMR ([D$_6$]DMSO, 200 MHz, TMS): δ = 14.20 (s, 1 H), 9.09 (dd, J_1 = 2, J_2 = 3 Hz, 2 H), 8.94 (dd, J_1 = 2, J_2 = 6 Hz, 2 H), 8.80 (d, J = 7.8 Hz, 1 H), 8.26 (d, J = 7.8 Hz, 2 H), 7.84 (m, 4 H), 7.57 (m, 4 H) ppm.

2-(1-Pyrenyl)-1*H*-imidazo[4,5-*f*][1,10]phenanthroline (pyip): A mixture of phen-dione (0.53 g, 2.50 mmol), 1-pyrenecarboxaldehyde (0.81 g, 3.50 mmol), ammonium acetate (3.88 g, 50.00 mmol), and glacial acetic acid (15 mL) was refluxed for 4 h The above solution was cooled to room temperature and diluted with water. Dropwise addition of concentrated aqueous ammonia gave a yellow precipitate, which was collected, washed with water, and dried. The crude product thus obtained was purified by recrystallization from pyridine/water (9:1, v/v) and dried. Yield: 0.71 g (68%). $C_{29}H_{16}N_4$ (420.48): calcd. C 82.77, H 3.81, N 13.32; found C 82.81, H 3.74, N 13.39. MALDI-TOF: *m*/*z* = 420 $[M]^+$. IR (KBr): $\tilde{\nu}$ = 3426 (N–H), 1602 (C=N) cm^{-1}. ^1H NMR ($CDCl_3$/[D$_6$]DMSO, 200 MHz, TMS): δ = 13.73 (s, 1 H), 9.28 (d, J = 9.8 Hz, 1 H), 9.12 (dd, J_1 = 5, J_2 = 6 Hz, 2 H), 8.93 (d, J = 8 Hz, 1 H), 8.52 (d, J = 8.8 Hz, 1 H), 8.18 (m, 8 H), 7.66 (dd, J_1 = 3.4, J_2 = 3.4 Hz, 2 H) ppm.

{2-(9-Anthryl)-1*H*-imidazo[4,5-*f*][1,10]phenanthroline}bis(1,10-phenanthroline)ruthenium(II) Bis(hexafluorophosphate) Dihydrate $[Ru(phen)_2(aip)](PF_6)_2\cdot 2H_2O$: This complex was prepared by refluxing aip (0.30 g, 0.76 mmol) with $[Ru(phen)_2Cl_2]\cdot 2H_2O$ (0.43 g, 0.75 mmol) in CH_3OH/H_2O (1:1, v/v) for 4 h. The resulting solution was cooled to room temperature, then 15 mL of water was added and the mixture filtered. Addition of a saturated solution of NH_4PF_6 to the filtrate precipitated bright orange-red crude $[Ru(phen)_2(aip)](PF_6)_2$, which was purified by column chromatography [alumina and acetonitrile/toluene (3:2, v/v)] and further recrystallized from acetone/diethyl ether (1:5, v/v). Yield: 0.48 g (54%). $C_{51}H_{36}F_{12}N_8O_2P_2Ru$ (1183.9): calcd. C 51.71, H 3.04, N 9.46; found C 51.86, H 2.98, N 9.53. MALDI-TOF: *m*/*z* = 1003 $[M - PF_6]^+$, 858 $[M - 2\ PF_6]^+$. IR (KBr): $\tilde{\nu}$ = 3381 (N–H), 1601 (C=N), 837 (PF_6) cm^{-1}. ^1H NMR ([D$_6$]DMSO, 200 MHz, TMS):

 © 2005 Wiley-VCH Verlag GmbH & Co. KGaA, Weinheim

δ = 8.97 (d, J = 7.5 Hz, 1 H), 8.81 (m, 4 H), 8.42 (s, 4 H), 8.26 (m, 4 H), 8.09 (m, 5 H), 7.82 (m, 9 H), 7.61 (m, 4 H) ppm.

Bis(1,10-phenanthroline){2-(1-pyrenyl)-1*H*-imidazo[4,5-*f*][1,10]phenanthroline}ruthenium(II) Bis(hexafluorophosphate) Dihydrate [Ru(phen)$_2$(pyip)](PF$_6$)$_2$·2H$_2$O: This mixed-ligand Ru^{II} complex was prepared by refluxing pyip (0.34 g, 0.82 mmol) with [Ru(phen)$_2$Cl$_2$]·2H$_2$O (0.45 g, 0.80 mmol) in CH$_3$OH/H$_2$O (1:1, v/v) for 4 h. The crude bright orange-red [Ru(phen)$_2$(pyip)](PF$_6$)$_2$ was obtained upon adding a saturated solution of NH$_4$PF$_6$. It was purified by column chromatography [alumina, acetonitrile/toluene (3:2, v/v)] and further recrystallized from acetone/diethyl ether (1:5, v/v). Yield: 0.49 g (53%). C$_{53}$H$_{36}$F$_{12}$N$_8$O$_2$P$_2$Ru (1207.9): calcd. C 52.67, H 2.98, N 9.28; found C 52.78, H 3.06, N 9.19. MALDI-TOF: m/z = 1026 [M – PF$_6$]$^+$, 883 [M – 2 PF$_6$]$^+$. IR (KBr): $\tilde{\nu}$ = 3377 (N–H), 1599 (C=N), 837 (PF$_6$) cm^{-1}. ^{1}H NMR ([D$_6$]DMSO, 200 MHz, TMS): δ = 9.43 (d, J = 10 Hz, 1 H), 9.19 (d, J = 7.6 Hz, 2 H), 8.80 (m, 4 H), 8.69 (d, J = 7.8 Hz, 1 H), 8.58 (d, J = 8.8 Hz, 1 H), 8.43 (m, 8 H), 8.15 (m, 6 H), 7.82 (m, 6 H), 7.20 (m, 2 H) ppm.

The hexafluorophosphate salts of the complexes were converted into the water-soluble chloride salts by treating the former salt solutions with an excess of TBACl in acetone. The chloride salts, which are insoluble in acetone, instantaneously precipitated from the solution. They were filtered and vacuum-dried before use. The yield was about 90% of the theoretical value in each case.

Spectroscopy and Electrochemistry: Care was taken to avoid the entry of direct, ambient light into the samples in all the spectroscopic and electrochemical experiments described below. Unless otherwise specified, all the experiments were carried out at 293 ± 3 K. Elemental analyses were performed with a Flash EA 1112 series CHNS (Thermo Finnigan/Eager 300) analyzer. Acetanilide was used as the reference standard. Mass (MALDI-TOF) spectra were recorded with a Kompact MALDI 4 mass spectrometer (Kratos Analytical Ltd.). The instrument was operated in reflection time-of-flight mode with an accelerating potential of 20 kV and in the negative ion recording mode. The IR spectra were recorded with a Jasco Model 5300 FT-IR spectrophotometer. The spectra of the solid samples were recorded by dispersing the samples as KBr pellets. The ^{1}H NMR spectra were recorded with a Bruker NR-200 AF-FT NMR spectrometer, with CDCl$_3$ or [D$_6$]-DMSO as the solvent and tetramethylsilane (TMS) as the internal standard. The UV/Vis spectra were recorded with a Shimadzu model UV-3101 spectrophotometer. A matched pair of quartz cuvettes (path length 1 cm) was employed. Steady-state fluorescence spectra were recorded with a Spex Fluoromax-3 spectrophotometer using a 1-cm quartz cell. Detection of emission was done at right angles to the incident beam. The excitation and emission slit widths employed were, typically, 5 nm. While hexafluorophosphate salts of the complexes were employed for the luminescence measurements in nonaqueous solvents (rigorously dried CH$_2$Cl$_2$, THF, 1,4-dioxane, CH$_3$CN, and DMF), the corresponding chloride salts were used for measurements in aqueous and aqueous buffered solutions. The optical densities of the samples were adjusted to ≤0.2 at the excitation wavelength in each case. Emission quantum yields (φ) were estimated by integrating the area under the fluorescence curves and by using the formula given in Equation (1),[52] where A is the area under the emission spectral curve and OD is the optical density of the compound at the excitation wavelength. 1,6-Diphenyl-1,3,5-hexatriene (dpht, φ = 0.80 in cyclohexane)[53] was used as the standard for the calculation of the quantum yield values of the new ligands aip and pyip. The standard used for emission quantum yield measurements for the ruthenium(II) complexes was [Ru(phen)$_3$](PF$_6$)$_2$ (φ = 0.028 in CH$_3$CN).[38] Refractive index corrections were incorporated when reporting the emission data in various solvents.[54]

$$\phi_{sample} = \frac{OD_{standard} \times A_{sample}}{OD_{sample} \times A_{standard}} \times \phi_{standard} \quad (1)$$

Cyclic and differential-pulse voltammetric experiments (CH$_3$CN/DMF/CH$_2$Cl$_2$, 0.1 M TBAP) were performed with a CH Instruments model CHI 620A electrochemical analyzer (working and auxiliary electrodes: Pt; reference electrode: SCE). The Fc$^+$/Fc (Fc = ferrocene) couple was used to calibrate the redox potential values.

DNA-Binding and Photocleavage Studies: The concentration of CT DNA was calculated from its known extinction coefficient at 260 nm (6600 M^{-1} cm^{-1}).[55] Unless otherwise specified, the concentration of DNA is expressed in base pairs (BP) throughout this manuscript. Buffer A (5 mM Tris, 50 mM NaCl, pH = 7.1), buffer B (1 mM phosphate, 2 mM NaCl, pH = 7.0), and buffer C (1.5 mM Na$_2$HPO$_4$, 0.5 mM NaH$_2$PO$_4$, 0.25 mM Na$_2$EDTA, pH = 7.0) were used for absorption and luminescence titration, thermal denaturation, and viscometric experiments, respectively. TAE (tris-acetate ethylenediaminetetraacetate) 1X buffer was used for gel electrophoresis cleavage and inhibition experiments. Absorption titration experiments were performed by maintaining a constant metal complex concentration (5 μM) and varying the nucleic acid concentration (0–100 μM). After the addition of DNA to the metal complex, the resulting solution was allowed to equilibrate at 25 °C for 10 min, after which the absorption readings were noted. The data were then fit to Equation (2) to obtain the intrinsic binding constant K_b,[56] where ε_a, ε_f, and ε_b are the apparent, free, and bound metal complex extinction coefficients, respectively.

$$[DNA]/(\varepsilon_a - \varepsilon_f) = [DNA]/(\varepsilon_b - \varepsilon_f) + 1/K_b(\varepsilon_b - \varepsilon_f) \quad (2)$$

A plot of [DNA]/(ε_a – ε_f) vs. [DNA] gave a slope of 1/(ε_b – ε_f) and a Y intercept equal to 1/K_b(ε_b – ε_f); K_b is the ratio of the slope to the Y intercept. Luminescence titration experiments were performed at a fixed metal complex concentration (7 μM) to which increments of a stock DNA solution (0–300 μM) containing the same concentration of the metal complex were added. After the addition of DNA to the metal complex, the resulting solution was allowed to equilibrate at 25 °C in the dark for 10 min before being excited by 450 ± 5 nm light. The data obtained were fitted to Equation (3), where C_T is the concentration of the complex added, C_F is the concentration of the free complex, and I_o and I are the fluorescence intensities in the absence and in the presence of DNA, respectively; P is the ratio of the observed fluorescence quantum yield of the bound complex to the free complex.

$$C_F = C_T[(I/I_o) - P]/[1 - P] \quad (3)$$

The value of P was obtained from a plot of I/I_o vs. 1/[DNA] such that the limiting fluorescence yield is given by the Y intercept. The amount of bound complex (C_B) at any concentration is equal to $C_T - C_F$. A plot of r/C_F vs. r, where $r = C_B$/[DNA], was constructed according to the modified Scatchard equation given by McGhee and Von Hippel [Equation (4)],[57] where K_b is the intrinsic binding constant and n is the binding-site size in base pairs.

$$r/C_F = K_b(1 - nr)\{(1 - nr)/[1 - (n - 1)r]\}^{n-1} \quad (4)$$

DNA melting experiments were carried out by monitoring the absorption (260 nm) of CT DNA (160 μM, nucleotide pairs, NP) with a Shimadzu model UV-160A spectrophotometer coupled with a

 © 2005 Wiley-VCH Verlag GmbH & Co. KGaA, Weinheim

temperature controller model Julabo-F12, at various temperatures, in the absence and presence of the complex. The melting temperature (T_m) and the curve width σ_T (temperature range where 10–90% of the absorption increase occurred) were calculated as described previously.[47,58] Viscometric titrations were performed at 25 ± 1 °C with a Cannon-Ubblehode viscometer. Titrations were performed for $[Ru(phen)_3]^{2+}$, $[Ru(phen)_2(aip)]^{2+}$, $[Ru(phen)_2(pyip)]^{2+}$, and ethidium bromide (EtBr; 3–40 μM). Each compound was introduced into the degassed DNA solution (300 μM) present in the viscometer using a Hamilton syringe fitted with a glass extender. Bubbling with nitrogen produced mixing of the drug and DNA. Flow times were measured, with a digital stopwatch, at least three times and were accepted if they agreed within 0.1 s. Reduced specific viscosities were calculated according to Cohen and Eisenberg.[59] Plots of $(\eta/\eta_o)^{1/3}$ (η and η_o are the reduced specific viscosities of DNA in the presence and absence of the drug, respectively) vs. [drug]/[DNA] were constructed. Plots of $(\eta/\eta_o)^{1/3}$ vs. [EtBr]/[DNA] and $[Ru(phen)_3]^{2+}$]/[DNA] were found to be similar to those reported in the literature.[46] For the gel electrophoresis experiments, supercoiled pBR 322 DNA (100 μM in nucleotides) in Tris-HCl buffer (pH = 8.0) was treated with the metal complex (10 μM) and the mixture was incubated in the dark for 1 h. The samples were analyzed by 0.8% agarose gel electrophoresis (Tris-acetate/EDTA buffer, pH = 8.0), stained with EtBr (1 μg/mL, 0.5 h) and then the data were documented with a UVITEC Gel Documentation system. Irradiation experiments were carried out by keeping the pre-incubated (dark, 1 h) samples inside the sample chamber of a JASCO model FP-777 spectrofluorimeter for 60 min (λ_{ex} = 450 ± 5 nm; slit width = 5 nm). The percentage of cleavage (C) was calculated according to Equation (5).

$$C = \frac{[\text{Form II}] + 2[\text{Form III}]}{[\text{Form I}] + [\text{Form II}] + 2[\text{Form III}]} \quad (5)$$

In order to identify the actual reactive oxygen species responsible for DNA damage, a number of control experiments were carried out using various types of quenchers ("inhibitor studies"). Nitrogen gas was used to flush out dioxygen, DABCO (10 mM) was used as a $^1O_2$ quencher, and DMSO (200 mM) and mannitol (100 mM) were used as ·OH scavengers. Tiron (10 mM) was used as a superoxide anion radical quencher.

Acknowledgments

Financial support received for this work from DST New Delhi is gratefully acknowledged. M. M. thanks CSIR for a research fellowship. The authors are thankful to the University Grant Commission, New Delhi, for the facilities provided under the Universities with Potential for Excellence (UPE) programme. We thank Prof. Samudranil Pal for his valuable suggestions.

[1] F. Scandola, C. Chiorboli, M. T. Indelli, M. A. Rampi, *Covalently Linked Systems Containing Metal Complexes*, in *Electron Transfer in Chemistry* (Ed.: V. Balzani), Wiley-VCH, Weinheim, **2001**.
[2] S. O. Kelly, J. K. Barton, in *Metal ions in Biological Systems* (Eds.: A. Sigel, H. Sigel), Marcel Dekker, New York, **1999**, vol. 39, p. 211.
[3] K. E. Erkkila, D. T. Odom, J. K. Barton, *Chem. Rev.* **1999**, *99*, 2777–2795.
[4] A. Kirsch de Mesmaeker, J.-P. Lecomte, J.-M. Kelly, *Top. Curr. Chem.* **1996**, *177*, 25.
[5] A. M. Pyle, J. K. Barton, in *Progress in Inorganic Chemistry* (Ed.: S. J. Lippard), Wiley-Interscience, New York, **1990**, vol. 38, pp. 413–474.
[6] D. S. Sigman, A. Mazumder, D. M. Perrin, *Chem. Rev.* **1993**, *93*, 2295–2316.
[7] S. Satyanarayana, J. C. Dabrowiak, J. B. Chaires, *Biochemistry* **1993**, *32*, 2573–2584.
[8] B. P. Hudson, C. M. Dupureur, J. K. Barton, *J. Am. Chem. Soc.* **1995**, *117*, 9379–9380.
[9] a) P. Lincoln, A. Broo, B. Norden, *J. Am. Chem. Soc.* **1996**, *118*, 2644–2653; b) E. Tuite, P. Lincoln, B. Norden, *J. Am. Chem. Soc.* **1997**, *119*, 239–240.
[10] C. M. Dupureur, J. K. Barton, *J. Am. Chem. Soc.* **1994**, *116*, 10 286–10 287.
[11] C. M. Dupureur, J. K. Barton, *Inorg. Chem.* **1997**, *36*, 33–43.
[12] N. A. P. Kane-Maguire, J. F. Wheeler, *Coord. Chem. Rev.* **2001**, *211*, 145–162.
[13] B. Norden, P. Lincoln, B. Akerman, E. Tuite, in *Metal Ions in Biological Systems* (Eds.: A. Sigel, H. Sigel), Marcel Dekker, New York, **1996**, vol. 33, pp. 177–252.
[14] C. Kaes, A. Katz, M. W. Hosseini, *Chem. Rev.* **2000**, *100*, 3553–3590.
[15] A. E. Friedman, J.-C. Chambron, J.-P. Sauvage, N. J. Turro, J. K. Barton, *J. Am. Chem. Soc.* **1990**, *112*, 4960–4962.
[16] Y. Jenkins, A. E. Friedman, N. J. Turro, J. K. Barton, *Biochemistry* **1992**, *31*, 10 809–10 816.
[17] R. M. Hartshorn, J. K. Barton, *J. Am. Chem. Soc.* **1992**, *114*, 5919–5925.
[18] S. Arounaguiri, B. G. Maiya, *Inorg. Chem.* **1999**, *38*, 842–843.
[19] A. Ambroise, B. G. Maiya, *Inorg. Chem.* **2000**, *39*, 4256–4263.
[20] A. Ambroise, B. G. Maiya, *Inorg. Chem.* **2000**, *39*, 4264–4272.
[21] C. V. Sastri, D. Eswaramoorthy, L. Giribabu, B. G. Maiya, *J. Inorg. Biochem.* **2003**, *94*, 138–145.
[22] B. M. Goldstein, J. K. Barton, H. M. Berman, *Inorg. Chem.* **1986**, *25*, 842–847.
[23] A. M. Pyle, J. P. Rehmann, R. Meshoyrer, C. V. Kumar, N. J. Turro, J. K. Barton, *J. Am. Chem. Soc.* **1989**, *111*, 3051–3058.
[24] Y. Xiong, L.-N. Ji, *Coord. Chem. Rev.* **1999**, *185–186*, 711–733.
[25] L.-N. Ji, X.-H. Zou, J.-G. Liu, *Coord. Chem. Rev.* **2001**, *216–217*, 513–536.
[26] Q.-Z. Zhen, B.-H. Ye, Q.-L. Zhang, J.-G. Liu, H. Li, L.-N. Ji, L. Wang, *J. Inorg. Biochem.* **1999**, *76*, 47–53.
[27] J.-Z. Wu, L. Li, T.-X. Zeng, L.-N. Ji, J.-Y. Zhou, T. Luo, R.-H. Li, *Polyhedron* **1997**, *16*, 103–107.
[28] J.-Z. Wu, B.-H. Ye, L. Wang, L.-N. Ji, J.-Y. Zhou, R.-H. Li, Z.-Y. Zhou, *J. Chem. Soc., Dalton Trans.* **1997**, 1395–1401.
[29] J.-G. Liu, Q.-L. Zhang, X.-F. Shi, L.-N. Ji, *Inorg. Chem.* **2001**, *40*, 5045–5050.
[30] H. Xu, K.-C. Zheng, Y. Chen, Y.-Z. Li, L.-J. Lin, H. Li, P.-X. Zhang, L.-N. Ji, *Dalton Trans.* **2003**, 2260–2268.
[31] V. Xu, K.-C. Zheng, H. Deng, L.-J. Lin, Q.-L. Zhang, L.-N. Ji, *New J. Chem.* **2003**, *27*, 1255–1263.
[32] E. A. Steck, A. R Day, *J. Am. Chem. Soc.* **1943**, *65*, 452–456.
[33] P. Didier, L. Jacquet, A. Kirsch de Mesmaeker, R. Hueber, A. V. Dorsselaer, *Inorg. Chem.* **1992**, *31*, 4803–4809.
[34] a) R. Wang, J. G. Vos, R. H. Schmehl, R. Hage, *J. Am. Chem. Soc.* **1992**, *114*, 1964–1970; b) L.-F. Tan, H. Chao, H. Li, Y.-J. Liu, B. Sun, W. Wei, L.-N. Ji, *J. Inorg. Biochem.* **2005**, *99*, 513–520.
[35] C. V. Kumar, E. H. A. Punzalan, W. B. Tan, *Tetrahedron* **2000**, *56*, 7027–7040.
[36] D. S. Tyson, J. Bialecki, F. N. Castellano, *Chem. Commun.* **2000**, 2355–2356.
[37] J. A. Mondal, G. Ramakrishna, A. K. Singh, H. N. Ghosh, M. Mariappan, B. G. Maiya, T. Mukherjee, D. K. Palit, *J. Phys. Chem. A* **2004**, *108*, 7843–7852.
[38] A. Juris, V. Balzani, F. Barigelletti, S. Campagna, P. Belser, A. V. Zelewsky, *Coord. Chem. Rev.* **1988**, *84*, 85–277.
[39] R. S. Nicholson, I. Shain, *Anal. Chem.* **1964**, *36*, 706–723.

 © 2005 Wiley-VCH Verlag GmbH & Co. KGaA, Weinheim

[40] D. P. Rillema, G. Allen, T. J. Meyer, D. C. Conrad, *Inorg. Chem.* **1983**, *22*, 1617–1622.
[41] B. K. Ghosh, A. Chakra-Vorty, *Coord. Chem. Rev.* **1989**, *95*, 239–294.
[42] S. Delaney, M. Pascaly, P. K. Bhattacharya, K. Han, J. K. Barton, *Inorg. Chem.* **2002**, *41*, 1966–1974.
[43] D. J. Patel, *Acc. Chem. Res.* **1979**, *12*, 118–125.
[44] A. L. Lehninger, *Biochemistry*, 2nd ed., Worth Publishers, New York, **1975**, pp. 873–875.
[45] C. V. Kumar, E. H. Asuncion, *J. Am. Chem. Soc.* **1993**, *115*, 8547–8553.
[46] S. Satyanarayana, J. C. Dabrowiak, J. B. Chaires, *Biochemistry* **1992**, *31*, 9319–9324.
[47] J. M. Kelly, A. B. Tossi, D. J. McConnell, C. OhUigin, *Nucl. Acid. Res.* **1985**, *13*, 6017–6034.
[48] B. Armitage, *Chem. Rev.* **1998**, *98*, 1171–1200.
[49] D. D. Perrin, W. L. F. Armarego, D. R. Perrin, *Purification of Laboratory Chemicals*, Pergamon, Oxford, **1986**.
[50] M. Yamada, Y. Tanaka, Y. Yoshimoo, S. Kuroda, I. Shimao, *Bull. Chem. Soc. Jpn.* **1992**, *65*, 1006–1011.
[51] B. P. Sullivan, D. J. Salmon, T. J. Meyer, *Inorg. Chem.* **1978**, *17*, 3334–3341.
[52] E. Austin, M. Gouterman, *Bioinorg. Chem.* **1978**, *9*, 281–298.
[53] I. B. Berlman, in *Handbook of Fluorescence Spectra of Aromatic Molecules*, Academic Press, New York, **1971**.
[54] J. R. Lackowicz, *Principles of Fluorescence Spectroscopy*, Plenum, New York, **1983**.
[55] M. E. Reichmann, S. A. Rice, C. A. Thomas, P. Doty, *J. Am. Chem. Soc.* **1954**, *76*, 3047–3053.
[56] A. Wolfe, G. H. Shimer, T. Meehan, *Biochemistry* **1987**, *26*, 6392–6396.
[57] J. D. McGhee, P. H. Von Hippel, *J. Mol. Biol.* **1974**, *86*, 469–489.
[58] J. Marmur, P. Doty, *J. Mol. Biol.* **1962**, *5*, 109–118.
[59] G. Cohen, H. Eisenberg, *Biopolymers* **1969**, *8*, 45–55.

Received: November 13, 2004

 © 2005 Wiley-VCH Verlag GmbH & Co. KGaA, Weinheim

Four Novel 3D Copper(II) Coordination Polymers with Different Topologies

Jin Yang,[a] Jian-Fang Ma,*[a] Ying-Ying Liu,[a] Shun-Li Li,[a] and Guo-Li Zheng[a]

Keywords: Coordination polymers / Copper / Self-assembly / Supramolecular chemistry / Topology

A series of Cu^{II} coordination polymers with different topologies, namely $[CuL(L^1)]\cdot 2H_2O$ (**1**), $[CuL_{1.5}(L^2)]\cdot 3H_2O$ (**2**), $[CuL(L^3)]\cdot 3H_2O$ (**3**) and $[Cu_2L_{2.5}(L^4)(H_2O)]\cdot 10H_2O$ (**4**) [L = 1,1′-(1,4-butanediyl)bis(imidazole), H_2L^1 = fumaric acid, H_2L^2 = 1,1′-ferrocenedicarboxylic acid, H_2L^3 = succinic acid, and H_4L^4 = pyromellitic acid], are presented. Different polymeric frameworks are obtained by varying the polycarboxylate anions. These include the threefold interpenetrated diamond structure of **1**, the rare twofold interpenetrated 4^66^4 network of **2**, and two planar four-connected networks of **3** and **4**, which display an unusual Archimedean-type $(6^58)(6^48^2)$ net containing two different types of nodes and a $(56^48)(5^26^28^2)_2(68^410)(5^46^2)$ net containing four different types of nodes, respectively. Thermogravimetric analysis (TGA) curves of **1**, **2**, **3**, and **4** exhibit three similar weight-loss stages.
(© Wiley-VCH Verlag GmbH & Co. KGaA, 69451 Weinheim, Germany, 2005)

Introduction

The construction of coordination networks with novel topologies is of particular current interest due to their intriguing structural diversity.[1] The analysis of network topology acts as an important role in the discussion and design of crystal structures. Wells has listed a large number of topologies in his classic monographs on networks.[2] Numerous reported fascinating archetypal structures, including diamond (6^6),[3] $SrSi_2$ (10^3-a),[4] α-$ThSi_2$ (10^3-b),[5] SiO_2 (6^48^2-b),[6] and PtS (4^28^4),[7] have provided experimental examples of these theoretical topologies. All of these extraordinary structures are of fundamental importance in structural design and in the understanding of structure–property correlations.

In recent years many rational synthetic strategies have been proposed for the design of metal-based coordination supramolecular structures. Application of these strategies allows the assembly of a target compound with novel topology.[8] However, general and precise principles for controlling the structures of the target products still need to be further classified and improved. An understanding of the factors that govern the assembly process is therefore necessary for the development of the synthetic strategies. In molecular self-assembly processes many factors influence the formation of the final architectures, such as the solvent system, template, central metal, and anion. We are particularly interested in the effects of anions on the architectures of the final complexes.[9] In an attempt to investigate the design and control of the preparation of coordination compounds, the first square-planar four-connected (8^6) or (8,4) nets have been rationally synthesized by Tong et al. and us.[10] As a continuation of our work, we present here four novel coordination polymers with different organic anions, namely $[CuL(L^1)]\cdot 2H_2O$ (**1**), $[CuL_{1.5}(L^2)]\cdot 3H_2O$ (**2**), $[CuL(L^3)]\cdot 3H_2O$ (**3**), and $[Cu_2L_{2.5}(L^4)(H_2O)]\cdot 10H_2O$ (**4**) [L = 1,1′-(1,4-butanediyl)bis(imidazole), H_2L^1 = fumaric acid, H_2L^2 = 1,1′-ferrocenedicarboxylic acid,[11] H_2L^3 = succinic acid, and H_4L^4 = pyromellitic acid; see Scheme 1]. Single-crystal X-ray analyses show that the organic anions play an important role in directing the final structural motifs of the polymers.

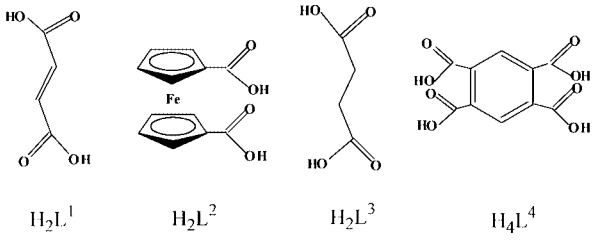

Scheme 1.

Results and Discussion

Syntheses and Characterization

Complexes **1**–**4** are insoluble in water and common organic solvents, and crystals suitable for X-ray diffraction analysis cannot be obtained by evaporating an appropriate solution of **1**–**4**. We found that they can be dissolved in a concentrated solution of ammonia by segregating the ligands from Cu^{II} cations owing to the coordinating role of ammonia toward the Cu^{II} cation. Their crystals were there-

[a] Department of Chemistry, Northeast Normal University, Changchun 130024, People's Republic of China
E-mail: jianfangma@yahoo.com.cn
Supporting information for this article is available on the WWW under http://www.eurjic.org or from the author.

 © 2005 Wiley-VCH Verlag GmbH & Co. KGaA, Weinheim **DOI: 10.1002/ejic.200400960**

fore obtained by an unusual crystallization process by evaporating an ammoniacal solution of **1**–**4**.

The elemental analysis data for the four compounds are in good agreement with the formulae $[CuL(L^1)]\cdot 2H_2O$ (**1**), $[CuL_{1.5}(L^2)]\cdot 3H_2O$ (**2**), $[CuL(L^3)]\cdot 3H_2O$ (**3**), and $[Cu_2L_{2.5}(L^4)(H_2O)]\cdot 10H_2O$ (**4**). In order to characterize the compounds **1**–**4** more fully in terms of thermal stability, we studied them by TGA. Compounds **1**–**4** were heated from 35 to 750 °C under N_2. When crystals of **1**–**4** were removed from the mother liquor, they lost some of their water molecules. TGA was performed with these partially dehydrated samples. As expected, the TGA curves of compounds **1**–**4** exhibit three similar weight-loss stages. The first weight loss, corresponding to the remaining water molecules, is observed over the wide temperature ranges 35–96 °C, 35–90 °C, 35–92 °C, and 35–89 °C for **1**–**4**, respectively. The second weight loss is 46.2% (calculated 43.6%) for **1** in the range 237–477 °C, 43.4% (calculated 42.2%) for **2** in the range 232–340 °C, 45.9% (calculated 44.8%) for **3** in the range 233–468 °C, and 47.3% (calculated 45.2%) for **4** in the range 227–330 °C, assigned to the release of L molecules. Drastic weight losses corresponding to the removal of L^1, L^2, L^3, and L^4 were observed from 477 to 530 °C for **1**, from 340 to 528 °C for **2**, from 468 to 530 °C for **3**, and from 400 to 505 °C for **4**, respectively.

Crystal Structures

Selected bond lengths and angles for complexes **1**–**4** are listed in Table 1. In the crystal structure of **1** there is one unique four-coordinate Cu^{II} atom. Each Cu^{II} center has a square-planar coordination sphere, with two nitrogen atoms from two L and two oxygen atoms from two L^1 ligands (see a in Figure 1), which provide the four-connected nodes resulting in an unsymmetrical adamantane-type 6^6 net (see b in Figure 1). Water molecules are found in the cage of the adamantane unit and distortions of the unit can arise from the application of different ligands (L and L^1).[12] The distance between the Cu^{II} centers is determined by the length of L (11.784 Å) or L^1 (9.714 Å). Three-fold interpenetration occurs for the 6^6 nets of **1** to diminish the void volume of the structure. Figure 1 (see c) shows that three independent equivalent networks are interpenetrated within the structure of **1**. Each pair of nets (I and II, II and III) display a normal mode of interpenetration.[13] For example, four rods from the node of net II inside the cavity of one adamantane unit of net I penetrate one six-membered window of the adamantane unit of net I.

The coordination environment of the Cu^{II} atom in **2** is shown in Figure 2 (see a). The copper(II) center adopts a distorted square pyramidal geometry by coordinating to three nitrogen atoms (N1, N3, and N5) from three L ligands and two oxygen atoms (O1 and O3A) from two L^2 ligands. The N1, N3, N5, and O1 atoms constitute the base of the pyramid, whereas O3A occupies the apical position at a Cu–O3A distance of 2.268(3) Å.

The Cu^{II} cations in **2** are bridged by L to form 2D (6,3) networks (see b in Figure 2). These 2D (6,3) networks are further connected by bridging L^2 ligands to give rise to a 3D network which can be classified as a 4^66^4 topological type based on pure five-connected nodes (see c in Figure 2). It is noteworthy that this 4^66^4 net is topologically analogous to the inorganic network B_2 in AlB_2.[13] Interestingly, as shown in Figure 2 (see d), the identical 4^66^4 networks are twofold interpenetrated to form an interlocked 3D structure. To the best of our knowledge, this structural topology is very rare in coordination polymer chemistry.[14]

The structure of **3** contains two crystallographically unique Cu^{II} cations, two unique L ligands, and one unique L^3 ligand. As shown in part a of Figure 3, each Cu^{II} cation is four-coordinate in a square-planar four-connected geometry with two nitrogen atoms from two L molecules and two oxygen atoms from two L^3 ligands. There exist some unique shortest six- and eight-membered circuits through Cu^{II} cations in **3** (see Figures S1–S4 in the Supporting Information). Figure 3 (see b) shows the unusual network displayed by the structure of **3**. This net contains two types of nodes (Cu1 and Cu2). For Cu1, each of four sets of *cis* links is contained in a six-membered ring (circuit II), and each of two sets of *trans* links is contained in an eight-membered

Table 1. Selected bond lengths [Å] and angles [°] for **1**–**4**.[a]

$[CuL(L^1)]\cdot 2H_2O$ (**1**)			
N(1)-Cu(1)	2.016(2)	O(1)-Cu(1)	1.996(2)
O(1)–Cu(1)–O(1)^{i}	93.0(1)	O(1)–Cu(1)–N(1)	174.61(7)
O(1)^{i}–Cu(1)–N(1)	91.02(8)	N(1)–Cu(1)–N(1)^{i}	85.2(1)
$[CuL_{1.5}(L^2)]\cdot 3H_2O$ (**2**)			
Cu(1)–N(1)	1.990(4)	Cu(1)–N(3)	2.087(4)
Cu(1)–N(5)	1.966(4)	Cu(1)–O(1)	2.016(3)
Cu(1)–O(3)^{i}	2.268(3)		
N(5)–Cu(1)–N(1)	176.1(2)	N(5)–Cu(1)–O(1)	89.5(1)
N(1)–Cu(1)–O(1)	88.0(1)	N(5)–Cu(1)–N(3)	94.0(2)
N(1)–Cu(1)–N(3)	89.8(2)	O(1)–Cu(1)–N(3)	144.6(2)
N(5)–Cu(1)–O(3)^{i}	90.0(1)	N(1)–Cu(1)–O(3)^{i}	89.0(2)
O(1)–Cu(1)–O(3)^{i}	123.8(1)	N(3)–Cu(1)–O(3)^{i}	91.5(1)
$[CuL(L^3)]\cdot 3H_2O$ (**3**)			
Cu(2)–N(1)	1.970(4)	Cu(1)–N(3)	1.970(3)
Cu(1)–O(2)	1.956(2)	Cu(2)–O(3)	2.000(3)
O(2)–Cu(1)–N(3)	91.2(1)	O(2)^{i}–Cu(1)–N(3)	90.5(1)
N(1)^{ii}–Cu(2)–O(3)	90.2(1)	N(1)–Cu(2)–O(3)	89.8(1)
$[Cu_2L_{2.5}(L^4)(H_2O)]\cdot 10H_2O$ (**4**)			
Cu(1)–N(2)	1.949(3)	Cu(2)–N(3)	2.009(3)
Cu(3)–N(6)	1.975(3)	Cu(2)–N(7)	1.996(3)
Cu(2)^{i}-N(10)	1.998(3)	Cu(1)–O(2)	1.928(2)
Cu(2)–O(4)	1.974(2)	Cu(3)–O(5)	1.981(2)
Cu(2)-Ow1	2.311(3)		
O(2)–Cu(1)–N(2)	91.4(1)	O(2)^{ii}–Cu(1)–N(2)	88.7(1)
O(4)–Cu(2)–N(10)^{iii}	89.9(1)	N(7)–Cu(2)–N(10)^{iii}	89.7(1)
O(4)–Cu(2)–N(3)	89.3(1)	N(7)–Cu(2)–N(3)	89.9(1)
N(10)^{iii}–Cu(2)–N(3)	170.5(1)	O(4)–Cu(2)–Ow1	92.0(1)
N(7)–Cu(2)–Ow1	95.6(1)	N(10)^{iii}–Cu(2)–Ow1	96.4(1)
N(3)–Cu(2)–Ow1	93.1(1)	O(4)–Cu(2)–N(7)	172.4(1)
N(6)^{iv}–Cu(3)–O(5)^{iv}	89.5(1)	N(6)–Cu(3)–O(5)^{iv}	90.5(1)
N(6)^{iv}–Cu(3)–O(5)	90.5(1)	N(6)–Cu(3)–O(5)	89.5(1)

[a] Symmetry codes for **1**: ^{i} $-x + 2$, y, $-z + 1/2$. Symmetry codes for **2**: ^{i} $x - 1$, y, z. Symmetry codes for **3**: ^{i} $-x + 1/2$, y, $-z + 1/2$; ^{ii} $-x + 1$, $-y$, $-z + 1$. Symmetry codes for **4**: ^{i} $x + 1$, y, z; ^{ii} $-x - 3$, $-y + 1$, $-z - 1$; ^{iii} $x - 1$, y, z; ^{iv} $-x$, $-y + 2$, $-z$.

 © 2005 Wiley-VCH Verlag GmbH & Co. KGaA, Weinheim

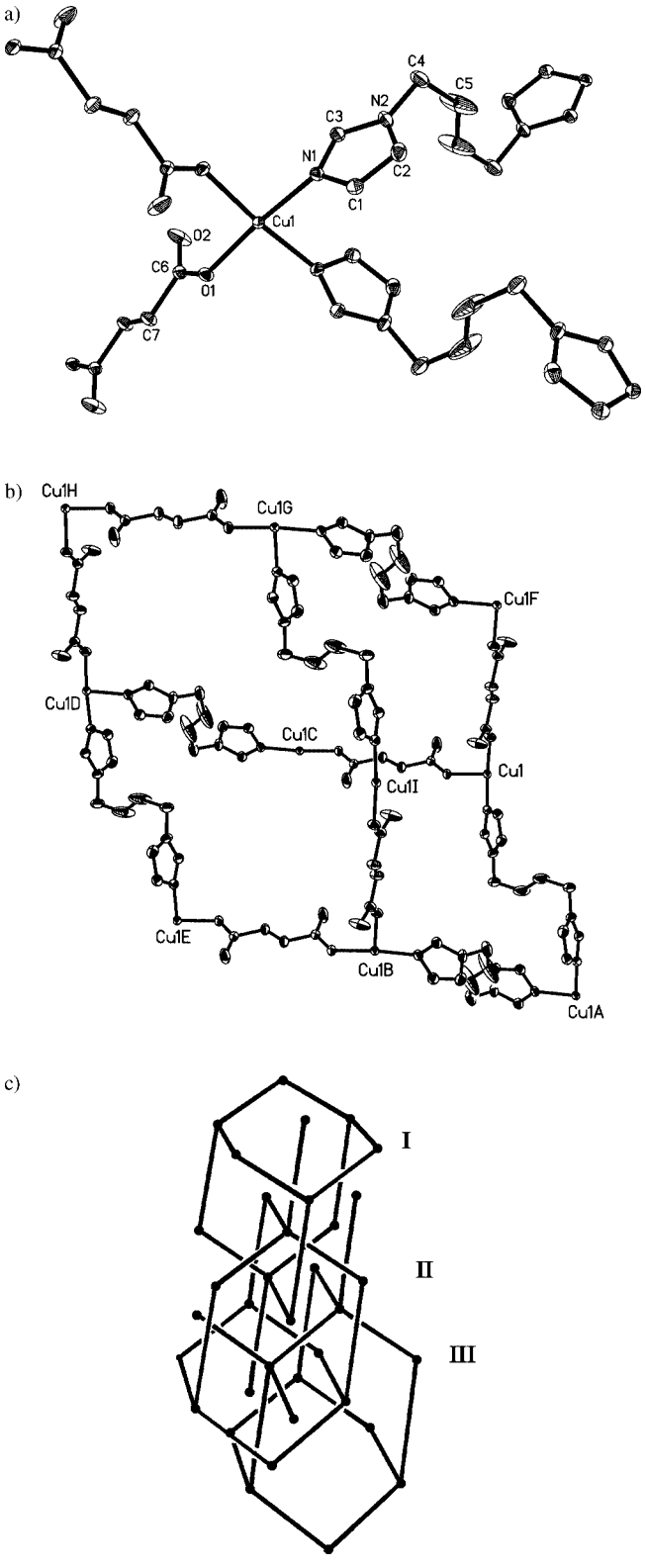

Figure 1. (a) ORTEP view of complex **1** showing 30% thermal probability ellipsoids. (b) View of the adamantane unit of **1**. (c) A schematic representation of the threefold interpenetration mode in **1**.

ring (circuit IV), so the square-planar four-connected Cu1 cation serves as an NbO-like node that also exists in the network of quartz (Schläfli symbol $6^4 8^2$).[15] For Cu2, each of four sets of *cis* links and one set of two *trans* links can be used to construct a six-membered ring (circuits I and II), and the other set of *trans* links is contained in an eight-membered ring (circuit III). Thus, the Cu2 cation can be described as a $CdSO_4$-like node (Schläfli symbol $6^5 8$).[15] Structures based solely on rare NbO or $CdSO_4$ have been explored, but networks containing both an NbO node and a $CdSO_4$ node have not previously been reported in coordination polymers.[15] The network of **3** based on Cu1 and Cu2 cations can be symbolized as an Archimedean-type $(6^5 8)(6^4 8^2)$ net with planar four-connected nodes.[2]

In the structure of **4**, there exist three crystallographically unique Cu^{II} cations (Cu1, Cu2, and Cu3), two unique L^4 ligands, and three unique L molecules. As shown in Figure 4a, each of the Cu1 and Cu3 cations is four-coordinate in a square-planar geometry with two nitrogen atoms from two L molecules and two oxygen atoms from two L^4 anions, while the Cu2 cation center has a distorted square-pyramid coordination sphere defined by one carboxylate oxygen atom, one water molecule, and three nitrogen atoms from three L molecules. The two unique L^4 anions display different coordination modes: one coordinates to four Cu^{II} cations through four carboxylate groups, acting as a tetradentate ligand, while the other coordinates to two Cu^{II} cations using two *para*-carboxylate groups and is a bidentate ligand.

For complex **4**, the benzene ring of the tetradentate L^4 anion can be considered as a four-connected node, thus there exist four kinds of planar four-connected nodes in the framework (Cu1, Cu2, Cu3 and the benzene ring of the L^4 anion). There exist some unique shortest five-, six-, eight-, and ten-membered circuits through nodes in **4** (see Figures S5–S12 in the Supporting Information). For Cu1, each of four sets of *cis* links is contained in a six-membered ring (circuit II), while two sets of *trans* links are contained in a five-membered ring (circuit I) and an eight-membered ring (circuit **III**), respectively (see Figure S13 in the Supporting Information). Thus, the Cu1 cation has the Schläfli symbol $5 6^4 8$. For Cu2, each of two sets of *cis* links is contained in a five-membered ring (circuit I), while each of the other two sets of *cis* links is contained in a six-membered ring (circuit IV); each of two sets of *trans* links is contained in an eight-membered ring (circuit V and circuit VI; see Figure S14 in the Supporting Information). Thus, the Cu2 cation has the Schläfli symbol $5^2 6^2 8^2$. For Cu3, each of four sets of *cis* links is contained in an eight-membered ring (circuit VI), while two sets of *trans* links are contained in a six-membered ring (circuit IV) and a 10-membered ring (circuit VII; see Figure S15 in the Supporting Information). Thus, Cu3 has the Schläfli symbol $6 8^4 10$. For the benzene ring of the tetradentate L^4 ligand, each of four sets of *cis* links is contained in a five-membered ring (circuit I), while each of two sets of *trans* links is contained in a six-membered ring (circuits II and VIII; see Figure S16 in the Supporting Information). Thus, the benzene ring of the tetradentate L^4 anion has the Schläfli symbol $5^4 6^2$. The molar ratio of these four kinds of nodes is 1:2:1:1, thus the network of complex **4** can be described as an Archimedean-type net with four kinds of nonequivalent points: $(56^4 8)(5^2 6^2 8^2)_2(68^4 10)(5^4 6^2)$

 © 2005 Wiley-VCH Verlag GmbH & Co. KGaA, Weinheim

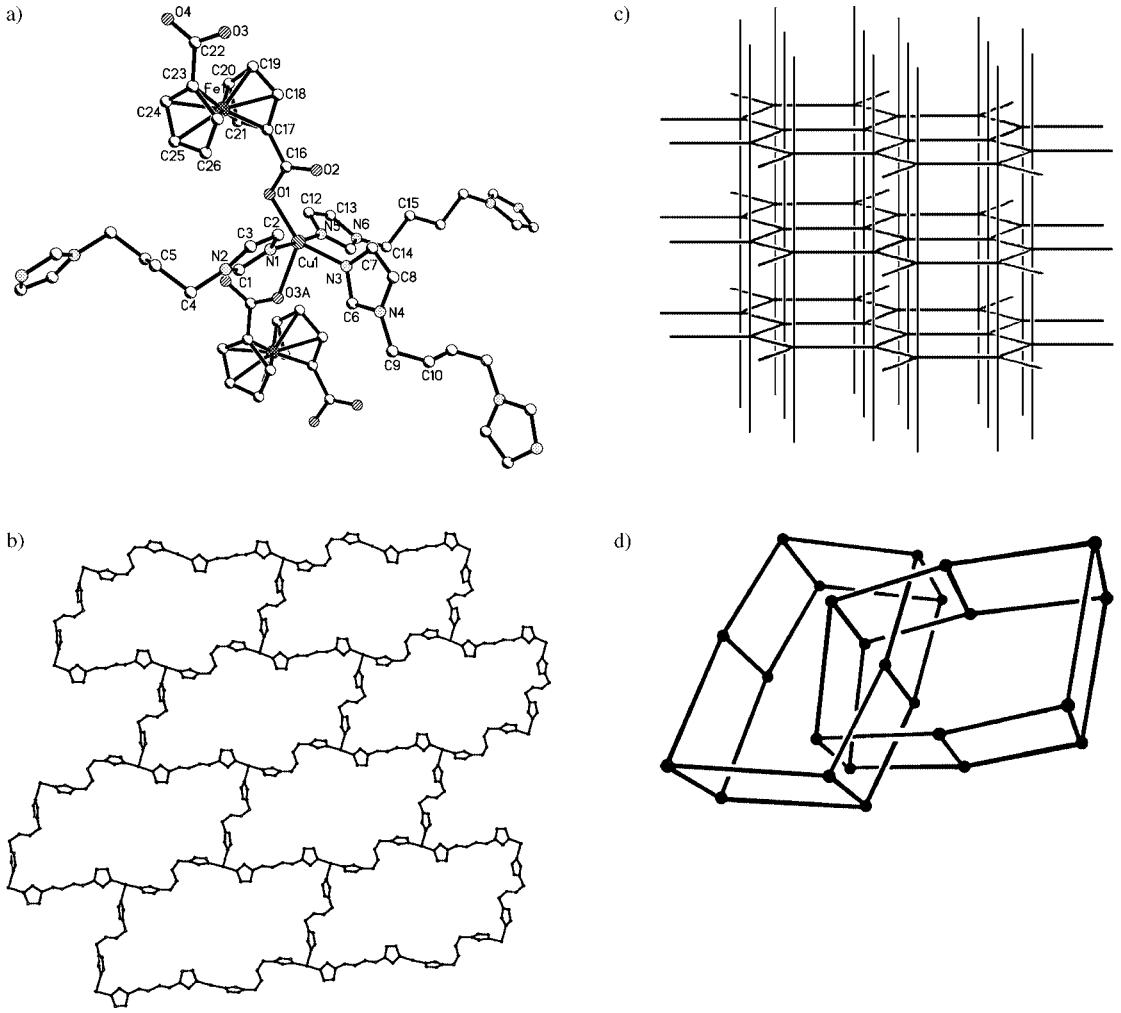

Figure 2. (a) Coordination environment of the copper(II) cation in **2**. (b) 2D (6,3) network containing Cu^{II} cations and L in **2**. (c) A schematic representation of the $4^6 6^4$ network of **2**. (d) A schematic representation of the twofold interpenetration mode in **2**.

(see b in Figure 4). To the best of our knowledge, complex **4** is the first example of a coordination polymer which displays a $(56^48)(5^26^28^2)_2(68^410)(5^46^2)$ topology.[1]

Role of the Anions in the Self-Assembly Processes

From the above descriptions it is clear that the choice of anions is critical in determining the molecular structures of the resultant complexes. In this study, the nature of the anions such as rigidity, flexibility, and the length of the spacer is the underlying reason behind the differences in the structure of this series of copper(II) complexes:·L^1 possesses rigidity due to the presence of a –C=C– spacer between the two carboxylate moieties, whereas L^3 possesses flexibility owing to the presence of a $–CH_2CH_2–$ spacer between the two carboxylate moiety;·L^2 is a ferrocene-based ligand, which can freely rotate around the organoferrocene "ball-joint" to meet the requirements of the coordination geometries of metal ions in the assembly process. Compared with L^1, L^2, and L^3, L^4 is a planar multi-carboxylate anion, which can adopt various coordination modes.

The ratios of Cu:L^n (n = 1, 2, 3, and 4) are determined by the negative charges of the anions. Thus, the ratios of Cu:L^n (n = 1, 2 and 3) are 1:1, and the ratio of Cu:L^4 is 2:1. Since the compounds are isolated by evaporation of the corresponding solutions, the Cu:L ratios of 1:1 for **1** and **3**, 1:1.5 for **2**, and 1:1.25 for **4** may be affected by the solubility of the compounds. The different network topologies of the compounds are related to the Cu:L:L^n ratios (n = 1, 2, 3 and 4). The topological difference between **1** and **3** should result from the structural features of L^1 and L^3: L^3 is more flexible than L^1, and due to its flexibility L^3 forms a $(6^58)(6^48^2)$ network with less void volume, and the rigid ligand L^1 forms a 6^6 network of **1** with large void volume, which is eliminated by the interpenetration. In addition, it should be pointed out that the change of copper(II) and L compositions used in the preparations of these complexes cannot have an effect on their final structures. Thus, the formation of these different frameworks is due solely to the effects of the organic anions.

 © 2005 Wiley-VCH Verlag GmbH & Co. KGaA, Weinheim

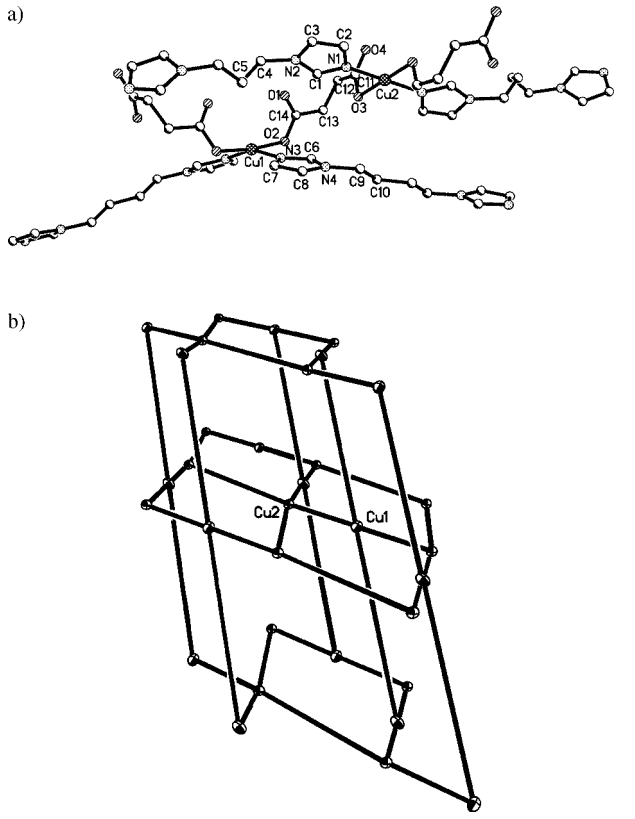

Figure 3. (a) View of the local coordination geometries of complex **3**. (b) The square-planar four-connected $(6^5 8)(6^4 8^2)$ net containing both NbO-like and $CdSO_4$-like nodes in complex **3**.

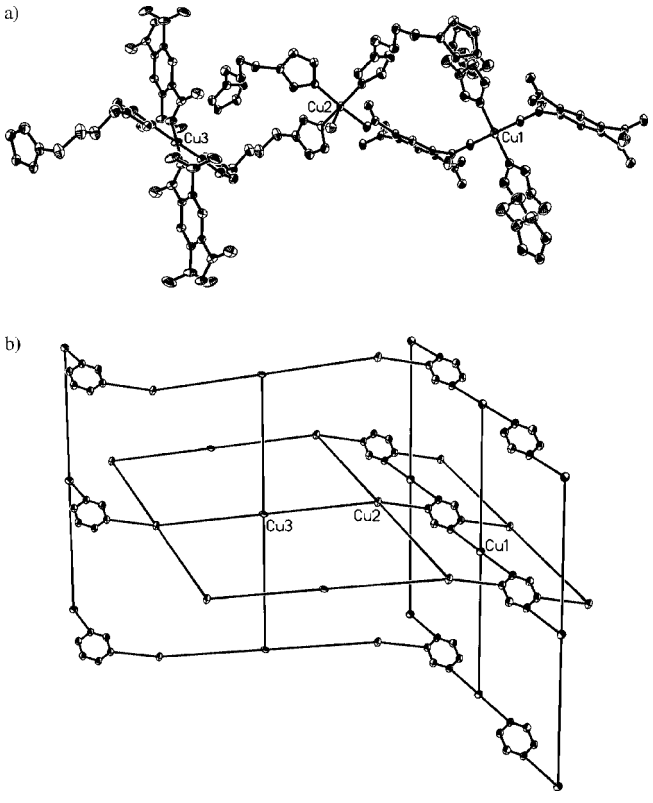

Figure 4. (a) View of the local coordination geometries of the Cu^{II} cations in **4**. (b) The planar four-connected $(56^4 8)(5^2 6^2 8^2)_2$-$(68^4 10)(5^4 6^2)$ net in **4**.

Conclusions

A series of Cu^{II} coordination polymers with different topologies has been synthesized due to the effect of the organic anions on the formation of the final frameworks. When L^1 was used as the bidentate carboxylate anion, a coordination polymer **1** with a threefold interpenetrated diamond structure was obtained. Coordination polymer **2**, containing a Cu^{II} atom and L^2, displays a rare twofold interpenetrated $4^6 6^4$ topology. Two planar, four-connected Cu^{II} coordination polymers **3** (with L^3) and **4** (with L^4) display an interesting Archimedean-type $(6^5 8)(6^4 8^2)$ net containing two different types of square-planar nodes and a $(56^4 8)(5^2 6^2 8^2)_2(68^4 10)(5^4 6^2)$ net containing four different types of square-planar nodes, respectively.

Experimental Section

Materials and Methods: All reagents and solvents for syntheses were purchased from commercial sources and used as received. A Perkin–Elmer 240 elemental analyzer was used to collect microanalytical data. TGA was performed on a Perkin–Elmer TG-7 analyzer in nitrogen. The FT-IR spectra were recorded from KBr pellets in the range 4000–400 cm^{-1} on a Mattson Alpha-Centauri spectrometer.

Synthesis of 1,1′-(1,4-Butanediyl)bis(imidazole) (L): A mixture of imidazole (3.4 g, 50 mmol) and NaOH (2.0 g, 50 mmol) in DMSO (10 mL) was stirred at 60 °C for 1 h, and then 1,4-dichlorobutane (3.2 g, 25 mmol) was added. The mixture was cooled to room temperature after stirring at 60 °C for 2 h and then poured into 200 mL of water. A white solid formed immediately, which weighed 4.1 g (86%) after drying in air. $C_{10}H_{14}N_4$ (190.25): calcd. C 63.16, H 7.37, N, 29.47; found C 63.11, H 7.42, N 29.31.

Synthesis of $[CuL(L^1)]\cdot 2H_2O$ (1): A mixture of $CuCl_2\cdot 2H_2O$ (0.171 g, 1 mmol), NaOH (0.080 g, 2 mmol), and fumaric acid (H_2L^1; 0.116 g, 1 mmol) in water was stirred for 10 min at 60 °C, then 1,1′-(1,4-butanediyl)bis(imidazole) (L; 0.190 g, 1 mmol) was added to the mixture. After stirring for 30 min, the blue precipitate was collected and dissolved in a minimum amount of ammonia (14 M). Blue single crystals of **1** were obtained by slow evaporation of the ammoniacal solution at ambient temperature. Yield: 66% (266 mg). $C_{14}H_{20}CuN_4O_6$ (403.88): calcd. C 41.60, H 4.99, N 13.87; found C 40.89, H 4.60, N 13.49. IR (KBr): 3436 cm^{-1} (s), 3125 (w), 2950 (m), 1619 (s), 1526 (m), 1451 (m), 1285 (w), 1238 (s), 1107 (vs), 948 (w), 849 (w), 771 (w), 756 (m), 664 (m).

Synthesis of $[CuL_{1.5}(L^2)]\cdot 3H_2O$ (2): The same procedure was used to synthesize compound **2** from 1,1′-ferrocenedicarboxylic acid (H_2L^2). Yield: 72% (324 mg). $C_{27}H_{35}CuFeN_6O_7$ (675.00): calcd. C 48.04, H 5.23, N 12.45; found C 48.43, H 5.63, N 12.79. IR (KBr): 3439 cm^{-1} (vs), 3127 (w), 2941 (m), 1606 (vs), 1561 (s), 1527 (m), 1454 (m), 1363 (s), 1237 (m), 1103 (s), 758 (m), 655 (m).

Synthesis of $[CuL(L^3)]\cdot 3H_2O$ (3): The same procedure was used to synthesize compound **3** from succinic acid (H_2L^3). Yield: 78% (331 mg). $C_{14}H_{24}CuN_4O_7$ (423.91): calcd. C 39.63, H 5.71, N 13.22; found C 39.29, H 5.60, N 13.49. IR (KBr): 3437 cm^{-1} (vs), 3123 (w), 2952 (m), 1617 (s), 1526 (m), 1453 (m), 1286 (w), 1240 (s), 1102 (vs), 952 (w), 846 (w), 773 (w), 659 (m).

Synthesis of $[Cu_2L_{2.5}(L^4)(H_2O)]\cdot 10H_2O$ (4): The same procedure was used to synthesize compound **4** from pyromellitic acid (H_4L^4).

 © 2005 Wiley-VCH Verlag GmbH & Co. KGaA, Weinheim

Table 2. Summary of X-ray crystallographic data for complexes **1**–**4**.

	1	**2**	**3**	**4**
Formula	$C_{14}H_{20}CuN_4O_6$	$C_{27}H_{35}CuFeN_6O_7$	$C_{14}H_{24}CuN_4O_7$	$C_{35}H_{59}Cu_2N_{10}O_{19}$
Mol. mass	403.88	675.00	423.91	1051.00
Space group	*C*2/*c*	$P2_1/c$	*P*2/*n*	$P\bar{1}$
a [Å]	14.272(3)	10.368(2)	8.9023(18)	10.702(2)
b [Å]	11.363(2)	18.377(4)	8.7362(17)	11.186(2)
c [Å]	11.432(2)	15.845(3)	24.059(5)	22.584(5)
α [°]	90.00	90.00	90.00	93.80(3)
β [°]	115.15(3)	96.86(3)	93.75(3)	90.13(3)
γ [°]	90.00	90.00	90.00	115.57(3)
V [Å^3]	1678.2(6)	2997.6(10)	1867.1(6)	2431.9(8)
Z	4	4	4	2
$D_{calcd.}$ [g cm^{-3}]	1.598	1.496	1.508	1.435
F(000)	836	1400	884	1098
Reflections obsd. [$I > 2\sigma(I)$]	1549	2405	2075	5975
GOF on F^2	1.072	0.819	0.821	0.928
R_1, wR_2 (obsd.)	0.0349, 0.0895	0.0485, 0.0742	0.0439, 0.1154	0.0498, 0.1335

Yield: 81% (340 mg). $C_{35}H_{59}Cu_2N_{10}O_{19}$ (1051.0): calcd. C 39.97, H 5.66, N 13.33; found C 39.71, H 5.53, N 13.48. IR (KBr): 3441 cm^{-1} (vs), 3133 (w), 2947 (m), 1609 (vs), 1559 (s), 1530 (m), 1452 (m), 1367 (s), 1240 (m), 1106 (s), 653 (m).

X-ray Crystallography: Single-crystal X-ray diffraction data for complexes **1**–**4** were recorded on a Rigaku RAXIS-RAPID image-plate diffractometer using the *ω*-scan technique with Mo-K_α radiation (λ = 0.71073Å). Absorption corrections were applied using the multi-scan technique. All structures were solved by direct methods with SHELXS-97[16] and refined by full-matrix least-squares techniques using the SHELXL-97 program.[17] All non-hydrogen atoms were refined with anisotropic temperature parameters; the hydrogen atoms of the ligands were refined as rigid groups. Further details of the structural analysis are summarized in Table 2.
CCDC-253915 (for **1**), -228776 (for **2**), -216566 (for **3**), and -216568 (for **4**) contain the supplementary crystallographic data for this paper. These data can be obtained free of charge from The Cambridge Crystallographic Data Centre via www.ccdc.cam.ac.uk/data_request/cif.

Powder X-ray Diffraction Analyses: The powder X-ray diffraction patterns for the polymers **1**–**4** agree well with those simulated. The diffraction peaks of both experimental and simulated patterns match well in position, thus indicating the phase purity of polymers **1**–**4**. The difference in reflection intensities between the simulated and experimental patterns is due to the different orientation of the crystals in the powder samples.

Supporting Information: Figures of circuits around the copper cations of **3** and **4** (Figures S1–S16).

Acknowledgments

We thank the National Natural Science Foundation of China (grant no. 20471014) and the Fok Ying Tung Education Foundation for financial support.

[1] a) O. R. Evans, W. Lin, *Acc. Chem. Res.* **2002**, *35*, 511–522; b) B. Moulton, M. J. Zaworotko, *Chem. Rev.* **2001**, *101*, 1629–1658; c) M. Eddaoudi, D. B. Moler, H. Li, B. Chen, T. M. Reineke, M. O'Keeffe, O. M. Yaghi, *Acc. Chem. Res.* **2001**, *34*, 319–330; d) L. Carlucci, G. Ciani, D. M. Proserpio, *Coord. Chem. Rev.* **2003**, *246*, 247–289; e) S. A. Barnett, N. R. Champness, *Coord. Chem. Rev.* **2003**, *246*, 145–168; f) S.-I. Noro, R. Kitaura, M. Kondo, S. Kitagawa, T. Ishii, H. Matsuzaka, M. Yamashita, *J. Am. Chem. Soc.* **2002**, *124*, 2568–2583.

[2] A. F. Wells, *Three-Dimensional Nets and Polyhedra*, Wiley-Interscience, New York, **1977**; A. F. Wells, *Further Studies of Three-dimensional Nets*, ACA Monograph 8, American Crystallographic Association, **1979**.

[3] P. J. Hagrman, D. Hagrman, J. Zubieta, *Angew. Chem. Int. Ed.* **1999**, *38*, 2638–2684.

[4] Z.-R. Qu, H. Zhao, Y.-P. Wang, X.-S. Wang, Q. Ye, Y.-H. Li, R.-G. Xiong, B. F. Abrahams, Z.-G. Liu, Z.-L. Xue, X.-Z. You, *Chem. Eur. J.* **2004**, *10*, 53–60.

[5] G. B. Gardner, D. Venkataraman, J. S. Moore, S. Lee, *Nature* **1995**, *374*, 792–795.

[6] S. R. Batten, R. Robson, *Angew. Chem. Int. Ed.* **1998**, *37*, 1460–1494.

[7] T. M. Reineke, M. Eddaoudi, M. O'Keeffe, O. M. Yaghi, *Angew. Chem. Int. Ed.* **1999**, *38*, 2590–2594.

[8] R. Kitaura, K. Seki, G. Akiyama, S. Kitagawa, *Angew. Chem. Int. Ed.* **2003**, *42*, 428–431.

[9] a) J.-F. Ma, J.-F. Liu, Y. Xing, H.-Q. Jia, Y.-H. Lin, *J. Chem. Soc., Dalton Trans.* **2000**, 2403–2407; b) J.-F. Ma, J.-F. Liu, Y.-C. Liu, Y. Xing, H.-Q. Jia, Y.-H. Lin, *New J. Chem.* **2000**, *24*, 759–763; c) M. L. Tong, B. H. Ye, J. W. Cai, X.-M. Chen, S. W. Ng, *Inorg. Chem.* **1998**, *37*, 2645–2650; d) T. L. Hennigar, D. C. MacQuarrie, P. Losier, R. D. Rogers, M. J. Zaworoko, *Angew. Chem. Int. Ed. Engl.* **1997**, *36*, 972–973.

[10] a) M.-L. Tong, X.-M. Chen, S. R. Batten, *J. Am. Chem. Soc.* **2003**, *125*, 16 170–16 171; b) J.-F. Ma, J. Yang, G.-L. Zheng, L. Li, J.-F. Liu, *Inorg. Chem.* **2003**, *42*, 7531–7534.

[11] a) G.-L. Zheng, J.-F. Ma, Z.-M. Su, L.-K. Yan, J. Yang, Y.-Y. Li, J.-F. Liu, *Angew. Chem. Int. Ed.* **2004**, *43*, 2409–2411; b) G.-L. Zheng, J.-F. Ma, J. Yang, Y.-Y. Li, X.-R. Hao, *Chem. Eur. J.* **2004**, *10*, 3761–3768.

[12] Z.-Y. Fu, X.-T. Wu, J.-C. Dai, S.-M. Hu, W.-X. Du, H.-H. Zhang, R.-Q. Sun, *Eur. J. Inorg. Chem.* **2002**, 2730–2735.

[13] W. B. Pearson, *The Crystal Chemistry and Physics of Materials and Alloys*, Wiley-Interscience, New York, **1972**.

[14] a) L. Pan, N. Ching, X. Huang, J. Li, *Chem. Commun.* **2001**, 1064–1065; b) M. J. Zaworotko, *Chem. Commun.* **2001**, 1–2; c) M. O'Keeffe, M. Eddaoudi, H. Li, T. Reineke, O. M. Yaghi, *J. Solid State Chem.* **2000**, *152*, 3–20; d) J.-C. Dai, X.-T. Wu, S.-M. Hu, Z.-Y. Fu, J.-J. Zhang, W.-X. Du, H.-H. Zhang, R.-Q. Sun, *Eur. J. Inorg. Chem.* **2004**, 2096–2106.

 © 2005 Wiley-VCH Verlag GmbH & Co. KGaA, Weinheim

[15] a) X.-H. Bu, M.-L. Tong, H.-C. Chang, S. Kitagawa, S. R. Batten, *Angew. Chem. Int. Ed.* **2004**, *43*, 192–195; b) L. Carlucci, G. Ciani, D. M. Proserpio, *Chem. Commun.* **2004**, 380–381; c) T.-Y. Niu, X.-Q. Wang, A. J. Jacobson, *Angew. Chem. Int. Ed.* **1999**, *38*, 1934–1937; d) B. Moulton, H. Abourahma, M. W. Bradner, J.-J. Lu, G. J. McManus, M. J. Zaworotko, *Chem. Commun.* **2003**, 1342–1343.

[16] G. M. Sheldrick, *SHELXS-97, Programs for X-ray Crystal Structure Solution*, University of Göttingen, Germany, **1997**.

[17] G. M. Sheldrick, *SHELXL-97, Programs for X-ray Crystal Structure Refinement*, University of Göttingen, Germany, **1997**.

Received: November 18, 2004

 © 2005 Wiley-VCH Verlag GmbH & Co. KGaA, Weinheim

Synthesis and Crystal Structures of Four Cyanide-Bridged Coordination Polymers

Xiang He,[a] Can-Zhong Lu,*[a] Da-Qiang Yuan,[a] Shu-Mei Chen,[a] and Jiu-Tong Chen[a]

Keywords: Bridging ligands / Coordination polymers / Copper / Cyanides / Heterometallic complexes

The hydrothermal reaction of $Cu(NO_3)_2 \cdot 3H_2O$, $K_3Fe(CN)_6$, and 1,10-phenanthroline (1,10-phen) or 2,2′-bipyridine (2,2′-bpy) gives rise to the three one-dimensional helical-chain complexes $[Cu_2Fe(CN)_4(1,10\text{-phen})_3]_n \cdot 0.5n\,H_2O$ (**1**), $[Cu_3(CN)_3(1,10\text{-phen})_3]_n$ (**2**), and $[Cu_3(CN)_3(2,2'\text{-bpy})_3]_n$ (**3**), and the two-dimensional layer complex $[Cu_3Fe(CN)_5(2,2'\text{-bpy})_2]_n$ (**4**). The structure of **1** contains a cyanide-bridged $Cu^I \cdots Fe^{II} \cdots Cu^I$ chain in which the two copper and one iron centers exhibit different coordination environments. The structures of **2** and **3** are both monometallic. Complex **4** is constructed alternately from fused 6- and 14-metal-membered nonplanar centrosymmetric rings that form a 2D layer architecture.

(© Wiley-VCH Verlag GmbH & Co. KGaA, 69451 Weinheim, Germany, 2005)

Introduction

The chemistry of spontaneously self-assembled supramolecular architectures based on transition metal complexes is currently an active and rapidly expanding research area. Transition metal cyanides have been studied for a long time because such compounds possess various interesting physical and chemical properties and have important applications in many fields, such as catalysis, molecular-based magnets, and zeolitic materials.[1–3] The cyanide group is a versatile ligand that can act as a monodentate ligand or as a bridging ligand adopting end-on (I) or end-to-end (II) modes to generate interesting complexes that may exhibit intriguing architectures and new topologies. As copper normally adopts three-, four-, five-, or sixfold coordination to form diverse geometric structures, much research has focused on the copper cyanide system from the viewpoint of structural engineering.[4,5] Helical structures have received special attention in the past decades as helicity is an essential element for bioactivity and also due to their potential applications in asymmetric catalysis and nonlinear optical materials.[6] To date, quite a few single- or double-helical chains have been generated,[7–9] with most helical polymers being obtained by using chiral ligands[10,11] or oligopyridines and other optically active ligands. In addition, the design and synthesis of novel coordination architectures can be controlled by varying the reaction conditions, including temperature,[12] metal-to-ligand ratio,[13] pH value,[14] solvents,[15] and counteranions.[16]

Generally, it is difficult to synthesise Fe^{II}-containing coordination polymers because the Fe^{II} ion is air-sensitive and hydrolyzes easily, and this might be the main reason why such Fe^{II} polymers are rare. In this article we report the syntheses and crystal structures of two Cu/Fe bimetallic cyanide-bridged coordination polymers − $[Cu_2Fe(CN)_4(1,10\text{-phen})_3]_n \cdot 0.5n\,H_2O$ (**1**) and $[Cu_3Fe(CN)_5(2,2'\text{-bpy})_2]_n$ (**4**) − and two copper polymers − $[Cu_3(CN)_3(1,10\text{-phen})_3]_n$ (**2**) and $[Cu_3(CN)_3(2,2'\text{-bpy})_3]_n$ (**3**).

To the best of our knowledge, compound **1** is the first example of a one-dimensional helical chain structure that contains different metal atoms with quite different coordination environments, while compound **4** is the first example of a bimetallic neutral 2D lamella framework compound built up by cyanide-bridged 6- and 14-metal rings.

Results and Discussion

Hydrothermal methods are important in the synthesis of novel multidimensional open-framework materials as a change of reaction conditions for the preparation of these complexes can also have an effect on their structures, although it is difficult to control and predict the crystal structures under hydrothermal methods. It is known that the architectures of the products depend on many factors, such as temperature, the anions involved, the molar ratios of the precursors, the pH etc., and subtle adjustments of these parameters often result in the formation of quite different structures. For example, Forster and his co-workers have carried out systematic studies on the effect of temperature on the structures of the products.[12] Our syntheses under hydrothermal conditions provide four novel compounds with different structural frameworks (Scheme 1). Interestingly, we obtained two monometallic compounds and two

[a] The State Key Laboratory of Structural Chemistry, Fujian Institute of Research on the Structure of Matter, the Chinese Academy of Sciences,
Fuzhou, Fujian, 350002, China
Fax: +86-591-83714946
E-mail: czlu@ms.fjirsm.ac.cn

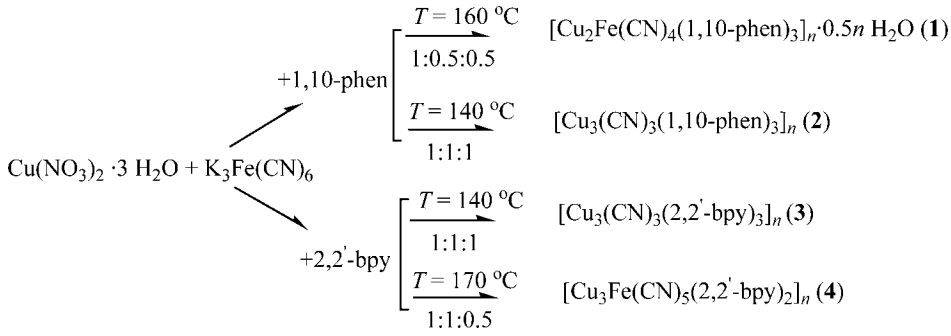

Scheme 1. Cyanide-bridged coordination polymers.

bimetallic materials from similar precursors. The reason for the different results obtained from these reactions is perhaps due to the temperature and the molar ratio of the precursors, although the details are not clear. From these processes $K_3Fe(CN)_6$ appears to be a promising precursor to obtain more new compounds.

The IR bands corresponding to CN stretching vibrations for compounds **1**–**4** appear in the range 2080–2116 cm^{-1}, which is typical for bridging cyanide groups. For **1**, two different absorptions at 2102 and 2080 cm^{-1} indicate the existence of two types of cyanide groups. The lower wavenumber band can be assigned to a terminal cyanide group, while the band at 2102 cm^{-1} is attributed to the stretching vibration of a linear bridging cyanide.

To study the stability of the polymers, thermogravimetric analysis (TGA) was performed for complexes **2**–**4**. These studies show that these complexes are stable up to 280 °C. The stabilities of these compounds make them potential candidates for practical applications.

Electron probe analyses revealed that there are two kinds of metals (copper and iron) in compounds **1** and **4**, the molar ratios of the two metals being 2:1 and 3:1, respectively, in agreement with the structural results. The magnetic susceptibilities of **1** and **4** are negative, which is typical of a diamagnetic behavior. This indicates that the iron atoms in these compounds are in the low-spin Fe^{II} ($S = 0$) state and the copper centers are in the Cu^{I} oxidation state.

$[Cu_2Fe(CN)_4(1,10\text{-phen})_3]_n \cdot 0.5n\,H_2O$ (1): A 1D Framework

The hydrothermal reaction of $Cu(NO_3)_2 \cdot 3H_2O$, $K_3Fe(CN)_6$, and 1,10-phen led to the formation of red crystals of compound **1**. X-ray analysis revealed that compound **1** has a one-dimension neutral helical-chain architecture. As the reaction was carried out under hydrothermal conditions, it is not surprising that the Cu^{II} and Fe^{III} ions have been reduced to Cu^{I} and Fe^{II} ions by cyanide or N-heterocyclic ligands, such as 1,10-phen or pyridine derivatives.[17–19] The cyanide in **1** is provided by the ferricyanide anions. A view of the metal coordination environment is presented in Figure 1. Two copper atoms have different co-

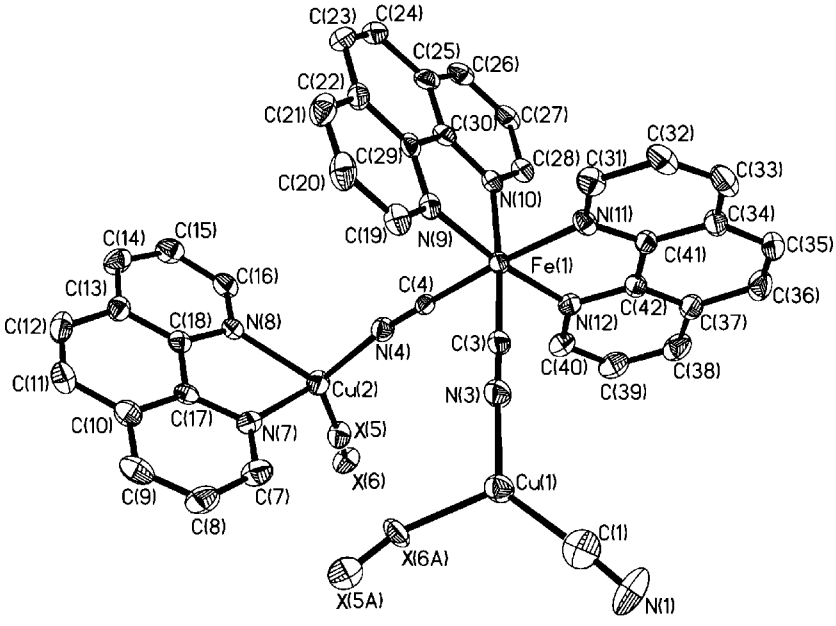

Figure 1. ORTEP representation of the polymeric structure of **1**, showing the coordination environments of the Cu and Fe centers (hydrogen atoms and solvent molecules have been omitted for clarity). Atoms from the disordered CN bridging groups are labeled as X.

 © 2005 Wiley-VCH Verlag GmbH & Co. KGaA, Weinheim

ordination environments: the first Cu^{I} is coordinated by two cyanide [Cu–X = 1.904(7) Å and Cu–N = 1.969(5) Å] and two nitrogen atoms from 1,10-phen [Cu–N = 2.128(5) Å] and exhibits a distorted tetrahedral coordination environment, whereas the second Cu^{I} is coordinated by three nitrogen atoms from three cyanides [Cu–X = 1.932(9)–1.989(6) Å] and exhibits a distorted trigonal planar coordination environment. The heterocyclic 1,10-phen ligand is planar and the copper atom lies within this plane. The bond lengths and angles within the 1,10-phen group are in agreement with those reported for the free 1,10-phen molecule.[20] An intramolecular hydrogen bonding interaction C(28)–H(28A)···N(12) of about 3.098(8) Å is also present.

Each iron atom exhibits a distorted octahedral coordination environment and is coordinated by the carbon atoms from two cyanides and four nitrogen atoms from two bidentate 1,10-phen ligands. The bond lengths for the iron atom [Fe–C = 1.903(6)–1.928(5) Å and Fe–N = 1.973(5)–2.006(5) Å] and the corresponding angle subtended by the bidentate 1,10-phen ligand [N–Fe–N = 81.9(2)–82.2(2)°] agree well with those reported for the low-spin iron(II) complex $[Fe(1,10\text{-phen})_2(CN)_2]$.[21]

The intrachain distances Cu1···Fe1, Fe1···Cu2, and Cu1···Cu2 across cyanide bridges are 5.033(3), 4.985(2), and 4.939(2) Å, respectively. Each pair of adjacent metal atoms is bridged by cyanides to form a helical chain along the *b* axis with a pitch of 10.267(1) Å (Figure 2). The shortest interchain iron–iron, iron–copper, and copper–copper distances are 8.778(3) Å [Fe1···Fe1 (0.5 – *x*, 0.5 + *y*, 0.5 – *z*)], 6.574(1) Å [Cu1···Fe1 (1 – *x*, 1 – *y*, –*z*)], and 5.998(3) Å [Cu1···Cu1 (1 – *x*, 1 – *y*, –*z*)], respectively.

$[Cu_3(CN)_3(1,10\text{-phen})_3]_n$ (2): A 1D Framework

Compound **2** was obtained by varying the temperature and the composition of the reaction mixture used for the preparation of **1**. The X-ray diffraction study revealed that the copper atom is coordinated by two cyanide [Cu–X = 1.914(7)–1.919(9) Å] and two nitrogen atoms from 1,10-phen [Cu–N = 2.096(8)–2.138(8) Å] to give a distorted tetrahedral coordination environment (Figure 3). The cyanide ligands are linearly coordinated [C–N–Cu angles range from 173.3(7)° to 175.4(5)°] and bridge adjacent Cu^{I} atoms to form a one-dimensional helical chain running along the *c* axis with a long pitch of 24.485(10) Å (see a in Figure 4). The intrachain Cu···Cu distance across the cyanide bridges is 4.962 Å. This chain is decorated by 1,10-phen ligands above and below the helical chain. Figure 4 (see part b) shows that five copper atoms form two approximately equilateral triangles that have the same vertex, with the butterfly shape viewed down the *c* axis. The shortest interchain copper–copper distance is 7.751(3) Å [Cu1···Cu1 (0.5 + *x*, 1.5 – *y*, 1 – *z*)].

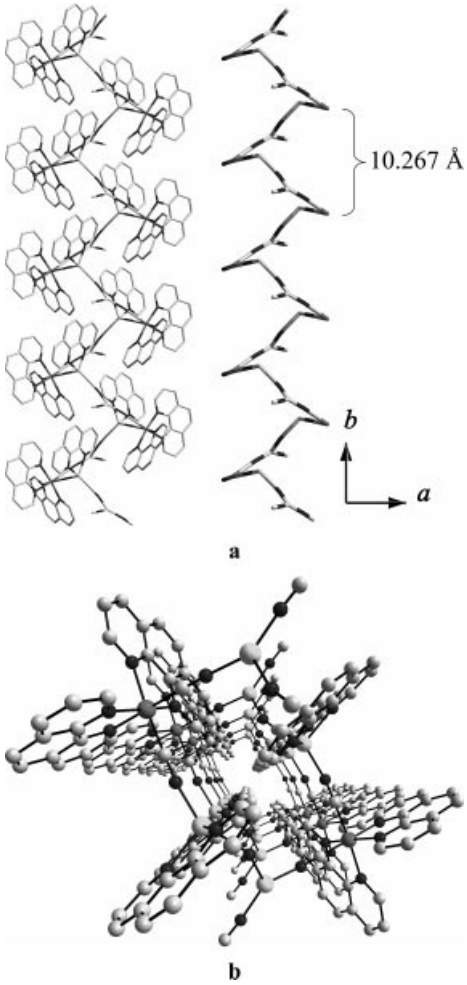

Figure 2. a) Schematic view of the helical chain of **1**. b) View along the helical axis.

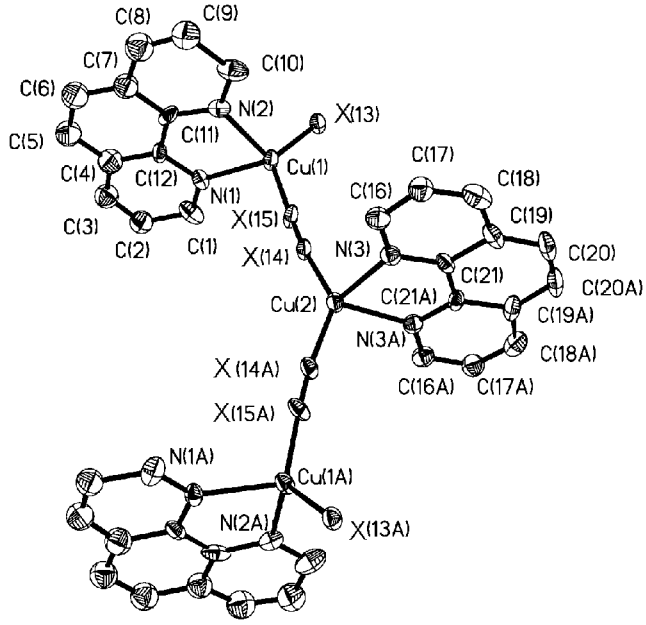

Figure 3. The coordination environments of the copper atoms in complex **2**.

 © 2005 Wiley-VCH Verlag GmbH & Co. KGaA, Weinheim

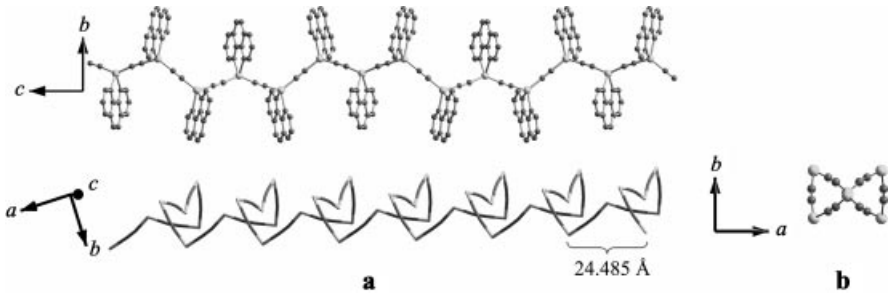

Figure 4. a) The 1D helical chain framework of **2**. b) View along the helical axis.

[Cu(CN)(2,2′-bpy)]$_n$ (3): A 1D Framework

X-ray analysis revealed that the asymmetric unit of compound **3** consists of three neutral mononuclear molecules with copper center in a distorted tetrahedral environment. As shown in Figure 5, each copper atom is coordinated by two cyanides [Cu–X = 1.882(6) Å–1.930(5) Å] and two nitrogen atoms from 2,2′-bpy [Cu–N = 2.078(6) and 2.112(5) Å]. Every two adjacent Cu^I atoms are bridged by cyanides to form a chiral helical chain along the 3_2 screw axis with a long pitch of 12.898(1) Å (see a in Figure 6). The intrachain Cu···Cu distance across cyanide bridges is 4.973(1) Å. The helical chain with only a Cu–Cu backbone has a trigonal shape when viewed down the *c* axis, with each copper atom as the vertex of an approximately equilateral triangle. The angle subtended at the copper atom by two cyanide linkages is reduced to 126.8(2)° (b in Figure 6). This chain is also decorated by 2,2′-bpy ligands along both sides of the chain. The shortest interchain copper–copper distance is 7.371(1) Å [Cu1···Cu3 (1 – *x* + *y*, 1 – *x*, – 0.66667 + *z*)], which is slightly shorter than that for compound **2**.

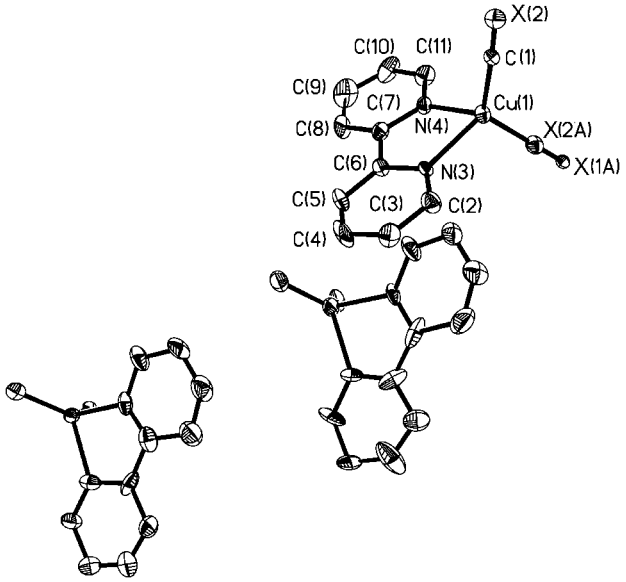

Figure 5. The coordination environments of the copper atoms in complex **3**.

[$Cu_3Fe(CN)_5(2,2'\text{-bpy})_2$]$_n$ (4): A 2D Network

Compound **4** was obtained by varying the temperature and the composition of the reaction mixture used for the preparation of **3**. The X-ray analysis revealed that the structure of **4** (Figure 7) consists of neutral corrugated sheets constructed alternately from fused 6- and 14-metal-membered nonplanar centrosymmetric rings, which are bridged by cyanide groups. Each 6-metal-ring contains two iron and four copper atoms, and the Fe^{II} atom is in a distorted octahedral environment containing four nitrogen atoms from two bipyridine ligands and two carbon atoms from two cyanide groups [Fe–N = 1.958(2)–1.986(3) Å; Fe–C = 1.909(3)–1.913(3) Å]. The values of the bond lengths in **4** for the iron atom are comparable to those found in compound **1** and other cyanide-bridged bimetallic complexes containing the [$Fe(bpy)_2(CN)_2$] building block.[22]

The two Cu^I atoms have two different coordination environments, with the first coordinated by three cyanide groups in a triangular geometry and the second coordinated by two cyanide groups in a linear geometry.

The Fe1···Cu1, Cu1···Cu4, Cu1···Cu2, and Cu2···Cu3 distances across cyanide bridges are 4.988(6), 4.870(7),

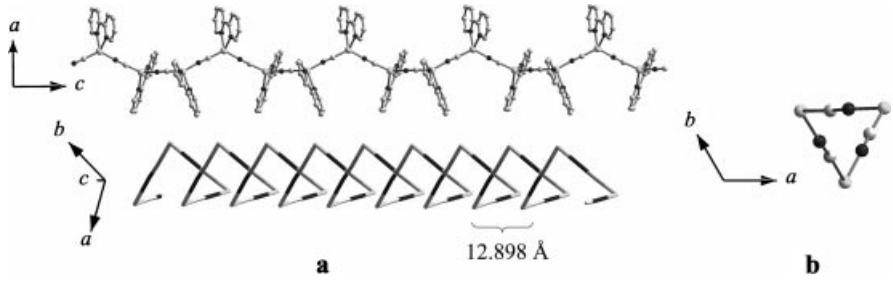

Figure 6. a) The 1D helical chain framework of **3**. b) View down the helical chain.

 © 2005 Wiley-VCH Verlag GmbH & Co. KGaA, Weinheim

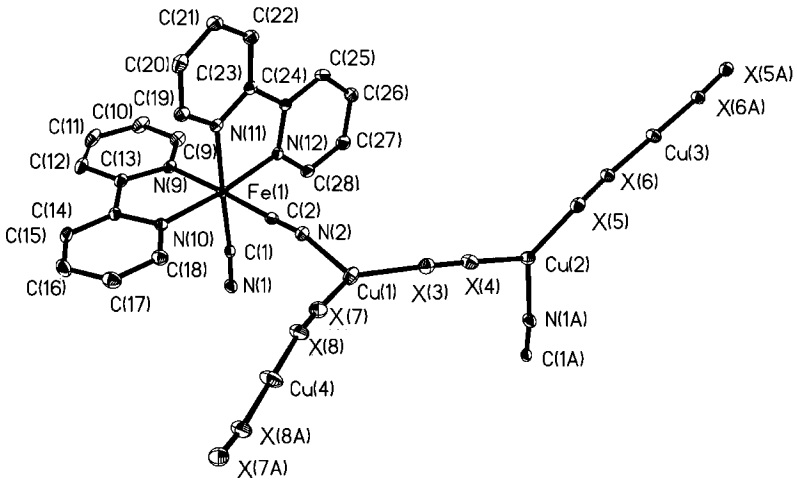

Figure 7. ORTEP representation of the polymeric structure of **4**, showing the coordination environments of the Cu and Fe atoms (hydrogen atoms have been omitted for clarity). Atoms from the disordered CN bridging groups are labeled as X.

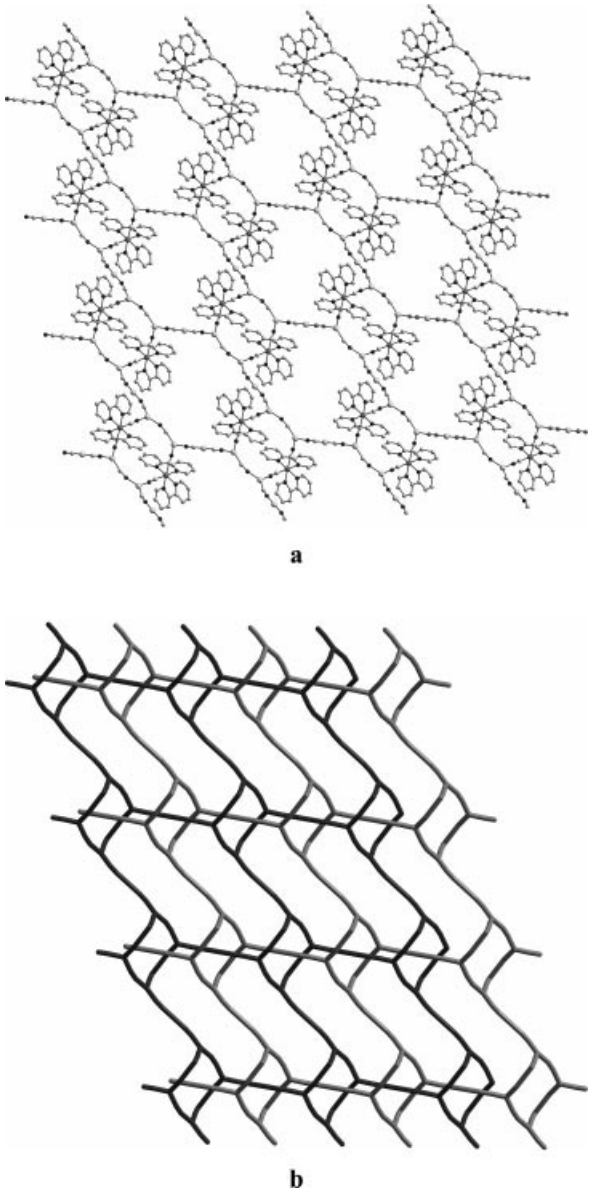

a

b

Figure 8. a) Perspective view of the 2D layer structure of **4**. b) Schematic representation of the interpenetrated 2D lamella framework.

4.901(13), and 4.840(16) Å, respectively. The structure consists of 2D layers, parallel to the *ac* plane, constructed by alternating 6- and 14-metal-membered centrosymmetric rings in which the metal centers are bridged by cyanide groups. The 6-metal rings adopt a chair conformation for the Cu···Fe···Cu···Cu···Fe···Cu unit. The size of these rings is about 8.9×8.0 Å^2. Four adjacent rings 6-metal rings add four two-coordinate copper atoms to form a larger 14-metal-membered ring {Fe-$(Cu)_6$-Fe-$(Cu)_6$} of approximately 13×22 Å^2. Each 14-metal-membered ring shares four sides with four adjacent 14-metal-membered rings and four sides with four adjacent 6-metal-membered rings; each 6-metal-membered ring shares all its edges with four 14-metal-membered rings to form a 2D framework. A view down the *b* axis shows that the actual crystal structure of compound **4** is a twofold interpenetrating 2D supramolecular framework (Figure 8). This is consistent with the fact that crystal structures with such large cavities are stabilized either by inclusion of suitable guests or by interpenetrating lattices.[23]

Intramolecular hydrogen-bonding interactions [C(9)–H(9A)···N(12) = 3.078(4) Å; C(19)–H(19A)···N(10) = 3.065(4) Å] also exist in **4**.

A method for preparing bimetallic compounds from hexacyanoferrate(III) under hydrothermal conditions has been reported previously.[24] Upon comparing the structure of **4** with the reported compound $[Fe(bipy)_2(CN)_4Cu_2]$, it can be seen that the latter compound is constructed by alternately fused 6- and 10-metal-membered rings to form an ABAB pattern layer instead of the twofold interpenetrating structure found in compound **4**.

Conclusions

Three novel one-dimensional helical-chain coordination polymers and one two-dimensional layer complex have been obtained by hydrothermal synthesis. Under hydrothermal conditions, high-valence ions are reduced to low-valence ions by N-heterocyclic ligands or cyanide from ferricyanide anions. Furthermore, slow release of CN^- might play an

 © 2005 Wiley-VCH Verlag GmbH & Co. KGaA, Weinheim

important role in the formation of these compounds. The successful isolation of these four compounds demonstrates that it is promising to use $K_3Fe(CN)_6$ as a precursor along with N-heterocyclic ligands, particularly derivatives of 2,2′-bpy and 1,10-phen, to construct novel coordination compounds under hydrothermal reaction conditions.

Experimental Section

General Remarks: All the syntheses were performed in poly(tetrafluoroethylene)-lined stainless steel autoclaves under autogenous pressure. Reagents were purchased commercially and were used without further purification. Elemental analyses of C and H were performed with an EA1110 CHNS-0 CE elemental analyzer. IR (KBr pellet) spectra were recorded on a Nicolet Magna 750FT-IR spectrometer. TGA analyses were carried out under nitrogen with a heating rate of 15 °C min^{-1} on a STA449C integration thermal analyzer. Electron probe analysis was performed with an EPM-810 EDAX9100 SHIMADZU electron probe microanalyzer. Variable-temperature (5–300K) magnetic susceptibility measurements were carried out on a Quantum Design MPMS-7 SQUID magnetometer at 5 T magnetic field using the SQUID method.

$[Cu_2Fe(CN)_4(1,10\text{-phen})_3]_n \cdot 0.5n\,H_2O$ (1): A mixture of $Cu(NO_3)_2 \cdot 3H_2O$ (0.02 g, 0.1 mmol), $K_3Fe(CN)_6$ (0.015 g, 0.05 mmol), and 1,10-phen (0.01 g, 0.05 mmol) in 20 mL of H_2O was stirred for 20 min at room temperature. The mixture was then transferred into a 30-mL, Teflon-lined stainless-steel vessel. The mixture was heated at 160 °C for two days under autogenous pressure. After the reaction mixture had slowly cooled down to room temperature, red prism-shaped crystals of **1** (0.02 g, 45% based on Cu) were collected. $C_{40}H_{25}Cu_2FeN_{10}O_{0.50}$ (863.65): calcd. C 57.42, H 3.01, Cu 15.19, N 16.74; found C 57.25, H 3.03, Cu 15.56, N 16.60. IR (KBr pellet): $\tilde{\nu}$ = 3552 m, 3421 m, 3049 m, 2102 vs, 2080 vs, 1628 m, 1421 s, 1342 m, 1205 m, 1142 m, 1051 m, 847 s, 777 w, 723 s, 633 w, 559 m cm^{-1}.

$[Cu_3(CN)_3(1,10\text{-phen})_3]_n$ (2): $Cu(NO_3)_2 \cdot 3H_2O$ (0.02 g, 0.1 mmol), $K_3Fe(CN)_6$ (0.03 g, 0.1 mmol), and 1,10-phen (0.02 g, 0.1 mmol) in 20 mL of H_2O were stirred for 20 min at room temperature. The mixture was then transferred into a 30-mL, Teflon-lined stainless-steel vessel. The mixture was heated at 140 °C for two days under autogenous pressure. After the reaction mixture had quickly cooled down to room temperature, red prism-shaped crystals were obtained (0.01 g, 45% based on Cu). $C_{39}H_{24}Cu_3N_9$ (809.29): calcd. C 57.88, H 2.99, Cu 23.56, N 15.58; found C 57.42, H 3.03, Cu 23.78, N 15.60. IR (KBr pellet): $\tilde{\nu}$ = 3415 m, 3057 m, 2107 vs, 2008 m, 1620 m, 1583 m, 1568 w, 1505 m, 1492 w, 1418 m, 1139 m, 841 s, 768 m, 727 s, 631 m cm^{-1}.

$[Cu_3(CN)_3(2,2'\text{-bpy})_3]_n$ (3): $Cu(NO_3)_2 \cdot 3H_2O$ (0.02 g, 0.1 mmol), $K_3Fe(CN)_6$ (0.03 g, 0.1 mmol), and 2,2′-bpy (0.016 g, 0.1 mmol) were added to 20 mL of H_2O. This mixture was stirred for 20 min at room temperature and was then transferred into a 30-mL, Teflon-lined stainless-steel vessel. The mixture was heated at 140 °C for two days under autogenous pressure. After the reaction mixture had slowly cooled down to room temperature, dark-red, prism-shaped crystals were obtained (0.01 g, 65% based on Cu). $C_{33}H_{24}Cu_3N_9$ (737.23): calcd. C 53.76, H 3.28, Cu 25.86, N 17.10; found C 54.02. H 3.36, Cu 25.53, N 17.53. IR (KBr pellet): $\tilde{\nu}$ = 3421 m, 3059 m, 2108 vs, 1593 m, 1470 m, 1439 s 1309 m, 1155 m, 1007 m, 764 s, 650 w, 417 w cm^{-1}.

$[Cu_3Fe(CN)_5(2,2'\text{-bpy})_2]_n$ (4): $Cu(NO_3)_2 \cdot 3H_2O$ (0.02 g, 0.1 mmol), $K_3Fe(CN)_6$ (0.03 g, 0.1 mmol), and 2,2′-bpy (0.008 g, 0.05 mmol) were added to 20 mL of H_2O. This mixture was stirred for 20 min at room temperature and was then transferred into a 30-mL, Teflon-lined stainless-steel vessel. The mixture was heated at 170 °C for two days under autogenous pressure. After the reaction mixture had slowly cooled down to room temperature, dark-red, prism-shaped crystals were obtained (0.006 g, 45% based on Cu). $C_{25}H_{16}Cu_3FeN_9$ (688.94): calcd. C 43.58, H 2.34, Cu 27.67, N 18.30; found C 43.56, H 2.64, Cu 27.89, N 18.49. IR (KBr pellet): $\tilde{\nu}$ = 3057 m, 2123 m, 2116 s, 2107 s, 1592 s, 1571 m, 1469 m, 1438 s, 1308 m, 1279 w, 1246 m, 1006 m, 792 s, 649 m cm^{-1}.

X-ray Crystallographic Study: Suitable single crystals of compounds with dimensions 0.34 × 0.32 × 0.30 mm (**1**), 0.30 × 0.20 × 0.20 mm (**2**), 0.50 × 0.18 × 0.10 mm (**3**), and 0.30 × 0.25 × 0.10 mm (**4**) were carefully selected and glued to thin glass fibers with epoxy resin. Crystal structure measurements for

Table 1. Crystal and structure-refinement data for compounds **1**–**4**.

Compound	**1**	**2**	**3**	**4**
Formula	$C_{40}H_{25}Cu_2FeN_{10}O_{0.5}$	$C_{39}H_{24}Cu_3N_9$	$C_{33}H_{24}Cu_3N_9$	$C_{25}H_{16}Cu_3FeN_9$
Mol. mass	863.65	809.29	737.23	688.94
Crystal system	monoclinic	orthorhombic	trigonal	triclinic
Space group	$P2_1/n$	$C222_1$	$P3_2$	$P\bar{1}$
a [Å]	13.1160(2)	8.515(4)	14.4307(8)	8.345(3)
b [Å]	10.2671(2)	16.616(9)	14.4307(8)	10.653(4)
c [Å]	25.7648(2)	24.485(10)	12.8975(11)	14.929(6)
α [°]				99.357(4)
β [°]	96.4740(10)			102.672(4)
γ [°]				93.668(4)
V [Å^3]	3447.45(9)	3464(3)	2326.0(3)	1270.8(8)
Z	4	4	3	2
D_c [g cm^{-3}]	1.612	1.552	1.579	1.800
$F(000)$	1692	1632	1116	684
μ [mm^{-1}]	1.687	1.868	2.078	3.070
GOF	1.048	1.104	1.040	1.072
R_1, wR_2 [$I > 2\sigma(I)$][a]	0.0616, 0.1279	0.0702, 0.1954	0.0552, 0.1465	0.0364, 0.0742
R_1, wR_2 (all data)[a]	0.0851, 0.1449	0.0791, 0.2027	0.0618, 0.1529	0.0504, 0.0821

[a] $R_1 = \Sigma(|F_o| - |F_c|)/\Sigma|F_o|$; $wR_2 = [\Sigma w(F_o^2 - F_c^2)^2/\Sigma w(F_o^2)^2]^{0.5}$.

 © 2005 Wiley-VCH Verlag GmbH & Co. KGaA, Weinheim

Table 2. Selected bond lengths [Å] and angles [°] for compounds **1**–**4**.[a]

		Compound **1**			
Fe(1)–C(3)	1.903(6)	C(3)–Fe(1)–C(4)	88.9(2)	N(9)–Fe(1)–N(11)	93.5(2)
Fe(1)–C(4)	1.928(5)	C(3)–Fe(1)–N(12)	91.8(2)	N(10)–Fe(1)–N(11)	92.30(18)
Fe(1)–N(12)	1.973(5)	C(4)–Fe(1)–N(12)	93.8(2)	C(1)–Cu(1)–N(3)	132.3(3)
Fe(1)–N(9)	1.981(5)	C(3)–Fe(1)–N(9)	94.0(2)	C(1)–Cu(1)–X(6)^{I}	118.2(3)
Fe(1)–N(10)	2.000(5)	C(4)–Fe(1)–N(9)	90.6(2)	N(3)–Cu(1)–X(6)^{I}	109.3(2)
Fe(1)–N(11)	2.006(5)	N(12)–Fe(1)–N(9)	172.8(2)	X(5)–Cu(2)–N(4)	124.8(2)
Cu(1)–C(1)	1.878(8)	C(3)–Fe(1)–N(10)	175.7(2)	X(5)–Cu(2)–N(8)	110.2(2)
Cu(1)–N(3)	1.941(6)	C(4)–Fe(1)–N(10)	89.6(2)	N(4)–Cu(2)–N(8)	111.27(19)
Cu(1)–X(6)^{I}	1.985(6)	N(12)–Fe(1)–N(10)	92.39(19)	X(5)–Cu(2)–N(7)	118.0(2)
Cu(2)–X(5)	1.904(7)	N(9)–Fe(1)–N(10)	81.9(2)	N(4)–Cu(2)–N(7)	104.7(2)
Cu(2)–N(4)	1.969(5)	C(3)–Fe(1)–N(11)	89.5(2)	N(8)–Cu(2)–N(7)	78.40(19)
Cu(2)–N(8)	2.128(5)	C(4)–Fe(1)–N(11)	175.7(2)	C(3)–N(3)–Cu(1)	175.0(6)
Cu(2)–N(7)	2.128(5)	N(12)–Fe(1)–N(11)	82.2(2)	C(4)–N(4)–Cu(2)	171.5(5)
		Compound **2**			
Cu(1)–X(13)	1.915(7)	X(13)–Cu(1)–N(15)	123.5(3)	X(13)^{III}–X(13)–Cu(1)	175.4(5)
Cu(1)–X(15)	1.919(9)	X(13)–Cu(1)–N(2)	111.5(3)	X(14)^{II}–Cu(2)–X(14)	136.1(4)
Cu(1)–N(2)	2.096(8)	X(15)–Cu(1)–N(2)	109.1(3)	X(14)^{II}–Cu(2)–N(3)	109.5(3)
Cu(1)–N(1)	2.116(7)	X(13)–Cu(1)–N(1)	117.1(3)	X(14)–Cu(2)–N(3)	104.4(3)
Cu(2)–X(14)	1.914(9)	X(15)–Cu(1)–N(1)	107.8(3)	N(3)–Cu(2)–N(3)^{II}	77.3(4)
Cu(2)–N(3)	2.138(8)	N(2)–Cu(1)–N(1)	78.9(3)		
		Compound **3**			
Cu(1)–X(2)	1.886(6)	Cu(3)–N(7)	2.088(5)	X(13)–Cu(2)–N(5)	105.3(3)
Cu(1)–X(1)	1.930(5)	Cu(3)–N(8)	2.105(6)	N(6)–Cu(2)–N(5)	77.1(2)
Cu(1)–N(4)	2.103(5)	X(2)–Cu(1)–X(1)	127.0(2)	X(35)–Cu(3)–X(36)	126.9(2)
Cu(1)–N(3)	2.112(5)	X(2)–Cu(1)–N(4)	115.2(2)	X(35)–Cu(3)–N(7)	113.2(2)
Cu(2)–X(14)	1.893(9)	X(1)–Cu(1)–N(4)	101.6(2)	X(36)–Cu(3)–N(7)	105.3(2)
Cu(2)–X(13)	1.926(9)	X(2)–Cu(1)–N(3)	111.6(2)	X(35)–Cu(3)–N(8)	108.7(2)
Cu(2)–N(6)	2.078(6)	X(1)–Cu(1)–N(3)	112.7(2)	X(36)–Cu(3)–N(8)	114.9(2)
Cu(2)–N(5)	2.083(6)	N(4)–Cu(1)–N(3)	77.36(18)	N(7)–Cu(3)–N(8)	76.6(2)
Cu(3)–X(35)	1.882(6)	X(14)–Cu(2)–X(13)	125.9(3)	C(3)–N(3)–C(7)	119.5(5)
Cu(3)–X(36)	1.929(6)	X(14)–Cu(2)–N(6)	109.7(3)	C(3)–N(3)–Cu(1)	124.1(4)
		X(13)–Cu(2)–N(6)	113.4(3)	C(7)–N(3)–Cu(1)	116.2(4)
		X(14)–Cu(2)–N(5)	114.9(3)		
		Compound **4**			
Fe(1)–C(2)	1.909(3)	Cu(2)–N(1)^{IV}	1.957(3)	N(12)–Fe(1)–N(9)	94.66(10)
Fe(1)–C(1)	1.913(3)	Cu(3)–X(6)	1.829(3)	C(2)–Fe(1)–N(11)	89.53(11)
Fe(1)–N(10)	1.958(2)	Cu(4)–X(8)	1.821(3)	C(1)–Fe(1)–N(11)	177.31(11)
Fe(1)–N(12)	1.966(2)	C(2)–Fe(1)–C(1)	91.00(12)	N(10)–Fe(1)–N(11)	94.13(10)
Fe(1)–N(9)	1.979(2)	C(2)–Fe(1)–N(10)	94.47(11)	N(12)–Fe(1)–N(11)	81.25(10)
Fe(1)–N(11)	1.986(3)	C(1)–Fe(1)–N(10)	88.46(11)	N(9)–Fe(1)–N(11)	89.71(10)
Cu(1)–X(7)	1.895(3)	C(2)–Fe(1)–N(12)	89.30(11)	X(7)–Cu(1)–X(3)	127.49(13)
Cu(1)–X(3)	1.909(3)	C(1)–Fe(1)–N(12)	96.11(11)	X(7)–Cu(1)–N(2)	115.01(12)
Cu(1)–N(2)	1.949(3)	N(10)–Fe(1)–N(12)	174.03(10)	X(3)–Cu(1)–N(2)	115.72(12)
Cu(2)–X(5)	1.892(3)	C(2)–Fe(1)–N(9)	175.81(11)	X(5)–Cu(2)–X(4)	131.55(12)
Cu(2)–X(4)	1.910(3)	C(1)–Fe(1)–N(9)	89.96(11)	X(5)–Cu(2)–N(1)^{IV}	118.61(12)
		N(10)–Fe(1)–N(9)	81.47(10)	X(4)–Cu(2)–N(1)^{IV}	109.83(11)

[a] Symmetry transformations used to generate equivalent atoms: I: $-x + 3/2$, $y + 1/2$, $-z + 1/2$; II: $-x$, y, $-z + 1/2$; III: x, $-y + 2$, $-z + 1$; IV: $-x + 2$, $-y$, $-z + 1$.

compounds **1**–**4** were performed on a Rigaku Mercury CCD diffractometer with graphite-monochromated Mo-K_α radiation (λ = 0.71073 Å) at room temperature. A total of 6060, 3051, 5435, and 5718 unique reflections were collected in the $\omega/2\theta$ scan mode for **1**–**4**, respectively. The structures were solved by direct methods and refined on F^2 with the SHELXL97 program.[25] For all complexes the bridging cyanide group between two Cu^{I} atoms was disordered with respect to the C and N termini; this disorder was treated by performing test refinements with C and N atoms with partial occupancies. The disordered CN atoms positions are labeled in the tables and drawings as X. All non-hydrogen atoms were refined with anisotropic displacement parameters, and the hydrogen atoms were treated as riding atoms using the SHELX97 default parameters. For **1**, the hydrogen atoms of the water molecules were neither found nor calculated. For **2**, rigid refinement about the next six carbon atoms C4, C5, C6, C7, C11, and C12 was used to form a phenyl ring. The absolute structure parameters of compound **2** and **3** are 0.05(5) and 0.00, respectively. The crystal data and details of refinement for compounds are summarized in Table 1; selected bond lengths and angles are listed in Table 2.

CCDC-236440 (for **1**), -227060 (for **2**), -227061 (for **3**), and -243534 (for **4**) contain the supplementary crystallographic data for this pa-

 © 2005 Wiley-VCH Verlag GmbH & Co. KGaA, Weinheim

per. These data can be obtained free of charge from The Cambridge Crystallographic Data Centre via www.ccdc.cam.ac.uk/data_request/cif.

Acknowledgments

This work was supported by the 973 Program of MOST (001CB108906), the National Natural Science Foundation of China (90206040, 20425313, 20333070, and 20303021), the NSF of Fujian, and the Chinese Academy of Sciences.

[1] K. R. Dunbar, R. A. Heintz, *Prog. Inorg. Chem.* **1997**, *45*, 283–391.
[2] M. Verdaguer, A. Bleuzen, V. Marvaud, J. Vaissermann, M. Seuleiman, C. Desplanches, A. Scuiller, C. Train, R. Garde, G. Gelly, C. Lomenech, I. Rosenman, P. Veillet, C. Cartier, F. Villain, *Coord. Chem. Rev.* **1999**, *190*, 1023–1047.
[3] M. Ohba, H. Okawa, *Coord. Chem. Rev.* **2000**, *198*, 313–328.
[4] A. J. Blake, N. R. Brooks, N. R. Champness, M. Crew, L. R. Hanton, P. Hubberstey, S. Parsons, M. Schroder, *J. Chem. Soc., Dalton Trans.* **1999**, 2813–2817.
[5] S. R. Batten, A. R. Harris, P. Jensen, K. S. Murray, A. Ziebell, *J. Chem. Soc., Dalton Trans.* **2000**, 3829–3835.
[6] J.-M. Lehn, *Supramolecular Chemistry*, Wiley-VCH, Weinheim, **1995**.
[7] V. Soghomonian, Q. Chen, R. C. Haushalter, J. Zubieta, C. J. O'Connor, *Science* **1993**, *259*, 1596–1599.
[8] C. Piguet, G. Bernardinelli, G. Hopfgartner, *Chem. Rev.* **1997**, *97*, 2005–2062.
[9] F. G. Gelalcha, M. Schulz, R. Kluge, J. Sieler, *J. Chem. Soc., Dalton Trans.* **2002**, 2517–2521.
[10] D. Sun, R. Cao, Y.-Q. Sun, W-H. Bi, X. Li, M.-C. Hong, Y.-J. Zhao, *Eur. J. Inorg. Chem.* **2003**, 38–41.
[11] a) D. L. Reger, R. F. Semeniuc, M. D. Smith, *Eur. J. Inorg. Chem.* **2002**, 543–546; b) J. M. Rowland, M. M. Olmstead, P. K. Mascharak, *Inorg. Chem.* **2002**, *41*, 1545–1549; c) C. S. A. Fraser, D. J. Eisler, M. C. Jennings, R. J. Puddephatt, *Chem. Commun.* **2002**, 1224–1225.
[12] P. M. Forster, A. R. Burbank, C. Livage, G. Férey, A. K. Cheetham, *Chem. Commun.* **2004**, 368–369.
[13] A. J. Blake, N. R. Brooks, N. R. Champness, P. A. Cooke, A. M. Deveson, D. Fenske, P. Hubberstey, W.-S. Li, M. Schröder, *J. Chem. Soc., Dalton Trans.* **1999**, 2103–2110.
[14] X.-X. Hu, J.-Q. Xu, P. Cheng, X.-Y. Chen, X.-B. Cui, J.-F. Song, G.-D. Yang, T.-G. Wang, *Inorg. Chem.* **2004**, *43*, 2261–2266.
[15] M. A. Withersby, A. J. Blake, N. R. Champness, P. A. Cooke, P. Hubberstey, W.-S. Li, M. Schröder, *Inorg. Chem.* **1999**, *38*, 2259–2266.
[16] J. R. Black, N. R. Champness, W. Levason, G. Reid, *J. Chem. Soc., Chem. Commun.* **1995**, 1277–1278.
[17] a) J. Tao, Y. Zhang, M.-L. Tong, X.-M. Chen, T. Yuen, C.-L. Lin, X.-Y. Huang, J. Li, *Chem. Commun.* **2002**, 1342–1343; b) J. Tao, X. Yin, R.-B. Huang, L.-S. Zheng, *Inorg. Chem. Commun.* **2002**, *5*, 1000–1002.
[18] S. M.-F. Lo, S. S.-Y. Chui, L.-Y. Shek, Z. Lin, X. Zhang, G. Wen, I. D. Williams, *J. Am. Chem. Soc.* **2000**, *122*, 6293–6294.
[19] E. Colacio, R. Kivekäs, F. Lloret, M. Sunberg, J. S. Varela, M. Bardaji, A. Laguna, *Inorg. Chem.* **2002**, *41*, 5141–5149.
[20] S. Nishigaki, H. Yoshioka, K. Nakatsu, *Acta Crystallogr., Sect. B* **1978**, *34*, 875.
[21] S.-Z. Zhan, Q.-J. Meng, X.-Z. You, G.-W. Wang, P.-J. Zheng, *Polyhedron* **1996**, *15*, 2655–2658.
[22] H. Oshio, H. Onodera, O. Tamada, H. Mizutani, T. Hikichi, T. Ito, *Chem. Eur. J.* **2000**, *6*, 2523–2530.
[23] a) J.-C. Dai, X.-T. Wu, Z.-Y. Fu, S.-M. Hu, W.-X. D, C.-P. Cui, L.-M. Wu, H.-H. Zhang, R.-Q. Sun, *Chem. Commun.* **2002**, 12–13; b) R. E. Melendez, C. V. K. Sharma, M. J. Zaworotko, C. Bauer, R. D. Rogers, *Angew. Chem. Int. Ed. Engl.* **1996**, *35*, 2213–2215.
[24] E. Colacio, J. M. Dominguez-Vera, F. Lloret, J. M. M. Sanchez, R. Kivekäs, A. Rodriguez, R. Sillanpää, *Inorg. Chem.* **2003**, *42*, 4209–4214.
[25] G. M. Sheldrick *SHELXS97 Program for Solution of Crystal Structures*; University of Göttingen, Göttingen, Germany, **1997**.

Received: November 24, 2004

 © 2005 Wiley-VCH Verlag GmbH & Co. KGaA, Weinheim

1,3,5-Triazapentadienes as Chelating Ligands: 1,2,4-Triphenyl-1,3,5-triazapentadiene Complexes of Cobalt(II), Nickel(II), Palladium(II), Copper(II) and Zinc(II)[‡]

Nadine Heße,[a] Roland Fröhlich,[a] Ionel Humelnicu,[b] and Ernst-Ulrich Würthwein*[a]

Dedicated to Prof. Paul v. R. Schleyer on the occasion of his 75th birthday

Keywords: Chelates / Ligand design / Triazapentadienes / N ligands / Tautomerism / DFT calculations

1,2,4-Triphenyl-1,3,5-triazapentadiene (**1a**), prepared from benzamidine and *N*-phenylbenzimidoyl chloride, was treated at room temperature with $CoCl_2$, $Ni(NO_3)_2$, Na_2PdCl_4, $CuCl_2$ and $ZnCl_2$ to form the corresponding six-membered 1:1 chelate complexes **1a·CoCl$_2$**, **1a·Ni(NO$_3$)$_2$**, **1a·PdCl$_2$**, **1a·CuCl$_2$**, and **1a·ZnCl$_2$**. In the solid state **1a·Ni(NO$_3$)$_2$** forms infinite linear chains, bridged by nitrate ions. From **1a** and $Cu(OTf)_2$ a 2:1 copper complex was obtained [(**1a**)$_2$·Cu(OTf)$_2$]. In all cases a proton shift from nitrogen atom N1 in the free ligand to N3 in the complex was observed. All complexes were completely characterized including X-ray crystallography. Quantum chemical DFT calculations indicate that triazapentadiene is a better ligand for $ZnCl_2$, $PdCl_2$ and $CuCl_2$ compared to β-diimines and *N*-acylamidines.

(© Wiley-VCH Verlag GmbH & Co. KGaA, 69451 Weinheim, Germany, 2005)

Introduction

1,3-Dicarbonyl derivatives and their nitrogen analogues (β-iminoketones and β-diimines) present valuable ligands for metal-ion chelation, either as neutral or as anionic species. Our synthetic interest is directed towards the development of analogous ligands, which bear a nitrogen atom in the central position instead of a carbon atom. From this point of view, diacylamines ("imides" in organic nomenclature) may be regarded as nitrogen analogues of β-diketones, *N*-acylamidines as nitrogen analogues of β-iminoketones (β-ketimino) and 1,3,5-triazapentadienes[1] (tap) as nitrogen analogues of β-diimines (Scheme 1). Some of these compounds have found intensive application in coordination chemistry, as they are quite potent bidentate chelating ligands [see, for example (β-diketiminato)metal complexes[2]]. The three nitrogen analogues deserve special attention of coordination chemists as they offer an additional coordination site at the central nitrogen atom, especially in their anionic form.

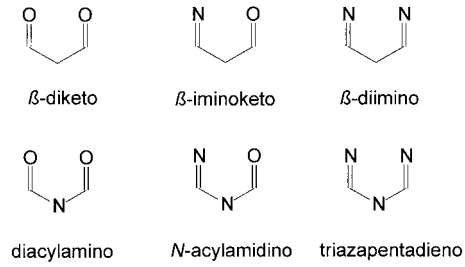

Scheme 1. Chelating ligands.

1,3,5-Triazapentadienes have rarely been used for the synthesis of metal complexes. However, already in 1907 Ley and Müller reported on the preparation of triazapentadienes and their successful complexation with cobalt(II) acetate, copper(II) acetate and nickel(II) acetate.[3] However, the nature of these complexes remained unclear. Many years later, Breuer and Small prepared a 1,3,5-triazapentadiene ligand starting from benzylamine, ethyl orthoformate and *N,N*-dibenzylformamide.[4] They obtained a blue (1,3,5-triazapentadiene)copper(II) chelate complex after treatment with copper(II) acetate in methanol. Siedle et al. treated a perfluorated imidoyl fluoride with 2 mol-equiv. of aniline to obtain a perfluorated 1,3,5-triazapendiene derivative, which may be converted into the corresponding 1,3,5-triazapentadienyl anion using *n*-butyllithium.[5] Treatment with silver oxide afforded the respective six-membered ring chelate silver complex, which in turn could be transmetallated to the

[‡] Unsaturated Hetero Chains, XII. Part XI: Ref.[19]

[a] Organisch-Chemisches Institut, Westfälische Wilhelms-Universität,
Corrensstraße 40, 48149 Münster, Germany
Fax: +49-251-83-39772
E-mail: wurthwe@uni-muenster.de
[b] Structure and Theoretical Chemistry Laboratory, Physical and Theoretical Chemistry Department, Faculty of Chemistry, "Al. I. Cuza" University of Iasi,
Carol I - 11, Iasi, 700506, Romania

corresponding Pd^{II}, Ir^{II} and Rh^{II} chelate complexes. Similarly, Fe^{II}, Co^{II} and Cu^{II} complexes were obtained by transmetallation of the corresponding potassium compound. Copper(I) and silver(I) complexes of fluorinated triazapentadienyl ligands were recently reported by Dias and Singh.[6,7]

However, there are several examples in the literature, where 1,3,5-triazapentadienes have been formed in situ from simpler amino compounds in the course of template reactions. For instance, Turnbull et al. treated $Cu(ClO_4)_2 \cdot 6H_2O$ with triazine in 95% methanol.[8] They obtained in 25% yield a 2:1 six-membered chelate Cu^{II} complex of the parent 1,3,5-triazapenta-1,4-diene, which was interpreted to be the result of copper(II)-catalyzed hydrolysis of triazine.[9] Analogously, tris(2-pyridyl)triazine may be hydrolyzed in the presence of copper(II) acetate to give bis[2,4-di(2-pyridyl)-1,3,5-triazapentadienyl]copper(II) complexes, either employing the corresponding triazapentadienes as neutral ligands or as anions after deprotonation.[10] Interestingly, the two nitrogen atoms in 1 and 5 position of the triazapentadiene act as coordination sites, not the 2-pyridyl subunits. Barker et al. reported on the in situ formation of the 2,4-diphenyl-1,3,5-triazapentadienyl ligand, when lithiobenzamidine was treated with $Pt(PhCN)_2Cl_2$ in ethereal solution. They isolated the 2:1 Pt^{II} chelate complex as a result of a nucleophilic attack of the benzamidine anion on the complexed benzonitrile. Similarly, a Pd^{II} complex was obtained from lithiobenzamidine and $Pd(PhCN)_2Cl_2$.[11] Acetamidine undergoes a self-condensation reaction to form a 2,4-dimethyl-1,3,5-triazapentadiene ligand when treated with nickel(II) chloride hexahydrate in methanol. The resulting Ni^{II} chloride chelate complex contains two neutral tautomers of the triazapentadiene units each with a proton at the central N3 position.[12] Nickel(II) chloride reacts with nitriles in the presence of oximes to form 2:1 chelate complexes.[13]

In this report we describe our experiments on the synthesis and thorough structural characterization of (1,3,5-triazapentadiene)metal complexes, of which some examples already were obtained by Ley and Müller in 1907.[3] These studies were part of an extended project concerning the application of 1,3,5-triazapentadienes for the synthesis of longer oligonitriles of the general formula $R_2N–(CR=N)_n–CR=NR$.[14]

Results and Discussion

As a typical, stable example 1,2,4-triphenyl-1,3,5-triazapentadiene (**1a**) was chosen as starting material for various complexation experiments. Its preparation is based on a procedure given by Ley and Müller,[3] according to which benzamidine is treated with *N*-phenylbenzimidoyl chloride. These authors used an equimolar surplus of amidine to trap the formed hydrochloride. In our experiments, this procedure did not work very successfully because of severe separation problems. We found it easier to use equimolar amounts of amidine and imidoyl chloride. Under these conditions mixtures of amidine hydrochloride and triazapentadienylium chloride **1a·HCl** are formed. However, the amidine hydrochloride was easily removed by washing with hot water in an ultrasonic bath. The free triazapentadiene **1a** was subsequently obtained in 29% yield after treatment with 2 N sodium hydroxide solution and repeated extraction with dichloromethane.

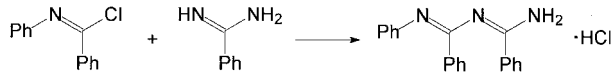

1a·HCl

Triazapentadienes are expected to be subject of tautomerism.[14] However, in our NMR, IR and X-ray studies all evidence is in favor for the indicated 1,3,5-triazapenta-1,3-diene structure **1a**. Indications for a tautomeric 1,3,5-triazpenta-1,4-diene structure were not observed.

Metal Complexes

Various metal complexes of triazapentadiene **1a** were easily obtained by co-dissolving metal salts with the ligand **1a** and crystallization, which was usually induced by adding less polar solvents to the reaction mixture.

Complex 1a·CoCl₂

The deep blue complex **1a·CoCl₂** is obtained from **1a** and cobalt(II) chloride hexahydrate after stirring of the components in acetonitrile in 72% yield as a fine precipitate. Recrystallisation from acetonitrile/DMF (1:1) and little diethyl ether produced a single crystal, suitable for X-ray analysis. The crystal system is triclinic ($P\bar{1}$) with two molecules in the unit cell. As Figure 1 shows, the ligand adopts now the tautomeric structure of a triazapenta-1,4-diene acting as a chelating ligand forming a six-membered 1:1 chelate with a tetrahedral Co^{II} moiety (compare ref.[15]).

Complex 1a·Ni(NO₃)₂

From equimolar amounts of **1a**, dissolved in DMF, and nickel(II) nitrate hexahydrate, dissolved in ethanol, an amorphous lilac precipitate **1a·Ni(NO₃)₂** is formed upon diffusion of diethyl ether. Dissolving in acetonitrile and repeated diffusion of diethyl ether yields turquoise needles in 76% yield, which are monoclinic ($P2_1/c$) and contain four molecules and four ethanol molecules in a unit cell. As Figures 2 and 3 display, a six-membered 1:1 chelate complex is formed and again a proton shift in the ligand from N1 to N3 is observed. In addition to ligand **1a**, one nitrate unit is coordinated in a bidentate fashion and two other ones are coordinated in a monodentate fashion to the Ni^{II} ion, forming an infinite chain structure with octahedral coordination sphere around Ni^{II}. A 2:1 nickel complex of another triazapentadiene system (acetimidoylacetamidine) has been reported by Norrestam.[12] Some of the corresponding diiminonickel complexes (β-iminoamino complexes) are known.[16]

 © 2005 Wiley-VCH Verlag GmbH & Co. KGaA, Weinheim

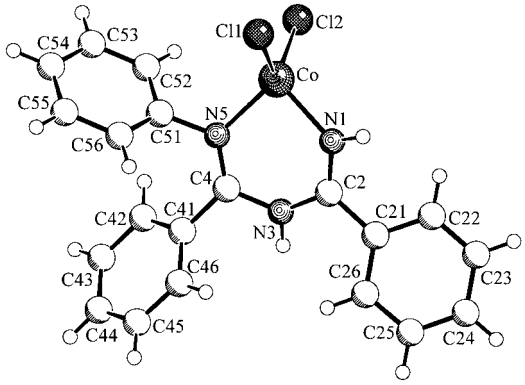

Figure 1. Molecular structure of complex **1a·CoCl$_2$** in the solid state (crystallographic numbering). Selected structural parameters: Bond lengths [Å] Co–Cl1 2.2472(5), Co–Cl2 2.2543(5), Co–N1 1.9785(14), Co–N5 2.0067(13), N1–C2 1.290(2), C2–N3 1.3836(19) N3–C4 1.3878(19) C4–N5 1.2923(19); bond angles [°] N1–Co–N5 91.68(5), N1–Co–Cl1 109.87(4), N5–Co–Cl1 115.55(4), N1–Co–Cl2 114.59(4), N5–Co–Cl2 109.25(4), Cl1–Co–Cl2 114.03(2), N1–C2–N3 121.34(14), C2–N3–C4 129.87(13), N3–C4–N5 121.88(13); torsional angles [°] Co–N1–C2–N3 –7.19, N1–C2–N3–C4 –15.96, C2–N3–C4–N5 21.57, N3–C4–N5–Co –3.18, N5–Co–N1–C2 16.83, N1–C2–C21–C22 –24.73, N5–C4–C41–C42 48.87, C4–N5–C51–C52 59.23.

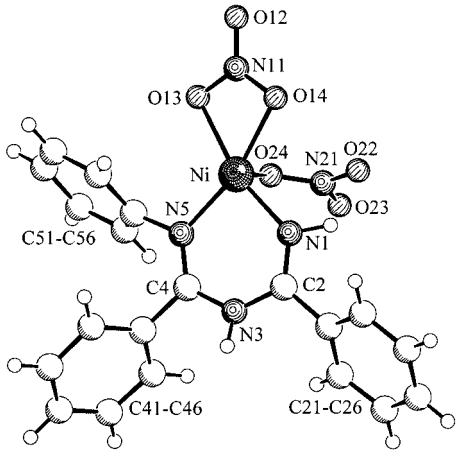

Figure 2. Molecular structure of one independent unit of **1a·Ni(NO$_3$)$_2$** in the solid state (crystallographic numbering). Selected structural parameters: Bond lengths [Å] Ni–O13 2.117(2), Ni–O14 2.124(2), Ni–O23* 2.090(2), Ni–O24 2.112(2), Ni–N1 1.969(3), Ni–N5 2.037(2), N1–C2 1.280(4), C2–N3 1.382(4), N3–C4 1.382(4), C4–N5 1.286(4); bond angles [°] N1–Ni–N5 90.69(11), N1–Ni–O23* 96.89(10), N5–Co–O23* 86.26(10), N1–Ni–O24 90.62(10), N5–Ni–O24 86.42(9), O23*-Ni–O24 169.57(8), N1–Ni–O13 164.70(10), N5–Ni–O13 104.15(10), N1–Ni–O14 104.16(10), N5–Ni–O14 165.02(10), O13–Ni–O14 61.19(9), N1–C2–N3 121.5(3), C2–N3–C4 130.3(3), N3–C4–N5 123.2(3); torsional angles [°] O12–N11–O13–Ni –179.47, O13–Ni–N1–C2 –168.54, O13–Ni–N5–C4 –176.35, Ni–N1–C2–N3 –3.53, N1–C2–N3–C4 7.59, C2–N3–C4–N5 –2.10, N3–C4–N5–Ni –6.41, N5–Ni–N1–C2 –2.50, N1–C2–C21–C26 38.18, N5–C4–C41–C46 –61.27, C4–N5–C51–C52–60.09.

Complex 1a·PdCl$_2$

A Pd^{II} complex was obtained from equimolar amounts of **1a** and Na_2PdCl_4 in DMF as solvent upon diffusion of diethyl ether into the reaction mixture. Orange small tiles

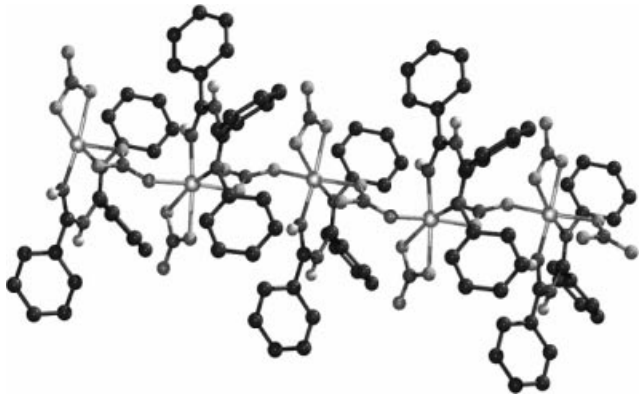

Figure 3. Plot of a part of the infinite chain structure of **1a·Ni(NO$_3$)$_2$** in the solid state.

were formed in 66% yield. They form a triclinic lattice ($P\bar{1}$) with two molecules and four DMF molecules in the unit cell. The X-ray diffraction of **1a·PdCl$_2$** (Figure 4) shows again the formation of a six-membered chelate 1:1 complex with a proton at the central nitrogen atom as a result of a proton shift. The chelate ring is not exactly planar, but slightly distorted with torsional angles up to 10° in a boat-shape fashion. As expected, Pd^{II} is square-planar coordinate. The corresponding (β-diimino)Pd^{II} complexes are reported to have catalytic activity in ethylene polymerization reactions.[17]

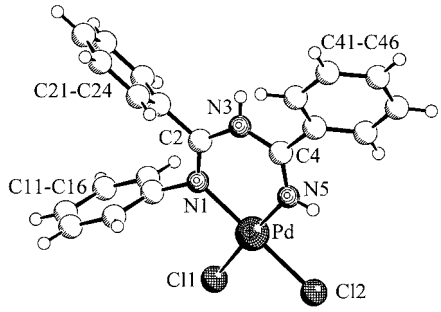

Figure 4. Molecular structure of one independent unit of **1a·PdCl$_2$** in the solid state (crystallographic numbering). Selected structural parameters: Bond lengths [Å] Pd–Cl1 2.2968(6), Pd–Cl2 2.3087(6), Pd–N1 2.0421(17), Pd–N5 1.9809(18), N1–C2 1.293(3), C2–N3 1.376(3), N3–C4 1.368(3), C4–N5 1.280(3); bond angles [°] N1–Pd–N5 89.49(7), N1–Pd–Cl1 93.51(5), N5–Pd–Cl1 176.96(6), N1–Pd–Cl2 175.85(5), N5–Pd–Cl2 87.70(6), Cl1–Pd–Cl2 89.33(2), N1–C2–N3 124.41(19), C2–N3–C4 129.36(18), N3–C4–N5 121.49(19); torsional angles [°] Pd–N1–C2–N3 0.78, N1–C2–N3–C4 –9.96, C2–N3–C4–N5 5.01, N3–C4–N5–Pd 8.79, N5–Pd–N1–C2 7.55, C2–N1–C11–C12 93.78, N1–C2–C21–C22 –66.94, N5–C4–C41–C46 39.49.

Complexes 1a·CuCl$_2$ and (1a)$_2$·Cu(OTf)$_2$

Equimolar amounts of ligand **1a** and copper(II) chloride dihydrate in ethanol yielded dark green little tiles in 46% yield after diffusion of diethyl ether. They crystallize in the triclinic space group $P\bar{1}$ with two molecules and two molecules of ethanol in the unit cell. Figure 5 shows the 1:1 chelate complex formed, again with a proton at N3 after a shift from position N1 of the free ligand. The six-membered

 © 2005 Wiley-VCH Verlag GmbH & Co. KGaA, Weinheim

chelate ring has a clear boat shape with Cu^{II} and N3 significantly above the plane of the four other atoms. The Cu^{II} ion displays a distorted tetrahedral coordination as a result of a Jahn–Teller distortion in this d^9 copper compound.

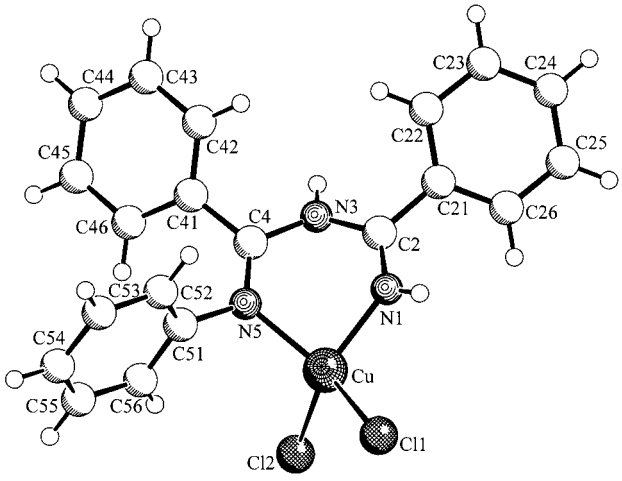

Figure 5. Molecular structure of one independent unit of **1a·CuCl$_2$** in the solid state (crystallographic numbering). Selected structural parameters: Bond lengths [Å] Cu–Cl1 2.2290(8), Cu–Cl2 2.2281(8), Cu–N1 1.928(2), Cu–N5 1.986(2), N1–C2 1.278(3), C2–N3 1.372(3), N3–C4 1.386(3), C4–N5 1.298(3); bond angles [°] N1–Cu–N5 87.90(9), N1–Cu–Cl1 97.87(8), N5–Cu–Cl1 142.89(7), N1–Cu–Cl2 138.42(8), N5–Cu–Cl2 99.28(7), Cl1–Cu–Cl2 100.21(3), N1–C2–N3 121.2(2), C2–N3–C4 126.5(2), N3–C4–N5 119.9(2); torsional angles [°] Cu–N1–C2–N3 19.50, N1–C2–N3–C4 19.74, C2–N3–C4–N5 –26.38, N3–C4–N5–Cu –5.96, N5–Cu–N1–C2 –35.97, N1–C2–C21–C26 37.39, N5–C4–C41–C46 –41.60, C4–N5–C51–C52 –70.68.

Reaction of ligand **1a** with copper(II) triflate in the molar ratio 2:1 in acetonitrile yielded a dark green solution, from which blue-violet rod-like crystals were obtained in 54% yield after diffusion of diethyl ether.[18] They crystallize in the triclinic space group $P\bar{1}$ with two molecules and two molecules of diethyl ether in the unit cell. From Figure 6 a 2:1 chelate complex can be derived. The ligands from two six-membered chelate rings with the mobile protons at position N3/N3*. Cu^{II} is square-planar coordinate with two additional longer contacts to the triflate counterions (2.498 Å). A 2:1 chelate complex of the parent 1,3,5-triazapentadiene, which was formed in situ by hydrolysis of triazine, has been reported by Turnbull et al.[8]

Complex 1a·ZnCl$_2$

Addition of a solution of zinc(II) chloride hydrate in ethanol to an ethanolic solution of triazapentadiene **1a** leads to a fine, colorless precipitate, from which a few single crystals **1a·ZnCl$_2$** were obtained after dissolving in little DMF and infusion of diethyl ether. **1a·ZnCl$_2$** crystallizes in the triclinic space group $P\bar{1}$ with two molecules in the unit cell. The X-ray analysis indicates the formation of a 1:1 chelate complex (Figure 7). The Zn^{II} ion displays a tetrahedral coordination. The complex **1a·ZnCl$_2$** is not planar, but shows a weak distortion towards boat shape. As in the other examples discussed before, a proton shift from the terminal amino group of **1a** to nitrogen atom N3 accompanies the

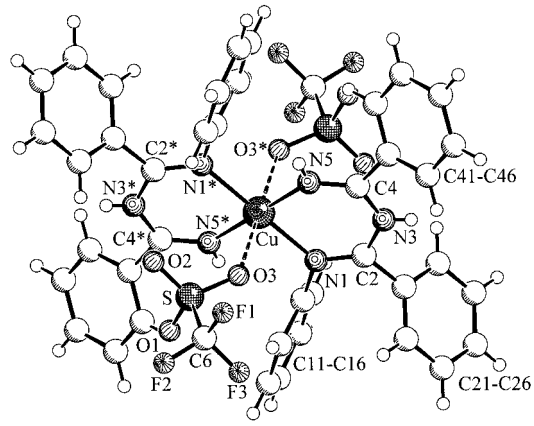

Figure 6. Molecular structure of one independent unit of **(1a)$_2$·Cu(OTf)$_2$** in the solid state (crystallographic numbering). Selected structural parameters: Bond lengths [Å] Cu–N1 2.0613(17), Cu–N5 1.9466(18), Cu–O3(18), 2.498(18), N1–C2 1.291(3), C2–N3 1.376(3), N3–C4 1.371(3), C4–N5 1.286(3); bond angles [°] N1–Cu–N5 86.36(7), N1–Cu–N1* 180.00(10), N5–Cu–N1* 93.64(7), N1–Cu–N5* 93.46(7), N5–Cu–N5* 180.00(10), N1*–Cu–N5* 86.36(7), N1–C2–N3 123.29(18), C2–N3–C4 127.62(18), N3–C4–N5 121.45(19); torsional angles [°] Cu–N1–C2–N3 9.89, N1–C2–N3–C4 2.08, C2–N3–C4–N5 –3.99, N3–C4–N5–Cu –7.47, N5–Cu–N1–C2 –14.13, C2–N1–C11–C12 –73.41, N1–C2–C21–C22 –63.75, N5–C4–C41–C42 –41.03, N1*–Cu–N5–C4 –166.64, N5*–Cu–N1–C2 165.87.

complexation. 2,4,6,8,8-Pentakis(dimethylamino)-1-oxa-3,5,7-aza-1,3,5,7-octatetraene, which may be regarded to include a triazapentadiene subunit, forms with $ZnCl_2$ a six-membered chelate complex, where $ZnCl_2$ bridges oxygen and nitrogen atoms.[19] (β-Diimino)Zn complexes are well known for their catalytic activity in CO_2/oxirane copolymerisations.[20]

Quantum Chemical Calculations

In order to rationalize the ability of the triazapentadiene ligand to coordinate to metal ions in comparison with similar systems (β-diimines, *N*-acylamidines) and to investigate their propensity for proton shifts in going from the free ligand to the chelate complex quantum chemical model calculations on the DFT level were performed. Zn^{II} and Pd^{II} complexes were investigated as typical (diamagnetic) examples of the complexes experimentally studied. The B3LYP hybrid functional was used together with the basis sets 6-31G*, 6-31+G(d,p), and MP2 and SCS-MP2[21]single points for the Zn^{II} compounds, and 6-31G*, 6-31+G(d,p) for C, H, N, O, Cl and the Stuttgart-Dresden Pd-ECP MWB[22] for the Pd^{II} complexes. All structures were completely optimized. The energies reported include zero point correction (no scaling). The G98 program[23] was employed using the build-in basis sets. BSSE effects[24] were considered using the counterpoise method as implemented in G03.[25]

As a measure for the tendency of the ligand to form chelate complexes simply the reaction energy of the complexation reaction was calculated, starting from free $ZnCl_2$ or

 © 2005 Wiley-VCH Verlag GmbH & Co. KGaA, Weinheim

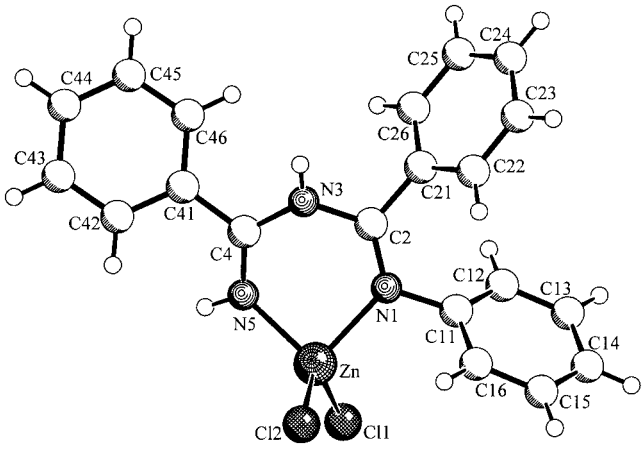

Figure 7. Molecular structure of one independent unit of **1a·$ZnCl_2$** in the solid state (crystallographic numbering). Selected structural parameters: Bond lengths [Å] Zn–Cl1 2.2221(4), Zn–Cl2 2.2394(5), Zn–N1 2.0615(12), Zn–N5 1.9818(12), N1–C2 1.2935(17), C2–N3 1.3903(18), N3–C4 1.3816(18), C4–N5 1.2856(18); bond angles [°] N1–Zn–N5 90.48(5), N1–Zn–Cl1 109.12(4), N5–Zn–Cl1 112.90(4), N1–Zn–Cl2 109.73(4), N5–Zn–Cl2 114.23(4), Cl1–Zn–Cl2 117.030(16), N1–C2–N3 121.88(12), C2–N3–C4 130.92(12), N3–C4–N5 120.93(12); torsional angles [°] Zn–N1–C2–N3 3.05, N1–C2–N3–C4 –20.12, C2–N3–C4–N5 12.14, N3–C4–N5–Zn 12.15, N5–Zn–N1–C2 11.87, C2–N1–C11–C12 –55.12, N1–C2–C21–C22 –49.66, N5–C4–C41–C42 22.42.

$PdCl_2$ in the gas phase and the free ligands in their lowest energy hydrogen-bonded conjugated form (Scheme 2).[16] For triazapentadiene and β-diimine two types of complexes were considered: first, the chelate complex involving a ligand after proton shift ("3*H* ligand"), second, a complex with a ligand in its original enolized form ("5*H* ligand") (Scheme 3). For the latter structures, at higher levels of DFT theory, the geometry optimizations opened the chelate structure in favor of hydrogen bonds from the chlorine atoms to the amino groups. In substituted derivatives as studied experimentally 5*H*-type structures were not observed (see above).

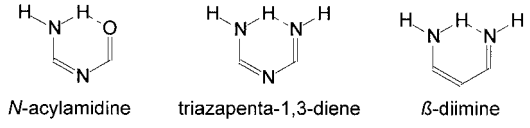

Scheme 2. Free ligands in their best gas phase structure (reference structures).

Among the $ZnCl_2$ compounds on all levels of theory triazapentadiene forms the strongest complexes acting as symmetrical ligand after proton shift from N1 to N3 (3*H* form) (Table 1). Indeed, this kind of coordination is experimentally observed (see above). The β-diimino ligand comes second in its two tautomeric forms, whereas (*N*-acylamidine) $ZnCl_2$ complexes are significantly less stable (by 5.0–5.7 kcal/mol). The β-diimino ligand is surprisingly differently treated by the theoretical methods employed. The DFT methods predict a better complexation energy for the ligand in its 5*H* form compared to the 3*H* form, probably

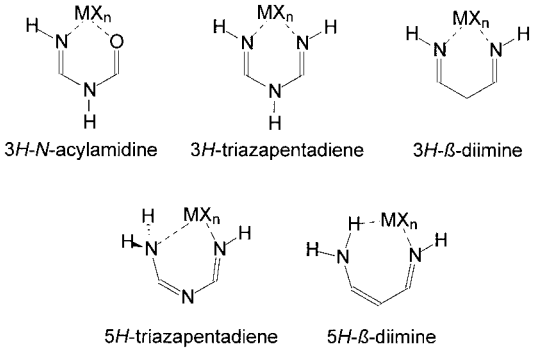

Scheme 3. Types of complexes (first row involving 3*H* ligands, second row 5*H* ligands.

due to the hydrogen bond formed. The MP2 single points, however, strongly favor the 3*H* form, which is known from many complexes.[2] The reason for this special behavior of the DFT methods remains unclear. For triazapentadiene, all methods prefer the 3*H* complexes over the 5*H* forms by 2.2–7 kcal/mol.

In the $PdCl_2$ series of chelate complexes (Table 2) a similar superiority of the triazapentadiene complex in its 3*H* form is found in accordance with the experimental findings (see above). Here, the β-diimine complexes come second (3.7–6.5 kcal/mol), whereas *N*-acylamidine forms the weakest complexes towards $PdCl_2$.[26,27] Both 5*H* forms of triazapentadiene and β-diimine bind significantly weaker than their 3*H* isomers and are therefore not expected to coordinate without tautomerism.

(*N*-Acylamidine)-[26] and (β-diimine)$PdCl_2$[17] complexes have found interest due to their potential as catalyst precursors.

For $CuCl_2$ preliminary UB3LYP/6-31+G(d,p) calculations (including ZPE and BSSE), which may probably be insufficient for such open-shell systems, indicate again best binding to triazapentadiene (–19.5 kcal/mol), whereas *N*-acylamidine and β-diimine coordinate weaker (–15.8 and –12.9 kcal/mol, respectively).

It is interesting to note that according to the gas-phase calculations triazapentadiene generally is a better ligand for $ZnCl_2$, $PdCl_2$ and $CuCl_2$ compared to β-diimine. Besides the electron-donating influence of the central nitrogen atom its abilility to allow π-conjugation over all five centers of the neutral ligand may be the reason for this observation. Thus, the introduction of the nitrogen atom in 3-position of β-diimine enhances the coordination ability of such chelating systems. This conclusion may be of importance with regard to the catalytic properties of such chelate complexes, e.g. as polymerization catalysts.

The comparison of the $ZnCl_2$, $PdCl_2$ and $CuCl_2$ complexation energies at similar levels of theory quantifies the common experience of significantly higher values for the $PdCl_2$ complexes as metal ion of the second transition row, whereas $CuCl_2$ and $ZnCl_2$ are coordinated with similar strength.

 © 2005 Wiley-VCH Verlag GmbH & Co. KGaA, Weinheim

Table 1. Quantum chemical complexation energies for $ZnCl_2$ model complexes at various computational levels including ZPE+BSSE [kcal/mol].

Ligand at $ZnCl_2$	B3LYP/6-31G(d)[a]	B3LYP/6-31+G(d,p)[a]	MP2/6-31+G(d,p)[b]	SCS-MP2/6-31+G(d,p)[b]
N-Acylamidine	–12.74	–13.95	–16.28	–16.22
3*H*-Triazapentadiene	–18.23	–19.64	–21.47	–21.21
5*H*-Triazapentadiene	–16.05	–17.35	–15.92	–14.88
3*H*-β-Diimine	–13.27	–12.33	–18.12	–18.68
5*H*-β-Diimine, H-bridged	–14.72	–17.19	–14.14	–13.01

[a] Fully geometry optimized. [b] Single points on B3LYP/6-31+G(d,p) geometries.

Table 2. Quantum chemical complexation energies for $PdCl_2$ model complexes at various computational levels including ZPE and BSSE (only column 4) [kcal/mol].

Ligand at $PdCl_2$	B3LYP/6-31G(d)/MWB[a]	B3LYP/6-31+G(d,p)/MWB[a]	B3LYP/6-31+G(d,p)/MWB[a]+BSSE
N-Acylamidine	–45.90	–40.19	–37.23
3*H*-Triazapentadiene	–63.37	–58.20	–54.51
5*H*-Triazapentadiene	–47.14	–41.08	–37.67
3*H*-β-Diimine	–59.73	–51.67	–48.19
5*H*-β-Diimine	–53.95	–47.53	–43.90

[a] Fully geometry optimized.

Conclusions

Triazapentadienes, easily prepared from amidines and imidoyl halides, are potent chelating ligands for metal complexation. 1,2,4-Triphenyl-1,3,5-triazapentadiene (**1a**) forms 1:1 six-membered chelate complexes with $CoCl_2$, $Ni(NO_3)_2$, Na_2PdCl_4, $CuCl_2$ and $ZnCl_2$, and additionally one 2:1 complex with $Cu(OTf)_2$. In the case of the Ni^{II} complex, a linear chain structure resulting from NO_3 bridging was observed. All new complexes have been fully characterized including X-ray crystallography.

By use of DFT-B3LYP calculations the relative complexation energies of model triazapentadiene, *N*-acylamidine and β-diimino ligands binding to $ZnCl_2$, $CuCl_2$ and $PdCl_2$ in the gas phase were evaluated. According to these theoretical results triazapentadiene binds stronger to these metal salts than β-diimine and *N*-acylamidine. For β-diimine and triazapentadiene, tautomeric complexes, characterized by the 3*H* and 5*H* form of the ligand, respectively, are discussed.

Experimental Section

Materials and Methods: IR: Nicolet 5DXC. ^{1}H NMR: Bruker WM 300 (300.13 MHz), Bruker AM 360 (360.13 MHz), Bruker AMX 400 (400.13 MHz) and Varian Unity plus (599.86 MHz), internal reference tetramethylsilane. ^{13}C NMR: Bruker WM 300 (75.47 MHz), Bruker AMX 400 (100.61 MHz) and Varian Unity 600 plus (150.85 MHz), internal reference tetramethylsilane or solvent. MS: MAT C 312, Finnigan (70 eV). ESI-MS: Quattro LC-Z, Micromass. MALDI (16–19 kV), nitrogen (337 nm, 3 ns); matrix: DTBC (2-[(2*E*)-3-(4-*tert*-butylphenyl)-2-methylprop-2-enylidene] malononitrile). UV/Vis: Cary 1 Bio, Varian. CHN: Elementar Vario El III. Melting points are uncorrected.

1,2,4-Triphenyl-1,3,5-triazapenta-1,3-diene (1a): In analogy to a literature procedure,[3] 7.73 g (64.7 mmol) of benzamidine was suspended in 20 mL of diethyl ether. 13.88 g (64.7 mmol) of *N*-phenylbenzimidoyl chloride,[28] dissolved in 40 mL of diethyl ether, was added dropwise. After stirring at room temperature for 2 h, the reaction mixture was heated to reflux for 1 h. The precipitate was removed by filtration and was treated with hot water in an ultrasonic bath in order to remove benzamidine hydrochloride. The remaining light yellow residue was separated and treated with 50 mL of 2 N sodium hydroxide solution. The suspension was extracted with portions of dichloromethane as long as solid was present in the reaction mixture. The combined organic layers were dried with magnesium sulfate. The solvent was removed under reduced pressure. Yield 5.54 g (18.5 mmol, 29%), light yellow solid, m.p. 143 °C (ref.[3] 152 °C). IR (KBr): $\tilde{\nu}$ = 3483, (s, NH_2), 3379 (s, NH_2), 3057 (m, $CH_{arom.}$), 3026 (w, $CH_{arom.}$), 2997 (w, $CH_{arom.}$), 1645 (vs, C=N), 1599 (vs, C=$C_{arom.}$), 1586 (vs, C=$C_{arom.}$), 1483 (m), 1448 (m), 1367 (s), 1315 (m), 1269 (m), 1227 (m), 1175 (w), 1074 (w), 1013 (m), 935 (w), 921 (w), 837 (m), 810 (m), 787 (m), 758 (s), 702 (vs) cm^{-1}. ^{1}H NMR (300 MHz, $CDCl_3$): δ = 6.80 (br., 2 H, NH_2), 6.93–6.99 (m, 1 H, $CH_{arom.}$), 7.05–7.08 (m, 2 H, $CH_{arom.}$), 7.22–7.28 (m, 2 H, $CH_{arom.}$), 7.41–7.51 (m, 6 H, $CH_{arom.}$), 7.78–7.81 (m, 2 H, $CH_{arom.}$), 8.01–8.05 (m, 2 H, $CH_{arom.}$) ppm. ^{13}C NMR (75.47 MHz, $CDCl_3$): δ = 122.0, 123.1, 128.0, 128.7, 128.9, 131.0, 131.3 ($C_{arom.}$), 135.4 (*i*-$C_{arom.}$), 136.9 (*i*-$C_{arom.}$), 151.8 (*i*-$C_{arom.}$), 154.7 (C=N), 161.7 (C=N) ppm. MS (70 eV): *m*/*z* (%) = 300 (14) [M^+ (^{13}C)], 299 (77) [M^+], 298 (83) [M^+ – 1], 196 (18) [M^+ – PhCN], 180 (100) [PhCNPh$^+$], 104 (57) [PhCN^+ + 1], 103 (25) [PhCN^+], 93 (32) [PhNH^+ + 2], 77 (84) [Ph^+], 51 (11) [$C_4H_3^+$]. $C_{20}H_{17}N_3$ (299.36): calcd. C 80.24 H 5.72 N 14.04; found C 80.13 H 5.38 N 14.03.

(1,2,4-Triphenyl-1,3,5-triazapenta-1,4-diene)cobalt(II) Chloride (1a·$CoCl_2$): 30 mg (0.10 mmol) of triazapentadiene **1a** and 24 mg (0.10 mmol) of cobalt(II) chloride hexahydrate were dissolved in 1 mL of acetonitrile. The resulting blue precipitate was filtered off. Yield 34 mg (0.07 mmol, 72%), blue powder, m.p. 208 °C. IR (KBr): $\tilde{\nu}$ = 3244 (s, NH), 3202 (m, NH), 3088 (m, $CH_{arom.}$), 3063 (m, $CH_{arom.}$), 3034 (m, $CH_{arom.}$), 1630 (vs, C=N), 1578 (s, C=$C_{arom.}$), 1504 (vs, C=$C_{arom.}$), 1493 (s, C=$C_{arom.}$), 1450 (m), 1375 (m), 1299 (m), 1275 (m), 1211 (m), 1138 (m), 852 (w), 781 (w), 752 (m), 696 (s) cm^{-1}. MS (MALDI, Matrix DCTB): *m*/*z* (%) = 393–397 [$C_{20}H_{16}N_3CoClH^+$], 358 [$C_{20}H_{16}N_3CoH^+$], 300 [$C_2H_{17}N_3H^+$]. UV/Vis (dichloromethane): λ_{max} ($\tilde{\nu}$, ε) = 621 (16103, 436), 542 (18450, 129), 364 (27473, 1124), 302 (33113, sh, 2351), 244 (40984,

20346), 227 (44053 cm^{-1}, sh, 14526 $M^{-1} cm^{-1}$) nm. $C_{20}H_{17}ClCoN_3 \cdot CH_3CN$ (470.25): calcd. C 55.97 H 3.99 N 9.79; found C 55.66 H 3.82 N 9.73.

X-ray Crystal Structure Analysis for 1a·$CoCl_2$:[29] Formula $C_{20}H_{17}Cl_2CoN_3 \cdot CH_3CN$, M = 470.25, blue crystal 0.30 × 0.20 × 0.15 mm, a = 10.064(1), b = 10.833(1), c = 11.996(1) Å, α = 105.12(1), β = 104.20(1), γ = 112.27(1)°, V = 1078.2(2) $Å^3$, $\rho_{calcd.}$ = 1.448 g cm^{-3}, μ = 10.59 cm^{-1}, empirical absorption correction (0.742 ≤ T ≤ 0.857), Z = 2, triclinic, space group $P\bar{1}$ (No. 2), λ = 0.71073 Å, T = 198 K, ω and φ scans, 12583 reflections collected (±h, ±k, ±l), [(sinθ)/λ] = 0.66 $Å^{-1}$, 5107 independent (R_{int} = 0.033) and 4512 observed reflections [$I \geq 2\sigma(I)$], 269 refined parameters, R = 0.029, wR_2 = 0.069, max. residual electron density 0.28 (–0.41) e·$Å^{-3}$, hydrogen atoms at N1 and N3 from difference Fourier calculations, others calculated and all refined as riding atoms.

(1,2,4-Triphenyl-1,3,5-triazapenta-1,4-diene)nickel(II) Nitrate [1a·$Ni(NO_3)_2$]: 30 mg (0.10 mmol) of triazapentadiene **1a** was dissolved in 0.5 mL of DMF and treated with 29 mg (0.10 mmol) of nickel(II) nitrate hexahydrate, dissolved in 1 mL of ethanol. After short shaking, a light-blue clear solution was formed. Diethyl ether was allowed to diffuse into the reaction mixture. After 1 d, a lilac precipitate was formed. It was filtered off and dissolved in 1 mL of acetonitrile. The solution turned blue. After repeated diffusion with diethyl ether, crystals were obtained. Yield 40 mg (0.08 mmol, 76%), turquoise needles, m.p. 209 °C (decomp.) IR (KBr): $\tilde{\nu}$ = 3350 (br., OH/NH), 1657 (s, C=N), 1614 (s, C=C_{arom}), 1587 (s, C=C_{arom}), 1555 (s, C=$C_{arom.}$), 1490 (s), 1441 (s), 1385 (vs), 1221 (m), 1024 (m), 779 (m), 752 (m), 696 (s) cm^{-1}. MS (MALDI, Matrix DCTB): m/z (%) = 655–661 (100) [$C_{40}H_{32}N_6NiH^+$], 300 (11) [$C_{20}H_{17}N_3H^+$]. UV/Vis (dichloromethane): λ_{max} ($\tilde{\nu}$, ε) = 342 (29240, sh, 651), 272 (36765, sh, 6897), 236 (42373, sh, 22873), 224 (44643 cm^{-1}, 23234 $M^{-1} cm^{-1}$) nm. $C_{20}H_{17}N_5NiO_6 \cdot C_2H_5OH$ (528.16): calcd. C 50.03 H 4.39 N 13.26; found C 50.84 H 4.53 N 13.25.

X-ray Crystal Structure Analysis for [1a·$Ni(NO_3)_2$]: Formula $C_{20}H_{17}N_5NiO_6 \cdot C_2H_5OH$, M = 528.16, light green crystal 0.50 × 0.15 × 0.05 mm, a = 11.961(1), b = 9.829(1), c = 22.025(1) Å, β = 100.63(1)°, V = 2544.9(4) $Å^3$, $\rho_{calcd.}$ = 1.378 g cm^{-3}, μ = 8.11 cm^{-1}, empirical absorption correction (0.687 ≤ T ≤ 0.961), Z = 4, monoclinic, space group $P2_1/c$ (No. 14), λ = 0.71073 Å, T = 198 K, ω and φ scans, 22808 reflections collected (±h, ±k, ±l), [(sinθ)/λ] = 0.68 $Å^{-1}$, 6386 independent (R_{int} = 0.037) and 5315 observed reflections [$I \geq 2\sigma(I)$], 311 refined parameters, R = 0.058, wR_2 = 0.179, max. residual electron density 1.98 (–0.85) e·$Å^{-3}$ close to solvent molecule, hydrogen atoms at N1 and N3 from difference Fourier calculations, others calculated and all refined as riding atoms, mixture of different solvents refined as disordered ethanol with isotropic thermal displacement parameters.

(1,2,4-Triphenyl-1,3,5-triazapenta-1,4-diene)palladium(II) Chloride (1a·$PdCl_2$): A mixture of 30 mg (0.10 mmol) of triazapentadiene **1a** and 29 mg (0.10 mmol) of disodium tetrachloropalladate(II) was dissolved in 1.7 mL of DMF. The orange solution was kept in a closed vial until a colorless precipitate was formed, which was filtered off. To the filtrate diethyl ether was allowed to diffuse. After 1 d, orange crystals had formed. Yield 41 mg (0.07 mmol, 66%), orange little tiles, m.p. 220 °C (decomp.). IR (KBr): $\tilde{\nu}$ = 3352 (m, NH), 3194 (m, NH), 3059 (m, $CH_{arom.}$), 2999 (m, $CH_{arom.}$), 2931 (m, $CH_{arom.}$), 1649 (vs, C=N), 1632 (vs, C=N), 1580 (m, C=$C_{arom.}$), 1516 (s, C=$C_{arom.}$), 1487 (s, C=$C_{arom.}$), 1444(m), 1387 (s), 1312 (m), 1255 (m), 1217 (m), 1156 (m), 1105 (m), 1026 (w), 868 (w), 773 (m), 719 (m), 700 (s) cm^{-1}. MS (MALDI, Matrix DCTB): m/z (%) = 436–447 [$C_{20}H_{16}N_3ClPdH^+$], 404 [$C_{20}H_{17}N_3^+$ + DCTB], 300 [$C_{20}H_{17}N_3^+$]. UV/Vis (dichlormethane): λ_{max} ($\tilde{\nu}$, ε) = 388 (25773, 308), 276 (36232, sh, 9829), 241 (41494, 31043), 228 (42860 cm^{-1}, sh, 27870 $M^{-1} cm^{-1}$) nm. $C_{20}H_{17}Cl_2N_3Pd \cdot 2C_3H_7NO$ (622.86): calcd. C 50.13 H 5.02 N 11.24; found C 49.88 H 5.07 N 11.13.

X-ray Crystal Structure Analysis for 1a·$PdCl_2$: Formula $C_{20}H_{17}Cl_2N_3Pd \bullet 2C_3H_7NO$, M = 622.86, yellow crystal 0.30 × 0.25 × 0.15 mm, a = 10.575(1), b = 11.341(1), c = 13.196(1) Å, α = 67.62(1), β = 82.38(1), γ = 71.68(1)°, V = 1389.1(2) $Å^3$, $\rho_{calcd.}$ = 1.489 g cm^{-3}, μ = 8.92 cm^{-1}, empirical absorption correction (0.776 ≤ T ≤ 0.878), Z = 2, triclinic, space group $P\bar{1}$ (No. 2), λ = 0.71073 Å, T = 198 K, ω and φ scans, 11495 reflections collected (±h, ±k, ±l), [(sinθ)/λ] = 0.66 $Å^{-1}$, 6419 independent (R_{int} = 0.035) and 5904 observed reflections [$I \geq 2\sigma(I)$], 335 refined parameters, R = 0.029, wR_2 = 0.073, max. residual electron density 0.72 (–0.84) e·$Å^{-3}$, hydrogen atoms at N3 and N5 from difference Fourier calculations, others calculated and all refined as riding atoms.

(1,2,4-Triphenyl-1,3,5-triazapenta-1,4-diene)copper(II) Chloride (1a·$CuCl_2$): A solution of 0.10 mmol (17 mg) of copper(II) chloride dihydrate in 1 mL of ethanol was added dropwise to a solution of 30 mg (0.10 mmol) of triazapentadiene **1a** in 5 mL of ethanol. The mixture turned dark green. After 1 d, dark green crystals had formed upon diffusion with diethyl ether. Yield 22 mg (0.05 mmol, 46%), green little tiles, m.p. 154 °C (decomp.). IR (KBr): $\tilde{\nu}$ = 3429 (br., s, OH), 3248 (s, NH), 3192 (sh, m, NH), 3061 (m, $CH_{arom.}$), 3034 (m, $CH_{arom.}$), 2962 (m, $CH_{aliph.}$), 2932 (m, $CH_{aliph.}$), 2883 (br.,$CH_{aliph.}$), 1654 (s, C=N), 1630 (vs, C=$C_{arom.}$), 1580 (m, C=$C_{arom.}$), 1497 (vs), 1447 (m), 1381 (m), 1319 (m), 1306 (m), 1281 (m), 1219 (m), 1138 (m), 1076 (m), 1055 (m), 1030 (m), 865 (sh), 854 (m), 787 (m), 771 (m), 750 (m), 716 (m), 700 (s) cm^{-1}. MS (MALDI, Matrix DCTB): m/z (%) = 362–365 [$C_{20}H_{16}N_3CuH^+$], 300 [$C_{20}H_{17}N_3H^+$]. UV/Vis (dichloromethane): λ_{max} ($\tilde{\nu}$, ε) = 407 (24570, 1415), 281 (35587, sh, 10370), 243 (41152 cm^{-1}, 24796 $M^{-1} cm^{-1}$) nm. $C_{20}H_{17}Cl_2CuN_3 \cdot C_2H_5OH$ (479.87): calcd. C 55.06 H 4.83 N 8.76; found C 54.69 H 4.49 N 8.70.

X-ray Crystal Structure Analysis for 1a·$CuCl_2$: Formula $C_{20}H_{17}Cl_2CuN_3 \cdot C_2H_5OH$, M = 479.87, green crystal 0.25 × 0.10 × 0.05 mm, a = 9.562(1), b = 10.099(1), c = 11.909(1) Å, α = 76.21(1), β = 78.15(1), γ = 83.05(1)°, V = 1089.9(2) $Å^3$, $\rho_{calcd.}$ = 1.462 g cm^{-3}, μ = 12.65 cm^{-1}, empirical absorption correction (0.743 ≤ T ≤ 0.939), Z = 2, triclinic, space group $P\bar{1}$ (No. 2), λ = 0.71073 Å, T = 198 K, ω and φ scans, 11413 reflections collected (±h, ±k, ±l), [(sinθ)/λ] = 0.66 $Å^{-1}$, 5134 independent (R_{int} = 0.043) and 3844 observed reflections [$I \geq 2\sigma(I)$], 272 refined parameters, R = 0.041, wR_2 = 0.085, max. residual electron density 0.36 (–0.51) e·$Å^{-3}$, hydrogen atoms at N1 and N3 from difference Fourier calculations, others calculated and all refined as riding atoms.

[Bis(1,2,4-triphenyl-1,3,5-triazapenta-1,4-diene)]copper(II) Triflate [$(1a)_2$·$Cu(OTf)_2$]: 30 mg (0.10 mmol) of triazapentadiene **1a** and 18 mg (0.05 mmol) of copper(II) triflate were dissolved in 1 mL of acetonitrile. Then diethyl ether was allowed to diffuse into the green solution. After 4 d, crystals were removed by filtration. Yield 30 mg (0.03 mmol, 54%), blue-violet rods, m.p. 211 °C (decomp.). IR (KBr): $\tilde{\nu}$ = 3339 (s, NH), 3204 (m, NH), 3099 (m, $CH_{arom.}$), 3061 (m, $CH_{arom.}$), 1655 (s, C=N), 1581 (m, C=$C_{arom.}$), 1520 (vs, C=$C_{arom.}$), 1447 (m), 1396 (m), 1313 (s), 1283 (vs), 1257 (vs), 1225 (vs), 1167 (s), 1155 (s), 1032 (vs), 921 (w), 852 (m), 810 (w), 783 (m), 721 (m), 696 (s) cm^{-1}. MS (MALDI, Matrix DCTB): m/z (%) = 660–664 (28) [$C_{40}H_{32}N_6CuH^+$], 362 (22) [$C_{20}H_{16}N_3CuH^+$], 300 (100) [$C_{20}H_{17}N_3H^+$]. UV/Vis (dichloromethane): λ_{max} ($\tilde{\nu}$, ε) = 373 (26810, 3117), 315 (31746, 11573), 248 (40323, 91178), 228

 © 2005 Wiley-VCH Verlag GmbH & Co. KGaA, Weinheim

(43860 cm^{-1}, sh, 59688 $M^{-1} cm^{-1}$) nm. $C_{42}H_{34}CuF_6N_6O_6S_2 \cdot 2C_4H_{10}O$ (1108.65): calcd. C 52.52 H 3.57 N 8.75; found C 52.49 H 3.30 N 8.74.

X-ray Crystal Structure Analysis for [(1a)$_2$·Cu(OTf)$_2$]: Formula $C_{40}H_{34}CuN_6 \cdot CF_3SO_3 \cdot 2C_4H_{10}O$, M = 1108.65, blue-purple crystal 0.35 × 0.30 × 0.25 mm, a = 10.607(1), b = 11.703(1), c = 12.758(1) Å, α = 99.27(1), β = 108.30(1), γ = 113.76(1)°, V = 1298.6(2) Å^3, $\rho_{calcd.}$ = 1.418 g cm^{-3}, μ = 5.81 cm^{-1}, empirical absorption correction ($0.823 \leq T \leq 0.868$), Z = 1, triclinic, space group $P\bar{1}$ (No. 2), λ = 0.71073 Å, T = 198 K, ω and φ scans, 9438 reflections collected ($\pm h$, $\pm k$, $\pm l$), [(sinθ)/λ] = 0.68 Å^{-1}, 6383 independent (R_{int} = 0.025) and 5446 observed reflections [$I \geq 2\sigma(I)$], 341 refined parameters, R = 0.048, wR_2 = 0.131, max. residual electron density 1.05 (–0.47) e·Å^{-3} close to the ether molecules, hydrogen atoms at N3 and N5 from difference Fourier calculations, other calculated and all refined as riding atoms.

(1,2,4-Triphenyl-1,3,5-triazapenta-1,4-diene)zinc(II) Chloride (1a·ZnCl$_2$): 30 mg (0.10 mmol) of triazapentadiene **1a** was dissolved in 4 mL of ethanol. Insoluble residues were filtered off. Then the solution was treated dropwise with a solution of 14 mg (0.10 mmol) of zinc(II) chloride hydrate in 0.4 mL of ethanol. A light colorless precipitate formed, which was dissolved by addition of as little as possible of DMF. After filtration, diethyl ether was allowed to diffuse, until colorless crystals formed. Low yield, not sufficient for complete analysis and spectroscopy. M.p. 193 °C. MS (MALDI, Matrix DTCB): m/z (%) = 398–404 (8) [$C_{20}H_{16}N_3ZnClH^+$], 300 (100) [$C_{20}H_{17}N_3H^+$].

X-ray Crystal Structure Analysis for 1a·ZnCl$_2$: Formula $C_{20}H_{17}Cl_2N_3Zn$, M = 435.64, colourless crystal 0.50 × 0.35 × 0.20 mm, a = 9.884(1), b = 10.390(1), c = 11.032(1) Å, α = 110.13(1), β = 98.74(1), γ = 107.80(1)°, V = 970.0(2) Å^3, $\rho_{calcd.}$ = 1.492 g cm^{-3}, μ = 15.50 cm^{-1}, empirical absorption correction ($0.511 \leq T \leq 0.747$), Z = 2, triclinic, space group $P\bar{1}$ (No. 2), λ = 0.71073 Å, T = 198 K, ω and φ scans, 7412 reflections collected ($\pm h$, $\pm k$, $\pm l$), [(sinθ)/λ] = 0.67 Å^{-1}, 4720 independent (R_{int} = 0.016) and 4409 observed reflections [$I \geq 2\sigma(I)$], 241 refined parameters, R = 0.024, wR_2 = 0.061, max. residual electron density 0.33 (–0.40) e·Å^{-3}, hydrogen atoms at N3 and N5 from difference Fourier calculations, others calculated and all refined as riding atoms.

Acknowledgments

The authors thank the Deutsche Forschungsgemeinschaft [Sonderforschungsbereich 424 and Graduate College "Hochreaktive Mehrfachbindungssysteme" (Postdoktorandenstipendium to I. H. 2001–2002)] and the Fonds der Chemischen Industrie (Frankfurt) for financial support.

[1] J. A. Elvidge, N. R. Barot, in *The Chemistry of Functional Groups*, Supplement A ("The Chemistry of the C=N Group"), Wiley, Chichester, **1989**, vol. 2, p. 1168–1249.
[2] L. Bourget-Merk, M. F. Lappert, J. R. Severn, *Chem. Rev.* **2002**, *102*, 3031.3066.
[3] H. Ley, F. Müller, *Ber. Dtsch. Chem. Ges.* **1907**, *40*, 2950–2958.
[4] S. W. Breuer, R. W. H. Small, *Acta Crystallogr. Sect. C* **1991**, *47*, 871–872.
[5] A. R. Siedle, R. J. Webb, F. E. Behr, R. A. Newmark, D. A. Weil, K. Erickson, R. Naujok, M. Brostrom, M. Mueller, S.-H. Chou, V. G. Young Jr., *Inorg. Chem.* **2003**, *42*, 932–934.
[6] H. V. R. Dias, S. Singh, *Inorg. Chem.* **2004**, *43*, 5786–5788.
[7] H. V. R. Dias, S. Singh, *Inorg. Chem.* **2004**, *43*, 7396–7402.
[8] M. M. Turnbull, M. Y. Wei, R. D. Willett, *J. Coord. Chem.* **1995**, *35*, 11–17.
[9] E. I. Lerner, S. J. Lippard, *J. Am. Chem. Soc.* **1976**, *98*, 5397–5398.
[10] T. Kajiwara, A. Kamiyama, T. Ito, *Chem. Commun.* **2002**, 1256–1257.
[11] J. Barker, M. Kilner, M. M. Mahmoud, S. C. Wallwork, *J. Org. Chem., Dalton Trans.* **1989**, 837–841.
[12] R. Norrestam, *Acta Crystallogr. Sect. C* **1984**, *40*, 955–957.
[13] M. N. Kopylovich, A. J. L. Pombeiro, A. Fischer, L. Kloo, V. Yu. Kukushkin, *Inorg. Chem.* **2003**, *42*, 7239–7248.
[14] N. Heße, Dissertation, Univ. Münster, **2004**.
[15] F. A. Cotton, L. M. Daniels, J. H. Matonic, X. Wang, C. A. Murillo, *Polyhedron* **1997**, *16*, 1177–1191.
[16] J. F. Parks, R. H. Holm, *Inorg. Chem.* **1968**, *7*, 1408–1416.
[17] J. Feldman, S. J. McLain, A. Parthasarathy, W. J. Marshall, C. J. Calabrese, S. D. Arthur, *Organometallics* **1997**, *16*, 1514.
[18] This substanz was first synthesized by J. K. Eberhardt, Ph. D. work, Univ. Münster, **2002**.
[19] Chr. Möllers, J. Prigge, B. Wibbeling, R. Fröhlich, A. Brockmeyer, H. J. Schäfer, E. Schmälzlin, C. Bräuchle, K. Meerholz, E.-U. Würthwein, *Eur. J. Org. Chem.* **2003**, 1198–1208.
[20] G. W. Coates, D. R. Moore, *Angew. Chem.* **2004**, *116*, 6784–6806; *Angew. Chem. Int. Ed.* **2004**, *43*, 6618–6639.
[21] S. Grimme, *J. Chem. Phys.* **2003**, *118*, 9095–9102.
[22] D. Andrae, U. Häußermann, M. Dolg, H. Stoll, H. Preuß, *Theor. Chim. Acta* **1990**, *77*, 123–141.
[23] M. J. Frisch, G. W. Trucks, H. B. Schlegel, G. E. Scuseria, M. A. Robb, J. R. Cheeseman, V. G. Zakrzewski, J. A. Montgomery, Jr., R. E. Stratmann, J. C. Burant, S. Dapprich, J. M. Millam, A. D. Daniels, K. N. Kudin, M. C. Strain, O. Farkas, J. Tomasi, V. Barone, M. Cossi, R. Cammi, B. Mennucci, C. Pomelli, C. Adamo, S. Clifford, J. Ochterski, G. A. Petersson, P. Y. Ayala, Q. Cui, K. Morokuma, N. Rega, P. Salvador, J. J. Dannenberg, D. K. Malick, A. D. Rabuck, K. Raghavachari, J. B. Foresman, J. Cioslowski, J. V. Ortiz, A. G. Baboul, B. B. Stefanov, G. Liu, A. Liashenko, P. Piskorz, I. Komaromi, R. Gomperts, R. L. Martin, D. J. Fox, T. Keith, M. A. Al-Laham, C. Y. Peng, A. Nanayakkara, M. Challacombe, P. M. W. Gill, B. Johnson, W. Chen, M. W. Wong, J. L. Andres, C. Gonzalez, M. Head-Gordon, E. S. Replogle, J. A. Pople, *Gaussian 98*, Revision A.11.3, Gaussian, Inc., Pittsburgh PA, **2002**.
[24] N. R. Kestner, J. E. Combariza, *Rev. Comput. Chem.* **1999**, *13*, 99–132.
[25] M. J. Frisch, G. W. Trucks, H. B. Schlegel, G. E. Scuseria, M. A. Robb, J. R. Cheeseman, J. A. Montgomery, Jr., T. Vreven, K. N. Kudin, J. C. Burant, J. M. Millam, S. S. Iyengar, J. Tomasi, V. Barone, B. Mennucci, M. Cossi, G. Scalmani, N. Rega, G. A. Petersson, H. Nakatsuji, M. Hada, M. Ehara, K. Toyota, R. Fukuda, J. Hasegawa, M. Ishida, T. Nakajima, Y. Honda, O. Kitao, H. Nakai, M. Klene, X. Li, J. E. Knox, H. P. Hratchian, J. B. Cross, C. Adamo, J. Jaramillo, R. Gomperts, R. E. Stratmann, O. Yazyev, A. J. Austin, R. Cammi, C. Pomelli, J. W. Ochterski, P. Y. Ayala, K. Morokuma, G. A. Voth, P. Salvador, J. J. Dannenberg, V. G. Zakrzewski, S. Dapprich, A. D. Daniels, M. C. Strain, O. Farkas, D. K. Malick, A. D. Rabuck, K. Raghavachari, J. B. Foresman, J. V. Ortiz, Q. Cui, A. G. Baboul, S. Clifford, J. Cioslowski, B. B. Stefanov, G. Liu, A. Liashenko, P. Piskorz, I. Komaromi, R. L. Martin, D. J. Fox, T. Keith, M. A. Al-Laham, C. Y. Peng, A. Nanayakkara, M. Challacombe, P. M. W. Gill, B. Johnson, W. Chen, M. W. Wong, C. Gonzalez, J. A. Pople, *Gaussian 03*, Revision C.01, Gaussian, Inc., Wallingford CT, **2004**.
[26] J. K. Eberhardt, R. Fröhlich, E.-U. Würthwein, *J. Org. Chem.* **2003**, *68*, 6690–6694.
[27] Unfortunately, the chelate complex of $PdCl_2$ with *N*-acylamidine $(CH_3)HN–CH=N–CHO$ was not considered in ref.[26] (Figure 2). Using the basis set B3LYP/6-31+G(d,p) for C,H,N,O,Cl and LANL2DZ + polarisation functions (A. W. Ehlers, M. Böhme, S. Dapprich, A. Gobbi, A. Höllwarth, V. Jonas, K. F. Köhler, R. Stegmann, A. Veldkamp, G. Frenking, *Chem. Phys. Lett.* **1993**, *208*, 111–114) and including ZPE, a total energy of

 © 2005 Wiley-VCH Verlag GmbH & Co. KGaA, Weinheim

E_{tot} = –1349.77981 au and a relative energy of only 0.16 kcal/mol with respect to best isomeric structure given there (**5a**) was obtained.

[28] R. A. Abramovitch, R. B. Rogers, *J. Org. Chem.* **1974**, *39*, 1802–1807.

[29] Data sets were collected with a Nonius KappaCCD diffractometer, equipped with a rotating anode generator. Programs used: data collection COLLECT (Nonius B. V., **1998**), data reduction Denzo-SMN (Z. Otwinowski, W. Minor, *Methods Enzymol.* **1997**, *276*, 307–326), absorption correction SORTAV (R. H. Blessing, *Acta Crystallogr., Sect. A* **1995**, *51*, 33–37; R. H. Blessing, *J. Appl. Crystallogr.* **1997**, *30*, 421–426), structure solution SHELXS-97 (G. M. Sheldrick, *Acta Crystallogr., Sect. A* **1990**, *46*, 467–473), structure refinement SHELXL-97 (G. M. Sheldrick, University of Göttingen, **1997**), graphics DIAMOND (K. Brandenburg, University of Bonn, **1997**) and SCHAKAL (E. Keller, University of Freiburg, **1997**). Crystallographic data (excluding structure factors) for the structures reported in this paper have been deposited with the Cambridge Crystallographic Data Centre as supplementary publication CCDC-254443 [**(1a)$_2$·Cu(OTf)$_2$**], -254444 (**1a·CuCl$_2$**), -254445 (**1a·ZnCl$_2$**), -254446 (**1a·PdCl$_2$**), -254447 [**1a·Ni(NO$_3$)$_2$**], and -254448 (**1a·CoCl$_2$**). These data can be obtained free of charge from The Cambridge Crystallographic Data Centre via www.ccdc.cam.ac.uk/data_request/cif..

Received: December 9, 2004

 © 2005 Wiley-VCH Verlag GmbH & Co. KGaA, Weinheim

Towards Understanding of the Selective Precipitation of Alkali Metal Cations in Presence of Dipicrylamine Anion

Suresh Eringathodi,[a] Pragati Agnihotri,[a] Bishwajit Ganguly,[a] Pragnya Bhatt,[a] Palani Sivagnana Subramanian,[a] Parimal Paul*[a] and Pushpito K. Ghosh*[a]

Keywords: Dipicrylamine / Alkali and alkaline earth metals / Selectivity / Single-crystal X-ray structure / Structure-selectivity correlation

Dipicrylamine anion (DPA^-) precipitates out [K(DPA)] with high selectivity from salt bitterns containing Na^+, K^+, and Mg^{2+}, whereas the same ligand shows poor selectivity towards K^+ – and much higher selectivity towards Cs^+ – in studies conducted with a mixture of K^+, Rb^+, and Cs^+. Their single-crystal structures reveal that the K^+ and Rb^+ salts have similar layered structures, with 8 oxygen atoms from seven DPA^- anions encapsulating the metal cation, whereas the Cs^+ salt possesses a channel-like structure with the metal ion encapsulated by ten oxygen atoms from six DPA^-. The conformation of DPA^- in the [Cs(DPA)] single crystal matches closely that of DPA in crystalline state. M···O and intermolecular C–H···O interactions together stabilize the structures. The ^{133}Cs NMR spectrum of the poorly soluble [Cs(DPA)] shows an upfield shift of the peak with respect to CsCl as a result of the interaction with the oxygen atoms of DPA^-, whereas ^{23}Na NMR spectrum of the highly soluble [Na(DPA)] shows no such upfield shift compared to NaCl. Powder XRD patterns of bulk [M(DPA)] (M = K^+, Rb^+, and Cs^+) precipitates show that these are similar to the patterns obtained by simulation of the single-crystal X-ray data. The selectivity of precipitation correlates qualitatively with the size and hydration enthalpies of the ions.

(© Wiley-VCH Verlag GmbH & Co. KGaA, 69451 Weinheim, Germany, 2005)

Introduction

Dipicrylamine (2,2′,4,4′,6,6′-hexanitrodiphenylamine, DPA) anion (Figure 1) has been used for the extraction of K^+ from sea bittern (mixture of K^+, Na^+, and Mg^{2+}).[1] The process of such extraction is depicted in Scheme 1. In a study conducted with a mixture of K^+, Rb^+, and Cs^+, it has been reported that the Cs^+ ion shows maximum selectivity towards DPA.[2] Indeed, recovery of Cs^+ from radioactive waste has been reported.[3] In spite of the large number of reports on the utility of DPA^-, little is known about the factors which control its selectivity towards the different alkali and alkaline earth metal ions.

DPA possesses some interesting structural features, namely: (i) six nitro groups that are flexible and can interact and adjust in the space, (ii) a secondary amine group that can be deprotonated with $Ca(OH)_2$ to form a water soluble salt, and (iii) partial delocalization of the resultant charge mediated by the aromatic rings, that may facilitate coordination of the oxygen atoms with suitable metal ions. Single-crystal X-ray structures of DPA and some of its organic

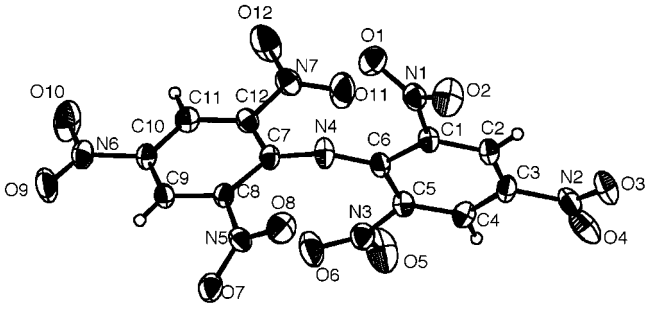

Figure 1. ORTEP view of the deprotonated dipicrylamine (DPA^-) showing atom numbering scheme.

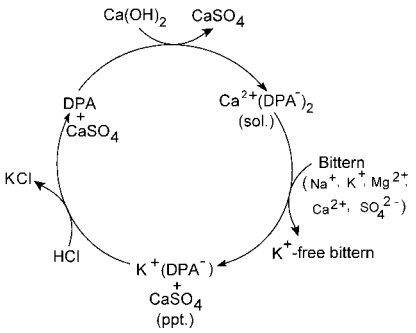

Scheme 1. Cyclic diagram showing extraction of KCl from bittern using DPA and $Ca(OH)_2$ and recycling of DPA.

[a] Analytical Science Discipline, Central Salt and Marine Chemicals Research Institute,
Bhavnagar 364002, India
E-Mail: pkghosh@csmcri.org (P. K. Ghosh)
ppaul@csmcri.org (P. Paul)

Supporting information for this article is available on the WWW under http://www.eurjic.org or from the author.

salts have been reported.[4] Computational study on the intermolecular interactions observed in the crystal structure of DPA has also been reported recently.[5] Crystal structures of K^+ and Ag^+ salts of DPA^- have been reported, although no detailed analysis of the former compound was carried out in absence of adequate refinement of the structure.[6a,6b] In the case of Rb^+ and Cs^+ salts of DPA^-, only unit cell parameters have been reported earlier.[6b–6d]

Herein, we report quantitative ion-chromatographic studies of DPA^- selectivity towards bittern and an equimolar aqueous mixture of K^+, Rb^+, and Cs^+ salts. We also report the synthesis and single-crystal X-ray structures of K^+, Rb^+, and Cs^+ salts of DPA^- to unravel the causes underlining selectivity, and further show that the powder XRD patterns simulated from these structures tally well with those of the bulk precipitated salts. ^{133}Cs and ^{23}Na solution NMR studies of the poorly soluble and highly soluble DPA^- salts of Cs^+ and Na^+, respectively, were also undertaken. These studies have enabled us to understand the possible factors that govern observed selectivity.

Results

Ion Selectivity

Ion selectivity was estimated by analyzing the composition of metal ions in the precipitate formed upon addition of $Ca(DPA)_2$ into aqueous mixtures of cations, as described in the experimental section. Our initial study was focused on the selectivity towards K^+ in bittern. The concentrations of Na^+, K^+, Mg^{2+}, and Ca^{2+} in bittern used for this study were estimated to be 0.8 M, 1.2 M, 2.1 M, and 0.2 M, respectively, from ion chromatographic analysis of the bittern. The precipitate obtained upon addition of $Ca(DPA)_2$ into bittern was similarly analyzed for the metal ion composition after destructive degradation of the complex. The chromatogram shows complete absence of Mg^{2+} despite its high concentration in bittern whereas the relative concentration of K^+ was found to 97.1% (Figure S1, Supporting Information, see also the footnote on the first page of this article). Na^+ and Ca^{2+} were present in the chromatograms to the extent of 2.7% and 0.2%, respectively, but these peaks were found even for a blank chromatogram with Milli Q water. The high selectivity evident for K^+ was reproducible on larger scale and corroborates earlier findings of high selectivity.[1] However, when the studies were conducted with equimolar mixture of KCl, RbCl, and CsCl, the observed selectivities were: 2.6%, 6.6%, and 90.7% for K^+, Rb^+, and Cs^+, respectively, i.e., very poor selectivity towards K^+ in marked contrast to the behavior found with bittern.[1]

Synthesis of the Complexes

[M(DPA)] [M = Na^+ (**1**), K^+ (**2**), Rb^+ (**3**), and Cs^+ (**4**)] salts of alkali metal ions were synthesized. The K^+, Rb^+, and Cs^+ salts **2**–**4** were synthesized by the reaction of the respective metal chloride salts with aqueous solution of the soluble $Ca(DPA)_2$. The K^+ salt has also been prepared following the same method using bittern instead of aqueous solution of metal chloride. The Na^+ salt **1** could not, however, be synthesized by this method because of its very high solubility in water. **1** was instead prepared from the reaction of NaOH and DPA in water followed by evaporation of solvent to dryness. All these compounds gave satisfactory elemental analysis. UV/Vis spectra of **1**–**4** in water were similar; the only band observed for all compounds showing similar λ_{max} (426 nm) and molar absorptivity ($\varepsilon \approx 3.5 \times 10^4$ $M^{-1}cm^{-1}$). X-ray quality single crystals of **2**, **3**, and **4** were grown by slow evaporation of the respective aqueous solutions at room temperature. However, attempts to grow the crystals of **1** were unsuccessful.

Crystal Structures

[K(DPA)]·0.5H_2O (2) and [Rb(DPA)]·H_2O (3): Crystallographic data for complexes **2, 3** and **4** are summarized in Table 4. Compounds **2** and **3** are isostructural. The DPA^- anions in these structures are arranged in a manner that allows the metal ions to interact strongly with eight nitro oxygen atoms of the DPA^- ligands, which is similar to that found in the crystal structure of [K(DPA)], reported earlier.[6a] PLUTO view of **2** showing the metal–oxygen interactions are illustrated in Figure 2. Oxygen atoms (O5 and O6) of one of the *o*-nitro groups (N3) are not involved in interaction with metal ion, otherwise at least one oxygen atom from all other nitro groups makes strong M···O interactions. The interacting metal–oxygen distances for **2** (Table 1) are in the range of 2.767 to 3.022 Å (average K–O distance is 2.916 Å), which is close to the value of 2.76 to 3.04 Å found earlier for [K(DPA)]. In the case of **3**, the Rb–O distances are in the range of 2.911 to 3.150 Å, with average Rb–O distance of 3.023 Å (Table 1). These values are comparable to the reported metal–oxygen distances.[7] In the case of N5 and N7 nitro groups, all of the four oxygen atoms (O7, O8, O11, and O12) interact with the metal ion, in which O7 shows μ-type interaction involving the neighboring metal ion. The K···K and Rb···Rb distances in **2** and **3** are 4.413 and 4.835 Å, respectively. Values of the mean plane distortion between the two phenyl rings of the DPA^- in **2** and **3** are 78.78° and 79.75°, respectively. The two *o*-nitro groups, N1–O1/O2 and N5–O7/O8, are rotated with respect to the phenyl rings to which they are attached by 33.7° and 32.40° in **2** and 34.22° and 31.3° in **3**, respectively.

Figure 3 shows the packing diagram of **2** viewed down the *a* axis. The metal ions and the lattice water molecules are located between the adjacent ligand layers running along the *c* axis in the overall layered architecture. The corrugated organic layer formed in the case of **2** is held in place by C–H···O interaction between the phenyl H11 hydrogen with the O10 nitro oxygen along *c*-direction, and between the phenyl H9 hydrogen and O3 nitro oxygen from the adjacent corrugated organic layer almost along *b* axis. These interactions create the layered architecture. The oxygen

 © 2005 Wiley-VCH Verlag GmbH & Co. KGaA, Weinheim

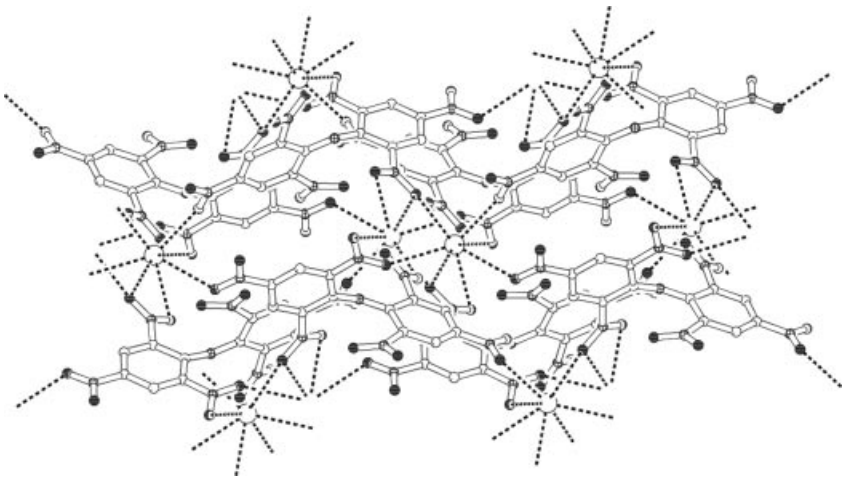

Figure 2. PLUTO view of [K(DPA)] (**2**) showing the interaction between the metal ion (open circle) and oxygen atoms (dark circles) of DPA^-.

Table 1. Metal–oxygen distances [Å] for **2**, **3**, and **4**.

Compound **2**			
K(1)–O(4)[a]	2.767(3)	K(1)–O(2)	2.814 (3)
K(1)–O(7)[b]	2.910(3)	K(1)–O(8)[b]	2.911(3)
K(1)–O(12)[c]	2.922(3)	K(1)–O(7)[d]	2.973(3)
K(1)–O(11)[e]	3.008(4)	K(1)–O(9)	3.022(3)
Compound **3**			
Rb(1)–O(3)	2.911(2)	Rb(1)–O(2)	2.941(2)
Rb(1)–O(11)[f]	3.001(2)	Rb(1)–O(7)	3.024(2)
Rb(1)–O(8)	3.050(2)	Rb(1)–O(9)	3.050(2)
Rb(1)–O(7)[g]	3.057(2)	Rb(1)–O(12)	3.150(3)
Compound **4**			
Cs(1)–O(1)	3.268(3)	Cs(1)–O(3)[l]	3.303(3)
Cs(1)–O(1)[h]	3.268(3)	Cs (1)–O(4)[k]	3.410(2)
Cs(1)–O(3)[i]	3.305(3)	Cs (1)–O(4)[l]	3.410(2)
Cs(1)–O(3)[j]	3.305(3)	Cs (1)–O(5)[m]	3.280(4)
Cs(1)–O(3)[k]	3.303(3)	Cs (1)–O(5)[n]	3.280(4)

[a] $x - 1/2, -y + 3/2, z - 1/2$. [b] $x - 1/2, -y + 1/2, z + 1/2$. [c] $x, y, z + 1$. [d] $-x + 1/2, y + 1/2, -z + 1/2$. [e] $-x, -y + 1, -z$. [f] $-x + 1, -y + 2, -z$. [g] $x + 2, -y + 2, -z$. [h] $-x, y, 1/2 - z$. [i] $1/2 + x, 1/2 + y, z$. [j] $-1/2 - x, 1/2 + y, 1/2 - z$. [k] $-1/2 - x, 1/2 - y, 1 - z$. [l] $1/2 + x, 1/2 - y, -1/2 + z$. [m] $x, 1 + y, z$. [n] $-x, 1 + y, 1/2 - z$.

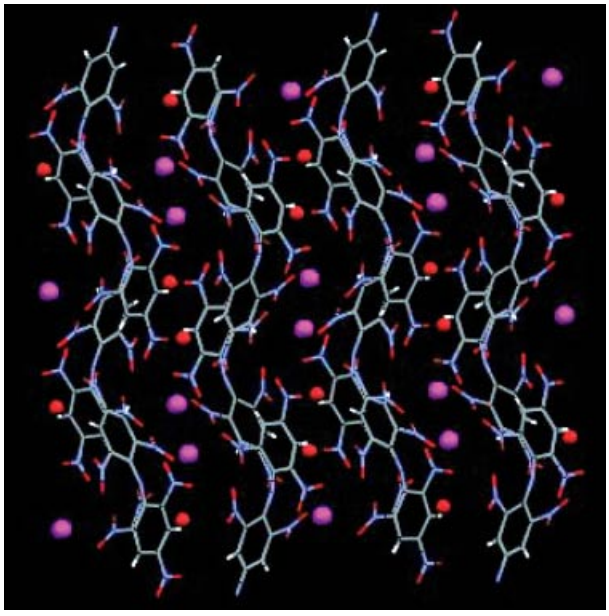

Figure 3. Molecular packing diagram of $[K(DPA)]\cdot 0.5H_2O$ (**2**) showing the architecture, in which the metal ions (purple) are encapsulated in regular intervals. Oxygen atoms of entrapped water molecules are shown in red.

Table 2. Parameters of C–H···O interactions for **2**, **3**, and **4**.

D–H···A [Å]	H···A [Å]	D···A [Å]	< D–H···A [°]
Compound **2**			
C(4)–H(4)···O(1)w[a]	H(4)···O(1)w = 2.44(4)	C(4)···O(1)w = 3.337(10)	C(4)–H(4)···O(1)w = 178 (4)
C(9)–H(9)···O(3)[b]	H(9)···O(3) = 2.58(4)	C(9)···O(3) = 3.417(5)	C(9)–H(9)···O(1)w = 176(4)
C(11)–H(11)···O(10)[c]	H(11)···O(10) = 2.51(4)	C(11)···O(11) = 3.389(6)	C(11)–H(11)···O(10) = 167(4)
Compound **3**			
C(4)–H(4)···O(1)w[d]	H(4)···O(1)w = 2.45(2)	C(4)···O(1)w = 3.337(4)	C(4)–H(4)···O(1)w = 175(2)
C(11)–H(11)···O(10)[e]	H(11)···O(10) = 2.43(3)	C(11)···O(11) = 3.400(3)	C(11)–H(11)···O(10) = 159(3)
Compound **4**			
C(4)–H(4)···O(1)[f]	H(4)···O(1) = 2.42(1)	C(4)···O(1) = 3.278(4)	C(4)–H(4)···O(1) = 154(2)

[a] x, y, z. [b] $1 - x, 1 - y, 1 - z$. [c] $-x, 1 - y, -z$. [d] $1- x, 1 - y, -z$.[e] $1 + x, y, z$. [f] $x, -y, 1/2 + z$.

 © 2005 Wiley-VCH Verlag GmbH & Co. KGaA, Weinheim

atom of the lattice water molecule also interacts with the H4 hydrogen of the phenyl ring. These observations are in contrast to the earlier report, where it was stated that no intermolecular interactions were found. The water molecule seen in the lattice of the present structure was also not observed in the earlier structure.[6a] In the case of **3**, only one C–H···O intermolecular interaction along *c* axis exists forming the corrugated layer as mentioned above for **2**, but no cross linking C–H···O interaction connecting the adjacent layers is observed. This could be due to the larger ionic radius of Rb^+ compared to K^+, and also inclusion of more water molecules between the layers, which prevents the sterically hindered ligands from coming closer to make such interaction along the *b* axis. The water molecules in **3** exhibit strong C–H···O interactions with a single DPA^- ligand, whereas in the case of **2** similar interactions of the water molecules with two DPA^- ligands are evident. Details of the H-bonding interactions found in complexes **2**, **3**, and **4** are given in Table 2.

[Cs(DPA)] (4): The molecule crystallises in centrosymmetric space group *C*2/*c* with Cs atom occupying a special position falling in the two-fold axis passing through the amino nitrogen atom of the deprotonated DPA moiety. Ten oxygen atoms of the surrounding nitro groups from six ligands make strong interactions with the metal ion. The PLUTO diagram showing the metal-oxygen interactions is depicted in Figure 4. At least one oxygen atom of each nitro group from the symmetry-related DPA ligand is involved in Cs···O interactions, the distances of which are in the range of 3.268 to 3.410 Å (average distance is 3.313 Å). These are in close agreement with the reported values.[7e,8] Oxygen atoms, O3 and O4, which are attached to N2, interact with the same metal ion; in addition O3 also makes μ-type of interaction involving the neighbouring metal ion. The Cs···Cs distance observed in this structure is 5.788 Å. The mean plane distortion between the phenyl rings of the DPA^- is 61.35°, while the *o*-nitro group N1–O1/O2 is rotated by 23.79° with respect to the phenyl ring to which it is attached.

The molecular packing (Figure 5) and C–H···O interactions in this molecule are quite different from that found in **2** and **3**. The H4 hydrogen atom shows strong intermolecular C–H···O interaction with O1 oxygen atoms of the *o*-nitro groups of a neighbouring molecule of DPA^-. Four such pairs of ligands assemble to create cavities down the *c* axis, in which the Cs^+ is encapsulated making interactions with the surrounding ten oxygen atoms from six ligands. The hydrogen bonding parameters with symmetry code is given in Table 2.

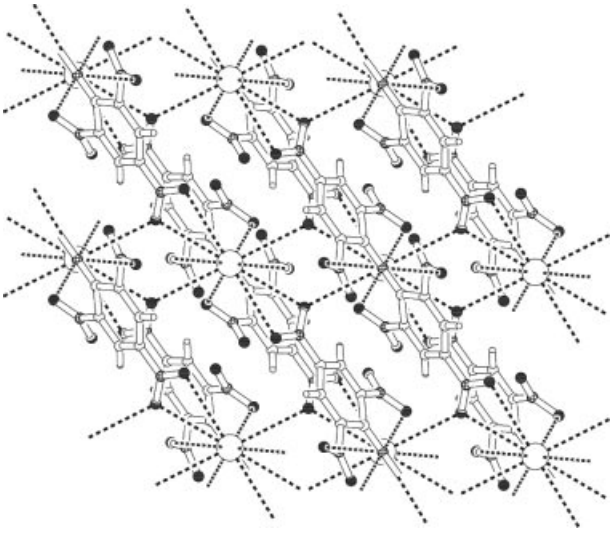

Figure 4. PLUTO view of [Cs(DPA)] (**4**) showing the interaction between the metal ion (open circles) and oxygen atoms (dark circles) of DPA^-.

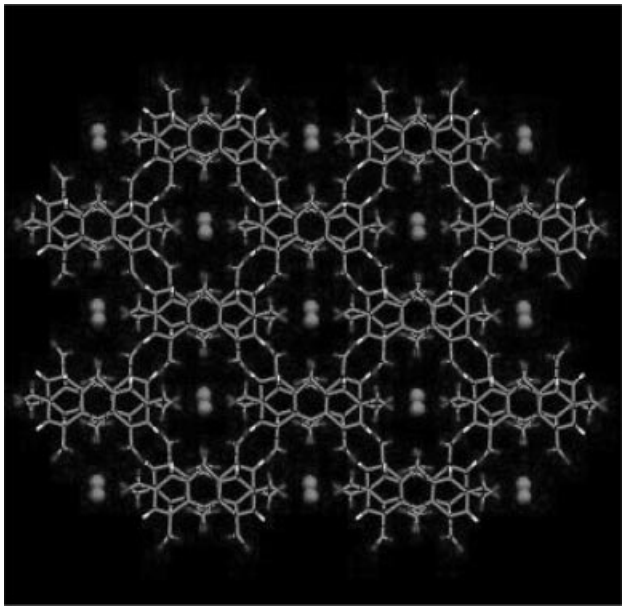

Figure 5. Molecular packing diagram of [Cs(DPA)] (**4**) showing the architecture, in which the metal ions (solid circles) are encapsulated in regular intervals.

NMR Study

To investigate possible differences in the coordination environments of metal ions in **1** and **4**, ^{23}Na and ^{133}Cs NMR spectra of the corresponding compounds were recorded and compared with those of NaCl and CsCl, respectively, in D_2O. ^{23}Na signal of **1** (Figure 6b′) appeared at the same position as of NaCl (Figure 6a′). In the case of **4**, on the other hand, the ^{133}Cs signal (Figure 6b) was shifted upfield significantly compared to that of CsCl (Figure 6a). Initially, soon after preparation of the solution, one signal was observed at –49.70 ppm (considering the signal of CsCl at 0.0 ppm), however, after 20 min, an additional signal appeared at –31.12 ppm (Figure 6c), and finally after 1 h, a third signal of low intensity appeared at –20.19 ppm (Figure 6d).

 © 2005 Wiley-VCH Verlag GmbH & Co. KGaA, Weinheim

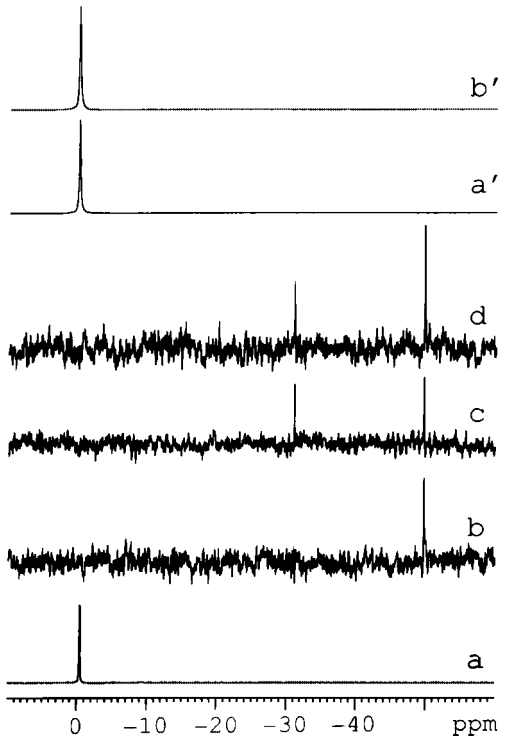

Figure 6. ^{133}Cs NMR spectra of CsCl (a) and [$Cs^+(DPA)^-$], recorded just after making solution (b), after 20 min (c) and after 60 min (d); and ^{23}Na NMR spectra of NaCl (a′) and [$Na^+(DPA)^-$] (b′). All spectra were recorded at room temperature in D_2O. Chemical shift position was taken as 0 ppm for the chloride salts of Na^+ and Cs^+.

Powder X-ray Diffraction

Powder XRD profiles of bulk precipitates of **2**–**4** obtained spontaneously upon addition of a solution of pure salt of the alkali metal ion into aqueous $Ca(DPA)_2$ were recorded. The XRD patterns of the same compounds **2**–**4** were also generated by simulation from the single-crystal X-ray data (Figure 7). The simulation was carried out following the method of Speak.[9] Good match between the experimental and simulated diffractograms was found. The diffractogram was also recorded of the highly water soluble **1** by evaporating the aqueous solution to dryness to obtain a solid powder. Unit cell parameters of **1**–**4** obtained from Powder XRD data and that of **2**–**4** obtained from single-crystal X-ray is shown in Table 3. The unit cell of **1** obtained from powder XRD data was found to be triclinic

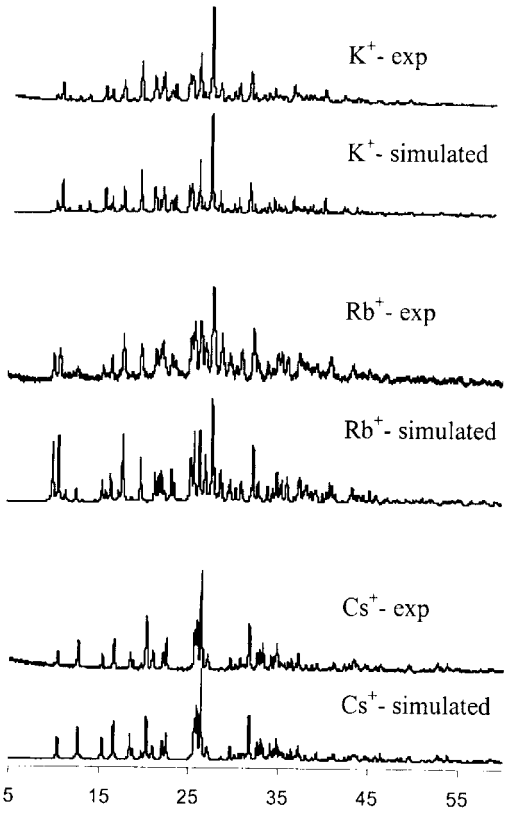

Figure 7. Experimental powder XRD data of bulk precipitates of K^+, Rb^+, and Cs^+ salts of DPA^- vs. powder XRD patterns simulated from the single-crystal X-ray data of the corresponding crystalline salts grown from the bulk precipitates.

Table 3. Crystal systems and unit cell parameters obtained from powder and single-crystal X-ray diffraction data for DPA and its compounds **1**–**4**.

DPA/complexes	Method	Crystal system	Unit cell dimensions *a*, *b*, and *c* [Å]	*α*, *β*, and *γ* [°]	Cell volume [Å^3]
DPA	SCXRD[a]	orthorhombic	7.370, 11.664, 18.894		1624.1
	PXRD[b]	orthorhombic	11.689, 18.992, 7.376		1637.5
[Na(DPA)]·H_2O	PXRD	triclinic	10.066, 17.247, 8.859	96.18, 93.48, 76.68	1487.0
[K(DPA)]·0.5H_2O	SCXRD	monoclinic	10.986, 13.054, 12.184	94.26	1742.5
	PXRD	monoclinic	12.181, 13.024, 10.968	94.37	1735.0
[Rb(DPA)]·H_2O	SCXRD	monoclinic	11.021, 13.262, 12.243	94.19	1784.6
	PXRD	monoclinic	12.287, 13.245, 11.005	94.16	1786.3
[Cs(DPA)]	SCXRD	monoclinic	13.885, 10.625, 11.500	91.63	1695.9
	PXRD	monoclinic	13.911, 10.643, 11.541	91.56	1707.9

[a] SCXRD = Single-crystal X-ray diffraction. [b] PXRD = Powder X-ray diffraction.

 © 2005 Wiley-VCH Verlag GmbH & Co. KGaA, Weinheim

whereas those of **2**–**4** were monoclinic, i.e., the same as that of single crystals of **2**–**4** reported above. The unit cell dimension and volume of the cell obtained from powder and single-crystal X-ray data also matched well.

Discussion

As mentioned above, selectivity was estimated through analysis of the precipitate obtained when a mixture of cations (bittern comprising mainly Na^+, K^+ and Mg^{2+} in one case and K^+, Rb^+ and Cs^+ in another case) was contacted with aqueous $Ca(DPA)_2$. When bittern is used, K^+ is found to be highly selective whereas Cs^+ is the most selective when the mixture comprises K^+, Rb^+ and Cs^+. To rationalize the observations of the second case, we sought to establish whether bulk precipitates are structurally similar to the single-crystal structures so that the latter may provide an understanding of selectivity. The similarity between experimental powder XRD data of bulk precipitates of **2**–**4** − that are formed almost instantaneously − and simulated diffractograms from the single-crystal data (Figure 7),[9] lead us to propose that the former are indeed structurally similar to the latter and, therefore, understanding of the crystal structures may provide vital clues on the selectivity trend. The unit cell dimensions obtained from powder X-ray data of **2**–**4** also matched well with those obtained from single-crystal X-ray data (Table 3) providing further support to this thesis. A similar comparison was not possible in the case of **1** in view of the inability to grow its single crystal.

As can be seen from the single-crystal structures of **2**–**4**, these structures are held in place by M···O and C–H···O interactions. Reduced exposure of the polar groups of the ligand to water by tying these up internally in the structure would lead to reduced solubility and, consequently, precipitation. The precipitation of $M^{n+}(DPA)_n$ can be depicted by Equation (1) (see also Scheme 1).

$$M^+_{(aq)} + [Ca(DPA)_2]_{aq} \rightarrow M(DPA)_n\downarrow + Ca^{2+}_{(aq)} \quad (1)$$

It can be seen from Equation (1) that the reaction will be favored with decrease in hydration enthalpy of $M_{(aq)}{}^+$. The values of hydration enthalpies follow the trend: M^{2+} (Mg, Ca) >> Na^+ (–97 kcal/mol) >K^+ (–77 kcal/mol) > Rb^+ (–70 kcal/mol) > Cs^+ (–63 kcal/mol). Thus for the mixture of K^+, Rb^+, and Cs^+, the selectivity would be highest for Cs^+ and least for K^+.[10] For the bittern system comprising Na^+, K^+, and Mg^{2+}, K^+ would be expected to have the highest selectivity on the basis of hydration enthalpy alone.

However, there are, other factors that also control selectivity besides hydration enthalpy. From packing diagrams of the K^+, Rb^+, and Cs^+ compounds **2**–**4**, space-filling models of the respective cavities comprising the metal ion and metal-bound oxygen atoms have been generated. The diagram for **4** is given in the figure in the table of contents of this issue and those of **2** and **3** are deposited as Supporting Information (Figures S4 and S5). The eight oxygen atoms around K^+/Rb^+ and ten oxygen atoms around Cs^+ make near-spherical cavities, the diameters of which can be determined from the respective distances between the *trans* oxygen atoms. The approximate diameters of the cavities (average of the distances between the *trans* oxygen atoms having O–M–O angle > 150°) are 5.720, 5.865, and 6.561 Å for K^+, Rb^+, and Cs^+, respectively. This increasing order of diameter of the cavities qualitatively follows the increasing order of the ionic sizes of these ions (2.66 Å, 2.94 Å, and 3.34 Å, for K^+, Rb^+, and Cs^+, respectively).[11] However, compared to the differences in the sizes of K^+ and Rb^+, the difference in the cavity diameters is less pronounced. Two opposite factors control cavity size: (i) short M···O distance and small size of the cation that can reduce the size of the cavity, and (ii) steric hindrance and electrostatic repulsion that prevent ligands from coming closer, and thereby increasing the cavity size. In the case of K^+, the latter may be the more dominant factor that prevents further shrinkage of the cavity diameter and weakens the M···O interactions which may, in addition to the hydration enthalpy difference, account for its lower selectivity in comparison to Rb^+, despite the similarities of the structures. Na^+, having smaller ionic size (1.94 Å), may be too small to fit in this cavity to make significant M···O interaction to form a stable assembly, if a similar structure were to apply in its case also. Alternative structures are, of course, possible, but comparative NMR study of **1** and NaCl suggests lack of metal-ligand interaction in solution, as ^{23}Na signal of both of them appeared at the same position, i.e., their environments are likely to be the same, namely Na^+ in hydrated state.

In the case of Cs^+, a large upfield shift (δ = 49.7 ppm) of the ^{133}Cs NMR signal of **4**, compared to CsCl, indicates strong metal-ligand interactions in solution. Ten oxygen atoms in the vicinity of the metal ion make strong Cs^+···O interactions, which decreases effective positive charge on the metal ion resulting in shielding of the Cs^+ ion. The additional NMR signals, which grow in with progress of the experiment, could be due to some new species formed in solution by dissociation of the supramolecular assembly. However, in all cases the observed peaks are shifted upfield indicating significant Cs^+···O interactions in solution state. Thus the selective formation may be assumed to originate in the solution phase and cascades to the solid precipitates. The larger cavity size in **4** allows for a higher coordination number (10) of Cs^+, which may lead to a greater degree of stabilization of the structure than with Rb^+ and K^+. Differences in ligand conformations may also have an effect on energetics and, consequently, selectivity. It is interesting to note that the DPA^- conformation in **4** has the closest match to that of DPA in crystalline state, the mean plane distortion being 61.35° compared to 50.5° for neutral DPA.[5] The deviations are much larger for **2** & **3**.

Alkaline earth metal ions, which are divalent in nature and have much higher hydration enthalpies ((Mg^{2+}, –459.1 mkcal/mol; Ca^{2+}, –376.9 kcal/mol; Sr^{2+}, –344.9 kcal/mol; Ba^{2+}, –311.9 kcal/mol),[10] are more difficult to complex with DPA^- which accounts for the high solubility of $Ca(DPA)_2$ and the lack of any $Mg(DPA)_2$ precipitation despite its high concentration in bittern. The relatively small ionic sizes of these cations may also be another factor that

 © 2005 Wiley-VCH Verlag GmbH & Co. KGaA, Weinheim

thwarts complex formation and precipitation. This is borne out by our preliminary studies with the larger Sr^{2+} and Ba^{2+} (ionic diameters: 2.26 and 2.68 Å, respectively) ions,[11] wherein crystals of $[Sr(DPA)_2]\cdot 4H_2O$ and $[Ba(DPA)_2]\cdot 4H_2O$ could be obtained from the solution on slow evaporation of the solvent.[12]

Conclusions

We conclude from the present study that the selectivity of formation of $[M^{n+}(DPA^-)_n]$ can be divided into two broad categories: (i) cations such as K^+, Rb^+, and Cs^+ that favorably form precipitates almost instantaneously upon contact and (ii) those such as Na^+ and Ca^{2+} that do not form any precipitate. The former case pertains to compounds where the cation and DPA^- readily form complexes. The latter case, as exemplified by the ^{23}Na NMR studies with aqueous Na(DPA) wherein the environment of Na^+ is the same as that of Na^+ in aqueous NaCl, pertains to the situation wherein complex formation is unfavorable for a variety of reasons such as large hydration enthalpy and unfavorable ionic size. Sr^{2+} and Ba^{2+} represent an intermediate case where the complexes are moderately soluble and crystal formation does occur, albeit sluggishly, upon slow evaporation of the solution. Where alkali metal ions precipitate instantaneously with DPA^-, the observed selectivities are nicely explained on the basis of the structures of the complexes, which, in turn, are controlled by the relative sizes and hydration enthalpies of the cations. Kinetic factors could also contribute to some degree towards the selectivities.

Experimental Section

Materials: Dipicrylamine was purchased from National Chemical Co., India and used as received. AR grade KCl, RbCl, CsCl, CaO, and NaOH were obtained from S. D. Fine Chemicals. Double distilled water was used for the synthesis of compounds and Milli-Q (Millipore Corporation) water was used for ion chromatographic study.

Instrumentation: Elemental analyses (C,H,N) were performed with a model 2400 Perkin–Elmer elemental analyzer. The UV/Vis spectra were recorded with a model 8452A Hewlett–Packard diode array spectrophotometer. Cation concentration was measured with a Dionex 500 ion chromatograph. NMR spectra were recorded in D_2O with a model DPX 200 Bruker FT NMR instrument. X-ray powder diffraction data were collected using Philips X′ Pert MPD system with Cu-K_α irradiation. Single-crystal structures were determined using either Enraf–Nonius CAD-4 or Bruker SMART APEX (CCD) diffractometers.

Selectivity Studies with DPA^-: Selectivity studies were carried out by precipitating metal ions as DPA^- salts from bittern (the mother liquor obtained after recovery of common salt from brine, which contains a mixture of Na^+, K^+, Mg^{2+}, Ca^{2+}, SO_4^{2-}, and Cl^-) and also from a solution containing equimolar amount of KCl, RbCl and CsCl. In a typical experiment $[Ca(DPA)_2]$ was prepared first by adding solid CaO (0.067 g, 1.2 mmol) into an aqueous (10 mL) suspension of DPA (0.439 g, 1 mmol) followed by stirring of the reaction mixture for 5 min. 10 mL of this (filtered) aqueous $[Ca(DPA)_2]$ (1 mmol) was added with stirring into bittern (20 mL) or into an aqueous solution (50 mL) containing 2 mmol each of KCl, RbCl, and CsCl. The precipitate, which was instantaneously separated, was isolated by filtration and washed with diethyl ether and dried in vacuo. 10 mg of this material was calcined at 550 °C in a furnace and the residue was dissolved in nitric acid, which was evaporated and the residue was further dissolved in deionised water (20 mL) and filtered through 0.2 μm filter paper. The concentrations of the metal ions in the filtrate were determined by ion chromatography using Ion Pac CS12 (2 mm) analytical column and 20 mM methylsulphonic acid as eluent with a flow rate of 0.25 mL/min. Quantification was made using standard solutions containing Na^+, K^+, Mg^{2+}, and Ca^{2+} in one case and K^+, Rb^+, and Cs^+ in the other case.

Synthesis of Metal Salts of DPA^-

$[Na(DPA)]\cdot H_2O$ (1): To an aqueous (10 mL) suspension of DPA (0.439 g, 1 mmol) 2 mL of NaOH (0.04 g) was added dropwise and the reaction mixture was stirred at room temperature for 2 h, during which a dark brown solution was formed. After stripping off the water in a rotavap, the dry mass was dissolved once again in 5 mL volume of water and filtered to remove traces of insoluble material. The water was then evaporated and the compound was dried in vacuo, yield 94% (0.45 g). $C_{12}H_6N_7NaO_{13}$ (479.0): calcd. C 30.09, H 1.26, N 20.46; found C 30.31, H 1.03, N 20.02. UV/Vis (H_2O): λ_{max} (ε) = 426 nm (3.3×10^4).

$[K(DPA)]\cdot 0.5H_2O$ (2). Method I, from Bittern: 10 mL of aqueous $[Ca(DPA)_2]$ (1 mmol) was added into bittern (10 mL) and stirred for 5 min. The brown precipitate, which formed almost instantaneously, was isolated by filtration, washed with water and diethyl ether and recrystallised from a large volume of water. Yield: 0.41 g (85%). **Method II, from KCl:** Solid KCl (0.075 g, 1 mmol) was added into the above-mentioned dark brown solution (Ca^{2+} salt of DPA^-) and stirring was continued for 5 min, during which a brown precipitate was separated. The precipitate was isolated and purified following the procedure mentioned in method I, yield 86% (0.4 g). $C_{12}H_5KN_7O_{12.5}$ (486.1): calcd. C 29.65, H 1.04, N 20.16; found C 29.70, H 0.95, N 19.90. UV/Vis (H_2O): λ_{max} (ε) = 426 nm (3.5×10^4).

$[Rb(DPA)]\cdot H_2O$ (3): This compound was synthesized following the same procedure as that described for method II of complex **2**, replacing KCl with RbCl, yield 85% (0.46 g). $C_{12}H_6N_7O_{13}Rb$ (541.5): C 26.61, H 1.12, N 18.09; found C 26.28, H 1.02, N 17. 86. UV/Vis (H_2O): λ_{max} (ε) = 426 nm (3.5×10^4).

$[Cs(DPA)]$ (4): This compound was synthesized following the same procedure as that described for method II of complex **2**, replacing KCl with CsCl, yield 84% (0.47 g). $C_{12}H_4CsN_7O_{12}$ (570.9): C 25.24, H 0.71, N 17.16; found C 25.19, H 0.86, N 17.11. UV/Vis (H_2O): λ_{max} (ε) = 426 nm (3.4×10^4).

X-ray Crystallography: Cell parameters and diffraction intensities for complex **2** were measured at room temperature with the CAD-4 X-ray diffractometer using graphite-monochromatised Mo-$K\alpha$ radiation (0.7107 Å) in the range θ = 2–25°, for complexes **3** and **4** data were collected on the CCD diffractometer (Table 4). In the case of complex **2**, 25 reflections with θ in the range 9–12° were used for getting the accurate cell dimensions. Three standard reflections were monitored after every 100 reflections during the entire period of data collection, which showed no significant variation, indicating the stability of the crystal. The crystal orientation, refinement of the cell parameters and intensity measurements were carried out using the program CAD-4 PC.[13] Raw intensity data were corrected for Lorentz polarization effects but not for absorp-

 © 2005 Wiley-VCH Verlag GmbH & Co. KGaA, Weinheim

tion. The Lorentz polarization corrections and data reduction were carried out using NRCVAX program.[14] The data for DPA and complexes **3** and **4** were corrected for Lorentz polarization and absorption effects. SHELXL-97[15] was used for structure solution and full-matrix least-squares refinement on F^2 for all these data. H atoms were included in the structure as riding model or obtained from the difference Fourier map.

Table 4. Summary of crystallographic data for **2**–**4**.

Compound	**2**	**3**	**4**
Empirical formula	$C_{12}H_4KN_7O_{12.5}$	$C_{12}H_4N_7O_{13}Rb$	$C_{12}H_4CsN_7O_{12}$
Molecular mass	485.32	539.69	571.13
Crystal system	monoclinic	monoclinic	monoclinic
Space group	$P2_1/n$	$P2_1/n$	$C2/c$
a [Å]	10.986 (4)	11.021(4)	13.885(5)
b [Å]	13.054(5)	13.262(5)	10.625(4)
c [Å]	12.184(3)	12.243(4)	11.500(4)
α [°]	90.0	90.0	90.0
β [°]	94.26(2)	94.190(5)	91.369(6)
γ [°]	90.0	90.0	90.0
Z	4	4	4
V [Å^3]	1742.5(10)	1784.6(11)	1695.9(11)
λ (Mo-K_α) [Å]	0.07107	0.7107	0.7107
$\rho_{calcd.}$ [g cm^{-3}]	1.850	2.869	2.276
μ [cm^{-1}]	8.930	28.69	22.76
T [K]	295(2)	295(2)	295(2)
R (F_o^2)[a]	0.0519	0.0342	0.0316
R_w (F_o^2)[b]	0.1302	0.0910	0.0788

[a] $R = \Sigma||F_o| - |F_c||/\Sigma|F_o|$, [b] $Rw = [Sw\ (F_o^2 - F_c^2)^2]/S\ [w(F_o^2)^2]^{1/2}$, $w = 1/\sigma(F_o)^2$:.

Powder X-ray Data Collection: Data were collected at room temperature in continuous scan mode in the 2θ range 5–60° with a step size of 0.02° 2θ and a count time of 4 s per step. Powder patterns were indexed using Visser-ITO[16] indexing program.

Simulation: Powder XRD pattern was simulated from single-crystal data by the method of Speak, using standard PLATON software.[9]

CCDC-264106 to -264108 (for **2**–**4**) contain the supplementary crystallographic data for this paper. These data can be obtained free of charge from The Cambridge Crystallographic Data Centre via www.ccdc.cam.ac.uk/data_request/cif.

Supporting Information Available: Ion chromatograms of a standard solution containing mixture of ions (Na^+, K^+, Mg^{2+}, Ca^{2+}), bittern and extracted (by DPA^-) material (Figure S1, see footnote on the first page of this article), PLUTO view of **3** showing metal–oxygen interactions (S2), molecular packing diagram of **3** showing the architecture, in which the metal ions are encapsulated (S3) and space filling models of the cavity consisting of metal ion and coordinated oxygen atoms for complexes **2** and **3** (Figures S4 and S5).

Acknowledgments

We are grateful to the Department of Science and Technology (DST), Government of India, for financial support. We thank Dr. M. M. Bhadbhade, NCL, Pune, for crystallographic data collection of complexes **3** and **4**. The assistance of Dr. P. Dastidar in generating some of the figures is gratefully acknowledged. We also thank the referees for their valuable suggestions.

[1] a) A. Winkel, D. I. H. Maas, *Angew. Chem.* **1936**, *49*, 827; b) J. Kielland, *Patent*, **1940**, No. Au 109552 19400110; **1941**, No. DE 715199 19411120; c) J. Kielland, W. Fleischer, *Patent*, **1940**, No. AU 112196 19401219; d) E. Berner, J. Kielland, *Patent*, **1942**, No. DE 726545 19420903; e) F. Massazza, B. Riva, *Ann. Chim. (Rome)* **1958**, *48*, 664; F. Massazza, B. Riva, *Ann. Chim. (Rome)* **1961**, *51*, 645; f) J. N. Kapoor, J. M. Sarkar, *Technology (Sindri, India)* **1966**, *3*, 177; g) S.-K. Chu, C.-T. Liaw, *Huaxue* **1969**, *4*, 106; h) J. Kielland, *Chem. Indust.* **1971**, 1309; i) M. Y. Bakr, A. A. Zatout, *Chemical Economy & Engineering Rev.* **1979**, *11*, 31.

[2] L. A. Bray, E. C. Martin, R. L. Moore, W. A. Richland, *U. S. At. Energy Commun.* **1962**, *HW-SA-2620*, p. 8.

[3] a) M. Kyrs, J. Pelcik, P. Polansky, *Czech. Collection Czechoslov. Chem. Communs.* **1960**, *25*, 2642; b) V. Kourim, J. Krtil, *Proc. U. N. Intern. Conf. Peaceful Uses At. Energy*, 2nd, Geneva, **1958**, *28*, 139; c) J. Rais, P. Selucky, *Patent*, **1973**, No. CZXXA9 CS 149403 19730715.

[4] a) M. L. Kundu, J. N. Kapoor, S. K. Ghosh, *Proc. Indian Acad. Sci., Chem. Sci.* **1982**, *91*, 65; b) K. Wozniak, H. He, J. Klinowski, W. Jones, E. Grech, *J. Phys. Chem.* **1994**, *98*, 13755.

[5] K. Wozniak, P. R. Mallinson, C. C. Wilson, E. Hovestreydt, E. Grech, *J. Phys. Chem. A* **2002**, *106*, 6897.

[6] a) M. L. Kundu, S. K. Ghosh, *Acta Crystallogr., Sect. B* **1980**, *36*, 941; b) V. P. Chalyi, F. G. Kramarenko, Yu. P. Krasan, L. L. Shevchenko, *Ukrainskii Khimicheskii Zhurnal* **1980**, *46*, 227; c) S. Furberg, P. Larssen, *Acta Chem. Scand.* **1952**, *6*, 965; d) V. P. Chalyi, G. N. Novitskaya, Yu. P. Krasan, L. L. Shevchenko, A. T. Pilipenko, *Zhurnal Strukturnoi Khimii* **1974**, *15*, 159.

[7] a) J. D. Owen, M. R. Truter, J. N. Wingfield, *Acta Crystallogr., Sect. C* **1984**, *40*, 1515; b) T. Sakamaki, Y. Inaka, Y. Nawata, *Acta Crystallogr. Sec. B* **1976**, *32*, 768; c) T. Sakamaki, Y. Inaka, Y. Nawata, *Chem. Lett.* **1972**, 1225; d) P. B. Hitchcock, M. F. Lappert, A. V. Protchenko, *J. Am. Chem. Soc.* **2001**, *123*, 189; e) K. Fukaya, T. Yamase, *Angew. Chem. Int. Ed.* **2003**, *42*, 654.

[8] a) P. R. A. Webber, G. Z. Chen, M. G. B. Drew, P. D. Beer, *Angew. Chem. Int. Ed.* **2001**, *40*, 2265; b) M. Cai, A. L. Marlow, J. C. Fettinger, D. Fabris, T. J. Haverlock, B. A. Moyer, J. T. Davis, *Angew. Chem. Int. Ed.* **2000**, *39*, 1283.

[9] A. L. Speak, *PLATON - A multipurpose crystallographic tool*, Ultrecht Univ., Ultrecht, The Netherland, *Acta Crystallogr., Sect. A* **1990**, *46*, C34.

[10] C. J. Pedersen, *J. Am. Chem. Soc.* **1967**, *89*, 7017.

[11] F. A. Cotton, W. Wilkinson, *Advanced Inorganic Chemistry, A comprehensive Text*, 3rd ed. **1979**, pp. 198, 645.

[12] Preliminary crystallographic data confirmed the compositions $[Sr(DPA)_2]\cdot 4H_2O$ and $[Ba(DPA)_2]\cdot 4H_2O$ with ten M···O interactions, however, well refined structures are yet to be obtained.

[13] *CAD4-PC Software*, Version 5, Enraf–Nonius, Delft, **1989**.

[14] E. I. Gabe, Y. Le Page, I. P. Charland, F. L. Lee, P. S. White, *J. Appl. Crystallogr.* **1989**, *22*, 384.

[15] G. M. Sheldrick, *SHELXL-97. Program for Crystal Structure Determination*, University of Göttingen, Germany, **1997**.

[16] J. W. Visser, *J. Appl. Crystallogr.* **1969**, *2*, 89.

Received: December 16, 2004

 © 2005 Wiley-VCH Verlag GmbH & Co. KGaA, Weinheim

Heterosite Effects in Novel Heteronuclear Clusters $[Os_2Ru(CO)_{11}(PPh_3)]$ and $[Os_2Ru(CO)_{10}$(2-acetylpyridine-*N*-isopropylimine)]

Frank W. Vergeer,[a,e] Martin Lutz,[b] Anthony L. Spek,[b] Maria J. Calhorda,[c,d] Derk J. Stufkens,[†][a] and František Hartl*[a]

Keywords: Cluster compounds / Density functional calculations / Time-resolved spectroscopy / Photochemistry / Spectroelectrochemistry

A new synthetic route towards the mixed-metal cluster $[Os_2Ru(CO)_{12}]$ is described together with the syntheses of its PPh_3 and *i*Pr-AcPy (*i*Pr-AcPy = 2-acetylpyridine-*N*-isopropylimine) derivatives. The molecular structures of the novel clusters $[Os_2Ru(CO)_{11}(PPh_3)]$ and $[Os_2Ru(CO)_{10}$(*i*Pr-AcPy)] were determined on the basis of crystalline solid solutions of the Os_2Ru and corresponding Os_3 species. The structures reveal that coordination of the Lewis bases occurs exclusively at the ruthenium site of $[Os_2Ru(CO)_{12}]$, which is in agreement with density functional theory (DFT) calculations on several structural isomers of these compounds. According to the time-dependent DFT results, the lowest optically accessible excited state of $[Os_2Ru(CO)_{10}$(*i*Pr-AcPy)] has a prevailing σ(Ru–Os2)-π*(*i*Pr-AcPy) character, with a partial σσ*(Ru–Os2) contribution. In weakly coordinating 2-chlorobutane, the excited state has a lifetime τ = 10.4 ± 1.2 ps and produces biradicals considerably faster than observed for $[Os_3(CO)_{10}$(*i*Pr-AcPy) (τ = 25.3 ± 0.7 ps). In coordinating acetonitrile, the excited state of $[Os_2Ru(CO)_{10}$(*i*Pr-AcPy)] decays mono-exponentially with a lifetime τ = 2.1 ± 0.2 ps. In contrast to $[Os_3(CO)_{10}$(*i*Pr-AcPy)] that forms biradicals as the main primary photoproduct even in strongly coordinating solvents, zwitterion formation from the solvated lowest excited state is observed for the heterometallic cluster. This is concluded from time-resolved absorption studies in the microsecond time domain. Due to the lower tendency of the coordinatively unsaturated $^{+}Ru(CO)_2$-(*i*Pr-AcPy$^{-/0}$) moiety to bind a Lewis base, the heteronuclear biradical and zwitterionic photoproducts live significantly shorter than their triosmium counterparts. The influence of the weaker Os2–Ru(*i*Pr-AcPy) bond on the redox reactivity is clearly reflected in very reactive radical anions formed upon electrochemical reduction of $[Os_2Ru(CO)_{10}$(*i*Pr-AcPy)]. The dimer $[^{-}Os(CO)_4$-$Os(CO)_4$-$Ru(CO)_2$(*i*Pr-AcPy)$]_2^{2-}$ is the only IR-detectable intermediate reduction product. The dinuclear complex $[Os_2(CO)_8]^{2-}$ and insoluble $[Ru(CO)_2$(*i*Pr-AcPy)$]_n$ are the ultimate reduction products, proving fragmentation of the Os_2Ru core.

(© Wiley-VCH Verlag GmbH & Co. KGaA, 69451 Weinheim, Germany, 2005)

Introduction

In the last four decades, considerable efforts have been made to develop general synthetic routes towards heteronuclear transition metal clusters.[1–4] The interest in this type of clusters where at least one metal–metal bond connects two different core metal atoms, has mainly originated from their possible application in both homogeneous and heterogeneous catalysis.[5] Apart from the general expectation that different transition metal atoms in close proximity of each other could initiate novel reactions by synergistic interactions, the different reactivity of adjacent metal centres in mixed-metal clusters may provide additional bi- or multifunctional activation pathways and increase the selectivity of substrate–cluster interactions.[6] Although catalysis by mixed-metal clusters in a number of cases indeed resulted in higher catalytic activity[7,8] or different product selectivity[9,10] than observed for their homonuclear analogues, the mechanistic insight into the role of the different metal centres in the catalytic cycle is generally limited. This problem mainly has its origin in scarcely available series of isostructural mixed-metal clusters, which precludes a systematic study of their bonding properties and reactivity.

One of the best known series of mixed-metal clusters is the family of group 8 triangular clusters $[M_3(CO)_{12}]$ (M = Fe, Ru, Os), where all possible metal combinations – except $[FeRuOs(CO)_{12}]$ – have been prepared.[3,11] Within this

[†] Deceased.
[a] Van't Hoff Institute for Molecular Sciences, University of Amsterdam,
Nieuwe Achtergracht 166, 1018 WV, Amsterdam, The Netherlands
Fax: +31-20-525-6456
E-mail: f.hartl@uva.nl
[b] Department of Crystal and Structural Chemistry, Utrecht University,
Padualaan 8, 3584 CH Utrecht, The Netherlands
[c] Instituto de Tecnologia Química e Biológica, Av. da República, EAN,
Apart. 127, 2781-901 Oeiras, Portugal
[d] Departamento de Química e Bioquímica, Faculdade de Ciências, Universidade de Lisboa,
1749-016 Lisboa, Portugal
[e] Current address: Physikalisches Institut, Westfälische Wilhelms-Universität Münster,
Wilhelm-Klemm-Strasse 10, 48149 Münster, Germany

series, the clusters $[Os_2Ru(CO)_{12}]$ and $[Ru_2Os(CO)_{12}]$ are of particular interest for our investigations, as the bonding properties, photochemistry and redox behaviour of the homonuclear dodecacarbonyl analogues and, in particular, their α-diimine-substituted derivatives $[M_3(CO)_{10}(\alpha\text{-diimine})]$ (M = Ru, Os), have been studied thoroughly in our groups.[12–21]

A continued systematic study of their heterometallic Ru/Os derivatives is desired in order to reveal the influence of the cluster core variation on the photochemistry and redox reactivity. However, one of the underlying reasons for the lacking studies of $[Os_2Ru(CO)_{12}]$ and $[Ru_2Os(CO)_{12}]$ is the serious difficulty to obtain these clusters in the pure form. Although several synthetic procedures have been reported, they yielded either hardly separable mixtures of $[Ru_3(CO)_{12}]$, $[Ru_2Os(CO)_{12}]$, $[Os_2Ru(CO)_{12}]$ and $[Os_3(CO)_{12}]$ in a nearly statistical 1:2:2:1 ratio[22–24] or gave the desired pure heterometallic clusters merely in very low yields ($\leq$ 5%).[25,26] Development of efficient novel synthetic routes toward these species is therefore compulsory.

Aimed at performing a comparative study of the heteronuclear cluster $[Os_2Ru(CO)_{10}(\alpha\text{-diimine})]$ and its homonuclear analogues $[M_3(CO)_{10}(\alpha\text{-diimine})]$ (M = Ru, Os), a novel route for the synthesis of $[Os_2Ru(CO)_{12}]$ (**1**) has been introduced, producing the cluster in a reasonable yield. Apart from the parent carbonyl cluster, we also report the syntheses and crystal structures of the substituted derivatives $[Os_2Ru(CO)_{11}(PPh_3)]$ (**2**) and $[Os_2Ru(CO)_{10}(i\text{Pr-AcPy})]$ (**3**) (*i*Pr-AcPy = 2-acetylpyridine-*N*-isopropylimine), schematically depicted in Figure 1. Both derivatives were prepared in order to establish the preferential coordination site of different Lewis bases in substitution reactions with $[Os_2Ru(CO)_{12}]$. The influence of the heteronuclear cluster core on the photo- and electrochemical reactivity of $[Os_2Ru(CO)_{10}(i\text{Pr-AcPy})]$ in comparison with the homonuclear derivatives is also described. Density functional theory (DFT) calculations provide direct insight into the bonding properties of $[Os_2Ru(CO)_{11}(PPh_3)]$ and $[Os_2Ru(CO)_{10}(i\text{Pr-AcPy})]$ and support the discussion of the experimental results.

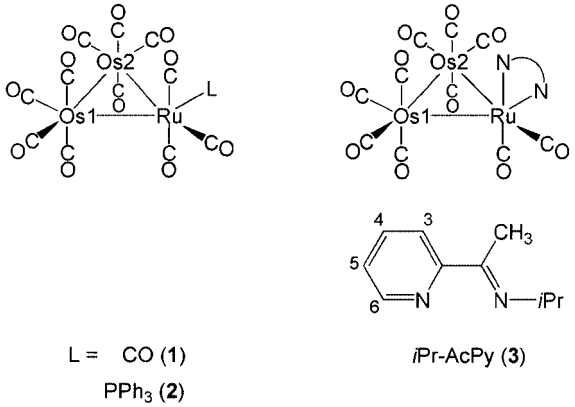

Figure 1. Schematic structures of the investigated clusters $[Os_2Ru(CO)_{11}(L)]$ [L = CO (**1**), PPh_3 (**2**)] and $[Os_2Ru(CO)_{10}(NN)]$ [NN = *i*Pr-AcPy (**3**)].

Results and Discussion

Synthesis of $[Os_2Ru(CO)_{12}]$ (1)

The heteronuclear cluster $[Os_2Ru(CO)_{12}]$ (**1**) was synthesized from its homonuclear analogues $[Os_3(CO)_{12}]$ and $[Ru_3(CO)_{12}]$ in a four-step reaction sequence (Scheme 1). Starting from $[Os_3(CO)_{12}]$, the linear cluster $[Os_3(CO)_{12}(Br)_2]$ was obtained by oxidation with Br_2 in refluxing CH_2Cl_2 [step (*i*)]. After the addition of Br_2, rapid removal of the heating bath is required in order to prevent the reaction of $[Os_3(CO)_{12}(Br)_2]$ with additional Br_2 producing at this stage undesired $[Os_2(CO)_8(Br)_2]$ that is known to transform into $[Os_2(CO)_6(Br)_2]$ at elevated temperatures.[27] Similar oxidative addition of X_2 (X = Cl, Br, I) to $[Ru_3(CO)_{12}]$ was reported[28,29] to yield the mononuclear complex *cis*-$[Ru(CO)_4(X)_2]$ as the initial product, which reflects the increasing stability of the metal–metal bonds towards oxidation on descending the periodic table. Unfortunately, the synthetic strategy depicted in Scheme 1 could therefore not be applied for the synthesis of the isostructural cluster $[Ru_2Os(CO)_{12}]$. The controlled formation of the dinuclear complex $[Os_2(CO)_8(Br)_2]$ was achieved by slight modification of the procedure described by Moss et al. [step (*ii*)].[30] Visible irradiation of $[Os_3(CO)_{12}(Br)_2]$ at $\lambda > 420$ nm was found to prevent excessive formation of the mononuclear complex *cis*-$[Os(CO)_4(Br)_2]$. The latter compound is not only obtained as an unavoidable side-product formed during irradiation of $[Os_3(CO)_{12}(Br)_2]$, but it can also be formed from $[Os_2(CO)_8(Br)_2]$ by UV/Vis irradiation of this complex in the presence of Br_2. In a third step, the powerful nucleophile $Na_2[Ru(CO)_4]$ was prepared from $[Ru_3(CO)_{12}]$ by reduction with sodium in liquid ammonia [step (*iii*)].[31] As $[Ru(CO)_4]^{2-}$ is extremely air- and moisture-sensitive and readily converts to $[Ru(CO)_4H]^-$, the reduction of $[Ru_3(CO)_{12}]$ was performed at reduced pressure (3×10^{-4} Pa) on a high-vacuum line. After the completion of the reaction, the product must be dried extensively, as small traces of ammonia proved to react instantaneously with $[Os_2(CO)_8(Br)_2]$, reducing the yield of $[Os_2Ru(CO)_{12}]$. In order to prevent thermal decomposition of $Na_2[Ru(CO)_4]$ during the drying process, the temperature was carefully kept below 273 K. Finally, $Na_2[Ru(CO)_4]$ was extracted in thoroughly dried THF and added to $[Os_2(CO)_8(Br)_2]$ by vacuum filtration, instantaneously producing $[Os_2Ru(CO)_{12}]$ (**1**) in reasonable yields (step (*iv*)).

Unfortunately, in some cases, cluster **1** was found to contain variable amounts of $[Os_3(CO)_{12}]$ and/or $[Ru_2Os(CO)_{12}]$ impurities. The latter cluster could result from incomplete reduction of $[Ru_3(CO)_{12}]$ by less than six equivalents of sodium. Thus, although the number of impurities and their percentages are significantly reduced in comparison with the established synthetic procedures,[22–24] the purity of cluster **1** and its substitution products remains difficult to control, even when employing this novel synthetic route.

In order to establish the preferred coordination site in cluster **1** for different Lewis bases (L), substituted derivatives with monodentate PPh_3 and chelating α-diimine = *i*Pr-

 © 2005 Wiley-VCH Verlag GmbH & Co. KGaA, Weinheim

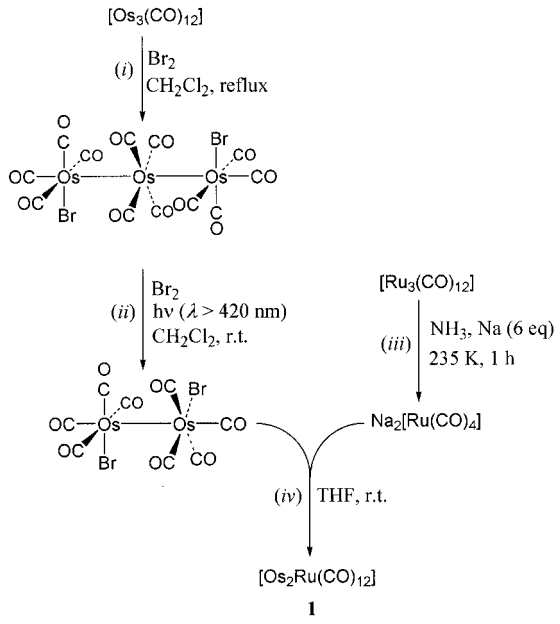

Scheme 1. Synthesis of $[Os_2Ru(CO)_{12}]$ (**1**).

AcPy ligands were prepared by a thermal reaction route involving precursor clusters $[Os_2Ru(CO)_{12-n}(MeCN)_n]$ (n = 1 for L = PPh_3; n = 2 for L = *i*Pr-AcPy). The substituted products $[Os_2Ru(CO)_{11}(PPh_3)]$ (**2**) and $[Os_2Ru(CO)_{10}(i$Pr-AcPy$)]$ (**3**) (see Figure 1) were characterised by IR and NMR spectroscopy and mass spectrometry. Their molecular structures were determined by single-crystal X-ray diffraction and compared with the optimised geometries resulting from DFT calculations.

Molecular Structure of $[Os_2Ru(CO)_{11}(PPh_3)]$ (2)

The crystal structure of cluster **2** is shown in Figure 2. This structure was determined on a mixture of $[Os_2Ru(CO)_{11}(PPh_3)]$ and $[Os_3(CO)_{11}(PPh_3)]$ in a ratio of 0.64:0.36. Selected bond lengths and angles are presented in Table 1. The structure of **2** exhibits disorder amounting to a 36% Os occupancy at the Ru atom site, being significantly distorted from the D_{3h} symmetry observed for $[M_3(CO)_{12}]$ (M = Ru, Os).[32,33] Most importantly, the crystal structure, in combination with (temperature-dependent) ^{31}P NMR spectra, reveals that the PPh_3 ligand in $[Os_2Ru(CO)_{11}(PPh_3)]$ occupies an equatorial position and is exclusively coordinated at Ru. This is in contrast with the results of Pereira et al. who obtained an 1:2 mixture of osmium- and ruthenium-substituted isomers after the reaction of PPh_3 with the tetranuclear mixed-metal cluster $[RuOs_3(\mu\text{-}H)_2(CO)_{13}]$ under similar conditions.[34]

The geometry around the phosphorus atom in cluster **2** is essentially tetrahedral, the phenyl groups being slightly bent away from the Ru atom [C–P–C angles are in the range 100.30(13)–104.64(14)°]. The average metal–metal bond length (2.894 Å) is longer than the unsubstituted homonuclear clusters $[M_3(CO)_{12}]$ [M = Ru: 2.8542 Å;[33] M = Os: 2.8771(27) Å[32]]. This is partly due to the substitution of a

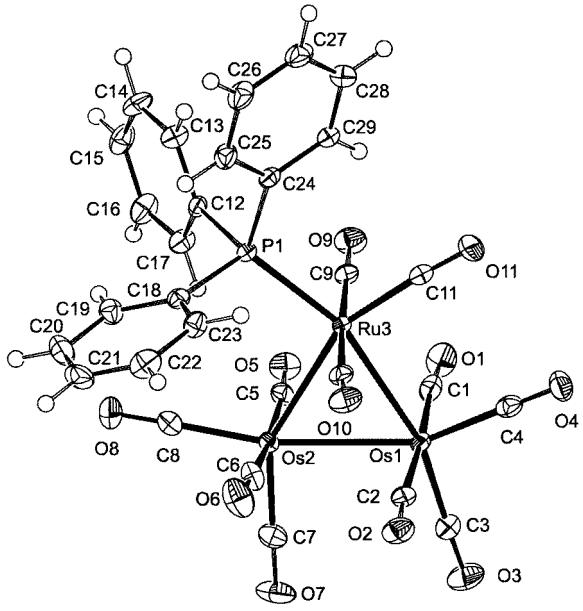

Figure 2. Molecular structure of the cluster $[Os_2Ru(CO)_{11}(PPh_3)]$ (**2**) in the crystal. Displacement ellipsoids are drawn at the 50% probability level. The site of Ru3 is occupied for 64% by Ru and for 36% by Os.

Table 1. Selected bond lengths [Å] and bond angles [°] for cluster **2**, with standard uncertainties in parentheses. For numbering see Figure 2. The site of Ru3 is occupied for 64% by Ru and for 36% by Os.

Ru3–Os1	2.88393(19)	Os1–Ru3–Os2	59.620(4)
Ru3–Os2	2.9147(2)	Os1–Os2–Ru3	59.660(4)
Os1–Os2	2.88275(16)	Ru3–Os1–Os2	60.721(5)
Ru3–P1	2.3683(7)	Ru3–P1–C12	116.70(9)
Ru3–C9	1.939(3)	Ru3–P1–C18	114.07(9)
Ru3–C10	1.940(3)	Ru3–P1–C24	116.04(9)
Ru3–C11	1.887(3)	C12–P1–C18	104.64(14)
P1–C12	1.842(3)	C18–P1–C24	103.18(13)
P1–C18	1.831(3)	C12–P1–C24	100.30(13)
P1–C24	1.826(3)		

π-accepting CO ligand by the much stronger σ-donor PPh_3, increasing the electron density on the metal core and resulting in expansion. Like in the corresponding homonuclear clusters $[M_3(CO)_{11}(PPh_3)]$ (M = Os, Ru),[35,36] the length of the metal–metal bond positioned *cis* to the PPh_3 ligand [Ru–Os2: 2.9147(2) Å] is increased to a larger extent than the other metal–metal bond lengths [Ru–Os1: 2.8839(2) Å; Os1–Os2: 2.8827(2) Å]. This difference has been attributed to steric interactions between the PPh_3 ligand and the *cis*-CO group on the adjacent metal atom.[35,36] The steric and electronic effects are also reflected in the marked shortening of the M–CO_{eq} bond *cis* to the PPh_3 ligand [Ru–C11 = 1.887(3) Å] compared to the average length of these bonds in, for example, $[Ru_3(CO)_{12}]$ [average Ru–CO_{eq}: 1.921(5) Å]. This shortening is ascribed to increased π-back-bonding to the CO ligand, resulting from the presence of the σ-donating phosphorus ligand attached to the same metal and to the sterically induced lengthening of the Ru–Os2 bond *trans* to this CO group.[35]

 © 2005 Wiley-VCH Verlag GmbH & Co. KGaA, Weinheim

The Ru–Os bond lenghts [2.9147(2) and 2.8839(2) Å] nicely fit within the values reported for the corresponding metal–metal bond lengths in the homonuclear analogues [$M_3(CO)_{11}(PPh_3)$] [M = Os: 2.918(1) and 2.891(1) Å, M = Ru: 2.907(3) and 2.876(3) Å]. This comparison is possible even though the reported Os–Ru distances do not correspond to "pure" [$Os_2Ru(CO)_{11}(PPh_3)$], but to a blend of Os_2Ru and Os_3 in solid solution (vide supra). The distortion from the D_{3h} symmetry, manifested by the twisting of the $Os(CO)_4$ units, is reflected in the C_{ax}–Os1–Os2–C_{ax} dihedral angles.[35] Just like for the metal–metal bond lengths, the values for C1–Os1–Os2–C5 (3.5°) and C2–Os1–Os2–C6 (12.8°) closely resemble those reported for the homonuclear analogues: 5.4° and 14.4° for Ru and 4.4° and 12.3° for Os, respectively.

The presence of [$Os_3(CO)_{11}(PPh_3)$], which was refined with a substitutional disorder model for the Ru/Os3 atom site, has most likely its origin in the formation of [$Os_3(CO)_{12}$] as a side-product during the preparation of **1** (vide supra). This is also reflected in the mass spectra of some of the [$Os_2Ru(CO)_{12}$] samples where a peak at *m*/*z* 908 is ascribed to the molecular ion of [$Os_3(CO)_{12}$]. The presence of ca. 35% [$Os_3(CO)_{11}(PPh_3)$] is also reflected in the $^{31}P\{H\}$ NMR and FD mass spectra of **2**, indicating that the observed ratio between the Os_3 and Os_2Ru phosphane-substituted clusters in the crystal structure is similar in the gas phase and in solution.

Density Functional Study of [$Os_2Ru(CO)_{11}(PPh_3)$] (2)

The density functional theory (DFT, ADF programme[37–43]) study of cluster **2** was performed with the aim to learn, whether the theory indeed predicts [$Os_2Ru(CO)_{11}(PPh_3)$] to be most stable with the PPh_3 ligand coordinated at the ruthenium centre at an equatorial site. The cluster [$Os_2Ru(CO)_{11}(PH_3)$] (**2a**) served as a model for **2**. Some features of the optimised geometry of **2a** slightly deviate from those of the crystal structure of **2** (Table 2, Figure 3). First of all, the calculated metal–metal bond lengths are slightly longer than the experimental ones (up to 0.05 Å), similar to the situation for [$Os_3(CO)_{12}$].[19,20] The Ru–Os bond *cis* to the PPh_3 ligand is calculated to be significantly longer than the other two metal–metal bonds, in agreement with the crystal structure. This trend points to the role of electronic effects apart from the expected steric influence. For, the differences in the metal–metal bond lengths should be smaller in the model **2a**, as the steric interactions of the PH_3 ligand with the *cis*-CO group on the adjacent metal atom are much less pronounced compared to the bulky PPh_3 ligand. Apart from this feature, the twisting of the $Os(CO)_4$ units in **2a** is much smaller than in the experimental structure. This is reflected in the orientation of the Os–CO_{ax} bonds in **2a**, which are almost perpendicular to the Os_2Ru plane (dihedral angles C1–Os1–Os2–C5 = 0.3° and C2–Os1–Os2–C6 = 0.5°). The larger distortion in the experimental structure has its origin presumably in the phenyl groups of the PPh_3 ligand. In the solid state, these phenyl rings interact with the phenyl rings of the two neighbouring clusters by four edge-to-face interactions to give a one-dimensional chain. Similar interactions, for example, have been reported for the cluster [$Os_3(CO)_{11}\{P(p\text{-}C_6H_4F)_3\}$].[44] Besides the crystal packing effects, not incorporated in the geometry optimisation of **2a**, the twist of the $M(CO)_4$ units also depends on the selected computational basis set.[19]

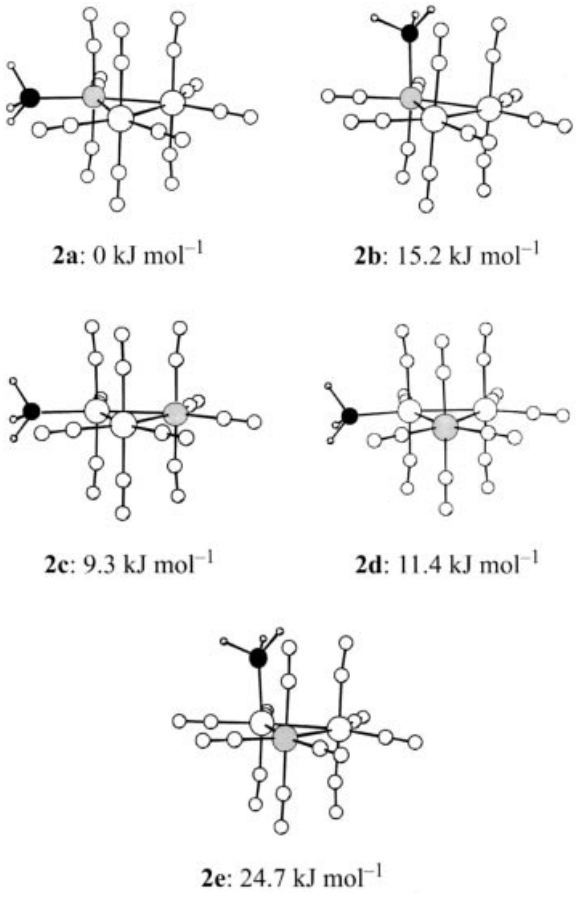

Figure 3. Optimised geometries and relative energies of the model cluster **2a** and its virtual isomers **2b**–**e**.

Table 2. Comparison of selected ADF/BP calculated bond lengths [Å] and angles [°] in cluster **2a** with the experimental crystallographic data.

Bond[a]	Calcd.	Exp.	Angle[a]	Calcd.	Exp.
Ru–Os1	2.913	2.88393(19)	Os1–Ru–Os2	60.0	59.620(4)
Ru–Os2	2.956	2.9147(2)	Os1–Os2–Ru	59.3	59.660(4)
Os1–Os2	2.933	2.88275(16)	Ru–Os1–Os2	60.8	60.721(5)
Ru–P	2.339	2.3683(7)			

[a] See Figure 2.

 © 2005 Wiley-VCH Verlag GmbH & Co. KGaA, Weinheim

In addition to the optimised model **2a**, the relative energies of several structural isomers **2b**–**e** have also been calculated (Figure 3). The isomers **2a** and **2b** have in common that the PH_3 ligand is coordinated to ruthenium, but they differ in the coordination of the ligand relative to the Os_2Ru plane (equatorial and axial, respectively). In isomers **2c**–**e**, the PH_3 ligand is coordinated at one of the osmium atoms, **2e** being the only model with the PH_3 ligand coordinated in an axial position. Isomers **2c** and **2d** have the PH_3 ligand coordinated in an equatorial position, but they differ in the orientation of the PH_3 ligand relative to the ruthenium centre. Importantly, isomer **2a** appeared to be more stable by 11.4 kJ·mol^{-1} than isomer **2d**, which proves the preferable coordination of the PH_3 ligand at ruthenium. Isomer **2c**, with the PH_3 ligand perpendicular to the Os1–Os2 bond, is in turn slightly more stable than isomer **2d**, where the position of the PH_3 ligand presents almost a continuation of the Os1–Os2 bond. The isomers **2b** and **2e**, with the PH_3 ligand occupying an axial site at Ru and Os, respectively, are highest in energy.

Although the difference in relative energy between the model structures **2a** and **2c** is relatively small, no experimental evidence has been obtained for $[Os_2Ru(CO)_{11}(PPh_3)]$ clusters with the phosphane ligand coordinated to osmium. However, as the relative energies calculated by DFT refer to isolated gas-phase molecules at zero Kelvin temperature, with PH_3 as the model for the PPh_3 ligand, the obtained values merely reflect a trend in the thermodynamic stability of the different isomers in solution at 293 K.

In order to investigate whether a chelating α-diimine ligand also prefers coordination at the ruthenium site of **1**, we synthesized the cluster $[Os_2Ru(CO)_{10}(i\text{Pr-AcPy})]$ (**3**) and determined its molecular geometry. Apart from its structure, the major interest in cluster **3** stems from our aim to reveal the influence of the heteronuclear cluster core on the photo- and redox reactivity of this compound. For a proper evaluation of this effect, the homonuclear clusters $[Os_3(CO)_{10}(\alpha\text{-diimine})]$ were used as a reference.

Molecular Structure of $[Os_2Ru(CO)_{10}(i\text{Pr-AcPy})]$ (3)

The molecular structure of cluster **3**, determined by single-crystal X-ray diffraction, is shown in Figure 4. Selected bond lengths and angles are collected in Table 3. As in compound **2**, the corresponding Os_3 compound, viz. $[Os_3(CO)_{10}(i\text{Pr-AcPy})]$, was also present in the crystal structure as a solid solution (occupancy 0.89:0.11 for Os_2Ru:Os_3). Importantly, the crystal structure reveals that the *i*Pr-AcPy ligand in $[Os_2Ru(CO)_{10}(i\text{Pr-AcPy})]$ is again bound at the ruthenium atom. Similar to 2,2′-bipyridine (bpy) and *N*,*N*′-diisopropyl-1,4-diaza-1,3-butadiene (*i*Pr-DAB) in the closely related $[Os_3(CO)_{10}(\alpha\text{-diimine})]$ clusters,[45,46] the asymmetric *i*Pr-AcPy ligand is coordinated to a single metal centre in a chelating fashion. The nitrogen atom of the pyridine ring and the imine nitrogen occupy axial and equatorial positions, respectively.

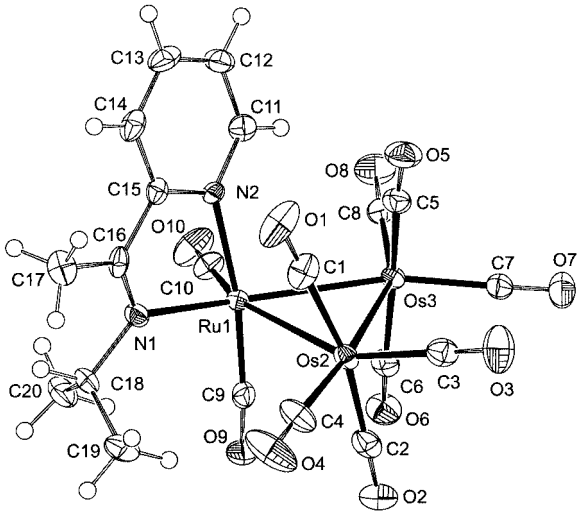

Figure 4. Molecular structure of the cluster $[Os_2Ru(CO)_{10}(i\text{Pr-AcPy})]$ (**3**) in the crystal. Displacement ellipsoids are drawn at the 50% probability level. The site of Ru1 is occupied for 89% by Ru and for 11% by Os.

Table 3. Selected bond lengths [Å] and angles [°] for cluster **3**, with standard uncertainties in parentheses. For numbering see Figure 4. The Ru1 site is occupied for 89% by Ru and for 11% by Os.

Ru1–Os3	2.8694(4)	N1–C16	1.307(5)
Ru1–Os2	2.9159(4)	N2–C15	1.358(5)
Os2–Os3	2.8815(2)		
Ru1–N1	2.141(4)	Os3–Os2–Ru1	59.328(8)
Ru1–N2	2.151(3)	Os2–Os3–Ru1	60.934(8)
Ru1–C9	1.846(5)	Os3–Ru1–Os2	59.738(8)
Ru1–C10	1.855(5)	N1–Ru1–Os3	157.77(10)
N2–C11	1.343(5)	N2–Ru1–Os2	101.98(9)
C11–C12	1.375(6)	N1–Ru1–C9	97.02(16)
C12–C13	1.380(6)	N2–Ru1–C9	171.47(16)
C13–C14	1.385(6)	N1–Ru1–N2	75.25(13)
C14–C15	1.383(6)	N1–C16–C15	115.7(4)
C15–C16	1.470(6)	N2–C15–C16	115.2(4)

Just as for cluster **2**, the observed substitutional disorder due to a small amount of the triosmium analogue most likely has its origin in the formation of $[Os_3(CO)_{12}]$ as a side-product during the preparation of **1**. Apart from the crystal structure, the presence of a small amount of $[Os_3(CO)_{10}(i\text{Pr-AcPy})]$ is also reflected in the FAB$^+$ mass spectrum of **3** where peaks at *m*/*z* 986.9 and 957.9 can be ascribed to $[M^+ - nCO]$ (M = $[Os_3(CO)_{10}(i\text{Pr-AcPy})]$; n = 1, 2). Moreover, the ^{1}H NMR spectrum of **3** in $CDCl_3$ displays small signals at δ = 9.50 (d, 1 H), 8.02 (d, 1 H), 7.86 (dd, 1 H), 7.11 (dd, 1 H) and 4.44 (m, 1 H) ppm, pointing to the presence of ca. 10–15% $[Os_3(CO)_{10}(i\text{Pr-AcPy})]$ (estimated from signal integrals). This proves that the ratio between $[Os_2Ru(CO)_{10}(i\text{Pr-AcPy})]$ and $[Os_3(CO)_{10}(i\text{Pr-AcPy})]$ in solution is very close to that in the solid state.

Density Functional Study of $[Os_2Ru(CO)_{10}(i\text{Pr-AcPy})]$ (3)

DFT calculations (ADF programme[37–43]) were performed in order to obtain more insight into the bonding

 © 2005 Wiley-VCH Verlag GmbH & Co. KGaA, Weinheim

properties of **3** and the influence of the Ru atom on the character of the frontier orbitals. The cluster $[Os_2Ru(CO)_{10}(H\text{-}PyCa)]$ (H-PyCa = pyridine-2-carbaldehyde-imine) (**3′**) was taken as a model, with the isopropyl and imine methyl groups of the *i*Pr-AcPy ligand replaced by hydrogen atoms. In order to determine whether the theoretical calculations indeed predict the coordination of *i*Pr-AcPy at the ruthenium centre instead of the osmium sites, the relative energies of the structural isomers **3′** and **3′′** were calculated, with **3′** having the α-diimine coordinated at ruthenium and **3′′** at osmium (Figure 5). In both model systems, H-PyCa is coordinated with the pyridine ring in the axial position. A recent DFT study of the related cluster $[Os_3(CO)_{10}(H\text{-}PyCa)]$[18] has shown that this geometric isomer is more stable than those with the pyridine ring equatorially bound or with both nitrogen atoms coordinated in the equatorial plane.

Geometry optimisation of both isomers with DFT revealed that **3′** is more stable than **3′′** by 22 kJ·mol^{-1}. This is in agreement with the experimental structure, showing that also the *i*Pr-AcPy ligand prefers coordination at the ruthenium site of $[Os_2Ru(CO)_{12}]$. The geometry of model **3′** is in good agreement with the experimental structure of **3** (Table 4, Figure 5).

The relatively large difference between the lengths of the two Ru–N bonds in **3′** (2.05 vs. 2.17 Å) indicates that the α-diimine ligand is coordinated in a more asymmetric fashion than in the experimental structure. The probable reason is the replacement of the isopropyl group by a hydrogen atom, shortening the Ru–N1 bond as a result of different steric and electronic effects.

From the ground-state DFT calculations, the composition of the molecular orbitals of **3′** has been obtained. The

Table 5. Characters and one-electron energies of selected frontier orbitals of $[Os_2Ru(CO)_{10}(H\text{-}PyCa)]$ (**3′**) as calculated by the ADF/BP method (L = LUMO, H = HOMO).

MO		*E* [eV]	Ru	Os1	Os2	H-PyCa	CO
111a	L+2	–2.70	0.5	0.1	0.6	87.7	6.0
110a	L+1	–3.04	23.4	7.3	4.5	9.5	44.6
109a	**L**	**–3.68**	**8.4**	**1.1**	**6.5**	**64.7**	**14.4**
108a	**H**	**–5.28**	**25.5**	**1.0**	**16.7**	**24.9**	**25.4**
107a	H-1	–5.77	24.4	21.9	17.1	3.4	26.7
106a	H-2	–5.84	38.3	16.1	3.2	7.8	30.2
105a	H-3	–6.22	52.8	7.0	10.9	5.8	17.1
104a	H-4	–6.46	35.6	9.6	19.8	1.8	26.5

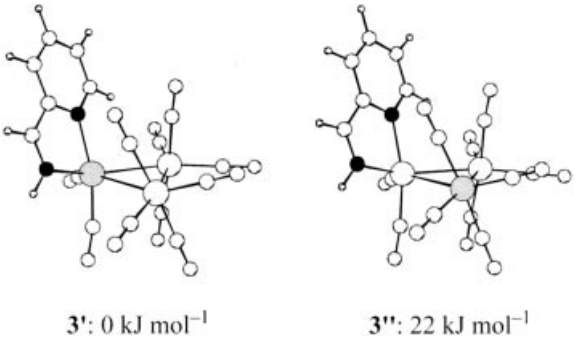

Figure 5. Optimised geometries and relative energies of the model clusters **3′** and **3′′**.

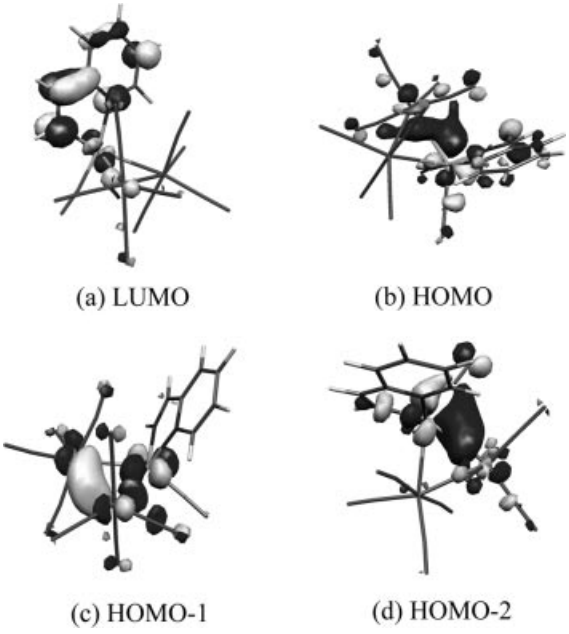

Figure 6. 3D representations of the LUMO (a), HOMO (b), HOMO-1 (c) and HOMO-2 (d) of $[Os_2Ru(CO)_{10}(H\text{-}PyCa)]$ (**3′**).

Table 4. Comparison of selected ADF/BP-calculated bond lengths [Å] and angles [°] in cluster **3′** with the experimental crystallographic data.

Bond[a]	Calcd.	Exp.	Bond/angle[a]	Calcd.	Exp.
Ru–Os3	2.896	2.8694(4)	N1–C16	1.314	1.307(5)
Ru–Os2	2.928	2.9159(4)	N2–C15	1.382	1.358(5)
Os3–Os2	2.913	2.8815(2)			
Ru–N1	2.049	2.141(4)	Os3–Os2–Ru	59.5	59.328(8)
Ru–N2	2.168	2.151(3)	Os2–Os3–Ru	60.5	60.934(8)
N2–C11	1.356	1.343(5)	Os3–Ru–Os2	60.0	59.738(8)
C11–C12	1.385	1.375(6)	N1–Ru–Os3	152.9	157.77(10)
C12–C13	1.405	1.380(6)	N2–Ru–Os3	96.8	97.41(9)
C13–C14	1.383	1.385(6)	N1–Ru–N2	75.2	75.25(13)
C14–C15	1.412	1.383(6)	N1–C16–C15	116.5	115.7(4)
C15–C16	1.426	1.470(6)	N2–C15–C16	113.9	115.2(4)

[a] See Figure 4.

 © 2005 Wiley-VCH Verlag GmbH & Co. KGaA, Weinheim

Table 6. TD-DFT calculated lowest-energy singlet excitation energies [eV] and oscillator strengths (O.S.) for $[Os_2Ru(CO)_{10}(H\text{-}PyCa)]$.

Transition	Composition	Energy [eV]	Wavelength [nm]	Exp. λ_{max}[a] [nm]	O.S.
1	63% (H→L); 26% (H-1→L)	2.09	594	581	0.085
2	55% (H-1→L); 23% (H-2→L);	2.16	573		0.021
3	63% (H-2→L); 28% (H→L+1)	2.24	553		0.010
4	49% (H→L+1); 16% (H-3→L); 11% (H→L)	2.46	504	520	0.050
5	76% (H-3→L)	2.63	471	[b]	0.027
6	85% (H→L+2)	2.72	456	[b]	0.020
7	64% (H-4→L); 25% (H-1→L+1)	2.84	436		0.011
8	46% (H-2→L+1); 27% (H-1→L+1)	2.90	428	434	0.038

[a] Absorption maxima of $[Os_2Ru(CO)_{10}(i\text{Pr-}AcPy)]$ observed in hexane at 298 K (Figure 8). [b] Nonresolved.

contribution of the relevant atomic wavefunctions to the frontier orbitals is given in Table 5, with the HOMO (H) and LUMO (L) being in boldface. Three-dimensional plots of the three highest occupied molecular orbitals (HOMO, HOMO-1 and HOMO-2) and of the lowest unoccupied molecular orbital (LUMO), are depicted in Figure 6. Notice that the cluster has a different orientation in Figure 6a–d. The HOMO of **3′** has large contributions from both the Ru and Os2 centres, while Os1 is almost not involved. Accordingly, the HOMO has a σ-bonding character with respect to the Ru–Os2 bond [σ(Ru–Os2)]. All three metal centres participate in the HOMO-1 that is mainly σ-bonding with regard to the Os1 and Os2 centres and will be denoted as σ(Os1–Os2). The Os2 centre is almost not involved in the HOMO-2 that receives large contributions from Ru, Os1 and the carbonyl ligands, being best described as a σ(Ru–Os1) bonding orbital.

The LUMO of **3′** mainly consists of the lowest π*(H-PyCa) orbital, while the LUMO+1 is delocalised over the cluster carbonyl core. Based on the contribution of the atomic wavefunctions to the frontier orbitals, the HOMO–LUMO transition has predominant σ(Ru–Os2)-to-π*(α-diimine) character. A comparison of the frontier orbitals with those of $[Os_3(CO)_{10}(H\text{-}PyCa)]$[18] shows that the HOMOs of both clusters are very similar, with only one specific metal–metal(α-diimine) bond involved in the bonding interactions. Notably, the ruthenium centre in **3′** contributes slightly more (25%) to the HOMO than the corresponding osmium centre in $[Os_3(CO)_{10}(H\text{-}PyCa)]$ (18%). The contributions of the π*(H-PyCa) orbital to the HOMO and the LUMO of both compounds are nearly identical. The excitation energies and the oscillator strengths of the low-lying electronic transitions of **3′** were calculated using TD-DFT and are presented in Table 6.

Electronic Absorption Spectra

The electronic absorption spectra of cluster **3** are characterised by a dominant lowest-energy band showing negative solvatochromism (Table 7) typical for charge transfer (CT) from transition metals to α-diimine ligands.

Table 7. Near-UV and visible absorptions of $[Os_2Ru(CO)_{10}(i\text{Pr-}AcPy)]$ (**3**) in different solvents.

Solvent	λ [nm]
hexane	323 (sh), 434 (sh), 520 (sh), 581
2-chlorobutane	322 (sh), 453 (sh), 562
tetrahydrofuran	323 (sh), 456, 535
acetonitrile	322 (sh), 457, 522

In order to evaluate the solvatochromism of the lowest-energy absorption band, we have plotted the experimentally determined transition energies against the empirical solvent parameter E^*_{MLCT} of Manuta et al. (Figure 7), which is based on the solvatochromism of the lowest MLCT band of $[W(CO)_4(bpy)]$.[47] The plot could be well fitted by linear regression. Its slope reflects the degree of solvatochromism, while the intercept at $E^*_{MLCT} = 0$ corresponds to the experimental transition energy (205.3 kJ·mol^{-1}, 582 nm) extrapolated to nonpolar isooctane interacting similarly weakly with both ground and excited states. The obtained extrapolated value is in good agreement with the calculated maximum of the lowest-energy transition (594 nm, Table 6) and the observed maximum of the lowest-energy absorption band of cluster **3** in hexane (581 nm, Table 7).

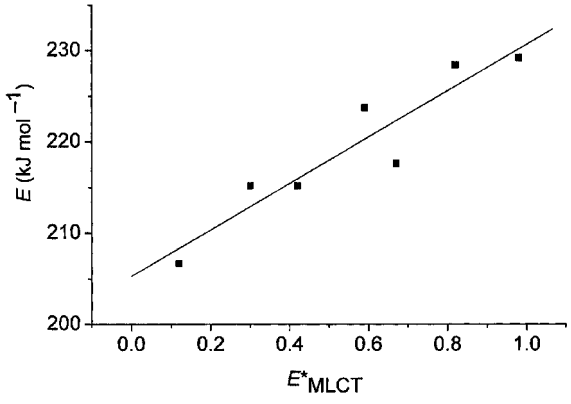

Figure 7. Solvatochromic behaviour of the lowest-energy absorption band of $[Os_2Ru(CO)_{10}(i\text{Pr-}AcPy)]$, based on the empirical solvent scale E^*_{MLCT} according to Manuta et al.[47] The solvents (with E^*_{MLCT} in parentheses) are CCl_4 (0.12), toluene (0.30), $CHCl_3$ (0.42), THF (0.59), CH_2Cl_2 (0.67), acetone (0.82) and acetonitrile (0.98).

 © 2005 Wiley-VCH Verlag GmbH & Co. KGaA, Weinheim

The experimental UV/Vis spectrum of cluster **3** in hexane and the corresponding spectrum simulated with SWizard[48] are shown in Figure 8. A comparison between the theoretical and experimental data (Table 6, Table 7 and Figure 8) shows that, besides the lowest-energy absorption band, there is also a good agreement between the calculated maxima of the higher-lying transitions (Table 6), the simulated SWizard spectrum, and the higher-lying band maxima of cluster **3** in hexane (Figure 8). As the absorption features in the visible region are generally broad and poorly resolved, the lowest-energy absorption band of **3** most likely consists of several allowed transitions of a prevailing charge transfer character, which is in line with its solvatochromism. A similar solvent dependence is observed for the higher-lying shoulder at 520 nm that corresponds with the calculated charge-transfer transition 4 (Table 6). The weak shoulder on the low-energy side of the intense near-UV absorption (434 nm in hexane) most likely consists of two differently composed transitions that mainly originate in the cluster core and are directed to the LUMO+1 (transitions 7 and 8, Table 6). Although the calculated excitation energies of the three different groups of electronic transitions (cluster model **3′**) slightly deviate from the experimental values (cluster **3**), the calculated oscillator strengths compare reasonably well with the observed band intensities and clearly predict that the lowest-energy, predominantly HOMO–LUMO transition, is the most intense one in the visible region. Due to their relatively small oscillator strengths and overlap, transitions 5 and 6 (Table 6) do not appear as distinct bands in the UV/Vis spectrum of **3**.

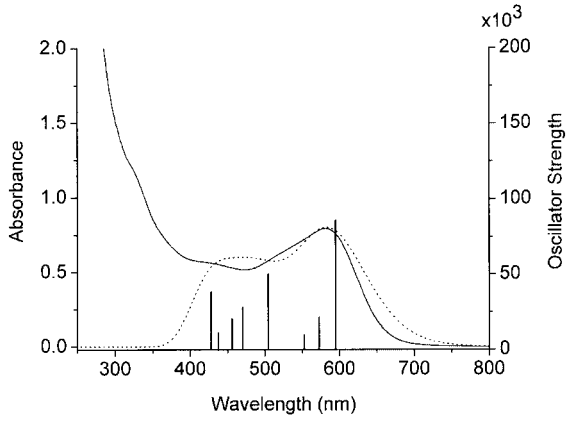

Figure 8. Electronic absorption spectrum of $[Os_2Ru(CO)_{10}(i$Pr-AcPy) in hexane at 293 K (−) together with the simulated SWizard spectrum (···) and the major electronic transitions of cluster **3′**, as calculated with the ADF programme (see Table 6).

Although the experimental results do not reveal whether the lowest-energy charge transfer transition originates from a molecular orbital with a predominant d_π(Ru) character or a delocalised σ(Ru–Os2) character, the TD-DFT results are clearly in favour of the latter assignment. The lowest-energy transition therefore belongs to a σπ* or sigma-bond-to-ligand charge transfer (SBLCT) transition, causing significant weakening of the Ru–Os2 bond in the excited state. Visible excitation of **3** is therefore expected to result efficiently in open-triangle photoproducts such as biradicals and zwitterions.

Time-Resolved Absorption Spectroscopy of Cluster 3 in Noncoordinating Solvents

Picosecond transient absorption (TA) spectra of cluster **3** were recorded in 2-chlorobutane (2-ClBu). Spectral changes following the 505 nm excitation were monitored in the region 510–710 nm. The spectra measured at 1–40 ps after the 130 fs laser pulse are depicted in Figure 9. Kinetic traces were obtained by plotting against time the ΔA values averaged over a small nanometer range. Due to the poor quality of the spectra, reliable lifetimes could only be obtained from the decay in the region 565–580 nm.

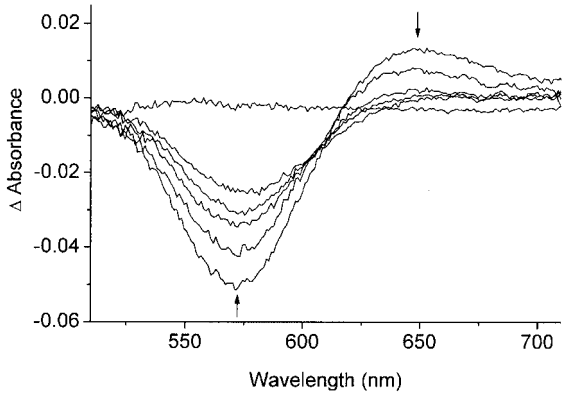

Figure 9. Transient difference absorption spectra of cluster **3** in 2-ClBu, recorded at time delays of –4 (baseline), 1, 3.5, 8.5, 16 and 31 ps, after 505 nm excitation (130 fs FWHM).

The TA spectrum at t_d = 1 ps (Figure 9) shows a bleach at about 570 nm, very close to the maximum of the ground-state absorption of the cluster in this solvent (562 nm), and an absorption with a maximum at 645 nm. The bleach partly disappears with a lifetime of 10.4 ± 1.2 ps. The remaining TA spectrum obtained at t_d = 31 ps, shows a bleach at 580 nm, which is approximately 47% of the initial signal and does not change significantly in the ps time domain. Thus, at least part of the transient species does not regenerate the parent cluster but instead converts into a second species. This is also evidenced by the long-wavelength absorption that transforms on the same time scale as the decay of the bleach into a much broader absorption without a distinct maximum. The ps TA spectra strongly resemble those of $[Os_3(CO)_{10}(i$Pr-AcPy)] in 2-ClBu.[16] This observation also implies that the 11% impurity of the latter cluster in the studied sample of **3** (vide supra) can hardly be distinguished by the TA method in this solvent.

In agreement with the results of the TD-DFT study, the initially observed broad transient absorption above 600 nm is assigned to an excited state having a predominant σπ* character. In this state, one electron has been transferred from the σ(Ru–Os2) bonding orbital (vide supra) to the lowest π* orbital of the *i*Pr-AcPy ligand. Such absorptions are characteristic for complexes in metal-to-α-diimine excited states[49–52] and for α-diimine radical anions contain-

 © 2005 Wiley-VCH Verlag GmbH & Co. KGaA, Weinheim

ing at least one aromatic group.[49,53,54] The remaining transient absorption in 2-ClBu is very similar to that observed in the ns TA spectra of **3** (vide infra) and is assigned to the biradical [˙Os(CO)$_4$–Os(CO)$_4$–$^+$Ru(CO)$_2$(α-diimine$^{\cdot-}$)], in accordance with the results for [Os$_3$(CO)$_{10}$(*i*Pr-AcPy)].[16] This assignment has also been verified by recording the ps TA spectra at 250, 500 and 750 ps delays after the laser pulse. These spectra do not differ from that obtained at t_d = 31 ps, thereby proving that the biradicals formed directly from the σπ* excited state do not disappear on the picosecond time scale. Although the TA spectra of **3** in 2-ClBu are very similar to those of the corresponding triosmium cluster, the excited-state lifetime of the former complex is significantly shorter (Os$_3$: τ = 25.3 ps vs. Os$_2$Ru: τ = 10.4 ps). This may be due to the fact that the Os2–Ru(α-diimine) bond is weaker and, thus, the energetic barrier for the biradical formation is lower. Assuming similar molar absorbance for the homo- and heteronuclear biradicals, the higher intensity of the remaining transient signal after the decay of the excited state (Os$_3$: 30% vs. Os$_2$Ru: 47%) also points to a more facile formation of the open-structure photoproducts in the case of cluster **3**.

The fate of the biradicals was studied in several weakly coordinating solvents (2-ClBu, THF, acetone) by nanosecond transient absorption (ns TA) spectroscopy. Spectra of **3** in acetone were obtained by excitation at 532 nm and the spectral changes were monitored in the 350–800 nm region. The difference absorption spectra, measured 0–900 ns after the laser pulse, are depicted in Figure 10. Kinetic traces were recorded after excitation at 532 nm and probed at 560 nm (bleach). The resulting lifetimes are collected in Table 8, together with the values for the corresponding homonuclear cluster [Os$_3$(CO)$_{10}$(*i*Pr-AcPy)].

The ns TA spectra of **3** in acetone reveal a strong bleaching between 440 and 600 nm due to the disappearance of **3**, and transient absorption below 440 nm and in the long-wavelength region. As stated above, the transient absorption is characteristic for α-diimine radical anions[49–52] and for α-diimine complexes in their metal-to-α-diimine excited state, provided the α-diimine ligand bears at least one heteroaromatic group.[49,53,54] As the ns TA spectra closely resemble those of [Os$_3$(CO)$_{10}$(*i*Pr-AcPy)] in acetone,[15] the transient absorption is again assigned to the open-structure biradical [˙Os(CO)$_4$–Os(CO)$_4$–$^+$Ru(Sv)(CO)$_2$(*i*Pr-AcPy$^{\cdot-}$)] (Sv = acetone). In addition, the ns TA spectrum at t_d = 5 ns in acetone is very similar to the TA spectrum of **3** at t_d = 31 ps in 2-ClBu. This confirms that the biradicals formed directly from the excited state, are present in both the ps and ns time domain. The decay of the nanosecond transient species in acetone almost completely regenerated the parent cluster with a lifetime of 228 ns. On changing the solvent to THF and 2-ClBu, the lifetime decreased to 95 and 27 ns, respectively. This result demonstrates that the lifetime of the biradical follows the coordinating ability of the solvent, increasing in the order 2-chlorobutane < THF < acetone. A further increase in the lifetime was found when **3** was irradiated in 2-ClBu in the presence of 1.0 M MeCN. The kinetic trace of this solution shows a decrease of the bleach on the μs time scale (τ = 6.8 μs), but not its complete disappearance. This means that the MeCN-stabilised biradicals did not convert back to the parent cluster but transformed into the corresponding MeCN-stabilised zwitterions, just as observed for [Os$_3$(CO)$_{10}$(*i*Pr-AcPy)].[16] In the case of the triosmium cluster, this process typically occurs for strong Lewis bases (MeCN, pyridine) and firmly coordinating olefins (styrene, octene).[15]

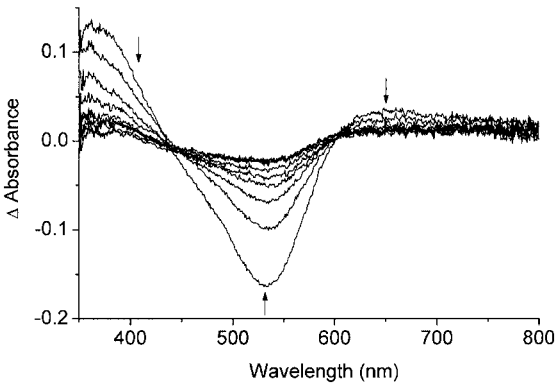

Figure 10. Nanosecond transient difference absorption spectra of cluster **3** in acetone, recorded in the time interval t = 0–900 ns after the 532 nm laser pulse; the time delay between the spectra is 100 ns.

Time-Resolved Spectroscopy in Strongly Coordinating Solvents

In addition to the experiments in 2-ClBu, ps TA spectra of cluster **3** were also recorded in strongly coordinating MeCN. The spectra measured at 1–5 ps after the 130 fs/505 nm laser pulse are depicted in Figure 11. Kinetic traces were extracted by plotting against time the ΔA values averaged in the range 605–615 nm.

Table 8. Lifetimes [ns] of the solvent-stabilised biradical photoproducts of cluster **3** and the reference compound [Os$_3$(CO)$_{10}$(*i*Pr-AcPy)], obtained from their kinetic profiles probed at 560 nm. Standard deviations are given in parentheses.

Solvent	[Os$_2$Ru(CO)$_{10}$(*i*Pr-AcPy)]	[Os$_3$(CO)$_{10}$(*i*Pr-AcPy)]
2-chlorobutane	27(4)	22(3)
THF	95(4)	104(7)
Acetone	228(8)	677(2)
2-chlorobutane/MeCN (1.0 M)	6.8 (0.1)[a]	13.5 (0.2)[a]

[a] Lifetime in μs.

 © 2005 Wiley-VCH Verlag GmbH & Co. KGaA, Weinheim

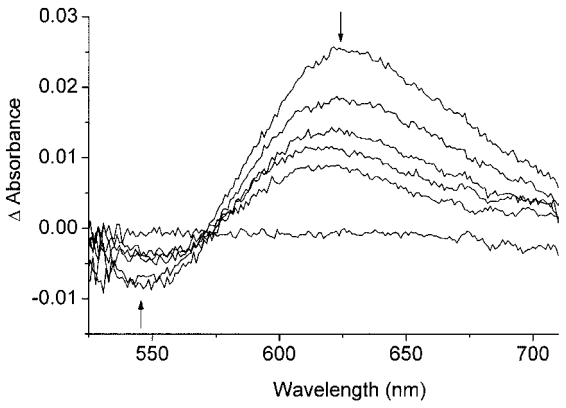

Figure 11. Transient difference absorption spectra of cluster **3** in MeCN, recorded at time delays of –1 (baseline), 1, 1.5, 2.5, 3.5 and 4.5 ps, respectively, after 505 nm excitation (130 fs FWHM).

The first TA spectra (Figure 11) are similar to those in 2-ClBu although the maxima of the bleach (550 nm) and the transient absorption (630 nm) are somewhat shifted. Although the TA spectra of **3** in MeCN resemble those obtained for $[Os_3(CO)_{10}(i\text{Pr-AcPy})]$ in this solvent,[16] the excited states of both clusters behave differently. For $[Os_3(CO)_{10}(i\text{Pr-AcPy})]$ the decay of the excited state in coordinating MeCN is bi-exponential. The slower process (τ = 21.4 ps) has been ascribed to biradical formation, having a lifetime similar to that observed in 2-ClBu.[16] The faster process (τ = 2.9 ps) has been assigned to the heterolytic cleavage of an Os–Os(α-diimine) bond from an MeCN-coordinated excited state with concomitant zwitterion formation; zwitterions were indeed observed in the ps TRIR spectra of $[Os_3(CO)_{10}(i\text{Pr-AcPy})]$.[55] The excited state of cluster **3** decays mono-exponentially in MeCN and its lifetime (τ = 2.1 ps) closely corresponds to the shorter 2.9 ps component of the bi-exponential decay of the excited state of $[Os_3(CO)_{10}(i\text{Pr-AcPy})]$. This points to the same process for both clusters and suggests that irradiation of **3** in neat MeCN gives rise to very fast formation of zwitterions as the only photoproduct. As will be shown hereinafter, TA studies in the nano- and microsecond time domain and rapid scan FTIR spectroscopic measurements confirm this presumption.

As described above, the kinetic trace of **3** in 2-ClBu in the presence of 1.0 M MeCN showed a decrease of the bleach on the μs time scale (τ = 6.8 μs) that, in accordance with the results for $[Os_3(CO)_{10}(i\text{Pr-AcPy})]$,[16] was assigned to the conversion of MeCN-stabilised biradicals into the corresponding MeCN-zwitterions. The MeCN-stabilised biradicals result in this case from the substitution of weakly coordinating 2-ClBu by MeCN within the lifetime of the solvent-stabilised biradicals $[^{\cdot}Os(CO)_4–Os(CO)_4–Ru^+(Sv)(CO)_2(i\text{Pr-AcPy}^{\cdot-})]$ (Sv = 2-ClBu). In neat MeCN, however, the kinetic trace of **3** does not show any change in signal intensity on the nano- and microsecond time scale (Figure 12), indicating that the pathway for zwitterion formation via the biradicals, similar to that observed for the triosmium analogue, does not exist. Thus, contrary to $[Os_3(CO)_{10}(i\text{Pr-AcPy})]$, cluster **3** affords a single photoproduct that does not convert into another species in the time domains studied. Based on our previous ns-μs TA studies of biradical and zwitterion photoproducts of $[Os_3(CO)_{10}(i\text{Pr-AcPy})]$ in MeCN,[12,15,16] the presence of 11% impurity of the latter cluster in the investigated sample of **3** should result in ΔA ca. 0.002 in Figure 12, which is difficult to resolve in the spectral noise.

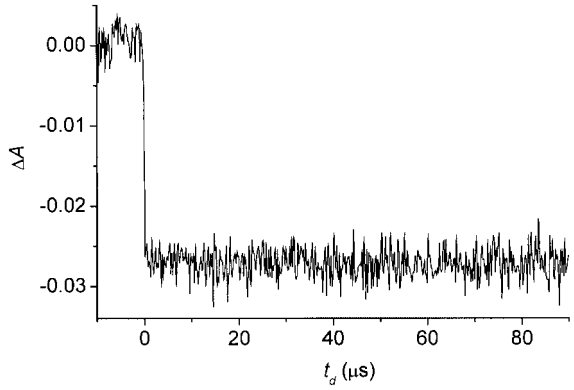

Figure 12. Transient kinetics at 560 nm measured for cluster **3** in MeCN, following irradiation at 532 nm with a Nd:YAG laser (7 ns FWHM, average of 10 shots at 10 s intervals, 2 mJ·pulse^{-1}).

In order to confirm that the single photoproduct is the zwitterion $[^{-}Os(CO)_4–Os(CO)_4–Ru^+(MeCN)(CO)_2(i\text{Pr-AcPy})]$, the photoreaction of **3** in MeCN was followed with rapid-scan IR spectroscopy in the (sub)second time domain. In addition, also pyridine was used as the solvent. Cluster **3** was irradiated for 2 s with an argon-ion laser (514.5 nm, 150 mW) and the IR spectral changes in the CO-stretching region were monitored in both solvents on the time scale of seconds to minutes. The difference IR spectra of **3** in pyridine, measured 0–93 s after the laser pulse, are depicted in Figure 13. Unfortunately, irradiation of **3** in MeCN at 293 K only resulted in the formation of very weak transient bands at 1997 (vw), 1970 (s) and 1874 (s, br) cm^{-1}, that decayed with a lifetime similar to that of the zwitterions formed upon irradiation of $[Os_3(CO)_{10}(i\text{Pr-AcPy})]$ (τ = 38 ± 1 s).[12] Based on the intensity of the transient signals and the observed lifetime, this transient species is assigned as the homonuclear zwitterion $[^{-}Os(CO)_4–Os(CO)_4–{}^{+}Os(MeCN)(CO)_2(i\text{Pr-AcPy})]$, originating from the 11% $[Os_3(CO)_{10}(i\text{Pr-AcPy})]$ impurity in the sample (vide supra). Repeating the experiment at 273 K resulted in similar, more intense product bands, whose decay was clearly bi-exponential. Both the transient absorptions and the parent bleaches rapidly decay within 5 s to approximately 15% of their initial intensity. In a second, slower process, the remaining transient fully regenerates the parent cluster with a lifetime of 54.6 ± 1.2 s, being very close to the lifetime of the zwitterions formed upon irradiation of pure $[Os_3(CO)_{10}(i\text{Pr-AcPy})]$ under these conditions. As the amplitudes of both processes nicely correspond with the observed ratio between $[Os_2Ru(CO)_{10}(i\text{Pr-AcPy})]$ and $[Os_3(CO)_{10}(i\text{Pr-AcPy})]$ in the ^{1}H NMR spectrum and crystal structure of **3**, the faster process is assigned to the decay of

 © 2005 Wiley-VCH Verlag GmbH & Co. KGaA, Weinheim

the heteronuclear zwitterions [$^{-}$Os(CO)$_4$–Os(CO)$_4$–$^{+}$Ru(MeCN)(CO)$_2$(*i*Pr-AcPy)]. In agreement with the lifetime, the slower process is then attributed to the decay of the homonuclear zwitterions originating from the [Os$_3$(CO)$_{10}$(*i*Pr-AcPy)] impurity.

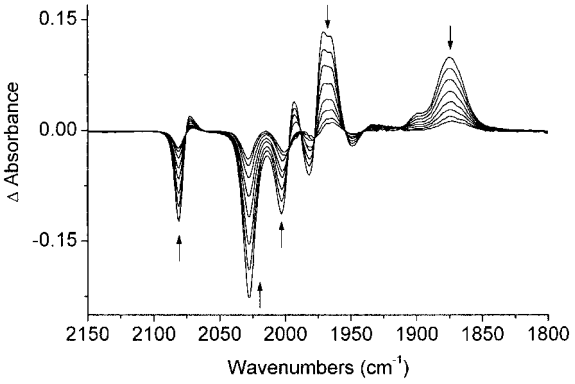

Figure 13. Difference rapid-scan IR spectra of cluster **3** in pyridine measured at time delays of 1.8, 6.6, 11.4, 18.6, 28.2, 40.2, 59.4 and 93.0 s after the 514.5 nm laser pulse.

Irradiation of **3** in strongly coordinating pyridine at room temperature resulted in similar spectral changes as observed in MeCN at 273 K (Figure 13). After excitation, the first spectra display instantaneous bleaching of the parent ν(CO) bands, together with transient absorption bands at 2073 (vw), 1994 (w), 1971 (s), 1965 (sh), 1898 (sh) and 1875 (s, br) cm^{-1}. Both the transient bands and parent bleaches decay again bi-exponentially. The lifetime of the heteronuclear zwitterion increased from a few seconds in MeCN to 23.0 ± 0.3 s in pyridine, which is consistent with the stronger coordination of the latter solvent. At the same time, the difference in the lifetimes of the heteronuclear and triosmium zwitterions has also increased significantly, the latter one living in pyridine for more than 30 minutes. The rapid-scan FTIR experiments thus clearly demonstrate that the irradiation of [Os$_2$Ru(CO)$_{10}$(*i*Pr-AcPy)] in strongly coordinating solvents like MeCN and pyridine results in the formation of solvent-stabilised zwitterions, with lifetimes much shorter than those of the corresponding triosmium zwitterions. The results of the combined time-resolved studies of cluster **3** are summarised in Scheme 2.

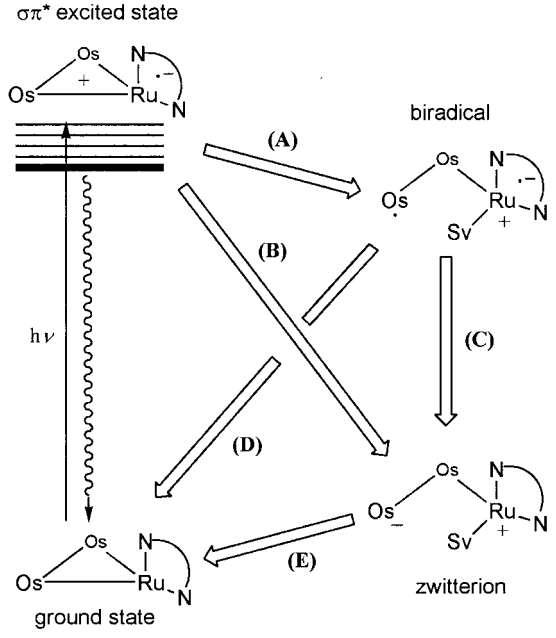

Scheme 2. Schematic representation of the photoreaction pathways established for the cluster [Os$_2$Ru(CO)$_{10}$(*i*Pr-AcPy)] (**3**). The separate reaction steps (**A**)–(**E**) depend on the solvent (Sv) used: (*i*) (**A**) + (**D**) in 2-ClBu, THF, acetone (293 K); (*ii*) (**B**) + (**E**) in MeCN; (*iii*) (**A**) + (**C**) + (**E**) in 2-ClBu + 1.0 M MeCN.

Stability of the Photoproducts

The observed photochemical reactivity of **3** differs significantly from that of the homonuclear clusters [Ru$_3$(CO)$_8$(μ-CO)$_2$(α-diimine)].[17] Although visible excitation of the latter clusters also resulted in the formation of open-structure photoproducts like biradicals and zwitterions, the efficiency of these processes is significantly lower due to the persistent presence of bridging carbonyl ligands in the excited state. Secondly, the triruthenium photoproducts could only be stabilised at low temperatures or in the presence of strongly coordinating Lewis bases or radical scavengers. Regarding the formation of open-structure photoproducts, the photoreactivity of **3** resembles more closely that of its triosmium analogue [Os$_3$(CO)$_{10}$(*i*Pr-AcPy)], for which fairly stable solvent-stabilised biradicals and zwitterions were observed upon excitation into its lowest-energy electronic transition.[12,15,16,55] The latter cluster therefore serves as a reference compound in order to evaluate the influence of the heteronuclear cluster core in **3** on the photoreactivity.

Interestingly, the solvent-stabilised biradicals of parent cluster **3** are significantly shorter-lived than their triosmium counterparts (Table 8). This difference in the biradical lifetime is most striking in acetone, where the lifetime of the heteronuclear biradical (τ = 228 ns) is merely 30% of the value found for [Os$_3$(CO)$_{10}$(*i*Pr-AcPy)] (τ = 677 ns). A much smaller difference is observed in THF (Os$_2$Ru: τ = 95 ns vs. Os$_3$: τ = 104 ns) while in weakly coordinating 2-ClBu the biradical lifetimes of both clusters are almost identical. These results clearly document that the difference in the biradical lifetime increases with the coordinating ability of the solvent. A similar trend applies for the lifetimes of the solvent-stabilised zwitterions. Whereas the lifetime of the heteronuclear zwitterion increases only slightly from a few seconds in MeCN to 23 s in pyridine, the lifetime of the triosmium zwitterion in pyridine amounts to more than 30 minutes compared to 38 s in MeCN. The shorter lifetimes of the heteronuclear photoproducts in better coordinating solvents indicate that the stabilisation of these products by solvent coordination is significantly reduced compared to the corresponding triosmium species. This is attributed to the higher tendency of the coordinatively unsaturated $^{+}$Os(CO)$_2$(*i*Pr-AcPy$^{\cdot-/0}$) moieties in the photoproducts to bind a Lewis base. A similar difference in Lewis base coordination on descending a transition metal group in the peri-

 © 2005 Wiley-VCH Verlag GmbH & Co. KGaA, Weinheim

odic table is observed, for example, for the coordinatively unsaturated radicals $[M(CO)_3(\alpha\text{-diimine})]\cdot$ (M = Mn, Re; α-diimine is, e.g., bpy, *i*Pr-PyCa, *i*Pr-DAB). Thus, while the unsaturated radicals $[Re(CO)_3(\alpha\text{-diimine})]\cdot$ form at room temperature fairly stable 18e paramagnetic species $[Re(CO)_3(\alpha\text{-diimine})(Sv)]\cdot$ (Sv = MeCN, PrCN),[56–58] analogous radicals were not observed for $[Mn(CO)_3(\alpha\text{-diimine})]\cdot$.[59]

Redox Behaviour of $[Os_2Ru(CO)_{10}(i\text{Pr-AcPy})]$ (3)

A combined cyclic voltammetric and IR spectroelectrochemical study of cluster **3** was performed in order to investigate the influence of the heteronuclear cluster core on the reduction pathway and stability of the reduction products. The redox potentials are presented in Table 9.

Table 9. Redox potentials of cluster **3** and its reduction products.

Cluster[a][b]	$E_{p,c}$ [V][c]	$E_{p,a}$ [V][c]
3	–1.87 (irr)	+0.27 (irr)
3[d]	–1.93 (irr)	+0.37 (irr)
$\mathbf{3b}^{2-}$ [d]		–1.50 (irr)
$[\mathbf{3b\text{-}3b}]^{2-}$		–1.17 (irr)
$[\mathbf{3b\text{-}3b}]^{2-}$ [d]		–0.85 (irr)

[a] Conditions and definitions: 10^{-3} mol·dm^{-3} solutions in THF (containing 10^{-1} M Bu_4NPF_6) at 293 K, unless stated otherwise; Pt disk microelectrode (0.42 mm^2); v = 100 mV s^{-1}; redox potentials vs. $E_{1/2}$ (Fc/Fc$^+$); $E_{p,c}$, cathodic peak potential for reduction of parent cluster; $E_{p,a}$, anodic peak potential for oxidation of parent cluster or its reduction products. [b] Assignments given in the main text. [c] Chemical irreversibility denoted by (irr). [d] T = 200 K.

The cyclic voltammogram of **3** in THF at room temperature (v = 100 mV·s^{-1}) showed a chemically irreversible two-electron reduction at $E_{p,c}$ = –1.87 V (cathodic peak R_1, see Figure 14a), most likely producing the open-core dianion $[^{-}Os(CO)_4\text{–}Os(CO)_4\text{–}Ru^{-}(CO)_2(i\text{Pr-AcPy})]^{2-}$ ($\mathbf{3b}^{2-}$). Similar dianions are formed upon reduction of the homonuclear clusters $[M_3(CO)_{10}(\alpha\text{-diimine})]$ (M = Ru, Os).[17,53] At room temperature, the dianion $\mathbf{3b}^{2-}$ was, however, not detectable on the reverse scan (vide infra). Instead, scan reversal behind R_1 resulted in the appearance of an anodic peak at –1.17 V (O_2') assigned, in accordance with the results for $[Os_3(CO)_{10}(i\text{Pr-PyCa})]$,[53] to the oxidation of the cluster dimer $[^{-}Os(CO)_4\text{–}Os(CO)_4\text{–}Ru(CO)_2(i\text{Pr-AcPy})]_2^{2-}$ ($[\mathbf{3b\text{-}3b}]^{2-}$) containing an (*i*Pr-AcPy)Ru–Ru(*i*Pr-AcPy) bond. Additional proof for this assignment was obtained from IR spectroelectrochemical experiments (vide infra), where the reduction of **3** resulted in the appearance of a ν(CO) band pattern closely resembling that of the photogenerated zwitterions with an open cluster core. On lowering the temperature to 200 K, the reduction of **3** remained chemically irreversible (Figure 14b). However, in contrast to the room-temperature scan, the anodic sweep showed an additional anodic peak at –1.50 V (O_2) assigned[53] to the oxidation of $\mathbf{3b}^{2-}$, the latter species being sufficiently stable at low temperatures. The minor anodic process denoted with the asterisk (Figure 14b) corresponds to the oxidation of unassigned species.

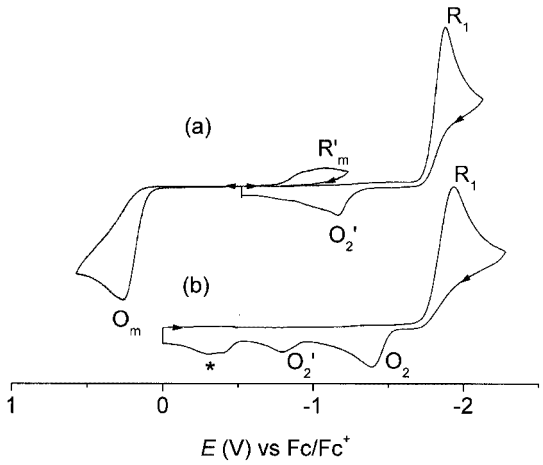

Figure 14. Cyclic voltammogram of cluster **3** at T = 293 K (a) and T = 200 K (b). Conditions: 10^{-3} M cluster in THF/10^{-1} M Bu_4NPF_6, Pt disk microelectrode (0.42 mm^2 apparent surface area), v = 100 mV s^{-1}.

Cyclic voltammetry thus documents that the closed-triangle radical anion of **3** cannot be stabilised even at 200 K and readily transforms into the open-structure dianion $\mathbf{3b}^{2-}$ (see Scheme 3). The latter dianion is also unstable and could only be produced in detectable amounts at low temperatures. This is in contrast with the results of $[Os_3(CO)_{10}(i\text{Pr-PyCa})]$, where the oxidation of the open-structure dianion is already clearly visible at 293 K.[53] Formation of dimer $[\mathbf{3b\text{-}3b}]^{2-}$, whose oxidation is observed at 200 K at $E_{p,a}$ = –0.85 V (O_2'), is known to take place by a rapid nucleophilic attack of dianion $\mathbf{3b}^{2-}$ at the yet nonreduced parent cluster **3**. A similar ECEC reduction path, for example, has been reported for the homonuclear clusters $[Os_3(CO)_{10}(\alpha\text{-diimine})]$.[53] Both $\mathbf{3b}^{2-}$ and $[\mathbf{3b\text{-}3b}]^{2-}$ are structurally related to the solvent-stabilised zwitterions

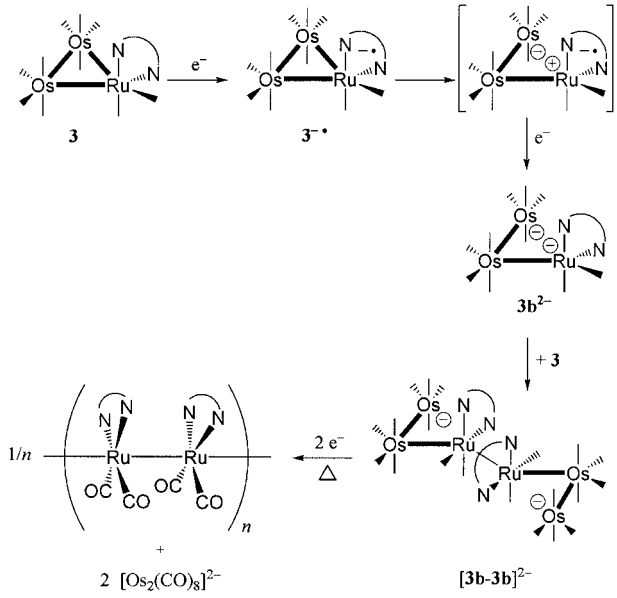

Scheme 3. Reduction path of cluster **3**.

 © 2005 Wiley-VCH Verlag GmbH & Co. KGaA, Weinheim

[$^{-}$Os(CO)$_4$–Os(CO)$_4$–$^{+}$Ru(Sv)(CO)$_2$(*i*Pr-AcPy)], the photoproduct of **3** in coordinating solvents (Sv) (vide supra).

For completeness, the oxidation of cluster **3** at the potential $E(O_m)$ is chemically irreversible, resulting in a secondary product reducible on the reverse cathodic scan at the potential $E(R'_m)$. These processes were not studied in detail.

In the course of corresponding IR spectroelectrochemical experiments, the reduction of **3** in THF at 250 K resulted in the appearance of transient ν(CO) bands at 2049 (m), 2009 (m), 1991 (m), 1965 (s), 1942 (sh) and 1864 (m) cm^{-1}, similarly to the IR ν(CO) spectrum reported for the open-core dimers [$^{-}$Ru(CO)$_4$–Ru(CO)$_4$–Ru(CO)$_2$(α-diimine)]$_2^{2-}$ (α-diimine = 2,2′-bipyridine, 2,2′-bipyrimidine).[17] Accordingly, these bands are assigned to the heteronuclear analogue [$^{-}$Os(CO)$_4$–Os(CO)$_4$–Ru(CO)$_2$(*i*Pr-AcPy)]$_2^{2-}$ ([**3b-3b**]$^{2-}$, Scheme 3). No IR bands attributable to the open-structure dianion **3b**$^{2-}$ were observed in the course of the reduction. This means that **3b**$^{2-}$ is unstable on the spectroelectrochemical time scale at 250 K and readily reacts with the parent cluster **3** to form the dimer [**3b-3b**]$^{2-}$. Actually, the latter species was also unstable and converted into another carbonyl product absorbing at 1938 (s) and 1863 (s, br) cm^{-1}. In agreement with the literature[31] and the results for [Os$_3$(CO)$_{10}$(α-diimine)],[60] this product is proposed to be the dinuclear complex [Os$_2$(CO)$_8$]$^{2-}$. As the highest-frequency ν(CO) band of the corresponding [Ru$_2$(CO)$_8$]$^{2-}$ complex is found at significantly lower wavenumber (Ru: 1930 cm^{-1} vs. Os: 1940 cm^{-1}),[31] the observation of [Os$_2$(CO)$_8$]$^{2-}$ provides another evidence that the α-diimine ligand in **3** is coordinated at ruthenium. Parallel to [Os$_2$(CO)$_8$]$^{2-}$, reduction of [**3b-3b**]$^{2-}$ most likely results in the formation of the polymeric chain [Ru(CO)$_2$(*i*Pr-AcPy)]$_n$, as indicated by the formation of a blue film at the working electrode and in its vicinity. Similar species are also formed as the ultimate reduction products of the clusters [M$_3$(CO)$_{10}$(α-diimine)] (M = Ru, Os), closely resembling [M(CO)$_2$(bpy)]$_n$, generated by electrochemical reduction of mononuclear complexes *trans*(Cl)-[M(CO)$_2$(bpy)(Cl)$_2$].[61–64]

The interest in these open-chain polymers [M(CO)$_2$(α-diimine)]$_n$ (M = Ru, Os) mainly derives from their electrocatalytic activity towards reduction of carbon dioxide.[63,65–67]

From the DFT results (Table 5, Figure 6) it is clear that the LUMO of cluster **3** is for about 65% the lowest π*(*i*Pr-AcPy) orbital. Further, the LUMO has also got a nonnegligible σ*(Ru–Os2) character. Single occupation of this orbital is therefore expected to result in largely α-diimine-localised radical anion **3**$^{\cdot-}$ with a weakened Ru–Os2 bond. This bond becomes readily cleaved, similar to the photoreactivity of cluster **3** (vide supra). While the photochemical cleavage is promoted by the partial σσ* character of the excited state, the driving force behind the electrochemical cleavage is probably the pronounced donor nature of the singly reduced *i*Pr-AcPy ligand in **3**$^{\cdot-}$ causing strong polarisation of the Ru–Os2 bond nearly perpendicular to the *i*Pr-AcPy plane. Unlike the corresponding homonuclear clusters [Os$_3$(CO)$_{10}$(*i*Pr-PyCa)][53] and [Ru$_3$(CO)$_8$(μ-CO)$_2$(α-diimine)][17] [α-diimine = 2,2′-bipyridine (bpy), 4,4′-dimethyl-2,2′-bipyridine (dmb), 2,2′-bipyrimidine (bpym)] forming fairly stable radical anions at moderately low temperatures, the reduction of **3** remains chemically irreversible even at 200 K. A comparison of the reduction potentials of the homonuclear [M$_3$(CO)$_{10}$(α-diimine)] clusters (M = Os,[68] Ru[17]) with that of **3** (–1.87 V) reveals that the π-acceptor capacity of the *i*Pr-AcPy ligand in **3** is similar to that of bpy (–1.85 V, M = Os, Ru) and dmb (–1.91 V, M = Ru). This implies that the higher reactivity of radical anions **3**$^{\cdot-}$ is not due to a limited donor power of the reduced *i*Pr-AcPy ligand but, probably, has its origin in the weak heterometallic Os2–Ru(*i*Pr-AcPy) bond.

Just as for the corresponding [Os$_3$(CO)$_{10}$(*i*Pr-PyCa)] cluster,[53] no open-structure dianions were detected by IR spectroscopy on the spectroelectrochemical time scale of minutes at 250 K, the dimer [**3b-3b**]$^{2-}$ being the initially observed reduction product. The triangular open-structure units in dimer [**3b-3b**]$^{2-}$ undergo fragmentation and linear chains [Ru(CO)$_2$(*i*Pr-AcPy)]$_n$ are ultimately formed, together with the dinuclear complex [Os$_2$(CO)$_8$]$^{2-}$.

Conclusions

Crystal structures of the novel clusters [Os$_2$Ru(CO)$_{11}$(PPh$_3$)] (**2**) and [Os$_2$Ru(CO)$_{10}$(*i*Pr-AcPy)] (**3**) clearly reveal, in agreement with DFT calculations on several structural isomers, that both PPh$_3$ and *i*Pr-AcPy prefer coordination at the ruthenium site of [Os$_2$Ru(CO)$_{12}$] (**1**). The Os2–Ru(*i*Pr-AcPy) bond in cluster **3** is weaker than the corresponding metal–metal(α-diimine) bonds in the homonuclear [Os$_3$(CO)$_{10}$(*i*Pr-AcPy)] and doubly CO-bridged triruthenium analogues. This factor contributes to the observed differences in the photo- and electrochemical reactivity of cluster **3** compared to the homonuclear cores; although, the general course of the photo- and redox reactions remains unchanged.

Regarding the photochemical formation of biradical and zwitterionic photoproducts, cluster **3** closely resembles its homonuclear analogue [Os$_3$(CO)$_{10}$(*i*Pr-AcPy)]. In weakly coordinating 2-ClBu, the lowest σπ* excited state decays with a lifetime of approximately 10 ps, resulting in the formation of solvent-stabilised biradicals. In contrast to its triosmium analogue, irradiation of **3** in coordinating solvents exclusively results in heterolytic splitting of the Os2–Ru(*i*Pr-AcPy) bond, producing solvent-stabilised zwitterions. Interestingly, the lifetimes of the biradical- and zwitterionic photoproducts of cluster **3** are significantly shorter than their triosmium counterparts. This difference results most likely from a lower tendency of the coordinatively unsaturated $^{+}$Ru(CO)$_2$(*i*Pr-AcPy$^{\cdot-/0}$) moieties in the photoproducts to bind a Lewis base. Electrochemically, the influence of the weak Os2–Ru(α-diimine) bond is clearly reflected in the low stability of the radical anions initially formed by one-electron reduction of **3**.

In general, the combination of experimental photo- and electrochemical techniques together with the theoretical support from DFT calculations have provided a good in-

 © 2005 Wiley-VCH Verlag GmbH & Co. KGaA, Weinheim

sight into the bonding properties of $[Os_2Ru(CO)_{10}(i$PrAcPy)]. Although the incorporation of a Ru centre into the cluster core does not induce drastic changes in the photo- and electrochemical reactivity pattern in comparison with the triosmium derivative, more pronounced heterosite effects may, for example, be expected for mixed-metal clusters combining transition metal centres from different groups of the periodic Table (e.g., Os_2Pt, Os_2Rh).

Experimental Section

Materials and Preparations: Solvents of analytical grade [Acros: acetone, acetonitrile (MeCN), dichloromethane (CH_2Cl_2), hexane, tetrahydrofuran (THF); Aldrich: 2-Chlorobutane (2-ClBu); Merck: pyridine] were dried with sodium wire (hexane), sodium/benzophenone (THF), $CaSO_4$ (acetone) and CaH_2 (MeCN, CH_2Cl_2, 2-ClBu, pyridine) and freshly distilled under nitrogen prior to use. $[Ru_3(CO)_{12}]$, $[Os_3(CO)_{12}]$ (Strem Chemicals), PPh_3, Br_2 (Aldrich), ferrocene (BDH) and NH_3 (Praxair) were used as received. Trimethylamine *N*-oxide, $Me_3NO{\cdot}2H_2O$ (Janssen), was dehydrated before use by vacuum sublimation. The supporting electrolyte Bu_4NPF_6 (Aldrich) was recrystallised twice from ethanol and dried in vacuo at 350 K overnight. Neutral aluminium oxide 90 (70–230 mesh, Merck) and silica 60 (70–230 mesh, Merck) for column chromatography were activated by heating in vacuo at 450 K overnight and stored under N_2. Preparative TLC was performed on Silica Gel G plates (20×20 cm, 1 μm, Analtech).

Synthetic Procedures: All syntheses were performed under dry nitrogen, using standard Schlenk techniques. The preparation of $Na_2[Ru(CO)_4]$ and the consecutive coupling with $[Os_2(CO)_8(Br)_2]$ were performed on a high-vacuum line at reduced pressure ($\approx 10^{-4}$ Pa). $[Os_3(CO)_{12}(Br)_2]$,[69] $[Os_2(CO)_8(Br)_2]$[30] and $Na_2[Ru(CO)_4]$[31] were prepared by modified literature procedures. $[Os_2Ru(CO)_{11}(MeCN)]$ and $[Os_2Ru(CO)_{10}(MeCN)_2]$ were prepared by similar procedures as used by Foulds et al. for the syntheses of $[Ru_3(CO)_{12-n}(MeCN)_n]$ (n = 1, 2).[70] Both clusters were prepared in situ and only characterised by IR spectroscopy (vide infra).

Synthesis of $[Os_3(CO)_{12}(Br)_2]$: In a typical experiment, a solution of $[Os_3(CO)_{12}]$ (500 mg, 0.55 mmol) in CH_2Cl_2 (350 mL) was heated to reflux for 20 min. After addition of Br_2 (40 μL, 0.78 mmol) the solvent was immediately removed in vacuo. The pale yellow residue was dissolved in CH_2Cl_2/hexane, 1:4 (400 mL) and precipitated at 190 K. The product was obtained as a pale yellow powder (412 mg, 70%) and used in the synthesis of $[Os_2(CO)_8(Br)_2]$ without further purification. IR (CH_2Cl_2): $\tilde{\nu}$ [ν(CO)] = 2149 (vw), 2119 (s), 2062 (vs, br), 2030 (s), 2002 (w) cm^{-1}.

Synthesis of $[Os_2(CO)_8(Br)_2]$: A solution of $[Os_3(CO)_{12}(Br)_2]$ (350 mg, 0.33 mmol) in CH_2Cl_2 (60 mL) was heated at 323 K to dissolve all starting material. After cooling to room temperature, Br_2 (14.5 μL, 0.28 mmol) was added and the solution was irradiated with a 125 W high-pressure Hg lamp using a $\lambda > 420$ nm cut-off filter. The reaction was monitored by IR spectroscopy and irradiation was stopped when no further increase of the product ν(CO) bands was observed (ca. 85% conversion). After removal of the solvent in vacuo, the crude yellow product was extracted with hexane (5×10 mL). The combined fractions were filtered and the solvents evaporated to dryness. The remaining solid was redissolved in hexane containing a few drops of CH_2Cl_2 and precipitated at 270 K. The product was obtained as a pale yellow powder (86 mg, 40%). IR (hexane): $\tilde{\nu}$ [ν(CO)] = 2118 (s), 2079 (vs), 2067 (s), 2063 (vs), 2052 (s), 2031 (s) cm^{-1}.

Synthesis of $Na_2[Ru(CO)_4]$ and $[Os_2Ru(CO)_{12}]$ (1): Two reaction vessels, equipped with Rotaflo® stopcocks and connected by a glass frit, were placed on a standard high-vacuum line. Under a continuous N_2 flow, $[Os_2(CO)_8(Br)_2]$ (200 mg, 0.26 mmol) was placed in one of the vessels while the other one contained $[Ru_3(CO)_{12}]$ (55.8 mg, 0.087 mmol) and metallic sodium (12 mg, 0.52 mmol). Anhydrous NH_3 (ca. 25 mL) was condensed in a separate vessel onto metallic sodium and frozen, using a liquid nitrogen bath. After closing the vessel containing $[Os_2(CO)_8(Br)_2]$, NH_3 was distilled under vacuum onto the sodium/$[Ru_3(CO)_{12}]$ mixture. Using an acetone/dry ice bath, the solution was slowly warmed to 235 K and stirred vigorously until the characteristic blue Na/NH_3 solution transformed into a yellow solution containing a white precipitate. This usually required about 30 minutes of reaction time. The mixture was stirred for another 30 minutes and remaining sodium, which splashed on the walls of the flask, was washed down by cold spotting with glass wool drenched with liquid nitrogen. After 1 h, NH_3 was evaporated by further warming to 260 K and the remaining cream-coloured solid was dried under high-vacuum conditions for another 3.5 h at this temperature. $Na_2[Ru(CO)_4]$ was then dissolved on the vacuum line in THF that had been pre-dried with sodium/benzophenone and thoroughly degassed in four consecutive freeze-pump-thaw cycles. The pale yellow solution was degassed once more to remove the last traces of ammonia. Finally, the THF solution was warmed to 273 K and added to $[Os_2(CO)_8(Br)_2]$ by filtration through the frit connecting the reaction vessels. Upon mixing, the solution turned red and gas was evolving. The solution was stirred overnight at 293 K, followed by evaporation of the solvent. Purification of the crude product was established by column chromatography (activated neutral alumina, hexane/CH_2Cl_2 gradient elution). After precipitation from THF at 190 K, the product was obtained as a yellow powder in yields varying between 86 and 135 mg (40–63% based on $[Os_2(CO)_8(Br)_2]$), depending on the quality of $Na_2[Ru(CO)_4]$ (vide supra). IR (hexane): $\tilde{\nu}$ [ν(CO)] = 2068(s), 2036 (s), 2015 (m), 2004 (m) cm^{-1}. UV/Vis (CH_2Cl_2): λ = 280 (sh), 329, 382 (sh) nm. MS (FD): m/z = 817 $[M]^+$ (calcd. 817.8). MS (EI): $m/z = [M^+ - n\text{CO}]$ (n = 0–12).

Synthesis of $[Os_2Ru(CO)_{11}(PPh_3)]$ (2): Me_3NO (5.5 mg, 0.07 mmol) in MeCN (2 mL) was added to a solution of $[Os_2Ru(CO)_{12}]$ (30 mg, 0.04 mmol) in THF (25 mL) at 200 K. After stirring the mixture for approximately 30 minutes, IR spectra revealed almost complete conversion to $[Os_2Ru(CO)_{11}(MeCN)]$. After addition of PPh_3 (10.6 mg, 0.04 mmol), the solution was warmed to room temperature. As IR spectra showed hardly any conversion after 60 minutes, additional PPh_3 was added (5.2 mg, 0.02 mmol) and the solution was stirred for two days in the dark. After removal of the solvent in vacuo, the residue was loaded on a silica 60 column packed in hexane. Gradient elution with hexane/THF resulted in the clean separation of three (yellow, orange and red) mobile bands. The yellow fraction was further purified by preparative TLC to remove free PPh_3. Recrystallisation of the yellow residue from petroleum ether 40–60 at 250 K yielded orange crystals of cluster **2** (15 mg, 40%). On the basis of their IR spectra, the orange and red fractions likely contained higher substituted compounds, but no detailed characterization of the mixtures was attempted.

$[Os_2Ru(CO)_{11}(MeCN)]$: IR (CH_2Cl_2): $\tilde{\nu}$ [ν(CO)] = 2104 (w), 2050 (vs), 2040 (vs), 2019 (s, sh), 2008 (vs), 1984 (m) cm^{-1}.

$[Os_2Ru(CO)_{11}(PPh_3)]$ (2): IR (CH_2Cl_2): $\tilde{\nu}$ [ν(CO)] = 2107 (m), 2054 (s), 2033 (s), 2017 (vs), 1999 (m), 1988 (m), 1977 (m), 1957 (w) cm^{-1}. ^1H NMR (300 MHz, $CDCl_3$, 293 K): δ = 7.35 (m, 15

 © 2005 Wiley-VCH Verlag GmbH & Co. KGaA, Weinheim

H) ppm. $^{31}P\{H\}$ NMR (300 MHz, $CDCl_3$, 293 K): δ = 29.6 ([$Os_2Ru(CO)_{11}(PPh_3)$]), –0.8 ([$Os_3(CO)_{11}(PPh_3)$]) ppm (ratio ca. 2:1). MS (FD): m/z = 1142 $[M]^+$ (M = [$Os_3(CO)_{11}(PPh_3)$]) (calcd. 1141.9), 1054 $[M]^+$ (M = [$Os_2Ru(CO)_{11}(PPh_3)$]) (calcd. 1053.9) (ratio ca.1:2).

Synthesis of [$Os_2Ru(CO)_{10}$(*i*Pr-AcPy)] (3): To a solution of [$Os_2Ru(CO)_{11}$(MeCN)] at 270 K, freshly prepared from [$Os_2Ru(CO)_{12}$] (100 mg, 0.12 mmol) and Me_3NO (18.6 mg, 0.25 mmol), a solution of Me_3NO (13.5 mg, 0.18 mmol) in CH_2Cl_2 was added dropwise. After stirring for 45 minutes IR spectra revealed [$Os_2Ru(CO)_{10}$(MeCN)$_2$] as the main product. After addition of *i*Pr-AcPy (200 mg, 1.2 mmol) the solution was stirred overnight while warming to room temperature. Purification of the crude product over silica using 2:3 hexane/THF as eluent gave [$Os_2Ru(CO)_{10}$(*i*Pr-AcPy)] as a purple powder (34 mg, 30%). Crystals were grown by slow diffusion of hexane into a saturated solution of [$Os_2Ru(CO)_{10}$(*i*Pr-AcPy)] in THF.

[$Os_2Ru(CO)_{10}$(MeCN)$_2$]: IR (CH_2Cl_2): $\tilde{\nu}$ [ν(CO)] = 2079 (w), 2019 (vs), 1984 (s), 1958 (m) cm^{-1}.

[$Os_2Ru(CO)_{10}$(*i*Pr-AcPy)] (3): IR (THF): $\tilde{\nu}$ [ν(CO)] = 2082 (m), 2028 (vs), 2002 (vs), 1990 (s), 1979 (s), 1962 (m), 1956 (sh), 1907 (w) cm^{-1}. ^1H NMR (300 MHz, $CDCl_3$, 293 K) {for numbering scheme see Figure 1; asterisks denote signals due to [$Os_3(CO)_{10}$(*i*Pr-AcPy)] (ca.10–15%)}: δ = 9.50* (d, 1 H), 9.23 (d, $^3J_{H,H}$ = 4.5 Hz, 1 H, H^6), 8.04 (d, $^3J_{H,H}$ = 8.1 Hz, 1 H, H^3), 8.02* (d, 1 H), 7.91 (dd, $^3J_{H,H}$ = 8.1, $^3J_{H,H}$ = 7.5 Hz, 1 H, H^4), 7.86* (dd, 1 H), 7.25 (dd, $^3J_{H,H}$ = 7.5, $^3J_{H,H}$ = 5 Hz, 1 H, H^5), 7.11* (dd, 1 H), 4.44* (m, 1 H), 3.73 (m, 1 H, C*H*(CH_3)$_2$), 2.66 (s, 3 H, N=C–C*H*$_3$), 1.40 [d, $^3J_{H,H}$ = 4.8 Hz, 6 H, CH(C*H*$_3$)$_2$] ppm. MS (FAB^+): m/z = 986.9 $[M + H]^+$–CO (M = [$Os_3(CO)_{10}$(*i*Pr-AcPy)]), 957.9 $[M + H]^+$ – 2CO (M = [$Os_3(CO)_{10}$(*i*Pr-AcPy)]), 925.91 $[M + H]^+$ (M = [$Os_2Ru(CO)_{10}$(*i*Pr-AcPy)]) (calcd. 925.89), $[M + H]^+$–*n*CO (n = 1–10) (M = [$Os_2Ru(CO)_{10}$(*i*Pr-AcPy)]).

X-ray Crystal Structure Determinations of Clusters 2 and 3: Intensities were measured with a Nonius KappaCCD diffractometer with rotating anode (Mo-K_α, λ = 0.71073 Å) at a temperature of 150(2) K up to a resolution of ($\sin\theta/\lambda$) = 0.65 $Å^{-1}$. The structures were solved with Patterson methods (DIRDIF-97)[71] and refined with the programme SHELXL-97[72] against F^2 of all reflections. Non-hydrogen atoms were refined freely with anisotropic displacement parameters, and hydrogen atoms as rigid groups. The drawings, structure calculations, and checking for higher symmetry were performed with the programme PLATON.[73] The ruthenium sites in both structures were partially occupied by osmium atoms. The ruthenium and the corresponding osmium atoms were constrained to the same coordinates and the same anisotropic displacement parameters. Then the partial occupancies were refined with the criterion that the total occupancy remains 1.0.

[$Os_2Ru(CO)_{11}(PPh_3)$] (2): $C_{29}H_{15}O_{11}Os_{2.36}PRu_{0.64}$; Fw = 1083.94; yellow plates, 0.36 × 0.21 × 0.12 mm^3; monoclinic, space group $C2/c$ (no. 15); cell parameters: a = 21.9824(1), b = 16.0859(1) Å, c = 17.2605(1) Å; β = 103.7064(3)°; V = 5929.62(6) $Å^3$; Z = 8; ρ = 2.428 g cm^{-3}; F(000) = 3996; 55381 reflections were measured, 6811 reflections were unique (R_{int} = 0.0519). An analytical absorption correction was applied (μ = 10.526 mm^{-1}, 0.08–0.39 transmission). 398 Refined parameters, no restraints. R (obsd. refl.): R_1 = 0.0196, wR_2 = 0.0425. R (all data): R_1 = 0.0230, wR_2 = 0.0434. Weighting scheme $w = 1/[\sigma^2(F_o^2) + (0.0165P)^2 + 11.6188P]$, where $P = (F_o^2 + 2F_c^2)/3$. GoF = 1.110. Residual electron density between –0.92 and 0.75 e/$Å^3$.

[$Os_2Ru(CO)_{10}$(*i*Pr-AcPy)] (3): $C_{20}H_{14}N_2O_{10}Os_{2.11}Ru_{0.89}$; Fw = 933.61; red needles, 0.39 × 0.03 × 0.03 mm^3; monoclinic, space group $P2_1/c$ (no. 14); cell parameters: a = 9.1117(1), b = 13.9915(1) Å, c = 20.7504(2) Å; β = 113.6862(4)°; V = 2422.54(4) $Å^3$; Z = 4; ρ = 2.560 g cm^{-3}; F(000) = 1710. 43532 reflections were measured, 5551 reflections were unique (R_{int} = 0.0740). An analytical absorption correction was applied (μ = 11.644 mm^{-1}, 0.20–0.78 transmission). 320 refined parameters, no restraints. R (obsd. refl.): R_1 = 0.0277, wR_2 = 0.0419. R (all data): R_1 = 0.0510, wR_2 = 0.0460. Weighting scheme $w = 1/[\sigma^2(F_o^2) + (0.0147P)^2]$, where $P = (F_o^2 + 2F_c^2)/3$. GoF = 0.996. Residual electron density between –0.95 and 1.01 e/$Å^3$.

CCDC-258240 (for **2**) and -258241 (for **3**) contain the supplementary crystallographic data for this paper. These data can be obtained free of charge from The Cambridge Crystallographic Data Centre via www.ccdc.cam.ac.uk/data_request/cif.

Spectroscopic Measurements: Electronic absorption spectra were recorded with a Hewlett–Packard 8453 diode-array spectrophotometer and FT-IR spectra with a Bio-Rad FTS-7 (16 scans at 2 cm^{-1} resolution) spectrometer. Rapid-scan FT-IR spectra were measured with a Bio-Rad FTS-60A spectrometer (equipped with a dual-source rapid-scan 896 interferometer and a liquid-nitrogen cooled MCT detector) after excitation of the sample by the 514.5 nm line of a Spectra Physics Model 2016 argon-ion laser. ^1H and $^{31}P\{H\}$ NMR spectra were recorded with a Bruker AMX 300 spectrometer. Field Desorption (FD), Fast Atom Bombardment (FAB) and Electron Impact (EI) mass spectra were collected with a JEOL JMS SX/SX102A four-sector mass spectrometer. For synthetic purposes, a Philips HPK 125-W high-pressure Hg lamp, equipped with appropriate cut-off filters to select the desired wavelength region, served as a light source.

Photochemistry: All photochemical samples were prepared under nitrogen, using standard inert-gas techniques, and cluster concentrations typically between 10^{-3}–10^{-4} mol·dm^{-3}. Nanosecond transient absorption (ns TA) spectra were obtained by irradiating the samples with 2 ns pulses of the 532 nm line (typically 5 mJ $pulse^{-1}$) of a tunable (420–710 nm) Coherent Infinity XPO laser and using a high-power EG&G FX-504 Xe lamp as probe light.[17] Nanosecond flash photolysis transient kinetics were measured by irradiating the sample with 7 ns (FWHM) pulses of a Spectra Physics GCR-3 Nd:YAG laser (10 Hz repetition rate) and using a pulsed Xe lamp perpendicular to the laser beam as probe light. The excitation wavelength in this case (532 nm) was obtained by frequency doubling. The 450-W Xe lamp was equipped with a Müller Electronik MSP05 pulsing unit, giving pulses of 0.5 ms. A shutter, placed between the lamp and the sample, was opened for 10 ms to prevent photomultiplier fatigue. Suitable pre- and post-cut-off filters and band-pass filters were used to minimize both the probe light and scattered light from the laser. The sampling rate was kept at a relatively long time (10 s intervals) to prevent accumulation of possible photo-induced intermediates. The light was collected in an Oriel monochromator, detected by a P28 PMT (Hamamatsu), and recorded with a Tektronix TDS3052 (500 MHz) oscilloscope. The laser oscillator, Q-switch, lamp, shutter and trigger were externally controlled with a home made digital logic circuit, which allowed for synchronous timing. The absorption transient were plotted as $\Delta A = \log(I_t/I_0)$ vs. time, where I_0 is the monitoring light intensity prior to the laser pulse and I_t is the observed signal at delay time t.

Picosecond transient absorption (ps TA) spectra were recorded using the set-up installed at the University of Amsterdam.[16] Part of the 800 nm output of a Ti-sapphire regenerative amplifier (1 kHz, 130 fs, 1 mJ) was focussed into a H_2O flow-through cell (10 mm; Hellma) to generate white light. The residual part of the

 © 2005 Wiley-VCH Verlag GmbH & Co. KGaA, Weinheim

800 nm fundamental was used to provide 505 nm (fourth harmonic of the 2020 OPA idler beam) excitation pulses with a general output of 5 μJ pulse^{-1}. After passing through the sample, the probe beam was coupled into a 400 μm optical fibre and detected by a CCD spectrometer (Ocean Optics, PC2000). The chopper (Rofin Ltd., f = 10–20 Hz), placed in the excitation beam, provided I and I_0, depending on the status of the chopper (open or closed). The excited state spectra were obtained by $\Delta A = \log(I/I_0)$. Typically two thousand excitation pulses were averaged to obtain the transient at a particular time delay.

Electrochemistry: Cyclic voltammograms (CV) of approximately 10^{-3} M parent cluster in 10^{-1} M Bu_4NPF_6 electrolyte solution were recorded in a gas-tight, single-compartment, three-electrode cell equipped with platinum microdisc (apparent surface 0.42 mm^2) working, coiled platinum wire auxillary and silver wire pseudo-reference electrodes. The cell was connected to a computer-controlled PAR Model 283 potentiostat. All redox potentials are reported against the ferrocene-ferrocenium (Fc/Fc^+) redox couple.[74,75] IR spectroelectrochemical measurements at variable temperatures were performed with previously described optically transparent thin-layer electrochemical (OTTLE) cells[76,77] equipped with a platinum minigrid working electrode (32 wires/cm) and CaF_2 windows. The potential during these measurements was controlled by a PA4 potentiostat (EKOM, Czech Republic). In the spectroelectrochemical experiments, cluster concentrations of 5×10^{-3} mol·dm^{-3} were used.

Computational Details: All density functional theory (DFT) calculations[78] were carried out with the Amsterdam Density Functional (ADF2000) programme.[37–43] Vosko, Wilk and Nusair's local exchange correlation potential was used.[79] Gradient-corrected geometry optimizations[80,81] were performed, using the Generalized Gradient Approximation (Becke's exchange[82] and Perdew's correlation[83,84] functionals). Relativistic effects were treated by the ZORA method[85] The core orbitals were frozen for Ru ([1–4]s, [2–4]p, 3d), Os ([1–4]s, [2–4]p, [3–4]d), P ([1–2]s, 2p), and C, N, O (1s). Triple ζ Slater-type orbitals (STO) were used to describe the valence shells of H (1s), C and O (2s and 2p), P (3s and 3p), Ru (4d, 5s and 5p) and Os (4f, 5d, 6s). A set of polarization functions was added: H (single ζ, 2p, 3d), C, N, O (single ζ, 3d, 4f), P(single ζ, 3d, 4f), Ru (single ζ, 5p, 4f) and Os (single ζ, 6p, 5f). Full geometry optimizations were performed without any symmetry constraints on models based on the available crystal structures. The UV/Vis spectrum was calculated using the SWizard programme,[48] revision 3.7. The half-band widths, $\Delta_{1/2,I}$, were taken to be equal to 3000 cm^{-1}, the default value of the programme. Three-dimensional representations of the orbitals were obtained with Molekel.[86]

Time-dependent DFT (TD-DFT)[87–89] calculations in the ADF implementation were used to determine the excitation energies. In all cases the ten lowest singlet-singlet excitation energies were calculated using the optimized geometries.

Acknowledgments

A. Hearley (University of Cambridge, UK) is gratefully acknowledged for valuable discussions regarding the synthesis of [$Os_2Ru(CO)_{12}$]. This work was undertaken as part of the European collaborative COST project (D14/0001/99). Financial support was received by F. W. V. and F. H. from the Council for Chemical Sciences of the Netherlands Organization for Scientific Research (CW-NWO, project No. 348–032).

[1] R. D. Adams, in *Comprehensive Organometallic Chemistry II*, vol. 10, Pergamon, New York, **1995**.
[2] W. L. Gladfelter, G. L. Geoffroy, *Adv. Organomet. Chem.* **1980**, *18*, 207–273.
[3] D. A. Roberts, G. L. Geoffroy, in *Comprehensive Organometallic Chemistry*, vol. 6, Pergamon, Oxford, **1982**.
[4] S. M. Waterman, N. T. Lucas, M. G. Humphrey, *Adv. Organomet. Chem.* **2000**, *46*, 47–143.
[5] P. Braunstein, J. Rosé, in *Catalysis by Di- and Polynuclear Metal Cluster Complexes* (Eds.: R. D. Adams, F. A. Cotton), Wiley-VCH, New York, **1998**, pp. 443–508.
[6] P. Braunstein, J. Rosé, in *Comprehensive Organometallic Chemistry II*, vol. 10, Pergamon, New York, **1995**.
[7] R. D. Adams, T. S. Barnard, Z. Li, W. Wu, J. H. Yamamoto, *J. Am. Chem. Soc.* **1994**, *116*, 9103–9113.
[8] M. A. Aubart, L. H. Pignolet, *J. Am. Chem. Soc.* **1992**, *114*, 7901–7903.
[9] S. Attali, R. Mathieu, *J. Organomet. Chem.* **1985**, *291*, 205–211.
[10] I. Ojima, Z. Zhang, *J. Org. Chem.* **1988**, *53*, 4422–4425.
[11] L. J. Farrugia, in *Comprehensive Organometallic Chemistry II*, vol. 10, Pergamon, New York, **1995**.
[12] J. Nijhoff, M. J. Bakker, F. Hartl, D. J. Stufkens, W.-F. Fu, R. van Eldik, *Inorg. Chem.* **1998**, *37*, 661–668.
[13] J. Nijhoff, F. Hartl, D. J. Stufkens, J. Fraanje, *Organometallics* **1999**, *18*, 4380–4389.
[14] J. Nijhoff, M. J. Bakker, F. Hartl, D. J. Stufkens, *J. Organomet. Chem.* **1999**, *572*, 271–281.
[15] M. J. Bakker, F. Hartl, D. J. Stufkens, O. S. Jina, X.-Z. Sun, M. W. George, *Organometallics* **2000**, *19*, 4310–4319.
[16] F. W. Vergeer, C. J. Kleverlaan, D. J. Stufkens, *Inorg. Chim. Acta* **2002**, *327*, 126–133.
[17] F. W. Vergeer, M. J. Calhorda, P. Matousek, M. Towrie, F. Hartl, *Dalton Trans.* **2003**, 4084–4099.
[18] M. J. Calhorda, E. Hunstock, L. F. Veiros, F. Hartl, *Eur. J. Inorg. Chem.* **2001**, 223–231.
[19] M. J. Calhorda, P. J. Costa, F. Hartl, F. W. Vergeer, *C. R. Chimie* **2005**, in the press.
[20] E. Hunstock, C. Mealli, M. J. Calhorda, J. Reinhold, *Inorg. Chem.* **1999**, *38*, 5053–5060.
[21] E. Hunstock, M. J. Calhorda, P. Hirva, T. A. Pakkanen, *Organometallics* **2000**, *19*, 4624–4628.
[22] G. A. Battiston, G. Bor, U. K. Dietler, S. F. A. Kettle, R. Rossetti, G. Sbrignadello, P. L. Stanghellini, *Inorg. Chem.* **1980**, *19*, 1961–1973.
[23] R. P. Ferrari, G. A. Vaglio, M. Valle, *J. Chem. Soc., Dalton Trans.* **1978**, 1164–1166.
[24] B. F. G. Johnson, R. D. Johnston, J. Lewis, I. G. Williams, P. A. Kilty, *Chem. Commun.* **1968**, 861–862.
[25] J. R. Fox, W. L. Gladfelter, G. L. Geoffroy, *Inorg. Chem.* **1980**, *19*, 2574–2578.
[26] H. Remita, R. Derai, M.-O. Delcourt, *Radiat. Phys. Chem.* **1991**, *37*, 221–225.
[27] J. R. Moss, W. A. G. Graham, *J. Chem. Soc., Dalton Trans.* **1977**, 89–94.
[28] B. F. G. Johnson, R. D. Johnston, P. L. Josty, J. Lewis, I. G. Williams, *Nature* **1967**, *213*, 901–902.
[29] B. F. G. Johnson, R. D. Johnston, J. Lewis, *J. Chem. Soc., A* **1969**, 792–797.
[30] J. R. Moss, M. L. Niven, E. E. Sutton, *Inorg. Chim. Acta* **1988**, *147*, 251–256.
[31] N. K. Bhattacharyya, T. J. Coffy, W. Quintana, T. A. Salupo, J. C. Bricker, T. B. Shay, M. Payne, S. G. Shore, *Organometallics* **1990**, *9*, 2368–2374.
[32] M. R. Churchill, B. G. DeBoer, *Inorg. Chem.* **1977**, *16*, 878–884.
[33] M. R. Churchill, F. J. Hollander, J. P. Hutchinson, *Inorg. Chem.* **1977**, *16*, 2655–2659.
[34] L. Pereira, W. K. Leong, S. Y. Wong, *J. Organomet. Chem.* **2000**, *609*, 104–109.
[35] M. I. Bruce, M. J. Liddell, C. A. Hughes, B. W. Skelton, A. H. White, *J. Organomet. Chem.* **1988**, *347*, 157–180.

 © 2005 Wiley-VCH Verlag GmbH & Co. KGaA, Weinheim

[36] E. J. Forbes, N. Goodhand, D. L. Jones, T. A. Hamor, *J. Organomet. Chem.* **1979**, *182*, 143–154.
[37] E. J. Baerends, D. Ellis, P. Ros, *Chem. Phys.* **1973**, *2*, 41–51.
[38] E. J. Baerends, P. Ros, *Int. J. Quantum Chem.* **1978**, *S12*, 169–190.
[39] E. J. Baerends, A. Bérces, C. Bo, P. M. Boerrigter, L. Cavallo, L. Deng, R. M. Dickson, D. E. Ellis, L. Fan, T. H. Fischer, C. Fonseca Guerra, S. J. A. van Gisbergen, J. A. Groeneveld, O. V. Gritsenko, F. E. Harris, P. van den Hoek, H. Jacobsen, G. van Kessel, F. Kootstra, E. van Lenthe, V. P. Osinga, P. H. T. Philipsen, D. Post, C. C. Pye, W. Ravenek, P. Ros, P. R. T. Schipper, G. Schreckenbach, J. G. Snijders, M. Sola, D. Swerhone, G. te Velde, P. Vernooijs, L. Versluis, O. Visser, E. van Wezenbeek, G. Wiesenekker, S. K. Wolff, T. K. Woo, T. Ziegler, *ADF 2000*, University of Amsterdam, Amsterdam, **2000**.
[40] C. Fonseca Guerra, O. Visser, J. G. Snijders, G. te Velde, E. J. Baerends, in *Methods and Techniques for Computational Chemistry* (Eds.: E. Clementi, C. Corongiu), STEF, Cagliari, **1995**, pp. 303–395.
[41] C. Fonseca Guerra, J. G. Snijders, G. te Velde, E. J. Baerends, *Theor. Chem. Acc.* **1998**, *99*, 391–403.
[42] P. M. Boerrigter, G. te Velde, E. J. Baerends, *Int. J. Quantum Chem.* **1988**, *33*, 87–113.
[43] G. te Velde, E. J. Baerends, *J. Comput. Phys.* **1992**, *99*, 84–98.
[44] V. M. Hansen, A. K. Ma, K. Biradha, R. K. Pomeroy, M. J. Zaworotko, *Organometallics* **1998**, *17*, 5267–5274.
[45] N. E. Leadbeater, J. Lewis, P. R. Raithby, G. N. Ward, *J. Chem. Soc., Dalton Trans.* **1997**, 2511–2516.
[46] R. Zoet, T. B. H. Jastrzebski, G. van Koten, T. Mahabiersing, K. Vrieze, D. Heijdenrijk, C. H. Stam, *Organometallics* **1988**, *7*, 2108–2117.
[47] D. M. Manuta, A. J. Lees, *Inorg. Chem.* **1983**, *22*, 3825–3828.
[48] S. I. Gorelsky, *SWizard programme*, revision 3.7, http://www.obbligato.com/software/swizard/.
[49] B. D. Rossenaar, D. J. Stufkens, A. Vlček Jr., *Inorg. Chim. Acta* **1996**, *247*, 247–255.
[50] B. D. Rossenaar, D. J. Stufkens, A. Vlček Jr., *Inorg. Chem.* **1996**, *35*, 2902–2909.
[51] B. D. Rossenaar, E. Lindsay, D. J. Stufkens, A. Vlček Jr., *Inorg. Chim. Acta* **1996**, *250*, 5–14.
[52] M. P. Aarnts, D. J. Stufkens, M. P. Wilms, E. J. Baerends, A. Vlček Jr., I. P. Clark, M. W. George, J. J. Turner, *Chem. Eur. J.* **1996**, *2*, 1556–1565.
[53] J. Nijhoff, F. Hartl, J. W. M. van Outersterp, D. J. Stufkens, M. J. Calhorda, L. F. Veiros, *J. Organomet. Chem.* **1999**, *573*, 121–133.
[54] A. Klein, W. Kaim, *Organometallics* **1995**, *14*, 1176–1186.
[55] F. W. Vergeer, C. J. Kleverlaan, P. Matousek, M. Towrie, D. J. Stufkens, F. Hartl, *Inorg. Chem.* **2005**, 44, 1319–1331.
[56] F. P. A. Johnson, M. W. George, F. Hartl, J. J. Turner, *Organometallics* **1996**, *15*, 3374–3387.
[57] G. J. Stor, F. Hartl, J. W. M. van Outersterp, D. J. Stufkens, *Organometallics* **1995**, *14*, 1115–1131.
[58] B. D. Rossenaar, F. Hartl, D. J. Stufkens, *Inorg. Chem.* **1996**, *35*, 6194–6203.
[59] B. D. Rossenaar, F. Hartl, D. J. Stufkens, C. Amatore, E. Maisonhaute, J.-N. Verpeaux, *Organometallics* **1997**, *16*, 4675–4685.
[60] F. Hartl, J. W. M. van Outersterp, unpublished results.
[61] S. Chardon-Noblat, A. Deronzier, D. Zsoldos, R. Ziessel, M. Haukka, T. Pakkanen, T. Venäläinen, *J. Chem. Soc., Dalton Trans.* **1996**, 2581–2583.
[62] C. Caix-Cecillon, S. Chardon-Noblat, A. Deronzier, M. Haukka, T. Pakkanen, R. Ziessel, D. Zsoldos, *J. Electroanal. Chem.* **1999**, *466*, 187–196.
[63] S. Chardon-Noblat, A. Deronzier, F. Hartl, J. van Slageren, T. Mahabiersing, *Eur. J. Inorg. Chem.* **2001**, 613–617.
[64] F. Hartl, T. Mahabiersing, S. Chardon-Noblat, P. Da Costa, A. Deronzier, *Inorg. Chem.* **2004**, *43*, 7250–7258.
[65] S. Chardon-Noblat, A. Deronzier, R. Ziessel, *Collect. Czech. Chem. Commun.* **2001**, *66*, 207–226.
[66] S. Chardon-Noblat, A. Deronzier, R. Ziessel, D. Zsoldos, *J. Electroanal. Chem.* **1998**, *444*, 253–260.
[67] M.-N. Collomb-Dunand-Sauthier, A. Deronzier, R. Ziessel, *Inorg. Chem.* **1994**, *33*, 2961–2967.
[68] J. W. M. van Outersterp, Ph. D. Thesis, University of Amsterdam, Amsterdam, **1995**.
[69] B. F. G. Johnson, J. Lewis, P. A. Kilty, *J. Chem. Soc., A* **1968**, 2859–2864.
[70] G. A. Foulds, B. F. G. Johnson, J. Lewis, *J. Organomet. Chem.* **1985**, *296*, 147–153.
[71] P. T. Beurskens, G. Admiraal, G. Beurskens, W. P. Bosman, S. Carcia-Granda, R. O. Gould, J. M. M. Smits, C. Smykalla, *The DIRDIF-97 programme system*, Technical Report of the Crystallography Laboratory, University of Nijmegen, The Netherlands, **1997**.
[72] G. M. Sheldrick, *SHELXL-97*, University of Göttingen, Göttingen, Germany, **1997**.
[73] A. L. Spek, *J. Appl. Crystallogr.* **2003**, *36*, 7–13.
[74] V. V. Pavlishchuk, A. W. Addison, *Inorg. Chim. Acta* **2000**, *298*, 97–102.
[75] G. Gritzner, J. Kůta, *Pure Appl. Chem.* **1984**, *56*, 461–466.
[76] F. Hartl, H. Luyten, H. A. Nieuwenhuis, G. C. Schoemaker, *Appl. Spectrosc.* **1994**, *48*, 1522–1528.
[77] M. Krejčík, M. Daněk, F. Hartl, *J. Electroanal. Chem. Interfacial Electrochem.* **1991**, *317*, 179–187.
[78] R. G. Parr, W. Yang, *Density Functional Theory of Atoms and Molecules*, Oxford University Press, New York, **1989**.
[79] S. H. Vosko, L. Wilk, M. Nusair, *Can. J. Phys.* **1980**, *58*, 1200–1211.
[80] L. Versluis, T. Ziegler, *J. Chem. Phys.* **1988**, *88*, 322–328.
[81] L. Fan, T. Ziegler, *J. Chem. Phys.* **1991**, *95*, 7401–7408.
[82] A. D. Becke, *J. Chem. Phys.* **1988**, *88*, 1053–1062.
[83] J. P. Perdew, *Phys. Rev. B* **1986**, *33*, 8822–8824.
[84] J. P. Perdew, *Phys. Rev. B* **1986**, *34*, 7406.
[85] E. van Lenthe, A. Ehlers, E. J. Baerends, *J. Chem. Phys.* **1999**, *110*, 8943–8953.
[86] S. Portmann, H. P. Lüthi, *Chimia* **2000**, *54*, 766–770.
[87] S. J. A. van Gisbergen, J. A. Groeneveld, A. Rosa, J. G. Snijders, E. J. Baerends, *J. Phys. Chem.* **1999**, *103*, 6835–6844.
[88] S. J. A. van Gisbergen, A. Rosa, G. Ricciardi, E. J. Baerends, *J. Chem. Phys.* **1999**, *111*, 2499–2506.
[89] A. Rosa, S. J. A. van Gisbergen, E. van Lenthe, J. A. Groeneveld, J. G. Snijders, *J. Am. Chem. Soc.* **1999**, *121*, 10356–10365.

Received: December 20, 2004

 © 2005 Wiley-VCH Verlag GmbH & Co. KGaA, Weinheim

Preparation and Characterization of Co^{II}, Ni^{II}, and Zn^{II} Complexes of Sterically Demanding Hexaazamacrocyclic Dithiophenolates

Mathias Gressenbuch,[a] Vasile Lozan,[a] Gunther Steinfeld,[b] and Berthold Kersting*[a]

Keywords: Binding pockets / Macrocyclic ligands / Cobalt / Nickel / Zinc

N-Alkylated variants of a Robson-type 24-membered hexaazamacrocyclic dinucleating dithiophenolate ligand bearing ethyl and propyl groups have been prepared and their ligating properties towards the 3d elements Ni, Co and Zn have been examined. The new ligands support the formation of dinuclear complexes of the type $[(L^R)M^{II}_2(L')]^+$, i.e. $[(L^{Et})Ni_2(Cl)]^+$ (**7**), $[(L^{Pr})Ni_2(Cl)]^+$ (**8**), $[(L^{Et})Ni_2(OAc)]^+$ (**9**), $[(L^{Pr})Ni_2(OAc)]^+$ (**10**), $[(L^{Et})Ni_2(O_2COMe)]^+$ (**11**), $[(L^{Et})Ni_2(O_2COEt)]^+$ (**12**), $[(L^{Et})Zn_2(OAc)]^+$ (**14**), $[(L^{Et})Co_2(Cl)]^+$ (**17**), and $[(L^{Et})Co_2(OAc)]^+$ (**18**), the overall structures of which are very similar to the corresponding complexes of the parent permethylated ligand system. The use of the longer alkyl chains expands the binding pocket of the complexes to a more conical, "calixarene"-like cavity and has allowed for the isolation of the trication $[(HL^{Et})Ni_2]^{3+}$ (**13**), which is an intermediate in the substitution reactions of **7**. Complex **13** reveals a new coordination mode of the supporting ligand with adjacent four- and five-coordinate nickel atoms. Its higher stability is presumably a consequence of the increased steric crowding imposed by the longer alkyl chains of $(L^{Et})^{2-}$. These results have thus demonstrated that these highly functionalized ligand systems allow for the stabilization of reactive intermediates. This information can now be used as a guide to further modulate the chemical reactivity of these compounds.

(© Wiley-VCH Verlag GmbH & Co. KGaA, 69451 Weinheim, Germany, 2005)

Introduction

Much effort is currently been invested in the design and development of supporting ligands for the construction of metal complexes with deep binding pockets.[1] Several suitable ligand systems have already been reported, as for instance the calixarenes,[2,3] the cyclodextrines[4,5] and some highly functionalized chelate ligands.[6,7] Recently, we reported that the Robson-type[8] macrocycles H_2L^H and its permethylated derivative H_2L^{Me} (see Scheme 1) can also be employed for this purpose.[9] Both ligands support the formation of $[(L^R)M_2(\mu\text{-}L')]^+$ complexes, whose ligand conformations are reminiscent of the "partial cone" and "cone" conformations of the calixarenes.

It has been observed that the binding pocket influences the coordination chemistry of the $[(L^R)M_2(\mu\text{-}L')]^+$ complexes significantly. For example, the substitution rates of the bridging coligands (L′) are drastically increased.[10] Likewise, it allows for the activation of small molecules such as carbon dioxide,[11] and it can mediate the course of substrate transformations as seen in the highly diastereoselective *cis*-bromination of α,β-unsaturated carboxylate coligands.[12]

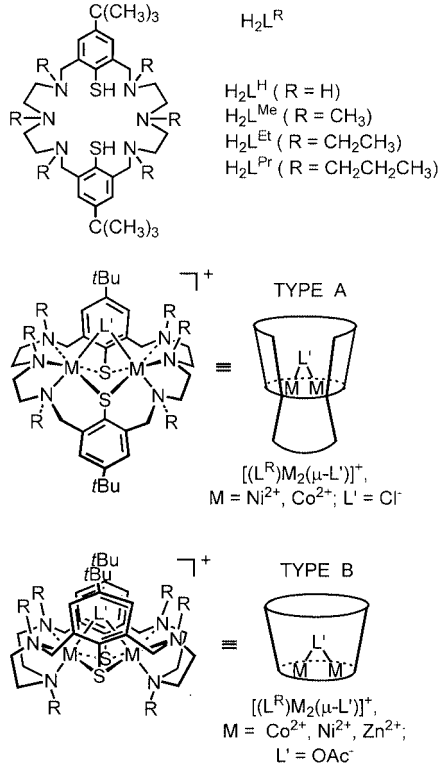

Scheme 1. Structure of the ligands (H_2L^R) and schematic representation of the structures of their corresponding metal complexes $[(L^R)M_2(\mu\text{-}L')]^+$. The cavity representation of the ligands $(L^R)^{2-}$ should not be confused with the one used for cyclodextrins.

[a] Institut für Anorganische Chemie, Universität Leipzig, Johannisallee 29, 04103 Leipzig, Germany
Fax: + 49-341-97-36199
E-Mail: b.kersting@uni-leipzig.de
[b] Institut für Anorganische und Analytische Chemie, Universität Freiburg,
Albertstr. 21, 79104 Freiburg

These results prompted us to expand the binding pocket of this versatile ligand system by using alkyl groups larger than methyl and to investigate the effect of this modification on the ligating properties. In this paper, we describe the synthesis and characterization of *N*-alkylated variants of H_2L^{Me} bearing ethyl and propyl groups in place of the methyl functions and report on their ligating properties towards the 3d elements Ni, Co and Zn (see Scheme 1 for abbreviations).

Results and Discussion

Ligand Synthesis

Two new derivatives of the parent hexaazamacrocyclic dithiophenolate H_2L^H with ethyl and propyl substituents were prepared in order to probe the influence of ligand structural variations on metal ion complexation and metal complex structures. For the bulkier ethyl and propyl derivatives a reaction sequence similar to that used for the alkylation of triazacyclononane[13] and cyclam[14] was used. The syntheses began with the acylation of known amine **1**,[15] with the anhydrides **2** (Scheme 2). The resulting amides **3** were then reduced with lithium aluminium hydride in refluxing THF solution to give the corresponding amines **4**. The thioether functions of the latter compounds were deprotected in the usual way[16] with sodium in liquid ammonia to afford the desired ligands which could be readily isolated as hydrochloride salts H_2L^R·6HCl (R = Et, Pr). All new compounds were characterized by elemental analysis, IR, ^1H and ^{13}C NMR spectroscopy. The hydrochloride salts of the ligands could not be obtained in analytically pure form. However, they were of sufficient purity for metal complex syntheses.

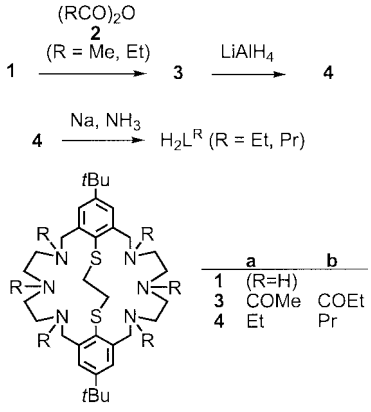

Scheme 2. Preparation of the ligands H_2L^{Et} and H_2L^{Pr}.

Synthesis of Complexes

The synthesized compounds and their labels are collected in Table 1. Of these, the compounds $[(L^{Me})Ni^{II}_2(\mu\text{-Cl})]ClO_4$ (**5**·ClO_4) and $[(L^{Me})Ni^{II}_2(\mu\text{-OAc})]ClO_4$ (**6**·ClO_4) were reported previously.[10,11] According to these procedures, the macrocycles H_2L^{Et} and H_2L^{Pr} were allowed to react with $NiCl_2$·$6H_2O$ and triethylamine in 1:2:8 molar ratios in methanolic solution according to Equation (1). In the case of the ethylated derivative H_2L^{Et}, the complexation reaction was complete after stirring at ambient temperature for 3 d. Upon addition of $LiClO_4$ to the bright yellow solution, yellow microcrystals of $[(L^{Et})Ni^{II}_2(\mu\text{-Cl})]ClO_4$ (**7**·ClO_4) could be obtained in 82% yield. The propylated ligand H_2L^{Pr} reacted similarly, generating the yellow species $[(L^{Pr})Ni^{II}_2(\mu\text{-Cl})]ClO_4$ (**8**·ClO_4), but stirring for 1 week was necessary to obtain it in comparable yields. In this respect, the two new ligands contrast the sterically less bulky ones which form dinuclear species more quickly. Characterization by elemental analysis, IR and UV/Vis spectroscopy {previously reported for $[(L^{Me})Ni^{II}_2(\mu\text{-Cl})]ClO_4$ (**5**·ClO_4)} are indicative of analogous bioctahedral structures of type A for these chloro-bridged compounds.

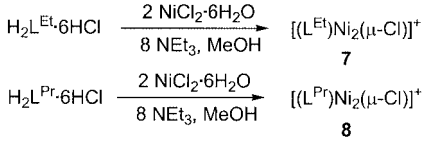

(1)

Table 1. Synthesized complexes, their labeling and selected structural data.[a]

Compound		Structure [*d*(M···M)/Å]	Ref.
5	$[(L^{Me})Ni^{II}_2(\mu\text{-Cl})]^+$	A [3.201]	[10]
6	$[(L^{Me})Ni^{II}_2(\mu\text{-OAc})]^+$	B [3.483]	[11]
7	$[(L^{Et})Ni^{II}_2(\mu\text{-Cl})]^+$	A[b]	this work
8	$[(L^{Pr})Ni^{II}_2(\mu\text{-Cl})]^+$	A[b]	this work
9	$[(L^{Et})Ni^{II}_2(\mu\text{-OAc})]^+$	B[c]	this work
10	$[(L^{Pr})Ni^{II}_2(\mu\text{-OAc})]^+$	B [3.513]	this work
11	$[(L^{Et})Ni^{II}_2(\mu\text{-}O_2COMe)]^+$	B[c]	this work
12	$[(L^{Et})Ni^{II}_2(\mu\text{-}O_2COEt)]^+$	B [3.520]	this work
13	$[(HL^{Et})Ni^{II}_2]^{3+}$	[3.319]	this work
14	$[(L^{Et})Zn^{II}_2(\mu\text{-OAc})]^+$	B [3.459]	this work
15	$[(L^{Me})Co^{II}_2(\mu\text{-Cl})]^+$	A [3.180]	[9b]
16	$[(L^{Me})Co^{II}_2(\mu\text{-OAc})]^+$	B [3.448]	[9b]
17	$[(L^{Et})Co^{II}_2(\mu\text{-Cl})]^+$	A[b]	this work
18	$[(L^{Et})Co^{II}_2(\mu\text{-OAc})]^+$	B [3.482]	this work

[a] The complexes were isolated as ClO_4^- or BPh_4^- salts. [b] The experimentally determined structures of **5** and **15** suggest that complexes **7**, **8** and **17** adopt the form A. [c] The experimentally determined structures of **10** and **12** suggest that complexes **9** and **11** adopt the form B.

The bridging halide ions in complexes **7** and **8** proved quite labile. Thus, the reactions of the respective $[(L)Ni_2(\mu\text{-Cl})]^+$ cations with sodium acetate proceeded smoothly and yielded green solutions, from which green crystals of $[(L^{Et})Ni_2(\mu\text{-OAc})]ClO_4$ (**9**·ClO_4) and $[(L^{Pr})Ni_2(\mu\text{-OAc})]ClO_4$ (**10**·ClO_4) were obtained in good yields [Equation (2)]. Later studies revealed that the same compounds can also be directly synthesized from the respective ligands and $Ni(OAc)_2$·$6H_2O$.

 © 2005 Wiley-VCH Verlag GmbH & Co. KGaA, Weinheim

$$[(L^{Et})Ni_2(\mu\text{-}Cl)]^+ \xrightarrow[MeOH]{NaOAc} [(L^{Et})Ni_2(\mu\text{-}OAc)]^+$$
7 **9**

$$[(L^{Pr})Ni_2(\mu\text{-}Cl)]^+ \xrightarrow[MeOH]{NaOAc} [(L^{Pr})Ni_2(\mu\text{-}OAc)]^+$$
8 **10** (2)

The methyl carbonate species **11** and its corresponding ethyl carbonate derivative **12** represent two further examples of nickel complexes of the ethylated macrocycle. Compound **11** was obtained by a carbonation reaction of the green μ-hydroxo species $[(L^{Et})Ni^{II}_2(\mu\text{-}OH)]^+$ (prepared in situ from **7** and sodium hydroxide; Equation (3)] and isolated as the pale-green perchlorate salt **11**·ClO_4 in 88% yield. The conversion of the methyl carbonate complex **11** into the ethyl carbonate species **12** was accomplished by a transesterification reaction with neat ethanol [Equation (4)]. Similar transformations were previously observed for the nickel complex **5** of the permethylated macrocycle. Thus, the rate of the substitution reactions and the ability to fix small molecules is not drastically altered by the longer alkyl chains.

$$[(L^{Et})Ni_2(\mu\text{-}Cl)]^+ \xrightarrow[\text{2. Air } (CO_2),\ MeOH\ \text{r.t., 24h, > 95\%}]{\text{1. NaOH}} [(L^{Et})Ni_2(\mu\text{-}O_2COMe)]^+$$
7 **11** (3)

$$[(L^{Et})Ni_2(\mu\text{-}O_2COMe)]^+ \xrightarrow[\text{r.t., 12h, > 95\%}]{EtOH} [(L^{Et})Ni_2(\mu\text{-}O_2COEt)]^+$$
11 **12** (4)

The compound $[(HL^{Et})Ni^{II}_2]^{3+}$ (**13**) formed rather unexpectedly during attempts to prepare a methanolato-bridged complex $[(L^{Et})Ni^{II}_2(\mu\text{-}OMe)]^+$ (Scheme 3). Instead of the anticipated compound the dark-green trication **13** was obtained. It could be isolated as the triperchlorate salt **13**·$(ClO_4)_3$ but only in low yield. This compound differs from the ones above in several respects. It bears no coligands, reveals a central $N_2Ni(\mu\text{-}S)_2NiN_3$ core structure with adjacent four- and five-coordinate Ni^{II} ions and shows one protonated (non-coordinating) amine function (see below). It reacts readily with Et_4NCl to regenerate the parent complex **7**, and produces the acetato-bridged compound **9** upon addition of sodium acetate (Scheme 3). Recall that **7** is a type A species whereas **9** is of the kind B. The reaction in Equation (2) therefore involves a conformational change of the macrocycle from A to B. It can be shown that this requires an inversion of the configurations of the tertiary nitrogen donor atoms; however, this can only proceed by dissociation of the metal–nitrogen bonds. The crystal structure of **13** reveals such non-coordinating nitrogen donor atoms. Thus, **13** is presumably an intermediate in the above substitution reactions [e.g. Equation (2)]. All attempts to isolate the analogous compound of the permethylated macrocylce have failed.[17] Therefore, the isolation of **13** can be traced back to the sterically more demanding ethyl functions. As we will show below, the use of H_2L^{Et} in place of H_2L^{Me} results in restricted access to the two metal ions which are buried inside a sterically more encumbered cavity. This clearly shows that these highly functionalized macrocycles allow for the stabilization of reactive intermediates.

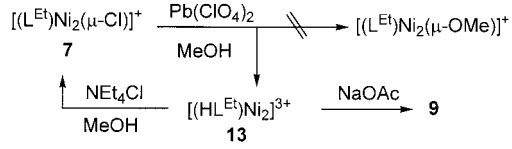

Scheme 3. Preparation and reactions of **13**.

To obtain some preliminary information on the solution structures, the synthesis of diamagnetic zinc complexes was devised next. The acetato-bridged dizinc complex **14** was obtained by the direct reaction of H_2L^{Et}·6HCl with $Zn(OAc)_2$·$2H_2O$ and triethylamine in methanol [Equation (5)]. Attempts to prepare a chloro-bridged complex such as $[(L^{Et})Zn^{II}_2(\mu\text{-}Cl)]^+$ were unsuccessful.

$$H_2L^{Et}\cdot 6HCl \xrightarrow[8\ NEt_3,\ MeOH]{2\ Zn(OAc)_2\cdot 2H_2O} [(L^{Et})Zn_2(\mu\text{-}OAc)]^+$$
14 (5)

The two Co^{II} complexes **17** and **18** represent the last two compounds of this study. These were prepared according to Equations (6) and (7). Both cations were isolated as their perchlorate salts in 83% and 74% yield, respectively. The structures of complexes $[(L^{Me})Co^{II}_2(\mu\text{-}Cl)]^+$ (**15**) and $[(L^{Me})Co^{II}_2(\mu\text{-}OAc)]^+$ (**16**) have previously been shown to be of type A and B, respectively.[18] On the basis of spectroscopic similarities (vide infra), analogous structures are likely for the complexes supported by H_2L^{Et}. This is confirmed by an X-ray crystal structure determination of $[(L^{Et})Co^{II}_2(\mu\text{-}OAc)]BPh_4$ (**18**·BPh_4, see below).

$$H_2L^{Et}\cdot 6HCl \xrightarrow[8\ NEt_3,\ MeOH]{2\ CoCl_2\cdot 6H_2O} [(L^{Et})Co_2(\mu\text{-}Cl)]^+$$
17 (6)

$$[(L^{Et})Co_2(\mu\text{-}Cl)]^+ \xrightarrow[MeOH]{NaOAc} [(L^{Et})Co_2(\mu\text{-}OAc)]^+$$
17 **18** (7)

All new complexes are stable in air both in solution and in the solid state. The perchlorate salts are very soluble in a range of common polar organic solvents (CH_3CN, EtOH, MeOH). The complexes with the longer alkyl chains also exhibit some solubility in apolar solvents such as cyclohexane or toluene. The new compounds gave satisfactory elemental analyses and were characterized by spectroscopic methods (IR, UV/Vis, ^1H and ^{13}C NMR spectroscopy) and compounds **10**·ClO_4, **12**·BPh_4, **13**·$(ClO_4)_3$, **14**·ClO_4, and **18**·BPh_4 also by X-ray structure analysis.

 © 2005 Wiley-VCH Verlag GmbH & Co. KGaA, Weinheim

Spectroscopic Characterization

Infrared Spectroscopy

The infrared spectra of all compounds display the bands expected for the macrocyclic ligands, counterions, carboxylate or alkyl carbonate coligands.[19] Selected Infrared data are listed in Table 2. The ClO_4^- ion gives rise to a broad band at 1100 cm^{-1} which is normal for this counterion. The IR spectra of the acetato-bridged complexes **6**, **9**, **10**, **14**, **16**, and **18** are very similar. Each spectrum displays two strong bands around 1590 and 1430 cm^{-1}. These bands are associated with the asymmetric [$\nu_{asym}(OAc^-)$] and symmetric stretching modes [$\nu_{sym}(OAc^-)$] of the carboxylate coligands.[20] The similarities to the IR spectrum of the dinickel complex **6** are indicative of $\mu_{1,3}$-bridging acetate groups. The IR spectra of complexes **7**, **8**, **15**, and **17** lack these two bands, which is in good agreement with the formulation of the chloro-bridged $[(L^{Me})M_2(\mu\text{-}Cl)]^+$ cations. As can be seen in Table 2, the asymmetric and symmetric stretching modes of the alkyl carbonate complexes **11** and **12** are shifted to higher and lower frequencies, respectively, when compared with the corresponding values for the acetato-bridged compounds. This trend has also been observed for the carboxylate and alkyl carbonate complexes of the permethylated macrocycle.[11] We finally note that the methyl and ethyl carbonate complexes can be easily distinguished by their IR spectra [e.g. by the frequency of the $\nu_{sym}(O_2CR)$ stretching mode].

UV/Vis Spectroscopy

All new complexes were further characterized by UV/Vis spectroscopy. The electronic absorption spectra of the complexes were recorded in the 300–1600 nm range in acetonitrile solution. Selected spectroscopic data are reported in Table 2. The data for complexes **5**, **6**, **15**, and **16** have been reported previously and are included for comparative purposes.

The spectra of the nickel complexes are similar but not identical. Each compound displays two weak absorption bands. One appears in the 620–670 nm range, the other one is observed between 1000 and 1180 nm. These absorptions can be attributed to the d-d transitions ν_2 [$^3A_{2g}(F) \rightarrow {}^3T_{1g}(F)$] and ν_1 [$^3A_{2g}(F) \rightarrow {}^3T_{2g}(F)$], respectively, of an octahedral nickel(II) (d^8) ion. For the chloro-bridged compounds the ν_1 absorption is split presumably due to lower symmetry. The higher energy features below 400 nm (not listed in Table 2) result from π-π* transitions within the $(L^R)^{2-}$ ligands. The slight differences in the position of the d-d transitions indicate that each complex retains its integrity in solution. This is also supported by the NMR spectroscopic data described below for the zinc complex **14**.

As expected, the UV/Vis spectrum of the $[(HL^{Et})Ni^{II}_2]^{3+}$ trication **13** is different from the bioctahedral complexes above. The spectrum is dominated by an intense absorption band at 574 nm, which can be tentatively assigned to a d-d transition of the planar four-coordinate NiN_2S_2 chromophore. It is a typical value for complexes containing planar NiN_2S_2 units.[21] This intense absorption presumably obscures the weaker d-d transition bands of the five-coordinate NiN_3S_2 fragment.[22]

The electronic absorption spectra of the four cobalt(II) complexes are again very similar. Each compound reveals a weak band at ca. 1260 nm which can be readily assigned to the $^4T_{1g}(F) \rightarrow {}^4T_{2g}$ transition of an octahedral high-spin cobalt(II) ion.[23] Further absorption bands are observed in the 500–600 nm range. These bands are attributable to components of the parent octahedral ligand field transitions, $^4T_{1g}(F) \rightarrow {}^4T_{1g}(P)$ and $^4T_{1g}(F) \rightarrow {}^4A_{2g}$, split by lower symmetry. The more intense band at ca. 450 nm most probably arises from a thiolate-to-cobalt(II) charge transfer (LMCT) transition and the feature at ca. 350 nm from a π-π* transition within the $(L^R)^{2-}$ ligand. Again, these spectroscopic findings clearly show that the coligands remain attached to the cobalt ions in the solution state.

NMR Spectroscopy

The ^1H NMR spectrum of the acetato-bridged zinc complex **14** displays only one set of signals, indicative of a single isomer. The four aromatic protons (C^{Ar}) and the *tert*-butyl protons [$C(CH_3)_3$] appear as singlets, implying C_{2v} sym-

Table 2. Selected UV/Vis and IR spectroscopic data for compounds **5**–**18**.

Compound	λ_{max}/nm (ε/M^{-1} cm^{-1})	ν_{as}, ν_s (O_2CR)
5	658 (41), 920 (59), 1002 (80)	–
6	649 (28), 1134 (55)	1588, 1426
7	659 (30), 930 (53), 1026 (76)	–
8	674 (26), 931 (54), 1023 (74)	–
9	660 (29), 1180 (79)	1589, 1426
10	662 (29), 1183 (77)	1593, 1428
11	668 (22), 1136 (84)	1638, 1330
12	668 (28), 1140 (79)	1637, 1316
13	574 (850), 1016 (50)	–
14	352 (2290)	1584, 1442
15	357 (1523), 468 (590), 545 (162), 571 sh (137), 1237 (23)	–
16	440 (467), 523 (170), 542 (121), 565 sh (64), 608 sh (21), 1262 (33)	1587, 1434
17	342 (2401), 470 (602), 548 (175), 578 sh (162), 1280 (28)	–
18	440 (610), 528 (204), 1288 (44)	1588, 1439

[a] The UV/Vis and IR spectra were recorded for the perchlorate salts.[b] Spectra were recorded in CH_3CN solution at 295 K. Concentration of solutions were ca. 1.0×10^{-3} M.

 © 2005 Wiley-VCH Verlag GmbH & Co. KGaA, Weinheim

metry for the $[(L^{Et})Zn_2(\mu\text{-OAc})]^+$ cation (i.e. structure type B). This is further supported by the fact that the $[(L^{Et})Zn_2]^{2+}$ fragment gives rise to only 13 ^{13}C signals (9 for the aliphatic and 4 for the aromatic carbon atoms). The appearance of the ^1H NMR signals for the methyl protons of the bridging acetato coligand at δ = 0.85 ppm is also worth mentioning. This signal is shifted to high field when compared with free sodium acetate (δ = 1.83 ppm). This can be understood in terms of the ring current. As can be seen from Figure 3, the methyl protons of the acetate groups are positioned in the binding cavity of the $[(L^{Et})Zn_2]^{2+}$ fragment slightly above the center of the two phenyl rings in the shielding region. Similar findings have been observed for the $[(L^{Me})Zn^{II}(\mu\text{-OAc})]^+$ cation.[24] In summary, the spectroscopic data have clearly established that all complexes exist as discrete and stable species with similar "cone"- and "partial-cone"-like conformations of the macrocycles. Thus, with the exception of complex **13**, the ligating properties of the new ligands are not very different from the parent $(L^{Me})^{2-}$ and $(L^{H})^{2-}$ ligands.

X-ray Crystallography

The formulations of the new compounds were further confirmed by X-ray diffraction studies. Single crystals of X-ray quality were obtained for the perchlorate salts of **10**, **13**, and **14** and for the tetraphenylborate salts of **12** and **18**. Selected crystallographic data are listed in Table 4. The molecular structures of the complexes are displayed in Figures 1, 2, 3, 4 and 5, and selected bond lengths and angles are given in Table 3.

Description of the Structures of the Bioctahedral $[(L^R)M_2(\mu\text{-}O_2CR)]^+$ Complexes

The structures of the bioctahedral species **10**, **12**, **14**, and **18** will be discussed first. A common labeling scheme for the $[(L^{Me})M_2]^{2+}$ fragments has been used to facilitate structural comparisons. The structure of the cation $[(L^{Me})Ni_2^{II}(\mu\text{-OAc})]^+$ (**6**) has been reported previously, and its metrical parameters are also given for comparison.

Structure of the $[(L^R)M_2]^{2+}$ Fragment

It is appropriate to describe the structures of the $[(L^R)M_2]^{2+}$ fragments first. The macrocycles adopt the conformation of type B, previously reported for the acetato-bridged complex **6** (Scheme 1).[11] In each case, the two metal ions are coordinated in a square-pyramidal fashion by the two *fac*-$N_3(\mu\text{-}S)_2$ donor sets of the doubly deprotonated macrocycles. The coordination of the exogenous coligands generates distorted octahedral environments for the metal ions. The metrical parameters of the central $N_3M(\mu\text{-}S)_2(\mu\text{-}O_2CR)MN_3$ cores are very similar (see Table 3). The diethylenetriamine units are *fac*-coordinated with one larger and two smaller N–M–N bond angles, which is most commonly observed in complexes with this tridentate unit.[25] Likewise, the M–N bonds involving the four benzylic nitrogen donors are invariably longer (by ca. 0.1 Å) than the ones comprising the central nitrogen atoms of the linking diethylenetri-

Figure 1. Two perspective side views of the structure of the dinickel complex **10** with thermal ellipsoids drawn at the 50% probability level. Hydrogen atoms are omitted for reasons of clarity.

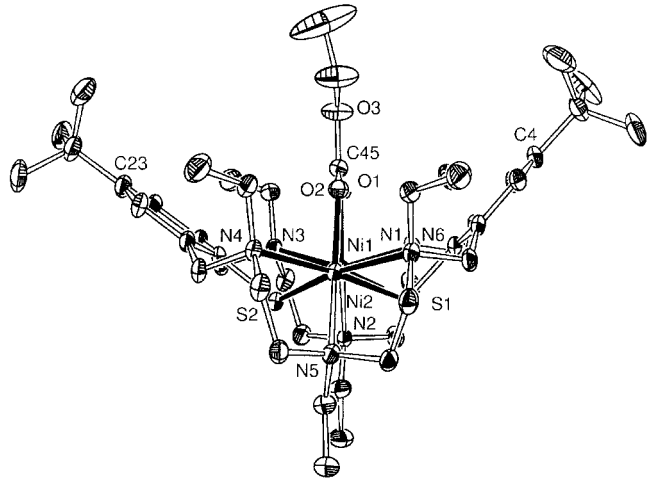

Figure 2. Structure of the dinickel complex **12** with thermal ellipsoids drawn at the 50% probability level. Hydrogen atoms are omitted for reasons of clarity.

 © 2005 Wiley-VCH Verlag GmbH & Co. KGaA, Weinheim

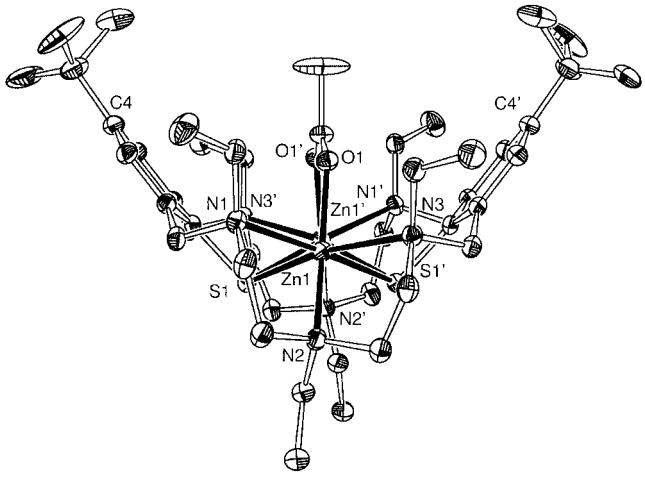

Figure 3. Structure of the dizinc complex **14** with thermal ellipsoids drawn at the 50% probability level. Only one orientation of the disordered *tert*-butyl group is displayed. Hydrogen atoms are omitted for reasons of clarity. Symmetry code used to generate equivalent atoms: $1 - x$, y, $0.5 - z$ ($'$).

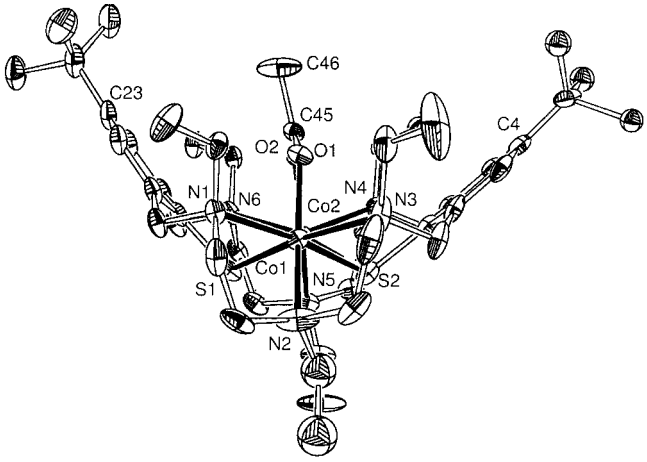

Figure 4. Structure of the dicobalt complex **18** with thermal ellipsoids drawn at the 50% probability level. Hydrogen atoms are omitted for reasons of clarity.

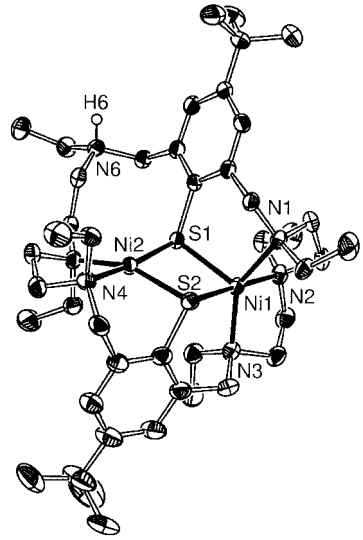

Figure 5. Structure of the dinickel complex **13** with thermal ellipsoids drawn at the 30% probability level. Only one orientation of the disordered *tert*-butyl and the *N*-propyl group is displayed. Selected bond lengths [Å] and angles [°]: Ni(1)···Ni(2) 3.319; Ni(1)–N(1) 2.051(3), Ni(1)–N(2) 2.138(3), Ni(1)–N(3) 2.060(3), Ni(1)–S(1) 2.2911(11), Ni(1)–S(2) 2.4065(13), Ni(2)–N(4) 1.991(3), Ni(2)–N(5) 1.997(3), Ni(2)–S(1) 2.2140(13), Ni(2)–S(2) 2.2129(12); N(5)–Ni(2)–S(2) 157.83(10), N(4)–Ni(2)–S(1) 171.76(10), N(2)–Ni(1)–S(2) 176.86(9), N(1)–Ni(1)–S(1) 100.57(9), N(3)–Ni(1)–S(1) 113.77(10), N(1)–Ni(1)–N(3) 145.55(12).

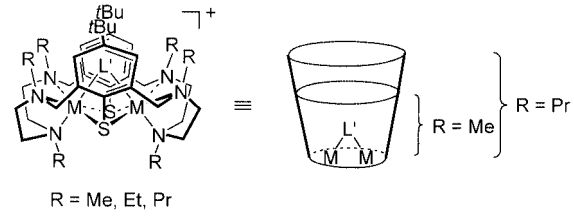

Scheme 4. Schematic representation of the expansion of the binding pocket of the $[(L^R)M_2(L')]^+$ complexes upoing going from the methylated (R = Me) to the propylated ligand system (R = Pr).

amine units. This is also normal for carboxylato-bridged structures of this ligand system {e.g. $[(L^{Me})M_2(\mu\text{-OAc})]^+$, M = Co^{II}, Ni^{II}, and Zn^{II}}. Hence, the differences in the metal–nitrogen bond lengths are due to steric constraints of the macrocycles.

Cavity Dimensions

As can be seen from Scheme 4, the four alkyl residues on the four benzylic nitrogen atoms align with the two phenyl rings. Thus, upon going from the methylated derivative to the *N*-propylated macrocycle the binding pocket of the $[(L^R)M_2]^{2+}$ fragment expands to a sterically more encumbered, conical, calixarene-like cavity as schematically illustrated in Scheme 4.

The dimensions of the binding cavities of the $[(L^{Me})M_2]^{2+}$ fragments can be described by the intramolecular distances between the two opposing aryl ring carbon atoms bearing the *tert*-butyl groups [e.g. the diameter of the pocket entrance, see for example, C(4)···C(26) in **10**]. The values range from 9.265 to 9.891 Å (Table 3). Two trends are apparent. Firstly, the diameter increases with increasing length of the *N*-alkyl residues (e.g. compare **6** with **10**). Secondly, the distances increase with increasing steric bulk of the coligand with this latter trend being the more important one (e.g. compare **10** with **12**). This is indicative of intramolecular steric repulsions between the residues of the bowl-shaped hosts and their guests.

Binding Mode of the Coligands

As expected, the acetate and ethyl carbonate coligands bind to the $[(L^{Me})M_2]^{2+}$ fragment as bidentate $\mu_{1,3}$-bridges. Consequently, the M···M separations are almost equidistant in these three compounds [average value is 3.491(1) Å]. The average metal–ligand bond lengths show no unusual features and compare well with those in **6**.

 © 2005 Wiley-VCH Verlag GmbH & Co. KGaA, Weinheim

Table 3. Selected bond lengths and angles of complexes **6**, **10**, **12**, **14** and **18**.

	6	**10**	**12**	**14**	**18**
M(1)–O(1)	1.998(2)	1.990(6)	2.020(3)	2.021(3)	1.993(3)
M(1)–N(1)	2.281(2)	2.321(7)	2.293(4)	2.362(3)	2.292(4)
M(1)–N(2)	2.152(2)	2.158(6)	2.156(4)	2.193(3)	2.212(4)
M(1)–N(3)	2.251(2)	2.238(9)	2.291(4)	2.418(3)	2.387(4)
M(1)–S(1)	2.493(1)	2.517(3)	2.494(1)	2.565(1)	2.495(2)
M(1)–S(2)	2.448(1)	2.423(2)	2.441(1)	2.535(1) (S1′)[b]	2.502(2)
M(2)–O(2)	2.008(2)	1.985(5)	2.030(3)	2.021(3) (Zn1′-O1′)[b]	2.004(3)
M(2)–N(4)	2.244(2)	2.247(6)	2.253(4)	2.362(3) (Zn1′-N1′)[b]	2.313(4)
M(2)–N(5)	2.158(2)	2.174(6)	2.160(4)	2.193(3) (Zn1′-N2′)[b]	2.191(6)
M(2)–N(6)	2.295(2)	2.334(7)	2.340(4)	2.418(3) (Zn1′-N3′)[b]	2.312(5)
M(2)–S(1)	2.493(1)	2.507(2)	2.475(1)	2.565(1) (Zn1′-S1)[b]	2.492(1)
M(2)–S(2)	2.451(1)	2.423(3)	2.430(1)	2.535(1) (Zn1′-S1′)[b]	2.538(2)
M–O	2.003(2)	1.988(6)	2.025(3)	2.021(3)	1.999(3)
M–N[a]	2.230(2)	2.245(7)	2.248(4)	2.324(3)	2.285(5)
M–S[a]	2.471(1)	2.468(3)	2.460(1)	2.550(3)	2.507(2)
M···M	3.483(1)	3.513(1)	3.520(1)	3.459(1) (Zn1–Zn1′)[b]	3.482(1)
C(4)···C(20)	9.306	9.622[d]	9.891[e]	9.265 (C4–C4′)[b]	9.563[e]
S(1)–M(1)–S(2)	79.49(4)	77.94(8)	78.26(5)	82.20(5) (S1–Zn1–S1′)	80.17(6
S(1)–M(2)–S(2)	79.45(3)	78.11(8)	78.83(5)	82.20(5) (S1–Zn1′–S1′)	79.55(5)
O(1)–M(1)–N(2)	163.89(7)	162.9(2)	164.81(14)	159.43(11)	158.40(15)
N(1)–M(1)–S(2)	170.28(5)	167.4(2)	168.21(11)	172.35(8) (N1–Zn1–S1′)	169.98(10)
N(3)–M(1)–S(1)	170.09(5)	168.1(2)	168.31(10)	168.60(8)	168.51(10)
O(2)–M(2)–N(5)	163.84(7)	160.9(2)	164.90(14)	159.4(1) (O1′-Zn1′-N2′)	159.7(2)
N(4)–M(2)–S(1)	170.86(5	168.2(2)	169.16(10)	172.35(8) (N3′-Zn1′-S1)	169.74(11)
N(6)–M(2)–S(2)	169.28(5)	167.68(16)	168.08(10	168.60(8) (N1′-Zn1′-N2′)	168.47(12)
Ph/Ph[c]	80.8	88.1	95.2	76.0	83.8

[a] Average values. [b] Symmetry code used to generate equivalent atoms: $1 - x$, $+y$, $0.5 - z$ (′). [c] Angle between the normals of the planes of the two aryl rings. [d] C(4)···C(26). [e] C(4)···C(23).

Description of the Crystal Structure of [(HL^{Et})Ni$_2$](ClO$_4$)$_3$·3MeOH·H$_2$O [13·(ClO$_4$)$_3$·3MeOH·H$_2$O]

This salt crystallizes in the triclinic space group $P\bar{1}$. The structure revealed the presence of discrete dinuclear $[(HL^{Et})Ni_2]^{3+}$ trications, perchlorate anions, and methanol and water molecules of solvent of crystallization. As can be seen in Figure 5, this complex bears no coligands and features two differently coordinated nickel atoms. One nickel atom is coordinated in a distorted planar fashion by two *cis*-oriented nitrogen atoms and two bridging thiophenolate sulfur atoms. The other nickel ion is five-coordinate. The protonated amine donor N(6) is out of range of bonding interactions with the metal atoms and points away from them.

The coordination geometry of the four-coordinate nickel ion is significantly distorted from square-planar towards tetrahedral, as indicated by an N–Ni–N/S–Ni–S dihedral angle of 23.80(2)° (mean deviation from plane 0.238 Å). This is a rather large distortion from planarity. Other nickel complexes with N_2S_2 coordination environments are more rigorously square-planar, the tetrahedral twists from the NiN_2S_2 planes not exceeding 15°.[26,27]

The coordination environment around the five-coordinate nickel atom is distorted trigonal-bipyramidal with S(1), N(1) and N(3) occupying the equatorial and S(2) and N(2) the axial positions. The angles in the equatorial plane deviate by as much as 25.6° [N(1)–Ni(1)–N(3)] from the ideal values of a perfect trigonal bipyramid. The average Ni–N and Ni–S distances of 2.083 and 2.349 Å are shorter than in the above bioctahedral species but compare well with those reported for [Ni^{II}(terpy)(S-2,4,6-(*i*Pr)$_3$C$_6$H$_2$)$_2$] (terpy = 2,2′,2″-terpyridine; Ni–N 2.057 Å, Ni–S 2.303 Å)[28] and other trigonal-bipyramidal $Ni^{II}N_3S_2$ complexes.[29] The metal–ligand bonds involving the equatorial donor atoms are shorter than the ones comprising the axial ones; an exactly analogous situation is found in the terpy complexes. As a consequence of the shorter metal–ligand bonds, the metal···metal separation is smaller at 3.319 Å. Finally, it should be noted that the two nickel(II) ions are almost completely surrounded by the apolar *N*-ethyl substituents from the macrocycle. This steric crowding about the coordinatively unsaturated dinickel site might explain its higher stability {relative to the very unstable $[(HL^{Me})Ni_2]^{3+}$ trication of the permethylated macrocycle}.

Summary and Conclusion

The following are the main findings of this investigation. a) *N*-Alkylated variants of H_2L^{Me} bearing ethyl and propyl groups in place of the methyl functions can be readily prepared by acylation of the parent hexaamine–dithioether compound **1** followed by reduction of the amide and thioether functions. b) The new ligands support the formation of dinuclear complexes of the type $[(L^R)M_2(\mu\text{-}L')]$ with a bowl-shaped structure. c) The binding pocket of the complexes expands to a more conical, "calixarene"-like cavity upon going from the permethylated to the perpropylated ligand system. d) The rate of the substitution reactions and the ability to fix small molecules is not drastically altered by the longer alkyl chains. e) Finally, it has been demonstrated that these highly functionalized ligand systems allow

 © 2005 Wiley-VCH Verlag GmbH & Co. KGaA, Weinheim

for the stabilization of reactive intermediates. These findings can now be used as a guide to further modulate the chemical reactivity of these compounds.

Experimental Section

Materials and Methods: Compound **1** was prepared as described in the literature.[9] All syntheses were carried out under argon. Melting points were determined in open glass capillaries and are uncorrected. NMR spectra were recorded with a Bruker AVANCE DPX-200 spectrometer at 300 K. Chemical shifts refer to solvent signals. Infrared spectra were recorded with a Bruker VECTOR 22 FT-IR spectrometer and electronic absorption spectra with a Jasco V-570 UV/VIS/NIR spectrometer. Elemental analyses were carried out with a VARIO EL elemental analyzer. ***CAUTION:*** *Perchlorate salts are potentially explosive and should therefore be prepared only in small quantities and handled with appropriate care!*

Compound 3a: A solution of **1** (9.44 g, 15.4 mmol) in acetic anhydride (90 mL) was stirred at 50 °C for 6 h. After the solvent was distilled off at reduced pressure, the residue was taken up in aqueous potassium hydroxide solution (3 M, 100 mL) and dichloromethane (100 mL). The layers were separated and the aqueous phase was extracted with dichloromethane (3 × 50 mL). The combined organic layers were washed with water (50 mL) and dried with anhydrous sodium sulfate. Evaporation of the solvent gave **3a** as a white solid (13.1 g, 98%). M.p. 236 °C. This material was used in the next step without further purification. ^{1}H NMR (200 MHz, $CDCl_3$): δ = 1.06–1.26 [m, 18 H, ArC(CH_3)$_3$], 1.94–2.23 (m, 18 H, NCOCH_3), 2.82–3.35 (m, 20 H, NCH_2CH_2 and SCH_2), 4.47–4.74 (m, 8 H, ArCH_2), 6.91–7.10 (m, 4 H, Ar*H*) ppm. IR (KBr): $\tilde{\nu}$ = 3456 m, 2963 s, 2871 w, 1652 vs, ν(CO), 1559 vw, 1474 m, 1418 s, 1363 m, 1313 vw, 1238 w, 1195 w, 1131 vw, 1094 vw, 1062 vw, 1035 vw, 988 vw, 950 vw, 878 vw, 603 w cm^{-1}. $C_{46}H_{68}N_6O_6S_2$·CH_3CO_2H (865.19 + 60.05): calcd. C 62.31, H 7.99, N 9.52, S 7.26; found C 62.33, H 8.79, N 9.23, S 6.66.

Compound 4a: A solution of **3a** (8.65 g, 10.0 mmol) in tetrahydrofuran (50 mL) was added dropwise to a suspension of lithium aluminium hydride (4.55 g, 120 mmol) in tetrahydrofuran (200 mL). The reaction mixture was refluxed for 12 h. To the hot reaction mixture was added water (10 mL) in small portions followed by 3 M aqueous potassium hydroxide solution (30 mL). Care should be taken during this step because of the violent reaction. The reaction mixture was refluxed for an additional hour to ensure complete hydrolysation of the aluminum salts. After cooling to room temperature, the organic layer was decanted from a white residue. This residue was extracted with boiling tetrahydrofuran (3 × 100 mL). The combined organic layers were dried with anhydrous sodium sulfate. Evaporation of the solvent gave the title compound as a yellowish oil which was used in the next step without further purification (6.80 g, 87%). ^{1}H NMR ($CDCl_3$, 200 MHz): δ = 0.85–1.00 (m, 18 H, NCH$_2$CH_3), 1.23 [s, 18 H, ArC(CH_3)$_3$], 2.29–2.55 (m, 28 H, NCH_2CH$_3$ and NCH_2CH_2N), 2.70 (s, 4 H, SCH_2), 3.62 (s, 8 H, ArCH_2N), 7.41 (s, 4 H, Ar*H*) ppm. ^{13}C{^{1}H}NMR (50 MHz, $CDCl_3$): δ = 13.6, 13.8 (CH_3), 32.5 [ArC(*C*H$_3$)$_3$], 35.8 [Ar*C*(CH$_3$)$_3$], 37.0 (ArS*C*H$_2$), 49.0 (CH_2), 51.0 (CH_2), 52.3 (CH_2), 53.0 (CH_2), 58.7 (CH_2), 125.8 (CH), 129.1 (C^{Ar}), 145.0 (C^{Ar}), 152.1 (C^{Ar}) ppm. IR (Nujol): $\tilde{\nu}$ = 3417 m, 2964 vs, 2869 s, 2809 s, 2354 vw, 2327 vw, 1730 vw, 1713 vw, 1691 vw, 1659 vw, 1642 vw, 1631 vw, 1600 w, 1555 vw, 1513 vw, 1463 m, 1383 m, 1363 m, 1292 w, 1262 s, 1223 w, 1173 w, 1096 s, 1073 s, 865 vw, 802 s, 710 vw, 663 vw cm^{-1}.

Compound H_2L^{Et}·6HCl: To a solution of sodium (3.45 g, 150.0 mmol) in liquid ammonia (150 cm^3) was added a solution of compound **4a** (3.91 g, 5.00 mmol) in tetrahydrofuran (50 cm^3) dropwise at –78 °C. The resulting blue reaction mixture was stirred at –78 °C for one additional hour to ensure complete deprotection of the macrocycle. Solid ammonium chloride was added in small portions at –78 °C to destroy excess reducing agent. The resulting colourless suspension was allowed to warm to room temperature. After 12 h, the remaining solvent was distilled off at reduced pressure. The residue was taken up in water (50 mL) and the pH of the suspension adjusted to ca. 1 to give a pale-yellow solution of H_2L^{Et} as the hexahydrochloride salt. To remove the inorganic salts, the solution was concentrated in vacuo to a volume of about 20 mL. Methanol (ca. 60 mL) was then added and the resulting solution was filtered from NaCl and NH_4Cl. The latter two steps were repeated several times in this order, until no more salts precipitated upon addition of MeOH. A 100-mL portion of ethanol was then added. Upon standing for 1–2 h, the product precipiated as a pale-yellow solid (2.82 g, 58%). ^{1}H NMR (200 MHz, D_2O): δ = 1.29 [s, 18 H, ArC(CH_3)$_3$], 1.39 (m, 18 H, CH$_2$CH_3), 3.33 (m, 12 H, CH_2CH$_3$), 3.75–3.90 [m, 16 H, N(CH_2CH_2)$_2$], 4.59 (s br, 8 H, ArCH_2N), 7.56 (s, 4 H, Ar*H*) ppm. ^{13}C{^{1}H} NMR (50 MHz, D_2O): δ = 9.09 (CH_3), 9.21 (CH_3), 31.49 [ArC(*C*H$_3$)$_3$], 34.90 [Ar*C*(CH$_3$)$_3$], 47.41 (CH_2), 48.73 (CH_2), 50.19 (CH_2), 50.39 (CH_2), 59.44 (CH_2), 131.74 (CH), 132.00 (C^{Ar}), 147.00 (C^{Ar}), 149.00 (C^{Ar}) ppm. This compound was pure enough for the preparation of the metal complexes. IR (KBr:) $\tilde{\nu}$ = 3407 vs, 2962 vs, 2624 vs, 1690 s, 1630 m, 1451 vs, 1400 vs, 1231 m, 1161 s, 1031 s, 898 vs, 801 vs, 565 vs cm^{-1}.

Compound 3b: The preparation of this compound was analogous to that of **3a**, except that propionic anhydride was used instead of acetic anhydride. **3b** was obtained as a white solid (8.92 g, 94%). M.p. 170–176 °C. This product was used in the next step without further purification. ^{1}H NMR (200 MHz, $CDCl_3$): δ = 1.17 (m, 18 H, NCOCH$_2$CH_3), 1.25–1.36 [m, 18 H, ArC(CH_3)$_3$], 2.70 (m, 12 H, NCOCH_2CH$_3$), 3.06–3.68 [m, 20 H, N(CH_2CH_2N)$_2$ + ArSCH_2], 4.90 (s, 8 H, ArCH_2N), 7.00–7.06 (m, 4 H, Ar*H*) ppm. IR (KBr): $\tilde{\nu}$ = 3441 w, 2967 m, 2939 m, 2876 w, 1724 vw, 1648 vs, 1563 vw, 1468 s, 1421 s, 1378 w, 1364 w, 1198 m, 1184 m, 1120 vw, 1079 w, 1052 w, 970 vw, 879 vw, 815 vw, 726 vw, 683 vw, 573 vw, 535 vw cm^{-1}. $C_{52}H_{80}N_6O_6S_2$ (949.36): calcd. C 65.79, H 8.49, N 8.85, S 6.76; found C 65.02, H 8.52, N 8.28, S 6.16.

Compound 4b: The preparation of this compound was analogous to **3b**. Compound **4b** was obtained as a yellowish oil which crystallized on standing. Recrystallization from ethanol gave 5.02 g (58%) of analytically pure material. M.p. 128 °C. ^{1}H NMR ($CDCl_3$, 200 MHz): δ = 0.77 (t, ^3J = 7.2 Hz, 18 H, NCH$_2$CH$_2$CH$_3$), 1.23 [s, 18 H, ArC(CH$_3$)$_3$], 1.14–1.40 (m, 12 H, NCH$_2$CH$_2$CH$_3$), 2.26 (t, ^3J = 7.2 Hz, 12 H, NCH$_2$CH$_2$CH$_3$), 2.48 (s, 16 H, NCH$_2$CH$_2$N), 2.63 (s, 4 H, ArSCH$_2$), 3.60 (s, 8 H, ArCH$_2$N), 7.45 (s, 4 H, ArH) ppm. ^{13}C{^{1}H} NMR ($CDCl_3$, 75 MHz): δ = 12.3 (NCH$_2$CH$_2$CH$_3$), 21.2(NCH$_2$CH$_2$CH$_3$), 21.6 (NCH$_2$CH$_2$CH$_3$), 31.8 [ArC(CH$_3$)$_3$], 35.2 [Ar*C*(CH$_3$)$_3$], 35.7 (ArSCH$_2$), 51.5 (CH_2), 52.4 (CH_2), 56.1 (CH_2), 58.2 (CH_2), 59.2 (CH_2), 124.7 (CH), 127.7 (C^{Ar}), 144.2 (C^{Ar}), 151.4 (C^{Ar}) ppm. IR (KBr): $\tilde{\nu}$ = 2958 s, 2933 s, 2870 m, 2817 m, 1460 m, 1404 w, 1380 w, 1361 w, 1079 m, 893 w, 647 w cm^{-1}. $C_{52}H_{92}N_6S_2$ (865.46): C 72.16, H 10.71, N 9.71, S 7.41; found C 71.92, H 10.86, N 9.60, S 7.30.

Compound H_2L^{Pr}·6HCl: The preparation of this compound was analogous to H_2L^{Et}·6HCl, except that **4b** (4.32 g, 5.00 mmol) was used as the starting material. The hydrochloride was obtained as a pale-yellow solid (3.33 g, 63%). ^{1}H NMR (200 MHz, D_2O): δ =

 © 2005 Wiley-VCH Verlag GmbH & Co. KGaA, Weinheim

0.71 (t, ^3J = 7.2 Hz, 18 H, $NCH_2CH_2CH_3$), 1.04 [s, 18 H, $C(CH_3)_3$], 1.60–1.35 (m, 12 H, $NCH_2CH_2CH_3$), 2.87 (m, 12 H, $NCH_2CH_2CH_3$), 3.44 (m, 16 H, NCH_2CH_2N), 4.30 (s, 8 H, $ArCH_2N$), 7.25 (s, 4 H, ArH) ppm. $^{13}C\{^1H\}$ NMR (50 MHz, D_2O): δ = 10.4 (CH_3), 17.2 (CH_2), 17.4 (CH_2), 30.7 [$ArC(CH_3)_3$], 34.8 [$ArC(CH_3)_3$], 35.5 (CH_2), 47.3 (CH_2), 48.7 (CH_2), 56.0 (CH_2), 59.6 (CH_2), 61.9 (CH_2), 131.1 (CH), 134.3 (C^{Ar}), 147.9 (C^{Ar}), 158.4 (C^{Ar}) ppm. IR (KBr): $\tilde{\nu}$ = 3427 w, 2967 vw, 2878 w ν(CH), 2465 w, 1629 s ν(CO), 1471 w, 1384 m, 1364 m, 1300 s, 1200 m, 1150 m, 1051 s, 996 s, 967 s, 806 vs, 755 vs, 601 vs cm^{-1}. This compound was pure enough for the preparation of the metal complexes.

$[(L^{Et})Ni_2(Cl)]ClO_4$ (7·ClO_4): To a suspension of H_2L^{Et}·6HCl (974 mg, 1.00 mmol) in methanol (40 mL) was added a solution of $NiCl_2$·$6H_2O$ (475 mg, 2.00 mmol) in methanol (2 mL). A solution of Et_3N (810 mg, 8.00 mmol) in methanol (2 mL) was then added to give a dark red solution. After stirring at room temperature for 3 d, the product was precipitated by the addition of solid $LiClO_4$·$3H_2O$ (2.50 g, 15.6 mmol). The yellow microcrystalline solid was isolated by filtration, washed with 5 mL of cold ethanol and 5 mL of ether, and dried in vacuo. This material was recrystallized once from a few milliliters of acetonitrile. Yield: 824 mg (82%). M.p. 305 °C (decomp.). IR (KBr) $\tilde{\nu}$ = 3445 m, 2961 m, 2894 w, 2361 vw, 1631 w, 1460 m, 1381 w, 1100 vs $\nu(ClO_4^-)$, 912 w, 884 w, 778 w, 733 w, 627 m cm^{-1}. UV/Vis (CH_3CN): λ_{max} (ε) = 384 (2070), 480 sh (430), 659 (30), 930 (53), 1026 nm (76 M^{-1} cm^{-1}). $C_{44}H_{76}Cl_2N_6Ni_2O_4S_2$ (1005.53): calcd. C 52.56, H 7.62, N 8.36, S 6.38; found C 52.40, H 7.47, N 8.42, S 6.49.

$[(L^{Pr})Ni_2(Cl)]ClO_4$ (8·ClO_4): The preparation of this compound was similar to that of **7**·ClO_4, except that the reaction mixture was stirred for 1 week. The compound was obtained as yellow microcrystals and purified by recrystallization from acetonitrile. Yield: 37%. M.p. 274 °C (decomp.). IR (KBr): $\tilde{\nu}$ = 3435 vs, 2964 vs, 2874 s, 2741 vw, 2665 vw, 2381 vw, 2179 vw, 2061 s, 1732 vw, 1630 s, 1607 s, 1464 s, 1365 m, 1328 vw, 1261 w, 1233 w, 1108 vs, 926 w, 912 w, 882 w, 805 m, 751 w, 629 s, 559 m cm^{-1}. UV/Vis (CH_3CN): λ_{max} (ε) = 674 (26), 931 (54), 1023 nm (74 M^{-1} cm^{-1}). $C_{50}H_{88}Cl_2N_6Ni_2O_4S_2$·$CH_3CN$·$3H_2O$ (1089.69 + 41.05 + 54.06): calcd. C 52.71, H 8.25, N 8.28; found C 52.90, H 8.35, N 8.17.

$[(L^{Et})Ni_2(OAc)]ClO_4$ (9·ClO_4): To a solution of **7**·ClO_4 (97.4 mg, 0.100 mmol) in methanol (25 mL) was added a solution of sodium acetate (16.4 mg, 0.200 mmol) in methanol (10 mL). After stirring for 2 h, solid $LiClO_4$·$3H_2O$ (160 mg, 1.00 mmol) was added. The resulting pale-green precipitate was isolated by filtration, washed with methanol and dried in air. This material was recrystallized once from a mixed acetonitrile/ethanol solvent system. Yield: 73.5 mg (66%). M.p. 332 °C (decomp.). IR (KBr): $\tilde{\nu}$ = 3446 m, 2964 vs, 2900 s, 2359 vw, 1714 vw, 1589 s $\nu_{asym}(OAc^-)$, 1426 s $\nu_{sym}(OAc^-)$, 1383 s, 1326 w, 1313 w, 1248 w, 1231 m, 1202 vw, 1187 vw, 1151 m, 1101 vs $\nu(ClO_4^-)$, 987 w, 949 w, 928 vw, 907 w, 878 w, 783 m, 756 vw, 664 w, 623 s, 581 vw, 558 vw cm^{-1}. UV/Vis (CH_3CN): λ_{max} (ε) = 345 (1596), 660 (29), 1180 nm (79 M^{-1} cm^{-1}). $C_{46}H_{79}ClN_6Ni_2O_6S_2$ (1029.13): calcd. C 53.69, H 7.74, N 8.17, S 6.23; found C 53.34, H 7.72, N 8.10, S 6.08.

$[(L^{Pr})Ni_2(\mu\text{-}O_2CCH_3)]ClO_4$ (10·ClO_4): This compound was prepared by the method detailed above for **9**·ClO_4. Yield: 75.7 mg (68%). M.p. 319 °C (decomp.). IR (KBr): $\tilde{\nu}$ = 3445 m, 2963 vs, 2872 m, 1589 s $\nu_{asym}(OAc^-)$, 1457 m, 1428 m $\nu_{sym}(OAc^-)$, 1365 w, 1312 w, 1332 w, 1151 m, 1092 vs $\nu_s(ClO_4^-)$, 1061 vs, 937 w, 911 w, 876 w, 813 w, 755 w, 663 w, 626 m, 529 w cm^{-1}. UV/Vis (CH_3CN): λ_{max} (ε) = 662 (29), 1183 nm (77 M^{-1} cm^{-1}). $C_{52}H_{91}ClNi_2N_6O_6S_2$ (1113.29): calcd. C 56.10, H 8.24, N 7.55, S 5.76; found C 56.49, H 8.42, N 7.17, S 5.48.

$[(L^{Et})Ni_2(\mu\text{-}O_2COMe)]ClO_4$ (11·ClO_4): To a solution of **7**·ClO_4 (201 mg, 0.200 mmol) in a mixture of MeOH/H_2O (40 mL/ 5 mL) was added finely ground NaOH (20 mg, 0.50 mmol). The color of the reaction mixture turned from yellow to green. The reaction mixture was exposed to air and stirred at room temperature for 24 h. A solution of $LiClO_4$·$3H_2O$ (1.00 g, 6.25 mmol) in methanol (2 mL) was then added. The green microcrystalline solid was isolated by filtration, washed with methanol and dried in vacuo. The yield was 182 mg (87%). M.p. 284–285 °C (decomp.). UV/Vis (CH_3CN): λ_{max} (ε) = 670 (20), 1138 nm (49 M^{-1} cm^{-1}). IR (KBr): $\tilde{\nu}$ = 3446 m, 2964 vs, 2901 m, 2357 vs, 1716 vw, 1638 vs $\nu_{asym}(CH_3OCO_2^-)$, 1450 vs, 1384 m, 1331 vs $\nu_{sym}(CH_3OCO_2^-)$, 1261 w, 1232 w, 1101 vs, $\nu(ClO_4^-)$, 987 vw, 950 vw, 908 vw, 979 vw, 785 s, 625 m, 581 vw, 560 vw cm^{-1}. UV/Vis (CH_3CN): λ_{max} (ε) = 350 (2384), 668 (22), 1136 nm (84 M^{-1} cm^{-1}). $C_{46}H_{79}ClN_6Ni_2O_7S_2$ (1045.13): calcd. C 52.86, H 7.62, N 8.04, S 6.14; found C 52.26, H 7.67, N 7.90, S 5.71.

$[(L^{Et})Ni_2(\mu\text{-}O_2COEt)]ClO_4$ (12·ClO_4): The complex **11**·ClO_4 (105 mg, 0.100 mmol) was dissolved in acetonitrile (20 mL). To the green solution was added ethanol (20 mL) and the reaction mixture was stirred at room temperature for 24 h. The solution was concentrated in vacuo to about 5 mL whereupon a pale-green precipitate formed. The precipitate was filtered, washed with a few milliliters of cold ethanol and dried in air. Yield: 75 mg (71%). M.p. 295 °C (decomp.). IR (KBr): $\tilde{\nu}$ = 3453 m, 2965 vs ν(CH), 2900 s, 1638 vs $\nu_{asym}(CH_3CH_2OCO_2^-)$, 1449 vs, 1384 m, 1330 vw, 1316 vs $\nu_{sym}(CH_3CH_2OCO_2^-)$, 1248 w, 1231 m, 1187 w, 1151 m, 1101 vs $\nu(ClO_4^-)$, 1056 s, 987 vw, 949 vw, 908 vw, 878 vw, 806 w, 785 m, 756 w, 628 m, 582 vs, 560 vs cm^{-1}. UV/Vis (CH_3CN): λ_{max} (ε) = 350 (2550), 668 (28), 1140 nm (79 M^{-1} cm^{-1}). $C_{47}H_{81}ClN_6Ni_2O_7S_2$ (1059.15): calcd. C 53.30, H 7.71, N 7.93, S 6.05; found C 52.48, H 7.65, N 7.76, S 5.85. The tetraphenylborate salt, $[(L^{Et})Ni_2(\mu\text{-}O_2COEt)]BPh_4$ (**12**·BPh_4), was prepared by adding $NaBPh_4$ (342 mg, 1.00 mmol) to a solution of $[(L^{Et})Ni_2(\mu\text{-}O_2COEt)]ClO_4$ (106 mg, 0.100 mmol) in methanol (40 mL). The pale-green microcrystalline solid was isolated by filtration, washed with ethanol and dried in air. Yield: 116 mg (91%). M.p. 293–294 °C (decomp). IR (KBr): $\tilde{\nu}$ = 3442 s ν(OH), 3056 s ν(ArH), 2968 vs ν(CH), 2903 s ν(CH), 1634 vs $\nu_{asym}(CH_3CH_2OCO_2^-)$, 1579 m, 1478 s, 1463 s, 1427 m, 1397 m, 1373 m, 1316 vs $\nu_{sym}(CH_3CH_2OCO_2^-)$, 1261 w, 1231 w, 1185 m, 1154 m, 1102 s, 1056 s, 948 vw, 909 vw, 879 vw, 854 vw, 803 w, 744 vs $\nu(BPh_4^-)$, 715 vs $\nu(BPh_4^-)$, 628 w, 612 w, 560 w cm^{-1}. UV/Vis (CH_3CN): λ_{max} (ε) = 668 (27), 1140 nm (70 M^{-1} cm^{-1}). The tetraphenylborate salt was additionally characterized by X-ray crystal structure analysis.

$[(HL^{Et})Ni_2](ClO_4)_3$ (13·$(ClO_4)_3$): To a solution of **7**·ClO_4 (101 mg, 0.100 mmol) in MeOH (30 mL) was added $Pb(ClO_4)_2$ (40.6 mg, 0.100 mmol). The resulting dark green solution was stored at room temperature for 12 h during which a few crystals of the title compound precipitated as dark green crystals. Yield: 16 mg (13%). The ^1H NMR spectra obtained for the trication are broad with chemical shifts ranging from δ = +200 to –50 ppm and almost completely collapse into the base line, indicative of a paramagnetic species. UV/Vis (CH_3CN): λ_{max} (ε) = 574 (850), 1016 nm (50 M^{-1} cm^{-1}). This compound was additionally characterized by X-ray crystal structure analysis.

$[(L^{Et})Zn_2(OAc)]ClO_4$ (14·ClO_4): To a suspension of H_2L^{Et}·6HCl (974 mg, 1.00 mmol) in methanol (50 mL) was added a solution of $Zn(OAc)_2$·$2H_2O$ (439 mg, 2.00 mmol) in methanol (5 mL). A solution of triethylamine (810 mg, 8.00 mmol) in methanol (1 mL) was added and the resulting clear solution was stirred at room temperaturefor 12 h. Solid $LiClO_4$·$3H_2O$ (1.60 g, 10.0 mmol) was then

 © 2005 Wiley-VCH Verlag GmbH & Co. KGaA, Weinheim

added. The resulting colorless precipitate was isolated by filtration, washed with methanol and dried in air. Yield: 830 mg (80%). M.p. 282–284 °C (decomp.). IR (KBr): $\tilde{\nu}$ = 3442 m, 2964 vs, 2899 s, 1585 s $\nu_{asym}(OAc^-)$, 1464 s, 1442 vw $\nu_{sym}(OAc^-)$, 1385 m, 1329 w, 1252 w, 1230 w, 1149 m, 1100 vs $\nu(ClO_4^-)$, 1056 vs, 947 vw, 906 w, 884 w, 782 w, 656 vw, 625 s, 578 vw, 553 vw cm^{-1}. ^1H NMR (300 MHz, CD_3CN, 25 °C, TMS): δ = 7.13 (s, 4 H, Ar*H*), 4.12 (d, ^2J = 12.0 Hz, 4 H, $ArCH_2$), 3.21 (d, ^2J = 12.0 Hz, 4 H, $ArCH_2$), 3.60–2.60 (m, 28 H, NCH_2CH_2 + NCH_2), 1.25 (t, ^3J = 7.0 Hz, 6 H, NCH_2CH_3), 1.23 [s, 18 H, $C(CH_3)_3$], 1.16, (t, ^3J = 7.0 Hz, 12 H, NCH_2CH_3), 0.83 (s, 3 H, CO_2CH_3) ppm. $^{13}C\{^1H\}$ NMR (75 MHz, CD_3CN, 25 °C, TMS): δ = 174.74 (C=O), 145.96 (C), 143.85 (C), 135.65 (C), 128.30 (CH), 54.96, 54.17, 53.47, 53.16, 47.53 (all CH_2), 34.53 [$C(CH_3)_3$], 31.55 [$C(CH_3)$], 23.12 ($COCH_3$), 6.87 ($ArCH_2NCH_2CH_3$), 4.58 (NCH_2CH_3). The tetraphenylborate salt, $[(L^{Et})Zn_2(OAc)]BPh_4$ (**14**·BPh_4), was prepared by adding $NaBPh_4$ (342 mg, 1.00 mmol) to a solution of $[(L^{Et})Zn_2(OAc)]ClO_4$ (104 mg, 0.100 mmol) in methanol (50 mL). The colorless, microcrystalline solid was isolated by filtration, washed with methanol and dried in air. Yield: 115 mg (91%). M.p. 246–248 °C (decomp.). IR (KBr): $\tilde{\nu}$ = 1582 s $\nu_{asym}(OAc^-)$, 1440 s $\nu_{sym}(OAc^-)$, 703, 732 $\nu(BPh_4^-)$ cm^{-1}. $C_{70}H_{99}BN_6O_2S_2Zn_2$ (1262.30): calcd. C 66.60, H 7.91, N 6.66, S 5.08; found C 66.89, H 7.85, N 6.45, S 4.84. Compound **14**·ClO_4 was also characterized by X-ray crystal structure analysis.

$[(L^{Et})Co_2(\mu\text{-}Cl)]ClO_4$ (17·ClO_4): To a suspension of H_2L^{Et}·6HCl (974 mg, 1.00 mmol) in methanol (40 mL) was added a solution of $CoCl_2$·$6H_2O$ (476 mg, 2.00 mmol) in methanol (2 mL). A solution of Et_3N (810 mg, 8.00 mmol) in methanol (2 mL) was then added to give a dark red solution. After stirring at room temperature for 3 d, the product was precipitated by the addition of solid $LiClO_4$·$3H_2O$ (2.50 g, 15.6 mmol). The red microcrystalline solid was isolated by filtration, washed with 5 mL of cold ethanol and 5 mL of ether, and dried in vacuo. This material was recrystallized once from a few milliliters of acetonitrile. Yield: 765 mg (76%). M.p. 313 °C (decomp.). IR (KBr): $\tilde{\nu}$ = 3443 s, 2963 vs, 2867 s, 2354 vw, 1730 vw, 1696 vw, 1634 w, 1556 vw, 1540 vw, 1518 vw, 1478 s, 1463 s, 1382 m, 1327 w, 1278 vw, 1251 w, 1231 w, 1202 vw, 1159 m, 1099 vs $\nu(ClO_4^-)$, 987 vw, 956 vw, 913 vw, 884 w, 803 vw, 776 m, 732 vw, 674 vw, 624 m cm^{-1}. UV/Vis (CH_3CN): λ_{max} (ε) = 342 (2401), 470 (602), 548 sh (174), 578 (161), 1280 nm (28 M^{-1} cm^{-1}). $C_{44}H_{76}Cl_2Co_2N_6O_4S_2$·$H_2O$ (1006.01 + 18.02): calcd. C 51.61, H 7.68, N 8.21, S 6.26; found C 51.20, H 7.39, N 8.37, S 6.25.

$[(L^{Et})Co_2(OAc)]ClO_4$ (18·ClO_4): A solution of sodium acetate (41 mg, 0.50 mmol) in methanol (5 mL) was added to a solution of $[(L^{Et})Co_2(\mu\text{-}Cl)]ClO_4$ (202 mg, 0.200 mmol) in methanol (40 mL). The mixture was stirred for 1 h, during which the color of the solution turned to light brown. A solution of $LiClO_4$·$3H_2O$ (320 mg, 2.00 mmol) in methanol (2 mL) was added. The resulting light brown solid was isolated by filtration, washed with cold methanol and dried in air. This compound was recrystallized once from a mixed acetonitrile/ethanol (1:1) solvent system. Yield: 152 mg (74%). M.p. 337–338 °C (decomp.). IR (KBr): $\tilde{\nu}$ = 3442 m, 2964 vs, 2898 s, 1588 vs $\nu_{asym}(OAc^-)$, 1440 vs $\nu_{sym}(OAc^-)$, 1384 s, 1361 m, 1326 w, 1314 w, 1249 w, 1230 s, 1187 vw, 1152 m, 1100 vs $\nu(ClO_4^-)$, 1055 s, 986 w, 948 w, 928 w, 906 w, 880 w, 783 m, 755 vw, 653 w, 626 s cm^{-1}. UV/Vis (CH_3CN): λ_{max} (ε) = 338 (2203), 440 (610), 528 (204), 1288 nm (44 M^{-1} cm^{-1}). CV (CH_3CN, 295 K, 0.1 M nBu_4NPF_6, ν = 100 mV/s; E (vs. SCE): $E^1_{1/2}$ = +0.27 V (ΔE_p = 0.126 V), $E^2_{1/2}$ = +0.64 V (ΔE_p = 0.131 V). The tetraphenylborate salt, $[(L^{Et})Co_2(OAc)]$ BPh_4 (**18**·BPh_4), was prepared by adding $NaBPh_4$ (342 mg, 1.00 mmol) to a solution of $[(L^{Et})Co_2(\mu\text{-}O_2CCH_3)]$ ClO_4 (103 mg, 0.100 mmol) in methanol (50 mL). The light brown microcrystalline solid was isolated by filtration, washed with methanol and dried in air. Yield: 113 mg (90%). M.p. 318–319 °C (decomp.). IR (KBr): $\tilde{\nu}$ = 3437 m, 3055 s ν(Ar), 2968 vs, 2866 s, 1582 vs $\nu_{asym}(OAc^-)$, 1440 vs $\nu_{sym}(OAc^-)$, 1383 m, 1326 w, 1310 w, 1248 w, 1231 w, 1185 vw, 1154 w, 1100 m, 1057 vs, 1033 w, 987 vw, 951 vw, 909 w, 882 w, 844 vw, 780 m, 732 s $\nu(BPh_4^-)$, 704 vs $\nu(BPh_4^-)$, 653 vw, 626 w, 612 m, 579 vw, 557 vw cm^{-1}. UV/Vis (CH_3CN): λ_{max} (ε) = 442 (597), 528 (196), 1294 nm (43 M^{-1} cm^{-1}). $C_{70}H_{99}BCo_2N_6O_2S_2$ (1249.38): calcd. C 67.29, H 7.99, N 6.73, S 5.13; found C 66.96, H 7.73, N 7.03, S 4.95.

Crystal Structure Determinations: Single crystals of $[(L^{Pr})Ni_2(OAc)]$·ClO_4·MeOH (**10**·ClO_4·MeOH), $[(HL^{Et})Ni_2]$·$3ClO_4$·3MeOH·H_2O (**13**·$3ClO_4$·3MeOH·H_2O) and $[(L^{Et})Zn_2(OAc)]$·ClO_4·MeOH

Table 4. Crystallographic data for complexes **10**, **12**, **13**, **14**, and **18**.

Compound	**10**·ClO_4·MeOH	**12**·BPh_4·MeCN·EtOH	**13**·$(ClO_4)_3$·3MeOH·H_2O	**14**·ClO_4·2MeOH	**18**·BPh_4·EtOH
Empirical formula	$C_{53}H_{95}ClN_6Ni_2O_7S_2$	$C_{75}H_{110}BN_7Ni_2O_4S_2$	$C_{47}H_{91}Cl_3N_6Ni_2O_{16}S_2$	$C_{47}H_{83}ClN_6O_7S_2Zn_2$	$C_{72}H_{102}BCo_2N_7O_2S_2$
M_r [g/mol]	1145.34	1366.05	1284.15	1074.50	1290.40
Space group	$P2_1/n$	$P2_1/n$	$P\bar{1}$	$C2/c$	$P2_1/c$
a [Å]	14.810(3)	16.346(3)	13.551(3)	16.385(3)	15.734(3)
b [Å]	20.793(4)	29.155(6)	14.076(3)	29.778(6)	26.293(5)
c [Å]	21.376(4)	16.945(3)	16.661(3)	13.310(3)	18.319(4)
α [°]	90	90	77.77(3)	90	90.00
β [°]	108.78(3)	114.22(3)	89.92(3)	123.56(3)	112.14(3)
γ [°]	90	90	75.24(3)	90	90.00
V [Å^3]	6232(2)	7365(2)	2999(1)	5412(2)	7019.7(24)
Z	4	4	2	4	4
$d_{calcd.}$ [g/cm^3]	1.221	1.232	1.421	1.358	1.221
Crystal size [mm]	0.45×0.30×0.30	0.30×0.15×0.15	0.20×0.20×0.20	0.35×0.26×0.18	0.30×0.20×0.20
μ(Mo-K_α) [mm^{-1}]	0.764	0.620	0.899	1.064	0.580
2θ limits [°]	3.50–56.76	2.80–56.66	3.06–56.62	4.58–56.70	2.80–56.62
Measured reflections	39885	46840	27268	17437	44376
Independent reflections	15063	17670	14028	6519	16817
Observed reflections[a]	3609	8078	7533	2860	6415
Number of parameters	604	791	697	341	748
$R1$[b] ($R1$ all data)	0.0774 (0.2867)	0.0779 (0.1497)	0.0540 (0.1117)	0.0434 (0.1373)	0.0717 (0.1676)
$wR2$[c] ($wR2$ all data)	0.1928 (0.2636)	0.1966 (0.2369)	0.1229 (0.1529)	0.0858 (0.1133)	0.1805 (0.2100)
Max/min peaks [e/Å^3]	1.237/–0.653	1.129/–1.888	0.770/–0.742	0.386/–0.523	1.583/–0.672

[a] Observation criterion: $I > 2\sigma(I)$. [b] $R1 = \Sigma||F_o| - |F_c||/\Sigma|F_o|$. [c] $wR2 = \{\Sigma[w(F_o^2 - F_c^2)^2]/\Sigma[w(F_o^2)^2]\}^{1/2}$.

 © 2005 Wiley-VCH Verlag GmbH & Co. KGaA, Weinheim

(**14**·ClO_4·MeOH) were taken directly from the reaction mixtures. Crystals of [(L^{Et})Ni_2(O_2COEt)]BPh_4·MeCN·EtOH (**12**·BPh_4·MeCN·EtOH) and [(L^{Et})Co_2(OAc)]BPh_4·EtOH (**18**·BPh_4·EtOH) were grown by recrystallization from an acetonitrile/ethanol (1:1) mixed solvent system. The crystals were mounted on glass fibers using perfluoropolyether oil. Intensity data were collected at 210(2) K, using a Bruker SMART CCD diffractometer. Graphite-monochromated Mo-K_α radiation (λ = 0.71073 Å) was used throughout. Crystallographic data of the compounds are listed in Table 4. The data were processed with SAINT[30] and corrected for absorption using SADABS[31] [transmission factors: 1.00–0.92 (**10**, **13**), 1.00–0.89 (**12**, **18**), 1.00–0.87 (**14**)]. The structures were solved by using the program SHELXS-86.[32] Refinements were carried out with the program SHELXL-97.[33] PLATON was used to search for higher symmetry.[34] ORTEP-3 was used for the artwork of the structures.[35] Where appropriate, all non-hydrogen atoms were refined anisotropically. Hydrogen atoms were assigned to idealized positions and given isotropic thermal parameters 1.2 times (1.5 times for CH_3 groups) the thermal parameter of the atoms to which they were attached. In the crystal structure of **10**·ClO_4·MeOH a propyl group, a *tert*-butyl group and a ClO_4^- ion were found to be disordered over two positions. The site occupancies of the respective positions were refined as follows: C(18a)–C(20A)/C(18b)–C(20b) 0.50(2)/0.50(2); C(48a)–C(50a)/C(48b)–C(50b): 0.55(2)/0.45(2); O(3a)–O(6a)/O(3b)–O(6b) 0.70(1)/0.30(1). The C and O atoms of the disordered groups and the solvate molecules were refined isotropically. In the crystal structure of **12**·BPh_4·MeCN·EtOH the C, N, and O atoms of the solvate molecules were refined isotropically. In the crystal structure of **13**·3ClO_4·3MeOH·H_2O one *tert*-butyl group and two methanol molecules of solvent of crystallization were found to be disordered over two positions [C(42a)–C(44a)/C(42b)–C(44b) 0.53(2)/0.47(2); O(14)–C(45a)/O(14)–C(45b) 0.57(2)/0.43(2), and O(15a)–C(46a)/O(15b)–C(46b) 0.47(2)/0.53(2)]. In the crystal structure of **14**·ClO_4·MeOH a *tert*-butyl group and the counteranion were found to be disordered over two positions [C(20a)–C(22a)/C(20b)–C(22b) 0.47(2)/0.53(2); O(2a),O(3a)/(O2b),O(3b) 0.71(2)/0.29(2)]. In the crystal structure of **18**·BPh_4·EtOH one *tert*-butyl group was found to be disordered over two positions at site occupancies of 0.53(2) [C(42a)-C(44a)] and of 0.47(2) [C(42b)-C(44b)]. The C and O atoms of the solvate molecule and the disordered groups were refined isotropically. CCDC-259281 (**10**), -259282 (**12**), -259283 (**13**), -259284 (**14**) and -259285 (**18**) contains the supplementary crystallographic data for this paper. These data can be obtained free of charge from The Cambridge Crystallographic Data Centre via www.ccdc.cam.ac.uk/data_request/cif.

Acknowledgments

We are particularly grateful to Prof. Dr. H. Vahrenkamp for providing facilities for NMR and X-ray crystallographic measurements. Financial support of this work from the Deutsche Forschungsgemeinschaft (Priority programme "Sekundäre Wechselwirkungen", KE 585/3-1,2) is gratefully acknowledged.

[1] J. W. Canary, B. C. Gibb, *Prog. Inorg. Chem.* **1997**, *45*, 1–83.
[2] a) B. R. Cameron, S. J. Loeb, G. P. A. Yap, *Inorg. Chem.* **1997**, *36*, 5498–5504; b) B. S. Hammes, D. Ramos-Maldonado, G. P. A. Yap, L. Liable-Sands, A. L. Rheingold, V. G. Young, Jr., A. S. Borovik, *Inorg. Chem.* **1997**, *36*, 3210–3211.
[3] a) S. Blanchard, L. Le Clainche, M.-N. Rager, B. Chansou, J.-P. Tuchagues, A. F. Duprat, Y. Le Mest, O. Reinaud, *Angew. Chem.* **1998**, *110*, 2861–2864; *Angew. Chem. Int. Ed. Engl.* **1998**, *37*, 2732–2735; b) Y. Rondelez, G. Bertho, O. Reinaud, *Angew. Chem.* **2002**, *114*, 1086–1088; *Angew. Chem. Int. Ed.* **2002**, *41*, 1044–1046.
[4] a) M. T. Reetz, S. R. Waldvogel, *Angew. Chem.* **1997**, *109*, 870–873; *Angew. Chem. Int. Ed. Engl.* **1997**, *36*, 865–867; b) M. T. Reetz, *Catal. Today* **1998**, *42*, 399.
[5] For reviews of cyclodextrins, see: *Chem. Rev.* **1998**, *98*, 1741–2076 (special issue).
[6] a) N. Kitajima, W. B. Tolman, *Prog. Inorg. Chem.* **1995**, *43*, 419–531; b) S. Trofimenko, *Scorpionates: The Coordination Chemistry of Polypyrazolylborate Ligands*; Imperial College Press, London, U. K., **1999**; c) H. Vahrenkamp, *Acc. Chem. Res.* **1999**, *32*, 589–596.
[7] P. Chaudhuri, K. Wieghardt, *Prog. Inorg. Chem.* **1987**, *35*, 329–436.
[8] N. H. Pilkington, R. Robson, *Aust. J. Chem.* **1970**, *23*, 2225–2236.
[9] a) M. H. Klingele, G. Steinfeld, B. Kersting, *Z. Naturforsch.* **2001**, *56b*, 901–907; b) B. Kersting, G. Steinfeld, *Inorg. Chem.* **2002**, *41*, 1140–1150; c) B. Kersting, *Z. Allg. Anorg. Chem.* **2004**, *630*, 765–780.
[10] B. Kersting, G. Steinfeld, *Chem. Commun.* **2001**, 1376–1377.
[11] B. Kersting, *Angew. Chem.* **2001**, *113*, 4109–4112; *Angew. Chem. Int. Ed.* **2001**, *40*, 3987–3990.
[12] G. Steinfeld, V. Lozan, B. Kersting, *Angew. Chem.* **2003**, *115*, 2363–2365; *Angew. Chem. Int. Ed.* **2003**, *42*, 2261–2263.
[13] K. Wieghardt, P. Chaudhuri, B. Nuber, J. Weiss, *Inorg. Chem.* **1982**, *21*, 3086–90.
[14] N. W. Alcock, A. C. Benninston, S. J. Grant, H. A. A. Omar, P. Moore, *J. Chem. Soc. Chem. Commun.* **1991**, 1573–1575.
[15] B. Kersting, G. Steinfeld, T. Fritz, J. Hausmann, *Eur. J. Inorg. Chem.* **1999**, 2167–2172.
[16] a) M. H. Klingele, G. Steinfeld, B. Kersting, *Z. Naturforsch.* **2001**, *56b*, 901–907; b) G. Siedle, B. Kersting, *Z. Anorg. Allg. Chem.* **2003**, *629*, 2083–2090.
[17] Complex **5**·ClO_4 is also readily dehalogenated with $Pb(ClO_4)_2$. However, the resulting [(HL^{Me})Ni_2]$^{3+}$ intermediate reacts instantaneously with a ClO_4^- anion to give the perchlorate complex [(L^{Me})Ni_2($\mu_{1,3}$-ClO_4)]$^+$. The structure of this compound will be reported elsewhere.
[18] B. Kersting, G. Steinfeld, *Inorg. Chem.* **2002**, *41*, 1140–1150.
[19] For a complete list of the IR absorptions, see Exp. Sect.
[20] K. Nakamoto, *Infrared and Raman Spectra of Inorganic and Coordination Compounds*, 5th ed., Wiley-VCH, New York, **1997**.
[21] a) I. Murase, S. Ueno, S. Kida, *Bull. Chem. Soc. Jpn.* **1983**, *56*, 2748–2751; b) G. A. Lawrance, M. Maeder, T. M. Manning, M. A. O'Leary, B. W. Skelton, A. H. White, *J. Chem. Soc. Dalton Trans.* **1990**, 2491–2495.
[22] M. D. Santana, G. Garcia, J. Perez, E. Molins, G. Lopez, *Inorg. Chem.* **2001**, *40*, 5701–5703.
[23] The high-spin d^7 configuration for the present cobalt(II) complexes is also supported by temperature-dependent magnetic susceptibility measurements. The results of these studies will be reported in due course.
[24] J. Hausmann, S. Käss, S. Klod, E. Kleinpeter, B. Kersting, *Eur. J. Inorg. Chem.* **2004**, 4402–4411.
[25] D. A. House, *Comprehensive Coordination Chemistry* (Eds.: G. Wilkinson, R. D. Gillard, J. A. McCleverty), Pergamon Press, Oxford, **1996**, vol. 2, p. 23–72.
[26] a) D. K. Mills, J. H. Reibenspies, M. Y. Darensbourg, *Inorg. Chem.* **1990**, *29*, 4364–4366; b) D. K. Mills, Y. M. Hsiao, P. J. Farmer, E. V. Atnip, J. H. Reibenspies, M. Y. Darensbourg, *J. Am. Chem. Soc.* **1991**, *113*, 1421–1423; c) R. M. Buonomo, I. Font, M. J. Maguire, J. H. Reibenspies, T. Tuntulani, M. J. Darensbourg, *J. Am. Chem. Soc.* **1995**, *117*, 963–973.
[27] C. A. Grapperhaus, M. J. Maguire, T. Tuntulani, M. Y. Darensbourg, *Inorg. Chem.* **1997**, *36*, 1860–1866.
[28] a) N. Baidya, M. M. Olmstead, P. K. Mascharak, *Inorg. Chem.* **1991**, *30*, 929–937; b) N. Baidya, M. M. Olmstead, J. P. White-

 © 2005 Wiley-VCH Verlag GmbH & Co. KGaA, Weinheim

head, C. Bagyinka, M. J. Maroney, P. K. Mascharak, *Inorg. Chem.* **1992**, *31*, 3612–3619.
[29] C. A. Marganian, H. Vazir, N. Baidya, M. M. Olmstead, P. K. Mascharak, *J. Am. Chem. Soc.* **1995**, *117*, 1584–1594.
[30] *SAINT+*, V6.02, Bruker AXS, Madison, WI, **1999**.
[31] *SADABS, An empirical absorption correction program*, part of SAINTPlus NT, version 5.10, Bruker AXS, Madison, WI, **1998**.
[32] G. M. Sheldrick, *Acta Crystallogr., Sect. A* **1990**, *46*, 467–473.
[33] G. M. Sheldrick, *SHELXL-97, Computer program for crystal structure refinement*, University of Göttingen, Göttingen, Germany, **1997**.
[34] A. L. Spek, *PLATON – A Multipurpose Crystallographic Tool*, Utrecht University, Utrecht, The Netherlands, **2000**.
[35] L. J. Farrugia, *J. Appl. Crystallogr.* **1997**, *30*, 565–568..
Received January 10, 2005

 © 2005 Wiley-VCH Verlag GmbH & Co. KGaA, Weinheim

Crystallographic and Electrochemical Characteristics of $La_{0.7}Mg_{0.3}Ni_{4.5-x}(Al_{0.5}Mo_{0.5})_x$ (x = 0–0.8) Hydrogen Storage Alloys

Xin-Bo Zhang,[a] Dan-Zi Sun,[b] Wen-Ya Yin,[a] Yu-Jun Chai,[a] and Min-Shou Zhao,*[a]

Keywords: High-rate dischargeability / Low-temperature dischargeability / Exchange current density / Hydrogen diffusion coefficient / Alloys / X-ray diffraction

The structure, hydrogen storage property, and electrochemical characteristics of the $La_{0.7}Mg_{0.3}Ni_{4.5-x}(Al_{0.5}Mo_{0.5})_x$ (x = 0, 0.2, 0.4, 0.6, 0.8) hydrogen storage alloys have been investigated systematically. The X-ray powder diffraction and Rietveld analysis results reveal that all the alloys mainly consist of the La(La, Mg)$_2$Ni$_9$ phase and the $LaNi_5$ phase. The electrochemical measurements show that the maximum discharge capacity increases first from 246.3 (x = 0) to 345.4 mAh/g (x = 0.6) and then decreases to 317.6 mAh/g (x = 0.8), which is consistent with the variation of the hydrogen storage capacity indicated by the P-C isotherms. For the discharge current density of 1200 mA/g, the high-rate dischargeability of the alloy electrodes increases linearly from 47.2 % (x = 0) to 73.8 % (x = 0.8). Moreover, according to the linear polarization curves, the exchange current density of the alloy electrodes also increases monotonously with increasing x. The hydrogen diffusion coefficient increases with increasing Al and Mo content, and thus increases the low-temperature dischargeability of the alloy electrodes.

(© Wiley-VCH Verlag GmbH & Co. KGaA, 69451 Weinheim, Germany, 2005)

Introduction

Hydrogen storage alloys have attracted considerable attention in view of their potential as a new energy storage material. Recently, the nickel-metal hydride battery (Ni-MH), in which a hydrogen storage alloy is employed as a negative electrode material, has become the focus of interest as a candidate consumer-used battery by virtue of its several advantages: high reversible energy storage density, high resistance to overcharging and overdischarging, good charge/discharge kinetics, environmental compatibility, and interchangeability with the nickel-cadmium battery.[1–6] To date, almost all commercial Ni-MH batteries are employing AB_5-type alloys as negative electrode materials because of their good overall electrode properties.[7] However, the electrochemical capacity of the AB_5-type alloys is limited by the single $CaCu_5$-type hexagonal structure;[8] the energy densities of the Ni-MH batteries cannot compete favorably with some other advanced secondary batteries. Therefore, new types of alloys with higher energy densities, faster activation, better rate dischargeabilities, and lower cost are urgently needed to replace the conventional rare-earth-based AB_5-type alloys.[9]

Recently, Kadir et al.[10–12] have reported the discovery of a new type of ternary alloys with the general formula RMg_2Ni_9 (R: rare earth, Ca, Y) with $PuNi_3$-type structure. It is found that some of the R–Mg–Ni-based ternary alloys can absorb–desorb 1.8–1.87 wt.-% H_2, which is much more than the $LaNi_5$ alloys (which can only absorb 1.4 wt.-% H_2), and are thus regarded as promising candidates for reversible gaseous hydrogen storage.[13,14] As for their electrochemical hydrogen storage, Chen et al.[6] have studied the electrochemical characteristics of LaCaMg(Ni, M)$_9$ [M = Al, Mn] alloys, and almost at the same time, Kohno et al.[3] have reported that the discharge capacity of the $La_{0.7}Mg_{0.3}Ni_{2.8}Co_{0.5}$ alloy reached 410 mAh/g. However, up to now, the La–Mg–Ni–Co-system hydrogen storage electrode alloys could not be used as the negative material of the Ni-MH secondary batteries due to their serious corrosion in KOH electrolyte,[15] and hence their cycling stability had to be upgraded for practical applications. In commercial AB_5-type alloys, the presence of 10 wt.-% Co has indeed improved the cycling life of Ni-MH batteries. However, it negatively influences the discharge capacity as well as initial activation, and it constitutes about 40% of the material cost.[16] Much effort has been devoted to search for a more cost-effective substitute element with high reliability of improving the cycling life of Ni-MH batteries. It is believed that Al is one of the best candidates for cobalt substitution.[17] However, the addition of Al is detrimental to the diffusion of hydrogen from the electrode surface to the alloy bulk, and thus inevitably decreases the high-rate dischargeability of the alloy electrode.[2] It is reported that the

[a] Key Laboratory of Rare Earth Chemistry and Physics, Changchun Institute of Applied Chemistry, Chinese Academy of Sciences, Graduate School of Chinese Academy of Sciences, Changchun 130022, P. R. China
E-mail: eboat@ciac.jl.cn
[b] State Key Laboratory of Electro-analytical Chemistry, Changchun Institute of Applied Chemistry, Chinese Academy of Sciences, Graduate School of Chinese Academy of Sciences, Changchun 130022, P. R. China

addition of Mo can remarkably increase the kinetic property[18] as well as the electrochemical capacity of the alloy electrode.[19] Therefore, it can be expected that the overall electrochemical properties of the La–Mg–Ni-type hydrogen storage alloys could be improved by substitution of Al and Mo for Ni in the alloys.

In this work, on the basis of our previous studies and the belief that the Al and Mo addition may result in some noticeable modifications, the structure and electrochemical characteristics of the $La_{0.7}Mg_{0.3}Ni_{4.5-x}(Al_{0.5}Mo_{0.5})_x$ (x = 0–0.8) hydrogen storage alloys has been investigated systematically.

Results and Discussion

Alloy Composition and Structure Characteristics

It is well known that the low-melting Mg metal will inevitably be lost during the sample preparation by arc melting. We have tried many ways to overcome this problem, for example, by using an Mg–Ni master alloy as an Mg additive, by decreasing the melting current, by adding a slight excess of Mg over sample composition, and so on. Among all these methods, we found that the latter is the most effective way to compensate evaporative loss of Mg. Several attempts were made until the optimum preparative conditions were found. In this paper, the weight lost during sample preparation is almost the same as excess Mg added. The results of the ICP-AES analysis for all compounds are given in Table 1. It can be seen that the final composition of all the alloys is identical to the original composition.

Table 1. Composition of the $La_{0.7}Mg_{0.3}Ni_{4.0-x}(Al_{0.5}Mo_{0.5})_x$ (x = 0–0.8) alloys.

Sample	La [mg/g]	Mg [mg/g]	Ni [mg/g]	Al [mg/g]	Co [mg/g]	La:Mg:Ni:Al:Mo[a]
x = 0.0	263.74	19.78	716.47	0	0	1.90:0.81:12.21:0:0
x = 0.2	263.35	19.75	683.61	7.31	25.98	1.90:0.81:11.65:0.27:0.27
x = 0.4	262.96	19.72	650.84	14.59	51.89	1.89:0.81:11.09:0.54:0.54
x = 0.6	262.56	19.69	618.17	21.86	77.72	1.89:0.81:10.53:0.81:0.81
x = 0.8	262.17	19.66	585.59	29.10	103.47	1.89:0.81:9.98:1.08:1.08

[a] Atomic ratio.

The crystal structures have been identified and refined by means of X-ray powder diffraction data. Figure 1 shows the Rietveld refinement pattern of the XRD profiles for the $La_{0.7}Mg_{0.3}Ni_{4.3}(Al_{0.5}Mo_{0.5})_{0.2}$ hydrogen storage alloy as a representative example of the $La_{0.7}Mg_{0.3}Ni_{4.5-x}(Al_{0.5}Mo_{0.5})_x$ (x = 0, 0.2, 0.4, 0.6, 0.8) hydrogen storage alloys. The results show that, besides an impurity Ni phase, the $La_{0.7}Mg_{0.3}Ni_{4.3}(Al_{0.5}Mo_{0.5})_{0.2}$ alloy mainly consists of two phases: a La_2MgNi_9 phase with a $PuNi_3$-type rhombohedral structure and a $LaNi_5$ phase with a $CaCu_5$-type hexagonal structure. The final Rietveld structure parameters of the La_2MgNi_9 phase are tabulated in Table 2. It can be easily found that the La atoms in La_2MgNi_9 are located not only at the 3a site (the Pu1 atom position of the $PuNi_3$ structure), but also at the 6c sites (the Pu2 atom position of the $PuNi_3$ structure), while the Mg atoms in the alloy exhibit a strong preference for the 6c site, which indicates that the alloy is an ordered compound with the same structure as the previously reported RMg_2Ni_9 (R = La, Ca, Y) alloys. Hence, the final formula of the La_2MgNi_9 phase can be designated as $La(La, Mg)_2Ni_9$. The characteristics of the alloy phases in the $La_{0.7}Mg_{0.3}Ni_{4.5-x}(Al_{0.5}Mo_{0.5})_x$ (x = 0–0.8) alloys are listed in Table 3. We find that all the alloys consist of an impurity Ni phase and two other main crystallographic phases, namely, the $La(La, Mg)_2Ni_9$ phase and the $LaNi_5$ phase. In addition, variations of the cell parameters and volume of the two main phases as a function of x in $La_{0.7}Mg_{0.3}Ni_{4.5-x}(Al_{0.5}Mo_{0.5})_x$ alloys is shown in Figure 2. It can be seen that the parameters a and c of both the $La(La, Mg)_2Ni_9$ phase and the $LaNi_5$ phase in the alloys increase linearly with an increase in x, which is mainly ascribed to the fact that the atomic radius of Al (1.432 Å) and Mo (1.363 Å) is larger than that of Ni (1.246 Å). Figure 3 shows the abundance of the $La(La, Mg)_2Ni_9$ phase and the $LaNi_5$ phase as a function of x in the alloys. As can be seen in Figure 3 and Table 3, it can be seen that the $La(La, Mg)_2Ni_9$ phase abundance decreases from 39.21% to 29.79% with increasing x, while the $LaNi_5$ phase abundance increases from 60.34% to 70.07%. These results may influence the hydrogen storage and electrochemical characteristics of the alloys studied.

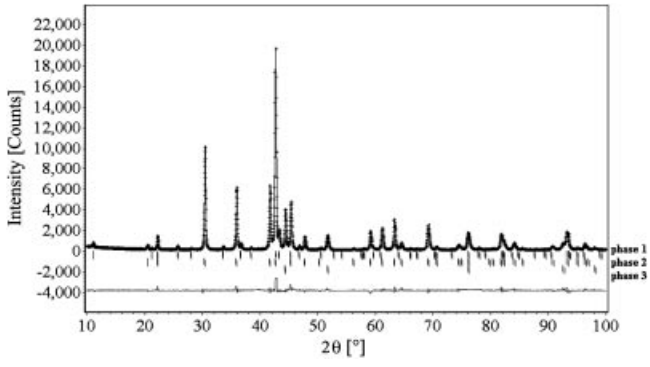

Figure 1. Rietveld refinement pattern of the XRD profiles for the $La_{0.7}Mg_{0.3}Ni_{4.3}(Al_{0.5}Mo_{0.5})_{0.2}$ hydrogen storage alloy (Phase 1: $La(La, Mg)_2Ni_9$; phase 2: $LaNi_5$; phase 3: Ni).

Table 2. Crystallographic parameters for La_2MgNi_9 by using X-ray diffraction Cu-$K_{\alpha 1}$ (λ = 1.5405981 Å) at 298 K with a space group of $R\bar{3}m$ and Z = 3.[a]

Atom	Site	Metal atom position			Occupancy
		x	y	z	
La1	3a	0	0	0	1
La2	6c	0	0	0.1427(2)	0.476
Mg1	6c	0	0	0.1427(2)	0.524
Ni1	6c	0	0	0.3311(2)	1
Ni2	3b	0	0	0.5	1
Ni3	18h	0.4996(5)	0.5004(5)	0.0855(6)	1

[a] Structure was refined by using the Rietveld refinement program Rietica. The pattern factor is 6.2, the weighted pattern factor is 8.1, and the goodness of fit S = 2.0.

 © 2005 Wiley-VCH Verlag GmbH & Co. KGaA, Weinheim

Table 3. Characteristics of alloy phases in $La_{0.7}Mg_{0.3}Ni_{4.5-x}(Al_{0.5}Mo_{0.5})_x$ (x = 0–0.8) alloys.

Samples	Phases	Phase abundance (wt.-%)	Lattice parameter [Å]			Cell volume [Å]
			A	*b*	*c*	
	$La(La, Mg)_2Ni_9$	39.21	4.989	4.989	24.093	519.34
x = 0.0	$LaNi_5$	60.34	5.064	5.064	4.025	89.39
	Ni	0.45	3.536	3.536	3.536	44.21
	$La(La, Mg)_2Ni_9$	36.85	5.013	5.013	24.369	530.35
x = 0.2	$LaNi_5$	62.90	5.073	5.073	4.042	90.09
	Ni	0.25	3.545	3.545	3.545	44.55
	$La(La, Mg)_2Ni_9$	33.59	5.043	5.043	24.410	537.62
x = 0.4	$LaNi_5$	65.83	5.078	5.078	4.045	90.33
	Ni	0.58	3.548	3.548	3.548	44.66
	$La(La, Mg)_2Ni_9$	32.41	5.077	5.077	24.622	549.63
x = 0.6	$LaNi_5$	67.32	5.091	5.091	4.070	91.35
	Ni	0.27	3.561	3.561	3.561	45.16
	$La(La, Mg)_2Ni_9$	29.79	5.124	5.124	24.713	561.92
x = 0.8	$LaNi_5$	70.07	5.097	5.097	4.078	91.75
	Ni	0.14	3.572	3.572	3.572	45.58

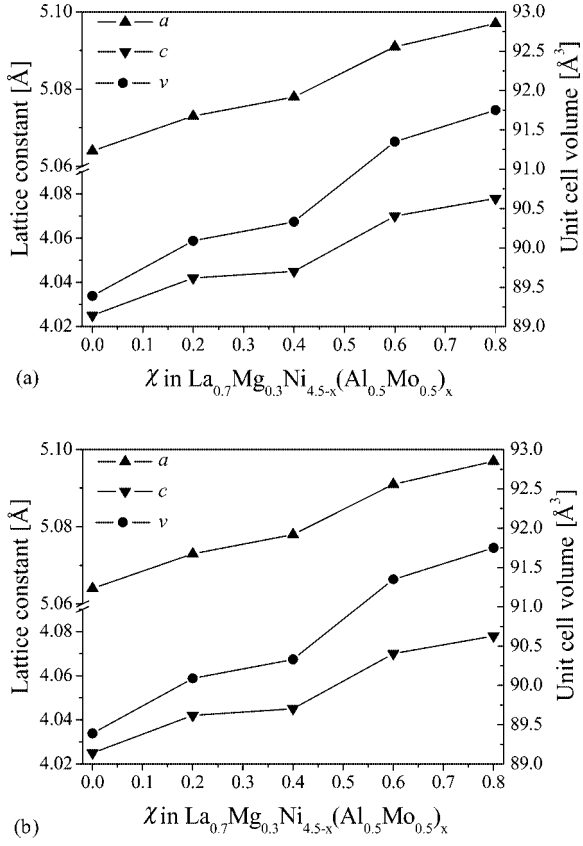

Figure 2. Variations of the cell parameters and volumes as a function of x in $La_{0.7}Mg_{0.3}Ni_{4.5-x}(Al_{0.5}Mo_{0.5})_x$ alloys (x = 0–0.8) (a) $La(La, Mg)_2Ni_9$ phase; (b) $LaNi_5$ phase.

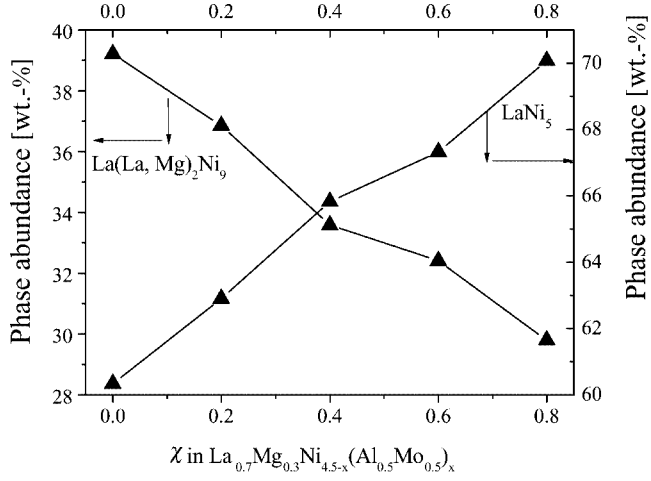

Figure 3. Phase abundance of the $La(La, Mg)_2Ni_9$ phase and the $LaNi_5$ phase existing in the $La_{0.7}Mg_{0.3}Ni_{4.5-x}(Al_{0.5}Mo_{0.5})x$ (x = 0–0.8) alloys.

P-C Isotherms

The electrochemical pressure-composition isotherm method is very useful for examining the charging and discharging levels of hydrogen in an anode, although the calculated pressures pertain to a quasi-equilibrium state.[17] Figure 4 shows the electrochemical P-C isotherms for $La_{0.7}Mg_{0.3}Ni_{4.5-x}(Al_{0.5}Mo_{0.5})_x$ (x = 0–0.8) alloy electrodes at 298 K. It can be seen that desorption pressure decreases continually as the addition of Al and Mo increases, which indicates that the stability of the hydrides of the alloys increases with the increasing Al and Mo content. The phenomenon observed here is consistent with those reported previously for AB_3 alloys[14] and most AB_5 alloys.[20] Moreover, it can be seen that there is only one plateau in each P-C curve as shown in Figure 4. Since the unit cell of the AB_3 compounds contains one-third of the AB_5 structure and two-thirds of the AB_2 structure,[6] it is perhaps concluded that the plateau pressure of the $La(La, Mg)_2Ni_9$ phase is similar to that of the $LaNi_5$ phase or that the difference between their plateau pressures of the AB_3 and AB_5 compounds is too small to be observed. With regard to the hydrogen storage capacity, it increases from 0.616 to 0.868 wt.-% as x increases from 0 to 0.6. This is mainly attributed to the enhancement of the intrinsic hydrogen storage capacity of the alloy, which results from the decrease in plateau pressure. However, as x increases further, the hydrogen storage capacity decreases to 0.799 wt.-% when x reaches 0.8. This is mainly attributed to the reasons

 © 2005 Wiley-VCH Verlag GmbH & Co. KGaA, Weinheim

as follows: it is known that the hydrogen storage capacity of the $LaNi_3$ phase (1.8–1.87 wt.-% H_2) is larger than that of the $LaNi_5$ phase (1.4 wt.-% H_2).[13–14] However, as shown in Figure 3 and Table 3, the La(La, $Mg)_2Ni_9$ phase abundance decreases while the $LaNi_5$ phase abundance increases with increasing x in the alloys.

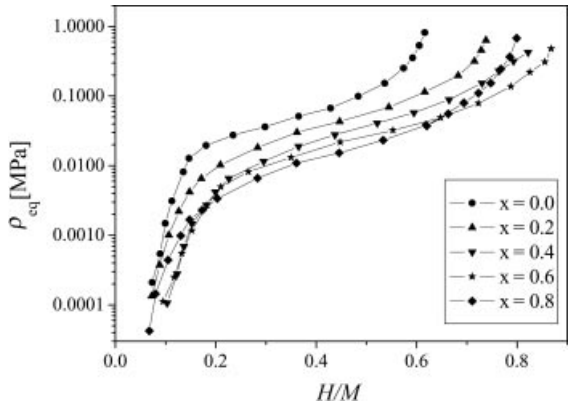

Figure 4. Electrochemical desorption P-C curves for the $La_{0.7}Mg_{0.3}Ni_{4.5-x}(Al_{0.5}Mo_{0.5})_x$ (x = 0, 0.2, 0.4, 0.6, 0.8) alloys at 298 K.

Discharge Capacity and Discharge Potential

The activation and maximum discharge capacity of the $La_{0.7}Mg_{0.3}Ni_{4.5-x}(Al_{0.5}Mo_{0.5})_x$ (x = 0–0.8) alloy electrodes are listed in Table 4. It can be seen that all these alloys can be easily activated to reach the maximum capacity within five cycles. The maximum discharge capacity C_{max} improves first and reaches a maximum at x = 0.6, and then decreases as x increases further. The variation of the maximum discharge capacity of the alloys is basically consistent with the variation of the H/M with the Al and Mo content in the alloys.

Table 4. Electrode performance of $La_{0.7}Mg_{0.3}Ni_{4.5-x}(Al_{0.5}Mo_{0.5})_x$ (x = 0–0.8) alloy electrodes.

Sample	H/M	C_{max} [mAh/g]	N_a[a]	HRD_{1200}[b] [%]	S_{70} [%]
x = 0.0	0.616	246.3	5	47.2	54.1
x = 0.2	0.738	294.8	4	50.6	54.7
x = 0.4	0.822	327.6	3	55.8	58.9
x = 0.6	0.868	345.4	2	64.7	62.3
x = 0.8	0.799	317.6	2	73.8	68.9

[a] The cycle numbers needed to activate the electrodes. [b] The high-rate dischargeability at a discharge current density of 1200 mA/g.

Figure 5 shows the discharge curves (fifth cycle) of the $La_{0.7}Mg_{0.3}Ni_{4.5-x}(Al_{0.5}Mo_{0.5})_x$ (x = 0–0.8) alloy electrodes at 60 mA/g and 298 K. Obviously, each curve has a wide discharge potential plateau based on the oxidation of desorbed hydrogen from the hydride. Besides, the discharge plateau shifts towards a more positive potential as Al and Mo addition increases in the alloys. As shown in Figure 5, the mid-discharge potential (potential at 50% depth of discharge) decreases from –0.8710 to –0.8194 V when x increases from 0 to 0.8, which is in good agreement with the reduction of the desorption plateau pressure with increasing Al and Mo content in the alloys.

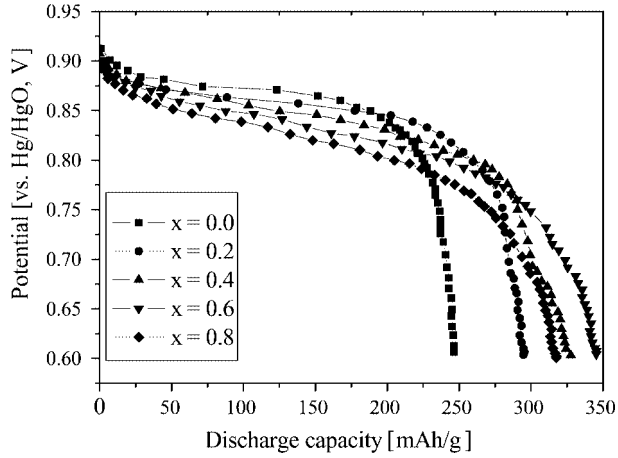

Figure 5. Discharge curves for the $La_{0.7}Mg_{0.3}Ni_{4.5-x}(Al_{0.5}Mo_{0.5})_x$ (x = 0–0.8) alloy electrodes at the discharge current density of 60 mA/g and 298 K.

Cyclic Stability

The cycling capacity retention rate, expressed as S_{70} (%) = C_{70}/C_{max} × 100 (where C_{max} is the maximum discharge capacity, C_{70} is the discharge capacity at the 70th cycle), after 70 cycles at 60 mA/g is also listed in Table 4. It can be seen that the capacity retention rate (S_{70}) increases noticeably from 54.1% to 68.9% as x increases from 0 to 0.8, which indicates that the cyclic stability of the La–Mg–Ni–Al–Mo-system alloys is improved markedly with the increase in Al and Mo content in the alloys. It is known that the capacity degradation of the La–Mg–Ni-type alloy electrode results primarily from two factors: the corrosion of Mg and La and the pulverization of the alloy particles.[20] The Al substitution results in the formation of a protective oxide (hydroxide) of Al on the alloy surface and a subsequent strong protection to the alloy from further corrosion of La and Mg. Moreover, the pulverization of the alloy particles can be improved effectively by substitution of Ni by Mo. In conclusion, the combined effect of the addition of Al and Mo results in the notable increase in the stability of the alloy electrodes. Further investigations in this aspect are going on in our research group.

High-Rate Dischargeability (HRD) and Electrochemical Kinetics

As an important kinetics property of the hydride electrode in batteries, it is very important to restrain the decrease in the discharge capacity even at high discharge cur-

 © 2005 Wiley-VCH Verlag GmbH & Co. KGaA, Weinheim

rent density. Figure 6 shows the relationship between the HRD and the discharge current density of the $La_{0.7}Mg_{0.3}Ni_{4.5-x}(Al_{0.5}Mo_{0.5})_x$ (x = 0–0.8) alloy electrodes. It can be seen that HRD of the alloy electrodes increases monotonously with increasing x. The HRD of the alloy electrodes at a discharge current density of 1200 mA/g are also listed in Table 4. It can be seen that as x increases, the HRD of the alloy electrodes increases from 47.2% (x = 0) to 73.8% (x = 0.8). It is well known that the HRD of metal hydride electrodes is influenced mainly by the electrochemical reaction kinetics on the alloy powder surface and the diffusion rate of hydrogen in the bulk of the alloy.[22] To examine the effect of the partial substitution of Ni by Al and Mo on the discharge kinetics, linear polarization was preformed on these alloy electrodes. Based on the measured linear polarization curves, values of the exchange current density I_0 and polarization resistance R_p were evaluated for the alloy electrodes and are summarized in Table 5. Figure 7 shows HRD and R_p as a function of I_0 for the hydrogen evolution reaction at the alloy electrodes. It can be seen that the HRD is a linear function of I_0. Moreover, we can find that the hydrogen diffusion coefficient (D) remains almost unchanged (13.1–13.6 × 10^{-10} cm^2/s). Iwakura et al.[23] have pointed out that, if the electrochemical reaction on the surface is the rate-determining factor, a linear dependence of the high-rate dischargeability on the exchange current density should be observed. In contrast, if the diffusion of hydrogen in the bulk is the rate-determining factor, the high-rate dischargeability should be constant, irrespective of exchange density. Therefore, in the present study, the HRD is essentially controlled by the charge-transfer reaction of hydrogen on the surface at a discharge current density of 1200 mAh/g. As the same time, from Figure 7, it can be seen that R_p decreases with increasing exchange current density, while HRD shows the reverse trend, which implies that the R_p value is closely related to HRD.

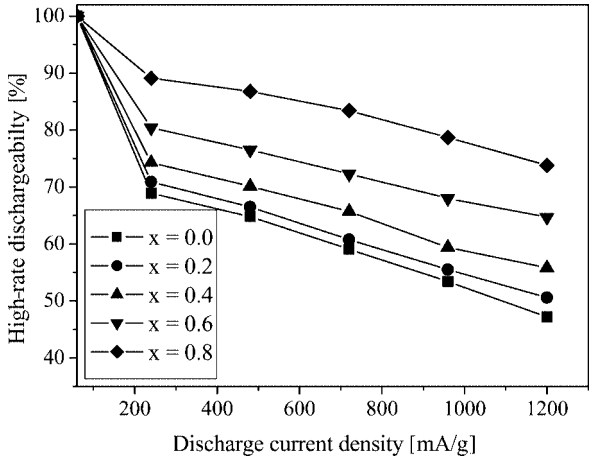

Figure 6. High-rate dischargeability of the $La_{0.7}Mg_{0.3}Ni_{4.5-x}(Al_{0.5}Mo_{0.5})_x$ (x = 0,0.2, 0.4, 0.6, 0.8) alloy electrodes at 298 K.

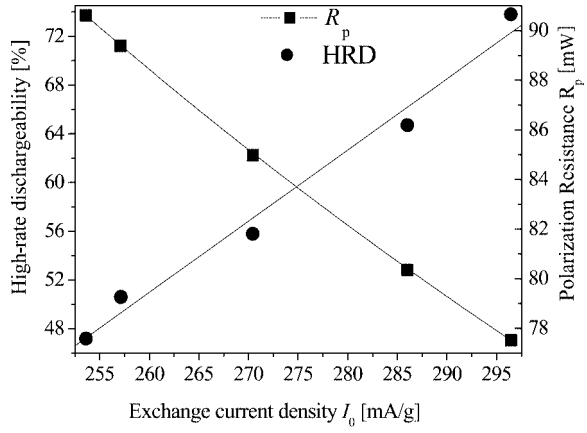

Figure 7. High-rate dischargeability and polarization resistance as a function of exchange current density for hydrogen evolution at $La_{0.7}Mg_{0.3}Ni_{4.5-x}(Al_{0.5}Mo0.5)_x$ (x = 0–0.8) alloy electrodes.

Low-Temperature Dischargeability (LTD)

It has been reported that the discharge capacity of the negative electrode in nickel-metal hydrides decreases drastically with decreasing temperature.[24] Sakai et al.[2] pointed out that the dischargeability of the negative electrodes at relatively low temperatures depended on hydrogen diffusion and/or the charge-transfer process occurring at the metal electrolyte interface. The value of D in the bulk is evaluated using the method described by Iwakura et al.[18] The LTD is expressed as LTD_{233} (%) = $C_{233}/C_{298} \times 100$ (where C_{233} and C_{298} are the discharge capacities at 233 K and 298 K, respectively). The values of D and I_0 for the $La_{0.7}Mg_{0.3}Ni_{4.5-x}(Al_{0.5}Mo_{0.5})_x$ (x = 0–0.8) alloy electrodes at 233 K are also listed in Table 5. It can be found that both I_0 and D are smaller than that at 298 K. Moreover, we find that I_0 remains almost unchanged (80.35–82.17 mA/g), whereas D increases remarkably with increasing x, which implies that hydrogen diffusion in the alloy probably be-

Table 5. Electrochemical kinetic parameters for the $La_{0.7}Mg_{0.3}Ni_{4.5-x}(Al_{0.5}Mo_{0.5})_x$ (x = 0–0.8) alloy electrodes.

Sample	Polarization resistance, R_p [mΩ]		Exchange current density, I_0 [mA/g]		Hydrogen diffusion coefficient, D [×10^{-10} cm^2/s]	
	298 K	233 K	298 K	233 K	298 K	233 K
x = 0.0	90.61	249.56	253.62	80.35	13.1	1.6
x = 0.2	89.38	248.20	257.12	80.79	13.1	3.0
x = 0.4	84.98	246.93	270.43	81.21	13.3	3.7
x = 0.6	80.36	245.62	286	81.64	13.5	4.8
x = 0.8	77.52	244.04	296.45	82.17	13.6	6.2

 © 2005 Wiley-VCH Verlag GmbH & Co. KGaA, Weinheim

comes the rate-determining factor for low-temperature dischargeability at 233 K. Figure 8 shows the LTD as a function of D in the alloy electrodes. It can be easily seen that D increases with an increase in x, which can be attributed to cell-volume expansion. The larger the value of D, the greater the LTD of the alloy electrodes.

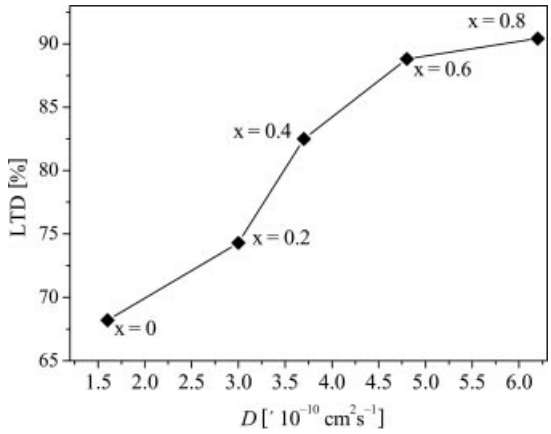

Figure 8. The low-temperautre dischargeability (LTD) as a function of hydrogen diffusion coefficient (D) of the $La_{0.7}Mg_{0.3}Ni_{4.5-x}$-$(Al_{0.5}Mo0.5)_x$ (x = 0, 0.2, 0.4, 0.6, 0.8) alloy electrodes at 233 K.

Conclusions

The structure, hydrogen storage characteristics, and electrochemical properties of the $La_{0.7}Mg_{0.3}Ni_{4.5-x}(Al_{0.5}Mo_{0.5})_x$ (x = 0, 0.2, 0.4, 0.6, 0.8) hydrogen storage alloys have been investigated systematically. It is found that, by X-ray powder diffraction and Rietveld analysis, all the $La_{0.7}Mg_{0.3}Ni_{4.5-x}(Al_{0.5}Mo_{0.5})_x$ alloys consist of an impurity Ni phase and two main crystallographic phases, namely, the La(La, $Mg)_2Ni_9$ phase and the $LaNi_5$ phase. Moreover, the lattice parameters and cell volumes of both the La(La, $Mg)_2Ni_9$ and the $LaNi_5$ phases increase with increasing Al and Mo content in the alloys. The P-C isotherm curves indicate that the hydrogen storage capacity first increases and then decreases with increasing x, while the desorption pressure always decreases with an increase in x. The electrochemical measurements show that the maximum discharge capacity increases from 246.3 (x = 0) to 345.4 mAh/g (x = 0.6), and then decreases to 317.6 mAh/g (x = 0.8). For a discharge current density of 1200 mA/g, the HRD of the alloy electrodes increases linearly from 47.2% (x = 0) to 73.8% (x = 0.4). Moreover, according to the linear polarization curves, the exchange current density of the alloy electrodes also increases monotonously with increasing x. The value of D increases with increasing Al and Mo content, and thus increases the LTD of the alloy electrodes.

Experimental Section

Alloy Preparation and X-ray Diffraction Analysis: All alloy samples were prepared by carefully arc-melting the constituent elements on a water-cooled copper hearth under argon, followed by annealing in vacuo for 100h at 770 °C. The purity of the metals, i.e. La, Mg, Ni, Al, and Mo is higher than 99.9 mass-%, respectively. The samples were all inverted and remelted 5 times to ensure good homogeneity. A slight excess of Mg over sample composition was needed in order to compensate for evaporative loss of Mg under the preparation conditions. Several attempts were performed to find the optimum preparative conditions. The final compounds were carefully checked by Inductively Coupled Plasma-Atomic Emission Spectrometry (ICP-AES) with a TJA Poems-type instrument. Thereafter, these alloy samples were crushed in a mortar into fine powders of 200–300 mesh.

Crystallographic characteristics of the hydrogen storage alloys were investigated by X-ray diffraction on a Rigaku D/Max 2500PC X-ray diffractometer (Cu-K_α radiation, Bragg–Brentano geometry, 2θ range 10–100°, step size 0.02°, backscattered rear graphite monochromator) by using JADE5 software.[25] The lattice constants and cell volume were calculated by the RIETICA program after internal θ calibration by using silicon as standard reference material.

Electrochemical Measurement: The alloy powder and carbonyl nickel powder were mixed well in a weight ratio of 1:5 and pressed into tablets as metal hydride electrodes, which had a diameter of 13 mm and a thickness of 1.5 mm; the weight of each electrode was about 0.9 g.

The electrochemical properties were then measured in a standard three-electrode cell consisting of a working electrode (metal hydride electrode), a counter electrode ($NiOOH/Ni(OH)_2$ electrode), and a reference electrode (Hg/HgO electrode). The electrolyte in the cell was a 6 M KOH aqueous solution. Charge and discharge tests were carried out on an automatic galvanostatic system (DC-5). The emphasis of these charge/discharge tests was on the electrochemical capacity and stability of the negative electrode, thus the capacity of the positive electrode plate was designed to be much higher than that of the negative electrode. At 298 K, these experimental cells were first charged at current of 60 mA/g for 7 h followed by a rest for 30 min, and were discharged at the same discharge current density to the cut-off voltage of –0.60 V vs. Hg/HgO.

Pressure-composition isotherm (P-C) curves were electrochemically obtained by converting the equilibrium potential of the metal hydride electrode into the equilibrium pressure of hydrogen on the basis of the Nernst equation by using electrochemical data[26] as reported in reference.[27] The equilibrium potential curves were obtained by alternating the following two processes: (1) a pulse discharge of (25 mA/g × 0.25 h), and (2) a rest period until the potential became almost constant. The equilibrium potential change of approximately 30 mV corresponds to the equilibrium pressure change by one order of magnitude. Since the measured potentials have an error of 1–2 mV, the calculated pressure values are accurate to within 10%.[27]

The high-rate dischargeability (HRD) was defined by the following formula:

$$HRD\ (\%) = C_n \times 100/(C_n + C_{60})$$

where C_n is the discharge capacities of the alloy electrode at a discharge current of n mA/g (n = 60, 240, 480, 720, 960, 1200); C_{60} is the additional discharge capacity measured subsequently at 60 mA/g after Cn was measured.

For investigating the electrocatalytic activity of the hydrogen electrode reaction, the linear polarization curves of the electrode were plotted on a EG&G PARC's Model 273 Potentiostat/Galvanostat station by scanning the electrode potential at the rate of 0.1mV/s

 © 2005 Wiley-VCH Verlag GmbH & Co. KGaA, Weinheim

from –5 to 5 mV (vs. open circuit potential) at 50% depth of discharge at 298 K and 233 K. The polarization resistance R_p can be obtained from the slope of the linear polarization curves. Moreover, the exchange current density (I_0), which is a measure of the catalytic activity of the electrode, was calculated from the slopes of the polarization curves by the following Equation (1),[17]

$$I_0 = \frac{RT}{FR_p} \quad (1)$$

where R is the gas constant; T is the absolute temperature; F is the Faraday constant; and R_p is the polarization resistance. The potentiostatic discharge technique was used to evaluate the coefficient of diffusion within the bulk of the alloy electrodes. After being fully charged followed by a 30 min open-circuit lay-aside, the test electrodes were discharged with a +500-mV potential-step for 500 s on a EG&G PARC's Model 273 Potentiostat/Galvanostat station, by using the M352 CorrWare electrochemical/corrosion software.

Acknowledgments

This work was financially supported by the National Natural Science Foundation of China (Grant No.20171042).

[1] J. J. G. Willems, K. H. J. Buschow, *J. Less-Common Met.* **1987**, *129*, 13–30.
[2] T. Sakai, H. Miyamura, N. Kuriyama, A. Kato, K. Oguro, H. Ishikawa, *J. Electrochem. Soc.* **1990**, *137*, 795–799.
[3] T. Kohno, H. Yoshida, F. Kawashima, T. Inaba, I. Sakai, M. Yamamoto, M. Kanda, *J. Alloys Compd.* **2000**, *311*, L5–L7.
[4] J. J. G. Willems, *Philips J. Res.* **1984**, *39*, 1–94.
[5] H. G. Pan, Y. F. Zhu, M. X. Gao, Q. D. Wang, *J. Electrochem. Soc.* **2002**, *149*, A829–A833.
[6] J. Chen, N. Kuriyama, H. T. Takeshita, H. Tanaka, T. Sakai, M. Haruta, *Electrochem. Solid-State Lett.* **2000**, *3*, 249–252.
[7] T. Sakai, I. Uehara, H. Iwakura, *J. Alloys Compd.* **1999**, *293–295*, 762–769.
[8] J. J. Reilly, G. D. Adzic, J. R. Johnson, T. Vogt, S. Mukerjee, J. McBreen, *J. Alloys Compd.* **1999**, *293–295*, 569–582.
[9] Y. F Liu, H. G. Pan, Y. F. Zhu, R. Li, Y. Q. Lei, *Mater. Sci. Eng. A* **2004**, *372*, 163–172.
[10] K. Kadir, T. Sakai, I. Uahara, *J. Alloys Compd.* **1997**, *257*, 115–121.
[11] K. Kadir, N. Nuriyama, T. Sakai, I. Uehara, L. Eriksson, *J. Alloys Compd.* **1999**, *284*, 145–154.
[12] K. Kadir, T. Sakai, I. Uahara, *J. Alloys Compd.* **1999**, *287*, 264–270.
[13] K. Kadir, T. Sakai, I. Uahara, *J. Alloys Compd.* **2000**, *302*, 112–117.
[14] J. Chen, H. T. Takeshita, H. Tanaka, N. Kuriyama, T. Sakai, *J. Alloys Compd.* **2000**, *302*, 304–313.
[15] B. Liao, Y. Q. Lei, L. X. Chen, G. L. Lu, H. G. Pan, Q. D. Wang, *J. Power Sources* **2004**, *129*, 358–367.
[16] P. H. Notton, P. Hokkeling, *J. Electrochem. Soc.* **1991**, *138*, 1877–1885.
[17] T. Sakai, H. Miyamura, N. Kuriyama, A. Kato, K. Oguro, H. Ishikawa, *J. Less-Common Met.* **1990**, *159*, 127–139.
[18] C. Iwakura, H. Senoh, K. Morimoto, Y. Hara, H. Inoue, *Electrochem.* **2002**, *70*, 2–7.
[19] M. T. Yeh, V. M. Beibutian, S. E. Hsu, *J. Alloys Compd.* **1999**, *293–295*, 721–723.
[20] J. J. Reilly, "Metal Hydrides Electrodes", in *Handbook of Battery Materials* (Ed.: J. O. Bessenhard), Wiley, New York, **2000**, pp. 123–127.
[21] H. G. Pan, Y. F. Liu, M. X. Gao, Y. Q. Lei, Q. D. Wang, *J. Electrochem. Soc.* **2003**, *150*, A565–A570.
[22] T. Sakai, H. Miyamura, N. Kuriyama, A. Kato, K. Oguro, H. Ishikawa, *J. Less-Common Met.* **1990**, *159*, 127–139.
[23] C. Iwakura, T. Oura, H. Inoue, M. Matsuoka, *Electrochim. Acta* **1996**, *41*, 117–121.
[24] H. Senoh, Y. Hara, H. Inoue, C. Iwakura, *Electrochim. Acta* **2001**, *46*, 967–971.
[25] *Materials Data JADE Realease 5, XRD Pattern Processing*, Materials Data Inc. (MDI), **1997**.
[26] T. Sakai, K. Oguro, H. Miyamura, N. Kuriyama, A. Kato, H. Ishikawa, C. Iwakura, *J. Less-Common Met.* **1990**, *161*, 193–202.
[27] H. G. Pan, Q. W. Jin, M. X. Gao, Y. F. Liu, R. Li, Y. Q. Lei, *J. Alloys Compd.* **2004**, *373*, 237–245.

Received: September 28, 2004

 © 2005 Wiley-VCH Verlag GmbH & Co. KGaA, Weinheim

Electrochemical Synthesis and Structural Characterisation of Cadmium and Mercury Complexes Containing Pyrimidine-2-thionate Ligands

Antonio Rodríguez,[a] Antonio Sousa-Pedrares,[a] José A. García-Vázquez,[a] Jaime Romero,[a] and Antonio Sousa*[a]

Dedicated to Professor V. I. Minkin on the occasion of his 70th birthday

Keywords: Cadmium / Electrochemistry / Heterocycles / Mercury / S ligands

The electrochemical oxidation of anodic metal (cadmium or mercury) in a cell containing an acetonitrile solution of the appropriate pyrimidine-2-thione (RpymSH) affords complexes [M(RpymS)$_2$] (M = Cd, Hg; R = 4-CF$_3$, 4,6-CF$_3$,Me and 4,6-CF$_3$,Ph). When 2,2′-bipyridine (bipy) or 1,10-phenanthroline (phen) was added to the electrolytic cell, adducts of cadmium and compounds with these coligands were obtained. All the compounds have been characterised by microanalysis, IR spectroscopy and, in the case of the compounds that were sufficiently soluble, by ^{1}H, ^{13}C and ^{199}Hg NMR spectroscopy. The compounds [Cd(4-CF$_3$pymS)$_2$] (**1**), [Cd(4,6-CF$_3$MepymS)$_2$(bipy)] (**4**), [Cd(4,6-CF$_3$PhpymS)$_2$-(phen)] (**6**) and [Hg(4,6-CF$_3$MepymS)$_2$] (**8**) were also characterised by X-ray diffraction. Compound **1** presents a polymeric structure with the polymer chains interconnected by intermolecular C–H···N interactions. Compounds **4** and **6** adopt mononuclear structures, with weak inter- and intramolecular C–H···π interactions, as well as π–π stacking interactions for compound **6**. Compound **8** also presents a mononuclear structure with intermolecular π–π interactions between the pyrimidine rings and additional weak Hg···Hg contacts (3.484 Å).
(© Wiley-VCH Verlag GmbH & Co. KGaA, 69451 Weinheim, Germany, 2005)

Introduction

The chemistry of metal–sulfur complexes has attracted much interest over the past decade because of the potential relevance of such compounds to active sites in metalloenzymes and also for their ability to adopt geometries of variable nuclearity and great structural complexity.[1–7] These latter features are the result of the tendency of thiolate ligands to bridge metal centres to yield oligomeric or polymeric species, a situation that makes it difficult to obtain and isolate crystals suitable for X-ray diffraction studies. It has been shown[8–10] that the degree of association depends intimately on both the reaction conditions and the nature of the thiolate ligands. Moreover, these association phenomena may be limited by incorporating steric constraints by appropriate ligand design or introducing coligands to block a number of coordination sites around the metal. Recently, a great deal of effort has been made[11–17] to modify the thiolate ligand by introducing a solubilizing group or a bulky substituent that might modify the aggregation process.

However, in comparison with the coordination chemistry of transition metals, the chemistry of the main-group metals with sulfur ligands remains much less developed.[18–22] In many cases, the interaction of toxic metals with biological systems involves bonding of the metal to the sulfydryl groups present in enzymes. Hence, an insight into the chemistry of main-group thiolate compounds is important in terms of understanding the aforementioned interaction and for the design of detoxifying agents.[23,24] The generally poor solubility of group 12 metal thiolate compounds makes it difficult to structurally characterise these systems.

As part of our continuing interest in the chemistry of sterically hindered thiolates,[25] we report here the electrochemical synthesis and characterisation of Cd and Hg complexes with a number of substituted pyrimidine-2-thiones (Scheme 1). This type of ligand, besides having solubilising and bulky groups that might modify the degree of aggregation as a result of steric constraints, is one of the most versatile sulfur ligands. These ligands can act as follows: (a) a neutral monodentate ligand coordinated through the sulfur atom,[26] through one of the nitrogen atoms,[27] and as a bridging ligand through sulfur[28] or as an N,S-chelating ligand,[29,30] and (b) as an anionic ligand, in which case it can be monodentate through the sulfur atom,[31] as an N,S-chelating ligand,[32] as a binuclear bridging ligand through

[a] Departamento de Química Inorgánica, Universidad de Santiago de Compostela,
15782, Santiago de Compostela, Spain

 DOI: 10.1002/ejic.200400848

nitrogen and sulfur,[33] or sulfur only,[34] as a binuclear triply bridging ligand through sulfur and one of the nitrogens[35] or the two nitrogen and sulfur atoms,[36,37] and as a trinuclear triply bridging system.[38]

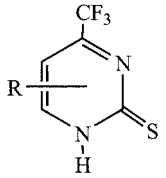

R = 4-CF_3, 4,6-CF_3, Me, 4,6-CF_3, Ph

Scheme 1.

In addition, and in order to reduce the nuclearity of the homoleptic cadmium(II) complexes, didentate N,N′-donor coligands, such as 2,2′-bipyridine or 1,10-phenanthroline, were added to the electrochemical cell. This modification results in the preparation of monomeric mixed cadmium(II) complexes in one step.

Results and Discussion

Cadmium and mercury complexes of general formula $[M(RpymS)_2]$ (M = Cd and Hg; R = 4-CF_3, 4,6-CF_3,Me and 4,6-CF_3,Ph) were easily prepared in reasonable yields by a simple, one-step electrochemical method. Mixed complexes of cadmium with 2,2′-bipyridine or 1,10-phenanthroline were also obtained by addition of the corresponding coligand to the cell. The compounds are air-stable and moderately soluble in organic non-polar solvents, but soluble in dimethyl sulfoxide or *N*,*N*′-dimethylformamide.

The values of the electrochemical efficiency, defined as the amount of metal dissolved per unit of charge, were close to 0.5 mol F^{-1} regardless of the presence or absence of additional ligand. This observation, along with the evolution of hydrogen at the cathode, is compatible with the following mechanism:

Cathode: 2 RpymSH + 2 $e^- \rightarrow$ 2 $RpymS^-$ + H_2

Anode: M + 2 $RpymS^- \rightarrow [M(RpymS)_2]$ + 2 e^-

(M = Cd, Hg)

or

M + 2 $RpymS^-$ + L $\rightarrow [M(RpymS)_2L]$ + 2 e^-

(M = Cd; L = bipy, phen)

Crystallographic Studies

Crystal and Molecular Structure of [Cd(4-CF_3pymS)$_2$] (1)

Figure 1 shows a perspective view of compound **1** along with the atomic labelling scheme used. A selection of bond lengths and angles (with estimated standard deviations) are given in Table 1.

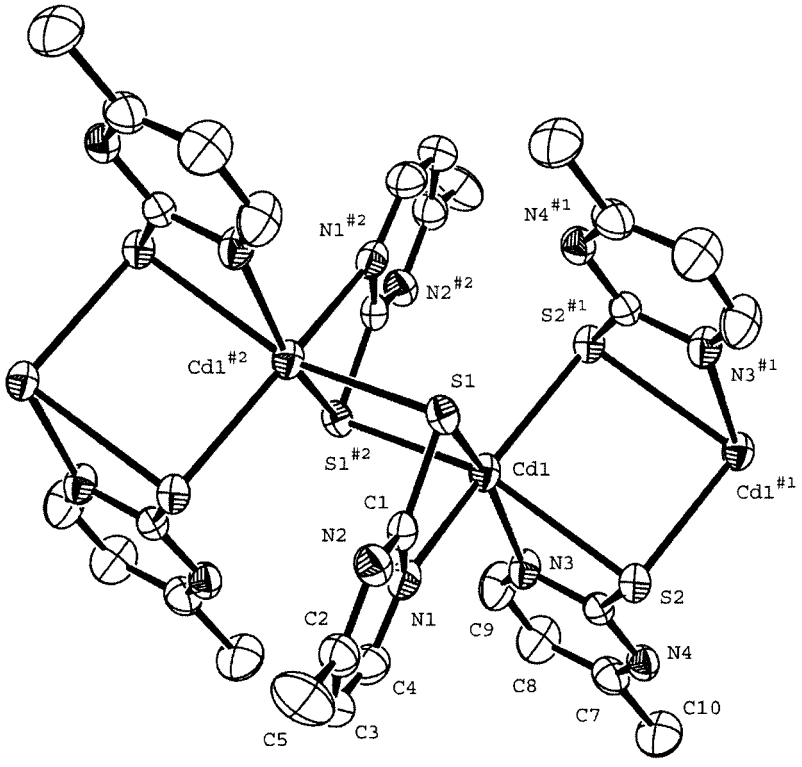

Figure 1. ORTEP diagram of the structure of $[Cd(4\text{-}CF_3pymS)_2]_x$ (**1**), showing 40% thermal ellipsoid probability. The hydrogen atoms and the CF_3 groups on C(5) and C(10) have been omitted for clarity. Symmetry codes: #1 = $-x + 2$, $-y$, $-z + 1$; #2 = $-x + 1$, $-y$, $-z + 1$.

 © 2005 Wiley-VCH Verlag GmbH & Co. KGaA, Weinheim

Table 1. Selected bond lengths [Å] and angles [°] for [Cd(4-CF_3pymS)$_2$] (**1**).[a]

Cd(1)–N(3)	2.336(4)	Cd(1)–N(1)	2.457(4)
Cd(1)–S(2)#1	2.6347(12)	Cd(1)–S(1)#2	2.6733(11)
Cd(1)–S(1)	2.6777(12)	Cd(1)–S(2)	2.8011(11)
S(2)–C(6)	1.745(4)	S(1)–C(1)	1.755(5)
N(3)–Cd(1)–S(2)#1	96.89(11)	N(1)–Cd(1)–S(2)#1	158.73(10)
N(3)–Cd(1)–S(1)#2	97.31(9)	N(1)–Cd(1)–S(1)#2	92.70(8)
S(2)#1-Cd(1)–S(1)#2	99.56(3)	N(3)–Cd(1)–S(1)	156.88(11)
N(1)–Cd(1)–S(1)	61.71(9)	S(2)#1-Cd(1)–S(1)	99.54(4)
S(1)#2-Cd(1)–S(1)	95.89(3)	N(3)–Cd(1)–S(2)	60.63(9)
N(1)–Cd(1)–S(2)	85.41(8)	S(2)#1-Cd(1)–S(2)	89.76(4)
S(1)#2-Cd(1)–S(2)	157.13(4)	S(1)–Cd(1)–S(2)	103.15(3)

[a] Symmetry codes: #1 = $-x + 2, -y, -z + 1$; #2 = $-x + 1, -y, -z + 1$.

The compound consists of polymeric chains along the *a* axis with the cadmium atom hexacoordinated by two nitrogen atoms from two different thionate ligands and four bridging sulfur atoms. Each ligand chelates one cadmium metal and bridges an adjacent cadmium atom through the exocyclic sulfur. A second ligand is almost perpendicular to the first one and also chelates this cadmium atom and bridges to the next cadmium atom in the chain. Each thionate ligand acts as a binuclear triply bridging μ_2-S,N(η^2-S;η^1-N) five-electron-donor ligand: each atom of cadmium is in a highly distorted [CdN_2S_4] octahedral environment with the nitrogen atoms in *cis* positions. The bond angles between the metal and the donor atoms that are in a *trans* disposition are in the range 151.6(3)–167.1(3)°, far from the ideal value of 180°. The values for the angles described by the donors in the *cis* positions are much lower than those expected for a regular octahedron, with values for the S–Cd–N angles of 61.1(3)° and 61.3(3)°.

Three of the four Cd–S bond lengths are very similar and are in the range 2.6347(12)–2.6777(12) Å. The other Cd–S distance is longer at 2.8011(11) Å. These values are within the range observed for other complexes containing CdN_2S_4 units with μ_2-S,N(η^2-S;η^1-N) bridging ligands; for example 2.638(6)–2.761(8) Å in the hexanuclear complex [{Cd(4,6-Me_2pymS)$_2$}$_6$][35] and 2.647–2.777 Å in other hexacoordinate thionate complexes.[39,40] However, the range for these distances in the complex [Cd(pyS)$_2$],[41] which has a similar chain structure, is much wider [2.543(5)–3.038(4) Å].

The Cd–N bond lengths of 2.336(4) and 2.457(4) Å are also close to the values found in other octahedral complexes of cadmium containing heterocyclic thionates as ligands; for example 2.42(2) and 2.53(2) Å in [Cd(pymS)$_2$(phen)],[42] [Cd(4,6-CF_3MepymS)$_2$(bipy)] and [Cd(4,6-CF_3PhpymS)$_2$-(phen)] (see below).

The S–C bond lengths of 1.755(5) and 1.745(4) Å are intermediate between the value found in free 4,6-dimethylpyrimidine-2-thione[30] [1.686(4) Å] and 1-phenyl-4,6-dimethylpyrimidine-2-thione[29] [1.676(2) Å], which exist in the thione form in the solid state, and the values of 1.781(2) Å and 1.782(3) Å found in bis(2-pyrimidyl) disulfide[43] and bis(4,6-dimethyl-2-pyrimidyl) disulfide,[44] both of which possess a simple C–S bond. This observation suggests that the ligand is coordinated in a way that is closer to the thionato form than to the thione form of the free ligand.

The packing structure of **1** (Figure 2) shows that every polymeric chain interacts with two parallel chains in the *b* direction through non-classical C–H···N hydrogen bonds. These interactions link the polymeric chains through weak C(8)–H···N(2) hydrogen bonds. The hydrogen bonds involve the uncoordinated pyrimidine nitrogen atoms, N(2), on alternate ligands in one chain that are parallel to one another and also parallel to the chain with the pyrimidyl protons bond at C(8) atom on ligands in the adjacent chains, which are again parallel between themselves but almost perpendicular to the first ones. The bond lengths and angles in this system are as follows: C···N = 3.422(7) Å, N···H = 2.58 Å and C–H···N = 150.3°.

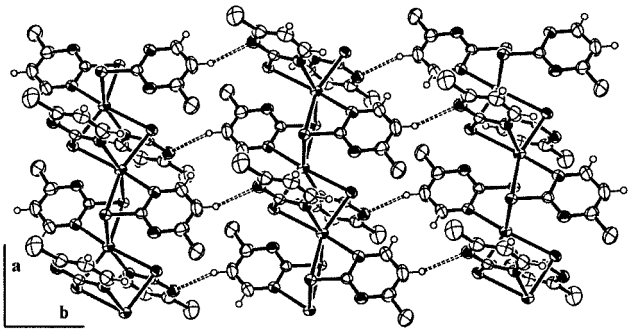

Figure 2. The crystal packing of **1** viewed along the *c* axis. Dashed lines show the C–H···N interactions.

These interactions result in the formation of layers parallel to the crystallographic *ab* plane that stack along the *c* axis.

A comparison of the structures of cadmium complexes with different pyridine and pyrimidine-2-thiones clearly demonstrates that the degree of aggregation depends to a large extent on the steric effects created by the ligand substituents. Thus, while the complex with pyridine-2-thione consists of [Cd(pyS)$_2$]$_x$,[41] a polymeric chain structure, the increased steric constraints introduced by the methyl groups in the case of 4,6-dimethylpyrimidine-2-thione reduce the tendency for polymerisation and the complex obtained is hexanuclear [Cd(4,6-Me_2pymS)$_2$]$_6$.[35] The metal atom in the latter complex is hexacoordinate as in [Cd(pyS)$_2$]$_x$.[41] A higher degree of steric hindrance, such as in 3-trimethylsilylpyridine-2-thione, produces a dimer [Cd(3-Me_3Sipyt)$_2$]$_2$,[45] with each cadmium atom in a five-coordinate environment. In the case of 4-trifluoromethylpyrimidine-2-thione, the presence of a CF_3 group in the 4-position produces greater steric hindrance than in pyridine-2-thione, but less hindrance than in 4,6-dimethylpyrimidine-2-thione. However, the steric hindrance introduced by the CF_3 group is not sufficient to reduce the aggregation level and the complex is also polymeric as in [Cd(pyS)$_2$]$_x$.[41] Naturally, other factors such as reaction conditions, kinetic factors, nature of the solvent, etc., can also play a role in the aggregation process.[25,45]

 © 2005 Wiley-VCH Verlag GmbH & Co. KGaA, Weinheim

Molecular Structures of [Cd(4,6-CF_3MepymS)$_2$(bipy)] (4) and [Cd(4,6-CF_3PhpymS)$_2$(phen)] (6)

Figure 3 and Figure 4 show perspective views of compounds **4** and **6**, respectively, together with the atomic labelling schemes used. A selection of bond lengths and angles (with estimated standard deviations) are given in Table 2 and Table 3, respectively.

The cadmium atoms in both **4** and **6** are located on a twofold rotation axis; accordingly, their asymmetric units contain one half of the bipyridine (**4**) or phenanthroline (**6**) ligand, one pyrimidine-2-thionate ligand and one half of the cadmium atom.

Table 2. Selected bond lengths [Å] and angles [°] for [Cd(4,6-CF_3MepymS)$_2$bipy] (**4**).[a]

Cd–N(3)	2.38(3)	N(2)–C(2)	1.35(4)
N(3)–C(7)	1.25(4)	Cd–S	2.523(10)
N(3)–C(11)	1.38(5)	Cd–N(l)	2.56(2)
S–C(l)	1.68(3)		
N(3)–Cd–N(3)#l	69.9(14)	N(3)–Cd–S	150.9(7)
N(3)#l-Cd–S	94.2(8)	N(3)–Cd–S#l	94.2(8)
S–Cd–S#l	109.4(6)	N(3)–Cd–N(l)#l	86.8(9)
S–Cd–N(l)#l	118.5(6)	N(3)–Cd–N(l)	90.6(10)
N(3)#l-Cd–N(l)	86.8(9)	S–Cd–N(l)	63.5(7)
S#l-Cd–N(l)	118.5(6)	N(l)#l-Cd–N(l)	176.9(14)

[a] Symmetry code: #1 = –*x*, –*y*, *z*.

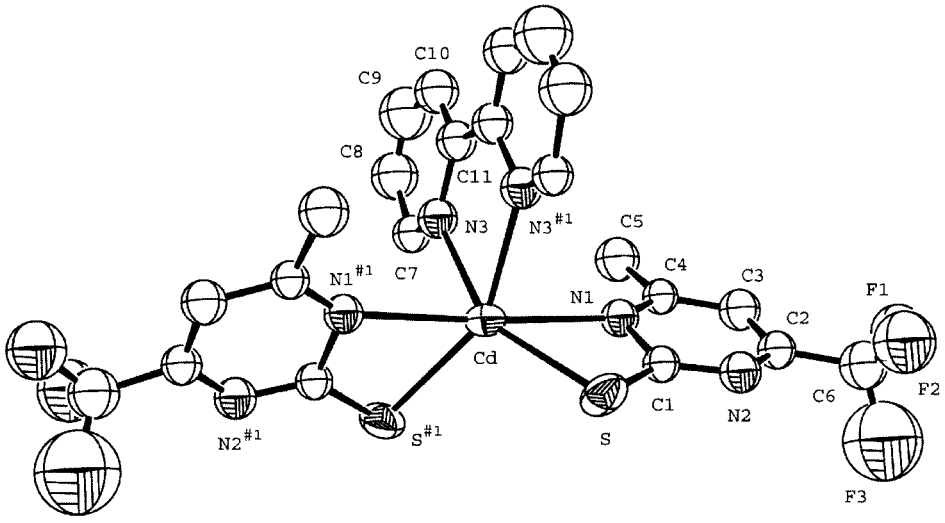

Figure 3. ORTEP diagram of the molecular structure of [Cd(4,6-CF_3MepymS)$_2$(bipy)] (**4**), with 40% thermal ellipsoid probability. The hydrogen atoms have been omitted for clarity. Symmetry code: #1 = –*x*, –*y*, *z*.

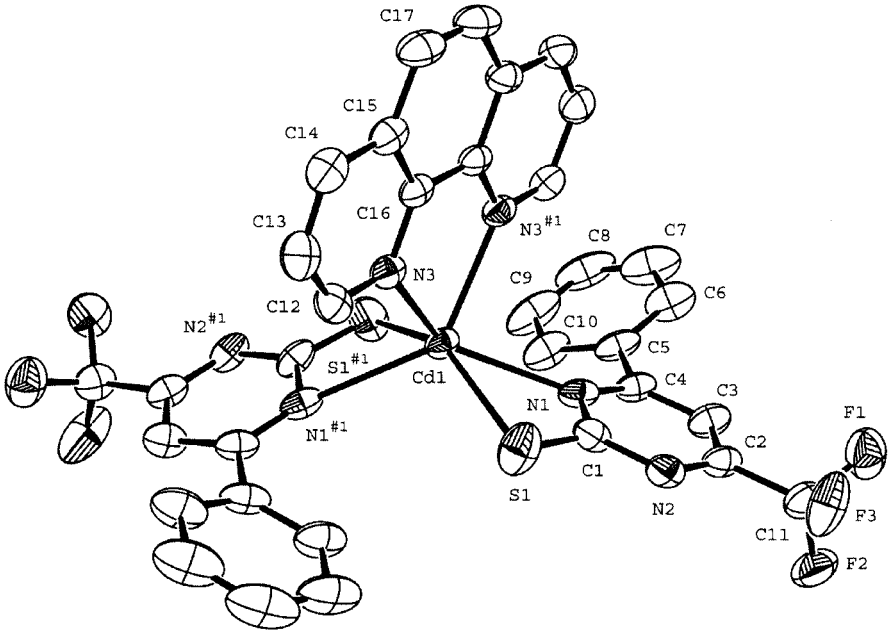

Figure 4. ORTEP diagram of the molecular structure of [Cd(4,6-CF_3PhpymS)$_2$(phen)] (**6**), with 30% thermal ellipsoid probability. The hydrogen atoms have been omitted for clarity. Symmetry code: #1 = –*x* + 2, *y*, –*z* + 1/2.

 © 2005 Wiley-VCH Verlag GmbH & Co. KGaA, Weinheim

Table 3. Selected bond lengths [Å] and angles [°] for [Cd(4,6-CF_3PhpymS)$_2$phen] (**6**).[a]

Cd(1)–N(3)#1	2.378(4)	Cd(1)–N(3)	2.378(4)
Cd(1)–S(1)	2.4758(17)	Cd(1)–S(1)#1	2.4758(17)
Cd(1)–N(1)	2.570(4)	Cd(1)–N(1)#1	2.570(4)
S(1)–C(1)	1.533(6)		
N(3)#1-Cd(1)–N(3)	70.62(19)	N(3)#1-Cd(1)–S(1)	113.99(10)
N(3)–Cd(1)–S(1)	94.92(10)	N(3)–Cd(1)–S(1)#1	113.99(10)
S(1)–Cd(1)–S(1)#1	144.89(11)	N(3)#1-Cd(1)–N(1)	87.86(12)
N(3)–Cd(1)–N(1)	136.46(11)	S(1)–Cd(1)–N(1)	59.18(8)
S(1)#1-Cd(1)–N(1)	104.96(9)	N(3)–Cd(1)–N(1)#1	87.86(12)
S(1)–Cd(1)–N(1)#1	104.96(9)	N(1)–Cd(1)–N(1)#1	130.17(16)

[a] Symmetry code: #1 = $-x + 2$, y, $-z + 1/2$.

In both cases the molecular structure consists of discrete molecular species, which shows that the presence of an additional didentate coligand inhibits the polymerisation of the complexes. In both compounds the cadmium atom is hexacoordinated by the chelating nitrogen donors of the coligand (bipy or phen) and two anionic pyrimidine-2-thionate ligands, which also act in a didentate chelating (S,N) manner.

The cadmium atom in compound **4** is in a distorted [CdS_2N_4] octahedral environment. The disposition of the ligands in **4** is such that the sulfur atoms occupy *cis* positions. The equatorial plane of the molecule can be considered as being formed by the two nitrogen atoms from the 2,2′-bipyridine molecule and two sulfur atoms from pyrimidine-2-thionato ligands; these four atoms are not exactly coplanar. In terms of the best plane that includes these four donor atoms and the cadmium centre, the atoms N(3) and S, which occupy *trans* positions, are both below this plane (by –0.514 and –0.318 Å respectively), while the atoms N(3#1) and S(#1) are located above this plane (by +0.514 and +0.318 Å respectively). The cadmium atom, however, is in the plane defined above.

These deviations produce N(3)–Cd–S and N(3#1)–Cd–S(#1) bond angles of 150.9(7)°, which differ from the ideal value of 180°. In addition, the small angles of the chelate rings, together with the elongation in the axial direction, cause the S–Cd–S′ and S–Cd–N(3#1) angles to deviate significantly from 90° [109.4(6) and 94.2(8)°, respectively].

In complex **6** the disposition of the 4-trifluoromethyl-6-phenylpyrimidine-2-thionate ligands differs from that found in [Cd(4,6-CF_3MepymS)$_2$(bipy)] (**4**). As in compound (**4**), the cadmium atom in **6** is also in a [CdS_2N_4] environment, although in this case the geometry is best described as distorted trigonal prismatic. This can clearly be seen by inspection of the twist angle between the two parallel faces of the coordination polyhedron, as shown in Figure 5. These values are 14.2° for N(3) and N(3#1), 10.5° for N(1) and S(1) and 10.5° for N(1#1) and S(1#1). The expected values are 0° for a regular trigonal-prismatic geometry and 60° for an octahedral one.

In the structure, the three didentate ligands (two pyrimidine-2-thionates and one phenanthroline) link the two triangular faces of the trigonal prism. The higher value of 14.2° for the twist angle involving the phenanthroline ligand

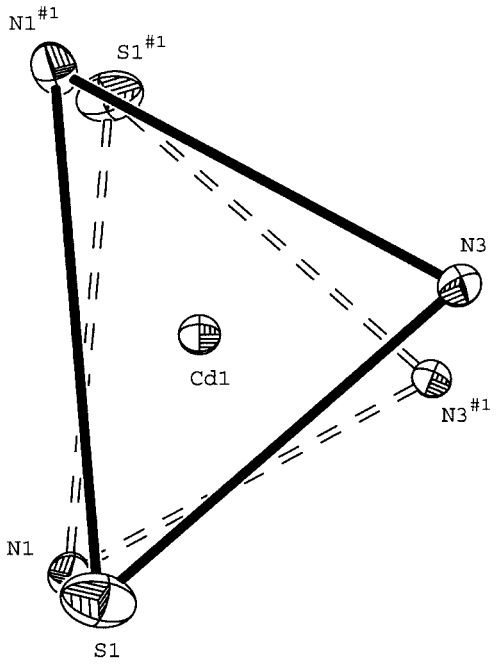

Figure 5. Distorted trigonal-prismatic environment for [Cd(4,6-CF_3PhpymS)$_2$(phen)] (**6**).

[N(3) and N(3#1)] can be explained by the formation of a rigid five-membered chelating ring, while the pyrimidine-2-thionate ligands form four-membered rings.

The Cd–S bond lengths [2.523(10) for **4** and 2.4578(17) Å for **6**] are similar to those found in other octahedral compounds of cadmium(II) with heterocyclic thionate ligands [2.588–2.5331 Å].[42,46] The Cd–N_{pymS} bond lengths [2.56(2) Å and 2.570(4) Å for **4** and **6**, respectively] are clearly longer than those involving the metal and the nitrogen atoms of the bipyridine in **4** or phenanthroline in **6** [Cd–N_{bipy} = 2.38(3) Å and Cd–N_{phen} = 2.378(4) Å]. This situation is probably due to the fact that the chelate coordination of the thionate ligand gives rise to a four-membered ring, which causes an elongation of the C–N bond as the interaction with sulfur is more favourable and the thionate ligand is rigid. However, these Cd–N_{bipy} and Cd–N_{phen} bond lengths [2.38(3) Å] do not differ significantly from those found in other octahedral cadmium(II) 2,2′-bipyridine and 1,10-phenanthroline complexes.[42,46]

The thionate ring is nearly planar and the exocyclic sulfur atom is also in the same plane. Other structural characteristics of the thionate ligand and the 2,2′-bipyridine or 1,10-phenanthroline unit are as one would expect and do not warrant further discussion.

Compound **6** shows a wide variety of intra- and intermolecular interactions that involve the π clouds of the aromatic rings.

A view of the crystal packing of this compound is shown in Figure 6. Each molecule in the crystal lattice interacts with four neighbouring molecules: two through the phenanthroline groups and two through the pyrimidine rings. Only the interactions between the phenanthroline rings are

 © 2005 Wiley-VCH Verlag GmbH & Co. KGaA, Weinheim

shown in the figure (upper part of Figure 6). The crystal packing is such that the phenanthroline rings are opposite one another and π–π stacking occurs between the outer rings of each phenanthroline unit (distance between centroids = 3.597 Å). The rings of the phenanthroline groups involved in the π interactions are arranged in such a way that the six atoms of the ring do not completely eclipse those of the other ring, meaning that the interaction is not "perfect face alignment" but "offset or slipped stacking" (distances between the corresponding atoms of the two rings of 3.587, 3.588 and 3.616 Å). Figure 7 shows a view perpendicular to the planes of the phenanthroline groups.

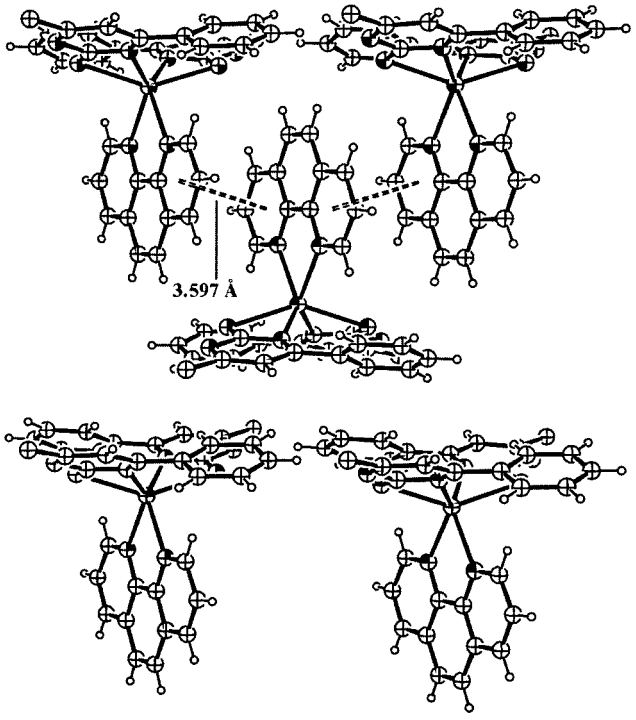

Figure 6. Crystal packing diagram of **6**; intermolecular π–π stacking interactions between phenanthroline rings are represented by dashed lines.

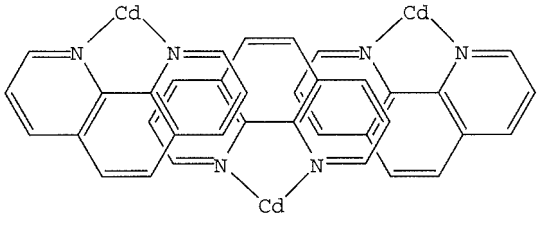

Figure 7. Overlapping between phenanthroline rings of three neighbouring molecules in **6**.

A view of the interactions between one molecule in the crystal lattice and neighbouring molecules through the pyrimidine rings is shown in Figure 8 (see also lower part of Figure 6).

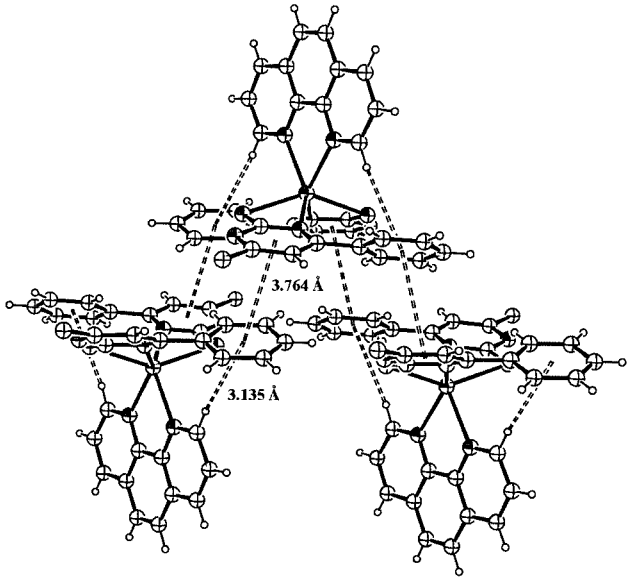

Figure 8. A view of complex **6** showing intramolecular C–H···π bonds and intermolecular π–π interactions between phenyl rings.

It can be seen from Figure 8 that, besides the π–π stacking interactions discussed above, each molecule in the crystal lattice is involved in two other interactions through the π clouds of the aromatic rings of the heterocyclic thione: one of these interactions is intramolecular and the other is intermolecular. The intramolecular interaction is of the C–H···π type and occurs between the protons *ortho* to the phenanthroline nitrogen (the most acidic protons in this unit) and the phenyl groups in the 6-position of the pyrimidine rings (H–centroid distance = 3.135 Å; C–centroid distance = 4.060 Å; C–H–centroid angle = 173.70°). It is interesting to note the high level of directionality of this interaction. In this situation each molecule is involved in two identical interactions of this type due to the presence of two pyrimidine units in each molecule.

As far as the intermolecular interaction is concerned, each pyrimidine ring takes part in a π–π stacking interaction with a phenyl ring in the 6-position of a pyrimidine ring in a neighbouring molecule. This π–π stacking interaction is of the most common offset or slipped-stacking type. This type of interaction is characterised by a distance between the centroids of the rings in question of about 3.8 Å. In the case under discussion here the distance between the centroids is 3.764 Å (the distances between the corresponding atoms ranges between 3.637 and 3.899 Å).

The compounds [Cd(4,6-CF_3MepymS)$_2$(bipy)] (**4**) and [Cd(4,6-CF_3PhpymS)$_2$(phen)] (**6**) (Figure 9) have different groups in the 6-position of the pyrimidine rings and, consequently, the disposition of the pyrimidine ligands in the two complexes is very different. These differences are clear when one considers the dihedral angles R–C–C′–R′, where R or R′ is the group in the 6-position (Me or Ph) and C or C′ is the carbon atom in the 6-position of the ring to which the substituent is attached. These angles have values of 110.0° when R = Me and 175.8° when R = Ph.

 © 2005 Wiley-VCH Verlag GmbH & Co. KGaA, Weinheim

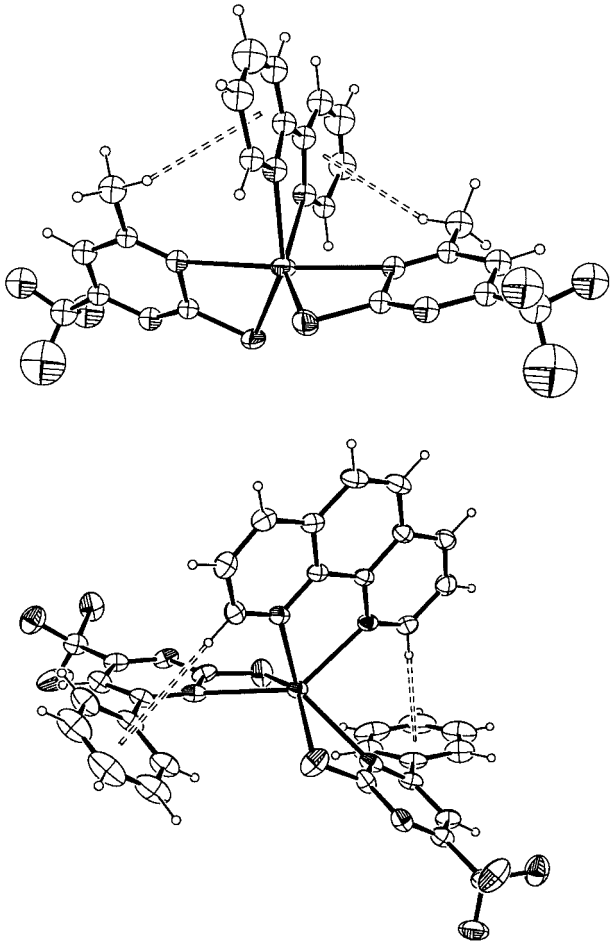

Figure 9. Views of complexes **4** (top) and **6** (bottom) illustrating the disposition of the pyrimidine rings.

Molecular structure of [Hg(4,6-CF_3MepymS)$_2$] (8)

Figure 10 shows a view of compound **8** together with the atomic numbering scheme. Selected bond lengths and angles (with estimated deviations) are given in Table 4.

Table 4. Selected bond lengths [Å] and angles [°] [Hg(4,6-CF_3MepymS)$_2$] (**8**).[a]

Hg–S#l	2.330(2)	N(1)–C(4)	1.325(9)
Hg–S	2.330(2)	Hg–N(1)	2.773(6)
N(2)–C(2)	1.320(9)	Hg–Hg#2	3.4845(5)
N(2)–C(1)	1.325(7)	Hg–Hg#3	3.4845(5)
S–C(l)	1.752(6)	N(1)–C(1)	1.333(9)
S#l-Hg–S	180.0	N(2)–C(2)–C(6)	114.3(8)
S#l-Hg–Hg#2	90.0	C(3)–C(2)–C(6)	120.6(6)
S–Hg–Hg#2	90.0	C(2)–C(3)–C(4)	115.1(6)
S#l-Hg–Hg#3	90.0	N(1)–C(4)–C(3)	122.3(6)
S–Hg–Hg#3	90.0	N(1)–C(4)–C(5)	115.2(7)
Hg#2-Hg–Hg#3	180.0	C(3)–C(4)–C(5)	122.6(7)
C(l)-S–Hg	94.2(2)		

[a] Symmetry codes: #1 = $-x + 1, -y + 1, -z + 1$; #2 = $-x + 1, y, -z + 1/2$; #3 = $-x + 1, y, -z + 3/2$.

In compound **8** the whole molecule, except F(2), lies on a mirror plane (symmetry code #4) and the mercury atom is located on a centre of symmetry (symmetry code #1); accordingly, the asymmetric unit contains one pyrimidine-2-thionate ligand (apart from one of the fluorine atoms of the CF_3 group) and one half of the mercury atom. In the molecule, the mercury atom is bonded to two sulfur atoms in a linear disposition. The Hg–S bond length [2.330(2) Å] is very similar to those found in other thionatomercury complexes with a linear geometry.[11,47–49]

In the complex the two ligands are on different sides of the line defined by the S–Hg–S bonds, and the pyrimidine rings are in a staggered conformation. The ligands are oriented in such a way that the N(1) atom is close to the mercury atom (distance of 2.773 Å). This value is larger than those observed in other mercury complexes containing heterocyclic donor nitrogen ligands, such as [Hg(pyS)(OAc)][50] (2.210 Å) or [HgMepy](NO_3)[51] [2.12(2) Å], but shorter than the sum of the van der Waals radii (3.23 Å),[52] and comparable to the distances in other mercury thiolate complexes characterised by weak intramolecular Hg···N interactions (2.798–2.980 Å).[46,53–55]

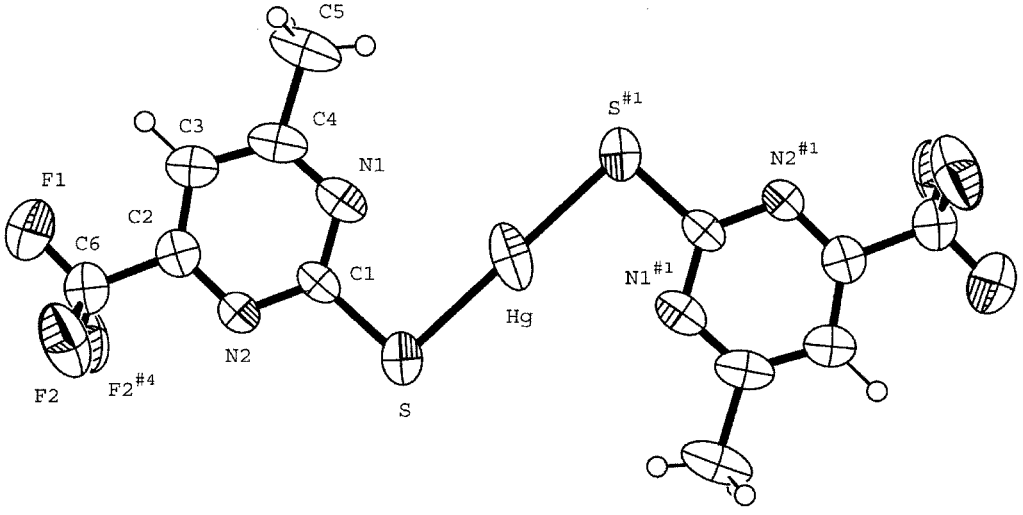

Figure 10. ORTEP diagram of the molecular structure of [Hg(4,6-CF_3MepymS)$_2$] (**8**), with 50% thermal ellipsoid probability. Symmetry codes: #1 = $-x + 1, -y + 1, -z + 1$; #4 = $x, y, -z + 1$.

 © 2005 Wiley-VCH Verlag GmbH & Co. KGaA, Weinheim

The Hg···Hg distance [3.4845(5) Å] is much longer than those found in elemental mercury[56] (3.02 Å), in mercury clusters with mercury in an oxidation state of zero or in dinuclear mercury(I) complexes (Hg_2^{2+}, 2.5 Å).[57] However, the distance is close to or shorter than the sum of the van der Waals radii (1.7–2.0 Å)[58] and even shorter than that observed in most other mercury(II) complexes (3.848–3.578 Å).[59–63] It is also similar to the shortest Hg···Hg distance found in the case of tris(1,3-dimethyluracil-5-yl)mercurioxonium salt, which dimerises in two different ways through weak Hg···Hg contacts [Hg···Hg distances in the range 3.4552(6) to 3.5974(5) Å].[64]

The pyrimidine rings are planar and the sulfur atoms are located in the same plane as the corresponding ring and the Hg atom. The S–C bond length (1.752 Å) is close to those found in many other complexes containing thionate ligands.

Each [Hg(4,6-CF_3MepymS)$_2$] unit is essentially planar given that the pyrimidine ring is planar and both rings in each unit are related by an inversion centre located on the mercury atom. The pyrimidine rings of each unit are parallel to the crystallographic *ab* plane. In the crystal packing of the complex these units are arranged parallel to one another (Figure 11). The units are not superimposable but are related through a rotation of 180° around an axis that passes through the Hg centres and is parallel to the *b* axis, followed by a translation about the *c* axis (1 – *x*, *y*, *z* + 0.5). In this arrangement the molecules are stacked in the direction of the crystallographic *c* axis. Two types of intermolecular interaction are responsible for the packing arrangement. On the one hand, an Hg–Hg interaction exists between two units and this results in the Hg atoms being in a linear arrangement parallel to the *c* axis (Hg–Hg distance = 3.484 Å). On the other hand, a π–π stacking interaction exists between the pyrimidine rings of the contiguous [Hg(4,6-CF_3MepymS)$_2$] units (distance between the centroids = 3.512 Å). In this case the π–π stacking interaction gives rise to "perfect facial alignment", as shown by the angle formed by the centroids of the three consecutive rings (165.56°). This angle is very close to the 180° that one would expect for a complete interaction. It should also be noted that, for each interaction of this type, each ring is rotated with respect to the adjacent ring, meaning that the groups present on one ring do not eclipse those on other rings. This situation can clearly be seen in the diagram below (Scheme 2), which shows a view perpendicular to the plane of the pyrimidine rings (along the crystallographic *c* axis).

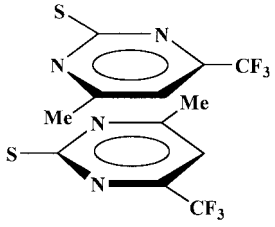

Scheme 2.

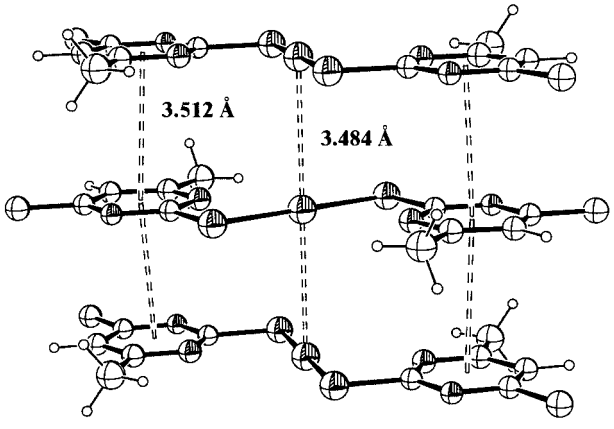

Figure 11. Partial packing diagram of **8** showing intermolecular π–π interactions and weak Hg···Hg contacts.

Spectroscopic Data

IR Spectra

The IR spectra of the complexes do not show bands due to ν(N–H), which in the free ligands appear between 3200 and 3050 cm^{-1}. This shows that deprotonation of the NH group has occurred during the synthesis and, therefore, that the ligand is coordinated in the thionato form. This conclusion is supported by the shift to smaller wavenumbers of the strong bands for ν(C=C) and ν(C=N), which appear at 1600–1550 and 1570–1525 cm^{-1}, respectively, in the free ligands, on going from the free ligands to the complexes. In addition, bands attributable to the ring breathing vibration at ca. 1000 and 630 cm^{-1} are observed. These shifts provide evidence that the nitrogen atom is bound to the metal atom.[65,66] In addition, the mixed complexes show bands typical for coordinated 2,2′-bypyridine[67] (770 and 730 cm^{-1}) and 1,10-phenanthroline[67,68] (1530–1505, 840 and 720 cm^{-1}).

NMR Spectra

The ^{1}H NMR spectra of the complexes do not contain a signal for the NH proton of the free ligand, which shows that the ligands are deprotonated in the complexes. The signals of all the protons of the pyrimidine ring and phenyl or methyl groups in the complexes are slightly shifted with respect to those of the free ligands. The NMR spectra of mixed complexes show additional signals for 2,2′-bipyridine and 1,10-phenanthroline at around δ = 7.6–9.2 ppm. These signals are slightly shifted to lower field in comparison to the corresponding signals in the free ligands. These changes again provide evidence of coordination of the ligands to the metal atom through the nitrogen atoms.[69–71] The ^{13}C NMR spectra of the free ligands 4,6-CF_3MepymSH and 4,6-CF_3PhpymSH show double the expected number of signals for C(2), C(6), CF_3 and CH_3, as the free ligands exist in two tautomeric forms. This doubling in the number of signals is not observed in the ^{13}C NMR spectra of the metal complexes. This situation provides evidence that, in solu-

 © 2005 Wiley-VCH Verlag GmbH & Co. KGaA, Weinheim

tion, the ligand is coordinated to the metal in the thionate form only.

The mercury complexes have $\delta(^{199}Hg)$ values in the δ = –1180 to –1213 ppm range. These values are similar to those found in other mercury(II) thionates in which a weak interaction between the metal atom and the heterocyclic nitrogen is observed.[11,49]

Mass Spectra

The cadmium and mercury complexes were also characterised by mass spectrometry using the positive-ion FAB technique in 3-nitrobenzyl alcohol (NBA) as matrix. The FAB spectra of $[Cd(RpymS)_2(bipy)]$ and $[Cd(RpymS)_2(phen)]$ show the molecular ion with the appropriate isotope distribution, as well as peaks due to the fragments produced by the loss of one and two thionate ligands. In the case of $[Cd(4,6\text{-}CF_3MepymS)_2(phen)]$ the peak due to the loss of the 1,10-phenanthroline is also observed at m/z = 294.

The FAB mass spectra of both of the mercury compounds, $[Hg(RpymS)_2]$, show the molecular ion peak at m/z = 561 (R = CF_3) and 589 (R = 4,6-CF_3,Me) along with peaks at m/z = 381 and 386, respectively, which are associated with [Hg(RpymS)] formed by loss of one thionate ligand.

Conclusions

In this report we have described the electrochemical synthesis of a series of homoleptic and heteroleptic neutral cadmium(II) complexes and homoleptic mercury complexes with pyrimidine-2-thione derivatives. The ligands differ in the nature, position and number of substituents in the heterocyclic ring.

In the case of $[Cd(4\text{-}CF_3pymS)_2]$ (**1**), the presence of the trifluoromethyl substituent is not sufficient to prevent the association process and, as a consequence, the compound is a polymer, with the metal atom in an $[S_4N_2]$ octahedral environment. However, the presence of coligands, such as 1,10-phenanthroline and 2,2′-bipyridine, in the coordination sphere of cadmium modifies the aggregation process and the complexes $[Cd(4,6\text{-}CF_3MepymS)_2bipy]$ (**4**) and $[Cd(4,6\text{-}CF_3PhpymS)_2bipy]$ (**6**) are monomers with the metal atom in a different $[S_2N_4]$ hexacoordinate environment for both compounds − distorted octahedral for **4** and distorted trigonal prismatic for **6**. The crystal packing of compound **6** shows the presence of C–H···π and π–π stacking interactions. The groups involved in the C–H···π interactions are in the 6-position of the pyrimidine rings.

Experimental Section

General Considerations: 4-Trifluoromethylpyrimidine-2-thione, 1,1,1-trifluoroacetone, 1,1,1-trifluoro-2,4-pentanedione, thiourea, benzaldehyde, 1,10-phenanthroline and 2,2′-bipyridine are all commercial products and were used as supplied. Cadmium (Aldrich) was used as 2 × 2 cm plates. Mercury metal, a commercial product, was washed with nitric acid and water prior to use.

Elemental analysis was performed with a Carlo–Erba EA microanalyser. IR spectra were recorded as KBr mulls on a Bruker IFS-66V spectrophotometer. ^1H and ^{13}C NMR spectra were recorded on a Bruker AMX 300 MHz instrument with $CDCl_3$ or $[D_6]$DMSO as solvent. Chemical shifts are given relative to TMS as the internal standard. ^{119}Hg NMR spectra were recorded on a Bruker AMX500 spectrometer with $CDCl_3$ as solvent. The mass spectra (FAB) were recorded on a Micromass Autospec spectrometer, with 3-nitrobenzyl alcohol as the matrix material.

[4,6-CF_3MepymSH]: This compound was obtained by direct reaction between thiourea (2.428 g, 32 mmol) and 1,1,1-trifluoro-2,4-pentanedione (5 g, 32 mmol) in ethanol in the presence of concentrated hydrochloric acid (1 mL) as a catalyst. The mixture was heated under reflux for 2 h and the resulting dusty yellow solid was filtered off. $C_6H_5F_3N_2S$ (194.17): calcd. C 37.11, H 2.60, N 14.43, S 16.51; found C 36.89, H 2.60, N 14.26, S 16.08. IR (KBr): $\tilde{\nu}$ = 3100–3200 (m, br), 1615 (vs), 1590 (vs), 1440 (m), 1350 (vs), 1320 (w), 1200(s, br), 1130 (m), 1100 (m), 1030 (w), 970 (s), 920 (m), 860 (w), 850 (m), 705 (w), 660 (w), 595 (w), 570 (w), 530 (m), 510 (w), 470 (m), 450 (m), 370 (w) cm^{-1}. ^1H NMR (300 MHz, $[D_6]$DMSO, 25°): δ = 14.40 (s, 1 H, NH), 7.19 (s, 1 H, H^5), 2.39 (s, 3 H, CH_3) ppm. ^{13}C NMR (300 MHz, $[D_6]$DMSO): δ = 181.00 and 172.13 (s, C^2), 155.86 and 153.72 (q $^2J_{^{13}C\text{-}^{19}F}$ = 35 Hz, C^4), 104.89 (s, C^5), 163.61 (s, C^6), 119.27 and 119.67 (q, $^1J_{^{13}C\text{-}^{19}F}$ = 275 Hz, CF_3), 23.45 and 18.46 (s, CH_3) ppm. MS (FAB): m/z = 194 (4,6-CF_3MepymSH).

[4,6-CF_3PhpymSH]: The precursor 1,1,1-trifluoro-4-phenyl-3-buten-2-one was prepared previously. Benzaldehyde (5.22 g, 49 mmol) and 1,1,1-trifluoroacetone (5.21 g, 49 mmol) were added to a solution of NaOH (9.93 g, 0.25 mol) in cold water (200 mL). The mixture was allowed to reach room temperature, stirred for 6 h and finally heated to 65 °C for 12 h. The organic compounds were extracted with CH_2Cl_2, dried ($MgSO_4$) and the solvent removed by vacuum distillation to give a colourless liquid. (yield: 3.81 g, 39%). ^1H NMR (300 MHz, $CDCl_3$): δ = 6.8 (d, olefinic protons), 6.9 (d, olefinic protons), 7.3 (m, Ph) ppm. ^{13}C NMR (300 MHz, $[D_6]$-DMSO): δ = 180.53 (q, CF_3), 150.44 (CO), 115–130 (C, phenyl ring), 34.42 and 38.42 (C, olefinic) ppm.

Dry ethanol (40 mL) was placed in a flame-dried round-bottomed flask purged with argon, and sodium (0.45 g, 19.9 mmol) was added at 0 °C. When effervescence had ceased, a solution of thiourea (0.38 g, 4.99 mmol) in dry ethanol (30 mL) was added by cannula and the mixture was stirred for 15 min at room temperature. A solution of the previously prepared 1,1,1-trifluoro-4-phenyl-3-buten-2-one (1 g, 5 mmol) in dry ethanol was added to the reaction mixture by cannula. The mixture was heated under reflux under argon for 24 h. When the reaction was complete, the solvent was removed and the resultant solid was added to water (50 mL). The suspension was filtered and the alkaline solution was acidified to pH 6 with AcOH. The resulting dusty yellow solid was filtered off and washed with water until the washings were neutral. The solid was dried under vacuum to give 1.1 g of a dusty orange solid. The product was recrystallized from ethanol to give an orange solid. Yield: 0.652 g (51%). $C_{11}H_7F_3N_2S$ (256.25): calcd. C 51.50, H 2.75, N 10.93, S 12.51; found C 51.40, H 2.81, N 11.02, S 12.39. IR (KBr): $\tilde{\nu}$ = 3100–3200 (m, br), 1645 (m), 1610 (s), 1570 (s), 1550 (m), 1530 (m), 1490 (m), 1460 (m), 1450 (w), 1390 (vs), 1350 (m), 1330 (m), 1310 (w), 1260 (s), 1190 (vs), 1140 (m), 1110 (m), 1000 (s), 970 (w), 900 (m), 870 (w), 830 (s), 720 (m), 710 (w), 690 (s), 630 (m), 580 (m), 470 (w), 410 (w) cm^{-1}. ^1H NMR (300 MHz, $[D_6]$-DMSO): δ = 13.0 (s, 1 H, NH), 7.8 (s, 1 H, H^5), 7.6 (m, Ph) ppm. ^{13}C NMR (300 MHz, $[D_6]$DMSO): δ = 169.30 (s, C^2), 167.31 (q,

 © 2005 Wiley-VCH Verlag GmbH & Co. KGaA, Weinheim

C^4), 110.42 (s, C^5), 163.85 (s, C^6), 118.54 (q, CF_3), 122.98–135.32 (phenyl ring) ppm. MS: m/z = 257.2 [M^+], 511 [M_2^+].

Electrochemical Synthesis: All complexes were obtained by an electrochemical procedure.[25] The cell was a 100-mL, tall-form beaker fitted with a rubber bung. An acetonitrile solution of the thione containing tetraethylammonium perchlorate (10 mg) was electrolysed using a platinum wire as the cathode and a cadmium plate as a sacrificial anode suspended from another platinum wire. For the synthesis of mercury compounds, the anode, which was in the bottom of the vessel, was also connected through a platinum wire. For the synthesis of mixed complexes, the corresponding co-ligand was added to the solution phase. In all cases, hydrogen was evolved at the cathode. The cells can be summarised as $M_{(+)}/CH_3CN$ + RpymSH + L′/$Pt_{(-)}$. During the electrolysis the yellow colour of the solution faded and, at the end of the reaction, the solids were isolated by filtration.

[Cd(4-CF_3pymS)$_2$] (1): Electrochemical oxidation of a cadmium anode in a solution of 4-(trifluoromethyl)pyrimidine-2-thione (4-CF_3pymSH; 0.150 g, 0.83 mmol) in acetonitrile (50 mL) at 14 V and 10 mA for 1.5 h caused 36 mg of cadmium to be dissolved (E_f = 0.52 mol F^{-1}). During the electrolysis hydrogen was evolved at the cathode and at the end of the experiment a crystalline solid, suitable for X-ray studies, had formed at the bottom of the vessel. The yellow solid was filtered off, washed with acetonitrile and diethyl ether and dried under vacuum. Yield: 0.102 g (52%). $C_{10}H_4CdF_6N_4S_2$ (470.69): calcd. C 25.5, H 0.9, N 11.9, S 13.6; found C 25.5, H 0.8, N 12.0, S 13.6. IR (KBr): $\tilde{\nu}$ = 1570 (s), 1550 (vs), 1420 (m), 1345 (s), 1325 (vs), 1200 (s), 1175 (m), 1145 (m), 1110 (s), 830 (vs), 780 (m), 730 (s), 670 (s), 470 (m), 440 (m) cm^{-1}. ^1H NMR (300 MHz, [D_6]DMSO): δ = 7.37 (d, 1 H, H^5), 8.53 (d, 1 H, H^6) ppm. ^{13}C NMR (300 MHz, [D_6]DMSO): δ = 183.34 (C^2), 168.68 (C^6), 154.17 (q, C^4), 114.95 (C^5), 120 (q, CF_3) ppm.

[Cd(4-CF_3pymS)$_2$(bipy)] (2): Electrolysis of an acetonitrile solution containing 4-CF_3pymSH (0.150 g, 0.83 mmol), 2,2′-bipyridine (0.065 g, 0.42 mmol) and a small amount of tetraethylammonium perchlorate (ca. 10 mg) at 10 mA and 16 V for 1.5 h dissolved 26 mg of cadmium (E_f = 0.44). At the end of the experiment the white solid was filtered off, washed with acetonitrile and dried in vacuo. The compound was characterised as [Cd(4-CF_3pymS)$_2$(bipy)] (**2**). Yield: 0.142 g (55%) $C_{20}H_{12}CdF_6N_6S_2$ (626.88): calcd. C 38.3, H 1.9, N 13.4, S 10.2; found C 38.0, H 1.9, N 13.5, S 10.2. IR (KBr): $\tilde{\nu}$ = 1585 (m), 1550 (vs), 1475 (w), 1460 (w), 1430 (m), 1415 (s), 1335 (vs), 1240 (w), 1200 (vs), 1165 (w), 1150 (w), 1130 (m), 1110 (m), 1010 (m), 970 (m), 830 (m), 820 (m), 760 (s), 730 (m), 670 (s), 645 (w), 620 (w) cm^{-1}. ^1H NMR (300 MHz, [D_6]DMSO): δ = 7.21 (d, 2 H, H^5), 8.51 (d, 2 H, H^6); bipy: 9.10 (d, 2 H, $H^6/H^{6'}$), 7.60 (dd, 2 H, $H^5/H^{5'}$), 8.10 (dd, 2 H, $H^4/H^{4'}$), 8.80 (d, 2 H, $H^3/H^{3'}$) ppm. ^{13}C NMR (300 MHz, [D_6]DMSO): δ = 168.67 (C^2), 162.10 (C^6), 154.45 (q, C^4), 121 (q, CF_3), 114.9 (C^5), 149.12 (bipy, $C^2/C^{2'}$); 139.16 (bipy, $C^5/C^{5'}$), 125.38 (bipy, $C^3/C^{3'}$), 118.55 (bipy, $C^4/C^{4'}$) ppm. MS (FAB): m/z = 448 [Cd(4-CF_3pymS)(bipy)], 627 [Cd(4-CF_3pymS)$_2$(bipy)].

[Cd(4-CF_3pymS)$_2$(phen)] (3): A similar experiment to that described above (12 V, 10 mA, 1.5 h) with 4-CF_3pymSH (0.150 g, 0.83 mmol) and phenanthroline (0.084 g, 0.467 mmol) in acetonitrile (50 mL) dissolved 27 mg of cadmium (E_f = 0.46). The solid was filtered off, washed with cold acetonitrile and diethyl ether, and dried under vacuum. Yield: 0.122 g (45%). $C_{22}H_{12}CdF_6N_6S_2$ (650.90): calcd. C 40.6, H 1.9, N 12.9, S 9.8; found C 40.6, H 1.8, N 12.9, S 9.9. IR (KBr): $\tilde{\nu}$ = 1610 (m), 1580 (m), 1550 (vs), 1525 (w), 1510 (w), 1500 (s), 1480 (m), 1415 (vs), 1335 (vs), 1320 (m), 1190 (s), 1160 (m), 1130 (w), 1110 (w), 1095 (w), 1070 (w), 1010 (m), 985 (m), 970 (w), 860 (m), 840 (s), 830 (s), 815 (s), 770 (m), 720 (vs), 665 (s), 635 (m), 460 (w), 430 (w), 415 (w), 350 (w), 310 (w) cm^{-1}. ^1H NMR (300 MHz, [D_6]DMSO): δ = 7.60 (d, 2 H, H^5), 8.60 (d, 2 H, H^6); phen: 8.87 (d, 2 H, H^2/H^9), 7.80 (dd, 2 H, H^3/H^8), 8.80 (d, 2 H, H^7/H^4), 8.00 (s, 2 H, H^6/H^5) ppm. ^{13}C NMR (300 MHz, [D_6]DMSO): δ = 170.12 (C^2), 162.11 (C^6), 154.21 (C^4), 114.96 (C^5), 127 (q, CF_3), 149.62 (phen, C^9/C^2), 139.80 (phen, C^{4b}/C^{6b}), 139.33 (C^4/C^7), 128.74 (phen, C^{4a}/C^{6a}), 127.05 (phen, C^5/C^6), 125.13 (phen, C^3/C^8) ppm. MS (FAB): m/z = 471 [Cd(4-CF_3pymS)(phen)], 650 [Cd(4-CF_3pymS)$_2$(phen)].

[Cd(4,6-CF_3MepymS)$_2$(bipy)] (4): Electrolysis of an acetonitrile solution containing 4,6-CF_3MepymSH (0.200 g, 1.03 mmol) and bipyridine (0.080 g, 0.51 mmol) at 10 mA and 32 V for 2.75 h dissolved 73 mg of cadmium (E_f = 0.56). At the end of the experiment the yellow solid was filtered off, washed with acetonitrile and diethyl ether, and dried in vacuo. The compound was characterised as [Cd(4,6-CF_3MepymS)$_2$(bipy)]. Yield: 0.128 g (38%). $C_{22}H_{16}CdF_6N_6S_2$ (654.93): calcd. C 40.3, H 2.5, N 12.8, S 9.8; found C 40.7, H 2.3, N 12.9, S 9.6. IR (KBr): $\tilde{\nu}$ = 1590 (m), 1565 (vs), 1540 (vs), 1465 (m), 1435 (s), 1380 (vs), 1360 (m), 1310 (m), 1270 (vs), 1255 (s), 1220 (m), 1190 (m), 1135 (s), 1100 (m), 1010 (m), 1000 (m), 970 (m), 910 (m), 845 (s), 760 (s), 730 (m), 705 (s), 645 (w), 540 (m), 460 (w), 405 (w) cm^{-1}. ^1H NMR (300 MHz, $CDCl_3$): δ = 2.53 (s, 6 H, CH_3), 6.87 (s, 2 H, H^5); bipy: 8.91 (d, 2 H, $H^6/H^{6'}$), 7.82 (dd, 2 H, $H^5/H^{5'}$), 8.05 (dd, 2 H, $H^4/H^{4'}$), 8.23 (d, 2 H, $H^3/H^{3'}$) ppm. ^{13}C NMR (300 MHz, $CDCl_3$): δ = 184.07 (C^2), 169.13 (C^6), 155.17 (q, C^4), 109.57 (s, C^5), 24.33 (s, CH_3), 122.49 (q, CF_3), 150.62 (bipy, $C^2/C^{2'}$), 150.03 (bipy, $C^6/C^{6'}$), 140.17 (bipy; $C^5/C^{5'}$), 126.4 (bipy, $C^3/C^{3'}$), 112.8 (bipy, $C^4/C^{4'}$) ppm. MS (FAB): m/z = 463 [Cd(4,6-CF_3MepymS)(bipy)], 499 [Cd(4,6-CF_3MepymS)$_2$], 655 [Cd(4,6-CF_3MepymS)$_2$(bipy)].

Crystals of [Cd(4,6-CF_3MepymS)$_2$(bipy)] (**4**) suitable for X-ray studies were obtained by recrystallisation of the initial product from *i*PrOH.

[Cd(4,6-CF_3MepymS)$_2$(phen)] (5): An acetonitrile solution of 4,6-CF_3MepymSH (0.200 g, 1.03 mmol) and phenanthroline (0.100 g, 0.55 mmol) was electrolysed at 10 mA during 2.75 h and 68 mg of cadmium was dissolved from the anode (E_f = 0.53). At the end of the electrolysis the solution was concentrated and the resulting green solid was filtered off, washed with cold acetonitrile and diethyl ether, dried under vacuum and identified as [Cd(4,6-CF_3MepymS)$_2$(phen)]. Yield: 0.269 g (79%). $C_{24}H_{16}CdF_6N_6S_2$ (678.95): calcd. C 42.3, H 2.4, N 12.4, S 9.4; found C 42.0, H 2.4, N 12.6, S 9.0. IR (KBr): $\tilde{\nu}$ = 1570 (s), 1540 (vs), 1525 (w), 1505 (m), 1420 (m), 1385 (vs), 1360 (s), 1300 (m), 1270 (vs), 1255 (vs), 1220 (m), 1175 (s), 1160 (m), 1005 (w), 970 (w), 915 (m), 840 (s), 770 (w), 725 (s), 705 (vs), 630 (w), 545 (m), 460 (m) cm^{-1}. ^1H NMR (300 MHz, [D_6]DMSO): δ = 7.09 (s, 2 H, H^5), 2.06 (s, 6 H, CH_3); phen: 9.22 (dd, 2 H, H^2/H^9), 8.80 (d, 2 H, H^4/H^7), 8.01 (dd, 2 H, H^8/H^3), 8.2 (s, 2 H, H^5/H^6) ppm. ^{13}C NMR (300 MHz, [D_6]DMSO): δ = 184.07 (C^2), 169.13(C^6), 155.42 (q, C^4), 122.50 (q, CF_3), 109.34 (C^5), 24.40 (CH_3), 150.15 (phen, C^9/C^2), 141.82 (phen, C^{4b}/C^{6b}), 139.29 (phen, C^4/C^7), 129.62 (phen, C^{4a}/C^{6a}), 127.50 (phen, C^5/C^6), 125.39(phen, C^3/C^8) ppm. MS (FAB): m/z = 180 [phen], 294 [Cdphen], 487 [Cd(4,6-CF_3MepymS)(phen)], 499 [Cd(4,6-CF_3MepymS)$_2$], 679 [Cd(4,6-CF_3MepymS)$_2$(phen)].

[Cd(4,6-CF_3PhpymS)$_2$(phen)] (6): A similar experiment (6 V, 10 mA, 1 h) with 4,6-CF_3PhpymSH (0.100 g, 0.55 mmol) and phen (0.035 g, 0.19 mmol) in acetonitrile (50 mL) dissolved 18 mg of cadmium (E_f = 0.48). Crystals suitable for X-ray studies were obtained directly from the cell. The solid was filtered off, washed with cool acetonitrile and diethyl ether, and dried under vacuum. Yield:

 © 2005 Wiley-VCH Verlag GmbH & Co. KGaA, Weinheim

0.119 g (36%). $C_{34}H_{20}CdF_6N_6S_2$ (803.08): calcd. C 50.8, H 2.5, N 10.4, S 8.0; found C 50.4, H 2.3, N 10.4, S 7.9. IR (KBr): $\tilde{\nu}$ = 1615 (s), 1559 (m), 1540 (w), 1515 (w), 1500 (m), 1430 (w), 1400 (w), 1380 (vs), 1318 (s), 1300 (m), 1241 (m), 1180 (s), 1150 (s), 1135 (s), 1000 (s), 840 (m), 810 (w), 780 (s), 720 (w), 730 (m), 715 (w), 700 (m), 650 (w), 640 (m) cm^{-1}. ^1H NMR (300 MHz, [D$_6$]DMSO): δ = 8.41 (s, 2 H, H^5); phen: 9.07 (dd, 2 H, H^2/H^9), 8.79 (d, 2 H, H^4/H^7), 8.00 (dd, 2 H, H^3/H^8), 8.20 (s, 2 H, H^5/H^6) ppm; signals at δ = 7.39–7.84 ppm were assigned to the phenyl group.

[Hg(4-CF$_3$pymS)$_2$] (7): A solution of acetonitrile (50 mL) containing 4-CF$_3$pymSH (0.150 g, 0.83 mmol) was electrolysed at 10 mA during 2 h. No precipitation occurred initially, but within several hours a white solid had formed and this was filtered off, washed with acetonitrile, dried and identified by elemental analysis. Yield: 0.096 g (41%). $C_{10}H_4F_6HgN_4S_2$ (558.87): calcd. C 21.5, H 0.7, N 10.0, S 11.5; found C 22.0, H 0.6, N 10.3, S 11.2. IR (KBr): $\tilde{\nu}$ = 1550 (vs), 1420 (s), 1350 (vs), 1330 (vs), 1280 (w), 1200 (s), 1175 (w), 1110 (s), 1005 (w), 975 (s), 845 (m), 830 (m), 750 (w), 730 (m), 670 (s), 630 (w), 455 (w), 365 (w) cm^{-1}. ^1H NMR (300 MHz, [D$_6$]DMSO): δ = 7.43 (d, 2 H, H^5), 8.61 (d, 2 H, H^6) ppm. ^{13}C NMR (300 MHz, [D$_6$]DMSO): δ = 176.95 (C^2), 160.45 (C^6), 153.85 (q, C^4), 111.98 (C^5), 121.49 (q, CF_3) ppm. ^{119}Hg NMR (500 MHz $CDCl_3$): δ = –1213 ppm. MS (FAB): m/z = 560 [Hg(4-CF$_3$pymS)$_2$], 381 [Hg(4-CF$_3$pymS)].

[Hg(4,6-CF$_3$MepymS)$_2$] (8): A similar procedure was used to that described for [Hg(4-CF$_3$pymS)$_2$]. 4,6-CF$_3$MepymSH (0.200 g, 1.03 mmol) was electrolysed at 10 mA during 2 h. At the end of the experiment a microcrystalline white solid had formed and this was filtered off, washed with acetonitrile, dried and identified by elemental analysis. Yield: 0.114 g (38%). $C_{12}H_8F_6HgN_4S_2$ (587.94): calcd. C 24.6, H 1.4, N 9.6, S 11.0; found C 24.6, H 1.2, N 9.5, S 11.1. IR (KBr): $\tilde{\nu}$ = 1580 (vs), 1535 (s), 1385 (vs), 1310 (w), 1270 (s), 1255 (m), 1220 (m), 1170 (m), 1140 (m), 1110 (m), 1025 (w), 975 (m), 920 (w), 865 (s), 845 (s), 780 (w), 750 (w), 710 (vs), 680 (w), 635 (w), 565 (w), 550 (m), 485 (w), 450 (w), 370 (w) cm^{-1}. ^1H NMR (300 MHz, $CDCl_3$): δ = 7.18 (s, 2 H, H^5), 2.47 (s, 6 H, CH_3) ppm. ^{13}C NMR (300 MHz, $CDCl_3$): δ = 177.13 (s, C^2), 170.80 (s, C^6), 155.60 (q, C^4), 118.70 (CF_3), 112.58 (s, C^5), 24.40 (s, CH_3) ppm. ^{119}Hg NMR (500 MHz, $CDCl_3$): δ = –1207 ppm. MS (FAB): m/z = 386 [Hg(4,6-CF$_3$MepymS)], 588 [Hg(4,6-CF$_3$MepymS)$_2$], 386 [Hg(4,6-CF$_3$MepymS)].

Crystallisation from ethanol/acetone gave monocrystals suitable for X-ray studies.

X-ray Crystal Structure Determinations: X-ray data were collected on a Bruker Smart CCD 1000 diffractometer for **1** and **6**, and on an Enraf–Nonius CAD4 diffractometer in the cases of **4** and **8**, with graphite-monochromated Mo-K_α radiation (λ = 0.71073 Å). The data were collected at 293 K for all structures. The ω-scan technique was employed to measure intensities for all crystals. Decomposition of the crystals did not occur during data collection. Absorption effects in compounds **1** and **6** were corrected with SADABS.[72] Absorption in **4** and **8** was corrected by semi-empirical Ψ scans. All the structures were solved by direct methods and refined[73] by full-matrix least-squares based on F^2. For all the complexes, hydrogen atoms were also included in idealised positions and refined with isotropic displacement parameters. All non-hydrogen atoms in the structures were refined anisotropically with the exception of compound **4**, in which only the heavy atoms (mercury and sulfur) were refined anisotropically due to the poor quality of the high-angle data. The CF_3 groups of compounds **1** and **6** are disordered over two positions with occupancies 51:49 and 57:43 for the groups on C(5) and C(10) in compound **1** and 63:37 for the CF_3 group in compound **6**. Atomic scattering factors and anomalous dispersion corrections for all atoms were taken from the International Tables for X-ray Crystallography.[74] The crystal data and summary of data collection and structure refinement for these compounds are given in Table 5. The structures were visualised with ORTEP3.[75]

CCDC-240151–240154 (for **1**, **4**, **6** and **8**, respectively) contain the supplementary crystallographic data for this paper. These data can be obtained free of charge from The Cambridge Crystallographic Data Centre via www.ccdc.cam.ac.uk/data_request/cif.

Table 5. Crystal data and structure refinement for **1**, **4**, **6** and **8**.

	1	**4**	**6**	**8**
Empirical formula	$C_{10}H_4CdF_6N_4S_2$	$C_{22}H_{16}CdF_6N_6S_2$	$C_{17}H_{10}Cd_{0.50}F_3N_3S$	$C_{12}H_8F_6HgN_4S_2$
Formula mass	470.69	654.93	401.54	587.94
Crystal System	triclinic	orthorhombic	monoclinic	orthorhombic
Space group	$P\bar{1}$	*Aba*2	*C*2/*c*	*Ibam*
a [Å]	7.0419(2)	15.911(3)	23.3377(11)	7.632(2)
b [Å]	10.3710(4)	17.930(4)	13.6311(7)	31.855(6)
c [Å]	11.3981(3)	9.098(2)	10.5163(5)	6.969(1)
a [°]	81.768(1)	90	90	90
β [°]	78.624(1)	90	108.391(1)	90
γ [°]	70.736(1)	90	90	90
Volume [Å^3]	767.63(4)	2595.5(9)	3174.6(3)	1684.3(6)
Z	2	4	8	4
D_c [Mg m^{-3}]	2.036	1.676	1.680	2.301
μ(Mo-K_α) [mm^{-1}]	1.758	1.069	0.891	9.395
F(000)	452	1296	1600	1096
Crystal size [mm]	0.25 × 0.05 × 0.05	0.42 × 0.26 × 0.06	0.35 × 0.20 × 0.10	0.80 × 0.25 × 0.05
T [K]	293	293	293	293
No. of reflections collected	5131	748	10 808	893
No. of indept. reflections	3674	432	3908	484
Goodness of fit on F^2	0.956	1.069	1.052	1.064
R[a]	0.0481	0.0836	0.0570	0.0212
$wR2$[b]	0.1092	0.1958	0.1476	0.0493

[a] $R = \Sigma(|F_o| - |F_c|)/\Sigma|F_o|$. [b] $wR2 = \{\Sigma[w(|F_o|^2 - |F_c|^2)^2]/\Sigma(w|F_o^2|^2)\}^{1/2}$.

 © 2005 Wiley-VCH Verlag GmbH & Co. KGaA, Weinheim

Acknowledgments

We thank the Ministerio de Educación y Cultura of Spain and the Xunta de Galicia for financial support.

[1] E. S. Raper, *Coord. Chem. Rev.* **1985**, *61*, 115–184.
[2] E. S. Raper, *Coord. Chem. Rev.* **1996**, *153*, 199–225.
[3] E. S. Raper, *Coord. Chem. Rev.* **1997**, *165*, 475–567.
[4] B. Krebs, G. Henkel, *Angew. Chem. Int. Ed. Engl.* **1991**, *30*, 769–788.
[5] I. G. Dance, *Polyhedron* **1986**, *5*, 1037–1104.
[6] P. G. Blower, J. R. Dilworth, *Coord. Chem. Rev.* **1987**, *76*, 121–185.
[7] J. R. Dilworth, J. Hu, *Adv. Inorg. Chem.* **1993**, *40*, 411–459.
[8] K. Tang, M. Aslam, E. Block, T. Nicholson, J. Zubieta, *Inorg. Chem.* **1987**, *26*, 1488–1497.
[9] E. Block, M. Gernon, H. Kang, S. Liu, J. Zubieta, *J. Chem. Soc. Chem. Commun.* **1988**, 1031–1033.
[10] E. Block, M. Gernon, H. Kang, G. Ofori-Okai, J. Zubieta, *Inorg. Chem.* **1989**, *28*, 1263–1271.
[11] E. Block, M. Brito, M. Gernon, D. McGowty, H. Kang, J. Zubieta, *Inorg. Chem.* **1990**, *29*, 3172–3181.
[12] I. Casals, P. González-Duarte, J. Sola, J. Vives, M. Font-Bardia, X. Solans, *Polyhedron* **1990**, *9*, 769–771.
[13] E. Block, M. Gernon, H. Kang, S. Liu, J. Zubieta, *Inorg. Chim. Acta* **1990**, *167*, 143–146.
[14] E. Block, M. Gernon, H. Kang, G. Ofori-Okai, J. Zubieta, *Inorg. Chem.* **1991**, *30*, 1736–1747.
[15] E. Block, G. Ofori-Okai, H. Kang, J. Zubieta, *Inorg. Chim. Acta* **1991**, *188*, 7–13.
[16] W. Wojnowski, B. Becker, L. Walz, K. Peters, E.-M. Peters, H. G. von Schnering, *Polyhedron* **1992**, *11*, 607–612.
[17] H.-O. Stephan, G. Henkel, *Inorg. Chim. Acta* **1994**, *219*, 1–2.
[18] A. Sousa-Pedrares, I. Casanova, J. A. García-Vázquez, M. L. Durán, J. Romero, A. Sousa, J. Silver, P. J. Titler, *Eur. J. Inorg. Chem.* **2003**, 678–686.
[19] D. Dakternieks, K. Jurkschat, R. Tozer, J. Hook, E. R. S. Tiekink, *Organometallics* **1997**, *16*, 3696–3706.
[20] J. Fernández, M. B. Hurthouse, M. Laguna, R. Terrota, *J. Organomet. Chem.* **1999**, *574*, 207–212.
[21] S. R. Foley, G. P. A. Yap, D. S. Richeson, *J. Chem. Soc. Dalton Trans.* **2000**, 1663–1668.
[22] R. Jurkschat, V. Pieper, S. Seemeyer, M. Schurmanm, M. Biesmans, I. Verbruggen, R. Willem, *Organometallics* **2001**, *20*, 868–880.
[23] E. Block, G. Ofori-Okai, J. Zubieta, *J. Am. Chem. Soc.* **1989**, *111*, 2327–2329.
[24] M. M. Jones, *Met. Ions Biol. Syst.* **1983**, *16*, 47–83.
[25] J. A. García-Vázquez, J. Romero, A. Sousa, *Coord. Chem. Rev.* **1999**, *193–195*, 691–745.
[26] R. López Garzón, M. D. Gutiérrez Valero, M. L. Godino-Salido, B. K. Kepler, B. Nuber, *J. Coord. Chem.* **1993**, *30*, 111–123.
[27] A. C. Skapski, K. A. Woode, *Acta Crystallogr. Sect. B* **1979**, *35*, 59–62.
[28] P. Karagiannidis, S. K. Hadjikakou, P. Aslanidis, A. Hountas, *Inorg. Chim Acta* **1990**, *178*, 27–34.
[29] L. R. Battaglia, R. Battistuzzi, A. Bonamartini Corradi, C. Rizzolie, P. Sgarabotto, *J. Crystallogr. Spectrosc. Res.* **1993**, *23*, 937–942.
[30] J. Abbot, D. M. L. Goodgame, Y. Jeeves, *J. Chem. Soc. Dalton Trans.* **1978**, 880–884.
[31] L. Petrilli, F. Caruso, E. Rivarola, *Main Group Met. Chem.* **1994**, *17*, 439–446.
[32] P. K. Baker, P. D. Jackson, M. E. Harman, M. B. Hursthouse, *J. Organomet. Chem.* **1994**, *468*, 171–174.
[33] H. Engelking, S. Karentzopoulos, G. Reusmann, B. Krebs, *Chem. Ber.* **1994**, *127*, 2355–2361.
[34] Y. K. Au, K. K. Cheung, W. T. Wong, *J. Chem. Soc. Dalton Trans.* **1995**, 1047–1057.
[35] R. Castro, J. A. García-Vázquez, J. Romero, A. Sousa, R. Pritchard, C. McAuliffe, *J. Chem. Soc. Dalton Trans.* **1994**, 1115–1120.
[36] A. Rodríguez, J. A. García-Vázquez, A. Sousa-Pedrares, J. Romero, A. Sousa, *Inorg. Chem. Commun.* **2003**, *6*, 619–622.
[37] A. Rodríguez, J. A. García-Vázquez, A. Sousa-Pedrares, J. Romero, A. Sousa, *J. Organomet. Chem.* **2004**, *689*, 557–563.
[38] R. Castro, M. L. Durán, J. A. García-Vázquez, J. Romero, A. Sousa, E. E. Castellano, J. Zukerman-Schpector, *J. Chem. Soc. Dalton Trans.* **1992**, 2559–2563.
[39] L. Raston, A. H. White, *Aust. J. Chem.* **1976**, *29*, 739–742.
[40] A. McCleverty, S. Gill, R. S. Z. Kowalski, N. A. Bailey, H. Adams, K. W Lumbard, M. A. Murphy, *J. Chem. Soc. Dalton Trans.* **1982**, 493–503.
[41] B. Hursthouse, O. F. Z. Khan, M. Mazid, M. Moteralli, P. O. O'Brien, *Polyhedron* **1990**, *9*, 541–544.
[42] R. Castro, M. L. Durán, J. A. García-Vázquez, A. Sousa, A. Castiñeiras, W. Hiller, J. Strähle, *Z. Naturforsch.* **1992**, *47b*, 1067–1074.
[43] S. Furberg, J. Solbakk, *Acta Chem. Scand.* **1973**, *27*, 2536–2542.
[44] J. A. Castro, J. Romero, J. A. García-Vázquez, A. Castiñeiras, A. Sousa, *Polyhedron* **1995**, *14*, 2841–2847.
[45] R. Castro, J. A. García-Vázquez, J. Romero, A. Sousa, A. Castiñeiras, W. Hiller, J. Strähle, *Inorg. Chim. Acta* **1993**, *211*, 47–54.
[46] A. Sousa-Pedrares, J. Romero, J. A. García-Vázquez, M. L. Durán, I. Casanova, A. Sousa, *Dalton Trans.* **2003**, 1379–1388.
[47] E. S. Gruff, S. A. Koch, *J. Am. Chem. Soc.* **1990**, *112*, 1245–1247.
[48] P. A. W. Dean, V. Manivannan, J. J. Vitall, *Inorg. Chem.* **1989**, *28*, 2360–2368.
[49] J. Tallón, J. A. García-Vázquez, J. Romero, M. S. Louro, A. Sousa, Q. Chen, Y. Chang, J. Zubieta, *Polyhedron* **1995**, *14*, 2309–2317.
[50] S. Wang, J. P. Fackler, *Inorg. Chem.* **1989**, *28*, 2615–2619.
[51] R. T. C. Brownlee, A. J. Canty, M. F. MacKay, *Aust. J. Chem.* **1978**, *31*, 1933–1036.
[52] A. Bondi, *J. Phys. Chem.* **1964**, *68*, 441–451.
[53] J. L. Atwood, D. E. Berry, S. R. Stobart, M. J. Zaworotko, *Inorg. Chem.* **1983**, *22*, 3480–3482.
[54] A. Castiñeiras, W. Hiller, J. Strähle, J. Bravo, J. S. Casas, M. Gayoso, J. Sordo, *J. Chem. Soc. Dalton Trans.* **1986**, 1945–1948.
[55] D. St. Black, G. B. Deacon, G. L. Edwards, B. M. Gatehouse, *Aust. J. Chem.* **1993**, *46*, 1323–1326.
[56] N. N. Greenwood, E. Earnshaw, *Chemistry of the Elements*, 2nd ed., **1997**, p. 1205.
[57] K. Wurst, J. Strähle, *Z. Anorg. Allg. Chem.* **1991**, *595*, 239–250, and references cited therein.
[58] A. J. Canty, G. B. Deacon, *Inorg. Chim. Acta* **1980**, *45*, L225–L227.
[59] R. D. Schluter, G. Krauter, W. S. Rees, *J. Cluster Sci.* **1997**, *8*, 123–154.
[60] J. S. Casas, A. Castiñeiras, I. Haiduc, A. Sánchez, J. Sordo, E. M. Vázquez-López, *Polyhedron* **1997**, *16*, 781–787.
[61] J. S. Casas, E. M. Vázquez-López, J. Zukerman-Schpector, *J. Chem. Soc. Dalton Trans.* **1996**, 1973–1978.
[62] P. Biscarini, E. Foresti, G. Pradella, *J. Chem. Soc. Dalton Trans.* **1984**, 953–957.
[63] A. J. Canty, C. L. Raston, A. H. White, *Aust. J. Chem.* **1978**, *31*, 677–684.
[64] F. Zamora, M. Sabat, M. Janik, C. Siethoff, B. Lippert, *Chem. Commun.* **1997**, 485–486.
[65] R. C. Paul, H. S. Makhni, P. Singh, S. L. Chadha, *Z. Anorg. Allg. Chem.* **1970**, *377*, 108–112 references cited therein.
[66] R. D. Kross, V. A. Fassel, M. Hargoshes, *J. Am. Chem. Soc.* **1956**, *78*, 1332–1335.

 © 2005 Wiley-VCH Verlag GmbH & Co. KGaA, Weinheim

[67] A. A. Schilt, R. C. Taylor, *J. Inorg. Nucl. Chem.* **1959**, *9*, 211–221.
[68] R. G. Inskeep, *J. Inorg. Nucl. Chem.* **1963**, *24*, 763–776.
[69] S. Yamazaki, *Polyhedron* **1985**, *4*, 1915–1923.
[70] T. A. Annan, R. K. Chadha, D. G. Tuck, K. D. Watson, *Can. J. Chem.* **1987**, *65*, 2670–2676.
[71] H. E. Mabrouk, D. G. Tuck, *J. Chem. Soc. Dalton Trans.* **1988**, 2539–2543.
[72] G. M. Sheldrick, *SADABS, An empirical absorption correction program for area detector data*, University of Göttingen, Germany, **1996**.
[73] G. M. Sheldrick, *SHELX-97, Program for the solution and refinement of crystal structures*, University of Göttingen, Germany, **1997**.
[74] *International Tables for X-ray Crystallography*, vol. C, Kluwer, Dordrecht, **1992**.
[75] ORTEP3 for Windows: L. J. Farrugia, *J. Appl. Crystallogr.* **1997**, *30*, 565.

Received: October 08, 2004

 © 2005 Wiley-VCH Verlag GmbH & Co. KGaA, Weinheim

Trigonal-Prismatic vs. Octahedral Geometry for Mn^{II} Complexes with Innocent Didentate Ligands: A Subtle Difference as Shown by XRD and DFT on $[Mn(acac)_2(bpy)]$

Remy van Gorkum,[a] Francesco Buda,[a] Huub Kooijman,[b] Anthony L. Spek,[b] Elisabeth Bouwman,*[a] and Jan Reedijk[a]

Keywords: Trigonal prism / Distorted octahedron / Density Functional Theory (DFT) / Manganese(II) / Packing effects

In this paper the first example of a mixed-ligand Mn^{II} complex, having a trigonal-prismatic coordination geometry with simple, innocent, didentate ligands is presented. The solution and solid-state structures of $[Mn(acac)_2(bpy)]$ as studied by EPR spectroscopy, magnetic susceptibility measurements and XRD are presented: single crystals are hexagonal, space group $P6_1$ with unit cell dimensions a = 8.0482(9) Å, c = 51.602(10) Å, V = 2894.6(7) Å^3 and Z = 6. The complex has the trigonal-prismatic geometry only in the solid state. Density functional theory (DFT) calculations were performed to address the question of the preference for a specific coordination geometry in the related Mn^{II} complexes $[Mn(acac)_2(bpy)]$ (trigonal prismatic) and $[Mn(acac)_2(phen)]$ (distorted octahedral). Based on the very small energy differences for the calculated trigonal-prismatic and octahedral structures it has been concluded that crystal packing effects must contribute largely in determining the trigonal-prismatic structure for $[Mn(acac)_2(bpy)]$.
(© Wiley-VCH Verlag GmbH & Co. KGaA, 69451 Weinheim, Germany, 2005)

Introduction

Even though the first observed example of a trigonal-prismatic complex, $[Re(1,2\text{-}S_2C_2Ph_2)_3]$, dates back from 1965,[1] mixed ligand trigonal-prismatic complexes with simple didentate ligands are still rare. Since 1965 several tris(dithiolene) complexes with trigonal-prismatic or distorted octahedral geometry have been reported.[2] In addition a limited, but growing number of examples of non-dithiolene $[M(didentate)_3]$ trigonal-prismatic compounds is known, for instance with buta-1,3-diene, methyl vinyl ketone or acetylacetonate as ligands.[3–6] A few mixed ligand trigonal-prismatic complexes of the form $[M(didentate1)_2(didentate2)]$ are known, for example the complexes with a diimine and two (substituted) catechol semiquinonates as ligands,[7–9] but they are definitely not as common as homoleptic tris(didentate) complexes. Most compounds mentioned above have either noninnocent ligands, or ligands that can easily participate in π-(back) bonding. Therefore, it is not unexpected that for these complexes the majority of arguments for favoring trigonal-prismatic over octahedral geometry are electronic in nature, as for example: The overall charge of the complex, ligand-field stabilization energy, matching of ligand and metal orbital energies, bonding between the ligand donor-atoms and π-bonding.[10,11] Even some examples of six-coordinate trigonal-prismatic complexes with monodentate ligands have been reported.[12,13] These complexes all contain d^0 metal ions and in these cases the preference for the trigonal-prismatic geometry has been ascribed to the absence of steric or π-bonding effects.

A well-known strategy for obtaining trigonal-prismatic complexes is using rigid, penta- or hexadentate ligands that force the trigonal-prismatic geometry upon a complex by means of steric constraints.[14–16] This successful strategy has resulted in many examples of trigonal-prismatic complexes.

While searching for novel manganese-based catalysts for the oxidative drying of alkyd paints,[17] the X-ray structure of the well-known compound $[Mn(acac)_2(bpy)]$ was determined. Although this complex has been claimed to have an octahedral coordination geometry,[18] it appears to be the first example of a mixed-ligand complex with innocent didentate ligands that possesses the trigonal-prismatic coordination geometry. Herein, we describe the crystal structure details and EPR spectra of the complex. DFT calculations have been performed to address the question of the preference for trigonal-prismatic vs. octahedral geometry, comparing this complex with the related octahedral phenanthroline complex, $[Mn(acac)_2(phen)]$.

[a] Leiden Institute of Chemistry, Leiden University,
P. O. Box 9502, 2300 RA, Leiden, The Netherlands,
Fax: +31-71-5274451
E-mail: Bouwman@chem.leidenuniv.nl
[b] Bijvoet Center for Biomolecular Research, Crystal and Structural Chemistry, Utrecht University,
Padualaan 8, 3584 CH Utrecht, The Netherlands
Supporting information for this article is available on the WWW under http://www.eurjic.org or from the author.

Results

Synthesis and Characterization: The synthesis of [Mn(acac)$_2$(bpy)] is best carried out under argon until the product is isolated and dried, since the complex is very sensitive to air-oxidation when moist or in solution. The dried complex is stable in air. The yield (67%) is satisfactory, as was the elemental analysis.

Spectroscopic Features: The infrared spectrum of [Mn(acac)$_2$(bpy)] is in agreement with literature,[18] with important IR peaks being ν(C–O) 1604, 1578 cm^{-1}, ν(C–C) 1516 cm^{-1}, ν(M–O) 647, 536, 415 cm^{-1} and ν(M–N) 403, 228 cm^{-1}. The electronic spectrum of the solid compound shows an MLCT band at 365 nm (27.4×10^3 cm^{-1}).

EPR: The room temperature powder spectrum of [Mn(acac)$_2$(bpy)] shows a strong, nonisotropic resonance signal at g = 3.25 and a very weak signal at high field, at g = 0.74, see Figure 1. The powder spectrum of [Mn(acac)$_2$(phen)] shows a single broad signal at g = 2 (see the inset in Figure 1).[19]

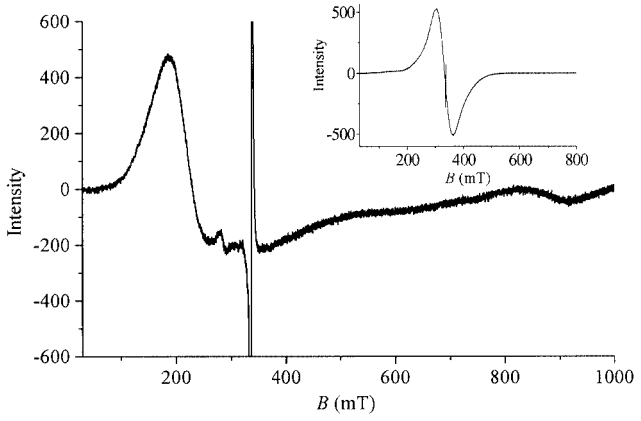

Figure 1. Room temperature powder EPR spectra of [Mn(acac)$_2$(bpy)] and [Mn(acac)$_2$(phen)] (inset). Important EPR parameters for both spectra: frequency 9.434 GHz, power 4 mW. The dpph reference can be seen as a sharp radical signal at 336 mT. The small signal at 280 mT is due to an impurity in the cavity.

The frozen-solution spectra (77 K, 0.001 M in CH_2Cl_2/toluene) of [Mn(acac)$_2$(bpy)] and [Mn(acac)$_2$(phen)] are nearly identical, showing a broad peak at g = 2.7 and a very broad signal (260–410 mT) centered around g = 2 (see supporting information for the frozen-solution EPR spectra of both compounds; for supporting information see also the footnote on the first page of this article). Overlapping the signal at g = 2 a six-line signal typical for octahedral manganese(II) is present, showing ^{55}Mn hyperfine structure and additional lines due to zero-field splitting.

Magnetic Susceptibility: A χT vs. T plot for [Mn(acac)$_2$(bpy)] shows a straight line which declines at low temperatures, most likely due to the zero-field splitting of the Mn^{II} ion.[20] Plotting χ^{-1} vs. T also results in a straight line and thus the compound obeys the Curie–Weiss law. Fitting the data, the Curie and Weiss constants are obtained, being C = 4.137 cm^{-3} K·mol^{-1} and θ = –1.35 K, respectively. The Curie constant allows for calculating the total molecular spin of the compound, and a value of S = 2.42 (ca. 5/2) is obtained. For [Mn(acac)$_2$(phen)] a value of μ_{eff} = 6.2 μ_b is given in the literature, which also confirms an S = 5/2 spin state.[21]

Description of the Crystal and Molecular Structure: The filtered reaction mixture was left stand overnight at –20 °C to yield single crystals of [Mn(acac)$_2$(bpy)] . The geometry of the complex and the atom labeling scheme are shown in Figure 2. Selected bond lengths and angles are collected in Table 1.

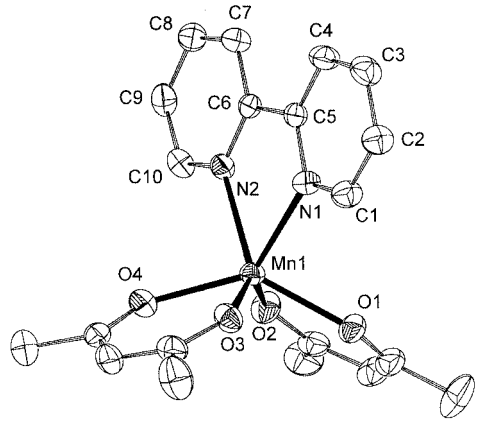

Figure 2. ORTEP plot of [Mn(acac)$_2$(bpy)], ellipsoids are shown at 50% probability. Hydrogen atoms are omitted for clarity.

Table 1. Selected bond lengths [Å] and angles [°] experimentally obtained with XRD compared to values obtained by DFT calculations.

	Prism			Octahedron		
	X-ray	Calculated		X-ray[22]	Calculated	
	bpy	bpy	phen	phen	bpy	phen
Mn1–O1	2.1480(16)	2.1380	2.1373	2.116(5)	2.1235	2.1259
Mn1–O2	2.1580(18)	2.1314	2.1281	2.152(5)	2.1358	2.1231
Mn1–O3	2.1534(16)	2.1316	2.1290	2.152(5)	2.1321	2.1275
Mn1–O4	2.1572(17)	2.1382	2.1361	2.116(5)	2.1182	2.1229
Mn1–N1	2.288(3)	2.3395	2.3603	2.307(5)	2.3549	2.3488
Mn1–N2	2.283(2)	2.3382	2.3603	2.307(5)	2.3713	2.3491
O1–Mn1–O2	81.69(6)	82.81	82.99	84.0(2)	84.34	84.88
O3–Mn1–O4	81.92(6)	82.79	83.01	84.0(2)	84.65	84.89
N1–Mn1–N2	70.41(8)	68.61	69.53	72.6(2)	68.80	70.60
N1–Mn1–O1	85.12(7)	83.88	82.77	93.4(2)	90.70	89.02
N1–Mn1–O2	129.76(8)	125.57	123.32	90.8(2)	94.13	95.37
N1–Mn1–O3	85.99(7)	83.98	83.55	86.6(2)	86.36	86.82
N1–Mn1–O4	134.44(7)	133.73	134.91	163.0(2)	156.55	156.71
N2–Mn1–O1	132.45(7)	133.71	134.89	163.0(2)	156.20	157.20
N2–Mn1–O2	83.83(8)	84.11	83.55	86.6(2)	85.21	86.92
N2–Mn1–O3	131.01(7)	125.40	123.35	90.8(2)	96.82	96.14
N2–Mn1–O4	85.20(7)	83.90	82.79	93.4(2)	90.82	88.68
O1–Mn1–O3	84.83(6)	85.54	86.20	98.1(2)	93.68	92.71
O1–Mn1–O4	136.62(7)	138.54	138.64	102.0(2)	111.44	113.07
O2–Mn1–O4	82.52(6)	85.41	86.22	98.1(2)	95.63	93.97
O2–Mn1–O3	139.97(8)	146.46	149.13	176.7(2)	177.95	176.71
Torsion angles						
N1–C5–C6–N2	3.0(3)	4.42	0.61	3.09	4.32	0.23
Ct1[a]–N2–N1–Ct2[b]	–2.1(3)	–5.92	–8.49	39.45	35.98	37.38
Ct1–O2–O1–Ct2	–1.9(3)	–5.44	–7.47	42.34	37.92	37.30
Ct1–O4–O3–Ct2	–2.5(3)	–5.54	–7.48	42.34	36.98	36.21

[a] Ct1 = Centroid of the triangular face O2–O4–N2. [b] Ct2 = centroid of triangular face O1–O3–N1.

The manganese(II) ion has an almost perfect N_2O_4 trigonal-prismatic coordination environment, with two acetylacetonate ligands and one bipyridine ligand. The manganese to nitrogen distances are 2.288(3) and 2.283(2) Å. The manganese to oxygen distance for the acetylacetonate li-

 © 2005 Wiley-VCH Verlag GmbH & Co. KGaA, Weinheim

gands is for each Mn–O bond almost the same, and lie in the range 2.1480(16)–2.1580(18) Å. The bite angles for each of the acetylacetonate ligands are also nearly identical, being 81.69(6)° (O1–Mn1–O2) and 81.92(6)° (O3–Mn1–O4). Since the bite angles are rather small and the Mn–O distance rather large, the Mn–O–C angles are also large, in the range 130.39(17)–131.78(16)°. The bipyridine ligand has a bite angle (N1–Mn1–N2) of 70.41°. The two acetylacetonate ligands are nearly planar, but the angle between the least-squares planes through the rings of the bipyridine ligand amounts to 3.79(12)°, and this ligand is thus not planar. For all three ligands, the atoms comprising the chelate rings deviate little from their least-squares mean plane. The obtuse angles between the least-squares mean planes of the chelate rings lie in the range 117.67(7)–121.30(6)°, in accordance with the trigonal-prismatic coordination geometry.

The two trigonal-faces of the prism constitute one oxygen atom of each of the acetylacetonate ligands and one nitrogen atom, thus forming O1–O3–N1 and O2–O4–N2. Figure 3 shows the trigonal-prismatic coordination geometry around manganese in more detail, and the dimensions and angles of the prism are tabulated in Table 2. The lengths of the triangular sides are in the range 2.901(2)–3.030(3) Å for the triangle O1–O3–N1 and 2.846(2)–3.007(3) Å for the triangle O2–O4–N2, all angles are in the range 56.88(7)–62.25(7)°. The four acetylacetonate oxygen atoms as make up an almost exact square, the sides of which are in the range 2.816(2)–2.901(2) Å. The remaining two faces of the prism are trapezoids consisting of two oxygen atoms of one acetylacetonate ligand and are joined by the two nitrogen atoms of bipyridine. Both faces have an O–O distance of 2.826(2) and 2.816(2) Å, an N–O distance in the range 2.968(3)–3.030(3) Å and a markedly shorter distance of 2.635(3) Å for the N1–N2 side. Since the N1–N2 side is shorter than the O–O sides of the trapezoid faces of the prism, the two triangular faces are not parallel. The planes defined by O1–N1–O3 and O2–N2–O4 make an angle of 4.04(10)°. The torsion angles about the centroids of the triangular faces and each of the corners [for example Ct1–N1–N2–Ct2 are –2.1(3)°, –1.9(3)° and –2.5(3)°] are faces exactly overlapping.. A perfect trigonal prism would have angles of 0°, the triangular faces exactly overlapping.

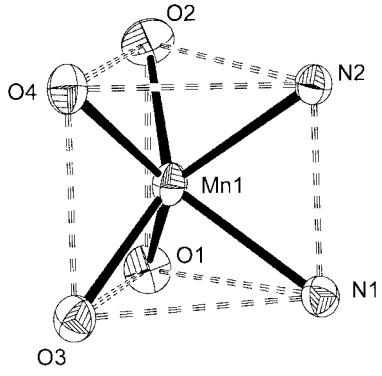

Figure 3. Trigonal-prismatic geometry of $[Mn(acac)_2(bpy)]$ in detail.

Table 2. Trigonal prism distances [Å] and angles [°] of $[Mn(acac)_2(L)]$, L = bpy (XRD & DFT data) or phen (only DFT).

	X-ray	Calculated	
	bpy	bpy	phen
O1–N1	3.002(3)	2.996	2.978
O1–O3	2.901(2)	2.899	2.915
O3–N1	3.030(3)	2.995	2.996
O2–N2	2.968(3)	2.998	2.978
O2–O4	2.846(2)	2.896	2.914
O4–N2	3.007(3)	2.996	2.978
N1–N2	2.635(3)	2.636	2.692
O1–O2	2.816(2)	2.824	2.826
O3–O4	2.826(2)	2.823	2.827
O3–O1–N1	61.74(6)	57.88	61.10
O3–O1–O2	90.22(6)	90.99	91.24
O2–O1–N1	87.51(8)	86.16	85.79
O1–O2–N2	88.99(8)	89.86	91.02
O4–O2–N2	62.25(7)	61.08	60.50
O4–O2–O1	89.91(6)	88.73	88.28
O1–O3–N1	60.76(6)	61.08	60.49
O1–O3–O4	88.61(6)	88.66	88.25
O4–O3–N1	88.77(7)	90.06	90.98
O2–O4–O3	91.17(6)	91.17	91.25
O2–O4–N2	60.88(7)	61.14	61.10
O3–O4–N2	87.56(7)	86.05	85.82
O1–N1–O3	57.50(6)	57.88	58.41
N2–N1–O3	90.63(9)	89.50	87.90
N2–N1–O1	91.78(10)	93.70	94.10
O2–N2–O4	56.88(7)	57.78	58.40
O2–N2–N1	91.65(9)	89.57	87.88
O4–N2–N1	92.93(9)	93.75	94.08

The crystal structure has a hexagonal unit cell and space group $P6_1$. Figure 4 and Figure 5 show the packing in the *a*, *b* and *c* directions. The structure is composed of right-handed helices along the *c*-axis and therefore is chiral. A single helix consists of six molecules of $[Mn(acac)_2(bpy)]$ per unit cell, due to the inherent hexagonal symmetry. The helices are tightly packed together in such a way that each molecule in the helix is part of a layer that extends in the *a* and *b* direction. Within such a layer, one can observe rows of $[Mn(acac)_2(bpy)]$ molecules with aligned bipyridine ligands, each bipyridine pointing in-between the acetylace-

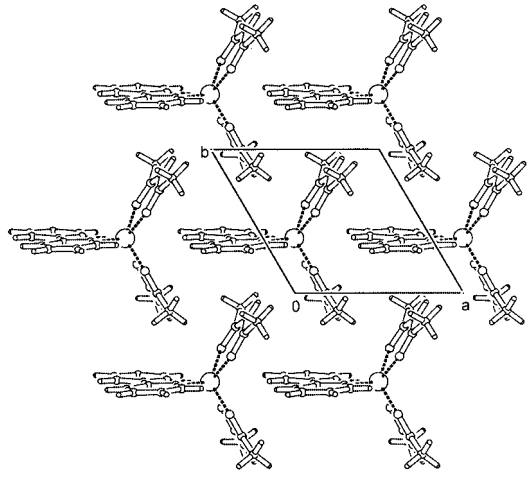

Figure 4. Crystal packing of $[Mn(acac)_2(bpy)]$ in the *a*,*b* plane. The acac methyl groups are packed together in rows along *a*.

 © 2005 Wiley-VCH Verlag GmbH & Co. KGaA, Weinheim

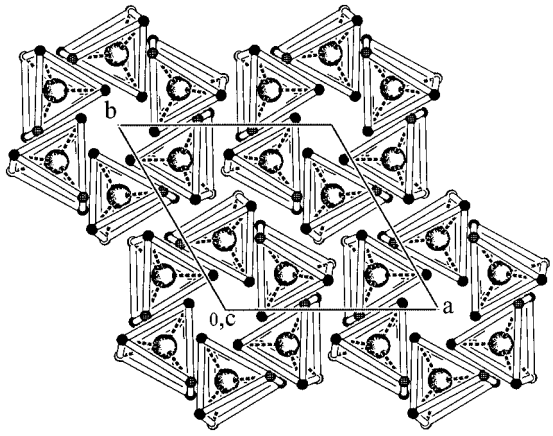

Figure 5. Projection of the crystal lattice of [Mn(acac)$_2$(bpy)] down the *c*-axis. The lattice is composed of right-handed helices in the *c* direction. Each complex in the helix is part of a layer in the *a*,*b* plane. Only the trigonal-prismatic polyhedra are shown for clarity.

tonate ligands of the following molecule in the row. Due to this orientation, all acetylacetonate methyl groups are also packed together in rows.

DFT Calculations: The DFT-B3LYP geometry optimization shows that the complex [Mn(acac)$_2$(bpy)] is stable in the trigonal-prismatic structure in vacuo and that the high-spin (S = 5/2) electronic state is the lowest energy configuration. Some of the theoretically predicted bond lengths and angles for this complex (in the vacuum) are reported in Table 2. The comparison between computed and experimental data in the crystal structure shows a good agreement. In particular the theory predicts that the bipyridine ligand is not planar, showing a small torsion angle of about 4° between its pyridine rings. The high-spin electronic configuration (S = 5/2) is important for the stability of the trigonal-prismatic geometry. Indeed, the optimized structure for S = 3/2 is found to be about 34 kcal/mol higher in energy than the S = 5/2 spin state. In the low-spin state S = 1/2, the trigonal-prismatic geometry is unstable and during the optimization the complex changes spontaneously towards an octahedral geometry.

To study the relative stability we have also optimized the complex [Mn(acac)$_2$(bpy)] in an octahedral coordination geometry in the vacuum. To obtain a relevant starting configuration the X-ray coordinates of the known octahedral compound [Mn(acac)$_2$(phen)] have been used,[22] removing C11 and C12 from the phen ligand in the coordinate file, thereby generating a bpy ligand. The final octahedral structure has an energy which is only a few tenths of a kcal/mol different from the energy of the trigonal-prismatic geometry. Given the typical accuracy of these calculations, the two structures can be considered energetically equivalent. The high-spin state is the lowest in energy also for the octahedral coordination geometry.

Subsequently the relative energy difference for the similar compound [Mn(acac)$_2$(phen)] was computed in a distorted-octahedral environment and in a trigonal-prismatic geometry for comparison. It turned out that for this compound the octahedral geometry is favoured by 1.5 kcal/mol over the trigonal-prismatic one, both again favoring the S = 5/2 spin state.

Discussion

Structural Features: The manganese to bipyridine distances 2.288(3) and 2.283(2) Å are not extraordinary and comparable to the Mn–N distances reported for the similar compound [Mn(acac)$_2$(phen)], which are 2.307 Å.[22] The bipyridine ligand has a bite angle N1–Mn1–N2 of 70.41°, which is quite small and can be related to the large ionic radius of Mn^{II}. Unsubstituted bipyridine ligands in manganese complexes commonly have bite angles varying between 72–80°.[23] Simple donor-atom to donor-atom repulsion energy considerations predict small bite angles for trigonal-prismatic complexes,[3] and indeed the average bite angle for the acetylacetonate ligands (81.81°) is among the lowest found for 2,4-pentanedionate coordinated to manganese(II).[23] The only other case found in literature where the 2,4-pentanedionato ligand coordinated to Mn^{II} has a bite angle smaller than 82°, is in the structure [Mn^{II}(Mn^{II}(acac)$_3$)$_2$], in which the two peripheral Mn^{II} ions also have a trigonal-prismatic coordination geometry.[24]

Trigonal Prism vs. Octahedron: Why does [Mn(acac)$_2$(bpy)] adopt a trigonal-prismatic coordination geometry in the solid phase, and why does the complex [Mn(acac)$_2$(phen)] not do so? The high-spin d^5 Mn^{II} ion has no ligand field stabilization and no large degree of π-bonding is present, since the magnetic data shows both complexes having a spin state of S = 5/2. This value would be lower if π-bonding would take place to the extent of that found in rhenium dithiolene complexes for example.[25]

The solid-state EPR spectra for the two complexes are quite different, reflecting the different coordination symmetries and thus the difference in the zero-field splitting parameters. The symmetry of the trigonal-prismatic complex is rhombic, which is the cause of the large EPR signal at g = 3.25. Although the exact magnitudes of the zero-field splitting parameters D, E and λ (= E/D) have not been calculated, it is clear from literature that D is likely to be significant ($0.05 < D < 0.15$ cm^{-1}) and λ will approach its limiting value of 1/3.[26] The complex [Mn(acac)$_2$(phen)] has a fairly regular octahedral coordination environment, which gives very small zero-field splitting values (D in the order of 10^{-2} cm^{-1}, λ approximately 0) and thus a resonance signal near the free electron value of g = 2 is observed.[26]

The similar solution-EPR spectra that are obtained demonstrate that in solution, the geometry around the Mn^{II} ion is comparable for both complexes.

The DFT calculations in vacuo show a slight (1.5 kcal/mol) preference for the octahedral geometry for [Mn(acac)$_2$(phen)], although this "octahedral" geometry is significantly trigonally distorted. The complex [Mn(acac)$_2$(bpy)] does not show a preference for either prism or octahedron, but there is some barrier for going from one to the other, since it does not adopt the trigonal-prismatic geometry when starting from the octahedral geometry. The calcu-

 © 2005 Wiley-VCH Verlag GmbH & Co. KGaA, Weinheim

lated octahedral complexes for both bpy and phen show a significant trigonal distortion of 37° (the average torsion angle between the centroids of the faces N1–O1–O3 and O2–N2–O4, see Table 1). This is even more than that for the starting configuration (the X-ray geometry of [Mn(acac)$_2$(phen)], see Figure 6) which has a trigonal distortion of 41.37° (for a regular octahedron this angle is 60°). Apparently, for both complexes there does seem to exist some driving force towards the trigonal-prismatic geometry. The calculations also show that the prismatic geometry is only stable for the high-spin complexes, the complex [Mn(acac)$_2$(bpy)] spontaneously adopts an octahedral geometry when the calculation is performed with $S = 1/2$. This behaviour is to be expected, since for the low-spin Mn^{II} ion ligand field stabilization energy does play a role and the octahedral geometry is now significantly lower in energy compared to the trigonal-prismatic conformation.[15]

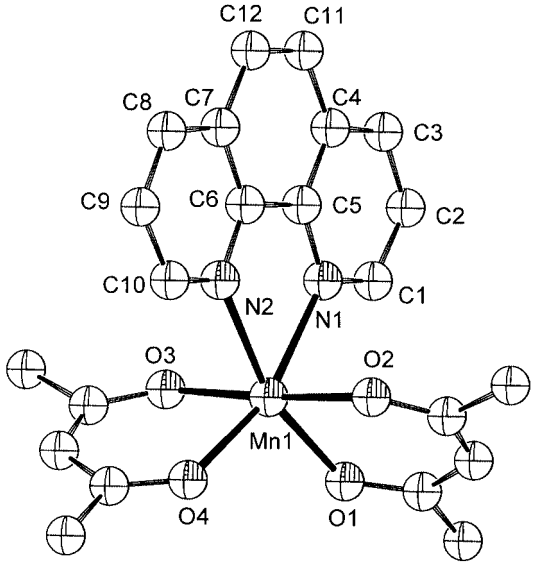

Figure 6. Molecular structure of [Mn(acac)$_2$(phen)]; hydrogen atoms are omitted for clarity; coordinates taken from the Cambridge structural database.

Contrary to expectation, the difference in rigidity between the bpy and phen ligand does not seem to have a large influence on the coordination geometry. Comparing the torsion angles for the calculated prismatic complexes in Table 2, it can be seen that the phen ligand can be regarded as more rigid than the bpy ligand, judging by the torsion angle N1–C5–C6–N2, which is 0.61° for phen vs. 4.42° for bpy. The same values are found for the calculated octahedral complexes. The deviation from a perfect prism is slightly larger for the phen complex, however, whereas for the calculated octahedral complexes the average trigonal distortion is identical. Furthermore, in the crystal structures the bpy and phen N1–C5–C6–N2 torsion angles are nearly identical, yet the coordination geometry is certainly different.

It thus seems that an important factor for determining the preference for octahedral vs. trigonal-prismatic geometry for the complexes [Mn(acac)$_2$(bpy)] and [Mn(acac)$_2$(phen)] is the crystal structure packing. In the *a*,*b* layer of the lattice of [Mn(acac)$_2$(bpy)], the bpy ligand fits precisely in-between the two acac ligands of the next molecule in the row (see Figure 4). The phenanthroline complex has a comparable *a*,*b* layer structure where the phenanthroline ligands of the complexes in the layer are aligned in rows and point towards, but do not fit in-between, the acac ligands of the next complex in the row.[22] The tighter packing that results for [Mn(acac)$_2$(bpy)] is likely stabilising the trigonal-prismatic geometry.

Conclusions

The trigonal-prismatic and octahedral environments in the compounds [Mn(acac)$_2$(bpy)] and [Mn(acac)$_2$(phen)] are both stable and very similar in energy for the high spin state. However, in the solid state [Mn(acac)$_2$(phen)] favours a (distorted) octahedral geometry whereas [Mn(acac)$_2$(bpy)] adopts a nearly perfect trigonal-prismatic geometry. Since the rigidity of the dinitrogen diimine ligand does not seem to play a role and the energy difference between different ligand environments for the complexes in the vacuum is quite small, packing effects in the crystal lattice must play an important role in determining the final solid-state structure.

Experimental Section

Materials: 2,2′-Bipyridine (bpy) and acetylacetone (Hacac) were purchased from Acros and used as received. [Mn^{II}(acac)$_2$(H$_2$O)$_2$] was prepared according to a literature procedure.[27] Methanol was distilled from CaH_2 and stored with 3-Å molecular sieves under argon prior to use.

Synthesis of [Mn(acac)$_2$(bpy)]: The title compound was synthesized using a slightly modified procedure from that published.[21] The reaction was performed under argon using standard Schlenk techniques. To a stirred, dark orange solution of [Mn(acac)$_2$(H$_2$O)$_2$] (1 g, 3.46 mmol) in 20 mL of methanol was added a solution of bpy (1.08 g, 6.92 mmol) in 10 mL of methanol. After 1 minute of stirring, [Mn(acac)$_2$(bpy)] precipitated as a bright yellow microcrystalline material. Stirring was continued for an additional 15 minutes and then the product was filtered under argon and dried for 24 hours at room temperature under reduced pressure. Yield: 0.95 g (67%). $C_{20}H_{22}MnN_2O_4$ (409.3): calcd. C 58.68, H 5.42, N 6.84; found C 58.51, H 5.26, N 7.08. The filtrate was stored overnight at –20 °C. Yellow, prismatic-shaped single crystals precipitated. One of these crystals was used to determine the crystal structure.

Physical Measurements: Elemental analyses on C, H and N was performed with a Perkin–Elmer series II CHNS/O Analyzer 2400. The IR spectrum was recorded with a Perkin–Elmer FT-IR Paragon 1000 spectrophotometer, using a CsI pellet (4000–200 cm^{-1}, resolution 1 cm^{-1}). Ligand field spectra were obtained with a Perkin–Elmer Lambda 900 spectrophotometer. The diffuse-reflectance technique was used with MgO as a reference for the solid compound. Electron paramagnetic resonance measurements were performed with a JEOL JES-RE2X ESR Spectrometer with a JEOL X-band microwave, a JEOL electromagnet and a JEOL ESPRIT 330 ESR Datasystem unit. A special quartz Dewar flask was used for measurements at liquid nitrogen temperature (77 K). Magnetic

 © 2005 Wiley-VCH Verlag GmbH & Co. KGaA, Weinheim

susceptibility measurements (5–300 K) were carried out using a Quantum Design MPMS-5 5T SQUID magnetometer (measurements carried out at 1000 Gauss). Data were corrected for magnetization of the sample holder and for diamagnetic contributions, which were estimated from the Pascal constants.

DFT Calculations: Density functional theory (DFT) calculations were performed to address the question of the preference for a specific coordination geometry in the Mn^{II} complex [$Mn(acac)_2$(bpy)]. The relative energy of the trigonal-prismatic vs. the octahedral coordination geometry was calculated for the complex [$Mn(acac)_2$-(bpy)] in the vacuum. For comparison the same relative energy difference was calculated for the related phenanthroline compound [$Mn(acac)_2$(phen)], which is known to have a distorted octahedral environment about the Mn atom in the solid state.[22]

The hybrid B3LYP exchange and correlation functional was used.[28] All self-consistent field (SCF) calculations were done using the 6-31G(d,p) gaussian basis set and were performed with the Gaussian 98 package.[29] The geometries of the various complexes were fully optimised without imposing any symmetry constraint. All calculations were spin unrestricted and the relative stability of the different spin states were checked.

X-ray Crystallographic Study: A crystal of dimensions $0.10 \times 0.15 \times 0.35$ mm was selected from a batch of yellow prisms, obtained from the filtrate of the reaction mixture overnight at –20 °C. Crystal data and details on data collection are listed in Table 3.

Table 3. Crystallographic data for [$Mn(acac)_2$(bpy)].

Formula	$C_{20}H_{22}MnN_2O_4$
Fw	409.34
Crystal system	hexagonal
Space group	$P6_1$
a [Å]	8.0482(9)
c [Å]	51.602(10)
V [Å^3]	2894.6(7)
Z	6
λ [Mo-K_α]	0.71073
T [K]	150
$\delta_{calcd.}$ [g cm^{-3}]	1.4089(3)
μ [mm^{-1}]	0.712
R [$I > 2\sigma(I)$][a]	0.0291
wR_2[b]	0.0584
GoF	1.035

[a] $R = \Sigma(||F_o| - |F_c||)/\Sigma|F_o|$. [b] $wR_2 = \{\Sigma[w(F_o^2 - F_c^2)^2]/\Sigma[w(F_o^2)^2]\}^{1/2}$.

Data were collected with an Enraf–Nonius KappaCCD area detector on a rotating anode. 30196 Reflections were measured ($1.0° < \theta < 25.37°$), 3375 of which were independent ($R_{int} = 0.0528$). The structure was solved by Patterson methods (DIRDIF[30]) and refined on F^2 by using SHELXL-97-2.[31] Hydrogen atoms were included in the refinement on calculated positions, riding on their carrier atoms. Methyl hydrogen atoms were refined as a rigid group, allowing for rotation around the C–C bond. Non-hydrogen atoms were refined with anisotropic displacement parameters Hydrogen atoms were refined with a fixed isotropic displacement parameter linked to the value of the equivalent isotropic displacement parameter of their carrier atoms. A total of 248 parameters were refined. All peaks in the final difference Fourier map were in the range $-0.19 < \Delta\rho < 0.18$ e·Å^{-3}. The Flack *x* parameter,[32] derived during the final structure-factor calculation, amounts to –0.012(14), indicating a correctly assigned absolute structure. Refinement of the inverse absolute structure resulted in an *x* parameter of 0.97(2) (value derived during the final structure-factor calculation). Figures of merit for this inverted structure are $R_1 = 0.0428$, $wR_2 = 0.1067$ and $S = 1.040$. CCDC-257462 contains the supplementary crystallographic data for this paper. These data can be obtained free of charge from The Cambridge Crystallographic Data Centre via www.ccdc.cam.ac.uk/data_request/cif.

Supporting Information (see also footnote on the first page of this article): The frozen-solution EPR spectra of [Mn(acac)2(bpy)] and [Mn(acac)2(phen)] are available as supporting information.

Acknowledgments

This work was carried out as part of the SENTER/Innovation Oriented Research Program on Heavy Metals (IOP) No. IZW99241c, sponsored by the Dutch Ministry of Economic Affairs. This work was supported in part (ALS) by the Council for the Chemical Sciences of the Netherlands Organisation for Scientific Research (CW-NWO). Mr. G. A. van Albada is kindly acknowledged for the magnetic susceptibility measurements.

[1] R. Eisenberg, J. A. Ibers, *J. Am. Chem. Soc.* **1965**, *87*, 3776–3778.
[2] C. L. Beswick, J. M. Schullman, E. I. Stiefel, in *Dithiolene Chemistry: Synthesis Properties and Applications* (Ed.: E. I. Stiefel), John Wiley & Sons Inc., Hoboken, New Jersey **2004**, vol. 52, p. 55–110.
[3] D. L. Kepert, in *Comprehensive Coordination Chemistry* (Ed.: G. Wilkinson), Pergamon, Oxford **1987**, vol. 1, p. 61.
[4] M. F. Lappert, C. L. Raston, B. W. Skelton, A. H. White, *J. Chem. Soc. Chem. Commun.* **1981**, 485–486.
[5] R. E. Moriarty, R. Bau, R. D. Ernst, *J. Chem. Soc. Chem. Commun.* **1972**, 1242–1244.
[6] P. S. Skell, M. J. McGlinchey, *Angew. Chem. Int. Ed.* **1975**, *14*, 195–199.
[7] A. S. Attia, C. G. Pierpont, *Inorg. Chem.* **1995**, *34*, 1172–1179.
[8] C. L. Simpson, C. G. Pierpont, *Inorg. Chem.* **1992**, *31*, 4308–4313.
[9] O. S. Jung, C. G. Pierpont, *Inorg. Chem.* **1994**, *33*, 2227–2235.
[10] M. L. Kirk, R. L. McNaughton, M. E. Helton, in *Dithiolene Chemistry: Synthesis Properties and Applications* (Ed.: E. I. Stiefel), John Wiley & Sons, Inc., Hoboken, New Jersey **2004**, vol. 52, p. 111–212.
[11] J. L. Martin, J. Takats, *Can. J. Chem.* **1989**, *67*, 1914–1923.
[12] P. M. Morse, G. S. Girolami, *J. Am. Chem. Soc.* **1989**, *111*, 4114–4116.
[13] J. C. Friese, A. Krol, C. Puke, K. Kirschbaum, D. M. Giolando, *Inorg. Chem.* **2000**, *39*, 1496–1500.
[14] S. G. Sreerama, S. Pal, *Inorg. Chem. Commun.* **2001**, *4*, 656–660.
[15] R. A. D. Wentwort, *Coord. Chem. Rev.* **1972**, *9*, 171–187.
[16] E. Larsen, G. N. Lamar, B. E. Wagner, R. H. Holm, J. E. Parks, *Inorg. Chem.* **1972**, *11*, 2652–2668.
[17] R. van Gorkum, E. Bouwman, J. Reedijk, *Inorg. Chem.* **2004**, *43*, 2456–2458.
[18] G. C. Percy, D. A. Thornton, *J. Mol. Struct.* **1971**, *10*, 39–48.
[19] K. Kaeriyama, *Bull. Chem. Soc., Japan* **1974**, *47*, 753–754.
[20] O. Kahn, *Molecular Magnetism*, Wiley-VCH Inc., New York **1993**, p. 14–26.
[21] F. P. Dwyer, A. M. Sargeson, *J. Proc. Roy. Soc., NSW* **1956**, *90*, 29–33.
[22] F. S. Stephens, *Acta Crystallogr. Sect. B* **1977**, *33*, 3492–3495.
[23] F. H. Allen, *Acta Crystallogr. Sect. B* **2002**, *58*, 380–388.
[24] S. Shibata, S. Onuma, H. Inoue, *Inorg. Chem.* **1985**, *24*, 1723–1725.
[25] E. I. Stiefel, R. Eisenberg, R. C. Rosenberg, H. B. Gray, *J. Am. Chem. Soc.* **1966**, *88*, 2956–2966.
[26] R. D. Dowsing, J. F. Gibson, D. M. Goodgame, M. Goodgame, P. J. Hayward, *Nature* **1968**, *219*, 1037–1038.

 © 2005 Wiley-VCH Verlag GmbH & Co. KGaA, Weinheim

[27] R. G. Charles, in *Inorg. Synth.* (Ed.: E. G. Rochow), McGraw-Hill, London **1960**, vol. VI, p. 164–166.
[28] P. J. Stephens, F. J. Devlin, C. F. Chabalowski, M. J. Frisch, *J. Phys. Chem.* **1994**, *98*, 11623–11627.
[29] M. J. Frisch, G. W. Trucks, H. B. Schlegel, G. E. Scuseria, M. A. Robb, J. R. Cheeseman, V. G. Zakrzewski, J. A. Montgomery Jr., R. E. Stratmann, J. C. Burant, S. Dapprich, J. M. Millam, A. D. Daniels, K. N. Kudin, M. C. Strain, Ö. Farkas, J. Tomasi, V. Barone, M. Cossi, R. Cammi, B. Mennucci, C. Pomelli, C. Adamo, S. Clifford, J. Ochterski, G. A. Petersson, P. Y. Ayala, Q. Cui, K. Morokuma, P. Salvador, J. J. Dannenberg, D. K. Malick, A. D. Rabuck, K. Raghavachari, J. B. Foresman, J. Cioslowski, J. V. Ortiz, A. G. Baboul, B. B. Stefanov, G. Liu, A. Liashenko, P. Piskorz, I. Komáromi, R. Gomperts, R. L. Martin, D. J. Fox, T. Keith, M. A. Al-Laham, C. Y. Peng, A. Nanayakkara, M. Challacombe, P. M. W. Gill, B. Johnson, W. Chen, M. W. Wong, J. L. Andres, C. Gonzalez, M. Head-Gordon, E. S. Replogle, J. A. Pople, *Gaussian 98*, Gaussian, Inc., Pittsburgh, PA **1998**.
[30] P. T. Beurskens, G. Admiraal, G. Beurskens, W. P. Bosman, S. García-Granda, R. O. Gould, J. M. M. Smits, C. Smykalla, The DIRDIF99 program system, University of Nijmegen, The Netherlands **1999**.
[31] G. M. Sheldrick, SHELXL-97-2, Program for crystal structure refinement, University of Göttingen, Germany **1997**.
[32] H. D. Flack, *Acta Crystallogr. Sect. A* **1983**, *39*, 876–881.
Received: December 06, 2004

 © 2005 Wiley-VCH Verlag GmbH & Co. KGaA, Weinheim

Complex Formation of ICL670 and Related Ligands with Fe^{III} and Fe^{II}

Stefan Steinhauser,[a] Uwe Heinz,[a] Mark Bartholomä,[a] Thomas Weyhermüller,[b] Hanspeter Nick,[c] Kaspar Hegetschweiler*[a]

Keywords: Iron / Ligand design / Chelates / N,O ligands / Redox chemistry

The pFe values of the two ligands H_3L^x and H_3L^y in section 2.3 on page 4183 of the original article[1] are incorrect; the corresponding sentence with the correct values should read as follows:

In general, the iron binding properties of H_3L^x and H_3L^y are indeed closely related: the pFe values[30] for H_3L^x and H_3L^y (total [L] = 10 μM, total [Fe] = 1 μM, pH = 7.4, H_2O, I = 0.1 M) are 23.5 and 22.6, respectively.

[1] S. Steinhauser, U. Heinz, M. Bartholomä, T. Weyhermüller, H. Nick, K. Hegetschweiler, *Eur. J. Inorg. Chem.* **2004**, 4177−4192.

Received: April 13, 2005
The Authors

[a] Anorganische Chemie, Universität des Saarlandes, Postfach 15 11 50, 66041 Saarbrücken, Germany
Fax: +49-681-302-2663
E-mail: hegetschweiler@mx.uni-saarland.de
[b] Max-Planck-Institut für Bioanorganische Chemie, Postfach 10 13 65, 45413 Mülheim an der Ruhr, Germany
[c] Novartis Institutes for BioMedical Research, WKL-136.P.72, Klybeckstrasse 141, 4002 Basel, Switzerland

 © 2005 Wiley-VCH Verlag GmbH & Co. KGaA, Weinheim **DOI: 10.1002/ejic.200500302**

EurJIC
European Journal of Inorganic Chemistry

Issue 12/2005

Pages 2265–2556

Papers available ahead of print in Early View at www.interscience.wiley.com

Earliest available Table of Contents: Automatically, free of charge by e-mail through www.interscience.wiley.com/alerts

COVER PICTURE

The cover picture shows how the isophthalate-bridged structures are tuned by various polydentate ligands from tetradentate ligand tpa to tridentate ligand tpm to bidentate ligand bpm, which results in one dinuclear and two one-dimensional complexes, $[Cu_2(tpa)_2(m\text{-bda})](ClO_4)_2$ (**1**), $\{[Cu_2(tpm)_2(m\text{-bda})_2]\cdot 2CH_3OH\cdot 4H_2O\}_n$ (**2**) and $\{[Cu_2(bpm)_2(m\text{-bda})_2(H_2O)]\cdot CH_3CN\cdot H_2O\}_n$ (**3**). The variable-temperature magnetic behavior reveals the existence of ferromagnetic interactions in them. Details of synthesis and characterization of these complexes are given in the article by P. Cheng et al. on p. 2297ff.

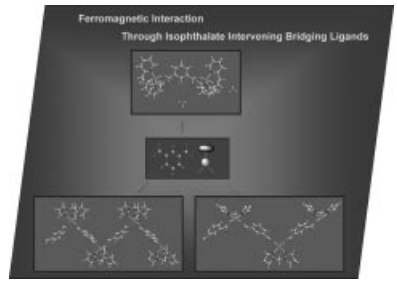

MICROREVIEW

Contents

2281 **R. K. O. Sigel***

Group II Intron Ribozymes and Metal Ions – A Delicate Relationship

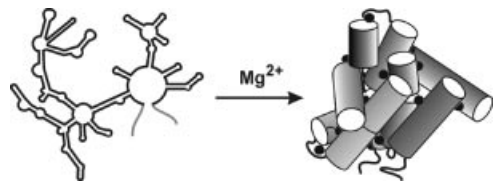

Keywords: Bioinorganic chemistry / Ribozymes / RNA structures / Metal ions / Calcium

 © 2005 Wiley-VCH Verlag GmbH & Co. KGaA, Weinheim

SHORT COMMUNICATION

2293 **L. Courthéoux, D. Amariei, S. Rossignol,* C. Kappenstein**

Facile Catalytic Decomposition at Low Temperature of Energetic Ionic Liquid as Hydrazine Substitute

Keywords: Platinum-based catalyst / Sol-gel synthesis / Ionic liquids / Alumina-silica / Catalyst activity

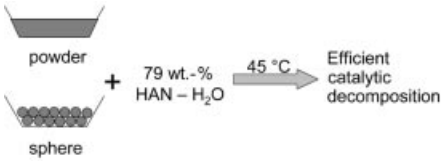

FULL PAPERS

2297 **W.-Z. Shen, X.-Y. Chen, P. Cheng,* S.-P. Yan, B. Zhai, D.-Z. Liao, Z.-H. Jiang**

A Structural and Magnetic Investigation of Ferromagnetically Coupled Copper(II) Isophthalates

Keywords: Copper / Magnetic properties / N ligands / Organic-inorganic hybrid composites

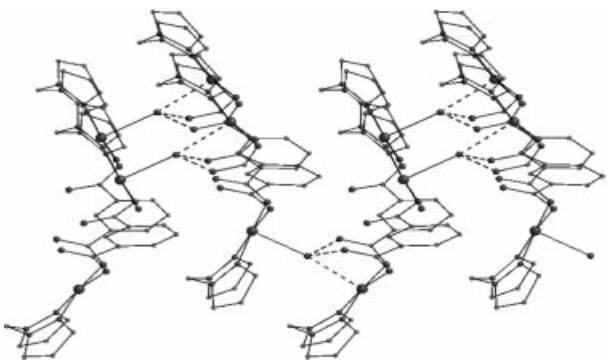

2306 **O. Fuhr,* L. Fernandez-Recio, D. Fenske**

New Copper Chalcogenide Clusters with a Selenide Core and a Sulfide Shell

Keywords: Cluster compounds / Chalcogens / Copper / S ligands

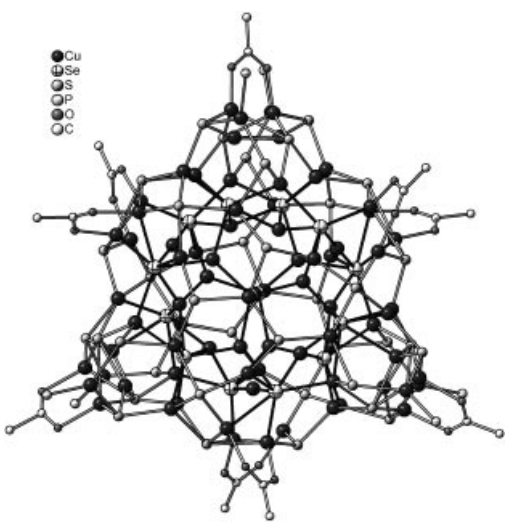

2315 **L. Flores-Santos, E. Martin,* A. Aghmiz, M. Diéguez, C. Claver, A. M. Masdeu-Bultó,* M. Muñoz-Hernández**

Cationic Iridium Complexes with Chiral Dithioether Ligands: Synthesis, Characterisation and Reactivity under Hydrogenation Conditions

Keywords: Chiral auxiliaries / S ligands / Iridium / Hydrides / Asymmetric catalysis

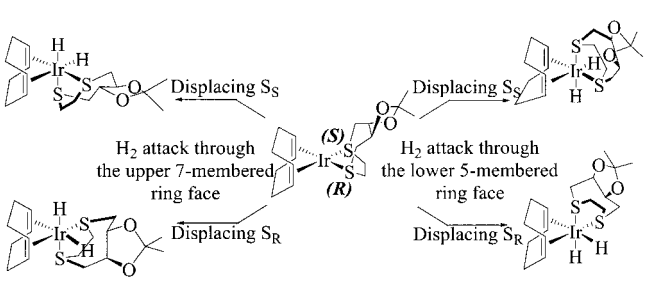

2324 **R. Poli,* I. Cacelli**

Orbital Splitting and Pairing Energy in Open-Shell Organometallics: A Study of Two Families of 16-Electron Complexes [Cp_2M] (M = Cr, Mo, W) and [$CpM(PH_3)$] (M = Co, Rh, Ir)

Keywords: Density functional calculations / Metallocenes / Open-shell organometallics / Pairing energy / Singlet−triplet gap

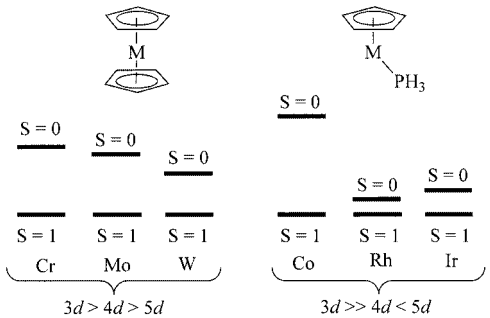

2332 **I. L. Fedushkin,* A. A. Skatova, G. K. Fukin, M. Hummert, H. Schumann***

Addition of Enolisable Ketones to (dpp-bian)-$Mg(THF)_3$ [dpp-bian = 1,2-Bis{(2,6-diisopropylphenyl)imino}acenaphthene]

Keywords: Enolisation / Ketones / Magnesium / N ligands

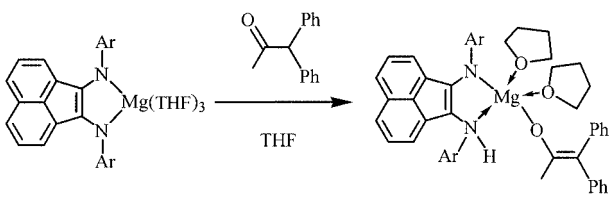

2339 **W. Lu, Z.-M. Yan, J. Dai,* Y. Zhang, Q.-Y. Zhu, D.-X. Jia, W.-J. Guo**

Coordination Assembly of TTF Derivatives through CuI Bridges

Keywords: Tetrathiafulvalene / Copper(I) complexes / Crystal structures / Molecular assembly

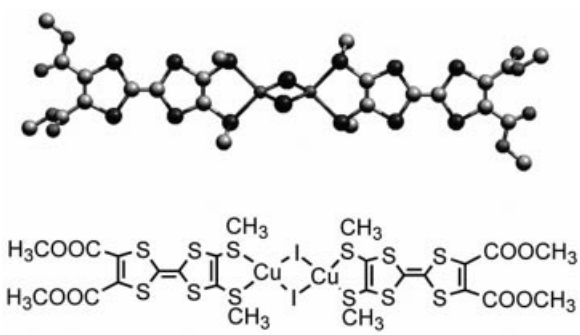

2346 **F. Meyer,* H. Pritzkow**

Bridging β-Lactam Coordination at Dinuclear Zinc Sites

Keywords: Dinuclear complexes / Metalloenzymes / N ligands / Pyrazolate ligands / Zinc

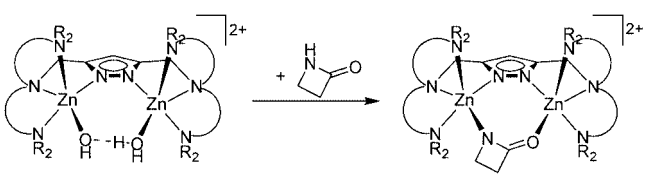

2352 **J. J. Schneider,* J. Engstler, K. P. Budna, C. Teichert, S. Franzka**

Freestanding, Highly Flexible, Large Area, Nanoporous Alumina Membranes with Complete Through-Hole Pore Morphology

Keywords: Alumina / Electrochemistry / Porous template / Oxidation

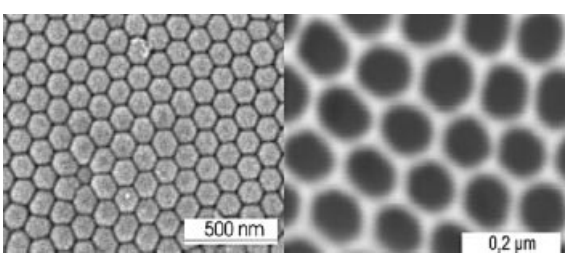

 © 2005 Wiley-VCH Verlag GmbH & Co. KGaA, Weinheim

2360 **G. Sánchez,* J. Vives, G. López, J. L. Serrano, L. García, J. Pérez**

Exploring the Reactivity towards Acidic Protic Ligands of the Di-μ-hydroxo Complex $[NBu_4]_2[Pd_2\{C_4(COOMe)_4\}_2(\mu\text{-}OH)_2]$: A Convenient Precursor in the Preparation of New Palladacyclopentadiene Complexes

Keywords: Palladacyclopentadiene complexes / Hydroxo complexes / Metallacycles / Cycloaddition

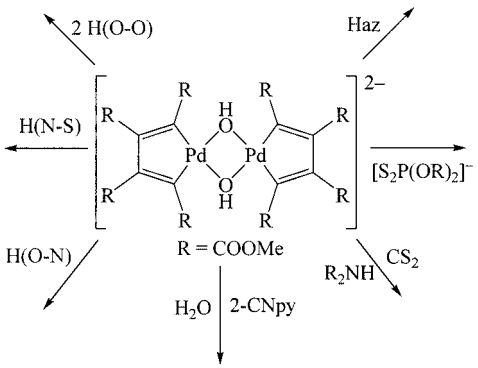

2368 **S. M. Nabavizadeh,* A. Akbari, M. Rashidi**

Thermodynamic Study of the Binding of Methyltrioxorhenium with Pyridine and Its Derivatives in Benzene Solution

Keywords: N ligands / Rhenium / Thermodynamics

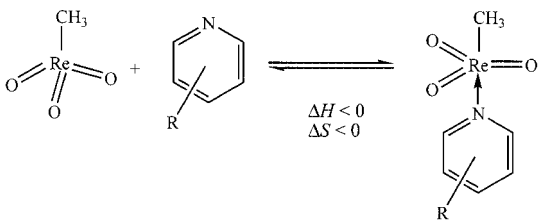

R = H; 4-Me; 3-Me; 4-C(CH$_3$)$_3$; 3-C(O)OMe; 3,4-Me$_2$; 3-Cl; 3-Ph and 4-CH$_2$Ph

2376 **S. Banerjee, M. G. B. Drew, C.-Z. Lu, J. Tercero, C. Diaz,* A. Ghosh***

Dinuclear Complexes of M^{II} Thiocyanate (M = Ni and Cu) Containing a Tridentate Schiff-Base Ligand: Synthesis, Structural Diversity and Magnetic Properties

Keywords: Copper / Nickel / N,N,O ligands / Schiff-base ligands / Magnetic properties / Crystal structures

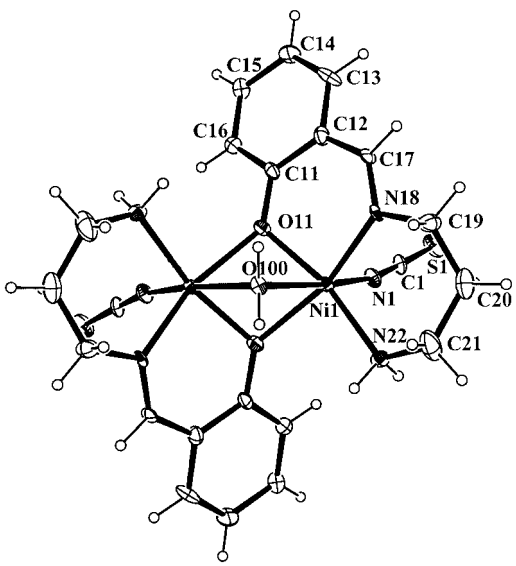

2384 **J. M. Harrowfield,* G. A. Koutsantonis, G. L. Nealon, B. W. Skelton, A. H. White**

Amphiphile Structures in the Solid State: Complex Cations with Lipophilic Substituents

Keywords: Cage complexes / Lipophilicity / Solid state structures

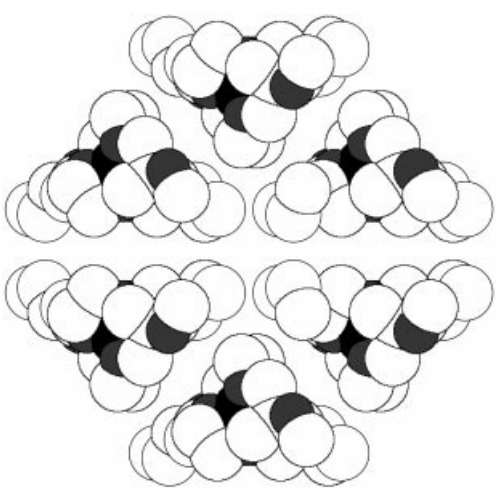

 © 2005 Wiley-VCH Verlag GmbH & Co. KGaA, Weinheim

2393 **D. Jiménez, R. Martínez-Máñez,* F. Sancenón, J. V. Ros-Lis, J. Soto, Á. Benito, E. García-Breijo**

Multi-Channel Receptors and Their Relation to Guest Chemosensing and Reconfigurable Molecular Logic Gates

Keywords: Cations / Chemosensing / Chromophores / Electrochemistry / Molecular logic gates

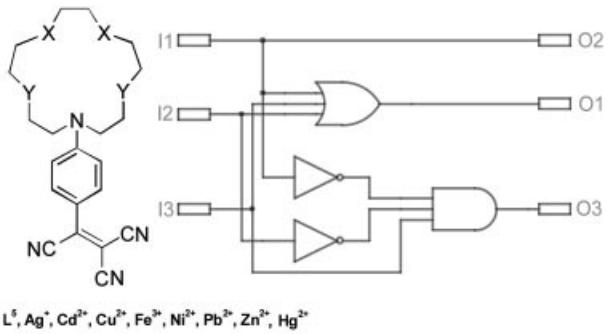

2404 **A. W. Addison,* R. J. Butcher, Z. Homonnay, V. V. Pavlishchuk, M. J. Prushan, L. K. Thompson**

The Hexakis(thiocyanato)ferrate(III) Ion: a Coordination Chemistry Classic Reveals an Interesting Geometry Pattern for the Thiocyanate Ligands

Keywords: Iron / Thiocyanate / X-ray diffraction / Magnetic properties / IR spectroscopy / Moessbauer spectroscopy / Coordination modes / Isomers

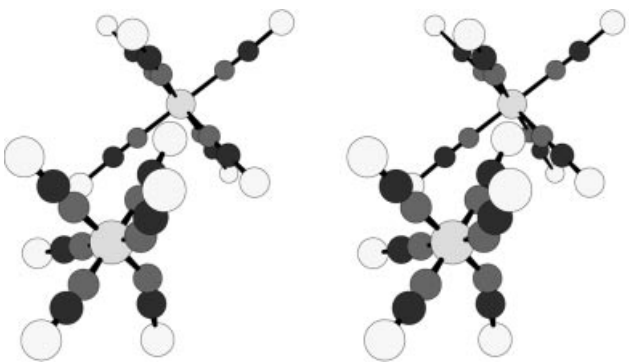

2409 **S. Tamburini,* U. Casellato, L. Bertolo, P. A. Vigato**

[1+1] Asymmetric Compartmental Macrocycles Bearing a Pendant Arm and Related *s,f*-Heterodinuclear Complexes Containing Lanthanide(III) and Sodium Ions

Keywords: Compartmental macrocycles / Lanthanides / Schiff bases / NMR of paramagnetic systems / Shift reagents / ^{23}Na NMR

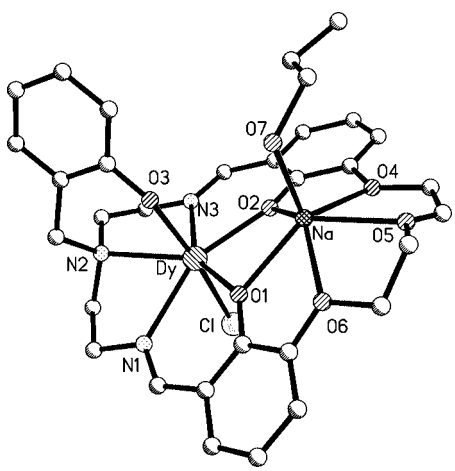

2423 **G. Tresoldi,* L. Baradello, S. Lanza, P. Cardiano**

Hemilabile Thioether Ligands Based on Pyrimidine and/or Pyridine Derivatives that Interconvert between *N,S*- and *N*-Coordination in Congested Ruthenium(II) Complexes

Keywords: Ruthenium / Pyridine thioether / Pyrimidine thioether / *N,S*-Coordination / *N*-Coordination

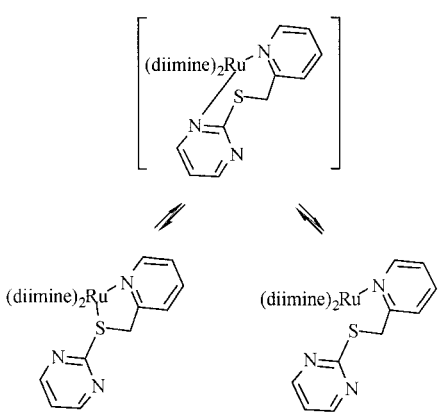

 © 2005 Wiley-VCH Verlag GmbH & Co. KGaA, Weinheim

2436 **V. Lloveras, A. Caballero, A. Tárraga, M. Desamparados Velasco, A. Espinosa, K. Wurst, D. J. Evans, J. Vidal-Gancedo, C. Rovira, P. Molina,* J. Veciana***

Synthesis and Characterization of Radical Cations Derived from Mono- and Biferrocenyl-Substituted 2-Aza-1,3-butadienes: A Study of the Influence of an Asymmetric and Oxidizable Bridge on Intramolecular Electron Transfer

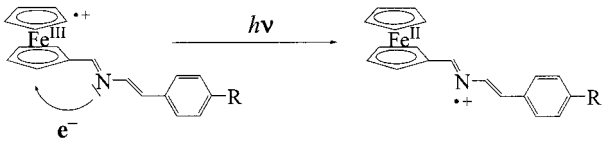

Keywords: Charge transfer / Electrochemistry / Electron transfer / Metallocenes / Optical spectroscopy

2451 **L. Bareille, P. Le Gendre,* P. Richard, C. Moïse***

Towards a Library of "Early-Late" Ti−Ru Bimetallic Complexes

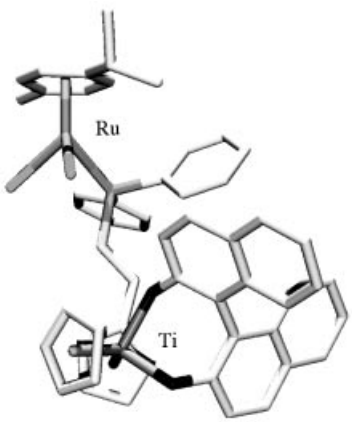

Keywords: Heterometallic complexes / Metallocenes / Ruthenium / Titanium

2457 **D. Pucci,* G. Barberio, A. Bellusci, A. Crispini, M. La Deda, M. Ghedini, E. I. Szerb**

Induction of Columnar Mesomorphism in Tetracoordinated Ionic Silver(I) Complexes Based on Chelate 4,4′-Disubstituted 2,2′-Bipyridines

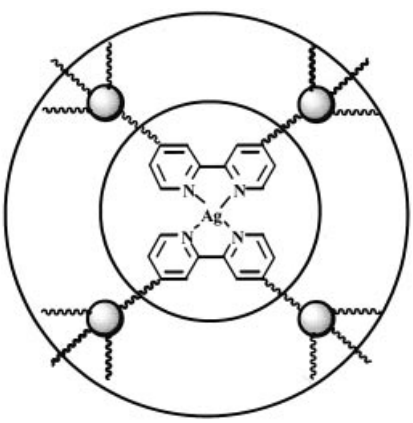

Keywords: Bipyridine ligands / Silver / Metallomesogens / Ionic / Luminescence

2464 **K. Koszinowski, M. Schlangen, D. Schröder, H. Schwarz***

Formation, Structure, and Reactivity of Gaseous $Ni_2O_2^+$

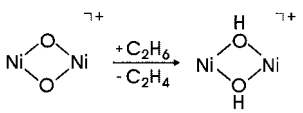

Keywords: Catalysis / C−H bond activation / Gas-phase reactions / Metal clusters / Nickel / Transition-metal oxides

 © 2005 Wiley-VCH Verlag GmbH & Co. KGaA, Weinheim

2470 **Y. Mulyana, C. J. Kepert,* L. F. Lindoy,* J. C. McMurtrie**

New Cadmium(II) and Iron(II) Coordination Frameworks Incorporating a Di(4-pyridyl)isoindoline Ligand

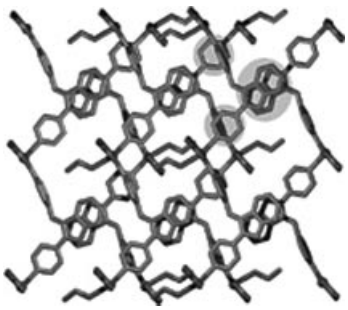

Keywords: Cadmium / Iron / Molecular framework

2476 **Y. V. Mironov, S. S. Yarovoi, D. Y. Naumov, N. V. Kuratieva, S. G. Kozlova, A. Simon, V. E. Fedorov***

First Examples of Chalcofluoride Rhenium Cluster Complexes with Cubane-Like Anions $[Re_4Q_4F_{12}]^{4-}$ (Q = S, Se)

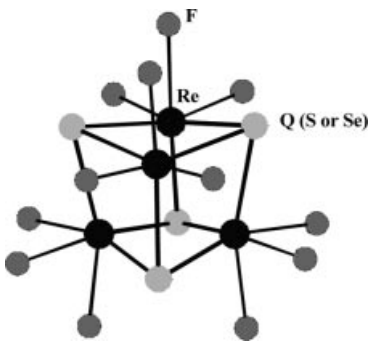

Keywords: Tetrahedral rhenium cluster / Chalcofluoride complexes / Density functional calculations

2480 **S. Groysman, E. Sergeeva, I. Goldberg, M. Kol***

Salophan Complexes of Group IV Metals

Keywords: Salophan / Tetradentate ligands / N,O ligands / Coordination modes / Octahedral complexes / Titanium / Zirconium

2486 **L. Brachais, M. Visseaux***

NMR T_1-Relaxation Measurements on Paramagnetic Organolanthanides: An Alternative Tool for Structure Determination in Solution

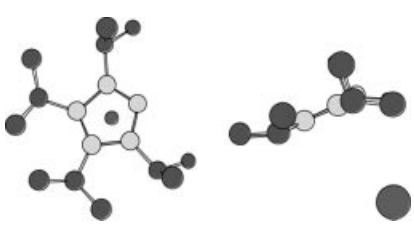

Keywords: Spin-lattice relaxation times / Paramagnetic complexes / Lanthanides / NMR spectroscopy

 © 2005 Wiley-VCH Verlag GmbH & Co. KGaA, Weinheim

2493 **B. Delavaux-Nicot,* J. Maynadié, D. Lavabre, C. Lepetit, B. Donnadieu**

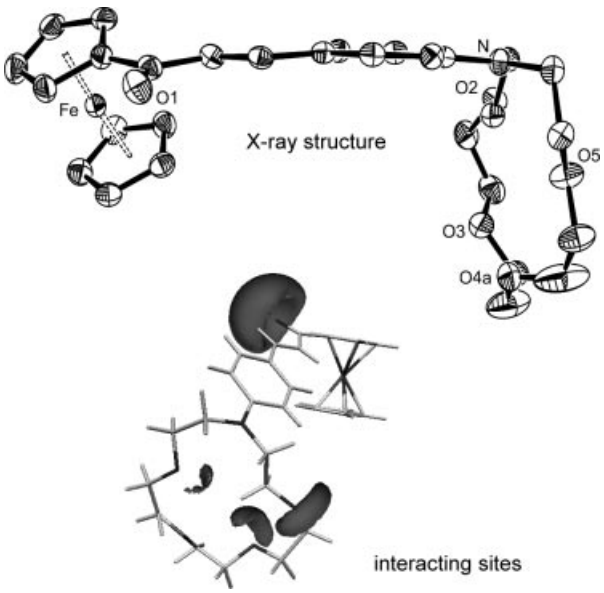

The First X-ray Characterized Monosubstituted Ferrocenyl Azacrown Chalcone: Focus on Its Calcium Interaction/Electrochemical Detection Studies

Keywords: Calcium / Cations / Crown compounds / Ferrocene / Sensors

2506 **P. Li, M. Wang,* C. He, G. Li, X. Liu, C. Chen, B. Åkermark, L. Sun***

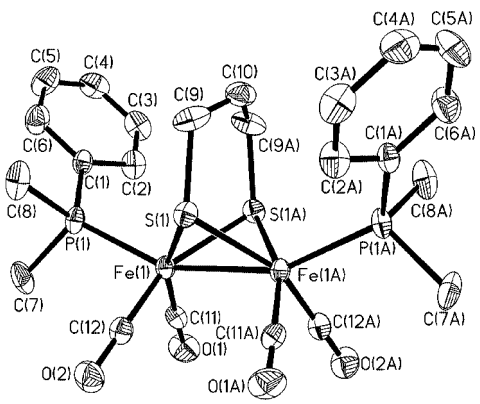

Influence of Tertiary Phosphanes on the Coordination Configurations and Electrochemical Properties of Iron Hydrogenase Model Complexes: Crystal Structures of $[(\mu\text{-}S_2C_3H_6)Fe_2(CO)_{6-n}L_n]$ (L = PMe_2Ph, n = 1, 2; PPh_3, $P(OEt)_3$, n = 1)

Keywords: Binuclear iron complexes / Bioinorganic chemistry / Carbonyl displacement / Fe-only hydrogenase / P ligands

2514 **Y. Steudel, M. W. Wong, R. Steudel***

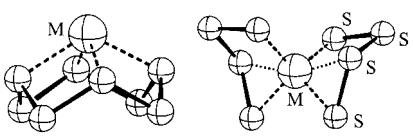

Coordination of Li^+, Ca^+, V^+, and Cu^+ to the Molecules S_8 and S_4 − A Computational Study

Keywords: Ab initio calculations / S ligands / Cluster compounds / Lithium / Calcium / Vanadium / Copper

2526 **M. Bera, W. T. Wong, G. Aromí, D. Ray***

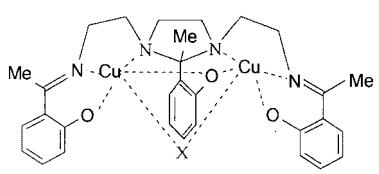

X = OAc^-, NO_3^-, Cl^-, $MeOCS_2^-$

μ-η^1:η^1-*N*,*N*′-Imidazolidine-Bridged Dicopper(II/III) Complexes of a New Dinucleating μ-Bis(tetradentate) Schiff Base Ligand: Synthesis, Structural Characterization, ^1H NMR Spectroscopy, and Magnetic Coupling

Keywords: N,O ligand / Imidazolidine / Copper complexes / Magnetic properties

 © 2005 Wiley-VCH Verlag GmbH & Co. KGaA, Weinheim

2536 T. Lébl,* P. Zoufalá, C. Bruhn

A Comparative Assessment of the Effect of the Lewis Acidity of the Central Tin Atom on Intramolecular Coordination of (3-Methoxypropyl)stannanes

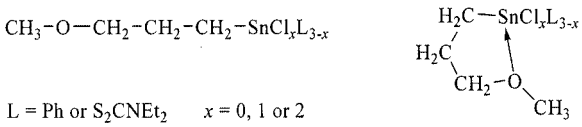

Keywords: Tin / Chelates / O ligands / Structure elucidation / Coordination modes

2545 F. A. Kiani, M. Hofmann*

The Additive Nature of Energy Penalties in 10-Vertex *nido*-(Car)boranes

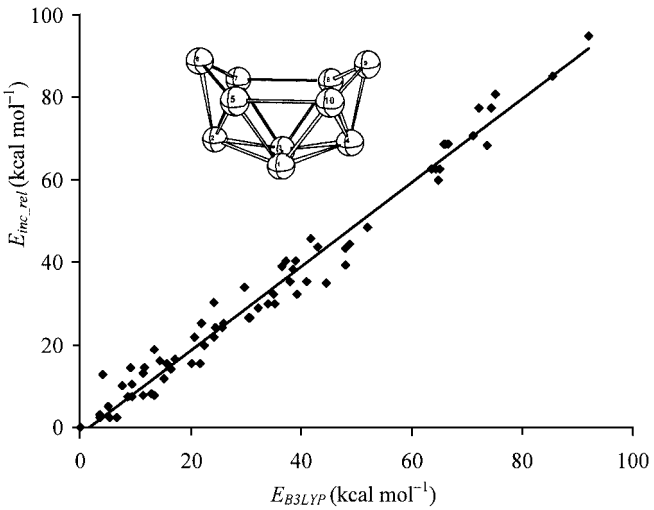

Keywords: Boranes / Carboranes / Density functional theory / Energy penalties / Structural increment system

 © 2005 Wiley-VCH Verlag GmbH & Co. KGaA, Weinheim

Group II Intron Ribozymes and Metal Ions – A Delicate Relationship

Roland K. O. Sigel*[a]

Keywords: Bioinorganic chemistry / Ribozymes / RNA structures / Metal ions / Calcium

Group II introns are naturally occurring ribozymes in plants, fungi, bacteria, and lower eukaryotes that undergo a fascinating array of reactions. These large molecular machines with a size ranging between 600 and 2500 nucleotides are self-splicing introns also capable of reinserting themselves into RNA or DNA, thus making them mobile genetic elements. The structural information available on group II intron ribozymes is very scarce. So far, only one crystal structure and one NMR solution structure of two domains located in the catalytic core are available. For proper folding and function, each intron requires specific concentrations of monovalent and divalent metal ions. Although most of these metal ions are used for charge screening, some are bound to distinct sites as has been shown by hydrolytic cleavage experiments. These specifically bound ions are crucial for tertiary contact formation and catalysis. This review will discuss the different metal-ion requirements of self-splicing group II introns, the available structural data and information on the binding location and affinity of metal ions, as well as the methods applied to investigate the metal-ion binding properties of these large RNAs. Due to the size of these introns, the richness of local structures, the catalytic versatility and the involvement of metal ions in all of the above-mentioned aspects, group II introns are an ideal target to be studied by combined means from the fields of Biochemistry, Molecular Biology, Analytical, and (Bio)Inorganic Chemistry.
(© Wiley-VCH Verlag GmbH & Co. KGaA, 69451 Weinheim, Germany, 2005)

1. Introduction

In contrast to the typical misconception that RNA is a stringy, single-stranded molecule without defined architecture, most functional RNA molecules are compact, stable, and tightly folded into a unique conformation.[1–4] Even mRNAs, which are normally thought of as linear "tapes" encoding for protein sequences, contain highly structured regions at their termini that serve as signals for regulating gene expression.[5,6] In the early 1980s, the research in RNA biochemistry "exploded" after the exciting discovery by Altman, Cech, and Pace that RNA is able to catalyze various reactions in living cells without the aid of amino acids.[7,8] Thus, the old dogma of only proteins being enzymes was overthrown and ribozymes were "born".

In the past twenty years, many more catalytic and noncatalytic functions of RNA in Nature have been and are still being discovered.[9] To name just a few: Aside from its diverse roles in protein synthesis (e.g., tRNA, rRNA), RNA is also involved in protein transport (signal recognition par-

[a] Institute of Inorganic Chemistry, University of Zürich,
Winterthurerstrasse 190, 8057 Zürich, Switzerland
Fax: +41-44-635-6802
E-mail: roland.sigel@aci.unizh.ch

Roland K. O. Sigel, born 1971 in Basel, Switzerland, graduated from the University of Basel with a Diploma in Chemistry in 1995. He carried out his Ph.D. thesis in the group of Professor Bernhard Lippert at the University of Dortmund, Germany, working on the effect of platinum(II) coordination on the acid-base and hydrogen-bonding properties of nucleobases and received his doctoral degree summa cum laude in 1999. During 2000–2002, he spent nearly three years as a postdoctoral fellow at Columbia University, New York, working with Professor Anna Marie Pyle (now Yale University) on ribozymes. During the six years abroad he received several fellowships, including a European TMR Fellowship covered by the Swiss National Science Foundation and the Swiss Federal Office for Education & Science as well as a fellowship from the Swiss Academy of Natural Sciences and the Swiss National Science Foundation. In early 2003, he returned to Switzerland and in April of this year he became an Assistant Professor of Inorganic Chemistry at the University of Zürich, endowed with a Förderungsprofessur of the Swiss National Science Foundation. His research interests are in Bioinorganic Chemistry and focus on the interrelations between metal ions and ribozymes, especially group II introns; his research group evaluates structural and catalytic impacts of metal ions by applying a broad combination of tools, including biochemical syntheses, stability-constant measurements, kinetic methods and 3-dimensional NMR spectroscopy. Since Volume 43 Roland K. O. Sigel is also an editor of the Metal Ions in Biological Systems series.

MICROREVIEWS: This feature introduces the readers to the authors' research through a concise overview of the selected topic. Reference to important work from others in the field is included.

ticle, SRP).[10] Furthermore, in the last couple of years, small RNAs composed of about 21–23 nucleotides in lengths were discovered to occur in periodic cycles within the cell. Such small interfering RNAs (siRNAs) play a key role in cell development (RNA interference, RNAi).[11,12] Only very recently, so-called coRNAs (coregulatory RNA) or riboswitches[13–19] were found to be important for gene regulation. Last, but not least, RNA molecules also fulfil diverse functions regarding RNA editing as well as RNA processing, i.e., they carry out post-transcriptional modifications. Catalytic RNAs are found among several of these groups; they are involved in protein synthesis, gene regulation, RNA editing, as well as RNA processing.[9] In all of these RNAs, catalytic or noncatalytic, metal ions play an essential role in their architectural assemblies and modes of action that are central to RNA biology.

Today, three different families of naturally occurring ribozymes are known: (i) The large phosphoryl transfer ribozymes (group I and group II introns, ribonuclease P), (ii) the small phosphoryl transfer ribozymes [hammerhead, hairpin, hepatitis delta, and Varkud satellite (VS) ribozyme], and (iii) the aminoacylesterase ribozymes (ribosome).[20] All these ribozymes either catalyze the cleavage and/or joining of RNA and DNA molecules through reactions at phosphate centers[20] or catalyze peptidyl transfers during protein synthesis, which involve the transfer of an activated ester at a carbon center.[21]

Very recently two new ribozymes have been discovered. First, the *glms* ribozyme, which belongs to the small phosphoryl transfer ribozymes [family (ii) mentioned above].[18] This ribozyme consists of a RNA motif found within a mRNA that self-cleaves upon binding to the reaction product of its encoded protein, therefore providing self-regulation in gene expression. Second, the co-transcriptional cleavage (CoTC) RNA motif that occurs in the 3′-flanking regions of primate β-globin genes and promotes transcription termination.[22] There is also strong evidence that another large ribonucleoprotein complex within the cell is a ribozyme – the so-called spliceosome.[23,24] This molecular machine, composed of five different snRNA molecules (small nuclear RNA) and numerous proteins, is found in all higher eukaryotes and is responsible for the correct splicing of freshly transcribed RNAs (thus belonging to the first mentioned family).[25,26]

As indicated in the above paragraphs, natural ribozymes encompass a surprisingly large chemical and functional repertoire in living organisms. The structures and reaction mechanisms of some of these ribozymes, like the Hammerhead, the Hairpin, or group I introns have been resolved to some detail in the past few years.[27–33] This short review focuses on group II introns, their occurrence, the reactions they catalyze, their structure, as well as on what is known about their delicate and complicated interaction with metal ions. For example, the Mg^{2+} requirements of different group II introns originating from the same gene within one organism can differ by a factor of more than ten. In addition, these large RNAs have one very remarkable quality: A group II intron broken into individual domains will reassemble into the catalytically active ribozyme! It is this modular behavior of the components, together with the anticipated richness of structural motifs and the strict requirement of metal ions for folding and catalysis that makes group II introns excellent systems to be studied by a combination of biochemical, analytical, and (bio)inorganic methods.

2. What are Group II Intron Ribozymes?

Group II introns are a very interesting class of naturally occurring ribozymes. These large molecular machines consist of about 600 to 2500 nucleotides and are second in size only to ribosomal RNAs. More than 750 gene locations of group II introns are known.[34] They are found primarily in organellar genes of plants, fungi, and lower eukaryotes, but also in many bacteria.[35] These RNAs are best known for their ability to undergo self-splicing, but they also perform a variety of other reactions including RNA and DNA hydrolysis as well as intron mobility into RNA and DNA substrates.[35,36]

RNA splicing is defined as follows: Most genes are transcribed into mRNA precursors that are not ready to undergo translation into proteins. Before translation, these mRNAs (as well as most tRNAs, rRNAs, and snRNAs) must undergo the process of splicing, in which noncoding introns (*in*tervening sequences) are removed from the coding exons (*ex*pressed regions). RNA splicing can be achieved by either autocatalytic introns (group I and group II introns), the eukaryotic spliceosome, or proteins (tRNA splicing).[37] The spliceosome releases the excised introns from the mRNA precursor as branched lariat molecules. This formation of lariat RNA resembles very much the splicing pathway of group II introns, with the only difference that the catalytic components responsible for splicing reside within the intron itself (Figure 1).[38–40]

In group II introns, the first step of the splicing reaction consists of a nucleophilic attack of the 2′-OH of a highly conserved adenosine located in a bulge within domain 6 (D6) (see below). In the second step, the 5′ and 3′ exons are ligated and the lariat intron is simultaneously released (Figure 1). Both steps of this branching reaction are highly reversible, explaining the fact that free lariat group II introns can catalytically insert themselves into RNA and DNA.[41–43] This ability makes group II introns infectious genetic elements that are capable of migrating into new hosts or new positions within a host genome.[44–50] Unlike other systems of genetic transposition, in group II introns, this process depends on the reactivity of the intron itself, which catalyzes its own reverse splicing into new genomic locations. Studies of intron mobility have shown that group II introns can be designed to target and insert themselves at any desired location, thereby either knocking out or transforming a gene.[45,48,51]

The transesterification reaction in group II intron splicing is in constant competition with an alternative hydrolytic pathway: A water molecule can readily react as nucleophile

 © 2005 Wiley-VCH Verlag GmbH & Co. KGaA, Weinheim

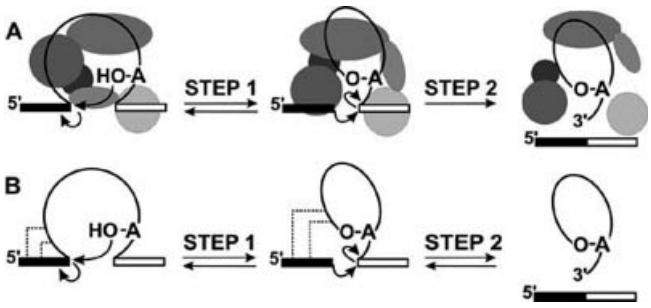

Figure 1. Comparison of the similar splicing pathways of the spliceosome and group II introns. **(A)** In higher eukaryotes the spliceosome removes introns and joins exons together. Five RNAs and several proteins assemble around the splice site and remove the intron as a lariat. An intronic 2′-OH of an adenosine serves as the nucleophile. After removal of the intron and joining of the exons, the RNAs and the proteins disassemble and then reassemble at the next splice site. **(B)** Group II introns fold into the active structure around the splice site. Correct cleavage site recognition by the EBS-IBS base pairings is indicated by dashed lines. In a first step, an internal 2′-OH of a conserved adenosine attacks the 5′-splice site to form a lariat. In a second step, the two exon pieces are joined and the intron removed as a lariat. Both steps are reversible, enabling group II introns to reinsert themselves into RNA or DNA.

during the first step of splicing (both in vitro and in vivo) making the two steps irreversible.[52–54] Although autocatalytic in vivo, group II introns often employ proteins to stabilize the intron structure or to enhance their functionality (e.g., reverse transcriptase activity during intron mobility).[36,55–57] Many group II introns have the innate capability to function in vitro, but only a few have been characterized in more detail. Among those best studied regarding folding, tertiary structure, and catalytic activity is ai5γ, which is located in the cytochrome oxidase 1 gene of mitochondria in baker's yeast *Saccharomyces cerevisiae*.[36,58]

Despite a relative lack of sequence conservation among group II introns they all possess a conserved set of six domains that contain well-defined secondary structural elements (Figure 2).[36,58] Each domain has a specific function: Domain 1 (D1) is an independent folding unit and a molecular scaffold for docking of the other domains.[59] In addition, this domain recognizes the 5′-exon through two EBS-IBS (exon/intron binding site) base pairing interactions, which are not conserved but always co-vary.[60] D1 contains components important for catalysis, including motifs involved in the λ[61] and ε[62] tertiary interactions, and forms together with domain 5 (D5) the minimal structure capable of supporting catalytic activity.[63,64] D2 lacks phylogenetic conservation but may aid to stabilize the tertiary structure of the folded intron.[64,65] D3 is a catalytic effector that increases the rate of catalysis by D1 and D5.[66–68] D4 does not contribute to self-splicing activity but often contains an open reading frame (ORF) encoding a maturase protein that aids in splicing and intron mobility in vivo.[69,70] Unlike the other domains of the intron, D5 is highly conserved and represents the most critical active-site component. It forms a very stable hairpin and binds through the ζ-ζ′[71] and the κ-κ′[72] tertiary interactions to the central region of D1 (Figure 2). Combination with the λ-λ′[61] (and ε-ε′)[62] interaction places the 5′ splice site right next to the "chemical face" of D5, i.e., to functional groups which have been identified to play a direct role in catalysis.[73,74] D6 contains the conserved bulged adenosine branch-point that serves as the nucleophile during the first step of branching.[38] The branch-point region of D6 contains conserved functionalities that position the bulged adenosine relative to the active-site components in D1 and D5.[72,75]

Group II introns have the interesting ability that their domains are independent folding units.[59] Thus the individual domains can be added together *in trans* (i.e. not covalently linked) and they will reassemble (at the proper metal-ion concentration) to the active three dimensional fold.[61,68,76] It should be added that the individual domains or combinations thereof can be easily synthesized by in vitro transcription from double-stranded DNA (dsDNA) templates, e.g. linearized plasmids or synthetic dsDNA, and purified by polyacrylamide gel electrophoresis (PAGE).[77,78] All these points make group II introns ideal targets to study with respect to either structure-function and/or metal-ion binding-function relationship.

3. The Need of Metal Ions in RNA Folding and Catalysis

Due to the polyanionic nature of the phosphate-sugar backbone metal ions are inextricably involved in the process of RNA folding and function. A simplified two-step folding pathway of large RNAs starts with the transition from a random coil to the secondary structure followed by the second step of compaction to the tertiary structure, in which specific long-range interactions orient all the structural elements in space (Figure 3).[79,80] Monovalent ions tend to play an important role in charge-screening, thereby allowing the secondary structure to form (Figure 3). Only recently one has begun to decipher the repertoire of tertiary interaction motifs that stabilize folded RNA molecules.[71,81] Tertiary structural elements are stabilized by interactions with divalent metal ions, preferably Mg^{2+}, but also the monovalent potassium appears to have an additional role in binding to high affinity sites.[82] The stabilization of nucleobase quartets by alkaline metal ions,[83,84] e.g. in telomeres,[85,86] is just one prominent example. In general, the formation of RNA tertiary structure is dependent on four parameters: (i) RNA sequence, (ii) metal-ion identity, (iii) metal-ion concentration, and (iv) the presence of RNA binding proteins and polyamines.[20] However, in addition to employing metal ions within structural elements, ribozymes also use them directly for catalysis.

One of the major differences between nucleic acids and proteins is that in DNA or RNA, due to the existence of only four nucleobase moieties (compared to 21 amino acids) a much smaller diversity of functional groups is present, none of which having a pK_a value near the physiological pH. This lack in diversity can be overcome by several factors: Stabilization of a protonated spezies by hydrogen

 © 2005 Wiley-VCH Verlag GmbH & Co. KGaA, Weinheim

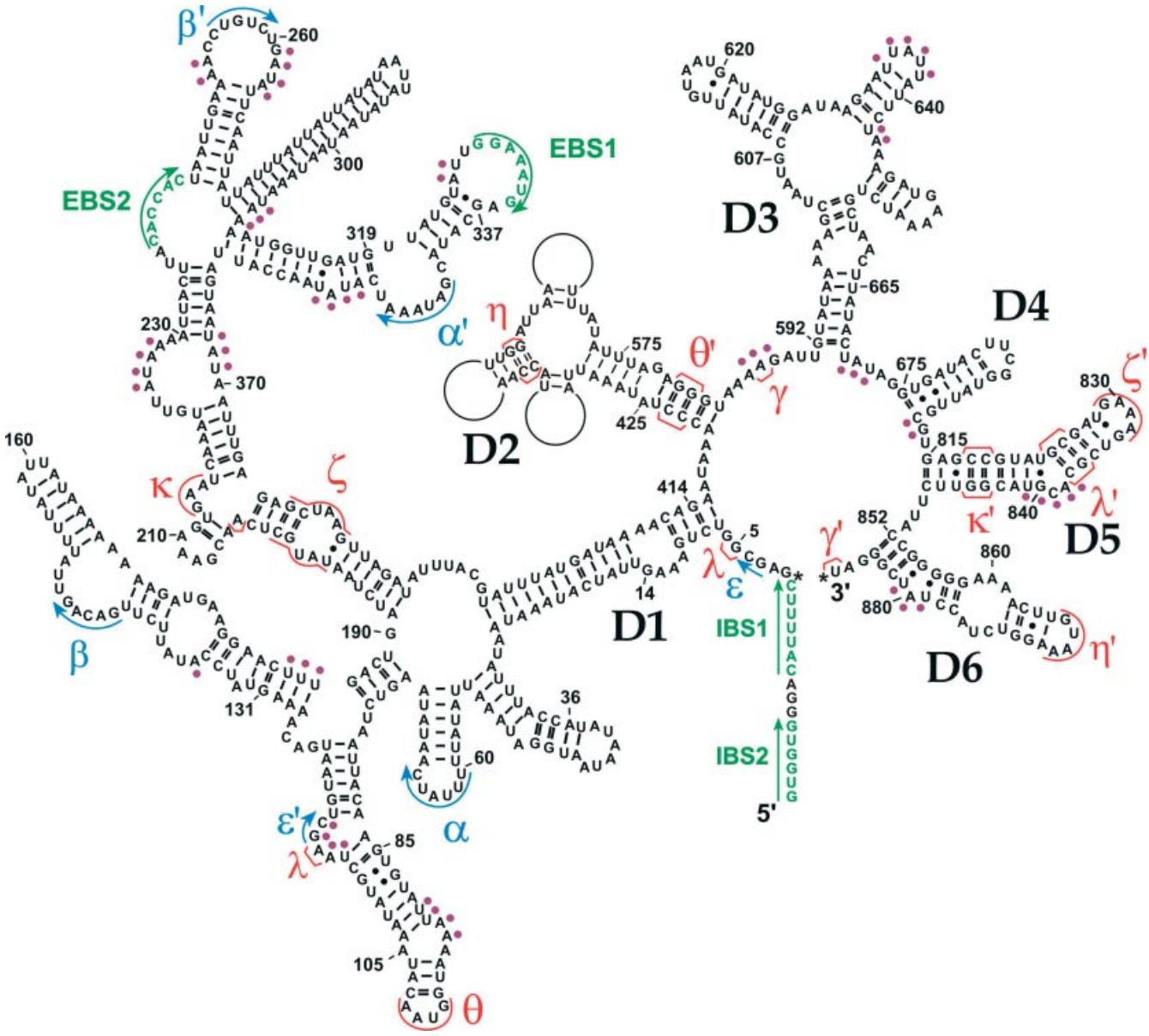

Figure 2. Secondary structure of a ribozyme derived from the group II intron ai5γ from *S. cerevisiae*. Domain 2 (D2) is only partly drawn; further regions making no known contacts to the other intronic domains are indicated as circles. Domain 4 (D4), which in some introns contains an open reading frame (ORF) is truncated and reduced to a hairpin, although the numbering of the nucleotides corresponds to that of the full lengths intron. The last sixteen nucleotides of the 5′ exon are also shown and separated from the intronic nucleotides by the splice site. Both, the 5′ and the 3′ splice sites are indicated by asterisks. Long-range tertiary contacts are labeled with pairs of Greek letters: Of the latter ones, intra-domain contacts are colored in blue, whereas inter-domain contacts are shown in red. Intron-exon interactions (IBS1-EBS1 & IBS2-EBS2) are shown in green. Sites of intense Tb^{3+} cleavage are marked by filled circles in magenta (see also ref.[78]).

bonding like in A·C$^+$ base pairs,[23] formation of a special fold with distinct electrostatic properties, and/or by the aid of metal ions.[87–89] Coordination of a metal ion to a nucleobase can lead to large pK_a shifts at amino and/or imino groups.[90–95] As a consequence, hydrogen bonding might be strengthened,[92,94,96,97] and/or rare tautomers stabilized[98] leading to new base pairing patterns.[96] In addition, such acidified protons could now participate directly in catalysis at a pH close to neutral. In fact, in most ribozymes structurally and/or biochemically investigated today, divalent metal ions are found within the catalytic core. There they are used, e.g., to activate the attacking nucleophile for phospho-diester cleavage, to stabilize the transition state, or the leaving group.[20,99,100] It follows that in nucleic acids not only kinetically inert metal ions, e.g. Pt^{2+},[101,102] but also labile metal ions[103] can coordinate in close neighborhood to each other,[104–106] sometimes even to the same nucleobase.[107] In a few cases, divalent metal ions can be replaced by high, i.e. molar, concentrations of monovalent ions, suggesting a mechanism where metal ions "only" have an electrostatic role and are thus probably not coordinated at the active site. However, it is unclear if under such conditions

 © 2005 Wiley-VCH Verlag GmbH & Co. KGaA, Weinheim

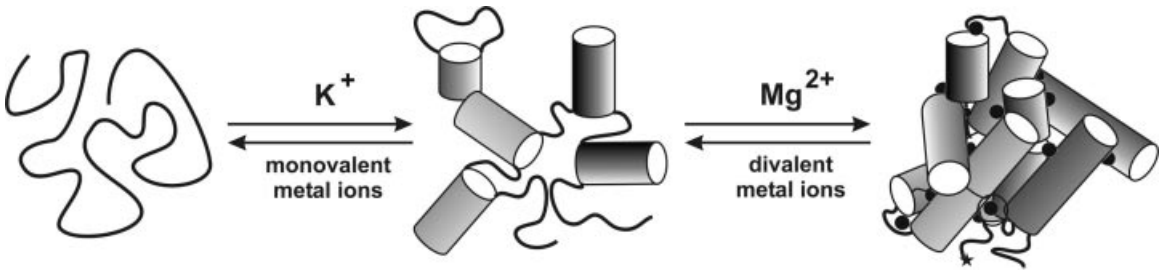

Figure 3. Schematic view of group II intron folding. Monovalent metal ions are needed for charge-screening and enable formation of the secondary structure. Tertiary structure formation to the catalytically active architecture only takes place in the presence of divalent metal ions like Mg^{2+}. Several Mg^{2+} ions (in some instances also K^+ ions) occupy specific binding sites stabilizing local structural motifs (adapted from ref.[79,80]).

of nonnatural high concentrations of M^+ ions, the mechanism of catalysis corresponds to the one in the presence of divalent ions.

To summarize, both Mg^{2+} and K^+ play an indispensable role in the world of RNA metabolism (see Figure 3), but in limited cases, also Na^+ and Li^+ (and NH_4^+) can contribute to correct folding of certain RNAs. Ca^{2+}, Mn^{2+}, Zn^{2+}, Cd^{2+}, and Pb^{2+} can sometimes substitute for Mg^{2+}, but they are rarely the natural cofactors.[108,109]

4. Metal Ions and Group II Introns

Large ribozymes like group II introns are particularly dependent on metal ions for function and are therefore ideal "targets" for study by bioinorganic chemists. It is interesting to note, although so far not understood, that different group II introns have rather different requirements for divalent and monovalent ions in vitro (see Table 1).[110–112] This specificity does not only relate to ribozymes from different organisms, but also to those originating from within one gene.[110] Considering the highly conserved secondary structure of these molecules, the range of Mg^{2+} concentrations varying between 0.1 and 100 mM is astonishing – even more so because there seems to be no correlation with the GC content of the nucleic acid sequence. Today, only one catalytic Mg^{2+} ion is known, which binds to the 3′-oxygen of the scissile phospho diester bond in both steps of splicing thereby stabilizing the 3′-oxoanion leaving group.[24] This Mg^{2+} coordination is observed in group II introns and the spliceosome, thus extending the parallels between these two splicing machineries.[24,113]

Binding studies of metal ions to folded RNA molecules are hampered because Mg^{2+} and K^+ are spectroscopically silent and are further complicated by the fact that these ions serve multiple roles (structural and catalytical) within the same molecule; hence, it is difficult to focus on one particular binding site. In addition, high Mg^{2+} concentrations are often required as Mg^{2+} binding is predominantly weak. Therefore, in experimental studies Mg^{2+} is often partly replaced by other metal ions. Besides d-transition metal ions, as well as Zn^{2+}, Cd^{2+}, and Pb^{2+}, lanthanides have lately become important mimics of Mg^{2+} to probe RNA structures and functions.[114,115] Like Mg^{2+}, lanthanide ions are mostly redox inactive and coordinate preferably to hard ligands such as phosphate oxygen atoms. Their +3 charge enables them to interact stronger with RNA than Mg^{2+}, but also leads to lower pK_a values for coordinated water molecules compared to the situation encountered with Mg^{2+}. The lanthanide hydroxide species can either directly attack the phospho diester bond, or alternatively depro-

Table 1. Concentrations of K^+ (or NH_4^+) and Mg^{2+} needed for achieving the best splicing activity in vitro with group II introns from different organisms. In column 1, the organism is given, in which the group II intron (column 2) belonging to one of the two subgroups (column 3) is found. The gene location is given in column 4. Optimal concentrations of K^+/NH_4^+ (column 5) and Mg^{2+} (column 6) are listed together with the tested concentration range, in which the ribozyme is active.

Organism	Group II intron	Subgroup	Location[a]	[K^+][M]	[Mg^{2+}][mM]	Ref.
Azotobacter vinelandii	Av.hsp60	IIB	hsp60	0.5	100	[111]
Chlamydomonas sp.	Chs.psbA1	IIB	psbA	1 (0.5–1.5)	25 (12–100)	[148]
Lactococcus lactis	Ll.ltrB	IIA	ltrB	0.5–1.5[b]	50	[51,149]
Podospora anserina	Pa.coI I1	IIA	cox1 su1	0.5–1.25[b]	60	[134]
Pylaiella littoralis	Pl.lsu/1	IIB	lsu rRNA	1	100	[110]
	Pl.lsu/2	IIB	lsu rRNA	1 (0.1–1)	5 (0.1–100)	[110]
Saccharomyces cerevisiae	aI1	IIA	cox1	1	100	[150]
	aI2	IIA	cox1	2[b]	100	[57]
	ai5γ	IIB	cox1	0.5	50–100	[112,132]
	bI1	IIB	cob	1.25[b]	10	[122]
Scenedesmus obliquus	So.lsu/1	IIB	lsu rRNA	1.25[b]	60[c]	[151]

[a] Hsp60, heat shock protein 60kD; psbA, photosystem II thylakoid protein domain 1; ltrB, relaxase gene of conjugative element pRS01; cox1, cytochrome oxidase 1; su1, subunit 1; lsu rRNA, large subunit of ribosomal RNA; cob, apocytochrome B. [b] NH_4Cl. [c] In the presence of 2 mM spermidine.

 © 2005 Wiley-VCH Verlag GmbH & Co. KGaA, Weinheim

tonate a 2′-hydroxy group, which itself can then act as a nucleophile to break the scissile phospho diester linkage. This reaction mechanism has two consequences: (i) only those metal-ion binding sites are detected, where the Ln^{III} ion is in close neighborhood to either the phospho diester or the 2′-OH, and (ii) under physiological conditions Ln^{3+} ions cleave RNA more efficiently at their coordination site than Mg^{2+}.[77,116,117]

Taking advantage of the above-mentioned properties of Ln^{3+} ions, we have applied them to locate the metal-ion binding sites in domains 1, 3, 5 and 6 of the group II intron ai5γ (Figure 4).[77] The ribozyme was labeled at either the 5′ or the 3′ end with ^{32}P and subsequently incubated with sufficient K^+ and Mg^{2+} at pH 7 to achieve the correct three-dimensional fold. Micromolar amounts of Tb^{3+} (or other lanthanides) were then added and the reaction mixture put on ice to protect the ribozyme from additional unspecific cleavage. As the natural Mg^{2+} ions are bound kinetically labile at their coordination sites, these ions are now in equilibrium with the higher charged Ln^{3+} ions. Binding of the lanthanide ions within the binding pocket subsequently leads to cleavage of the phospho diester backbone close to their binding site. The resulting RNA pieces of different length can then be separated by denaturing polyacrylamide gel electrophoresis (PAGE) and thus the multiple metal-ion binding sites within the RNA can be located.

Analysis of the PAGE gels shows that some sites are cleaved with high specificity whereas other regions are completely protected from hydrolysis.[77] When plotting the determined metal-ion binding sites onto the secondary structure of the RNA, it is striking to see that the metals are spread out all over the intron and are located mostly at single-stranded regions, suggesting unspecific cleavage (Figure 2). However, comparison with biochemical data from footprinting experiments[118] shows that almost all binding sites are located in the inner core of the active three dimensional architecture. Furthermore, the cleaved nucleotides are mostly known to be either crucial for long-range or tertiary contact formation via diverse hydrogen bonding patterns, or to take part in catalysis itself. Additional evidence that Ln^{3+} ions bind to the same sites as Mg^{2+} ions in the active structure is given by the fact that only the corresponding hydrolytic cleavage experiments with Mg^{2+} yield the same sites, though the cleavage intensities are much lower than with, e.g., Tb^{3+} and the gels therefore more difficult to interpret.[77] Hence, it is reasonable to assume that indeed $Ln^{3+}$and Mg^{2+} ions bind to the same sites in group II introns and RNA in general.

Divalent d-transition metal ions, as well as Zn^{2+} and Pb^{2+}, have also been applied in metal-mediated cleavage reactions of the RNA backbone.[119–122] These metal ions usually have a well defined coordination geometry but often prefer the softer nitrogen donor atoms instead of the harder oxygen atoms of the phosphate and carbonyl groups, which are the predominant binding partners of Mg^{2+}. In contrast, Ln^{3+} ions have the distinct advantage of preferentially binding to oxygen atoms as well. Although their preferred coordination geometry does not fit the one of Mg^{2+}, it is very

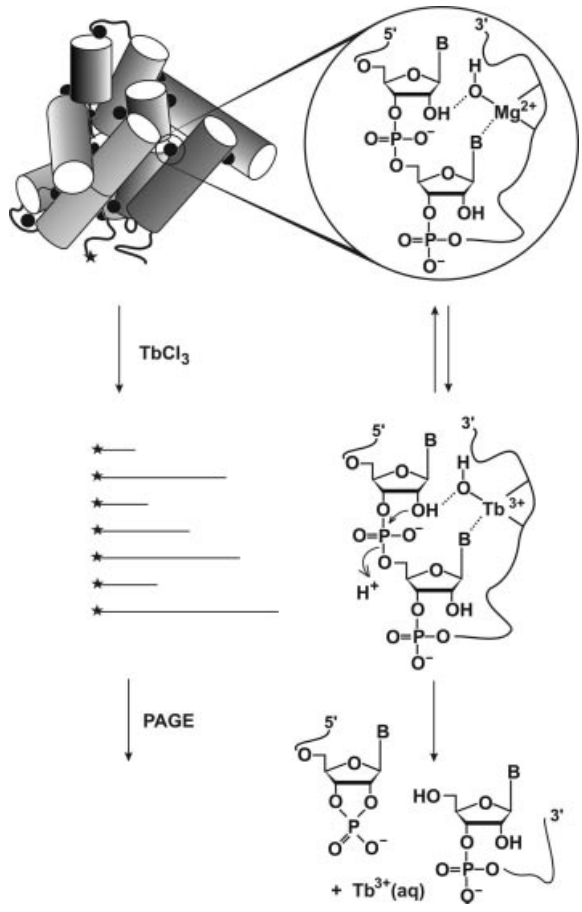

Figure 4. Lanthanide(III)-mediated cleavage of the phosphate-sugar backbone of large RNA molecules. The ribozyme, which is labeled with ^{32}P either at its 5′ or 3′ end (indicated by an asterisk), is folded to its active three-dimensional structure in the presence of K^+ and Mg^{2+}. Subsequently added Tb^{3+} competes with Mg^{2+} at its binding sites and cleaves the phosphate-sugar backbone by hydrolysis (B indicates the nucleobase moiety). The resulting RNA fragments of different lengths are separated by denaturing polyacrylamide gel electrophoresis (PAGE) and visualized with a phosphoimager. The cleavage sites, and thus coordination sites, of the Tb^{3+} ions appear as dark bands and these can be correlated with their position in the intron by a nuclease T1 digest run in parallel.[77]

flexible and can thus adopt easily to different environments. Thus, lanthanide ions seem to preserve the prefolded tertiary structure and not to disturb the local geometry within the binding pocket. The relative rigidity of the coordination sphere of Pb^{2+} is reflected by the fact that in case of the group II intron ai5γ, backbone cleavage induced by this metal ion leads to fewer detectable sites but these being identical with those induced by Tb^{3+} or Mg^{2+}.[77]

With another group II intron, bI1 from the cob gene in yeast, Mn^{2+} and Zn^{2+} were used to test for metal-ion binding sites.[122] In this case not the primary cleavage pattern was investigated, but a primer extension analysis was chosen. Although primer extension is not as sensitive as the direct observation, this method has the advantage that it can be applied to very large RNAs.[116,122] In the case of bI1, Mn^{2+} and Zn^{2+} induced cleavage revealed the same sites. However, some sites detected with Tb^{3+} did not show

 © 2005 Wiley-VCH Verlag GmbH & Co. KGaA, Weinheim

up, like the one in the bulge of domain 5, which is part of the catalytic center (see also below).[77]

Tb^{3+} has another striking feature: When applied at millimolar concentrations, Tb^{3+} nonspecifically cleaved also intronic regions with a high AU content. Most of these regions are not crucial for catalysis; they are believed to lie on the surface of the ribozyme and are therefore likely to be dynamic or disordered in secondary structure. Under such conditions of high concentration, Tb^{3+} coordinates unspecifically to the surface nucleotides of the intron, leading to an enhanced hydrolysis of the phospho diester bridges at these positions. Thus, depending on the concentration applied, Tb^{3+} can also be readily used as a probe for unstructured regions within a large folded RNA.

In addition to their use to determine metal-ion binding sites in large RNA molecules like group II introns, hydrolytic cleavage experiments with Ln^{3+} ions also yield information about the affinity of these ions to the RNA at each specific site.[114] Variation of the Tb^{3+} concentration shows that at some sites cleavage already occurs at low micromolar concentrations, whereas at other sites high micromolar or even millimolar amounts of this lanthanide(III) ion are needed to cleave the backbone.[114] Assuming a 1:1 binding behavior, the dependence of cleavage intensity on the Tb^{3+} concentration can be fitted with a nonlinear least-squares fit and affinity constants for each site determined. It is interesting to see that the intensity of the cleavage does not coincide with the affinities of Tb^{3+} at the single sites. This simply means that at some sites the Tb^{3+} ion is geometrically ideally positioned to promote cleavage but that this positioning is independent from its affinity at the site.[114] To conclude, in such experiments it is always important to perform Tb^{3+} titrations over a large concentration range, as the cleavage picture/intensity at just a single concentration can easily be misleading regarding the affinity of the metal ion to a given site.

5. Structure and Metal Ion-Binding Properties of the Catalytic Domain 5

5.1. The Role of Magnesium Ions

Domain 5 (D5) (see Section 2 and Figure 2) is the phylogenetically most conserved region of group II introns and is an essential active-site component for any reaction catalyzed by these ribozymes. D5 forms a hairpin-loop structure with usually about 34 nucleotides in length.[36,75] This hairpin always consists of two helical stems separated by a two-nucleotide bulge and is closed on one side by a GNRA tetraloop (N = any nucleotide, R = purine). Almost every nucleotide within D5 has at least one functional group, which is important for either catalysis itself or for binding of D5 to other intronic domains. Close to the 5′ end of D5, the so-called AGC, or catalytic, triad is located. These three nucleotides are almost invariable and their major groove functional groups have been shown to be crucial for the catalytic step.[74] D5 has a nanomolar affinity for the other intronic components,[123] of which advantage is taken in so-called *trans*-splicing experiments, where D5 acts as the "enzyme" in Michaelis–Menten-type kinetics.[76] The major interaction between D5 and the central region within D1 is a tetraloop-tetraloop receptor interaction, which is highly dependent on the presence of divalent metal ions.[124] In addition, further contacts between these two domains are known.[61,72] There are no phylogenetic covariations of Watson–Crick base pairing between nucleotides in D5 and other intronic or exonic regions, thus, these interactions are made through conserved hydrogen bonding patterns, which can be rather stable,[102] involving nucleobase and sugar moieties thus building higher order structures like base triples.[61,62,71,72]

Only few of these inter domain contacts are structurally characterized, mainly based on nucleotide analog interference mapping studies (NAIM).[72] Indeed, any structural information on group II introns is very scarce.[78,125] Regarding D5, phylogenetic alignment clearly shows a two-helix structure. However, the secondary structure around the bulge is still a matter of debate (Figure 5). On the one hand a GU wobble pair leaving the adjacent A and C unpaired, and on the other hand an AU Watson–Crick pair with flipped out C and G nucleobases is proposed. In favor of the first base pairing scheme with the GU wobble is a crystal structure of a permuted D5D6 construct.[125] The first helix is closed by the wobble pair between U823 and G840 and the second helix is stacked on top thus forming one straight long helix with two flipped out nucleotides A and C in the middle. The two flipped out nucleotides form crystal lattice contacts with neighboring molecules, possibly mimicking similar contacts within the whole ribozyme (Figure 5B).[125] In the NMR solution structure of D5 in the presence of Mg^{2+} the bulge adopts a hitherto unknown structure.[78] The two bulged AC nucleotides are stacked within the hairpin and the downstream G840 does not form a wobble pair but instead is in a *syn* conformation and thus flipped down into the major groove of stem 1 (Figure 5C). As a consequence, the two helixes are slightly twisted against each other, exposing the AU base pair below to the solvent providing a possible platform for stacking interactions with incoming nucleotides of the above λ-λ′ contact. In support of the flipped down *syn*-G840 is the biochemical observation that the NH_2 group of G840 is known to be crucial for catalysis.[72,126] In the NMR structure the exocyclic amino group is very close to the AGC triad[78] and thus, to the reaction center.[61] In addition, Tb^{3+} cleavage experiments of D5 alone and in the presence of D1 both revealed a metal-ion binding site in the bulge, suggesting that D5 adopts a similar structure in solution as in the ribozyme.[77]

Several metal-ion binding sites have been detected in D5. Thio rescue experiments revealed a Mg^{2+} coordinated to the S_p-oxygen atom of the A816 phosphate group within the AGC triad, thus being important for binding of D5 to the other domains.[127] Titration studies of D5 with $MgCl_2$ by NMR revealed further binding sites of Mg^{2+} within D5.[78,128] In fact, such sites may closely neighbor each other.[107] The recording of 2D $^1H,^1H$-NOESY spectra al-

 © 2005 Wiley-VCH Verlag GmbH & Co. KGaA, Weinheim

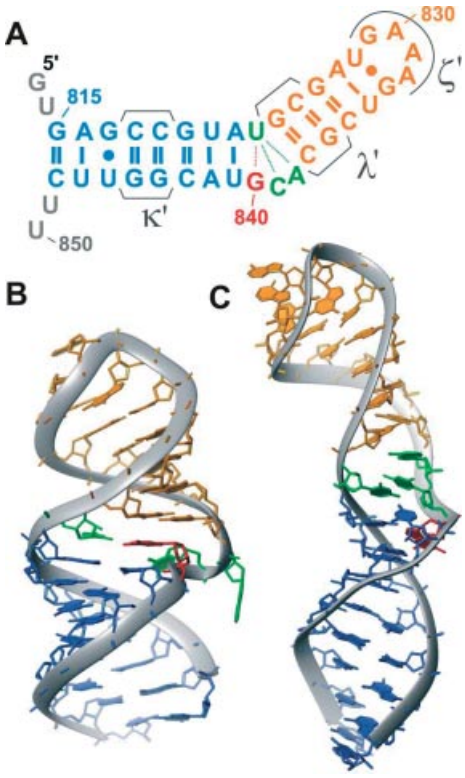

Figure 5. Solution and crystal structures of D5 together with its secondary structure. (**A**) Secondary structure of D5 from ai5γ together with its numbering scheme and tertiary contacts with other domains indicated by Greek letters (see also Figure 2). Helix one is colored in blue, helix two in orange, G840 in red, and the other bulge nucleotides in green. Nucleotides shown in grey, flanking D5, are not included in the two structures. (**B**) In the crystal structure (pdb entry 1KXK),[125] D5 adopts a straight helix with the two bulge nucleotides A838 and C839 flipped out making lattice contacts with neighboring molecules. (**C**) The NMR structure (pdb entry 1R2P)[78] reveals a more flexible structure with the two helices slightly kinked as all bulge-nucleotides are found within the helix. The syn-G840 is flipped down into the major groove. Both structures were drawn with the program MOLMOL,[147] based on the pdb entries given above.

lowed us to follow the chemical shift changes of the aromatic nucleobase, as well as the aliphatic sugar protons and yielded therefore a very detailed picture not only about the location, but also about the strength of the binding.[78,128] Almost all protons in D5 are affected by the addition of Mg^{2+} implying that in general Mg^{2+} binds unspecifically to the phosphate groups of this oligonucleotide. However, some chemical shifts show a much larger dependence on Mg^{2+} concentration, e.g., resonances belonging to nucleotides around the bulge, the tetraloop and the tandem GC pairs in helix 1. In line with the above-mentioned results from the Tb^{3+} cleavage experiments[77] and the structural orientation of the bulge, is the strong metal-ion binding in this region (log $K = 2.52 \pm 0.12$ M^{-1})[77] for Mg^{2+}, K being the stability constant), which is high compared to e.g., $Mg(pUpU)^-$ (log $K = 1.84 \pm 0.04$ M^{-1}).[129] Indeed, several carbonyl oxygen atoms are positioned in the minor groove of the bulge, providing possible multiple coordination sites for the hard Mg^{2+} ion. The large chemical shift changes of about 0.3 ppm may be indicative of a structural change in the bulge upon Mg^{2+} binding, although the NOESY pattern did not change up to 7.5 mM $MgCl_2$ added. Metal-ion coordination within the bulge region together with a hydrophobic stacking interaction of incoming nucleotides with the below lying AU platform, might facilitate the formation of the λ-λ′ tertiary contact by providing charge compensation for the anionic backbone.

5.2. The Effect of Other Metal Ions on Group II Intron Reactivity

Monovalent cations are primarily used for charge screening, but in a few cases also very specific binding sites for, e.g., K^+ ions, are known.[130] In living cells, the concentration of Na^+ and K^+ is (depending on the organism and kind of cell) usually between 2 and 150 mM. In addition, polyamines and RNA binding proteins are abundant in the cell to stabilize large three dimensional RNA structures such as group II introns. For in vitro splicing, much higher salt concentrations are needed; usually between 500 and 1500 mM (see Table 1 and refs. therein). However, also for in vitro splicing, usually 100 mM Mg^{2+} (Table 1) can be partly replaced (e.g. 10 mM $MgCl_2$ total) by either polyamines like spermidine (2 mM)[38] or protamine (5 nM),[53] or RNA binding proteins: Experiments with the Ll.ltrB intron have shown that the self-encoded maturase protein LtrA binds to intronic sequences in D4 and enables splicing also under reduced salt conditions (450 mM NaCl, 5 mM $MgCl_2$).[131]

KCl can be replaced in most instances by ammonium salts like NH_4Cl or $(NH_4)_2SO_4$ without much loss of overall activity, but having an effect on the chosen splicing pathway: Ammonium sulfate favors transesterification (branching), KCl the hydrolytic pathway, whereas NH_4Cl yields the products of both pathways in similar amounts.[53,132–134] Thus, for many biochemical experiments, like NAIM (nucleotide analog interference mapping), NAIS (nucleotide analog interference suppression), as well as for reverse-splicing reactions ammonium salts are preferred.[72,131] In intron insertion reactions into DNA, i.e. in the presence of a self-encoded maturase protein, Na^+ is readily used (at low Mg^{2+} concentrations). However, there are only few examples of in vitro splicing reactions where Na^+ is used instead of K^+ (or NH_4^+),[131] as the presence of high amounts of Na^+ can lead to a loss in activity.[110] Li^+ can promote folding of some RNAs,[135] but it is only rarely employed. However, one should be aware that, although not specifically reported, sodium (and lithium) ions are almost always present to some extent: Many lithium and sodium salts of nucleotide triphosphates and of buffers are used during transcription and purification of the RNA as well as in the splicing reaction itself (MOPS, Edta, to name just two).

All group II introns investigated up to now need Mg^{2+} to perform splicing or branching. However, other divalent metal ions are often added in low millimolar amounts, e.g., in thio-rescue, hydrolytic cleavage experiments, and NAIS/

 © 2005 Wiley-VCH Verlag GmbH & Co. KGaA, Weinheim

NAIM studies. In thio-rescue experiments, mainly $CdCl_2$ and $MnCl_2$ are used in concentrations between 2 and 10 mM in the presence of 100 mM Mg^{2+}.[72,127,136] Under such conditions, both branching and splicing still take place. It should be added here that it is a common misconception that Mn^{2+} is significantly more thiophilic than Mg^{2+}. Mn^{2+} does not show an increased affinity towards thiophosphate groups compared to phosphate groups.[137] However, due to its position in the Irving–Williams series, its affinity to (thio)phosphate groups is slightly higher than that of Mg^{2+}, explaining the few observed "rescue" effects (related results are given in refs.[137–140]).

5.3. The Special Effects of Calcium Ions

Above, the need of group II introns for K^+/NH_4^+ and Mg^{2+} as well as the use and effect of various mimicking metal ions has been summarized. But what about other alkaline earth metal ions? For example, Ca^{2+} is abundant in Nature, although in living cells the free calcium concentration is normally kept low. Ca^{2+} is slightly larger than Mg^{2+}, but it also prefers oxygen donors as ligands and therefore effectively binds carbonyl groups.[141] Complexes of Ca^{2+} with monophosphate groups[142] are known to be weaker by a factor of about 0.75 compared to those with Mg^{2+}. For the simultaneous coordination to several phosphate groups like in a nucleoside triphosphate, the factor between Mg^{2+} and Ca^{2+} is further reduced to about 0.4.[143] One would therefore assume that small amounts of Ca^{2+} have only little effect on the reactivity of group II introns. Surprisingly, the opposite is observed. We have performed *trans* cleavage assays, in which the 5′-exon is cleaved from the intronic domains 1, 2, and 3 upon addition of D5 (Figure 6).[144,145] Such a setup has been shown to be an excellent mimic for the first step of splicing obeying Michaelis–Menten kinetics, when D5 is added in excess.[76]

Under saturating conditions of D5 (500 mM KCl, 100 mM $MgCl_2$) the observed rate constant $k_{obsd.}$ equals 0.044 ± 0.002 min^{-1}.[76,144,145] In the presence of only 1 mM Ca^{2+} (and, 99 mM Mg^{2+}), the rate of the reaction decreases significantly (Figure 6).[144,145] The slightly decreased concentration of Mg^{2+} cannot be the reason for reduced catalysis, especially as at concentrations down to 50 mM Mg^{2+} the ribozyme still remains folded and active.[112] The mode of inhibition by Ca^{2+} is unclear. The displacement of Mg^{2+} from the active site is a first possibility, although a less likely one. Nevertheless, it is evident that, despite having normally a lower affinity towards the constituents of nucleic acids, Ca^{2+} must somehow alter the three dimensional fold of a local metal-ion binding motif or even of the whole ribozyme, for example by binding to (additional) carbonyl groups due to its larger size and higher coordination number. This observation proves that group II intron ribozymes indeed are a very delicate molecular machinery being extremely sensitive to small changes in its environment, and despite its size show a high specificity for certain metal ions.

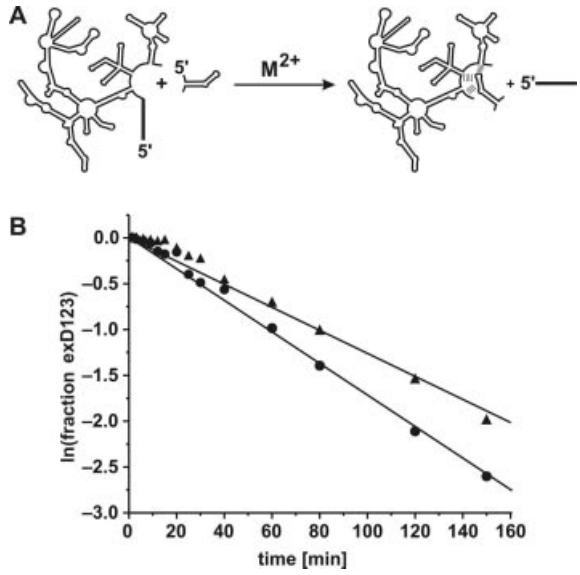

Figure 6. Effect of Ca^{2+} on the splicing reaction of the group II intron ai5γ. (**A**) Reaction scheme of the *trans* splicing reaction of exD123 upon addition of D5 in the presence of divalent metal ions. (**B**) Comparison of the observed rate of the above reaction in the presence of only Mg^{2+} (100 mM, ●) and a ratio of Ca^{2+}:Mg^{2+} = 1 mM:99 mM (▲). The fraction of precursor is drawn vs. time. The reaction is clearly slower in the presence of Ca^{2+}.[144,145]

6. Conclusions and Outlook

In this review, I have tried to show why group II introns are fascinating molecules and worthwhile targets for studies by Bioinorganic Chemists. After a short summary of the diverse array of reactions catalyzed by group II intron ribozymes, the role of metal ions in folding and activity of these catalytic RNAs was discussed. In living cells only concentrations in the lower millimolar range of monovalent and divalent metal ions are needed, as polyamines and RNA binding proteins support the folding of these large RNAs to the active three dimensional structure. Such stabilizing effects by biomolecules other than RNA are usually replaced in vitro by high concentrations of metal ions, also supporting catalysis. However, it is reasonable to assume that both in vivo and in vitro, metal ions are occupying the same key sites within the catalytic core or regions of tertiary interactions.

In the light of the highly conserved secondary structure of group II introns it is not understood why introns from different organisms and gene loci exhibit such a diverse need regarding the concentration of Mg^{2+}. A set of minor groove binding sites for metal ions has been determined by hydrolytic cleavage experiments for the ai5γ and bI1 introns from yeast.[77,122] Not all binding sites appear to correspond to each other. However, as different metal ions have been used for the promoted backbone hydrolysis as well as different methods to visualize the cleavage sites, a thorough interpretation is difficult.

It will be interesting to see if group II introns from different organisms have high affinity binding sites for metal ions at different locations within the intronic domains. One

 © 2005 Wiley-VCH Verlag GmbH & Co. KGaA, Weinheim

can speculate if group II introns do not manifest one particular fold and reaction pathway, but rather that there might be subtle differences in the structure depending on the subgroup and the origin of a particular group II intron. Such a scenario is quite well possible, as two existing models of the catalytic centers of ai5γ and Pl.lsu/2 cannot be superimposed.[118,146] The two structures of single domains of the group II intron ai5γ solved so far,[78,125] together with the two models of the catalytic core,[118,146] are first important steps in the direction of building a structural basis for these molecular machines. Indeed, more structural information is highly needed for the interpretation of metal-ion binding necessary for folding and catalysis. It is evident that much work needs to be done because at present hardly any exact binding site is known; for example, if a divalent metal ion binds to a G unit, where is the metal ion exactly located? At N1, O6, N7 or even at N3? Is the phosphate group also involved? Only if we are able to answer these questions down to the atomic level we shall be able to characterize and understand the reaction processes in detail.

Acknowledgments

I thank Dr. Eva Freisinger, as well as the members of my enthusiastic group Michèle Erat, Maya Furler, Sofia Gallo, Dr. Bernd Knobloch, Daniela Kruschel, and Miriam Steiner for helpful comments and discussions regarding this manuscript. Financial support by the Swiss National Science Foundation (SNF-Förderungsprofessur PP002–68733/1) is gratefully acknowledged.

[1] Abbreviations and Definitions: For names and locations of group II introns see Table 1; CoTC RNA, co-transcriptional cleavage RNA; dsDNA, double-stranded DNA; Edta, ethylenediamine-*N*,*N*,*N*′,*N*′-tetraacetic acid; MOPS, 3-(*N*-morpholino)propanesulfonic acid; NAIM, nucleotide analogue interference mapping, NAIS, nucleotide analogue interference suppression; ORF, open-reading frame; PAGE, polyacrylamide gel electrophoresis; RNA, ribonucleic acid; RNAi, RNA interference; coRNA, co-regulatory RNA; mRNA, messenger RNA; rRNA, ribosomal RNA; siRNA, small interfering RNA; snRNA, small nuclear RNA; tRNA, transfer RNA.

[2] B. L. Golden, A. R. Gooding, E. R. Podell, T. R. Cech, *Science* **1998**, *282*, 259–264.
[3] J. H. Cate, A. R. Gooding, E. Podell, K. Zhou, B. L. Golden, C. E. Kundrot, T. R. Cech, J. A. Doudna, *Science* **1996**, *273*, 1678–1685.
[4] J. A. Latham, T. R. Cech, *Science* **1989**, *245*, 276–282.
[5] T. A. Edwards, S. E. Pyle, R. P. Wharton, A. K. Aggarwal, *Cell* **2001**, *105*, 281–289.
[6] N. K. Gray, M. W. Hentze, *Mol. Biol. Rep.* **1994**, *19*, 195–200.
[7] K. Kruger, P. J. Grabowski, A. J. Zaug, J. Sands, D. E. Gottschling, T. R. Cech, *Cell* **1982**, *31*, 147–157.
[8] C. Guerrier-Takada, K. Gardiner, T. Marsh, N. Pace, S. Altman, *Cell* **1983**, *35*, 849–857.
[9] R. F. Gesteland, T. R. Cech, J. F. Atkins, *The RNA World*, 2nd ed.; Cold Spring Harbor Press: **1999**; vol. 37, pp. 1–709.
[10] R. J. Keenan, D. M. Freymann, R. M. Stroud, P. Walter, *Annu. Rev. Biochem.* **2001**, *70*, 755–775.
[11] G. Hutvagner, J. McLachlan, A. E. Pasquinelli, E. Balint, T. Tuschl, P. D. Zamore, *Science* **2001**, *293*, 834–838.
[12] E. G. Moss, *Curr. Biol.* **2001**, *11*, R772-R775.
[13] A. Herbert, *Nat. Genet.* **2004**, *36*, 19–25.
[14] S. Brantl, *Trends Microbiol.* **2004**, *12*, 473–475.
[15] R. Micura, *Angew. Chem. Int. Ed.* **2004**, *43*, 4692–4694.
[16] M. Mandal, R. R. Breaker, *Nature Rev. Mol. Cell Biol.* **2004**, *5*, 451–463.
[17] E. Nudler, A. S. Mironov, *Trends Biochem. Sci.* **2004**, *29*, 11–17.
[18] W. C. Winkler, A. Nahvi, J. A. Collins, R. R. Breaker, *Nature* **2004**, *428*, 281–286.
[19] R. T. Batey, S. D. Gilbert, R. K. Montange, *Nature* **2004**, *432*, 411–415.
[20] A. M. Pyle, *Met. Ions Biol. Syst.* **1996**, *32*, 479–519.
[21] P. Nissen, J. Hansen, N. Ban, P. B. Moore, T. A. Steitz, *Science* **2000**, *289*, 920–930.
[22] A. Teixeira, A. Tahiri-Alaoui, S. West, B. Thomas, A. Ramadass, I. Martianov, M. Dye, W. James, N. J. Proudfoot, A. Akoulitchev, *Nature* **2004**, *432*, 526–530.
[23] A. Huppler, L. J. Nikstad, A. M. Allmann, D. A. Brow, S. E. Butcher, *Nat. Struct. Biol.* **2002**, *9*, 431–435.
[24] E. J. Sontheimer, P. M. Gordon, J. A. Piccirilli, *Genes Dev.* **1999**, *13*, 1729–1741.
[25] M. Azubel, S. G. Wolf, J. Sperling, R. Sperling, *Mol. Cell* **2004**, *15*, 833–839.
[26] A. Stoltzfus, *Curr. Biol.* **2004**, *14*, R351–R352.
[27] P. L. Adams, M. R. Stahley, A. B. Kosek, J. Wang, S. A. Strobel, *Nature* **2004**, *430*, 45–50.
[28] B. L. Golden, H. Kim, E. Chase, *Nat. Struct. Biol.* **2005**, *12*, 82–89.
[29] F. Guo, A. R. Gooding, T. R. Cech, *Mol. Cell* **2004**, *16*, 351–362.
[30] J. A. Doudna, T. R. Cech, *Nature* **2002**, *418*, 222–228.
[31] E. A. Doherty, J. A. Doudna, *Annu. Rev. Biophys. Biomol. Struct.* **2001**, *30*, 457–475.
[32] R. G. Kuimelis, L. W. McLaughlin, *Chem. Rev.* **1998**, *98*, 1027–1044.
[33] M. J. Fedor, *Curr. Opin. Struct. Biol.* **2002**, *12*, 289–295.
[34] J. J. Cannone, S. Subramanian, M. N. Schnare, J. R. Collett, L. M. D′Souza, Y. Du, B. Feng, N. Lin, L. V. Madabus, K. M. Muller, N. Pande, Z. Shang, N. Yu, R. R. Gutell, *BMC Bioinformatics* **2002**, *3*.
[35] F. Michel, J. L. Ferat, *Annu. Rev. Biochem.* **1995**, *64*, 435–461.
[36] K. Lehmann, U. Schmidt, *Critical Rev. Biochem. Mol. Biol.* **2003**, *38*, 249–303.
[37] T. R. Cech, *Structure and mechanism of the larger catalytic RNAs: Group I and group II introns and ribonuclease P* in: *The RNA World* (Eds.: R. Gesteland, J. Atkins), Cold Spring Harbor Press: Cold Spring Harbor, **1993**; pp. 239–270.
[38] C. L. Peebles, P. S. Perlman, K. L. Mecklenburg, M. L. Petrillo, J. H. Tabor, K. A. Jarrell, H. L. Cheng, *Cell* **1986**, *44*, 213–223.
[39] C. Schmelzer, R. J. Schweyen, *Cell* **1986**, *46*, 557–565.
[40] R. Van der Veen, A. C. Arnberg, G. Van der Horst, L. Bonen, H. F. Tabak, L. A. Grivell, *Cell* **1986**, *44*, 225–234.
[41] K. Chin, A. M. Pyle, *RNA* **1995**, *1*, 391–406.
[42] M. Mörl, C. Schmelzer, *Cell* **1990**, *60*, 629–636.
[43] Y. Aizawa, Q. Xiang, A. M. Lambowitz, A. M. Pyle, *Mol. Cell* **2003**, *11*, 795–805.
[44] A. M. Lambowitz, *Cell* **1989**, *56*, 323–326.
[45] R. Eskes, L. Liu, H. Ma, M. Y. Chao, L. Dickson, A. M. Lambowitz, P. S. Perlman, *Mol. Cell. Biol.* **2000**, *20*, 8432–8446.
[46] S. Zimmerly, H. Guo, R. Eskes, J. Yang, P. S. Perlman, A. M. Lambowitz, *Cell* **1995**, *83*, 529–538.
[47] J. Yang, S. Zimmerly, P. S. Perlman, A. M. Lambowitz, *Nature* **1996**, *381*, 332–335.
[48] H. Guo, M. Karberg, M. Long, J. P. Jones, III, B. Sullenger, A. M. Lambowitz, *Science* **2000**, *289*, 452–457.
[49] N. Toro, *Env. Microbiol.* **2003**, *5*, 143–151.
[50] L. Dai, N. Toor, R. Olson, A. Keeping, S. Zimmerly, *Nucleic Acids Res.* **2003**, *31*, 424–426.
[51] M. Matsuura, R. Saldanha, H. Ma, H. Wank, J. Yang, G. Mohr, S. Cavanagh, G. M. Dunny, M. Belfort, A. M. Lambowitz, *Genes Dev.* **1997**, *11*, 2910–2924.

 © 2005 Wiley-VCH Verlag GmbH & Co. KGaA, Weinheim

[52] M. Podar, V. T. Chu, A. M. Pyle, P. S. Perlman, *Nature* **1998**, *391*, 915–918.
[53] D. L. Daniels, W. J. Michels, Jr., A. M. Pyle, *J. Mol. Biol.* **1996**, *256*, 31–49.
[54] J. Vogel, T. Borner, *EMBO J.* **2002**, *21*, 3794–3803.
[55] P. Boeck-Taferner, H. Wank, *Biol. Chem.* **2004**, *385*, 615–621.
[56] K. Perron, M. Goldschmidt-Clermont, J.-D. Rochaix, *RNA* **2004**, *10*, 704–711.
[57] H.-r. Huang, M. Y. Chao, B. Armstrong, Y. Wang, A. M. Lambowitz, P. S. Perlman, *Mol. Cell. Biol.* **2003**, *23*, 8809–8819.
[58] P. Z. Qin, A. M. Pyle, *Curr. Opin. Struct. Biol.* **1998**, *8*, 301–308.
[59] P. Z. Qin, A. M. Pyle, *Biochemistry* **1997**, *36*, 4718–4730.
[60] F. Michel, K. Umesono, H. Ozeki, *Gene* **1989**, *82*, 5–30.
[61] M. Boudvillain, A. de Lencastre, A. M. Pyle, *Nature* **2000**, *406*, 315–318.
[62] A. Jacquier, F. Michel, *J. Mol. Biol.* **1990**, *213*, 437–447.
[63] W. J. Michels, A. M. Pyle, *Biochemistry* **1995**, *34*, 2965–2977.
[64] J. L. Koch, S. C. Boulanger, S. D. Dib-Hajj, S. K. Hebbar, P. S. Perlman, *Mol. Cell. Biol.* **1992**, *12*, 1950–1958.
[65] M. Costa, F. Michel, *EMBO J.* **1997**, *16*, 3289–3302.
[66] E. A. Griffin, Z.-F. Qin, W. A. Michels, A. M. Pyle, *Chem. Biol.* **1995**, *2*, 761–770.
[67] M. Podar, S. Dib-Hajj, P. S. Perlman, *RNA* **1995**, *1*, 828–840.
[68] O. Fedorova, T. Mitros, A. M. Pyle, *J. Mol. Biol.* **2003**, *330*, 197–209.
[69] A. M. Lambowitz, M. Belfort, *Annu. Rev. Biochem.* **1993**, *62*, 587–622.
[70] M. Belfort, V. Derbyshire, M. M. Parker, B. Cousineau, A. M. Lambowitz, *Mobile DNA II* **2002**, 761–783.
[71] M. Costa, F. Michel, *EMBO J.* **1995**, *14*, 1276–1285.
[72] M. Boudvillain, A. M. Pyle, *EMBO J.* **1998**, *17*, 7091–7104.
[73] D. L. Abramovitz, R. A. Friedman, A. M. Pyle, *Science* **1996**, *271*, 1410–1413.
[74] B. B. Konforti, D. L. Abramovitz, C. M. Duarte, A. Karpeisky, L. Beigelman, A. M. Pyle, *Mol. Cell* **1998**, *1*, 433–441.
[75] V. T. Chu, C. Adamidi, Q. Liu, P. S. Perlman, A. M. Pyle, *EMBO J.* **2001**, *20*, 6866–6876.
[76] A. M. Pyle, J. B. Green, *Biochemistry* **1994**, *33*, 2716–2725.
[77] R. K. O. Sigel, A. Vaidya, A. M. Pyle, *Nat. Struct. Biol.* **2000**, *7*, 1111–1116.
[78] R. K. O. Sigel, D. G. Sashital, D. L. Abramovitz, A. G. Palmer III, S. E. Butcher, A. M. Pyle, *Nat. Struct. Mol. Biol.* **2004**, *11*, 187–192.
[79] J. Pan, D. Thirumalai, S. A. Woodson, *J. Mol. Biol.* **1997**, *273*, 7–13.
[80] J. Pan, M. L. Deras, S. A. Woodson, *J. Mol. Biol.* **2000**, *296*, 133–144.
[81] R. T. Batey, R. P. Rambo, J. A. Doudna, *Angew. Chem. Int. Ed.* **1999**, *38*, 2327–2343.
[82] R. Shiman, D. E. Draper, *J. Mol. Biol.* **2000**, *302*, 79–91.
[83] E. Freisinger, A. Schimanski, B. Lippert, *J. Biol. Inorg. Chem.* **2001**, *6*, 378–389.
[84] H. Witkowski, E. Freisinger, B. Lippert, *Chem. Commun.* **1997**, 1315–1316.
[85] R. H. Shafer, I. Smirnov, *Biopolymers* **2001**, *56*, 209–227.
[86] M. P. Horvath, S. C. Schultz, *J. Mol. Biol.* **2001**, *310*, 367–377.
[87] G. J. Narlikar, D. Herschlag, *Annu. Rev. Biochem.* **1997**, *66*, 19–59.
[88] P. C. Bevilacqua, T. S. Brown, S.-i. Nakano, R. Yajima, *Biopolymers* **2004**, *73*, 90–109.
[89] E. M. Moody, J. T. J. Lecomte, P. C. Bevilacqua, *RNA* **2005**, *11*, 157–172.
[90] R. K. O. Sigel, B. Lippert, *Chem. Commun.* **1999**, 2167–2168.
[91] R. K. O. Sigel, E. Freisinger, B. Lippert, *J. Biol. Inorg. Chem.* **2000**, *5*, 287–299.
[92] M. S. Lüth, M. Willermann, B. Lippert, *Chem. Commun.* **2001**, 2058–2059.
[93] M. G. Añorbe, M. S. Lüth, M. Roitzsch, M. M. Cerda, P. Lax, G. Kampf, H. Sigel, B. Lippert, *Chem. Eur. J.* **2004**, *10*, 1046–1057.
[94] M. Roitzsch, B. Lippert, *J. Am. Chem. Soc.* **2004**, *126*, 2421–2424.
[95] B. Lippert, *Prog. Inorg. Chem.* **2005**, in press.
[96] R. K. O. Sigel, E. Freisinger, S. Metzger, B. Lippert, *J. Am. Chem. Soc.* **1998**, *120*, 12000–12007.
[97] W. Brüning, R. K. O. Sigel, E. Freisinger, B. Lippert, *Angew. Chem. Int. Ed.* **2001**, *40*, 3397–3399.
[98] W. Brüning, E. Freisinger, M. Sabat, R. K. O. Sigel, B. Lippert, *Chem. Eur. J.* **2002**, *8*, 4681–4692.
[99] S.-O. Shan, A. V. Kravchuk, J. A. Piccirilli, D. Herschlag, *Biochemistry* **2001**, *40*, 5161–5171.
[100] A. M. Pyle, *J. Biol. Inorg. Chem.* **2002**, *7*, 679–690.
[101] R. K. O. Sigel, S. M. Thompson, E. Freisinger, B. Lippert, *Chem. Commun.* **1999**, 19–20.
[102] R. K. O. Sigel, S. M. Thompson, E. Freisinger, B. Lippert, *Chem. Eur. J.* **2000**, *7*, 1968–1980.
[103] H. Sigel, *Pure Appl. Chem.* **2004**, *76*, 1869–1886.
[104] S.-O. Shan, A. Yoshida, S. Sun, J. A. Piccirilli, D. Herschlag, *Proc. Natl. Acad. Sci. U. S. A.* **1999**, *96*, 12299–12304.
[105] J. H. Cate, R. L. Hanna, J. A. Doudna, *Nat. Struct. Biol.* **1997**, *4*, 553–558.
[106] C. C. Correll, B. Freeborn, P. B. Moore, J. A. Steitz, *Cell* **1997**, *91*, 705–712.
[107] B. Knobloch, R. K. O. Sigel, B. Lippert, H. Sigel, *Angew. Chem. Int. Ed.* **2004**, *43*, 3793–3795.
[108] D. Smith, A. B. Burgin, E. S. Haas, N. R. Pace, *J. Biol. Chem.* **1992**, *267*, 2429–2436.
[109] C. A. Grosshans, T. R. Cech, *Biochemistry* **1989**, *28*, 6888–6894.
[110] M. Costa, J. M. Fontaine, S. L. Goër, F. Michel, *J. Mol. Biol.* **1997**, *274*, 353–364.
[111] C. Adamidi, O. Fedorova, A. M. Pyle, *Biochemistry* **2003**, *42*, 3409–3418.
[112] J. F. Swisher, L. J. Su, M. Brenowitz, V. E. Anderson, A. M. Pyle, *J. Mol. Biol.* **2002**, *315*, 297–310.
[113] P. M. Gordon, E. J. Sontheimer, J. A. Piccirilli, *RNA* **2000**, *6*, 199–205.
[114] R. K. O. Sigel, A. M. Pyle, *Met. Ions Biol. Syst.* **2003**, *40*, 477–512.
[115] D. A. Harris, N. G. Walter, Terbium(III) footprinting as a probe of RNA structure and metalbinding sites, in *Handbook of RNA Biochemistry* (Eds.: A. Bindereif, R. Hartmann, A. Schön, E. Westhof), Wiley-VCH, Weinheim, **2005**, pp. 205–213.
[116] S. Dorner, A. Barta, *Biol. Chem.* **1999**, *380*, 243–251.
[117] N. G. Walter, N. Yang, J. M. Burke, *J. Mol. Biol.* **2000**, *298*, 539–555.
[118] J. Swisher, C. M. Duarte, L. J. Su, A. M. Pyle, *EMBO J.* **2001**, *20*, 2051–2061.
[119] R. S. Brown, B. A. Hingerty, J. C. Dewan, A. Klug, *Nature* **1983**, *303*, 543–546.
[120] J. Ciesiolka, W. D. Hardt, J. Schlegl, V. A. Erdmann, R. K. Hartmann, *Eur. J. Biochem.* **1994**, *219*, 49–56.
[121] A. Vaidya, H. Suga, *Biochemistry* **2001**, *40*, 7200–7210.
[122] M. Hertweck, M. W. Mueller, *Eur. J. Biochem.* **2001**, *268*, 4610–4620.
[123] S. D. Dib-Hajj, S. C. Boulanger, S. K. Hebbar, C. L. Peebles, J. S. Franzen, P. S. Perlman, *Nucleic Acids Res.* **1993**, *21*, 1797–1804.
[124] P. Z. Qin, S. E. Butcher, J. Feigon, W. L. Hubbell, *Biochemistry* **2001**, *40*, 6929–6936.
[125] L. Zhang, J. A. Doudna, *Science* **2002**, *295*, 2084–2088.
[126] U. Schmidt, M. Podar, U. Stahl, P. S. Perlman, *RNA* **1996**, *2*, 1161–1172.
[127] P. M. Gordon, J. A. Piccirilli, *Nat. Struct. Biol.* **2001**, *8*, 893–898.

 © 2005 Wiley-VCH Verlag GmbH & Co. KGaA, Weinheim

[128] R. K. O. Sigel, A. G. Palmer, A. M. Pyle, manuscript in preparation.
[129] B. Knobloch, D. Suliga, A. Okruszek, R. K. O. Sigel, *Chem. Eur. J.* **2005**, in press.
[130] S. Basu, R. P. Rambo, J. Strauss-Soukup, J. H. Cate, A. R. Ferre-D'Amare, S. A. Strobel, J. A. Doudna, *Nat. Struct. Biol.* **1998**, *5*, 986–992.
[131] H. Wank, J. SanFilippo, R. N. Singh, M. Matsuura, A. M. Lambowitz, *Mol. Cell* **1999**, *4*, 239–250.
[132] K. A. Jarrell, C. L. Peebles, R. C. Dietrich, S. L. Romiti, P. S. Perlman, *J. Biol. Chem.* **1988**, *263*, 3432–3439.
[133] J. Bachl, C. Schmelzer, *J. Mol. Biol.* **1990**, *212*, 113–125.
[134] U. Schmidt, B. Riederer, M. Moerl, C. Schmelzer, U. Stahl, *EMBO J.* **1990**, *9*, 2289–2298.
[135] J. R. Lorsch, J. W. Szostak, *Biochemistry* **1994**, *33*, 973–982.
[136] P. M. Gordon, E. J. Sontheimer, J. A. Piccirilli, *Biochemistry* **2000**, *39*, 12939–12952.
[137] C. P. Da Costa, A. Okruszek, H. Sigel, *ChemBioChem.* **2003**, *4*, 593–602.
[138] V. L. Pecoraro, J. D. Hermes, W. W. Cleland, *Biochemistry* **1984**, *23*, 5262–5271.
[139] R. K. O. Sigel, B. Song, H. Sigel, *J. Am. Chem. Soc.* **1997**, *119*, 744–755.
[140] C. P. Da Costa, D. Krajewska, A. Okruszek, W. J. Stec, H. Sigel, *J. Biol. Inorg. Chem.* **2002**, *7*, 405–415.
[141] B. Knobloch, H. Sigel, *J. Biol. Inorg. Chem.* **2004**, *9*, 365–373.
[142] H. Sigel, B. Song, *Met. Ions Biol. Syst.* **1996**, *32*, 135–206.
[143] H. Sigel, *Pure & Appl. Chem.* **2004**, *76*, 375–388.
[144] M. C. Erat, M. Wächter, R. K. O. Sigel, *CHIMIA* **2004**, *58*, 479.
[145] M. C. Erat, R. K. O. Sigel, to be published.
[146] M. Costa, F. Michel, E. Westhof, *EMBO J.* **2000**, *19*, 5007–5018.
[147] R. Koradi, M. Billeter, K. Wüthrich, *J. Mol. Graphics* **1996**, *14*, 29–32 and 51–55.
[148] O. W. Odom, D. L. Shenkenberg, J. A. Garcia, D. L. Herrin, *RNA* **2004**, *10*, 1097–1107.
[149] R. Saldanha, B. Chen, H. Wank, M. Matsuura, J. Edwards, A. M. Lambowitz, *Biochemistry* **1999**, *38*, 9069–9083.
[150] S. K. Hebbar, S. M. Belcher, P. S. Perlman, *Nucleic Acids Res.* **1992**, *20*, 1747–1754.
[151] U. Kück, I. Godehardt, U. Schmidt, *Nucleic Acids Res.* **1990**, *18*, 2691–2697.

Received: December 07, 2004
Published Online: April 25, 2005

 © 2005 Wiley-VCH Verlag GmbH & Co. KGaA, Weinheim

Facile Catalytic Decomposition at Low Temperature of Energetic Ionic Liquid as Hydrazine Substitute

Laurence Courthéoux,[a] Dan Amariei,[a] Sylvie Rossignol*[a] and Charles Kappenstein[a]

Keywords: Platinum-based catalyst / Sol-gel synthesis / Ionic liquids / Alumina-silica / Catalyst activity

Platinum supported on doped alumina catalysts were prepared and evaluated for the decomposition of NH_3OHNO_3/water energetic liquid. Powdered and shaped catalysts remain active after 23 injections at 45 °C.

(© Wiley-VCH Verlag GmbH & Co. KGaA, 69451 Weinheim, Germany, 2005)

Energetic liquid compounds known as monopropellants are used for propulsion and gas generator purposes. For example, the orbit and attitude control of satellites is obtained through small thruster engines using the catalytic decomposition of hydrazine, N_2H_4, on supported iridium catalysts. The high toxicity of hydrazine induces high costs and its replacement by a less toxic propellant is of current interest.[1,2] The most currently proposed and studied hydrazine substitutes are energetic aqueous ionic liquids and a representative mixture contains hydroxylammonium nitrate (or $NH_3OH^+NO_3^-$, HAN) as oxidizer, water and a fuel.[3–5] Nevertheless, the use of such mixtures involves more drastic conditions than for hydrazine, due to the high temperature reached during the decomposition (up to 1400 °C) and the need of frequent restarts that involve a preheating of the catalyst (300–400 °C). Therefore, a high catalytic activity at low temperature (20–200 °C) associated with a high thermal stability of shape formed catalysts remain critical parameters for the future development of new engines.

Previous studies performed by our group have revealed that platinum supported on thermally stable Si-doped alumina displays a good activity at low temperatures[6,7] The powder or shaped Si-doped alumina (xerogel) are obtained by sol-gel procedure and were demonstrated to be stable at high temperature (1200 °C, 5 h);[8] the metallic phase (10 wt.-% Pt) is added by the wet impregnation procedure. These catalysts have been evaluated for the decomposition of HAN/water solutions in a lab-made constant volume batch reactor,[9] and lead to decomposition at very low temperatures, less than 60 °C,[10] whereas the thermal decomposition temperature is in the range 115–120 °C.[4] Another key point concerns the long-term stability of the catalysts, particularly in the presence of a large amount of propellant. In this paper, we present the activity of powdered and shaped (spheres) catalysts for successive HAN/water injections. These successive injections were carried out to simulate the pulse mode of the satellite thrusters. The catalysts (160 mg) are preheated at 45 °C during 1 h, then 100 μL (150 mg) of a binary 79 wt.-% HAN/water mixture (i.e. 1.23 mmol) was injected manually 23 times, using a syringe, in the constant volume reactor (167 cm^3). Each injection is made after the thermal re-equilibration (approximately 4 min); the number of injections is limited by the pressure gauge and by the size of the sample holder.

The evolution of pressure and temperature (catalyst and gas phase) as a function of time during the successive injections using the sphere-shaped catalyst are represented in part a of Figure 1. Each peak corresponds to the decomposition following the injection, with an ignition delay of about 0.5 s; the catalysts are still active after all the injections. The decomposition reaction can form the thermodynamic products N_2, O_2 and H_2O [Equation (1)] or give additional kinetic products, in the form of nitrogen oxides [i.e. Equation (2)]. The calculated values of pressure increase (gas phase temperature: 25 °C) using the perfect gas formula are 365 mbar and 91 mbar, respectively, for a reaction giving thermodynamic [Equation (1)] and kinetic [Equation (2)] products.[11]

$$NH_2OHNO_3(aq) \rightarrow N_2(g) + O_2(g) + 2\ H_2O(l) \quad (1)$$

$$NH_3OHNO_3(aq) \rightarrow NO_2(g \text{ or } aq) + 0.5\ N_2(g) + 2\ H_2O(l) \quad (2)$$

Moreover, in both cases, the reaction produces water, which stay for the main part in the sample holder. An enlargement of a catalytic decomposition peak is given in Figure 1b; for each peak, the pressure increase (ΔP) due to the formation of gaseous products[10] and the rate of the decomposition (slope: $\Delta P/\Delta t$ in mbar·s^{-1}) between the points 1 and 2 are determined. The catalyst temperature-

[a] Laboratoire de Catalyse par les Métaux, University of Poitiers, LACCO UMR 6503,
40 Avenue du Recteur Pineau, 86022 Poitiers Cedex, France
Fax: +33-5-49454157
E-mail: sylvie.rossignol@univ-poitiers.fr

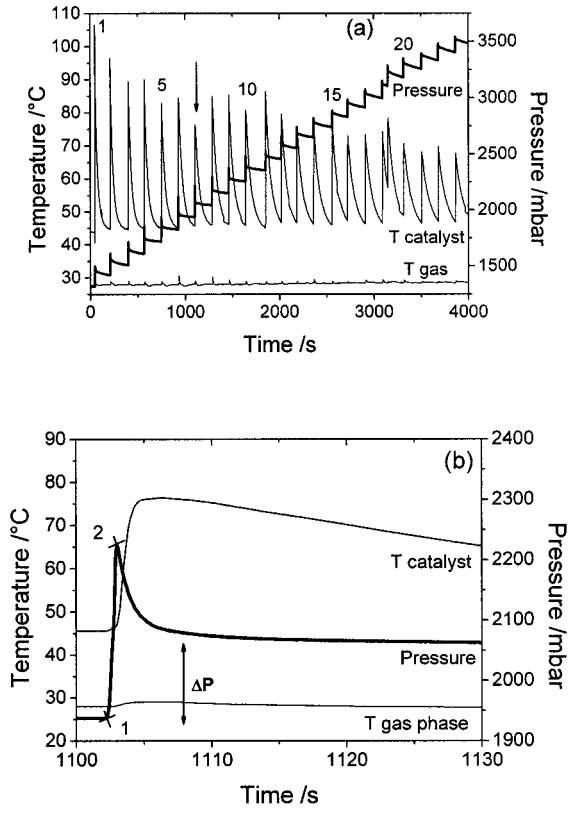

Figure 1. (a) Catalytic decomposition of 79 wt.-% HAN/H_2O at 45 °C with the sphere-shaped sample (23 injections) and (b) enlargement of one decomposition peak (see arrow, part a): Determination of pressure increase and the slope between points 1 and 2.

decrease is due to the heat transfer to the reactor; the progressive reduction of the temperature maxima (106 to 70 °C; Figure 1a) is related to the increasing amount of water in the sample holder. The pressure increase (ΔP) variations of the two catalysts are similar, as shown in Figure 2. The values gradually decrease from 140 mbar at the beginning, to 110 mbar at the end of the 23 injections, corresponding to 0.94 and 0.74 mmol of gaseous product formed during the decomposition reaction. This decrease can be explained by a small deactivation of the catalyst related to the increasing amount of water in the sample holder. The pressure-increase values for both samples are close to the kinetic value (91 mbar), indicating the formation of nitrogen oxides. Other experiments carried out in a dynamic reactor with on-line MS analysis are in progress in order to determine the gas phase composition during the decomposition reaction. The first results show the formation of kinetics products, such as NO, NO_2 and lower amounts of N_2O.[12]

The evolution of the decomposition rate (measured by the $\Delta P/\Delta t$ slope) during the 23 successive injections on both catalysts is given in Figure 3. Whatever the catalyst, an increase of the reaction rate is evidenced until the seventh injection to reach 434 mbar·s^{-1} for the sphere-shaped sample and 323 mbar·s^{-1} for the powder, indicating a fast reaction rate. Then, the slope values oscillate between 200 and

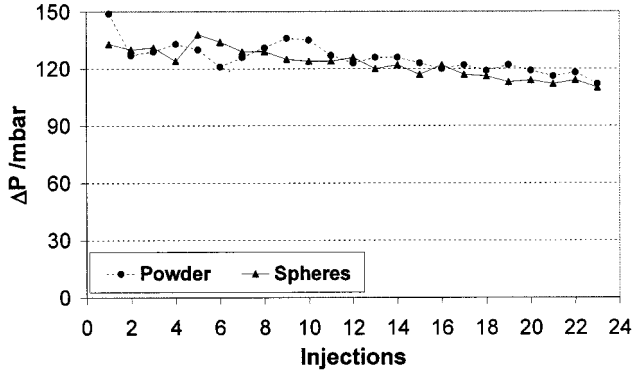

Figure 2. Evolution of pressure increase (ΔP) values during the 23 successive injections of 79 wt.-% HAN/H_2O at 45 °C on both catalysts.

400 mbar·s^{-1}. The nonreproducible oscillations are due to the manual injection procedure. An automatic injection system using a microburette failed for this pulse injection mode. These results show the very good efficiency of both catalysts and the noninhibiting effect of the shaping. Nevertheless, mechanical breaking of the spheres has been observed during the reaction probably due to the strong exothermic decomposition of the HAN/H_2O solution. This mechanical breaking could be avoided by a preheating at 100 °C.

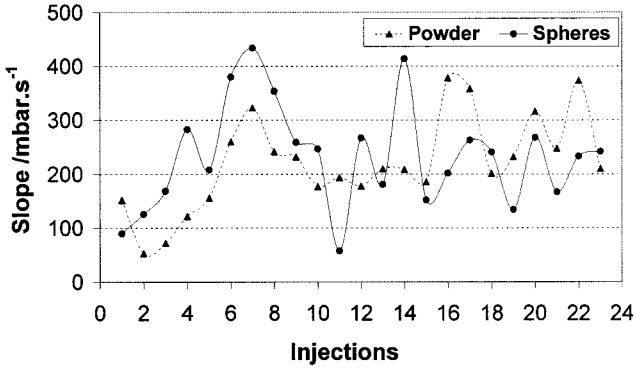

Figure 3. Evolution of $\Delta P/\Delta t$ slopes during the successive injections of HAN/H_2O at 45 °C on the powder and sphere-shaped catalysts.

All these experiments display the very good activity and stability of our catalysts. Indeed they allowed the efficient decomposition of the HAN/water solution at low temperature (45 °C) even in presence of a large amount of solution. Moreover, these materials remain active, showing a high reaction rate and an important pressure increase, after 23 monopropellant injections which remains a challenge for the development of new satellites thrusters. Nevertheless, the breaking of the sphere implies to find a more mechanically stable shaped catalyst support.

 © 2005 Wiley-VCH Verlag GmbH & Co. KGaA, Weinheim

Acknowledgments

The authors wish to thank the CTI Company for the shape forming of the samples, the French Space Agency (CNES, Nicolas Pillet) and the European Space Agency (Mark Ford) for funding this study.

[1] V. Bombelli, D. Simon, J. Moerel, T. Maree, *AIAA Pap.* **2003**, 4783.
[2] AIAA papers are available from the American Institute for Aeronautics and Astronautics website: http://www.aiaa.org/content.cfm?pageid = 413.
[3] D. M. Zube, E. J. Wucherer, B. Reed, *AIAA Pap.* **2003**, 4643.
[4] H. Lee, T. A. Litzinger, *Combust. Flame* **2001**, *127*, 2205–2222.
[5] Y. P. Chang, K. K. Kuo, *AIAA Pap.* **2001**, 3272.
[6] L. Courthéoux, F. Popa, E. Gautron, S. Rossignol, C. Kappenstein, *J. Non-Cryst. Solids* **2004**, *350*, 113–119.
[7] F. Popa, L. Courthéoux, E. Gautron, S. Rossignol, C. Kappenstein. *Eur. J. Inorg. Chem.* **2005**, 543–554.
[8] F. Popa, S. Rossignol, C. Kappenstein, *J. Mater. Chem.* **2002**, *12*(*10*), 2866–2868.
[9] R. Eloirdi, S. Rossignol, C. Kappenstein, D. Duprez, N. Pillet, *J. Propul. Power* **2003**, *19*, 213-219.
[10] L. Courthéoux, S. Rossignol, C. Kappenstein, N. Pillet, *AIAA Pap.* **2003**, 4645.
[11] E. S. Kim, H. S. Lee, C. F. Mallery, S. T. Thynell, *Combust. Flame* **1997**, *110*, 239–255.
[12] Y. Batonneau, L. Courthéoux, P. Esteves, S. Rossignol, L. Pirault-Roy, C. Kappenstein, N. Pillet, *AIAA Pap.* **2004**, 3835.
Received: January 28, 2005

 © 2005 Wiley-VCH Verlag GmbH & Co. KGaA, Weinheim

A Structural and Magnetic Investigation of Ferromagnetically Coupled Copper(II) Isophthalates

Wei-Zheng Shen,[a] Xiao-Yan Chen,[a] Peng Cheng,*[a] Shi-Ping Yan,[a] Bin Zhai,[a] Dai-Zheng Liao,[a] and Zong-Hui Jiang [a]

Keywords: Copper / Magnetic properties / N ligands / Organic-inorganic hybrid composites

Dinuclear and one-dimensional copper complexes $[Cu_2(tpa)_2(m\text{-bda})](ClO_4)_2$ (**1**), $[\{Cu_2(tpm)_2(m\text{-bda})_2\}\cdot 2CH_3OH\cdot 4H_2O]_n$ (**2**), and $[\{Cu_2(bpm)_2(m\text{-bda})_2(H_2O)\}\cdot CH_3CN\cdot H_2O]_n$ (**3**) [tpa: tris(2-pyridylmethyl)amine; tpm: tris(pyrazolyl)methane; bpm: bis(pyrazolyl)methane; *m*-bda: isophthalate dianion] have been prepared from various polydentate terminal ligands. Complex **1** crystallizes in the monoclinic $P2_1/c$ space group with a = 14.003(6), b = 17.201(7), c = 20.654(9) Å, Z = 4, R_1 = 0.0678, wR_2 = 0.1751. Complex **2** crystallizes in the triclinic $P\bar{1}$ space group with a = 10.250(7), b = 15.078(10), c = 15.190(10) Å, Z = 2, R_1 = 0.0571, wR_2 = 0.1288. Complex **3** crystallizes in the orthorhombic *Pnma* space group with a = 17.956(6), b = 17.615(5), c = 10.776(4) Å, Z = 4, R_1 = 0.0554, wR_2 = 0.0845. In these complexes the isophthalate anion acts as a bis(monodentate) ligand bridging copper(II) centers. The variable temperature magnetic behavior reveals the existence of ferromagnetic interactions in **1**–**3**. The best fittings to the experimental magnetic susceptibilities give J = 1.02 cm^{-1} (**1**), 2.58 cm^{-1} (**2**), and 35.5 cm^{-1} (**3**). In light of the structural data it can be concluded that the magnetic coupling via the isophthalate bridging ligand is negligibly small, and the abnormally large ferromagnetic interaction in complex **3** may be due to the hydrogen bonding between copper centers via carboxylic groups through a spin-polarization mechanism.

(© Wiley-VCH Verlag GmbH & Co. KGaA, 69451 Weinheim, Germany, 2005)

Introduction

The study of superexchange interactions between paramagnetic ions in a variety of magnetic systems has been a vital field in inorganic chemistry in the last decades driven by the need to understand the fundamental science associated with magnetic interactions between metal centers and develop structure-function relationships that enable the rational design of new magnetic materials.[1] Owing to its fundamental importance, the study of long-range magnetic interactions has also been an active field of research,[2] in which phenyldicarboxylate ligands have been extensively studied.[3–6] Alhough magnetic interactions transmitted through phenyldicarboxylate bridges are usually weak,[2,6–8] the magnitude and nature of the coupling interactions can be influenced by a series of factors, such as the separation of the metal centers, bridging modes, degree of coplanarity between the coordination basal planes and the ligand, the dihedral angles between the carboxylato planes and the phenyl ring, and the angle between the planes of the two carboxylato groups of each phthalato bridge.[9–12]

In copper phthalates, magnetic systems with terephthalate as bridges are the most abundant, whereas those with isophthalate have been less widely reported.[5,6,13,14] In fact, compounds of phenyldicarboxylates are mostly dinuclear and oligonuclear, while those with polymeric structures and transition metal varieties are still relatively limited, especially for isophthalic acid. In a previous report,[14] we systematically investigated the influence of various isomers of phthalic acids on magnetic properties, and found that the structural differences caused by the bridging ligands lead to unexpected magnetic behavior, including changes from ferromagnetic to antiferromagnetic couplings. As a continuation of this magneto-structural relationship study, we initiated a systematic experimental approach in an attempt to design μ-isophthalato-Cu^{II} magnetic systems to investigate the factors that influence the isophthalate-bridged complexes. Three ferromagnetically coupled complexes $[Cu_2(tpa)_2(m\text{-bda})](ClO_4)_2$ (**1**), $[\{Cu_2(tpm)_2(m\text{-bda})_2\}\cdot 2CH_3OH\cdot 4H_2O]_n$ (**2**), and $[\{Cu_2(bpm)_2(m\text{-bda})_2(H_2O)\}\cdot CH_3CN\cdot H_2O]_n$ (**3**) [tpa: tris(2-pyridylmethyl)amine; tpm: tris(pyrazolyl)methane; bpm: bis(pyrazolyl)methane; *m*-bda: isophthalate dianion] were prepared. The coordination geometries of the Cu^{II} centers are tuned by the various polydentate terminal ligands, which ultimately leads to the different crystal structures and magnetic properties.

Results and Discussion

Complexes **1**–**3** were prepared with the same bridging ligand, the isophthalate dianion, and three different terminal

[a] Department of Chemistry, Nankai University, Tianjin 300071, P. R. China
Fax: +86-22-23502458
E-mail: pcheng@nankai.edu.cn

ligands, tris(pyrazolyl)methane, tris(2-pyridylmethyl)amine and bis(pyrazolyl)methane. Since tris(pyrazolyl)methane is a tridentate ligand, it reacts very easily with 0.5 equiv. of the metal ion to form the sandwich complex $M(tpm)_2$. On the other hand, the isophthalate dianion is not an active bridging ligand in neutral environments. In this paper, we successfully obtained a half-sandwich structure by making the pH basic. This solution also works when we change the terminal ligand into tris(2-pyridylmethyl)amine or bis(pyrazolyl)methane.

The X-ray crystal structure analyses reveal a dinuclear unit for **1** and one-dimensional zigzag chain motifs for **2** and **3**. The copper(II) ions in **1** and **2** are all five-coordinate, whereas there are two types of crystallographically different copper atoms − four-coordinate and five-coordinate − in **3**.

Crystal Structure of $[Cu_2(tpa)_2(m\text{-bda})](ClO_4)_2$ (1)

The structure of **1** contains a $[Cu_2(tpa)_2(m\text{-bda})]^{2+}$ cation and a ClO_4^- anion. The $[Cu_2(tpa)_2(m\text{-bda})]^{2+}$ unit is shown in Figure 1. The tpa ligand acts as a quadridentate terminal ligand with four nitrogen atoms ligated at the copper center. The *m*-bda group acts as a bis(monodentate) ligand, and bridges copper(II) ions to form a dinuclear complex. The coordination geometry around the copper atom is distorted trigonal-bipyramidal. The apical sites of the trigonal bipyramid are occupied by the N4 and O1 atoms [Cu1–N4 = 2.033(6) Å; Cu1–O1 = 1.901(5) Å]. The best equatorial plane is defined by atoms N1, N2, and N3, with an average Cu–N bond length and N–Cu–N bond angle of 2.085(7) Å and 117.3(3)°, respectively. The Cu1 atom is 0.091(6) Å out of this plane. The distance between two copper(II) ions is 10.557(5) Å.

$[\{Cu2(tpm)2(m\text{-bda})2\}\cdot 2CH_3OH\cdot 4H_2O]_n$ (2)

In the structure of **2**, tpm is a tridentate terminal ligand. The isoelectronic tris(pyrazolyl)methane ligand is formally derived from tris(pyrazolyl)borate ligands by replacing the central boron anion with a carbon atom, and has received considerably less attention.[15–17] Surprisingly, 1D or multidimensional polymers with tpm as terminal ligand have seldom been reported so far, which is probably due to the fact that tpm is such a strong tridentate, chelating, six-electron donor that it can effectively prevent building blocks from constructing infinite aggregates. In principle, the half-sandwich complexes containing tpm can be extended into infinite structures through appropriate bridging ligands. Here, the *m*-bda anion, as a bis(monodentate) ligand, bridges copper(II) ions to form a one-dimensional zigzag chain-like structure, as shown in Figure 2. The coordination geometry around the copper atom is distorted square pyramidal. The apical site of the square pyramid around the Cu1 atom is occupied by N3 [Cu1–N3 = 2.414(5) Å]. Other Cu–N bond lengths vary slightly, from 1.984(5) to 1.991(4) Å. The Cu–O bond lengths [Cu1–O1 = 1.899(4) Å, Cu1–O5 = 1.905(14) Å] are somewhat shorter than in other *m*-bda-bridged complexes,[5,6,13] which may be due to the distorted square pyramid geometry caused by the rigid tridentate tpm ligand. The best equatorial plane is defined by N1, N5, O1, and O5. The largest deviation from the mean plane is 0.2261 Å for O5, and the Cu1 atom is 0.0023 Å out of this plane. The distance between copper(II) ions along the chain is 10.403 Å, which is much longer than the shortest interchain distance (6.644 Å) between copper ions.

$[\{Cu_2(bpm)_2(m\text{-bda})_2(H_2O)\}\cdot CH_3CN\cdot H_2O]_n$ (3)

The polymeric $[Cu_2(bpm)_2(m\text{-bda})_2(H_2O)\}$ unit of **3** is shown in Figure 3. The bpm ligand acts as a bidentate terminal ligand. There are two kinds of crystallographically different Cu^{II} ions in **3**: Cu1 (five-coordinate) and Cu2 (four-coordinate). The coordination geometry around Cu1 is perfectly square pyramidal, with two nitrogen atoms from bpm [Cu1–N1(N1A) = 2.081(3) Å] and two oxygen atoms from *m*-bda [Cu1–O1(O1A) = 1.937(3) Å] composing the equatorial plane. The Cu1 atom is 0.0541(4) Å out of this plane. The apical site of this square pyramid is occupied by the oxygen atom from the coordinated water molecule [Cu1–O5 = 2.394(4) Å]. The coordination geometry around Cu2 is a distorted square plane with two nitrogen atoms from bpm [Cu2–N3(N3B) = 2.009(3) Å] and two oxygen

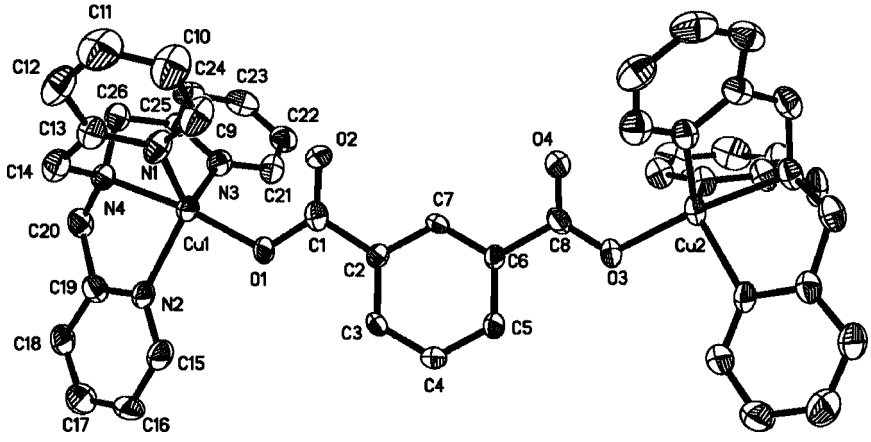

Figure 1. ORTEP drawing of $[Cu_2(tpa)_2(m\text{-bda})](ClO_4)_2$ (**1**); ClO_4^- and H atoms have been omitted for clarity.

 © 2005 Wiley-VCH Verlag GmbH & Co. KGaA, Weinheim

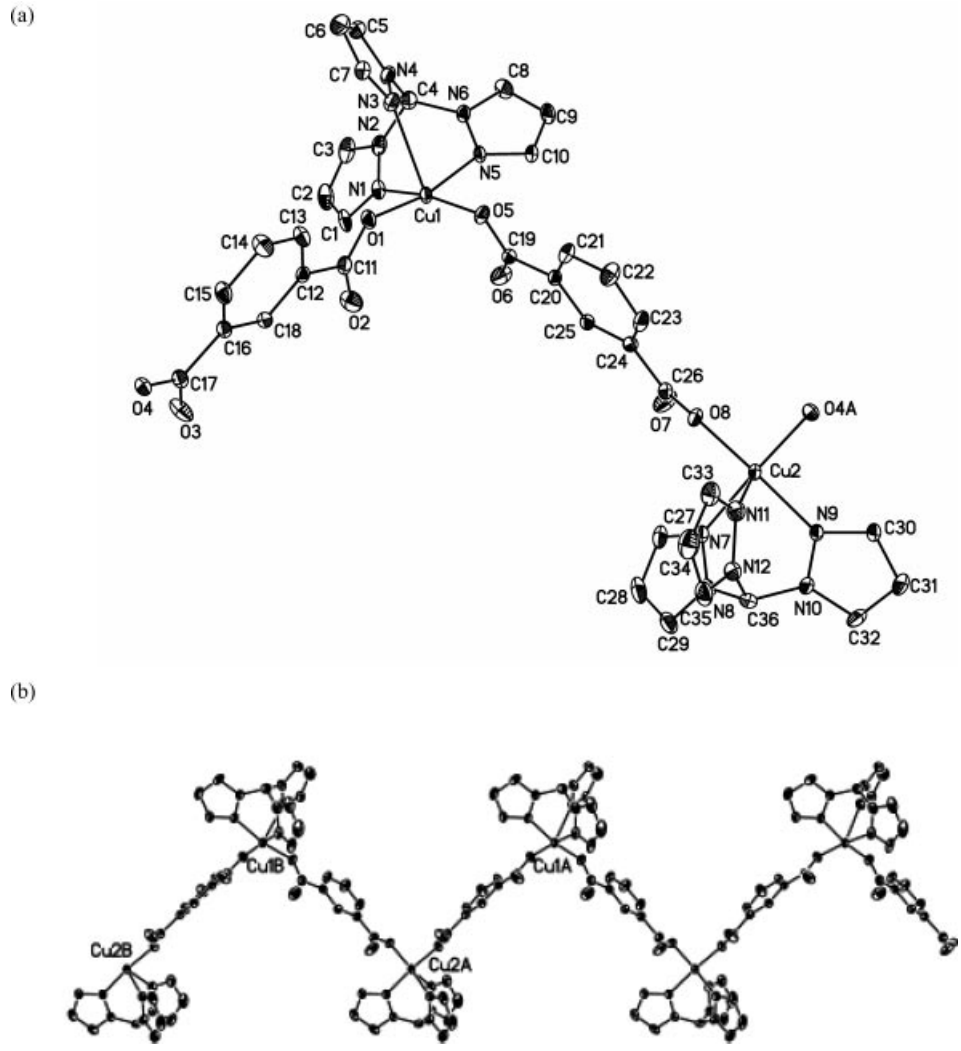

Figure 2. (a) ORTEP drawing of $[\{Cu_2(tpm)_2(m\text{-bda})_2\}\cdot 2CH_3OH\cdot 4H_2O]_n$ (**2**); solvent molecules and H atoms have been omitted for clarity. (b) Zigzag chain structure of **2**.

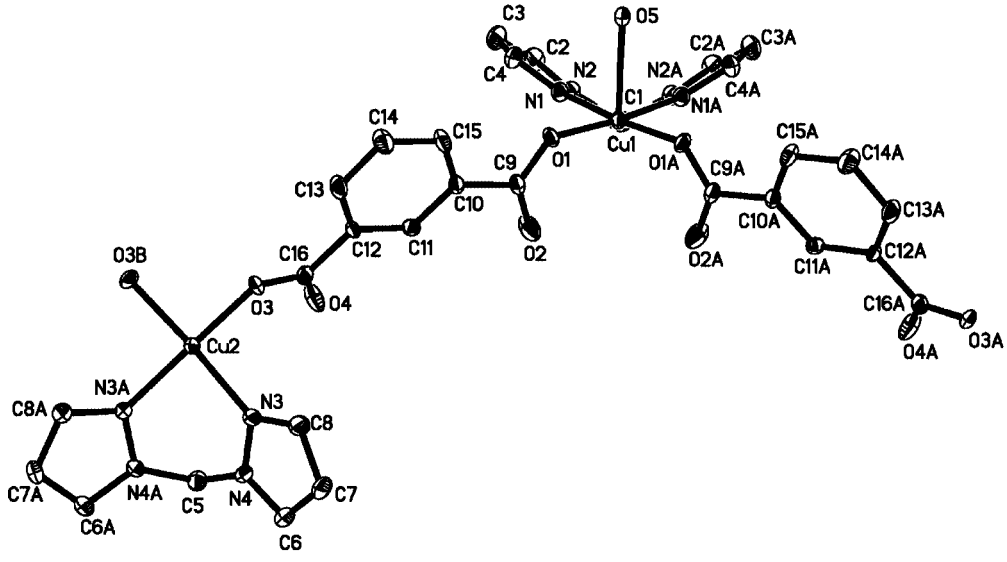

Figure 3. ORTEP drawing of $[\{Cu_2(bpm)(m\text{-bda})_2(H_2O)\}\cdot CH_3CN\cdot H_2O]_n$ (**3**); solvent molecules and H atoms have been omitted for clarity.

 © 2005 Wiley-VCH Verlag GmbH & Co. KGaA, Weinheim

atoms from *m*-bda [Cu2–O3(O3B) = 1.939(9) Å]. The Cu2 atom is 0.1514 Å out of the plane. The *m*-bda group acts as a bis(monodentate) ligand and bridges two crystallographically different copper(II) ions alternately to form a one-dimensional zigzag chain (Figure 3). The distance between copper(II) ions along the chain is 10.643 Å, which is much longer than the shortest interchain distance [4.936(4) Å] between copper ions.

There are two kinds of weak interactions between neighboring copper chains: (i) Cu–O···Cu weak coordination bonds, where the oxygen atom from the coordinated water molecule of the five-coordinate Cu atom forms a weak coordination bond with the four-coordinate Cu atom of the neighboring chain [Cu···O 2.552(7) Å, bold dashed line in Figure 4]. The Cu···Cu distance is 4.936(4) Å, and the Cu–O···Cu angle is 172.7(8)°; (ii) hydrogen bonds, with a distance of 2.692(3) Å between the oxygen atom of the H_2O coordinated to one Cu and the nonbonded carboxylate oxygen atoms of the adjacent Cu center. Such a distance strongly suggests the occurrence of H-bonding between these units (thin dashed line in Figure 4).

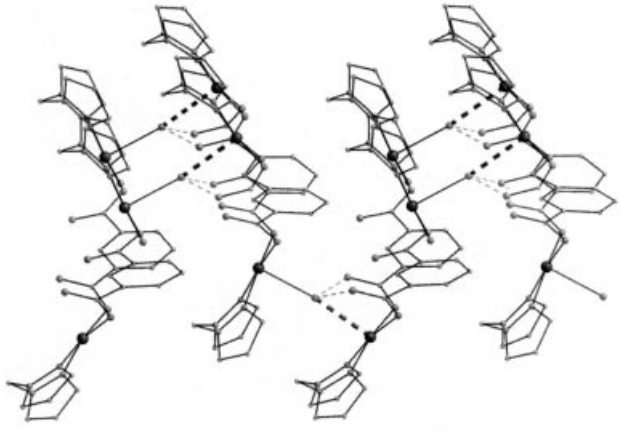

Figure 4. Packing arrangement of **3** along the *ac* plane.

The terminal ligands play an important role during the structure formation. For **1**, the terminal ligand is tetradentate tpa, and the large steric hindrance prevents the formation of infinite chainlike polymer; a dinuclear complex **1** is therefore obtained. For complex **2**, tpm is a tridentate ligand, and the steric hindrance is smaller than tpa. The copper centers are five-coordinate, with two oxygen atoms from an *m*-bda ligand which bridges copper centers into a 1D chain. We have previously published a series of phthalic acid bridged complexes − $[\{Cu_4(tacn)_4(o\text{-bda})_2\}(ClO_4)_4(H_2O)_2]_n$, $[\{Cu(tacn)(m\text{-bda})\}(CH_3OH)_{0.5}(H_2O)_{0.5}]_n$, and $[\{Cu_2(tacn)_2(p\text{-bda})\}(ClO_4)_2]_n$ (tacn = 1,4,7-triazacyclononane, bda = benzenedicarboxylic acid)[14] − in which the terminal ligand tacn is also a tridentate ligand and leads to the formation of one-dimensional chains. For complex **3**, bpm is a bidentate ligand, and the steric hindrance is the smallest, which allows a water molecule to coordinate to Cu1 while Cu2 is square planar. In general, tetradentate tpa ligands create a binuclear complex, whereas tridentate tpm and tacn ligands favor the formation of 1D chains, and the bidentate bpm ligand permits the formation of a 2D layer composed of weak interactions.

Magnetic Properties

The molar magnetic susceptibilities, χ_M, were measured in a field of 5000 G for **2** and 10000 G for **1** and **3**; plots of χ_M and μ_{eff} vs. T are shown below.

For **1**, the μ_{eff} is 2.55 μ_B at room temperature, which is similar to the spin-only value of 2.45 μ_B for two uncoupled copper(II) ions (Figure 5). It increases slightly on cooling to 18 K, and then decreases to 2.45 μ_B at 6 K. Intermolecular antiferromagnetic coupling results in the decrease of μ_{eff} be-

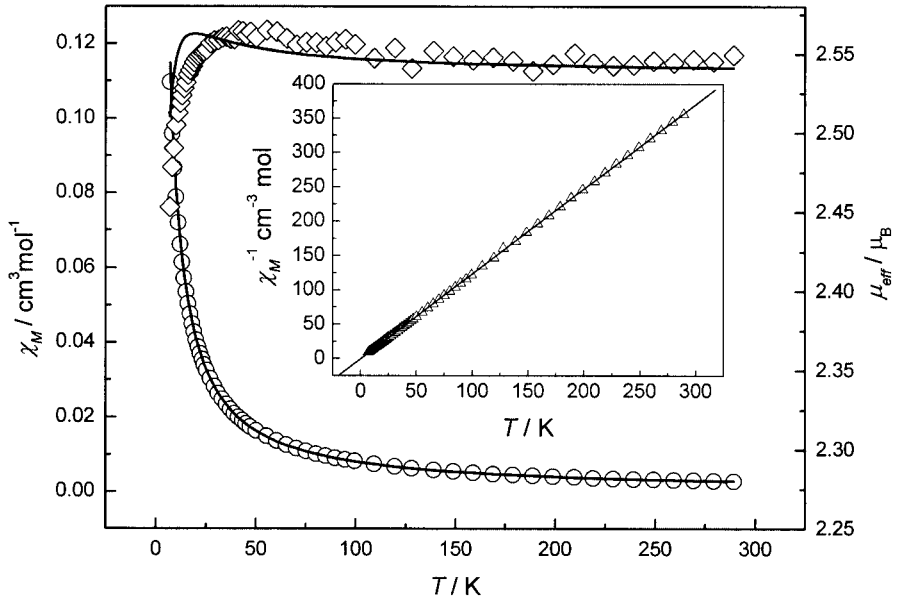

Figure 5. Plots of χ_M (O) and μ_{eff} (◊) vs. T and χ_M^{-1} vs. T (Δ) (inset) for **1**. The solid line represents the theoretical curve with the best-fit parameters.

 © 2005 Wiley-VCH Verlag GmbH & Co. KGaA, Weinheim

low 18 K. The χ^{-1} data for **1** obey the Curie–Weiss law with a Curie–Weiss temperature, θ, of 0.2 K and a Curie constant, C, of 0.81 emu K mol^{-1} (see inset of Figure 5). The Curie constant is larger than the expected value for two uncoupled Cu^{2+} spins (C_{theor} = 0.75 emu K mol^{-1}). The positive sign of the Weiss constant suggests the presence of ferromagnetic interactions between two copper centers. The magnetic parameters were estimated from a least-squares fitting of the susceptibility data by the equation for dinuclear Cu^{II} complexes [Equation (1)],[18] considering the decrease of μ_{eff} below 18 K, a temperature independent susceptibility term ($N\alpha$) was applied and set as 1.2×10^{-4} cm^3 mol^{-1}. A molecular field approximation [Equation (2)] was also used. The best fit was obtained for J = 1.02 cm^{-1}, zJ' = –0.05 cm^{-1}, g = 2.08, and $R = 3.6\times10^{-3}$ [agreement factor, defined as $\Sigma(\chi_M^{obs} - \chi_M^{calc})^2/\Sigma(\chi_M^{obs})^2$].

$$\chi_M = \frac{2Ng^2\beta^2}{kT}\left[3+\exp(-2J/kT)\right]^{-1} + N\alpha \quad (1)$$

$$\chi_M = \chi_{chain}/(1 - zJ'\chi_{chain}/NG^2\beta^2)$$
$$H = -2JS_1S_2 \quad (2)$$

For **2**, the effective magnetic moment is 1.83 μ_B at room temperature, which is close to that of an isolated Cu^{II} ion (1.73 μ_B). As the temperature is lowered, μ_{eff} of **2** smoothly increases to the maximum value of 1.91 μ_B at 24 K, and then decreases to 1.84 μ_B at 5.2 K (Figure 6). The increase of μ_{eff} is due to intrachain ferromagnetic coupling, while the interchain antiferromagnetic coupling results in the decrease of μ_{eff} below 24 K. The χ^{-1} data above 24 K for **2** obey the Curie–Weiss law, with a Curie–Weiss temperature of 1.4 K and a Curie constant of 0.42 emu K mol^{-1} (see inset of Figure 6). The Curie constant is larger than the expected value for one uncoupled Cu^{2+} spin (S = 1/2, C_{theor} = 0.375 emu K mol^{-1}), and the positive sign of the Weiss constant suggests ferromagnetic interactions between copper centers.

The magnetic susceptibility data of **2** were fitted approximately by the equation for a ferromagnetic chain [Equation (3)] with S = 1/2 and a molecular field correction equation [Equation (4)][19] in which A = 5.7979916, B = 16.902653, C = 29.376885, D = 29.832959, E = 14.036918, A' = 2.7979916, B' = 7.0086780, C' = 8.6538644, D' = 4.5743114, and $x = 2|J|/KT$. A temperature-independent susceptibility term ($N\alpha$) was also included and set as 60×10^{-6} cm^3 mol^{-1}. The other symbols have their usual meanings.

$$\chi_{chain} = \frac{Ng^2\beta^2}{4KT}\left[\frac{1+Ax+Bx^2+Cx^3+Dx^4+Ex^5}{1+A'x+B'x^2+C'x^3+D'x^4}\right]^{2/3} + N\alpha \quad (3)$$

$$\chi_M = \chi_{chain}/(1 - zJ'\chi_{chain}/NG^2\beta^2) \quad (4)$$

The best fit to the magnetic susceptibility data yielded J = 2.58 cm^{-1}, zJ' = –0.9 cm^{-1}, g = 2.13, and $R = 9.8\times10^{-4}$. These results confirmed the weak ferromagnetic coupling between adjacent copper(II) ions through the bridging isophthalate ligand, while $zJ' < 0$ indicates the weaker antiferromagnetic interaction between the chains.

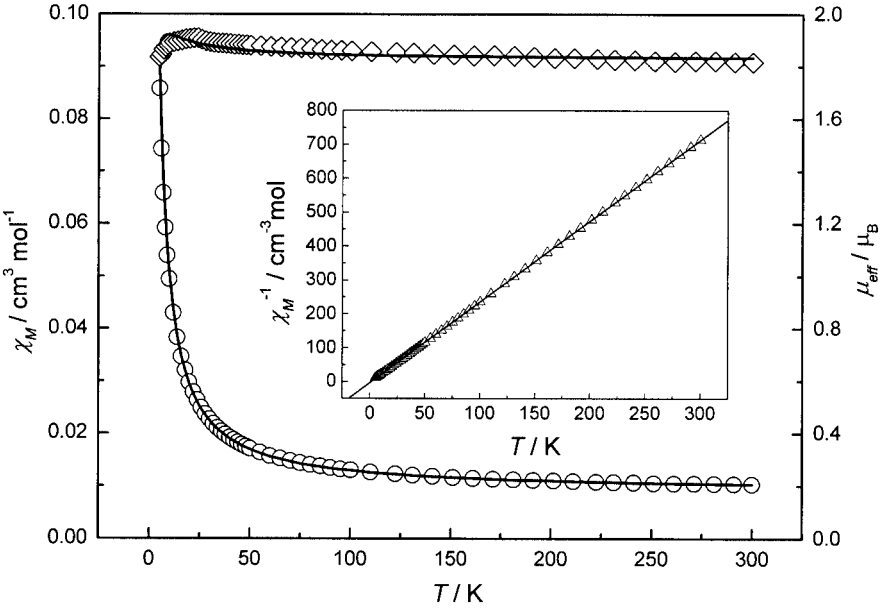

Figure 6. Plots of χ_M (O) and μ_{eff} (◊) vs. T and χ_M^{-1} vs. T (Δ) (inset) for **2**. The solid line represents the theoretical curve with the best-fit parameters.

 © 2005 Wiley-VCH Verlag GmbH & Co. KGaA, Weinheim

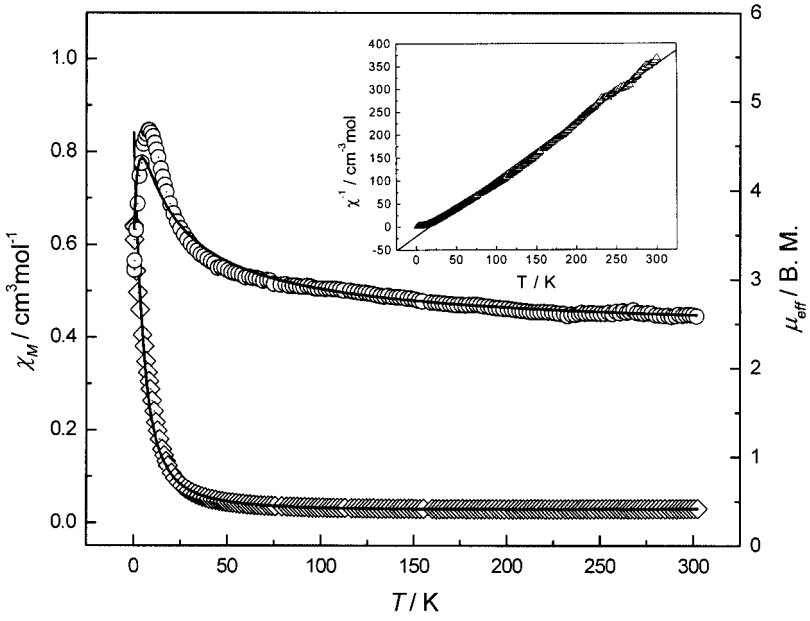

Figure 7. Plots of χ_M (O) and μ_{eff} (◊) vs. T and χ_M^{-1} vs. T (Δ) (inset) for **3** from Equation (1). The solid line represents the theoretical curve with the best-fit parameters.

The effective magnetic moment of **3** is 2.56 μ_B at room temperature, which is close to the value of two isolated Cu^{II} ions (2.45 μ_B). As the temperature is lowered, μ_{eff} of **3** increases to a maximum value of 4.79 μ_B at 9.5 K, and then decreases to 3.15 μ_B at 2 K (Figure 7). The increase of μ_{eff} indicates a ferromagnetic coupling between the copper centers. The χ^{-1} data obey the Curie–Weiss law, with a Curie–Weiss temperature of 16.2 K and a Curie constant of 0.42 emu K mol^{-1}. The positive sign of the Weiss constant also suggests the presence of ferromagnetic interactions between copper centers. Although the one-dimensional zigzag chain structure of **3** is similar to that of **2**, and the neighboring Cu···Cu distances are almost equal, the magnetic behavior is significantly different from that of **2**. First, we attempted to analyze the susceptibilities by the same equation as for complex **2** with the best-fit parameters of J = 33.9 cm^{-1}, zJ' = –2.73 cm^{-1}, g = 2.00, and $R = 9.38 \times 10^{-3}$. In our previous published results, we obtained an *m*-bda-bridged complex [{Cu(tacn)(*m*-bda)}$(CH_3OH)_{0.5}(H_2O)_{0.5}]_n$ (**4**) (tacn = 1,4,7-triazacyclononane).[14] Like tpm, tacn is a tridentate ligand, and the crystal structure of complex **4** is similar to that of **2**. Consequently, J was found to be 1.2 cm^{-1}, which is also close to that of **2**. The selected magnetostructural data of **1**–**4** are listed in Table 1; τ_1, τ_2, and δ are defined in Scheme 1. Comparing the terminal ligands, we can see that although the steric hindrance of the tetradentate ligand tpa prevents the formation of infinite aggregates for **1**, a long bridge through the benzene ring exists at the same time for **1**–**4**, which leads to a similar intramolecular metal–metal separation; in **1**, **2**, and **4** it is the only exchange pathway.

Table 1. Selected structural and magnetic parameters of *m*-bda-bridged copper(II) complexes.

	1	**2**	**3**	**4**
Bridging mode	bis(monodentate)	bis(monodentate)	bis(monodentate)	bis(monodentate)
Terminal ligand	tetradentate	tridentate	bidentate	tridentate
Cu:*m*-bda:terminal ligand	2:2:1	1:1:1	1:1:1	1:1:1
Coordination number	5	5	4, 5	5
Coordination geometry	trigonal-bipyramid	square pyramid	square pyramid, square plane	square pyramid
Cu–O(*m*-bda)$_{av}$ [Å]	1.912(5)	1.898(4)	1.937(3)	1.888(9)
τ_1 [°]	2.9(7), 4.1(2)	1.8(4), 17.9(8)	12.8(5), 17.9(3)	17.8(3), 26.3(8)
τ_2 [°]	7.3(8)	16.3(6)	27.7(3)	43.8(5)
δ [°]	119.9(5), 120.4(5)	129.4(4), 110.1(4)	123.4(3), 123.6(3)	135.6(9), 128.5(15)
d_{intra} [Å]	10.557	10.403	10.643	10.783
d_{inter} [Å]	–	6.644	4.936	7.171
J [cm^{-1}]	1.02	2.58	33.9/38.5	1.2
zJ' [cm^{-1}]	–0.05	–0.9	–2.37/–2.25	–0.18
g	2.08	2.13	2.00/2.06	2.07

 © 2005 Wiley-VCH Verlag GmbH & Co. KGaA, Weinheim

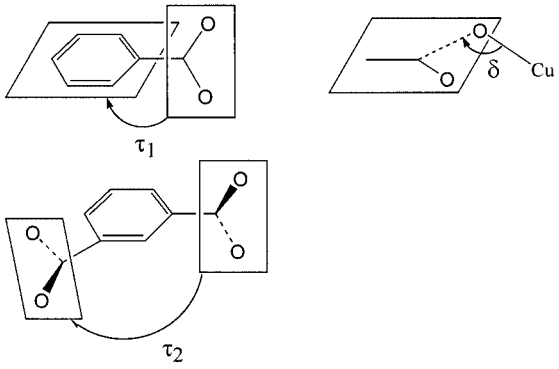

Scheme 1.

Despite the anomalously different τ_1, τ_2, and δ angles, the J values of **1**, **2** and **4** are similar. This implies that the coordination geometry of the metal centers and *m*-bda bridging configuration has no effect on the magnitude of the exchange coupling via the *m*-bda ligand. Accordingly, isophthalic acid is not an efficient bridging ligand for the transmission of electronic effects. The presence of weak ferromagnetic interactions in **1**, **2**, and **4** could be the result of the accidental orthogonality of the magnetic orbitals, while the unusually strong ferromagnetic interaction observed for complex **3** is not possible for the simple exchange pathway through the *m*-bda bridge. A similar condition has been observed by Bakalbassis et al.[20] By calculating the energies of the frontier MOs of $[Cu_2(\mu\text{-TPHA})(bpy)_2(OH_2)_2](ClO_4)_2$ (TPHA = terephthalato and bpy = 2,2′-bipyridine) on the basis of the EHMO method, they ascribed the unexpectedly strong antiferromagnetic interaction ($2J = -51.8\ cm^{-1}$) to the orbital interactions located on the intermolecular Cu–O···Cu moieties and came to the conclusion that the terephthalato bridging unit has an unfavorable character to transmit electronic effects over long distances owing to the very low electron density delocalization on the bridging unit of each magnetic orbital. As for our complex **3**, in the Cu–O···Cu weak coordination bonds the bridging oxygen atom occupies an axial coordination site on both Cu^{II} ions, but the magnetic orbital for Cu^{II} is not located along the z axis, and therefore only a very weak exchange interaction can be expected. The contribution of intrachian interactions via the *m*-bda bridge is insignificant to the overall magnetic behavior of **3**. Thus, the hydrogen bonding between copper centers via carboxylic groups may account for the ferromagnetic interactions through a spin-polarization mechanism. Accordingly, the magnetic data of **3** were fitted again by the same equation as for complex **1** for dinuclear Cu^{II} complexes.[18] Considering the decrease of μ_{eff} in the low-temperature region, a molecular field correction was applied. A fit of the data gave $J = 35.5\ cm^{-1}$, $zJ' = -2.0\ cm^{-1}$, $g = 2.08$, and $R = 3.0 \times 10^{-3}$.

Cano et al. have also proposed that the relatively strong antiferromagnetic coupling observed for terephthalate-bridged Cu^{II} complexes is due to the carboxylate-assisted loss of the coordinated water molecule and subsequent carboxylate dimerization.[8] In light of the peculiar coordination geometry of Cu^{II} in **3** (four- and five-coordinate), the presence of hydrogen bonds between copper centers via carboxylic groups through a spin-polarization mechanism is feasible.

Conclusions

In summary, three copper isophthalates have been prepared and characterized by variable-temperature susceptibility measurements. The above discussion shows that isophthalic acid can be used as an appropriate bridging unit to design magnetic systems with a separation of about 11 Å between the two paramagnetic centers. However the magnetic interactions are, as with the terephthalate-bridged systems, negligibly small. The small steric hindrance of the terminal ligand bpm leads to hydrogen bonding between Cu^{II} centers, which accounts for the abnormally large ferromagnetic coupling of complex **3**.

Experimental Section

General Remarks: Copper(II) perchlorate hexahydrate, tpm, bpm, and tpa were obtained by literature methods.[21–24] These ligands were analyzed by elemental analysis and NMR spectroscopy. Isophthalic acid and other reagents were obtained from commercial sources and used without further purification. Analyses for C, H, and N were carried out on a Perkin–Elmer analyzer at the Institute of Elemento-Organic Chemistry, Nankai University. Variable-temperature magnetic susceptibilities were measured on a Quantum Design MPMS-7 SQUID magnetometer. Diamagnetic corrections were made with Pascal's constants for all the constituent atoms.

Synthesis of $[Cu_2(tpa)_2(m\text{-bda})](ClO_4)_2$ (1): Tpa·3 $HClO_4$ (0.059 g, 0.1 mmol) was dissolved in 10 mL of methanol and triethylamine (1.572 g, 1.55 mmol) was added. $Cu(ClO_4)_2 \cdot 6H_2O$ (0.0371 g, 0.1 mmol) and dipotassium isophthalate (0.0105 g, 0.05 mmol) were added to the resulting solution. The mixture was stirred for 30 min and then filtered. After several weeks, green crystals suitable for X-ray analysis were obtained. Yield: 0.012 g (32% based on Cu). IR (KBr): $\tilde{\nu}$ = 1603 (s) cm^{-1}, 1560 (m), 1475 (w), 1435 (m), 1356 (s), 1315 (w), 1280 (w), 1085 (s), 1010 (m), 815 (w), 760 (s). $C_{44}H_{40}Cl_2Cu_2N_8O_{12}$ (1070.8): calcd. C 49.35, H 3.74, N 10.46; found C49.10, H 3.71, N 10.48.

Synthesis of $[\{Cu_2(tpm)_2(m\text{-bda})_2\} \cdot 2CH_3OH \cdot 4H_2O]_n$ (2): An aqueous solution of $CuCl_2 \cdot 2H_2O$ (0.171 g, 1.0 mmol) was added to NaOH (0.040 g, 2.0 mmol) in H_2O (5 mL), then isophthalic acid (0.166 g, 1.0 mmol) was added. After stirring for 2 h at room temperature, tpm (0.214 g, 1.0 mmol) in MeOH (15 mL) was added dropwise and stirred for 1 h. The mixture was then filtered. Blue crystals suitable for X-ray structure analysis were obtained by slow evaporation of the filtrate. Yield: 0.066 g (39% based on Cu). IR (KBr): $\tilde{\nu}$ = 1600 (s) cm^{-1}, 1568 (m), 1440 (w), 1400 (s), 1360 (w), 1290 (s), 1240 (w), 1080 (m), 850 (s). $C_{37}H_{40}Cu_2N_{12}O_{13}$ (987.89): calcd. C 44.94, H 4.05, N 17.65; found C 44.48, H 4.04, N 17.50.

Synthesis of $[\{Cu_2(bpm)_2(H_2O)(m\text{-bda})_2\} \cdot CH_3CN \cdot H_2O]_n$ (3): A solution of $Cu(ClO_4)_2 \cdot 6H_2O$ (0.0742 g, 0.2 mmol) in CH_3CN (5 mL) was added to bpm (0.214 g, 1.0 mmol) in CH_3CN (5 mL), then an aqueous solution of isophthalic acid (0.166 g, 1.0 mmol) was added. After stirring for 15 min, NaOH (0.1 M) was added to adjust the pH value to 7. The mixture was stirred for 2 h at room

 © 2005 Wiley-VCH Verlag GmbH & Co. KGaA, Weinheim

temperature and the precipitates were filtered off. Blue crystals suitable for X-ray structure analysis were obtained by slow evaporation of the filtrate. Yield: 0.030g (40% based on Cu). IR (KBr): $\tilde{\nu}$ = 1620 (s) cm^{-1}, 1572 (m), 1460 (w), 1410 (s), 1350 (w), 1300 (s), 1250 (w), 1100 (m), 850 (s). $C_{32}H_{31}Cu_2N_9O_{10}$ (828.74): calcd. C 44.34, H 3.74, N 15.20; found C 44.56, H 3.35, N 15.32.

Crystallographic Studies: Crystals of complexes **1**, **2**, and **3** were mounted on a Bruker Smart 1000 diffractometer equipped with a CCD camera. The determination of unit-cell parameters and data collection were performed with Mo-K_α radiation (λ = 0.71073 Å). The structures were solved primarily by direct methods and secondly by Fourier difference techniques and refined by the full-ma-

Table 2. Data collection and processing parameters for **1, 2** and **3**.

	1	**2**	**3**
Empirical formula	$C_{44}H_{40}Cl_2Cu_2N_8O_{12}$	$C_{37}H_{40}Cu_2N_{12}O_{13}$	$C_{32}H_{31}Cu_2N_9O_{10}$
Formula mass	1070.82	987.89	828.74
Temperature (K)	298(2)	273(2)	293(2)
Wavelength [Å]	0.71073	0.71073	0.71073
Crystal system	monoclinic	triclinic	orthorhombic
Space group	*P*21/*c*	$P\bar{1}$	*Pnma*
a [Å]	14.003(6)	10.250(7)	17.956(6)
b [Å]	17.201(7)	15.078(10)	17.615(5)
c [Å]	20.654(9)	16.2328(6)	10.776(4)
α [°]	90	114.241(12)	90
β [°]	90.637(9)	90.212(13)	90
γ [°]	90	108.389(11)	90
V [$Å^3$]	4975(4)	2007(2)	3408.5(18)
Z	4	2	4
$D_{calcd.}$ [$mg\,m^{-3}$]	1.430	1.635	1.615
Crystal size (mm^3)	0.25×0.10×0.20	0.35×0.25×0.10	0.24×0.20×0.08
θ	1.45–25.03	1.49–25.03	2.20–26.48
Reflections collected	20495	7529	15588
Independent reflections	8652 [*R*(int.) = 0.3379]	6809 [*R*(int.) = 0.0326]	3632 [*R*(int.) = 0.1157]
Max. and min. transmission	0.9797 and 0.7830	0.8943 and 0.6905	1.0000 and 0.8112
Data/restraints/parameters	8652/0/613	6809/0/595	3632/0/256
Goodness-of-fit on F^2	0.997	0.975	1.009
R_1, wR_2 [$I > 2\sigma(I)$]	0.0678, 0.1751	0.0571, 0.1288	0.0554, 0.0845
R_1, wR_2 (all data)	0.1851, 0.2138	0.1135, 0.1543	0.1208, 0.1011
Largest diff. peak and hole ($e\,Å^{-3}$)	0.823 and –0.455	0.513 and –0.422	0.420 and –0.556

[a] $R_1 = \Sigma||F_o| - |F_C||/\Sigma|F_o|$, $wR_2 = (\Sigma[w(F_o^2 - F_c^2)^2]/\Sigma(F_o^2)^2]^{1/2}$, $w = 1/[\sigma^2(F_o^2) + (0.0880P)^2 + 0.0000P]$ where $P = (F_o^2 + 2F_c^2)/3$ for **1**; $w = 1/[\sigma^2(F_o^2) + (0.0728P)^2 + 0.0000P]$, $P = (F_o^2 + 2F_c^2)/3$ for **2**; $w = 1/[\sigma^2(F_o^2) + (0.1000P)^2 + 0.0000P]$, $P = (F_o^2 + 2F_c^2)/3$ for **3**.

Table 3. Selected bond lengths [Å] and angles [°] for **1**, **2** and **3**.

1		**2**[a]		**3**[b]	
Cu(1)–O(1)	1.901(5)	Cu(1)–O(1)	1.899(4)	Cu(1)–O(1)	1.937(3)
Cu(1)–N(4)	2.033(6)	Cu(1)–O(5)	1.905(4)	Cu(1)–N(1)	2.018(3)
Cu(1)–N(2)	2.068(6)	Cu(1)–N(1)	1.984(5)	Cu(1)–O(5)	2.394(4)
Cu(1)–N(3)	2.086(7)	Cu(1)–N(5)	1.991(4)	Cu(2)–O(3)	1.937(3)
Cu(1)–N(1)	2.101(7)	Cu(1)–N(3)	2.414(5)	Cu(2)–N(3)	2.018(3)
Cu(2)–O(3)	1.922(5)	Cu(2)–O(8)	1.891(4)		
Cu(2)–N(8)	2.040(6)	Cu(2)–O(4)#1	1.897(4)		
Cu(2)–N(6)	2.073(7)	Cu(2)–N(9)	1.976(4)		
Cu(2)–N(5)	2.081(7)	Cu(2)–N(7)	1.981(5)		
Cu(2)–N(7)	2.085(7)	Cu(2)–N(11)	2.434(5)		
O(1)–Cu(1)–N(4)	172.8(2)	O(1)–Cu(1)–O(5)	89.97(17)	O(1)–Cu(1)–N(1)	88.80(13)
O(1)–Cu(1)–N(2)	92.3(2)	O(1)–Cu(1)–N(1)	95.33(18)	O(1)#1–Cu(1)–O(1)	94.99(16)
N(4)–Cu(1)–N(2)	80.5(3)	O(5)–Cu(1)–N(1)	166.53(19)	O(1)#1–Cu(1)–N(1)	175.01(13)
O(1)–Cu(1)–N(3)	102.2(3)	O(1)–Cu(1)–N(5)	166.82(19)	N(1)–Cu(1)–N(1)#1	87.2(2)
N(4)–Cu(1)–N(3)	80.7(3)	O(5)–Cu(1)–N(5)	91.04(18)	O(1)–Cu(1)–O(5)	89.41(11)
N(2)–Cu(1)–N(3)	115.2(3)	N(1)–Cu(1)–N(5)	86.62(19)	N(1)–Cu(1)–O(5)	87.39(12)
O(1)–Cu(1)–N(1)	104.3(3)	O(1)–Cu(1)–N(3)	86.31(18)	O(3)#2–Cu(2)–O(3)	90.29(17)
N(4)–Cu(1)–N(1)	80.2(3)	O(5)–Cu(1)–N(3)	110.42(18)	O(3)#2–Cu(2)–N(3)	171.07(14)
N(2)–Cu(1)–N(1)	121.8(3)	N(1)–Cu(1)–N(3)	82.3(2)	O(3)–Cu(2)–N(3)	90.48(12)
N(3)–Cu(1)–N(1)	114.8(3)	N(5)–Cu(1)–N(3)	81.02(19)	N(3)–Cu(2)–N(3)#2	87.40(19)
O(3)–Cu(2)–N(8)	173.1(3)	O(8)–Cu(2)–O(4)#1	89.95(18)	C(4)–N(1)–Cu(1)	128.4(3)
O(3)–Cu(2)–N(6)	102.2(3)	O(8)–Cu(2)–N(9)	165.91(19)	N(2)–N(1)–Cu(1)	123.9(3)
N(8)–Cu(2)–N(6)	79.8(3)	O(4)#1-Cu(2)–N(9)	91.56(18)	C(8)–N(3)–Cu(2)	130.7(3)
O(3)–Cu(2)–N(5)	91.7(3)	O(8)–Cu(2)–N(7)	95.05(18)	N(4)–N(3)–Cu(2)	123.5(3)
N(8)–Cu(2)–N(5)	81.5(3)	O(4)#1–Cu(2)–N(7)	166.64(19)	C(16)–O(3)–Cu(2)	123.6(3)
N(6)–Cu(2)–N(5)	116.3(3)	N(9)–Cu(2)–N(7)	86.61(19)		

[a] #1 *x*, *y*, *z* + 1; #2 *x*, *y*, *z* – 1. [b] #1 *x*, –*y* + 1/2, *z*; #2 *x*, –*y* + 3/2, *z*.

 © 2005 Wiley-VCH Verlag GmbH & Co. KGaA, Weinheim

trix least-squares method. The computations were performed with the SHELXL-97 program.[25,26] All non-hydrogen atoms were refined anisotropically. The hydrogen atoms were set in calculated positions and refined as riding atoms with a common fixed isotropic thermal parameter. The crystal parameters and details of the data collections and refinement for the complexes are listed in Table 2. Selected bond lengths are listed in Table 3.

CCDC-257849 (for **1**), -196145 (for **2**), and -196147 (for **3**) contain the supplementary crystallographic data for this paper. These data can be obtained free of charge from The Cambridge Crystallographic Data Center via www.ccdc.cam.ac.uk/data_request/cif.

Acknowledgments

This work was supported by the National Natural Science Foundation of China (grant no. 20425103).

[1] a) D. Gatteschi, O. Kahn, J. Miller, F. Palacio, *Molecular Magnetic Materials*, Kluwer, Dordrecht, **1991**; b) J. Ribas, A. Escuer, M. Monfort, R. Vicente, R. Cortés, L. Lezama, T. Rojo, *Coord. Chem. Rev.* **1999**, *193–195*, 1027–1068.
[2] a) L. Deakin, A. M. Arif, J. S. Miller, *Inorg. Chem.* **1999**, *38*, 5072–5077; b) R. H. Groeneman, L. R. MacGillivray, J. L. Atwood, *Inorg. Chem.* **1999**, *38*, 208–209; c) N. Ohata, H. Masuda, Y. Osamu, *Angew. Chem. Int. Ed. Engl.* **1996**, *35*, 531–532; d) M. Eddaoudi, H. Li, O. M. Yaghi, *J. Am. Chem. Soc.* **2000**, *122*, 1391–1397.
[3] a) O. M. Yaghi, C. E. Davis, G. Li, H. Li, *J. Am. Chem. Soc.* **1997**, *119*, 2861–2868; b) H. J. Choi, M. P. Suh, *J. Am. Chem. Soc.* **1998**, *120*, 10 622–10 628; c) O. M. Yaghi, H. L. Li, C. Davis, D. Richardson, T. L. Groy, *Acc. Chem. Res.* **1998**, *31*, 474–484; d) E. G. Bakalbassis, D. G. Paschalidis, *Inorg. Chem.* **1998**, *37*, 4735–4737.
[4] a) S. S.-Y. Chui, S. M.-F. Lo, J. P. H. Charmant, A. G. Orpen, I. D. Williams, *Science* **1999**, *283*, 1148–1150; b) R. H. Groeneman, L. R. MacGillivray, J. L. Atwood, *Chem. Commun.* **1998**, 2735–2736.
[5] a) H. X. Zhang, B. S. Kang, A. W. Xu, Z. N. Chen. Z. Y. Zhou, A. S. C. Chan, K. B. Yu, C. Ren, *J. Chem. Soc. Dalton Trans.* **2001**, 2559–2566; b) X. M. Chen, G. F. Liu, *Chem. Eur. J.* **2002**, *8*, 4811–4817; c) C. B. Ma, C. N. Chen, Q. T. Liu, D. Z. Liao, L. C. Li, L. C. Sun, *New J. Chem.* **2003**, *27*, 890–894.
[6] X.-S. Tan, J. Sun, D.-F. Xiang, W.-X. Tang, *Inorg. Chim. Acta* **1997**, *255*, 157–161.
[7] L. C. Francesconi, D. R. Corbin, A. W. Clauss, D. N. Hendrickson, G. D. Stucky, *Inorg. Chem.* **1981**, *20*, 2078–2083.
[8] J. Cano, G. D. Munno, J. L. Sanz, R. Ruiz, J. Faus, F. Lloret, M. Julve, A. Caneschi, *J. Chem. Soc. Dalton Trans.* **1997**, 1915–1924.
[9] C. E. Xanthopulos, M. P. Sigalas, G. A. Katsoulos, C. A. Tsipis, A. Terzis, M. Mentzafos, A. Hountas, *Inorg. Chem.* **1993**, *32*, 5433–5436.
[10] E. G. Bakalbassis, J. Mrozinski, C. A. Tsipis, *Inorg. Chem.* **1986**, *25*, 3684–3690.
[11] C. S. Hong, S.-K. Son, Y. S. Lee, M.-J. Jun, Y. Do, *Inorg. Chem.* **1999**, *38*, 5602–5610.
[12] S. K. Shakhatreh, E. G. Bakalbassis, I. Brüdgam, H. Hartl, J. Mrozinski, C. A. Tsipis, *Inorg. Chem.* **1991**, *30*, 2801–2806.
[13] Y. T. Li, D. Z. Liao, Z. H. Jiang, G. L. Wang, *Synth. React. Inorg. Met.-Org. Chem.* **1995**, *25*, 319–326.
[14] P. Cheng, S. P. Yan, C. Z. Xie, B. Zhao, X. Y. Chen, X. W. Liu, C. H. Li, D. Z. Liao, Z. H. Jiang, G. L. Wang, *Eur. J. Inorg. Chem.* **2004**, 2369–2378.
[15] N. Kitajima, Y. Moro-oka, *Chem. Rev.* **1994**, *94*, 737–757.
[16] D. L. Reger, C. A. Little, V. G. Young, P. Maren, *Inorg. Chem.* **2001**, *40*, 2870–2874.
[17] D. L. Reger, R. F. Semeniuc, V. Rassolov, M. D. Smith, *Inorg. Chem.* **2004**, *43*, 537–554.
[18] O. Kahn, *Molecular Magnetism*, Wiley-VCH, New York, **1993**.
[19] D. D. Swank, C. P. Landee, R. D. Willet, *Phys. Rev. B: Condens. Matter* **1979**, *20*, 2154–2162.
[20] E. G. Bakalbassis, C. A. Tsipis, J. Mrozinski, *Inorg. Chem.* **1985**, *24*, 4231–4233.
[21] J. R. Bethrendt, S. K. Madan, *J. Inorg. Nucl. Chem.* **1950**, *20*, 195–202.
[22] J. E. Richman, T. J. Atkins, *J. Am. Chem. Soc.* **1974**, *96*, 2268–2270.
[23] D. L. Reger, T. C. Grattan, *J. Organomet. Chem.* **2000**, *607*, 120–128.
[24] B. G. Gafford, R. A. Holwerda, *Inorg. Chem.* **1989**, *28*, 60–66.
[25] G. M. Sheldrick, *SHELXS 97, Program for the Solution of Crystal Structures*, University of Göttingen, Germany, **1997**.
[26] G. M. Sheldrick, *SHELXL 97, Program for the Refinement of Crystal Structures*, University of Göttingen, Germany, **1997**.

Received: December 11, 2004
Published Online: May 11, 2005

 © 2005 Wiley-VCH Verlag GmbH & Co. KGaA, Weinheim

New Copper Chalcogenide Clusters with a Selenide Core and a Sulfide Shell

Olaf Fuhr,*[a] Lucia Fernandez-Recio,[a] and Dieter Fenske[a,b]

Keywords: Cluster compounds / Chalcogens / Copper / S ligands

The reaction of copper(I) acetate with mixtures of $PhSSiMe_3$ and $Se(SiMe_3)_2$ in the presence of PPh_3 leads to a series of new cluster compounds consisting of a copper selenide core surrounded by a sulfide shell: $[Cu_{17}Se(SPh)_{15}(PPh_3)_4]$, $[Cu_{20}Se(SPh)_{12}(OAc)_6(PPh_3)_4]$, $[Cu_{28}Se_6(SPh)_{16}(PPh_3)_8]$, $[Cu_{36}Se_8(SPh)_{20}(PPh_3)_8]$, $[Cu_{54}Se_8(SPh)_{30}(OAc)_8(PPh_3)_6]$, and $[Cu_{72}Se_{14}(SPh)_{36}(OAc)_8(PPh_3)_6]$. They have been structurally characterized by single-crystal X-ray analysis. The two smallest clusters have a ball-like structure with one selenium atom in the center totally enclosed by sulfur atoms. In the other clusters the inner copper–selenium core is surrounded by an incomplete sulfur shell varying between 53 and 87 % coverage.

(© Wiley-VCH Verlag GmbH & Co. KGaA, 69451 Weinheim, Germany, 2005)

Introduction

Within the last few years there has been a lot of interest in the synthesis and properties of nanoparticles consisting of binary compounds that are known to be semiconductors as bulk substances.[1–3] Investigations of their optical properties show that the quantum yield of their fluorescence can be improved enormously by surrounding them with a thin shell (one or two monolayers) of a compound that has a larger bandgap than the core material.[4–6]

In the corresponding field of binary-ligand-protected cluster compounds a large number of species have been synthesized and structurally characterized by single-crystal X-ray analysis.[7,8] In these systems the size regime of the larger clusters overlaps with the size regime of the smaller nanoparticles (having diameters of 1–3 nm). An investigation of a series of different sized cadmium selenide clusters has shown that their absorption properties are mainly dominated by the metal chalcogenide core, whereas the very weak fluorescence is due to processes in the organic ligand shell.[9–11] Further studies of clusters with the composition $[Cd_{10}E_4(E'Ph)_{12}(PEt_3)_4]$ (E, E′ = S, Se, Te) have found that the absorption is dependent upon the inner Cd_6E_4 core; the surrounding shell with its E′Ph groups has only a small influence on the absorption.[12]

In this paper we describe the synthesis and structure of six copper chalcogen clusters having a copper selenide core surrounded by a copper sulfide shell.

[a] Forschungszentrum Karlsruhe, Institut für Nanotechnologie, Postfach 3640, 76021 Karlsruhe, Germany
E-mail: olaf.fuhr@int.fzk.de
[b] Universität Karlsruhe (TH), Institut für Anorganische Chemie, Engesserstraße Gebäude Nr 30.45, 76128 Karlsruhe, Germany

Results and Discussion

The reactions of copper(I) acetate with a mixture of the disilylated selenium compound $Se(SiMe_3)_2$ and the monosilylated sulfur species $PhSSiMe_3$ lead to the formation of several new copper chalcogenide clusters. As usual in the chemistry of cluster formation these reactions are highly dependent on the stoichiometry used. Scheme 1 summarizes the reactions leading to compounds **1**–**6**.

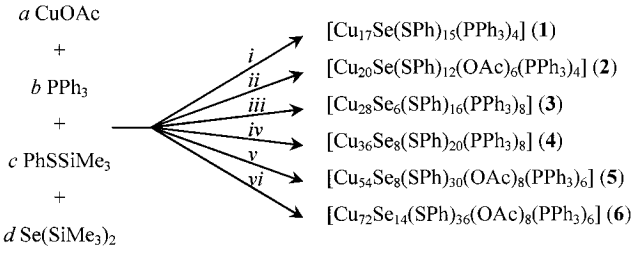

Scheme 1. Reactions leading to compounds **1**–**6**; ratios of the coefficients a:b:c:d i) 20:10:15:1, ii) 24:8:12:1, iii) 30:25:16:5, iv) 10:10:5:2, v) 60:15:30:5. iv) 40:10:18:7.

All compounds were crystallized and their structure determined by single-crystal X-ray analysis. Due to the different number of $SiMe_3$ groups in the chalcogen sources used, the selenium compound $Se(SiMe_3)_2$ reacts to give Se^{2-} ions whereas the sulfur species $PhSSiMe_3$ keeps its phenyl ring to form SPh^- groups. Therefore, all of the new compounds consist of an inner copper(I) selenide core surrounded by a sulfide shell. The phenyl groups of the SPh units and the PPh_3 ligands form an organic layer around the inorganic copper chalcogenide part. In some cases (**2**, **5**, **6**) there are additional acetate groups integrated into the ligand shell.

 © 2005 Wiley-VCH Verlag GmbH & Co. KGaA, Weinheim **DOI: 10.1002/ejic.200400758**

The cluster $[Cu_{17}Se(SPh)_{15}(PPh_3)_4]$ (**1**) crystallizes as yellow bars in the trigonal space group $R\bar{3}$ with six formula units per elemental cell. Figure 1 shows the molecular structure of the heavy atom framework and in the upper right corner the chalcogenide substructure.

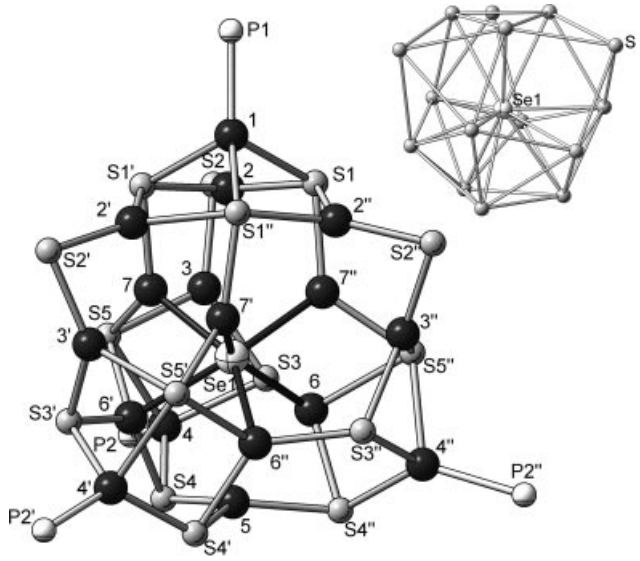

Figure 1. The molecular structure of the core of compound **1** (C and H atoms omitted for clarity); upper right: the chalcogenide substructure of **1** (same line of vision). Bond lengths [pm] in **1**: Cu–Se 239.8(3) (Cu7–Se1) and 262.8(3) (Cu6–Se1); Cu–S 221.2(7) (Cu3–S2) to 234.7(3) (Cu2–S1′); average Cu–P: 219.5.

There is a threefold axis running through the atoms Cu1, Cu5, Se1, and P1. A selenium atom (Se1) is present at the center of the cluster, and is surrounded by six copper atoms to form a skewed trigonal prism. The trigonal faces of this prism (formed by Cu6, Cu6′, Cu6′′ and Cu7, Cu7′, Cu7′′) are twisted by 17.1° against each other. The Se–Cu distances are 239.8(3) pm (Se1–Cu7) and 262.8(3) pm (Se1–Cu6). This inner (Cu_6Se) core is surrounded by a shell of the composition $[Cu_{11}(SPh)_{15}]$; four of the outer copper atoms (Cu1, Cu4, Cu4′, Cu4′′) have additional phosphane ligands. In compound **1** the metal atoms either have a nearly trigonal planar (Cu2, Cu3, Cu5, Cu6) or a skewed tetrahedral coordination sphere (Cu1, Cu4, Cu7). The sulfur atoms within the shell bond to either two (S2), three (S3, S4), or four (S1, S5) copper atoms in addition to a phenyl group.

Compound **2** crystallizes as yellow octahedra with eight molecules per unit cell in the cubic space group *Pa*3, with a C_3 axis running through the atoms Cu1, Cu7, Se1, and P1. Figure 2 illustrates the molecular structure of **2** and the arrangement of the chalcogen atoms.

Compound **2** has a shell-like construction with the central selenium atom Se1 surrounded by copper atoms Cu6, Cu6′, Cu6′′, and Cu7 that form a slightly distorted tetrahedron with bond lengths of 237.5(3) pm (Cu7–Se1) and 239.1(1) pm (Cu6–Se1). Around this polyhedron the twelve sulfur atoms of the SPh groups form a cube octahedron, whereby the four inner copper atoms are located beneath trigonal faces of the sulfur polyhedron. The distances between the sulfur atoms and the inner metal atoms vary from 236.0(3) pm (Cu6–S2) to 246.1(3) pm (Cu6–S1). The core can also be viewed as a section of a cubic closest packing of chalcogen atoms with half of the tetrahedral holes filled with copper atoms. The outer shell of the heavy atom framework of **2** is again formed by copper atoms. The four copper atoms (Cu1, Cu8, Cu8′, Cu8′′) that are additionally bonded to phosphane ligands cap the trigonal faces of the sulfur cube octahedron that are not bridged by the inner metal atoms (average Cu–S distance: 255.7 pm). The remaining twelve copper atoms are bound by acetate ligands to form six (Cu_2OAc) units, which cap the six tetragonal faces of the sulfur polyhedron. The average Cu–Cu distance in these units is about 279 pm, which is significantly longer than the corresponding distance in copper(I) acetate (255.6 pm);[13,14] the bonds between these copper atoms and the sulfur shell are about 224.8 pm long.

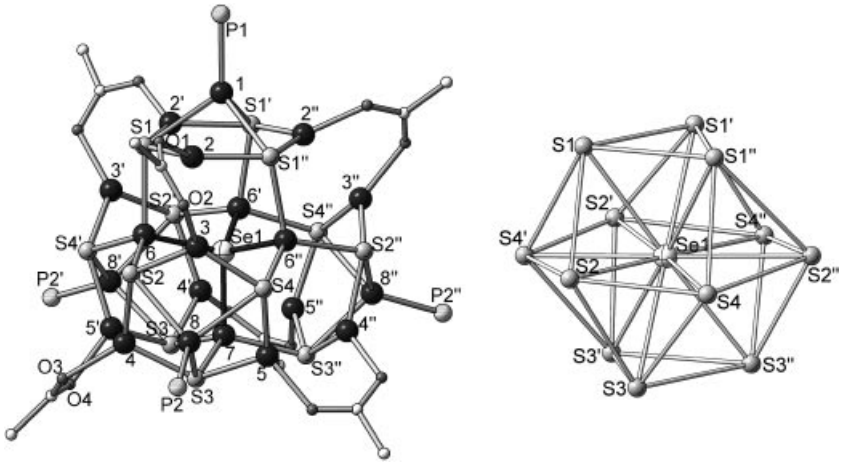

Figure 2. Left: The molecular structure of compound **2** (phenyl groups omitted for clarity); right: the chalcogenide substructure of **2** (same line of vision). Bond lengths [pm] in **2**: Cu–Se 237.5(3) (Cu7–Se1) and 2.391(2) (Cu6–Se1); Cu–S 219.5(3) (Cu2–S1′′) to 258.3(3) (Cu1–S1); average Cu–P: 222.5; average Cu–O: 195.8.

 © 2005 Wiley-VCH Verlag GmbH & Co. KGaA, Weinheim

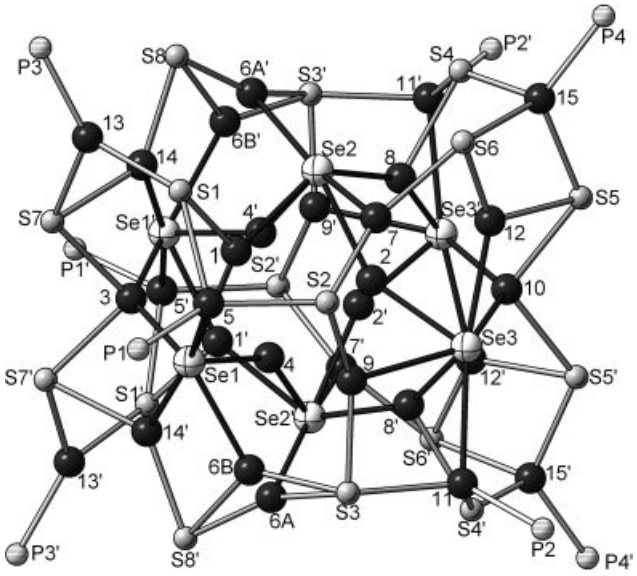

Figure 3. The molecular structure of the core of compound **3** (C and H atoms omitted for clarity). Bond lengths [pm] in **3**: Cu–Se 233.1(2) (Cu4–Se1) to 289.9(3) (Cu6A′–Se2); Cu–S 212.7(6) (Cu6A–S8′) to 2.469(9) (Cu6B–S8′); average Cu–P: 223.1.

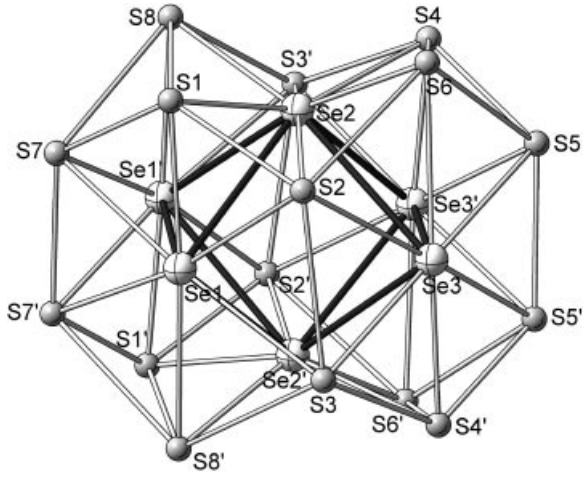

Figure 4. The chalcogenide substructure of **3**.

Recently, a copper–selenium structure with a similar composition and structure has been published: $[Cu_{20}Se(SePh)_{12}(OAc)_6(Ph_2PC_6H_4SMe)_2]$.[15]

Cluster **3** contains 28 copper atoms and crystallizes in the orthorhombic space group *Pnn*2 as red blocks with two formula units per elemental cell. A crystallographic C_2 axis runs through the atoms Cu3 and Cu10. Figure 3 shows the heavy atom framework and Figure 4 the arrangement of the selenium and sulfur atoms in **3**.

The selenium substructure formed by six atoms can be described as two-edge sharing tetrahedra. Except for the shared one, all edges are μ_2-bridged by copper atoms. The four atoms Cu2, Cu2′, Cu4 and Cu4′ are located inside the selenium polyhedron and do not have any further associations. The other copper atoms of this $Cu_{10}Se_6$ core are either coordinated by one additional sulfur atom in a trigonal planar way (Cu1, Cu1′, Cu8, Cu8′) or by two extra sulfur atoms (Cu3, Cu10) to form a tetrahedral sphere.

The sulfide shell in **3** consists of 16 sulfur atoms that form a polyhedron made out of four trigonal and six hexagonal faces (see Figure 4). Four of the hexagonal faces are nearly planar, whereas the other two are highly folded. In the center of each of these six-membered rings there is a selenium atom of the core structure. Therefore in **3**, in contrast to compounds **1** and **2**, the sulfide shell surrounding the selenium core is incomplete. Four (Cu13, Cu13′, Cu15, Cu15′) of the eight copper atoms coordinated to phosphane

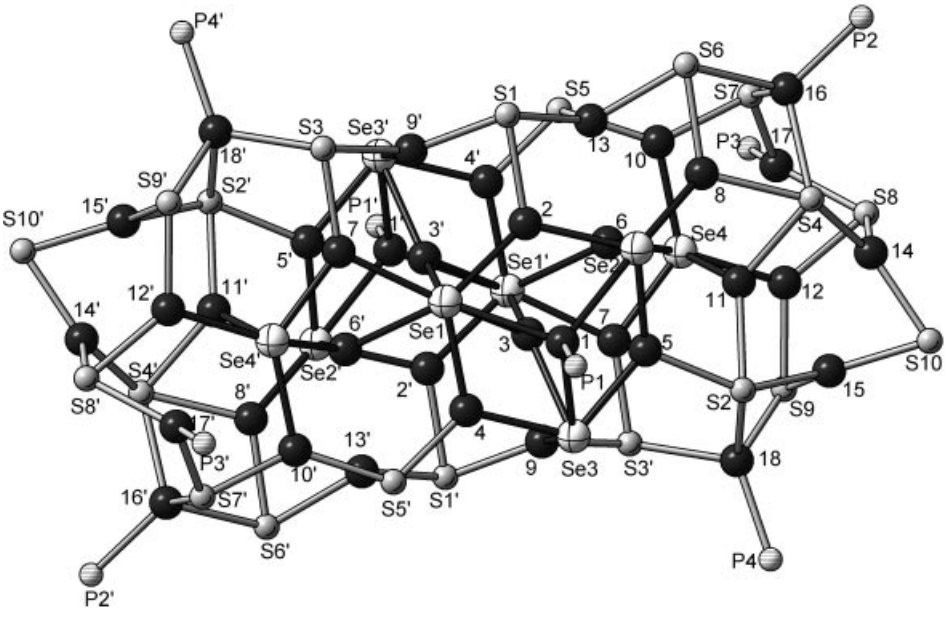

Figure 5. The molecular structure of compound **4** (C and H omitted for clarity). Bond lengths [pm] in **4**: Cu–Se 235.9(2) (Cu3–Se1′) to 281.8(2) (Cu3–Se1); Cu–S 220.6(3) (Cu4–S5′) to 246.0(3) (Cu18–S2); average Cu–P: 223.4.

 © 2005 Wiley-VCH Verlag GmbH & Co. KGaA, Weinheim

ligands are located above the trigonal faces of the sulfur polyhedron. Whereas for Cu15 and Cu15′ one finds two short (about 232 pm) and one long (271 pm) Cu–S distance, for Cu13 and Cu13′ one can only speak of bonding towards two sulfur atoms (230 pm); the distance to the third sulfur atom (S8) is too long (334 pm) to be considered as a real bond. The other four copper atoms having phosphane ligands (Cu5, Cu5′, Cu11, Cu11′) are each acting as μ_3-bridges between two sulfur and one selenium atom. All other copper atoms are located inside the chalcogenide polyhedron and have (except for the already mentioned twofold and fourfold coordinated atoms) a trigonal planar sphere formed either by two sulfur and one selenium atom or by one sulfur and two selenium atoms. One copper atom (Cu6) is disordered over two positions and has been refined with an occupation of Cu6A:Cu6B of 2:1. The same phenomenon has been observed in repeated X-ray measurements of different crystals. Therefore it can be said that this disorder is a principle characteristic of compound **3** and not simply a defect of a single individual crystal.

Compound **4** crystallizes in the monoclinic space group $P2_1/n$ with two cluster molecules per unit cell. There are also noncoordinating solvent molecules (DME) in the crystal lattice which are disordered over four crystallographic positions. A symmetry center is located in the middle of the cluster (Figure 5).

The chalcogenide substructure, which is shown in two different projections in Figure 6, can be described as a stack of two skewed hexagonal layers that are shifted against each other like inside a closest packing. The eight selenium atoms are located in the middle of the chalcogenide substructure and, similar to **3**, six of them (Se1, Se2, Se3 and their symmetry equivalents) form two edge-sharing tetrahedra. The remaining two (Se4, Se4′) are found above the edges formed by Se1 and Se2, and Se1′ and Se2′, respectively. As in **3** the sulfide shell surrounding the selenide core is incomplete.

All copper atoms that do not have phosphane ligands are coordinated to three chalcogen atoms in all different combinations ranging from three selenium through to three sulfur atoms. The Cu–Se distances are found to be between 239.2(2) and 281.9(2) pm, and the Cu–S distances are between 220.7(3) and 245.9(4) pm. The copper atoms Cu17 and Cu17′ also form a trigonal planar sphere by acting as a μ_2-bridge over one S–S edge of the chalcogenide frame [Cu17–S7 229.1(3) pm, Cu17–S8 228.4(4) pm]; they also have an additional bond to a phosphane ligand. Only the copper atoms Cu1, Cu16, and Cu18, and their symmetry equivalents, show a skewed tetrahedral coordination sphere: Cu1 binds to Se1, Se2, Se3 and the phosphorus atom P1, whereas Cu16 and Cu18 bind to three sulfur and one phosphorus atom each. The copper–chalcogen distances of these atoms are, on average, about 16 (Cu–Se) and 9 pm (Cu–S) longer than those of the triply coordinated copper atoms. The remaining electron density found in the refinement (largest peak 2.095 e Å^{-3}) is located in the area between the cluster molecules, thus indicating that the additional DME molecule might be disordered over more than the refined positions.

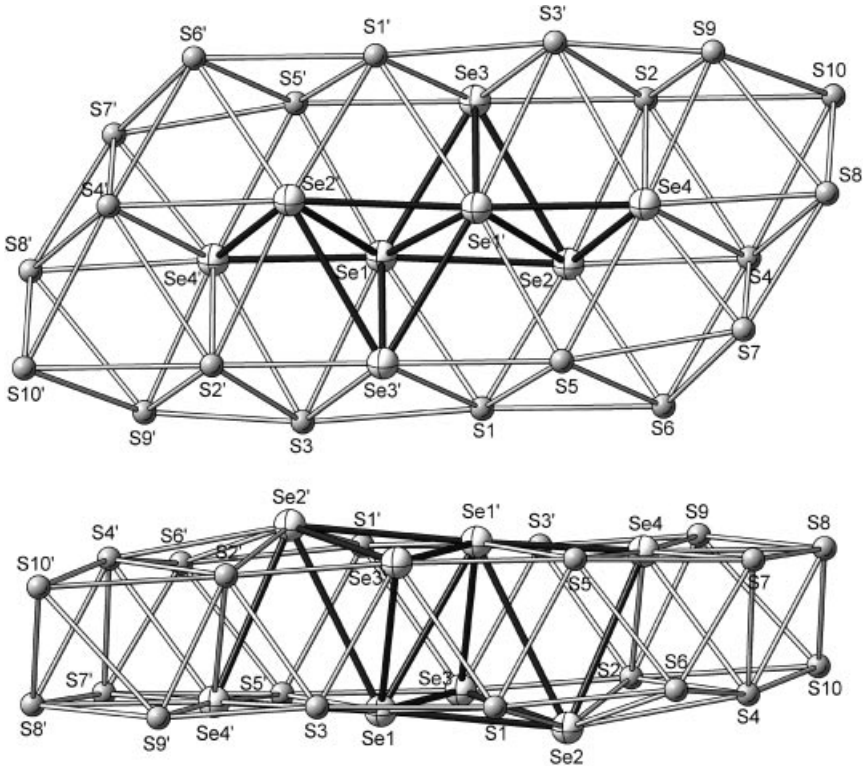

Figure 6. Two different views of the chalcogenide layer structure of **4**.

 © 2005 Wiley-VCH Verlag GmbH & Co. KGaA, Weinheim

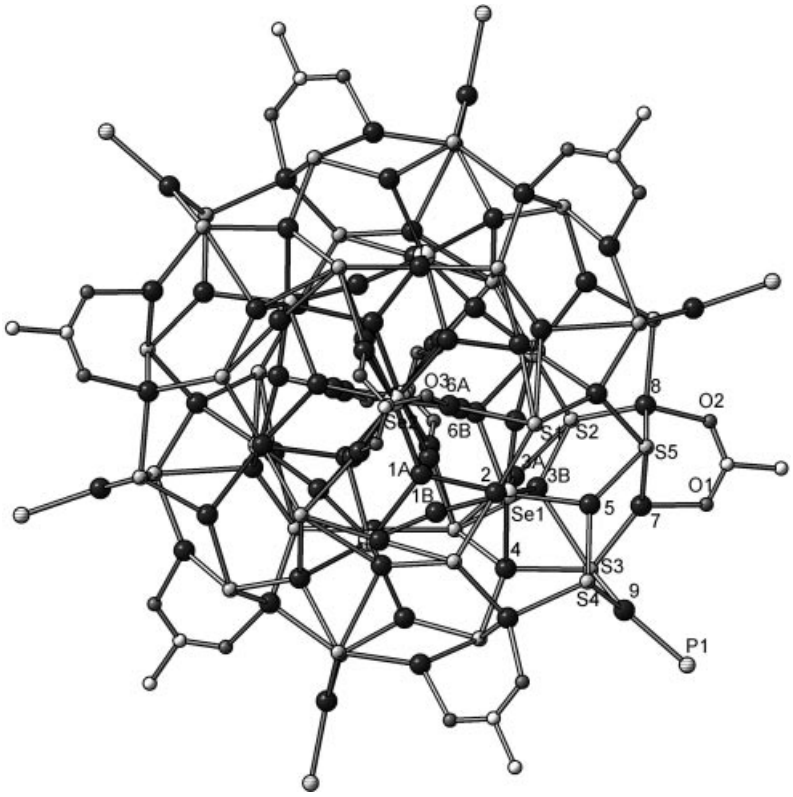

Figure 7. The molecular structure of compound **5** (phenyl groups omitted for clarity; only the atoms of the asymmetric unit are labeled). Bond lengths [pm] in **5**: Cu–Se 195.4(6) (Cu1B–Se1′) to 248.4(2) (Cu3A–Se1); Cu–S 213.3(8) (Cu6B–S1) to 266.8(8) (Cu3B–S1′); Cu–P 223.5(3); average Cu–O: 196.1.

The dark-red compound **5** crystallizes with three formula units per elemental cell in the trigonal space group $R\bar{3}$. The crystallographic $\bar{3}$ axis runs through the atoms Se2, Se2′, C3, C3′, C4, and C4′. The heavy-atom framework of **5** is shown in Figure 7 and the chalcogenide substructure in Figure 8.

Compound **5** appears to be discus-like in shape with the copper chalcogenide core having a diameter of 1.6 nm and a height of 0.7 nm. In the middle of the cluster eight selenium atoms form a highly compressed hexagonal bipyramid in which six copper atoms are embedded. These are disordered and were refined over two positions where they are either occupying a face of the bipyramid (pos. A), where they are coordinated by three selenium atoms, or an edge, with two neighboring selenium atoms (pos. B). The inner Cu_6Se_8 core is surrounded by a copper–sulfur shell consisting of 30 copper atoms and the 30 sulfur atoms from the SPh groups. In this shell the coordination spheres of the copper atoms vary. The tetrahedral copper atoms are bonded to three sulfur and one selenium atom (Cu–Se: av. 242.2 pm; Cu–S: av. 245.3 pm), whilst the trigonal copper atoms are bonded to one selenium and two sulfur atoms (Cu–Se: av. 245.1 pm; Cu–S: av. 225.4 pm). The remaining copper atoms are either bonded to one phosphane ligand and two sulfur atoms or form Cu_2OAc groups, as in compound **2**. At the top and bottom of the discus-like copper chalcogenide core are two acetate units whose two oxygen atoms are disordered over three positions, consistent with

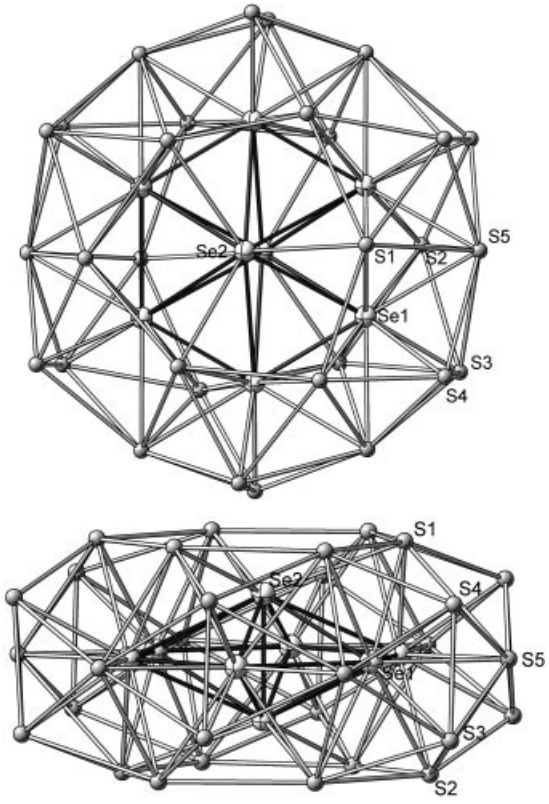

Figure 8. Two different views of the chalcogenide substructure of **5**.

 © 2005 Wiley-VCH Verlag GmbH & Co. KGaA, Weinheim

the threefold symmetry of the cluster. The copper atoms binding to these ligands are also disordered and occupy one position (Cu6A), with coordination to a sulfur, a selenium, and an oxygen atom, or are coordinated linearly (Cu6B) to only the two chalcogen atoms. Due to all of these disordering phenomena, all of which were observed in several crystals, the structure solution ends up with poor quality factors and additional electron density near to the disordered copper atoms [distance between largest peak (2.329 e Å^{-3}) and Cu3B: 0.75 Å].

Compound **6**, which contains 72 copper atoms, crystallizes in the monoclinic space group $P2_1/n$ with four formula units per elemental cell as large black blocks. Figure 9 shows the heavy-atom framework.

The whole cluster has pseudo-C_3 symmetry with a (pseudo) axis running through the atoms Cu54, Cu56, Cu72, Se13, and Se14. The selenide core in **6** has the shape of a hexagonal antiprism (hexagonal faces formed by Se1–Se6 and Se7–Se12) with one additional selenium atom at the center of each hexagonal face (Se13 and Se14, respectively). Thus, the mantle as well as the top and the bottom faces of the selenium polyhedron consist of nearly equilateral triangles. At the center of the selenide core there is a linearly coordinated copper atom (Cu72); further doubly coordinated copper atoms are located on the edges of the mantle faces of the selenium prism (Cu39 between Se2 and Se8; Cu43 between Se4 and Se10; Cu47 between Se6 and Se12). Another twelve copper atoms (Cu60–Cu71) are located inside the selenium polyhedra, with each being coordinated by three selenium atoms. These copper atoms form an icosahedron which is highly compressed in the direction of the (pseudo)-C_3 axis. The $Cu_{16}Se_{14}$ core described above is shown in Figure 10, and the chalcogenide substructure is shown in Figure 11.

The first copper shell surrounding the selenium core consists of eight atoms (Cu13, Cu15, Cu17, Cu19, Cu21, and Cu23) which each bonded to one sulfur and two selenium atoms. Furthermore, there are 44 copper atoms bonded to only one selenium atom. Three different coordination

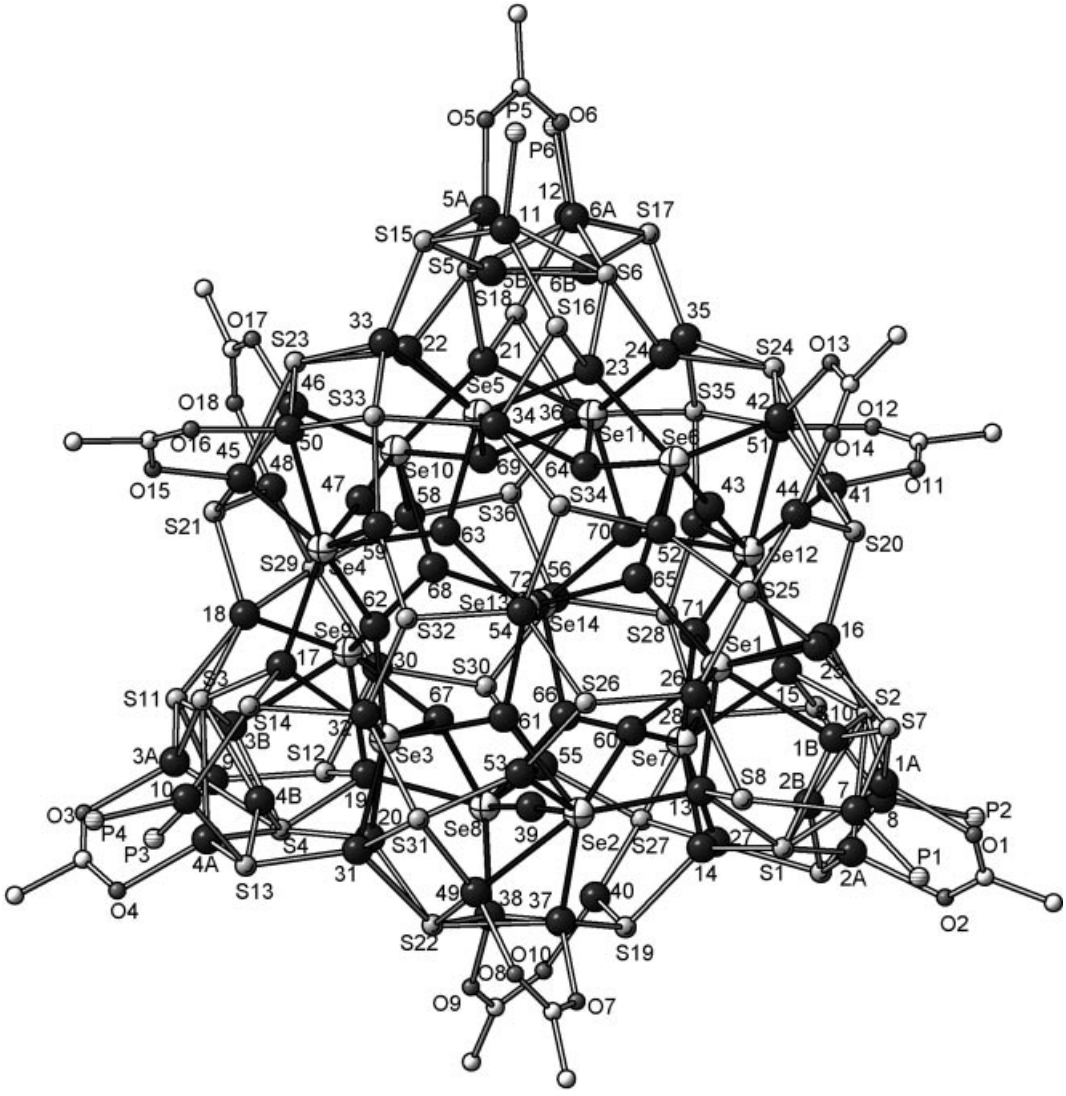

Figure 9. The molecular structure of compound **6** (phenyl groups omitted for clarity). Bond lengths (pm) in **6**: Cu–Se 232.7(4) (Cu72–Se13) to 291.4(7) (Cu44–Se6); Cu–S 192(3) (Cu1B–S7) to 276(1) (Cu2A–S2); average Cu–P 220; average: Cu–O 201.

 © 2005 Wiley-VCH Verlag GmbH & Co. KGaA, Weinheim

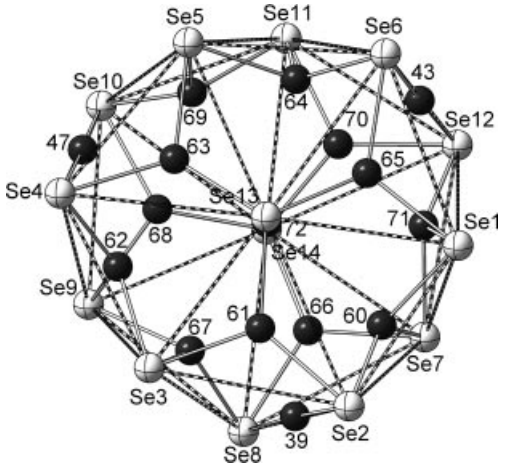

Figure 10. The inner $Cu_{16}Se_{14}$ core of **6**.

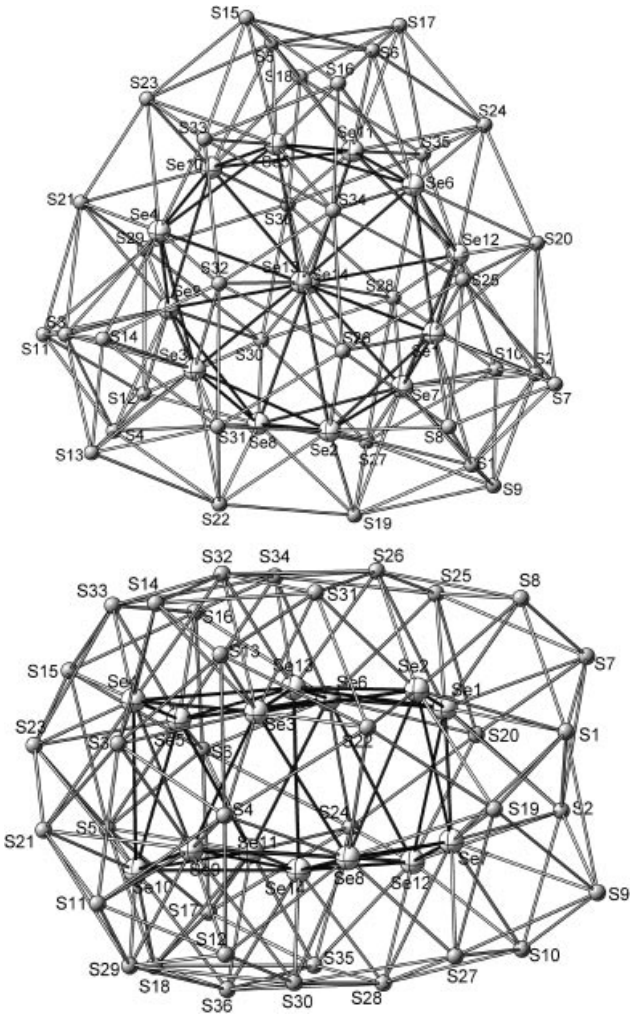

Figure 11. Two different views of the chalcogenide substructure of **6**.

spheres are observed within this group. The first contains trigonal-planar copper atoms coordinated by two additional sulfur atoms, whilst in the second the copper atoms have a tetrahedral geometry, binding to three more sulfur atoms. The remaining twelve copper atoms form six Cu_2OAc units with coordination spheres comprising one selenium, two sulfur, and one oxygen atom each. Not all of the copper atoms in the sulfide shell bond to the core selenium atoms. On the one hand Cu7–Cu12 are coordinated by two sulfur atoms and one phosphorus atom, while on the other hand Cu1A–Cu6A bond to two sulfur atoms and one oxygen atom of an acetate group. As in clusters **3** and **5** it is found that some of the copper atoms present in **6** are disordered. In this case, it is the atoms Cu1–Cu6, which have been refined using occupations between 0.1 and 0.9 for positions A and B. Position A has already been described above. Those copper atoms in position B are located further inside the cluster and again interact with two sulfur atoms along with a core selenium atom. Assuming that the corresponding positions A and B have a total occupancy of one copper atom, the total number of copper atoms for the whole cluster is 72. Considering **6** to be electrically neutral there must be eight acetate units; six of these were refined with satisfying vibration factors. The remaining two acetate groups are split over three possible positions, with bonds to the partially occupied copper positions A.

Due to disordering the refinement has poor R values (R_1 = 0.141, wR_2 = 0.393), with additional electron density near to the areas of disordered copper atoms [distance between largest peak (3.772 e Å^{-3}) and Cu2A: 0.78 Å]. Similar results were obtained with crystals from other reactions.

Conclusions

We have described six new cluster compounds. All of them have a selenide core consisting of 1 to 14 selenium atoms. In compound **2** the one selenium atom in the center is surrounded by twelve sulfur atoms to form a cube octahedron. Compared with the corresponding fcc lattice, this means that there is one complete shell formed around the central atom. In **1** there are 15 sulfur atoms in more than one layer. In the other compounds the covering of the interior selenide core is less than one layer of sulfur atoms. The approximate completeness of the covering in all compounds is summarized in Table 1.

Table 1. Comparison of the completeness of the sulfide shell covering the selenide core in **1**–**6**.

Compound	Se in core	S in shell	Coverage [%]
1	1	15	>100
2	1	12	100
3	6	16	53
4	8	20	53
5	8	30	83
6	14	36	67

The colors of the compounds vary from yellow (**1**, **2**) to different shades of red (**3**–**5**), and black (**6**). Investigations into the optical properties of these compounds are an area of current work.

Experimental Section

Due to the high oxygen and moisture sensitivity of the compounds used, all reactions were performed under a dry, oxygen-free nitro-

gen using standard Schlenk techniques. Solvents were dried with sodium/benzophenone and freshly distilled. Copper(I) acetate (CuOAc),[16] $Se(SiMe_3)_2$,[17]and $PhSSiMe_3$[18] were synthesized according to literature procedures. All reactions described below are very sensitive to small variations of the starting material ratio such that in some cases mixtures of different compounds were obtained.

Synthesis of $[Cu_{17}Se(SPh)_{15}(PPh_3)_4]$ (1): At room temperature, copper(I) acetate (0.365 g, 2.98 mmol) and PPh_3 (0.39 g, 1.49 mmol) were suspended in DME (100 mL). $PhSSiMe_3$ (0.42 mL, 2.23 mmol) and $Se(SiMe_3)_2$ (0.034 mL, 0.15 mmol) were then added. The bright yellow solution was stirred for 24 h and then its volume was reduced. After some hours **1** crystallized as yellow rods. Yield: 0.23 g (40%). $C_{162}H_{135}Cu_{17}P_4S_{15}Se$ (3845.6): calcd. C 50.59, H 3.54, S 12.51; found C 51.32, H 3.78, S 12.59.

Synthesis of $[Cu_{20}Se(SPh)_{12}(OAc)_6(PPh_3)_4]$ (2): $PhSSiMe_3$ (0.54 mL, 2.87 mmol) and $Se(SiMe_3)_2$ (0.057 mL, 0.24 mmol) were dissolved in DME (10 mL) and added to a suspension of CuOAc (0.703 g, 5.73 mmol) and PPh_3 (0.50 g, 1.91 mmol) in DME (100 mL) at –30 °C. After stirring for five minutes the mixture was filtered and allowed to warm up to 4 °C. Within several hours **2** crystallized as small, yellow octahedra. Yield: 0.35 g (36%). found C 46.87, H 3.98, S 9.14; $C_{156}H_{138}Cu_{20}O_{12}P_4S_{12}Se$ (4063.2): calcd. C 46.11, H 3.42, S 9.47%).

Synthesis of $[Cu_{28}Se_6(SPh)_{16}(PPh_3)_8]$ (3): CuOAc (0.329 g, 2.68 mmol) and PPh_3 (0.59 g, 2.22 mmol) were suspended in DME (50 mL). After adding $PhSSiMe_3$ (0.27 mL, 1.43 mmol) and $Se(SiMe_3)_2$ (0.11 mL, 0.45 mmol) all solids were dissolved resulting a dark red solution. Within several days one got **3** as red coffin shaped crystals. Yield: 0.19 g (41%). $C_{244}H_{208}Cu_{28}O_2P_8S_{16}Se_6$ (**3**·DME) (6185.7): calcd. C 47.37, H 3.39, S 8.29; found C 46.61, H 3.50, S 8.42.

Synthesis of $[Cu_{36}Se_8(SPh)_{20}(PPh_3)_8]$ (4): CuOAc (0.342 g, 2.79 mmol) and PPh_3 (0.73 g, 2.79 mmol) were dissolved in DME (100 mL). Addition of $PhSSiMe_3$ (0.26 mL, 1.39 mmol) led to a yellow solution, which turned dark red after addition of $Se(SiMe_3)_2$ (0.13 mL, 0,56 mmol). Within some days **4** crystallized directly from the reaction mixture as red plates. Yield: 0.15 g (30%). $C_{268}H_{230}Cu_{36}O_2P_8S_{20}Se_8$ (**4**·DME) (7290.6): calcd. C 44.15, H 3.18, S 8.80; found C 44.43, H 3.25, S 8.79.

Synthesis of $[Cu_{54}Se_8(SPh)_{30}(OAc)_8(PPh_3)_6]$ (5): CuOAc (0.55 g, 4.49 mmol) and PPh_3 (0.29 g, 1.12 mmol) were suspended in DME (75 mL) and stirred for two hours. $PhSSiMe_3$ (0.42 mL, 2.24 mmol) and $Se(SiMe_3)_2$ (0.089 mL, 0.37 mmol) were added within two minutes resulting a dark-red solution with no solids left. Within a few minutes a yellow precipitate had formed. After five hours the mixture was filtered and within one day square, red plates of **5** crystallized. Yield: 0.11 g (25%). $C_{304}H_{264}Cu_{54}O_{16}P_6S_{30}Se_8$ (9383.6): calcd. C 38.91, H 2.84, S 10.25; found C 38.43, H 2.81, S 10.49).

Synthesis of $[Cu_{72}Se_{14}(SPh)_{36}(OAc)_8(PPh_3)_6]$ (6): $PhSSiMe_3$ (0.24 mL, 1.28 mmol) and $Se(SiMe_3)_2$ (0.12 mL, 0.50 mmol) were dissolved in DME (10 mL) and added to a suspension of CuOAc (0.347 g, 2.83 mmol) and PPh_3 (0.19 g, 0.71 mmol) in DME (50 mL) at 0 °C. After one hour the resulting dark solution was allowed to warm up to room temperature. Within some days **6** crystallized as big black blocks. Yield: 0.11 g (26%). $C_{344}H_{304}Cu_{72}O_{18}P_6S_{36}Se_{14}$ (**6**·DME) (11747.1): calcd. C 35.17, H 2.61, S 9.83; found C 35.19, H 2.67, S 9.69.

X-ray Structure Determination: Crystals were removed from the reaction flask under a stream of N_2 gas and immediately covered with a layer of perfluoropolyether oil (Riedel-de Haën). A suitable crystal was selected, attached to a glass fiber, and immediately placed in the low-temperature nitrogen stream. The data were collected with a STOE IPDS II diffractometer using Mo-K_α (λ = 0.71073 Å) radiation, either from a common X-ray tube at 2 kW (compounds **1**–**3**, **5**) or a rotating anode run at 4.8 kW (**4**, **6**). Structure solution and refinement against F^2 were carried out using shelxs and shelxl software.[19] Molecular drawings were prepared with Diamond 2.1[20] and PaintShopPro 7AE;[21] in the figures cop-

Table 2. Crystallographic data for **1**–**3**.

	1	**2**	**3**·DME
Formula	$C_{162}H_{135}Cu_{17}P_4S_{15}Se$	$C_{156}H_{138}Cu_{20}O_{12}P_4S_{12}Se$	$C_{244}H_{208}Cu_{28}O_2P_8S_{16}Se_6$
Formula mass	3845.62	4063.02	6185.7
Temperature [K]	200	200	200
Crystal system	trigonal	cubic	orthorhombic
Space group	$R\bar{3}$	$Pa3$	$Pnn2$
a [pm]	1873.5(3)	3189.4(4)	3298.7(7)
b [pm]	1873.5(3)	3189.4(4)	1916.3(4)
c [pm]	8318.3(17)	3189.4(4)	2025.1(4)
α [°]	90	90	90
β [°]	90	90	90
γ [°]	120	90	90
Volume [10^6 pm^3]	25286(7)	32444(7)	12801(4)
Z	6	8	2
Density [g cm^{-3}]	1.515	1.664	1.605
μ [mm^{-1}]	2.580	3.033	3.351
$2\theta_{max}$ [°]	48	50	54.4
$F(000)$	11604	16288	6160
Reflections collected	9218	65717	40096
Indep. reflections	4063 [R_{int} = 0.0457]	9507 [R_{int} = 0.1717]	19915 [R_{int} = 0.1691]
Indep. refl. with $F_o > 4\sigma(F_o)$	2612	4076	13909
Restraints/parameters	0/535	0/618	1/1669
GooF on F^2	1.020	0.842	1.038
R_1 [$I > 2\sigma(I)$]	0.0599	0.0558	0.0690
wR_2 (all data)	0.1969	0.1648	0.2079
Largest diff. peak and hole (e Å^{-3})	0.936/–0.527	1.454/–0.771	1.117/–1.278
Flack parameter			0.001(17)

 © 2005 Wiley-VCH Verlag GmbH & Co. KGaA, Weinheim

Table 3. Crystallographic data for **4**–**6**.

	4·DME	**5**	**6**·DME
Formula	$C_{268}H_{230}Cu_{36}O_2P_8S_{20}Se_8$	$C_{304}H_{264}Cu_{54}O_{16}P_6S_{30}Se_8$	$C_{344}H_{304}Cu_{72}O_{18}P_6S_{36}Se_{14}$
Formula mass	7290.60	9383.61	11747.05
Temperature [K]	200	200	100
Crystal system	monoclinic	trigonal	monoclinic
Space group	$P2_1/n$	$R\bar{3}$	$P2_1/n$
a [pm]	2177.0(4)	2946.9(4)	2660.4(5)
b [pm]	2975.2(6)	2946.9(4)	4445.7(9)
c [pm]	2412.6(5)	3964.7(8)	3820.4(8)
α [°]	90	90	90
β [°]	106.05(3)	90	98.49(3)
γ [°]	90	120	90
Volume [10^6 pm^3]	15017(5)	29818(8)	44690(15)
Z	2	3	4
Density [g cm^{-3}]	1.612	1.568	2.629
μ [mm^{-1}]	3.683	3.775	4.714
$2\theta_{max}$ [°]	48	50	48
F(000)	7220	13872	22592
Reflections collected	48076	35133	197207
Independent reflections	24151 [R_{int} = 0.0743]	11519 [R_{int} = 0.0663]	68063 [R_{int} = 0.1467]
Indep. refl. with $F_o > 4\sigma(F_o)$	11358	6581	38849
Restraints/parameters	0/1537	0/743	11/2518
GooF on F^2	0.906	0.987	0.978
R_1 [$I > 2\sigma(I)$]	0.0598	0.0846	0.1413
wR_2 (all data)	0.1922	0.2917	0.3928
Largest diff. peak and hole (e Å^{-3})	2.095/–0.787	2.329/–2.076	3.772/–1.758

per atoms are represented only by their numbers, other elements are named with symbols and numbers. In the figures showing the chalcogenide substructures the lines between neighboring atoms do not represent bonds. The crystal and refinement data of **1**–**6** are summarized in Tables 2 and 3.

CCDC-260742 (for **1**), -260743 (for **2**), -260744 (for **3**), -260745 (for **4**), -260746 (for **5**), and -260747 (for **6**) contain the supplementary crystallographic data for this paper. These data can be obtained free of charge from The Cambridge Crystallographic Data Centre via www.ccdc.cam.ac.uk/data_request/cif.

Acknowledgments

This work was supported by the Deutsche Forschungsgemeinschaft (Centrum für funktionelle Nanostrukturen) and the Deutsch–Israelisches Programm (DIP).

[1] C. B. Murray, D. J. Norris, M. G. Bawendi, *J. Am. Chem. Soc.* **1993**, *115*, 8706–8715.
[2] H. Weller, *Angew. Chem.* **1993**, *105*, 43–55; *Angew. Chem. Int. Ed. Engl.* **1993**, *32*, 41–52.
[3] A. A. Guzelian, U. Banin, A. V. Kadavanich, X. Peng, A. P. Alivisatos, *Appl. Phys. Lett.* **1996**, *69*, 1432–1434.
[4] D. V. Talapin, A. L. Rogach, A. Kornowski, M. Haase, H. Weller, *Nanolett.* **2001**, *1*, 207–211.
[5] Y. W. Cao, U. Banin, *J. Am. Chem. Soc.* **2000**, *122*, 9692–9702.
[6] M. A. Hines, P. Guyot-Sionnest, *J. Phys. Chem.* **1996**, *100*, 468–471.
[7] S. Dehnen, A. Eichhöfer, D. Fenske, *Eur. J. Inorg. Chem.* **2002**, 279–317.
[8] D. Fenske, C. Persau, S. Dehnen, C. E. Anson, *Angew. Chem.* **2004**, *116*, 309–313; *Angew. Chem. Int. Ed.* **2004**, *43*, 305–309.
[9] V. N. Soloviev, A. Eichhöfer, D. Fenske, U. Banin, *Phys. Status Solidi B* **2001**, *224*, 285–289.
[10] V. N. Soloviev, A. Eichhöfer, D. Fenske, U. Banin, *J. Am. Chem. Soc.* **2001**, *123*, 2354–2364.
[11] V. N. Soloviev, A. Eichhöfer, D. Fenske, U. Banin, *J. Am. Chem. Soc.* **2000**, *122*, 2673–2674.
[12] A. Eichhöfer, A. Aharoni, U. Banin, *Z. Anorg. Allg. Chem.* **2002**, *628*, 2415–2421.
[13] R. D. Mountz, T. Ogura, Q. Fernando, *Inorg. Chem.* **1974**, *13*, 803–805.
[14] M. G. B. Drew, D. A. Edwards, R. Richards, *J. Chem. Soc., Chem. Commun.* **1973**, 124–125.
[15] O. Fuhr, A. Meredith, D. Fenske, *J. Chem. Soc., Dalton Trans.* **2002**, 4091–4094.
[16] D. A. Edwards, R. Richards, *J. Chem. Soc., Dalton Trans.* **1973**, 2463–2468.
[17] H. Schmidt, H. Ruf, *Z. Anorg. Allg. Chem.* **1963**, *321*, 270–273.
[18] N. Miyoshi, H. Ishii, K. Kondo, S. Mui, N. Sonoda, *Synthesis* **1979**, 301.
[19] a) G. M. Sheldrick, *SHELXS-97, Program for Crystal Structure Solution*, University of Göttingen, **1997**; b) G. M. Sheldrick, *SHELXL-97, Program for Crystal Structure Refinement*, University of Göttingen, **1997**.
[20] K. Brandenburg, Diamond 2.1d, Visual Crystal Structure Information System, Bonn, 2000.
[21] PaintShopPro 7AE, Jasc Software, Eden Prairie, **2001**.

Received: September 13, 2004

 © 2005 Wiley-VCH Verlag GmbH & Co. KGaA, Weinheim

Cationic Iridium Complexes with Chiral Dithioether Ligands: Synthesis, Characterisation and Reactivity under Hydrogenation Conditions

Leticia Flores-Santos,[a] Erika Martin,*[a] Ali Aghmiz,[b] Montserrat Diéguez,[b] Carmen Claver,[b] Anna M. Masdeu-Bultó,*[b] and Miguel Ángel Muñoz-Hernández[c]

Keywords: Chiral auxiliaries / S ligands / Iridium / Hydrides / Asymmetric catalysis

A series of cationic Ir^I complexes containing chiral dithioether ligands have been prepared in order to study the influence of the sulfur substituents and the metallacycle size on the acetamidoacrylate hydrogenation reaction. In the case of complexes **6**, **7** and **10**, a mixture of diastereomers is observed in solution due to the sulfur inversion processes. In contrast, this fluxional behaviour is efficiently controlled by using bicyclic ligands which inhibit the S-inversion in complexes **8** and **9**. The solid-state structure of complex **10b** shows only one diastereomer with the sulfur substituents in a relative *anti* disposition and in an overall configuration of $S_CS_CS_SS_S$ at the coordinated dithioether ligand. Iridium complexes containing seven- and six-membered metallacycles (**6b**–**d**, **7b**,c, **10a**,**b**) react with the substrate through S-ligand substitution, and the rate of this substitution is related to the position of the fluorine atom on the aromatic ring. On the contrary, complexes containing a *bis*metallacycle (**8** and **9**) are not displaced by the substrate. The catalytic hydrogenation activity of complexes **8** and **9** is analysed in terms of the high stability of the corresponding dihydride complexes (**13** and **14**). In both cases, only two of the four possible diastereomeric dihydride species are formed in solution.
(© Wiley-VCH Verlag GmbH & Co. KGaA, 69451 Weinheim, Germany, 2005)

Introduction

The study of chiral sulfur transition-metal complexes as asymmetric catalysts has notably increased during the last decades.[1,2] In particular, complexes containing thioether mixed-donor ligands such as the P,S-,[3–8] N,S-[9–17] and O,S-[18–22] donors have been successfully applied in asymmetric hydrogenation,[5,6,23] allylic substitutions[7–10,18] and enantioselective hydrosilylation of ketones.[4,23] In contrast, catalysts with chiral bidentate thioether ligands have been scarcely investigated,[24–32] although some have shown promising catalytic properties. In fact, we have recently shown that metal complexes with chiral dithioether ligands afford up to 81% *ee* in palladium-catalysed asymmetric allylic substitutions[24] and 68% *ee* in iridium-catalysed asymmetric hydrogenation reactions.[25,26]

Upon coordination to a metal, thioether ligands generate a stereogenic centre at the sulfur atom, whose close proximity to the metal coordination sphere may be advantageous for enantioinduction; however, these centres are not configurationally stable, since sulfur inversion has a low energy barrier. In the case of chiral dithioether complexes, the presence of two stereogenic centres at sulfur atoms, in addition to the carbon stereogenic centres at the ligand backbone, can lead to mixtures of diastereomers. The presence of mixtures of diasteromeric species and the difficulty to control their interconversion in solution have been regarded as a problem for asymmetric induction in catalytic reactions. In spite of this behaviour, enantioinductions have been improved when the configuration at the sulfur atom is controlled by steric effects.[24,31,32] Unfortunately, having few examples of S,S-homodonor ligands, which also differ considerably in their skeleton size and rigidity, makes it difficult to elucidate the structure-performance relationship.

In order to understand the influence of structural and electronic factors on the reactivity of chiral dithioether-containing catalysts, in the present work we prepared a series of cationic iridium complexes with chiral dithioether ligands **1**–**5** (Figure 1) derived from L-(+)-diethyltartrate[33] and (2*R*,4*R*)-2,4-pentanediol.[34] These ligands were selected in order to study electronic and ring size effects and sulfur inversion control, by the following strategies: (i) introduction of fluorine atoms at *ortho*- *meta*- or *para*- positions of a thioether aromatic ring in order to change the donor/acceptor electronic properties of sulfur atoms (ligands **1a–c** and **2a**–**c**); (ii) evaluation of two ring sizes to tune the rigidity of the molecular backbone (ligands **1a**–**d** and **2a**–**c** vs.

[a] Departamento de Química Inorgánica, Facultad de Química, Universidad Nacional Autónoma de México, Cd. Universitaria, 04510 México DF, México
Fax: +52-55-5622-3720
E-mail: erikam@servidor.unam.mx
[b] Departament de Química Física i Inorgànica, Universitat Rovira i Virgili,
c/Marcel·lí Domingo s/n, 43005 Tarragona, Spain
Fax: +34 977-559563
E-mail: masdeu@quimica.urv.es
[c] Centro de Investigaciones Químicas, Universidad Autónoma del Estado de Morelos,
Av. Universidad 1001 Col. Chamilpa, Cuernavaca, México
Fax: +52-77-7329-7998
E-mail: mamund2@ciq.uaem.mx

5); (iii) effective stereocontrol at sulfur atoms in metal intermediates by using cyclic chiral thioether ligands which eliminate pyramidal inversion and also allow a backbone rigidity modulation (ligands **3** and **4**).

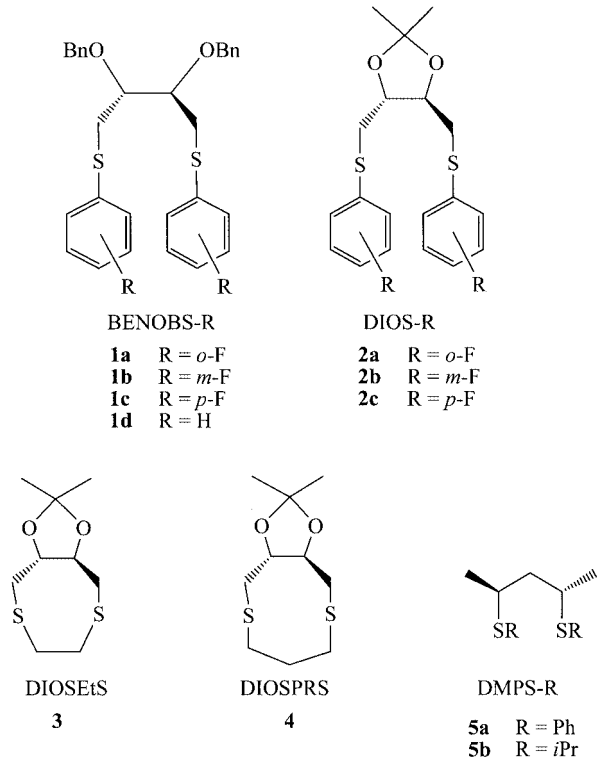

Figure 1. Dithioether ligands **1–5**.

The reactivity of the synthesised complexes [Ir(dithioether)(cod)]BF_4 towards acrylic acid derivatives and dihydrogen is discussed in relation to the activity and selectivity observed under catalytic hydrogenation conditions.

Results and Discussion

Iridium Complexes [Ir(cod)(dithioether)]BF_4

Ligands **3**, **4** and **5a**,**b** reacted with dichloromethane solutions of [Ir(cod)$_2$]BF_4 to form the corresponding [Ir(cod)(dithioether)]BF_4 complexes **8**, **9** and **10a**,**b** by cod substitution (Scheme 1). The complexes were isolated as relatively air-stable, yellow or orange solids by addition of hexane or diethyl ether with yields ranging from 50 to 99%. In contrast, ligands **1a–d** and **2a–c** did not react with dichloromethane solutions of [Ir(cod)$_2$]BF_4 unless hydrogen was bubbled through the solution to reduce cod and promote its substitution. These results can be rationalised according to the lower stability of the seven-membered metallacycle formed in the case of ligands **1** and **2**. A similar behaviour was observed for the non-fluorinated derivative of ligands **2**.[25] In the case of ligands **3** and **4**, the generation of [7,5]- and [7,6]-membered rings, respectively, increases the chelate stability. Dithioethers **1a** and **2a** did not form the iridium complexes, probably because of steric hindrance in addition to the electron-withdrawing effect of the *ortho*-fluoro substitution.

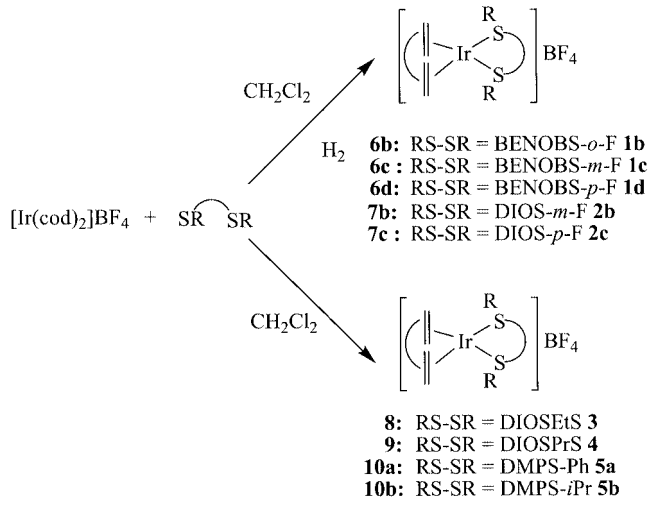

Scheme 1. Syntheses of complexes **6–10**.

FAB mass spectra confirmed the formation of the mononuclear species in all cases. Complexes were characterised in solution by ^1H and ^{13}C NMR spectroscopy. ^{19}F NMR spectroscopy was also used for complexes **6b**,**c** and **7b**,**c**. The full assignment of ^1H and ^{13}C NMR parameters was performed by using homo- and heteronuclear two-dimensional spectroscopy techniques (^1H,^1H-COSY, HETCOR and NOESY).

The coordination of the dithioether ligands to the metal generates a stereogenic centre at each sulfur atom. Therefore, a mixture of diastereomers with different spatial arrangements of the sulfur substituents and conformations of the chelate ring could exist in solution (Figure 2). Taking into account that ligands **1** and **2** have absolute *RR*-configuration at their asymmetric carbon centres and two possible configurations at the sulfur atoms, three diastereomers could be formed: $R_CR_CR_SR_S$ and $R_CR_CS_SS_S$ (both attributed to the *anti* isomers) and $R_CR_CR_SS_S$ or $R_CR_CS_SR_S$ (corresponding to the *syn* isomer). This analysis applies also for complexes with ligands **5**, which have absolute *SS* configuration at their asymmetric carbon centres, therefore three possible diastereomers, $S_CS_CR_SR_S$ and $S_CS_CS_SS_S$ (*anti* isomers), and $S_CS_CR_SS_S$ or $S_CS_CS_SR_S$ (*syn* isomer) can be formed. In contrast, for complexes containing ligands **3** and **4**, there is only one possible *syn* isomer with $R_CR_CR_SS_S$ or $R_CR_CS_SR_S$ configuration, since the inversion at both sulfur atoms is inhibited.

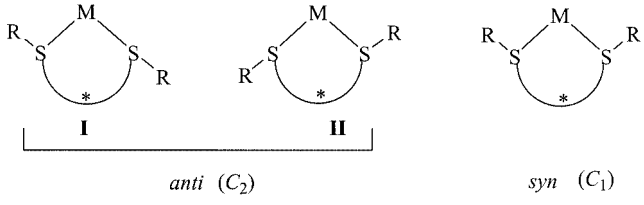

Figure 2. Possible diastereomers for metal complexes with ligands **1–5**.

 © 2005 Wiley-VCH Verlag GmbH & Co. KGaA, Weinheim

In fact, variable temperature NMR studies (down to –80 °C) performed on complexes **8** and **9** are in accordance with the presence of only one diastereomer in solution, which corresponds to a C_1-symmetry molecule with $R_CR_CR_SS_S$ configuration. Full assignment of ^{1}H and ^{13}C spectra was achieved by homo- and heteronuclear 2D NMR techniques and the conformation of both rings was determined by using NOE experiments (Figure 3). The seven-membered ring has a twisted chair conformation in both complexes. The second ring is either a five-membered chelate ring with an envelope conformation in **8** (NOE contact between H^4 with H^1 and H^2) or a six-membered ring with a chair conformation in **9** (NOE contact between H^1 and H^7).

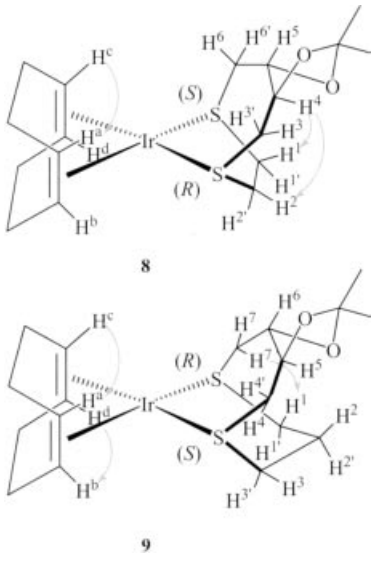

Figure 3. Structures proposed for complexes **8** and **9** showing the NOE contacts.

For complexes **10a**,**b** containing a six-membered metallacycle, variable temperature ^{1}H NMR spectra (–40 to +25 °C) exhibited patterns corresponding to the presence of only one species with C_2 symmetry, which may be attributed to one of the two possible *anti* diastereomers $S_SS_CS_CS_CS_S$ or $R_SS_CS_CR_S$ with equatorial–equatorial or axial–axial conformations, or to the chair equatorial–axial conformers interchanging fast in solution. VT NMR spectra of **10b** in CD_2Cl_2 were invariant in the temperature range studied. NOE experiments suggested that an equatorial–equatorial species was likely to be present in solution; nevertheless, the possibility of rapid equilibration with other species could not be discarded. Moreover, the structure in the solid state of **10b**, determined by X-ray diffraction (see following section), confirmed that the sulfur substituents were *anti* with an equatorial–axial disposition.

The ^{1}H and ^{19}F NMR spectra of complexes **6b**,**c** and **7b**,**c** show in all cases broad signals at room temperature. It is interesting to note that the chemical shifts of the cod methynic protons are not sensitive to the position of the fluoro substituent on the dithioether ligands. Nevertheless, the reactivity towards acrylic acid derivatives depends on the position of the fluorine atom in the aromatic ring.

The ^{13}C NMR spectra for complexes **6b–d** showed only two signals for cod methylenic carbons and two signals for cod methynic carbons, which can be attributed to the presence of only one *anti* diastereomer or a fast exchange between both *anti* diastereomers. However, the ^{19}F NMR experiments in the temperature range of +30 °C to –60 °C show two different signals for complexes **6b** and **6c** in the ratios 10:6 and 10:9.1, respectively, proving the presence of two *anti* diastereomers in solution (**I** and **II**). The rate of isomer interconversion for complex **6b** was very low and invariant in the temperature range studied ($k = 1.10^{-3}$ s^{-1}) [35], and for complex **6c** the rate could not be calculated, since no significant change in the shape of the spectra was observed in the same range of temperatures. Although no splitting of signals in ^{1}H and ^{13}C NMR spectra was observed for complex **6d**, by analogy with **6c**,**d**, two diastereomers could also be present in solution.

In the case of complexes **7b** and **7c**, two isomers, **I** and **II**, were also detected at low temperature. The exchange rates ranged from 5.26×10^2 s^{-1} (at –60 °C) to 1.22×10^4 s^{-1} (at 30 °C) for **7b** and from 8.22×10^2 s^{-1} (–60 °C) to 5×10^4 s^{-1} (30 °C) for **7c**. The values of the Gibbs activation energy ($\Delta G^{\neq}$, evaluated by the Eyring equation) are 50.4 ± 1.0 kJ mol^{-1} for **7b** and 48.1 ± 1.3 kJ mol^{-1} for **7c**, and are in the range reported for sulfur inversion in thioether complexes.[36,37] Therefore, the dynamic behaviour in solution of **7b** and **7c** is independent of the position of the fluorine atom in the aromatic ring.

Crystal Structure of [Ir(cod)(5b)]BF$_4$ (10b)

Single crystals of **10b** suitable for X-ray diffraction were obtained by slow diffusion of *n*-hexane into an ethyl acetate solution of the complex. The cationic structure is shown in Figure 4, and selected bond lengths and angles are listed in Table 1. The iridium atom shows a slightly distorted square-planar environment. The sulfur atoms are in a *cis* configuration and the cyclooctadiene ligand occupies the other two coordination sites. For the latter ligand, using the centroids of the C12–C13 and C16–C17 double bonds, X1a and X1b, respectively, a twist of 4.8° of the dihedral planes S1–Ir1–S2 and X1a–Ir1–X1b is found. A similar situation was observed for the Ir complex [Ir(cod){C[P(S)(Ph)$_2$]$_3$}],[38] which showed a twist of 9.0°. The distortion is also evident from the deviation from 90° observed in the following bond angles: X1a–Ir1–S1 86.8°, X1b–Ir1–S2 99.6° and X1a–Ir1–X1b 85.6°, which is more pronounced than in [Ir(cod)-{[P(S)(Ph)$_2$]$_3$C}] (89.5, 88.3 and 87.5°, respectively)[38] and the Rh complex [Rh(cod){CH[P(S)(Ph)$_2$]$_2$}] (86.4, 88.3 and 86.7°, respectively).[39] The Ir–S and Ir–C average bond lengths [2.3537(19) and 2.131(9) Å, respectively] are in the range reported for related Ir^{I} complexes.[38,40,41] Furthermore, similar Ir–S distances were reported for Ir^{I} cyclooctadiene complexes with thiolate bridging ligands.[42,43] The average angle C–S–Ir [110.0(3)°] is close to the tetrahedral angle, indicating sp^3 hybridization at the sulfur atom.

 © 2005 Wiley-VCH Verlag GmbH & Co. KGaA, Weinheim

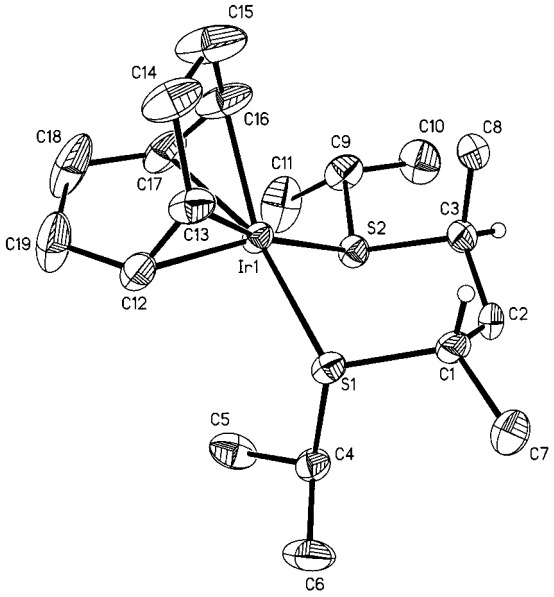

Figure 4. ORTEP representation (50% probability) of iridium complex **10b**. Hydrogen atoms and BF_4^- are omitted.

Table 1. Selected bond lengths [Å] and angles [°] for complex **10b**.

Bond lengths	[Å]	Bond angles	[°]
Ir(1)–C(16)	2.116(11)	C(16)–Ir(1)–C(12)	95.5(4)
Ir(1)–C(12)	2.126(8)	C(17)–Ir(1)–C(13)	88.4(4)
Ir(1)–C(17)	2.141(9)	C(16)–Ir(1)–S(2)	98.6(3)
Ir(1)–C(13)	2.141(8)	C(17)–Ir(1)–S(2)	99.6(3)
Ir(1)–S(2)	2.344(2)	C(12)–Ir(1)–S(1)	85.9(2)
Ir(1)–S(1)	2.3633(18)	C(13)–Ir(1)–S(1)	87.9(2)
		S(2)–Ir(1)–S(1)	88.18(8)
		C(1)–S(1)–C(4)	105.0(4)
		C(1)–S(1)–Ir(1)	108.3(3)
		C(4)–S(1)–Ir(1)	111.3(3)
		C(3)–S(2)–C(9)	105.4(4)
		C(3)–S(2)–Ir(1)	104.4(3)
		C(9)–S(2)–Ir(1)	116.1(3)

The solid structure shows only one diastereomer with the sulfur substituents in a relative *anti* disposition. The metallacycle adopts a chair conformation with an overall configuration $S_C S_C S_S S_S$.

Catalytic Experiments and Reactivity of the Iridium Complexes

The catalytic activity of iridium complexes **6b**–**d**, **7b**,**c**, **8**, **9**, **10a**,**b** in the hydrogenation of acrylic acid derivative **11a** at 25 °C and 1 atm of hydrogen pressure was examined (Scheme 2).

All catalyst precursors show low conversions even at 12 h of reaction (Figure 5). Regarding the influence of the fluoro-substitution on the aromatic ring, the *meta*-fluoro derivatives **6b** and **7b** showed higher conversion than their analogous *para*-fluoro derivatives **6c** and **7c**, in the same reaction time. The complex **6d** without the fluoro-substituted ligand showed higher conversion than the *meta*- and *para*-fluoro complexes **6b** and **6c**.

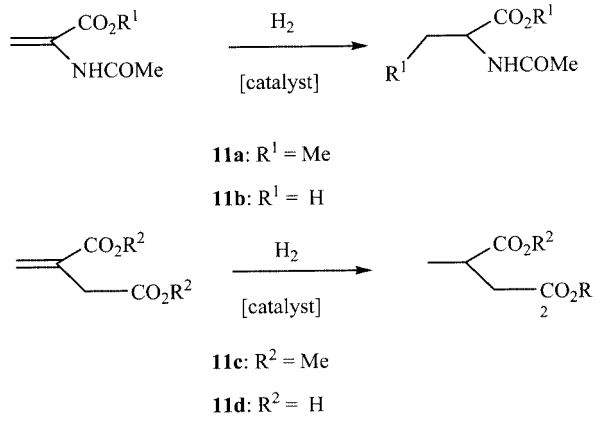

Scheme 2. Hydrogenation of acrylic acid derivatives **11a**–**d**.

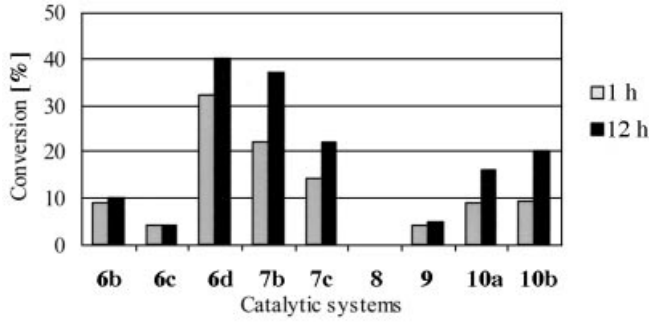

Figure 5. Catalytic hydrogenation of methyl acetamidoacrylate (**11a**) by using dithioether iridium complexes. Conditions: [{Ir(cod)L}BF_4] = 4.3 mM, [Substrate] = 175 mM, T = 25 °C and $p(H_2)$ = 1 atm.

The activity is also modified by the dithioether skeleton; complexes **7b**,**c** provided higher conversion than **6b**,**c** and complex **10a**, with a smaller six-membered metallacycle, showed lower conversion than the seven-membered chelate complex **6d**. Finally, complexes **8** and **9**, which contain metallabicycles, provided less active catalytic systems. In all cases, the enantioinduction was practically nonexistent.

These catalytic results can be explained in terms of the stability of the complexes. Catalytic systems **6**, **7** and **10** decomposed gradually during the catalytic reaction to form Ir^0 with the consequent loss of the chiral ligand. This was confirmed for the fluorinated precursors (**6b**,**c** and **7b**,**c**) by analysis of the catalytic mixture at the end of the hydrogenation reactions through ^{19}F NMR spectroscopy, which showed the presence of the free ligand as a distinct species. The decoordination of the dithioether ligands is promoted by substrate coordination, since the addition of **11a** to dichloromethane solutions of complexes **6**, **7** and **10** under nitrogen generates free dithioether ligands and [Ir(**11a**)(cod)]$^+$, detected by ^{19}F NMR spectroscopy or by ^1H and ^{13}C NMR.

In an attempt to recoordinate the dithioether ligand by forcing cod reduction, H_2 was bubbled into a solution containing **6b** and **11a**, but the signal of the free dithioether

 © 2005 Wiley-VCH Verlag GmbH & Co. KGaA, Weinheim

remained unaltered, and the formation of metallic iridium was observed.

For purposes of comparison, the catalytic activity of complex $[Ir(cod)_2]^+$ (**12**) was studied under the same catalytic conditions and was found to be the highest (45% conversion at 1 h). Since the conversion obtained with **12** is higher than that found with the dithioether complexes and it has been demonstrated that these dithioether ligands are replaced by the substrate to yield $[Ir(\mathbf{11a})(cod)]^+$, the increasing conversion can be related to a higher rate of dithioether substitution. Thus, the less active systems are those in which the rate of substitution is lower, suggesting that the dithioether ligand is more strongly coordinated to the metal. Consequently, in the case of seven-membered complexes, catalytic precursors **6** lead to more active systems probably because of the formation of weaker M–S bonds. The same situation is observed when the more stable six-membered complex **10a** is compared with the seven-membered complex **6b**. Concerning the electronic factors, the lower activity of the fluorinated systems may be related to a stronger M–S interaction due to an enhancement of the π-acceptor ability of these ligands.

In contrast to the above-mentioned behaviour, bicyclic systems **8** and **9** do not decompose to Ir^0 under catalytic conditions, and the dithioether ligands are not replaced by substrate **11a**. Therefore, the catalytic hydrogenation of **11b**–**d** was studied by using **8** and **9**. For these substrates, the conversions ranged from modest to low and only for the acid substrates **11b** and **11d**, the *ee* reached up to 15% (*R*), with **8** as catalyst precursor. In order to understand the catalytic performance of these *bis*metallacycles, we studied the species formed in the presence of hydrogen.

Reactivity of Complexes 8 and 9 with Hydrogen

Complexes **8** and **9** reacted with H_2 at –70 °C to form the corresponding dihydride species $[Ir(H)_2(\mathbf{8})(cod)]BF_4$ (**13**) and $[Ir(H)_2(\mathbf{9})(cod)]BF_4$ (**14**) (Scheme 3). Similar reactivity was reported for other dithioether iridium complexes.[25,26]

$$[Ir(COD)(L)]BF_4 + H_2 \longrightarrow [Ir(H)_2(COD)(L)]BF_4$$

8: L = DIOSEtS **3** — **13**: L = DIOSEtS **3**
9: L = DIOSPrS **4** — **14**: L = DIOSPrS **4**

Scheme 3. Reaction of complexes **8** and **9** with H_2.

Taking into account the two different faces of the coordination plane (named seven-membered- and five-membered ring faces) four diastereomers can be formed (Figure 6).

The hydride region of the ^1H NMR spectra of complex **13** showed four signals at –70 °C which were attributed to the presence of two different isomers: a major isomer (δ = –11.37 and –13.83 ppm) and a minor one (δ = –11.56 and –13.78 ppm) in a 5:3 ratio. The measurement of relaxation times, T_1 (see Experimental Section), confirmed the formation of "classical hydride ligands".[44–48] Moreover, signals at δ = –11.37 and –11.56 ppm showed similar T_1 values (0.31 s) and the same was observed for T_1 values (0.2 s) of

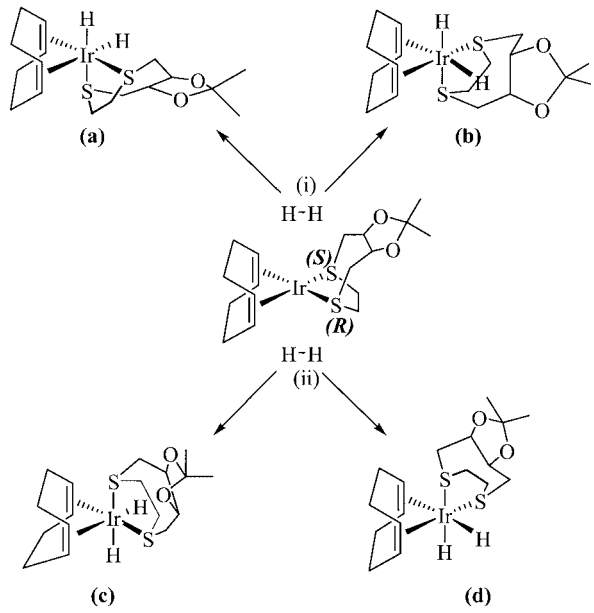

Figure 6. Attack of H_2 (i) through the "upper" seven-membered ring face with displacement of the (a) S_S (**13-I**) and (b) S_R atoms (**13-II**); (ii) through the "lower" five-membered ring face with displacement of the (c) S_S (**13-III**) and (d) S_R (**13-IV**) atoms.

signals at δ = –13.83 and –13.78 ppm, suggesting similar chemical environments for each couple sharing equal T_1 values.

NOE experiments allowed identification of the major isomer as **13-I**, formed by the attack of H_2 through the seven-membered ring face with displacement of the sulfur with absolute *S* configuration (Figure 7). In particular, NOE contacts between the methynic proton H^5 with $H^{3'}$ and the hydride ligand H^f, indicated the proximity of the seven-membered ring face to the hydride ligand. The methynic proton H^4 showed contacts with the ethyl protons $H^1$and H^2. The minor isomer corresponds to isomer **13-II**, formed also by the attack of H_2 through the seven-membered ring face but with displacement of the sulfur with absolute *R* configuration. The NOE contacts H^f–H^5, H^2–H^4–H^1 and H^b-$H^{3'}$ allowed determination of the minor isomer structure.

The dihydride complexes **13-I** and **13-II** were very stable; the hydride signals remained in the ^1H NMR spectra up to 25 °C after 24 h. The high stability of these complexes may account for the very low activity of **8** in the hydrogenation of acrylic acid derivatives. Although the oxidative addition takes place readily at –70 °C, the 1,2-insertion of the hydride ligands in the M-alkene (cod) bond to hydrogenate the cod ligand is very slow.

Similar results were obtained in the reactivity study of complex **9** with H_2 to form the dihydride complex **14**. The ^1H NMR in the hydride region also showed four signals corresponding to two isomers in a 5:3 ratio. In this case, the NOE contacts suggested that hydrogen attack also takes place through the seven-membered ring face for both isomers. The structure assignment of the major and minor isomers was not possible because the hydride NOE signals

 © 2005 Wiley-VCH Verlag GmbH & Co. KGaA, Weinheim

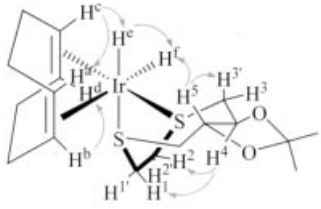

13-I

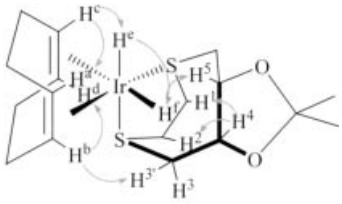

13-II

Figure 7. Representation of complexes of **13-I** and **13-II**, showing the NOE contacts.

were superimposed. Upon increasing the temperature up to 0 °C, the hydride signals disappeared, and both signals of cyclooctane and complex **9** were observed. This corresponds to two parallel reactions, the hydrogenation of cod and the reversible reductive elimination of H_2.

As has been shown, the approach of dihydrogen to complexes **8** and **9** takes place through the seven-membered ring face, which is presumably the more hindered. Nevertheless, upon formation of the dihydride complex, the reorganization of the dithioether cyclic ligand leads to a less hindered structure than when the approach is through the five- (for complex **8**) or six- (for complex **9**) -membered ring face. In this latter case, the bicyclic moiety of the resulting structure would be bent towards the cod coordinated ligand while in the other case, this fragment is launched outside the coordination sphere (Figure 6), which may favour the formation of the observed isomers. The low enantioselectivity obtained with both systems is probably related to the formation of different dihydrido complexes in solution.

Conclusion

Cationic iridium(I) complexes containing chiral dithioether ligands were prepared and their fluxional behaviour in solution was efficiently controlled by using bicyclic ligands, which form configurationally stable sulfur stereocentres upon coordination to the metal. The systematic study of the reactivity of these complexes allowed to establish that: (i) seven-membered chelating ligands are displaced in all cases by methyl acetoamidoacrylate to form the species $[Ir(substrate)(cod)]^+$, which is responsible for the catalytic activity in the hydrogenation of this substrate; (ii) the position of the fluorine atoms in the aromatic rings affects the substitution rate of the dithioether, thus modifying the catalytic activity directly; (iii) the dithioether substitution does not occur in the more rigid complexes containing cyclic dithioligands; however, these systems show poor activities and enantioselectivities; (iv) the low activity of the *bis*-metallacycles is directly related to the high stability of the corresponding dihydride species; (v) only two diastereomeric dihydride species (5:3) are formed in both cases; (vi) in the *bis*metallacycle systems the enantioinduction is slightly improved using the more rigid [7,5]- in comparison to the [7,6]-*bis*metallacycle.

Experimental Section

General Remarks: All iridium complexes were prepared by standard Schlenk techniques under nitrogen. The complex $[Ir(cod)_2]BF_4$ was prepared by methods described in the literature.[49] The syntheses of ligands **1a–d**, **2a–c**, **3** and **4** were reported previously.[33] The syntheses of ligands **5a** and **5b** will be described elsewhere.[34] Solvents were dried over standard drying agents and were freshly distilled and deoxygenated prior to use. All other reagents were used as commercially supplied. ^1H, ^{13}C, and ^{19}F NMR spectra were measured with Varian 300 or 400 MHz spectrometers operating at 300 or 400 MHz (^1H), 75 or 100 MHz (^{13}C), 282 or 376 MHz (^{19}F). Chemical shifts are relative to TMS δ = 0 ppm (^1H), CD_2Cl_2 δ = 55 ppm (^{13}C) and $CFCl_3$ δ = 0 ppm (^{19}F). All species were studied in deuterated dichloromethane unless otherwise indicated. Infrared spectra were measured with a Nicolet AVATAR 320 FT-IR spectrometer. Electronic Impact and FAB^+ mass spectra were recorded with a Jeol SX102A inverse geometry spectrometer and VG Autospect using a 3-nitrobenzyl alcohol matrix. Elemental analyses were performed with an AE FISONS CHNS-0 equipment or a Carlo–Erba EA-1108 microanalyser. Gas chromatography analyses were performed with a Hewlett–Packard 5890A instrument. Enantiomeric excesses (*ee*) were determined with a fused silica capillary column Permabond L-Chirasil-Val (25 m × 0.25 mm) for substrates **11a**,**b**, and Chiraldex-G-TA (30 m × 0.25 mm) for substrates **11c**,**d**.

Synthesis of Complexes [Ir(cod)(dithioether)]BF_4 (dithioether = 1b–d, 2b,c, 3–5)

Procedure A: A solution of the corresponding ligand (**1b–d, 2b**,**c**, 0.08 mmol) in dichloromethane (3 mL) was added to a solution of $[Ir(cod)_2]BF_4$ (40 mg, 0.08 mmol) in dichloromethane (5 mL) under nitrogen. The solution was stirred for 30 min, and then hydrogen was bubbled into the solution for 15 s in order to hydrogenate the 1,5-cyclooctadiene ligand and coordinate the dithioether to iridium. The solution was filtered to remove Ir^0, and the solvent was evaporated. The residue was thoroughly washed with hexane and recrystallised from dichloromethane/hexane to yield the products as yellow microcrystalline solids.

[Ir(cod)(1b)]BF_4 (6b): Colour: yellow; yield: 33.5 mg, 46%. IR [KBr (cm^{-1})]: (ν_{B-F}) 1064 (s). ^1H NMR (400 MHz): δ = 7.59 (m, 18 H, H_{ar}), 4.87 (m, 4 H, CH_2–C_6H_5), 4.19 (m, 2 H, CH), 3.95 (m, 4 H, CH_2), 3.82 (m, 4 H, CH cod), 2.3 (m, 2 H, CH_2 cod), 2.24 (m, 2 H, CH_2 cod), 1.81 (m, 2 H, CH_2 cod), 1.7 (m, 2 H, CH_2 cod) ppm. $^{13}C\{^1H\}$ NMR (100 MHz): δ = 162.83 (Ci-F, $J_{C,F}$ = 250.4), 137.16 (Ci-S), 131.66 (Ci), 129.2 (C_m-S), 128.9 (C_o), 128.7 (C_p), 128.56 (C_m), 118.19 (C_o–S, C*p*-S), 75.79 (CH), 74.65 (CH cod), 73.97 (CH cod), 73.67 (CH_2–C_6H_5), 31.14 (CH_2 cod), 31.08 (CH_2 cod), 29.46 (CH_2) ppm. ^{19}F NMR (376 MHz, –60 °C): δ = –109.45 (m, **6b-I**), –111.77 (m, **6b-II**) ppm; **6b-I**/**6b-II** = 5:3. FAB^+: *m*/*z* (%) = 823 ($M–BF_4$). $C_{38}H_{40}BF_6IrO_2S_2$ (909.88): calcd. C 50.16, H 4.43, S 7.05; found C 49.74, H 4.40, S 7.00.

[Ir(cod)(1c)]BF_4 (6c): Colour: yellow; yield: 26.2 mg, 36%. IR [KBr (cm^{-1})]: (ν_{B-F}) 1061 (s). ^1H NMR (400 MHz): δ = 7.34 (m, 18 H,

 © 2005 Wiley-VCH Verlag GmbH & Co. KGaA, Weinheim

CH_{ar}), 4.57 (m, 4 H, CH_2–C_6H_5), 3.87 (m, 2 H, CH), 3.68 (m, 4 H, CH_2), 3.6 (m, 4 H, CH cod), 2.4 (m, 2 H, CH_2 cod), 2.1 (m, 1 H, CH_2 cod), 1.99 (m, 1 H, CH_2 cod), 1.58 (m, 2 H, CH_2 cod), 1.46 (m, 2 H, CH_2 cod) ppm. $^{13}C\{^1H\}$ NMR (100 MHz): δ = 137.67 (Ci), 134.68 (C_o–S), 129.79 (Ci-S), 129.14 (C_o), 128.87 (C_p), 128.79 (C_m), 117.63 (C_m-S), 76.43 (CH), 74.68 (CH cod), 73.87 (CH_2–C_6H_5), 73.74 (CH cod), 31.38 (CH_2 cod), 31.34 (CH_2 cod), 31.05 (CH_2) ppm. ^{19}F NMR (376 MHz, –60 °C): δ = –108.0 (m, **6c-I**), –113.89 (m, **6c-II**) ppm; **6c-I/6c-II** = 10:9.1. FAB$^+$: *m/z* (%) = 823 (M–BF_4). $C_{38}H_{40}BF_6IrO_2S_2$ (909.88): calcd. C 50.16, H 4.43, S 7.05; found C 49.69, H 4.43, S 7.13.

[Ir(cod)(1d)]BF_4 (6d): Colour: yellow; yield: 38.9 mg, 47%. IR [KBr (cm^{-1})]: (ν_{B-F}) 1063(s). ^1H NMR (400 MHz): δ = 7.42 (m, 20 H, H_{ar}), 4.62 (m, 4 H, CH_2–C_6H_5), 3.95 (m, 2 H, CH), 3.69 (m, 4 H, CH_2), 3.62 (m, 4 H, CH cod), 2.11 (m, 2 H, CH_2 cod), 1.98 (m, 2 H, CH_2 cod), 1.58 (m, 2 H, CH_2 cod), 1.47 (m, 2 H, CH_2 cod) ppm. $^{13}C\{^1H\}$ NMR (100 MHz): δ = 137.47 (Ci), 132.34 (Ci-S), 130.47 (C_o), 129.58 (C_o–S), 129.2 (C_m-S), 128.97 (C_p, C_p-S), 128.85 (C_m), 76.22 (CH), 74.84 (CH cod), 74.17 (CH cod), 73.82 (CH_2–C_6H_5), 31.39 (CH_2 cod), 31.33 (CH_2 cod), 29.74 (CH_2) ppm. FAB$^+$: *m/z* (%) = 787 (M–BF_4). $C_{38}H_{42}BF_4IrO_2S_2$ (873.9): calcd. C 52.23, H 4.84, S 7.34; found C 52.75, H 4.84, S 7.27.

[Ir(cod)(2b)]BF_4 (7b): Colour: yellow; yield: 53 mg, 86%. IR [KBr (cm^{-1})]: (ν_{B-F}) 1085 (s), (ν_{B-F}) 1055 (s). ^1H NMR (400 MHz): 7.26 (m, 18 H, H_{ar}), 4.23 (m, 2 H, CH), 4.05 (m, 4 H, CH cod), 3.54 (m, 4 H, CH_2), 2.25 (m, 4 H, CH_2 cod), 1.76 (m, 4 H, CH_2 cod), 1.42 (s, 6 H, CH_3) ppm. $^{13}C\{^1H\}$ NMR (100 MHz): δ = 161.0 (Ci-F, $J_{C,F}$ = 250.3), 132.17 (C_m), 130.17 (Ci), 127.03 (C_p-F), 118.11 (C_p), 117.88 (C_o–S), 111.90 ($C(CH_3)_2$), 80.57 (CH cod), 80.31 (CH cod), 78.52 (CH), 40.22 (CH_3), 31.56 (CH_2 cod), 27.22 (CH_2) ppm. ^{19}F NMR (376 MHz, –80 °C): δ = –108.3 (m, **7b-I**), –111.41 (m, **7b-II**) ppm; **7b-I/7b-II** = 10:3.8. $\Delta H^{\neq}$ = 16.4 ± 1 kJ mol^{-1}, $\Delta S^{\neq}$ = –0.1 kJ mol^{-1} K^{-1}, $\Delta G^{\neq}_{298.15}$ = 50.4 ± 1 kJ mol^{-1}. FAB+: *m/z* (%) = 683 (M–BF_4).

[Ir(cod)(2c)]BF_4 (7c): Colour: yellow; yield: 50.5 mg, 82%. IR [KBr (cm^{-1})]: (ν_{B-F}) 1084 (s), (ν_{B-F}) 1057 (s). ^1H NMR (400 MHz) 7.62 (m, 4 H, H_{ar}), 7.19 (m, 4 H, H_{ar}), 4.2 (m, 2 H, CH), 3.96 (m, 4 H, CH cod), 3.66 (m, 2 H, CH_2), 3.47 (m, 2 H, CH_2), 2.25 (m, 4 H, CH_2 cod), 1.77 (m, 4 H, CH_2 cod), 1.41 (s, 6 H, CH_3) ppm. $^{13}C\{^1H\}$ NMR (100 MHz): δ = 163.89 (Ci-F, $J_{C,F}$ = 249.5), 134.06 (C_o, $^3J_{C,F}$ = 6.3), 130.16 (Ci-S, $^4J_{C,F}$ = 2.3), 117.54 (C_m, $^2J_{C,F}$ = 16.6), 111.12 ($C(CH_3)_2$), 79.72 (CH cod), 79.78 (CH cod), 78.59 (CH), 40.61 (CH_3), 31.53 (CH_2 cod), 31.23 (CH_2) ppm. ^{19}F NMR (376 MHz, –80 °C): δ = –107.41 (m, **7c-I**), –115.62 (m, **7c-II**) ppm; **7c-I/7c-II** = 10:3.5. $\Delta H^{\neq}$ = 19.4 ± 1.3 kJ mol^{-1}, $\Delta S^{\neq}$ = –0.1 kJ mol^{-1} K^{-1}, $\Delta G^{\neq}_{298.15}$ = 48.1 ± 1.3 kJ mol^{-1}. FAB$^+$: *m/z* (%) = 683 (M–BF_4).

Procedure B: A solution of the corresponding ligand (**3**, **4**, 0.08 mmol) in dichloromethane (3 mL) was added to a solution of [Ir(cod)$_2$]BF_4 (40 mg, 0.08 mmol) in dichloromethane (5 mL) under nitrogen. After stirring for 40 min, the colour of the solution turned yellow-orange. The volume was reduced, and hexane was added to precipitate the product, which was collected by filtration, washed with additional hexane and vacuum dried.

[Ir(cod)(3)]BF_4 (8): Colour: yellow-orange; yield: 39.9 mg, 82%. IR [KBr (cm^{-1})]: (ν_{B-F}) 1054 (s). ^1H NMR (400 MHz, –80 °C, refer to Figure 3 for assignments): δ = 4.87 (m, 1 H, CH_a cod), 4.64 (m, 1 H, CH_d cod), 4.64 (m, 1 H, CH *5*), 4.50 (m, 1 H, CH_b cod) 4.45 (m, 1 H, CH_c cod), 4.14 (m, 1 H, CH *4*), 3.77 (m, 1 H, CH_2 *3*), 3.59 (m, 1 H, CH_2 *6*), 3.28 (m, 3 H, CH_2 *6′,1, 2′*), 3.07 (m, 1 H, CH_2 *2*), 2.82 (m, 1 H, CH_2 *1′*), 2.58 (m, 1 H, CH_2 *3′*) 2.17 (m, 4 H, CH_2 cod), 2.02 (m, 2 H, CH_2 cod), 1.89 (m, 2 H, CH_2 cod), 1.34 (s, 3 H, CH_3), 1.36 (s, 3 H, CH_3) ppm; (20 °C): δ = 4.95 (m, 1 H, CH_a cod), 4.75 (m, 1 H, CH_d cod), 4.68 (m, 1, CH *5*), 4.61 (m, 1 H, CH_b cod) 4.44 (m, 1 H, CH_c cod), 4.19 (m, 1 H, CH *4*), 3.83 (m, 1 H, CH_2 *3*), 3.62 (m, 1 H, CH_2 *6*), 3.36 (m, 3 H, CH_2 *6′,1, 2′*), 3.17 (m, 1 H, CH_2 *2*), 2.89 (m, 1 H, CH_2 *1′*), 2.61 (m, 1 H, CH_2 *3′*) 2.26 (m, 4 H, CH_2 cod), 2.05 (m, 4 H, CH_2 cod), 1.41 (s, 6 H, CH_3) ppm. $^{13}C\{^1H\}$ NMR (100 MHz): δ = 111.09 ($C(CH_3)_2$), 83.43 (CH_a cod), 83.14 (CH, *5*), 81.29 (CH_d cod), 78.61 (CH_b cod), 76.73 (CH_c cod), 76.31 (CH, *4*), 46.54 (CH_2 *6*), 41.04 (CH_2 *3*), 36.55 (CH_2 *2*), 33.08 (CH_2 *1*), 32.41 (CH_2 cod), 32.11 (CH_2 cod), 31.66 (CH_2 cod), 31.34 (CH_2 cod), 28.56 (CH_3) ppm. FAB$^+$: *m/z* (%) = 521 (M–BF_4). High resolution FAB$^+$: *m/z* (%) = 521.1226; $C_{17}H_{28}IrO_2S_2$ (Err [ppm/mmu] = +12.7/+6.6). $C_{17}H_{28}BF_4IrO_2S_2$ (607.56): calcd. C 33.61, H 4.65, S 10.56; found C 33.71, H 4.63, S 10.60.

[Ir(cod)(4)]BF_4 (9): Colour: yellow-orange; yield: 49.3 mg, 99%. IR [KBr (cm^{-1})]: (ν_{B-F}) 1053 (s). ^1H NMR (300 MHz, refer to Figure 3 for assignments): δ = 4.91 (m, 1 H, CH *5*), 4.61 (m, 1 H, CH_a CH_a CH_a CH_a cod), 4.58 (m, 1 H, CH *6*), 4.93 (m, 1 H, CH_d cod), 4.21 (m, 1 H, CH_b cod), 4.06 (m, 1 H, CH_c cod), 3.75 (m, 1 H, CH_2 *7′*), 3.54 (m, 1 H, CH_2 *4*), 3.46 (m, 2 H, CH_2 *1,3*), 3.44 (m, 1 H, CH_2 *4′*), 3.24 (m, 2 H, CH_2 *2,2′*), 3.0 (m, 2 H, CH_2 *1,3*), 2.71 (m, CH_2 *7*), 2.40–2.19 (m, 8 H, CH_2 cod), 1.43 (s, 6 H, CH_3) ppm. $^{13}C\{^1H\}$ NMR (75 MHz): δ = 106.06 ($C(CH_3)_2$), 79.31 (CH_a cod), 78.46 (CH, *5*), 77.94 (CH_d cod), 73.84 (CH_b cod), 73.71 (CH_c cod), 72.04 (CH, *6*), 38.28 (CH_2, *7*), 34.09 (CH_2 *4*), 30.09 (CH_2 *2*), 28.57 (CH_2 *1*), 27.7 (CH_2, cod), 27.03 (CH_2 cod), 26.71 (CH_2 cod), 24.96 (CH_2 *3*), 24.62 (CH_2 cod) 22.24 (CH_3), 21.90 (CH_3) ppm. FAB$^+$: *m/z* (%) = 535 (M–BF_4). High resolution FAB$^+$: *m/z* (%) = 535.1344; $C_{18}H_{30}IrO_2S_2$ (Err [ppm/mmu] = +5.1/+2.7).

Procedure C: The corresponding ligand (**5a**,**b**, 0.12 mmol) was added to a solution of [Ir(cod)$_2$]BF_4 (40 mg, 0.08 mmol) in dichloromethane (5 mL) under nitrogen. After stirring for 30 min, the colour of the solution turned yellow-orange. Diethyl ether was added to precipitate the product, which was collected by filtration, washed with additional diethyl ether and vacuum dried.

[Ir(cod)(5a)]BF_4.CH_2Cl_2 (10a.CH_2Cl_2): Colour: yellow; yield: 29.2 mg, 48%. ^1H NMR ($CDCl_3$, 300 MHz): δ = 7.7 (m, 10 H, C_6H_5), 4.0 (m, 6 H, CH + CH cod), 2.4 (t, 2 H, CH_2, $J_{H,H}$ = 5.1 Hz), 2.28 (m, 4 H, CH_2 cod), 1.8 (m, 4 H, CH_2 cod), 1.48 (d, 6 H, CH_3, $J_{H,H}$ = 6.3 Hz) ppm. $^{13}C\{^1H\}$ NMR ($CDCl_3$, 75 MHz): δ = 133.68 (C*o*), 131.78 (C*m*), 130.38 (C*p*), 79.06 (CH cod), 78.52 (CH cod), 44.17 (CH), 38.83 (CH_2), 31.58 (CH_2 cod), 30.75 (CH_2 cod), 20.57 (CH_3) ppm. FAB$^+$: *m/z* (%) = 589 (M–BF_4). $C_{25}H_{32}BF_4IrS_2$·CH_2Cl_2 (760.63): calcd. C 41.06, H 4.51, S 8.44; found C 41.30, H 4.70, S 8.04.

[Ir(cod)(5b)]BF_4 (10b): Colour: orange; yield: 26.7 mg, 55%. ^1H NMR ($CDCl_3$, 300 MHz,): δ = 4.37 (m, 2 H, CH cod), 4.13 (m, 2 H, CH cod), 3.76 (sextuplet, 2 H, CH, $J_{H,H}$ = 5.4 Hz), 3.55 (sept, 2 H, *i*Pr CH, $J_{H,H}$ = 6.9 Hz), 2.56 (t, 2 H, CH_2, $J_{H,H}$ = 5.4 Hz), 2.3 (m, 4 H, CH cod), 2.02 (m, 2 H, CH_2 cod), 1.78 (m, 2 H, CH cod), 1.61 (d, *i*Pr CH_3, $J_{H,H}$ = 6.6 Hz), 1.54 (d, 6 H, *i*Pr CH_3, $J_{H,H}$ = 6.4 Hz) 1.53 (d, 6 H, *i*Pr CH_3, $J_{H,H}$ = 6.5 Hz) ppm. $^{13}C\{^1H\}$ NMR ($CDCl_3$, 75 MHz): δ = 78.24 (CH cod), 75.39 (CH cod), 41.53 (CH_2), 41.0 (CH), 40.06 (*i*Pr CH), 32.75 (CH_2 cod), 30.42 (CH_2 cod), 24.20 (CH_3), 23.26 (*i*Pr CH_3), 22.84 (*i*Pr CH_3) ppm. FAB$^+$: *m/z* (%) = 521 (M–BF_4). $C_{19}H_{36}BF_4IrS_2$ (607.65): calcd. C 37.56, H 5.97, S 10.55; found C 37.98, H 6.57, S 10.91.

Synthesis of [Ir(H)$_2$(cod)(dithioether)]BF_4 (dithioether = 3, 4)

General Procedure: Hydrogen was bubbled into an NMR tube containing a solution of [Ir(cod)(dithioether)]BF_4 (ditihioether = **3**, **4**)

 © 2005 Wiley-VCH Verlag GmbH & Co. KGaA, Weinheim

(0.066 mmol) in deuterated dichloromethane at –72 °C for 20 min, obtaining yellow solutions in both cases. The tube was introduced into the NMR equipment at –80 °C and spectra were acquired. The relaxation time, T_1, was determined at –70 °C, and then the temperature was increased by 10 °C intervals, recording spectra at each successive temperature, until 25 °C was reached. 2D NMR spectra were acquired at 25 °C for complex $[Ir(H)_2(cod)(\mathbf{3})]BF_4$ and at 0 °C for complex $[Ir(H)_2(cod)(\mathbf{4})]BF_4$.

$[Ir(H)_2(cod)(3)]BF_4$ (13): ^{1}H NMR (300 MHz, –70 °C, refer to Figure 3 and Figure 7 for assignments): δ = 4.85 (m, 1 H, CH_a cod), 4.64 (m, 1 H, CH_d cod), 4.50 (m, 1, CH *5*), 4.41 (m, 1 H, CH_b cod) 4.41 (m, 1 H, CH_c cod), 4.13 (m, 1 H, CH *4*), 3.77 (m, 1 H, CH_2 *3*), 3.59 (m, 1 H, CH_2 *6*), 3.28 (m, 3 H, CH_2 *6′,1, 2′*), 3.07 (m, 1 H, CH_2 *2*), 2.80 (m, 1 H, CH_2 *1′*), 2.59 (m, 1 H, CH_2 *3′*) 2.06 (m, 4 H, CH_2 cod), 1.91 (m, 4 H, CH_2 cod), 1.34 (s, 3 H, CH_3), 1.33 (s, 3 H, CH_3), –11.37 [s, 1 H, complex **13-I**, H*f*, T_1 = 0.3112 s (err = 0.008368)], –11.56 [s, 1 H, complex **13-II**, H*f*, T_1 = 0.3112 s (err = 0.009975)], –13.78 [s, 1 H, complex **13-II**, H*e*, T_1 = 0.222 s (err = 0.006233)], –13.83 [s, 1 H, complex **13-I**, H*e*, T_1 = 0.2087 s (err = 0.003677)] ppm; **13-I/13-II** = 5:3. ^{1}H NMR (CD_2Cl_2, 300 MHz, 20 °C): δ = 4.93 (m, 1 H, CH_a cod), 4.76 (m, 1 H, CH_d cod), 4.66 (m, 1, CH *5*), 4.60 (m, 1 H, CH_b cod) 4.43 (m, 1 H, CH_c cod), 4.17 (m, 1 H, CH *4*), 3.81 (m, 1 H, CH_2 *3*), 3.34 (m, 1 H, CH_2 *6*), 3.316 (m, 3 H, CH_2 *6′,1, 2′*), 3.15 (m, 1 H, CH_2 *2*), 2.91 (m, 1 H, CH_2 *1′*), 2.61 (m, 1 H, CH_2 *3′*) 2.24 (m, 4 H, CH_2 cod), 2.06 (m, 4 H, CH_2 cod), 1.39 (s, 6 H, CH_3), –11.39 (s, 1 H, complex **1**, H*f*), –11.59 (s, 1 H, complex **2**, H*f*), –13.87 (s, 1 H, complex **2**, H*e*), –13.85 (s, 1 H, complex **1**, H*e*) ppm.

$[Ir(H)_2(cod)(4)]BF_4$ (14): ^{1}H NMR (400 MHz, 0 °C, refer to Figure 3 for assignments): δ = 4.91 (m, 1 H, CH *5*), 4.6 (m, 2 H, CH_a cod + CH *6*), 4.94 (m, 1 H, CH_d cod), 4.18 (m, 1 H, CH_b cod), 4.07 (m, 1 H, CH_c cod), 3.76 (m, 1 H, CH_2 *7′*), 3.57 (m, 1 H, CH_2 *4*), 3.38 (m, 2 H, CH_2 *1,3*), 3.35 (m, 1 H, CH_2 *4′*), 3.29 (m, 2 H, CH_2 *2, 2′*), 3.03 (m, 2 H, CH_2 *1, 3*), 2.78 (m, CH_2 *7*), 2.38–1.91 (m, 8 H, CH_2 cod), 1.43, 1.41 (s, 6 H, CH_3, *0.5:1*), –12.57 [s, 1 H, complex **14-I/II**, H*f*, T_1 = 0.4089 s (err = 0.01158)], –12.72 [s, 1 H, complex **14-I/II**, H*f*, T_1 = 0.3934 s (err = 0.009862)], –12.84 [s, 1 H, complex **14-I/II**, H*e*, T_1 = 0.2825 s, (err = 0.009123)], –13.28 [s, 1 H, complex **14-I/II**, H*e*, T_1 = 0.2846 s (err = 0.007316)] ppm.

Catalysis: A standard hydrogenation experiment was performed in the following manner.[25] A solution in dichloromethane (6 mL) containing the complex $[Ir(cod)L]BF_4$ (L = dithioether or cod, 0.026 mmol) and the substrate (1.05 mmol) was introduced into the evacuated hydrogenation system which was filled up to atmospheric pressure with hydrogen. The mixture was vigorously stirred using a wrist-shaker and it was analysed directly by GC in the case of substrates **11a** and **11c**. The final mixtures resulting from the hydrogenation of acid substrates **11b** and **11d** were transformed into the esters by the following procedure: trimethylsilyldiazomethane (0.3 mL, 2 M in hexane) and MeOH (0.1 mL) were added to the final catalytic solution (0.5 mL). This mixture was stirred for 30 min at room temperature, filtered through silica and analysed by GC.

Crystal Data for Complex 10b: Suitable crystals of complexes **10b** were grown by slow diffusion of *n*-hexane into a solution of the complex in ethyl acetate and mounted on a glass fiber. The X-ray data were collected at 293.5 K with a Bruker APEX instrument (Mo-K_α radiation, λ = 0.71073 Å). The SHELXTL v. 6.1 program package was used for structure solution and refinement. An absorption correction was applied using SADABS. The structure was solved by direct methods and refined by full-matrix least-squares procedures. All non-hydrogen atoms were refined anisotropically. $C_{19}H_{36}BF_4IrS_2$, M = 607.61, Monoclinic space group $P2_1$, a = 9.2855(12), b = 12.5844(17), c = 10.0187(13) Å, β = 97.892(2)°, V = 1159.6(3) Å^3, Z = 2, D_c = 1.740 Mg/m^3, 11295 reflections measured, 4057 unique (R_{int} = 0.0492) which were used in all calculations; the final R value was 0.0331 [$F > 4\sigma(F)$] and 0.0501 (all data). The ORTEP diagram was generated using ORTEP-3.[50]

CCDC-239321 contains the supplementary crystallographic data for this paper. These data can be obtained free of charge from The Cambridge Crystallographic Data Centre via www.ccdc.cam.ac.uk/data_request/cif.

Acknowledgments

This work was financially supported by CONACyT from Mexico (Ref. 34982), and Ministerio de Educación y Cultura from Spain (PB97-0407-C05-01 and PB98-0641). L. F.-S. appreciates the fellowship of DGEP-UNAM and CONACyT.

[1] J. C. Bayón, C. Claver, A. M. Masdeu-Bultó, *Coord. Chem. Rev.* **1999**, *193–195*, 73–195.
[2] A. M. Masdeu-Bultó, M. Diéguez, E. Martin, M. Gómez, *Coord. Chem. Rev.* **2003**, *242*, 159–201.
[3] P. Barbaro, A. Currao, H. Jörg, R. Nesper, P. S. Pregosin, R. Salzmann, *Organometallics* **1996**, *15*, 1879–1888.
[4] M. Hiraoka, A. Mishikawa, T. Marimoto, K. Achiwa, *Chem. Pharm. Bull.* **1998**, *46*, 704–706.
[5] E. Hauptman, P. J. Fagan, W. Marshall, *Organometallics* **1999**, *18*, 2061–2073.
[6] O. Pámies, M. Diéguez, G. Net, A. Ruiz, C. Claver, *Organometallics* **2000**, *19*, 1488–1496.
[7] A. Albinati, P. S. Pregosin, K. Wick, *Organometallics* **1996**, *15*, 2419–2421.
[8] D. A. Evans, K. R. Campos, J. S. Tedrow, F. E. Michael, M. R. Gagné, *J. Am. Chem. Soc.* **2000**, *122*, 7905–7920.
[9] K. Boog-Wick, P. S. Pregosin, G. Trabesinger, *Organometallics* **1998**, *17,* 3254–3264.
[10] S.-L. You, X.-L. Hou, L.-X. Dai, Y.-H. Yu, W. Xia, *J. Org. Chem.* **2002**, *67*, 4684–4695.
[11] B. K. Vriesema, M. Lemaire, J. Buter, R. M. Kellog, *J. Org. Chem.* **1986**, *51*, 5169–5177.
[12] C. G. Frost, J. M. J. Williams, *Tetrahedron: Asymmetry* **1993**, *4,* 1785–1788.
[13] C. G. Frost, G. Christopher, J. M. J. Williams, *Tetrahedron Lett.* **1993**, *34*, 2015–2018.
[14] G. J. Dawson, C. G. Frost, C. J. Martin, J. M. J. Williams, S. J. Coote, *Tetrahedron Lett.* **1993**, *34,* 7793–7795.
[15] J. V. Allen, J. F. Bower, J. M. J. Williams, *Tetrahedron: Asymmetry* **1994**, *5*, 1895–1898.
[16] J. V. Allen, S. J. Coote, G. J. Dawson, C. G. Frost, C. J. Martin, J. M. J. Williams, *J. Chem. Soc. Perkin Trans. 1* **1994**, 2065–2072.
[17] H. Adams, J. C. Anderson, R. Cubbon, D. S. James, J. P. Mathias, *J. Org. Chem.* **1999**, *64*, 8256–8262.
[18] C. G. Frost, J. M. J. Williams, *Synlett* **1994**, *7*, 551–552.
[19] O. Pàmies, G. Net, A. Ruiz, C. Claver, S. Woodward, *Tetrahedron: Asymmetry* **2000**, *11*, 871–877.
[20] S. M. W. Bennett, S. M. Brown, A. Cunningham, M. R. Dennis, J. P. Muxworthy, M. A. Oakley, S. Woodward, *Tetrahedron* **2000**, *56*, 2847–2855.
[21] C. Börner, M. R. Dennis, E. Sinn, S. Woodward, *Eur. J. Org. Chem.* **2001**, 2435–2446.
[22] C. Börner, W. A. König, S. Woodward, *Tetrahedron Lett.* **2001**, *42*, 327–329.
[23] D. A. Evans, F. E. Michael, J. S. Tedrow, K. R. Campos, *J. Am. Chem. Soc.* **2003**, *125*, 3534–3543.
[24] S. Jansat, M. Gómez, G. Muller, M. Diéguez, A. Aghmiz, C. Claver, A. M. Masdeu-Bultó, L. Flores-Santos, E. Martin,

M. A. Maestro, J. Mahía, *Tetrahedron: Asymmetry* **2001**, *12*, 1469–1474.
[25] M. Diéguez, A. Orejón, A. M. Masdeu-Bultó, R. Echarri, S. Castillón, C. Claver, A. Ruiz, *J. Chem. Soc. Dalton Trans.* **1997**, 4611–4618.
[26] M. Diéguez, A. Ruiz, C. Claver, M. M. Pereira, A. M. d′A. Rocha Gonsalves, *J. Chem. Soc. Dalton Trans.* **1998**, 3517–3522.
[27] N. Ruiz, A. Aaliti, J. Forniés-Cámer, A. Ruiz, C. Claver, C. J. Cardin, D. Fabbri, S. Gladiali, *J. Organomet. Chem.* **1997**, *545*, 79–87.
[28] O. Pàmies, M. Diéguez, G. Net, A. Ruiz, C. Claver, *J. Chem. Soc. Dalton Trans.* **1999**, 3439–3444.
[29] D. Enders, R. Peters, R. Lochtman, G. Raabe, J. Runsink, J. W. Bats, *Eur. J. Org. Chem.* **2000**, 3399–3426.
[30] W. Li, J. P. Waldkirch, X. Zhang, *J. Org. Chem.* **2002**, *67*, 7618–7623.
[31] N. Khiar, C. S. Araujo, E. Alvarez, I. Fernández, *Tetrahedron Lett.* **2003**, *44*, 3401–3404.
[32] R. Siedlecka, E. Wojaczyńska, J. Skarżewski, *Tetrahedron: Asymmetry* **2004**, *15*, 1437–1444.
[33] L. Flores-Santos, E. Martin, M. Diéguez, A. M. Masdeu-Bultó, C. Claver, *Tetrahedron: Asymmetry* **2001**, *12*, 3029–3034.
[34] F. Fernández, M. Gómez, S. Jansat, G. Muller, L. Flores-Santos, A. Acosta-Ramirez, P. García-Reynaldos, E. Martin, A. Aghmiz, M. Giménez-Pedrós, M. Diéguez, C. Claver, A. M. Masdeu-Bultó, M. A. Maestro, *Organometallics*, in preparation.
[35] Calculated by gNMR software (P. H. M. Budzelaar, Cherwell Scientific Publishing, **1995**–**1997**).
[36] E. W. Abel, S. K. Bhargava, K. G. Orrell in *Progress in Inorganic Chemistry* (Ed.: S. J. Lippard), John Wiley & Sons, **1984**, vol. 32, p. 1.
[37] K. G. Orrell, *Coord. Chem. Rev.* **1989**, *96*, 1–48.
[38] S. O. Grim, P. B. Kettler, J. S. Merola, *Inorg. Chim. Acta* **1991**, *185*, 57–61.
[39] M. Abbas, P. A. Chaloner, C. Claver, P. Hitchcock, A. M. Masdeu, A. Ruiz, T. Saballs, *J. Organomet. Chem.* **1991**, *403*, 229.
[40] H. A. Jenkins, S. J. Loeb, *Organometallics* **1994**, *13*, 1840–1850.
[41] A. J. Blake, M. A. Halcrow, M. Schröder, *J. Chem. Soc. Chem. Commun.* **1991**, 253–256.
[42] F. A. Cotton, P. Lahuerta, J. Latorre, M. Sanaú, I. Solana, W. Schwotzer, *Inorg. Chem.* **1988**, *27*, 2131–2135.
[43] E. Fernández, A. Ruiz, S. Castillón, C. Claver, J. F. Piniella, A. Alvarez-Larena, G. Germain, *J. Chem. Soc. Dalton Trans.* **1995**, 2137–2142.
[44] G. J. Kubas, *Acc. Chem. Res.* **1988**, *21*, 120–128.
[45] D. G. Hamilton, R. H. Crabtree, *J. Am. Chem. Soc.* **1988**, *110*, 4126–4133.
[46] P. J. Desrosiers, L. Cai, Z. Lin, R. Richards, J. Halpern, *J. Am. Chem. Soc.* **1991**, *113*, 4173–4184.
[47] R. H. Crabtree, *Angew. Chem. Int. Ed. Engl.* **1993**, *32*, 789–805.
[48] D. M. Heinekey, A. Liegeois, M. van Room, *J. Am. Chem. Soc.* **1994**, *116*, 8388–8389.
[49] M. Green, T. A. Kuc, S. H. Taylor, *J. Chem. Soc. A* **1971**, 2334–2337.
[50] *ORTEP-3 for Windows*: L. J. Farrugia, *J. Appl. Crystallogr.* **1997**, *30*, 565–565.

Received: October 5, 2004

 © 2005 Wiley-VCH Verlag GmbH & Co. KGaA, Weinheim

Orbital Splitting and Pairing Energy in Open-Shell Organometallics: A Study of Two Families of 16-Electron Complexes [Cp_2M] (M = Cr, Mo, W) and [$CpM(PH_3)$] (M = Co, Rh, Ir)

Rinaldo Poli*[a] and Ivo Cacelli[b]

Keywords: Density functional calculations / Metallocenes / Open-shell organometallics / Pairing energy / Singlet–triplet gap

The singlet–triplet gap for two families of 16-electron organometallic complexes has been examined in detail by DFT calculations at the B3LYP level with polarized basis sets on both metal and ligands. For the first family, the group 6 metallocenes (Cp_2M with Cp = η^5-C_5H_5 and M = Cr, Mo, W), the singlet–triplet gap ($E_S - E_T$) is always positive and decreases continuously on going from Cr to Mo to W. For the family of group 9 $CpM(PH_3)$, on the other hand, there is a decrease on going from Co to Rh, followed by a slight increase on going further to Ir. These trends have been analyzed in qualitative monoelectronic terms as a function of the competition between the pairing energy and the orbital gap. While the pairing energy decreases as expected in the order 3d >> 4d > 5d, the orbital gap varies in a different way for the two families and, though quantitatively less important, is responsible for the different trends. It is argued that changes in orbital gap are system-dependent for open-shell organometallic systems, thus it is not possible to establish a universal trend of singlet–triplet gaps for a homologous series of complexes with a group of transition metals.
(© Wiley-VCH Verlag GmbH & Co. KGaA, 69451 Weinheim, Germany, 2005)

Introduction

Reaction selectivities and catalytic activities can be tuned by the relative stabilization of the reaction intermediates and transition states. The most typical situation encountered in organometallic chemistry involves reaction intermediates that are less electronically saturated than the reagents and products; for instance a saturated, 18-electron compound may generate a 16-electron intermediate by a ligand dissociation, or reductive elimination, or migratory insertion, etc. Although most organometallic reactions involve reagents, products and intermediates having a diamagnetic ground state, it is now well appreciated that compounds with fewer than 18-electrons and a paramagnetic ground state are also involved in all sorts of stoichiometric and catalytic transformations.[1,2] Even when the reagents and the products are saturated, diamagnetic systems, it is possible that a reaction takes place via more than one potential energy surface, through open-shell intermediates in a different spin state.[3–7]

Three distinct factors are recognized to play a role in the energetic stabilization of open-shell compounds, relative to more saturated ones. Steric pressure, enforced by encumbering ligands, destabilizes higher coordination numbers and therefore stabilizes less saturated intermediates in a relative sense. Ligands possessing inactive electron pairs for the saturated systems (e.g. π-symmetry lone pairs), may stabilize the less saturated intermediates by becoming engaged in bonding with the metal orbital associated with the open coordination site. Finally, a third factor is present when the system undergoes a changes of spin state on going from the reagent to the intermediate. The binding energy lost during the formation of the open coordination site can be partially recovered by unpairing two electrons. In the qualitative, single-electron framework, the promotion of one electron to a higher-energy orbital may be more than compensated by the lower electron–electron coulombic repulsion (J) and by a gain in exchange energy (K). The combination of these factors is known by the general term "pairing energy".

The concept of pairing energy has a solid place in the chemistry of Werner-type coordination compounds to understand the preference of a low- vs. high-spin configuration for octahedral or tetrahedral complexes, as a function of the orbital splitting between the t_{2g} and e_g orbitals (Δ_O) or between the e and t_2 orbitals (Δ_T), respectively. In particular, it is widely appreciated that, whereas this separation increases down a series of transition metals (e.g. $3d \leqslant 4d \leqslant 5d$ for elements within the same group), the pairing energy correspondingly decreases.[8] Therefore, both factors concur for the stabilization of the low-spin state relative to the high-spin one on going from the lighter to the heavier element.

[a] Laboratoire de Chimie de Coordination, UPR CNRS 8241, 205 Route de Narbonne, 31077 Toulouse Cedex, France
Fax: +33-561-553-003
E-mail: poli@lcc-toulouse.fr
[b] Dipartimento di Chimica e Chimica Industriale, Università di Pisa,
Via Risorgimento 35, 56126 Pisa, Italy

However, the same trend does not appear to be valid in general for open-shell organometallic compounds. Few families of ML_n complexes within the same group of transition metals have been studied in terms of high spin–low spin energy gap at the same level of theory. The trend of the Werner complexes seems reproduced for the organometallic group 8 $M(CO)_4$ systems, the energy difference ($E_S - E_T$, in kcal mol^{-1}) being 1.7 for Fe, –13.1 for Ru, and –16.2 for Os at a nonlocal DFT level.[9] On the other hand, a nonmonotonous variation of the same quantity results for the group 9 CpM(CO) series at various computational levels, for instance 11.2 for Co, –5.9 for Rh, and 0.3 for Ir using a CI calculation combined with a couple pair functional to correct the lack of size consistency.[10] It is generally known that the pairing energy decreases on going from the lighter to the heavier element, because of the cloud expansion (nephelauxetic) effect on going from lower (e.g. 3d) to higher (e.g. 5d) valence shells. It is also known that this effect is particularly strong on going from the 3d to the 4d element.[8] This trend is common to the Werner-type octahedral and tetrahedral complexes mentioned above. On the other hand, it is not clear how the orbital splitting should change along a homologous series of open-shell organometallic compounds.

There is an important difference between Werner-type complexes and open-shell organometallic compounds. For the Werner-type systems, the higher-energy orbitals whose occupation increases in the higher spin state have metal-ligand antibonding character (strong for the octahedral e_g orbitals, weaker for the tetrahedral t_2 orbitals), while those losing electrons in the same process are nonbonding (or π-bonding in the presence of π-acceptor ligands). Thus, the well-known increase of metal–ligand binding energy on going from the lighter to the heavier metal[11,12] results in an energy increase for the higher-energy orbitals and possibly in an energy decrease for the lower-energy ones, both effects contributing to raise the orbital gap. On the other hand, both the high energy and the low energy orbitals involved in the spin transition for open-shell organometallic compounds generally have similar characteristics with respect to metal-ligand bonding (essentially σ nonbonding; possibly π bonding), thus the variation of this orbital gap along a group of transition metals cannot be easily predicted a priori.

For this reason, we set out to study two representative families of homologous 16-electron complexes, the group 6 metallocenes Cp_2M (M = Cr; Mo, W) and the Group 9 "one-legged piano stools" $CpM(PH_3)$ (M = Co, Rh, Ir), that are models of the more widely studied PMe_3 complexes. A variety of calculations at different levels of theory[13–19] have already shown that these complexes, or at least some of them, adopt a spin-triplet ground state configuration. In this contribution, we examine for the first time the details of how orbital gap and pairing energy vary along the two homologous series, and compare these findings with the computed singlet–triplet gaps. It will be shown that the trends of the singlet–triplet energy difference are qualitatively reproduced by the approximate one-electron formula, which expresses the energy difference as a combination of orbital energy gap and a pairing energy term. Thus, the qualitative thinking that is often applied to Werner-type coordination compounds can be successfully extended to open-shell organometallics. However, although the pairing energies trends are as expected, the trends of orbital gaps are found to be family-dependent. Therefore, a universal trend for the singlet–triplet gap upon descending a group of transition metals cannot be established.

Results and Discussion

DFT Calculations: Electronic and Molecular Structures

Our investigation makes use of the DFT approach, using the B3LYP functional and polarized basis sets, which has proven effective for the computation of several other cases of spin-state dichotomy in coordination and organometallic chemistry.[7,10,20,21] The optimized geometries for all systems are shown in Figure 1 for the group 6 metallocenes and Figure 2 for the group 9 $CpM(PH_3)$ systems.

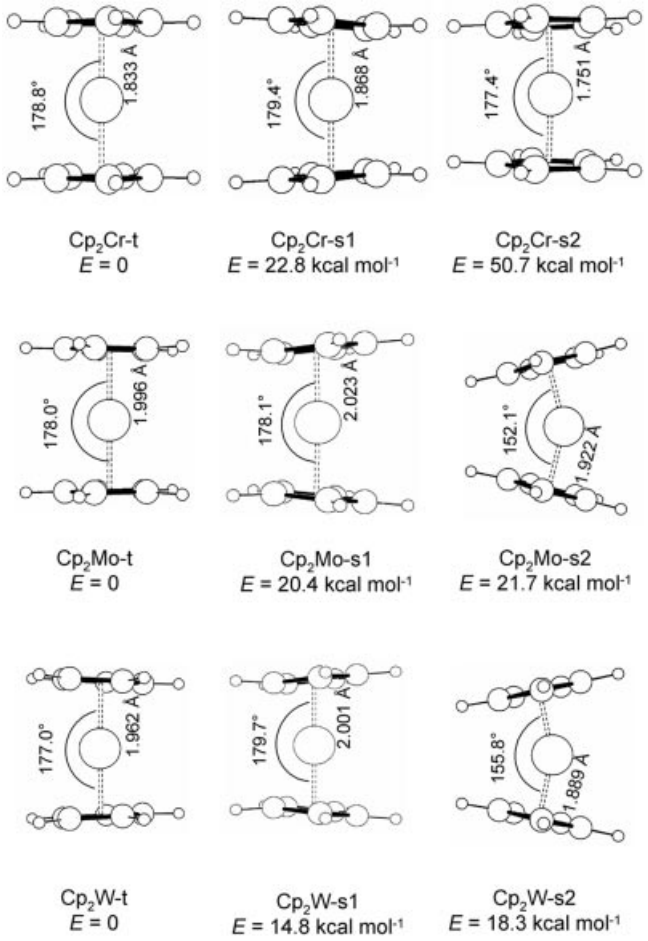

Figure 1. Views of the optimized geometries, relative energies, and selected bonding parameters for the Cp_2M systems (M = Cr, Mo, W; s = singlet, t = triplet). The distance of the metal from the Cp ring is calculated from the ring centroid (CNT).

 © 2005 Wiley-VCH Verlag GmbH & Co. KGaA, Weinheim

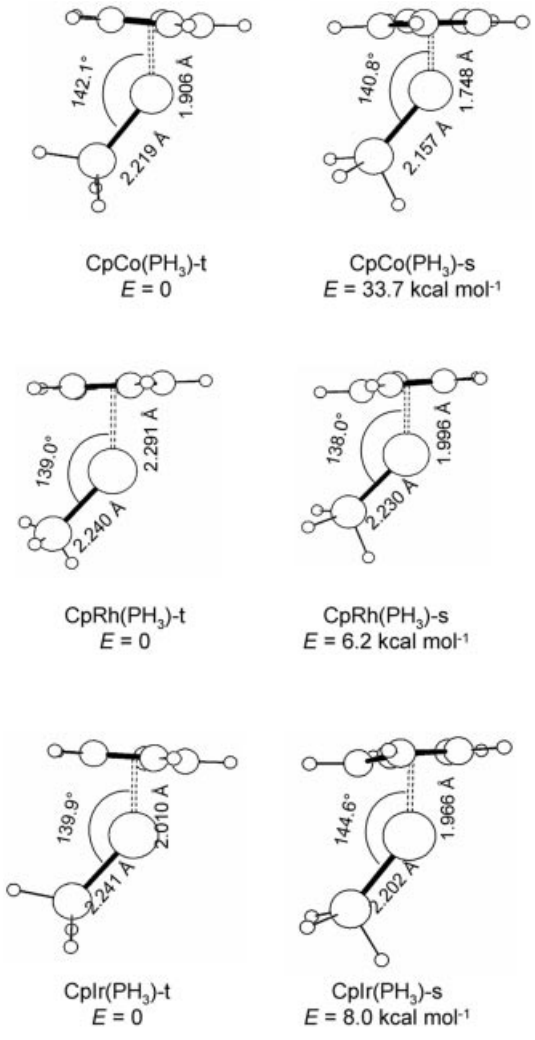

Figure 2. Views of the optimized geometries, relative energies, and selected bonding parameters for the $CpM(PH_3)$ systems (M = Co, Rh, Ir; s = singlet, t = triplet). The distance of the metal from the Cp ring is calculated from the ring centroid (CNT).

The energies obtained at the chosen level of theory favor a triplet ground state for all systems. From the experimental point of view, chromocene is a stable triplet compound[22] whereas molybdenocene and tungstenocene cannot be isolated. However, a magnetic circular dichroism study demonstrates their triplet ground state.[23,24] The calculated Cr–Cp (center) distance of 1.833 Å for triplet Cp_2Cr is in relatively good agreement with the experimentally determined one of 1.791(4) Å.[25] There is no experimental information on any 16-electron $CpM(PR_3)$ system, to the best of our knowledge.

All metallocene molecules yielded two different stable minima (termed s1 and s2 in Figure 1) that differ by their orbital occupation, as shown in Figure 3. It is noteworthy that, with only one exception for chromocene,[21] all previously published computational studies on the group 6 metallocenes report only one energy minimum for both the singlet and the triplet state.[15,26] The recent report by Reiher et al.,[21] which probed the effect of the exact exchange admixture parameter c_3 on the singlet–triplet gap for various first row metallocenes, mentions the location of a second singlet minimum for chromocene at low c_3 values. However, neither the energy difference between these two minima, nor the optimized geometry of either minimum, were reported.

It is curious that the two chromocene minima s1 and s2 were obtained starting with the same input geometry and guess orbitals, at the same computational level, and using the closely related Gaussian98 and Gaussian03 programs, respectively. With particular care in the choice of alternative input geometries, or by artificially altering the list of filled and empty guess orbitals, both energy minima were eventually obtained with both program packages. The molybdenocene and tungstenocene molecules only yielded the s2 minima initially. They provided the lower-energy s1 minima only by artificially altering the list of filled and empty guess orbitals, and, in particular, by substituting the LUMO for the HOMO in the guess density of the self-consistent procedure. This example serves to illustrate that one has to be very careful about checking all considered states in close-to-degeneracy situations.

The origin of the double-singlet minimum can be related to the observed geometrical distortions as follows. In an ideal symmetric top geometry (D_{5x} with $x = h$ or d or nothing, depending on the dihedral angle), the metallocene electronic structure is well known.[27] The metal frontier orbitals (z^2, xy and $x^2 - y^2$) are partitioned into a singly degenerate (z^2, a_1-type) orbital and a doubly degenerate (xy, $x^2 - y^2$, e-type) set, their complete symmetry label depending on the point group (e.g. a_1' or a_{1g} for z^2 in D_{5h} and D_{5d}, respectively). However, a molecular distortion that lowers the symmetry to C_{2v} splits the e-set into an a_1 and a b_2 orbital.[28] This symmetry lowering allows orbital mixing with a consequent energy lowering, a phenomenon known as the pseudo-Jahn–Teller effect (or second-order Jahn–Teller effect).[29] Different levels of mixing lead to different orbital energies and consequently to different geometries and orbital occupations. The s1 minimum corresponds to the configuration $(x^2 - y^2)^2(z^2)^2$, whereas the s2 minimum has the configuration $(x^2 - y^2)^2(xy)^2$ (we maintain the same orientation of the principal axes as in the higher-symmetry molecule). The same double-minimum phenomenon has been described previously for several other 16-electron organometallic complexes such as a variety of d^6 ML_5 complexes,[30,31] $[(arene)Nb(CO)_3]^+$,[32] and $[CpMo(L)_2X]$ (L = CO, PH_3; X = H, CH_3, Cl, Br, I, etc.).[33,34] For the latter two systems in particular, Hasanayn was able to show that the second-order Jahn–Teller distortion generates two different symmetry states for both the singlet and the triplet electronic configurations. In principle, more than one triplet minimum could also exist for the metallocenes. However, only a single minimum with the same relative orbital ordering as the s1 singlet could be located, yielding the $(x^2 - y^2)^2(z^2)^1(xy)^1$ configuration ($^3B_2$). Numerous attempts, starting with differently populated guess geometries, either linear or bent, led to the same optimized minimum.

 © 2005 Wiley-VCH Verlag GmbH & Co. KGaA, Weinheim

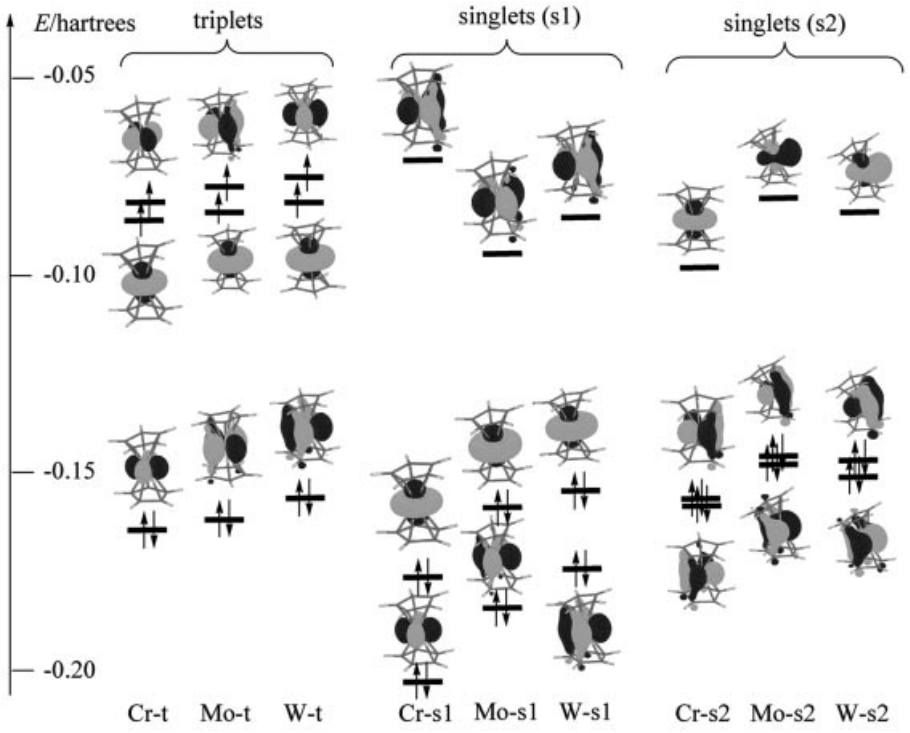

Figure 3. Electronic structure (frontier orbital region) of the singlet and triplet metallocenes. The orbital energies shown for the triplet states were obtained at the ROB3LYP level.

The metal orbital mixing, resulting from the geometrical distortion, is only very slight for all triplets and also for the s1 singlets. The Mo and W metallocenes of s2 type show a significant participation of the p orbital that points along the symmetry C_2 axis (a_1 type) in the LUMO (see Figure 3). There is no significant mixing of this kind, on the other hand, for the chromocene s2 minimum. This orbital mixing is reflected in the molecular geometry, which is severely bent (CNT-M-CNT << 180°) for the molybdenocene and tungstenocene s2 minima (see Figure 1).

On the other hand, all triplets and s1 singlets, as well as the chromocene s2 minimum, are very close to linear. The different orbital occupancy reflects very strongly on the Cp–M distance: the double occupation of the z^2 orbital, which has a slight Cp-M σ* character, considerably lengthens the M–CNT distance in Cp_2M-s1 relative to Cp_2M-s2. This distance is, in fact, even longer in Cp_2M-s1 than in Cp_2M-t.

A second interesting effect is that the Cp rings are differently tilted from the ideal arrangement, with equivalent M–C distances, in which the metal lies on the C_5 symmetry axis of the Cp moiety. The s2 singlets do not display any significant tilting, the angle between the M–CNT vector and the Cp least-squares plane being 90.0° for all three metals. On the other hand, the distortion is significant for the triplets (85.4°, 85.9°, and 85.9° for Cr, Mo, and W, respectively) and even more so for the s1 singlets (76.4°, 84.3°, and 81.1° for Cr, Mo, and W, respectively). This effect can be attributed to δ-type M–Cp back-bonding interactions, as previously highlighted by Hoffmann et al.[35] These interactions can be established by the $x^2 - y^2$ and xy orbitals. When both orbitals are filled, as in the s2 singlets, the δ back-bonding has cylindrical symmetry and no major distortion occurs. This cylindrical symmetry is broken by the molecular distortion to C_{2v} symmetry for the molybdenocene and tungstenocene, resulting in a slight ring tilting, but both back-bonding interactions are still present, as can be appreciated from Figure 3. The triplets and the s1 singlets, on the other hand, have a reduced population of the xy orbitals, thus the prevalence of the back-bonding interaction from the $x^2 - y^2$ orbital causes the ring tilting. It is noteworthy that neither Cp_2Cr-s1 nor Cp_2Cr-s2 correspond to the optimized geometry obtained by the previous calculation reported by Green and Jardine,[26] which is bent like those of the Mo and W analogs, with an inter-ring angle of 26.8°. Our s1 and s2 minima have inter-ring angles of 10.1° and 2.7°, respectively.

It should be noted that the higher-energy s2 singlets for molybdenocene and tungstenocene are better pre-organized than the corresponding s1 singlets for the interaction with molecules of L or X–Y type, leading to L addition or X–Y oxidative addition to generate saturated $Cp_2M(L)$ or $Cp_2M(X)(Y)$ products. The metallocene is bent as in the final products and the LUMO is geometrically well disposed to receive electron density from the L or X–Y donating orbital. Thus, a reaction coordinate leading from the free Cp_2M triplet molecule to the above singlet products should involve crossing of the reagent triplet surface with the higher-energy s2 singlet surface, rather than with the lower-energy one. A similar situation has been described for the addition of CO and N_2 to triplet $[CpMo(PH_3)_2Cl]$,[33] which is isoelectronic with the metallocenes studied here.

 © 2005 Wiley-VCH Verlag GmbH & Co. KGaA, Weinheim

The energy of the frontier orbitals for the Cp_2M triplet systems increases regularly on going from the 3d to the 5d metal (see Figure 3), following the analogous trend of the atomic orbitals which contribute almost totally to their composition. On the other hand, the orbital energies for the singlet systems show a different and more complex trend, which is probably related to the different degree of orbital mixing and geometrical distortions discussed above. The chromocene s1 system is anomalous for having a higher-energy LUMO than the heavier congeners. Within the s2 series, on the other hand, tungstenocene unexpectedly shows lower energies for all frontier orbitals relative to molybdenocene.

For each member of the group 9 $CpM(PH_3)$ series, we located only one singlet and one triplet minimum. We did not exhaustively explore the possibility of other minima in any of the two spin-states. Since the geometry of these molecules is much farther from a pseudo-symmetry situation than for the metallocenes, less complications of this kind are anticipated. The optimized geometries (Figure 2) are very close to those obtained for the same systems at other levels of theory. All metal–ligand bonds shorten slightly on going from the triplet to the singlet, as expected.

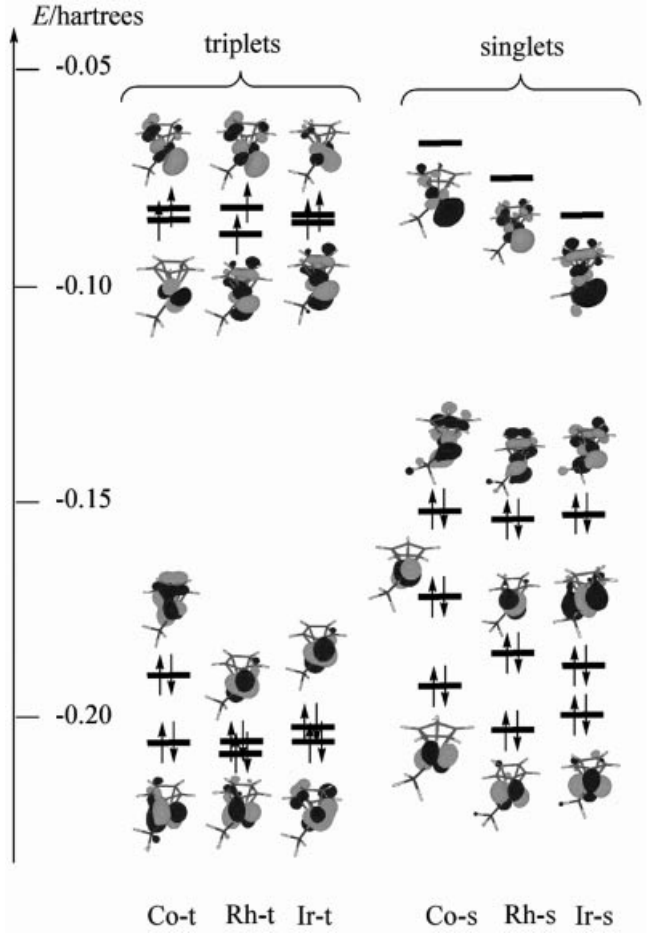

Figure 4. Electronic structure (frontier orbital region) of the singlet and triplet $CpM(PH_3)$ systems (M = Co, Rh, Ir). The orbital energies shown for the triplet states were obtained at the ROB3LYP level.

The main structural changes observed upon changing spin state have been amply discussed previously.[16] The electronic and molecular structures of the $CpM(PH_3)$ systems do not deserve any further discussion. The orbital energies, shapes, and occupations in both spin states are shown in Figure 4. The electronic structure remains unchanged along the series for both triplets and singlets. The orbital analysis agrees with that already reported by Ziegler et al.[16] for $CpRh(PH_3)$, although in this paper we find a somewhat larger mixing between the metal and the Cp orbitals. Notice, however, that in that work a reverse order was found for the singlet–triplet energy gap: the singlet was found to be the most stable state. The rationalization of the orbital energies is found in the interaction of the metal orbitals with different types of Cp orbitals, with minor effects of the σ- and σ*-orbitals of PH_3. For instance, the HOMO in the singlet state shows a small antibonding metal-Cp character, indicating a destabilization due to the interaction with the occupied π-orbitals of Cp. On the contrary, metal-Cp bonding character, due to interaction with the empty π*-orbitals, is observed for the low-lying, metal-based molecular orbitals. The most notable change in the series is the stabilization of the LUMO for the singlet system on going from Co to Ir, whereas the HOMO remains approximately at the same energy. Consequently, the HOMO–LUMO gap decreases.

DFT Calculations: Singlet–Triplet Gaps

As far as we are aware, experimental determinations of the singlet–triplet gap are unavailable for any of the compounds examined here. As anticipated in the introduction, there is no clear monotonous trend of singlet–triplet gap on going from the 3d through the 4d to the 5d system within each family. The gap is larger for the 3d system, relative to the heavier congeners, within each family of complexes. On going from the 4d to the 5d system, on the other hand, the calculations predict a slight decrease for the metallocene series and a slight increase for the $CpM(PH_3)$ series. In previous computational work on the same systems, the singlet state was found to be higher than the triplet for all Cp_2M systems (M = Cr, 34.8; Mo, 16.4; W, 17.9 kcal mol^{-1}).[26] Our own previous calculations on Cp_2M (M = Mo, W) gave a lower-energy triplet by 24.1 and 19.1 kcal mol^{-1} at the B3LYP/LANL2DZ level, or by 23.0 and 19.6 kcal mol^{-1} at the same level used here, except that polarization functions on the metal atoms were not used (those calculations dealt only with the singlet structure that corresponds to the s2 minimum reported herein).[15] For the $CpM(PH_3)$ series, the Co system was found as a ground-state triplet, 33.0 kcal mol^{-1} more stable than the singlet at the B3LYP/LANL2DZ level.[13] For the Rh and Ir systems, the triplet was reported to be more stable by 8.17 and 20.1 kcal mol^{-1} at the MP2/LANL1DZ level,[18] and by 13.2 and 16.9 kcal mol^{-1} at the B3LYP/LANL2DZ level,[19] respectively. However, another report on the Ir system gives a relative stability for the triplet of 6.4 or 8.4 kcal mol^{-1} by using B3LYP and the LANL2DZ or TZV basis sets.[14] In all re-

 © 2005 Wiley-VCH Verlag GmbH & Co. KGaA, Weinheim

ported cases, except one,[26] the stability of the triplet state relative to the singlet on going from the 4d to the 5d metal *decreases* for the Cp_2M system and *increases* for the $CpM(PH_3)$ system.

Analysis of the Orbital Gaps and Pairing-Energy Factors

Using the qualitative concepts of orbital splitting and pairing energy, the singlet–triplet gap for the neutral system can be approximately expressed as in Equation (1), where the relevant orbital energies, ε, and the two-electron coulombic (J) and exchange (K) integrals appear.

$$\Delta E_{ST} = E_S - E_T = (J_{11} - J_{12} + K_{12}) - (\varepsilon_2 - \varepsilon_1) \quad (1)$$

In this simple expression the pairing energy ($J_{11} - J_{12} + K_{12}$) is defined as the change of electrostatic energy in going from a $\varphi_1\alpha\varphi_2\alpha$ (triplet) to a $\varphi_1\alpha\varphi_1\beta$ (singlet) configuration irrespective of the one-electron potential arising from the nuclei and from the other electrons (core electrons). The latter is accounted for by the orbital energy gap ($\varepsilon_1 - \varepsilon_2$), which includes also the kinetic energy of the orbitals entering Equation (1). This equation is, of course, a rather drastic approximation because both the orbital relaxation and the electronic correlation between the two active electrons, which may be of crucial importance for low singlet–triplet energy gaps, are completely neglected. In addition, the core electrons are considered frozen, i.e. their distribution is assumed to be independent of the configuration of the two active electrons. Nevertheless, this simple picture has a great appeal, and in several cases can furnish a fashioned model to rationalize a number of results, the best known application in coordination chemistry being the rationalization and prediction of high-spin vs. low-spin magnetic properties for octahedral complexes of d^4–d^7 metal ions.[8] Assuming $\varepsilon_1 < \varepsilon_2$, it is apparent that high orbital energy gaps favor the singlet state, i.e. the one-electron terms stabilize the singlet state. Conversely, the pairing energy expression contains the $J_{11} - J_{12}$ term, which is generally positive and accounts for the larger electron–electron repulsion energy of the singlet, as well as the K_{12} exchange term, which further stabilizes the triplet state; greater values for J and K integrals therefore lead to a stronger preference for the higher spin state.

Once the model has been well characterized, a second important problem arises. How can the active orbitals to be used in Equation (1) be determined? One possibility was originally suggested and implemented by Hall et al.[36] in order to analyze nephelauxetic effects in the series of compounds $[Ti(dmpe)_2X_2]$ (X = Cl, OPh),[36] and later applied by us to a family of [CpCr(NO)XY] compounds (X, Y = Cl, alkyl, amido).[37] In this approach, the active orbitals are the LUMO and LUMO+1 of a simple HF calculation with $n - 2$ electrons (dication in our case). As pointed out by the authors,[36] this choice provides an unbiased determination of the active orbitals, which proved to predict qualitatively correct singlet–triplet splittings. One other possibility that we suggest here is based on the DFT approach which, in the Kohn–Sham (KS) scheme, furnishes a set of orbitals and a set of orbital energies which can be recognized to have a physical meaning. For instance, in Slater's transition state method,[38] the basic Equation (2) shows that the change in the total energy, E, due to an infinitesimal increase of charge in the KS orbital φ_i, corresponds to its eigenvalue ε_i. This equation gives a real physical meaning to the KS orbitals and recognizes the orbital energies of the occupied orbitals as true ionization potentials.[39–41] The extension to unoccupied orbitals is trivial and HOMO and LUMO KS orbital energies are currently used to estimate a number of molecular properties. Therefore, the B3LYP KS eigenvalues and the corresponding orbitals obtained for the dication can be inserted in Equation (1) in order to look for some rationale for the energy splittings. This choice, while preserving the simplicity of such an expression, has the clear advantage, with respect to the previous choice based on HF results, of using orbitals that represent a more accurate density function and are thus expected to give more reliable estimates of the quantities entering Equation (1). As a matter of fact, we found that the KS orbitals are generally a bit more contracted than the HF ones and lead to slightly higher values of the Coulomb and exchange integrals. This finding can be rationalized as the effect of the electronic correlation, which optimizes the inter-electronic repulsion energy and allows the density to better accumulate in the wells of the nuclear potential.

$$\frac{\delta E}{\delta n_i} = \varepsilon_i \quad (2)$$

In view of the approximations contained in Equation (1), only general and clear trends may be physically meaningful; conversely, some caution must be used in order to draw conclusions based on strongly method-dependent quantities. For instance, the comparison between the results for the different systems can be meaningful only if the active orbitals in the dication systems (LUMO and LUMO+1) have the same nature, i.e. show similar lobes along each series. In addition, these orbitals should be pure metal orbitals, in order for the resulting J and K values to have a stronger significance. The only cases where we found this set of conditions to be satisfied, for the Cp_2M systems, are for the B3LYP calculations of the dication using either the s1 optimized structures or the optimized triplet structures of the neutral complexes. This is probably because the three geometries follow a regular trend in these cases. The orbital order found in the dications is the same as that observed for the neutral triplets and s1 singlets (Figure 3), with z^2 below xy. For the $CpMPH_3$ systems, the best trend was observed for the singlet optimized geometries and these were then used for the dication calculations. The results are shown in Table 1. The results obtained with the triplet geometries for the metallocene series (not reported) are nearly identical to those obtained with the s1 geometries.

Despite the approximations just described, it is possible to analyze trends of orbital gap and pairing energy along both series of isoelectronic complexes and draw some reasonable conclusions. As stated in the introduction, conventional wisdom tells us that the J values should decrease on

 © 2005 Wiley-VCH Verlag GmbH & Co. KGaA, Weinheim

Table 1. Orbital energies and relevant J and K integrals (in kcal mol^{-1}) for the Cp_2M (M = Cr, Mo, W) and $CpM(PH_3)$ complexes. The reported quantities arise from B3LYP calculation of the 2+ ion at the geometries of the neutral complex.

	Cp_2M[a]			$CpM(PH_3)$[b]		
M	Cr	Mo	W	Co	Rh	Ir
ε_2	–318.5	–328.3	–321.2	–316.3	–303.7	–299.0
ε_1	–330.6	–329.9	–326.1	–333.1	–330.6	–323.7
J_{11}	435.5	289.7	264.1	275.4	208.3	194.2
J_{12}	383.3	271.1	252.9	249.9	188.6	176.8
K_{12}	16.8	17.1	18.8	9.6	9.2	10.0
$(\varepsilon_2 - \varepsilon_1)$	12.1	1.5	4.9	16.7	26.9	24.7
PE[c]	69.0	35.7	30.0	35.1	29.0	27.5
ΔE_{ST}[d]	56.9	34.2	25.1	18.4	2.1	2.8

[a] Using the singlet (s1) optimized geometries. [b] Using the singlet optimized geometries. [c] PE = Pairing energy = $J_{11} - J_{12} + K_{12}$. [d] Estimated singlet–triplet energy gap from Equation (1).

going from the 3d to the 4d element, and then again (though by a smaller extent) on going from the 4d to the 5d element. This is indeed what our calculations reveal (see Table 1). It can also be seen that, as expected, J_{11} is greater than J_{12} for all systems and that the J values are much greater than the K values.

It is apparent from the data of Table 1 that the simple Equation (1) is able to reproduce the correct energy trends for both systems: the triplet is always the most stable state (see Figures 1 and 2). For the metallocene systems, the ΔE_{ST} values from Table 1 must be compared with the gap between the triplet state and the s1 state, because that is the state having the same orbital ordering as the triplet state, used for the ΔE_{ST} calculation by Equation (1).

For the Cp_2M series, ΔE_{ST} is dominated by the pairing energy whose decrease is mainly due to the difference between J_{11} and J_{12}, since K_{12} is almost constant. Notice that the orbital gap is of the same order as those of the RO-B3LYP triplet calculations on the neutral molecule (3–4 kcal mol^{-1}) and is much smaller than the HOMO–LUMO gap of the singlet s1, which involves the same orbitals. This can be expected because the two involved orbitals have the same occupancy in the triplet and in the dication (1 and 0, respectively). Thus, unlike the neutral singlets, their near degeneracy is preserved.

For the $CpM(PH_3)$ systems, the PE decreases whereas the orbital energy gap increases on going from 3d to 4d and changes little from 4d to 5d. It is somewhat surprising that the trend of this gap is in contrast with the HOMO–LUMO gap of the neutral singlet calculation, which shows a monotonic decrease. However, the different meaning of the orbital energies in the dication (empty orbitals include interactions with $n - 2$ core orbitals only) and of the neutral singlet system (empty and occupied orbitals feel the effect of n and $n - 1$ electrons, respectively, for Self Interaction free methods) do not allow a significant comparison. Differently from the Cp_2M systems, the orbital energy gaps are greater than the (HOMO – 1)–HOMO gaps of the neutral triplet state: this is possibly related to the geometry used for the dication (neutral singlet) which can remove the near degeneracy. Calculations of the dications at the neutral triplet geometry indeed show generally lower energy gaps. All in all we do not see any systematic trend in the orbitals leading to a rationale for the variation of the energy splitting along the $CpM(PH_3)$ series.

The different trend of the PE and orbital energy gap for $CpM(PH_3)$ generates a nonmonotonic behavior of ΔE_{ST} along the series. Whereas for Co the PE dominates and favors the triplet state, for Rh and Ir complexes the two terms practically cancel each other out, leading to near degenerate triplet and single states. This feature agrees with the DFT calculations of the neutral systems, whose relative energies are reported in Figure 2: 33.7, 6.2, and 8.0 kcal mol^{-1} for Co, Rh, and Ir, respectively.

Conclusions

This contribution reports the first analysis of the electronic structure of families of open-shell organometallic complexes in terms of the variations of the pairing energy and the orbital gap. On one side, there is always a monotonous decrease of the pairing energy on going from the 3d to the 4d and further to the 5d orbitals, the biggest change occurring between 3d and 4d. On the other side, the variations of the orbital gap are smaller upon descending the group and may occur, in principle, in either direction (increase or decrease). As a result, a very different trend of the low-spin–high-spin energy gap, relative to the Werner-type octahedral and tetrahedral complexes, may result on going from the 3d to the 5d element within a group of transition metals. In some cases, like the group 9 $CpM(PH_3)$ complexes examined here, a nonmonotonous change may result. While the pairing-energy effect seems to dominate the situation on going from the 3d to the 4d complex, such that the lighter complex seems to always favor the higher-spin ground state to a greater extent, the low-spin–high-spin energy gap may decrease or increase on going from the 4d to the 5d metal, depending on the system under consideration. A universal model allowing us to predict this trend for any structure is not available at the moment, thus one must examine this problem on a case-by-case basis.

Computational Details

All geometry optimizations were performed using the B3LYP three-parameter hybrid density functional method of Becke,[42] as implemented in the Gaussian03 suite of programs.[43] However, many calculations were also carried out with the previous version (Gaussian98) of the program. With one exception (see Results section), both programs gave the same optimized geometry and energy, within insignificant fractions of 1 kcal mol^{-1}. All calculations were performed with no symmetry restrictions and all optimized geometries were characterized as local minima of the potential energy surface (PES) by verifying that all second derivatives of the energy were positive. The unrestricted formulation was used for the triplet states, whereas singlet states were obtained within the restricted formulation. For the purpose of computing and visualizing the shape of the Kohn–Sham orbitals, the calculations for all triplet states were also carried out by the Restricted Open (RO)

 © 2005 Wiley-VCH Verlag GmbH & Co. KGaA, Weinheim

method at the fixed unrestricted optimized geometry (these energies were generally 1–2 kcal mol^{-1} higher than the unrestricted ones). All reported relative energies are relative to the unrestricted computations. Numerical integrations were performed using the "ultrafine" grid of Gaussian98 and Gaussian03, consisting of 99 radial shells and 590 angular points per shell, and the default values were chosen both for the self consistency and for the geometry optimization convergence criteria. The basis sets used for the geometry optimizations are the standard 6-31G** for C, H, and P atoms, and the standard LANL2DZ basis set, which includes the Hay and Wadt effective core potentials (ECP),[44] for the metal atoms. To the latter, however, was added a single *f*-type polarization function (α = 0.8) in order to obtain a balanced basis set and to improve the angular flexibility of the metal functions. In the model calculations for the study of the trends in the metal series a newly coded program (SPINETTA) was used to read the results of the DFT calculations, to sort the relevant orbitals, and to compute the one- and two-electron necessary integrals.

Acknowledgments

R. P. thanks CINES (Montpellier) and CICT (Project CALMIP, Toulouse) for granting free CPU time, and Dr. Odile Eisenstein, whose question at the end of a lecture inspired the present study. We are grateful to the reviewers for helpful comments.

[1] R. Poli, *Chem. Rev.* **1996**, *96*, 2135–2204.
[2] R. Poli, *J. Organomet. Chem.* **2004**, *689*, 4291–4304.
[3] S. Shaik, D. Danovich, A. Fiedler, D. Schröder, H. Schwarz, *Helv. Chim. Acta* **1995**, *78*, 1393–1407.
[4] D. Schröder, S. Shaik, H. Schwarz, *Acc. Chem. Res.* **2000**, *33*, 139–145.
[5] H. Schwarz, *Int. J. Mass Spectrom.* **2004**, *237*, 75–105.
[6] J. N. Harvey, R. Poli, K. M. Smith, *Coord. Chem. Rev.* **2003**, *238–239*, 347–361.
[7] R. Poli, J. N. Harvey, *Chem. Soc. Rev.* **2003**, *32*, 1–8.
[8] J. E. Huheey, E. A. Keiter, R. L. Keiter, *Inorganic Chemistry. Principles of Structure and Reactivity*, 4th ed., Harper & Row, New York, **1993**.
[9] J. Li, G. Schreckenbach, T. Ziegler, *J. Am. Chem. Soc.* **1995**, *117*, 486–494.
[10] P. E. M. Siegbahn, *J. Am. Chem. Soc.* **1996**, *118*, 1487–1496.
[11] J. A. Connor, *Topics Curr. Chem.* **1971**, *71*, 71–110.
[12] J. A. Martinho Simões, J. L. Beauchamp, *Chem. Rev.* **1990**, *90*, 629–688.
[13] R. Poli, K. M. Smith, *Eur. J. Inorg. Chem.* **1999**, 877–880.
[14] K. M. Smith, R. Poli, J. N. Harvey, *Chem. Eur. J.* **2001**, *7*, 1679–1690.
[15] J. C. Green, J. N. Harvey, R. Poli, *J. Chem. Soc., Dalton Trans.* **2002**, 1861–1866.
[16] T. Ziegler, V. Tschinke, L. Fan, A. D. Becke, *J. Am. Chem. Soc.* **1989**, *111*, 9177–9185.
[17] R. Jiménez-Cataño, M. B. Hall, *Organometallics* **1996**, *15*, 1889–1897.
[18] M.-D. Su, S.-Y. Chu, *J. Phys. Chem. A* **1997**, *101*, 6798–6806.
[19] M.-D. Su, S.-Y. Chu, *Chem. Eur. J.* **1999**, *5*, 198–207.
[20] J. Harvey, M. Aschi, *Faraday Discuss. Chem. Soc.* **2003**, *124*, 129–143.
[21] O. Salomon, M. Reiher, B. A. Hess, *J. Chem. Phys.* **2002**, *117*, 4729–4737.
[22] H. P. Fritz, K.-E. Schwarzhans, *J. Organomet. Chem.* **1964**, *1*, 208–211.
[23] P. A. Cox, P. Grebenik, R. N. Perutz, M. D. Robinson, R. Grinter, D. R. Stern, *Inorg. Chem.* **1983**, *22*, 3614–3620.
[24] P. Grebenik, R. Grinter, R. N. Perutz, *Chem. Soc. Rev.* **1988**, *17*, 453–490.
[25] K. R. Flower, P. B. Hitchcock, *J. Organomet. Chem.* **1996**, *507*, 275–277.
[26] J. C. Green, C. N. Jardine, *J. Chem. Soc., Dalton Trans.* **1999**, 3767–3770.
[27] T. A. Albright, J. K. Burdett, M. H. Whangbo, *Orbital Interactions in Chemistry*, J. Wiley & Sons, New York, **1985**.
[28] Although all calculations were carried out in the C_1 point group, the optimized geometries essentially maintain the higher C_{2v} symmetry throughout the optimization.
[29] I. B. Bersuker, *Chem. Rev.* **2001**, *101*, 1067–1114.
[30] I. El-Idrissi, O. Eisenstein, Y. Jean, *New J. Chem.* **1990**, *14*, 671–677.
[31] J.-F. Riehl, Y. Jean, O. Eisenstein, M. Pélissier, *Organometallics* **1992**, *11*, 729–737.
[32] F. Abu-Hasanayn, P. H. Y. Cheong, M. Oliff, *Angew. Chem. Int. Ed.* **2002**, *41*, 2120–2122.
[33] V. R. Jensen, R. Poli, *J. Phys. Chem. A* **2003**, *107*, 1424–1432.
[34] F. Hasanayn, M. Z. Markarian, R. Al-Rifai, *Inorg. Chem.* **2004**, *43*, 3691–3696.
[35] P. Kubácek, R. Hoffmann, Z. Havlas, *Organometallics* **1982**, *1*, 180–188.
[36] C. Q. Simpson II, M. B. Hall, M. F. Guest, *J. Am. Chem. Soc.* **1991**, *113*, 2898–2903.
[37] P. Legzdins, W. S. Mcneil, K. M. Smith, R. Poli, *Organometallics* **1998**, *17*, 615–622.
[38] J. C. Slater, *Adv. Quantum Chem.* **1972**, *6*, 1–47.
[39] D. P. Chong, O. V. Gritsenko, E. J. Baerends, *J. Chem. Phys.* **2002**, *116*, 1760–1772.
[40] J. F. Janak, *Phys. Rev. B* **1978**, *18*, 7165–7168.
[41] J. P. Perdew, R. G. Parr, M. Levy, J. L. Balduz Jr., *Phys. Rev. Lett.* **1982**, *49*, 1691–1694.
[42] A. D. Becke, *J. Chem. Phys.* **1993**, *98*, 5648–5652.
[43] M. J. Frisch, G. W. Trucks, H. B. Schlegel, G. E. Scuseria, M. A. Robb, J. R. Cheeseman, J. Montgomery, J. A., T. Vreven, K. N. Kudin, J. C. Burant, J. M. Millam, S. S. Iyengar, J. Tomasi, V. Barone, B. Mennucci, M. Cossi, G. Scalmani, N. Rega, G. A. Petersson, H. Nakatsuji, M. Hada, M. Ehara, K. Toyota, R. Fukuda, J. Hasegawa, M. Ishida, T. Nakajima, Y. Honda, O. Kitao, H. Nakai, M. Klene, X. Li, J. E. Knox, H. P. Hratchian, J. B. Cross, C. Adamo, J. Jaramillo, R. Gomperts, R. E. Stratmann, O. Yazyev, A. J. Austin, R. Cammi, C. Pomelli, J. W. Ochterski, P. Y. Ayala, K. Morokuma, G. A. Voth, P. Salvador, J. J. Dannenberg, V. G. Zakrzewski, S. Dapprich, A. D. Daniels, M. C. Strain, O. Farkas, D. K. Malick, A. D. Rabuck, K. Raghavachari, J. B. Foresman, J. V. Ortiz, Q. Cui, A. G. Baboul, S. Clifford, J. Cioslowski, B. B. Stefanov, G. Liu, A. Liashenko, P. Piskorz, I. Komaromi, R. L. Martin, D. J. Fox, T. Keith, M. A. Al-Laham, C. Y. Peng, A. Nanayakkara, M. Challacombe, P. M. W. Gill, B. Johnson, W. Chen, M. W. Wong, C. Gonzalez, J. A. Pople, *Gaussian 03, Revision B.04*, Gaussian, Inc., Pittsburgh PA, **2003**.
[44] P. J. Hay, W. R. Wadt, *J. Chem. Phys.* **1985**, *82*, 270–283.

Received: October 06, 2004

 © 2005 Wiley-VCH Verlag GmbH & Co. KGaA, Weinheim

Addition of Enolisable Ketones to (dpp-bian)Mg(THF)$_3$ [dpp-bian = 1,2-Bis{(2,6-diisopropylphenyl)imino}acenaphthene]

Igor L. Fedushkin,*[a] Alexandra A. Skatova,[a] Georgii K. Fukin,[a] Markus Hummert,[b] and Herbert Schumann*[b]

Dedicated to Prof. Dr. Alexei N. Egorochkin on the occasion of his 70th birthday

Keywords: Enolisation / Ketones / Magnesium / N ligands

The enolates [(dpp-bian)(H)]Mg[OC(=CHPh)CH$_2$Ph](THF)$_2$ (**6**), [(dpp-bian)(H)]Mg[OC(=CPh$_2$)CH$_3$](THF)$_2$ (**7**) and [(dpp-bian)(H)]Mg(camphor)(py)$_2$ (**8**) were prepared by treating (dpp-bian)Mg(THF)$_3$ (**1**) with equimolar amounts of dibenzyl ketone, 1,1-diphenylacetone and camphor, respectively. Single-crystal X-ray structure analyses showed these enolates to be five-coordinate, trigonal bipyramidal magnesium complexes with terminal, nonbridging enolate ligands. In solutions of **6** and **7** the proton, which in the solid-state is attached to only one of the two nitrogen atoms of the dpp-bian ligand, is delocalised between both nitrogen atoms.

(© Wiley-VCH Verlag GmbH & Co. KGaA, 69451 Weinheim, Germany, 2005)

Introduction

Besides fundamental chemical knowledge, the chemistry of metal complexes prepares the way for applied material science, bioinorganic and synthetic organic chemistry. Traditionally, metal complexes have been widely used in organic synthesis[1] and, so far, this area of research has not lost its topical interest. Nowadays, it is difficult to find a complex organic molecule, the synthesis of which does not involve transition metal mediated key steps.[2] The electronic differences between transition and non-transition metal atoms cause the differences in the reactivity of their corresponding organic complexes. In general, the main group metals hold quite distinct oxidation states in their complexes, thus preventing oxidative addition and reductive elimination processes which play a very important role in transition metal chemistry. The application of organometallic compounds of the alkali, alkaline earth and group 13 metals in organic synthesis is primarily based on their ability to transfer organic groups, whereas transition metal complexes are mainly used in transformation reactions of various organic molecules including catalytic processes.

A short time ago, we became interested in the preparation of main group metal complexes which would be able to compete with the reactivity modes of transition metal complexes. The idea was to design a complex in which the central main group metal atom with all its advantages such as Lewis acidity, vacant coordination sites and ability to form thermodynamically stable but reactive metal-to-carbon bonds, is coordinated by a ligand which would adopt certain features of transition metals especially their oxidative and reductive power and their ability to add protons, Lewis acids and Lewis bases. Ligands which meet these requirements to a high degree are the 1,2-bis(arylimino)-acenaphthenes. These ligands possess (a) a conformationally rigid, chelating diimine fragment, (b) lone pairs of electrons at the nitrogen atoms capable of coordinating to metals or capturing protons, and (c) a conjugated π system acting as an electron tank.

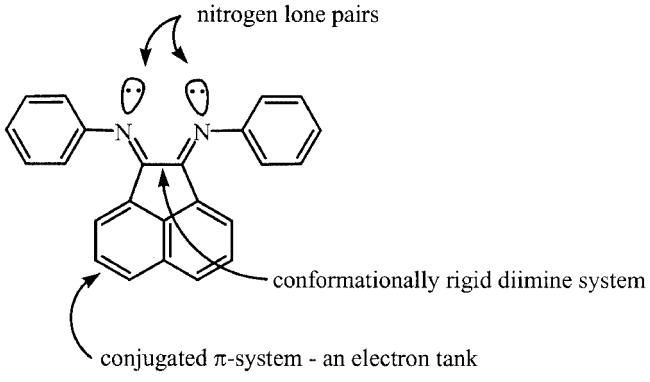

[a] G. A. Razuvaev Institute of Organometallic Chemistry of Russian Academy of Sciences,
Tropinina 49, 603950 Nizhny Novgorod GSP-445, Russia
Fax: +7-8312-127-497
E-mail: igorfed@imoc.sinn.ru
[b] Institut für Chemie der Technischen Universität Berlin,
Strasse des 17. Juni 135, 10623 Berlin, Germany
Fax: +49-30-3142-2168
E-mail: schumann@chem.tu-berlin.de
Supporting information for this article is available at http://www.eurjic.org or from the author.

 © 2005 Wiley-VCH Verlag GmbH & Co. KGaA, Weinheim **DOI: 10.1002/ejic.200400948**

During the last decade, 1,2-bis(arylimino)acenaphthens have been used in transition metal chemistry as ancillary ligands. The corresponding nickel and palladium complexes show high catalytic activity in a number of important organic reactions including the polymerisation of olefins.[3] Very recently, we reported several alkali,[4a,4b] alkaline earth[4c–4e] and germanium(II) complexes[4f,4g] with different charged 1,2-bis[(2,6-diisopropylphenyl)imino]acenaphthene (dpp-bian) anions as ligands. Following our initial idea that dpp-bian complexes of the main group metals might show unique reactivity, we began to study the reactions of (dpp-bian)Mg(THF)$_3$ (**1**), a complex which is easy to prepare from activated magnesium and dpp-bian in THF[4c] with organic substrates. We were able to demonstrate that **1** reduces diphenyl ketone with simultaneous oxidation of the dianionic dpp-bian ligand to a radical-anionic ligand, thus affording the pinacolate complex [(dpp-bian)$^{\bullet-}$Mg(THF)]$_2$-[μ-$O_2C_2Ph_4$] (**2**).[5a] On the other hand, the reaction of **1** with 9(10*H*)-anthracenone causes deprotonation of the respective phenolic tautomer yielding the 9-anthracenolato complex [(dpp-bian)$^{\bullet-}$Mg($OC_{14}H_9$)$(THF)_2$] (**3**).[5a]

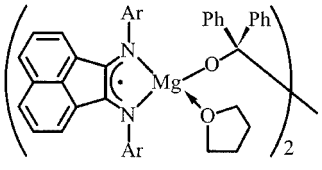

2

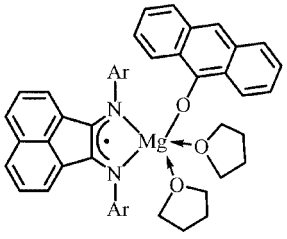

3

Owing to the Lewis basicity of **1**, it also adds phenylacetylene to give the phenylethynyl derivative [dpp-bian(H)]-Mg(C≡CPh)$(THF)_2$ (**4**) which in turn reacts with diphenyl ketone with insertion into the magnesium carbon bond, elimination of the *N*-bonded hydrogen and oxidation of the dianionic dpp-bian ligand to the radical anion affording the carbonilate (dpp-bian)$^{\bullet-}$Mg[OC(Ph_2)CCPh](THF) (**5**).[5b]

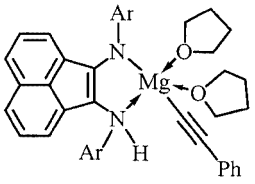

4

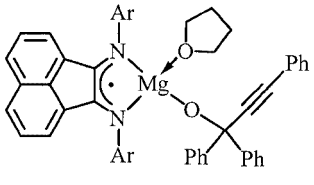

5

Recently we observed the unprecedented elimination of isopropyl radicals from (dpp-bian)$^{\bullet-}$(MgPr-*i*)(Et_2O) accompanied by the reduction of the radical anionic dpp-bian ligand to the dianion.[5c]

From the short survey of the reactivity of **1** given above the following two important conclusions can be drawn: (1) in all the reactions the dpp-bian ligand remains coordinated to the metal and (2) the reactions occur not only at the metal but also at the ligand.

Continuing our studies on the reactivity of **1** towards organic substrates, we report in this paper the reactions of **1** with aliphatic ketones containing C–H bonds in α-position to the carbonyl group.

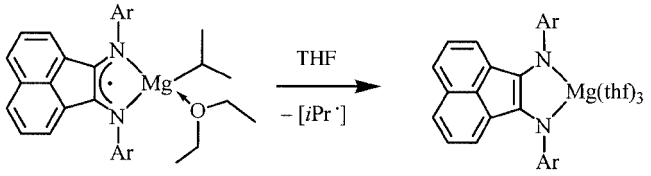

1

Results and Discussion

Reactions of Enolisable Ketones with (dpp-bian)Mg(THF)$_3$ (1)

Complex **1**, prepared by treating activated magnesium metal with dpp-bian in THF,[4c] was used in situ for the reactions with ketones. Addition of one equiv. of acetone, butan-2-one, or pentan-3-one to THF solutions of **1** caused a quick colour change from deep green to deep blue. Unfortunately, we did not succeed in isolating these products since they are highly soluble in THF and aromatic solvents and too little soluble in Et_2O and hexane. Attempts to isolate the products from THF/hexane or THF/Et_2O resulted in their decomposition into dpp-bian$(H)_2$ and colourless, insoluble solids. However, since a similar change in colour from green to blue was observed in the reaction of **1** with phenylacetylene yielding **4**, it can be suggested that the reactions proceed in a comparable way by protonation of one of the two nitrogen atoms of the dpp-bian ligand and attachment of the respective enolate anion to magnesium. Fortunately, the reactions of **1** with equimolar amounts of dibenzyl ketone, 1,1-diphenylacetone and camphor in THF allowed the successful isolation of the enolates [(dpp-bian)-(H)]Mg[OC(=CHPh)CH_2Ph]$(THF)_2$ (**6**), [(dpp-bian)(H)]-Mg[OC(=CPh_2)CH_3]$(THF)_2$ (**7**) and [(dpp-bian)(H)]-Mg(camphor)$(py)_2$ (**8**), respectively (Scheme 1). In the case of the reaction of **1** with dibenzyl ketone and 1,1-diphenylacetone, the colour of the reaction mixture immediately changed from green to deep blue, whereas in the reaction with camphor the respective change in colour was not to observed until the mixture was heated to 60 °C for some minutes. Using two equiv. of the ketone caused a violet colour which might indicate double protonation of the ligand forming the diimine (dpp-bian)H_2.

Compounds **6** and **7** were crystallised from diethyl ether and isolated in yields of 72 and 79%, respectively, as deep blue, almost black crystals. The crude camphor derivative was treated first with pyridine and then crystallised from benzene affording **8** in 43% yield. In the solid-state as well as in solution **6**–**8** are extremely sensitive towards moisture and air but thermally quite stable. They decompose (**6**) or melt (**7**, **8**) above 115 °C and are stable in THF at reflux for several minutes. The single-crystal X-ray structure determinations indicated the formation of magnesium enolates each supported by a dpp-bian amido/amino ligand. The ^1H

 © 2005 Wiley-VCH Verlag GmbH & Co. KGaA, Weinheim

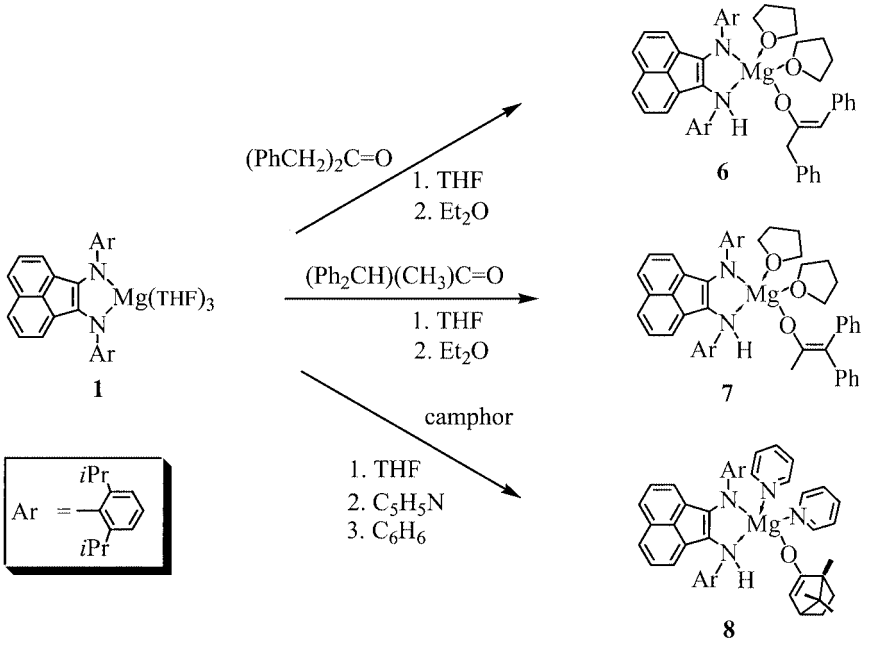

Scheme 1.

NMR spectra of **6** and **7** discussed below indicate delocalisation of the amino hydrogen in solution between both nitrogen atoms.

Henderson and co-workers reported the formation of magnesium enolates by amine elimination from enolisable ketones and magnesium amides such as iPr$_2$NMgBr, (iPr$_2$N)$_2$Mg, and [(Me$_3$Si)$_2$N]$_2$Mg.[6] Since both nitrogen atoms of the dpp-bian ligand in **1** and **6**–**8** are part of a conformationally rigid chelating system, an amine elimination cannot take place. Despite the protonation of one of the nitrogen atoms of the dpp-bian system in **6**, **7** and **8**, the system still acts as a chelating ligand.

Molecular Structures of 6, 7 and 8

The molecular structures of **6**, **7** and **8** are depicted in Figures 1, 2 and 3, respectively. The crystallographic, collection and structure refinement data are listed in Table 1, selected bond lengths and bond angles are collected in Table 2.

The magnesium atoms in the molecules of the complexes **6**, **7** and **8** are five-coordinate with slightly distorted trigonal bipyramidal geometries. In **6** and **7** the axial positions of the bipyramids are occupied by the atoms N(2) and O(3) and in **8** by the atoms N(2) and N(4). The angles between the axially positioned atoms are 177.32(13)° in **6**, 176.09(7)° in **7**, and 172.22(8)° in **8**. The significant differences in the lengths of the two Mg–N bonds in **6**, **7** and **8** [**6**: Mg–N(1), 2.066(3) Å, Mg–N(2), 2.369(4) Å; **7**: Mg–N(1), 2.051(2) Å, Mg–N(2), 2.410(2) Å; **8**: Mg–N(1), 2.055(2) Å, Mg–N(2), 2.436(2) Å] reflect the different strengths of the metal coordination to the amido [N(1)] and the amino functions [N(2)]. The long Mg–N(2)(amino) bonds are always to the N atoms in the axial positions. The differences between the

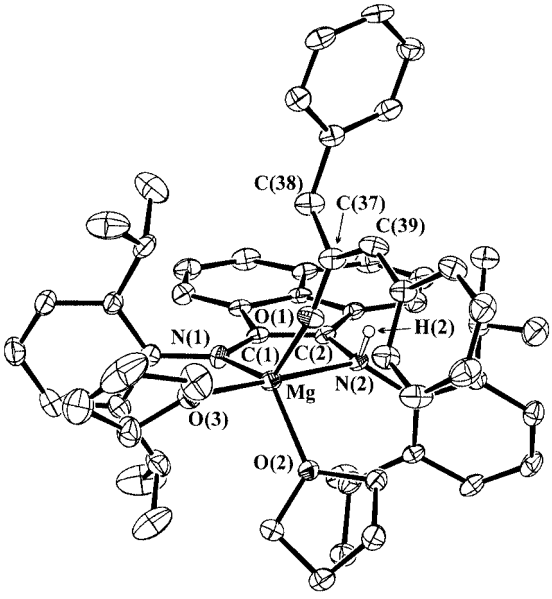

Figure 1. ORTEP drawing of **6** with thermal ellipsoids drawn at the 30% probability level. Hydrogen atoms with the exception of H(2) are omitted for clarity.

N(amido)–metal and the N(amino)–metal distances correspond well with those found for **4** (2.355 and 2.045 Å), obtained by addition of phenylacetylene to **1**.[5b] The short amido Mg–N(1) bonds in **6**, **7** and **8** are close to the Mg–N bond lengths in the starting complex **1** (2.045 and 2.105 Å).[4c] In **6** as well as in **7**, the Mg–O(2) bond of the equatorially positioned THF molecule is shorter than the Mg–O(3) bond to the THF molecule situated in the axial position [**6**: Mg–O(2) 2.075(3), Mg–O(3) 2.114(3) Å; **7**: Mg–O(2) 2.042(2), Mg–O(3) 2.137(2) Å]. The difference in the lengths of the Mg–N coordination bonds of the two equato-

 © 2005 Wiley-VCH Verlag GmbH & Co. KGaA, Weinheim

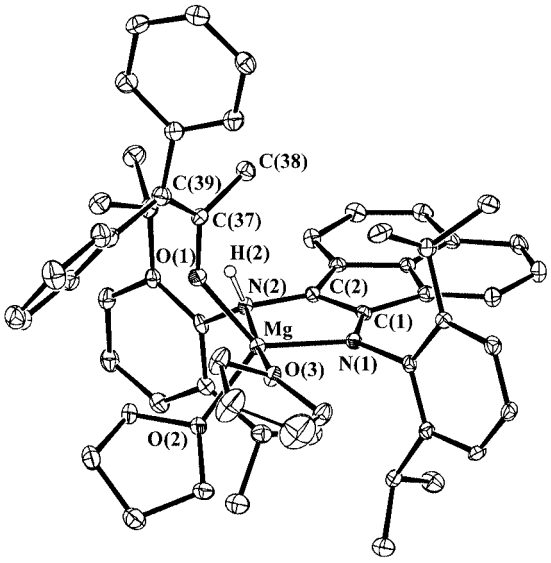

Figure 2. ORTEP drawing of **7** with thermal ellipsoids drawn at the 30% probability level. Hydrogen atoms with the exception of H(2) are omitted for clarity.

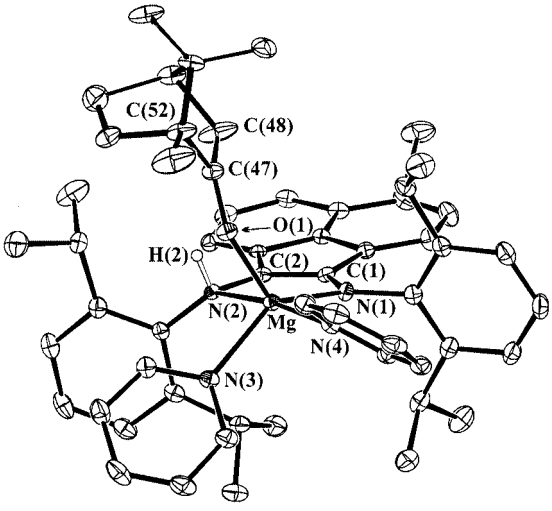

Figure 3. ORTEP drawing of **8** with thermal ellipsoids drawn at the 30% probability level. Hydrogen atoms with the exception of H(2) are omitted for clarity.

rially and axially positioned pyridine molecules in **8** is far less pronounced [Mg–N(3) 2.151(2) and Mg–N(4) 2.195(2) Å]. In **6**, **7** and **8** the enolate ligand and the amine hydrogens H(2) are located on the same side of the plane formed by the metallacycle Mg–N(1)–C(1)–C(2)–N(2). The torsion angles H(2)–N(2)–Mg–O(1) are 7.0° (**6**), 17.2° (**7**) and 8.1° (**8**), respectively. Whereas the enolate group in the four magnesium enolates studied crystallographically up to now – [{*t*Bu(CH$_2$)CO}MgBr{(Me$_2$N)$_3$PO}]$_2$,[6a] [Mes(CH$_2$)CO]$_8$Mg$_4${OC(Mes)(Me)}$_2$,[6c] [{*t*Bu(CH$_3$CH)CO}MgBr(Et$_2$O)]$_2$[7a] and [{CH(CMeN-C$_6$H$_3$-2,6-*i*Pr$_2$)$_2$}Mg(μ-OC$_6$H$_9$)]$_2$[7b] – is acting as a μ$_2$-bridging ligand, the enolate group in **6**, **7** and **8** is a terminal group. This is clearly due to steric crowding imposed by the 2,6-diisopropylphenyl substituents on the nitrogen atoms of the ligand. The terminal Mg–O(1) bonds are 1.902(3), 1.921(2) and 1.890(2) Å for **6**, **7**, and **8**, respectively, and are somewhat shorter than the Mg–O(μ$_2$-enolate) bonds in two of the above mentioned magnesium enolates [{*t*Bu(CH$_2$)CO}MgBr{(Me$_2$N)$_3$PO}]$_2$ [1.956(4) and 1.981(4) Å][6a] and [{CH(CMeNC$_6$H$_3$-2,6-*i*Pr$_2$)$_2$}Mg(μ-OC$_6$H$_9$)]$_2$ [1.970(2) and 1.994(2) Å].[7b] The carbon-carbon double bonds formed as a consequence of the enolisation of the ketones are longer in **6** and **7** [C(37)–C(39): 1.368(6) (**6**), 1.373(3) Å (**7**)] than in **8** [C(47)–C(48) 1.333(4) Å] probably due to π conjugation of those double bonds in **6** and **7** with the phenyl rings of the dpp-bian unit. The conjugation is evident from the small dihedral angle of only 0.6° between the plane formed by the phenyl ring attached to C(39) and the plane formed by O(1)–C(37)–C(39).

^{1}H NMR Spectroscopic Studies on Solutions of 6 and 7

As indicated by the X-ray structural analyses, the molecules of **6**, **7** and **8** exhibit asymmetric amido/amino structures in the solid-state. Proceeding on the assumption that this general molecular structure will be maintained in solution, the ^{1}H NMR spectra of the compounds should reveal nonequivalence for all aromatic ring protons as well as for the four methine protons and the eight CH$_3$ groups of the isopropyl substituents at the phenyl groups of the dpp-bian ligand. It was expected, however, that in analogy to the ^{1}H NMR spectroscopic results obtained for the closely related compound [(dpp-bian)(H)]Mg(C≡CPh)(THF)$_2$ (**4**), the complexes **6** and **7** would adopt more symmetric structures in solution with the amino hydrogen not being fixed at one dpp-bian nitrogen atom but being delocalised between both nitrogen atoms of the ligand. Such a fast proton transfer (on the NMR time scale) between both nitrogen atoms results in a general structure with a plane of symmetry bisecting the N–Mg–N angle thus dividing the dpp-bian ligand into two equal parts. The ^{1}H NMR spectra of **6** and **7** are depicted in the supporting information.

According to our expectations, the ^{1}H NMR spectrum of **6** in [D$_8$]toluene revealed two septets for the methine protons centred at δ = 3.97 and 3.32 ppm. The low field signal overlaps with the THF signal at δ = 3.39 ppm but can be clearly assigned by means of the ^{1}H ^{1}H COSY spectrum. Each septet has cross peaks with two pairs of doublets in the range of δ = 1.4 to 1.0 ppm which can be assigned to the methyl protons and appear together with signals of THF and Et$_2$O. The signal of the delocalised N–H proton appears as a singlet at δ = 6.10 ppm and overlaps partially with a doublet signal of the aromatic protons at δ = 6.15 ppm. The protons of the CH and CH$_2$ groups of the enolate ligand give rise to singlets at δ = 5.31 and 3.53 ppm, respectively.

In agreement with the spectroscopic results obtained for **6**, the ^{1}H NMR spectrum of **7** in [D$_8$]THF shows two septets for the isopropyl methine protons at δ = 3.79 and 3.67 ppm, four doublets for the protons of the isopropyl methyl groups at δ = 1.30, 1.22, 0.98 and 0.92 ppm, a singlet

 © 2005 Wiley-VCH Verlag GmbH & Co. KGaA, Weinheim

for the protons of the CH_3 group of the enolate ligand at δ = 1.99 ppm and a singlet separated from other resonances for the delocalised NH proton at δ = 6.42 ppm. The ^1H NMR spectra of **6** and **7** indicate the presence of small amounts of (dpp-bian)H_2 probably due to partial hydrolysis of the compounds during sample preparation.

Conclusions

We have been able to demonstrate that the recently prepared magnesium complex (dpp-bian)Mg(THF)$_3$ containing the dianionic 1,2-bis[(2,6-diisopropylphenyl)imino]acenaphthene ligand can serve as an enolising reagent towards aliphatic ketones such as dibenzyl ketone, 1,1-diphenylacetone or camphor. In contrast to the reactions of magnesium amides with enolisable ketones which proceed with amine elimination,[6] the above reactions proceed by addition of the enols with formation of magnesium enolate bonds and simultaneous protonation of one of the acenaphthene nitrogen atoms of the stabilising ligand. These reactions are the first examples of such a reaction pathway in transition as well as non-transition metal chemistry. The magnesium enolates [dpp-bian(H)]MgOR formed from dibenzyl ketone and 1,1-diphenylacetone are labile in solution. The proton attached only to one nitrogen atom of the dpp-bian ligand in the solid-state is delocalised between the two nitrogen atoms of the ligand in solution. We intend to investigate the potential of the compounds reported here as reagents for aldol reactions.

Experimental Section

General Remarks: All manipulations were carried out under vacuum using Schlenk ampoules. The solvents THF and diethyl ether were dried by distillation from sodium benzophenone. The deuterated solvents [D_8]THF (Aldrich) and [D_8]toluene (Aldrich) used for the NMR measurements were dried with sodium benzophenone at ambient temperature and, just prior to use, condensed under vacuum into the NMR tubes already containing the respective compound, the spectrum of which could then be recorded. Melting points were measured in sealed capillaries. 1,2-Bis[(2,6-diisopropylphenyl)imino]acenaphthene was prepared according to the published procedure.[8] The IR spectra were recorded on a Specord M80 spectrometer and the ^1H NMR spectra on a Bruker DPX-200 NMR spectrometer.

(dpp-bian)Mg(THF)$_3$ (1): Magnesium shavings (2.4 g, 100 mmol) and CH_2I_2 (0.8 g, 2.98 mmol) were placed in a Schlenk-like ampoule (ca. 100 mL volume) equipped with a Teflon stopcock. After evacuation of the ampoule (at 10^{-1} Torr for ca. 1 min), THF (40 mL) was added by condensation and the mixture was stirred for 2 h. The $MgI_2(THF)_n$ formed was decanted together with the

Table 1. Crystal data and structure refinement details for **6**, **7** and **8**.

	6	**7**	**8**
Empirical formula	$C_{61}H_{75}MgN_2O_{3.5}$	$C_{63}H_{80}MgN_2O_4$	$C_{59}H_{69}MgN_4O$
Formula mass	916.58	953.60	874.4
Temperature [K]	173(2)	100(2)	100(2)
Wavelength [Å]	0.71073	0.71073	0.71073
Crystal system	monoclinic	monoclinic	monoclinic
Space group	$P2_1/n$	$C2/c$	$P2_1/n$
a [Å]	12.1786(2)	46.217(2)	12.8143(15)
b [Å]	23.4643(1)	14.4134(7)	21.868(3)
c [Å]	19.1081(3)	16.1226(8)	18.509(2)
β [°]	103.6480(10)	90.1870(10)	102.247(3)
Volume [Å^3]	5306.19(12)	10740.0(9)	5068.5(11)
Z	4	8	4
$\rho_{calcd.}$ [g cm^{-3}]	1.147	1.180	1.146
μ [mm^{-1}]	0.086	0.083	0.079
F(000)	2166	4128	1884
Crystal size [mm]	0.50 × 0.44 × 0.08	0.25 × 0.20 × 0.05	0.50 × 0.45 × 0.20
$\theta_{min}/\theta_{max}$	1.81/25.00	1.76/23.00	1.77/25.00
Index ranges	$-13 \le h \le 14$	$-50 \le h \le 50$	$-13 \le h \le 15$
	$-17 \le k \le 27$	$-15 \le k \le 15$	$-26 \le k \le 25$
	$-21 \le l \le 22$	$-17 \le l \le 14$	$-18 \le l \le 22$
Reflections collected	31042	24617	27335
Independent reflections	9326	7467	8900
R_{int}	0.1524	0.0584	0.0318
Completeness to θ_{max} [%]	99.8	99.9	99.7
Absorption correction	SADABS	SADABS	SADABS
Max./min. transmission	0.953674/0.611385	0.9959/0.9797	0.9844/0.9617
Refinement method	Full-matrix least-squares on F^2	Full-matrix least-squares on F^2	Full-matrix least-squares on F^2
Data/restraints/parameters	9327/2/623	7467/16/944	8900/24/638
GOF on F^2	0.956	0.965	1.218
Final R indices [$I > 2\sigma(I)$]	R_1 = 0.0798	R_1 = 0.0427	R_1 = 0.0835
	wR_2 = 0.1475	wR_2 = 0.0927	wR_2 = 0.1719
R indices (all data)	R_1 = 0.0798	R_1 = 0.0771	R_1 = 0.0929
	wR_2 = 0.1895	wR_2 = 0.1021	wR_2 = 0.1748
Largest diff. peak/hole [e Å^{-3}]	0.530/–0.301	0.426/–0.321	0.639/–0.670

 © 2005 Wiley-VCH Verlag GmbH & Co. KGaA, Weinheim

solvent and the residual metal was washed three times with THF (40 mL). A suspension of dpp-bian (0.5 g, 1.0 mmol) in THF (30 mL) was then added to the activated magnesium metal and the mixture was heated to reflux. Over the course of about 30 min, the reaction mixture turned deep green due to the formation of **1**. The solution was then cooled to ambient temperature, decanted from the excess magnesium and used in situ for the reactions with ketones.

[(dpp-bian)(H)]Mg[OC(=CHPh)CH$_2$Ph](THF)$_2$ (6): To a THF solution of **1** [prepared from 0.5 g (1.0 mmol) of dpp-bian in 30 mL THF] was added dibenzyl ketone (0.21 g, 1.0 mmol) with stirring. The solution immediately turned deep blue. Evaporation of the solvent and crystallisation of the crude product from diethyl ether (40 mL) at room temperature yielded 0.66 g (72%) of **6**(Et$_2$O)$_{0.5}$ as deep blue crystals. M.p. >115 °C (dec.). IR (Nujol): $\tilde{\nu}$ = 1580 (s), 1510 (s), 1405 (m), 1315 (m), 1290 (w), 1240 (m), 1180 (s), 1110 (w), 1080 (w), 1040 (w), 1012 (m), 935 (w), 920 (w), 905 (m), 895 (m), 870 (s), 825 (m), 805 (w), 770 (s), 745 (s), 695 (s), 660 (w), 620 (w), 565 (w), 515 (m), 465 (m), 420 (w) cm^{-1}. ^{1}H NMR (200 MHz, [D$_8$]toluene, 20 °C): δ = 7.56 (d, J = 6.8 Hz, 2 H, C–H Ar.), 7.33–6.76 (m, 18 H, C–H Ar.), 6.38 (d, J = 7.0 Hz, 1 H, C–H Ar.), 6.15 (d, J = 6.5 Hz, 1 H, C–H Ar.), 6.10 (s, 1 H, N–H), 5.31 (s, 1 H, C*H*Ph), 3.97 [sept, J = 6.8 Hz, 2 H, C*H*(CH$_3$)$_2$], 3.53 (s, 2 H, C*H*$_2$ Ph), 3.39 (m, 8 H, α-THF), 3.32 [sept, 2 H, C*H*(CH$_3$)$_2$], 3.23 (q, 4 H, Et$_2$O), 1.32 [d, J = 6.8 Hz, 6 H,CH(C*H*$_3$)$_2$], 1.24–1.09 (m, 8 H, β-THF; 12 H, CH(C*H*$_3$)$_2$; 6 H, Et$_2$O), 1.03 (d, J = 6.8 Hz, 6 H, CH(C*H*$_3$)$_2$). C$_{59}$H$_{70}$MgN$_2$O$_3$·(C$_4$H$_{10}$O)$_{0.5}$ (916.58): calcd. C 79.94, H 8.25; found C 80.03, H 8.14.

[(dpp-bian)(H)]Mg[OC(=CPh$_2$)CH$_3$](THF)$_2$ (7): Diphenylacetone (0.21 g, 1.0 mmol) was added with stirring to a THF solution of **1** (prepared in situ from 0.5 g (1.0 mmol) of dpp-bian in 40 mL THF). The solution instantly turned deep blue. The residue remaining after removal of the solvent in vacuo was crystallised from diethyl ether (40 mL) affording 0.72 g (79%) of **7**(Et$_2$O) as deep blue crystals. M.p. 142–144 °C. IR (Nujol): $\tilde{\nu}$ = 1560 (s), 1515 (s), 1330 (m), 1290 (m), 1275 (m), 1240 (m), 1185 (s), 1170 (m), 1105 (s), 1080 (w), 1045 (w), 1030 (m), 1010 (s), 970 (m), 935 (w), 915 (w), 865 (s), 835 (m), 815 (w), 800 (w), 760 (s), 700 (vs), 660 (w), 615 (m), 570 (w), 525 (m), 500 (m), 485 (m) cm^{-1}. ^{1}H NMR (200 MHz, [D$_8$]THF, 20 °C): δ = 7.37–6.67 (m, 20 H, C–H Ar.), 6.42 (s, 1 H, N–H), 5.96 (d, J = 7.0 Hz, 1 H, C–H Ar.), 5.75 (d, J = 6.3 Hz, 1 H, C–H Ar.), 3.79 [sept, J = 6.8 Hz, 2 H, C*H*(CH$_3$)$_2$], 3.67 [sept, J = 6.8 Hz, 2 H, C*H*(CH$_3$)$_2$] 3.39 [q, J = 7.0 Hz, 4 H, (CH$_3$C*H*$_2$)$_2$O], 1.99 (s, 3 H, C*H*$_3$), 1.30 [d, J = 6.8 Hz, 6 H, CH(C*H*$_3$)$_2$], 1.22 [d, J = 6.8 Hz, 6 H, CH(C*H*$_3$)$_2$], 1.10 [t, J = 7.0 Hz, 6 H, (C*H*$_3$CH$_2$)$_2$O], 0.98 [d, J = 6.8 Hz, 6 H, CH(C*H*$_3$)$_2$], 0.92 [d, J = 6.8 Hz, 6 H, CH(C*H*$_3$)$_2$]. C$_{59}$H$_{70}$MgN$_2$O$_3$·(C$_4$H$_{10}$O) (953.60): calcd. C 79.35, H 8.46; found C 79.72, H 8.61.

[(dpp-bian)(H)]Mg(camphor)(py)$_2$ (8): Camphor (0.15 g, 1.0 mmol) was added with stirring to a THF solution of **1** [prepared in situ from 0.5 g (1.0 mmol) of dpp-bian in 40 mL THF]. The solution was heated to 60 °C for 1 h. During heating, the solution turned deep blue. The solvent was then removed in vacuo and the residue was dissolved in pyridine (10 mL). After removal of pyridine and all other volatiles in vacuo, a waxy residue remained which was dried in vacuo at room temperature for 1 h. Subsequently the solid was dissolved in benzene (20 mL). The resultant solution was concentrated to 10 mL in vacuo at 50 °C. Crystallisation at room temperature afforded 0.37 g (43%) of **8**(C$_6$H$_6$)$_{0.5}$ as deep blue crystals. M.p. 172–174 °C. C$_{56}$H$_{66}$MgN$_4$O·0.5(C$_6$H$_6$) (874.40): calcd. C 81.03, H 7.95; found C 81.38, H 8.09. IR (Nujol): $\tilde{\nu}$ = 1595 (vs), 1510 (s), 1325 (m), 1305 (w), 1240 (m), 1190 (s), 1135 (w), 1100 (m), 1060 (m), 1035 (m), 1005 (w), 970 (w), 930 (w), 905 (m), 880 (m), 860 (w), 830 (w), 815 (w), 800 (w), 770 (s), 745 (s), 700 (s), 675 (s), 455 (m) cm^{-1}.

Single Crystal X-ray Structure Determinations of 6, 7 and 8: The crystal data and details of data collection are given in Table 1, selected bond lengths and bond angles are collected in Table 2. The data for **6** were collected on a Siemens SMART CCD diffractometer (graphite-monochromated Mo-K_α radiation, ω-scan technique, λ = 0.71073 Å) at 173 K. The data for **7** and **8** were collected on a Bruker SMART APEX diffractometer (graphite-monochromated Mo-K_α radiation, ω- and Φ-scan technique, λ = 0.71073 Å) at 100 K. The structures were solved by direct methods using SHELXS-97[9] and were refined on F^2 using SHELXL-97.[10] All non-hydrogen atoms were refined anisotropically and the hydrogen atoms were placed in calculated positions and assigned to an isotropic displacement parameter of 0.08 Å^2. SADABS[11] was used to perform area detector scaling and absorption corrections. The geometrical aspects of the structures were analysed by using the PLATON program.[12] CCDC-259974 (for **6**), -259975 (for **7**) and -259976 (for **8**) contain the supplementary crystallographic data for this paper. These data can be obtained free of charge from The Cambridge Crystallographic Data Centre via www.ccdc.cam.ac.uk/data_request/cif.

Supporting Information Available: ^{1}H NMR spectra of **6** and **7**.

Table 2. Selected bond lengths [Å] and angles [°] for **6**, **7** and **8**.

Compound	**6**	**7**	**8**
	Bond length		
Mg–N(1)	2.066(3)	2.051(2)	2.055(2)
Mg–N(2)	2.369(4)	2.410(2)	2.436(2)
Mg–O(1)	1.902(3)	1.9212(18)	1.8902(19)
Mg–O(2)	2.075(3)	2.0420(17)	
Mg–O(3)	2.114(3)	2.1370(17)	
Mg–N(3)			2.151(2)
Mg–N(4)			2.195(2)
N(1)–C(1)	1.359(5)	1.356(3)	1.352(3)
N(2)–C(2)	1.453(5)	1.449(3)	1.449(3)
C(1)–C(2)	1.391(5)	1.386(3)	1.384(3)
O(1)–C(37)	1.320(5)	1.321(3)	
O(1)–C(47)			1.307(3)
C(37)–C(38)	1.514(5)	1.501(3)	
C(37)–C(39)	1.368(6)	1.373(3)	
C(47)–C(48)			1.333(4)
C(47)–C(52)			1.540(3)
N(2)–H(2)	0.840	0.886	0.888
	Bond angles		
N(1)–Mg–N(2)	80.33(13)	79.16(7)	79.31(8)
N(1)–Mg–O(1)	123.48(13)	129.83(8)	122.43(8)
N(2)–Mg–O(1)	86.28(14)	84.96(7)	90.17(8)
N(1)–Mg–O(2)	128.49(14)	124.50(8)	
N(2)–Mg–O(3)	177.32(13)	176.09(7)	
N(1)–Mg–N(3)			135.32(9)
N(2)–Mg–N(4)			172.22(8)
Mg–O(1)–C(37)	156.1(3)	138.23(15)	
Mg–O(1)–C(47)			144.63(17)

Acknowledgments

This work was supported by the Russian Foundation for Basic Research (Grant No. 03-03-32246A), the Russian Science Support Foundation (ILF), the Fonds der Chemischen Industrie, and the Deutsche Forschungsgemeinschaft (Graduiertenkolleg "Syntheti-

 © 2005 Wiley-VCH Verlag GmbH & Co. KGaA, Weinheim

sche, mechanistische und reaktionstechnische Aspekte von Metallkatalysatoren").

[1] Ch. Elschenbroich, A. Salzer, *Organometallics*, 2nd ed., Wiley-VCH: Weinheim, **1992**.

[2] L. S. Hegedus, *Transition Metals in the Synthesis of Complex Organic Molecules*, 2nd ed., University Science Books: Sausalito, California, **1999**.

[3] a) M. W. van Laren, C. J. Elsevier, *Angew. Chem.* **1999**, *111*, 3926–3929; *Angew. Chem. Int. Ed.* **1999**, *38*, 3715–3717; b) R. van Belzen, H. Hoffmann, C. J. Elsevier, *Angew. Chem.* **1997**, *109*, 1833–1835; *Angew. Chem. Int. Ed. Engl.* **1997**, *36*, 1743–1745; c) G. A. Grasa, R. Singh, E. D. Stevens, S. P. Nolan, *J. Organomet. Chem.* **2003**, *687*, 269–279; d) A. Heumann, L. Giordano, A. Tenaglia, *Tetrahedron Lett.* **2003**, *44*, 1515–1518; e) A. E. Cherian, E. B. Lobkovsky, G. W. Coates, *Chem. Commun.* **2003**, 2566–2567; f) M. D. Leatherman, S. A. Svejda, L. K. Johnson, M. Brookhart, *J. Am. Chem. Soc.* **2003**, *125*, 3068–3081; g) J. Kiesewetter, W. Kaminsky, *Chem. Eur. J.* **2003**, *9*, 1750–1758.

[4] a) I. L. Fedushkin, A. A. Skatova, V. A. Chudakova, G. K. Fukin, *Angew. Chem.* **2003**, *115*, 3416–3420; *Angew. Chem. Int. Ed.* **2003**, *42*, 3294–3298; b) I. L. Fedushkin, A. A. Skatova, V. A. Chudakova, V. K. Cherkasov, G. K. Fukin, M. A. Lopatin, *Eur. J. Inorg. Chem.* **2004**, 388–393; c) I. L. Fedushkin, A. A. Skatova, V. A. Chudakova, G. K. Fukin, S. Dechert, H. Schumann, *Eur. J. Inorg. Chem.* **2003**, 3336–3346; d) I. L. Fedushkin, V. A. Chudakova, A. A. Skatova, N. M. Khvoinova, Yu. A. Kurskii, T. A. Glukhova, G. K. Fukin, S. Dechert, M. Hummert, H. Schumann, *Z. Anorg. Allg. Chem.* **2004**, *630*, 501–507; e) I. L. Fedushkin, A. A. Skatova, A. N. Lukoyanov, V. A. Chudakova, S. Dechert, M. Hummert, H. Schumann, *Russ. Chem. Bull.* **2004**, *53*, 2751–2762; f) I. L. Fedushkin, N. M. Khvoinova, A. Yu. Baurin, G. K. Fukin, V. K. Cherkasov, M. P. Bubnov, *Inorg. Chem.* **2004**, *43*, 7807–7815; g) I. L. Fedushkin, A. A. Skatova, V. A. Chudakova, N. M. Khvoinova, A. Yu. Baurin, S. Dechert, M. Hummert, H. Schumann, *Organometallics* **2004**, *23*, 3714–3718.

[5] a) I. L. Fedushkin, A. A. Skatova, V. K. Cherkasov, V. A. Chudakova, S. Dechert, M. Hummert, H. Schumann, *Chem. Eur. J.* **2003**, *9*, 5778–5783; b) I. L. Fedushkin, N. M. Khvoinova, A. A. Skatova, G. K. Fukin, *Angew. Chem.* **2003**, *115*, 5381–5384; *Angew. Chem. Int. Ed.* **2003**, *42*, 5223–5226; c) I. L. Fedushkin, A. A. Skatova, M. Hummert, H. Schumann, *Eur. J. Inorg. Chem.* **2005**, 1601–1608.

[6] a) J. F. Allan, W. Clegg, K. W. Henderson, L. Horsburgh, A. R. Kennedy, *J. Organomet. Chem.* **1998**, *559*, 173–179; b) J. F. Allan, K. W. Henderson, A. R. Kennedy, *Chem. Commun.* **1999**, 1325–1326; c) J. F. Allan, K. W. Henderson, A. R. Kennedy, S. J. Teat, *Chem. Commun.* **2000**, 1059–1060.

[7] a) P. G. Willard, J. M. Salvino, *J. Chem. Soc., Chem. Commun.* **1986**, 153–154; b) M. H. Chisholm, J. Gallucci, K. Phomphrai, *Inorg. Chem.* **2002**, *41*, 2785–2794.

[8] A. A. Paulovicova, U. El-Ayaan, K. Shibayama, T. Morita, Y. Fukuda, *Eur. J. Inorg. Chem.* **2001**, 2641–2646;

[9] G. M. Sheldrick, *SHELXS-97 Program for the Solution of Crystal Structures*, University of Göttingen, **1990**.

[10] G. M. Sheldrick, *SHELXL-97 Program for the Refinement of Crystal Structures*, University of Göttingen, **1997**

[11] G. M. Sheldrick, *SADABS Program for Empirical Absorption Correction of Area Detector Data*, University of Göttingen, **1996**.

[12] A. L. Spek, *PLATON A Multipurpose Crystallographic Tool*, Utrecht University, **2000**.

Received: November 10, 2004

 © 2005 Wiley-VCH Verlag GmbH & Co. KGaA, Weinheim

Coordination Assembly of TTF Derivatives through CuI Bridges

Wen Lu,[a] Zhe-Min Yan,[a] Jie Dai,*[a–c] Yong Zhang,[a] Qin-Yu Zhu,[a] Ding-Xian Jia,[a] and Wen-Juan Guo[a]

Keywords: Tetrathiafulvalene / Copper(I) complexes / Crystal structures / Molecular assembly

The sulfur-rich ligand $C_{12}H_{12}O_4S_6$ (**1**) and complexes $[(C_{12}H_{12}O_4S_6)CuI]_2$ (**2**) and $[(C_7H_6O_4S_3)CuI]_\infty$ (**3**) have been synthesized and characterized crystallographically. Molecules of compound **1,** a tetrathiafulvalene (TTF) derivative, have a boat-shaped configuration and are packed discretely within the crystal. Compound **1** coordinates to a rhomboid CuI center forming a dimeric TTF derivative **2**. In complex **2** the boat-shaped configuration of **1** is flattened. Molecules of **2** are packed regularly and compactly in the crystal and are arranged side by side with short S···S contacts, which assemble the molecules into a 1D ribbon structure. This provides evidence that metal coordination or assembly is a useful stratagem for changing the molecular configuration and packing that further influence the intermolecular interactions. Complex **3** has a step-like polymeric structure formed by copper-iodine bridges and copper-sulfur bridges (coordinated thiocarbonyl).

(© Wiley-VCH Verlag GmbH & Co. KGaA, 69451 Weinheim, Germany, 2005)

Introduction

Although tetrathiafulvalene (TTF) and its derivatives have been intensively investigated for several decades, these unique functional molecules continue to attract great attention. So far, much research on the design and preparation of dimeric and oligomeric TTFs has been reported by organic chemists. The reported dimeric TTFs can be roughly divided into two types: one is linked through conjugated π systems and the other through nonconjugated σ chains.[1–4] Recently, a new kind of dimeric TTF has been reported, in which two TTF units are connected by metal coordination. Great efforts in synthesis and characterization have revealed the wide application of TTF derivatives with additional groups having coordinating properties. The incorporation of TTF units into dithiolate ligands is one of the successful examples (see a in Scheme 1) and a series of metal coordinated bis-TTF complexes was reported by Kobayashi et al.[5–9] The metal coordination extends and enhances the π conjugation of the sulfur-rich system, and hence provides the complexes with novel conductive and magnetic properties. Furthermore, the coordination of TTF derivatives to metal ions is expected to give new bis-TTF or polymolecular systems with improved inter- or intra- molecular interactions. The synthesis of a number of metal complexes of TTF derivatives with coordinating groups of alkylthiole,[10–13] phenylphosphite,[14,15] pyridine[16–18] or alkylsilyl[19] (see b in Scheme 1) has provided insight into the role of metal ions in molecular assembly.

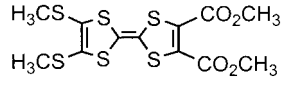

1

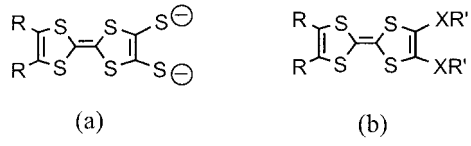

(a) (b)

X = S, R' = Me, Et or ~py

X = P, R' = ph_2

X = Si, R' = Me_2H

Scheme 1.

The synthesis and coordination properties of TTF derivatives attracted our interest.[20–22] Here, structures of dimethyl 2-[4,5-bis(methylthio)-1,3-dithiol-2-ylidene]-1,3-dithiole-4,5-dicarboxylate (**1**) and its derivatives are studied. Detailed discussions about the roles of metal coordination in the molecular assembly are presented.

[a] Department of Chemistry, Suzhou University,
P. O. Box 174, 1 Shizi Street, Suzhou 215006, P.R. China
E-mail: daijie@suda.edu.cn
[b] State Key Laboratory of Coordination Chemistry, Nanjing University,
Nanjing 210093, P.R. China
[c] Laboratory of Organic Solids, Center for Molecular Sciences, Institute of Chemistry, Chinese Academy of Sciences,
Beijing 100080, P. R.China

Results and Discussion

Synthesis and Characterization

Some methods for synthesizing the asymmetric compound **1** have been reported.[23,24] However, the detailed procedures have only recently been reported by Hudhomme et al. and McCullough et al.[25,26] Followed these latter methods, the compound was synthesized successfully in our laboratory. The details can be found in the experimental section. Single crystals of **1** were obtained and its molecular structure was reported for the first time (see next section).

Scheme 2 exhibits the synthetic routes for compounds **1**, **2** and **3**. Compound **2** (D-σ-D type) was synthesized by refluxing a mixture of **1** and CuI in acetonitrile under argon. The inorganic-organic hybrid compound **2** was stable under ambient conditions. The cyclic voltammetry of **2** was studied in acetonitrile containing 0.1 mol dm^{-3} Et_4NClO_4. Two reversible redox peaks were detected and the results are listed in Table 1 together with the data of the free ligand **1**. The potential shift of **1** for the methylthio group coordinated with the Cu^I ion was not observed, which was different from the electrochemical behavior of the dithiolate complexes.[27] This might be a result of the complex dissociating to free ligand **1** and solvated CuI in a dilute solution of acetonitrile at a concentration of ca. 10^{-3} mol dm^{-3}. This indicates that the coordination of the methylthiol group to copper(I) is not as strong as that of thiolate. It should be also pointed out that the oxidation of Cu^I was not observed from cyclic voltammetry. In the IR spectra of **2**, the stretching band of C=C was observed at 1431 cm^{-1} with a slightly red shift compared to that of **1** at 1439 cm^{-1}. It is well known that the central C=C stretching of TTF undergoes a large down-shift in frequency on oxidation (normally more than 50–100 cm^{-1}).[28,29] Therefore, the ligand in the CuI complex is in neutral state, which is in agreement with the molecular composition deduced from microanalysis. A slightly blue shift was observed for the C=O stretching bands of the carboxyl group. The complex **3** was synthesized by a similar method to that of **2** in acetonitrile, the reaction proceeded readily at room temperature due to the strong tendency of the C=S group to coordinate to Cu^I ions. The C=S vibrational mode of complex **3** appears at 1065 cm^{-1} which is shifted to a lower frequency in comparison with that of the free ligand at 1088 cm^{-1}.

Table 1. Data from cyclic voltammetry of compound **1** and **2** in acetonitrile (V, vs. SCE).

	$E_{1/2}(1)$	$E_{pa}(1)$	$E_{pc}(1)$	$E_{1/2}(2)$	$E_{pa}(2)$	$E_{pc}(2)$
1	0.596	0.638	0.554	0.854	0.896	0.811
2	0.594	0.641	0.548	0.842	0.892	0.792

Description of Structures

$C_{12}H_{12}O_4S_6$ (1): The ORTEP view of **1** and atom labeling scheme are shown in Figure 1. Atom pair O(3)/O(3′) is presented with occupancies of 0.60 and 0.40, respectively, due to the C=O bond disorders over two orientations. The distances of the C=C double bonds are 1.344(4), 1.337(4) and 1.341(4) Å for C(1)–C(2), C(3)–C(4) and C(5)–C(6), respectively (Table 2). The central C=C bond is slightly shorter than the others. The TTF moiety takes on a boat-shaped configuration formed by three planes defined as plane 1: S(3), S(4) C(3), C(4), S(5), S(6) (central plane), plane 2: S(1), S(2) C(1), C(2), S(3), S(4) and plane 3: S(5), S(6), C(5), C(6), C(9), C(11). Their mean deviations are 0.0107, 0.0395 and 0.0389 Å, respectively. The planes 1 and 2 share a common line along S(3)–S(4) with a dihedral angle of 19.15(3)° and the planes 1 and 3 share a common line along S(5)–S(6) with a dihedral angle of 11.39(7)° (Figure 2, top). The contributions of the TTF fragment to the boat shaped configuration, are the envelope configurations, on C(3) or C(4), of both of the five-membered dithiol rings. In the crystal structure, four molecules are contained in a unit cell with different orientations, being a direct consequence of the symmetrical operation of a $P2_1/c$ (no.14) space group.

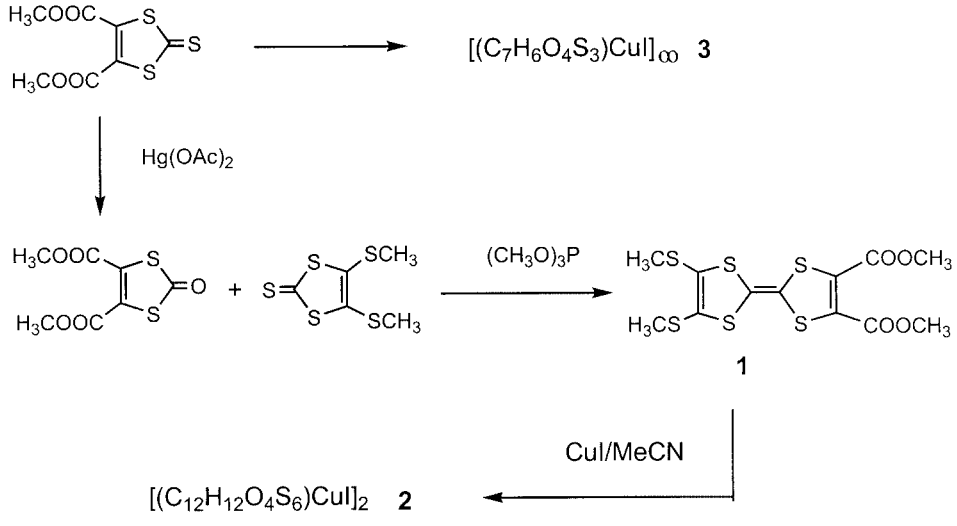

Scheme 2.

Table 2. Selected bond lengths [Å] and angles [°] and the important interaction distances for **1**–**3**.

1		**2**		**3**	
S(1)–C(1)	1.745(3)	Cu(1)–I(1)	2.5676(10)	Cu(1)–I(1)	2.6223(7)
S(2)–C(2)	1.741(3)	Cu(1)–S(1)	2.3497(16)	Cu(1)–S(1)	2.2806(11)
C(1)–C(2)	1.344(4)	Cu(1)–S(2)	2.3604(16)	S(1)–C(1)	1.653(4)
C(3)–C(4)	1.337(4)	Cu(1)–I(1^{ii})	2.6030(12)	Cu(1)–I(1^{iv})	2.6650(7)
C(5)–C(6)	1.341(4)	S(1)–C(3)	1.763(5)	Cu(1)–I(1^{v})	2.6450(7)
		S(2)–C(4)	1.760(5)		
S(1)–C(1)–C(2)	122.6(2)	C(5)–C(6)	1.343(6)	Cu(1)–S(1)–C(1)	108.48(13)
S(2)–C(2)–C(1)	123.9(2)			S(1)–Cu(1)–I(1)	120.04(4)
		S(1)–Cu(1)–S(2)	91.36(5)	I(1^{iv})–Cu(1)–I(1^{v})	110.54(2)
O(2)···O(4^{i})	3.031(2)	I(1)–Cu(1)–I(1^{ii})	118.42(3)		
		Cu(1)–I(1)–Cu(1^{ii})	61.58(3)	Cu(1)···Cu(1^{iv})	3.0053(8)
		S(1)–C(3)–C(4)	125.6(4)	Cu(1)···Cu(1^{v})	3.0053(8)
		S(2)–C(4)–C(3)	125.1(4)	S(1)···S(3^{vi})	3.591(3)
				S(1)···I(1)	3.707
		Cu(1)···Cu(1^{ii})	2.6469(15)		
		S(2)···S(6^{iii})	3.586(2)		
		S(4)···S(6^{iii})	3.599(2)		

^{i} x, 1 + y, z; ^{ii} 1 – x, 1 – y, –z; ^{iii} 1 – x, 1 – y, 1 – z; ^{iv} x – 1/2, –y + 1/2, 1 – z; ^{v} x + 1/2, –y + 1/2, 1 – z; ^{vi} x – 1/2, 3/2 – y, 1 – z

The shortest S···S distance between two molecules is 4.072 Å, significantly longer than the van der Waals radius sum (3.7 Å). Thus, the S···S interaction within this crystal is negligible.

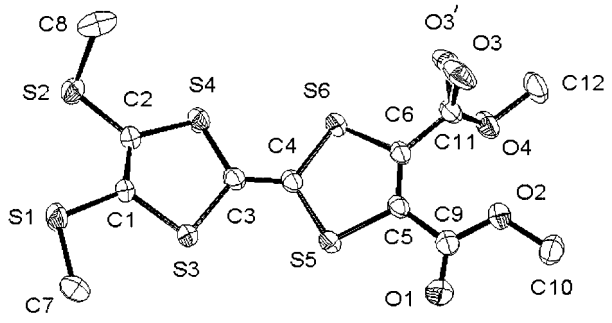

Figure 1. An ORTEP view of **1** showing the atom labeling scheme. Non-H atoms are shown as 50% probability displacement ellipsoids. H-atoms have been omitted for clarity.

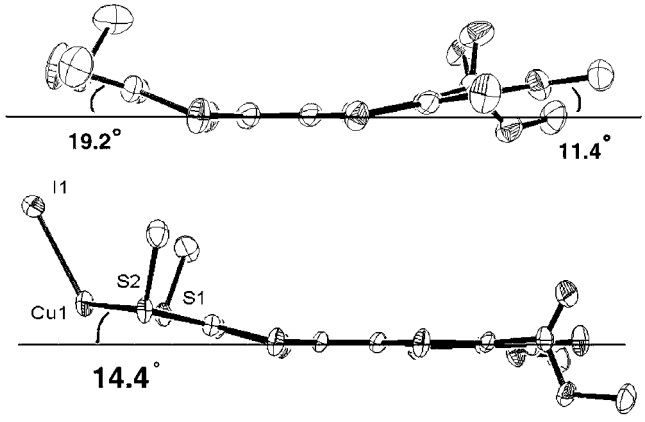

Figure 2. Side views of **1** (top) and **1**·CuI (**2**) (bottom) showing the change in the dihedral angles of the ligand.

[($C_{12}H_{12}O_4S_6$)CuI]$_2$ (2): An ORTEP view of complex **2** with atom labeling is shown in Figure 3. The methylthiol groups of ligand **1** are coordinated to the coppers of rhomboid Cu_2I_2 to produce a dimeric structure. The geometry around the copper atom is a distorted tetrahedron with an I–Cu–I angle of 118.42(3)° and S–Cu–S angle of 91.36(5)°. The Cu–I and Cu–S distances are in agreement with those of the corresponding compounds.[3,12]

Some changes are found by comparing the structures of complex **2** and the ligand **1**. When the coordination bonds are formed, the S(1)–C(1) and S(2)–C(2) distances of **1** [1.745(3) and 1.741(3) Å] are elongated to 1.763(5) and 1.760(5) Å, respectively. Correspondingly the angles of S(1)–C(1)–C(2) and S(2)–C(2)–C(1) [122.6(2) and 123.9(2)°] are enlarged to 125.6(4) and 125.1(4)°, respectively (Table 2). The boat configuration of **1** is flattened in complex **2**. The dihedral angle changes from 19.15(3)° to 14.44(5)° at the methylthio-side and on the carboxyl ester side plane 3 is completely coplanar with plane 1 (b in Figure 2). The mean deviation of the new plane, C(3)–C(6), S(3)–S(6), C(9), C(11), is 0.0269 Å. These changes enhance the delocalization of the conjugated π electrons of the TTF derivative.

The boat-shaped configuration might be one of the important reasons for the discrete packing of **1** (no S···S contacts). However, the molecular packing of **2** is very regular and compact. The bis-TTF compound approximately resembles a planar ruler and twelve sulfur atoms lie on the sides. The molecules are further arranged side by side and S···S contacts are shown between S(2), S(6^{iii}) (3.586(2) Å, iii: 1 – x, 1 – y, 1 – z) and S(4), S(6^{iii}) [3.599(2) Å], which assembles the molecules into a 1D ribbon structure along the [001] direction (Figure 4). Sulfur atoms from two neighboring molecules are alternately contacted as an occluded slide fastener. Between these ribbons, only weak C–H···O and C–H···I interactions are found.

A similar compound was reported by Delhaès,[30] who studied the crystal structure and properties of the radical salt, but unfortunately the chemical composition of those radical salts were not characterized. However, the crystal structure of the neutral complex can be compared with that

 © 2005 Wiley-VCH Verlag GmbH & Co. KGaA, Weinheim

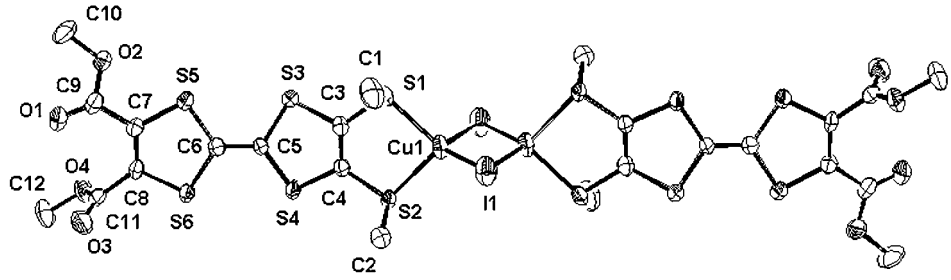

Figure 3. An ORTEP view of **2** showing the atom labeling scheme. Non-H atoms are shown as 50% probability displacement ellipsoids. H-atoms have been omitted for clarity.

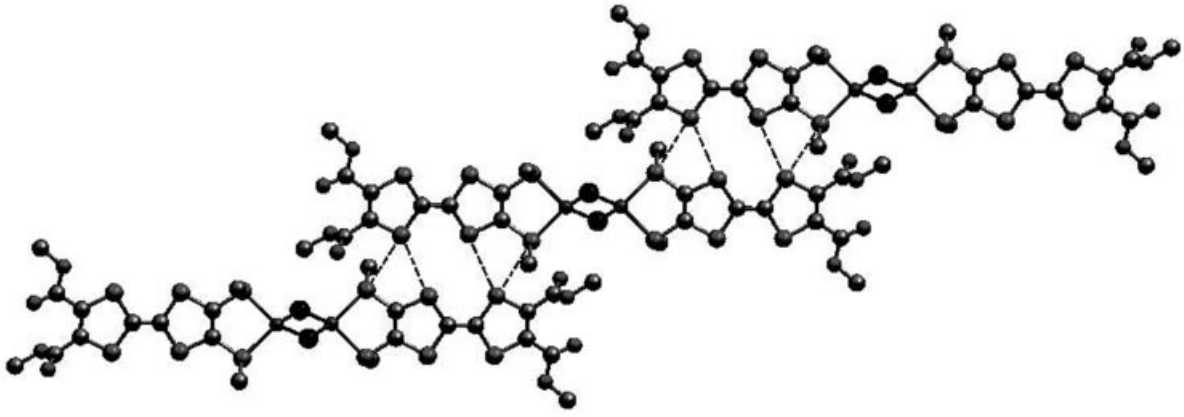

Figure 4. Part of an intermolecular contacts assembled ribbon. Dashed lines are used to represent short S···S contacts.

of **2**. Although the difference between these two molecules is only at the terminal substituted groups, ethylenedithiol group instead of di(methyl carboxylate) of **2**, the crystal systems and molecular packing of them are completely different from each other.

$[(C_7H_6O_4S_3)CuI]_\infty$ (3): Figure 5 gives the ORTEP view of the unit of complex **3** with selected atom labeling. The geometry around the copper atom is a distorted tetrahedron with three iodide ions and a thiocarbonyl sulfur atom from the ligand. Through iodine bridges, the $C_7H_6O_4S_3CuI$ units form a step-like polymeric structure (or chain) propagated in the direction of the *a* axis (Figure 6). The Cu(1)–I(1) distance, 2.6223(7) Å, for **3** is somewhat shorter than those for $[(C_5H_4S_5)CuI]$[31] and $[(C_5H_6S_5)CuI]$,[32] sulfur-rich complexes with ligands of 4,5-bisalkylthiol-1,3-dithiole-2-thione. The Cu–S (thiocarbonyl sulfur) distance of 2.2806(11) Å and the S(1)=C(1) distance of 1.653(4) Å are within the expected values for these kinds of CuI complexes.[13,14]

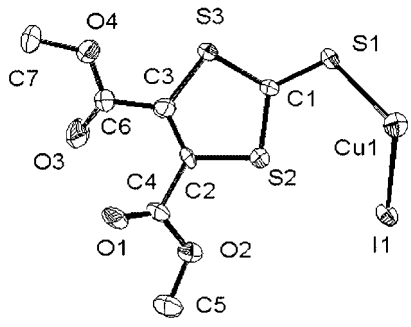

Figure 5. An ORTEP view of **3** showing the atom labeling scheme. Non-H atoms are shown as 50% probability displacement ellipsoids. H-atoms have been omitted for clarity.

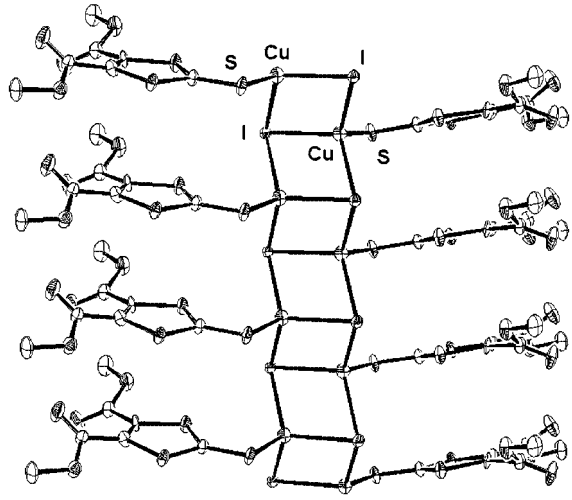

Figure 6. The $C_7H_6O_4S_3CuI$ units of **3** form a step-like chain structure propagated in the direction of the *a* axis.

Unlike $[(C_5H_6S_5)CuI]$, no significant S···S contacts exist between the ligands within the chains, however short interchains, S···S contacts, occur between S(1) and S(3^{vi}), 3.591(3) Å (vi: $x - 1/2, 3/2 - y, 1 - z$). With these contacts,

 © 2005 Wiley-VCH Verlag GmbH & Co. KGaA, Weinheim

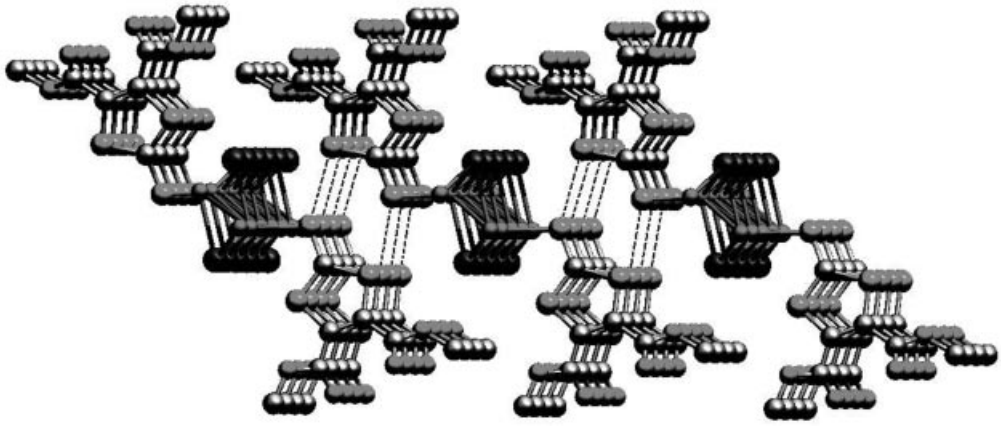

Figure 7. The representation shows the short S···S contacts (dashed lines) between the 1D chains, viewed along the direction of the chains.

a novel two-dimensional network is formed. Figure 7 shows the molecular packing and the intermolecular S···S contacts, when looking along the *a* axis.

Conclusions

Although the copper halogen frameworks are dramatically changed due to the coordination of different halogen ions and other ligands, only two types of CuI coordination centers, rhomboid and step-like structures, have been reported for sulfur-rich compounds (TTF derivatives).[3,31,32] The thiocarbonyl sulfur coordination usually produces step-like structures, whereas the chelate coordination of *ortho*-bis(alkylthiol) groups prefer a rhomboid structure. The Cu–S (thiocarbonyl) coordination bond is stronger than the Cu–S (methylthio) bond. In the case where both groups exist, the thiocarbonyl group predominantly coordinates to Cu^{I}, giving a step-like polymeric structure.[32] Both the change in the substituted groups, and also metal coordination are useful stratagems for rearranging the molecular packing, which further influences the intermolecular interactions of the TTF derivatives. Besides the molecular packing, the configuration of the TTF moiety is also affected by these stratagems. The room temperature conductivity (σ_{RT}) of I_2 doped **2** (1.0×10^{-3} S cm^{-1}) is one order of magnitude greater than that of the I_2 doped ligand **1** (2.0×10^{-4} S cm^{-1}), under the same conditions. The results also illustrate the effects of metal coordination on the molecular arrangement and the intermolecular interactions in crystals.

Experimental Section

General Remarks: The reagents, 4,5-bis(methylthio)-1,3-dithiole-2-thione ($C_5H_6S_5$), dimethyl 2-thioxo-1,3-dithiole-4,5-dicarboxylate ($C_7H_6O_4S_3$) and dimethyl 2-oxo-1,3-dithiole-4,5-dicarboxylate ($C_7H_6O_5S_2$), were prepared according to the literature.[33–35] Acetonitrile was dried by a standard method and distilled before use. Elemental analyses of C, H and N were performed with an MOD 1106 elemental analyzer. The IR spectra were recorded as KBr discs on a Nicolet Magma 550 FT-IR spectrometer. ^{1}H NMR spectra were recorded with an INOVA-400 spectrophotometer. Cyclic voltammetry (CV) was performed with a model CHI600 electrochemistry workstation, with a cell containing a Pt plate as the working electrode, a Pt wire as the counter electrode and saturated calomel electrode (SCE) as a reference electrode. The electrical conductivity was measured with a conventional two-probe method at room temperature with compressed discs.

Synthesis of Compounds

$C_{12}H_{12}O_4S_6$ (1): The compound was synthesized by a coupling reaction from 4,5-bis(methylthio)-1,3-dithiole-2-thione ($C_5H_6S_5$) and dimethyl 2-oxo-1,3-dithiole-4,5-dicarboxylate ($C_7H_6O_5S$), using a similar method to that reported.[25,26] A mixture of the reactants (1 mmol, respectively) was refluxed for 2 h in trimethyl phosphite (10 mL) and toluene (10 mL) under argon. The dark purple solution was then evaporated and the residue was purified by chromatography on a silica gel column (CH_2Cl_2). $C_{12}H_{12}O_4S_6$ (412.58) dark-red crystals, (yield: 145 mg, 35%). ^{1}H NMR: δ = 3.43 (s, CH_3S–), 3.85 (s, CH_3O–) ppm. IR: 1726 (s, C=O), 1708 (s, C=O), 1272 (s, COOC), 1438 (m, C=C) cm^{-1}; m.p. 86–87 °C; calcd. C 34.93, H 2.93; found C 34.85, H 3.06%.

$[(C_{12}H_{12}O_4S_6)CuI]_2$ (2): Ligand **1** (41.2 mg, 0.1 mmol) in acetonitrile (5.0 mL) was added to an acetonitrile solution (5.0 mL) of CuI (19.3 mg, 0.1 mmol). The mixture was stirred for 2 h while refluxing under argon. The red filtrate was evaporated slowly under ambient conditions. Orange crystals suitable for X-ray crystal determination were obtained after two days, which were filtered and washed with acetonitrile, and finally dried in vacuo (yield: 48 mg, 40%). IR: 1743 (s, C=O), 1725 (s, C=O), 1251 (s, COOC), 1431 (m, C=C) cm^{-1}. $C_{24}H_{24}O_8S_{12}Cu_2I_2$ (1206.07): calcd. C 23.90, H 2.01; found C 23.67, H 2.26%.

$[(C_7H_6O_4S_3)CuI]_\infty$ (3): A solution of the ligand $C_7H_6O_4S_3$ (25 mg, 0.1 mmol) in acetonitrile (5.0 mL) was added to an acetonitrile solution (5.0 mL) of CuI (19.1 mg, 0.1 mmol). The mixture was stirred for 30 min at room temperature under argon. The red filtrate was evaporated slowly under ambient conditions. Red crystals suitable for X-ray crystal determination were obtained after several days, which were filtered and washed with acetonitrile, and finally dried in vacuo (yield: 27 mg, 60%). IR: 1759 (s, C=O), 1728 (s, C=O), 1258 (s, COOC), 1065 (m, C=S) cm^{-1}. $C_7H_6O_4S_3CuI$ (440.75): calcd. C 19.10, H 1.38; found C 19.05, H 1.36%.

X-ray Crystallographic Study: All measurements were carried out with a Rigaku Mercury CCD diffractometer at 193 K with graphite-monochromated Mo-K_α (λ = 0.71073 Å) radiation. X-ray crystallographic data for compounds **1**–**3** were collected and processed

 © 2005 Wiley-VCH Verlag GmbH & Co. KGaA, Weinheim

Table 3. Crystallographic data for compounds **1**–**3**.

Compound	**1**	**2**	**3**
Empirical formula	$C_{12}H_{12}O_4S_6$	$C_{24}H_{24}O_8S_{12}Cu_2I_2$	$C_7H_6O_4S_3CuI$
Formula mass	412.58	1206.07	440.75
Color, habit	dark-red, platelet	orange, prism	red, platelet
Crystal system	monoclinic	triclinic	orthorhombic
Crystal size [mm]	$0.60\times0.21\times0.09$	$0.15\times0.10\times0.10$	$0.40\times0.40\times0.15$
Space group	$P2_1/c$ (no. 14)	$P\bar{1}$ (no. 2)	$P\,2_1\,2_1\,2_1$ (no. 19)
a [Å]	14.371(2)	7.981(3)	4.0923(6)
b [Å]	4.2903(4)	8.394(4)	9.2312(11)
c [Å]	27.876(3)	15.107(6)	31.897(5)
α [°]	90	86.77(1)	90
β [°]	94.023(5)	77.646(11)	90
γ [°]	90	81.566(12)	90
Z	4	1	4
T [K]	193	193	193
V [Å^3]	1714.4(3)	977.7(7)	1205.0(3)
$D_{calcd.}$ [mg m^{-3}]	1.598	2.048	2.429
μ [mm^{-1}]	0.809	3.350	4.887
$F(000)$	848.00	588.00	840.00
Reflections collected	13688	6842	8755
Unique reflections	3212	3567	2640
Observations [$I > 2\sigma(I)$]	3100	3146	2624
Variables	213	222	148
R_1 [$I > 2\sigma(I)$]	0.0433	0.0416	0.0268
wR_2	0.0850	0.0826	0.0604
Goodness of fit indicator	1.168	1.117	1.146

$R_1 = \Sigma||F_o| - |F_c||/\Sigma\,|F_o$ and $wR_2 = [\Sigma(w(F_o^2 - F_c^2)^2)/\Sigma w(F_o^2)^2]^{1/2}$

using CrystalClear (Rigaku).[36] The structures were solved by direct methods using SHELXS-97[37] and the refinements against all reflections of the compounds were performed using SHELXL-97.[38] The non-hydrogen atoms were refined anisotropically and hydrogen atoms were refined using the theoretical riding model. A summary of the experimental details and selected results for compounds **1**–**3** is given in Table 3. The selected bond lengths and angles are listed in Table 2.

CCDC No. 256152–256154 contains the supplementary crystallographic data for this paper. These data can be obtained free of charge from The Cambridge Crystallographic Data Centre via www.ccdc.cam.ac.uk/data_request/cif.

Measurements of Conductivity: To confirm the effect of coordination assembly, compounds **1** and **2**, as precursors, were doped by iodine using the gaseous diffusion method at 50 °C. The dark-red color of compound **2** turned gradually into black after a week. The conductivity (σ_{RT}) of the I_2 doped compound **2** was 1.0×10^{-3} S cm^{-1} which was measured by a conventional two-probe method for compacted pellets at room temperature. The conductivity of the I_2 doped ligand **1** was 2.0×10^{-4} S cm^{-1}, doped and measured under the same experimental conditions.

Acknowledgments

This work was supported by the National Natural Science Foundation (20071024, 20371033), P. R. China. The authors are also grateful to the Key Laboratory of Organic Synthesis of Jiangsu Province, Suzhou University, for financial support.

[1] M. B. Nielsen, C. Lomholt, J. Becher, *J. Chem. Soc. Rev.* **2000**, *29*, 153–164.
[2] M. Adam, K. Müllen, *Adv. Mater.* **1994**, *6*, 439–459.
[3] T. Otsubo, Y. Aso, K. Takimiya, *Adv. Mater.* **1996**, *8*, 203–211.
[4] J. L. Segura, N. Martín, *Angew. Chem. Int. Ed.* **2001**, *40*, 1372–1409.
[5] H. Tanaka, Y. Okano, H. Kobayashi, W. Suzuki, A. Kobayashi, *Science* **2001**, *291*, 285–287.
[6] E. Fujiwara, A. Kobayashi, H. Fujiwara, H. Kobayashi, *Inorg. Chem.* **2004**, *43*, 1122–1129.
[7] W. Suzuki, E. Fujiwara, A. Kobayashi, Y. Fujishiro, E. Nishibori, M. Takata, M. Sakata, H. Fujiwara, H. Kobayashi, *J. Am. Chem. Soc.* **2003**, *125*, 1486–1487.
[8] H. Tanaka, H. Kobayashi, A. Kobayashi, *J. Am. Chem. Soc.* **2002**, *124*, 10002–10003.
[9] A. Kobayashi, E. Fujiwara, H. Kobayashi, *Chem. Rev.* **2004**, *104*, 5243–5264.
[10] M. Munakata, T. Kuroda-Sowa, M. Maekawa, A. Hirota, S. Kitagawa, *Inorg. Chem.* **1995**, *34*, 2705–2710.
[11] X.-M. Gan, M. Munakata, T. Kuroda-Sowa, M. Maekawa, Y. Misaki, *Polyhedron* **1995**, *14*, 1343–1350.
[12] X.-M. Gan, M. Munakata, T. Kuroda-Sowa, M. Maekawa, *Bull. Chem. Soc. Jpn.* **1994**, *67*, 3009–3011.
[13] L. P. Wu, J. Dai, M. Munakata, T. Kuroda-Sowa, M. Maekawa, Y. Suenaga, Y. Ohno, *J. Chem. Soc., Dalton Trans.* **1998**, 3255–3261.
[14] J. M. Asara, C. E. Uzelmeier, K. R. Dunbar, J. Allison, *Inorg. Chem.* **1998**, *37*, 1833–1840.
[15] M. Fourmigué, C. E. Uzelmeier, K. Boubekeur, S. L. Bartley, K. R. Dunbar, *J. Organomet. Chem.* **1997**, *529*, 343–350.
[16] S.-X. Liu, S. Dolder, P. Franz, A. Neels, H. Stoeckli-Evans, S. Decurtins, *Inorg. Chem.* **2003**, *42*, 4801–4803.
[17] F. Iwahori, S. Golhen, L. Ouahab, R. Carlier, J.-P. Sutter, *Inorg. Chem.* **2001**, *40*, 6541–6542.
[18] F. Setifi, L. Ouahab, S. Golhen, Y. Yoshida, G. Saito, *Inorg. Chem.* **2003**, *42*, 1791–1793.
[19] M. J. Jayaswal, H. N. Peindy, F. Guyon, M. Knorr, N. Avarvari, M. Fourmigué, *Eur. J. Inorg. Chem.* **2004**, 2646–2651.
[20] J. Dai, T. Kuroda-Sowa, M. Munakata, M. Maekawa, Y. Suenaga, Y. Ohno, *J. Chem. Soc., Dalton Trans.* **1997**, 2363–2368.
[21] G. Q. Bian, J. Dai, Q. Y. Zhu, W. Yang, Z. M. Yan, M. Munakata, M. Maekawa, *Chem. Commun.* **2002**, 1474–1475.

 © 2005 Wiley-VCH Verlag GmbH & Co. KGaA, Weinheim

[22] Q. Y. Zhu, G. Q. Bian, J. Dai, D. X. Jia, J. S. Zhang, L. Guo, *Inorg. Chim. Acta* **2003**, *351*, 177–182.
[23] H. Muller, A. Lerf, H. P. Fritz, K. Andres, *Synth. Metals* **1991**, *42*, 2381–2384.
[24] P. Blanchard, M. Sallé, G. Duguay, M. Jubault, A. Gorgues, *Tetrahedron Lett.* **1992**, *33*, 2685–2688.
[25] P. Hudhomme, S. L. Moustarder, C. Durand, N. Gallego-Planas, N. Mercier, P. Blanchard, E. Levillain, M. Allain, A. Gorgues, A. Riou, *Chem. Eur. J.* **2001**, *7*, 5070–5083.
[26] R. D. McCullough, M. A. Petruska, J. A. Belot, *Tetrahedron* **1999**, *55*, 9979–9998.
[27] J. Dai, M. Munakata, Y. Ohno, G. Q. Bian, Y. Suenaga, *Inorg. Chim. Acta* **1999**, *285*, 332–335.
[28] A. R. Siedle, T. J. Kistenmacher, R. M. Metzger, C. S. Kuo, R. P. V. Duyne, T. Cape, *Inorg. Chem.* **1980**, *19*, 2048–2051.
[29] G. Matsubayashi, K. Yokoyama, T. Tanaka, *J. Chem. Soc., Dalton Trans.* **1988**, 3059–3062.
[30] J. Ramos, V. M. Yartsev, S. Golhen, L. Ouahab, P. Delhaès, *J. Mater. Chem.* **1997**, *7*, 1313–1319.
[31] J. Dai, M. Munakata, L. P. Wu, T. Kuroda-Sowa, *Inorg. Chim. Acta* **1997**, *258*, 65–69.
[32] J. Dai, W. Yang, Z. G. Ren, Q. Y. Zhu, D. X. Jia, *Polyhedron* **2004**, *23*, 1447–1451.
[33] N. Svenstrup, K. M. Rasmussen, T. K. Hansen, J. Becher, *Synthesis* **1994**, 809–812.
[34] N. Svenstrup, J. Becher, *Synthesis* **1995**, 215–235;.
[35] L. R. Melby, H. D. Hartzler, W. A. Sheppard, *J. Org. Chem.* **1974**, *39*, 2456–2458.
[36] Rigaku Corporation, **1999**, *CrystalClear Software User's Guide*, *Molecular Structure Corporation*, **2000**; J. W. Pflugrath, *Acta Crystallogr. Sect. D* **1999**, *55*, 1718–1725.
[37] G. M. Sheldrick, *SHELXS-97*, *Program for Structure Solution*, University of Göttingen, Germany, **1997**.
[38] G. M. Sheldrick, *SHELXL-97*, *Program for Structure Refinement*, University of Göttingen, Germany, **1997**.

Received: December 05, 2004

 © 2005 Wiley-VCH Verlag GmbH & Co. KGaA, Weinheim

Bridging β-Lactam Coordination at Dinuclear Zinc Sites

Franc Meyer,*[a] and Hans Pritzkow[b]

Dedicated to Professor Heinrich Vahrenkamp on the occasion of his 65th birthday

Keywords: Dinuclear complexes / Metalloenzymes / N ligands / Pyrazolate ligands / Zinc

Two highly preorganized dizinc scaffolds based on compartmental pyrazolate ligands are found to incorporate 2-azetidinone in its deprotonated β-lactamide form as an N,O-bridging ligand within the dimetallic pocket. Both dizinc β-lactamide complexes **3**·$(ClO_4)_2$ and **4**·$(ClO_4)_2$ have been characterized structurally and spectroscopically, revealing a strengthening of the β-lactamide C–N bond and a weakening of the C=O bond relative to free 2-azetidinone. These findings contrast the reverse geometrical changes observed recently by Brombacher and Vahrenkamp for β-lactamide *N*-bound to only a single zinc ion, thus underlining the particular dimetallic effect that is achieved by the cooperativity of two adjacent metal ions.

(© Wiley-VCH Verlag GmbH & Co. KGaA, 69451 Weinheim, Germany, 2005)

Introduction

β-Lactamases are a class of enzymes that efficiently catalyze the hydrolytic opening of β-lactam rings.[1,2] Since the β-lactam motif is a crucial subunit of the largest group of therapeutically useful antibiotics comprising the penicillin, cephalosporin, and carbapenem families, bacteria express β-lactamases in order to escape the action of those important drugs. Nowadays, increasing resistance against β-lactam antibiotics poses a serious clinical problem.[3–5] Unfortunately, most clinically useful inhibitors are inactive towards a particular class of β-lactamases, which depend on one or two zinc(II) ions within their active site.[6–8] These so-called metallo-β-lactamases hydrolyze a wide range of substrates, and insight into the binding and transformation of β-lactam compounds by such zinc active sites is considered not only of fundamental interest, but may also contribute to the development of efficient mechanism-based inhibitors.

Detailed information about the active-site structure of several metallo-β-lactamases has been gained from X-ray crystallography and other methods, in particular for the enzymes from *Bacillus cereus* and *Bacteroides fragilis*.[8,9] The majority of these sites have similar unsymmetrical dizinc binding motifs and a shared water/hydroxide ligand in a typical bridging position (**A**),[10–15] but structural evidence has also been reported for a nonbridged form with a loose ligand arrangement and a larger Zn···Zn distance of 4.4 Å.[14] The latter configuration has been reproduced in theoretical models by an O_2H_3 unit between the two zinc ions (**B**; Scheme 1),[16] and such an O_2H_3 moiety has indeed been proposed as a possible functional motif in oligozinc hydrolases.[17–19]

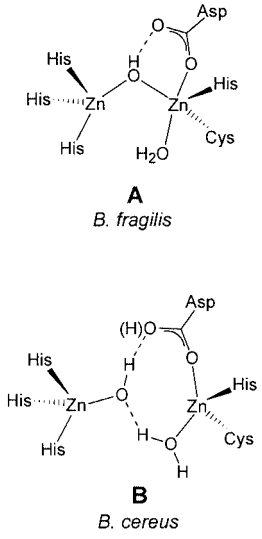

Scheme 1.

Although the dizinc form of the metallo-β-lactamases from *B. fragilis* and *B. cereus* is usually considered as the biologically active form, the role of the second Zn^{2+} re-

[a] Institut für Anorganische Chemie der Georg-August-Universität, Tammannstrasse 4, 37077 Göttingen, Germany
Fax: +49-551-39-3012
E-mail: franc.meyer@chemie.uni-goettingen.de
[b] Anorganisch-Chemisches Institut der Ruprecht-Karls-Universität, Im Neuenheimer Feld 270, 69120 Heidelberg, Germany

mains controversial,[20,21] and distinct mechanisms may be relevant for the mono- and dimetallic forms.[9,21–23] Details of the catalysis by dizinc metallo-β-lactamases are still a subject of debate, although it is generally postulated that interaction of the β-lactam carbonyl group with a zinc ion polarizes the C–O bond and allows nucleophilic attack by a metal-bound hydroxide ion with fission of the C–N bond. Subsequent protonation of the β-lactam N atom and dissociation of the acyl group would liberate the ring-opened product (Scheme 2).[22] A ring-opened form of the substrate has been detected as an intermediate in the hydrolysis of nitrocefin by the *B. fragilis* enzyme;[24] its identity as a zinc(II)-bound *N*-deprotonated species formed by C–N bond cleavage was corroborated by model studies.[25]

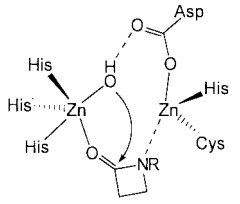

Scheme 2. Proposed β-lactam cleavage step of dizinc metallo-β-lactamase.

The pH profiles of the *B. cereus* reaction indicate that the second zinc(II) center is not required for nucleophile activation, but its role in orienting the attacking nucleophile and in stabilizing reaction intermediates has been proposed.[22,26–28] While several groups have dealt with the hydrolysis or methanolysis of β-lactams by simple transition-metal salts, including Zn^{2+} salts,[29,30] very few studies have employed preorganized dinuclear zinc(II) complexes as functional mimics of metallo-β-lactamases.[25,31–33] Such models might provide valuable insights into, inter alia, the mechanistic role of the second Zn^{2+} ion, cooperative effects of the adjacent metal ions, and possible binding modes of the substrate. Lippard et al. recently reported an in-depth study of nitrocefin hydrolysis mediated by some phenol- and naphthyridine-based dizinc complexes.[31,32] Preferential metal ion coordination of typical β-lactam substrates through a monodentate carboxylate group was inferred from ^{13}C NMR and IR spectroscopy.[31,32]

Structure–activity correlations have been deduced for the hydrolytic cleavage of penicillin G (pen; Scheme 3) mediated by a series of pyrazolate-based dizinc(II) complexes with tunable Zn···Zn distances.[33] The drastic differences in activity for the various systems were explained on the basis of the necessity of suitably oriented, accessible coordination sites that are required to bind and activate both the nucleophile and the substrate. The molecular structures of several adducts of such pyrazolate-based dizinc scaffolds with the small substrate analog oxazetidinyl acetate (oaa) confirmed that binding of the zinc ion to the carboxylate group is favored over binding to the β-lactam amide group. However, additional zinc coordination by the β-lactam amide O atom may still be induced under suitable circumstances, and was observed crystallographically for the first time in the tetranuclear complex **C** (Scheme 4), which reveals significant

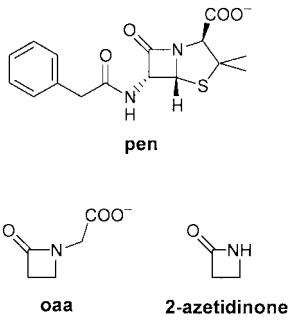

Scheme 3. β-Lactams used in this and previous work with dizinc complexes **1** and **2**.

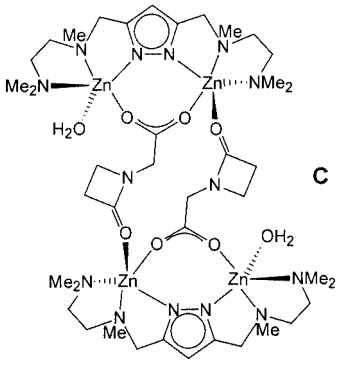

Scheme 4. Complex **C** featuring β-lactam amide-O coordination of oaa.[33]

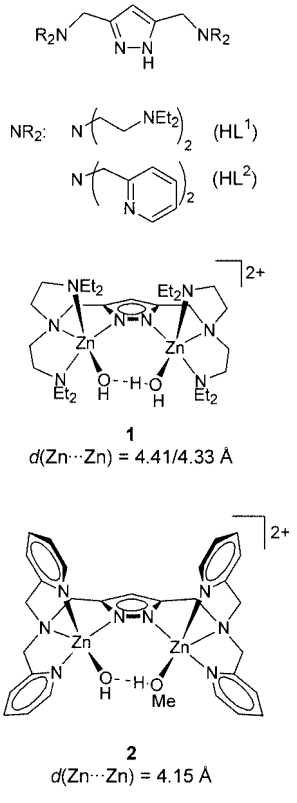

Scheme 5. Ligands and complexes used in this work.

 © 2005 Wiley-VCH Verlag GmbH & Co. KGaA, Weinheim

changes of the internal geometry of the β-lactam moiety that are likely to facilitate subsequent hydrolytic ring cleavage.[33]

In this contribution we report the synthesis and crystallographic characterization of adducts between the most simple β-lactam, 2-azetidinone, and two highly preorganized dizinc complexes **1** and **2** (Scheme 5)[34,35] that mimic the loosely bridged type **B** form (Scheme 1) of the active site of the *B. cereus* β-lactamase.

Results and Discussion

Complexes **1** and **2** were prepared in situ from the respective ligand HL, 2 equiv. of base (KO*t*Bu), and 2 equiv. of $Zn(ClO_4)_2 \cdot 6H_2O$; 1 equiv. of 2-azetidinone was then added to the reaction mixture, and colorless single crystals of **3**·$(ClO_4)_2$·MeOH and **4**·$(ClO_4)_2$·acetone could be obtained upon recrystallization of the resulting complexes from methanol or acetone solutions, respectively (Scheme 6). The FAB mass spectra of solid samples show prominent peaks at *m*/*z* = 818 (**3**) and 786 (**4**) with an isotopic distribution pattern characteristic for the ions $[L^1Zn_2(C_3H_4NO)(ClO_4)]^+$ and $[L^2Zn_2(C_3H_4NO)(ClO_4)]^+$, respectively, suggesting the formation of 1:1 adducts between the dizinc complexes and deprotonated 2-azetidinone. The IR spectrum of **3**·$(ClO_4)_2$ reveals a strong absorption at 1606 cm^{-1} for the β-lactam $\nu(C{=}O_{amide})$ stretch, which is significantly shifted to lower frequency compared to free 2-azetidinone (IR: $\tilde{\nu}$ = 1723 cm^{-1}; Raman: $\tilde{\nu}$ = 1697 cm^{-1}).[36,37] This shift indicates Zn coordination by the lactam O atom. In the case of **4**·$(ClO_4)_2$, the $\nu(C{=}O_{amide})$ vibration cannot be identified unambiguously, since several strong bands of the pyridyl groups also appear in that region (1629, 1606, 1589, 1565 cm^{-1}). The molecular structures of **3** and **4** were elucidated by X-ray crystallography and are depicted in Figures 1 and 2, respectively.

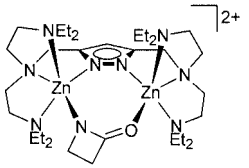

3
d(Zn···Zn) = 4.28 Å

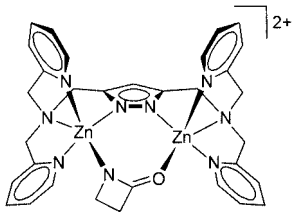

4
d(Zn···Zn) = 4.02 Å

Scheme 6. Complexes **3** and **4** prepared in this work.

In both cases the $\{LZn_2\}$ entities of the starting complexes **1** and **2** are fully conserved. The 2-azetidonone is

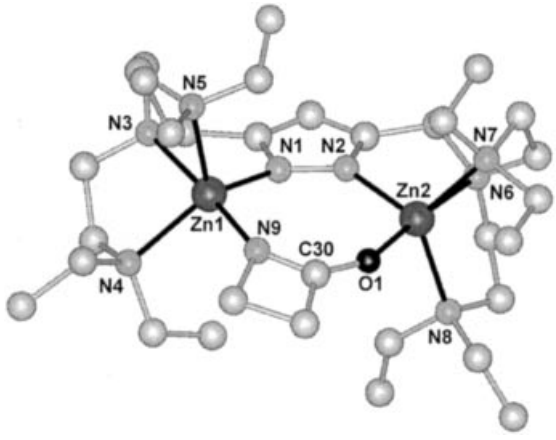

Figure 1. View of the molecular structure of **3**. In the interests of clarity, all protons have been omitted. Selected interatomic distances [Å] and angles [°]: Zn1–N1 2.051(3), Zn1–N3 2.294(4), Zn1–N4 2.187(4), Zn1–N5 2.164(4), Zn1–N9 2.032(4), Zn2–N2 2.009(4), Zn2–N6 2.238(4), Zn2–N7 2.161(5), Zn2–N8 2.155(5), Zn2–O1 1.958(4), C30–O1 1.239(7), C30–N9 1.292(7); N9–C30–O1 131.5(5).

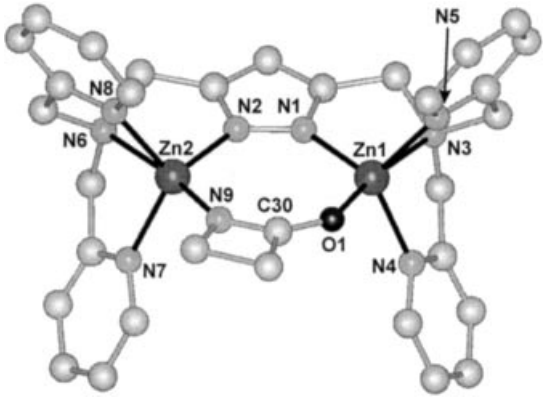

Figure 2. View of the molecular structure of **4**. In the interests of clarity, all protons have been omitted. Selected interatomic distances [Å] and angles [°]: Zn1–N1 1.984(4), Zn1–N3 2.281(5), Zn1–N4 2.062(5), Zn1–N5 2.056(5), Zn1–O1 1.973(4), Zn2–N2 1.993(5), Zn2–N6 2.303(5), Zn2–N7 2.074(5), Zn2–N8 2.081(5), Zn2–N9 1.980(6), C30–O1 1.245(8), C30–N9 1.274(8); N9–C30–O1 130.9(6).

incorporated in its *N*-deprotonated lactamide form within the dimetallic pocket and bridges the two zinc ions in an N,O-fashion at a Zn···Zn distance of 4.277(1) Å (**3**) and 4.015(1) Å (**4**). A similar Zn···Zn distance of 4.180 Å was observed in a carbonato-bridged complex of a related pyrazolate ligand.[18] All zinc ions in **3** and **4** are found in a slightly distorted trigonal-bipyramidal coordination environment (**3**: τ = 0.88 for Zn1 and 0.94 for Zn2; **4**: τ = 0.90 for Zn1 and 0.87 for Zn2).[38] The bond lengths between the zinc ions and the N-donor atoms of the dinucleating ligand scaffolds L are in the normal range, with bonds between Zn and the pyrazolate N atom being the shortest [1.984(4)–2.051(3) Å] and bonds between Zn and the backbone N3/N6 atoms being the longest [2.238(4)–2.303(5) Å]. In the latter case, the Zn–N bonds *trans* to the lactamide N

 © 2005 Wiley-VCH Verlag GmbH & Co. KGaA, Weinheim

atom are somewhat longer than those *trans* to the lactamide O atom.

The most interesting metric parameters are those of the bound β-lactamide, which can be compared to those of free 2-azetidinone[39] and to the β-lactamide subunit of a $Tp^{Cum,Me}$Zn(β-lactamide) complex **D** reported recently by Brombacher and Vahrenkamp [Scheme 7; $Tp^{Cum,Me}$ = tris(3-cumyl-5-methylpyrazolyl)borate].[40] It should be noted that no other structurally characterized zinc β-lactamide complex has been reported in the literature, and complexes featuring a bridging β-lactamide between other metal ions are very scarce.[41] In **D** the β-lactamide is bound through its N atom to a single zinc ion, while the lactamide O atom remains uncoordinated. This reduces conjugation within the amide moiety and hence leads to lengthening of the C–N bond [1.363(4)/1.356(4) Å in **D** vs. 1.333(2) Å in free 2-azetidinone] and a shortening of the C=O bond [1.214(5)/1.227(4) Å in **D** vs. 1.226(2) Å in free 2-azetidinone]. Binding of a second zinc ion to the β-lactamide O atom, as observed in complexes **3** and **4**, reverses this trend: the C–N bond is shortened [1.274(8)/1.292(7) Å] and the C=O bond is clearly elongated [1.238(7)/1.245(8) Å]. At the same time the N–C–O bond angle of 131.5(5)° (**3**) or 130.9(6)° (**4**) remains unchanged [131.7(4)/131.1(3)° in **D**]. A CSD search reveals that many organic molecules containing a β-lactam subunit have been characterized crystallographically, and both the C=O and C–N bond lengths are found to vary considerably, with most C=O bonds in the range 1.15–1.27 Å (mean value 1.207 Å) and most C–N bonds in the range 1.30–1.45 Å (mean value 1.370 Å). Overall, the lactamide ligand within the dimetallic clamp of **3** and **4** features a relatively long C=O bond and a short C–N bond that is close to the lower limit of the above range.

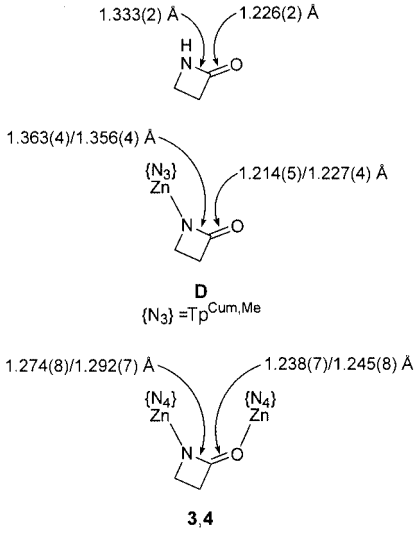

Scheme 7. C–N and C=O bond lengths of 2-azetidinone,[39] complex **D**,[40] and complexes **3** and **4**.

In line with these structural findings, the β-lactam ν(C=O) stretch in **D** (1709 cm^{-1}) is barely shifted from those of free 2-azetidinone, while the ν(C=O) vibrations of **3** and **4** appear at much lower frequency, as mentioned above. Apparently, changes in the β-lactam unit (and possible activation towards subsequent reactions, such as hydrolysis) differ dramatically depending on whether the β-lactamide is bound to a single or two adjacent zinc ions. Although initial experiments with **3** and **4** did not reveal any activation of the β-lactam ring towards hydrolytic cleavage (as expected due to the anionic character of the *N*-deprotonated species), the present findings once more underline the particular ability of highly preorganized dinuclear scaffolds to accommodate and polarize small substrate molecules within their dimetallic binding pocket, which is distinct from activation at a single metal ion.

Experimental Section

General Remarks: Manipulations were carried out under dry nitrogen by employing standard Schlenk techniques. Solvents were dried according to established procedures. Complexes **1** and **2** were prepared in situ starting from HL^1 and HL^2;[42,43] all other chemicals were used as purchased. Microanalyses: Mikroanalytische Laboratorien des Organisch-Chemischen Instituts der Universität Heidelberg. IR spectra: Perkin–Elmer 983G; recorded as KBr pellets. UV/Vis spectra: Perkin–Elmer Lambda 19. FAB mass spectra: Finnigan MAT 8230.

Caution! Although no problems were encountered in this work, perchlorate salts are potentially explosive and should be handled with proper precautions.

Synthesis of $[L^1Zn_2(C_3H_4NO)](ClO_4)_2$·MeOH (3): A solution of HL^1 (260 mg, 0.50 mmol) in MeOH (30 mL) was treated with 2 equiv. of KO*t*Bu (112 mg, 1.00 mmol) and 2 equiv. of $Zn(ClO_4)_2$·$6H_2O$ (372 mg, 1.00 mmol). After stirring the mixture at room temperature for 30 min, 1 equiv. of 2-azetidinone (36 mg, 1.01 mmol) was added, and stirring continued for 2 h. The reaction mixture was then concentrated to dryness and the residue was taken up in methanol (20 mL) and filtered. Layering of the resulting clear solution with diethyl ether afforded colorless crystals of the product **3**·MeOH at room temperature over a period of several days (320 mg, 67%). MS (FAB+): *m*/*z* (%) = 818 (100) $[L^1Zn_2(C_3H_4NO)(ClO_4)]^+$. IR (KBr): $\tilde{\nu}$ = 3523 (w, CH_{MeOH}), 2973 (m), 2938 (m), 2877 (m), 1606 (s, C=O), 1516 (w), 1468 (m), 1384 (m), 1348 (w), 1331 (w), 1283 (w), 1263 (w), 1225 (w), 1181 (w), 1091 (vs, ClO_4), 970 (m), 909 (m), 818 (m), 795 (m), 778 (m), 734 (m), 622 (s), 546 (w) cm^{-1}. $C_{32}H_{65}Cl_2N_9O_9Zn_2$·MeOH (953.6): calcd. C 41.56, H 7.29, N 13.22; found C 41.10, H 7.13, N 13.43.

Synthesis of $[L^2Zn_2(C_3H_4NO)](ClO_4)_2$·acetone (4): A solution of HL^2 (245 mg, 0.50 mmol) in MeOH (30 mL) was treated with 2 equiv. of KO*t*Bu (112 mg, 1.00 mmol) and 2 equiv. of $Zn(ClO_4)_2$·$6H_2O$ (372 mg, 1.00 mmol). After stirring the mixture at room temperature for 30 min, 1 equiv. of 2-azetidinone (36 mg, 1.01 mmol) was added, and stirring continued for 2 h. The reaction mixture was then concentrated to dryness and the residue was taken up in acetone (20 mL) and filtered. Layering of the resulting clear solution with light petroleum afforded colorless crystals of the product **4**·acetone at room temperature over a period of several days (180 mg, 38%). MS (FAB+): *m*/*z* (%) = 786 (10) $[L^2Zn_2(C_3H_4NO)(ClO_4)]^+$, 307 (100). IR (KBr): $\tilde{\nu}$ = 3108 (w), 3069 (w), 2957 (w), 2904 (w), 2857 (w), 1704 (m, $C{=}O_{acetone}$), 1629 (s), 1606 (s), 1589 (s), 1565 (m), 1504 (w), 1479 (m), 1438 (m), 1378 (w), 1314 (w), 1259 (m), 1218 (w), 1159 (w), 1090 (vs, ClO_4), 1024 (m), 974 (w), 954 (w), 899 (w), 880 (w), 811 (w), 768 (m), 650 (m), 622 (s), 527

 © 2005 Wiley-VCH Verlag GmbH & Co. KGaA, Weinheim

Table 1. Crystal data and refinement details for **3** and **4**.

	3	**4**
Empirical formula	$C_{32}H_{65}N_9Cl_2O_9Zn_2$·MeOH	$C_{32}H_{33}N_9Cl_2O_9Zn_2$·acetone
M_r [g mol]	953.61	947.39
Crystal size [mm]	0.44 × 0.32 × 0.26	0.27 × 0.26 × 0.17
Crystal system	monoclinic	monoclinic
Space group	$P2_1/c$	$P2_1/c$
a [Å]	19.4962(15)	17.3710(15)
b [Å]	14.1066(11)	15.5745(14)
c [Å]	16.1861(12)	15.0981(13)
β [°]	102.261(2)	105.685(2)
Volume [Å^3]	4350.0(6)	3932.6(6)
$\rho_{calcd.}$ [g cm^{-3}]	1.456	1.600
Z	4	4
F(000)	2016	1944
Temperature [K]	173(2)	173(2)
λ(Mo-K_α) [Å]	0.71073	0.71073
hkl range	–25 to 25, 0 to 18, 0 to 21	–20 to 19, 0 to 18, 0 to 17
θ range [°]	1.9–28.3	1.8–25.0
Measured reflections	42844	21922
Unique reflections (R_{int})	10734 (0.036)	6946 (0.074)
Observed reflections [$I > 2\sigma(I)$]	8935	4588
Refined parameters	549	529
Residual electron density [e Å^{-3}]	1.56	1.35
R_1 [$I > 2\sigma(I)$]	0.0755	0.0634
wR_2 (all data)	0.1851	0.1931
Goodness-of-fit	1.105	1.060

(w), 502 (w), 487 (w), 415 (w) cm^{-1}. $C_{32}H_{33}Cl_2N_9O_9Zn_2$·acetone (947.4): calcd. C 44.37, H 4.15, N 13.31; found C 43.88, H 4.32, N 12.75.

X-ray Crystallographic Study: Data collection was carried out with a Bruker AXS CCD diffractometer at 173 K using graphite-monochromated Mo-K_α radiation (λ = 0.71073 Å). Structures were solved by direct methods (SHELXS-97) and refined by full-matrix least-squares techniques based on F^2 (SHELXL-97).[44] Atomic coordinates and thermal parameters of the non-hydrogen atoms were refined in fully anisotropic models. Hydrogen atoms were included using the riding model. Some of the ethyl groups in **3** are disordered. Crystal data and refinement details are listed in Table 1. CCDC-258281 (**3**) and -258282 (**4**) contain the supplementary crystallographic data for this paper. These data can be obtained free of charge from The Cambridge Crystallographic Data Centre via www.ccdc.cam.ac.uk/data_request/cif.

Acknowledgments

We sincerely thank the DFG (project Me1313/5-1) and the Fonds der Chemischen Industrie for support of this work.

[1] M. I. Page, *Acc. Chem. Res.* **1984**, *17*, 144–151.
[2] M. I. Page, A. P. Laws, *Chem. Commun.* **1998**, 1609–1617.
[3] D. J. Payne, *J. Med. Microbiol.* **1993**, *39*, 93–99.
[4] J. M. Frère, *Mol. Microbiol.* **1995**, *16*, 385–395.
[5] K. Bush, *Curr. Pharm. Des.* **1995**, *5*, 839–845.
[6] K. Bush, *Clin. Infect. Dis.* **1998**, *27*, 48–53.
[7] Z. Wang, W. Fast, A. M. Valentine, S. J. Benkovic, *Curr. Opin. Chem. Biol.* **1999**, *3*, 614–622.
[8] J. A. Cricco, A. J. Vila, *Curr. Pharm. Des.* **1999**, *5*, 915–927.
[9] J. A. Cricco, E. G. Orellano, R. M. Rasia, E. A. Ceccarelli, A. J. Vila, *Coord. Chem. Rev.* **1999**, *190–192*, 519–535.
[10] A. Carfi, S. Pares, E. Duée, M. Galleni, C. Duez, J. M. Frère, O. Dideberg, *EMBO J.* **1995**, *14*, 4914–4921.
[11] N. O. Concha, B. A. Rasmussen, K. Bush, O. Herzberg, *Structure* **1996**, *4*, 823–836.
[12] J. H. Ullah, T. R. Walsh, I. A. Taylor, D. C. Emery, C. S. Verma, S. J. Gamblin, J. Spencer, *J. Mol. Biol.* **1998**, *284*, 125–136.
[13] A. Carfi, E. Duée, M. Galleni, J.-M. Frère, O. Dideberg, *Acta Crystallogr., Sect. D* **1998**, *54*, 313–323.
[14] S. M. Fabiane, M. K. Sohi, T. Wan, D. J. Payne, J. H. Bateson, T. Mitchell, B. J. Sutton, *Biochemistry* **1998**, *37*, 12 404–12 411.
[15] N. O. Concha, C. A. Janson, P. Rowling, S. Pearson, C. A. Cheever, B. P. Clarke, C. Lewis, M. Galleni, J.-M. Frère, D. J. Payne, J. H. Bateson, S. S. Abdel-Meguid, *Biochemistry* **2000**, *39*, 4288–4298.
[16] a) N. Diaz, D. Suárez, K. M. Merz, Jr., *J. Am. Chem. Soc.* **2000**, *122*, 4197–4208; b) D. Suárez, N. Diaz, K. M. Merz, Jr., *J. Comput. Chem.* **2002**, *23*, 1587–1600; c) D. Suárez, E. N. Brothers, K. M. Merz, Jr., *Biochemistry* **2002**, *41*, 6615–6630.
[17] M. Ruf, K. Weis, H. Vahrenkamp, *J. Am. Chem. Soc.* **1996**, *118*, 9288–9294.
[18] F. Meyer, P. Rutsch, *Chem. Commun.* **1998**, 1037–1038.
[19] S. Erhardt, E. Jaime, J. Weston, *J. Am. Chem. Soc.* **2005**, *127*, 3654–3655.
[20] G. S. Baldwin, A. Galdes, A. O. Hill, B. E. Smith, S. G. Waley, E. P. Abraham, *Biochem. J.* **1978**, *175*, 441–447.
[21] R. M. Rasia, A. J. Vila, *Biochemistry* **2002**, *41*, 1853–1860.
[22] Z. Wang, W. Fast, S. J. Benkovic, *Biochemistry* **1999**, *38*, 10 013–10 023.
[23] M. H. Valladares, M. Kiefer, U. Heinz, R. P. Soto, W. Meyer-Klaucke, H. F. Nolting, M. Zeppezauer, M. Galleni, J.-M. Frère, G. M. Rossolini, G. Amicosante, H.-W. Adolph, *FEBS Lett.* **2000**, *467*, 221–225.
[24] Z. Wang, W. Fast, S. J. Benkovic, *J. Am. Chem. Soc.* **1998**, *120*, 10 788–10 789.
[25] N. V. Kaminskaia, B. Spingler, S. J. Lippard, *J. Am. Chem. Soc.* **2001**, *123*, 6555–6563.
[26] R. M. Rasia, A. J. Vila, *J. Biol. Chem.* **2004**, *279*, 26 046–26 051.
[27] C. Prosperi-Meys, J. Wouters, M. Galleni, J. Lamotte-Brasseur, *Cell. Mol. Life Sci.* **2001**, *58*, 2136–2143.

 © 2005 Wiley-VCH Verlag GmbH & Co. KGaA, Weinheim

[28] G. L. Estiú, R. M. Rasia, J. A. Cricco, A. J. Vila, M. C. Zerner, *Int. J. Quantum Chem.* **2002**, *88*, 118–132.
[29] M. I. Page, *Acc. Chem. Res.* **1984**, *17*, 144–151.
[30] a) A. A. M. García, P. G. Navarro, P. J. Martínez de las Parras, R. G. Ortiz, I. H. Blázquez, *Recent Res. Dev. Pure Appl. Anal. Chem.* **2002**, *4*, 89–106; b) P. J. Montoya-Pelaez, G. T. T. Gibson, A. A. Neverov, R. S. Brown, *Inorg. Chem.* **2003**, *42*, 8624–8632; c) N. Diaz, T. L. Sordo, D. Suárez, R. Méndez, J. Marin-Vallacorta, *New J. Chem.* **2004**, *28*, 15–25.
[31] N. V. Kaminskaia, C. He, S. J. Lippard, *Inorg. Chem.* **2000**, *39*, 3365–3373.
[32] N. V. Kaminskaia, B. Spingler, S. J. Lippard, *J. Am. Chem. Soc.* **2000**, *122*, 6411–6422.
[33] B. Bauer-Siebenlist, S. Dechert, F. Meyer, *Chem. Eur. J.*, in press.
[34] B. Bauer-Siebenlist, F. Meyer, E. Farkas, D. Vidovic, J. A. Cuesta-Seijo, R. Herbst-Irmer, H. Pritzkow, *Inorg. Chem.* **2004**, *43*, 4189–4202.
[35] B. Bauer-Siebenlist, F. Meyer, E. Farkas, D. Vidovic, S. Dechert, *Chem. Eur. J.*, **2005**, in press.
[36] K. Hanai, Y. Maki, A. Kuwae, *Bull. Chem. Soc. Jpn.* **1985**, *58*, 1367–1375.
[37] The noncoincidence of the IR and Raman frequencies of the C=O stretch of 2-azetidinone has been explained by the presence of cyclic H-bonded dimers with a center of symmetry. The C=O vibration that is symmetric with respect to the center of symmetry is then observed at 1697 cm^{-1} in the Raman spectrum, while the asymmetric mode is observed at 1723 cm^{-1} in the IR spectrum.[36]
[38] The angular structural parameter, τ, is defined as $\tau = (\beta - \alpha)/60$, where α and β represent two basal angles with $\beta > \alpha$. It is a measure of the degree of trigonality: a perfect TB-5 structure is associated with $\tau = 1$, while $\tau = 0$ is expected for an idealized SPY-5 geometry: A. W. Addision, T. N. Rao, J. Reedijk, J. van Rijn, G. C. Verschoor, *J. Chem. Soc., Dalton Trans.* **1984**, 1349–1356.
[39] Q.-C. Yang, P. Seiler, J. D. Dunitz, *Acta Crystallogr., Sect. C* **1987**, *43*, 565–567.
[40] H. Brombacher, H. Vahrenkamp, *Inorg. Chem.* **2004**, *43*, 6054–6060.
[41] a) D. M. L. Goodgame, S. P. W. Hill, D. J. Williams, *Polyhedron* **1992**, *11*, 1841–1847; b) W. Henderson, A. G. Oliver, C. E. F. Rickard, *Inorg. Chim. Acta* **2000**, *307*, 144–148.
[42] F. Meyer, S. Beyreuther, K. Heinze, L. Zsolnai, *Chem. Ber./Recueil* **1997**, *130*, 605–613.
[43] J. Ackermann, F. Meyer, H. Pritzkow, *Inorg. Chim. Acta* **2004**, *357*, 3703–3711.
[44] G. M. Sheldrick, *SHELXS-97, Program for Crystal Structure Solution*, University of Göttingen, **1997**; G. M. Sheldrick, *SHELXL-97, Program for Crystal Structure Refinement*, University of Göttingen, **1997**.

Received: December 15, 2004

 © 2005 Wiley-VCH Verlag GmbH & Co. KGaA, Weinheim

Freestanding, Highly Flexible, Large Area, Nanoporous Alumina Membranes with Complete Through-Hole Pore Morphology

Jörg J. Schneider,*[a] Jörg Engstler,[a] Karl P. Budna,[a,b] Christian Teichert,[c] and Steffen Franzka[d]

Keywords: Alumina / Electrochemistry / Porous template / Oxidation

Electrochemical anodic oxidation of aluminium metal sheets leads to the formation of compact and dense, but highly porous alumina surfaces on top of the anode. The alumina surfaces obtained by anodic oxidation can be detached from the bare metal by using a voltage detachment procedure, without employing chemical etching techniques. This procedure leads to large area porous alumina membranes with closed backsides. Prestructuring of the aluminium base metal leads to ordered pore regions at anodisation voltages of 25, 40 and 50 V, resulting in porous alumina membranes with pore diameters of 33, 40 and 72 nm. The careful opening of the backside alumina membranes can be realised by acid treatment leading to highly flexible large area porous alumina membranes with complete through-hole pore morphology. The backside pore-opening process realised by chemical etching is strongly dependent on time and acid concentration and is best monitored routinely by microscopy techniques in order to gain control over the process.
(© Wiley-VCH Verlag GmbH & Co. KGaA, 69451 Weinheim, Germany, 2005)

Introduction

Over the last few years mesoporous alumina has attracted much scientific interest in materials chemistry because of its compact and highly ordered porous structure.[1] These features, in combination with the possibility to vary the pore size of the individual alumina pores between 10 and 300 nm, as well as its high temperature and chemical resistance, makes this material attractive as a template material for the synthesis of one-dimensional ordered nanoscaled functional materials such as wires, tubes, fibres and particles.[2] The thickness of the porous alumina membrane which determines the pore length as well as the pore diameter is controlled by the electrochemical synthesis conditions of the anodic oxidation process. Aside from the electrochemical parameters, a dependence of its properties on temperature, pH, time of the process, as well as the aluminium metal surface conditions is observed. It is highly desirable to have as much experimental control as possible over the complex alumina formation process, because the alumina pore morphology controls the morphology of the templated guest materials incorporated within the pores. Therefore it is necessary to control the synthetic anodisation process as well as the detachment and pore conditioning process in its crucial parameters: (a) pore size, (b) membrane thickness, (c) regular arrangement of the pores, (d) detachment of the *p*orous *a*lumina *ox*ide (PAOX) membrane from the aluminium base metal and (e) generation of a complete through-hole pore morphology of the PAOX membrane. Point (e) is especially important for employing PAOX membranes in controlled gas phase processes, for example in a chemical vapour deposition nanoreactor in which gaseous species are transported through or reacted within the PAOX membrane. Examples in this area are the formation of carbon nanotubes[3] or polymer fibres derived from [2.2] paracyclophane[4] as well as catalytic gas phase hydrogenation and CO oxidation reaction.[5]

Herein we present our investigations on the synthesis of alumina membranes with regular hexagonal pore order. These membranes are produced at 25, 40 and 50 V anodisation voltage giving rise to 33, 40 and 72 nm diameter pores. To the best of our knowledge and despite the intensive use of the unique pore system of PAOX membranes in synthetic materials chemistry, no detailed studies dealing with backside pore opening of PAOX membranes has been reported. One goal is to establish reliable experimental protocols for PAOX alumina backside pore opening. This is necessary in order to employ PAOX membranes on a broader basis, for example as a nanoporous template platform in synthetic as well as catalytic gas phase processes. A qualitative model of the stepwise pore opening is developed herein which offers for the first time an experimental verifi-

[a] Fachbereich Chemie, Eduard-Zintl-Institut für Anorganische und Physikalische Chemie, Technische Universität Darmstadt, Petersenstraße 18, 64287 Darmstadt, Germany
Fax: +49-06151-16-3470
E-mail: joerg.schneider@ac.chemie.tu-darmstadt.de
[b] Current address: Institut für Metallkunde und Werkstoffprüfung, Montanuniversität Leoben, 8700 Leoben, Austria
[c] Institut für Physik, Montanuniversität Leoben, 8700 Leoben, Austria
[d] Fachbereich Chemie, Institut für Physikalische Chemie, Universität Duisburg-Essen, 45117 Essen, Germany

cation of the dissolution processes of the different dense alumina compositions which constitute the PAOX pore walls. This procedure allows the experimental realisation of freestanding, large area PAOX membranes with enhanced mechanical flexibility (area size of several 10 cm^2) and complete through-hole pore morphology.

General Features of Porous Anodic Alumina

Figure 1 represents a schematic top view on the surface of the open pore side of a PAOX membrane. The membrane is constructed of individual alumina cells with hexagonal cell shape. In the centre of these hexagonal cells are uniform uniaxially rounded pores. The diameter of the PAOX cells as well as the diameter of the PAOX pores is directly proportional to the applied anodisation voltage.[6] The pore walls consist of two different types of alumina.[7] On the one hand is a relatively pure anion-free dense alumina which makes up the hexagonal body of the cell. This material is not in direct contact with the pore itself. On the other hand, in the inner cell region is an electrolyte-contaminated less dense alumina, which forms the pore wall. Figure 1 (part a) shows a cross-section of the PAOX membrane with the unidirectional pore arrangement. At the bottom the pores are separated from the aluminium metal base by the barrier layer, which seals the PAOX membrane on one side. To obtain a total through-hole pore morphology (i) the PAOX membrane has to be detached from the aluminium metal base and (ii) a pore opening process has to be employed which dissolves the barrier layer and forms a uniform pore diameter *without* destroying the overall porous backside structure. Steps (i) and (ii) have to be applied consecutively in two independent processes.

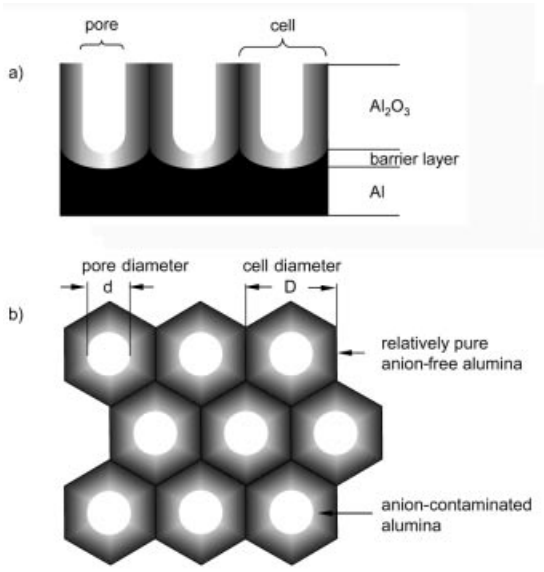

Figure 1. Schematic view of the characteristics of an idealised PAOX membrane pore geometry. (a) Schematic of the cross section of the unidirectional pore arrangement of a PAOX membrane. The pores are sealed on one side by the convex shaped barrier layer, which forms the connection of the PAOX membrane to the aluminium metal base. (b) Top view of the surface showing the hexagonal cells with the central through-hole pores. The alumina consists of two different types: (i) relatively pure dense alumina which constitutes the outer cell region cell and (ii) anion-contaminated, less dense alumina, which forms the surrounding through-hole pore material which is in direct contact with the inner pore. This different material composition is schematically shown by the greyish colour graduation.

Results and Discussion

Our first experimental step in the synthesis of alumina membranes is the high temperature annealing of commercial aluminium sheets at 400 °C. This procedure relaxes the surface of the aluminium base metal from defects.[8] Figure 2 (part a) shows an SEM picture of as-received aluminium (99.93%, PURALUX®). The general roughness of the surface as measured by AFM is 47 nm. Part b of Figure 2 shows an SEM picture of the same aluminium sheet after heat treatment under air (400 °C) for 1 h. Its roughness has increased. The general roughness of the heat-treated aluminium is about 100 nm as compared to 47 nm before this treatment. This difference can be explained by a thermal expansion of the aluminium sheet during the heat treatment followed by subsequent contraction of the metal surface while cooling down to room temperature.[9] This relaxes stresses within the surface, but on the other hand results in a folding of the surface which increases the overall roughness in comparison to the untreated material.

To remove this surface roughness the heat-treated metal specimen is electropolished in a solution of perchloric acid in ethanol.[10] Electropolishing is used in deburr processes

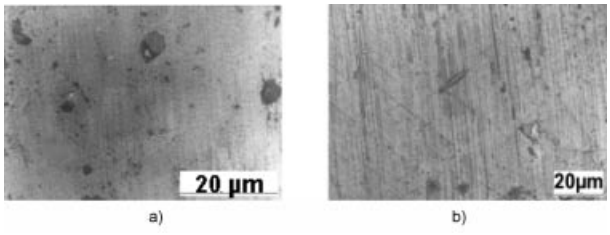

Figure 2. SEM pictures of (a) aluminium PURALUX® as received, (b) PURALUX® surface after heat treatment of 450 °C for 1 h. The roughness of the surface has increased.

of metals, where cutting edges of metals are flattened. This treatment removes the induced roughness of the Al metal sheet surface by chemical etching. The roughness of the aluminium surface after electropolishing is about 29 nm as detected by AFM (part a in Figure 3). However, what is most important here for the alumina surface is that the electropolishing procedure pretextures the metallic surface on a nanoscale [Figure 3, parts a (AFM) and b (SEM)]. This pretexturing is dependent on the applied voltage. The diameter of the concave spots on the electropolished aluminium surface (SEM, Figure 3, part b) is about 55 nm at 40 V. A direct connection exists between the electropolishing conditions employed and the formation of the PAOX membranes by the follow-up anodic oxidation process (see below and upcoming section on PAOX membrane formation).

 © 2005 Wiley-VCH Verlag GmbH & Co. KGaA, Weinheim

Nevertheless, other recent reports on the formation of PAOX membranes claim no significant effect of electropolishing on the prestructuring of the aluminium metal surface.[11]

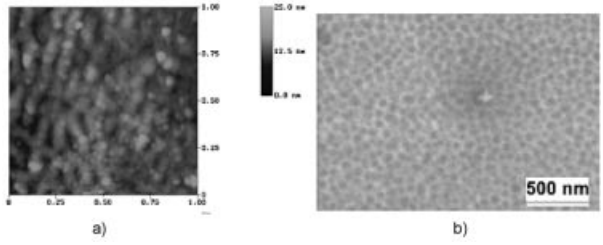

Figure 3. (a) AFM picture of an electropolished aluminium surface (1×1 μm^2 scan, height bar 0–25 nm). The roughness of the surface is 30 nm. (b) Concave structures (diameter 60 nm) on the top of the surface are visible by SEM. The diameter of the concave part is in the range of 60 nm.

Figure 4 shows an SEM of an aluminium surface which was first electropolished (see Exp. Section) followed by long-term anodic oxidation for 24 h, followed by detachment of the thus formed alumina membrane from the aluminium metal base by reversing the initially applied anodisation voltage (see Exp. Section).[12] This procedure leaves the aluminium metal base with a characteristic starting pore geometry on top (Figure 4). The diameter of the concave hollows on the metal surface is 80 nm, which is in fair agreement with the theory of voltage versus cell/pore size relationship of PAOX films. For an anodic oxidation voltage of 40 V, as in the present experiments, values of 51.6 nm for the pore diameter and 110.8 nm for the overall cell diameter are expected.[6] The mean diameter of the experimentally observed concave hollow structures (80 nm) on the aluminium surface is between these two values.

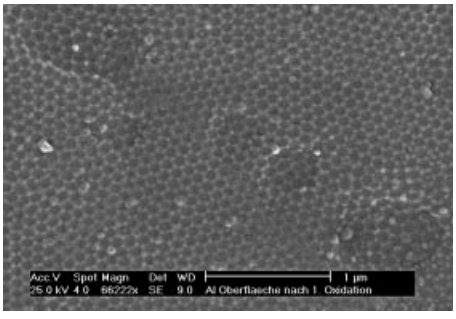

Figure 4. SEM picture of an aluminium surface after first anodisation and detachment of the resulting alumina membrane.

These results show that the different steps of pretreatment of the aluminium base metal have an enormous effect on the structure of the surface. It is interesting to note that the concave oxidic hollows on the underlying aluminium metal base generated by detachment of the PAOX membrane may serve as future template structures for depositing ordered nanodots of equivalent dot size.

Preparation of Freestanding PAOX Membranes with Through-Hole Morphology

After having studied the initial steps of porous oxide formation, we investigated the formation of PAOX membranes with hexagonally ordered pores at anodisation voltages of 25, 40 and 50 V in more detail. For pretexturing the electropolished aluminium surface we carried out the above-described process involving electropolishing followed by an anodic anodisation for 24 h, followed by detachment of the resulting membrane from the aluminium backside by reverse voltage technique (see Exp. Section). This procedure results in aluminium metal sheets with hexagonal textured structures on top (Figure 4). To obtain PAOX membranes from such prestructured metal surfaces we then performed a final anodisation step under the same electrolysis conditions as before with such a prestructured aluminium surface. The complete procedure was carried out for PAOX membranes under anodisation conditions of 40, 50 and finally 20 V.

40-V PAOX Membranes from Prestructured Aluminium Surfaces

Prestructured aluminium metal sheets (see above) were finally anodised for 20 h/10 °C/40 V anodisation voltage (see experimental). The resulting PAOX membrane was then detached from the aluminium base by reversing the voltage (Figure 5). We have optimised this technique and found that membrane detachment by the voltage reversal has significant advantages over chemical detachment methods using $HgCl_2$ or $CuBr_2$ often employed to obtain freestanding PAOX membranes. Detachment by careful voltage reversal allows production of up to several square centimetres of sized flexible PAOX membranes which may find use in future large area template applications (Figure 6).

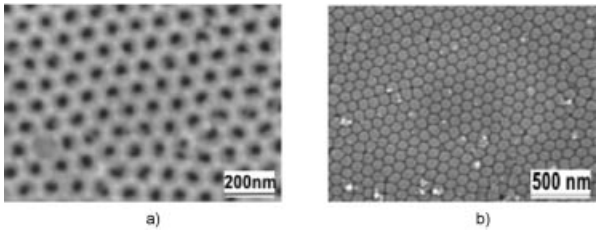

Figure 5. SEM pictures of a detached PAOX membrane prepared in a second anodisation step at 40 V. (a) Front side with hexagonally ordered open pores, (b) rear side with closed hexagonally ordered pores.

In Figure 5 the hexagonally ordered open pores of the PAOX membrane can be seen. The uniform diameter of the pores is 36 nm (±2 nm) and the cell diameter is 105 nm (±4 nm). It is known that the pore walls of PAOX membranes contain varying amounts of electrolyte.[7,13,14] The contrast-rich region of the SEM picture, next to the middle of the neighbouring pores, represents electrolyte-free dense alumina (see Figure 1). The less contrast-rich part of the inner pore region corresponds to the electrolyte-containing

 © 2005 Wiley-VCH Verlag GmbH & Co. KGaA, Weinheim

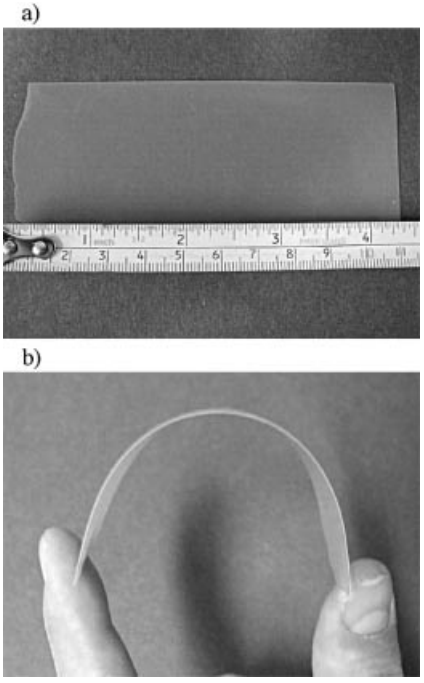

Figure 6. (a) Photo of a freestanding PAOX membrane (size about 40 cm^2). (b) Same sized PAOX membrane under manual mechanical torsion.

part of alumina. Their distinction in the SEM is due to the scattering behaviour of the electron beam for different dense materials. Figure 5b shows the rear side of a detached PAOX membrane. The hexagonally arranged pores are closed because of the presence of the barrier layer. Figure 7 (pos. 1, pos. 2) shows regions in which highly ordered domains are separated from unordered domains by different unordered boundary pore arrangements, for example, a flowerlike arrangement (Figure 7, pos. 1) and a linear arrangement of pores (Figure 7, pos. 2). We have observed such morphologies separating well ordered, hexagonally arranged pore regions from each by lower ordered regions throughout the whole PAOX membrane structure over cm^2 large areas in several independent experiments. The pore formation process in PAOX membranes has been studied theoretically by applying the mathematical theory of Voronoi.[14,15] Similar disordered pore structures are expected

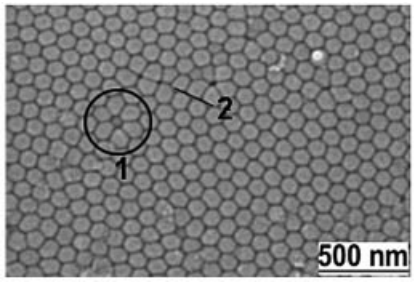

Figure 7. SEM of a backside of a detached PAOX membrane showing different ordered domains. Several kinds of disorder can be observed at the boundaries of the domains. Defects labelled with 1 have a flowerlike structure, and those labelled 2 display a linear structure.

by the theoretical model reported therein, and are also found experimentally by others.[15] This inherent and characteristic domain disorder of PAOX membranes can be overcome to a significant extent by using a prestructured alumina metal base which is available, for example, by embossing techniques using mechanically hard master stamps (produced e.g. by e-beam lithography), as has been shown by Masuda et al. for the first time.[16]

Figure 8 shows a cross-section of a typical PAOX membrane generated at 40 V exhibiting an all through parallel pore morphology. The nearly perfect parallel pore structure running orthogonal to the PAOX membrane surface is evident.

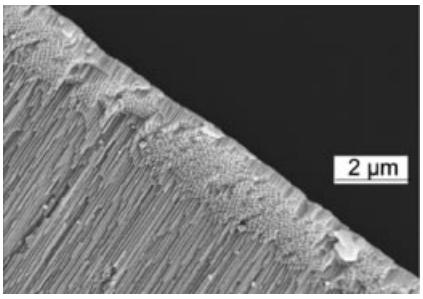

Figure 8. SEM of a cross-section of a detached PAOX membrane generated at 40 V. The pore channels are nearly perfectly parallel and orthogonally aligned to the surface which is seen partly in the foreground of the image. The channels are running from the top to the bottom of the image.

50-V PAOX Membrane from Prestructured Aluminium Surfaces

Figure 9 (parts a, b) show the front side of such a membrane. A hexagonal order of pores in μm^2-sized domains can be seen. The pore diameter is 57 nm (±4 nm) and the cell diameter is 114 nm (±4 nm), both corresponding to the values expected theoretically, which are 64.5 nm for the pore diameter and 138.5 nm for the cell diameter.[6] Part c of Figure 9 depicts the closed backside of a PAOX membrane detached from the aluminium metal base by the voltage reversal technique. The hexagonal ordering of the pores is again nearly perfect. Figure 9 (part d) shows the massive parallel pore arrangement of such a PAOX channel system.

We also routinely generated hexagonally ordered alumina membranes at 25-V anodisation voltage with the same morphological characteristics as discussed for the 40- and 50-V membranes (SEM, AFM topological characterisation not shown). Their pore diameter is 36 nm (±3 nm) and the cell diameter 64 nm (±2 nm), both in good agreement with the theoretical values of 32 and 69 nm for the cell and pore diameters, respectively.

Controlled Dissolution Studies of the Barrier Layer from Freestanding PAOX Membranes

For detachment of the alumina membrane after their synthesis we generally use the reversing voltage technique

 © 2005 Wiley-VCH Verlag GmbH & Co. KGaA, Weinheim

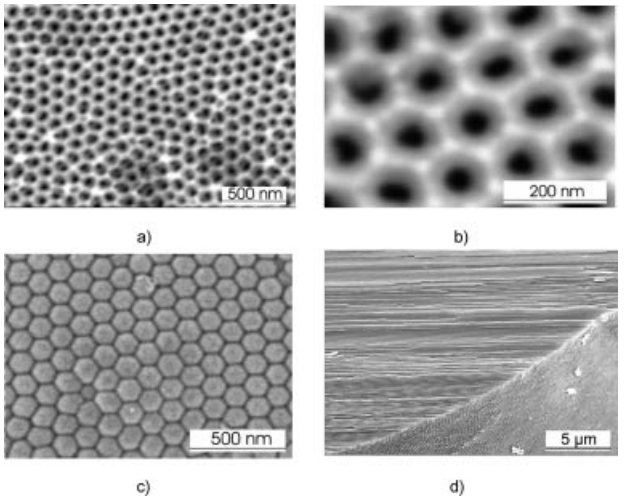

Figure 9. SEM of hexagonally ordered pores of a detached PAOX membrane generated at 50 V with complete through-hole morphology. (a) Front side of a PAOX membrane generated at 50 V with hexagonally ordered open pores; (b) as (a), but higher magnification; (c) back side of a PAOX membrane (50 V) with closed barrier layer; (d) cross-section of the same membrane with parallel pore arrangement.

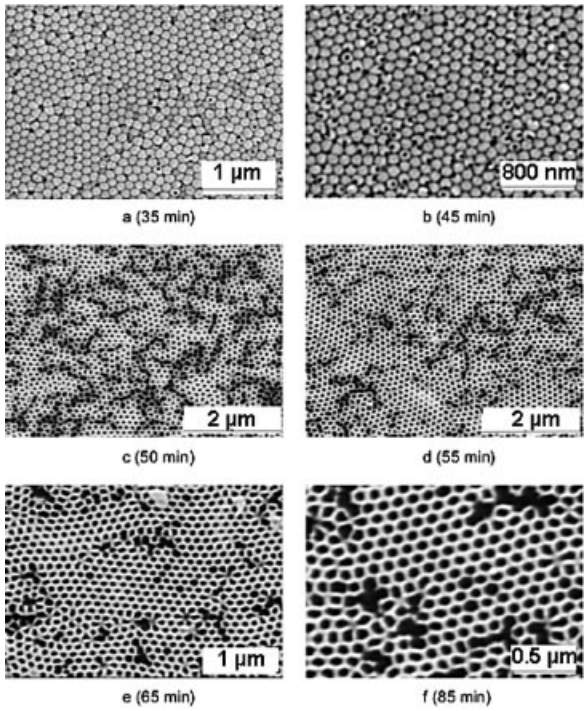

Figure 10. SEM images of the barrier layer of a PAOX membrane (50 V) at different intervals of backside pore opening (5% H_3PO_4). After 45 min of acid treatment (9a and 10b) the majority of the pores are still closed. After 50 min (c) pores are fully opened and pore widening of the inner pores starts to take place. (d) Further etching leads to an increased pore widening and subsequent destruction of the opened alumina membrane backside. This occurs predominantly in areas of hexagonal disorder [e and f (scale bar 200 nm)].

(see before). This results in the formation of a freestanding PAOX membrane with a *single* open pore side. The open pore side represents the initial oxidation front of the electrochemical anodisation process and reflects in its cell size and overall surface structure the unsteady electrolysis conditions present during the beginning of the aluminium oxidation when equilibrium conditions for pore cell formation have not been reached. The closed side of the PAOX membrane, the barrier side, represents the front of the ongoing oxidation process directly attached to the aluminium metal substrate. Therefore the backside typically shows well-arranged pore cells, because electrolysis conditions reach an equilibrium state during the ongoing anodisation.

Time-Dependent Acid Etch of the Barrier Layer

In numerous experiments we have found that the process of pore opening of the backside of PAOX membranes is experimentally the most difficult procedure in obtaining PAOX membranes with a complete through-hole morphology.[16] It depends crucially on the acid strength, and time and type of contact in order to open the closed backside in a controlled and reproducible way. Control over this process by straightforward chemical etching techniques is desirable in order to have access to through-hole open pore geometries with different pore diameters.

To obtain PAOX membranes with a continuous through-hole pore morphology we studied dissolution of the barrier layer over different time intervals. In our experiments we studied hexagonally arranged PAOX membranes that were generated at 50 V and the barrier layer was dissolved with 5% H_3PO_4 (aq.) over time. Figure 10 (parts a–f) show SEM micrographs at different time intervals representing different stages of barrier layer dissolution.

35 min of Acid Treatment

The initial dissolution process starts by producing hole structures in the convex domes of the barrier layer (Figure 10, part a). The location of the holes in the individual pores appear as black dots distributed inhomogeneously over the membrane surface, for example holes can be observed in the centre of one pore, as well at the edges of individual pores. The majority of the backside pore domes, however, are still unaffected after that time interval.

45–55 min of Acid Treatment

After 45 min the number of partially opened backside pore domes has increased significantly (Figure 10, part b). Interestingly the dimensions of the already opened pore domes from the first etch period (35 min) are nearly unaffected. After 50 and 55 min of dissolution (Figure 10, parts c and d) the barrier layer is completely removed and all pores are opened. However different stages of pore opening are detectable after these times. Some pores are opened to such an extent that connecting neighbouring pores are already affected. This effect is observed to a significantly large extent in domain areas where cell disorder is found. Ordered domain areas show a more even pore dissolution characteristic. This effect is even more pronounced after

 © 2005 Wiley-VCH Verlag GmbH & Co. KGaA, Weinheim

65 min (Figure 10, part e) and after 85 min (Figure 10, part f) of pore dome dissolution. With ongoing acid treatment, not only are the disordered parts of the membrane dissolved, but the structure of the inner pore walls of the ordered regions also becomes larger. This is due to an ongoing dissolution of alumina from the already opened pores. This process is generally known as pore widening and is caused by the dissolution of the electrolyte-rich inner alumina phase. In Figure 10f the inner alumina phase is nearly completely dissolved, leaving the electrolyte-free outer alumina portion of the pore cell structure, which is not prone to dissolution under these conditions, unaffected.

Based on the results of these dissolution experiments we have developed a scheme illustrating the acid dissolution process of the PAOX membrane backside over time (Figure 11).

The first step of the dissolution process is a slow thinning of the outer electrolyte-free alumina, which represents the top of the barrier layer of the convex dome structures as shown in (a) on the left-hand side of Figure 11. Until dissol-

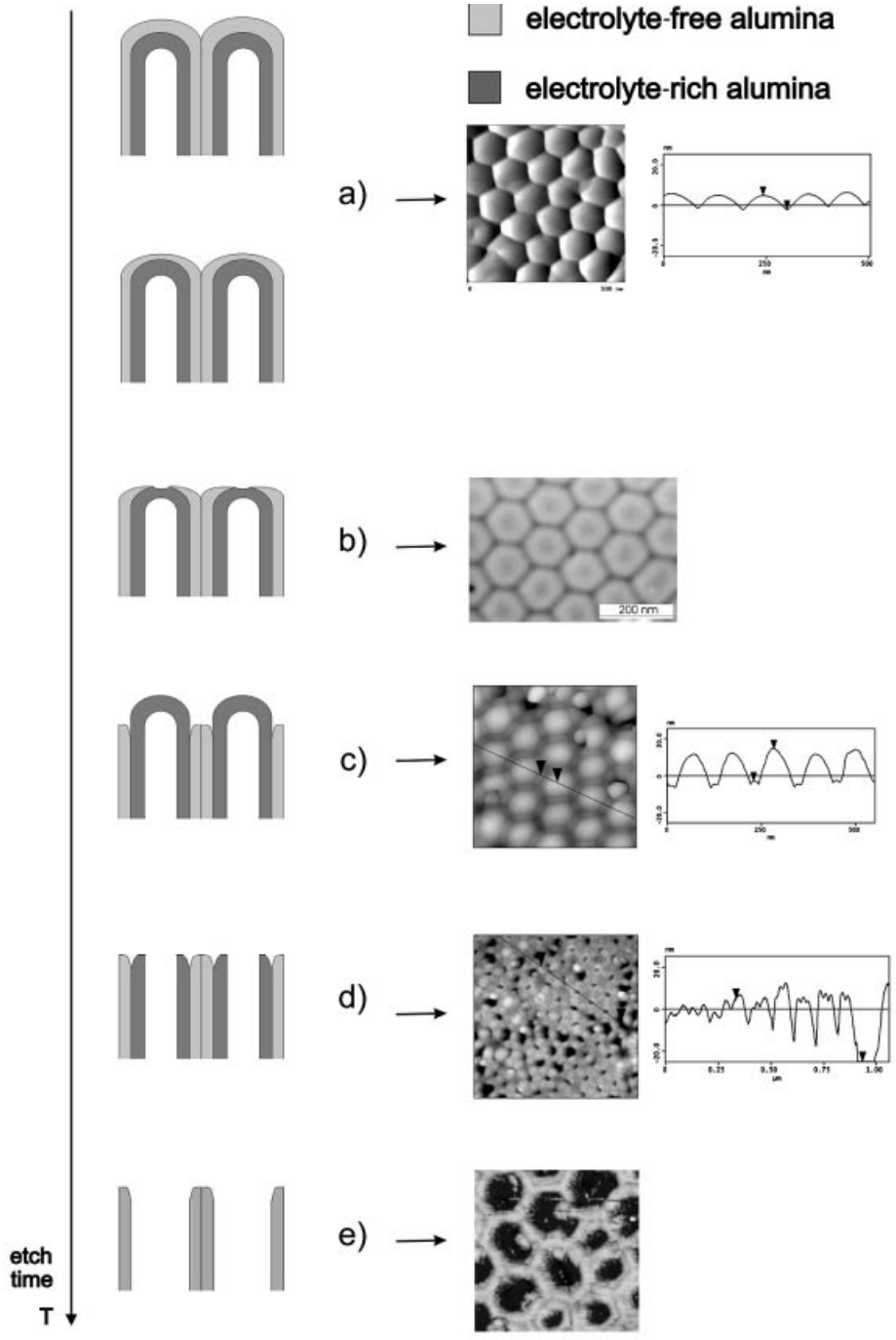

Figure 11. Scheme of the dissolution process leading to a pore opening by acid treatment (see text for details). (a) Line scan 0–500 nm, height bar 0–20 nm; (b) scale bar SEM 200 nm; (c) line scan 0–500 nm, height bar 0–20 nm; (d) line scan 0–1 μm, height bar 0–20 nm.

 © 2005 Wiley-VCH Verlag GmbH & Co. KGaA, Weinheim

ution of the alumina dome caps of the backside has progressed significantly, we are not able to detect any significant change in morphology using AFM. After increasing reaction time the dome caps are dissolved to a significant extent, which can be visualised by SEM (Figure 11b). The initial process of dome cap opening needs a significantly longer time compared to the next steps of the overall dissolution process finally leading to the complete opening of the PAOX membrane backside. A rationale for this can be found in the different compositions of the outer and inner alumina compositions of the PAOX cell structure (see Figure 1). The dome caps of the alumina cells are composed of electrolyte-free (Figure 11, light grey region) and electrolyte-contaminated alumina (Figure 11, dark grey region). The former is more resistant towards acidic dissolution than the inner pore walls of the cells. Once the outlying, more dense, electrolyte-free alumina part of the dome caps has been completely dissolved, the overall backside dissolution process leading to complete pore opening proceeds very quickly.

Part c of Figure 11 shows the situation of a strongly dissolved, electrolyte-free alumina dome cap structure. The pore walls are already strongly dissolved in comparison to the still closed underlying dome cap of the electrolyte-containing alumina (see AFM cross-section analysis, Figure 11, part c, right side). The interface region separates two neighbouring, still closed pores in which the electrolyte-free alumina is completely dissolved.

The next step in the dissolution process is the beginning of the complete pore opening which produces the desired through-hole morphology of the PAOX membrane (AFM, Figure 11, part d; right side). Ongoing dissolution opens the pores to a further significant extent (Figure 11, part e). This last dissolution step is the so-called pore-widening step because it enlarges the entrance part of the opened pores over their regular sized dimensions (the 'pore size', see Figure 1) by dissolving interior material from the alumina pores. Obviously the pore-opening model developed here is in good agreement with the dissolution process as it is verified experimentally in Figure 10.

The required times for total pore opening and widening (Figure 11, part e) for 25-, 40- and 50-V PAOX membranes are summarised in Table 1. With increasing pore diameter and barrier-layer thickness, the time for pore opening increases. However, no linear correlation between dissolution time, anodisation voltage and thickness of the barrier layer was found. To obtain reproducible PAOX membrane properties we check the PAOX morphology by routine interval SEM studies to watch the ongoing dissolution process in a stepwise manner. These checks allow simple but efficient control of the pore-opening process and give the possibility of varying pore entrance diameters at will just by stopping the chemical etching process at a certain time. To the best of our knowledge such control over pore entrance diameters in PAOX membranes has only been reported by using grazing angle Ar ion milling[17] of a closed PAOX membrane backside. This technique is able to produce certain degrees of pore openings. However, this is a technique that is not applicable over several cm^2-large PAOX membrane areas as we have reported herein with the time-controlled etching method.

Table 1. Typical time intervals for generation of a PAOX membrane with complete through-hole pore morphology generated from a detached PAOX membrane with closed backside at different anodisation voltages viz. different pore and cell diameters.

Anodisation voltage [V]	Time of acid treatment [min]
25	23
40	75
50	85

Another point of importance for the pore-opening procedure is the occurrence of domain boundaries between ordered pore regions. They represent areas of local disorder in which alumina surrounding these areas is dissolved more quickly than alumina in higher ordered areas. This effect is demonstrated in Figure 12 in which the initial start period of a PAOX backside dissolution process is shown. Dissolution is predominant in areas where disordered structures are present (boundary regions), denoted by dark circles.

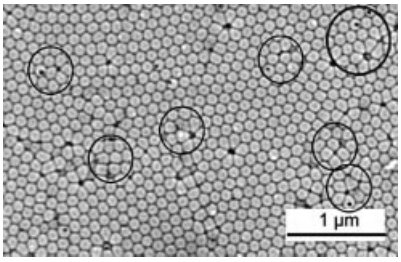

Figure 12. SEM picture of alumina membrane barrier layer at an early stage of backside pore opening. The circles mark positions where pore opening is observed preferentially. This is dominantly α or β to a location of pore disorder.

Conclusion

We have synthesised freestanding, large area sized PAOX membranes with an all through pore arrangement by electrochemical anodic oxidation of aluminium followed by detachment and selective pore opening. We have shown that hexagonally ordered pores over several square µm regions can be obtained at anodisation voltages of 25, 40 and 50 V, resulting in PAOX membranes with pore diameters of 33, 40 and 72 nm.

It has also been shown by AFM and SEM investigations that pretreatment (annealing and electropolishing) of the aluminium metal substrate, especially the applied voltage in the electropolishing step, has a significant influence on the quality and order of the pores of the PAOX membrane. By using the reversing voltage technique for detachment of the prepared alumina membrane, samples with an open pore side and a closed barrier side are obtained. We investigated a time resolved dissolution of the barrier layer with AFM and SEM. Based on these results we have proposed a mechanism for the successive dissolution of the closed pores

 © 2005 Wiley-VCH Verlag GmbH & Co. KGaA, Weinheim

with H_3PO_4. This allows access to flexible, freestanding, large area PAOX membranes with ordered pore geometries and completes through-hole pore morphology on a routine experimental basis by straightforward chemical techniques.

Experimental Section

General Information: Aluminium (99.93%, PURALUX Quality) was from AMAG, Ranshofen, Austria. For SEM characterisation the PAOX membranes were sputter coated with gold using a Cressington 108a sputter coater. SEM was carried out with a Zeiss Gemini DSM 982 and AFM was done with a DI Nanoscope IIIa in the tapping mode. Pore and cell diameter measurements of PAOX membranes were made on a statistical basis determining up to 20 structures in different domain areas of the membrane.

Electropolishing of the Aluminium Base Metal: This was performed in a mixture of ethanol and perchloric acid (4:1, vol.-%) at 0 °C. The distance of the aluminium electrodes was fixed at 9 cm. The best results for polishing were obtained with current densities between 0.25 and 0.40 A cm^{-2}. The polishing voltage was the same as for the following anodisation step. After 3 min of polishing the anode was removed while voltage was still on and was rapidly rinsed with water and acetone.

PAOX Sample Preparation (General Preparation Procedure): $10 \times 3 \times 0.13$ cm aluminium base metal sheets were first degreased with acetone and subsequently annealed at 400 °C for one hour. Following the electropolishing of the sample (current density between 7 and 30 mA cm^{-2}) a first anodisation was carried out for 24 h followed by voltage reversal at the same voltage to detach the membrane from the alumina base. Time for detachment varies between 12 and 24 h, depending on the degree of pore opening. The final anodisation of the prestructured aluminium metal base under identical conditions (see Table 2) was followed again by detachment of the formed membrane from the aluminium metal base through the voltage reversal technique.

Table 2. Experimental conditions for aluminium anodisation leading to PAOX membranes with hexagonal pore geometry.

Electrolyte	Concentration [wt.-%]	Anodisation voltage [V]; time	Temperature [°C]
H_2SO_4	10	(25)[a]; 15–30	(5); 10–25
$H_2C_2O_4$	4	(40, 50); 30–60	(5); 0–25

[a] Number in parentheses: this work; others: possible temperature window which can be also used to form PAOX membranes under otherwise same conditions.

Dissolution of the Barrier Layer: To open the backside of the PAOX membrane the barrier layer was treated with a 5% phosphoric acid solution at 30 °C. Therefore the membrane was placed with the barrier layer face down on the phosphoric acid solution (see Table 1 for time intervals). After the time necessary for dissolution of the backside PAOX membrane it was carefully lifted off the acid bath, rinsed with distilled water for 30 min and thereafter washed with acetone.

Acknowledgments

We thank AMAG, Ranshofen, Austria for donation of the PURALUX aluminium metal sheets. Use of the SEM facility in the Dep. of Geology (Prof. Piller), Karl-Franzens-University Graz, Austria, is also acknowledged with gratitude.

[1] a) H. Masuda, K. Fukuda, *Science* **1995**, *268*, 1466; b) H. Masuda, H. Asoh, M. W. Watanabe, K. Nishio, M. Nakao, T. Tamamura, *Adv. Mater.* **2001**, *13*, 189; c) G. D. Sulka, S. Stroobants, V. Moshchalkov, G. Borghs, J. Celis, *J. Electrochem. Soc.* **2002**, *149*, D97; d) C. H. Martin, *Science* **1996**, *8*, 1739; e) M. Kang, S. Yu, N. Li, C. R. Martin, *Small* **2005**, *1*, 1–4; f) J. Yan, G. V. Rama Rao, M. Barela, D. A. Brevnov, Y. Jiang, H. Xu, G. P. López, P. B. Atanassov, *Adv. Mater.* **2003**, *15*, 2015–2018.
[2] See for example: a) J. Li, C. Papadopoulos, J. Xu, M. Moskovits, *Appl. Phys. Lett.* **1999**, *75*, 367; b) G. L. Hornyak, A. C. Dillon, P. A. Parilla, K. M. Jones, F. S. Fasoon, M. J. Heben, J. J. Schneider, N. Czap, *Nanostruct. Mater.* **1999**, *12*, 83; c) H. Masuda, M. Ohya, H. Asoh, M. Nohtomi, T. Tamamura, *Jpn. J. Appl. Phys.* **1999**, *38*, L1403; d) G. L. Hornyak, M. Kröll, R. Pugin, T. Sawitowski, G. Schmid, J.-O. Bovin, G. Karsson, H. Hofmeister, S. Hopfe, *Chem. Eur. J.* **1997**, *3*, 1951.
[3] T. Yanagishita, M. Sasaki, K. Nishio, H. Masuda, *Adv. Mater.* **2004**, *16*, 429–432.
[4] A. H. Greiner, J. H. Wendorf, M. Steinhart, *Nachr. Chem.* **2004**, *52*, 426.
[5] H.-P. Kormann, G. Schmid, K. Pelzer, K. Philippot, B. Chaudret, *Z. Anorg. Allg. Chem.* **2004**, *630*, 1913.
[6] J. P. O'Sullivan, G. C. Wood, *Proc. R. Soc.* **1970**, *A317*, 511.
[7] a) S. Ono, N. Masuko, *Corros. Sci.* **1992**, *33*, 503; b) S. Ono, H. Ichinose, N. Masuko, *Corros. Sci.* **1992**, *33*, 841; c) H. Uchi, T. Kanno, R. S. Alwitt, *J. Electrochem. Soc.* **2001**, *148*, B17–B23.
[8] H. Hu, in: *Metals Handbook*, 9th ed., American Society for Metals, Metals Park, OH, **1985**, vol. 9, pp. 692–699.
[9] D. Altenpohl, *Aluminium*, 4th ed., Aluminium-Verlag, Düsseldorf, **1979**, ch. 10, pp. 122–137.
[10] F. Li, L. Zhang, R. M. Metzger, *Chem. Mater.* **1998**, *10*, 2470.
[11] I. H. Yuan, F. Y. He, D. E. Sun, X. H. Xia, *Chem. Mater.* **2004**, *16*, 1841.
[12] T. Kyotani, W. H. Xu, Y. Yokoyama, J. Inahara, H. Touhara, A. Tomita, *J. Membr. Sci.* **2002**, *196*, 231–239.
[13] Y. C. Sui, B. Z. Cui, L. Martínez, R. Perez, D. J. Sellmyer, *Thin Solid Films* **2002**, *406*, 64–69.
[14] J. Randon, P. P. Mardilovich, A. N. Govyadinov, R. Paterson, *J. Colloid Interface Sci.* **1995**, *169*, 335.
[15] A. P. Li, F. Müller, A. Birner, K. Nielsch, U. Gösele, *J. Vac. Sci. Technol. A* **1999**, *17*, 1428.
[16] H. Masuda, H. Yamada, M. Satoh, H. Asoh, M. Nakao, T. Tamamura, *Appl. Phys. Lett.* **1997**, *71*, 2770.
[17] T. Xu, G. Zangari, R. M. Metzger, *Nano Lett.* **2002**, *2*, 37–41.
Received: December 22, 2004

 © 2005 Wiley-VCH Verlag GmbH & Co. KGaA, Weinheim

Exploring the Reactivity towards Acidic Protic Ligands of the Di-μ-hydroxo Complex $[NBu_4]_2[Pd_2\{C_4(COOMe)_4\}_2(\mu\text{-}OH)_2]$: A Convenient Precursor in the Preparation of New Palladacyclopentadiene Complexes

Gregorio Sánchez,*[a] Jorge Vives,[a] Gregorio López,[a] José Luis Serrano,[b] Luis García,[b] and José Pérez[b]

Keywords: Palladacyclopentadiene complexes / Hydroxo complexes / Metallacycles / Cycloaddition

The dinuclear hydroxo complex $[NBu_4]_2[Pd_2\{C_4(COOMe)_4\}_2(\mu\text{-}OH)_2]$ (**I**) reacts in a 1:2 molar ratio with a wide variety of protic electrophiles H(L) bearing different sets of donor atoms (L = O^O, N^S or O^N) to give the mononuclear anionic palladium(II) derivatives with the general formula $[Pd\{C_4(COOMe)_4\}(L)]^-$ [O^O = salycilaldehydate (sal) (**1**), acetohydroxamate (ahx) (**2**) and benzohydroxamate (bhx) (**3**); N^S = 2-pyridinthiolate (spy) (**4**), 2-pyrimidinthiolate (spym) (**5**), 3-methyl-2-imidazolin-thiolate (meimt) (**6**) and 2-aminothiophenolate (2-atp) (**7**); O^N = *N*-phenylsalycilaldiminate (*N*-phsal) (**8**), *N*-*p*-chlorophenylsalycilaldiminate (*N*-clsal) (**9**), *N*-*p*-tolylsalycilaldiminate (*N*-tolsal) (**10**), 2-aminophenolate (2-atp) (**11**), 2-pyrrole-carboxaldeydate (2-pcal) (**12**), 8-hydroxiquinolinate (oxin) (**13**), picolinate (2-pic) (**14**)]. Structural characterisation by X-ray diffraction of complexes **5**, **8** and **13** confirmed the proposed formula. Dinuclear complexes $[NBu_4]_2$ $[Pd\{C_4(COOMe)_4\}(\mu\text{-az})]_2$ (az = pyrazolate (pz) (**15**), triazolate (tz) (**16**) and 3,5-dimethylpyrazolate (3,5-Me_2pz) (**17**) were obtained when treating **I** with azoles in the same molar ratio, and also treating the hydroxo complex with chloranilic acid (chl) (**18**) and squarate (sq) (**19**) in 1:1 proportion to yield compounds $[NBu_4]_2[Pd\{C_4(COOMe)_4\}\{(\mu\text{-O–O})\}]$ with the ligands acting as *bis*-bidentate ones. A related process takes place when (**I**) reacts with ammonium *O*,*O*′-dialkyldithiophosphates in acetone under mild conditions and complexes $[NBu_4][Pd\{C_4(COOMe)_4\}\{S(S)P(OR)_2\}]$ (R = Me (**20**), Et (**21**), *i*Pr (**22**)) are obtained. Deprotonation of secondary amines Et_2NH, Pr_2NH, piperidine or morpholine by (**I**) in the presence of carbon disulfide leads to the corresponding dithiocarbamate complexes $[Pd\{C_4(COOMe)_4\}(S_2CNR_2)]$ **23**–**26**. (**I**) also promotes the nucleophilic addition of water to pyridine-2-carbonitrile and a mononuclear complex **27** containing the pyridine-2-carboxamidate ligand is formed. Its structure has been determined by a single-crystal diffraction study. The new complexes were fully characterised by analytical and spectroscopic techniques (FAB-MS, IR; ^1H, ^{13}C and ^{31}P-NMR).

(© Wiley-VCH Verlag GmbH & Co. KGaA, 69451 Weinheim, Germany, 2005)

Introduction

The chemistry of metallacycles has received growing interest during the last few years, as a result of their involvement in catalytic processes and their applications in organic synthesis.[1] The cycloaddition of two unsaturated fragments to a metal unit is one of the most useful methods of metallacycle synthesis, since it gives access to relatively complex structures starting from small unsaturated molecules.[1a] In particular, the oxidative cycloaddition of acetylenic esters such as dimethylacetylenedicarboxylate (dmad) to Ni, Pd and Pt has received attention in the past,[2,3] in part because of its involvement in different oligomerization and co-oligomerization catalytic reactions,[4] and also because of the interesting behaviour as precursors in organometallic chemistry of the compounds formed. Specifically, the polymeric palladacyclopentadiene complex [1,2,3,4-tetrakis(methoxycarbonyl)-1,3-butadiene-1,4-diyl]palladium(II) (TCPC) $[Pd(C_4(COOMe)_4)]_n$, obtained in the reaction of dmad with $Pd(dba)_2$ (dba = dibenzylidenacetone) reacts with a wide range of donor ligands to give soluble discrete molecules,[2,3,5,6] although to date, just a few crystal structures of such palladacyclopentadiene compounds are known.[7,8] Other interesting features recently studied are their use as catalysts in several types of reactions. Thus, intramolecular carbametalation and [2 + 2 + 2] cycloaddition,[9] enyne metathesis accompanied by skeletal rearrangement,[10,11] co-cyclotrimerization of various alkynes[5], and hydrostannation of cyclopropenes,[12] have employed TCPC amongst other derivatives as the catalyst. In this sense, in the frame of our collaboration with Fairlamb and co-workers, we have reported the first application of mononuclear palladacyclopentadiene complexes containing

[a] Departamento de Química Inorgánica, Universidad de Murcia, 30071 Murcia, Spain
E-mail: gsg@um.es
[b] Departamento de Ingeniería Minera, Geológica y Cartográfica, Área de Química Inorgánica, Universidad Politécnica de Cartagena,
30203 Cartagena, Spain
E-mail: jose.serrano@upct.es

imidato ligands as catalysts in standard Stille cross-coupling reactions,[13]stating that yields and reaction times are dependent on the presence and type of these ligands. The exceptional catalytic properties of related dinuclear derivatives are currently under investigation, and suggest potential applications of compounds presented here.

On the other hand, in addition to their interest related to applied fields such antitumour activity of Pt^{II} complexes or catalytic processes,[14] the synthetic value of palladium(II) and platinum(II) di-μ-hydroxo complexes is a subject of growing study. For example, Sharp[15,16] and later others[17] have employed several such complexes as precursors in the preparation of scarce oxo and imido derivatives that are also relevant to C–O and C–N bond forming reactions in catalytic processes.[14] The reactivity towards protic substrates of dinuclear compounds $[Pd(\mu\text{-}OH)L^n]_2$ (L^n = orthometallated imine-based ligands) provides a general route to obtain dinuclear complexes with double and mixed bridges that have shown liquid crystal behaviour.[18] In this sense, during the last few years we have also been developing the usefulness of binuclear hydroxo complexes of palladium in the preparation of an extensive selection of new compounds, by means of a simple acid-base reaction.[19] Our more recent contribution to the area has been the synthesis of the dinuclear complex $[Pd_2\{C_4(COOMe)_4\}_2(\mu\text{-}OH)_2][NBu_4]_2$ and its use in the preparation of new palladacyclopentadiene derivatives that, as mentioned above, have shown interesting catalytic properties.[13] We expand in this paper on the reactivity of this complex towards several protic electrophiles and describe other related reactions, like that against amines in the presence of carbon disulfide or the addition of water experienced by pyridine-2-carbonitrile when $[Pd_2\{C_4(COOMe)_4\}_2(\mu\text{-}OH)_2][NBu_4]_2$ is present in the reaction.

Results and Discussion

The palladacyclopentadiene complex $[Pd_2\{C_4(COOMe)_4\}_2(\mu\text{-}OH)_2]^{2-}$ (**I**) was conveniently prepared by reaction of the polymeric complex $[Pd\{C_4(COOMe)_4\}]_n$ with NBu_4OH in water.[13] Its reactivity was easily followed by the disappearance of both an IR stretching vibration at 3600 cm^{-1} and a high-field shielded ^1H NMR resonance at δ = –0.85 ppm. The reactions explored in this paper are displayed in Scheme 1 and specific conditions followed for each of them are collected in the experimental section.

The hydroxo complex reacts with weak protic acids H(L) to give mono- or binuclear species depending on whether the deprotonated acid $(L)^-$ is *exo*- or *endo*-bidentate. These reactions can be viewed as an initial proton abstraction by (**I**) that provides $(L)^-$ and the metal substrate, subsequently trapped by the anion to form the new complexes. The protonation at the nucleophilic oxygen atom of the bridging OH should give an initial *aqua* complex that experiences H_2O replacement by the *endo*- or *exo*-bidentated $(L)^-$ leading to the formation of $[Pd\{C_4(COOMe)_4\}(L)]^-$ (**1**–**14**) or $[Pd\{C_4(COOMe)_4\}(\mu\text{-}L)]_2^{2-}$ (**15**–**17**) respectively. Similarly, the use of ligands able to coordinate in a *bis*-bidentate mode reacting with the precursor (**I**) in a 1:1 molar ratio allows the obtention of complexes **18** and **19**. The considerable nucleophilicity of the bridging OH groups of **I** makes it also

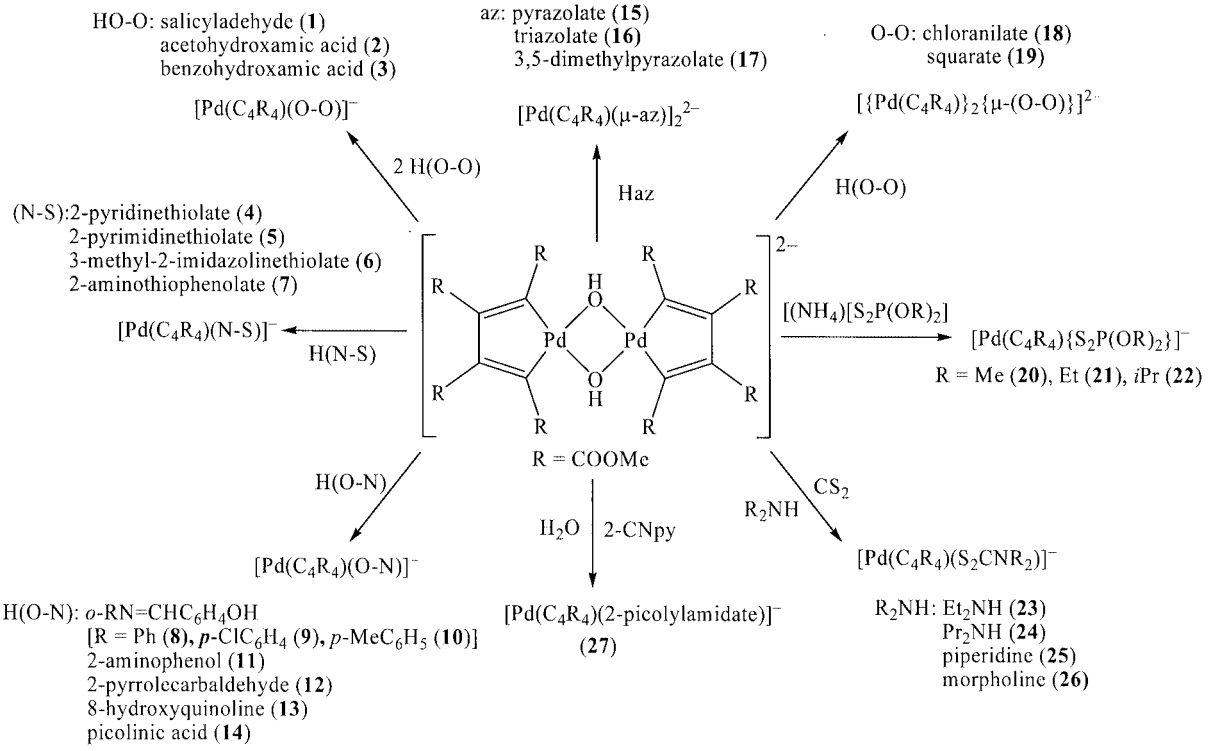

Scheme 1. Reactivity of the hydroxo complex $[NBu_4]_2[Pd_2\{C_4(COOMe)_4\}_2(\mu\text{-}OH)_2]$ (**I**).

 © 2005 Wiley-VCH Verlag GmbH & Co. KGaA, Weinheim

reactive towards ammonium *O,O′*-dialkyldithiophosphates, yielding complexes **20**–**22** with the concomitant release of NH_3 and H_2O. The preparation of the dithiocarbamate complexes **23**–**26** should involve a first step of amine deprotonation, followed by nucleophilic attack of R_2N^- to carbon disulfide to form the dithiocarbamate anion. On the other hand, the activation of nitriles with respect to attack by nucleophiles in the coordination sphere of metal ions has attracted considerable interest.[20] We have described the attack of OH^- and MeO^- on benzonitrile coordinated to Pt^{II}[21] and the use of the hydroxo complex $[\{Ni(C_6F_5)_2(\mu\text{-}OH)\}_2]^{2-}$ in the formation of complexes containing amidate ligands,[22] and now we employ a similar reaction between **I** and pyridine-2-carbonitrile in acetone/water to prepare complex **27**.

The new palladium complexes are air-stable and their IR spectra show two very strong bands [ν(CO)] around 1700 cm^{-1} characteristic of the carboxylate groups,[2] in some cases partly overlapped by those absorptions attributed to the incoming deprotonated ligands (see Exp. Section). The ^{1}H-NMR spectra show the corresponding signals of these ligands, and as a common feature the characteristic chemical shifts of the methoxycarbonyl groups, which act as a preliminary probe for the compounds geometry, i.e., symmetric complexes show two signals and asymmetric show four resonances, in accordance with previous results.[7,8]

The proposed nuclearity of the new complexes is also confirmed by FAB mass spectrometry and the negative FAB-MS data of the complexes with the *m/z* values for the observed fragments are collected in the experimental section. The abundance of the signals around the parent ion are consistent in all cases with the natural isotopic abundances. This technique has special relevance conferring the mononuclearity of complexes with heterocyclic-2 thiolate ligands **4**–**7**, as NMR spectroscopic data would be compatible with either mononuclear complexes with the ligands acting in a chelating mode or dinuclear complexes with bridging ligands. This extent has been further proved by X-ray diffraction analysis of compound **5** whose structure and selected bond lengths and angles are shown in Figure 1 and Table 1. The Pd–N and Pd–S distances are slightly longer than the ones found for related Pd^{II} complexes with this ligand[23] and the N(1)–Pd–S(1) angle is considerably smaller than 90°, in agreement with previously reported data for four-membered N,S-chelate rings.[24,25]

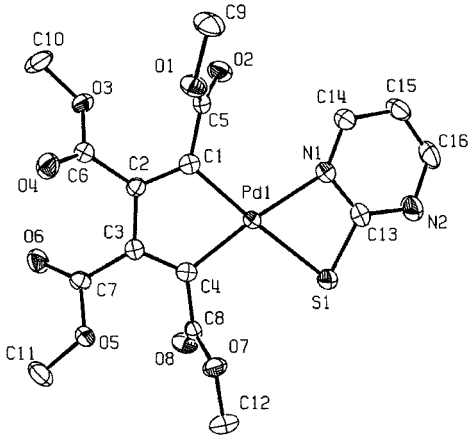

Figure 1. ORTEP diagram of anion complex **5** with the atom numbering Scheme; thermal spheres are drawn at the 50% probability level.

The mononuclear nature of complexes **8** and **13** that contain chelating ON donor ligands has also been confirmed by single-crystal X-ray analysis. The ORTEP diagrams of the two anions are shown in Figure 2 and Figure 3, while the relevant bond lengths and angles are reported in

Table 1. Selected bond lengths [Å] and angles [°] for complexes **5**, **8**, **13**, **20** and **27**.

	5	**8**	**13**	**20**	**27**
Pd(1)–C(1)	2.023(3)	2.007(3)	2.019(2)	2.05(3)	2.036(7)
Pd(1)–C(4)	1.986(3)	2.002(3)	1.981(2)	2.00(2)	1.741(6)
Pd(1)–N(1)	2.114(3)	2.111(2)	2.122(2)		1.882(5)
Pd(1)–N(2)					2.040(5)
Pd(1)–S(1)	2.3734(8)			2.406(8)	
Pd(1)–S(2)				2.396(7)	
Pd(1)–O(9)		2.0636(19)	2.0689(17)		
C(4)–Pd(1)–C(1)	79.29(12)	79.46(11)	79.30(9)	79.9(4)	79.6(3)
C(4)–Pd(1)–N(1)	172.48(11)	178.80(10)	171.32(9)		172.4(3)
C(4)–Pd(1)–N(2)					96.9(3)
C(1)–Pd(1)–N(1)	107.37(11)	101.51(10)	106.33(9)		107.1(2)
C(1)–Pd(1)–N(2)					176.4(2)
C(4)–Pd(1)–O(9)		90.83(10)	94.00(8)		
C(1)–Pd(1)–O(9)		167.91(9)	172.73(8)		
C(4)–Pd(1)–S(1)	103.85(8)			177.8(7)	
C(1)–Pd(1)–S(1)	176.77(9)			99.6(8)	
C(4)–Pd(1)–S(2)				97.0(7)	
C(1)–Pd(1)–S(2)				176.5(7)	
N(1)–Pd(1)–N(2)					76.5(2)
N(1)–Pd(1)–S(1)	69.45(7)				
O(9)–Pd(1)–N(1)		88.12(8)	80.66(7)		
S(1)–Pd(1)–S(2)				83.53(10)	

 © 2005 Wiley-VCH Verlag GmbH & Co. KGaA, Weinheim

Table 1. The torsion angles of the six-membered ring chelate in (**8**) suggest for it a distorted sofa conformation.[26]

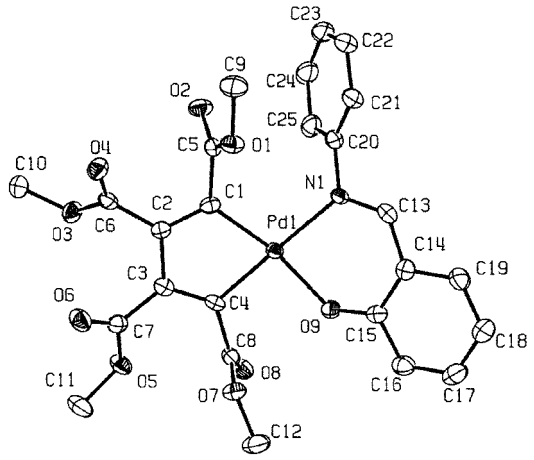

Figure 2. X-ray crystal structure of **8**. Thermal ellipsoids are drawn at 50% probability. Hydrogens omitted for clarity.

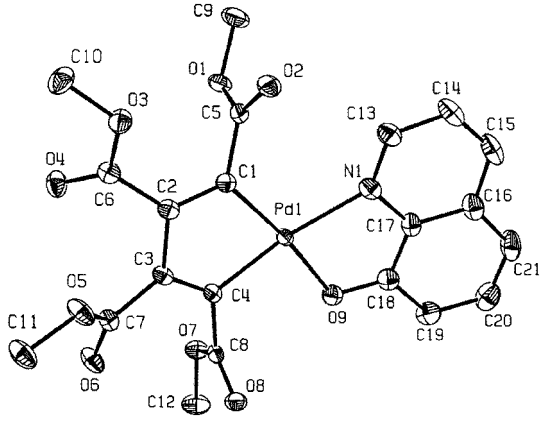

Figure 3. An ORTEP representation of **13**.

The structure of the dimethyldithiophosphate complex **20** has been established and is shown in Figure 4. The Pd–S distances are slightly longer than those found in related complexes (Table 1).[27] It can be inferred from this Table that the Pd–C bond lengths in complexes **5**, **8**, **13**, **21** are

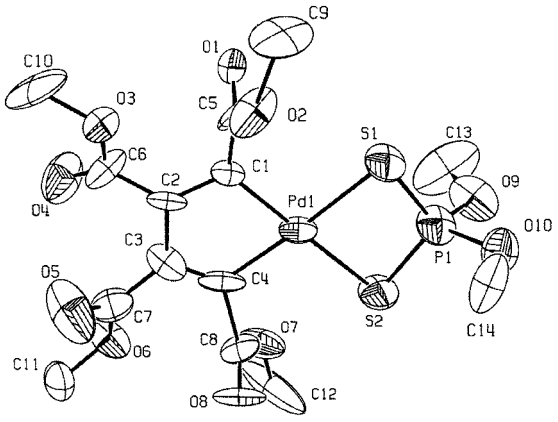

Figure 4. ORTEP diagram of **20**; thermal ellipsoids are drawn at the 50% probability level.

all similar with values of ca. 2 Å, with independence of the donor atom placed in *trans*- to the metallacyclic carbon. However, the distance Pd(1)–C(4) in complex **27** *trans*- to the pyridinic nitrogen is comparatively shorter. In this structure (Figure 5) is also found a short Pd(1)–N(1) distance if compared with the analogous one in complex **5** with the 2-pyrimidinthiolate ligand described above.

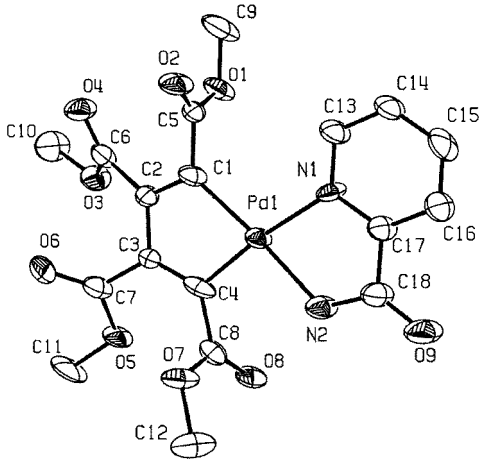

Figure 5. Structure of the $[Pd\{C_4(COOMe)_4\}(2\text{-}HNCOpy)]^-$ anion in the single crystal structure of **27**. All hydrogen atoms have been omitted for clarity.

The five new structures may be described as nearly planar, and their deviation from the planar coordination has been quantified by the $N_1{*}C_1C_4Pd_1$ and $E{**}C_4C_1Pd_1$ improper torsion angles (see Table 2).[28]

Table 2. Distortion parameters from square-planar coordination.

Improper torsion angles [°]	**5**	**8**	**13**	**20**	**27**
N(1)[a] C(1)–C(4)–Pd(1)	2.19	–0.47	4.17	–1.55	–2.14
E[b] C(4)–C(1)–Pd(1)	–0.53	5.19	1.98	–1.19	–0.60

[a] Except **20** (S1). [b] E = S(1) **5**; O(9) **8**, **13**; S(2) **20** and N(2) **27**.

Experimental Section

General Remarks for Synthesis: C,H,N,S analyses were carried out with a Carlo–Erba model 1108 microanalyser. IR spectra were recorded with a Perkin–Elmer spectrophotometer 16F PC FT-IR, using Nujol mulls between polyethylene sheets. NMR spectroscopic data were recorded on Bruker Avance 200, 300 and 400 spectrometers. Mass spectrometric analyses were performed with a Fisons VG Autospec double-focusing spectrometer, operated in the negative mode. Ions were produced by fast atom bombardment (FAB) with a beam of 25-keV Cs atoms. The mass spectrometer was operated with an accelerating voltage of 8 kV and a resolution of at least 1000. The hydroxo complex precursor $[NBu_4]_2[Pd_2\{C_4(COOMe)_4\}_2(\mu\text{-}OH)_2]$ was prepared by a published method.[13] Reagents were purchased from commercial sources and used directly unless otherwise stated in the text.

Preparations

Complexes $[NBu_4][Pd[C_4(COOMe)_4\}(O–O)]$ [O–O: Salycilaldehydate (sal) (1), Acetohydroxamate (ahx) (2) and Benzohydroxamate (bhx) (3)]: These mononuclear complexes were obtained according

 © 2005 Wiley-VCH Verlag GmbH & Co. KGaA, Weinheim

to the following general method. To an acetone solution (10 mL) of hydroxo complex (0.07 g, 0.054 mmol) the stoichiometric amount of H(O–O) (molar ratio 1:2) was added. The solution was stirred at room temperature for 30 min and the solvent was partly evaporated under reduced pressure. The addition of diethyl ether caused the formation of yellow-orange solids, which were filtered off, washed with diethyl ether and air-dried. The compounds were recrystallised from dichloromethane/diethyl ether.

[NBu$_4$][Pd(C$_4${COOMe}$_4$)(sal)] (1): Yield 0.072 g (88%), m.p. 153 °C (dec.). $C_{35}H_{53}NO_{10}Pd$ (754.2): calcd. C 55.7, H 7.1, N 1.9; found C 55.5, H 7.0, N 2.0. IR (Nujol) $\tilde{\nu}$ = 1692 (vs), 1612 (vs), 1596 (vs), 1556 (vs) cm^{-1}. ^{1}H NMR (300 MHz, $CDCl_3$): δ = 3.60 (s, 6 H, COOMe), 3.75 (s, 3 H, COOMe), 3.80 (s, 3 H, COOMe), 6.39 (m, 1 H, aromatic), 6.64 (d, 1 H, aromatic, J = 8.8 Hz), 7.17–7.27 (m, 2 H, aromatics), 9.06 (s, 1 H, CH=O) ppm. ^{13}C NMR (300 MHz, $CDCl_3$): δ = 50.9 (COO*Me*), 51.0 (COO*Me*), 51.2 (COO*Me*) ppm. FAB-MS (negative mode): *m*/*z* (%) = 512 [Pd{C_4(COOMe)$_4$}(sal)]$^-$ + 1.

[NBu$_4$][Pd(C$_4${COOMe}$_4$)(ahx)] (2): Yield 0.068 g (89%), m.p. 180 °C (dec.). $C_{30}H_{52}N_2O_{10}Pd$ (707.2): calcd. C 50.9, H 7.4, N 4.0; found C 50.6, H 7.3, N 4.0. IR (Nujol) $\tilde{\nu}$ = 3155 (m) (ν NH), 1726 (vs), 1709 (vs), 1688 (vs), 1592 (vs) cm^{-1}. ^{1}H NMR (400 MHz, $CDCl_3$): δ = 1.92 (s, 3 H, Me), 3.58 (s, 6 H, COOMe), 3.65 (s, 3 H, COOMe), 3.74 (s, 3 H, COOMe), 10.42 (br., 1 H, NH) ppm. ^{13}C NMR (400 MHz, $CDCl_3$): δ = 16.7 (Me), 50.7 (COO*Me*), 50.8 (COO*Me*), 51.0 (COO*Me*), 51.1 (COO*Me*) ppm. FAB-MS (negative mode): *m*/*z* (%) = 463 [Pd{C_4(COOMe)$_4$}(ahx)]$^-$ – 1; 448 [Pd{C_4(COOMe)$_4$}(O–NH–CO)]$^-$ – 1.

[NBu$_4$][Pd(C$_4${COOMe}$_4$)(bhx)] (3): Yield 0.063 g (76%), m.p. 203 °C (dec.). $C_{35}H_{54}N_2O_{10}Pd$ (769.2): calcd. C 54.6, H 7.1, N 3.6; found C 54.8, H 7.3, N 3.8. IR (Nujol) $\tilde{\nu}$ = 3268 (s) cm^{-1} (ν NH), 1698 (vs), 1682 (vs), 1596 (vs), 1572 (vs) cm^{-1}. ^{1}H NMR (200 MHz, CD_3CN): δ = 3.55 (s, 6 H, COOMe), 3.61 (s, 3 H, COOMe), 3.71 (s, 3 H, COOMe), 7.38–7.49 (m, 3 H, aromatics), 7.66–7.69 (m, 2 H, aromatics), 10.38 (br., 1 H, NH) ppm. ^{13}C NMR (200 MHz, $CDCl_3$): δ = 50.1 (COO*Me*), 50.2 (COO*Me*) ppm. FAB-MS (negative mode): *m*/*z* (%) = 526 [Pd{C_4(COOMe)$_4$}(bhx)]$^-$.

Complexes [NBu$_4$][Pd{C$_4$(COOMe)$_4$}(N–S)] [N–S: 2-Pyridinthiolate (spy) (4), 2-Pyrimidinthiolate (spym) (5) 3-Methyl-2-imidazolinthiolate (meimt) (6) and 2-Aminothiophenolate (2-atp) (7)]: The complexes were obtained by treating [NBu$_4$]$_2$[Pd$_2${C$_4$(COOMe)$_4$}$_2$(μ-OH)$_2$] (0.100 g, 0.077 mmol) with the corresponding heterocyclic-2-thione or 2-aminothiophenol (molar ratio 1:2) in acetone (10 mL). The solution was stirred at room temperature for 30 min and then concentrated under reduced pressure until half volume. Slow addition of diethyl ether caused the formation of yellow complexes, which were filtered off, washed with diethyl ether and air-dried. The compounds were recrystallised from dichloromethane/diethyl ether.

[NBu$_4$][Pd{C$_4$(COOMe)$_4$}(spy)] (4): Yield 0.086 g (75%), m.p. 131 °C (dec.). $C_{33}H_{52}N_2O_8PdS$ (743.26): calcd. C 53.3, H 7.0, N 3.8, S 4.3; found C 53.2, H 7.0, N 3.7, S 4.4. IR (Nujol) $\tilde{\nu}$ = 1716 (vs), 1694 (vs), 1594 (s), 1578 (s) cm^{-1}. ^{1}H NMR (200 MHz, $CDCl_3$): δ = 3.62 (s, 3 H, COOMe), 3.64 (s, 3 H, COOMe), 3.68 (s, 3 H, COOMe), 3.77 (s, 3 H, COOMe), 6.61 (m, 1 H, spy), 6.79 (m, 1 H, spy), 7.23 (m, 1 H, spy), 7.79 (m, 1 H, spy) ppm. ^{13}C NMR (200 MHz, $CDCl_3$): δ = 51.0 (COO*Me*), 51.3 (COO*Me*) ppm. FAB-MS (negative mode): *m*/*z* (%) = 500 [Pd{C_4(COOMe)$_4$}(spy)]$^-$.

[NBu$_4$][Pd{C$_4$(COOMe)$_4$}(spym)] (5): Yield 0.082 g (72%), m.p. 130 °C (dec.). $C_{32}H_{51}N_3O_8PdS$ (744.25): calcd. C 51.6, H 6.9, N 5.6, S 4.3; found C 51.4, H 6.8, N 5.6, S 4.2. IR (Nujol) $\tilde{\nu}$ = 1712 (vs), 1698 (vs), 1570 (s), 1554 (s) cm^{-1}. ^{1}H NMR (200 MHz, $CDCl_3$): δ = 3.61 (s, 3 H, COOMe), 3.63 (s, 3 H, COOMe), 3.67 (s, 3 H, COOMe), 3.72 (s, 3 H, COOMe), 6.61 (m, 1 H, spym), 8.01 (dd, 1 H, spym, J^3 = 5.0, J^4 = 2.5 Hz), 8.24 (dd, 1 H, spym, J^3 = 5.0, J^4 = 2.5 Hz) ppm. ^{13}C NMR (200 MHz, $CDCl_3$): δ = 51.0 (COO*Me*), 51.2 (COO*Me*) ppm. FAB-MS (negative mode): *m*/*z* (%) = 501 [Pd{C_4(COOMe)$_4$}(spym)]$^-$.

[NBu$_4$][Pd{C$_4$(COOMe)$_4$}(meimt)] (6): Yield 0.087 g (76%), m.p. 135 °C. $C_{32}H_{53}N_3O_8PdS$ (746.26): calcd. C 51.5, H 7.2, N 5.6, S 4.3; found C 51.2, H 7.3, N 5.9, S 4.2. IR (Nujol) $\tilde{\nu}$ = 1694 (vs), 1532 (s) cm^{-1}. ^{1}H NMR (300 MHz, $CDCl_3$): δ = 3.09 (s, 3 H, Me), 3.41 (s, 3 H, COOMe), 3.42 (s, 3 H, COOMe), 3.47 (s, 3 H, COOMe), 3.63 (s, 3 H, COOMe), 6.21 (d, 1 H, meimt, J = 1.4 Hz), 6.36 (d, 1 H, meimt, J = 1.4 Hz) ppm. ^{13}C NMR (300 MHz, $CDCl_3$): δ = 34.3 (meimt), 48.0 (COO*Me*), 49.1 (COO*Me*), 49.2 (COO*Me*), 49.3 (COO*Me*) ppm. FAB-MS (negative mode): *m*/*z* (%) = 501 [Pd{C_4(COOMe)$_4$}(meimt)]$^-$.

[NBu$_4$][Pd{C$_4$(COOMe)$_4$}(2-atp)] (7): Yield 0.087 g (75%), m.p. 145 °C (dec.). $C_{34}H_{54}N_2O_8PdS$ (757.29): calcd. C 53.9, H 7.2, N 3.7, S 4.2; found C 54.1, H 7.5, N 3.8, S 4.4. IR (Nujol) $\tilde{\nu}$ = 3292 (m), 3252 (m), 1674 (s), 1592 (s) cm^{-1}. ^{1}H NMR (300 MHz, $CDCl_3$): δ = 3.60 (s, 3 H, COOMe), 3.69 (s, 3 H, COOMe), 3.72 (s, 3 H, COOMe), 3.77 (s, 3 H, COOMe), 4.64 (s, 2 H, NH_2), 6.70 (m, 1 H, 2-atp), 6.89 (m, 1 H, 2-atp), 6.97 (m, 1 H, 2-atp), 7.42 (m, 1 H, 2-atp) ppm. ^{13}C NMR (300 MHz, $CDCl_3$): δ = 50.8 (COO*Me*), 50.9 (COO*Me*), 51.0 (COO*Me*), 51.1 (COO*Me*) ppm. FAB-MS (negative mode): *m*/*z* (%) = 514 [Pd{C_4(COOMe)$_4$}(2-atp)]$^-$.

Complexes [NBu$_4$][Pd{C$_4$(COOMe)$_4$}(N–O)] [H(N–O): *N*-Phenylsalycilaldimine (*N*-phsal) (8), *N*-*p*-Chlorophenylsalycilaldimine (*N*-clsal) (9), *N*-*p*-Tolylsalycilaldimine (*N*-tolsal) (10), 2-Aminophenol (2-ap) (11), 2-Pyrrolecarboxaldeyde (2-pcal) (12), 8-Hydroxiquinoline (oxin) (13), Picolinic Acid (2-pic) (14): The complexes were obtained by treating [NBu$_4$]$_2$[Pd$_2${C$_4$(COOMe)$_4$}$_2$(μ-OH)$_2$] (0.100 g, 0.077 mmol) with the corresponding protic ligand (HO–N) (molar ratio 1:2) in acetone (10 mL). The solution was stirred at room temperature for 30 min and then concentrated under reduced pressure until ca. one fifth of the initial volume. Slow addition of diethyl ether caused the formation of yellow complexes, which were filtered off, washed with diethyl ether and air-dried. The compounds were recrystallised from dichloromethane/diethyl ether.

[NBu$_4$][Pd{C$_4$(COOMe)$_4$}(*N*-phsal)] (8): Yield 0.106 g (83%), m.p. 175 °C (dec.). $C_{41}H_{58}N_2O_9Pd$ (829.33): calcd. C 59.4, H 7.0, N 3.4; found C 59.2, H 7.2, N 3.7. IR (Nujol) $\tilde{\nu}$ = 1700 (vs), 1686 (vs), 1606 (s), 1586 (s), 1530 (s) cm^{-1}. ^{1}H NMR (200 MHz, $CDCl_3$): δ = 2.84 (s, 3 H, COOMe), 3.56 (s, 3 H, COOMe), 3.59 (s, 3 H, COOMe), 3.90 (s, 3 H, COOMe), 6.40 (m, 1 H, *N*-phsal), 6.77 (d, 1 H, *N*-phsal, J = 8.4 Hz), 7.08 (m, 1 H, *N*-phsal), 7.15 (m, 2 H, *N*-phsal), 7.32 (m, 4 H, *N*-phsal), 7.94 (s, 1 H, CH=N) ppm. ^{13}C NMR (200 MHz, $CDCl_3$): δ = 50.7 (COO*Me*), 50.9 (COO*Me*) ppm. FAB-MS (negative mode): *m*/*z* (%) = 586 [Pd{C_4(COOMe)$_4$}(*N*-phsal)]$^-$.

[NBu$_4$][Pd{C$_4$(COOMe)$_4$}(*N*-clsal)] (9): Yield 0.105 g (80%), m.p. 160 °C (dec.). $C_{41}H_{57}ClN_2O_9Pd$ (863.77): calcd. C 57.0, H 6.6, N 3.2; found C 57.3, H 6.9, N 3.0. IR (Nujol) $\tilde{\nu}$ = 1688 (vs), 1606 (s), 1572 (s), 1526 (s) cm^{-1}. ^{1}H NMR (300 MHz, $CDCl_3$): δ = 3.00 (s, 3 H, COOMe), 3.63 (s, 3 H, COOMe), 3.64 (s, 3 H, COOMe), 3.95 (s, 3 H, COOMe), 6.46 (m, 1 H, *N*-clsal), 6.82 (d, 1 H, *N*-clsal, J = 8.5 Hz), 7.25 (m, 6 H, *N*-clsal), 7.95 (s, 1 H, CH=N) ppm. ^{13}C NMR (300 MHz, $CDCl_3$): δ = 50.5 (COO*Me*), 50.8 (COO*Me*), 50.9 (COO*Me*), 51.0 (COO*Me*) ppm. FAB-MS (negative mode): *m*/*z* (%) = 622 [Pd{C_4(COOMe)$_4$}(*N*-clsal)]$^-$.

 © 2005 Wiley-VCH Verlag GmbH & Co. KGaA, Weinheim

[NBu_4][Pd{C_4(COOMe)$_4$}(*N*-tolsal)] (10): Yield 0.097 g (75%), m.p. 136 °C (dec.). $C_{42}H_{60}N_2O_9Pd$ (843.35): calcd. C 59.8, H 7.2, N 3.3; found C 59.9, H 7.4, N 3.4. IR (Nujol) $\tilde{\nu}$ = 1702 (vs), 1686 (s), 1600 (s), 1586 (s), 1530 (s) cm^{-1}. ^1H NMR (300 MHz, $CDCl_3$): δ = 2.33 (s, 3 H, Me), 2.86 (s, 3 H, COOMe), 3.57 (s, 3 H, COOMe), 3.59 (s, 3 H, COOMe), 3.90 (s, 3 H, COOMe), 6.40 (m, 1 H, *N*-tolsal), 6.76 (d, 1 H, *N*-tolsal, *J* = 8.4 Hz), 7.16 (m, 6 H, *N*-tolsal), 7.93 (s, 1 H, CH=N) ppm. ^{13}C NMR (300 MHz, $CDCl_3$): δ = 20.8 (Me), 50.5 (COO*Me*), 50.9 (COO*Me*), 51.0 (COO*Me*) ppm. FAB-MS (negative mode): *m*/*z* (%) = 600 [Pd{C_4(COOMe)$_4$}(*N*-tolsal)]$^-$.

[NBu_4][Pd{C_4(COOMe)$_4$}(2-ap)] (11): Yield 0.102 g (90%), m.p. 165 °C (dec.). $C_{34}H_{54}N_2O_9Pd$ (741.22): calcd. C 55.1, H 7.3, N 3.8; found C 55.3, H 7.5, N 3.6. IR (Nujol) $\tilde{\nu}$ = 3310 (m), 3260 (m), 1688 (s), 1598 (s), 1538 (s) cm^{-1}. ^1H NMR (200 MHz, $CDCl_3$): δ = 3.61 (s, 3 H, COOMe), 3.67 (s, 3 H, COOMe), 3.68 (s, 3 H, COOMe), 3.82 (s, 3 H, COOMe), 4.18 (s, 2 H, NH_2), 6.25 (m, 1 H, 2-ap), 6.60 (d, 1 H, 2-ap, *J* = 7.8 Hz), 6.87 (m, 2 H, 2-ap) ppm. ^{13}C NMR (200 MHz, $CDCl_3$): δ = 51.1 (COO*Me*), 51.2 (COO*Me*), 51.3 (COO*Me*) ppm. FAB-MS (negative mode): *m*/*z* (%) = 499 [Pd{C_4(COOMe)$_4$}(2-ap)]$^-$.

[NBu_4][Pd{C_4(COOMe)$_4$}(2-pcal)] (12): Yield 0.075 g (67%), m.p. 155 °C (dec.). $C_{33}H_{52}N_2O_9Pd$ (727.19): calcd. C 54.5, H 7.2, N 3.8; found C 54.7, H 7.3, N 4.0. IR (Nujol) $\tilde{\nu}$ = 1694 (vs), 1564 (s) cm^{-1}. ^1H NMR (200 MHz, $CDCl_3$): δ = 3.63 (s, 3 H, COOMe), 3.64 (s, 3 H, COOMe), 3.78 (s, 3 H, COOMe), 3.80 (s, 3 H, COOMe), 6.24 (d, 1 H, 2-pcal, *J* = 4.0 Hz), 6.96 (d, 1 H, 2-pcal, *J* = 4.0 Hz), 7.05 (m, 1 H, 2-pcal), 8.53 (s, 1 H, CHO) ppm. ^{13}C NMR (200 MHz, $CDCl_3$): δ = 50.9 (COO*Me*), 51.0 (COO*Me*), 51.2 (COO*Me*), 51.3 (COO*Me*) ppm. FAB-MS (negative mode): *m*/*z* (%) = 484 [Pd{C_4(COOMe)$_4$}(2-pcal)]$^-$.

[NBu_4][Pd{C_4(COOMe)$_4$}(oxin)] (13): Yield 0.091 g (76%), m.p. 205 °C (dec.). $C_{37}H_{54}N_2O_9Pd$ (777.25): calcd. C 57.2, H 7.0, N 3.6; found C 57.3, H 7.2, N 3.6. IR (Nujol) $\tilde{\nu}$ = 1708 (vs), 1694 (vs), 1570 (s), 1498 (s) cm^{-1}. ^1H NMR (200 MHz, $CDCl_3$): δ = 3.64 (s, 3 H, COOMe), 3.65 (s, 3 H, COOMe), 3.81 (s, 3 H, COOMe), 3.86 (s, 3 H, COOMe), 6.77 (d, 1 H, oxin, *J* = 7.8 Hz), 6.84 (d, 1 H, oxin, *J* = 7.0 Hz), 7.31 (m, 2 H, oxin), 8.10 (d, 1 H, oxin, *J* = 8.4 Hz), 8.33 (m, 1 H, oxin) ppm. ^{13}C NMR (200 MHz, $CDCl_3$): δ = 50.9 (COO*Me*), 51.1 (COO*Me*), 51.2 (COO*Me*) ppm. FAB-MS (negative mode): *m*/*z* (%) = 534 [Pd{C_4(COOMe)$_4$}(oxin)]$^-$.

[NBu_4][Pd{C_4(COOMe)$_4$}(2-pic)] (14): Yield 0.087 g (5%), m.p. 130 °C (dec.). $C_{34}H_{52}N_2O_{10}Pd$ (755.20): calcd. C 54.1, H 6.9, N 3.7; found C 54.1, H 7.1, N 3.9. IR (Nujol) $\tilde{\nu}$ = 1698 (vs), 1644 (vs), 1600 (vs) cm^{-1}. ^1H NMR (200 MHz, $CDCl_3$): δ = 3.62 (s, 3 H, COOMe), 3.65 (s, 3 H, COOMe), 3.77 (s, 3 H, COOMe), 3.80 (s, 3 H, COOMe), 7.44 (m, 1 H, 2-pic), 7.89 (m, 1 H, 2-pic), 8.15 (d, 1 H, 2-pic, *J* = 7.2 Hz), 8.35 (d, 1 H, 2-pic, *J* = 4.7 Hz) ppm. ^{13}C NMR (200 MHz, $CDCl_3$): δ = 50.9 (COO*Me*), 51.0 (COO*Me*), 51.1 (COO*Me*), 51.4 (COO*Me*) ppm. FAB-MS (negative mode): *m*/*z* (%) = 512 [Pd{C_4(COOMe)$_4$}(2-pic)]$^-$.

Complexes [NBu_4]$_2$[Pd_2{C_4(COOMe)$_4$}$_2$(μ-az)] [az = Pyrazolate (pz) (15), Triazolate (tz) (16) and 3,5-Dimethylpyrazolate (3,5-Me_2pz) (17)]: These dinuclear complexes were obtained according to the following general method. To a solution of hydroxo complex (0.07 g, 0.054 mmol) in dichloromethane (10 mL) was added the corresponding azolate (molar ratio 1:2). The solution was stirred at room temperature for 20 min and then concentrated under reduced pressure until about one fifth of the initial volume. Slow addition of diethyl ether caused the formation of yellow complexes, which were filtered off, washed with diethyl ether and air-dried. The compounds were recrystallised from dichloromethane/diethyl ether.

[NBu_4]$_2$[Pd(C_4{COOMe}$_4$)(μ-pz)]$_2$ (15): Yield 0.051 g (68%), m.p. 160 °C (dec.). $C_{62}H_{102}N_6O_{16}Pd_2$ (1400.34): calcd. C 53.2, H 7.3, N 6.0; found C 53.4, H 7.5, N 6.3. IR (Nujol) $\tilde{\nu}$ = 1688 (vs), 1616 (s) cm^{-1}. ^1H NMR (200 MHz, $CDCl_3$): δ = 3.37 (s, 12 H, COOMe), 3.58 (s, 12 H, COOMe), 5.89 (m, 2 H, pz), 7.26 (m, 4 H, pz) ppm. ^{13}C NMR (200 MHz, $CDCl_3$): δ = 50.6 (COO*Me*), 50.7 (COO*Me*), 101.3 (pz), 137.3 (pz) ppm. FAB-MS (negative mode): *m*/*z* (%) = 1158 [(NBu_4)Pd_2{C_4(COOMe)$_4$}$_2$(μ-pz)$_2$]$^-$, 917 [Pd_2{C_4(COOMe)$_4$}$_2$(μ-pz)$_2$]$^-$ + 1, 849 [Pd_2{C_4(COOMe)$_4$}$_2$(μ-pz)]$^-$.

[NBu_4]$_2$[Pd(C_4{COOMe}$_4$)(μ-tz)]$_2$ (16): Yield 0.055 g (72%), m.p. 167 °C (dec.). $C_{60}H_{100}N_8O_{16}Pd_2$ (1402.3): calcd. C 51.4, H 7.2, N 8.0; found C 51.6, H 7.2, N 8.3. IR (Nujol) $\tilde{\nu}$ = 1692 (vs), 1552 (s) cm^{-1}. ^1H NMR (200 MHz, $CDCl_3$): δ = 3.40 (s, 12 H, COOMe), 3.59 (s, 12 H, COOMe), 7.73 (m, 4 H, tz) ppm. ^{13}C NMR (200 MHz, $CDCl_3$): δ = 50.5 (COO*Me*), 50.7 (COO*Me*), 150.0 (tz) ppm. FAB-MS (negative mode): *m*/*z* (%) = 1160 [(NBu_4)-Pd_2{C_4(COOMe)$_4$}$_2$(μ-tz)$_2$]$^-$, 919 [Pd_2{C_4(COOMe)$_4$}$_2$(μ-tz)$_2$]$^-$ + 1, 851 [Pd_2{C_4(COOMe)$_4$}$_2$(μ-tz)]$^-$.

[NBu_4]$_2$[Pd(C_4{COOMe}$_4$)(μ-3,5-Me_2pz)]$_2$ (17): Yield 0.053 g (67%), m.p. 167 °C (dec.). $C_{66}H_{110}N_6O_{16}Pd_2$ (1456.45): calcd. C 54.4, H 7.6, N 5.8; found C 54.5, H 7.7, N 6.0. IR (Nujol) $\tilde{\nu}$ = 1698 (vs), 1642 (s), 1546 (s) cm^{-1}. ^1H NMR (200 MHz, $CDCl_3$): δ = 2.18 (s, 12 H, 3,5-Me_2pz) 3.37 (s, 12 H, COOMe), 3.57 (s, 12 H, COOMe), 5.34 (s, 2 H, 3,5-Me_2pz) ppm. ^{13}C NMR (200 MHz, $CDCl_3$): δ = 14.1 (3,5-Me_2pz), 50.4 (COO*Me*), 50.5 (COO*Me*), 100.4 (3,5-Me_2pz), 146.6 (3,5-Me_2pz) ppm. FAB-MS (negative mode): *m*/*z* (%) = 1214 [(NBu_4)Pd_2{C_4(COOMe)$_4$}$_2$(μ-3,5-Me_2pz)$_2$]$^-$, 973 [Pd_2{C_4(COOMe)$_4$}$_2$(μ-3,5-Me_2pz)$_2$]$^-$ + 1, 877 [Pd_2-{C_4(COOMe)$_4$}$_2$(μ-3,5-Me_2pz)]$^-$.

Complexes [NBu_4]$_2$[Pd_2{C_4(COOMe)$_4$}$_2$(μ-O–O)] [O–O = Chloranilate (chl) (18) and Squarate (sq) (19)]: These dinuclear complexes were obtained according to the following general method. To an acetone solution (10 mL) of hydroxo complex (0.07 g, 0.054 mmol) the stoichiometric amount of H(O–O) (molar ratio 1:1) was added. The solution was stirred at room temperature for 30 min and the solvent was partly evaporated under reduced pressure. The addition of diethyl ether caused the formation of yellow-orange solids, which were filtered off, washed with diethyl ether and air-dried. The compounds were recrystallised from dichloromethane/diethyl ether.

[NBu_4]$_2$[Pd_2(C_4{COOMe}$_4$)$_2$(μ-chl)] (18): Yield 0.057 g (72%), m.p. 215 °C (dec.). $C_{62}H_{96}Cl_2N_2O_{20}Pd_2$ (1473.2): calcd. C 50.5, H 6.6, N 1.9; found C 50.6, H 6.9, N 2.2. IR (Nujol) $\tilde{\nu}$ = 1703 (vs), 1504 (vs) cm^{-1}. ^1H NMR (200 MHz, $CDCl_3$): δ = 3.63 (s, 12 H, COOMe), 3.76 (s, 12 H, COOMe) ppm. ^{13}C NMR (200 MHz, $CDCl_3$): δ = 51.1 (COO*Me*), 51.2 (COO*Me*) ppm. FAB-MS (negative mode): *m*/*z* (%) = 1230 [(NBu_4)Pd_2{C_4(COOMe)$_4$}$_2$(μ-chl)]$^-$.

[NBu_4]$_2$[Pd_2(C_4{COOMe}$_4$)$_2$(μ-sq)] (19): Yield 0.060 g (81%), m.p. 150 °C (dec.). C60H96N2O20Pd2 (1378.2): calcd. C 52.3, H 7.0, N 2.0; found C 52.4, H 7.2, N 2.2. IR (Nujol) $\tilde{\nu}$ = 1736 (vs), 1704 (vs), 1556 (vs), 1494 s cm^{-1}. ^1H NMR (200 MHz, $CDCl_3$): δ = 3.65 (s, 12 H, COOMe), 3.71 (s, 12 H, COOMe) ppm. ^{13}C NMR (200 MHz, $CDCl_3$): δ = 51.2 (COO*Me*), 51.6 (COO*Me*) ppm. FAB-MS (negative mode): *m*/*z* (%) = 1138 [(NBu_4)Pd_2{C_4(COOMe)$_4$}$_2$(μ-sq)]$^-$ +2; 895 [Pd_2{C_4(COOMe)$_4$}$_2$(μ-sq)]$^-$ + 1; 502 [Pd{C_4(COOMe)$_4$}-(sq)]$^-$.

Complexes [NBu_4][Pd{C_4(COOMe)$_4$}{S_2P(OR)$_2$}] [R: Me (20), Et (21), *i*Pr (22)]: To a solution of the precursor [NBu_4]$_2$[Pd_2-{C_4(COOMe)$_4$}$_2$(μ-OH)$_2$] (0.100 g, 0.077 mmol) in dichloromethane (10 mL) was added the corresponding ammonium dialkyldithiophosphate (molar ratio 1:2). The solution was refluxed for 30 min and then concentrated under reduced pressure until ca. one

 © 2005 Wiley-VCH Verlag GmbH & Co. KGaA, Weinheim

fifth of the initial volume. Slow addition of diethyl ether caused the formation of yellow complexes, which were filtered off, washed with diethyl ether and air-dried. The compounds were recrystallised from dichloromethane/diethyl ether.

[NBu$_4$][Pd{C$_4$(COOMe)$_4$}{S$_2$P(OMe)$_2$}] (20): Yield 0.099 g (82%), m.p. 140 °C (dec.). $C_{30}H_{54}NO_{10}PPdS_2$ (790.27): calcd. C 45.6, H 6.9, N 1.8, S 8.1; found C 45.7, H 7.1, N 1.9, S 8.3. IR (Nujol) $\tilde{\nu}$ = 1698 (vs), 1022 (vs), 654 (vs) cm^{-1}. ^{1}H NMR (200 MHz, $CDCl_3$): δ = 3.61 (s, 6 H, COOMe), 3.69 (s, 6 H, COOMe), 3.70 (d, 6 H, Me, J_{PH} = 14.6 Hz) ppm. ^{31}P NMR (200 MHz, $CDCl_3$): δ = 109.3 (s, 1P) ppm. FAB-MS (negative mode): *m*/*z* (%) = 547 [Pd{C$_4$(COOMe)$_4$}{S$_2$P(OMe)$_2$}]$^-$.

[NBu$_4$][Pd{C$_4$(COOMe)$_4$}{S$_2$P(OEt)$_2$}] (21): Yield 0.101 g (80%), m.p. 128 °C (dec.). $C_{32}H_{58}NO_{10}PPdS_2$ (818.33): calcd. C 47.0, H 7.1, N 1.7, S 7.8; found C 47.1, H 7.4, N 2.0, S 8.1. IR (Nujol) $\tilde{\nu}$ = 1692 (vs), 1012 (vs), 652 (vs) cm^{-1}. ^{1}H NMR (200 MHz, $CDCl_3$): δ = 1.30 (t, 6 H, Et), 3.61 (s, 6 H, COOMe), 3.69 (s, 6 H, COOMe), 4.10 (m, 4 H, Et) ppm. ^{31}P NMR (200 MHz, $CDCl_3$): δ = 104.5 (s, 1P) ppm. FAB-MS (negative mode): *m*/*z* (%) = 575 [Pd{C$_4$(COOMe)$_4$}{S$_2$P(OEt)$_2$}]$^-$.

[NBu$_4$][Pd{C$_4$(COOMe)$_4$}{S$_2$P(O*i*Pr)$_2$}] (22): Yield 0.079 g (61%), m.p. 143 °C (dec.). $C_{34}H_{62}NO_{10}PPdS_2$ (846.38): calcd. C 48.2, H 7.4, N 1.6, S 7.6; found C 48.4, H 7.5, N 1.9, S 7.9. IR (Nujol) $\tilde{\nu}$ = 1692 (vs), 1011 (vs), 645 (vs) cm^{-1}. ^{1}H NMR (200 MHz, $CDCl_3$): δ = 2.60 (d, 12 H, *i*Pr, *J* = 6.2), 3.61 (s, 6 H, COOMe), 3.69 (s, 6 H, COOMe), 4.74 (m, 2 H, *i*Pr) ppm. ^{31}P NMR (200 MHz, $CDCl_3$): δ = 101.1 (s, 1P) ppm. FAB-MS (negative mode): *m*/*z* (%) = 603 [Pd{C$_4$(COOMe)$_4$}{S$_2$P(O*i*Pr)$_2$}]$^-$.

Complexes [NBu$_4$][Pd{C$_4$(COOMe)$_4$}(S$_2$CNR$_2$)] [R$_2$NH: Et$_2$NH (23), Pr$_2$ (24), Piperidine (25), Morpholine (26)]: In separate experiments, to a solution of complex [NBu$_4$]$_2$[Pd$_2${C$_4$(COOMe)$_4$}$_2$(μ-OH)$_2$] (0.100 g, 0.077 mmol) in acetone (10 mL) was added the corresponding amine (molar ratio 1:2) and a slight excess of carbon disulfide. The solution was refluxed for 30 min and then concentrated under reduced pressure until ca. one fifth of the initial volume. Slow addition of diethyl ether caused the formation of yellow complexes, which were filtered off, washed with diethyl ether and air-dried. The compounds were recrystallised from dichloromethane/diethyl ether.

[NBu$_4$][Pd{C$_4$(COOMe)$_4$}(S$_2$CNEt$_2$)] (23): Yield 0.082 g (69%), m.p. 132 °C (dec.). $C_{33}H_{58}N_2O_8PdS_2$ (781.37): calcd. C 50.7, H 7.5, N 3.6, S 8.2; found C 50.9, H 7.7, N 3.7, S 8.4. IR (Nujol) $\tilde{\nu}$ = 1724 (vs), 1706 (vs), 1505 (vs) cm^{-1}. ^{1}H NMR (200 MHz, $CDCl_3$): δ = 1.19 (t, 6 H, Et), 3.60 (s, 6 H, COOMe), 3.67 (s, 6 H, COOMe), 3.74 (q, 4 H, Et) ppm. ^{13}C NMR (200 MHz, $CDCl_3$): δ = 12.4 (Et), 43.9 (Et), 50.8 (COO*Me*), 50.9 (COO*Me*) ppm. FAB-MS (negative mode): *m*/*z* (%) = 539 [Pd{C$_4$(COOMe)$_4$}(S$_2$CNEt$_2$)]$^-$ + 1.

[NBu$_4$][Pd{C$_4$(COOMe)$_4$}(S$_2$CNPr$_2$)] (24): Yield 0.086 g (69%), m.p. 182 °C (dec.). $C_{35}H_{62}N_2O_8PdS_2$ (809.43): calcd. C 51.9, H 7.7, N 3.5, S 7.9; found C 51.9, H 7.8, N 3.6, S 8.1. IR (Nujol) $\tilde{\nu}$ = 1694 (vs), 1504 (vs) cm^{-1}. ^{1}H NMR (200 MHz, $CDCl_3$): δ = 0.90 (t, 6 H, Pr), 1.64 (m, 4 H, Pr), 3.62 (m, 10 H, Pr + COOMe), 3.69 (s, 6 H, COOMe) ppm. ^{13}C NMR (200 MHz, $CDCl_3$): δ = 11.1 (Pr), 20.5 (Et), 50.8 (COO*Me*), 50.9 (COO*Me*), 51.1 (Pr) ppm. FAB-MS (negative mode): *m*/*z* (%) = 566 [Pd{C$_4$(COOMe)$_4$}-(S$_2$CNPr$_2$)]$^-$.

[NBu$_4$][Pd{C$_4$(COOMe)$_4$}(S$_2$CNC$_5$H$_{10}$)] (25): Yield 0.094 g (77%), m.p. 165 °C (dec.). $C_{34}H_{58}N_2O_8PdS_2$ (809.43): calcd. C 51.5, H 7.4, N 3.5, S 8.1; found C 51.7, H 7.4, N 3.7, S 8.0. IR (Nujol) $\tilde{\nu}$ = 1694 (vs), 1500 (vs) cm^{-1}. ^{1}H NMR (200 MHz, $CDCl_3$): δ = 1.65 (m, 6 H, S$_2$CNC$_5$H$_{10}$), 3.45 (s, 6 H, COOMe), 3.49 (s, 6 H, COOMe), 3.85 (t, 4 H, S$_2$CNC$_5$H$_{10}$) ppm. ^{13}C NMR (200 MHz, $CDCl_3$): δ = 15.2 (S$_2$CNC$_5$H$_{10}$), 16.5 (S$_2$CNC$_5$H$_{10}$), 38.6 (S$_2$CNC$_5$H$_{10}$), 50.5 (COO*Me*), 50.7 (COO*Me*) ppm. FAB-MS (negative mode): *m*/*z* (%) = 551 [Pd{C$_4$(COOMe)$_4$}(S$_2$CNC$_5$H$_{10}$)]$^-$ + 1.

[NBu$_4$][Pd{C$_4$(COOMe)$_4$}(S$_2$CNC$_4$H$_8$O)] (26): Yield 0.099 g (82%), m.p. 186 °C (dec.). $C_{33}H_{56}N_2O_9PdS_2$ (795.36): calcd. C 49.8, H 7.1, N 3.5, S 8.1; found C 50.1, H 7.3, N 3.6, S 8.3. IR (Nujol) $\tilde{\nu}$ = 1694 (vs), 1499 (vs) cm^{-1}. ^{1}H NMR (200 MHz, $CDCl_3$): δ = 3.62 (s, 6 H, COOMe), 3.68 (m, 10 H, S$_2$CNC$_4$H$_8$O + COOMe), 4.00 (t, 4 H, S$_2$CNC$_4$H$_8$O) ppm. ^{13}C NMR (200 MHz, $CDCl_3$): δ = 47.2 (S$_2$CNC$_4$H$_8$O), 50.9 (COO*Me*) ppm. FAB-MS (negative mode): *m*/*z* (%) = 552 [Pd{C$_4$(COOMe)$_4$}(S$_2$CNC$_4$H$_8$O)]$^-$.

Hydration of pyridine-2-carbonitrile: Complex [NBu$_4$][Pd-{C$_4$(COOMe)$_4$}(2-HNCOpy)] (27): To a solution of [NBu$_4$]$_2$-[Pd$_2${C$_4$(COOMe)$_4$}$_2$(μ-OH)$_2$] (0.100 g, 0.077 mmol) in acetone/H$_2$O (10:0.5 mL) was added pyridine-2-carbonitrile (0.018 g, 0.154 mmol). The resultant clear solution was stirred for 30 min at room temperature and then concentrated under reduced pressure until ca. one fifth of the initial volume. Slow addition of diethyl ether caused the formation of yellow complexes, which were filtered

Table 3. Crystal data and structure refinement for compounds **5**, **8**, **13**, **20** and **27**.

	5	**8**	**13**	**20**	**27**
Formula	$C_{32}H_{51}N_3O_8PdS$	$C_{41}H_{58}N_2O_9Pd$	$C_{37}H_{54}N_2O_9Pd$	$C_{30}H_{54}NO_{10}PPdS_2$	$C_{34}H_{53}N_3O_9Pd$
Molecular mass	744.22	829.29	777.22	790.23	754.19
Crystal system	monoclinic	monoclinic	monoclinic	monoclinic	orthorhombic
Space group	$P2_1/c$	$P21/n$	$P2_1/c$	Cc	$Pcab$
a [Å]	10.3174(6)	9.6870(10)	10.8804(6)	8.9363(7)	20.002(2)
b [Å]	20.4166(16)	11.3580(10)	9.1196(5)	22.938(2)	17.359(3)
c [Å]	17.3615(19)	36.978(2)	38.995(2)	18.9201(17)	21.299(2)
β [°]	100.486(9)	91.78	95.3460(10)	102.281(6)	90
V [Å^3]	3596.1(5)	4066.5(6)	3852.4(4)	3789.4(6)	7395.3(16)
Z	4	4	4	4	8
T [K]	173(2)	173(2)	100(2)	173(2)	173(2)
Reflections collected	7028	9782	23503	3566	7553
μ [mm^{-1}]	0.624	0.511	0.535	0.692	0.556
Independent reflections	6324	7155	8645	2495	6504
Final $R1$	0.0328	0.0335	0.0405	0.0631	0.0633
$wR2$ [$I > 2\sigma(I)$]	0.0770	0.0768	0.0838	0.1676	0.1603
R indices (all data)	$R1$ = 0.0488	$R1$ = 0.0482	$R1$ = 0.0451	$R1$ = 0.0937	$R1$ = 0.1103
	$wR2$ = 0.0823	$wR2$ = 0.0814	$wR2$ = 0.0859	$wR2$ = 0.1916	$wR2$ = 0.1767

 © 2005 Wiley-VCH Verlag GmbH & Co. KGaA, Weinheim

off, washed with diethyl ether and air-dried. The compounds were recrystallised from acetone/diethyl ether.

Complex [NBu_4][Pd{C_4(COOMe)$_4$}(2-HNCOpy)] (27): Yield 0.091 g (78%), m.p. 123 °C. $C_{34}H_{53}N_3O_9Pd$ (754.22): calcd. C 54.1, H 7.1, N 5.6; found C 54.2, H 7.4, N 5.8. IR (Nujol) $\tilde{\nu}$ = 3352 (vs), 1698 (vs), 1630 (vs), 1596 (vs), 1586 (vs), 1566 (vs) cm^{-1}. ^1H NMR (200 MHz, $CDCl_3$): δ = 3.63 (s, 6 H, COOMe), 3.76 (s, 3 H, COOMe), 3.78 (s, 3 H, COOMe), 5.24 (br., 1 H, NH), 7.37 (m, 1 H, 2-HNCOpy), 7.87 (m, 1 H, 2-pic), 8.08 (m, 1 H, 2-HNCOpy), 8.38 (m, 1 H, 2-HNCOpy) ppm. ^{13}C NMR (200 MHz, $CDCl_3$): δ = 50.9 (COO*Me*), 51.0 (COO*Me*), 51.1 (COO*Me*), 51.3 (COO*Me*) ppm. FAB-MS (negative mode): *m*/*z* (%) = 511 [Pd{C_4(COOMe)$_4$}(2-HNCOpy)]$^-$.

X-ray Structure Analysis: Suitable crystals of **5**, **8**, **13**, **20** and **27** were grown from dichloromethane/ether liquid diffusion. The crystals were mounted onto the tip of a glass fibre, and the data collection was performed with a Siemens P4 diffractometer for **5**, **8**, **20** and **27**, the scan mode was θ-2θ. Data collection for **13** was performed with a Bruker Smart CCD diffractometer with a nominal crystal to detector distance of 4.5 cm. Diffraction data were collected with a ω scan run. A total of 1371 frames were collected at 0.3° intervals and 10°s per frame. The diffraction frames were integrated using the SAINT package[29] and corrected for absorption with SADABS.[30] The structures were solved by direct methods SHELXS-97[31] and refined by full-matrix least-squares SHELXL-97[31] (Table 3). Hydrogen atoms were included using a riding model. CCDC-258720 (for **5**) -258721 (for **8**), -258722 (for **13**), -258723 (for **20**) and -258724 (for **27**) contain the supplementary crystallographic data for this paper. These data can be obtained free of charge from The Cambridge Crystallographic Data Centre via www.ccdc.cam.ac.uk/data_request/cif.

Acknowledgments

Financial support of this work by Dirección General de Investigación (Spain) (project-BQU2001–0979-C02–01/02) is gratefully acknowledged.

[1] a) J. Cámpora, P. Palma, E. Carmona, *Coord. Chem. Rev.* **1999**, *195*, 207–281; b) P. W. Jennings, L. L. Johnson, *Chem. Rev.* **1994**, *94*, 2241–2290; c) I. Ojima, M. Tzmarioudaki, Z. Li, R. Donovan, *Chem. Rev.* **1996**, *96*, 635–662.
[2] K. Moseley, P. M. Maitlis, *J. Chem. Soc. Dalton Trans.* **1974**, 169–175.
[3] T. S. Ito, S. Hasegawa, Y. Takashi, Y. Ishii, *J. Chem. Soc. Chem. Commun.* **1972**, 629–630.
[4] K. Itoh in *Fundamental Research in Organometallic Chemistry* (Eds.: M. Tsutsui, Y. Ishii, H. Yaozeng), Science Press, Van Nostrand Reinhold Company, New York, **1982**, p. 149.
[5] H. tom Dieck, C. Munz, C. Müller, *J. Organomet. Chem.* **1990**, *384*, 243–255.
[6] H. Suzuki, K. Itoh, Y. Ishii, K. Simon, J. A. Ibers, *J. Am. Chem. Soc.* **1976**, *98*, 8494–8500.
[7] R. van Belzen, R. A. Klein, H. Kooijman, N. Veldman, A. L. Speck, C. J. Elsevier, *Organometallics* **1998**, *17*, 1812–1825 and references cited therein.
[8] G. Sánchez, J. Vives, J. L. Serrano, J. Pérez, G. López, *Inorg. Chim. Acta* **2002**, *328*, 74–80.
[9] B. M. Trost, G. J. Tanoury, *J. Am. Chem. Soc.* **1987**, *109*, 4753–4755.
[10] a) B. M. Trost, M. K. Trost, *J. Am. Chem. Soc.* **1991**, *113*, 1850–1852; b) B. M. Trost, M. Yanai, K. Hoogsteen, *J. Am. Chem. Soc.* **1993**, *115*, 5294–5295; c) B. M. Trost, V. K. Chang, *Synthesis* **1993**, 824–832; d) B. M. Trost, A. S. K. Hashmi, *Angew. Chem. Int. Ed. Engl.* **1993**, *32*, 1085–1087.
[11] A. Fürstner, F. Stelzer, H. Szillat, *J. Am. Chem. Soc.* **2001**, *123*, 11863–11869.
[12] M. Rubina, M. Rubin, V. Gevorgyan, *J. Am. Chem. Soc.* **2002**, *124*, 11566–11567.
[13] J. L. Serrano, I. J. S. Fairlamb, G. Sánchez, L. García, J. Pérez, J. Vives, G. López, C. M. Crawforth, R. J. K. Taylor, *Eur. J. Inorg. Chem.* **2004**, 2706–2715.
[14] a) S. Kannan, A. J. James, P. R. Sharp, *Inorg. Chim. Acta* **2003**, *345*, 8–14; b) S. Kannan, A. J. James, P. R. Sharp, *Polyhedron* **2000**, *19*, 155–163 and references cited therein.
[15] U. Anandhi, T. Holbert, D. Lueng, P. R. Sharp, *Inorg. Chem.* **2003**, *42*, 1282–1295.
[16] P. R. Sharp, *J. Chem. Soc. Dalton Trans.* **2000**, 2647–2657.
[17] B. Longato, G. Bandoli, A. Dolmella, *Eur. J. Inorg. Chem.* **2004**, 1092–1099.
[18] L. Díez, P. Espinet, J. A. Miguel, *J. Chem. Soc. Dalton Trans.* **2001**, 1189–1195.
[19] a) J. Ruiz, V. Rodriguez, N. Cutillas, M. Pardo, J. Pérez, G. López, P. Chaloner, P. B. Hitchcock, *Organometallics* **2001**, *20*, 1973–1982; b) J. Ruiz, V. Rodríguez, G. López, J. Casabó, E. Molins, C. Miravitlles, *Organometallics* **1999**, *18*, 1177–1184 .and references cited therein; c) J. Ruiz, N. Cutillas, V. Rodríguez, J. Sampedro, G. López, P. A. Chalonner, P. B. Hitchcock, *J. Chem. Soc. Dalton Trans.* **1999**, 2939–2946; d) G. Sánchez, J. L. Serrano, J. García, G. López, J. Pérez, E. Molins, *Inorg. Chim. Acta* **1999**, *287*, 37–46; e) G. Sánchez, J. L. Serrano, J. Pérez, M. C. Ramírez de Arellano, G. López, E. Molins, *Inorg. Chim. Acta* **1999**, *295*, 136–145.
[20] G. Sánchez, J. L. Serrano, M. C. Ramírez de Arellano, J. Pérez, G. López, *Polyhedron* **2000**, *19*, 1395–1406 and references cited therein.
[21] G. López, J. Ruiz, G. García, C. Vicente, J. M. Martí, J. A. Hermoso, A. Vegas, M. Martínez-Ripoll, *J. Chem. Soc. Dalton Trans.* **1992**, 53–58.
[22] G. Sánchez, F. Ruiz, M. C. Ramírez de Arellano, G. López, *Helv. Chim. Acta* **1997**, *80*, 2477–2485.
[23] J. L. Serrano, J. Pérez, G. Sánchez, J. F. Martínez, G. López, E. Molins, *Transition Met. Chem.* **2002**, *27*, 105–109.
[24] A. L. Rheingold, C. J. Baldacchini, J. M. O'Connor, J. Huang, *Acta Crystallogr. Sect C* **1989**, *45*, 1626–1628.
[25] G. López, G. Sánchez, G. García, J. García, A. Martínez, J. A. Hermoso, M. Martínez-Ripoll, *J. Organomet. Chem.* **1992**, *435*, 193–202.
[26] F. H. Allen, R. Taylor, *Acta Crystallogr. Sect. B* **1991**, *47*, 404–412.
[27] a) S. Narayan, V. K. Jain, K. Panneergelvam, T. Huey Lu, S-F. Tung, *Polyhedron* **1999**, *18*, 1253–1258; b) K. Panneerselvam, T. Huey Lu, S-F. Tung, S. Narayan, V. K. Jain, *Acta Crystallogr.Sect. C* **1999**, *55*, 541–543.
[28] J. Pérez, L. García, E. Pérez, J. L. Serrano, J. F. Martínez, G. Sánchez, G. López, A. Espinosa, M. Liu, F. Sanz, *New J. Chem.* **2003**, *27*, 1490–1496.
[29] SAINT, Version 6.22, Bruker AXS Inc.
[30] G. M. Sheldrick, SADABS, University of Göttingen, **1996**.
[31] G. M. Sheldrick, SHELX-97. Programs for Crystal Structure Analysis (Release 97–2), University of Göttingen, Germany, **1998**.

Received: December 22, 2004

 © 2005 Wiley-VCH Verlag GmbH & Co. KGaA, Weinheim

Thermodynamic Study of the Binding of Methyltrioxorhenium with Pyridine and Its Derivatives in Benzene Solution

S. Masoud Nabavizadeh,*[a] Alireza Akbari,[a] and Mehdi Rashidi[a]

Keywords: N ligands / Rhenium / Thermodynamics

A spectrophotometric study of the interaction of methyltrioxorhenium (MTO) with pyridine and its derivatives in benzene solution has been carried out at various temperatures. The stability constants of the resulting 1:1 complexes were determined by analysis of spectrophotometric data and found to vary in the order 3,4-Me_2Py > 4-*t*BuPy > 4-MePy > 3-MePy > 4-BenzylPy > Py > 3-PhPy > 3-C(O)OMePy > 3-ClPy. The enthalpy and entropy of adduct formation were determined from the temperature dependence of the stability constants. All complexes formed were enthalpy stabilized but entropy destabilized.

(© Wiley-VCH Verlag GmbH & Co. KGaA, 69451 Weinheim, Germany, 2005)

Introduction

Methyltrioxorhenium (MTO) has found numerous applications in various catalytic processes, especially the oxidation of olefins,[1,2] alcohols,[3,4] arenes[5] and carbonylmetal compounds.[6,7] Epoxidations with MTO/H_2O_2 has several advantages. For instance, MTO is easily available and is active at low concentrations of both MTO and H_2O_2. It works within a broad temperature range (–40 to +90 °C) and is stable in aqueous acidic solution as well as in basic media in special cases. Furthermore, the MTO/H_2O_2 system works in a broad variety of solvents, ranging from highly polar solvents (e.g. nitromethane, water) to solvents with low polarity (e.g., toluene). A major advantage of MTO, however, is that it does not decompose hydrogen peroxide. The most important drawback of the MTO-catalyzed process is the concomitant formation of diols instead of the desired epoxides, especially in the case of more sensitive substrates.[8] It has been reported that the use of Lewis base adducts of MTO significantly decreases the formation of diols due to the reduced Lewis acidity of the catalyst system. It has also been found that addition of a significant excess of pyridine as Lewis base not only hampers the formation of diols but also increases the reaction velocity in comparison to MTO as catalyst precursor.[9,10] In addition, it has been shown that 3-cyanopyridine, and especially pyrazole, as Lewis bases are even more effective and less problematic than pyridine itself, while pyridine *N*-oxides are less efficient.[11–14] The Brønsted basicity of pyridines lowers the activity of hydronium ions, thus reducing the rate of opening of the epoxide ring.[15] MTO forms trigonal-bipyramidal adducts with monodentate N-bases and (distorted) octahedral adducts with bidentate Lewis bases.[16–19] MTO and its monodentate Lewis base adducts react with H_2O_2 to form mono- and bisperoxo complexes. The activity of the bisperoxo complexes (with coordinated Lewis base) in olefin epoxidation depends on the nature, concentration, and redox stability of the Lewis bases. High selectivity (epoxide vs. diol) can be attained by temperature control, trapping of water, or the use of certain additives, such as aromatic Lewis-base ligands, which additionally accelerate the epoxidation reactions.[20] The pK_a of the Lewis base used is important in achieving ligand-accelerated catalysis since the extent of interaction between rhenium and the Lewis base can be correlated to the latter's pK_a: more basic Lewis bases tend to deactivate the MTO.[21] In this regard, we have recently presented a convincing correlation between log *K* of the binding constant, *K*, of the ligand L to MTO and the pK_a of L.[19] Considering the important applications of the pyridine–MTO complexes in catalytic processes, and the effect of temperature on olefin epoxidation, in the present work we have obtained the stability constants of adduct formation of MTO with pyridine derivatives at different temperatures and studied their thermodynamics.

[a] Department of Chemistry, College of Sciences, Shiraz University,
Shiraz, 71454, Iran
Fax: +98-711-228-6008
E-mail: nabavi@chem.susc.ac.ir

Results and Discussion

Adduct Formation with Electron Donors

(η^1-Organo)rhenium(VII) trioxides are Lewis acids with two free coordination sites. Reaction with Lewis bases leads to electronic and steric saturation of the Re center. Ligands, especially those with oxygen or nitrogen donor atoms, form Lewis acid–base adducts with MTO.[22–25] Although both sites of bidentate ligands, such as 2,2′-bipyridine, can bind

 © 2005 Wiley-VCH Verlag GmbH & Co. KGaA, Weinheim DOI: 10.1002/ejic.200500004

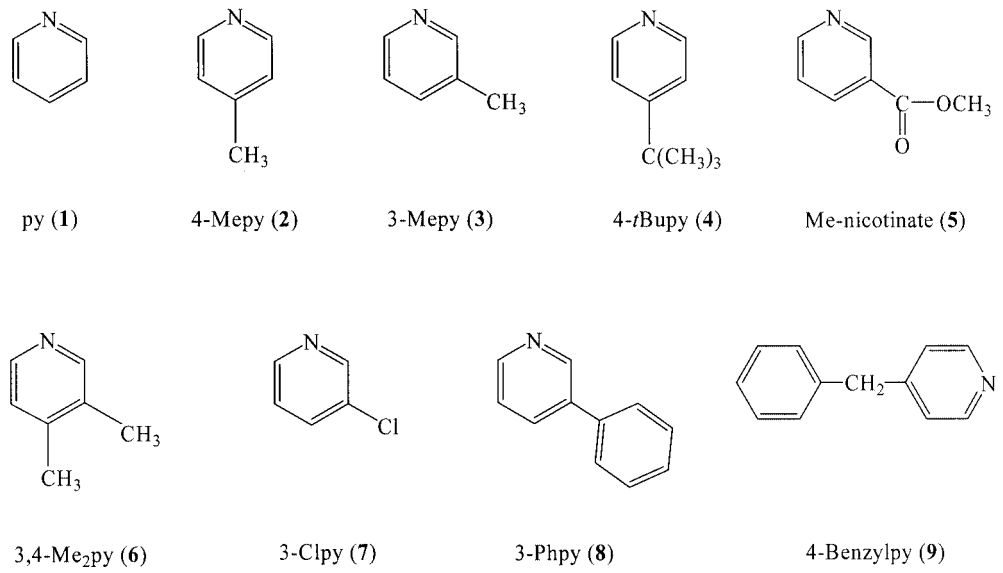

Scheme 1. Structural formulae of pyridine and its derivatives.

to the rhenium center to form a distorted octahedral complex,[26] usually only a single monodentate ligand coordinates to the rhenium atom when a monodentate ligand is used. The lack of formation of MTO·L_2 (L = monodentate ligands) is probably caused by steric factors. Adducts of the composition MTO·L_2 are only known for very small Lewis bases, for example NH_3.[24,25] Special attention has been paid to these adducts because they have proven to be highly selective oxidation catalysts.[23] The reaction of MTO with various pyridine derivatives in benzene affords 1:1 adducts of the composition [CH_3ReO_3]·N [N = pyridine (**1**), 4-picoline (**2**), 3-picoline (**3**), 4-*tert*-butylpyridine (**4**), methyl nicotinate (**5**), 3,4-dimethylpyridine (**6**), 3-chloropyridine (**7**), 3-phenylpyridine (**8**), and 4-benzylpyridine (**9**); see Scheme 1].

The interaction between MTO and several pyridines at different temperatures was studied by UV/Vis spectroscopy. The reaction between MTO and pyridines produces the indicated adduct; the crystal structure for the 4-*tert*-butyl analog has been reported previously.[16] In solution, however, these reactions do not proceed to completion. With UV/Vis detection, an increase in N-donor concentration caused more adduct to form. A series of experiments was carried out with various pyridine derivatives containing substitution in the 3- or 4-position. The values of the stability constants at different temperatures were evaluated for the reaction represented in Scheme 2.

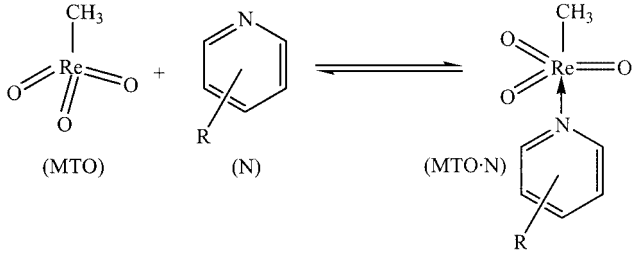

Scheme 2.

The corresponding stability constant, K_{eq}, is given by Equation (1).

$$K_{eq.} = \frac{[MTO{\cdot}N]}{[MTO][N]} \quad (1)$$

where [MTO·N], [MTO], and [N] represent the equilibrium molar concentrations of adduct (CH_3ReO_3·N), free MTO, and free (uncomplexed) pyridine or other ligand, respectively. The absorbance changes in the UV/Vis spectra were analyzed by a nonlinear least-squares fitting according to Equation (2):[19]

$$Abs_{eq} = \frac{\varepsilon_{MTO}([MTO]+[MTO{\cdot}N]) + \varepsilon_{MTO{\cdot}N} K_{eq}[N]([MTO]+[MTO{\cdot}N])}{1+K_{eq}[N]} \quad (2)$$

where Abs_{eq} is the absorbance of a solution at equilibrium, and ε_{MTO} and $\varepsilon_{MTO{\cdot}N}$, are molar absorptivities for the MTO and MTO·N species at the corresponding wavelength. The data for pyridine fit well to Equation (2), affording these values for the parameters: K_{eq} = 677.6 ± 9.7 L mol^{-1} and $\varepsilon_{MTO{\cdot}py}$ = 964.4 ± 2.7 L mol^{-1} cm^{-1} in benzene at 20 °C. Figure 1 shows the fit to Equation (2) of the absorbance values at corresponding wavelength for pyridine at different temperatures.

Derivatives of pyridine [4-Me, 3-Me, 4-C(CH_3)$_3$, 3-C(O)OMe, 3,4-Me_2, 3-Cl, 3-Ph and 4-CH_2Ph] also interact with MTO to a greater or lesser extent. These data were also treated by the same procedure used for pyridine. The resulting parameters are indicated in Table 1.

As shown before,[19] stability constants are sensitive to both steric and electronic effects. For N-donor ligands, a linear relationship between log K_{eq} and pK_a at given temperature is expected, as expressed by Equation (3).

$$\log K_{eq} = m(pK_a) + b \quad (3)$$

 © 2005 Wiley-VCH Verlag GmbH & Co. KGaA, Weinheim

Table 1. Stability constants[a] for the coordination of substituted pyridines to MTO at different temperatures in benzene.

Entry	Ligand	K_{eq} [L mol^{-1}] at 10 °C	K_{eq} [L mol^{-1}] at 20 °C	K_{eq} [L mol^{-1}] at 30 °C	K_{eq} [L mol^{-1}] at 40 °C	pK_a[b]	σ[c]
1	pyridine	**1036.7 ± 34.1**	**677.6 ± 9.7**	**408.4 ± 5.0**	**250.6 ± 6.4**	5.23	0
2	4-picoline	**2056.8 ± 76.5**	**1248.8 ± 38.5**	**791.5 ± 6.9**	**510.9 ± 5.0**	5.89	–0.17
3	3-picoline	**2020.2 ± 188.6**	**1082.7 ± 53.1**	**696.5 ± 38.6**	**408.7 ± 13.6**	5.79	–0.07
4	4-*tert*-butylpyridine	**2542.9 ± 68.5**	**1637.9 ± 156.5**	**1043.5 ± 22.0**	**724.7 ± 14.2**	5.99	–0.20
5	methyl nicotinate	**220.8 ± 6.7**	**117.3 ± 3.3**	**66.5 ± 6.7**	**39.7 ± 2.8**	3.13	0.32
6	3,4-dimethylpyridine	**2848.6 ± 102.2**	**2082.5 ± 162.7**	**1698.7 ± 90.4**	**888.2 ± 89.2**	6.46	–0.24[d]
7	3-chloropyridine	**171.4 ± 7.6**	**89.0 ± 2.2**	**46.2 ± 3.5**	**29.1 ± 2.6**	2.84	0.37
8	3-phenylpyridine	**831.8 ± 7.2**	**494.3 ± 8.9**	**293.8 ± 4.7**	**185.4 ± 5.2**	4.80	0.06
9	4-benzylpyridine	**1649.5 ± 39.6**	**980.4 ± 42.9**	**537.2 ± 37.4**	**312.7 ± 19.6**	5.59	[e]
10	3,5-dibromopyridine	32.9	15.2	6.7	4.3	0.82	0.78[d]
11	4-$Me_2NC_5H_4N$	39219.3	33250.6	26921.6	17382.0	9.61	–0.83
12	3,5-dichloropyridine	29.1	13.3	5.8	3.8	0.67	0.74[d]
13	3-fluoropyridine	186.0	99.7	51.0	32.9	2.97	0.34
14	3-cyanopyridine	54.6	26.4	12.2	7.8	1.45	0.56
15	4-cyanopyridine	76.0	37.7	17.9	11.6	1.86	0.66
16	3-iodopyridine	233.1	127.4	66.4	42.9	3.25	0.35
17	4-phenylpyridine	1487.6	952.8	582.8	376.3	5.55	–0.01
18	3-methoxypyridine	866.9	530.1	309.6	199.9	4.88	0.12
19	4-methoxypyridine	3523.7	2429.9	1600.3	1033.2	6.62	–0.27
20	4-phenoxypyridine[f]	4653.7	3470.6	2423.3	1483.2	[g]	–0.32
21	3-acetylpyridine	220.3	119.8	62.2	40.2	3.18	0.38
22	4-acetylpyridine	287.4	159.9	84.9	54.8	3.51	0.50
23	3-aminopyridine	2190.3	1450.2	916.8	591.9	6.03	–0.16
24	4-aminopyridine	26212.0	21468.4	16791.9	10841.8	9.11	–0.66
25	3-pyridinecarboxyaldehyde[f]	319.9	188.3	101.2	62.7	[g]	0.25
26	4-pyridinecarboxyaldehyde	242.6	133.0	69.6	44.9	3.30	0.45
27	3-nitropyridine	32.6	15.1	6.6	4.3	0.81	0.71
28	4-nitropyridine	62.2	30.3	14.1	9.1	1.61	0.78
29	3-bromo-5-methoxypyridine	138.1	72.1	35.9	23.2	2.60	0.51[d]
30	3-methyl-4-nitropyridine	101.6	51.7	25.1	16.2	2.22	0.71[d]
31	4-amino-3-bromopyridine	4943.1	3509.1	2379.1	1536.0	7.04	–0.27[d]

[a] Experimental values are given in bold; the others are redundant values calculated from them at a given temperature according to Equation (3). [b] K_a applies to the reaction $HL^+ \rightleftharpoons H^+ + L$ in aqueous solution. Data are from ref.[27,28]. [c] The σ_m parameter was used for substitution at C(3), and the σ_p parameter was used for substitution at C(4). [d] These substituent parameters were obtained by adding the individual σ_m or σ_p values for both substituents. [e] Not defined. [f] Values of K_{eq} for these N-donor ligands were calculated with the Hammett equation [log $(K/K_0) = \rho\sigma$]. [g] Not known.

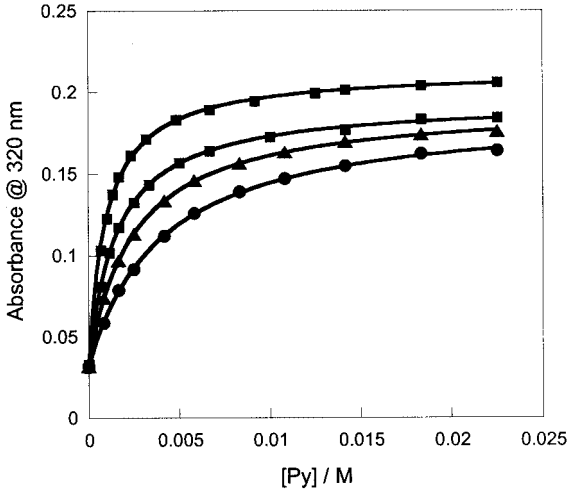

Figure 1. Change in absorbance at 320 nm on addition of pyridine (**1**) to MTO in benzene at T = 10, 20, 30, and 40 °C (temperature increases reading downward); the solid lines show the fit of the spectrophotometric data to Equation (2).

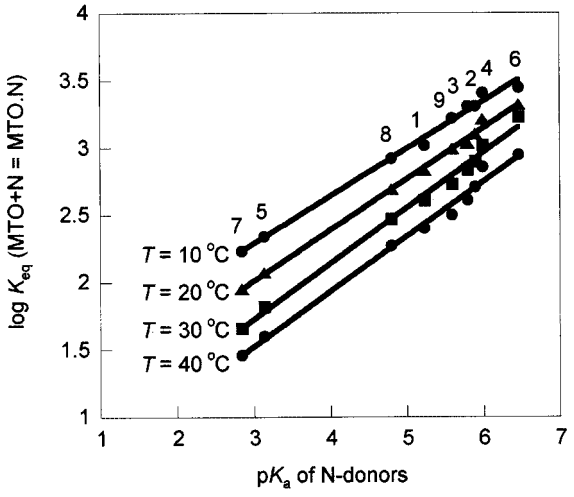

Figure 2. Plot showing a correlation between the stability constants (on the logarithmic scale) for adduct formation of MTO with different N-donors in benzene and pK_a of the same ligands.

 © 2005 Wiley-VCH Verlag GmbH & Co. KGaA, Weinheim

In Figure 2, the values from Table 1 for log K_{eq} are plotted against pK_a at various temperatures. It is evident that the data for MTO·N fit on a straight line. The experimental results listed in Table 1 were used to calculate the straight-line equations summarized in Table 2 by least-squares procedures. These equations allow calculation of the expected stability constant for an adduct of any monodentate N-donor ligand from its pK_a. In Table 1, 36 values of K_{eq} at different temperatures are derived from experiments and the remaining 88 values of K_{eq} are redundant and were calculated directly from these 36 experimental values; of course, the calculated ones will have higher error limits owing to the propagation of errors.

Table 2. Straight-line correlations for stability constants of MTO with monodentate N-donors and ligand basicities[a] at different temperatures in benzene.

Temp. [°C]	m	b	R[b]
10	0.35 ± 0.01	1.23 ± 0.06	0.992
20	0.38 ± 0.01	0.87 ± 0.04	0.997
30	0.41 ± 0.02	0.49 ± 0.07	0.992
40	0.41 ± 0.02	0.30 ± 0.09	0.989

[a] The slopes (m) and intercepts (b) for the straight reference lines from plots of log K_{eq} vs. pK_a were calculated by the least-squares procedure from the data listed in Table 1. [b] Correlation coefficient.

From Table 1, it is obvious that the MTO–ligand interaction is considerably weakened at higher temperatures. The pyridine adducts of MTO are considerably less stable towards moisture and temperature than MTO itself. This enhanced sensitivity has also been observed for other N-donor adducts of MTO.[29]

Linear Free-Energy Relationship (LFER)

An attempted linear free-energy relationship (LFER) correlation according to the Hammett equation at 20 °C is displayed in Figure 3. The slopes of the line of log (K/K_0) vs. σ (substituent constant) are –2.04 ± 0.14 (R = 0.985), –2.22 ± 0.09 (R = 0.986), –2.42 ± 0.11 (R = 0.987) and –2.41 ± 0.07 (R = 0.992) at T = 10, 20, 30, and 40 °C, respectively, which are the reaction constants (ρ). The ρ values for these plots have an absolute magnitude greater than 1, thus indicating that the equilibrium is more sensitive to electronic effects than ionization of benzoic acid. The negative reaction constant for the pyridines' equilibrium indicates that a positive charge develops on the pyridine nitrogen in the adduct as compared with the free molecule. As expected, the Re^{VII} center acts as an electron acceptor, attracting electrons upon coordination. MTO is believed to be a hard Lewis acid on the basis of its strong interactions with N- and O-donor ligands and its weak interaction with S-donor ligands.[15] Therefore, the affinity for the hard N-atom in the N-donor ligands investigated here is expected to be quite high.

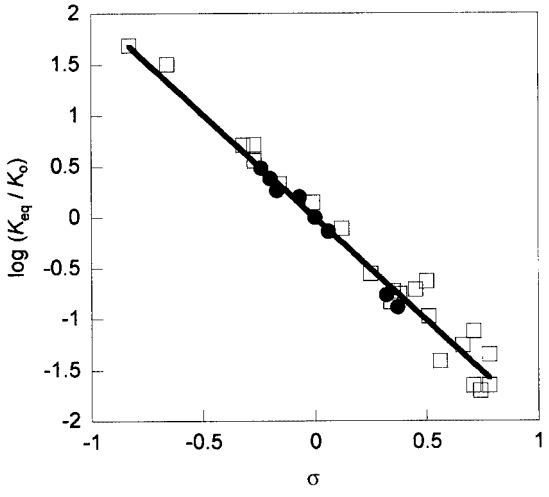

Figure 3. Hammett plot based on the stability constants (●: experimental values; □: calculated values) for the binding of substituted pyridines to MTO in benzene at 20 °C. The reaction constant (for ligands **1**–**9**) is –2.22 ± 0.09.

Effect of Donor

In this work, we have nine donors with different electron-donating capabilities due to different substitution on pyridine. We chose to examine only adducts with pyridines substituted in the *p*- and *m*- positions in order to minimize the steric influence of the Lewis base on the adducts. It is believed that the interaction between MTO and these donors is governed by the electron density on the nitrogen atom of the pyridine ring. On the basis of this description, the following sequence was confirmed from ΔG (20 °C, from Table 3) and K_{eq} (20 °C) values for the interaction of MTO with monodentate N-donors.

	MTO+(**5**)	MTO+(**1**)	MTO+(**4**)
K_{eq} (20 °C) /L mol^{-1}	117.3	677.6	1637.9
ΔG (20 °C) /kJ mol^{-1}	–11.6	–15.9	–18.1

Thermodynamic Parameters

In order to have a better understanding of the thermodynamics of adduct-formation reactions of monodentate N-donors with MTO, it is useful to consider the enthalpic and entropic contributions to these reactions. The ΔH and ΔS values for the adduct formation reactions were evaluated from the corresponding temperature data by applying a linear ln K_{eq} least-squares analysis according to the van't Hoff equation [Equation (4)].

$$\ln K_{eq} = \frac{-\Delta H}{RT} + \frac{\Delta S}{R} \quad (4)$$

Plots of ln K_{eq} vs. 1/T for different MTO·N systems were linear for all cases studied (Figure 4). The enthalpies and entropies of adduct formation were determined in the usual manner from the slopes and intercepts of the plots and the

 © 2005 Wiley-VCH Verlag GmbH & Co. KGaA, Weinheim

Table 3. ΔH, ΔS, and ΔG values for adduct formation of MTO with pyridine derivatives in benzene.

Entry	Ligand	ΔH [kJ mol^{-1}]	ΔS [J K^{-1} mol^{-1}]	ΔG [kJ mol^{-1}][a]
1	pyridine	**–35.1 ± 1.6**	**–65.9 ± 5.3**	**–15.9 ± 0.1**
2	4-picoline	**–34.2 ± 0.1**	**–57.3 ± 0.4**	**–17.4 ± 0.1**
3	3-picoline	**–38.6 ± 1.4**	**–73.2 ± 4.8**	**–17.0 ± 0.1**
4	4-*tert*-butylpyridine	**–31.1 ± 0.6**	**–44.6 ± 1.9**	**–18.1 ± 0.3**
5	methyl nicotinate	**–42.1 ± 0.5**	**–104.1 ± 1.6**	**–11.6 ± 0.2**
6	3,4-dimethylpyridine	**–27.1 ± 5.3**	**–29.0 ± 17.9**	**–18.6 ± 0.2**
7	3-chloropyridine	**–44.1 ± 1.7**	**–113.1 ± 5.7**	**–10.9 ± 0.1**
8	3-phenylpyridine	**–37.0 ± 0.3**	**–74.9 ± 1.1**	**–15.1 ± 0.1**
9	4-benzylpyridine	**–41.2 ± 1.4**	**–83.6 ± 4.5**	**–16.8 ± 0.1**
10	3,5-dibromopyridine	–51.0	–151.4	–6.6
11	4-$Me_2NC_5H_4N$	–19.4	19.9	–25.4
12	3,5-dichloropyridine	–51.5	–154.2	–6.31
13	3-fluoropyridine	–43.3	–109.5	–11.2
14	3-cyanopyridine	–48.8	–139.2	–7.9
15	4-cyanopyridine	–47.3	–131.2	–8.8
16	3-iodopyridine	–42.3	–104.1	–11.8
17	4-phenylpyridine	–34.0	–59.2	–16.7
18	3-methoxypyridine	–36.4	–72.3	–15.3
19	4-methoxypyridine	–30.2	–38.4	–19.0
20	4-phenoxypyridine	–27.8	–27.6	–19.8
21	3-acetylpyridine	–42.5	–105.4	–11.6
22	4-acetylpyridine	–41.3	–99.0	–12.4
23	3-aminopyridine	–32.3	–49.9	–17.7
24	4-aminopyridine	–21.2	10.2	–24.3
25	3-pyridinecarboxyaldehyde	–40.6	–95.3	–12.8
26	4-pyridinecarboxyaldehyde	–42.1	–103.1	–11.9
27	3-nitropyridine	–51.0	–151.6	–6.6
28	4-nitropyridine	–48.2	–136.0	–8.3
29	3-bromo-5-methoxypyridine	–44.6	–116.7	–10.4
30	3-methyl-4-nitropyridine	–46.0	–124.1	–9.6
31	4-amino-3-bromopyridine	–28.6	–30.2	–19.9

[a] At 20 °C.

results are summarized in Table 3. The values of ΔH and ΔS for ligands **1**–**9** were calculated directly from experimental values of K_{eq} and for ligands **10**–**31** they were derived from calculated K_{eq} values at different temperatures. These data allow calculation of the enthalpy and entropy changes for an adduct of any N-donor ligand from its K_{eq} and pK_a. From the data given in Table 3, it is readily obvious that the MTO·N adducts formed in benzene solution are enthalpy stabilized but entropy destabilized. It should be noted that, to the best of our knowledge, no published values of ΔH and ΔS for the adduct formation of MTO are available for comparison with the results obtained here. The ΔG values, calculated from $\Delta G = -RT \ln K_{eq}$ at 20 °C, are included in Table 3.

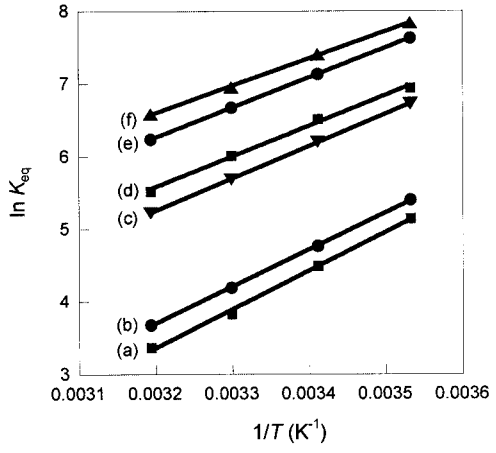

Figure 4. van't Hoff plots for adduct formation of MTO with pyridine derivatives [(a) 3-chloropyridine; (b) methylnicotinate; (c) 3-phenylpyridine; (d) pyridine; (e) 4-methylpyridine; (f) 4-*tert*-butylpyridine] in benzene.

Thermodynamic Analysis of the Adduct-Formation Reaction

Solvation Energy

An Onsager's reaction field model[33–35] was introduced to estimate the solvation energy. The reaction field model expresses solvation energy by

$$\Delta E_{solv} = \frac{2\mu^2}{r^3}\left(\frac{\varepsilon_r - 1}{\varepsilon_r + 2} - \frac{n^2 - 1}{n^2 + 2}\right) \quad (5)$$

where ε_r and n are the dielectric constant and refractive index, respectively, of the solvent and μ and r represent the dipole moment and the diameter, respectively, of the solute. Since the solvent (benzene) is the same for all the systems (MTO + N ⇌ MTO·N), the parentheses term of Equation (5) becomes constant. Thus, solvation energy is assumed to depend only on the μ^2/r^3 term. Since the radii will change only slightly, one can approximate $r_{MTO\cdot N} = r_{MTO}$

 © 2005 Wiley-VCH Verlag GmbH & Co. KGaA, Weinheim

+ r_N, and the solvation energy can therefore be expressed as a linear function of μ (see Table 4).

Table 4. Dipole moments of some pyridine derivatives.

Ligand	$\mu_{calcd.}$ [D][a]	$\mu_{exp.}$ [D][b]
Pyridine	2.35	2.20
4-Picoline	2.78	2.68
3-Picoline	2.61	2.45
4-*tert*-Butylpyridine	2.89	
Methyl nicotinate	0.70	
3,4-Dimethylpyridine	3.05	
3-Chloropyridine	2.16	2.02
3-Phenylpyridine	2.48	
4-Benzylpyridine	2.64	

[a] The μ values for N-donors were obtained from B3LYP/6-311++G** calculations with the Gaussian 98 program package.[30] [b] Available experimental data are from refs.[31,32]

For reactions of the type considered in this work $\Delta G = \Delta G^i - \Delta G^s$, where ΔG^i is the Gibbs free energy change of the adduct formation reaction without solvation and ΔG^s is the additional term due to the effect of solvation. We performed a trial plot of ΔG against μ according to Equation (5) for nine different N-donors (**1**–**9**), shown in Figure 5, to determine if there exists any correlation between ΔG (or ΔG^s) and μ. The plot shows a good linear relationship. Therefore, we concluded that ΔG, and hence ΔG^s, are controlled by μ of the N-donor after the reaction field model.

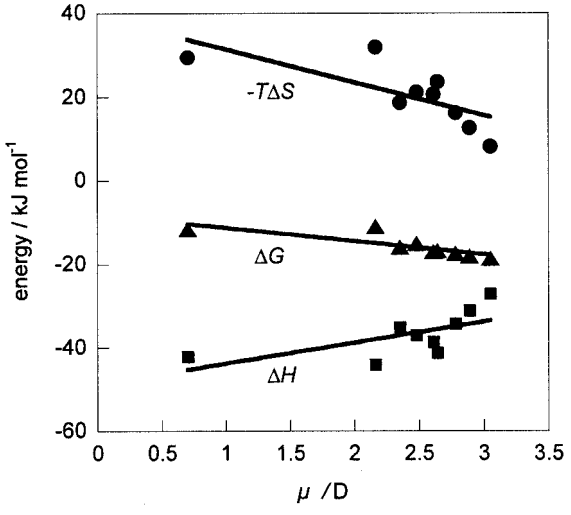

Figure 5. Correlation between ΔH, ΔG, or $T\Delta S$ and dipole moment. Data were taken from Tables 3 and 4 (for ligands **1**–**9**) at 20 °C and fitted to a linear relation.

Enthalpy and Entropy Contributions

The stabilization model by solvation seems to explain the μ-dependence of ΔG in the MTO·N-donor adduct formation. Since the Gibbs free energy consists of enthalpy and entropy terms ($\Delta G = \Delta H - T\Delta S$), we discuss the solvation effect by considering the two terms separately and try to understand how these thermodynamic terms (ΔH and ΔS) of the reaction depend on the dipole moment of the N-donors.

For a given reaction, the enthalpy and entropy changes can be considered to be composed of intrinsic (ΔH^i and ΔS^i) and solvation (ΔH^s and ΔS^s) terms:

$$\Delta H = \Delta H^i + \Delta H^s$$

$$\Delta S = \Delta S^i + \Delta S^s$$

In the enthalpy term, the second term is for the solvation energy and is possibly proportional to μ. We plot the ΔH values against μ in Figure 5 to find some correlation between ΔH and μ. Figure 5 shows a reasonable linear dependence of ΔH upon μ. Therefore, we concluded that ΔH is controlled by μ of the N-donors, and the reaction field model seems valid in the adduct formation MTO + N-donor → Adduct. Since the slope in the plot of ΔH vs. μ is positive, the solvation energy of the reactants is larger than that of the adduct. We discuss this result according to Equation (5). Since the refractive index, n, and the dielectric constant, ε_r, of the solvent are constant, we consider only the μ^2/r^3 term. This formula means that the solvation energy depends on the dipole moment and the volume. We discuss these factors separately. The volumes of MTO and the N-donor are smaller than the adduct, although one can assume that this factor, compare to the dipole moment, is not very important, because $r_{MTO\cdot N} \approx r_{MTO} + r_N$. Thus, the solvation energy for the reactants is larger than that of the adduct. The dipole moment plays an important role in the solvation. The dipole moment of the adduct is probably smaller than the reactants due to the structure of the adduct. The dipoles of MTO and N-donors may be antiparallel and cancel each other out in the adduct. Also, the ΔH value for the adduct MTO·3,4-dimethylpyridine is less negative (–27.1 kJ mol^{-1}) than the others (i.e. MTO·3-ClPy: ΔH = –44.1 kJ mol^{-1}), although the formation constant is the highest (2082.5 L mol^{-1} at 20 °C). It seems that this donor is better solvated, due to its larger dipole moment, and this reduces the overall enthalpy.

The ΔS values, which are negative in the present association reaction, apparently depend on μ and change from –104.1 to –29.0 (J K^{-1} mol^{-1}) as μ increases from 0.7 to 3.05 D, for ligands **5** and **6** respectively. We qualitatively discuss the relation between enthalpy change (ΔH^s) and entropy change (ΔS^s) by solvation. The ΔH values are plotted against ΔS in Figure 6. The absolute value of ΔH (or exothermicity of the reaction) increases as the entropy change decreases, which indicates that solvation controls not only ΔH but also ΔS. When the N-donor has negligibly small μ, the enthalpy changes of solvation ΔH^s for the reactants and the adduct are negligible, and the solvent molecules are loosely bound to the reactants and the adduct. Thus, the solvent molecules are not well aligned with the reactants or with the adduct (negligible ΔS^s). This is the case of the "small μ limit" as shown in the energy diagrams in Figure 7. On the other hand, for the N-donor having large μ, the solvation energy becomes much larger, according to Onsager's reaction field model (negative and larger ΔH^s), and the solvent molecules are tightly trapped by the reactants and the adduct. Thus, the solvent molecules are well aligned

 © 2005 Wiley-VCH Verlag GmbH & Co. KGaA, Weinheim

with the reactants and with the adduct (negative and large ΔS^s). This is the case of the "large μ limit" in Figure 7. As a result, the absolute magnitudes of ΔH and ΔS values decrease when μ changes from the small μ limit to the large μ limit. It might be worthy to note that: (1) both ΔH and $T\Delta S$ contribute similarly to ΔG, and that (2) these contributions cancel out each other, resulting in a rather constant ΔG value against μ. This feature is visualized in Figure 5, where ΔG, ΔH, or $-T\Delta S$ are plotted against μ values; the ΔH and $T\Delta S$ contributions vary, but ΔG does not vary greatly for various N-donors with different μ. All these phenomena can be reasonably explained in the thermodynamical terms described above.

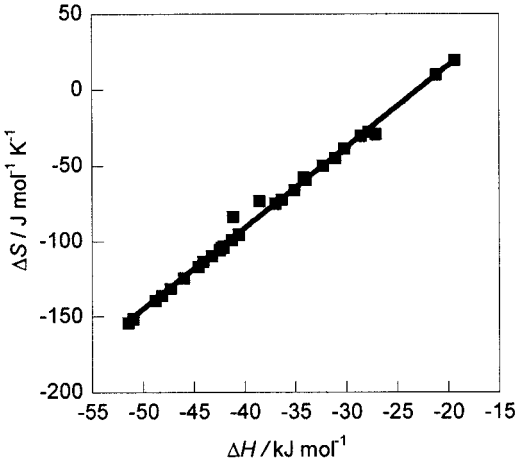

Figure 6. Correlation between ΔH and ΔS (enthalpy–entropy compensation) for adduct formation of MTO with pyridine derivatives. The data are listed in Table 3.

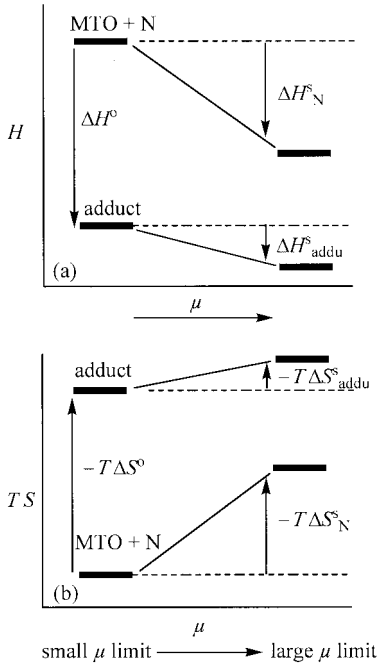

Figure 7. Energy diagrams of the reactants and the adduct: (a) enthalpy changes upon adduct formation; (b) entropy changes upon adduct formation. Both ΔH and $T\Delta S$ are small for N-donors with large μ.

The enthalpy–entropy compensation plot of adduct formation of MTO with pyridine derivatives, which is shown in Figure 6, gives a good straight line. This may be taken as evidence for the operation of a common structure–activity relationship in this series of complexes.[36,37]

Conclusions

Lewis-base adducts of MTO are known to be more rigid at lower temperatures and less strongly coordinated at higher temperatures. The stability of the adducts formed by pyridine and its derivatives with MTO is entirely due to a negative ΔH, while ΔS counteracts the adduct formation investigated here. ΔH and ΔS are controlled by the dipole moments of pyridine derivatives. Both ΔH and ΔS are small for N-donors with large μ.

Experimental Section

The compound methyltrioxorhenium ($MeReO_3$ or MTO) was synthesized according to a literature procedure.[22] The pyridine derivatives were purchased from commercial sources (Merck or Fluka) and were used as received. Benzene (Merck, quality: for spectroscopy) was used as solvent throughout this study and the data were obtained at different temperatures (10, 20, 30, and 40 °C). A Perkin–Elmer Lambda 25 spectrophotometer with temperature control using an EYELA NCB-3100 constant temperature bath was used to record UV/Vis spectra. Typically, a 2×10^{-4} M solution of the MTO in benzene contained in a quartz cuvette with a 1-cm path length was treated with successive aliquots of a solution of the N-donor ligand, of known concentration, in the same solvent. The values of stability constants and the extinction coefficient of adducts at different wavelengths were determined by fitting the equilibrium absorbance to Equation (2) by the method of nonlinear least-squares.

Acknowledgments

We thank the Shiraz University Research Council, Iran (Grant No. 82-SC-1664-C259) for financial support. We also thank Dr. Ghatee for his key help in purchasing the UV/Vis spectrometer.

[1] W. A. Herrmann, R. W. Fischer, D. W. Marz, *Angew. Chem. Int. Ed. Engl.* **1991**, *30*, 1638–1641.
[2] W. A. Herrmann, R. W. Fischer, W. Scherer, M. U. Rauch, *Angew. Chem. Int. Ed. Engl.* **1993**, *32*, 1157–1160.
[3] W. A. Herrmann, J. P. Zoller, R. W. Fischer, *J. Organomet. Chem.* **1999**, *579*, 404–407.
[4] T. H. Zauche, J. H. Espenson, *Inorg. Chem.* **1998**, *37*, 6827–6831.
[5] W. Adam, W. A. Herrmann, J. Lin, C. R. Saha-Möller, R. W. Fischer, J. D. G. Correia, *Angew. Chem. Int. Ed. Engl.* **1994**, *33*, 2475–2476.
[6] W. R. Thiel, R. W. Fischer, W. A. Herrmann, *J. Organomet. Chem.* **1993**, *459*, C9-C11.
[7] W. A. Herrmann, J. D. G. Correia, F. E. Kühn, G. R. J. Artus, C. C. Romão, *Chem. Eur. J.* **1996**, *2*, 168–173.
[8] W. A. Herrmann, R. W. Fischer, M. U. Rauch, W. Scherer, *J. Mol. Catal.* **1994**, *86*, 243–266.

 © 2005 Wiley-VCH Verlag GmbH & Co. KGaA, Weinheim

[9] J. Rudolph, K. L. Reddy, J. P. Chiang, K. B. Sharpless, *J. Am. Chem. Soc.* **1997**, *119*, 6189–6190.
[10] H. Adolfsson, A. Converso, K. B. Sharpless, *Tetrahedron Lett.* **1999**, *40*, 3991–3994.
[11] C. Copéret, H. Adolfsson, K. B. Sharpless, *J. Chem. Soc., Chem. Commun.* **1997**, 1565–1566.
[12] W. A. Herrmann, H. Ding, R. M. Kratzer, F. E. Kühn, J. J. Haider, R. W. Fischer, *J. Organomet. Chem.* **1997**, *549*, 319–322.
[13] W. A. Herrmann, F. E. Kühn, M. R. Mattner, G. R. J. Artus, M. Geisberger, J. D. G. Correia, *J. Organomet. Chem.* **1997**, *538*, 203–209.
[14] H. Adolfsson, C. Copéret, J. P. Chiang, A. K. Yudin, *J. Org. Chem.* **2000**, *65*, 8651–8658.
[15] W. D. Wang, J. H. Espenson, *J. Am. Chem. Soc.* **1998**, *120*, 11 335–11 341.
[16] F. E. Kühn, A. M. Santos, P. W. Roesky, E. Herdtweck, W. Scherer, P. Gisdakis, I. V. Yudanov, C. Di Valentin, N. Rösch, *Chem. Eur. J.* **1999**, *5*, 3603–3615.
[17] P. Ferreira, W. M. Xue, É. Bencze, E. Herdtweck, F. E. Kühn, *Inorg. Chem.* **2001**, *40*, 5834–5841.
[18] A. M. Santos, F. E. Kühn, W. M. Xue, E. Herdtweck, *J. Chem. Soc., Dalton Trans.* **2000**, 3570–3574.
[19] S. M. Nabavizadeh, *Inorg. Chem.* **2003**, *42*, 4204–4208.
[20] F. E. Kühn, A. Scherbaum, W. A. Herrmann, *J. Organomet. Chem.* **2004**, *689*, 4149–4164.
[21] B. S. Lane, K. Burgess, *Chem. Rev.* **2003**, *103*, 2457–2473.
[22] W. A. Herrmann, in *Applied Homogeneous Catalysis with Organometallic Compounds* (Eds.: B. Cornils, W. A. Herrmann), 2nd ed., vol. 3, Wiley-VCH, Weinheim, **2002**, p. 1319.
[23] W. A. Herrmann, F. E. Kühn, *Acc. Chem. Res.* **1997**, *30*, 169–180.
[24] W. A. Herrmann, J. G. Kuchler, G. Weichselbaumer, E. Herdtweck, P. Kiprof, *J. Organomet. Chem.* **1989**, *372*, 351–370.
[25] W. A. Herrmann, G. Weichselbaumer, E. Heerdtweck, *J. Organomet. Chem.* **1989**, *372*, 371–389.
[26] C. C. Romão, F. E. Kühn, W. A. Herrmann, *Chem. Rev.* **1997**, *97*, 3197–3246.
[27] R. M. Smith, A. E. Martell, *Critical Stability Constants*, Plenum Press, New York, **1974**.
[28] *CRC Handbook of Chemistry and Physics* (Editor-in-Chief: D. R. Lide), 81st ed., CRC Press, Boca Raton, FL, **2000**.
[29] H. Rudler, J. R. Gregorio, B. Denise, J. M. Brégeault, A. Deloffre, *J. Mol. Catal. A* **1998**, *133*, 255–265.
[30] M. J. Frisch, G. W. Trucks, H. B. Schlegel, G. E. Scuseria, M. A. Robb, J. R. Cheeseman, V. G. Zakrzewski, J. A. Montgomery Jr., R. E. Stratmann, J. C. Burant, S. Dapprich, J. M. Millam, A. D. Daniels, K. N. Kudin, M. C. Strain, O. Farkas, J. Tomasi, V. Barone, M. Cossi, R. Cammi, B. Mennucci, C. Pomelli, C. Adamo, S. Clifford, J. Ochterski, G. A. Petersson, P. Y. Ayala, Q. Cui, K. Morokuma, D. K. Malick, A. D. Rabuck, K. Raghavachari, J. B. Foresman, J. Cioslowski, J. V. Ortiz, A. G. Baboul, B. B. Stefanov, G. Liu, A. Liashenko, P. Piskorz, I. Komaromi, R. Gomperts, R. L. Martin, D. J. Fox, T. Keith, M. A. Al-Laham, C. Y. Peng, A. Nanayakkara, C. Gonzalez, M. Challacombe, P. M. W. Gill, B. Johnson, W. Chen, N. W. Wong, J. L. Andres, M. Head-Gordon, E. S. Replogle, J. A. Pople, Gaussian 98, Revision A.7, Gaussian, Inc., Pittsburgh, PA, **1998**.
[31] I. Pápai, G. Jancsó, *J. Phys. Chem. A* **2000**, *104*, 2132–2137.
[32] V. V. Prezhdo, E. V. Vaschenko, O. V. Prezhdo, A. Puszko, *J. Mol. Struct.* **1998**, *471*, 127–137.
[33] L. Onsager, *J. Am. Chem. Soc.* **1936**, *58*, 1486–1493.
[34] J. N. Wilson, *Chem. Rev.* **1939**, *25*, 377–406.
[35] E. G. McRae, *J. Phys. Chem.* **1957**, *61*, 562–572.
[36] L. Liu, Q. X. Guo, *Chem. Rev.* **2001**, *101*, 673–696.
[37] J. H. Espenson, *Chemical Kinetics and Reaction Mechanisms*, McGraw-Hill, New York, 2nd ed., **1995**.

Received: January 04, 2005

 © 2005 Wiley-VCH Verlag GmbH & Co. KGaA, Weinheim

Dinuclear Complexes of M^{II} Thiocyanate (M = Ni and Cu) Containing a Tridentate Schiff-Base Ligand: Synthesis, Structural Diversity and Magnetic Properties

Suparna Banerjee,[a] Michael G. B. Drew,[b] Can-Zhong Lu,[c] Javier Tercero,[d] Carmen Diaz,*[d] and Ashutosh Ghosh*[a]

Keywords: Copper / Nickel / N,N,O ligands / Schiff-base ligands / Magnetic properties / Crystal structures

A dinuclear Ni^{II} complex, $[Ni_2(\mathbf{L})_2(H_2O)(NCS)_2]\cdot 3H_2O$ (**1**) in which the metal atoms are bridged by one water molecule and two μ_2-phenolate ions, and a thiocyanato-bridged dimeric Cu^{II} complex, $[Cu(\mathbf{L})NCS]_2$ (**2**) [**L** = tridentate Schiff-base ligand, *N*-(3-aminopropyl)salicylaldimine, derived from 1:1 condensation of salicylaldehyde and 1,3-diaminopropane], have been synthesized and characterized by IR and UV/Vis spectroscopy, cyclic voltammetry and single-crystal X-ray diffraction studies. The structure of **1** consists of dinuclear units with crystallographic C_2 symmetry in which each Ni^{II} atom is in a distorted octahedral environment. The Ni–O distance and the Ni–O–Ni angle, through the bridged water molecule, are 2.240(11) Å and 82.5(5)°, respectively. The structure of **2** consists of dinuclear units bridged asymmetrically by di-$\mu_{1,3}$-NCS ions; each Cu^{II} ion is in a square-pyramidal environment with τ = 0.25. Variable-temperature magnetic susceptibility studies indicate the presence of dominant ferromagnetic exchange coupling in complex **1** with J = 3.1 cm^{-1}, whereas complex **2** exhibits weak antiferromagnetic coupling between the Cu^{II} centers with J = –1.7 cm^{-1}.
(© Wiley-VCH Verlag GmbH & Co. KGaA, 69451 Weinheim, Germany, 2005)

Introduction

Dinuclear metal complexes and ligands facilitating their formation have been extensively investigated due to their potential applications in many field of chemistry.[1–10] The essential requirements for the formation of these dimeric complexes are an unsaturated coordination environment of the single-coordinated metal ion and the presence of bridging atoms or groups. The bridging abilities of the phenolate oxygen atom[11] and polyatomic moieties[12–15] (e.g. N_3, NCO, NCS, NCSe) have been exploited extensively for the synthesis of dinuclear species. However, it is very difficult to predetermine the structure of the self-assembled species when both types of bridging groups are present. Parameters that should be considered to achieve the desired species in such cases include the nature of the metal ions and their coordination requirement. In order to have an insight into the controlling parameters we have synthesized complexes of Ni^{II} and Cu^{II} with thiocyanate and the tridentate Schiff-base ligand **L** (Scheme 1), prepared by 1:1 condensation of salicylaldehyde and 1,3-propanediamine. We have found that Ni^{II} forms a phenolate-bridged dinuclear complex with thiocyanate acting as terminal ligand, whereas Cu^{II} yields an end-to-end thiocyanato-bridged dinuclear species having phenoxo as the terminal ligand.

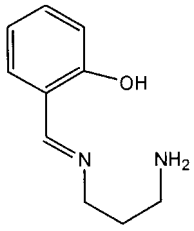

Scheme 1. Ligand **L**.

The structural and magnetic properties of dinuclear nickel(II) complexes with bridging ligands have received considerable attention over the past two decades. Magneto-structural correlations have been made and interesting trends have emerged. Among these compounds, the azide group has been predominant due to its versatility as a ligand. When the N_3^- anion acts as bridging ligand, normally the end-to-end 1,3-coordination mode gives antiferromagnetic coupling, while the end-on 1,1-mode gives ferromagnetic coupling, but for very large M–$\mu_{1,3}$-N_3–M bond angles the magnetic coupling may be reversed.[16–19] For the SCN^- anion the bridging mode usually involves a 1,3-coordination mode with both nitrogen and sulfur atom bound to the metal ions. From crystal structures it has been shown

[a] Department of Chemistry, University College of Science and Technology, University of Calcutta, 92, A. P. C. Road, Kolkata 700009, India
[b] School of Chemistry, The University of Reading, P. O. Box 224, Whiteknights, Reading RG6 6AD, UK
[c] The State Key Laboratory of Structural Chemistry, Fujian Institute of Research on the Structure of Matter, The Chinese Academy of Sciences, Fuzhou, Fujian 350002, P. R. China
[d] Departament de Química Inorgànica, Universitat de Barcelona, Martí I Franquès 1–11, 08028 Barcelona, Spain

 © 2005 Wiley-VCH Verlag GmbH & Co. KGaA, Weinheim **DOI: 10.1002/ejic.200500080**

experimentally that in Ni^{2+} dinuclear complexes, all dinuclear $[Ni_2(\mu\text{-}NCS)_2]$ cores have approximately the same angles and distances, and they generally show low ferromagnetic behavior, which was explained by Ginsberg et al.[19d] and Duggan et al.[19e] Ferromagnetic interactions have been found, generally, in octahedrally coordinated dimeric nickel(II) complexes with 1,3-thiocyanate[16a,17] and -selenocyanate bridges.[18]

When the phenolate acts as a bridging ligand through the oxygen atom in dinuclear nickel(II) complexes, generally antiferromagnetic behaviour was found;[20–23] only three complexes showing ferromagnetic coupling have been described in the literature.[24] Complex **1**, is, to the best of our knowledge, the first dinuclear complex in which the octahedral Ni^{2+} ions share a face, and it is therefore of considerable interest that its magnetic behavior is ferromagnetic.

The study of polynuclear complexes of Cu^{II} with pseudohalogen bridges has received considerable attention in recent years.[25–29] Again, there are many examples of such complexes in which the azide group acts as a bridge. By contrast the literature available for magneto-structural studies on Cu^{II} complexes containing the bridging thiocyanate groups is scarce, as this ligand is less versatile and also less efficient as a transmitter of magnetic interactions than the azide.[26,27] Most of the previously reported asymmetric end-to-end 1,3-thiocyanate-bridged Cu^{II} compounds have octahedral geometry and exhibit very low values of *J* or paramagnetic behavior.[26a,28,29] There are only a few examples of double bridged end-to-end thiocyanato dimers in which the Cu^{II} atoms are five-coordinate.[28,30] The design of molecule-based magnets relies on the presence of both intra- and intermolecular coupling. Therefore, the identification of structural features that can be correlated with the strength and sign of this interaction clearly constitutes a necessary step in such design.

Results and Discussion

Synthesis

The monocondensed ligand *N*-(3-aminopropyl)salicylaldimine (**L**) was prepared as $[NiL_2]$ by the reaction of Ni^{II} nitrate, salicylaldehyde and 1,3-propanediamine (see Exp. Sect.). $[NiL_2]$ reacted readily with $Ni(SCN)_2$ in a 1:1 molar ratio in methanolic solution to produce the μ_2-phenolato- and aqua-bridged complex $[Ni_2(L)_2(H_2O)(NCS)_2]\cdot 3H_2O$ (**1**). The free ligand (**L**) which was isolated by removing nickel as bis(dimethylglyoximato)nickel(II) from $[NiL_2]$, on reaction with the methanolic solution of copper acetate followed by ammonium thiocyanate yielded the thiocyanato-bridged dinuclear complex $[Cu(L)NCS]_2$ (**2**).

IR Spectra

In the IR spectrum of complex **1**, a strong band at 2091 cm^{-1} is due to ν(CN) of the *N*-bonded thiocyanate and a band at 1626 cm^{-1} is due to ν(CO) of the phenolato-bridged ligand. The broad band in the range 3391–3340 cm^{-1} is assigned to the O–H stretching vibrations of uncoordinated and bridged water molecules.

In complex **2**, only one ν(CN) vibration at 2094 cm^{-1} is observed, due to the presence of bridging thiocyanato ligands and the ν(CS) is assigned at 782 cm^{-1}. The C=N stretch of the phenolate ligand is observed near 1630 cm^{-1} in both complexes. The two primary NH_2 stretching modes are clearly seen in **2** near 3310 and 3185 cm^{-1} for the asymmetric and symmetric vibrations respectively.

Description of Structure 1

The molecular structure of **1** is shown in Figure 1. Selected bond lengths and angles are summarized in Table 1. The dimeric structure shows a crystallographic two-fold

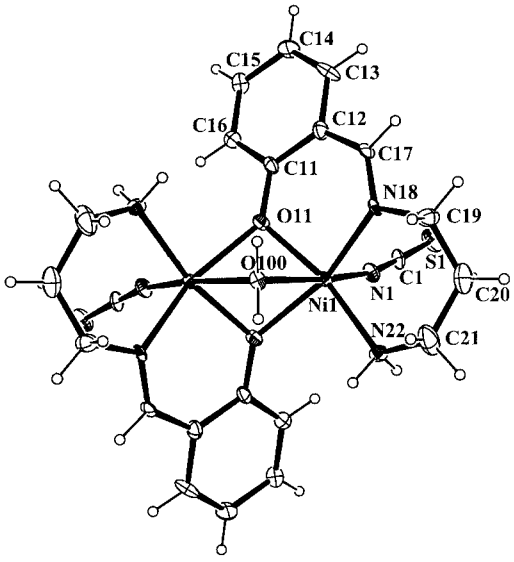

Figure 1. Perspective view of the complex **1** (30% thermal probability ellipsoids, for clarity hydrogen atoms and uncoordinated water molecules are omitted).

Table 1. Selected bond lengths [Å] and angles [°] for compound $[Ni_2(L)_2(H_2O)(NCS)_2]\cdot 3H_2O$ (**1**).

Ni1–O11	1.990(10)	Ni1–O11A	2.131(9)
Ni1–N18	2.035(10)	Ni1–O100	2.240(11)
Ni1–N1	2.039(12)	Ni1–Ni1A	2.953(4)
Ni1–N22	2.085(11)		
O11–Ni1–N18	91.5(4)	O11A-Ni1–O100	75.5(3)
O11–Ni1–N1	92.6(4)	N18–Ni1–N1	91.3(5)
O11–Ni1–N22	167.8(4)	N18–Ni1–N22	98.6(5)
N1–Ni1–N22	93.9(5)	O11A-Ni1–O11	76.3(4)
N18–Ni1–O11A[a]	163.8(4)	C11–O11–Ni1	124.8(8)
N1–Ni1–O11A	99.7(4)	C11–O11–Ni1A	141.2(8)
N22–Ni1–O11A	92.5(4)	Ni1–O11–Ni1A	91.5(4)
O11–Ni1–O100	78.3(3)	N18–Ni1–O100	91.8(4)
N1–Ni1–O100	170.5(4)	N22–Ni1–O100	94.5(4)
Ni1–O100–Ni1A	82.2(5)		

[a] A represents symmetry element $-x, y, 0.5 - z$.

 © 2005 Wiley-VCH Verlag GmbH & Co. KGaA, Weinheim

axis through the bridging water molecule O100. The dinuclear unit is formed by two Ni^{II} atoms labeled Ni1 and Ni1A, bridged by this water molecule and by the two μ_2-phenolato oxygen atoms O11 and O11A of the Schiff-base ligands. The two equivalent nickel atoms have distorted octahedral environments. The basal plane $Ni_2N_2O_2$ is formed by the two nitrogen atoms N18 and N22 and the two oxygen atoms O11 and O11A of the bridging phenoxo ligands. The N1 atom of the thiocyanato terminal ligand and the O100 atom of the bridging aqua ligand occupy the axial positions. The two Ni atoms are separated by 2.953(4) Å with two Ni–O11–Ni bridge angles of 91.5(4)° and one Ni–O100–Ni bridge angle of 82.5(5)°. The basal bond lengths around the Ni atom are in the range of 1.990(10)–2.131(9) Å. The apical bond lengths are Ni1–N1 2.039(12) Å and Ni1–O100 2.240(11) Å, the bond angle being O100–Ni1–N1 170.5(4)°. The Ni–NCS distance, 2.039(12) Å, is as expected. However, the Ni–OH_2 distance, 2.240(11) Å, although comparable to those found in some aqua-bridged dinuclear Ni^{II} complexes,[31] is much longer than the range 2.09–2.16 Å reported for few other known examples of water bridges in Ni^{II} structures.[32] Some of this bond lengthening can be accounted for by the involvement of the bridging water molecule in hydrogen bonds to another water molecule O101. Another water molecule O102 is also hydrogen-bonded to the nitrogen atom of the thiocyanato ligand (Figure 2). The *cis* angles in the nickel polyhedra are all within 15° of 90° (Table 1). These distortions can be rationalized as resulting from the ligand constraints in the molecule, particularly in the bridging system.

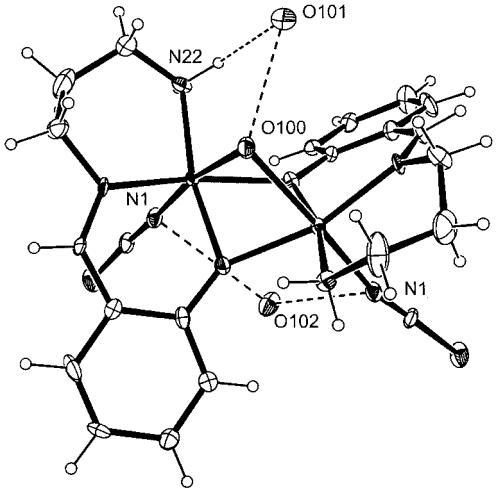

Figure 2. Hydrogen bonding in complex **1** involving uncoordinated water molecules (30% thermal probability ellipsoids, water molecules uninvolved in hydrogen bonding are omitted for clarity).

Description of Structure 2

Figure 3 shows an NCS-bridged copper dimer $[Cu_2(\mathbf{L})_2(\mu\text{-NCS})_2]$, in which the asymmetric units are related by a centre of inversion. Selected bond lengths and angles are summarized in Table 2. The intradimer Cu–Cu distance is 5.863 Å. The copper atoms are located in a distorted square-pyramidal environment as revealed by the trigonal index, $\tau = 0.25$. The value of τ is defined as the difference between the two largest donor–metal–donor angles divided by 60, a value which is 0 for the ideal square pyramid and 1 for the trigonal bipyramid[33] In the present case τ is calculated as (176.8 – 161.4)/60 = 0.25. The elongated square-pyramidal (4 + 1) geometry of the copper(II) centers is constructed from a basal plane containing three ligating atoms, O, N2, N3 of the tridentate Schiff-base ligand and a nitrogen atom, N1 from the thiocyanate group. In addition, the elongated apical position is occupied by the weakly bonded sulfur donor atom S′ from the other centrosymmetrically related thiocyanato bridge at a distance of 2.952(1) Å (symmetry operation: $^1/_2 - x$, $^1/_2 - y$, $1 - z$); the bond angle at the axially coordinated Cu–S′–C1′ being 102.6(1)°. The metal–nitrogen and metal–oxygen distances involving the equatorial plane ($CuON_3$) agree well with those generally found in five-coordinate Cu^{II} complexes.[26a,30] The metal atom is 0.064 Å above the basal plane in the direction of the apex, which is usual for square-pyramidal geometry. The dimeric units are related by translation along the *y* axis to form extended chains by strong interdimer hydrogen bonding between the amine nitrogen atom of one dimeric unit and the phenolate oxygen atom of the adjacent dimeric unit (N2A···O = 2.938 Å, H2A···O = 2.067 Å, ∠N2–H2A···O′ = 162.67°) (Figure 4). The shortest interdinuclear Cu^{II}–Cu^{II} distance between the two H-bonded units is

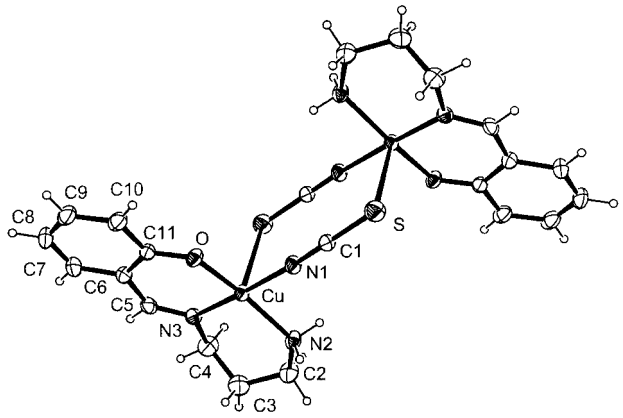

Figure 3. Perspective view of complex **2** (30% thermal probability ellipsoids).

Table 2. Selected bond lengths [Å] and angles [°] for compound $[Cu(\mathbf{L})NCS]_2$ (**2**).

Cu–O	1.910(2)	Cu–N2	2.019(3)
Cu–N3	1.964(3)	Cu–S′[a]	2.952(1)
Cu–N1	1.995(3)		
O–Cu–N3	93.33(11)	N1–Cu–N2	85.04(12)
O–Cu–N1	86.57(11)	S′–Cu–N1	92.15(10)
N3–Cu–N1	176.77(12)	S′–Cu–O	101.08(8)
O–Cu–N2	161.37(12)	S′–Cu–N3	84.70(9)
N3–Cu–N2	95.97(12)	S–Cu–N2	95.8310)

[a] The primes (′) refer to atoms related by the symmetry operation: $^1/_2 - x$, $^1/_2 - y$, $1 - z$.

 © 2005 Wiley-VCH Verlag GmbH & Co. KGaA, Weinheim

3.571 Å. Numerous (thiocyanato)Cu^{II} complexes have been described in the literature; however, it is worth noting that most of them are made up of dinucluear entities and have octahedral coordination around Cu^{II} containing di-$\mu_{1,3}$-NCS bridges[17] whereas in the present complex end-to-end thiocyanato-bridged dimer the Cu^{II} atoms are five-coordinate.

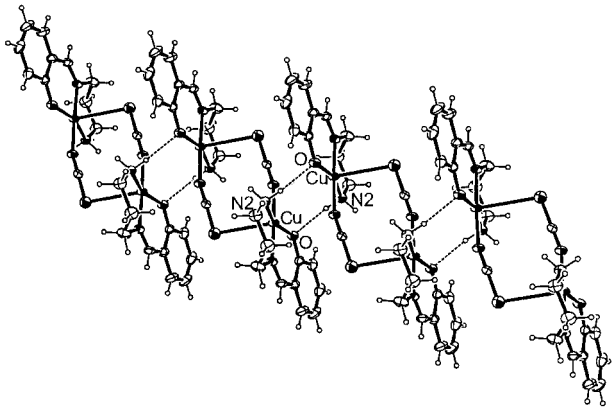

Figure 4. Molecular packing view of **2** along the *y* direction; the intermolecular hydrogen bonds are shown as dashed lines.

Electronic Spectra

The peaks in the electronic spectrum, taken in the solid state (Nujol mull) and in acetonitrile solution are similar in the two complexes.

The dinickel complex **1** exhibits two distinct bands at 610 and 874 nm and a weaker band near 773 nm. The first two bands can be assigned to the spin-allowed d-d transition $^3T_2 \leftarrow {}^3A_{2g}$ and $^3T_{1g} \leftarrow {}^3A_{2g}$, respectively, and the weaker band to the spin-forbidden transition $^1E_g \leftarrow {}^3A_{2g}$. These values are in agreement with the literature values for octahedral Ni^{II} compounds.[34]

The dicopper complex **2** shows a d-d transition around 612 nm. The UV absorption band observed at 358 nm can be assigned to the charge transfer transition. Strong absorption bands in the region 280 nm are clearly also due to charge transfer.

Electrochemical Study

The cyclovoltammogram of complex **1** in acetonitrile solution (Pt electrode) under nitrogen displays a electrochemically irreversible (ΔE_p = 120 mV) oxidative response attributed to the Ni^{II}/Ni^{III} couple at +0.70 V vs. SCE.

The cyclovoltammogram of the copper complex **2** recorded in dry acetonitrile solution (vs. SCE) at ambient temperature exhibits a reversible signal at +1.1 V (ΔE_p = 80 mV). The redox process is assigned to Cu^{2+}/Cu^{3+} oxidation. No reductive response of either Cu^{2+}/Cu^{1+} or Cu^{2+}/Cu was observed in the cathode sweep.

To ascertain the stoichiometry of the redox couple of the Cu^{II} complex **2** we performed constant potential exhaustive electrolysis at +1.25 V under ambient conditions. The coulomb count of the experiment revealed one electron oxidative transfer from Cu^{2+} resulting in the formation of Cu^{III} analogs. The oxidized Cu^{III} compound, however, is not isolable at room temperature but stable enough for EPR study at 77 K (toluene/acetonitrile mixture) to determine the metal valence. The oxidized compound is EPR-inactive under frozen glass conditions (77 K), thereby confirming the formation of a diamagnetic Cu^{III} species.

The other possibility of ligand oxidation has been far outweighed from this experimental observation, which otherwise would have resulted in an odd electron paramagnetic species (s = 1/2), sensitive towards EPR measurement. Therefore, it is justified to conclude the oxidative response at +1.1 V to be associated with a Cu^{II}/Cu^{III} oxidation instead of an energetically unfavourable phenolate moiety based ligand oxidation event.

Magnetic Properties

The variable-temperature magnetic properties $\chi_M T$ vs. T of **1** and **2** are illustrated in Figures 5 and 6, respectively.

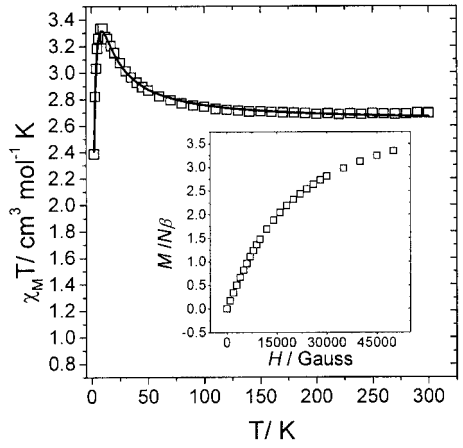

Figure 5. Plot of $\chi_M T$ [cm^3 mol^{-1} K] vs. T [K] in the range 2–300 K for **1**. The solid line is generated from the best-fit magnetic parameters. Inset: Plot of $M/N\beta$ vs. H for complex **1**.

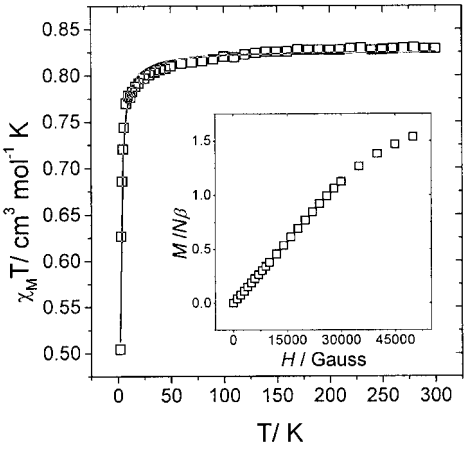

Figure 6. Plot of $\chi_M T$ [cm^3 mol^{-1} K] vs. T [K] in the range 2–300 K for **2**. The solid line is generated from the best-fit magnetic parameters. Inset: plot of $M/N\beta$ vs. H for complex **2**.

 © 2005 Wiley-VCH Verlag GmbH & Co. KGaA, Weinheim

In complex **1** the $\chi_M T$ values (χ_M is the molar susceptibility for two Ni^{II} ions) show a gradual increase from a room-temperature value of 2.70 $cm^{-1} mol^{-1} K$ to 3.25$cm^{-1} mol^{-1} K$ at 6 K, followed by a drop at lower temperature. This behavior is typical of a system exhibiting dominant intramolecular ferromagnetic exchange coupling. The $\chi_M T$ vs. temperature curve for **1** was least-squares-fitted {by minimizing the function $R = \Sigma[(\chi_M T)_{exp.} - (\chi_M T)_{calcd.}]^2/\Sigma(\chi_M T)_{exp.}^2\}$ to the theoretical expression of magnetic susceptibility of Ginsberg et al.,[35] from the Hamiltonian

$$H = -2JS_1S_2 - D(S_{1Z}^2 + S_{2Z}^2) - g\beta H(S_1 + S_2) - Z'J'S\langle S\rangle$$

in which J is the intradimer exchange parameter, D the single-ion zero-field splitting, and $Z'J'$ the parameter for effective interdimer exchange; it is assumed that $g_x = g_y = g_z = g$. The resulting χ_M expression is:

$$\chi_M = 2Ng^2\beta^2/3k[F_1/(T - 4Z'J'F_1) + 2F'/(1 - 4Z'J'F')$$

F_1 and F' being complicated functions of temperature, zero-field splitting, and the intradimer exchange parameter J.

The best-fitting parameters obtained are $J = 3.1(1)$ cm^{-1}, $g = 2.29(1)$, $D = 1.8(1)$ cm^{-1}, $Z'J' = -0.2(1)$ cm^{-1} with $R = 1.8 \times 10^{-5}$. These values should be considered with caution because, although the Ginsberg expression gives accurate values of J and g, the parameters D and $Z'J'$ are not well determined from magnetic susceptibility data.[35b,35c] The value of the reduced molar magnetization is 3.55 $N\beta$ when the field is 5 T (inset, Figure 5). This small value can be explained by the presence of either parameter D or antiferromagnetic interdimer interactions or by a combination of the two.

For complex **2** the value of $\chi_M T$ at 300 K is 0.83, which is expected for two magnetically quasi-isolated spin doublets ($g > 2.00$). This value remains practically constant upon cooling and then decreases sharply in the low-temperature region attaining a value of 0.50 at 2 K; no maximum of the magnetic susceptibility (χ_M vs. T) is observed. These observed features are characteristic of very weak antiferromagnetic interactions between copper(II) ions. We have analyzed the magnetic data through a simple Bleaney–Bowers expression for a copper(II) dimer,[36] derived through the isotropic Hamiltonian $H = -JS_1S_2$, where J is the exchange coupling parameter and $S_1 = S_2 = 1/2$ (interacting local spins). Least-squares fitting leads to the following parameters: $J = -1.71(1)$ cm^{-1}, $g = 2.10(1)$, and $R = 3 \times 10^{-5}$ {R is the agreement factor defined as: $R = \Sigma[(\chi_M T)_{exp.} - (\chi_M T)_{calcd.}]^2/\Sigma(\chi_M T)_{exp.}^2\}$. Considering that in complex **2** the dinuclear entities are linked by structurally strong hydrogen bonds, the fit of the magnetic data has been carried out, too, by the Bleaney–Bowers expression taking into account the J' intermolecular parameter. The best-fit parameter obtained was $J = -1.8$ cm^{-1}, $J' = 0.10$ cm^{-1}, $g = 2.10$ and the same R value. The small positive J' value indicates that the hydrogen intermolecular interactions could be ferromagnetic. The value of the reduced molar magnetization is 1.55 $N\beta$ when the field is 5 T (inset in Figure 6). The shape of the curve formed by the experimental points does not follow the Brillouin formula. This feature is also indicative of the small antiferromagnetic coupling.

Discussion

Complex 1

The demonstration of a linear dependence of the exchange coupling constant (J) with the Cu–O–Cu bridge angle in planar dihydroxy-bridged dicopper(II) complexes has turned out to be one of the most useful and best known magneto-structural correlations.[37] Unlike hydroxo- and alkoxo-bridged Cu^{II} dinuclear complexes[38] structural modeling and magneto-structural correlations are scarce in nickel(II) complexes, due to fewer number of known complexes and to the large number of structural parameters that affect the superexchange mechanism in these systems. Dinuclear nickel(II) complexes in which one or two phenolate groups act as bridges are generally found to be antiferromagnetic.[20–23] Ferromagnetic behavior has been found in only three complexes[24] of which one has not been structurally characterized,[24a] while the other two have one of the nickel ions in a five-coordinate, trigonal-bipyramidal coordination environment. Correlations of the superexchange coupling in centrosymmetric Ni–O–Ni dinuclear nickel(II) complexes made by Nanda et al.,[21] and a quantumchemical ab initio study by Wang el al.,[39] show that the value of the exchange coupling constants is directly proportional to the Ni–O–Ni bridge angles or Ni···Ni distance. The results (at least qualitatively) are in very good agreement with nearly all measurements on such complexes: Thus, for Ni–O–Ni angles in the region of 90° the coupling is ferromagnetic with J values in the order of 10 cm^{-1}. The magnetic properties of **1**, which contain a distorted octahedral geometry around the Ni^{2+} ions and with a noncentrosymmetric structure, are interpreted in terms of two different bridges, the phenolate and the H_2O. The Ni–O–Ni′ bridge angle through the phenolato ligand is 91.5(4)° and the Ni···Ni distance is 2.953(4) Å. The Ni–O100–Ni′ bridge angle through the oxygen atom of the water molecule is 82.2(4)° and the Ni–O100 distance is 2.240(11) Å. Taking into account the small Ni···Ni distance and the small angles in the bridges, it is reasonable to assume a ferromagnetic exchange through the two kinds of bridges.

Complex 2

A weak but significant interaction between the copper(II) centers is observed through the end-to-end thiocyanato intrametallic bridges. Complex **2** shows the following features: (a) the copper(II) centers are bridged by two thiocyanate ions in an asymmetric end-to-end fashion, (b) the copper(II) ions are five-coordinated, (c) the nitrogen atom of the SCN bridge ligand lies in the equatorial plane and the sulfur li-

 © 2005 Wiley-VCH Verlag GmbH & Co. KGaA, Weinheim

gand occupies the axial position. Few complexes with these characteristics are reported in the literature.[30]

The majority of the complexes described in the literature with NCS^--bridged ligand(s) with an N(basal)–S(apical) disposition, exhibit either very low values of J or paramagnetic behavior.[26a,28,29] This behaviour is characteristic of all complexes and does not seem to depend on either the topology of the copper(II) centers (usually octahedral) or the existence of single or double μ-NCS bridges.

EPR Measurements

The X-band EPR spectra of complexes **1** and **2** were recorded on microcrystalline powders at temperatures from 280 to 4 K.

It is of interest to note that in complex **1** the spectrum, recorded at low temperature, shows only one absorption at very low field (Figure 7a). For an axial integer $S = 2$ spin system, the zero-field interaction (D parameter) splits the m_s levels into two doublets $m_s = |\pm2\rangle$ and $|\pm1\rangle$ and one $m_s = 0$ state. Transitions between these Kramer doublets are not possible due to the D value expected for the nickel(II) ion. For a rhombic distortion, the E parameter splits the $m_s = |\pm2\rangle$ and $m_s = |\pm1\rangle$ Kramer doublets giving a Δ_2 and Δ_1 gap at zero field. The value of Δ_1 is strongly dependent on E and is usually much greater than the $g\beta H$ energy of an X-band measurement. In contrast, the Δ_2 increases as a function of E^2/D and the ±2 transition usually lies in the low-field region of the spectra.[40] This type of EPR spectrum is similar to that previously reported for manganese(III), iron(IV), and tetranuclear cobalt(II) spectra.[24b,41]

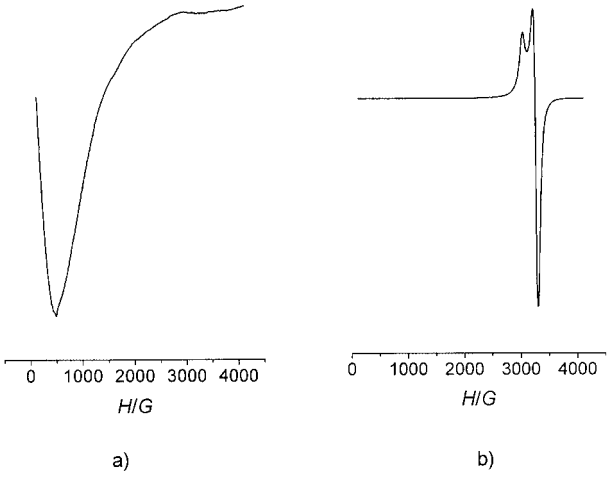

Figure 7. EPR spectra of polycrystalline complexes **1** (a) and **2** (b) at 4 K.

The X-band EPR spectra of complex **2** shown in Figure 7b shows absorption features of axial symmetry with $g_{\|} = 2.22$ and $g_{\perp} = 2.08$. The observed g inequality ($g_{\|} > g_{\perp}$) is consistent with the square-pyramidal geometry of complex **2** with the unpaired electron residing in the $3d_{x^2-y^2}$ orbital thereby making $^2B_{1g}$ the ground state.

Conclusions

Two new complexes of Ni^{II} and Cu^{II} thiocyanate have been synthesized using an N,N,O-donor Schiff-base ligand. The tridentate ligand is chelated and the thiocyanate ion is coordinated to metal centers through the nitrogen atom in both complexes, as expected. However, the construction of the dinuclear entities occurs in very different ways. In complex **1** two Ni ions are bridged through the phenolate oxygen atom, and a water molecule acts as an additional bridge to complete the hexacoordination around the nickel ion. On the other hand, the sulfur atom of the *N*-bonded thiocyanato ligand coordinates axially to bridge the two copper atoms in complex **2**. The weak axial coordination and consequently the square-pyramidal geometry around Cu^{II} is probably dictated by the active Jahn–Teller effect of the d^9 system. Thus, the nature of the metal ion plays a very important role in the self-assembly of the mononuclear units into the dinuclear complex. From the magnetic point of view complex **1** is the first example where dinucluear Ni^{II}, simultaneously bridged by phenolato and aqua ligands, exhibits ferromagnetic behaviour.

Experimental Section

Starting Materials: Salicylaldehyde, 1,3-diaminopropane, $Cu(OAc)_2{\cdot}H_2O$, ammonium thiocyanate and Ni^{II} salts were purchased from commercial sources and used as received. HPLC grade acetonitrile, was used for electrochemical and UV/Vis measurements and all other solvents were of reagent grade and were used without further purification.

Physical Measurements: Spectral measurements were carried out using the following equipments: UV/Vis (both in acetonitrile solution and solid), Hitachi-U 3501 Spectrophotometer. IR (KBr disc), Perkin–Elmer RXI FT-IR spectrometer and Nicolet Magna IR 750 Series II. A Perkin–Elmer 240C elemental analyzer was used for microanalysis (C, H, N). The magnetic measurements were carried out in the "Servei de Magnetoquimica (Universitat de Barcelona)" on polycrystalline samples (20 mg) with a Quantum Design SQUID MPMSXL susceptometer in the temperature range of 2–300 K and the magnetic field was 1 T. Magnetization measurements were carried out in the same instrument at 2 K. EPR spectra were recorded on powder samples at X-band frequency with a Bruker 300E automatic spectrometer, varying the temperature between 4 and 300 K. Electrochemical measurements were performed under nitrogen using a PAR model Versastat-2 electrochemical analyzer, with a platinum working electrode under dry nitrogen. The supporting electrolyte was tetraethylammonium perchlorate (TEAP), and the potentials are referenced to the saturated calomel electrode (SCE) without junction correction.

***N*-(3-Aminopropyl)salicylaldimine (L):** The complex bis(3-aminopropylsalicylideneiminato)nickel(II) ($C_{20}H_{26}N_4Ni$) was prepared by the method of Elder.[42] A solution of the ligand (10 mmol) was obtained by refluxing the Ni^{II} complex (2.06 g, 5 mmol) with 2 equiv. of DMG (1.16 g, 10 mmol) in methanol (20 mL) for 2 h and filtering the precipitated bis(dimethylglyoximato)nickel(II) according to the procedure of Burke and McMillin.[43]

$[Ni_2(L)_2(H_2O)(NCS)_2]{\cdot}3H_2O$ (1): $Ni(SCN)_2$ (0.351 g, 1.5 mmol), dissolved in 10 mL of hot methanol, was added to a methanolic solution (10 mL) of bis(3-aminopropylsalicylideneiminato)nickel(II)

 © 2005 Wiley-VCH Verlag GmbH & Co. KGaA, Weinheim

(0.619 g, 1.5 mmol) and stirred for 10 min. The colour of the solution turned to light green. The resulting solution, on keeping at room temperature for several hours, yielded a dark green crystalline solid. It was filtered and dissolved in a minimum volume of acetonitrile and kept in a refrigerator. Upon slow evaporation of the solvent, dark green crystals of complex **1,** suitable for X-ray analysis appeared after 2 d. Yield: 0.529 g (86%). $C_{22}H_{34}N_6Ni_2O_6S_2$ (660.06): calcd. C 40.03, H 5.19, N 12.73; found C 39.90, H 5.14, N 12.72.

[Cu(L)NCS]$_2$ (2): To a solution of **L** (0.534 g, 3 mmol) in methanol (10 mL), $Cu(OAc)_2 \cdot H_2O$ (0.598 g, 3 mmol), dissolved in a minimum volume of hot methanol, was added and stirred for 30 min. To the resulting solution, a methanolic solution of NH_4SCN (456 mg, 6 mmol) was added. The blue solution yielded needle-shaped crystals on keeping at room temperature for 24 h. Yield: 0.824 g (92%). $C_{11}H_{13}CuN_3OS$ (298.02): calcd. C 44.21, H 4.38, N 14.06; found C 44.15, H 4.30, N 14.51.

X-ray Crystallography: Data for both crystals were measured with Mo-K_α radiation (λ = 0.71073 Å) using a MARresearch Image Plate System for **1** and a Siemens SMART CCD diffractometer for **2**. For **1** the crystals were positioned at 70 mm from the image plate. 100 frames were measured at 2° intervals with a counting time of 2 min. Data analysis for **1** was carried out with the XDS program[44] and for **2** with the SHELXAL™ V.5.03 program.[45] The structures were solved by direct methods (SHELX-86 program for **1**[46] and SHELXTL for **2**). Absorption corrections were carried out using DIFABS[47] for **1** and SADABS for **2**[48] The structures were then refined to convergence on F^2 using SHELXL for **1**[49] and SHELXTL for **2**. The non-hydrogen atoms were refined with anisotropic thermal parameters in all cases. For **1** the hydrogen atoms bonded to carbon atoms were included in geometric positions and given thermal parameters equivalent to 1.2 times those of the atoms to which they are attached. All calculations were carried out using SHELX-86, SHELXL-93, PLATON-99 for **1** and Siemens SHELXTL, Bruker SHELXTL for **2**. Selected bond lengths and bond angles of the crystals are presented in Tables 1 and 2. while selected crystallographic data for the two complexes are summarized in Table 3. Repeated recrystallization from acetonitrile failed to produce good-quality crystals of **1**. The poor quality of the crystals of **1** gave rise to misshapen large spots in the diffraction pattern which in turn led to high *R* values. CCDC-256766 (**1**) and -256767 (**2**) contain the supplementary crystallographic data for this paper. These data can be obtained free of charge from The Cambridge Crystallographic Data Centre via www.ccdc.cam.ac.uk/data_request/cif.

Table 3. Crystallographic data for complexes **1** and **2**.

	1	**2**
Empirical formula	$C_{22}H_{34}N_6Ni_2O_6S_2$	$C_{11}H_{13}CuN_3OS$
M	660.09	298.84
System	monoclinic	monoclinic
Space group	*C*2/*c*	*C*2/*c*
a [Å]	8.735(11)	20.5473(10)
b [Å]	15.950(17)	7.2149(3)
c [Å]	21.31(2)	18.0073(7)
β [°]	100.807(10)	108.0170(10)
V [Å^3]	2916(6)	2538.62(19)
Z	4	8
D [mg m^{-3}]	1.503	1.564
T [K]	293(2)	293(2)
μ [mm^{-1}]	1.480	1.871
Independent reflections	2438	2216
R_{int}	0.0796	0.0166
Collected reflections	6483	3888
$[I > 2\sigma(I)]$, R_1, wR_2	0.1423, 0.3010	0.0425, 0.1078

Acknowledgments

This work was supported by the University Grants Commission (UGC), India (Fellowship for S. B., Sanction No. UGC/548/jr. Fellow Sc 2001/2002). We like to thank the Spanish government (Grant BQU2003-00539) and EPSRC, the University of Reading for funds for the image plate system. We are thankful to Dr. S. Chaudhuri, RSIC, Bose Institute, Kolkata, India, for useful discussion on crystallography.

[1] P. Dapporto, M. Formica, V. Fusi, L. Giothi, M. Micheloni, P. Paoli, R. Pontellini, P. Rossi, *Inorg. Chem.* **2001**, *40*, 6186.
[2] C. J. Pedersen, *J. Am. Chem. Soc.* **1967**, *89*, 7017.
[3] J. M. Lehn, *Pure Appl. Chem.* **1977**, *49*, 857.
[4] D. J. Gam, J. M. Gam, *Science* **1984**, *183*, 4127.
[5] J. M. Lehn, *Angew. Chem. Int. Ed. Engl.* **1988**, *27*, 89.
[6] P. Guerriero, S. Tamburini, P. A. Vigato, *Coord. Chem. Rev.* **1993**, *110*, 17.
[7] C. Bazzsicalupi, A. Bencini, V. Fusi, C. Giorgi, P. Paoletti, B. Vattacoli, *Inorg. Chem.* **1998**, *37*, 941 and references cited therein.
[8] D. A. Nation, A. E. Martell, R. I. Carroll, A. Clearfield, *Inorg. Chem.* **1996**, *35*, 7246.
[9] T. Koike, M. Inoue, E. Kimura, M. Shiro, *J. Am. Chem. Soc.* **1996**, *118*, 3091.
[10] a) C. Bazzsicalupi, A. Bencini, A. Bianchi, V. Fusi, E. Gracia-Espana, C. Giorgi, M. J. Llinares, J. A. Ramirez, B. Valtancoli, *Inorg. Chem.* **1999**, *38*, 620 and references cited therein; b) A. Bianchi, K. James-Bowman, E. Garcia-Espana, *Supramolecular Chemistry of Anions*, Wiley-VCH, New York, **1997**.
[11] a) A. S. Hay, *J. Polym. Sci., Part A: Polym. Chem.* **1998**, *36*, 505; b) H. Higashimura, M. Kubota, A. Shiga, K. Fujisawa, Y. Morooka, H. Uyama, S. Kobayashi, *Macromolecules* **2000**, *33*, 1986 and refercences therein; c) B. A. Jazdzewski, W. B. Tolman, *Coord. Chem. Rev.* **2000**, *200–202*, 633.
[12] a) J. Ribas, M. Monfort, I. Resino, X. Solans, P. Rabu, F. Maingot, M. Drillan, *Angew. Chem. Int. Ed. Engl.* **1996**, *35*, 2520; b) G. De Munno, M. Julve, G. Viau, F. Lloret, J. Faus, D. Viterbo, *Angew. Chem. Int. Ed. Engl.* **1996**, *35*, 1807.
[13] a) E. A. Mauro, I. S. Klein, A. C. Saldana, D. Simone, J. Zukerman-Schpector, E. E. Castellano, *Polyhedron* **1990**, *9*, 2937; b) R. Vicente, A. Escuer, E. Penalba, X. Solans, M. Font-Badia, *J. Chem. Soc., Dalton Trans.* **1994**, 3005.
[14] a) M. Monfort, J. Ribas, X. Solans, *Inorg. Chem.* **1994**, *33*, 4271; b) R. Vicente, A. Escuer, J. Ribas, X. Solans, *J. Chem. Soc., Dalton Trans.* **1994**, 259.
[15] a) J. Ribas, C. Diaz, X. Solans, M. Font-Bardia, *J. Chem. Soc., Dalton Trans.* **1997**, 35; b) J. Ribas, C. Diaz, R. Costa, X. Tercero, X. Solans, M. Font-Bardia, *Inorg. Chem.* **1998**, *37*, 233.
[16] a) R. Cortes, T. I. Ruiz de Larramendi, L. Lezama, T. Rojo, K. Urtiaga, M. I. Arriortua, *J. Chem. Soc., Dalton Trans.* **1992**, 2723; b) M. I. Arriortua, R. Cortes, L. Lezama, T. Rojo, X. Solans, M. Font-Bardia, *Inorg. Chim. Acta* **1990**, *174*, 263.
[17] M. I. Arriortua, R. Cortes, J. L. Mesa, L. Lezama, T. Rojo, G. Villenueve, *Transition Met. Chem. (Weinheim, Ger.)* **1988**, *13*, 371.
[18] a) M. D. Duggan, D. N. Hendrickson, *Inorg. Chem.* **1974**, *13*, 2929; b) A. E. Shrelashvili, M. A. Porii-Koshits, A. S. Antsyshkina, *J. Struct. Chem. (Engl. Transl.)* **1969**, *10*, 552; c) T. Rojo, R. Cortes, L. Lezama, I. M. Arriortua, G. Villenueve, *J. Chem. Soc., Dalton Trans.* **1991**, 1779.
[19] a) C. G. Pierpont, D. N. Hendrickson, D. M. Duggan, F. Wagner, E. K. Barefield, R. L. Martin, *Inorg. Chem.* **1975**, *14*, 604; b) P. Chaudhuri, M. Gottmann, D. Ventur, K. Wieghardt,

B. Nuber, J. Weiss, *J. Chem. Soc., Chem. Commun.* **1985**, 1618; c) J. Ribas, A. Escuer, M. Monfort, R. Vicente, R. Cortés, L. Lezama, T. Rojo, *Coord. Chem. Rev.* **1999**, *193–195*, 1027–1068; d) A. P. Ginsberg, R. W. Brookes, R. C. Sherwood, *Inorg. Chem.* **1972**, *11*, 2884; e) D. M. Duggan, D. N. Hendrickson, *Inorg. Chem.* **1974**, *13*, 2929.

[20] a) S. L. Lambert, D. N. Hendrickson, *Inorg. Chem.* **1979**, *18*, 2683; b) C. L. Spiro, S. L. Lambert, T. J. Smith, E. N. Duesler, R. R. Gagne, D. N. Hendrickson, *Inorg. Chem.* **1981**, *20*, 1229.

[21] a) K. K. Nanda, L. K. Thompson, J. N. Bridson, K. Nag, *J. Chem. Soc., Chem. Commun.* **1994**, 1337; b) K. K. Nanda, R. Das, K. Venkatsubramanium, P. Paul, K. Nag, *Inorg. Chem.* **1994**, *33*, 1188 and references cited therein.

[22] E. Berti, A. Caneschi, C. Daiguebonne, P. Dapporto, M. Formica, V. Fusi, L. Giorgi, A. Guerri, M. Micheloni, P. Paoli, R. Pontelli, P. Rossi, *Inorg. Chem.* **2003**, *42*, 348.

[23] a) T. Koga, H. Furutachi, T. Nakamura, N. Fukita, M. Ohba, K. Takahaski, H. Okawa, *Inorg. Chem.* **1998**, *37*, 989; b) S. K. Dey, N. Mondal, M. S. El Fallah, R. Vicente, A. Escuer, X. Solans, M. Font-Bardia, V. Gramlich, S. Mitra, *Inorg. Chem.* **2004**, *43*, 2427.

[24] a) K. K. Nanda, A. W. Addison, N. Paterson, E. Sinn, L. K. Thompson, U. Sakaguchi, *Inorg. Chem.* **1998**, *37*, 1028; b) D. Volkmer, B. Hammerich, K. Griesar, W. Haase, B. Krebs, *Inorg. Chem.* **1996**, *35*, 3792.

[25] a) A. H. Norbury, A. I. P. Q. Sinha, *Rev. Chem. Soc.* **1970**, *24*, 69; b) O. Kahn, Y. Pei, Y. Journaux, in: *Inorganic Materials*, 2nd ed. (Eds.: W. Q. Bruce, D. O'Hare), John Wiley, Chichester, U. K. **1997.**

[26] a) M. Julve, M. Verdaguer, G. De Munno, J. A. Real, G. Bruno, *Inorg. Chem.* **1993**, *32*, 795; b) M. Cannas, G. Carta, G. Marongis, *J. Chem. Soc., Dalton Trans.* **1973**, 556; c) M. Kabesova, M. Dunaj-Jurco, J. Soldanova, *Inorg. Chim. Acta* **1987**, *130*, 105; d) L. Walz, W. Haase, *J. Chem. Soc., Dalton Trans.* **1985**, 1243.

[27] a) J. G. Haasnoot, W. L. Driessen, J. Reedijk, *Inorg. Chem.* **1984**, *23*, 2803; b) C. Harding, D. Mc Dowell, J. Nelson, S. Raghunathan, C. Stevenson, M. G. B. Drew, P. C. Yates, *J. Chem. Soc., Dalton Trans.* **1990**, 2521.

[28] a) N. N. Karan, S. Mitra, T. Matsushita, V. Gramlich, G. Rosair, *Inorg. Chim. Acta* **2002**, *332*, 87; b) P. Domiano, A. Musatti, M. Nardelli, C. Pelizzi, G. predieri, *J. Chem. Soc., Dalton Trans.* **1975**, 2357; c) J. A. R. Navarro, M. A. Romero, J. M. Salas, M. Quiros, E. R. T. Tickink, *Inorg. Chem.* **1997**, *36*, 4988; d) P. Gomez-Saiz, J. Garcia-Tojal, F. J. Arnaiz, M. A. Maestro, L. Lezama, T. Rojo, *Inorg. Chem. Commun.* **2003**, *6*, 558; e) R. Vicente, A. Escuer, E. Penalba, X. Solans, M. Font-Bardia, *Inorg. Chim. Acta* **1997**, *7*, 255.

[29] a) S. Ferlay, G. Francese, H. W. Schamalle, S. Decurtis, *Inorg. Chim. Acta* **1999**, *286*, 108; b) C. Diaz, J. Ribas, N. Sanz, X. Solans, M. Font-Bardia, *Inorg. Chim. Acta* **1999**, *286*, 169; c) H. Grove, M. Julve, F. Lloret, P. E. Kruger, K. W. Tornroos, J. Sletten, *Inorg. Chim. Acta* **2001**, *325*, 115; d) Z. E. Serna, R. Cotes, M. K. Urtiaga, M. G. Barandika, L. Lezama, M. I. Arriortua, T. Rojo, *Eur. J. Inorg. Chem.* **2001**, 865; e) M. Soibinet, I. Dechamps-Oliver, E. Goillon, J. P. Barbier, M. Aplicourt, F. Chuburu, M. Le Baccen, H. Handel, *Eur. J. Inorg. Chem.* **2003**, 1984; f) P. G. Saiz, J. Garcia-Tojal, F. J. Arnaiz, M. A. Maestro, L. Lezama, T. Rojo, *Inorg. Chim. Acta* **2003**, *6*, 558.

[30] a) M. B. Cingi, A. M. Manotti Lanfredi, A. Tiripicchio, J. G. Haasnoot, J. Reedijk, *Inorg. Chim. Acta* **1983**, *72*, 81; b) R. Vicente, A. Escuer, E. Penalba, X. Solans, M. Font-Bardia, *Inorg. Chim. Acta* **1997**, *255*, 7; c) J. G. Haasnoot, W. L. Driessen, J. Reedijk, *Inorg. Chem.* **1984**, *23*, 2803.

[31] a) E. D. Mckenzie, *Inorg. Chim. Acta* **1979**, *32*, 253; b) D. Volkmer, B. Hommerich, K. Griesar, W. Haase, B. Krebs, *Inorg. Chem.* **1996**, *35*, 3792; c) A. M. Barrios, S. J. Lippard, *J. Am. Chem. Soc.* **1999**, *121*, 11751.

[32] a) U. Turpeinen, *Finn. Chem. Lett.* **1976**, 173; U. Turpeinen, *Finn. Chem. Lett.* **1977**, 36; U. Turpeinen, *Finn. Chem. Lett.* **1977**, 123; b) M. Ahlgren, R. Hamalainen, U. Turpeinen, *Cryst. Struct. Commun.* **1977**, *6*, 829.

[33] A. W. Addison, T. Nageswara Rao, J. Reedijk, J. Vanrijn, G. C. Verschoor, *J. Chem. Soc., Dalton Trans.* **1984**, 1349.

[34] a) W. Henke, D. Reinen, *Z. Anorg. Allg. Chem.* **1977**, *436*, 187; b) A. B. P. Lever, *Inorganic Electronic Spectroscopy*, Elsevier, Amsterdam, **1986**.

[35] a) A. P. Ginsberg, *Inorg. Chim. Acta* **1971**, *5*, 45; b) M. D. Duggan, E. K. Barefield, D. N. Hendrickson, *Inorg. Chem.* **1973**, *12*, 985; c) L. P. Battaglia, A. Bianchi, A. Bonamartini-Corradi, E. Garcia-Espana, M. Micheloni, M. Julve, *Inorg. Chem.* **1988**, *27*, 4174.

[36] B. Bleaney, K. D. Bowers, *Proc. R. Soc. London, Ser. A* **1952**, *214*, 451.

[37] a) V. H. Crawford, H. W. Richardson, J. R. Wasson, D. J. Hodgson, W. E. Hatfield, *Inorg. Chem.* **1976**, *15*, 2107; b) D. J. Hodgson, *Prog. Inorg. Chem.* **1975**, *19*, 173.

[38] a) E. Ruiz, P. Alemany, S. Alvarez, J. Cano, *Inorg. Chem.* **1997**, *36*, 3683; b) E. Ruiz, P. Alemany, S. Alvarez, J. Cano, *J. Am. Chem. Soc.* **1997**, *119*, 1297.

[39] C. Wang, K. Fink, V. Staemmler, *Chem. Phys.* **1995**, *192*, 25.

[40] A. Abragam, B. Bleaney, in: *Electron Paramagnetic Resonance of Transition Ions*, Oxford University Press, New York, **1986**, pp. 209–216.

[41] a) S. L. Dexheimer, J. W. Gohdes, K. S. Hagen, W. H. Amstrong, M. P. Klein, *J. Am. Chem. Soc.* **1989**, *111*, 8923; b) K. L. Kostka, B. G. Fox, M. P. Hendrich, T. J. Collins, C. E. F. Rickard, L. J. Wright, E. Munch, *J. Am. Chem. Soc.* **1993**, *115*, 6746; c) G. S. Papaefstathiou, A. Escuer, C. P. Raptopoulou, A. Terzis, S. P. Perlepes, R. Vicente, *Eur. J. Inorg. Chem.* **2001**, 1567.

[42] R. C. Elder, *Aust. J. Chem.* **1978**, *31*, 35.

[43] P. J. Burke, D. R. Mcmillin, *J. Chem. Soc., Dalton Trans.* **1980**, 1794.

[44] W. Kabsch, *J. Appl. Crystallogr.* **1988**, *21*, 916.

[45] G. M. Sheldrick, *SHELXTL*™, V.5.03, Bruker Analytical X-ray Systems, Madison, WI, USA, **1994**.

[46] *SHELX86*: G. M. Sheldrick, *Acta Crystallogr., Sect. A* **1990**, *46*, 467.

[47] *DIFABS*: N. Walker, D. Stuart, *Acta Crystallogr., Sect. A* **1983**, *39*, 158.

[48] G. M. Sheldrick, *SADABS, Aborption Correction Program*, University of Göttingen, Germany, **1996**.

[49] G. M. Sheldrick, *SHELXL, program for crystal structure refinement*, University of Göttingen, **1993**.

Received: January 25, 2005

 © 2005 Wiley-VCH Verlag GmbH & Co. KGaA, Weinheim

Amphiphile Structures in the Solid State: Complex Cations with Lipophilic Substituents

Jack M. Harrowfield,*[a,b] George A. Koutsantonis,[a] Gareth L. Nealon,[a] Brian W. Skelton,[a] and Allan H. White[a]

Keywords: Cage complexes / Lipophilicity / Solid state structures

Structural characterisation of hexamine cage complexes, two containing diamagnetic Co^{III} and one containing paramagnetic Cu^{II}, to which both rather short (C_4) and relatively long (C_{13}) alkyl substituents have been attached, shows that while the longer "tail" introduces an anticipated bilayer form to the crystalline solid, even the shorter tail can be associated with a form of aggregation of lipophilic entities in the crystal. The short tail at least may also be involved in interactions with anions of a complex type. As surfactants, functionalised cage complexes contain a head group, which is a multi-site hydrogen-bonding entity, and which can thus provide a mechanism for further aggregation concomitant with that of any apolar functionality.

(© Wiley-VCH Verlag GmbH & Co. KGaA, 69451 Weinheim, Germany, 2005)

Introduction

As potential head groups for surfactant molecules, complex cations and anions offer the chance to introduce entities, often chiral, of unusually high charge, of variable spectroscopic and magnetic properties, and with structures that may facilitate specific forms of association of counterions with those head groups.[1] The same virtues apply, of course, in the design of metallomesogens.[2] The kinetic inertness and ease of functionality of cage amine complexes[3] render them particularly appealing for use as head groups, and it has been shown that surfactants derived from Co^{III} cage complexes can have unusual physical and biological properties.[4] In seeking to expand this field of chemistry, we have investigated alternative syntheses of amphiphiles and what might be termed "reverse" bola-amphiphiles[5,6] based on cage amine complexes of various metals and have sought to characterise these materials in detail, in the solid state, through X-ray crystallography. This report is specifically concerned with some structural results, which have uncovered both expected and unexpected properties concerning the cage amines **1**–**3**

The broad basis of the present work was an effort to develop methods for the synthesis of functionalised cage amines, which continued to exploit the advantages associated with the selective protection of nucleophilic centres by metal ion coordination,[3,4] while avoiding the commonly encountered difficulty[3f,7] of the need for extreme conditions in order to remove the new ligands from the metal centre on which they are formed. In the case of reductive alkylation reactions of amine centres as presently described, the use of a metal (Mg^{II}) easily removed[7] from the cage as an agent to protect endocyclic amine centres introduces problems in that even the mildly acidic conditions normally applied in $RCHO/NaBH_3CN$ reactions[8] cause its loss from the reactant cage. However, the value of the syntheses described herein is that they demonstrate that Mg^{II}, under weakly basic conditions, can be used to selectively protect multiple N-donor sites, while efficient reductive alkylation still occurs at unprotected centres.

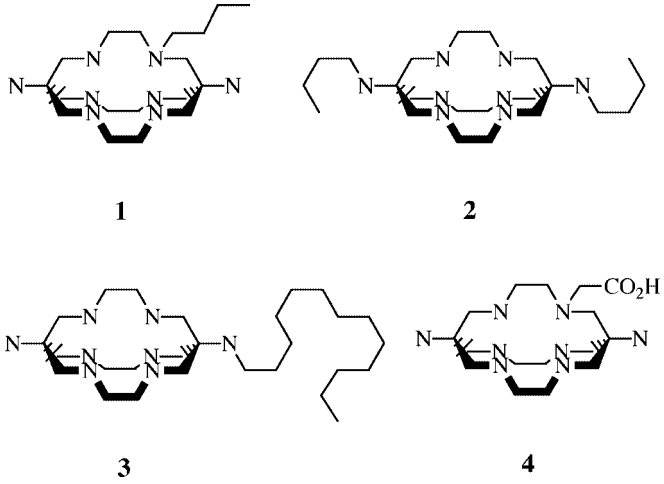

1 **2** **3** **4**

Results and Discussion

Perhaps fortuitously, the use of non-acidic conditions for the reductive alkylation of "free" diaminosarcophagine by

[a] Chemistry M313, School of Biomedical and Chemical Sciences, University of Western Australia,
35 Stirling Highway, Crawley, Perth, WA 6009, Australia
[b] Current address: Laboratoire de Chimie Supramoléculaire, ISIS, Université Louis Pasteur,
8, allée Gaspard Monge, 67083 Strasbourg, France
E-mail: harrowfield@isis.u-strasbg.fr

$CH_3(CH_2)_2CHO/NaBH_3CN$ in large excess results in quite efficient monoalkylation. As in simple alkylation reactions,[3f] this monofunctionalisation appears to occur predominantly on a secondary and not a primary amine centre of the reactant, generating the ligand **1**. The reaction was studied in order to establish a model procedure for alkylations involving long-chain aldehydes, although it in fact did not prove particularly useful for this purpose. As expected for a ligand-containing tertiary nitrogen donor centres,[3c,3f,9] significant distortions of the coordination sphere of a bound metal result, this being reflected in the beautiful crimson (not yellow) colour (λ_{max} 502 nm) of the Co^{III} complex, $[Co(\mathbf{1})]^{3+}$. Given the presence of a lipophilic (albeit short) substituent on **1**, the high water-solubility of all simple salts of $[Co(\mathbf{1})]^{3+}$ was surprising and thus the crystal structure of $[Co(\mathbf{1})][Sm(dipic)_3]\cdot 15\,H_2O$ was studied in order both to characterise the Co^{III} coordination sphere and to determine what interactions with the butyl chain might be involved. The high degree of hydration of this material is typical of compounds containing $[Ln(dipic)_3]^{3-}$ species,[10,11] though it was not immediately clear that this should be the only consideration here. The discovery that $[Sm(dipic)_3]^{3-}$ in particular could be used to obtain a crystalline solid from $[Co(\mathbf{1})]^{3+}$ was purely a matter of good fortune, resulting from the availability of hydrated $Na_3[Sm(dipic)_3]$ in the laboratory, and was not a consequence of any logic other than "charge matching" of the anion and cation (Table 1).

The complex, a racemate in a non-centrosymmetric space group, crystallises with one formula unit, devoid of crystallographic symmetry, comprising the asymmetric unit of the structure. Projections of the cation, the anion, and the unit cell, viewed variously, are presented in Figure 1, with hydrogen bonding summarised in Table 2. The cation presented in part (a) of Figure 1 is very similar to that found in the complex of 3-carboxymethyl-1,8-diaminosarcophagine (**4**), in $[Co(\mathbf{4})]Cl(S_2O_6)\cdot 4.5\,H_2O$.[3f] The bond to the tertiary donor [Co–N(3b), 2.063(4) Å] is elongated compared to those to the secondary donors [1.974–2.000(4), <> 1.986(11) Å], though in the present case by only ca. 0.07 Å rather than ca. 0.09 Å. The cation again has the lel_3 configuration, with two NH units (3a,3b′) H bonding to one water molecule [O(6) ($^1/_2 - x$, $\bar{y}$, $z - {}^1/_2$)], two others (3c,3a′) H bonding to separate water molecules H-bonded to one another [O(1,4)], and the remaining NH (3c′) interacting with an uncoordinated carboxylate-*O* [O(14)] of an adjacent complex anion. Bridging of NH units by H-bond acceptors appears to be a significant feature concomitant with adoption of the lel_3 form.[3f] The primary amino groups are also involved in H bonding to both water and carboxylate groups, as part of the extended H bonding array in the heavily hydrated crystal, which resembles overall that found in other $[Ln(dipic)_3]^{3-}$ derivatives. The *N*-butyl substituent is extended and remote from water molecules, projecting towards a neighbouring complex anion, the terminal methyl group appearing to contact at least one pyridine ring, with C···ring centroid 3.76 Å (CH···π interaction?), and the adjacent methylene carbon atom [C(33b)] being 3.361(7) Å from a coordinated carboxylate-*O* [O(13)] (CH···O bonding?). The anion geometry is similar to those reported for related $[Ln(dipic)_3]^{3-}$ species,[10,11] with Sm–N 2.551–2.556(3), <> 2.554(3) Å; Sm–O 2.420–2.478(4), <> 2.45(2) Å.

When viewed down *a* and *b* [part (b) of Figure 1], the lattice of $[Co(\mathbf{1})][Sm(dipic)_3]\cdot 15\,H_2O$ appears to contain separate columns of the two metals, Co and Sm, running parallel to *a*. Two Sm columns nearly superimpose and may be considered as one column gently undulating about *a*. Along *c*, these columns are separated by double columns of Co atoms which can also be considered as in a markedly zig-zagged array of a single column down *a*. The alternations in both these "columns" are associated with the fact

Table 1. Crystal data, details of data collection and structure refinement.

Complex	$[Co(\mathbf{1})][Sm(dipic)_3]\cdot 15\,H_2O$	$[Co(\mathbf{2}H_2)]Cl_5\cdot 6\,H_2O$	$[Cu(\mathbf{3}H)][Cu(\mathbf{3}H_2)](ClO_4)_7\cdot 6\,H_2O$
Formula	$C_{39}H_{81}CoN_{11}O_{27}Sm$	$C_{22}H_{64}Cl_5CoN_8O_6$	$C_{54}H_{135}Cl_7Cu_2N_{16}O_{34}$
M	1345.4	773.0	1928.0
Crystal system	orthorhombic	monoclinic	triclinic
Space group	$Pca2_1$	C2/*m*	*P*-1
a [Å]	18.890(3)	14.0970(7)	8.664(2)
b [Å]	10.439(2)	24.911(1)	8.727(2)
c [Å]	28.014(5)	12.1088(6)	32.942(7)
α [°]			93.318(4)
β [°]		116.495(1)	93.178(4)
γ [°]			119.555(4)
V [Å^3]	5524	3777	2153
D_c [g cm^{-3}]	1.61_7	1.35_9	1.48_6
Z	4	4	2
Size [mm]	0.50 × 0.45 × 0.40	0.32 × 0.18 × 0.14	0.50 × 0.28 × 0.12
μ_{Mo} [cm^{-1}]	14.5	8.5	8.0
Transmission (min./max.)	0.77	0.82	0.63
$2\theta_{max}$ [°]	75	75	50
N_t	114531	39324	20637
N (R_{int})	14810 (0.059)	10071 (0.022)	7540 (0.063)
N_o	11393	8184	5916
R	0.037	0.044	0.10
R_w (n_w)	0.048 (2)	0.069 (2)	0.13 (0.4)

 © 2005 Wiley-VCH Verlag GmbH & Co. KGaA, Weinheim

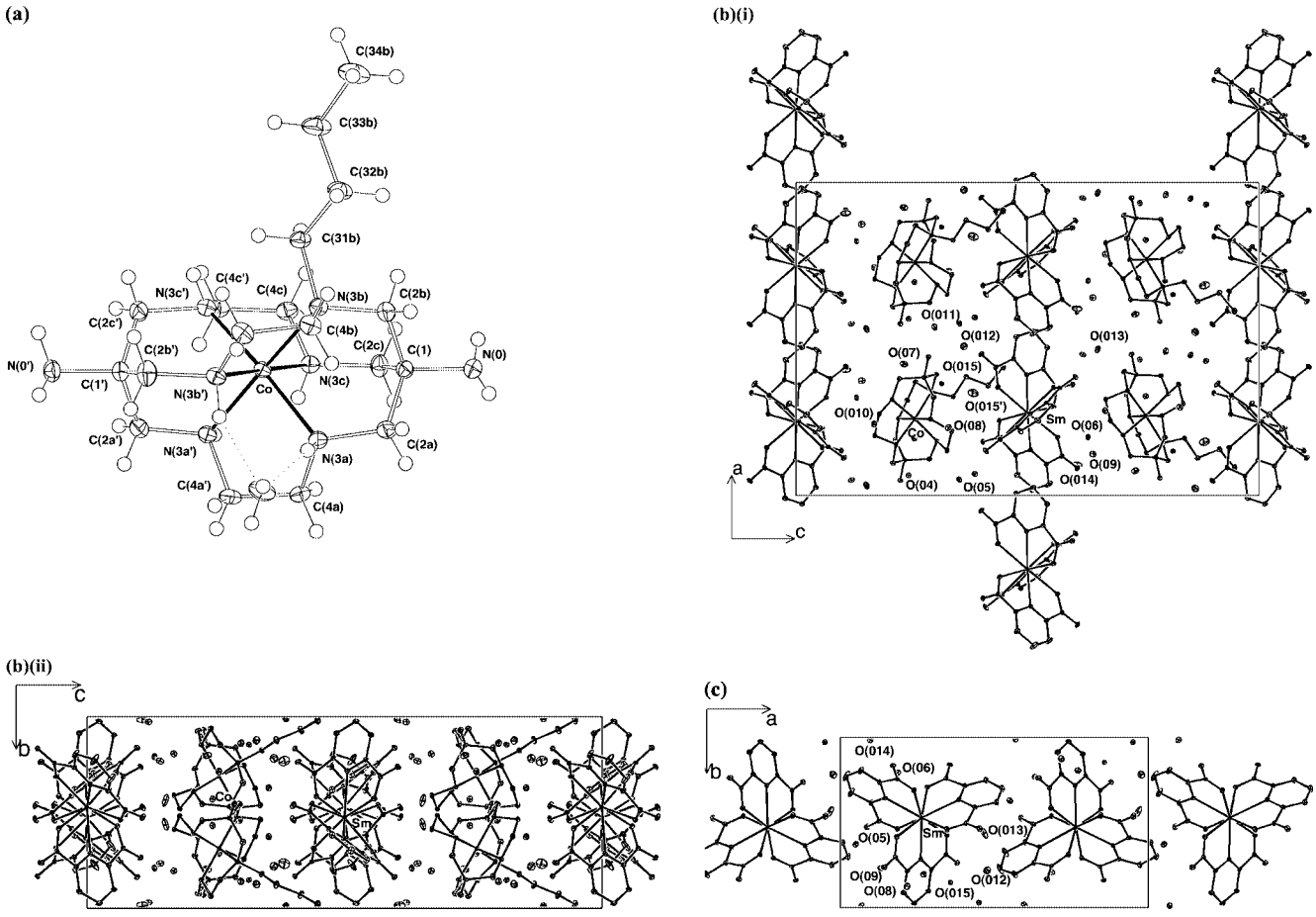

Figure 1. (a) Projection of the $[Co(\mathbf{1})]^{3+}$ cation, showing the lel_3 ligand conformation and the "chelated" associated water molecule. (b) Unit cell contents of $[Co(\mathbf{1})][Sm(dipic)_3]\cdot 15\,H_2O$ projected down (i) *b*, (ii) *a*. (c) The layer of anions about $z = 0.5$.

that the metals are the centres of chiral entities (cationic for Co, anionic for Sm), such that the undulation/zig-zag can be described as ···Δ–Λ–Δ–Λ–Δ–Λ–Δ–Λ··· in both cases. Columnar arrays, more often homochiral {as in the closely-related $[Co(sar)][Eu(dipic)_3]\cdot 13\,H_2O$;[10] and see below} than heterochiral as here, are very commonly seen in structures of $[Ln(dipic)_3]^{3-}$ derivatives,[10,11] interactions (stacking and edge-to-face[12]) of the heteroaromatic ligands, as seen in many similar helical complexes,[13] possibly being one factor favouring their presence. Given its persistence, it is perhaps appropriate to regard this array as a kind of "molecular register" which, in the present case, determines the associated array of chiral cations. Along *c*, the necessarily polar cation array is such that the butyl substituents of both Δ and Λ species are oriented to the one side of each zig-zag column, creating two different "sides" to the undulating Sm complex columns (perpendicular to the undulation plane). For a given Sm centre, its nearest Co neighbour [at 7.027(1) Å] to one side is from a complex unit of the same chirality for which the butyl substituent approaches the dipicolinate ligand atoms on the Sm. To the other side, a slightly more remote Co [at 7.392(1) Å] is the centre of a complex cation of the opposite chirality. Interactions here occur through a pair of H-bonded water molecules which is H-bonded to a cation NH and an uncoordinated carboxylate-*O* of the anion.

A possibly simpler analysis of the lattice is provided in the view down *b*, from which it appears that the two metals can also be considered to form true columns parallel to *b*. The complexes in these columns are all of the same chirality, species contacts within the columns all seemingly the result of H bonding involving lattice water, so that the (homochiral) Sm···Sm distance, *b* [10.439(2) Å], is longer than the (heterochiral) separation, *a*/2 [= 18.890(2)/2 Å], associated with aromatic/aromatic interactions in the undulating column parallel to *a*. Homo- and hetero-chiral Co···Co separations, *b* and 10.235(2) Å, respectively, differ much less, perhaps reflecting the fact that H bonding (via water) is the common cause of contact.

A feature lacking in the lattice of $[Co(\mathbf{1})][Sm(dipic)_3]\cdot 15\,H_2O$ is any sign of close contact between the butyl substituents of the cations. This is consistent with the lack of any evidence for surfactant properties of $[Co(\mathbf{1})]^{3+}$ or the related dibutylated complex $[Co(\mathbf{2})]^{3+}$ in aqueous solution, and with the expectation that a butyl chain would be too short to induce such properties in a cage complex.[4] Though the difficulty of obtaining adequate crystals means that relatively limited structural data are available for true

 © 2005 Wiley-VCH Verlag GmbH & Co. KGaA, Weinheim

Table 2. Hydrogen-bonding in [Co(**1**)][Sm(dipic)$_3$]·15 H_2O(N,O···H est.).

Atoms	Distance [Å]	Atoms	Distance [Å]
(a) To the terminal NH_2 groups			
O(04),H(04B)···N(0^{i})	2.052(6), 2.1	O(07),H(07A)···N(0′^{ii})	2.808(6), 2.1
(b) From the other (NH) amine groups			
N(0),H(0A)···O(07)	3.053(6), 2.3	N(0′),H(0A′)···O(02^{iii})	3.143(6), 2.3
N(0),H(0B)···O(24)	3.194(6), 2.4	N(0′),H(0B′)···O(011^{iv})	3.017(6), 2.1
N(3a),H(3a)···O(06^{iii})	2.879(5), 2.0	N(3a′),H(3a′)···O(04)	2.919(5), 2.1
		N(3b′),H(3b′)···O(06^{iii})	2.922(5), 2.1
N(3c),H(3c)···O(01)	2.902(5), 2.1	N(3c′),H(3c′)···O(14)	2.925(5), 2.4
(c) To the (uncoordinated) anion oxygen atoms			
O(09),H(09A)···O(12)	2.832(6), 2.1	O(03),H(03A)···O(14)	2.717(6), 2.0
O(013),H(013A)···O(12)	2.742(7), 2.2		
O(02),H(02A)···O(22)	2.753(5), 2.0	O(05^{ii}),H(05B^{ii})···O(24)	2.863(6), 2.0
		O(012),H(012A)···O(24)	2.801(7), 2.1
O(02^{v}),H(02B^{v})···O(32)	2.832(5), 2.0	O(03^{v}),H(03B^{v})···O(34)	2.815(6), 1.9
		O(05),H(05A)···O(34)	2.760(6), 2.1
		O(08),H(08B)···O(34)	2.915(6), 2.1
[O(06),H(06A)···O(21)	2.904(5), 2.2]		
(d) Between water molecules			
O(01),H(01A)···O(08)	2.738(6), 1.8	O(04),H(04A)···O(013^{iii})	2.632(6), 2.0
O(01),H(01B)···O(04)	2.703(5), 2.0	O(06),H(06B)···O(014)	2.708(7), 2.0
O(07),H(07B)···O(09^{iii})	2.775(6), 1.9	O(08),H(08A)···O(015)	2.692(8), 2.0
O(09),H(09B)···O(07^{vi})	2.775(6), 2.2	O(08),H(08A)···O(015′)	2.80(2), 2.0
O(010),H(010A)···O(09^{iii})	2.750(6), 2.7	O(011),H(011A)···O(05^{ii})	2.864(6), 2.0
O(010),H(010B)···O(01)	2.777(6), 2.1	O(011),H(011B)···O(03^{vii})	2.843(6), 2.1
O(014),H(014A)···O(09^{viii})	2.837(7), 2.1	O(012),H(012B)···O(015)	2.733(8), 1.9
O(014),H(014B)···O(02^{iv})	2.808(7), 2.7	O(013),H(013B)···O(04^{vi})	2.632(6), 2.7
O(014),H(014B)···O(06)	2.708(7), 2.7		

Transformations of the asymmetric unit: i: $x - {}^1/_2$, $1 - y$, z. ii : $x + {}^1/_2$, $1 - y$, z. iii: ${}^1/_2 - x$, $\bar{y}$, $z - {}^1/_2$. iv: $x - {}^1/_2$, $\bar{y}$, z. v: x, $1 + y$, z. vi: ${}^1/_2 - x$, y, ${}^1/_2 + z$. vii: ${}^1/_2 + x$, y, z. viii: x, $y - 1$, z.

surfactant complexes,[1,14] these do show prominent aggregation of the lipophilic moieties in the lattice. It is somewhat surprising, therefore, that the crystal structure of [Co(**2**H_2)]Cl_5·6H_2O does provide evidence for association of the butyl substituents. In this complex, one half of the formula unit comprises the asymmetric unit of the structure. The cation present in this compound [part (a) of Figure 2], disposed with the central Co on a crystallographic *2*-axis, adopts the relatively uncommon but still quite familiar *ob*$_3$ conformation,[3b–3f] but has properties otherwise completely unexceptional for a Co^{III} complex of a cage amine. The *ob*$_3$ conformation, as in other cases, appears to result from the abundance of H-bond acceptors within the lattice, this leading in particular to the absence of any bridging interactions involving the secondary NH entities of a given complex unit. Such bridging "chelation" of chloride anions by *lel*$_3$ cations formally results, in several instances,[3] in the presence of D_3-symmetric {Co(L)Cl_3} ion quartets, but here the coordinated NH centres of the cation separately hydrogen-bond to chloride ions [N,H(3a)···Cl(1) 3.149(2), 2.3; N,H(3b)···Cl(1) (${}^1/_2 + x$, ${}^1/_2 - y$, z) 3.202(1), 2.3$_5$; N,H(3c)···Cl(2) 3.144(1), 2.3 Å], while the terminal ammonio groups contact both Cl [N(0),H(0a)···Cl(3) 3.058(2), 2.2 Å] and water molecule oxygen [N(0),H(0b)···O(01) 2.791(2), 1.9 Å], displacement amplitudes of all non-hydrogen atoms in this cation/anion/solvent system being small ($U_{eq} \leq 0.031$ Å^2), the cation "tail" excepted. Amplitudes in the latter increase markedly towards its periphery [parts (b) and (c) in Figures 2] and are high, as are those of the remaining anion, Cl(4), (which, located on a "special position" of the lattice, may be susceptible to unresolved disorder) and the remaining water molecules, many of these modelled as disordered fragments and forming a much less well-defined segment of the array. Cl(1–3), in fact, all have bridging functions, Cl(1) bridging a pair of cations as indicated above, while Cl(2,3), both located on symmetry elements – a mirror plane and a *2*-axis, respectively – link the symmetry images, via NH···Cl interactions. Other close contacts to the chlorides are sparse (Table 3), involving for Cl(1,3) a further pair of water molecules (or fragments), symmetry-related for Cl(3).

The lattice of [Co(**2**H_2)]Cl_5·6H_2O can be regarded as built up from alternating sheets parallel to the [–2,0,1] plane, one sheet containing complex cations and some chloride anions, the other water molecules and chloride ions. Viewed down *b*, the sheets are seen edge-on, with the cations extended in the *ac* plane. Within the cation sheets, there are regions where all polar entities, including chloride, are excluded and the butyl chains aggregate. These "greasespot" regions (Figure 3) are defined by laterally compressed hexagonal clusters of essentially coplanar cation units, which alternate in chirality Δ–Λ–Δ–Λ–Δ–Λ around the hexagon. The arrays in adjacent cation planes are displaced such that each greasespot contacts carbon atoms of ethylene links of the complex cations, two sets thereof in each plane above and below, creating thus a "greaseball". Closest C···C contacts within this greaseball range from 3.7–4.3 Å, very similar to analogous contacts in structures of true surfactants,[1] with the shortest present contact being 3.743(4) Å between the 3-carbon atoms of adjacent butyl chains. Though the greaseball structure may be a conse-

 © 2005 Wiley-VCH Verlag GmbH & Co. KGaA, Weinheim

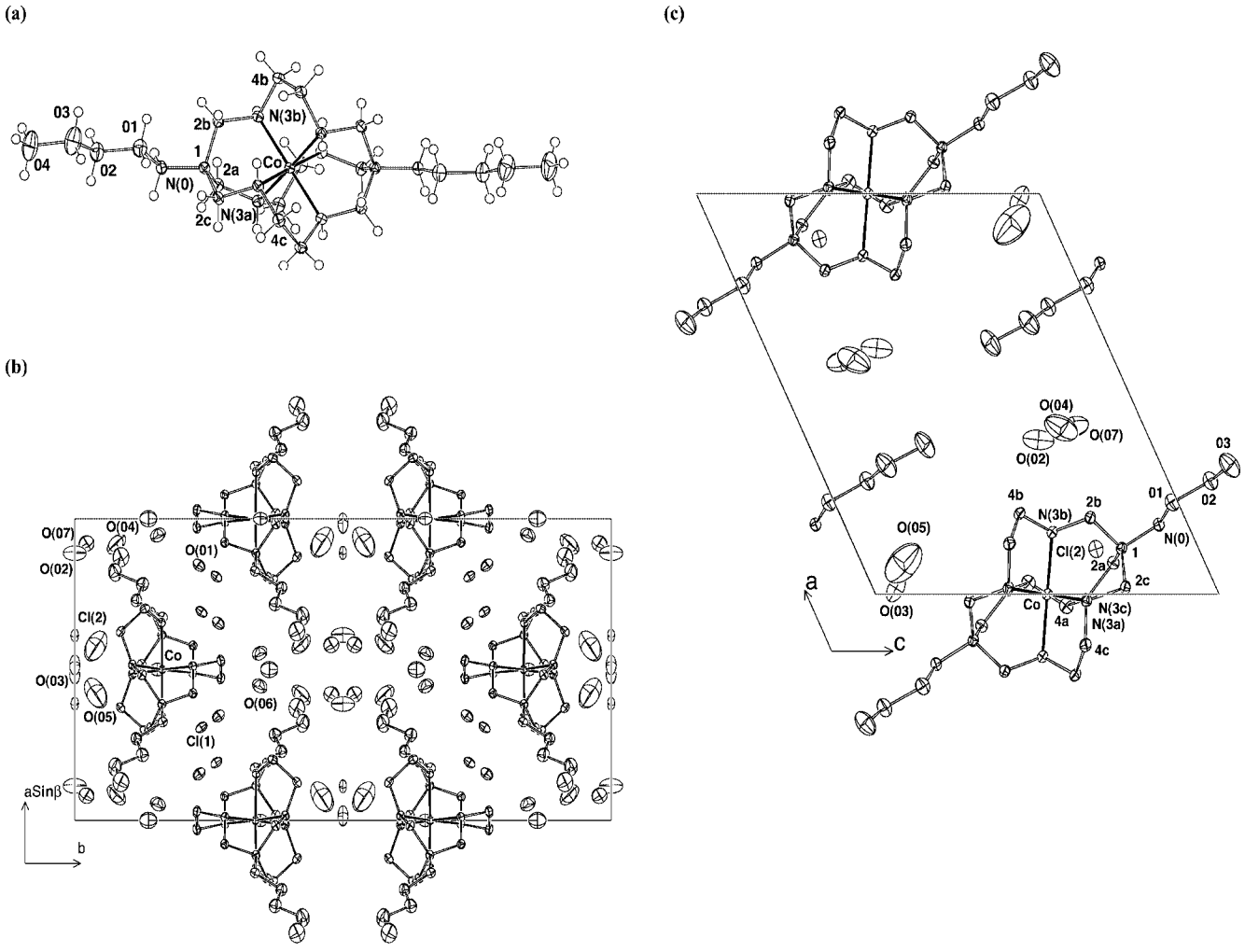

Figure 2. (a) The $[Co(\mathbf{2}H_2)]^{5+}$ cation, which lies disposed on a crystallographic *2*-axis passing through the mid-point of the ligand string "a", showing the ob_3 ligand conformation. (b) Unit cell contents of $[Co(\mathbf{2}H_2)]Cl_5{\cdot}6H_2O$, projected down *c*. (c) A slice of the cell, about $y = 0.5$, projected down *b*.

Table 3. Hydrogen-bonding in $[Co(\mathbf{2})]Cl_5{\cdot}6H_2O$.

Atoms	Distance [Å]	Atoms	Distance [Å]
(a) From the terminal nBuNH$_2^+$ group			
N(0),H(0A)···Cl(3)	3.058(2), 2.2	N(0),H(0B)···O(01)	2.791(2), 1.9
(b) From the other (NH) amino groups			
N(3a),H(3a)···Cl(1)	3.149(2), 2.3	N(3b),H(3b)···Cl(1^{i})	3.202(1), 2.4
N(3c),H(3c)···Cl(2)	3.144(1), 2.3		
(c) Other components of the chloride environments (Cl···O < 3.4 Å)			
Cl(1)···O(01^{ii})	3.223(2)	Cl(3)···O(05)	3.175(9)
Cl(1)···O(06)	3.230(8)		
Transformations of the asymmetric unit: i, ii $x \pm {}^1/_2$, ${}^1/_2 - y$, z.			

quence of the multitudinous interactions occurring in the solid state, it is unlike that of a conventional micelle and may indicate that rather particular forms of aggregation are possible for metal complex surfactants in solution.

Some further particularities of complex ions as surfactant headgroups are apparent in the crystal structure of the Cu^{II} complex of the ligand **3**, a complex which, unlike those of **1** and **2**, displays typical surfactant properties, readily forming aqueous emulsions and foams. The synthesis of **3**,

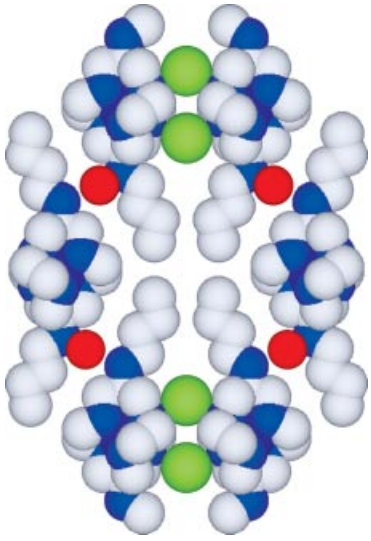

Figure 3. A simplified, space-filling representation of the "grease-spot region" of the lattice of $[Co(\mathbf{2}H_2)]Cl_5{\cdot}6H_2O$, showing the segregation of polar and apolar entities. Atom code: C = white; Cl = green; Co = dark blue; N = blue; O = red.

 © 2005 Wiley-VCH Verlag GmbH & Co. KGaA, Weinheim

based on the use of Mg^{II} to protect the secondary amino group nitrogen atoms of the reactant, illustrates a problem presumably due to association in the preparative medium. Thus, dialkylation predominates even in media where the reactant ratio is 1:1, a result which may be explicable if initially-formed mono-alkylated complex associates with unreacted aldehyde and so favours its attack on the other primary amino group of the same complex entity. (Note that the dialkylated product is the symmetrical 1,8 isomer.) The complex as crystallised, modelled as $[Cu(\mathbf{3}H)][Cu(\mathbf{3}H_2)](ClO_4)_7{\cdot}6H_2O$, contains formally a 1:1 mixture of diprotonated and monoprotonated cations [part (a) of Figure 4], a circumstance encountered in various unfunctionalised cage complexes[15] and, presumably, another indication of the important influence of H bonding on the form of the lattices, since the "additional" proton is taken to be shared between pairs of monoprotonated complex cations. The lattice, as viewed down *c*, for example, [part (b) in Figure 4] shows multiple layering, one aspect of which is the double layer of cage units formed by the (amino) head-to-head H-bonded array of complex cations. Consistent with related known structures[3c,3f,15,16] and the susceptibility of Cu^{II} to Jahn–Teller distortions, the CuN_6 environment (Table 4) in the cage is not only irregular, but disordered with the chiral, *lel*$_3$ complex cations distributed equally as Δ and Λ species over the available sites. The cores of the cations are disposed about copper atoms lying at (approximately) $z = {}^1/_3, {}^2/_3$, forming layers encompassing perchlorates 1,3 which lie close and equidistant to either side [*z*(Cl(1,3)) 0.27, 0.40], the "inwardly" directed oxygen atoms O(11–13;31–33) interacting directly with the cation or a translation image within the layer by way of hydrogen bonds with the core NH centres, and in such a way that the interaction is with one or other of the disordered components. Thus, O(11) contacts H(3a,3cB), O(12) contacts H(3b,3aB) ($x - 1$, $y - 1$, z) and O(13) contacts H(3c,2bB) (where "B" atoms belong to the Λ form of the cation, otherwise Δ) among the unprimed $(NH)_{3(2/2)}$ triad, while O(31) contacts H(3a′,3b′B) ($x - 1$, $y - 1$, z), O(32) H(3b′,3c′B) ($x - 1$, $y - 1$, z), and O(33) H(3c′,3a′B) among the primed, all at distances of 2.1–2.4 Å. No disorder is resolvable in these two perchlorates, U_{eq} among the hydrogen-bonded oxygens all ≤ 0.08 Å^2, excepting O(31) (0.13). Displacement amplitudes on perchlorate 2 are also ≤ 0.1 Å^2, presumably in consequence of its proximity to water molecules 1,2 [O(21)···O(02); O(23)···O(01) both 2.96(1) Å, hydrogen atoms not located] but anion **4** is modelled with half-occupancy, presumed disordered in concert with O(03,04) (water) about $z = 0.5$, this plane also imaging the $NH_2{\cdots}H{\cdots}H_2N$ cation components.

Between the polar layers just described, the tridecyl chains aggregate to form a lipophilic layer about 13 Å thick, the extended, *transoid* chains being bent away from the *pseudo-C$_3$* axis of the head group complexes so as to lie, with their neighbours down *a*, in sheets which confront similar, parallel sheets arising from the next layer of complex units. As in some[14,17] but not all[1] related complex structures, there is no interdigitation of the chains, and closest

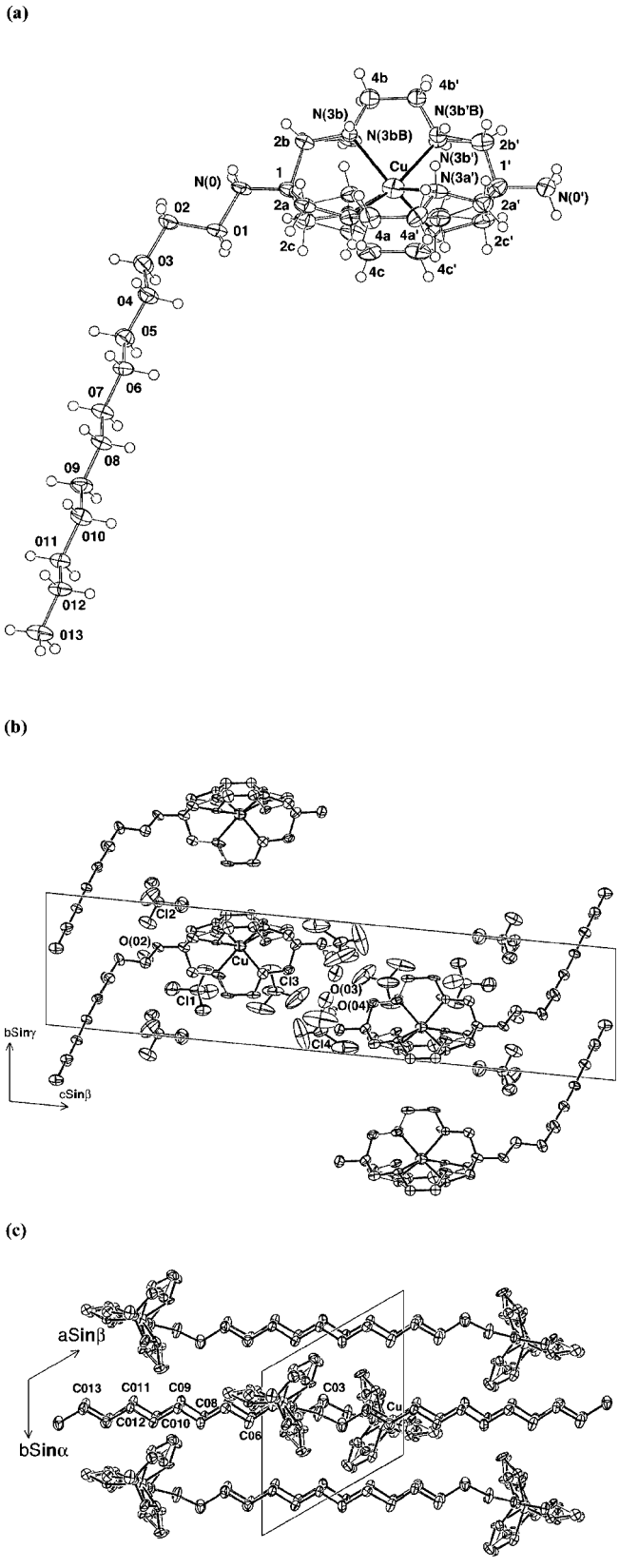

Figure 4. (a) The [Cu(**3**)] species, shown as the tetrapositive cation. (b) Unit cell contents of $[Cu(\mathbf{3})]_2H(ClO_4)_7{\cdot}6H_2O$, projected down *a*. (c) A slice of the cell about $y = 0$, projected down *c*.

 © 2005 Wiley-VCH Verlag GmbH & Co. KGaA, Weinheim

Table 4. Selected bond lengths and bond angles for [Cu(**3**H)][Cu(**3**H_2)]$(ClO_4)_7$·6H_2O.

Atoms	Bond lengths [Å]	Atoms	Bond angles [°]
Cu–N(3a)	2.17(1)	N(3a)–Cu–N(3a′)	79.4(5)
Cu–N(3aB)	2.16(1)	N(3aB)–Cu–N(3a′B)	80.8(5)
Cu–N(3a′)	2.24(2)	N(3b)–Cu–N(3b′)	83.2(4)
Cu–N(3a′B)	2.27(1)	N(3bB)–Cu–N(3b′B)	82.3(4)
Cu–N(3b)	2.16(1)	N(3c)–Cu–N(3c′)	82.9(4)
Cu–N(3bB)	2.15(1)	N(3cB)–Cu–N(3c′B)	80.7(5)
Cu–N(3b′)	2.15(1)		
Cu–N(3b′B)	2.151(9)		
Cu–N(3c)	2.21(1)		
Cu–N(3cB)	2.10(1)		
Cu–N(3c′)	2.07(1)		
Cu–N(3c′B)	2.18(1)		

C···C within and between chain layers lie in the range ca. 4.1–4.3 Å, presumably indicative of extensive but rather weak dispersion interactions (as found in other systems, interdigitated or not). For a given H-bonded pair of complex cations bridging a layer the tails are oppositely oriented, so as to make a centrosymmetric entity.

Conclusions

The high aqueous solution solubility of simple salts of [Co(**1**)]$^{3+}$ is presumably indicative of a low lattice energy for the solids, since substitution of N(butyl) for NH in the cation would, again presumably, not enhance its hydration energy. A low lattice energy could result from the particular regioisomeric form being such as to inhibit association between butyl entities and other components present (e.g. water, chloride) not being capable of significant interactions with butyl, so that the apparent CH_3-π and CH···O interactions of the butyl group observed in [Co(**1**)][Sm(dipic)$_3$]·15H_2O may be important determinants of its insolubility. Although yet to be quantified, such effects are of potential interest for the systematic construction of crystalline solids, in particular for the use of a "molecular register" defined by columnar arrays of $\{[Ln(dipic)_3]^{3-}\}_n$.[18] The structure of [Co(**2**H_2)]Cl_5·6H_2O shows that a butyl substituent upon a cage complex is not too short to be involved in lipophilic aggregation processes and indicates that there may be novel ways for such "reverse bola-amphiphile" complexes to aggregate in solution, possibly more readily exploited in systems with alkyl-functionalised chelate arms. Association of relatively water-soluble cage complexes in solution may be a more useful means of creating a multi-electron redox catalyst than that of linking cage units through kinetically inert scaffolds.[19] The structure of the true surfactant species [Cu(**3**H)][Cu(**3**H_2)]$(ClO_4)_7$·6H_2O shows both that introduction of a sufficiently long alkyl-chain substituent gives rise to solid state aggregation of a familiar form, and that, when considered with the other structures presently described, a cage complex head group is not a simple cationic centre and may be involved in a variety of interactions which could provide mechanisms for the control of solution aggregation processes.

Experimental Section

Instrumentation and Procedures: ^1H and ^{13}C NMR spectra were recorded with a Bruker ARX 500 instrument (^1H at 500.13 MHz, ^{13}C at 75.5 MHz) using solvent resonances [CH_3OH (^1H: 3.34 ppm, ^{13}C: 49.50 ppm); $(CH_3)_2CO$ (^1H: 2.22 ppm, ^{13}C: 215.94, 30.89)] as internal references. Tridecanal was freed of contaminant acid by washing its dichloromethane solution with aqueous $NaHCO_3$. Cation exchange chromatography was conducted under gravity flow in glass columns using either Na^+-form SP Sephadex C25 or H^+-form Dowex 50Wx2 resins.

Synthesis: 1,8-Diamino-3-butylsarcophagine (**1**), and its Co^{III} Complex, [Co(1)][Sm(dipic)$_3$]·15H_2O (dipic = pyridine-2,6-dicarboxylate, dipicolinate). $(NH_2)_2$sar[7] (0.53 g) and large excesses of butanal (3.0 mL) and $NaBH_3CN$ (0.25 g) were dissolved in absolute ethanol (50 mL) and the mixture heated at reflux under Ar for 24 h. The solvent was then removed under reduced pressure and the oily brown residue acidified with concentrated HCl. The resulting mixture of a clear brown solution and a small amount of brown oil was again taken to dryness and *cis*-[$CoCl_2(OH_2)_4$]·2H_2O (0.44 g) in water (20 mL) added, followed by sufficient ethanol to give a homogeneous solution. After aerating and heating (steam bath) the mixture for 30 min, the deep pink-red supernatant solution was decanted from some residual brown oil, diluted with water (500 mL) and passed through a column of Na^+ form SP Sephadex C25 cation exchange resin. The absorbed complexes were then eluted with 0.1 mol L^{-1} Na_2HPO_4. A small amount of Co^{II} was rapidly eluted first, followed by a trace amount of a pink species which was not further characterised beyond recording its ^1H NMR spectrum, which indicated that it did contain (probably mono-) alkylated cage ligand. The bulk of the product was in the third eluted fraction, from which the complex was recovered as its chloride by H^+ form Dowex 50Wx2/HCl chromatography. This material proved to be extremely soluble in water and no efficient way of precipitating the cation from solution was found other than to crystallise it as its $[Sm(dipic)_3]^{3-}$ derivative. Thus, the residue obtained by evaporating a 3 mol L^{-1} HCl solution of the complex to dryness was dissolved in water and an excess of $Na_3[Sm(dipic)_3]$[10] added. The precipitate which formed immediately (due to acid decomposition of the Sm complex), was dissolved by the dropwise addition of aqueous NH_3 (2 mol L^{-1}) and the deep pink solution formed was allowed stand overnight as small, pink tablet-like crystals, as used for the X-ray work, deposited. Sample drying prior to analysis appeared to cause some loss of water relative to the composition found from the crystal structure determination: [Co(1)][Sm(dipic)$_3$]·8H_2O = $C_{39}H_{67}CoN_{11}O_{20}Sm$ (1219.3): calcd. C 38.42, H 5.54, N 12.64; found C 38.3, H 5.4, N 12.4. NMR spectra were recorded on the residue obtained by evaporating a solution of the chloride salt after it had been re-evaporated (twice) from D_2O. ^1H NMR (D_2O): δ = 0.96 (t, 3 H), 1.42 (m, 2 H), 1.75–2.00 (m, 2 H), 2.85–3.70 (m, 26 H) ppm. $^{13}C\{^1H\}$ NMR (D_2O): δ = 13.66, 20.37, 24.82, 51.22, 51.51, 52.46, 53.02, 53.29, 53.83, 54.09 (br. s, possibly two unresolved resonances), 54.93, 55.07, 55.68, 56.60, 60.27, 61.22, 61.38 ppm.

1,8-Di(butylamino)sarcophagine (2) and its Co^{III} Complex [Co(2H_2)]Cl_5·*n*H_2O: [Co{$(NH_2)_2$sar}]$(OAc)_3$·6.5H_2O[3b] (626 mg), a large excess of butanal (20 mL) and an excess of $NaBH_3CN$ (170 mg) were dissolved in absolute EtOH (50 mL) and the reaction mixture heated at reflux under Ar for 24 h. The mixture was dried, treated with concentrated HCl (ca. 50 mL), and then dried again before adding water (ca. 100 mL). The brown mixture was then extracted with CH_2Cl_2 (4 × 150 mL), and after discarding the organic extracts, the aqueous layer was applied to a column of Na^+ SP

 © 2005 Wiley-VCH Verlag GmbH & Co. KGaA, Weinheim

Sephadex cation exchange resin. Elution with 0.1 M Na_2HPO_4 solution removed a very broad orange band, in which dialkylated product appeared to lead monalkylated but with imperfect separation, so that the leading third of the band was taken to obtain an eluate of predominantly the dialkylated species. Purification by absorption on H^+ Dowex 50Wx2 resin, elution with 5 M HCl, evaporation to dryness and crystallisation (twice) from the minimum quantity of hot water by addition of EtOH, gave a fine yellow powder of $[Co(\mathbf{2}H_2)]Cl_5{\cdot}nH_2O$ (50 mg; the total yield of mixed species was 270 mg) in a form which, after vacuum desiccation, appeared to be a trihydrate of the fully protonated complex. $C_{22}H_{52}Cl_5CoN_8{\cdot}3H_2O$ (719.0): calcd. C 36.75, H 8.13, N 15.59; found C 37.1 , H 7.1, N 15.5. ^{1}H NMR (D_2O): δ = 0.87 (t, 6 H), 1.35 (m, 2 H), 1.53 (m, 2 H), 2.85–3.20 (m, 16 H), 3.40–3.75 (m, 16 H) ppm. $^{13}C\{^1H\}$ NMR (D_2O): δ = 15.04 (CH_3), 21.43 (CH_2), 30.46 (CH_2), 45.05 (CH_2), 52.18 (CH_2), 55.52 (CH_2), 62.65 (4 C) ppm. Crystals for the structure determination were obtained by vapour diffusion of ethanol into a concentrated solution of the complex in 1 mol L^{-1} HCl, the structure solution being consistent with the tentative formulation of the crystalline material as an ethanol sesquisolvate trihydrate, $[Co(\mathbf{2}H_2)]Cl_5{\cdot}3H_2O{\cdot}1.5CH_3CH_2OH$. An inadvertent discovery appreciated only after completion of further structural work was that it would appear possible to separate the mono- and dialkylated complexes by fractional crystallisation of their chlorides. Thus, in an attempt to obtain crystals of the monoalkylated complex, vapour diffusion of ethanol into an aqueous solution of the residue from the trailing third of the SP Sephadex/Na_2HPO_4 chromatography band (indicated by ^{1}H NMR to be at least 90% monoalkylated complex) gave crystals subsequently shown, by means of the structure recorded herein, to be essentially those of the dialkylated species as its pentachloride hexahydrate.

Tridecylation of Diaminosarcophagine to give 1-Alkylated and 1,8-Dialkylated Derivatives 3 and 4, respectively: $(NH_2)_2$sar (1.02 g), $Mg(OAc)_2$ (1.89 g), tridecanal (0.990 mL) and $NaBH_3CN$ (215 mg) were dissolved in absolute EtOH (50 mL) and the reaction mixture heated at reflux for 24 h under argon. The white precipitate of magnesium acetate hydroxide was filtered off, the solution dried, and the oily white residue treated with concentrated HCl (ca. 10 mL). The mixture was again dried, and the white solid extracted with $CHCl_3$ (3 × 50 mL; discarded) and 1 mol L^{-1} HCl (3 × 10 mL), leaving a residue of dialkylated ligand hydrochloride. This was recrystallised from boiling methanol to give a white, waxy solid (762 mg). $(C_{13}H_{27}NH)_2$sar·4 HCl·3 H_2O = $[\mathbf{4}H_4]Cl_4{\cdot}3H_2O$ = $C_{40}H_{96}Cl_4N_8O_3$ (879.1): calcd. C54.65, H 11.01, Cl 16.13, N12.75; found 54.7, H 9.3, Cl 16.1, N 12.7. ^{1}H NMR (CD_3OD): δ = 0.90 (t, 6 H), 1.29 (m, br., 36 H), 1.39 (m, 4 H), 1.66 (m, 4 H), 2.75–3.50 (m, 28 H), 4.50 (m., br., NH) ppm. $^{13}C\{^1H\}$ NMR (CD_3OD): δ = 14.44, 23.73, 27.55, 28.00, 30.20, 30.47, 30.50, 30.62, 30.74, 30.77, 33.06, 42.88, 49.88, 53.19, 58.2 ppm. To isolate the pure monoalkylated ligand (as its Cu^{II} complex), the 1 mol L^{-1} HCl extracts of the bulk product were dried, the residue dissolved in water (ca. 30 mL) and excess $Cu(OAc)_2$ added. Concentrated ammonia (ca. 1 mL) was added and the blue solution was heated to boiling, producing a green precipitate of copper acetate hydroxide. After filtration, concentrated $HClO_4$ (ca. 1 mL) was added to the filtrate, producing a blue precipitate of the monoalkylated ligand complex. Yield: 144 mg. [Cu{(1-tridecylammonio)(8-ammonio)sar}][Cu{(1-tridecylammonio)(8-amino)sar}]$(ClO_4)_7{\cdot}6H_2O$ = $[Cu(\mathbf{3}H)][Cu(\mathbf{3}H_2)](ClO_4)_7{\cdot}6H_2O$ = $C_{54}H_{135}Cl_7Cu_2N_{16}O_{34}$ (1928.0): calcd. 33.64, H 7.06, Cl 12.87, N 11.62; found C 34.1, H 6.9, Cl, 13.7, N 11.6. ESMS: *m*/*z* (658.7) = $[Cu(\mathbf{3})(ClO_4)]^+$; *m*/*z* (320.8) = $[Cu(\mathbf{3})(CH_3CN)_2]^{2+}$; *m*/*z* (300.4) = $[Cu(\mathbf{3})(CH_3CN)]^{2+}$. The filtrate from the bulk of the rather insoluble Cu^{II} complex was allowed to evaporate slowly, producing blue crystals as used for the X-ray work. In order to obtain NMR spectra for the (coordinated) ligand, the complex was dissolved in hot water and converted into the zinc complex by addition of Zn powder. After heating and stirring the mixture for 15 minutes on the steam bath, the solid was filtered off and the clear filtrate was dried. The white solid obtained was only slightly soluble in D_2O, so the solution was acidified with a few drops of concentrated DCl, causing the solid to dissolve rapidly. ^{1}H NMR (D_2O/DCl): δ = 0.82 (t, 3 H), 1.25 (br. 20 H), 1.67 (br., 2 H), 2.50–3.70 (m, br. 26 H), 4.28 (br., ≈ 5 H, NH) ppm. $^{13}C\{^1H\}$ NMR (D_2O): 14.36, 23.11, 26.90, 27.12, 29.70, 29.99, 30.04, 30.30, 30.32, 30.37, 30.43, 32.44, 42.55, 49.20, 51.70, 53.12, 54.81, 56.49 ppm. It again appears that two methylene-C signals may superimpose but the important aspect of this $^{13}C\{^1H\}$ NMR spectrum is the appearance of two distinct quaternary carbons at δ = 51.70 and 56.49.

Structure Determinations: Full spheres of "low"-temperature CCD area-detector diffractometer data were recorded (Bruker AXS instrument, ω-scans; monochromatic Mo-K_α radiation, λ = 0.7107$_3$ Å; *T* ca. 153 K) yielding $N_{t(otal)}$ reflections, merging to *N* unique (R_{int} cited) after "empirical"/multiscan absorption correction (proprietary software), N_o with $F > 4\sigma(F)$ considered "observed" and used in the full-matrix least-squares refinements, refining anisotropic displacement parameter forms for the non-hydrogen atoms, $(x, y, z, U_{iso})_H$ (where defined) constrained at estimates. Conventional residuals *R*, R_w on |*F*| are cited at convergence {weights: $[\sigma^2(F_o) + 10^{-3}n_w F_o^2]^{-1}$}. Neutral atom complex scattering factors were employed within the Xtal 3.7 program system.[20] Pertinent results are given below and in the Tables and Figures, the latter showing 50% probability amplitude displacement envelopes, hydrogen atoms having arbitrary radii of 0.1 Å. Individual diversities in procedure are noted below (variata).

Variata: $[Co(\mathbf{1})][Sm(dipic)_3]{\cdot}15H_2O$. The residue assigned as water molecule oxygen 15 was modelled as disordered over a pair of sites of equal occupancy separated by 2.17(2) Å, associated hydrogen atoms not being located. Hydrogen atoms were located in association with all other water molecule oxygen atoms. "Friedel" data being retained distinct, x_{abs} refined to 0.062(8).

Variata: $[Co(\mathbf{2}H_2)]Cl_5{\cdot}6H_2O$ (crystallised from a solution containing largely the monoalkylated complex). Difference map residues were refined as (disordered) water molecule oxygen atom fragments. The O(01) site was fully occupied, with associated hydrogen atoms resolvable; for the remainder, no credible hydrogen atom complement could be resolved, occupancies being set at 0.5 [O(02–05)] or 0.25 [O(06–07)], after trial refinement. The possibility that the lattice contained both mono- and dialkylated species was a cause of some concern, the site occupancies of the "tail" components having little impact on the refinement for a range between 85 and 100%, though being finally set at the latter. As noted above, material more confidently assigned as fully dialkylated was also studied, being formulated in the refinement as an ("isomorphous") mixed ethanol/water solvate. Displacement parameters on the solvent component were very high, however, and the overall precision of the determination appreciably lower, so that the "hexahydrate" determination was ultimately preferred and presented, there being otherwise no non-trivial differences in cation model and geometries.

Variata: $[Cu(\mathbf{3}H)][Cu(\mathbf{3}H_2)](ClO_4)_7{\cdot}6H_2O$. The coordinated nitrogen atoms were modelled as disordered over pairs of sites, occupancies set at 0.5 after trial refinement. Perchlorate **4** was modelled over two sets of sites, occupancies set at 0.5, as also for water molecule oxygen residues O(03,04). Hydrogen atoms were not located in association with water molecule oxygen atoms; the stoichiometry

 © 2005 Wiley-VCH Verlag GmbH & Co. KGaA, Weinheim

of the compound is rationalised in terms of the proximity of the amine cap N(0′) lying in the vicinity of an inversion image, distance 2.86(1) Å, postulating the array as $–NH_2\cdots H\cdots H_2N–$ or derivative.

For the latter two compounds, attempted refinement in lower symmetry was (inherently) unfruitful, the bulk of the structure (including the major species) being generally well-behaved in refinement except as detailed.

CCDC-194249, -194250 and -261886 contain the supplementary crystallographic data for this paper. These data can be obtained free of charge from The Cambridge Crystallographic Data Centre via www.ccdc.cam.ac.uk/data_request/cif.

[1] H. J. Choi, M. P. Suh, *Inorg. Chem.* **2003**, *42*, 1151–1156 and references cited therein.

[2] a) See, for example, R. Ziessel, L. Douce, A. El-ghayoury, A. Harriman, A. Skoulios, *Angew. Chem. Int. Ed.* **2000**, *39*, 1489–1493; b) J. L. Serrano, *Metallomesogens*, Wiley-VCH, Weinheim, **1996**.

[3] As recent publications, see: a) P. S. Donnelly, J. M. Harrowfield, *J. Chem. Soc., Dalton Trans.* **2002**, 906–913; b) S. Burnet, M.-H. Choi, P. S. Donnelly, J. M. Harrowfield, I. Ivanova, S.-H. Jeong, Y. Kim, M. Mocerino, B. W. Skelton, A. H. White, C. C. Williams, Z.-L. Zeng, *Eur. J. Inorg. Chem.* **2001**, 1869–1181; c) P. S. Donnelly, J. M. Harrowfield, B. W. Skelton, A. H. White, *Inorg. Chem.* **2001**, *40*, 5645–5652; d) N. Di Bartolo, A. M. Sargeson, T. M. Donlevy, S. V. Smith, *J. Chem. Soc., Dalton Trans.* **2001**, 2303–2309; e) P. M. Angus, A. J. Elliott, A. M. Sargeson, A. C. Willis, *J. Chem. Soc., Dalton Trans.* **2000**, 2933–2938; f) P. S. Donnelly, J. M. Harrowfield, B. W. Skelton, A. H. White, *Inorg. Chem.* **2000**, *39*, 5817–5830. See also ref.[4a]

[4] a) G. W. Walker, R. J. Geue, A. M. Sargeson, C. A. Behm, *J. Chem. Soc., Dalton Trans.* **2003**, 2992–3001; b) C. A. Behm, P. F. L. Boreham, I. I. Creaser, B. R. Korybut-Daszkiewicz, D. J. Maddalena, A. M. Sargeson, G. M. Snowdon, *Aust. J. Chem.* **1995**, *48*, 1009–1030; c) C. A. Behm, I. I. Creaser, B. R. Korybut-Daszkiewicz, R. J. Geue, A. M. Sargeson, G. W. Walker, *J. Chem. Soc., Chem. Commun.* **1993**, 1844–1846.

[5] a) J.-H. Fuhrhop, T. Wang, *Chem. Rev.* **2004**, *104*, 2901–2937; b) J.-H. Fuhrhop, D. Fritsch, *Acc. Chem. Res.* **1986**, *19*, 130–137.

[6] P. Bandyopadhyay, P. K. Bharadwaj, *Langmuir* **1998**, *14*, 7537–7538 and references cited therein.

[7] G. A. Bottomley, I. J. Clark, I. I. Creaser, L. M. Engelhardt, R. J. Geue, K. S. Hagen, J. M. Harrowfield, G. A. Lawrance, P. A. Lay, A. M. Sargeson, A. J. See, B. W. Skelton, A. H. White, F. R. Wilner, *Aust. J. Chem.* **1994**, *47*, 143–179.

[8] L. A. Paquette (Ed.), *Encyclopedia of Reagents for Organic Synthesis*, John Wiley & Sons, New York, **1995**, vol. 7.

[9] D. Meyerstein, *Coord. Chem. Rev.* **1999**, *185–186*, 141–147.

[10] P. A. Brayshaw, J.-C. G. Bünzli, P. Froidevaux, J. M. Harrowfield, Y. Kim, A. N. Sobolev, *Inorg. Chem.* **1995**, *34*, 2068–2076.

[11] a) P. A. Brayshaw, J. M. Harrowfield, A. N. Sobolev, *Acta Crystallogr., Sect. C* **1995**, *51*, 1799–1802; b) J. M. Harrowfield, Y. Kim, B. W. Skelton, A. H. White, *Aust. J. Chem.* **1995**, *48*, 807–824; c) J. Albertsson, *Acta Chem. Scand.* **1970**, *24*, 1213–1229 and references cited therein.

[12] W. B. Jennings, B. M. Farrell, J. F. Malone, *Acc. Chem. Res.* **2001**, *34*, 885–894.

[13] a) V. Russell, M. Scudder, I. Dance, *J. Chem. Soc., Dalton Trans.* **2001**, 789–799 and references cited therein; b) D. Gut, A. Rudi, J. Kopilov, I. Goldberg, M. Kol, *J. Am. Chem. Soc.* **2002**, *124*, 5449–5456.

[14] N. Arulsarny, D. S. Bohle, P. A. Goodson, D. A. Jaeger, V. B. Reddy, *Inorg. Chem.* **2001**, *40*, 836–842.

[15] B. W. Skelton, A. H. White, unpublished.

[16] P. V. Bernhardt, R. Bramley, L. M. Engelhardt, J. M. Harrowfield, D. C. R. Hockless, B. R. Korybut-Daszkiewicz, E. R. Kraus, T. Morgan, A. M. Sargeson, B. W. Skelton, A. H. White, *Inorg. Chem.* **1995**, *34*, 3589–3599.

[17] D. S. Bohle, P. A. Goodson, D. A. Jaeger, A. Zafar, *Inorg. Chim. Acta* **2001**, *312*, 210–214.

[18] P. A. Brayshaw, A. K. Hall, W. T. A. Harrison, J. M. Harrowfield, D. Pearce, T. M. Shand, B. W. Skelton, C. R. Whitaker, A. H. White, *Eur. J. Inorg. Chem.* **2005**, 1127–1141. Related work concerning structural studies of $[Co(phen/bipy)_3][Ln(dipic)_3]\cdot n H_2O$ and $[Co(polyamine)_n][Ln(dipic)_3]\cdot n H_2O$ species is under submission.

[19] P. S. Donnelly, J. M. Harrowfield, B. W. Skelton, A. H. White, *Aust. J. Chem.* **2001**, *54*, 15–17.

[20] S. R. Hall, D. J. du Boulay, R. Olthof-Hazekamp (Eds.), *The Xtal 3.7 System*, University of Western Australia, **2001**.

Received: January 26, 2005

 © 2005 Wiley-VCH Verlag GmbH & Co. KGaA, Weinheim

Multi-Channel Receptors and Their Relation to Guest Chemosensing and Reconfigurable Molecular Logic Gates

Diego Jiménez,[a] Ramón Martínez-Máñez,*[a] Félix Sancenón,*[a] José V. Ros-Lis,[a] Juan Soto,[a] Ángel Benito,[a] and Eduardo García-Breijo[b]

Keywords: Cations / Chemosensing / Chromophores / Electrochemistry / Molecular logic gates

The synthesis and characterisation of a family of multi-channel receptors containing crown-cation binding sites anchored to a 1-aminophenyl-1,2,2-tricyanoethylene group is reported. The ligands L^1–L^6 bear a 1-aminophenyl-1,2,2-tricyanoethylene scaffolding which is simultaneously a redox-active group (showing reduction processes at moderately modest potentials) and an acceptor moiety in the 1-aminophenyl-1,2,2-tricyanoethylene chromophore. Additionally, dyes L^1–L^6 also show fluorescence emission. The colour variation of L^1–L^6 in acetonitrile in the presence of the metal cations Ag^+, Cd^{2+}, Cu^{2+}, Fe^{3+}, Hg^{2+}, Pb^{2+} and Zn^{2+} has been studied. Selective hypsochromic shifts were found for the systems L^4-Pb^{2+}, L^5-Hg^{2+} and L^6-Hg^{2+}. For Hg^{2+} with L^5 and L^6 and Pb^{2+} with L^4, emission fluorescence enhancements most likely associated with metal coordination to the anilinium nitrogen were observed. The electrochemical behaviour of receptors L^1–L^6 was studied in acetonitrile with platinum as working electrode and $[Bu_4N][BF_4]$ as supporting electrolyte. This family of receptors shows a one-electron reversible reduction process at around –0.70 V vs. SCE, attributed to the reduction of the tricyanovinyl group. Additionally, all the receptors also show the oxidation of the anilinium moiety at about 1.2–1.4 V vs. SCE. Significant anodic shifts of both reduction and oxidation waves were found in the presence of certain metal cations. The relationship of these multiple-channel signalling receptors with guest chemosensing and reconfigurable molecular-based logic gates is discussed.

(© Wiley-VCH Verlag GmbH & Co. KGaA, 69451 Weinheim, Germany, 2005)

Introduction

One of the most interesting and expanding fields in supramolecular chemistry is related to the management of input/output signals and their relationship with molecular information. This double "signal-information" concept has, for instance, been applied to different research fields, such as those of molecular logic gates[1] and chemosensing.[2] In the former, chemical species are used as inputs and the output is usually a light signal (emission or colour variation). In chemosensing protocols, light (emission or colour variation) or an electrochemical signal can be considered as input events which are related to the presence of certain chemical species (output information). In many cases these molecular input/output transducers have in common the presence of "binding sites" and "signalling" units.

In the development of chemosensors, the binding site is specifically designed to achieve a high degree of complementarity with target ions, whereas the signalling unit is capable of transducing the (usually selective) binding event into a signal.[3] Following this approach, a number of examples have been described in recent years on the synthesis of cation[4] and anion chemosensors.[5] A large number of coordination sites have been designed that are dependent on the nature of the guest. Three groups of reporters have been mainly used as signalling units: fluorescent groups[6] (the signal is an emission fluorescence change), dyes (the signal is a colour variation) and redox-active groups[7] (the signal upon guest coordination is a shift in the redox potential of the redox-active groups). Advances in this area have been described as important for the selective and sensitive development of target molecular probes.

However and despite the development of individual chromogenic, fluorogenic and electrochemical molecular sensors, there are few examples of receptors capable of displaying two or more output signals upon guest binding. Towards the development of multi-signalling receptors, we have recently reported chemosensors containing both anthracene (as fluorescent) and ferrocene (as electroactive) subunits.[8] Some other recent examples of multi-signalling include the work of Delavaux-Nicot et al., who have developed cation chemosensors containing ferrocene and *N*,*N*-diethylbenzene fluorescent groups.[9] A similar approximation has been used by Beer et al. by synthesising redox-

[a] GDDS, Departamento de Química, Centro de Investigación en Química Molecular Aplicada, Universidad Politécnica de Valencia,
Camino de Vera s/n, 46071 Valencia, Spain
Fax: +34-963879349
E-mail: rmaez@qim.upv.es
fsanceno@upvnet.upv.es
[b] Grupo de Microelectrónica Híbrida, Departamento de Ingeniería Electrónica, Universidad Politécnica de Valencia,
Camino de Vera s/n, 46071 Valencia, Spain

active and photoactive ruthenium(II) and osmium(II) bipyridylferrocene and -cobaltocene-containing macrocycles capable of sensing anionic guests by electrochemical and fluorescence techniques.[10] Also remarkable are the papers published by Shimidzu and Lehn.[11] Chemosensors functionalised with only one subunit capable of displaying two or more observable events (usually two-channel fluorescence – colour changes) upon addition of a certain guest are commonly observed in the so-called intrinsic sensors, in which at least one coordination atom from the binding site is also part of the signalling subunit (usually a dye scaffolding). For example, Fabbrizzi et al. recently reported the synthesis of a chemodosimeter for copper(II), composed of a cyclam unit functionalised with 7-nitrobenzo[1,2,5]oxadiazol-4-ylamine chromophore, which operates through two different channels − colour change and fluorescence quenching of the chromophore.[12] A pH sensor operating through both absorption and emission and based on 1,3-diaryl-5-pyridyl-4,5-dihydropyrazole has been reported by de Silva.[13] However, as far we know, chemosensors operating through three different channels (colour, fluorescence and redox) are very rare and are not common in the literature.[14] We report here the synthesis and characterisation of a family of multichannel receptors containing different crown cation binding sites anchored to a 1-aminophenyl-1,2,2-tricyanoethylene group, which is simultaneously a redox-active group (showing reduction processes at moderately modest potentials) and an acceptor moiety in the 1-aminophenyl-1,2,2-tricyanoethylene chromophore. Additionally, the synthesised receptors also show fluorescence emission. An advance report of the results shown here has recently been published.[14] These multi-signalling systems are not only of interest in sensing protocols but could also be of importance for the development of "reconfigurable" molecular-based logic gates.

Results and Discussion

Receptors L^2–L^6 are built of macrocyclic binding sites (of different sizes, also containing different heteroatoms; nitrogen, oxygen and sulfur) and an (aminophenyl)tricyanovinyl signalling reporter (Scheme 1). Ligands L^1 and L^3 have previously been synthesised by Charles[15a] and Beer,[15b] respectively. Receptor L^1 has an *N*,*N*-dimethylamino moiety and was selected as a model compound in order to study the selectivity towards metal cations imposed by the nature of the binding rings. The Richman–Atkins procedure was used to synthesise the phenyl-functionalised macrocyclic subunits.[16] Aza-oxa macrocycles were synthesised in high dilution procedures by deprotonation of *N*,*N*-phenyldiethanolamine (**3**) with sodium hydride followed by reaction with the methylsulfonyl ester derived from the corresponding polyethylene glycol (**2a**–**2c**; see Scheme 2). The macrocycles used to obtain receptors L^3 and L^4 were previously synthesised in 1978 by Vögtle.[17] The macrocycles used to obtain receptors L^5 and L^6, which contain sulfur atoms in their structures, were synthesised by a modified procedure in which 3,6-dioxaoctane-1,8-dithiol (**6a**) and 3,6-dithiaoctane-1,8-diol (**6b**) were deprotonated with potassium carbonate and sodium hydride, respectively, followed by treatment with the methylsulfonyl ester of *N*,*N*-phenyldiethanolamine (**5**) to give the sulfur-containing macrocycles **7a** and **7b**. *N*,*N*-Dimethylaniline and the synthesised phenyl-containing macrocycles were treated with tetracyanoethylene in warm DMF (60 °C) to give the corresponding receptors L^1–L^6, which were isolated as dark-reddish solids.

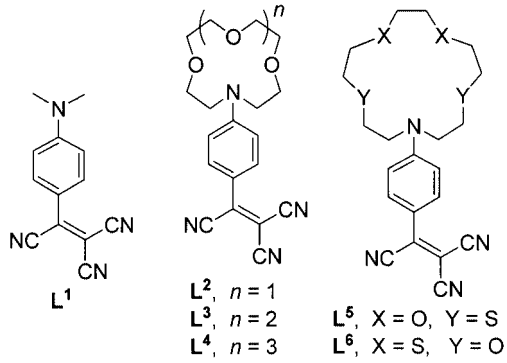

Scheme 1.

The ^{1}H NMR spectra of receptors L^2–L^6 show macrocyclic protons in the range of δ = 2.6 to 3.8 ppm, with two clearly defined zones − the methylene protons adjacent to the sulfur atoms at δ = 2.6–2.9 ppm and the methylene protons adjacent to nitrogen and oxygen atoms in the range δ = 3.5–3.8 ppm. Two doublets at δ = 6.70 and 8.00 ppm indicate the presence of a 1,4-disubstituted aromatic benzene ring. In the ^{13}C NMR spectrum the methylenes adjacent to the sulfur atoms appear in the range δ = 30–35 ppm, whereas the methylenes adjacent to nitrogen and oxygen show signals in the δ = 51–73 ppm range. The aromatic and cyanide carbons appear in the δ = 113–155 ppm range. The most significant signals are the three cyanide carbons centred at δ = 113.7, 114.0 and 114.5 ppm and the signals at δ = 117.8 and 137.3 ppm attributed to the quaternary carbons of the tetrasubstituted double bond.

Despite their easy synthesis and extensive application in different fields, such as optical recording materials or in electrophotography,[18] tricyanovinyl dyes have scarcely been used for sensing purposes. Phenyltricyanoethylene dyes coupled with a phenylboronic acid have previously been used as chromogenic reagents for carbohydrate sensing.[19] Additionally, receptors L^1 and L^3 have previously been used for electrochemical studies in the presence of Na^+, K^+ and Mg^{2+} cations.[15b]

The crystal structure of receptor L^5 was solved by single-crystal X-ray procedures. Suitable crystals for X-ray diffraction were obtained by slow diffusion of diethyl ether into dichloromethane solutions of the receptor L^5. The compound crystallises in the space group $P\bar{1}$ with two molecules of L^5 per asymmetric unit. Figure 1 shows a view of one of the two molecules. The aromatic ring, the double bond and the three cyanide moieties that form the chromogenic subunit are planar within the experimental error. This chromo-

 © 2005 Wiley-VCH Verlag GmbH & Co. KGaA, Weinheim

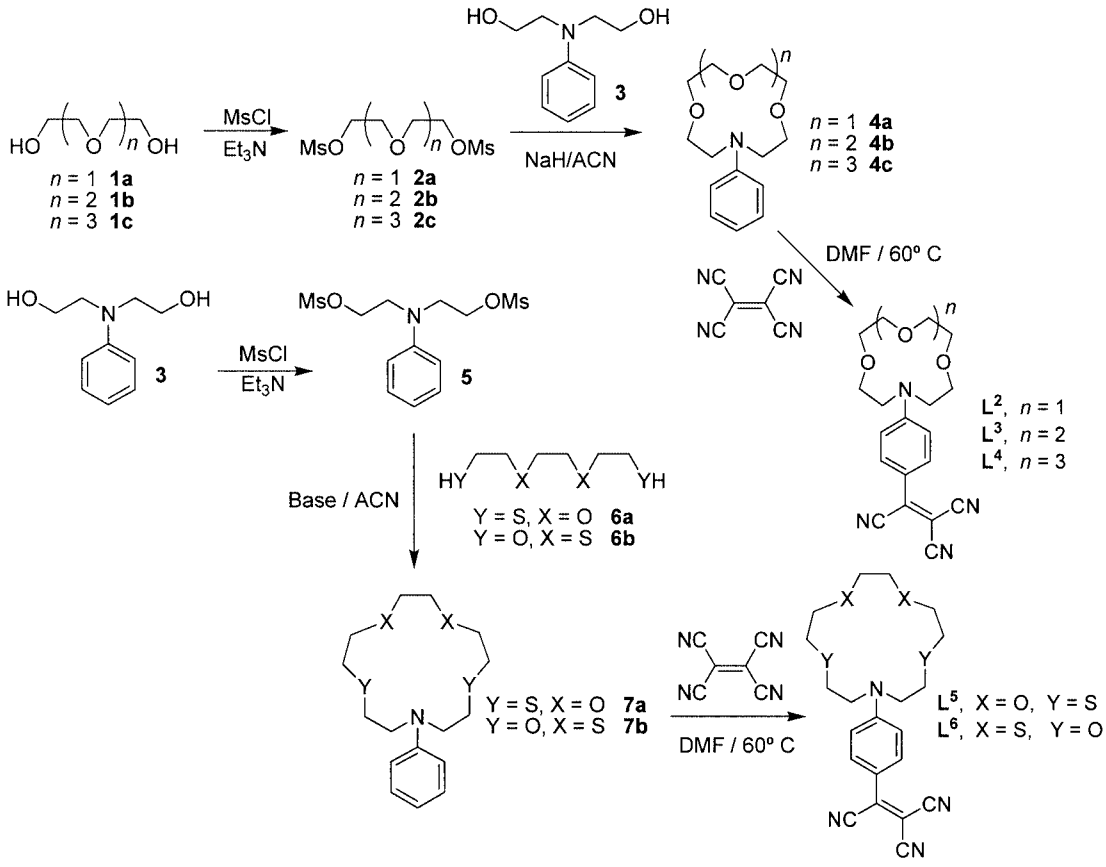

Scheme 2.

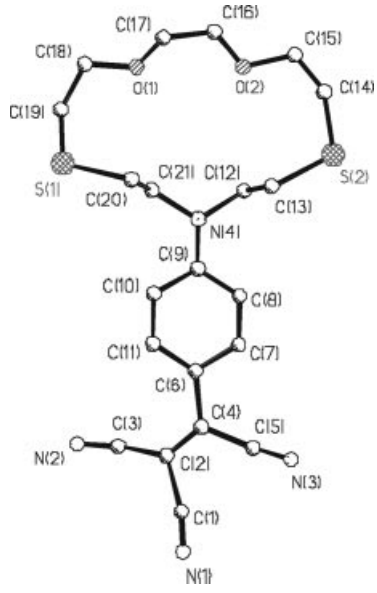

Figure 1. Crystal structure of receptor L^5. Two molecules of L^5 were found in the asymmetric unit but only one is shown. Selected distances [Å]: C(1)–N(1) 1.118(9), C(3)–N(2) 1.115(9), C(5)–N(3) 1.130(8), C(2)–C(1) 1.434(10), C(2)–C(3) 1.419(11), C(4)–C(2) 1.356(10), C(4)–C(5) 1.497(10), C(4)–C(6) 1.431(19), C(9)–N(4) 1.350(8), S(1)–C(19) 1.772(8), S(1)–C(20) 1.848(9), S(2)–C(14) 1.781(7), S(2)–C(13) 1.794(7).

genic subunit is linked to the macrocycle by a nitrogen atom.

Chromogenic Signaling

The visible spectrum of the chemosensors L^1–L^6 in acetonitrile solutions (5.0×10^{-5} M) is characterised by a band centred at about 520 nm which can tentatively be assigned to a charge-transfer band from the donor anilinium group to the acceptor tricyanovinyl moiety.[20] This visible band is responsible for the red-pink colour shown by the receptors in acetonitrile solution.

Addition of equimolar quantities of alkali (Li^+, Na^+, K^+) or alkaline-earth (Ca^{2+}, Ba^{2+}, Mg^{2+}) cations to acetonitrile solutions of receptors L^1–L^6 produced negligible changes in this band. The visible behaviour was also studied in the presence of the metal cations Cd^{2+}, Cu^{2+}, Hg^{2+}, Ni^{2+}, Pb^{2+}, Zn^{2+} and Ag^+. The model compound L^1, without a macrocyclic cavity in its structure, shows three different behaviours (see Figure 2 and Table 1); namely no changes with Ag^+ and Cd^{2+}, a slight hyperchromic effect (intensity enhancement of the visible band centred at 516 nm) in the presence of Zn^{2+}, Pb^{2+} and Hg^{2+}, and the apparition of a shoulder at 468 nm in the presence of Fe^{3+} and Cu^{2+} (see Figure 2) attributed to metal coordination with the donor nitrogen atom of the aniline group.[6] Upon titration of a

 © 2005 Wiley-VCH Verlag GmbH & Co. KGaA, Weinheim

solution of receptor L^1 with Cu^{2+} cation, clear isosbestic points were obtained. The presence of these isosbestic points is indicative of the formation of only one complex, with a 1:2 stoichiometry (cation:receptor). Monitoring the changes at 468 nm upon Cu^{2+} addition, a logarithm of the stability constant of 4.53 ± 0.03 for the formation of the $[Cu(L^1)_2]^{2+}$ complex was obtained.[21] Studies with Fe^{3+} gave no clear isosbestic points, most likely due to the simultaneous formation of complexes with different stoichiometries.

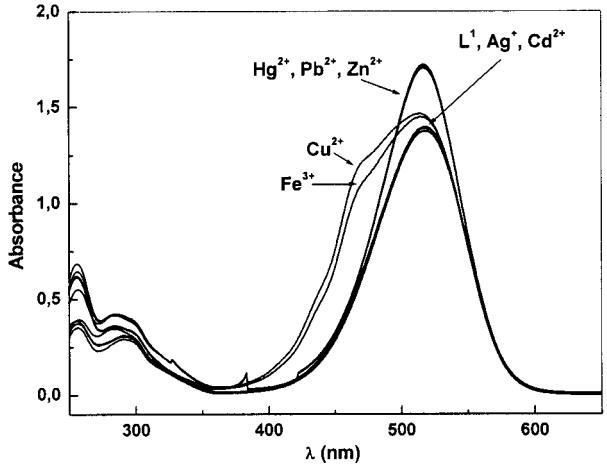

Figure 2. Changes in the UV/Vis spectra of receptor L^1 upon addition of equimolar quantities of metal cations in acetonitrile (5.0×10^{-5} M).

Table 1. Absorption λ_{max} [nm]and ε [$L\,mol^{-1}\,cm^{-1}$] for receptors L^1 to L^6 and their variation upon addition of metal cations in acetonitrile solutions.

	L^1	L^2	L^3	L^4	L^5	L^6
λ_{max}	517	523	518	520	520	518
ε	32500	47300	29900	33500	35200	37500
Ag^+	517	523	518	520	520	518
Cd^{2+}	517	523	518	520	520	518
Cu^{2+}	↓490[a]	523	518	520	520	518
Fe^{3+}	↓490[a]	↓519[a]	↓518[a]	↓513[a]	520	518
Hg^{2+}	517	523	518	520	394	504
Pb^{2+}	517	523	518	475	520	518
Zn^{2+}	517	523	518	520	520	518

[a] The downward pointing arrows indicate a significant hypochromic change in the visible band with respect to that of the free ligand.

On changing from the receptor L^1 to those containing macrocycles, important changes in the selectivity trends were found. Thus, addition of equimolar quantities of Cd^{2+}, Cu^{2+}, Hg^{2+}, Ni^{2+}, Pb^{2+}, Zn^{2+} or Ag^+ to acetonitrile solutions of L^2 produced negligible changes in the UV/Vis spectrum, whereas the presence of equimolar quantities of Fe^{3+} resulted in a remarkable hypochromic change (diminution of the visible band intensity of 60% for Fe^{3+}). A concomitant unremarkable hypsochromic shift of the band centred at 523 nm to 519 nm was also observed for Fe^{3+}. Studies on the variation of the intensity at 523 nm upon addition of increasing amounts of this cation suggested the formation of well-defined 1:1 complexes. A $\log K$ value of 4.69 ± 0.09 was determined for the formation of the $[Fe(L^2)]^{3+}$ complex (see Table 2).[21] These results for L^2, which has a relatively small coordination ring, are somehow related to the characteristics of the Fe^{3+} metal cation, which is, of all the metal cations studied, that with the smallest ionic radius (0.64 Å). The perfect fitting of the Fe^{3+} cation within the macrocyclic subunit of L^2 probably induces Fe–N interactions that could be the responsible for the hypsochromic shift observed. The lack of response in the presence of Cu^{2+} shown by L^2 (when compared to L^1) could be due to the poorer tendency of the Cu^{2+} cation to fit within the macrocyclic cavity (Cu^{2+} ionic radius = 0.69 Å), although steric constraints could make the Cu–N interaction less effective.

For L^3 − the macrocycle in L^3 contains one oxygen atom and one methylene unit more than the macrocycle in L^2 − only Fe^{3+} is able to induce a hypochromic change in the visible band at 518 nm similar to that observed for L^2 (no hypsochromic shifts were found). A $\log K$ of 4.63 ± 0.15 for the formation of the $[Fe(L^3)]^{3+}$ complex was obtained from the intensity changes of the 518 nm band (see Figure 3). The addition of equimolar quantities of the other metal cations tested induced negligible changes.

A more selective and remarkable behaviour was found for chemosensor L^4, which contains the largest macrocyclic cavity of all the receptors studied. A selective colour variation from red-pink to yellow-orange (hypsochromic shift from 520 to 475 nm) was observed upon addition of the heavy metal cation Pb^{2+} (see Figure 4).[22] This result is in agreement with the larger radius of Pb^{2+}, which apparently fits well into the large binding cavity of L^4. The correct combination of ring and cation size would result in a suitable coordination to the nitrogen atom of the macrocyclic subunit, thus inducing the hypsochromic shift of the charge-transfer band.[6] UV/Vis titration experiments for the system Pb^{2+}-L^4 showed clear isosbestic points indicative of the formation of 1:1 ligand-to-metal species. The $\log K$ for the formation of the $[Pb(L^4)]^{2+}$ complex, obtained by nonlinear least-squares treatment of the titration profile, is 6.42 ± 0.03 (see Figure 5).[21] The presence of Fe^{3+} results in

Table 2. Logarithm of the stability constant for the formation of $[M(L^n)]^{m+}$ complexes.

	L^1	L^2	L^3	L^4	L^5	L^6
Cu^{2+}	4.53 ± 0.03[a]	–	–	–	–	–
Fe^{3+}	–	4.69 ± 0.09	4.63 ± 0.15	4.97 ± 0.10	–	–
Hg^{2+}	–	–	–	–	7.57 ± 0.02	5.60 ± 0.05
Pb^{2+}	–	–	–	6.42 ± 0.03	–	–

[a] 2:1 (receptor:cation) stoichiometry for the complex formed between L^1 and Cu^{2+}.

 © 2005 Wiley-VCH Verlag GmbH & Co. KGaA, Weinheim

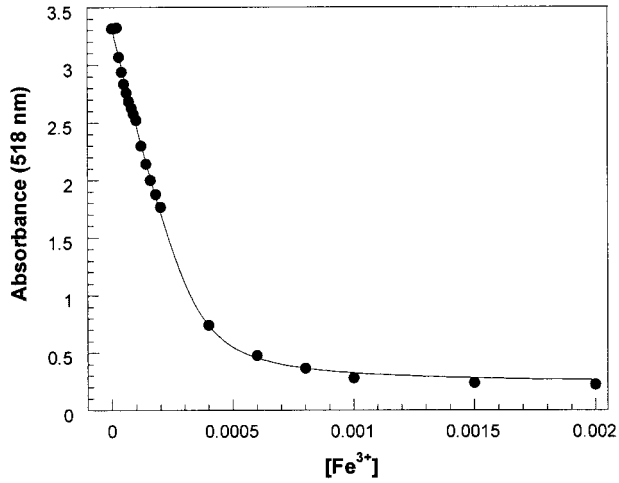

Figure 3. Variation of the intensity at 518 nm for receptor L^3 upon addition of increasing amounts of Fe^{3+} cation in acetonitrile (5.0×10^{-5} M).

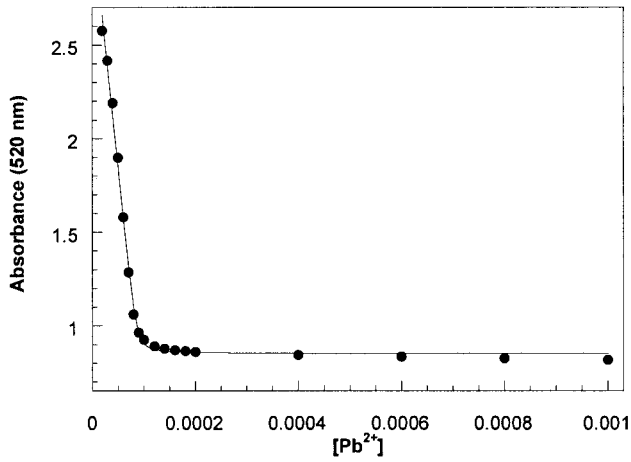

Figure 5. Variation of the intensity at 520 nm for receptor L^4 upon addition of increasing amounts of Pb^{2+} cation in acetonitrile (5.0×10^{-5} M).

a hypochromic effect and an unremarkable hypsochromic shift of less than 10 nm. Monitoring the intensity changes at 520 nm upon addition of Fe^{3+} gave moderate log K values (4.97 ± 0.10). Addition of other metals such as Ag^+, Cu^{2+}, Cd^{2+}, Hg^{2+}, Ni^{2+} and Zn^{2+} to acetonitrile solutions of L^4 gave no change in the colour of the solutions.

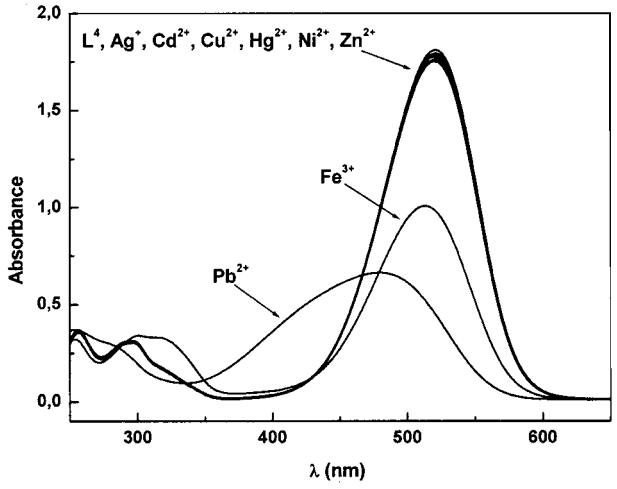

Figure 4. Changes in the UV/Vis spectra of receptor L^4 upon addition of equimolar amounts of metal cations in acetonitrile (5.0×10^{-5} M).

The receptors L^5 and L^6, which bear oxathiaaza crowns, were synthesised in an attempt to colourimetrically recognise additional thiophilic cations such as Hg^{2+}.[23] Thus, red-pink acetonitrile solutions of L^5 changed to yellow upon addition of Hg^{2+} due to a hypsochromic shift of the visible band upon cation binding (see Figure 6). Other metal cations (Li^+, Na^+, K^+, Ca^{2+}, Ba^{2+}, Mg^{2+},Cd^{2+}, Pb^{2+}, Ni^{2+}, Cu^{2+}, Zn^{2+}, Ag^+ and Fe^{3+}) induced no significant changes.[24] The behaviour of acetonitrile solutions of receptor L^6 in the presence of equimolar quantities of metal cations was very similar to that found for L^5: only Hg^{2+} induced a significant hypsochromic shift of the band centred at 518 nm to 504 nm associated with a change in colour from pink to orange. This lesser hypsochromic shift shown by L^6 when compared to L^5 can be ascribed to the position of the sulfur atoms in the macrocyclic subunit. Hypsochromic shifts of a charge-transfer band are observed upon a suitable interaction (for instance coordination) with the donor group. In receptor L^5, the sulfur atoms are placed in the vicinity of the anilinium nitrogen that is part of the chromogenic unit. This spatial proximity might favour the interaction (orbital overlap) of the nitrogen with the Hg^{2+} cation. In receptor L^6, however, the sulfur atoms are separated from the anilinium nitrogen by oxygen atoms and the corresponding methylene subunits. In this case, a preferential coordination of the highly thiophilic Hg^{2+} cation with these sulfur atoms would result in a weaker interaction with the anilinium nitrogen, with concomitant smaller changes in the UV/Vis spectra. As in the above cases, the hypsoch-

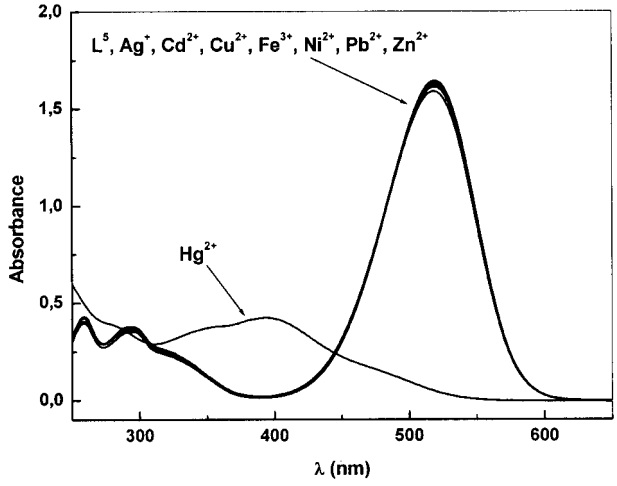

Figure 6. Changes in the UV/Vis spectra of receptor L^5 upon addition of equimolar amounts of metal cations in acetonitrile (5.0×10^{-5} M).

 © 2005 Wiley-VCH Verlag GmbH & Co. KGaA, Weinheim

romic shift of the visible band upon Hg^{2+} coordination is consistent with a decrease in the donor strength of the donor group.[6] UV/Vis titrations showed clear isosbestic points, indicating the formation of 1:1 L^5-to-Hg^{2+} complexes. A log K of 7.57 ± 0.02 was calculated for the formation of the $[Hg(L^5)]^{2+}$ complex (see Figure 7); 1:1 complexes were also formed between L^6 and Hg^{2+}. In this case, log K for the formation of the $[Hg(L^6)]^{2+}$ complex, calculated by nonlinear least-squares treatment of the titration profiles, was 5.60 ± 0.05.

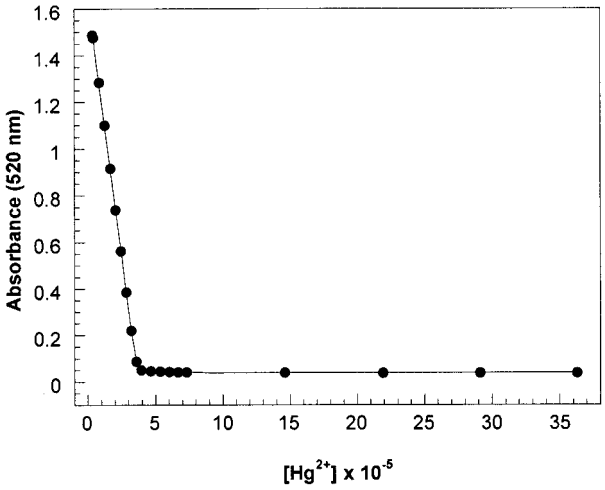

Figure 7. Variation of the intensity at 518 nm for receptor L^5 upon addition of increasing amounts of Hg^{2+} cation in acetonitrile (5.0×10^{-5} M).

Fluorogenic Signalling

The 1-aminophenyl-1,2,2-tricyanoethylene chromophore also shows fluorescence emission upon excitation at the visible absorption band. Fluorescence studies were carried out with acetonitrile solutions (ca. 3.0×10^{-5}M) of the receptors by addition of equimolar quantities of the corresponding metal cation. L^1 shows dual emission features in acetonitrile upon excitation at 517 nm, with a broad, unstructured emission band centred at 610 nm and another more-intense, red-shifted band centred at 690 nm. This red-shifted emission can tentatively be ascribed to formation of an excimer by interaction of an excited state fluorophore with a fluorophore in the ground state.[25] Addition of Ag^+, Pb^{2+}, Zn^{2+}, Ni^{2+} or Cd^{2+} resulted in no significant variation in the emission intensity profiles, whereas the presence of Fe^{3+}, Hg^{2+} or Cu^{2+} inhibited the formation of the excimer and caused an almost complete quenching of the red-shifted band centred at 690 nm.

The emission behaviour of receptors functionalised with macrocyclic subunits (L^2–L^6) is somewhat different to that of L^1 and, upon excitation, only an emission band centred at 600 nm was found; the red-shifted emission found in L^1 was not observed. This could be related to steric factors due to the presence of the bulky macrocyclic moieties, which might prevent excimer formation in the L^2–L^6 receptors. The emission behaviour of acetonitrile solutions of L^2 and L^3 (excitation at 518 and 515 nm for L^2 and L^3, respectively) upon addition of metal cations was unexciting, with only minor changes in the emission intensity (centred at 610 nm) upon addition of the Fe^{3+} cation (see Table 3).

Table 3. Fluorescence emission intensity variation (as % of that of the receptor) obtained for L^1–L^6 upon addition of metal cations in acetonitrile solutions.

	$L^{1[a]}$	$L^{2[a]}$	$L^{3[a]}$	$L^{4[a]}$	$L^{5[a]}$	$L^{6[a]}$
Ag^+	<5	<5	<5	<5	<5	<5
Cd^{2+}	<5	<5	<5	<5	<5	<5
Cu^{2+}	↓ 90[b]	<5	<5	↓ 16[b]	<5	<5
Fe^{3+}	↓ 90[b]	↓ 11[b]	↓ 18[b]	↓ 22[b]	<5	<5
Hg^{2+}	↓ 90[b]	<5	<5	<5	↑ 90[b]	↑ 20[b]
Pb^{2+}	<5	<5	<5	↑ 45[b]	<5	<5
Zn^{2+}	<5	<5	<5	↑ 10[b]	<5	<5

[a] Excitation wavelengths of 517, 518, 515, 467, 450 and 470 nm for L^1, L^2, L^3, L^4, L^5 and L^6, respectively. [b] The upward and downward pointing arrows indicate increase and quenching, respectively, of the emission intensity (690 nm for L^1 and 610 nm for L^2–L^6).

A more significant and selective behaviour was observed with receptors L^4 and L^5. The isosbestic points obtained in the UV/Vis titrations of L^4 with Pb^{2+} (467 nm) and L^5 with Hg^{2+} (450 nm) were chosen as excitation wavelengths. Upon excitation unstructured emission bands centred at 610 and 605 nm were observed for L^4 and L^5, respectively. The results obtained upon addition of one equivalent of the corresponding metal cations are shown in Table 3. The most remarkable effect was the selective enhancement of the emission intensity (90%), coupled with a moderate 10-nm hypsochromic shift of the emission band (from 605 to 595 nm) observed upon addition of Hg^{2+} to solutions of L^5 (Figure 8). Other metal cations tested (Ag^+, Cd^{2+}, Cu^{2+}, Fe^{3+}, Pb^{2+} and Zn^{2+}) induced negligible variations (less than 5%) in the fluorescence emission of this receptor. The excitation spectra (λ_{exc} = 610 nm) measured upon addition of one equivalent of Hg^{2+} cation to an acetonitrile solution of receptor L^5 show the apparition of a band centred at 380 nm, indicating that the $[Hg(L^5)]^{2+}$ complex is the emissive species that induces the apparition of the emission band centred at 605 nm. With L^4, the addition of equimolar quantities of Pb^{2+} or Zn^{2+} induced enhancement in the emission intensity (45% with Pb^{2+} and 10% with Zn^{2+}) with a very low hypsochromic shifts in the emission band (2 nm for Pb^{2+} and negligible with Zn^{2+}), whereas the presence of Cu^{2+} or Fe^{3+} induced moderate quenching and hypsochromic shifts (5 and 10 nm for Cu^{2+} and Fe^{3+} respectively). The fluorescent behaviour of receptor L^6 in the presence of metal cations is very similar to that found for L^5. Upon excitation at the isosbestic point obtained from UV/Vis titrations of L^6 with the mercuric cation (470 nm), a broad emission band centred at 614 nm developed. Of all the metal cations tested, only Hg^{2+} induces a 20% enhancement of the emission intensity, with a hypsochromic shift of the emission band to 604 nm.

 © 2005 Wiley-VCH Verlag GmbH & Co. KGaA, Weinheim

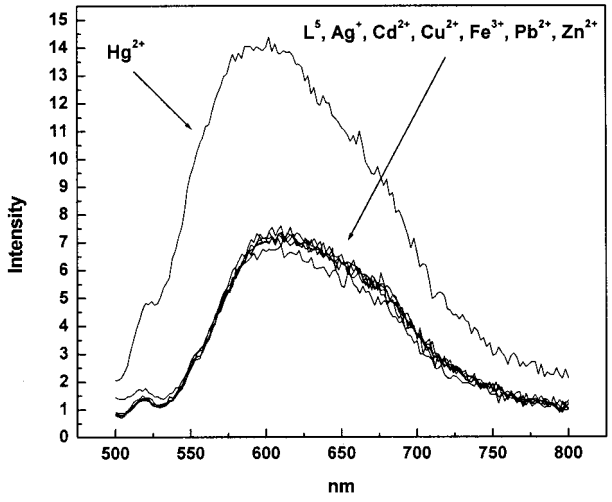

Figure 8. Emission spectra of receptor L^5 (λ_{ex} = 450 nm) upon addition of equimolar amounts of metal cations in acetonitrile (3.0×10^{-5} M).

Table 3 shows that only Hg^{2+}, Pb^{2+} and Zn^{2+} display fluorescence enhancement effects. This is in agreement with their d^{10} electronic configuration, for which electron-transfer or energy-transfer processes usually do not occur.[26] For Hg^{2+} with L^5 and L^6, and Pb^{2+} with L^4, the emission fluorescence enhancement is remarkable and is most likely associated with a strong metal coordination to the anilinium nitrogen (this is also supported by the UV/Vis studies, see above). On the other hand, quenching was observed with the redox-active metal cations Fe^{3+} and Cu^{2+}, for which electron-transfer processes involving the d-orbitals of the metals and the excited state of the fluorophore can occur.[26]

Electrochemical Signalling

The electrochemical behaviour of the tricyanovinyl receptors was studied in acetonitrile with platinum as working electrode and $[Bu_4N][BF_4]$ as supporting electrolyte. This family of receptors shows a one-electron reversible reduction process at about –0.70 V vs. SCE attributed to the reduction of the tricyanovinyl group.[15b] They also show a reversible oxidation process at 1.2–1.4 V vs. SCE due to the oxidation of the anilinium moiety.[27] This electrochemical interpretation is in agreement with molecular modelling and orbital calculations performed on L^1 at the PM3 level.

A detailed electrochemical study in the presence of the metal cations Ag^+, Cd^{2+}, Cu^{2+}, Fe^{3+}, Hg^{2+}, Pb^{2+} and Zn^{2+} was carried out with ligands L^4, L^5 and L^6, which are those that show a more remarkable optical behaviour (see above). A summary of the electrochemical responses is shown in Table 4. For ligand L^5, three different cation-induced electrochemical behaviours were observed. The first type of behaviour was found in the presence of Hg^{2+}, with a remarkable anodic shift (340 mV) of the reduction wave of L^5 along with a significant drop in the reduction wave intensity. Additionally, in the presence of this metal cation the oxidation peak of L^5 "disappears" (the wave is shifted anodically out of the solvent redox window). As is well-known, cation coordination with redox-active molecules results in significant electrochemical anodic shifts of either oxidation or reduction processes.[28] A simple explanation of this effect is related to the idea that it is easier to reduce and more difficult to oxidize the positively charged $[Hg(L^5)]^{2+}$ complex than the corresponding neutral ligand. Therefore, coordination of Hg^{2+} to the oxathiaaza ring would give rise to both an anodic shift in the oxidation wave of the aniline (the shift is so large that the new wave is not observed) and an anodic shift of the reduction process (340 mV). This strong Hg^{2+}–N interaction in L^5, suggested by the electrochemical results, is in agreement with the selective chromogenic results found for this cation (see above).

Table 4. Anodic shifts of the reduction wave (ΔE in mV) obtained for L^4, L^5 and L^6 in the presence of metal cations in acetonitrile solutions.

	$\Delta E(L^4)$[a]	$\Delta E(L^5)$[a]	$\Delta E(L^6)$[a]
Ag^+	10	17	<10
Cd^{2+}	170	120	80
Cu^{2+}	40	25	20
Fe^{3+}	340	240	<10
Hg^{2+}	370	340	200
Pb^{2+}	360	330	160
Zn^{2+}	160	140	20

[a] $\Delta E(L^n) = E(L^n + M^{n+}) - E(L^n)$.

A second sort of electrochemical behaviour was observed for L^5 upon addition of cations such as Pb^{2+}, Zn^{2+}, Fe^{3+} and Cd^{2+}. In this case, there is also a significant anodic shift of the reduction wave, but there is no significant shift of the oxidation peak of L^5. A drop of the peak intensity was found for both the oxidation and reduction waves. This intensity drop (attributed to the formation of species with a lower diffusion coefficient), along with the anodic shift of the reduction wave suggests that there must be some kind of interaction between these metal cations and L^5. Additionally, the absence of changes in the oxidation wave suggests that this interaction is not with the anilinium nitrogen. Tentatively, this interaction can be assigned to a weak coordination of the metal cations with either remote donor atoms from the ring, such as S or O, or due to some interaction with the electron-rich cyano groups. The absence of significant shifts observed in the oxidation wave is often indicative of CE (chemical electrochemical) processes (decoordination and oxidation of the free ligand) favoured by a weak metal–ligand interaction in these cases. Finally, for cations such as Ag^+, Al^{3+} and Cu^{2+} no remarkable changes were observed in either the oxidation or reduction peaks of L^5.

Ligand L^6 shows a somehow similar behaviour to L^5, although in this case, in general, smaller anodic shifts of the reduction wave are observed. The most remarkable are the anodic shifts of 200 and 160 mV of the reduction wave observed for L^5 in the presence of Hg^{2+} and Pb^{2+} cations, respectively.

L^4 shows a notably large anodic shift of the reduction wave of 370 mV with the metal cations Hg^{2+}, Pb^{2+} and

 © 2005 Wiley-VCH Verlag GmbH & Co. KGaA, Weinheim

Fe^{3+}. Addition of Cd^{2+} and Zn^{2+} cations induced a less-important redox shift (170 and 160 mV for Cd^{2+} and Zn^{2+}, respectively). Of all these metal cations, Pb^{2+} is the only one capable of inducing a significant anodic shift of the oxidation peak (140 mV), strongly suggesting coordination of the Pb^{2+} cation with the anilinium nitrogen, in agreement with the chromogenic results. Ag^{+} and Cu^{2+} cations gave unremarkable variations of the electrochemical behaviour of L^4.

Triple Signalling

A very remarkable aspect is that, in their molecular interaction with metal cations, the receptors gave a somewhat different response depending on the transduction channel studied (electrochemical, chromogenic or fluorogenic). In order to explain this effect, it has to be taken into account that the specific response observed in each case strongly depends on the particularities of each coordination-transduction process. Thus, for instance, chromogenic transduction (hypsochromic shift) would be expected when there is a strong enough interaction of a certain metal cation with the anilinium nitrogen (the donor group involved in the anilinotricyanoethylene chromophore). On the other hand, the electrochemical transduction is related to a coulombic-type interaction between the reduced form of the redox-active group (the tricyanovinyl moiety in this case) and the metal cation. This means that the interaction of a certain metal cation with "remote" binding sites, such as the oxygen and sulfur atoms or the cyano groups, might result in an electrochemical response, but in a poor optical variation. Also remarkable is that, in certain cases, the response obtained by fluorescence is also somehow different to that found chromogenically. Thus, for L^4 the coordination of d^{10} cations such as Pb^{2+} induces emission enhancement, whereas redox-active cations such as Fe^{3+} induce significant quenching, probably by interaction with the photo-excited L^4 receptor through energy or photoelectron transfer processes.

As we have commented above, there is a recent interest in the development of molecules with intrinsic logic capabilities. This concept has become widespread since it was realized that the interaction of a receptor molecule with certain species (input) and the observed response (output) can follow Boolean logic rules.[29] Since then a number of examples have been described, most of them using two inputs (usually the presence of protons and a certain metal cation) that cooperatively control the output observed (usually an optical signal). It is also common to many described molecular logic systems to be related to just one Boolean function, whereas it is less common to observe different logical expressions from one unique molecular entity. However the development of "reconfigurable" molecular logic gates could be of interest.[30] In this context, some of the multichannel signalling chemosensors described above might lead to the expression of different logical truth tables by selecting different types of output. This is, for instance, observed in Table 5, which shows the changes in receptor L^4 upon addition, as inputs, of the metal cations Pb^{2+} and Hg^{2+}. A two-input OR logic gate is observed when the output is electrochemical, whereas a TRANSFER gate is found for colour variation outputs. Table 5 also shows changes in L^4 upon addition of Pb^{2+} and Fe^{3+} input cations. An OR, TRANSFER and INHIBIT logic gate is obtained when the electrochemical, colour and emission quenching outputs are selected, respectively. These multi-channel systems can be seen as reconfigurable versatile logic systems. More-complex, three-input reconfigurable molecular logic systems can also be obtained, as shown in Table 6, where the logic gates OR, TRANSFER and INHIBIT are found for just one molecular entity (receptor L^4) by selecting the output channel.

Table 5. Two-input logical truth tables associated with electrochemical, colour and emission quenching measurements using receptor L^4 and different metal cations as input signals.

Input 1	Input 2	$\Delta E > 300$ mV	Colour variation
Pb^{2+}	Hg^{2+}	O1	O2
0	0	0	0
1	0	1	1
0	1	1	0
1	1	1	1

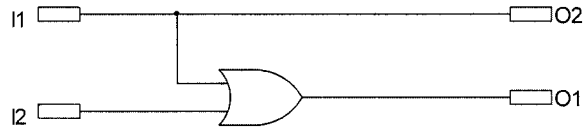

Input 1	Input 2	$\Delta E > 300$ mV	Colour variation	Emission quenching
Pb^{2+}	Fe^{2+}	O1	O2	O3
0	0	0	0	0
1	0	1	1	0
0	1	1	0	1
1	1	1	1	0

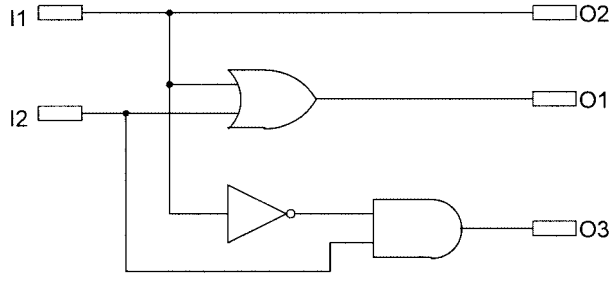

A related aspect is that multi-channel signalling receptors such as L^4 and L^5 can give multiple signalling expressions (combination of different signals) that can be used for sensing purposes. This is also depicted in Table 6, where the equivalence between the output observed and the sensing information one can obtain can be seen. Thus a 1/1/0 output pattern (ΔE larger than 300 mV/colour variation/emission quenching) would only be observed in the presence of Pb^{2+}. In the absence of lead (no colour variation), 1/0/0 and 1/0/1 patterns would be indicative of the presence of Hg^{2+} and Fe^{3+}, respectively. Some other combinations (not shown in Table 6) are possible; for instance, and despite the

 © 2005 Wiley-VCH Verlag GmbH & Co. KGaA, Weinheim

Table 6. Three-input logical truth tables associated with electrochemical, colour and emission measurements using receptor L^4.

Input 1	Input 2	Input 3	$\Delta E > 300$ mV	Colour variation	Emmission quenching
Pb^{2+}	Hg^{2+}	Fe^{3+}	O1	O2	O3
0	0	0	0	0	0
1	0	0	1	1	0
0	1	0	1	0	0
1	1	0	1	1	0
0	0	1	1	0	1
1	0	1	1	1	0
0	1	1	1	0	0
1	1	1	1	1	0

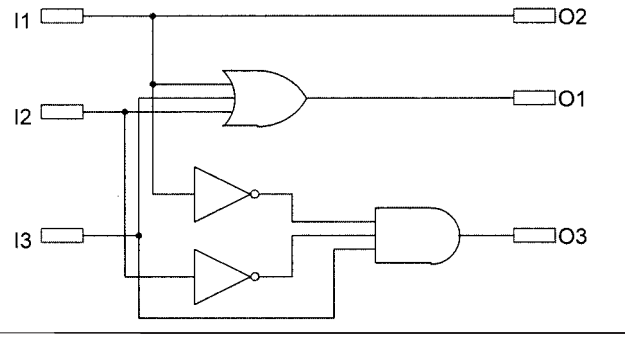

low quenching found for copper, a 0/0/1 combination would be observed with Cu^{2+}; a 0/0/0 pattern, but with variations of ΔE of about 100 mV. can indicate the presence of Cd^{2+} or Zn^{2+} cations. L^4 therefore acts as a prototype of molecular chemosensors capable of sensing several single guests by multiple signalling combinations. Similar observations can be made with other receptors and a suitable combination of input signals.

Table 6 shows how reconfigurable logic gates or multichannel signalling receptors are both intimately related concepts. This is indicated by using tricyanoethylene receptors, which are rare electro-optical signalling systems capable of reporting molecular interaction by a triple-channel transduction. These studies suggest that the development of receptors containing a number of reporter groups might open new perspectives in the design of a new generation of multichannel signalling molecules capable of being used as either prototypes of "reconfigurable" molecular logic gates or as multi-channel guest reporting systems by the use of different output signals from just one molecular entity.

Conclusions

A family of receptors based on functionalised tricyanoethylene moieties has been synthesised and characterised and their interaction with metal cations monitored by optical (colour and fluorescence) and electrochemical changes. A selective chromogenic response was found for the L^4-Pb^{2+}, L^5-Hg^{2+} and L^6-Hg^{2+} systems in acetonitrile, whereas fluorescence and electrochemical responses were usually less selective. A final discussion suggests that receptors containing several reporter channels (multi-channel signalling molecules) can be used for studying the intimately related concepts of multi-channel signalling and reconfigurable logic gates.

Experimental Section

General Remarks: All commercially available reagents were used without further purification. Air/water-sensitive reactions were performed in flame-dried glassware under argon. Acetonitrile was dried with CaH_2 and distilled prior to use.

Physical Measurements: Metal cations (Ag^+, Cd^{2+}, Fe^{3+}, Ni^{2+}, Pb^{2+} as perchlorate salts and Cu^{2+}, Hg^{2+}, Zn^{2+} as triflate salts) were used to obtain approximately 1.0×10^{-3} M acetonitrile solutions. UV/Vis studies were carried out with a Perkin–Elmer Lambda 35 spectrometer. The concentration of ligands used in the measurements was about 5.0×10^{-5} M in acetonitrile. UV/Vis spectra were recorded in the presence of equimolar quantities of the corresponding ligand and metal cation or anion. The fluorescence behaviour was studied with an FS900CDT Steady State T-Geometry Fluorimeter from Edinburgh Analytical Instruments. All solutions for photophysical studies were previously degassed. The concentration of ligands was about 3.0×10^{-5} M in acetonitrile. Fluorescence emission spectra were recorded in the presence of equimolar quantities of ligand and the corresponding metal cation. Electrochemical data were recorded fors previously degassed dry acetonitrile solution, with a programmable function generator Tacussel IMT-1, connected to a Tacussel PJT 120–1 potentiostat. The concentration of ligands and metal ions was about 1.0×10^{-3} M in acetonitrile (the metal ions were perchlorate or triflate salts of Ag^+, Cd^{2+}, Cu^{2+}, Fe^{3+}, Hg^{2+}, Pb^{2+} and Zn^{2+}). Electrochemical studies were carried out in the presence of equimolar quantities of ligand and the corresponding metal cation. The working electrode was platinum connected to a saturated calomel reference electrode separated from the test solution by a salt bridge containing the solvent and the supporting electrolyte (0.25 M $[Bu_4N][BF_4]$). The auxiliary electrode was a platinum wire.

The ^1H and ^{13}C NMR spectra were recorded with a Varian Gemini spectrometer. Chemical shifts are reported in ppm downfield from TMS signal. Spectra recorded in $CDCl_3$ were referenced to residual $CHCl_3$.

Synthetic Procedures: The syntheses of 2-(2-methylsulfonyloxyethoxy)ethyl methanesulfonate (**2a**),[31] 2-[(2-methylsulfonyloxyethyl)phenylamino]ethyl methanesulfonate (**5**),[31] 13-phenyl-1,4,7,10-tetraoxa-13-azacyclopentadecane (**4b**)[17] and 16-phenyl-1,4,7,10,13-pentaoxa-16-azacycloheptadecane (**4c**)[17] have been previously published. Compound **3** is commercially available.

Synthesis of 10-Phenyl-1,4,7-trioxa-10-azacyclododecane (4a): *N*,*N*-phenyldiethanolamine (**3**; 10 g, 0.05 mol) was dissolved in dry acetonitrile (400 mL) and then sodium hydride (3.3 g, 0.137 mol) was slowly added over 60 min with vigorous stirring at room temperature. The mixture formed was heated to reflux and then, over 4 h, 2-(2-methylsulfonyloxyethoxy)ethyl methanesulfonate (**2a**; 14.4 g, 0.055 mol) dissolved in dry acetonitrile was added. The crude reaction mixture was refluxed overnight. The mixture was then filtered and the filtrate concentrated in vacuo to dryness to give an orange sticky oil that was purified by column chromatography on aluminium oxide with dichloromethane and dichloromethane/ethanol (50:1 v/v) as eluents to give 10-phenyl-1,4,7-trioxa-10-azacyclododecane (3.8 g, 0.015 mol) as a yellowish oil. Yield: 30%. ^1H NMR (300 MHz, $CDCl_3$): δ = 3.55 (t, J = 7.5 Hz, 4 H, O-CH_2-CH$_2$-N), 3.64 (m, J = 7.5 Hz, 8 H, O-CH_2-CH_2-O-CH_2-CH_2-O), 3.83 (t, J = 7.5 Hz, 4 H, O-CH$_2$-CH_2-N), 6.68 (t, J = 6 Hz, 2 H, C_6H_5), 6.70

 © 2005 Wiley-VCH Verlag GmbH & Co. KGaA, Weinheim

(d, J = 6 Hz, 1 H, C_6H_5), 7.18 (t, J = 6 Hz, 2 H, C_6H_5) ppm. $^{13}C\{^1H\}$ NMR (75 MHz, $CDCl_3$): δ = 52.35 (CH_2-N), 69.55 (CH_2-O), 69.77 (CH_2-O), 71.46 (CH_2-O), 112.24 (C_6H_5), 116.03 (C_6H_5), 128.98 (C_6H_5), 148.44 (C_6H_5) ppm. MS: m/z = 251 [M^+], 220, 176, 162, 150, 132, 120, 105, 91 [C_6H_5N], 77 [C_6H_5]. $C_{14}H_{21}NO_3$ (251): calcd. C 66.91, H 8.42, N 5.57; found C 66.62, H 8.37, N 5.60.

Synthesis of 10-Phenyl-1,4-dioxa-7,13-dithia-10-azacyclopentadecane (7a): 3,6-Dioxaoctane-1,8-dithiol (**6a**; 3.6 g, 0.022 mol) and anhydrous potassium carbonate (12.2 g, 0.088 mol) were dissolved in dry acetonitrile (400 mL) and heated to reflux. Then, 2-[(2-methylsulfonyloxyethyl)phenylamino]ethyl methanesulfonate (**5**; 7.4 g, 0.022 mol) was added over 4 h. The crude reaction mixture was refluxed overnight. The resultant mixture was then filtered and the filtrate concentrated in vacuo to dryness to give a yellow sticky oil that was purified by column chromatography on silica with dichloromethane as eluent to give 10-phenyl-1,4-dioxa-7,13-dithia-10-azacyclopentadecane (2.9 g, 0.009 mol) as a white solid. Yield: 40%. ^1H NMR (300 MHz, $CDCl_3$): δ = 2.73 (t, J = 7 Hz, 4 H, O-CH_2-CH_2-S), 2.88 (t, J = 7 Hz, 4 H, N-CH_2-CH_2-S), 3.62 (s, 4 H, O-CH_2-CH_2-O), 3.64 (t, J = 7 Hz, 4 H, O-CH_2-CH_2-S), 3.79 (t, J = 7 Hz, 4 H, N-CH_2-CH_2-S), 6.63 (m, 3 H, C_6H_5), 7.20 (d, J = 6 Hz, 2 H, C_6H_5) ppm. $^{13}C\{^1H\}$ NMR (75 MHz, $CDCl_3$): δ = 29.29 (CH_2-S), 30.95 (CH_2-S), 51.63 (CH_2-N), 70.56 (CH_2-O), 74.11 (CH_2-O), 111.57 (C_6H_5), 115.98 (C_6H_5), 129.29 (C_6H_5), 146.46 (C_6H_5) ppm. MS: m/z = 327 [M^+], 204, 192, 179, 164, 149, 132, 119, 105, 91 [C_6H_5N], 77 [C_6H_5]. $C_{16}H_{25}NO_2S_2$ (327): calcd. C 58.68, H 7.69, N 4.28; found C 58.60, H 7.61, N 4.23.

Synthesis of 4-Phenyl-1,7-dioxa-10,13-dithia-4-azacyclopentadecane (7b): 3,6-Dithiaoctane-1,8-diol (**6b**; 3.6 g, 0.022 mol) was dissolved in dry acetonitrile (400 mL) and then sodium hydride (1.6 g, 0.066 mol) was slowly added over 1 h with vigorous stirring at room temperature. The mixture formed was heated to reflux and then, over 4 h methanesulfonic acid 2-[(2-methylsulfonyloxy-ethyl)phenylamino]ethyl methanesulfonate (**5**; 7.4 g, 0.022 mol) dissolved in dry acetonitrile was added. The crude reaction mixture was refluxed overnight, filtered, and the filtrate concentrated in vacuo to dryness to give a yellow sticky oil that was purified by column chromatography on silica with dichloromethane as eluent to give 4-phenyl-1,7-dioxa-10,13-dithia-4-azacyclopentadecane (1.8 g, 0.0055 mol) as a yellowish oil. Yield: 25%. ^1H NMR (300 MHz, $CDCl_3$): δ = 2.72 (t, J = 7 Hz, 4 H, O-CH_2-CH_2-S), 2.88 (s, 4 H, S-CH_2-CH_2-S), 3.60–3.82 (m, 12 H, N-CH_2-CH_2-O), 6.63 (m, 3 H, C_6H_5), 7.20 (d, J = 6 Hz, 2 H, C_6H_5) ppm. $^{13}C\{^1H\}$ NMR (75 MHz, $CDCl_3$): δ = 31.50 (CH_2-S), 32.72 (CH_2-S), 51.06 (CH_2-N), 69.73 (CH_2-O), 72.02 (CH_2-O), 112.02 (C_6H_5), 116.33 (C_6H_5), 129.18 (C_6H_5), 148.02 (C_6H_5) ppm. MS: m/z = 327 [M^+], 204, 192, 179, 164, 149, 132, 119, 105, 91 [C_6H_5N], 77 [C_6H_5]. $C_{16}H_{25}NO_2S_2$ (327): calcd. C 58.68, H 7.69, N 4.28; found C 58.55, H 7.73, N 4.31.

General Procedure for the Synthesis of Tricyanovinyl Dyes: *N*,*N*-Dimethylaniline or the corresponding phenyl macrocycle (1.0 mmol) and tetracyanoethylene (192 mg, 1.5 mmol) were dissolved in dry DMF (12 mL) and heated at 60 °C for 90 min. The crude reaction mixture was concentrated in vacuo to dryness and purified by column chromatography as indicated below. Receptors L^1 and L^3 were previously synthesised by Beer et al. in 1990. ***CAUTION:*** *Synthesis of L^2 to L^6 occurs with elimination of HCN.*

Receptor L^2: Flash chromatography (dichloromethane/acetonitrile, 9:1 v/v) on silica gel gave a dark reddish solid. Yield: 65%. ^1H NMR (300 MHz, $CDCl_3$): δ = 3.58 (m, 8 H, O-CH_2-CH_2-O), 3.73 (t, J = 4.9 Hz, 4 H, O-CH_2-CH_2-N), 3.92 (t, J = 4.9 Hz, 4 H, O-CH_2-CH_2-N), 6.86 (d, J = 9.4 Hz, 2 H, C_6H_4), 8.01 (d, J = 9.4 Hz, 2 H, C_6H_4) ppm. $^{13}C\{^1H\}$ NMR (75 MHz, $CDCl_3$): δ = 53.19 (CH_2-N), 69.08 (CH_2-O), 69.81 (CH_2-O), 71.24 (CH_2-O), 113.41 (C_6H_4), 113.76 (CN), 114.03 (CN), 114.48 (CN), 117.79 (C=C), 132.70 (C_6H_4), 137.30 (C=C), 154.91 (C_6H_4) ppm. MS (FAB$^+$): m/z (%) = 353 (100) [M^+ + 1]. HRMS: calcd. for $C_{19}H_{20}N_4O_3$ 353.1614; found 353.1608.

Receptor L^4: Flash chromatography (dichloromethane/acetonitrile, 8:2 v/v) on silica gel gave a dark reddish oil. Yield: 68%. ^1H NMR (300 MHz, $CDCl_3$): δ = 3.53–3.64 (m, 16 H, O-CH_2-CH_2-O), 3.73 (t, J = 4.7 Hz, 4 H, O-CH_2-CH_2-N), 3.80 (t, J = 4.7 Hz, 4 H, O-CH_2-CH_2-N), 6.80 (d, J = 9.4 Hz, 2 H, C_6H_4), 8.00 (d, J = 9.4 Hz, 2 H, C_6H_4) ppm. $^{13}C\{^1H\}$ NMR (75 MHz, $CDCl_3$): δ = 51.80 (CH_2-N), 68.40 (CH_2-O), 70.61 (CH_2-O), 70.72 (CH_2-O), 70.76 (CH_2-O), 70.92 (CH_2-O), 112.74 (C_6H_4), 113.84 (CN), 114.08 (CN), 114.47 (CN), 117.54 (C=C), 132.92 (C_6H_4), 137.10 (C=C), 154.31 (C_6H_4) ppm. MS (FAB$^+$): m/z (%) = 440 (100) [M^+ + 1]. HRMS: calcd. for $C_{23}H_{28}N_4O_5$ 440.2060; found 440.2057.

Receptor L^5: Flash chromatography (dichloromethane) on silica gel gave a dark reddish solid. Yield: 58%. ^1H NMR (300 MHz, $CDCl_3$): δ = 2.75 (t, J = 4.8 Hz, 4 H, O-CH_2-CH_2-S), 2.89 (t, J = 7.9 Hz, 4 H, N-CH_2-CH_2-S), 3.62 (s, 4 H, O-CH_2-CH_2-O), 3.76–3.83 (m, 8 H, O-CH_2-CH_2-S and N-CH_2-CH_2-S), 6.70 (d, J = 9.4 Hz, 2 H, C_6H_4), 8.04 (d, J = 9.4 Hz, 2 H, C_6H_4) ppm. $^{13}C\{^1H\}$ NMR (75 MHz, $CDCl_3$): δ = 29.65 (CH_2-S), 31.88 (CH_2-S), 52.40 (CH_2-N), 70.64 (CH_2-O), 74.30 (CH_2-O), 112.54 (C_6H_4), 113.58 (CN), 113.84 (CN), 114.36 (CN), 117.76 (C=C), 133.14 (C_6H_4), 137.51 (C=C), 153.03 (C_6H_4) ppm. MS (FAB$^+$): m/z (%) = 429 (100) [M^+ + 1]. HRMS: calcd. for $C_{21}H_{24}N_4O_2S_2$ 429.1419; found 429.1426.

Receptor L^6: Flash chromatography (dichloromethane) on silica gel gave a dark reddish solid. Yield: 61%. ^1H NMR (300 MHz, $CDCl_3$): δ = 2.72 (t, J = 5.7 Hz, 4 H, O-CH_2-CH_2-S), 2.81 (s, 4 H, N-CH_2-CH_2-S), 3.70 (t, J = 5.7 Hz, 4 H, O-CH_2-CH_2-O), 3.77 (t, J = 4.7 Hz, 4 H, O-CH_2-CH_2-S), 3.85 (t, J = 4.7 Hz, 4 H, N-CH_2-CH_2-S), 6.78 (d, J = 9.4 Hz, 2 H, C_6H_4), 8.03 (d, J = 9.4 Hz, 2 H, C_6H_4) ppm. $^{13}C\{^1H\}$ NMR (75 MHz, $CDCl_3$): δ = 31.93 (CH_2-S), 32.96 (CH_2-S), 51.73 (CH_2-N), 69.23 (CH_2-O), 72.16 (CH_2-O), 112.65 (C_6H_4), 113.50 (CN), 113.78 (CN), 114.35 (CN), 117.80 (C=C), 132.93 (C_6H_4), 137.52 (C=C), 154.26 (C_6H_4) ppm. MS (FAB$^+$): m/z (%) = 429 (100) [M^+ + 1]. HRMS: calcd. for $C_{21}H_{24}N_4O_2S_2$ 429.1419; found 429.1413.

Structure Determination of L^5: $C_{21}H_{24}N_4O_2S_2$, M = 428.56, triclinic space group $P\bar{1}$, a = 9.654(4), b = 13.643(6), c = 17.196(5) Å, α = 96.68(3)°, β = 102.98(3)°, γ = 97.72(3)°, Z = 4, V = 2161.7(14) Å^3, $D_{calcd.}$ = 1.317 g cm^{-3}, λ(Mo-K_α) = 0.71073 Å, T = 293(2) K, μ(Mo-K_α) = 0.271 mm^{-1}. Measurements were carried out with a Siemens P4 diffractometer with graphite-monochromated Mo-K_α radiation on a crystal of dimensions 0.17 × 0.17 × 0.15 mm^3. A total of 5963 reflections was collected of which 5558 were independent (R_{int} = 0.0468). Lorentz, polarisation and absorption (ψ-scan, max. and min. transmission 0.295 and 0.210) corrections were applied. The structure was solved by direct methods (SHELXTL) and refined by full-matrix least-squares analysis on F^2 (SHELXTL).[32] The refinement converged at R_1 = 0.090 [$F > 4\sigma(F)$] and wR_2 = 0.2494 (all data). Largest peak and hole in the final difference map +0.58 and –0.37 e Å^3.

CCDC-252155 contains the supplementary crystallographic data for this paper. These data can be obtained free of charge from The Cambridge Crystallographic Data Centre via www.ccdc.cam.ac.uk/data_request/cif.

 © 2005 Wiley-VCH Verlag GmbH & Co. KGaA, Weinheim

Acknowledgments

We wish to thank the Ministerio de Ciencia y Tecnología (MAT2003-08568-C03 and REN2002-04237-C02-01) and the Generalitat Valenciana (GRUPOS03/035) for support. F.S. wishes to thank the Ministerio de Ciencia y Tecnología for the award of a Ramón y Cajal contract.

[1] a) F. M. Raymo, S. Giordani, *Molecular Logic Gates, Encyclopedia of Nanoscience and Nanotechnology* **2004**, vol. 5, p. 677; b) A. P. de Silva, B. McCaughan, B. O. T. McKinney, M. Querol, *Dalton Trans.* **2003**, 1902.
[2] J. P. Desvergne, A. W. Czarnik *Chemosensors for Ion and Molecule Recognition*, NATO Asi Series, Series C, Kluwer Academic Publisher, London, **1997**.
[3] a) L. Fabbrizzi, A. Poggi, *Chem. Soc. Rev.* **1995**, 197; b) R. A. Bissell, A. P. de Silva, H. Q. N. Gunaratne, P. L. M. Lynch, G. E. M. Maguire, K. R. A. S. Sandanayake, *Chem. Soc. Rev.* **1992**, 187.
[4] A. P. de Silva, H. Q. N. Gunaratne, T. Gunnlaugsson, A. J. M. Huxley, C. P. McCoy, J. T. Rademacher, T. E. Rice, *Chem. Rev.* **1997**, *97*, 1515.
[5] a) R. Martínez-Máñez, F. Sancenón, *Chem. Rev.* **2003**, *103*, 4419; b) P. D. Beer, P. A. Gale, *Angew. Chem. Int. Ed.* **2001**, *40*, 486.
[6] a) B. Valeur, I. Leray, *Coord. Chem. Rev.* **2000**, *205*, 3; b) A. W. Czarnik, *Acc. Chem. Res.* **1994**, *27*, 302; c) K. Rurack, U. Resch-Genger, *Chem. Soc. Rev.* **2002**, *31*, 116.
[7] a) P. D. Beer, *Chem. Commun.* **1996**, 689; b) R. Martínez-Máñez, J. Soto, J. M. Lloris, T. Pardo, *Trends Inorg. Chem.* **1998**, *5*, 183; c) P. D. Beer, *Coord. Chem. Rev.* **2000**, *205*, 131.
[8] F. Sancenón, A. Benito, F. J. Hernández, J. M. Lloris, R. Martínez-Máñez, T. Pardo, J. Soto, *Eur. J. Inorg. Chem.* **2002**, 866.
[9] a) J. Maynadie, B. Delavaux-Nicot, S. Fery-Forgues, D. Lavabre, R. Mathieu, *Inorg. Chem.* **2002**, *41*, 5002; b) B. Delavaux-Nicot, S. Fery-Forgues, *Eur. J. Inorg. Chem.* **1999**, 1821.
[10] a) P. D. Beer, A. R. Graydon, L. R. Sutton, *Polyhedron* **1996**, *15*, 2457; b) P. D. Beer, F. J. Szemes, *J. Chem. Soc., Chem. Commun.* **1995**, 2245; c) P. D. Beer, A. R. G. Graydon, A. O. M. Johnson, D. K. Smith, *Inorg. Chem.* **1997**, *36*, 2112.
[11] a) T. Saika, T. Iyoda, K. Honda, T. Shimidzu, *J. Chem. Soc., Perkin Trans. 2* **1993**, 1181; b) T. Iyoda, T. Saika, K. Honda, T. Shimidzu, *Tetrahedron Lett.* **1989**, *30*, 5429; c) T. Shimidzu, T. Iyoda, K. Honda, *Pure Appl. Chem.* **1988**, *60*, 1025; d) F. P. Funeriu, J. M. Lehn, K. M. Fromm, D. Fenske, *Chem. Eur. J.* **2000**, *6*, 2103; e) J. M. Lehn, *Chem. Eur. J.* **2000**, *6*, 2097.
[12] M. Boiocchi, L. Fabbrizzi, M. Licchelli, D. Sacchi, M. Vázquez, C. Zampa, *Chem. Commun.* **2003**, 1812.
[13] A. P. de Silva, H. Q. N. Gunaratne, M. Lynch, *J. Chem. Soc., Perkin Trans. 2* **1995**, 685.
[14] D. Jiménez, R. Martínez-Máñez, F. Sancenón, J. Soto, *Tetrahedron Lett.* **2004**, *45*, 1257.
[15] a) R. G. Charles, *Org. Synth.* **1959**, *39*, 61; b) P. D. Beer, H. Sikanyika, *Polyhedron* **1990**, *9*, 1747.
[16] K. E. Krakowiak, J. S. Bradshaw, D. J. Zamecka-Krakowiak, *Chem. Rev.* **1989**, *89*, 929.
[17] J. P. Dix, F. Vögtle, *Angew. Chem. Int. Ed. Engl.* **1978**, *17*, 857.
[18] a) S. Maeda, *Jpn. Kokai Tokkyo Koho*, **1998**, JP 10244752; b) L. Vanmaele, W. Janssens, *Eur. Pat. Appl.*, **1994**, EP 594238.
[19] C. J. Wood, P. Patel, T. D. James, *Org. Lett.* **2002**, *4*, 477.
[20] J. Aihara, K. Araya, Y. Matsunaga, *Bull. Chem. Soc. Jpn.* **1981**, *54*, 615.
[21] J. Bourson, J. Pouget, B. Valeur, *J. Phys. Chem.* **1993**, *97*, 4552.
[22] a) A. Mason, A. Sheridan, J. O. Sutherland, A. Vincent, *J. Chem. Soc., Chem. Commun.* **1994**, 2627; b) N. J. van der Veen, R. J. M. Egberink, J. F. J. Engbersen, F. J. C. M. Van Veggel, D. N. Reinhoudt, *Chem. Commun.* **1999**, 681.
[23] a) F. Sancenón, R. Martínez-Máñez, J. Soto, *Angew. Chem. Int. Ed.* **2002**, *41*, 1416; b) A. B. Descalzo, R. Martínez-Máñez, R. Radeglia, K. Rurack, *J. Am. Chem. Soc.* **2003**, *125*, 3418.
[24] a) M. J. Choi, M. Y. Kim, S. K. Chong, *Chem. Commun.* **2001**, 1664; b) O. Brümmer, J. J. La Clair, K. D. Janda, *Org. Lett.* **1999**, *1*, 415; c) F. Sancenón, R. Martínez-Máñez, J. Soto, *Chem. Commun.* **2001**, 2262.
[25] a) *Principles of Fluorescence Spectroscopy* (Ed.: J. R. Lakowicz), Plenum Publishers Corporation, New York, **1999**; b) B. Valeur, *Top. Fluoresc. Spectrosc.* **1994**, *4*, 21.
[26] L. Fabbrizzi, M. Licchelli, P. Pallavicini, L. Parodi, A. Taglietti *Transition Metals in Supramolecular Chemistry*, John Wiley & Sons Ltd, New York, **1999**, p. 93.
[27] We have found (unpublished results) oxidation values for products **4a**, **4b**, **4c**, **7a** and **7b** of +0.8–0.9 V in acetonitrile. However, in the electrochemical studies carried out with L^1–L^6 there was no oxidation peak in this anodic region − the first anodic peak was found at +1.2–1.4 V and attributed to the oxidation of the anilinium moiety. The different nature of the ligands and the existence of CE (chemical electrochemical) mechanisms (the anilinium oxidation peak is not reversible) might account for this difference between the oxidation peaks of the anilinum crowns **4a**, **4b**, **4c**, **7a**, **7b** and those of L^1–L^6.
[28] J. M. Lloris, R. Martínez-Máñez, M. E. Padilla-Tosta, T. Pardo, J. Soto, P. D. Beer, J. Cadman, D. K. Smith, *J. Chem. Soc., Dalton Trans.* **1999**, *23*, 2359.
[29] A. P. de Silva, N. D. McClenaghan, *Chem. Eur. J.* **2004**, *10*, 574.
[30] a) G. J. Brown, A. P. de Silva, S. Pagliari, *Chem. Commun.* **2002**, 2461; b) F. Pina, M. J. Melo, M. Maestri, R. Ballardini, V. Balzani, *J. Am. Chem. Soc.* **1997**, *119*, 5556; c) F. M. Raymo, S. Giordani, A. J. P. White, D. J. Williams, *J. Org. Chem.* **2003**, *68*, 4158; d) A. Saghatelian, N. H. Voelcker, K. M. Guckian, V. S.-Y. Lin, M. R. Ghadiri, *J. Am. Chem. Soc.* **2003**, *125*, 346; e) S. Ami, M. Hliwa, C. Joachim, *Chem. Phys. Lett.* **2003**, *367*, 662; f) K. Rurack, A. Kovalchuck, J. L. Bricks, J. L. Slominskii, *J. Am. Chem. Soc.* **2001**, *123*, 6205; g) S. Alves, F. Pina, M. T. Albelda, E. García-España, C. Soriano, S. V. Luis, *Eur. J. Inorg. Chem.* **2001**, 405; h) A. P. de Silva, N. D. McClenaghan, *Chem. Eur. J.* **2002**, *8*, 4935.
[31] P. E. Stott, J. S. Bradshaw, W. W. Parish, *Heterocycles* **1981**, *15*, 179.
[32] SHELXTL, version 5.03, Siemens Analytical X-ray Instruments, Madison, WI, **1994**.

Received: October 07, 2004

 © 2005 Wiley-VCH Verlag GmbH & Co. KGaA, Weinheim

The Hexakis(thiocyanato)ferrate(III) Ion: a Coordination Chemistry Classic Reveals an Interesting Geometry Pattern for the Thiocyanate Ligands

Anthony W. Addison,*[a] Raymond J. Butcher,[b] Zoltán Homonnay,[c] Vitaly V. Pavlishchuk,*[d] Michael J. Prushan,[e] and Laurence K. Thompson[f]

Keywords: Iron / Thiocyanate / X-ray diffraction / Magnetic properties / IR spectroscopy / Moessbauer spectroscopy / Coordination modes / Isomers

$(NMe_4)_3[Fe(NCS)_6]$ crystallizes from ethanol in the monoclinic space group *C*2/*c*. Two different types of complex ions are contained in the unit cell, though both possess exclusively *N*-coordination of the thiocyanate ligands. In one ion, the thiocyanate ligands are all essentially linearly bound, with an Fe–N–C angle of 174 ± 4°, while in the other, there are two *cis*-thiocyanate ligands with a notably small Fe–N–C angle of 146.5°. The EPR and Mössbauer results show that all the iron(III) centers maintain the high-spin state down to 80 K, while the magnetic susceptibility confirms this to 2 K. Infrared and Mössbauer spectra provide evidence for an unusually "soft" lattice. Traditional criteria for interpretation of the infrared frequencies are not strictly applicable for this compound.
(© Wiley-VCH Verlag GmbH & Co. KGaA, 69451 Weinheim, Germany, 2005)

Introduction

Given that the $[Fe(NCS)_6]^{3-}$ ["iron(III) rhodanide"] ion is a classical Werner complex of fundamental significance, there has hardly been an overwhelming number of studies of it since Krüsz and Moraht[1] first described its isolation as (the apparently double) salt $Na_3[Fe(NCS)_6]\cdot 6NaNCS\cdot 4H_2O$ over a century ago. Other cations' $[Fe(NCS)_6]^{3-}$ salts were subsequently prepared by Rosenheim and Cohen,[2] while spectrophotometric studies, originated in 1931,[3] moved forward to define the d-d (940 nm, 570 nm) and LMCT (480, 320, 250 nm) bands.[4–9] Forster and Goodgame[6] also demonstrated the high-spin nature of $(NMe_4)_3[Fe(NCS)_6]$ at ambient temperature (μ = 5.92 μ_B). From the LMCT spectroscopy of the $Fe(NCS)_6^{3-}$ ion doped into the analogous lanthanide lattices $(R_4E)_3[Ln(NCS)_6]$, Walker and McCarthy[10] noted a photosensitivity which they ascribed to NCS^- dissociation, yielding $[Fe(NCS)_5]^{2-}$. In hyperbaric studies of $[Me_4N]_3[Fe(NCS)_6]$[11] and $K_3[Fe(NCS)_6]$[12] by infrared and Mössbauer spectroscopy, respectively, Hellner et al.[11] and Fung and Drickamer[12] detected responses which they attributed to an intramolecular redox process (presumably corresponding to hyperbaric stabilisation of the LMCT excited state Fe^{II}–NCS·–; cf. ref.[10]) and also to the linkage isomerisation Fe–NCS ⇌ Fe–SCN. The assignment of this remarkable isomerisation was based on the shifting of ν_{Fe-NCS} and ν_{C-N}[6,11] to frequencies traditionally associated with M–*S*CN rather than M–*N*CS bonding.[13]

Thiocyanatometallates are capable of acting as ligands (i.e., thiocyanato-bridged Fe–M systems), in this regard bearing an analogy to hexacyanoferrates, which have been used extensively in supramolecular lattice construction.[14] In connection with our interest in the potential of $[Fe(NCS)_6]^{3-}$ as a building block for supramolecular lattices, we present here the results of a crystallographic characterisation of a salt of this anion.

Questions which we anticipated might thus be addressed included: (1) is any *S*-thiocyanato coordination present under ambient conditions, or is coordination exclusively via the nitrogen atoms? and (2) if the latter is the case, does spin-crossover occur for $[Fe(NCS)_6]^{3-}$ at sub-ambient temperatures?

As we considered it important to avoid coordinative interactions between $[Fe(NCS)_6]^{3-}$ and any metal countercation, we sought tetraalkylammonium salts of $[Fe(NCS)_6]^{3-}$, of which the tetramethylammonium one, $(Me_4N)_3[Fe(NCS)_6]$, indeed proved amenable to crystallography.

Results and Discussion

$(Me_4N)_3[Fe(NCS)_6]$ crystallises from ethanol as unsol vated monoclinic crystals belonging to the space group *C*2/*c*

[a] Chemistry Department, Drexel University, Philadelphia, PA 19104-2875, USA
[b] Chemistry Department, Howard University, Washington, DC 20059, USA
[c] Department of Nuclear Chemistry, Eötvös Loránd University, Pázmány P. s 1/A, 1117 Budapest, Hungary
[d] L.V. Pisarzhevskii Institute of Physical Chemistry, Ukrainian Academy of Sciences, Prospekt Nauki 31, Kiev, 03028 Ukraine
[e] Department of Chemistry & Biochemistry, LaSalle University, Philadelphia, PA 19141, USA
[f] Chemistry Department, Memorial University, St. John's NFD, A1B 3X7 Canada

(Table 1). One of the tetramethylammonium ions is disordered.

Table 1. Crystal Data for $(Me_4N)_3[Fe(NCS)_6]$ (CCDC-252536).

Empirical formula: $C_{18}H_{36}FeN_9S_6$
Formular mass: 626.77
a = 24.9838(18) Å
b = 9.3117(7) Å
c = 28.624(2) Å
β = 100.245(1)°
V = 6553.0(8) Å^3
Z = 8
Crystal dimensions: 0.4 × 0.18 × 0.1 mm
Absorption coefficient = 0.865 mm^{-1}
$\rho_{calcd.}$ = 1.271
T = 295(2) K
R(all) = 0.107
R_w(all) = 0.147
Final R = 0.0548
Final R_w = 0.127
Goodness-of-fit = 1.032

Table 2. Selected bond lengths [Å] and angles (°) in $(Me_4N)_3[Fe(NCS)_6]$.

A anions			
Fe(1)–N(13)	2.046(4)	C(13)–N(13)–Fe(1)	173.9(4)
Fe(1)–N(11)	2.050(4)	N(13)–Fe(1)–N(13′)	179.4(2)
Fe(1)–N(12)	2.061(4)	N(13)–Fe(1)–N(11)	88.81(16)
S(11)–C(11)	1.611(5)	N(13)–Fe(1)–N(11′)	91.58(16)
S(12)–C(12)	1.605(5)	N(11)–Fe(1)–N(11′)	92.7(2)
S(13)–C(13)	1.604(5)	N(13)–Fe(1)–N(12)	89.66(16)
N(11)–C(11)	1.125(5)	N(11)–Fe(1)–N(12′)	177.84(16)
N(12)–C(12)	1.147(5)	N(11)–Fe(1)–N(12)	88.87(16)
N(13)–C(13)	1.130(5)	N(11)–C(11)–S(11)	178.2(5)
C(11)–N(11)–Fe(1)	146.5(4)	N(12)–C(12)–S(12)	177.6(4)
C(12)–N(12)–Fe(1)	175.4(4)	N(13)–C(13)–S(13)	177.8(5)
B anions[a]			
Fe(2)–N(21)	2.045(4)	C(23)–N(23)–Fe(2)	178.4(4)
Fe(2)–N(23)	2.052(4)	N(21)–Fe(2)–N(23)	91.33(15)
Fe(2)–N(22)	2.057(4)	N(21)–Fe(2)–N(23)	88.67(15)
S(21)–C(21)	1.611(5)	N(21)–Fe(2)–N(22)	89.09(14)
S(22)–C(22)	1.627(5)	N(23)–Fe(2)–N(22)	89.58(15)
S(23)–C(23)	1.629(5)	N(21)–Fe(2)–N(22)	90.91(14)
N(21)–C(21)	1.152(5)	N(23)–Fe(2)–N(22)	90.42(15)
N(22)–C(22)	1.142(5)	N(21)–C(21)–S(21)	179.1(4)
N(23)–C(23)	1.148(5)	N(22)–C(22)–S(22)	178.1(4)
C(21)–N(21)–Fe(2)	169.9(4)	N(23)–C(23)–S(23)	179.0(5)
C(22)–N(22)–Fe(2)	175.2(4)		

[a] The *trans*-N–Fe–N angles are obligatorily 180°.

The most notable feature of the Fe coordination is that there are two types of anions present in the unit cell. In one set of anions (*B*, Fe[1]; Figure 1, Table 2), the thiocyanate ligands are all essentially "linearly" coordinated to iron(III), with Fe–N–C angles ranging from 170 to 179°.

In the other half of the $[Fe(NCS)_6]^{3-}$ population (anions *A*, possessing C_2 symmetry), a mutually *cis* pair of the NCS^- ligands are in a "bent" mode, with the Fe–N–C angle at 146.5(4)°. Such structural diversity within the unit cell is reminiscent of previously reported instances, such as $[Cu(Dipica)_2](BF_4)_2$,[15] and $[Ni(CN)_5]^{2-}$.[16] M–N–C angles of 160–175° are common in the literature,[17,18] including cases[19] where different thiocyanate ligands in the same complex display significantly different angles. On the other hand, M–N–C angles of 130–150° are encountered less frequently (almost exclusively for M = Cd),[20] and a difference of 30° in M–N–C angles within the same molecule, as observed in the present case, is unusual, if not unique.

Sulfur coordination is not seen in either complex anion, any ligand N/S-orientation ambiguity in this regard being mitigated by the clear differentiation between N–C and C–S bonds in the lattice (1.14 ± 0.01 Å vs. 1.62 ± 0.01 Å, respectively) The thiocyanate ligands (particularly the sulfur atoms) show some librational mobility, principally in one of the local (coordination octahedron) Cartesian directions. For the bent thiocyanate ligands, this occurs at right-angles to the Fe–N–C angle, so is not connected with any intrinsic variation in the Fe–N–C angle. Even in the more

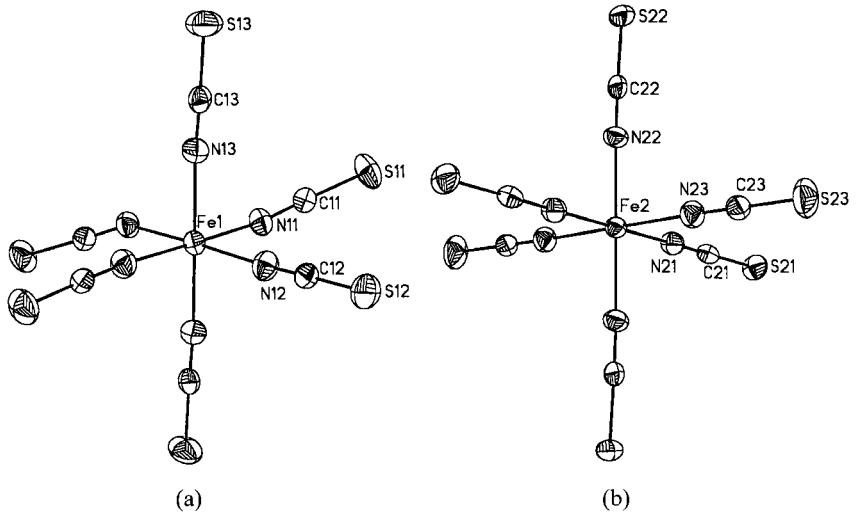

Figure 1. ORTEP diagrams of (a) the "*A*" anion in $(Me_4N)_3[Fe(NCS)_6]$, displaying the four "linear" and the two "bent" *cis*-Fe–*N*–CS linkages, and (b) the "*B*" anion, displaying the six linear Fe–*N*–CS linkages. In each ion, there is a unique facial set of NCS^- ligands with the opposite set symmetry-related to them. The ellipsoids are displayed at the 20% level.

 © 2005 Wiley-VCH Verlag GmbH & Co. KGaA, Weinheim

symmetric *B* anions, the FeN_6 moiety is not homometric, the thiocyanate ligands being arranged (via their local inversion symmetry) as *trans* pairs, with the intermediate Fe–N distance (2.052 Å) being the mean of the shorter (2.045 Å) and longer (2.059 Å) values. Although static Jahn–Teller distortion is not expected (depending on the spin state, vide infra), the possibility of lattice dynamism should not be ruled out, and may be a factor relevant to the various spectroscopic results.[11,12] We do not consider the difference (0.004 Å) between the average Fe–N distances in the *A* anions vs. the *B* anions to be chemically significant. Perhaps unexpectedly, the mutually *trans*-linear Fe–NCS in the *A* anion display the shortest (2.040 Å) Fe–N linkages, the Fe–N (bent) distances (2.046 Å) being hardly unique, but close to the average (2.050 ± 0.007 Å) of the six discrete Fe–N values in the unit cell. All the thiocyanate ligands are linear within 2° (N–C–S).

Magnetic susceptometry of $(Me_4N)_3[Fe(NCS)_6]$ yielded a susceptibility ($\chi_{m,c} = 14.5 \times 10^{-3}$ cm^3·mol^{-1}) at ambient temperature, corresponding closely to the high-spin moment reported previously.[6] The variable-temperature results are shown in Figure 2; the value of χT (4.37 cm^3·K·mol^{-1}) is essentially constant from ambient temperature down to 15 K, and may be compared with the value (4.375 cm^3·K·mol^{-1}) expected for a $g = 2.0$, $S = 5/2$ ion.

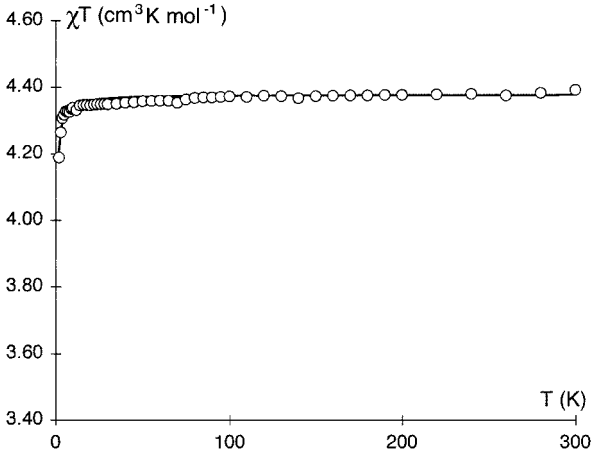

Figure 2. Plot of χT vs. T for $(Me_4N)_3[Fe(NCS)_6]$. The solid line is the fit computed with $g = 2.00(5)$, the circles being the experimental data. The goodness-of-fit index used was R^2 (on χT) = $\Sigma(\chi T_{obsd.} - \chi T_{calcd.})^2/\Sigma(\chi T_{obsd.})^2 = 4 \times 10^{-6}$.

Below 15 K, χT decreases noticeably, reaching 4.19 cm^3·K·mol^{-1} at 2 K. The data accede to a Curie–Weiss law, with $C = 4.375$ and $\theta = +0.07$ K. The downturn in χT at very low temperature could be attributed to the onset of weak intermolecular antiferromagnetic ordering (cf. θ value). However, we advocate a more informative interpretation, in which the departure from simple paramagnetism is due to zero-field splitting of the $S = 5/2$ state:[21]

$$\chi_m = \frac{Ng^2\beta^2}{12kT} \cdot \frac{75e^{-10D/3kT} + 27e^{2D/3kT} + 3e^{8D/3kT}}{e^{-10D/3kT} + e^{2D/3kT} + e^{8D/3kT}}$$

Polycrystalline $(Me_4N)_3[Fe(NCS)_6]$ at 77 K yielded a powder ESR spectrum with broad resonances (ΔH_{p-p} of 25–70 mT) typical of iron(III). An intense bisignate resonance at $g = 2.08$ is assigned to the (M_s) –1/2→+1/2 transition of $S = 5/2$ Fe^{III}, for which the ZFS parameter D is expected to be small ($D < h\nu$) when the ion is close to O_h symmetry.[22] A band at $g = 5.68$ and shoulder near $g = 3.2$ are indicative of a non-O_h component, the g values for Fe^{III} being highly sensitive to D.[23] If the D value for the *A* anions, for instance, dominates that from the more symmetric *B* anions, then attribution of the low-T downturn in the χT value to the ZFS of the *A* anions yields $D = +0.051(2)$ cm^{-1}. A first-order estimate of the resonance fields (Table 3) reveals that the observed EPR spectrum is in turn consistent with this interpretation, when the more anisotropic component has $D \approx 0.05$ cm^{-1}. (There is no unique solution yielding values for both D_A and D_B; the solution yields only that $D_A + D_B \approx 0.05$ cm^{-1}.)

Table 3. Resonance fields with $D > 0$.

Transition	Energy	$g_{app./calcd.}$[a]	$g_{obsd.}$
–1/2 → +1/2	gβH	2.08	2.08
–1/2 ↔ –3/2	±(2D – gβH)	3.05	3.17
–3/2 ↔ –5/2	±(4D – gβH)	5.69	5.68
+3/2 ↔ +5/2	4D + $g\beta H$	1.27	[b]

[a] Using $g = 2.08$, $D = 0.0485$ cm^{-1} at $\nu = 9.15$ GHz. [b] Not observed.

The data thus confirm a high-spin state for iron(III) at all temperatures, so that it is clear that there is no spin-crossover. The results also militate against any static Jahn–Teller distortion, which would require an inhomogeneous spin population in the e_g or t_{2g} subshell ($S = 1/2$, t_{2g}^5).

The Mössbauer spectroscopic results for $(Me_4N)_3[Fe(NCS)_6]$ displayed in Table 4 and Figure 3 are in consonance with the bulk magnetochemical results. Data were obtained at both 300 K and 80 K, and the isomer shift is characteristic of iron(III).

Table 4. Mössbauer results.

Temp.	Isomer shift [mm·s^{-1}]	Line width [mm·s^{-1}]	Relative mössbauer effect (area/baseline)
300 K	+0.46	1.54	0.6%
80 K	+0.57	1.66	3.4%

Although the ambient-temperature data could be fitted with a non-zero quadrupole splitting (0.45 mm·s^{-1}), its difference from zero was not of great statistical significance, and the quadrupole splitting actually diminished to essentially zero for the 80 K spectrum. Thus, the electronic field symmetry of the iron center is close to spherical, which matches its homoleptic, high-spin d^5 situation. However, the linewidths are unusually large, and there is a notable difference in sensitivity (amplitude response) between 80 K (higher) and 300 K (lower). This indicates a very low Debye temperature and the presence of numerous low-energy lattice phonon modes which serve as relaxation pathways for the γ-absorption recoil energy. This is especially so at room

 © 2005 Wiley-VCH Verlag GmbH & Co. KGaA, Weinheim

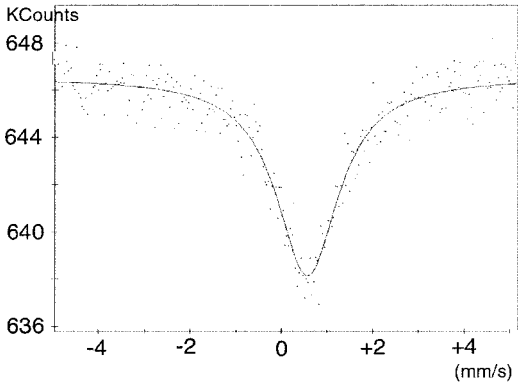

Figure 3. Mössbauer spectrum of $(Me_4N)_3[Fe(NCS)_6]$ at 80 K. The abscissa is the isomer shift, relative to α-Fe.

temperature, though the large linewidth would also require that the consequent polarisability be transmitted to the metal ion itself. This observation is consistent with the hypothesis of lattice dynamism (vide supra) – and the previously observed effects of applied pressure – i.e., the lattice is mechanically "soft".

Similarly to prior reports for $[Fe(NCS)_6]^{3-}$ salts,[6,11,24] the infrared spectrum of $(Me_4N)_3[Fe(NCS)_6]$ displayed very strong absorption in the ν_{CN} region, consisting of a band at 2060 cm^{-1}, along with a well-defined but lesser intensity absorption at 2012 cm^{-1}. Frequencies near 2050 cm^{-1} are traditionally considered typical of *N*-coordinated thiocyanate, while S-coordination shifts the frequency to near 2100 cm^{-1}, the ν_{CN} pattern in any case being much more dependent on the NCS^- binding mode than on molecular symmetry considerations.[13] From an orbital hybridisation viewpoint (as implied by the resonance structures in Scheme 1), the higher C–N bond order can be associated with the more intense band assigned to the majority of the thiocyanate ligands coordinated in the linear mode [Scheme 1(b)], which, by requiring sp hybridisation at the nitrogen atom, elevates the C–N bond order. Thus, the two ν_{CN} bands' frequencies and relative intensities are actually quite consistent with the difference in ligand electronic structure between linear and bent NCS^- coordination. A similar correlation, between spin state and ν_{CN} (with ν_{CN} = 2110 cm^{-1}), was seen for some (triaryltriazole)iron(II) *N*-thiocyanates.[18] Inasmuch as the molar volume of an $[M(NCS)_6]^{n-}$ anion should decrease when ligands transform from the linear to the bent coordination mode, such a transformation may well contribute to any hyperbaric reorganisation pathway. However, the facts that (a) these frequencies are slightly different from those reported previously for the tetra*ethyl*ammonium salt,[24] and (b) the previous Mössbauer study[12] was performed on the *potassium* salt brings forward the likelihood that the precise coordination geometry in $[Fe(NCS)_6]^{3-}$ is actually countercation-dependent, opening the way for validation of further studies on a variety of $[Fe(NCS)_6]^{3-}$ salts.

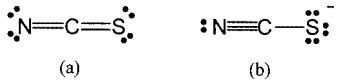

Scheme 1.

In acetonitrile solution at the 1 mM level, a quasireversible Fe^{III}/Fe^{II} redox couple was observed at +0.11 V vs. the nonaqueous Ag^+/Ag electrode (+0.41 V vs. SCE[26]).

Conclusions

In $(Me_4N)_3[Fe(NCS)_6]$, two different types of complex ions are contained in the unit cell, though both possess exclusively *N*-coordination of the thiocyanate ligands. In one ion, the thiocyanate ligands are all essentially linearly bound, with an Fe–N–C angle of 174 ± 4°, while in the other, two of the thiocyanate ligands are *cis*, with an Fe–N–C angle of 146.5°. The EPR, magnetic susceptibility and Mössbauer results show that all the iron(III) centers maintain the high-spin state down to 2 K. Infrared and Mössbauer spectra provide evidence for a lattice of unusual mechanical softness. Traditional criteria for interpretation of the infrared frequencies are not strictly applicable for this compound.

Experimental Section

$(NMe_4)_3[Fe(NCS)_6]$ was prepared according to Forster and Goodgame,[6] using tetramethylammonium thiocyanate obtained by metathesis between KNCS and Me_4NCl in ethanol. The product was recrystallised from ethanol, yielding crystals which indeed in reflected light appear olive-green, with a metallic lustre. Infrared spectra were obtained from powdered crystals and nujol oil mulls (to minimise pressurization) with a Thermo Nicolet Avatar 360 FT-IR equipped also with a Nicolet Smart MIRacle ATR diamond crystal accessory. Magnetic susceptibilities were measured with a Pd-standard-calibrated Quantum Design MPMS5S SQUID magnetometer, at a field of 0.1 T. EPR spectra were obtained with a Varian E-12 X-band instrument, calibrated with diphenylpicrylhydrazyl radical and chloropentaamminechromium(III) chloride. Mössbauer spectra were obtained in the transmission mode with a constant-acceleration-type spectrometer (Wissel), a liquid nitrogen cooled, bath-type cryostat being used for low-temperature spectra. An 800 MBq $^{57}Co(Rh)$ sample was used as the γ-ray source, while isomer shifts are referred to α-iron at room temperature. The sample was measured in the form of a fine powder in order to avoid texture effects in the spectra. Spectra were deconvoluted using the MossWin 3.0 code,[25] applying Lorentzian lineshape. Cyclic voltammetry was performed at 25 °C in deoxygenated CH_3CN solution with 0.1–0.2 M Et_4NClO_4 as supporting electrolyte using a Bioanalytical Systems BAS 100A electrochemical analyzer. The three-electrode assembly comprised a Pt-wire working electrode, an Ag^+ (0.01 M, 0.1 M Et_4NClO_4, CH_3CN)/Ag reference electrode ("APE")[26] and a Pt auxiliary electrode. For X-ray diffraction, a suitable crystal was mounted on a glass fiber with epoxy cement and attached to a goniometer head of a Siemens P4S diffractometer utilising a CCD area detector and graphite-monochromated Mo-K_α radiation (λ = 0.71073 Å). Cell constants and orientation matrices were obtained by least-squares procedures using φ and ω scans, the data collection and reduction being controlled by Bruker SMART software. Absorption corrections (μ = 0.865 mm^{-1}) were obtained with SHELXA.[27] A total of 28471 reflections were collected (–29

 © 2005 Wiley-VCH Verlag GmbH & Co. KGaA, Weinheim

$\leq h \leq 29$, $-10 \leq k \leq 10$, $-33 \leq l \leq 33$) in the θ range 1.45–24.71°. Solution, refinement and outputting were performed using the SHELX suite of programmes.[27] The structure was refined with direct methods using full-matrix least-squares procedures, on F^2 against 5576 independent reflections with $F^2 > 2\sigma(F^2)$. H atoms were initially emplaced geometrically and then included in subsequent cycles of refinement.

Acknowledgments

A. W. A. and V. V. P. thank Drexel University for support, and R. B. C. and S. H. for demonstration of the consequences of differing degrees of mechanical resistance.

[1] G. Krüsz, H.Moraht, *Justus Liebigs Ann. Chem.* **1890**, *260*, 209.
[2] Rosenheim, R. Cohen, *Z. Anorg. Chem.* **1901**, *27*, 295.
[3] H. I. Schlesinger, H. B. van Valkenburgh, *J. Am. Chem. Soc.* **1931**, *53*, 1215.
[4] L. M. Kul'berg, A. K. Gorlinskii, *J. Gen. Chem. U.S.S.R.* **1939**, *9*, 1707.
[5] H. H. Schmidtke, *Ber. Bunsenges. Phys. Chem.* **1967**, *71*, 1138.
[6] D. Forster, D. M. L. Goodgame, *J. Chem. Soc.* **1965**, 268.
[7] K. B. Yatsimirskii, S. V. Volkov, J. I. Maslowska, N. I. Buryak, *Roczniki Chemii* **1972**, *46*, 1999.
[8] B. Csiszar, V. Gutmann, E. Wychera, *Monatsh. Chem.* **1967**, *98*, 12.
[9] J. Hennion; J. Nicole, G. Tridot, *C. R. Seances Acad. Sci., Sci. Chim.* **1974**, *C278*, 235.
[10] I. M. Walker, P. J. McCarthy, *Inorg. Chem.* **1984**, *23*, 1842.
[11] E. Hellner, H. Ahsbas, G. Dehnicke, K. Dehnicke, *Naturwissenschaften* **1974**, *61*, 502.
[12] S. C. Fung, H. G. Drickamer, *Proc. Natl. Acad. Sci. U.S.A.* **1969**, *62*, 38.
[13] K. Nakamoto, *Infrared and Raman Spectra of Inorganic and Coordination Compounds*, 4th ed., Wiley-Interscience, New York, **1997**, part B, pp. 117–119.
[14] a) C. C. Chang, B. Pfennig, A. B. Bocarsly, *Coord. Chem. Rev.* **2000**, *208*, 33; b) H.-Z. Kou, W.-M. Bu, S. Gao, D.-Z. Liao, Z-H. Jiang, S.-P. Yan, Y.-G. Fan, G.-L. Wang, *J. Chem. Soc., Dalton Trans.* **2000**, 2996.
[15] M. Palaniandavar, R. J. Butcher, A. W. Addison, *Inorg. Chem.* **1996**, *35*, 467; Dipica is bis(2′-picolyl)amine.
[16] K. N. Raymond, P. W. R. Corfield, J. A. Ibers, *Inorg. Chem.* **1968**, *7*, 1362.
[17] K. Vrieze, G. van Koten, in: *Comprehensive Coordination Chemistry* (Eds.: G. Wilkinson, R. D. Gillard, J. A. McCleverty), Pergamon Press, Oxford, New York, **1987**, vol. 2, pp. 226–234.
[18] D. Zhu, Y. Xu, Z. Yu, Z. Guo, H. Sang, T. Liu, X. You, *Chem. Mater.* **2002**, *14*, 838.
[19] a) E. Freire, S. Baggio, L. Suescun, R. Baggio, *Acta Crystallogr., Sect. C* **2001**, *57*, 905; b) P. Manikandan, K. R. J. Thomas, P. T. Manoharan, *Acta Crystallogr., Sect. C* **2000**, *56*, 3087; c) J.-C. Liu, G.-C. Guo, J.-S. Huang, X.-Z. You, *Inorg. Chem.* **2003**, *42*, 235; d) A. J. Leong, L. F. Lindoy, D. C. R. Hockless, G. F. Swiegers, S. B. Wild, *Inorg. Chim. Acta* **1996**, *246*, 371.
[20] a) A. E. Shvelashvili, M. A. Porai-Koshits, A. I. Kvitashvili, B. M. Shchedrin, L. P. Sarishvili, *J. Struct. Chem.* **1974**, *15*, 293; b) M. Cannas, G. Carta, A. Cristini, G. Marongiu, *Inorg. Chem.* **1977**, *16*, 228.
[21] $$\chi_m = \frac{Ng^2\beta^2}{12kT} \cdot \frac{\sum a_i e^{-E_i/kT}}{\sum b_j e^{-E_j/kT}}$$
where the exponential terms represent the Boltzmann distribution over the M_s states of the Fe^{III} center, at $-8D/3$ ($M_s = \pm 1/2$), $-2D/3$ ($M_s = \pm 3/2$) and $+10D/3$ ($M_s = \pm 5/2$). The TIP was taken to be zero for this $^6A_{1g}$ term: A. Earnshaw, *Introduction to Magnetochemistry*, Academic Press, London, New York, **1968**, p. 67.
[22] H. Levanon, G. Stein, Z. Luz, *J. Am. Chem. Soc.* **1968**, *90*, 5292–5293.
[23] G. Palmer, "Electron Paramagnetic Resonance of Metalloproteins", in: *Physical Methods in Bioinorganic Chemistry* (Ed.: L. Que Jr.), University Science Books, Sausalito, California, **2000**, pp. 149.
[24] R. A. Bailey, S. L. Kozak, T. W. Michelsen, W. N. Mills, *Coord. Chem. Rev.* **1971**, *6*, 407.
[25] Z. Klencsár, E. Kuzmann, A. Vértes, *J. Radioanal. Nucl. Chem.* **1996**, *A210*, 105.
[26] V. V. Pavlishchuk, A. W. Addison, *Inorg. Chim. Acta* **2000**, *298*, 97.
[27] G. M. Sheldrick, *SHELX-97, Programs for the Solution and Refinement of Crystal Structures*, Universität Göttingen, **1997**.
Received: October 14, 2004

 © 2005 Wiley-VCH Verlag GmbH & Co. KGaA, Weinheim

[1+1] Asymmetric Compartmental Macrocycles Bearing a Pendant Arm and Related *s,f*-Heterodinuclear Complexes Containing Lanthanide(III) and Sodium Ions

Sergio Tamburini,*[a] Umberto Casellato,[a] Laura Bertolo,[a] and Pietro Alessandro Vigato[a]

Keywords: Compartmental macrocycles / Lanthanides / Schiff bases / NMR of paramagnetic systems / Shift reagents / ^{23}Na NMR

[1+1] Asymmetric compartmental macrocycles and/or related mononuclear, homodinuclear and sodium(I)-lanthanide(III) heterodinuclear complexes are reported and their properties investigated by SEM-EDS microscopy and ^{1}H, ^{13}C and ^{23}Na NMR spectroscopy. These ligands bear a pendant arm, represented by a -CH_2COOH (H_3L_A), -$CH_2C_5H_4N$ (H_2L_B) or -$CH_2C_6H_4OH$ (H_3L_C) group bonded to the aminic nitrogen, and contain an O_2O_3 crown-ether-like chamber and an N_3XO_2 (where X = O, N) Schiff-base chamber. It was found that the lanthanide(III) ion resides in the N_3XO_2 chamber while the sodium(I) ion fills the O_2O_3 crown-ether-like chamber, as ascertained for the complex [DyNa(L_C)(PrOH)(Cl)] by a single-crystal X-ray structural investigation. The complex is monoclinic, space group $P2_1/c$, with a = 9.601(2), b = 12.927(2), c = 26.638(4) Å, β = 99.55(3)°. The dysprosium ion is seven-coordinate in the N_3O_2 site, showing a pentagonal-bipyramid-coordination polyhedron and bonded, in the axial positions, to a chlorine ion and to the oxygen of the pendant phenolic group of the ligand. The sodium ion is six-coordinate in the O_3O_2 site and bonded to the propyl alcohol oxygen. Furthermore, the potential use of these complexes as molecular probes for the selective recognition of specific metal ions has been tested. In particular, their ability to act as shift reagents towards Na^+ was investigated by ^{23}Na NMR spectroscopy. The relationship between the structure of these complexes in the solid state and in solution is reported.
(© Wiley-VCH Verlag GmbH & Co. KGaA, 69451 Weinheim, Germany, 2005)

Introduction

Macrocyclic compounds have attracted an increasing interest owing to their role in the understanding of the molecular processes that occur in different scientific fields, ranging from chemistry to biochemistry and medicine, from material science to hydrometallurgy.[1–9]

In the past, dinucleating macrocyclic systems attracted great interest. In particular, the physico-chemical properties arising from the proximity of two metal ions closely coordinated within an appropriate organic moiety were investigated. This molecular aggregation can mediate certain chemical reactions better (or in a different manner) than those in isolated centres. Moreover, it significantly contributes to the knowledge of cooperative effects in the activation, transport and separation of specific molecules with different complexity, in the selective recognition of neutral and charged species, in the design of probes and devices capable of operating at molecular level.[10–17]

Furthermore, dinucleating macrocyclic ligands have been used for the synthesis of compounds with specific spectroscopic and magnetic properties. It was demonstrated that complexes containing dinuclear (or polynuclear) magnetic entities at appropriate distances and/or with well-defined stereochemistry exhibit peculiar magnetic properties, arising from the nature and magnitude of the interactions between the metal ions within the molecular unit.[10,12]

In this field, a particular role was played by compartmental macrocyclic ligands, that is, systems with two adjacent coordination chambers capable of coordinating two metal ions, interacting through the appropriate bridging donor atoms of these ligands. This interaction can be tuned by changing the donor atoms of the two chambers, the flexibility of the ligands, the metal ions, the distance between the two chambers and/or the metal ions themselves.[10,12]

These compartmental ligands can be symmetric or asymmetric in nature, depending on the difference in the donor set and/or in the aliphatic or aromatic chains of the two adjacent coordination chambers; the symmetric ligating systems give rise almost exclusively to homo-dinuclear complexes. Only under specific, experimental conditions can they form mononuclear complexes, which, however, easily turn into the homo-dinuclear analogues.

Unsymmetrical modifications of these symmetric systems were designed in order to achieve a different recognition process at the two adjacent chambers and consequently to favour the formation of hetero-dinuclear complexes. The type and the extent of dissymmetry introduced in the coor-

[a] Istituto di Chimica Inorganica e delle Superfici – C.N.R., Corso Stati Uniti 4, 35127 Padova, Italy
Fax: +39-0498702911
E-mail: sergio.tamburini@icis.cnr.it

dination moiety can influence and modify considerably the coordination selectivity of the two sites, allowing the formation of pure hetero-dinuclear species, not otherwise accessible.[11,12,18]

Recently we have started a project aimed at the preparation of molecular probes for selective recognition of alkali or alkaline metal ions. In particular, we have prepared the [1+1] asymmetric cyclic ligands H_2L_D and H_2L_E by reaction of 3,3′-(3-oxapentane-1,5-diyldioxy)bis(2-hydroxybenzaldheyde) or 3,3′-(3,6-dioxaoctane-1,8-diyldioxy)bis(2-hydroxybenzaldheyde) with 1,5-diamino-3-azamethylpentane. They contain an N_3O_2 Schiff-base chamber and an O_2O_n (where n = 3, 4) crown-ether-like chamber and react with $LnCl_3{\cdot}nH_2O$ in alcoholic solution, giving rise to the related mononuclear complexes $[Ln(H_2L_D)(Cl)_3(H_2O)_4]$ or $[Ln(H_2L_E)(Cl)_3(H_2O)_4]$, where the lanthanide(III) ion invariantly occupies the O_2O_n crown-ether-like chamber, as ascertained also by X-ray diffractometric investigations.[19,20] However, when this chamber is already occupied by a suitable metal ion [i.e. sodium(I) or calcium(II) ion] the lanthanide(III) ion is forced into the N_3O_2 Schiff-base chamber with the consequent formation of the hetero-dinuclear complexes $[Ln^{III}Na^{I}(L_D)(Cl)_2(CH_3OH)]$ or $[Ln^{III}Ca^{II}(L_D)(Cl)_3]$.[16,17]

The alkali metal cations Na^+ and K^+ and the alkaline metal cations Mg^{2+} and Ca^{2+} are ubiquitous in living systems. The role of sodium and potassium stems essentially in their unequal distributions in the intra- and extracellular compartments and related transmembrane transport processes. The divalent magnesium and calcium cations possess a more marked binding ability towards macromolecules, polyelectrolytes and biological surfaces and thus their role is more differentiated. Under the form of aqua complexes, Mg^{2+} is concentrated in the cells, whereas Ca^{2+} is excluded. The distribution of alkaline and alkaline-earth ions in the inner- and outer-cell compartments is crucial to the viability of any organism. Thus, their qualitative and quantitative determination is essential, and NMR spectroscopy offers unique tools to reach this goal. The separation of the NMR signals from the two compartments is possible when their magnetic environments are made different by the presence of a paramagnetic agent, which selectively distributes in one compartment only. A successful separation of in- and out-signals is strongly dependent upon the interaction that the cation of interest is able to set up with the paramagnetic agent. In this context, compartmental ligands can be very useful. In fact, one may design systems containing a suitable lanthanide(III) ion endowed with a high magnetic moment and a non-*S* electronic configuration in one chamber, whereas the second chamber is available for coordination of an alkaline or alkaline-earth ion, possibly involved in an exchange process with the "bulk".

By this procedure quite interesting and powerful shift reagents (LIS reagents) have been proposed, in particular for Na^+.[21–23] The lanthanide(III) ions offer the unique possibility of progressively modifying their physical properties (and hence their ability to act as shift reagents), while maintaining the same chemical properties.

Most of the work was carried out on heterodinuclear lanthanide(III) complexes containing sodium(I).[24,25] More recently, some very encouraging results have been obtained with analogous complexes containing lithium(I), potassium(I) or calcium(II) ions instead of sodium(I).[26]

Unfortunately, these systems are sparingly soluble and not very stable in water. Consequently, in order to overcome these problems, we have functionalized the macrocyclic ligand by inserting pendant arms, which also bear additional donor groups. An additional, not negligible result of these functionalizations is that they further diversify the two coordination chambers, thus introducing more precise and selective recognition properties at the two chambers.

This paper deals with the design, synthesis and characterization of hetero-dinuclear sodium(I)-lanthanide(III) complexes with the ligands H_3L_A, H_2L_B,[27] H_3L_C, containing an O_2O_3 crown-ether-like chamber and an N_3XO_2 (X = O, N) Schiff-base chamber, where the pendant arm is represented by $-CH_2COOH$, $-CH_2C_5H_5N$, $-CH_2C_6H_4OH$, respectively, directly bound to the central aminic nitrogen as described in Scheme 1. The ligand H_2L_D and related complexes have been already studied and are here included for comparison purposes only.

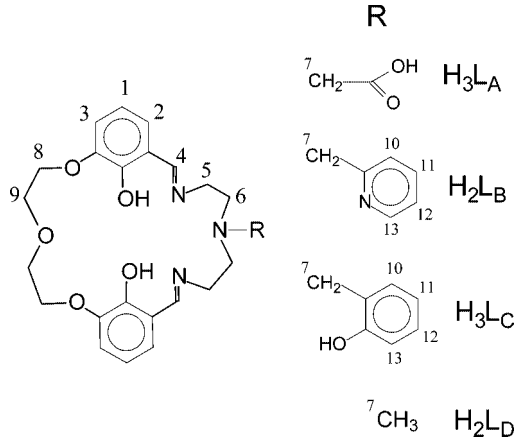

Scheme 1. The prepared ligands with the numbering scheme used to assign the peaks of the NMR spectra.

Results and Discussion

H_3L_A, H_2L_B, H_3L_C and/or Related Sodium(I) Derivatives

While the macrocyclic ligand H_3L_A was not obtained in acceptable quantities by condensation of the appropriate diformyl and polyamine precursors, the related trisodium derivative Na_3L_A was synthesised in a considerable amount by treating the disodium diformyl precursor Na_2L' with the functionalized polyamine *i*-DTMA·3 HCl in the presence of NaOH. The crude product can be purified by crystallization from *i*PrOH. Its IR spectrum shows a strong band at 1623 cm^{-1} ($\upsilon_{C=N}$) and two intense bands at 1594 cm^{-1} (υ_{asymm} COO) and at 1396 cm^{-1} (υ_{symm} COO); two additional strong bands at 1213 and 1096 cm^{-1} are due to the υ_{C-O} of the crown-ether groups. The ^1H NMR spectroscopic data

 © 2005 Wiley-VCH Verlag GmbH & Co. KGaA, Weinheim

in CD_3OD show a peak at δ = 8.41 ppm due to the formation of the CH=N group; the contemporary absence of the CH=O resonance at δ = 10 ppm proves that the condensation process is complete. As for the macrocycle Na_3L_A, the NMR spectroscopic data indicate that the Na^+ ion is not strongly coordinated to the etheric chamber and is bound only to phenolato groups. In fact, the molecules are very flexible in solution (fast exchange on the NMR timescale) and there is no evidence of geminal multiplets in the aliphatic region, due to the characteristic stereochemical rigidity of Na^+ when it is fully coordinated in the etheric site. The ESI-MS spectrum in MeOH shows a peak at *m*/*z* (%) = 473 (5) due to the free ligand $[H_4L_A]^+$, an intense peak at *m*/*z* (%) = 495 (100) due to the species $[NaH_2L_A]$ and two additional peaks at *m*/*z* (%) = 517 (20) $[Na_2HL_A]$ and *m*/*z* (%) = 538 (20) $[Na_3L_A]$.

Attempts to isolate the ligand H_2L_B or its sodium derivative Na_2L_B by self-condensation of the precursors, using different experimental conditions, failed. The ligand can only be obtained under template conditions, as mononuclear or dinuclear lanthanide(III) complexes as a result of the experimental conditions used, as reported in the subsequent paragraph.

The phenol-containing ligand H_3L_C was obtained as the sodium derivatives $[Na_2(HL_C)]$ or $[Na(H_2L_C)]$ by treating the appropriate precursors in the presence of NaOH in two different synthetic ways: $[Na_2(HL_C)]$ was prepared by condensation of Na_2L' and Moden·3HCl in methanol, whereas for $[Na(H_2L_C)]$, H_2L', Moden·3HCl and NaOH were dissolved in a minimum amount of methanol, but the condensation reaction was conducted in diethyl ether. Once more, the completion of the condensation reaction is proved by the presence of the infrared $\upsilon_{C=N}$ band at 1624 cm^{-1} for $[Na_2(HL_C)]$ and at 1639 cm^{-1} for $[Na(H_2L_C)]$, which indicates, for the latter, that the Na^+ is not bound to the iminic nitrogen and quite probably resides in the crown-ether site. The ESI-MS spectrum of $[Na(H_2L_C)]$ in MeOH shows the parent peak at *m*/*z* (%) = 542 (55) due to $[Na(H_3L_c)]^+$. The ^1H NMR spectrum in CD_3OD of both sodium derivatives, together with the bidimensional experiments COSY, NOESY and HMQC, allow us to correctly assign the observed proton and carbon peaks. The CH=N resonance at δ = 8.26 ppm proves that the condensation process has occurred, while 2D data demonstrate that the phenol pendant arm resonances at δ = 7.15 (10-H), 6.93 (12-H), 6.68 (11-H) and 6.30 (13-H) ppm are connected via the methylenic (7-H) resonance at δ = 3.81 ppm to the other methylenic groups of the Schiff base moiety at δ = 2.98 (6-H) and 3.88 (5-H) ppm and via the iminic resonance at δ = 8.26 (4-H) ppm to the phenolic protons.

Mononuclear or Homodinuclear Lanthanide(III) Complexes

Complexes with $[L_A]^{3-}$

Owing to the availability of Na_3L_A and the difficulty in obtaining a suitable amount of H_3L_A, the complexation reactions were carried out using the tris-sodium derivative. Na_3L_A reacts with the appropriate $LnCl_3{\cdot}nH_2O$ in methanol in a 1:1 molar ratio to yield, after a 2 h reflux, $[LnNa(NaL_A)(Cl)_2]{\cdot}nH_2O{\cdot}x$ NaCl (where NaL_A indicates the diphenolate macrocycle with a sodium acetate group and Ln = Y, Lu, Yb) and, after a 12 h reflux, $[Ln_2(L_A)(Cl)_3]{\cdot}nH_2O{\cdot}x$ NaCl (where Ln = Y, Lu, Yb, Nd) (see Scheme 2). Attempts to isolate the LnNa heterodinuclear complexes by template synthesis failed. Furthermore, attempts to crystallize homo- and hetero-dinuclear complexes under a variety of experimental procedures failed. However, careful SEM-EDS investigations prove an Ln/Cl = 1:2 ratio together with well-detectable NaCl grains for the heterodinuclear LnNa and an Ln/Cl = 2:3 ratio for the homodinuclear LnLn complexes.

The properties of the Ln-Na complexes will be discussed in detail in the appropriate paragraph.

In the homodinuclear lanthanide(III) complexes, the $\upsilon_{C=N}$ is found at 1624–1654 cm^{-1} and the stretchings of the etheric groups occur at 1230–1223 cm^{-1} and at 1094–1090 cm^{-1}. Surprisingly, the $\upsilon_{C=N}$ of the homodinuclear complexes lies at higher wavelength in relation to the heterodinuclear Ln-Na analogues, where the same bands lie at 1625–1637 cm^{-1}. The long refluxing time required for the preparation of the homodinuclear complexes resulted in the loss of the sodium ion from the complex and consequent formation of NaCl, as shown by SEM and elemental analyses.

The carboxylate group quite probably participates in the coordination to the lanthanide ion as a monodentate group. The $\upsilon_{asymm}(COO)$ is found at1601–1618 cm^{-1} whereas the $\upsilon_{symm}(COO)$ is at 1415–1459 and 1460–1500 cm^{-1}.

It may be suggested that, in the formation of the homodinuclear species, the first event to take place is the formation of the heterodinuclear LnNa complex with the lanthanide ion probably lying in the mean equatorial plane of the N_3O_2 donor set of the Schiff base, as already found for similar lanthanide complexes.[25] This is followed, as a consequence of the prolonged reflux and subsequent release of the Na^+ ion, by the coordination of a second lanthanide in the free O_3O_2 site, which is the favourite site of the lanthanide(III) ion, as already ascertained.[27] The macrocycle does not have the correct coordination shape to encapsulate both metal ions firmly into the mean equatorial plane. Consequently, the lanthanide ion coordinated to the Schiff-base site, owing to the steric hindrance caused by the incoming second lanthanide ion, is pushed away from the N_3O_2 mean plane toward the acetate group. This causes a coordination lowering of the iminic nitrogen to the central metal ion with the consequent shift of the $\upsilon_{C=N}$ toward higher wavelengths. The NMR spectroscopic data of $[Lu_2(L_A)(Cl)_3]{\cdot}0.3$ PrOH in $MeOD_4$ show that the compound is not stable in solution. The complexity of the aromatic and iminic region proves the presence of several species deriving from the demetalation reaction, with the formation of mononuclear complexes with different coordination sets. Another proof of this instability comes from the ESI-MS spectra of these complexes where no peak attributable to the homodinuclear specie was found.[28]

 © 2005 Wiley-VCH Verlag GmbH & Co. KGaA, Weinheim

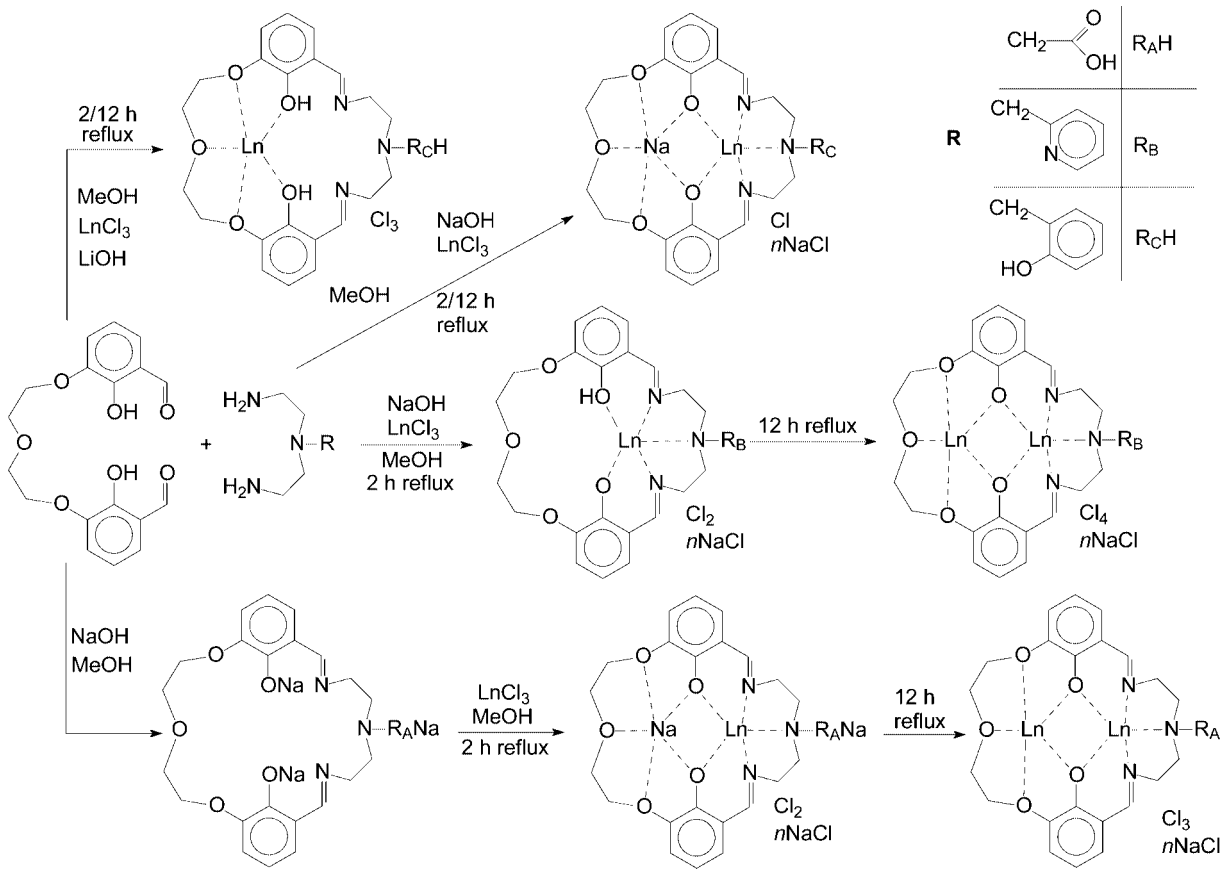

Scheme 2. Preparation of mononuclear and homo- or hetero-dinuclear complexes.

Complexes with $[L_B]^{2-}$

As H_2L_B or Na_2L_B are not available, the pyridine-containing macrocycle was prepared by a template synthesis in the presence of the desired lanthanide(III) chloride hydrate in alcoholic solution. It was found that when the diformyl and amine precursor are condensed in the presence of NaOH and $LnCl_3 \cdot n H_2O$ in methanol (molar ratio 1:1:3:1), and the reaction mixture is allowed to reflux for 1–2 h, the mononuclear complexes $[Ln(HL_B)(Cl)_2] \cdot n NaCl \cdot m H_2O$ are obtained (Ln = Y, Yb, Lu, Tm, Tb, La, Ce); on the contrary, when the reflux is continued for 12 h, the homodinuclear complexes $[Ln_2(L_B)Cl_4] \cdot n NaCl \cdot m H_2O$ are collected (Ln = Y, Lu, Tb, La; see Scheme 2). Again, careful SEM-EDS investigations prove an Ln/Cl = 1:1 ratio for both complexes together with well-detectable NaCl grains.

The IR spectra of these mononuclear and dinuclear complexes are comparable to those obtained for the similar complexes with Na_3L_A. In particular, the mononuclear complexes show a strong $\upsilon_{C=N}$ absorption at 1617–1655 cm^{-1}. This band is generally higher in the dinuclear analogue; it lies for instance at 1625 cm^{-1} in $[La(HL_B)(Cl)_2] \cdot 2.5 H_2O$ and at 1647 cm^{-1} in $[La_2(L_B)(Cl)_4] \cdot 3.9 H_2O$.

The close proximity of the two metal ions in the dinuclear complexes, and the consequent steric hindrance, push a lanthanide ion partially out of its N_4O_2 coordination plane, causing a wavelength increase of the $\upsilon_{C=N}$ stretching band. A similar trend is observed in the related ^1H NMR spectrum in [D4]MeOH: the peak at δ = 8.15 ppm due to the iminic groups of the mononuclear complexes is shifted to δ = 8.60 ppm in the homodinuclear analogue.

The NMR experiments in the diamagnetic La, Y and Lu complexes also show that the impurities present in the mononuclear complexes are mainly the homodinuclear analogues. The NMR spectra of these dinuclear species, in fact, match perfectly those of the impurities present in the mononuclear complexes. The main differences in these spectra are localized in the Schiff-base protons. This confirms the above assumption that the Schiff-base site is only partially involved in the coordination. The solution instability of the dinuclear species represents a severe limitation to an exhaustive description of the behaviour of these complexes in solution.

In the mononuclear complexes, no evidence of Na^+ coordinated in the crown-ether moiety was found, probably because it may be more easily released than in the complexes with Na_3L_A, facilitating the formation of mononuclear lanthanide complexes. The lability of Na^+ in the crown-ether moiety, also verified by ^{23}Na NMR spectroscopy, is quite important in the determination of interesting LIS properties as reported above.

A study of the ^1H, $^{13}C\{^1H\}$ and 2D COSY, NOESY, HMQC NMR spectra in [D4]MeOH allows a complete assignment and interpretation of the peaks occurring in the mononuclear $[Ln(HL_B)(Cl_2)]$ and dinuclear diamagnetic

 © 2005 Wiley-VCH Verlag GmbH & Co. KGaA, Weinheim

and paramagnetic $[Ln_2(L_B)(Cl)_4]$ complexes (see Exp. Sect.).

The study of the weak paramagnetic complex $[Ce(HL_B)(Cl)_2]\cdot 7H_2O$ is particularly indicative of the lanthanide coordination. On the basis of 2D NOESY, acquired at several mixing times and HMQC experiments, it was possible to fully assign 13 resonances in the ^1H NMR spectrum. The very low-field 21.30 ppm shift of protons 4-H and the severe shift (δ = 8.01 and –11.46 ppm) and broadening of methylenic protons of the Schiff-base moiety strongly support the thesis of lanthanide coordination in the Schiff-base site, also confirmed by the usual position of 8-H and 9-H resonances (δ = 3.66 and 4.77 ppm) of the O_3O_2 site. Furthermore, the downfield shift of pyridinic protons 13-H, 12-H, 11-H and 10-H (δ = 11.50, 8.62, 9.27, and 9.10 ppm) suggests that the pendant arm is involved in such coordination.

ESI-MS spectra of these samples show the presence of signals related to the sodium or lanthanide mononuclear complexes; this proves the real occurrence of the mononuclear lanthanide(III) complexes. Moreover, in a few cases the mononuclear lanthanide complexes encapsulate a methanol or chloride and/or water molecule.[28] As for the L_A^{3-} ligand, no evidence of homodinuclear species was found.

Complexes with $[L_C]^{3-}$

The mononuclear complexes $[Ln(H_3L_C)(Cl)_3]$ (where Ln = Lu, Eu, Tb, Y, La) were synthesised by [1+1] condensation of the triamine precursor (Moden·3HCl), neutralized with LiOH, with the diformyl precursor (H_2L') in the presence of $LnCl_3\cdot n H_2O$. SEM-EDS data confirm the Ln/Cl = 1: 3 ratio (see Scheme 2). The key of this synthesis is the use of LiOH as a neutralizing agent of the aminic precursor instead of NaOH; Li^+ is not a suitable competitor of the lanthanide(III) ion for the hard site and hence it allows the coordination of the lanthanide ion to the crown-ether site. On the contrary, Na^+ strongly competes with the lanthanide(III) ion and makes the coordination of the 4f ion very problematic or impossible.

Long refluxing times do not yield homodinuclear species, as for the previous ligands H_3L_A or H_2L_B. The complexes recovered after a 12 h reflux always produce the mononuclear or the heterodinuclear Ln-Na complexes when LiOH or NaOH, respectively, are used.

Quite interestingly, when a higher LiOH/ligand ratio is used, the coordination site of the lanthanide ion can be chosen. More precisely, under basic conditions (LiOH/Moden·3HCl/H_2L'/$LnCl_3$ = 6:1:1:1), complexes have been invariantly obtained where the NMR (iminic proton at higher field shifts and appearance of geminal peaks in the Schiff base methylenic region) and IR ($\upsilon_{C=N}$ at 1620–1625 cm^{-1}) spectra clearly indicate that the lanthanide ion resides in the Schiff-base site. Unfortunately, the compounds prepared always contain a low amount of mononuclear species with the lanthanide coordinated in the crown-ether moiety.

Less basic conditions (LiOH/Moden·3HCl/H_2L'/$LnCl_3$ = 3:1:1:1) always lead to pure mononuclear complexes in which the crown ether site is occupied by the lanthanide(III) ion. IR data corroborate the coordination in the O_3O_2 site: in fact, the $\upsilon_{C=N}$ IR band in these complexes lies between 1647 and 1653 cm^{-1}, which is higher than the analogue LnNa derivatives ($\upsilon_{C=N}$ at 1619–1626 cm^{-1}), where the lanthanide was found to reside in the Schiff-base site.

This hypothesis is in agreement with the study of the ^1H NMR spectrum of the paramagnetic $[Eu(H_3L_C)(Cl)_3]$ in $[D_4]$MeOH. In fact, the coordination of the Eu^{III} ion in the crown ether moiety shifts and widens the peak at δ = 11.83 ppm related to aliphatic protons (8-H) and (9-H). On the other hand, protons of the pendant arm do not seem to be involved in the coordination of europium since they do not undergo any change in bandwidth or chemical shift [they are found at δ = 7.42 (10-H), 7.06 (12-H), 6.67 (11-H, 13-H) ppm; (see part a of Figure 1).

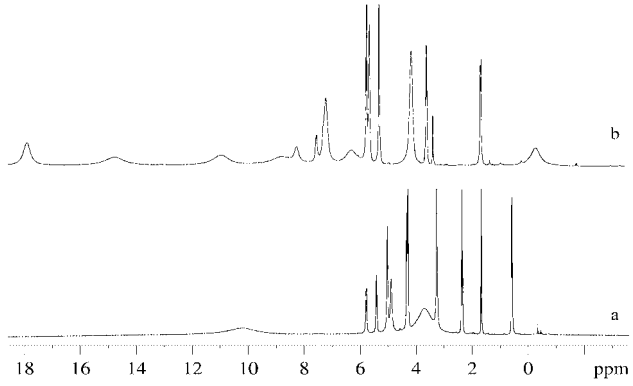

Figure 1. ^1H NMR spectra of $[Eu(H_3L_C)(Cl)_3]$ in CD_3OD at 293 K (a) and 253 K (b).

The europium(III) coordination was further clarified by the NMR spectrum acquired at 253 K. The broad peak centered at δ = 11.83 ppm generated four peaks at 17.75, 14.53, 10.84 and –0.34 ppm assigned, on the basis of 2D NOESY acquired at several mixing times and HMQC experiments, to the geminal axial and equatorial 8-H and 9-H methylenic protons of the O_3O_2 site. At that temperature, the other broad resonance at δ = 5.33 ppm, assigned to the 5-H and 6-H methylenic protons of the N_3O_3 site, is shifted to 6.22 and 4.08 ppm but still unresolved (see part b of Figure 1).

Heterodinuclear Lanthanide(III)–Sodium(I) Derivatives

Complexes with $[L_A]^{2-}$

As reported above, the reaction of Na_3L_A with the appropriate $LnCl_3\cdot n H_2O$ in methanol and in a 1:1 molar ratio, under a 2 h reflux, yields $[LnNa(NaL_A)(Cl)_2]\cdot n H_2O$, where it is likely that one sodium ion resides in the crown-ether chamber and the other is linked to the carboxylate group (see Scheme 2). These complexes always contain variable amounts of NaCl, clearly detected as grains by SEM-EDS microscopy. These measurements also prove that the complexes possess the right Na/Ln/Cl = 2:1:2 metal ratio (excluding NaCl crystals present in the sample).

 © 2005 Wiley-VCH Verlag GmbH & Co. KGaA, Weinheim

The IR spectra of the LnNa complexes show a strong $\upsilon_{C=N}$ absorption at 1631–1619 cm^{-1}, supporting a complexation of the lanthanide(III) ion inside the Schiff-base site. The broadening of this band also suggests that the $\upsilon_{symm}(COO)$ occurs at these wavenumbers. Furthermore, strong bands at 1221–1217 cm^{-1} and at 1093–1090 cm^{-1}, due to the stretching of the crown-ether C–O groups, have been observed, together with $\upsilon_{symm}(COO)$ absorption at 1410–1417 cm^{-1}.

NMR 2D data in CD_3OD of the diamagnetic LuNa complex resemble those obtained for the Na_3L_A precursor, allowing a complete assignment and interpretation of the peaks (see Exp. Sect.). Furthermore, the NMR spectroscopic data of the EuNa complex give a good indication of the site occupancy of the metal ions. In particular, the remarkable upfield shift of the iminic proton (δ = 28.28 ppm) and the presence of geminal methylenic protons between δ = –6.96 and –20.12 ppm indicate that the europium ion is coordinated to the Schiff-base site. Furthermore, geminal methylenic protons in the range δ = 2.33 to –0.36 ppm suggest that the etheric region of the macrocycle is rigidly coordinated to the sodium(I) ion. The peak at δ = 28.99 ppm of the remaining methylenic protons of the acetate pendant arm is very interesting and the considerable shift indicates that the acetate group is probably involved in the coordination of the paramagnetic ion. Moreover, the absence of methylenic geminal protons in the diamagnetic lutetium and lanthanum complexes suggests that the coordination proposed for the europium ion could be unrealistic for other LnNa complexes. The parent peaks at 644 and 666 *m*/*z* in the ESI-MS spectra of the europium and lutetium complexes, respectively, confirm the occurrence of a heterodinuclear $[(LnNaL_A)]^+$ species.

Surprisingly, the ^{23}Na NMR spectra in methanol of the paramagnetic complexes $[LnNa(Na_xL_A)(Cl)_{1+x}]$ (where Ln = Yb, Tm, Tb; x = 0, 1) do not show any ^{23}Na shift, thus proving that no interaction between the two metal ions occurs. The reason for this failure is not easily explainable. Certainly it is due to a wrong Ln···Na alignment. It could also be due to the fact that the coordination observed in the NMR spectroscopic data of the europium complex is not maintained in other complexes and the acetate group is competing with the O_3O_2 site in coordinating the sodium ion, thus determining an incorrect stereochemistry for obtaining a relevant ^{23}Na shift. Alternatively, even if the lanthanide(III) ion were in the Schiff-base site, its displacement from the equatorial plane toward the carboxylate group would give rise to an incorrect alignment.

Complexes with $[L_B]^{2-}$

Heterodinuclear Ln-Na complexes were not obtained with L_B^{2-}, but SEM-EDS measurements clearly prove the presence of NaCl in $[Yb(HL_B)(Cl)_2]\cdot 7\,NaCl\cdot 0.1\,H_2O\cdot 1.6\,EtOH$ and $[Tm(HL_B)(Cl)_2]\cdot 7.6\,NaCl\cdot EtOH$. As reported above, we have proved, by 2D NMR measurements on these paramagnetic complexes, that the lanthanide(III) ion, probably owing to the presence of a pyridinic pendant arm, prefers the Schiff-base site rather than the etheric one. Consequently, in methanolic solution, the sodium ion related to NaCl is partially coordinated to the Ln complex and this coordination causes a high isotropic ^{23}Na shift (δ = 330 ppm for the Tm complex at –20 °C). Furthermore, as expected, the ^{23}Na chemical shift linearly decreases with the increasing temperature. This behaviour is similar to that observed in the $[LnNa(L_D)(Cl)_2(MeOH)]$ complexes described in a previous paper,[25] where X-ray structural determinations show that the lanthanide(III) ion resides in the N_3O_2 Schiff-base chamber and the sodium(I) ion is in the crown-ether-like chamber. Thus we can reasonably suggest that heterodinuclear complexes are formed and that a site occupancy similar to that ascertained for $[LnNa(L_D)(Cl)_2(MeOH)]$ occurs, taking into account that the similar positional isomeric complexes with H_2L_D, where the lanthanide(III) ion resides in the O_3O_2 chamber and the sodium(I) ion in the crown-ether site, show a negligible ^{23}Na chemical shift.

The formation of an LnNa hetero-dinuclear coordination is also proved by the ESI-MS spectra in methanol of the complexes. The presence of peaks at 331.4 and 349.8 *m*/*z* (where z = 2) of the La and Yb complexes, respectively, is convincing evidence of the formation of $[LnNa(L_B)]^{2+}$ species.

The lability of Na^+, mentioned above, is an interesting and useful feature in order to obtain powerful molecular shift devices as they need a quick complexation–decomplexation process of the species to be characterized.

Complexes with $[L_C]^{3-}$

The heterodinuclear complexes $[LnNa(L_C)(Cl)]\cdot x\,NaCl$ (where Ln = Y, Yb, Lu, Tm, Tb, Dy, Eu, Er, La, Ce) were synthesised by condensation of the triamine precursor (Moden·3 HCl), with the diformyl precursor (H_2L') in the presence of NaOH and the appropriate $LnCl_3\cdot n\,H_2O$ in a 1:1:5:1 ratio (see Scheme 2) in methanolic solution.

The IR spectra of the LnNa complexes show a strong $\upsilon_{C=N}$ absorption at 1626–1619 cm^{-1}, supporting a complexation of the lanthanide(III) ion inside the Schiff-base site. These complexes always contain variable amounts of NaCl, detected as grains by SEM-EDS electron microscopy. The ESI-MS spectra in MeOH for each complex clearly show the parent peak due to the appropriate $[LnNaL_C]^+$ molecule, bearing in mind that additional NaCl or solvent molecules present in the sample are not directly involved in the coordination. In agreement with the related systems containing H_3L_A or H_2L_D and with the literature,[25] the presence of Na^+, which preferentially fills the O_2O_3 site, forces the lanthanide(III) ion into the Schiff-base moiety; this coordination is strengthened by the further coordination of the phenolic group, as confirmed by X-ray diffractometry structural studies in the solid state and in solution by NMR spectroscopy.

The complexes are very soluble in methanol and sparingly soluble in water. Consequently, NMR spectra were carried out in CD_3OD. Moreover, the complexes are soluble and stable for a long period of time in a CD_3OD/D_2O (1:1)

 © 2005 Wiley-VCH Verlag GmbH & Co. KGaA, Weinheim

solution; the results in this solution completely parallel those obtained in CD_3OD.

In order to clarify the coordination in solution of the lanthanide ion, ^1H and ^{13}C NMR bidimensional studies were carried out on the paramagnetic complex [EuNa(L_C)(Cl)]·6.5 NaCl in CD_3OD. On the basis of COSY, HMQC and several NOESY spectra with different mixing times and starting from the two doublets at δ = 0.52 ppm (d) and 1.98 ppm (d) (with identical T_1 = 450 ms), assigned respectively to protons 2-H and 3-H, we find the triplet related to proton 1-H at δ = 4.20 ppm (m), proton 4-H at δ = –29.90 ppm (s) (dipolar correlation with 2-H; see Figure 2, line a) and geminal proton 8e-H at δ = 2.63 ppm (t) [scalar coupled with 8a-H at δ = 4.42 ppm (m)] (dipolar correlation with 3-H). Geminal protons 9e-H at 3.95 (m) and 9a-H at δ = 5.67 ppm (m) are then assigned by scalar correlation with protons 8-H. Again, 2D NOESY spectra reveal the aliphatic geminal protons 5e-H, at δ = –9.57 ppm (s) (dipolar coupling with 4-H; see Figure 2, line b) and 5a-H, at δ = 4.22 ppm (m), and 6a-H, at δ = –1.00 ppm (s), and 6e-H, at δ = 19.46 ppm [(s); see Figure 2, line e]. Then proton 7-H lies at δ = –12.87 ppm [(s) dipolar correlation with 6a-H; see Figure 2, line c], which correlates with proton 10-H at δ = 4.20 ppm [(m); see Figure 2, line d]. Protons 11-H, 12-H and 13-H are found at δ = 5.67 (m), 5.31 (t) and 11.37 ppm (d), respectively.

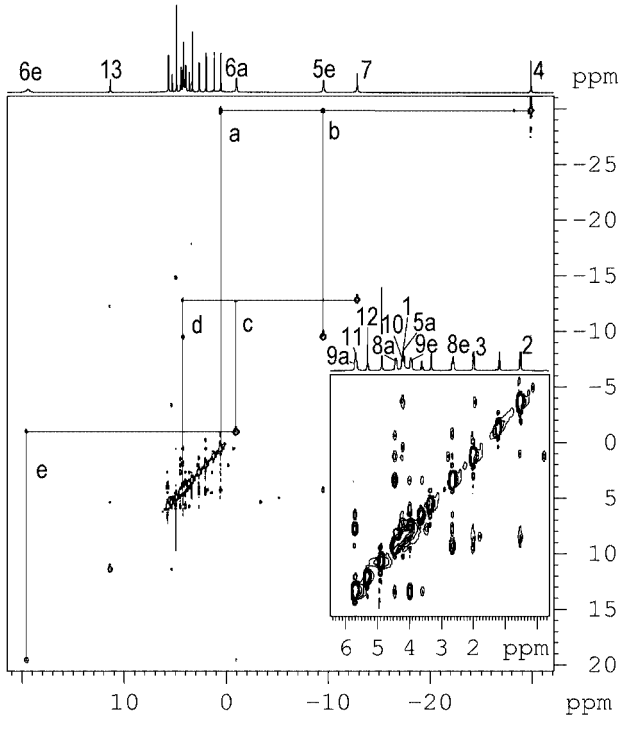

Figure 2. 2D ^1H NOESY NMR spectra of [EuNa(L_C)(Cl)] in CD_3OD at 293 K. Main window: mixing time = 60 ms; small window: mixing time = 220 ms.

NMR spectroscopy of paramagnetic Eu complexes is a powerful tool for a satisfactory understanding of the site occupancy of the lanthanide(III) ions. In contrast to [Eu(H_3L_C)($Cl)_3$], where it was clearly demonstrated that the europium ion occupies the O_3O_2 site, in [EuNa(L_C)(Cl)] the europium ion, due to the large shift of 5-H, 6-H (from δ = –9.57 to 19.46 ppm) and 4-H (δ = –29.90 ppm) resonances, lies in the N_3O_3 site. Furthermore, the pendant arm, owing to the large shift of the 10-H, 11-H, 12-H and 13-H resonances (from δ = 4.20 to 11.37 ppm), quite different from the diamagnetic one, is clearly coordinated to the europium(III) ion. Finally, the occurrence of a geminal resonance for each methylenic group proves that the complex is very rigid in solution and that both coordination sites are firmly occupied by a metal ion.

^{23}Na NMR spectra of the [LnNa(L_C)(Cl)] complexes (where Ln = Yb, Tm, Tb, Dy) show that complexes with L_C^{3-} have the same behaviour as those with L_B^{2-}. The presence of a broad resonance with a large shift from the free-ion peak arises from the coordination of Na^+ in the O_3O_2 site of the complexes, resulting in a slow exchange at room temperature on the NMR timescale.

The slow exchange is confirmed by the peak at δ = 0 ppm corresponding to the free ion, which originates from the presence of NaCl in the sample. The observed isotropic shift is very large as far as the Tm, Dy and Tb complexes are concerned, whereas it is smaller for the Yb complex; numerical values of these shifts are: [TmNa(L_C)(Cl)] +270 ppm (room temp.), +360 ppm (–20 °C); [DyNa(L_C)(Cl)] –158 ppm (room temp.), –200 ppm (–20 °C); [TbNa(L_C)(Cl)] –258 ppm (room temp.), –352 ppm (–20 °C); [YbNa(L_C)(Cl)] +50 ppm (room temp.), +61 ppm (–20 °C; see Figure 3).

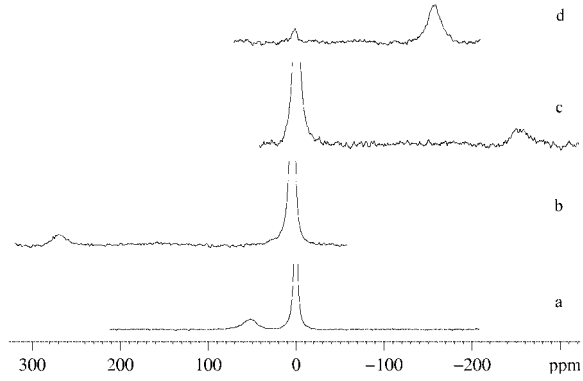

Figure 3. ^{23}Na NMR spectra at 293 K of [YbNa(L_C)(Cl)] (a), [TmNa(L_C)(Cl)] (b), [TbNa(L_C)(Cl)] (c), [DyNa(L_C)(Cl)] (d).

The ^{23}Na NMR spectroscopic data in CD_3OD/D_2O (1:1) containing NaCl are comparable with those in CD_3OD reported above; the most remarkable difference is a considerable broadening of the signal of the bound sodium ion due to the high Na_{bound}/Na_{free} exchange.

Crystal Structure

Crystals of [DyNa(L_C)(PrOH)(Cl)] were obtained from slow evaporation of 1-propanol solutions. The ORTEP representation of the crystal-structure complex and coordination geometries are shown in Figure 4.

 © 2005 Wiley-VCH Verlag GmbH & Co. KGaA, Weinheim

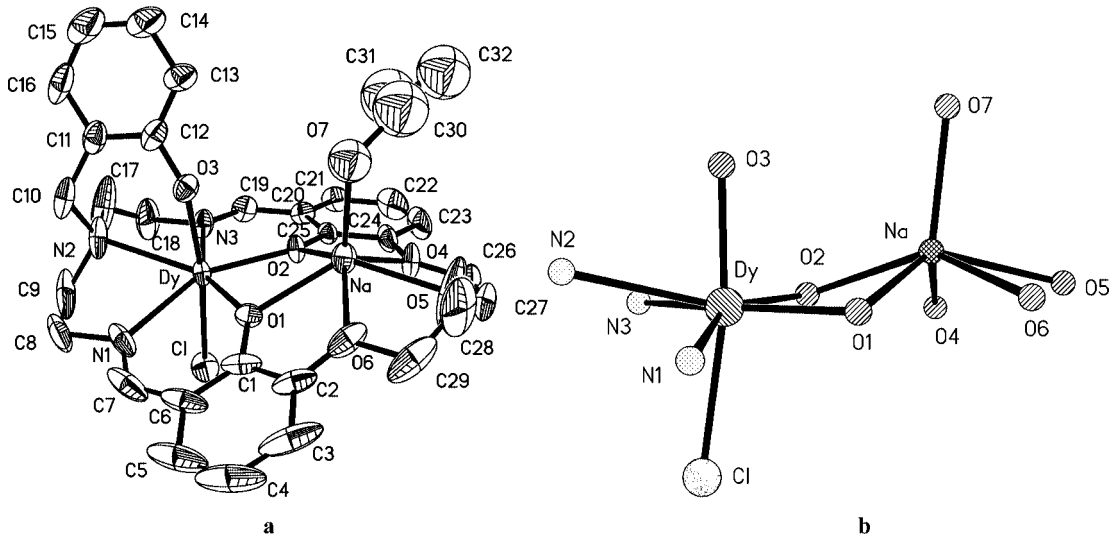

Figure 4. ORTEP representation of the (a) crystal structure of the complex [DyNa(L_C)(PrOH)(Cl)] and (b) coordination geometries.

The sodium ion is located in the O_2O_3 crown-like site of the macrocyclic ligand and reaches the coordination number of six by bonding to five oxygen atoms from the ligand and one oxygen atom from the 1-propanol molecule. The oxygen atoms O(4), O(5) and O(6), are etheric, whereas O(1) and O(2) are phenolic. The coordination geometry around the sodium ion can be described as a distorted pentagonal pyramid with the 1-propanol oxygen atom as apex; the sodium atom is displaced by 0.765 Å from the basal mean plane. The seven-coordination of the dysprosium ion is achieved by three nitrogen atoms, two phenolic oxygens [O(1) and O(2)] that act as a bridge, the pendant phenolic oxygen of the ligand and one chlorine ion. The coordination polyhedron around the dysprosium ion is better depicted as a distorted pentagonal bipyramid with the chlorine ion and the phenolic pendant oxygen, O(3), as apices. The total four positive charges of the two metal ions are neutralized by the three, negatively charged phenyl oxygens and by the chlorine ion.

As for other similar complexes,[25] the molecule adopts a butterfly shape with the two benzene rings as wings that form a dihedral angle of 34.6°. The pendant system, beginning from N(2) and coordinated to Dy by the O(3) atom is placed on the convex part of the molecule and influences the conformation of the torsion angles involving the nitrogen atoms of the Schiff-base chamber.

The mean plane formed by the five, donor atoms [O(1), O(2), N(1), N(2), N(3)] bonded to the dysprosium atom includes this ion (displacement –0.0083 Å) while the displacements of the five atoms range between +0.416 and –0.456 Å. The mean plane formed by the five oxygen atoms bonded to the sodium ion [O(1), O(2), O(4), O(5), O(6)] is more planar; the displacements vary between +0.197 and –0.169 Å. The sodium ion is –0.7651 Å far from the plane.

The Dy–O distances are similar in the atoms involved in the bridge [O(1) 2.236(5) Å and O(2) 2.226(4) Å], while the Dy–O(3) bond is shorter, 2.185(6) Å [the O(3) atom is negatively charged and non-bridging]. Minor differences are present in the Dy–N distances; in fact the Dy–N(iminic) bonds are similar [Dy–N(1) 2.474(8) Å and Dy–N(3) 2.494(7) Å], while the Dy–N(2) (aminic) is 2.556(7) Å.

The Na–O(etheric) distances vary between 2.376(8) and 2.410(7) Å.

Owing to the interesting LIS data found for these complexes, structural data of the [DyNa(L_C)(PrOH)(Cl] complex have been compared with the similar [LnNa(L_D)-($Cl)_2$(MeOH)] (where Ln = Nd, Eu, Gd, Yb) complexes[25] that present a comparable ^{23}Na NMR shift. All the complexes have shown that the sodium environment is always preserved with very similar coordination distances and angles, while some differences, as foreseen, are detected about the bond lengths around the lanthanide ions. These, in fact, follow the constant decreasing of the ionic radii along the lanthanide series with a decrease of the coordination bond lengths in going from Nd to Yb complexes. In the [LnNa(L_D)($Cl)_2$(MeOH)] complexes, the conformation of the torsion angles N(1)–C(8)–C(9)–N(2) and N(2)–C(17)–C(18)–N(3) are g^- and g^+, respectively, while they are g^- (–47.6°) and g^- (–42.6°) in [DyNa(L_C)(PrOH)(Cl]. Other differences with the structure described here are present in the bond angles of coordinated atoms and are mainly due to the geometrical constrains of the pendant phenolate group. The contact distance Ln···Na of L_D complexes has a mean value 3.55 Å compared to the 3.496(3) Å of Dy···Na found in the [DyNa(L_C)(PrOH)(Cl] crystal.

Conclusion

A series of heterodinuclear sodium-lanthanide complexes, together with the related mononuclear and/or homodinuclear lanthanide complexes with three different [1+1] asymmetric macrocyclic ligands, containing two adjacent cavities, an O_3O_2 crown-ether site and an N_3XO_2 Schiff-base site, where X is N or O of a pendant arm (-CH_2COOH for H_3L_A, -$CH_2C_5H_4$N for H_2L_B and -$CH_2C_6H_4$OH for

 © 2005 Wiley-VCH Verlag GmbH & Co. KGaA, Weinheim

H_3L_C) bonded to the aminic nitrogen, were synthesised by different routes, that is, self-condensation of the precursors followed by the reaction of the cyclic Schiff base with the appropriate lanthanide(III) ion or template synthesis [the lanthanide(III) ion used as templating agent]; both methods lead to the same products.

Remarkably, the use of NaOH as a base also introduces an Na^+ ion into the crown-ether cavity for both L_A^{3-} and L_C^{3-}, but not for L_B^{2-} (which generates only mononuclear and homodinuclear lanthanide complexes). Mononuclear lanthanide(III) complexes with L_C^{3-} were synthesised only when NaOH was substituted by LiOH, as the Li^+ ion is not as tightly coordinated as Na^+ to the crown-ether moiety, thus it forces the lanthanide(III) ion to reside in the Schiff-base site, as confirmed by the X-ray structure of [DyNa-$(L_C)(Cl)(CH_3OH)$].

The refluxing time appears to be very important in determining the reaction pathway for complexes with L_A^{3-} and L_B^{2}. Thus, when the appropriate reactants were refluxed for 2 h, the heterodinuclear LnNa (for L_A^{3-}) or the mononuclear Ln (for L_B^{2-}) complexes were obtained, whereas a prolonged reflux (12 h) led to the homodinuclear Ln_2 complexes of both ligands. Neither heterodinuclear LnNa complexes with L_B^{2-}, nor mononuclear Ln complexes with L_A^{3-} were obtained. Under similar conditions, no homo-dinuclear lanthanide complexes were obtained with L_C; the hetero dinuclear NaLn or the mononuclear Ln complexes were invariantly obtained.

In all complexes, the presence of the lanthanide ion in the Schiff-base site is favoured only when the ligand is fully deprotonated. The formation of strong hydrogen bonds between phenolic hydrogen and iminic nitrogen or imine protonation probably prevent the coordination of the lanthanide in the N_3O_2 site.

There is not a clear explanation of the impossibility of obtaining the heterodinuclear LnNa complexes with L_B^{2-}. It must be stressed that this ligand, under particular conditions (i.e. a prolonged reflux in methanol), forms exclusively the dinuclear lanthanide(III) complexes. The partial occupancy of the crown-ether site by a lanthanide(III) ion may prevent a stable sodium encapsulation in the crown-ether moiety. The presence of a basic pendant arm may favour partial deprotonation of the phenolic oxygen and hence an easier formation of homodinuclear species, instead of heterodinuclear LnNa analogues. In any case, the coordination of sodium to the crown-ether moiety, whether it occurs, appears weak.

The introduction of a pendant arm containing a coordinating group in the macrocyclic system improves the solubility in relation to the complexes $[LnNa(L_D)(Cl)_2(MeOH)]$. Complexes with L_C^{3-} show the best solubility in alcohol, but the heterodinuclear LnNa complexes are still insoluble in water (whereas mononuclear Ln complexes are slightly water-soluble). The solubility in H_2O/MeOH (1:1), however, is very good and the complexes are stable for many days. The stability of the LnNa complexes with the phenol pendant arm seems to increase significantly as well, though this is not a general trend with pendant arms.

The behaviour of $[LnNa(L_C)(Cl)]$ in solution was carefully studied especially by ^1H and ^{13}C NMR spectra. It was pointed out that in $[LnNa(L_C)(Cl)]$, the phenol pendant arm is tightly coordinated to the lanthanide ion. Evidence of a rigid system also comes from the quite simple ^1H NMR spectral pattern which denotes the presence of a symmetry plane perpendicular to the molecule and passing through the Ln-Na axis. These data show that the behaviour of these complexes in solution parallels that observed in the solid state.

While the ^{23}Na NMR spectra of the paramagnetic $[LnNa(L_A)(Cl)]$ (where Ln = Yb, Tm, Tb) do not show any ^{23}Na shift, probably for an incorrect alignment of Ln^{3+} and Na, as already described, those of $[Ln(HL_B)(Cl)_2]\cdot n$NaCl (Ln = Yb, Tm) prove that the NaCl present in these complexes is partially coordinated to the crown-ether moiety, thereby causing a high isotropic ^{23}Na shift.

We have already observed that the mononuclear complexes $[Ln(HL_D)(Cl)_2(MeOH)]$,[25] where the lanthanide(III) resides in the O_3O_2 crown-ether chamber, do not strongly coordinate Na^+ in the N_3O_2 Schiff-base site (or in a correct way). In fact, only a negligible ^{23}Na shift was detected in these complexes. Thus, the mononuclear complexes with L_B^{2-}, on prolonged reflux, may prefer to coordinate a second lanthanide instead of an Na^+ ion. Moreover, Na^+ is not able to transmetallate the Ln^{3+} from the crown-ether moiety. Nevertheless, the mononuclear complexes, once formed, when reacted with Na^+ in $[D_4]$MeOH, give rise to a significant ^{23}Na shift, which proves that a correct geometry is reached at least in solution with the Na^+ ion in the crown-ether moiety.

The coordination lability of Na^+, together with its relevant ^{23}Na shift, testifies that it could be an excellent molecular device for sodium detection in solution.

In the paramagnetic complexes $[LnNa(L_C)(Cl)]$ (where Ln = Yb, Tm, Tb, Dy), the ^{23}Na NMR resonance of the bound cation is markedly shifted from that of the free ion, and the shift itself is greater than that observed for L_B^{2-} and for L_D^{2-} complexes.

The formation of solution-stable LaNa complexes with H_3L_C testifies also that the $N–CH_2–C_6H_4O^-$ arm, which forms a six-membered ring with the lanthanide(III) ion, is quite suitable to suppress molecular movements of the metal ions, assuring a correct stereochemistry that favours the interaction between the Ln^{3+} ion and Na^+ that makes the paramagnetic complexes $[LnNa(L_C)(Cl)]$ the best ^{23}Na shift reagents prepared so far.

The ^{23}Na paramagnetic shift depends on the geometrical position of the sodium ion in relation to the magnetic symmetry axis of the complex and on the Ln–Na distance. Under the simplified hypothesis that the lanthanide complex is characterized by an effective axial symmetry (often a good approximation),[29] the magnitude of the shift is proportional to a term of the type $D_1(3\cos^2\theta - 1)/r^3$, where θ is the angle between the Ln–Na vector and the principal magnetic axis of the complex and r is the Ln–Na distance. In the heterodinuclear $[LnNa(L_C)(Cl)]$ complexes, the distance r is only 3.496(3) Å, shorter than that found in similar

 © 2005 Wiley-VCH Verlag GmbH & Co. KGaA, Weinheim

$[LnNa(L_D)(Cl)_2(MeOH)]$ (Ln = Nd, Eu, Gd, Yb) complexes[25] (ca. 3.55 Å) and much shorter than that estimated for the corresponding polyaminopolycarboxylic (ca. 3.9 Å) and polyoxa tetraaza macrocyclic complexes (5.3 Å).[30] Furthermore, the negative sign of the hyperfine ^{23}Na shifts for the Tb and Dy complexes ($D_1 > 0$) and the positive sign of the Tm complex ($D_1 < 0$) suggests that the angle θ is close to 90° and thus that the principal magnetic susceptibility axis of the complex is orthogonal to the molecular plane. For the Yb complex ($D_1 > 0$) the sign of the ^{23}Na shift is positive (in contrast with the negative sign found in $[YbNa(L_D)(Cl)_2(MeOH)]$). In this case the principal magnetic susceptibility axis is parallel to the molecular plane (probably due to the fact that Yb has the smallest ionic radius) and this is supported by the ^1H NMR spectrum of the Yb complex (for which the dipolar contribution to the paramagnetic shift has the largest contribution), where the resonances have positive chemical shift values.

In conclusion, the introduction of suitable, coordinating pendant arms at the periphery of the coordination moiety of the [1+1] asymmetric compartmental macrocycles containing one N_3O_2 and one O_3O_2 adjacent coordination sites, increases the solubility and, for the complexes with H_2L_B and H_3L_C, the ^{23}Na shift. Unfortunately, the three pendant arms do not confer enough solubility to the LnNa complexes to allow NMR spectroscopy experiments in water. The quite stimulating, preliminary results obtained in CD_3OD/H_2O (1:1), however, force us to shift our efforts toward a deeper investigation of the complexes with H_3L_C in water-containing solvents.

Experimental Section

Materials: The solvents, the inorganic and organic compounds and the lanthanide chloride hydrates were commercial products, supplied by Aldrich, Riedel-de Haën, Carlo–Erba or Fluka. They were used as received, without further purification. Dimethyl sulfoxide, used in the preparation of the diformyl precursors, was purified according to the literature.[31]

Physico-Chemical Measurements: Elemental analyses were carried out using a Fison 1108 analyzer. IR spectra were recorded as KBr pellets on a Mattson FTIR spectrometer. All NMR spectra (^1H, ^{13}C, ^{23}Na) were recorded on a Bruker AMX300 spectrometer equipped with direct and inverse broad-band multinuclear probes and variable-temperature unit, with lanthanide(III) complexes dissolved in CD_3OD, used also as internal reference. The T1 longitudinal relaxation times and the mixing times of NOESY experiments of paramagnetic europium and cerium complexes were measured using the standard inversion recovery pulse sequence. All ESI-MS mass spectrometric measurements were performed using an LCQ mass spectrometry (Finnigam) and methanolic solutions of the samples (10^{-5} M). The morphology, homogeneity and the Ln/Cl or Ln/Na/Cl ratio of the complexes were investigated using a Philips XL40 model scanning electron microscope equipped with an EDAXDXPRIME energy dispersive spectrometer.

Diformyl and Amine Precursors: The diformyl precursor 3,3′-(3-oxapentane-1,5-diyldioxy)bis(2-hydroxybenzaldheyde) (H_2L') and its disodium derivative Na_2L' were prepared according to the literature.[13,17] The diformyl precursor was purified by chromatography on silica gel using $CHCl_3$ as eluent. The amine precursors: 4-diethylenetriaminoacetic acid·3 HCl (i-DTMA·3 HCl), 1,7-bis-(aminoethyl)-2-(aminomethyl)pyridine·3 HCl (DETPY·3 HCl),*N*,*N*-bis(2-aminoethyl)-2-hydroxybenzylamine·3 HCl (Moden·3HCl) were prepared according to the literature.[32] Elemental analysis, ESI-MS, IR and NMR spectroscopic data agree with the proposed formulation.

Macrocyclic Ligands

Preparation of H_3L_A: *i*-DTMA·3 HCl (0.10×10^{-2} mol) and NaOH (0.30×10^{-2} mol) were added to a methanolic solution of the diformyl precursor H_2L' (0.10×10^{-2} mol) and the solution was refluxed for 3 h. The solvent was then evaporated to dryness and the resulting solid was dissolved in CH_2Cl_2. The solution was clarified by filtration and the solvents evaporated to dryness. The yellow solid obtained was collected by filtration, dried in vacuo and recrystallised from a methanol/diethyl ether solution. Owing to the difficult purification, the ligand was obtained in very low yield (<5%). IR $\tilde{\nu}$ = 1646 (C=N) cm^{-1}. $C_{25}H_{36}N_3O_{9.5}$: calcd. C 56.60, H 6.84, N 7.92; found C 56.82, H 6.97, N 8.34. ^1H NMR (CD_3OD): δ = 8.42 (s, 2 H, 4-H), 6.96 (d, 2 H,3-H), 6.91 (d, 2 H, 2-H), 6.56 (t, 2 H, 1-H), 4.21 (m, 4 H, 8-H), 4.00 (m, 4 H, 9-H), 3.85 (m, 4 H, 5-H), 3.56 (s, 2 H, 6-H), 3.35 (m, 4 H, 7-H) ppm.

Preparation of Na_3L_A: *i*-DTMA·3 HCl (0.10×10^{-2} mol) was dissolved in methanol (30 mL) at a pH adjusted to ≈ 7 by NaOH. Then it was added to a methanolic solution of Na_2L' (0.30×10^{-2} mol) and the resulting solution was refluxed for 2 h. The solvent was evaporated to dryness and the yellow solid obtained was dissolved in CH_2Cl_2. The solution, clarified by filtration, was evaporated to dryness. 2-Propanol was added to the residue and the mixture heated until a clear solution was obtained. The yellow product, crystallised by cooling the solution, was filtered and dried in vacuo. IR $\tilde{\nu}$ = 1623 (C=N) cm^{-1}. $C_{24.9}H_{31.2}N_3O_{8.7}Na_3 \cdot 1.4\,H_2O \cdot 0.3\,PrOH$: calcd. C 51.51, H 5.42, N 7.24; found C 51.44, H 5.07, N 6.47. ^1H NMR (CD_3OD): δ = 8.41 (s, 2 H, 4-H), 6.95 (d, 2 H, 3-H), 6.91 (d, 2 H, 2-H), 6.57 (t, 2 H, 1-H), 4.19 (m, 4 H, 8-H), 3.99 (m, 4 H, 9-H), 3.84 (m, 4 H, 5-H), 3.56 (s, 4 H, 6-H), 3.29 (m, 2 H, 7-H) ppm. ^{13}C NMR (CD_3OD): δ = 166.34 (C-4), 176.24 (C-13), 114.18 (C-2), 114.39 (1), 124.83 (3), 115.97 (C-10), 149.46 (C-11), 163.29 (C-12), 68.70 (C-8), 63.33 (C-9), 56.24 (C-5), 52.37 (C-6), 57.66 (C-7) ppm.

Preparation of Na_2HL_C: Methanolic solutions of NaOH (0.90×10^{-3} mol) and Na_2L' (0.30×10^{-3} mol) were added in succession to a methanolic solution of Moden·3 HCl (0.30×10^{-3} mol). The resulting yellow solution was refluxed for 3 h, then reduced in volume. The subsequent addition of 3 mL of ethanol formed a precipitate that was filtered off. The solution was evaporated to dryness and the residue treated with 1-propanol. The solution, clarified by filtration, was evaporated to dryness; the yellow solid obtained was filtered, washed twice with 1-propanol and dried in vacuo. IR $\tilde{\nu}$ = 1624 (C=N) cm^{-1}. $C_{37.5}H_{55}N_3O_{9.5}Na_{2.5}Cl_{0.5}$: calcd. C 58.12, H 7.15, N 5.42; found C 58.05, H 7.14, N 6.60. ^1H NMR (CD_3OD): δ = 8.26 (s, 2 H, 4-H), 7.19 (d, 1 H, 10-H), 7.01 (d, 2 H, 3-H), 6.90 (m, 1 H, 12-H), 6.86 (d, 2 H, 2-H), 6.66 (t, 1 H, 1-H), 6.65 (t, 1 H, 11-H), 6.34 (d, 1 H, 13-H), 4.24 (m, 4 H, 8-H), 4.03 (m, 4 H, 9-H), 3.90 (m, 4 H, 5-H), 3.81 (s, 2 H, 7-H), 2.97 (m, 4 H, 6-H) ppm.

Preparation of NaH_2L_C: Methanolic solutions of Moden·3 HCl (0.30×10^{-3} mol) neutralized with NaOH (0.90×10^{-3} mol) and H_2L' (0.30×10^{-3} mol) were added dropwise to a flask containing Et_2O. The suspension was stirred for 2 h at room temp. The white precipitate was filtered, dried in vacuo and then dissolved in $CHCl_3$. The resulting solution was clarified by filtration and re-

 © 2005 Wiley-VCH Verlag GmbH & Co. KGaA, Weinheim

duced in volume, then petroleum ether was added and the yellow solid obtained was filtered and dried in vacuo. IR $\tilde{\nu}$ = 1639 (C=N) cm^{-1}. $C_{29}H_{32}N_3O_6Na_{12.5}Cl_{11.5}$: calcd. C 28.70, H 2.66, N 3.46; found 28.91, H 2.63, N 3.04. MS: *m*/*z* (%) = 542 (55) $[Na(H_3L_C)]^+$. ^1H NMR (CD_3OD): δ = 8.27 (s, 2 H, 4-H), 7.15 (d, 1 H, 10-H), 7.03 (d, 2 H, 3-H), 6.93 (m, 1 H, 12-H), 6.87 (d, 2 H, 2-H), 6.72 (t, 1 H, 1-H), 6.68 (t, 1 H, 11-H), 6.30 (d, 1 H, 13-H), 4.24 (m, 4 H, 8-H), 3.99 (m, 4 H, 9-H), 3.88 (m, 4 H, 5-H), 3.81 (s, 2 H, 7-H), 2.98 (m, 4 H, 6-H) ppm. ^{13}C NMR (CD_3OD): δ = 166.85 (C-4), 128.62 (C-10), 128.10 (C-12), 124.16 (C-2), 119.42 (C-11), 115.85 (C-1), 115.29 (C-13), 113.83 (C-3), 68.31 (C-9), 66.58 (C-8), 55.94 (C-6), 55.15 (C-7), 52.11 (C-5) ppm.

Complexes

Preparation of $[LnNa(Na_xL_A)(Cl)_{1+x}]\cdot nH_2O$ (x = 0, 1): $LnCl_3\cdot 6H_2O$ (0.20×10^{-3} mol) (where Ln = Y, Lu, Yb, Tm, Tb, Eu) in methanol (20 mL) was added to a methanolic solution (20 mL) of Na_3L_A (0.20×10^{-3} mol). The solution obtained was refluxed for 2 h, then evaporated to dryness and the resulting residue was treated twice with 1-propanol. The yellow precipitate was filtered, washed with diethyl ether and dried in vacuo. The reported stoichiometry and the Na/Ln/Cl ratio were ascertained by SEM-EDS together with elemental analysis.

$[YNa(NaLA)(Cl)_2]\cdot 3NaCl\cdot 2H_2O$: IR $\tilde{\nu}$ = 1636 (C=N) cm^{-1}. $C_{24}H_{30}N_3O_9Na_5Cl_5Y$: calcd. C 32.55, H 3.41, N 4.74; found C 32.00, H 3.34, N 4.63. ^1H NMR (CD_3OD): δ = 8.34 (s, 2 H, 4), 7.13 (d, 2 H, 2), 7.00 (d, 2 H, 3), 6.67 (t, 2 H, 1), 4.27 (m, 4 H, 8), 4.04 (m, 4 H, 9), 3.96 (m, 4 H, 5), 3.79 (s, 2 H, 7), 2.75 (m, 4 H, 6) ppm.

$[LuNa(NaL_A)(Cl)_2]\cdot 4.5NaCl\cdot PrOH$: IR $\tilde{\nu}$ = 1625 (C=N) cm^{-1}. $C_{27}H_{34}N_3O_8Na_{6.5}Cl_{6.5}Lu$: calcd. C 29.93, H 3.16, N 3.88; found C 29.41, H 2.76, N 3.60.

$[YbNa(NaL_A)(Cl)_2]\cdot 1.3NaCl\cdot 3.2H_2O$: IR $\tilde{\nu}$ = 1637 (C=N) cm^{-1}. $C_{24}H_{32.4}N_3O_{10.2}Na_{3.3}Cl_{3.3}Yb$: calcd. C 34.34, H 3.89, N 5.01; found: C 34.60, H 3.68, N 4.95.

$[TmNa(L_A)(Cl)]\cdot 5.5NaCl\cdot 2.5H_2O$: IR $\tilde{\nu}$ = 1625 (C=N) cm^{-1}. $C_{24}H_{31}N_3O_{9.5}Na_{6.5}Cl_{6.5}Tm$: calcd. C 27.14, H 2.94, N 3.96; found C 27.10, H 2.95, N 3.05.

$[TbNa(L_A)(Cl)]\cdot 0.6NaCl\cdot 0.3H_2O$: IR $\tilde{\nu}$ = 1625 (C=N) cm^{-1}. $C_{24}H_{26.6}N_3O_{7.3}Na_{1.6}Cl_{1.6}Tb$: calcd. C 39.69, H 3.69, N 5.79; found: C 39.54, H 3.68, N 4.21.

$[EuNa(L_A)(Cl)]$: IR $\tilde{\nu}$ = 1619 (C=N) cm^{-1}. $C_{24}H_{26}N_3O_7NaClEu$: calcd. C 42.46, H 3.86, N 6.19; found: C 43.10, H 3.66, N 4.50. ^1H NMR (CD_3OD): δ = 28.99 (s, 2 H, 7-H), 3.46 (t, 2 H, 1-H), 2.33 (t, 2 H, 8-H), 1.23 (d, 2 H, 9-H), 1.09 (d, 2 H, 9-H), 0.97 (d, 2 H, 3-H), 0.25 (t, 2 H, 2-H), –0.36 (t, 2 H, 8-H), –6.96 (s, 2 H, 6-H), –8.68 (s, 2 H, 5-H), –19.93 (s, 2 H, 6-H), –20.12 (s, 2 H, 5-H), –28.28 (s, 2 H, 4-H) ppm.

Preparation of $[Ln_2(L_A)(Cl)_3]\cdot nH_2O\cdot m$PrOH: The same synthetic procedure used for $[LnNa(NaL_A)(Cl)]\cdot nH_2O$, but a 12 h reflux (when Ln = Y, Lu, Yb, Nd) leads to the homodinuclear complexes $[Y_2(L_A)(Cl)_3]\cdot 1NaCl\cdot 7.7H_2O$; $[Lu_2(L_A)(Cl)_3]\cdot 4.8NaCl\cdot 0.3$PrOH; $[Yb_2(L_A)(Cl)_3]\cdot 4NaCl\cdot 1.3H_2O$; $[Nd_2(L_A)(Cl)_3]\cdot 1.2NaCl\cdot 1.2$PrOH.

$[Y_2(L_A)(Cl)_3]\cdot NaCl\cdot 7.7H_2O$: IR $\tilde{\nu}$ = 1655 cm^{-1} (C=N) cm^{-1}. $C_{24}H_{41.4}N_3O_{14.7}NaCl_4Y_2$: calcd. calcd.C 30.35, H 4.39, N 4.42; found C 30.26, H 4.39, N 5.08.

$[Lu_2(L_A)(Cl)_3]\cdot 4.8NaCl\cdot 0.3$PrOH: IR $\tilde{\nu}$ = 1639 (C=N) cm^{-1}. $C_{24.9}H_{28.4}N_3O_{7.3}Na_{4.8}Cl_{7.8}Lu_2$: calcd. C 24.45, H 2.34, N 3.43; found C 24.37, H 2.27, N 2.92.

$[Yb_2(L_A)(Cl)_3]\cdot 4NaCl\cdot 1.3H_2O$: IR $\tilde{\nu}$ = 1624 cm^{-1} (C=N) cm^{-1}. $C_{24}H_{28.6}N_3O_{8.3}Na_4Cl_7Yb_2$: calcd. C 24.47, H 2.45, N 3.57; found C 24.58, H 2.45, N 2.98.

$[Nd_2(L_A)(Cl)_3]\cdot 1.2NaCl\cdot 1.2$PrOH: IR $\tilde{\nu}$ = 1654 (C=N) cm^{-1}. $C_{27.6}H_{35.6}N_3O_{8.2}Na_{1.2}Cl_{4.2}Nd_2$: calcd. C 32.97, H 3.57, N 4.18; found C 32.88, H 3.59, N 4.05.

Preparation of $[Ln(HL_B)(Cl)_2]\cdot xNaCl\cdot yH_2O$: NaOH in methanol (20 mL) was added to a methanolic solution (20 mL) of DETPY·3 HCl (0.10×10^{-2} mol) until pH = 7–8. The appropriate lanthanide chloride hydrate $LnCl_3\cdot nH_2O$ (0.10×10^{-2} mol) (where Ln = Y, Yb, Lu, Tm, Tb with n = 6 and Ln = La, Ce with n = 7), and the diformyl derivative H_2L' (0.10×10^{-2} mol) were added in succession and the resulting solution refluxed for 2 h. The solution was clarified by filtration, then evaporated to dryness. The solid obtained was washed twice with ethanol. The yellow precipitate was filtered, washed with diethyl ether and dried in vacuo. The reported stoichiometry and the Ln/Cl ratio were ascertained by SEM-EDS together with elemental analysis.

$[Y(HL_B)(Cl)_2]\cdot 2.9NaCl\cdot 0.6H_2O$: IR $\tilde{\nu}$ = 1647 (C=N) cm^{-1}. $C_{27}H_{32.2}N_4O_{5.6}Na_{2.9}Cl_{4.9}Y$: calcd. C 39.00, H 3.90, N 6.74; found C 39.86, H 3.80, N 4.76. ^1H NMR (CD_3OD): δ = 8.66 (s, 2 H, 4-H), 8.45 (d, 1 H, 13-H), 7.93 (t, 1 H, 11-H), 7.58 (d, 1 H, 10-H), 7.37 (m, 1 H, 12-H), 7.33 (d, 2 H, 3-H) 7.15 (2-H), 6.78 (t, 2 H, 1-H), 4.55 (m, 8 H, 8-H + 9-H), 4.08 (s, 2 H, 7-H), 4.00 (m, 4 H, 5-H), 3.04 (m, 4 H, 6-H) ppm. ^{13}C NMR (CD_3OD): δ = 171.97 (4), 151.79 (16), 135.31 (14), 128.80 (13), 127.45 (15), 130.29 (3), 120.08 (2), 118.41 (1), 73.78 (8), 68.75 (9), 57.03 (6), 52.29 (5), 61.86 (7) ppm. Similar results were obtained for the diamagnetic complexes $[La(HL_B)(Cl)_2]\cdot 10NaCl\cdot 2.5H_2O$, and for the paramagnetic $[Ce(HL_B)(Cl)_2]\cdot 6.4NaCl\cdot 7H_2O$, $[Yb(HL_B)(Cl)_2]\cdot 7NaCl\cdot 0.1H_2O\cdot 1.6$EtOH, $[Tb(HL_B)(Cl)_2]\cdot 7.7NaCl\cdot 5.3H_2O$, $[Tm(HL_B)(Cl)_2]\cdot 7.6NaCl\cdot$EtOH. IR $\tilde{\nu}$ = 1617 (C=N, Tm complex)–1652 (C=N, Tb complex) cm^{-1}.

$[La(HL_B)(Cl)_2]\cdot 10NaCl\cdot 2.5H_2O$: IR $\tilde{\nu}$ = 1625 (C=N) cm^{-1}. $C_{27}H_{36}N_4O_{7.5}Na_{10}Cl_{12}La$: calcd. C 24.37, H 2.73, N 4.21; found C 25.02, H 2.72, N 3.84.

$[Ce(HL_B)(Cl)_2]\cdot 6.4NaCl\cdot 7H_2O$: IR $\tilde{\nu}$ = 1638 (C=N) cm^{-1}. $C_{27}H_{45}N_4O_{12}Na_{6.4}Cl_{8.4}Ce$: calcd. C 29.96, H 3.77, N 4.66; found C 27.71, H 3.73, N 6.39. ^1H NMR (CD_3OD): δ = 21.30 (s, 2 H, 4-H), 11.50 (d, 1 H, 13-H), 11.36 (d, 2 H, 2-H), 9.27 (t, 1 H, 11-H), 9.10 (d, 1 H, 10-H), 9.04 (d, 2 H, 3-H), 8.62 (m, 3 H, 12-H + 1-H), 4.77 (m, 4 H, 9-H), 5.01 (s, 2 H, 7-H), 3.66 (m, 4 H, 8-H), 8.01 (broad, 4 H, aliph.), –11.46 (broad, 4 H, aliph.) ppm.

$[Yb(HL_B)(Cl)_2]\cdot 7NaCl\cdot 0.1H_2O\cdot 1.6$EtOH: IR $\tilde{\nu}$ = 1624 (C=N) cm^{-1}. $C_{31.8}H_{40.8}N_4O_{6.7}Na_7Cl_9Yb$: calcd. C 29.79, H 3.37, N 4.59; found C 29.73, H 3.37, N 3.63.

$[Tb(HL_B)(Cl)_2]\cdot 7.7NaCl\cdot 5.3H_2O$: IR $\tilde{\nu}$ = 1652 (C=N) cm^{-1}. $C_{27}H_{41.6}N_4O_{10.3}Na_{7.7}Cl_{9.7}Tb$: calcd. C 25.60, H 3.31, N 4.42; found C 25.63, H 3.32, N 4.72.

$[Tm(HL_B)(Cl)_2]\cdot 7.6NaCl\cdot$EtOH: IR $\tilde{\nu}$ = 1617 (C=N) cm^{-1}. $C_{29}H_{37.4}N_4O_{6.2}Na_{10.5}Cl_{10.5}Tm$: calcd. C 28.51, H 3.05, N 4.59; found C 28.58, H 2.95, N 3.23.

Preparation of $[Ln_2(L_B)(Cl)_4]\cdot xNaCl\cdot yH_2O$: The same procedure was used as for $[Ln(HL_B)(Cl)_2]$, but a 12 h reflux of the appropriate solution (when Ln = Y, Lu, Dy with n = 6 and Ln = La with n = 7) leads to the homodinuclear complexes $[La_2(L_B)(Cl)_4]\cdot 8NaCl\cdot 3.9H_2O$, $[Y_2(L_B)(Cl)_4]\cdot 0.6NaCl\cdot 7.5H_2O\cdot 3$MeOH, $[Lu_2(L_B)(Cl)_4]\cdot 2.7NaCl\cdot 6.6H_2O$, $[Dy_2(L_B)(Cl)_4]\cdot 4.5\ NaCl\cdot 9H_2O\cdot$MeOH.

$[La_2(L_B)(Cl)_4]\cdot 8NaCl\cdot 3.9H_2O$: IR $\tilde{\nu}$ = 1647 (C=N) cm^{-1}. $C_{27}H_{37.8}N_4O_{8.9}Na_8Cl_{12}La_2$: calcd. C 22.40, H 2.63, N 3.87; found

 © 2005 Wiley-VCH Verlag GmbH & Co. KGaA, Weinheim

C 22.71, H 2.63, N 3.78. ^{1}H NMR (CD_3OD): δ = 8.53 (s, 2 H, 4-H), 8.46 (d, 1 H, 13-H), 7.91 (d, 1 H, 11-H), 7.61 (d, 1 H, 10-H), 7.39 (t, 1 H, 12-H), 7.27 (d, 2 H, 3-H), 7.09 (d, 2 H, 2-H), 6.71 (t, 2 H, 1-H), 4.51 (m, 8 H, 8-H + 9-H), 4.09 (s, 2 H, 7-H), 4.02 (m, 4 H, 5-H), 3.09 (m, 4 H, 6-H) ppm.

$[Y_2(L_B)(Cl)_4]\cdot 0.6\,NaCl\cdot 7.5\,H_2O\cdot 3\,MeOH$: IR ṽ = 1654 (C=N) cm^{-1}. $C_{30}H_{57}N_4O_{15.5}Na_{0.6}Cl_{4.6}Y_2$: calcd. C 33.48, H 5.34, N 5.20; found C 33.65, H 5.34, N 5.12.

$[Lu_2(L_B)(Cl)_4]\cdot 2.7\,NaCl\cdot 6.6\,H_2O$: IR ṽ = 1658 (C=N) cm^{-1}. $C_{27}H_{43.2}N_4O_{11.6}Na_{2.7}Cl_{6.7}Lu_2$: calcd. C 25.76, H 3.46, N 4.45; found C 25.65, H 3.45, N 4.65.

$[Dy_2(L_B)(Cl)_4]\cdot 4.5\,NaCl\cdot 9\,H_2O\cdot MeOH$: IR ṽ = 1655 (C=N) cm^{-1}. $C_{28}H_{52}N_4O_{15}Na_{4.5}Cl_{8.5}Dy_2$: calcd. C 23.78, H 3.71, N 3.96; found C 23.69, H 3.67, N 4.34.

Preparation of $[LnNa(L_C)(Cl)]\cdot x\,NaCl\cdot y\,H_2O$: $LnCl_3\cdot nH_2O$ (5×10^{-2} mol) (where Ln = Y, Yb, Lu, Tm, Tb, Dy, Eu, Er with n = 6 and Ln = La, Ce with n = 7) dissolved in methanol was added to a methanolic solution of Na_2HL_C (5×10^{-2} mol). The solution was refluxed for 3 h, then evaporated to dryness. The crude product was treated with 1-propanol and the yellow solid obtained was filtered, washed with 2-propanol and dried in vacuo. The reported stoichiometry and the Na/Ln/Cl ratio were ascertained by SEM-EDS together with elemental analysis.

$[LuNa(L_C)(Cl)]\cdot 4.2\,NaCl\cdot 1.7\,H_2O$: IR ṽ = 1626 (C=N) cm^{-1}. $C_{29}H_{33.4}N_3O_{7.7}Na_{5.2}Cl_{5.2}Lu$: calcd. C 33.95, H 3.28, N 4.10; found C 33.91, H 3.28, N 3.68. ^{1}H NMR (CD_3OD): δ = 8.35 (s, 2 H, 4-H), 7.13 (d, 2 H, 3-H), 7.02 (d, 1 H, 10-H), 6.96 (d, 2 H, 2-H), 6.93 (m, 1 H, 12-H), 6.62 (t, 2 H, 1-H), 6.51 (t, 1 H, 11-H), 6.34 (d, 1 H, 13-H), 4.30 (m, 4 H, 8-H), 4.13 (m, 2 H, 5-H), 4.08 (m, 4 H, 9-H), 3.85 (m, 2 H, 5-H), 3.76 (s, 2 H, 7-H), 3.23 (m, 2 H, 6-H), 2.84 (m, 2 H, 6-H) ppm. ^{13}C NMR (CD_3OD): δ = 171.71 (4), 132.05 (10), 130.89 (12), 128.80 (2), 119.37 (13), 117.34 (11), 116.45 (3), 115.52 (1), 70.21 (9), 67.07 (8), 57.97 (7), 57.05 (5), 55.04 (6) ppm. ESI-MS: m/z (%) = 715 (100) $[LuNa(L_C)]^+$.

$[YNa(L_C)(Cl)]\cdot 2.2\,NaCl\cdot 0.7\,MeOH$: IR ṽ = 1625 (C=N) cm^{-1}. $C_{29.7}H_{32.8}N_3O_{6.7}Na_{3.2}Cl_{3.2}Y$: calcd. C 43.78, H 4.06, N 5.16; found C 43.81, H 4.04, N 4.72. Similar results were obtained for the paramagnetic complexes $[YbNa(L_C)(Cl)]\cdot 4.1\,NaCl$, $[TbNa(L_C)(Cl)]\cdot 1.5\,NaCl$, $[TmNa(L_C)]Cl\cdot 4.3\,NaCl$, $[DyNa(L_C)(Cl)]\cdot 2.3\,NaCl$, $[EuNa(L_C)(Cl)]\cdot 6.5\,NaCl$. IR $\upsilon_{C=N}$ varies within the range 1620–1629 cm^{-1}.

$[EuNa(L_C)(Cl)]\cdot 6.5\,NaCl$: IR ṽ = 1623 (C=N) cm^{-1}. $C_{29}H_{30}N_3O_6Na_{7.5}Cl_{7.5}Eu$: calcd. C 31.47, H 2.73, N 3.80; found C 31.60, H 2.73, N 3.56. ^{1}H NMR (CD_3OD), paramagnetic: δ = 19.46 (s, 2 H, 6-H), 11.37 (d, 1 H, 13-H), 5.67 (m, 2+ 1 H, 9-H + 11-H), 5.31 (t, 1 H, 12-H), 4.42 (m, 2 H, 8-H), 4.22 (m, 2 H, 5-H), 4.21 (t, 2 H, 1-H), 4.19 (t, 1 H, 10-H), 3.95 (m, 2 H, 9-H), 2.63 (t, 2 H, 8-H), 1.98 (d, 2 H, 3-H), 0.52 (d, 2 H, 2-H), –1.00 (s, 2 H, 6-H), –9.57 (s, 2 H, 5-H), –12.87 (s, 2 H, 7-H), –29.90 (s, 2 H, 4-H) ppm. ^{13}C NMR (CD_3OD): δ = 152.38 (4), 134.24 (10), 131.98 (2), 124.39 (12), 119.55 (6), 113.57 (11), 110.98 (3), 106.16 (1), 92.04 (5), 77.10 (13), 76.90 (7), 70.99 (9), 66.90 (8) ppm.

$[YbNa(L_C)(Cl)]\cdot 4.1\,NaCl$: IR ṽ = 1626 (C=N) cm^{-1}. $C_{29}H_{30}N_3O_6Na_{5.1}Cl_{5.1}Yb$: calcd. C 35.27, H 3.06, N 4.25; found C 35.29, H 2.76, N 3.86. ESI-MS: m/z (%) = 713 (100) $[YbNa(L_C)]^+$.

$[TbNa(L_C)(Cl)]\cdot 1.5\,NaCl$: IR ṽ = 1623 (C=N) cm^{-1}. $C_{29}H_{30}N_3O_6Na_{2.5}Cl_{2.5}Tb$: calcd. C 42.40, H 3.68, N 5.11; found C 42.72, H 3.64, N 4.74. ESI-MS: m/z (%) = 699 (100) $[TbNa(L_C)]^+$.

$[TmNa(L_C)(Cl)]\cdot 4.3\,NaCl$: IR ṽ = 1625 (C=N) cm^{-1}. $C_{29}H_{30}N_3O_6Na_{5.3}Cl_{5.3}Tm$: calcd. C 35.00, H 3.04, N 4.22; found C 35.03, H 2.53, N 3.69. ESI-MS: m/z (%) = 708 (100) $[TmNa(L_C)]^+$.

$[DyNa(L_C)(Cl)]\cdot 2.3\,NaCl$: IR ṽ = 1623 (C=N) cm^{-1}. $C_{29}H_{30}N_3O_6Na_{3.3}Cl_{3.3}Dy$: calcd. C 39.95, H 3.47, N 4.82, found C 40.07, H 3.22, N 4.23. ESI-MS: m/z (%) = 704 (100) $[DyNa(L_C)]^+$.

Preparation of $[Ln(H_3L_C)(Cl)_3]\cdot x\,LiCl\cdot y\,EtOH$: LiOH ($0.9\times10^{-3}$ mol) dissolved in ethanol was added to an ethanolic suspension of Moden·3 HCl (0.3×10^{-3} mol) up to pH ≈ 8. $LnCl_3\cdot n\,H_2O$ (0.3×10^{-3} mol) (where Ln = Lu, Eu, Tb, Y with n = 6, Ln = La with n = 7) was added to an ethanolic solution of H_2L' (0.3×10^{-3} mol) and the two solutions were mixed and refluxed for 5 h. The yellow solution, reduced in volume under reduced pressure, separated a yellow precipitate which was filtered, washed with ethanol and dried in vacuo. The reported stoichiometry and the Ln/Cl ratio were ascertained by SEM-EDS together with elemental analysis.

$[Eu(H_3L_C)(Cl)_3]\cdot 0.6\,LiCl$: IR ṽ = 1647 (C=N) cm^{-1}. $C_{29}H_{33}N_3O_6Li_{0.6}Cl_{3.6}Eu$: calcd. C 43.36, H 4.14, N 5.23; found C 43.40, H 4.03, N 4.91. ^{1}H NMR (CD_3OD), paramagnetic: δ = 11.83 (s, broad, 8 H, aliph.), 7.42 (d, 1 H, 13-H), 7.06 (t, 1 H, 12-H), 6.67 (m, 2 H, 10-H + 11-H), 6.53 (m, 2 H, 7-H), 5.96 (d, 2 H, 2-H), 5.93 (s, 2 H, 4-H), 5.33 (s, broad, 8 H, aliph.), 4.00 (t, 2 H, 1-H), 2.22 (d, 2 H, 3-H) ppm.

$[Lu(H_3L_C)(Cl)_3]\cdot 1\,LiCl\cdot 1.4\,H_2O$: IR ṽ = 1651 (C=N) cm^{-1}. $C_{29}H_{35.8}N_3O_{7.4}LiCl_4Lu$: C 40.11, H 4.15, N 4.84; found C 40.36, H 4.15, N 4.39. ^{1}H NMR (CD_3OD): δ = 8.63 (s, 2 H, 4-H), 7.39 (d, 2 H, 3-H), 7.17 (d, 2 H, 2-H), 7.16 (d, 1 H, 10-H), 6.89 (t, 1 H, 12-H), 6.81 (t, 2 H, 1-H), 6.75 (d, 1 H, 13-H), 6.66 (t, 1 H, 11-H), 4.67 (m, 4 H, 8-H), 4.56 (m, 4 H, 9-H), 4.13 (m, 4 H, 5-H), 3.85 (s, 2 H, 7-H), 3.04 (m, 4 H, 6-H) ppm.

$[La(H_3L_C)(Cl)_3]\cdot 1.8\,LiCl\cdot 2.9\,H_2O$: IR ṽ = 1645 (C=N) cm^{-1}. $C_{29}H_{38.8}N_3O_{8.9}Li_{1.8}Cl_{4.8}La$: calcd. C 41.20, H 4.63, N 4.97; found C 41.15, H 4.61, N 5.24.

$[Tb(H_3L_C)(Cl)_3]\cdot 0.2\,LiCl\cdot EtOH$: IR ṽ = 1653 (C=N) cm^{-1}. $C_{31}H_{39}N_3O_7Li_{0.2}Cl_{3.2}Tb$: calcd. C 44.36, H 4.68, N 5.01; found C 44.48, H 4.67, N 5.00.

$[Er(H_3L_C)(Cl)_3]\cdot 2\,LiCl\cdot H_2O\cdot EtOH$: IR 1652 (C=N) cm^{-1}. $C_{31}H_{41}N_3O_8Li_2Cl_5Er$: calcd. C 39.52, H 4.39, N 4.46; found C 40.00, H 4.39, N 4.42.

X-ray Crystallographic Study: Diffraction data were collected at room temperature on a Philips PW1100 automatic four-circle diffractometer (FEBO System) using the graphite-monochromated Mo-Kα radiation and ω-2θ scan method. Lattice parameters were obtained from least-squares refinement of the setting angles of 30 reflections with $10 \le 2\theta \le 24°$. Table 1 lists a summary of the crystallographic data and structure refinement. No sign of crystal deterioration was revealed by monitoring three standard reflections after every 200 measurements but the quality of the crystals was very poor, even after several attempts with different crystals. The structure was solved by standard Patterson methods and subsequently completed by a combination of least-squares techniques and Fourier syntheses with SHELX program.[33,34] All the benzene rings were refined as rigid bodies, the hydrogen atoms were included in the idealized positions with fixed C–H distances (C–H = 0.93 Å) and isotropic temperature factors fixed to $1.2\times U$(eq) of the preceding carbon atom.

The poor quality of the crystals did not give very good data. In particular, serious disorder in the C3–C5, O5 atoms and the coordinated propanol molecule was found and high values of thermal parameters were maintained to absorb the disorder.

 © 2005 Wiley-VCH Verlag GmbH & Co. KGaA, Weinheim

Listing of selected bond lengths and angles pertinent to the coordination sphere are summarized in Table 2. Additional crystallographic data, atomic coordinates, anisotropic thermal parameters, and full listings of bond lengths and angles are provided as supplementary material to CCDC. Final geometrical calculations and drawings were carried out with the PARST program[35] and the XP utility of the Siemens package[36] respectively, running on a DIGITAL ALPHA-AXP 300 computer.

CCDC-251962 contains the supplementary crystallographic data for this paper. These data can be obtained free of charge from The Cambridge Crystallographic Data Centre via www.ccdc.cam.ac.uk/data_request/cif.

Table 1. Crystal and intensity data for the DyNa complex.

Empirical formula	$C_{32}H_{30}ClDyN_3NaO_7$
Formula mass	789.53
Crystal system	monoclinic
Space group	$P2_1/c$ (no. 14)
a [Å]	9.601(2)
b [Å]	12.927(2)
c [Å]	26.638(4)
β [°]	99.55(3)
V [Å^3]	3260(1)
Z	4
Calcd. density [g cm^{-3}]	1.609
μ [mm^{-1}] (Mo-$K\alpha$)	2.437
Range of rel. transm. factors[a] [%]	88–100
θ limits [°]	6.3–52
Data collected/unique	6749/6606
Data observed	6443 [$F \geq 3\sigma(F)$]
No. of parameters (obsd. per parameter)	351 (9.8)
$R(\Sigma(\|F_o\| - \|F_c\|) / \Sigma\|F_o\|)$	0.059
$R_w[\Sigma w(\|\|F_o\| - \|F_c\|)^2 / \Sigma w(F_o)^2]^{1/2}$	0.130
Highest map residual [e Å^{-3}]	1.12

[a] Corrections: Lorentz-polarization and absorption (empirical, ψ scan).

Table 2. Selected bond lengths [Å] and angles [°] of the DyNa complex .

Bond lengths [Å]			
Dy–O(1)	2.236(5)	Na–O(1)	2.354(6)
Dy–O(2)	2.226(4)	Na–O(2)	2.323(5)
Dy–O(3)	2.185(6)	Na–O(4)	2.410(7)
Dy–N(1)	2.474(8)	Na–O(5)	2.40(1)
Dy–N(2)	2.556(7)	Na–O(6)	2.376(8)
Dy–N(3)	2.494(7)	Na–O(7)	2.33(1)
Dy–Cl	2.719(2)		
		N(1)–C(7)	1.24(2)
Dy···Na	3.496(3)	N(3)–C(19)	1.26(1)
Angles [°]			
O(1)–Dy–O(2)	79.2(2)	O(1)–Na–O(2)	74.9(1)
O(1)–Dy–N(1)	74.3(3)	O(2)–Na–O(4)	66.2(2)
N(1)–Dy–N(2)	70.5(3)	O(4)–Na–O(5)	63.6(4)
N(2)–Dy–N(3)	68.3(2)	O(5)–Na–O(6)	68.4(4)
N(3)–Dy–O(2)	73.7(2)	O(1)–Na–O(6)	66.2(3)
O(1)–Dy–O(3)	88.7(2)	O(1)–Na–O(7)	115.2(4)
N(1)–Dy–O(3)	98.5(2)	O(2)–Na–O(7)	113.9(4)
N(2)–Dy–O(3)	75.0(3)	O(4)–Na–O(7)	113.8(3)
N(3)–Dy–O(3)	94.8(2)	O(5)–Na–O(7)	96.8(6)
O(2)–Dy–O(3)	92.3(2)	O(6)–Na–O(7)	102.5(4)
Cl–Dy–O(1)	98.5(1)		
Cl–Dy–O(2)	93.5(1)		
Cl–Dy–N(1)	79.2(2)	Line Cl–Dy / Dy–O(3) 171	
Cl–Dy–N(2)	96.4(2)		
Cl–Dy–N(3)	80.9(2)		

Acknowledgments

We thank Mr. A. Aguiari, Mrs. O. Biolo and Mrs A. Moresco for technical assistance. We also thank Prof. V. Fusi for the kind cooperation in the synthesis of *N,N*-bis(2-aminoethyl)-2-hydroxybenzylamine·3HCl and then MIUR project FIRB-RBNE019H9K for financial support.

[1] O. Kahn, *Advances in Inorganic Chemistry* (Ed.: A. G. Sykes), Academic Press, S. Diego (U. S. A.), **1995**, *43*, 179–259.
[2] K. S. Murray, *Advances in Inorganic Chemistry* (Ed.: A. G. Sykes), Academic Press, S. Diego (U. S. A.), **1995**, *43*, 261–358.
[3] P. D. Beer, D. K. Smith, *Prog. Inorg. Chem.* (Ed.: K. D. Karlin), J. Wiley & Sons, New York (U. S. A.), **1997**, *46*, 1–96.
[4] J. Nelson, V. McKee, G. Morgan, *Prog. Inorg. Chem.* (Ed.: K. D. Karlin), J. Wiley & Sons, New York (U. S. A.), **1998**, *47*, 167–316.
[5] T. A. Kaden, *Top. Cur. Chem.* **1984**, *121*, 175–179.
[6] D. E. Fenton, *Advances in Inorganic and Bioinorganic Mechanism* (Ed.: A. G. Sykes), Academic Press, S. Diego (U. S. A.), **1983**, *43*, 187.
[7] P. Zanella, S. Tamburini, P. A. Vigato, G. A. Mazzocchin, *Coord. Chem. Rev.* **1987**, *77*, 165–273.
[8] F. L. Urbach, *Metal Ions in Biological Systems. Copper Proteins* (Ed.: H. Sigel), Marcel Dekker, Basel, **1981**, *13*, 73–115 and references cited therein.
[9] T. M. Sorrel, *Tetrahedron* **1989**, *45*, 3–68.
[10] V. Alexander, *Chem. Rev.* **1995**, *95*, 273–342.
[11] P. Guerriero, S. Tamburini, P. A. Vigato, *Coord. Chem. Rev.* **1995**, *139*, 17–243.
[12] H. Okawa, H. Furutachi, D. E. Fenton, *Coord. Chem. Rev.* **1998**, *174*, 51–75.
[13] D. M. Rudkevic, J. D. Mercher-Chalmers, W. Verboom, R. Ungaro, F. De Jong, D. N. Reinhoudt, *J. Am. Chem. Soc.* **1995**, *117*, 6124–6125.
[14] D. M. Rudkevic, Z. Brozka, M. Palys, C. H. Visser, W. Verboom, D. N. Reinhoudt, *Angew. Chem.* **1994**, *106*, 480; *Angew. Chem. Int. Ed. Engl.* **1994**, *33*, 467–468.
[15] D. M. Rudkevic, W. Verboom, D. N. Reinhoudt, *J. Org. Chem.* **1994**, *59*, 3683–3686.
[16] D. M. Rudkevic, W. P. R. V. Stauthamer, J. F. J. Engbersen, S. Harkema, D. N. Reinhoudt, *J. Am. Chem. Soc.* **1992**, *114*, 9671–9673.
[17] D. M. Rudkevic, W. Verboom, Z. Brozka, M. Palys, W. P. R. V. Stauthamer, G. J. Van Hummel, S. M. Franken, S. Harkema, J. F. J. Engbersen, D. N. Reinhoudt, *J. Am. Chem. Soc.* **1994**, *116*, 4341–4351.
[18] P. A. Vigato, S. Tamburini, *Coord. Chem. Rev.* **2004**, *248*, 1717–2128.
[19] U. Casellato, S. Tamburini, P. Tomasin, P. A. Vigato, S. Aime, M. Botta, *Inorg. Chem.* **1999**, *38*, 2906–2916.
[20] N. Brianese, U. Casellato, S. Tamburini, P. Tomasin, P. A. Vigato, *Inorg. Chem. Commun.* **1999**, *2*, 149–152.
[21] A. D. Sherry, C. F. G. C. Geraldes, *Lanthanide Probes in Life, Chemical and Earth Sciences* (Eds.: J.-C. G. Bünzli, G. R. Choppin), Elsevier, Amsterdam, **1989**, 93–124.
[22] J. Ren, A. D. Sherry, *Inorganica Chimica Acta* **1996**, *246*, 331–341.
[23] T. Knubovets, H. Shinar, G. Navon, *Journal of Magnetic Resonance* **1998**, *131*, 92–96.
[24] U. Casellato, S. Tamburini, P. Tomasin, P. A. Vigato, S. Aime, A. Barge, M. Botta, *Chem. Commun.* **2000**, 145–146.
[25] U. Casellato, C. Scalco, S. Tamburini, P. Tomasin, P. A. Vigato, S. Aime, A. Barge, M. Botta, *Chem. Eur. J.* **2002**, *8/17*, 3917–3926.

 © 2005 Wiley-VCH Verlag GmbH & Co. KGaA, Weinheim

[26] A. Barge, M. Botta, U. Casellato, S. Tamburini, P. A. Vigato, *Eur. J. Inorg. Chem.* **2005**, 1492–1499.
[27] M. Gatos, L. Bertolo, S. Tamburini, P. A. Vigato, work in progress.
[28] A. Di Tullio, S. Tamburini, S. Reale, L. Bertolo, P. A. Vigato, F. De Angelis, work in progress.
[29] J. A. Peters, J. Huskens, D. J. Raber, *Prog. NMR Spectrosc.* **1996**, *28*, 283.
[30] R. M. Sink, D. C. Buster, A. D. Sherry, *Inorg. Chem.* **1990**, *29*, 3645–3649.
[31] D. D. Perrin, W. L. Armarego, D. R. Perrin, *Purification of Laboratory Chemicals*, 2nd ed., Pergamon Press, Oxford (UK), **1982**.
[32] Q. Zeng, M. Quian, S. Gou, H-K. Fun, C. Duan, X. You, *Inorg. Chim. Acta* **1999**, *294*, 1–7.
[33] G. M.Sheldrick, *SHELX-86 Crystallographic Computing 3* (Eds.: C. Kruger, R.Goddard), Oxford University Press, London, **1985**, 175.
[34] G. M.Sheldrick *SHELXL-93 Program for Crystal Structure Refinement,* University of Göttingen, Göttingen, Germany, **1993**.
[35] M. Nardelli, *J. Appl. Crystallogr.* **1995**, *28*, 659.
[36] G. M. Sheldrick, *SHELXTL-PLUS, Version 4.2;* Siemens Analytical X-ray Instruments Inc.: Madison, WI, **1991**.
Received: November 16, 2004

 © 2005 Wiley-VCH Verlag GmbH & Co. KGaA, Weinheim

Hemilabile Thioether Ligands Based on Pyrimidine and/or Pyridine Derivatives that Interconvert between *N*,*S*- and *N*-Coordination in Congested Ruthenium(II) Complexes

Giuseppe Tresoldi,*[a] Laura Baradello,[a] Santo Lanza,[a] and Paola Cardiano[a]

Keywords: Ruthenium / Pyridine thioether / Pyrimidine thioether / *N*,*S*-Coordination / *N*-Coordination

The thioether ligands **L** [**L** = 2-pyridylmethyl 2′-pyridyl sulfide (**L_1**), 2-pyridylmethyl 2′-pyrimidyl sulfide (**L_2**) and 2-pyridylmethyl 2′-(4-methylpyrimidyl) sulfide (**L_3**)] react with *cis*-[Ru(*N*,*N*-diimine)$_2$Cl$_2$] {diimine = 2,2′-bipyridine (bipy), di-2-pyrimidyl sulfide (dprs), 2,2′-bis(5-ethylpyrimidyl) sulfide (5edprs)} to give compounds [Ru(*N*,*N*-diimine)$_2$L][PF$_6$]$_2$ {diimine = bipy, **L** =**L_1** (**1**), **L_2** (**2**), **L_3** (**3**); diimine = dprs, **L** = **L_1** (**4**); diimine = 5edprs, **L** = **L_1** (**5**); diimine = dprs, **L** = **L_2** (**6**), **L** = **L_3** (**7**); diimine = 5edprs, **L** = **L_2** (**8**), **L** = **L_3** (**9**)}. NMR investigations show that these potentially tridentate ligands act as *N*,*S*-bidentate species, to form a five-membered RuSCCN(*Ru–N*) ring, and in certain cases, as *N*-monodentate species coordinated to the ruthenium through the 2-pyridylmethyl group. The *N*,*S*-chelated species contain chiral sulfur and ruthenium atoms with (*R*) and (*S*), and Δ and Λ configurations, respectively. Two invertomers and two sets of NMR signals in the slow-exchange region are expected. However, the low-temperature ^{1}H NMR spectra show that sulfur inversion is fast. The variable-temperature ^{1}H NMR spectra allow two species to be observed (**6a** + **6b**, **7a** + **7b**, **8a** + **8b** and **9a** + **9b**), which exhibit different abundances. In the minor species (**6b**, **7b**, **8b**, and **9b**), **L_2** or **L_3** exhibits an *N*-monodentate coordination, while in the major species, the usual *N*,*S*-coordination. At low temperatures, the population ratio is about 85:15, while when the temperature increases, the abundance of the minor species grows rapidly. The one-dimensional band-shape analysis of the exchanging methylene proton signals shows that the energy-barrier for the interchange process ($\Delta G^{\#}_{298}$) for **6a** + **6b**, **7a** + **7b**, **8a** + **8b**, and **9a** + **9b** is practically the same (ca. 59.5 kJ·mol^{-1}), while the $\Delta S^{\#}$ values are negative or near to zero. The possible mechanisms for the process are discussed. The NMR spectroscopic findings strongly support the formation of an *N*,*N*-chelated labile intermediate.
(© Wiley-VCH Verlag GmbH & Co. KGaA, 69451 Weinheim, Germany, 2005)

Introduction

The coordination chemistry of chelated ligands containing mixed functionalities in transition-metal complexes is an active area of research. In particular, the chemistry of hemilabile ligands, which contain both inert and labile groups, has received considerable attention.[1] Since one group bonds strongly to a metal center, the substitutionally labile group, which can be displaced from the metal center, remain available for recoordination. Thus the hemilability of a chelate can be observed as a dynamic process that involves the dissociation and recoordination of weakly bound moieties. When the hemilabile ligand contains two or more weakly bonding groups, it may undergo intramolecular ligand-exchange reactions. These processes often have been referred to as "wind-screen wiper" or "tick-tock" mechanisms,[2–9] and "opening and closing" or "rotation" mechanisms.[8–10] Furthermore, hemilability through ligand-interchange reactions involving equilibria between weakly bonding groups of the ligand and coordinating counterions, small molecules, or solvent molecules has been observed.[10,11]

There are many reasons for studying hemilabile ligands. Since these ligands can furnish open coordination sites and stabilize reactive transition-metal centers throughout the course of the reaction, their complexes can be utilized in catalytic reactions. Complexes containing hemilabile ligands have been shown to be active, for example, toward hydrogenation,[12] methanol carbonylation,[13] hydroformylation,[14] dimerization of ethene,[15] isomerization of alkene,[16] allylation,[17] and epoxidation of alkenes.[18] Furthermore, the labile fragments of these ligands are often displaced easily and reversibly from the metal center by small molecules, and the corresponding complexes are useful for small molecule activation[19] and sensing.[20]

N-heterocyclic donors are often good ligands for many transition-metal centers, and ligands containing inert *N*-heterocyclic moieties, in particular, pyridine or bipyridine groups are the most common type of nitrogen-based hemilabile ligands.[21] Hybrid S/N/S ligands consisting of substitutionally inert pyridine moieties and labile sulfur moieties are known.[22–25] In these complexes, the S–S switching, in

[a] Dipartimento di Chimica Inorganica, Chimica Analitica e Chimica Fisica, Università di Messina,
Salita Sperone 31, 98166 Vill. S. Agata, Messina, Italy
Fax: +39-090393756
E-mail: tresoldi@chem.unime.it

addition to sulfur inversion, was often observed.[23–25] Although the thioether-containing aromatic nitrogen heterocycles such as di-2-pyridyl sulfide (dps) usually adopts the *N*,*N*-bidentate coordination,[26–32] it can exhibit a variety of bonding modes to a metal, for example, monodentate[29–31] and bridging modes.[30–34] However, the hemilability of dps has been addressed in a few cases, and only the pyridine moieties have been utilized as inert and labile, bound groups.[29–31] Recently we demonstrated that dps, under the proper conditions, binds the ruthenium metal in an *N*,*S*-chelate fashion, leaving one of the rings uncoordinated.[35] In such species some dynamic processes occur, as shown by the temperature dependence of the NMR spectra, but only the restricted uncoordinated ring rotation could be studied and the total dynamic stereochemistry remained unclear.[35] We have been able to obtain activation-energy data for the pyramidal inversion at the coordinated sulfur atom[36] as well as for the restricted rotation of the pendant ring[37] when the ruthenium(II) center is *N*,*S*-chelated by thioether ligands based on pyridine or pyrimidine, and benzyl or phenyl derivatives.

We have now turned our attention to metal complexes that contain unsymmetrical NSN or NSNN thioethers; we are interested in studying the hemilability of these ligands and consequently the interchange process between chemically distinct coordination species. Since the potentially polydentate ligands **L** [**L** = 2-methylpyridyl pyridyl sulfide (**L_1**), 2-methylpyridyl pyrimidyl sulfide (**L_2**) and 2-methylpyridyl 2-(4-methylpyrimidyl) sulfide (**L_3**)] may bind to the ruthenium center through nitrogen atoms[27,28,32,35–37] or nitrogen and sulfur atoms,[35–37] an NMR spectroscopic study has been carried out to identify the different coordination species obtained when **L** reacts with $Ru(bipy)_2Cl_2$, $Ru(dprs)_2Cl_2$, and $Ru(5edprs)_2Cl_2$ and to examine any dynamic process which might lead to their interconversion.

Results

Synthesis of the Compounds

The air-stable compounds **1–9** were obtained by the reactions of *cis*-[$RuCl_2$(*N*,*N*-diimine)$_2$] and **L** as depicted in Scheme 1.

The complexes are yellow or orange solids that are soluble in acetone or acetonitrile. They were characterized by elemental analysis, conductivity measurements in acetonitrile solutions with values characteristic of 1:2 electrolytes (315–350 $S cm^2 mol^{-1}$), IR spectroscopy, which shows the

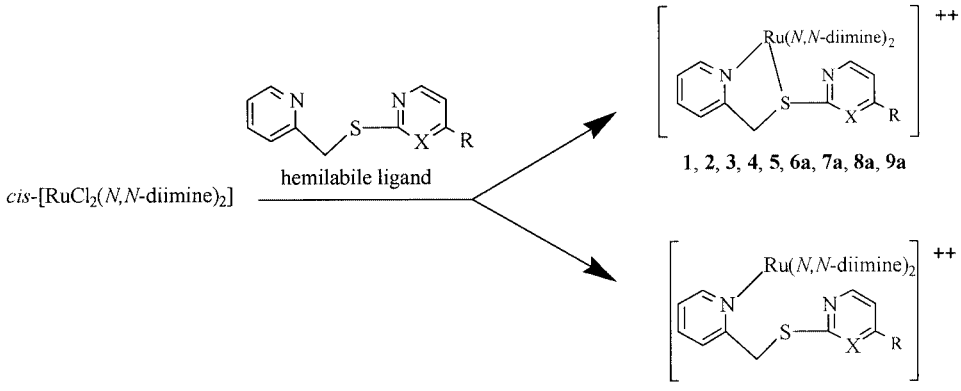

cis-[$RuCl_2$(*N*,*N*-diimine)$_2$]	hemilabile ligand	Complex
cis-[Ru(*N*,*N*-bipy)$_2$$Cl_2$]	**L_1** (X = CH, R = H)	**1**
	L_2 (X = N, R = H)	**2**
	L_3 (X = N, R = Me)	**3**
cis-[$RuCl_2$(*N*,*N*-dprs)$_2$]	**L_1**	**4***
cis-[$RuCl_2$(*N*,*N*-5edprs)$_2$]	**L_1**	**5***
cis-[$RuCl_2$(*N*,*N*-dprs)$_2$]	**L_2**	**6a** + **6b**
	L_3	**7a** + **7b**
cis-[$RuCl_2$(*N*,*N*-5edprs)$_2$]	**L_2**	**8a** + **8b**
	L_3	**9a** + **9b**

* At low temperatures only the *N*,*S*-chelated species are observed

Scheme 1.

 © 2005 Wiley-VCH Verlag GmbH & Co. KGaA, Weinheim

bands of PF_6^- (ca. 844 and 558 cm^{-1}) and those characteristic of thioether ligands in the range (1630–1540 and 780–720 cm^{-1}). These data indicate that the ligands bipy, dprs, and 5edprs act as *N*,*N*-chelate ligands.[26–32] These findings were confirmed by subsequent ^1H and ^{13}C NMR spectroscopic studies.

Coordination of L_1 in $[Ru(bipy)_2(N,S/L_1)][PF_6]_2$ (1), $[Ru(bipy)_2(N,S/L_2)][PF_6]_2$ (2), and $[Ru(bipy)_2(N,S/L_3)][PF_6]_2$ (3).

The crystal structure of $[Ru(N,N\text{-dps})_2(N,S/L_1)][PF_6]_2$[37] has shown that $\mathbf{L_1}$ is *N*,*S*-chelated to the ruthenium atom forming the five-membered ring RuSCCN*(Ru–N)*. Further-

Table 1. ^1H NMR spectroscopic data.

Compound[a]	*T*/K	Ring	Positions					*J*(CH_2)/Hz	Ring	Positions			
			3	4	5	6	CH_2			3	4	5	6
L_1	298	A	7.49	7.67	7.19	8.44	4.56		B[b]	7.28	7.59	7.07	8.48
L_2	298	A	7.52	7.69	7.21	8.49	4.54		B[c]		8.59	7.15	8.59
L_3	298	A	7.52	7.69	7.22	8.49	4.52		B[c]		2.42[d]	7.03	8.42
1	223	A	8.07	7.99	7.22	7.55	5.80	*J* = 16.6	B[b]	6.78	7.37	7.27	8.10
		C	8.32	8.16	7.65	8.31	5.02		D	8.34	8.01	7.45	8.02
		E	8.94	8.36	7.90	9.75			F	8.89	8.23	7.53	7.92
2	298	A	8.07	7.97	7.25	7.59	5.64	*J* = 17.2	B[c]		8.29	7.27	8.29
		C	8.46	8.10	7.47	8.05	5.17		D	8.48	8.07	7.48	7.96
		E	8.85	8.34	7.92	9.64			F	8.80	8.21	7.55	7.87
3	298	A	8.05	7.97	7.25	7.58	5.68	*J* = 17.2	B[c]		2.15[d]	7.13	8.13
		C	8.47	8.11	7.52	8.02	5.15		D	8.51	8.08	7.48	8.08
		E	8.86	8.35	7.92	9.64			F	8.82	8.22	7.55	7.88
4[e]	203	A	7.53	8.01	7.64	9.27	4.55	*J* = 16.9	B[b]	8.15	7.95	7.27	7.55
		C		8.46	7.48	9.33	3.69		D		8.99	7.50	8.84
		E		9.13	7.65	9.06			F		8.94	7.76	9.69
5[e]	228	A	7.50	7.98	7.61	9.36	4.57	*J* = 16.9	B[b]	8.10	7.93	7.26	7.53
		C	1.04[f]	8.41	2.53[g]	9.28	3.83		D	0.87[f]	8.93	2.35[g]	8.78
		E	0.91[f]	9.06	2.40[g]	8.96			F	1.15[f]	8.90	2.58[g]	9.64
6a	218	A	7.55	8.03	7.63	9.22	4.89	*J* = 17.2	B[c]		8.42	7.41	8.42
		C		8.49	7.47	9.28	3.93		D		9.01	7.49	8.84
		E		9.12	7.65	9.05			F		8.94	7.75	9.62
6b[h]	218	A	7.90	8.15	7.63	9.37	5.08	*J* = 15.2	B[c]		8.89	7.70	8.89
							4.18		F		8.66	7.05	7.84
6a + 6b	330	A	7.72	8.05	7.64	9.05	4.99	*J* = 16.4	B[c]		8.51	7.44	8.51
		C		8.98	7.41	8.74	4.01		D		9.05	7.55	8.90
		E		8.82	7.48	8.90			F		8.61	7.40	9.07
7a	215	A	7.55	8.05	7.65	9.23	4.84	*J* = 17.2	B[c]		1.87[d]	7.26	8.44
		C		8.50	7.49	9.29	3.90		D		9.00	7.51	8.86
		E		9.11	7.65	9.06			F		8.95	7.76	9.62
7b[h]	215	A	7.90	8.14	7.60	9.37	5.03	*J* = 15.3	B[c]		2.40[d]	7.70	8.76
		C		8.88			4.14		D		9.10		8.93
		E		9.16	7.71	9.18			F		8.65		7.80
7a + 7b	323	A	7.73	8.06	7.63	9.04	5.00	*J* = 16.7	B[c]		2.18[d]	7.28	8.38
		C		8.98	7.42	8.75	4.03		D		9.04	7.54	8.90
		E		8.82	7.48	8.90			F		8.60	7.40	9.06
8a	228	A	7.51	8.00	7.63	9.33	4.83	*J* = 17.2	B[c]		8.40	7.39	8.40
		C	1.00[f]	8.44	2.60[g]	9.23	3.91		D	0.87[f]	8.94	2.36[g]	8.77
		E	0.90[f]	9.06	2.37[g]	8.97			F	1.14[f]	8.90	2.69[g]	9.57
8b[h]	228	A	7.90	8.10	7.70	9.48	5.11	*J* = 14.9	B[c]		8.98	7.80	8.98
		C	1.08[f]	8.83		9.08	4.22		D				8.81
		E				9.07			F	0.75[f]	8.68		7.73
8a + 8b	328	A	7.65	8.03	7.67	9.18	4.86	*J* = 16.6	B[c]		8.54	7.48	8.54
		C	1.11[f]	8.75	2.52[g]	8.83	3.89		D	0.98[f]	8.80	2.47[g]	8.98
		E	1.03[f]	8.91	2.49[g]	8.54			F	1.09[f]	8.53	2.62[g]	8.96
9a	228	A	7.52	8.01	7.62	9.34	4.76	*J* = 17.2	B[c]		1.89[d]	7.26	8.42
		C	1.04[f]	8.52	2.59[g]	9.23	3.87		D	0.87[f]	8.95	2.35[g]	8.77
		E	0.91[f]	9.06	2.39[g]	8.96			F	1.15[f]	8.91	2.70[g]	9.57
9b[h]	228	A	7.92	8.13	7.71	9.46	5.10	*J* = 14.9	B[c]		2.46[d]	7.69	8.84
		C		8.83		9.08	4.20		D				8.82
		E				9.08			F	0.70[f]	8.68	1.82[g]	7.81
9a + 9b	330	A	7.68	8.04	7.66	9.18	4.84	*J* = 16.6	B[c]		2.23[d]	7.34	8.40
		C	1.09[f]	8.75	2.54[g]	8.85	3.87		D	0.98[f]	8.93	2.47[g]	8.57
		E	1.03[f]	8.81	2.54[g]	8.98			F	1.09[f]	8.55	2.58[g]	8.95

[a] At 300.13 MHz in $[D_6]$acetone, δ in ppm with respect to TMS, coupling constant (Hz). Ring A = picolyl ring in the free and coordinated hemilabile ligands; the coupling constant values are: $J_{6,5} \approx 4.8$, $J_{6,4} \approx 1.9$, $J_{6,3} \approx 0.7$, $J_{5,4} = 7.5$, $J_{5,3} \approx 1.1$, $J_{4,3} \approx 8.0$ (in the free ligands) and $J_{6,5} \approx 5.6$, $J_{6,4} \approx 1.3$, $J_{6,3} \approx 0.7$, $J_{5,4} \approx 7.5$, $J_{5,3} \approx 0.8$, $J_{4,3} \approx 7.8$ (coordinated ligands). Ring C, D, E, and F are pyrimidine rings, $J_{6,5} \approx 6.1$, $J_{6,4} \approx 2.1$, $J_{4,5} \approx 4.6$. [b] S-pyridyl fragment. [c] Pyrimidyl or methylpyrimidyl fragment, $J_{6,5} \approx 4.9$. [d] Methyl of *N*,*S*-ligand. [e] Signal for minor isomer is not observed. [f] Methyl signals of 5edprs. *J* (between methyl and methylene protons) ≈ 7.50. [g] Methylene signals of 5edprs. [h] Minor isomer; only some signals are assigned.

 © 2005 Wiley-VCH Verlag GmbH & Co. KGaA, Weinheim

more, in the compounds $[Ru(diimine)_2(N,S/L')][PF_6]_2$ [diimine = dps, 4-mdps, 5-mdps, dprs and 5edprs; **L′** = 2-pyrimidylmethyl *p*-tolyl sulfide and *p*-chlorophenyl 2-pyrimidylmethyl sulfide], **L′** is *N,S*-chelated to Ru and forms a five-membered ring.[37] These data suggest that the present ligands **L** can adopt an *N,S*-coordination in the complexes $Ru(bipy)_2(N,S\text{-}L)][PF_6]_2$. However, the NMR spectra of the complexes $Ru(dprs)_2(N,S\text{-}L)][PF_6]_2$ and $Ru(5edprs)_2(N,S\text{-}L)][PF_6]_2$ (see infra) show the presence of two different coordination species. Thus, in the absence of the crystal structure data of **1**, **2** and **3**, we performed several NMR spectroscopic experiments at various temperatures to exclude the presence of different coordination species.

Identification of the coordination mode of $\mathbf{L_1}$, $\mathbf{L_2}$ and $\mathbf{L_3}$ in compounds **1**, **2** and **3**, respectively, was based preliminarily on the analysis of the ^{1}H NMR spectra. In particular: i) the H(6) and H(4) pyrimidine protons of $\mathbf{L_2}$ in **2** are equivalent in that the pyrimidine ring is uncoordinated, ii) the H(3) signal of the uncoordinated pyridine ring of $\mathbf{L_1}$ appears at an unusually low frequency δ = 6.78 ppm (in the free ligand δ = 7.28 ppm); this upfield shift is consistent with increased shielding as the proton lies above the π cloud of the bipyridine ring C or F in the two invertomers (see infra), iii) the temperature has a negligible effect on the methylene proton signals which appear, at all the temperatures, as a single AB system (for instance in **2** at 223 K, δ = 5.61 and 5.18 ppm, J = 17.3 Hz, and at 330 K, δ = 5.65 and 5.17 ppm, J = 17.2 Hz, see also Table 1). Since **1**, **2** and **3** contain a stereogenic sulfur atom [(*R*) and (*S*) configurations] of the unsymmetrical thioether *N,S*-coordinated ligands and a stereogenic tris-chelated ruthenium center (Δ and Λ configurations), two invertomers are expected as enantiomeric couples (ΔR, ΛS) and (ΔS, ΛR). They should give two set of signals in the low-temperature ^{1}H NMR spectra and, in particular, two AB systems for the methylene protons of the two slowly exchanging invertomers. However, the spectra show a single AB system. This can indicate the presence of: 1) only one invertomer, 2) two invertomers that give superimposed signals, 3) two rapidly exchanging invertomers at low temperatures. From literature precedents,[23–25,36] the presence of only one invertomer or two invertomers that have similar resonances is unlikely. Thus, a fast sulfur inversion occurs, even at low temperatures, which is in accordance with the presence of a flexible five-membered chelate ring.[37,38]

On the other hand, the splitting patterns of the methylene protons at higher temperatures (single AB system) rule out the possibility of racemization ($\Delta \rightleftharpoons \Lambda$), which should average the environments of the methylene protons.

The ^{1}H NMR spectra of **1**, **2**, and **3**, in the range 210–330 K (Table 1) show the absence of different coordination species and dynamic processes of interconversion. Furthermore, in the NOESY phase-sensitive experiments of the compounds, positive cross-peaks due to chemical exchange of magnetization are absent.

The NOESY spectrum of **1** at 223 K is shown in Figure 1. Strong NOEs include intraring *ortho* interactions (6–5, 5–4 and 4–3) in the pyridine rings as well as interactions between the methylene protons. Most significantly, it shows interactions between: 1) the H(3) proton of the uncoordinated pyridine ring (labelled B in Table 1) of $\mathbf{L_1}$ at δ = 6.78 ppm, and that of the coordinated pyridine ring (A) at δ = 8.07 ppm; 2) the last proton and the methylene protons at δ = 5.02 and 5.80 ppm, respectively, and the H(6) proton of the bipyridine ligand at δ = 8.31 ppm (ring C); 3) the H(6) bipyridine proton at δ = 9.75 ppm (ring E) and the methylene proton at δ = 5.02 ppm. Weak interactions are observed between the H(3) proton of the uncoordinated pyridine group of $\mathbf{L_1}$ at δ = 6.78 ppm and the methylene proton at δ = 5.80 ppm and the H(6) bipyridine proton at δ = 9.75 ppm (ring E). Furthermore, the NOEs between the H(3) bipyridine protons at δ = 8.32 and 8.34 ppm, and those at δ = 8.94 and 8.89 ppm were used to identify the H(3) protons in the same bipyridine ligand (rings C, D and E, F, respectively).

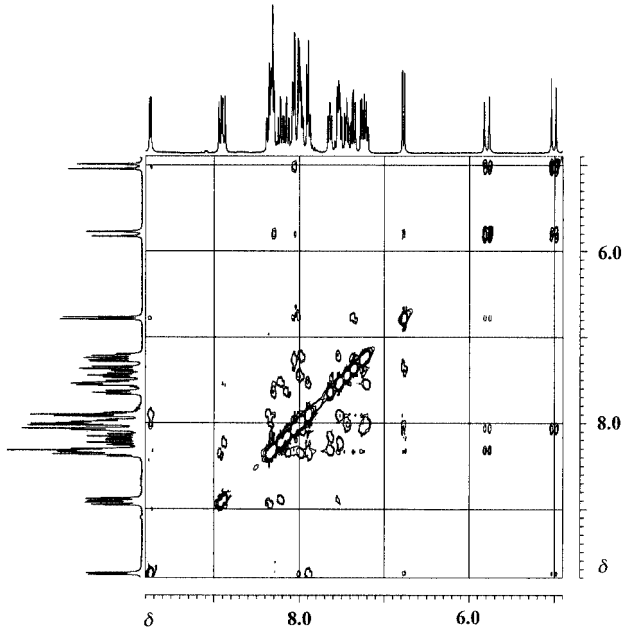

Figure 1. 2D NOESY of $[Ru(bipy)_2L_1][PF_6]_2$ (**1**) at 223 K in $[D_6]$-acetone.

On the basis of 2D phase-sensitive NOESY, 2D COSY, decoupling experiments and monodimensional ^{1}H NMR spectra at various temperatures the *N,S*-coordination of $\mathbf{L_1}$, $\mathbf{L_2}$ and $\mathbf{L_3}$ ligands resulting in the formation of the five-membered ring was assigned. In one invertomer, the uncoordinated pyridine ring B has a *cis* conformation with respect to the pyridine ring labelled C; in the other invertomer, ring B has a *cis* conformation with respect to ring F. Rings and proton positions of **1**, **2** and **3** are listed in Table 1.

Solution Structure of $[Ru(N,N\text{-dprs})_2(N,S/L_1)][PF_6]_2$ (4) and $[Ru(N,N\text{-5edprs})_2(N,S/L_1)][PF_6]_2$ (5) at Low Temperatures

The signal assignments for **4** and **5** were performed with the help of the aforementioned experiments, and the results are listed in Table 1. The portion of the NOESY spectrum of $[Ru(N,N\text{-dprs})_2\mathbf{L_1}][PF_6]_2$ (**4**), performed at 233 K in $(CD_3)_2$-

 © 2005 Wiley-VCH Verlag GmbH & Co. KGaA, Weinheim

CO, shown in Figure 2, displays the proton signals of the pyridyl rings labelled A (coordinated ring) and B (uncoordinated ring), the pyrimidyl rings C and D of the same dprs (the first ring is near ring B, Figure 3), and the rings E and F of the other ligand (E is *trans* with respect to the sulfur atom, Figure 3). 6A (δ = 9.27 ppm, $\Delta\delta$ with respect to the free ligand is 0.79 ppm) displays a high-frequency shift due to coordination and short contact with the 6C proton of the pyrimidine ring at δ = 9.33 ppm. The strong NOEs include: a) intraring *ortho* interactions: 6–5, 5–4, and 4–3 in the pyridine rings, 6–5 and 5–4 in the pyrimidine rings; b) geminal interaction of the methylene protons; c) adjacent-group interaction of the methylene proton at δ = 4.55 and 3A at δ = 7.53; d) interaction between the H(6) protons of the pyrimidine rings (6A and 6C, 6F at δ = 9.69 ppm and 6E at δ = 8.84 ppm, 6C and 6D at δ = 9.06 ppm).

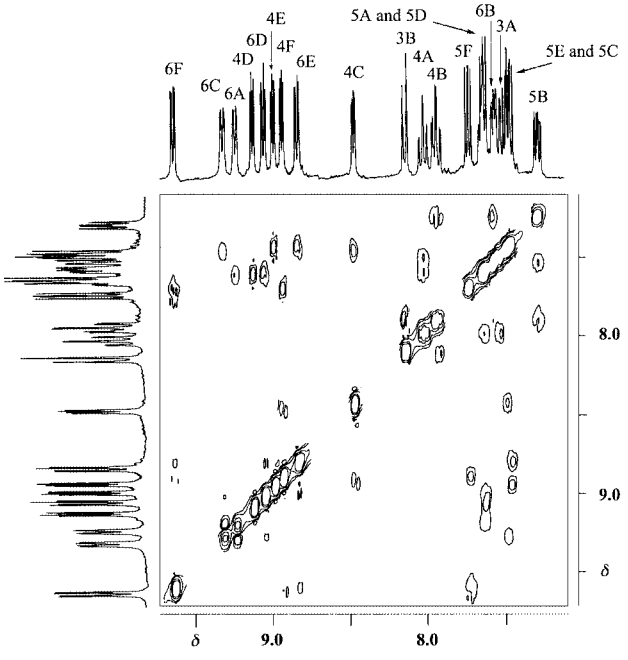

Figure 2. 2D NOESY of $[Ru(dprs)_2L_1][PF_6]_2$ (**4**) at 233 K in $[D_6]$-acetone.

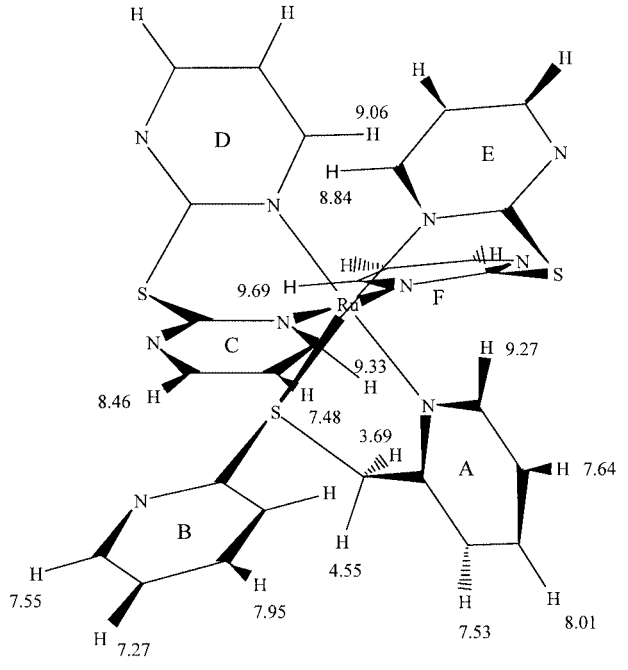

Figure 3. Proposed structure of an invertomer of **4**.

Solution Behaviour of 6a + 6b, 7a + 7b, 8a + 8b and 9a + 9b

Variable-temperature ^{1}H NMR spectra of the compounds were obtained in $(CD_3)_2CO$ in the range 215–330 K and in CD_3CN (220–370 K). At low temperature in $(CD_3)_2CO$ or CD_3CN, the ^{1}H NMR spectra of the complexes consist of two sets of signals; one set is much more intense than the other, and this is in agreement with the presence of two different coordination species, one of which was predominant in solution (**6a**, **7a**, **8a**, or **9a**). Identification of these pairs of species was based primarily on the analysis of the proton signals of $\mathbf{L_2}$ or $\mathbf{L_3}$. The shift at high frequencies of the pyridyl proton signals of $\mathbf{L_2}$ and $\mathbf{L_3}$ with respect to the free ligand is in agreement with the pyridyl coordination in both the species. The equivalence, of the pyrimidyl protons 4B and 6B, as well as 4B′ and 6B′ of $\mathbf{L_2}$, suggests that pyrimidyl ring is uncoordinated in both species.

The ^{1}H NMR spectrum of **6a** + **6b** at 218 K in $(CD_3)_2CO$ is shown in Figure 4. All the proton signals of **6a** and some signals of **6b** are labelled. The data are listed in Table 1. According to the presence of two species (population ratio 87:13), four doublets appear in the methylene region: two doublets of major intensity at δ = 4.89 and 3.93 ppm (J = 17.2 Hz), labelled M and N, respectively, and two doublets at δ = 5.08 and 4.18 ppm (J = 15.2 Hz), labelled M′ and N′, respectively. In the aromatic region, the multiplets of major intensity were all assigned, with the help of NOESY, COSY and decoupling experiments, to the 19 protons of **6a**: 12 nonequivalent pyrimidyl protons of *N*,*N*-chelated dprs ligands (with the coupling constants $J_{4,5} \approx 4.6$, $J_{4,6} \approx 2.1$, and $J_{5,6} \approx 6.0$ Hz) and seven protons of $\mathbf{L_2}$; of the latter protons, four are pyridyl protons at δ = 7.55 (3A), 8.03 (4A), 7.63 (5A), and 9.22 ppm (6A) and three are pyrimidyl protons (5B at δ = 7.41 ppm and the equivalent 4B and 6B at δ = 8.42 ppm). These signals are clearly associated to the coordination species containing the five-membered ring RuSCCN(*Ru–N*) and the uncoordinated pyrimidyl ring. In the same aromatic region, full assignment of the minor intensity signals was not possible due to their weakness and numerous partial or complete overlap of these signals with the more intense signals. The assignment of some significant signals was made on the basis of the cited experiments and the multiplet structures of these signals which matched those of their major counterparts. In particular, the pyridyl signals of $\mathbf{L_2}$ in **6b** are at δ = 9.37 (6A′), 8.15 (4A′), 7.90 (3A′), and 7.63 ppm (5A′) (the last masked by the signal of the corresponding proton of the major isomer) and the pyrimidyl signals at δ = 7.70 (5B′) and 8.88 ppm (4B′ and 6B′).

The 2D NOESY spectrum of **6a** + **6b** (Figure 5) was obtained at 243 K. At this temperature, some significant signals

 © 2005 Wiley-VCH Verlag GmbH & Co. KGaA, Weinheim

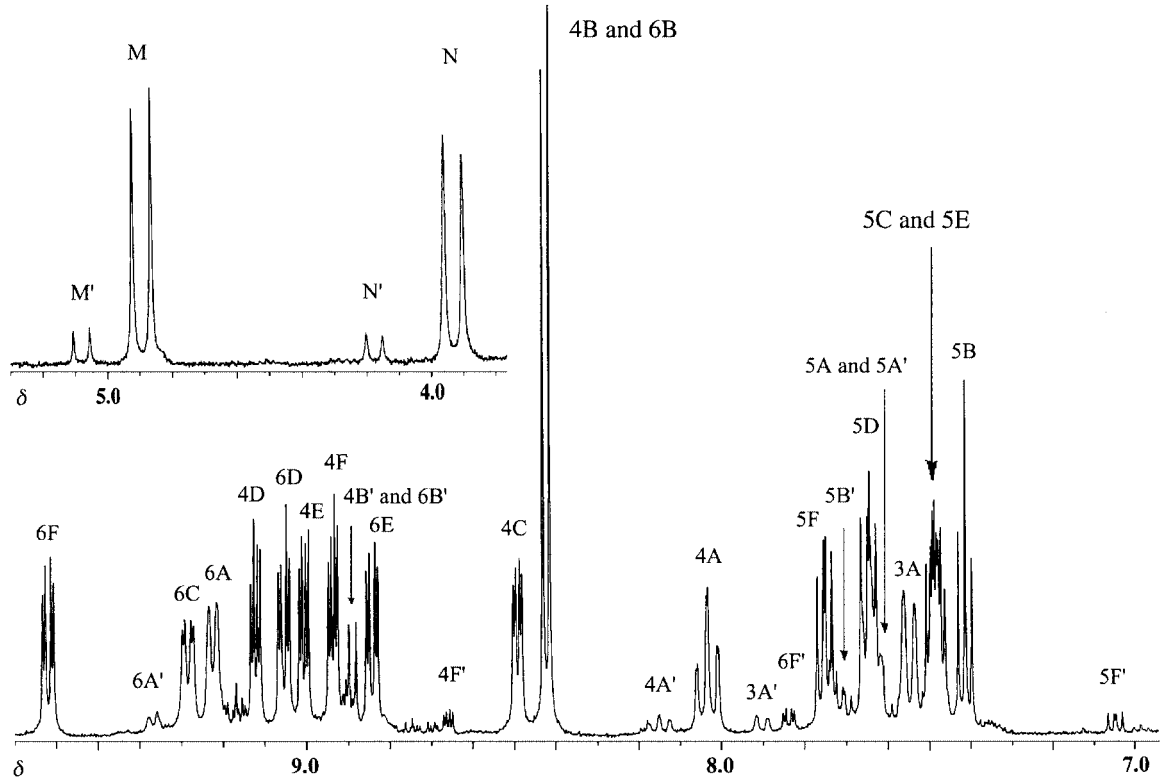

Figure 4. ^{1}H NMR spectrum of $[Ru(dprs)_2L_2][PF_6]_2$ (**6a** + **6b**) at 218 K in $[D_6]$acetone.

of the two species are well separated, and the interchange process is slow. The cross peaks, resulting from chemical exchange of magnetization (grey in Figure 5), are detected in the methylene region between the proton signals M–M′ and N–N′, whereas in the aromatic region (see Figure 4), well-resolved cross peaks are observed between the corresponding $\mathbf{L_2}$ proton signals of the two species (6A – 6A′, 4A – 4A′, 3A – 3A′, 6B and 4B – 6B′ and 4B′, 5B – 5B′) and between 6F (δ = 9.62) and 6F′ (δ = 7.84 ppm), 4F (δ = 8.94 ppm) and 4F′ (δ = 8.66 ppm) and 5F (δ = 7.75 ppm) and 5F′ (δ = 7.05 ppm).

The strong NOEs (black in Figure 5), for the major species, include interactions between the methylene protons, intraring interactions (e.g. 6–5, 5–4 and 4–3 in the pyridine ring and 6–5 and 4 –5 in the pyrimidine rings) and, most significantly, the following interactions between: methylene proton at δ = 4.89 ppm and 3A δ = 7.55 ppm, methylene proton at δ = 3.93 ppm and 6F, equivalent protons (6B and 4B at δ = 8.42 ppm) and 5B at δ = 7.41 ppm.

We assume that the sulfur inversion is fast in the major species even at the low temperatures as observed in **1**, **2**, **3**, **4**, **5**, and similar complexes.[37,38] In fact, the methylene protons of **6a** give only one AB system. On the contrary, if slow inversion occurs at low temperatures, the presence of two diasteroisomers ΔR (ΛS) and ΔS (ΛR) should produce two AB systems in the methylene region of the spectrum.[36] There is no restricted rotation of ring B at 218 K. Restricted rotation of the pyrimidine ring probably occurs below this temperature. Unfortunately, experimental difficulties and, in particular, solubility problems ruled out the possibility of performing NMR experiments below 215 K. In terms of fast inversion and rotation, 4B and 6B are equivalent.

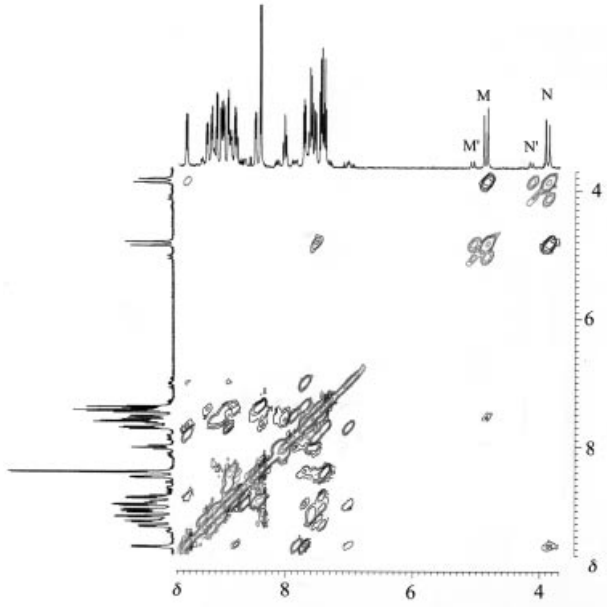

Figure 5. 2D NOESY of $[Ru(dprs)_2L_2][PF_6]_2$ (**6a** + **6b**) at 243 K in $[D_6]$acetone.

The equivalence of 4B′ and 6B′ indicates that the coordination of $\mathbf{L_2}$ does not involve the pyrimidyl group in **6b** also. Since the sulfur inversion and the pyrimidyl rotation are fast, it is unlikely that the minor species is an invertomer or rotamer of the major species. On the other hand, the minor

 © 2005 Wiley-VCH Verlag GmbH & Co. KGaA, Weinheim

species is very different from the major species. In particular, the coupling constants of the methylene protons in the two species are different (for instance, the coupling constant value in **6a** is 17.2 Hz, whereas in **6b**, 15.2 Hz). Some corresponding signals are very different (the signals of the ring A, B and F with respect to those of rings A′, B′ and F′). Thus, in the minor species, the pyrimidyl coordination as well as the *N*,*S*-coordination are unlikely. Since the complete dissociation of $\mathbf{L_2}$ or $\mathbf{L_3}$ by the minor species can be excluded because free ligand addition allows for the observation of separate signals for the free and coordinated ligands (Figure 6), the possible species to be considered are the monodentate ones with *N*-(pyridine)- or *S*-coordination. The *N*-coordination is assigned on the basis of: i) the nitrogen of the pyridyl group is a better donor atom than the sulfur atom towards these ruthenium centers;[23,27,28,35–38] ii) the ^{1}H NMR spectra show downfield shifts of the H(6) protons of isomers **6b**, **7b**, **8b**, and **9b** (see Table 1 and 6A′ in Figure 4); iii) the minor species containing the uncoordinated pyrimidine group attached to the sulfur is favored with respect to that containing the pyridine group, whereas a weakening of the Ru–S bond is expected when the pyridine group is replaced by the better electron-withdrawing pyrimidine group.

On warming the solutions, all the spectral lines in the ^{1}H NMR spectra broaden but the signal intensity of the minor species increases. The methylene signals M′ and N′ of **6b** disappear at ca 288 K.

Figure 6 shows the ^{1}H NMR spectrum of **6a** + **6b** in the presence of a small amount of free ligand ($\mathbf{L_2}$) at 330 K, the highest temperature reached. Eighteen signals in the aromatic region and two averaged doublets in the methylene region are observed. Moreover, some signals for free ligand $\mathbf{L_2}$ are observed (in particular, the methylene signal at δ = 4.55 ppm). These NMR findings are in line with the presence of an exchange between the major species containing the five-membered ring RuSCCN(*Ru–N*) and the minor containing the *N*-monodentate ring, in the range 218–330 K. Furthermore, the averaged methylene signals for $\mathbf{L_2}$ at 330 K are observed at δ = 4.99 and 4.01 ppm. These values are the weighted means of 4.89 (M) and 5.08 (M′), and 3.93 (N) and 4.18 (N′) if the population ratio, at this temperature, is 55:45 (see Table 2), whereas at 218 K the ratio is 87:13.

The rates for the process were deduced by band-shape analysis of the methylene signals. Some experimental and computer-simulated spectra of **6a** + **6b** are shown in Figure 7. In the temperature range 218–243 K, the rates are very

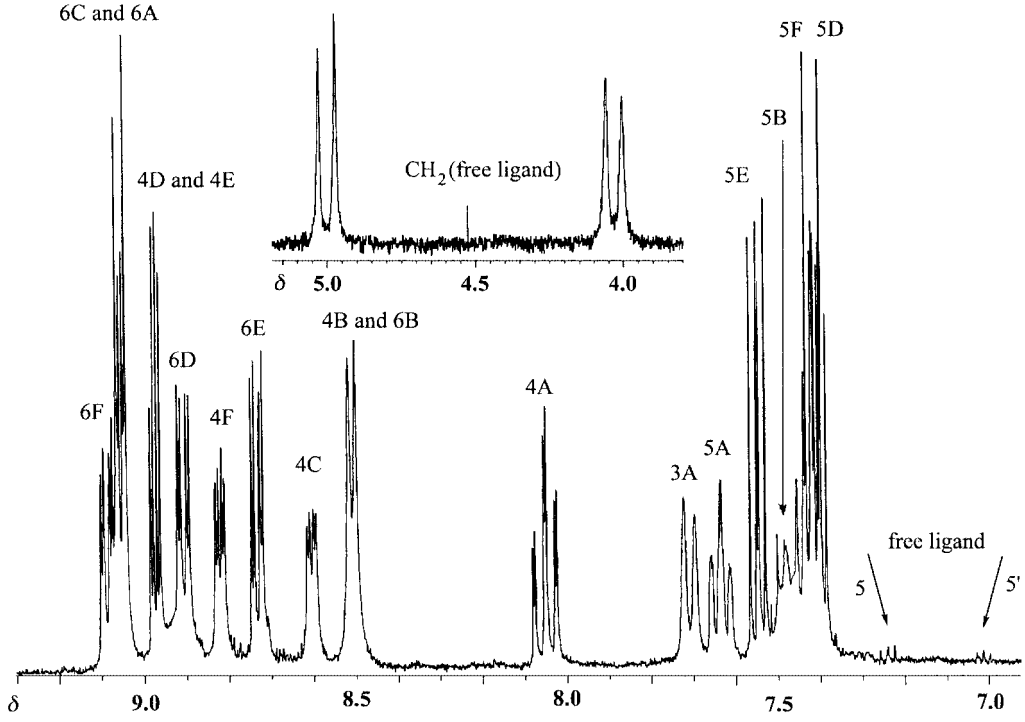

Figure 6. ^{1}H NMR spectrum of $[Ru(dprs)_2L_2][PF_6]_2$ (**6a** + **6b**) at 330 K in $[D_6]$acetone, with small amount of free $\mathbf{L_2}$.

Table 2. Activation energy data.

Species	Population (%) at 218 K	Population (%) at 330 K	$\Delta G^{\#}_{298\ K}$ (kJ·mol^{-1})	$\Delta H^{\#}$ (kJ·mol^{-1})	$\Delta S^{\#}$ (kJ mol^{-1})
6a + **6b**	87:13	55:45	59.1± 0.05	50.5± 1.1	–28.8±3.8
7a + **7b**	82:18	51:49	59.8± 0.10	51.1± 1.3	–29.1±4.8
8a + **8b**	84:16	60:40	59.3± 0.01	57.7± 0.9	–5.4±3.0
9a + **9b**	84:16	60:40	59.5± 0.02	59.0± 1.3	–1.7+4.4

 © 2005 Wiley-VCH Verlag GmbH & Co. KGaA, Weinheim

low; however, the population ratio is temperature dependent. To correct for this temperature dependence, a linear interpolation was used.[39] This correction gives the ratio 55:45 at 330 K. Activation parameters were calculated from 15 independent fittings in the temperature range 218–330 K. The activation parameters for the mixtures **7a** + **7b**, **8a** + **8b**, and **9a** + **9b** were obtained in a similar manner and are collected in Table 2.

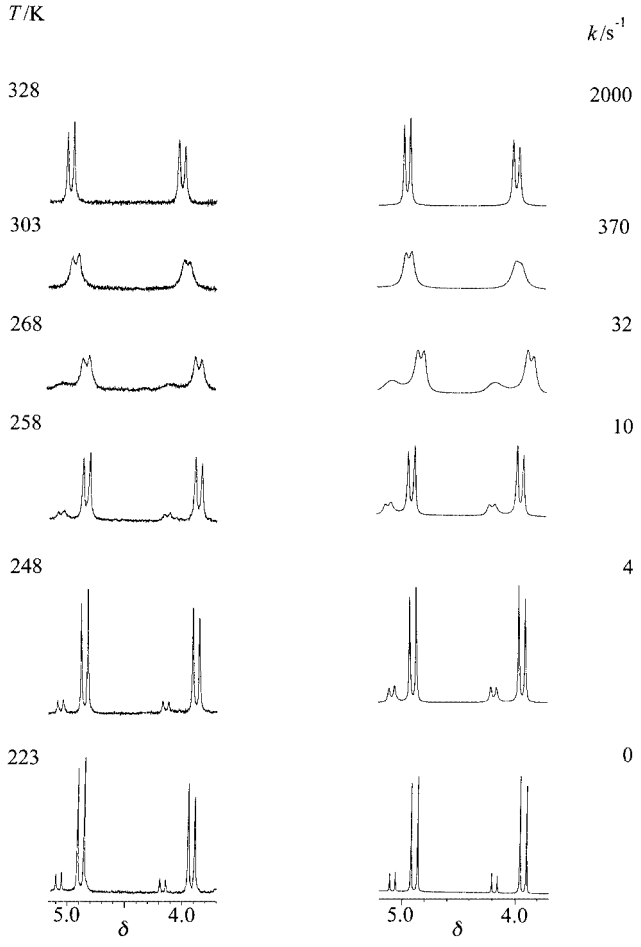

Figure 7. The methylene region of the experimental (left) and computer generated (with the gNMR program, right) ^{1}H NMR spectra of [Ru(dprs)$_2$L$_2$][PF$_6$]$_2$ (**6a** + **6b**) in [D$_6$]acetone.

The ^{13}C NMR spectra of the *N*,*S*-chelate species were interpreted easily (Table 3) by comparison of the spectra of these compounds with those of the free ligand and similar complexes containing *N*,*S*-chelate ligands.[37] Furthermore, although some carbon signals of the minor species are not observed, the ^{13}C NMR spectra show the equivalence of the H(4) and H(6) pyrimidine carbons of **L$_2$** from the presence of uncoordinated pyrimidine ring in the species **6b** and **8b**.

Discussion

We have found that in the complexes [Ru(*N*,*N*-diimine)$_2$(*N*,*S*-pySCH$_2$R)][PF$_6$]$_2$[36] (diimine = dps or dprs, py = pyridine or pyrimidine, and R = phenyl derivative), the ligand pySCH$_2$R is *N*,*S*-coordinated and forms the four-membered ring RuSCN(*Ru–N*). Furthermore, since the ruthenium and sulfur atoms are stereogenic centers, with Δ and Λ, and *R* and *S* configurations, respectively, they lead to the formation of four isomers: Δ*R*, Λ*S*, Λ*R* and Δ*S*. The NMR spectra at various temperatures showed that the pyramidal inversion at the sulfur atom produces an exchange between the diasteroisomers Δ*R* and Λ*S*, as well as between Λ*R* and Δ*S*. The low values of $\Delta G^{\#}_{298}$ (50–55 kJ·mol^{-1}) were explained in terms of the simultaneous presence of the congested Ru(*N*,*N*-dprs)$_2$ fragment and sterically demanding *N*,*S*-coordinated thioethers, which have a high-energy ground state.

In the compounds [Ru(diimine)$_2$(*N*,*S*/L)][PF$_6$]$_2$ [diimine = dps, 4-mdps, 5-mdps, dprs, and 5edprs; L = 2-pyrimidylmethyl *p*-tolyl sulfide (**a**) and *p*-chlorophenyl 2-pyrimidylmethyl sulfide (**b**)], **a** and **b** are *N*,*S*-chelated and form a five-membered ring RuSCCN(*Ru–N*). A restricted phenyl rotation, which exchanges *ortho* as well as *meta* phenyl protons, was also observed. The values of $\Delta G^{\#}_{298}$ are 49–55 kJ·mol^{-1}.

In the present compounds **1**, **2** and **3**, the ligands 2-pyridylmethyl 2′-pyridyl sulfide (**L$_1$**), 2-pyridylmethyl 2′-pyrimidyl sulfide (**L$_2$**), and 2-pyridylmethyl 2′-(4-methylpyrimidyl) sulfide (**L$_3$**) adopt only the *N*,*S*-coordination and form five-membered rings RuSCCN(*Ru–N*) as observed in the crystal structure of [Ru(dps)$_2$(2-pyridylmethyl 2′-pyridyl sulfide)][PF$_6$]$_2$.[37]

The expected invertomers Δ*R* and Λ*S*, and Δ*S* and Λ*R* give only one set of signals in the ^{1}H NMR spectra even at low temperatures as a result of fast sulfur inversion. For the complexes **4**–**9**, two fast exchanging *N*,*S*-chelated invertomers are present, as observed in similar species containing flexible five-membered *N*,*S*-chelated ring.[37]

Although the NMR spectra at low temperatures of **4** and **5** are in agreement with *N*,*S*-coordination, in the range 290–310 K, the proton signals broaden, particularly, the H(6) signal of the dprs ring F. These NMR findings are likely to be associated with the presence of the *N*-monodentate species at high temperature. It is pertinent to note at this point that a strong temperature dependence of the population ratio is normally observed in these systems (see population ratio of **6a** + **6b**, **7a** + **7b**, **8a** + **8b** and **9a** + **9b** in Table 2). Furthermore, very different resonances are observed for corresponding protons 6F and 6F′ of the two different coordination species (Table 1). In other words, at low temperature the *N*,*S*-chelated species of **4** and **5** largely predominates, the concentration of the *N*-monodentate species increases on warming; the H(6) signals of ring F are sensitive to this process.

For **4** and **5**, we cannot calculate the activation parameters of the process, as we do not know the population ratio and difference in the chemical shifts of the two species at low temperatures.

With regard to a mechanism that is consistent with the exchange of the two different coordination species (**6a** + **6b**, **7a** + **7b**, **8a** + **8b** and **9a** + **9b**), we base our suggestion preliminarily on the following observations: i) The $\Delta G^{\#}_{298}$ values for these mixtures are almost the same, approximately equal to 59,5 kJ·mol^{-1}; ii) the $\Delta S^{\#}$ values are negative for **6a** + **6b** and **7a** + **7b** and close to zero for **8a** + **8b** and **9a** + **9b**.

 © 2005 Wiley-VCH Verlag GmbH & Co. KGaA, Weinheim

Table 3. ^{13}C NMR spectroscopic data.

Complex[a]	Asymmetric thioether ligand						Other ligands				
T [K]	C(2)	C(3)	C(4)	C(5)	C(6)	CH_2	C(2)	C(3)	C(4)	C(5)	C(6)
L_1	158.8[b]	123.4[b]	136.9[b]	122.1[b]	149.8[b]	36.0[b]	158.8[c]	122.4[c]	136.7[c]	120.1[c]	149.6[c]
L_2	158.1[b]	123.3[b]	136.8[b]	122.4[b]	149.6[b]	36.8[b]	171.7[d]		157.8[d]	117.4[d]	157.8[d]
L_3	158.7[b]	123.6[b]	137.0[b]	122.6[b]	149.9[b]	37.1[b]	171.4[d]	23.7[e]	168.3[d]	117.0[d]	157.6[d]
1	162.8[b]	128.4[b]	139.3[b]	125.4[b]	153.4[b]	39.4[b]	157.2	125.6	138.4	124.2	151.6
	148.4[c]	125.5[c]	138.4[c]	123.9[c]	150.9[c]		157.3	127.7	138.5	124.3	152.0
							157.6	128.3	138.6	124.4	152.6
							158.1	128.4	139.1	125.3	152.9
2	162.9[b]	128.9[b]	138.7[b]	125.5[b]	151.8[b]	41.4[b]	157.7	125.6	138.7	124.4	152.2
	171.6[d]		159.4[d]	120.9[d]	159.4[d]		157.8	125.9	138.8	124.5	152.3
							158.0	127.7	139.3	125.3	153.0
							158.2	128.4	139.5	125.4	153.9
3	163.2[b]	129.0[b]	138.7[b]	125.7[b]	151.9[b]	41.4[b]	157.9	125.9	138.8	124.4	152.3
	170.4[e]	23.4[d]		120.6[e]	158.5[e]		157.9	127.8	138.9	124.5	152.5
							158.1	128.4	139.4	125.5	153.2
							158.3	128.9	139.6	125.6	153.9
4[h]	163.0[b]	129.6[b]	138.3[b]	123.4[b]	154.8[b]	44.3[b]	168.7		156.9	121.6	164.1
233	151.5[c]	124.8[c]	138.1[c]	120.2[c]	149.2[c]		169.5		158.4	121.7	164.8
							169.6		158.4	122.3	164.9
							169.7		158.8	123.1	165.0
5[h]	165.4[b]	126.5[b]	139.9[b]	125.2[b]	157.1[b]	46.8[b]	166.9	15.5[f]	158.5	138.8	163.6
325	153.7[c]		140.0[c]	125.0[c]	151.0[c]		167.4	15.7[f]	159.8	139.8	165.1
		23.6[g]	23.5[g]	23.4[g]	23.3[g]		169.3	16.0[f]	159.8	140.1	165.2
							169.8	16.1[f]	160.5	140.7	165.2
6a	163.5[b]	124.1[b]	138.7[b]	123.9[b]	155.3[b]	44.1[b]	169.3		157.6	122.0	164.6
243	172.3[d]		158.9[d]	120.8[d]	158.9[d]		170.1		159.0	122.1	165.5
							170.2		159.0	122.3	165.5
							170.7		159.4	122.9	165.9
6b[i]			139.0[b]			44.4[b]	169.1[j]	170.4[j]	158.0[k]		158.2[k]
243			159.8[d]	121.1[d]	159.8[d]		169.4[j]	170.4[j]	158.0[k]		158.2[k]
6a + 6b	164.4[b]	125.9[b]	140.2[b]	125.8[b]	156.9[b]	45.4[b]	170.8		159.9	122.9	166.4
325			160.2[d]	122.2[d]	160.2[d]		170.8		160.1	123.0	166.5
							172.0		160.5	123.1	166.6
							172.0		160.9	124.0	166.7
7a	163.3[b]	123.8[b]	138.3[b]	123.7[b]	155.0[b]	43.9[b]	169.1		157.3	121.0	164.8
243	172.5[d]	22.5[e]	161.7[d]	120.3[d]	159.1[d]		169.9		158.1	121.9	165.2
							170.0		158.7	122.1	165.3
							170.7		158.7	122.6	165.3
7b[i]	163.1[b]	124.8[b]	139.3[b]	124.4[b]	155.9[b]	43.7[b]	168.8[j]	169.5[j]		165.0[l]	165.1[l]
243		23.1[e]		120.7[d]	159.6[d]		170.2[j]	170.8[j]		165.7[l]	166.0[l]
7a + 7b		125.9[b]	140.1[b]	125.8[b]	156.7[b]	45.2[b]	170.7		159.2	122.3	164.7
323	172.5[d]	23.9[e]		122.0[d]	160.7[d]		171.3		159.5	123.0	166.3
							171.9		159.8	123.1	166.5
							172.0		160.0	124.0	166.5
8a		124.5[b]	139.1[b]	124.0[b]	155.8[b]	44.3[b]	169.0	15.1[f]	158.0	137.8	164.7
243			158.8[d]	121.3[d]	158.8[d]		169.2	15.2[f]	158.1	137.9	165.0
							160.9	15.3[f]	158.5	138.2	165.5
							170.1	15.6[f]	158.7	138.6	166.0
8b[i]		125.0[b]	139.9[b]	124.9[b]	156.8[b]	44.0[b]	168.9[j]	169.5[j]			
243			159.8[d]	121.8[d]	159.8[d]		170.0[j]	170.6[j]			
8a + 8b		125.6[b]	140.3[b]	125.6[b]	157.4[b]	45.9[b]	168.1	15.4[f]	159.3	139.0	163.4
325			160.3[d]	123.1[d]	160.3[d]		169.8	15.7[f]	159.8	139.5	165.1
		23.6[g]	23.5[g]	23.3[g]	23.3[g]		169.9	15.9[f]	159.9	140.1	165.3
							170.2	16.1[f]	160.7	140.8	165.5
9a	163.9[b]	123.5[b]	138.0[b]	122.9[b]	155.1[b]	43.6[b]		15.1[f]	157.7	136.6	164.7
233		22.4[e]	162.1[d]	120.8[d]	158.6[d]			15.2[f]	157.8	138.4	165.2
		22.0[g]	21.8[g]	21.8[g]	21.6[g]			15.2[f]	158.2	138.5	167.3
								15.6[f]	158.3	139.0	168.6
9b[i]	163.9[b]	122.5[b]	139.1[b]	123.7[b]	156.7[b]	42.3[b]			164.3[l]	136.3	166.2[l]
233		23.4[e]	162.1[d]	120.9[d]	159.3[d]						168.0[l]
9a + 9b	164.8[b]	125.7[b]	140.2[b]	125.5[b]	157.3[b]	45.8[b]		15.4[f]	158.9	138.7	163.3
325		24.1[e]	164.2[d]	122.4[d]	160.7[d]			15.7[f]	159.5	139.5	165.1
		23.6[b]	23.5[g]	23.4[g]	23.3[g]			15.7[f]	159.7	140.0	165.3
								16.1[f]	159.8	140.8	165.5

[a] Recorded at 75.56 MHz in [D_6]acetone and 298 K unless stated otherwise. [b] CH_2-pyridyl fragment. [c] S-pyridyl fragment. [d] Pyrimidyl fragment. [e] Methyl signal of **L_3**. [f] Methyl signal of 5edprs. [g] Methylene signal of 5edprs. [h] The signals for the minor isomer is not observed. [i] Minor isomer, only a few signals are assigned. [j] C(2) signal of dprs or 5edprs. [k] C(4) signal of dprs. [l] C(6) signal of dprs.

 © 2005 Wiley-VCH Verlag GmbH & Co. KGaA, Weinheim

We propose that the mechanism for the interconversion involves the formation of a labile *N*,*N*-intermediate, and subsequent fast dissociation of the Ru–N(pyrimidine) bond, which gives rise to the *N*-monodentate species (Scheme 2). The hemilabile ligands $\mathbf{L_2}$ or $\mathbf{L_3}$ contain three different types of bonding groups. The pyridine group bonds strongly to a metal center, whereas the sulfur and the pyrimidine nitrogen atoms are substitutionally labile groups. In other words, the ruthenium atom undergoes a 1,3-shift between the N(pyrimidine) atom and the sulfur atom, whereas the N(pyridine) atom is always coordinated to the metal, as a result of the ligand attempting, but failing, to adopt a terdentate bonding. The labile *N*,*N*-intermediate involves a seven-coordinate metal transition-state in which S and N(pyrimidine) atom contribute to the bonding. Furthermore, as a consequence of the rotation of the pyrimidine ring in the *N*,*S*-chelate and the *N*-monodentate species, involvement of the both N(pyrimidine) atoms in the coordination is achieved. A substantially stronger Ru–N(pyridine) bond than the Ru–S and Ru–N(pyrimidine) bonds would favor this mechanism.

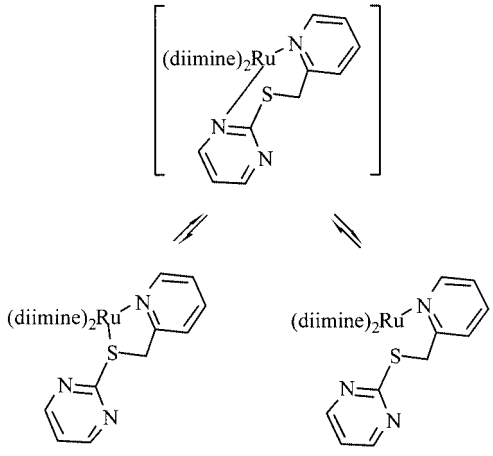

Scheme 2. Proposed mechanism of the interconversion between the different coordination species.

The negative or close to zero $\Delta S^{\#}$ values reflect the formation of a seven-coordinate metal transition-state, while the $\Delta G^{\#}_{298}$ values, practically unchanged by substitution of $\mathbf{L_2}$ with $\mathbf{L_3}$, are compatible with the a similar congested nature of the transition state in all the complexes.

A simple dissociative mechanism involving rupture of the Ru–S bond in the *N*,*S*-chelated species is unlikely, not only because the $\Delta S^{\#}$ values are negative or close to zero, but also because of the following NMR findings: 1) the ^{1}H NMR signals are temperature-reversible and concentration-independent; 2) the process is clearly the same in acetone and acetonitrile below 345 K (in acetonitrile above this temperature some decomposition is observed); 3) the substitution of the uncoordinated pyridine ring with the pyrimidine ring favors the dynamic process.

Although electronic effects can be invoked to explain this behavior, these effects are not observed when the H(4) pyrimidyl proton of $\mathbf{L_2}$ is substituted with the methyl group or when the H(5) pyrimidyl proton of dprs is substituted with the ethyl group.

It is important to note at this point that the process is present only in congested ruthenium cores in which the *N*,*S*-chelated ligand must contain at least three donor atoms, and is favored by the presence of two donor atoms in the uncoordinated pyrimidine ring. The pyrimidine group bonded to the sulfur atom not only weakens the Ru–S bond but also increases the statistical probability of the *N*,*N*-intermediate.

On the other hand, an associative mechanism, involving solvent, anion, or free ligand, is incompatible with the following observations: a) addition of free ligand or PF_6^- anion does not affect the rates of the process; b) separate signals for the free and coordinated ligand were observed in the range 200–330 K (Figure 6). Therefore, the mechanism, consistent with the experimental results, appears to involve the labile *N*,*N*-chelated intermediate.

Conclusions

The reactions of thioethers bearing CH_2Py and pyridine or pyrimidine groups with $Ru(dprs)_2Cl_2$ has allowed us to extend the chemistry of octahedral congested ruthenium(II) compounds containing *N*,*S*-chelated ligands with a five-membered chelate ring. The ring size of *N*,*S*-chelated ligands plays a determining role for sulfur inversion. In the five-membered chelate ring, the process is fast, in the four-membered ring, it is much slower.[36] The NMR experiments show that a minor species containing the *N*-monodentate thioether is favored by the presence of two nitrogen atoms in the uncoordinated ring, whereas it is not observed when the nitrogen atoms are absent.[37] Further experiments are in progress with the aim of studying the effect of the nature of congested $Ru(N,N\text{-dimmine})_2$ cores on the interconversion between different coordination species.

Experimental Section

General Remarks: Bis(2-pyrimidyl) sulfide,[35] 2-pyridylmethyl 2′-pyridyl sulfide ($\mathbf{L_1}$),[40] 2,2′-bis(5-ethylpyrimidyl) sulfide (5edprs),[37] $[Ru(dprs)_2Cl_2]\cdot 2H_2O$,[35] and $[Ru(5edprs)_2Cl_2]$[37] were prepared according to published methods. $Ru(bipy)_2Cl_2$ and other reagents and solvents were used as received. All the syntheses were performed under N_2, and all the complexes were dried over P_4O_{10} under vacuum. Elemental analyses were carried out by Redox Microanalytical Laboratory of Cologno Monzese (Milano). Conductivity measurements were done on a Metrohm 644 conductometer. Infrared spectra were recorded with a Perkin–Elmer RX I FT-IR spectrophotometer with samples as Nujol mulls placed between KBr plates, and the ^{1}H and ^{13}C NMR spectra were recorded with a Bruker AMX 300 spectrometer. Simulations of static and dynamic spectra were performed by the gNMR program.

Preparations

The known[40] 2-pyridylmethyl 2′-pyrimidyl sulfide ($\mathbf{L_2}$) was prepared with the following procedure: 2-sulfanylpyrimidine (5.6 g, 0.05 mol), 2-picolyl chloride hydrochloride (8.2 g, 0.05 mol), and K_2CO_3

 © 2005 Wiley-VCH Verlag GmbH & Co. KGaA, Weinheim

(9.67 g, 0.07 mol) were vigorously stirred in DMF (30 cm^3) at 100 °C for 6 h. The solvent was distilled under reduced pressure, and the residue extracted with CH_2Cl_2 (200 cm^3). This was then concentrated (ca. 5 cm^3) and added to the top of the chromatography column (diameter 2 cm) packed with aluminium oxide (35 g; Aldrich neutral, STD grade, 150 mesh). Elution with CH_2Cl_2/hexane (5:2) gave a pale yellow band, which was collected. The solvent was removed in vacuo, and the remaining yellow oil was kept at –24 °C until a solid was formed (ca. 2 d). Yield 4.57 g (45%). Selected IR data (KBr): $\tilde{\nu}$ = 1670 vs, 1590 vs, 1563 vs, 1548 vs, 1257 s, 1199 vs, 1184 vs, 1091 vs, 994 s, 799 vs, 773 vs, 749 vs, 734 s and 588 ms cm^{-1}.

2-Pyridylmethyl 2′-(4-Methylpyrimidyl) Sulfide (L_3): Prepared similarly starting from 2-mercapto-4-methylpyrimidine hydrochloride (8.13 g, 0.05 mol), 2-picolyl chloride hydrochloride (8.20 g, 0.05 mol), and K_2CO_3 (16.7 g, 0.12 mol). Yield 4.35 g (40%). Selected IR data (KBr): $\tilde{\nu}$ = 1592 vs, 1568 vs, 1541 vs, 1223 s, 1206 vs, 1091 s, 995 s, 881 s, 785 s, 771 s, 750 vs, 713 vs, 698 s, 590 s, 547 s and 406 s cm^{-1}. $C_{11}H_{11}N_3S$ (217.29), calcd. C 60.80, H 5.10, N 19.34, S 14.75; found C 60.70, H 5.20, N 19.50, S 14.70.

$[Ru(bipy)_2(L_1)][PF_6]_2$ (1): $[Ru(bipy)_2Cl_2]\cdot 2H_2O$ (0.174 g, 0.33 mmol) in degassed ethanol/water (3:2, 50 cm^3) was heated under reflux for 1 h. 2-pyridylmethyl 2′-pyridyl sulfide (0.178 g, 0.882 mmol) was then added, and the mixture was heated under reflux for a further 4 h. The hot solution was filtered, and the filtrate was added to water (50 cm^3) containing NH_4PF_6 (0.98 g, 6.0 mmol). An orange precipitate was obtained, filtered, washed with water, and dried overnight. The solid was dissolved in acetone (15 cm^3), precipitated with diethyl ether (100 cm^3), and washed with diethyl ether (70 cm^3). Yield 0.181 g (60%). Selected IR data (KBr): $\tilde{\nu}$ = 1605 s, 1575 s, 1560 ms, 1548 ms, 1515 s, 1315 s, 1243 s, 1162 s, 1125 s, 845 br, 764 vs, 740 ms, 730 s, 558 vs cm^{-1}. $C_{31}H_{26}F_{12}N_6P_2RuS$ (905.65), calcd. C 41.11, H 2.89, N 9.28, S, 3.54; found: C 40.90, H 3.00, N 9.30, S 3.60. Conductivity: Λ_M (MeCN, 2×10^{-4} mol·dm^{-3}, 20 °C) = 333 S·cm^2·mol^{-1}.

$[Ru(bipy)_2(L_2)][PF_6]_2$ (2): This compound was obtained in the same way as that described above starting from $[Ru(bipy)_2Cl_2]\cdot 2H_2O$ (0.302 g, 0.623 mmol) and 2-pyridylmethyl 2′-pyrimidyl sulfide (0.630 g, 3.100 mmol). Yield 0.339 g (60%). Selected IR data (KBr): $\tilde{\nu}$ = 1605 s, 1561 s, 1557 vs, 1315 ms, 1243 ms, 1164 s, 1108 s, 838 br, 764 vs, 731 s, 558 vs cm^{-1}. $C_{30}H_{25}F_{12}N_7P_2RuS$ (906.64), calcd. C 39.74, H 2.78, N 10.81, S, 3.53; found: C 39.70, H 2.80, N 10.85, S 3.60. Conductivity: Λ_M (MeCN, 2×10^{-4} mol·dm^{-3}, 25 °C) = 310 S·cm^2·mol^{-1}.

$[Ru(bipy)_2(L_3)][PF_6]_2$ (3): The compound was obtained in the same way as that described above starting from $[Ru(bipy)_2Cl_2]\cdot 2H_2O$ (0.200 g, 0.413 mmol) and 2-pyridylmethyl 2′-(4-methylpyrimidyl) sulfide (0.510 g, 2.34 mmol). Yield 247 (65%). Selected IR data (KBr): $\tilde{\nu}$ = 1603 ms, 1575 s, 1534 ms, 1163 ms, 844 br, 768 vs, 732 ms, 558 vs cm^{-1}. $C_{31}H_{27}F_{12}N_7P_2RuS$ (920.66), calcd. C 40.44, H 2.95, N 10.65, S, 3.48; found: C 40.40, H 2.90, N 10.65, S 3.50. Conductivity: Λ_M (MeCN, 2×10^{-4} mol·dm^{-3}, 25 °C) = 340 S·cm^2·mol^{-1}.

$[Ru(dprs)_2(L_1)][PF_6]_2$ (4): $[Ru(dprs)_2Cl_2]\cdot 2H_2O$ (0.196 g, 0.33 mmol) and 2-pyridylmethyl 2′-pyridyl sulfide (0.178 g, 0.882 mmol) in ethanol/water (3:2, 50 cm^3) were heated under reflux under N_2 for 4 h. The hot solution was filtered, and the filtrate was added to water (50 cm^3) containing NH_4PF_6 (0.65 g, 4 mmol). An orange precipitate was obtained, filtered, washed with cold water (30 cm^3), and dried overnight. The solid was then dissolved in acetone (15 cm^3), precipitated with diethyl ether (100 cm^3), washed with diethyl ether (70 cm^3), and dried over P_4O_{10} under vacuum. Yield 0.195 g (60%). Selected IR data (KBr): $\tilde{\nu}$ = 1654 br, 1575 s, 1549 s, 1168 s, 1127 s, 1085 ms, 847 br, 767 s, 753 s, 721 ms, 559 vs cm^{-1}. $C_{27}H_{22}F_{12}N_{10}P_2RuS_3$ (973.72), calcd. C 33.31, H 2.28, N 14.38, S, 9.88; found: C 33.30, H 2.30, N 14.20, S 9.80. Conductivity: Λ_M (MeCN, $2\cdot10^{-4}$ mol·dm^{-3}, 25 °C) = 320 S·cm^2·mol^{-1}.

$[Ru(5edprs)_2(L_1)][PF_6]_2$ (5): The compound was obtained in the same way as **4** starting from $[Ru(5edprs)_2Cl_2]$ (0.219 g, 0.33 mmol) and 2-pyridylmethyl 2′-pyridyl sulfide (0.178 g, 0.882 mmol). Yield 0.215 g (60%). Selected IR data (KBr): $\tilde{\nu}$ = 1653 br, 1574 s, 1548 vs, 1242 s, 1145 vs, 1061 vs, 878 vs, 845 br, 780 s, 765 s, 721 ms, 558 vs cm^{-1}. $C_{35}H_{38}F_{12}N_{10}P_2RuS_3$ (1085.93), calcd. C 38.71, H 3.53, N 12.90, S, 8.86; found: C 38.60, H 3.60, N 12.80, S 8.80. Conductivity: Λ_M (MeCN, $2\cdot10^{-4}$ mol·dm^{-3}, 25 °C) = 315 S·cm^2·mol^{-1}.

$[Ru(dprs)_2(L_2)][PF_6]_2$ (6a + 6b): The procedure used in this synthesis was similar to that described for **4** starting from $[Ru(dprs)_2Cl_2]\cdot 2H_2O$ (0.196 g, 0.33 mmol) and 2-pyridylmethyl 2′-pyrimidyl sulfide (0.178 g, 0.882 mmol.) Yield 0.195 g (60%). Selected IR data (KBr): $\tilde{\nu}$ = 1654 br, 1578 vs, 1561 s, 1549 vs, 1169 vs, 1085 s, 845 br, 769 ms, 754 s, 723 ms, 558 vs cm^{-1}. $C_{26}H_{21}F_{12}N_{11}P_2RuS_3$ (974.71), calcd. C 32.04, H 2.17, N 15.81, S 9.87; found C 32.00, H 2.20, N 15.60, S 9.80. Conductivity: Λ_M (MeCN, $2\cdot10^{-4}$ mol·dm^{-3}, 25 °C) = 318 S·cm^2·mol^{-1}.

$[Ru(dprs)_2(L_3)][PF_6]_2$ (7a + 7b): The procedure used in this synthesis was similar to that described above with an equivalent quantity of 2-pyridylmethyl 2′-(4-methylpyrimidyl) sulfide (0.192 g, 0.882 mmol) used in place of L_2. Yield 0.190 g (68%). Selected IR data (KBr): $\tilde{\nu}$ = 1575 vs, 1549 vs, 1261 s, 1167 vs, 1086 s, 846 br, 767 ms, 753 s, 721 ms, 558 vs cm^{-1}. $C_{27}H_{23}F_{12}N_{11}P_2RuS_3$ (988.74), calcd. C 32.80, H 2.34, N 15.58, S 9.73; found C 32.60, H 2.40, N 15.60, S 9.80. Conductivity: Λ_M (MeCN, $2\cdot10^{-4}$ mol·dm^{-3}, 25 °C) = 321 S·cm^2·mol^{-1}.

$[Ru(5edprs)_2(L_2)][PF_6]_2$ (8a + 8b): $[Ru(5edprs)_2Cl_2]$ (0.219 g, 0.33 mmol) and 2-pyridylmethyl 2′-pyrimidyl sulfide (0.178 g, 0.882 mmol) in ethanol/water (3:2, 50 cm^3) were heated under reflux for 2 h. $AgPF_6$ (0.167 g 0.66 mmol) was then added, and the mixture was stirred for 1 h at 50 °C in the dark. After filtration of the solution into water (50 cm^3) containing NH_4PF_6 (0.65 g, 4.0 mmol), an orange precipitate was obtained, filtered, washed with cold water (30 cm^3), and dried overnight. Aluminium oxide (0.200 g) was added to the crude product dissolved in acetone (15 cm^3), and the mixture was stirred for 15 min. The solution was then filtered, and the aluminium oxide was washed with acetone (5 cm^3). The solution and washing liquids were concentrated (5 cm^3), and diethyl ether (50 cm^3) was added. The precipitate was collected and washed with diethyl ether. Yield 0.108 g (30%). Selected IR data (KBr): $\tilde{\nu}$ = 1580 s, 1556 s, 1549 vs, 1260 vs, 1093 vs, 1061 s, 1022 vs, 845 br, 777 s, 754 s, 740 ms, 721 s, 558 vs cm^{-1}. $C_{34}H_{37}F_{12}N_{11}P_2RuS_3$ (1086.93), calcd. C 37.57, H 3.43, N 14.18, S 8.85; found C 37.60, H 3.55, N 14.10, S 8.80. Conductivity: Λ_M (MeCN, $2\cdot10^{-4}$ mol·dm^{-3}, 25 °C) = 343 S·cm^2·mol^{-1}.

$[Ru(5edprs)_2(L_3)][PF_6]_2$ (9a + 9b): The procedure used in this synthesis was similar to that described above with an equivalent quantity of 2-pyridylmethyl 2′-(4-methylpyrimidyl) sulfide (0.192 g, 0.882 mmol) used in place of L_2. Yield 0.134 g (37%). Selected IR data (KBr): $\tilde{\nu}$ = 1575 vs, 1548 vs, 1143 s, 1061 s, 841 br, 757 s, 740 ms, 721 ms, 558 vs cm^{-1}. $C_{35}H_{39}F_{12}N_{11}P_2RuS_3$ (1100.95), calcd. C 38.18, H 3.57, N 13.99, S 8.74; found C 38.20, H 3.60, N 13.90, S 8.80. Conductivity: Λ_M (MeCN, $2\cdot10^{-4}$ mol·dm^{-3}, 25 °C) = 350 S·cm^2·mol^{-1}.

 © 2005 Wiley-VCH Verlag GmbH & Co. KGaA, Weinheim

Acknowledgments

This work was supported by the Università di Messina, Italy (PRA, 2002).

[1] C. S. Slone, D. A. Weimberg, C. A. Mirkin, *Prog. Inorg. Chem.* **1999**, *48*, 233–350.
[2] E. W. Abel, N. J. Long, K. G. Orrell, A. G. Osborne, H. M. Pain, V. Sik, *J. Chem. Soc. Chem. Commun.* **1992**, 303–304.
[3] E. W. Abel, V. S. Dimitrov, N. J. Long, K. G. Orrell, A. G. Osborne, V. Sik, M. B. Hursthouse, M. A. Mazid, *J. Chem. Soc. Dalton Trans.* **1993**, 291–298.
[4] E. W. Abel, K. A. Hylands, M. D. Olsen, K. G. Orrel, A. G. Osborne, W. Sik, G. N. Ward, *J. Chem. Soc. Dalton Trans.* **1994**, 1079–1090.
[5] E. W. Abel, A. Gelling, K. G. Orrell, A. G. Osborne, V. Sik, *J. Chem. Soc. Chem. Commun.* **1996**, 2329–2330.
[6] P. J. Heard, D. A. Tocher, *J. Chem. Soc. Dalton Trans.* **1998**, 2169–2176.
[7] M. L. Creber, K. G. Orrell, A. G. Osborne, V. Sik, M. B. Hursthouse, K. M. A. Malik, *J. Chem. Soc. Dalton Trans.* **2000**, 4218–4226.
[8] P. J. Heard, J. Cameron, *J. Chem. Soc. Dalton Trans.* **1997**, 1083–1091.
[9] P. J. Heard, P. M. King, A. D. Bain, P. Hazendonk, D. A. Tocher, *J. Chem. Soc. Dalton Trans.* **1999**, 4495–4501.
[10] J. H. Groen, P. W. N. M. van Leeun, K. Vrieze, *J. Chem. Soc. Dalton Trans.* **1998**, 113–117.
[11] a) S. J. Chadwell, S. J. Coles, P. G. Edwards, M. B. Hursthouse, *J. Chem. Soc. Dalton Trans.* **1996**, 1105–1112; b) R. Jaouhari, P. G. Edwards, *Recl. Trav. Chim. Pays-Bas* **1988**, *107*, 511–513; c) N. W. Alcock, A. W. G. Platt, P. Pringle, *J. Chem. Soc. Dalton Trans.* **1987**, 2273–2280; d) J. P. Farr, F. E. Wood, A. L. Balch, *Inorg. Chem.* **1983**, *22*, 3387–3393.
[12] a) T. B. Rauchfuss, J. Clements, S. F. Agnew, D. M. Roundhill, *Inorg. Chem.* **1977**, *16*, 775–778; b) E. Lindner, U. Schober, R. Fawzi, W. Hiller, U. Englert, P. Wegner, *Chem. Ber.* **1987**, *120*, 1621–1628; c) L. Horner, G. Simons, *Z. Naturforsch. B: Anorg. Chem. Org. Chem.* **1984**, *39*, 497–503; d) M. Alvarez, N. Lugan, R. Mathieu, *J. Organomet. Chem.* **1994**, *468*, 249–256; e) B. D. Vineyard, W. S. Knoweles, M. J. Sabacky, G. L. Bachman, D. J. Weinkauff, *J. Am. Chem. Soc.* **1977**, *99*, 5946–5952; f) H. Yang, M. Alvarez-Gressier, N. Lugan, R. Mathieu, *Organometallics* **1997**, *16*, 1401–1409; g) H. Yang, M. Alvarez, N. Lugan, R. Mathieu, *J. Chem. Soc. Chem. Commun.* **1995**, 1721–1722; h) M. A. Esteruelas, A. M. Lòpez, L. A. Oro, A. Perez, M. Schulz, H. Werner, *Organometallics* **1993**, *12*, 1823–1830; i) E. Lindner, Q. Wang, H. A. Mayer, A. Bader, H. Kühbauch, P. Wegner, *Organometallics* **1993**, *12*, 3291–3296; j) J. M. Brown, P. A. Chaloner, G. Descotes, R. Glaser, D. Lafont, D. Sinou, *J. Chem. Soc. Chem. Commun.* **1979**, 611–613.
[13] a) E. Lindner, S. Meyer, P. Wegner, B. Karle, A. Sickinger, B. Steger, *J. Organomet. Chem.* **1987**, *335*, 59–70; b) E. Lindner, A. Sickinger, P. Wegner, *J. Organomet. Chem.* **1986**, *312*, C37–C40; c) R. W. Wegman, A. G. Abatjoglou, A. M. Harrison, *J. Chem. Soc. Chem. Commun.* **1987**, 1891–1892; d) E. Lindner, H. A. Mayer, P. Wegner, *Chem. Ber.* **1986**, *119*, 2616–2630; e) S. Bischoff, A. Weigt, H. Miebner, B. Lücke, *J. Mol. Catal.* **1996**, *107*, 339–346; f) J. Freiberg, A. Weigt, H. Dilcher, *J. Prakt. Chem.* **1993**, *335*, 337–344; g) E. Lindner, A. Bader, H. Bräunling, R. Jira, *J. Mol. Catal.* **1990**, *57*, 291–300; h) E. Lindner, A. Bader, E. Glaser, P. Wegner, *J. Mol. Catal.* **1989**, *56*, 86–94; i) E. Lindner, J.-P. Reber, *Z. Naturforsch. B: Anorg. Chem. Org. Chem.* **1991**, *46b*, 1581–1584; j) E. Lindner, H. Norz, *Chem. Ber.* **1990**, *123*, 459–465.
[14] a) M. Alvarez, N. Lugan, B. Donnadieu, R. Mathieu, *Organometallics* **1995**, *14*, 365–370; b) C. Abu-Gnim, I. Amer, *J. Chem. Soc. Chem. Commun.* **1994**, 115–117; c) C. Abu-Gnim I. Amer, *J. Mol. Catal.* **1993**, *85*, L275–L278; d) S. Gladiali, L. Pinna, C. G. Arena, E. Rotondo, F. Faraone, *J. Mol. Catal.* **1991**, *66*, 183–190.
[15] S. Meking, W. Keim, *Organometallics* **1996**, *15*, 2650–2656.
[16] a) H. Adams, N. A. Bailey, M. Colley, P. A. Scofield, C. White, *J. Chem. Soc. Dalton Trans.* **1994**, 1445–1451; b) M. C. Bonnet, B. Stitou, I. Tkatchenko, *J. Organomet. Chem.* **1985**, *279*, C1–C4.
[17] K. Burgess, M. J. Ohlmeyer, K. H. Whitmire, *Organometallics* **1992**, *11*, 3588–3600.
[18] M. Bressan, A. Morvillo, *J. Chem. Soc. Chem. Commun.* **1988**, 650–651.
[19] a) G. P. C. M. Dekker, A. Buijs, C. J. Elsevier, K. Vrieze, P. W. N. M. van Leeuwen, W. J. J. Smeets, A. J. Spek, Y. F. Wang, C. H. Stam, *Organometallics* **1992**, *11*, 1937–1948; b) S. Park, D. Hedden, H. M. Roundhill, *Organometallics* **1986**, *5*, 2151–2152; c) E. Lindner, B. Keppeler, H. A. Mayer, K. Gierling, R. Fawzi, M. Steimann, *J. Organomet. Chem.* **1996**, *526*, 175–186; d) H. Werner, M. Schulz, B. Windmüller, *Organometallics* **1995**, *14*, 3659–3668.
[20] K. R. Dunbar, S. C. Haefner, A. Quillevèrè, *Polyhedron* **1990**, *9*, 1695–1702; K. R. Dunbar, *Comments Inorg. Chem.* **1992**, *13*, 313–357.
[21] R. S. Vagg, in Comprehensive Coordination Chemistry: The *Synthesis* Reactions, Properties & Application of Coordination Compounds, G. Wilkinson, R. G. Gillard, J. A. McCleverty, Eds., Pergamon, Oxford, UK, **1987**, Vol. 2, pp 793–812.
[22] a) E. C. Constable, R. P. G. Henney, D. A. Tocher, *J. Chem. Soc. Chem. Commun.* **1989**, 913–914; b) E. C. Constable, S. J. Dunne, D. G. F. Rees, C. X. Schmitt, *J. Chem. Soc. Chem. Commun.* **1989**, 1169–1170; c) E. C. Constable, R. P. G. Henney, D. A. Tocher, *J. Chem. Soc. Dalton Trans.* **1992**, 2467–2474.
[23] E. W. Abel, D. Ellis, K. G. Orrell, *J. Chem. Soc. Dalton Trans.* **1992**, 2243- 2249.
[24] E. W. Abel, P. J. Heard, K. G. Orrell, M. B. Hursthouse, M. A. Mazid, *J. Chem. Soc. Dalton Trans.* **1993**, 3795–3801.
[25] E. W. Abel, E. S. Blackwall, M. L. Creber, P. J. Heard, K. G. Orrell, *J. Organomet. Chem.* **1995**, *490*, 83–88.
[26] a) D. C. Black, *Aust. J. Chem.* **1967**, *20*, 2101–2107; b) R. Driver, W. R. Walker, *Aust. J. Chem.* **1968**, *21*, 2101–2107; c) M. E. Bridson, W. R. Walker, *Aust. J. Chem.* **1970**, *23*, 1191–1197; d) G. C. Pappalardo, A. Seminara, *J. Inorg. Nucl. Chem.* **1976**, *38*, 1993 – 1995; e) A. Forchioni, V. Librando, G. C. Pappalardo, *J. Chem. Soc. Dalton Trans.* **1977**, 638–641; f) F. Nicolò, G. Bruno, G. Tresoldi, *Acta Crystallogr. Sect C* **1996**, *52*, 2188–2191; g) M. Kondo, S. Kawata, S. Kitagawa, H. Kiso, M. Munukata, *Acta Crystallogr. Sect C* **1995**, *51*, 567–569; h) O. S. Jung, D. H. Jo, Y. A. Lee, B. J. Conklin, C. G. Pierpoint, *Inorg. Chem.* **1997**, *36*, 19–24; i) G. Tresoldi, S. Lo Schiavo, P. Piraino, *Inorg. Chim. Acta* **1997**, *254*, 381–385.
[27] a) G. Bruno, F. Nicolò, G. Tresoldi, *Acta Crystallogr. Sect C* **2000**, *56*, 282- 283; b) G. Bruno, F. Nicolò, G. Tresoldi, S. Lanza, *Acta Crystallogr. Sect C* **2002**, *58*, M56–M58.
[28] G. Bruno, F. Nicolò, S. Lo Schiavo, M. S. Sinicropi, G. Tresoldi, *J. Chem. Soc. Dalton Trans.* **1995**, 17–24.
[29] G. Tresoldi, E. Rotondo, P. Piraino, M. Lanfranchi, A. Tiripicchio, *Inorg. Chim. Acta* **1992**, *194*, 233–241.
[30] G. Tresoldi, P. Piraino, E. Rotondo, F. Faraone, *J. Chem. Soc. Dalton Trans.* **1991**, 425–430.
[31] G. De Munno, G. Bruno, E. Rotondo, G. Giordano, S. Lo Schiavo, P. Piraino, G. Tresoldi, *Inorg. Chim. Acta* **1993**, *208*, 67–75.
[32] G. Tresoldi, S. Lo Schiavo, P. Piraino, P. Zanello, *J. Chem. Soc. Dalton Trans.* **1996**, 885–892.
[33] W. M. Teles, N. G. Fernandes, A. Abras, C. A. L. Filgueiras, *Trans. Met. Chem.* **1999**, *24*, 321–325.
[34] R. J. Anderson P. J. Steel, *Acta Crystallogr. Sect C* **1996**, *54*, 2188- 2191.
[35] R. Scopelliti, G. Bruno, C. Donato, G. Tresoldi, *Inorg. Chim. Acta* **2001**, *313*, 43–55.

 © 2005 Wiley-VCH Verlag GmbH & Co. KGaA, Weinheim

[36] G. Tresoldi, S. Lo Schiavo, S. Lanza, P. Cardiano, *Eur. J. Inorg. Chem.* **2002**, 181–191.
[37] L. Baradello, S. Lo Schiavo, F. Nicolò, S. Lanza, G. Alibrandi, G. Tresoldi, *Eur. J. Inorg. Chem.* **2004**, 3358–3369.
[38] E. W. Abel, S. K. Bhargava, K. G. Orrell, *Prog. Inorg. Chem.* **1984**, *32*, 1–118.
[39] G. Binsch, H. Kessler, *Angew. Chem. Int. Ed. Engl.* **1980**, *19*, 411–494.
[40] F. Haviv, R. W. DeNet, R. J. Micaels, J. J. D. Ratajczyk, G. W. Carter, P. R. Young, *J. Med. Chem.* **1983**, *26*, 218–222.
Received: November 23, 2004

 © 2005 Wiley-VCH Verlag GmbH & Co. KGaA, Weinheim

Synthesis and Characterization of Radical Cations Derived from Mono- and Biferrocenyl-Substituted 2-Aza-1,3-butadienes: A Study of the Influence of an Asymmetric and Oxidizable Bridge on Intramolecular Electron Transfer

Vega Lloveras,[a] Antonio Caballero,[b] Alberto Tárraga,[b] M. Desamparados Velasco,[b] Arturo Espinosa,[b] Klaus Wurst,[c] David J. Evans,[d] José Vidal-Gancedo,[a] Concepció Rovira,[a] Pedro Molina,*[b] and Jaume Veciana*[a]

Keywords: Charge transfer / Electrochemistry / Electron transfer / Metallocenes / Optical spectroscopy

The synthesis and study of structural and electronic properties of mono-ferrocenyl π-conjugated complexes **5a**–**d**, whose electronic characteristics have been systematically varied by introducing an electron-donating or electron-withdrawing substituent either at the 1-position or at the 4-position of the 2-aza-1,3-butadiene moiety linked to the ferrocenyl unit, are presented. The structural and electronic properties of the homobimetallic complex **5f**, with two ferrocene units linked through the asymmetric and oxidizable 2-aza-1,3-butadiene bridge, is also reported. The crystal structures of complexes **5b**, **5d**, and **5f** show a large degree of conjugation in this family of compounds. Complexes **5** show a rich electrochemical behavior due both to the oxidation of ferrocenyl units and the 2-aza-1,3-butadiene bridge, as revealed by cyclic voltammetry. Radical cations $\mathbf{5}^{+\cdot}$ were prepared from **5** by coulometric oxidations following their generation by absorption spectroscopy. The electronic properties of all reported neutral and oxidized π-conjugated complexes have been investigated by means of UV/Vis–near-IR, EPR and ^{57}Fe Mössbauer spectroscopy. The detailed study of mono-oxidized species $\mathbf{5a}^{+\cdot}$–$\mathbf{5f}^{+\cdot}$ has permitted the determination of the influence of an asymmetric bridge with an electroactive character on the intramolecular electron transfer (IET) phenomenon, thus demonstrating that the 2-aza-1,3-butadiene bridge promotes the IET between the two metallic units of $\mathbf{5f}^{+\cdot}$ through two different pathways. The experimental data and conclusions are supported by DFT computations (B3LYP/3-21G*) and time-dependent DFT methods.
(© Wiley-VCH Verlag GmbH & Co. KGaA, 69451 Weinheim, Germany, 2005)

Introduction

Currently, there is considerable interest in the study of the properties of compounds bearing multiple redox centers separated by an organic bridge and, in particular, those that are able to produce mixed-valence species.[1] Such species are interesting not only because of their importance in producing new valuable materials, such as molecular wires and switches, that show intramolecular electron transfer (IET) phenomena, but also to understand the role of biologically relevant mixed-valence compounds.[2] One of the richer areas of metallocene chemistry is the study of general strategies for assembling two or more such electroactive metal fragments in close proximity in order to determine the type of electronic interactions between the metal fragments.[3] Among the various possibilities to bridge two cyclopentadienyl-type (Cp) ligands, emphasis has been laid on the electronic and steric properties of organic bridges because both will influence the interaction between the metal fragments bound to the Cp's and, in many cases, these factors will not be independent.

It is worth noting that IET can be monitored by the study of optical transitions occurring in mixed-valence complexes,[4] and that intervalence charge-transfer (IV-CT) bands may be observed in both σ- and π-bridged systems. In the former case, a through-space mechanism is generally believed to be responsible, such that low-energy bands at the near-IR are usually only observed in species that are sufficiently flexible to allow the two metal centers to come into close proximity. In π-bridged systems, near-IR bands are much more widely observed, even when the metals are well separated by rigid bridges, thereby suggesting that through-bond mechanisms are involved. IET in such π-bridged systems may proceed either by a superexchange and/or a hopping mechanism.[5] In the superexchange

[a] Institut de Ciència de Materials de Barcelona (CSIC), Campus Universitari de Bellaterra,
08193, Cerdanyola, Spain
Fax: +34-93-580-5729
E-mail: vecianaj@icmab.es
[b] Universidad de Murcia, Departamento de Química Orgánica, Facultad de Química,
Campus de Espinardo, 30100 Murcia, Spain
Fax: +34-968-364149
E-mail: pmolina@um.es
[c] Institut für Allgemeine Anorganische und Theoretische Chemie, Universität Innsbrück,
6020, Innrain 52a, Innsbruck, Austria
[d] Department of Biological Chemistry, John Innes Centre, Norwich Research Park, Colney, Norwich, NR4 7UH, UK
Supporting information for this article is available on the WWW under http://www.eujic.org/ or from the author.

 © 2005 Wiley-VCH Verlag GmbH & Co. KGaA, Weinheim **DOI: 10.1002/ejic.200400992**

mechanism the bridge serves solely to mediate the wavefunctions of the two electroactive centers that act as electron-donor and -acceptor groups; the electron (or hole) is never vibronically localized on the bridge. In contrast, in the hopping mechanism the electron (or hole) is located at the bridge for a short time (vibronically localized) during its journey from one redox center to the other. The former mechanism is generally the origin of many of the observed IV-CT bands in mixed-valence species, while the hopping one is much less common, probably because of the strict structural and electronic requirements that must be fulfilled by the bridge. Nowadays there is a great interest in the development of organic bridges that favor the hopping mechanism between the two electroactive centers since they could provide new molecular devices that act as electronic relays to promote IETs over large distances.

A large number of bis-metallocenes and metallocenes linked by saturated carbon bridges have been synthesized and studied with respect to metal–metal interactions. It has been demonstrated that, compared to bis-metallocenes, species linked by a single carbon bridge show substantially weaker metal–metal interactions.[6] In general, stronger electrochemical metal–metal interactions occur when two linkages are made between two metallocenes and the metals are brought into closer proximity. On the other hand, IV-CT absorptions are usually not observed in the mono-oxidized derivatives of ferrocenes with insulating hydrocarbon bridges.[7] Most bis-metallocenes linked by saturated carbon bridges belong to class I in the Robin–Day classification,[8] the only interaction detected being at the electrochemical level and which can be attributed only to electrostatic and inductive effects. In contrast, ferrocenyl groups linked by unsaturated bridges show slightly larger metal–metal interactions than those with analogous saturated bridges,[2c,9–13] and the corresponding mono-oxidized olefin-bridged species show IV-CT absorptions in the near-IR region. Thus, many such species belong to class II, in which there is a moderate coupling between the two electroactive centers mediated by the organic bridge through a superexchange mechanism. Intermetallic interactions of different magnitudes have been observed in diferrocene complexes in which the two metallocene units are linked through a symmetric spacer with two conjugated double bonds (e.g. butadiene,[14] 1,4-diaza-1,3-butadiene,[15] 2,3-diaza-1,3-butadiene,[16] and others[17]). However, no examples have been reported of metal–metal interactions between metallocene units linked by an asymmetric spacer like the 2-aza-1,3-butadiene bridge.

Here we wish to present the synthesis and study of structural and electronic properties of ferrocenyl (Fc) π-conjugated complexes **5a**–**d**, whose electronic properties have been systematically varied by introducing an electron-donating or electron-withdrawing substituent, either at the 1-position or at the 4-position of the 2-aza-1,3-butadiene moiety linked to the ferrocenyl unit. We also wish to present here a study of the homobimetallic complex **5f**, which contains two ferrocene units linked by the asymmetric 2-aza-1,3-butadiene bridge. The mono-oxidized species of this complex, $\mathbf{5f}^{+\bullet}$, has permitted the study of the influence of an asymmetric bridge with an electroactive character on the intramolecular electron transfer (IET) phenomenon, demonstrating that the 2-aza-1,3-butadiene bridge favors the IET between the two metallic centers.

Results and Discussion

Synthesis and Characterization

Compounds **5** were all prepared from the readily available diethyl aminomethylphosphonate (**1**),[18] which was condensed with the appropriate aromatic or organometallic aldehyde **2** to give the corresponding *N*-substituted diethyl aminomethylphosphonate **3** in excellent yields (85–95%). Generation of the metalloenamine by treatment with *n*BuLi at –78 °C and subsequently with one equivalent of the aldehyde **4** provided the 1,4-disubstituted 2-aza-1,3-butadienes **5** in yields ranging from 40% to 90% (Scheme 1). While two individual operations are required in the latter synthesis, it is possible to execute the entire sequence of reactions in a single flask without isolation of the intermediates **3** without affecting the yield. However, in this case, isolation of compounds **5** proved to be more difficult. Compounds **5**, recrystallized from dichloromethane/diethyl ether (1:10), were characterized by mass spectroscopy and ^{1}H and ^{13}C NMR spectroscopy, as well as by elemental analyses.

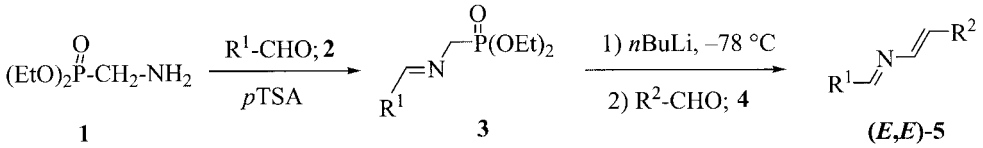

	R^1
3a	4-H_3CO-C_6H_4
3b	4-O_2N-C_6H_4
3c	Fc

	R^1	R^2
5a	4-H_3CO-C_6H_4	Fc
5b	4-O_2N-C_6H_4	Fc
5c	Fc	4-H_3CO-C_6H_4
5d	Fc	4-O_2N-C_6H_4
5e	4-H_3CO-C_6H_4	4-H_3CO-C_6H_4
5f	Fc	Fc

Scheme 1.

 © 2005 Wiley-VCH Verlag GmbH & Co. KGaA, Weinheim

Assignment of the configuration of the double bonds present in the 1,4-disubstituted 2-aza-1,3-butadienes **5** was achieved by inspection of the ^{1}H NMR spectroscopic data. It is well established that the condensation reaction between a primary amine and an aldehyde is not stereoselective, hence both (*E*)- and (*Z*)-aldimine isomers are generally present in the reaction product. However, it must be emphasized that the condensation reaction between **1** and the appropriate aldehyde **2** takes place stereoselectively to give exclusively the (*E*)-isomer, as ascertained by ^{1}H NMR spectroscopy. Indeed, an NOE effect is observed to the methylene group on irradiation of the aldiminic proton of **3a**. On the other hand, *N*-substituted diethyl aminophosphonates **3**, after deprotonation with *n*BuLi, react smoothly in THF with the corresponding aldehyde **4** to give only the *trans* configured carbon-carbon double bond, as is expected in a Horner–Wadsworth–Emmons olefination process. This configuration was confirmed by the characteristic vicinal coupling constants (J = 14.0 Hz) in the ^{1}H NMR spectrum. In addition, NOE and two-dimensional NOESY experiments on a solution of compound **5f** in $CDCl_3$ confirmed not only the (*E*,*E*)-configuration of the double bonds present in the bridge, but also the *s-cis*-conformation in this solvent. Thus, on irradiation at δ = 7.04 ppm (H_4) an NOE effect is observed on the aldiminic H_1; no NOE effect is observed to H_1 when irradiation takes place at δ = 6.63 ppm (H_3).

X-ray Crystal Structures

Single crystals of compounds **5b**, **5d**, and **5f**, suitable for X-ray structure determination, were grown from diffusion of *n*-hexane into a solution of the compound in CH_2Cl_2. The crystal data and details of data collection and structure refinement are given as Supporting Information (Table S1). Attempts to grow good-quality single crystals of **5a** and **5c** for X-ray determination were unsuccessful.

Compound **5b** crystallizes in the triclinic space group $P\bar{1}$ with four molecules in the unit cell. Two independent molecules were found per asymmetric unit. Figure 1 (see a) shows the ORTEP drawing of the molecular structure of **5b** with the atomic numbering scheme. The molecular structure reveals that **5b** is present as the (*E*,*E*)-isomer, as is observed in solution by ^{1}H NMR spectroscopy, and has an *s-trans* configuration in the solid state. The interatomic distances and bond angles of **5b** are close to those previously observed for ferrocene[19] and other substituted ferrocene

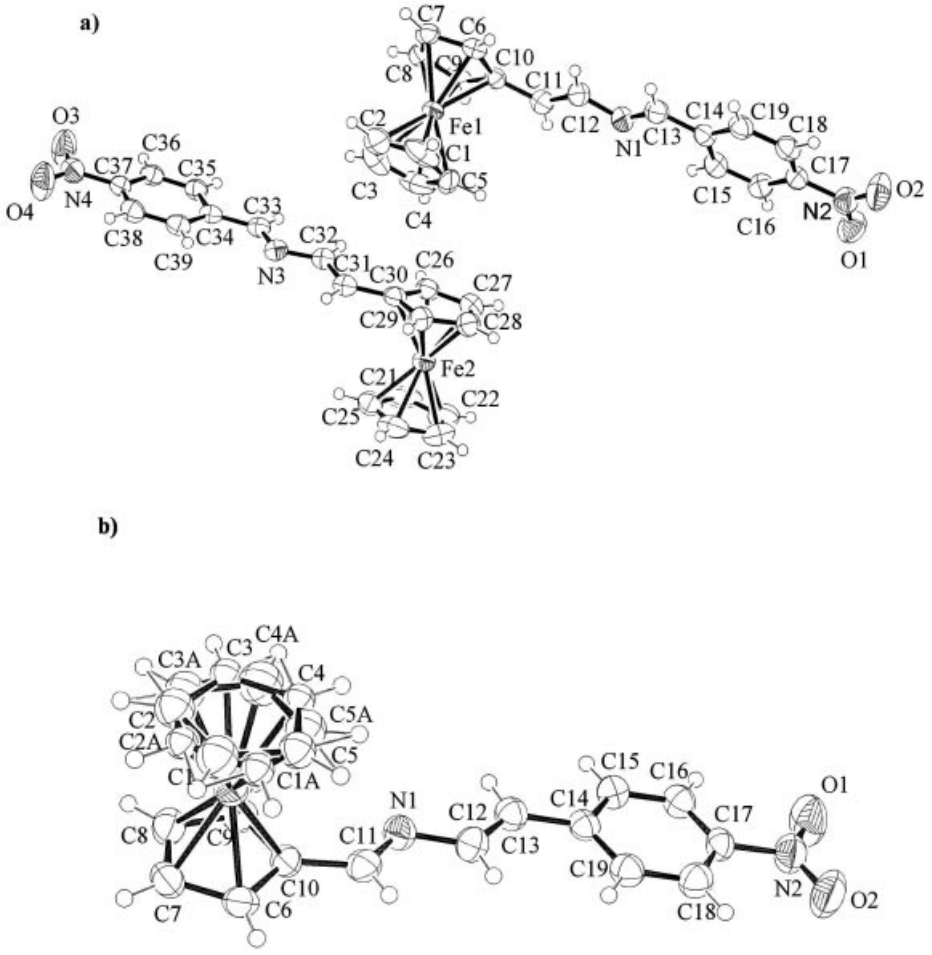

Figure 1. ORTEP views of the asymmetric unit of **5b** showing the atom numbering scheme (a) and of **5d** showing the atom numbering scheme (b). Thermal ellipsoids are drawn at the 50% probability level.

 © 2005 Wiley-VCH Verlag GmbH & Co. KGaA, Weinheim

compounds.[20] The most interesting structural feature of **5b** is that all atoms of the 2-aza-1,3-butadiene bridge and the two attached rings are disposed in a planar configuration, thus indicating a large degree of π-conjugation and rigidity of this organic ligand.

Compound **5d** crystallizes in the monoclinic space group *P*21/*n* with four molecules in the unit cell. Figure 1 (see b) shows the ORTEP drawing with the atomic numbering scheme. Molecules of this compound are also present as the (*E*,*E*)-isomer, as observed in solution by ^{1}H NMR spectroscopy, and have an *s-trans* configuration in the solid state. The bond and dihedral angles reveal that all the atoms of the bridge and the two linked rings are disposed in a planar configuration, as in compound **5b**, thus indicating a large degree of conjugation in the π-system.

Compound **5f** crystallizes in the monoclinic space group *P*21/*c* with two molecules in the unit cell. Figure 2 shows the ORTEP drawing of **5f** with the atomic numbering scheme. The molecular structure of **5f** reveals a 1:1 disorder of the two atoms C12 and N1 at the same position. The crystallographic asymmetric unit is only one half of the molecule, since the other half is generated by a symmetry operation with a center of symmetry, as shown in Figure 2. Since the molecule does not really possess a symmetry center it must be disordered, therefore C12 and N1 were refined each with an occupancy of 0.5 with the same coordinates and temperature factors. Molecules of **5f** are also present as the (*E*,*E*)-isomer, as observed in solution by ^{1}H NMR spectroscopy, but in the solid state they adopt an *s-trans* conformation in contrast to the major conformation adopted in solution (vide supra). One of the two equivalent possibilities of the molecule is shown in Figure 2.

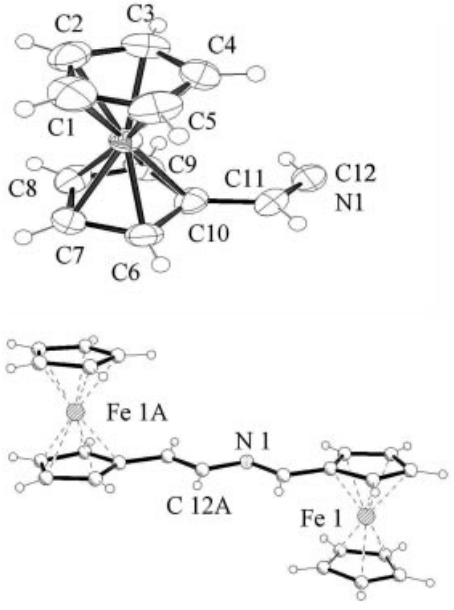

Figure 2. Top: ORTEP view of the asymmetric unit of **5f** showing the atom numbering scheme. Thermal ellipsoids are drawn at the 50% probability level. Bottom: drawing of a complete molecule of **5f**.

Theoretical Calculations

Geometry optimizations at the DFT level were carried out for neutral 2-aza-1,3-butadienes **5** as well as for the oxidized species **5**$^{\bullet+}$; the resulting geometrical parameters are gathered in Table 1. For those compounds whose X-ray structures are reported here, a high degree of coincidence is observed with the calculated values, as shown by the following critical geometrical parameters: the calculated N(bridge)···Fe distances for **5b**, **5d**, and **5f** are 5.309, 3.868, and 3.885 (Fe_1) and 5.380 Å (Fe_4), while the corresponding experimental distances are 5.242, 3.893, and 3.967 and 5.169 Å, respectively; the calculated Fe_1···Fe_4 distance in **5f** is 9.225 Å, while the experimental one is 9.107 Å. The other two calculated structures **5a** and **5c** display similar values (5.350 and 3.860 Å, respectively) for the N(bridge)···Fe distance. On the other hand, all calculated structures have a pure *s-trans* conformation (C1–N2–C3–C4 dihedral angles of 179.7°, 178.3°, 177.5°, 178.6°, and 179.2° for **5a**–**d** and **5f**, respectively), with the substituted phenyl rings almost parallel to the 2-aza-1,3-butadiene plane (angles between mean planes of 0.3°, 3.5°, 4.7°, and 1.4° for **5a**–**d**, respectively) and the bridge-attached Cp rings with small twisting angles (13.6°, 5.6°, 7.8°, 3.5°, 1.4°, and 12.1° for **5a**–**d** and Fc_1 and Fc_4 in **5f**, respectively). Where available, all experimental ring (Cp or substituted phenyl) twisting angles are systematically higher than the corresponding calculated values. From these calculations it is possible to conclude that both neutral 2-aza-1,3-butadienes **5** and oxidized species **5**$^{\bullet+}$ show planar structures exhibiting a large conjugation and a high structural rigidity (Table 1).

Electronic Spectroscopy

The UV/Visible data obtained in CH_2Cl_2 for **5a**–**d** and **5f** are collected in Table 2. These spectra are characterized by a very strong absorption with a maximum between 336 and 375 nm, which is assigned to a localized π-π* excitation mainly within the 2-aza-1,3-butadiene bridge. In addition to this band, another weaker absorption is visible between 469 and 535 nm, which is assigned to another localized excitation with a lower energy produced either by two nearly degenerate transitions, an Fe^{II} d-d transition[21] (e.g. HOMO–1 → LUMO+3 in **5a**), or by a metal-to-ligand charge transfer (MLCT) process (d_π-π*)[22] (e.g. HOMO–3 → LUMO+1 in **5a**). By comparison of the compounds with the ferrocenyl unit in the same position of the bridge it is easy to conclude that the presence of an electron-donating methoxy group (**5a** and **5c**) results in a significant decrease of the wavelength of the absorption maximum relative to the compounds with a nitro substituent (**5b** and **5d**). On the other hand, the compounds with the ferrocenyl group at the 4-position of the bridge show a shift of the absorption maxima to longer wavelengths relative to the compounds with the ferrocenyl group at the 1-position. Therefore, the calculated energy gap between HOMO and LUMO in the first position (3.6558 and 2.8194 eV for **5a** and **5b**, respectively) is slightly smaller than in the second position (3.6889 and

 © 2005 Wiley-VCH Verlag GmbH & Co. KGaA, Weinheim

Table 1. Selected calculated[a] and geometrical parameters[b] for neutral 2-aza-1,3-butadienes **5** and oxidized species $\mathbf{5}^{+\cdot}$.

	R^1–C^1	C^1–N^1	N^2–N^3	C^3–C^4	C^4–R^4	$C^1N^2C^3$	$C^1N^2C^3C^4$	$R^{1\#}Azd^{\#}$	$Azd^{\#}R^{4\#}$	$Fe^1\cdots N^2$	$Fe^4\cdots N^2$	$Fe^1\cdots Fe^4$
5a	1.457	1.294	1.399	1.348	1.447	119.8	179.7	0.3	13.6		5.350	
5b	1.462	1.293	1.395	1.350	1.443	120.6	178.3	3.5	5.6		5.309	
	(1.454)	(1.280)	(1.387)	(1.335)	(1.447)	(117.7)	(176.7)	(5.2)	(9.6)		(5.242)	
5c	1.444	1.294	1.401	1.348	1.459	119.5	177.5	7.8	4.7	3.860		
5d	1.439	1.297	1.398	1.349	1.458	119.0	178.6	3.5	1.4	3.868		
	(1.442)	(1.282)	(1.394)	(1.320)	(1.460)	(117.1)	(179.2)	(3.9)	(4.2)	(3.893)		
5f	1.439	1.297	1.398	1.349	1.458	119.0	178.6	1.4	12.1	3.885	5.380	9.225
	(1.442)	(1.282)	(1.394)	(1.320)	(1.460)	(117.1)	(179.2)	(8.1)	(8.1)	(3.967)	(5.169)	(9.107)
$\mathbf{5a}^{+\cdot}$	1.431	1.313	1.370	1.366	1.424	119.5	177.5	1.0	7.4		5.445	
	(–0.026)	(+0.019)	(–0.029)	(+0.018)	(–0.023)	(–0.3)	(–2.2)	(+0.7)	(–6.2)		(+0.095)	
$\mathbf{5c}^{+\cdot}$	1.433	1.308	1.374	1.367	1.436	121.3	178.3	4.2	2.1	3.984		
	(–0.011)	(+0.014)	(–0.027)	(+0.019)	(–0.023)	(+1.8)	(+0.8)	(–3.6)	(–2.6)	(+0.124)		
$\mathbf{5d}^{+\cdot}$	1.446	1.296	1.392	1.354	1.455	121.0	179.9	7.6	1.0	3.900		
	(+0.007)	(–0.001)	(–0.006)	(+0.005)	(–0.003)	(+2.0)	(+1.3)	(+4.1)	(–0.4)	(+0.032)		
$\mathbf{5f}^{+\cdot}$	1.420	1.314	1.373	1.364	1.425	118.8	176.1	3.4	9.0	3.842	5.456	9.261
	(–0.024)	(+0.020)	(–0.028)	(+0.017)	(–0.022)	(–0.8)	(–3.1)	(+2.0)	(–1.6)	(–0.043)	(+0.076)	(+0.036)
$\mathbf{5f}^{2+}$	1.412	1.409	1.295	1.458	1.415	119.3	178.1	24.5[c]	35.7[c]	3.057	4.124	7.172
	(–0.008)	(+0.094)	(–0.078)	(+0.094)	(–0.010)	(+0.5)	(–0.2)	(+21.1)	(+26.7)	(–0.785)	(–1.332)	(–2.089)

[a] The experimental values for neutral compounds, where available, and, for oxidized species, the calculated absolute difference in relation to the precedent structure before one-electron oxidation, are given in parentheses. [b] Distances [Å] and bond and dihedral angles [°]; # stands for the azadiene skeleton (Azd), Cp or substituted-phenyl mean planes. [c] Unusually large angles between mean planes do not reflect a twisting rotation around a C_{Cp}–C_{Azd} bond, but a bending distortion of the exocyclic substituent towards Fe atom in order to alleviate the electron deficiency. See for instance ref.[49]

Table 2. Calculated and experimental electronic absorption bands of neutral compounds **5a**–**d** and **5f**.

Compound	R^1	R^2	Calculated λ_{max} [nm] (oscillator strength)	Experimental[a] λ_{max} [nm] (10^{-3} ε, $M^{-1}cm^{-1}$)
5a	4-$CH_3OC_6H_4$	Fc	343.6 (0.7961), 375.8 (0.1944), 469.7 (0.0052)	345 (24.5), 360 (sh), 470 (2.1)
5b	4-$NO_2C_6H_4$	Fc	378.7 (0.4862), 526.9 (0.0965)	375 (16.9), 535 (4.4)
5c	Fc	4-$CH_3OC_6H_4$	341.3 (1.2479), 369.2 (0.0132), 470.3 (0.0033)	342 (20.7), 356 (sh), 469 (1.9)
5d	Fc	4-$NO_2C_6H_4$	366.1 (0.5466), 522.6 (0.0690)	371 (18.7), 504 (4.5)
5f	Fc	Fc	336.2 (0.0415), 339.9 (0.1006), 476.2 (0.0033)	336 (25.5), 346 (sh), 478 (3.6)

[a] In CH_2Cl_2.

2.9889 eV for **5c** and **5d**, respectively) and this gap is greatly increased by the presence of an electron-donating substituent at the aromatic ring. Finally, the homobimetallic complex **5f** shows an absorption spectrum that is very similar to those of complexes **5a** and **5c**, as expected from the similar electron-donor abilities of ferrocenyl and *p*-methoxyphenyl groups (calculated HOMO–LUMO gap of 3.7785 eV for **5f**).

At this point, it is useful to consider the electronic transitions in terms of the molecular orbitals involved. Analysis of the electronic transitions by time-dependent DFT methods (TDDFT) gave essentially identical results for each studied compound between experimental and calculated transitions (summarized in Table 2). The agreement between calculated optical transitions and the experimentally observed results lends credence to the used theoretical level as well as to the attained geometries and the molecular-orbital model developed to explain such optical transitions. In addition, such an agreement confirms the assignation previously made to each optical transition.

Electrochemistry

Compounds **5** are all expected to show electroactivity due both to the Fe^{II}/Fe^{III} couple and the oxidation of the 2-aza-1,3-butadiene bridge. Indeed, monoferrocenyl derivatives **5a**–**d** show two oxidation waves in the range 0–1.5 V vs. SCE; their potentials are collected in Table 3. The first oxidation wave for all compounds is reversible and occurs at potentials close to that of the Fe^{II}/Fe^{III} couple in ferrocene (0.460 V vs. SCE, or 0.530 V vs. decamethylferrocene, DMFc).[23] Therefore, this wave is assigned to the Fe^{II}/Fe^{III} redox couple. The oxidation potentials of the ferrocenyl units of these compounds show a dependence on the position of the 2-aza-1,3-butadiene bridge to which they are attached and also on the electron-donating ability of the aromatic group linked to the bridge. Thus, higher potentials are observed when the ferrocenyl is attached at the 1-position of the bridge and when the substituent of the aromatic ring is a nitro group. In contrast to the first oxidation wave, the second wave is clearly not reversible for **5a**–**c** under the conditions of our experiments, since only the anionic peak appears in the cyclic voltammogram. Taking into account that the *p*-methoxyphenyl moiety is the most "ferrocene-like" group in terms of its electron-donating capability, as demonstrated experimentally by the similarity of the UV/Vis spectra of **5a**, **5c**, and **5f** (vide supra), and also by independent non-linear optical measurements,[24] the 1,4-bis(*p*-methoxyphenyl)-2-aza-1,3-butadiene **5e** was also studied for comparison purposes. The CV of this compound shows two

 © 2005 Wiley-VCH Verlag GmbH & Co. KGaA, Weinheim

irreversible oxidation waves at 1.084 and 1.440 V vs. DMFc that may be assigned to the oxidation of the N atom of the bridge and the *p*-methoxyphenyl group, respectively. This assignment is based on the fact that when the N atom of **5e** is protonated under acidic conditions the first oxidation peak disappears while the second remains unchanged. On the basis of these observations, the second wave observed in the CVs of compounds **5a**–**c** is also assigned to the oxidation of the 2-aza-1,3-butadiene group, the potential of which varies from 1.090 V to 1.416 V vs. DMFc and also shows a dependence on the substituents of the aromatic ring and on the relative position of the ferrocenyl and aromatic groups. Such an irreversible oxidation wave is not observed for compound **5d**, probably because it appears at a potential more positive than +1.5 V vs. DMFc due to the strong electron-withdrawing character of the nitro group.

Table 3. Cyclic voltammogram data for compounds **5a**–**f** in CH_2Cl_2.

Compound	R^1	R^2	$^1E_{1/2}$ (Fc^+/Fc)[a]	$^2E_{ap}$ (irrev)[a]
5a	4-$CH_3OC_6H_4$	Fc	0.530	1.090
5b	4-$NO_2C_6H_4$	Fc	0.590	1.190
5c	Fc	4-$CH_3OC_6H_4$	0.698	1.416
5d	Fc	4-$NO_2C_6H_4$	0.704	–
5e	4-$CH_3OC_6H_4$	4-$CH_3OC_6H_4$	–	1.084, 1.440
5f	Fc	Fc	0.560 0.770	1.116

[a] $E_{1/2}$ [V] vs. decamethylferrocene.

To gain further insight into the nature of the irreversible oxidation wave, the electrochemical behavior of compounds **5a**–**d** was investigated in the presence of HBF_4. Upon protonation, the potential shift of the ferrocenyl unit present in these compounds was found to be strongly dependent on its position in the 2-aza-1,3-butadiene bridge. When it is placed at the 4-position a $\Delta E_{1/2}$ (L – LH^+) of 70 mV (**5a**) and 80 mV (**5b**) was observed, while when it is placed at the 1-position the corresponding shifts are 300 mV (**5c**) and 320 mV (**5d**). Additionally, in all these cases, the irreversible wave associated with the oxidation of the bridge disappeared upon protonation, except for **5c**, which seems to be due to the oxidation of the methoxy group present in the ring.

The species formed during the irreversible oxidation waves of **5a**–**c** are probably the radical cations centered mainly at the N atom of the 2-aza-1,3-butadiene bridge, species which must be relatively unstable under the experimental conditions used. Although no electrochemical oxidation study of the 2-aza-1,3-butadiene fragment has been reported, this description is based on the fact that the anodic oxidation of the closely related *N*-benzylidene-*p*-anisidine Schiff bases show two irreversible anodic peaks at 1.08–1.25 and 1.41–1.61 V vs. SCE. The peak potentials of the first wave, which show good linearity against the σ^+ values of the substituent in the benzylidene ring, are ascribed to the formation of a radical cation centered at the nitrogen atom, whereas the second peak is attributed to the oxidation of the substituent in the aromatic ring.[25] In this sense, the electrochemical behaviors of compound **5e** and *N*-*p*-methoxybenzylidene-*p*-anisidine are almost identical, since the CV displays two irreversible oxidation peaks at 1.08 and 1.52 V vs. SCE.

The CV of **5f**, which contains two ferrocenyl groups, was recorded in two different experiments. Firstly, the CV (see a in Figure 3) scanned from 0–1 V shows two closely spaced reversible one-electron oxidations corresponding to the oxidation of the ferrocenyl units present in the molecule. Secondly, when the CV was run from 0.0–1.6 V, after the first scan, three oxidation waves were observed: two for the ferrocenyl units and one for the oxidation of the bridge. The cathodic return wave is, in general, higher and thinner than the anodic forward wave, which can be attributed to some adsorption of the oxidized compound onto the electrode surface in the ferrocenium form. The difference between the anodic and cathodic peak potentials (ΔE_p) is lower than the 58 mV value expected for a reversible single-electron wave of an electroactive species in solution at 20 °C (the fully adsorbed redox species would ideally have a ΔE_p value of zero). However, it is important to emphasize that the results obtained in the latter experiment could only be reproduced when the electrode was cleaned before subsequent scans were run. Otherwise, the wave corresponding to the oxidation of the bridge disappears, indicating that the electrode behaves as an insulator in the region in which the azadiene moiety is oxidized. The protonation process of **5f** was also followed by cyclic voltammetry. Upon protonation, the three waves present in the neutral ligand evolve into two waves in the protonated derivative, the latter wave appearing at almost the same potential region as that corresponding to the bridge in the neutral ligand. In order to understand the nature of the unit causing that wave, Osteryoung square-wave voltammetry (OSWV) experiments were carried out by protonation of **5f** (see b in Figure 3). While the neutral ligand exhibits only two oxidation waves at 0.560 and 0.770 V vs. DMFc, stepwise addition of HBF_4 resulted in a clear evolution of the first oxidation wave from 0.560 V to 0.630 V and the disappearance of the second oxidation wave, accompanied by concomitant appearance of a new oxidation wave at 1.060 V. The peak intensity of the new oxidation wave increases with the concentration of the acid added up to until two equivalents. At this point, the original oxidation waves disappear and the new ones reach full development. The resulting two oxidation waves, with a 1:1 ratio and a separation of 0.430 V, are due to the oxidation of the two ferrocenyl moieties in the protonated complex. Again, for reproducibility, it is very important to clean the electrode after each scan.

It is worth mentioning that the difference between the first two reversible oxidation waves in compound **5f** ($\Delta E_{1/2}$ = 210 mV) is much larger than those observed for most bis-ferrocenyl compounds with four-membered π-conjugated bridges, such as 1,4-bis(ferrocenyl)butadiene (129 mV),[14] 1,4-bis(ferrocenyl)butadiyne (120 mV),[10] 1,4-bis(ferrocenyl)-1,4-diazabutadiene (60 mV),[15] and 1,4-bis(ferrocenyl)-2,3-diaza-1,4-dimethylbutadiene (90 mV).[16] The origin of this large $\Delta E_{1/2}$ value must be ascribed to the asym-

 © 2005 Wiley-VCH Verlag GmbH & Co. KGaA, Weinheim

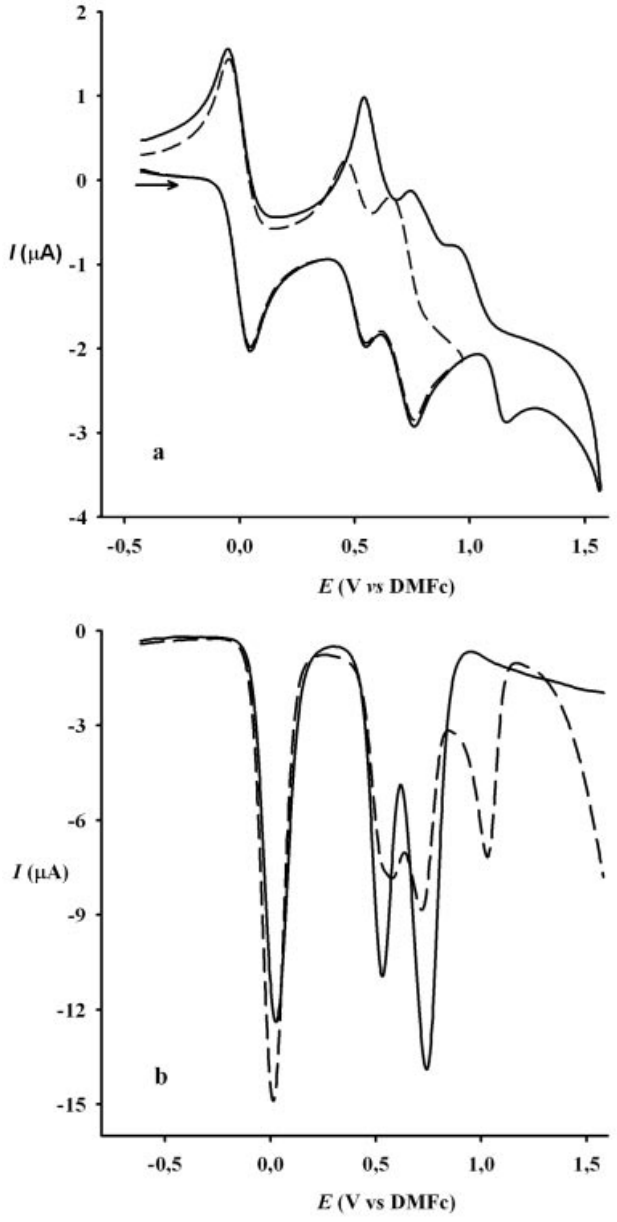

Figure 3. a) Cyclic voltammogram of compound **5f** (1 mM) in $CH_2Cl_2/[(nBu)_4N]ClO_4$ scanned at 0.1 $V s^{-1}$ from –0.5 V to 0.9 V (dash) and from –0.5 V to 1.6 V (solid). b) OSWV of compound **5f** (1 mM) in $CH_2Cl_2/[(nBu)_4N]ClO_4$ recorded at 0.1 $mV s^{-1}$ before (solid) and after (dash) addition of 1 equiv. of HBF_4. Decamethylferrocene (DMFc) was used as an internal standard.

metry of the bridge linking the two ferrocenyl groups. Thus, the distinct position of the N atom with respect to the two ferrocenyl groups should perturb the two ferrocenyl moieties to a different extent.

Optically Induced Intramolecular Electron Transfer in $5a^{\cdot+}$–$d^{\cdot+}$

It has been demonstrated that in electrochemically active ferrocenylthiophene derivatives, in which the gap between the metal and the organic bridge oxidation potentials is relatively small, it is possible, upon oxidation of the ferrocenyl group, to induce optically an electron transfer from the thienyl group to the Fe^{III} center.[26] This IET has an associated low-energy ligand-to-metal charge transfer (LMCT) band in the near-IR, which is very similar to those observed in symmetrical mixed-valence complexes. Moreover, it has been reported recently that the electrochemical oxidation of Fe^{II} centers of mono- or bis(ferrocenylethynyl)oligothiophenes, in which the potential difference between the reversible oxidation of the ferrocenyl group and the irreversible oxidation of the thienyl ring varies from 0.38 V to 1.12 V, yields the corresponding radical cations, which also exhibit oligothiophene-to-Fe^{III} charge-transfer LMCT bands in the near-IR region.[27] Taking into account that in compounds **5a**–**d** the potential differences between the two successive oxidation waves are in the range of 0.3–0.7 V (Table 3), and that these values are comparable to those of oligothiophene-substituted ferrocenes, the oxidized ferrocenyl derivatives $\mathbf{5a}^{\cdot+}$–$\mathbf{d}^{\cdot+}$ were considered suitable candidates to study the optically induced IET from the 2-aza-1,3-butadiene bridge to the Fe^{III} center. In favor of such an expectation is the recently reported fact that ferrocenyl derivatives containing a $-CH_2-N(R)-CH_2-$ bridge undergo intramolecular electron transfer between the Fe^{III} center and the nitrogen atom in the electrochemically oxidized state to give an intermediate containing an Fe^{II} center and a nitrogen with a radical cation character.[28]

The generation of the oxidized species derived from **5a**–**d** was performed electrochemically and monitored by absorption spectroscopy. Stepwise coulometric titrations were performed on ca. 2×10^{-3} M solutions of complexes **5a**–**d** in CH_2Cl_2, with $[(nBu)_4N]PF_6$ (0.15 M) as supporting electrolyte, and the absorption spectra were regularly recorded for different average number ($0 \le n \le 1$) of removed electrons. The UV/Vis–near-IR spectroscopic data of $\mathbf{5a}^{\cdot+}$–$\mathbf{d}^{\cdot+}$ are collected in Table 4. The spectra of $\mathbf{5a}^{\cdot+}$–$\mathbf{d}^{\cdot+}$ show three absorption bands, one in the UV region in the range of 371–418 nm of strong intensity, another in the visible region between 518 and 685 nm, with a weaker intensity, and an even weaker additional band in the near-IR region between 973–1219 nm. The latter band is not observed for $\mathbf{5d}^{\cdot+}$. The high-energy absorptions in the UV appear at similar wavelengths and have comparable intensities to those shown by the corresponding neutral complexes **5a**–**d** and, therefore, they are assigned to localized π-π* transitions at the 2-aza-1,3-butadiene group. The absorptions appearing in the visible region are similar to the bands shown by other oxidized ferrocenyl derivatives and, consequently, are assigned to Cp → Fe^{III} ligand-to-metal charge transfer (LMCT) transitions.[21] Finally, the absorption band in the near-IR, which is not observed in the neutral complexes and is likely to take place after the creation of an electronic vacancy in the HOMO, is assigned to a 2-aza-1,3-butadiene → Fe^{III} LMCT transition. This assignment is based on the following considerations: (i) during the course of the oxidations of **5a**–**c** these low-energy bands increase continuously in intensity, achieving a maximum when the oxidation process is complete (see

 © 2005 Wiley-VCH Verlag GmbH & Co. KGaA, Weinheim

Figure 4); (ii) defined isosbestic points at 385 and 487 nm are maintained during the course of the oxidations (see Figure 4); and (iii) similar low-energy transitions have been observed in the near-IR region in other Fe^{III} and Ru^{III} complexes with conjugated oligothiophene ligands[26,27] and with a -CH_2-N(*R*)-CH_2- bridge.[28] Therefore, the absorption bands in the near-IR shown by **5a**$^{\cdot+}$–**c**$^{+}$ correspond to an optically induced electron transfer from the 2-aza-1,3-butadiene to the Fe^{III} center, as schematically shown in Figure 5 using the Marcus–Hush model.[4] We have assumed that during this optical transition one electron from the localized pair of nonbonding electrons on the N atom of the 2-aza-1,3-butadiene bridge is transferred to the Fe^{III} d_π orbital of the ferrocene moiety. This assumption is supported by the presence of a high-energy filled orbital in oxidized complexes **5a**$^{\cdot+}$–**d**$^{+}$ (e.g. HOMO–2 in **5a**$^{\cdot+}$ and HOMO–3 in **5c**$^{\cdot+}$) that is mainly localized on this N atom, as pointed out by theoretical calculations. Such calculations also show an absolute energetic minimum on the potential energy hypersurface essentially corresponding to the respective neutral top after the appropriate geometrical reorganization to redistribute the electronic density. Only a rough correlation with the experimental absorption values was claimed from time-dependent DFT calculations performed on some of these structures (see Table 4), due to the reported inaccuracy of these types of methods in particular cases.[29] Although there is only a rough correlation between the experimental and calculated values of absorption bands for oxidized complexes **5a**$^{\cdot+}$–**d**$^{\cdot+}$, the results of the time-dependent DFT calculations confirmed the assignations of optical transitions previously given for **5a**$^{\cdot+}$–**d**$^{\cdot+}$, based on experimental facts.

Table 4. Calculated and experimental electronic absorptions of oxidized species **5a**$^{+\cdot}$–**d**$^{+\cdot}$ and **5f**$^{+\cdot}$.

Compound	Calculated λ_{max} [nm] (oscillator strength)		Experimental[a] λ_{max} [nm] (10^{-3} ε, $M^{-1}cm^{-1}$)	
5a$^{+\cdot}$	418.8 (0.1538), 421.1 (0.1415), 486.6 (0.0560), 527.7 (0.0002), 566.0 (0.0014), 618.0 (0.3043)	947.5 (0.0210)	418 (8.5), 481 (3.8), 519 (2.8), 575 (1.9), 618 (0.9)	975 (1.0)
5b$^{+\cdot}$	–	–	259 (16.7), 330 (10.24), 390(sh), 518 (2.29), 685 (0.70)	1219 (0.30)
5c$^{+\cdot}$	269.6 (0.3447), 286.9 (0.1123), 360.0 (0.3045), 414.9 (0.2880), 556.8 (0.2648)	974.5 (0.0275)	259 (9.8), 293 (7.3), 383(7.2), 536 (2.2)	973 (0.13)
5d$^{+\cdot}$	–	–	263 (19.7), 286 (sh), 371(25.2), 549 (4.2)	–
5f$^{+\cdot}$	349.3 (0.1272), 374.2 (0.0753), 425.8 (0.0428), 549.5 (0.0101)	846.0 (0.0027), 1249.4 (0.0017)	327 (12.8), 369 (sh), 429 (sh), 547 (4.9)	764 (0.33), band A; 1250 (0.64) band B
5f^{2+}	–	–	297 (sh), 365 (11.4), 558 (3.7)	764 (0.60), band A; 971 (0.36); band C

[a] In CH_2Cl_2.

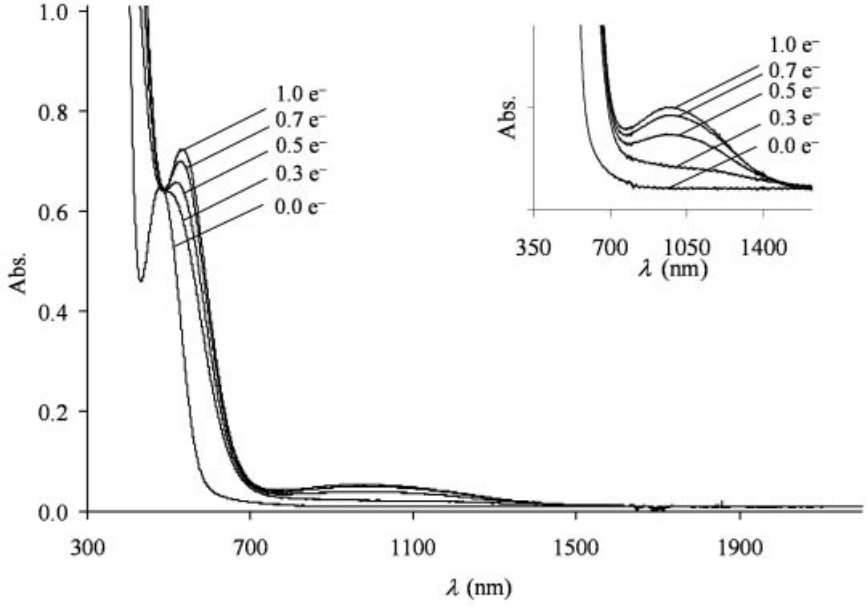

Figure 4. Evolution of Vis-near-IR spectra during the course of the oxidation of compound **5c**. The average number of removed electrons is given on each spectrum. Inset: NIR region enlargement.

 © 2005 Wiley-VCH Verlag GmbH & Co. KGaA, Weinheim

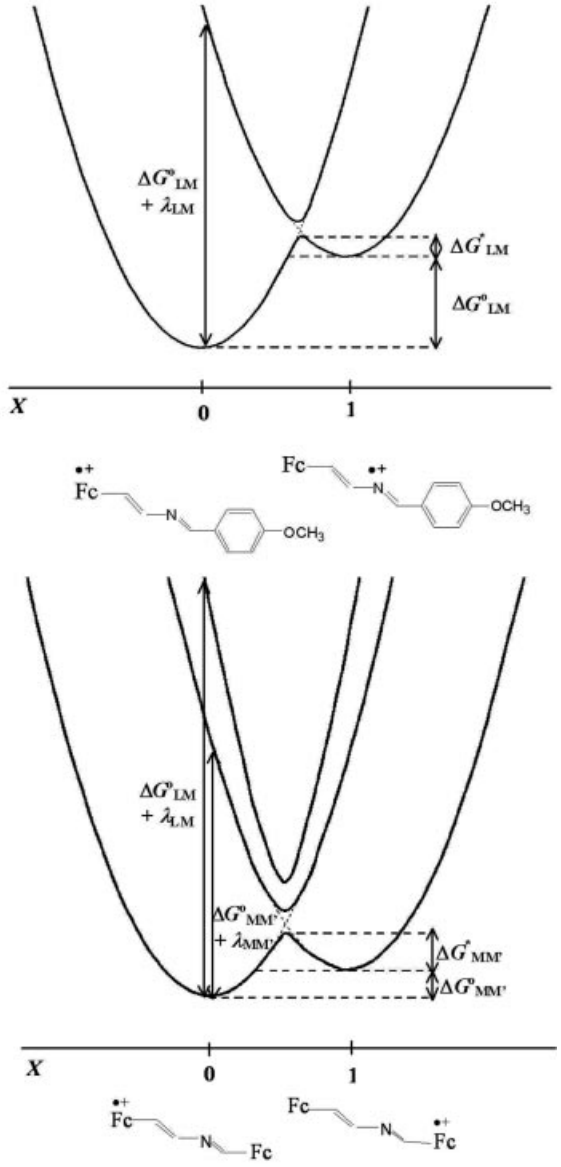

Figure 5. Marcus–Hush model used to describe IET in asymmetric oxidized complexes **5a**$^{\cdot+}$–**d**$^{\cdot+}$ (top) and in oxidized homobimetallic complex **5f**$^{\cdot+}$ (bottom).

The Marcus–Hush model can be used to describe the classical intramolecular electron-transfer process when the electron is coupled between a donor and an acceptor group via a single oscillator having the same frequency in both initial and final states.[4] Originally developed for the interpretation of intervalence charge transfer (IV-CT) bands in extended solids, the Marcus–Hush model has been extended and applied to IV-CT in mixed-valence organometallic[30,31] and organic compounds,[1g,32] as well as to LMCT and metal-to-ligand charge transfer (MLCT) processes in charge-localized asymmetric complexes.[33,34] In accordance with such precedents we have also used the Marcus–Hush model to study the IET of asymmetric complexes **5a**$^{\cdot+}$–**d**$^{\cdot+}$. As schematized in Figure 5, such species exist in two states having the charge/hole localized either on the metal (M) or a particular region of the organic ligand (L), which are separated by the relative free enthalpy $\Delta G°_{LM}$. The electronic coupling between the two electroactive centers (M and L) is measured by the V_{LM} term and the optical transition energy of the LMCT band at its maximum ($h\nu_{max}$; in cm^{-1}), corresponds to the sum of $\Delta G°_{LM}$ and the vertical reorganization energy λ_{LM} (i.e. $h\nu_{max} = \Delta G°_{LM} + \lambda_{LM}$).

The spectral data of LMCT bands of **5a**$^{\cdot+}$–**d**$^{\cdot+}$, summarized in Table 5, can be used to determine the electronic coupling parameter, V_{LM}, and the reorganization energy, λ_{LM}, for each oxidized compound. This was accomplished by deconvoluting the LMCT bands[35] using the classical procedure (see Figure S2 in the Supporting Information) assuming that the effective electron-transfer distance is the distance between the Fe and N atoms. Such distances can be determined from the crystal structures of **5b**, **5d**, and **5f** (5.2 and 3.9 Å for the complexes with the ferrocenyl groups attached to the 4- and 1-positions, respectively). The relative free enthalpies of the two vibronically localized electronic states for compounds **5a**–**c** can be estimated, in a first approximation, from the difference of electrochemical potentials corresponding to the oxidation of the 2-aza-1,3-butadiene center (L) and to the ferrocenyl center (M) of neutral complexes. Due to the experimental impossibility of measuring the L^0/L^{+1} couple of the 2-aza-1,3-butadiene when it is linked to a neutral ferrocenyl group, the corresponding oxidation potential was assumed to be 40 mV less positive than the anionic peak of compound **5e**, observed at +1.084 V, since the *p*-methoxyphenyl and ferrocenyl groups have similar electron-donor capabilities but the first group is not electrochemically active at potentials lower than +1.4 V (vide supra). An inspection of the resulting V_{LM} val-

Table 5. LMCT and IV-CT band parameters, obtained from the spectral deconvolution, and calculated IET parameters for radical cations **5a**$^{+\cdot}$–**d**$^{+\cdot}$and **5f**$^{+\cdot}$.

	R^1	R^2	ΔG^0_{LM} [cm^{-1}]	$h\nu_{max}$ [cm^{-1}]	λ_{LM} [cm^{-1}]	ε_{max} [M^{-1} cm^{-1}]	$\Delta\nu_{1/2}$ [cm^{-1}]	f[a]·10^3	d [Å]	V_{LM} [cm^{-1}]
5a$^{+\cdot}$	4-$CH_3OC_6H_4$	Fc	4150	10260	6110	1000	2640	12.1	5.2	650
5b$^{+\cdot}$	4-$NO_2C_6H_4$	Fc	3660	8200	4540	300	2090	2.9	5.2	280
5c$^{+\cdot}$	Fc	4-$CH_3OC_6H_4$	2790	10280	7490	130	3800	2.3	3.9	380
5d$^{+\cdot}$	Fc	4-$NO_2C_6H_4$	2740	–	–	–	–	–	–	–
5f$^{+\cdot}$	Fc	Fc	3900	13090[b] (band A)	9190[b]	330[b]	3450[b]	5.2[b]	5.2	480[b]
			1110	8000[c] (band B)	6890[c]	640[c]	2500[c]	7.4[c]	9.1	260[c]

[a] Total oscillator strength obtained by $f = 4.6\times10^{-9}\ \varepsilon_{max}\cdot\Delta\nu_{1/2}$. [b] LMCT band corresponding to an electron transfer between L and M units. [c] IV-CT band corresponding to an electron transfer between M and M′ units.

 © 2005 Wiley-VCH Verlag GmbH & Co. KGaA, Weinheim

ues for complexes **5a**–**c** (Table 5) shows that electronic couplings between the ferrocenyl and the 2-aza-1,3-butadiene ligand are moderate, such that all these complexes belong to class II.[8] In addition, the electronic coupling of complexes **5a**–**c** is influenced by the position to which the ferrocenyl is attached, as well as on the electron-donor capability of the substituent on the phenyl group. It should be noted from the spectral analysis that the charge-transfer transition oscillator strengths clearly increase for complexes **5a**–**d**. Complex **5d** apparently does not show any LMCT band. This can be ascribed to the presence of a nitro group linked to the 4-position of the bridge, which drains some electron density from the 2-aza-1,3-butadiene chain, thus lowering the effective overlap between diabatic orbitals and decreasing the probability of the transition. This effect has indeed been predicted theoretically for other electron-withdrawing groups, such as the cyano group.[36]

Intramolecular Electron Transfer in the Mixed-Valence Compound $5f^{+\cdot}$

Oxidized species derived from **5f** were generated electrochemically and their formation followed by absorption spectroscopy. Thus, a stepwise coulometric titration was performed on a 2×10^{-3} M solution of **5f** in CH_2Cl_2, with $[(n\text{Bu})_4\text{N}]PF_6$ (0.15 M) as supporting electrolyte, and absorption spectra were regularly recorded for a different average number ($0 \le n \le 2$) of removed electrons. Figure 6a shows the evolution of the spectra during the oxidation of **5f** in the $0 \le n \le 1$ range, with an increase of the Cp → Fe^{III} LMCT band appearing at 547 nm, characteristic of a ferrocenium ion, and a decrease of the band that corresponds to a localized excitation of a ferrocene group at 478 nm. Along with the changes of these bands, the appearance and maintenance of two well-defined isosbestic points at 425 and 501 nm was observed. Nevertheless, the most interesting feature is that during the oxidation of **5f** two new weak and broad bands centered at 764 nm (band A) and at 1250 nm (band B) appear, and these increase continuously in intensity until one electron has been removed (i.e. when the formation of $\mathbf{5f}^{+\cdot}$ is complete). As also shown in Figure 6, on removing more electrons ($1 \le n \le 2$) the intensity of band A continues to increase until its intensity has doubled, while band B decreases until it disappears (when the dication $\mathbf{5f}^{2+}$ is completely formed). At the same time, another new weak and broad band at 971 nm (band C) increases until the fully oxidized species $\mathbf{5f}^{2+}$ is formed. Table 4 collects all the spectroscopic data for oxidized complexes $\mathbf{5f}^{+\cdot}$ and $\mathbf{5f}^{2+}$. The deconvolution of the experimental spectra of $\mathbf{5f}^{+\cdot}$, performed on spectral intensity times wavenumber vs. wavenumber, assuming Gaussian shapes (Figure 6c), allows an accurate determination of the position, width, and intensity of bands A and B, which are gathered in Table 5.[35,37] These spectral parameters are relevant for the characterization of intramolecular electron transfer in $\mathbf{5f}^{+\cdot}$

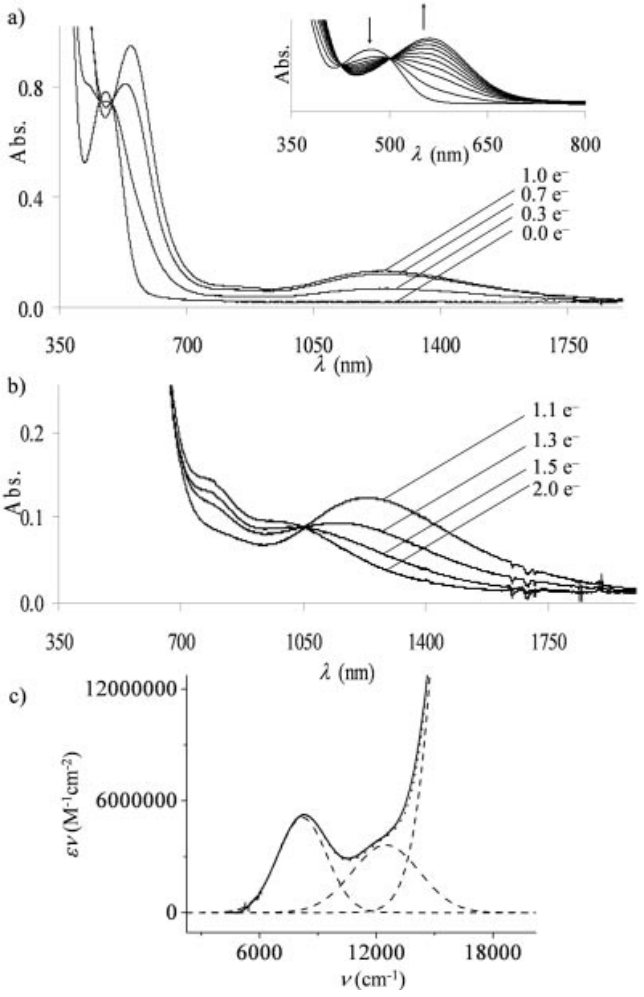

Figure 6. Evolution of Vis-near-IR spectra upon oxidation of **5f**: a) oxidation of **5f** until the maximum ($n = 1$) of the mixed-valence species $\mathbf{5f}^{+\cdot}$ is achieved. Inset: Expanded spectra of the visible region showing the two isosbestic points; b) oxidation until the maximum ($n = 2$) of the fully oxidized species $\mathbf{5f}^{2+}$ is achieved; c) deconvolution of the NIR spectrum of the $\mathbf{5f}^{+\cdot}PF_6^{-\cdot}$ salt. The experimental spectrum was deconvoluted by means of three Gaussian functions (dashed lines) using spectral intensity times wavenumber vs. wavenumber. The sum of the dashed lines (dotted line) closely matches the experimental spectrum (solid line).

The presence of several near-IR bands in the spectrum of a mixed-valence complex is not uncommon, and their occurrence is generally explained by one of three different possible causes.[38,39] One could be the presence of a strong spin-orbit coupling effect, which becomes important only for complexes containing third-row transition metals.[38] A second source could be the presence of a double-exchange mechanism,[39] a mechanism that becomes more probable as the bridge length and the level of π-orbitals increases. Finally, such multiple near-IR bands might be caused by the presence of a bridge with accessible redox state levels, as has been recently proposed to explain the rich absorption spectrum of certain mixed-valence compounds with redox-active bridges.[1g] Based on the behaviors of $\mathbf{5a}^{+\cdot}$–$\mathbf{c}^{+\cdot}$, the latter source seems to be the most probable origin for the

 © 2005 Wiley-VCH Verlag GmbH & Co. KGaA, Weinheim

two near-IR bands of **5f**$^{+\cdot}$. Accordingly, and also based on the spectral evolution observed during the oxidation of **5f**, the band A is assigned to a 2-aza-1,3-butadiene → Fe^{III} LMCT transition, which implies an electron transfer from the N atom of the 2-aza-1,3-butadiene bridge to the Fe^{III} site linked at the 4-position of the bridge, whereas band B is attributed to the bridge-mediated superexchange between the two coupled iron sites (M and M′) − an IET between the two iron sites.

In order to estimate the effectiveness of both IET pathways we used the Marcus–Hush model, as schematized in Figure 5, where the reorganization energies of both transitions, λ_{LM} and $\lambda_{MM'}$, were determined from the absorption maxima of the bands A and B. For the free-energy difference between the two electronic states of **5f**$^{+\cdot}$ having the charge localized on each Fe site we used, in a first approximation, the value of $\Delta G°_{MM'}$ (1113 cm^{-1}) obtained from the difference of the first oxidation potentials of **5c** and **5f**. For $\Delta G°_{LM}$ we used a value of 3904 cm^{-1}, which was determined by employing the same approximations as for **5a**$^{+\cdot}$–**c**$^{+\cdot}$ (vide supra). The spectral parameters of bands A and B were also used to determine the effective electronic coupling parameters V_{LM} and $V_{MM'}$, taking as effective electron-transfer distances those measured between the N and the two Fe atoms in the crystal structure of **5f**. Both effective electronic couplings are moderate, indicating that the mixed-valence **5f**$^{+\cdot}$ also belongs to class II.[8] The relative values of V_{LM} and $V_{MM'}$ indicate that the IET may proceed through the two different pathways. The IET mediated by the bridge through a superexchange is apparently less effective than that in which the electron jumps into the bridge. It is also of interest to compare the effective electronic coupling between the two iron sites of **5f**$^{+\cdot}$ with that of the mixed-valence compound derived from 1,4-diferrocenyl-1,3-butadiene, i.e., $[Fc(CH=CH)_2Fc]^{+\cdot}$.[14] The latter compound has a $V_{MM'}$ of 430 cm^{-1}, which is larger than that of **5f**$^{+\cdot}$, suggesting that the replacement of an sp^2 C atom by an N atom in the 1,3-butadiene bridge results in a decrease of the interaction between both ferrocenes, probably because of a poorer overlap between the diabatic orbitals of the two ferrocenes with the orbital of the bridge involved in the superexchange mechanism. Indeed, in both types of systems the HOMO of the neutral molecule is the bridge-centered superexchange involved MO, which can be considered as being formed by a combination of the higher energy MO of π-type at the bridge and two $3e_2'$-based MOs of both ferrocene subunits (Figure 7). At the level of theory used, the latter is 0.953 eV higher in energy than the HOMO in 1,3-butadiene, but 1.587 eV higher than HOMO–1 in the 2-aza-1,3-butadiene, the HOMO being that containing the electron lone-pair at the N atom. (See Figure S3 in the Supporting Information). This leads to a poorer, although still significant, overlap between the diabatic orbitals of the two ferrocenes with the orbital of the bridge involved in the superexchange mechanism.

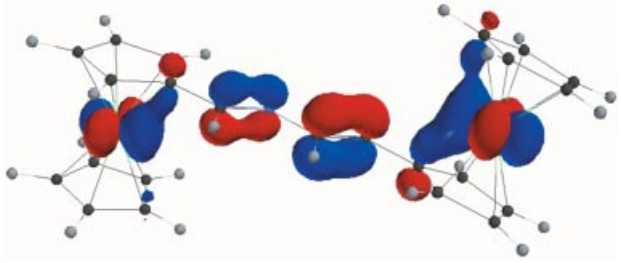

Figure 7. Superexchange-responsible MO (HOMO) in compound **5f** at a 0.050 isovalue.

For the mixed-valence **5f**$^{+\cdot}$ the free energy difference between the two electronic states having the charge localized on each Fe site is 3.2 kcal mol^{-1}. This relatively large value suggests that, at 300 K, the population of the state with the positive charge located on the iron attached to the 4-position of the 2-aza-1,3-butadiene bridge is dominant, with just a very small population (<0.1%) of the state with the charge on the other iron site. In addition, we can make a crude estimation of the thermal activation energy barrier for the interconversion of such two states, using the Marcus–Hush model.[40,41] The resulting thermal energy barrier of about 7.4 kcal mol^{-1} suggests a rate constant of about 10^8 s^{-1} at 300 K and hence any spectroscopic technique with a time scale faster than 10^9 s^{-1} should show the valence-localized mixed-valence complex **5f**$^{+\cdot}$, with the positive charge trapped on the Fe site attached at the 4-position of the bridge, at this temperature. This effect would be even more pronounced at temperatures below 100 K, so that with spectroscopic techniques such ^{57}Fe Mössbauer and EPR the valence should appear to be localized, as is indeed the case (see Supporting Information).

Conclusion and Perspectives

The presence of low-energy LMCT and IV-CT bands in the oxidized forms **5a**$^{+\cdot}$–**d**$^{+\cdot}$ and **5f**$^{+\cdot}$ of mono- and bis-ferrocenyl derivatives attached to a 2-aza-1,3-butadiene bridge indicates the existence of optically induced IETs between the metal units and the organic linkers. This important result demonstrates that the introduction of a heteroatom, like the N atom, in a conjugated organic bridge is an attractive strategy for promoting IET through an alternative pathway. This finding may have implications in the design of molecular electron-transfer materials and, in particular, in the development of new molecular devices that act as electronic relays which promote IET over large distances. Efforts in this direction are in progress in our laboratories using symmetrical compounds with two electroactive units attached to oxidizable, symmetrical, and conjugated organic bridges containing two heteroatoms.

Experimental Section

General Procedures: All reactions were carried out under N_2 and using solvents which were dried by routine procedures. All melting points were determined on a Kofler hot-plate melting point apparatus and are uncorrected. IR spectra were determined as Nujol emulsions or films on a Nicolet Impact 400 spectrophotometer. UV/Vis–near IR spectra were recorded on a Varian Cary 5 E spec-

 © 2005 Wiley-VCH Verlag GmbH & Co. KGaA, Weinheim

trophotometer. ^{1}H and ^{13}C NMR spectra were recorded on a Bruker AC200, 300, or 400 spectrometer (200, 300, or 400 MHz for ^{1}H). Chemical shifts are referenced to signals of tetramethylsilane in the case of ^{1}H and ^{13}C NMR spectra and to 85% aqueous phosphoric acid in the case of ^{31}P NMR spectra. The EI and FAB$^+$ mass spectra were recorded on a Fisons AUTOSPEC 500 VG spectrometer, using 3-nitrobenzylalcohol as matrix. EPR spectra were obtained with an X-Band Bruker ESP 300E spectrometer equipped with a TE_{102} microwave cavity, a Bruker variable temperature unit, a field frequency lock system Bruker ER 033 M; line positions were determined with an NMR Gaussmeter Bruker ER 035 M. The modulation amplitude was kept well below the line width, and the microwave power was well below saturation. Crystallographic measurements were made at 233(2) K on a Bruker diffractometer equipped with an area detector positioned at the window of a rotating anode generator using Mo-K_α radiation (λ = 0.71073 Å). Mössbauer spectra were recorded on an ES-Technology MS-105 spectrometer, with a 100 MBq ^{57}Co source, in a rhodium matrix. Solid samples were prepared by grinding with boron nitride. Spectra were referenced to natural iron at 298 K. Parameters were obtained by fitting the data with Lorentzian lines; errors <0.01 mm s^{-1}. Microanalyses were performed on a Perkin–Elmer 240C instrument. The cyclic voltammetric measurements were performed on a QUICELTRON potentiostat/galvanostat controlled by a personal computer and driven by dedicated software. Cyclic voltammetry was performed with a conventional three-electrode configuration consisting of platinum working and auxiliary electrodes and an SCE reference electrode. The experiments were carried out with a 10^{-3} M solution of sample in dry CH_2Cl_2 containing 0.1 M $[N(nC_4H_9)_4]ClO_4$ as supporting electrolyte. Deoxygenation of the solutions was achieved by bubbling nitrogen for at least 10 min and the working electrode was cleaned after each run. The cyclic voltammograms were recorded with a scan rate increasing from 0.05 to 1.00 V s^{-1}. The square-wave voltammograms were recorded before and after addition of sequential additions of an aliquot of 0.1 equiv. of 2.5×10^{-2} M solutions of $HBF_4 \cdot Et_2O$ in CH_3CN. ΔE_s = 4 mV, ΔE_p = 25 mV, and f = 15 Hz. Decamethylferrocene (DMFe) (–0.07 V vs. SCE) was used as an internal reference both for potential calibration and for reversibility criteria. Oxidations were performed by electrolysis in a three-electrode cell under argon using dry CH_2Cl_2 as solvent and 0.15 M $[N(n\text{-}C_4H_9)_4]ClO_4$ as supporting electrolyte. The progress of the oxidation was followed coulometrically (or chronoamperometrically) by 263A of EG&PAR potentiostat-galvanostat. The reference electrode and the counter electrode were separately immersed in the solvent containing the supporting electrolyte and isolated from the bulk solution by a glass frit. The working electrode was a platinum grid. UV/Vis–near IR absorption spectra were regularly recorded by transferring a small aliquot of the solution contained in the electrochemical cell into a UV quartz cell for a different average number of removed electrons.

Theoretical Calculations: Geometry optimizations were performed with the Spartan'02 package (Spartan'02, build 119, Wavefunction Inc., Irvine, CA). For neutral compounds **5a**–**f** a preliminary optimization was done at the semi-empirical PM3(d) level and the obtained geometries were then refined at the DFT level of theory,[42] which has proved to be remarkably successful in reproducing experimental ground-state geometries and rotational barriers for ferrocenes.[43] The B3LYP functional[44] (Becke's three-parameter hybrid functional[45] with the Lee–Yang–Parr[46] correlation functional) and the 3-21G* basis set were used. Harmonic frequency calculations verified the nature of the stationary points as minima (all real frequencies).[47] The geometry of oxidized radical-cation species **5a**$^{+\cdot}$, **5c**$^{+\cdot}$, **5d**$^{+\cdot}$, and **5f**$^{+\cdot}$ were optimized starting from the corresponding neutral minimized structures with the appropriate charge and multiplicity constraints. Structure **5b**$^{+\cdot}$ was not calculated due to systematic failures in the SCF convergence. Similarly, **5f**$^{+\cdot}$ was used as the initial geometry for the fully oxidized **5f**$^{2+}$. Time-dependent DFT methods (TDDFT), as contained within the Gaussian 98 program suite,[48] performed as an SPE calculation at the same level as the minimized structures, were employed to study the excited states and model the UV/Vis–NIR electronic transitions in both neutral and oxidized species.

General Procedure for the Preparation of Diethyl *N*-Arylidene- and [(Ferrocenylmethylidene)aminomethyl]phosphonates 3: A mixture of diethyl aminomethylphosphonate (0.78 g, 4.64 mmol), an equimolar amount of the appropriate aldehyde **2**, and *p*-toluenesulfonic acid (0.01 g, 0.058 mmol) in dry benzene (50 mL) was stirred at room temperature for 4 h. Then, the flask was fitted with a Dean–Stark trap and a reflux condenser and heated overnight, atr reflux temperature, with constant removal of water. The reaction mixture was allowed to cool to room temperature and the solvent was removed under vacuum to give the corresponding diethyl phosphonates **3** as colored oils, which were used without further purification in the next step.

Diethyl [(*p*-Methoxybenzylidene)aminomethyl]phosphonate (3a): Yield: 95%. IR (Nujol): $\tilde{\nu}$ = 1641, 1609, 1577, 1524, 1444, 1422, 1396, 1316, 1252, 1166, 1102, 969 cm^{-1}. ^{1}H NMR ($CDCl_3$): δ = 1.34 (t, $^4J_{H,P}$ = 6.5 Hz, 6 H), 3.84 (s, 3 H), 4.07 (d, $^1J_{H,P}$ = 16.8 Hz, 2 H),4.19–4.09 (m, 4 H), 6.91 (d, J = 8.6 Hz, 2 H), 7.68 (d, J = 8.6 Hz, 2 H), 8.22 (d, $^4J_{H,P}$ = 4.7 Hz, 1 H) ppm. ^{13}C NMR ($CDCl_3$): δ = 16.5 (d, $^3J_{P,C}$ = 5.6 Hz, CH_3), 55.3 (CH_3O), 57.4 (d, $^1J_{P,C}$ = 152.6 Hz, NCH_2), 62.4 (d, $^2J_{P,C}$ = 6.7 Hz, OCH_2), 114.0 (CH_{Ar}), 128.7 (q), 130.0 (CH_{Ar}), 162.0 (q), 164.9 (d, $^3J_{P,C}$ = 16.0 Hz, CH=N) ppm. ^{31}P NMR ($CDCl_3$): δ = 22.68 ppm. EIMS: m/z (%) = 285 (100) [M$^+$], 152 (82), 148 (61), 125 (90), 121 (80), 97 (44), 91 (19), 78 (25).

Diethyl [(*p*-Nitrobenzylidene)aminomethyl]phosphonate (3b): Yield: 85%. IR (Nujol): $\tilde{\nu}$ = 1654, 1604, 1523, 1454, 1404, 1360, 1266, 1097, 1016, 966, 847 cm^{-1}. ^{1}H NMR ($CDCl_3$): δ = 1.34 (t, $^4J_{H,P}$ = 6.9 Hz, 6 H), 4.01–4.24 (m, 6 H), 7.91 (d, J = 8.0 Hz, 2 H), 8.26 (d, J = 8.0 Hz, 2 H), 8.40 (d, $^4J_{H,P}$ = 5.1 Hz, 1 H) ppm. ^{13}C NMR ($CDCl_3$): δ = 16.4 (d, $^3J_{P,C}$ = 5.7 Hz, CH_3), 57.7 (d, $^1J_{P,C}$ = 152.7 Hz, NCH_2), 62.7 (d, $^2J_{P,C}$ = 6.6 Hz, OCH_2), 123.8 (CH_{Ar}), 130.5 (CH_{Ar}), 140.9 (q), 149.2 (q), 163.2 (d, $^3J_{P,C}$ = 22.0 Hz, CH=N) ppm. ^{31}P NMR ($CDCl_3$): δ = 21.77 ppm. EIMS: m/z (%) = 300 (36) [M$^+$], 163 (60), 152 (96), 125 (82), 108 (100), 90 (95), 81 (42).

Diethyl [(Ferrocenylmethylidene)aminomethyl]phosphonate (3c): Yield: 94%. IR (Nujol): $\tilde{\nu}$ = 1642, 1473, 1448, 1398, 1241, 1166, 1035, 972, 828, 778 cm^{-1}. ^{1}H NMR ($CDCl_3$): δ = 1.38 (t, $^4J_{H,P}$ = 3.3 Hz, 6 H), 3.92 (d, 2 H, $^2J_{H,P}$ = 18 Hz), 4.08–4.25 (m, 4 H), 4.23 (s, 5 H), 4.36 (t, J = 1.8 Hz, 2 H), 4.64 (t, J = 1.8 Hz, 2 H), 8.19 (d, $^4J_{H,P}$ = 4.8 Hz, 1 H) ppm. ^{13}C NMR ($CDCl_3$): δ = 16.3 (d, $^3J_{P,C}$ = 5.7 Hz, CH_3), 57.2 (d, $^1J_{P,C}$ = 150.7 Hz, NCH_2), 62.4 (d, $^2J_{P,C}$ = 6.5 Hz, OCH_2), 68.5 (2 × CH, Cp), 69.1 (5 × CH, Cp), 70.6 (2 × CH, Cp), 79.7 (d, $^4J_{P,C}$ = 9 Hz, q, Cp), 166.2 (d, $^3J_{P,C}$ = 19.5 Hz, CH=N) ppm. ^{31}P NMR ($CDCl_3$): δ = 22.77 ppm. EIMS: m/z (%) = 363 (86) [M$^+$], 298 (100), 224 (39), 260 (48), 121 (63), 81 (25), 65 (9), 56 (24).

General Procedure for the Preparation of 1,4-Disubstituted-2-aza-1,3-butadienes 5: *n*-Butyllithium (1.6 M in hexane, 3 mL) was added dropwise to a solution of the appropriate diethyl phosphonate **3** (4.64 mmol) in dry THF (20 mL) at –78 °C under nitrogen. A solution of an equimolar amount of the appropriate aldehyde **4** (4.64 mmol) in dry THF (10 mL) was added dropwise to this stirred

 © 2005 Wiley-VCH Verlag GmbH & Co. KGaA, Weinheim

solution and the mixture was stirred for 1.5 h. Then, the reaction mixture was allowed to reach room temperature and was heated at reflux temperature overnight. After the solution had cooled to room temperature, the solvent was evaporated under reduced pressure and the crude product was stirred with water (50 mL) and then extracted with dichloromethane (4 × 50 mL). The combined organic layers were dried with anhydrous Na_2SO_4 and, after filtration, the solution was concentrated to dryness to give a crude product which was crystallized from dichloromethane/diethyl ether (1:10).

4-Ferrocenyl-1-(*p*-methoxyphenyl)-2-aza-1,3-butadiene (5a): Yield: 90%; m.p. 175–176 °C. IR (Nujol): $\tilde{\nu}$ = 1605, 1511, 1456, 1395, 1240, 1162, 1107, 1074, 1046, 1024, 990, 985, 830, 741 cm^{-1}. ^1H NMR ($CDCl_3$): δ = 3.86 (s, 3 H), 4.15 (s, 5 H), 4.28 (t, J = 1.6 Hz, 2 H), 4.43 (t, J = 1.6 Hz, 2 H), 6.70 (d, J = 14.0 Hz, 1 H), 6.94 (d, J = 8.0 Hz, 2 H), 7.18 (d, J = 14.0 Hz, 1 H), 7.75 (d, J = 8.0 Hz, 2 H), 8.18 (s, 1 H) ppm. ^{13}C NMR ($CDCl_3$): δ = 55.3 (CH_3O), 67.0 (2 × CH, Cp), 69.0 (2 × CH, Cp), 69.3 (5 × CH, Cp), 81.5 (q, Cp), 114.2 (CH_{Ar}), 128.3 (CH=CH), 129.4 (q), 129.9 (CH_{Ar}), 139.7 (CH=CH), 158.0 (q), 161.5 (CH=N) ppm. EIMS: m/z (%) = 345 (100) [M^+], 280 (77), 278 (10), 121 (31), 56 (23). $C_{20}H_{19}FeNO$ (345.22): calcd. C 69.58, H 5.55, N 4.06; found C 69.35, H 5.40, N 4.15.

4-Ferrocenyl-1-(*p*-nitrophenyl)-2-aza-1,3-butadiene (5b): Yield: 50%; m.p. 223–224 °C. IR (Nujol): $\tilde{\nu}$ = 1600, 1514, 1454, 1335, 1182, 1109, 1030, 957, 745, 698 cm^{-1}. ^1H NMR ($CDCl_3$): δ = 4.12 (s, 5 H), 4.32 (t, J = 1.6 Hz, 2 H), 4.42 (t, J = 1.6 Hz, 2 H), 6.87 (d, J = 13.0 Hz, 1 H), 7.21 (d, J = 13.0 Hz, 1 H), 7.89 (d, J = 8.1 Hz, 1 H), 8.22 (s, 1 H), 8.23 (d, J = 8.1 Hz, 1 H) ppm. ^{13}C NMR ($CDCl_3$): δ = 67.5 (2 × CH, Cp), 69.6 (5 × CH, Cp), 69.9 (2 × CH, Cp), 80.4 (q), 124.2 (CH_{Ar}), 128.5 (CH_{Ar}), 134.0 (CH=CH), 138.6 (CH=CH), 142.3 (q), 148.5 (q), 154.7 (CH=N) ppm. EIMS: m/z (%) = 360 (100) [M^+], 330 (19), 295 (23), 265 (21), 192 (34), 165 (30), 121 (62). $C_{19}H_{16}FeN_2O_2$ (360.19): calcd. C 63.36, H 4.48, N 7.78; found C 63.54, H 4.35, N 7.69.

1-Ferrocenyl-4-(*p*-methoxyphenyl)-2-aza-1,3-butadiene (5c): Yield: 85%; m.p. 102–103 °C. IR (Nujol): $\tilde{\nu}$ = 1645, 1605, 1565, 1514, 1250, 1176, 1107, 1038, 969, 826 cm^{-1}. ^1H NMR ($CDCl_3$): δ = 3.82 (s, 3 H), 4.22 (s, 5 H), 4.47 (t, J = 1.6 Hz, 2 H), 4.73 (t, J = 1.6 Hz, 2 H), 7.34 (d, J = 14.0 Hz, 1 H), 7.40 (d, J = 8.0 Hz, 2 H), 7.82 (d, J = 14.0 Hz, 1 H), 7.88 (d, J = 8.0 Hz, 2 H), 8.21 (s, 1 H) ppm. ^{13}C NMR ($CDCl_3$): δ = 55.2 (CH_3O), 68.7 (2 × CH, Cp), 68.9 (5 × CH, Cp), 71.1 (2 × CH, Cp), 80.4 (q), 114.1 (CH_{Ar}), 127.5 (CH_{Ar}), 127.6 (CH=CH), 129.3 (q), 141.0 (CH=CH), 159.0 (q), 161.5 (CH=N) ppm. EIMS: m/z (%) = 345 (100) [M^+], 318 (40), 279 (24), 278 (14), 186 (43), 121 (66), 56 (39). $C_{20}H_{19}FeNO$ (345.22): calcd. C 69.58, H 5.55, N 4.06; found C 69.33, H 5.28, N 4.21.

1-Ferrocenyl-4-(*p*-nitrophenyl)-2-aza-1,3-butadiene (5d): Yield: 40%; m.p. 182–183 °C. IR (Nujol): $\tilde{\nu}$ = 1561, 1508, 1438, 1337, 1225, 1177, 1123, 1107, 1033, 750, 696 cm^{-1}. ^1H NMR ($CDCl_3$): δ = 4.24 (s, 5 H), 4.56 (t, J = 1.6 Hz, 2 H), 4.78 (t, J = 1.6 Hz, 2 H), 6.87 (d, J = 13.4 Hz, 1 H), 7.52 (d, J = 8.0 Hz, 2 H), 7.55 (d, J = 13.4 Hz, 1 H), 8.18 (d, J = 8.0 Hz, 2 H), 8.35 (s, 1 H) ppm. ^{13}C NMR ($CDCl_3$): δ = 69.4 (2 × CH, Cp), 69.6 (5 × CH, Cp), 72.1 (2 × CH, Cp), 79.6 (q), 124.2 (CH_{Ar}), 125.2 (CH=CH), 126.6 (CH_{Ar}), 143.7 (q), 146.4 (q), 146.5 (CH=CH), 165.9 (CH=N) ppm. EIMS: m/z (%) = 360 (100) [M^+], 333 (22), 192 (22), 186 (34), 165 (27), 120 (63), 56 (33). $C_{19}H_{16}FeN_2O_2$ (360.19): calcd. C 63.36, H 4.48, N 7.78; found C 63.19, H 4.29, N 7.62.

1,4-Bis(*p*-methoxyphenyl)-2-aza-1,3-butadiene (5e): Yield: 85%; m.p. 170–172 °C. IR (Nujol): $\tilde{\nu}$ = 1647, 1609, 1553, 1510, 1454, 1423, 1373, 1311, 1280, 1255, 1174, 1111, 1024, 986, 943, 875, 813 cm^{-1}. ^1H NMR ($CDCl_3$): δ = 3.80 (s, 3 H), 3.84 (s, 3 H), 6.86 (d, J = 8.0 Hz, 2 H), 6.91 (d, J = 14.1 Hz, 1 H), 6.94 (d, J = 8.0 Hz, 2 H), 7.40 (d, J = 8.0 Hz, 2 H), 7.44 (d, J = 14.1 Hz, 1 H), 7.76 (d, J = 8.0 Hz, 2 H), 8.25 (s, 1 H) ppm. ^{13}C NMR ($CDCl_3$): δ = 55.2, 55.3, 114.0, 114.1, 127.8, 129.2, 129.4, 130.0, 140.4, 159.2, 159.7, 161.8 ppm. EIMS: m/z (%) = 267 (100) [M^+], 252 (44), 236 (28), 160 (69), 121 (35), 91 (28). $C_{17}H_{17}NO_2$ (267.33): calcd. C 76.38, H 6.41, N 5.24; found C 76.20, H 6.67, N 5.12.

1,4-Bis(ferrocenyl)-2-aza-1,3-butadiene (5f): Yield: 87%; m.p. 253–255 °C. IR (Nujol): $\tilde{\nu}$ = 1649, 1580, 1102, 1023, 1041, 1003, 966, 829, 810 cm^{-1}. ^1H NMR ($CDCl_3$): δ = 4.15 (s, 5 H), 4.22 (s, 5 H), 4.27 (s, 2 H), 4.40 (s, 2 H), 4.45 (s, 2 H), 4.72 (s, 2 H), 6.60 (d, J = 13.2 Hz, 1 H), 7.05 (d, J = 13.2 Hz, 1 H), 8.11 (s, 1 H) ppm. ^{13}C NMR ($CDCl_3$): δ = 66.80 (2 × CH, Cp), 68.61 (2 × CH, Cp), 69.00 (2 × CH, Cp), 69.20 (10 × CH, Cp), 71.00 (2 × CH, Cp), 80.81 (q, Cp), 82.11 (q, Cp), 126.32 (CH=), 140.32 (=CH-N), 159.82 (CH=N) ppm. EIMS: m/z (%) = 423 (100) [M^+], 358 (60), 212 (32), 186 (28), 121 (64), 56 (25). $C_{23}H_{21}Fe_2N$ (423.12): calcd. C 65.29, H 5.00, N 3.31; found C 65.40, H 4.88, N 3.50.

Preparation of the Mixed-Valence Compound $5f^+I_3^-$: A sample of this mixed-valence compound was prepared by adding a solution of iodine (0.030 g, 0.12 mmol) in dry benzene (5 mL) to a solution of 1,4-diferrocenyl-2-aza-1,3-butadiene (0.1 g, 0.24 mmol) in the same solvent (50 mL). The reaction mixture was stirred at room temperature under nitrogen for 1 h and the dark-purple microcrystals formed were collected by filtration and washed with three portions of benzene and one portion of diethyl ether. The solid obtained was dried in a dessicator overnight. FAB MS: m/z (%) = 424 (100) [M^+ + 1]. $C_{23}H_{21}Fe_2I_3N$ (803.82): calcd. C 34.33, H 2.61, N 1.74; found C 34.23, H 2.38, N 1.58.

Supporting Information: Crystal data of **5b**, **5d**, and **5f**, optical absorption data of oxidized species and the procedure for their analysis with the Marcus–Hush model, and ^{57}Fe Mössbauer and EPR spectra are provided.

Acknowledgments

We gratefully acknowledge the financial support of the DGI, Ministerio de Ciencia y Tecnología, Spain (projects MAT2003-04699 and CTQ2004-02201), the Fundación Séneca (CARM) (project no. PB/72/FS/02), and DGR, Catalunya (2001 SGR00362). The Biotechnology and Biological Sciences Research Council, UK, is also thanked for funding (D.J.E.).

[1] a) D. Segal, A. Nitzan, W. B. Davis, M. R. Wasielewski, M. A. Ratner, *J. Phys. Chem. B.* **2000**, *104*, 3817–3829; b) M. N. Paddow-Row, in *Electron Transfer in Chemistry* (Ed.: V. Balzani), Wiley-VCH, Weinheim, **2001**, pp. 179–271; c) L. DeCola, P. Belser, in *Electron Transfer in Chemistry* (Ed.: V. Balzani), Wiley-VCH, Weinheim, **2001**, pp. 97–136; d) K. Kilsa, J. Kajanus, A. N. Macpherson, J. Martensson, B. Albinsson, *J. Am. Chem. Soc.* **2001**, *123*, 3069–3080; e) J.-P. Launay, *Chem. Soc. Rev.* **2001**, *30*, 386–397; f) M. D. Newton, *Chem. Rev.* **1991**, *91*, 767–792; g) S. F. Nelsen, R. F. Ismagilov, D. F. Powell, *J. Am. Chem. Soc.* **1998**, *120*, 1924–1925; h) W. B. Davis, W. A. Svec, M. A. Ratner, M. R. Wasielewski, *Nature* **1998**, *396*, 60–53; i) D. S. Weiss, J. R. Cowdery, R. H. Young, in *Electron Transfer in Chemistry* (Ed.: V. Balzani), Wiley-VCH, Weinheim, **2001**, pp. 379–471; j) H. Bassler, in *Semiconducting Polymers* (Eds.: G. Hadziioannou, P. F. van Hutten), Wiley-VCH, Weinheim, **2000**, pp. 365–410.

 © 2005 Wiley-VCH Verlag GmbH & Co. KGaA, Weinheim

[2] a) U. T. Müller-Westerhoff, *Angew. Chem. Int. Ed. Engl.* **1986**, *25*, 702–717; b) E. E. Bunel, P. Campos, J. Ruz, L. Valle, I. Chadwick, M. Santa Ana, G. Gonzalez, J. M. Manriquez, *Organometallics* **1988**, *7*, 474–476; c) E. E. Bunel, L. Valle, N. L. Jones, P. J. Carroll, M. Gonzalez, N. Muñoz, J. M. Manriquez, *Organometallics* **1988**, *7*, 789–791; d) H. Atzkern, B. Huber, F. H. Köhler, G. Müller, R. Müller, *Organometallics* **1991**, *10*, 238–244; e) J. Hiermeier, F. H. Köhler, G. Müller, *Organometallics* **1991**, *10*, 1787–1793.

[3] a) A. C. Benniston, V. Goulle, A. Harriman, J. M. Lehn, B. Marczinke, *J. Phys. Chem.* **1994**, *98*, 7798–7804; b) M. Haga, M. M. Ali, S. Koseki, K. Fujimoto, A. Yoshimura, K. Nozaki, T. Ohno, K. Nakajima, D. J. Stufkens, *Inorg. Chem.* **1996**, *35*, 3335–3347; c) M. E. Elliot, D. L. Derr, S. Ferrere, M. D. Newton, Y. P. Liu, *J. Am. Chem. Soc.* **1996**, *118*, 5221–5228; d) C. Pataoux, C. Coudret, J. P. Launay, C. Joachim, A. Gourdon, *Inorg. Chem.* **1997**, *36*, 5037–5049; e) J.-P. Sauvage, J.-P. Collin, J.-C. Chambron, S. Guillerez, C. Coudret, *Chem. Rev.* **1994**, *94*, 993–1019; f) N. S. Hush, *Coord. Chem. Rev.* **1985**, *64*, 135–157; g) A. C. Ribou, J. P. Launay, K. Takhashi, T. Nihira, S. Tarutani, C. W. Spangler, *Inorg. Chem.* **1994**, *33*, 1325–1329.

[4] a) C. Creutz, *Prog. Inorg. Chem.* **1983**, *30*, 1–73; b) R. J. Crutchley, *Adv. Inorg. Chem.* **1994**, *41*, 273–325; c) S. Barlow, D. O'Hare, *Chem. Rev.* **1997**, *97*, 637–669; d) N. S. Hush, *Prog. Inorg. Chem.* **1967**, *8*, 391–444.

[5] a) C. Lambert, G. Nöll, J. Schelter, *Nat. Mater.* **2002**, *1*, 69–73; b) P. J. Low, M. A. J. Paterson, H. Puchmann, A. E. Goeta, J. A. K. Howard, C. Lambert, J. C. Cherryman, D. R. Tackley, S. Leeming, B. Brown, *Chem. Eur. J.* **2004**, *10*, 83–91.

[6] W. H. Morrison, S. Krogsrud, D. N. Hendrickson, *Inorg. Chem.* **1973**, *12*, 1998–2004.

[7] a) F. Delgado-Pena, D. R. Talham, D. O. Cowan, *J. Organomet. Chem.* **1983**, *253*, C43–C46; b) M. F. Moore, S. R. Wilson, D. N. Hendrickson, U. T. Mueller-Westerhoff, *Inorg. Chem.* **1984**, *23*, 2918–2920; c) M. F. Moore, S. R. Wilson, M. J. Cohn, T. Y. Dong, U. T. Mueller-Westerhoff, D. N. Hendrickson, *Inorg. Chem.* **1985**, *24*, 4559–4565.

[8] M. Robin, P. Day, *Adv. Inorg. Radiochem.* **1967**, *10*, 247–422.

[9] a) T. Y. Dong, T. J. Ke, S. M. Peng, S. K. Yeh, *Inorg. Chem.* **1989**, *28*, 2103–2106; b) B. Floris, P. Tagliatesta, *J. Chem. Res., Synop.* **1993**, 42–43.

[10] C. Le Vanda, K. Bechgaard, D. O. Covan, *J. Org. Chem.* **1976**, *41*, 2700–2704.

[11] I. Motoyama, M. Watanabe, H. Sano, *Chem. Lett.* **1978**, 513–516.

[12] C. Jutz, *Tetrahedron Lett.* **1959**, 1–4.

[13] a) J. Lukasser, H. Angleitner, H. Schottenberger, H. Kopacka, M. Schweiger, B. Bildstein, K. H. Ongania, K. Wurst, *Organometallics* **1995**, *14*, 5566–5578; b) A. Tárraga, P. Molina, J. L. López, A. Espinosa, D. J. Evans, *Tetrahedron Lett.* **2002**, *43*, 4717–4720.

[14] A. C. Ribou, J. P. Launay, M. L. Sachtleben, H. Li, C. W. Spangler, *Inorg. Chem.* **1996**, *35*, 3735–3740.

[15] B. Bildstein, M. Malaun, H. Kopacka, M. Fontani, P. Zanello, *Inorg. Chim. Acta* **2000**, *300–302*, 16–22.

[16] a) A. G. Osborne, M. W. da Silva, M. B. Hursthouse, K. M. A. Malik, G. Opromolla, P. J. Zanello, *J. Organomet. Chem.* **1996**, *516*, 167–176; b) V. A. Sauro, M. S. Worketin, *Can. J. Chem.* **2002**, *80*, 250–256.

[17] a) A. Tárraga, P. Molina, D. Curiel, M. D. Velasco, *Organometallics* **2001**, *20*, 2145–2152; b) A. Tárraga, P. Molina, D. Curiel, M. D. Velasco, *Tetrahedron Lett.* **2002**, *43*, 8453–8457.

[18] S. K. Davidsen, G. W. Phillips, S. F. Martin, *Org. Synth.* **1993**, *8*, 451–458.

[19] P. Séller, J. D. Dunitz, *Acta Crystallogr., Sect. B* **1982**, *38*, 1741.

[20] J. L. López, A. Tárraga, A. Espinosa, M. D. Velasco, P. Molina, V. Lloveras, J. Vidal-Gancedo, C. Rovira, J. Veciana, D. J. Evans, K. Wurst, *Chem. Eur. J.* **2004**, *10*, 1815–1826.

[21] a) G. L. Geoffroy, M. S. Wrighton, *Organometallic Photochemistry*, Academic Press, New York, **1979**; b) Y. S. Sohn, D. N. Hendrickson, H. B. Gray, *J. Am. Chem. Soc.* **1971**, *93*, 3603–3612.

[22] S. Barlow, H. E. Bunting, C. Ringham, J. C. Green, G. U. Bublitz, S. G. Boxer, J. W. Perry, S. R. Marder, *J. Am. Chem. Soc.* **1999**, *121*, 3715–3723.

[23] N. G. Connelly, W. E. Geiger, *Chem. Rev.* **1996**, *96*, 877–910.

[24] V. Alain, A. Fort, M. Barzoukas, T.-H. Chen, S. R. Blanchard-Desce, S. R. Marder, J. W. Perry, *Inorg. Chim. Acta* **1996**, *242*, 43–49.

[25] M. Masui, H. J. Ohmori, *J. Chem. Soc., Perkin Trans. 2* **1972**, 1882–1887.

[26] a) Y. B. Zu, M. O. Wolff, *Chem. Mater.* **1999**, *11*, 2995–3001; b) Y. B. Zu, D. B. Millet, M. O. Wolf, S. J. Rettig, *Organometallics* **1999**, *18*, 1930–1938.

[27] Y. B. Zu, M. O.Wolf, *J. Am. Chem. Soc.* **2000**, *122*, 10121–10125.

[28] a) I. Yamaguchi, T. Sakano, H. Ishii, K. Osakada, T. Yamamoto, *J. Organomet. Chem.* **1999**, *584*, 213–216; b) M. Horie, T. Sakano, K. Osakada, H. Nakao, *Organometallics* **2004**, *23*, 18–20; c) M. Horie, Y. Suzaki, K. Osakada, *J. Am. Chem. Soc.* **2004**, *126*, 3684–3685.

[29] M. Turki, C. Daniel, S. Zalis, A. Vicek, J. van Slageren, D. J. Stufkens, *J. Am. Chem. Soc.* **2001**, *123*, 11431–11440.

[30] M. C. B. Colbert, J. Lewis, N. J. Long, P. R. Raithby, M. Younus, A. J. P. White, D. J. Williams, N. N. Payne, L. Yellowlees, D. Beljonne, N. Chawdhury, R. H. Friend, *Organometallics* **1998**, *17*, 3034–3043.

[31] Y. Zhu, O. Clot, M. O. Wolf, G. P. A. Yap, *J. Am. Chem. Soc.* **1998**, *120*, 1812–1821.

[32] C. Lambert, G. Nöll, *J. Am. Chem. Soc.* **1999**, *121*, 8434–8442.

[33] a) P. Desjardins, G. P. A. Yap, R. J. Crutchley, *Inorg. Chem.* **1999**, *38*, 5901–5905; b) C. E. B. Evans, M. L. Naklicki, R. J. Crutchley, *Inorg. Chem.* **1995**, *34*, 1350–1354.

[34] T. Ito, N. Imai, T. Yamagushi, T. Hamaguchi, C. H. Londergan, C. P. Kubiak, *Angew. Chem. Int. Ed.* **2004**, *43*, 1376–1381 and references cited therein.

[35] I. R. Gould, D. Noukakis, L. Gómez-Jahn, R. H. Young, J. L. Goodman, S. Farid, *Chem. Phys.* **1993**, *176*, 439–456.

[36] C. Joachim, *Thesis*, Université Paul Sabatier, Tolouse, France, **1990**, pp. 146, 211, and 214.

[37] The proportion of mixed-valence species at half-oxidation (*P*), where $P = K_c^{1/2}/(2 + K_c^{1/2})$ is generally used to compute the intensity of corrected spectra. The comproportionation constant, K_c, which is related to the thermodynamic stability of the mixed-valence compound, of the equilibrium of comproportionation, $[Fe^{II}\text{-L-}F^{II}] + [Fe^{III}\text{-L-}F^{III}] \leftrightharpoons 2[Fe^{II}\text{-L-}F^{III}]$, was calculated for **5f** from the electrochemical data, giving a value of 3.6×10^3. With such a high value of K_c, *P* is almost 100% so that the dependency on K_c is very small and it is not necessary to correct the intensity of the spectrum.

[38] a) E. M. Kober, K. A. Goldsby, D. N. S. Narayane, T. J. Meyer, *J. Am. Chem. Soc.* **1983**, *105*, 4303–4309; b) P. A. Lay, R. H. Magnuson, H. Taube, *Inorg. Chem.* **1988**, *27*, 2364–2371; c) W. M. Laidlaw, R. G. Denning, *J. Chem. Soc., Dalton Trans.* **1994**, 1987–1994.

[39] a) D. E. Richardson, H. Taube, *J. Am. Chem. Soc.* **1983**, *105*, 40–51; b) J. Halpern, L. E. Orgel, *Discuss. Faraday Soc.* **1960**, *29*, 32–41.

[40] According to Hush and Marcus, for symmetrical weakly coupled class II mixed-valence complexes the activation barrier to electron transfer is given by $\Delta G_{MM'}^* = \lambda_{MM'}/4 - V_{MM'} + (V_{MM'}^2/\lambda_{MM'})$; see ref.[41]. With the parameters given in Table 5 for $\mathbf{5f}^{+\cdot}$, a value of $\Delta G_{MM'}^* + \Delta G^\circ_{MM'} = 7.4$ kcal mol^{-1} is obtained for the 4-Fe^{3+} + 1-Fe^{2+} → 4-Fe^{2+} + 1-Fe^{3+} process. The corresponding first-order rate constant (k_{th})can be calculated from $k_{th} = k \cdot \nu_n \cdot \exp(-\Delta G_{MM'}^*/RT)$ where $k = 1$, since the reaction is adiabatic, and the nuclear frequency factor, ν_n, is $2.00 \times 10^{+13}$ s^{-1}, as determined from $\nu_n = [2(V_{MM'})^2/h] \cdot [(\pi^3/\lambda_{MM'}RT)^{1/2}]$. This gives a value for k_{th} of $8.8 \times 10^{+7}$ s^{-1} at 300 K.

 © 2005 Wiley-VCH Verlag GmbH & Co. KGaA, Weinheim

[41] a) R. A. Marcus, *J. Chem. Phys.* **1956**, *24*, 966–978; b) R. A. Marcus, *J. Chem. Phys.* **1965**, *43*, 679; c) R. A. Marcus, N. Sutin, *Inorg. Chem.* **1975**, *14*, 213–216; d) C. Creutz, M. D. Newton, N. Sutin, *J. Photochem. Photobiol. Sect. A* **1994**, *82*, 47–59.
[42] a) E. J. Baerends, D. E. Ellis, P. Ros, *Chem. Phys.* **1973**, *2*, 41–51; b) W. Kohn, A. D. Becke, R. G. Parr, *J. Phys. Chem.* **1996**, *100*, 12974–12980.
[43] a) A. Berces, T. Ziegler, L. Fan, *J. Phys. Chem.* **1994**, *98*, 1584–1595; b) A. Berces, T. Ziegler, *Top. Curr. Chem.* **1996**, *182*, 41–85; c) U. Hohm, D. Goebel, S. Grimme, *Chem. Phys. Lett.* **1997**, *272*, 328–334; d) C. A. Morrison, S. F. Bone, D. W. H. Rankin, H. E. Robertson, F. Parsons, R. A. Coxall, S. Fraser, J. A. S. Howell, P. C. Yates, N. Fey, *Organometallics* **2001**, *20*, 2309–2320.
[44] L. J. Bartolotti, K. Fluchick, in *Reviews in Computational Chemistry* (Eds.: K. B. Lipkowitz, B. D. Boyd), VCH Publishers, New York, **1996**, vol. 7, pp. 187–216.
[45] A. D. Becke, *J. Chem. Phys.* **1993**, *98*, 5648–5652.
[46] C. Lee, W. Yang, R. G. Parr, *Phys. Rev. B* **1988**, *37*, 785–789.
[47] J. W. McIver, A. K. Komornicki, *J. Am. Chem. Soc.* **1972**, *94*, 2625–2633.
[48] Gaussian 98, Revision A.9, M. J. Frisch, G. W. Trucks, H. B. Schlegel, G. E. Scuseria, M. A. Robb, J. R. Cheeseman, V. G. Zakrzewski, J. A. Montgomery Jr., R. E. Stratmann, J. C. Burant, S. Dapprich, J. M. Millam, A. D. Daniels, K. N. Kudin, M. C. Strain, O. Farkas, J. Tomasi, V. Barone, M. Cossi, R. Cammi, B. Mennucci, C. Pomelli, C. Adamo, S. Clifford, J. Ochterski, G. A. Petersson, P. Y. Ayala, Q. Cui, K. Morokuma, D. K. Malick, A. D. Rabuck, K. Raghavachari, J. B. Foresman, J. Cioslowski, J. V. Ortiz, A. G. Baboul, B. B. Stefanov, G. Liu, A. Liashenko, P. Piskorz, I. Komaromi, R. Gomperts, R. L. Martin, D. J. Fox, T. Keith, M. A. Al-Laham, C. Y. Peng, A. Nanayakkara, M. Challacombe, P. M. W. Gill, B. Johnson, W. Chen, M. W. Wong, J. L. Andres, C. Gonzalez, M. Head-Gordon, E. S. Replogle, J. A. Pople, Gaussian, Inc., Pittsburgh PA, **1998**.
[49] R. Gleiter, R. Seeger, *Helv. Chim. Acta* **1971**, *54*, 1217–1220..
Received: November 30, 2004

 © 2005 Wiley-VCH Verlag GmbH & Co. KGaA, Weinheim

Towards a Library of "Early-Late" Ti–Ru Bimetallic Complexes

Laurianne Bareille,[a] Pierre Le Gendre,*[a] Philippe Richard,[a] and Claude Moïse*[a]

Keywords: Heterometallic complexes / Metallocenes / Ruthenium / Titanium

A series of new titanocene phosphanes **3**–**6** have been prepared by replacing both chloride atoms at the titanium atom of the complexes [$TiCl_2(\eta^5\text{-}C_5H_5)\{\eta^5\text{-}C_5H_4(CH_2)_2PR_2\}$] (**1**: R = Ph; **2**: R = Cy) by sodium fluoride or sodium benzoate in two-phase systems. Treatment of these new metalloligands with the binuclear complex [(*p*-cymene)$RuCl_2]_2$ affords the targeted titanocene difluoride and titanocene dibenzoate bimetallic ruthenium complexes **8**–**11**. The first chiral Ti–Ru bimetallic complex **12** bearing a binaphthyloxy ligand at the titanium centre has been synthesised in this way. In each series, an X-ray crystal structure has been determined.

(© Wiley-VCH Verlag GmbH & Co. KGaA, 69451 Weinheim, Germany, 2005)

Introduction

Complexes containing early as well as late transition metals are particularly attractive materials owing to their potential application in homogeneous catalysis.[1–3] Indeed, the coordination of the substrate to one of the two metals may increase its reactivity towards the other. Such compounds, which often show a cooperative effect, may constitute a new class of catalysts that are able to improve the efficiency of known processes or to give new reactions. Nevertheless, probably because of their laborious access, only a few early–late bimetallic complexes have been tested in catalysis.[4] Our strategy to construct such systems was to first synthesise a titanocene dichloride phosphane complex and then to treat these early metal ligands with the binuclear complex [(*p*-cymene)$RuCl_2]_2$.[5] We obtained a series of Ti–Ru heterobimetallic complexes in sufficient amounts to carry out a screening of their catalytic behaviour.[6–8] Another aspect of interest of this approach is the structural flexibility of the titanocene phosphane as regards a possible tuning of the bimetallic complexes towards the target catalytic reaction. Indeed, by replacing the two chloride atoms on the titanium atom by other ligands it should be possible to design new phosphanes and therefore to expand substantially this class of bimetallic complexes. Here we report the synthesis and the characterisation of a series of new Ti–Ru bimetallic complexes by using this strategy.

Results and Discussion

Titanocene dibenzoate can be synthesised, in good yields, from the reaction of titanocene dichloride with sodium benzoate in a biphasic system ($CHCl_3/H_2O$).[9] Therefore we carried out the reaction with the titanocene dichloride phosphanes **1** and **2** under similar conditions (Scheme 1). The colour of the reaction mixture, initially red, turned slowly to orange. After this treatment, titanocene dibenzoate phosphanes **3** and **4**, respectively, were isolated as orange powders in good yields. The NMR spectroscopic data of **3** and **4** are very similar to their dichloride counterparts **1** and **2**, with additional resonances for the benzoate hydrogens. The IR spectra exhibit two (COO) stretching bands around 1630 and 1320 cm^{-1}, consistent with the monodentate coordination of the benzoate ligands.[10] Thus, in one step, both the steric and electronic features of the titanocene phosphanes **1** and **2** have been modified. In an extension of this procedure, we conducted a reaction between sodium fluoride and the titanocene dichloride phosphanes **1** and **2** under similar conditions. The halide exchange proceeded smoothly and led to the titanocene difluoride phosphanes **5**, and **6**, respectively, in very good yields. The $^{19}F\{^1H\}$ NMR spectrum of **5** shows singlets at δ = 64.3 ppm in the range reported for [Cp_2TiF_2].[11] The $^{19}F\{^1H\}$ NMR spectrum of **6** also contains a singlet but with a chemical shift shifted slightly downfield at δ = 86.8 ppm. All other NMR spectroscopic data of **5** and **6** are in accordance with their structural features. At this point we should mention that [Cp_2TiF_2] has recently been converted, under mild conditions, into [Cp_2TiH], which has proved to be a very effective catalyst for the hydrosilylation of lactones[12] and the dehydropolymerisation of silanes.[13] The potential of the bimetallic complexes constructed with the fluorinated titanocene phosphane is thus reinforced.

These results prompted us to use the same strategy to convert the titanocene dichloride phosphanes **1** and **2** into optically active ligands. According to well-known procedures for the resolution of titanium metallocenes,[14–18] we carried out the reaction of one equivalent of sodium bi-

[a] Laboratoire de Synthèse et Electrosynthèse Organométalliques, LSEO-UMR 5188, Université de Bourgogne
Faculté des Sciences Gabriel, 6 bd Gabriel, 21000 Dijon, France
Fax: +33-3-8039-6880
E-mail: pierre.le-gendre@u-bourgogne.fr

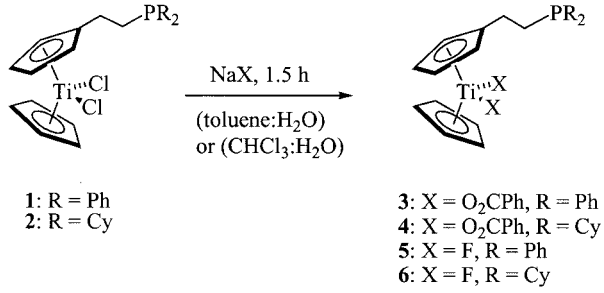

Scheme 1.

naphtholate with **1** in THF at room temperature to afford the desired titanocene binaphtholate phosphane **7**. However, a careful study of the ^{1}H NMR spectrum of the crude product revealed that a partial loss of the $Cp(CH_2)_2PPh_2$ moiety occurs in this reaction. At this step, purification by chromatography is effective but led to a dramatic loss of yield. Therefore we conducted this reaction under milder conditions and used binaphthol directly along with imidazole as an HCl trap (Scheme 2). The reaction proceeded cleanly without any side product formation and in very good yield. The ^{1}H NMR spectrum of **7** differs from that of the precursor phosphane **1** in that it displays four signals for the substituted Cp instead of two. This anisochrony is indicative of a loss of symmetry due to the introduction of binaphthol. The $^{31}P\{^1H\}$ NMR spectrum of **7** displays a single peak at δ = –14.3 ppm, which is shifted slightly downfield with respect to **1**. Thus, starting from a readily commercially available chiral diol, a pure optically active phosphane is available without the usual difficulties of chiral ligand synthesis (resolution, measurement of optical purity, etc.). Finally, it is worth mentioning that all attempts to convert **2** into an optically active phosphane by either the sodium binaphtholate or imidazole routes were unsuccessful.

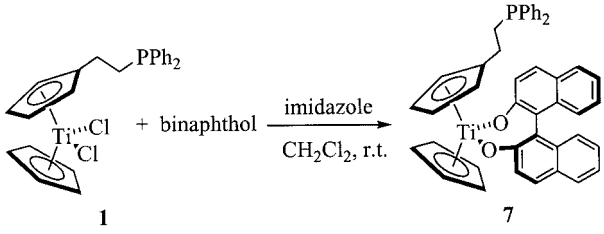

Scheme 2.

Once this series of new titanocene phosphanes had been prepared, we investigated their complexation with ruthenium by following the procedure previously described for the titanocene dichloride phosphanes **1** and **2**.[5,6] Thus, the treatment of **3**–**6** with 0.5 molar equivalents of the binuclear complex $[(p\text{-cymene})RuCl_2]_2$ in benzene gave the targeted early–late bimetallic complexes **8**–**11**, respectively, in good yields (Scheme 3). The ^{31}P NMR chemical shifts of these complexes, in the δ = 20 ppm range, correspond to a downfield shift of 30–40 ppm relative to the free ligands. As expected, the two carboxylate stretching bands in the IR spectra of **8** and **9** are similar to those reported for the free titanocene phosphanes. The $^{19}F\{^1H\}$ NMR chemical shifts of **10** and **11** show signals in the range of $[Cp_2TiF_2]$ at δ = 62.3 and 62.5 ppm, respectively. This suggests that the dicyclohexylphosphane group is responsible for the deshielding of the signal in the $^{19}F\{^1H\}$NMR spectrum of **6**. All other spectroscopic data of the bimetallic complexes **8**–**11** are in accordance with their structural features.

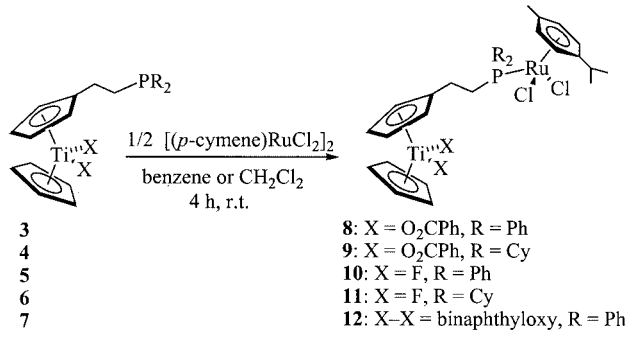

Scheme 3.

We then carried out the reaction of the optically active phosphane **7** with 0.5 molar equivalents of the binuclear complex $[(p\text{-cymene})RuCl_2]_2$ in CH_2Cl_2. Purification of the crude product by flash chromatography on silica, in order to remove an excess of $[(p\text{-cymene})RuCl_2]_2$, allowed the isolation of the first chiral Ti–Ru bimetallic complex **12**. The $^{31}P\{^1H\}$ NMR spectrum of **12** shows a single peak at δ = 24.7 ppm, which is shifted downfield with respect to **7**. The ^{1}H NMR spectrum of **12** exhibits a marked anisochrony not only for the substituted Cp, as for **7**, but also for the *p*-cymene fragment on the ruthenium centre − a chemical shift gap of 0.25 ppm between both methyl protons of the isopropyl group is observed. At this point, we should mention that the synthesis and the characterisation of chiral early–late bimetallic complexes are remarkably scarce in the literature.[19,20]

Crystals of **8** suitable for X-ray measurements were obtained by slow diffusion of pentane into a saturated dichloromethane solution of the complex. The asymmetric unit contains the bimetallic complex, one dichloromethane solvate and one benzoic acid molecule (originally present as an impurity in the sample). The structure of the complex consists of two fragments: a titanocene moiety with a tetrahedral geometry and a ruthenium moiety with a usual three-legged piano stool structure (Figure 1).[21,22] These two blocks are tethered together through a phosphanylethylene bridge. Most of the structural features of the titanocene dibenzoate fragment within the bimetallic complex **8** are similar to those reported for $[Cp_2Ti(O_2CPh)_2]$,[9,10] as the lengths of the C–O bonds to the coordinated and uncoordinated oxygen atoms are significantly different, the angles at the coordinated oxygen atoms (Ti–O–C) are large and both benzoate ligands tilt with respect to the O(1)–Ti–O(2) plane, with dihedral angles of 42.6(2)° and 29.9(2)°, respectively. Despite the fact that benzoate ligands are rather bulkier than chloride atoms, the phosphorus atom

remains located on the open side of the titanocene but not exactly in the bisecting plane. This asymmetry is induced by a π-stacking effect observed between one phenyl ring of a benzoate ligand and one phenyl ring of a diphenylphosphanyl group. Finally, the cocrystallised benzoic acid molecule forms a hydrogen bond with the oxygen atom O(2) of one benzoate ligand.

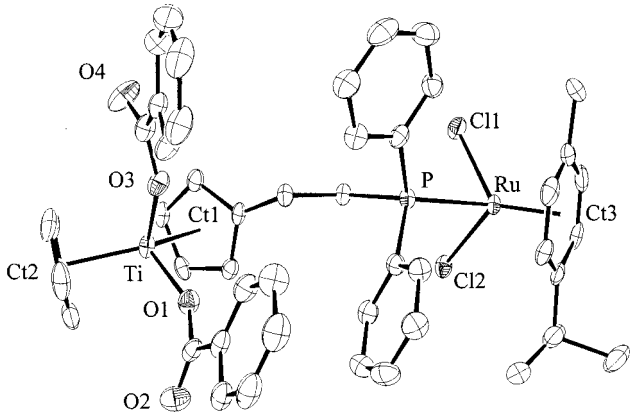

Figure 1. Molecular structure of complex **8**. The CH_2Cl_2 solvate molecule and the benzoic acid have been omitted for clarity. Selected bond lengths [Å] and angles [°]: Ti–Ct1 2.049(3), Ti–Ct2 2.054(4), Ti–O1 1.947(2), Ti–O3 1.956(2), Ru–Ct3 1.707(3), Ru–P 2.3516(8), Ru–Cl1 2.4182(9), Ru–Cl2 2.4211(8); Ct1–Ti–Ct2 132.4(2), O1–Ti–O3 90.8(1), Ct3–Ru–P 130.6(1), Ct3–Ru–Cl1 127.3(1), Ct3–Ru–Cl2 124.7(1), P–Ru–Cl1 85.25(3), P–Ru–Cl2 85.89(3), Cl(1)–Ru–Cl(2), 89.16(3) Ti–O(1)–C(35) 152.9(2), Ti–O3–C42 142.4(2).

Crystals of **10** suitable for an X-ray study were also obtained by layering techniques with $CDCl_3$/hexane (the sample came from a NMR solution). The asymmetric unit contains two independent complexes of **10** and six $CDCl_3$ solvate molecules. The two molecules exhibit an almost identical conformation with opposite orientations of the *p*-cymene ligand. The molecular structure of complex **10**, represented in Figure 2, is very similar to the one with two chlorides.[5] The diphenylphosphanyl group is on the open side of the titanocene, near a bisecting position, with both phenyls rings directed toward the titanium atom and the ruthenium away from it in the least congested environment. As expected, the Ti–F bond lengths [<Ti–F> = 1.91(2) Å, mean over four distances] are shorter than the Ti–Cl bond lengths [2.35(3) Å] and the F–Ti–F angle [95(1)°, mean over two angles] similar to the one with chlorides [Cl–Ti–Cl = 95.26(8)°]. These structural parameters are close to those observed for other titanocene difluoride derivatives.[23,24]

Recrystallisation attempts of **12**, starting from a racemic mixture, proved to be difficult, but finally succeeded by slow evaporation under air of a CH_2Cl_2/pentane solution of the crude product. Its molecular structure is shown in Figure 3. The asymmetric unit contains the bimetallic Ti–Ru compound, one additional binaphthol molecule and 2.5 dichloromethane solvates. Contrary to the bimetallic complexes **8** and **10**, the PPh_2 substituent is rotated from the bisecting position, leading to a dihedral angle between the Ct(1)–Ti–Ct(2) plane and the Ct(1)–C(11)–Ct(2) one [C(11) being the

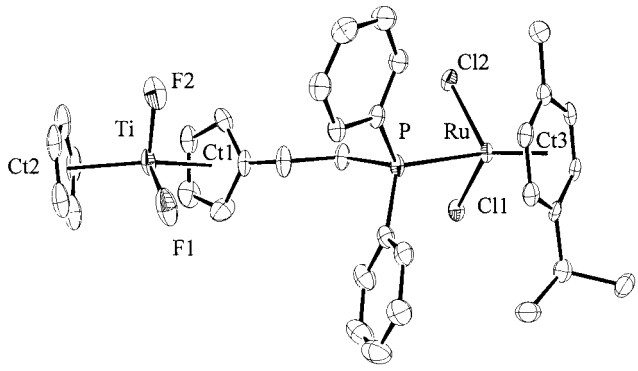

Figure 2. Molecular structure of complex **10**. The $CDCl_3$ solvate molecules have been omitted for clarity. Selected bond lengths [Å] and angles [°] [data in square brackets correspond to the second indepedent molecule]: Ti–Ct1 2.050(5) [2.055(5)], Ti–Ct2 2.065(5) [2.056(5)], Ti–F1 1.891(3) [1.905(4)], Ti–F2 1.937(3) [1.896(4)], Ru–Ct3 1.707(4) [1.709(4)], Ru–P 2.347(1) [2.344(1)], Ru–Cl1 2.4180(12) [2.4093(13)], Ru–Cl2 2.4126(13) [2.4200(11)]; Ct1–Ti–Ct2 132.6(2) [136.2(2)], F1–Ti–F2 93.70(14) [95.7(2)], Ct3–Ru–P 131.0(1) [130.6(1)], Ct3–Ru–Cl1 126.1(1) [126.1(1)], Ct3–Ru–Cl2 127.7(1) [127.3(1)], P–Ru–Cl1 84.35(3) [83.47(3)], P–Ru–Cl2 86.92(4) [86.74(4)], Cl1–Ru–Cl2 86.80(4) [86.84(4)].

methylene carbon atom attached to the Cp ring] of 67°. Thus, the areneruthenium moiety lies in an open area and not above the bulky binaphtholate group. The structural parameters of the chelate ring formed are similar to those described in the literature.[14–17] The bite angle O(1)–Ti–O(2) is equal to 92.0(1)° and the dihedral angle between the naphthalene planes [64.8(1)°] is contracted from that of cocrystallised "free" binaphthol (90° is generally observed). It is noteworthy that two different Ti–O bond lengths are observed [Ti–O(1) = 1.915(2) Å and Ti–O(2) = 1.981(2) Å]. This can be explained by the presence of a hydrogen bond pointing from a hydroxide group of the "free" binaphthol molecule toward the O(2) atom [O(3)–H···O(2) = 1.75 Å]. In fact, this binaphthol molecule plays an active role in the crystallisation process in connecting two adjacent molecules: the second hydroxy group points between the two chlorine atoms of the Ru moiety of an adjacent complex [O(4)–H···Cl(1) = 2.35 Å and O(4)–H···Cl(2) = 2.70 Å].[25]

Conclusions

This study provides a straightforward access to a series of new early–late transition metal complexes. The substitution of both chloride atoms of a titanocene phosphane by other ligands such as benzoate, fluoride or binaphtholate is the key step of this new route. The phosphanes so formed react readily with the binuclear complex [(*p*-cymene)-$RuCl_2$]$_2$ to give the targeted bimetallic complexes. The structures of three of them have been confirmed by X-ray diffraction studies. Assessment of the catalytic behaviour of these early–late bimetallic complexes is currently being studied in our laboratory. The design of new titanocene phosphanes inspired by the fruitful chemistry of $[Cp_2TiCl_2]$ is also in progress.

 © 2005 Wiley-VCH Verlag GmbH & Co. KGaA, Weinheim

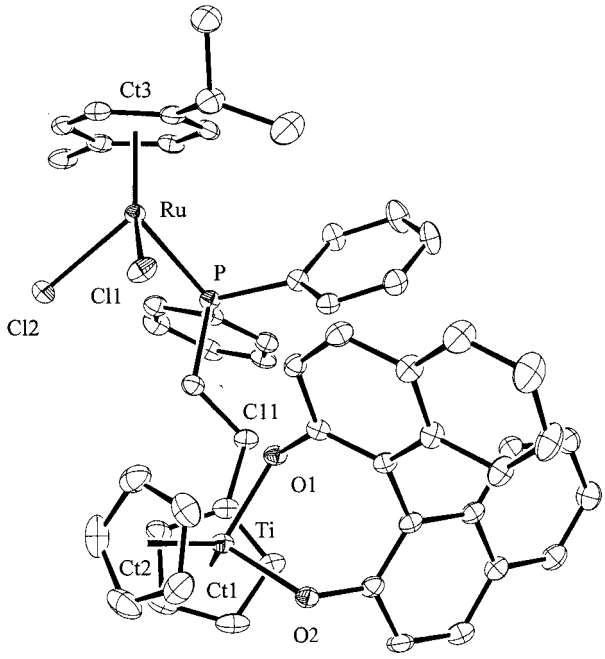

Figure 3. Molecular structure of complex *rac*-**12**. Only one enantiomer is shown for clarity. The free binaphthol molecule and the CH_2Cl_2 solvate molecules are also not shown. Selected bond lengths [Å] and angles [°]: Ti–Ct1 2.099(3), Ti–Ct2 2.088(4), Ti–O1 1.915(2), Ti–O2 1.981(2), Ru–Ct3 1.703(3), Ru–P 2.3442(8), Ru–Cl1 2.4210(7), Ru–Cl2 2.4157(8); Ct1–Ti–Ct2 130.48(13), O1–Ti–O2 91.96(9), Ct3–Ru–P 130.95(9), Ct3–Ru–Cl1 126.04(9), Ct3–Ru–Cl2 126.42(9), P–Ru–Cl1 84.97(3), P–Ru–Cl2 86.80(3), Cl1–Ru–Cl2 87.22(3).

Experimental Section

General Remarks: All reactions were carried out under an atmosphere of purified argon. The solvents and eluents were dried by the appropriate procedures and distilled under argon immediately before use. Standard Schlenk techniques and conventional glass vessels were employed. Elemental analyses were carried out with a EA 1108 CHNS-O FISONS Instruments. ^{1}H (500 MHz), ^{19}F (282 MHz) and ^{31}P{^{1}H} (202 MHz) spectra were collected on a Bruker 500 MHz Avance DRX spectrometer. Chemical shifts are quoted relative to internal TMS (^{1}H), external $CFCl_3$ (^{19}F) or external H_3PO_4 (^{31}P). IR spectra were obtained with a Bruker IFS 66v spectrometer. The titanocene phosphanes **1** and **2** were synthesised as reported previously.[5,6]

[Ti(O$_2$CPh)$_2$(η^5-C$_5$H$_5$){η^5-C$_5$H$_4$(CH$_2$)$_2$PPh$_2$}] (3): A 100-mL flask was charged with $PhCO_2Na$ (0.3 g, 2 mmol), [$TiCl_2$(η^5-C_5H_5){η^5-$C_5H_4(CH_2)_2PPh_2$}] (**1**; 0.4 g, 1 mmol), 5 mL of degassed water and 44 mL of $CHCl_3$. The mixture was stirred for 1.5 h during which time the colour turned to orange. Then, the organic phase was removed, washed with 5 mL of water, dried with $MgSO_4$, filtered and the solvents evaporated to dryness to yield an orange powder (0.45 g, 75% yield). IR (KBr): ν(COO) = 1634, 1324 cm^{-1}. ^{1}H NMR ($CDCl_3$): δ = 2.17 (t, $^3J_{H,H}$ = 8 Hz, 2 H, CH_2), 2.61 (pseudo q, $^3J_{H,H}$ = $^2J_{H,P}$ = 8 Hz, 2 H, CH_2), 6.42 (pseudo t, $^3J_{H,H}$ = $^4J_{H,H}$ = 3 Hz, 2 H, C_5H_4), 6.59 (s, 5 H, C_5H_5), 6.61 (pseudo t, $^3J_{H,H}$ = $^4J_{H,H}$ = 3 Hz, 2 H, C_5H_4), 7.16–7.20 (m, 10 H, PPh_2), 7.44 (pseudo t, $^3J_{H,H}$ = 7 Hz, 4 H, Ph), 7.54 (t, $^3J_{H,H}$ = 7 Hz, 2 H, Ph), 8.03 (d, $^3J_{H,H}$ = 7 Hz, 4 H, Ph) ppm. ^{31}P{^{1}H} NMR ($CDCl_3$): δ = –14.87 (s, PPh_2) ppm. $C_{38}H_{33}O_4PTi$ (632.51): calcd. C 72.16, H 5.26; found C 72.00, H 5.02.

[Ti(O$_2$CPh)$_2$(η^5-C$_5$H$_5$){η^5-C$_5$H$_4$(CH$_2$)$_2$PCy$_2$}] (4): This compound was obtained following the above procedure but with [$TiCl_2$(η^5-C_5H_5){η^5-$C_5H_4(CH_2)_2PCy_2$}] (**2**) and toluene/H_2O as the biphasic system (0.38 g, 62% yield). IR (KBr): ν(COO) = 1635, 1326 cm^{-1}. ^{1}H NMR (C_6D_6): δ = 1.10–1.90 (m, 24 H, Cy + CH_2), 2.85 (pseudo q, $^3J_{H,H}$ = $^2J_{H,P}$ = 8 Hz, 2 H, CH_2), 6.14 (pseudo t, $^3J_{H,H}$ = $^4J_{H,H}$ = 3 Hz, 2 H, C_5H_4), 6.28 (s, 5 H, C_5H_5), 6.41 (pseudo t, $^3J_{H,H}$ = $^4J_{H,H}$ = 3 Hz, 2 H, C_5H_4), 7.35 (t, $^3J_{H,H}$ = 8 Hz, 2 H, Ph), 7.39 (pseudo t, $^3J_{H,H}$ = 8 Hz, 4 H, Ph), 8.54 (d, $^3J_{H,H}$ = 8 Hz, 4 H, Ph) ppm. ^{31}P{^{1}H} NMR (C_6D_6): δ = –3.79 (s, PCy_2) ppm. $C_{38}H_{45}O_4PTi$ (644.60): calcd. C 70.80, H 7.04; found C 70.54, H 7.16.

[TiF$_2$(η^5-C$_5$H$_5$){η^5-C$_5$H$_4$(CH$_2$)$_2$PPh$_2$}] (5): A 100-mL flask was charged with NaF (0.065 g, 1.54 mmol), [$TiCl_2$(η^5-C_5H_5){η^5-$C_5H_4(CH_2)_2PPh_2$}] (**1**; 0.36 g, 0.78 mmol), 4 mL of degassed water and 36 mL of $CHCl_3$. The mixture was stirred for 1.5 h during which time the colour turned to deep yellow. Then, the organic phase was removed, washed with 5 mL of water, dried with $MgSO_4$, filtered and the solvents evaporated to dryness to yield a yellow powder (0.16 g, 50% yield). ^{1}H NMR ($CDCl_3$): δ = 2.29 (t, $^3J_{H,H}$ = 8 Hz, 2 H, CH_2), 2.65 (pseudo q, $^3J_{H,H}$ = $^2J_{H,P}$ = 8 Hz, 2 H, CH_2), 6.05 (pseudo s, 2 H, C_5H_4), 6.38 (m, 7 H, C_5H_5 + 2 H C_5H_4), 7.25–7.35 (m, 6 H, PPh_2), 7.37–7.44 (m, 4 H, PPh_2) ppm. ^{19}F NMR ($CDCl_3$): δ = 64.28 (s, TiF_2) ppm. ^{31}P{^{1}H} NMR ($CDCl_3$): δ = –14.99 (s, PPh_2) ppm. $C_{24}H_{23}F_2PTi$ (428.28): calcd. C 67.31, H 5.41; found C 66.82, H 5.26.

[TiF$_2$(η^5-C$_5$H$_5$){η^5-C$_5$H$_4$(CH$_2$)$_2$PCy$_2$}] (6): This compound was obtained following the above procedure but with [$TiCl_2$(η^5-C_5H_5){η^5-$C_5H_4(CH_2)_2PCy_2$}] (**2**) and toluene/H_2O as the biphasic system (0.17 g, 50% yield). ^{1}H NMR (C_6D_6): δ = 1.10–1.27 (m, 12 H, Cy), 1.55–1.84 (m, 12 H, Cy+CH_2), 2.87 (pseudo q, $^3J_{H,H}$ = $^2J_{H,P}$ = 8 Hz, 2 H, CH_2), 5.84 (pseudo s, 4 H, C_5H_4), 5.99 (s, 5 H, C_5H_5) ppm. ^{19}F NMR (C_6D_6): δ = 86.76 (s, TiF_2) ppm. ^{31}P{^{1}H} NMR (C_6D_6): δ = –3.41 (s, PCy_2) ppm. $C_{24}H_{35}F_2PTi$ (440.37): calcd. C 65.46, H 8.01; found C 65.15, H 8.22.

[Ti{(*R*)-Binaphtholate)}(η^5-C$_5$H$_5$){η^5-C$_5$H$_4$(CH$_2$)$_2$PPh$_2$}] (7): Imidazole (0.14 g, 2.15 mmol) in 10 mL of dichloromethane and (*R*)-binaphthol (0.32 g, 1.13 mmol) in 25 mL of dichloromethane were successively added to a solution of [$TiCl_2$(η^5-C_5H_5){η^5-C_5H_4-$(CH_2)_2PPh_2$}] (**1**; 0.52 g, 1.13 mmol) in 25 mL of dichloromethane at room temperature. The mixture was stirred for 4 h. After filtration, the solvent was removed from the filtrate under reduced pressure and 40 mL of toluene was added to the resulting product. Filtration through celite and evaporation of the solvent afforded **7** (0.5 g, 70% yield) as a red solid. ^{1}H NMR ($CDCl_3$, 500 MHz): δ = 1.65–1.75 (m, 2 H, CH_2), 2.20–2.35 (m, 2 H, CH_2), 5.28–5.35 (m, 1 H, C_5H_4), 5.85–5.95 (m, 1 H, C_5H_4), 5.98–6.04 (m, 1 H, C_5H_4), 6.09 (s, 5 H, C_5H_5), 6.60–6.66 (m, 1 H, C_5H_4), 7.15–8.15 (m, 22 H, phenyl-*H* and binaphthyl-*H*) ppm. ^{31}P{^{1}H} NMR ($CDCl_3$, 202 MHz): δ = –14.3 (s, PPh_2) ppm. $C_{44}H_{35}PTiO_2$ (674.59): calcd. C 78.34, H 5.23; found C 78.48, H 5.29. $[\alpha]_D^{20}$ = –2163 (*c* = 0.1, CH_2Cl_2).

[(*p*-Cymene)RuCl$_2$}{(η^5-C$_5$H$_5$)[μ-η^5:η^1-C$_5$H$_4$(CH$_2$)$_2$PPh$_2$[Ti(O$_2$CPh)$_2$}] (8): A 25-mL Schlenk flask was charged under argon with **3** (0.45 g, 0.71 mmol), [(*p*-cymene)$RuCl_2$]$_2$ (0.16 g, 0.27 mmol) and degassed benzene. The mixture was stirred at room temperature for 4 h, during which time a brick-red precipitate slowly formed. The solvent was removed by filtration and the red residue was dried under vacuum (0.38 g, 75% yield). IR (KBr): ν(COO) = 1636, 1355 cm^{-1}. ^{1}H NMR (500 MHz, $CDCl_3$): δ = 0.74 [d, $^3J_{H,H}$ = 7 Hz, 6 H, CH-

(CH_3)$_2$], 1.81 (s, 3 H, CH_3), 2.17 (m, 2 H, CH_2), 2.45 [sept, $^3J_{H,H}$ = 7 Hz, 1 H, CH(CH$_3$)$_2$], 2.63 (m, 2 H, CH_2), 5.01 (d, $^3J_{H,H}$ = 6 Hz, 2 H, *p*-cymene), 5.18 (d, $^3J_{H,H}$ = 6 Hz, 2 H, *p*-cymene), 6.14 (pseudo t, $^3J_{H,H}$ = $^4J_{H,H}$ = 2 Hz, 2 H, C$_5H_4$), 6.48 (pseudo t, $^3J_{H,H}$ = $^4J_{H,H}$ = 2 Hz, 2 H, C$_5H_4$), 6.49 (s, 5 H, C$_5H_5$), 7.19 (pseudo t, $^3J_{H,H}$ = 6 Hz, 4 H, PPh$_2$), 7.25–7.35 (m, 6 H, PPh$_2$), 7.49 (t, $^3J_{H,H}$ = 8 Hz, 2 H, Ph), 7.56 (pseudo t, $^3J_{H,H}$ = 8 Hz, 4 H, Ph), 7.82 (d, $^3J_{H,H}$ = 8 Hz, 4 H, Ph) ppm. ^{31}P{^{1}H} NMR (202 MHz, CDCl$_3$): δ = 24.99 (s, PPh$_2$) ppm. $C_{48}H_{47}Cl_2O_4PRuTi$ (938.70): calcd. C 61.42, H 5.05; found C 60.92, H 5.21.

[(*p*-Cymene)RuCl$_2$\{(η^5-C$_5$H$_5$)[μ-η^5:η^1-C$_5$H$_4$(CH$_2$)$_2$PCy$_2$]Ti(O$_2$CPh)$_2$\}] (9): This compound was obtained following the above procedure but with **4** (0.41 g, 80% yield). IR (KBr): ν(COO) = 1635, 1328 cm^{-1}. ^{1}H NMR (CDCl$_3$): δ = 0.85–2.17 (m, 24 H, Cy + CH_2), δ = 1.24 [d, $^3J_{H,H}$ = 7 Hz, 6 H, CH(CH_3)$_2$], 2.02 (s, 3 H, CH_3), 2.60 (m, 2 H, CH_2), 2.75 [sept, $^3J_{H,H}$ = 7 Hz, 1 H, CH(CH$_3$)$_2$], 5.01 (pseudo s,, 4 H, *p*-cymene), 6.37 (pseudo t, $^3J_{H,H}$ = $^4J_{H,H}$ = 3 Hz, 2 H, C$_5H_4$), 6.55 (pseudo t, $^3J_{H,H}$ = $^4J_{H,H}$ = 3 Hz, 2 H, C$_5H_4$), 6.60 (s, 5 H, C$_5H_5$), 7.46 (pseudo t, $^3J_{H,H}$ = 8 Hz, 4 H, Ph), 7.50 (t, $^3J_{H,H}$ = 8 Hz, 2 H, Ph), 8.07 (d, $^3J_{H,H}$ = 8 Hz, 4 H, Ph) ppm. ^{31}P{^{1}H} NMR (CDCl$_3$): δ = 25.84 (s, PCy$_2$) ppm. $C_{48}H_{59}Cl_2O_4PRuTi$ (950.80): calcd. C 60.23, H 6.25; found C 60.43, H 6.55.

[(*p*-Cymene)RuCl$_2$\{(η^5-C$_5$H$_5$)[μ-η^5:η^1-C$_5$H$_4$(CH$_2$)$_2$PPh$_2$]TiF$_2$\}] (10): This compound was obtained following the procedure described for the synthesis of **8** but with **5** (0.33 g, 83% yield). ^{1}H NMR (500 MHz, CDCl$_3$): δ = 0.80 [d, $^3J_{H,H}$ = 7 Hz, 6 H, CH(CH_3)$_2$], 1.90 (s, 3 H, CH_3), 2.25 (m, 2 H, CH_2), 2.52 [sept, $^3J_{H,H}$ = 7 Hz, 1 H, CH(CH$_3$)$_2$], 2.74 (m, 2 H, CH_2), 5.09 (d, $^3J_{H,H}$ = 8 Hz, 2 H, *p*-cymene), 5.28 (d, $^3J_{H,H}$ = 8 Hz, 2 H, *p*-cymene), 5.93 (pseudo s, 2 H, C$_5H_4$), 6.25 (pseudo s, 2 H, C$_5H_4$), 6.36 (s, 5 H, C$_5H_5$), 7.48 (m, 6 H, PPh$_2$), 7.90 (m, 4 H, PPh$_2$) ppm. ^{19}F NMR (CDCl$_3$): δ = 62.29 (s, TiF_2) ppm. ^{31}P{^{1}H} NMR (202 MHz, CDCl$_3$): δ = 24.57 (s, PPh$_2$) ppm. $C_{34}H_{37}Cl_2F_2PRuTi$ (734.47): calcd. C 55.60, H 5.08; found C 55.10, H 4.90.

[(*p*-Cymene)RuCl$_2$\{(η^5-C$_5$H$_5$)[μ-η^5:η^1-C$_5$H$_4$(CH$_2$)$_2$PCy$_2$]TiF$_2$\}] (11): This compound was obtained following the procedure described for the synthesis of **8** but with **6** (0.24 g, 60% yield). ^{1}H NMR (CDCl$_3$): δ = 1.10–2.31 (m, 24 H, Cy + CH_2), δ = 1.24 [d, $^3J_{H,H}$ = 7 Hz, 6 H, CH(CH_3)$_2$], 2.11 (s, 3 H, CH_3), 2.65 (m, 2 H, CH_2), 2.85 [sept, $^3J_{H,H}$ = 7 Hz, 1 H, CH(CH$_3$)$_2$], 5.58 (pseudo s, 4 H, *p*-cymene), 6.14 (pseudo t, $^3J_{H,H}$ = $^4J_{H,H}$ = 3 Hz, 2 H, C$_5H_4$), 6.31 (pseudo t, $^3J_{H,H}$ = $^4J_{H,H}$ = 3 Hz, 2 H, C$_5H_4$), 6.42 (s, 5 H, C$_5H_5$) ppm. ^{19}F NMR (CDCl$_3$): δ = 62.54 (s, TiF_2) ppm. ^{31}P{^{1}H} NMR (CDCl$_3$): δ = 25.88 (s, PCy$_2$) ppm. $C_{34}H_{49}Cl_2F_2PRuTi$ (746.57): calcd. C 54.70, H 6.61; found C 54.55, H 6.41.

[(*p*-Cymene)RuCl$_2$\{(η^5-C$_5$H$_5$)[μ-η^5:η^1-C$_5$H$_4$(CH$_2$)$_2$PPh$_2$]Ti[(*R*)-binaphtholate)]\}] (12): [(*p*-cymene)RuCl$_2$]$_2$ (0.041 g, 0.07 mmol) in 5 mL of dichloromethane was added to a solution of **7** (0.1 g, 0.15 mmol) in 10 mL of dichloromethane at 0 °C. The mixture was stirred at room temperature for 4 h. The solvent was then removed in vacuo. Purification by flash chromatography on silica (toluene/THF, 50:50) under argon and at 10 °C afforded **12** as an orange solid (0.070 g, 50% yield). Complex **12** in its racemic form, which was used to obtain suitable crystal for X-ray diffraction, was prepared in a similar way. ^{1}H NMR (CDCl$_3$, 500 MHz): δ = 0.70 [d, $^3J_{H,H}$ = 7 Hz, 3 H, CH(CH_3)$_2$], 0.95 [d, $^3J_{H,H}$ = 7 Hz, 3 H, CH(CH_3)$_2$], 1.67–1.80 (m, 1 H, CH_2), 1.87 (s, 3 H, CH_3), 2.00–2.19 (m, 1 H, CH_2), 2.45–2.65 (m, 1 H, CH_2), 2.54 [sept, $^3J_{H,H}$ = 7 Hz, 1 H, CH(CH$_3$)$_2$], 2.74–2.96 (m, 1 H, CH$_2$), 4.76–4.81 (m, 1 H, C$_5H_4$), 4.88 (d, $^3J_{H,H}$ = 6 Hz, 1 H, *p*-cymene), 5.19 (d, $^3J_{H,H}$ = 6 Hz, 1 H, *p*-cymene), 5.28 (d, $^3J_{H,H}$ = 6 Hz, 1 H, *p*-cymene), 5.39 (d, $^3J_{H,H}$ = 6 Hz, 1 H, *p*-cymene), 5.97–6.04 (m, 1 H, C$_5H_4$), 6.09–6.15 (m, 1 H, C$_5H_4$), 6.20 (s, 5 H, C$_5H_5$), 6.49–6.57 (m, 1 H, C$_5H_4$), 6.80–8.00 (m, 22 H, Ph and binaphthyl) ppm. ^{31}P{^{1}H} NMR (CDCl$_3$, 202 MHz): δ = 24.66 (s) ppm. $C_{54}H_{49}Cl_2O_2PRuTi$ (980.78): calcd. C 66.13, H 5.04; found C 66.60, H 5.10. $[\alpha]_D^{20}$ = –1920 (*c* = 0.1, CH_2Cl_2).

X-ray Crystallographic Study of 8: $C_{48}H_{47}Cl_2O_4PRuTi\cdot C_7H_6O_2\cdot 0.5(CH_2Cl_2)$, *MW* = 1103.28, monoclinic, space group *C*2/*c*, *a* = 25.0136(3), *b* = 18.9231(2), *c* = 21.2279(3) Å, β = 98.595(1)°, *V* = 9935.1 (2) Å^3, *Z* = 8, D_{calc} = 1.475 g cm^{-3}; *F*(000) = 4536. The structure was solved by the heavy-atom method using SHELXS97.[26] Refinement, based on F^2, was carried out by full-matrix least-squares with the SHELXL97 and WINGX programs.[26,27] Non-hydrogen atoms were refined anisotropically. H atoms were included in calculated positions and included in the refinement with a riding-motion model with U_{iso} = 1.2U_{eq} of the carrier atom (1.5 for methyl groups and OH). Convergence was reached at wR_2 = 0.125 for all data (11386 intensities), R_1 = 0.047 for 7904 intensities with $I > 2\sigma(I)$ and *S* = 1.044 for 615 parameters. The residual electron density in the final difference Fourier map was 1.12 and –1.18 e Å^{-3}.

X-ray Crystallographic Study of 10: $C_{34}H_{37}Cl_2F_2PRuTi\cdot 3(CHCl_3)$, *MW* = 1092.6, triclinic, space group $P\bar{1}$; *a* = 9.716(5), *b* = 17.008(5), *c* = 28.927(5) Å, α = 75.609(5)°, β = 82.660(5)°, γ = 81.094(5)°, *V* = 4554 (3) Å^3, *Z* = 4, D_{calc} = 1.593 g cm^{-3}; *F*(000) = 2192. The structure was solved by the heavy-atom method using SHELXS97.[26] Refinement, based on F^2, was carried out by full-matrix least-squares with the SHELXL97 and WINGX programs.[26,27] Non-hydrogen atoms were refined anisotropically. H atoms were included in calculated positions and included in the refinement with a riding-motion model with U_{iso} = 1.2U_{eq} of the carrier atom (1.5 for methyl groups). Two independent molecules of **10** are present in the asymmetric unit and one of them has a disordered cyclopentadienyl ring over two positions with occupancies refined to 0.53:0.47. Among the six chloroform solvates present in the asymmetric unit, three are disordered over two positions with occupancies refined to 0.59:0.41, 0.90:0.10 and 0.90:0.10. The chlorine atoms with occupancies equal to 0.10 were isotropically refined Convergence was reached at wR_2 = 0.119 for all data (18928 intensities), R_1 = 0.051 for 15240 intensities with $I > 2\sigma(I)$ and *S* = 1.039 for 1047 parameters. The residual electron density in the final difference Fourier map was 1.25 and –1.03 e Å^{-3}.

X-ray Crystallographic Study of 12: $C_{54}H_{49}Cl_2O_2PRuTi\cdot C_{20}H_{14}O_2\cdot 2.5(CH_2Cl_2)$, *MW* = 1479.4, triclinic, space group $P\bar{1}$; *a* = 12.8350(4), *b* = 15.5480(5), *c* = 19.4240(6) Å, α = 112.361(2)°, β = 97.889(2)°, γ = 105.773(2)°, *V* = 3321.2 (2) Å^3, *Z* = 2, D_{calc} = 1.479 g cm^{-3}; *F*(000) = 1518. The structure was solved by the heavy-atom method using SHELXS97.[26] Refinement, based on F^2, was carried out by full-matrix least-squares with the SHELXL97 and WINGX programs.[26,27] Non-hydrogen atoms were refined anisotropically. H atoms were included in calculated positions and included in the refinement with a riding-motion model with U_{iso} = 1.3U_{eq} of the carrier atom. Two of the three dichloromethane solvates are disordered: one, located close to an inversion centre, was refined with an occupation factor of 0.5, the other is disordered over two positions with occupancies refined to 0.77:0.23. Convergence was reached at wR_2 = 0.129 for all data, R_1 = 0.049 for 12707 intensities with $I > 2\sigma(I)$ and *S* = 1.053 for 841 parameters. The residual electron density in the final difference Fourier map was 1.8 and –1.7 e Å^{-3} close to a disordered dichloromethane solvate.

CCDC-256921 (for **8**), -256922 (for **10**) and -225303 (for **12**) contain the supplementary crystallographic data for this paper. These

 © 2005 Wiley-VCH Verlag GmbH & Co. KGaA, Weinheim

data can be obtained free of charge from The Cambridge Crystallographic Data Centre via www.ccdc.cam.ac.uk/data_request/cif.

[1] R. Choukroun, D. Gervais, P. Kalck, F. Senocq, *J. Organomet. Chem.* **1987**, *335*, C9–C12.
[2] A. M. Trzeciak, J. J. Ziolkowski, R. Choukroun, *J. Mol. Catal.* **1996**, *110*, 135–139.
[3] B. E. Bosch, I. Brümmer, K. Kunz, G. Erker, R. Fröhlich, S. Kotila, *Organometallics* **2000**, *19*, 1255–1261.
[4] N. Wheatley, P. Kalck, *Chem. Rev.* **1999**, *99*, 3379–3419.
[5] P. Le Gendre, P. Richard, C. Moïse, *J. Organomet. Chem.* **2000**, *605*, 151–156.
[6] P. Le Gendre, M. Picquet, P. Richard, C. Moïse, *J. Organomet. Chem.* **2002**, *643–644*, 231–236.
[7] P. Le Gendre, V. Comte, A. Michelot, C. Moïse, *Inorg. Chim. Acta* **2003**, *350*, 289–292.
[8] J. Goux, P. Le Gendre, P. Richard, C. Moïse, *J. Organomet. Chem.* **2004**, in press.
[9] K. Döppert, H. P. Klein, U. Thewalt, *J. Organomet. Chem.* **1986**, *303*, 205–211.
[10] D. M. Hoffman, N. D. Chester, R. C. Fay, *Organometallics* **1983**, *2*, 48–52.
[11] A. Herzog, F. Q. Liu, H. W. Roesky, A. Demsar, K. Keller, M. Noltemeyer, F. Pauer, *Organometallics* **1994**, *13*, 1251–1256.
[12] X. Verdaguer, M. C. Hansen, S. C. Berk, S. L. Buchwald, *J. Org. Chem.* **1997**, *62*, 8522–8528.
[13] F. Lunzer, C. Marschner, S. Landgraf, *J. Organomet. Chem.* **1998**, *568*, 253–255.
[14] F. R. W. P. Wild, L. Zsolnai, G. Huttner, H. H. Brintzinger, *J. Organomet. Chem.* **1982**, *232*, 233–247.
[15] M. E. Huttenloch, B. Dorer, U. Rief, M. H. Prosenc, K. Schmidt, H. H. Brintzinger, *J. Organomet. Chem.* **1997**, *541*, 219–232.
[16] M. S. Erickson, F. R. Fronczek, M. L. McLaughlin, *J. Organomet. Chem.* **1991**, *415*, 75–85.
[17] B. A. Kuntz, R. Ramachandran, N. J. Taylor, J. Guan, S. Collins, *J. Organomet. Chem.* **1995**, *497*, 133–142.
[18] S. Collins, B. A. Kuntz, Y. Hong, *J. Org. Chem.* **1989**, *54*, 4154–4158.
[19] A. Kless, C. Lefeber, A. Spannenberg, R. Kempe, W. Baumann, J. Holz, A. Börner, *Tetrahedron* **1996**, *52*, 14599–14606.
[20] M. Quirmbach, A. Kless, J. Holz, V. Tararov, A. Börner, *Tetrahedron: Asymmetry* **1999**, *10*, 1803–1811.
[21] J. F. Mai, Y. Yamamoto, *J. Organomet. Chem.* **1998**, *560*, 223–232.
[22] J. F. Mai, Y. Yamamoto, *J. Organomet. Chem.* **1997**, *545*, 577–579.
[23] C. H. Winter, X. X. Zhou, M. J. Heeg, *Inorg. Chem.* **1992**, *31*, 1808–1815.
[24] A. J. Edwards, N. J. Burke, C. M. Dobson, K. Prout, S. J. Heyes, *J. Am. Chem. Soc.* **1995**, *117*, 4637–4653.
[25] G. Aullon, D. Bellamy, L. Brammer, E. A. Bruton, A. G. Orpen, *Chem. Commun.* **1998**, 653–654.
[26] G. M. Sheldrick, SHELX97 (includes SHELXS97, SHELXL97); Programs for Crystal Structure Analysis (Release 97-2); University of Göttingen, Göttingen, Germany, **1998**.
[27] L. J. Farrugia, *J. Appl. Crystallogr.* **1999**, *32*, 837–838.

Received: December 14, 2004

 © 2005 Wiley-VCH Verlag GmbH & Co. KGaA, Weinheim

Induction of Columnar Mesomorphism in Tetracoordinated Ionic Silver(I) Complexes Based on Chelate 4,4′-Disubstituted 2,2′-Bipyridines

Daniela Pucci,*[a] Giovanna Barberio,[a] Anna Bellusci,[a] Alessandra Crispini,[a] Massimo La Deda,[a] Mauro Ghedini,[a] and Elisabeta Ildyko Szerb[a]

Keywords: Bipyridine ligands / Silver / Metallomesogens / Ionic / Luminescence

The reaction of silver triflate (AgOTf) and silver dodecyl sulfate (AgDOS) with two nonmesomorphic 4,4′-disubstituted 2,2′-bipyridines, L^n, yielded a series of bis-chelate ionic silver complexes $[Ag(L^n)_2]X$. Complexation induced columnar mesomorphism in all the silver(I) tetra-branched bipyridine derivatives and the role of the counterion proved to be crucial in the generation of different symmetries of the mesophase. Remarkably, all silver(I) complexes exhibit emission at room temperature both in solution and in the solid state.

(© Wiley-VCH Verlag GmbH & Co. KGaA, 69451 Weinheim, Germany, 2005)

Introduction

Metallomesogens are a fascinating branch of nanostructure materials research,[1] as they join a current goal in supramolecular chemistry,[2] such as the self-assembly of coordinated species, with new functionalities provided from liquid crystalline properties.[3]

Our interest in this field has recently prompted us to employ nonmesogenic 4,4′-disubstituted 2,2′-bipyridines as building blocks in the synthesis of new coordination complexes, the mesomorphic properties of which are induced through the self-assembly of half-disc shaped $[LMCl_2]$ complexes (M = Pd, Pt, Ni, Zn) to full disc-shaped supramolecules, by the complementary shape approach. The complexes are liquid crystals regardless of the metal ion coordination geometry. The molecular organisation in the mesophase was mainly driven by intermolecular attractive interactions, with small structural variations having only subtle effects on the overall properties.[4]

Encouraged by these results, an electrostatic interaction was introduced to the molecular architecture and consequently to the supramolecular assembly. The synthesis of coordinatively saturated homoligand silver(I) complexes based on 2,2′-bipyridine ligands functionalised with amidic substituents in 4,4′-positions and with triflate as the counterion has been reported previously.[5] For the first time metallomesogens with tetracoordination around the silver(I) centre, based on chelate bipyridine ligands, were obtained. For these novel ionic liquid crystals a tetra-branched geometry induced mesomorphic molecular structures, such as columns. However, the presence of the amidic substituents introduced order in the structure, probably because of the ability to form H-bonding interactions, which lead to high transition temperatures.[5]

Novel examples of silver(I) complexes based on the nonmesomorphic 2,2′-bipyridines functionalised in 4,4′-positions with different substituents have been synthesised, as an alternative route to obtain low-temperature nonconventional ionic thermotropic metallomesogens. Four cationic bis-chelate silver complexes $[Ag(L^n)_2]X$ (Scheme 1) displaying columnar mesomorphism induced upon complexation are described here. These complexes are mesogenic even though they show pseudo-tetrahedral geometry around the metal centre, which would usually prevent the appearance of mesomorphic behaviour.[6]

The synthesis of metal complexes represents a challenge for obtaining new functional liquid crystalline materials where a wide choice of combinations of both metals and ligands would enhance preselected properties such as charge transport or luminescence.[1] Among the few reports on photoactive metallomesogens, few systems involve the use of the silver(I) ion,[7] although the various coordination modes of Ag^I, combined with the presence within the Ag complexes of large π systems as ligands,[8] would represent an ideal mode to expand the applicability of metallomesogens in the field of electro-optics.

Because many practical applications require liquid crystalline materials luminescent at room temperature, our investigations have reached this goal, giving rise to silver(I) complexes which exhibit emission at room temperature.

Moreover, the effect of the triflate (OTf) and the dodecyl sulfate (DOS) counterions on the mesogenic and photophysical properties have been investigated.

In the description of the $[Ag(L^n)_2]X$ complexes, dendrimeric terminology has been used in order to distinguish be-

[a] Centro di Eccellenza CEMIF.CAL-LASCAMM, Unità INSTM della Calabria, Dipartimento di Chimica, Università della Calabria,
87030 Arcavacata (CS), Italy

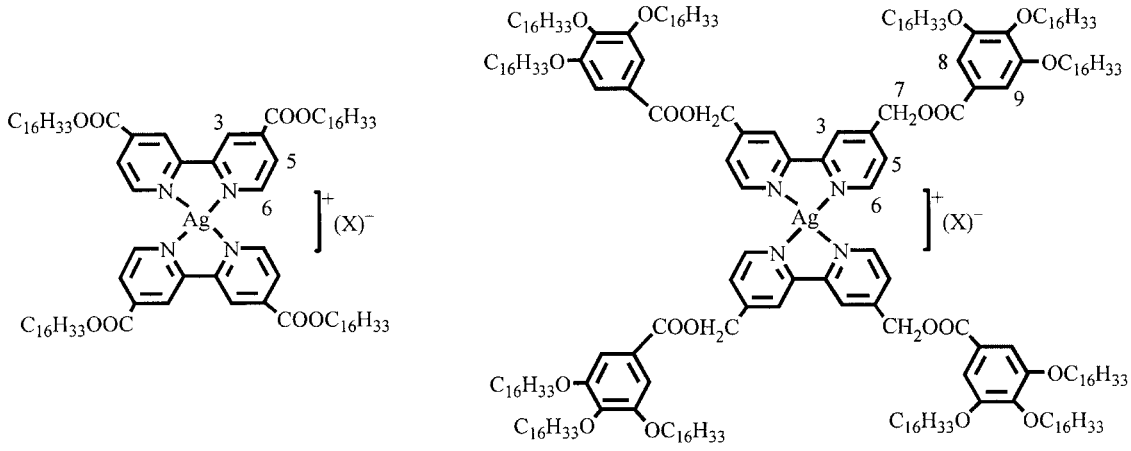

Scheme 1.

tween the different types of substituents on the bipyridine cores. Therefore all the silver derivatives are referred to as first-generation tetra-branched compounds, and the L^2 derivatives, **3** and **4**, as second-generation 12-branched compounds (Scheme 2).

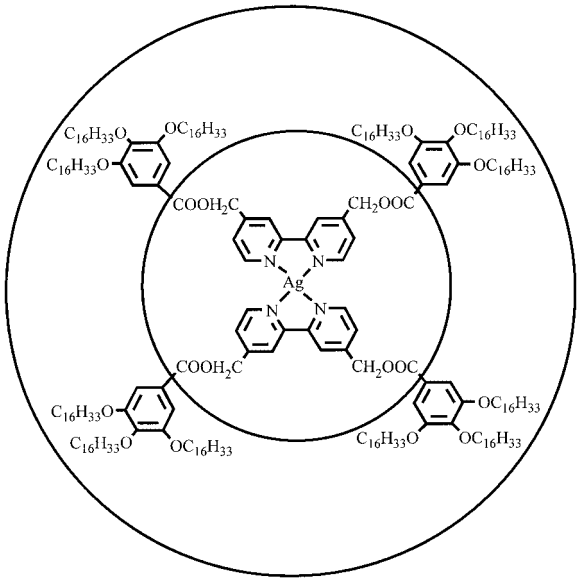

Scheme 2.

Results and Discussion

Synthesis

The reaction of L^n ligands with the appropriate silver salts (AgOTf and AgDOS) in a 1:2 metal-to-ligand stoichiometry, in dichloromethane, led to the formation of $[Ag(L^n)_2][X]$ complexes, **1**–**4**, in very good yields. The stoichiometry and purity of all compounds were confirmed using elemental analyses, IR and ^1H NMR spectroscopy. In these cationic bis-chelate silver derivatives, the silver atom is in a distorted tetrahedral geometry coordinated by four nitrogen atoms of the two bipyridines, as already found in the crystal structure determination of nonsubstituted 2,2′-bipyridine silver complexes with anions such as $(BF_4)^-$ and $(PF_6)^-$.[9,10]

Liquid Crystalline and Photophysical Properties

Although the ligands L^n are not liquid crystals, the complexation to different silver salts gave rise to the new series of complexes, **1**–**4**, which all showed thermally reproducible mesomorphism, characterised by a combination of optical microscopy (POM), differential scanning calorimetry (DSC) and powder X-ray diffraction analysis at variable temperature (PXRD). The thermal data of the $[Ag(L^n)_2]X$ series are summarised in Table 1 and the relative phase diagram is reported in Figure 1.

All the complexes **1**–**4** showed, after a crystal-to-crystal transition, enantiotropic columnar phases, with melting temperatures under 100 °C. The results from POM suggested, for both triflate complexes (**1** and **3**), the presence of a hexagonal mesophase with the typical fan-shaped optical texture with homeotropic areas (Plate 1 in Figure 2). As regards the dodecyl sulfate derivatives (**2** and **4**), they exhibit a different optical behaviour: for complex **2**, a texture with Maltese crosses appeared after annealing on cooling from the isotropic melt, which developed in the fingerprint texture reported in Figure 2 (plate 2); while complex **4** exhibits a fine columnar fan-like texture (plate 3 in Figure 2).

The columnar nature of the mesophases shown by complexes **1**–**4** has been confirmed by PXRD at variable temperature; the X-ray diffraction data are listed in Table 2.

The XRD patterns of the triflate complexes, **1** and **3**, are typical of a two-dimensional hexagonal lattice with the three peaks in the low angle region in the ratio $1:(3)^{1/2}:2$. In both cases, the wide angle region displayed a broad halo centred at 4.6–4.7 Å, typical of liquid-like correlations be-

 © 2005 Wiley-VCH Verlag GmbH & Co. KGaA, Weinheim

Table 1. Optical and thermal data of complexes **1**–**4**.

Complex[a]	Transition[a]	T/°C[a]	ΔH/kJ mol^{-1}
$[Ag(L^1)_2](OTf)$ (**1**)	Cr–Cr′	33	14.4
	Cr′–Col_h	59	8.14
	Col_h–I	71	56.7
	I–Col_h + Cr[b]	48	44.3
$[Ag(L^1)_2](DOS)$ (**2**)	Cr–Cr′	77	16.8
	Cr′–Col_r	81	98.5
	Col_r–I	85	62.2
	I–Col_r	64	41.2
	Col_r–Cr	48	39.3
$[Ag(L^2)_2](OTf)$ (**3**)	Cr–Cr′	49	111.9
	Cr′–Col_h	69	10.0
	Col_h–I	97	3.3
	I–Col_h	96	3.2
	Col_h–Cr	44	118.7
$[Ag(L^2)_2](DOS)$ (**4**)	Cr–Cr′	58	85.0
	Cr′–Col_r	77	34.9
	Col_r–I	90	2.3
	I–Col_r + Cr[b]	55	135.2

[a] Cr: crystal; Col: columnar; I: isotropic liquid. [b] Only a broad peak for the two transitions.

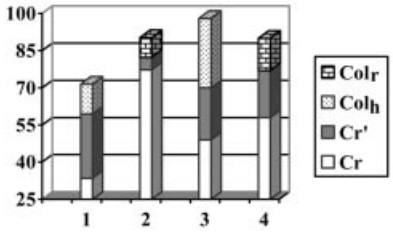

Figure 1. Phase diagram of complexes **1**–**4**.

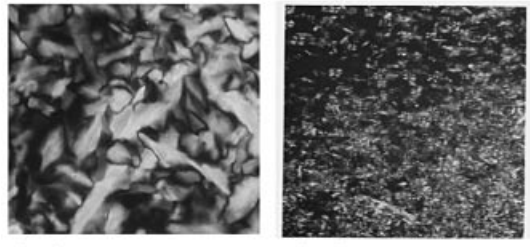

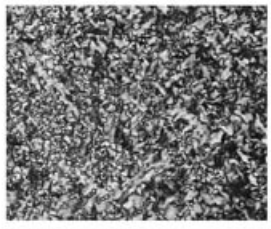

Figure 2. Polarised light optical photomicrograph of the textures exhibited by complex **3** at 85 °C on cooling (Plate 1); by complex **2** at 60 °C on cooling (Plate 2); and by complex **4** at 85 °C on heating (Plate 3).

Table 2. X-ray diffraction data of complexes **1**–**4**.

Complex	Mesophase lattice constants/Å	$d_{obsd.}$/Å ($d_{calcd.}$/Å)	Miller indices
1		43.7 (43.7)	(1 0)
	Col_h at 68 °C	26.6 (25.2)	(1 1)
	(on heating)	22.2 (21.8)	(2 0)
		14.8 (14.3)	(3 0)
	a = 51.6	ca. 4.7	broad
	n = 3.0[a]	ca. 3.6	broad
2		38.7 (38.7)	(1 1)
	Col_r at 83 °C	29.1 (29.1)	(2 0)
	(on heating)	19.2 (19.3)	(2 2)
		12.9 (12.9)	(0 4)
	a = 58.3	4.6	
	b = 51.6	4.3	
		4.0	
3		37.3 (37.3)	(1 0)
	Col_h at 86 °C	21.4 (21.5)	(1 1)
	(on cooling)	18.9 (18.6)	(2 0)
		ca. 4.6	broad
	a = 43.2		
	n = 1.1[a]		
4		48.4 (48.4)	(2 0)
	Col_r at 84 °C	36.5 (36.5)	(1 1)
	(on heating)	25.2 (25.0)	(3 1)
		20.7 (20.6)	(4 1)
	a = 96.8	16.6 (16.8)	(3 2)
	b = 39.4	ca. 4.7	broad
		ca. 4.1	broad

[a] Number of molecules calculated according to the formula $n = V_{cell}(N_A/M)\rho$ assuming a density of 1 g cm^{-3}, where N_A is the Avogadro constant; V_{cell} is calculated assuming a height of 3.6 Å for **1** and 4.6 Å for **3**.

tween side chains, while only in the case of complex **1** is a peak present at 3.6 Å, corresponding to the distance between adjacent cores. These differences account for a more ordered hexagonal phase in the case of complex **1**, in which there is a reduced number of aliphatic peripheral chains around the central core. The crystallinity of the mesophase in this case is also confirmed by the huge difference in the transition enthalpy values for the Col_h–I transitions of **1** and **3**, as reported in Table 1. Remarkably, the lattice parameter of **1** (a_{hex} = 51.6 Å) is significantly greater than that of complex **3** (a_{hex} = 43.2 Å), which has bulkier substituents on the 2,2′-bipyridines and greater side-chain density. This difference, which has already been observed in other polycatenar compounds with variable length alkyl chains,[11] reflects the different organisation of the molecules within the columns depending on the number of the alkyl chains. For the Col_h phase of **1**, approximately three molecules instead of just the one calculated for complex **3** can be found in the cross-section of the columns when the height of the columnar slice is assumed to be 4.6 Å (Table 2), indicating that the overall organisation between the molecular cores is of an edge-to-edge type. In the case of the second-generation 12-branched complex **3**, the four phenyl rings and 12 chains per molecule can completely sur-

 © 2005 Wiley-VCH Verlag GmbH & Co. KGaA, Weinheim

round the molecular cores, reducing the number of molecules in the cross-section of each unit cell.

The symmetry of the columnar mesophases changes on going from the OTf to the DOS derivatives. In fact, both DOS derivatives **2** and **4** showed X-ray diffraction patterns of a rectangular columnar mesophase, characterised by two sharp fundamental peaks in the low angle region (Figure 3).

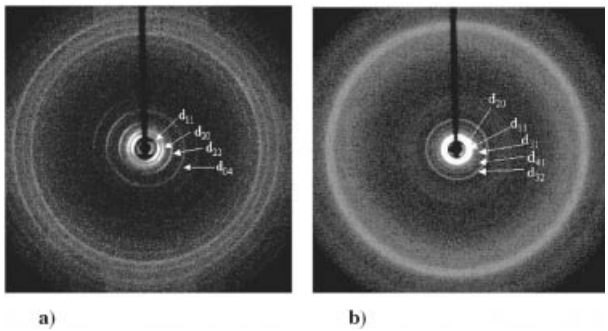

Figure 3. X-ray diffraction patterns of nonaligned samples of the rectangular columnar phases of (a) complex **2** at 87 °C on heating and (b) complex **4** at 84 °C on heating.

.

The change in the shape of the counterion destabilises the hexagonal phase, favouring rectangular phases at higher temperatures. The mesophase crossover from Col_r to Col_h is generally associated with the increase of the side-chain lengths or with the different size of the metal centres,[5,12,13] and, in both cases, the effect is a greater core–core interaction, which favours the formation of the Col_r phase. In a Col_h phase a rotationally averaged shape of the molecules gives a circular projection along the column's axis and the mesogenic plane is perpendicular to the column's axis. A distortion from Col_h to a Col_r is obtained when the molecules project an elliptical shape along the column's axis (Figure 4).[14]

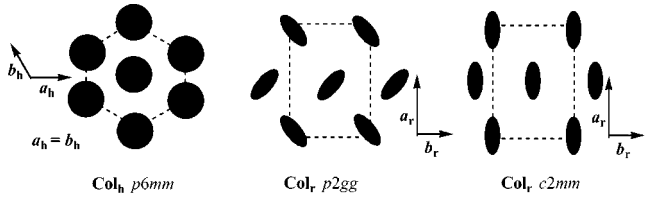

Figure 4. Schematic representation of the 2D lattices of the different columnar mesophases observed and their associated plane groups.

In this case the presence of the DOS counterion, which because of its shape can be organised with the flexible aliphatic chain aligned in the direction of the aliphatic periphery of the cation, hinders the molecular rotation of the nondisclike molecules, generating an elliptical cross-section. Within the rectangular arrangements, two different symmetries characterised by two different plane groups can be distinguished. The indexation of the two spectra showed that the reflection conditions for the *c2mm* plane group are verified in the case of complex **2**, with the (11) reflection being at a smaller angle ($d_{11} > d_{20}$), while the *p2gg* plane group is assigned to the Col_r phase of the second-generation 12-branched complex **4** (Table 2). Indeed the presence of a further aliphatic chain of the DOS counterion induces a more pronounced effect on the second-generation tetrabranched complex **2** with respect to the second-generation 12-branched complex, in which the volume fraction of the flexible chains completely surrounds the polar inner sphere.

Another important feature of the two rectangular columnar mesophases is the notable difference in the organisation within the columns evidenced by the high angle region of the XRD spectra. While in the XRD spectrum of **4** only a broad halo centred at 4.7 Å is present, typical of liquid-like correlations between side chains; in the case of **2**, three distinct reflections are observable at 4.6, 4.3 and 4.0 Å, indicative of a crystalline rectangular mesophase (Figure 3). This is confirmed also by the difference in the enthalpy values associated with the transitions to the isotropic liquid (Table 1).

A photophysical study has been performed on compounds **1**–**4**, in dichloromethane solution at room temperature, to assess the absorption and luminescence properties of the single subunits (Table 3).

The absorption features of the ligands are very similar to each other, and characteristics of these chromophores:[4b] π–π* excitations on aromatic rings give rise to two main bands at 240 and 300 nm (Table 3), which appear with a shoulder because of a vibrational progression. A weak low-energy band at about 330 nm is assigned to an n–π* transition. In the L^2 spectrum some differences are found: in particular, the band maximum at 278 nm is blue-shifted and more intense with respect to the corresponding band in L^1; this is attributed to the introduction of three hexadecyloxybenzyl substituents which stabilise the π orbital on the pyridine ring by exerting a weak electron-donating effect. Moreover, the aromatic transitions localised on the phenyl rings of the substituents contribute to the intensity of the

Table 3. Photophysical data.

Compound	Solution Abs., λ/nm (ε/L mol^{-1} cm^{-1})[a]	Em, λ/nm (Φ)	Solid Abs., λ/nm	Em, λ/nm
1	250 (sh), 275 (sh), 310 (21000), 315 (sh), 330 (sh)	350 (1.0%)	310, 320	350
2	250 (sh), 275 (sh), 310 (16800), 315 (sh), 330 (sh)	350 (0.8%)	310, 320, 340	365
3	250 (sh), 280 (66270), 290 (sh)	355 (3.5%)	280	367
4	250 (sh), 280 (82860), 290 (sh)	355 (3.0%)	280	367

[a] sh: shoulder.

 © 2005 Wiley-VCH Verlag GmbH & Co. KGaA, Weinheim

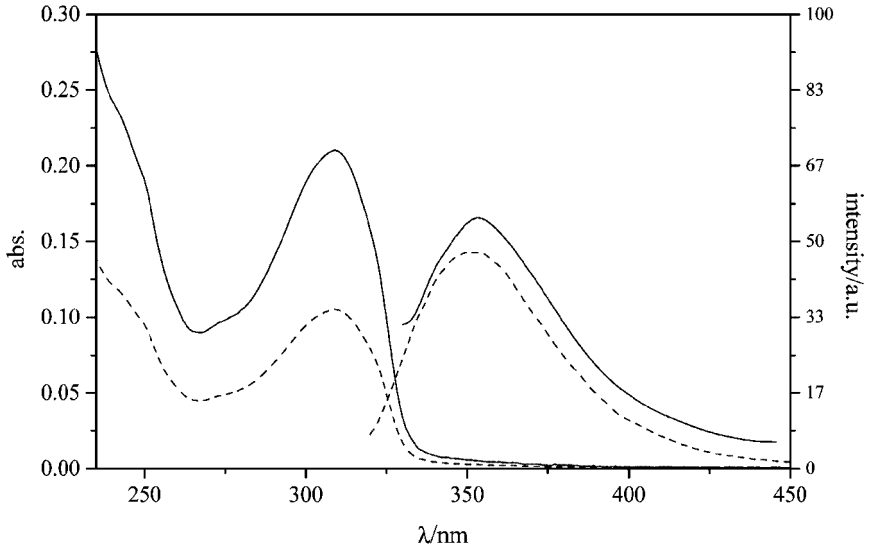

Figure 5. Absorption and emission spectra of **1** (solid line) and **3** (dashed line) in dichloromethane solution.

278-nm band. Metal complexation of both ligands induces a slight red-shift of the absorption bands in their derivatives (Figure 5), while, as expected, in solution no appreciable spectral differences are attributed to the influence of the two counterions. In the spectra of complexes **1** and **2** a weak band is visible at 275 nm, attributed to a ligand-to-metal-charge transfer;[15] the same feature in the spectra of **3** and **4** is probably hidden by the intense band at 278 nm.

The emission spectra of the ligands show a maximum at 350 (L^1) and 355 nm (L^2), which is ascribable to the deactivation of the π–π*-related state (Table 3); the measured quantum yields are comparable with those found for similar compounds.[4b] All the first-generation tetra-branched complexes showed the same luminescence observed in their corresponding ligands,[4b] and attributed to a ^{1}LC (ligand centred) transition. The observed quantum yields for these complexes are reduced because of the presence of the heavy atoms which induce $^1LC \rightarrow {}^3LC$ intersystem crossing.[16] In solution, no spectral differences are attributable to the counterion and the differences among Φ-values of the L^1 and L^2 derivatives are within the range of experimental uncertainty. Remarkably, in analogy to the corresponding ligands, the second-generation 12-branched complexes **3** and **4** have a quantum yield higher than that of complexes **1** and **2**.

A study of the photophysical properties of both ligands and complexes **1**–**4** has been performed also in the solid state, with the intention of examining the influence of the crystal packing on the luminescence features. No significant differences have been recorded with respect to the spectra in solution (Table 3).

Conclusions

The general preference of the silver(I) ion in liquid crystals reported to date is for linear 2-coordination or for tetra-coordination in macrocycle derivatives.[1,17] However, often the structure and packing of the ionic silver complexes are influenced by the argentophilic interaction (Ag–Ag contacts) and by the presence of coordinating counterions, which can induce the coordination number to increase up to six. This change in the network dimensionality has led to a drawback for the silver complexes, namely that their high clearing temperatures and their poor thermal stability have meant that their physical properties have been scarcely investigated.

We have recently reported a new class of chelate silver bipyridine with a coordinative saturation around the metal centre. These complexes exhibited columnar mesomorphism at very high temperatures, as the presence of amidic functionalities on the bipyridine ligands gives rise to H-bonding interactions.[5] In order to overcome this structural limitation new ligands with different substituents have been used for the synthesis of a novel class of ionic $[Ag(L^n)_2][X]$ complexes with a tetracoordination around the silver centre. The coordination of the two nonmesomorphic ligand units, with different molecular features, namely rod-like for L^1 and hemi-disc for the hexacatenar L^2, to the silver atom gives rise to a starlike molecular shape because of the pseudo-tetrahedral coordination around the metal centre, and induces liquid crystalline behaviour in the resulting complexes. In particular, it seems that the difference in the molecular anisotropy and the volume of the cationic cores of the two ligands L^n does not perturb the molecular arrangement and the mesophase induction. Thus, all complexes show columnar mesomorphism, regardless of the nature and number of branchings on the organic ligand with a lowering by 100–200 °C of the clearing temperatures with respect to the similar amidic Ag^I complexes.[5]

However, the enhancement of the aliphatic periphery in the second-generation 12-branched compounds allows the transition from crystalline to liquid crystalline mesophases.

 © 2005 Wiley-VCH Verlag GmbH & Co. KGaA, Weinheim

The symmetry of the mesophase of the four derivatives strongly depends on the structural role of the counterion, which drives the organisation of both the single molecular units and of the overall supramolecular motifs. Indeed the triflate anion has been found to promote the hexagonal phase while rectangular phases seem to be stabilised by the dodecyl sulfate anion which, because of its shape, can be organised with the flexible aliphatic chain aligned in the direction of the aliphatic periphery of the cation, hindering the molecular rotation of the nondisclike molecules and thus generating an elliptical cross-section. This change of mesophase morphology is related to the balance between the two microsegregate regions of the molecules, as evidenced by the different perturbation induced by the DOS anion on the two derivatives. Indeed for the second-generation 12-branched complex **4**, in which the volume fraction of the flexible chains completely surrounds the polar inner sphere, the presence of the aliphatic chain of the DOS counterion induces a less pronounced effect on the symmetry (*p2gg* lattice) than that on complex **2** (*c2mm* lattice).

The influence of the counteranion on thermal behaviour follows the same trend: the molecular arrangement in the solid phase of the dodecyl sulfate derivatives is more effective than that of the triflate complexes, which tend to melt at lower temperatures and show a wider mesophase range with respect to the homologues in the dodecyl sulfate series.

Moreover, complexes **1**–**4** show luminescence at room temperature both in solution and in the solid state, which is not a common feature for Ag^{I} derivatives,[8] and therefore they represent interesting materials for applicative purposes requiring room temperature luminescent liquid crystals.

Experimental Section

Materials and Measurements: Silver triflate (AgOTf) was purchased from Aldrich and used as received. Also the solvents were used as received from commercial sources without further purification. Ligands, dihexadecyl 2,2′-bipyridine-4,4′-dicarboxylate (L^1) and 4,4′-bis(3,4,5-trihexadecyloxybenzoyloxymethyl) 2,2′-bipyridine (L^2) were synthesised as previously reported.[4a,4c]

Infrared spectra were recorded with a Spectrum One FT-IR Perkin–Elmer spectrometer and ^{1}H NMR spectra with a Bruker AVANCE-300 spectrometer, in $CDCl_3$ solution, with TMS as internal standard. Elemental analyses were performed with a Perkin–Elmer 2400 analyser.

The textures of the mesophases were studied with a Zeiss Axioscope polarising microscope equipped with a Linkam CO 600 heating stage. The transition temperatures and enthalpies were measured with a Perkin–Elmer Pyris 1 Differential Scanning Calorimeter with a heating and cooling rate of 10 °C/min. The apparatus was calibrated with indium. Two or more heating/cooling cycles were performed on each sample.

Spectrofluorimetric grade dichloromethane (Acros Organics) was used for the photophysical investigations in solution, at room temperature. A Perkin–Elmer Lambda 900 spectrophotometer was employed to obtain the absorption spectra, while the uncorrected emission spectra, all confirmed by excitation ones, were recorded with a Perkin–Elmer LS 50B spectrofluorimeter, equipped with a Hamamatsu R928 photomultiplier tube. Emission quantum yields were determined using the optically dilute method[18a] on aerated solutions with absorbance at excitation wavelengths <0.1; $Ru(bipy)_3Cl_2$ (bipy = 2,2′-bipyridine) in water was used as standard (Φ = 0.028).[18b] The experimental uncertainty on the molar extinction coefficients is 10%, while on the emission quantum yields it is 15%. The examined compounds are fairly stable in dichloromethane, as demonstrated by the constancy of their absorption spectra over a week.

The powder X-ray diffraction patterns were obtained by using a Bruker AXS General Area Detector Diffraction System (D8 Discover with GADDS) with Cu-K_α radiation; the high sensitive area detector was placed at a distance from the sample of 10 cm and equipped with a CalCTec (Italy) heating stage. The samples were heated at a rate of 5.0 °C min^{-1} to the appropriate temperature. Measurements were performed by charging samples in Lindemann capillary tubes with an inner diameter of 0.5 mm.

Synthesis of Complexes: All silver complexes were prepared in a similar fashion from the appropriate ligands and silver salts. The synthesis of complex **1** is described in detail below while for all others only yields, ^{1}H NMR, IR and elemental analysis data are reported.

Bis(dihexadecyl 2,2′-bipyridyl-4,4′-dicarboxylate)silver(I) Triflate [$(L^1)_2$Ag](OTf) (1): A solution of AgOTf (15 mg, 0.0575 mmol) and L^1 (80 mg, 0.115 mmol) in dichloromethane (10 mL) was stirred under nitrogen (24 h, 40 °C), with the vessel protected from light. The mixture was then filtered through Celite and concentrated under reduced pressure. The product was collected as a yellow solid in 96% yield (90 mg) after precipitation by diethyl ether; thermotropic behaviour is shown in Table 1. ^{1}H NMR (300 MHz, $CDCl_3$, 25 °C, TMS): δ = 0.87 (t, $^3J_{H,H}$ = 6.4 Hz, 12 H, CH_3), 1.25 (m, 104 H, $(CH_2)_{13}CH_3$), 1.84 (m, 8 H, $CH_2(CH_2)_{13}CH_3$), 4.43 (t, $^3J_{H,H}$ = 6.8 Hz, 8 H, OCH_2), 8.07 (d, $^3J_{H,H}$ = 5.1 Hz, 4 H, H-5), 8.81 (s, 4 H, H-3), 8.92 (d, $^3J_{H,H}$ = 5.1 Hz, 4 H, H-6). IR (KBr): $\tilde{\nu}$ = 1726 cm^{-1} (C=O), 1288, 1255 cm^{-1} (OTf). $C_{89}H_{144}AgF_3N_4O_{11}S$ (1643.07): calcd. C 65.06, H 8.83, N 3.41; found C 65.16, H 8.90, N 3.34.

Bis(dihexadecyl 2,2′-bipyridyl-4,4′-dicarboxylate)silver(I) Dodecyl Sulfate [$(L^1)_2$Ag](DOS) (2): The product was collected as a pale yellow solid in 82% yield (83 mg); thermotropic behaviour is shown in Table 1. ^{1}H NMR (300 MHz, $CDCl_3$, 25 °C, TMS): δ = 0.87 (t, $^3J_{H,H}$ = 6.8 Hz, 15 H, CH_3), 1.25 (m, 122 H, $(CH_2)_nCH_3$), 1.84 (m, 10 H, $CH_2(CH_2)_nCH_3$), 4.10 (t, $^3J_{H,H}$ = 6.8 Hz, 2 H, O_3SOCH_2), 4.45 (t, $^3J_{H,H}$ = 6.6 Hz, 8 H, OCH_2), 8.10 (dd, $^3J_{H,H}$ = 5.1, $^4J_{H,H}$ = 1.5 Hz, 4 H, H-5), 8.86 (s, 4 H, H-3), 9.07 (d, $^3J_{H,H}$ = 5.1 Hz, 4 H, H-6). IR (KBr): $\tilde{\nu}$ = 1720 cm^{-1} (C=O), 1254, 1230 cm^{-1} (DOS). $C_{100}H_{169}AgN_4O_{12}S$ (1759.39): calcd. C 68.27, H 9.68, N 3.18; found C 68.33, H 9.58, N 3.05.

Bis[4,4′-bis(3,4,5-trihexadecyloxybenzoyloxymethyl)-2,2′-bipyridyl]-silver(I) Triflate [$(L^2)_2$Ag](OTf) (3): The product was collected as a white solid in 92% yield (211 mg); thermotropic behaviour is shown in Table 1. ^{1}H NMR (300 MHz, $CDCl_3$, 25 °C, TMS): δ = 0.85 (t, $^3J_{H,H}$ = 6.2 Hz, 36 H, CH_3), 1.25 (m, 312 H, $(CH_2)_{13}CH_3$), 1.83 (m, 24 H, $CH_2(CH_2)_{13}CH_3$), 4.02 (t, $^3J_{H,H}$ = 6.8 Hz, 24 H, OCH_2), 5.53 (s, 8 H, H-7), 7.32 (s, 8 H, H-8,9), 7.57 (d, $^3J_{H,H}$ = 4.9 Hz, 4 H, H-5), 8.32 (s, 4 H, H-3), 8.64 (d, ^3J = 5.0 Hz, 4 H, H-6). IR (KBr): $\tilde{\nu}$ = 1709 cm^{-1} (C=O), 1252, 1220 cm^{-1} (OTf). $C_{245}H_{424}AgF_3N_4O_{23}S$ (3991.00): calcd. C 73.73, H 10.71, N 1.40; found C 73.52, H 10.56, N 1.41.

Bis[4,4′-bis(3,4,5-trihexadecyloxybenzoyloxymethyl)-2,2′-bipyridyl]-silver(I) Dodecyl Sulfate, [$(L^2)_2$Ag](DOS) (4): The product was collected as a beige solid in 78% yield (184 mg); thermotropic behav-

 © 2005 Wiley-VCH Verlag GmbH & Co. KGaA, Weinheim

iour is shown in Table 1. ^{1}H NMR (300 MHz, $CDCl_3$, 25 °C, TMS): δ = 0.89 (t, $^3J_{H,H}$ = 6.6 Hz, 39 H, CH_3), 1.27 (m, 330 H, $(CH_2)_nCH_3$), 1.79 (m, 26 H, $CH_2(CH_2)_nCH_3$), 4.04 (m, 26 H, OCH_2), 5.51 (s, 8 H, H-7), 7.34 (s, 8 H, H-8,9), 7.48 (d, $^3J_{H,H}$ = 5.1 Hz, 4 H, H-5), 8.43 (s, 4 H, H-3), 8.70 (d, ^3J = 5.1 Hz, 4 H, H-6). IR (KBr): $\tilde{\nu}$ = 1709 cm^{-1} (C=O), 1254, 1221 cm^{-1} (DOS). $C_{256}H_{449}AgN_4O_{24}S$ (4107.32): calcd. C 74.86, H 11.02, N 1.36; found C 75.05, H 10.97, N 1.61.

Acknowledgements

This work was partly supported by the Italian Ministero dell′Istruzione, dell′Università e della Ricerca (MIUR) through the INSTM-FIRB and Centro di Eccellenza CEMIF.CAL grants.

[1] a) J. L. Serrano, *Metallomesogens*, Wiley-VCH, Weinheim, **1996**; b) B. Donnio, D. W. Bruce, "Metallomesogens" in *Structure and Bonding* vol. 95 (Liquid Crystals II) (Ed.: D. M. P. Mingos), Springer, Heidelberg, **1999**; c) B. Donnio, D. Guillon, R. Deschenaux, D. W. Bruce, "Metallomesogens" in *Comprehensive Coordination Chemistry II*, vol. 6 (Eds.: J. A. McCleverty, T. J. Meyer), Elsevier, Oxford, **2003**.

[2] J. M. Lehn, *Science* **2002**, *295*, 2400–2415.

[3] T. Kato, N. Mizoshita, *Curr. Opin. Sol. State Mater. Sci.* **2002**, *6*, 579–587.

[4] a) D. Pucci, G. Barberio, A. Crispini, O. Francescangeli, M. Ghedini, *Mol. Cryst. Liq. Cryst.* **2003**, *395*, 155–165; b) D. Pucci, G. Barberio, A. Crispini, O. Francescangeli, M. Ghedini, M. La Deda, *Eur. J. Inorg. Chem.* **2003**, 3649–3661; c) G. Barberio, A. Bellusci, A. Crispini, M. Ghedini, A. Golemme, P. Pruss, D. Pucci, *Eur. J. Inorg. Chem.* **2005**, 181–188.

[5] D. Pucci, G. Barberio, A. Bellusci, A. Crispini, M. Ghedini, E. I. Szerb, *Mol. Cryst. Liq. Cryst.* **2005**, in press.

[6] A. Pegenau, T. Hegmann, C. Tschierske, S. Diele, *Chem. Eur. J.* **1999**, *5*, 1643–1651.

[7] P. K. Sudhadevi Antharjanam, V. Ajay Mallia, S. Das, *Chem. Mater.* **2002**, *14*, 2687–2692.

[8] a) X.-C. Huang, S.-L. Zheng, J.-P. Zhang, X.-M. Chen, *Eur. J. Inorg. Chem.* **2004**, 1024–1029; b) Y. Kang, C. Seward, D. Song, S. Wang, *Inorg. Chem.* **2003**, *42*, 2789–2797.

[9] E. C. Constable, C. E. Housecroft, M. Neuburger, I. Poleschak, M. Zehnder, *Polyhedron* **2003**, *22*, 93–108.

[10] H.-P. Wu, C. Janiak, G. Rheinwald, H. Lang, *J. Chem. Soc. Dalton Trans.* **1999**, 183–190.

[11] T. Hegmann, J. Kain, S. Diele, B. Schubert, H. Bögel, C. Tschierske, *J. Mater. Chem.* **2003**, *13*, 991–1003.

[12] C. K. Lai, C.-H. Tsai, Y.-S. Pang, *J. Mater. Chem.* **1998**, *8*, 1355–1360.

[13] H. Zheng, C. K. Lai, T. M. Swager, *Chem. Mater.* **1995**, *7*, 2067–2077.

[14] D. Goldmann, D. Janietz, C. Schmidt, J. H. Wendorff, *J. Mater. Chem.* **2004**, *14*, 1521–1525.

[15] a) V. W. W. Yam, *Pure Appl. Chem.* **2001**, *73*, 543–548; b) C. R. Wang, K. K. W. Lo, V. W. W. Yam, *Chem. Phys. Lett.* **1996**, *262*, 91–96.

[16] N. Armaroli, M. A. J. Rodgers, P. Ceroni, V. Balzani, C. O. Dietrich-Buchecker, J. M. Kern, A. Bailal, J. P. Sauvage, *Chem. Phys. Lett.* **1995**, *241*, 555–558.

[17] F. Neve, *Adv. Mater.* **1996**, *8*, 277–289.

[18] a) J. N. Demas, G. A. Crosby, *J. Phys. Chem.* **1971**, *75*, 991–1024; b) K. Nakamaru, *Bull. Soc. Chem. Jpn.* **1982**, *5*, 2697–2705.

Received: January 03, 2005

 © 2005 Wiley-VCH Verlag GmbH & Co. KGaA, Weinheim

Formation, Structure, and Reactivity of Gaseous $Ni_2O_2^+$

Konrad Koszinowski,[a,b] Maria Schlangen,[a] Detlef Schröder,[a] and Helmut Schwarz*[a]

In memoriam Chava Lifshitz

Keywords: Catalysis / C–H bond activation / Gas-phase reactions / Metal clusters / Nickel / Transition-metal oxides

The dinuclear metal dioxide $Ni_2O_2^+$ is prepared by the reaction of gaseous Ni_2^+ with N_2O in a Fourier-transform ion-cyclotron-resonance (FT-ICR) mass spectrometer. The title compound oxidizes CO, thus proving the catalytic activity of Ni_2^+ for mediating oxygen-atom transfer from N_2O to CO. Whereas $Ni_2O_2^+$ does not react with H_2 and CH_4, it accomplishes C–H bond activation of ethane, propane, and *n*-butane. In comparison to the previously studied metal-oxide clusters $Mn_2O_2^+$ and $Fe_2O_2^+$, $Ni_2O_2^+$ exhibits an enhanced reactivity, which is ascribed to a lower oxygen-binding energy.

(© Wiley-VCH Verlag GmbH & Co. KGaA, 69451 Weinheim, Germany, 2005)

1. Introduction

For more than two decades, the gas-phase chemistry of diatomic transition-metal oxide cations MO^+ has been an area of active research.[1–5] The interest in these species mainly results from the fact that they are the simplest conceivable model compounds for catalytically active transition-metal oxides in the condensed phase, whose structural complexity often is prohibitive for direct mechanistic studies.

With routine methods for the generation of gaseous metal clusters at hand today,[6,7] polynuclear $M_mO_n^+$ species can be investigated as well. These cluster ions are supposed to be more realistic models for neutral, bulk transition-metal oxides than isolated MO_n^+ species, because they exhibit lower charge densities and incorporate some degree of aggregation. Nonetheless, the number of reactivity studies on $M_mO_n^+$ clusters still is limited.[8] So far, research activities have focused on $V_mO_n^+$,[9,10] their heavier homologues $Nb_mO_n^+$ and $Ta_mO_n^+$,[9] $Mn_2O_2^+$,[11] $Fe_mO_n^+$,[12,13] and Pt_mO^+.[14] In addition, reactions of the dinuclear cluster ions $Ti_2O_2^+$ and $Co_2O_2^+$ have been investigated;[15,16] however, these studies did not address the problems of C–H bond activation or oxygen-atom transfer, which are prime challenges in the context of catalysis.[17]

In the present contribution, we report on the gas-phase synthesis and reactivity of $Ni_2O_2^+$. As a group 10 element, nickel has a rather high electronegativity and is less oxophilic than earlier 3*d* metals. It will be interesting to see whether the accordingly expected lower stability of $Ni_2O_2^+$, compared to the previously studied cations $Mn_2O_2^+$ and $Fe_2O_2^+$, results in an enhanced reactivity of the title compound.

[a] Institut für Chemie der Technischen Universität Berlin, Strasse des 17. Juni 135, 10623 Berlin, Germany
E-mail: Helmut.Schwarz@mail.chem.tu-berlin.de
[b] Present address: Department of Chemistry, Stanford University, Stanford, CA 94305-5080, USA

2. Results and Discussion

2.1 Formation of $Ni_2O_2^+$

Ni_2^+ reacts with N_2O by oxygen-atom transfer, Equation (1). The resulting Ni_2O^+ continues to abstract oxygen from N_2O, thereby forming $Ni_2O_2^+$, Equation (2), as the final product under ICR conditions.

$$Ni_2^+ + N_2O \rightarrow Ni_2O^+ + N_2 \quad (1)$$

$$Ni_2O^+ + N_2O \rightarrow Ni_2O_2^+ + N_2 \quad (2)$$

The occurrence of these processes under thermal conditions implies $D_0(Ni_2^+–O) \geq D_0(N_2–O) = 161$ kJ·mol^{-1}[18] as well as $D_0(Ni_2O^+–O) \geq D_0(N_2–O)$; the first lower limit is completely in line with $D_0(Ni_2^+–O) = 457.6 \pm 3$ kJ·mol^{-1} reported by Vardhan et al.[19] Both reactions exhibit rather moderate efficiencies (Table 1). Interestingly, several mononuclear transition-metal cations M^+, including Ni^+, have been found not to react at all with N_2O at thermal energies, although oxygen transfer is allowed thermochemically.[2,20,21] The existence of barriers associated with these processes has been rationalized by spin restrictions,[22] as MO^+ correlates with atomic $O(^3P)$, whereas N_2O yields $O(^1D)$ upon adiabatic oxygen release.[2,23] Possibly, the presence of more electronic states in the Ni_2^+ cluster opens new spin-allowed reaction paths not available for the mononu-

 DOI: 10.1002/ejic.200500040

clear system and thus leads to the enhanced reactivity observed.

Table 1. Bimolecular rate constants k, efficiencies φ, and branching ratios (b.r.) for reactions of dinuclear nickel clusters at 298 K.

Reactants	k [cm^3 s^{-1}][a]	φ	Products	b.r. (%)
$Ni_2^+ + N_2O$	3.0×10^{-11}	0.04	$Ni_2O^+ + N_2$	100[b]
$Ni_2O^+ + N_2O$	9.3×10^{-11}	0.13	$Ni_2O_2^+ + N_2$	100
$Ni_2{}^{16}O_2^+ + {}^{18}O_2$	8.0×10^{-13}	0.0015	$Ni_2{}^{16}O{}^{18}O^+ + {}^{16}O{}^{18}O$	100
$Ni_2O^+ + CO$	3.5×10^{-11}	0.050	$Ni_2^+ + CO_2$	100
$Ni_2O_2^+ + CO$	2.1×10^{-11}	0.030	$Ni_2O^+ + CO_2$	100
$Ni_2O_2^+ + C_2H_6$	1.4×10^{-10}	0.14	$Ni_2H_2O_2^+ + C_2H_4$	100
$Ni_2O_2^+ + C_3H_8$	3.8×10^{-10}	0.38	$NiC_3H_6^+ + [Ni,H_2,O_2]$	10
			$Ni_2H_2O_2^+ + C_3H_6$	90
$Ni_2O_2^+ + n\text{-}C_4H_{10}$	6.7×10^{-10}	0.64	$NiC_4H_6^+ + [Ni,H_4,O_2]$	15
			$Ni_2H_2O_2^+ + C_4H_8$	65
			$Ni_2C_4H_6^+ + 2\ H_2O$	10
			$Ni_2C_4H_8O^+ + H_2O$	10

[a] Uncertainties of the absolute rate constants estimated at 30%.[40] [b] In addition, $Ni(N_2O)^+$ is formed, see text for discussion.

In addition to oxygen-atom transfer, Ni_2^+ undergoes two side reactions. The first one yields atomic Ni^+ (ca. 7% branching ratio, b.r.) such that the neutral byproduct(s) cannot be inferred unambiguously. One possible suggestion for the latter might be NiO and N_2. According to this assignment, the formation of Ni^+ would result from spontaneous fission of part of the Ni_2O^+ clusters generated after initial O-atom transfer. For this reaction to be exothermic, the relation $D_0(Ni^+–Ni) + D_0(N_2–O) = 393 \pm 2$ kJ·mol^{-1} ≤ $D_0(Ni–O)$ should hold, which is consistent with the reported value $D_{298}(Ni–O) = 382 \pm 17$ kJ·mol^{-1} within error bars.[18] As a direct probe for the involvement of Ni_2O^+ in the generation of Ni^+, the former is subjected to a double-resonance experiment.[24] In this experiment, continuous resonant irradiation ejects all Ni_2O^+ ions formed and thus prevents the build-up of any consecutive products. The effectiveness of this measure is clearly seen from the complete removal of $Ni_2O_2^+$ upon resonant irradiation on Ni_2O^+. In contrast, the amount of Ni^+ generated is not affected, which disproves the involvement of Ni_2O^+ as its precursor, unless the dissociation of Ni_2O^+ occurs faster than the time scale of ion ejection, $\Delta_{eject}t \approx 1$ ms. Alternatively, the formation of Ni^+ can be rationalized by reaction with residual traces of oxygen present in the high vacuum system, Equation (3). The exoergicity of this process has been demonstrated previously.[19]

$$Ni_2^+ + O_2 \rightarrow Ni^+ + NiO_2 \quad (3)$$

However, we cannot rigorously rule out the possible origin of Ni^+ from electronically excited reactant Ni_2^+ either. The thermochemical relations so far discussed rely on the assumption that all reactant cluster ions are in the electronic ground state. Yet, this assumption not necessarily appears valid in light of the results presented next.

The second side reaction (ca. 15% b.r.) leads to the formation of NiN_2O^+. As the abundance of this ion is not affected by continuous ejection of Ni_2O^+ in a double-resonance experiment, the former cannot be generated in a consecutive reaction of neither Ni_2O^+ (nor $Ni_2O_2^+$). Furthermore, NiN_2O^+ cannot result from a consecutive reaction of Ni^+ either because direct association processes are highly unlikely given the small size of the molecular systems under study as well as the low pressure regime of the experiments (and are observed neither for Ni_2^+, Ni_2O^+, nor $Ni_2O_2^+$). Last but not least, the temporal evolution of the abundance of NiN_2O^+ agrees with that of a primary product within the limits of the kinetic scheme applied[25] in that it appears to be formed by a formally direct exchange of Ni for N_2O, Equation (4). At longer reaction times, the yield of NiN_2O^+ declines while NiH_2O^+ emerges as new product ion. A double-resonance experiment confirms that the latter originates from the former. Because traces of water, like oxygen, are inevitably present in the vacuum system, the formation of NiH_2O^+ can obviously be rationalized by a substitution of N_2O for H_2O, Equation (5). The facile occurrence of this exchange suggests that NiN_2O^+ contains an intact N_2O ligand and the ion is thus assigned to correspond to a $Ni(N_2O)^+$ complex.[26]

$$Ni_2^+ + N_2O \rightarrow Ni(N_2O)^+ + Ni \quad (4)$$

$$Ni(N_2O)^+ + H_2O \rightarrow Ni(H_2O)^+ + N_2O \quad (5)$$

Whereas the secondary exchange reaction is substantially exothermic, $D_{298}(Ni^+–H_2O) = 184 \pm 3$ kJ·mol^{-1}[27] vs. $D_0(Ni^+–N_2O) = 105.7 \pm 0.3$ kJ·mol^{-1},[28] the first one is strongly endothermic for ground-state Ni_2^+ ($D_0(Ni^+–Ni) = 204 \pm 10$ kJ·mol^{-1})[29] and should therefore not take place at ambient temperatures. The occurrence of this reaction may thus point to the presence of thermally not equilibrated reactants. Although the generation of electronically excited, long-lived metal clusters in a Smalley-type cluster ion source has not been reported to the best of our knowledge,[30] its involvement might be considered in the present case and warrants further investigation.

In order to assess the effect of the thermalization procedure on the reaction channel in question, the number of argon pulses applied was varied between 0 and 20. Yet, no decrease in the combined abundances of $Ni(N_2O)^+$ and $Ni(H_2O)^+$ was observed. This result is in fact not at all surprising because the Ni_2^+ ions present in the analyzer cell of the FT-ICR mass spectrometer already have undergone a large number of collisions with helium atoms in the supersonic expansion occurring in the Smalley-type cluster-ion source. If any electronically excited $Ni_2{}^+$* survived these conditions, it should not be quenched by collisions with argon atoms either. The absence of any reaction with argon also suggests a lower limit for the bond dissociation energy of the hypothetical excited $Ni_2{}^+$* cluster (if the operation of kinetic barriers is neglected), whereas the substitution of one Ni atom by N_2O according to Equation (4) yields an upper limit of $D_0(Ni^+–Ar) = 54.69 \pm 0.06 \leq D_0(Ni^+–Ni^*) \leq 105.7 \pm 0.3$ kJ·mol^{-1}.[28,31] Ligands L stronger than N_2O then should react with $Ni_2{}^+$* in a similar manner to afford NiL^+ complexes. However, the nickel dimer prepared did neither react with Xe, CO, nor H_2O, although at least the latter two clearly bind Ni^+ more strongly than N_2O does [$D_0(Ni^+–CO) = 175 \pm 11$ kJ·mol^{-1},[29] $D_{298}(Ni^+–H_2O) = 184$

 © 2005 Wiley-VCH Verlag GmbH & Co. KGaA, Weinheim

± 3 kJ·mol^{-1}].[27] Hence, these experiments do not support the generation of electronically excited, long-lived Ni_2^+ in the cluster-ion source.

An alternative explanation for the formation of $Ni(N_2O)^+$ borrows from a recent study of Bohme and coworkers, in which termolecular processes were reported to account for the coupling of two or more NO_x molecules by transition-metal ions.[32] With respect to the present case, a plausible scenario for the formation of $Ni(N_2O)^+$ would involve a reaction of ground-state Ni_2^+ with two molecules of N_2O to yield NiO + N_2 as neutral byproducts. However, the low pressures sampled in the present experiments render the occurrence of termolecular reactions highly improbable, in contrast to the conditions applied by Bohme and coworkers.[32]

None of the different suggestions discussed above achieves a conclusive explanation of all experimental findings. Possible other rationalizations include the involvement of impurities and/or fast reacting intermediates that escape attention within the kinetic limits of the ICR studies.[25] Given the low efficiency of $Ni(N_2O)^+$ formation (only ≈ 6 out of 1000 collisions are successful), these factors might indeed be important while difficult to probe. Additional insight could possibly be gained from the application of other mass spectrometric techniques. Note, however, that the unknown origin of NiN_2O^+ by no means affects the reactivity studies of the title compound $Ni_2O_2^+$ which are described in the next section.

2.2 Structure and Reactivity of $Ni_2O_2^+$

The first aspect to be discussed is the structure of the $Ni_2O_2^+$ cluster formed upon reaction of Ni_2^+ with N_2O. Two alternatives appear most likely: The dioxide species **1** or the peroxide **2** (Scheme 1). To distinguish between these alternative structures, $Ni_2O_2^+$ is subjected to CID, which yields Ni^+ and Ni_2O^+ as ionic fragments, respectively (Equation 6).

$$Ni_2O_2^+ \rightarrow Ni^+ + NiO_2 \ 85\%$$
$$Ni_2O_2^+ \rightarrow Ni_2O^+ + O \ 15\% \quad (6)$$

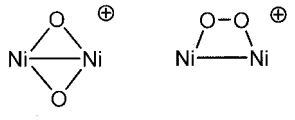

1 **2**

Scheme 1.

This fragmentation pattern is consistent with the parent ion having structure **1**, whereas an additional channel under expulsion of O_2 might be expected for a peroxide species, **2**. As a further probe, $Ni_2O_2^+$ is exposed to $^{18}O_2$. In case of the peroxide **2**, a relatively facile exchange of the O_2 unit might occur. In contrast, the reaction observed experimentally is very slow (Table 1) and only brings about stepwise $^{16}O/^{18}O$ exchange, Equation (7). Therefore, the dioxide structure **1** is assumed most plausible for $Ni_2O_2^+$.[7,33]

$$Ni_2{}^{16}O_2^+ + {}^{18}O_2 \rightarrow Ni_2{}^{16}O{}^{18}O^+ + {}^{16}O{}^{18}O \quad (7)$$

For an evaluation of the oxidative power of $Ni_2O_2^+$, first its reaction with carbon monoxide is studied. While the efficiency of this process is low, $Ni_2O_2^+$ indeed succeeds in the oxidation of CO, Equation (8). Moreover, the resulting Ni_2O^+ also accomplishes oxygen-atom transfer to CO, Equation (9), though even less efficiently than $Ni_2O_2^+$. The stepwise release of atomic oxygen from $Ni_2O_2^+$ is yet another piece of evidence for the dioxide structure **1** rather than that of the peroxide **2** for the ionic reactant.

$$Ni_2O_2^+ + CO \rightarrow Ni_2O^+ + CO_2 \quad (8)$$

$$Ni_2O^+ + CO \rightarrow Ni_2^+ + CO_2 \quad (9)$$

As N_2O spontaneously re-oxidizes Ni_2^+ and Ni_2O^+, gaseous Ni_2^+ in effect catalyzes the oxidation of CO by N_2O. Similar catalytic activities have been reported for several mononuclear transition-metal cations[1,17] as well as for anionic[8] and cationic platinum clusters.[14] In contrast to $Ni_2O_2^+$, $Fe_2O_2^+$ does not transfer an oxygen atom to CO. This difference is a first indication that $Ni_2O_2^+$ is a more powerful oxidant than $Fe_2O_2^+$, as already an analysis of the formal oxidation numbers of the metals would suggest. The average formal oxidation state of +2.5 adopted by the metals in $M_2O_2^+$ is energetically more favorable for iron, whereas nickel strongly prefers an oxidation state of +2 in its compounds.[34] Vann et al. also investigated the reactivity of $Ni_mO_n^+$ clusters towards NO, but could not clearly establish the occurrence of oxygen-transfer processes.[35]

Next, $Ni_2O_2^+$ is exposed to hydrogen. From the absence of any reaction, an upper limit of $k \leq 3\times10^{-14}$ cm^3·s^{-1} can be derived which corresponds to $\varphi \leq 2\times10^{-5}$. For NiO^+, the reaction with H_2 to produce Ni^+ and H_2O does occur, but proceeds only with low efficiency although it is highly exothermic.[36] An analogous situation is encountered for the thoroughly studied system $FeO^+ + H_2$ where the interplay of potential-energy surfaces with different spins turns out to be crucial;[4,22] a similar importance of spin restrictions might be assumed for the reactions of NiO^+ and $Ni_2O_2^+$ with H_2. Unlike the case of oxygen transfer from N_2O towards Ni^+ vs. Ni_2^+, the transition from mononuclear NiO^+ to its dinuclear counterpart does not appear to weaken the effect of these spin restrictions in the particular case of H_2 oxidation.

The remaining reactions explored here are discussed in the context of C–H bond activation. To probe the reactivity of $Ni_2O_2^+$ in this regard, its reactions with CH_4, C_2H_6, C_3H_8, and n-C_4H_{10} are considered. First insights can be gained just from inspection of the overall efficiencies observed (Table 1). While no measurable reaction takes place in the case of methane ($k \leq 1\times10^{-13}$ cm^3·s^{-1}, $\varphi \leq 1\times10^{-4}$), the efficiencies rapidly increase for the larger alkanes and closely approach unity for *n*-butane. This trend correlates with C–H binding energies decreasing as a function of chain length.[18] In addition, a mere size effect can be ex-

 © 2005 Wiley-VCH Verlag GmbH & Co. KGaA, Weinheim

pected to further enhance the increase in reactivity. Because of their higher number of internal degrees of freedom, larger substrates can dissipate intramolecularly the energy released upon complexation more effectively and thus lower the probability for dissociation back to the reactants. For NiO^+, unity efficiency is already reached in the reaction with ethane; the increased reactivity of NiO^+ is also reflected in its ability to activate methane.[3] Attenuation of reactivity associated with the transition from mononuclear to dinuclear transition-metal oxides is a general trend also observed for manganese[11] and iron.[12,13] The lower charge densities of the cluster ions and their higher degrees of valence saturation are likely reasons for the more moderate reactivities.[37] As stated initially, exactly these properties add to their attractiveness as model compounds for real catalysts in the condensed phase.

While $Mn_2O_2^+$, $Fe_2O_2^+$, and $Ni_2O_2^+$ have in common lower reactivities towards alkanes than their mononuclear counterparts, they nonetheless also show clear differences in their efficiencies. In contrast to the moderate to high efficiencies observed for the reactions of $Ni_2O_2^+$ with C_nH_{2n+2}, n = 2–4, those reported for the reactions of $Fe_2O_2^+$ are much smaller and even in the case of *n*-butane do not exceed $\varphi = 0.03$.[14] With respect to $Mn_2O_2^+$, only the reaction with *i*-C_4H_{10} was studied, but it did not occur at a measurable rate at all.[11] Thus, $Ni_2O_2^+$ proves to be the most reactive of the $M_2O_2^+$ clusters of late *3d* metals investigated so far.

The main product channel of the reactions of $Ni_2O_2^+$ with the alkanes studied yields $Ni_2H_2O_2^+$ and the corresponding alkene, Equation (10) with n = 2–4, thus corresponding to an oxidative dehydrogenation of the alkane. For the reduced product cluster, $Ni_2(OH)_2^+$ or $Ni_2O(H_2O)^+$ structures seem most likely.

$$Ni_2O_2^+ + C_nH_{2n+n} \rightarrow Ni_2H_2O_2^+ + C_nH_{2n} \quad (10)$$

In addition, mononuclear species $NiC_nH_{2n}^+$ are formed in the reactions with C_3H_8 and *n*-C_4H_{10}, Equation (11) with n = 3 and 4. Apparently, hydrogen transfer and complexation of the metal by the resulting alkene provide sufficient energy to cleave the Ni–Ni bond. In the case of *n*-C_4H_{10}, single and double dehydration occurs as well, Equation (12) and (13).

$$Ni_2O_2^+ + C_nH_{2n+2} \rightarrow NiC_nH_{2n}^+ + NiH_2O_2 \quad (11)$$

$$Ni_2O_2^+ + n\text{-}C_4H_{10} \rightarrow Ni_2C_4H_8O^+ + H_2O \quad (12)$$

$$Ni_2O_2^+ + n\text{-}C_4H_{10} \rightarrow Ni_2C_4H_6^+ + 2\ H_2O \quad (13)$$

An analysis of the kinetic data as well as a double-resonance experiment show that $Ni_2C_4H_8O^+$ also results from a secondary reaction of $Ni_2H_2O_2^+$. This process combines expulsion of H_2O with dehydrogenation of the organic substrate, Equation (14), thus demonstrating an appreciable reactivity of the primary product ion $Ni_2H_2O_2^+$. In addition, this species yields $Ni_2C_4H_{10}O_2^+$ upon reaction with *n*-C_4H_{10}, Equation (15). While this consecutive process formally corresponds to a substitution of H_2 by *n*-C_4H_{10}, it is better interpreted as a dehydrogenation of the alkane leading to a $Ni_2H_2O_2^+(C_4H_8)$ complex.

$$Ni_2H_2O_2^+ + n\text{-}C_4H_{10} \rightarrow Ni_2C_4H_8O^+ + H_2 + H_2O \quad (14)$$

$$Ni_2H_2O_2^+ + n\text{-}C_4H_{10} \rightarrow Ni_2C_4H_{10}O_2^+ + H_2 \quad (15)$$

In another secondary reaction with *n*-C_4H_{10}, $Ni_2C_4H_6^+$ forms $Ni_2C_8H_{12}^+$, Equation (16). This process is remarkable as it shows that $Ni_2C_4H_6^+$, though supposedly already binding 1,3-butadiene as a bifunctional ligand, still is capable of double dehydrogenation of *n*-butane.

$$Ni_2C_4H_6^+ + n\text{-}C_4H_{10} \rightarrow Ni_2C_8H_{12}^+ + 2\ H_2 \quad (16)$$

The reactions of $Ni_2O_2^+$ with C_3H_8 and *n*-C_4H_{10} display several similarities compared to the processes observed for $Fe_2O_2^+$ (for the latter, no reaction products could be detected upon exposure to C_2H_6).[13] For both clusters, dehydrogenation of the alkanes yielding $M_2H_2O_2^+$ corresponds to the main reaction channel, compare Equation (10). In analogy to Equation (12), $Fe_2O_2^+$ also accomplishes dehydration of *n*-C_4H_{10}. Sufficiently exothermic reactions of $Fe_2O_2^+$ with larger hydrocarbons lead to the cleavage of the metallic cluster core, thereby resembling the formation of $NiC_nH_{2n}^+$ in Equation (11). However, there are also some interesting differences between the reactivities of $Ni_2O_2^+$ and $Fe_2O_2^+$. The reactions of $Fe_2O_2^+$ with *n*-butane and larger alkanes yield protonated alkenes, thus allowing an estimation of the proton affinity of Fe_2HO_2, $PA(Fe_2HO_2) \approx 750$–815 kJ·mol^{-1}.[13] From the absence of $C_4H_9^+$ in the reaction of $Ni_2O_2^+$ with *n*-C_4H_{10}, one could infer the inequality $PA(Ni_2HO_2) > PA(Fe_2HO_2)$ under the assumption that protonation of the resulting olefin by $Ni_2H_2O_2^+$ is prevented on thermochemical rather than kinetic grounds. Another product in the reaction of $Fe_2O_2^+$ with *n*-C_4H_{10} is $Fe_2C_2H_6O_2^+$,[13] whereas $Ni_2O_2^+$ exclusively reacts in terms of C–H bond activation and thus exhibits a higher selectivity than $Fe_2O_2^+$, although it is clearly more reactive in terms of the overall reaction efficiency.

3. Conclusions

The cluster cation $Ni_2O_2^+$ can be generated by a gas-phase reaction of Ni_2^+ with N_2O. Analogous procedures might also be used for the efficient preparation of other $M_2O_2^+$ species (compare ref.[12] for the case of $Fe_2O_2^+$, however), whereas most synthetic protocols reported so far directly introduce oxygen in the cluster source[15] or alternatively rely on volatile metal carbonyls.[11,13,16] Evidence is presented that $Ni_2O_2^+$ prepared by the method described here exhibits a genuine dioxide structure.

The observed reactions of $Ni_2O_2^+$ probed can be divided into two classes: Oxygen-atom transfer and C–H bond activation. The first reaction type is operative in the oxidation of CO, a process which could easily be made catalytic if N_2O were provided for the regeneration of $Ni_2O_2^+$. C–H bond activation occurs upon reaction of $Ni_2O_2^+$ with the hydrocarbons ethane, propane, and *n*-butane. In contrast

 © 2005 Wiley-VCH Verlag GmbH & Co. KGaA, Weinheim

to its smaller homologue NiO^+, $Ni_2O_2^+$ does not activate methane, however, thus demonstrating the moderating effect of the transition from mononuclear ions to clusters. In a more general sense, this attenuation in reactivity can be considered as a closer resemblance to the behavior of transition-metal oxides in the condensed phase and thus as an improvement of the gas-phase model for applied catalysis. In comparison to $Mn_2O_2^+$ and $Fe_2O_2^+$, the reactivity of $Ni_2O_2^+$ still is remarkably high, which can be ascribed to a lowered stability of this compound with a formal oxidation state exceeding the value of +2 preferred for nickel.

Experimental Section

Experiments are performed by means of a Spectrospin CMS 47X Fourier-transform ion cyclotron resonance (FT-ICR) mass spectrometer[38] equipped with a Smalley-type[6] cluster-ion source developed by Bondybey, Niedner-Schatteburg, and co-workers.[7,10] In brief, the fundamental of a pulsed Nd:YAG laser (λ = 1064 nm, Spectron Systems) is focused onto a rotating nickel target. The metal plasma thereby generated is entrained in a synchronized helium pulse (15 bar backing pressure) and cooled by supersonic expansion. After passing a skimmer, the cationic components of the molecular beam are transferred into the analyzer cell where they are trapped in the field of a 7.05 T superconducting magnet.

After mass selection of the $^{58}Ni_2^+$ cluster by means of the FERETS ion-ejection technique,[39] argon gas is pulsed-in for ion thermalization. Ni_2^+ is then exposed to N_2O at a static pressure $p \approx 3\times10^{-7}$ mbar. Based on the pseudo first-order kinetic approximation, the temporal evolution of Ni_2^+, the primary product Ni_2O^+, and the consecutive product $Ni_2O_2^+$ is compared to a fit that yields bimolecular rate constants k for both the primary and consecutive reaction with absolute errors estimated to $\pm 30\%$.[40] Reaction efficiencies $\varphi = k/k_{cap}$ are calculated according to capture theory.[41] For the reactivity studies, $Ni_2O_2^+$ is generated by pulsing N_2O to mass-selected, thermalized $^{58}Ni_2^+$ and mass-selected prior to exposure to the static neutral substrate. Bimolecular rate constants and efficiencies are derived as described for the reaction of Ni_2^+ with N_2O. Collision-induced dissociation (CID) of $Ni_2O_2^+$ is accomplished by collision of the kinetically excited ions with pulsed-in argon gas.

Acknowledgments

Support by the Deutsche Forschungsgemeinschaft (DFG) and the Fonds der Chemischen Industrie is gratefully acknowledged. K. K. particularly thanks the DFG for an Emmy Noether fellowship (KO, 2875/1–1).

[1] M. M. Kappes, R. H. Staley, *J. Am. Chem. Soc.* **1981**, *103*, 1286.
[2] P. B. Armentrout, L. F. Halle, J. L. Beauchamp, *J. Chem. Phys.* **1982**, *76*, 2449.
[3] D. Schröder, H. Schwarz, *Angew. Chem.* **1995**, *107*, 2126; *Angew. Chem. Int. Ed. Engl.* **1995**, *34*, 1973.
[4] D. Schröder, H. Schwarz, S. Shaik, *Struct. Bonding (Berlin)* **2000**, *97*, 91.
[5] G. K. Koyanagi, D. Caraiman, V. Blagojevic, D. K. Bohme, *J. Phys. Chem. A* **2002**, *106*, 4581.
[6] S. Maruyama, L. R. Anderson, R. E. Smalley, *Rev. Sci. Instrum.* **1990**, *61*, 3686.
[7] C. Berg, T. Schindler, M. Kantlehner, G. Niedner-Schatteburg, V. E. Bondybey, *Chem. Phys.* **2000**, *262*, 143.
[8] For an example of reactivity studies of transition-metal cluster anions $M_mO_n^-$, see: Y. Shi, K. M. Ervin, *J. Chem. Phys.* **1998**, *108*, 1757.
[9] K. A. Zemski, D. R. Justes, A. W. Castleman, Jr., *J. Phys. Chem. B* **2002**, *106*, 6136.
[10] M. Engeser, T. Weiske, D. Schröder, H. Schwarz, *J. Phys. Chem. A* **2003**, *107*, 2855.
[11] B. Chiavarino, M. E. Crestoni, S. Fornarini, *Chem. Eur. J.* **2002**, *8*, 2740.
[12] O. Gehret, M. P. Irion, *Chem. Eur. J.* **1996**, *2*, 598.
[13] P. Jackson, J. N. Harvey, D. Schröder, H. Schwarz, *Int. J. Mass Spectrom.* **2001**, *204*, 233.
[14] O. P. Balaj, I. Balteanu, T. J. J. Roßteuscher, M. K. Beyer, V. E. Bondybey, *Angew. Chem.* **2004**, *116*, 6681; *Angew. Chem. Int. Ed.* **2004**, *43*, 6519.
[15] B. C. Guo, K. P. Kerns, A. W. Castleman, Jr., *Int. J. Mass Spectrom. Ion Processes* **1992**, *117*, 129.
[16] J. J. Klaassen, D. B. Jacobson, *Inorg. Chem.* **1989**, *28*, 2022.
[17] For a recent review of gas-phase catalysis by metal ions, see: D. K. Böhme, H. Schwarz, *Angew. Chem.* **2005**, *117*, 2388; *Angew. Chem. Int. Ed.* **2005**, *44*, 2336.
[18] S. G. Lias, J. E. Bartmess, J. F. Liebman, J. L. Holmes, R. D. Levin, W. G. Mallard, *J. Phys. Chem. Ref. Data* **1988**, *17*, Suppl. 1.
[19] D. Vardhan, R. Liyanage, P. B. Armentrout, *J. Chem. Phys.* **2003**, *119*, 4166.
[20] G. K. Koyanagi, D. Caraiman, V. Blagojevic, D. K. Bohme, *J. Phys. Chem. A* **2002**, *106*, 4581.
[21] V. V. Lavrov, V. Blagojevic, G. K. Koyanagi, G. Orlova, D. K. Bohme, *J. Phys. Chem. A* **2004**, *108*, 5610.
[22] For a recent review on the role of spin-forbidden reactions in the gas phase, see: H. Schwarz, *Int. J. Mass Spectrom.* **2004**, *237*, 75.
[23] I. Kretzschmar, A. Fiedler, J. N. Harvey, D. Schröder, H. Schwarz, *J. Phys. Chem. A* **1997**, *101*, 6252.
[24] M. B. Comisarow, V. Grassi, G. Parisod, *Chem. Phys. Lett.* **1978**, *57*, 413.
[25] J. Schwarz, D. Schröder, H. Schwarz, C. Heinemann, J. Hrušák, *Helv. Chim. Acta* **1996**, *79*, 1110.
[26] See also: V. Baranov, G. Javahery, A. C. Hopkinson, D. K. Bohme, *J. Am. Chem. Soc.* **1995**, *117*, 12801.
[27] N. F. Dalleska, K. Honma, L. S. Sunderlin, P. B. Armentrout, *J. Am. Chem. Soc.* **1994**, *116*, 3519.
[28] D. Bellert, T. Buthelezi, V. Lewis, K. Dezfulian, P. J. Brucat, *Chem. Phys. Lett.* **1995**, *240*, 495.
[29] P. B. Armentrout, B. L. Kickel, in: *Organometallic Ion Chemistry*, (Ed.: B. S. Freiser), Kluwer, Dordrecht, **1995**, p. 1.
[30] Y. M. Ibrahim, E. H. Alsharaeh, M. S. El-Shall, *J. Phys. Chem. B* **2004**, *108*, 3959, and references therein.
[31] R. L. Asher, D. Bellert, T. Buthelezi, P. J. Brucat, *Chem. Phys. Lett.* **1994**, *228*, 599.
[32] a) V. V. Lavrov, V. Blagojevic, G. K. Koyanagi, G. Orlova, D. K. Bohme, *J. Phys. Chem. A* **2004**, *108*, 5610; b) V. Blagojevic, J. Y. Michael, E. Flaim, G. K. Koyanagi, V. V. Lavrov, D. K. Bohme, *Angew. Chem. Int. Ed.* **2003**, *42*, 4923.
[33] Also see: a) D. Schröder, A. Fiedler, J. Schwarz, H. Schwarz, *Inorg. Chem.* **1994**, *33*, 5094; b) A. Fiedler, I. Kretzschmar, D. Schröder, H. Schwarz, *J. Am. Chem. Soc.* **1996**, *118*, 9941; c) M. Brönstrup, D. Schröder, I. Kretzschmar, H. Schwarz, J. N. Harvey, *J. Am. Chem. Soc.* **2001**, *123*, 142.
[34] N. N. Greenwood, A. Earnshaw, *Chemistry of the Elements*, Pergamon, Oxford, **1984**, p. 1334.
[35] W. D. Vann, R. C. Bell, A. W. Castleman, Jr., *J. Phys. Chem. A* **1999**, *103*, 10846.

 © 2005 Wiley-VCH Verlag GmbH & Co. KGaA, Weinheim

[36] D. Schröder, A. Fiedler, M. F. Ryan, H. Schwarz, *J. Phys. Chem.* **1994**, *98*, 68.
[37] V. E. Bondybey, M. K. Beyer, *J. Phys. Chem. A* **2001**, *105*, 951.
[38] K. Eller, W. Zummack, H. Schwarz, *J. Am. Chem. Soc.* **1990**, *112*, 621.
[39] R. A. Forbes, H. F. Laukien, J. Wronka, *Int. J. Mass Spectrom. Ion Processes* **1988**, *83*, 23.
[40] D. Schröder, H. Schwarz, D. E. Clemmer, Y.-M. Chen, P. B. Armentrout, V. I. Baranov, D. K. Böhme, *Int. J. Mass Spectrom. Ion Processes* **1997**, *161*, 175.
[41] a) T. Su, *J. Chem. Phys.* **1988**, *88*, 4102; b) T. Su, *J. Chem. Phys.* **1988**, *89*, 5355.

Received: January 13, 2005

 © 2005 Wiley-VCH Verlag GmbH & Co. KGaA, Weinheim

New Cadmium(II) and Iron(II) Coordination Frameworks Incorporating a Di(4-pyridyl)isoindoline Ligand

Yanyan Mulyana,[a] Cameron J. Kepert,*[a] Leonard F. Lindoy,*[a] and John C. McMurtrie[a,b]

Keywords: Cadmium / Iron / Molecular framework

The metal-directed assembly of molecular frameworks incorporating the ditopic heterocyclic ligand 1-(4-pyridyl)imino-2-(4-pyridyl)isoindoline (**L**) associated with nonlinear coordination vectors, is presented. Two infinite metallo-arrays of empirical formula $[Cd\mathbf{L}(NO_3)_2(EtOH)]_n\cdot(1.4\,H_2O)_n$ and $[Fe\mathbf{L}_2(NCS)_2]_n\cdot\{(2\,CHClCCl_2)\cdot(1.4\,MeOH)\cdot(2.9\,H_2O)\}_n$ have been characterised. The X-ray structures of both arrays are reported. The cadmium(II) framework consists of co-aligned 1D coordinate polymer chains while the iron(II) framework consists of rhombic grids with 2D polymeric connectivity.
(© Wiley-VCH Verlag GmbH & Co. KGaA, 69451 Weinheim, Germany, 2005)

Introduction

The assembly of metal-organic frameworks is an area of much current interest[1a–1k,2] since the porous structures characteristic of such materials frequently show selective guest molecule uptake (or exchange) from vapours,[3a–3e] solution[3a–3e] and gases[4a,4b] as well as promoting heterogeneous catalysis in a number of cases.[5] While a wide range of organic components has now been incorporated in such frameworks, nitrogen-containing heterocycles have been particularly common and a variety of derivatives of this latter type are available that provide coordination angles that range from 60° to 180°.[6a–6d]

We now report the synthesis of two new coordination frameworks incorporating iron(II) and cadmium(II) that are based on the new heterocyclic nitrogen derivative 1-(4-pyridyl)imino-2-(4-pyridyl)isoindoline (**L**). In comparison with the "classical" prototypical (linear) bis(pyridyl) ligand, 4,4′-bipyridyl,[6a–6d] the positions of the two pyridyl functions in **L** are more separated and the relative orientation of the coordination vectors is now angular. As occurs for other nonlinear bis(pyridyl) ligands such as 4,4′-dipyridyl sulfide,[7a,7b] a number of structural variations in the frameworks formed by **L** appeared possible. In part, the exploration of these possibilities provided a motivation for the investigation now reported.

[a] Centre for Heavy Metals Research, School of Chemistry, University of Sydney,
NSW 2006, Australia
E-mail: lindoy@chem.usyd.edu.au
[b] School of Physical and Chemical Sciences, Queensland University of Technology,
GPO Box 2434, Brisbane 4001, Australia
Supporting information for this article is available on the WWW under http://www.eurjic.org or from the author.

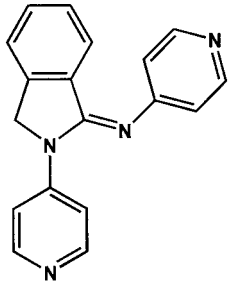

L

Results and Discussion

Ligand Synthesis

Isoindoline ring generation has been reported previously from the reaction of aniline with *o*-phthalaldehyde.[8] Using this methodology, *o*-phthalaldehyde was condensed with 4-aminopyridine in the present study to yield the isoindoline derivative **L**; the ESI mass spectral, ^1H NMR and microanalysis results confirmed the successful synthesis of this product.

Synthesis and Structures of the Frameworks

Treatment of **L** with cadmium(II) nitrate in ethanol produced colourless crystals of $[Cd\mathbf{L}(NO_3)_2(EtOH)]_n\cdot(1.4\,H_2O)_n$ that were stable in air at room temperature and proved suitable for an X-ray diffraction study. An ORTEP[9] representation of the asymmetric unit, plus a diagram illustrating the cadmium(II) coordination geometry, are presented in Figure 1. Pertinent geometric details are listed in Table 1.

The isoindoline derivative **L** bridges cadmium(II) centres creating a 1D chain-like coordination polymer (see a and b

 © 2005 Wiley-VCH Verlag GmbH & Co. KGaA, Weinheim **DOI: 10.1002/ejic.200500108**

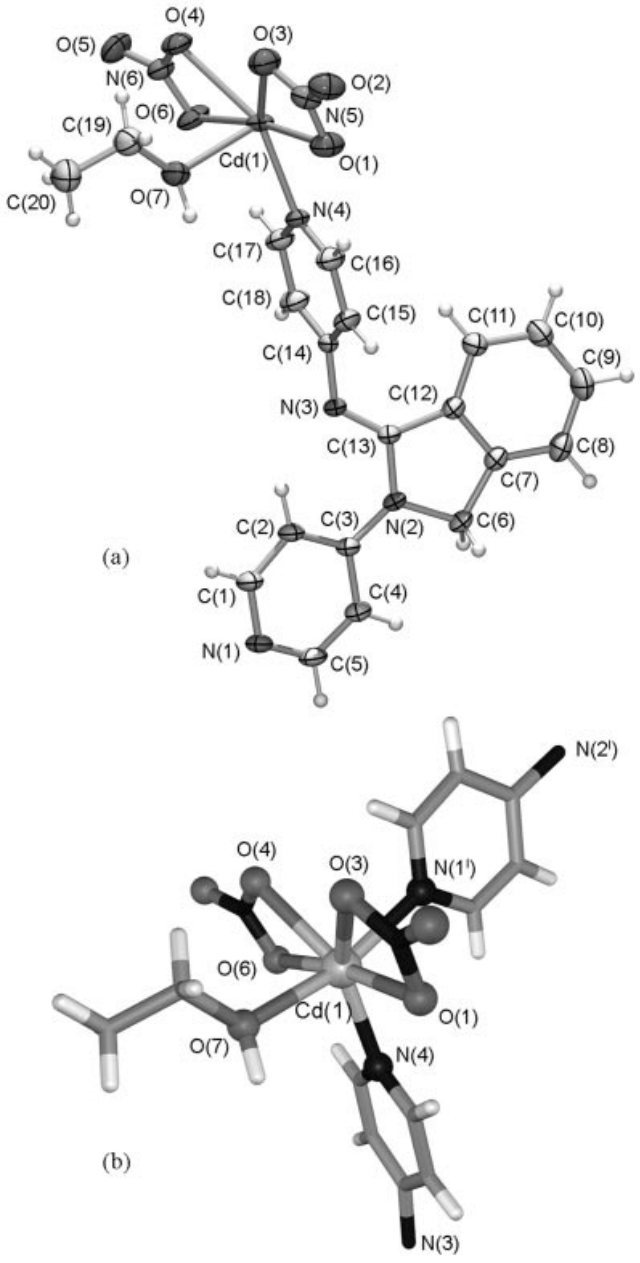

Figure 1. (a) An ORTEP representation of the asymmetric unit for the structure of $[Cd\mathbf{L}(NO_3)_2(EtOH)]_n\cdot(1.4\,H_2O)_n$ (50% ellipsoid probability, water solvate not shown). (b) Illustration of the approximate pentagonal bipyramidal cadmium(II) coordination geometry. The isoindoline ligands that coordinate via N(4) and N(1^I) have been truncated at N(3) and N(2^I) respectively. Symmetry code; ^{I} x, y, z + 1.

in Figure 2) with a repeating $[Cd\mathbf{L}(EtOH)(NO_3)_2]$ fragment that propagates parallel to the crystallographic c axis. The cadmium(II) ions are seven coordinate with approximate pentagonal bipyramidal stereochemistry. The pyridyl nitrogen atom N(4) binds within the pentagonal plane along with two nitrate anions (both bidentate). One pyramidal apex is occupied by an ethanol ligand while the other is occupied by the pyridyl nitrogen N(1) from an adjacent ligand in the chain. The individual chains propagate in a zigzag pattern reflecting the ca. 120° angle between the N donor atoms of the pyridyl groups which, in turn, is countered by a combination of the N(1^I)–Cd–N(4) coordination angle (104°) combined with a conformational contribution from the ligand (ca. 16°).

Table 1. Selected geometry details; bond lengths [Å] and angles [°] for $[Cd\mathbf{L}(NO_3)_2(EtOH)]_n\cdot(1.4\,H_2O)_n$.

Cd(1)–N(1^I)	2.283(2)	Cd(1)–O(4)	2.430(2)
Cd(1)–N(4)	2.279(2)	Cd(1)–O(6)	2.402(2)
Cd(1)–O(1)	2.476(2)	Cd(1)–O(7)	2.314(2)
Cd(1)–O(3)	2.462(2)		
		N(4)–Cd(1)–O(7)	90.62(8)
N(1^I)–Cd(1)–N(4)	104.76(8)	O(1)–Cd(1)–O(3)	51.85(8)
N(1^I)–Cd(1)–O(1)	89.49(9)	O(1)–Cd(1)–O(4)	133.18(8)
N(1^I)–Cd(1)–O(3)	83.75(9)	O(1)–Cd(1)–O(6)	171.61(8)
N(1^I)–Cd(1)–O(4)	88.11(8)	O(1)–Cd(1)–O(7)	88.01(9)
N(1^I)–Cd(1)–O(6)	96.68(9)	O(3)–Cd(1)–O(4)	81.44(8)
N(1^I)–Cd(1)–O(7)	164.19(9)	O(3)–Cd(1)–O(6)	134.36(8)
N(4)–Cd(1)–O(1)	85.71(8)	O(3)–Cd(1)–O(7)	82.44(9)
N(4)–Cd(1)–O(3)	137.02(9)	O(4)–Cd(1)–O(6)	53.06(7)
N(4)–Cd(1)–O(4)	139.73(8)	O(4)–Cd(1)–O(7)	82.27(8)
N(4)–Cd(1)–O(6)	87.22(8)	O(6)–Cd(1)–O(7)	87.56(9)

^{I} x, y, z + 1

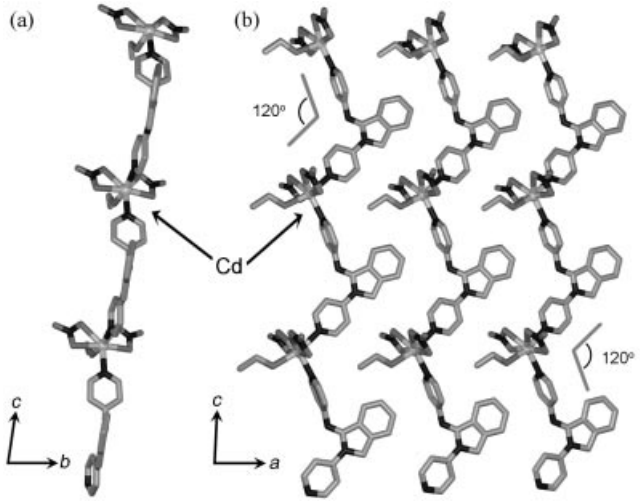

Figure 2. (a) The 1D coordinate polymer chains in $[Cd\mathbf{L}(NO_3)_2(EtOH)]_n\cdot(1.4\,H_2O)_n$ propagate parallel to the c axis. (b) Adjacent chains are aligned in sheets parallel to the ac plane. The individual chains display a 120° zigzag motif that derives from the angle between the N-donor directions countered predominantly by the coordination geometry at the cadmium(II) centre.

Adjacent 1D chains are co-aligned to produce sheets parallel to the ac plane.

These sheets are paired by a combination of offset face-to-face (π···π) interactions between the isoindoline components and edge-to-face (CH···π) interactions between the pyridyl groups of ligands in adjacent sheets (see Figure 1S in the Supporting Information). The isoindoline components involved in the offset face-to-face interactions are arranged with crystallographic inversion symmetry so that the five-membered rings overlap the six-membered rings with a mean plane-plane distance of 3.60 Å. The edge-to-face interactions between pyridyl groups occur with a CH_{edge}–

 © 2005 Wiley-VCH Verlag GmbH & Co. KGaA, Weinheim

Py_{plane} distance of ca. 2.91 Å. Both distances fall in the normal range for each interaction type.[10,11]

The crystal lattice is depicted in Figure 3. Pairs of sheets stack parallel to the *ac* plane to produce channels, occupied by disordered water molecules, that run parallel to the *a* axis (see Figure 2S, Supporting Information). The solvent accessible volume in these channels constitutes approximately 21% of the total crystal volume.

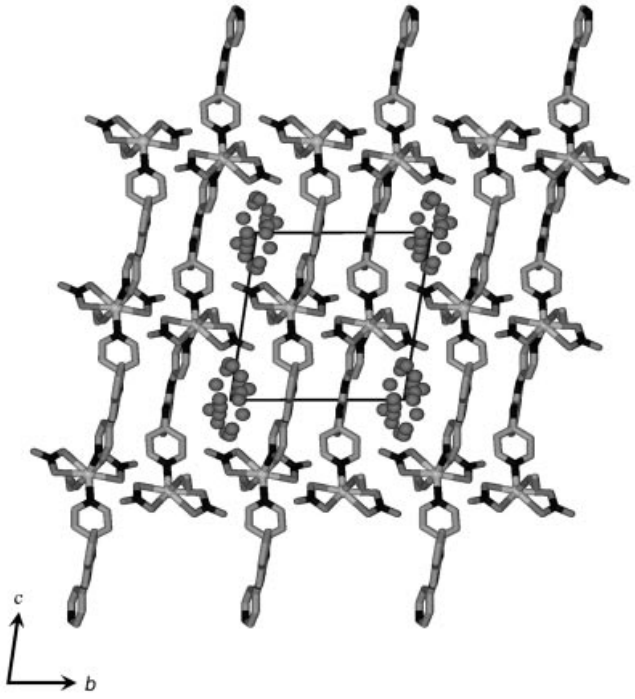

Figure 3. The crystal lattice viewed along the *a* axis. Disordered water molecules occupy channels between the paired sheets of polymeric complexes.

On reaction with iron(II) thiocyanate, **L** yielded the porous framework, $[Fe\mathbf{L}_2(NCS)_2]_n \cdot \{(2\,CHClCCl_2) \cdot (1.4\,MeOH) \cdot (2.9\,H_2O)\}_n$, in which the iron(II) ions subtend with two-dimensional polymeric connectivity. An ORTEP representation of the asymmetric unit and an illustration of the coordination geometry of the iron(II) centre are provided in Figure 4. Pertinent geometry details are listed in Table 2. The iron(II) centre has approximate octahedral stereochemistry with four pyridyl nitrogen atoms (from four separate ligand molecules) coordinated in equatorial positions and thiocyanato ligands *N*-coordinated in axial positions.

The above coordination connectivity results in infinite 2D rhombic grids (Figure 5) that propagate parallel to the *ab* plane; the grids have diagonal dimensions of 13 Å and 22 Å. The rhombic grids stack in the third dimension (along the *c* axis) with contiguous grids alternately offset. The observation of stacked rhombic grids is in contrast to our previous observation of an interpenetrated network structure with *trans*-4,4′-azopyridine (L′) of type $Fe_2(L')_4(NCS)_4 \cdot$(guest) which displays guest-dependent spin crossover.[2]

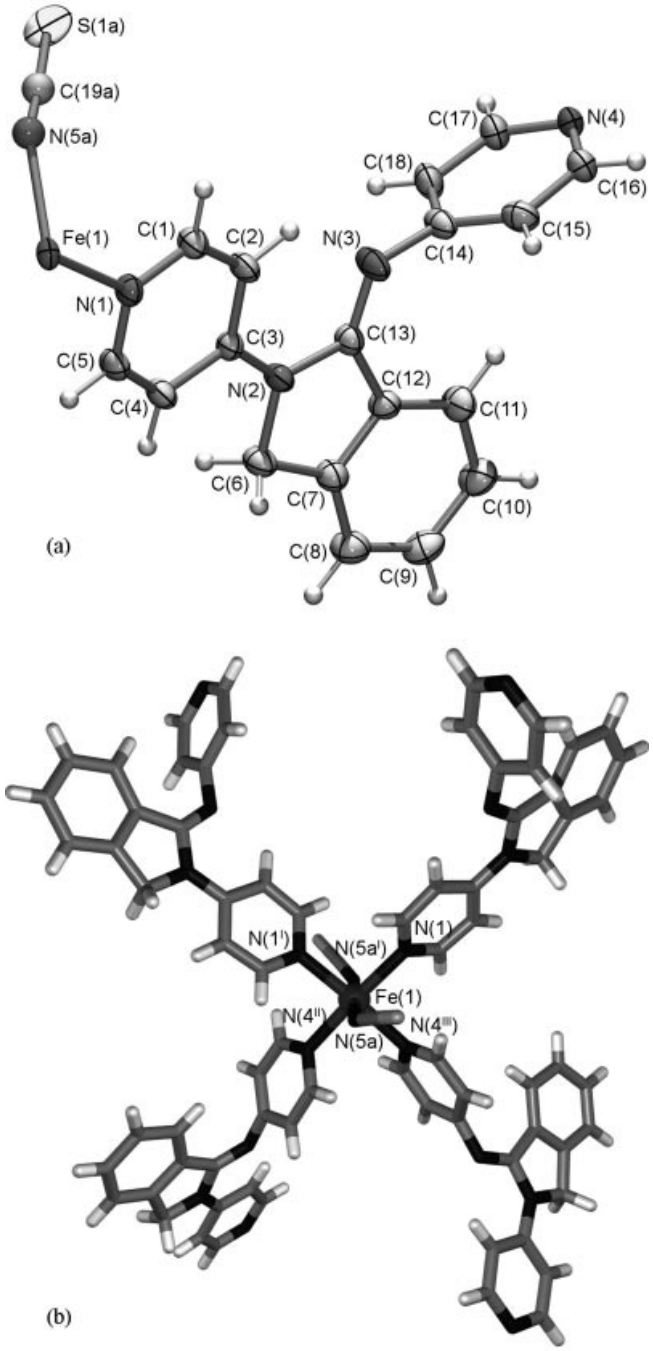

Figure 4. (a) An ORTEP representation of the asymmetric unit in $[Fe\mathbf{L}_2(NCS)_2]_n \cdot \{(2\,CHClCCl_2) \cdot (1.4\,MeOH) \cdot (2.9\,H_2O)\}_n$ (50% probability ellipsoids, solvent and the lower occupancy position of the disordered thiocyanato ligand omitted). (b) The coordination geometry at the iron(II) centre is approximately octahedral. Each iron(II) atom is equatorially bound to four pyridyl nitrogen atoms of four independent isoindoline ligands. Axial positions are occupied by thiocyanato groups.

A SQUID magnetism study of a vacuum-dried sample of the present framework was undertaken from 5 K to 300 K and showed a constant magnetic moment value corresponding to high spin iron(II) of μ_{eff}/μ_B = 5.2 between 80 and 300 K with no evidence for spin-crossover behaviour (zero-field splitting, rather than spin crossover, caused an

 © 2005 Wiley-VCH Verlag GmbH & Co. KGaA, Weinheim

Table 2. Selected geometry details (bond lengths in Å, angles in °) for $[FeL_2(NCS)_2]_n \cdot \{(2\,CHClCCl_2) \cdot (1.4\,MeOH) \cdot (2.9\,H_2O)\}_n$.

Fe(1)–N(1)	2.202(4)	Fe(1)–N(5a)	2.137(5)
Fe(1)–N(4^{II})	2.223(4)		
		N(1)–Fe(1)–N(4^{III})	88.83(15)
N(1)–Fe(1)–N(5a)	88.8(3)	N(1^{I})–Fe(1)–N(4^{II})	88.83(15)
N(1)–Fe(1)–N($5a^{I}$)	91.0(2)	N(1^{I})–Fe(1)–N(4^{III})	176.80(15)
N(5a)–Fe(1)–N($5a^{I}$)	179.7(5)	N(4^{II})–Fe(1)–N(4^{III})	88.1(2)
N(1^{I})–Fe(1)–N($5a^{I}$)	88.8(3)	N(4^{II})–Fe(1)–N(5a)	91.8(3)
N(1^{I})–Fe(1)–N(5a)	91.0(2)	N(4^{III})–Fe(1)–N($5a^{I}$)	91.8(3)
N(1)–Fe(1)–N(1^{I})	94.3(2)	N(4^{II})–Fe(1)–N($5a^{I}$)	88.4(2)
N(1)–Fe(1)–N(4^{II})	176.80(15)	N(4^{III})–Fe(1)–N(5a)	88.4(2)

^{I} $-x + 1, y, -z + 3/2$; ^{II} $x - 1/2, y - 1/2, -z + 3/2$; ^{III} $-x + 3/2, y - ½, z$

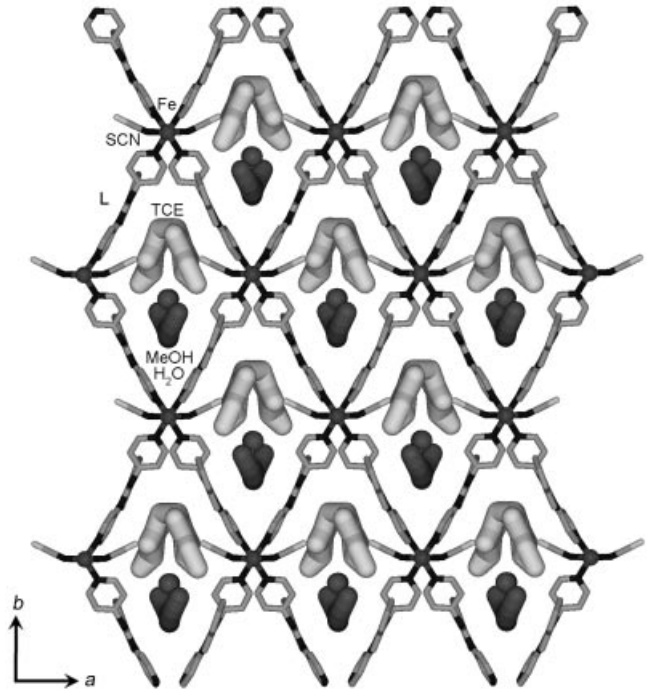

Figure 5. The difunctional isoindoline ligands connect iron atoms to produce rhombic grids. A section of each pore in the grid is occupied by disordered trichloroethylene and the remaining space in the pore is occupied by disordered water and methanol.

abrupt downturn in the effective magnetic moment below 50 K).

The pores in the present grid are solvated with a combination of water, methanol and trichloroethylene molecules. The polar water and methanol molecules are positioned on one side of each pore while the hydrophobic trichloroethylene molecules are positioned on the other. The overlap of the grids produces cavities occupied by trichloroethylene and continuous channels occupied by the water and methanol (this is illustrated in Figure 3S, Supporting Information). The solvent accessible regions in this framework constitute 42% of the total crystal volume and it is noted that solvent is rapidly lost from this product in air at room temperature with loss of crystallinity. Presumably the extensive solvation within the structure in this case provides an alternative to the formation of an interpenetrated arrangement that might otherwise serve to reduce the void volume.

Conclusions

Two new infinite molecular systems, one containing cadmium(II) and another containing iron(II), based on the nonlinear bis(pyridyl) ligand derivative **L** have been synthesised. The cadmium(II) framework is comprised of coaligned 1D coordinate polymer chains while the iron(II) framework consists of rhombic grids with 2D polymeric connectivity. Both crystal lattices are porous; the solvent accessible channels in the cadmium(II) framework constitute 21% of the crystal while those in the iron(II) framework constitute 42%.

Experimental Section

Reagents and Instrumentation: All reagents used for synthesis were obtained commercially and used without further purification. NMR spectra were recorded at 300 K on a Bruker DX300 Spectrometer. Low resolution electrospray mass spectra (ESI-MS) were obtained with a Finnigan LCQ-8 spectrometer. FTIR (DRIFTS) were collected with a Bio-Rad FTS-7 spectrometer. Magnetic susceptibility data were obtained using a Quantum Design MPMS SQUID magnetometer under an applied field of 1 T. The sample was first dispersed in petroleum jelly to prevent it from losing solvent. Diamagnetic corrections for the sample and sample holder were applied using Pascal constants. The magnetic susceptibility was measured from 5 K to 300 K. The final plot was obtained as μ_{eff}/μ_B value (where μ_{eff} is effective magnetic moment that equals to $(\chi_M T)^{1/2}$ and μ_B is Bohr magneton) as a function of temperature (K).

1-(4-Pyridyl)imino-2-(4-pyridyl)isoindoline Dihydrate (L·2H$_2$O): A mixture of *o*-phthalaldehyde (1.0 g, 0.007 mol), 4-aminopyridine (1.4 g, 0.014 mol), and glacial acetic acid (0.5 mL) in xylene (30 mL) was heated under reflux for 5 h to yield a yellow solution. Water was removed from the two-phase reaction using a Dean–Stark apparatus until the initial (two-phase) solution was homogeneous. The solution was then filtered and cooled in a refrigerator. The crude yellow product that precipitated was recrystallised from toluene to give a yellow microcrystalline solid of **L** as its dihydrate. Yield 1.5 g; 75%. $C_{18}H_{18}N_4O_2$ (322.4): calcd. C 67.07, H 5.63, N 17.38; found C 67.39, H 5.23, N 17.16. ^{1}H NMR (300 MHz, $CDCl_3$, 25 °C): δ = 8.54 (t, 5 H), 7.9 (dd, J = 1.65, 1.53 Hz, 2 H), 7.5 (m, 2 H), 7.16 (m, 1 H), 6.93 (m, 2 H), 4.97 (s, 2 H, CH_2) ppm. Mass Spectrum (ESI-MS): Found 287.3 m/z, $[M + H]^+$ requires 287.13 m/z.

[CdL(NO$_3$)$_2$]$_n$·(0.5H$_2$O)$_n$: Ligand **L** (0.02 g) was dissolved in ethanol (1 mL) and the solution placed in one side of a H-shaped glass cell. In the other side was placed a solution of cadmium(II) nitrate tetrahydrate (0.02 g) in ethanol (1 mL). The tube was then slowly filled with ethanol so that minimal mixing of the solution took place. A small quantity of colourless crystals (yield ca. 10%) with formula $[CdL(NO_3)_2(EtOH)]_n \cdot (1.4\,H_2O)_n$ suitable for X-ray analysis formed over a period of two weeks. The crystals were isolated and appeared stable in air over several days. They were dried under vacuum over P_2O_5 before microanalysis. The ethanol ligand and 0.9 water molecules per cadmium(II) were lost from the sample during

 © 2005 Wiley-VCH Verlag GmbH & Co. KGaA, Weinheim

drying. $C_{18}H_{16}CdN_6O_{6.5}$ (532.8): calcd. C 40.58, H 3.03, N 15.77; found C 40.25, H 2.46, N 15.38.

$[FeL_2(NCS)_2]_n\cdot(H_2O)_n$: Iron(II) thiocyanate (0.08 mmol) in a mixture of trichloroethylene/methanol (2:1) 10 mL) was added to a solution of **L** (0.07 mmol) in the same solvent mixture (10 mL). The resulting red-orange solution slowly changed colour to red and after several days and orange crystals with formula $[Fe\mathbf{L}_2(NCS)_2]_n\cdot\{(2\,CHClCCl_2)\cdot(1.4\,MeOH)\cdot(2.9\,H_2O)\}_n$ suitable for X-ray structure determination formed. The crystals (0.03 g, 78%) were isolated and dried under vacuum over P_2O_5, resulting in loss of all solvate except one water molecule (per iron(II)), prior to microanalysis. $C_{38}H_{30}FeN_{10}OS_2$ (762.7): calcd. C 59.84, H 3.96, N 18.36; found C 59.19, H 3.56, N 18.13. A second preparation of this complex was carried out using a dichloromethane/methanol (2:1) solvent mixture. The unit cell constants for a crystal from this batch were determined to be the same as those in crystals obtained from the trichloroethylene/methanol crystallisation experiment.

X-ray Crystallographic Study: Data were collected at 150(2) K with ω scans to approximately 56° 2θ using a Bruker SMART 1000 diffractometer employing graphite-monochromated Mo-$K\alpha$ radiation generated from a sealed tube (0.71073 Å). Data integration and reduction were undertaken with SAINT and XPREP[12] and subsequent computations were carried out using the WinGX-32 graphical user interface.[13a,13b] Multi-scan empirical absorption corrections were applied to the data using the program SADABS.[14] The structures were solved by direct methods using SIR97[15] then refined and extended with SHELXL-97.[16]

In general, ordered non-hydrogen atoms were refined anisotropically. Partial occupancy non-hydrogen atoms were refined isotropically. Carbon-bound hydrogen atoms were included in idealised positions and refined using a riding model. Refinement residuals are defined as $R_1 = \Sigma||F_o| - |F_c||/\Sigma|F_o|$ for $F_o > 2\sigma(F_o)$ and $wR_2 = \{\Sigma[w(F_o^2 - F_c^2)^2]/\Sigma[w(F_c^2)^2]\}^{1/2}$ where $w = 1/[\sigma^2(F_o^2) + (\mathbf{A}P)^2 + \mathbf{B}P]$, $P = (F_o^2 + 2F_c^2)/3$ and A and B are listed with the crystal data for each structure.

$[CdL(NO_3)_2(EtOH)]_n\cdot(1.4\,H_2O)_n$: Formula $C_{20}H_{20}CdN_6O_7\cdot(H_2O)_{1.4}$, M = 594.04, triclinic, space group $P\bar{1}$ (no. 2), a = 9.105(2) Å, b = 12.106(3) Å, c = 12.494(3) Å, α = 80.891(4)°, β = 86.483(3)°, γ = 80.048(4), V = 1338.5(5) Å^3, D_c = 1.474 g cm^{-3}, Z = 2, crystal size 0.265 × 0.184 × 0.162 mm, colour colourless, habit multi-faced, temperature 150(2) K, λ(Mo-K_α) = 0.71073, μ(Mo-K_α) 0.869 mm^{-1}, T(empirical)$_{min,max}$ = 0.712, 0.869, $2\theta_{max}$ = 56.6, hkl range –11 to 12, –15 to 15, –16 to 16, N = 13064, N_{ind} = 6101 (R_{merge} = 0.0214), $N_{obsd.}$ = 5490 [$I > 2\sigma(I)$], N_{var} = 341, residuals $R_1(F, 2\sigma)$ = 0.0380, $wR_2(F^2$, all) = 0.1131, A = 0.0705, B = 0.7933, GoF(all) = 1.117, $\Delta\rho_{min,max}$ = –0.674, 1.014 e$^-$Å^{-3}.

Individual details: The water solvate is diffuse and was modelled with oxygen atoms in ten different positions, O(1W)–O(10W), with site occupancies between 0.1 and 0.2 to a total occupancy of 1.4 water molecules per asymmetric unit. H(7OE) attached to the ethanol oxygen atom O(7), was located in the difference map and refined (isotropically) with a 1.0 Å O–H bond length restraint.

$[FeL_2(NCS)_2]_n\cdot\{(2\,CHClCCl_2)\cdot(1.4\,MeOH)\cdot(2.9\,H_2O)\}_n$: Formula $C_{38}H_{28}FeN_{10}S_2\cdot(C_2HCl_3)_2\cdot(CH_4O)_{1.4}\cdot(H_2O)_{2.9}$, M = 1104.54, orthorhombic, space group *Pbcn* (no. 60), a = 13.045(3) Å, b = 22.026(5) Å, c = 17.824(4) Å, V = 5121(2) Å^3, D_c = 1.433 g cm^{-3}, Z = 4, crystal size 0.216 × 0.143 × 0.110 mm, colour orange, habit irregular, temperature 150(2) K, λ(Mo-K_α) = 0.71073, μ(Mo-K_α) 0.741 mm^{-1}, T(empirical)$_{min,max}$ = 0.810, 0.920, $2\theta_{max}$ = 56.6, hkl range –17 to 17, –29 to 29, –23 to 23, N = 20669, N_{ind} = 6279 (R_{merge} = 0.0571), $N_{obsd.}$ = 4288 [$I > 2\sigma(I)$], N_{var} = 270, residuals $R_1(F, 2\sigma)$ = 0.1017, $wR_2(F^2$, all) = 0.3240, A = 0.1762, B = 25.8136, GoF(all) = 1.038, $\Delta\rho_{min,max}$ = –1.781, 1.478 e$^-$Å^{-3}.

Individual details: The asymmetric unit comprises half of one iron(II) atom (Fe on twofold site), one ligand **L** and one thiocyanato ligand. The thiocyanato ligand displays minor disorder and was modelled in two positions, N(5a)–C(19a)–S(1a) and N(5b)–C(19b)–S(1b), with site occupancies of 0.8 and 0.2 respectively. The asymmetric unit also contained regions of smeared electron density associated with diffuse solvent molecules. Using three possible solvents (trichloroethylene, methanol and water), attempts were made to model this diffuse solvent. The most plausible model comprises 1 trichloroethylene (three positions with occupancies 0.5, 0.3 and 0.2), 0.7 methanol (two positions with occupancies 0.4 and 0.3) and 1.45 water (five positions with occupancies 0.4, 0.3, 0.25, 0.25 and 0.25) molecules per asymmetric unit. For comparative purposes, the electron density associated with the disordered solvent was removed from the intensity data using the SQUEEZE function of PLATON.[17a,17b] The cell void volume (in the absence of modelled solvent) was determined to be *c*. 2160 Å^3 which constitutes 42% of the total unit cell volume. The approximate electron count (determined by PLATON) associated with the cell void is 816 electrons (i.e. 102 electrons per asymmetric unit). This is reasonably consistent with the total count of electrons used in the disordered solvent model (87 electrons per asymmetric unit). The residuals obtained upon structure refinement after the application of SQUEEZE [$R_1(F,2\sigma)$ = 0.0463, $wR_2(F^2$,all) = 0.1240] were very acceptable and considerably lower than the residuals obtained upon refinement of the solvated model [$R_1(F,2\sigma)$ = 0.1017, $wR_2(F^2$,all) = 0.3240]. It appears from the SQUEEZE analysis that the high residuals in the reported structure are artefacts of (unavoidable) inadequacies in the solvent model. All disordered components (except water) were refined as rigid groups.

CCDC-258885 and -258886 contain the supplementary crystallographic data for this paper. These data can be obtained free of charge from The Cambridge Crystallographic Data Centre via www.ccdc.cam.ac.uk/data_requst/cif.

Supporting Information (see also footnote on the first page of this article): Figures showing how the sheets in $[Cd\mathbf{L}(NO_3)_2(EtOH)]_n\cdot(1.4\,H_2O)_n$ are paired through offset face-to-face π interactions and edge-to-face π interactions; the surface contours of the solvent accessible channels in $[Cd\mathbf{L}(NO_3)_2(EtOH)]_n\cdot(1.4\,H_2O)_n$ and a view of the $[Fe\mathbf{L}_2(NCS)_2]_n\cdot\{(2\,CHClCCl_2)\cdot(1.4\,MeOH)\cdot(2.9\,H_2O)\}_n$ lattice parallel to the *c* axis. In the latter case the grids stack along the *c* axis with adjacent grids offset from one another. The effect of this is to enclose the trichloroethylene in noncontinuous cavities while the water and methanol molecules occupy the continuous channels in the porous framework.

Acknowledgments

We thank the Australian Research Council for support and Prof. K. S. Murray and Dr. B. Moubaraki of Monash University for undertaking the variable temperature magnetic measurements.

[1] a) M. Fujita, Y. J. Kwon, S. Washizu, K. Ogura, *J. Am. Chem. Soc.* **1994**, *116*, 1151; b) J. Lu, T. Paliwala, S. C. Lim, C. Yu, T. Niu, A. J. Jacobson, *Inorg. Chem.* **1997**, *36*, 923; c) R.-D. Schnebeck, L. Randaccio, E. Zangrado, B. Lippert, *Angew. Chem. Int. Ed. Engl.* **1998**, *37*, 119; d) K. N. Power, T. L. Hennigar, M. J. Zaworotko, *New J. Chem.* **1998**, *22*, 177; e) M. Kondo, M. Shimamura, S. Noro, S. Minakoshi, A. Asami, K. Seiki, S. Kitagawa, *Chem. Mater.* **2000**, *12*, 1288; f) Y. Zhang,

 © 2005 Wiley-VCH Verlag GmbH & Co. KGaA, Weinheim

L. Jianmin, M. Nishiura, T. Imamoto, *J. Mol. Struct.* **2000**, *519*, 219; g) A. N. Khlobystov, A. J. Blake, N. R. Champness, D. A. Lemenovskii, A. G. Majouga, N. V. Zyk, M. Schröder, *Coord. Chem. Rev.* **2001**, *222*, 155; h) S. A. Barnett, N. R. Champness, *Coord. Chem. Rev.* **2003**, *246*, 145; i) S. L. James, *Chem. Soc. Rev.* **2003**, *32*, 276; j) G. S. Papaefstathiou, L. R. MacGillivray, *Coord. Chem. Rev.* **2003**, *246*, 169; k) M. J. Rosseinsky, *Microporous Mesoporous Mater.* **2004**, *73*, 15.

[2] G. J. Halder, C. J. Kepert, B. Moubaraki, K. S. Murray, J. D. Cashion, *Science* **2002**, *298*, 1762.

[3] a) H. J. Choi, T. S. Lee, M. P. Suh, *Angew. Chem. Int. Ed.* **1999**, *38*, 1405; b) C. J. Kepert, M. J. Rosseinsky, *Chem. Commun.* **1999**, 375; c) K. S. Min, M. P. Suh, *J. Am. Chem. Soc.* **2000**, *122*, 6834; d) E. J. Cussen, J. B. Claridge, M. J. Rosseinsky, C. J. Kepert, *J. Am. Chem. Soc.* **2002**, *124*, 9574; e) C. Janiak, *Dalton Trans.* **2003**, 2781.

[4] a) M. Eddaoudi, J. Kim, N. Rosi, D. Vodak, J. Wachter, M. O'Keefe, O. M. Yaghi, *Science* **2002**, *295*, 469; b) N. L. Rosi, J. Eckert, M. Eddaoudi, D. T. Vodak, J. Kim, M. O'Keefe, O. M. Yaghi, *Science* **2004**, *300*, 1127.

[5] J. S. Seo, D. Whang, H. Lee, S. I. Jun, J. Oh, Y. J. Jeon, K. Kim, *Nature* **2000**, *404*, 982.

[6] a) P. J. Stang, B. Olenyuk, *Acc. Chem. Res.* **1997**, *30*, 502; b) S. Leininger, B. Olenyuk, P. J. Stang, *Chem. Rev.* **2000**, *100*, 853; c) J. A. R. Navarro, B. Lippert, *Coord. Chem. Rev.* **2001**, *222*, 219; d) S. R. Seidel, P. J. Stang, *Acc. Chem. Res.* **2002**, *35*, 972.

[7] a) C. S. Lai, E. R. T. Tiekink, *Cryst. Eng. Commun.* **2004**, *6*, 593; b) S. Muthu, Z. Ni, J. J.Vittal, *Inorg. Chim. Acta* **2005**, *358*, 595.

[8] S. Nan′ya, T. Tange, E. Maekawa, *J. Heterocycl. Chem.* **1985**, *22*, 449.

[9] ORTEP-3, L. J. Farrugia, *J. Appl. Crystallogr.* **1997**, *30*, 565.

[10] C. Janiak, *J. Chem. Soc. Dalton Trans.* **2000**, 3885.

[11] M. Nishio, M. Hirota, Y. Umezawa, The CH/pi interaction, Wiley-VCH, New York, **1998**.

[12] Bruker; SMART, SAINT and XPREP: Area detector control and data integration and reduction software, Bruker Analytical X-ray Instruments Inc., Madison, Wisconsin, USA, **19<95**.

[13] a) WinGX-32: System of programs for solving, refining and analysing single-crystal X-ray diffraction data for small molecules; b) L. J. Farrugia, *J. Appl. Crystallogr.* **1999**, *32*, 837.

[14] G. M. Sheldrick, SADABS: empirical absorption and correction software, University of Göttingen, Göttingen, Germany, **1999**.

[15] A. Altomare, M. C. Burla, M. Camalli, G. L. Cascarano, C. Giocavazzo, A. Guagliardi, A. G. C. Moliterni, G. Polidori, S. Spagna, *J. Appl. Crystallogr.* **1999**, *32*, 115.

[16] G. M. Sheldrick, SHELX-97: programs for crystal structure analysis, University of Göttingen, Göttingen, Germany, **1998**.

[17] a) A. L. Spek, *Acta Crystallogr. Sect. C* **1990**, *46*, 34; b) P. van der Sluis, A. L. Spek, *Acta Crystallogr.* **1990**, *46*, 194.

Received: February 03, 2005

 © 2005 Wiley-VCH Verlag GmbH & Co. KGaA, Weinheim

First Examples of Chalcofluoride Rhenium Cluster Complexes with Cubane-Like Anions $[Re_4Q_4F_{12}]^{4-}$ (Q = S, Se)

Yuri V. Mironov,[a] Spartak S. Yarovoi,[a] Dmitry Y. Naumov,[a] Natalia V. Kuratieva,[a] Svetlana G. Kozlova,[a,b] Arndt Simon,[c] and Vladimir E. Fedorov*[a,d]

Dedicated to Professor James A. Ibers on the occasion of his 75th birthday

Keywords: Tetrahedral rhenium cluster / Chalcofluoride complexes / Density functional calculations

Two rhenium tetrahedral cluster chalcofluoride compounds, $K_4[Re_4S_4F_{12}]\cdot 3.4H_2O$ (**1**) and $K_4[Re_4Se_4F_{12}]\cdot 6H_2O$ (**2**), have been synthesized for the first time by a reaction of $Re_4Q_4(TeCl_2)_4Cl_8$ (Q = S, Se) with molten KHF_2. Both compounds have been characterized by single-crystal X-ray diffraction methods. Compound **1** crystallizes in the trigonal space group $R\bar{3}$ with 24 formula units per cell [$a = b = 23.6503(3)$ Å, $c = 25.2697(7)$ Å, $V = 12240.6(4)$ Å^3 ($T = 293$ K)]; compound **2** crystallizes in the monoclinic space group $P\bar{1}$ with four formula units per cell [$a = 10.6451(3)$ Å, $b = 14.6853(4)$ Å, $c = 16.9349(5)$ Å, $\alpha = 66.8420(10)°$, $\beta = 84.8460(10)°$, $\gamma = 85.5740(10)°$, $V = 2421.69(12)$ Å^3 ($T = 293$ K)]. Hydrophilic terminal fluoride ligands of cluster anions are included in the hydrogen bond systems of their hydrate shells.

(© Wiley-VCH Verlag GmbH & Co. KGaA, 69451 Weinheim, Germany, 2005)

Introduction

Chalcohalide cluster complexes of the early transition metals like triangular $[M_3Q_7L_6]^{2-}$, tetrahedral $[M_4Q_4L_{12}]^{4-}$, and octahedral $[M_6Q_8L_6]^{4-}$ (M = Mo, W, Re; Q = S, Se, Te) complexes are well known in the literature.[1–6] In these complexes the outer ligands L are most often halide ions (Cl^-, Br^-, I^-) and some other simple ligands such as CN^- and SCN^-. Complexes with organic ligands L are known also. Whereas F^- in both inner and outer positions has been known for a long time from the solid state compounds $Nb_6F^i_{12}F^a_{6/2}$,[7] up to now none was known where a fluoride ion played the role of an outer L ligand in complexes, except for the recently described Mo_3 triangular thiofluoride complex $K_5[Mo_3S_4F_7(FHF)_2]\cdot 2H_2O$ and Re_6 octahedral thiofluoride complexes $[Re_6S_8F_6]^{4-}$ and $[Re_6S_8F_2(H_2O)_4]$.[8,9]

Here we present the successful syntheses, crystal structures, and some properties of the first representatives of tetrahedral chalcofluoride cluster complexes of rhenium $[Re_4Q_4F_{12}]^{4-}$ (Q = S, Se). Cubane-like chalcofluoride rhenium(IV) complexes with cluster anions $[Re_4S_4F_{12}]^{4-}$ and $[Re_4Se_4F_{12}]^{4-}$ were obtained by the reaction of $Re_4Q_4(TeCl_2)_4Cl_8$ (Q = S, Se) with molten potassium bifluoride KHF_2. These anionic complexes were isolated as potassium salts of compositions $K_4[Re_4S_4F_{12}]\cdot 3.4H_2O$ (**1**) and $K_4[Re_4Se_4F_{12}]\cdot 6H_2O$ (**2**) from aqueous solutions. Compounds **1** and **2** are the first examples of cubane-like clusters with fluoride ligands in the outer sphere of a cluster core $\{Re_4Q_4\}$.

Results

The prepared anionic complexes **1** and **2** are the first examples of cubane-like clusters with fluoride ligands in the outer sphere of a cluster core $\{Re_4Q_4\}$, namely $[Re_4S_4F_{12}]^{4-}$ and $[Re_4Se_4F_{12}]^{4-}$ (Figure 1).

Compound **1** crystallizes in the trigonal space group $R\bar{3}$. In the structure there are two different cluster anions $[Re_4S_4F_{12}]^{4-}$ with symmetries C_1 and C_3 respectively, however they are geometrically closely related. Re–Re distances are in the range 2.7277(5)–2.7448(5) Å, and Re–(μ_3-S) distances are in the range 2.310(2)–2.336(2) Å, which are close to those in the starting compound and analogous distances in related cubane rhenium thiohalides. The Re–F distances [1.980(5)–2.020(5) Å] are slightly greater than analogous bond lengths in mononuclear octahedral hexafluororhenates(IV) such as K_2ReF_6 (1.953 Å)[10] and K_3ClReF_6

[a] Nikolaev Institute of Inorganic Chemistry, Siberian Branch of Russian Academy of Sciences,
Novosibirsk 630090, Russia
E-mail: yuri@che.nsk.su
[b] Boreskov Institute of Catalysis, Siberian Branch of Russian Academy of Sciences,
Novosibirsk 630090, Russia
[c] Max-Planck-Institut für Festkorperforschung,
Heisenbergsstrasse 1, 70569 Stuttgart, Germany
E-mail: A.Simon@fkf.mpg.de
[d] Novosibirsk State University,
Novosibirsk 630090, Russia

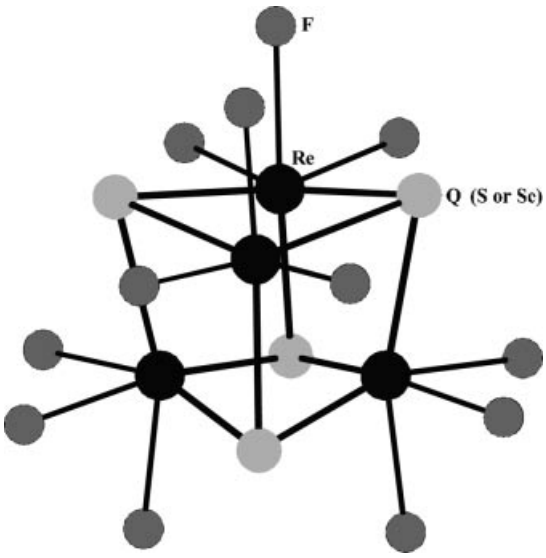

Figure 1. The structure of cluster anions $[Re_4Q_4F_{12}]^{4-}$ (Q = S, Se) in compounds **1** and **2**.

(1.837 Å).[11] In the structure the anions form slightly corrugated hexagonal parallel planes (001) which are linked through potassium cations and hydrogen bonds with additional water molecules.

The K atoms are mainly surrounded by O atoms of water molecules and F atoms of cluster anions. The K8 atom is located on the threefold axis and has a honeycomb-like arrangement of cluster anions (Figure 2).

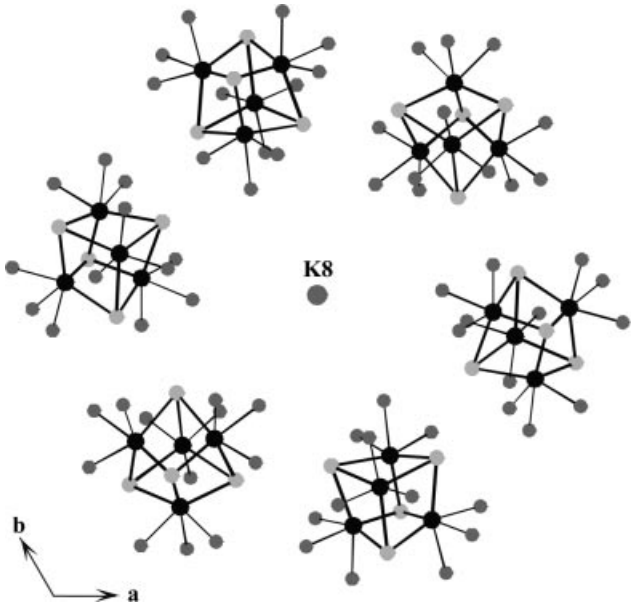

Figure 2. A fragment of the unit cell with honeycomb arrangement of the K8 atom in a projection along the *c* axis in compound **1**.

Compound **2** crystallizes in the triclinic space group $P\bar{1}$. There are two crystallographically independent cluster anions $[Re_4Se_4F_{12}]^{4-}$ in the unit cell. A general view of the mutual arrangement of the clusters in the structure of **2** is given in Figure 3. In the cluster complex the main interatomic distances like Re–Re [2.7527(5)–2.7817(5) Å], Re–(μ_3-Se) [2.4315(10)–2.4454(9) Å], and Re–F [1.987(5)–2.027(5) Å] are in good agreement with those for starting and related compounds. The environment of K atoms consists of fluorine atoms of cluster anions and oxygen atoms of water molecules.

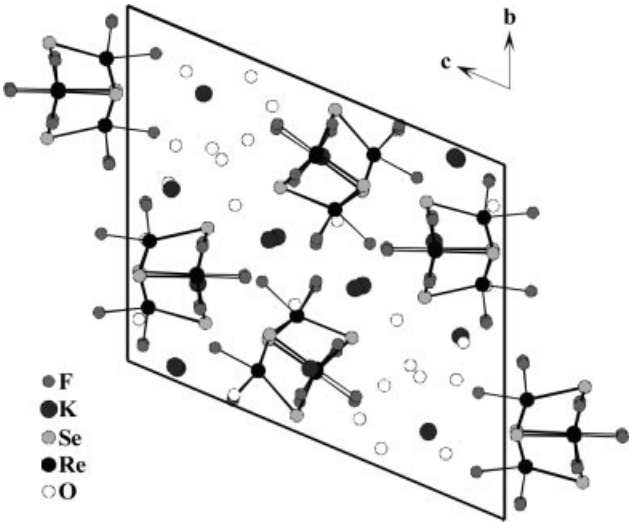

Figure 3. View of the unit cell in a projection along the *a* axis in compound **2**.

In both structures potassium atoms and water molecules connect the cluster anions through potassium ions and hydrogen bonds F···H–O and O···H–O.

NMR

Aqueous solutions of both compounds were studied by NMR on ^{19}F. The spectra of both solutions exhibit only one intensive line with chemical shifts δ^1_{iso} = –227 ppm (compound **1**) and δ^2_{iso} = –252 ppm (compound **2**) and a number of lines with relative intensities less than 0.5% of the strong lines (Figure 4). This experiment was repeated after one month to test the stability of the compounds in the solution, with no changes found in the spectra. It is worth noting that the experimental difference of the chemicals shifts, $\Delta\delta = \delta^1_{iso} - \delta^2_{iso}$ = 25 ppm, correlates with the

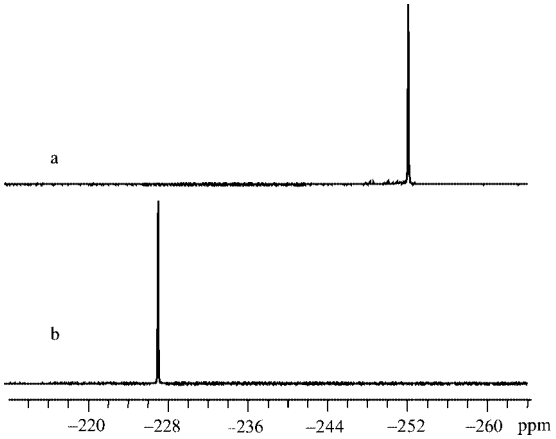

Figure 4. ^{19}F NMR spectra of compounds **1** (a) and **2** (b).

 © 2005 Wiley-VCH Verlag GmbH & Co. KGaA, Weinheim

DFT calculated difference of the isotropic NMR nuclear shielding, $\Delta\sigma = \sigma^2_{iso} - \sigma^1_{iso} = 21$ ppm, for the optimized structures of $[Re_4Q_4F_{12}]^{4-}$ models with symmetry T_d ($\sigma^1_{iso} = 337.9$ ppm and $\sigma^2_{iso} = 358.4$ ppm).

Electronic Structure

The calculated bond energies of the complexes $[Re_4Q_4F_{12}]^{4-}$ indicate that the bonding is energetically feasible, and it is stronger for the S complex (–113.40 eV) than for the Se complex (–109.64 eV). The calculated HOMO–LUMO gap is 2.55 eV for $[Re_4S_4F_{12}]^{4-}$ and 2.42 eV for $[Re_4Se_4F_{12}]^{4-}$. The calculated ionization potentials for these complexes are –5.9 eV (S) and –5.8 eV (Se).

The third degenerated HOMOs, $40t_2$ and $46t_2$, are antibonding in character for S and Se complexes and are largely centered on the rhenium atoms (65% of the 5d-valence orbitals), with the F and Q p-valence orbital contributions (Figure 5). The vacant MOs are formed from the valence orbitals of all atoms also. The exception is represented at levels $24a_1$ (for S) and $27a_1$ (for Se), which are formed mainly from atomic s orbitals of rhenium, chalcogen, and fluorine atoms. The calculated charge distribution suggests that these complexes can be formulated as $Re_4^{0.21+}S_4^{0.11-}F_{12}^{0.37-}$ and $Re_4^{0.19+}S_4^{0.09-}F_{12}^{0.37-}$. The value of a charge on Re atoms is slightly positive and on Q is slightly negative. This indicates the essentially covalent nature of bonding for a cluster core $\{Re_4Q_4\}$.

The dipole-allowed excitation energies for systems with a T_d symmetry are depicted in Figure 5. The energies calculated for proposed transitions are in qualitative agreement with experimental UV/Vis spectra. The uninterrupted weak absorption in the visible range (700–400 nm, $\varepsilon \leq 2\times10^2$) can be explained by electron-dipole transitions between HOMO and a nearby vacant MO (LUMO_LUMO2). The most intensive transitions occur in the UV region of absorption ($\varepsilon > 1\times10^3$) and can involve electron-dipole transitions between the HOMO and vacant MOs.

Experimental Section

$Re_4Q_4(TeCl_2)_4Cl_8$ (Q = S, Se) compounds were prepared as described previously.[12] All other reagents used were commercially available products of reagent grade quality. All experiments were performed in air. UV/Vis spectra were recorded in H_2O with an Ultraspec 3300 Pro spectrometer at room temperature in the range 200–1100 nm. Infrared spectra were recorded with a Bruker IFS-85. ^{19}F NMR spectra of aqueous solutions were obtained with a Bruker MSL-400 spectrometer in a magnetic field of 9.4 T at room temperature. The resonance frequency for ^{19}F was 376.308 MHz, pulse width (90°) 8 μs with a 2-s repetition rate for 3000 transients. Chemical shifts are reported with respect to an external standard C_6F_6. EMA = Electron microprobe analysis.

Preparation of $K_4[Re_4S_4F_{12}]\cdot3.4H_2O$ (1): $Re_4S_4(TeCl_2)_4Cl_8$ (0.35 g, 0.18 mmol) was heated with an excess of KHF_2 (5 g, 64 mmol) in a carbon glass vessel in air for 2 h at 300–310 °C. The fusion cake was washed with water (20 mL), and the remaining solid was dissolved in water (40 mL) to yield a green solution which was filtered and left for a day. A green precipitate formed; it was filtered and dried in air. Yield: 0.19 g (76%). Single crystals of **1** were obtained by dissolving the pure product in water with the addition of a small amount of KHF_2. The solution was left for 3 days in an open polyethylene tube. Dark brown crystals that formed were filtered and dried in air. EMA: $K_{4.1}Re_4S_{3.9}F_{12.1}$. Microanalysis for $H_{6.8}F_{12}K_4O_{3.4}Re_4S_4$: calcd. F 17.29, S 9.73; found F 16.95, S 9.90. IR (KBr): $\tilde{\nu}$ = (Re–F) = 512 (s), 466 (s) cm^{-1}. ^{19}F NMR (ppm): –227. UV/Vis (H_2O): λ, nm (ε, $L\,mol^{-1}\,cm^{-1}$): 230 (5458), 267 (5368), 317 (1965), 363 (1143) (700–400 uninterrupted weak absorption).

Preparation of $K_4[Re_4Se_4F_{12}]\cdot6H_2O$ (2): $Re_4Se_4(TeCl_2)_4Cl_8$ (0.6 g, 0.31 mmol) was treated as described for compound **1** (Yield: 0.29 g (58%)) and single dark green plate crystals of **2** were obtained in the same way as for compound **1**. EMA: $K_{4.1}Re_4Se_{3.8}F_{12.5}$. Microanalysis for $H_{12}F_{12}K_5O_6Re_4Se_4$: calcd. F 14.32; found F 14.68. IR

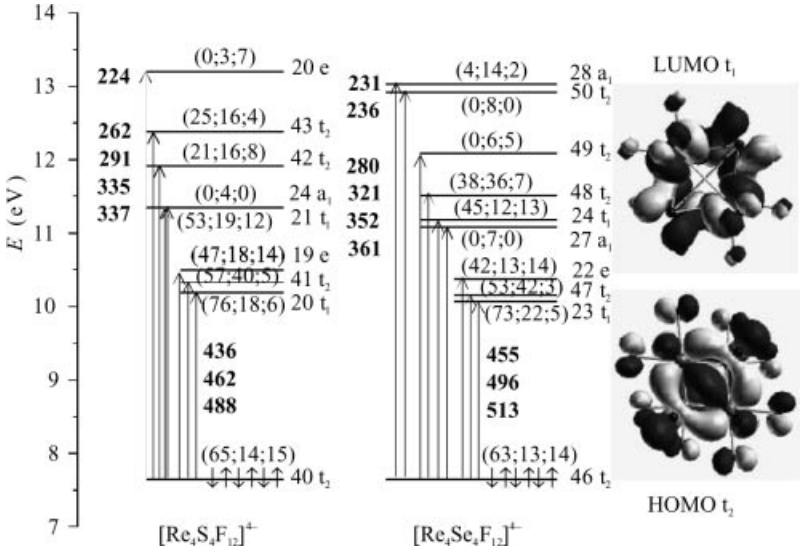

Figure 5. Electronic level schemes for $[Re_4Q_4F_{12}]^{4-}$ models and schematic figures of one from third degenerated HOMO and LUMO. The numbers and symmetry types of the calculated MOs are indicated. Numbers in brackets indicate the percentage of the contributing valence orbitals – 5d Re; 3p S; 4p Se; 2p F, respectively. The vertical arrows and integers (nm) show the calculated transitions.

 © 2005 Wiley-VCH Verlag GmbH & Co. KGaA, Weinheim

(KBr): $\tilde{\nu}$ = (Re–F) = 500 (s), 455 (s) cm^{-1}. ^{19}F NMR (ppm): –252. UV/Vis (H_2O): λ, nm (ε, $L\,mol^{-1}\,cm^{-1}$): 265 (2667), 294 (3686), 334 (2429), 381 (sh) (750–430 uninterrupted weak absorption).

X-ray Structure Determination: Diffraction data for **1** and **2** were collected with a Bruker–Nonius X8Apex equipped with a 4-K CCD area detector with graphite-monochromated Mo-K_α radiation (λ = 0.71073 Å) at room temperature using standard techniques (Table 1). An empirical absorption correction using the SADABS program was applied. The structures were solved by direct methods employing difference Fourier syntheses and refined anisotropically by full-matrix least-squares techniques on F^2 using the SHELXL-97 Release 97-2 software package.[13] The hydrogen atoms of water molecules were not located. Crystal data, experimental details, and refinement results are summarized in Table 1 and have been deposited with the Fachinformationszentrum Karlsruhe.[14]

Table 1. Crystal data and structure refinement for $K_4[Re_4S_4F_{12}]\cdot 3.4\,H_2O$ (**1**) and $K_4[Re_4Se_4F_{12}]\cdot 6\,H_2O$ (**2**).

Compound	**1**	**2**
Chemical formula	$H_{6.76}F_{12}K_4O_{3.38}Re_4S_4$	$H_{12}F_{12}K_4O_6Re_4Se_4$
Formula mass	1318.24	1553.14
a [Å]	23.6503(3)	10.6451(3)
b [Å]		14.6853(4)
c [Å]	25.2697(7)	19.763(3)
α [°]	66.8420(10)	66.842(1)
β [°]		84.846(1)
γ [°]		85.574(1)
V [Å^3]	12240.6(4)	2421.7(1)
$d_{calcd.}$ ($g\,cm^3$)	4.292	4.260
Space group	$R\bar{3}$	$P\bar{1}$
Z	24	4
μ (mm^{-1})	24.991	26.735
T (K)	293(2)	293(2)
$R_1(F)$ ($F_o^2 > 2\sigma(F_o^2)$)	0.0374	0.0415
$R_w(F^2)$ (all data)	0.0886	0.1010

DFT Calculations: Density functional spin-restricted calculations (DFT) were carried out on $[Re_4Q_4F_{12}]^{4-}$ models by using the ADF2002 code.[15] The local-exchange VWN correlation potential was used for the local density (LDA) approximation;[16] Becke's nonlocal corrections to the exchange energy[17] and Perdew's nonlocal corrections to the correlation energy were added.[18] The ZORA (zeroth-order relativistic approximation) method was used to account for the scalar relativistic effects.[19] The STO basic set without core potentials was used for all atoms (ZORA/TZ2P). The tetrahedral symmetry, T_d, was imposed on the full geometry optimization of the ground electronic states for the $[Re_4Q_4F_{12}]^{4-}$ and $[Re_4Q_4F_{12}]^{3-}$ models. Calculations of the electronic binding energy were performed as $\Delta E_n = [Re_4Q_4F_{12}]^{n-} - (4Re + 4Q + 12F)$. The ionization potentials were computed as the energy differences between the $[Re_4Q_4F_{12}]^{3-}$ and $[Re_4Q_4F_{12}]^{4-}$, IP = $\Delta E_3 - \Delta E_4$. The atomic net charges for $[Re_4Q_4F_{12}]^{4-}$ complexes were obtained using the Hirshfeld analysis.[20] The isotropic NMR nuclear shieldings (^{19}F σ_{iso}) were calculated by the method of gauge including atomic orbitals (GIAO) with scalar relativistic effects.[21]

Acknowledgments

This work was supported by the Russian Foundation "Universities of Russia" (grant UR.05.01.208) and by the Division of Chemistry and Materials Science of the RAS (project No.15 of Program 4.1).

[1] Y. V. Mironov, V. E. Fedorov, *Russ. Chem. Bull., Int. Ed.* **2002**, *51*, 569–580.
[2] J.-C. P. Gabriel, K. Boubekeur, S. Uriel, P. Batail, *Chem. Rev.* **2001**, *101*, 2037–2066.
[3] M. N. Sokolov, V. P. Fedin, A. G. Sykes, in *Comprehensive Coordination Chemistry II* (Eds: J. A. McCleverty, T. J. Meyer), Elsevier, New York, **2003**, vol. 4, pp. 768–824.
[4] T. G. Gray, *Coord. Chem. Rev.* **2003**, *243*, 213–235.
[5] M. H. Chisholm (Ed.), *Early Transition Metal Clusters with π-Donor Ligands*, VCH Verlagsgesellschaft, Weinheim (Germany), **1995**, pp. 289.
[6] N. Prokopuk, D. F. Shriver, *Adv. Inorg. Chem.* **1998**, *37*, 1–49.
[7] H. Schaefer, H. G. Schnering, K.-J. Niehues, H. G. Nieder-Vahrenholz, *J. Less-Common Met.* **1965**, *9*, 95–104.
[8] Yu. V. Mironov, S. S. Yarovoi, S. F. Solodovnikov, V. E. Fedorov, *J. Mol. Struct.* **2003**, *656*, 195–199.
[9] Y. V. Mironov, S. S. Yarovoi, S. F. Solodovnikov, Y. V. Gatilov, O. Oeckler, A. Simon, V. E. Fedorov, *Proceedings of Int. Conf. "Advanced Inorganic Fluorides"*, Novosibirsk, Russia, April 2–4, **2003**, 135–137.
[10] G. R. Clark, D. R. Russell, *Acta Crystallogr. B* **1978**, *34*, 894–895.
[11] H. Mueller, S. Abberger, *Indian J. Chem.* **1995**, *34*, 563–566.
[12] Y. V. Mironov, T. E. Albrecht-Schmitt, J. A. Ibers, *Inorg. Chem.* **1997**, *36*, 944–946.
[13] G. M. Sheldrick, *SHELXTL* DOS/Windows/NT, Version 5.10; Bruker Analytical X-ray Instruments, Inc., Madison, WI, **1997**.
[14] Crystallographic data (excluding structure factors) for the structures reported in this paper have been deposited with the Fachinformationszentrum Karlsruhe, 76344 Eggenstein-Leopoldshafen, Germany, and can be obtained on quoting the depository numbers CSD-415122 and -415123.
[15] *Amsterdam Density Functional (ADF) program*, Release 2002.02, Vrije Universteit, Amsterdam, The Netherlands, **2002**.
[16] S. H. Vosko, L. Wilk, M. Nusair, *Can. J. Phys.* **1980**, *58*, 1200–1211.
[17] A. D. Becke, *Phys. Rev. A* **1988**, *38*, 3098–3100.
[18] J. P. Perdew, *Phys. Rev. B* **1986**, *33*, 8822–8824.
[19] E. van Lenthe, A. E. Ehlers, E. J. Baerends, *J. Chem. Phys.* **1999**, *110*, 8943–8951.
[20] F. L. Hirshfeld, *Theor. Chim. Acta* **1977**, *44*, 129–138.
[21] G. Schreckenbach, T. Ziegler, *J. Phys. Chem.* **1995**, *99*, 606–611.

Received: February 12, 2005

 © 2005 Wiley-VCH Verlag GmbH & Co. KGaA, Weinheim

Salophan Complexes of Group IV Metals

Stanislav Groysman,[a] Ekaterina Sergeeva,[a] Israel Goldberg,[a] and Moshe Kol*[a]

Keywords: Salophan / Tetradentate ligands / N,O ligands / Coordination modes / Octahedral complexes / Titanium / Zirconium

The coordination chemistry of tetradentate Salophan ligands with titanium and zirconium alkoxides is described for the first time. Three new Salophan ligand precursors featuring different phenolate substituents (*ortho*-Me, *ortho,para*-di-Cl, *ortho,para*-di-*t*Bu) were synthesized in addition to the known prototypical Salophan precursor, by a sequence of condensation and reduction. All ligand precursors were reacted with the metal alkoxides $Ti(OiPr)_4$ and $Zr(OtBu)_4$. The unsubstituted Salophan led to a complex product mixture for both titanium and zirconium. The methyl-substituted ligand led to a clean complex only with zirconium, and the other ligands gave well-defined coordination chemistry with both metals. NMR analysis indicated that these Salophans acted as dianionic ligands, giving rise to hexa-coordinate complexes of C_2-symmetry. X-ray analysis of three complexes supported this view, and revealed that the ligands wrapping mode was *fac-fac* and that the orientation of the labile groups was *cis*. A partial hydrolysis of one of the titanium complexes led to a dinuclear bridging oxo complex in which the ligand wrapping mode had changed to *fac-mer*, as revealed from its crystal structure.

(© Wiley-VCH Verlag GmbH & Co. KGaA, 69451 Weinheim, Germany, 2005)

Introduction

Tetradentate diamino-diphenolate [ONNO]-type ligands exhibit a versatile chemistry with many transition and main-group elements.[1–4] Salan-type ligands bind to early transition metals almost exclusively in a *fac-fac* geometry, forming octahedral C_2-symmetrical complexes with the two labile groups in a *cis* geometry. This disposition is suitable for olefin polymerization catalysis.[2,5] In contrast, Salen-type ligands exhibit mostly a *mer-mer* geometrical preference, leading to *trans* disposition of the labile groups.[6] It would thus seem that the hybridization at the nitrogen atom, i.e. sp^2 or sp^3, plays a major role on the [ONNO] ligand wrapping mode.[7] In this regard, the coordination mode of Salan-type ligands, featuring an aromatic spacer between the two nitrogen donors (also known as Salophan ligands), is intriguing when compared with the common Salan ligands possessing an aliphatic spacer.

Lig^1H_2, the prototypical Salophan ligand that features no substituents on the phenolate rings, was studied by several research groups,[8,9] and its coordination behavior was reported to be versatile. Atwood and co-workers have shown that, upon binding to group III alkyls (Al, Ga), this ligand normally acts as a tetra-anionic ligand, forming complexes of varying nuclearity.[8a–8c] In most cases, the ligand was found to bind to the "central" Al in a "flat" fashion, forming the basis of a square-pyramidal complex. For Zn, this ligand acted as a dianionic ligand, forming a dimeric pentacoordinate complex.[8d] For Mo^{VI}, Lig^1H_2 may bind as a tetradentate dianionic ligand, wrapping around the metal in a *fac-fac* fashion forming octahedral complex, or as a tridentate tri-anionic ligand (one of the phenolates unbound and protonated), forming a *mer*-bis(homoleptic) complex.[9] As part of our continuing interest in various [ONNO]-type ligands, we report herein on the preparation of new Salophan-type ligands, and describe our initial results concerning their chemistry with Group IV metals.

Results and Discussion

Two readily available complexes, $Ti(OiPr)_4$ and $Zr(OtBu)_4$, were used as metal precursors for alcoholysis reactions with the ligand precursors. All reactions were performed by adding an ethereal solution of the corresponding ligand to a stirred solution of the metal precursor at –30 °C, followed by warming to room temp. and stirring for an additional hour. At first, we explored the reactivity of the prototypical ligand, Lig^1H_2. The reaction between Lig^1H_2 and $Ti(OiPr)_4$ led to the formation of a red material whose NMR spectra indicated a complex mixture featuring at least six different methyl groups. Under the same conditions, the reaction of Lig^1H_2 and $Zr(OtBu)_4$ also led to a complex mixture. We therefore turned to substituted ligands.

For this purpose, we prepared three additional Salophan-type ligands, having varying steric and electronic influence. In comparison to Lig^1H_2, Lig^2H_2 features electron-donating methyl groups at the *ortho* positions of the phenolate

[a] School of Chemistry, Raymond and Beverly Sackler Faculty of Exact Sciences, Tel Aviv University,
Tel Aviv 69978, Israel
E-mail: moshekol@post.tau.ac.il

rings, Lig^3H_2 features electron-withdrawing chloro groups at the *ortho*, *para* positions, and Lig^4H_2 bears bulky electron-donating *t*Bu groups at the *ortho*, *para* positions. The ligands were prepared by a two-step route involving condensation between the corresponding 2-hydroxybenzaldehyde and 1,2-phenylenediamine, followed by reduction with sodium borohydride (Scheme 1). For Lig^1H_2 – Lig^3H_2, this route is practical, and leads to the desired ligand precursors smoothly in high yields. For Lig^4H_2, this route is not very effective, as the reduction of the Schiff-base intermediate is very slow, and leads to additional products. Fortunately, the solubility of Lig^4H_2 in methanol is low, so it may be purified by methanol washings of the crude product, or by column chromatography.

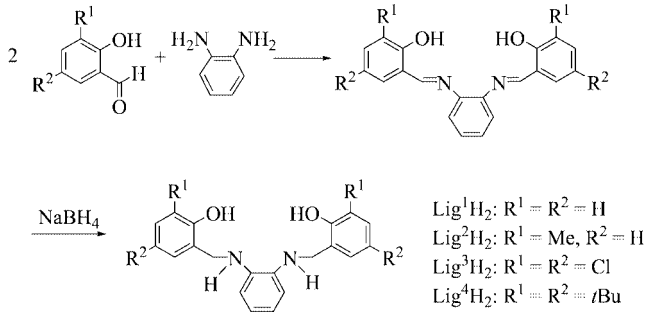

Scheme 1. Synthesis of Salophan ligands Lig^1H_2 – Lig^4H_2.

The reaction between Lig^2H_2 bearing methyl substituents and Ti(O*i*Pr)$_4$ led to an initial off-white solid whose color changed within a few minutes to deep-red. The ^{1}H NMR spectrum of this product exhibited broad signals that may indicate some equilibrating species. Recrystallization of this product from cold ether yielded bright-yellow crystals (**2**-Ti), whose solid-state structure was consistent with all subsequent structures (vide supra). However, dissolving these bright-yellow crystals in deuteriobenzene led to a deep red color in seconds, and the spectrum was consistent with the spectrum of the crude product, containing only broad absorptions. In contrast, the initially-formed Zr complex of this ligand, **2**-Zr, did not change color either in the solid phase or in solution for prolonged periods of time, and its ^{1}H NMR spectrum featured sharp absorptions. Interestingly, Lig^3H_2 that carries chloro groups, reacted cleanly with both titanium and zirconium to giving the well-defined **3**-Ti and **3**-Zr, respectively, albeit the smaller size of the Cl groups. The bulky Lig^4H_2, carrying *t*Bu groups near the metal center, also presented a well-behaved reactivity with both metals, yielding the species **4**-Ti and **4**-Zr cleanly.

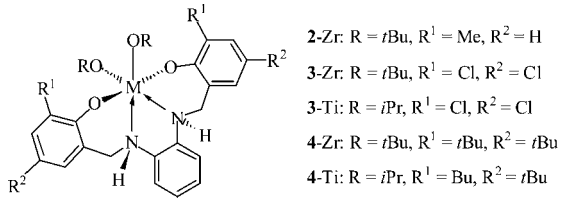

Figure 1. The C_2-symmetrical structure of Salophan-Group IV metal complexes.

Thus, relative to Lig^2H_2, both the electron withdrawing ligand Lig^3H_2 and the bulky ligand Lig^4H_2 lead to well defined products. The stable Salophan complexes obtained in this work are outlined in Figure 1.

The ^{1}H and ^{13}C NMR spectra support a C_2-symmetry of all these complexes as judged by the presence of two distinct aromatic doublets for the phenolate hydrogens, an AB system for the ligand methylene protons, and a single type of labile groups. The diastereotopic methyl groups of the isopropoxide ligands give rise to two peaks in both ^{1}H and ^{13}C NMR spectra of the titanium complexes. According to the presence of NH signals in the ^{1}H NMR spectra and the number of labile groups, these ligands bind to the metal centers in a dianionic fashion. Interestingly, the ligand methylene protons present an additional splitting, seemingly from the NH proton, and this splitting is different for the diastereotopic CH_2 protons. In the sterically congested **4**-Ti complex, two types of splitting are clearly observed (1.2 Hz, 2.7 Hz), while in the more open **3**-Ti complex, only one type of splitting (2.1 Hz) could be observed. For the zirconium species, only one of the AB signals exhibits this additional splitting, and it is consistent throughout the series (3.0–4.0 Hz).

X-ray quality crystals of the complexes **3**-Zr, and **4**-Ti, were obtained upon recrystallization from pentane, and their crystal structures were solved, in addition to the structure of **2**-Ti, obtained upon recrystallization from ether (for the crystal structures see Figure 2, Figure 3 and Figure 4). In agreement with the NMR spectroscopic data, the Salophan ligands wrap around the Group IV metals in a *fac-fac* mode to afford non-crystallographic C_2-symmetrical complexes. As previously observed for the complexes of the Salan series, the phenolate oxygen atoms are located mutually *trans* (160° for **2**-Ti, 156° for **3**-Zr, 160° for **4**-Ti), and the monodentate ligands are mutually *cis* (106° in **2**-Ti, 108° in **3**-Zr, 105° in **4**-Ti), and *trans* to the amine donors (159–166°). Thus, the exchange of the aliphatic spacer between

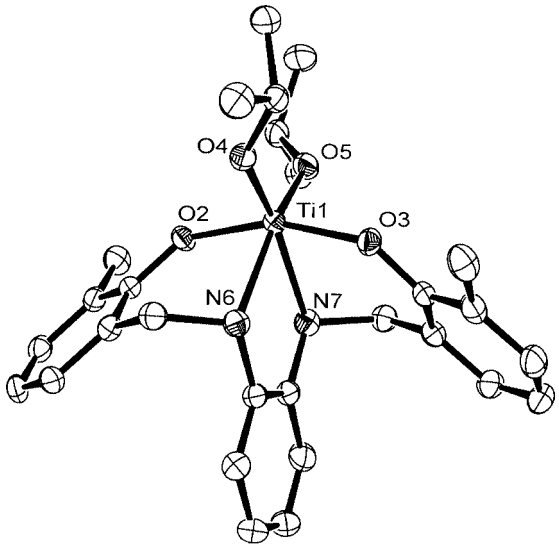

Figure 2. ORTEP representation (50% probability ellipsoids) of **2**-Ti; hydrogen atoms are omitted for clarity.

 © 2005 Wiley-VCH Verlag GmbH & Co. KGaA, Weinheim

two amine donors by an aromatic one preserves the overall binding mode in this ligand family. Moreover, the N–M dative bonds for the potentially poorer σ-donor (aniline) are very close to the N–M dative bonds in the complexes featuring ethylene diamine backbone (2.31 Å for **4**-Ti vs. 2.29 Å for the analogous complex with the ethylene diamine backbone).[2b] The M–OPh bond lengths are also comparable to those reported for Salan complexes, with a slight difference for Zr {2.05 Å for **3**-Zr vs. 2.01 Å for [Salan]-$Zr(CH_2Ph)_2$}[2a] probably resulting from the bulkier monodentate ligands. Most notably, the metal is coplanar with the phenylene diamine unit for the sterically open **2**-Ti and **3**-Zr, while for the sterically congested **4**-Ti, the metal lies slightly outside the phenyl plane (see Figure 5).

We found that the titanium complexes are relatively unstable to hydrolysis. For example, the sterically congested complex **4**-Ti undergoes a slow decomposition when stored in a paraffin-sealed NMR tube outside the glovebox. The resulting main product, **4**-Ti-a, which is only slightly soluble in benzene, crystallizes out to give yellow crystals. The NMR spectrum of this compound is complicated, and shows a low symmetry of the ligand backbone, being composed of four *t*Bu peaks, two N–H signals, and four different methylene signals (coupled to two carbon atoms). In addition, the spectrum contains a single isopropoxide group. The X-ray structure determination disclosed a dinuclear structure with a $[Ti_2O]$ μ-oxo core (see Figure 6). Each Ti center is of nearly octahedral geometry, being surrounded by a bridging oxo ligand (Ti1–O 1.848 Å, Ti2–O 1.834 Å), and the isopropoxo ligand, in addition to the [ONNO] donor set of the Salophan ligand. The Ti–OPh distances differ significantly, with the Ti–OPh bond length *trans* to the oxo ligand being longer (1.928 Å vs. 1.847 Å).

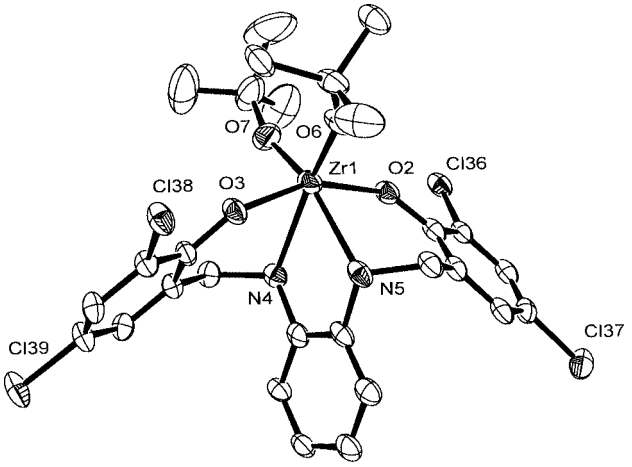

Figure 3. ORTEP representation (30% probability ellipsoids) of **3**-Zr. A second, chemically identical molecule, that is present in the asymmetric unit, crystallization solvent and the hydrogen atoms are omitted for clarity.

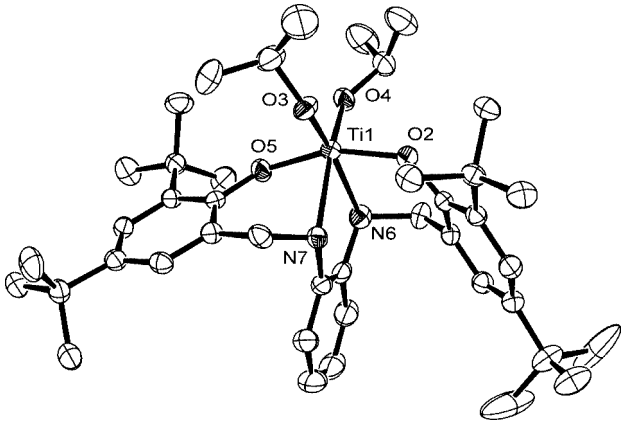

Figure 4. ORTEP representation (50% probability ellipsoids) of **4**-Ti; hydrogen atoms were omitted for clarity.

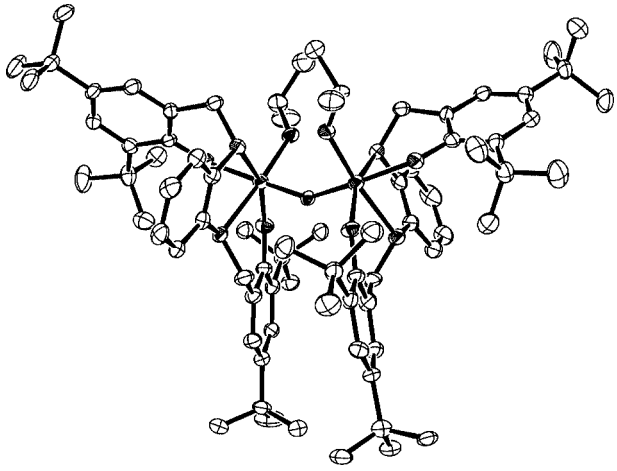

Figure 6. ORTEP representation of **4**-Ti-a, 50% probability; hydrogen atoms, and the crystallization solvent are omitted for clarity. One of the *t*Bu groups is disordered.

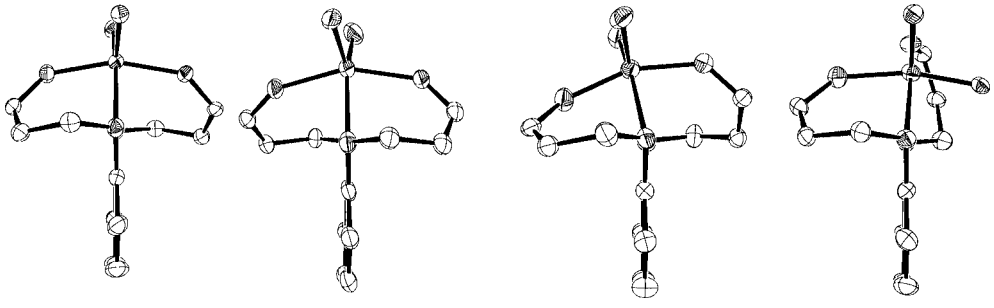

Figure 5. ORTEP representations of the cores of **2**-Ti, **3**-Zr, **4**-Ti, **4**-Ti-a (from left to right, respectively) along the plane of the phenylene ring, demonstrating the relative conformations of the phenylene diamine unit and the metal.

 © 2005 Wiley-VCH Verlag GmbH & Co. KGaA, Weinheim

Most significantly, the ligand binds to the metal in a *fac-mer* mode for the first time. The Ti–N bond lengths are relatively different in this disposition: the Ti–N bond in the *mer* fragment is longer than in the *fac* fragment (2.275 and 2.278 Å for the former, and 2.211 and 2.222 Å for the latter), possibly indicating a stronger binding in the *fac* disposition. Finally, the metal is coplanar with the phenylene diamine unit in both parts of the molecule (Figure 5), as previously encountered in **2**-Ti and **3**-Zr complexes, and in contrast to its sterically congested precursor, **4**-Ti.

In conclusion, we have prepared a variety of new Salophan-type ligands, and their titanium and zirconium complexes. The coordination chemistry of these ligands with Group IV metals was found to depend on the phenolate substituents: The substituents-free Lig[1] led to complex mixtures, while the 2,4-dichloro- or di-*t*Bu-substituted ligands Lig[3] or Lig[4] led to a clean chemistry for both metals. The ligand bearing *ortho*-methyl groups Lig[2] formed a stable zirconium complex, and an unstable titanium complex. In all cases in which stable complexes were formed, they possessed C_2-symmetry on the NMR timescale, and their wrapping mode, being supported by X-ray structures, was found to be *fac-fac*, as previously found in Salan-Group IV complexes. The sterically congested di(isopropoxo) titanium complex **4**-Ti was found to undergo a facile (partial) hydrolysis, forming a μ-oxo product, in which the Salophan ligand coordinates to the metal in a *fac-mer* fashion. We are currently investigating the reactivity of these species, and exploring the chemistry of the newly prepared Salophan ligands with other early transition metals.

Experimental Section

Materials and Instrumentation: All syntheses of metal complexes were performed under dry nitrogen in a nitrogen-filled glovebox. Ether was purified by reflux and distillation under dry argon from Na/benzophenone. Pentane was washed with HNO_3/H_2SO_4 prior to distillation from Na/benzophenone/tetraglyme. Ti(O*i*Pr)$_4$ and Zr(O*t*Bu)$_4$ were purchased from Aldrich Inc and used without purification. NMR spectroscopic data for the ligand precursors were recorded with a Bruker AC-200 spectrometer in $CDCl_3$ and referenced to TMS (δ = 0.00) in proton spectra, or to the chemical shift of $CDCl_3$ in carbon NMR spectroscopy. NMR spectroscopic data for the metal complexes were recorded with a Bruker AC-200 or Bruker Avance 400 spectrometers and referenced to protio impurities in [D$_6$]benzene (δ, 7.15), and to ^{13}C chemical shift of benzene (δ, 128.70). Elemental analyses were performed by the microanalytical laboratory of the Hebrew University of Jerusalem. The metal complexes were analyzed within a few hours of being taken out of the freezer of the glovebox. The X-ray diffraction measurements were performed on a Nonius Kappa CCD diffractometer system, using Mo-K_α (λ = 0.7107 Å radiation). The analyzed crystals were embedded within a drop of viscous oil and freeze-cooled to ca. 110 K. The structures were solved by a combination of direct methods and Fourier techniques using the SIR-92 software,[10] and were refined by full-matrix least-squares with SHELXL-97.[11] The crystal data are summarized in Table 1. The crystals of **3**-Zr and **4**-Ti-a contain partly disordered *t*Bu groups, and partly disordered solvent, thus affecting to some extent the precision of the structure determination.

Lig^{1}H$_2$: A solution of salicylaldehyde (4.60 g, 38 mmol) and 1,2-phenylenediamine (2.05 g, 19 mmol) in 60 mL of methanol was placed in a 100 mL round-bottomed flask equipped with a magnetic stir-bar and a reflux condenser. After several minutes, a yellow solution had formed, followed by formation of an orange precipitate (Salophen intermediate). The reaction mixture was allowed to stand for 30 min at room temp. and sodium borohydride (2.86 g, 5 equiv.) was added in small portions to the stirred heterogeneous mixture. The orange precipitate gradually disappeared, and a bright yellow transparent solution formed. The reaction mixture was poured into 100 mL of water, and allowed to stand for several hours. The resulting white solid was isolated by vacuum filtration, washed several times with water, and dried under vacuum at 50 °C for 2 h, yielding 4.99 g of Lig^{1}H$_2$ (82% yield). The ^{1}H/^{13}C NMR spectra indicated its sufficient purity, being consistent with those previously described.[8]

Table 1. Crystallographic experimental details.

	2-Ti	**3**-Zr	**4**-Ti	**4**-Ti-a
Empirical formula	$C_{28}H_{36}N_2O_4Ti$	$C_{30.5}H_{38}Cl_4N_2O_4Zr$	$C_{42}H_{64}N_2O_4Ti$	$C_{45}H_{63}N_2O_{3.50}Ti$
Formula mass	512.49	729.65	708.85	735.87
a [Å]	10.1360(2)	12.093(1)	9.8910(2)	14.2740(8)
b [Å]	18.9990(5)	17.124(1)	15.8450(3)	16.8810(8)
c [Å]	14.4670(3)	19.413(1)	26.8520(6)	19.2770(10)
α (°)	90.00	99.682(5)	90.00	89.727(3)
β (°)	108.9220(15)	93.196(4)	97.691(1)	102.663(3)
γ (°)	90.00	103.812(3)	90.00	109.904(3)
Crystal system	monoclinic	triclinic	monoclinic	triclinic
Space group	$P2_1/n$	$P\bar{1}$	$P2_1/n$	$P\bar{1}$
V [Å^3]	2635.41(10)	3828.8(4)	4170.5 (2)	4248.9(4)
$D_{calcd.}$ [g cm^{-1}]	1.292	1.266	1.464	1.150
μ [cm^{-1}]	0.360	0.598	0.245	0.242
Z	4	4	4	2
No. of measd. reflns.	6263	13401	9865	18165
No. of reflns. [$I > 2\sigma(I)$]	4717	7095	5384	6917
R_1 [$I > 2\sigma(I)$]	0.0473	0.0906	0.0737	0.0770
wR_2 [$I > 2\sigma(I)$]	0.1257	0.2425	0.1549	0.1551
GOF	1.033	1.005	0.992	0.935

 © 2005 Wiley-VCH Verlag GmbH & Co. KGaA, Weinheim

Lig^{2}H$_2$: A solution of 2-methylsalicylaldehyde (0.95 g, 7.1 mmol) and 1,2 phenylenediamine (0.38 g, 3.5 mmol) in 30 mL of methanol was placed in a 100 mL round-bottomed flask equipped with a magnetic stir-bar and a reflux condenser. The resulting bright yellow solution was heated to reflux for 2 h. Upon cooling to room temp. an orange crystalline solid had formed. The solid was collected by vacuum filtration, and identified by ^{1}H NMR as a Salophen intermediate. The orange intermediate product was suspended in 60 mL of methanol, and ca. 5 equiv. of sodium borohydride were added. The reaction mixture became entirely homogeneous and colorless. The solution was poured into 100 mL of water, and the resulting white solid was isolated by vacuum filtration, and dried under vacuum. The yield of Lig^{2}H$_2$ was 0.49 g (40%). $C_{22}H_{24}N_2O_2$ (348.44): calcd. C 75.83, H 6.94, N 8.04; found C 75.81, H 6.92, N 8.18. ^{1}H NMR (200 MHz, $CDCl_3$): δ = 8.21 (s, 2 H, O–*H*), 7.09 (d, $^3J_{H,H}$ = 7.6 Hz, 2 H), 7.04 (d, $^3J_{H,H}$ = 7.6 Hz, 2 H), 6.94 (s, 4 H), 6.79 (t, $^3J_{H,H}$ = 7.5 Hz, 2 H), 4.38 (d, $^3J_{H,H}$ = 5.4 Hz, 4 H), 3.66 (t, $^3J_{H,H}$ = 5.2 Hz, 2 H), 2.21 (s, 6 H) ppm. ^{13}C NMR (50.29 MHz, $CDCl_3$): δ = 154.8 (*C*), 136.8 (*C*), 130.8 (*C*H), 126.9 (*C*H), 125.4 (*C*), 122.1 (*C*), 121.8 (*C*H), 119.9 (*C*H), 114.4 (*C*H), 48.2 (CH_2), 15.8 (CH_3) ppm.

Lig^{3}H$_2$: 2,4-Dichlorosalicylaldehyde (4.92 g, 26 mmol) was dissolved in ca. 30 mL of methanol and added dropwise to a stirred suspension of 1,2-phenylenediamine (1.41 g, 13 mmol) in 20 mL of methanol. The reaction color changed immediately, and the deep-orange Salophen intermediate crystallized out. The reaction mixture was allowed to stand for 20 min. Sodium borohydride (3 equiv., 2.78 g) was added in small portions to the vigorously stirred heterogeneous mixture. The resulting homogeneous bright yellow solution was poured into 100 mL of water, and extracted with two 50 mL portions of dichloromethane. The combined (yellow) organic phase was dried with anhydrous magnesium sulfate, filtered, and the solvent was removed. The resulting yellow solid was dried under vacuum at 50 °C for 2 h, yielding 3.22 g of pure Lig^{3}H$_2$ (54% yield). $C_{20}H_{16}Cl_4N_2O_2{\cdot}H_2O$ (476.18): calcd. C 50.45, H 3.81, N 5.88; found C 50.74, H 3.55, N 5.95. ^{1}H NMR (200 MHz, $CDCl_3$): δ = 7.28 (d, $^4J_{H,H}$ = 2.5 Hz, 2 H), 7.14 (d, $^4J_{H,H}$ = 2.4 Hz, 2 H), 6.90 (m, 2 H), 6.79 (m, 2 H), 4.37 (s, 4 H) ppm. ^{13}C NMR (50.29 MHz, $CDCl_3$): δ = 150.0 (*C*), 136.5 (*C*), 128.4 (*C*H), 127.7 (*C*H), 126.6 (*C*), 125.2 (*C*), 121.6 (*C*H), 121.4 (*C*), 114.4 (*C*H), 46.4 (CH_2) ppm.

Lig^{4}H$_2$: A homogeneous bright yellow solution of 3.98 g (17 mmol) of 2,4-di-*tert*-butylsalicylaldehyde and 0.89 g (8.5 mmol) of 1,2 phenylenediamine in 50 mL of methanol was heated to reflux in a 100 mL round-bottomed flask equipped with a magnetic stir-bar and a reflux condenser for 2 h, and then left at room temp. overnight. The orange solid that had formed was collected by vacuum filtration, and identified by ^{1}H NMR as a Salophen intermediate. The yield was 1.54 g (33%). The orange intermediate product was suspended in 60 mL of methanol, and ca. 10 equiv. of sodium borohydride were added, and the reaction mixture was stirred overnight. After hydrolysis, the bright-yellow solid was isolated by vacuum filtration. According to ^{1}H NMR, the solid contained at least two different products. The solid was washed several times with methanol, yielding the insoluble Lig^{4}H$_2$. Alternatively, Lig^{4}H$_2$ could be isolated by flash chromatography, using chloroform as an eluent; however, in this case the yield was lower. Drying under vacuum for 2 h at 100 °C, yielded 0.5 g of Lig^{4}H$_2$ (34% relative to the corresponding Salophen). $C_{36}H_{52}N_2O_2{\cdot}0.5\,H_2O$ (553.82): calcd. C 78.07, H 9.65, N 5.06; found C 78.43, H 9.67, N 5.12. ^{1}H NMR (200 MHz, $CDCl_3$): δ = 7.98 (s, 2 H), 7.26 (d, $^4J_{H,H}$ = 2.2 Hz, 2 H), 7.04 (d, $^4J_{H,H}$ = 2.2 Hz, 2 H), 6.97 (s, 4 H), 4.35 (d, $^3J_{H,H}$ = 5.9 Hz, 4 H), 3.57 (t, $^3J_{H,H}$ = 5.9 Hz, 2 H), 1.37 (s, 18 H), 1.28 (s, 18 H) ppm. ^{13}C NMR (50.29 MHz, $CDCl_3$): δ = 153.3 (*C*), 142.0 (*C*), 136.9 (*C*), 136.4 (*C*), 124.2 (*C*H), 124.0 (*C*H), 122.3 (*C*), 121.9 (*C*H), 114.6 (*C*H), 49.0 (CH_2), 35.1 (*C*), 34.4 (*C*), 31.8 (CH_3), 29.9 (CH_3) ppm.

2-Zr: 80 mg (0.17 mmol) of Lig^{2}H$_2$ was treated with 67 mg (0.17 mmol) of Zr(O*t*Bu)$_4$. The resulting white solid was washed with a small volume of pentane. The yield was 105 mg (0.15 mmol, 89%). $C_{30}H_{40}N_2O_4Zr$ (583.87): calcd. C 61.71, H 6.91, N 4.80; found C 61.72, H 6.85, N 4.85. ^{1}H NMR (200 MHz, C_6D_6): δ = 7.00 (t, $^3J_{H,H}$ = 4.6 Hz, 2 H), 6.54 (m, 2 H), 6.44 (d, $^3J_{H,H}$ = 4.7 Hz, 2 H), 6.30 (m, 2 H), 4.69 (d, $^2J_{H,H}$ = 11.9 Hz, 2 H), 3.58 (br. s, 2 H), 3.46 (dd, $^2J_{1,H-H}$ = 12.2, $^3J_{2,H-H}$ = 4.0 Hz, 2 H), 2.33 (s, 6 H), 1.51 (s, 18 H) ppm. ^{13}C NMR (50.29 MHz, C_6D_6): δ = 161.3 (*C*), 141.3 (*C*), 131.3 (CH), 128.4 (*C*H), 127.3 (*C*H), 126.6 (*C*), 125.7 (*C*H), 122.1 (*C*)116.8 (*C*H), 75.5 (*C*), 53.5 (CH_2), 33.3 (CH_3), 16.9 (CH_3) ppm.

3-Zr: 69 mg (0.15 mmol) of Lig^{3}H$_2$ was treated with 58 mg (0.15 mmol) of Zr(O*t*Bu)$_4$. The yield was 105 mg (0.15 mmol, 100%). X-ray quality crystals were obtained upon recrystallization from a minimal volume of pentane at –30 °C. $C_{28}H_{32}N_2O_4Cl_4Zr$ (693.60): calcd. C 48.49, H 4.65, N 4.04; found C 48.61, H 4.79, N 3.97. ^{1}H NMR (200 MHz, C_6D_6): δ = 7.07 (d, $^4J_{H,H}$ = 2.6 Hz, 2 H), 6.36 (m, 2 H), 6.29 (d, $^4J_{H,H}$ = 2.6 Hz, 2 H), 6.02 (m, 2 H), 4.65 (d, $^2J_{H,H}$ = 12.8 Hz, 2 H), 3.58 (br. s, 2 H), 3.10 (dd, $^2J_{H,H}$ = 12.9, $^3J_{H,H}$ = 3.5 Hz, 2 H), 1.57 (s, 18 H) ppm. ^{13}C NMR (50.29 MHz, $CDCl_3$): δ = 156.9 (*C*), 139.8 (*C*), 129.7 (*C*H), 128.9 (*C*H), 128.2 (*C*H), 126.2 (*C*H), 124.9 (*C*), 123.7 (*C*), 120.9 (*C*), 76.8 (*C*), 52.9 (CH_2), 33.0 (CH_3) ppm.

4-Zr: Lig^{4}H$_2$ (63 mg, 0.12 mmol) was treated with Zr(O*t*Bu)$_4$ (53 mg, 0.13 mmol). The yield was 83 mg (0.11 mmol, 89%). $C_{44}H_{68}N_2O_4Zr$ (780.25): calcd. C 67.73, H 8.78, N 3.59; found C 67.67, H 8.91, N 3.71. ^{1}H NMR (200 MHz, C_6D_6): δ = 7.30 (d, $^4J_{H,H}$ = 2.5 Hz, 2 H), 6.46 (m, 4 H), 6.36 (m, 2 H), 4.94 (d, $^2J_{H,H}$ = 12.3 Hz, 2 H), 3.73 (br. s, 2 H, N–H), 3.46 (dd, $^2J_{H,H}$ = 12.3, $^4J_{H,H}$ = 3.2 Hz, 2 H), 1.72 (s, 18 H), 1.55 (s, 18 H), 1.17 (s, 18 H) ppm. ^{13}C NMR (50.29 MHz, C_6D_6): δ = 159.0 (*C*), 141.2 (*C*), 138.3 (*C*), 136.3 (*C*), 127.1 (*C*H), 126.4 (*C*H), 126.1 (*C*H), 123.4 (*C*H), 122.7 (*C*), 75.7 (*C*), 54.3 (CH_2), 35.5 (*C*), 34.1 (*C*), 33.5 (CH_3), 31.9 (CH_3), 30.1 (CH_3) ppm.

3-Ti: Lig^{3}H$_2$ (45 mg, 0.10 mmol) was treated with Ti(O*i*Pr)$_4$ (28 mg, 0.10 mmol). The yield was 60 mg (0.10 mmol, 100%). $C_{26}H_{28}N_2O_4Cl_4Ti$ (622.19): calcd. C 50.19, H 4.54, N 4.50; found C 50.59, H 4.61, N 4.51. ^{1}H NMR (200 MHz, C_6D_6): δ = 7.10 (d, $^4J_{H,H}$ = 2.6 Hz, 2 H), 6.39 (m, 2 H), 6.34 (d, $^4J_{H,H}$ = 2.6 Hz, 2 H), 6.13 (m, 2 H), 5.29 (s, $^3J_{H,H}$ = 6.1 Hz, 2 H), 4.66 (br. d, $^2J_{H,H}$ = 12.9 Hz, 2 H), 3.78 (br. s, 2 H), 3.13 (dd, $^2J_{1,\ H-H}$ = 13.2, $^3J_{2,\ H-H}$ = 1.9 Hz, 2 H), 1.51 (d, $^3J_{H,H}$ = 6.2 Hz, 6 H), 1.43 (d, $^3J_{H,H}$ = 6.2 Hz, 6 H) ppm. ^{13}C NMR (50.29 MHz, C_6D_6): δ = 158.4 (*C*), 141.0 (*C*), 130.1 (*C*H), 129.1 (*C*H), 129.0 (*C*H), 128.8 (*C*), 126.2 (*C*H), 125.9 (*C*), 123.5 (*C*), 122.0 (*C*), 79.9 (*C*H), 53.7 (CH_2), 26.9 (CH_3), 26.8 (CH_3) ppm.

4-Ti: Lig^{4}H$_2$ (47 mg, 0.09 mmol) was treated with Ti(O*i*Pr)$_4$ (24 mg, 0.09 mmol). The yield was 63 mg (0.09 mmol, 100%). Recrystallization from pentane (ca. 1 mL) afforded yellow-orange crystals of X-ray quality. $C_{44}H_{68}N_2O_4Ti$ (708.84): calcd. C 71.17, H 9.10, N 3.95; found C 71.42, H 9.14, N 3.96. (400 MHz, C_6D_6): δ = 7.31 (d, $^4J_{H,H}$ = 2.5 Hz, 2 H), 6.55 (d, $^4J_{H,H}$ = 2.4 Hz, 2 H), 6.48 (s, 4 H), 5.03 (s, $^3J_{H,H}$ = 6.1 Hz, 2 H) 4.79 (dd, $^2J_{H,H}$ = 12.5, $^3J_{H,H}$ = 1.2 Hz, 2 H), 4.00 (br. s, 2 H), 3.51 (dd, $^2J_{H,H}$ = 12.6, $^3J_{H,H}$

 © 2005 Wiley-VCH Verlag GmbH & Co. KGaA, Weinheim

= 2.8 Hz, 2 H), 1.74 (s, 18 H), 1.49 (d, $^3J_{H,H}$ = 6.0 Hz, 6 H), 1.39 (d, ^3J = 6.1 Hz, 6 H), 1.17 (s, 18 H) ppm. ^{13}C NMR (50.29 MHz, C_6D_6): δ = 160.1 (C), 142.1 (C), 138.9 (C), 135.9 (C), 127.1 (CH), 125.6 (CH), 125.4 (CH), 123.1 (CH), 123.1 (C), 77.4 ($CH(CH_3)_2$), 54.3 (CH_2), 35.4 (C), 34.1 (C), 31.9 ($CH(CH_3)_3$), 30.2 ($CH(CH_3)_3$), 26.9 ($CH(CH_3)_2$), 26.5 ($CH(CH_3)_2$) ppm.

4-Ti-a: Lig^{4}H$_2$ (84 mg, 0.15 mmol) was treated with Ti(O*i*Pr)$_4$ (43 mg, 0.15 mmol) . The solvent was removed, and the crude product was re-dissolved in deuteriobenzene and kept outside the glovebox in a paraffin-sealed capped vial. After two days, bright-yellow crystals had formed. The crystals were separated from the solution, washed with cold ether and dried in vacuo to give 23 mg of **4Ti-a** (23% yield). ^{1}H NMR (400 MHz, C_6D_6): δ = 9.66 (s, 1 H, N–*H*), 7.37 (d, $^4J_{H,H}$ = 2.4 Hz, 1 H), 7.34 (d, $^3J_{H,H}$ = 7.84 Hz, 1 H), 7.21 (d, $^4J_{H,H}$ = 2.4 Hz, 1 H), 6.96 (t, $^3J_{H,H}$ = 7.8 Hz, 1 H), 6.77 (d, $^4J_{H,H}$ = 2.4 Hz, 2 H), 6.60 (t, $^3J_{H,H}$ = 7.8 Hz, 1 H), 6.34 (d, $^3J_{H,H}$ = 7.8 Hz, 1 H), 5.30 (s, $^3J_{H,H}$ = 5.9 Hz, 1 H, $(CH_3)_2CH$), 4.90 (d, $^2J_{H,H}$ = 12.5 Hz, 1 H), 4.60 (t, $J_{H,H}$ = 13.0 Hz, 1 H), 4.20 (dd, $^2J_{H,H}$ = 12.7, $^3J_{H,H}$ = 2.2 Hz, 1 H), 3.58 (d, $^3J_{H,H}$ = 13.2 Hz, 1 H, N–*H*), 3.54 (d, $^2J_{H,H}$ = 13.4 Hz, 1 H), 1.87 (d, $^3J_{H,H}$ = 6.0 Hz, 3 H, $(CH_3)_2CH$), 1.42 (m, 12 H), 1.38 (s, 9 H), 1.34 (s, 9 H), 1.20 (s, 9 H) ppm. ^{13}C NMR (100.58 MHz, C_6D_6): δ = 160.2, 159.6, 144.4, 142.8, 139.98, 138.7, 135.8, 135.5, 128.2, 128.0, 126.6, 125.9, 125.4, 124.8, 124.4, 123.9, 123.3, 123.3, 74.9, 55.9, 55.1, 35.4, 35.3, 34.4, 34.2, 32.1, 31.9, 30.2, 29.9, 27.8, 27.7 ppm.

CCDC-266239 to -266242 (for complexes **3**-Zr, **4**-Ti, **4**-Ti-a, and **2**-Ti, respectively) contain the supplementary crystallographic data for this paper. These data can be obtained free of charge from The Cambridge Crystallographic Data Centre via www.ccdc.cam.ac.uk/data_request/cif.

Acknowledgments

We thank the Israel Science Foundation for financial support.

[1] a) P. Subramanian, J. T. Spence, R. Ortega, J. H. Enemark, *Inorg. Chem.* **1984**, *28*, 2564; b) C. J. Hinshaw, G. Peng, R. Singh, J. T. Spence, J. H. Enemark, M. Bruck, J. Kristofzski, S. L. Merbs, R. B. Ortega, P. A. Wexler, *Inorg. Chem.* **1989**, *28*, 4483.
[2] a) E. Y. Tshuva, I. Goldberg, M. Kol, *J. Am. Chem. Soc.* **2000**, *122*, 10706; b) S. Segal, I. Goldberg, M. Kol, *Organometallics* **2004**, *24*, 200.
[3] J. Balsells, P. Carroll, P. J. Walsh, *Inorg. Chem.* **2001**, *40*, 5568.
[4] R. García-Zarracino, J. Ramos-Quiñones, H. Höpfl, *J. Organomet. Chem.* **2002**, *664*, 188.
[5] V. Busico, R. Cipullo, V. Romanelli, S. Ronca, M. Togrou, *J. Am. Chem. Soc.* **2005**, *127*, 1608.
[6] T. Katsuki, *Adv. Synth. Catal.* **2002**, *344*, 131.
[7] A. Yeori, S. Gendler, S. Groysman, I. Goldberg, M. Kol, *Inorg. Chem. Commun.* **2004**, *7*, 280.
[8] a) D. A. Atwood, D. Rutherford, *Organometallics* **1995**, *14*, 2880; b) D. A. Atwood, D. Rutherford, *Organometallics* **1995**, *14*, 3988; c) D. A. Atwood, D. Rutherford, *Organometallics* **1996**, *15*, 4763; d) A. L. Singer, D. A. Atwood, *Inorg. Chim. Acta* **1998**, *277*, 157.
[9] S. F. Gheller, T. W. Hambley, M. R. Snow, K. S. Murray, A. G. Wedd, *Aust. J. Chem.* **1984**, *37*, 911.
[10] A. Altomare, G. Cascarano, C. Giacovazzo, A. Guagliardi, M. C. Burla, G. Polidori, M. Camali, *J. Appl. Crystalogr.* **1994**, *27*, 435.
[11] G. M. Sheldrick, *SHELXL-97 Program*, University of Göttingen, Germany, **1996**.

Received: March 20, 2005

 © 2005 Wiley-VCH Verlag GmbH & Co. KGaA, Weinheim

NMR T_1-Relaxation Measurements on Paramagnetic Organolanthanides: An Alternative Tool for Structure Determination in Solution

Laurent Brachais[a] and Marc Visseaux*[a,b]

Keywords: Spin-lattice relaxation times / Paramagnetic complexes / Lanthanides / NMR spectroscopy

^{1}H NMR investigations were conducted on four paramagnetic organolanthanides, all bearing the tetraisopropylcyclopentadienyl ligand Cp^{4i} (HC_5iPr_4) in order to verify whether or not interactions observed in the solid state are maintained in solution. In some cases variable-temperature experiments were necessary to enhance the resolution and determine the best conditions for the study. The 1D NMR spectrum could be interpreted in every case. Complementary 2D COSY experiments allowed the full attribution of the signals. T_1 (^{1}H) relaxation values were determined for all the paramagnetic complexes at the most suitable temperature, and compared with those of the diamagnetic KCp^{4i}. The same tendency was observed, with particular features concerning the isopropyl groups. Among the four methyl groups, one exhibits a much higher T_1 value and one a much lower value; the two others are intermediate. This was interpreted as the result of a privileged conformation of the Cp^{4i} ligand: the two α-isopropyl groups take up a spatial orientation with one methyl group in the *exo* position, opposite to the metal atom, whereas the methyl groups of the two β-isopropyl groups are equidistant from the metal atom. Whatever the nature of the metal (Nd, Sm), the oxidation state (Sm^{II}, Sm^{III}) or the temperature (298, 363 K), this conformation is retained. The structure in solution seems to be different from that previously determined in the solid state.

(© Wiley-VCH Verlag GmbH & Co. KGaA, 69451 Weinheim, Germany, 2005)

Introduction

Organolanthanide complexes have recently received a growing interest, due in part to their use as catalysts for polymerisation.[1–4] Investigations of the catalytic mechanisms are conducted starting from their molecular structures usually computed from X-ray diffraction data. However, these data reflect a solid-state organisation that is often different from the solution structure involved during reactions.

We recently synthesised a series of complexes bearing the voluminous Cp^{4i} ligand (Cp^{4i} = HC_5iPr_4).[5,6] X-ray studies showed a particular behaviour for several of them: one methyl(Cp^{4i})–lanthanide interaction, possibly agostic, was observed in the X-ray structure of [Ln(Cp^{4i})$_2$(BH_4)] (Ln = Nd, Sm), as well as in divalent [Sm(Cp^{4i})$_2$], whereas [Ln(cot)Cp^{4i}] (cot = C_8H_8) displays an unusually short cot–metal distance. We also established that organolanthanides bearing this Cp^{4i} ligand afford highly *trans*-stereospecific catalysts toward isoprene polymerisation upon activation with BuLi,[6] which is in accordance with the steric hindrance around the metal atom.[7,8] Moreover, [Sm(Cp^{4i})$_2$] was found to be efficient for ε-caprolactone polymerisation, whereas it remained unsolvated in the presence of THF.[5] It was therefore of interest to study thoroughly the stereoelectronic environment of the metal atom in such complexes, and whether or not the interactions observed were maintained in solution, since molecular complexes of lanthanides often behave differently in solution with respect to the solid state.[9]

NMR spectroscopy is a powerful technique that can give additional information, and is thus a complement to X-ray diffraction for studying three-dimensional structures in solution.[10] NMR studies on organolanthanide compounds are still mainly restricted to the diamagnetic derivatives (La, Lu, Y, Sc),[11] while the best catalysts are obtained in the more paramagnetic neodymium and samarium series.[12–14] However, even if the results usually suffer from the loss of resolution of the spectra due to the intrinsic properties of the lanthanide atom, this paramagnetism is able to give some information concerning the complex geometry.[15,16] NMR spectroscopy of paramagnetic molecules has been widely studied and discussed, particularly in terms of chemical shifts,[17] and many lanthanide complexes are used as shift reagents. Paramagnetic metals are also involved in a large number of natural compounds, such as proteins, and their presence usually complicates the study of such compounds. Bertini and co-workers have recently reviewed the

[a] Laboratoire de Synthèse et Electrosynthèse Organométalliques – UMR 5188 CNRS, Université de Bourgogne,
B. P. 47870, 21078 Dijon, France
Fax: +33-3-8039-6084
E-mail: laurent.brachais@u-bourgogne.fr
[b] Present address: Laboratoire de Catalyse de Lille, UMR CNRS 8010, ENSCL
B. P. 108, 59652 Villeneuve d'Ascq Cedex, France
Fax: +33-3-2043-6585
E-mail: marc.visseaux@ensc-lille.fr

Table 1. Molecular complexes under study.

Complex[a]	Metal (ox. state)	Ligand 1 (charge)	Ligand 2 (charge)	Ligand 3 (charge)	Temperature for T_1 measurements [K]
KCp^{4i}	K (+I)	Cp^{4i} (–I)			298
$[Sm(cot)Cp^{4i}]$	Sm (+III)	Cp^{4i} (–I)	cot (–II)		298
$[Sm(Cp^{4i})_2(BH_4)]$	Sm (+III)	Cp^{4i} (–I)	Cp^{4i} (–I)	BH_4 (–I)	298/363
$[Nd(cot)Cp^{4i}]$	Nd (+III)	Cp^{4i} (–I)	cot (–II)		363
$[Sm(Cp^{4i})_2]$	Sm (+II)	Cp^{4i} (–I)	Cp^{4i} (–I)		373

[a] cot = C_8H_8, Cp^{4i} = HC_5iPr_4.

field of paramagnetic NMR spectroscopy of biological compounds.[18] It has been increasingly recognized that, besides contributing to line broadening, the electron–nucleus interactions contain useful structural information. Many of the relevant effects that the presence of paramagnetic metals has on the behaviour of the compound nuclei have to do with the metal's magnetic susceptibility. Most of these effects have been well known since the1950s and 1960s, but a few have been described more recently. Concerning lanthanide complexes, the effect of paramagnetism on the spin–lattice relaxation has been studied but mostly with coordination complexes in aqueous media.[19]

Different techniques have been found to calculate distances from T_1 relaxation rates.[20,21] These methods are, however, complicated to undertake due to the high number of parameters they involve. In particular, the comparison of T_1 values obtained for different compounds should be made at the condition of T_{1min}. This is an important problem in the case of paramagnetic compounds because the T_{1min} is usually only reached at low temperature, which induces an additional loss of resolution, and the poor resolution observed prevents the computation of T_1.

In the present study we compare the molecular structures of several organolanthanide complexes in solution, based on their paramagnetic ^1H NMR spectroscopic data. Moreover, we examine paramagnetic samarium and neodymium complexes to overturn the general idea that comprehensive NMR studies are not possible for compounds of these metals.

The choice of organometallic complexes, presented in Table 1, allows the study of different parameters and their influence on the structure. These parameters are: the metal, the oxidation state of the metal, the nature of the ligands (cot, Cp^{4i}), the solvent and the temperature.

Results and Discussion

Choice of Temperature and Signal Assignment

As a first approach, the temperature dependence of the chemical shifts of the complexes was studied. It is well known that paramagnetic organolanthanides display temperature-dependent NMR spectra with respect to both chemical shifts and resolution.[17]

The goal of this experiment was to determine the best temperature for T_1 measurement, i.e., the temperature at which the spectrum exhibits a good enough resolution with no signal overlaps. For most of the complexes this was reached near the highest temperature of the study, typically a few degrees below the solvent boiling point (near 363 K, Figure 1). This was particularly the case of the neodymium complex $[Nd(cot)Cp^{4i}]$ due to the strong paramagnetic character of this metal. In fact, this latter complex gives broad lines even at high temperature but it was possible to distinguish all signals with only two recovering lines, while at room temperature most of the lines could not be distinguished from the noise.

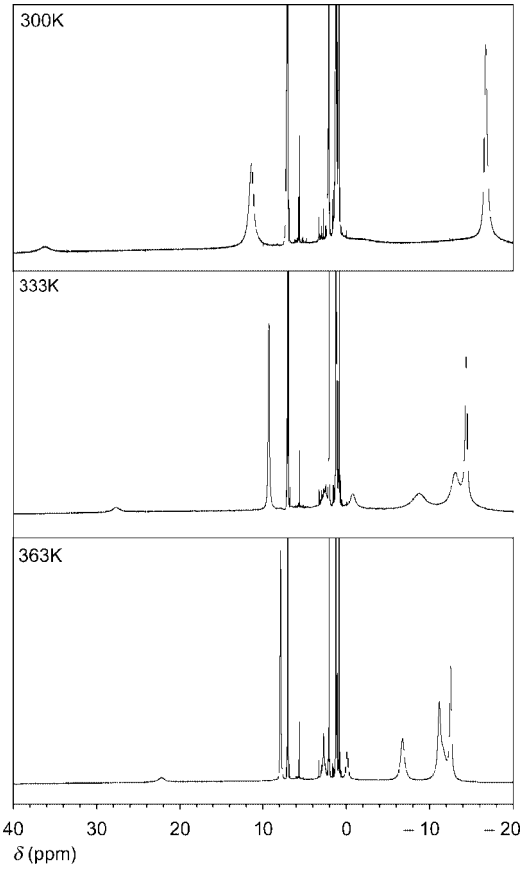

Figure 1. Evolution of the ^1H NMR spectrum of $[Nd(cot)Cp^{4i}]$ (in C_7D_8) with temperature.

After the temperature had been chosen, it was necessary to complete the assignment. Actually, whatever the complex, there are four non-equivalent methyl groups and two non-equivalent methyne groups all belonging to the four isopropyl groups attached to the Cp unit. This indicates that there are two different types of isopropyl groups. Ac-

 © 2005 Wiley-VCH Verlag GmbH & Co. KGaA, Weinheim

cording to the symmetry of the Cp^{4i} ligand, two equivalent isopropyl groups are located in an α-position to the Cp methyne group (HCp) and the second type is attributed to both isopropyl groups located in the β-position of the HCp group (Scheme 1).

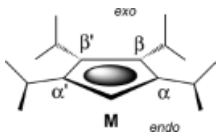

Scheme 1. Representation of the Cp^{4i} ligand showing the different types of isopropyl groups and the two different sides of the molecule when a metal atom is coordinated.

The presence of four non-equivalent methyl groups for two non-equivalent isopropyl groups means that both methyl groups belonging to the same isopropyl group are non-equivalent (Figure 2). This is explained by the presence of the metal atom located on one side of the Cp plane. Thus, there are two different Cp sides: one *endo* side and one *exo* side. Such a molecular arrangement obviously affords a diastereotopic system of methyl groups.[22,23]

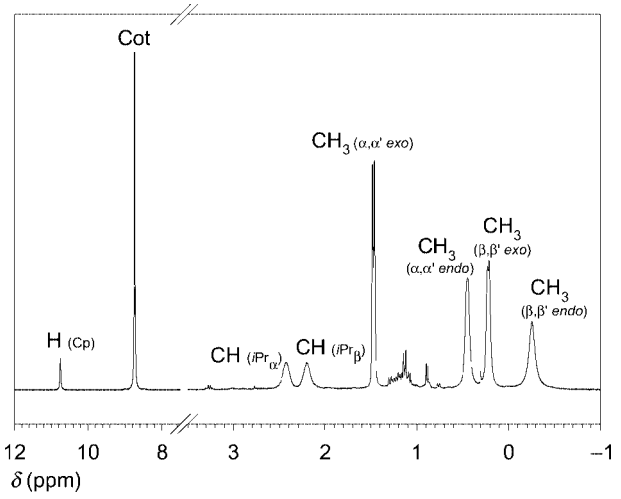

Figure 2. 500 MHz ^{1}H NMR spectrum and assignment of the complex [Sm(cot)Cp^{4i}] recorded at 298 K.

It is noteworthy that the spectrum of KCp^{4i} displays only signals of two types of methyl groups: one type corresponding to the α-isopropyl groups and the other one to the β-isopropyl groups. The geometry of this compound is different from that of the complexes under study as KCp^{4i} is an ionic compound, which means that the potassium ion is not linked to the Cp ring, as neodymium or samarium can be, and therefore *endo* and *exo* sides do not exist. The NMR spectrum can be explained in terms of symmetry if the potassium ion is not coordinated face-on to the Cp ring, with both sides becoming equivalent, or if it alternatively roams quickly from one side to the other in THF.[24] Finally, the methyl groups belonging to the same isopropyl group are enantiotopic in KCp^{4i}.

The next step in the assignment procedure was to connect methyl groups with methyne groups of the same isopropyl group. This was done with a 2D-COSY experiment, which gives correlations between coupled protons (Figure 3). For some complexes, like [Nd(cot)Cp^{4i}], no correlation could be observed due to the very fast relaxation occurring in this compound. As a matter of fact, the incremental delay placed in the 2D sequence to create the second dimension results in a complete relaxation of protons prior to the acquisition step and thus no signal could be detected. Assignment could be achieved for Sm complexes as well as for the potassium salt.

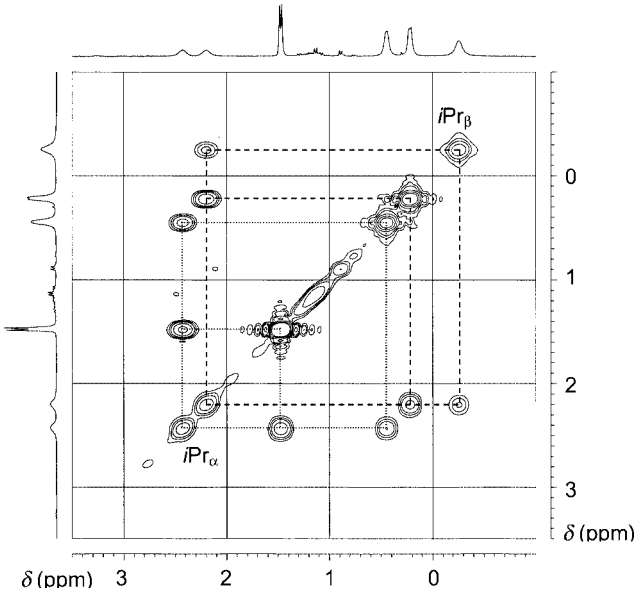

Figure 3. 2D COSY map of the complex [Sm(cot)Cp^{4i}] recorded at 298 K. Assignments of both types of isopropyl groups are shown.

Two uncertainties still remained at this stage of our studies, namely the identification of the α- and the β-isopropyl groups and the *exo*- and *endo*-methyl groups. The first problem was solved by performing an NOE-difference experiment in which the HCp signal was irradiated. We observed a significant variation of one H(*i*Pr) signal intensity, and this isopropyl group was thus assigned to the closest (α and α′) position. Such an experiment could not be conducted on all complexes due to fast relaxation but was unambiguous for [$Sm(BH_4)(Cp^{4i})_2$]. These results were further generalized to the other complexes. The identification of *endo* and *exo* groups was achieved by measuring T_1 values (see below).

Relaxation Study

The non-paramagnetic KCp^{4i} was first studied as a reference. As we remarked previously, the potassium cation does not generate the asymmetry at the Cp ring that is the origin of the *endo* and *exo* sides noticed in the other complexes. Moreover, the metal should have very little influence on the Cp^{4i} relaxation rates since it is not paramagnetic, in contrast with the other complexes under study. The relaxation times of KCp^{4i} are reported in Table 2. These values are similar to those usually observed for small organic molecules. The α- and β-methyne signals exhibit relaxation times

 © 2005 Wiley-VCH Verlag GmbH & Co. KGaA, Weinheim

Table 2. T_1 data [ms] of molecular complexes at 298 K.

Complex	H_{Cp}	CH_α	CH_β	CH_3 (α,α′-*exo*)	CH_3 (α,α′-*endo*)	CH_3 (β,β′-*exo*)	CH_3 (β,β′-*endo*)	cot/BH_4
[Sm(cot)Cp^{4i}]	53.4	212.8	236.4	515.5	208.8	303.0	227.8	73.7
[Sm(Cp^{4i})$_2$(BH_4)]	27.5	201.2	152.9	471.7	173.3	–[c]	217.4	3.6
[Sm(Cp^{4i})$_2$(BH_4)][a]	34.5	244.5	240.4	800.0	248.1	392.2	308.6	2.6
[Nd(cot)Cp^{4i}][a]	1.8	7.7	7.1	32.9	9.8	15.3	11.5	6.8
[Sm(Cp^{4i})$_2$][b]	11.4	37.1	–[c]	176.8	34.0	53.0	37.6	–
KCp^{4i}	4169	2775	2111	1605 (α,α′)		1839 (β,β′)		–

[a] Recorded at 363 K. [b] Recorded at 373 K. [c] Signal overlapped.

of 2.77 and 2.11 s, respectively, which are rather different. However, in such diamagnetic compounds dipolar relaxation is predominant over other relaxation processes, and this can explain the observed difference. The β-methyne protons feel the influence of methyl groups belonging to the same isopropyl group as well as that of methyl groups belonging to both neighbouring isopropyl groups. In the case of α-methyne protons, however, there is only one neighbouring isopropyl group, which induces a less efficient dipolar relaxation. The α- and β-methyl groups display relaxation times of 1.60 and 1.84 s, respectively; this small difference seems to be not very significant. The relaxation times measured for KCp^{4i} are of no structural interest but are interesting for comparison with those measured for paramagnetic complexes.

As expected, all paramagnetic complexes display relaxation times that are drastically smaller than those reported for KCp^{4i}. This decrease is due to the presence of the paramagnetic metal, although the distances between the protons and the metal atom may also have a strong influence.

Straight lines corresponding to relaxation of [Sm(cot)Cp^{4i}] protons are shown in Figure 4 as an example; the relaxation times of the different complexes under study are reported in Table 2.

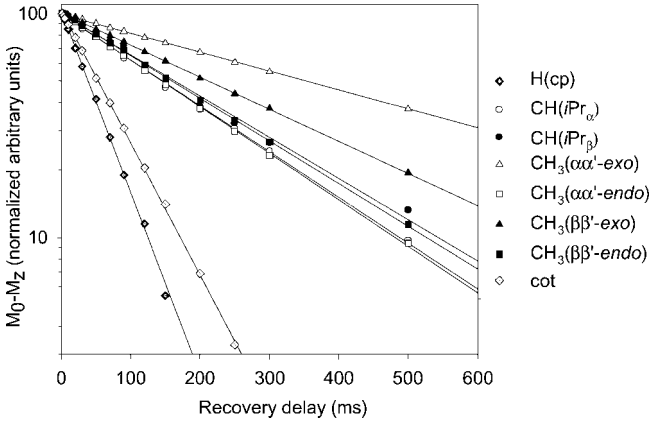

Figure 4. [Sm(cot)Cp^{4i}] T_1 (^{1}H) relaxation plots recorded at 298 K.

As regards to the variety of the complexes under study, the nature of the metal can be evaluated by comparing both [Sm(cot)Cp^{4i}] and [Nd(cot)Cp^{4i}]. Samarium complexes usually give ^{1}H NMR spectra that are better resolved than those corresponding to neodymium derivatives, which display spectra with very broad lines.[5,6,25] From this consideration, one would expect smaller T_1 values for neodymium than for samarium complexes; the T_1 values reported in Table 2 confirm this. As a matter of fact, [Nd(cot)Cp^{4i}] T_1 values are much smaller than those observed for [Sm(cot)Cp^{4i}]. The ratio T_1([Sm(cot)Cp^{4i}])/T_1([Nd(cot)Cp^{4i}]) has values of between 10, for the cot protons, and 30, for the isopropyl methyne groups. Nevertheless, it is noteworthy that in both complexes the same tendency in the T_1 distribution is observed: the HCp proton has the shortest T_1 relaxation in both compounds, followed by the cot protons. Such small HCp T_1 values were not observed for KCp^{4i}. Obviously, the diamagnetic character of the compound explains the larger T_1 values, but in the case of KCp^{4i} HCp exhibits the largest T_1 value. As explained previously, dipolar relaxation is the most important relaxation mechanism in KCp^{4i} and HCp is the most distant proton from the other ones, thus explaining the lack of efficiency in its relaxation mechanism. In the cases of both [Sm(cot)Cp^{4i}] and [Nd(cot)Cp^{4i}], paramagnetic relaxation dominates and the smaller HCp T_1 values, as compared to those of other nuclei, indicate that HCp is the nearest proton to the metal ion. This is valid for all complexes under study since they all display very small HCp T_1 values.

Other interesting T_1 values are those of the methyl groups. In all complexes T_1 values corresponding to the four non-equivalent types of methyl groups could be measured, leading each time to the same tendency: i) one value is much higher than the others; ii) two types of methyl groups have intermediate values of the same order; iii) the last type of methyl groups exhibits a T_1 value a little bit smaller than the intermediate value; iv) the methyl groups exhibiting the smallest and largest T_1 values belong to the same type of isopropyl groups located in the α-position to HCp, and thus methyl groups with intermediate T_1 values belong to isopropyl groups in the β-position to HCp.

These results give important information concerning the complexes' geometry. It seems that α-isopropyl groups take an orientation in which one methyl group is far from the paramagnetic centre while the other one is much closer to the metal atom. Taking into consideration that the metal atom is located beneath the Cp ring plane, this means that the α-isopropyl groups take an orientation in which one methyl group (with the largest T_1 value) is located on the *exo* side of the Cp ring plane while the other one (with the smallest T_1 value) is located on the *endo* side of this plane. This conformation most likely places the *exo*-methyl group in the plane perpendicular to the Cp ring. In this situation, this methyl group is located as far as possible from the para-

 © 2005 Wiley-VCH Verlag GmbH & Co. KGaA, Weinheim

magnetic centre. It is noteworthy, given the tetrahedral geometry of sp^3-carbon atoms, that in this case the *endo*-methyl groups are not as close as possible to the metal atom. Also, this conformation places the α-isopropyl methyne groups slightly on the *endo* side but not far from the Cp ring plane (Scheme 2). Thus, whereas the diastereotopic nature of the methyl groups does not give any information about possible free rotation of isopropyl groups on the basis of chemical shifts, the fact that such a T_1 difference can be observed for methyl groups belonging to the same isopropyl groups clearly indicates a tendency to hindered rotation.

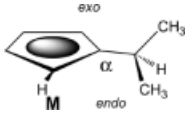

Scheme 2. Conformation of the α-isopropyl group, with one methyl group as far as possible from the metal atom.

We can see that β-isopropyl methyne groups have relaxation times close to those measured for α-methyne groups. If we consider that paramagnetic relaxation, and thus the proximity of the metal atom, is the predominant mechanism of relaxation, this indicates that α- and β-methyne groups are approximately at the same distance from the metal atom. Nevertheless, β-methyl groups adopt a quite different orientation from their α homologues, since they display relaxation times between both values observed for α-methyl groups. Moreover, the difference between both methyl groups belonging to the same β-isopropyl group is smaller than that measured between α-isopropyl methyl groups. This suggests an orientation of the β-isopropyl groups in which the methyl groups probably have positions not far from the plane of the Cp ring. According to the fact that the α-*endo*-methyl groups have the shortest relaxation time (as compared to other methyl groups), the β-methyl groups might be on the *exo* side due to their larger T_1 value (Scheme 3).

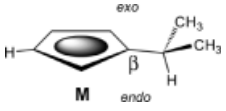

Scheme 3. Conformation of the β-isopropyl group, with the two methyl groups nearly equidistant to the metal atom.

All these structural considerations are valid for the complete series of paramagnetic complexes under study, whatever the metal or its oxidation state. A comparison of [Sm(cot)Cp^{4i}] and [Sm(Cp^{4i})$_2$(BH_4)] shows the influence that other ligands might have on the Cp^{4i} relaxation. In fact, replacing the cyclooctatetraenyl ligand by a borohydride and a second Cp^{4i} ligand induces a small decrease of the T_1 values. This indicates that if the general geometry of Cp^{4i} is the same, the distances between the metal atom and the Cp^{4i} ligand should be different in both complexes. Actually, the Sm–CP distances have been found to be 2.40 Å in [Sm(cot)Cp^{4i}][5] and 2.44 and 2.47 Å in [Sm(Cp^{4i})$_2$(BH_4)][6] (CP is the centroid of the Cp^{4i} ring). Although the distance is slightly shorter in the cot complex, the T_1 values are higher. However, the geometry of the two complexes is different: [Sm(cot)Cp^{4i}] is a metallocene of Sm^{III}, while [Sm(Cp^{4i})$_2$(BH_4)] bears one additional ligand.

X-ray diffraction analyses also indicate that [Sm(Cp^{4i})$_2$(BH_4)] exhibits one very short Sm–H(CH_3) distance (2.50 Å). This could be due to an agostic interaction. A similar feature, though less pronounced, has also been detected in other [Ln(cot)Cp^{4i}] complexes (Ln = Nd, Sm). According to our NMR experiments, it seems that such an interaction, which should lead to a much smaller T_1 value, is not retained in solution.

Changing the oxidation state of the metal also has important effects on the relaxation times. [Sm(Cp^{4i})$_2$] has a much lower relaxation time than [Sm(Cp^{4i})$_2$(BH_4)], while its Sm–CP distances are slightly longer, as expected for Sm^{II} (2.51 Å);[5] the more pronounced paramagnetism of Sm^{II} against Sm^{III} is responsible for the important decrease of the T_1 values.

As previously noticed, these changes do not influence the Cp geometry; the differences in relaxation times are undoubtedly due to the different electronic configurations of the metal to which the paramagnetism is strongly bound.

Finally, [Sm(Cp^{4i})$_2$(BH_4)] was submitted to T_1 measurements at two different temperatures (room and high temperature), while other complexes were generally studied at high temperature only due to the better resolution under these conditions. This was done mainly to verify that the geometry of the complexes does not change in the range 298–373 K. Obviously, some differences are to be expected when comparing T_1 values measured at both temperatures since temperature influences the motion of the complexes. However, whatever the temperature of the study, the same conclusions can be drawn concerning the [Sm]-Cp^{4i} geometry. The most probable conformation of the Cp^{4i} ligand in all the complexes under study is represented in Figure 5.

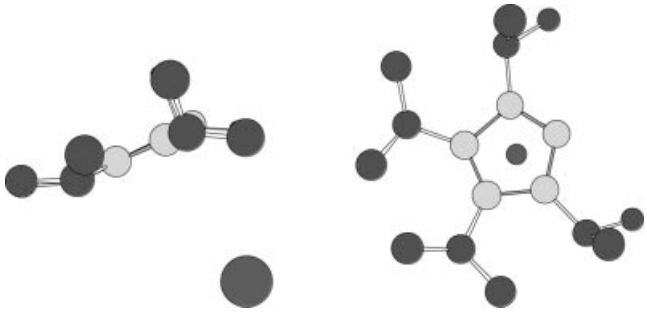

Figure 5. 3D representation of the [Cp^{4i}-Sm] moiety of [Sm(cot)-Cp^{4i}] orthogonally to the Cp ring (left) and in the Cp ring plane (right).

In order to validate our approach, Ln–H distances were calculated from T_1 data. It is well known that relaxation rates are proportional to $1/r^6$, where r can be considered as the metal–H distance, since paramagnetic relaxation is the dominant relaxation process.[21] Under our experimental conditions, only relative distances are easily accessible. For each complex under study, we took as reference the Ln–H(Cp) distance found in its X-ray structure. Among all Ln–

 © 2005 Wiley-VCH Verlag GmbH & Co. KGaA, Weinheim

Table 3. Metal–H distances [Å] (calculated from NMR T_1/determined from X-ray).

Complex	H_{Cp}[a]	CH_α	CH_β	CH_3 (α,α′-*exo*)	CH_3 (α,α′-*endo*)	CH_3 (β,β′-*exo*)	CH_3 (β,β′-*endo*)	cot/BH_4
[Sm(cot)Cp^{4i}]	3.19	4.02/3.87	4.09/3.95	4.65/5.39	4.00/4.11	4.26/5.39	4.06/3.82	3.37/3.29
[Sm(Cp^{4i})$_2$(BH_4)][b]	3.19	4.45/4.06	4.25/3.90	5.13/5.46	4.34/4.31	–/5.49	4.51/4.13	2.28/2.68
[Nd(cot)Cp^{4i}]	3.26	4.15/3.95	4.10/4.01	5.29/5.44	4.32/4.10	4.66/5.40	4.44/3.79	4.07/3.32
[Sm(Cp^{4i})$_2$]	3.27	3.98/3.92	–/4.04	5.16/5.49	3.92/4.20	4.22/5.43	3.99/3.76	–/–

[a] X-ray data, used as reference for NMR-computed distances. [b] From T_1 recorded at 363 K.

H distances, the latter is supposed to fluctuate the least from the solid state to the solution due to the rigid plane structure of the Cp ring. All other distances given in Table 3 were calculated from this reference. One can see that the computed distances fit quite well with those determined from X-ray studies. As expected, a significant difference is found between *endo*- and *exo*-CH_3αα′. On the other hand, whereas in the solid state the Cp^{4i} ligand displays *endo*- and *exo*-CH_3ββ′, this seems to be no longer the case in solution. The Ln–H(CH_3ββ′) distances take values that are quite similar, which corresponds well to methyl groups both located close to the plane of the Cp ring.

Conclusions

Structural information for four paramagnetic organolanthanides has been deduced by ^{1}H NMR spectroscopy. Despite the paramagnetism, the molecular conformation of the hyperbulky tetraisopropylcyclopentadienyl ligand involved in these complexes was fully resolved from 1D, 2D COSY and T_1 relaxation experiments.

The specific conformation is retained at high temperature, whatever the other surrounding ligands and the nature (neodymium or samarium) and the oxidation state (divalent or trivalent) of the lanthanide atom. The molecular structure in solution differs from that previously observed in the solid state. Such a conclusion can be drawn thanks to T_1 relaxation experiments.

This contribution shows that structural features may not be retained in solution in the case of the bigger early lanthanides, and this should be taken into consideration when performing mechanistic studies. Finally, the paramagnetism of lanthanide complexes does not necessarily preclude extensive NMR investigations for the determination of their conformation in solution.

Experimental Section

General Remarks: All complexes were prepared as published.[5,6] The potassium derivative KCp^{4i} was obtained by the classical reaction of KH with HCp^{4i} in THF. All samples were dissolved in [D_8]-toluene previously dried with Na/K alloy. Toluene was chosen as solvent due to its higher boiling point than benzene. Toluene transfer was performed by vacuum distillation into NMR tubes equipped with a Teflon valve (Young). After transfer, samples were stored under argon pressure. For KCp^{4i} [D_8]THF was used as solvent due to its poor solubility in toluene or benzene. All NMR experiments were recorded with a Bruker Avance 500 spectrometer working at a field of 11 T. Initially, several spectra were recorded as a function of temperature in order to determine the best conditions for the relaxation-time measurements. The highest resolution, and thus the best conditions, were usually reached at 363 or 373 K, depending on the nature of the complex. Assignment of the proton signals was performed with a 2D COSY experiment. The classical sequence using magnitude correction was used. No gradients were used for the complexes containing a paramagnetic metal because the additional delays involved in the pulse sequence result in a complete loss of magnetisation due to the very short relaxation time of the compounds under study. A gradient field 2D-COSY pulse sequence was used for the only non-paramagnetic complex (KCp^{4i}). In this case, the *Z*-gradient powers were set to 10% while the gradient pulse and the delay for gradient recovery were 1 ms and 100 μs, respectively. In order to complete the assignment of the *exo* and *endo* substituents, a 1D NOE-difference experiment was performed; the HCp signal was irradiated to indicate the closest α-and α′-isopropyl groups. Pulse lengths were calibrated prior to each relaxation-time measurement. Typically, the 90° proton pulse was 5.6 μs at an attenuation of 0 dB. T_1 measurements were performed by using the conventional inversion recovery technique. Several experiments of 256 scans were recorded with 20 different durations between the 180° and the 90° pulses. These experiments were recorded in a random order of the durations to minimize errors due to adjustment drifts occurring as a function of the time. The delay between each scan was chosen to be much larger than five times T_1. After Fourier transformation, the intensities of the different signals were collected and the curves $\ln(M_0 - M_Z)$ were drawn as a function of the delay between the 180° and the 90° pulses. The constant M_0 was evaluated by averaging two experiments involving long delays much larger than five times the T_1. The slopes of the obtained straight lines were then computed and led thus to the T_1 values, which are known to be the opposite reverse of the slopes ($-1/T_1$).

Acknowledgments

The authors wish to thank Prof. H. Sitzmann for a gift of the Cp^{4i} ligand and Prof. A. Dormond and Dr. D. Barbier-Baudry for helpful discussions.

[1] P. L. Watson, G. W. Parshall, *Acc. Chem. Res.* **1985**, *18*, 51–56.
[2] H. Yasuda, *J. Organomet. Chem.* **2002**, *647*, 128–138.
[3] G. G. Hlatky, *Coord. Chem. Rev.* **2000**, *199*, 235–329.
[4] Z. Hou, Y. Wakatsuki, *J. Organomet. Chem.* **2002**, *647*, 61–70.
[5] M. Visseaux, D. Barbier-Baudry, O. Blacque, A. Hafid, P. Richard, F. Weber, *New J. Chem.* **2000**, *24*, 939–942.
[6] D. Barbier-Baudry, O. Blacque, A. Hafid, A. Nyassi, H. Sitzmann, M. Visseaux, *Eur. J. Inorg. Chem.* **2000**, 2333–2336.
[7] S. Kaita, N. Koga, Z. Hou, Y. Doi, Y. Wakatsuki, *Organometallics* **2003**, *22*, 3077–3082.
[8] F. Bonnet, M. Visseaux, A. Pereira, F. Bouyer, D. Barbier-Baudry, *Macromol. Rapid Commun.* **2004**, *25*, 873–877.

 © 2005 Wiley-VCH Verlag GmbH & Co. KGaA, Weinheim

[9] W. J. Evans, D. G. Giarikos, J. W. Ziller, *Organometallics* **2001**, *20*, 5751–5758.
[10] V. I. Bakhmutov, M. Visseaux, D. Baudry, A. Dormond, P. Richard, *Inorg. Chem.* **1996**, *35*, 7316–7324.
[11] S. Arndt, J. Okuda, *Chem. Rev.* **2002**, *102*, 1953–1976.
[12] F. Bonnet, M. Visseaux, D. Barbier-Baudry, E. Vigier, M. M. Kubicki, *Chem. Eur. J.* **2004**, *10*, 2428–2434.
[13] Z. Hou, Y. Wakatsuki, *Coord. Chem. Rev.* **2002**, *231*, 1–22.
[14] Z. Shen, *Inorg. Chim. Acta* **1987**, *140*, 7–14.
[15] A. Steudel, E. Siebel, R. D. Fischer, G. Paolucci, V. Lucchini, *J. Organomet. Chem.* **1998**, *556*, 229–238.
[16] M. Visseaux, D. Baudry, A. Dormond, C. T. Qian, *C. R. Acad. Sci. Paris* **1996**, *323*, 415–419.
[17] J. P. Jesson, in *NMR of Paramagnetic Molecules: Principles and Applications* (Eds.: G. N. La Mar, W. D. Horrocks, Jr., R. H. Holm), Academic Press, New York, **1973**.
[18] I. Bertini, C. Luchinat, M. Piccioli, *Methods Enzymol.* **2001**, *339*, 314–340.
[19] S. Aime, L. Barbero, M. Botta, G. Ermondi, *J. Chem. Soc., Dalton Trans.* **1992**, *2*, 225–228.
[20] V. L. Bakhmutov, E. V. Vorontsov, G. I. Nikonov, D. A. Lemenovskii, *Inorg. Chem.* **1998**, *37*, 279–282.
[21] P. J. Desrosiers, L. Cai, Z. Lin, R. Richards, J. Halpern, *J. Am. Chem. Soc.* **1991**, *113*, 4173–4184.
[22] G. Devriese, R. Ottinger, D. Zimmermann, J. Reisse, K. Mislow, *Bull. Soc. Chim. Belg.* **1976**, *85*, 167–178.
[23] M. J. McGlinchey, *Can. J. Chem.* **2001**, *79*, 1295–1309.
[24] H. Günther, in: *La Spectroscopie de RMN*, Masson, Paris, **1994**, pp. 366.
[25] D. Barbier-Baudry, S. Heiner, M. M. Kubicki, E. Vigier, M. Visseaux, A. Hafid, *Organometallics* **2001**, *20*, 4207–4210.

Received: July 19, 2004

 © 2005 Wiley-VCH Verlag GmbH & Co. KGaA, Weinheim

The First X-ray Characterized Monosubstituted Ferrocenyl Azacrown Chalcone: Focus on Its Calcium Interaction/Electrochemical Detection Studies

Béatrice Delavaux-Nicot,*[a] Jérôme Maynadié,[a] Dominique Lavabre,[b] Christine Lepetit,[a] and Bruno Donnadieu[a,c]

Keywords: Calcium / Cations / Crown compounds / Ferrocene / Sensors

The first X-ray characterization of an azacrown ferrocenyl chalcone [$(C_5H_5)Fe(C_5H_4COCH{=}CHC_6H_4$-*p*-aza-15-crown-5)] (**2**) is reported. Its cation electrochemical detection capabilities have been evaluated and its behaviour towards protonation and calcium addition has been thoroughly examined. The uncommon ligand–Ca^{2+} interaction process involves three species of different stoichiometry in equilibrium in solution. Their association constants have been calculated. These species are formed by interaction of calcium with both the azacrown and CO functions of compound **2**, as evidenced by NMR and IR spectroscopy. The theoretical MESP analysis also suggests that, contrary to its *N*-ethyl-substituted homologue [$(C_5H_5)Fe(C_5H_4COCH{=}CHC_6H_4NEt_2)$] (**1a**), both coordination sites of **2** are involved in this interaction process. The study highlights that the CO group of **2** improves the selectivity of the cation electrochemical detection when compared to the known compound [$(C_5H_5)Fe(C_5H_4$-$CH{=}CHC_6H_4$-*p*-aza-15-crown-5)].
(© Wiley-VCH Verlag GmbH & Co. KGaA, 69451 Weinheim, Germany, 2005)

Introduction

Although a plethora of redox-active or fluorescent molecules have proved their usefulness as ion sensors,[1] ferrocenyl receptors that contain two types of signaling units, i.e. electroactive and fluorescent, are rare.[2] They could be the keystone of new families of ion chemo-sensors that can either sense different guests or display two or more macroscopic observable events upon addition of a certain analyte.[2c,3a] The fabrication of these systems and their integration into different supports (e.g. electronically conducting polymeric supports and optical fiber) would lead to novel prototype molecular sensory devices for commercial use.[1b,2a]

Recently, we have investigated the synthesis of electroactive receptors that combine a ferrocenyl unit and a purely organic fluorescent ion sensor subunit containing an R-amino complexing moiety (-$COCH{=}CHC_6H_4$-*p*-R):[2b] In particular, the disubstituted compound [$Fe(C_5H_4$-$COCH{=}CHC_6H_4NEt_2)_2$] behaves as a new type of multiresponsive calcium-sensing device in CH_3CN.[4] Its monosubstituted counterpart [$(C_5H_5)Fe(C_5H_4COCH{=}CHC_6H_4$-$NEt_2)$] (**1a**) is not fluorescent. However, interposition of the conjugated -$COCH{=}CHC_6H_4$- spacer between the ferrocene unit and the NEt_2 ionophore in this compound allows an electronic communication through the link.[2b] This important property suggests that molecules containing this fluorescent organic fragment could be electrochemical sensors. Other research teams have also shown a great deal of interest in the studies of related compounds (analogs of **1a**) incorporating a CO function directly linked to a ferrocenyl moiety,[5] and tested these compounds in applications such antimalarial activity[6] or as potential anticancer drugs.[7] However, none of these compounds was evaluated for electrochemical sensing.

In an earlier study,[8] we focused on the effect of the insertion of a -CH=CH- unit into the conjugated link of compound **1a**, and evaluated three *N*-alkyl ferrocenyl derivatives with a variable spacer length towards cation electrochemical detection (Scheme 1).

Redox-active ionophores based on covalently linked crown ether–metallocene systems have received much attention in recent years because they provide a good selective electrochemical response to the presence of a guest cation.[9] In the present study, we have investigated the influence of the substituent of the nitrogen atom on the cation electrochemical detection and have replaced the diethylamino group of **1a** by the aza-15-crown-5 residue to synthesize compound **2** (Scheme 2). Furthermore, we have pursued our interest in understanding and quantifying the nature of the complex process leading to the calcium electrochemical detection. To the best of our knowledge, this is not a

[a] Laboratoire de Chimie de Coordination du CNRS, UPR 8241, 205, route de Narbonne, F-31077, Toulouse cedex 04, France
Fax: +33-5-6155-3003
E-mail: delavaux@lcc-toulouse.fr
[b] Laboratoire des Interactions Moléculaires et Réactivité Chimique et Photochimique, UMR 5623 du CNRS, Université Paul Sabatier,
118 route de Narbonne, 31062, Toulouse cedex, France
[c] Present address: University of California, Riverside, Department of Chemistry,
324 Pierce Hall Building Riverside, CA 92521, USA
Supporting information for this article is available on the WWW under http://www.eurjic.org or from the author.

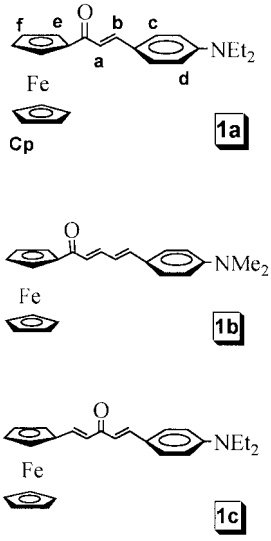

Scheme 1. Compounds **1a**–**c**.

common approach in this research field of ferrocenyl chemistry.

In this paper we report the X-ray and electrochemical characterization of the azacrown compound **2**, together with its cation electrochemical detection abilities. We describe the preparation and characterization of its protonated derivative [**2**H][BF_4] (**3**) and the investigation of thorough ^1H and ^{13}C NMR measurements concerning the interaction of compound **2** with calcium. In addition, we have recorded mass and IR spectral data that provide interesting information about the complex equilibrium that occurs during this interaction. Finally, we compare these results with those obtained in the previous study concerning the *N*-substituted methyl and ethyl compounds.[8] Furthermore, in agreement with experimental data, the theoretical MESP analysis of compounds **1a** and **2** indicates that both coordination sites of **2** are involved in this interaction process.

Results and Discussion

Synthesis and Characterization of Compound 2

We synthesized compound **2** by treatment of acetylferrocene with the appropriate crown aldehyde according to the improved procedure reported for **1a**–**c**[8] (Scheme 2). This new procedure allows a significant improvement on the isolated yield of **2** when compared to our original procedure.[2b] The product was isolated in good yield (65%) as a red powder. The IR spectrum of molecule **2** exhibits a ν(CO) stretching vibration at 1647 cm^{-1} in CH_3CN or in KBr. This low value is due to the conjugation of the CO bond with the double bonds of the π-system (-CH=CHC_6H_4- moiety) in the molecule.[2b,10a–10d] We could observe clearly both the characteristic strong stretching vibrations associated with the methylene groups of the crown in the 2873–2941 cm^{-1} range in CH_3CN[11a] and the asymmetrical stretching C–O–C vibrations as a broad band near 1125 cm^{-1}.[11b]

2D NMR experiments were undertaken in CD_3CN in order to provide a complete assignment of each signal (see Experimental Section). In comparison to compound **1a**, which has nearly the same signals in this solvent, the three CH_2 crown signals observed at δ = 3.57 (br. s), 3.62 (m), and 3.74 (t) ppm, respectively, appear as the ^1H NMR signature of the compound **2** (see Figure S1 in the Supporting Information). Interestingly, a low-field HMQC experiment allowed the verification of a clean correlation between the C_{ipso}-N carbon atom of the phenyl ring and the protons of the CH_2 crown groups α to the nitrogen atom (H_p). This feature is also observed for **1a** and **1c** between the C_{ipso}-N carbon atom and the protons of the CH_2 ethyl groups. Variable temperature NMR experiments in CD_3CN gave no further information.

Crystals of **2** suitable for X-ray structural analysis were obtained by slow recrystallization from CH_3CN. A perspective view of the molecule is shown in Figure 1, crystallographic data for compound **2** are provided in Table 1, and selected bond lengths and angles are listed in Table 2.

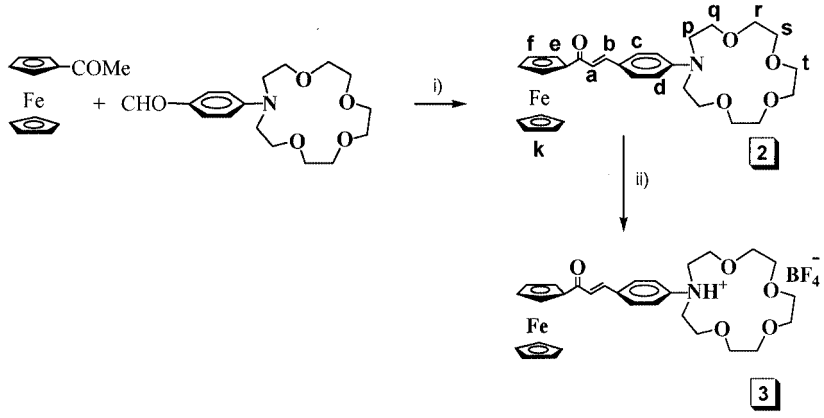

Scheme 2. Synthetic route to compounds **2** and **3**. Reagents and conditions: i) NaOH (5 equiv.), EtOH, 20 °C; ii) HBF_4 (1 equiv.), Et_2O, CH_3CN, 20 °C.

 © 2005 Wiley-VCH Verlag GmbH & Co. KGaA, Weinheim

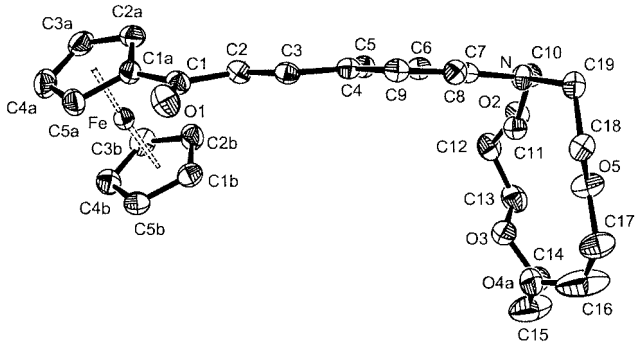

Figure 1.Molecular view of the structure of compound **2** (ORTEP 3) with 50% thermal ellipsoids.

Table 1. Crystallographic data for Compound **2**.

Empirical formula	$C_{29}H_{35}NO_5Fe$
Molecular mass	532.42
Crystal system	orthorhombic
Space group	*Pbca*
a [Å]	15.03434(9)
b [Å]	12.9933(8)
c [Å]	26.589(2)
V [Å^3]	5193.6(6)
$\rho_{calcd.}$ [mg m^{-3}]	1.362
Z	8
μ [mm^{-1}]	0.620
T [K]	160(2)
R_1 [$I > 2\sigma(I)$]	0.0381
wR_2 [$I > 2\sigma(I)$]	0.0850
R_1 (all data)[a]	0.0636
wR_2 (all data)[b]	0.0933

[a] $R_1 = \Sigma||F_o| - |F_c||/\Sigma|F_o|$. [b] $wR_2 = [\Sigma\{w(F_o^2 - F_c^2)^2/\Sigma[w(F_o^2)^2]\}]^{1/2}$.

Table 2. Selected bond lengths [Å] and angles [°] for compound **2** with esd's in parentheses.

Bond lengths [Å]		Bond angles [°]	
C1a–C(1)	1.477(4)	O(1)–C(1)–C(2)	122.6(3)
O(1)–C(1)	1.231(4)	O(1)–C(1)–C(1a)	120.3(3)
C(1)–C(2)	1.464(4)	C(2)–C(3)–C(4)	127.2(3)
C(2)–C(3)	1.339(4)	C(4)–C(5)–C(6)	122.1(3)
C(3)–C(4)	1.449(4)	C(6)–C(7)–C(8)	116.6(3)
C(4)–C(5)	1.403(5)	C(7)–C(8)–C(9)	121.3(2)
C(5)–C(6)	1.370(4)	C(6)–C(7)–N	121.5(3)
C(8)–C(9)	1.369(4)	C(8)–C(7)–N	121.8.(2)
C(7)–N	1.375(4)	N–C(10)–C(11)	114.0(2)
N–C(19)	1.462(4)	N–C(19)–C(18)	115.1(2)

The Cp rings of the compound are nearly eclipsed, with a tilt angle of 7°. The bond lengths within the ferrocenyl moieties[12] as well as the C=O, C_5H_4–C_1, and C=C distances compare well with values reported in the literature[12,13] and values obtained for the *N*-alkyl compounds **1b** and **1c**.[8] In compound **2**, the ethylenic bond is *cis* to the CO function, as for the two structurally characterized compounds **1b** and **1c**, and the conjugated organic chain is also almost planar. The crown moiety is essentially perpendicular to this link, with a torsion angle of 103° and 76° for C7–N–C10–C11 and C7–N–C19–C18, respectively. The observed disorder of the oxygen ring atoms illustrates the degree of flexibility of the crown moiety.[14] Its C–C and C–O distances are in the expected range of values.[15] To the best of our knowledge, this molecule is the fourth structurally characterized example of a monosubstituted compound presenting a $C_5H_4COCH{=}CHC_6H_4$ linkage.[8,12a] The C–N distance in **2** [1.375(4) Å] is close to the values observed for **1b**, **1c**, and $[(C_5H_5)Fe(C_5H_4COC_6H_4NH_2)]$[10d] [1.385(4), 1.384(5), and 1.368(9) Å, respectively]. As expected, these distances are longer than that in $[(C_5H_5)Fe(C_5H_4\text{-}COCH{=}CHC_6H_4NO_2)]$[12a] [1.224(11) Å], which bears an electron-withdrawing NO_2 function.

It is noteworthy that the C1a–N distance of around 9.0 Å is significantly shorter than in **1b** and **1c** (11.5 and 11.4 Å, respectively). The distance between the iron atom and the crown carbons (C11, C12) is approximately 9.5 Å. The shortest distance between the Cp unit and the crown ring is the C2B–C12 distance of 7.8 Å.

Electrochemical Studies: Characterization of Compound 2

The electrochemical properties of compound **2** were investigated in CH_3CN (Table 3) and a typical voltammogram of this species is shown in Figure 2. The shape of the cyclic voltammogram is not altered either by multiple successive scans or by change of the scan rate. As shown in Figure 2 and Table 3, compounds **1a** and **2** exhibit similar electrochemical characteristics. For these compounds the first wave observed in the cyclic voltammograms (CV), at $E_{pa} \approx 0.70$ V, is due to the oxidation of the ferrocene moiety and corresponds to a quasi-reversible process whose $E_{1/2}$ value was determined by linear voltammetry. The first irreversible oxidation process of compound **2**, whose $E_{1/2}$ value is 0.92 V, may be attributed to the oxidation potential of the organic amine moiety ($E_{1/2}$ Org).[8] Moreover, it lies in the range of values reported for the oxidation of some azaferrocenyl compounds.[16] Interesting studies on the oxidation of organic and ferrocenyl aromatic and aliphatic amines[17–20] and our previous results[1d,8] suggest that different and/or competitive mechanisms (e.g. amine protonation or radical coupling) may be responsible for the second and third well-defined irreversible organic oxidation waves situated at E_{pa} = 1.20 V and 1.65 V. In reduction, the single wave observed (E_{pa} = –1.76 V) is attributed to a reduction process mainly located on the CO function.

As illustrated by the first organic oxidation potential, the organic moiety of compound **2** is slightly more difficult to oxidize than that of **1a**. This is probably due to the presence of the electron-withdrawing oxygen atom, which decreases the donor strength of the nitrogen atom. Under similar conditions, the same phenomenon is also observed in the case of the organic compounds $[CHOC_6H_4NEt_2]$ and $[CHOC_6H_4\text{-}p\text{-aza-15-crown-5}]$. An anodic shift (60 mV) of the oxidation potential of the organic moiety is observed for the second compound when compared to the first one. It is noticeable that the E_{pa} value of the "CO" reduction process of **2** may vary but its $E_{1/2}$ is always very close to that of the *N*-alkyl compound **1a**.

 © 2005 Wiley-VCH Verlag GmbH & Co. KGaA, Weinheim

Table 3. Selected electrochemical characteristics of compounds **1a** and **2** in CH_3CN.[a]

	Fe				Org		CO	
	E_{pa}	$E_{1/2}$ (P)	ΔE_p	RI_p	E_{pa}	$E_{1/2}$ (P)	E_{pa}	$E_{1/2}$ (P)
1a	0.70	0.64 (*52*)	63	1.0	0.92; 1.60	0.84 (*47*); 1.50 (*106*)	–1.78	–1.69 (*46*)
2	0.70	0.63 (*54*)	84	1.0	0.99; 1.20*; 1.65	0.92 (*37*); #; 1.50 (*47*)	–1.76	–1.67 (*47*)

[a] P, ΔE_P [mV]; $E_{1/2}$, E_{pa} [V]. $\Delta E_p = E_p$(backward) – E_p(forward) = $E_{pc} - E_{pa}$. $RI_p = |I_p(\text{backward})/I_p(\text{forward})| = |I_{Pred}/I_{Pox}|$. P = slope of the linear regression of $E = f(\log|i/i_d - i|)$. Org = oxidation processes of the organic part of the molecule. Conditions: [complexes] = 10^{-3} M; Pt electrode (1 mm diameter); scan rate in cyclic voltammetry: 100 mV s^{-1}, in linear voltammetry: 5 mV s^{-1}; solution of 0.1 M nBu$_4$NBF$_4$ in CH_3CN; reference electrode SCE. * = residual wave; # = $E_{1/2}$ not determined.

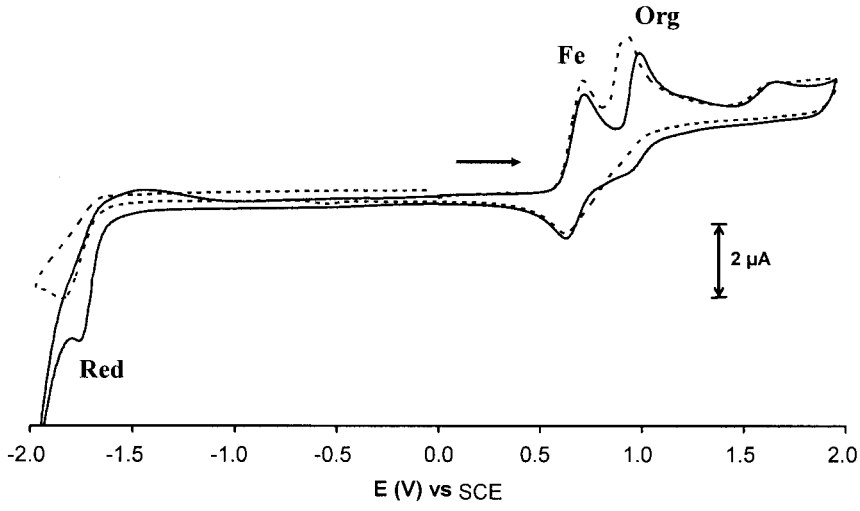

Figure 2. Cyclic voltammograms of compounds **1a** (dashed line) and **2** (solid line). Experimental conditions: Pt electrode (1 mm diameter) in 0.1 M solution of nBu$_4$NBF$_4$ in CH_3CN; scan rate 100 mV s^{-1}; ligand concentration 10^{-3} M; reference electrode SCE.

Electrochemical Calcium Recognition Ability of Compound 2

Electrochemical tests were first performed with **2** (10^{-3} M) in acetonitrile in the presence of various cations (Li^+, Na^+, K^+, Ba^{2+}, Mg^{2+}, Ca^{2+}, Cu^+, Cu^{2+}, and Zn^{2+}). Complex changes occurred in the presence of copper cations and give rise to unclear detections that have not been studied further. As for compound **1a**, compound **2** is poorly sensitive to the presence of cations other than Mg^{2+} and Ca^{2+}. The design of chemosensors that are specific to these biologically relevant cations is a challenging task for many groups.[21] However, for the Mg^{2+} cation, the detection was rather inefficient and peculiar: with one equivalent of salt the iron potential very slowly shifted anodically ($\Delta E_{1/2}$ = 50 mV after 2 h), whereas an incomplete decrease of the intensity of the organic wave was observed, even in salt excess.

As the Ca^{2+} electrochemical sensing was very clear for compound **2** we were especially interested in it. Addition of one equiv. of $Ca(OSO_2CF_3)_2$ to compound **2** induced a clear shift of the $Fe^{II/III}$ couple to anodic potential ($\Delta E_{1/2}$ = 70 mV; Figure 3). This shifted wave still corresponds to a quasi-reversible process ($E_{1/2}$ = 0.70 V, ΔE_p = 81 mV, R_{Ip} = 1.0). Simultaneously, the waves corresponding to the oxidation processes of the organic part of the molecule disappeared. The reduction process is also strongly perturbed (see Figure S2 in the Supporting Information): a very broad, ill-defined reduction wave could be observed around –0.8 V while a new reduction process appeared at –0.19 V (vide infra). Furthermore, when an equimolar mixture of Li^+, Na^+, K^+, Ba^{2+}, Zn^{2+} (4 equiv.) in the presence of 1 equiv. of Ca^{2+} was added to an acetonitrile electrochemical solution of **2**, the same electrochemical characteristics as those induced by Ca^{2+} alone were obtained.

The results obtained here are similar to those obtained for **1a** upon calcium addition. Consequently, in this family of compounds, the cation detection is more sensitive to the nature of the Fe–N spacer than to the nature of the aza group.

Upon comparing the reported data concerning the electrochemical detection of lithium by [(C_5H_5)Fe-$(C_5H_4CH{=}CHC_6H_4NMe_2)$][16] and by [$Fe(C_5H_4CONR_2)_2$][22] with the changes observed by cyclic voltammetry for compound **2** upon calcium addition, it appears that the Ca^{2+} complexation process could involve the whole organic part of molecule **2** since *both* its oxidation and reduction processes are entirely perturbed. Therefore, to determine in particular whether the azacrown moiety and/or the CO function were involved in this complexation (or interaction) process, a thorough NMR study was undertaken.

 © 2005 Wiley-VCH Verlag GmbH & Co. KGaA, Weinheim

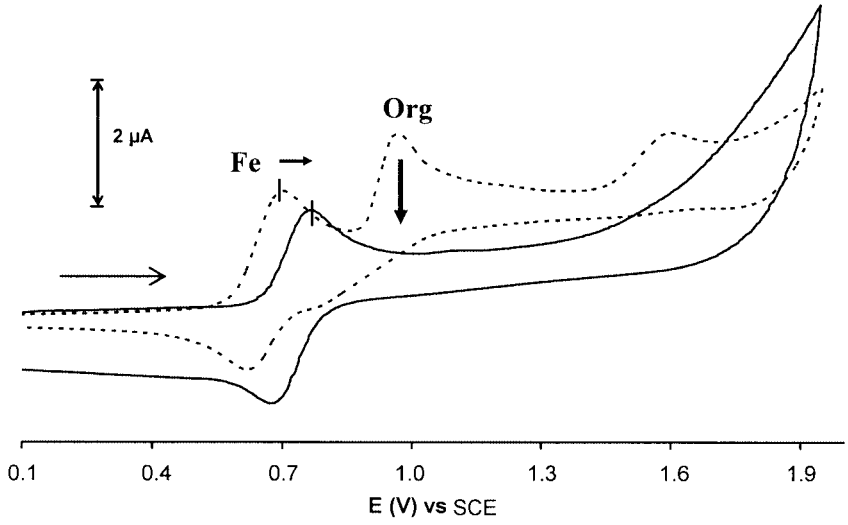

Figure 3. Segmented cyclic voltammograms of compound **2** (dashed line), and **2** + 1 equiv. of $Ca(OSO_2CF_3)_2$ (solid line). Experimental conditions: Pt electrode (1 mm diameter) in 0.1 M solution of nBu_4NBF_4 in CH_3CN; scan rate 100 mV s^{-1}; ligand concentration 10^{-3} M; reference electrode SCE.

NMR Spectroscopic Study: Treatment of Compound 2 with H^+ and Ca^{2+}

To investigate the complexation at the nitrogen atom, compound **2** was protonated. In CH_3CN, treatment of compound **2** with $HBF_4{\cdot}Et_2O$ in a 1:1 stoichiometry turned the solution from red to pink and afforded the protonated species [**2**H][BF_4] (**3**; Scheme 2). This new compound was isolated in good yield (80%). As described in the Experimental Section, elemental analyses and mass spectra are also in agreement with the proposed formula for **3**. In the solid state (IR spectrum, KBr), its elongation vibration ν(NH^+) could be located in the expected range 3030–3100 cm^{-1}.[1d,2b,23a]

The characterization of this compound was fully achieved by ^1H and ^{13}C 2D NMR measurements. In the ^1H NMR spectrum (CD_3CN, 293 K, 400 MHz) the protonation reaction was confirmed by the presence of a new signal at δ = 8.48 ppm attributed to the proton of the NH^+ group.[1d,23b] The NCH_2 crown protons α to the nitrogen atom H_p appear as a downfield-shifted multiplet (δ = 3.90 ppm) compared to **2**, as shown in Figure 4. The HMQC measurements indicated that the H_q and H_r protons of the crown groups are diastereotopic (see Experimental Section).

Tables 4 and 5 clearly highlight that compounds **2** and **1a** have a similar NMR behaviour towards protonation. However, the $\Delta(\delta CH_p)$ value of **2** is smaller than that of **1**, which is probably due to the flexibility of the crown moiety. Stronger perturbations of the phenyl ring of **2** are observed upon protonation: the $\Delta(\delta H_d)$ values are 1.16 ppm and 0.82 ppm for **2** and **1a**, respectively. For both compounds, the CH_d and C_{ipso}-C carbon shifts are also sensitive to the important structural variations that occur.[9] Finally, the CH_c, CH_e, CH_f, and CO groups present the smallest variations.

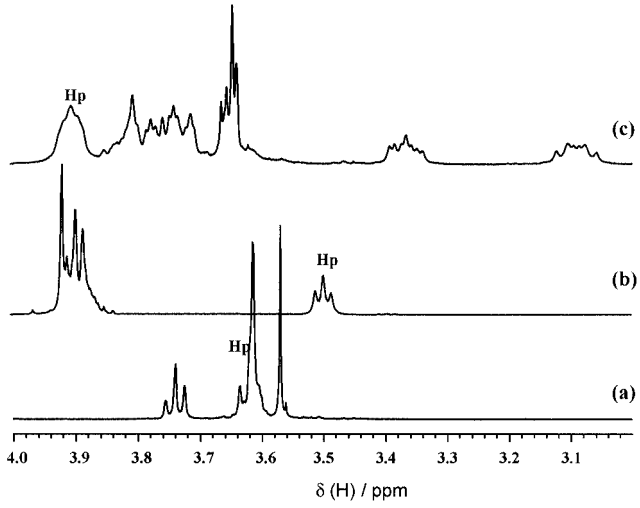

Figure 4. ^1H NMR (400 MHz, CD_3CN) spectra in the δ = 3.0–4.0 ppm range: crown region of (a) **2**, (b) **2** + 1 equiv. Ca^{2+}(c) **2** + 1 equiv. H^+.

Table 4. ^1H NMR (400.13 MHz, CD_3CN, 293 K) shift variations [$\Delta\delta$, in ppm] of selected groups of compounds **1a** and **2** upon a) protonation and b) calcium addition (1 equiv.). [L] = 5×10^{-3} M. See group labeling in Scheme 2.

	H_a	H_b	H_c	H_d	H_p[a]	H_e	H_f
a) Protonation							
1a	0.31	0.11	0.40	0.82	0.23	0.05	0.10
2	0.31	0.12	0.40	1.16	0.28	0.06	0.11
b) Calcium addition							
1a	–0.01	0.17	0.01	–0.02	0	0.11	0.09
2	0.11	–0.02	0.15	0.59	–0.15	0.06	0.11

[a] H_p: protons α to the N atom.

 © 2005 Wiley-VCH Verlag GmbH & Co. KGaA, Weinheim

Table 5. ^{13}C NMR (100.62 MHz, CD_3CN, 293 K) shift variations [$\Delta\delta$, in ppm] of selected groups of compounds **1a** and **2** upon a) protonation and b) calcium addition (1 equiv.). [L] = 5×10^{-3} M. See group labeling in Scheme 2.

Compound	CH_a	CH_b	CH_c	CH_d	CH_p	CH_e	CH_f	CO	C_{ipso}-C	C_{ipso}-N
a) Protonation										
1a	8.46	–3.50	–0.07	11.62	9.96	0.35	1.01	–0.07	16.08	–11.84
2	7.92	–3.31	–0.15	12.21	5.94	0.33	0.92	–0.12	15.72	–13.92
b) Calcium addition										
1a	–1.07	2.67	0.71	0.03	0.07	0.68	1.16	2.77	–0.36	0.55
2	4.05	–0.44	–0.46	9.04	0.23	0.56	1.09	1.48	7.34	1.80

To get an insight into the ligand–Ca^{2+} interaction process responsible for the electrochemical detection of calcium, the ^1H NMR spectra of this compound were recorded in CD_3CN both with and without one equivalent of calcium salt. To properly ascertain the variations of the shift observed, 2D NMR measurements were also performed (see Experimental Section).

As indicated in Table 4, the H_a, H_c, and H_d protons of compound **2** present similar downfield shift variations upon addition of Ca^{2+} as those induced by protonation of **2**, but with smaller magnitudes. In addition, calcium addition induces drastic downfield shifts of the H_d aromatic protons and of the azacrown protons H_{q-t}, and an upfield shift for the H_p crown protons adjacent to the nitrogen atom (see Figure 4). This phenomenon has been previously ascribed to conformational changes resulting from Ca^{2+} crown complexation.[24] This is also reminiscent of the NMR behaviour of organic aza-15-crown-5 compounds[25] and of the ferrocenylazacrown compound $[(C_5H_4CH_2N(C_{12}H_{24}O_5)Fe(C_5H_4)]_2$[26] towards alkali or alkaline-earth metal cations.

Tables 4 and 5 also illustrate how alkyl compound **1a** and crown compound **2** behave differently upon addition of one equivalent of calcium. In particular, the noticeable differences for compound **2** are that (i) the H_p shift occurs, (ii) the H_b proton is not affected, and (iii) the CH_d carbon atoms are strongly perturbed whereas the CO group is only moderately perturbed. The observed shifts with a 1:1 stoichiometry suggest that a preferred azacrown interaction occurs but that a competitive CO interaction may also exist. The studies of the effect of salt concentration presented in the two following sections reinforce this interpretation.

Mass Spectrometry, IR Spectroscopy, and a Theoretical Approach

First, to confirm that strong enough interactions may exist between ligand **2** and the $Ca(OSO_2CF_3)^+$ unit, mass spectra were recorded with samples of **2** (10^{-2} M) containing 0.5, 1, 2, and 4 equivalents of salt, respectively. These mass measurements revealed peaks for the three following species **2**M, $(\mathbf{2})_2$M, and $\mathbf{2}M_2$, where M is the calcium salt (see Experimental Section). This also indicates that different adducts may be present in these mixtures.

In order to confirm further the above NMR hypothesis, complementary investigations were performed. For the IR studies, stepwise addition of Ca^{2+} to a solution of **1a** at the NMR concentration led to a decrease in the intensity of the ν(CO) vibration at 1647 cm^{-1} and to the appearance of a new band located at 1630 cm^{-1}. An excess of salt (up to 10 equiv.) increased the intensity of this new vibration at the expense of the original ν(CO) vibration of the free ligand, which still remained. This is consistent with the proposed equilibrium between the two main species: the free form **1a**, and its 1:1 complexed form [**1a**$Ca(OSO_2CF_3)_2$].[8] In this case, interaction of Ca^{2+} with the CO function classically induces the lowering of the wavenumber.

In contrast, addition of one equivalent of Ca^{2+} to a solution of the crown compound **2** first led to a decrease of its main ν(CO) vibration at 1647 cm^{-1} while a new band appeared at higher wavenumber (1655 cm^{-1}, see Figure 5, part a). This is consistent with a preferred N-crown complexation,[27] which decreases the force constant of the C_{ipso}-N bond and the resonance with the conjugated system, thus strengthening the ν(CO) vibration mode. Furthermore, protonation of **1** and **2** at the nitrogen site also induces a significant shift of the ν(CO) vibration mode to higher wavenumber (from 1647 cm^{-1} to 1659 cm^{-1}). These latter results strengthen our interpretation.

When more calcium salt was added, the main feature observed was the increase of a new broad band centered at 1640 cm^{-1}; the intensity of the band situated at 1655 cm^{-1} also increased slightly (see part b of Figure 5). This latter phenomenon may be interpreted as the result of the formation of one species where Ca^{2+} is now interacting with CO. It is also consistent with the formation of a $\mathbf{2}M_2$ adduct which could potentially interact at high salt concentration through both its CO and azacrown groups. In conclusion, the CO group acts here as a Ca^{2+} IR sensitive probe.

Thus, the IR studies show that Ca^{2+} interacts with both possible coordination sites of **2**. As shown below, this is supported by a comparative theoretical investigation of the molecular electrostatic potential (MESP) of compounds **2** and **1a**.

The gas-phase molecular electrostatic potential (MESP) was computed for the experimental geometries of **1a** and **2** at the B3PW91/6-31G** level. The MESP has been shown to be weakly sensitive to the level of calculation.[28] A MESP minimum value of –0.101 a.u. is obtained for **1a**. Part a of Figure 6 displays the MESP isosurface for a value of –0.080 a.u. There is a continuous negative MESP region formed by the joining of the two lone-pair regions of the oxygen atom of the carbonyl moiety. This suggests that the minima of the MESP are located near the lone pairs of the

 © 2005 Wiley-VCH Verlag GmbH & Co. KGaA, Weinheim

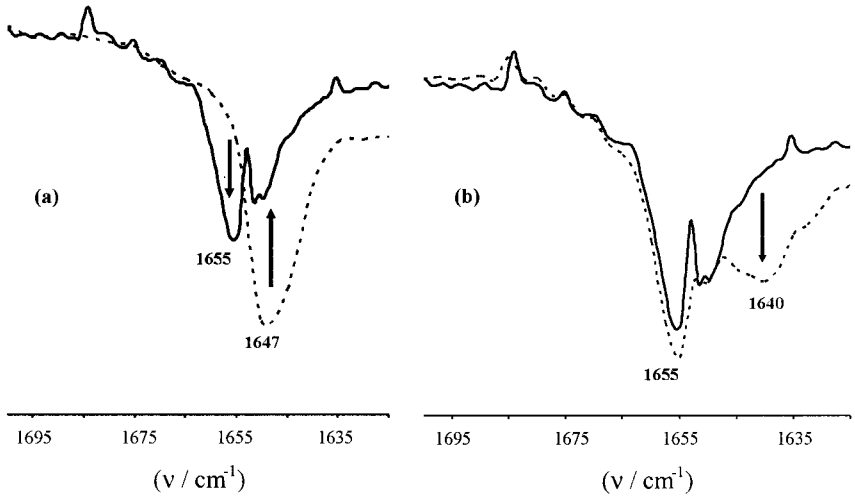

Figure 5. Segmented IR spectra of: (a) **2** (dashed line), **2** + 1 equiv. of $Ca(OSO_2CF_3)_2$ (solid line); (b) **2** + 1 equiv. of $Ca(OSO_2CF_3)_2$ (solid line), **2** + 4 equiv. of $Ca(OSO_2CF_3)_2$ (dashed line) in CH_3CN at NMR concentration.

oxygen atom of the carbonyl group. The carbonyl group is therefore expected to be the preferential binding site of the calcium cation. The picture is different for **2**. A similar MESP minimum value of –0.104 a.u. was computed at the same level. Again, the minima of the MESP are located near the lone pairs of the oxygen atom of the carbonyl group. However, as shown in part b of Figure 6, the lone pairs of the oxygen atoms of the crown moiety display a slightly less negative value of MESP than that of the carbonyl group. This suggests that these sites will now compete with CO for the calcium cation binding.

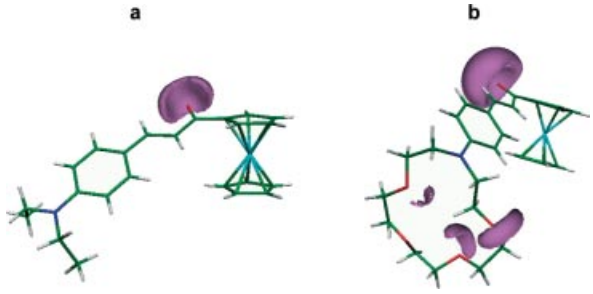

Figure 6. a) compound **1a**, MESP isosurface (–0.080 a.u.) and b) compound **2**, MESP isosurface (–0.055 a.u.), computed at the B3PW91/6-31G**level. Iron atom in sky-blue, nitrogen atom in deep blue, oxygen atom in red, and carbon atoms in green.

Analysis of the ^{13}C NMR Data and Proposition of a Ca^{2+} Interaction Model

To determine the number, the stoichiometry, and the values of the association constants of the calcium adducts involved, this interaction process was further studied by NMR spectroscopy. The variation of the ^1H and ^{13}C NMR chemical shifts was studied when changing the $Ca(OSO_2CF_3)_2$ concentration in CD_3CN. At 293 K, contrary to compound **1a**, the width of the ^1H NMR peaks observed for compound **2** was sometimes too great to allow an accurate assignment. Fortunately, the chemical shift variations of seven protons of **2** at 323 K could be successfully plotted against the calcium concentration. Figure 7 clearly illustrates a decreasing effect following the order $\Delta\delta H_d > \Delta\delta H_p > \Delta\delta H_c > \Delta\delta H_a > \Delta\delta H_b \approx \Delta\delta H_e, \Delta\delta H_f$, thereby corroborating a preferred crown complexation. It is noteworthy that the H_p protons are also the only protons of the crown ring whose shift variation can be clearly followed vs. the salt concentration at 323 K.

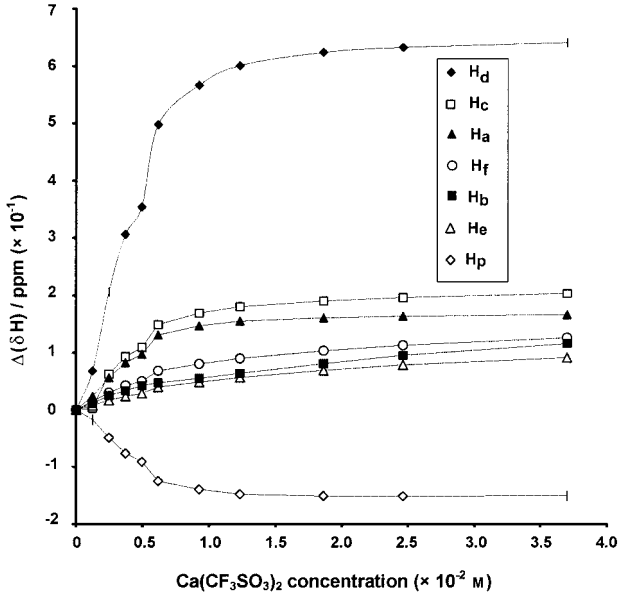

Figure 7. ^1H NMR chemical shift variations of the mentioned protons of **2** (6.2×10^{-3} M) vs. the $Ca(OSO_2CF_3)_2$ concentration in CD_3CN at 323 K. See atom labeling in Scheme 2.

At 293 K, as shown in Figure 8, the ^{13}C NMR study provides more information about the azacrown compound. As expected, the largest carbon shift variations occur for the CH_d and C_{ipso}-C carbons. The main feature is that the CO and the CH_b carbon shifts vs. Ca^{2+} concentration yield values larger than those observed for the CH_p groups involved in the crown complexation. This feature clearly indicates

 © 2005 Wiley-VCH Verlag GmbH & Co. KGaA, Weinheim

that a Ca^{2+}–CO interaction also occurs.[4,8] Thus, Figures 7 and 8 illustrate clearly the resulting effect of a double-site interaction process that involves not only the crown ring but also the CO conjugated moiety. To the best of our knowledge, this is the first time that a thorough ^{13}C NMR investigation has shown the possibility of such a competitive process with a ferrocenyl ligand.

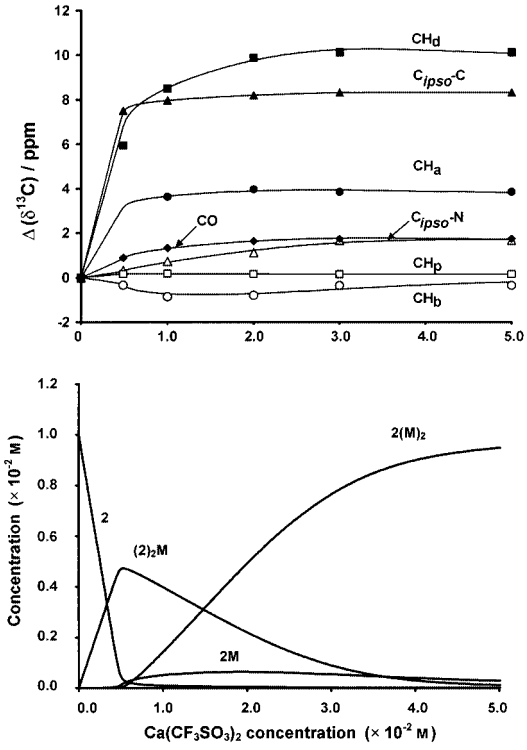

Figure 8. Top: ^{13}C NMR chemical shift variations of the mentioned protons of **2** (1×10^{-2} M) vs. the $Ca(OSO_2CF_3)_2$ concentration in CD_3CN at 293 K. Experimental values (dots) and calculated (lines) curves obtained by fitting the data. See atom labeling in Scheme 2. Bottom: Concentration of the formed species vs. calcium concentration. [**2**] = (1×10^{-2} M).

The continuous shifts of the sharp peaks observed during the calcium titration experiments are indicative of the presence of fast equilibria on the NMR timescale. So, for each calcium concentration, only a time-averaged spectrum of the ligand and/or the ligand–calcium complexes is observed. For example, in the ^{13}C NMR spectra, any observed chemical shift δC_i (where i corresponds to a specific site) is, in fact, a mole fraction weighted average of the shifts observed in the free and complexed molecules, see Equation (1).

$$\delta C_i = \sum(\delta C_{ij} X_j \alpha_j) = \delta C_i^{L} X_L + \delta C_i^{LM} X_{LM} + 2\delta C_i^{L2M} X_{L2M} + \delta C_i^{LM2} X_{LM2} \quad (1)$$

where L is the ferrocenyl ligand **2**, M is the calcium cation, and X the mole fraction of the considered species, and α_j its stoichiometric coefficient.The clear advantage of the global curve-fitting method, i.e. the simultaneous fitting of the data related to all signals, is that it can discriminate between several L_nM_m complex binding models.[29] We have previously reported the method used to determine the association constants for the different L_nM_m complexes present in solution.[30,31] In the present work, the fitted data were the δC_i for the seven curves shown in Figure 8. The following equilibria were considered and are described in the expressions below.

$$L + M \rightleftharpoons LM \qquad K_1$$

$$LM + L \rightleftharpoons L_2M \qquad K_2$$

$$LM + M \rightleftharpoons LM_2 \qquad K_3$$

In Figure 8, we display the ^{13}C NMR experimental data points together with the corresponding theoretical fit curves. A complete agreement between theory and experiment could only be obtained by taking into account the existence of three species [**2**M, (**2**)$_2$M, **2**M$_2$] of different stoichiometries and their corresponding association constants ($K_1 = 1.99\times10^3$, $K_2 = 8.09\times10^4$, $K_3 = 1.07\times10^3$ M^{-1}; values given with ±15% error). The other unknowns are the seven calculated δC_i values for each of the three species [**2**M, (**2**)$_2$M, **2**M$_2$] as indicated in Equation (1). Their adjusted $\Delta\delta C_i$ values are given in the Supporting Information (Table S6). The set of association constant values also gave a good curve fit in the case of the ^1H NMR spectroscopic data (see Figure S3). However, since the experimental temperature is different, the equilibrium can be modified. Therefore, this latter result must be considered with caution. As shown in Figure 8 (bottom), the calculated concentrations of the formed species vs. calcium concentration indicate that while (**2**)$_2$M is the main stoichiometry at low concentration, **2**M$_2$ is the major compound at high calcium concentration as for the alkyl compound **1c**.[8] Contrary to the alkyl compounds **1a**–**c**, (**2**)$_2$M may exist in significant amounts.

The model used to calculate the association constants does not make any distinction between the two sites of interaction – azacrown ring and unsaturated ligand CO system. However, association constants two to four orders of magnitude larger than for the alkyl compounds **1a**–**c** were found under the same experimental conditions.[8] The main difference is that these latter compounds do not interact through their nitrogen site. This suggests that the preferential complexation of the azacrown moiety stabilizes the formed adducts of **2**. It should be noted that for the **2**M compound, the calcium ion diameter of 1.98 Å closely fits the crown-ether cavity, which is 1.7–2.2 Å,[32] and the double charge of this cation promotes a good electrostatic interaction. This may explain the stability of such a complex. Considering a **L**$_2$M species, high values of the association constants have also been found for related *organic* ligands after treatment of their UV/Vis data.[30] In conclusion, in the range of ligand concentrations considered (from 6.2×10^{-3} to 1×10^{-2} M), several species compete. In a future paper, we will show that this NMR analysis is in full agreement with the results of a UV/Vis spectroscopic study realized with compound **2** and Ca^{2+}.

From a coordination point of view, as previously demonstrated, the Ca^{2+}–ligand interaction may occur with the crown moiety and/or with the unsaturated CO moiety. Con-

 © 2005 Wiley-VCH Verlag GmbH & Co. KGaA, Weinheim

sidering first the CO–Ca^{2+} interaction, a screening of the CCDC database shows that the Ca^{2+} cation may interact with six to nine donor atoms of an organic ligand exhibiting a –C=C–C=O linkage.[33] Considering now the crown group, although numerous calcium-containing structures are known, the X-ray structures of only a few azacrown calcium complexes have been reported.[15,24,34] In these latter references, concerning purely organic ligands, the calcium is complexed to the crown moiety and the coordination shell of the calcium is completed (or not) with oxygen provided by another part of the organic ligand, or by a solvent molecule (methanol or water). Otherwise, a sandwich complex of Ca^{2+} with two 18-crown-5 ligands has been recently structurally characterized by Akutagawa et al.,[35] which suggests that a similar arrangement may exist for the $(\mathbf{2})_2$M azacrown compound. Moreover, under our experimental conditions, the triflate ion may also interact with the Ca^{2+} cation, for example through its O or F atoms, thereby increasing the number and nature of possible donor atoms and interacting modes.[36]

Unfortunately, it was not possible to obtain any X-ray structure of $\mathbf{2}Ca^{2+}$, but in the light of the above cited references[15,24,34–36] we may infer that several interacting formulations can be considered for one definite stoichiometry. For example, the $(\mathbf{2})_2$M species could be formed by interaction of two carbonyl groups of two different ligands with the same calcium, by interaction of one CO group of one ligand and one crown group of another ligand with calcium, or by sandwich complexation of calcium by two crown groups of different ligands.

As far as the $\mathbf{2}M_2$ species is concerned, the possibility of having two coordination sites of the same ligand simultaneously involved in the Ca^{2+} interaction, one located close to the negative site (CO) and the other to the positive (azacrown) site of **2**, is supported by the recent description of a dimeric X-ray structure of an interesting $[LPb^{2+}]_2$ chemosensor.[37]

In conclusion, to satisfy a required stoichiometry and to complete the calcium coordination sphere, one or both interacting sites, different anion binding modes, solvent molecules, or, if necessary, several ligands can be involved. However, in the reported equilibria, electrostatic interactions or weak intermolecular interactions (for example with adjacent phenyl groups), rather than classical complexation reactions, may also be considered. Finally, let us remark that the IR data corroborate the NMR analysis when increasing the Ca^{2+} concentration.

NMR tests were also performed with **2** in the presence of lithium, sodium, and potassium triflate, and showed weak proton-shift variations when compared to those due to the interaction with calcium (see Figures S4 and S5). Therefore, in these cases, a thorough NMR study was not appropriate. However, for example, the $\mathbf{2}Na^+$ adduct could be detected by mass spectrometry by a peak situated at m/z = 556 (FAB, and ES positive mode). For the $Ba(OSO_2CF_3)_2$ salt, a good ligand–Ba^{2+} interaction exists (see Figure S4) and the **2**M, $(\mathbf{2})_2$M, and $\mathbf{2}M_2$ species were detected by mass spectroscopy (ES). Because the Ba^{2+} electrochemical detection was not efficient, the **2**–Ba^{2+} interaction was not studied. As far as the Mg^{2+} cation is concerned, a thorough NMR study was not appropriate.

Pathway Between Calcium Interaction and Its Electrochemical Detection

In the above sections, we have shown that the protonation of ligand **2** affords the well-defined product **3**, whereas interaction of ligand **2** with calcium triflate affords different products (see also Figure 4). It must be pointed out that, in contrast, under our standard electrochemical conditions the protonated compound **3** leads to similar electrochemical characteristics as **2** in the presence of one equivalent of calcium triflate. In particular, for compound **3**, a new reduction wave at $E_{1/2}$ = –0.19 V (ΔE_p = 224 mV) was also clearly detected (vide supra), and is attributed to the NH^+ reduction process. How could these two different reactions − calcium interaction with ligand **2** and its protonation − lead to the same electrochemical characteristics (detection)?

In light of the outcome of the electrochemical detection of calcium by alkyl compounds **1a**–**c**,[8] we suspected a peculiar role of the nBu$_4$NBF$_4$ electrolyte in the $Ca(OSO_2CF_3)_2$ electrochemical detection. Therefore, for compound **2**, the calcium interaction process with $Ca(OSO_2CF_3)_2$ was re-examined in the presence of the nBu$_4$NBF$_4$ supporting electrolyte, following the same procedure as that detailed previously.[8] The main conclusion is that, as for the alkyl compounds **1a**–**c**, the three components in the mixture (Ca^{2+}, BF_4^-, H_2O) are responsible for the formation of the protonated species **3** (as a selected representative illustration see Figure 9). The small amount of water can be provided by the electrochemical or the NMR medium. There is no interaction between ligand **2** and the nBu$_4$NBF$_4$ electrolyte salt. In fact, the protonation reaction follows the $Ca(OSO_2CF_3)_2$ interaction process with ligand **2** only when the BF_4^- anion is present in the medium. Thus, in this case, the protonation reaction is the ultimate reaction step. Consequently, in the presence of the nBu$_4$NBF$_4$ electrolyte, the observed electrochemical calcium detection does not directly correspond to the $Ca(OSO_2CF_3)_2$ interaction process but is induced by it. The positive potential shift ($\Delta E_{1/2}$) of iron observed for ligand **2** upon Ca^{2+} addition corresponds, in fact, to that induced by ligand protonation. Thus, the $\Delta E_{1/2}$ of the Fe^{II}/Fe^{III} couple represents the difference of the oxidation potential between the protonated form [$Fe^{II}NH^+$] and the neutral form of the compound. For compounds **1a**–**c**, increasing the distance between the redox center and the amino site decreases the $|\Delta E_{1/2}|$ value of the Fe oxidation process. We have shown here with compound **2** that modifying the nature of the amine has no effect on the electrochemical detection. In fact, the C1–N distance in the new compound **2** is close to that of **1a**. According to the rule devised by Plenio et al.[38], the through-bond electronic communication along the conjugated chain responsible for the detection must be the same for **1a** and **2**, and is effec-

 © 2005 Wiley-VCH Verlag GmbH & Co. KGaA, Weinheim

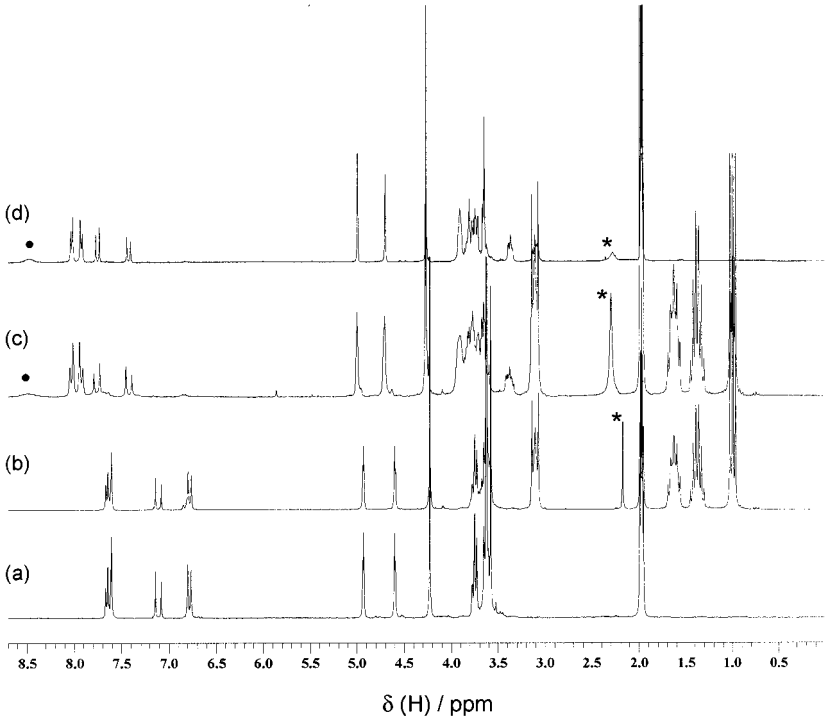

Figure 9. ^{1}H NMR (250 MHz, CD_3CN) spectra in the δ = 0–8.7 ppm range of (a) **2**, (b) **2** + 1 equiv. of nBu$_4$NBF$_4$, (c) mixture (b) + 1 equiv. of Ca(OSO$_2$CF$_3$)$_2$ after 4 h, (d) compound **3**. * H_2O, · NH^+.

tively better than that for **1b**,**c**, which have a longer C1–N distance. Our findings are also in agreement with those obtained for the Mg^{2+} electrochemical detection by compounds [(C_5H_5)Fe(C_5H_4CH=CHC_6H_4R)] (R = NMe_2 and N-azacrown-5), leading to the same $\Delta E_{1/2}$ value, and for which a through-bond electronic communication has been proposed.[39]

Concluding Remarks

We have evaluated the first structurally characterized ferrocenyl azacrown chalcone compound **2** for its electrochemical cation detection ability. A remarkable sensing of the Ca^{2+} cation is possible. This sensing relies on a complex interaction that involves not only the CO moiety of this receptor, as for its simple alkyl homologues **1a**–**c**, but also the azacrown ring, as evidenced by IR spectroscopy and MESP calculations. This interaction gives rise to the formation of three species of different stoichiometry in equilibrium in solution. This kind of phenomenon is not usual for ferrocenyl compounds. This was especially evidenced by experiments varying the ligand/cation concentration ratio and using different techniques such as mass spectrometry and IR and 2D NMR spectroscopy.

In our compounds the CO function plays a role as a coordination site for the interaction and does not interrupt the electronic communication between the terminal N donor and the ferrocenyl center, which can sense the variation of the electronic density. In contrast, the CO group can change the selectivity for the cation electrochemical detection. In fact, under our experimental conditions, the CO-free compound [(C_5H_5)Fe(C_5H_4CH=CHC_6H_4-*p*-aza-15-crown-5)] detects the Li^+[16] Na^+ and K^+[39] cations through crown–cation interactions with a magnitude of the cathodic shifts of 110, 60, and 20 mV, respectively, for the Fe^{II}/Fe^{III} couple. One reason for this difference may be that for compound **2** these N–cation interactions are weakened by the charge transfer due to the presence of the electron-withdrawing CO group. For compound **2**, in these cases, the CO–cation interactions are also probably too weak to be electrochemically detected or to promote the final protonation responsible their detection.

In comparison to the **2**–Ca^{2+} interactions, **2**–Ba^{2+} interactions are probably different because the Ba^{2+} cation is larger, has a lower charge density, and a preference for intermolecular associations. These kinds of interactions do not allow the final Ba^{2+} electrochemical detection by compound **2**. The stability of these **2**–Ba^{2+} interactions is demonstrated by the addition of the nBu$_4$NBF$_4$ supporting electrolyte, which does not induce any change of the NMR spectra.

Overall, regarding the field of ferrocenyl chemistry, we have reported solid evidence for a novel and rare example of a ligand–cation complex equilibrium. Furthermore, we have also shown that this new X-ray characterized ferrocenyl azacrown ligand leads to a peculiar and rather selective electrochemical calcium detection in which the CO function plays a key role. These results also clearly highlight that the Ca^{2+}detection or sensing by ligand **2** is not a simple Ca^{2+} molecular interaction or recognition process.

 © 2005 Wiley-VCH Verlag GmbH & Co. KGaA, Weinheim

Experimental Section

Materials: Toluene and THF were distilled from over sodium/benzophenone, whereas pentane, dichloromethane, and CH_3CN (pure SDS) were distilled from over CaH_2 and stored under argon. EtOH (analytical grade, purex SDS) was simply degassed. [$(C_5H_5)Fe(C_5H_4COMe)$] (95%; Aldrich), [C_6H_5-*p*-aza-15-crown-5] (98%; Acros), and HBF_4 (54% in Et_2O; Aldrich) were obtained from the indicated suppliers. $Ca(OSO_2CF_3)_2$ (96%; Strem) was used without purification. $LiOSO_2CF_3$ (99%; Strem), $NaOSO_2CF_3$ (97%; Fluka), $Ba(OSO_2CF_3)_2$ (97%; Fluka), $KOSO_2CF_3$ (99%; Acros), $Zn(OSO_2CF_3)_2$ (98%; Aldrich), and $Mg(OSO_2CF_3)_2$ (98%; Fluka) were obtained as indicated. All these salts were dried under vacuum, weighed, and added to solution under an argon atmosphere. [$CHOCH{=}CHC_6H_4$-*p*-aza-15-crown-5] was prepared according to the published procedure.[40]

General Instrumentation and Procedures: All syntheses were performed under a nitrogen atmosphere using standard Schlenk tube techniques. IR spectra were recorded on a Perkin–Elmer GX FT-IR spectrophotometer. Samples were run as KBr pellets or in CH_3CN. Elemental analyses were carried out on a Perkin–Elmer 2400 B analyzer at the L. C. C. Microanalytical Laboratory in Toulouse. Mass spectra were obtained at the Service Commun de Spectrométrie de Masse de l'Université Paul Sabatier et du CNRS de Toulouse (fast atom bombardment, FAB>0; or desorption chemical ionization, DCI) were performed on a Nermag R 10-10H spectrometer. A 9 kV xenon atom beam was used to desorb samples from the 3-nitrobenzyl alcohol matrix. Other spectra were performed on a triple quadrupole mass spectrometer (Perkin–Elmer Sciex API 365) using electrospray as the ionization mode. The infusion rate was 5 μL min^{-1}. ^{1}H and ^{13}C NMR spectra were recorded on Bruker AC 200, AM 250, DPX 300, and AMX 400 spectrometers and are referenced to external tetramethylsilane. For 2D NMR experiments, the observation frequencies were in the range 400.13 MHz for ^{1}H and 100.62 MHz for ^{13}C.

Electrochemical Studies: Voltammetric measurements were carried out with a home-made potentiostat[41] using the interrupt method to minimize the uncompensated resistance (iR drop). Experiments were performed at room temperature in an airtight three-electrode cell connected to a vacuum/argon line. The reference electrode consisted of a saturated calomel electrode (SCE) separated from the solution by a bridge compartment filled with the same solvent and supporting electrolyte solution. The counter electrode was a platinum wire of about 1 cm^2 apparent surface. The working electrode was a Pt electrode (1 mm diameter). The supporting electrolyte [nBu$_4$NBF$_4$ (99%; Fluka electrochemical grade) or Et$_4$NBF$_4$ (99%; Aldrich)] was melted and dried under vacuum for one hour. All solutions measured were 1.0×10^{-3} M in the organometallic complex and 0.1 M in supporting electrolyte. The solutions were degassed by bubbling argon before experiments. With the above reference, a value of $E_{1/2}$ = 0.45 V vs. SCE was obtained for 1 mM ferrocene (estimated experimental uncertainty of ±10 mV). Cyclic voltammetry was performed in the potential range –2 to 2 V vs. SCE scanning from 0 toward 2 V/SCE for oxidation studies (and from 0 towards –2 V/SCE for reduction studies) at 0.1 V s^{-1}, at room temperature. Before each measurement, the electrode was polished with Emery paper (Norton A621). To calculate the half-wave potential ($E_{1/2}$), the method is as follows: a quasi-steady-state behavior (at Pt working electrode: 1 mm of diameter) was obtained by the use of linear voltammetry at 5 mV s^{-1}.

Proton NMR Titration Studies: Proton and carbon NMR titrations were typically performed as followed. A solution (500 μL) of the receptor in a deuterated solvent (10^{-2} M) was added with a microsyringe to NMR tubes containing the appropriate quantities of solid $Ca(OSO_2CF_3)_2$ under inert atmosphere, and the NMR spectrum of the receptor was monitored. The samples of calcium salt were prepared by evaporating the corresponding calculated volumes of a standard solution (10^{-2} M) in acetonitrile. Stability constants were evaluated from titration data using the method indicated in the text.

[$(C_5H_5)Fe(C_5H_4COCH{=}CHC_6H_4$-*p*-aza-15-crown-5)] (2): A mixture of [$(C_5H_5)Fe(C_5H_4COMe)$] and $CHOC_6H_4$-*p*-(aza-15-crown-5) (1:1; 0.66×10^{-3} M), and five equiv. of NaOH was dissolved in ethanol (15 mL) and stirred for 24 h at room temperature. The mixture was evaporated to dryness and the residue was dissolved in dichloromethane (10 mL). The solution was filtered off and the solvent evaporated to dryness (twice). The product was purified by column chromatography on alumina (eluent: pentane/CH_2Cl_2) and the obtained red phase was extracted with THF as eluent. After evaporation of the solvent, the product was washed with pentane (30 mL) and dried to afford the desired product as a deep orange powder in 65% yield. ^{1}H NMR (CD_3CN, 293 K): δ = 3.57 (m, 4 H, H$_t$), 3.62 (m, 8 H, H$_p$, H$_s$), 3.63 (m, 4 H, H$_r$), 3.74 (t, $^3J_{Hp,Hq}$ = 6.3 Hz, 4 H, H$_q$), 4.22 (s, 5 H, C_5H_5), 4.59 (t, $^3J_{He,Hf}$ = 1.9 Hz, 2 H, H$_f$), 4.93 (t, $^3J_{He,Hf}$ = 1.9 Hz, 2 H, H$_e$), 6.77 (d, $^3J_{Hc,Hd}$ = 9.0 Hz, 2 H, H$_d$), 7.11 (d, $^3J_{Ha,Hb}$ = 15.5 Hz, 1 H, H$_a$), 7.62 (d, $^3J_{Hc,Hd}$ = 9.0 Hz, 2 H, H$_c$), 7.63 (d, $^3J_{Ha,Hb}$ = 15.5 Hz, 1 H, H$_b$) ppm. ^{13}C{^{1}H} NMR (CD_3CN, 293 K): δ = 52.86 (CH$_p$), 68.48 (CH$_q$), 69.76 (CH$_e$), 69.78 (CH$_t$), 70.21 (C_5H_5), 70.30 (CH$_s$), 70.96 (CH$_r$), 72.63 (CH$_f$), 83.35 (C_{ipso}-C_5H_4), 112.05 (CH$_d$), 118.59 (CH$_a$), 122.84 (C_{ipso}-C), 130.64 (CH$_c$), 141.06 (CH$_b$), 150.00 (C_{ipso}-N), 192.50 (CO) ppm. IR (KBr): $\tilde{\nu}$ = 1522, 1553, 1577, 1610, 1647 (ν_{CO}), 2855–2946 cm^{-1} (ν_{CH}); (CH_3CN): 1521, 1579, 1609, 1647 (ν_{CO}), 2873–2941 cm^{-1} (ν_{CH}). MS (DCI): m/z = 534 [M + H]$^+$. $C_{29}H_{35}FeNO_5$: calcd. C 65.30, H 6.61, N 2.63; found C 65.42, H 6.54, N 2.70.

Interaction of One Equivalent of Ca^{2+} with Compound 2: ^{1}H NMR (CD_3CN, 293 K): δ = 3.47 (s, 4 H, Hp), 3.84–3.92 (m, 16 H, H$_q$, H$_r$, H$_s$, H$_t$), 4.25 (s, 5 H, C_5H_5), 4.70 (t, $^3J_{He,Hf}$ = 1.9 Hz, 2 H, H$_f$), 4.99 (t, $^3J_{He,Hf}$ = 1.9 Hz, 2 H, H$_e$), 7.22 (d, $^3J_{Ha,Hb}$ = 15.6 Hz, 1 H, H$_a$), 7.36 (d, $^3J_{Hc,Hd}$ = 8.8 Hz, 2 H, H$_d$), 7.61 (d, $^3J_{Ha,Hb}$ = 15.6 Hz, 1 H, H$_b$), 7.77 (d, $^3J_{Hc,Hd}$ = 8.8 Hz, 2 H, H$_c$) ppm. ^{13}C{^{1}H} NMR (CD_3CN, 293K): δ = 53.09 (CH$_p$), 68.38, 68.96, 69.03, and 69.86 (CH$_q$, CH$_r$, CH$_s$, and CH$_t$), 70.32 (CH$_e$), 70.58 (C_5H_5), 73.72 (CH$_f$), 81.11 (C_{ipso}-C_5H_4), 121.09 (CH$_d$), 122.84 (CH$_a$), 130.18 (C_{ipso}-C, CH$_c$), 140.62 (CH$_b$), 151.80 (C_{ipso}-N), 193.98 (CO) ppm.

[$(C_5H_5)Fe(C_5H_4COCH{=}CHC_6H_4$-*p*-aza-15-crown-5)H][$BF_4$] (3): $HBF_4{\cdot}Et_2O$ (1 equiv.) was slowly syringed into a stirred solution of **2** (0.19×10^{-3} M) in acetonitrile (10 mL). The light-protected mixture was stirred for 4 h. After solvent evaporation, the product was washed with diethyl ether (30 mL) and pentane (40 mL), and dried under vacuum. A violet powder was obtained in 80% yield. ^{1}H NMR (400 MHz, CD_3CN, 293 K): δ = 3.09 (m, 2 H, H$_q$), 3.37 (m, 2 H, H$_r$), 3.64 (m, 4 H, H$_s$), 3.72 (m, 2 H, H$_r'$), 3.74 (m, 4 H, H$_t$), 3.79 (m, 2 H, H$_q'$), 3.90 (m, 4 H, H$_p$), 4.26 (s, 5 H, C_5H_5), 4.70 (t, $^3J_{He,Hf}$ = 2.0 Hz, 2 H, H$_f$), 4.99 (t, $^3J_{He,Hf}$ = 2.0 Hz, 2 H, H$_e$), 7.42 (d, $^3J_{Ha,Hb}$ = 16.0 Hz, 1 H, H$_a$), 7,75 (d, $^3J_{Ha,Hb}$ = 16.0 Hz, 1 H, H$_b$), 7.93 (d, $^3J_{Hc,Hd}$ = 8.4 Hz, 2 H, H$_d$), 8,02 (d, $^3J_{Hc,Hd}$ = 8.4 Hz, 1 H, H$_c$), 8.48 (br. s, 1 H, NH$^+$) ppm. ^{13}C{^{1}H} NMR (100.6 MHz, CD_3CN, 293 K): δ = 58.80 (CH$_p$), 68.90 (CH$_s$), 69.12 (CH$_q$), 70.09 (CH$_e$), 70.43 (C_5H_5), 70.43 (CH$_t$), 70.59 (CH$_r$), 73.55 (CH$_f$), 81.40 (C_{ipso}-C_5H_4), 124.26 (CH$_d$), 126.51 (CH$_a$), 130.49 (CH$_c$), 136.08 (C_{ipso}-N), 137.75 (CH$_b$), 138.56 (C_{ipso}-C), 192.38 (CO) ppm. IR (CH_3CN): $\tilde{\nu}$ = 1516, 1597, 1608, 1659 (ν_{CO}), 2880–2942(ν_{CH}), 3052–3149 cm^{-1} (ν_{NH^+}). MS-FAB: m/z = 534 [M – BF_4]$^+$.

 © 2005 Wiley-VCH Verlag GmbH & Co. KGaA, Weinheim

$C_{29}H_{36}BF_4FeNO_5$: calcd. C 56.07, H 5.84, N 2.25; found C 55.96, H 5.78, N 2.23.

Mass Spectrometry: Interaction of Compound 2 with Ca^{2+}: The samples used were those of the NMR titrations. MS (ES, CH_3CN): m/z = 287 [**2** + Ca^{2+}], 722 [**2**M – $CF_3SO_3^-$], 1060 [(**2**)M_2 – $CF_3SO_3^-$], 1255 [(**2**)$_2$M – $CF_3SO_3^-$].

Computational Details: The molecular electrostatic potential (MESP) has been extensively used by chemists for probing molecular structure and reactivities.[42] It is the potential generated by the molecular charge distribution as experienced by a positive charge. The topological analysis of the MESP, proposed by Gadre at al.,[43] is a very valuable tool for exploring the sites of reactivity of a molecule as well as their relative strengths. The deepest minimum in the MESP distribution can generally be taken as the most favorable position for an approaching positive charge. The minima in the MESP indicate localization of electron density and can be treated as potent sites of electrophilic attack. The molecular electrostatic potential (MESP) was computed for the experimental geometries at the B3PW91/6-31G** level using Gaussian98.[44] Visualization of the MESP isosurfaces was performed with molekel.[45]

Curve-Fitting Method: In the cited references 4, 8, 30, and 31, D. Lavabre has performed all the simulations and parametric adjustments by relying on his homemade software, SA version 3.

Crystallographic Study: Data were collected at low-temperature (160 K) on a four-circle Kappa CCD XCALIBUR diffractometer from Oxford Diffraction using graphite-monochromated Mo-K_α radiation (λ = 0.71073 Å) and equipped with a nitrogen low-temperature device (CRYOSET). Final unit-cell parameters were obtained by means of a least-squares refinement of 5768 reflections. The structure was solved by direct methods using SIR92[46] and subsequent Fourier maps. The model was refined by least-squares procedures on F^2 using SHELXL97[47] implemented in WinGX.[48] Atomic scattering factors were taken from the International Tables for X-ray Crystallography.[49] All hydrogen atoms attached to carbon were introduced at their idealized positions [d(CH) = 0.93 Å] and were refined using a riding model. They were given isotropic thermal parameters 20% higher than those of the atom to which they are attached. The oxygen atom O(4) was found to be statistically distributed over two sites and was refined accordingly. All non-hydrogen atoms were anisotropically refined, and the weighting scheme used in the last refinement cycles was $w = 1/[\sigma^2(F_o^2) + (aP)^2 + bP]$, where $P = (F_o^2 + 2F_c^2)/3$. For all compounds the criteria for a satisfactory complete analysis were the ratios of the root-mean-square shift standard deviation being less than 0.1 and no significant features in final difference Fourier maps. Drawing of the molecule was realized with the help of ORTEP3[50] with 50% probability displacement ellipsoids for non-hydrogen atoms.

CCDC-245554 contains the supplementary crystallographic data for this paper. These data can be obtained free of charge from The Cambridge Crystallographic Data Center via www.ccdc.cam.ac.uk/data_request/cif.

Supporting Information (see also the footnote on the first page of this article): Figure S1. The ^{1}H NMR spectra of compounds **1a** and **2** in the δ = 1–8 ppm range. Figure S2. The cyclic voltammogram of **2** after Ca^{2+} addition, in reduction. Figure S3. The calculated curves obtained by fitting the ^{1}H NMR spectroscopic data of compound **2** at 323 K. Figure S4. The compared NMR spectra of compound **2** with 1 equiv. of Li^+, Na^+, K^+, Ba^{2+} and Ca^{2+}, respectively. Table S5. The ^{1}H NMR shift variations of compound **2** upon addition of one equiv. of the indicated salts. Table S6 shows the calculated $\Delta\delta C_i$ values for the three species **2**M, (**2**)$_2$M, and **2**M_2. S7 shows the NMR shifts for the interaction of one equiv. of $Ca^{2+}$with compound **2**, in CD_3CN at 323 K.

Acknowledgments

The authors would like to thank CALMIP (calcul intensif en Midi-Pyrénées, Toulouse, France) for use of their computing facilities and Professor Gadre for fruitful discussions.

[1] For examples of redox-active molecules see: a) P. D. Beer, *Adv. Inorg. Chem.* **1992**, *39*, 79–157; b) P. D. Beer, J. Cadman, *Coord. Chem. Rev.* **2000**, *205*, 131–155; c) J. C. Medina, T. T. Goodnow, M. T. Rojas, J. L. Atwood, B. C. Lynn, A. E. Kaifer, G. W. Gokel, *J. Am. Chem. Soc.* **1992**, *114*, 10583–10595; d) B. Delavaux-Nicot, A. Bigeard, A. Bousseksou, B. Donnadieu, G. Commenges, *Inorg. Chem.* **1997**, *36*, 4789–4797 and references cited therein. For examples of fluorescent molecules see: e) A. Prasanna de Silva, H. Q. N. Gunaratne, T. Gunnlaugsson, A. J. M. Huxley, C. P. McCoy, J. T. Rademacher, T. E. Rice, *Chem. Rev.* **1997**, *97*, 1515–1566; f) A. Czarnik, *Fluorescent Chemosensors for Ion and Molecule Recognition*, ACS Symposium Ser. 538, Washington DC, **1993**; g) R. Y. Tsien, in *Methods in Cell Biology* (Eds.: D. Taylor, Y.-L. Wang), Academic Press, London, **1989**, vol. 30, 127.

[2] a) P. D. Beer, F. Szemes, V. Balzani, C. M. Salà, M. G. B. Drew, S. W. Dent, M. Maestri, *J. Am. Chem. Soc.* **1997**, *119*, 11864–11875; b) B. Delavaux-Nicot, S. Fery-Forgues, *Eur. J. Inorg. Chem.* **1999**, 1821–1825; c) S. Fery-Forgues, B. Delavaux-Nicot, *J. Photochem. Photobiol. A: Chem.* **2000**, *132*, 137–159.

[3] a) F. Sancenon, A. Benito, F. J. Hernandez, J. M. Lloris, R. Martinez-Manez, T. Pardo, R. Soto, *Eur. J. Inorg. Chem.* **2002**, 866–875; b) J. Gan, H. Tian, Z. Wang, K. Chen, J. Hill, P. A. Lane, M. D. Rahn, A. M. Fox, D. D. C. Bradley, *J. Organomet. Chem.* **2002**, *645*, 168–175.

[4] J. Maynadié, B. Delavaux-Nicot, S. Fery-Forgues, D. Lavabre, R. Mathieu, *Inorg. Chem.* **2002**, *41*, 5002–5004.

[5] For example: a) A. G. Nagy, S. Toma, *J. Organomet. Chem.* **1984**, *266*, 257–268; b) A. G. Nagy, *J. Organomet. Chem.* **1985**, *291*, 335–340; c) J. P. C. G. Dubosc, U. S. Patent, **1967**, 3,335,008; d) A. N. Nesmeyanov, G. B. Shulp'in, L. V. Rybin, N. T. Gubenko, M. I. Rybinskaya, P. V. Petrovkii, V. I. Robas, *J. Gen. Chem. USSR* **1974**, *44*, 1994–2001; e) S. Toma, A. Perjessy, *Chem. Zvesti* **1969**, *23*, 343–351; f) J. Boichard, J. P. Monin, J. Tirouflet, *Bull. Soc. Chim. Fr.* **1963**, *4*, 851–856.

[6] X. Wu, P. Wilairat, M.-L. Go, *Bioorg. Med. Chem. Lett.* **2002**, *12*, 2299–2302.

[7] A. Ferle-Vidovic, M. Poljak-Blazi, V. Rapic, D. Skare, *Cancer Biother. Radiopharm.* **2000**, *15*, 617–624.

[8] J. Maynadié, B. Delavaux-Nicot, D. Lavabre, B. Donnadieu, J. C. Daran, A. Sournia-Saquet, *Inorg. Chem.* **2004**, *43*, 2064–2077.

[9] M. C. Grossel, D. G. Hamilton, J. I. Fuller, E. Millan-Barios, *J. Chem. Soc., Dalton Trans.* **1997**, 3471–3477 and references cited therein.

[10] a) R. M. Silverstein, G. C. Bassler, T. C. Morril, in *Spectrometric Identification of Organic Compounds*, 4th ed., John Wiley & Sons, New York, **1981**, chapter 3, 117–118; b) P. D. Harvey, J. G. Sharman, *Can. J. Chem.* **1990**, *68*, 223–227; c) D. Prim, A. Auffrant, Z. F. Plyta, J. P. Tranchier, F. Rose-Munch, E. Rose, *J. Organomet. Chem.* **2001**, *624*, 124–130; d) M. Ansorge, K. Polborn, T. J. J. Müller, *Eur. J. Inorg. Chem.* **2000**, 2003–2009.

[11] a) R. M. Silverstein, G. C. Bassler, T. C. Morril, in *Spectrometric Identification of Organic Compounds*, 4th ed., John Wiley & Sons, New York, **1981**, chapter 3, p 107; b) R. M. Silverstein, G. C. Bassler, T. C. Morril, in *Spectrometric Identification of Organic Compounds*, 4th ed., John Wiley & Sons, New York, **1981**, chapter 3, p. 115.

 © 2005 Wiley-VCH Verlag GmbH & Co. KGaA, Weinheim

[12] a) S. V. Lindeman, R. E. Bozak, R. J. Hicks, S. Husebye, *Acta Chem. Scand.* **1997**, *51*, 966–968; b) F. H. Allen, O. Kennard, D. G. Watson, L. Brammer, G. A. Orpen, R. Taylor, *J. Chem. Soc., Perkin Trans. 2* **1987**, *12*, S1–S19.
[13] a) H. Shottenberger, M. R. Buchmeiser, H. Angleitner, K. Wurst, R. H. Herber, *J. Organomet. Chem.* **2000**, *605*, 174–183; b) A. C. Bényei, C. Glidewell, P. Lightfoot, B. J. L. Royles, D. M. Smith, *J. Organomet. Chem.* **1997**, *539*, 177–186; c) E. Gyepes, T. Glowiak, S. Toma, *J. Organomet. Chem.* **1986**, *316*, 163–168.
[14] *Crown Compounds Toward Future Applications* (Ed.: S. R Cooper.), VCH Publishers, Inc., New York, **1992**.
[15] S. Itoh, H. Kumey, S. Nagatomo, T. Kitagawa, S. Fukuzumi, *J. Am. Chem. Soc.* **2001**, *123*, 2165–2175.
[16] M. P. Andrews, C. Blackburn, J. F. McAleer, V. D. Patel, *J. Chem. Soc., Chem. Commun.* **1987**, 1122–1124.
[17] S. D. Ross, M. Finkelstein, E. J. Rudd, *Anodic Oxidation*, Academic Press, New York, **1975**, vol. 32, chapter 8, p. 189.
[18] a) R. Prins, A. R. Koorswagen, A. G. T. G. Kortbeek, *J. Organomet. Chem.* **1972**, *39*, 335–344; b) R. Prins, *Mol. Phys.* **1970**, *19* 603–620.
[19] M. Spescha, N. W. Duffy, B. H. Robinson, J. Simpson, *Organometallics* **1994**, *13*, 4895–4904.
[20] N. W. Duffy, J. Harper, P. Ramani, R. Ranatunge-Bandarage, B. H. Robinson, J. Simpson, *J. Organomet. Chem.* **1998**, *564*, 125–131.
[21] a) A. Ajayaghosh, E. Arunkumar, J. Daub, *Angew. Chem. Int. Ed.* **2002**, *41*, 1766–1769; b) A. Chesney, M. R. Bryce, A. S. Batsanov, J. A. K. Howard, L. M. Goldenberg, *Chem. Commun.* **1998**, 677–678.
[22] P. D. Beer, H. Sikanyika, C. Blackburn, J. F. McAleer, *J. Organomet. Chem.* **1988**, *350*, C15–C19.
[23] a) H.-J. Bruegge, D. Carboo, K. von Deuten, A. Knöchel, J. Kopf, W. Dreissig, *J. Am. Chem. Soc.* **1986**, *108*, 107–112; b) R. M. Silverstein, G. C. Bassler, T. C. Morril, in *Spectrometric Identification of Organic Compounds*, 4th ed., John Wiley & Sons, New York, **1981**, chapter 3, p. 198.
[24] C. D. Hall, A. Leineweber, J. H. R. Tucker, D. Williams, *J. Organomet. Chem.* **1996**, *523*, 13–22.
[25] K. Rurack, J. L. Bricks, G. Reck, R. Radeglia, U. Resch-Genger, *J. Phys. Chem.* **2000**, *104*, 3087–3109.
[26] T.-Y. Dong, C.-K. Chang, C.-H. Cheng, K.-J. Lin, *Organometallics* **1999**, *18*, 1911–1922.
[27] M. C. Grossel, M. R. Goldspink, J. A. Hriljac, S. C. Weston, *Organometallics* **1991**, *10*, 851– 860.
[28] S. A. Kulkarni, S. R. Gadre, *Chem. Phys. Lett.* **1997**, *274*, 255–263.
[29] a) M. J. Hynes, *J. Chem. Soc., Dalton Trans.* **1993**, 311; b) L. Fielding, *Tetrahedron* **2000**, *56*, 6151–6170.
[30] N. Marcotte, S. Fery-Forgues, D. Lavabre, S. Marguet, V. G. Pivovarenko, *J. Phys. Chem. A* **1999**, *103*, 3163–3170.
[31] S. Fery-Forgues, D. Lavabre, D. Rochal, *New J. Chem.* **1998**, *22*, 1531–1538.
[32] a) C. J. Pedersen, H. K. Frendsdorff, *Angew. Chem. Int. Ed. Engl.* **1972**, *11*, 16–25; b) B. Dietrich, *J. Chem. Educ.* **1985**, *62*, 954–964.
[33] See, for example: a) T. Sato, H. Takeda, K. Sakai, T. Tsubomura, *Inorg. Chim. Acta* **1996**, *246*, 413–421; b) V.-C. Arunasalam, I. Baxter, S. R. Drake, M. B. Hursthouse, K. M. A. Malik, S. A. S. Miller, D. M. P. Mingos, D. J. Otway, *J. Chem. Soc., Dalton Trans.* **1997**, 1331–1335.
[34] J. Hu, L. J. Barbour, R. Ferdani, G. W. Gokel, *Chem. Commun.* **2002**, 1806–1807.
[35] T. Akutagawa, N. Takamatsu, K. Shitagami, T. Hasegawa, T. Nakamura, T. Inabe, W. Fujita, K. Awaga, *J. Mater. Chem.* **2001**, *11*, 2118–2124.
[36] a) G. A. Lawrance, *Chem. Rev.* **1986**, *86*, 17–33; b) A. D. Frankland, P. B. Hitchcock, M. F. Lappert, G. A. Lawless, *J. Chem. Soc., Chem. Commun.* **1994**, 2435–2436; c) A. Onoda, Y. Yamada, M. Doi, T. Okamura, N. Ueyama, *Inorg. Chem.* **2001**, *40*, 516–521.
[37] C.-T. Chen, W.-P. Huang, *J. Am. Chem. Soc.* **2002**, *124*, 6246–6247.
[38] H. Plenio, J. Yang, R. Diodone, J. Heinze, *Inorg. Chem.* **1994**, *33*, 4098–4104.
[39] P. D. Beer, C. Blackburn, J. F. McAleer, H. Sikanyika, *Inorg. Chem.* **1990**, *29*, 378–381.
[40] J. P. Dix, F. Vögtle, *Chem. Ber.* **1980**, *113*, 457–470.
[41] P. Cassoux, R. Dartiguepeyron, D. de Montauzon, J. B. Tommasino, P. L. Fabre, *Actual. Chim.* **1994**, *1*, 49–55.
[42] a) E. Sorocco, J. Tomasi, *Advances in Quantum Chemistry* (Ed.: P. O. Löwdin), Academic Press, New York, **1978**, vol. 11, 116 (115–193); b) E. Sorocco, J. Tomasi, in *Chemical Applications of Atomic and Molecular Electrostatic potentials* (Eds.: P. Politzer, D. G. Thruhlar), Plenum, New York, **1981**.
[43] a) S. R. Gadre, S. A. Kulkarni, I. H. Shrivastava, *J. Chem. Phys.* **1992**, *96*, 5253–5260; b) S. R Gadre, in *Computational Chemistry Reviews in Current Trends* (Ed.: J. Leczynski), World Scientific, Singapore, **1999**, vol. 4, p. 1; c) S. R. Gadre, R. N. Shirsat, in *Electrostatics of Atoms and Molecules*, Universities Press, Hyderabad, India, **2000**.
[44] M. J. Frisch, G. W. Trucks, H. B. Schlegel, G. E. Scuseria, M. A. Robb, J. R. Cheeseman, V. G. Zakrzewski, J. A. Montgomery Jr., R. E. Stratmann, J. C. Burant, S. Dapprich, J. M. Millam, A. D. Daniels, K. N. Kudin, M. C. Strain, O. Farkas, J. Tomasi, V. Barone, M. Cossi, R. Cammi, B. Mennucci, C. Pomelli, C. Adamo, S. Clifford, J. Ochterski, G. A. Petersson, P. Y. Ayala, Q. Cui, K. Morokuma, D. K. Malick, A. D. Rabuck, K. Raghavachari, J. B. Foresman, J. Cioslowski, J. V. Ortiz, A. G. Baboul, B. B. Stefanov, G. Liu, A. Liashenko, P. Piskorz, I. Komaromi, R. Gomperts, R. L. Martin, D. J. Fox, T. Keith, M. A. Al-Laham, C. Y. Peng, A. Nanayakkara, C. Gonzalez, M. Challacombe, P. M. W. Gill, B. Johnson, W. Chen, M. W. Wong, J. L. Andres, C. Gonzalez, M. Head- E. S. Gordon, J. A. Replogle, Pople, Gaussian 98, Revision A7, Gaussian, Inc., Pittsburgh PA, **1998**.
[45] P. F. Flükiger, S. Portman, Molekel 4.3, University of Geneva and CSCS/ETHZ, Switzerland, **2002**.
[46] SIR92, A program for crystal structure solution: A. Altomare, G. Cascarano, G. Giacovazzo, A. Guagliardi, *J. Appl. Cryst.* **1993**, *26*, 343–350.
[47] G. M. Sheldrick, SHELXL-97, *Program for the Refinement of Crystal Structures*; University of Göttingen, Göttingen, Germany, **1997**.
[48] WINGX 1.63 Integrated System of Windows Programs for the Solution, Refinement and Analysis of Single Crystal X-ray Diffraction Data: L. Farrugia, *J. Appl. Crystallogr.* **1999**, *32*, 837–838.
[49] International Tables for X-ray Crystallography, **1974**, vol. IV, Kynoch Press, Birmingham, England.
[50] ORTEP3 for Windows:L. Farrugia, *J. Appl. Crystallogr.* **1997**, *30*, 565.

Received: September 21, 2004

 © 2005 Wiley-VCH Verlag GmbH & Co. KGaA, Weinheim

Influence of Tertiary Phosphanes on the Coordination Configurations and Electrochemical Properties of Iron Hydrogenase Model Complexes: Crystal Structures of $[(\mu\text{-}S_2C_3H_6)Fe_2(CO)_{6-n}L_n]$ (L = PMe_2Ph, n = 1, 2; PPh_3, $P(OEt)_3$, n = 1)

Ping Li,[a] Mei Wang,*[a] Chengjiang He,[a] Guanghua Li,[b] Xiaoyang Liu,[a,b] Changneng Chen,[c] Björn Åkermark,[d] and Licheng Sun*[a,e]

Keywords: Binuclear iron complexes / Bioinorganic chemistry / Carbonyl displacement / Fe-only hydrogenase / P ligands

A series of mono- and disubstituted diiron complexes $[(\mu\text{-pdt})Fe_2(CO)_5L]$ [pdt = 1,3-propanedithiolato; L = PMe_3 (**2**), PMe_2Ph (**3**), PPh_3 (**4**), $P(OEt)_3$ (**5**)] and $[(\mu\text{-pdt})Fe_2(CO)_4L_2]$ [L = PMe_2Ph (**6**), PPh_3 (**7**), $P(OEt)_3$ (**8**)] were prepared as Fe-only hydrogenase-active-site models by controllable CO displacement of $[(\mu\text{-pdt})Fe_2(CO)_6]$ by tertiary phosphanes. The coordination configurations of **3**–**6** were characterized by X-ray crystallography. Disubstituted diiron complex **6** features an apical/apical coordination mode, instead of the typical *transoid* basal/basal configuration. The electrochemistry of **2**–**6** and **8** was studied by cyclic voltammetry to evaluate the effects of different tertiary phosphane ligands on the redox properties of the iron atoms of model complexes.

(© Wiley-VCH Verlag GmbH & Co. KGaA, 69451 Weinheim, Germany, 2005)

Introduction

The Fe-only hydrogenases, which can effectively catalyze the reduction of protons to dihydrogen in numerous microorganisms,[1,2] are of significance to the economical production of H_2. The composition and the structure of the active site of Fe-only hydrogenases have been established by high-resolution X-ray crystallographic and spectroscopic studies of Fe-only hydrogenases isolated from *Desulfovibrio desulfuricans* and *Clostridium pasteurianum*.[3,4] These achievements in molecular biology and protein crystallography provide an opportunity for chemists to chemically mimic the structure and function of the Fe-only hydrogenase-active site and to explore cheap and efficient catalyst candidates for proton reduction.

The propanedithiolato-bridged dinuclear complex $[(\mu\text{-pdt})Fe_2(CO)_6]$ (**1**) bears remarkable structural similarities with the active site of Fe-only hydrogenase. The introduction of good donor ligands, such as cyanide, tertiary phosphanes and isonitriles, in the $[(\mu\text{-pdt})Fe_2(CO)_6]$ complex renders the iron atoms more electron-rich and more protophilic. In recent years, there have been numerous reports regarding the CO displacement of $[(\mu\text{-pdt})Fe_2(CO)_6]$ by CN^-,[5–9] PR_3[10–13] and CNR,[14,15], as well as the protonation and electrochemistry of the CN^-- and PR_3-substituted derivatives.[16–19] Tertiary phosphane ligands are preferably used in many model complexes of the Fe-only hydrogenase-active site for the following reasons: 1) The electronic characteristics of tertiary phosphane ligands towards the Fe atom are similar to those of CN^- ligands. 2) The steric and electronic properties of PR_3 are tunable by changing the R groups. 3) The replacement of CN^- by PR_3 can avoid the complications of protonation on the cyanide nitrogen atom. Although CO-displacement reactions of $[(\mu\text{-SR})_2Fe_2(CO)_6]$ with tertiary phosphanes have been extensively studied since the 1970s,[19–23] to the best of our knowledge, only a limited number of structurally characterized PR_3-monosubstituted derivatives of diiron dithiolate complexes have been reported in the literature.[11–13] In addition to the crystal structures of PMe_3-disubstituted complexes $[(\mu\text{-SR})_2Fe_2(CO)_4(PMe_3)_2]$ (R = Me, Et)[17,24] and $[(\mu\text{-SRS})Fe_2(CO)_4(PMe_3)_2]$ (R = CH_2CH_2, $CH_2CH_2CH_2$),[10,17] the coordination configurations of other PR_3-disubstituted complexes, $[(\mu\text{-pdt})Fe_2(CO)_4L_2]$ (L = PMe_2Ph, PPh_3), are still not known. Albeit complex $[(\mu\text{-pdt})Fe_2(CO)_4(PMe_2Ph)_2]$ was reported recently[17] and the PPh_3-disubstituted complexes $[(\mu\text{-SR})Fe_2(CO)_4(PPh_3)_2]$ (R = Me, Ph) were pre-

[a] State Key Laboratory of Fine Chemicals, Dalian University of Technology,
Zhongshan Road 158–46, Dalian 116012, China
E-mail: symbueno@vip.sina.com
[b] State Key Laboratory of Inorganic Synthesis and Preparative Chemistry, Jilin University,
Changchun 130012, China
[c] State Key Laboratory of Structural Chemistry, Fujian Institute of Research on the Structure of Matter,
Fuzhou 350002, China
[d] Department of Organic Chemistry, Arrhenius Laboratory, Stockholm University,
10691 Stockholm, Sweden
[e] KTH Chemistry, Organic Chemistry, Royal Institute of Technology,
10044 Stockholm, Sweden

pared in the early 1970s,[25–27] the coordination positions of PMe_2Ph and PPh_3 in these diiron complexes are hitherto unknown. A series of PR_3-substituted diiron complexes, [(μ-pdt)$Fe_2(CO)_5$L] [L = PMe_3 (**2**), PMe_2Ph (**3**), PPh_3 (**4**), $P(OEt)_3$ (**5**)] and [(μ-pdt)$Fe_2(CO)_4L_2$] [L = PMe_2Ph (**6**), PPh_3 (**7**), $P(OEt)_3$ (**8**)], were prepared for a systematic study of the influence of phosphane ligands on the coordination structures and the redox potentials. Here we describe the preparation, spectroscopic characterization and the coordination configurations of complexes **2**–**8**, as well as the electrochemical properties of complexes **2**–**6** and **8**. The X-ray crystallographic study shows that the PMe_2Ph ligands on the Fe atoms of **6** are in an apical/apical coordination mode, which is in contrast with the *transoid* basal/basal configuration of [(μ-pdt)$Fe_2(CO)_4(PMe_3)_2$][10] and the recently reported complex [(μ-pdt)$Fe_2(CO)_4(PTA)_2$] (PTA = 1,3,5-triaza-7-phosphaadamantane).[12]

Results and Discussion

Preparation and Spectroscopic Characterization of Complexes 2–8

Monosubstituted complexes [(μ-pdt)$Fe_2(CO)_5$L] (**2**–**5**) were readily prepared in moderate to good yields by treating **1** with PR_3, according to literature procedures (see Scheme 1).[20,26] Different solvents, namely, hexane, benzene and toluene, were used for the individual reactions in the light of the solubility of the tertiary phosphanes. The reaction of **1** with 1 equiv. of a less bulky tertiary phosphane (L = PMe_3, PMe_2Ph) can be controlled at the monosubstituted stage at room temp. Complex **5** was obtained by treating **1** with 1 equiv. of $P(OEt)_3$ in refluxing toluene. PPh_3 (2 equiv.) is required to obtain **4** in good yield for the displacement of CO in **1** by PPh_3 in refluxing toluene. The PMe_2Ph-disubstituted complex **6** was obtained in satisfactory yield either by treatment of the monosubstituted complex **3** with an additional equiv. of PMe_2Ph in refluxing toluene (see Scheme 2) or by a straightforward reaction of the all-CO complex **1** with 4 equiv. of PMe_2Ph. The formation of PPh_3-disubstituted complex **7** is more difficult than that of the PMe_3-[10] and PMe_2Ph-disubstituted derivatives,[17] presumably due to the large bulk of the PPh_3 ligand. The reaction of **1** with PPh_3 in a molar ratio of 1:4 (**1**/PPh_3) in refluxing toluene for 5 h afforded the PPh_3-monosubstituted complex **4** as a major product together with a low yield of the PPh_3-disubstituted complex **7**. With the PPh_3-monosubstituted complex **4** as a starting reactant, the reaction also gave **7** in low yield after 10 h of reflux in toluene but the major part of **4** did not react, even in excess PPh_3. A similar behaviour to PPh_3 was found for the double CO-displacement of **1** by $P(OEt)_3$. The reaction of **1** with 4 equiv. of $P(OEt)_3$ in refluxing toluene gave **5** as the major product and the $P(OEt)_3$-disubstituted complex **8** in low yield. All complexes (**2**–**8**) are relatively thermo- and air-stable in the solid state. The PPh_3 derivatives, **4** and **7**, are less stable in solution than their analogous PMe_3-, PMe_2Ph- and $P(OEt)_3$-substituted diiron complexes. In toluene at room temp., dissociation of the PPh_3 ligand in **4** and **7** was indicated by ^{31}P NMR spectral studies.

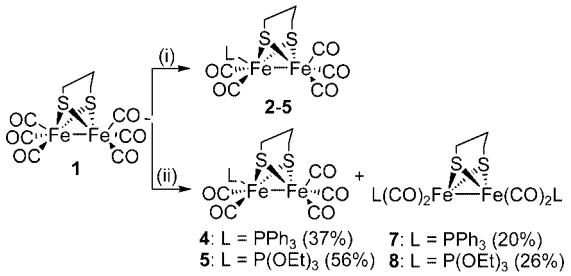

Scheme 1. Reagents and conditions: (i) for **2**, L = PMe_3 (1 equiv.), hexane, room temp., 5 h; for **3**, L = PMe_2Ph (1 equiv.), benzene, room temp., 10 h; for **4**, L = PPh_3 (2 equiv.), toluene, reflux, 6 h; for **5**, L = $P(OEt)_3$ (1 equiv.), toluene, reflux, 3 h; (ii) L = PPh_3, $P(OEt)_3$ (4 equiv.), toluene, reflux, 6 h.

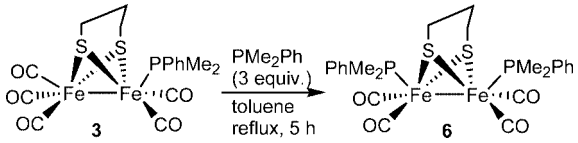

Scheme 2.

The products obtained were characterized by IR, ^1H and ^{31}P NMR spectroscopy and elemental analysis. The results of the elemental analyses for all products are in good agreement with the supposed compositions. Complexes **2**–**8** each show three or four infrared bands in the ν(CO) stretching region (1900–2050 cm^{-1}). The IR data of ν(CO) for **2**–**8** are listed in Table 1 for a comparison, together with the ν(CO) data of [(μ-pdt)$Fe_2(CO)_6$] and [(μ-pdt)$Fe_2(CO)_4L_2$] [L = PMe_3 (**9**)].[10,28,29] The ν(CO) bands are considered as a useful indicator for detecting the variation in the electron density of the Fe atoms in the model complexes of the Fe-only hydrogenase-active site. A comparison of the ν(CO) bands for the four subsets of mono- and disubstituted homologues in Table 1 (**2** vs. **9**, **3** vs. **6**, **4** vs. **7** and **5** vs. **8**) indicates that the introduction of a phosphane ligand has a considerable effect on the ν(CO) bands, while the difference in phosphane ligands appears to have a smaller influence on the shift values of the ν(CO) bands of **2**–**8**. The red shifts of 44–58 cm^{-1} for the first ν(CO) bands and of 29–38 cm^{-1} for the second ones are observed (see Table 1) as the monosubstituted complexes **2**–**5** are converted into their disubstituted homologues **6**–**9**. Compared with the all-carbonyl complex **1**, the average values of the three strong ν(CO) bands for the PR_3-disubstituted complexes are lowered by about 95, 89, 75, and 69 cm^{-1} for **9**, **6**, **7**, and **8**, respectively. The order of the red-shift values of the ν(CO) bands for **6**–**9** is consistent with the electron-donating capabilities of different phosphane ligands, which exhibit a clear ranking of $PMe_3 > PMe_2Ph > PPh_3 > P(OEt)_3$.

 © 2005 Wiley-VCH Verlag GmbH & Co. KGaA, Weinheim

Table 1. Comparison of ν(CO) bands in PR_3-mono- and -disubstituted complexes of **1**.[a]

Complex	ν(CO) [cm^{-1}]	$\Delta\nu$[b] [cm^{-1}]		Note
		$\Delta\nu$ of 1st ν(CO)	$\Delta\nu$ of 2nd ν(CO)	
1	2074(m), 2036(s), 1995(s)	–	–	ref.[29]
2	2037(s), 1980(s), 1919(m)	–37	–56	this work
3	2040(s), 1980(s), 1921(m)	–34	–56	this work
4	2044(s), 1984(s), 1931(m)	–30	–52	this work
5	2046(s), 1989(s), 1936(m)	–28	–47	this work
6	1982(s), 1946(s), 1910(s)	–58	–34	this work
7[c]	1997(s), 1951(s), 1933(s)	–47	–33	this work
8	2002(s), 1960(s), 1935(s)	–44	–29	this work
9	1979(s), 1942(s), 1898(s)	–58	–38	ref.[10]

[a] The spectra were measured in CH_3CN unless stated otherwise. [b] For the PR_3-monosubstituted complexes **2**–**5**: $\Delta\nu = \nu(CO)_{mono} - \nu(CO)_{allCO}$ and for the PR_3-disubstituted complexes **6**–**9**: $\Delta\nu = \nu(CO)_{di} - \nu(CO)_{mono}$. [c] The spectrum was measured in $CHCl_3$.

Molecular Structures of Complexes 3–6

Complexes **4** and **6** were previously prepared according to the same reactions,[11,17] but until now their coordination configurations had not been structurally characterized. As the coordination positions of the phosphane ligands in the diiron complexes cannot be determined solely by the spectroscopic data, X-ray diffraction studies were undertaken for **3**–**6**. The molecular structures of **3**–**6** are displayed in Figure 1 and selected bond lengths and angles are listed in Tables 2 and 3. The central 2Fe2S structures of four complexes are all in the butterfly conformation as in previously reported models,[9–17] and each iron atom is coordinated with a pseudo-square-pyramidal geometry. The CO displacement by one or two molecules of tertiary phosphane ligands has only a small effect on the Fe–Fe distances [2.5048(10) Å in **3**, 2.5247(6) Å in **4**, 2.5142(9) Å in **5** and 2.5198(13) Å in **6**] as compared to that of [(μ-pdt)Fe_2-$(CO)_6$] [2.5103(11) Å].[28]

The coordination configurations of the monosubstituted complexes **3**, **4** and **5** are essentially identical with that of

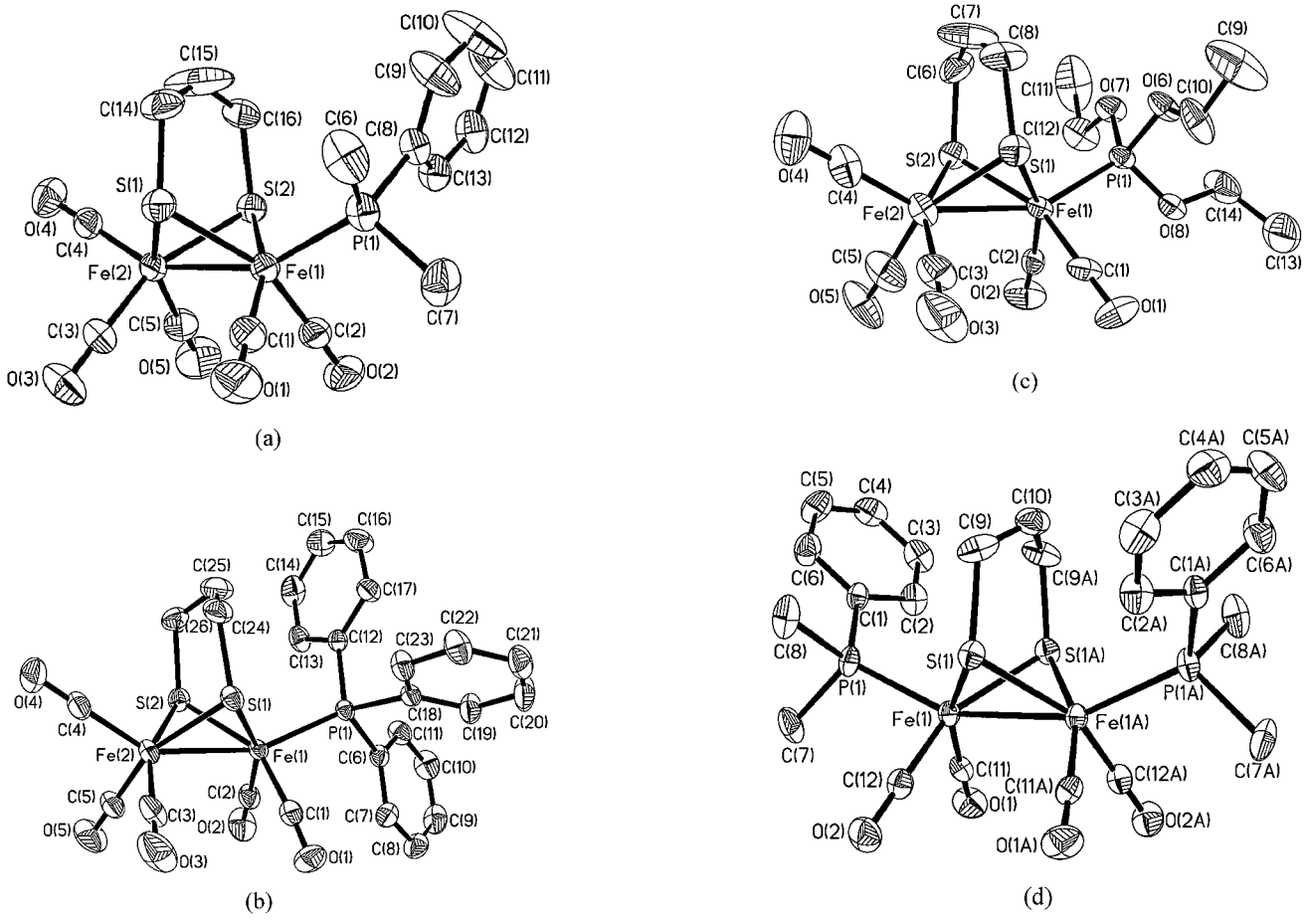

Figure 1. Molecular structures of **3** (a), **4** (b), **5** (c) and **6** (d).

Table 2. Selected bond lengths [Å] and angles [°] for complexes **3**–**5**.

Complex	**3**	**4**	**5**
Bond lengths			
Fe(1)–Fe(2)	2.5048(10)	2.5247(6)	2.5142(9)
Fe(1)–S(2)	2.2653(14)	2.2639(10)	2.253(4)
Fe(1)–S(1)	2.2617(13)	2.2700(9)	2.267(4)
Fe(2)–S(1)	2.2653(14)	2.2598(9)	2.276(4)
Fe(2)–S(2)	2.2707(13)	2.2629(10)	2.259(4)
Fe(1)–P(1)	2.2222(15)	2.2566(9)	2.1696(12)
Fe(1)–C(1)	1.791(5)	1.759(4)	1.771(14)
Fe(1)–C(2)	1.772(5)	1.756(4)	1.779(15)
Fe(2)–C(3)	1.776(6)	1.786(4)	1.785(12)
Fe(2)–C(4)	1.788(6)	1.797(4)	1.800(7)
Fe(2)–C(5)	1.797(6)	1.771(5)	1.770(19)
Bond angles			
P(1)–Fe(1)–S(1)	107.04(6)	107.13(3)	104.86(15)
P(1)–Fe(1)–S(2)	105.45(5)	111.79(4)	105.42(14)
P(1)–Fe(1)–C(1)	93.1(2)	97.15(12)	98.0(5)
P(1)–Fe(1)–C(2)	97.61(19)	94.94(13)	94.9(4)
S(1)–Fe(1)–C(1)	87.72(18)	89.37(12)	87.7(5)
S(1)–Fe(1)–C(2)	155.34(19)	157.80(13)	160.2(4)
S(2)–Fe(1)–C(1)	161.3(2)	150.99(12)	156.5(5)
S(2)–Fe(1)–C(2)	88.31(18)	85.34(13)	88.5(4)
S(1)–Fe(1)–Fe(2)	56.47(4)	55.94(3)	56.56(11)
S(2)–Fe(1)–Fe(2)	56.59(4)	56.08(3)	56.24(11)
S(1)–Fe(2)–C(3)	88.2(2)	86.70(13)	83.0(5)
S(1)–Fe(2)–C(4)	105.37(16)	101.93(12)	103.7(5)
S(1)–Fe(2)–C(5)	155.3(2)	157.88(14)	155.8(6)
S(2)–Fe(2)–C(3)	154.8(2)	158.12(16)	154.2(5)
S(2)–Fe(2)–C(4)	104.59(17)	101.73(14)	106.3(5)
S(2)–Fe(2)–C(5)	85.4(2)	87.53(14)	89.4(5)

Table 3. Selected bond lengths [Å] and angles [°] for complex **6**.

Complex	**6**
Bond lengths	
Fe(1)–Fe(1A)	2.5198(13)
Fe(1)–S(1)	2.2750(14)
Fe(1)–S(1A)	2.2691(14)
Fe(1)–P(1)	2.2286(13)
Fe(1)–C(11)	1.757(5)
Fe(1)–C(12)	1.724(5)
Bond angles	
P(1)–Fe(1)–S(1)	103.81(5)
P(1)–Fe(1)–S(1A)	110.50(5)
P(1)–Fe(1)–C(11)	96.54(18)
P(1)–Fe(1)–C(12)	93.24(17)
S(1)–Fe(1)–C(11)	159.64(17)
S(1)–Fe(1)–C(12)	88.53(18)
S(1A)–Fe(1)–C(11)	87.96(16)
S(1A)–Fe(1)–C(12)	156.21(17)
S(1)–Fe(1)–Fe(1A)	56.43(4)
S(1A)–Fe(1)–Fe(1A)	56.21(4)

their analogues [{μ-S(C_6H_3-*m*-CH_3)S}$Fe_2(CO)_5(PPh_3)$],[11] [(μ-pdt)$Fe_2(CO)_5$(PTA)][12] and [{(μ-SCH_2)$_2$N(C_6H_4-4-Br)}-$Fe_2(CO)_5(PPh_3)$].[13] Tertiary phosphane ligands PMe_2Ph, PPh_3 and $P(OEt)_3$ are coordinated to an apical site on Fe(1) and roughly *trans* to the Fe–Fe bond. Both ^{31}P NMR and X-ray crystallographic analyses of **3**–**5** suggest that one CO displacement by tertiary phosphane in [(μ-pdt)$Fe_2(CO)_6$] affords only an apical isomer, as shown in Figure 1(a–c). One of the phenyl groups of the apical PPh_3 ligand in **4** and the sole phenyl group of the apical PMe_2Ph ligand in **3** are approximately facing the six-membered ring of the propanedithiolate. The angles of C(14)S(1)Fe(1) [114.9(2)°] and C(16)S(2)Fe(1) [114.04(18)°] in **3** are a bit wider than the corresponding angles of C(14)S(1)Fe(2) [110.7(2)°] and C(16)S(2)Fe(2) [111.93(19)°]. Compared with **3**, even larger differences between the counterpart angles C(24)S(1)Fe(1) [116.29(15)°] vs. C(24)S(1)Fe(2) [108.84(15)°] and C(26)S(2)-Fe(1) [116.62(15)°] vs. C(26)S(2)Fe(2) [109.71(15)°] are observed for the structure of **4**. It shows that the six-membered ring of the propanedithiolate in **3** and **4** is pushed away from the site occupied by an apical PMe_2Ph or PPh_3 ligand, leading to the tilt of the propanedithiolate ring towards the $Fe(CO)_3$ site. The P(1)Fe(1)Fe(2) angle is 10.17(17)° larger than the C(4)Fe(2)Fe(1) angle in **4**, while the difference between two angles is only 1.99(34) and 0.57(21)° for **3** and **5**, respectively. The PR_3 ligands used in the present work display the steric effects on the coordination structures in the order $PPh_3 >> PMe_2Ph > P(OEt)_3$. The Fe(1)–P(1) bond lengths of 2.2222(15) Å in **3**, 2.2566(9) Å in **4** and 2.1696(12) Å in **5** are similar to the values of Fe–P bond lengths reported for PR_3-coordinating diiron complexes.[9–13,17–19] The average Fe(2)–C(CO) bonds, 1.785–1.787 Å for **3**–**5**, are slightly shorter than in [(μ-pdt)$Fe_2(CO)_6$] [av. 1.800(3) Å],[28] and the average Fe(1)–C(CO) distance [1.757(9) Å] of **4** is considerably shortened by coordination of PPh_3 to Fe(1).

Theoretically, there are four possible coordination configurations for double-CO displacement by two identical non-carbonyl ligands on each iron atom of [(μ-pdt)$Fe_2(CO)_6$], that is, ap/ap, ap/ba, *transoid* and *cisoid* ba/ba configurations (see Scheme 3).[17] The first three possible configurations can each be related to one or two well-characterized examples, reported in recent years as biomimetic models of the Fe-only hydrogenase-active site.[5,10,12,15] The structurally characterized diiron propanedithiolate with an Fe–Fe bond for the *cisoid* ba/ba configuration model has not yet been reported. Only a protonated diiron complex with double-CO displacement by PMe_3 and CN^- on two iron atoms was found in a *cisoid* ba/ba configuration.[18] The X-ray single-crystal analysis shows that the PMe_2Ph-disubstituted complex **6** possesses an ap/ap coordination configuration, which is identical to the coordination mode of the large isocyanide ligand *t*BuNC,[15] but in contrast with the *transoid* ba/ba configuration of [(μ-pdt)$Fe_2(CO)_4(PMe_3)_2$] and [(μ-pdt)$Fe_2(CO)_4$(PTA)$_2$],[10,12] presumably due to the steric requirement of PMe_2Ph. It could be predicted that for tertiary phosphane ligands of large volume an ap/ap configuration should be sterically less crowded than a ba/ba and an ap/ba configuration. It is noteworthy that the complex [(μ-pdt)$Fe_2(CO)_4(CN)_2$]$^{2-}$ with two small CN^- ligands on each iron atom features an ap/ba configuration,[5] implying that not only the steric requirement but also the electronic effects of a ligand can influence the coordination configurations of diiron propanedithiolates. Another noticeable fact is that although the protonated species [(μ-H)(μ-pdt)$Fe_2(CO)_4(PMe_2Ph)_2$] is in a *transoid* ba/ba configuration in the crystalline state,[17] the coordination structure of its parent complex [(μ-pdt)$Fe_2(CO)_4(PMe_2Ph)_2$] is in an

 © 2005 Wiley-VCH Verlag GmbH & Co. KGaA, Weinheim

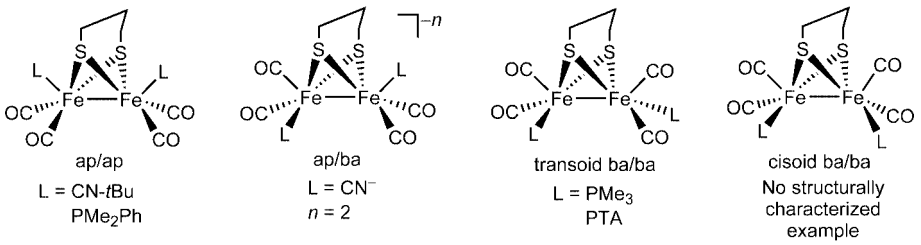

Scheme 3. Four possible coordination configurations resulting from the L orientation.

ap/ap geometry in the crystalline state. In solution, the coordination configurations of the PR_3-substituted diiron complexes might be mobile structural forms.[12] It is unambiguous that there exists a rotation of CO and PMe_2Ph ligands during the protonation process of iron atoms in **6**, just as in the very recently reported isomerization in the protonation process of diruthenium propanedithiolate.[30]

The phenyl groups of the apical PMe_2Ph ligands in **6** both face the inner top side of the molecule, framing a glider-shape conformation with a C_2 symmetry. The dihedral angle between the S(1)C(9)C(9A)S(1A) and S(1A)-Fe(1)S(1) planes and the counterpart angle between the planes of S(1A)C(9)C(9A)S(1) and S(1A)Fe(1A)S(1) are found to have the same value (131.5°) for **6**. The average Fe–C(CO) bond of 1.741 Å in **6** is shortened, and meanwhile the average C–O bond [1.163(1) Å in **6**] is elongated by coordination of the PMe_2Ph ligands to the iron atoms, as compared with [(μ-pdt)$Fe_2(CO)_6$] [Fe–$C(CO)_{av.}$ 1.800(3) Å and C–$O_{av.}$ 1.136(1) Å].[28] The CO displacement by the better donating tertiary phosphane ligands enhances electron accumulation on the iron centers of a diiron dithiolate model, resulting in stronger back-bonding from the metal atoms to the CO ligands and at the same time weakening the CO triple bonds.

Cyclic Voltammograms of Complexes 2–6 and 8

The redox properties of model complexes are one of the interesting features in the structural and functional mimics of the Fe-only hydrogenase-active site. The cyclic voltammograms (CV) of complexes **2**–**6** and **8** were studied to evaluate the effects of different phosphane ligands on the redox properties of the central iron atoms. The CV measurements were carried out in CH_3CN and scanned in the cathodic direction as indicated in Figures 2, 3 and 4. The redox potentials of **2**–**6** and **8**, as well as their parent complex [(μ-pdt)$Fe_2(CO)_6$], are given in Table 4. A good CV of the PPh_3-disubstituted complex **7** was not obtained because of the poor solubility of **7** in CH_3CN.

Each phosphane-monosubstituted diiron complex displays four irreversible peaks, two oxidative and two reductive peaks. Compared with the electrochemical data of the all-carbonyl diiron complex **1** and other analogues,[9,29,31,32] the peaks at 0.33–0.52 V are assigned to the one-electron oxidation process of Fe^IFe^I to $Fe^{II}Fe^I$, and the more anodic peaks at 0.70–0.74 V are proposed to be the response of the further oxidation process of $Fe^{II}Fe^I$ to

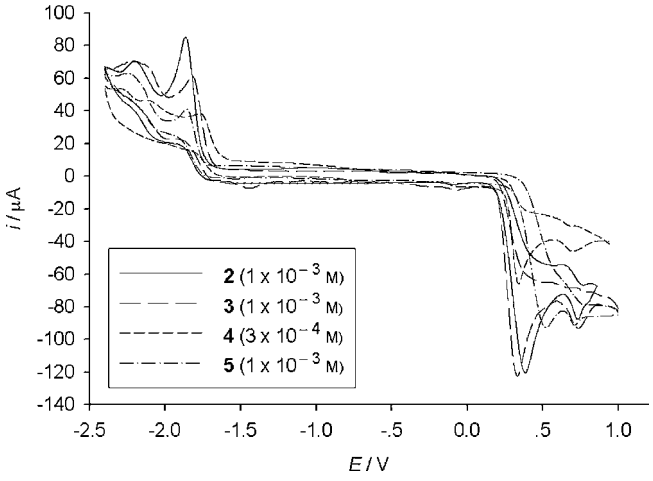

Figure 2. Cyclic voltammograms of complexes **2**–**5**.

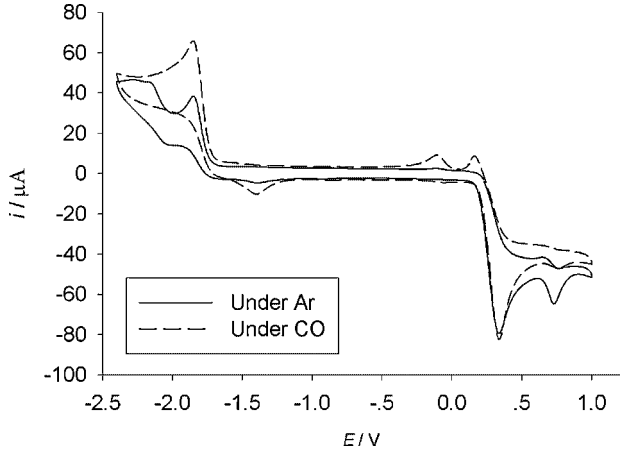

Figure 3. Cyclic voltammograms of **3** (1×10^{-3} M) under Ar and CO.

$Fe^{II}Fe^{II}$. Complexes **2**–**5** exhibit the first reductive peaks at –1.86, –1.82, –1.76 and –1.73 V, respectively, which are attributed to the reduction process of Fe^IFe^I to Fe^0Fe^I (E_1). The second reductive peaks for **2**–**5** in the range of –2.06 to –2.19 V, detected under Ar, were not observed when the CV measurement was carried out under CO (Figure 3). The CV control studies of **2**–**5** suggest that the more negative peaks at –2.06 to –2.19 V might be raised by the one-electron reduction process of Fe^IFe^I/Fe^IFe^0 for a CH_3CN-substituted species, [(μ-pdt)[$Fe(CO)_2(PR_3)$][$Fe(CO)_2$-$(NCCH_3)$].[12] The assignment of the third irreversible reductive peak for complex **4** at ca. –2.29 V is not clear. The first reduction potential is shifted in a cathodic direction

 © 2005 Wiley-VCH Verlag GmbH & Co. KGaA, Weinheim

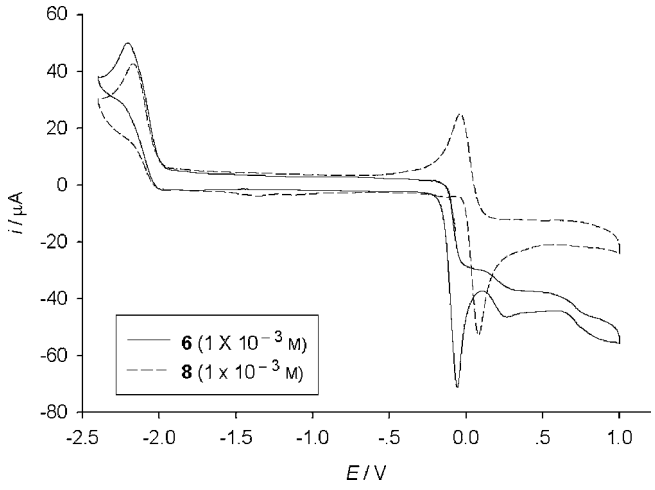

Figure 4. Cyclic voltammograms of complexes **6** and **8**.

Table 4. Redox potentials of complexes **1**–**6** and **8**.[a]

Complex	E_{pa} [V] $Fe^{II}Fe^{I}/Fe^{II}$- Fe^{II}	E_{pa} [V] $Fe^{I}Fe^{I}/Fe^{II}$- Fe^{I}	E_{pc} [V] $Fe^{I}Fe^{I}$/ $Fe^{0}Fe^{I}$
1	+0.84	–	–1.57
2	+0.73	+0.39	–1.86
3	+0.74	+0.33	–1.82
4	+0.70	+0.34	–1.76
5	+0.71	+0.52	–1.73
6	+0.28	–0.06	–2.22
8	–	+0.08	–2.19

[a] nBu$_4$NPF$_6$ (0.1 M) in CH_3CN; scan rate: 0.1 V s^{-1}; working electrode: glassy carbon electrode of diameter 3 mm; reference electrode: non-aqueous Ag/Ag$^+$ electrode (0.01 M $AgNO_3$ in CH_3CN); counter electrode: platinum wire.

by ca. 290, 250, 190 and 160 mV for **2**–**5**, respectively, as compared to that of the all-carbonyl parent complex.[31] The better donor character of PMe_3 and PMe_2Ph renders the reduction of the iron core more difficult. Complexes **4** and **5**, with either a PPh_3 or a $P(OEt)_3$ ligand, display smaller cathodic shifts in CV relative to **2** and **3**. The reduction potential (E_1) for **5** is obviously less cathodic than that for complex **2** by 130 mV, indicative of a considerable influence of different phosphane ligands on the redox properties of the iron atoms of Fe-only hydrogenase-active-site model complexes.

As for previously reported CVs of PMe_3-disubstituted derivatives,[29] **6** and **8** each show only one reductive peak at ca. –2.2 V, which is attributed to the reduction process of $Fe^{I}Fe^{I}$ to $Fe^{0}Fe^{I}$. The second reductive peaks of **6** and **8** are not accessible within the solvent window in Figure 4. The first reductive peaks of **6** and **8** apparently move to more negative potentials by 400 and 460 mV, respectively, as compared with that of the corresponding monosubstituted homologues **3** and **5**. It suggests that the introduction of the second tertiary phosphane ligand exerts a stronger influence on the redox potentials of diiron complexes than the introduction of the first one. With the conversion of mono- to disubstituted derivatives, the anodic peak, assigned to the oxidation of $Fe^{I}Fe^{I}$ to $Fe^{II}Fe^{I}$, shifts from +0.33 to –0.06 V for the conversion of **3** to **6** and from +0.52 to +0.08 V for **5** to **8**. Another oxidative peak at +0.28 V for **6**, with a cathodic shift of 460 mV compared with the corresponding peak of **3**, is tentatively ascribed to the oxidation process of $Fe^{II}Fe^{I}$ to $Fe^{II}Fe^{II}$.

Experimental Section

General Procedures: All reactions and operations related to organometallic complexes were carried out under dry, oxygen-free dinitrogen with standard Schlenk techniques. Solvents were dried and distilled prior to use according to the standard methods. Commercially available chemicals, 1,3-propanedithiol, [$Fe(CO)_5$] and all tertiary phosphanes and phosphite, were reagent grade and used as received. The starting compound [(μ-pdt)$Fe_2(CO)_6$] (**1**) was prepared according to the literature.[28,33] Infrared spectra were recorded from KBr pellets with a JASCO FT/IR 430 spectrophotometer. ^{1}H and ^{31}P NMR spectra were collected with a Varian INOVA 400 NMR spectrometer. Elemental analyses were performed with a Thermoquest-Flash EA 1112 elemental analyzer.

Synthesis of [(μ-pdt)$Fe_2(CO)_5$L] [L = PMe_3 (2), PMe_2Ph (3)]: Trimethylphosphane (46 mg, 0.6 mmol) was added to a solution of hexacarbonyldiiron dithiolate **1** (240 mg, 0.6 mmol) in hexane (30 mL). The red solution was stirred for 5 h and the color turned dark red. After the solution was concentrated by solvent evaporation in vacuo, the crude product was purified by flash column chromatography on silica gel, first with hexane and then with hexane/CH_2Cl_2 (6:1) as eluents. Product **2** was obtained by cooling the concentrated hexane solution to –20 °C. Yield: 0.16 g (61%). $C_{11}H_{15}O_5PS_2Fe_2$ (434.0): calcd. C 30.44, H 3.48; found C 31.28, H 3.57. IR (KBr, νCO): $\tilde{\nu}$ = 2037, 1980, 1919 cm^{-1}. ^{1}H NMR ($CDCl_3$): δ = 1.95 (m, 4 H, SCH_2), 1.71 (m, 2 H, CCH_2C), 1.48 (d, J_{P-H} = 9.19 Hz, 9 H, CH_3) ppm. ^{31}P NMR ($CDCl_3$): δ = 24.96 (PMe_3) ppm. Complex **3** was prepared by a procedure similar to that of **2**. The reaction of **1** (3.0 g, 7.8 mmol) with PMe_2Ph (1.07 g, 7.8 mmol) was carried out in benzene (100 mL). Analytically pure complex **3** was obtained by column chromatography on silica gel, with hexane and then hexane/CH_2Cl_2 (3:1) as eluents. Yield: 2.8 g (72%). $C_{16}H_{17}Fe_2O_5PS_2$ (496.1): calcd. C 38.74, H 3.45; found C 38.90, H 3.51. IR (KBr, νCO): $\tilde{\nu}$ = 2040, 1980, 1921 cm^{-1}. ^{1}H NMR ($CDCl_3$): δ = 7.57, 7.41 (2 s, br., 5 H, Ph), 1.94 (m, 4 H, SCH_2), 1.80 (s, br., 6 H, CH_3), 1.66 (m, 2 H, CCH_2C) ppm. ^{31}P NMR ($CDCl_3$): δ = 32.66 (PMe_2Ph) ppm.

Synthesis of [(μ-pdt)$Fe_2(CO)_5$L] [L = PPh_3 (4), $P(OEt)_3$ (5)]: Triphenylphosphane (2.0 g, 6.5 mmol) was added to a solution of **1** (1.3 g, 3.2 mmol) in toluene (100 mL). The solution was refluxed for 6 h and the color turned purple-red. After the solution was concentrated by solvent evaporation in vacuo, the crude product was purified by flash column chromatography on silica gel with CH_2Cl_2 as eluent. Purple crystals of **4** were obtained by recrystallization in hexane/CH_2Cl_2. Yield: 1.2 g (64%). $C_{26}H_{21}O_5PS_2Fe_2$ (620.2): calcd. C 50.35, H 3.41; found C 50.29, H 3.45. IR (KBr, νCO): $\tilde{\nu}$ = 2044, 1984, 1931 cm^{-1}. ^{1}H NMR ($CDCl_3$): δ = 7.69, 7.43 (2 s, 15 H, Ph), 1.73 (m, 4 H, SCH_2), 1.54 (m, 2 H, CCH_2C) ppm. ^{31}P NMR ($CDCl_3$): δ = 65.74 (PPh_3) ppm. Complex **5** was prepared by a procedure similar to that for **4**. The reaction of **1** (386 mg, 1.0 mmol) with $P(OEt)_3$ (0.17 mL, 1.0 mmol) was carried out in toluene (20 mL) for 3 h. Analytically pure complex **5** was obtained by recrystallization of the product in hexane/CH_2Cl_2 at –20 °C. Yield: 0.158 g (33%). $C_{14}H_{21}Fe_2O_8PS_2$ (524.1): calcd. C 32.08, H 4.04; found C 32.04, H 4.04. IR (KBr, νCO): $\tilde{\nu}$ = 2046,

 © 2005 Wiley-VCH Verlag GmbH & Co. KGaA, Weinheim

Table 5. Crystallographic data and processing parameters for complexes **3**–**6**.

Complex	**3**	**4**	**5**	**6**
Empirical formula	$C_{16}H_{17}Fe_2O_5PS_2$	$C_{26}H_{21}Fe_2O_5PS_2$	$C_{14}H_{21}Fe_2O_8PS_2$	$C_{23}H_{28}Fe_2O_4P_2S_2$
M_w	496.09	620.22	524.10	606.21
T [K]	293(2)	293(2)	293(2)	293(2)
Crystal system	triclinic	monoclinic	monoclinic	orthorhombic
Space group	$P\bar{1}$	$P2(1)/c$	$C2$	$Fdd2$
a [Å]	9.061(2)	9.2533(4)	20.5038(8)	25.633(5)
b [Å]	9.155	17.5257(6)	13.8441(7)	27.503(6)
c [Å]	14.067(4)	16.8340(6)	8.4154(5)	7.7193(15)
α [°]	106.5720(10)	90.00	90.00	90.00
β [°]	96.578(2)	102.7620(10)	103.953(4)	90.00
γ [°]	108.048(2)	90.00	90.00	90.00
V [Å^3]	1036.81(4)	2662.54(17)	2318.3(2)	5441.8(19)
Z	2	4	4	8
$\rho_{calcd.}$ [g cm^{-3}]	1.589	1.547	1.502	1.480
F (000)	504	1264	1072	2496
Crystal size [mm]	0.09 × 0.10 × 0.28	0.07 × 0.15 × 0.20	0.05 × 0.08 × 0.13	0.18 × 0.25 × 0.34
$\theta_{min/max}$ [°]	1.55/25.04	1.70/25.06	1.79/28.30	3.18/27.48
Reflections collected/unique	5375/3607	7906/4204	8384/ 5091	11919/2893
Parameters refined	235	325	244	154
Goodness-of-fit on F^2	1.019	1.036	0.920	1.050
Final R_1 [$I > \sigma(I)$]	0.0461	0.0386	0.0447	0.0500
Final wR_2	0.1268	0.0931	0.0981	0.1038
Residual electron density [e Å^{-3}]	0.524, –0.416	0.621, –0.344	0.581, –0.356	0.481, –0.514

1989, 1936 cm^{-1}. ^{1}H NMR ($CDCl_3$): δ = 4.13 (s, 6 H, OCH_2), 2.05 (m, 4 H, SCH_2), 1.76 (m, 2 H, CCH_2C), 1.37 (s, 9 H, CH_3) ppm. ^{31}P NMR ($CDCl_3$): δ = 171.09 [P(OEt)$_3$] ppm.

Synthesis of [(μ-pdt)Fe$_2$(CO)$_4$(PMe$_2$Ph)$_2$] (6): Product **6** can be prepared directly from [(μ-pdt)Fe$_2$(CO)$_6$] in one pot according to the reported protocol[17] or by a stepwise CO displacement with **3** as a starting compound. The crystal suitable for X-ray analysis was obtained from a solution of hexane at –20 °C.

Synthesis of [(μ-pdt)Fe$_2$(CO)$_4$L$_2$] [L = PPh$_3$ (7), P(OEt)$_3$ (8)]: Compound **1** (2.5 g, 6.5 mmol) was dissolved in toluene (150 mL) and then an excess of PPh_3 (6.8 g, 26.0 mmol) was added. The red solution was refluxed for 6 h and the color turned dark red. The solution was concentrated by solvent evaporation in vacuo. Mono- and disubstituted complexes **4** and **6** were separated by column chromatography on silica gel with hexane/CH_2Cl_2 (2:1) and then CH_2Cl_2 as eluents. Product **4** was obtained from the first band (1.5 g, 37%) and **7** from the second band (1.1 g, 20%). $C_{43}H_{36}Fe_2O_4P_2S_2$ (854.5): calcd. C 60.44, H 4.25; found C 60.27, H 4.28. IR (KBr, νCO): $\tilde{\nu}$ = 1997, 1951, 1933 cm^{-1}. ^{1}H NMR ($CDCl_3$): δ = 7.69, 7.34 (2s, 30 H, Ph), 1.85 (m, 4 H, SCH_2), 1.56 (m, 2 H, CCH_2C) ppm. ^{31}P NMR ($CDCl_3$): δ = 62.79 (PPh$_3$) ppm. Essentially the same procedure as for **7** was applied for the preparation of **8**, by refluxing a toluene solution (35 mL) of **1** (1.3 g, 3.4 mmol) and P(OEt)$_3$ (2.0 mL, 11.6 mmol) for 6 h. Product **5** was obtained from the first band (1.0 g, 56%) and **8** from the second band (0.57 g, 26%). $C_{19}H_{36}Fe_2O_{10}P_2S_2$ (662.3): calcd. C 34.46, H 5.48; found C 34.64, H, 5.63. IR (KBr, νCO): $\tilde{\nu}$ = 2002, 1960, 1935 cm^{-1}. ^{1}H NMR ($CDCl_3$): δ = 4.15 (s, 12 H, OCH_2), 1.95 (m, 4 H, SCH_2), 1.70 (m, 2 H, CCH_2C), 1.36 (s, 18 H, CH_3) ppm. ^{31}P NMR ($CDCl_3$): δ = 175.43 [P(OEt)$_3$] ppm.

Crystal Structure Determination of Complexes 3, 4 and 6: The single-crystal X-ray diffraction data were collected with a Siemens SMART CCD diffractometer for **3** and **4** and with an AFE5R Rigaku diffractometer for **5** and **6** with graphite-monochromated Mo-K_α radiation (λ = 0.71073 Å) at 293 K using the ω-2θ scan mode. Data processing was accomplished with the SAINT processing program.[34] Intensity data were corrected for absorption by the SADABS program.[35] The structure was solved by direct methods and refined on F^2 against full-matrix least-squares methods by using the SHELXTL97 program package.[36] All non-hydrogen atoms were refined anisotropically. Hydrogen atoms were located by geometrical calculation, but their positions and thermal parameters were fixed during the structure refinement. Crystal data and parameters for data collections and refinements of complexes **3**–**6** are listed in Table 5. CCDC-218501 (**3**), -228422 (**4**), -255204 (**5**) and -253139 (**6**) contain the supplementary crystallographic data for this paper. These data can be obtained free of charge from The Cambridge Crystallographic Data Centre via www.ccdc.cam.ac.uk/data_request/cif.

Electrochemistry Studies of Complexes 2–6 and 8: Acetonitrile (Aldrich, spectroscopy grade) used for electrochemical measurements was dried with molecular sieves and then freshly distilled from CaH_2 under N_2. A solution of 0.1 M nBu$_4$NPF$_6$ (Fluka, electrochemical grade) in CH_3CN was used as electrolyte, which was degassed by bubbling with dry argon for 10 min before measurement. Electrochemical measurements were recorded using a BAS-100W electrochemical potentiostat at a scan rate of 200 mV/s. Cyclic voltammograms were obtained in a three-electrode cell under argon. The working electrode was a glassy carbon disc (diameter 3 mm) successively polished with 3- and 1-μm diamond pastes and sonicated in ion-free water for 10 min. The reference electrode was a non-aqueous Ag/Ag$^+$ electrode (0.01 M $AgNO_3$ in CH_3CN) and the auxiliary electrode was a platinum wire.

Acknowledgments

We are grateful to the Chinese National Natural Science Foundation (Grant nos. 20471013 and 20128005), the Swedish Energy Agency and the Swedish Research Council for financial supports of this work.

[1] R. Cammack, *Nature* **1999**, *397*, 214–215.
[2] M. Frey, *ChemBioChem* **2002**, *3*, 153–160.

[3] J. W. Peters, W. N. Lanzilotta, B. J. Lemon, L. C. Seefeldt, *Science* **1998**, *282*, 1853–1858.
[4] Y. Nicolet, C. Piras, P. Legrand, C. E. Hatchikian, J. C. Fontecilla-Camps, *Structure* **1999**, *7*, 13–23.
[5] M. Schmidt, S. M. Contakes, T. B. Rauchfuss, *J. Am. Chem. Soc.* **1999**, *121*, 9736–9737.
[6] A. L. Cloirec, S. P. Best, S. Borg, S. C. Davies, D. J. Evans, D. L. Hughes, C. J. Pickett, *J. Chem. Soc., Chem. Commun.* **1999**, 2285–2286.
[7] E. J. Lyon, I. P. Georgakaki, J. H. Reibenspies, M. Y. Darensbourg, *J. Am. Chem. Soc.* **2001**, *123*, 3268–3278.
[8] M. Y. Darensbourg, E. J. Lyon, X. Zhao, I. P. Georgakaki, *Proc. Natl. Acad. Sci.* **2003**, *100*, 3683–3688.
[9] F. Gloaguen, J. D. Lawrence, M. Schmidt, S. R. Wilson, T. B. Rauchfuss, *J. Am. Chem. Soc.* **2001**, *123*, 12518–12527.
[10] X. Zhao, I. P. Georgakaki, M. L. Miller, J. C. Yarbrough, M. Y. Darensbourg, *J. Am. Chem. Soc.* **2001**, *123*, 9710–9711.
[11] M. M. Hasan, M. B. Hursthouse, S. E. Kabir, K. M. A. Malik, *Polyhedron* **2001**, *20*, 97–101.
[12] R. Mejia-Rodriguez, D. Chong, J. H. Reibenspies, M. P. Soriaga, M. Y. Darensbourg, *J. Am. Chem. Soc.* **2004**, *126*, 12004–12014.
[13] S. Ott, M. Borgström, M. Kritikos, R. Lomoth, J. Bergquist, B. Åkermark, L. Hammarström, L. Sun, *Inorg. Chem.* **2004**, *43*, 4683–4692.
[14] J. D. Lawrence, T. B. Rauchfuss, S. R. Wilson, *Inorg. Chem.* **2002**, *41*, 6193–6195.
[15] J. L. Nehring, D. M. Heinekey, *Inorg. Chem.* **2003**, *42*, 4288–4292.
[16] F. Gloaguen, J. D. Lawrence, T. B. Rauchfuss, *J. Am. Chem. Soc.* **2001**, *123*, 9476–9477.
[17] X. Zhao, I. P. Georgakaki, M. L. Miller, R. Mejia-Rodriguez, C. Y. Chiang, M. Y. Darensbourg, *Inorg. Chem.* **2002**, *41*, 3917–3928.
[18] F. Gloaguen, J. D. Lawrence, T. B. Rauchfuss, M. Benard, M. M. Rohmer, *Inorg. Chem.* **2002**, *41*, 6573–6582.
[19] X. Zhao, C. Y. Chiang, M. L. Miller, M. V. Rampersad, M. Y. Darensbourg, *J. Am. Chem. Soc.* **2003**, *125*, 518–524.
[20] J. A. de Beer, R. J. Haines, *J. Organomet. Chem.* **1972**, *37*, 173–181.
[21] P. C. Ellgen, J. N. Gerlach, *Inorg. Chem.* **1973**, *12*, 2526–2532.
[22] M. S. Arabi, P. Mathieu, R. Poilblanc, *J. Organomet. Chem.* **1979**, *177*, 199–209.
[23] R. Hourihane, G. Gray, T. Spalding, T. Deeney, *J. Organomet. Chem.* **2002**, *642*, 40–47.
[24] G. L. Borgne, D. Grandjean, R. Mathieu, R. Poilblanc, *J. Organomet. Chem.* **1977**, *131*, 429–438.
[25] J. A. de Beer, R. J. Haines, R. Greatrex, N. N. Greenwood, *J. Organomet. Chem.* **1971**, *27*, C33–35.
[26] J. A. de Beer, R. J. Haines, *J. Organomet. Chem.* **1972**, *36*, 297–312.
[27] J. A. de Beer, R. J. Haines, R. Greatrex, N. N. Greenwood, *J. Chem. Soc. A* **1971**, 3271–3282.
[28] E. J. Lyon, I. P. Georgakaki, J. H. Reibenspies, M. Y. Darensbourg, *Angew. Chem. Int. Ed.* **1999**, *38*, 3178–3180.
[29] D. Chong, I. P. Georgakaki, R. Mejia-Rodriguez, J. Sanabria-Chinchilla, M. P. Soriaga, M. Y. Darensbourg, *J. Chem. Soc., Dalton Trans.* **2003**, 4158–4163.
[30] A. K. Justice, R. C. Linck, T. B. Rauchfuss, S. R. Wilson, *J. Am. Chem. Soc.* **2004**, *126*, 13214–13215.
[31] T. Liu, M. Wang, Z. Shi, H. Cui, W. Dong, J. Chen, B. Åkermark, L. Sun, *Chem. Eur. J.* **2004**, *10*, 4474–4479.
[32] A. Darchen, H. Mousser, H. Patin, *J. Chem. Soc., Chem. Commun.* **1988**, 968–970.
[33] L. E. Bogan, D. A. Lesch, T. B. Rauchfuss, *J. Organomet. Chem.* **1983**, *250*, 429–438.
[34] *Software packages SMART and SAINT*, Siemens Energy & Automation Inc., Madison, Wisconsin, **1996**.
[35] G. M. Sheldrick, *SADABS Absorption Correction Program*, University of Göttingen, Germany, **1996**.
[36] G. M. Sheldrick, *SHELXTL97 Program for the Refinement of Crystal Structure*, University of Göttingen, Germany, **1997**.

Received November 10, 2004

 © 2005 Wiley-VCH Verlag GmbH & Co. KGaA, Weinheim

Coordination of Li^+, Ca^+, V^+, and Cu^+ to the Molecules S_8 and S_4 – A Computational Study

Yana Steudel,[a] Ming Wah Wong,*[b] and Ralf Steudel*[a]

Keywords: Ab initio calculations / S ligands / Cluster compounds / Lithium / Calcium / Vanadium / Copper

The complex formation between the Li^+ cation and the sulfur homocycle S_8 has been studied by ab initio MO calculations at the G3X(MP2) level of theory. Starting with various isomers of S_8, the formation of LiS_8 heterocycles and clusters is preferred over complexes with a monodentate ligand. The binding energies of the cation in the 23 complexes investigated range from –95 to –217 kJ·mol^{-1}. The global minimum structure of $[LiS_8]^+$ is of C_{4v} symmetry with the S_8 homocycle in the well-known crown conformation and four Li–S bonds of length 254.2 pm (binding energy: –156.5 kJ·mol^{-1}). The S–S bonds of the various ligands are slightly weakened by the complex formation and a more or less strong bond length alternation is induced. Relatively unstable isomers of S_8 (chair, tub, *exo–endo* ring, branched rings, triplet chain) are partly stabilized and partly destabilized by complex formation with Li^+. The interaction between the cation and the S_8 ligands is mainly due to ion–dipole attraction with little to moderate charge transfer (0.04–0.27 electrostatic units). In the four most stable isomers of $[LiS_8]^+$, the number of sulfur–sulfur bonds is at a maximum and the coordination number of Li^+ is either 4 or 3. Complexes of the type $[Li(S_4)_2]^+$ are much less stable than isomers with an eight-atomic ligand. The Li–S bond lengths in all of these complex cations (230–273 pm) depend on the coordination number of Li and on the atomic charge of the donating sulfur atom(s). In contrast to $[LiS_8]^+$, the complexes of composition $[MS_8]^+$ with M = Ca, V, and Cu are more stable as $[M(S_4)_2]^+$ than with an eight-atomic crown-shaped ligand.
(© Wiley-VCH Verlag GmbH & Co. KGaA, 69451 Weinheim, Germany, 2005)

Introduction

There are numerous metal complexes with *anionic* sulfur-containing ligands such as sulfide (S^{2-}), thiolate (RS^-), or polysulfide anions (S_n^{2-}).[1] These species are of tremendous importance in inorganic and biological chemistry, in geology and mineralogy as well as in industrial chemistry. However, the interaction of metal cations with *neutral* sulfur molecules S_n has not been studied systematically. This unsatisfactory situation is probably due to the fact that the interaction of neutral molecules with metal cations is comparably weak. Consequently, only a few solid coordination compounds are known in which sulfur molecules S_n function as neutral ligands. Examples include several silver salts with the cations $[AgS_8]^+$ and $[Ag(S_8)_2]^+$, respectively, and weakly coordinating anions,[2,3] the rhenium complexes $[Re_2X_2(CO)_6(S_8)]$ (X = Br, I)[4] and the rhodium compounds $[Rh_2(O_2CCF_3)_4]_n(S_8)_m$ with n/m = 1:1 and 3:2.[5] The X-ray structure determinations of these compounds revealed that the S_8 ligands exhibit basically the same crown-shaped ring conformation as the molecules in orthorhombic *cyclo*-octasulfur, and S_8 functions as either bi-, tri-, or tetradentate ligands or as a bridging ligand between two metal centers. The mean S–S bond lengths in these complexes are practically identical to the value determined for orthorhombic S_8 (205 pm[6]). The binding energy of gaseous $[Ag(S_8)]^+$ (C_{4v} symmetry) with respect to the free components has been calculated by various density functional and ab initio MO methods as between –208 and –247 kJ·mol^{-1}.[3] Related solid complexes with other sulfur ring sizes have not been reported.

However, a large number of complexes of univalent metal cations with various sulfur ligands, $[MS_n]^+$ with n = 1–21, have been generated in the gas phase and detected by ion cyclotron resonance (ICR) mass spectrometry. The metals include Ca, Sc, Ti, V, Cr, Mn, Fe, Co, Ni, Zn, Cu and many rare-earth elements.[7–10] The structures and relative energies of these complexes are only partially known from preliminary reports on density functional calculations of calcium-, scandium-, vanadium-, and copper-containing polysulfur cations.[9,10] These calculations (of which no details have been released yet) show that Ca^+ forms complexes with the S_3 ligand in a planar geometry and with the crown-shaped *cyclo*-S_8 ligand in a bi-, tri-, and tetradentate manner. Complexes of compositions $[Ca(S_3)]^+$, $[Ca(S_8)]^+$, $[Ca(S_3)(S_8)]^+$, and $[Ca(S_3)_3]^+$ have been found to be local energy minima on the potential energy surfaces (PES). The

[a] Institut für Chemie, Technische Universität Berlin, Sekr. C2, 10623 Berlin, Germany
Fax: +49-30-31426519
E-mail: steudel@sulfur-research.de
[b] Department of Chemistry, National University of Singapore, 3 Science Drive 3, Singapore 117543
E-mail: chmwmw@nus.edu.sg
Supporting information for this article is available on the WWW under http://www.eurjic.org or from the author.

 © 2005 Wiley-VCH Verlag GmbH & Co. KGaA, Weinheim **DOI: 10.1002/ejic.200401017**

most stable cationic complexes of Sc, V, and Mn with between four and eight sulfur atoms have been predicted to contain the sulfur exclusively in the form of S_2 ligands; for the vanadium complexes a singlet ground state has been assumed. In the case of copper, the ion of composition $[Cu(S_{12})]^+$ was predicted to be most stable as a 12-membered sulfur ring with the metal ion at the center.

To elucidate the possible structures of complexes between a univalent cation and a sulfur homocycle, we have previously studied the various isomers of composition $[LiS_6]^+$.[11] In this work we have investigated theoretically the interaction of the sulfur homocycle S_8 with gaseous Li^+ which serves as a simple model ion to allow calculations at a high level of theory. Besides S_6,[11] only the coordination of gaseous S_3 to Li^+ has been investigated previously by quantum-chemical calculations: $[LiS_3]^+$ is of C_{2v} symmetry.[12] In the case of $[LiS_6]^+$, 15 isomeric structures have been identified on the potential energy hypersurface (PES). The most stable structure is of C_{3v} symmetry and contains a chair-like S_6 ligand of similar geometry as that of solid S_6. The metal ion is linked to three equivalent sulfur atoms resulting in a binding energy of –134 kJ·mol^{-1}.[11] We define here the (adiabatic) binding energy as the energy difference between the complex and the sum of the energies of the two separated components in the same (or closest) conformation as found in the complex.

In the present work, we investigate the interaction of Li^+ with various isomers of S_8 to find out whether an activation of these molecules takes place. We did not intend to scan the total PES of this system. Instead, using existing knowledge of the various isomers of $[LiS_6]^+$[11] we investigated mainly the coordination of Li^+ to the previously studied isomeric cyclic forms of S_8 and to only one of the eight-atomic chains. In agreement with our earlier results (topological analysis),[11] all Li–S distances above 280 pm will be treated as nonbonding. In addition to the Li^+ complexes, we report on preliminary calculations of univalent cations of composition $[MS_8]^+$ with M = Ca, V, and Cu.

Results and Discussion

Structures and Energies

There are at least nine isomeric structures on the PES of the S_8 molecule.[13] The five stable eight-membered rings are of D_{4d} (**1**), C_s (**3**), C_2 (**4**), D_{2d} (**5**), and C_{2h} (**6**) symmetry (Figure 1). The crown-shaped structure (**1**) is the global energy minimum, while a spiral cluster with C_2 symmetry (**2**) is the next most stable structure. The two branched rings of the type S_7=S (**7** and **8**) are of C_1 symmetry and are much less stable. The least stable is the triplet open chain of C_2 symmetry (**9**). These isomers and their relative energies are shown in Figure 1.

Using the various S_8 isomers as ligands, we have located 20 isomeric structures on the PES of $[LiS_8]^+$ with coordination numbers (CN) of the metal atom of between 1 and 4. In addition, three cations with two S_4 ligands each were found to be minima on this PES. The absolute energies are given in Table S1 in the Supporting Information. The symmetries, relative energies, binding energies and dipole moments of all investigated Li^+ complexes are listed in Table 1. In the following discussion these various isomers will be discussed approximately in the order of increasing relative energy.

The global minimum structure of $[LiS_8]^+$ (**8a**) is of C_{4v} symmetry with a crown-shaped S_8 ligand and four Li–S

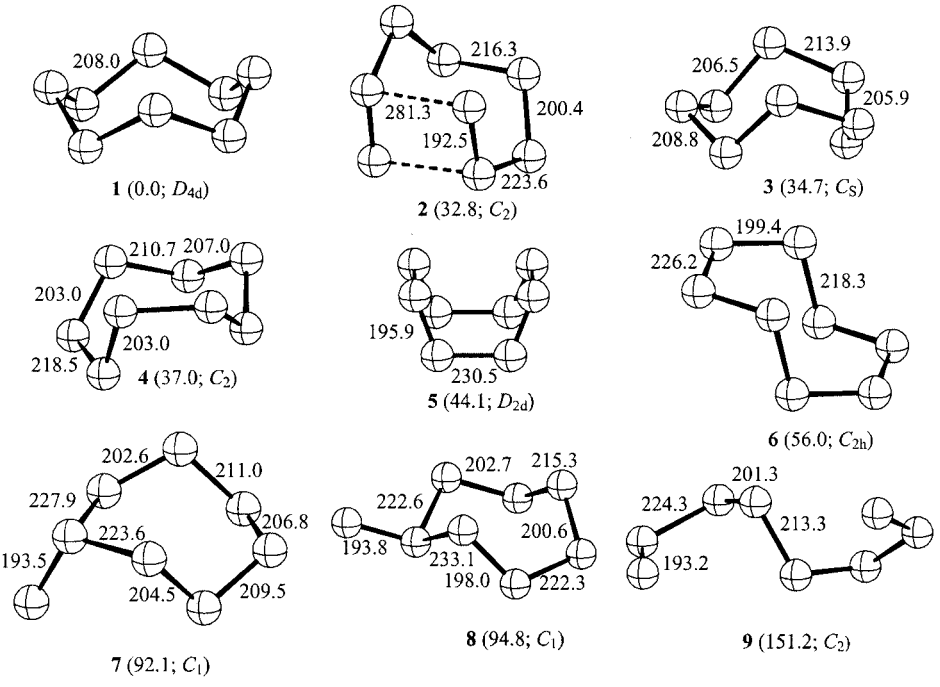

Figure 1. Various cyclic and chain-like isomers of the S_8 molecule with relative energies (kJ·mol^{-1}) and symmetries (according to ref.[13]).

 © 2005 Wiley-VCH Verlag GmbH & Co. KGaA, Weinheim

Table 1. Symmetries, relative energies (ΔE_o) and binding energies (kJ·mol^{-1}) as well as dipole moments (Debye) of 22 isomers of composition $[LiS_8]^+$, calculated by the G3X(MP2) method (CN is the coordination number of the lithium atom).

Species	Symmetry	CN(Li)	Relative energy ΔE_o	Binding energy[a]	Dipole moment[b]
$[LiS_8]^+$ (**8a**)	C_{4v}	4	0.0	–156.5 (**1**)	3.15
$[LiS_8]^+$ (**8b**)	C_1	2+2	34.4	–141.2 (**4**)	3.64
$[S_7SLi]^+$ (**8c**)	C_1	1+2	37.5	–151.8 (**2**)	3.43
$[LiS_8]^+$ (**8d**)	C_s	3	50.0	–141.2 (**3**)	4.41
$[LiS_8]^+$ (**8e**)	C_2	2	57.4	–99.2 (**1**)	12.25
$[LiS_8]^+$ (**8f**)	C_{2v}	4	60.4	–140.2 (**5**)	3.86
$[LiS_8]^+$ (**8g**)	C_s	4	60.5	–152.1 (**6**)	3.68
$[LiS_8]^+$ (**8h**)	C_s	1	61.6	–94.9 (**1**)	14.04
$[S_7$–$Sli]^+$ (**8i**)	C_1	1+2	65.6	–182.9 (**7**)	2.93
$[LiS_8]^+$ (**8j**)	C_1	2	71.3	–104.2 (**7**)	10.27
$[S_7$–$Sli]^+$ (**8k**)	C_1	1+1	72.3	–176.3 (**4**)	7.05
$[LiS_8]^+$ (**8l**)	C_1	2	84.3	–116.2 (**5**)	11.26
$[LiS_8]^+$ (**8m**)	C_s	2	91.9	–120.7 (**6**)	9.77
$[S_7$–$Sli]^+$ (**8n**)	C_s	1+2	93.4	–155.2 (**7**)	3.69
$[LiS_8]^+$ (**8o**)	C_1	2	104.4	–108.2 (**6**)	11.77
$[S_7$–$Sli]^+$ (**8p**)	C_s	1	116.4	–132.2 (**7**)	13.68
$[LiS_7 = S]^+$ (**8q**)	C_1	2+1	121.9	–126.6 (**7**)	5.16
$[LiS_7 = S]^+$ (**8r**)	C_s	2	129.0	–119.6 (**7**)	8.95
$[Li(\eta^2\text{-}S_4)_2]^+$ (**8s**)	D_{2d}	4	132.9	–216.7	0.0
$[LiS_8]^+$ (**8t**)	C_2	2+2	142.5	–165.3	1.05
$[Li(\eta^1\text{-}S_4)_2]^+$ (**8u**)	C_2	2	146.0	–203.6	0.63
$[Li(\eta^2\text{-}S_4)(\eta^1\text{-}S_4)]^+$ (**8v**)	C_1	3	178.9	–212.0	3.12

[a] The numbers in parentheses indicate the S_8 isomer (Figure 1), which has been used to calculate the binding energy. [b] B3LYP/6-31G(2df,p) values.

bonds of length 263.1 pm (Figure 2). The metal atom is located on the upper lobes of the lone-pair orbitals of the four ring atoms no. 1, 3, 5, and 7. These orbitals form the HOMO of the S_8 molecule. In this way, the HOMO(S_8)–LUMO(cation) interaction is maximized, resulting in a binding energy of –156.5 kJ·mol^{-1}. The calculated S–S bond length of 209.1 pm is slightly larger than that calculated for the free S_8 molecule (208.0 pm), indicating a certain degree of activation. Bond angles and torsion angles of the Li^+ complexes are presented in Table 2.

The calculated structure of isomer **8a** is in agreement with the experimentally determined structure of the cation $[AgS_8]^+$, which is also of C_{4v} symmetry in solid $[AgS_8]$-[Al(hfip)] (hfip = hexafluoroisopropanolate)[3], and with the theoretically predicted structure of $[Ca(S_3)(S_8)]^+$.[10] On the other hand, the cation $[VS_8]^+$ has been predicted by density functional calculations to prefer the connectivity $[V(S_2)_4]^+$ (assuming a singlet electronic state) while a structure analogous to **8a** was not considered.[9] Below we show that the latter results are probably incorrect.

A structure with the Li^+ ion at the geometrical center of the S_8 ring is a first-order saddle point of D_{4d} symmetry (**TS1**) which connects two equivalent structures of the global minimum **8a** with a barrier height of 72.5 kJ·mol^{-1} (Figure 2). Via this transition state the Li^+ ion is able to oscillate back and forth through the center of the S_8 ligand. In **TS1**, Li^+ has the coordination number 8 with Li–S distances of 247.9 pm. A structure analogous to **TS1** with CN(V) = 8 was predicted as a high-energy minimum on the singlet PES of $[VS_8]^+$,[9] but we were unable to reproduce this result (see below).

The first equilibrium structure (**8b**) above the global minimum consists of an asymmetric twisted ring with the Li cation coordinated to four sulfur atoms with distances of between 247.3 and 272.9 pm (Figure 2). To a first approximation, this structure of relative energy 34.4 kJ·mol^{-1}, derived from the twist-form of S_8 (**4**), can be considered as a distortion of structure **8a**. The S–S bond lengths vary between 203.2 and 226.9 pm; the longest bond is characterized by an unusually small SSSS torsion angle of 6.3°. The overall motif of the homocycle (the order of signs of the torsion angles) is –+–++–++. The coordination pattern of the metal atom is pyramidal and the sum of the four neighboring SLiS angles is 303.3° (360° would result in a planar coordination sphere).

The second structure above the global minimum of $[LiS_8]^+$ is a complex containing the cluster-like S_8 ligand **2** (see Figure 1) with the Li atom coordinated to three sulfur atoms (isomer **8c** in Figure 2). The ligand has the same conformation as the related molecule S_7=O which has been studied by X-ray crystallography of single crystals.[14] The Li–S distances below 280 pm are 239.1, 250.8 and 260.8 pm. There are two S–S–S–S torsion angles close to zero (–2.6° at atoms 5678 and 7.4° at atoms 1287) while S–S bonds usually prefer a torsion angle close to 90°.[15] As a consequence, the S–S bond lengths vary between 193.0 and 246.9 pm. Structure **8c** is less stable than **8a** by only 37.5 kJ·mol^{-1}, while the cluster-like S_8 isomer **2** is less stable than the crown **1** by only 32.8 kJ·mol^{-1}. The binding energy with respect to **2** is –151.8 kJ·mol^{-1}. For the bond angles of **8c**, see Table 2.

The $[LiS_8]^+$ structure **8d** contains the eight-membered sulfur ring in an *exo–endo* conformation resulting in CN = 3 for the metal atom (Figure 2). This ion is of C_s symmetry and less stable than **8a** by 50.0 kJ·mol^{-1}. In this case, the metal atom is approximately located on the upper lobes of

 © 2005 Wiley-VCH Verlag GmbH & Co. KGaA, Weinheim

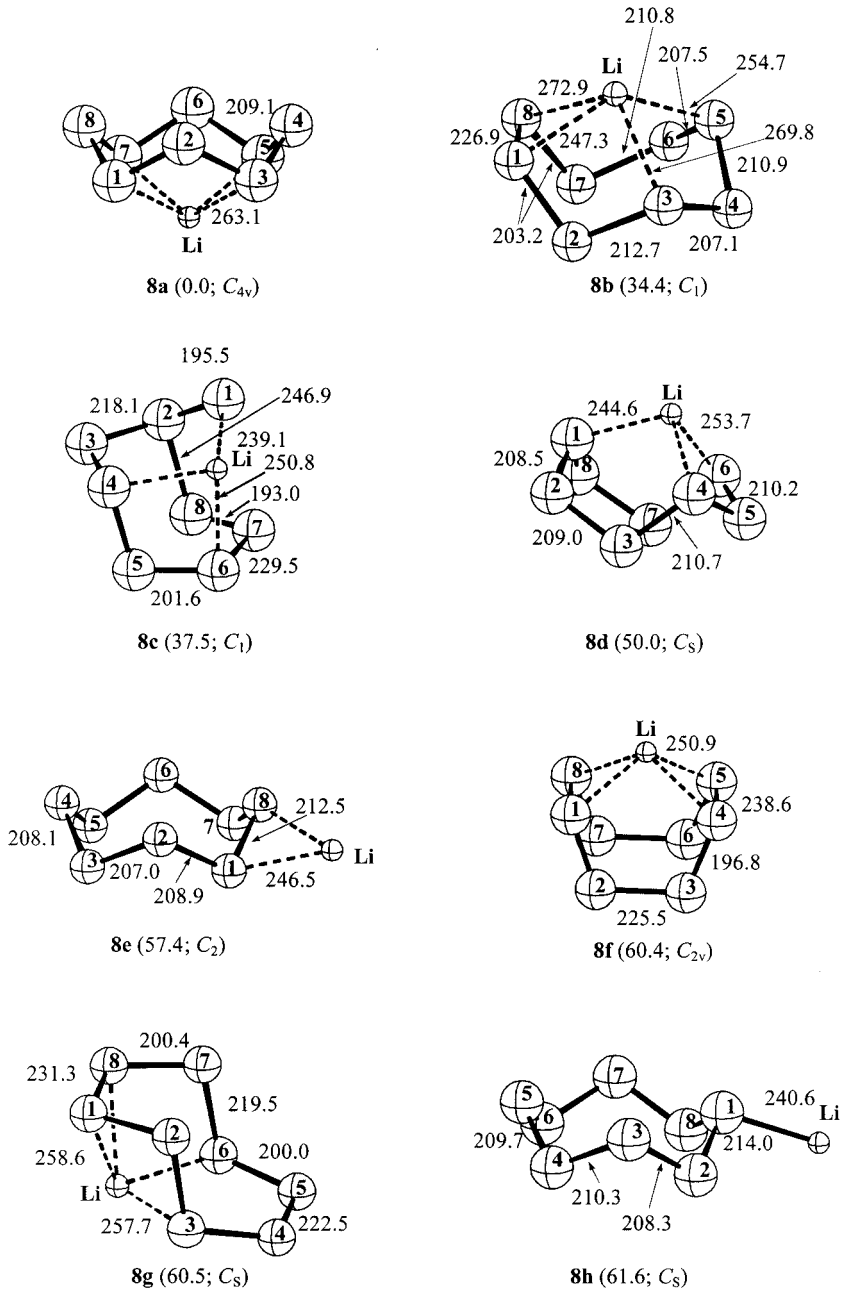

Figure 2. Structures of the eight lowest-energy isomers (**8a**–**h**) of composition $[LiS_8]^+$ (relative energies in kJ·mol^{-1} and symmetries are given in parentheses). Bond lengths in pm.

the lone-pair orbitals of the three ring atoms 1, 4, and 6. The three shortest Li–S distances are 244.6 pm (1) and 253.7 pm (2). As a consequence of the asymmetric coordination, the S–S bonds are no longer equivalent but their lengths range from 208.5 to 210.7 pm. This range is narrower than in the free ligand of identical conformation containing S–S bonds of between 205.9 and 213.9 pm. The free *exo–endo* shaped ligand is less stable than the crown structure by 34.7 kJ·mol^{-1}.[13] In other words, the coordination to Li^+ destabilizes the *exo–endo* form by 15.3 kJ·mol^{-1} because only three Li–S bonds are formed compared to four in **8a**. The binding energy of **8d** is –141.2 kJ·mol^{-1}.

The $[LiS_8]^+$ isomer **8e** consists of a crown-shaped S_8 ring with the Li cation located on one of the C_2 axes of the ring and bridging just one S–S bond, which becomes the longest bond in the ligand (212.5 pm). Because of the lower coordination number of 2, the binding energy of –99.2 kJ·mol^{-1} is significantly smaller (by 37%) than in the case of **8a** with CN = 4.

There are two $[LiS_8]^+$ isomers formally derived from the tub- or boat-like S_8 isomer **5** shown in Figure 1. Structure **8f** is of C_{2v} symmetry with CN(Li) = 4 and Li–S distances of 250.9 pm (Figure 2). The S–S bond lengths range from 196.8 to 238.6 pm. This structure is less stable than isomer

 © 2005 Wiley-VCH Verlag GmbH & Co. KGaA, Weinheim

Table 2. Selected bond angles and torsional angles [°] of the $[LiS_8]^+$ isomers **8a**–**v** [B3LYP/6-31G(2df,p) optimized geometries]. For the numbering of the sulfur atoms, see Figures 2–5.

Species	Bond angles (α) and torsion angles (τ)
8a	α_{123} = 105.6, α_{234} = 110.2, α_{1Li3} = 78.6, τ_{1234} = –98.9
8b	α_{123} = 104.7, α_{234} = 108.8, α_{345} = 102.7, α_{456} = 109.3, α_{567} = 109.3, α_{678} = 108.1, α_{782} = 105.9, α_{812} = 109.2, α_{1Li3} = 78.8, α_{1Li5} = 125.9, α_{1Li8} = 51.3, τ_{1234} = –107.9, τ_{2345} = 83.8, τ_{3456} = –108.1, τ_{4567} = 64.4, τ_{5678} = 59.5, τ_{6781} = –108.1, τ_{7812} = 6.3, τ_{8123} = 92.9
8c	α_{123} = 112.2, α_{234} = 106.9, α_{345} = 107.6, α_{456} = 103.9, α_{567} = 105.2, α_{678} = 107.0, α_{782} = 101.4, α_{1Li6} = 119.0, α_{1Li4} = 96.1, α_{21Li} = 103.4, τ_{1234} = –38.1, τ_{2345} = –76.1, τ_{3456} = 108.8, τ_{4567} = –83.9, τ_{5678} = –2.4, τ_{6782} = 88.0, τ_{7821} = 7.5
8d	α_{123} = 108.6, α_{234} = 106.7, α_{345} = 103.9, α_{456} = 110.0, α_{1Li4} = 98.3, α_{4Li6} = 85.4, τ_{1234} = 50.6, τ_{2345} = –116.2, τ_{3456} = 84.3, τ_{56Li1} = 110.6
8e	α_{123} = 105.6, α_{234} = 108.6, α_{345} = 107.9, α_{812} = 108.5, α_{1Li8} = 51.1, τ_{1234} = –93.4, τ_{2345} = 100.1, τ_{3456} = –103.6, τ_{1876} = 97.9, τ_{2187} = –106.1
8f	α_{123} = 110.4, α_{812} = 104.1, α_{1Li8} = 56.8, α_{1Li4} = 92.5, τ_{1234} = 0, τ_{2345} = –84.6, τ_{3456} = 0
8g	α_{123} = 101.3, α_{234} = 108.3, α_{345} = 110.0, α_{812} = 107.2, α_{1Li3} = 77.9, α_{1Li8} = 53.1, α_{3Li6} = 88.4, α_{6Li8} = 77.9, τ_{1234} = –141.0, τ_{2345} = 81.6, τ_{8123} = 87.8
8h	α_{123} = 106.9, α_{234} = 107.9, α_{345} = 108.0, α_{456} = 108.1, α_{21Li} = 99.4, α_{218} = 110.7, τ_{1234} = 96.1, τ_{2345} = –98.7, τ_{3456} = 100.6, τ_{321Li} = 155.1, τ_{2187} = 99.5
8i	α_{123} = 111.1, α_{234} = 104.9, α_{345} = 105.4, α_{456} = 105.3, α_{567} = 104.5, α_{678} = 103.3, α_{781} = 112.5, α_{821} = 99.3, α_{1Li8} = 81.8, τ_{1234} = –30.8, τ_{2345} = –106.0, τ_{3456} = 80.5, τ_{4567} = –77.6, τ_{5678} = 105.0, τ_{6782} = –82.6, τ_{821Li} = –36.9, τ_{3287} = 5.4, τ_{Li123} = 73.6
8j	α_{123} = 109.1, α_{234} = 109.6, α_{345} = 107.0, α_{456} = 103.4, α_{567} = 108.5, α_{678} = 105.8, α_{781} = 109.0, α_{78Li} = 101.2, α_{1Li8} = 56.5, τ_{1234} = –64.1, τ_{2345} = –62.8, τ_{3456} = 110.9, τ_{4567} = –82.9, τ_{5678} = 103.2, τ_{6781} = –99.3, τ_{678Li} = –163.0, τ_{7812} = 4.0, τ_{Li123} = 165.8
8k	α_{123} = 107.6, α_{234} = 105.2, α_{345} = 103.7, α_{456} = 105.6, α_{567} = 105.8, α_{678} = 109.4, α_{782} = 106.4, α_{1Li7} = 93.4, α_{21Li} = 102.7, τ_{1234} = –37.0, τ_{2345} = –79.9, τ_{3456} = 112.1, τ_{4567} = –84.6, τ_{5678} = 0.4, τ_{6782} = 92.0, τ_{1287} = 8.4, τ_{Li128} = 29.1
8l	α_{123} = 104.0, α_{234} = 106.4, α_{345} = 105.5, α_{456} = 105.5, α_{567} = 106.4, α_{678} = 104.0, α_{781} = 103.1, α_{78Li} = 135.8, α_{1Li8} = 48.1, τ_{Li123} = 72.8, τ_{1234} = 83.9, τ_{2345} = –2.2, τ_{3456} = –85.2, τ_{4567} = –2.0, τ_{5678} = 83.9, τ_{6781} = 3.8, τ_{7812} = –91.0, τ_{8123} = 4.0, τ_{678Li} = 72.6
8m	α_{812} = 106.8, α_{123} = 103.9, α_{234} = 104.1, α_{345} = 108.0, α_{1Li8} = 57.8, τ_{8123} = 85.0, τ_{1234} = –143.9, τ_{2345} = 86.0
8n	α_{123} = 109.3, α_{234} = 104.7, α_{354} = 109.1, α_{456} = 109.9, α_{21Li} = 97.0, α_{4Li7} = 86.7, τ_{Li123} = –57.6, τ_{1234} = 45.3, τ_{2345} = 103.5, τ_{3456} = –81.2, τ_{4567} = 0.0
8o	α_{812} = 1105.4, α_{123} = 105.4, α_{234} = 1104.8, α_{345} = 1108.2, α_{456} = 1107.5, α_{567} = 103.0, α_{678} = 104.5, α_{781} = 104.5, α_{1Li2} = 48.8, τ_{7812} = –14.8, τ_{8123} = 96.7, τ_{1234} = –136.2, τ_{2345} = 87.1
8p	α_{123} = 107.0, α_{234} = 105.4, α_{345} = 107.1, α_{456} = 108.5, α_{21Li} = 99.6, τ_{1234} = 47.6, τ_{2345} = 103.5, τ_{3456} = –84.2, τ_{4567} = 0.0, τ_{321Li} = 121.6
8q	α_{123} = 109.2, α_{234} = 101.1, α_{345} = 106.7, α_{456} = 103.5, α_{567} = 105.6, α_{678} = 107.5, α_{782} = 100.3, α_{821} = 112.0, α_{4Li7} = 106.5, α_{6Li7} = 53.5, τ_{1234} = 170.0, τ_{5678} = 7.7
8r	α_{123} = 106.2, α_{234} = 99.0, α_{345} = 107.8, α_{456} = 113.2, α_{45Li} = 101.4, τ_{1234} = 24.7, τ_{2345} = 103.7, τ_{3456} = –79.1, τ_{4567} = 2.7, τ_{345Li} = –143.9
8s	α_{123} = 112.6, α_{21Li} = 112.1, α_{1Li4} = 90.6, α_{1Li8} = 119.7
8t	α_{1Li8} = 153.7, α_{4Li5} = 51.3, α_{Li12} = 112.5, α_{123} = 112.4, α_{234} = 108.0, α_{345} = 104.5, τ_{Li123} = –8.6, τ_{1234} = –8.4, τ_{2345} = 88.3, τ_{3456} = 148.7, τ_{8Li12} = 174.8
8u	α_{123} = 109.2, α_{234} = 104.7, α_{34Li} = 99.5, τ_{34Li5} = –117.1
8v	α_{123} = 112.9, α_{234} = 112.9, α_{21Li} = 110.6, α_{1Li4} = 92.8, α_{1Li5} = 149.3, α_{567} = 110.5, α_{678} = 112.3

8a by 60.4 kJ·mol^{-1} compared to the relative energy of only 44.1 kJ·mol^{-1} for the free ligand.[13] The other isomer with a boat-shaped S_8 ligand (**8l**) has a relative energy of 84.3 kJ·mol^{-1}. This structure has no symmetry at all and contains a two-coordinate Li^+ ion with Li–S distances of 245.0 and 245.1 pm. The tub-like S_8 rings in **8f** and **8l** can approximately be thought of as being composed of four S_2 units because the S–S bond lengths alternate between rather small (194.0–199.8 pm) and much larger values (230.5–238.6 pm). As expected, the binding energy of **8l** (–116.2 kJ·mol^{-1}) is smaller than that of **8f** (–140.2 kJ·mol^{-1}). When we tried to optimize the geometry of a cube-like structure with connectivity $[Li(S_2)_4]^+$ (metal ion at the center of an arrangement of four parallel but independent S_2 molecules; starting symmetry D_{4h}) in analogy to the reported $[V(S_2)_4]^+$ structure,[9] we obtained structure **8f** instead.

A crown-shaped S_8 ring is also present in structure **8h** which is of C_s symmetry and less stable than **8a** by 61.6 kJ·mol^{-1} (see Figure 2). This structure resembles that of the S_8=O molecule[16] but the metal atom is in an equatorial position with an Li–S distance of 240.6 pm. Owing to the lower coordination number of 1, the binding energy is only –94.9 kJ·mol^{-1}, the lowest value among all complexes studied in this work. As expected, the distortion of the eight-membered ring by the metal ion induces a symmetrical S–S bond length alternation with the two longest bonds (214.0 pm) neighboring the Li–S bond (Figure 2). The average S–S bond length of 210.6 pm is now considerably larger than in free S_8 (208.0 pm). Attempts to optimize a similar structure with Li^+ in an axial position (as the oxygen atom in solid S_8O) resulted in isomer **8a**.

We found three isomeric $[LiS_8]^+$ cations derived from the chair conformation of S_8 (structure **6** in Figure 1; motif00–+–0+–+). The most stable of these, **8g**, with a relative energy of 60.5 kJ·mol^{-1}, contains the Li cation pyramidally coordinated to four sulfur atoms with distances in the narrow range of 257.7–258.6 pm (Figure 2). The other two iso-

mers with CN = 2 (**8m** and **8o**) are considerably less stable than **8g**, by 31.5 and 44.0 kJ·mol^{-1}, respectively (see Figure 3). The binding energies decrease in the order of decreasing relative stability (Table 1).

As has been shown previously, a characteristic feature of Li^+ complexes with sulfur-rich ligands is the bridging of single S–S bonds by the metal ion.[11] This type of bonding can also be seen in structure **8j** (Figure 3), which is a derivative of the twisted S_8 isomer **4** shown in Figure 1. Complex **8j** is characterized by an LiS_2 triangle with Li–S bonds of lengths 242.9 and 243.3 pm bridging a dramatically lengthened S–S bond of 230.2 pm. The remaining S–S bonds alternate in length symmetrically to a plane through the lithium atom and the midpoint of bond S4–S5 (symmetry C_s). This isomer with a binding energy of –104.2 kJ·mol^{-1} is less stable than **8a** by 71.3 kJ·mol^{-1}.

The asymmetrical structure **8i** is the most stable $[LiS_8]^+$ isomer with an S_7=S ligand with a relative energy of 65.6 kJ·mol^{-1}. It has the largest binding energy (–182.9 kJ·mol^{-1}) among all the $[LiS_8]^+$ structures. The metal ion coordinates to the exocyclic sulfur atom and very weakly also to two ring atoms. The seven-membered ring is considerably distorted compared to free S_7 and free S_7=S (**7**), as the SS bond lengths vary between 201.4 and 234.1 pm (Figure 3). The related isomer **8k** with the relative energy of 72.3 kJ·mol^{-1} contains the S_7 = S ligand in another connectivity (Figure 3). The metal atom is linked by a short bond (234.5 pm) to the exocyclic sulfur atom and by a much longer bond (250.3 pm) to one of the two atoms at which the HOMO of the S_7=S molecule is centered, resulting in a bicyclic structure similar to that of isomer **8c**. There are four additional complex cations containing various conformations and isomers of the S_7=S ligand. As a free molecule, S_7=S exists as two conformers (Figure 1) which are less stable then the S_8 crown (**1**) by 92.1 and 94.8 kJ·mol^{-1}, respectively.[13] The ion **8n** is of C_s symmetry (Figure 3). The metal atom is linked to the exocyclic sulfur atom with a rather short bond of 236.1 pm and to two ring

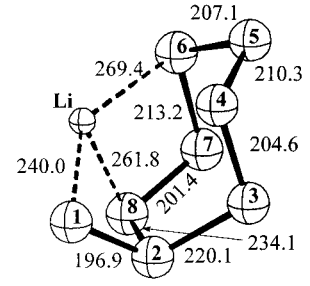

8i (65.6; C_1)

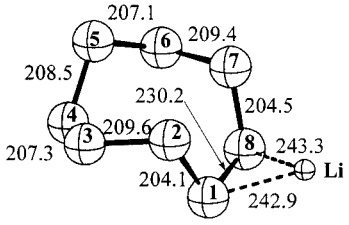

8j (71.3; C_1)

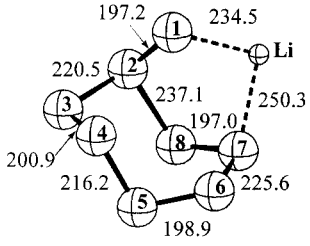

8k (72.3; C_1)

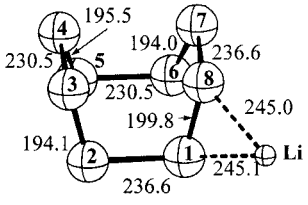

8l (84.3; C_1)

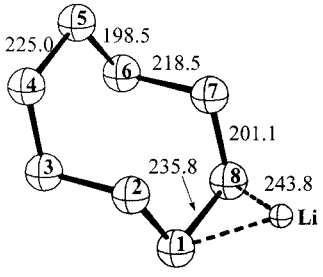

8m (91.9; C_S)

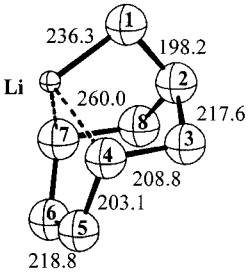

8n (93.4; C_s)

Figure 3. Isomeric structures **8i**–**n** of composition $[LiS_8]^+$ (relative energies in kJ·mol^{-1} and symmetries are given in parentheses). Bond lengths in pm.

 © 2005 Wiley-VCH Verlag GmbH & Co. KGaA, Weinheim

atoms with bond lengths of 260.1 pm forming a tricyclic structure. This type of interaction results in a binding energy of –155.2 kJ·mol^{-1}. The conformation of the seven-membered ring is very similar to that of the free S_7 molecule,[17] with one torsion angle of zero and a strong and symmetrical bond length alternation. The compact and cluster-like geometry of **8n** is less stable than **8a** by 93.4 kJ·mol^{-1}. This relative energy is practically identical to the relative energy of the most stable conformation of the free S_7=S ligand compared to the crown-shaped S_8 molecule.[13] Structure **8p** contains the metal atom coordinated just to the exocyclic sulfur atom of S_7=S, which carries the highest negative charge in the free ligand.[13] The exocyclic sulfur atom is in an axial position which is stabilized by the anomeric effect. The corresponding structure with the LiS group in an equatorial position (**8p′**) is also a minimum on the PES but slightly less stable than **8p**. Interestingly, on the PES of $[HS_8]^+$ a structure similar to **8p** with the hydrogen atom coordinated just to the exocyclic sulfur atom represents the global minimum structure.[18] We notice that the field strength of Li^+ is evidently not high enough to stabilize the S_7=S structure over the crown-shaped eight-membered ring as the proton does. Even less stable than **8p** are two isomers with other coordination patterns (structures **8q**,**r** in Figure 4 and Table 1). These structures will not be discussed in detail.

We found three minimal energy structures of composition $[LiS_8]^+$, each containing two S_4 ligands (Figure 5). However, these isomers are much less stable than all the complexes with the undissociated S_8 ligand, despite their larger binding energies (Table 1). This finding is in agreement with the corresponding results obtained for $[LiS_6]^+$ complexes.[11] The most stable of the $[Li(S_4)_2]^+$ complexes (isomer **8s**), with a relative energy of 132.9 kJ·mol^{-1}, is of D_{2d} symmetry with two planar LiS_4 heterocycles joined by a common Li atom. These two rings are perpendicular to each other. The *cis*-planar conformation of the two S_4 ligands corresponds to the global minimum structure of the free S_4 molecule.[19] The same holds for the most remarkable structure **8u** in which the two S_4 ligands are monodentate. This nine-atomic chain of C_2 symmetry consists of two planar segments of six atoms each, having the central three-atom unit S–Li–S in common. The torsion angle between the two planes is 126.5°. The relative energy of **8u** is 146.0 kJ·mol^{-1}. Complex **8v**, on the other hand, contains one chelating and one open-chain S_4 ligand, the latter in the *trans*-planar conformation (Figure 4) resulting in a relative energy of 178.9 kJ·mol^{-1}. In species **8v** the torsion angle between the two planar S_4 units is 159.8°. The binding energies of **8s**,**u**,**v** (–216.7, –203.6, and –212.0 kJ·mol^{-1}, respectively) are much higher than for the $[LiS_8]^+$ complexes with the eight-atomic ligands.

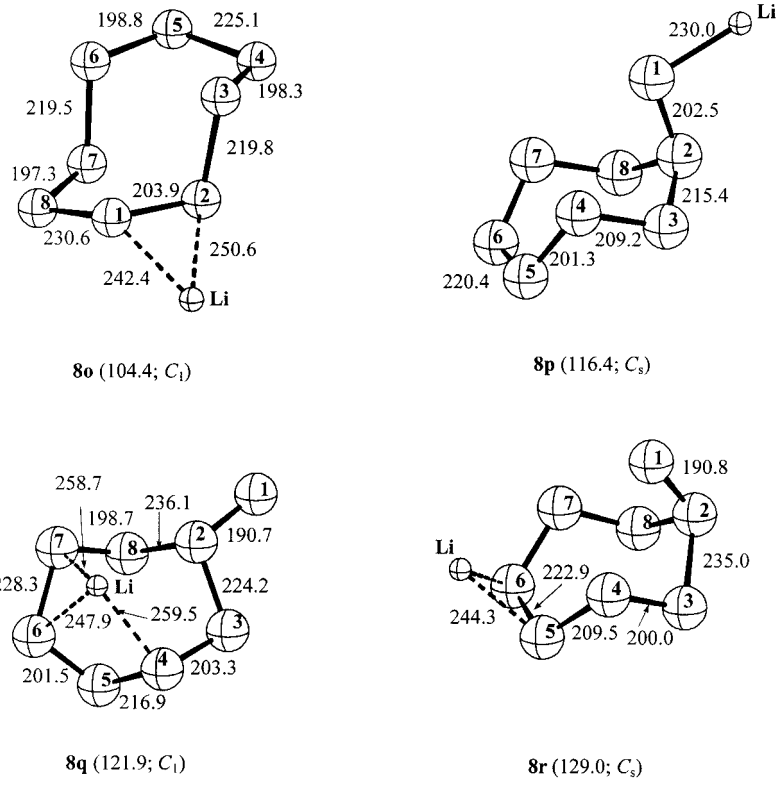

8o (104.4; C_1) **8p** (116.4; C_s)

8q (121.9; C_1) **8r** (129.0; C_s)

Figure 4. Isomeric structures **8o**–**r** of composition $[LiS_8]^+$ (relative energies in kJ·mol^{-1} and symmetries are given in parentheses). Bond lengths in pm.

 © 2005 Wiley-VCH Verlag GmbH & Co. KGaA, Weinheim

It is worth noting that the related complex of composition $[LiS_4]^+$ also exists as two isomers with either a monodentate or a bidentate S_4 ligand (see Figure 5). Both isomers are planar. The five-membered heterocycle **4a** (binding energy –124.7 kJ·mol^{-1}) is more stable than **4b** (binding energy –113.2 kJ·mol^{-1}). Addition of another S_4 to **4a** with formation of **8s** liberates –92.0 kJ·mol^{-1}.

Because the S_8 molecule can also exist as a triplet chain (structure **9** in Figure 1), we have investigated its ability to coordinate to Li^+. The resulting triplet cation (**8t**) forms an eight-membered heterocycle with CN(Li) = 2+2 (Figure 5). Six torsion angles of this ring are within 10° of either 0° or 180°, that is, planarity (Table 2). Thus, this heterocycle is rather flat. The relative energy of 142.5 kJ·mol^{-1} is slightly lower than the corresponding energy of **9** (151.2 kJ·mol^{-1}). However, the binding energy (–165.3 kJ·mol^{-1}) is higher than in the case of the global minimum structure **8a** by 10 kJ·mol^{-1}. We did not consider other possible triplet chain structures with lower coordination numbers as they are expected to have lower binding energies. However, a singlet nine-membered $[LiS_8]^+$ heterocycle is less stable than the global minimum structure **8a** by only 81.7 kJ·mol^{-1}. Finally, we would like to mention that the connectivity $[Li(S_6)(S_2)]^+$ represents also a minimum on the PES of $[LiS_8]^+$, but this structure is even less stable than **8v**.

The present results and the calculations on complexes of the types $[LiS_6]^+$[11] and $[LiS_7]^+$[20] indicate that the global minimum structures always contain the most stable conformation of the ligand donating electron density to the metal atom through three or four atoms. Hence, we expect that other alkali metal cations form analogous symmetrical complexes with sulfur homocycles. However, univalent transition-metal polysulfur cations seem to prefer other structures and different compositions (see below).

Our present data together with previous results[11] allow the calculation of the reaction energy of the following gas-phase sulfurization reaction between the most stable species involved:

$[LiS_6]^+$ (**6a**) + ¼ S_8 (**1**) → $[LiS_8]^+$ (**8a**)

ΔE_o = –49.0 kJ·mol^{-1}, $\Delta H°_{298}$ = –47.8 kJ·mol^{-1}, $\Delta G°_{298}$ = –33.5 kJ·mol^{-1}

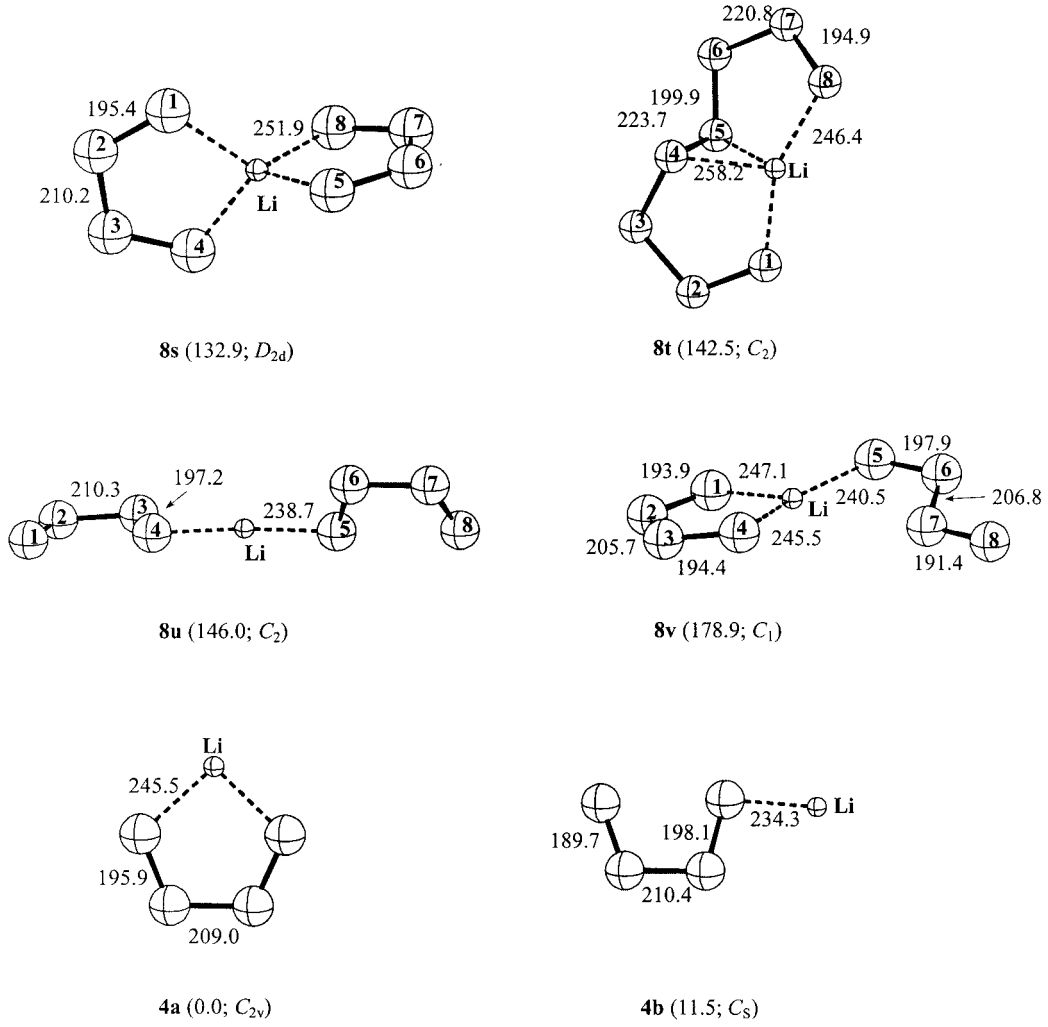

8s (132.9; D_{2d}) **8t** (142.5; C_2)

8u (146.0; C_2) **8v** (178.9; C_1)

4a (0.0; C_{2v}) **4b** (11.5; C_s)

Figure 5. Isomeric structures **8s**–**v** of composition $[LiS_8]^+$ and **4a**–**b** of composition $[LiS_4]^+$, all containing chain-like ligands (relative energies in kJ·mol^{-1} and symmetries are given in parentheses). Bond lengths in pm.

 © 2005 Wiley-VCH Verlag GmbH & Co. KGaA, Weinheim

One, therefore, would expect the cation $[LiS_6]^+$ to be unstable in the presence of an excess of S_8, for example in a mass spectrometric experiment. The lithium cation basicity of S_8 (**1**), that is, the negative Gibbs energy of the addition of Li^+ to S_8 producing **8a** at 298 K, is 122.7 kJ·mol^{-1}.

Atomic Charges

The atomic charges of the 23 complexes of composition $[LiS_8]^+$ calculated by the NBO approach are listed in Table S2 in the Supporting Information. The charge transfer from the polysulfur ligand(s) to the metal atom varies between 0.04 and 0.27 electrostatic units. In the various isomers all sulfur atoms linked to Li^+ are negatively charged while all others are positive or practically neutral, with the exception of exocyclic and terminal atoms, which are always negative. The metal ion clearly polarizes the valence electrons of the ligand(s) and thus induces dipole moments directed towards this cation. This can be seen, for example, in the charge distribution of the global minimum structure **8a**. The three-coordinate sulfur atoms bear a small negative charge of –0.03, while the two-coordinate atoms have a positive charge of +0.07 and Li^+ has gained 0.18 electrons from the ligand. Exocyclic sulfur atoms as in S_7=S are always negatively charged; therefore, Li^+ prefers to bind to these atoms except in the high-energy isomers **8q** and **8r**. A high degree of charge separation is also found in the three cations with S_4 ligands **8s**,**u**,**v**. In these complexes the charge differences between the metal atom and the coordinating sulfur atoms are considerably larger than 1 electrostatic unit. The structures of the latter three ions can be reproduced readily using point-charge model calculations.

Vibrational Spectra

To identify the species **8a** or similar cations containing crown-shaped S_8, one may use vibrational spectroscopy, as the bonds between two-coordinate sulfur atoms are excellent Raman scatterers and the metal–sulfur bonds will give rise to vibrations of high infrared intensity. In addition, the vibrational spectrum of a ligand contains information about the influence of the metal ion on the ligand. Therefore, we have compared the vibrational spectra of S_8 (**1**) and $[LiS_8]^+$ (**8a**) in Table 3. The additional atom increases the number of vibrational degrees of freedom by 3. Taking the lowering of the symmetry from D_{4d} to C_{4v} into account, the irreducible representation $2A_1 + B_1 + B_2 + 2E_1 + 3E_2 + 2E_3$ of S_8[21] changes to $4A_1 + A_2 + 3B_1 + 3B_2 + 5E$ for $[LiS_8]^+$. The three E_2 modes of S_8 split into B_1 and B_2 modes in $[S_8Li]^+$ while all E_1 and E_3 modes of S_8 end up as E modes in the cation. The vibrational transitions introduced by the Li atom are calculated at 254 cm^{-1} (A_1) and 222 cm^{-1} (E). As can be seen from the data in Table 3, the wavenumbers of the S_8 ligand are very similar to those of the free S_8 molecule in agreement with the weak interaction deduced above from the internuclear distances and the atomic charges.

Table 3. Calculated harmonic fundamental vibrations (cm^{-1}) of S_8 (D_{4d} symmetry) and of $[S_8Li]^+$ (C_{4v}) as well as infrared intensities (km·mol^{-1}) of the latter. Observed wavenumbers of S_8 (dissolved in CS_2) are given in parentheses (according to ref.[21]).

S_8	Symmetry	$[S_8Li]^+$	Symmetry	Infrared intensity
474 (476)	A_1	465	A_1	0.0
466 (471)	E_1	462	B_1	0.0
462 (476)	E_2	460	E	0.9
		453	B_2	0.0
415 (444)	E_3	415	E	2.2
389 (–)	B_1	385	A_2	0.0
		254	A_1 (LiS_3)	20.7
247 (248)	E_3	251	E	5.5
		222	E (LiS_3)	19.4
241 (243)	B_2	220	A_1	12.9
213 (218.5)	A_1	196	A_1	45.0
189 (191)	E_1	171	E	4.7
145 (152.5)	E_2	155	B_1	0.0
		141	B_2	0.0
72 (86)	E_2	94	B_2	0.0
		68	B_1	0.0

Other Metal Ions

To investigate the dependence of the reported structures on the metal ion, we have carried out preliminary calculations on some ions of composition $[MS_8]^+$ with M = Ca, V, and Cu using calculations at the CCSD(T)/6-31G*//B3LYP/6-31G*+ZPE level after mass spectrometric observations of such species have been reported (see Introduction). In particular, we were interested in the relative stabilities of isomeric complexes containing either one crown-shaped S_8 ligand or two chain-like chelating S_4 ligands. The thermodynamic results are summarized in Tables 4 and S3 (Supporting Information), and the molecular structures are shown in Figure 6. For the free metal ions, the most stable electronic configuration[22] was used to calculate the binding energies. It turned out that for all three cations, the complex with the connectivity $[M(S_4)_2]^+$ is more favorable energetically than the structures analogous to **8a**. The binding energy for $[Li(S_8)]^+$ is now obtained as –164.3 kJ·mol^{-1} rather than –156.5 kJ·mol^{-1} at the G3X(MP2) level (Table 1). The interaction of Ca^+ with S_8 (**1**) is relatively weak (binding energy only –71.4 kJ·mol^{-1}). In the case of Cu^+, the symmetry of the S_8 complex is only C_{2v} rather than C_{4v}, and $[V(S_8)]^+$ is even of C_s symmetry. The complexes $[Ca(S_2)_4]^+$ and $[Cu(S_2)_4]^+$ contain planar S_4 ligands and the metal atoms are tetrahedrally coordinated. $[V(S_4)_2]^+$ has an interesting although asymmetrical geometry (Figure 6) with the higher coordination number 6 for the metal atom and two tridentate S_4 ligands explaining its remarkable binding energy of –586.5 kJ·mol^{-1}. This nonplanar ion with SSSS torsion angles of 57° and 63° has a triplet ground state while the isomeric complex with the eight-atomic crown-shaped ligand is a quintet (Table 4), as is the free V^+ ion. Even more stable than $[V(S_4)_2]^+$ are the isomeric complexes $[V(S_2)(S_6)]^+$ and $[V(S_3)(S_5)]^+$ (not shown) which both prefer the singlet state. In contrast to the report by Dance et al.,[9] we could not locate a minimum structure

 © 2005 Wiley-VCH Verlag GmbH & Co. KGaA, Weinheim

Table 4. Relative energies ΔE_o and binding energies ($kJ \cdot mol^{-1}$) of complexes of composition $[MS_8]^+$ with M = Li, Ca, V, Cu calculated at the CCSD(T)/6-31G*//B3LYP/6-31G*+ZPE level of theory. The relative energy of the complex with an eight-atomic crown-shaped S_8 ligand was set equal to zero in all cases.

Metal ion	Relative energy of $[M(S_4)_2]^+$	Binding energy of $[M(S_8)]^+$	Binding energy of $[M(S_4)_2]^+$
Li^+ (^1S)	+73.4	–164.3	–269.1
Ca^+ (^2S)	–49.0	–71.4	–298.6
V^+ (^5D)	–213.3	–195.0[a]	–586.5[b] –656.6[c]
Cu^+ (^1S)	–58.2	–304.5	–540.9

[a] Quintet ground state. [b] Triplet ground state. [c] Calculated with respect to triplet V^+.

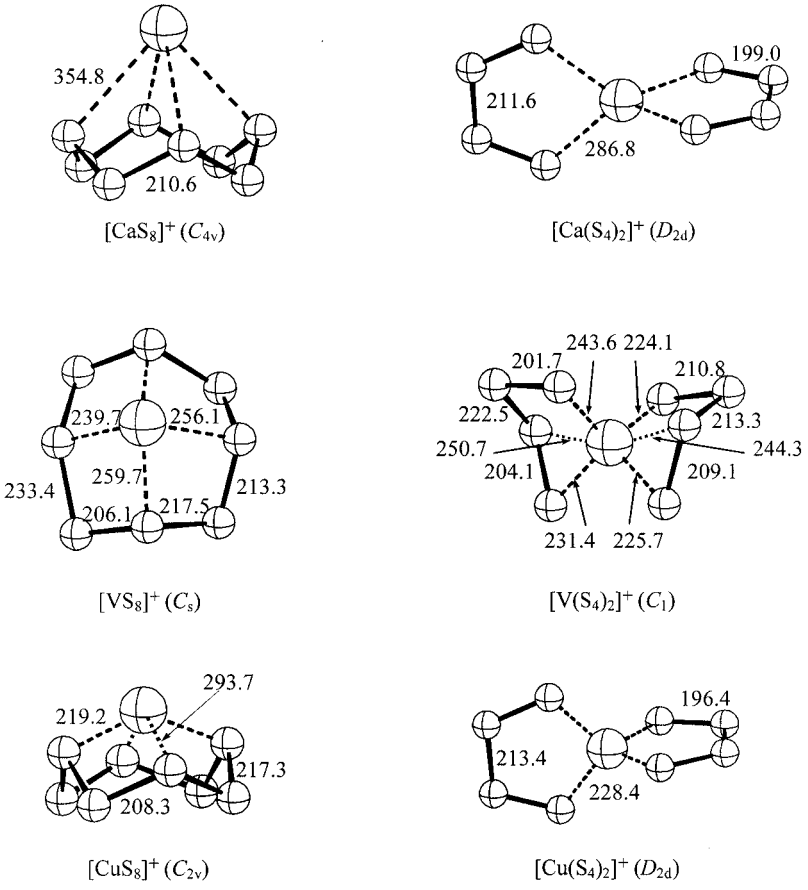

Figure 6. Structures of the complexes $[M(S_8)]^+$ and $[M(S_4)_2]^+$ with M = Ca, V, Cu, calculated at the B3LYP/6-31G* level. Bond lengths in pm.

for $[V(S_2)_4]^+$. More details on the polysulfur complexes of transition metals will be published elsewhere.

Conclusions

Lithium cations form stable complexes with neutral sulfur molecules such as various isomers of S_8 and S_4 with binding energies ranging from –95 to –217 $kJ \cdot mol^{-1}$. The crown-shaped S_8 ring of D_{4d} symmetry coordinates to Li^+ as a tetradentate ligand resulting in a complex of C_{4v} symmetry, which represents the global minimum on the PES of $[LiS_8]^+$. The interaction is explained by ion–dipole attraction with a charge transfer of only 0.18 electrostatic units. Consequently, the vibrational spectrum of the S_8 ligand changes only slightly on complex formation, reflecting however the lower symmetry. Higher-energy conformers and isomers of *cyclo*-S_8 such as twisted, chair- and tub-like eight-membered rings, branched seven-membered rings (S_7=S) as well as the triplet and singlet chains also form complexes with Li^+ with the coordination number of the metal atom varying between 1 and 4. In general, the conformation of the ligand changes only very little on complex formation but the relative energy changes are sometimes considerable. Complexes of composition $[LiS_8]^+$ containing two S_4 ligands are much less stable than those with one S_8 or S_7=S ligand. The planar S_4 unit may coordinate either as a chelating dihapto ligand or as a chain-like monohapto ligand of either *cis*- or *trans*-conformation. Consequently, there are several types of $[Li(S_4)_2]^+$ complexes. We should note that our calculations may relate directly to experiments

 © 2005 Wiley-VCH Verlag GmbH & Co. KGaA, Weinheim

in the gas phase, but not in a condensed phase, as Li^+ is strongly solvated in a dielectric medium. As a result, the lithium binding energies are expected to be absolutely smaller in solution. Complexes of composition $[MS_8]^+$ with M = Ca, V, and Cu prefer the connectivity $[M(S_4)_2]^+$ over $[M(S_8)]^+$ with CN(M) = 4 or 6 and binding energies in the range –266 to –586 kJ·mol^{-1}, but in the case of vanadium even more stable isomers of connectivities $[V(S_2)(S_6)]^+$ and $[V(S_3)(S_5)]^+$ have been located on the PES.

Computational Methods

Standard ab initio and density functional calculations were carried out with the GAUSSIAN 98 and 03 series of programs[23] at the G3X(MP2) level of theory.[24] This theory corresponds effectively to QCISD(T)/G3XL//B3LYP/6-31G(2df,p) energy together with zero-point vibrational and higher-level corrections. The G3X(MP2) theory represents a modification of the G3(MP2) theory,[25] with three important modifications: (1) B3LYP/6-31G(2df,p) geometry, (2) B3LYP/6-31G(2df,p) zero-point energy, and (3) addition of a *g* polarization function to the G3Large basis set for the second-row atoms at the Hartree–Fock level. These features are particularly important for the proper description of the sulfur-containing compounds examined in this work.[13,18,19] For instance, the geometries and stabilities of several cluster species are poorly predicted by the MP2 theory.[13]

Harmonic frequencies were calculated at the B3LYP/6-31G(2df,p) level to characterize stationary points as equilibrium structures, with all wavenumbers real, or transition states, with one imaginary wavenumber. The binding energy (ΔE) of the metal ion complexes were computed as the difference between the energy of the lithiated species and the total energy of the two free monomers in the same conformation as found in the complex. The Gibbs energy differences (ΔG) were computed from the equation $\Delta G_T = \Delta H_T - T\Delta S$, where ΔS is the entropy change and $\Delta H_T = \Delta H_0 + (H_T - H_0)$. The thermal correction ($H_{298} - H_0 = 6.197$ kJ·mol^{-1}) and the entropy value ($S_{298} = 133.017$ J·mol^{-1}·K^{-1}) of the lithium cation were taken from the JANAF compilation.[26] Unless otherwise noted, all relative energies of S_n molecules and $[LiS_8]^+$ ions reported in this publication are given as ΔE_o and correspond to the G3X(MP2) level, while all reported structural parameters of these species correspond to the B3LYP/6-31G(2df,p) level. The structures of all complexes of composition $[MS_8]^+$ (M = Ca, V, Cu) were examined by the density functional method B3LYP with the 6-31G* basis set with higher-level single-point energy calculations obtained at the CCSD(T)/6-31G* level. All structures were optimized initially without any symmetry constraint and were reoptimized with a higher symmetry after a local energy minimum was obtained. In the case of vanadium, the singlet, triplet, and quintet states have been investigated for both $[M(S_8)]^+$ and $[M(S_4)_2]^+$ species.

Supporting Information (see also footnote on the first page of this article): Absolute energies and atomic charges of the isomers of composition $[LiS_8]^+$ and total energies as well as zero-point energies (ZPE) of the complexes $[M(S_8)]^+$ and $[M(S_4)_2]^+$ and related species.

Acknowledgments

This work has been supported by the Deutsche Forschungsgemeinschaft, the Norddeutscher Verbund für Hoch- und Höchstleistungsrechnen, the Fonds der Chemischen Industrie, and the National University of Singapore.

[1] a) M. Schröder, "S-Donor-Ligands", in *Encyclopedia of Inorganic Chemistry*, (Ed.: B. R. King), John Wiley & Sons, New York, **1985**, vol. 7, pp. 3577–3594; b) M. Draganjac, T. B. Rauchfuss, *Angew. Chem.* **1985**, *97*, 745–760; *Angew. Chem. Int. Ed. Engl.* **1985**, *24*, 742–757; c) A. Müller, E. Diemann, *Adv. Inorg. Chem.* **1987**, *31*, 89–122; d) M. G. Kanatzidis, S.-P. Huang, *Coord. Chem. Rev.* **1994**, *130*, 509–621; e) E. I. Stiefel, K. Matsumoto (Eds.), *Transition Metal Sulfur Chemistry*, ACS Symposium Series, **1996**, vol. 653; f) N. Takeda, N. Tokitoh, R. Okazaki, *Top. Curr. Chem.* **2003**, *231*, 153–202; g) T. B. Rauchfuss, *Inorg. Chem.* **2004**, *43*, 14–26.
[2] H. W. Roesky, M. Thomas, J. Schimkowiak, P. G. Jones, W. Pinkert, G. M. Sheldrick, *J. Chem. Soc. Chem. Commun.* **1982**, 895–896.
[3] T. S. Cameron, A. Decken, I. Dionne, M. Fang, I. Krossing, J. Passmore, *Chem. Eur. J.* **2002**, *8*, 3386–3401.
[4] A. Bacchi, W. Baratta, F. Calderazzo, F. Marchetti, G. Pelizzi, *Inorg. Chem.* **2002**, *41*, 3894–3900.
[5] F. A. Cotton, E. V. Dikarev, M. A. Petrukhina, *Angew. Chem.* **2001**, *113*, 1569–1571; *Angew. Chem. Int. Ed.* **2001**, *40*, 1521–1523.
[6] P. Coppens, Y. W. Yang, R. H. Blessing, W. F. Cooper, F. K. Larsen, *J. Am. Chem. Soc.* **1977**, *99*, 760–766.
[7] a) T. J. MacMahon, T. C. Jackson, B. S. Freiser, *J. Am. Chem. Soc.* **1989**, *111*, 421–427; b) Z. Yu, N. Zhang, X. Wu, Z. Gao, Q. Zhu, F. Kong, *J. Chem. Phys.* **1993**, *99*, 1765–1770.
[8] a) I. G. Dance, K. J. Fisher, G. D. Witt, *Inorg. Chem.* **1996**, *35*, 4177–4184; b) I. Dance, *ACS Symp. Ser.* **1996**, *653*, 135–152; c) K. Fisher, I. Dance, G. Willett, *J. Chem. Soc. Dalton Trans.* **1998**, 975–980; d) P. Liu, C. Han, Z. Gao, F. Kong, Q. Zhu, *J. Phys. Chem. B* **1999**, *103*, 3337–3339.
[9] I. Dance, K. Fisher, G. Willett, *Angew. Chem.* **1995**, *107*, 215–218; *Angew. Chem. Int. Ed. Engl.* **1995**, *34*, 201–203.
[10] I. G. Dance, K. J. Fisher, G. D. Willett, *J. Chem. Soc. Chem. Commun.* **1995**, 975–976.
[11] Y. Steudel, M. W. Wong, R. Steudel, *Chem. Eur. J.* **2005**, *11*, 1281–1293.
[12] O. P. Charkin, M. L. McKee, N. M. Klimenko, P. v. R. Schleyer, *Russ. J. Inorg. Chem.* **1998**, *43*, 240–247.
[13] M. W. Wong, Y. Steudel, R. Steudel, *Chem. Phys. Lett.* **2002**, *364*, 387–392.
[14] a) R. Steudel, R. Reinhardt, T. Sandow, *Angew. Chem.* **1977**, *89*, 757–758; *Angew. Chem. Int. Ed. Engl.* **1977**, *16*, 716; b) R. Steudel, *Top. Curr. Chem.* **2003**, *231*, 203–230.
[15] R. Steudel, *Angew. Chem.* **1975**, *87*, 683–692; *Angew. Chem. Int. Ed. Engl.* **1975**, *14*, 655–664.
[16] P. Luger, H. Bradaczek, R. Steudel, M. Rebsch, *Chem. Ber.* **1976**, *109*, 180–184.
[17] R. Steudel, J. Steidel, J. Pickardt, F. Schuster, R. Reinhardt, *Z. Naturforsch. B* **1980**, *35*, 1378–1383.
[18] M. W. Wong, Y. Steudel, R. Steudel, *J. Chem. Phys.* **2004**, *121*, 5899–5907.
[19] M. W. Wong, R. Steudel, *Chem. Phys. Lett.* **2003**, *379*, 162–169.
[20] M. W. Wong, Y. Steudel, R. Steudel, *Inorg. Chem.*, submitted.
[21] Review: B. Eckert, R. Steudel, *Top. Curr. Chem.* **2003**, *231*, 31–98.
[22] http://physics.nist.gov/cgi-bin/AtData/main_asd.
[23] M. J. Frisch, G. W. Trucks, H. B. Schlegel, G. E. Scuseria, M. A. Robb, J. R. Cheeseman, V. G. Zakrzewski, J. A. Montgomery, Jr., R. E. Stratmann, J. C. Burant, S. Dapprich, J. M. Millam, A. D. Daniels, K. N. Kudin, M. C. Strain, O. Farkas, J. Tomasi, V. Barone, M. Cossi, R. Cammi, B. Mennucci, C. Pomelli, C. Adamo, S. Clifford, J. Ochterski, G. A. Petersson, P. Y. Ayala, Q. Cui, K. Morokuma, D. K. Malick, A. D. Rabuck, K. Raghavachari, J. B. Foresman, J. Cioslowski, J. V. Ortiz, A. G. Baboul, B. B. Stefanov, G. Liu, A. Liashenko, P. Pis-

 © 2005 Wiley-VCH Verlag GmbH & Co. KGaA, Weinheim

korz, I. Komaromi, R. Gomperts, R. L. Martin, D. J. Fox, T. Keith, M. A. Al-Laham, C. Y. Peng, A. Nanayakkara, C. Gonzalez, M. Challacombe, P. M. W. Gill, B. Johnson, W. Chen, M. W. Wong, J. L. Andres, C. Gonzalez, M. Head-Gordon, E. S. Replogle, J. A. Pople, *GAUSSIAN 98*, Gaussian Inc., Pittsburgh, PA, **1998**.

[24] L. A. Curtiss, P. C. Redfern, K. Raghavachari, J. A. Pople, *J. Chem. Phys.* **2001**, *114*, 108–117.

[25] L. A. Curtiss, P. C. Redfern, K. Raghavachari, V. Rassolov, J. A. Pople, *J. Chem. Phys.* **1999**, *110*, 4703–4709.

[26] NIST-JANAF Thermochemical Tables, 4th ed. (Ed.: M. W. Chase), National Institute of Standards and Technology, New York, **1998**.

Received: December 10, 2004

 © 2005 Wiley-VCH Verlag GmbH & Co. KGaA, Weinheim

μ-η¹:η¹-*N*,*N*′-Imidazolidine-Bridged Dicopper(II/III) Complexes of a New Dinucleating μ-Bis(tetradentate) Schiff Base Ligand: Synthesis, Structural Characterization, ^{1}H NMR Spectroscopy, and Magnetic Coupling

Manindranath Bera,[a] Wing Tak Wong,[b] Guillem Aromí,[c] and Debashis Ray*[a]

Keywords: N,O ligand / Imidazolidine / Copper complexes / Magnetic properties

The copper coordination chemistry of a new imidazolidine-based doubly bridging μ-bis(tetradentate) ligand, H_3mhbai is studied. A new family of pentacoordinate dinuclear complexes of formula $[Cu^{II}_2(\mu\text{-mhbai})(\mu\text{-X})]\cdot 2H_2O$ (**1**–**4**) [X = OAc, NO_3, Cl, S_2COMe], where H_3mhbai stands for 2-(2-hydroxyphenyl)-1,3-bis[4-(2-hydroxyphenyl)-4-methyl-3-aza-but-3-enyl]-2-methyl-1,3-imidazolidine, were synthesized from the ligand, H_3mhbai in air. The complex **1** was structurally characterized by X-ray crystallography. The μ-η¹:η¹-*N*,*N*′-imidazolidine bridging mode between two copper(II) ions has been identified in this complex along with a nonhelical binding mode of the μ-bis(tetradentate) ligand. Variable temperature (2–300 K) magnetic susceptibility data of **1** show the presence of a weak antiferromagnetic exchange interaction between the two triply bridged magnetically isolated copper(II) (S = 1/2) ions. The $\chi_m T$ values start to drop at temperature below 50 K, to reach a value of 0.55 $cm^3 K mol^{-1}$ at 2 K for a coupling constant value of J = –2.2 cm^{-1}. The ^{1}H NMR spectrum of the weakly coupled complex **1** shows a total of seventeen hyperfine shifted peaks, as expected from the idealized C_s symmetry of the compound, spread over a very large window of chemical shift, spanning about 130 ppm.

(© Wiley-VCH Verlag GmbH & Co. KGaA, 69451 Weinheim, Germany, 2005)

Introduction

Synthesis and characterization of novel dicopper(II/III) complexes of new diaza heterocyclic bridge[1] incorporated bis(polydentate) ligands is an active area of synthetic inorganic chemistry research during the last couple of years.[2–8] Studies on dicopper complexes of imidazolidine bridging ligands bearing additional chelating side arms in the 1- and 3-positions of the heterocycle are unknown. Dimetal complexes have the potential to provide new reactivity patterns and physical properties that could not be achieved with similar type of mononuclear complexes.[9] It is convenient to classify dinucleating ligands by the number and types of bridging groups that are used to assemble dimetal complexes. For an intimate dimetal complex having small metal–metal separation the maximum number of bridging groups is three. The diaza heterocyclic bridge containing new bis(polydentate) ligands can be developed from the known[10] imidazolidine ring formation reaction on the ethylenediamine segment of the tetramine backbone of the parent hexadentate ligand. This is some kind of chelate elaboration on the potential heterocycle bridge by Schiff base formation using ketones for the first time. Recently we have shown[11] that in absence of the imidazolidine bridging backbone the parent hexadentate ligand can give μ_4-oxo-bridged tetracopper(II) complex through ligand self-assembly. Double helical binding of the hexadentate ligand was also observed there. Dinuclear copper complexes with two metal ions in close proximity have received a great deal of attention in recent times.[12–15] Unlike other potential bridging units such as phthalazine, pyridazine, oxadiazole, thiadiazole, 1,8-naphthyridine,[9] neutral imidazolidine bridge-supported dicopper(II/III) complexes are unknown till date. Here, we report the coordination chemistry of μ-η¹:η¹-*N*,*N*′-imidazolidine-bridged dicopper(II/III) complexes of a new μ-bis(tetradentate) ligand, H_3mhbai {2-(2-hydroxyphenyl)-1,3-bis[4-(2-hydroxyphenyl)-4-methyl-3-azabut-3-enyl]-2-methyl-1,3-imidazolidine} (Scheme 1).

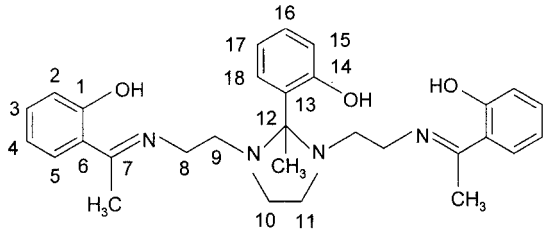

Scheme 1. 2-(2-hydroxyphenyl)-1,3-bis[4-(2-hydroxyphenyl)-4-methyl-3-azabut-3-enyl]-2-methyl-1,3-imidazolidine (H_3mhbai).

[a] Department of Chemistry, Indian Institute of Technology, Kharagpur 721 302, India,
E-mail: dray@chem.iitkgp.ernet.in
[b] Department of Chemistry, University of Hong Kong, Pokfulam Road, Pokfulam, Hong Kong SAR, P.R. China
[c] Departament de Química Inorgànica, Universitat de Barcelona, Diagonal, 647, 08028 Barcelona, Spain

This dinucleating ligand feature a 2-(hydroxyphenyl)-imidazolidine bridge, linking two arms of imine-phenol groups and support dimetallic structures with a variety of exogenous bridging ligands. The complex also binds a water dimer showing a novel example of simple near-linear self-assembled water cluster $(H_2O)_2$ in a crystalline dimetal complex.[16] Recently, it has been discovered that certain imidazole compounds can stabilize similar infinite 1D water chains[17] as potential models of biologically relevant proton wires. Similar tetrameric water structure has also been identified recently in an organic macrocyclic ligand crystal host.[18] The present work also reports the X-ray structural characterization of a dicopper(II/III) complex of a new non-macrocyclic dinucleating ligand satisfying four coordination sites around each copper center and two of which are bridging. From variable temperature magnetic measurement a weak antiferromagnetic (J = –2.2 cm^{-1}) coupling was observed for complex **1** in a distorted square-pyramidal geometry. ^1H NMR study of complex **1** also shows that at room temperature the system remains largely paramagnetic due to the very weak nature of the observed antiferromagnetic coupling.

Results and Discussion

Syntheses and Spectroscopic Characterization Studies

The μ-bis(tetradentate) ligand H_3mhbai was synthesized by the known imidazolidine ring formation reaction with 2-hydroxyacetophenone and triethylenetetramine in a mol ratio of 3:1 under reflux for 5 h and isolated in the solid form following a modified Bailer route[19] (Scheme 2). The resulting Schiff base incorporated an imidazolidine ring from the reaction of the third ketone with the two inner adjacent secondary amine nitrogen atoms of trien.[20] The parent hexadentate ligand (H_2bahped) reported earlier[11] producing novel μ_4-oxo-bridged tetracopper(II) was synthesized as a yellow oil from a similar Schiff base condensation reaction of 2-hydroxyacetophenone and triethylenetetramine (trien) in a 2:1 mol ratio under reflux for 0.5 h. In the IR spectrum of the ligand H_3mhbai, the phenolic O–H stretchings of the two terminal rings are observed at 3443 cm^{-1}. The C=N stretching frequency of the ligand is observed at 1616 cm^{-1}. In the EI-MS of the ligand, the molecular ion peak (*m*/*z*) was observed at 500, confirming the formation of the desired imidazolidine ring containing ligand. In ^1H NMR spectra the characteristic central methyl protons and terminal methyl protons both appear as singlet at δ = 1.38 and 2.21 ppm, respectively. The characteristic central methyl carbon and terminal methyl carbon atoms appear at δ = 14.51 and 26.58 ppm in ^{13}C NMR spectra, respectively. The imidazolidine ring carbon at the hydroxyphenyl substitution appears at δ = 116.83 ppm. The imine carbon appears at δ = 164.29 ppm. Both ^1H and ^{13}C NMR spectroscopic data are comparable with the literature values.[10,21] The signals due to aromatic ring protons were observed in the 6.74–7.40 ppm region. The hydrogen atoms on the imidazolidine backbone appeared as a complex set of overlapping triplet resonance signals at 2.74–2.80 ppm. The reaction of different copper(II) salts with this hitherto unknown ligand in 2:1 molar ratio in alcoholic media at room temperature affords green $[Cu^{II}_2(\mu\text{-mhbai})(\mu\text{-X})]\cdot 2H_2O$ (**1**–**3**) [X = OAc, NO_3, Cl]. Use of a stoichiometric amount of $MeCOS_2^-$ in the reaction of H_3mhbai and $CuCl_2\cdot 2H_2O$ yields $[Cu^{II}_2(\mu\text{-mhbai})(\mu\text{-}S_2COMe)]\cdot 2H_2O$ (**4**) (Scheme 2). They represent a new family of 2-phenolate-substituted imidazolidine-bridged dicopper(II/III) complexes. All the complexes are insoluble in water and separate immediately from the reaction medium. The complexes are soluble in MeCN, DMF and DMSO. The molar conductivity values in DMF are in the range 12 to 29 $\Omega^{-1}cm^2mol^{-1}$ (28 °C), consistent with the nonelectrolytic formulations of the complexes. The infrared spectrum of the complex **1** shows stretching frequencies at 1586 and 1405 cm^{-1} corresponding to asymmetric and symmetric mode of OAc^- ion present.

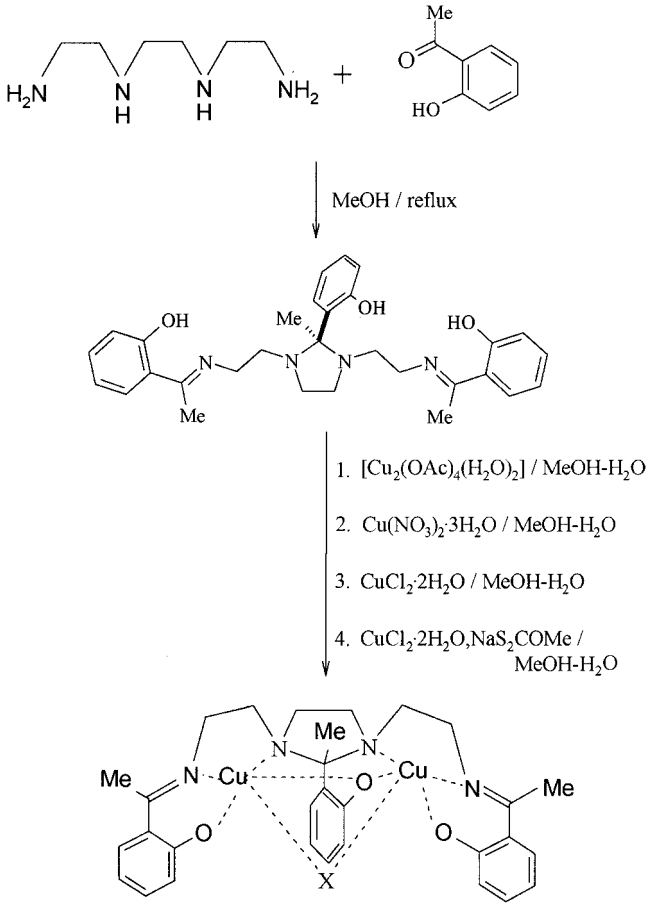

Compound	X
1	OAc^-
2	NO_3^-
3	Cl^-
4	$MeOCS_2^-$

Scheme 2.

 © 2005 Wiley-VCH Verlag GmbH & Co. KGaA, Weinheim

For complex **2**, the characteristic $\nu_{(N=O)}$ frequencies for bridging NO_3^- group appear at 1378 cm $^{-1}$ and 843 cm^{-1}, respectively, and are similar to the reported values.[22] Complex **4** shows a group of bands between 1021 and 1203 cm^{-1} assigned to ν_{C-O} and ν_{C-S} coupled modes similar to the reported values[23] which are absent in complex **3**. The room temperature magnetic moments per Cu for all the four complexes are in the range of 1.66–1.98 μ_B. Electronic spectra of the complexes **1**–**4** in dimethylformamide solutions show several intense absorption bands in the visible region which are assigned to the allowed d-d and charge transfer transitions. All the complexes exhibit similar type broad bands in 602–627 nm region with molar extinction coefficient of 230–385 L mol^{-1} cm^{-1} for d-d transitions. The higher intensity charge transfer transitions are obtained at 359–370 nm and 268–274 nm range with molar extinction coefficients of 5170–10945 L mol^{-1} cm^{-1} and 15170–24730 L mol^{-1} cm^{-1}, respectively.

X-ray Structure of Cu^{II}_2(μ-mhbai)(μ-OAc)]·2 H_2O

The identity of the compound **1** is established through X-ray structure determination. An ORTEP view of **1** is shown in Figure 1. The selected bond length and bond angles are given in Table 1. Complex **1** consists of a neutral dinuclear [Cu_2(μ-mhbai)(μ-OAc)] molecule with a hydrogen-bonded water dimer. Each copper(II) atom is in a square-pyramidal N_2O_3 environment, made up of one amine nitrogen, one imine nitrogen, one terminal phenol oxygen atom from the dinucleating ligand and one axial acetate oxygen. The exogenous acetate group binds two copper atoms in μ-*syn*-*syn*-η^1:η^1-fashion. The μ-η^1:η^1-*N*,*N*′-imidazolidine and the phenolate groups bridge two copper atoms along the edge of the bi-square-pyramid. Two axial oxygen atoms, from the acetate group, complete the triply bridging motif in the dicopper complex. The μ-bis(tetradentate) ligand connects the copper atoms through μ-η^1:η^1-*N*,*N*′-imidazolidine and phenoxy bridges. The acetate bridging in *syn*-*syn* bidentate mode is common in diiron and dimanganese complexes[24] and also found in dicopper(II/III) complexes.[25,26] The dinucleating μ-bis(tetradentate) ligand shows a nonhelical binding mode for the dicopper(II/III) complex as against the double helical binding of two parent hexadentate ligands for a tetracopper[(II)$_4$] complex reported recently by us.[11] Two nitrogen atoms, one terminal and one bridging phenolate oxygen atom from one-half of the ligand are coordinated to one metal center forming one five-membered (N–Cu–N) and two six-membered (N–Cu–O) terminal and bridging chelate rings. The chelate bite angle for the five-membered ring is in the range

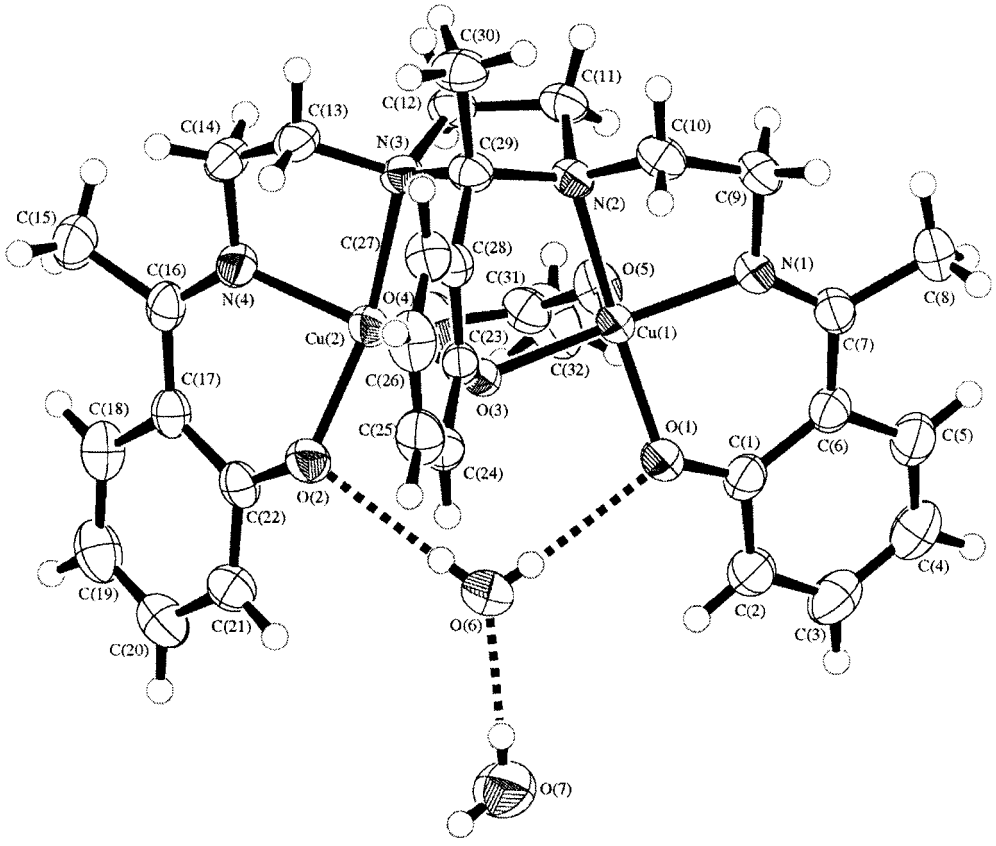

Figure 1. An ORTEP drawing of the neutral molecule [Cu^{II}_2(μ-mhbai)(μ-OAc)]·2 H_2O (**1**) with H bond indicated as dashed lines. Ellipsoids are drawn at 50% probability.

 © 2005 Wiley-VCH Verlag GmbH & Co. KGaA, Weinheim

Table 1. Selected bond lengths and angles for $[Cu^{II}_2(\mu\text{-mhbai})(\mu\text{-OAc})]\cdot 2H_2O$ (**1**).

Bond lengths [Å]	
Cu(1)–O(1)	1.911(2)
Cu(1)–O(5)	2.190(2)
Cu(1)–N(2)	2.116(2)
Cu(2)–O(3)	1.955(2)
Cu(2)–N(3)	2.203(2)
Cu(1)–O(3)	1.953(1)
Cu(1)–N(1)	1.946(2)
Cu(2)–O(2)	1.934(2)
Cu(2)–O(4)	2.132(2)
Cu(2)–N(4)	1.955(2)
Bond angles [°]	
O(1)–Cu(1)–O(3)	89.70(7)
O(1)–Cu(1)–N(1)	91.66(9)
O(3)–Cu(1)–O(5)	102.64(7)
O(3)–Cu(1)–N(2)	89.98(7)
O(5)–Cu(1)–N(2)	96.80(9)
O(2)–Cu(2)–O(3)	91.29(8)
O(2)–Cu(2)–N(3)	156.85(8)
O(3)–Cu(2)–O(4)	101.46(7)
O(3)–Cu(2)–N(4)	160.18(8)
O(4)–Cu(2)–N(4)	97.90(8)
O(1)–Cu(1)–O(5)	94.60(9)
O(1)–Cu(1)–N(2)	168.38(9)
O(3)–Cu(1)–N(1)	161.74(9)
O(5)–Cu(1)–N(1)	95.39(8)
N(1)–Cu(1)–N(2)	85.07(9)
O(2)–Cu(2)–O(4)	98.34(9)
O(2)–Cu(2)–N(4)	90.07(9)
O(3)–Cu(2)–N(3)	86.70(8)
O(4)–Cu(2)–N(3)	104.67(8)
N(3)–Cu(2)–N(4)	84.33(9)

of 84.33(9)–85.07(9)° and for the six-membered rings it is in the range of 90.07(9)–91.66(9)° for terminal and 86.70(8)–89.98(7)° for bridging. The *cis* angles around the Cu(1) ion range from 85.07(9) to 102.64(7)° with an average value of 93.23° and that around the Cu(2) ion range from 84.33(9) to 104.67(8)° with an average value of 94.34°. The average *trans* angles around Cu(1) ion are 87.38 and 90.82° and that around Cu(2) ion are 87.81 and 88.38°. For acetate coordination the Cu(l)-O(5) distance of 2.190(2) Å differs from the Cu(2)–O(4) distance of 2.132(2) Å by 0.058 Å.

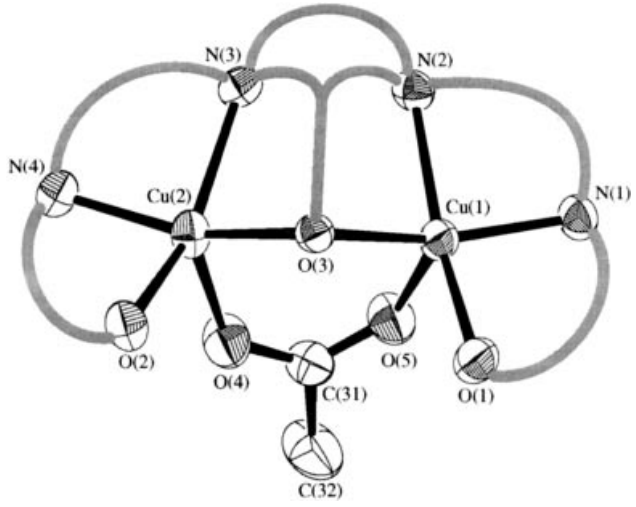

Figure 2. The core of the dinuclear complex $[Cu^{II}_2(\mu\text{-mhbai})(\mu\text{-OAc})]\cdot 2H_2O$ (**1**).

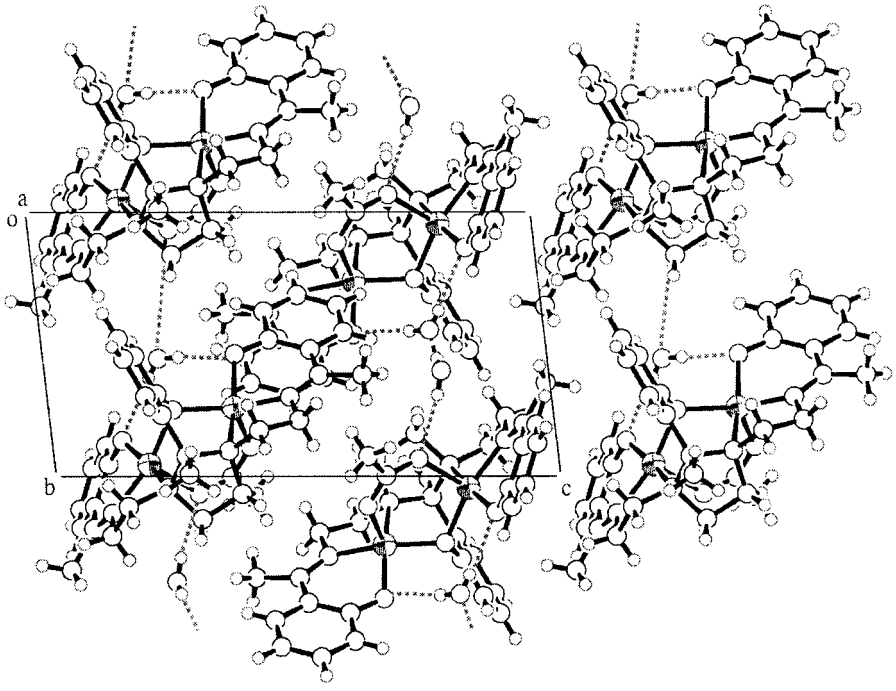

Figure 3. The packing diagram along *b* axis of the neutral molecule $[Cu^{II}_2(\mu\text{-mhbai})(\mu\text{-OAc})]\cdot 2H_2O$ (**1**) showing H bonding with water molecules.

 © 2005 Wiley-VCH Verlag GmbH & Co. KGaA, Weinheim

This difference in bond length of the two metal ions to the oxygen atoms of the *syn-syn* bidentate carboxylate bridge is usually not larger than 0.10 Å as in other diiron or dimanganese complexes. Endogenous phenolato and exogenous acetato bridging support the formation of the imidazolidine-bridged homodinuclear assembly. The Cu–Cu distance is 3.298(4) Å, which is in the normal range for other triply bridging molecules.[2,27] Longer Cu–N distances [Cu(1)–N(2) = 2.116(2) Å; Cu(2)–N(3) = 2.203(2) Å][28–31] are observed for the tertiary amine nitrogen atoms of the imidazolidine ring to both the copper(II) ions. The Cu–N_{imine} and Cu–O_{phenol} distances are in the normal range. The Cu–O distances for the bridging phenolate coordination indicate that the bridge is practically symmetric [Cu(1)–O(3) = 1.953(1) Å; Cu(2)–O(3) = 1.955(2) Å] for a dicopper complex. Similarly, the Cu(1)–O(5) and Cu(2)–O(4) distances show a high degree of symmetry with respect to the acetate bridge (Figure 2). The complex **1** shows an intricate hydrogen bonding between two water molecules and two terminal phenolic oxygen atoms, attaching a water dimer to the compound. The first water molecule O(6) gives rise intramolecular interactions with both the terminal phenolic oxygen atoms (Figure 1) [O(6)···O(1) = 2.889(3) Å; O(6)···O(2) = 2.931(3) Å]. The hydrogen bonded water molecule provides a pseudo macrocyclic ligand environment around two copper(II) centers. The second water molecule is further hydrogen bonded to the first one [O(7)···O(6) = 2.820(3) Å] and the distance is in between that of liquid water and regular ice (about 2.85 and 2.74 Å).[32] A unit cell packing pattern (Figure 3) is obtained for the complex **1** due to the involvement of the water dimer in the hydrogen bonding network with the complex. Intermolecular hydrogen bonding is operative between the second water molecule O(7) and one of the acetate oxygen atom of another dicopper molecule.

Magnetochemistry of Cu^{II}_2(μ-mhbai)(μ-OAc)]·2H_2O

The degree of magnetic superexchange interaction within the dinuclear complex [Cu^{II}_2(μ-mhbai)(μ-OAc)]·2H_2O (**1**) was evaluated by means of variable temperature bulk magnetic susceptibility measurements in the 2–300 K temperature range, under a constant magnetic field of 0.8 T. The results are presented in Figure 4 in a form of $\chi_m T$ vs. T plot, where χ_m is the molar magnetic susceptibility after correction for the diamagnetic contribution and that of temperature independent paramagnetism (which were combined in one unique parameter). In this plot, $\chi_m T$ remains almost constant over most of the temperature range, at its 300 K value of 0.88 $cm^3 K mol^{-1}$, consistent with two magnetically isolated Cu^{II} (S = 1/2) centers in the molecule. The product $\chi_m T$ starts drop at temperatures below 50 K, to reach a value of 0.55 $cm^3 K mol^{-1}$ at 2 K. These results indicate that the coupling between Cu^{II} ions within **1** is very weak and antiferromagnetic in nature. A quantitative description of this behavior was performed by fitting the experimental data to a theoretical model using the Bleaney–Bowers equation[33,34] as the expression for $\chi_m = f(T)$. The convention employed for the phenomenological description of the magnetic coupling is conveyed by the Heisenberg-Spin Hamiltonian $\boldsymbol{H} = -2\boldsymbol{J}\boldsymbol{S}_1\boldsymbol{S}_2$. Satisfactory fits could only be obtained when the data at lowest temperatures were excluded. This is presumably because at such temperatures, weaker effects begin to surface, which are not included in the model, such as intermolecular interactions. Thus, a least-squares procedure was carried out to model the data above 8 K. The best fit (Figure 4, solid line) ensued from J = –2.2 cm^{-1} and g = 2.17. The magnetic superexchange in dinuclear systems such as complex **1** has been explained in numerous previous examples in terms of the overlap between the magnetic orbitals of the Cu^{II} ions through the intermediacy of the bridging ligands.[35] In complex **1**, the metal ions are in a distorted square-pyramidal geometry, the apical positions being occupied by the oxygen atoms from the μ–AcO^- bridge. Therefore, the magnetic orbitals are $d_{x^2-y^2}$ and can only interact via the phenol bridging moiety. A magneto-structural study has established the correlation existing between the Cu–O–Cu angle and J in bis-(phenoxide)-bridged [Cu_2] complexes, and has shown the strong antiferromagnetic character of this coupling.[36] In the mentioned study, both μ-phenoxide groups occupy equatorial coordination positions from Cu^{II}, thereby providing for two strong exchange pathways. Complex **1** however, belongs to the smaller group of compounds displaying one phenoxide and one η^1:η^1:μ_2-acetate bridge. In this family, the magnetic coupling has been found to be much weaker[37–39] and in very few exceptions a ferromagnetic type of exchange has been claimed.[40] This is consistent with the fact that in these compounds there is only one possible pathway for the exchange. In addition, it has been argued that the angle between the equatorial planes around Cu^{II} exerts a significant influence on the magnitude of J.[41] In particular, a deviation of this angle from zero degrees causes the decrease of the energy gap between the symmetric (φ_s) and the antisymmetric (φ_a) combination of magnetic orbitals, diminishing the antiferromagnetic nature of the coupling. In compound **1**, the idealized Cu^{II} equatorial planes are significantly bent, forming an angle 38.32°, to which

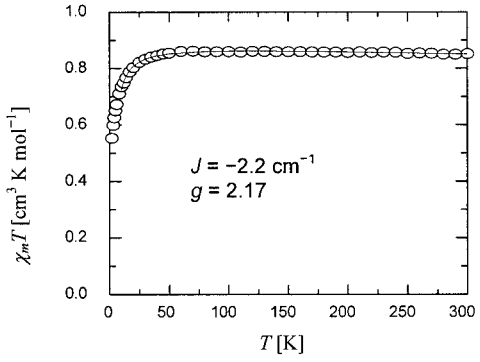

Figure 4. Plot of $\chi_m T$ vs. T per mol of complex [Cu^{II}_2(μ-mhbai)(μ-OAc)]·2H_2O (**1**). Data have been corrected for sample diamagnetic contributions and temperature independent paramagnetism. The solid line is the best fit to the experimental data above 8 K (see text for details).

 © 2005 Wiley-VCH Verlag GmbH & Co. KGaA, Weinheim

could be ascribed the small value of J calculated above. Comparisons of complex **1** with previous systems, however, are thwarted by the unique structural features imposed on this assembly by the dinucleating ligand. This is perhaps most evident in the unconventional orientation of the C–O bond of the bridging phenoxide with respect to the plane containing the Cu–O–Cu atoms from that bridge. Useful for this discussion could be the suggestion that μ-acetates and alkoxide bridges, when simultaneously present in this type of $[Cu_2]$ complexes, are *counter-complementary*, leading to a reduction of the $\varphi_s - \varphi_a$ energy gap and therefore, of the absolute value of J.[42] In the present case however, this mechanism can not operate because the AcO^- group is bound to the axial positions of Cu^{II} and, therefore, is not interacting with the magnetic orbitals of the metals.

EPR Spectroscopy of Cu^{II}_2(μ-mhbai)(μ-OAc)]·2H_2O

Powder X-Band (9.7857 GHz) EPR spectra were collected for complex **1** at room temperature and 77 K. The latter one is shown in Figure 5. In both the cases, the obtained spectra could be interpreted in terms of mononuclear Cu^{II} chromophores in a *quasi* axial geometry, which is in line with the above revelation that at these temperatures, the ions within the complex are essentially uncoupled. Thus, consistent with the asymmetric square-pyramidal geometry of the metal centers in **1**, with a *cis*-N_2O_2 equatorial donor set, three components of g can be observed, with $g = 2.17$ and $g_\perp$ split in two; $g_x = 2.12$ and $g_y = 2.07$. The lower field side of the parallel signal shows a shoulder that could be interpreted as the manifestation of small hyperfine splitting of this signal as a result of the coupling with the nuclear spin from $^{3/2}$Cu. The average isotropic g-factor resulting from these measured values is $g = 2.12$, which is in reasonable agreement with the value calculated from fitting the bulk magnetization measurements (see above).

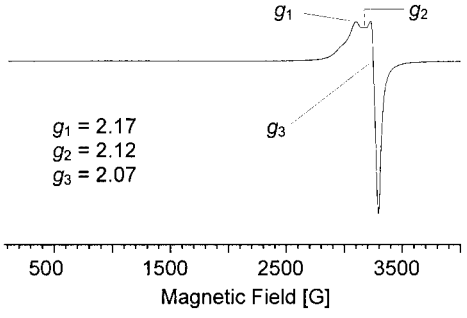

Figure 5. Powder X-band EPR spectrum of complex [Cu^{II}_2(μ-mhbai)(μ-OAc)]·2H_2O (**1**) at ca 77 K.

^{1}H NMR Spectroscopy of Cu^{II}_2(μ-mhbai)(μ-OAc)]·2H_2O

^{1}H NMR spectroscopy has been shown to be applicable to characterization of the structure and reactivity of dicopper(II/II) complexes with magnetic coupling that ranges from weakly ferromagnetic to strongly antiferromagnetic.[43] Few reports have described copper(II) complexes that produce narrow ^{1}H NMR resonances.[44–49] Paramagnetic NMR of dinuclear copper complexes has been used extensively in order to establish their relevance as models for metal sites in copper enzymes.[50] Construction of a library of compounds along with their NMR properties is beneficial in the context of bioinorganic modeling of naturally occurring metallo-enzymes. 250-MHz ^{1}H NMR spectroscopic data of complex **1** were collected in [D_4]methanol at room temperature. The T_1 value of almost every observed resonance has been determined for helping in the assignment of the spectrum. For this, it was taken into consideration that the relaxation time T_1 of protons within paramagnetic complexes is proportional to r^{-6}, where r is the distance from the observed H nucleus to the metallic center. The T_1 values and the chemical shifts, δ, of all resonances are collected in Table 2, whereas the spectrum with the assignment of the signals are shown in Figure 6. Complex **1** is only scarcely soluble in MeOH, therefore, a large number of scans needed to be collected before an acceptable signal-to-noise ratio could be attained. The spectrum of **1** shows a total of seventeen hyperfine shifted peaks, as expected from the idealized C_s symmetry of the compound, spread over a very large window of chemical shift, spanning about 130 ppm. This reflects the fact that at room temperature the system remains largely paramagnetic as a result of the very weak nature of the observed antiferromagnetic coupling. In addition, peaks attributed to MeOH and free ligand were detected. The assignment of the latter peaks was made on the basis of their smaller relative intensity with respect to the rest of the signals. The signals from the solvent were used as internal reference. Inspection of the intensity integrals of these seventeen resonances allowed their grouping into four sets of one (a), two (b), ten (c), and four (d) signals, respectively, integrating for six, three, two and one proton, as predicted from the structure of **1** (Figure 6, top). These groups correspond to the following categories of protons: Group "a", only one signal, which integrates for six protons, corresponding to the two equivalent methyl groups in α to the imine N atoms, and which was readily assigned; group "b", two signals with intensities equivalent to three protons each, arising from two inequivalent methyl groups, respectively. These correspond to the μ-acetate and to the methyl attached to the central five-membered ring of the ligand. The assignment of these two signals to either of both groups remains ambiguous since the distances of the protons to the Cu^{II} ions is very similar in both cases; group "c" is the most numerous. It includes ten signals with intensity ratios for two H nuclei. These result from the hydrogen atoms attached to the amine groups (six signals) and from those attached to the two external phenyl rings (which are equivalent). The peaks from the first sub-group are broader than these of the second, since the protons causing the former are crystallographically closer to the metal centers. Again, the assignment could be made almost unambiguously on the basis of the T_1 values. Where T_1 was so small that could not be measured, the broadness of the peaks was used as an approximate measure of the relative relaxation times. The resonances of the other sub-group are sharper

 © 2005 Wiley-VCH Verlag GmbH & Co. KGaA, Weinheim

and show the alternation of chemical shifts characteristic of π-delocalization mechanisms.[51] This, along with relaxation time data helped in the assignment of the resonances; group "d" is the last set of signals, which includes the four peaks from the central phenyl ring of the ligand (one proton per signal). Here is also evident a mechanism of π-delocalization of the electronic spin, which was useful in the assignment of the peaks. With this study, complex **1** enters the small group of binuclear [Cu_2] complexes of which, the ^{1}H NMR spectrum could be explained almost unambiguously and is a valuable contribution to the growing body of spectroscopic data which can be useful in the functional and structural study of the metallo-enzymes.

Table 2. ^{1}H NMR data of [Cu^{II}_2(μ-mhbai)(μ-OAc)]·2H_2O (**1**).

Signal	δ [ppm]	T_1 [ms]	Signal	δ [ppm]	T_1 [ms]
a	–12.7	20	c_7	16.6	31
b_1	38.1	49	c_8	5.2	t.s.[a]
b_2	10.7	8.2	c_9	1.3	t.s.[a]
c_1	184	t.f.[b]	c_{10}	–10.8	7.5
c_2	123	t.f.[b]	d_1	33.4	26
c_3	122	t.f.[b]	d_2	17.7	17
c_4	91	4.5	d_3	–20.5	21
c_5	78	5.0	d_4	–26.6	t.f.[b]
c_6	28	2			

[a] Too slow to be measured within the time scale of the experiment. [b] Too fast to be measured within the time scale of the experiment.

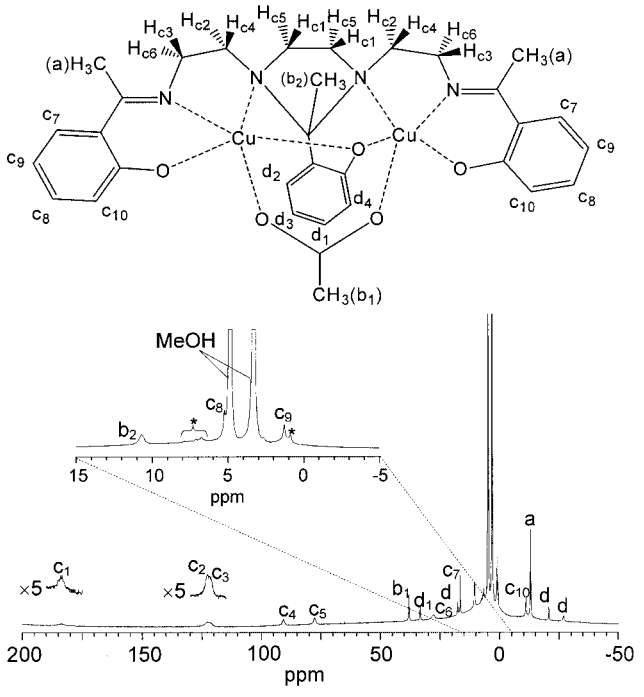

Figure 6. Scheme of complex **1**, where all protons have been labeled according to the group (a, b, c or d) where they pertain, depending on their integration. At the bottom is a labeled 250 MHz 1H NMR spectrum of **1**. Asterisks * denote signals from free ligand (See text and Table 2 for details on the assignment).

Electrochemistry of [Cu^{II}_2(μ-mhbai)(μ-S_2COMe)]·2H_2O

The electron-transfer behaviour of the complex [Cu^{II}_2(μ-mhbai)(μ-S_2COMe)]·2H_2O (**4**) in dimethylformamide has been studied by cyclic voltammetry. A glassy-carbon working electrode with tetraethylammonium perchlorate (TEAP) as supporting electrolyte at 298 K were used. The cyclic voltammogram was recorded in the potential range of 0.0 to +0.9 V vs. saturated calomel electrode (SCE) at a scan rate of 50 mV s^{-1}. Complexes **1**–**3** do not display any characteristic cyclic voltammetric response within the above-mentioned potential window. Only the xanthate-bridged complex **4** exhibits a quasi-reversible response at $E_{1/2}$ = 0.504 V (ΔE_p = 132 mV). The observed quasi-reversible peak is assigned to an one electron transfer process [Equation (1) for ligand oxidation.The ligand centered oxidation is known in several sulfur-based ligand systems where thiyl radical formation is predicted for an instance when ligand-based oxidation occurs rather than metal-based.[52]

$$[Cu^{II}\{\mu\text{-MeO(C=S)S}^-\}Cu^{II}]^{3+} - e^- \leftrightarrow [Cu^{II}\{\mu\text{-MeO(C=S)S}^{\cdot}\}Cu^{II}]^{4+} + e^- \quad (1)$$

The quasi-reversible nature of the voltammogram indicate the formation of a methoxythiyl radical coordinated to a metal ion with a weak Cu–$^{-}$S(C=S)OMe bond. The absence of any voltammetric response in analogous acetate-bridged complex (**1**) also shows the easy oxidizing nature of thio derivatives.[52] At 298 K the oxidized species is stable at the voltammetric time-scale only.

Concluding Remarks

The results presented here demonstrate the synthesis, structural characterization and magnetic behaviour of imidazolidine-bridged Cu^{II}–Cu^{II} triply-bridged intimate complex supported by a new μ-bis(tetradentate) Schiff-base ligand. Complex **1** is the example of a new structurally characterized μ-η^1:η^1-*N*,*N*′-imidazolidine-bridged dicopper(II/III) complex. Neither triply-bridged structure nor the imidazolidine bridge is responsible for any strong magnetic interaction. Two copper(II) ions at a distance of 3.2984 Å show only a weak magnetic interaction. The isolated new dicopper(II/III) complexes have [Cu_2(μ-imidazolidine)]$^{4+}$ core and currently we are engaged in synthesizing analogues complexes of other 3d and 4d metal ions to explore the role of bridging imidazolidine moiety in the molecular structure and physical properties of new complexes.

Experimental Section

Materials and Physical Measurements: The chemicals used were obtained from the following sources: Triethylenetetramine and carbon disulfide from S.D. Fine Chem, India. 2-Hydroxyacetophenone from Spectrochem, Mumbai, India. Cupric acetate hydrate and cupric chloride dihydrate from SRL, India. Cupric nitrate trihydrate from E. Merck, India. All other chemicals and solvents were reagent grade materials and were used as received without further purification. The elemental analyses (C, H, N) were performed with

 © 2005 Wiley-VCH Verlag GmbH & Co. KGaA, Weinheim

a Perkin–Elmer model 240 C elemental analyzer. ^{1}H and ^{13}C NMR spectra of the ligand were obtained with a Bruker AC 200 NMR spectrometer using TMS as the internal standard. ^{1}H NMR spectra of the complex were collected with a 250 MHz Bruker DXR 250 spectrometer. Longitudinal relaxation times (T_1) were measured using an inversion-recovery pulse sequence (180-τ-90°) with a 300 MHz Varian Unity-300 spectrometer. In all cases, the protio-solvent signal was used as reference and chemical shifts were quoted on the δ scale (down field shifts are positive). IR spectra were recorded with a Perkin–Elmer 883 spectrophotometer. The solution electrical conductivity and electronic spectra were obtained with a Unitech type U131C digital conductivity meter with a solute concentration of about 10^{-3} M and a Shimadzu UV 3100 UV/Vis-NIR spectrophotometer, respectively. Mass spectra were obtained with a Finnigan MAT 8200 (electron ionization, EIMS) instrument. The room temperature magnetic susceptibilities in the solid state were measured using a home built Gouy balance fitted with a polytronic d.c. power supply. The experimental magnetic susceptibilities were corrected for the diamagnetic response using Pascal's constants.[53] Magnetic measurements were carried out at the "Servei de Magnetoquímica (Universitat de Barcelona)" on polycrystalline samples (ca. 40 mg) by using a Quantum Design MPMS XL-5 SQUID susceptometer operating at a constant magnetic field of 0.8 T between 2 and 300 K. The experimental magnetic moment was corrected for the diamagnetic contribution from the sample holder. X-Band EPR measurements (9.7857 GHz) were performed at room temperature and ca. 77 K on powdered samples a Bruker Spectrometer (ESR, 300E), working with an oxford helium liquid cryostat for variable temperature. Electrochemical measurements were made using a PAR model 173 potentiostat/galvanostat, 175 universal programmer, 178 electrometer, and 377-cell system. A glassy carbon working-electrode, a platinum-wire auxiliary-electrode, and an aqueous saturated calomel reference electrode (SCE) were used in a three-electrode configuration. A digital series 2000 Omni Graphic recorder was used to trace the voltammograms. Electrochemical measurements were made under nitrogen.

Synthesis of 2-(2-Hydroxyphenyl)-1,3-bis[4-(2-hydroxyphenyl)-4-methyl-3-azabut-3-enyl]-2-methyl-1,3-imidazolidine (H_3mhbai): A solution of triethylenetetramine (3.7 g, 25.3 mmol) in methanol (25 mL) was added dropwise to a methanolic solution (25 mL) of 2-hydroxyacetophenone (10.2 g, 74.9 mmol) with stirring at room temperature. The yellow solution was then refluxed for 5 h. The solvent was evaporated in air. The yellow solid was separated by filtration through G4 sintered bed and washed thoroughly with hexane and water. Finally the isolated compound was dried in vacuo with P_4O_{10}. Yield 9.3 g (75%), m.p. 184–186 °C. $C_{30}H_{36}N_4O_3$ (500.6): calcd. C 71.97, H 7.25, N 11.19; found C 71.51, H 7.62, N 11.49. Mass spectrum (EI): *m/z* 500 ($M^+ = L^+$). IR (cm^{-1}, KBr disk): $\tilde{\nu}$ = 3443 [w, ν(phenolic OH)], 1616 [s, ν(C=N)], 1371 [s, ν(phenolic C–O)], 835 [m, ν(CH_2)], 745 [m, ν(aromatic CH)]. ^{1}H NMR ($CDCl_3$, ppm): δ = 16.13 (s, 2 H, terminal phenolic OH), 12.03 (s, 1 H, pendant phenolic OH), 7.21–7.48 (m, 8 H, H^{2-5}), 6.74–6.89 (m, 4 H, H^{15-18}), 3.47–3.55 (m, 4 H, H^8), 2.86 (t, 4 H, H^9), 2.74–2.80 (m, 4 H, H^{10} and H^{11}), 2.21 (s, 6 H, $H_{terminal\ methyl}$), 1.138 (s, 3 H, $H_{central\ methyl}$). ^{13}C NMR ($CDCl_3$, ppm): δ = 164.29 (C^7), 162.38 ($C^{1,14}$), 132.48 (C^6), 130.68 ($C^{16,18}$), 128.00 ($C^{3,5}$), 119.18 (C^{17}), 118.88 (C^4), 118.39($C^{2,15}$), 116.83 (C^{12}), 49.61 (C^8), 49.44 (C^9), 49.10 (C^{10}), 26.58 ($C_{terminal\ methyl}$), 14.51 ($C_{central\ methyl}$).

Synthesis of the Complexes: A general procedure was followed for the preparation and isolation of all complexes of type [Cu^{II}_2(μ-mhbai)(μ-X)]·2H_2O. Details are given below for the representative cases.

[Cu^{II}_2(μ-mhbai)(μ-OAc)]·2H_2O (1): An aqueous solution (10 mL) of $Cu(OAc)_2$·H_2O (0.399 g, 1.9 mmol) was slowly added dropwise at ambient temperature to a magnetically stirred warm methanolic solution (15 mL) of H_3L (0.5 g, 0.9 mmol) during a period of 15 min. After complete addition a dark green compound was seen separating in solution. The whole reaction mixture was stirred for 1 h at room temperature. The solvent was evaporated in air. The green precipitate was filtered through a glass frit and washed with water followed by ethanol and hexane and finally dried in vacuo over P_4O_{10}. Yield: 0.61 g (85%). $C_{32}H_{40}Cu_2N_4O_7$ (719.8): calcd. C 53.40, H 5.60, N 7.78, Cu 17.65; found C 52.91, H 5.36, N 7.37, Cu 17.90. IR (cm^{-1}, KBr disk): $\tilde{\nu}$ = 3415 (b), 1605 (vs), 1586 (s), 1532 (s), 1405 (s), 1312 (s), 1201 (s), 869 (s), 755 (s). Molar conductance, Λ_M: (DMF) = 16.36 ohm^{-1}cm^{2}mol^{-1}. UV/Vis (DMF): λ_{max} (ε, L mol^{-1}cm^{-1}) = 616 (385), 368 (10945), 300 (11780) sh, 273 nm (24730). μ_{eff} (tot.): 2.43 μ_B; μ_{eff}/Cu: 1.71 μ_B.

[Cu^{II}_2(μ-mhbai)(μ-NO_3)]·2H_2O (2): This compound was prepared following the above procedure using $Cu(NO_3)_2$·3H_2O and triethylamine. The stirring was continued for 1 h. Yield: 0.54 g (75%). $C_{30}H_{37}Cu_2N_5O_8$ (722.7): calcd. C 49.85, H 5.16, N 9.69, Cu 17.58; found C 49.51, H 4.96, N 9.37, Cu 17.01. IR (cm^{-1}, KBr disk): $\tilde{\nu}$ = 3438 (b), 1611 (vs), 1588 (s), 1539 (s), 1453 (s), 1403 (s), 1378 (s), 1297 (s), 1201 (s), 824 (s), 735 (s). Molar conductance, Λ_M: (DMF) = 12.48 ohm^{-1}cm^{2}mol^{-1}. UV/Vis (DMF): λ_{max} (ε, L mol^{-1}cm^{-1})] = 602 (230), 361 (7045), 268 nm (16505). μ_{eff} (tot.): 2.35 μ_B; μ_{eff}/Cu: 1.66 μ_B.

[Cu^{II}_2(μ-mhbai)(μ-Cl)]·2H_2O (3): This compound was prepared following the above procedure using $CuCl_2$·2H_2O. The stirring was continued for 1 h. Yield: 0.56 g (80%). $C_{30}H_{37}ClCu_2N_4O_5$ (696.2): calcd. C 51.76, H 5.36, N 8.05, Cu 19.24; found C 51.33, H 5.67, N 8.34, Cu 19.18. IR (cm^{-1}, KBr disk): $\tilde{\nu}$ = 3396 (b), 1602 (vs), 1530 (s), 1319 (s), 1277 (s), 891 (s), 734 (s). Molar conductance, Λ_M: (DMF) = 29.26 ohm^{-1}cm^{2}mol^{-1}. UV/Vis(DMF): λ_{max} (ε, L mol^{-1}cm^{-1}) = 623 (110), 359 (5170), 272 nm (15170). μ_{eff} (tot.): 2.81 μ_B; μ_{eff}/Cu: 1.98 μ_B.

[Cu^{II}_2(μ-mhbai)(μ-S_2COMe)]·2H_2O (4): This compound was prepared following the above procedure, using $CuCl_2$·2H_2O and NaS_2COMe. The stirring was continued for 1 h. Yield: 0.59 g (77%). $C_{32}H_{40}Cu_2N_4O_6S_2$ (767.9): calcd. C 50.05, H 5.25, N 7.29, Cu 16.55; found C 50.41, H 4.96, N 7.81, Cu 16.62. IR (cm^{-1}, KBr disk): $\tilde{\nu}$ = 3410 (b), 1607 (vs), 1527 (s), 1318 (s), 1203 (s), 1144 (s), 1021 (s), 861 (s), 724 (s). Molar conductance, Λ_M: (DMF) = 20.18 ohm^{-1}cm^{2}mol^{-1}. UV/Vis (DMF): λ_{max} (ε, L mol^{-1}cm^{-1}) = 627 (225), 370 (8350), 315 (10380), 274 nm (19225). μ_{eff} (tot.): 2.68 μ_B; μ_{eff}/Cu: 1.89 μ_B.

X-ray Crystallographic Procedures for [Cu^{II}_2(μ-mhbai)(μ-OAc)]·2H_2O (1): The green plate-like single crystals of complex [Cu^{II}_2(μ-mhbai)(μ-OAc)]·2H_2O suitable for the X-ray analysis were grown by the slow evaporation of a acetonitrile/water solution of the complex. The intensity data of the complex were collected on Bruker SMART CCD X-ray diffractometer using a single crystal with dimensions $0.01 \times 0.22 \times 0.25$ mm^3 that uses graphite-monochromated Mo-K_α radiation (λ = 0.71073 Å) by ω-scan method. Precise unit cell dimensions were determined by least-squares refinement of 25 strong reflections having 2θ values. Data were collected at 298 K. A total of 7019 reflections were recorded with Miller indices h_{min} = 0, h_{max} = 11, k_{min} = –14, k_{max} = 14, l_{min} = –21, l_{max} = 21. In the final cycles of full-matrix least-squares on F^2 all non-hydrogen atoms were assigned anisotropic thermal parameters and refinement converged at R = 0.034. The residual electron density is in the range +0.73 to –0.64 e·Å^{-3}. The positions of the H atoms bonded to C atoms were calculated (C–H distance

 © 2005 Wiley-VCH Verlag GmbH & Co. KGaA, Weinheim

0.96 Å). The structure was solved on a PC 486 by using the DIRDIF92-PATTY programme system[54] and refined by full-matrix least-squares methods with use of the programme SHELX-97[55]/TEXSAN.[56] Analytical expressions of neutral-atom scattering factors were employed, and anomalous dispersion corrections were incorporated.[57] Information concerning X-ray data collection and structure refinement of the compound is summarized in Table 3.

Table 3. Crystallographic data for compound $[Cu^{II}_2(\mu\text{-mhbai})(\mu\text{-OAc})]\cdot 2H_2O$ (**1**).

Emoirical formula	$C_{32}H_{40}Cu_2N_4O_7$
Molecular mass	719.78
Crystal system	triclinic
Space group	*P*-1(2)
a [Å]	8.879(1)
b [Å]	11.329(2)
c [Å]	16.412(2)
α [°]	99.40(1)
β [°]	93.57(1)
γ [°]	107.520(1)
V [Å^3]	1542.2(4)
$D_{calcd.}$ [g cm^{-3}]	1.550
Z	2
F(000)	748.00
Λ [Å]	0.71073
T [K]	298(1)
Crystal size [mm]	0.01×0.22×0.25
μ [mm^{-1}]	1.434
R[a], R_w [$I > 2\sigma(I)$][b]	0.034, 0.040
GOF	1.043
Final difference map	
Max./min. resid. electron density [e·Å^{-3}]	0.73/–0.64

[a] $R = \Sigma(||F_o| - |F_c||)/\Sigma|F_o|$. [b] $R_w = [\Sigma w(|F_o| - |F_c|)^2/\Sigma w(F_o)^2]^{1/2}$. $w = 0.75/(\sigma^2(F_o) + 0.0010F_o^2)$.

CCDC-259334 contains the supplementary crystallographic data for this paper. These data can be obtained free of charge from The Cambridge Crystallographic Data Centre via www.ccdc.cam.ac.uk/data_request/cif.

Acknowledgments

We are thankful to the Council of Scientific and Industrial Research, New Delhi, for the financial support. W. T. W. acknowledges the financial support from the Hong Kong government. This work was also supported by the Spanish Ministry of Science in form of a "Ramóny Cajal" contract.

[1] F. Meyer, H. Pritzkow, *Angew. Chem. Int. Ed.* **2000**, *39*, 2112.
[2] L. K. Thompson, F. L. Lee, E. J. Gabe, *Inorg. Chem.* **1988**, *27*, 39.
[3] C. He, S. J. Lippard, *Inorg. Chem.* **2000**, *39*, 5225.
[4] C. A. Salata, M. T. Youinou, C. J. Burrows, *Inorg. Chem.* **1991**, *30*, 3454.
[5] J. L. Chou, D. N. Horng, J. P. Chyn, K. M. Lee, F. L. Urbach, G. H. Lee, H. L. Tsai, *Inorg. Chem. Commun.* **1999**, *2*, 392.
[6] L. K. Thompson, S. S. Tandon, M. E. Manuel, *Inorg. Chem.* **1995**, *34*, 2356.
[7] C. J. Sumby, P. J. Steel, *Inorg. Chem. Commun.* **2003**, *6*, 127.
[8] W. M. E. Koomen-van Oudenniel, R. A. G. de Graaff, J. G. Haasnoot, R. Prins, J. Reedijk, *Inorg. Chem.* **1989**, *28*, 1128.
[9] A. L. Gavrilova, B. Bosnich, *Chem. Rev.* **2004**, *104*, 349.
[10] E. Wong, S. Liu, T. Lugger, F. E. Hahn, C. Orvig, *Inorg. Chem.* **1995**, *34*, 93.
[11] M. Bera, W. T. Wong, G. Aromi, J. Ribas, D. Ray, *Inorg. Chem.* **2004**, *43*, 4787.
[12] P. A. Vigato, S. Tamburini, D. Fenton, *Coord. Chem. Rev.* **1990**, *106*, 25–170.
[13] J. E. Bol, W. L. Driessen, J. Reedijk, *J. Chem. Soc., Chem. Commn.* **1995**, 1365.
[14] S. Torelli, C. Belle, I. Gautier-Luneau, J. L. Pierre, *Inorg. Chem.* **2000**, *39*, 3526.
[15] Y. C. Chou, S. F. Huang, R. Koner, G. H. Lee, Y. Wang, S. Mohanta, H. Wei, *Inorg. Chem.* **2004**, *43*, 2759.
[16] S. Manikumari, V. Shivaiah, S. K. Das, *Inorg. Chem.* **2002**, *41*, 6953.
[17] L. E. Cheruzel, M. S. Pometun, M. R. Cecil, M. S. Mashuta, R. J. Wittebort, R. M. Buchanan, *Angew. Chem. Int. Ed.* **2003**, *42*, 5452.
[18] S. Pal, N. B. Sankaran, A. Samanta, *Angew. Chem. Int. Ed.* **2003**, *42*, 1741.
[19] B. D. Sarma, J. C. Bailar, Jr., *J. Am. Chem. Soc.* **1955**, *77*, 5476.
[20] D. F. Evans, D. A. Jakubovic, *J. Chem. Soc., Dalton Trans.* **1988**, 2927.
[21] U. Mukhopadhay, L. R. Falvello, D. Ray, *Euro. J. Inorg. Chem.* **2001**, 2823.
[22] a) L. L. Borer, J. Kong, E. Sinn, *Inorg. Chim. Acta* **1986**, *122*, 145; b) M. Y. Chow, Z. Y. Zhou, T. C. W. Mak, *Inorg. Chem.* **1992**, *31*, 4900.
[23] A. A. Mohamed, I. Kani, A. O. Ramirez, J. P. Fackler, Jr., *Inorg. Chem.* **2004**, ASAP.
[24] a) K. Weighardt, K. Pohl, W. Gebert, *Angew. Chem. Int. Ed. Engl.* **1983**, *22*, 727; b) Y. Gultneh, A. Farooq, S. Liu, K. D. Karlin, J. Zubieta, *Inorg. Chem.* **1992**, *31*, 3607; c) W. H. Armstrong, S. J. Lippard, *J. Am. Chem. Soc.* **1983**, *105*, 4837; d) A. S. Borovic, M. P. Hendrich, T. R. Holman, E. Munck, V. Papaefthymiou, L. Que, Jr., *J. Am. Chem. Soc.* **1990**, *112*, 6031.
[25] a) J. D. Crane, D. E. Fenton, J. M. Latour, A. J. Smith, *J. Chem. Soc., Dalton Trans.* **1991**, 2979; b) Y. Nishida, T. Tokii, Y. Mori, *J. Chem. Soc., Chem. Commun.* **1988**, 675.
[26] a) T. M. Rajendiran, R. Kannappan, R. Venkatesan, P. Sambasiva Rao, M. Kandaswamy, *Polyhedron* **1999**, *18*, 3085; b) A. Elmali, C. T. Zeyrek, Y. Elerman, *J. Mol. Struct.* **2004**, *693*, 225.
[27] D. Ajo, A. Bencini, F. Mani, *Inorg. Chem.* **1988**, *27*, 2437.
[28] M. Fondo, A. M. Garcia-Deibe, M. R. Bermejo, J. Sanmartin, A. L. Liamas-Saiz, *J. Chem. Soc., Dalton Trans.* **2002**, 4746.
[29] E. P. Copeland, I. A. Kahwa, J. T. Mague, G. L. Mcpherson, *J. Chem. Soc., Dalton Trans.* **1997**, 2849.
[30] U. Mukhopadhyay, L. Govindasamy, K. Ravikumar, D. Velmurugan, D. Ray, *Inorg. Chem. Commun.* **1998**, *1*, 152.
[31] B. Chiari, O. Piovesana, T. Tarantelli, P. F. Zanazzi, *Inorg. Chem.* **1982**, *21*, 2444.
[32] R. Ludwig, *Angew. Chem. Int. Ed.* **2001**, *40*, 1808.
[33] B. Bleaney, K. D. Bowers, *Proc. Roy. Soc., (London) Ser. A* **1952**, *214*, 451.
[34] O. Kahn, in: *Molecular Magnetism*; VCH: New York **1993**.
[35] M. Verdaguer, *Polyhedron* **2001**, *20*, 1115.
[36] L. K. Thompson, S. K. Mandal, S. S. Tandon, J. N. Bridson, M. K. Park, *Inorg. Chem.* **1996**, *35*, 3117.
[37] Y. Nishida, H. Shimo, H. Maehara, S. Kida, *J. Chem. Soc., Dalton Trans.* **1985**, 1945.
[38] K. Bertoncello, G. D. Fallon, J. H. Hodgkin, K. S. Murray, *Inorg. Chem.* **1988**,*27*, 4750.
[39] M. Lubben, R. Hage, A. Meetsma, K. Byma, B. L. Feringa, *Inorg. Chem.* **1995**, *34*, 2217.
[40] L. S. Cai, W. G. Xie, H. Mahmoud, Y. Han, D. J. Wink, S. C. Li, C. J. Oconnor, *Inorg. Chim. Acta* **1997**, *263*, 231.
[41] M. F. Charlot, S. Jeannin, Y. Jeannin, O. Kahn, J. Lucreceabaul, J. Martinfrere, *Inorg. Chem.* **1979**, *18*, 1675.
[42] Y. Nishida, M. Takeuchi, K. Takahashi, S. Kida, *Chem. Lett.* **1985**, 631.
[43] J. H. Satcher, Jr., A. L. Balch, *Inorg. Chem.* **1995**, *34*, 3371.

[44] M. Maekawa, S. Kitigawa, M. Munakata, H. Masuda, *Inorg. Chem.* **1989**, *28*, 1904.
[45] A. L. Balch, M. Mazzanti, B. C. Noll, M. O. Olmstead, *J. Am. Chem. Soc.* **1993**, *115*, 12206.
[46] R. C. Holz, J. M. Brink, *Inorg. Chem.* **1994**, *33*, 4609.
[47] R. A. Zelonka, M. C. Baird, *Inorg. Chem.* **1972**, *11*, 134.
[48] S. Wang, Z. Pang, J. C. Zheng, M. J. Wagner, *Inorg. Chem.* **1993**, *32*, 5975.
[49] R. C. Holz, J. M. Brink, F. T. Gobena, C. J. O'Connor, *Inorg. Chem.* **1994**, *33*, 6086.
[50] J. M. Brink, R. A. Rose, R. C. Holz, *Inorg. Chem.* **1996**, *35*, 2878.
[51] R. W. Kluiber, W. D. Horrocks, *Inorg. Chem.* **1967**, *6*, 430.
[52] S. Kimura, E. Bill, E. Bothe, T. Weyhermuller, K. Wieghardt, *J. Am. Chem. Soc.* **2001**, *123*, 6025.
[53] R. L. Carlin, *Magnetochemistry,* (Springer-Verlag, New York).**1986**.
[54] P. T. Beurskens, G. Admiraal, G. Beurskens, W. P. Bosman, S. Garcia-Granda, R. O. Gould, J. M. M. Smits, C. Smykalla, *The DIRDIF program system, Technical Report of the Crystallography Laboratory*, University of Nijmegen, The Netherlands, **1992**.
[55] G. M. Sheldrick, SHELXS-97, *Program for the Refinement of Crystal Structures*, University of Göttingen, Germany, **1997**.
[56] Molecular Structure Corporation, TEXSAN. Crystal Structure Analysis Package, Molecular Structure Corporation,The Woodlands, TX, USA, **1992**.
[57] *International tables for X-ray Crystallography*, Kynoch, Birmingham, **1974**, vol. 4, pp. 55, 99, 149 (now distributed by Kluwer; Dordrecht).

Received: January 26, 2005

 © 2005 Wiley-VCH Verlag GmbH & Co. KGaA, Weinheim

A Comparative Assessment of the Effect of the Lewis Acidity of the Central Tin Atom on Intramolecular Coordination of (3-Methoxypropyl)stannanes

Tomáš Lébl,*[a,c] Petra Zoufalá,[a] and Clemens Bruhn[b]

Keywords: Tin / Chelates / O ligands / Structure elucidation / Coordination modes

The recently studied set of (3-methoxypropyl)stannanes of general formula R_xSnCl_{4-x} [R = $(CH_2)_3OCH_3$, x = 4 (**1**), x = 3 (**2**), x = 2 (**3**) and x = 1 (**4**)] is extended with two new sets of (3-methoxypropyl)stannanes of general formula $RPh_{3-x}SnCl_x$ [x = 0 (**5**), x = 1 (**6**) and x = 2 (**7**)] and $RSn(S_2CNEt_2)_{3-x}Cl_x$ [x = 0 (**8**), x = 1 (**9**) and x = 2 (**10**)]. The molecular structures of **6**, **7**, **9** and **10** in the solid state were determined by X-ray diffraction. In compounds **6** and **7**, the 3-methoxypropyl ligand forms a C,O-chelate and the tin atom is coordinated as a distorted trigonal bipyramid with the oxygen and one chlorine atom in the axial positions. Compounds **9** and **10** are hexacoordinate with a distorted octahedral ligand arrangement. While the 3-methoxypropyl ligand in **10** also forms a C,O-chelate, the oxygen atom in **9** is not coordinated to the central tin atom. The structures in a non-coordinating ($CDCl_3$) and a coordinating solvent ([D_6]DMSO) were studied by multinuclear ^{1}H, ^{13}C and ^{119}Sn NMR spectroscopy. It is proposed that the structures found in the solid state are retained upon dissolution in $CDCl_3$. Compounds **5**, **8** and **9** also preserve their structures in [D_6]DMSO. On the other hand, an equilibrium, in which one or more molecules of solvent enter the coordination sphere of the central tin atom and cleave the oxastannacycle, is established in [D_6]DMSO solutions of **6**, **7** and **10**. A comparison of the $J_{^1H,^{119}Sn}$ coupling constants obtained from 1D ^{1}H,^{119}Sn HMQC and 2D ^{1}H,^{119}Sn J-HMBC spectra and the $J_{^{13}C,^{119}Sn}$ coupling constants derived from conventional 1D ^{13}C NMR spectra shows that the best indicator of the O→Sn donor–acceptor interaction in 3-methoxypropylstannanes is the $^3J_{^{13}C,^{119}Sn}$ value.
(© Wiley-VCH Verlag GmbH & Co. KGaA, 69451 Weinheim, Germany, 2005)

Introduction

Organotin complexes containing C,Y-chelating ligands (i.e. organic substituents with a donor atom Y at a position where it is capable of intramolecular donor–acceptor interaction with the central metal atom) have been known for about thirty years.[1] Nevertheless, their manifold structures are still being intensively studied. Complexes of both transition and main-group metals are the subject of these studies. There are a number of reports detailing organostannanes containing either aromatic pincer-type ligands[2] or alkyl ligands substituted by a Lewis-basic heteroatom Y in a position enabling formation of five- or even six-membered heterostannacycles.[3]

Recently, we reported the synthesis and structures of the first set of (3-methoxypropyl)stannanes of the general formula R_xSnCl_{4-x} [R = $(CH_2)_3OCH_3$, x = 4 (**1**), x = 3 (**2**), x = 2 (**3**) and x = 1 (**4**)], which were studied for their considerable water solubility and appreciable in vitro trypanocidal activity.[4] We showed that the 3-methoxypropyl group can be bonded either as a monodentate ligand (Scheme 1, **A**) or as a bidentate C,O-chelating ligand (Scheme 1, **B**), and that this is dependent on the Lewis acidity of the central tin atom. However, the ^{119}Sn chemical shift gives unambiguous evidence for an O→Sn donor–acceptor interaction only if no other potentially bidentate ligand, such as a carboxylate group, is present in the coordination sphere. Moreover, even for R_4Sn (**1**), where the 3-methoxypropyl ligands do not form a chelate, all protons display ^{1}H-^{119}Sn HMQC correlations.[5] Therefore, the existence of the correlation itself cannot prove the existence of the oxastannacycle, and to distinguish between these two bonding modes (Scheme 1) in solution is a crucial issue of structural research.

In the case of the monodentate 3-methoxypropyl group (Scheme 1, **A**), there is only one scalar coupling pathway, that through the covalent bonds of the 3-methoxypropyl chain. On the other hand, if the oxastannacycle is closed (Scheme 1, **B**) there are two scalar coupling pathways − through the covalent bonds and through the coordinative O→Sn bond − which could be reflected in the magnitude of the $J_{^1H,^{119}Sn}$ and $J_{^{13}C,^{119}Sn}$ coupling constants.[5,6] The long-range $^{6+3}J_{^1H,^{119}Sn}$ coupling constants of 0.52, 1.86 and 2.24 Hz obtained for **1**, **3** and **4**, respectively, show that this parameter increases with the strength of the O→Sn interac-

[a] Department of General and Inorganic Chemistry, University of Pardubice,
Čs. Legií 565, 53210 Pardubice, Czech Republic
Fax: +420-40-603-7068
E-mail: petra.zoufala@upce.cz
[b] Department of Inorganic Chemistry, Martin-Luther-Universität Halle-Wittenberg,
Kurt-Mothes-Straße 2, 06120 Halle (Saale), Germany
E-mail: bruhn@chemie.uni-halle.de
[c] Curent address: School of Chemistry, University of St Andrews, Purdie Building, KY16 9ST, St Andrews, Scotland, UK
E-mail: tl12@st-andrews.ac.uk

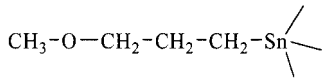

A

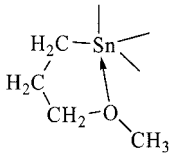

B

Scheme 1.

tion.[4] Since this limited set of results does not allow us to draw any final conclusion, two more sets of (3-methoxypropyl)stannanes were prepared. In the first set, of general formula $RPh_{3-x}SnCl_x$ [x = 0 (**5**), x = 1 (**6**) and x = 2 (**7**)], there is only one 3-methoxypropyl group in the coordination sphere and the Lewis acidity of the central tin atom is varied by substitution of phenyl groups by chlorine atoms. The latter set, of general formula $RSn(S_2CNEt_2)_{3-x}Cl_x$ [x = 0 (**8**), x = 1 (**9**) and x = 2 (**10**)], is composed of monorganotin compounds and variation of the Lewis acidity of tin is achieved by changing the number of chlorine atoms and strongly chelating *N*,*N*-diethyldithiocarbamate groups in the coordination sphere. These complexes were studied by X-ray diffraction, ^{13}C and ^{119}Sn CP/MAS NMR spectroscopy in the solid state and multinuclear ^{1}H, ^{13}C and ^{119}Sn NMR spectroscopy in solution in non-coordinating ($CDCl_3$) and coordinating ([D_6]DMSO) solvent. The obtained parameters are compared and are discussed with the aim of finding an indicator of the strength of the O→Sn donor–acceptor interaction.

Results and Discussion

Syntheses

(3-Methoxypropyl)triphenylstannane (**5**) was synthesised as shown in Scheme 2. Treatment of chlorotriphenylstannane with excess (3-methoxypropyl)magnesium chloride, which was previously prepared from 1-chloro-3-methoxypropane and magnesium chips in THF, provided tetraorganostannane **5**, which was isolated as a white powder in a yield of 85% with respect to Ph_3SnCl.

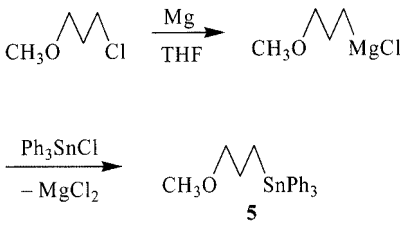

Scheme 2.

Chloro(3-methoxypropyl)phenylstannanes **6** and **7** were prepared from **5** by stepwise cleavage of phenyl groups upon treatment with HCl in $CHCl_3$ at room temperature (Scheme 3). The reaction proceeded selectively and both compounds were obtained as white crystals in yields of over 95%.

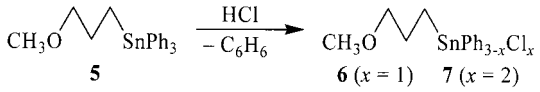

Scheme 3.

Treatment of **4** with an appropriate stoichiometric amount of sodium *N*,*N*-diethyldithiocarbamate in acetone at room temperature afforded carbamate complexes **8**, **9** and **10** (Scheme 4) as white or yellowish crystals in yields of 80, 83 and 59%, respectively.

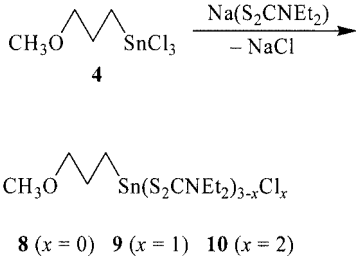

Scheme 4.

Solid-State Structures

In the case of **5**, isolation of a single crystal suitable for X-ray crystal structure determination was unsuccessful. However, considering that **5** is a tetraorganotin compound, any coordination of oxygen to tin and consequent increase of its coordination number above four can be easily excluded, and thus it can be assumed that the structure is close to tetrahedral as in the majority of tetraorganotin compounds.[7]

The molecular structures of **6** and **7**, as determined by X-ray diffraction, are shown in Figures 1 and 2, respectively. Selected bond lengths and angles are given in Table 1.

Both complexes consist of discrete molecules with a structure that is very like that of **4**.[4] The central tin atom is coordinated as a distorted trigonal-bipyramid with the oxygen atom and one chlorine atom in the axial positions [Cl–Sn–O: 170.37(4)° and 172.6(1)°] (Figure 1). Compound **6** has a rather symmetrical equatorial plane containing two carbons of phenyl groups and one carbon of the 3-methoxypropyl group [C–Sn–C: 122.67(11)°, 119.48(11)°, 111.56(10)°]. However, the phenyl rings have different orientations: while one lies practically within the equatorial plane [C10–C5–Sn–C1: 4.2(3)°] the second one is oriented nearly along the axis of the trigonal bipyramid [C12–C11–Sn–O: –10.8(2)°]. This means that the tin atom is a stereocentre and **6** is chiral in the solid state. This asymmetry is also revealed in the ^{13}C CP/MAS NMR spectrum, where twelve signals are observed in the aromatic region. For compound

 © 2005 Wiley-VCH Verlag GmbH & Co. KGaA, Weinheim

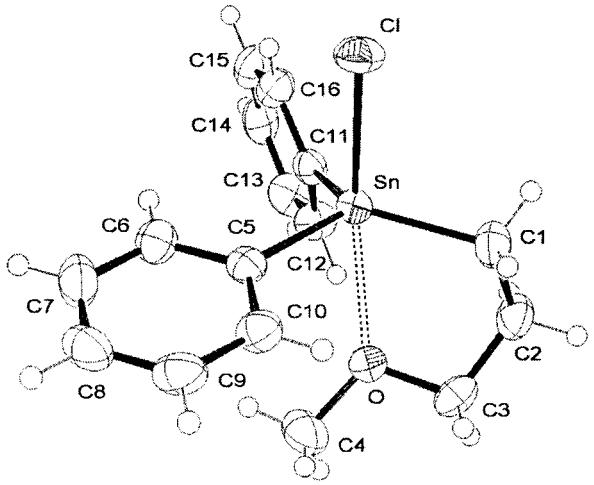

Figure 1. Solid-state structure of **6**.

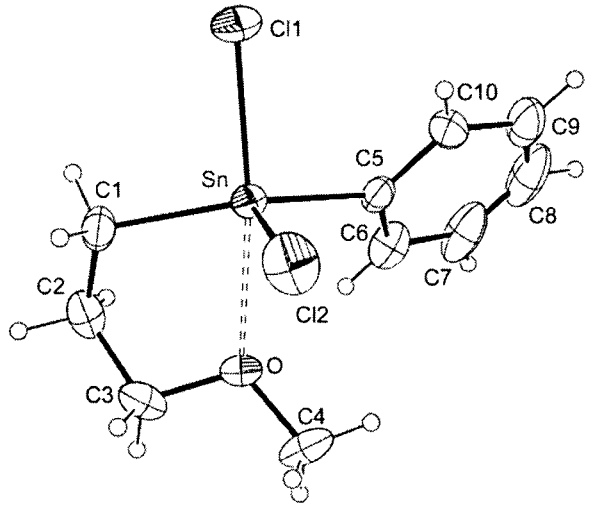

Figure 2. Solid-state structure of **7**.

7 (Figure 2), one phenyl group is replaced by the second chlorine atom and, consequently, the equatorial plane is less symmetrical [C–Sn–C: 140.2(2)°]. However, **7** still lacks a mirror plane and an inversion centre and therefore it is also chiral. The unit cells in crystals of both compounds consist of pairs of enantiomers, and thus **6** and **7** are racemates. The sum of angles in the equatorial plane of **6** and **7** (353.71° and 354.1°, respectively) is considerably smaller then 360° because both coordination polyhedra have the whole equatorial plane tilted towards the oxygen atom in a similar fashion to **4**.

In the case of **7**, the *trans* influence of the coordinated oxygen atom of the 3-methoxypropyl group causes the apical chlorine atom to have a slightly weaker bond to the central tin atom [Sn–Cl1: 2.425(2) Å] than the corresponding equatorial one [Sn–Cl2: 2.365(2) Å]. An analogous phenomenon is observed for compound **4**, where the Sn–Cl distance for the axial chlorine atom is 2.3904(12) Å while the distances for the equatorial bonds are 2.3317(14) and 2.3274(12) Å.[4] Although the structures of **6**, **7** and **4** are very similar, they differ markedly in the strength of the O→Sn coordination [Sn–O: 2.5505(18), 2.461(4) and 2.394(3) Å, respectively], which increases with the number of chlorine atoms in the coordination sphere, i.e. with the Lewis acidity of the central tin atom. Nevertheless, all the Sn–O bonds are slightly shorter than those found in **3** [Sn–O: 2.559(4) and 2.556(4) Å], where both oxygen atoms are coordinated to tin in a *cis* configuration.[4]

The crystal structure of $[RSn(S_2CNEt_2)_3]$ (**8**) was published recently.[8] An Sn–O intramolecular interaction is precluded [Sn–O: 5.427(1) Å] in this complex because of the penchant of dithiocarbamate to chelate tin and the steric crowding, given that the tin is already seven-coordinate. Thus, the 3-methoxypropyl group is bonded to tin only through carbon as a monodentate ligand and the structure is very close to those of other monorganotin tris(*N*,*N*-diethyldithiocarbamate) complexes such as $[MeSn(S_2CNEt_2)_3]$, $[BuSn(S_2CNEt_2)_3]$ and $[PhSn(S_2CNEt_2)_3]$.[9,10]

The molecular structures of the next two carbamate complexes in the set, $[RSn(S_2CNEt_2)_2Cl]$ (**9**) and $[RSn(S_2CNEt_2)Cl_2]$ (**10**), determined by X-ray diffraction, are shown in Figures 3 and 4, respectively. Selected bond lengths and angles are given in Table 2.

Complexes **9** and **10** also exist as discrete molecules. However, in contrast to previously discussed compounds, the tin atoms are hexacoordinate with a distorted octahedral ligand arrangement. The crystal structure of **9** resembles those of other monoorganotin complexes with two dithiocarbamate ligands and a chlorine atom in the coordination sphere, such as $[PhSn(S_2CNEt_2)_2Cl]$[11] and $[(MeO_2CCH_2CH_2)Sn(S_2CNMe_2)_2Cl]$.[12] The central tin atom is coordinated by four sulfur atoms from two bidentate dithiocarbamate ligands, the carbon atom of the 3-methoxypropyl substituent and the chlorine atom; the latter donor atoms are mutually *cis* [C11–Sn–Cl: 93.3(2)°]. The deviation of the coordination polyhedron from the ideal octahedral

Table 1. Selected bond lengths [Å] and angles [°] for compound **6** and **7**.

6				**7**			
Sn–O	2.5505(18)	Sn–C5	2.122(3)	Sn–O	2.461(4)	Sn–C1	2.126(6)
Sn–Cl	2.4412(8)	Sn–C11	2.139(2)	Sn–Cl1	2.425 (2)	Sn–C5	2.120(5)
Sn–C1	2.139(3)			Sn–Cl2	2.365(2)		
Cl–Sn–O	170.37(4)	C1–Sn–C5	122.67(11)	Cl1–Sn–O	172.6(1)	C1–Sn–C5	140.2(2)
Cl–Sn–C1	98.94(8)	C1–Sn–C11	119.48(11)	Cl1–Sn–C1	98.3(2)	C1–Sn–Cl2	108.0 (2)
Cl–Sn–C5	97.28(7)	C5–Sn–C11	111.56(10)	Cl1–Sn–C5	97.1(2)	C5–Sn–Cl2	105.9 (2)
Cl–Sn–C11	98.87(7)	C1–Sn–O	73.34(9)	Cl1–Sn–Cl2	97.85(9)	C1–Sn–O	74.9(2)

 © 2005 Wiley-VCH Verlag GmbH & Co. KGaA, Weinheim

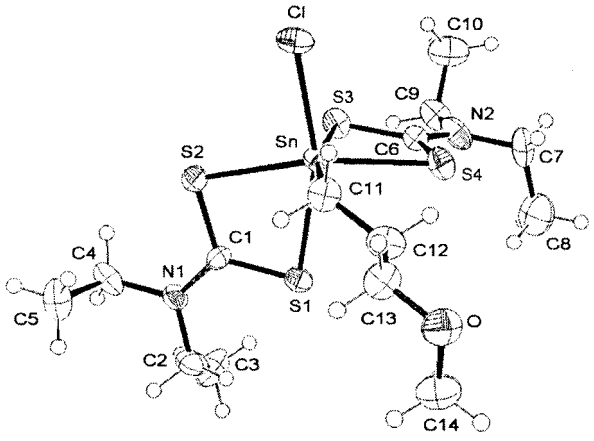

Figure 3. Solid-state structure of **9**.

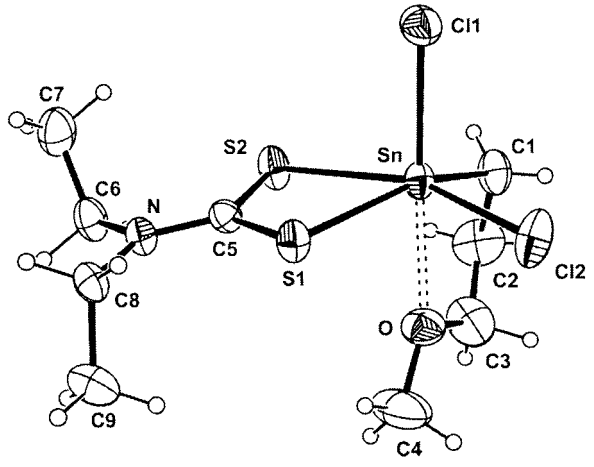

Figure 4. Solid-state structure of **10**.

geometry is especially apparent for the angles S2–Sn–S4, Cl–Sn–S1 and C11–Sn–S3, which are 153.86(6)°, 161.82(6)° and 166.2(2), respectively, instead of 180°. This distortion of the geometry is constrained by the small bite angles [S1–Sn–S2: 69.98(6)°, S3–Sn–S4: 69.86(6)°] of the dithiocarbamate ligands, which are typical for organotin dithiocarbamates.[10] The two dithiocarbamate groups are not equivalent, as becomes evident in the ^{13}C CP/MAS NMR spectrum (Figure 5), where four sets of signals for ethyl groups and two signals for the CS_2 group are observed. Nevertheless, they form unusually symmetrical chelates [Sn–S: 2.5658(18), 2.5980(19), 2.5693(19) and 2.615(2) Å].

The Sn–C [2.167(7) Å] and Sn–Cl [2.468(2) Å] bonds are longer than those of chloro(3-methoxypropyl)phenylstannanes **6** and **7**, and this can be ascribed to the lower Lewis acidity of the tin atom. On the other hand, the average Sn–S distance in **9** [2.587(15) Å] is considerably shorter than the comparable distance of 2.680(5) Å found for **8**,[8] which is a result of the higher Lewis acidity of the central tin atom caused by replacement of one dithiocarbamate ligand by chloride. In spite of this increased Lewis acidity, the oxygen atom of the 3-methoxypropyl group is not coordinated to tin as in **8**.

In the case of **10**, the distorted octahedral neighbourhood of the tin atom is composed of two chlorine atoms in mutual *cis* positions [Cl–Sn–Cl: 94.82(4)°], a four-membered chelate ring of the bidentate dithiocarbamate ligand and a five-membered chelate ring of the 3-methoxypropyl ligand arising from coordination of oxygen to tin. Thus, the molecular structure of **10** is very close to that of [(MeO$_2$CCH$_2$CH$_2$)Sn(S$_2$CNMe$_2$)Cl$_2$], where the ester carbonyl oxygen is also coordinated to tin.[13] Similarly to other organotin dithiocarbamate complexes, the dithiocarbamate ligand is bonded asymmetrically [Sn–S: 2.4728(10) and 2.6405(10) Å], with a typically small bite angle of 70.27(3)°, which is in part responsible for the distortion of the octahedral geometry.[10] The second most apparent deviation from an ideal octahedron is the bite angle of the 3-methoxypropyl ligand [C–Sn–O: 74.60(13)°]. In the solid-state structure of **10**, the ethyl groups are also non-equivalent and, consequently, the molecule lacks a mirror plane and inversion centre (Figure 4). In the ^{13}C CP/MAS NMR spectrum this is not shown for the CH_3 groups, and two signals were found only for the CH_2 groups. The unit cell in the crystal structure of **10** consist of a pair of enantiomers and thus it is also a racemate.

There is a considerable difference between the Sn–Cl distances [Sn–Cl: 2.4128(11) and 2.4309(10) Å] due to the different *trans* influence of sulfur and oxygen. Nevertheless, both distances are shorter than those found in **9** due to the higher Lewis acidity of the central tin atom in **10**. This is also demonstrated by the average Sn–S bond length of 2.557 Å, which is slightly shorter than that of **9** [2.587(15) Å] and **8** [2.680(5) Å]. Considering that the Sn–O bond length in **10** [2.475(3) Å] is longer than that of **4** and **7** [Sn–O: 2.394(3) and 2.461(4) Å, respectively], but shorter than that of **3** and **6** [Sn–O: 2.559(4), 2.556(4) and 2.5505(18) Å, respectively], it can be concluded that the

Table 2. Selected bond lengths [Å] and angles [°] for compounds **9** and **10**.

9				**10**			
Sn–S1	2.615(2)	Sn–O	5.560(6)	Sn–O	2.475(3)	Sn–S1	2.4728(10)
Sn–S2	2.5693(19)	Sn–Cl	2.468(2)	Sn–Cl1	2.4128(11)	Sn–S2	2.6405(10)
Sn–S3	2.5658(18)	Sn–C11	2.167(7)	Sn–Cl2	2.4309(10)	Sn–C1	2.138(3)
Sn–S4	2.5980(19)						
Cl–Sn–S1	161.82(6)	C11–Sn–Cl	93.3(2)	Cl1–Sn–Cl2	94.82(4)	S1–Sn–S2	70.27(3)
C11–Sn–S3	166.2(2)	C11–Sn–S4	96.41(9)	Cl1–Sn–C1	102.51(12)	S2–Sn–C1	95.71(11)
S2–Sn–S4	153.86(6)	C11–Sn–S2	103.3(2)	Cl1–Sn–S1	97.82(4)	C1–Sn–Cl2	100.65(11)
S1–Sn–S2	69.98(6)	S2–Sn–S3	90.30(6)	Cl1–Sn–S2	95.72(4)	Cl2–Sn–S1	89.33(4)
S3–Sn–S4	69.86(6)			Cl1–Sn–O	177.07(7)	C1–Sn–O	74.60(13)

 © 2005 Wiley-VCH Verlag GmbH & Co. KGaA, Weinheim

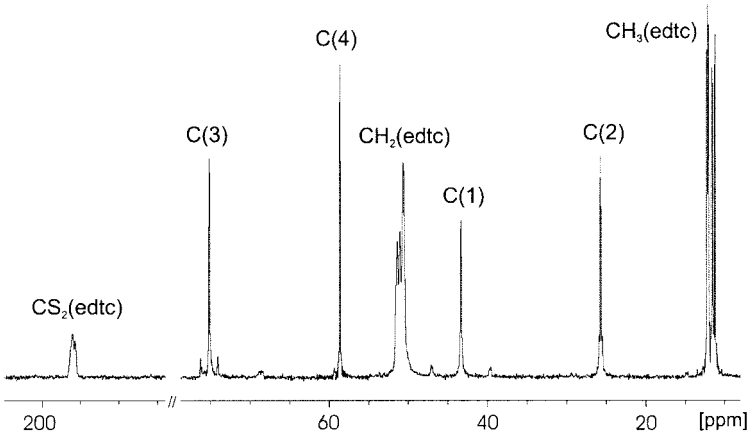

Figure 5. ^{13}C CP/MAS NMR spectrum of [RSn(S_2CNEt_2)$_2$Cl] (**9**) (edtc = *N*,*N*-diethyldithiocarbamate).

Lewis acidity of the central tin atom in **10** is in-between the Lewis acidities of the tin atoms in these compounds.

NMR Spectroscopy and Structures in Solution

The (3-methoxypropyl)stannanes were fully characterised in $CDCl_3$ solution by ^{1}H and ^{13}C NMR spectroscopy; the values of the ^{1}H and ^{13}C chemical shifts for **5**–**7**, **9** and **10** are given in the Experimental Section. The parameters for the other compounds have been published elsewhere.[4,8] In order to evaluate solution structures both in non-coordinating and coordinating solvents, ^{119}Sn NMR spectra were measured in $CDCl_3$ and [D_6]DMSO and also in the solid state. The values of the ^{119}Sn chemical shifts are summarised in Table 3. The coordinative behaviour of the 3-methoxypropyl ligand will be discussed in light of the $J_{^1H,^{119}Sn}$ coupling constants obtained from 1D ^{1}H,^{119}Sn HMQC and 2D ^{1}H,^{119}Sn J-HMBC NMR spectra[5] (Table 4) and $J_{^{13}C,^{119}Sn}$ values derived from conventional 1D ^{13}C NMR spectra (Table 5). The numbering used for the hydrogen and carbon atoms is given in Scheme 5.

Table 3. ^{119}Sn chemical shifts [ppm] for (3-methoxypropyl)stannanes in the solid state, $CDCl_3$ and [D_6]DMSO.

Compound	δ_{Sn} (solid state)	δ_{Sn} ($CDCl_3$)	δ_{Sn} ([D_6]DMSO)
1[4]	[a]	–4.3	–1.2
2[4]	[a]	49.0	27.4
3[4]	–133[d]	–108.6	–170.5
4[4]	–157	–138.5	–445.6
5	[c]	–99.6	–97.6
6	–82.4[d]	–79.5	–137.3
7	–121.7	–83.0	–281.1
8[8]	–828.3, –832.0	–774.2	–769.5
9	–593.9[d]	–582.1	–575.4
10	–405.6	–392.4	–470.3, –575.2[b]

[a] Oily substance. [b] Two signals observed due to the dynamic equilibrium discussed in the text. [c] Not measured. [d] Splitting due to the interaction of ^{119}Sn nuclei with one or two $^{35/37}$Cl spins observed according to ref.[14]

Table 4. $^nJ_{^1H,^{119}Sn}$ coupling constants [Hz] for selected protons in (3-methoxypropyl)stannanes.

Compound	H1[a] $n = 2$	H2[a] $n = 3$	H3[b] $n = 4$	H4[b] $n = 6$
1[4]	51.2	47.8	[c]	0.52
2[4]	60.8	86.2	1.31	[d]
3[4]	95.9	195.8	7.73	1.86
4[4]	104.9	254.2	5.07	2.24
5	56.8	65.6	< 0.5	< 0.5
6	76.8	134.5	5.12	1.32
7	86.6	169.3	5.65	1.73
8[8]	107.3	151.8	< 1.5	1.06
9	102.0	153.9	5.41	2.46
10	105.2	283.1	7.84	3.24

[a] Obtained from the 1D ^{1}H,^{119}Sn HMQC spectra. [b] Obtained from the 2D ^{1}H,^{119}Sn J-HMBC NMR spectra. [c] Not obtained due to an overlap. [d] Not obtained probably due to the existence of the fast dynamic equilibrium discussed in the text.

Table 5. $^nJ_{^{13}C,^{119}Sn}$ coupling constants for selected carbons in (3-methoxypropyl)stannanes.

Compound	Solvent	C1 $n = 1$	C2 $n = 2$	C3 $n = 3$
1[4]	$CDCl_3$	324.5	18.6	59.3
	[D_6]DMSO	325.3	19.3	52.3
2[4]	$CDCl_3$	434.6	26.5	55.7
	[D_6]DMSO	456.5	27.2	65.2
3[4]	$CDCl_3$	731.6	42.7	34.0
	[D_6]DMSO	840.4	44.7	95.1
4[4]	$CDCl_3$	845,2	67.0	79.3
	[D_6]DMSO	[a]	62.5	229.6
5	$CDCl_3$	404.9	21.6	56.3
	[D_6]DMSO	412.4	23.2	53.4
6	$CDCl_3$	539.8	31.1	25.5
	[D_6]DMSO	[a]	31.3	78.3
7	$CDCl_3$	640.9	40.8	43.5
	[D_6]DMSO	1028.0	53.7	104.7
8[8]	$CDCl_3$	1005.2	61.8	247.8
	[D_6]DMSO	1008.0	62.2	239.6
9	$CDCl_3$	960.5	54.5	223.9
	[D_6]DMSO	[b]	54.4	211.6
10	$CDCl_3$	985.9	71.9	75.2
	[D_6]DMSO	[a]	56.6	216.0

[a] Not obtained probably due to the existence of the dynamic equilibrium discussed in the text. [b] Not obtained due to an overlap.

 © 2005 Wiley-VCH Verlag GmbH & Co. KGaA, Weinheim

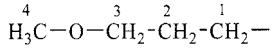

Scheme 5.

Although complex **7** (Figure 2) is chiral in the solid state, the inequivalency of the CH_2 hydrogen atoms is not seen in the 500 MHz ^1H NMR spectra of $CDCl_3$ solutions. On the other hand, there are only moderate differences between the ^{119}Sn chemical shifts in $CDCl_3$ solution and in the solid state (Table 3). Even the largest difference (57.2 ppm), found for **8,** is still far from that corresponding to a change of coordination number[14,15] and is probably caused only by crystal-packing forces. Therefore, it can be assumed that the structures found in the solid state are retained upon dissolution in $CDCl_3$.

The non-equivalence of the ethyl groups in **9** and **10** found in the solid-state structures (Figures 3 and 4) and in ^{13}C CP/MAS spectra disappears in solution due to a free rotation of the C–N bonds and was not observed even in [D_8]toluene at 180 K.

In the case of compounds **1**, **5**, **8** and **9**, where the 3-methoxypropyl group is bonded to the central tin atom only through carbon, the ^{119}Sn resonances in [D_6]DMSO are only slightly shifted to higher frequency with respect to those in $CDCl_3$ (Table 3). This shows that these compounds preserve their structures even in a strongly coordinating solvent such as [D_6]DMSO. On the other hand, the remaining compounds, i.e. those where the chelate ring of the 3-methoxypropyl ligand is closed in the solid state and in $CDCl_3$ solution, have ^{119}Sn resonances in [D_6]DMSO that are more or less shifted to lower frequency. This shows that the dynamic equilibrium already described in our previous paper[4] is established in which one or more molecules of solvent enter the coordination sphere of the central tin atom and cleave the oxastannacycle.

While only one broad ^{119}Sn resonance was observed in most cases, there is one broad resonance (δ = –470.3 ppm) and one sharp resonance (δ = –575.2 ppm) in the ^{119}Sn NMR spectrum of **10**. This likely indicates that an equilibrium of at least three species is established in [D_6]DMSO solution of **10** (Scheme 6). The broad signal with a chemical shift of δ = –470.3 ppm probably arises due to the equilibrium between hexacoordinate species **A** and **B**, which is fast on the NMR timescale. The difference between the chemical shifts of the observed resonances is 105 ppm (19.5 kHz) and therefore the sharp resonance at δ = –575.2 ppm could be assigned to heptacoordinate complex **C**, which is in a slow exchange regime on the NMR timescale.

The values of the $^2J_{^1H,^{119}Sn}$ coupling constants obtained for proton H1 (Table 4) clearly show that this parameter is mainly influenced by the number of polar groups (Cl, Et_2NCS_2) bonded to the central tin atom, and by the coordination number, and therefore do not bring any information about the O→Sn coordination. Comparison of $^3J_{^1H,^{119}Sn}$ coupling constants found for proton H2 in heptacoordinate and hexacoordinate compounds **8**, **9** and **10** (151.8, 153.9 and 283.1 Hz, respectively) denote that the closure of the oxastannacycle results in a considerable increase of this parameter. However, the 3-methoxypropyl group in pentacoordinate compounds **6** and **7** also forms a chelate but the values of the $^3J_{^1H,^{119}Sn}$ coupling constants observed for proton H2 (134.5 and 169.3 Hz) are similar to those in **8** and **9**, where the oxygen is not coordinated to tin, while another pentacoordinate compound with a chelating 3-methoxypropyl group (**4**) has this parameter almost two times higher (254.2 Hz). Thus, it is evident that $^3J_{^1H,^{119}Sn}$ coupling constants are also still strongly influenced by the coordination environment of the central tin atom and it is impossible to use this parameter to evaluate the coordinative behaviour of the 3-methoxypropyl ligand. Surprisingly, the changes of long-range $^4J_{^1H,^{119}Sn}$ coupling constants obtained for proton H3 (Table 4) do not exhibit any trend that could enable conclusions to be drawn about the coordination of oxygen to tin.

For the methoxy group of tetraorganotin compound **5**, it was impossible to obtain the exact value of the long-range $^6J_{^1H,^{119}Sn}$ coupling constant, but the trace of the sine modulation obtained from an $^1H,^{119}Sn$ J-HMBC experiment enabled us to estimate that the value is lower than 0.5 Hz. On the other hand, the values of this parameter in **6** and **7** (1.32 and 1.73 Hz, respectively) are considerably higher and increase with the strength of donor–acceptor bonding between the oxygen atom of the 3-methoxypropyl ligand and the central tin atom [Sn–O: 2.5505(18) and 2.461(4) Å, respectively] but they are still smaller than that of **4** (2.24 Hz), where the closure of the oxastannacycle is even more firm [Sn–O: 2.394(3) Å]. Thus, it seems that the long-range $^6J_{^1H,^{119}Sn}$ coupling constants of proton H4 reflect the strength of the O→Sn coordinative bond and the conclusions made on the basis of the values obtained for the first

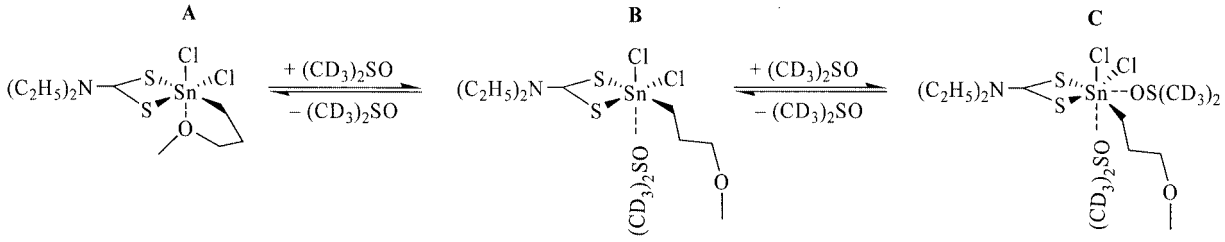

Scheme 6.

 © 2005 Wiley-VCH Verlag GmbH & Co. KGaA, Weinheim

set of (3-methoxypropyl)stannanes (**1**–**4**) are confirmed.[4] However, all dithiocarbamate complexes **8**, **9** and **10** have rather large long-range $^{6}J_{^{1}H,^{119}Sn}$ coupling constants (1.06, 2.46 and 3.24 Hz, respectively) for proton H4 even though the 3-methoxypropyl ligand forms a chelate only in the last one. Moreover, the value of 3.24 Hz obtained for **10** is significantly higher than that for **4** (2.24 Hz), where the O→Sn donor–acceptor interaction is stronger [Sn–O: 2.475(3) and 2.394(3) Å, respectively]. Thus, it is evident that this long-range coupling constant is also markedly dependent on the neighbourhood of the central tin atom and is also not very useful as an indicator of intermolecular donor–acceptor interactions.

The values of the $^{1}J_{^{13}C,^{119}Sn}$ and $^{2}J_{^{13}C,^{119}Sn}$ coupling constants obtained for carbons C1 and C2, respectively (Table 5), are influenced especially by the neighbourhood of the central tin atom and no effect of the coordinative behaviour of the 3-methoxypropyl ligand is apparent. In our previous paper,[4] we remarked that the compounds with an oxastannacycle of a 3-methoxypropyl ligand (**3** and **4**) have values of $^{3}J_{^{13}C,^{119}Sn}$ for carbon C3 lower than the corresponding values for 1-butyltin. This also holds true for new compounds **6**, **7** and **10** (Table 5). As in **3**, compound **6** has $^{3}J_{^{13}C,^{119}Sn}$ lower than $^{2}J_{^{13}C,^{119}Sn}$ (i.e., opposite to the trend usually observed for 1-butylstannanes).[15] It has been suggested that this phenomenon is caused by the sum of two scalar coupling pathway contributions − through the covalent bonds of the 3-methoxypropyl chain and through the coordinative O→Sn bond − of opposite signs. In [D_6]-DMSO solutions of **3**, **4**, **6**, **7** and **10**, the $^{3}J_{^{13}C,^{119}Sn}$ coupling constants increase by between 53 and 150 Hz (Table 5). This considerable change can be ascribed to the cleavage of the oxastannacycle because of the equilibrium discussed above in which the donor oxygen atom of the 3-methoxypropyl substituent is replaced by the stronger Lewis base [D_6]DMSO. On the contrary, compounds **1**, **5**, **8** and **9**, where the 3-methoxypropyl ligand does not form a chelate and which do not change structures upon dissolution in [D_6]DMSO, have values of this parameter in [D_6]DMSO even slightly lower than in $CDCl_3$ (Table 5). Thus, $^{3}J_{^{13}C,^{119}Sn}$ coupling constants seem to be a useful indicator of the strength of the O→Sn donor–acceptor interaction in (3-methoxypropyl)stannanes.

Experimental Section

General: THF was distilled from sodium benzophenone ketyl. $CHCl_3$ was distilled from P_2O_5. Other solvents were used without purification. The solution of HCl in $CHCl_3$ was prepared by absorption of dry gaseous HCl which was obtained by dropwise addition of hydrochloric acid into concentrated sulfuric acid. Mg chips, 1,2-dibromomethane, chlorotriphenylstannane and sodium *N*,*N*-diethyldithiocarbamate trihydrate were obtained from commercial sources. Preparation of 1-chloro-3-methoxypropane, tetrakis(3-methoxypropyl)stannane (**1**), chlorotris(3-methoxypropyl)-stannane (**2**), dichlorobis(3-methoxypropyl)stannane (**3**) and trichloro(3-methoxypropyl)stannane (**4**) has been described elsewhere.[4]

Microanalyses (C, H, N, S, Cl) were carried out using a Fison EA 1108 instrument in the Microanalytical Laboratory at the University of Pardubice.

Synthesis of (3-Methoxypropyl)triphenylstannane RPh_3Sn (5): A solution of 1-chloro-3-methoxypropane (3.00 g, 27.63 mmol) in THF (6 mL) was added to Mg chips (0.83 g, 34.14 mmol) which were previously activated by I_2 vapours. About 20% of the solution was added at once and the reaction was started by addition of 2 drops of 1,2-dibromethane. The rest of the solution was added dropwise in order to maintain the reflux. Then, the reaction mixture was refluxed for a further hour. After cooling to –50 °C, a solution of chlorotriphenylstannane (7.18 g, 18.63 mmol) in THF (6 mL) was added dropwise and the reaction mixture was then refluxed for 8 h. After cooling to room temperature, the reaction mixture was filtered and water (40 mL) was added. The mixture was extracted with diethyl ether (3 × 20 mL). The organic part was separated, dried with anhydrous Na_2SO_4 and the solvents were removed by rotary evaporation. The residue was recrystallised from $CHCl_3$/hexane solution and **1** (6.56 g, yield 85%) was obtained as white crystals, m.p. 49–51 °C. ^{1}H NMR ($CDCl_3$, 25 °C): δ = 1.84 (m, 2 H, $SnCH_2CH_2$), 2.31 (m, 2 H, $SnCH_2CH_2$), 3.17 (s, 3 H, OCH_3), 3.38 (t, $^{3}J_{HH}$ = 6.5 Hz, 2 H, CH_2OCH_3), 7.37 (m, 9 H, *m*-Ph, *p*-Ph), 7.56 (m, 6 H, *o*-Ph) ppm. ^{13}C NMR ($CDCl_3$, 25 °C): δ = 7.32 ($SnCH_2$), 26.4 ($SnCH_2CH_2$), 58.1 (OCH_3), 75.0 (CH_2OCH_3), 128.3 (*m*-Ph), 128.6 (*p*-Ph), 136.9 (*o*-Ph), 139.2 (*i*-Ph) ppm. $C_{22}H_{24}OSn$ (423.14): calcd. C 62.45, H 5.72; found C 62.25, H 5.53.

Synthesis of Chloro(3-methoxypropyl)phenylstannanes $RPh_{3-x}SnCl_x$ 6 and 7: A solution of HCl in dry $CHCl_3$ [10 mL (0.169 M) for **6**; 19 mL (0.169 M) for **7**] was added to **1** (0.5 g, 1.20 mmol) and the mixture was stirred at room temperature for 2 d. The solvent was then removed by rotary evaporation. The residue was recrystallised from $CHCl_3$/hexane solution.

Chloro(3-methoxypropyl)diphenylstannane (6): Yield: 0.43 g (96%), white crystals, m.p. 93–95 °C. ^{1}H ($CDCl_3$, 25 °C): δ = 1.79 (m, 2 H, $SnCH_2$), 2.15 (m, 2 H, $SnCH_2CH_2$), 2.96 (s, 3 H, OCH_3), 3.53 (t, $^{3}J_{HH}$ = 6.0 Hz, 2 H, CH_2OCH_3), 7.41 (m, 2 H, *p*-Ph), 7.43 (m, 4 H, *m*-Ph), 7.71 (m, 4 H, *o*-Ph) ppm. ^{13}C NMR ($CDCl_3$, 25 °C): δ = 14.7 ($SnCH_2$), 25.3 ($SnCH_2CH_2$), 73.0 (CH_2OCH_3), 128.6 (*m*-Ph), 129.2 (*p*-Ph), 135.6 (*o*-Ph), 140.4 (*i*-Ph) ppm. $C_{16}H_{19}ClOSn$ (381.48): calcd. C 50.38, H 5.02, Cl 9.29; found C 49.95, H 4.89, Cl 9.01.

Dichloro(3-methoxypropyl)phenylstannane (7): Yield: 0.42 g (98%), white crystals, m.p. 99–101 °C. ^{1}H ($CDCl_3$, 25 °C): δ = 1.96 (m, 2 H, $SnCH_2$), 2.19 (m, 2 H, $SnCH_2CH_2$), 3.29 (s, 3 H, OCH_3), 3.61 (t, $^{3}J_{HH}$ = 5.4 Hz, 2 H, CH_2OCH_3), 7.45 (m, 1 H, *p*-Ph), 7.64 (m, 2 H, *m*-Ph), 7.80 (m, 2 H, *o*-Ph) ppm. ^{13}C NMR ($CDCl_3$, 25 °C): δ = 22.2 ($SnCH_2$), 24.9 ($SnCH_2CH_2$), 58.5 (OCH_3), 71.7 (CH_2OCH_3), 129.0 (*m*-Ph), 130.6 (*p*-Ph), 134.8 (*o*-Ph), 141.0 (*i*-Ph) ppm. $C_{10}H_{14}Cl_2OSn$ (339.83): calcd. C 35.35, H 4.15, Cl 20.87; found C 35.03, H 3.95, Cl 20.63.

Synthesis of (3-Methoxypropyl)stannyl *N*,*N*-Diethyldithiocarbamates $RSn(S_2CNEt_2)_{3-x}Cl_x$ (8–10): A mixture of **4** (0.5 g, 1.67 mmol) and sodium *N*,*N*-diethyldithiocarbamate [1.19 g (5.29 mmol) for **8**; 0.76 g (3.37 mmol) for **9**; 0.38 g (1.69 mmol) for **10**] in acetone (10 mL) was stirred at room temperature for 2 h. The reaction mixture was then filtered and the solvent was removed by rotary evaporation. The residue was recrystallised from $CHCl_3$/hexane solution.

(3-Methoxypropyl)stannyl Tris(*N*,*N*-diethyldithiocarbamate) (8): Yield: 0.86 g (80%), yellowish crystals, m.p. 92–93 °C (for further characterisation of **8** see ref.[8]).

 © 2005 Wiley-VCH Verlag GmbH & Co. KGaA, Weinheim

Table 6. Experimental details for the X-ray crystal structure determination of **6**, **7**, **9** and **10**.

	6	**7**	**9**	**10**
Empirical formula	$C_{16}H_{19}ClOSn$	$C_{10}H_{14}Cl_2OSn$	$C_{14}H_{29}ClN_2OS_4Sn$	$C_9H_{19}Cl_2NOS_2Sn$
Formula mass	381.45	339.80	523.83	410.96
Crystal system	monoclinic	monoclinic	triclinic	monoclinic
Space group	$P2_1/n$	$P2_1/n$	$P\bar{1}$ (no. 2)	$P2_1/c$
a [Å]	9.6368(19)	9.4591(5)	10.416(3)	8.0136(18)
b [Å]	17.639(4)	8.3341(16)	10.670(3)	14.738(4)
c [Å]	9.786(2)	16.5793(10)	11.849(3)	13.858(5)
α [°]	90	90	93.39(3)	90
β [°]	99.87(2)	93.126(6)	114.34(3)	100.42(3)
γ [°]	90.00	90.00	107.15(3)	90.00
V [Å^3]	1638.9(6)	1305.1(3)	1121.5(7)	1609.7(8)
Z	4	4	2	4
D_c [g cm^{-3}]	1.546	1.729	1.551	1.696
μ [mm^{-1}]	1.712	2.336	1.635	2.161
T [K]	223	297	223	203
Reflections collected	11464	4609	7914	6382
Independent reflections	2759 (R_{int} = 0.047)	2122 (R_{int} = 0.069)	3658 (R_{int} = 0.102)	2838 (R_{int} = 0.046)
Goodness of fit	1.007	1.113	1.130	1.066
R_1, wR_2 [$I > 2\sigma(I)$]	0.022, 0.055	0.056, 0.156	0.050, 0.152	0.024, 0.061
R_1, wR_2 (all data)	0.028, 0.058	0.063, 0.172	0.054, 0.166	0.028, 0.065

Chloro(3-methoxypropyl)stannyl Bis(*N*,*N*-diethyldithiocarbamate) (9): Yield: 0.72 g (83%), yellowish crystals, m.p. 66–69 °C. ^{1}H (CDCl$_3$, 25 °C): δ = 1.28 (t, $^3J_{HH}$ = 6.9 Hz, 12 H, CH$_2$C*H*$_3$), 1.83–1.96 (m, 4 H, SnC*H*$_2$C*H*$_2$), 3.28 (s, 3 H, OC*H*$_3$), 3.38 (t, $^3J_{HH}$ = 5.8 Hz, 2 H, C*H*$_2$OCH$_3$), 3.69 (q, $^3J_{HH}$ = 6.9 Hz, 8 H, NC*H*$_2$) ppm. ^{13}C NMR (CDCl$_3$, 25 °C): δ = 11.7 (CH$_2$*C*H$_3$), 25.9 (SnCH$_2$*C*H$_2$), 42.4 (Sn*C*H$_2$), 50.7 (N*C*H$_2$), 58.1 (O*C*H$_3$), 73.8 (*C*H$_2$OCH$_3$), 196.8 (N*C*S$_2$) ppm. $C_{14}H_{29}ClN_2OS_4Sn$ (523.82): calcd. C 32.10, H 5.58, Cl 6.77, N 5.35, S 24.48 ; found C 31.93, H 5.35, Cl 6.43, N 5.03, S 24.35.

Dichloro(3-methoxypropyl)stannyl *N*,*N*-Diethyldithiocarbamate (10): Yield: 0.40 g (59%), white crystals, m.p. 135–136 °C. ^{1}H (CDCl$_3$, 25 °C): δ = 1.35 (t, $^3J_{HH}$ = 7.1 Hz, 6 H, CH$_2$C*H*$_3$), 1.77 (m, 2 H, SnC*H*$_2$), 2.19 (m, 2 H, SnCH$_2$C*H*$_2$), 3.67 (t, $^3J_{HH}$ = 6.0 Hz, 2 H, C*H*$_2$OCH$_3$), 3.72 (q, $^3J_{HH}$ = 7.1 Hz, 4 H, NC*H*$_2$), 3.74 (s, 3 H, OC*H*$_3$) ppm. ^{13}C NMR (CDCl$_3$, 25 °C): δ = 11.7 (CH$_2$*C*H$_3$), 24.1 (SnCH$_2$*C*H$_2$), 35.2 (Sn*C*H$_2$), 51.7 (N*C*H$_2$), 58.6 (O*C*H$_3$), 71.4 (*C*H$_2$OCH$_3$), 192.8 (N*C*S$_2$) ppm. $C_9H_{19}Cl_2NOS_2Sn$ (411.00): calcd. C 26.3, H 4.66, Cl 17.25, N 3.41, S 15.60; found C 26.11, H 4.53, Cl 17.19, N 3.32, S 15.52.

NMR Spectroscopy: ^{1}H, ^{13}C and ^{119}Sn NMR spectra were recorded in a 5-mm tuneable probe with a Bruker AMX 360 (^{1}H: 360.14 MHz; ^{13}C: 90.57 MHz; ^{119}Sn: 134.28 MHz) or a Bruker AVANCE 500 spectrometer (^{1}H: 500.13 MHz; ^{13}C: 125.77 MHz; ^{119}Sn: 186.48 MHz). ^{1}H and ^{13}C chemical shifts are given in ppm with respect to Me$_4$Si, and ^{119}Sn chemical shifts with respect to Me$_4$Sn. The gradient-assisted 1D ^{1}H,^{119}Sn HMQC and 2D ^{1}H,^{119}Sn J-HMBC spectra were recorded as explained elsewhere,[5] with the Bruker AVANCE 500 spectrometer. ^{13}C and ^{119}Sn CP/MAS NMR spectra were recorded with a Bruker AVANCE 500 spectrometer equipped with a double-bearing CP/MAS probe at room temperature. The ^{119}Sn chemical shifts were calibrated indirectly to tetracyclohexyltin (δ = –97.35 ppm) and were allocated approximately to the centre of gravity of the signals.

X-ray Crystallography: Single crystals were prepared by diffusion of hexane into CHCl$_3$ solutions of the complexes. The diffraction experiments were carried out using Mo-K_α radiation (λ = 0.71073 Å) on a Stoe IPDS (for **6** and **9**) or a Stoe STADI (for **7** and **10**) diffractometer. The structures were solved by direct methods (SHELXS-86)[16] and refined by full-matrix least-squares on F^2 (SHELXL-97)[17] with anisotropic displacement parameters for all non-H atoms. Hydrogen atoms were placed in calculated positions and refined according to the riding model (Table 6).

CCDC-238979 (for **10**), -238980 (for **7**), -238981 (for **9**) and -238982 (for **6**) contain the supplementary crystallographic data for this paper. These data can be obtained free of charge from The Cambridge Crystallographic Data Centre via www.ccdc.cam.ac.uk/data_request/cif.

Acknowledgments

Financial support from the Ministry of Education, Youth and Sports of the Czech Republic (project LN 00 A028) and the Grant Agency of the Czech Republic (grant 203/04/0223) is gratefully acknowledged. We are grateful to J. Brus from the Institute of Macromolecular Chemistry of the Academy of Sciences of the Czech Republic for measuring ^{13}C and ^{119}Sn CP/MAS NMR spectra. T. L. and P. Z. thank Aleš Smička, who suddenly and tragically died on June 19th 2001 in Pardubice, for starting their investigations on (3-methoxypropyl)stannanes, and Prof. Jaroslav Holeček for fruitful discussions about chemistry and life, and all that helped us to finish this paper.

[1] J. T. B. H. Jastrzebski, G. van Koten, *Adv. Organomet. Chem.* **1993**, *35*, 241–294 and references cited therein.

[2] a) G. van Koten, J. G. Noltes, *J. Am. Chem. Soc.* **1976**, *98*, 5393–5395; b) J. T. B. H. Jastrzebski, J. Boersma, P. M. Esch, G. van Koten, *Organometallics* **1991**, *10*, 930–935; c) A. Růžička, V. Pejchal, J. Holeček, A. Lyčka, K. Jacob, *Collect. Czech. Chem. Commun.* **1998**, *63*, 977–989; d) R. Jambor, I. Císařová, A. Růžička, J. Holeček, *Acta Crystallogr., Sect. C* **2001**, *57*, 373–374; e) M. Mehring, M. Schürmann, K. Jurkschat, *Organometallics* **1998**, *17*, 1227–1236; f) M. Mehring, C. Löw, M. Schürmann, K. Jurkschat, *Eur. J. Inorg. Chem.* **1999**, 887–898; g) M. Mehring, C. Löw, F. Uhlig, M. Schürmann, K. Jurkschat, B. Mahieu, *Organometallics* **2000**, *19*, 4613–4623; h) M. Mehring, I. Vrasidas, D. Horn, M. Schürmann, K. Jurkschat, *Organometallics* **2001**, *20*, 4647–4653; i) R. Jambor, L. Dostál, A. Ružička, I. Císařová, J. Brus, M. Holčapek, J. Holeček, *Organometallics* **2002**, *21*, 3996–4004.

[3] a) U. Kolb, M. Dräger, M. Dargatz, K. Jurkschat, *Organometallics* **1995**, *14*, 2827–2834; b) N. Pieper, C. Klaus-Mrestani,

 © 2005 Wiley-VCH Verlag GmbH & Co. KGaA, Weinheim

M. Schürmann, K. Jurkschat, M. Biesemans, I. Verbruggen, J. C. Martins, R. Willem, *Organometallics* **1997**, *16*, 1043–1056; c) K. Jurkschat, N. Pieper, S. Seemeyer, M. Schürmann, M. Biesemans, I. Verbruggen, R. Willem, *Organometallics* **2001**, *20*, 868–880; d) M. Seibert, K. Merzweiler, Ch. Wagnert, H. Weichmann, *J. Organomet. Chem.* **2002**, *650*, 25–36; e) M. Biesemans, R. Willem, S. Damoun, P. Geerling, M. Lahcini, P. Jaumier, B. Jousseaume, *Organometallics* **1996**, *15*, 2237–2245; f) M. Biesemans, R. Willem, S. Damoun, P. Geerling, E. R. T. Tiekink, P. Jaumier, M. Lahcini, B. Jousseaume, *Organometallics* **1998**, *17*, 90–97; g) R. Willem, M. Biesemans, P. Jaumier, B. Jousseaume, *J. Organomet. Chem.* **1999**, *572*, 233–238; h) J. Susperregui, M. Bayle, J. M. Léger, G. Déléris, M. Biesemans, R. Willem, M. Kemmer, M. Gielen, *J. Organomet. Chem.* **1997**, *545–546*, 559–565.

[4] T. Lébl, A. Smička, J. Brus, C. Bruhn, *Eur. J. Inorg. Chem.* **2003**, 143–148.

[5] J. C. Martins, M. Biesemans, R. Willem, *Progr. Nucl. Magn. Reson. Spectrosc.* **2000**, *36*, 271–322.

[6] M. Biesemans, J. C. Martins, R. Willem, A. Lyčka, A. Růžička, J. Holeček, *Magn. Reson. Chem.* **2002**, *40*, 65–69.

[7] A. G. Davies, P. J. Smith, in *Comprehensive Organometallic Chemistry* (Eds.: G. Wilkinson, F. Gordon, A. Stone, E. W. Abel), Pergamon, New York, **1982**, vol. 2, p. 535.

[8] P. Zoufalá, I. Císařová, A. Růžička, *Main Group Met. Chem.* **2003**, *26*, 53–58.

[9] a) J. S. Morris, E. O. Schlemper, *J. Cryst. Mol. Struct.* **1978**, *8*, 295–307; b) J. S. Morris, E. O. Schlemper, *J. Cryst. Mol. Struct.* **1979**, *9*, 1.

[10] E. R. T. Tiekink, *Main Group Met. Chem.* **1992**, *15*, 161–186.

[11] P. G. Harrison, A. Mangia, *J. Organomet. Chem.* **1976**, *120*, 211–216.

[12] O. S. Jung, J. H. Jeong, Y. S. Sohn, *Acta Crystallogr., Sect. C* **1990**, *46*, 31–33.

[13] O. S. Jung, J. H. Jeong, Y. S. Sohn, *Polyhedron* **1989**, *8*, 1413–1417.

[14] R. K. Harris, A. Sebald, D. Furlani, G. Tagliavini, *Organometallics* **1988**, *7*, 388–394.

[15] a) V. Pejchal, J. Holeček, M. Nádvorník, A. Lyčka, *Collect. Czech. Chem. Commun.* **1995**, *60*, 1492–1501; b) M. Nádvorník, J. Holeček, K. Handlíř, A. Lyčka, *J. Organomet. Chem.* **1984**, *275*, 43–51; c) J. Holeček, M. Nádvorník, K. Handlíř, A. Lyčka, *J. Organomet. Chem.* **1986**, *315*, 299–308.

[16] G. M. Sheldrick, *SHELXS-86*, *A Program for Crystal Structure Solution,* University of Göttingen, Germany, **1986**.

[17] G. M. Sheldrick, *SHELXL-97*, *A Program for Crystal Structure Refinement,* University of Göttingen, Germany, **1997**.

Received: October 18, 2004

 © 2005 Wiley-VCH Verlag GmbH & Co. KGaA, Weinheim

The Additive Nature of Energy Penalties in 10-Vertex *nido*-(Car)boranes

Farooq A. Kiani[a,b] and Matthias Hofmann*[a]

Keywords: Boranes / Carboranes / Density functional theory / Energy penalties / Structural increment system

A structural increment system, i.e. quantitative rules that govern the relative stabilities of 10-vertex *nido*-boranes and -carboranes, has been determined. Density functional theory computations at the B3LYP/6-311+G(d,p)//B3LYP/6-31G(d) level with ZPE corrections were carried out for 81 different boron hydride and carborane structures from $[B_{10}H_{12}]^{2-}$ to $C_3B_7H_{11}$ to determine their relative stabilities. A set of eleven disfavored geometrical features that destabilize a cluster structure relative to a hypothetical ideal situation were identified and weighted by so-called energy penalties. The latter show good additive behavior and allow us to reproduce the DFT computed relative energies mostly with an accuracy of 6.0 kcal mol^{-1}. Some unknown 10-vertex *nido*-carboranes that are thermodynamically more stable than their known isomers are also identified.

(© Wiley-VCH Verlag GmbH & Co. KGaA, 69451 Weinheim, Germany, 2005)

Introduction

Assuming a hypothetical, ideal cluster and additive destabilizations caused by deviating structural features, one can derive corresponding energy penalties that allow an easy estimation of the thermodynamic stabilities of cluster isomers. Such quantitative rules weighting different disfavored structural features of a particular heteroborane cluster have already been determined for 6-[1] and 11-vertex[2] *nido*-(car)boranes and 11-vertex *nido*-hetero(car)boranes.[3] These rules not only indicate the thermodynamically most stable isomer for a given formula,[2,3] but also describe the relative stabilities of different isomers quite accurately.[1–3] These systematic studies also identified some still unknown clusters of competitive thermodynamic stability which might be synthesized in the future.[2,3] Some structural features have similar energy penalties in 6- and 11-vertex *nido*-boranes, -carboranes, and even -heterocarboranes.

Here we extend the structural increment approach to the more complex 10-vertex *nido* cluster; 6- and 11-vertex *nido* clusters are quite simple as they have only one kind of cage (i.e., of the same connectivity, identified by k_c) and one kind of peripheral (k_p) vertex. A *nido* 6-vertex cluster has five $3k_p$ and one $5k_c$ vertices ($\Delta k = 2$), and an 11-vertex *nido* cluster has five $4k_p$ and six $5k_c$ vertices ($\Delta k = 1$). The situation is more complicated in the 10-vertex *nido* family, however, due to two different types of peripheral vertices, i.e. two $3k_p$ ($\Delta k = 2$) and four $4k_p$ ($\Delta k = 1$) next to the four $5k_c$ vertices (see Figure 1). These three different types of vertices make the 10-vertex *nido* cluster more complex and therefore some new and additional structural features need to be introduced. These features and their corresponding energy penalties have been derived and are discussed in this paper.

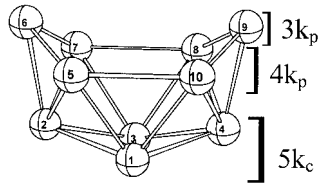

Figure 1. Cluster shape and numbering scheme for 10-vertex *nido*-boranes and -carboranes; 3*k*, 4*k*, and 5*k* indicate connectivities of peripheral (p) and cluster (c) vertices with respect to other cluster atoms.

Results and Discussion

Structural Features for 10-Vertex *nido*-Boranes and -Carboranes

Eleven energy increments corresponding to disfavoring structural features are sufficient to reproduce the relative stability order, as derived by DFT computations, for eighty-one 10-vertex *nido*-boranes and -carboranes ranging from $[B_{10}H_{12}]^{2-}$ to $C_3B_7H_{11}$. These energy penalties are listed in Table 1 and the corresponding structural features are illustrated in Figure 2.

The energy penalties can be divided into three main groups: *carbon structural features*, arising due to carbon-

[a] Anorganisch-Chemisches Institut, Ruprecht-Karls-Universität Heidelberg
Im Neuenheimer Feld 270, 69120 Heidelberg, Germany
Fax: +49-6221-544955
E-mail: matthias.hofmann@aci.uni-heidelberg.de
farooq.kiani@aci.uni-heidelberg.de
[b] Department of Chemistry, Quaid-I-Azam University, Islamabad 45320, Pakistan

Supporting information for this article is available on the WWW under http://www.eurjic.org or from the author.

Table 1. A comparison of energy penalties for 6-, 10- and 11-vertex *nido* clusters.

Increment name	Symbol	Energy penalties [kcal mol^{-1}]		
		6-vertex *nido*[a]	11-vertex *nido*[b]	10-vertex *nido*[c]
Carbon atom at 5*k* instead of 3*k*	$C_{3k\rightarrow5k}$	33	–	40.4
Carbon atom at 4*k* instead of 3*k*	$C_{3k\rightarrow4k}$	–	–	16.1
Carbon atom at 5*k* instead of 4*k*	$C_{4k\rightarrow5k}$	–	28.0	24.3[d]
endo-CH	CH_2	30	33.2	32.6
C(*endo*-CH)	$C(CH_2)$	10	(11.6)	–
C(*endo*-CH)C	$C(CH_2)C$	(17)	(20.4)	–
Bridge CH–B	CH–B	27	33.1	32.1
Bridge C–HB	C–HB	35	–	–
C(bridge-CH–B)	C(CH–B)	5	(7.3)	–
Adjacent carbon atoms.	CC	15	16.0	14.1
Adjacent carbon atoms (3*k*–5*k*)	CC(3–5)	–	–	3.3
endo-BH	BH_2	11	2.3	5.0
C(*endo*-BH)	$C(BH_2)$	7	(4.6)	–
C(*endo*-BH)C	$C(BH_2)C$	25	28.8	–
BHB(*endo*-H)BHB	H(*endo*-H)H	–	23.9	–
$(BHB)_2$(0–62)	HA_0	7	–	–
$(BHB)_2$	HH	–	25.9	2.9
C(BHB)	C(H)	–	2.2	–
5*k*C$(BHB)_2$(0–62)	5*k*(HA_0)	5	–	–
$(BHB)_2$(1–43)	HA_1	11	–	–
5*k*C$(BHB)_2$(1–43)	5*k*(HA_1)	(2)	–	–
BHB(c)BHB	H(C)H	–	–	8.7
BHB connected to 4*k* vertices	H(4–4)	–	–	12.7
3*k*(open-face BHB)	3*k*C(H)	–	–	13.7

[a] See ref.[1] [b] See ref.[2] [c] This work. [d] $C_{4k\rightarrow5k}$ is not an independent structural feature in the 10-vertex *nido* cluster, but results as the difference between $C_{3k\rightarrow4k}$ and $C_{3k\rightarrow5k}$.

atom positions, *hydrogen structural features*, arising due to hydrogen-atom placement, and *mixed structural features*, which involve both carbon and hydrogen atoms.

Carbon Structural Features

$C_{3k\rightarrow5k}$

A carbon atom at a 5*k* (vertices 1 through 4) rather than a 3*k* position (vertices 6 and 9) destabilizes a structure by 40.4 kcal mol^{-1}.

$C_{3k\rightarrow4k}$

A carbon atom has an energy penalty of 16.1 kcal mol^{-1} when it is at a 4*k* position (i.e. positions 5, 7, 8, or 10) rather than a 3*k* position.

CC and CC(3–5)

Two adjacent carbon atoms are unfavorable, but the amount of destabilization depends upon the carbon atoms' connectivities: for $\Delta k = 0$ and 1 the CC energy penalty is 14.1 kcal mol^{-1}, whereas for $\Delta k = 2$, (i.e., adjacent 3*k* and 5*k* C atoms), a considerably smaller CC(3–5) energy penalty of only 3.3 kcal mol^{-1} is found.

Hydrogen Structural Features

H(4–4)

A hydrogen atom bridging to two 4*k* vertices (rather than a 3*k* and a 4*k* boron vertex) results in an increased energy of the cluster by 12.7 kcal mol^{-1}.

BH_2

An *endo*-terminal hydrogen atom attached to a boron atom has an energy penalty of 5.0 kcal mol^{-1}.

HH

Adjacent hydrogen atoms are accompanied by an energy penalty of 2.9 kcal mol^{-1}.

Mixed Structural Features

CH_2

An *endo*-terminal hydrogen atom at a carbon atom results in an energy penalty of 32.6 kcal mol^{-1}. In all structures considered here, except **JR**, the CH_2 group is located at a 3*k* vertex.

CH–B

An *endo*-hydrogen atom bound to a carbon atom but bent towards a boron atom, i.e. bridging between a carbon atom and a boron atom, is disfavored by 32.1 kcal mol^{-1}.

3kC(H)

A 3*k* carbon atom in the presence of one or more bridging hydrogen atoms at the open face results in a 13.7 kcal mol^{-1} destabilization.

H(C)H

One or two carbon atoms entrapped between two hydrogen bridges through one connection only, incorporate a penalty of 8.7 kcal mol^{-1}.

 © 2005 Wiley-VCH Verlag GmbH & Co. KGaA, Weinheim

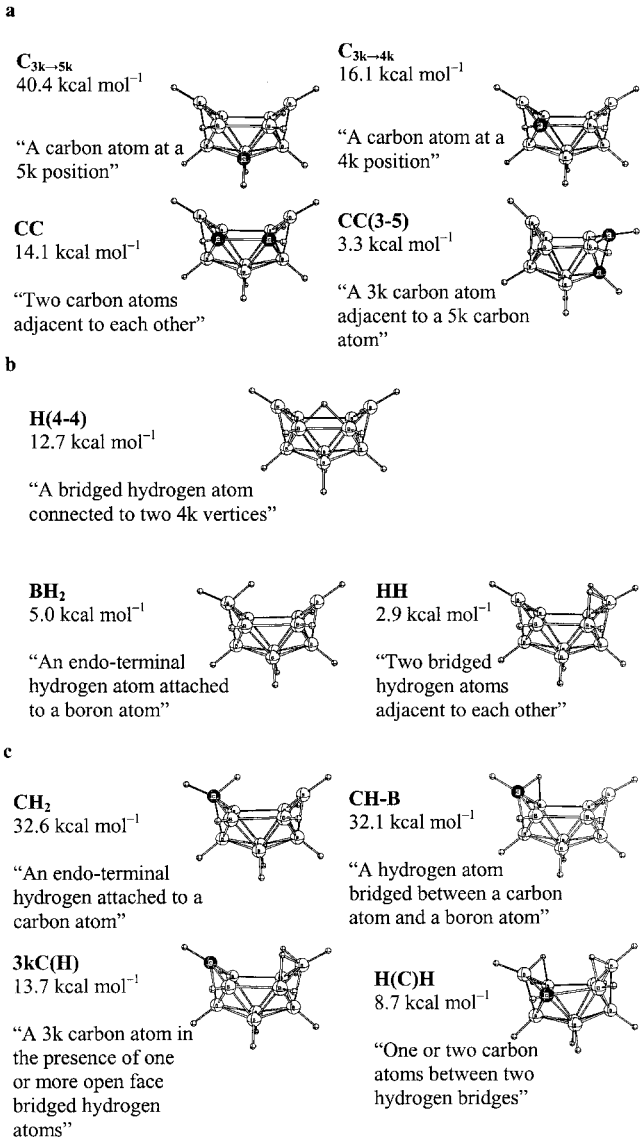

Figure 2. a) Carbon, b) hydrogen, and c) mixed structural features and their energy penalties.

A Comparison of Energy Penalties Between the 10-Vertex *nido* Cluster and the 6- and 11-Vertex *nido* Clusters

Some structural features in the 10-vertex *nido* cluster are also present in the 6- and/or 11-vertex *nido* clusters, i.e. HH, CC, BH_2, CH–B, and $C_{3k\rightarrow5k}$. All the features that were identified for all three cluster sizes are summarized in Table 1. Four comparable features are carbon structural features, one is a hydrogen structural feature, and two are mixed structural features. The remainder are entirely new and are described in the next section.

$C_{3k\rightarrow4k}$

Moving a carbon atom from a 3*k* vertex to a 4*k* vertex in the 10-vertex *nido* cluster requires 16.1 kcal mol^{-1}. This energy penalty is not observed in 6- or 11-vertex *nido* clusters because they lack 4*k* and 3*k* vertices, respectively.

$C_{3k\rightarrow5k}$

Moving a carbon atom from a 3*k* position to a 5*k* position involves an energy penalty of 40.4 kcal mol^{-1} in the 10-vertex *nido* cluster. The corresponding energy penalty in the 6-vertex *nido* cluster is 33 kcal mol^{-1}.

$C_{4k\rightarrow5k}$

This is not an independent structural feature of the 10-vertex *nido* cluster, but an energy penalty of 24.3 kcal mol^{-1} can be derived for it as the difference between $E_{inc}[C_{3k\rightarrow4k}]$ and $E_{inc}[C_{3k\rightarrow5k}]$. This value is quite close to the value of 28.0 kcal mol^{-1} for $C_{4k\rightarrow5k}$ in the 11-vertex *nido* cluster.[2]

CC

The CC energy penalty is essentially independent of the cluster size: values of 15, 14.1, and 16.0 kcal mol^{-1} apply for the 6-, 10-, and 11-vertex *nido* clusters, respectively.

HH

Two hydrogen bridges adjacent to each other, HH, have an energy penalty of 7 kcal mol^{-1} in the case of 6-vertex *nido*-boranes and -carboranes. This value is much larger (25.9 kcal mol^{-1}) in the case of 11-vertex *nido*-boranes and -carboranes. For the 10-vertex *nido* cluster, the energy penalty associated with HH is 2.9 kcal mol^{-1}. Hence, HH has very different energy penalties for the 6-, 10-, and 11-vertex *nido* clusters, although it should be kept in mind that the bridged hydrogen atoms have different connectivities in all these cases. In the case of 6-vertex *nido* clusters the bridged hydrogen atoms are connected to 3*k* peripheral vertices, whereas in the 11-vertex *nido* cluster the bridged hydrogen atoms are attached to all 4*k* peripheral vertices. In the case of a 10-vertex *nido* cluster, however, they are connected to a 3*k* vertex (6 or 9) on one side and to a 4*k* vertex on the other side.

CH–B

This has very similar energy penalties of 27, 32.1, and 33.1 kcal mol^{-1} in the 6-, 10-, and 11-vertex *nido* clusters, respectively.

CH_2

An *endo*-terminal hydrogen atom attached to a carbon atom in the 10-vertex *nido* cluster has an energy penalty of 32.6 kcal mol^{-1}, which is quite close to the CH_2 energy penalty of 30 kcal mol^{-1} and 33.2 kcal mol^{-1}for the 6-vertex and 11-vertex *nido* clusters, respectively. In the structure **JM**, there are two CH_2 moieties, each accompanied by one imaginary frequency.

In summary, carbon-related and mixed structural features are independent of cluster size.

New Structural Features for the 10-Vertex *nido* Cluster

There are four architectural features in the 10-vertex *nido*-boranes and -carboranes that are not present or not important in 6- and 11-vertex *nido*-boranes and -carbor-

 © 2005 Wiley-VCH Verlag GmbH & Co. KGaA, Weinheim

anes. These features are H(4–4), CC(3–5), 3*k*C(H), and H(C)H (see Figure 2). H(4–4) will be discussed later and H(C)H has already been discussed above. Here only CC(3–5) and 3*k*C(H) will be discussed.

CC(3–5)

When a 3*k* and a 5*k* carbon atom are adjacent to each other in the 10-vertex *nido* cluster, the energy penalty (3.3 kcal mol^{-1}) is only about one fourth of the CC value. This characteristic feature is accompanied by the distortion of the cluster structure in such a way that the 3*k* carbon atom lies almost in the plane of the 4*k* vertices [5,7,8,10, see Figure 2a, CC(3–5)]. This distortion counteracts the destabilization of the CC relationship and results in a diminished E_{inc}[CC(3–5)]. For the 6-vertex *nido* cluster a 3*k*–5*k* CC behaves the same way as a 3*k*–3*k* CC, but CC(3–3) is not possible in the 10-vertex cluster. Similarly, in the case of the 11-vertex *nido* cluster the energy penalty for a 4*k*–4*k* CC is the same as for 4*k*–5*k* CC or 5*k*–5*k* CC. In the 10-vertex *nido* cluster, CC(3–5) leads to significantly less destabilization as compared to more homogeneous CC relationships (3*k*–4*k*, 4*k*–4*k*, 4*k*–5*k*).

3kC(H)

A carbon atom at a 3*k* vertex in the presence of one or more open-face hydrogen bridges results in a thermodynamic stability reduction of 13.7 kcal mol^{-1}. This feature is not observed in $[C_2B_8H_{10}]^{2-}$, where there are no open-face hydrogen bridges, although it is present in 6,9-$C_2B_8H_{12}$ (Figure 3, **JS**). When there is an *endo*-terminal hydrogen atom at a 3*k* carbon atom (CH_2), or a bridged hydrogen atom between a carbon atom and a boron atom (CH–B), the 3*k*C(H) feature is not possible and no extra energy penalty is counted.

Hydrogen Placement Patterns

Hydrogen Bridges Occupy the Positions of Least Connectivity

In the 6- and 11-vertex clusters, there is only one kind of peripheral vertex each, and consequently all open-face edges are equally suited for hydrogen bridges. However, the open-face edges available for hydrogen bridges are not equivalent in the 10-vertex *nido* cluster due to different peripheral vertices. In all thermodynamically most stable isomers, the hydrogen bridges are located at 3*k*–4*k* edges. A hydrogen bridge between two 4*k* vertices, H(4–4), is 12.7 kcal mol^{-1} less stable [see Figure 2b, H(4–4)].

Hydrogen Placement Patterns are Primary to Carbon Placement Patterns

Williams' qualitative carbon placement rules[4,5] are quantitatively covered by $C_{3k\rightarrow4k}$, $C_{3k\rightarrow5k}$ and CC (see above). In the presence of extra hydrogen atoms, however, some more rules are needed. Figure 3 shows the 6,9- and 5,7-isomers of $C_2B_8H_{12}$[6,7] and their dianions.[8,9] A comparison of $[C_2B_8H_{10}]^{2-}$ and $C_2B_8H_{12}$ isomers demonstrates that carbon atoms occupy the least coordinated positions only when extra hydrogen atoms are absent. For example, *nido*-$[C_2B_8H_{10}]^{2-}$ (**HA**), without any *endo*-hydrogen atom, is the most stable $[C_2B_8H_{10}]^{2-}$ isomer as carbon atoms favor the positions of least connectivity. The doubly protonated *nido*-6,9-$C_2B_8H_{12}$ (**JS**), with bridging hydrogen atoms at positions 5/10 and 7/8, accumulates three structural features [H(4–4), 3kC(H), and H(C)H, each present twice], corresponding to a total energy penalty of 70.2 kcal mol^{-1}. This is 35.1 kcal mol^{-1} more than that of the most stable 5,7-$C_2B_8H_{12}$ (**JA**), where the carbon atoms are at positions of higher connectivity, i.e. $C_{3k\rightarrow4k}$ and HH are present. The computed energy difference is 44.5 kcal mol^{-1}.

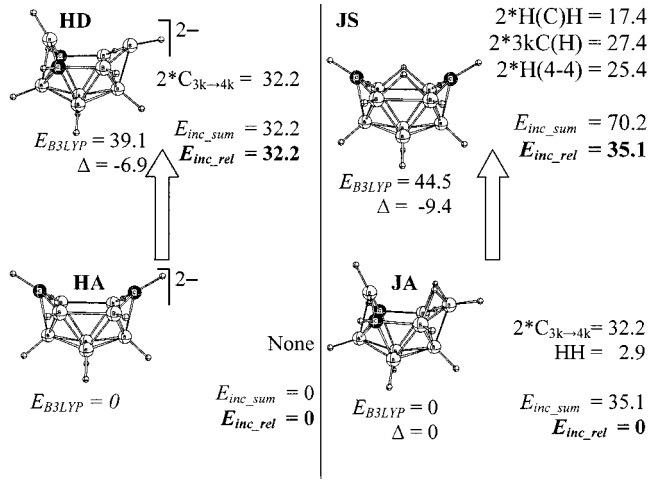

Figure 3. 6,9- and 5,7-isomers of $[C_2B_8H_{10}]^{2-}$ and $C_2B_8H_{12}$.

Comparisons of Relative Stabilities from Empirical Energy Penalties (E_{inc_rel}) and from DFT-Calculated Values (E_{B3LYP}) for 10-Vertex *nido*-Boranes and -Carboranes

Initially, energy penalties for those structural features that were already found to be important for 6- and 11-vertex *nido*-boranes and -carboranes[1,2] were considered. 10-Vertex *nido*-boranes and -carboranes were found to have some features common with their 6- and 11-vertex counterparts, but some additional features are needed. The final set of structural features is shown in Figure 2 and listed in Tables 2–6 (see below). A total of eighty-one 10-vertex *nido*-borane and -carborane isomers from $[B_{10}H_{12}]^{2-}$ to $C_3B_7H_{11}$ were computed, ten of which are known experimentally. The sum of energy penalties for all structural features gives E_{inc_sum} for each structure, which relative to the most stable isomer (isomer with least E_{inc_sum}) gives E_{inc_rel}. Computed relative energies are listed as E_{B3LYP}. The difference between E_{inc_rel} and E_{B3LYP} (E_{diff}) is equal to, or larger than, 6 kcal mol^{-1} in only six cases. The largest deviation (Δ = –9.4 kcal mol^{-1}) is found for **JS** (6,9-$C_2B_8H_{12}$). Three $C_4B_6H_{10}$ isomers were computed but four carbon atoms in

 © 2005 Wiley-VCH Verlag GmbH & Co. KGaA, Weinheim

the 10-vertex *nido* cluster behave far less additively and cause large deviations (see Table 6 below). Tetracarboranes seem to have considerable hydrocarbon character. In the case of 6-vertex and 11-vertex *nido* clusters, the largest deviations are also observed for tetracarboranes. Our 10-vertex *nido*-(car)boranes study concentrates on mono- to tricarboranes.

nido-$[B_{10}H_{10+x}]^{(4-x)-}$ (x = 2–4) Isomers

Three structures have already been computed for *nido*-$[B_{10}H_{12}]^{2-}$ and the correct solution structure was reported to have μ-H: 5/6, 8/9 (**AA**, Figure 4).[10] Our increment system also predicts **AA** to be the most stable due to the absence of any structural feature (Table 2). Structure **AB** is slightly higher in energy than **AA** due to the structural feature HH. **AC**, with one imaginary frequency, has the structural feature H(4–4) twice due to two hydrogen atoms bridging two 4*k* vertices.

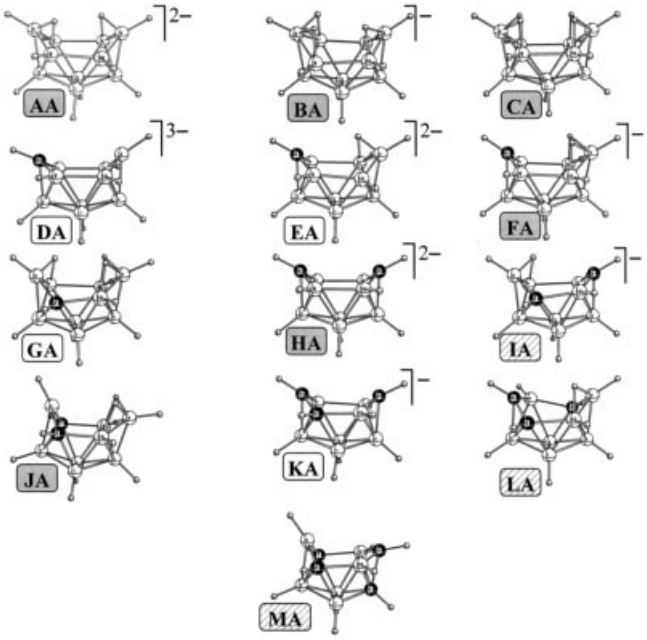

Figure 4. Most-stable isomers from *nido*-$[B_{10}H_{12}]^{2-}$ to -$C_4B_6H_{10}$. Known isomers are labeled with gray boxes. Those filled diagonally with grey lines are strong candidates for synthesis.

$B_{10}H_{14}$ (**CA**) can be easily deprotonated to give $[B_{10}H_{13}]^-$.[11] **BA**, (Figure 4) with bridging hydrogen atoms at the 5/6, 6/7, and 8/9 positions,[12] is the most stable $[B_{10}H_{13}]^-$ structure,[10] with only one structural feature, i.e. HH, as two hydrogen bridges at the 5/6 and 6/7 positions are adjacent to each other (Table 2). Hydrogen bridges at the 5/10, 6/7, and 8/9 positions (**BB**) involve one structural feature H(4–4). **BC** with one *endo*-H (structural feature BH_2) at position number 5 (a 4*k* vertex) is the transition state for a facile hydrogen rearrangement from the structure with bridging hydrogen atoms in the 5/6, 6/7, and 8/9 positions (**BA**) to the structure with bridging hydrogen atoms in the 6/7, 8/9, and 5/10 bridging positions (**BB**). **BD**, with BH_2 and HH, is the least favorable of the four isomers considered here. Two $B_{10}H_{14}$ structures were computed and the experimentally found structure[13] with four hydrogen atoms bridging to B5/6, B6/7, B8/9, and B9/10 positions (**CA**) was found to be computationally more stable than the structure with bridging hydrogen atoms at the 7/8 and 5/10 positions and an *endo*-H at 6,9 (**CB**, which corresponds to the prototypical 10-vertex *arachno* structure) by 38.1 kcal mol^{-1}. **CA** has the structural feature HH twice, but **CB** has the structural features $2BH_2$ + 2H(4–4), with an E_{inc_rel} of 29.6 kcal mol^{-1} with respect to **CA**. The difference between the computed and incremented relative energies (E_{diff}) is 8.5 kcal mol^{-1}.

nido-$[CB_9H_{10+x}]^{(3-x)-}$ (x = 0–3) Isomers

nido-6-$[CB_9H_{10}]^{3-}$ (**DA**, Figure 4) is the most stable $[CB_9H_{10}]^{3-}$ isomer, with the carbon atom at a 3*k* position (Table 3). *nido*-5-$[CB_9H_{10}]^{3-}$ (**DB**), with the $C_{3k\rightarrow4k}$ structural feature [$E_{inc}(C_{3k\rightarrow4k})$ = 16.1 kcal mol^{-1}], is thermodynamically 17.1 kcal mol^{-1} less stable than **DA**. The carbon atom is at a 5*k* position (structural feature $C_{3k\rightarrow5k}$) in *nido*-2-$[CB_9H_{10}]^{3-}$ (**DC**) and *nido*-1-$[CB_9H_{10}]^{3-}$ (**DD**), although **DC** is slightly more favorable. A "fine tuning increment" may be applied to differentiate between a 5*k* carbon atom at positions 1,3 (less favorable) and a 5*k* carbon atom at positions 2,4. A similar effect was also reported for the 11-vertex *nido* cluster where all vertices next to the apex (vertex number 1) are 5*k* but two vertices next to positions 2–6 are 4*k* and hence the apical position is slightly less favorable than positions 2–6.[2,3]

Table 2. Structural features and relative energies [kcal mol^{-1}] for $[B_{10}H_{12}]^{2-}$ and $[B_{10}H_{13}]^-$ isomers.

	Compound	Extra hydrogen atoms	Symmetry	H(4-4)	BH_2	HH	E_{inc_sum}	E_{inc_rel}	E_{B3LYP}	E_{diff}[a]
				12.7	5.0	2.9				
AA[b]	$B_{10}H_{12}^{2-}$	μ-H: 5/6, 8/9	C_2				0	0	0	0
AB	$B_{10}H_{12}^{2-}$	μ-H: 8/9, 9/10	C_s			1	2.9	2.9	3.4	–0.5
AC[c]	$B_{10}H_{12}^{2}$	μ-H: 5/10, 7/8	C_s	2			25.4	25.4	21.8	3.8
BA[a]	$B_{10}H_{13}^{1-}$	μ-H: 5/6, 6/7, 9/10	C_1			1	2.9	0	0	0
BB	$B_{10}H_{13}^{1-}$	μ-H: 5/10, 6/7, 8/9	C_1	1			12.7	12.7	3.9	7.8
BC[c]	$B_{10}H_{13}^{1-}$	μ-H: 6/7, 8/9 *endo*-H: 5	C_1		1		5.0	5.0	4.9	1.0
BD[c]	$B_{10}H_{13}^{1-}$	μ-H: 5/6, 6/7 *endo*-H: 9	C_s		1	1	7.9	7.9	13.4	–5.5
CA[b]	$B_{10}H_{14}$	μ-H: 5/6, 6/7, 8/9, 9/10	C_{2v}			2	5.8	0.0	0.0	0.0
CB	$B_{10}H_{14}$	μ-H: 7/8, 5/10, *endo*-H: 6,9	C_{2v}	2	2		35.4	29.6	38.1	–8.5

[a] E_{diff} is the difference between E_{inc_rel} and E_{B3LYP}. [b] Experimentally known structures. [c] **AC**, **BC**, and **BD** possess imaginary frequencies.

 © 2005 Wiley-VCH Verlag GmbH & Co. KGaA, Weinheim

Table 3. Structural features and relative energies [kcal mol^{-1}] for $[CB_9H_{10+x}]^{3-x}$ (x = 0–3) isomers.

	Compound	Extra hydrogen atoms	Symmetry	H(4–4)	BH_2	HH	$C_{3k\rightarrow5k}$	$C_{3k\rightarrow4k}$	CH_2	CH–B	3*k*C(H)	H(C)H	E_{inc_sum}	E_{inc_rel}	E_{B3LYP}	E_{diff}[a]
				12.7	5.0	2.9	40.4	16.1	32.6	32.1	13.7	8.7				
DA	6-$CB_9H_{10}^{3-}$	–	C_s										0.0	0.0	0.0	0.0
DB	5-$CB_9H_{10}^{3-}$	–	C_1					1					16.1	16.1	17.1	–1.0
DC	2-$CB_9H_{10}^{3-}$	–	C_s				1						40.4	40.4	37.1	3.3
DD	1-$CB_9H_{10}^{3-}$	–	C_s				1						40.4	40.4	38.9	1.5
EA	6-$CB_9H_{11}^{2-}$	μ-H: 8/9	C_1								1		13.7	0	0	0
EB	5-$CB_9H_{11}^{2-}$	*endo*-H: 9	C_1		1			1					21.1	7.4	8.6	–1.2
EC	6-$CB_9H_{11}^{2-}$	*endo*-H: 6	C_s						1				32.6	18.9	13.3	5.6
ED	1-$CB_9H_{11}^{2-}$	μ-H: 7/8	C_s	1			1						53.1	39.4	48.1	–8.7
FA[b]	6-$CB_9H_{12}^{1-}$	μ-H: 8/9, 9/10	C_s			1					1		16.7	0	0	0
FB	5-$CB_9H_{12}^{1-}$	μ-H: 8/9, 9/10	C_1			1		1					19.1	2.4	6.6	–4.2
FC	5-$CB_9H_{12}^{1-}$	μ-H: 6/7, 9/10	C_1					1				1	24.8	8.2	12.7	–4.5
FD	6-$CB_9H_{12}^{1-}$	μ-H: 5/6, 8/9	C_1							1			32.1	15.5	15.6	–0.1
FE	2-$CB_9H_{12}^{1-}$	μ-H: 8/9, 9/10	C_s			1	1						43.4	26.7	30.5	–3.7
FF	1-$CB_9H_{12}^{1-}$	μ-H: 8/9, 9/10	C_1			1	1						43.4	26.7	30.7	–4.0
GA	5-CB_9H_{13}	μ-H: 6/7, 8/9, 9/10	C_1			1		1				1	27.8	0	0	0
GB[c]	6-CB_9H_{13}	μ-H: 8/9, 9/10; *endo*-H: 6	C_s			1			1				35.6	7.8	11.2	–3.4
GC	2-CB_9H_{13}	μ-H: 6/7, 8/9, 9/10	C_1			1	1						43.4	15.6	20.1	–4.5
GD	1-CB_9H_{13}	μ-H: 6/7, 8/9, 9/10	C_1			1	1						43.4	15.6	21.6	–6.0
GE	1-CB_9H_{13}	μ-H: 5/6, 7/8, 9/10	C_s	1				1				1	61.8	34.0	29.6	4.5

[a] E_{diff} is the difference between E_{inc_rel} and E_{B3LYP} [b] **FA** is an experimentally known structure. [c] **GB** has one imaginary frequency.

The most stable *nido*-6-$[CB_9H_{11}]^{2-}$ structure (**EA**, Figure 4) has one structural feature, i.e. 3*k*C(H), as a 3*k* carbon atom and a bridged hydrogen atom are present. *nido*-5-$[CB_9H_{11}]^{2-}$ (**EB**) has an *endo* hydrogen atom (structural feature BH_2) in addition to $C_{3k\rightarrow4k}$. **EC** differs with respect to the most stable isomer **EA** only in the positions of the hydrogen atom on the open face (the *endo*-terminal hydrogen atom on the carbon atom results in the high-energy structural feature CH_2 in **EC**). *nido*-1-$[CB_9H_{11}]^{2-}$ (**ED**) is highly unstable due to the presence of a carbon atom at a 5*k* position ($C_{3k\rightarrow5k}$).

Experimentally known[14] *nido*-6-$[CB_9H_{12}]^-$ (**FA**, Figure 4) has two structural features, HH and 3*k*C(H), each once. Both **FB** and **FC** have the carbon atom at vertex number 5 ($C_{3k\rightarrow4k}$), but different hydrogen positions result in one HH (two adjacent hydrogen bridges) in the former and H(C)H (a carbon atom between two hydrogen bridges) in the latter. The energy penalty for H(C)H is larger than that for HH, and therefore **FC** is suggested to be more favorable than **FB**, both computationally as well as by the increment system. The basic skeleton of *nido*-6-$[CB_9H_{12}]^-$ (**FD**) is identical to that of the most stable **FA** except that hydrogen atoms are bridging positions 5/6 and 8/9 in the latter but 8/9 and 9/10 in the former. The special hydrogen position in **FD** (a hydrogen atom is bridging a carbon atom and a boron atom) gives rise to the structural feature CH–B, with E_{inc}(CH–B) = 32.1 kcal mol^{-1}, and is responsible for the high relative energy of the cluster even though the carbon atom is situated at a least connected vertex. Each of the *nido*-2-$[CB_9H_{12}]^-$ (**FE**) and *nido*-1-$[CB_9H_{12}]^-$ (**FF**) clusters possess the structural features HH and $C_{3k\rightarrow5k}$, but the carbon atom at position 1 in **FF** is slightly more disfavoring.

The experimentally unknown *nido*-5-CB_9H_{13} (**GA**, Figure 4) is the most favorable CB_9H_{13} structure. The structural features, corresponding energy penalties, and relative stabilities of the five computed CB_9H_{13} isomers are listed in Table 3.

The relative stabilities of the 6- and 5-isomers of *nido*-$[CB_9H_{10+x}]^{3-x}$ (x = 0–3) are as follows: *nido*-6-$[CB_9H_{10}]^{3-}$ (**DA**) is 17.1 kcal mol^{-1} more stable than *nido*-5-$[CB_9H_{10}]^{3-}$ (**DB**), and *nido*-6-$[CB_9H_{11}]^{2-}$ (**EA**) and *nido*-6-$[CB_9H_{12}]^-$ (**FA**) are 8.6 and 6.6 kcal mol^{-1} more stable than their 5-isomers (**EB** and **FB**, respectively). However, in the case of the neutral clusters, 6-CB_9H_{13} (**GB**) is 11.2 kcal mol^{-1} less stable than *nido*-5-CB_9H_{13} (**GA**). An increased hydrogen content on the open face results in highly connected carbon atoms in the most stable isomer, as is observed in the case of 11-vertex *nido*-$CB_{10}H_{14}$.[2] This can be well explained in terms of the structural features. E_{inc_sum} for the different structural features of **DB**, **EB**, and **FB** is less than that of **DA**, **EA**, and **FA**; however, E_{inc_sum} favors 5-CB_9H_{13} (**GA**; E_{inc_sum} = 27.8 kcal mol^{-1}) rather than 6-CB_9H_{13} (**GB**; E_{inc_sum} = 35.6 kcal mol^{-1}) mainly due to the high-energy structural feature (CH_2) in the latter. No *nido*-CB_9H_{13} isomer is experimentally known. However, the computed (HF/6-31G*) geometry for *nido*-6-CB_9H_{13} (**GB**) has been reported.[15]

nido-$[C_2B_8H_{10+x}]^{(2-x)-}$ (x = 0–2)

Two structures, i.e. the most stable *nido*-6,9-$[C_2B_8H_{10}]^{2-}$ (**HA**, Figure 4),[8] and *nido*-5,7-$[C_2B_8H_{10}]^{2-}$ (**HD**),[9] are experimentally known. Three structural features, i.e. $C_{3k\rightarrow4k}$, $C_{3k\rightarrow5k}$, and CC reproduce the relative stability of any possible $C_2B_8H_{10}^{2-}$ isomer (see Table 4) as there are no hydrogen atoms. *nido*-6,9-$[C_2B_8H_{10}]^{2-}$ (**HA**) has no structural features as the carbon atoms are at the nonadjacent least-connected vertices. Addition of one bridging hydrogen atom to **HA** makes the situation highly unfavorable in *nido*-6,9-$[C_2B_8H_{11}]^-$ (**IC**) due to one H(4–4) and two 3*k*C(H) structural features. One carbon atom is located at a 4*k* vertex in the most stable *nido*-5,9-$[C_2B_8H_{11}]^-$ (**IA**, Figure 4), for which the sum of the energy penalties is less than that of **IC**. Experimentally known *nido*-5,6-$[C_2B_8H_{11}]^-$ (**ID**)[16] is higher in energy than its three unknown isomers *nido*-5,9-$[C_2B_8H_{11}]^-$ (**IA**), *nido*-5,7-$[C_2B_8H_{11}]^-$ (**IB**), and *nido*-6,9-$[C_2B_8H_{11}]^-$ (**IC**). *nido*-2,6-$[C_2B_8H_{11}]^-$ (**IE**), which contains the structural feature CC(3–5) as well as $C_{3k\rightarrow5k}$ and 3*k*C(H), is the highest-energy structure.

nido-5,7-$C_2B_8H_{12}$ (**JA**, Figures 3 and 4)[6] is the most stable neutral dicarba isomer (Table 5). *nido*-5,6-$C_2B_8H_{12}$

Table 4. Structural features and relative energies [kcal mol^{-1}] for $[C_2B_8H_{10+x}]^{2-x}$ (x = 0, 1) isomers.

	Compound	Extra hydrogen atoms	Symmetry	H(4–4)	BH_2	HH	$C_{3k\rightarrow5k}$	$C_{3k\rightarrow4k}$	CC	CC(3–5)	3kC(H)	E_{inc_sum}	E_{inc_rel}	E_{B3LYP}	E_{diff}[a]
				12.7	5.0	2.9	40.4	16.1	14.1	3.3	13.7				
HA[b]	6,9-$C_2B_8H_{10}^{2-}$	–	C_{2v}									0	0	0	0
HB[c]	5,9-$C_2B_8H_{10}^{2-}$	–	C_1					1				16.1	16.1	14.4	1.7
HC[c]	5,8-$C_2B_8H_{10}^{2-}$	–	C_2					2				32.2	32.2	35.0	–2.8
HD[b]	5,7-$C_2B_8H_{10}^{2-}$	–	C_s					2				32.2	32.2	39.1	–6.9
HE	2,6-$C_2B_8H_{10}^{2-}$	–	C_s				1			1		43.8	43.8	43.0	0.8
HF	5,10-$C_2B_8H_{10}^{2-}$	–	C_s					2	1			43.3	43.3	48.0	–4.7
HG	1,5-$C_2B_8H_{10}^{2-}$	–	C_1				1	1	1			70.7	70.7	71.0	–0.3
HH	2,4-$C_2B_8H_{10}^{2-}$	–	C_{2v}				2					80.9	80.9	75.0	5.9
HI	1,3-$C_2B_8H_{10}^{2-}$	–	C_{2v}				1		1			95.0	95.0	92.0	3.0
IA[c]	5,9-$C_2B_8H_{11}^{1-}$	μ-H: 6/7	C_1					1			1	29.8	0	0	0
IB[c]	5,7-$C_2B_8H_{11}^{1-}$	*endo*-H: 9	C_s		1			2				37.2	7.4	9.4	–2.0
IC[c]	6,9-$C_2B_8H_{11}^{1-}$	μ-H: 7/8,	C_s	1							2	40.1	10.3	9.4	0.8
ID[b]	5,6-$C_2B_8H_{11}^{1-}$	μ-H: 8/9	C_1					1	1		1	43.9	14.1	16.4	–2.3
IE	2,6-$C_2B_8H_{11}^{1-}$	μ-H: 8/9	C_1				1			1	1	57.4	27.5	29.9	–2.4

[a] E_{diff} is the difference between E_{inc_rel} and E_{B3LYP}. [b] Experimentally known isomers. [c] Strong candidates for synthesis.

Table 5. Structural features and relative energies [kcal mol^{-1}] for $C_2B_8H_{12}$ isomers.

	Compound	Extra hydrogen atoms	Symmetry	H(4–4)	BH_2	HH	$C_{3k\rightarrow5k}$	$C_{3k\rightarrow4k}$	CC	CC(3–5)	CH_2	CH–B	3kC(H)	H(C)H	E_{inc_sum}	E_{inc_rel}	E_{B3LYP}	E_{diff}[a]
				12.7	5.0	2.9	40.4	16.1	14.1	3.3	32.6	32.1	13.7	8.7				
JA[b]	5,7-$C_2B_8H_{12}$	μ-H: 8/9, 9/10	C_s			1		2							35.1	0	0	0
JB[c]	5,9-$C_2B_8H_{12}$	μ-H: 6/7, 9/10	C_1					1				1			48.2	13.1	11.3	1.8
JC[c]	5,8-$C_2B_8H_{12}$	μ-H: 6/7, 9/10	C_1					2						1	49.6	14.5	11.6	3.0
JD[b]	5,6-$C_2B_8H_{12}$	μ-H: 8,9, 9/10	C_1			1		1	1				1		46.8	11.7	15.1	–3.4
JE	1,6-$C_2B_8H_{12}$	μ-H: 8/9, 9/10	C_1			1	1						1		57.0	21.9	20.7	1.2
JF	5,10-$C_2B_8H_{12}$	μ-H: 6/7, 8/9	C_s					2	1					1	55.1	20.0	22.3	–2.4
JG	4,6-$C_2B_8H_{12}$	μ-H: 8/9, 9/10	C_s			1	1						1		59.4	21.9	24.2	–2.3
JH	1,7-$C_2B_8H_{12}$	μ-H: 8/9, 9/10	C_1			1	1	1							59.4	24.3	24.3	0
JI	2,10-$C_2B_8H_{12}$	μ-H: 5/6, 6/7	C_1			1	1	1							59.4	24.3	25.7	–1.4
JJ	2,6-$C_2B_8H_{12}$	μ-H: 8/9, 9/10	C_s			1	1			1			1		60.3	25.2	26.0	–0.8
JK	6,9-$C_2B_8H_{12}$	μ-H: 6/7, 8/9	C_s									2			64.2	29.1	32.1	–0.7
JL	1,7-$C_2B_8H_{12}$	μ-H: 5/6, 8/9	C_1				1	1						1	65.2	30.1	33.8	–3.7
JM[d]	6,9-$C_2B_8H_{12}$	*endo*-H: 6,9	C_{2v}								2				65.2	30.1	35.3	–5.2
JN	1,7-$C_2B_8H_{12}$	μ-H: 5/10; *endo*-H:9	C_1	1	1		1	1							74.1	39.0	36.4	2.7
JO	2,7-$C_2B_8H_{12}$	μ-H: 5/6, 9/10	C_1				1	1	1						70.6	35.5	37.9	–2.4
JP	2,7-$C_2B_8H_{12}$	μ-H: 8/9, 9/10	C_1			1	1	1	1						73.5	38.4	38.4	0
JQ	1,5-$C_2B_8H_{12}$	μ-H: 6/7, 8/9	C_1				1	1	1						70.6	35.5	41.0	–5.5
JR	6,8-$C_2B_8H_{12}$	μ-H: 5/6; *endo*-H: 8	C_1					1			1	1			80.8	45.7	41.7	4.0
JS	6,9-$C_2B_8H_{12}$	μ-H: 5/10, 7/8	C_{2v}	2									2	2	70.2	35.1	44.5	–9.4
JT	3,7-$C_2B_8H_{12}$	μ-H: 5/6, 8/9	C_1				1	1	1					1	79.4	44.3	48.7	–4.4
JU	2,4-$C_2B_8H_{12}$	μ-H: 8/9, 9/10	C_s			1	2								83.7	48.6	52.1	–3.5
JV	1,3-$C_2B_8H_{12}$	μ-H: 8/9, 9/10	C_s			1	2		1						97.8	62.7	63.5	–0.8
JW	1,2-$C_2B_8H_{12}$	μ-H: 8/9, 9/10	C_1			1	2		1						97.8	62.7	64.4	–1.7
JX	1,2-$C_2B_8H_{12}$	μ-H: 5/6, 8/9	C_1				2		1						94.9	59.8	64.8	–5.0
JY	1,2-$C_2B_8H_{12}$	μ-H: 5/6, 6/7	C_1			1	2		1						97.8	62.7	65.2	–2.5
JZ	1,2-$C_2B_8H_{12}$	μ-H: 5/10, 6/7	C_1				2		1					1	1.03.7	68.8	65.8	2.7
JAA	1,3-$C_2B_8H_{12}$	μ-H: 6/7, 8/9	C_s				2		1					1	1.03.7	68.8	66.0	2.6
JAB	1,3-$C_2B_8H_{12}$	μ-H: 5/6, 8/9	C_2				2		1					1	103.7	68.8	66.5	2.1
JAC	1,2-$C_2B_8H_{12}$	μ-H: 5/10; *endo*-H: 6	C_1	1	1		2		1						112.6	77.5	72.1	5.4
JAD	1,2-$C_2B_8H_{12}$	μ-H: 5/6, 9/10	C_1				2		1					1	103.7	68.6	73.5	–5.0
JAE	1,2-$C_2B_8H_{12}$	μ-H: 5/10; *endo*-H: 9	C_1	1	1		2		1						112.6	77.5	74.3	3.1
JAF	1,3-$C_2B_8H_{12}$	μ-H: 7/8, 5/10	C_{2v}	2			2		1						120.3	85.2	85.5	–0.3

[a] E_{diff} is the difference between E_{inc_rel} and E_{B3LYP}. [b] Experimentally known isomer. [c] Strong candidate for synthesis. [d] **JM** has two imaginary frequencies.

(**JD**) and *nido*-5,7-$C_2B_8H_{12}$ (**JA**) represented the first case of skeletal isomers in *nido*-carboranes.[7] A large number of $C_2B_8H_{12}$ isomers (Table 5) was computed in order to obtain a reliable structural increment system for 10-vertex *nido*-carboranes. Calculated (HF/6-31G*) geometries for *nido*-6,9-$C_2B_8H_{12}$ (**JM**) and *nido*-6,9-$C_2B_8H_{12}$ (**JS**) have been reported before.[15]

nido-$[C_3B_7H_{10}]^-$ and -$C_3B_7H_{11}$

Three $[C_3B_7H_{10}]^-$ isomers have been computed, of which 5,6,9-$[C_3B_7H_{10}]^-$ (**KA**, Figure 4) is the most stable structure. Two *nido*-$C_3B_7H_{11}$ isomers are known: *nido*-5,6,9-$C_3B_7H_{11}$ (**LA**, Figure 4)[17] and *nido*-5,6,10-$C_3B_7H_{11}$ (**LD**), with a bridging hydrogen atom at the 7/8 position.[18] The increment system quite successfully reproduces the relative stability order of *nido*-$[C_3B_7H_{10}]^-$ and -$C_3B_7H_{11}$ structures (Table 6).

nido-$C_4B_6H_{10}$

The only known $C_4B_6H_{10}$ isomer is 5,6,8,9-$C_4B_6H_{10}$ (**MB**) reported by Stibr et al.,[19] but the 4,5,7,9-isomer (**MA**, Figure 4) is computed to be slightly preferred energetically (by 2.5 kcal mol^{-1}). For tetracarbaboranes from **MA** to **MG** (Table 6), deviations between the E_{B3LYP} and E_{inc_rel} are large when only the increments discussed above are applied. In the case of $C_4B_6H_{10}$, the four carbon atoms in a cluster result in a change of the behavior of carboranes, due to considerable hydrocarbon character. Hence, the additivity required by the increment system to be useful is not followed strictly and deviations of between 10.3 and

 © 2005 Wiley-VCH Verlag GmbH & Co. KGaA, Weinheim

Table 6. Structural features and relative energies [kcal mol^{-1}] for 10-vertex *nido*-tri- and -tetracarboranes.

	Compound	Extra hydrogen atoms	Symmetry	$C_{3k\rightarrow5k}$	$C_{3k\rightarrow4k}$	CC	CC(3–5)	CH–B	3kC(H)	$(CC)_2$	E_{inc_sum}	E_{inc_rel}	E_{B3LYP}	E_{diff}[a]
				40.4	16.1	14.1	3.3	32.1	13.7	18.1				
KA	5,6,9-$C_3B_7H_{10}^{1-}$	–	C_1		1	1					30.2	0.0	0.0	0.0
KB	1,6,9-$C_3B_7H_{10}^{1-}$	–	C_s	1							40.4	10.2	7.6	2.4
KC	6,7,8-$C_3B_7H_{10}^{1-}$	–	C_1		2	2					60.4	30.2	24.0	6.2
LA[b]	5,6,8-$C_3B_7H_{11}$	μ-H: 9/10	C_1		2	1			1		60.0	0	0	0
LB[b]	5,6,9-$C_3B_7H_{11}$	μ-H: 6/7	C_1		1	1		1			62.3	2.3	3.4	–1.1
LC[c]	5,7,8-$C_3B_7H_{11}$	μ-H: 9/10	C_1		3	1					62.4	2.4	5.3	–2.9
LD[b]	5,6,10-$C_3B_7H_{11}$	μ-H: 8/9	C_1		2	2			1		74.1	14.1	9.0	5.2
MA[c]	4,5,7,9-$C_4B_6H_{10}$	–	C_1	1	2		1				76.0	0.0	0	0.0
MB[b]	5,6,8,9-$C_4B_6H_{10}$	–	C_2		2	2				1	78.5	2.5	2.5	0.0
MC	5,6,7,9-$C_4B_6H_{10}$	–	C_s		2	2				1	78.5	2.5	9.5	–7.0
MD	1,6,7,9-$C_4B_6H_{10}$	–	C_1	1	1	1					70.7	–5.3	11.1	–16.4
ME	1,5,7,9-$C_4B_6H_{10}$	–	C_1	1	2	1					86.8	10.8	11.8	–1.0
MF	5,7,8,10-$C_4B_6H_{10}$	–	C_{2v}		4	2				1	110.7	34.7	26.9	7.8
MG	2,4,6,9-$C_4B_6H_{10}$		C_{2v}	2			2			1	105.7	29.7	30.5	–0.8

[a] E_{diff} is the difference between E_{inc_rel} and E_{B3LYP}. [b] Experimentally known isomer. [c] Strong candidate for synthesis.

25.1 kcal mol^{-1} are observed. However, applying an extra increment [$(CC)_2$ = 18.1 kcal mol^{-1}] for the adjacent carbon atoms in the cluster twice lowers the energy differences considerably (Table 6), and only **MD** remains with a large deviation. Larger deviations of tetracarbaboranes are also observed in 6- and 11-vertex *nido* clusters.

Conclusions

An increment system has been established for 10-vertex *nido*-boranes and -carboranes. Eleven architectural features have been identified (eight of major importance, with $E_{inc} > 5$ kcal mol^{-1}, and three of minor importance). The corresponding energy penalties have allowed us to accurately estimate the relative stabilities of 81, and probably more, 10-vertex *nido* isomers from $[B_{10}H_{12}]^{2-}$ to $C_3B_7H_{11}$. Applying our increment system, ten carboranes have been identified that are not yet known experimentally but are thermodynamically more stable than known isomers and hence should be synthesizable.

The relative energies of 10-vertex *nido*-carboranes can be accurately predicted from $[B_{10}H_{12}]^{2-}$ to $C_3B_7H_{11}$ using the increment approach (Figure 5). In all the above examples, there are six cases where the difference between the estimated relative energy based on increments (E_{inc_rel}) and computed relative energy (E_{B3LYP}) is equal to, or more than, 6 kcal mol^{-1}. The difference between the E_{inc_rel} and E_{B3LYP} is less than 2 kcal mol^{-1} in 31 cases. The largest deviation, namely 9.4 kcal mol^{-1}, is found for 6,9-$C_2B_8H_{12}$ (**JS**). The stability order is mostly the same according to the B3LYP-computed results and to the increment approach. However, it is slightly different in many $C_2B_8H_{12}$ cases where the energetic separations of the many isomers considered is very small (see Table 5). The energy penalties for three features – CC, CH–B, and CH_2 – are very similar to those derived for the 6- and 11-vertex *nido*-(car)boranes. A fourth feature, $C_{4k\rightarrow5k}$, also has an energy penalty quite similar to the 11-vertex *nido*-(car)borane value. This increment system is not limited to the representative 81 isomers it was derived from, but can be applied to many 10-vertex *nido*-carborane structures. A similar kind of increment system might be derivable for 10-vertex *nido*-heterocarboranes.

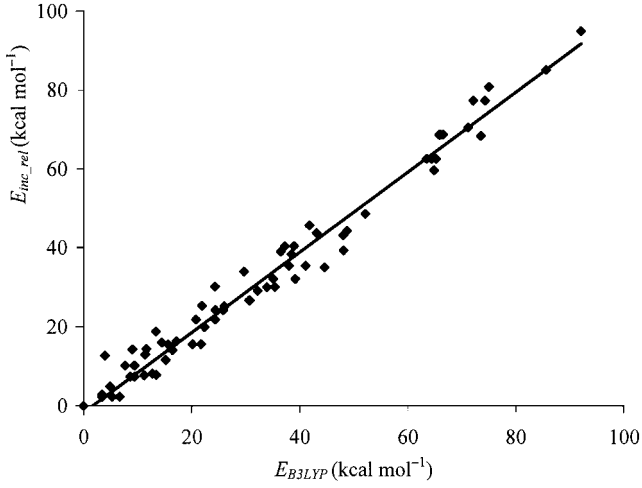

Figure 5. Structural increments accurately reproduce the relative stabilities of 10-vertex *nido*-(car)boranes computed by DFT methods.

Computational Details

Density functional theory was employed for successive optimization of all geometries at the B3LYP/3-21G and B3LYP/6-31G(d) levels, respectively, using the Gaussian 98 program.[20] Symmetry restrictions for different geometries, where applied, are given in Tables 2–6. All the structures, except five (**AC**, **BC**, **BD**, **GB** and **JM**, Tables 2, 3, and 5), presented in this paper are local minima at the B3LYP/6-31G(d) level as determined by frequency calculations. Single-point energies computed at the B3LYP/6-311+G(d,p) level, together with zero-point corrections at the B3LYP/6-31G(d) level, were used to derive relative energies for all the isomers. These computed relative energies are to be reproduced by a structural increment system. Certain geometrical features were identified and assigned reasonable preliminary energy penalties by comparison with suitable isomeric clusters. The values were refined through a statistical fitting procedure in order to obtain the final increment system. The Cartesian coordinates of structures fully optimized at the RB3LYP/6-31G(d) level and corresponding absolute energies

 © 2005 Wiley-VCH Verlag GmbH & Co. KGaA, Weinheim

from RB3LYP/6-311+G(d,p) energy computations are provided as Supporting Information.

Acknowledgments

Financial support by the Deutsche Forschungsgemeinschaft (DFG) is gratefully acknowledged.

[1] M. Hofmann, M. A. Fox, R. Greatrex, P. v. R. Schleyer, R. E. Williams, *Inorg. Chem.* **2001**, *40*, 1790–1801.
[2] F. A. Kiani, M. Hofmann, *Inorg. Chem.* **2004**, *43*, 8561–8571.
[3] F. A. Kiani, M. Hofmann, *Inorg. Chem.*, submitted.
[4] R. E. Williams, *J. Am. Chem. Soc.* **1965**, *87*, 3513–3515.
[5] R. E. Williams, in *Progress in Boron Chemistry* (Eds.: R. J. Brotherton, H. Steinberg), Pergamon Press, England, **1970**, vol. 2, chapter 2, p. 57.
[6] P. M. Garrett, G. S. Ditta, M. F. Hawthorne, *J. Am. Chem. Soc.* **1971**, *93*, 1265–1266.
[7] R. R. Rietz, R. Schaeffer, *J. Am. Chem. Soc.* **1973**, *95*, 6254–6262.
[8] B. Štíbr, J. Plešek, S. Heřmánek, *Collect. Czech. Chem. Commun.* **1973**, *38*, 338–342.
[9] B. Štíbr, Z. Janousek, K. Base, S. Heřmánek, J. Plešek, I. A. Zakharova, *Collect. Czech. Chem. Commun.* **1984**, *49*, 1891–1894.
[10] M. Hofmann, P. v. R. Schleyer, *Inorg. Chem.* **1998**, *37*, 5557–5565.
[11] G. A. Guter, G. W. Schaeffer, *J. Am. Chem. Soc.* **1956**, *78*, 3456.
[12] A. J. Wynd, A. J. Welch, *Acta Crystallogr., Sect. C* **1989**, *45*, 615–617.
[13] J. S. Kasper, C. M. Lucht, D. Harker, *Acta Crystallogr.* **1950**, *3*, 436–455.
[14] K. Base, B. Štíbr, J. Dolansky, J. Duben, *Collect. Czech. Chem. Commun.* **1981**, *46*, 2345–2353.
[15] M. L. McKee, *Inorg. Chem.* **1994**, *33*, 6213–6218.
[16] J. Zbyněk, P. Kaszynski, J. D. Kennedy, B. Štíbr, *Collect. Czech. Chem. Commun.* **1999**, *64*, 986–992.
[17] S. O. Kang, G. T. Furst, L. G. Sneddon, *Inorg. Chem.* **1989**, *28*, 2339–2347.
[18] A. E. Wille, L. G. Sneddon, *Collect. Czech. Chem. Commun.* **1997**, *62*, 1214–1228.
[19] B. Štíbr, T. Jelínek, E. Drdakova, S. Heřmánek, J. Plešek, *Polyhedron* **1988**, *7*, 669–670.
[20] M. J. Frisch, G. W. Trucks, H. B. Schlegel, G. E. Scuseria, M. A. Robb, J. R. Cheeseman, V. G. Zakrzewski, J. A. Montgomery Jr., R. E. Stratmann, J. C. Burant, S. Dapprich, J. M. Millam, A. D. Daniels, K. N. Kudin, M. C. Strain, O. Farkas, J. Tomasi, V. Barone, M. Cossi, R. Cammi, B. Mennucci, C. Pomelli, C. Adamo, S. Clifford, J. Ochterski, G. A. Petersson, P. Y. Ayala, Q. Cui, K. Morokuma, D. K. Malick, A. D. Rabuck, K. Raghavachari, J. B. Foresman, J. Cioslowski, B. J. V. Ortiz, B. Stefanov, G. Liu, A. Liashenko, P. Piskorz, I. Komaromi, R. Gomperts, R. L. Martin, D. J. Fox, T. Keith, M. A. Al-Laham, C. Y. Peng, A. Nanayakkara, C. Gonzalez, M. Challacombe, P. M. W. Gill, B. Johnson, W. Chen, M. W. Wong, J. L. Andres, C. Gonzalez, M. Head-Gordon, E. S. Replogle, J. A. Pople, *Gaussian 98*, Revision A.6, Gaussian, Inc., Pittsburgh PA, **1998**..

Received: November 26, 2004

 © 2005 Wiley-VCH Verlag GmbH & Co. KGaA, Weinheim

EurJIC
European Journal of Inorganic Chemistry

Issue 13/2005

Pages 2557–2764

Papers available ahead of print in Early View at www.interscience.wiley.com

Earliest available Table of Contents:
Automatically, free of charge by e-mail through
www.interscience.wiley.com/alerts

COVER PICTURE

The cover picture shows the proposed mechanism of the Co(salen)-catalyzed oxidation of a lignin model compound in water, as elucidated by several in-situ spectroscopic techniques. Catalytic oxygen activation can help to prevent the formation of hazardous side products in organic oxidations, especially if harmless solvents are used. The target in this work is lignin, which is found in wood and must be removed as selectively as possible before paper production. In view of avoiding chlorine as the oxidant, the idea is to catalytically enhance the oxygen delignification stage in the pulp bleaching sequence. Details are discussed in the article by T. Repo, B. M. Weckhuysen et al. on p. 2591ff.

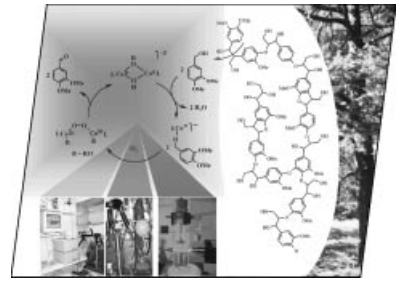

MICROREVIEW

Contents

2573 **Hong Xue, Jean'ne M. Shreeve***

Ionic Liquids with Fluorine-Containing Cations

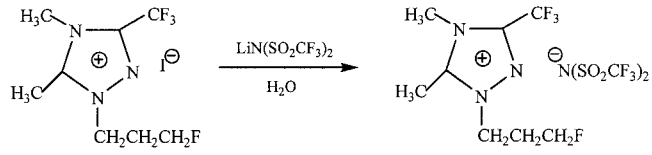

Keywords: Ionic liquids / Fluorine / Cations / Quaternization

 © 2005 Wiley-VCH Verlag GmbH & Co. KGaA, Weinheim

SHORT COMMUNICATIONS

2581 **P. Cai, M.-X. Li, C.-Y. Duan,* F. Lu, Q.-J. Meng**

Synthesis and Properties of the Geometrically Controlled Mixed-Valence Tetrahedral Ru^{II}_2-$Ru^{III}_2L_6$ Cluster

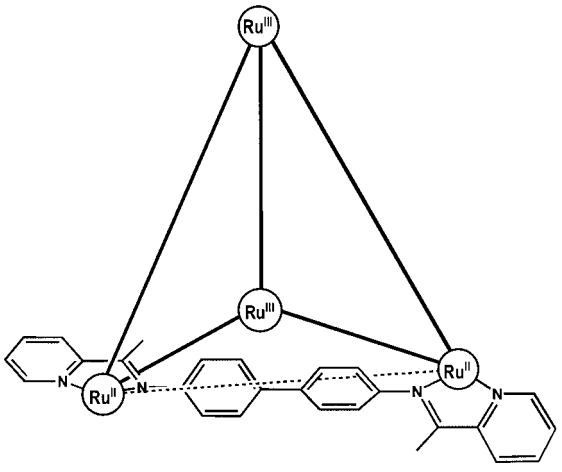

Keywords: Ruthenium / Mixed-valent compounds / Tetrahedral cluster

2586 **G. Beobide, O. Castillo,* U. García-Couceiro, J. P. García-Terán, A. Luque, M. Martínez-Ripoll, P. Román**

A Binuclear Copper(II) Complex Containing the Pyrazine-2,5-dicarboxylate Ligand: Study of the Magnetic Exchange through the Pyrazine Bridge

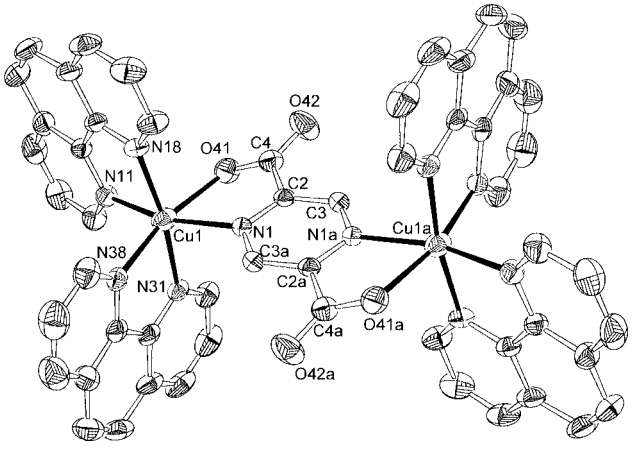

Keywords: Copper / Density functional calculations / Magnetic properties / N ligands / Pyrazine

FULL PAPERS

2591 **K. Kervinen, H. Korpi, J. G. Mesu, F. Soulimani, T. Repo,* B. Rieger, M. Leskelä, B. M. Weckhuysen***

Mechanistic Insights into the Oxidation of Veratryl Alcohol with Co(salen) and Oxygen in Aqueous Media: An in-situ Spectroscopic Study

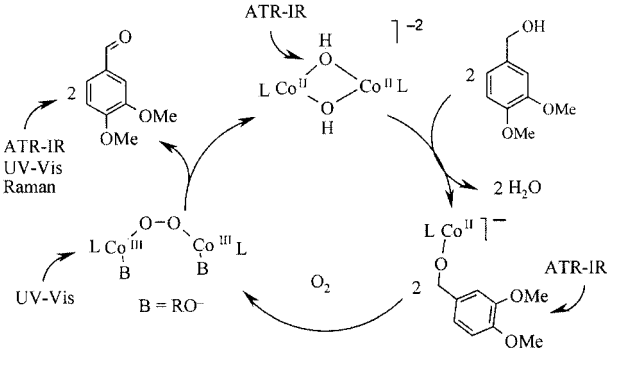

Keywords: Cobalt complexes / Schiff bases / Homogeneous catalysis / IR spectroscopy / Raman spectroscopy / UV/Vis spectroscopy

 © 2005 Wiley-VCH Verlag GmbH & Co. KGaA, Weinheim

2600 **J. A. Alonso,* M. J. Martínez-Lope, M. T. Casais, J. L. Martínez, V. Pomjakushin**

Synthesis, Structural, and Magnetic Characterization of $YCrMnO_5$

Keywords: Magnetic properties / Ferrimagnetic ordering / High-oxygen-pressure synthesis / Crystal structure refinement / Neutron powder diffraction / X-ray diffraction

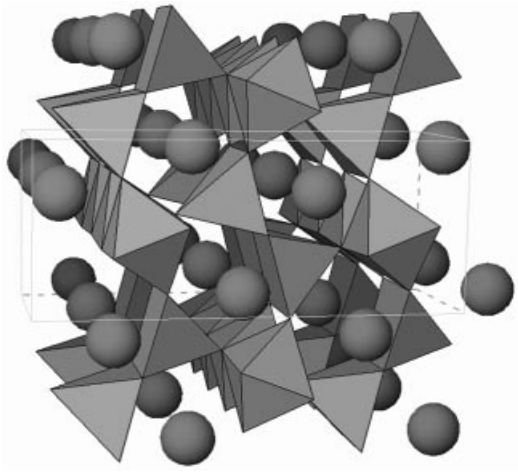

2607 **C. Schulze Isfort, T. Pape, F. E. Hahn***

Synthesis and X-ray Molecular Structure of $(PNP)_2[Mo^{IV}(C_6H_4S_2\text{-}1,2)_3]$ Completing the Structural Characterization of the Series $[Mo(C_6H_4S_2\text{-}1,2)_3]^{n-}$ (n = 0, 1, 2)

Keywords: Molybdenum / S ligands / X-ray diffraction / Coordination modes

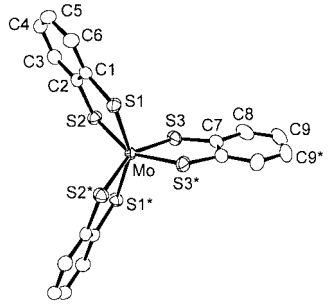

2612 **Y. Bian, L. Li, D. Wang, C.-F. Choi, D. Y. Y. Cheng, P. Zhu, R. Li, J. Dou, R. Wang, N. Pan, D. K. P. Ng, N. Kobayashi, J. Jiang***

Synthetic, Structural, Spectroscopic, and Electrochemical Studies of Heteroleptic Tris(phthalocyaninato) Rare Earth Complexes

Keywords: Phthalocyanines / Sandwich complexes / Rare earths / Triple-decker complexes / Heteroleptic complexes

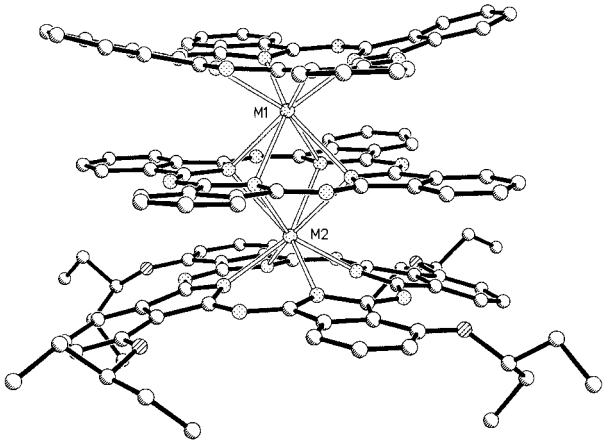

2619 **D. Martin, H. Gornitzka, A. Baceiredo,* G. Bertrand***

C-Phosphoniophosphaalkenes as Precursors of $1\sigma^4,3\sigma^2$-Diphosphaallenes: Scope and Limitations

Keywords: Phosphorus / Phosphaalkenes / Phosphacumulenes / Phosphorus ylides

 © 2005 Wiley-VCH Verlag GmbH & Co. KGaA, Weinheim

2625 **H. Hou, Q. Peng, S. Zhang, Q. Guo, Y. Xie***

A "User-Friendly" Chemical Approach Towards Paramagnetic Cobalt Phosphide Hollow Structures: Preparation, Characterization, and Formation Mechanism of Co_2P Hollow Spheres and Tubes

Keywords: Cobalt / Materials science / Nanostructures / Phosphides

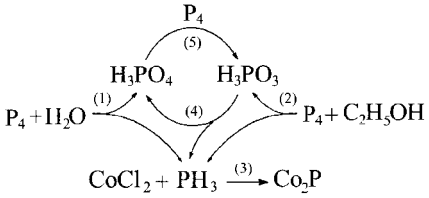

2631 **M. Jiménez-Tenorio, M. C. Puerta, P. Valerga***

C−H vs. N−H Bond Activation in Aminophosphane Ligands: Reaction of $[Cp^*Ru(MeCN)_2(PR^1{}_2NHR^2)]^+$ (R^1 = Ph, *i*Pr; R^2 = Ph, C_6F_5) with Alkynes

Keywords: Alkyne ligands / C−H activation / Half-sandwich complexes / Phosphane ligands / Ruthenium

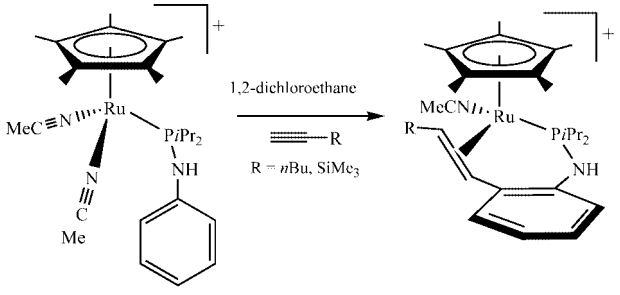

2641 **A. Mourran, U. Ziener, M. Möller,* E. Breuning, M. Ohkita, J.-M. Lehn***

Two Morphologies of Stable, Highly Ordered Assemblies of a Long-Chain-Substituted [2 × 2]-Grid-Type Fe^{II} Complex Adsorbed on HOPG

Keywords: Iron / Long alkyl chains / Scanning tunneling microscopy / Highly oriented pyrolytic graphite / Nanopatterning / Self-assembly

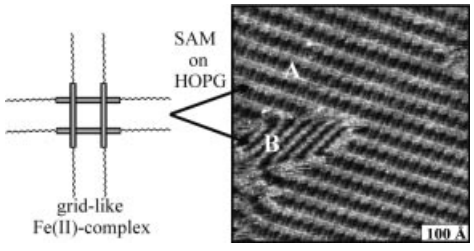

2648 **A. C. G. Hotze, E. P. L van der Geer, H. Kooijman, A. L. Spek, J. G. Haasnoot, J. Reedijk***

Characterization by NMR Spectroscopy, X-ray Analysis and Cytotoxic Activity of the Ruthenium(II) Compounds $[RuL_3](PF_6)_2$ (L = 2-Phenylazopyridine or *o*-Tolylazopyridine) and $[Ru'_2L'']](PF_6)_2$ (L′, L″ = 2-Phenylazopyridine, 2,2′-Bipyridine)

Keywords: Ruthenium / Tris(chelate) complexes / 2D NMR / Cytotoxicity

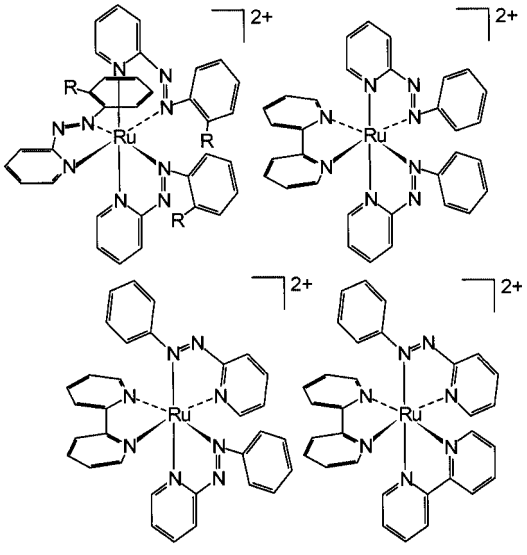

 © 2005 Wiley-VCH Verlag GmbH & Co. KGaA, Weinheim

2658 **S. El Ghachtouli, C. Cadiou, I. Déchamps-Olivier, F. Chuburu,* M. Aplincourt, V. Turcry, M. Le Baccon, H. Handel**

Spectroscopy and Redox Behaviour of Dicopper(II) and Dinickel(II) Complexes of Bis(cyclen) and Bis(cyclam) Ligands

Keywords: Copper / Nickel / Bis(cyclen) ligands / Bis(cyclam) ligands / Electrochemistry / EPR spectroscopy

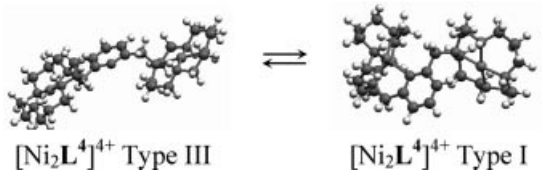

2669 **D. S. Jacob, S. Makhluf, I. Brukental, R. Lavi, L. A. Solovyov, I. Felner, I. Nowik, R. Persky, H. E. Gottlieb, A. Gedanken***

Sonochemical Synthesis and Characterization of $Ni(C_4H_6N_2)_6(PF_6)_2$, $Fe(C_4H_6N_2)_6(BF_4)_2$, and $Ni(C_4H_6N_2)_6(BF_4)_2$ in 1-Butyl-3-methylimidazole with Hexafluorophosphate and Tetrafluoroborate

Keywords: Ionic liquids / Sonochemistry / Iron / Nickel / Imidazole / X-ray powder diffraction / Structure analysis

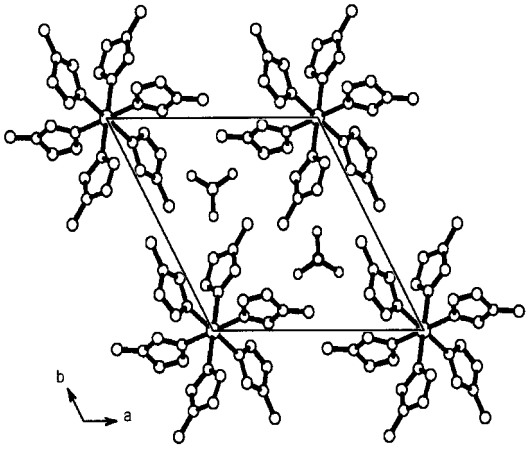

2678 **D. Li, Y. Wang,* X. Luan, P. Liu, C. Zhou, H. Ma, Q. Shi**

1-D Open-Channeled 3-D Supramolecular Self-Assembled Frameworks Encapsulating Unprecedented Cyclic $(H_2O)_8$ Clusters or Solvent Molecules

Keywords: Hydroxybutanedioic acid / Copper / Bipyridine / Phenanthroline / Self-assembly / 1-D open channel

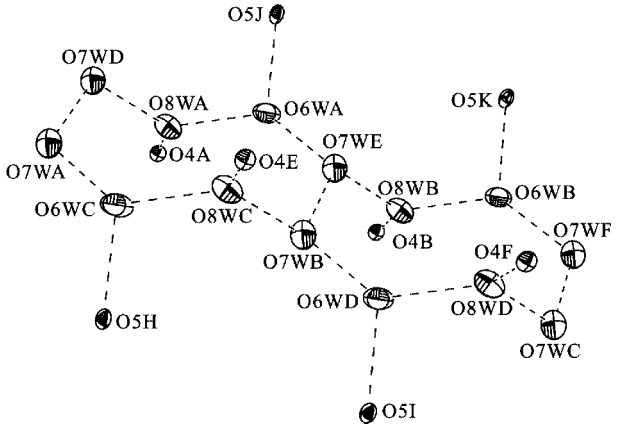

2685 **T. Storr, B. R. Cameron,* R. A. Gossage, H. Yee, R. T. Skerlj, M. C. Darkes, S. P. Fricker, G. J. Bridger, N. A. Davies, M. T. Wilson, K. P. Maresca, J. Zubieta**

Ru^{III} Complexes of Edta and Dtpa Polyaminocarboxylate Analogues and Their Use as Nitric Oxide Scavengers

Keywords: Bioinorganic chemistry / Ruthenium / Polyaminocarboxylates / Nitric oxide scavenging

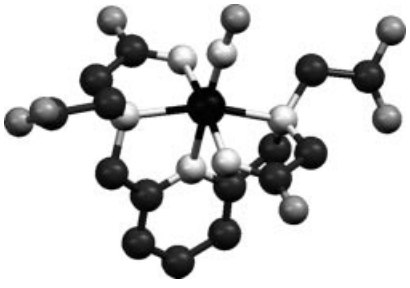

 © 2005 Wiley-VCH Verlag GmbH & Co. KGaA, Weinheim

2698 **Y. Mosqueda, E. Pérez-Cappe, P. Aranda, E. Ruiz-Hitzky***

Preparation of an $Li_{0.7}Ni_{0.8}Co_{0.2}O_2$ Electrode Material From a New Li−Co−Ni Mixed-Citrate Precursor

Keywords: Citrates / Electrode materials / Lithium batteries / Mixed-valent compounds / Oxides

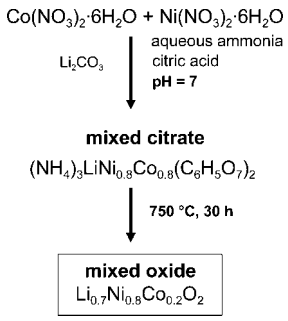

2706 **S.-C. Xiang, S.-M. Hu, J.-J. Zhang, X.-T. Wu,* J.-Q. Li**

A New Spherical Metallacryptate Compound $[Na⊂\{Cu_6(Thr)_8(H_2O)_2(ClO_4)_4\}]·ClO_4·5H_2O$: Magnetic Properties and DFT Calculations

Keywords: Spherical metallacryptate / Magnetic properties / Density functional calculations / Broken symmetry / Threonine

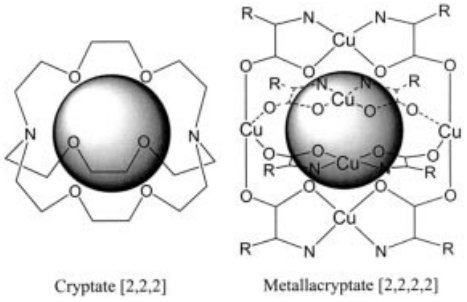

2714 **J. Goulon,* C. Goulon-Ginet, A. Rogalev, F. Wilhelm, N. Jaouen, D. Cabaret, Y. Joly, G. Dubois, R. J. P. Corriu, G. David, S. Brandés, R. Guilard***

A Study Using X-ray Absorption and Emission Spectroscopy of Dioxygen-Binding Xerogels Incorporating Cyclam Units Complexed with Copper Salts

Keywords: X-ray absorption spectroscopy / Tetraazamacrocyclic ligand / Dioxygen binding / Peroxo ligand / Copper

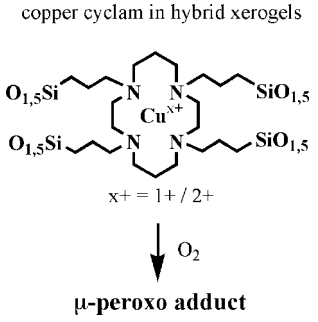

2727 **K. Vehlow, K. Köhler*, S. Blechert, S. Dechert, F. Meyer**

Trialkoxysilyl-Functionalized Silver(I) Carboxylates: New Building Blocks for the Synthesis of Immobilizable and Immobilized Homogeneous Catalysts

Keywords: Silver / Carboxylate ligands / Fluorinated ligands / Immobilization / Silica / Catalysis

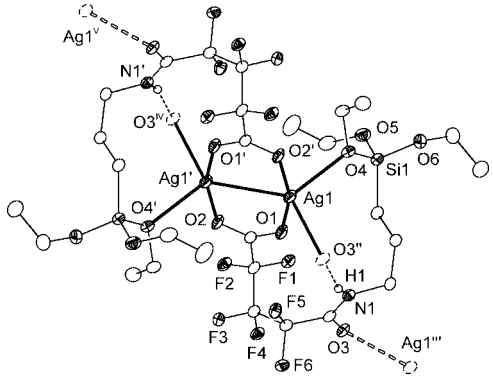

 © 2005 Wiley-VCH Verlag GmbH & Co. KGaA, Weinheim

2737 **D. Braga,* S. L. Giaffreda, M. Polito, F. Grepioni***

Design, Preparation and Characterization of the Adducts of the Bis-Amido Cobalticinium Complex $[Co^{III}(\eta^5\text{-}C_5H_4CONHC_5H_4N)_2][PF_6]$ with Fumaric and Maleic Acids

Keywords: Organometallic complexes / Amides / Hydrogen bonding / Crystal engineering / Supramolecular chemistry

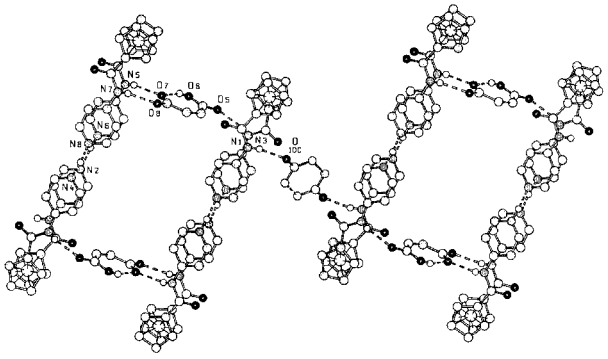

2747 **U. Caruso, R. Centore,* B. Panunzi, A. Roviello, A. Tuzi**

Grafting Poly(4-vinylpyridine) with a Second-Order Nonlinear Optically Active Nickel(II) Chromophore

Keywords: N ligands / Nickel / Nonlinear optics / Poly(4-vinylpyridine)

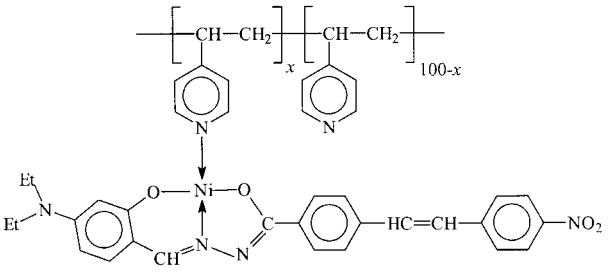

Metallo-polymers for second-order nonlinear optics

2754 **H. Braunschweig,* M. Kraft, K. Radacki, S. Stellwag**

[1]Borahafnocenophanes: Synthesis, Structure and Catalytic Activity

Keywords: Boron / Hafnium / Metallocenophanes / *ansa*-Metallocenes / Ethylene polymerisation

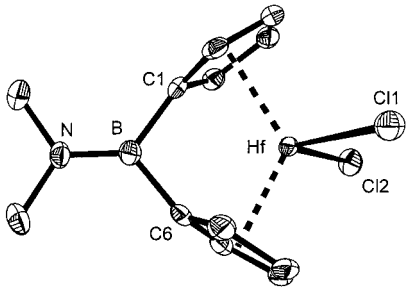

 © 2005 Wiley-VCH Verlag GmbH & Co. KGaA, Weinheim

Ionic Liquids with Fluorine-Containing Cations

Hong Xue[a] and Jean'ne M. Shreeve*[a]

Keywords: Ionic liquids / Fluorine / Cations / Quaternization

Interest in ionic liquids with fluorine-containing cations has grown markedly in recent years. The syntheses, characterization and properties of quaternary fluoroalkyl-substituted ammonium, imidazolium, triazolium, pyridinium, pyrazinium, pyridazinium, pyrimidinium, piperazinium, pyrrolidinium, oxazolidinium, and morpholinium salts have been studied in detail. By modifying the anion or the fluorine-containing substituent on the cation, a wide range of properties of fluorine-containing ionic liquids can be tuned, including viscosity, melting point, density, conductivity, solubility, liquid range, thermal and hydrolytic stability. They are promising solvents for electrochemical, photovoltaic, surfactant and synthetic applications. In this Microreview, only the literature dealing with ionic liquids that involve fluorine-containing cations is presented.

(© Wiley-VCH Verlag GmbH & Co. KGaA, 69451 Weinheim, Germany, 2005)

1. Introduction

Ionic liquids are salts with low melting points (< 100 °C). Since ionic liquids exhibit extremely low vapor pressures, long liquid ranges, and are highly polar yet noncoordinating, they are good solvents for a wide range of organic and inorganic materials. These interesting compounds are achieved either by incorporating a bulky asymmetric cation into the structure in order to preclude good crystal packing and/or by selecting an anion in which there is considerable delocalization of the electron cloud over the molecular backbone that tends to decrease interionic interaction, e.g., bis(trifluoromethylsulfonyl)-amide or polyfluoro-β-diketonate. Results described in current publications indicate that replacing an organic solvent by an ionic liquid may lead to remarkable improvement in well-known processes. A number of reviews that cover the history, properties, and uses of ionic liquids are available.[1–9] These amazing liquids have been utilized not only as clean solvents, but also as catalysts for green chemistry and electrolytes for batteries, photochemistry, and electrosynthesis, and even as advanced heat transfer fluids and lubricants. Many of these types of ionic liquids are available commercially,[10] see, for example, Acros, Aldrich, Cytec, Strem and Merck.

[a] Department of Chemistry, University of Idaho,
Moscow, Idaho 83843-2343, USA
Fax: +1-208-885-9146
E-mail: jshreeve@uidaho.edu

Hong Xue was born in 1969 in Changchun, China, and received his Ph. D. in polymer chemistry from Dalian University of Technology (China) in 1999. He held a postdoctoral position for two years at Changchun Institute of Applied Chemistry, Chinese Academy of Sciences, and worked on living polymerization and chiral polymer materials. In 2002, he joined the group of Professor Jean'ne M. Shreeve as a postdoctoral fellow. His current research focuses on the syntheses and application of organofluorine compounds, ionic liquids and energetic materials.

Jean'ne M. Shreeve is a Montana native. She received a BA in chemistry from the University of Montana, MS in analytical chemistry from the University of Minnesota, and Ph. D. in inorganic chemistry from the University of Washington, Seattle. She joined the University of Idaho faculty in 1961, became department head in 1973, and, in 1987, assumed the role of Vice-President for Research and Graduate Studies. In January 2000, she returned to full time research. She was privileged to have worked with three of the finest gentlemen of fluorine chemistry – Professors George H. Cady, Harry J. Emeléus, and Oskar Glemser. Her research interests include the syntheses, characterization and reactions of new fluorine-containing compounds as exemplified by more than 370 refereed publications. In July 2004, she became Jean'ne M. Shreeve Chemistry Professor.

MICROREVIEWS: This feature introduces the readers to the authors' research through a concise overview of the selected topic. Reference to important work from others in the field is included.

Earlier generations of ionic liquids were extremely water-sensitive – most often due to the presence of polychlorometallates as the anions. However, recently developed ionic liquids without halometallates, are water- and air-insensitive and possess remarkably high thermal stability. Typically, they are composed of bulky 1,3-dialkylimidazolium, alkylammonium, alkylphosphonium, or alkylpyridinium organic cations and inorganic/organic anions, such as NO_3^-, ClO_4^-, $CF_3SO_3^-$, PF_6^-, BF_4^-, $(CF_3SO_2)_2N^-$, $CF_3CO_2^-$.[1–9] Until now, the ionic liquid field has been extensively dominated by imidazolium salts with anions most frequently being fluorine-containing. Somenew fluoroanions, such as fluorohydrogenates,[11] tetrakis{*p*-[dimethyl(1*H*,1*H*,2*H*,2*H*-perfluorooctyl)silyl]-phenyl}borate,[12] perfluoroalkyl-β-diketonates,[13] tris(perfluoroalkyl) trifluorophosphates,[14] and perfluoroalkyl trifluoroborates,[15] have been reported as useful in the synthesis of new low melting salts.

Following the syntheses of the first fluorine-containing ionic liquids, 3-methyl-1-(2,2,2-trifluoroethyl)imidazolium salts, which were characterized as hydrophobic, highly conductive ambient-temperature molten materials,[16] the interest in ionic liquids with fluoroalkyl-substituted cations has grown markedly.[17–36] By modifying the anion or the fluorine-containing substituent on the cation, a wide range of properties of fluorine-containing ionic liquids can be tuned, including, for example, viscosity, melting point, density, conductivity, solubility, liquid range, thermal and hydrolytic stability, and heat of formation. The influence of inter-ion hydrogen bonding can be diminished by introducing fluorine-containing groups into the cation and especially when employing anions such as bis(trifluorosulfonyl)amide and perfluoroalkyldiketonate.[13,37] Excellent reviews of room-temperature ionic liquids with alkylimidazolium cations and fluoroanions are available.[38,39] A U.S. patent issued in 1998 claims a vast number of "hydrophobic ionic liquids," many of which have fluorine-containing cations.[22] In summarizing the inventions described in the patent, the authors conclude that when the cation and/or the anion is fluorinated, the hydrophobic ionic liquids of the invention have certain additional special properties, including 1) inertness to organic solvents and oxidizing agents; 2) resistance to corrosive acids and bases; and 3) resistance to extremes of temperature and pressure. The applications for the perfluorinated hydrophobic ionic liquids claimed in the patent encompass superior hydraulic, inert liquid diluents for highly reactive chemicals and solvents with a high capacity for dissolved gases such as oxygen, and useful for catalysis and for oil and gas separations where the desired product is partitioned between an aqueous and hydrophobic perfluorinated ionic liquid phase. These applications are, of course, in addition to all of those suggested for conventional ionic liquids. These points provide the raison d'être for further syntheses, characterization and study of new ionic liquids that contain the element fluorine. In this paper, only the literature dealing with ionic liquids that involve fluorine-containing cations is reviewed.

2. Syntheses and Properties of Quaternary (Fluoroalkyl)ammonium Salts

Since the report of a liquid ammonium salt, $EtNH_3^+NO_3^-$, early in the last century,[40] many additional quaternary ammonium salts have been synthesized and studied. Typically, introduction of greater asymmetry into the ionic species by decreasing the symmetry of the cation results in lowering of the melting point.[41] Until very recently only a very few (fluoroalkyl)ammonium salts, such as $(CH_3)_3(CH_2F)N^+X^-$ (X = Br, I), had been reported.[42] Selected quaternary ammonium salts containing polyfluoroalkyl groups (Figure 1), such as dimethylbis-(4,4,5,5,6,6,7,7,7-nonafluoroheptyl)ammonium chloride (m.p. 70–72 °C), were claimed in a patent.[43] However, the characterization was limited.

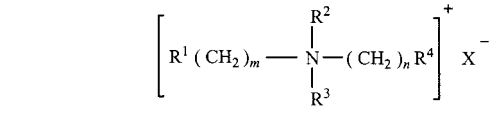

R^1, R^4 = fluoroalkyl; R^2 = alkyl; R^3 = alkyl or $R^1(CH_2)_m$-; X = anion

Figure 1. Quaternary ammonium salts containing polyfluoroalkyl groups.

Now a series of water- and thermally stable low-melting salts based on quaternary trialkyl(polyfluoroalkyl)ammonium cations has been synthesized and characterized. Metathetical reactions of the iodide salts with fluorine-containing anions resulted in new liquid salts (Scheme 1). The marked variations in melting points appear to be a function of the anion primarily and is essentially independent of the substituents on the cation. In this series, iodide salts of the triisooctyl(polyfluoroalkyl)amines are also liquids at 25 °C.[18] In some cases, the viscosities of these salts are remarkably low. Another novel iodide, diallyl(4,4,5,5,6,6,7,7,8,8,9,9,10,10,11,11,11-heptadecafluoroundecyl)(methyl)ammonium iodide (m.p. 65–68 °C) has been described as an effective antimicrobial agent.[19]

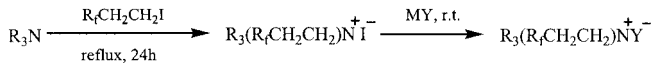

R = *n*-C_3H_7, *n*-C_4H_9, i-C_8H_{17}

R_f = $(CF_2)_xCF_3$, *x* = 3, 7, 9

M = Ag, Li; Y = $N(CF_3SO_2)_2$, CF_3SO_3, $C_3F_7CO_2$

R	R_f	Y	Yield[a]	*d*[b]	T_m (T_g)[c]	T_d[d]
n-C_4H_9	$CF_3(CF_2)_3$	I	80	–	82	252
n-C_4H_9	$CF_3(CF_2)_7$	I	85	–	91	260
i-C_8H_{17}	$CF_3(CF_2)_3$	I	83	1.1	22.5	270
i-C_8H_{17}	$CF_3(CF_2)_7$	I	80	1.0	20.1	265
i-C_8H_{17}	$CF_3(CF_2)_9$	I	78	1.0	18.2	279
n-C_4H_9	$CF_3(CF_2)_7$	Bu_fCO_2[e]	80	1.4	(–48)	345
n-C_4H_9	$CF_3(CF_2)_3$	NTf_2[f]	90	1.2	15.5	374
n-C_4H_9	$CF_3(CF_2)_7$	NTf_2	90	1.3	22.1	290
i-C_8H_{17}	$CF_3(CF_2)_7$	NTf_2	90	1.0	(–62.6)	358

[a] %. [b] g/cm^3, pycnometer; 25°C. [c] Melting point (phase transition) [°C]. [d] Thermal decomposition [°C]. [e] Heptafluorobutyrate. [f] Bis(trifluoromethanesulfonyl)amide.

Scheme 1.

 © 2005 Wiley-VCH Verlag GmbH & Co. KGaA, Weinheim

3. Syntheses and Properties of Quaternary Fluoroalkyl-Substituted Imidazolium Salts

An ionic liquid in which the cation is a polyfluoroalkyl-substituted imidazolium species derived from the antifungal drug miconazole becomes a soft yellow wax over a period of hours but is readily reliquified by heating to 92–96 °C (Scheme 2[20] It is stable in air to ≥ 150 °C. It also exhibits lyotropic liquid-crystalline behavior while inducing the gelation of benzene. 1-Alkyl-3-(polyfluoroalkyl)imidazolium hexafluorophosphates were employed as surfactants to promote the formation and stabilization of dispersions of perfluorocarbons in a conventional ionic liquid, such as 1-hexyl-3-methylimidazolium hexafluorophosphate [(6-mim)-PF_6] (Figure 2).[21]

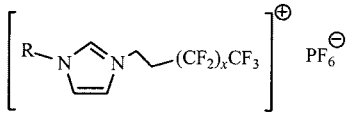

R = Me, *n*Bu; *x* = 5, 7

Figure 2. 1-Alkyl-3-(polyfluoroalkyl)imidazolium hexafluorophosphates.

The presence of fluorine markedly increases the density of fluoroalkyl-substituted imidazolium ionic liquids and, in some cases, may cause increases in the melting points even in the presence of a constant anion (Scheme 3).[23] Some of the bis(polyfluoroalkyl)imidazolium salts are liquids with higher densities, e. g., the density of *N*,*N*′-bis(3,3,3-trifluoropropyl)imidazolium bis(trifluoromethylsulfonyl)amide (m.p. –62 °C) is 1.85 g cm^{-3}.

Among several highly halogenated, low-melting imidazolium salts which exhibit densities ranging from 1.95 to 2.80 g cm^{-3} are two highly brominated (polyfluoroalkyl)-imidazolium bis(trifluoromethylsulfonyl)amides with densities of 2.11 and 2.35 g cm^{-3} (Scheme 4). These dense, viscous liquids are thermally and hydrolytically remarkably stable.[24]

Quaternization of 1-(tetrafluoroethyl)imidazole with electrophiles such as RI (R = Me, Et, *n*Pr, *i*Pr, *n*Bu) followed by metathesis with $LiNTf_2$ or $AgBF_4$ gives rise to the first examples of ionic liquids with substituents at the nitrogen atom bonded through –CF_2–, i.e., CF_2CF_2H.[25]

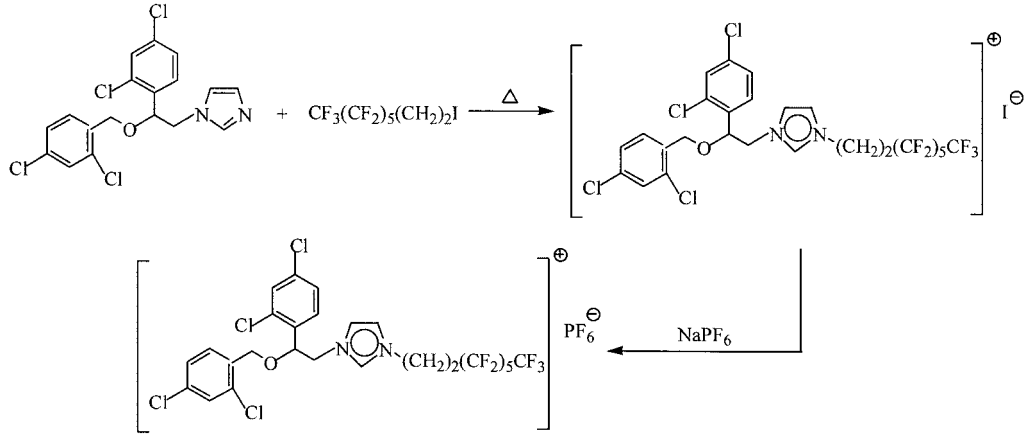

Scheme 2.

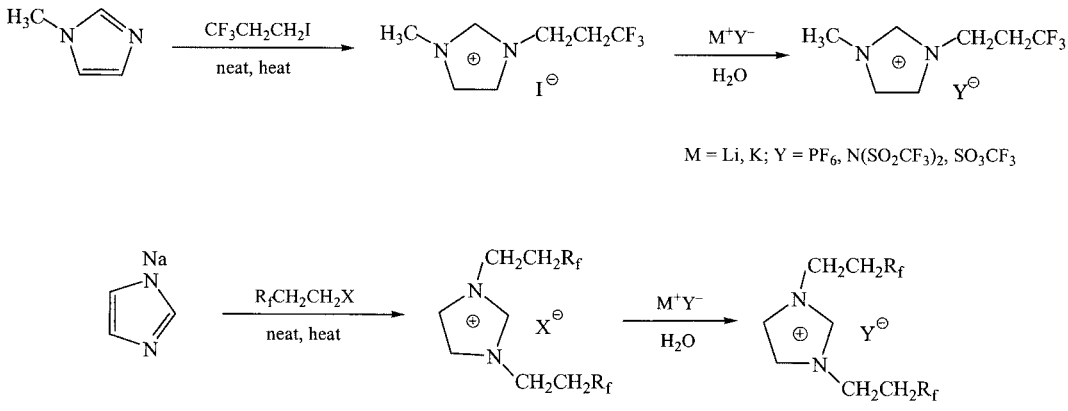

Scheme 3.

 © 2005 Wiley-VCH Verlag GmbH & Co. KGaA, Weinheim

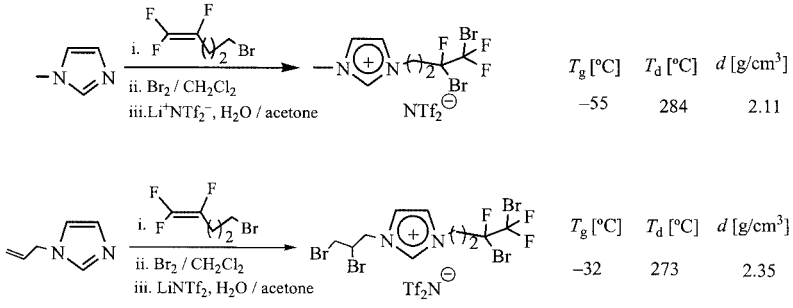

Scheme 4.

Bis[(4,4,4-trifluorobutyl)imidazolium] quaternary salts based on *p*-*tert*-butylcalix[4]arenes have melting points >100 °C.[26]

A number of structurally different trimethylsilylated and tris[(oxyethyl)imidazolium] and tris[(oxyethyl)ammonium] ionic liquids built on the triazine ring, including polyfluorinated ones, were prepared and characterized (Scheme 5).[27] The physical and thermal properties were studied in this work, and the densities of the polyfluorinated triquaternary salts on the triazine frame were shown to lie between 1.69 and 1.88 g cm^{-3}.

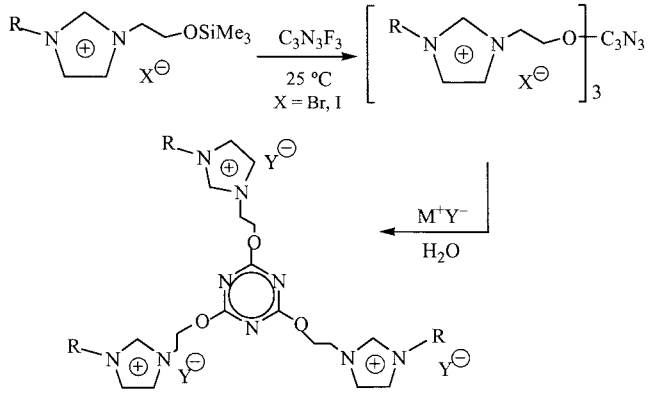

R	Y	T_g [°C]	T_d [°C]	d [g/cm^3]
$CH_2CH_2CH_2F$	NTf_2	–35	300	1.72

Scheme 5.

4. Syntheses and Properties of Quaternary Fluoroalkyl-Substituted Triazolium Salts

Until recently, there were very few triazolium quaternary salts with melting points < 100 °C, especially polyfluoroalkylated or perfluoroalkylated triazolium compounds. Considerable attention has been devoted to changes in the properties of polyfluoroalkyl-1,2,4-triazolium ionic liquids as a function of the chain length and extent of fluorination of the chain, as well as the impact of a variety of anions (Scheme 6).[28] As the number of carbon atoms in the alkyl and polyfluoroalkyl substituent chains on the cation increases resulting in concomitantly less efficient packing in the solid, the melting points are observed to decrease. The density increases with elongation of the fluoroalkyl substituent and the degree of fluorination of the chain and decreases as the alkyl group becomes bulkier. The liquid ranges and the thermal stabilities of these ionic liquids are impressive covering, in many cases, over 400 °C and frequently decomposing at > 400 °C.

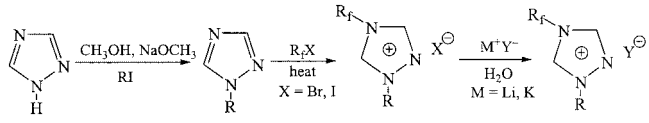

R	R_f	Y	T_m (T_g)[a]	T_d[b]
CH_3	$(CH_2)_2CF_3$	NTf_2	(–58)	376
$CH_3(CH_2)_3$	$(CH_2)_2CF_3$	NTf_2	(–67)	395
$CH_3(CH_2)_6$	$(CH_2)_2CF_3$	NTf_2	(–67)	402
$CH_3(CH_2)_9$	$(CH_2)_2CF_3$	NTf_2	(–68)	400
$CH_3(CH_2)_3$	$(CH_2)_2(CF_2)_3CF_3$	NTf_2	69	394
$CH_3(CH_2)_6$	$(CH_2)_2(CF_2)_3CF_3$	NTf_2	55	396
$CH_3(CH_2)_9$	$(CH_2)_2(CF_2)_3CF_3$	NTf_2	53	396
CH_3	$(CH_2)_2(CF_2)_5CF_3$	NTf_2	62	381
$CH_3(CH_2)_3$	$(CH_2)_2(CF_2)_5CF_3$	NTf_2	28	368
$CH_3(CH_2)_6$	$(CH_2)_2(CF_2)_5CF_3$	NTf_2	22	405
$CH_3(CH_2)_6$	$(CH_2)_2F$	NTf_2	(–70)	359
$CH_3(CH_2)_9$	$(CH_2)_2F$	NTf_2	(–62)	425
$CH_3(CH_2)_9$	$(CH_2)_2F$	OTf	46	362
$CH_3(CH_2)_6$	$(CH_2)_2F$	BF_4	52	336
$CH_3(CH_2)_3$	$(CH_2)_2CF_3$	OTf	33	379

[a] Melting point/phase transition temperature [°C]. [b] Thermal degradation [°C].

Scheme 6.

An efficient procedure for the syntheses of a family of perfluoroalkyl-containing triazolium quaternary salts, 1-alkyl-4,5-dimethyl-3-(perfluoroalkyl)-1,2,4-triazolium salts was developed (Scheme 7).[29] Although the molecular weight of the cation of 1-alkyl-4,5-dimethyl-3-(perfluorooctyl)-1,2,4-triazolium tetrafluoroborate is threefold greater than that of the 3-(trifluoromethyl) derivative, its melting point is 32 °C lower (98 °C vs. 130 °C) (Figure 3). In general, these ionic salts are not miscible with nonpolar organic liquids such as hexane but miscible with acetone and water.

4-Functionalized 1-alkyl- or 1-(polyfluoroalkyl)-1,2,4-triazolium salts were synthesized to give a series of triazolium cations that contain covalently bound anionic sites, such as sulfonate, fluorohomoallylic, fluorocarboxy, and fluoroalkanol groups, and were converted by metathesis with fluorine-containing salts to a wide range of low-melting salts (Scheme 8).[30] These functionalized triazolium salts possess many characteristics of excellent ionic liquids with respect to air, water, and thermal stability. Most of them exhibit phase-transition temperatures between –22 and ca. –68 °C,

 © 2005 Wiley-VCH Verlag GmbH & Co. KGaA, Weinheim

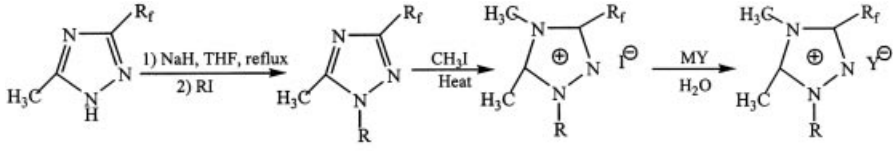

R_f	R	MY	T_m[a]	T_d[b]
CF_3	CH_3	$LiNTf_2$	70	368
CF_3	$CH_2CH_2CH_2F$	$LiNTf_2$	49	323
C_8F_{17}	CH_3	$LiNTf_2$	81	313
C_8F_{17}	CH_3	$AgClO_4$	90	294
C_8F_{17}	CH_3	$AgBF_4$	98	306

[a] Melting point [°C]. [b] Thermal degradation [°C].

Scheme 7.

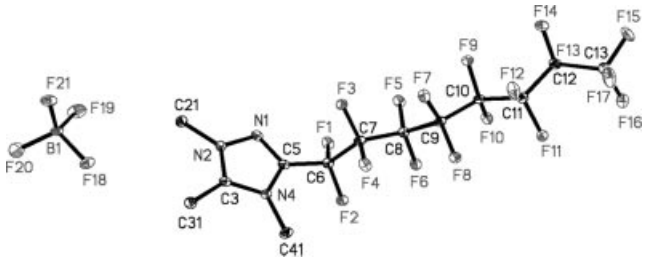

Figure 3. 1,4,5-Trimethyl-3-perfluorooctyl-1,2,4-triazolium tetrafluoroborate.

have decomposition temperatures between 254 and 408 °C, and densities between 1.45 and 1.61 g cm^{-3}.

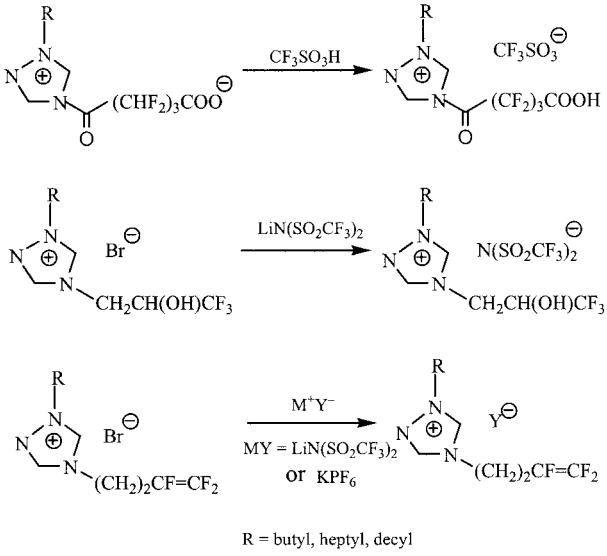

Scheme 8.

5. Syntheses and Properties of Quaternary Fluoroalkyl-Substituted Pyridinium and Bipyridinium Salts

(Fluoroalkyl)pyridinium salts that melt at > 100 °C have been studied for more than 20 years.[44] However, in a one-step method using the powerful alkylating reagent, phenyl-(trifluoroethyl)iodonium bis(trifluoromethylsulfonyl)amide, direct trifluoroethylation of pyridine derivatives gave the 4-methyl-*N*-(trifluoroethyl)pyridinium salts, whose melting points are lower than 100 °C (Scheme 9).[31]

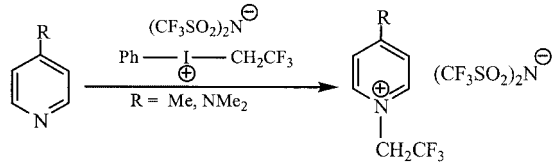

Scheme 9.

In addition, several bridged tetraquaternary salts derived from *N*,*N*′-bis(polyfluoroalkyl)-4,4′-bipyridine were found to meet the melting point criterion for ionic liquids (Scheme 10).[32]

All of the 4,4′-bipyridinium salts are stable in water and air and are thermally stable up to 340 °C as determined by DSC. They are generally soluble in acetone, ethyl acetate, DMF, and DMSO. The polyfluoroalkylated mono-, di-, and tetraquaternary 4,4′-bipyridinium salts are likely to have a considerable practical chemistry.

6. Syntheses and Properties of Quaternary Fluoroalkyl-Substituted Pyrazinium, Pyridazinium, Pyrimidinium, Piperazinium and Pyrrolidinium Salts

A variety of new quaternized salts of pyridazine, pyrazine, pyrimidine and 1,4-dimethylpiperazine that contain polyfluoroalkyl and alkyl substituents were synthesized and characterized (Scheme 11).[33] Many of these quaternary salts melt below 100 °C and therefore fall into the ionic liquid class. The thermal stability is largely a function of the cation with the pyridazinium compounds being the most stable. These salts also have the lowest melting points, and were prepared under the mildest reaction conditions. The pyridazinium bis(trifluoromethylsulfonyl)amide salts exhibit relatively high densities between 1.81 and 2.13 g/cm^3. The latter is one of the most dense ionic liquids excluding the hydrolytically unstable metal salts. Pyrazinium and pyridazinium salts are much less susceptible to hydrogen/deute-

 © 2005 Wiley-VCH Verlag GmbH & Co. KGaA, Weinheim

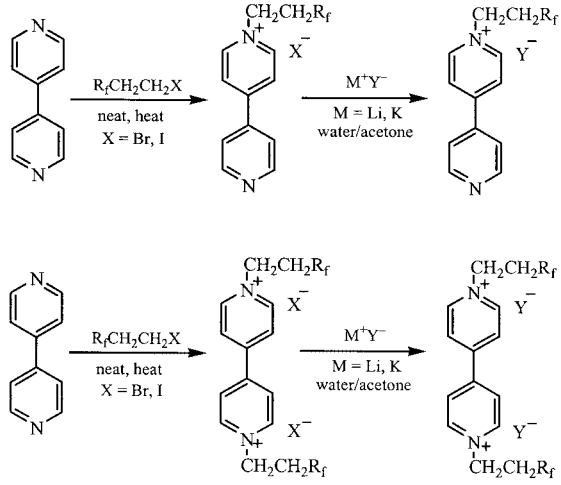

R_f	Y	T_m [°C]
CH_2F	NTf_2	62
CF_3	NTf_2	67
C_6F_{13}	NTf_2	52
C_8F_{17}	NTf_2	94
CH_2F	SO_3CF_3	88
CF_3	SO_3CF_3	98

R_f	Y	T_m [°C]
CH_2F	NTf_2	64
CF_3	NTf_2	96
CH_2F	SO_3CF_3	89

Scheme 10.

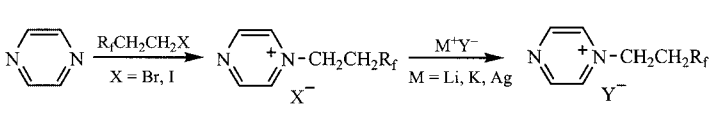

R_f	Y	T_m [°C]
F	NTf_2	–48 (T_g)
F	ClO_4	72
CF_3	NTf_2	95

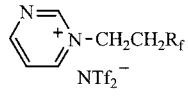

R_f	T_m[°C]
F	–19 (T_g)
CF_3	55

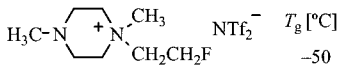

T_g [°C]: –50

Scheme 11.

rium exchange than the analogous imidazolium compounds which may allow for applications of the former liquid salts where the latter may not be suitable.

N-Alkylpyrrolidines are also readily quaternized with fluoroalkyl bromides and iodides to give ionic liquids when metathesized with lithium bis(trifluoromethylsulfonyl)-amide.[34]

7. Syntheses and Properties of Quaternary Salts Containing the Pentafluorosulfanyl (SF_5) Group

The first quaternary salts of pyridine, *N*-methylimidazole, *N*-propyltriazole, and pyridazine that contain the pentafluorosulfanyl (SF_5) group were found to be low melting (Scheme 12).[35] The presence of the pentafluorosul-

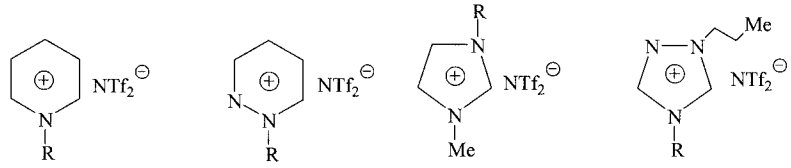

R	T_m (T_g) [°C]	d [g/cm^3]	T_g [°C]	d [g/cm^3]	T_g [°C]	d [g/cm^3]	T_g [°C]	d [g/cm^3]
$SF_5(CF_2)_2(CH_2)_4$	18	2.02	–41.7	1.87	–56.7	2.01	–54.8	1.89
$SF_5(CF_2)_2(CH_2)_2$	33	1.96	–14	1.93	–55.5	2.00		
$SF_5(CF_2)_4(CH_2)_2$	36.1 (–39.7)	1.97			–50	1.97		
$CF_3CH_2CH_2$			–64	1.85	–74	1.44	–67	1.60
$CF_3(CF_2)_5(CH_2)_2$	38.4		–13	2.13	–50	1.77	28	

Scheme 12.

 © 2005 Wiley-VCH Verlag GmbH & Co. KGaA, Weinheim

fanyl group markedly increases the densities of the bis(trifluoromethylsulfonyl)amide salts. The methylimidazolium, pyridinium, and pyridazinium salts exhibit densities of ca. 2 g cm^{-3}. However, $CF_3(CF_2)_5(CH_2)_2$– as a substituent on the ring also plays a major role in increasing the liquid densities relative to the C_8 alkyl or to shorter polyfluoroalkyl substitutents and, in some cases, to the polyfluoro(pentafluorosulfanyl)alkyl substitutents.

8. Syntheses and Properties of Fluoroalkyl-Substituted Oxazolidinium and Morpholinium Salts

A series of *N*-alkyl- and *N*-(fluoroalkyl)-substituted oxazolidinium- and morpholinium-based quaternary salts and their corresponding ionic liquids as well as ionic liquids obtained from quaternization of alkoxyethyl- and (fluoroalkoxy)ethyl-substituted morpholine compounds have been studied (Scheme 13).[36] All of the morpholinium bis(trifluoromethylsulfonyl)amide products are liquids at 25 °C and have interesting physical properties. They are stable thermally and have long liquid ranges. Overall, these ionic liquids with saturated core rings tend to exhibit greater thermal stabilities than those composed of unsaturated rings. This property plus the concomitant higher viscosities suggests higher temperature fluids applications.

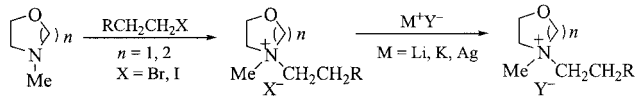

n	R	Y	T_m (T_g)[a]	T_d[b]	*d* [g/cm^3]	Viscosity[c]
1	F	NTf_2	(< –78)	330	1.63	287
1	F	PF_6	(–56)	191		
1	F	NO_3	(< –78)	245	1.49	
1	F	ClO_4	(< –78)	268	1.46	
1	F	OTf	(< –78)	283		
2	F	NTf_2	(–51)	342	1.69	
2	F	PF_6	80	196		
2	F	NO_3	58	289		
2	F	ClO_4	(< –78)	276	1.50	
2	F	OTf	68	293		
2	OCH_2CF_3	NTf_2	(–53)	412	1.69	
2	OCH_2CF_3	PF_6	72	268		
2	$OCH_2(CF_2)_3CHF_2$	NTf_2	(–53)	400	1.86	970
2	$OCH_2(CF_2)_3CHF_2$	PF_6	62	260		

[a] Melting point/phase transition temperature [°C]. [b] Thermal degradation [°C]. [c] cP.

Scheme 13.

9. Applications of Fluorocationic Ionic Salts

The fluorocationic ionic liquids reviewed here are still being investigated in different research fields. Fluorinated quaternary ammonium salts are useful as phase-transfer reaction catalysts, especially in basic media,[43] as surfactants,[42] or as antimicrobials.[19] Fluoroalkyl-substituted imidazolium salts have also been reported as surfactants in conventional ionic liquids.[21] Triazine-based polyfluorinated triquaternary imidazolium liquid salts were used as solvents in the rhodium-catalyzed hydroformylation of 1-octene which resulted in a significant increase in selectivity with preference for 1-nonanal.[27] Highly hydrophobic ionic liquids, such as some imidazolium, pyrazolium, triazolium, thiazolium, oxazolium, pyridinium, pyridazinium, pyrimidinium and pyrazinium salts, have applications in non-aqueous batteries, electrochemical capacitors, electroplating, catalysis and chemical separations.[16,22] A recent review (> 350 references), which essentially ignores ionic liquids with fluorine-containing cations, reports adequately on the syntheses of non-fluorine-containing ionic liquids and chemical and biochemical transformations in them.[45]

10. Conclusion

In conclusion, ionic liquids with fluorine-containing cations have many special and valuable characteristics in comparison with their non-fluorine analogues. It has been shown that by changing the fluoroalkyl chain or fluorine-containing moiety on the cation or the inorganic and organic anion, a wide range of tunable properties of these novel ionic liquids can be obtained. They are promising solvents for electrochemical, photovoltaic, surfactant and synthetic applications.

Acknowledgments

The authors gratefully acknowledge the support of AFOSR (F49620-03-1-0209), NSF (CHE0315275), and ONR (N00014-02-1-0600).

[1] T. Welton, *Chem. Rev.* **1999**, *99*, 2171–2083.
[2] P. Wasserscheid, W. Keim, *Angew. Chem. Int. Ed.* **2000**, *39*, 3772–3789.
[3] P. Wasserscheid, T. Welton, *Ionic Liquids in Synthesis*, Wiley-VCH, Weinheim, Germany, **2003**.
[4] R. D. Rogers, K. R. Seddon, *Ionic Liquids as Green Solvents: Progress and Prospects*, ACS Symposium Series 856, American Chemical Society, Washington, DC, **2003**.
[5] R. D. Rogers, K. R. Seddon, *Ionic Liquids: Industrial Applications to Green Chemistry*, ACS Symposium Series 818, American Chemical Society, Washington, DC, **2002**.
[6] R. A. Sheldon, *Chem. Commun.* **2001**, 2399–2407.
[7] N. Jain, A. Kumar, S. Chauhan, S. M. S. Chauhan, *Tetrahedron* **2005**, *61*, 1015–1060.
[8] P. Kubisa, *Prog. Polym. Sci.* **2004**, *29*, 3–12.
[9] J. H. Davis, Jr., *Chem. Lett.* **2004**, *33*(9), 1072–1077.
[10] J. H. Davis, Jr.; P. A. Fox, *Chem. Commun.* **2003**, 1209–1212.
[11] R. Hagiwara, K. Matsumoto, Y. Nakamori, T. Tsuda, Y. Ito, H. Matsumoto, K. Momota, *Proceedings-Electrochemical Society*, **2002**, *2002–19* (Molten Salts XIII),1007–1013.
[12] J. van den Broeke, F. Winter, B. J. Deelman, G. V. Koten, *Org. Lett.* **2002**, *4*, 3851–3854.
[13] O. D. Gupta, B. Twamley, J. M. Shreeve, *Tetrahedron Lett.* **2004**, *45*, 1733–1736.
[14] N. V. Ignat'ev, W. R. Pitner, Urs Welz-Biermann, M. Weiden, O. Sheppard, C. Hardacre, Abstracts of Papers, 228th ACS National Meeting, Philadelphia, PA, United States, August 22–26, **2004**, ORGN-546.
[15] a) Z. B. Zhou, M. Takeda, M. Ue, *J. Fluorine Chem.* **2004**, *125*, 471–476; b) Z. B. Zhou, H. Matsumoto, K. Tatsumi, *Chem. Eur. J.* **2005**, *11*, 752–766.

 © 2005 Wiley-VCH Verlag GmbH & Co. KGaA, Weinheim

[16] P. Bonhôte, A. P. Dias, N. Papageorgiou, K. Kalyanasundaram, M. Grätzel, *Inorg. Chem.* **1996**, *35*, 1168–1178.
[17] T. L. Merrigan, J. H. Davis, Jr., Abstracts of Papers, 220th ACS National Meeting, Washington, DC, United States, August 20–24, **2000**, CHED-176.
[18] O. D. Gupta, P. D. Armstrong, J. M. Shreeve, *Tetrahedron Lett.* **2003**, *44*, 9367–9370.
[19] H. Shao, L. Jiang, W. D. Meng, F. L. Qing, *J. Fluorine Chem.* **2003**, *124*, 89–91.
[20] J. H. Davis, Jr., K. J. Forrester, T. Merrigan, *Tetrahedron Lett.* **1998**, *39*, 8955–8958.
[21] T. Merrigan, E. D. Bates, S. C. Dorman, J. H. Davis, Jr., *Chem. Commun.* **2000**, 2051–2052.
[22] V. R. Koch, C. Nanjundiah, R. T. Carlin, U. S. Patent 5,827,602, **1998**. The very broad claims in this patent cover "hydrophobic ionic liquids" with pyridinium, pyridazinium, pyrimidinium, pyrazinium, imidazolium, pyrazolium, thiazolium, oxazolium, and triazolium cores where the rings are frequently substituted with fluorine and/or perfluoro- and polyfluoroalkyl or other fluorine-containing moieties.
[23] a) R. P. Singh, S. Manandhar, J. M. Shreeve, *Tetrahedron Lett.* **2002**, *43*, 9497–9499; b) R. P. Singh, S. Manandhar, J. M. Shreeve, *Synthesis* **2003**, *10*, 1579–1585.
[24] C. Ye, J. M. Shreeve, *J. Org. Chem.* **2004**, *69*, 6511–6513.
[25] K. I. Petko, T. M. Sokolenko, L. M. Yagupolskii, 14th European Symposium on Fluorine Chemistry, Poznan, Poland, July 11–16, **2004**, Absract A-O-15.
[26] C. M. Jin, J. M. Shreeve, *Inorg. Chem.* **2004**, *43*, 7532–7538.
[27] B. A. Omotowa, J. M. Shreeve, *Organometallics* **2004**, *23*, 783–791.
[28] a) Y. R. Mirzaei, B. Twamley, J. M. Shreeve, *J. Org. Chem.* **2002**, *67*, 9340–9345; b) Y. R. Mirzaei, J. M. Shreeve, *Synthesis* **2003**, *1*, 24–26.
[29] H. Xue, B. Twamley, J. M. Shreeve, *J. Org. Chem.* **2004**, *69*, 1397–1400.
[30] Y. R. Mirzaei, H. Xue, J. M. Shreeve, *Inorg. Chem.* **2004**, *43*, 361–367.
[31] J. Zhang, G. R. Martin, D. D. DesMarteau, *Chem. Commun.* **2003**, 2334–2335.
[32] a) R. P. Singh, J. M. Shreeve, *Chem. Commun.* **2003**, 1366–1367; b) R. P. Singh, J. M. Shreeve, *Inorg. Chem.* **2003**, *42*, 7416–7421.
[33] Y. Gao, J. M. Shreeve, *Synthesis* **2004**, *7*, 1072–1082.
[34] R. P. Singh, S. D. Meshri, D. T. Meshri, 14th European Symposium on Fluorine Chemistry, Poznan, Poland, **2004**, Abstract C-P-04.
[35] R. P. Singh, R. W. Winter, G. L. Gard, Y. Gao, J. M. Shreeve, *Inorg. Chem.* **2003**, *42*, 6142–6146.
[36] J. Kim, R. P. Singh, J. M. Shreeve, *Inorg. Chem.* **2004**, *43*, 2960–2966.
[37] a) R. M. Pomaville, C. F. Poole, *J. Chromatogr.* **1989**, *468*, 261–278; b) R. M. Pomaville, C. F. Poole, *J. Chromatogr.* **1990**, *468*, 749–759.
[38] R. Hagiwara, Y. Ito, *J. Fluorine Chem.* **2000**, *105*, 221–227.
[39] R. Hagiwara, Y. Ito, *Electrochemistry (Tokyo)* **2002**, *70*(2), 130–136.
[40] P. Walden, *Bull. Acad. Imper. Sci. (St. Petersburg)* **1914**, 1800.
[41] a) J. Sun, M. Forsyth, D. R. MacFarlane, *J. Phys. Chem. B* **1998**, *102*, 8858–8864; b) J. Sun, M. Forsyth, D. R. MacFarlane, *Molten Salt Forum* **1998**, *5/6*, 585–588; c) A. P. Abbott, G. Capper, D. L. Davies, H. L. Munro, R. K. Rasheed, V. Tambyrajah, *Chem. Commun.* **2001**, 2010–2011; d) H. Matsumoto, M. Yanagida, K. Tanimoto, M. Nomura, Y. Kitagawa, Y. Miyazaki, *Chem. Lett.* **2000**, 922–923; e) B. M. Quinn, A. Ding, R. Moulton, A. J. Bard, *Langmuir* **2002**, *18*, 1734–1742; f) Z. B. Zhou, H. Matsumoto, K. Tatsumi, *Chem. Lett.* **2004**, *33*(7), 886–887.
[42] H. Böhme, M. Hilp, *Chem. Ber.* **1970**, *103*, 104–111; H. Niederpruem, P. Voss, V. Beyl, *Ger. Offen.* DE 1966931, **1975**.
[43] W. M. Qiu, *U. S. Patent* 6,054,615, **2000**.
[44] a) Sagami Chemical Research Center, Japan, Jpn. Kokai Tokkyo Koho, *JP 58039664* A2, **1983**; b) L. Strekowski, A. S. Kiselyov, *Advances in Heterocycl. Chem.* **1995**, *62*, 1–17; c) T. Umemoto, K. Harasawa, G. Tomizawa, K. Kawada, K. Tomita, *J. Fluorine Chem.* **1991**, *53*, 369–377; d) C. Rocaboy, F. Hampel, J. A. Gladysz, *J. Org. Chem.* **2002**, *67*, 6863–6870; e) S. Alunni, V. Laureti, L. Ottavi, R. Ruzziconi, *J. Org. Chem.* **2003**, *68*, 718–725.
[45] N. Jain, A. Kumar, S. Chauhan, S. M. S. Chauhan, *Tetrahedron* **2005**, *61*, 1015–1060, and references cited therein.

Received February 12, 2005
Published Online: April 27, 2005

 © 2005 Wiley-VCH Verlag GmbH & Co. KGaA, Weinheim

Synthesis and Properties of the Geometrically Controlled Mixed-Valence Tetrahedral $Ru^{II}_2Ru^{III}_2L_6$ Cluster

Ping Cai,[a] Ming-xue Li,[a,b] Chun-ying Duan,*[a] Feng Lu,[a] and Qing-jin Meng[a]

Keywords: Ruthenium / Mixed-valent compounds / Tetrahedral cluster

The reaction of $Ru(DMSO)_4Cl_2$ and *N,N′*-bis[1-(pyridin-2-yl)-ethylidene]benzidine (L) in the presence of $NaClO_4$ afforded the tetranuclear ruthenium compound, $Ru_4L_6{\cdot}10ClO_4$, by self-assembly. Magnetic and electrochemical measurements clearly indicated the presence of both Ru^{II} and Ru^{III} moieties within the tetrahedral ruthenium cluster. The Robin-Day Class II mixed-valence behavior was supported by the UV/Vis-NIR spectra with the electronic coupling parameter V_{ab} of 200 cm^{-1}. It is demonstrated that the mixed-valence $Ru^{II}_2Ru^{III}_2L_6$ cation was stabilized by controlling the coordination geometries of the ruthenium ions between octahedral and trigonal prismatic to fit the supramolecular structure of the tetranuclear cluster.

(© Wiley-VCH Verlag GmbH & Co. KGaA, 69451 Weinheim, Germany, 2005)

Introduction

It is well established that the self-assembly processes may generate, in a spontaneous and direct manner,[1] well-defined architectures that are dependent on numerous factors such as the nature of the coordination sites, the structures of the bridging ligands, the geometric preferences of the metal ions, and the weak noncovalent interactions. The application of metal–ligand interactions has proved particularly fruitful, and a considerable variety of frequently predesigned molecular architectures have been assembled.[2] Among them, polygonal and polyhedral compounds formed by self-assembly of transition metals have many special functional properties such as luminescence, redox activity and magnetism in addition to their particular structural features.[3] As the simplest platonic polyhedrons, tetrahedral clusters formed by self-assembly of the transition metals have attracted more attention because of their intrinsic beauty and interesting host–guest chemistry, as well as the fact that they illustrate some basic construction principles necessary to assemble high-symmetry clusters.[4]

On the other hand, mixed-valence species have played a dominant role as simple model systems in the investigation of electron-transfer (ET) processes.[5] With respect to the artificial ET model systems consisting of two redox centers separated by saturated or unsaturated spacers, enormous effort and ingenuity have gone into studying the details of the factors influencing the metal–metal interaction, and a great deal of progress has been made.[6] However, relatively little is known about the process of electron transfer between a single donor and acceptor as influenced by their inclusion into larger supramolecular assemblies.[7] In an effort to study electron delocalization in more symmetric polynuclear systems, we have adopted a synthetic approach to assembling high-nuclear mixed-valent metallomacrocycles.[8]

In this contribution, we report a new tetrahedral Ru_4L_6 complex assembled from the rigid imine-based ligand L, *N,N′*-bis[1-(pyridin-2-yl)ethylidene]benzidine, (Scheme 1) with two binding sites separated by a biphenyl group.[9] It is expected that the rigidity of the designed ligand imposes a special geometry on the metal centers by fitting them into the tetrahedral geometry of the cluster (Scheme 1) and that

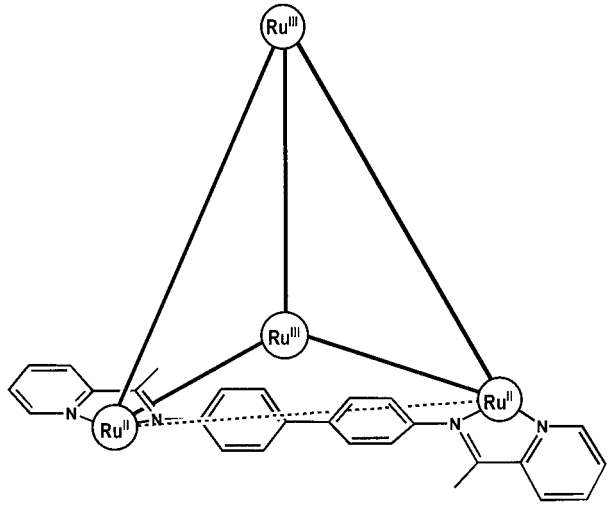

Scheme 1. The tetrahedral structure of complex **1** including a perchlorate anion within its cavity.

[a] Coordination Chemistry Institute, The State Key Laboratory of Coordination Chemistry,
Nanjing University, Nanjing 210093, P. R. China
E-mail: duancy@nju.edu.cn
[b] College of Pharmacy, Henan University,
Kaifeng 475004, P. R. China

 DOI: 10.1002/ejic.200500113 © 2005 Wiley-VCH Verlag GmbH & Co. KGaA, Weinheim

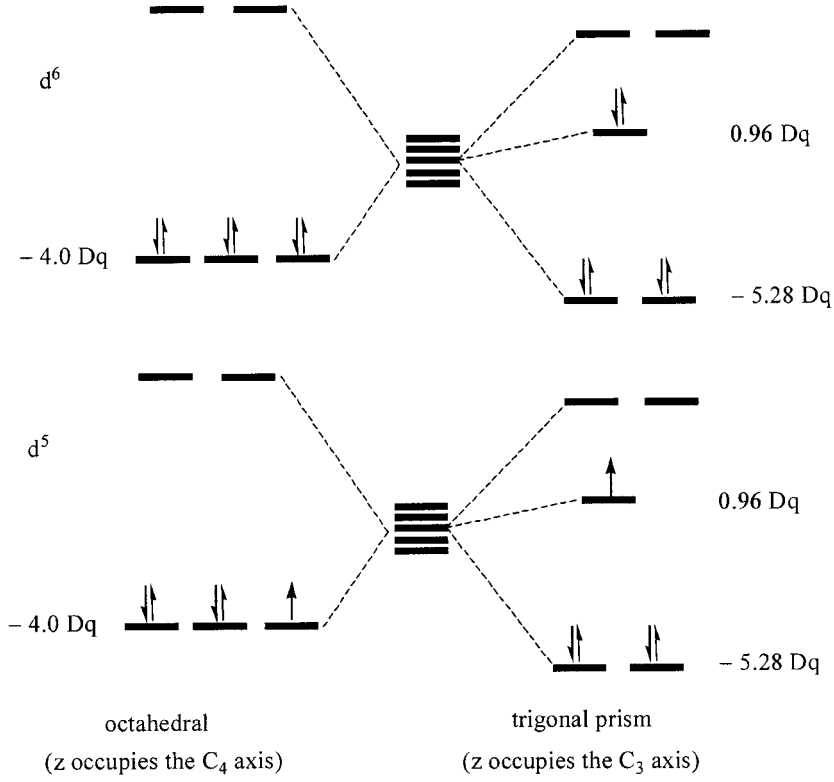

Scheme 2. The energy level of the *d* orbitals in the octahedral and trigonal prismatic coordination fields.

the resulting conformational restriction allows the modification of the redox potentials to form the mixed-valence species, similar to some metal proteins as well as many synthetic analogs.[8,10] In fact, tetranuclear copper and zinc cations $Cu_4L_6^{8+}$ and $Zn_4L_6^{8+}$ have been reported, in which the geometry at the metal center is between octahedral and trigonal prismatic,[9] but mixed-valence behavior was not exhibited, owing to the lack of suitable electronic structures. On the basis of the electronic structures of the d^5 and d^6 metal centers in the octahedral and trigonal prismatic coordination fields (Scheme 2),[11] it should be suggested that the Ru^{II} and Ru^{III} ions coexist in the clusters, because the Ru^{III} ion is more stable than the Ru^{II} ion in the trigonal prismatic coordination field, whereas the Ru^{II} ion has higher stability relative to the Ru^{III} ion in the octahedral coordination field.

Results and Discussion

Treatment of $Ru(DMSO)_4Cl_2$ with the imine-based ligand L in the presence of $NaClO_4$ afforded the tetranuclear ruthenium compound **1** in 44% yield by self-assembly. Elemental analysis and spectroscopic studies suggested the formula $Ru_4L_6{\cdot}10ClO_4$ for compound **1**. The ESI-MS spectrum exhibited an intense peak at *m*/*z* 316.4 corresponding to $[Ru_4L_6{\subset}ClO_4]^{9+}$, which was consistent with the formation of the tetrahedral species. The perchlorate anion was included within the cavity of the cluster like that of the copper and zinc analogs.[9] The tetrahedral ruthenium cation was the major species in the solution, even under the conditions of electrospraying. To determine the coexistence of Ru^{II} and Ru^{III} ions as well as their molar ratio, the temperature-dependent magnetic behavior of compound **1** was investigated (Figure 1). The effective magnetic moment (μ_{eff}) at room temperature of 2.58 μ_B was consistent with the

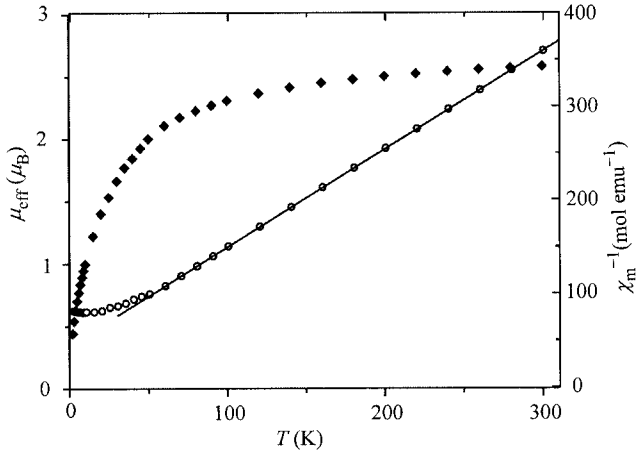

Figure 1. The temperature dependence of the molar magnetic susceptibility μ_{eff} and the reciprocal of the effective magnetic moment χ_m^{-1} for **1**. Open points represent the observed results, and the solid line represents the fitting curve based on the Curie–Weiss law.

 © 2005 Wiley-VCH Verlag GmbH & Co. KGaA, Weinheim

value expected for two independent Ru^{III} ions. The value of μ_{eff} decreased slightly with decreasing temperature (2.17 μ_B at 70 K). Below 70 K, the μ_{eff} decreased rapidly and reached 0.44 μ_B at 2 K. It seemed that the two Ru^{III} ions exhibited antiferromagnetic coupling, which was further suggested by a negative Weiss constant [θ = –35.5(2) K] using the data for temperatures greater than 70 K.

In the cyclic voltammograms (CV) of complex **1**, two metal-based reduction waves were observed in the region between 0.4 and 0.7 V and one metal-based broad wave at about 0.9 V. In order to obtain more accurate values of the reduction/oxidation peaks, the differential pulse voltammetry (DPV) technique was employed.[12] DPV measurements (Figure 2) of complex **1** exhibited three main peaks at 0.46, 0.60, and 0.89 V (vs. SCE). Considering the results of the CV experiments, it was helpful to confirm by DPV that the peaks at 0.6 and 0.46 V were reduction peaks, whereas the peak at 0.89 V corresponded to oxidation. Not surprisingly, the first redox potential is much smaller than that of the $[Ru(bpy)_3]^{2+}$ moiety and most of the mononuclear and polynuclear bpy–Ru complexes,[13] since the ruthenium centers in complex **1** are coordinated in a geometry between octahedral and trigonal prismatic, like those of the tetranuclear zinc and copper M_4L_6 complexes.[9] It seems that the peaks at 0.46 and 0.60 V of complex **1** were assigned to the single-electron reduction processes $[Ru^{II}_3Ru^{III}]/[Ru^{II}_4]$ and $[Ru^{II}_2Ru^{III}_2]/[Ru^{II}_3Ru^{III}]$, respectively. The broad peak at 0.89 V was due to the two overlapping single-electron oxidation processes $[Ru^{II}Ru^{III}_3]/[Ru^{II}_2Ru^{III}_2]$ and $[Ru^{III}_4]/[Ru^{II}Ru^{III}_3]$ (Gaussian deconvolution of such a band gives two peaks at 0.79 V and 0.91 V, respectively). It is postulated that such a conformation makes the Ru^{III} moiety exhibit higher stability relative to the common octahedrally coordinated geometry.

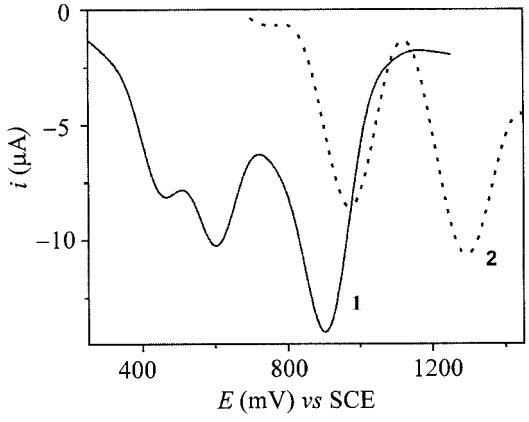

Figure 2. DPV of complexes **1** and **2** in CH_3CN solution (0.1 M NBu_4ClO_4; scan rate 20 mV/s).

To test such a hypothesis, the dinuclear ruthenium complex $[Ru_2(bpy)_4L](ClO_4)_4$ **2**, in which the ruthenium atom is octahedrally coordinated, was synthesized and characterized. DPV measurements for **2** exhibited two oxidation peaks at 0.93 and 1.30 V (vs. SCE) (Figure 2). The first oxidation potential of complex **2** was too high for the Ru^{III} species to be stable in the usual conditions. The ESI-MS spectrum of **2** exhibited one strong peak at *m*/*z* 304.5 corresponding to $[Ru_2(bpy)_4L]^{4+}$, which confirmed that there was no Ru^{III} ion in complex **2**. Clearly, the difference in the coordinative conformation of the metal centers in the two complexes was the important factor on controlling the redox potentials of the Ru^{III}/Ru^{II} couples.

The UV/Vis spectrum of complex **1** exhibits metal-to-ligand charge-transfer (MLCT) for Ru^{II} at 570 nm with a shoulder at about 520 nm, which is red-shifted relative to the same peak for complex **2** (460 nm) (Figure 3). Such results agree well with the related electrochemistry studies, which indicate that the coordination geometries of the ruthenium atoms in the two complexes are significantly different. In the near-IR region, complex **2** does not exhibit any obvious absorption band. However, complex **1** exhibits a LMCT absorption band corresponding to the Ru^{III} moiety at about 11000 cm^{-1} (ε = 5500 cm^2/mol) and a MMCT band at about 7500 cm^{-1} (ε = 2000 $cm^2 \cdot mol^{-1}$) with half-width of 4000 cm^{-1}, respectively. Intervalence charge-transfer bands in mixed-valence Ru^{III}/Ru^{II} complexes generally occurred in the near-IR region of the electronic spectra and had extinction coefficients of several hundred or a few thousand mol/$dm^3 \cdot$cm,[5,6] so both the position and the intensity of the 7500 cm^{-1} peak are consistent with an IT band. Assuming that the MV compound behaves as a Robin-Day Class II compound,[14] the IT absorption band of MV compounds can be modeled by classical Marcus-Hush theory[15] to obtain the electronic coupling parameter.[16] However, there are two Ru^{II} and two Ru^{III} in the complete tetrahedron. This means that the effective concentration in ion pairs Ru^{II}-Ru^{III} is actually four times the actual concentration (ε = 500 cm^2/mol). Considering that the Hush formula is valid for a simple binuclear system, i.e. a single Ru^{II}–Ru^{III} pair, the electronic coupling parameter of compound **1** can be given as 200 cm^{-1}. Significantly, the coordination environment of the metal centers in geometrically

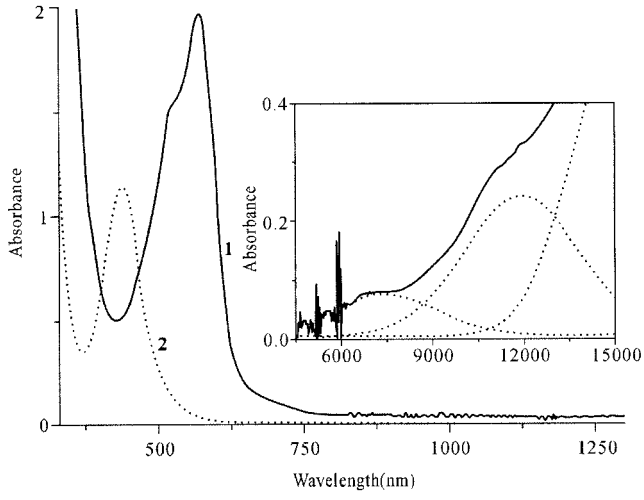

Figure 3. The UV/Vis-NIR spectra of the complexes **1** and **2** in acetonitrile (2.0×10^{-5} M). The insert showed the near-IR spectrum of the complex **1** in acetonitrile (5.0×10^{-5} M). The Gaussian fits (the dot lines) showed the LMCT band at 11000 cm^{-1} and the MMCT band at 7500 cm^{-1}, respectively.

 © 2005 Wiley-VCH Verlag GmbH & Co. KGaA, Weinheim

constrained tetrahedral architectures plays an important role in controlling the redox potential of the Ru^{III}/Ru^{II} couples and modifying metal–metal interactions.

In summary, this paper describes a modular approach to a mixed-valence compound implemented by controlling the coordination geometry of ruthenium ions to fit the architecture in the tetranuclear cluster. Mixed-valence compounds have played a crucial role not only in the exploration of electron-transfer theory but also for addressing contemporary issues in electron-transfer research, especially when the emphasis in this field has shifted away from simple dinuclear MV species and focused on multinuclear supramolecular species.[17,18]

Experimental Section

General: All chemicals were of reagent grade quality; they were obtained from commercial sources and used without further purification. $Ru(DMSO)_4Cl_2$,[19] the ligand[9] and *cis*-$Ru(bipy)_2Cl_2 \cdot 2H_2O$[20] were synthesized according the literature methods. The elemental analyses of C, H, and N were performed with a Perkin–Elmer 240C elemental analyzer at the Analysis Center of Nanjing University. Electrospray mass spectra were recorded with a LCQ system (Finnigan MAT, USA) using methanol as the mobile phase. IR spectra were recorded with a Nicolet 170SX FT-IR spectrophotometer with KBr pellets in the 4000–400 cm^{-1} region. Variable-temperature magnetic susceptibility data were obtained on polycrystalline samples at 2–300 K in a magnetic field of 10 Koe after zero-field cooling using a MagLab System 2000 magnetometer. Diamagnetic corrections were estimated from Pascal's constants. Differential pulse voltammetry (DPV) was done with an EG and GPAR model 273 instrument in a three-electrode cell with a pure Ar gas inlet and outlet. The working electrode and counter electrode were Pt spirals, and the reference electrode was a saturated calomel electrode (SCE). DPV experiments were performed with a scan rate of 20 mV/s. Uv/Vis-NIR spectra were obtained in acetonitrile solution at room temperature with a Shimadzu 3100 spectrophotometer.

Preparation of Complex 1: The ethanol solution of the mixture $Ru(DMSO)_4Cl_2$ (0.58 g, 1.2 mmol) and the ligand L (0.71 g, 1.8 mmol) was refluxed for 12 h. Dark blue precipitate $(Ru_4L_6)(ClO_4)_{10}$ was formed when the solution was added to a saturated ethanol solution of $NaClO_4$. Purification was performed by chromatography on a neutral alumina column (20 × 1.5 cm) with CH_3CN/MeOH, 1:1 (v/v) as eluent. The dark-blue fraction was collected and concentrated to a small volume. Upon addition of ethanol, complex **1** was obtained as a dark solid. Yield 0.48 g (44%). $Ru_4C_{156}H_{132}Cl_{10}N_{24}O_{40}$ (3738.2): calcd. C 50.1, H 3.6, N 9.0; found C 49.8, H 4.1, N 8.7. UV/Vis (logε) in methanol: 287 (4.8), 448 (4.3), 481 (4.6) nm. IR: 3444 (ν_{C-H}), 1634, 1539, 1504, 1463 ($\nu_{C=C}$, $\nu_{C=N}$, ν_{C-N}), 1092, (ν_{Cl-O}), 837, 770, 736 (δ_{C-H}) cm^{-1}.

Preparation of Complex 2: $[Ru(bpy)_2Cl_2] \cdot 2H_2O$ (0.15 g, 0.31 mmol) and L (0.06 g, 0.15 mmol) were refluxed in ethanol (50 mL) for 12 h under nitrogen. When this solution was added to a saturated ethanol solution of $NaClO_4$, $[Ru_2(bipy)_4L](ClO_4)_4$ separated out as a red precipitate, which was collected by filtration, washed with water and ethanol for several times, and dried in vacuo over P_4O_{10}. Yield: 0.15 g (68%). $C_{66}N_{12}H_{54}Ru_2Cl_4O_{16}$ (1614.1): calcd. C 49.1, H 3.4, N 10.4; found C 49.2, H 3.2, N 10.3. ^1H NMR ([D$_6$]DMSO): δ = 8.87 (t, 2 H, Py), 8.67 (d, 2 H, Py), 8.62 (d, 2 H, Py), 8.50 (t, 4 H, bipy), 8.22 (m, 8 H, bipy), 8.01 (d, 4 H, Ph), 7.96 (m, 4 H, bipy), 7.86 (d, 2 H, Py), 7.72 (d, 4 H, bipy), 7.68 (d, 4 H, Ph), 7.35 (t, 2 H, bipy), 6.90 (d, 2 H, bipy), 6.84 (d, 4 H, bipy), 6.69 (d, 4 H, bipy), 1.62 (s, 6 H, CH_3) ppm. UV/Vis (log ε) in CH_3CN: 289 (4.2), 347 (3.2), 466 (3.4) nm. IR: 3426 (ν_{C-H}), 1464, 1445, 1422 ($\nu_{C=C}$, $\nu_{C=N}$, ν_{C-N}), 858, 766, 624 (δ_{C-H}), 1092, (ν_{Cl-O}) cm^{-1}.

Caution! Although no problems were encountered in this work, perchlorates are potentially explosive and should be handled with care.

Acknowledgments

This work was supported by the National Natural Science Foundation of China and the Ministry of Education of China.

[1] a) J. L. Atwood, J. E. D. Davies, D. D. MacNicol, F. Vögtle, J.-M. Lehn, *Comprehensive Supramolecular Chemistry Pergamon*, Oxford, **1996**, vol. 9, pp. 165; b) G. F. Swiegers, T. J. Malefetse, *Chem. Rev.* **2000**, *100*, 3483–3537.

[2] a) M. Fujita, N. Fujita, K. Ogura, K. Yamaguchi, *Nature* **1999**, *400*, 52–55; b) B. Olenyuk, J. A. Whiteford, A. Fechtenkötter, P. J. Stang, *Nature* **1999**, *398*, 796–799; c) S. Leininger, B. Olenyuk, P. J. Stang, *Chem. Rev.* **2000**, *100*, 853–907 and references cited therein.

[3] a) K. D. Benkstein, J. T. Hupp, C. L. Stern, *Angew. Chem. Int. Ed.* **2000**, *39*, 2891–2893; b) E. Lengo, B. Milani, E. Zangrando, S. Geremia, E. Alessio, *Angew. Chem. Int. Ed.* **2000**, *39*, 1096–1099; c) C. S. Campos-Fernander, R. Clerac, K. R. Dunbar, *Angew. Chem. Int. Ed.* **1999**, *38*, 3477–3479; d) R. V. Slone, K. D. Benkstein, S. Belanger, J. T. Hupp, I. A. Guzei, A. L. Rheingold, *Coord. Chem. Rev.* **1998**, *171*, 221–243 and reference therein.

[4] a) A. J. Terpin, M. Ziegler, D. W. Johnson, K. N. Raymond, *Angew. Chem. Int. Ed.* **2001**, *40*, 157–160; b) R. W. Saalfrank, R. Burak, S. Reihs, N. Löw, F. Hampel, H. D. Stachel, J. Lentmaier, K. Peters, E. M. Peters, H. G. von Schnering, *Angew. Chem. Int. Ed. Engl.* **1995**, *34*, 993–995; c) J. S. Fleming, K. L. V. Mann, C. A. Carraz, E. Psillakis, J. J. C. Jeffery, A. McCleverty, M. D. Ward, *Angew. Chem. Int. Ed.* **1998**, *37*, 1279–1281; d) Y. Bai, D. Guo, C. Y. Duan, D. B. Dang, Q. J. Meng, *Chem. Commun.* **2004**, 186–187.

[5] a) B. S. Brunschwig, C. Cruetz, N. Sutin, *Chem. Soc. Rev.* **2002**, *31*, 168–184; b) J.-P. Launay, *Chem. Soc. Rev.* **2001**, *30*, 386–397; c) K. D. Demadis, C. M. Hartshorn, T. J. Meyer, *Chem. Rev.* **2001**, *101*, 2655–2685; d) W. Kaim, A. Klein, G. Marcus, *Acc. Chem. Res.* **2000**, *33*, 755–763.

[6] a) S. Fraysse, C. Coudret, J. P. Launay, *J. Am. Chem. Soc.* **2003**, *125*, 5880–5888; b) T. Morita, S. Kimura, *J. Am. Chem. Soc.* **2003**, *125*, 8732–8733; c) C. Lambert, G. Noll, *J. Am. Chem. Soc.* **1999**, *121*, 8434–8442; d) C. E. B. Evans, M. L. Naklicki, A. R. Rezvani, C. A. White, V. V. Kondratiev, R. J. Crutchley, *J. Am. Chem. Soc.* **1998**, *120*, 13096–13097.

[7] a) C. Lambert, G. Noll, J. Schelter, *Nature Materials* **2002**, *1*, 69–73; b) C. Lambert, G. Noll, *J. Chem. Soc., Perkin Trans. 2* **2002**, 2039–2043; c) M. Holzapfel, C. Lambert, C. Selinka, D. Stalke, *J. Chem. Soc., Perkin Trans. 2* **2002**, 1553–1561.

[8] a) D. Guo, C. Q. Qian, C. Y. Duan, K. L. Pang, Q. J. Meng, *Inorg. Chem.* **2003**, *42*, 2024–2030; b) G. Han, D. Guo, C. Y. Duan, H. Mo, Q. J. Meng, *New J. Chem.* **2002**, *26*, 1371–1377.

[9] C. He, L. Y. Wang, Z. M. Wang, Y. Liu, C. S. Liao, C. H. Yan, *J. Chem. Soc., Dalton Trans.* **2002**, 134–135.

[10] a) S. Zahn, J. W. Canary, *Science* **2000**, *288*, 1404–1407; b) R. H. Holm, P. Kennepohl, E. I. Solomon, *Chem. Rev.* **1996**, *96*, 2239–2314; c) D. W. Randall, S. D. George, B. Hedman, K. D. Hodgson, K. Fujisawa, E. I. Solomon, *J. Am. Chem. Soc.* **2000**, *122*, 11620–11631; d) P. L. Holland, W. B. Tolman, *J. Am. Chem. Soc.* **2000**, *122*, 6331–6332.

[11] H. L. Chen, B. Y. Yu, *Theoretical Inorganic Chemistry* **1989**, Chapter 2.

 © 2005 Wiley-VCH Verlag GmbH & Co. KGaA, Weinheim

[12] a) B. R. Serr, K. A. Andersen, C. M. Elliott, O. P. Anderson, *Inorg. Chem.* **1988**, *27*, 4499–4504; b) D. E. Richardson, H. Taube, *Inorg. Chem.* **1981**, *20*, 1278–1285.
[13] For example: a) F. P. Dwyer, E. C. Gyarafas, *J. Am. Chem. Soc.* **1954**, *76*, 6320–6321; b) S. Ernst, V. Kasack, W. Kaim, *Inorg. Chem.* **1988**, *27*, 1146–1148; c) A. Guerzo, S. Leroy, F. R. Fages, H. Schmell, *Inorg. Chem.* **2002**, *41*, 359–366; d) D. M. Dalessandro, L. S. Kelso, F. R. Keene, *Inorg. Chem.* **2001**, *40*, 6841–6844.
[14] M. B. Robin, P. Day, *Adv. Inorg. Chem. Radiochem.* **1967**, *10*, 247–249.
[15] a) N. S. Hush, *Coord. Chem. Rev.* **1985**, *64*, 135–158; b) R. A. Marcus, *J. Chem. Phys.* **1956**, *24*, 966–978; c) R. A. Marcus, N. Sutin, *Inorg. Chem.* **1975**, *14*, 213–216; d) N. S. Hush, *Prog. Inorg. Chem.* **1967**, *8*, 391–392.
[16] Calculated from the Hush formula: $V_{ab} = 0.0205 \times [(\varepsilon_{max}\tilde{\nu}_{max}\Delta\nu_{1/2})^{1/2}]/R$, where ε_{max}, $\tilde{\nu}_{max}$, and $\Delta\nu_{1/2}$ are the actual molar extinction coefficient, the absorption maximum in wavenumbers, and the bandwidth at half-maximum height, respectively; and R is the metal–metal separation, which is taken as 13 Å from the crystal structure of the tetranuclear zinc complex in ref.[9]
[17] a) R. A. Marcus, *Angew. Chem.* **1993**, *105*, 1161–1163; b) C. Creutz, M. D. Newton, N. Sutin, *J. Photochem. Photobiol. A* **1994**, *82*, 47–49; c) R. J. Cave, M. D. Newton, *Chem. Phys. Lett.* **1996**, *249*, 15–19; d) D. V. Matyushov, B. M. Ladanyi, *J. Phys. Chem. A* **1998**, *102*, 5027–5039; e) M. D. Newton, *Adv. Chem. Phys.* **1999**, *106*, 303–375.
[18] a) C. Lambert, G. Nöll, F. Hampel, *J. Phys. Chem. A* **2001**, *105*, 7751–7758; b) E. Grunwald, *J. Am. Chem. Soc.* **1985**, *107*, 125–133; c) J. P. Guthrie, *J. Am. Chem. Soc.* **1996**, *118*, 12878–12885.
[19] E. Alessio, B. Milani, M. Bolle, *Inorg. Chem.* **1995**, *34*, 4722–4734.
[20] W. J. Stratton, D. H. Busch, *J. Am. Chem. Soc.* **1958**, *80*, 3191–3195.

Received: February 4, 2005
Published Online: May 27, 2005

 © 2005 Wiley-VCH Verlag GmbH & Co. KGaA, Weinheim

A Binuclear Copper(II) Complex Containing the Pyrazine-2,5-dicarboxylate Ligand: Study of the Magnetic Exchange through the Pyrazine Bridge

Garikoitz Beobide,[a] Oscar Castillo,*[a] Urko García-Couceiro,[a] Juan P. García-Terán,[a] Antonio Luque,[a] Martín Martínez-Ripoll,[b] and Pascual Román[a]

Keywords: Copper / Density functional calculations / Magnetic properties / N ligands / Pyrazine

The compound $[Cu_2(\mu\text{-pzdc})(phen)_4](NO_3)_2\cdot 10H_2O$ (**1**; pzdc = pyrazine-2,5-dicarboxylato; phen = 1,10-phenanthroline) has been structurally and magnetically characterised. Theoretical calculations have allowed us to establish a plausible magneto-structural correlation for pyrazine-bridged complexes.

(© Wiley-VCH Verlag GmbH & Co. KGaA, 69451 Weinheim, Germany, 2005)

Introduction

A lot of work has been devoted to the study of the magnetic interactions between two paramagnetic centres bridged by an aromatic ring.[1] The study of the spin delocalisation and polarisation effects is helpful in order to understand the nature of these magnetic interactions. The spin-polarisation mechanism itself provides a key tool for predicting the kind of magnetic interactions in high-spin organic molecules, and therefore for designing molecule-based magnets.[2] Nevertheless, the application of this strategy to transition metal complexes, which provide a more stable spin source than those based on organic radicals, is more tricky, and the spin-delocalisation effect must also be taken into account.[3] Metal complexes containing pyrazine-2,5-dicarboxylate (pzdc) ligands have seldom been investigated.[4] Until now, as far as we aware, a three-dimensional Mn^{II} complex[5] and a binuclear V^{V} complex[6] are the only structurally characterised examples with this ligand.

We report here the synthesis,[7] crystal structure[8] and magnetic properties of a complex with formula $[Cu_2(\mu\text{-pzdc})(phen)_4](NO_3)_2\cdot 10H_2O$ (**1**). In addition, a plausible magneto-structural correlation for pyrazine-bridged complexes is analysed by DFT methods.

Results and Discussion

The structure of compound **1** consists of water molecules of crystallisation, nitrate counterions and centrosymmetric $[Cu_2(\mu\text{-pzdc})(phen)_4]^{2+}$ binuclear units (Figure 1) in which a bidentate pzdc ligand bridges two copper atoms with an M···M distance of 7.112 Å. The distorted octahedral environment around each copper atom is completed by four nitrogen atoms of two phen ligands (phen1 and phen2). We can distinguish two long bonds in the *trans* position formed by an oxygen of the carboxylate group and a nitrogen of the phen2 ligand [Cu1–O41 2.271(3) Å, Cu1–N38 2.210(3) Å]. The four shortest bonds are nearly coplanar and are to two N atoms from phen1 [Cu1–N11 2.115(3) Å, Cu1–N18 2.011(2) Å], another one from phen2 [Cu1–N31 2.003(2) Å] and a one from the bridging ligand [Cu1–N1 2.184(2) Å]. This equatorial plane is almost perpendicular to the mean plane of the pzdc ligand [dihedral angle 81.7(2)°]. Similar distorted octahedral environments have been reported for other phen or 2,2′-bipyridine copper complexes.[9] The deviation of the metal atom from the pyrazine ring is quite significant [0.209(1) Å], probably due to the steric hindrance of the terminal ligands.

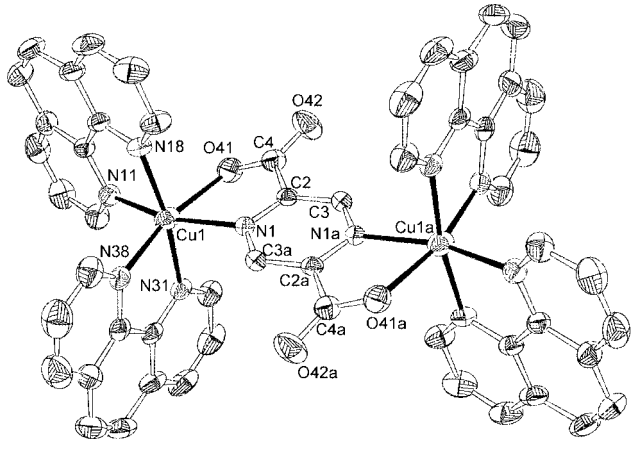

Figure 1. ORTEP view of the dimeric entity in compound **1**.

[a] Departamento de Química Inorgánica, Universidad del País Vasco,
Apartado 644, 48080, Bilbao, Spain
Fax: +34-946-012-000
E-mail: qipcacao@lg.ehu.es
[b] Grupo de Cristalografía Molecular y Biología Estructural, Instituto de Química-Física Rocasolano, CSIC,
Serrano 119, 28006 Madrid, Spain

Supporting information for this article is available on the WWW under http://www.eurjic.org or from the author.

 DOI: 10.1002/ejic.200500119

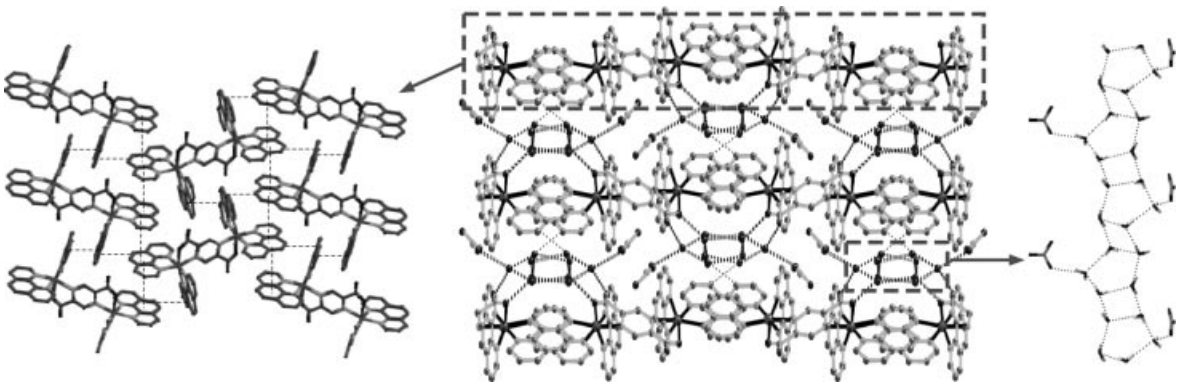

Figure 2. Crystal structure viewed along the [001] direction showing π–π interactions (dashed lines) within the cationic layers and hydrogen-bonded (dotted lines) chains of water molecules.

In the crystal structure (Figure 2), the cationic complexes are held together by means of face-to-face and edge-to-face π–π interactions between the aromatic phen ligands to form corrugated layers parallel to the *bc* plane. The water molecules are inserted in the interlayer space and are linked themselves by O_w–H···O_w hydrogen bonds to form zig-zag strips comprised of an alternating sequence of fused water pentamers and tetramers running along the [001] direction. The nitrate anions are attached to the edges of the pentagonal water ring by a hydrogen bond. There are no significant interactions between adjacent strips, therefore the water strips act as bridges between the cationic layers by means of a highly complex network of non-covalent interactions. Compound **1** shows a different crystal packing to those described in a recent study[10] of the most common packings of complexes based on phen ligands, and bears a very close resemblance to the compound [{Cu(ox)(phen)$_2$}·5H_2O].[11] Both compounds show a similar π–π interaction scheme within the corrugated complex layers. Due to this conformation, there is a similarity between the hydrophilic holes in the interlayer space, which leads to a similar arrangement of the solvated water molecules.

Variable-temperature magnetic-susceptibility measurements (2–200 K) show the presence of weak antiferromagnetic coupling, with values of $J = -5.7$ cm^{-1} and $g = 2.14$ obtained from the Bleaney–Bowers expression ($H = -JS_A \cdot S_B$) for a binuclear copper(II) complex. This antiferromagnetic coupling is mainly attributed to the magnetic interaction through the pyrazine ring. The contribution of the carboxylate groups can be considered negligible due to the long magnetic pathway involving these groups.

DFT methods have shown to give good estimates of the magnetic interactions.[12] A detailed description of the computational strategy adopted in this work is given elsewhere.[13] For the evaluation of the coupling constant, two separate DFT calculations were carried out, from which the energy of the highest spin (E_{HS}) and broken-symmetry singlet configuration (E_{BS}) are obtained. The magnetic coupling constant results from the energy difference between the triplet and singlet states ($E_{HS} - E_{BS} = -J$). The hybrid B3LYP method, as implemented in Gaussian 03, was used in all calculations.[14] The exact Hartree–Fock-type exchange was mixed with Becke's expression for the exchange functional and the Lang–Yong–Parr correlation functional was used. A basis set of double-ζ quality (triple-ζ for the transition metal atoms), proposed by Schäfer et al.,[15] was employed throughout.

The calculations were performed for an isolated $[Cu_2(phen)_4(\mu\text{-pzdc})]^{2+}$ dimer with an experimental geometry of $C\bar{1}$ symmetry, leading to a value of the magnetic interaction ($J_{calc} = -8.4$ cm^{-1}) similar to the experimental one ($J_{exp} = -5.7$ cm^{-1}). Figure 3 illustrates the spin densities for the ground state ($S = 0$) of the title compound. The spin-density distribution around the metal centre resembles a $d_{x^2-y^2}$ orbital with a significant contribution of d_{z^2}. The coordinated Cu1 and pzdc atoms (N1 and O41) carry spin densities with the same sign due to the spin-delocalisation effect. This situation is in sharp contrast to that of organic high-spin materials bridged by *m*-phenylenes,[2] in which the spin density alternates throughout the π-conjugated hydrocarbon network, as predicted by the spin-polarisation mechanism.

Most of the previously reported Cu^{II} complexes with pyz-type (pyz = pyrazine) bridging ligands coordinated at

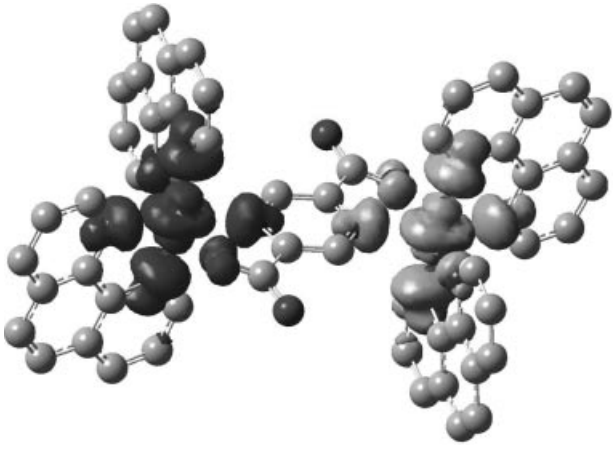

Figure 3. Calculated spin-density distribution for the ground state ($S = 0$) of $[Cu_2(phen)_4(\mu\text{-pzdc})]^{2+}$ with a surface threshold level of 0.001. Hydrogen atoms have been omitted for clarity. Spin densities: Cu1 0.667, N31 0.105, N11 0.057, N18 0.099, O41 0.025, N1 0.043, N38 0.020, C2 –0.006, C3a –0.008.

 © 2005 Wiley-VCH Verlag GmbH & Co. KGaA, Weinheim

the equatorial sites show very weak antiferromagnetic interactions ($|J| < 4$ cm^{-1}).[16] However, there are a handful of pyz-bridged Cu^{II} complexes, specially with the tppz ligand [1,3,5,6-tetra(2-pyridyl)pyrazine], that present unusually large antiferromagnetic interactions,[17] with J values ranging from –35 to –61 cm^{-1}. A common structural feature of the latter compounds is the large displacement of the metal from the mean plane of the pyrazine bridge (0.34–0.56 Å) and/or the distortion of the pyrazine ring (dihedral angles between the two C–N–C planes of the pyz ring range between 8.8 and 11.0°). Due to the structural features of the title compound, we have restricted the present work to the analysis of the former structural parameter, which allows a σ-overlap between the metal $d_{x^2-y^2}$ orbital and the π-orbitals of the pyrazine ring; in an ideal planar system this d_σ–p_π overlap is not allowed (part a in Scheme 1). Taking into account these facts, the observed values of J could be attributable to an important contribution of the π-orbitals of the pyz-type ligand through a d_σ–p_π interaction, which is allowed by the structural distortion (Scheme 1, part b). The title compound represents an intermediate situation between the negligible values commonly observed and the cited unusually high values.

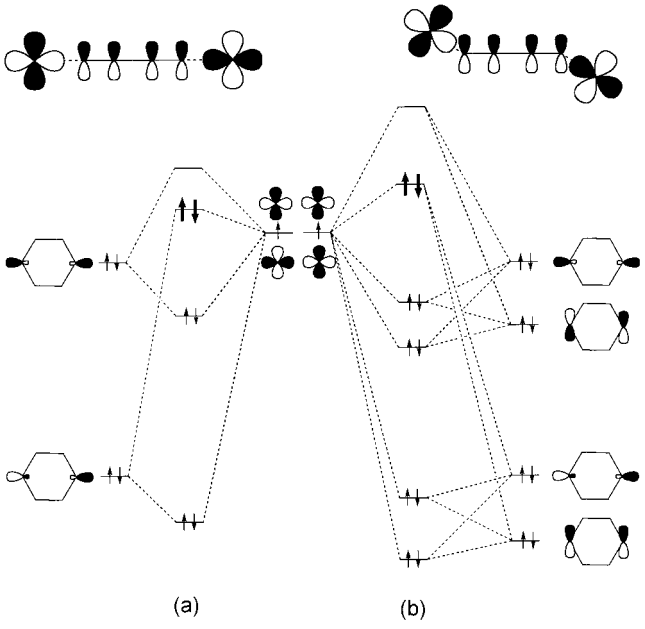

Scheme 1. Orbital interaction diagram showing the interaction between the two Cu $d_{x^2-y^2}$ orbitals and a) the σ-symmetry orbitals and b) the σ- and π-orbitals.

In order to determine the contribution of the π-orbitals of the bridging ligand to the magnetic behaviour, we carried out DFT calculations on a pyrazine-bridged dimeric Cu^{II} model for different values of the Cu–N_{pyz}···N_{pyz} angle (see details in Figure 4). The values obtained for the magnetic coupling constant indicate an exponential increase of the J value with a decrease of the Cu–N_{pyz}···N_{pyz} angle. The J value is –6.8 cm^{-1} at 180°, but reaches values as high as –144 cm^{-1} for an angle of 130°.

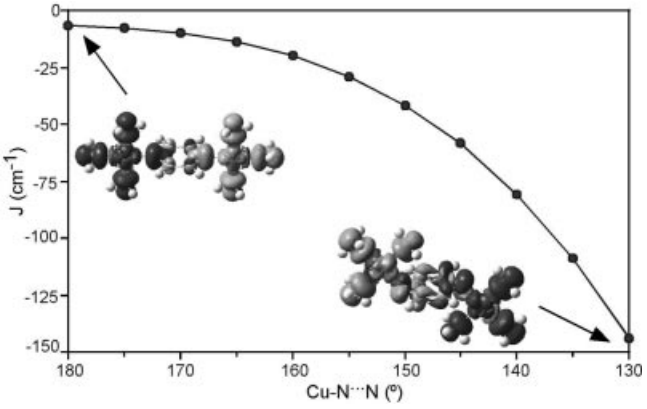

Figure 4. Calculated coupling constants for $[Cu_2(NH_3)_6(\mu\text{-pyz})]^{4+}$ as a function of the Cu–N_{pyz}···N_{pyz} angle. The inset graphics represent the spin-density distribution for the two extreme angles. Calculations have been performed in an idealised C_{2h} symmetry using the following bond lengths [Å] and angles [°]: Cu–N 2.00, C–N: 1.35, C–C 1.42, C–H 1.00, N–H 1.00, N–Cu–N 90.0, N–Cu–N–C 90.0, Cu–N_{pyz}···N_{pyz} 130.0–180.0.

As depicted in Scheme 1 (part a), when the Cu–N_{pyz}···N_{pyz} angle is 180°, the two Cu $d_{x^2-y^2}$ orbitals overlap with the two symmetry-adapted σ-orbitals of the pyrazine. The energy of these σ-orbitals is not equal, leading to a substantial energy difference between the two singly occupied orbitals of the dimer and, consequently, an antiferromagnetic coupling through the pyrazine is observed. If the Cu–N_{pyz}···N_{pyz} angle is not linear the overlap of the two Cu $d_{x^2-y^2}$ orbitals involves the symmetry-adapted σ- and π-orbitals of the bridge, and the energy difference between the two SOMOs increases, leading to an increase of the antiferromagnetic interaction (part b in Scheme 1). No simple relation between the spin density at the pyrazine bridge and the magnetic coupling constant has been found.

The experimental J value (–5.7 cm^{-1}) is comparable to that obtained for the model compound with a similar Cu–N_{pyz}···N_{pyz} angle (–9.8 cm^{-1}) taking into account the small singlet–triplet gap. In agreement with the trend shown in Figure 4, the pyrazine-bridged complex with the highest J value[16a] (–61.1 cm^{-1}) shows the greatest deviation of the metal from the mean plane of the pyrazine. However, the values of other tppz-based complexes cannot be fitted easily, due to the high distortion that the pyrazine ring presents.

Other structural factors, such as the Cu–N_{pyz} distance, the dihedral angle between the Cu^{II} equatorial plane and the pyrazine plane, the influence of the axial ligand, etc. seem to have a less decisive role on the magnetic properties (see Supporting Information).

Acknowledgments

This work was supported by the Spanish Ministerio de Ciencia y Tecnología (MAT2002–03166) and the Universidad del País Vasco/Euskal Herriko Unibertsitatea (9/UPV 00169.310-15329-2003). G. B. thanks to the Eusko Jaurlaritza/Gobierno Vasco for a doctoral fellowship.

 © 2005 Wiley-VCH Verlag GmbH & Co. KGaA, Weinheim

[1] a) A. M. W. Cargill Thompson, D. Gatteschi, J. A. McCleverty, J. A. Navas, E. Rentschler, M. D. Ward, *Inorg. Chem.* **1996**, *35*, 2701–2703; b) O. Kahn, *Molecular Magnetism*, VCH Publishers, Inc., New York, **1993**.
[2] a) S. K. Silverman, D. A. Dougherty, *J. Phys. Chem.* **1993**, *97*, 13273–13283; b) H. Iwamura, *Adv. Phys. Org. Chem.* **1990**, *26*, 179–253; c) A. Rajca, *Chem. Rev.* **1994**, *94*, 871–893.
[3] J. Cano, E. Ruiz, S. Álvarez, M. Verdaguer, *Comments Inorg. Chem.* **1998**, *20*, 27–56.
[4] a) L. R. Harlow, S. H. Simonsen, *Acta Crystallogr. Sect. B* **1974**, *30*, 1370–1372; b) H. Ptasiewicz-Bak, J. Leciejewicz, *J. Coord. Chem.* **1998**, *44*, 299–309; c) H. Ptasiewicz-Bak, J. Leciejewicz, *J. Coord. Chem.* **1998**, *44*, 237–246.
[5] G. Beobide, O. Castillo, A. Luque, U. García-Couceiro, J. P. García-Terán, P. Román, *Inorg. Chem. Commun.* **2003**, *6*, 1224–1227.
[6] G. Süss-Fink, L. González Cuervo, B. Therrien, H. Stoeckli-Evans, G. B. Shul′pin, *Inorg. Chim. Acta* **2004**, *357*, 475–484.
[7] Compound **1** was prepared in aqueous solution (30 mL) from the stoichiometric reaction between H_2pzdc·$2H_2O$, $Cu(NO_3)_2$·$3H_2O$ and phen. The reaction yielded a blue, polycrystalline precipitate of compound **1**. After filtering off the precipitate the resulting solution was allowed to stand at room temperature. Single crystal growth was observed after six days. Yield: 65%. $C_{54}H_{54}Cu_2N_{12}O_{20}$: calcd. C 48.97, H 3.99, Cu 9.51, N 12.69; found C 49.20, H 4.13, Cu 9.64, N 12.75.
[8] Crystal data for **1**: Monoclinic, space group $P2_1/c$, a = 10.421(1), b = 26.566(3), c = 10.718(2) Å, β = 108.24(1)°, U = 2818.1(7) Å^3, Z = 2, μ(Cu-K_α) = 1.5418 mm^{-1}. Final R [4330 with $I \geq 2\sigma(I)$] = 0.0496 and wR_2 (4687 unique reflections) = 0.1337. CCDC-254764 contains the supplementary crystallographic data for this paper. These data can be obtained free of charge from The Cambridge Crystallographic Data Centre via www.ccdc.cam.ac.uk/data_request/cif.
[9] a) D. Choquesillo-Lazarte, M. J. Sánchez-Moreno, E. Bugella-Altamirano, M. J. Moyano-Gallego, J. D. Martín-Ramos, J. M. González-Pérez, R. Carballo, J. Niclos-Gutiérrez, *Z. Anorg. Allg. Chem.* **2003**, *629*, 291–296; b) H. J. He, L. G. Zhu, *Chin. J. Inorg. Chem.* **2003**, *19*, 317–320; c) O. Costisor, M. Brezeanu, Y. Journaux, K. Mereiter, P. Weinberger, W. Linert, *Eur. J. Inorg. Chem.* **2001**, 2061–2066.
[10] V. Russel, M. Scudder, I. Dance, *J. Chem. Soc., Dalton Trans.* **2001**, 789–799.
[11] O. Castillo, A. Luque, P. Román, *J. Mol. Struct.* **2001**, *559–601*, 181–188.
[12] E. Ruiz, J. Cano, S. Álvarez, P. Alemany, *J. Comput. Chem.* **1999**, *20*, 1391–1400.
[13] a) E. Ruiz, P. Alemany, S. Álvarez, J. Cano, *J. Am. Chem. Soc.* **1997**, *119*, 1297–1303; b) E. Ruiz, A. Rodríguez-Fortea, J. Cano, S. Álvarez, P. Alemany, *J. Comput. Chem.* **2003**, *24*, 982–989.
[14] M. J. Frisch, G. W. Trucks, H. B. Schlegel, G. E. Scuseria, M. A. Robb, J. R. Cheeseman, J. A. Montgomery, Jr., T. Vreven, K. N. Kudin, J. C. Burant, J. M. Millam, S. S. Iyengar, J. Tomasi, V. Barone, B. Mennucci, M. Cossi, G. Scalmani, N. Rega, G. A. Petersson, H. Nakatsuji, M. Hada, M. Ehara, K. Toyota, R. Fukuda, J. Hasegawa, M. Ishida, T. Nakajima, Y. Honda, O. Kitao, H. Nakai, M. Klene, X. Li, J. E. Knox, H. P. Hratchian, J. B. Cross, C. Adamo, J. Jaramillo, R. Gomperts, R. E. Stratmann, O. Yazyev, A. J. Austin, R. Cammi, C. Pomelli, J. W. Ochterski, P. Y. Ayala, K. Morokuma, G. A. Voth, P. Salvador, J. J. Dannenberg, V. G. Zakrzewski, S. Dapprich, A. D. Daniels, M. C. Strain, O. Farkas, D. K. Malick, A. D. Rabuck, K. Raghavachari, J. B. Foresman, J. V. Ortiz, Q. Cui, A. G. Baboul, S. Clifford, J. Cioslowski, B. B. Stefanov, G. Liu, A. Liashenko, P. Piskorz, I. Komaromi, R. L. Martin, D. J. Fox, T. Keith, M. A. Al-Laham, C. Y. Peng, A. Nanayakkara, M. Challacombe, P. M. W. Gill, B. Johnson, W. Chen, M. W. Wong, C. Gonzalez, J. A. Pople, Gaussian 03, Revision B.04, Gaussian, Inc., Pittsburgh PA, **2003**.
[15] a) A. Schäfer, H. Horn, R. Ahlrichs, *J. Chem. Phys.* **1992**, *97*, 2571–2577; b) A. Schaefer, C. Huber, R. Ahlrichs, *J. Chem. Phys.* **1994**, *100*, 5829–5835.
[16] a) H. Grove, J. Sletten, M. Julve, F. Lloret, *J. Chem. Soc., Dalton Trans.* **2000**, 515–522; b) T. Okubo, M. Kondo, S. Kitawaga, *Synth. Met.* **1997**, *85*, 1661–1662; c) J. Suárez-Varela, E. Colacio, A. Romerosa, J. C. Ávila-Rosón, M. A. Hidalgo, J. Romero, *Inorg. Chim. Acta* **1994**, *217*, 39–44.
[17] a) M. Graf, H. Stoeckli-Evans, A. Escuer, R. Vicente, *Inorg. Chim. Acta* **1997**, *257*, 89–97; b) E. Burkholder, V. Golub, C. J. O'Connor, J. Zubieta, *Inorg. Chem.* **2003**, *42*, 6729–6740; c) J. Carranza, J. Sletten, C. Brennan, F. Lloret, J. Cano, M. Julve, *Dalton Trans.* **2004**, 3997–4005.

Received: February 7, 2005
Published Online: May 24, 2005

 © 2005 Wiley-VCH Verlag GmbH & Co. KGaA, Weinheim

Mechanistic Insights into the Oxidation of Veratryl Alcohol with Co(salen) and Oxygen in Aqueous Media: An in-situ Spectroscopic Study

Kaisa Kervinen,[a,b] Heikki Korpi,[a] J. Gerbrand Mesu,[b] Fouad Soulimani,[b] Timo Repo,*[a] Bernhard Rieger,[c] Markku Leskelä,[a] and Bert M. Weckhuysen*[b]

Keywords: Cobalt complexes / Schiff bases / Homogeneous catalysis / IR spectroscopy / Raman spectroscopy / UV/Vis spectroscopy

Many transition-metal complexes can perform catalytic oxidations, but their corresponding reaction pathways are still not clear. In this study, the mechanism of Co(salen)-catalyzed [salen = *N*,*N*′-bis(salicylidene)ethylenediamine] oxidization of veratryl alcohol (3,4-dimethoxybenzyl alcohol) by dioxygen in alkaline aqueous solution was elucidated with in-situ ATR-IR, Raman and UV/Vis spectroscopy. The mechanism of this reaction seems to start by formation of a bis-μ-hydroxo[(Co(salen)]$_2$ species, which explains the dramatic effect of pH on the reaction rate. Substrate coordination to this species leads to formation of a cobalt-bound veratryl alkoxo intermediate, to which oxygen molecule can bind. Formation of a μ-peroxo bridge between two such Co(salen) substrate units is observed in the UV/Vis spectra. Transfer of a hydrogen atom from the substrate to the peroxo bridge results in detachment of the product aldehyde and regeneration of the initial bis-μ-hydroxo[(Co(salen)]$_2$ species. In the overall cycle two substrate molecules are oxidized to aldehyde and molecular oxygen is reduced to water. The rate-limiting step is the detachment of the product molecule, which is aided by the methoxy substituents in the aromatic ring of the benzylic alcohol.
(© Wiley-VCH Verlag GmbH & Co. KGaA, 69451 Weinheim, Germany, 2005)

Introduction

Activation of molecular oxygen by transition-metal complexes for selective oxidations in water is an environmentally benign and economical alternative for many present day industrial processes.[1–3] Nevertheless, organic solvents are more commonly used, as stability and solubility of transition-metal complexes is often a problem in aqueous solutions.[2–7] Despite the importance, the mechanisms of transition-metal complex-catalyzed oxidation reactions are still not fully understood.[4] For example, Co(salen) [salen = *N*,*N*′-bis(salicylidene)ethylenediamine] has long been known to reversibly bind and activate dioxygen and its oxygen adducts are well characterized,[8–10] but it is not clear how these catalytic reactions proceed.[4,11] It has been suggested that the mononuclear superoxo species is usually responsible for catalyst activity in the oxidation of phenolic substrates, but no direct evidence is yet available.[3,4,12–14] There are less examples on the oxidation of benzylic substrates. It has been noted that the reaction mechanisms depend greatly on the nature of the substrate and its substituents.[3,15]

In this study, Co(salen) is used as a catalyst to oxidize a lignin model compound, veratryl alcohol (3,4-dimethoxybenzyl alcohol), to an aldehyde in alkaline water solution. Selective oxidation of lignin would be attractive for catalytic pulp bleaching[16–18] and for the search of renewable raw materials.[3,12] This reaction proceeds in the presence of molecular oxygen to reach TOF = 10–15 at optimum conditions (TOF = turnover frequency, moles of product per mol of catalyst per hour).[16] The effect of reaction conditions observed previously for this system suggest that a mononuclear superoxo complex is not responsible for catalytic activity.[16–17] However, direct proof for the intermediates involved in the catalytic cycle is lacking. Temperature and pH have a dramatic effect on the catalytic activity of this system, and thus it is vital that the mechanism is studied under real experimental conditions. Therefore, the Co(salen)-catalyzed reaction (Scheme 1) has been studied with a combination of in-situ ATR-IR, Raman and UV/Vis spectroscopy in aqueous solution at pH 12 and 80 °C.

The use of complementary techniques is a powerful way to monitor a catalytic reaction.[20–21] Different species show more intense absorptions in different regions of the electromagnetic spectrum. Electronic transitions usually give rise to absorption or emission in the ultraviolet or visible regions, whereas molecular vibrations give rise to absorption bands throughout most of the infrared region. Symmetrical

[a] Laboratory of Inorganic Chemistry, Department of Chemistry, University of Helsinki,
P. O. Box 55, 00014 Helsinki, Finland
E-mail: timo.repo@helsinki.fi
[b] Department of Inorganic Chemistry and Catalysis, Debye Institute, University of Utrecht,
Sorbonnelaan 16, 3584 CA Utrecht, The Netherlands
E-mail: b.m.weckhuysen@chem.uu.nl
[c] Department of Materials and Catalysis, University of Ulm,
Albert-Einstein-Allee 11, 89069 Ulm, Germany

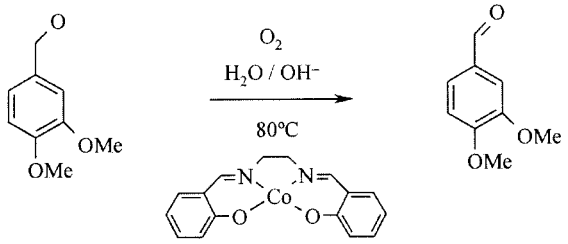

Scheme 1. Oxidation of veratryl alcohol by Co(salen) (**1**) and dioxygen in water.

molecules can be totally IR inactive, but exhibit intense vibrations in the Raman spectrum.[19] In this work, UV/Vis spectroscopy was used to study the reaction at low concentrations, whereas ATR-IR and Raman techniques require higher concentrations. Based on the combination of results, a mechanism for veratryl alcohol oxidation by Co(salen) in alkaline aqueous solution is proposed (Scheme 1).

Results and Discussion

ATR-IR Spectroscopy

Carbonyl compounds have distinct vibrations in the IR range, and therefore it is attractive to study the veratraldehyde formation by in-situ IR spectroscopy.[22–24] Metal-dioxygen complexes have also been extensively characterized by vibrational spectroscopic techniques.[24–28] [Co(salen)B]$_2O_2$ (B = py, pyO, DMF or other axial base) exhibits its ν(O–O) at 888–910 cm^{-1} and the oxygen bridge is regarded as a peroxo bridge. [Co(salen)]$_2O_2$ exhibits ν(O–O) at 1010 cm^{-1} and this bridge is regarded as being an intermediate between peroxo and superoxo species.[27] The superoxo-cobalt complexes exhibit ν(O–O) at a typical range of 1075–1122 cm^{-1}.[28]

Figure 1 shows a typical set of ATR-IR spectra obtained for the Co(salen)-catalyzed oxidation of veratryl alcohol with oxygen in water as a function of time. Mainly two vibrations are observed to form during the reaction. As expected, the aldehyde C=O vibration peak is appearing at 1675 cm^{-1}. A second strong vibration peak, which increases with reaction time, was observed at 993 cm^{-1}. The rate of formation of the peak at 993 cm^{-1} is faster than that of the peak at 1675 cm^{-1} (Figure 1), indicating that they belong to two different species. The change in the vibrations of the aromatic ring, of the methoxy groups and of the C–H bonds in the aldehyde compared to the alcohol are seen as shifts in vibration frequencies.[29]

Interestingly, the vibration at 993 cm^{-1} only appears when both, Co(salen) and veratryl alcohol, are present. This is shown in Figure 2. A weak vibration peak at 984 cm^{-1} is observed to appear when only Co(salen) is stirred at pH 12 in the absence of oxygen, but when substrate is added, a strong vibration peak forms at 993 cm^{-1} and the vibration at 984 cm^{-1} can no longer be observed. Neither one of the peaks is observed at a lower pH (no addition of NaOH, corresponds to a pH of about 9.5).

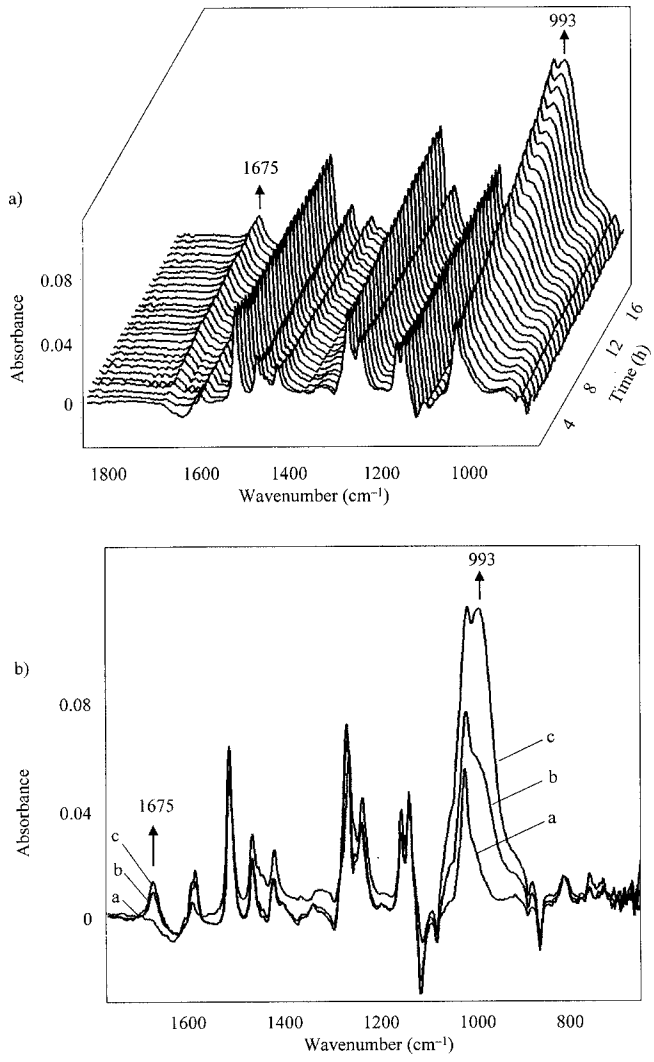

Figure 1. a) 3D plot of time-resolved ATR-IR spectra of the veratryl alcohol oxidation by Co(salen) and dioxygen in water at 80 °C and pH 12. b) Sample spectra were taken at 0 h (a), 8 h (b) and 16 h (c). (150 mg Co(salen) and 3 mL of veratryl alcohol in 90 mL of water/dioxane (5:1) mixture).

Hydroxo-metal complexes exhibit the MOH bending mode below 1200 cm^{-1}. If the hydroxo group is bridging two metal ions, the bending mode moves to lower energies and is seen at 955 cm^{-1} for bis-μ-hydroxo[Cu(bipy)$_2$] type complexes.[24] Thus, we assign the 984 cm^{-1} vibration to bis-μ-hydroxo[Co(salen)]$_2$ species as it appears in aqueous solution of Co(salen) at pH 12. Metal-bound alkoxides (M–OR) exhibit ν(C–O) at ca. 1000 cm^{-1}.[24] As the 993 cm^{-1} vibration appears in solutions of veratryl alcohol and Co(salen) at pH 12 under argon, we assign this vibration to a cobalt-bound veratryl alkoxo group.

If this assignment is valid, the vibration at 993 cm^{-1} should behave differently in the absence or presence of oxygen. This is indeed the case, as illustrated in Figure 3. The rate of formation of the 993 cm^{-1} peak decreases after the addition of oxygen. This is also the point at which the production of aldehyde starts. The peak at 993 cm^{-1} does not

 © 2005 Wiley-VCH Verlag GmbH & Co. KGaA, Weinheim

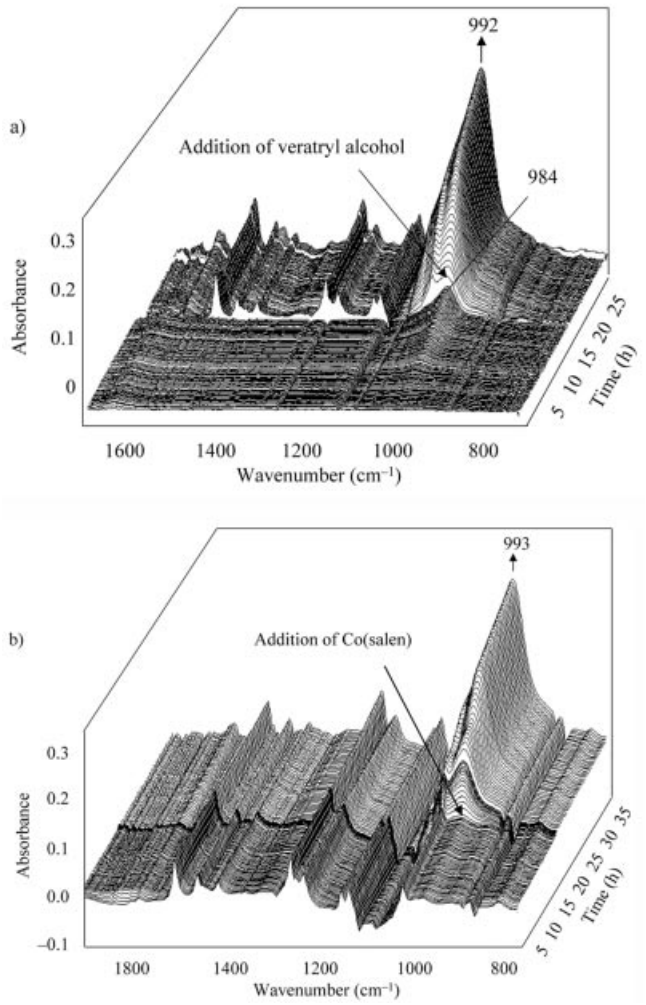

Figure 2. A strong vibration peak at 993 cm^{-1} appears after addition of veratryl alcohol (a) or Co(salen) (b) to the reaction mixture with other reagents. [150 mg Co(salen) and 3 mL of veratryl alcohol in 90 mL of water/dioxane (5:1) mixture at 80 °C and pH 12 under argon].

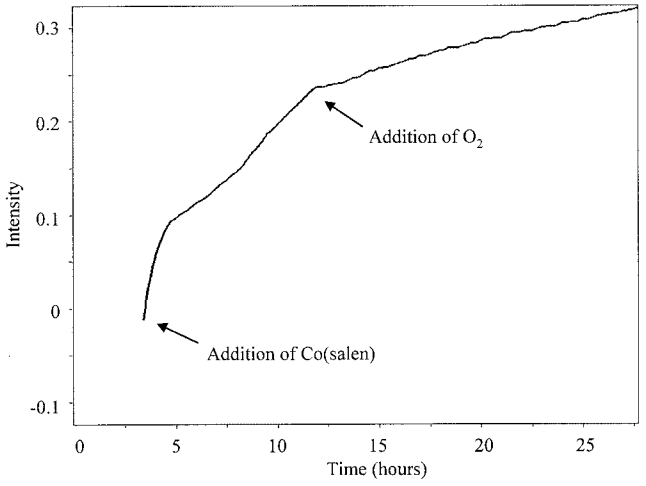

Figure 3. Appearance and increase in intensity of the vibration peak at 993 cm^{-1} monitored in a Co(salen) reaction in the absence and presence of oxygen. (150 mg Co(salen) and 3 mL of veratryl alcohol in 90 mL of water/dioxane (5:1) mixture at 80 °C and pH 12 initially under argon).

appear at temperatures lower than 70 °C nor at low pH values (with no addition of NaOH).

Summarizing, a vibration at 993 cm^{-1} appears at a temperature and pH range of an active system, but forms faster in the absence of oxygen. Thus it does not arise from the product nor from a oxygen-cobalt species, but from an interaction between the substrate and the complex. We assign this species to alkoxo-cobalt intermediate (Figure 3).

Raman Spectroscopy

Different oxygen bridges are more Raman or IR active depending on their symmetry and therefore it is important to use both techniques to determine the presence of oxygen-bridged cobalt complexes.[19,24] Raman spectroscopy is, however, even less sensitive than ATR-IR spectroscopy, and therefore a high concentration of reagents had to be used. The substrate exhibits vibrations at about the same frequencies as in the IR spectra. Figure 4 shows, that the only changes observed after an overnight measurement are the formation of a weak carbonyl vibration at 1675 cm^{-1} and shifts in the vibration peaks of the substrate.[29] Thus no peroxo or superoxo bridges could be observed in the Raman spectra of the Co(salen)-catalyzed reaction.

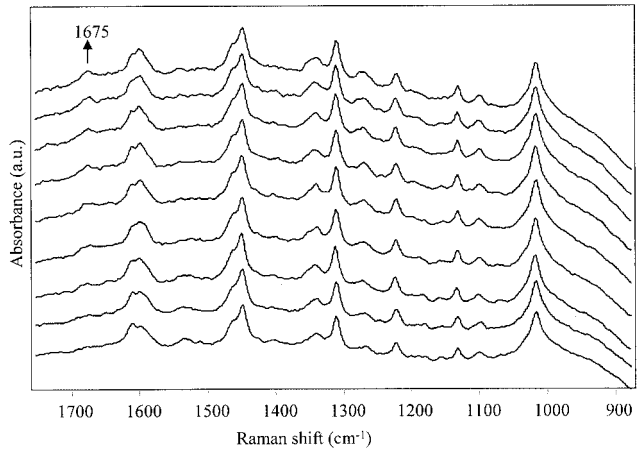

Figure 4. Raman spectra of Co(salen)-catalyzed veratryl alcohol oxidation. Vibration at 1675 cm^{-1} corresponds to the C=O bond of the product. Other peaks observed belong to the substrate.[29] (200 mg Co(salen) and 5 mL veratryl alcohol in 90 mL of water/dioxane mixture (3:1) at 80 °C and pH 12).

UV/Vis Spectroscopy

The oxygen complexes of cobalt have been widely studied by UV/Vis spectroscopy.[30–33] According to Lever and Gray, the bridging superoxo complexes of cobalt exhibit a single intense band in the electronic spectra in the region 300–400 nm, whereas a bridging peroxo has two absorption bands, at about 320 nm and 400 nm. A doubly bridged μ-hydroxo-μ-peroxo (OH, O_2^{2-}) has only one intense absorption band at about 375 nm and a shoulder at higher energies (about 290 nm).[30] Aldehydes also exhibit absorptions in the UV range arising from the n → π* transitions of the

 © 2005 Wiley-VCH Verlag GmbH & Co. KGaA, Weinheim

free electron pair of the carbonyl oxygen and thus product formation can also be monitored by UV/Vis spectroscopy.[34]

Figure 5 shows the UV/Vis spectra of an experiment, in which NaOH was added to the reaction solution of Co(salen) and veratryl alcohol before oxygen (reactions 1–4). Co(salen) and veratryl alcohol in water at 80 °C and under argon exhibit absorption bands of similar intensity at 339 nm and 392 nm (1). At pH 12 the intensity of the absorption bands is enhanced, but they do not shift (2). Addition of an oxygen atmosphere shifts the absorption bands to 324 nm and 378 nm (3). Under argon the reaction solution is very reddish brown, but it turns to dark brown along exposure to oxygen. Under prolonged oxygen exposure the intensity of the absorption band at 324 nm decreases to a shoulder, while the band at 378 nm remains (4). This change suggests that a monobridged peroxo species transforms into a doubly bridged species. At these conditions this is most likely a μ-hydroxo-μ-peroxo bridge.[35]

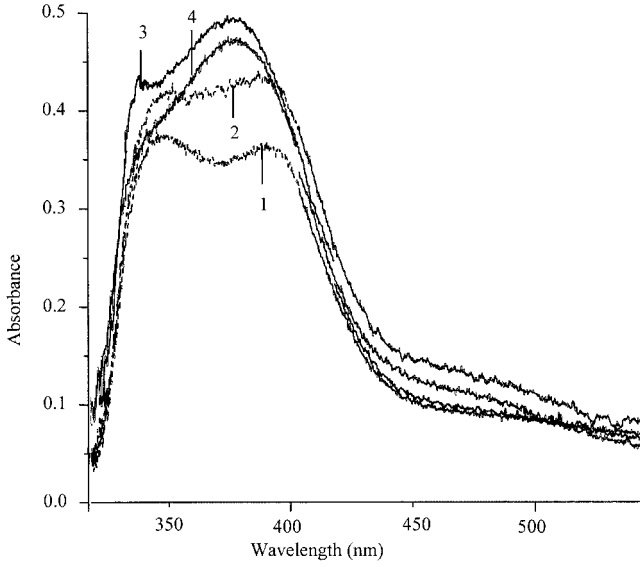

Figure 5. In-situ UV/Vis spectra of a solution of Co(salen) and veratryl alcohol in water under argon (1), after addition of NaOH to adjust pH to 12 (2), after addition of oxygen (3) and after 1 h of oxygen exposure (4). (10 mg of Co(salen) and 2 mL of veratryl alcohol in 120 mL of water at 80 °C).

If oxygen is added to a solution of Co(salen) and veratryl alcohol at low pH (no addition of NaOH), the absorption bands at 339 nm and 390 nm (5) are shifted to 300 nm and 378 nm (6). This implies that oxygen coordinates to the cobalt complex. After the addition of NaOH, the band at 378 nm does not shift, but an absorption band at 308 nm starts to arise, which is assigned to the n $\rightarrow$ π^* transitions in the C=O group of the aldehyde (7, Figure 6).[34,36]

Aldehyde formation can be monitored by UV/Vis spectroscopy as the appearance and growth of the absorption band at 308 nm and Figure 7 shows that the reaction rate increases with increasing reaction temperature. At 40 °C the rate of the reaction is so slow that practically no aldehyde is produced. Instead, at 60 °C the absorption band at

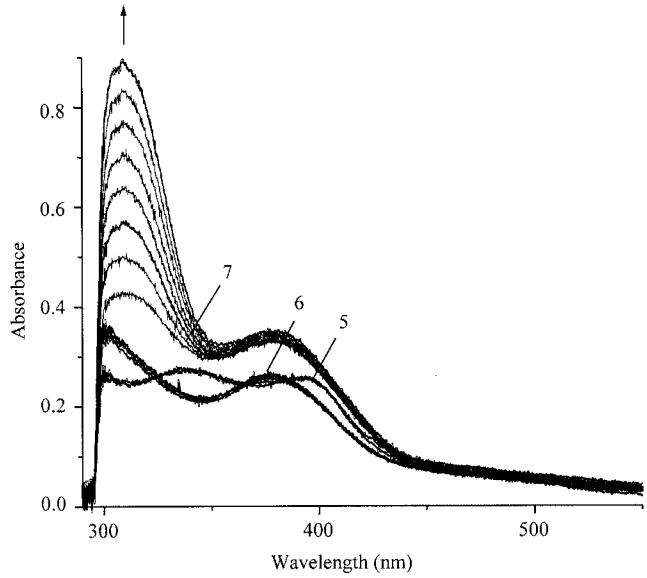

Figure 6. In-situ UV/Vis spectra of a solution of Co(salen) and veratryl alcohol in water at 80 °C under argon (5), after addition of oxygen (6) and after addition of NaOH to adjust pH to 12 (7). (10 mg of Co(salen) and 2 mL of veratryl alcohol in 120 mL of water at 80 °C).

308 nm starts to appear and at 80 °C its formation rate increases dramatically.

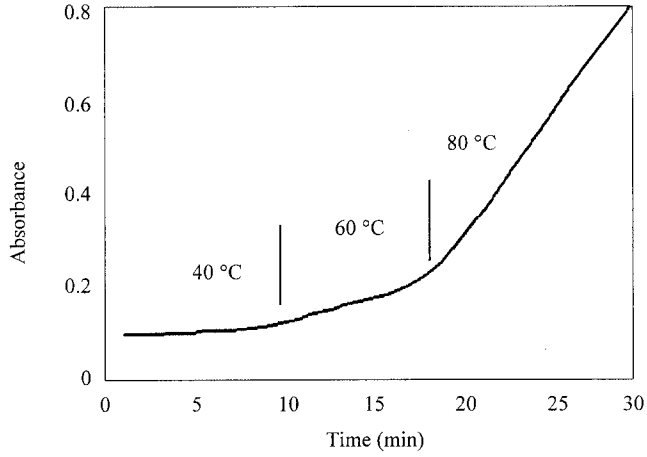

Figure 7. The rate of formation of the absorption band at 308 nm at different reaction temperatures.

Summarizing, a μ-peroxo bridge is observed to form when oxygen is introduced to the solution of Co(salen) and veratryl alcohol in water at 80 °C and pH 12. With time, a second bridge appears between the cobalt centers forming a doubly bridged μ-hydroxo-μ-peroxo species. Coordination of veratryl alcohol to the cobalt center followed by insertion of oxygen can also be seen at lower pH, but aldehyde formation does start before adjusting the pH to 12. Increasing temperature considerably enhances the rate of aldehyde production.

Reaction Monitoring Experiments

In our earlier studies it has been shown that substrate concentration strongly affects the activity of the system. It

 © 2005 Wiley-VCH Verlag GmbH & Co. KGaA, Weinheim

was especially noted that the substrate to Co(salen) ratio needs to be high for higher activity.[16] The formation of high amounts of an intermediate, in which the substrate is coordinated to cobalt at high reagent concentrations, can be observed in the ATR-IR spectra. Addition of oxygen slows down the formation of this species and initiates the formation of the aldehyde. At high concentrations of all reagents a oxygen-cobalt species is not observed, whereas at the low concentrations of the UV/Vis experiments oxygen insertion is seen to occur. Thus, to study the influence of oxygen pressure on the reaction at high and low concentrations, reaction-monitoring experiments were performed with a set-up from which samples can be taken during the experiment under higher oxygen pressures. The initial rates of reaction were also calculated.[37] Figure 8 summarizes the results of these experiments. At low concentrations [0.14 mM Co(salen) and 14 mM veratryl alcohol] the reaction rate is about the same under 1 and 10 bar oxygen pressure (Figure 8, experiments **1** and **2,** initial rates of 9.5 and 9.6 TOF_0, respectively[37]). At higher concentrations [0.41 mM Co(salen) and 41 mM veratryl alcohol] oxygen pressure significantly enhances the reaction rate (Figure 8, experiments **3** and **4**, initial rates of 1.8 and 16 TOF_0, respectively).

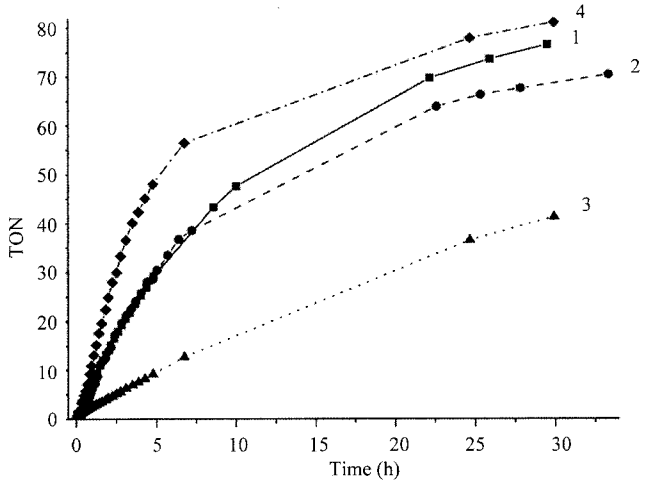

Figure 8. Oxidation activity (expressed as turnover number, TON, the moles of product per one mol of catalyst) at (1) 0.14 mM Co(salen), 14 mM veratryl alcohol and 1 bar oxygen, (2) 0.14 mM Co(salen), 14 mM veratryl alcohol and 10 bar oxygen, (3) 0.41 mM Co(salen), 41 mM veratryl alcohol and 1 bar oxygen and (4) 0.41 mM Co(salen), 41 mM veratryl alcohol and 10 bar oxygen.

Higher catalyst activity at low concentrations and low impact of added oxygen pressure on the catalytic system at low concentrations support the involvement of 2:1 $Co:O_2$ species in the catalytic cycle as the active species. In case of a mononuclear superoxo complex, increasing oxygen pressure should increase the reaction rate.[38]

As we have previously reported, the optimum pH for Co(salen)-catalyzed oxidation of veratryl alcohol is about 12.5.[16] The initial oxidation rate of Co(salen) increases from 5.2 h^{-1} to 9.6 h^{-1} when the pH is increased from 11.2 to 12.4. If the activity and the change in pH of the reaction are monitored simultaneously (Figure 9), it can be seen that the product formation and the OH^- ion consumption proceed hand in hand but no reasonable correlation between the conversions and the change in pH can be deduced.[39] Figure 9 also shows that the decrease in OH^- concentration slows down the reaction rate. Addition of NaOH at the end of a reaction restarts the oxidation activity.[16]

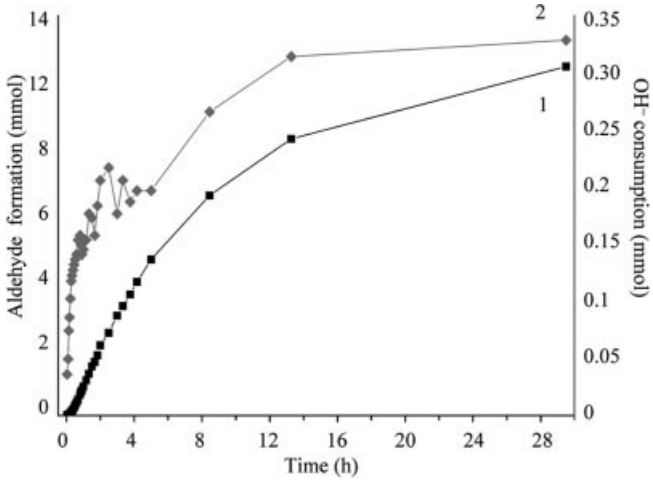

Figure 9. Rate of oxidation and total OH^- consumption in the Co(salen)-catalyzed reaction: (1) Formation of veratraldehyde and (2) consumption of OH^- ions. [0.14 mM Co(salen) and 14 mM veratryl alcohol at pH 11.6[40] and 80 °C] (TON: turnover number).

Discussion

Based on the presented results and supported by our earlier studies,[16–17] the oxidation of veratryl alcohol in water catalyzed by Co(salen) and oxygen is suggested to proceed through the steps described in Scheme 2.

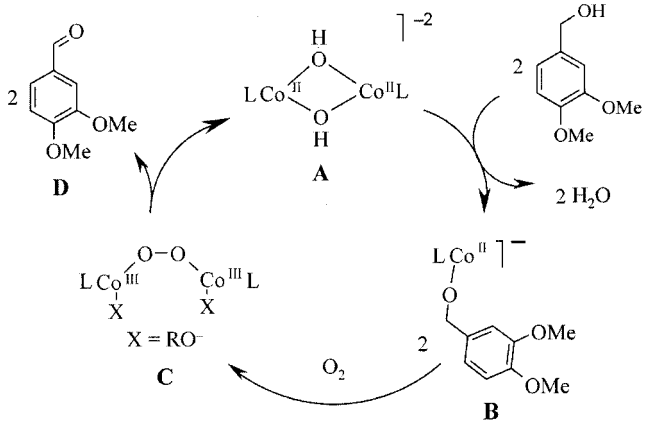

Scheme 2. Suggested mechanism for veratryl alcohol oxidation by Co(salen) and dioxygen in alkaline aqueous solution.

The cycle of veratryl alcohol oxidation starts with a bis-μ-hydroxo[Co(salen)]$_2$ complex **A**, which can deprotonate a substrate molecule at temperature higher than 60 °C forming an alkoxo intermediate **B** and water. The intermediate **B** can be observed in the ATR-IR spectra. In the absence of oxygen, this species accumulates in the reaction. After

 © 2005 Wiley-VCH Verlag GmbH & Co. KGaA, Weinheim

introduction of oxygen, the formation of a nonplanar μ-peroxo bridge between two alkoxy-Co(salen) units can be observed in UV/Vis spectra (intermediate **C**). The peroxo bridge of species **C** abstracts a proton from each substrate and veratraldehyde is formed as a product (**D**).

In the overall reaction, one activated oxygen molecule oxidizes two veratryl alcohol molecules to veratraldehyde, water is produced as the side product and the initial bis-μ-hydroxo[Co(salen)]$_2$ complex is regenerated in the cycle. The rate-limiting step seems to be the detachment of the product molecule. The methoxy substituents in the aromatic ring of veratryl alcohol seem to aid this step.[41] Table 1 summarizes the spectroscopic fingerprints of species **A**–**D**. Below the proposed steps of the mechanistic cycle are discussed in more detail.

Table 1. Spectroscopic fingerprints of species **A**–**D** (sh = shoulder).

Species	ATR-IR [cm^{-1}]	Raman [cm^{-1}]	UV/Vis [nm]
A	984	–	316, 375, 490 sh
B	993	–	339, 392
C	–	–	324, 378
D	1675	1677	308

Formation of Complex A

The reaction does not start before the addition of NaOH, and therefore it is apparent that OH^- ions are directly involved in generating the active species and not only acting as stoichiometric proton acceptors. As the pH gets lower during the reaction, possibly due to the formation of small amounts of veratrylic acid,[16] the concentration of the active species decreases and consequently the reaction rate slows down.

The catalytic activity can be regained by adding NaOH to the solution,[16] which is a clear indication that the active catalytic species is present only at higher pH. It has been shown that at higher pH values the Co(salen) complex exists rather as a hydroxo complex.[35,42] As the pH decreases the concentration of the hydroxo complex also decreases and the reaction slows down, whereas addition of NaOH shifts the equilibrium back towards the hydroxo species and the rate of reaction increases again. At the applied conditions in the beginning of the reaction, it is reasonable to expect, that the Co(salen) hydroxo complex exists most likely as a dimeric bis-μ-hydroxo[Co(salen)]$_2$ species **A**.[35,38,43] This species exhibits a vibration at 984 cm^{-1} (arising from bridging OH groups) and absorption bands at 316 nm and 375 nm with a shoulder at 490 nm.

Formation of the Intermediate B

According to UV/Vis spectroscopy, the substrate can replace the hydroxy group from the first coordination sphere of the cobalt center. This is seen as a shift of the absorption bands at 316 nm and 375 nm to 336 nm and 392 nm after addition of veratryl alcohol to the solution of Co(salen) at pH 12. It was already suggested before, that substrate coordination must be necessary for the reaction to occur as the strongly binding axial bases inhibit the reaction and the high substrate to metal ratio enhances it.[16–17] ATR-IR spectra show clearly that an intermediate species is formed between veratryl alcohol and Co(salen). This intermediate **B** exhibits a strong vibration at 993 cm^{-1} corresponding to the C–O bond of the metal-bound alkoxo group.[24] The vibration at 993 cm^{-1}, however, is observed to accumulate, especially in the absence of oxygen. The rate at which the intermediate **B** forms decreases after introduction of oxygen, as from that point on the aldehyde production starts. Nevertheless, the vibration peak at 993 cm^{-1} still grows. In other words, formation of species **B** is a fast step compared to the formation of species **C** and **D**.

The need of higher reaction temperatures is due to the formation of the alkoxo-metal intermediate **B**. The formation of the strong vibration peak at 993 cm^{-1} is not observed at 60 °C, but at 80 °C it accumulates. Also, a high pH is needed for the vibration 993 cm^{-1} to appear. Coordination of the substrate as an alcohol to cobaltcenter occurs also at low pH, as seen in UV/Vis spectra, but formation of the alkoxo species **B** requires deprotonation of the substrate. This seems to take place only at high temperature and pH, as seen by the appearance of the 993 cm^{-1} peak. UV/Vis spectroscopy shows as well that no aldehyde is formed at temperature below 60 °C and that raising temperature to 80 °C dramatically increases the rate of the reaction. Thus, the rate of reaction is dependent on the rate at which the substrate deprotonates and forms the intermediate **B**.

Formation of the Intermediate C

As discussed above, the introduction of oxygen atmosphere is needed to start the production of aldehyde.[34] UV/Vis spectra show shifts in the absorption bands of cobalt after addition of oxygen to a solution formerly under argon. These shifts suggest a formation of a peroxo bridge between two Co(salen) complexes.[30–32] Absorptions at 300 nm and 380 nm are observed when oxygen is added to a solution of Co(salen) and veratryl alcohol at low pH (below 10). Aldehyde production does not start in this solution before addition of NaOH. When oxygen is added to a solution of Co(salen) and veratryl alcohol at pH 12, absorption bands form at 324 nm and 392 nm. These absorptions are defined as arising from monobridged μ-peroxo complexes.[30,33] Thus, it is apparent that an oxygen bridge forms between two Co(salen) complexes under these reaction conditions and that the formation of the intermediate **C** is needed for the aldehyde production to start. A similar species has been reported in the oxidation of benzyl alcohol by $Co^{II}(bipy)_2$ complexes.[44]

The charge and geometry of the oxygen-bridged complex should be observable from the ATR-IR and Raman spectra. Superoxo and peroxo bridges exhibit vibrations at frequency ranges of 1100–1200 cm^{-1} and 760–920 cm^{-1}, respectively.[24] Nevertheless, no vibration peaks are ob-

 © 2005 Wiley-VCH Verlag GmbH & Co. KGaA, Weinheim

served to form in these regions in neither ATR-IR nor Raman spectra. The reason arises from the effect of concentration on the activity of the system. At the high concentrations needed for the ATR-IR and Raman measurements, the oxidation activity is quite low without an added oxygen pressure, as seen in Figure 8. The intermediate **B** forms in high amounts in these conditions and it could be regarded as a "dormant" species, whenever there is not enough oxygen to take the reaction further. Therefore, at the conditions of ATR-IR and Raman measurements the concentration of the oxygen-bridged species **C** is too low to be observed. However, the UV/Vis spectra are recorded at low concentrations and in these spectra the oxygen-bridged species **C** can easily be observed.

According to the literature, the peroxo bridge most probably forms through a mononuclear superoxo complex.[8,12] Oxygen molecule binds first to one cobalt center as a superoxo radical, which then binds to another cobalt complex forming a peroxo species. At these reaction conditions the dinuclear species is more stable and it forms fast. Thus the superoxo complex is so short-lived that it cannot be observed with the applied spectroscopic methods.

The Rate-Limiting Step

Alkoxo-metal species as a reaction intermediate have also been suggested for Co complexes mimicking horse liver alcohol dehydrogenase. In these reactions the product dissociation from the metal center was observed to be the rate-limiting step.[45] This is apparently also the case for the reaction under study. We have observed that a alkoxo-metal species similar to intermediate **B** is also formed in the reaction of Co(salen) with benzyl alcohol, although benzaldehyde is not produced by this system.[41] Thus, the reaction with benzyl alcohol seems to stop at the intermediate **B**, while with veratryl alcohol the aldehyde production starts directly after oxygen is introduced to the system. Thus, the methoxy substituents in veratryl alcohol aid the detachment of the product from the Co(salen) complex. Moreover, no alkoxo-metal intermediate is observed in the ATR-IR spectra of a similar system, in which (phenanthroline)copper-type [Cu(phen)] complexes are used as catalysts.[46] These complexes are more active than Co(salen) and can also catalyze the oxidation of benzyl alcohol to some extent. This implies that the alkoxo-metal intermediate is less stable or that such species does not even form in the Cu(phen)-catalyzed system.[23,46] The detachment step is preceded by abstraction of a hydrogen from the coordinated alkoxyl by the peroxo bridge. Thus, the methoxy substituents can be involved in making the α-H in the benzylic position more labile and easier to abstract.

The Regeneration of Complex A

High pH is needed to generate the bis-μ-hydroxo[Co(salen)]$_2$ species **A**, which can deprotonate the substrate. It seems that the overall OH^- consumption and alcohol oxidation are closely related, but the molar ratio of formed aldehyde and OH^- ions consumed varies from tens to hundreds.[16,39] This indicates that actually only a few substrate molecules are deprotonated by OH^- ions or that the OH^- ions are recovered during the reaction cycle. The latter suggestion supports the idea, that peroxo-bridged species **C** regenerates the bis-μ-hydroxo[Co(salen)]$_2$ species by abstracting a hydrogen from each of the two coordinated substrate molecules. Therefore, after initiation no "external" hydroxide ions are consumed in the reaction. Nevertheless, if the pH gets too low due to small amount veratryl acid formed as a side-product, the cobalt complex prefers to stay as a peroxo-bridged species **C** and the reaction stops. Thus addition of NaOH increases the reaction rate as it enhances the deprotonation step and keeps the species **A** as the dominating species in the solution.

A drawback of the Co(salen) catalytic system is that it suffers from irreversible oxidation. We have observed that this system can stay active for about 72–96 h, after which there is no more oxidation occurring even with further addition of NaOH. Thus, there is all the time a competing mechanistic path present, which causes the catalyst to deactivate. This could occur via the formation of doubly bridged μ-hydroxo-μ-peroxo species, which can be very stable.[35] UV/Vis spectra show a transformation in the bridging type of the oxygen complex from singly bridged peroxo towards a doubly bridged species. The presence of the substrate seems to protect the complex from deactivation. The activity is higher if the substrate to Co(salen) ratio is kept high.[16] Possibly, the coordinated substrate can prevent the insertion of a second bridge between cobalt centers. Careful balancing of the reaction conditions can minimize the damage caused by deactivation. For example, keeping the Co(salen) concentration low and veratryl alcohol concentration high dramatically improves the lifetime of the catalyst.[16]

Conclusions

The activities of transition-metal complex-catalyzed alcohol oxidations have remained low, normally in the order of TOF = 10 h^{-1} or less,[47] and therefore it is imperative to study the mechanisms of these reactions to be able to develop more active systems. In this work, the mechanism of Co(salen)-catalyzed oxidation of veratryl alcohol in alkaline aqueous solution was investigated in detail by in-situ spectroscopy. It was shown, that the combination of complementary in-situ spectroscopic techniques is a powerful approach to study a complicated catalytic system.

The obtained data support strongly a mechanism, in which substrate coordination is a key step in the catalytic cycle. Deprotonation and coordination of the substrate have been suggested before as reaction steps in similar systems, but direct proof is hard to find. Combination of in-situ UV/Vis and ATR-IR spectroscopy show, that veratryl alcohol is located in the coordination sphere of cobalt already at low pH values, but deprotonation and consequent alkoxo-

 © 2005 Wiley-VCH Verlag GmbH & Co. KGaA, Weinheim

cobalt intermediate formation occurs only at pH 12 and above. The spectroscopic data also suggests that a dinuclear μ-peroxo[Co(salen)]$_2$ complex is involved in this oxidation reaction instead of the mononuclear superoxo-Co(salen) complex, which is usually assumed to be responsible for catalytic activity. The mononuclear superoxo complex can still be formed initially, but its lifetime is too short to be observed. Nevertheless, the effect of reaction conditions presented in earlier papers point strongly to the dinuclear peroxo species over the mononuclear superoxo complex as the active intermediate in the catalytic cycle of this particular reaction.[16–17] Thus, both the optimum reaction conditions and the spectroscopic data support the mechanism described in Scheme 2. Further studies with different benzylic alcohols can give more insight into the effect of substituents on the rate-limiting step. Also, additional spectroscopic methods, such as EXAFS, could give further evidence for the involvement of the dinuclear species in this reaction.

Experimental Section

Co(salen) (**1**) was purchased from Aldrich and used as received without further purification. 3,4-Dimethoxybenzyl alcohol (veratryl alcohol) was purchased from ACROS and Aldrich in 97% purity. The 3% impurity is veratraldehyde, which has been taken into account when calculating conversions and turnover numbers. 1,4-Dioxane, 3,4-dimethoxybenzaldehyde and 3,4-dimethoxybenzylic acid were purchased from Aldrich and used as received. The oxygen gas was obtained from AGA in Finland and from Hoek–Loos in The Netherlands and had a purity of 99%. Online ATR-IR spectra were recorded with a Mettler Toledo ReactIR™1000 spectrometer with a DiComp™ probe, which was fitted in a 100-mL two-neck round-bottomed flask containing the reaction solution. The measurements were done with a scan program of 128 scans per measurement at selected intervals with a resolution of 4 cm^{-1}. The wavelength range covered was 650–4000 cm^{-1}. The diamond absorption prevents to observe any vibrations at a wavelength range of 1900–2400 cm^{-1}. A more detailed description of the ATR-IR setup and the procedure of the oxidation experiments is presented elsewhere.[16–17,21] The solvent used in all ATR-IR experiments was a water/dioxane mixture (5:1) at 80°C, which was in all cases subtracted as the background. The amounts of reagents varied, and therefore their exact concentrations are specified at the appropriate sections of this paper or in relevant Figure captions. Oxygen was installed by the balloon technique.[16] All reagents were degassed and under argon when working in the absence of oxygen. The IR spectra were analyzed with the program ReactIR 2.2. The UV/Vis spectra were recorded with a Varian CARY50 spectrometer equipped with an optical fibre and an insertion probe with variable path lengths. The same procedure for the oxidation experiments was used as with the ATR-IR technique. The Raman spectra were recorded with a Kaiser RXN dispersive system with a Peltier element-cooled Andor CCD camera for detection and a laser of 532 nm (60 mW). In these experiments, the reaction was monitored from the outside of the glass flask by using a laser objective. The resolution was about 2 cm^{-1} and 10 scans were accumulated with an exposure time of 15 s. The reaction monitoring experiments were performed in a 500-mL glass vessel equipped with a magnetic stir-bar fitted inside a 1-L steel autoclave. 200 mL of 0.05 M NaOH (pH, 12.4) was used as solvent. Depending on the experiment, 86.9 mg (0.275 mmol) or 269 mg (0.83 mmol) of Co(salen) was used. Veratryl alcohol was added in 100:1 molar ratio to Co(salen). The autoclave was placed in an oil bath and the reaction mixture was stirred at 80 °C under 10 bar of oxygen pressure. Samples were cooled to room temperature and prepared for GC analysis by a method described earlier.[23] GC measurements were conducted with a GC/Fid Agilent 6890N instrument using a HP-5 (30 m × 320 μm × 0.25 μm) capillary column and equipped with a FID detector.

Acknowledgments

Financial support from University of Helsinki, Academy of Finland (grant 204408, T.R.), Finnish Cultural Foundation (K. K.), Magnus Ehnrooth Foundation (K. K.), Acta Chemica Scandinavica (K. K.) and Finnish Technology Development Agency TEKES (H. K.) is gratefully acknowledged. B.M. W. and J.G.M. acknowledge funding from CW-NWO (VICI and Van der Leeuw grants) and NRSC-C. The authors also thank Dr. Tom Visser and Dr. Markus Allmendinger for valuable discussions.

[1] J. Ebner, D. Riley, in: *Active Oxygen in Chemistry*, (Eds.: C. S. Foote, J. S. Valentine, A. Greenberg, J. F. Liebman); SEARCH series, vol. 1, Chapman & Hall, **1995**, pp. 204–248.
[2] R. A. Sheldon, I. W. C. E. Arends, G.-J. ten Brink, A. Dijksman, *Acc. Chem. Res.* **2002**, *35*, 774–781.
[3] T. Elder, J. J. Bozell, *Holzforschung* **1996**, *50*, 24–30.
[4] *Advances in Catalytic Activation of Dioxygen by Metal Complexes* (Ed.: L. I. Simandi), Kluwer, Dordrecht, **2003**.
[5] A. Lubineau, J. Augé, in: *Aqueous-Phase Organometallic Catalysis* (Eds.: B. Cornils, W. A. Herrmann), Wiley-VCH, Weinheim, **1998**.
[6] A. Dijksman, A. Marino-González, A. Mairata i Payeras, I. W. C. E. Arends, R. A. Sheldon, *J. Am. Chem. Soc.* **2001**, *123*, 6826–6833.
[7] B. A. Steinhoff, S. R. Fix, S. S. Stahl, *J. Am. Chem. Soc.* **2002**, *124*, 766–767.
[8] R. Sheldon, J. Kochi, *Metal-Catalyzed Oxidations of Organic Compounds*, Academic Press, **1981**.
[9] A. Martell, in: *Oxygen Complexes and Oxygen Activation by Transition Metals*, (Eds.: A. Martell, D. Sawyer), Plenum Press, **1987**.
[10] T. Tsumaki, *Bull. Chem. Soc. Jpn* **1938**, *13*, 252–257.
[11] D. Chen, A. E. Martell, *Inorg. Chem.* **1987**, *26*, 1026–1030.
[12] J. Bozell, B. R. Hames, D. R. Dimmel, *J. Org. Chem.* **1995**, *60*, 2398–2404.
[13] D. E. Hamilton, R. S. Drago, A. Zombeck, *J. Am. Chem. Soc.* **1987**, *109*, 374–379.
[14] A. Zombeck, R. S. Drago, B. B. Corden, J. H. Gaul, *J. Am. Chem. Soc.* **1981**, *103*, 7580–7585.
[15] M. M. Whittaker, J. W. Whittaker, *Biochemistry* **2001**, *40*, 7140–7148.
[16] K. Kervinen, H. Korpi, M. Leskelä, T. Repo, *J. Mol. Catal. A: Chemical* **2003**, *203*, 9–19.
[17] K. Kervinen, P. Lahtinen, T. Repo, M. Svahn, M. Leskelä, *Catal. Today* **2002**, *75*, 183–188.
[18] Y. Cui, R. Patt, R. Chen, J. Gratzl, *J. Mol. Catal. A: Chemical* **1999**, *144*, 411.
[19] *Introduction to Infrared and Raman Spectroscopy* (Eds.: N. B. Colthup, L. H. Daly, S. E. Wiberley), Academic Press, Inc., San Diego, **1990**.
[20] B. M. Weckhuysen, *Phys. Chem. Chem. Phys.* **2003**, *5*, 4351–4360.
[21] *In-situ Spectroscopy of Catalysts* (Ed.: B. M. Weckhuysen), American Scientific Publishers, Stevenson Ranch, **2004**.
[22] K. Kervinen, M. Allmendinger, M. Leskelä, T. Repo, T. B. Rieger, *Phys. Chem. Chem. Phys.* **2003**, *5*, 4450–4454.

 © 2005 Wiley-VCH Verlag GmbH & Co. KGaA, Weinheim

[23] H. Korpi, P. Lahtinen, V. Sippola, O. Krause, M. Leskelä, T. Repo, *Appl. Catal. A General* **2004**, *268*, 199–206.
[24] *Infrared and Raman Spectra of Inorganic and Coordination Compounds, Part B: Applications in Coordination, Organometallic and Bioinorganic Chemistry* (Ed.: K. Nakamoto), John Wiley & Sons, Inc., New York, **1997**.
[25] N. N. Greenwood, A. Earnshaw, *Chemistry of the Elements*, Pergamon Press, Oxford, **1984**.
[26] E. M. Nour, R. E. Hester, *J. Mol. Struct.* **1980**, *62*, 77–79.
[27] M. Suzuki, T. Ishiguro, M. Kozuka, K. Nakamoto, *Inorg. Chem.* **1981**, *20*, 1993–1996.
[28] C. G. Barraclough, G. A. Lawrence, P. A. Lay, *Inorg. Chem.* **1978**, *17*, 3317–3322.
[29] The reference spectra measured at pH 12.5 in water/dioxane mixture (75 mL:15 mL) show the following vibrations for a 0.4 M solution of veratryl alcohol (cm^{-1}): 2948 (w), 2923 (w), 2892 (w), 2848 (w), 1596 (w), 1517 (s), 1468 (m), 1445 (w), 1424 (m), 1335 (m), 1266 (s), 1239 (m), 1158 (m-s), 1140 (m-s), 1025 (s), 816 (w). Veratraldehyde exhibits vibrations at (cm^{-1}): 2960 (w), 2854 (w), 1729 (w), 1673 (m), 1588 (d, m), 1513 (m-s), 1468 (m), 1455 (w), 1428 (w), 1345 (w), 1272 (s), 1245 (w), 1160 (w), 1140 (m), 1071 (w), 1017 (m). Similar shifts are observed in the Raman spectra, but the intensities of the vibrations can differ.
[30] A. B. P. Lever, H. B. Gray, *Acc. Chem. Res.* **1978**, *11*, 348–355.
[31] *Inorganic Electronic Spectroscopy* (Ed.: A. B. P. Lever), Elsevier, Amsterdam, **1986**.
[32] G. McLendon, R. J. Motekaitis, A. E. Martell, *Inorg. Chem.* **1975**, *14*, 1993–1996.
[33] V. M. Miskowski, J. L. Robbins, I. M. Treitel, H. B. Gray, *Inorg. Chem.* **1975**, *14*, 2318–2321.
[34] *Spectroscopic Methods in Organic Chemistry* (Eds.: D. H. Williams, I. Fleming); McGraw-Hill Book Company, London, **1989**.
[35] R. D. Jones, D. S. Summerville, F. Basolo, *Chem. Rev.* **1979**, *79*, 139–179.
[36] The commercial veratraldehyde exhibits absorption maxima at 268 nm and 308 nm with a shoulder at 290 nm. Veratrylic acid shows absorption maximum at 250.4 nm with shoulders at 295 nm and 330 nm.
[37] The initial oxidation rates were calculated from the derivatives at time zero for the functions presenting the conversion of the aldehyde as a function of time. These functions were obtained from the linear fit for the conversion points as a function of time during the first 10% of aldehyde formation. The rate of the reaction decreases after the conversion of aldehyde is over 15%. The slope of the plot was multiplied with the substrate/metal molar ratio to get result in the form of TON/h = TOF (1/h).
[38] E. C. Niederhoffer, J. H. Timmons, A. E. Martell, *Chem. Rev.* **1984**, *84*, 137–203.
[39] If the reaction is monitored according to the consumption of hydroxide ions vs. amount of aldehyde produced, more than ten equivalents of aldehyde is formed per consumed OH^- ion. For example, in an overall reaction in which pH decreased from 11.2 to 10.0, 30 moles of aldehyde was produced per 1 mol of hydroxide consumed.
[40] In these reactions initial pH 11.6 (0.005 M NaOH) was applied, as even modern pH electrodes seem to be too inaccurate for such a study in pH higher than 12.
[41] Although unsubstituted benzyl alcohol is not oxidized by this catalytic system, the vibration peak at 993 cm^{-1} is also visible in the corresponding ATR-IR spectra.
[42] R. J. Motekaitis, A. E. Martell, *Inorg. Chem.* **1988**, *27*, 2718–2724.
[43] *Comprehensive Coordination Chemistry: the synthesis, reactions, properties and applications of coordination compounds* (Ed.: G. Wilkinson); vol. 4, Pergamon Press, **1987**.
[44] A. Sobkowiac, D. T. Sawyer, *J. Am. Chem. Soc.* **1991**, *113*, 9520–9523.
[45] M. Gerber, M. Zeppezauer, M. F. Dunn, *Inorg. Chim. Acta* **1983**, *79*, 161–164.
[46] H. Korpi, K. Kervinen, T. Repo, M. Leskelä, *J. Chem. Soc., Dalton Trans*, submitted to.
[47] R. A. Sheldon, I. W. C. E. Arends, A. Dijksman, *Catal. Today* **2000**, *57*, 157–166.

Received: January 13, 2005
Published Online: April 25, 2005

 © 2005 Wiley-VCH Verlag GmbH & Co. KGaA, Weinheim

Synthesis, Structural, and Magnetic Characterization of $YCrMnO_5$

José A. Alonso,*[a] María J. Martínez-Lope,[a] María T. Casais,[a] José L. Martínez,[a] and Vladimir Pomjakushin[b]

Keywords: Magnetic properties / Ferrimagnetic ordering / High-oxygen-pressure synthesis / Crystal structure refinement / Neutron powder diffraction / X-ray diffraction

A new oxide of nominal stoichiometry $YCrMnO_5$ has been prepared in polycrystalline form by wet-chemistry procedures followed by thermal treatments under high-oxygen-pressure conditions. This material has been characterized by X-ray and neutron powder diffraction (NPD), magnetotransport and magnetization measurements. $YCrMnO_5$ is isostructural with RMn_2O_5 oxides (R = rare earths); its crystal structure has been Rietveld refined from NPD data in the space group *Pbam*, and it contains infinite chains of $(Cr,Mn)^{4+}O_6$ octahedra sharing edges, linked together by $(Mn,Cr)^{3+}O_5$ pyramids and YO_8 units. An important level of cationic disorder has been found between both metallic sites; the refined crystallographic formula is $Y[Mn_{0.47(1)}Cr_{0.53(1)}]_{oct}$-$[Cr_{0.37(1)}Mn_{0.63(1)}]_{pyr}O_5$. The magnetic susceptibility indicates the onset of magnetic ordering below $T_c \approx 85$ K; the magnetization isotherms are characteristic of a weakly ferrimagnetic material reaching a net magnetization of 0.25 μ_B/f.u. for $H = 50$ kOe. Low-temperature NPD patterns do not exhibit any additional magnetic contribution, confirming that a long-range magnetic ordering is not fully established.

(© Wiley-VCH Verlag GmbH & Co. KGaA, 69451 Weinheim, Germany, 2005)

Introduction

The family of RMn_2O_5 (R = rare earths) oxides was first described in the 1960s by Bertaut et al.,[1,2] that already recognized the extraordinary flexibility of the structure with regard to the substitutions of both R and Mn atoms allowing, for instance, the preparation of $RMnTiO_5$ phases. Some RMn_2O_5 materials have recently been revisited since they are among the few oxides that show a significant magneto-ferroelectric effect,[3–7] which implies a coupling between ferroelectricity and magnetic order in the system: the application of an external magnetic field leads to the appearance of an electrical polarization. The orthorhombic crystal structure of RMn_2O_5 (space group *Pbam*) is very interesting, since it contains infinite chains of $Mn^{4+}O_6$ octahedra, linked through $[Mn^{3+}O_5]$ pyramidal units and bicapped antiprisms $[RO_8]$. The shortest metal–metal distance seen in this family is Mn1–Mn1 = 2.750(2) Å in the Nd compound. Important implications on the physical properties of these oxides can be presumed from such short distances. RMn_2O_5 compounds are antiferromagnets at low temperatures,[8] and the magnetic structures, studied from neutron diffraction data, are rather complex and incommensurate with the chemical unit cell.[9] For most of these oxides, the magnetic structure is defined by the propagation vector $k = (1/2,0,\tau)$, with τ depending on the type of R.[10,11] The ordering of the Mn ions is helicoidal, and the magnetic moments are contained on the *ab* plane. The rare-earth ions also become ordered at lower temperatures according to a sinusoidal magnetic structure. The magnetic structure was subsequently revisited for R = Er and Tb,[12] and Dy,[13] and it seems that the amplitude of the moments for the Mn ions is also modulated. Exceptionally, $BiMn_2O_5$[9,14] and $LaMn_2O_5$[15] display a commensurate magnetic arrangement, defined by the propagation vectors $k = (1/2,0,1/2)$ and $k = (0,0,1/2)$, respectively.

With the aim to induce new magnetic interactions in the members of the RMn_2O_5 family, we recently designed and prepared $YFeMnO_5$,[16] which is obtained by replacing Mn^{3+} by Fe^{3+} in YMn_2O_5. A NPD study complemented with magnetic measurements demonstrated that $YFeMnO_5$ is a ferrimagnet below $T_c \approx 165$ K, and is characterized by the propagation vector $k = 0$.[16] This is the first reported member of a novel $RFeMnO_5$ (R = rare earths) series, where Mn^{4+} occupies the octahedral positions, whereas Fe^{3+} is placed at the pyramidal sites of the structure. In this paper we report on the preparation of a new material with stoichiometry $YCrMnO_5$, which is isostructural with the RMn_2O_5 compounds and is obtained by substitution of Cr by Mn cations. This oxide must be prepared under high O_2 pressure, and it has been characterized, from the structural point of view, from NPD data, complemented with macroscopic magnetic susceptibility and transport measurements.

[a] Instituto de Ciencia de Materiales de Madrid, CSIC, Cantoblanco, 28049 Madrid, Spain
E-mail: ja.alonso@icmm.csic.es
[b] Laboratory for Neutron Scattering, ETHZ & PSI, 5232 Villigen PSI, Switzerland

Results

Preparation

$YCrMnO_5$ was obtained as a dark brown, polycrystalline powder. The preparation from the precursor powders requires the presence of moderate O_2 pressures in order to partially oxidize Mn and Cr to the tetravalent oxidation states. The presence of the competitive $YMnO_3$ perovskite, nominally containing Mn^{3+}, was minimized with thermal treatments under O_2 pressure. The final O_2 pressure is an important parameter, which was tuned after several unsuccessful trials: treatments at O_2 pressures above 55 bar led to an increase in the competitive $YCrO_4$ phase, which contains Cr^{5+}. Further, the use of finely divided and homogeneous precursors was found to be extremely important for a successful synthesis: the oxygenation process and the formation of the complex oxide are favoured by the use of reactive and homogeneous precursors. Figure 1 shows the XRD pattern of $YCrMnO_5$. It can be indexed in an orthorhombic unit cell, isotypic to RMn_2O_5, with no additional peaks that could indicate the presence of superstructures or departure from the mentioned symmetry. Minor impurities of the competitive $YMnO_3$ and $YCrO_4$ phases were always identified in the patterns.

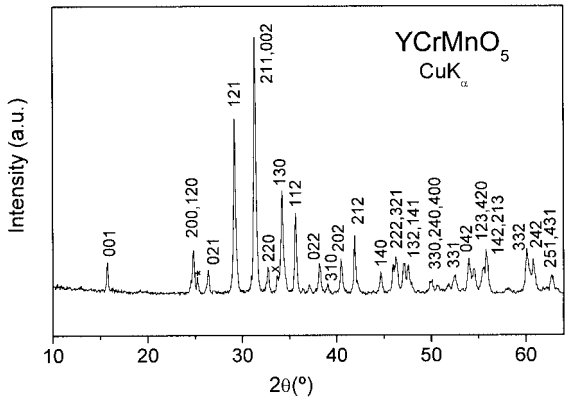

Figure 1. XRD pattern of $YCrMnO_5$, indexed in an orthorhombic unit cell with a = 7.2335(5) Å, b = 8.4953(5) Å, and c = 5.7069(4) Å. The star and the cross indicate the most intense reflections of $YCrO_4$ and $YMnO_3$, respectively.

Magnetic Measurements

The thermal variation of the *dc* susceptibility is shown in Figure 2. The magnetic susceptibility undergoes a remarkable increase below 100 K, revealing the onset of a magnetic transition at $T_C \approx 85$ K, determined from the susceptibility derivative, and an additional abrupt increment below 10 K. A linear Curie–Weiss fit in the high-temperature range 200–400 K gives a Weiss constant of $\theta_{Weiss} = -113(8)$ K, suggesting the presence of strong antiferromagnetic correlations, and an effective moment $\mu_{eff} = 5.60\ \mu_B$/f.u. In order to make clear the nature of the magnetic transitions, isothermal magnetization curves have also been measured. As can be seen in Figure 3, a hysteresis cycle is observed in the magnetization curves at 20 and 1.7 K, indicating the presence of a ferromagnetic component; in particular, at T = 1.7 K, the magnetization reaches 0.25 μ_B/formula at 50 kOe. The absence of saturation of the magnetic moments for the highest applied magnetic fields (50 kOe) is characteristic of ferrimagnetic materials or strongly canted ferromagnets. Above T_C, the magnetization curves at 150 K and 250 K present a linear behavior, corresponding to a paramagnetic state.

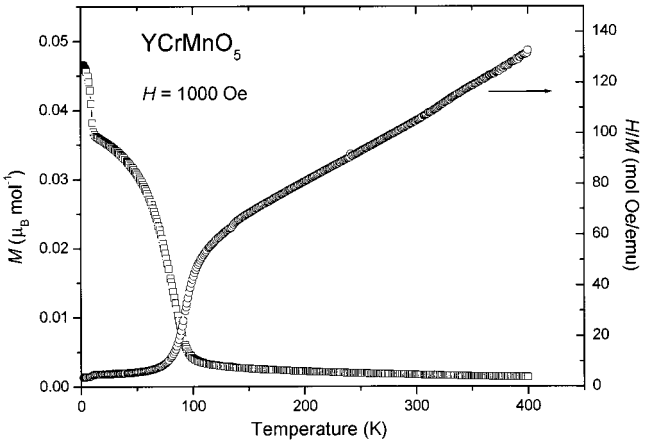

Figure 2. Thermal evolution of the magnetic susceptibility measured under a 1-kOe magnetic field. The right axis corresponds to the reciprocal susceptibility.

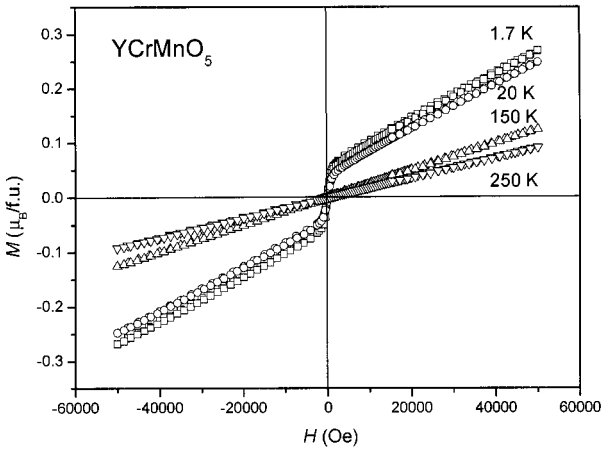

Figure 3. Isothermal magnetization curves.

Transport Properties

The temperature dependence of the electrical resistivity is shown in Figure 4. A semiconducting behavior is observed in the temperature range 160–385 K. A considerably high resistivity of $10^4\ \Omega$cm is observed at room temperature; below 160 K, the resistivity increases above $5 \times 10^6\ \Omega$cm and falls out of the measuring range of our equipment. The plot of ln ρ is linear with the reciprocal temperature, suggesting a thermally activated behavior; an Arrhenius fit gives an activation energy of 0.30 eV. The application of an external magnetic field of up to 90 kOe did not show any significant change in the resistivity, which ex-

 © 2005 Wiley-VCH Verlag GmbH & Co. KGaA, Weinheim

cluded the presence of magnetoresistance in the measured temperature range, well above T_C.

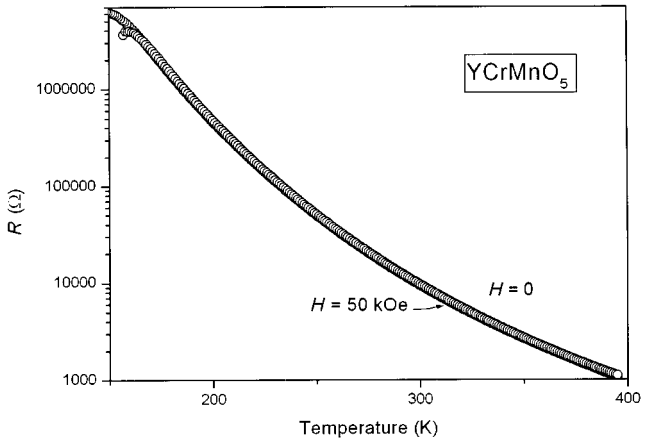

Figure 4. Thermal variation of the resistivity of $YCrMnO_5$. The curves for $H = 0$ and $H = 50$ KOe perfectly overlap.

Room-Temperature Neutron Diffraction: Crystallographic Structure

The crystallographic structure has been refined from the NPD pattern acquired at room temperature with wavelength $\lambda = 1.494$ Å. The pattern was fitted in the orthorhombic space group *Pbam*, with unit-cell parameters $a = 7.2335(5)$ Å, $b = 8.4953(5)$ Å and $c = 5.7069(4)$ Å. The crystal structure of $NdMn_2O_5$ was used as a starting model.[17,18] In the first refinement, Y atoms were placed at 4*g* (*x*,*y*,0) positions, Mn at 4*f* (0,½,*z*) sites, Cr at 4*h* (*x*,*y*,½) positions, and the four crystallographically independent oxygen atoms at 4*e* (0,0,*z*), 4*g*, 4*h* and 8*i* (*x*,*y*,*z*) positions. An unsatisfactory agreement between the calculated and observed patterns was found for this atomic distribution, leading to a discrepancy R_{Bragg} factor of 15%. The presence of antisite disorder between Cr and Mn cations was then checked; the refinement improved considerably, reaching a R_{Bragg} of 4.65%: In fact, the degree of antisite disordering was found to be extremely important in this sample, as shown in Table 1. In the final refinement, the partial occupancy of Cr/Mn at 4*f* and 4*h* positions was decoupled, allowing for the independent refinement of the occupancy factor at both sites; by doing so, the final refined stoichiometry was somewhat different to the nominal Cr/Mn = 1:1 composition, but the quality of the final refinement warrants the validity of this result. The refined crystallographic formula can be written as $Y[Mn_{0.47(1)}Cr_{0.53(1)}]_{4f}[Cr_{0.37(1)}Mn_{0.63(1)}]_{4h}O_5$, which corresponds to an empirical formula $YCr_{0.90(1)}Mn_{1.10(1)}O_5$. It is worth emphasizing that the refinement of the mixed occupancy factors of Cr and Mn over the same crystallographic site, which would be unfeasible by X-ray diffraction, is very precise by neutron diffraction given the opposite values of the scattering lengths for Cr (3.635 fm) and Mn (–3.73 fm). By the same reason, and given the comparable amounts of Cr and Mn found in both sites, the average scattering length of both sites is very weak, and the error in the determination of the corresponding positions and thermal factors is huge. As a result, in the final refinement, we fixed the positions to those determined by X-ray diffraction for both the 4*f* and 4*h* sites, and the thermal factors were fixed to 0.3 Å^2. The main structural parameters obtained in the fit are presented in Table 1. A selection of the most important atomic distances and angles is listed in Table 2. The goodness of the fit after the Rietveld refinement from the NPD data is displayed in Figure 5. The two minor impurities $YCrO_4$ (space group $I4_1/amd$, ref.[19]) and $YMnO_3$ (space group *Pbnm*, ref.[20]) were included in the refinement as second and third crystallographic phases;

Table 2. Selected interatomic distances [Å] and angles [°] for $YCrMnO_5$ at 295 K.

$(Cr,Mn)_{4f}O_6$ octahedra		YO_8	
Cr–O2 (x2)	1.973(8)	Y–O1 (x2)	2.362(5)
Cr–O3 (x2)	1.870(8)	Y–O2	2.319(6)
Cr–O4 (x2)	1.940(3)	Y–O2	2.392(6)
<Cr–O>	1.927	Y–O4 (x2)	2.337(4)
$(Mn,Cr)_{4h}O_5$ pyramids		Y–O4 (x2)	2.493(4)
Mn–O1 (x2)	1.930(7)	<Y–O>	2.387
Mn–O3	1.932(8)	Cr1–Cr1	2.96(1)
Mn–O4 (x2)	1.884(6)	Cr1–Cr1	2.74(1)
<Mn–O>	1.912	Mn2–Mn2	2.86(1)
Mn–O1–Mn	95.6(5)		
Cr–O2–Cr	97.4(14)	Cr–O3–Mn	132.0(5)
Cr–O3–Cr	94.3(7)	Cr–O4–Mn	123.0(5)

Table 1. Structural parameters after the refinement of NPD data for $YCrMnO_5$ at 295 K refined in the *Pbam* space group.

Atoms	Positions	*x*	*y*	*z*	*B* [Å^2]	Occupancy
Y	*4g*	0.1386(5)	0.1726(4)	0.00000	1.00(6)	1.0
Cr	*4f*	0.0000	0.5000	0.260(2)	0.30	0.53(1)
Mn′	*4f*	0.0000	0.5000	0.260(2)	0.30	0.47(1)
Mn	*4h*	0.4056(8)	0.3521(9)	0.50000	0.30	0.63(1)
Cr′	*4h*	0.4056(8)	0.3521(9)	0.50000	0.30	0.37(1)
O1	*4e*	0.0000	0.0000	0.2729(9)	0.98(7)	1.0
O2	*4g*	0.1678(6)	0.4444(5)	0.00000	0.41(8)	1.0
O3	*4h*	0.1534(7)	0.4270(5)	0.50000	0.75(9)	1.0
O4	*8i*	0.3918(3)	0.2088(3)	0.2487(7)	0.79(5)	1.0
Unit cell	$a = 7.2335(5)$ Å	$b = 8.4953(5)$ Å	$c = 5.7069(4)$ Å	$V = 350.69(4)$ Å^3		
Discrepancy factors	$R_p = 1.96\%$	$R_{wp} = 2.52\%$	$R_{Bragg} = 4.6\%$	$\chi^2 = 1.45$		

 © 2005 Wiley-VCH Verlag GmbH & Co. KGaA, Weinheim

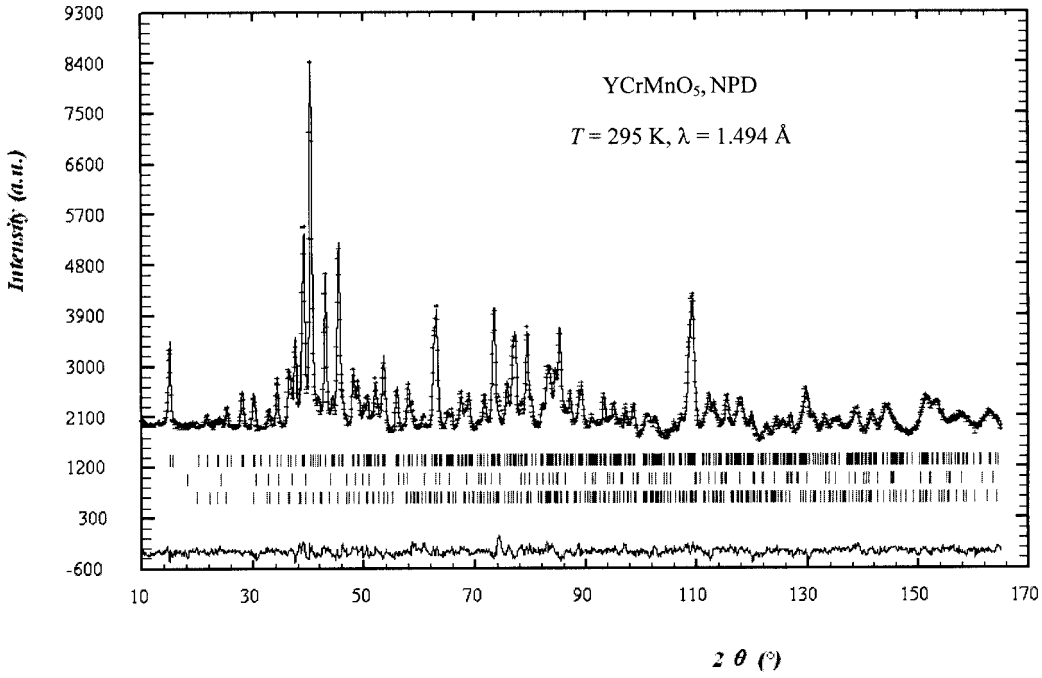

Figure 5. Observed (crosses), calculated (solid line) and difference (bottom line) NPD patterns at room temperature. The second and third series of Bragg positions correspond to the minor impurities $YCrO_4$ and $YMnO_3$, respectively.

from the scale factors, an amount of 1.34% and 2.03% of both impurities was estimated, respectively.

A view of the crystallographic structure along the *c* axis is displayed in Figure 6. There are two different oxygen environments for the atoms that occupy the 4*f* and 4*h* sites. At the 4*f* site, the $(Cr,Mn)^{4+}$ ions are inside the $M^{4+}O_6$ distorted octahedra, whereas at the 4*h* site, the $(Mn,Cr)^{3+}$ ions form $M^{3+}O_5$ distorted tetragonal pyramids. We assume that the Mn and Cr cations at the octahedral positions adopt a tetravalent oxidation state, whereas the metals at the pyramidal positions adopt a trivalent oxidation state, in order to preserve the electroneutrality of this oxide. Notice that the octahedral 4*f* positions are about half occupied by Cr and Mn, whereas the pyramidal 4*h* are about 2/3 occupied by Mn, probably because this irregular environment is well suited for the Jahn–Teller Mn^{3+} cation. The pyramids share edges to form dimer units M_2O_{10}, linked through O1 oxygen atoms. The structure contains infinite chains of $M^{4+}O_6$ octahedra, which share edges through the O2 and O3 oxygen atoms, that run along the *c* axis. The different chains of $M^{4+}O_6$ are interconnected through the M_2O_{10} pyramidal dimer units through the O3 and O4 oxygen atoms.

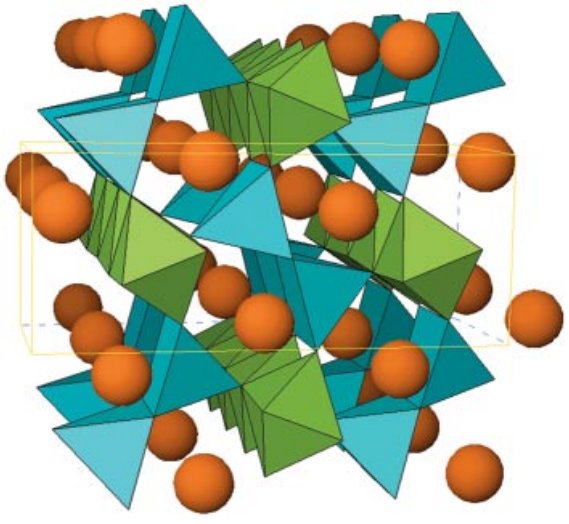

Figure 6. A view of the crystallographic structure of $YCrMnO_5$, approximately along the *c* axis. Octahedra (green) and tetragonal (turquoise) pyramids correspond to $(Cr,Mn)^{4+}O_6$ and $(Mn,Cr)^{3+}O_5$ polyhedra, respectively. Octahedra share edges, forming infinite chains along the *c* axis. Pyramids form dimer units, linking together the chains of the octahedra. Orange spheres represent the Y atoms.

Low-Temperature Neutron Diffraction Refinements

Three neutron diffraction patterns were collected below room temperature, with the hope of gaining information about the arrangement of Mn and Cr spins below the ordering temperature, T_C = 90 K. However, the low-temperature patterns collected at T = 1.5 K and 20 K did not contain any additional information, extra peaks or additional intensity on low angle Bragg reflections that could be attributed to the establishment of a long-range, ordered magnetic structure; the three patterns collected with λ = 1.886 Å could be perfectly refined by considering the crystal structure alone, with the expected shifts in unit-cell parameters and thermal factors. The upper limit of the ordered magnetic moments was determined from a simulation of a ferrimagnetic structure involving both magnetic sublattices. For the *Pbam* space group, there are two ferromagnetic Shubnikov groups: *Pb′a′m* and *Pb′am′*. The 4*f* and 4*h* sites have

 © 2005 Wiley-VCH Verlag GmbH & Co. KGaA, Weinheim

Table 3. Unit cell, positional, and thermal parameters for $YCrMnO_5$, refined in the orthorhombic *Pbam* space group, from NPD data below room temperature.

T [K]	1.5	20	120
a [Å]	7.2116(6)	7.2114(6)	7.2171(5)
b [Å]	8.4970(6)	8.4963(6)	8.4953(5)
c [Å]	5.7037(4)	5.7032(4)	5.7042(4)
V [Å^3]	349.50(4)	349.44(4)	349.73(4)
Y	*4 g* (*x*,*y*,0)		
x	0.1389(5)	0.1395(5)	0.1392(5)
y	0.1720(5)	0.1711(5)	0.1714(5)
B [Å^2]	0.72(8)	0.72(8)	0.78(8)
(Mn,Cr)	*4f* (0,½,*z*)		
z	0.25972	0.25972	0.25972
B [Å^2]	0.300	0.300	0.300
(Cr,Mn)	*4h* (*x*,*y*, ½)		
x	0.40562	0.40562	0.40562
y	0.35210	0.35210	0.35210
B [Å^2]	0.300	0.300	0.300
O1	*4e* (0,0,*z*)		
z	0.274(1)	0.274(1)	0.274(1)
B [Å^2]	0.9(1)	0.8(1)	0.9(1)
O2	*4g* (*x*,*y*,0)		
x	0.1668(8)	0.1672(8)	0.1667(8)
y	0.4430(5)	4430(5)	0.4433(5)
B [Å^2]	0.2(1)	0.2(1)	0.2(1)
O3	*4h* (*x*,*y*,½)		
x	0.1557(9)	0.1551(9)	0.1548(9)
y	0.4297(6)	0.4301(6)	0.4287(6)
B [Å^2]	0.9(1)	1.1(1)	1.1(1)
O4	*8i* (*x*,*y*,*z*)		
x	0.3921(4)	0.3923(4)	0.3922(4)
y	0.2076(4)	0.2076(4)	0.2080(4)
z	0.2454(7)	0.2453(7)	0.2454(7)
B [Å^2]	0.75(8)	0.67(8)	0.64(7)
Reliability factors			
χ^2	3.71	3.57	3.07
R_{Bragg} (%)	4.82	5.03	4.93

symmetries 2 and *m*, respectively. This means that the admissible moment directions for both sites are along the *z* axis for *Pb′a′m*, and perpendicular to the *z* axis for *Pb′am′*. After trying both possibilities, the estimation for the upper limit was found to be similar in both cases, $\mu < 0.4\ \mu_B$. Table 3 lists the main structural parameters after the refinement. Figure 7 illustrates the quality of the Rietveld fit at 1.5 K; the main crystallographic phase and the two minor impurity phases, $YCrO_4$ and $YMnO_3$, are considered in the same way as those in the room temperature refinement.

Discussion

$YCrMnO_5$ is derived from the parent YMn_2O_5 oxide (containing one Mn^{3+} and one Mn^{4+} cation per formula) by full replacement of approximately half the Mn atoms by Cr atoms. The crystal structure of $YCrMnO_5$, refined from NPD data, is closely related to that of RMn_2O_5 oxides, as expected from the comparable ionic sizes for Cr^{3+} and Mn^{3+} (0.615 and 0.645 Å, respectively), and Mn^{4+} and Cr^{4+} (0.53 and 0.55 Å, respectively) in a sixfold coordination and in the high-spin state for both cations.[21] Since no structural details on the parent YMn_2O_5 have been reported, a comparison can be established with the crystal structure of $HoMn_2O_5$,[8] given the similarity in the ionic sizes of Y^{3+} (1.019 Å) and Ho^{3+} cations (1.015 Å) in an eightfold coordination.[23] In $HoMn_2O_5$ (and other RMn_2O_5 compounds), the $Mn^{4+}O_6$ octahedra are fairly flattened,[8,19] with two bonds significantly shorter than the remaining four bonds [e.g. a Mn1–O3 bond length of 1.836(8) Å for the Ho compound]; the average Mn–O distance is 1.902 Å. The same configuration is observed in $YCrMnO_5$, although

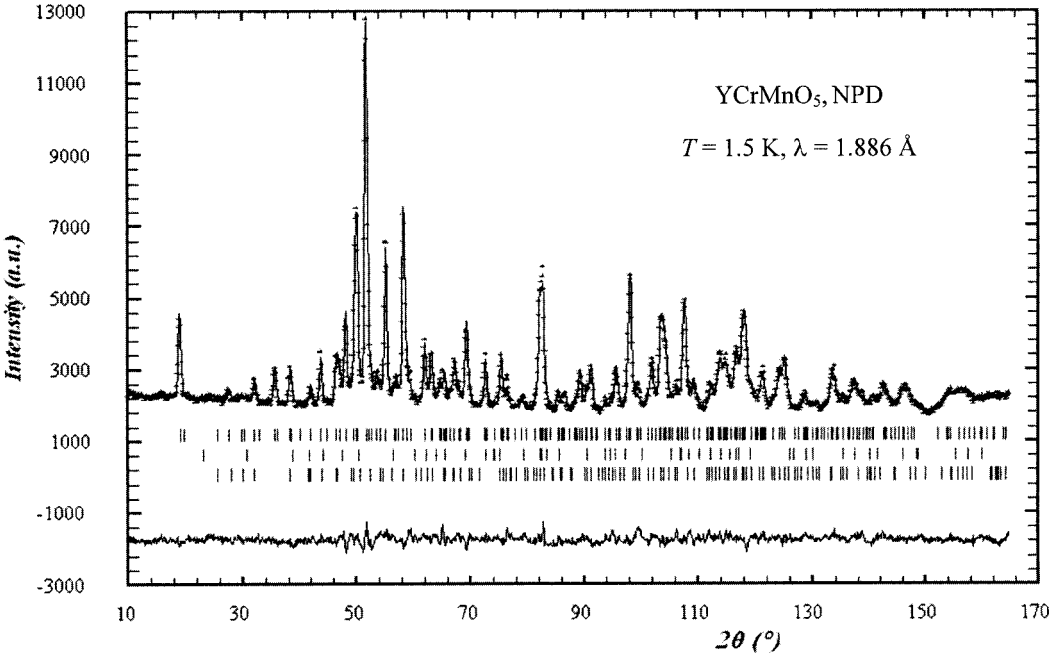

Figure 7. Observed (crosses), calculated (solid line) and difference (bottom line) NPD patterns for *T* = 1.5 K. The three series of Bragg positions correspond to $YCrMnO_5$, $YCrO_4$, and $YMnO_3$, respectively.

 © 2005 Wiley-VCH Verlag GmbH & Co. KGaA, Weinheim

the individual and average $(Cr,Mn)^{4+}$–O distances are slightly longer, scaling with the greater size of Cr^{4+} cations; the average bond length is 1.927 Å. With regard to the tetragonal pyramids, $(Mn,Cr)^{3+}O_5$, the equatorial (Mn,Cr)–O1 and (Mn,Cr)–O4 bond lengths (forming the square basis of the pyramid) are similar to the corresponding Mn–O distances in the $Mn^{3+}O_5$ units of the RMn_2O_5 compounds, whereas the axial (Mn,Cr)–O3 bond length [1.932(8) Å] is shorter than that observed in $HoMn_2O_5$, where the Mn^{3+}–O3 bond in the axial position is the longest one in the $Mn^{3+}O_5$ pyramid [2.024(8) Å]. This is probably related to the Jahn–Teller character of Mn^{3+} cations, favoring an increase in the axial bond lengths in the $Mn^{3+}O_5$ pyramids, in contrast with the non-Jahn–Teller character of Cr^{4+} ($3d^5$ configuration). With respect to the oxygen coordination of the Y^{3+} cations, it can be described as $Y^{3+}O_8$ bicapped prisms, with average <Y–O> distances of 2.387 Å, which are in good agreement with the <Ho–O> bond lengths of 2.381 Å observed in $HoMn_2O_5$.

One of the most remarkable features of $YCrMnO_5$ is the high degree of antisite disordering exhibited by this compound, which implies that the octahedral positions are occupied by roughly 50% of Mn and Cr cations, and the pyramidal groups contain two thirds Mn and one third Cr cations. This feature could only be unraveled by a neutron diffraction study, thanks to the contrasting neutron scattering lengths of Cr and Mn. The trend of Cr and Mn cations sharing the same crystallographic positions is opposite to that found in $YFeMnO_5$, where a clear preference of Mn^{4+} for the octahedral positions and Fe^{3+} for the tetrahedral sites was observed.[16] The reason of this difference could be found in the relative ease of Cr vs. Fe to adopt the tetravalent oxidation state for incorporation into the octahedral positions.

The Cr/Mn antisite disordering has a dramatic influence on the magnetic properties of $YCrMnO_5$. It shows a ferromagnetic-like behavior, with $T_C \approx 85$ K and a weak magnetization at 1.7 K of 0.25 μ_B/f.u. for $H = 50$ kOe. This is reminiscent of the ferrimagnetic behavior determined for $YFeMnO_5$, which shows a superior magnetic ordering temperature of $T_C \approx 165$ K, and a saturation magnetization at low temperatures of 0.81 μ_B/formula: In $YFeMnO_5$, a NPD study demonstrated that Mn and Fe magnetic moments, at the 4*f* and 4*h* crystallographic sites of the *Pbam* space group, respectively, lie along the *z* direction and are antiferromagnetically coupled, giving rise to a global ferrimagnetic structure. Assuming a ferrimagnetic coupling between the magnetic moments at the octahedral and pyramidal positions in $YCrMnO_5$, the net magnetization could vary from zero for the hypothetical composition $YCr^{3+}Mn^{4+}O_5$ ($S = 3/2$ for Cr^{3+}; $S = 3/2$ for Mn^{4+}) to 2 μ_B/f.u. for the hypothetical $YCr^{4+}Mn^{3+}O_5$ ($S = 1$ for Cr^{4+}; $S = 2$ for Mn^{3+}) stoichiometry. Given the actual level of antisite disordering found by neutron diffraction, the net magnetization for ferrimagnetic ordering between octahedral and pyramidal positions in $Y[Mn_{0.47(1)}Cr_{0.53(1)}]_{oct}[Cr_{0.37(1)}Mn_{0.63(1)}]_{pyr}O_5$ would be of 1.16 μ_B/f.u.: This is significantly higher than that found experimentally. This fact, together with the absence of magnetic reflections in the neutron diagrams collected below T_C (at 1.5 and 20 K) demonstrate that there is only a partial long-range magnetic ordering, giving rise to ordered moments below the detection limit of the neutron diffraction technique (0.5–1 μ_B). The random occupancy of both octahedral and pyramidal positions by Cr and Mn cations hinders the establishment of a full long-range ferrimagnetic ordering between both magnetic sublattices below $T_C \approx 85$ K. For the same reason, the NPD technique does not provide any insight on the nature of the second anomaly observed in the susceptibility curve below 10 K; this probably results from a spin reorientation in the complex system, although an effect coming from the observed impurities cannot be disregarded.

Conclusions

We describe a new oxide obtained by replacing Mn by Cr in the parent YMn_2O_5 compound. The crystal structure of $YCrMnO_5$ is isotypic with that of RMn_2O_5 materials (space group *Pbam*), and contains chains of edge-linked $(Cr,Mn)^{4+}O_6$ octahedra connected by dimer groups of square pyramids $(Mn,Cr)^{3+}O_5$. A feature of the Cr compound is that the square pyramids are not elongated, showing shorter axial distances relative to the $Mn^{3+}O_5$ pyramids in RMn_2O_5. $YCrMnO_5$ is semiconducting with a large room-temperature resistivity; the magnetic susceptibility reveals the onset of a ferrimagnetic structure below $T_c \approx 85$ K. The low-temperature NPD patterns do not show any magnetic contribution, indicating that a full long-range magnetic ordering is not established down to 1.5 K, although the presence of ferrimagnetic interactions between two distinct sublattices are clearly displayed in the magnetization curves.

Experimental Section

$YCrMnO_5$ was prepared in polycrystalline form from citrate precursors obtained by a wet-chemistry procedure. Stoichiometric amounts of analytical grade Y_2O_3, $Cr(NO_3)_3{\cdot}9H_2O$, and $MnCO_3$ were dissolved in citric acid; the solution was evaporated slowly, leading to an organic resin which was dried at 120 °C and decomposed at temperatures of up to 600 °C in air. High oxygen pressure treatments were performed in a VAS furnace. About 2 g of the precursor powder was contained in a gold can during the oxygenation process. The sample was slowly heated up to 900 °C at a final pressure of 55 bar, and held at this temperature for 12 h. The product was finally cooled, under pressure, down to room temperature at 300 °C h^{-1}. Finally, the oxygen pressure was released.

The dc susceptibility measurements were performed in a commercial SQUID magnetometer. They were obtained under a 1 kOe magnetic field under field-cooling conditions and for the temperature interval $1.8 < T < 400$ K. Different isothermal magnetization curves were measured under magnetic fields ranging from –50 kOe to 50 kOe and at $T = 1.7$, 20, 150, and 250 K. Transport measurements were performed by the conventional four-probe technique in a pellet sintered under the synthesis conditions (900 °C under 55 bar O_2). Magnetotransport measurements were carried out un-

 © 2005 Wiley-VCH Verlag GmbH & Co. KGaA, Weinheim

der magnetic fields of up to 90 kOe in a PPMS system from Quantum Design.

Neutron powder diffraction (NPD) diagrams were collected with the high resolution HRPT diffractometer of the SINQ spallation source, at the Paul Scherrer Institute, Villigen, Switzerland. The sample (2 g) was packed in a cylindrical vanadium holder with a 6-mm diameter. The room temperature pattern was collected with a wavelength of 1.494 Å. The sample was then cooled down in an orange cryostat, and three patterns were collected at 1.5, 20, and 120 K with a wavelength of 1.886 Å. In all cases, the high-intensity mode was used; the collection time was 4 h per diagram. The neutron diffraction patterns were analyzed with the Rietveld method,[22] using the FULLPROF program.[23] For the refinement of the profile, a pseudo-Voigt function was used to simulate the peak shape, and the background was fitted with a fifth-degree polynomial function. The coherent scattering lengths for Y, Cr, Mn, and O were, 7.75, 3.635, –3.73, and 5.803 fm, respectively. In the final run, the following parameters were refined: Background coefficients, zero-point, half-width, pseudo-Voigt, and asymmetry parameters for the peak shape; scale factor, positional, thermal factors, and unit-cell parameters.

Acknowledgments

We thank CICyT for the financial support for the project MAT2004–0479. This work was partially performed at the spallation source SINQ, Paul Scherrer Institute, Villigen, Switzerland. This research project has been supported by the European Commision under the 6th Framework Programme through the Key Action: Strengthening the European Research Area, Research Infrastructures; contract no. R113-CT-2003-505925.

[1] S. Quezel-Ambrunaz, E. F. Bertaut, G. Buisson, *C. R. Acad. Sci.* **1964**, *258*, 3025.
[2] E. F. Bertaut, G. Buisson, A. Durif, A. Mareschal, M. C. Montmory, S. Quezel-Ambrunaz, *Bull. Soc. Chim. Fr.* **1965**, 1132.
[3] A. Kadomtseva, Y. F. Popov, G. P. Vorobev, K. I. Kamilov, P. N. Makhov, M. M. Tehranchi, A. Phirouznia, *Physica B: Condensed Matter* **2003**, *329–333*, 856.
[4] K. Saito, K. Kohn, *J. Phys. Condens. Matter* **1995**, *7*, 2855.
[5] A. Inomata, K. Kohn, *J. Phys. Condens. Matter* **1996**, *8*, 2673.
[6] Y. F. Popov, A. M. Kadomtseva, S. S. Krotov, G. P. Vorob′ev, M. M. Lukina, *Ferroelectrics* **2002**, *279*, 147.
[7] Y. F. Popov, A. M. Kadomtseva, S. S. Krotov, G. P. Vorob′ev, K. I. Kamilov, M. M. Lukina, M. M. Tegranchi, *J. Exp. Theor. Phys.* **2003**, *96*, 961.
[8] J. A. Alonso, M. T. Casais, M. J. Martínez-Lope, J. L. Martínez, M. T. Fernández-Díaz, *J. Phys. Condens. Matter* **1997**, *9*, 8515.
[9] A. Muñoz, M. T. Casais, M. J. Martínez-Lope, J. L. Martínez, J. A. Alonso, M. T. Fernández-Díaz, *Phys. Rev. B* **2002**, *65*, 144423.
[10] G. Buisson, *Phys. Status Solidi A* **1973**, *16*, 533.
[11] G. Buisson, *Phys. Status Solidi A* **1973**, *17*, 191.
[12] P. P. Gardner, C. Wilkinson, J. B. Forsyth, B. M. Wanklyn, *J. Phys. C: Solid State Phys.* **1988**, *21*, 5653.
[13] C. Wilkinson, F. Sinclair, P. P. Gardner, J. B. Forsyth, B. M. Wanklyn, *J. Phys. C: Solid State* **1981**, *14*, 1671.
[14] E. F. Bertaut, G. Buisson, S. Quezel-Ambrunaz, G. Quezel, *Solid State Commun.* **1967**, *5*, 25.
[15] A. Muñoz, J. A. Alonso, M. T. Casais, M. J. Martínez-Lope, J. L. Martínez, M. T. Fernández-Díaz, *J. Mater. Chem*. 2004, in press.
[16] A. Muñoz, J. A. Alonso, M. J. Martínez-Lope, J. L. Martínez, *Chem. Mater.* **2004**, *16*, 4087.
[17] P. Euzen, P. Leone, Ch. Gueho, P. Palvadeau, *Acta Crystallogr. C* **1993**, *49*, 1875.
[18] J. A. Alonso, M. T. Casais, M. J. Martínez-Lope, I. Rasines, *J. Solid State Chem.* **1997**, *129*, 105.
[19] G. Buisson, E. F. Bertaut, J. Mareschal, *C. R. Acad. Sci.* **1964**, *259*, 411.
[20] J. A. Alonso, M. J. Martínez-Lope, M. T. Casais, M. T. Fernández-Díaz, *Inorg. Chem.* **2000**, *39*, 917.
[21] R. D. Shannon, *Acta Crystallogr., Sect. A* **1976**, *32*, 751.
[22] H. M. Rietveld, *J. Appl. Crystallogr.* **1969**, *2*, 65.
[23] J. Rodríguez-Carvajal, *Physica B* **1993**, *192*, 55.

Received: December 28, 2004

 © 2005 Wiley-VCH Verlag GmbH & Co. KGaA, Weinheim

Synthesis and X-ray Molecular Structure of $(PNP)_2[Mo^{IV}(C_6H_4S_2\text{-}1,2)_3]$ Completing the Structural Characterization of the Series $[Mo(C_6H_4S_2\text{-}1,2)_3]^{n-}$ (n = 0, 1, 2)

Christian Schulze Isfort,[a] Tania Pape,[a] and F. Ekkehardt Hahn*[a]

Keywords: Molybdenum / S ligands / X-ray diffraction / Coordination modes

The tris(benzene-1,2-dithiolato) complex $(Li)_2[Mo^{IV}(C_6H_4S_2\text{-}1,2)_3]$ {$(Li)_2[Mo^{IV}(bdt)_3]$} (bdt^{2-} = $C_6H_4S_2$-1,2 dianion) was synthesized from $[MoCl_4(CH_3CN)_2]$, (H_2bdt), and *n*BuLi in THF. Complex $(Li)_2[Mo^{IV}(bdt)_3]$ undergoes aerial oxidation to give $Li[Mo^{V}(bdt)_3]$. Both complexes were crystallized from methanol as the salts $(PNP)_2[Mo^{IV}(bdt)_3]$ and $(PNP)[Mo^{V}(bdt)_3]$ {PNP^+ = bis(triphenylphosphoranylidene)ammonium cation}, and their molecular structures were determined by X-ray diffraction. The molybdenum(IV) complex $[Mo^{IV}(bdt)_3]^{2-}$ assumes a distorted trigonal prismatic coordination geometry (average twist angle φ = 24.8°) while the coordination geometry of $[Mo^{V}(bdt)_3]^-$ is best described as distorted octahedral (average twist angle φ = 34.1°).

(© Wiley-VCH Verlag GmbH & Co. KGaA, 69451 Weinheim, Germany, 2005)

Introduction

The first trigonal prismatic (TP) tris(dithiolene) metal complex, tris(*cis*-1,2-diphenylethylene-1,2-dithiolato)rhenium, was reported in 1965.[1] Ever since, the reasons for the formation of complexes with trigonal prismatic coordination geometry over octahedral complexes has been a subject for discussion.[2] Early explanations based on molecular orbital schemes indicated that metal centers with a *formal* d^0 electron configuration preferentially form trigonal prismatic tris(dithiolene) transition metal complexes. In the series of tris(benzene-1,2-dithiolato) complexes, $[W^{VI}(bdt)_3]$ is trigonal prismatic (twist angle φ = 0°),[3] while the geometry of $[W^{V}(bdt)_3]^-$ was found to be closer to octahedral (average twist angle φ = 33°) than to trigonal prismatic.[4] Surprisingly, the $[W^{IV}(bdt)_3]^{2-}$ complex exhibits a geometry close to perfect trigonal prismatic (average twist angle φ = 3.5°).[5] In the homologous series of molybdenum complexes $[Mo^{V}(bdt)_3]^-$ assumes a geometry analogous to the W^V complex, between octahedral and trigonal prismatic (average twist angle φ = 33.5°),[6] while the complex $[Mo^{VI}(bdt)_3]$ is, as expected, trigonal prismatic (average twist angle φ = 0°).[7] The molecular structure of $[Mo^{IV}(bdt)_3]^{2-}$ has not been reported. The pseudooctahedral geometry of the d^0 complex $[Zr^{IV}(bdt)_3]^{2-}$ is rather unexpected[8] when compared to the trigonal prismatic[9] d^0 complex $[Nb^{V}(bdt)_3]^-$. It appears that the stepwise reduction of the *formal* d^0 center in $[M^{VI}(bdt)_3]$ (M = Mo, W) complexes does not generally enhance the tendency for the formation of octahedral complexes, and that the geometry of a particular complex is not governed only by electronic factors. Ligand constraints,[10] matching of ligand and metal d orbital energies, symmetry of ligand π orbitals, inter-donor interactions, and the overall charge of the complex have been suggested to be additional important factors.[11]

The situation is further complicated by the non-innocent nature of the bdt^{2-} ligand. Wieghardt has shown that an intramolecular redox reaction can convert coordinated bdt^{2-} into a coordinated *o*-dithiobenzosemiquinonate(1–) radical anion by the reduction of the metal center. Under such conditions, the *spectroscopic* oxidation state of the metal differs from the formal oxidation state. The geometrical changes within the ligand that are associated with the intramolecular redox reaction have been outlined for square planar bdt^{2-} complexes.[12]

As part of our ongoing effort to shed light on the relationship between the *formal* oxidation state of the metal and the molecular structure of $[M(bdt)_3]^{n-}$ (M = Mo, W) complexes, we present here the preparation and molecular structure of the yet unknown derivative $(PNP)_2[Mo^{IV}(bdt)_3]^{2-}$. In addition, the previously described[6] complex anion $[Mo^{V}(bdt)_3]^-$ was prepared again, and the crystal structure of the salt $(PNP)[Mo^{V}(bdt)_3]$ was elucidated and compared to the molecular structure reported for $(nBu_4N)[Mo^{V}(bdt)_3]$.[6a]

Results and Discussion

Transition metal tris(benzene-1,2-dithiolato) complexes have been synthesized by the reaction of the hexahalides

[a] Institut für Anorganische und Analytische Chemie, Westfälische Wilhelms–Universität Münster,
Wilhelm Klemm Strasse 8, 48149 Münster, Germany
Fax: +49-251-833-3108
E-mail: fehahn@uni-muenster.de

MX_6 with an excess of benzene-1,2-dithiol (H_2bdt) in CCl_4, a reaction that liberates gaseous HCl.[2d] Later Sellmann et al. showed that benzene-1,2-dithiol that is deprotonated with *n*BuLi (Li_2bdt) reacts with $[MoCl_4(THF)_2]$ to give $(Li)_2[Mo^{IV}(bdt)_3]$, while the reaction of benzene-1,2-dithiol with $[MoCl_4(THF)_2]$ gives $[Mo^{VI}(bdt)_3]$.[6b] Complex $[Mo^{VI}(bdt)_3]$ can be reduced to the complexes $[Mo^{V}(bdt)_3]^-$ and $[Mo^{IV}(bdt)_3]^{2-}$ with *n*BuLi.

We prepared $(Li)_2[Mo^{IV}(bdt)_3]$ by the deprotonation of H_2bdt with *n*BuLi at –78 °C in THF followed by the the dropwise addition of a DMF solution of $[MoCl_4(CH_3CN)_2]$ at –78 °C (Scheme 1). Below –40 °C the reaction mixture remained unchanged and colorless. Warming to above –40 °C led to a color change in the reaction mixture to deep blue, which is typical for solutions containing the $[Mo^{IV}(bdt)_3]^{2-}$ anion.[6b] The solution was warmed to room temperature, stirred at this temperature overnight, and then heated under reflux for 1 h. Standard workup procedures gave $(Li)_2[Mo^{IV}(bdt)_3]$ in 76% yield. Blue, air-sensitive crystals of $(PNP)_2[Mo^{IV}(bdt)_3]\cdot 6\,MeOH$ suitable for X-ray analysis were obtained by addition of a methanolic solution of PNPCl to a methanolic solution of $(Li)_2[Mo^{IV}(bdt)_3]$. Aerial oxidation of $(Li)_2[Mo^{IV}(bdt)_3]$ in methanol gave a green solution of $(Li)[Mo^{V}(bdt)_3]$. Addition of a methanolic solution of PNPCl yielded green, air-stable crystals of $(PNP)[Mo^{V}(bdt)_3]$ (Scheme 1).

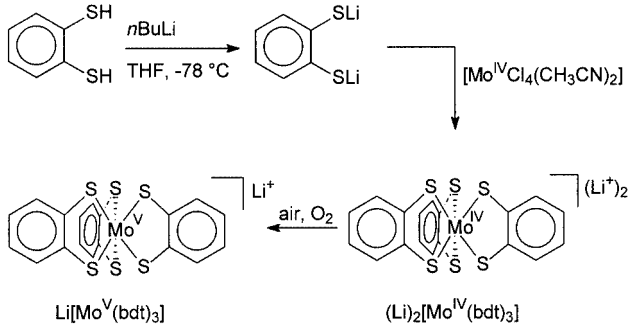

Scheme 1. Preparation of $(Li)_2[Mo^{IV}(bdt)_3]$ and $(Li)[Mo^{V}(bdt)_3]$.

The ^1H NMR spectrum of complex $(Li)_2[Mo^{IV}(bdt)_3]$ exhibits two multiplets at δ = 7.37 ppm and δ = 6.57 ppm for the benzene protons, and the coupling pattern corresponds to a symmetrical AA′XX′ spin system (Figure 1). Two resonances for the benzene carbon atoms were observed in the ^{13}C NMR spectrum at δ = 119.8 ppm and δ = 126.5 ppm in addition to the signal for the *ipso*-carbon atom at δ = 155.1 ppm. The difference in the line widths of these signals appears to be an artifact of the data acquisition method.

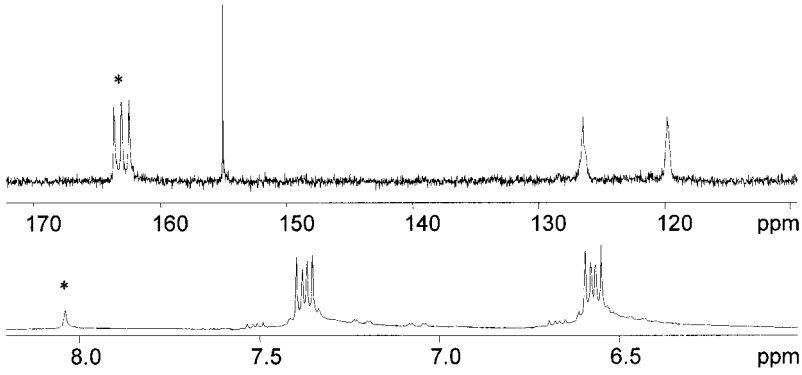

Figure 1. ^{13}C NMR (top) and ^1H NMR spectra (bottom) of $(Li)_2[Mo^{IV}(bdt)_3]$ (* = solvent).

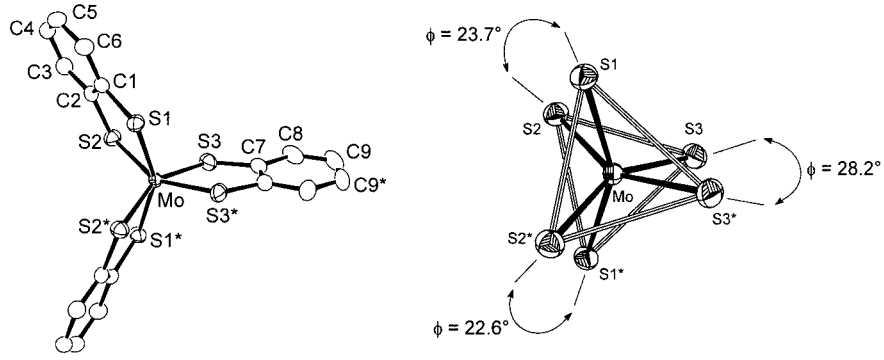

Figure 2. Left: molecular structure of the $[Mo^{IV}(bdt)_3]^{2-}$ anion with the crystallographic numbering scheme. Hydrogen atoms have been omitted. The anion resides on a twofold axis which bisects the C9–C9* bond (symmetry code *: 1 – *x*, *y*, 1/2 – *z*). Selected bond lengths [Å] and angles [°]: Mo–S1 2.3952(14), Mo–S2 2.3981(12), Mo–S3 2.3940(12), S1–C1 1.765(3), S2–C2 1.761(3), S3–C7 1.750(4); S1–Mo–S2 81.06(4), S1–Mo–S3 115.68(4), S1–Mo–S1* 152.33(5), S1–Mo–S2* 84.93(5), S1–Mo–S3* 85.96(4), S2–Mo–S3 83.22(5), S2–Mo–S1* 84.93(5), S2–Mo–S2* 118.70(5), S2–Mo–S3* 153.06(3), S3–Mo–S3* 81.31(6). Right: drawing of the MoS_6 core showing the twist angle φ between the S_3 planes.

 © 2005 Wiley-VCH Verlag GmbH & Co. KGaA, Weinheim

The ^1H NMR resonances correspond well to the values reported for $(NEt_4)_2[W(bdt)_3]$.[5] The molecular structure of $(PNP)_2[Mo(bdt)_3]\cdot 6\,MeOH$ was determined by X-ray diffraction (Figure 2).

The overall solid state molecular structure of the complex anion $[Mo^{IV}(bdt)_3]^{2-}$ differs from that of the heavier homologue $[W^{IV}(bdt)_3]^{2-}$. The molybdenum(IV) ion in $[Mo(bdt)_3]^{2-}$ is coordinated by six sulfur atoms from three bdt^{2-} ligands in a strongly distorted trigonal prismatic fashion. The average twist angle φ[13] (see Figure 2, right) is 24.8° for $[Mo(bdt)_3]^{2-}$ compared to φ = 3.5° for $[W(bdt)_3]^{2-}$.[5] The three different twist angles observed for $[Mo(bdt)_3]^{2-}$ result from the noncoplanar arrangement of the two S_3 planes. The bending of the S–C–C–S plane away from the S–Mo–S–plane is small in $[Mo^{IV}(bdt)_3]^{2-}$ (about 0.8°) while large bending angles were observed for $[Mo^{VI}(bdt)_3]$ (13.1, 21.1, 30.0°)[7] and $[W^{VI}(bdt)_3]$ (13.5, 22.6, 32.1°).[3] On the basis of Fenske–Hall MO calculations it has been suggested that the bending of the ligand can be viewed as a second-order Jahn–Teller distortion, which is most favored for d^0 metal centers in a trigonal prismatic coordination environment.[14] While the electronic factors provide the principal driving force, the bulk of the dithiolate ligand also plays a role in determining the molecular structures. This becomes obvious when the three different bending angles for $[M^{VI}(bdt)_3]$ (M = Mo, W) complexes are considered.

For a comparison of the bond parameters in $[Mo^{IV}(bdt)]^{2-}$ and $[Mo^{V}(bdt)]^{-}$, which have been obtained under similar conditions (153–173 K) and with identical counterions, we determined the molecular structure of $(PNP)[Mo^{V}(bdt)_3]$ (Figure 3). The molecular structure of $(nBu_4N)[Mo^{V}(bdt)_3]$ has been determined previously at room temperature.[6a]

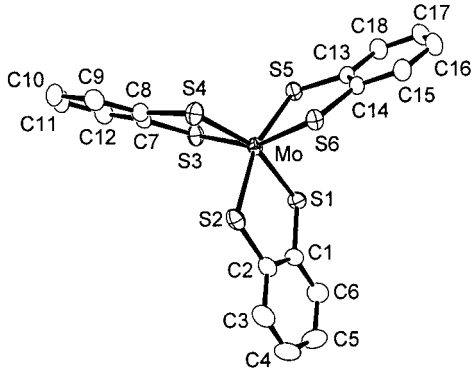

Figure 3. Molecular structure of $[Mo^{V}(bdt)_3]^{-}$ with the crystallographic numbering scheme. Hydrogen atoms have been omitted. Selected bonds lengths [Å] and angles [°]: Mo–S1 2.3880(8), Mo–S2 2.4020(8), Mo–S3 2.3702(7), Mo–S4 2.3778(8), Mo–S5 2.3999(8), Mo–S6 2.3785(7); S1–Mo–S2 81.81(3), S1–Mo–S3 95.42(3), S1–Mo–S4 160.05(3), S1–Mo–S5 82.89(3), S1–Mo–S6 102.93(3), S2–Mo–S3 107.72(3), S2–Mo–S4 79.91(3), S2–Mo–S5 162.41(3), S2–Mo–S6 92.28(2), S3–Mo–S4 82.64(3), S3–Mo–S5 82.31(3), S3–Mo–S6 154.62(3), S4–Mo–S5 116.31(3), S4–Mo–S6 85.78(3), S5–Mo–S6 82.73(2).

In both the PNP^+ and the nBu_4N^+ salts, the structure of the anion $[Mo(bdt)_3]^{-}$ is an unsymmetrical polyhedron, exhibiting a geometry between trigonal prismatic and octahedral (average twist angle φ = 34.1° for the PNP^+ salt and φ = 33.5° for the nBu_4N^+ salt). However, the $[Mo^{V}(bdt)_3]^{-}$ anions in the two salts show a considerable difference regarding the orientation of the S_3 planes that define the twist angle φ (Figure 2). While the anion in the nBu_4N^+ salt exhibits three rather similar angles (30.4, 34.4, 35.6°), which indicates an almost coplanar arrangement of the S_3 planes, three significantly different values were observed for $(PNP)[Mo(bdt)_3]$ (18.4, 36.3, 47.8°). The S1/S3/S5 plane in this complex is tilted by 7.2° with respect to the S2/S4/S6 plane. Crystal packing effects might be responsible for this observation, which again illustrates that electronic effects are not solely responsible for the molecular structure of $[M(bdt)_3]^{n-}$ complexes.

The "innocent" and "non-innocent" nature of ligands like bdt^{2-} has recently been discussed intensively.[12] For *O,O′*-coordinated catecholates or *o*-benzosemiquinonate(1–)-π-radicals a number of typical structural and spectroscopic features have been described, which allow the detection and identification of such ligands in coordination compounds.[15] The picture was not so clear for the corresponding *o*-dithio derivatives like bdt^{2-}. Recently square-planar complexes of the type $[M(bdt)_2]^{n-}$ ($M = Au^{III}$, Ni^{II})[12] have been described, and structural parameters associated with dithiolato(2–) and *o*-dithiobenzosemiquinonato(1–) coordination have been worked out. This allows, in principle, the assignment of the oxidation level of a benzene-1,2-dithiolato ligand in a complex. For complexes of the type $[M(bdt)_2]^{n-}$ this assignment becomes complicated if a benzene-1,2-dithiolate and an *o*-dithiobenzosemiquinonate ligand are coordinated at the same time, as the structural differences between the two ligand types are small. Statistical disorder problems may hamper the identification of the different oxidation levels of the ligand and this becomes even more complicated for complexes of the type $[M(bdt)_3]^{n-}$ with three bdt^{2-} ligands, each of which can undergo intramolecular oxidation.

We have studied the structural parameters in the series $[Mo(bdt)_3]^{n-}$ (n = 0, 1, 2, Figure 4) and found some trends in the Mo–S, S–C and C–C bond lengths. On the basis of the geometric parameters of the *o*-dithiolato ligands in $[Mo^{VI}(bdt)_3]$ and the paramagnetism observed for the complex, Bennet et al.[7] proposed, as early as 1976, the presence of a dithioketonic ligand species in $[Mo^{VI}(bdt)_3]$. On the basis of Wieghardt's investigations,[12] we believe that the ligand in $[Mo^{VI}(bdt)_3]$ is best described as an *o*-dithiobenzosemiquinonate(1–) radical anion.

In the series of $[Mo(bdt)_3]^{n-}$ complexes, the C–S bond lengths increase as the metal oxidation state changes from Mo^{VI} to Mo^{IV} (Figure 4). Mo^{VI} is capable of oxidizing the *o*-dithiolato ligand to a higher degree than Mo^{IV}, leading to a thioketonic ligand which is detectable by the decrease in the C–S bond lengths. This postulate is corroborated by an evaluation of the C–C bond lengths within the aromatic ring. In summary, the trends in the structural parameters

 © 2005 Wiley-VCH Verlag GmbH & Co. KGaA, Weinheim

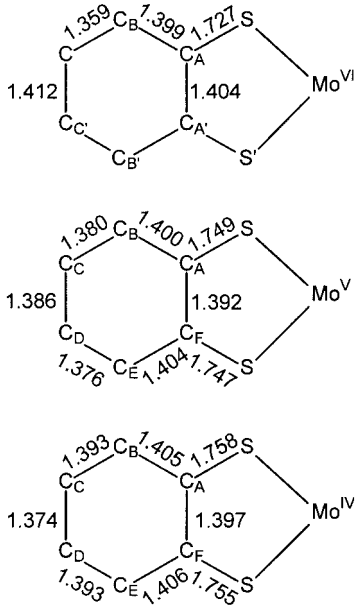

Figure 4. Average bond lengths [Å] for complexe anions of the type $[Mo(bdt)_3]^{n-}$ (n = 2, 1, 0) including literature data for $[Mo^{VI}(bdt)_3]$.[7]

indicate that the bdt^{2-} ligand is at least partially oxidized upon coordination to transition metals in high oxidation states (Mo^{VI}).

From the variation of the twist angle φ in the series $[Mo(bdt)_3]^{n-}$ (n = 0, 1, 2) it appears that the *formal* d electron configuration is not the only governing principle for the formation of certain coordination polyhedra. These results indicate once more that the stabilization of a trigonal prismatic coordination geometry does not only depend on the electronic situation at the central metal atom, but instead must be considered a complicated process involving various factors, including the counterions that are present.

Experimental Section

General Remarks: Unless stated otherwise, all manipulations were carried out under dry argon by means of standard Schlenk techniques. THF was freshly distilled from Na/benzophenone prior to use. Methanol was dried over magnesium and freshly distilled. The DMF purchased contained molecular sieves and was used as received. $[MoCl_4(CH_3CN)_2]$ was purchased from Aldrich.

$(Li)_2[Mo^{IV}(bdt)_3]$: A sample of benzene-1,2-dithiol (423 mg, 3.0 mmol) was dissolved in THF (20 mL). The solution was cooled to –78 °C and *n*BuLi (6.0 mmol, 2.4 mL of a 2.5 M solution in hexane) was added dropwise. $[MoCl_4(CH_3CN)_2]$ (320 mg, 1 mmol) in DMF (5 mL) was then added, and the reaction mixture was allowed to warm slowly to ambient temperature. While warming, the color of the solution turned deep blue. The reaction mixture was stirred overnight and then heated under reflux for 1 h. Thereafter all solvents were removed and the crude reaction product was washed with diethyl ether and dried in vacuo. Yield: 403 mg (0.76 mmol, 76%). $C_{18}H_{12}Li_2MoS_6$ (530.48): calcd. C 40.76, H 2.28; found C 41.43, H 2.40. ^1H NMR (200 MHz, [D$_7$]DMF): δ = 7.37 (dd, ^3J = 8.8, ^4J = 2.4 Hz, 6 H, Ar–H), 6.57 (dd, ^3J = 8.8, ^4J = 2.4 Hz, 6 H, Ar–H). ^{13}C NMR (50 MHz, [D$_7$]DMF): δ = 155.1 (*ipso*-C), 126.5 (Ar–C), 119.8 (Ar–C).

$(PNP)_2[Mo^{IV}(bdt)_3]\cdot 6\,MeOH$: Slow diffusion of a methanolic solution of PNPCl (PNPCl = bis(triphenylphosphoranylidene)ammonium chloride) into a solution of $(Li)_2[Mo^{IV}(bdt)_3]$ in methanol led to the precipitation of deep blue, air-sensitive single crystals of $(PNP)_2[Mo^{IV}(bdt)_3]\cdot 6$ MeOH which were suitable for an X-ray diffraction study. These crystals were characterized by X-ray diffraction only.

$(PNP)[Mo^{V}(bdt)_3]$: Complex $(Li)_2[Mo^{IV}(bdt)_3]$ dissolved in methanol was oxidized by exposure to air. A green solution of $Li[Mo^{V}(bdt)_3]$ resulted. Green crystals of $(PNP)[Mo^{V}(bdt)_3]$ were obtained by the slow addition of a methanolic solution of PNPCl.

X-ray Crystallographic Study of $(PNP)_2[Mo^{IV}(bdt)_3]\cdot 6\,MeOH$: A suitable crystal ($0.20\times0.10\times0.07$ mm^3) was mounted on a Bruker AXS APEX diffractometer equipped with a rotating molybdenum anode (λ = 0.71073 Å), a cooling device, and a graphite monochromator. $(PNP)_2[Mo(bdt)_3]\cdot 6$ MeOH, $C_{96}H_{96}N_2MoO_6P_4S_6$, M_r = 1785.93 g mol^{-1}, monoclinic, $C2/c$, a = 22.901(14), b = 16.245(8), c = 25.800(13) Å, β = 113.385(14)°, V = 8810(8) Å^3, Z = 4, $\rho_{calcd.}$ = 1.346 g cm^{-3}, μ = 0.419 mm^{-1}. 34636 structure factors ($-27 \le h \le 27$, $-19 \le k \le 19$, $-30 \le l \le 30$, 2θ-range 3.2–50.0°) were collected at –100 °C. An empirical absorption correction applied (T_{min} = 0.921, T_{max} = 0.971) before merging the data gave 7754 unique intensities (R_{int} = 0.058). Structure solution was performed with SHELXS,[16] and the subsequent refinement of 522 parameters against F^2 with 7754 unique intensities [6289 observed intensities $I > 2\sigma(I)$] was conducted with SHELXL.[17] The anisotropic thermal parameters for all non-hydrogen atoms were refined. Hydrogen atoms were added to the structure model at calculated positions. Final residuals: R_{all} = 0.0600, R_{obs} = 0.0460, $R_{w,obs}$ = 0.1182, *GOF* = 1.106. The molybdenum atom resides on a special position, namely, a twofold axis which bisects one of the benzene-1,2-dithiolato ligands. The asymmetric unit contains one half $[Mo^{IV}(bdt)_3]^{2-}$ anion, one PNP^+ cation, and three molecules of MeOH.

X-ray Crystallographic Study of (PNP)[2]: A suitable crystal ($0.48\times0.08\times0.02$ mm^3) was mounted on a Bruker AXS APEX diffractometer equipped with a rotating molybdenum anode (λ = 0.71073 Å), a cooling device, and a graphite monochromator. (PNP)[Mo(bdt)$_3$], $C_{54}H_{42}MoNP_2S_6$, M_r = 1055.13 g mol^{-1}, triclinic, $P\bar{1}$, a = 11.036(1), b = 13.882(2), c = 16.041(2) Å, α = 87.969(3), β = 75.861(3), γ = 87.512(3)°, V = 2380.0(5) Å^3, Z = 2, $\rho_{calcd.}$ = 1.472 g cm^{-3}, μ = 0.645 mm^{-1}. 19324 structure factors ($-13 \le h \le 13$, $-16 \le k \le 16$, $-19 \le l \le 19$, 2θ-range 3.0–50.0°) were collected at –120 °C. An empirical absorption correction applied (T_{min} = 0.747, T_{max} = 0.987) before merging the data gave 8382 unique intensities (R_{int} = 0.035). Structure solution was performed with SHELXS,[16] and subsequent refinement of 577 parameters against F^2 with 8382 unique intensities [6757 observed intensities $I > 2\sigma(I)$] was conducted with SHELXL.[17] The anisotropic thermal parameters for all non-hydrogen atoms were refined. Hydrogen atoms were added to the structure model at calculated positions. Final residuals: R_{all} = 0.0476, R_{obs} = 0.0335, $R_{w,obs}$ = 0.0757, *GOF* = 1.007. The asymmetric unit contains one molecule of (PNP)[Mo(bdt)$_3$].

CCDC-260986 (for $(PNP)_2[Mo^{IV}(bdt)_3]\cdot 6$ MeOH) and CCDC-260987 (for $(PNP)[Mo^{V}(bdt)_3]$) contain the supplementary crystallographic data for this paper. These data can be obtained free of charge from The Cambridge Crystallographic Data Centre via www.ccdc.cam.ac.uk/data_request/cif.

 © 2005 Wiley-VCH Verlag GmbH & Co. KGaA, Weinheim

Acknowledgments

This work was financially supported by the Deutsche Forschungsgemeinschaft (IGK, 673).

[1] a) R. Eisenberg, J. A. Ibers, *J. Am. Chem. Soc.* **1965**, *87*, 3776–3778; b) R. Eisenberg, J. A. Ibers, *Inorg. Chem.* **1966**, *5*, 411–416.

[2] a) D. L. Kepert, *Inorganic Stereochemistry; Inorganic Chemistry Concepts 6*; Springer Verlag: Berlin, **1982**, chapter 8; b) D. L. Kepert, *Progr. Inorg. Chem.* **1977**, *23*, 1–65; c) G. N. Schrauzer, V. P. Mayweg, *J. Am. Chem. Soc.* **1966**, *88*, 3235–3242; d) E. I. Stiefel, R. Eisenberg, R. C. Rosenberg, H. B. Gray, *J. Am. Chem. Soc.* **1966**, *88*, 2956–2966.

[3] H. V. Huynh, T. Lügger, F. E. Hahn, *Eur. J. Inorg. Chem.* **2002**, 3007–3009.

[4] a) T. E. Burrow, R. H. Morris, A. Hills, D. L. Hughes, R. L. Richards, *Acta Crystallogr. Sect. C* **1993**, *49*, 1591–1594; b) F. Knoch, D. Sellmann, W. Kern, *Z. Kristallogr.* **1992**, *205*, 300–302.

[5] C. Lorber, J. P. Donahue, C. A. Goddard, E. Nordlander, R. H. Holm, *J. Am. Chem. Soc.* **1998**, *120*, 8102–8112.

[6] a) A. Cervilla, E. Llopis, D. Marco, F. Perez, *Inorg. Chem.* **2001**, *40*, 6525–6528; b) D. Sellmann, L. Zapf, *Z. Naturforsch. Teil B* **1985**, *40*, 380–388.

[7] M. Cowie, M. J. Bennett, *Inorg. Chem.* **1976**, *15*, 1584–1589.

[8] M. Cowie, M. J. Bennett, *Inorg. Chem.* **1976**, *15*, 1595–1603.

[9] M. Cowie, M. J. Bennett, *Inorg. Chem.* **1976**, *15*, 1589–1595.

[10] a) T. J. McMurry, M. W. Hossaini, T. M. Garrett, F. E. Hahn, Z. E. Reyes, K. N. Raymond, *J. Am. Chem. Soc.* **1987**, *109*, 7196–7198; b) T. B. Karpishin, T. D. P. Stack, K. N. Raymond, *J. Am. Chem. Soc.* **1993**, *115*, 182–192.

[11] J. L. Martin, J. Takats, *Can. J. Chem.* **1989**, *67*, 1914–1923.

[12] a) P. Gosh, A. Begum, D. Herebian, E. Bothe, K. Hildenbrand, T. Weyhermüller, K. Wieghardt, *Angew. Chem.* **2003**, *115*, 581–585; *Angew. Chem. Int. Ed.* **2003**, *42*, 563–567; b) K. Ray, T. Weyhermüller, A. Goossens, M. W. J. Craje, K. Wieghardt, *Inorg. Chem.* **2003**, *42*, 4082–4087; c) V. Bachler, G. Olbrich, F. Neese, K. Wieghardt, *Inorg. Chem.* **2002**, *41*, 4179–4193.

[13] E. Larsen, G. N. La Mar, B. E. Wagner, J. E. Park, R. H. Holm, *Inorg. Chem.* **1972**, *11*, 2652–2668.

[14] S. Campbell, S. Harris, *Inorg. Chem.* **1996**, *35*, 3285–3288.

[15] C. G. Pierpont, C. W. Lange, *Prog. Inorg. Chem.* **1994**, *41*, 331–442.

[16] G. M. Sheldrick, SHELXS-97, *Acta Crystallogr. Sect. A* **1990**, *46*, 467–473.

[17] G. M. Sheldrick, SHELXL-97, University of Göttingen, **1997**.

Received: January 26, 2005
Published Online: May 24, 2005

 © 2005 Wiley-VCH Verlag GmbH & Co. KGaA, Weinheim

Synthetic, Structural, Spectroscopic, and Electrochemical Studies of Heteroleptic Tris(phthalocyaninato) Rare Earth Complexes

Yongzhong Bian,[a] Lei Li,[a] Daqi Wang,[b] Chi-Fung Choi,[c] Diana Y. Y. Cheng,[c] Pehua Zhu,[a] Renjie Li,[a] Jianmin Dou,[b] Rongming Wang,[a] Na Pan,[a,d] Dennis K. P. Ng,[c] Nagao Kobayashi,[d] and Jianzhuang Jiang*[a]

Keywords: Phthalocyanines / Sandwich complexes / Rare earths / Triple-decker complexes / Heteroleptic complexes

Three heteroleptic tris(phthalocyaninato) rare-earth triple-decker complexes [(Pc)M(Pc)M{Pc(α-$OC_5H_{11})_4$}] [M = Sm, Gd, Lu; Pc = phthalocyaninate; Pc(α-$OC_5H_{11})_4$ = 1,8,15,22-tetrakis(3-pentyloxy)phthalocyaninate] have been prepared as racemic mixtures by treating [M{Pc(α-$OC_5H_{11})_4$}(acac)], generated in situ, with the bis(phthalocyaninato) rare-earth double-decker complex [M$(Pc)_2$] in refluxing *n*-octanol. The molecular structures of the gadolinium and lutetium complexes have been determined by single-crystal X-ray diffraction analysis, both of which adopt the asymmetrical structure [(Pc)M(Pc)M{Pc(α-$OC_5H_{11})_4$}]. The outer Pc and Pc(α-$OC_5H_{11})_4$ rings are significantly domed, while the inner Pc ring is essentially planar. The ring-to-ring separation between the two adjacent Pc rings, as defined by the two N_4 mean planes, diminishes from [(Pc)Gd(Pc)Gd{Pc(α-$OC_5H_{11})_4$}] to [(Pc)Lu(Pc)Lu{Pc(α-$OC_5H_{11})_4$}] as a result of the smaller Lu^{III} ion. The decreased molecular symmetry for these complexes has also been revealed by the NMR spectra of the samarium and lutetium analogs, in which four sets of signals appear for the inner Pc ring protons due to the special disposition of the neighboring Pc(α-$OC_5H_{11})_4$ ring. Electrochemical studies have revealed four one-electron oxidations and up to five one-electron reductions for these complexes. The dependence of the phthalocyanine Q band as well as the first and second oxidation potentials on the size of the metal center indicates that substantial π-π interactions are present in these compounds.

(© Wiley-VCH Verlag GmbH & Co. KGaA, 69451 Weinheim, Germany, 2005)

Introduction

While monomeric chiral porphyrin and phthalocyanine derivatives have received increasing research interest in the past years,[1] chiral, sandwich-type tetrapyrrole metal complexes, however, still remain extremely rare.[2–4] Recently, we have reported a series of heteroleptic bis(phthalocyaninato) rare-earth complexes [M(Pc){Pc(α-$OC_5H_{11})_4$}] (M = Y, Sm–Lu) with a C_4 molecular symmetry.[5] As part of our continuing efforts in this regard, we have devised and prepared a new series of heteroleptic tris(phthalocyaninato) rare-earth triple-decker complexes [(Pc)M(Pc)M{Pc(α-$OC_5H_{11})_4$}] (M = Sm, Gd, Lu; Figure 1). In this paper, we report in detail the synthesis, structures, spectroscopic properties, and electrochemistry of these novel complexes. Due to the introduction of four 3-pentyloxy groups at the α-position of the outer Pc(α-$OC_5H_{11})_4$ ring, and the sandwich triple-decker molecular structure, these compounds are also intrinsically chiral in nature. However, due to the very small difference between the two enantiomers, they could not be separated and these triple-decker complexes have been found to exist as a pair of enantiomers co-crystallizing in the monoclinic *C*2/*c* system.

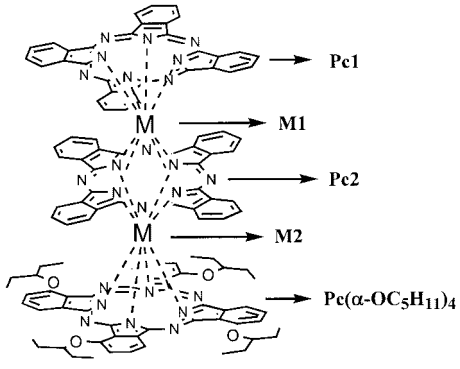

Figure 1. A schematic structure of the heteroleptic rare-earth triple-decker complexes [(Pc)M(Pc)M{Pc(α-$OC_5H_{11})_4$}] (**1**–**3**).

It is also worth pointing out that tris(phthalocyaninato) rare-earth triple-deckers were first briefly characterized by

[a] Department of Chemistry, Shandong University, Jinan 250100, China
Fax: +86-531-856-5211
E-mail: jzjiang@sdu.edu.cn
[b] Department of Chemistry, Liaocheng University, Liaocheng 252000, China
[c] Department of Chemistry, The Chinese University of Hong Kong, Shatin, N.T., Hong Kong, China
[d] Department of Chemistry, Graduate School of Science, Tohoku University, Sendai 980-8578, Japan
Supporting information for this article is available on the WWW under http://www.eurjic.org or from the authors.

mass spectroscopy in the 1980s.[6] Since then, both homoleptic and especially the heteroleptic complexes developed very recently have attracted increasing research interest as good systems to study the interactions between two 4f electronic systems in an isolated environment and as a new category of single molecular magnets.[7a,7b,8] To the best of our knowledge, only a very few tris(phthalocyaninato) triple-deckers have been structurally characterized, including the homoleptic tris[tetra(15-crown-5)phthalocyaninato]lutetium compound $[Lu_2\{Pc(15\text{-}C\text{-}5)_4\}_3]$ reported by Troyanov et al.[9] and the heteroleptic [(Pc)M{Pc(OC_8H_{17})$_8$}M′(Pc)] (M = Er, M′ = Lu; M = M′ = Er or Lu) reported by us.[7c] The present work adds the structural data of the intrinsically chiral [(Pc)M(Pc)M{Pc(α-OC_5H_{11})$_4$}] [M = Gd (2), Lu (**3**)]. These novel systems will also be of interest for further studies.

Results and Discussion

Synthesis of [(Pc)M(Pc)M{Pc(α-OC_5H_{11})$_4$}] [M = Sm (1), Gd (2), Lu (3)]

Two synthetic pathways have been reported to prepare heteroleptic rare earth(III) triple-decker complexes with two different kinds of phthalocyaninato ligands [(Pc′)M(Pc′)M(Pc′′)] or [(Pc′)M(Pc′′)M(Pc′)] (Pc′ ≠ Pc′′ = general phthalocyaninate). The first method involves the reaction between the monomeric [M(Pc′)X] and the metal-free H_2Pc′′ in a suitable ratio. This method has only been applied to prepare the lutetium triple-decker [(Pc)Lu{Pc(15-C-5)$_4$}Lu(Pc)].[10] The second pathway involves treatment of the monomeric [M(Pc′)X] with the double-decker [M(Pc′′)$_2$]. This method has been generally utilized to prepare a series of different kinds of tris(phthalocyaninato) rare-earth compounds recently,[7,8] and is also a convenient and efficient methodology to prepare mixed (porphyrinato)(phthalocyaninato) rare-earth triple-deckers, including [M_2(Pc′)$_2$(Por)] and [M_2(Pc′)(Por)$_2$] (Por = general porphyrinate).[11] In the present work, we employed the second methodology, using [M{Pc(α-OC_5H_{11})$_4$}(acac)] (M = Sm, Gd, Lu), generated in situ from the corresponding [M(acac)$_3$]·$n$$H_2$O (M = Sm, Gd, Lu) and metal-free H_2Pc(α-OC_5H_{11})$_4$, and [M(Pc)$_2$] as starting materials. Reaction of [M{Pc(α-OC_5H_{11})$_4$}(acac)] with the corresponding [M(Pc)$_2$] in refluxing *n*-octanol led to the heteroleptic triple-deckers [(Pc)M(Pc)M{Pc(α-OC_5H_{11})$_4$}] (M = Sm, Gd, Lu) in relatively good yields (24–42%). The reaction yield of these compounds is dependent on the size of the metal center: the yield is higher for lanthanides with a moderate size such as Sm and Gd, while the late lanthanide Lu analog gave a lower yield (Table 1). This result is in good accord with the trend observed for the mixed (porphyrinato)(phthalocyaninato) rare-earth triple-deckers [M_2(Pc)$_2$(TClPP)] and [M_2(Pc)(TClPP)$_2$] [TClPP = 5,10,15,20-tetrakis(4-chlorophenyl)porphyrinate].[12]

Spectroscopic Characterization

All the three new heteroleptic triple-deckers **1**–**3** were characterized by elemental analysis and various spectroscopic methods. Table 1 summarizes the analytical and mass spectroscopic data. The MALDI-TOF mass spectra of these compounds clearly show intense signals for the molecular ion $[M]^+$ or protonated molecular ion $[MH]^+$.

The diamagnetic lutetium(III) triple-decker [(Pc)Lu(Pc)Lu{Pc(α-OC_5H_{11})$_4$}] (**3**) gives a well-resolved ^{1}H NMR spectrum in $CDCl_3$. As shown in the ^{1}H-^{1}H COSY spectrum (Figure 2), the four most downfield signals (the doublets at δ = 9.07 and 8.86 ppm, and the triplets at δ = 8.71 and 8.64 ppm) are inter-correlated and can be attributed to one of the Pc rings. The other Pc rings' protons resonate as two typical AA′BB′ multiplets at δ = 8.48–8.50 and 8.00–8.03 ppm. The appearance of two sets of signals for the Pc rings confirms that the compound adopts an unsymmetrical structure, i.e. [(Pc)Lu(Pc)Lu{Pc(α-OC_5H_{11})$_4$}]. The former set of signals is tentatively assigned to the inner Pc ring as it is expected that the C_{4h} symmetry of the Pc(α-OC_5H_{11})$_4$ ring may impose a different environment to its neighboring ring protons, leading to four different signals. The remaining three aromatic signals from δ = 7.3 to 7.9 ppm are clearly due to the ring protons of Pc(α-OC_5H_{11})$_4$.

The aliphatic protons' signals can also be assigned unambiguously with the help of the ^{1}H-^{1}H COSY spectrum (Figure 2). The virtual quintet at δ = 4.46 ppm is due to the OCH proton, and the two multiplets at δ = 2.12–2.22 and 2.33–2.42 ppm can be ascribed to one set of the two diastereotopic methylene protons, which are correlated with the methyl protons resonating as a virtual triplet at δ = 1.50 ppm. The other set of methylene protons resonates as a quintet at δ = 1.68 ppm and its neighboring methyl protons resonate as a triplet at δ = 0.53 ppm. These results clearly show that a lowering of the symmetry of triple-decker complexes gives rise to more NMR signals.

Table 1. Analytical and mass spectroscopic data for the heteroleptic triple-deckers **1**–**3**.[a]

Compound	Yield [%]	$[M^+]$ or $[MH^+]$ [*m*/*z*]	Analysis [%][b] C	H	N
[(Pc)Sm(Pc)Sm{Pc(α-OC_5H_{11})$_4$}] (**1**)	40	2182.8 (2182.9)[b]	62.55 (62.39)[d]	4.04 (3.98)[d]	14.91 (14.99)[d]
[(Pc)Gd(Pc)Gd{Pc(α-OC_5H_{11})$_4$}] (**2**)	42	2197.6 (2197.7)[c]	60.75 (60.35)[e]	3.97 (3.99)[e]	13.67 (14.32)[e]
[(Pc)Lu(Pc)Lu{Pc(α-OC_5H_{11})$_4$}] (**3**)	24	2233.3 (2233.1)[c]	59.95 (59.39)[f]	4.21 (4.18)[f]	12.39 (13.46)[f]

[a] Calculated values given in parentheses. [b] Mass corresponding to the most abundant isotopic peak of the molecular ion $[M^+]$. [c] Mass corresponding to the most abundant isotopic peak of the protonated molecular ion $[MH^+]$. [d] Contains 0.5 equiv. of $CHCl_3$. [e] Contains 1.0 equiv. of $CHCl_3$ and 1.0 equiv. of CH_3OH. [f] Contains 1.5 equiv. of $CHCl_3$ and 1.0 equiv. of *n*-C_6H_{14}.

 © 2005 Wiley-VCH Verlag GmbH & Co. KGaA, Weinheim

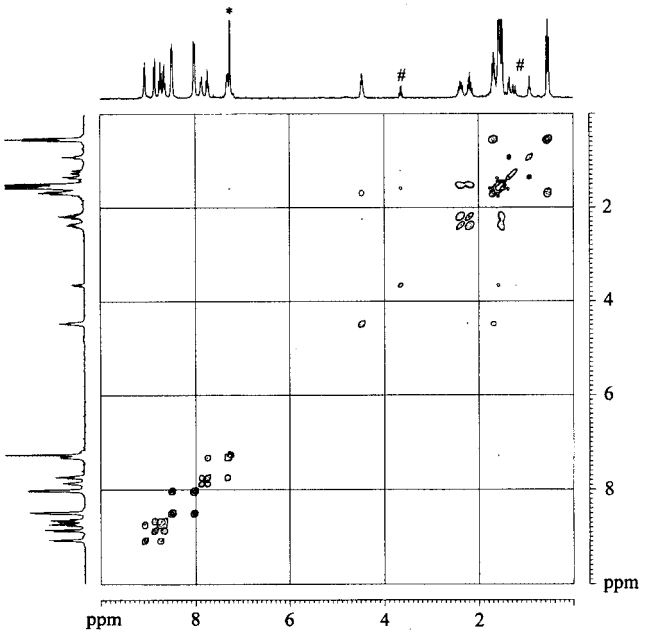

Figure 2. ^{1}H-^{1}H COSY spectrum of [(Pc)Lu(Pc)Lu{Pc(α-O-$C_5H_{11})_4$}] (**3**) in $CDCl_3$. The signals due to residual $CHCl_3$ and some impurities are denoted as * and #, respectively.

The ^{1}H NMR spectrum of the samarium(III) analog **1** shows similar spectral features, but some of the aromatic signals are overlapped and assignment could only be made by 2D NMR techniques. The total correlation spectroscopy (TOCSY)[13] spectrum (Figure S1a; see Supporting Information), in which the cross peaks indicate correlations between protons that belong to a common spin-system, is particularly useful. The spectrum clearly reveals that the two multiplets at δ = 7.92–7.97 and 7.62–7.69 ppm are correlated and can be assigned to the H_α and H_β protons of the outer Pc ring, respectively. The triplet at δ = 7.80 ppm, multiplet at δ = 7.62–7.69 ppm (overlapped with the outer Pc-H_β protons' signals), and the two doublets at δ = 7.52 and 7.11 ppm belong to a common spin system and can be attributed to the inner Pc ring. The multiplet at δ = 7.24–7.34 ppm contains overlapping signals for residual $CHCl_3$ and two sets of aromatic signals for Pc(α-$OC_5H_{11})_4$, which are correlated with the doublet at δ = 6.99 ppm. These correlations and the assignments are in agreement with the ^{1}H-^{1}H COSY spectrum (see Figure S1b in the Supporting Information).

The electronic absorption and MCD data of this series of compounds were measured in $CHCl_3$ and are shown in Figure 3. In general, the metal-dependent spectral features are analogous to those reported for related compounds [(Pc)M{Pc($OC_8H_{17})_8$}M{Pc($OC_8H_{17})_8$}],[7a] and thus could be assigned in the same manner. All the spectra of **1**–**3** show a typical Soret band at about 335 nm with a shoulder at the higher energy side at around 295 nm. The phthalocyanine Q bands appear around 643–652 nm as a very strong absorption with a weak satellite around 695–723 nm. Along with the decrease in the rare-earth ionic size from Sm to Lu, the Soret band for the three triple-deckers remains almost unchanged. In contrast, the main Q absorption band undergoes a blue shift and the satellite Q band is shifted to the red.

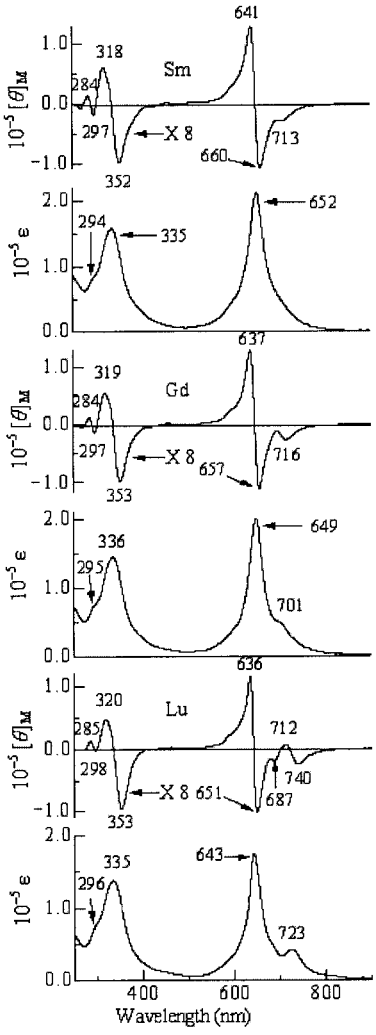

Figure 3. Electronic absorption and MCD spectra of [(Pc)M-(Pc)M{Pc(α-$OC_5H_{11})_4$}] (**1**–**3**) in $CHCl_3$.

The MCD spectra of **1**–**3** are different from those of the symmetrical mono(phthalocyaninato) metal and bis-(phthalocyaninato) rare-earth complexes in that splitting of the absorption bands appears in the Q-band region. It is also different from that of H_2Pc in that the MCD spectra clearly show the presence of pseudo Faraday-*A* terms. A symmetrical and intense pseudo *A* term is observed for **1**–**3** at 643–652 nm. Another unsymmetrical and weaker *A* term is also observed corresponding to the second Q band at 695–723 nm, which is well resolved for the Lu compound. In the Soret region, two symmetrical and weak pseudo *A* terms appear in the MCD spectra of **1**–**3**, corresponding to the Soret band at about 335 nm and its shoulder at around 295 nm. In the case of a cofacial eclipsed Pc dimer of low symmetry,[14] it has previously been found that both the electronic absorption and MCD spectra do not reflect the symmetry of the constituent Pc units. As shown by the X-ray structures (to be discussed in the following

 © 2005 Wiley-VCH Verlag GmbH & Co. KGaA, Weinheim

section), compounds **1**–**3** have C_s symmetry so that Faraday *A* terms are not expected theoretically. However, since pseudo Faraday *A* terms are observed in Figure 3, we can further conclude that the absorption and MCD spectra of cofacial trimers do not reflect the molecular symmetry.

Structural Studies

Single crystals of [(Pc)M(Pc)M{Pc(α-$OC_5H_{11})_4$}] [M = Gd (**2**), Lu (**3**)] suitable for X-ray diffraction analysis were obtained by slow diffusion of MeOH into the corresponding $CHCl_3$ solutions. These compounds crystallize in the monoclinic system with a *C*2/*c* space group, but unfortunately two pairs of enantiomeric triple-decker molecules are contained in each unit cell,. Attempts to resolve the two enantiomers of the these triple-deckers by HPLC using a silica gel column coated with cellulose 2,3,6-tris(3,5-dimethylphenylcarbamate) were not successful due to the very small differences between the two enantiomers. The crystal structure of these compounds also contained solvated chloroform molecules, which come from the solvents used for recrystallization. The gadolinium and lutetium compounds have similar crystal structures.

The molecular structure of [(Pc)Gd(Pc)Gd{Pc(α-$OC_5H_{11})_4$}] (**2**) is shown in Figure 4. Each gadolinium ion is sandwiched between an outer phthalocyanine ligand, Pc or Pc(α-$OC_5H_{11})_4$, and the inner Pc ring. However, the two gadolinium ions in this compound are not exactly identical

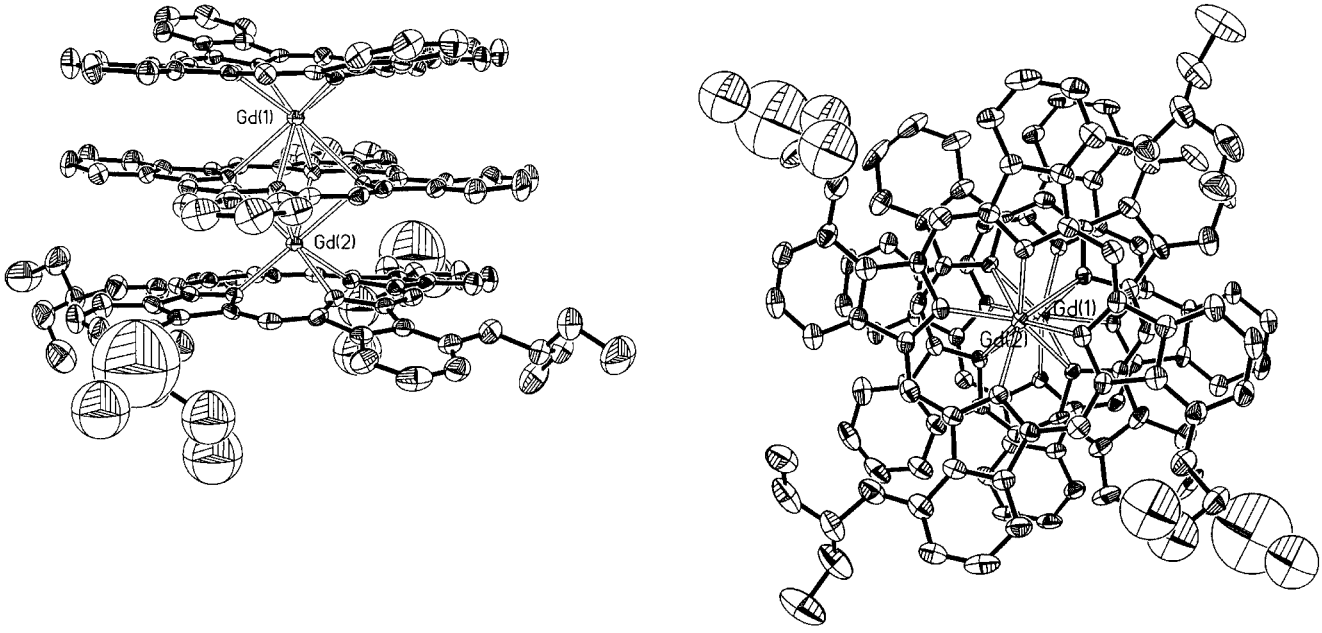

Figure 4. Molecular structure of [(Pc)Gd(Pc)Gd{Pc(α-$OC_5H_{11})_4$}] (**2**) in two different perspective views showing the 30% probability thermal ellipsoids for all non-hydrogen atoms.

Table 2. Comparison of the structural data for **2** and **3**.

	2	**3**
Average M1–N(Pc1) bond length [Å]	2.386	2.297
Average M1–N(Pc2) bond length [Å]	2.634	2.588
Average M2–N(Pc2) bond length [Å]	2.654	2.588
Average M2–N[Pc(α-$OC_5H_{11})_4$] bond length [Å]	2.364	2.307
M1–N_4(Pc1) plane distance [Å]	1.301	1.198
M1–N_4(Pc2) plane distance [Å]	1.765	1.721
M2–N_4(Pc2) plane distance [Å]	1.795	1.722
M2–N_4[Pc(α-$OC_5H_{11})_4$] plane distance [Å]	1.243	1.174
Interplanar distance N_4(Pc1)–N_4(Pc2)(Å)	3.067	2.920
Interplanar distance N_4(Pc2)–N_4 [Pc(α-$OC_5H_{11})_4$] [Å]	3.034	2.896
Dihedral angle between N_4(Pc1)–N_4(Pc2) [°]	0	0
Dihedral angle between N_4(Pc2)–N_4[Pc(α-$OC_5H_{11})_4$]	0	0
Average dihedral angle φ for the Pc1 ring [°][a]	9.1	10.1
Average dihedral angle φ for the Pc2 ring [°][a]	1.2	1.35
Average dihedral angle φ for the Pc(α-$OC_5H_{11})_4$ ring [°][a]	9.2	10.45
Average twist angle between Pc1 ring and Pc2 ring [°][b]	46.4	44.35
Average twist angle between Pc2 ring and Pc(α-$OC_5H_{11})_4$ ring [°][b]	41.4	47.5

[a] The average dihedral angle of the individual isoindole rings with respect to the corresponding N_4 mean plane. [b] Defined as the rotation angle of one ring away from the eclipsed conformation of the two rings.

 © 2005 Wiley-VCH Verlag GmbH & Co. KGaA, Weinheim

in terms of the distance from the inner and outer phthalocyanine ligands because of the difference in the ring-to-ring interaction between the inner and the two different outer phthalocyanine rings (Table 2). Both the outer Pc and Pc(α-$OC_5H_{11})_4$ rings adopt conformations that are domed toward the gadolinium cations (φ = 9.1 and 9.2°). The two unsubstituted Pc rings connected by Gd1 are rotated by an angle of 46.4°, and the central Pc and the outer Pc(α-$OC_5H_{11})_4$ ligands connected by Gd2 are rotated by 41.4°. The coordination polyhedra of both Gd1 and Gd2 are therefore a slightly distorted square antiprism. The displacements of the two gadolinium ions with respect to the three isoindole–nitrogen mean planes are Gd1–N_4(Pc1) = 1.295 Å, Gd1–N_4(Pc2) = 1.762 Å, Gd2–N_4(Pc2) = 1.800 Å, and Gd2–N_4[Pc(α-$OC_5H_{11})_4$] = 1.247 Å. The average Gd1–N(Pc1) bond length (2.376 Å) is significantly shorter than the average Gd1–N(Pc2) distance (2.634 Å), and the Gd2–N[Pc(α-$OC_5H_{11})_4$] (2.363 Å) bond length is shorter than Gd2–N(Pc2) (2.659 Å), as the central phthalocyanine ligand (Pc2) is shared by two gadolinium ions rather than one metal ion for the outer Pc1 or Pc(α-$OC_5H_{11})_4$ ligand. Similar data were obtained for the lutetium triple-decker **3**.

Electrochemical Properties

The redox behavior of the heteroleptic triple-deckers **1**–**3** was studied by cyclic voltammetry (CV) and differential pulse voltammetry (DPV) in CH_2Cl_2. All the compounds exhibit four quasi-reversible one-electron oxidations and up to five quasi-reversible one-electron reductions, which can be attributed to the successive removal of electrons from, and addition of electrons to, the ligand-based orbitals, respectively. Figure 5 shows the voltammograms for [(Pc)-Lu(Pc)Lu{Pc(α-$OC_5H_{11})_4$}] (**3**), which are typical for the other rare-earth counterparts. Table 3 collects the half-wave potentials of all these processes for these triple-deckers. As can be seen, while the half-wave potentials of the third and fourth oxidations of [(Pc)M(Pc)M{Pc(α-$OC_5H_{11})_4$}] remain virtually unchanged, the half-wave potentials of the first and second oxidations correlate linearly with the ionic size of the rare-earth metal center and are slightly shifted in the cathodic direction with a decrease in the rare-earth ionic size. The half-wave potentials of all the reductions for **1**–**3** appear to reveal no systematic trends with ionic radius. The potential difference between Oxd_1 and Red_1 ($\Delta E_{1/2}$) for the three heteroleptic triple-deckers **1**–**3** is also dependent on the central rare-earth ionic size, diminishing from 1.02 V for the Sm compound to 0.84 V for the Lu analog, indicating an increase in the ring-to-ring π-π interaction in the same order.[15]

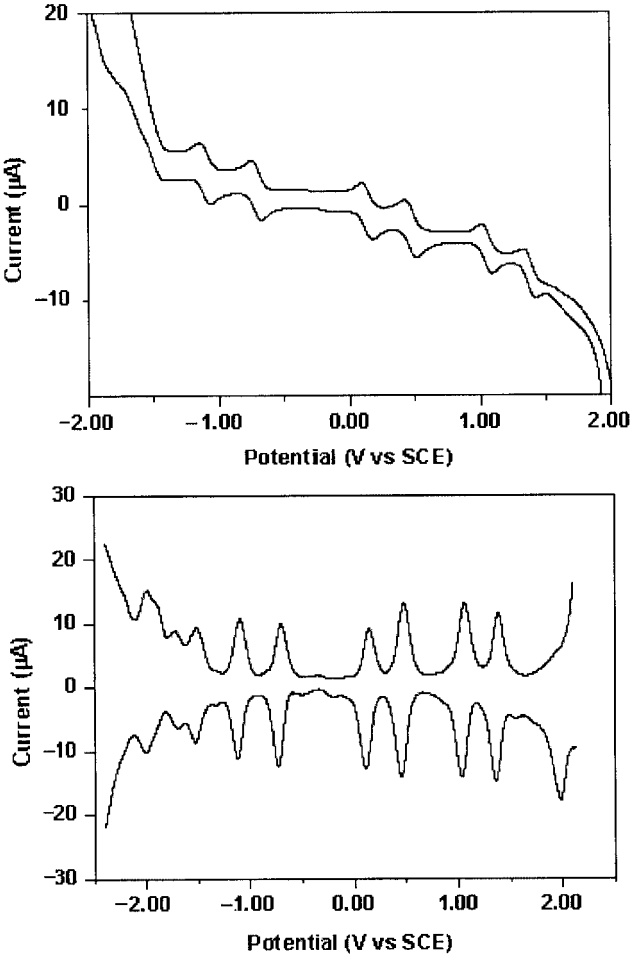

Figure 5. Cyclic voltammogram and differential pulse voltammogram of [(Pc)Lu(Pc)Lu{Pc(α-$OC_5H_{11})_4$}] (**3**) in CH_2Cl_2 containing 0.1 M $[Bu_4N][ClO_4]$ at a scan rate of 20 and 10 mV s^{-1}, respectively.

Conclusions

In summary, we have prepared novel heteroleptic tris-(phthalocyaninato) rare-earth complexes [(Pc)M(Pc)-M{Pc(α-$OC_5H_{11})_4$}] (M = Sm, Gd, Lu) as racemic mixtures. The compounds have been fully characterized by vari-

Table 3. Half-wave redox potentials of **1**–**3** (mV vs. SCE) in CH_2Cl_2 containing 0.1 M TBAP.

	Oxd_4	Oxd_3	Oxd_2	Oxd_1	Red_1	Red_2	Red_3	Red_4	Red_5	$\Delta E^{o}_{1/2}$[a]
1	1.39 (74)[b]	1.10 (66)[b]	0.64 (66)[b]	0.32 (68)[b]	–0.70 (66)[b]	–1.09 (74)[b]	–1.42 (73)[c]	–1.62[c]	–1.84[c]	1.02
2	1.37 (78)[b]	1.06 (75)[b]	0.57 (64)[b]	0.25 (66)[b]	–0.72 (64)[b]	–1.11 (70)[b]	–1.45 (76)[c]	–1.61[c]		0.97
3	1.38 (81)[b]	1.06 (76)[b]	0.48 (62)[b]	0.13 (68)[b]	–0.71 (64)[b]	–1.11 (74)[b]	–1.52 (75)[c]	–1.71[c]	–1.93[c]	0.84

[a] $\Delta E^{o}_{1/2}$ is the potential difference between the first oxidation and first reduction processes, i.e. the HOMO–LUMO gap of the corresponding molecules. [b] Cathodic to anodic peak separation given in parentheses [mV] relative to the value of 60 mV for Fe^{+}/Fe. [c] Recorded by DPV.

 © 2005 Wiley-VCH Verlag GmbH & Co. KGaA, Weinheim

ous spectroscopic and electrochemical methods. The molecular structures of the Gd and Lu analogs with a lower molecular symmetry have also been determined by X-ray diffraction analysis and NMR spectroscopy. Introduction of four 3-pentyloxy groups onto the α-positions of one outer phthalocyanine ring in the tris(phthalocyaninato)-rare-earth compounds induces a chirality in the resulting triple-decker molecules. Trials on the separation of the two enantiomers have not yet been successful.

Experimental Section

General: *n*-Pentanol and *n*-octanol were distilled from over sodium. Hexane used for chromatography was distilled from anhydrous $CaCl_2$. Column chromatography was carried out on silica gel columns (Merck, Kieselgel 60, 70–230 mesh) with the indicated eluents. Dichloromethane for voltammetric studies was freshly distilled from CaH_2 under nitrogen. All other reagents and solvents were used as received. The compounds 3-(3-pentyloxy)phthalonitrile,[16] $H_2Pc(\alpha\text{-}OC_5H_{11})_4$,[17] $M(acac)_3{\cdot}nH_2O$,[18] and $Li_2(Pc)$[19] were prepared according to the literature procedures.

Electronic absorption spectra were recorded on a Hitachi U-4100 spectrophotometer. Magnetic circular dichroism (MCD) spectra were recorded on a Jasco J-725 spectrodichrometer, with a Jasco electromagnet that produces a magnetic field of up to 1.09 T. The magnitude of this was expressed in terms of molecular ellipticity per tesla, $[\theta]_M$/deg dm^3 mol^{-1} cm^{-1} T^{-1}. MALDI-TOF mass spectra were recorded on a Bruker BIFLEX III ultra-high resolution Fourier transform ion cyclotron resonance (FT-ICR) mass spectrometer with α-cyano-4-hydroxycinnamic acid as matrix. Elemental analyses were performed by the Institute of Chemistry, Chinese Academy of Sciences. Electrochemical measurements were carried out with a BAS CV-50W voltammetric analyzer. The cell comprised inlets for a glassy carbon disk working electrode of 2.0 mm in diameter and a silver-wire counter electrode. The reference electrode was Ag/Ag$^+$, which was connected to the solution by a Luggin capillary whose tip was placed close to the working electrode. It was corrected for junction potentials by being referenced internally to the ferrocenium/ferrocene (Fe^+/Fe) couple [$E_{1/2}$ (Fe^+/Fe) = 501 mV vs. SCE]. Typically, a 0.1 M solution of $[Bu_4N][ClO_4]$ in CH_2Cl_2 containing 0.5 mM of sample was purged with nitrogen for 10 min, then the voltammograms were recorded at ambient temperature. The scan rate was 20 and 10 mV s^{-1} for CV and DPV, respectively.

General Procedure for the Preparation of Triple-Decker Complexes 1–3: In a typical procedure, a mixture of $M(acac)_3{\cdot}nH_2O$ (M = Sm, Gd, Lu) (25 mg, ca. 0.05 mmol) and phthalonitrile (39 mg, 0.30 mmol) in *n*-pentanol (4 cm^3) was heated at 140 °C under nitrogen for about 8 h. The solvent was then removed in vacuo and the residue was subjected to chromatography on a silica gel column using $CHCl_3$ as eluent. The double-decker complex $M(Pc)_2$ was isolated and further purified by recrystallization from a mixture of $CHCl_3$/MeOH. The complex $M(Pc)_2$ (60 mg, ca. 0.05 mmol) was then treated with $M(acac)_3{\cdot}nH_2O$ (M = Sm, Gd, Lu) (25 mg, ca. 0.05 mmol) and metal-free phthalocyanine $H_2Pc(\alpha\text{-}OC_5H_{11})_4$ (43 mg, 0.05 mmol) in refluxing *n*-octanol (5 cm^3) for 3 h. After cooling to room temperature, the mixture was evaporated under reduced pressure and the residue was chromatographed on a silica gel column using $CHCl_3$ as eluent. Following two green fractions containing a small amount of $H_2Pc(\alpha\text{-}OC_5H_{11})_4$ and $M(Pc)_2$, respectively, a blue band containing the target heteroleptic triple-deckers [(Pc)M(Pc)M{$Pc(\alpha\text{-}OC_5H_{11})_4$}] was developed, which was collected and the solvents evaporated. The crude product was purified by repeated chromatography followed by recrystallization from $CHCl_3$/MeOH or hexane, giving black needles.

X-ray Crystallography: Crystal data and details of data collection and structure refinement are given in Table 4. Data were collected on a Bruker SMART CCD diffractometer with an Mo-K_α sealed tube (λ = 0.71073 Å) at 293 K, using a ω-scan mode with an increment of 0.3°. Preliminary unit-cell parameters were obtained from 45 frames. Final unit-cell parameters were derived by global refinements of reflections obtained from integration of all the frame data. The collected frames were integrated using the preliminary cell-orientation matrix. The SMART software was used for collecting frames of data, indexing reflections, and determination of lattice constants, SAINT-PLUS for integration of intensity of reflections and scaling,[20] SADABS for absorption correction,[21] and SHELXL for space group and structure determination, refinements, graphics, and structure reporting.[22] All the H-atoms in these compounds were obtained geometrically. These H-atoms were included in the subsequent least-squares refinement as fixed contributors. The final refinement with anisotropic temperature factors for non-H atoms led to R values of 0.0726–0.0757 for these compounds.

Table 4. Crystallographic data for **2** and **3**.

	2·2CHCl$_3$	**3**·2CHCl$_3$
Formula	$C_{118}H_{90}Cl_6Gd_2N_{24}O_4$	$C_{118}H_{90}Cl_6Lu_2N_{24}O_4$
M_r	2435.34	2470.78
Crystal size [mm^3]	0.23 × 0.17 × 0.11	0.32 × 0.28 × 0.13
Crystal system	monoclinic	monoclinic
Space group	*C*2/*c*	*C*2/*c*
a [Å]	17.521(12)	17.366(14)
b [Å]	21.717(14)	21.293(19)
c [Å]	30.90(2)	30.58(3)
β [°]	106.472(13)	106.470(13)
V [Å]	11273(13)	10843(17)
Z	4	4
F(000)	4912	4968
$D_{calcd.}$ [Mg·m^{-3}]	1.435	1.514
μ [mm^{-1}]	1.373	2.025
Data collection range [°]	1.53 to 25.00	1.39 to 25.00
Reflections collected	28196	28229
Independent reflections	9919 [R_{int} = 0.0783]	9566 [R_{int} = 0.0935]
parameters	695	690
R_2 [$I > 2\sigma(I)$]	0.0757	0.0726
wR_2 [$I > 2\sigma(I)$]	0.2051	0.2014
Goodness of fit	1.088	1.030

CCDC-239882 (for **2**) and -239883 (for **3**) contain the supplementary crystallographic data for this paper. These data can be obtained free of charge from The Cambridge Crystallographic Data Centre via www.ccdc.cam.ac.uk/data_request/cif.

Acknowledgments

We thank Prof. Sherlock S. L. Lam for helpful discussion for the NMR spectroscopic data. Financial support from the National Science Foundation of China (grant numbers 20171028, 20325105, and 20431010), the National Ministry of Science and Technology of China (grant number 2001CB6105-04), the Ministry of Education of China, Shandong University, and The Chinese University of Hong Kong is gratefully acknowledged. This work was also partially supported by the Ministry of Education, Culture, Sports, Science and Technology, Japan, as a Grant-in-Aid COE project.

 © 2005 Wiley-VCH Verlag GmbH & Co. KGaA, Weinheim

[1] a) N. Kobayashi, *Coord. Chem. Rev.* **2001**, *219–221*, 99–123 and references cited therein; b) H. Liu, Y. Liu, M. Liu, C. Chen, F. Xi, *Tetrahedron Lett.* **2001**, *42*, 7083–7086; c) M. Kimura, T. Kuroda, K. Ohta, K. Hanabusa, H. Shirai, N. Kobayashi, *Langmuir* **2003**, *19*, 4825–4830.
[2] a) K. Tashiro, K. Konishi, T. Aida, *Angew. Chem. Int. Ed. Engl.* **1997**, *36*, 856–858; b) K. Tashiro, K. Konishi, T. Aida, *J. Am. Chem. Soc.* **2000**, *122*, 7921–7926.
[3] a) M. Takeuchi, M. Ikeda, A. Sugasaki, S. Shinkai, *Acc. Chem. Res.* **2001**, *34*, 865–873 and references cited therein; b) M. Ikeda, M. Takeuchi, S. Shinkai, F. Tani, Y. Naruta, S. Sakamoto, K. Yamaguchi, *Chem. Eur. J.* **2002**, *8*, 5541–5550.
[4] V. M. Negrimovskii, M. Bouvet, E. A. Luk'yanets, J. Simon, *J. Porphyrins Phthalocyanines* **2001**, *5*, 423–427.
[5] a) Y. Bian, R. Wang, J. Jiang, C.-H. Lee, J. Wang, D. K. P. Ng, *Chem. Commun.* **2003**, 1194–1195; b) Y. Bian, R. Wang, D. Wang, P. Zhu, R. Li, J. Dou, W. Liu, C.-F. Choi, H.-S. Chan, C. Ma, D. K. P. Ng, J. Jiang, *Helv. Chim. Acta* **2004**, *87*, 2581–2596.
[6] K. Kasuga, M. Ando, H. Morimoto, M. Isa, *Chem. Lett.* **1986**, 1095–1098.
[7] a) W. Liu, J. Jiang, D. P. Arnold, N. Pan, *Inorg. Chim. Acta* **2000**, *310*, 140–146; b) D. P. Arnold, J. Jiang, *J. Phys. Chem. A* **2001**, *105*, 7525–7533; c) P. Zhu, N. Pan, R. Li, J. Dou, Y. Zhang, D. Y. Y. Cheng, D. Wang, D. K. P. Ng, J. Jiang, *Chem. Eur. J.* **2005**, *11*, 1425–1432.
[8] a) N. Ishikawa, T. Iino, Y. Kaizu, *J. Am. Chem. Soc.* **2002**, *124*, 11440–11447; b) N. Ishikawa, T. Iino, Y. Kaizu, *J. Phys. Chem. A* **2002**, *106*, 9543–9550; c) N. Ishikawa, T. Iino, Y. Kaizu, *J. Phys. Chem. A* **2003**, *107*, 7879–7884; d) N. Ishikawa, S. Otsuka, Y. Kaizu, *Angew. Chem. Int. Ed.* **2005**, *44*, 731–733.
[9] S. L. Troyanov, L. A. Lapkina, V. E. Larcenko, A. Yu. Tsivadze, *Dokl. Akad. Nauk* (in Russian) **1999**, *367*, 644–648; *Doklady Chem*. (in English) **1999**, *367*, 192–196.
[10] N. Ishikawa, Y. Kaizu, *Chem. Phys. Lett.* **1994**, *228*, 625–632.
[11] a) D. K. P. Ng, J. Jiang, *Chem. Soc. Rev.* **1997**, *26*, 433–442; b) J. Jiang, K. Kasuga, D. P. Arnold, in *Supramolecular Photosensitive and Electroactive Materials* (Ed.: H. S. Nalwa), Academic Press, New York, **2001**, pp. 113–210; c) J. Jiang, W. Liu, D. P. Arnold, *J. Porphyrins Phthalocyanines* **2003**, *7*, 459–473.
[12] X. Sun, R. Li, D. Wang, J. Dou, P. Zhu, F. Lu, C. Ma, D. K. P. Ng, N. Kobayashi, J. Jiang, *Eur. J. Inorg. Chem.* **2004**, 3806–3813.
[13] L. Braunschweiler, R. R. Ernst, *J. Magn. Reson.* **1983**, *53*, 521–528.
[14] N. Kobayashi, M. Togashi, T. Osa, K. Ishii, S. Yamauchi, H. Hino, *J. Am. Chem. Soc.* **1996**, *118*, 1073–1085.
[15] P. Zhu, N. Pan, C. Ma, X. Sun, D. P. Arnold, J. Jiang, *Eur. J. Inorg. Chem.* **2004**, 518–523.
[16] W. O. Siegl, *J. Heterocycl. Chem.* **1981**, *18*, 1613–1618.
[17] K. Kasuga, M. Kawashima, K. Asano, T. Sugimori, K. Abe, T. Kikkawa, T. Fujiwara, *Chem. Lett.* **1996**, 867–868.
[18] J. G. Stites, C. N. McCarty, L. L. Quill, *J. Am. Chem. Soc.* **1948**, *70*, 3142–3143.
[19] P. A. Barrett, D. A. Frye, R. P. Linstead, *J. Chem. Soc.* **1938**, 1157–1163.
[20] *SMART and SAINT for Windows NT Software Reference Manuals*, Version 5.0, Bruker Analytical X-ray Systems, Madison, WI, **1997**.
[21] G. M. Sheldrick, *SADABS, A Software Program for Empirical Absorption Correction*, University of Göttingen, **1997**.
[22] *SHELXL Reference Manual*, Version 5.1, Bruker Analytical X-ray Systems, Madison, WI, **1997**.

Received: November 1, 2004
Published Online: May24, 2005

 © 2005 Wiley-VCH Verlag GmbH & Co. KGaA, Weinheim

C-Phosphoniophosphaalkenes as Precursors of $1\sigma^4,3\sigma^2$-Diphosphaallenes: Scope and Limitations

David Martin,[a,b] Heinz Gornitzka,[a] Antoine Baceiredo,*[a] and Guy Bertrand*[a,b]

Keywords: Phosphorus / Phosphaalkenes / Phosphacumulenes / Phosphorus ylides

The study of a general synthetic route to $1\sigma^4,3\sigma^2$-diphosphaallenes involving the reaction of LiHMDS with *C*-phosphoniophosphaalkenes is reported. The choice of the base is critical since the precursors are highly electrophilic species that react cleanly with methyl-, butyl-, mesityl-, or *tert*-butyllithium to afford *C*-phosphanylphosphonium ylides. The role of the substituents at the σ^4-phosphorus centre has also been studied. The resulting phosphaallenes react cleanly with a Lewis acid and undergo [3+2] cycloaddition with azides to afford a five-membered heterocycle in a three-step process.

(© Wiley-VCH Verlag GmbH & Co. KGaA, 69451 Weinheim, Germany, 2005)

Introduction

Among the possible neutral heterocumulenes featuring the PCP sequence, $1\sigma^4,3\sigma^4$-diphosphaallenes (carbodiphosphoranes) **A**[1] and $1\sigma^2,3\sigma^2$-diphosphaallenes **B**[2] have been known for many years. Recently, we reported the synthesis and characterisation of the first $1\sigma^4,3\sigma^2$-diphosphaallene **C** (Scheme 1), which features two different types of phosphorus–carbon "double" bonds.[3,4] Derivative **C** was prepared by elimination of N_2 from the phosphanyl(chlorophosphanyl)diazomethane **D**, which first leads to the corresponding transient carbene that then undergoes a 1,3-chlorine shift from one phosphorus to the other. However, the scope of this synthetic strategy is very limited in terms of starting materials (diazo precursors and chlorine migrating group).

Although phosphoniophosphaalkenes **E** can be readily prepared in high yields,[5] their reactivity has not been explored in detail. In particular, *C*-hydrogenophosphoniophosphaalkenes could afford the desired heterocumulene **C** by a simple deprotonation. Herein, we describe our results concerning this new and more general synthetic way to $1\sigma^4,3\sigma^2$-diphosphaallenes.

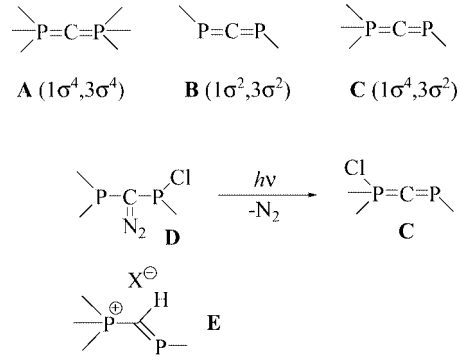

Scheme 1.

Results and Discussion

Phosphoniophosphaalkenes **3** were prepared in two steps by the method described by Grützmacher et al.[5] Two equivalents of phosphonium ylides **1** react with bis(diisopropylamino)chlorophosphane to give the corresponding *C*-phosphanyl phosphorus ylides **2**, with one equivalent of ylide **1** acting as a base to deprotonate the transiently formed *C*-phosphanylphosphonium salts. In the second step, the heterolytic cleavage of a P–N bond is achieved by addition of two equivalents of $BF_3{\cdot}OEt_2$, which affords the corresponding phosphoniophosphaalkenes **3** in good yields (72–95%) (Scheme 2). In the ^{31}P NMR spectra, compounds **3** display an AX system, with a low-field signal ($\delta \approx$ 300 ppm) characteristic of the phosphaalkene moiety, and a phosphorus–phosphorus coupling constant of about 130 Hz. In the ^{13}C NMR spectra, the signal for the PCP carbon atom appears as a doublet of doublets, with chemical shifts in the range δ = 95–100 ppm.

[a] Laboratoire Hétérochimie Fondamentale et Appliquée, (UMR, 5069), Université Paul Sabatier,
118 Route de Narbonne, 31062 Toulouse Cedex 04, France
Fax: +33-5-61-55-82-04
E-mail: baceired@chimie.ups-tlse.fr
[b] UCR-CNRS Joint Research Chemistry Laboratory (UMR, 2282), Department of Chemistry, University of California Riverside, CA 92521-0403, USA
Fax: +1-951-827-2725
E-mail: gbertran@mail.ucr.edu

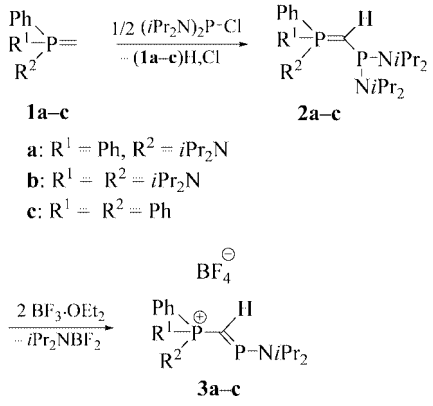

Scheme 2.

Phosphoniophosphaalkenes **3** are highly electrophilic species; they can be regarded as phosphenium salts substituted by a phosphonium ylide fragment (**3′**). Addition of methyl-, *n*-butyl- and mesityllithium to **3a** did not lead to the expected cumulenes; instead, the quantitative formation of the *C*-phosphanylphosphonium ylides **4**–**6** was observed (Scheme 3). This was indicated by the NMR spectroscopic data, in particular the disappearance of the characteristic low-field signal for the σ^2-phosphorus atom of compounds **3a** in the ^{31}P NMR spectrum. When the more sterically demanding *tert*-butyllithium was used, the *C*-phosphanylphosphonium ylide **7**,[6] featuring a P–H bond, was obtained in near quantitative yield. In the ^{31}P ^{1}H-coupled NMR spectrum, derivative **7** presents a characteristic doublet of doublets ($^2J_{P,P}$ = 160, $^1J_{P,H}$ = 220 Hz) at high-field (δ = –18 ppm) for the σ^3-phosphorus atom.

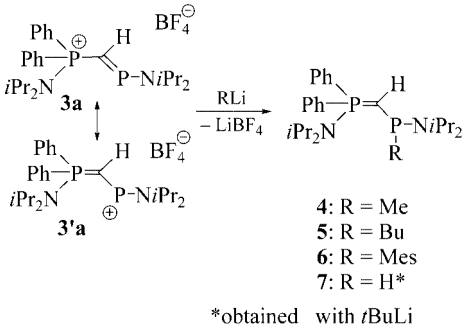

Scheme 3.

In order to prevent the nucleophilic attack at the σ^2-phosphorus atom we turned our attention to the bulky, but not reducing, lithium hexamethyldisilazide (LiHMDS). Addition of one equivalent of this strong base to a THF solution of **3a** afforded a mixture of compounds **8a** and **9a** in a 70:30 ratio (Scheme 4). The spectroscopic data for **9a** are again indicative of a phosphanylphosphonium ylide structure resulting from the addition of LiHMDS to the σ^2-phosphorus atom of **3a**. However, the major compound **8a** displays an AX system at δ = 313 and 41 ppm ($^2J_{P,P}$ = 190 Hz) in the ^{31}P NMR spectrum, the low-field signal being characteristic of a phosphaalkene moiety (Table 1). This new diphosphaallene **8a** was isolated as yellow crystals from a pentane solution in 55% yield, and its structure was unambiguously established by a single-crystal X-ray diffraction study (Figure 1).

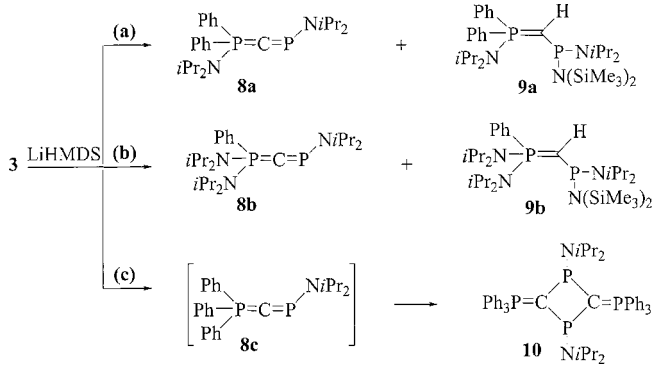

Scheme 4.

Table 1. ^{31}P and ^{13}C NMR spectroscopic data (δ in ppm and J in Hertz), and selected structural parameters [bond lengths (pm) and bond angles (°)] for derivatives **8a**, **8b** and **8d**.[4]

	$\delta_{^{31}P}$ ($J_{P,P}$)	$\delta_{^{13}C}$ ($J_{P,C}$)	(σ^4)P–C	(σ^2)P–C	P–C–P
8a	313, 41 (190)	167 (37, 14)	168.4	164.1	115.0
8b	295, 59 (166)	163 (70)	166.9	162.9	125.3
8d	303, 61 (240)	170 (37, 10)	165.0	164.3	120.9

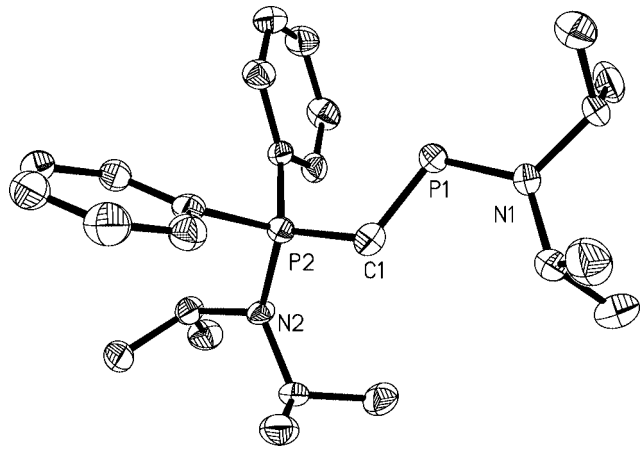

Figure 1. Structure of diphosphaallene **8a** (thermal ellipsoids drawn at 50% probability for non-hydrogen atoms; hydrogen atoms omitted for clarity).

Taking this result into account, one equivalent of LiHMDS was added to phosphoniophosphaalkene **3b**, in which one phenyl group has been replaced by a diisopropylamino substituent, as one would expect to have a more stabilized phosphonium fragment, and thus a less electrophilic σ^2-phosphorus centre. However, similar results were observed, and we isolated the phosphacumulene **8b** and the phosphanylphosphonium ylide **9b** in a 40:60 ratio (Table 1). Diphosphaallene **8b** was crystallised from a cold pentane solution, and its structure was established by an X-ray dif-

fraction study (Figure 2). With the more acidic phosphoniophosphaalkene **3c**, in which the σ^4-phosphorus atom is substituted by three phenyl groups, we did not observe any addition reaction. However, the expected cumulene **8c** was also not detected, even at low temperature, and the four-membered ring **10**[3] was characterised in solution. In this case the steric protection is probably not sufficient, and **8c** undergoes a head-to-tail dimerisation to afford heterocycle **10**,[3] as demonstrated by the presence of an A_2X_2 spin system at δ = 49 and 9 ppm ($^2J_{P,P}$ = 120 Hz) in the ^{31}P NMR spectrum.

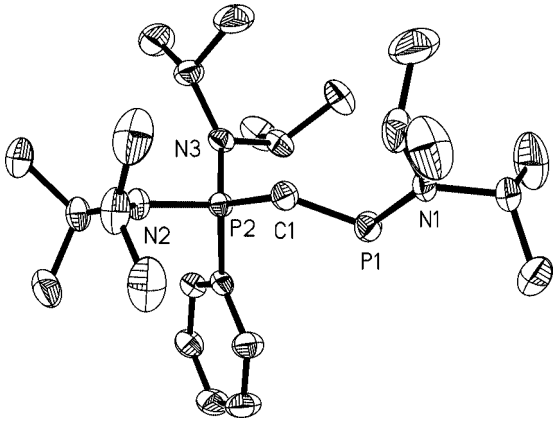

Figure 2. Structure of diphosphaallene **8b** (thermal ellipsoids drawn at 50% probability for non-hydrogen atoms; hydrogen atoms omitted for clarity).

Derivatives **8a** and **8b** present very similar NMR spectroscopic data (Table 1) to those observed for the already known diphosphacumulene **8d**, which features two diisopropylamino and a chloro group bonded to the σ^4-phosphorus atom.[4] Their molecular structures are also very similar, with very short (σ^2)P–C bond lengths (162.9–164.1 pm); the values of the PCP angles (115.0–125.3°) are in good agreement with an sp^2-hybridized carbon atom.

Thanks to its ylidic character, compound **8a** readily reacts with Lewis acids, such as BF_3, to afford the corresponding complex **11**, which was characterised by multinuclear NMR spectroscopy. Of particular interest is the quadruplet observed in the ^{19}F NMR spectrum at δ = –49 ppm ($^1J_{F,B}$ = 40 Hz), which is characteristic of alkylfluoroborate complexes (Scheme 5).[7] On the other hand, the P=C π-bond of **8a** acts as a dipolarophile upon treatment with trimethylsilyl azide to afford the [3+2]-cycloadduct **12**, which was detected by ^{31}P NMR spectroscopy at low temperature (δ = 110 and 31 ppm, $J_{P,P}$ = 200 Hz). Above –20°C, compound **12** undergoes a clean fragmentation into iminophosphane **13** ($\delta_{^{31}P}$ = 283 ppm)[8] and diazomethylenephosphorane **14** ($\delta_{^{31}P}$ = 23 ppm; IR: $\tilde{\nu}$ = 2200 cm^{-1}).[9] Note that **14** can also act as a 1,3-dipole for the diphosphacumulene **8a** to afford heterocycle **15**,[10] which was isolated as a deep-red oil in 80% yield. In the ^{31}P NMR spectrum, compound **15** displays a doublet of doublets at δ = 5.9 ppm ($^2J_{P,P}$ = 157 and 148 Hz) for the phosphane fragment and two doublets centred at δ = 30 ppm for the two inequivalent phosphonium ylides. The absence of symmetry is probably due to the pyramidalisation of both the phosphane and the ylidic carbons, which appear as doublets of doublets at δ = 94 ppm ($J_{P,C}$ = 137 and 23 Hz) in the ^{13}C NMR spectrum. Heterocycle **15** was also obtained (75%) when half an equivalent of trimethylsilyl azide was added to **8a**.

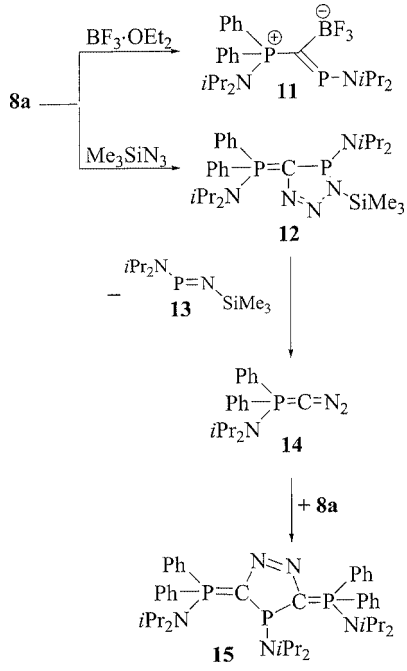

Scheme 5.

Conclusions

In conclusion, we have demonstrated that phosphoniophosphaalkenes **3** are convenient precursors for $1\sigma^4,3\sigma^2$-diphosphaallenes of type **C**. The presence of bulky substituents at the σ^4-phosphorus centre is required to prevent dimerisation. Future work will focus on the preparation of new types of cumulenes using the potential reactivity of the σ^2-phosphorus atom of these phosphoniophosphaalkenes.

Experimental Section

General Remarks: All manipulations were performed under an inert atmosphere of argon using standard Schlenk techniques. Dry, oxygen-free solvents were employed. ^{1}H, ^{13}C and ^{31}P NMR spectra were recorded on Bruker AC80, AC200, WM250 or AMX400 spectrometers. ^{1}H and ^{13}C chemical shifts are reported in ppm relative to Me_4Si as external standard. ^{31}P NMR downfield chemical shifts are expressed with a positive sign, in ppm, relative to external 85% H_3PO_4. ^{19}F chemical shifts are reported in ppm relative to F_3CCO_2H as external standard. IR spectra were recorded on a Perkin–Elmer spectrometer.

Preparation of *C*-Phosphanyl Phosphorus Ylides 2a,c: In a typical experiment, a THF solution of bis(diisopropylamino)chlorophosphane (0.2 g, 1 mmol) was added dropwise at –78 °C to a THF solution of two equivalents of ylide **1a**,**c**. The mixture was then warmed to room temperature. After stirring overnight, the solvent

 © 2005 Wiley-VCH Verlag GmbH & Co. KGaA, Weinheim

was removed under vacuum and the product was extracted with pentane. Compounds **2a,c** were purified by recrystallisation from hot acetonitrile.

2a: Yield: 0.47 g (89%), orange crystals, m.p. 98–100 °C. ^{1}H NMR (C_6D_6): δ = 1.90 (dd, $^2J_{P,H}$ = 4, $^2J_{P,H}$ < 1 Hz, 1 H, PC*H*P), 1.06 (d, $^3J_{H,H}$ = 7 Hz, 12 H, NCC*H*$_3$), 1.12 (d, $^3J_{H,H}$ = 7 Hz, 12 H, NCC*H*$_3$), 1.28 (d, $^3J_{H,H}$ = 7 Hz, 12 H, NCC*H*$_3$), 3.6 (d sept, $^2J_{P,H}$ = 7, $^3J_{H,H}$ = 7 Hz, 4 H, NC*H*), 4.0 (sept, $^3J_{H,H}$ = 7 Hz, 2 H, NC*H*), 7.80 (m, 4 H, H_{aro}), 7.12 (m, 6 H, H_{aro}) ppm. ^{13}C{^{1}H} NMR (C_6D_6): δ = 20.1 (dd, $^1J_{C,P}$ = 134 and 13 Hz, P*C*P), 24.2 (d, $^3J_{C,P}$ = 3 Hz, NCH*C*H$_3$), 25.0 (d, $^3J_{C,P}$ = 5 Hz, NCH*C*H$_3$), 46.0 (d, $^2J_{C,P}$ = 11 Hz, N*C*H), 127.8 (s, *C*H$_p$), 130.0 (d, $^3J_{C,P}$ = 3 Hz, *C*H$_m$), 132.9 (dd, $^2J_{C,P}$ = 93, $^4J_{C,P}$ = 3 Hz, *C*H$_o$), 134.0 (dd, $^1J_{C,P}$ = 100, $^3J_{C,P}$ = 3 Hz, *C*$_i$) ppm. ^{31}P{^{1}H} NMR (C_6D_6): δ = 50 and 35 (d, $^2J_{P,P}$ = 190 Hz).

2b: Yield: 0.53 g (96%), yellow powder, m.p. 113–115°C. ^{1}H NMR (C_6D_6): δ = 1.12 (d, $^3J_{H,H}$ = 7 Hz, 12 H, NCC*H*$_3$), 1.24 (d, $^3J_{H,H}$ = 7 Hz, 12 H, NCC*H*$_3$), 1.28 (d, $^3J_{H,H}$ = 7 Hz, 12 H, NCC*H*$_3$), 1.40 (d, $^3J_{H,H}$ = 7 Hz, 12 H, NCC*H*$_3$), 1.8 (dd, $^2J_{P,H}$ = 9 and 2 Hz, 1 H, PC*H*P), 3.86 (d sept, $^2J_{P,H}$ = 6, $^3J_{H,H}$ = 7 Hz, 4 H, NC*H*), 4.13 (d sept, $^2J_{P,H}$ = 13, $^3J_{H,H}$ = 7 Hz, 4 H, NC*H*), 7.1 (m, 2 H, H_{aro}), 8.0 (m, 3 H, H_{aro}) ppm. ^{31}P{^{1}H} NMR ($CDCl_3$): AB system centred at 56.0 ($^2J_{P,P}$ = 137 Hz).

2c: Spectroscopic data were identical to those reported in the literature.[5]

Preparation of *C*-Phosphoniophosphaalkenes 3a,c: In a typical experiment, a freshly distilled BF_3·OEt_2 solution (2 equiv.) was added dropwise at –78 °C to a CH_2Cl_2 solution of ylide **2a,c** (1 mmol). The mixture was warmed to room temperature and the volatile materials were removed under vacuum. The crude product was dissolved in CH_2Cl_2 and precipitated by vigorous stirring with Et_2O. The resulting powder was washed with Et_2O and dried under vacuum. Compounds **3a,c** were recrystallised from a CH_2Cl_2/Et_2O mixture at –30 °C.

3a: Yield: 0.37 g (72%), yellow crystals, m.p. 168 –170 °C. ^{1}H NMR ($CDCl_3$): δ = 1.24 (d, $^3J_{H,H}$ = 7 Hz, 12 H, NCC*H*$_3$), 3.6 (d sept, $^2J_{P,H}$ = 16, $^3J_{H,H}$ = 7 Hz, 4 H, NC*H*), 6.75 (dd, $^2J_{P,H}$ = 12, $^2J_{P,H}$ = 4 Hz, 1 H, PC*H*P), 7.80 (m, 10 H, H_{aro}) ppm. ^{13}C{^{1}H} NMR ($CDCl_3$): δ = 23.4 (broad, NCH*C*H$_3$), 49.2 (d, $^2J_{C,P}$ = 6 Hz, N*C*H), 95.5 (dd, $^1J_{C,P}$ = 105 and 56 Hz, P*C*P), 124.5 (dd, $^1J_{C,P}$ = 106, $^3J_{C,P}$ = 5 Hz, *C*$_i$), 129.8 (dd, $^2J_{C,P}$ = 13 Hz, *C*H$_{aro}$), 133.2 (d, $^3J_{C,P}$ = 10 Hz, *C*H$_{aro}$), 134.2 (s, *C*H$_p$) ppm. ^{31}P{^{1}H} NMR ($CDCl_3$): δ = 308 and 40 (d, $^2J_{P,P}$ = 133 Hz).

3b: Yield: 0.51 g (95%), colourless powder, m.p. 176–178 °C. ^{1}H NMR ($CDCl_3$): δ = 1.28 (d, $^3J_{H,H}$ = 7 Hz, 12 H, NCC*H*$_3$), 1.40 (d, $^3J_{H,H}$ = 7 Hz, 6 H, NCC*H*$_3$), 3.7 (d sept, $^2J_{P,H}$ = 16, $^3J_{H,H}$ = 7 Hz, 4 H, NC*H*), 3.9 (broad, 4 H, NC*H*), 6.22 (dd, $^2J_{P,H}$ = 12 and 6 Hz, 1 H, PC*H*P), 7.7 (m, 10 H, H_{aro}) ppm. ^{13}C{^{1}H} NMR ($CDCl_3$): δ = 23.6 (d, $^2J_{C,P}$ = 3 Hz, NC*C*H$_3$), 24.2 (broad, NCH*C*H$_3$), 48.7 (d, $^2J_{C,P}$ = 5 Hz, N*C*H), 50.0 (broad, N*C*H), 99.8 (dd, $^1J_{C,P}$ = 119 and 50 Hz, P*C*P), 124.2 (dd, $^1J_{C,P}$ = 125, $^3J_{C,P}$ = 3 Hz, *C*$_i$), 129.3 (d, $^2J_{C,P}$ = 14 Hz, *C*H$_{aro}$), 133.3 (d, $^3J_{C,P}$ = 6 Hz, *C*H$_{aro}$), 134.4 (s, *C*H$_{aro}$) ppm. ^{31}P{^{1}H} NMR ($CDCl_3$): δ = 303 and 53 (d, $^2J_{P,P}$ = 125 Hz).

3c: Spectroscopic data were identical to those reported in the literature.[5]

General Procedure for the Synthesis of Adducts 4–7: In a typical experiment, one equivalent of organolithium derivative (**4**: MeLi; **5**: *n*BuLi; **6**: MesLi; **7**: *t*BuLi;) in solution in hexanes was added to a THF solution of the phosphaalkene **3a** (0.43 g, 1 mmol) at –78 °C. The mixture was warmed to room temperature and the solvent was removed under vacuum. The resulting product was extracted with pentane and dried under vacuum. Derivatives **4**–**7** were obtained as orange oils and used without further purification.

4: Yield: 0.43 g (97%). ^{1}H NMR (C_6D_6): δ = 1.01 (d, $^3J_{H,H}$ = 7 Hz, 6 H, CHC*H*$_3$), 1.05 (d, $^3J_{H,H}$ = 6 Hz, 6 H, CHC*H*$_3$), 1.14 (d, $^3J_{H,H}$ = 7 Hz, 6 H, CHC*H*$_3$), 1.16 (d, $^3J_{H,H}$ = 5 Hz, 6 H, CHC*H*$_3$), 1.43 (d, $J_{P,H}$ = 7 Hz, 3 H, PC*H*$_3$), 1.65 (dd, $J_{P,H}$ = 9 and 3 Hz, 1 H, PC*H*P), 3.5 (m, 4 H, NC*H*), 7.1 (m, 6 H, H$_{aro}$), 7.7 (m, 4 H, H$_{aro}$) ppm. ^{13}C{^{1}H} NMR (C_6D_6): δ = 22.8 (dd, $^1J_{P,C}$ = 131 and 10 Hz, P*C*P), 23.0 (dd, $J_{P,C}$ = 14 and 20 Hz, P*C*H$_3$), 23.4 (s, CH*C*H$_3$), 23.7 (d, $J_{P,C}$ = 2 Hz, CH*C*H$_3$), 24.6 (s, CH*C*H$_3$), 24.8 (s, CH*C*H$_3$), 44.6 (d, $J_{P,C}$ = 8 Hz, N*C*H), 47.0 (d, $J_{P,C}$ = 5 Hz, N*C*H), 127.7 (s, *C*$_{aro}$H), 130.0 (dd, $J_{P,C}$ = 6 and 2 Hz, *C*$_{aro}$H), 132.0 (d, $J_{P,C}$ = 8 Hz, *C*$_{aro}$H), 132.9 (dd, $J_{P,C}$ = 9 and 2 Hz, *C*$_{aro}$H), 135.0 (dd, $J_{P,C}$ = 92 and 3 Hz, *C*$_i$) ppm. ^{31}P{^{1}H} NMR ($CDCl_3$): δ = 35 and 6 (d, $^2J_{P,P}$ = 107 Hz).

5: Yield: 0.44 g (90%). ^{1}H NMR (C_6D_6): δ = 0.8–1.1 (m, 33 H, butyl and CH$_3$), 2.57 (dd, $J_{P,H}$ = 9 and 8 Hz, 1 H, PC*H*P), 3.40 (d sept, $J_{H,H}$ = 8 Hz and $J_{P,H}$ = 10 Hz, 2 H, NC*H*), 3.60 (m, 2 H, NC*H*), 7.1 (m, 4 H, H_{aro}), 7.8 (m, 6 H, H_{aro}) ppm. ^{13}C{^{1}H} NMR(C_6D_6): δ = 14.4 (s, CH$_3$), 21.7 (dd, $J_{P,C}$ = 114 and 16 Hz, P*C*HP), 23.3 (broad, NCH*C*H$_3$), 23.7 (s, NCH*C*H$_3$), 24.7 (s, CH$_2$), 29.5 (d, $J_{P,C}$ = 17 Hz, CH$_2$), 36.9 (dd, $J_{P,C}$ = 17 and 7 Hz, PCH$_2$), 44.8 (d, $J_{P,C}$ = 8 Hz, N*C*H), 47.0 (d, $J_{P,C}$ = 5 Hz, N*C*H), 127.7 (s, *C*$_{aro}$H), 130.1 (dd, $J_{P,C}$ = 9 and 3 Hz, *C*$_{aro}$H), 132.6 (d, $J_{P,C}$ = 9 Hz, *C*$_{aro}$H), 134.2 (dd, $J_{P,C}$ = 103 and 8 Hz, *C*$_{ipso}$) ppm. ^{31}P{^{1}H} NMR (C_6D_6): δ = 38 and 15 (d, $^2J_{P,P}$ = 150 Hz).

6: Yield: 0.54 g (98%). ^{1}H NMR (C_6D_6): δ = 0.88 (d, $^3J_{H,H}$ = 8 Hz, 6 H, CHC*H*$_3$), 0.95 (d, $^3J_{H,H}$ = 8 Hz, 6 H, CHC*H*$_3$), 1.03 (d, $^3J_{H,H}$ = 5 Hz, 6 H, CHC*H*$_3$), 1.08 (d, $^3J_{H,H}$ = 5 Hz, 6 H, CHC*H*$_3$), 2.15 (s, 3 H, C$_{aro}$C*H*$_3$), 2.16 (s, 6 H, C$_{aro}$C*H*$_3$), 2.48 (dd, $J_{P,H}$ = 9 and 7 Hz, 1 H, PC*H*P), 3.4 (d sept, $J_{H,H}$ = 7, $J_{P,H}$ = 14 Hz, 2 H, NC*H*), 3.7 (m, 2 H, JC*H*), 6.8 (s, 2 H, H_{aro}), 7.1 (m, 6 H, H_{aro}), 7.8 (m, 4 H, H_{aro}) ppm. ^{13}C{^{1}H} NMR (C_6D_6): δ = 21.6 (dd, $J_{P,C}$ = 151 and 47 Hz, P*C*P), 23.6 (s, CH*C*H$_3$), 24 (m, *C*H$_3$), 46.9 (d, $J_{P,C}$ = 5 Hz, N*C*H), 47.0 (d, $J_{P,C}$ = 5 Hz, N*C*H), 47.4 (d, $J_{P,C}$ = 10 Hz, N*C*H), 127.3 (s, *C*$_{aro}$H), 127.4 (s, *C*$_{aro}$H), 130.7 (s, *C*$_{aro}$H), 132.8 (d, $J_{P,C}$ = 8 Hz, *C*$_{aro}$H), 129.9 (d, $J_{P,C}$ < 1 Hz, *C*$_{aro}$H), 134 (m, *C*$_{aro}$), 136.0 (s, *C*$_{aro}$), 141.3 (d, $J_{P,C}$ = 18 Hz, *C*$_{aro}$) ppm. ^{31}P{^{1}H} NMR (C_6D_6): δ = 39 and 18 (d, $^2J_{P,P}$ = 202 Hz).

7: Yield: 0.41 g (95%) ppm. ^{1}H NMR (C_6D_6): δ = 1.06 (d, $^3J_{H,H}$ = 7 Hz, 6 H, CHC*H*$_3$), 1.11 (d, $^3J_{H,H}$ = 6 Hz, 6 H, CHC*H*$_3$), 1.13 (d, $^3J_{H,H}$ = 7 Hz, 6 H, CHC*H*$_3$), 1.19 (d, $^3J_{H,H}$ = 7 Hz, 6 H, CHC*H*$_3$), 2.00 (pseudo t, $J_{P,H}$ = 9 Hz, 1 H, PC*H*P), 3.4 (m, 4 H, NC*H*), 6,01 (ddd, $J_{P,H}$ = 220, $J_{H,H}$ = 8 Hz, 1 H, P*H*), 7.1 (m, 6 H, H_{aro}), 7.7 (m, 4 H, H_{aro}) ppm. ^{13}C{^{1}H} NMR(C_6D_6): δ = 20.0 (dd, $J_{P,C}$ = 126 and 16 Hz, P*C*P), 23.3 (s, CH*C*H$_3$), 23.4 (s, CH*C*H$_3$), 24.0 (s, CH*C*H$_3$), 24.1 (s, CH*C*H$_3$), 24.2 (s, CH*C*H$_3$), 24.3 (s, CH*C*H$_3$), 47.7 (d, $J_{P,C}$ = 5 Hz, N*C*H), 49.2 (d, $J_{P,C}$ = 8 Hz, N*C*H), 128.4 (s, *C*$_{aro}$H), 130.7 (s, *C*$_{aro}$H), 132.8 (d, $J_{P,C}$ = 8 Hz, *C*$_{aro}$H), 133.1 (dd, $J_{P,C}$ = 7 and 2 Hz, *C*$_{aro}$H), 134.5 (dd, $J_{P,C}$ = 53 and 4 Hz, *C*$_i$) ppm. ^{31}P{^{1}H} NMR (C_6D_6): δ = 38 and –18 (d, $^2J_{P,P}$ = 160 Hz).

Reaction of LiMHDS with Phosphoniophosphaalkenes 3a,c: THF (6 mL) was added to a solid mixture of phosphaalkene **3a**,**c** (1.9 mmol) and LiHMDS·Et_2O (1.9 mmol), at –90 °C, and the solution was warmed to room temperature. The solvent was removed under vacuum and the crude product was immediately extracted with pentane.

8a: Yield: 0.45 g (55%), yellow needles from pentane/THF at 4 °C, m.p. 64–66 °C. ^{1}H NMR (C_6D_6): δ = 1.23 (d, $^3J_{H,H}$ = 7 Hz, 12 H, NCC*H*$_3$), 1.33 (br. d, $^3J_{H,H}$ = 7 Hz, 12 H, NCC*H*$_3$), 3.5 (d sept,

$^2J_{P,H}$ = 16, $^3J_{H,H}$ = 7 Hz, 4 H, NC*H*), 7.0 (m, 6 H, H_{aro}), 7.9 (m, 4 H, H_{aro}) ppm. $^{13}C\{^1H\}$ NMR (C_6D_6): δ = 23.3 (s, NCH*C*H$_3$), 47.6 (d, $^2J_{C,P}$ = 4 Hz, N*C*H), 128.1 (s, *C*H$_p$), 130.0 (d, $^3J_{C,P}$ = 3 Hz, *C*H$_m$), 132.1 (dd, $^2J_{C,P}$ = 12, $^4J_{C,P}$ < 1 Hz, *C*H$_o$), 135.0 (dd, $^1J_{C,P}$ = 93, $^3J_{C,P}$ = 3 Hz, C_i), 166.5 (dd, $^1J_{C,P}$ = 37 and 14 Hz, P*C*P) ppm. $^{31}P\{^1H\}$ NMR (C_6D_6): δ = 313 and 41 (d, $^2J_{P,P}$ = 190 Hz) ppm. $C_{54}H_{84}N_4OP_4$: calcd. C 69.80, H 9.11, N 6.03; found C 69.75, H 9.04, N 6.10.

9a: Yield: 0.28 g (25%). ^1H NMR (C_6D_6): δ = 0.22 (s, 9 H, SiCH$_3$), 0.41 (s, 9 H, SiCH$_3$), 1.03 (d, $^3J_{H,H}$ = 6 Hz, 12 H, NCC*H*$_3$), 1.07 (d, $^3J_{H,H}$ = 6 Hz, 12 H, NCC*H*$_3$), 1.13 (d, $^3J_{H,H}$ = 6 Hz, 12 H, NCC*H*$_3$), 2.39 (dd, $^2J_{P,H}$ = 12 and 2 Hz, 1 H, PCHP), 3.73 (d sept, $^2J_{P,H}$ = 7, $^3J_{H,H}$ = 6 Hz, 4 H, NC*H*), 3.80 (d sept, $^2J_{P,H}$ = 14, $^3J_{H,H}$ = 6 Hz, 2 H, NC*H*),7.2 (m, 6 H, H_{aro}), 7.6 (m, 4 H, H_{aro}) ppm. $^{13}C\{^1H\}$ NMR (C_6D_6): δ = 4.22 (s, Si*C*H$_3$), 4.48 (s, Si*C*H$_3$), 23.2 (s, NCH*C*H$_3$), 23.8 (s, NCH*C*H$_3$), 47.0 (d, $^2J_{C,P}$ = 5 Hz, N*C*H), 47.8 (d, $^2J_{C,P}$ = 4 Hz, N*C*H), 127.8 (d, $J_{C,P}$ = 6 Hz, *C*H$_{aro}$), 129.8 (dd, $J_{C,P}$ = 15 and 3 Hz, *C*H$_{aro}$), 130.0 (d, $J_{C,P}$ = 2 Hz, *C*H$_{aro}$) ppm. $^{31}P\{^1H\}$ NMR (C_6D_6): δ = 80 and 40 (d, $^2J_{P,P}$ = 200 Hz) ppm.

8b: Yield: 0.14 g (17%), yellow needles from pentane/THF, m.p. 80–82°C. ^1H NMR (C_6D_6): δ = 1.20 (d, $^3J_{H,H}$ = 7 Hz, 24 H, NCC*H*$_3$), 1.35 (d, $^3J_{H,H}$ = 7 Hz, 12 H, NCC*H*$_3$), 4.0 (m, 6 H, NC*H*), 7.1 (m, 6 H, H_{aro}), 8.0 (m, 4 H, H_{aro}) ppm. $^{13}C\{^1H\}$ NMR (C_6D_6): δ = 23.9 (s, NCH*C*H$_3$), 24.5 (s, NCH*C*H$_3$), 45.5 (broad, N*C*H), 46.8 (d, $^2J_{C,P}$ = 5 Hz, N*C*H), 127.6 (s, *C*H$_{aro}$), 129.5 (dd, $^3J_{C,P}$ = 8 and 2 Hz, *C*H$_{aro}$), 132.4 (dd, $^2J_{C,P}$ = 10, $^4J_{C,P}$ < 1 Hz, *C*H$_{aro}$), 136.0 (d, $^1J_{C,P}$ = 125 Hz, C_i), 162.4 (d, $^1J_{C,P}$ = 70 Hz, P*C*P) ppm. $^{31}P\{^1H\}$ NMR (C_6D_6): δ = 295 and 59 (d, $^2J_{P,P}$ = 166 Hz) ppm. $C_{25}H_{47}N_3P_2$: calcd. C 66.49, H 10.49, N 9.30; found C 66.55, H 10.53, N 9.27.

9b: Yield: 0.46 g (40%), yellow needles from pentane/THF, m.p. 121–122 °C. ^1H NMR (C_6D_6): δ = 0.53 (s, 9 H, SiCH$_3$), 0.55 (s, 9 H, SiCH$_3$), 1.06 (d, $^3J_{H,H}$ = 8 Hz, 12 H, NCC*H*$_3$), 1.15 (d, $^3J_{H,H}$ = 8 Hz, 12 H, NCC*H*$_3$), 1.24 (d, $^3J_{H,H}$ = 7 Hz, 6 H, NCC*H*$_3$), 1.26 (d, $^3J_{H,H}$ = 7 Hz, 6 H, NCC*H*$_3$), 1.79 (dd, $^2J_{P,H}$ = 9 and 2 Hz, 1 H, PCHP), 3.7–4.2 (m, 6 H, NC*H*), 7.2 (m, 3 H, H_{aro}), 8.1 (m, 2 H, H_{aro}) ppm. $^{31}P\{^1H\}$ NMR (C_6D_6): δ = 83 and 54 ($^2J_{P,P}$ = 170 Hz) ppm.

BF_3 Complex 11: One equivalent of $BF_3{\cdot}OEt_2$ was added to a THF solution (5 mL) of cumulene **8a** (0.8 g, 2 mmol) at room temperature. After stirring the mixture for 1 h, the solvent was removed under vacuum and the crude product was extracted with Et_2O. The solvent was removed under vacuum, and complex **11** was obtained as a yellow powder (0.6 g, 62%). M.p. 89–91 °C. ^1H NMR ($CDCl_3$): δ = 1.14 (br. d, $^3J_{H,H}$ = 7 Hz, 12 H, NCC*H*$_3$), 1.17 (d, $^3J_{H,H}$ = 7 Hz, 12 H, NCC*H*$_3$), 3.6 (br. m, 4 H, NC*H*), 4.0 (d sept, $^2J_{P,H}$ = 14, $^3J_{H,H}$ = 7 Hz, 4 H, NC*H*), 7.0 (m, 6 H, H_{aro}), 7.9 (m, 4 H, H_{aro}) ppm. $^{13}C\{^1H\}$ NMR ($CDCl_3$): δ = 23.2 (s, NCH*C*H$_3$), 49 (d, $^2J_{C,P}$ = 6 Hz, N*C*H), 128.1 (d, $J_{C,P}$ = 20 Hz, *C*H$_{aro}$), 129.0 (dd, $^1J_{C,P}$ = 115, $^3J_{C,P}$ = 8 Hz, C_i), 131.9 (s, *C*H$_{aro}$), 135.0 (d, $J_{C,P}$ = 10 Hz, *C*H$_{aro}$) ppm. ^{19}F NMR ($CDCl_3$): δ = –49 (q, $^1J_{B,F}$ = 40 Hz) ppm. $^{31}P\{^1H\}$ NMR ($CDCl_3$): δ = 326 (d, $^2J_{P,P}$ = 195 Hz), 57 (dq, $^2J_{P,P}$ = 195, $^3J_{P,F}$ = 8 Hz) ppm.

Heterocycle 15: Freshly distilled Me_3SiN_3 (13 μL, 0.1 mmol) was added to a THF solution (1 mL) of cumulene **8a** (80 mg, 0.2 mmol) at –78 °C. After warming to room temperature, the volatile materials were removed under vacuum to give compound **15** as a deep-red oil (110 mg (80%). ^1H NMR (C_6D_6): δ = 1.07 (d, $^3J_{H,H}$ = 7 Hz, 12 H, NCCH$_3$), 1.30 (d, $^3J_{H,H}$ = 7 Hz, 12 H, NCCH$_3$), 1.60 (d, $^3J_{H,H}$ = 7 Hz, 12 H, NCCH$_3$), 3.8 (d sept, $^2J_{P,H}$ = 16, $^3J_{H,H}$ = 7 Hz, 4 H, NCH), 7.0 (m, 6 H, CH$_{aro}$), 8.0 (m, 4 H, CH$_{aro}$), 8.4 (m, 4 H, CH$_{aro}$) ppm. $^{13}C\{^1H\}$ NMR (C_6D_6): δ = 24.1 (s, CH$_3$), 24.8 (s, CH$_3$), 47.6 (d, $J_{P,C}$ = 5 Hz, NCH), 94.0 (dd, $J_{P,C}$ = 137 and 23 Hz, PCP), 130.1 (s, HC$_{aro}$), 130.8 (s, HC$_{aro}$), 133.0 (dd, $J_{P,C}$ = 108 and 75 Hz, C$_i$), 134.8 (d, $J_{P,C}$ = 50 Hz, HC$_{aro}$), 134.9 (d, $J_{P,C}$ = 60 Hz, HC$_{aro}$) ppm. $^{31}P\{^1H\}$ NMR (C_6D_6): δ = 30.0 (dd, $^2J_{P,P}$ = 157 and 148 Hz), 5.9 (dd, $^2J_{P,P}$ = 157 and 148 Hz) ppm.

Crystallographic Data for 8a: $C_{54}H_{84}N_4OP_4$, M = 929.13, monoclinic, $P2_1/c$, a = 23.882(2), b = 7.920(1), c = 28.678(2) Å, β = 94.061(1)°, V = 5410.6(6) Å^3, Z = 4, T = 173(2) K. 22828 Reflections (7276 independent, R_{int} = 0.0698) were collected. Largest electron density residue: 0.305 e Å^{-3}, R_1 [for $I > 2\sigma(I)$] = 0.0641 and wR_2 = 0.1519 (all data) with $R_1 = \Sigma||F_o| - |F_c||/\Sigma|F_o|$ and $wR_2 = [\Sigma w(F_o^2 - F_c^2)^2/\Sigma w(F_o^2)^2]^{0.5}$.

Crystallographic Data for 8b: $C_{25}H_{47}N_3P_2$, M = 451.60, triclinic, $P\bar{1}$, a = 8.158(1), b = 12.372(2), c = 15.531(2) Å, α = 112.822(2)°, β = 95.436(2)°, γ = 102.054(2)°, V = 1385.8(4) Å^3, Z = 2, T = 193(2) K. 9920 Reflections (5404 independent, R_{int} = 0.0336) were collected. Largest electron density residue: 0.377 e Å^{-3}, R_1 [for $I > 2\sigma(I)$] = 0.0457 and wR_2 = 0.1180 (all data).

All data for both structures were collected at low temperatures using an oil-coated shock-cooled crystal on a Bruker-AXS CCD 1000 diffractometer with Mo-K_α radiation (λ = 0.71073 Å). The structure was solved by direct methods (SHELXS-97)[11] and all non hydrogen atoms were refined anisotropically using the least-squares method on F^2.[12]

CCDC-259732 (for **8a**) and -259733 (for **8b**) contain the supplementary crystallographic data for this paper. These data can be obtained free of charge from The Cambridge Crystallographic Data Centre via www.ccdc.cam.ac.uk/data_request/cif.

Acknowledgments

Thanks are due to the ACS/PRF (38192-AC4) and the CNRS for financial support of this work.

[1] a) F. Ramirez, N. B. Desai, B. Hansen, N. McKelvie, *J. Am. Chem. Soc.* **1961**, *83*, 3539; b) O. I. Kolodiazhnyi, in *Phosphorus Ylides* (Ed.: O. I. Kolodiazhnyi), Wiley-VCH, Weinheim, **1999**; c) A. W. Johnson, W. C. Kaska, K. A. O. Starzewski, D. A. Dixon, in *Ylides and Imines of Phosphorus* (Ed.: A. W. Johnson), Wiley-Interscience, New York, **1993**; d) H. J. Bestmann, R. Zimmermann, in *Methoden Org. Chem.* (Houben-Weyl), 4th ed., vol. E1, **1982**, pp.752–758.

[2] See for example: a) J. Escudié, H. Ranaivonjatovo, L. Rigon, *Chem. Rev.* **2000**, *100*, 3639; b) M. Yoshifuji, K. Toyota, N. Inamoto, *J. Chem. Soc., Chem. Commun.* **1984**, 689; c) H. H. Karsh, H. U. Reisacher, G. Müller, *Angew. Chem. Int. Ed. Engl.* **1984**, *23*, 618; d) M. Gouygou, M. Koenig, J. Escudié, C. Couret, *Heteroatom Chem.* **1991**, *2*, 221.

[3] H. P. Schrödel, G. Jochem, A. Schmidpeter, H. Nöth, *Angew. Chem. Int. Ed. Engl.* **1995**, *34*, 1853.

[4] T. Kato, H. Gornitzka, A. Baceiredo, G. Bertrand, *Angew. Chem. Int. Ed.* **2000**, *39*, 3319.

[5] H. Grützmacher, H. Pritzkow, *Angew. Chem. Int. Ed. Engl.* **1989**, *28*, 740.

[6] a) E. J. Corey, S. M. Albonico, U. Koelliker, T. K. Schaaf, R. K. Varmer, *J. Am. Chem. Soc.* **1971**, *93*, 1491; b) M. Soleilhavoup, A. Baceiredo, G. Bertrand, *Angew. Chem. Int. Ed. Engl.* **1993**, *32*, 1167.

[7] N. Kuhn, G. Henkel, T. Kratz, J. Kreutzberg, R. Boese, A. H. Maulitz, *Chem. Ber.* **1993**, *126*, 2041.

[8] L. N. Markovskii, V. D. Romanenko, A. V. Ruban, *Chemistry of Acyclic Compounds of Two-Coordinate Phosphorus*, Naukova Dumka, Kiev, **1988**.

 © 2005 Wiley-VCH Verlag GmbH & Co. KGaA, Weinheim

[9] J. M. Sotiropoulos, A. Baceiredo, G. Bertrand, *J. Am. Chem. Soc.* **1987**, *109*, 4711.
[10] H.-P. Schroedel, A. Schmidpeter, *Chem. Ber.* **1997**, *130*, 1519.
[11] G. M. Sheldrick, *Acta Crystallogr. Sect. A* **1990**, *46*, 467–473.
[12] *SHELXL-97, Program for Crystal Structure Refinement*, G. M. Sheldrick, University of Göttingen, Germany, **1997**.
Received: January 6, 2005
Published Online: May 27, 2005

 © 2005 Wiley-VCH Verlag GmbH & Co. KGaA, Weinheim

A "User-Friendly" Chemical Approach Towards Paramagnetic Cobalt Phosphide Hollow Structures: Preparation, Characterization, and Formation Mechanism of Co_2P Hollow Spheres and Tubes

Hongwei Hou,[b] Qi Peng,[c] Shuyuan Zhang,[b] Qixun Guo,[b] and Yi Xie*[a,b]

Keywords: Cobalt / Materials science / Nanostructures / Phosphides

User-friendly chemistry principles have been implemented for the synthesis of hollow Co_2P structures. In comparison with the original organometallic approach, the resulting alternative route is safe, simple, and inexpensive. The X-ray diffraction (XRD) pattern, X-ray photoelectron spectra (XPS), field emission scanning electron microscope (FESEM) images, and transmission electronic microscope (TEM) images were used to characterize the products, which exhibit paramagnetic behavior down to 2 K, as determined with a commercial superconducting quantum interference device (SQUID) magnetometer. The experimental investigations suggest that the formation of Co_2P hollow structures, hollow spheres, and tubes can be explained by an aggregation mechanism and a thermodynamically governed regime. Initially formed Co_2P nanoparticles are driven to aggregate into Co_2P hollow spheres by the gas bubbles produced. The formation of Co_2P tubes then occurs from the hollow spheres via hollow vessels in a thermodynamically governed process. (© Wiley-VCH Verlag GmbH & Co. KGaA, 69451 Weinheim, Germany, 2005)

Introduction

Inorganic materials with hollow structures have opened up a new and challenging field in chemistry, biotechnology, and materials science due to their potential applications in controlled-release capsules, medical imaging, artificial cells, chemical sensors, encapsulation of products (cosmetics, inks, and dyes), shape-selective adsorbents, and catalysts.[1–4] Recently, the preparation of magnetic hollow structures has become a promising approach for investigating magnetic properties due to the formation of unusual magnetic domains, the generation of quantum effects, and other phenomena.[5] Besides magnetic functions, they have potential applications in catalysis, coatings, and composite materials, etc., owing to their low density and large surface area.[6] To the best of our knowledge, the studies on hollow structures of transition metal phosphides are much less advanced in comparison to other magnetic materials because of their difficult synthesis.[7–9] All the above factors have driven us to explore the possibility of the preparation of hollow structures of transition metal phosphides under mild conditions.

[a] School of Chemical & Materials Engineering, Southern Yangtze University,
Wuxi, Jiangsu 214036, P. R. China
[b] Department of Nanomaterials and Nanochemistry, Hefei National Laboratory for Physical Sciences at Microscale, University of Science and Technology of China,
Hefei, Anhui 230026, P. R. China
Fax: +86-551-3603987
E-mail: yxielab@ustc.edu.cn
[c] Fujian Institute of Research on the Structure of Matter, Chinese Academy of Sciences,
Fuzhou, Fujian 350002, P. R. China.

Up to now, organometallic approaches have been applied to grow transition metal phosphides. Recently, FeP nanorods and nanowires were synthesized in a trioctylphosphane oxide (TOPO)/trioctylphosphane (TOP) solvent system from $Fe(CO)_5$ by a solution-phase injection route.[10] Fe_2P nanorods produced by thermal decomposition of $Fe(CO)_5$ using a syringe pump have also been reported.[11] MnP nanoparticles have been produced by the reaction of $Mn_2(CO)_{10}$ with $P(SiMe_3)_3$ in TOPO/myristic acid.[12] However, the synthetic approach using zero-valent transition metal carbonyl complexes in coordinating solvents possesses several intrinsic disadvantages.[13] For instance, sophisticated equipment such as a glove box or a syringe pump are required, as is an inert gas. Secondly, the reactions are not easy to control. Furthermore, for the tubular structures, controlling this process is difficult and the internal cavity is not always continuous throughout the length.[14] For these fundamental and practical reasons, an alternative route using a "user-friendly" chemical method is much anticipated. This concept, which refers to the synthetic and processing procedures, is different to the traditional "green chemistry".

Among M_2P compounds (M = Mn, Fe, CO, Ni), only Co_2P has a C_{23} orthorhombic structure; the others have a C_{22} hexagonal structure.[15,16] Our previous research on Co_2P nanocrystallites and nanorods gave some interesting results,[17,18] and these attracted us to the unexplored Co_2P nanostructures with special morphologies. Here, for the first time, we report the formation of Co_2P hollow spheres and tubes from metal halides and yellow phosphorus in a mixture of absolute ethanol and water as solvent. We have man-

aged to eliminate the use of toxic carbonyl complexes, and have developed an easy process for the formation of Co_2P hollow spheres and tubes under solvothermal conditions. On the basis of a series of comparison experiments, a mechanism of formation of Co_2P hollow spheres and tubes was proposed and investigated. We expect that the novel tubular nature of Co_2P together with the tunable interior nanoparticle size of these hollow spheres may make them ideal entities for incorporating other species or surface modification, which might bring novel optical, electronic, and magnetic properties in the near future.

Results and Discussion

The typical XRD patterns of the samples obtained at 220 °C for 30 h and 48 h are shown in Figures 1a and b, respectively. All the diffraction peaks can be indexed to orthorhombic Co_2P [space group *Pnam*(62)] in the JCPDS card no.74-287. Compared with the standard diffraction patterns, no characteristic peaks for impurities such as P or CoP_3, can be detected.

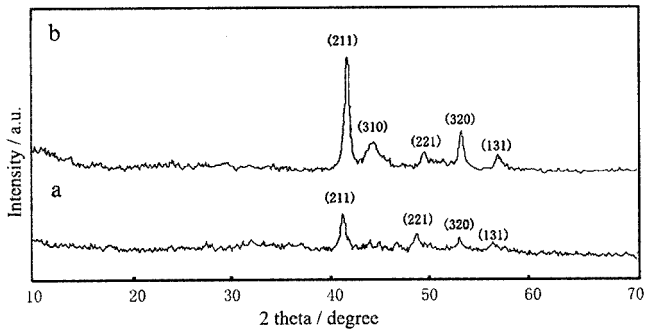

Figure 1. XRD patterns of the as-produced Co_2P hollow spheres (a) and tubes (b).

The purity and elemental composition of the products were determined by X-ray photoelectron spectroscopy (XPS); the XPS spectra of Co_2P are shown in Figures 2a and b. The Co $2p_{3/2}$ binding energy is 778.2 eV, which is in good agreement with the literature,[19] and the P 2p binding energy is 129.8 eV, consistent with our previous results (129.1 eV). From the integral peak areas of Co and P in the XPS spectra, the Co_2P samples obtained at 220 °C for 30 h have a Co/P molar ratio of 1.80:1 − the Co_2P samples obtained at 220 °C for 48 h have a molar ratio of 1.95:1 − both of which are close to the expected stoichiometry of Co_2P. No obvious impurities such as chloride or phosphate could be detected in any of the samples.

The morphology of the Co_2P samples obtained at 220 °C for 30 h is shown in Figure 3. The panoramic FESEM images (Figure 3a) show that the sample consists of a large quantity of nearly uniform spheres and clearly indicate that the spheres have diameters of around 1.2 μm; the TEM image (Figure 3b) reveals their partly overlapped hollow nature. The three obvious diffraction rings in the SAED pattern (Figure 3c) recorded from the hollow spheres can be identified as the (211), (310), and (131) planes of orthorhombic Co_2P. The HRTEM image (Figure 3d) clearly shows that the hollow spheres are aggregates of small particles with a size of 3–4 nm.

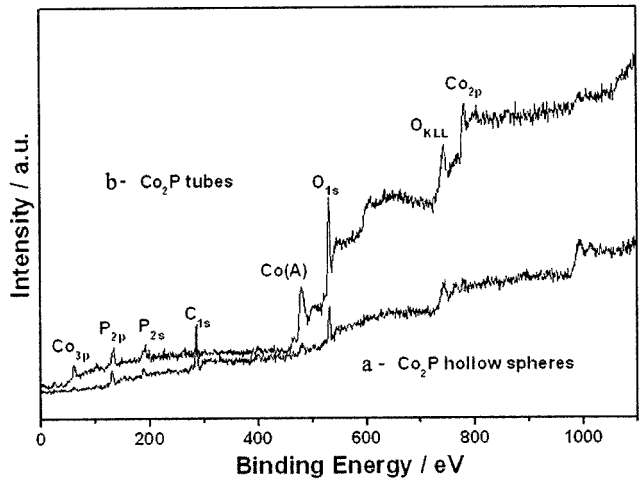

Figure 2. XPS analysis of the as-produced Co_2P hollow spheres (a) and tubes (b).

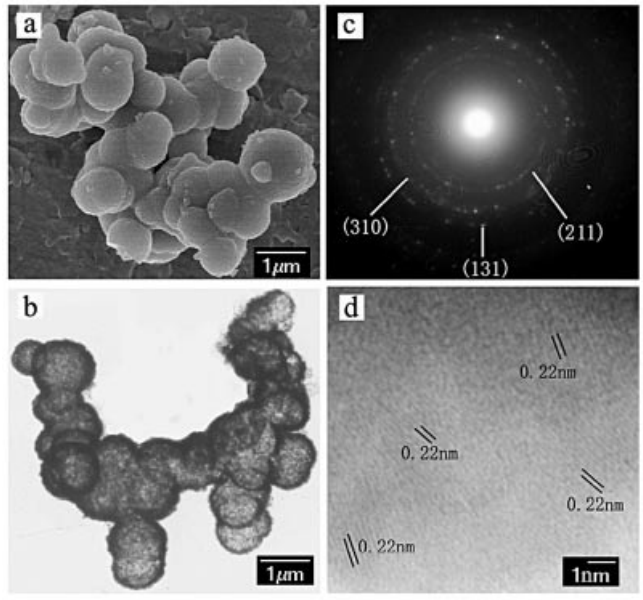

Figure 3. Morphology of the Co_2P hollow spheres formed at 220 °C after 30 h: (a) FESEM image; (b) TEM image; (c) SAED patterns; (c) HRTEM image.

The morphology of the Co_2P samples obtained at 220 °C for 48 h is shown in Figure 4. Both the FESEM and TEM images of the sample (Figure 4a–c) show that Co_2P here is present as tubular structures with a diameter of around 1 μm and length of 3–7 μm. The SAED patterns recorded from the tubes (Figure 4d) clearly show that the tubes are polycrystalline. Six easily observed diffraction rings can be identified as the (211), (310), (221), (131), (232), and (422) diffractions of orthorhombic Co_2P. The direct observation of the structure of the Co_2P tubes was performed by HRTEM, as shown in Figure 4e, which clearly shows that the tubes are aggregates of small particles.

 © 2005 Wiley-VCH Verlag GmbH & Co. KGaA, Weinheim

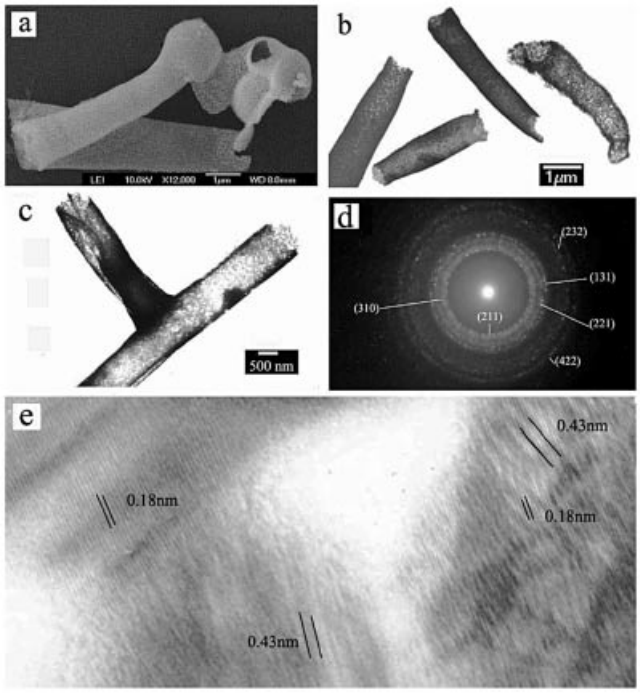

Figure 4. Morphology of the Co_2P tubes formed at 220 °C after 48 h: (a) FESEM image; (b) TEM image; (c) a typical tubular structure; (d) SAED patterns; (e) HRTEM image.

The magnetic properties of the Co_2P hollow spheres and tubes, which have similar properties, were measured with a commercial SQUID magnetometer (Quantum Design, MPMS). The temperature dependence of the magnetization for Co_2P hollow spheres and tubes measured in an applied magnetic field of 500 Oe between 2 K and 300 K is shown in Figure 5a, and the magnetic-field dependence of magnetization (M vs. H) at 2 K for both Co_2P hollow spheres and tubes is shown in Figure 5b. Both reveal that the Co_2P hollow spheres and tubes have no ferromagnetic characteristics and can be expressed as paramagnetic moments.[7–9] The results can be well described by the Curie–Weiss law, and agree well with those obtained from the M vs. H data. The Co_2P hollow spheres and tubes are paramagnetic with no evidence of ferromagnetic ordering, due to their C_{23} orthorhombic structure.[15] This is in agreement with the magnetic properties of Co_2P reported by Fujii, who reported that Co_2P exhibits ferromagnetism only in its hexagonal structure, and that orthorhombic Co_2P is a Pauli paramagnet.[16] The tube structures have stronger paramagnetic properties than the hollow spheres due to their better crystallinity.

The experimental investigations suggest that the formation of Co_2P hollow spheres and tubes can be explained as an aggregation mechanism in a thermodynamically governed process. Initially formed Co_2P nanoparticles are driven to aggregate into Co_2P hollow spheres by the bubbles of PH_3 and C_2H_4 produced. The formation of the Co_2P tubes is suggested to occur from the hollow spheres via hollow vessels in a thermodynamically governed process.

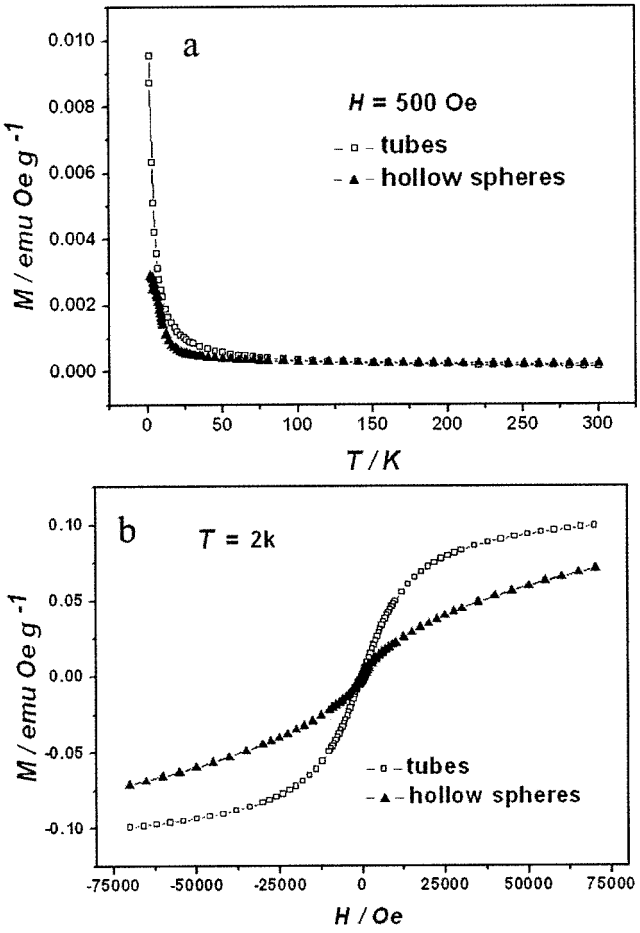

Figure 5. Magnetic properties of the Co_2P hollow spheres and tubes: (a) temperature dependence of magnetization under an applied magnetic field of 500 Oe; (b) magnetic-field dependence of the magnetization at 2 K.

In the present route the synthesis of Co_2P is based on the reaction of Co^{2+} with PH_3, which is produced by the reaction of yellow phosphorus with water and ethanol at 220 °C. Yellow phosphorus (melting point 44.1 °C and boiling point 280 °C) could form droplets dispersed in the aqueous solution to give a heterogeneous liquid–liquid two-phase system at elevated temperature. Obviously, the reactions easily occur at the interfaces of these two phases.

The reaction of phosphorus with water at high temperature and pressures has been studied by several authors who were primarily interested in the overall reaction and its products.[20–22] It is well known that ethanol reacts with yellow phosphorus at high temperatures and pressures.[23] In our approach, the system provides the appropriate conditions to initiate the reactions shown in Equations (1) and (2). Once generated, PH_3 would immediately react with the cobalt ion to form Co_2P, as shown in Equation (3). The by-product, H_3PO_3, undergoes a circular reaction with H_3PO_4, shown in Equations (4) and (5), which increases the amount of PH_3 and accelerates the reaction of PH_3 with the cobalt ion.[24,25] Reaction (3) continues until one of the raw materials runs out. The whole process can be formulated as shown in Scheme 1.

 © 2005 Wiley-VCH Verlag GmbH & Co. KGaA, Weinheim

$$2\ P_4 + 12\ H_2O \rightarrow 3\ H_3PO_4 + 5\ PH_3 \quad (1)$$

$$P_4 + 6\ C_2H_5OH \rightarrow 2\ H_3PO_3 + 2\ PH_3 + 6\ C_2H_4 \quad (2)$$

$$12\ CoCl_2 + 7\ PH_3 \rightarrow 6\ Co_2P + PCl_3 + 21\ HCl\ (pH = 2) \quad (3)$$

$$4\ H_3PO_3 \rightarrow PH_3 + 3\ H_3PO_4 \quad (4)$$

$$P_4 + 6\ H_3PO_4 + 6\ H_2O \rightarrow 10\ H_3PO_3 \quad (5)$$

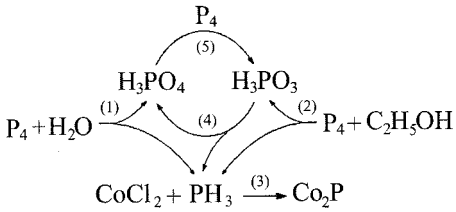

Scheme 1. Schematic growth path of Co_2P. (1)–(5) represent the corresponding reactions in the text.

After the initial nucleation, the newly formed Co_2P nuclei grow into nanoparticles. When the reaction was carried out at 220 °C for between 12 and 24 h, the nanoparticles grew gradually, as shown in Figures 6a and b. When the reaction time was prolonged to 30 h, a large quantity of nearly uniform hollow spheres of Co_2P was formed, as shown by the corresponding TEM images in Figure 6c. When the reaction time was extended further to 36 h, congregated hollow spheres were found in the product, as shown in Figure 6d.

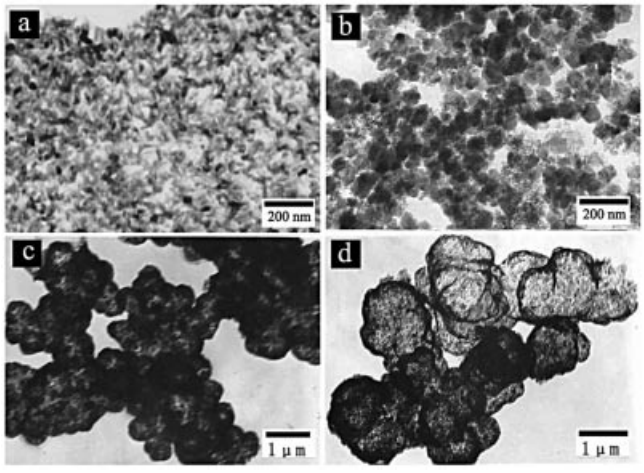

Figure 6. TEM images of the Co_2P structures formed in ethanol at 220 °C at different reaction times: (a) particles after 12 h; (b) particles after 24 h; (c) hollow spheres after 30 h; (d) congregated hollow spheres after 36 h.

Based on these observations and the structure of the hollow spheres we were able to propose an aggregation mechanism, as shown in Scheme 2. The TEM results suggested that these newly formed nanoparticles have a tendency to aggregate at the interface of the gas bubbles and the solution. Similar to the reported case of monodispersed SiO_2 or ZnSe microspheres aggregating under the effects of gas bubbles,[26,27] the gas aggregation centers are the PH_3 and C_2H_4 bubbles in our approach. The mixture of ethanol and water used as solvent could effectively form the bubble templates that are important for the formation of hollow spheres. In comparison with our previous work on Co_2P nanorods,[18] it is easy to show that the gaseous C_2H_4 produced in this approach is the linchpin of the bubble templates as it is not involved in any further reaction and thus can provide the gas aggregation center. Driven by the minimization of interfacial energy, newly formed Co_2P nanoparticles may aggregate around the gas–liquid interface between the gas bubbles and the solution and then form Co_2P hollow spheres.

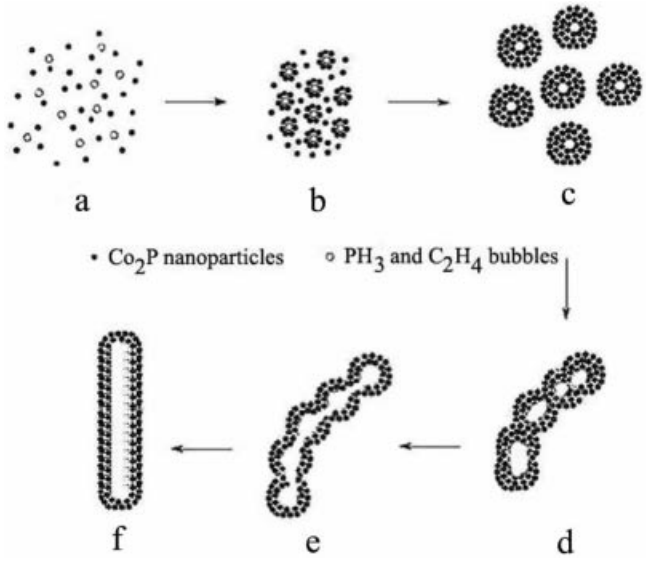

Scheme 2. Schematic illustration of a proposed mechanism for the formation of hollow Co_2P structures: (a) nanoparticles; (b) aggregated nanoparticles around the gas–liquid interface between PH_3 and C_2H_4 bubbles and the solution; (c) hollow spheres; (d) congregated hollow spheres; (e) connected hollow spheres; (f) tubes.

It was well known that in a thermodynamic process hollow spheres are generally less stable than tubes as they possess a higher internal energy; this favors the transformation of hollow spheres into tubes. When the reaction time was increased from 40 h to 42 h at 220 °C, these hollow spheres became attached end-to-end and a borderline could be detected only dimly (Figure 7a and b). When the reaction time was raised to 46 h, the tubular conductive structure had obviously formed (Figure 7c), as shown by the incurvate walls of the vessels and lack of borderline of the hollow microspheres. Finally, the rough vessels grew into smooth tubular structures (Figure 7d) after 48 h. The whole growth procedure from hollow spheres to Co_2P tubes is illustrated in Scheme 2.

 © 2005 Wiley-VCH Verlag GmbH & Co. KGaA, Weinheim

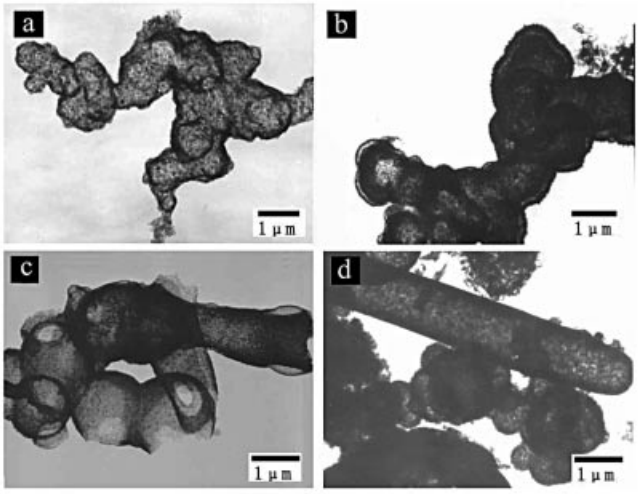

Figure 7. TEM images of the Co_2P structures formed in ethanol at 220 °C at different reaction times: (a) connected hollow spheres after 40 h; (b) connected hollow spheres after 42 h; (c) hollow vessels after 46 h; (d) tubes after 48 h.

Conclusions

In summary, we developed a "user-friendly" one-pot chemical approach to synthesize Co_2P hollow spheres and tubes, which exhibit paramagnetic behavior down to 2 K. In comparison with the original organometallic approach, this route is safe, simple, and inexpensive. The experimental investigations suggest that Co_2P hollow spheres are formed from the initially formed nanoparticles under the effect of PH_3 and C_2H_4 bubbles, and the Co_2P tubes form from the hollow spheres via hollow vessels in a thermodynamically governed process. The use of gas bubbles produced during the reaction to provide aggregation centers is a novel and effective method to fabricate hollow structures. Compared to other templated synthetic methods, this template-free method is very simple and convenient and avoids the introduction of impurities. It is therefore suitable for modern chemical synthesis. This idea might be extended to other solution systems in which easily aggregated monodispersed nanocrystals are produced during the reaction.

Experimental Section

Details of a typical experiment are as follows: $CoCl_2{\cdot}6H_2O$ (0.475 g, 2 mmol) and yellow phosphorus (1.24 g, 10 mmol) were placed into a 40-mL, Teflon-lined autoclave, which was then filled with absolute ethanol up to 80% of its capacity. To obtain Co_2P hollow spheres, the autoclave was heated to 220 °C for 30 h; To obtain Co_2P tubes, the autoclave was maintained at 220 °C for 48 h. In both cases the autoclave was then allowed to cool to room temperature, and the black precipitate was collected and washed with absolute ethanol and distilled water in sequence to remove any by-products and possible impurities. The final products were dried in vacuo at 60 °C for 3–4 h. The yields of the products synthesized by this method were above 80%.

The phase identification of the samples was performed with a Rigaku D/max-γA X-ray diffractometer equipped with Cu-K_α radiation (λ = 1.54178 Å). The purity and components were determined by X-ray Photoelectron Spectroscopy (XPS) with an ESCALab MKII X-ray photoelectron spectrometer with Mg-K_α radiation as the excitation source. The morphology of the products was determined with a field emission electron microscope (FESEM JEOL JSM-6700F) and transmission electron microscope (TEM Hitachi H-800). Further structural analysis was performed with a high-resolution transmission electron microscope (HRTEM JEOL-2010) and by selected area electron diffraction (SAED). The magnetic properties were measured with a commercial superconducting quantum interference device (SQUID) magnetometer (Quantum Design, MPMS).

Acknowledgments

Financial support from the National Natural Science Foundation of China is gratefully acknowledged.

[1] *Hollow and Solid Spheres and Microspheres: Science and Technology Associated with Their Fabrication and Application* (Eds.: D. L. Wilcox, M. Berg, T. Bernat, D. Kellerman, J. K. Cochran), Materials Research Society Proceedings, Pittsburgh, **1995**, 372.
[2] A. Krishnan, E. Dujardin, M. M. J. Treacy, J. Hugdahl, S. Lynum, T. W. Ebbesen, *Nature* **1997**, *388*, 451–454.
[3] F. Caruso, R. A. Caruso, H. Möhwald, *Science* **1998**, *282*, 1111–1114.
[4] H. Y. Huang, E. E. Remsen, T. Kowalewski, K. L. Wooley, *J. Am. Chem. Soc.* **1999**, *121*, 3805–3806.
[5] H. Yoshikawa, K. Hayashida, Y. Kozuka, A. Horiguchi, K. Awaga, S. Bandow, S. Iijima, *Appl. Phys. Lett.* **2004**, *85*, 5287–5289.
[6] S. W. Kim, M. Kim, W. Y. Lee, T. Hyeon, *J. Am. Chem. Soc.* **2002**, *124*, 7642–7643.
[7] *Borides, Silicides and Phosphides* (Eds.: B. Aronsson, T. Lundstrom, S. Rundqvist), Wiley, New York, **1965**.
[8] *Chemistry of the Elements* (Eds.: N. N. Greenwood, A. Earnshaw), Pergamon, New York, **1994**.
[9] C. Stinner, R. Prins, T. Weber, *J. Catal.* **2001**, *202*, 187–194.
[10] C. Qian, F. Kim, L. Ma, F. Tsui, P. D. Yang, J. Liu, *J. Am. Chem. Soc.* **2004**, *126*, 1195–1198.
[11] J. Park, B. Koo, Y. Hwang, C. Bae, K. An, J.-G. Park, H. M. Park, T. Hyeon, *Angew. Chem. Int. Ed.* **2004**, *43*, 2282–2285.
[12] S. C. Perera, G. Tsoi, L. E. Wenger, S. L. Brock, *J. Am. Chem. Soc.* **2003**, *125*, 13960–13961.
[13] X. G. Peng, *Chem. Eur. J.* **2002**, *8*, 334–339.
[14] B. Liu, H. C. Zeng, *J. Phys. Chem. B.* **2004**, *108*, 5867–5874.
[15] T. Hōkabe, *J. Sci. Hiroshima Univ., Ser. A: Phys. Chem.* **1978**, *42*, 1–5.
[16] S. Fujii, S. Ishida, S. Asano, *J. Phys. F: Met. Phys.* **1988**, *18*, 971–980.
[17] X. F. Qian, Y. Xie, Y. T. Qian, X. M. Zhang, W. Z. Wang, L. Wang, *Mater. Sci. Eng.* **1997**, *B49*, 135–137.
[18] H. W. Hou, Q. Yang, C. R. Tan, G. B. Ji, B. X. Gu, Y. Xie, *Chem. Lett.* **2004**, *33*, 1272–1273.
[19] *Handbook of X-ray Photoelectron Spectroscopy* (Eds.: C. D. Wagner, W. M. Rings, L. E. Dabis, J. F. Moulder, G. E. Muilenberg), Perkin–Elmer Corporation, Physical Electronics Division, Eden Prairie, Minnesota, **1979**.
[20] *Phosphorus and its Compounds*, vol. I ("Chemistry") (Ed.: J. R. V. Wazer), Interscience Publishers, Inc., New York, **1958**, p. 99–100.
[21] S. Brunauer, J. F. Schultz, *Ind. Eng. Chem.* **1941**, *33*, 828–829.
[22] C. Kroger, *Z. Anorg. Allg. Chem.* **1932**, *206*, 289–290.

 © 2005 Wiley-VCH Verlag GmbH & Co. KGaA, Weinheim

[23] *Important Inorganic Reactions* (Ed.: S. C. Chen), 3rd ed., Shanghai Science and Technology Press, China, **1994**, p. 1765–1775.
[24] S. M. Gao, J. Lu, N. Chen, Y. Zhao, Y. Xie, *Chem. Commun.* **2002**, 3064–3065.
[25] C. M. Lukehart, S. B. Milne, S. R. Stock, *Chem. Mater.* **1998**, *10*, 903–908.
[26] M. Ocana, R. Rodriguez-Clemente, C. J. Serna, *Adv. Mater.* **1995**, *7*, 212–216.
[27] Q. Peng, Y. J. Dong, Y. D. Li, *Angew. Chem. Int. Ed.* **2003**, *42*, 3027–3030.

Received: January 12, 2005
Published Online: May 27, 2005

 © 2005 Wiley-VCH Verlag GmbH & Co. KGaA, Weinheim

C–H vs. N–H Bond Activation in Aminophosphane Ligands: Reaction of $[Cp^*Ru(MeCN)_2(PR^1{}_2NHR^2)]^+$ (R^1 = Ph, *i*Pr; R^2 = Ph, C_6F_5) with Alkynes

Manuel Jiménez-Tenorio,[a] M. Carmen Puerta,[a] and Pedro Valerga*[a]

Dedicated to the memory of Prof. Francisco González García (Universidad de Sevilla)[‡]

Keywords: Alkyne ligands / C–H activation / Half-sandwich complexes / Phosphane ligands / Ruthenium

The reaction of the complexes $[Cp^*Ru(MeCN)_2(PR^1{}_2NHR^2)]^+$ (R^1 = R^2 = Ph **1**; R^1 = *i*Pr, R^2 = C_6F_5 **2**; R^1 = *i*Pr, R^2 = Ph **3**) with 1-alkynes HC≡CR (R = H, *n*Bu, $SiMe_3$) or diynes $HC{\equiv}CCH_2XCH_2C{\equiv}CH$ (X = O, CH_2, CH_2CH_2) yields different products depending on the nature of the aminophosphane ligand. In some cases, alkyne coupling involving migration of the phosphane and N–H activation occurs, yielding amidobutadiene complexes of the type $[Cp^*Ru\{\eta^4\text{-}C_4H_3(R)_2\text{-}PR^1{}_2NR^2\text{-}\kappa^1N\}]^+$ or $[Cp^*Ru\{\eta^4\text{-}C_4H_3(CH_2XCH_2)PR^1{}_2NR^2\text{-}\kappa^1N\}]^+$. The complexes $[Cp^*Ru\{\eta^4\text{-}C_4H_3(CH_2OCH_2)\text{-}PPh_2NPh\text{-}\kappa^1N\}][PF_6]$ (**1a**) and $[Cp^*Ru\{\eta^4\text{-}C_4H_3(CH_2\text{-}OCH_2)PiPr_2NC_6F_5\text{-}\kappa^1N\}][PF_6]$ (**2a**) have been structurally characterized by X-ray crystallography. In other cases, for example the reaction of **3** with HC≡CR (R = *n*Bu, $SiMe_3$), C–H bond activation at the *ortho*-position of the phenyl ring of the phenylamino moiety and coupling to the alkyne fragment takes place. This results in the formation of the novel π-alkene complexes $[Cp^*Ru(MeCN)\{\eta^2\text{-}RCH{=}CH(C_6H_4)\text{-}NHPiPr_2\text{-}\kappa^1P\}]^+$ (R = *n*Bu **4**, $SiMe_3$ **5**), formally derived from the insertion of the alkyne into the *ortho*-C–H bond of the phenyl ring. The derivative $[Cp^*Ru(MeCN)\{\eta^2\text{-}nBuCH{=}CH(C_6H_4)NHPiPr_2\text{-}\kappa^1P\}][BPh_4]$ has been structurally characterized by X-ray crystallography. These compounds are related to the also structurally characterized olefin complex $[Cp^*Ru(MeCN)(\eta^2\text{-}MeOOCCH{=}CH_2)(PPh_2NHPh)][PF_6]$ (**6**), generated by reaction of **1** with methyl acrylate.
(© Wiley-VCH Verlag GmbH & Co. KGaA, 69451 Weinheim, Germany, 2005)

Introduction

Complexes of the type $[(C_5R_5)Ru(MeCN)_2(L)]^+$ (R = H, Me; L = CO, PR_3, $AsPh_3$, $SbPh_3$) are regarded as synthons for the corresponding cationic 14-electron fragments $[(C_5R_5)Ru(L)]^+$ due to the substitutionally labile character of the acetonitrile ligands.[1] The reactivity of these systems towards alkynes has been thoroughly studied both from the experimental and theoretical points of view.[1–5] The derivatives $[(C_5R_5)Ru(MeCN)_2(L)]^+$ react with alkynes to yield bis(π-alkyne) adducts which readily undergo oxidative alkyne coupling of the two alkyne ligands to form cationic ruthenacyclopentatriene complexes.

Ruthenacyclopentatriene complexes are key intermediates in the overall process, and the final products of the reaction are determined by the nature of L, the use of Cp or Cp* as co-ligands, and the nature of the substituents present in the alkyne.[1] When L is PR_3, migration of the phosphane from Ru to C occurs in most cases, generating

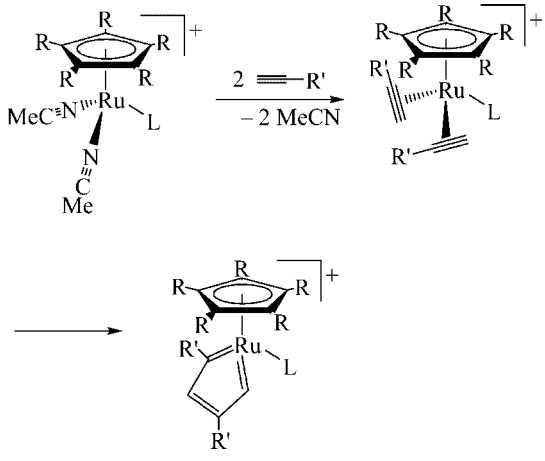

allyl carbene species.[2–4] These species behave as masked coordinatively unsaturated complexes that are capable of activating C–H bonds. In cyclopentadienyl complexes containing tertiary phosphane ligands the C–H activation process takes place at one of the aryl or alkyl substituents of the phosphane.[4,6]

At variance with this, in pentamethylcyclopentadienyl derivatives the C–H activation occurs at one of the methyl

[a] Departamento de Ciencia de Materiales e Ingeniería Metalúrgica y Química Inorgánica, Facultad de Ciencias, Universidad de Cádiz,
Apartado 40, 11510 Puerto Real, Cádiz, Spain
Fax: +34-956-016288
E-mail: pedro.valerga@uca.es
[‡] For his contribution to the development of Inorganic Chemistry in Spain.

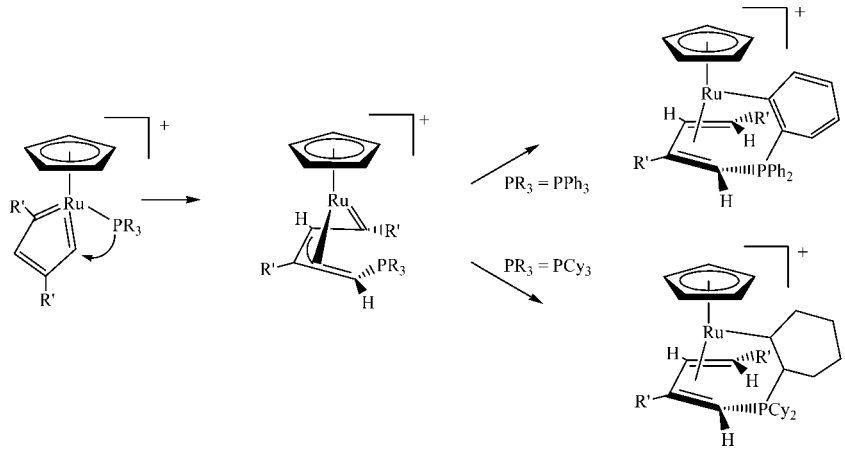

substituents of the Cp* ring to yield η^6-fulvene complexes.[6]

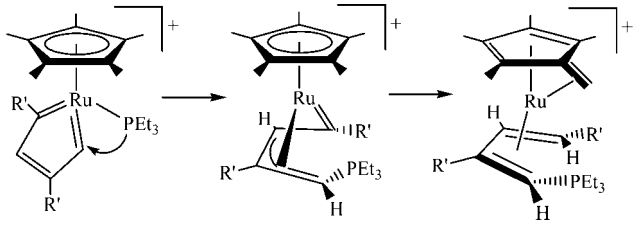

In all cases, the result of the phosphane migration to the organic fragment and the subsequent C–H activation process is the formation of η^4-butadiene species. Very recently, Kirchner and co-workers have reported the activation of alkynes by the aminophosphane complex $[CpRu(MeCN)_2(PPh_2NHPh)]^+$, which results in the formation of η^4-amidobutadiene complexes.[7] In this case phosphane migration also occurs, and is followed by an N–H bond activation process in the amino group rather than C–H bond activation.

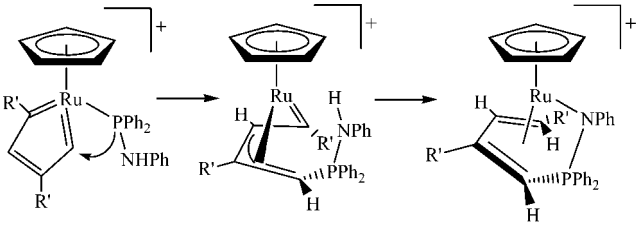

Given the previously observed behavior differences between $[CpRu(MeCN)_2(PR_3)]^+$ and the homologous $[Cp^*Ru(MeCN)_2(PR_3)]^+$ complexes with respect to the C–H activation processes,[6] we have addressed the question of whether N–H or C–H activation should occur in the case of Cp* complexes containing aminophosphane ligands. Hence, we have studied the interaction of 1-alkynes with the cationic complexes $[Cp^*Ru(MeCN)_2(PR^1{}_2NHR^2)]^+$. We have found that either N–H or C–H activation may take place depending upon the aminophosphane ligand and the substituent on the alkyne. The detailed results are discussed below.

Results and Discussion

The complexes $[Cp^*Ru(MeCN)_2(PR^1{}_2NHR^2)]^+$ ($R^1 = R^2$ = Ph **1**; R^1 = *i*Pr, $R^2 = C_6F_5$ **2**; R^1 = *i*Pr, R^2 = Ph **3**) were prepared by treatment of $[Cp^*Ru(MeCN)_3][PF_6]$ with a stoichiometric amount of the corresponding aminophosphane in dichloromethane; they were isolated either as their PF_6^- (**1** and **2**) or BPh_4^- (**3**) salts.

Treatment of **1**, **2**, or **3** with either propargyl ether or 1,6-heptadiyne led to the isolation after purification, in moderate yields, of the corresponding amidobutadiene complexes $[Cp^*Ru(\eta^4\text{-}C_4H_3(X)PR^1{}_2NR^2\text{-}\kappa^1N)]^+$ [$R^1 = R^2$ = Ph, X = CH_2OCH_2 **1a**, $(CH_2)_3$ **1b**; R^1 = *i*Pr, $R^2 = C_6F_5$, X = CH_2OCH_2 **2a**, $(CH_2)_3$ **2b**; R^1 = *i*Pr, R^2 = Ph, X = CH_2OCH_2 **3a**, $(CH_2)_3$ **3b**]. In analogous fashion, treatment of **1** and **3** with 1,7-octadiyne also led to the corresponding amidobutadiene complexes **1c** and **3c**, respectively, whereas the reaction of **2** with 1,7-octadiyne yielded a mixture from which no pure compound could be isolated. The reaction of **1** with HC≡CR (R = H, *n*Bu) also afforded the corresponding amidobutadiene complexes $[Cp^*Ru\{\eta^4\text{-}C_4H_3(R)_2\text{-}PPh_2NPh\text{-}\kappa^1N\}][PF_6]$ (R = H **1d**, *n*Bu **1e**). All these compounds were characterized by NMR spectroscopy. The ^1H and $^{13}C\{^1H\}$NMR spectra are consistent with those reported for the related cyclopentadienyl amidobutadiene complexes.[7] One of the most distinctive spectral features of these complexes is the resonance for H^1 and C^1 in their respective ^1H and $^{13}C\{^1H\}$ NMR spectra. Given the fact that C^1 is the carbon atom to which the phosphorus atom is bonded, its $^{13}C\{^1H\}$ resonance appears as a doublet with a rather large $^1J_{C,P}$ coupling constant in the range 100–115 Hz. The hydrogen atom attached to C^1 appears as a doublet with a value for the $^2J_{H,P}$ coupling constant of around 16 Hz. C^2 is a quaternary carbon atom in all cases except for compound **1d**. In this case, the hydrogen atom attached to C^2 displays a large $^3J_{H,P}$ coupling constant of 28 Hz with the phosphorus atom in the *trans*-position. The $^{31}P\{^1H\}$ NMR spectra consist of one singlet in all cases, which is shifted to high-field by 20 to 35 ppm with respect

 © 2005 Wiley-VCH Verlag GmbH & Co. KGaA, Weinheim

to the position of the $^{31}P\{^1H\}$ NMR resonance for the corresponding bis(acetonitrile) parent compound **1**, **2**, or **3** respectively. This is fully consistent with the fact that migration of phosphorus from ruthenium to carbon has occurred.

The X-ray crystal structures of **1a** and **2a** were determined. ORTEP views of the cations $[Cp^*Ru\{\eta^4\text{-}C_4H_3(CH_2OCH_2)PPh_2NPh\text{-}\kappa^1N\}]^+$ and $[Cp^*Ru\{\eta^4\text{-}C_4H_3(CH_2OCH_2)PiPr_2NC_6F_5\text{-}\kappa^1N\}]^+$ are shown in Figures 1 and 2, respectively, together with a listing of selected bond lengths and angles.

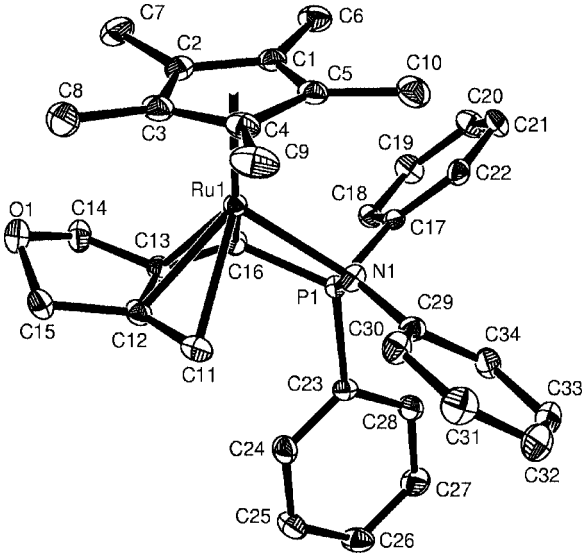

Figure 1. ORTEP drawing (50% thermal ellipsoids) of the cation $[Cp^*Ru\{\eta^4\text{-}C_4H_3(CH_2OCH_2)\text{-}PPh_2NPh\text{-}\kappa^1N\}]^+$ in complex **1a**. Hydrogen atoms have been omitted. Selected bond lengths [Å] and angles [°] with estimated standard deviations in parentheses: Ru1–C2 2.182(2), Ru1–C3 2.188(2), Ru1–C4 2.210(2), Ru1–C1 2.218(2), Ru1–C5 2.245(2), Ru1–N1 2.164(1), Ru1–C11 2.244(2), Ru1–C12 2.216(2), Ru1–C13 2.223 (2), Ru1–C16 2.217(2), P1–C16 1.766(2), C11–C12 1.401(3), C12–C13 1.420(3), C13–C16 1.413(3), N1–P1 1.599(2); Ru1–N1–P1 96.89(7), N1–Ru1–C16 72.30(7), N1–P1–C16 100.23(8), C11–C12–C13 128.1(2), C12–C13–C16 129.5(2).

The structures of the complex cations are very similar to those of the related cyclopentadienyl amidobutadiene complexes $[CpRu\{\eta^4\text{-}C_4H_3(CH_2CH_2CH_2)PPh_2NPh\text{-}\kappa^1N\}]^+$ and $[CpRu\{\eta^4\text{-}C_4H_3(n\text{Bu})_2PPh_2NPh\text{-}\kappa^1N\}]^+$.[7] The dimensions of the butadiene fragment are consistent with the delocalization of the double bonds, matching the values reported for the cyclopentadienyl complexes. The Ru1–N1 separation of 2.242(3) Å in **2a** is significantly longer than the corresponding Ru–N bond lengths observed in **1a** and in the cyclopentadienyl derivatives. This difference reflects the effect of the electron-attracting C_6F_5 group attached to the nitrogen atom in **2a**. On the other hand, all P–N and P–C separations have similar values, and are unexceptional.

The reactions of the pentamethylcyclopentadienyl bis(acetonitrile) complexes **1**–**3** with diynes or 1-alkynes examined so far seem to follow a pathway identical to that of the cyclopentadienyl derivative $[CpRu(MeCN)_2(PPh_2NHPh)]^+$, with phosphane migration, formation of an allyl carbene species, and an N–H bond activation process leading to the final amidobutadiene products.[7] However, we have found that in certain cases a different reaction pathway that leads to products other than amidobutadiene complexes is feasible.

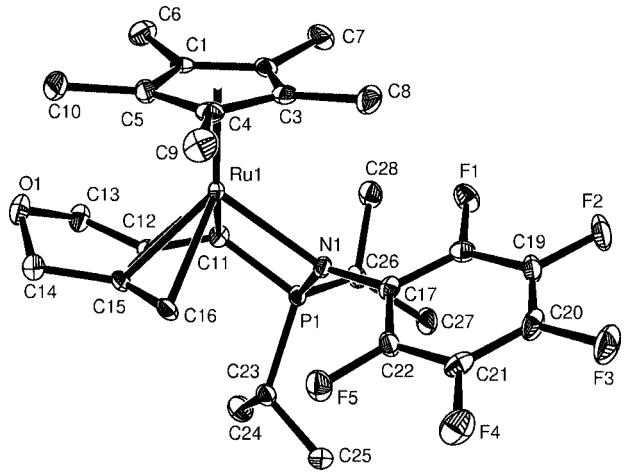

Figure 2. ORTEP drawing (50% thermal ellipsoids) of the cation $[Cp^*Ru\{\eta^4\text{-}C_4H_3(CH_2OCH_2)\text{-}PiPr_2NC_6F_5\text{-}\kappa^1N\}]^+$ in complex **2a**. Hydrogen atoms have been omitted. Selected bond lengths [Å] and angles [°] with estimated standard deviations in parentheses: Ru1–C1 2.167(4), Ru1–C5 2.189(3), Ru1–C2 2.198(4), Ru1–C4 2.216(4), Ru1–C3 2.242(4), Ru1–N1 2.242(3), Ru1–C16 2.208(4), Ru1–C15 2.227(4), Ru1–C12 2.219(4), Ru1–C11 2.208(4), P1–C11 1.771(4), C15–C16 1.392(5), C12–C15 1.425(5), C11–C12 1.410(5), N1–P1 1.605(3); Ru1–N1–P1 97.0(1), C11–Ru1–N1 70.2(1), N1–P1–C11 98.35(16), C16–C15–C12 128.1(3), C15–C12–C11 129.5(3).

The reaction of **3** with 1-hexyne or $HC{\equiv}CSiMe_3$ in dichloroethane yielded yellow materials that show one singlet in their respective $^{31}P\{^1H\}$ NMR spectra slightly above δ = 100 ppm. This indicates that migration of the aminophosphane ligands does not take place in these two cases, at variance with all the other reactions studied in this work. Furthermore, the observed patterns in the ^1H and $^{13}C\{^1H\}$ NMR spectra of these substances are remarkably different from the expected ones for amidobutadiene complexes. The NMR spectra are consistent with the presence of coordinated acetonitrile and NH groups. A series of multiplet resonances in the ^1H NMR spectra in the range δ = 2.6 to 3.9 ppm are correlated to two tertiary carbon resonances in their respective $^{13}C\{^1H\}$ NMR spectra, as inferred from DEPT and gHSQC NMR experiments, thereby suggesting the presence of an η^2-CH=CH group in the complexes. The X-ray structure analysis performed on crystals resulting from the reaction of **3** with 1-hexyne revealed the formation of the complex $[Cp^*Ru(MeCN)\{\eta^2\text{-}n\text{BuCH=CH}(C_6H_4)\text{-}NHPiPr_2\text{-}\kappa^1P\}][BPh_4]$ (**4**). The product resulting from the reaction of **3** with $HC{\equiv}CSiMe_3$ was then identified as $[Cp^*Ru(MeCN)\{\eta^2\text{-}Me_3SiCH=CH(C_6H_4)NHPiPr_2\text{-}\kappa^1P\}][BPh_4]$ (**5**).

An ORTEP view of the cation $[Cp^*Ru(MeCN)\{\eta^2\text{-}n\text{BuCH=CH}(C_6H_4)NHPiPr_2\text{-}\kappa^1P\}]^+$ is shown in Figure 3, together with a listing of selected bond lengths and angles. The ruthenium atom in the complex cation is bonded to one acetonitrile ligand, to the phosphorus atom of the aminophosphane, and to an olefin ligand η^2-*n*BuCH=CH re-

 © 2005 Wiley-VCH Verlag GmbH & Co. KGaA, Weinheim

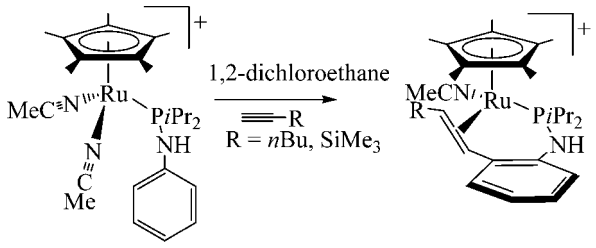

sulting formally from the insertion of the triple bond of a 1-hexyne molecule into one of the *ortho*-CH bonds of the NHPh group of the aminophosphane. The stereochemistry of the olefin ligand is *trans*. The C11–C12 separation of 1.42(1) Å, and the Ru1–C11 and Ru1–C12 bond lengths of 2.233(8) Å and 2.198(8) Å, respectively, compare well with the values found in other half-sandwich ruthenium η^2-alkene complexes, such as $[Cp^*Ru(\eta^2\text{-}CH_2{=}CH_2)(dippe)]^+$ [C–C: 1.43(2) Å; Ru–C: 2.24(1) Å and 2.25(1) Å; dippe = 1,2-bis(diisopropylphosphanyl)ethane][8] or $[Cp^*Ru(\eta^2\text{-}CH_2{=}CH_2)(CO)(PMe{i}Pr_2)]^+$ [C–C: 1.416(13) Å; Ru–C: 2.197(8) Å and 2.204(7) Å].[9]

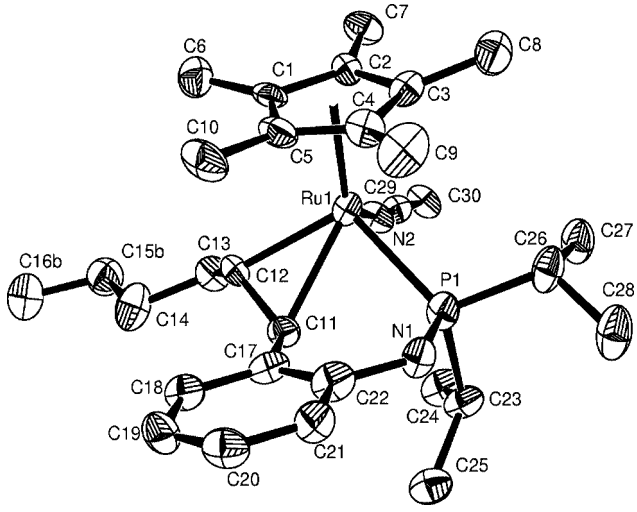

Figure 3. ORTEP drawing (50% thermal ellipsoids) of the cation $[Cp^*Ru(MeCN)\{\eta^2\text{-}n\text{BuCH=CH}(C_6H_4)NHPiPr_2\text{-}\kappa^1P\}]^+$ in complex **4**. Hydrogen atoms have been omitted. Selected bond lengths [Å] and angles [°] with estimated standard deviations in parentheses: Ru1–C1 2.227(8), Ru1–C2 2.254(8), Ru1–C3 2.247(9), Ru1–C4 2.227(8), Ru1–C5 2.208(9), Ru1–N2 2.032(7), Ru1–C11 2.233(8), Ru1–C12 2.198(8), Ru1–P1 2.327(2), P1–N1 1.688(7), C11–C12 1.42(1); Ru1–P1–N1 108.1(3), Ru1–N2–C29 169.1(7), C11–C12–C13 123.5(8), C12–C11–C17 122.7(8), C13–C12–C11–C17 139.2(9).

Complexes **4** and **5**, which incorporate only one alkyne molecule, are isolated even when compound **3** is allowed to react with an excess of the corresponding 1-alkyne. This fact indicates that the ruthenacyclopentatriene complex, which is a key intermediate in the process of formation of allyl carbene species, is not generated in the course of the reaction of **3** with 1-hexyne or $HC{\equiv}CSiMe_3$, and therefore an alternative reaction pathway leading to **4** and **5** is feasible.

For these processes we propose the reaction sequence shown in Scheme 1. After substitution of the first acetonitrile ligand by one alkyne molecule, the second acetonitrile molecule dissociates from the metal to generate a coordinatively unsaturated complex. If the addition of the second alkyne ligand is fast, then the resulting 18-electron bis(alkyne) complex undergoes oxidative alkyne coupling to yield a ruthenacyclopentatriene complex, and the course of the reaction would be as described previously.[1,7] However, in certain cases involving systems containing the strong electron-releasing aminophosphane iPr_2PNHPh, the metal center in the 16-electron intermediate is electron-rich enough to activate one C–H bond in the *ortho*-position of the phenyl ring to yield an orthometalated hydrido complex as a result of the oxidative addition reaction. This Ru^{IV} species is most likely in dynamic equilibrium with the 16-electron complex. Insertion of the alkyne into the ruthenium–hydride bond yields an alkenyl complex, which, upon addition of acetonitrile and reductive coupling of the alkenyl and phenyl fragments, leads to the final reaction product **4** or **5**. In the reaction of **3** with potentially chelating diynes the addition of the second alkyne to the 16-electron intermediate seems to be faster than the oxidative addition of the phenyl C–H and the subsequent alkyne insertion, and hence the amidobutadiene complexes **3a**–**c** are obtained.

The fact that reaction products similar to **4** or **5** are not observed in the course of the reaction of **1** or **2** with alkynes might be due to the following reasons: 1) in **1**, the PPh_2NHPh ligand is less basic than iPr_2PNHPh, and hence the corresponding 16-electron intermediate complex is probably not electron-rich enough to cleave *ortho*-C–H bonds prior to the entry of the second alkyne molecule, and 2) in the case of compound **2**, a final product analogous to **4** or **5** would involve C–F bond activation, a process which has a higher activation energy barrier than C–H bond activation.[10]

We must remark here that the proposed reaction sequence shown in Scheme 1, although reasonable, is only tentative. However, we must also point out the fact that spectroscopic evidence for the involvement of hydrido complexes in the formation of **4** has been obtained. In some instances, compound **4** was isolated accompanied by small amounts of other material which exhibits one hydride doublet resonance at $\delta = -10.89$ ppm, with a $^2J_{H,P}$ coupling constant of 43.9 Hz, in the ^1H NMR spectrum (Figure 4). The relatively large value of the $^2J_{H,P}$ coupling constant suggests a *transoid* disposition of the hydride and phosphane ligands. One singlet resonance at $\delta = 135.8$ ppm in the $^{31}P\{^1H\}$ NMR spectrum was attributed to this hydrido complex.

The reaction of **3** with an excess of 1-hexyne in [D_2]tetrachloroethane was monitored between 0 and 60 °C. Several intermediate species giving rise to singlets in the $^{31}P\{^1H\}$ NMR spectra were detected. One of these intermediate species is responsible for the doublet hydride resonance observed in the ^1H NMR spectrum. Although the isolation of any of these intermediate species was not possible, there is little doubt about the involvement of hydride species in the

 © 2005 Wiley-VCH Verlag GmbH & Co. KGaA, Weinheim

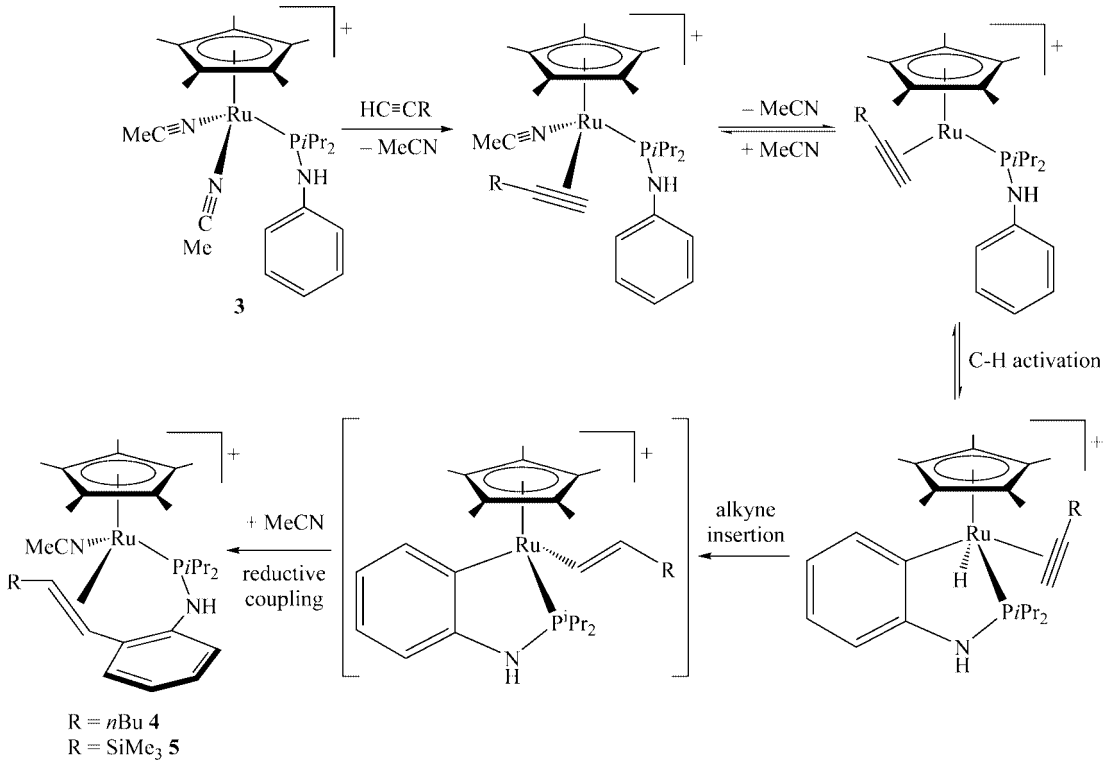

Scheme 1. Proposed reaction sequence for the formation of **4** or **5** by C–H activation.

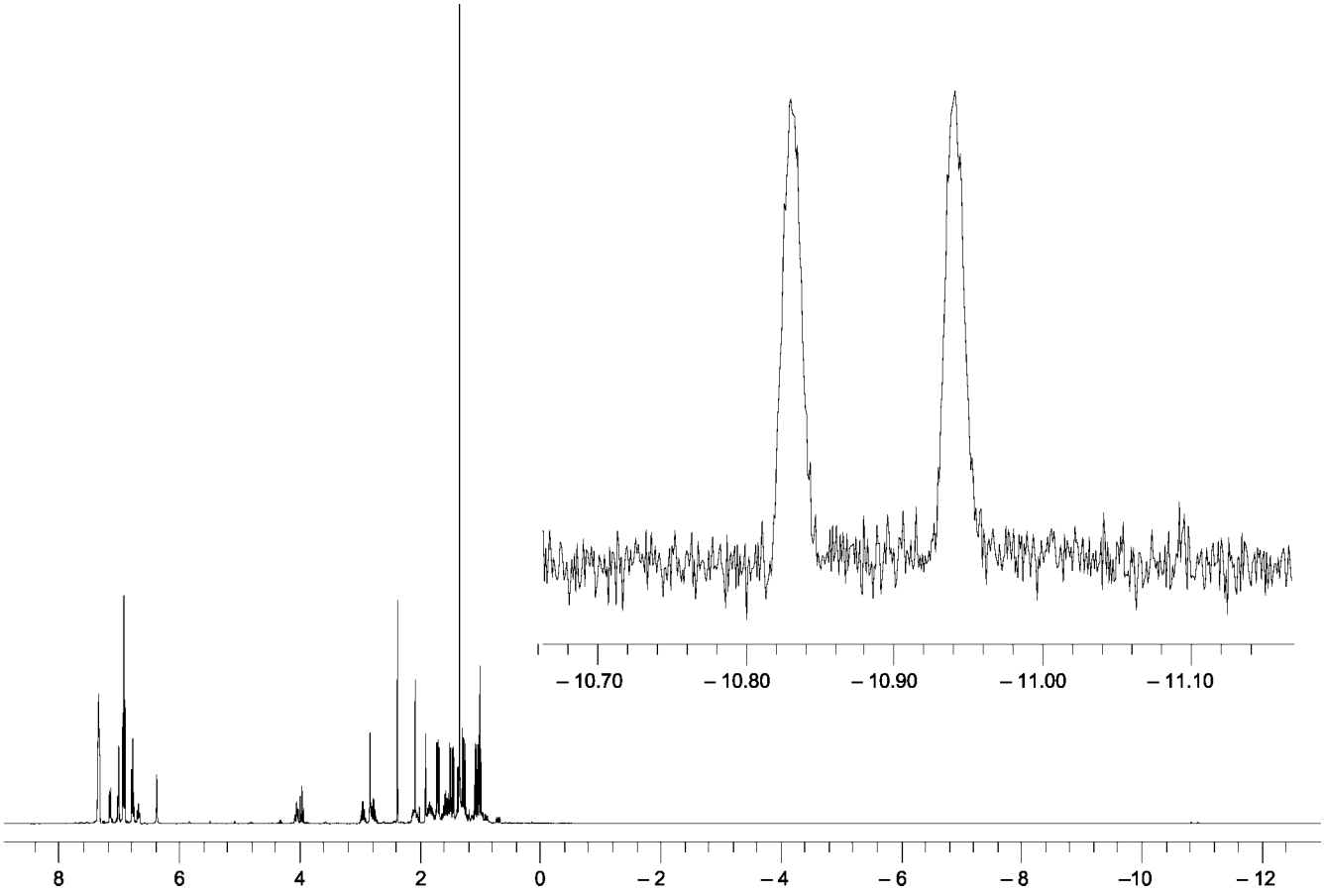

Figure 4. ^{1}H NMR spectrum (400 MHz) of crude compound **4** in [D_6]acetone, showing the presence of minor amounts of a hydrido complex.

 © 2005 Wiley-VCH Verlag GmbH & Co. KGaA, Weinheim

process. Orthometalation processes at coordinatively unsaturated metal centers leading to hydrido-phenyl species have been well documented in the literature.[11–14]

We also carried out reactions of **1**, **2**, and **3** with several olefins. The only characterized product from these reactions was the η^2-alkene complex [Cp*Ru(MeOOCCH=CH_2)(MeCN)(PPh_2NHPh)][PF_6] (**6**), which was obtained from the reaction of **1** with methyl acrylate. The substitution of only one acetonitrile ligand in **1** was accomplished irrespective of the metal to methyl acrylate ratio used in the reaction. The protons of the η^2-CH=CH_2 group of the methyl acrylate ligand appear as multiplets at δ = 2.61, 3.45, and 3.52 ppm in the ^{1}H NMR spectrum, whereas the resonances for the carbon atoms appear as doublets at δ = 46.5 and 52.2 ppm, with $J_{C,P}$ coupling constant values of 5.4 Hz and 17 Hz, respectively.

The crystal structure of **6** was determined. An ORTEP view of the cation [Cp*Ru(η^2-MeOOCCH=CH_2)(MeCN)(PPh_2NHPh)]$^+$ is shown in Figure 5, together with a listing of selected bond lengths and angles. The coordination sphere around ruthenium is very similar to that of complex **4**, consisting of one Cp*, one acetonitrile ligand, one aminophosphane ligand, and the η^2-methyl acrylate ligand. The dimensions of the alkene ligand compare well with the values found for **4**, and for other compounds reported in the literature.[8,9] Only one diastereoisomer is present in the crystal. The methylcarboxylate group faces the acetonitrile ligand in an *exo*-disposition, pointing away from the Cp* group in order to minimize steric repulsions. The closest contacts between the methyl acrylate ligand and any atom from the aminophosphane ligand are around 3 Å or longer, which indicates no significant interaction between the aminophosphane and the olefin in this complex.

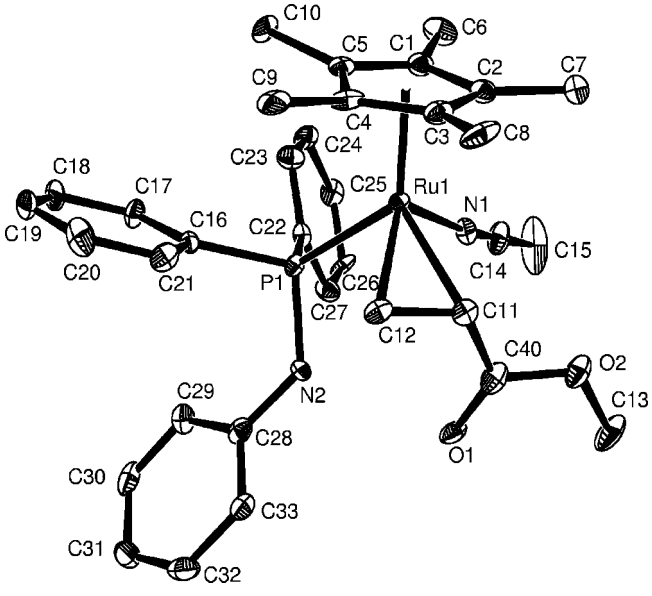

Figure 5. ORTEP drawing (50% thermal ellipsoids) of the cation [Cp*Ru(MeCN)(η^2-MeOOCCH=CH_2)(P*i*Pr_2NHPh)]$^+$ in complex **6**. Hydrogen atoms have been omitted. Selected bond lengths [Å] and angles [°] with estimated standard deviations in parentheses: Ru1–C2 2.200(5), Ru1–C1 2.215(5), Ru1–C3 2.229(5), Ru1–C4 2.245(5), Ru1–C5 2.282(6), Ru1–P1 2.342(1), Ru1–C11 2.185(5), Ru1–C12 2.181(5), Ru1–N1 2.063(4), C11–C12 1.411(7), C11–C40 1.456(8), N1–C14 1.143(7), N2–P1 1.675(5); Ru1–P1–N2 112.1(2), Ru1–N1–C14 173.0(5), C12–C11–C40 121.3(5).

We also studied the reactions of **5** with alkynes in order to check the possibility of alkene–alkyne coupling. However, this does not occur. The reaction of **5** with propargyl ether yielded red-orange crystals of the amidobutadiene complex **1a**. Likewise, the reaction with acetylene afforded the corresponding amidobutadiene derivative **1d**. Hence, the methyl acrylate and acetonitrile ligands behave as good leaving groups in these reactions, and are readily substituted by alkynes to give bis(alkyne) complexes, which follow the previously discussed reaction pathway to form amidobutadiene complexes by N–H activation.

Conclusions

We can conclude that the products of the reactions of [Cp*Ru(MeCN)$_2$(PR^1_2NHR^2)]$^+$ with alkynes are sensitive to the nature of the substituents in the aminophosphane ligand and in the alkyne. In some cases amidobutadiene complexes are generated by N–H activation, consistent with the behavior observed for their Cp counterparts. However, in other cases an alternative reaction pathway involving C–H activation is feasible. This process most likely involves orthometalation of the phenyl ring of an NHPh group and formation of Ru^{IV} hydrido species which are intermediates in the formation of the final products: η^2-alkene complexes formally derived from the insertion of one alkyne into the *ortho*-C–H bond of the NHPh group. Given the fact that the η^2-MeOOCCH=CH_2 ligand in the complex [Cp*Ru(η^2-MeOOCCH=CH_2)(MeCN)(PPh_2NHPh)]$^+$ (**6**) behaves as a good leaving group, it is reasonable to assume that the new ligands *i*Pr_2PNHC_6H_4CH=CHR (R = *n*Bu, $SiMe_3$) in complexes **4** and **5** should display a hemilabile character,[15] and hence their complexes might have potential catalytic activity, a possibility which is currently under investigation.

Experimental Section

General: All synthetic operations were performed under dry dinitrogen or argon following conventional Schlenk techniques. Tetrahydrofuran, diethyl ether, and petroleum ether (boiling point range 40–60 °C) were distilled from the appropriate drying agents. All solvents were deoxygenated immediately before use. The complex [Cp*Ru(MeCN)$_3$][PF_6] was obtained according to the literature.[16] The ligands PPh_2NHPh, P*i*Pr_2NHPh, and P*i*$Pr_2NHC_6F_5$, were prepared following suitable adaptations of published procedures.[17–21] 1-Alkynes, diynes, and methyl acrylate were purchased from Aldrich and used as received. NMR spectra were recorded on a Varian Unity 400 MHz or Varian Gemini 300 MHz spectrometer. Chemical shifts are given in ppm relative to $SiMe_4$ (^{1}H and $^{13}C\{^1H\}$), 85% H_3PO_4 ($^{31}P\{^1H\}$), or $CFCl_3$ (^{19}F). Microanalysis was performed on an elemental analyzer model LECO CHNS-932 at the Servicio Central de Ciencia y Tecnología, Universidad de Cádiz.

[Cp*Ru(MeCN)$_2$(PR^1_2NHR^2)][PF_6] (R^1 = R^2 = Ph 1; R^1 = *i*Pr, R^2 = C_6F_5 2): A stoichiometric amount of either PPh_2NHPh for **1** (1.67 g, 6 mmol), or *i*$Pr_2NHC_6F_5$ for **2** (1.79 g, 6 mmol), was

 © 2005 Wiley-VCH Verlag GmbH & Co. KGaA, Weinheim

added to a solution of [Cp*Ru(MeCN)$_3$][PF$_6$] (3 g, ca. 6 mmol) in dichloromethane (25 mL). The mixture was stirred at room temperature for 1 h. The solvent was then removed in vacuo. The residue was washed with several portions of diethyl ether, and finally with one portion of petroleum ether to give a yellow powder, which was dried in vacuo.

1: Yield: 4 g, ca. 90%. $C_{32}H_{37}F_6N_3P_2Ru$: calcd. C 51.89, H 5.04, N 5.7; found C 52.1, H 5.15, N 5.4. ^{1}H NMR (CD$_3$COCD$_3$, 298 K): δ = 1.45 [d, $J_{H,P}$ = 1.5 Hz, 15 H, C$_5$(C*H*$_3$)$_5$], 2.41 (d, $J_{H,P}$ = 1.5 Hz, 6 H, C*H*$_3$CN), 5.66 (d, $J_{H,P}$ = 13.8 Hz, 1 H, N*H*), 6.74, 7.01, 7.46, 7.71 (m, 15 H, C$_6$*H*$_5$) ppm. ^{13}C{^{1}H} NMR (CD$_3$COCD$_3$, 298 K): δ = 3.6 (s, *C*H$_3$CN), 9.1 [s, C$_5$(*C*H$_3$)$_5$], 87.9 [d, $J_{C,P}$ = 2.4 Hz, *C*$_5$(CH$_3$)$_5$], 119.1, 126.6, 128.7, 129.0, 130.4, 132.2 (*C*$_6$H$_5$) ppm. ^{31}P{^{1}H} NMR (CD$_3$COCD$_3$, 298 K): δ = 78.7 ppm (s).

2: Yield: 3.4 g, ca. 75%. $C_{26}H_{36}F_{11}N_3P_2Ru$: calcd. C 40.95, H 4.76, N 5.5; found C 40.8, H 4.88, N 5.3. ^{1}H NMR (CDCl$_3$, 298 K): δ = 1.61 [s, 15 H, C$_5$(C*H*$_3$)$_5$], 1.0–1.2 [m, 12 H, P{CH(C*H*$_3$)$_2$}$_2$], 2.39 [m, 2 H, P{C*H*(CH$_3$)$_2$}$_2$], 2.41 (s, 6 H, C*H*$_3$CN), 3.41 (d, $J_{H,P}$ = 12.7 Hz, 1 H, N*H*) ppm. ^{13}C{^{1}H} NMR (CDCl$_3$, 298 K): δ = 3.9 (s, *C*H$_3$CN), 10.3 [s, C$_5$(*C*H$_3$)$_5$], 17.4 [s, P{CH(*C*H$_3$)$_2$}$_2$], 29.0 [d, $J_{C,P}$ = 21.3 Hz, P{*C*H(CH$_3$)$_2$}$_2$], 86.0 [s, *C*$_5$(CH$_3$)$_5$] ppm. ^{19}F NMR (CDCl$_3$, 298 K): δ = –146.6, –161.0, –163.8 ppm. ^{31}P{^{1}H} NMR (CDCl$_3$, 298 K): δ = 116.5 ppm (s).

[Cp*Ru(MeCN)$_2$(P*i*Pr$_2$NHPh)][BPh$_4$] (3): This compound was prepared in a fashion analogous to that for **1** and **2**, starting from [Cp*Ru(MeCN)$_3$][PF$_6$] (1.5 g, ca. 3 mmol) and a stoichiometric amount of *i*Pr$_2$PNHPh (1.2 mL, 3 mmol) in dichloromethane (20 mL). The solvent was removed in vacuo and the residue washed with diethyl ether. Then, it was conveniently transformed into its [BPh$_4$]$^-$ salt by addition of MeOH and an excess of solid NaBPh$_4$ (1.5 g). The yellow precipitate was filtered, washed with EtOH and petroleum ether, and dried in vacuo. Yield: 2.16 g, 85%. $C_{50}H_{61}BN_3PRu$: calcd. C 70.91, H 7.26, N 5.0; found C 70.8, H 7.15, N 4.9. ^{1}H NMR (CD$_3$COCD$_3$, 298 K): δ = 1.45 [d, $J_{H,P}$ = 1.5 Hz, 15 H, C$_5$(C*H*$_3$)$_5$], 2.41 (d, $J_{H,P}$ = 1.5 Hz, 6 H, C*H*$_3$CN), 5.66 (d, $J_{H,P}$ = 13.8 Hz, 1 H, N*H*), 6.74, 7.01, 7.46, 7.71 (m, 15 H, C$_6$*H*$_5$) ppm. ^{13}C{^{1}H} NMR (CDCl$_3$, 298 K): δ = 3.2 (s, *C*H$_3$CN), 10.8 [s, C$_5$(*C*H$_3$)$_5$], 18.2, 18.3 [s, P{CH(*C*H$_3$)$_2$}$_2$], 29.7 [d, $J_{C,P}$ = 20.6 Hz, P{*C*H(CH$_3$)$_2$}$_2$], 93.5 [s, *C*$_5$(CH$_3$)$_5$], 121.6, 126.0, 135.7 (*C*$_6$H$_5$) ppm. ^{31}P{^{1}H} NMR (CD$_3$COCD$_3$, 298 K): δ = 101.1 ppm (s).

[Cp*Ru{η^4-C$_4$H$_3$(CH$_2$OCH$_2$)PPh$_2$NPh-κ^1*N*}][PF$_6$] (1a): A slight excess over the stoichiometric amount of propargyl ether (57 μL, 0.55 mmol) was added to a solution of **1** (0.37 g, 0.5 mmol) in dichloromethane (12 mL) and the mixture was stirred for 1 h at room temperature. The solvent was then removed in vacuo, and the residue washed with two portions of diethyl ether and one portion of petroleum ether. A red-orange powder was obtained, which was filtered off and dried in vacuo. It was recrystallized from a mixture of acetone and petroleum ether. Yield: 0.16 g, 44%. $C_{34}H_{37}F_6NOP_2Ru$: calcd. C 54.26, H 4.95, N 1.9; found C 53.9, H 5.04, N 1.7. ^{1}H NMR (CD$_3$COCD$_3$, 298 K): δ = 1.67 [s, 15 H, C$_5$(C*H*$_3$)$_5$], 2.79 (d, $J_{H,H}$ = 3.1 Hz, 1 H, H^{4endo}), 4.32, 5.15 (d, $J_{H,H}$ = 13.2 Hz, 1 H each, C*H*$_2$), 4.35, 5.26 (d, $J_{H,H}$ = 12.8 Hz, 1 H each, C*H*$_2$), 4.47 (d, $J_{H,P}$ = 17.6 Hz, 1 H, H^1), 4.94 (d, $J_{H,H}$ = 3.1 Hz, 1 H, H^{4exo}), 6.68–8.00 (m, 15 H, C$_6$*H*$_5$) ppm. ^{13}C{^{1}H} NMR (CD$_3$COCD$_3$, 298 K): δ = 9.7 [s, C$_5$(*C*H$_3$)$_5$], 26.6 (d, $J_{C,P}$ = 115.5 Hz, *C*^{1}), 50.0 (s, *C*^{4}), 75.1 (s, *C*H$_2$), 75.7 (d, $J_{C,P}$ = 11.4 Hz, *C*H$_2$), 86.3 (s, *C*^{3}), 99.4 [s, *C*$_5$(CH$_3$)$_5$], 114.8 (s, *C*^{2}), 120.7, 123.6, 123.8, 129.6, 130.5, 132.4, 132.6, 132.7, 134.9, 135.1, 142.4 (*C*$_6$H$_5$) ppm. ^{31}P{^{1}H} NMR (CD$_3$COCD$_3$, 298 K): δ = 42.7 ppm (s).

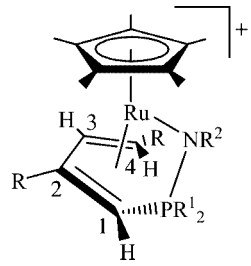

[Cp*Ru{η^4-C$_4$H$_3$(CH$_2$)$_3$PPh$_2$NPh-κ^1*N*}][PF$_6$] (1b): This compound was obtained in a fashion analogous to **1a**, but using 1,6-heptadiyne instead of propargyl ether. Yield: 53%. $C_{35}H_{39}F_6NP_2Ru$: calcd. C 56.00, H 5.24, N 1.9; found C 55.8, H 5.04, N 1.8. ^{1}H NMR (CD$_3$COCD$_3$, 298 K): δ = 1.37 (m, 2 H, C*H*$_2$), 1.68 [s, 15 H, C$_5$(C*H*$_3$)$_5$], 2.42 (m, 2 H, C*H*$_2$), 2.75 (d, $J_{H,H}$ = 3.1 Hz, 1 H, H^{4endo}), 3.48 (m, 2 H, C*H*$_2$), 4.10 (d, $J_{H,P}$ = 16.9 Hz, 1 H, H^1), 4.76 (d, $J_{H,H}$ = 3.1 Hz, 1 H, H^{4exo}), 6.68–8.00 (m, 15 H, C$_6$*H*$_5$) ppm. ^{13}C{^{1}H} NMR (CD$_3$COCD$_3$, 298 K): δ = 9.6 [s, C$_5$(*C*H$_3$)$_5$], 21.1 (s, *C*H$_2$), 26.5 (d, $J_{C,P}$ = 112.7 Hz, *C*^{1}), 36.2 (s, *C*H$_2$), 38.0 (d, $J_{C,P}$ = 12 Hz, *C*H$_2$), 51.8 (s, *C*^{4}), 98.8 [s, *C*$_5$(CH$_3$)$_5$], 99.9 (s, *C*^{3}), 115.3 (s, *C*^{2}), 120.2, 120.7, 124.0, 129.5, 129.9, 130.4, 132.4, 132.6, 134.7, 134.9, 142.6 (*C*$_6$H$_5$) ppm. ^{31}P{^{1}H} NMR (CD$_3$COCD$_3$, 298 K): δ = 47.7 ppm (s).

[Cp*Ru{η^4-C$_4$H$_3$(CH$_2$)$_4$PPh$_2$NPh-κ^1*N*}][PF$_6$] (1c): This compound was obtained in a fashion analogous to **1a**, but using 1,7-octadiyne instead of propargyl ether. Yield: 43%. $C_{36}H_{41}F_6NP_2Ru$: calcd. C 56.54, H 5.40, N 1.8; found C 56.5, H 5.33, N 1.8. ^{1}H NMR (CD$_3$COCD$_3$, 298 K): δ = 1.48 (m, 2 H, C*H*$_2$), 1.69 [s, 15 H, C$_5$(C*H*$_3$)$_5$], 1.95 (m, 2 H, C*H*$_2$), 2.23 (m, 2 H, C*H*$_2$), 2.60 (d, $J_{H,H}$ = 2.8 Hz, 1 H, H^{4endo}), 3.13 (m, 2 H, C*H*$_2$), 3.71 (d, $J_{H,P}$ = 14 Hz, 1 H, H^1), 4.62 (d, $J_{H,H}$ = 2.8 Hz, 1 H, H^{4exo}), 6.8–7.9 (m, 15 H, C$_6$*H*$_5$) ppm. ^{13}C{^{1}H} NMR (CD$_3$COCD$_3$, 298 K): δ = 10.0 [s, C$_5$(*C*H$_3$)$_5$], 22.0, 22.3 (s, *C*H$_2$), 28.2 (d, $J_{C,P}$ = 109 Hz, *C*^{1}), 31.4, 31.5 (s, *C*H$_2$), 54.1 (s, *C*^{4}), 99.7 [s, *C*$_5$(CH$_3$)$_5$], 108.7 (s, *C*^{3}), 115.8 (s, *C*^{2}), 121.5, 125.3, 129.4, 129.8, 130.5, 132.3, 132.6, 134.6, 135.0, 143.2 (*C*$_6$H$_5$) ppm. ^{31}P{^{1}H} NMR (CD$_3$COCD$_3$, 298 K): δ = 50.6 ppm (s).

[Cp*Ru(η^4-C$_4$H$_5$PPh$_2$NPh-κ^1*N*)][PF$_6$] (1d): Acetylene was bubbled through a solution of **1** (0.37 g, 0.5 mmol) in dichloromethane (15 mL) and the mixture was stirred under acetylene for 1 h at room temperature. The solution was then filtered in order to remove a black solid in suspension [most likely poly(acetylene)]. The solvent was removed in vacuo, and the residue washed with two portions of diethyl ether and one portion of petroleum ether. A red-orange powder was obtained, which was filtered off and dried in vacuo. It was recrystallized from a mixture of acetone and petroleum ether. Yield: 0.19 g, ca. 54%. $C_{32}H_{35}F_6NP_2Ru$: calcd. C 54.08, H 4.96, N 2.0; found C 53.8, H 5.06, N 1.8. ^{1}H NMR (CDCl$_3$, 298 K): δ = 1.66 [s, C$_5$(C*H*$_3$)$_5$], 2.45 (dd, $J_{H,H}$ = 11, $J_{H,H'}$ = 2.7 Hz, 1 H, H^{4endo}), 3.63 (dd, $J_{H,P}$ = 16.3, $J_{H,H}$ = 9.9 Hz, 1 H, H^1), 4.47 (dd, $J_{H,H}$ = 9.2, $J_{H,H'}$ = 2.7 Hz, 1 H, H^{4exo}), 5.41 (m, 1 H, H^3), 5.88 (ddd, $J_{H,P}$ = 28, $J_{H,H}$ = 9.9, $J_{H,H'}$ = 7.5 Hz, 1 H, H^2), 6.64–7.76 (m, C$_6$*H*$_5$) ppm. ^{13}C{^{1}H} NMR (CDCl$_3$, 298 K): δ = 9.8 [C$_5$(*C*H$_3$)$_5$], 31.5 (d, $J_{C,P}$ = 112.2 Hz, *C*^{1}), 58.2 (s, *C*^{4}), 98.2 (s, *C*^{3}), 98.9 [*C*$_5$(CH$_3$)$_5$], 103.8 (s, *C*^{2}), 120.6, 123.4, 123.5, 128.8, 129.1, 129.2, 129.6, 129.7, 131.2, 131.3, 131.4, 133.9, 134.2, 142.6 (*C*$_6$H$_5$) ppm. ^{31}P{^{1}H} NMR (CDCl$_3$, 298 K): δ = 41.6 ppm (s).

[Cp*Ru{η^4-C$_4$H$_3$(*n*Bu)$_2$PPh$_2$NPh-κ^1*N*}][PF$_6$] (1e): 1-Hexyne (126 μL, 1.10 mol) was added to a solution of **1** (0.37 g, 0.5 mmol) in dichloromethane (15 mL) and the mixture was stirred for 1 h at room temperature. The solvent was then removed in vacuo, and the

 © 2005 Wiley-VCH Verlag GmbH & Co. KGaA, Weinheim

residue washed with two portions of diethyl ether and one portion of petroleum ether. A yellow-orange powder was obtained, which was filtered off and dried in vacuo. It was recrystallized from a mixture of acetone and petroleum ether. Yield: 0.14 g, 35%. $C_{40}H_{51}F_6NP_2Ru$: calcd. C 58.39, H 6.25, N 1.7; found C 58.2, H 6.12, N 1.6. ^{1}H NMR ($CDCl_3$, 298 K): δ = 1.58 [s, $C_5(CH_3)_5$], 3.39 (m, 1 H, H^4), 3.45 (d, $J_{H,P}$ = 15.9 Hz, 1 H, H^1), 5.10 (d, $J_{H,H}$ = 11.3 Hz, 1 H, H^3), 6.58–7.70 (m, C_6H_5) ppm. ^{13}C{^{1}H} NMR ($CDCl_3$, 298 K): δ = 9.8 [s, $C_5(CH_3)_5$], 13.7, 13.9 [s, $(CH_2)_3CH_3$], 21.7 (s), 22.4 (s), 33.5 (s), 34.5 (s), 35.8 (s), 41.7 (d, $J_{C,P}$ = 9.8 Hz) [$(CH_2)_3CH_3$], 29.6 (d, $J_{C,P}$ = 112.2 Hz, C^1), 81.9 (s, C^4), 96.5 [$C_5(CH_3)_5$], 99.5 (s, C^3), 116.1 (s, C^2), 120.6, 123.2, 123.4, 128.7, 128.9, 129.0, 129.7, 129.8, 131.0, 133.7, 134.3, 142.6 (C_6H_5) ppm. ^{31}P{^{1}H} NMR ($CDCl_3$, 298 K): δ = 42.4 ppm (s).

[Cp*Ru{η^4-C$_4$H$_3$(CH$_2$OCH$_2$)P*i*Pr$_2$NC$_6$F$_5$-κ^1*N*}][PF$_6$] (2a): Propargyl ether (57 μL, 0.55 mmol) was added to a solution of **2** (0.38 g, ca. 0.5 mmol) in dichloromethane (12 mL) and the mixture was stirred for 1 h at room temperature. The solvent was then removed in vacuo, and the residue washed with two portions of diethyl ether and one portion of petroleum ether. A red-orange powder was obtained, which was filtered off and dried in vacuo. It was recrystallized from a mixture of acetone and petroleum ether. Yield: 0.16 g, ca. 42%. $C_{28}H_{36}F_{11}NOP_2Ru$: calcd. C 43.42, H 4.68, N 1.8; found C 43.3, H 4.77, N 1.5. ^{1}H NMR ($CDCl_3$, 298 K): δ = 0.90, 1.34, 1.54 [m, 12 H, P{CH(CH_3)$_2$}$_2$], 1.49 [s, 15 H, $C_5(CH_3)_5$], 2.49 [m, 2 H, P{CH(CH$_3$)$_2$}$_2$], 3.61 (d, $J_{H,H}$ = 4.5 Hz, 1 H, H^{4endo}), 4.11, 5.14 (d, $J_{H,H}$ = 13.2 Hz, 1 H each, CH_2), 4.29, 5.12 (d, $J_{H,H}$ = 14.2 Hz, 1 H each, CH_2), 4.38 (d, $J_{H,P}$ = 16.5 Hz, 1 H, H^1), 4.41 (d, $J_{H,H}$ = 4.5 Hz, 1 H, H^{4exo}) ppm. ^{13}C{^{1}H} NMR ($CDCl_3$, 298 K): δ = 8.9 [s, $C_5(CH_3)_5$], 14.9, 15.6, 16.4, 17.0 [s, P{CH(*C*H$_3$)$_2$}$_2$], 19.7 (d, $J_{C,P}$ = 105 Hz, C^1), 31.5 [d, $J_{C,P}$ = 44 Hz, P{*C*H(CH$_3$)$_2$}$_2$], 32.1 [d, $J_{C,P}$ = 42 Hz, P{*C*H(CH$_3$)$_2$}$_2$], 48.1 (s, C^4), 74.8 (s, *C*H$_2$), 75.2 (d, $J_{C,P}$ = 8.9 Hz, *C*H$_2$), 98.4 [s, $C_5(CH_3)_5$], 114.0 (s, C^2) ppm.^{19}F NMR ($CDCl_3$, 298 K): δ = –144.1, –162.3, –162.7 ppm. ^{31}P{^{1}H} NMR ($CDCl_3$, 298 K): δ = 84.7 ppm (s).

[Cp*Ru{η^4-C$_4$H$_3$(CH$_2$CH$_2$CH$_2$)P*i*Pr$_2$NC$_6$F$_5$-κ^1*N*}][PF$_6$] (2b): This compound was obtained in a fashion analogous to **2a**, but using 1,6-heptadiyne instead of propargyl ether. Yield: 50%. $C_{29}H_{38}F_{11}NP_2Ru$: calcd. C 45.08, H 4.96, N 1.8; found C 44.8, H 5.06, N 1.7. ^{1}H NMR ($CDCl_3$, 298 K): δ = 0.87, 1.32, 1.54 [m, 12 H, P{CH(CH_3)$_2$}$_2$], 1.21 (m, 2 H, CH_2), 1.45 [s, 15 H, $C_5(CH_3)_5$], 2.01, 2.16 [m, 1 H each, P{CH(CH$_3$)$_2$}], 2.62, 3.26 (m, 2 H each, CH_2) 3.59 (d, $J_{H,H}$ = 4.6 Hz, 1 H, H^{4endo}), 4.14 (d, $J_{H,P}$ = 16.4 Hz, 1 H, H^1), 4.37 (d, $J_{H,H}$ = 4.6 Hz, 1 H, H^{4exo}) ppm. ^{13}C{^{1}H} NMR ($CDCl_3$, 298 K): δ = 8.7 [s, $C_5(CH_3)_5$], 14.7, 15.8, 16.2 [s, P{CH(*C*H$_3$)$_2$}$_2$], 20.3 (s, *C*H$_2$), 21.5 (d, $J_{C,P}$ = 102.8 Hz, C^1), 31.5 [d, $J_{C,P}$ = 44.5 Hz, P{*C*H(CH$_3$)$_2$}], 34.0 [d, $J_{C,P}$ = 39.8 Hz, P{*C*H(CH$_3$)$_2$}], 35.4 (s, *C*H$_2$), 36.6 (d, $J_{C,P}$ = 7.7 Hz, *C*H$_2$), 54.6 (s, C^4), 97.0 [s, $C_5(CH_3)_5$], 116.4 (s, C^2) ppm. ^{19}F NMR ($CDCl_3$, 298 K): δ = –144.0, –162.4, –163.2 ppm. ^{31}P{^{1}H} NMR ($CDCl_3$, 298 K): δ = 85.1 ppm (s).

[Cp*Ru{η^4-C$_4$H$_3$(CH$_2$OCH$_2$)P*i*Pr$_2$NPh-κ^1*N*}][BPh$_4$] (3a): Propargyl ether (57 μL, 0.55 mmol) was added to a solution of **3** (0.42 g, ca. 0.5 mmol) in dichloromethane (15 mL) and the mixture was stirred for 1 h at room temperature. The solvent was then removed in vacuo, and the residue washed with two portions of diethyl ether and one portion of petroleum ether. A yellow-orange powder was obtained, which was filtered off and dried in vacuo. It was recrystallized from a mixture of acetone and petroleum ether. Yield: 0.22 g, 48%. $C_{57}H_{61}BNOPRu$: calcd. C 74.50, H 6.69, N 1.5; found C 74.2, H 6.58, N 1.3. ^{1}H NMR ($CDCl_3$, 298 K): δ = 0.60, 0.71, 1.10, 1.27 [m, 3 H each, P{CH(CH_3)$_2$}$_2$], 1.37 [s, 15 H, $C_5(CH_3)_5$], 1.74, 2.32 [m, 1 H each, P{CH(CH$_3$)$_2$}$_2$], 2.63 (d, $J_{H,H}$ = 3.6 Hz, 1 H, H^{4endo}), 3.20 (d, $J_{H,P}$ = 16 Hz, 1 H, H^1), 3.69, 4.64 (d, $J_{H,H}$ = 13.6 Hz, 1 H each, CH_2), 3.79, 4.75 (d, $J_{H,H}$ = 13.6 Hz, 1 H each, CH_2), 4.06 (d, $J_{H,H}$ = 3.6 Hz, 1 H, H^{4exo}), 6.36, 6.73, 7.02 (m, 5 H, C_6H_5) ppm. ^{13}C{^{1}H} NMR ($CDCl_3$, 298 K): δ = 9.5 [s, $C_5(CH_3)_5$], 16.2, 16.3, 16.8, 17.5 [s, P{CH(*C*H$_3$)$_2$}$_2$], 16.5 (d, $J_{C,P}$ = 104.3 Hz, C^1), 31.6 [d, $J_{C,P}$ = 47.7 Hz, P{*C*H(CH$_3$)$_2$}], 32.3 [d, $J_{C,P}$ = 34 Hz, P{*C*H(CH$_3$)$_2$}], 47.9 (s, C^4), 74.6 (s, *C*H$_2$), 74.9 (d, $J_{C,P}$ = 9 Hz, *C*H$_2$), 98.2 [s, $C_5(CH_3)_5$], 108.7 (s, C^3), 113.5 (s, C^2), 120.6, 122.7, 129.0, 142.2 (C_6H_5) ppm. ^{31}P{^{1}H} NMR ($CDCl_3$, 298 K): δ = 76.7 ppm (s).

[Cp*Ru{η^4-C$_4$H$_3$(CH$_2$CH$_2$CH$_2$)P*i*Pr$_2$NPh-κ^1*N*}][BPh$_4$] (3b): This compound was obtained in a fashion analogous to **3a**, but using 1,6-heptadiyne instead of propargyl ether. Yield: 55%. $C_{58}H_{63}BNPRu$: calcd. C 75.97, H 6.92, N 1.5; found C 76.1, H 7.04, N 1.5. ^{1}H NMR ($CDCl_3$, 298 K): δ = 0.78, 0.91, 1.37, 1.49 [m, 3 H each, P{CH(CH_3)$_2$}$_2$], 1.22 (m, 2 H, CH_2), 1.53 [s, 15 H, $C_5(CH_3)_5$], 2.11 (m, 2 H, CH_2), 1.92, 2.55 [m, 1 H each, P{CH(CH$_3$)$_2$}$_2$], 2.75 (d, $J_{H,H}$ = 3.2 Hz, 1 H, H^{4endo}), 3.19 (m, 2 H, CH_2), 3.53 (d, $J_{H,P}$ = 16 Hz, 1 H, H^1), 4.21 (d, $J_{H,H}$ = 3.2 Hz, 1 H, H^{4exo}), 6.51, 7.11, 7.21 (m, 5 H, C_6H_5) ppm. ^{13}C{^{1}H} NMR ($CDCl_3$, 298 K): δ = 9.6 [s, $C_5(CH_3)_5$], 16.2, 16.7, 16.9, 17.8 [s, P{CH(*C*H$_3$)$_2$}$_2$], 17.9 (d, $J_{C,P}$ = 103 Hz, C^1), 20.3 (s, *C*H$_2$), 31.7, 32.3 [m, P{*C*H(CH$_3$)$_2$}$_2$], 36.0 (s, *C*H$_2$), 37.1 (d, $J_{C,P}$ = 7.8 Hz, *C*H$_2$), 49.9 (s, C^4), 93.5 (s, C^3), 97.4 [s, $C_5(CH_3)_5$], 113.7 (s, C^2), 119.6, 120.4, 123.1, 126.0, 135.7, 142.8 (C_6H_5) ppm. ^{31}P{^{1}H} NMR ($CDCl_3$, 298 K): δ = 77.9 ppm (s).

[Cp*Ru{η^4-C$_4$H$_3$(CH$_2$)$_4$-P*i*Pr$_2$NPh-κ^1*N*}][BPh$_4$] (3c): This compound was obtained in a fashion analogous to **3a**, but using 1,7-octadiyne instead of propargyl ether. Yield: 48%. $C_{59}H_{65}BNPRu$: calcd. C 76.11, H 7.04, N 1.5; found C 76.1, H 6.98, N 1.4. ^{1}H NMR ($CDCl_3$, 298 K): δ = 0.64, 0.74, 1.04, 1.34 [s, 3 H each, P{CH(CH_3)$_2$}$_2$], 1.12 (m, 2 H, CH_2), 1.34 [s, 15 H, $C_5(CH_3)_5$], 1.69 (m, 2 H, CH_2), 1.72, 2.26 [m, 1 H each, P{CH(CH$_3$)$_2$}], 2.54 (m, 2 H, CH_2), 2.57 (d, $J_{H,H}$ = 3.2 Hz, 1 H, H^{4endo}), 2.74 (m, 2 H, CH_2), 2.79 (d, $J_{H,P}$ = 13.6 Hz, 1 H, H^1), 3.97 (d, $J_{H,H}$ = 3.2 Hz, 1 H, H^{4exo}), 6.45, 7.02, 7.11 (m, 5 H, C_6H_5) ppm. ^{13}C{^{1}H} NMR ($CDCl_3$, 298 K): δ = 9.8 [s, $C_5(CH_3)_5$], 14.8, 16.4, 17.6, 17.7 [P{CH(*C*H$_3$)$_2$}$_2$], 20.4 (d, $J_{C,P}$ = 98.6 Hz, C^1), 21.0, 21.4 (s, *C*H$_2$), 30.7 (d, $J_{C,P}$ = 8.1 Hz, *C*H$_2$), 30.9 (s, *C*H$_2$), 32.2 [d, $J_{C,P}$ = 48.5 Hz, P{*C*H(CH$_3$)$_2$}], 32.6 [d, $J_{C,P}$ = 43 Hz, P{*C*H(CH$_3$)$_2$}], 50.9 (s, C^4), 98.3 [s, $C_5(CH_3)_5$], 106.8 (s, C^3), 114.6 (s, C^2), 123.0, 124.4, 128.9, 135.7, 142.6 (C_6H_5) ppm. ^{31}P{^{1}H} NMR ($CDCl_3$, 298 K): δ = 81.7 ppm (s).

[Cp*Ru(MeCN){η^2-*n*BuCH=CH(C$_6$H$_4$)NHP*i*Pr$_2$-κ^1*P*}][BPh$_4$] (4): 1-Hexyne (65 μL, ca. 0.57 mmol) was added to a solution of **3** (0.42 g, 0.5 mmol) in 1,2-dichloroethane (8 mL). The mixture was stirred for 5 min at 60 °C and then for 1 h at room temperature. The solvent was removed in vacuo, and the residue washed with diethyl ether and petroleum ether until a yellow-orange powder was obtained. This material was filtered off and dried in vacuo. Yellow crystals of **4**·Me$_2$CO were obtained by recrystallization of the crude material from acetone/petroleum ether. Yield: 0.18 g, 40%. $C_{57}H_{74}BN_2OPRu$: calcd. C 72.36, H 7.88, N 3.0; found C 72.2, H 7.73, N 2.9. ^{1}H NMR ($CDCl_3$, 298 K): δ = 1.15 (s, 3 H, CH_3CN), 1.19 [d, $J_{H,P}$ = 1.5 Hz, 15 H, $C_5(CH_3)_5$], 0.87, 1.20, 1.33, 1.54 [m, 3 H each, P{CH(CH_3)$_2$}$_2$], 0.92, 1.51, 1.76 [m, 2 H each, (CH_2)CH_3], 1.00 [t, $J_{H,H}$ = 7.3 Hz, 3 H, (CH$_2$)CH_3], 2.45, 2.70 [m, 1 H each, P{CH(CH$_3$)$_2$}$_2$], 3.80 (m, 1 H, =CH*n*Bu), 3.84 (m, 1 H, =CHC$_6$H$_4$), 4.89 (s, 1 H, NH), 6.64, 6.70, 7.02, 7.21 (m, 1 H each, C_6H_4) ppm. ^{13}C{^{1}H} NMR ($CDCl_3$, 298 K): δ = 2.8 (s, *C*H$_3$CN), 8.9 [s, $C_5(CH_3)_5$], 14.2 [s, $(CH_2)_3CH_3$], 16.6, 18.2, 20.4, 21.5

 © 2005 Wiley-VCH Verlag GmbH & Co. KGaA, Weinheim

[P{CH(CH_3)$_2$}$_2$], 22.5, 33.6, 35.7 [s, (CH_2)$_3CH_3$], 32.5 [t, $J_{C,P}$ = 21.9 Hz, P{CH(CH_3)$_2$}$_2$], 57.4 (d, $J_{C,P}$ = 11 Hz, =CH*n*Bu), 67.1 (s, =CHC_6H_4), 93.8 [s, $C_5(CH_3)_5$], 116.5, 118.7, 128.1, 128.2, 135.7, 142.9 (C_6H_4) ppm. $^{31}P\{^1H\}$ NMR ($CDCl_3$, 298 K): δ = 101.7 ppm (s).

[Cp*Ru(MeCN){η^2-Me$_3$SiCH=CH(C$_6$H$_4$)NHP*i*Pr$_2$-κ^1*P*}][BPh$_4$] (5): This compound was obtained in a fashion analogous to **4**, but using HC≡CSiMe$_3$ instead of 1-hexyne. Yield: 53%. $C_{53}H_{68}BN_2PRuSi$: calcd. C 70.41, H 7.58, N 3.1; found C 70.2, H 7.64, N 3.0. ^1H NMR ($CDCl_3$, 298 K): δ = 0.01 [s, 9 H, Si(CH_3)$_3$], 0.93 (d, $J_{H,P}$ = 1 Hz, 3 H, CH_3CN), 1.07 [d, $J_{H,P}$ = 1.5 Hz, 15 H, C_5(CH_3)$_5$], 0.90, 1.04, 1.28, 1.42 [m, 3 H each, P{CH(CH_3)$_2$}$_2$], 2.27, 2.61 [m, 1 H each, P{CH(CH_3)$_2$}$_2$], 2.61 (m, 1 H, =CHSiMe$_3$), 3.91 (m, 1 H, =CHC_6H_4), 4.81 (s, 1 H, N*H*), 6.53, 6.60, 6.83, 6.92 (m, 1 H each, C_6H_4) ppm. $^{13}C\{^1H\}$ NMR ($CDCl_3$, 298 K): δ = 0.7 [s, Si(CH_3)$_3$], 2.5 (s, CH_3CN), 9.3 [s, C_5(CH_3)$_5$], 17.0 (d), 19.0 (d), 20.6 (s), 21.1 [s, P{CH(CH_3)$_2$}$_2$], 32.9, 34.5 [d, $J_{C,P}$ = 24.4 Hz, P{CH(CH_3)$_2$}$_2$], 54.0 [s, =$CHSi(CH_3)_3$], 62.1 (d, $J_{C,P}$ = 9.8 Hz, =CHC_6H_4), 94.4 [s, $C_5(CH_3)_5$], 116.4, 118.8, 127.8, 128.2, 129.8, 143.3 (C_6H_4) ppm. $^{31}P\{^1H\}$ NMR ($CDCl_3$, 298 K): δ = 107.7 ppm (s).

[Cp*Ru(MeCN)(η^2-MeOOCCH=CH$_2$)(PPh$_2$NHPh)][PF$_6$] (6): An excess of methyl acrylate (180 μL, ca. 1 mmol) was added to a solution of **1** (0.37 g, 0.5 mmol) in dichloromethane (10 mL) and the mixture was stirred for 30 min at room temperature. It was then filtered through celite and layered with petroleum ether. Yellow crystals of **6** were obtained after 3–4 days. The crystals were separated from the liquor, washed with petroleum ether, and dried in vacuo. Yield: 0.22 g, 56%. $C_{34}H_{40}F_6N_2O_2P_2Ru$: calcd. C 51.97, H 5.13, N 3.6; found C 51.9, H 5.14, N 3.5. IR: ν(C=O) = 1687 cm^{-1}. ^1H NMR ($CDCl_3$, 298 K): δ = 1.34 [d, $J_{H,P}$ = 1.5 Hz, 15 H, C_5(CH_3)$_5$], 2.44 (d, $J_{H,P}$ = 1.5 Hz, 3 H, CH_3CN), 3.78 (s, COOCH_3), 2.61, 3.45, 3.52 (m, 1 H each, CH=CH_2), 6.78 (d, $J_{H,P}$ = 15.9 Hz, 1 H, N*H*), 6.43, 6.68, 6.91 (m, 5 H, NHC_6H_5), 7.40–7.62 [m, 10 H, P(C_6H_5)$_2$] ppm. $^{13}C\{^1H\}$ NMR ($CDCl_3$, 298 K): δ = 3.7 (s, CH_3CN), 8.3 [s, C_5(CH_3)$_5$], 46.6 (d, $J_{C,P}$ = 5.4 Hz, =CH_2), 52.1 (d, $J_{C,P}$ = 17 Hz, =$CHCOOCH_3$), 52.3 (s, COOCH_3), 98.0 [s, C_5(CH_3)$_5$], 118.3, 120.8, 128.8, 128.9, 129.0, 129.1, 131.4, 131.7, 132.0, 132.1, 142.7 (C_6H_5), 178.1 ($COOCH_3$) ppm. $^{31}P\{^1H\}$ NMR ($CDCl_3$, 298 K): δ = 76.4 ppm (s).

X-ray Structure Determinations: Crystal data and experimental details are given in Table 1. X-ray diffraction data were collected on a Bruker SMART APEX three-circle diffractometer (graphite-monochromated Mo-K_α radiation, λ = 0.71073 Å) with a CCD area detector at the Servicio Central de Ciencia y Tecnología de la Universidad de Cádiz. Hemispheres of the reciprocal space were measured by omega scan frames with $\delta(\omega)$ 0.30°. Corrections for absorption and crystal decay (insignificant) were applied by semi-empirical methods from equivalents using the program SADABS.[22] The structures were solved by direct methods, completed by subsequent difference Fourier synthesis, and refined on F^2 by full-matrix least-squares procedures using the program SHELXTL.[23] The ligand *i*Pr$_2$PNH(C_6H_4)CH=CH*n*Bu in compound **4** showed orientation disorder at the end of the *n*Bu group. The set C(15)H$_2$ and C(16)H$_3$ was refined as two ethyl groups in complementary positions. Final refinements gave approximately 50% of each position. In this compound all non-hydrogen atoms except C15 and C15b were refined anisotropically, and hydrogen atoms were included at idealized positions and refined using a riding model. In the case of compounds **1a**, **2a**, and **6**, all non-hydrogen atoms were refined with anisotropic displacement coefficients, and all the remaining hydrogen atoms were refined using the SHELX riding model. The program ORTEP-3[24] was used for plotting.

CCDC260375 (for **1a**), -260376 (for **2a**), -260377 (for **4**), and -260378 (for **6**) contain the supplementary crystallographic data for this paper. These data can be obtained free of charge from The

Table 1. Summary of crystallographic data for **1a, 2a**, **4**, and **6**.

Compound	**1a**	**2a**	**4**	**6**
Formula	$C_{34}H_{37}F_6NOP_2Ru$	$C_{28}H_{36}F_{11}NOP_2Ru$	$C_{57}H_{74}BN_2OPRu$	$C_{34}H_{40}F_6N_2O_2P_2Ru$
Mol. mass	752.66	774.59	946.03	785.69
T [K]	100(2)	100(2)	100(2)	100(2)
Crystal size [mm]	0.44×0.31×0.28	0.41×0.15×0.03	0.23×0.22×0.06	0.32×0.15×0.06
Crystal system	orthorhombic	triclinic	monoclinic	orthorhombic
Space group	$Pna2_1$ (no. 33)	$P\bar{1}$ (no. 2)	$P2_1/c$ (no.14)	$Pna2_1$ (no. 33)
a [Å]	17.193(1)	8.378(2)	12.366(2)	21.133(1)
b [Å]	10.3496(6)	10.031(2)	17.846(2)	12.5882(7)
c [Å]	17.812(1)	17.976(4)	23.178(3)	12.9869(7)
α [°]		88.35(3)		
β [°]		86.22(3)	99.166(3)	
γ [°]		85.71(3)		
V [Å^3]	3169.4(3)	1502.9(5)	5049.8(1)	3454.8(3)
Z	4	2	4	4
ρ_{calc} [g cm^{-3}]	1.577	1.712	1.243	1.511
μ(Mo-K_α) [cm^{-1}]	6.61	7.22	3.83	6.12
F(000)	1536	784	2008	1608
Max. and min. transmission factors	1.04–0.93	1–0.83	0.98–0.73	1.18–0.91
Theta range for data collection	$2.28 < \theta < 27.56$	$2.04 < \theta < 25.06$	$1.67 < \theta < 23.27$	$1.88 < \theta < 27.52$
Reflections collected	27732	12886	30663	30365
Unique reflections	7085 (R_{int} = 0.0210)	5265 (R_{int} = 0.0337)	7221 (R_{int} = 0.1075)	7385 (R_{int} = 0.0532)
No. of observed reflections [$I > 2\sigma(I)$]	7007	4986	5948	7117
No.of parameters	411	409	592	431
Final $R1$, $wR2$ values [$I > 2\sigma(I)$]	0.0206, 0.0529	0.0413, 0.0821	0.0959, 0.1743	0.0524, 0.1171
Final $R1$, $wR2$ values (all data)	0.0210, 0.0531	0.0447, 0.0836	0.1237, 0.1890	0.0554, 0.1189
Residual electron density peaks (e Å^{-3})	+0.508, –0.286	+0.573, –0.785	+0.611, –1.191	+0.921, –1.287

 © 2005 Wiley-VCH Verlag GmbH & Co. KGaA, Weinheim

Cambridge Crystallographic Data Centre via www.ccdc.cam.ac.uk/data_request/cif.

Acknowledgments

We thank the Ministerio de Educación y Ciencia (DGI, Project CTQ2004-00776/BQU) and the Junta de Andalucía (PAI FQM188) for financial support, and Johnson Matthey plc for generous loans of ruthenium trichloride.

[1] R. Schmid, K. Kirchner, *Eur. J. Inorg. Chem.* **2004**, 2609–2626 and references cited therein.
[2] E. Becker, K. Mereiter, M. Puchberger, R. Schmid, K. Kirchner, *Organometallics* **2003**, *22*, 2124–2133.
[3] E. Becker, E. Rüba, K. Mereiter, R. Schmid, K. Kirchner, *Organometallics* **2001**, *20*, 3851–3853.
[4] K. Mauthner, K. M. Soldouzi, K. Mereiter, R. Schmid, K. Kirchner, *Organometallics* **1999**, *18*, 4681–4683.
[5] E. Rüba, K. Mereiter, R. Schmid, V. N. Sapunov, K. Kirchner, H. Schottenberger, M. J. Calhorda, L. F. Veiros, *Chem. Eur. J.* **2002**, *8*, 3948–3961.
[6] E. Rüba, K. Mereiter, R. Schmid, K. Kirchner, E. Bustelo, M. C. Puerta, P. Valerga, *Organometallics* **2002**, *21*, 2912–2920.
[7] S. Pavlik, K. Mereiter, R. Schmid, K. Kirchner, *Organometallics* **2003**, *22*, 1771–1774.
[8] I. de los Ríos, M. Jiménez-Tenorio, J. Padilla, M. C. Puerta, P. Valerga, *Organometallics* **1996**, *15*, 4565–4574.
[9] M. Jiménez-Tenorio, M. D. Palacios, M. C. Puerta, P. Valerga, *Organometallics* **2004**, *23*, 504–510.
[10] J. L. Kiplinger, T. G. Richmond, C. E. Osterberg, *Chem. Rev.* **1994**, *94*, 373–431.
[11] M. Jiménez-Tenorio, M. C. Puerta, P. Valerga, *Eur. J. Inorg. Chem.* **2004**, 17–32.
[12] R. F. R. Jazzar, S. A. Macgregor, M. F. Mahon, S. P. Richards, M. K. Whittlesey, *J. Am. Chem. Soc.* **2002**, *124*, 4944–4945.
[13] R. F. R. Jazzar, M. F. Mahon, M. K. Whittlesey, *Organometallics* **2001**, *20*, 3745–3751.
[14] J. N. Coalter, J. C. Huffmann, K. G. Caulton, *Organometallics* **2000**, *19*, 3569–3578.
[15] M. Bassetti, P. Álvarez, J. Gimeno, E. Lastra, *Organometallics* **2004**, *23*, 5127–5134.
[16] B. Steinmetz, W. A. Schenk, *Organometallics* **1999**, *18*, 943–946.
[17] W. Wiegrabe, H. Bock, *Ber. Dtsch. Chem. Ges.* **1968**, *101*, 1414–1427.
[18] M. S. Balakrishna, R. M. Abhyankar, J. T. Mague, *J. Chem. Soc., Dalton Trans.* **1999**, 1407–1412.
[19] M. R. I. Zubiri, H. L. Milton, D. J. Cole-Hamilton, A. M. Z. Slawin, J. D. Woollins, *Polyhedron* **2004**, *23*, 693–699.
[20] S. Miyano, M. Nawa, H. Hashimoto, *Chem. Lett.* **1980**, 729–730.
[21] S. Miyano, M. Nawa, A. Mori, H. Hashimoto, *Bull. Chem. Soc. Jpn.* **1984**, *57*, 2171–2176.
[22] G. M. Sheldrick, SADABS, **2001** version, Univ. of Göttingen, Germany.
[23] G. M. Sheldrick, SHELXTL version 6.10, Crystal Structure Analysis Package, Bruker AXS, Madison, WI, **2000.**
[24] ORTEP-3 for Windows, version 1.076: L. J. Farruggia, *J. Appl. Cryst.* **1997**, *30*, 565.

Received: January 12, 2005
Published Online: May 24, 2005

 © 2005 Wiley-VCH Verlag GmbH & Co. KGaA, Weinheim

Two Morphologies of Stable, Highly Ordered Assemblies of a Long-Chain-Substituted [2×2]-Grid-Type Fe^{II} Complex Adsorbed on HOPG

Ahmed Mourran[a][‡] Ulrich Ziener,[a] Martin Möller,*[a][‡] Esther Breuning,[b] Masakazu Ohkita,[b,c] and Jean-Marie Lehn*[b]

Keywords: Iron / Long alkyl chains / Scanning tunneling microscopy / Highly oriented pyrolytic graphite / Nanopatterning / Self-assembly

The programmed self-assembly of a multimetallic grid-type supramolecular architecture and its hierarchical organization on graphite are described. The doubly functionalized 4,6-bis(2,2′-bipyridyl-6-yl)-2-phenylpyrimidine derivative **1**, equipped with $CH_2OC_{16}H_{33}$ moieties at the terminal pyridine rings, was designed as a new bis(tridentate) ligand and synthesized using Stille-type coupling reactions. Treatment of ligand **1** with $Fe(BF_4)_2{\cdot}6H_2O$ in $CHCl_3/CH_3CN$ led to the spontaneous formation of a [2×2]-grid-type Fe^{II} complex **2** in quantitative yield. The self-assembled tetranuclear complex **2** was adsorbed onto highly oriented pyrolytic graphite (HOPG) and studied by scanning tunneling microscopy (STM), which showed two morphologies of highly ordered two-dimensional arrays of the metallo-supramolecular architectures. The resulting monolayers of the grid-type complex **2** are much more stable than that obtained from the corresponding unsubstituted grid-type complex owing to the additional attractive forces between the hexadecyl moieties in **2** and the HOPG surface. Moreover, the reproducibility of the STM images of the hexadecyl-substituted grid **2** was strongly improved compared to the unsubstituted one. These results suggest that the introduction of long alkyl chains into metallo-supramolecular architectures would have general advantages for their organization and STM investigation on HOPG. Details of the preparation and the STM investigation of ligand **1** are also presented.
(© Wiley-VCH Verlag GmbH & Co. KGaA, 69451 Weinheim, Germany, 2005)

Introduction

The design and formation of ordered nanoscaled structures with functional properties have attracted considerable attention in materials science and nanotechnology.[1] A bottom-up approach based on the self-assembly of simple building units to nanometric-size objects is expected to be a powerful tool, instead of microfabrication as a top-down approach, for producing functional materials with great technological advantages. Especially interesting is a sequential application of different self-organization principles for the preparation of hierarchically structured materials. This would be realized by the controlled use of relatively strong, directional interactions (such as hydrogen bonds and coordinative interactions) as well as weak, nondirectional interactions (such as van der Waals force and hydrophobic interaction). In this study we examined the hierarchical organization of a self-assembled multimetallic supramolecular architecture on graphite.

We have previously shown that the self-assembly of bis(tridentate) ligands, based on terpyridine-like binding sites, with octahedrally coordinated metal ions such as Fe^{II}, Co^{II}, and Zn^{II} leads to [2×2]-grid-type complexes.[2–4] These complexes present interesting electronic, redox, and magnetic properties such as electronic interactions between the metal centers,[2] multilevel electrochemical reduction up to 10 reversible steps,[5] antiferromagnetic transition at low temperatures,[6] and spin crossover phenomena triggered by temperature, pressure, and light.[7] For technological application a further 2D or 3D ordering of these supramolecular complexes is required. Several strategies have been examined to obtain such ordered arrangement of the grid-type supramolecular architectures, including self-assembly at the air-water interface,[8] hydrogen-bonded crystal formation,[9] and adsorption on graphite.[10,11] An excellent method to visualize such assemblies with submolecular resolution on for example highly ordered pyrolytic graphite (HOPG) is represented by scanning tunneling microscopy (STM).[12] However, the stabilities of the monolayers obtained from unsubstituted [2×2]-grid-type complexes[10] and its pyridyl-

[a] Organische Chemie III/Makromolekulare Chemie, Universität Ulm,
Albert-Einstein-Allee 11, 89081 Ulm, Germany
[b] Laboratoire de Chimie Supramoléculaire, ISIS, Université Louis Pasteur 8,
Allée Gaspard Monge, B. P. 70028, 67083 Strasbourg cedex, France
Fax: +33-3-90245140
E-mail: lehn@isis.u-strasbg.fr
[c] Department of Applied Chemistry, Nagoya Institute of Technology,
Nagoya 466-8555, Japan
[‡] Present address: Deutsches Wollforschungsinstitut, RWTH Aachen,
Pauwelsstraße 8, 52056 Aachen, Germany

substituted derivatives[11] are low, and thus their STM images are obtained only with low reproducibility. To address these problems, we have designed as a new ligand 4,6-bis(2,2′-bipyridyl-6-yl)-2-phenylpyrimidine (**1**), equipped with $CH_2OC_{16}H_{33}$ moieties at the terminal pyridine rings. The long alkyl chains are expected to result in better adsorption on graphite.[13] Herein, we describe the details of the nanopatterning of HOPG by the long-chain-substituted [2×2]-grid-type complex **2**, together with the preparation and STM investigation of ligand **1**.

Results and Discussion

Synthesis of Ligand 1 and Self-Assembly of [2×2]-Grid-Type Fe^{II} Complex 2

The synthesis of the long-chain-substituted ligand **1** is outlined in Scheme 1. Deprotonation of 2-bromo-5-(hydroxymethyl)pyridine (**3**), which was readily accessible from commercially available 2-hydroxy-5-pyridinecarboxylic acid,[14] with sodium hydride in DMF followed by treatment with hexadecyl iodide afforded ether **4** in 66% yield. Stannylation of **4** with a hexamethyldistannane/$Pd(PPh_3)_4$ system in refluxing toluene produced **5**, which was in turn coupled with 2,6-dibromopyridine in the presence of $Pd(PPh_3)_4$ to afford bipyridine derivative **6** in 52% yield. Twofold Stille coupling of 4,6-dichloro-2-phenylpyrimidine[15] with 2 equiv. of **7**, which was prepared by stannylation of **6** with a hexamethyldistannane/$Pd(PPh_3)_4$ system, in refluxing toluene in the presence of $Pd(PPh_3)_4$ gave the desired ligand **1** in 57% yield.

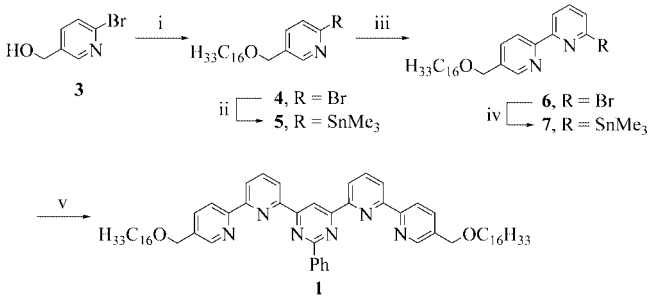

Scheme 1. Synthesis of ligand **1**, i) NaH, DMF, then $C_{16}H_{33}I$; ii) $Me_3SnSnMe_3$, $Pd(PPh_3)_4$, toluene; iii) 2,6-dibromopyridine, $Pd(PPh_3)_4$; iv) $Me_3SnSnMe_3$, $Pd(PPh_3)_4$, toluene; v) 4,6-dichloro-2-phenylpyrimidine, $Pd(PPh_3)_4$.

Reaction of **1** with $Fe(BF_4)_2{\cdot}6H_2O$ in acetonitrile/chloroform (1:1) proceeded smoothly and cleanly to yield the corresponding [2×2]-grid-type complex **2** in quantitative yield, as similarly shown earlier for the formation of related complexes (Scheme 2).[2–4] The electrospray mass spectrum of **2** confirms its [2×2]-grid-like structure in solution.[16]

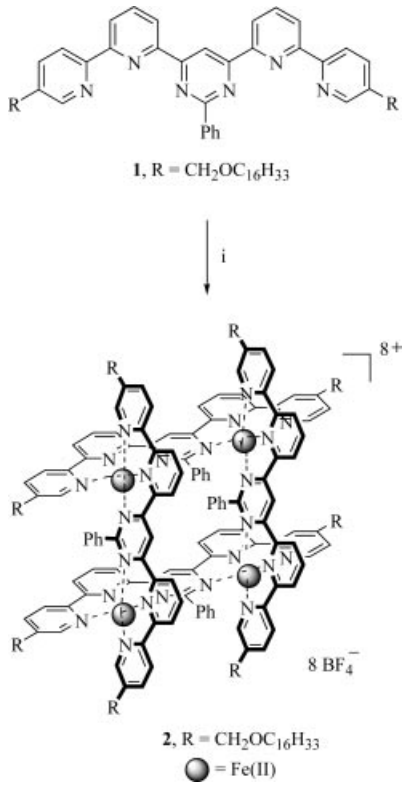

Scheme 2. Formation of the [2×2]-grid-type Fe^{II} complex **2**, i) $Fe(BF_4)_2{\cdot}6H_2O$, $CHCl_3/CH_3CN$ (1:1).

.

STM Investigation of Ligand 1 Adsorbed on HOPG

Self-assembly of ligand **1** on HOPG results in a highly ordered structure; the representative STM image of **1** is shown in Figure 1. Brighter and darker lamellae alternate within the image, where a bright color represents higher electron density. The periodicity of the lamellae is 55 Å. The brighter moiety exhibits a width of 25 Å and the darker moiety a width of 30 Å. The bright stripe shows a structured pattern with numerous small bright spots and is attributed to the aromatic rings. The darker stripe presents

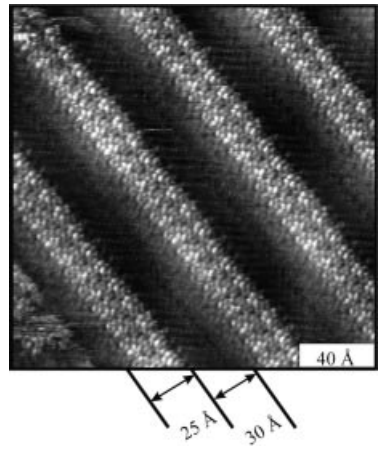

Figure 1. STM image of **1** on HOPG from 1,2,4-trichlorobenzene: Lamellar widths: 25 and 30 Å; V_{bias} = –362 mV, I_{set} = 23.8 pA.

 © 2005 Wiley-VCH Verlag GmbH & Co. KGaA, Weinheim

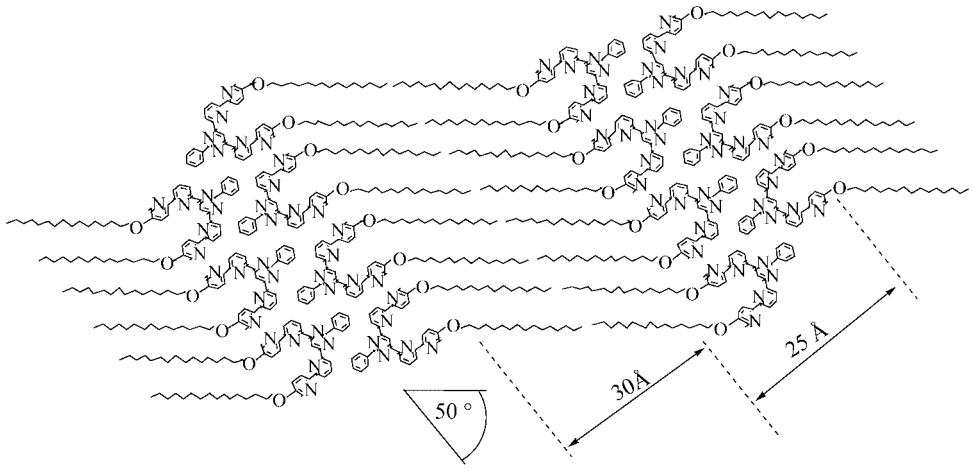

Scheme 3. Proposed model for the conformation and ordering of **1** on graphite.

.

an additional pattern of linear arrays of spots, which form an angle of 50° with the ribbons. These linear arrays are assigned to the alkyl chains in **1**. The image can be interpreted as a flat arrangement of the aromatic rings on the surface, which is expected for optimal contact between the monolayer and the basal plane of graphite. The alkyl chains in **1** are ordered commensurately with the graphite lattice.[13] The conformation of the aromatic units of **1** on the surface would be analogous to those observed for related compounds both in solution and in the solid state, i.e., a *transoid* conformation of the NC–CN bonds connecting the heterocycles, as indicated in our previous studies.[11,17–19] In the lower left corner of the STM image (Figure 1<yigr1>) a defect can be observed.

A plausible model for the arrangement of **1** on the surface is shown in Scheme 3. In this model, the bright stripes are formed by the aromatic part of two rows of molecules of **1**, which may be stabilized by weak intramolecular C–H···N interactions.[11,17–19] The alkyl chains form an angle of 50° with this stripe. From geometrical estimations the expected widths of the ribbons fit very well with the experimental values. The tilt angle of the alkyl chains with the main axis of the lamellae allows the optimal contact of ca. 4.5 Å between neighboring chains.[11] The comparison of the length of the alkyl chains in **1** and the observed width of the darker stripes in the image suggests a noninterdigitated assembly of the alkyl chains.

STM Investigation of [2×2]-Grid-Type Fe^{II} Complex 2 Assembled on HOPG

Representative STM images of the [2×2]-grid-type Fe^{II} complex **2** on HOPG are shown in Figure 2. The large scan area exhibits two domains of alternating brighter and darker ribbons (Figure 2a). On the first glimpse both domains seem to represent the same structure with changing preferred directions. A closer look reveals that the periodicities of the ribbons differ between 42 Å (domain A) and 23 Å (domain B), respectively, but both domains can be easily distinguished from the features of ligand **1** (Figure 1). Hence, we assume that **2** forms at the solution/HOPG interface at least two different morphologies. The formation of (pseudo)polymorphs[20] in 2D monolayers – sometimes depending on the solvent[21] – is known but the grid-like complexes of HOPG polymorphism were only observed in the case of different substituents in the periphery and in the center of the complexes, respectively.[10]

A detailed view of domain A (Figure 2b) shows that the brighter stripes are built from square-like entities with an edge length of 22 to 24 Å whereas the darker ribbons are structured by more narrow and broader stripes perpendicular to the ribbon direction. Because of the differences in electron density we attribute the brighter ribbons to the grid-like structure of the aromatic part of **2** and the darker bands to the alkyl substituents.

Regarding a reasonable model for the arrangement of **2** in domain A the fourfold symmetry of the square-like entities in Figure 2b gives hints for an arrangement of **2** with the C_4 axis perpendicular to the substrate surface (Scheme 4c). In Scheme 4a the geometrical dimensions of the grid core of **2** show that we expect an edge length for the squares without the alkyl chains of 18 Å. The larger size of the square-like shapes in Figure 2b suggests that each grid-like complex is rotated along the C_4 axis so that the ligands are no longer parallel and orthogonal, respectively, to the main direction of the bright stripes but form an angle of 20–30° and 110–120°, respectively (Scheme 4c). A further stripy fine structure of the square-like bright areas in the direction of one set of two parallel ligands per complex molecule with the above given angles supports this assumption. There is no optimal contact possible between the alkyl chains and the graphite surface due to the nonplanar structure of **2**. We suggest that the chains adopt a conformation similar to that shown in Scheme 4b, which exhibits the side view of one ligand molecule **1** in its conformation in complex **2**. Such conformation allows close contact between a part of an alkyl chain and graphite. The width of the darker ribbons of 18 Å is too small for a noninterdigitated arrange-

 © 2005 Wiley-VCH Verlag GmbH & Co. KGaA, Weinheim

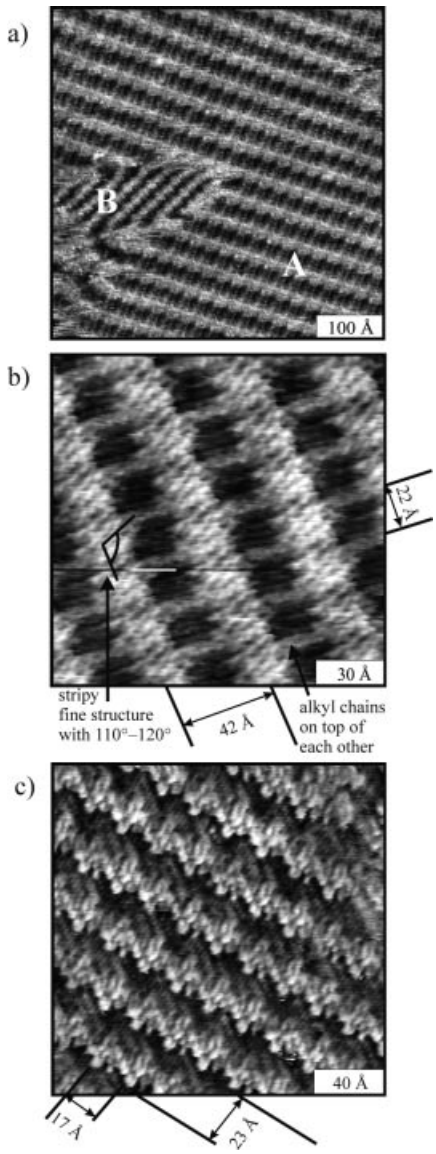

Figure 2. STM images of **2** on HOPG from 1,2,4-trichlorobenzene: Large-scan-area image with two different domains A and B (V_{bias} = –651 mV, I_{set} = 39.4 pA) (a), detailed view of domain A with a lamellar structure (periodicity: 42 Å) and a periodic fine structure within each lamella (periodicity: 22 Å), a stripy fine structure with an angle of ca. 115° with respect to the lamella axis is visible, too (V_{bias} = –410 mV, I_{set} = 36.6 pA) (b), detailed view of domain B with a lamellar structure (periodicity: 23 Å) and a periodic fine structure within each lamella (periodicity: 17 Å; V_{bias} = –344 mV, I_{set} = 44.1 pA) (c).

ment of the alkyl chains despite the above suggested conformation. Hence, we assume interdigitation which on the other side would lead, with the assumed orientation of the grid-like complexes, to a partial bumping of the alkyl chains (see Scheme 4c). Though the resolution of the STM image in Figure 2b does not give enough information on the exact ordering of the alkyl chains we suppose that at these positions the alkyl chains are approximately on top of each other. This might cause the contrast of brighter stripes within the darker ribbons in Figure 2b because of the topography and not primarily due to higher electron density.

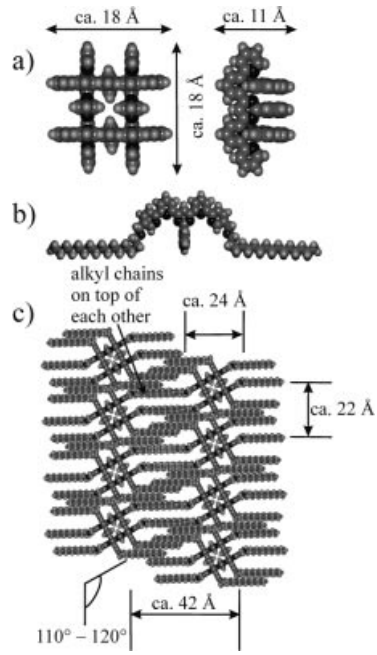

Scheme 4. Proposed model for the arrangement of **2** on HOPG in domain A: top view of one grid-like complex along the C_2 axis (a, left), side view of one grid-like complex (a, right), side view of one ligand **1** with the proposed conformation of the alkyl chains ensuring close contact between the surface and the alkyl chains (b), top view of the arrangement of the grid-like complexes on HOPG (c).

A detailed view of domain B shows lamellae which are built from a bright and a dark band, the dark formed by fine stripes with an angle of 40° with respect to the ribbons (Figure 2c). Theses stripes are assigned to the alkyl chains. The bright parts are attributed to the high electron density aromatic moieties of complex **2** showing an additional fine structure with a periodicity of 17 Å.

Comparing with the much larger periodicity of the ribbons in domain A (42 Å, Figure 2b), we suggest an edge-on arrangement of the complexes on the graphite in domain B (periodicity 23 Å, Figure 2c), though we cannot assign unambiguously the fine structure of the bright parts to the structure of the grid-like complex. The edge-on arrangement of the complexes on the graphite may be accompanied by a tilt angle of up to 70° which would lead to a projected area of 17×18 Å (Scheme 5). This arrangement should lead to an improved contact between the two alkyl chains next to the graphite and the graphite surface at the expense of the other six alkyl chains which are bent to come at least partially into contact with the graphite surface. An additional consequence of such an arrangement is a stacking of the complexes which should be advantageous due to their highly charged character. Within one ribbon the complexes are assumed to be parallel to each other. Comparing adjacent ribbons a shift between two neighboring molecules of ca. 6 Å can be found which might be caused by the packing of the alkyl chains.

The two arrangements of complex **2** coexist on HOPG (see Figure 2a) but we do not yet know how the formation of one or the other morphology can be controlled. The

 © 2005 Wiley-VCH Verlag GmbH & Co. KGaA, Weinheim

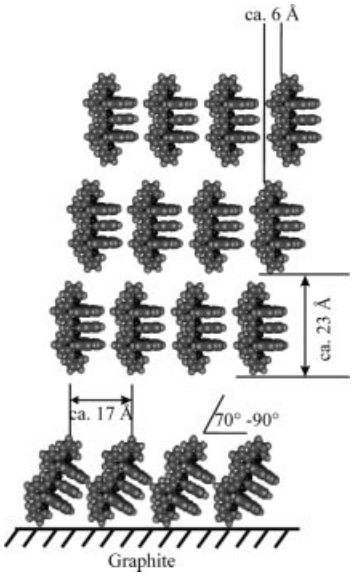

Scheme 5. Proposed model for the arrangement of **2** on HOPG in domain B: top view of the arrangement of the grid-like complexes (top), side view of the arrangement of the grid-like complexes parallel to the graphite surface with an angle of 70° resulting in a projected area of 17×18 Å (bottom). Only the grid cores are shown, the alkyl chains are omitted for clarity.

forms are stable enough not to be transformed into each other by the STM tip or any other external trigger present in the course of our STM experiments.

Conclusions

The doubly functionalized ligand **1**, having $CH_2OC_{16}H_{33}$ moieties at the terminal pyridine rings, was designed as a new bis(tridentate) ligand and synthesized. Treatment of **1** with $Fe(BF_4)_2{\cdot}6H_2O$ in $CHCl_3/CH_3CN$ led to the spontaneous formation of a [2×2]-grid-type Fe^{II} complex **2** in a quantitative yield. The STM investigations of both ligand **1** and the Fe^{II} complex **2** on graphite revealed their stable, regular arrangements on the surfaces. Complex **2** shows two different morphologies – a flat and an edge-on assembly of the grid-like complexes on HOPG. We do not yet know the factors determining the formation of one or the other arrangement. Importantly, stability of the monolayers of the long-chain-substituted complex **2**, and thus, reproducibility of their STM images have been significantly enhanced compared to the corresponding unsubstituted complex. Therefore, the present results suggest that the introduction of long alkyl chains into the ligand would be a useful strategy for the STM investigations of the related grid-type complexes as well as other metallo-supramolecular architectures on HOPG surfaces.

Experimental Section

General: Melting points were measured with a digital Electrotherma apparatus and are uncorrected. ^{1}H NMR spectra were recorded with a Bruker AC200 spectrometer in $CDCl_3$ at 200 MHz under ambient conditions; chemical shifts are given in ppm using TMS as reference. ^{13}C NMR spectra were recorded with a Bruker AC200 spectrometer in $CDCl_3$ at 50 MHz, also under ambient conditions; chemical shifts are given in ppm using the solvent peak as reference. Fast atom bombardment (FAB) mass spectra were recorded with a ZAB-HF VG spectrometer with *m*-nitrobenzyl alcohol as the matrix. Electrospray (ES) mass spectra were recorded with a triple quadrupole mass spectrometer Quattro II. The microanalyses were carried out at the Service Central de Microanalyse du CNRS, Faculté de Chimie, Strasbourg. Column chromatography was carried out on Merck silica gel 60 or Merck alumina activity II–III. 2-Bromo-5-(hydroxymethyl)pyridine (**3**)[14] and 4,6-dichloro-2-phenylpyrimidine[15] were prepared according to known procedures.

2-Bromo-5-(hexadecyloxymethyl)pyridine (4): To a suspension of sodium hydride (128 mg, 5.32 mmol, 60% dispersion in oil) in anhydrous DMF (6 mL) was added 2-bromo-5-(hydroxymethyl)pyridine (**3**)[14] (500 mg, 2.7 mmol) and the reaction mixture was stirred at room temperature for 1 h. The suspension was cooled to 0 °C and hexadecyl iodide (1.06 g, 3.0 mmol) was added to it. The mixture was then allowed to warm to room temperature and stirred for 44 h. After evaporation of the solvent, the residue was subjected to chromatography on silica gel eluting with hexane/EtOAc (4:1, v/v) to afford **4** as a colorless powder (723 mg, 66%). M.p. 47 °C. ^{1}H NMR (200 MHz, $CDCl_3$): δ = 0.84 (t, J = 6.7 Hz, 3 H, CH_3), 1.22 (m, 26 H, CH_2), 1.57 (quint, J = 6.7 Hz, 2 H, OCH$_2$CH_2), 3.44 (t, J = 6.4 Hz, 2 H, OCH_2), 4.42 (s, 2 H, C_{py}CH_2O), 7.41 (d, J = 8.2 Hz, 1 H, 4-H), 7.51 (dd, J = 8.2 and 2.4 Hz, 1 H, 3-H), 8.28 (d, J = 1.8 Hz, 1 H, 6-H). ^{13}C NMR (50 MHz, $CDCl_3$): δ = 14.0, 22.6, 26.1, 29.3, 29.4, 29.6, 31.9, 69.4, 71.0, 127.8, 133.5, 137.8, 141.1, 149.2. MS (FAB): *m*/*z* (%) = 412.1 (100) $[M + H]^+$. IR (KBr): $\tilde{\nu}$ = 2954, 2916, 2851, 1586, 1566, 1473, 1458, 1388, 1110, 1089, 1026, 842, 824, 716, 630 cm^{-1}. $C_{22}H_{38}BrNO$ (412.46): calcd. C 64.20, H 9.31, N 3.41; found C 64.07, H 9.46, N 3.38.

2-Bromo-6-[5′-(hexadecyloxymethyl)pyrid-2′-yl]pyridine (6): A mixture of **4** (1 g, 2.42 mmol), hexamethyldistannane (880 mg, 2.66 mmol), and $Pd(PPh_3)_4$ (70 mg, 0.060 mmol) in toluene (16 mL) under argon was refluxed for 4 h. 2,6-Dibromopyridine (1.26 g, 5.32 mmol) and $Pd(PPh_3)_4$ (120 mg, 0.11 mmol) were added to the mixture and the reaction mixture was further refluxed under argon for 20 h. After evaporation of the solvent, the residue was subjected to chromatography on silica gel eluting with hexane/EtOAc (9:1, v/v) to afford **6** as a colorless powder (620 mg, 52%). M.p. 67 °C. ^{1}H NMR (200 MHz, $CDCl_3$): δ = 0.88 (t, J = 6.1 Hz, 3 H, CH_3), 1.25 (m, 26 H, CH_2), 1.56–1.72 (m, 2 H, OCH$_2$CH_2), 3.50 (t, J = 6.4 Hz, 2 H, OCH_2), 4.57 (s, 2 H, C_{py}CH_2O), 7.47 (dd, J = 7.9 and 1.2 Hz, 1 H, 3′- or 5′-H), 7.65 (t, J = 7.9 Hz, 1 H, 4′-H), 7.79 (dd, J = 8.2 and 2.4 Hz, 1 H, 3-H), 8.37 (dd, J = 7.6 and 0.9 Hz, 1 H, 3′- or 5′-H), 8.38 (d, J = 8.2 Hz, 1 H, 4-H), 8.62 (d, J = 2.1 Hz, 1 H, 6-H). ^{13}C NMR (50 MHz, $CDCl_3$): δ = 14.0, 22.6, 26.1, 29.3, 29.4, 29.6, 31.8, 70.0, 70.8, 119.5, 120.9, 127.7, 134.7, 136.0, 139.0, 141.4, 148.3, 153.6, 157.1. MS (FAB): *m*/*z* (%) = 489.4 (100) $[M + H]^+$. IR (KBr): $\tilde{\nu}$ = 2953, 2916, 2849, 1600, 1570, 1545, 1470, 1434, 1387, 1124, 1026, 988, 801, 777, 754, 718, 672 cm^{-1}. $C_{27}H_{41}BrN_2O$ (489.54): calcd. C 66.25, H 8.44, N 5.72; found C 66.17, H 8.32, N 5.74.

4,6-Bis{6′-[5′′-(hexadecyloxymethyl)pyrid-2′′-yl]pyrid-2′-yl}-2-phenylpyrimidine (1): A mixture of **6** (300 mg, 0.61 mmol), hexamethyldistannane (221 mg, 0.64 mmol), and $Pd(PPh_3)_4$ (21 mg, 0.018 mmol) in toluene (4 mL) under argon was refluxed for 25 min. After evaporation of the solvent, the resultant crude stannylated product **7** was used for the following coupling reaction

 © 2005 Wiley-VCH Verlag GmbH & Co. KGaA, Weinheim

without further purification. ^{1}H NMR (200 MHz, $CDCl_3$): δ = 0.39 [s, 9 H, Sn(CH_3)$_3$], 0.89 (t, J = 6.1 Hz, 3 H, CH_3), 1.26 (m, 26 H, CH_2), 1.63 (quint, J = 6.7 Hz, 2 H, OCH_2CH_2), 3.50 (t, J = 6.4 Hz, 2 H, OCH_2), 4.57 (s, 2 H, $C_{py}CH_2O$), 7.44 (dd, J = 7.3 and 1.5 Hz, 1 H, 3′- or 5′-H), 7.64 (t, J = 7.3 Hz, 1 H, 4′-H), 7.80 (dd, J = 8.2 and 2.4 Hz, 1 H, 3-H), 8.27 (dd, J = 7.9 and 1.2 Hz, 1 H, 3′- or 5′-H), 8.54 (d, J = 7.9 Hz, 1 H, 4-H), 8.62 (d, J = 1.5 Hz, 1 H, 6-H). A mixture of **7** (334 mg, 0.58 mmol), 4,6-dichloro-2-phenylpyrimidine (**8**)[15] (66 mg, 0.29 mmol), and $Pd(PPh_3)_4$ (34 mg, 0.029 mmol) in toluene (5 mL) under argon was refluxed for 21 h. After evaporation of the solvent, the residue was taken up in $CHCl_3$ and filtered through a short pad of alumina. The solvent was evaporated, the residue was taken up in MeOH/acetone (1:1, v/v), and the precipitate formed was centrifuged off, washed with MeOH/acetone and dried in vacuo. The crude product thus obtained was further purified by column chromatography on alumina eluting with hexane/$CHCl_3$ (1:1, v/v) to afford **1** as a colorless powder (162 mg, 57%). M.p. 141 °C. ^{1}H NMR (200 MHz, $CDCl_3$): δ = 0.87 (t, J = 5.8 Hz, 6 H, CH_3), 1.24 (m, 52 H, CH_2), 1.67 (quint, J = 7.0 Hz, 4 H, OCH_2CH_2), 3.56 (t, J = 6.4 Hz, 4 H, OCH_2), 4.64 (s, 4 H, $C_{py}CH_2O$), 7.56–7.65 (m, 3 H, *m*- and *p*-H), 7.87 (d, J = 6.7 Hz, 2 H, 3′- or 5′-H), 8.05 (t, J = 7.9 Hz, 2 H, 4′-H), 8.60 (d, J = 7.9 Hz, 2 H, 3′- or 5′-H), 8.71–8.80 (m, 8 H, *o*-, 3′′-, 4′′- and 6′′-H), 9.62 (s, 1 H, 5-H). ^{13}C NMR (50 MHz, $CDCl_3$): δ = 14.1, 22.7, 26.2, 29.3, 29.5, 29.6, 29.6, 29.6, 29.7, 29.8, 31.9, 70.3, 70.9, 111.5, 120.8, 121.7, 122.4, 128.4, 128.4, 130.6, 134.4, 136.0, 137.9, 137.9, 148.5, 153.8, 155.3, 155.4, 163.9, 164.1. MS (FAB): *m*/*z* (%) = 973.7 (100) $[M + H]^+$. IR (KBr): $\tilde{\nu}$ = 3060, 2918, 2850, 1720, 1556, 1540, 1471, 1377, 1263, 1115, 1022, 994, 814, 50, 718, 690, 652, 634 cm^{-1}. HR-MS (FAB): $C_{64}H_{89}N_6O_2$ (1022.51): calcd. *m*/*z* = 973.704702, found *m*/*z* = 973.705754 $[M + H]^+$.

[2×2]-Grid-Type Fe^{II} Complex (2): A mixture of **1** (5 mg, 5.14 μmol) and $Fe(BF_4)_2$·$6H_2O$ (1.73 mg, 5.14 μmol) in $CHCl_3$ (0.4 mL) and CH_3CN (0.4 mL) under argon was refluxed. The reaction was monitored by ^{1}H NMR spectroscopy and ES mass spectrometry and was proven to be completed after 15 h. Evaporation of the solvents afforded pure complex **2** in a quantitative yield as a dark green powder. ^{1}H NMR (200 MHz, $CDCl_3$/CD_3CN): δ = –17.8, –10.2, 0.0, 2.3, 2.8, 5.6, 7.3, 13.4, 14.2, 17.5, 55.5, 60.0, 66.4, 74.5. MS (ESI): *m*/*z* = 2318.7 $[M - 2\ BF_4]^{2+}$, 1517.0 $[M - 3\ BF_4]^{3+}$, 1116.4 $[M - 4\ BF_4]^{4+}$, 876.3 $[M - 5\ BF_4]^{5+}$.

STM Investigations: STM measurements were carried out under ambient conditions with a low-current RHK 1000 control system. STM imaging of the adlayers was performed at the internal interface between HOPG and a concentrated solution of the ligand **1**, dissolved in 1,2,4-trichlorobenzene, according to the procedure of Rabe.[13a] A drop of the solution was placed on a freshly cleaved HOPG surface, while the surface had already been scanned by STM under the conditions that allowed atomic resolution of the graphite surface structure. A potential of $U = \pm 1$ V was applied to the substrate. The scan rate was varied between 0.2 and 0.6 μm s^{-1}. The tunneling current set point was 8–20 pA. All images presented were obtained at constant current mode using a Pt/Ir (90:10) tip, which was mechanically sharpened. Complex **2** was dissolved in acetonitrile at a concentration less than 1 wt.-%. A drop of the solution was deposited on a freshly cleaved surface of graphite. The substrates were dried in the presence of acetonitrile vapor over 1 h (in a covered Petri dish with a few mL of acetonitrile next to the sample). Then the sample was taken out of the Petri dish and dried fully under ambient conditions. The molecular structure of the adlayer was probed by STM under air. The distances and angles were determined by using an internal calibration. The overall error of these determinations is estimated below ±5% for distances and angles.

Acknowledgments

We thank the Ministry of Education, Science, Sports, and Culture of Japan (M. O.), Université Louis Pasteur (M. O.), and the Ministère de l'Education Nationale, de la Recherche et de la Technologie (E. B.). The work was further supported by the Deutsche Forschungsgemeinschaft within the framework of the Sonderforschungsbereich 569 at the University of Ulm and is part of the Marie Curie Research Training Network program BioPolySurf, which is financially supported by the EU under contract no. MRTN-CT-2004-005516. We also thank P. Maltèse (NMR) and H. Nierengarten (ES MS) for their spectroscopic measurements.

[1] J.-M. Lehn, *Supramolecular Chemistry: Concepts and Perspectives*, VCH, Weinheim, **1995**.
[2] G. S. Hanan, D. Volkmer, U. S. Schubert, J.-M. Lehn, G. Baum, D. Fenske, *Angew. Chem.* **1997**, *109*, 1929–1931; *Angew. Chem. Int. Ed. Engl.* **1997**, *36*, 1842–1844.
[3] a) D. M. Bassani, J.-M. Lehn, K. Fromm, D. Fenske, *Angew. Chem.* **1998**, *110*, 2534–2537; *Angew. Chem. Int. Ed.* **1998**, *37*, 2364–2367; b) J. Rojo, F.-J. Romero-Salguero, J.-M. Lehn, G. Baum, D. Fenske, *Eur. J. Inorg. Chem.* **1999**, 1421–1428.
[4] For a recent review, see: M. Ruben, J. Rojo, F. J. Romero-Salguero, L. H. Uppadine, J.-M. Lehn, *Angew. Chem. Int. Ed.* **2004**, *43*, 3644–3662.
[5] M. Ruben, E. Breuning, J.-P. Gisselbrecht, J.-M. Lehn, *Angew. Chem.* **2000**, *112*, 4312–4315; *Angew. Chem. Int. Ed.* **2000**, *39*, 4139–4142.
[6] O. Waldmann, J. Hassmann, P. Müller, G. S. Hanan, D. Volkmer, U. S. Schubert, J.-M. Lehn, *Phys. Rev. Lett.* **1997**, *78*, 3390–3393.
[7] E. Breuning, M. Ruben, J.-M. Lehn, F. Renz, Y. Garcia, V. Ksenofontov, P. Gutlich, E. Wegelius, K. Rissanen, *Angew. Chem.* **2000**, *112*, 2563–2566; *Angew. Chem. Int. Ed.* **2000**, *39*, 2504–2507.
[8] I. Weissbuch, P. N. W. Baxter, S. Cohen, H. Cohen, K. Kjaer, P. B. Howes, J. Als-Nielsen, G. S. Hanan, U. S. Schubert, J.-M. Lehn, L. Leiserowitz, M. Lahav, *J. Am. Chem. Soc.* **1998**, *120*, 4850–4860.
[9] E. Breuning, U. Ziener, J.-M. Lehn, E. Wegelius, K. Rissanen, *Eur. J. Inorg. Chem.* **2001**, 1515–1521.
[10] A. Semenov, J. P. Spatz, M. Möller, J.-M. Lehn, B. Sell, D. Schubert, C. H. Weidl, U. S. Schubert, *Angew. Chem.* **1999**, *111*, 2701–2705; *Angew. Chem. Int. Ed.* **1999**, *38*, 2547–2550.
[11] U. Ziener, J.-M. Lehn, A. Mourran, M. Möller, *Chem. Eur. J.* **2002**, *8*, 951–957.
[12] See recent reviews on this method at the solid-liquid interface: a) S. De Feyter, F. C. De Schryver, *J. Phys. Chem. B* **2005**, *109*, 4290–4302; b) S. De Feyter, M. M. S. Abdel-Mottaleb, N. Schuurmans, B. J. V. Verkuijl, J. H. v. Esch, B. L. Feringa, F. C. De Schryver, *Chem. Eur. J.* **2004**, *10*, 1124–1132; c) P. Samori, *J. Mater. Chem.* **2004**, *14*, 1353–1366; d) S. De Feyter, F. C. D. Schryver, *Chem. Soc. Rev.* **2003**, *32*, 139–150; e) S. De Feyter, A. Gesquiere, M. M. Abdel-Mottaleb, P. C. M. Grim, F. C. De Schryver, C. Meiners, M. Sieffert, S. Valiyaveettil, K. Müllen, *Acc. Chem. Res.* **2000**, *33*, 520–531; f) L. C. Giancarlo, G. W. Flynn, *Annu. Rev. Phys. Chem.* **1998**, *49*, 297–336; g) D. M. Cyr, B. Venkataraman, G. W. Flynn, *Chem. Mater.* **1996**, *8*, 1600–1615.
[13] Adsorption of long-chain alkanes and related molecules on HOPG substrates often leads to very well ordered layers that can be readily imaged at high resolution in the STM investigation, see: a) J. P. Rabe, S. Buchholz, *Science* **1991**, *253*, 424–

 © 2005 Wiley-VCH Verlag GmbH & Co. KGaA, Weinheim

427; b) G. C. McGonigal, R. H. Bernhardt, D. J. Thompson, *Appl. Phys. Lett.* **1990**, *57*, 28–30.
[14] D. Funeriu, Ph.D. Thesis, Université Louis Pasteur (France), **1999**.
[15] D. B. Harden, M. J. Mokrosz, L. Strekowski, *J. Org. Chem.* **1988**, *53*, 4137–4140.
[16] E. Breuning, G. S. Hanan, F. J. Romero-Salguero, A. M. Garcia, P. N. W. Baxter, J.-M. Lehn, E. Wegelius, K. Rissanen, H. Nierengarten, A. Van Dorsselaer, *Chem. Eur. J.* **2002**, *8*, 3458–3466.
[17] G. S. Hanan, J.-M. Lehn, N. Kyritsakas, J. Fischer, *J. Chem. Soc., Chem. Commun.* **1995**, 765–766.
[18] D. M. Bassani, J.-M. Lehn, G. Baum, D. Fenske, *Angew. Chem.* **1997**, *109*, 1931–1933; *Angew. Chem. Int. Ed. Engl.* **1997**, *36*, 1845–1847.
[19] M. Ohkita, J.-M. Lehn, G. Baum, D. Fenske, *Chem. Eur. J.* **1999**, *5*, 3471–3481.
[20] a) K. E. Plass, K. Kim, A. J. Matzger, *J. Am. Chem. Soc.* **2004**, *126*, 9042–9053; b) K. Kim, K. E. Plass, A. J. Matzger, *Langmuir* **2005**, *21*, 647–655.
[21] W. Mamdouh, H. Uji-i, A. E. Dulcey, V. Percec, S. D. Feyter, F. C. D. Schryver, *Langmuir* **2004**, *20*, 7678–7685.

Received: January 20, 2005
Published Online: May 27, 2005

 © 2005 Wiley-VCH Verlag GmbH & Co. KGaA, Weinheim

Characterization by NMR Spectroscopy, X-ray Analysis and Cytotoxic Activity of the Ruthenium(II) Compounds $[RuL_3](PF_6)_2$ (L = 2-Phenylazopyridine or *o*-Tolylazopyridine) and $[RuL'_2L'']](PF_6)_2$ (L′, L′′ = 2-Phenylazopyridine, 2,2′-Bipyridine)

Anna C. G. Hotze,[a,c] Erwin P. L. van der Geer,[a] Huub Kooijman,[b] Anthony L. Spek,[b] Jaap G. Haasnoot,[a] and Jan Reedijk*[a]

Keywords: Ruthenium / Tris(chelate) complexes / 2D NMR / Cytotoxicity

Tris(ligand) complexes $[RuL_3](PF_6)_2$ (L = 2-phenylazopyridine or *o*-tolylazopyridine) and mixed ligand $[RuL'_2L'']](PF_6)_2$ (L′ and L′′ are 2-phenylazopyridine or 2,2′-bipyridine) have been synthesized, structurally characterized and investigated for cytotoxic activity. These complexes are important to study the hypothesis that the compound α-$[Ru(azpy)_2Cl_2]$ (azpy = 2-phenylazopyridine) exhibits a high cytotoxicity due to its two *cis* chloride ligands, which might be exchanged for biological targets as DNA. Molecular structures of *mer*-$[Ru(azpy)_3](PF_6)_2$ (**1**) and *mer*-$[Ru(tazpy)_3](PF_6)_2$ (**5**) (tazpy = *o*-tolylazopyridine) have been determined by X-ray diffraction. Series of complexes $[RuL_3](PF_6)_2$ and $[RuL'_2L'']](PF_6)_2$ show interesting NMR spectroscopic data; e.g. the spectrum of *mer*-$[Ru(azpy)_3](PF_6)_2$ (**1**) shows extremely broadened resonances at room temp. but sharpened resonances at low temperature. In the ^1H NMR spectra of compounds $[Ru(azpy)_2(bpy)]^{2+}$ and $[Ru(bpy)_2(azpy)]^{2+}$ (bpy = 2,2-bipyridine), respectively, less broadened (room temp.) or completely sharp resonances (room temp.) occur in comparison to **1** (under same conditions). By selecting the right temperature and/or concentration, NMR spectra of these series of compounds have been resolved using 2D COSY and NOESY NMR spectroscopy. Remarkably, the cytotoxicity data against a series of human tumor cell lines (A498, EVSA-T, H226, IGROV, M19, MCF-7 and WIDR) show a moderate cytotoxicity for these series of tris(ligand) complexes. So, even though no chloride ligands are present in these tris(ligand) complexes, a considerable cytotoxic activity is observed. This would imply that the 2-phenylazopyridine ruthenium(II) complexes act by a completely different mechanism than the well-known cisplatin. This finding is important, because an anticancer compound acting via a different mechanism is a prerequisite in designing new anticancer drugs.

(© Wiley-VCH Verlag GmbH & Co. KGaA, 69451 Weinheim, Germany, 2005)

Introduction

The dichlorobis(2-phenylazopyridine)ruthenium(II) complexes, $[Ru(azpy)_2Cl_2]$ are under renewed investigation due to their cytotoxic activity in a panel of human tumor cell lines.[1,2] In particular the α configuration (Figure 1, α indicating the pairs of coordinating Cl, Npy and Nazo atoms in a mutual *cis*, *trans*, *cis* orientation) of the $[Ru(azpy)_2Cl_2]$ complexes is the most promising isomer, as this isomer displays a very high cytotoxicity, stability and a reasonable solubility.[1,2] The mechanisms underlying the cytotoxicity of the $[Ru(azpy)_2Cl_2]$ complexes and in particular of the α-$[Ru(azpy)_2Cl_2]$ are not known yet. In analogy to cisplatin[3] it has been hypothesized that two labile *cis* chloride ligands contribute to the overall activity of the compound, as in the tumor cell these labile chloride ligands will be replaced by water ligands and subsequently replaced by the nucleotides of the DNA. To confirm or reject this hypothesis it was decided to replace the chloride ligands of the *cis*-$[Ru(azpy)_2Cl_2]$ complexes by a third azpy or bpy ligand, unable to dissociate, and investigate this series tris(ligand)rutheni-

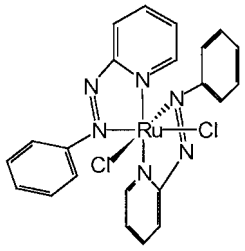

Figure 1. Schematic representation of the compound α-$[Ru(azpy)_2Cl_2]$.

[a] Leiden Institute of Chemistry, Gorlaeus Laboratories, Leiden University,
P. O. Box 9502, 2300 RA Leiden, The Netherlands
[b] Bijvoet Center for Biomolecular Research, Crystal and Structural Chemistry, Utrecht University,
Padualaan 8, 3584 CH, Utrecht, The Netherlands
[c] Current address: Bijvoet Center of Biomolecular Research, Department of NMR Spectroscopy, Utrecht University,
Padualaan 8, 3584 CH, Utrecht, The Netherlands
Supporting information for this article is available on the WWW under http://www.eurjic.org or from the author.

um(II) compounds for their cytotoxicity. This will result in a series of compounds, which will give more insights in the structure-activity relationships of these type of complexes.

Perhaps the most frequently considered binding interaction of heavy metals with DNA is that of coordinative binding to the bases of the DNA.[4] In addition to this interaction, intercalation is a common mode of association of small molecules with DNA; a flat aromatic heterocyclic moiety inserts and stacks in between the DNA base pairs.[4] Already in 1974 Lippard and co-workers[5,6] determined that platinum(II) complexes containing an aromatic heterocyclic ligand, such as terpyridine, could intercalate in DNA. This intercalation is not restricted to completely flat square-planar complexes, but partial intercalation of ligands coordinated to octahedral metal centers is also possible.[7] A ruthenium compound very thoroughly studied for its interaction with DNA is the tris(phenanthroline)ruthenium(II) complex. Depending on its enantiomeric form it binds to DNA by two non-coordinative modes, one described as a surface- or groove-bound interaction in the minor groove of the helix and the other appearing to be an intercalative interaction in the major groove of the helix.[4,7–9] However, the exact DNA binding mode of even a simple species like $[Ru(phen)_3]^{2+}$ remains an issue of debate.[10]

The compound $[Ru(azpy)_3](PF_6)_2$ theoretically exists in two different isomeric forms disregarding ΔΛ enantiomerism, i.e. the *mer* and *fac* isomers (Figure 2). The symmetry properties of the two isomers are markedly different; *fac*-$[Ru(azpy)_3](PF_6)_2$ belongs to the C_3 point group and hence has three equivalent azpy ligands. The *mer* isomer on the other hand is of C_1 symmetry, and all azpy ligands are inequivalent. The *fac* isomer formation of $[Ru(azpy)_3]^{2+}$ appears unlikely, also because previous studies have reported[11,12] that the *fac* isomer of $[Ru(azpy)_3]^{2+}$ is sterically unfavorable due to crowding of the three phenyl groups.

Several papers report the synthesis of $[Ru(azpy)_3]^{2+}$-like complexes. The first described[13] synthesis of $[Ru(azpy)_3]^{2+}$ dates from 1982; $[Ru(azpy)_3](PF_6)_2$ was synthesized using azpy and a crude mixture of isomers of $[Ru(azpy)_2Cl_2]$ with one isomer (probably α) in excess. The product is described as "a mixture" which has been characterized by IR and UV/Vis, which unfortunately does not say anything about the possible obtained *mer* or *fac* isomer(s). A one-pot synthesis using $RuCl_3$ and $[Ag(azpy)_2]^+$ as synthon has also been reported, but in this paper the possibility of the formation of both *fac* and *mer* isomers was not even discussed.[14] A recent publication appeared[11] after the present experimental work was carried out and showed the crystal structure of *mer*-$[Ru(azpy)_3](ClO_4)_2$. Except this crystal structure only a few more crystal structures of the type $[M(azpy)_3]^{n+}$ (with M any metal) have been reported, i.e. the rhenium structure[15] *fac*-$[Re(azpy)_3](ClO_4)$, the iron compound[16] $[Fe_2(CO)_2(4\text{-}CH_3\text{-}2\text{-phenylazopyridine})_3]$, the compound[11] *mer*-$[Ru(HL)_3](ClO_4)_2$ {HL = 2-[(4-(methoxyamino)phenyl)azopyridine} and the rhenium compound[17] *fac*-$[Re(apy)_3]I$ (apy = 2,2′-azobipyridine). Another type of tris(ligand) complexes are the mixed ligand complexes of the type $RuLL'_2$ (with L and L′ both didentate ligands with one of them containing the azo functionality) of which the crystal structures of $[Ru(bpy)(MeaaiMe)_2](ClO_4)_2$ [MeaaiMe = 1-methyl-2-(*p*-methylazo)imidazole], $[Ru(bpy)_2(p\text{-}MeaaiCH_2ph)](ClO_4)_2\cdot H_2O$, $[Ru(phen)(HaaiMe)_2](ClO_4)_2$, $[Ru(azpy)_2(H_2biim)](ClO_4)_2\cdot 3CH_2Cl_2$ (H_2Biim = 2,2′-biimidazole) and $[Ru(HL)(bpy)_2](ClO_4)_2$ {HL = 2-[(4-(arylamino)phenyl)azopyridine} are nice examples[11,18–21] of compounds structurally related to the series of compounds

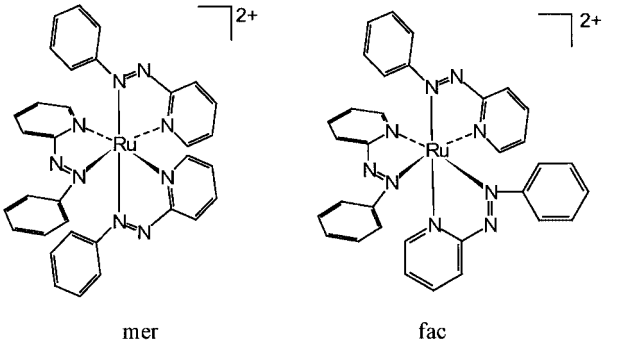

Figure 2. *mer*- and *fac*-$[Ru(azpy)_3]^{2+}$ (only Δ isomers shown).

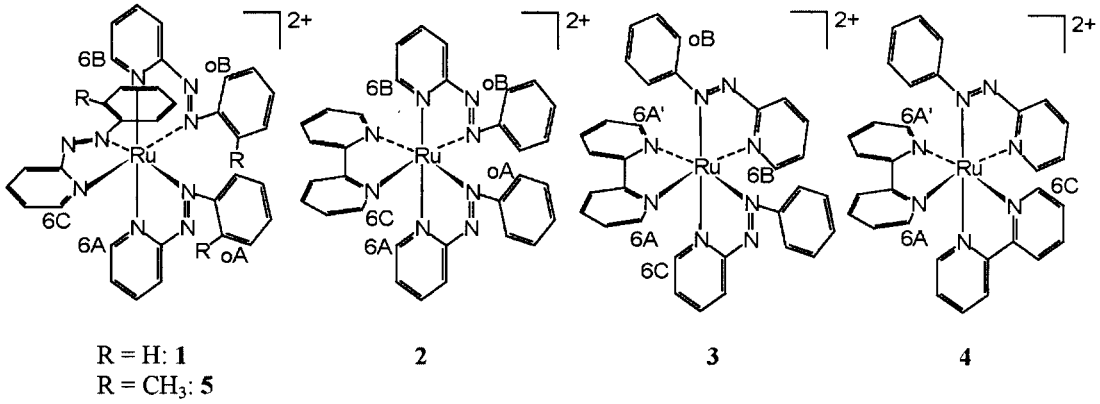

Figure 3. A series of tris(ligand) ruthenium(II) complexes (from left to right): mer-$[Ru(azpy)_3](PF_6)_2$ (**1**) and *mer*-$[Ru(tazpy)_3](PF_6)_2$ (**5**), α-$[Ru(azpy)_2(bpy)](PF_6)_2$ (**2**), β-$[Ru(azpy)_2(bpy)](PF_6)_2$ (**3**) and $[Ru(azpy)(bpy)_2](PF_6)_2$ (**4**); some hydrogen atoms, important for NMR assignments, are indicated.

 © 2005 Wiley-VCH Verlag GmbH & Co. KGaA, Weinheim

described in this paper. Till now, no 2D NMR characterization or cytotoxicity tests have ever been reported on any kind of above mentioned tris(ligand) complexes.

To design new anticancer drugs and to develop structure-activity relationships for 2-phenylazopyridine ruthenium(II) complexes, a series (Figure 3) of newly synthesized tris(ligand) ruthenium(II) complexes, i.e. *mer*-[Ru(azpy)$_3$](PF$_6$)$_2$ (**1**), α-[Ru(azpy)$_2$(bpy)](PF$_6$)$_2$ (**2**), β-[Ru(azpy)$_2$(bpy)](PF$_6$)$_2$ (**3**), [Ru(azpy)(bpy)$_2$](PF$_6$)$_2$ (**4**) and *mer*-[Ru(tazpy)$_3$](PF$_6$)$_2$ (**5**, tazpy = *o*-tolylazopyridine) are synthesized and characterized by 2D NMR spectroscopy. X-ray diffraction analysis of **1** and **5** have been performed. The synthesis of these complexes is known from early work,[12,13,22] but the full NMR characterization using variable temperature NMR and 2D NMR techniques and especially the correlations made to antitumor research are new. The cytotoxicity of the complexes will be discussed in relation to the very cytotoxic dichlorobis(azpy)ruthenium(II) complexes.

Results and Discussion

General Considerations

One of the syntheses described in this paper is the synthesis of *mer*-[Ru(azpy)$_3$](PF$_6$)$_2$ from α-[Ru(azpy)$_2$(NO$_3$)$_2$] and azpy. Since only the *mer* isomer of [Ru(azpy)$_3$](PF$_6$)$_2$ has two azpy ligands positioned according to the α configuration (pairs of pyridine N atoms *trans* and Nazo atoms *cis*) this synthetic route theoretically excludes *fac* isomer formation, assuming that no isomerization[23] takes place. Moreover, *fac* isomer formation remains unlikely, also because previous studies have reported[11,12] that the *fac* isomer of [Ru(azpy)$_3$](PF$_6$)$_2$ is sterically unfavorable due to crowding of the three phenyl groups (vide infra). As anticipated only pure *mer*-[Ru(azpy)$_3$](PF$_6$)$_2$ was obtained.

Crystal Structures of 1 and 5

The cations of the crystal structures of *mer*-[Ru(azpy)$_3$](PF$_6$)$_2$ (**1**) and *mer*-[Ru(tazpy)$_3$](PF$_6$)$_2$ (**5**) are redrawn in Figure 4. For clarity, only the Λ enantiomers are shown, while the unit cell actually contains the Λ and Δ enantiomer. Furthermore the two PF_6^- counterions of which one is disordered have been omitted. The X-ray data of *mer*-[Ru(azpy)$_3$](ClO$_4$)$_2$ have been published by Das et al,[11] but has a different crystal system (monoclinic) and space group ($P2_1/c$) than **1** (resp. triclinic and $P\bar{1}$). However, the bond lengths of the cation of *mer*-[Ru(azpy)$_3$](ClO$_4$)$_2$ show a great deal of similarity with **1**. It is interesting to compare the X-ray data of **1** with *mer*-[Ru(tazpy)$_3$](PF$_6$)$_2$ (**5**) (see Figure 4). Crystallographic data of **1** and **5** are listed in Table 1. Selected bond lengths and angles of **1** and **5** are listed in Table 2 and Table 3, respectively.

In order to draw a comparison of the tris(ligand) complexes **1** and **5** with the related bis(azpy) complexes, like α-[Ru(azpy)$_2$Cl$_2$], α-[Ru(azpy)$_2$(NO$_3$)$_2$] and β-[Ru(azpy)$_2$Cl$_2$] (β indicating coordinating pairs Cl, Npy, Nazo in mutual *cis*, *cis cis* orientation), some distances within these complexes are listed in Table 4. In the crystal structures[24,25] of the bis(azpy) complexes the Ru–Nazo bonds were found to be significantly shorter than the Ru–Npy bonds. These short Ru–Nazo bonds can be attributed to substantial π-back bonding of the ruthenium through an azo nitrogen [Ru(t_{2g})-π*azpy]. In complexes **1** and **5** the lengths of the Ru–Nazo bonds are, on average, more similar to the Ru–Npy bond lengths. Therefore, no significant π-back bonding effects on the coordination bonds of **1** and **5** are visible. This is probably caused by a greater competition for Ru(t_{2g}) electrons in the tris(ligand) complexes. A *trans* N(azo)–M–N(azo) arrangement is quite rare as can be directly seen from the fact that from the five isomers of [Ru(azpy)$_2$Cl$_2$] the less common isomers, i.e.[26] δ-[Ru(azpy)$_2$Cl$_2$] and the

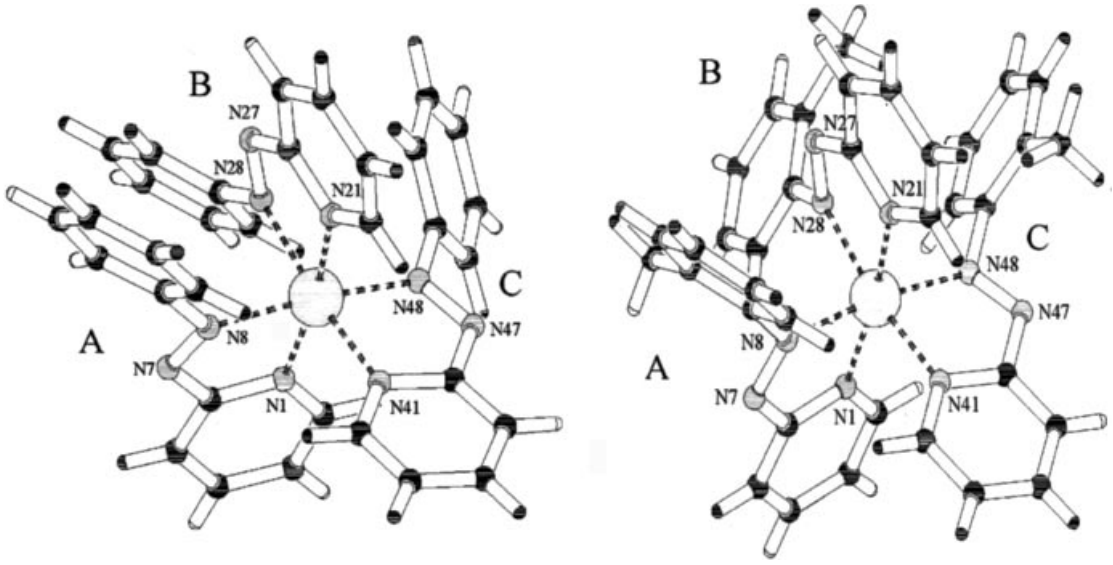

Figure 4. Crystal structures of **1** (left) and **5** (right). Only the Λ isomers are shown. To facilitate discussion the three (t)azpy ligands are denoted with A, B and C.

 © 2005 Wiley-VCH Verlag GmbH & Co. KGaA, Weinheim

Table 1. Crystallographic data for crystal structure determinations of **1** and **5**.

Compound	**1**	**5**
Empirical formula	$C_{33}H_{27}N_9Ru{\cdot}2PF_6$	$C_{36}H_{33}N_9Ru{\cdot}2PF_6$
Formula mass	940.65	982.72
Crystal system	triclinic	triclinic
Space group	$P\bar{1}$ (No. 2)	$P\bar{1}$ (No. 2)
a [Å]	9.4164(12)	10.8271(10)
b [Å]	10.1664(12)	11.9490(10)
c [Å]	19.230(3)	15.866(2)
α [°]	86.606(10)	95.902(6)
β [°]	88.751(10)	99.356(6)
γ [°]	88.105(10)	93.930(9)
V [Å]^3	1836.3(4)	2007.0(4)
D_c [g cm^{-3}]	1.701	1.626
Z	2	2
μ (Mo-K_α) [mm^{-1}]	0.615	0.567
Crystal color	dark red	black
Crystal size [mm]	$0.1\times0.3\times0.3$	$0.10\times0.25\times0.35$
Total data	23859	43393
Total unique data	6474	9124
R_{int}	0.035	0.0455
No. of refined parameters	537	544
R_1[a] [$I > 2\sigma(I)$]	0.0312 [5629 refl.]	0.0271 [7824 refl.]
wR_2[b] (all data)	0.0732	0.0631
GoF	1.074	1.032

[a] $R_1 = \Sigma||F_o| - |F_c||/\Sigma|F_o|$. [b] $wR_2 = [\Sigma\,[w(F_o^2 - F_c^2)^2]/\Sigma\,[w(F_o^2)^2]]^{1/2}$.

Table 2. Selected bond lengths [Å] and angles [°] of **1**.

Ru(1)–N(1)	2.067(2)	N(1)–Ru(1)–N(28)	99.69(8)
Ru(1)–N(8)	2.0776(19)	N(1)–Ru(1)–N(41)	90.45(8)
Ru(1)–N(21)	2.046(2)	N(1)–Ru(1)–N(48)	95.65(8)
Ru(1)–N(28)	2.049(2)	N(8)–Ru(1)–N(21)	96.19(8)
Ru(1)–N(41)	2.053(2)	N(8)–Ru(1)–N(28)	80.30(8)
Ru(1)–N(48)	2.0216(19)	N(8)–Ru(1)–N(41)	103.65(8)
N(7)–N(8)	1.278(3)	N(8)–Ru(1)–N(48)	170.94(8)
N(27)–N(28)	1.281(3)	N(21)–Ru(1)–N(28)	76.16(8)
N(47)–N(48)	1.282(3)	N(21)–Ru(1)–N(41)	93.95(8)
		N(21)–Ru(1)–N(48)	92.86(8)
		N(28)–Ru(1)–N(41)	169.79(8)
N(1)–Ru(1)–N(8)	75.30(8)	N(28)–Ru(1)–N(48)	101.91(8)
N(1)–Ru(1)–N(21)	171.16(8)	N(41)–Ru(1)–N(48)	75.68(8)

Table 3. Selected bond lengths [Å] and angles [°] of **5**.

Ru(1)–N(1)	2.0651(15)	N(1)–Ru(1)–N(28)	102.28(6)
Ru(1)–N(8)	2.0278(14)	N(1)–Ru(1)–N(41)	85.51(6)
Ru(1)–N(21)	2.0500(15)	N(1)–Ru(1)–N(48)	100.02(6)
Ru(1)–N(28)	2.0695(15)	N(8)–Ru(1)–N(21)	95.11(6)
Ru(1)–N(41)	2.0665(14)	N(8)–Ru(1)–N(28)	90.04(6)
Ru(1)–N(48)	2.0379(14)	N(8)–Ru(1)–N(41)	95.57(6)
N(7)–N(8)	1.282(2)	N(8)–Ru(1)–N(48)	171.73(6)
N(27)–N(28)	1.285(2)	N(21)–Ru(1)–N(28)	76.18(6)
N(47)–N(48)	1.280(2)	N(21)–Ru(1)–N(41)	96.85(6)
		N(21)–Ru(1)–N(48)	88.88(6)
		N(28)–Ru(1)–N(41)	170.84(6)
N(1)–Ru(1)–N(8)	76.08(6)	N(28)–Ru(1)–N(48)	97.95(6)
N(1)–Ru(1)–N(21)	171.11(6)	N(41)–Ru(1)–N(48)	75.73(6)

probable existing[27] ε-$[Ru(azpy)_2Cl_2]$ (δ indicating Cl, Npy and Nazo, *trans*, *trans*, *trans* and ε has the pairs of Cl, Npy and Nazo *cis*, *cis*, *trans*) have this *trans* Nazo-M–Nazo grouping. Also in the meridional tris(ligand) complexes this *trans* N(azo)–M–N(azo) arrangement occurs, e.g. the iron compound[16] $[Fe_2(CO)_2(4\text{-}CH_3\text{-}2\text{-phenylazopyridine})_3]$ and the compound[11] *mer*-$[Ru(azpy)_3](ClO_4)_2$. Especially in the *trans* Nazo–M–Nazo arrangement the two azo bonds are thought to compete for the back bonding of the Ru^{II} (4d) t2g electron density, resulting in, in theory, relatively long Ru–Nazo bond lengths.

Table 4. Comparison of selected bond lengths [Å] from the crystallographic data[24,25] of α-$[Ru(azpy)_2Cl_2]$, α-$[Ru(azpy)_2(NO_3)_2]$, β-$Ru(azpy)_2Cl_2]$, **1** and **5**. Distances are reported in Å, with standard uncertainties in parentheses. β-$Ru(azpy)_2Cl_2$ has two independent molecules.

	Ru–Naza	Ru–Npy	Naza-Naza
α-$Ru(azpy)_2Cl_2]$	1.977(4)	2.045(4)	1.279(7)
	1.984(4)	2.051(4)	1.283(6)
α-$Ru(azpy)_2(NO_3)_2]$	2.014(4)	2.031(4)	1.282(5)
	1.960(4)	2.059(4)	1.270(5)
β-$Ru(azpy)_2Cl_2]$ (mol, 1)	1.960(9)	2.059(9)	1.30(1)
	2.003(9)	2.020(9)	1.29(1)
β-$Ru(azpy)_2Cl_2]$ (mol, 2)	1.958(9)	2.069(9)	1.31(1)
	1.96(1)	2.028(9)	1.30(2)
1	2.0776(19)	2.067(2)	1.278(3)
	2.049(2)	2.046(2)	1.281(3)
	2.0216(19)	2.053(2)	1.282(3)
5	2.0278(14)	2.0651(15)	1.282(2)
	2.0695(15)	2.0500(15	1.285(2)
	2.0379(14)	2.0665(14)	1.280(2)

^{1}H NMR Characterization of the Tris(ligand)ruthenium(II) Complexes

General Information

At room temperature, the resonances of the tris(ligand) complexes **1**,**2** and **5** were found to be significantly broadened at room temperature. The variable-temperature ^{1}H NMR spectra in $[D_6]$acetone of **1** and **2** are depicted in Figure 5. This broadening seems to be dependent on both concentration and temperature.

For example compound **1** shows really broad resonances at room temperature but cooling the sample results in marked sharpening of the resonances (Figure 5). Till now, no thorough NMR characterization has been reported about *mer*-$[Ru(azpy)_3]^{2+}$ type of compounds. For example the reported ^{1}H NMR spectrum of the compound[12] *mer*-$[Ru(tap)_3]^{2+}$ (tap = *m*-tolylazopyridine) shows two methyl resonances and the absence of one more methyl signal (as all three ligands in the *mer* isomer should be distinguishable) has been explained by the fact that in practice two rings become equivalent. By using pure β-$[Ru(tap)_2(H_2O)_2]^{2+}$ the occurrence of both *mer* and (a small amount of) *fac*-$[Ru(tap)_3]^{2+}$ have been reported which have been characterized by ^{1}H NMR spectroscopy.[12] However, this NMR characterization was not very clear. Only the high field region of the ^{1}H NMR spectrum was shown, which is quite inconvenient with respect to the broadening of especially the aromatic resonances observed for this type of complexes (vide infra).[12] Also the recent publication of Das et al. does not show any NMR spectroscopic data of *mer*-$[Ru(azpy)_3]$-

 © 2005 Wiley-VCH Verlag GmbH & Co. KGaA, Weinheim

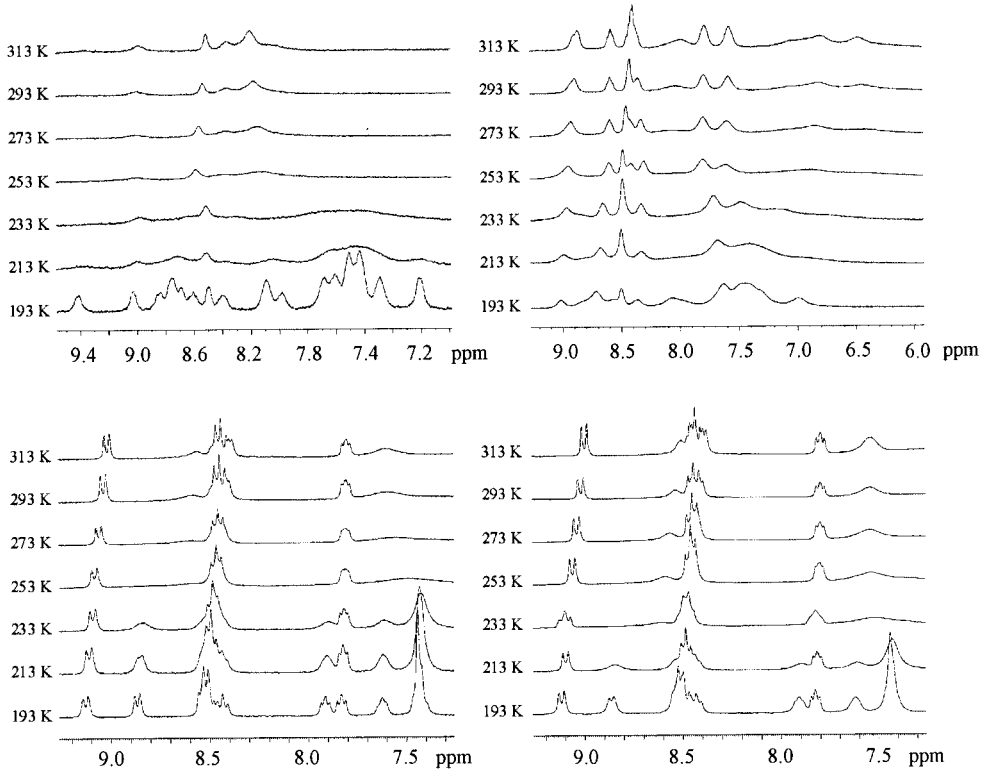

Figure 5. Temperature-dependent ^{1}H NMR spectra (300 MHz) of **1** (upper spectra) and **2** (lower spectra) at 2 mM (left) and 6 mM (right) in [D_6]acetone.

$(ClO_4)_2$. In general, for tris(ligand) complexes with 2-phenylazopyridine- or 2-phenylazoimidazole-like ligands only ^{1}H NMR chemical shift data are mentioned,[19–21,28] without performing 2D NMR experiments and no broadening is mentioned. In our opinion the ^{1}H NMR spectroscopic data of these very complicated spectra[19–21,28] are questionable. Therefore, an extensive description of the assignment of the tris(ligand) complexes mentioned in this paper using several 2D NMR techniques seems to be useful.

The ^{1}H NMR chemical shift values (600 MHz) of the complexes **1**, **2**, **3** and **4** (samples of **1** and **2** recorded at low temperatures) are listed in Table 5 (the resonances belonging to the azpy ligands are denoted with A, B or C, e.g. 6A or *o*B; the resonances belonging to the bpy ligands are denoted by only a number). The assignment of *mer*-[Ru(tazpy)$_3$](PF$_6$)$_2$ has not been attempted, as the broadening in this case was even more complicated probably due to additional steric hindrance due to the methyl group of the phenyl rings and under no conditions sharp resonances were observed. The assignment of the resonances of **1** at low temperature will be described in detail to show the common way of assigning such complicated spectra. It

Table 5. ^{1}H NMR chemical shift values (600 MHz) of **1**, **2**, **3** and **4** in [D_6]acetone. The spectrum of **1** has been recorded recorded at 183 K, 2 at 195 K and **3** and **4** at room temperature.

Compound (ligand)	azpy bpy 6 6	5 5	4 4	3 3	*o* 6′	*m* 5′	*p* 4′	3′
1 (A)	8.70	7.99	8.40	8.78	7.53	7.44	7.68	
(B)	8.51	8.10	8.62	8.87	7.02	7.29	7.50	
(C)	9.06	8.08	8.75	9.44	7.42	7.61	7.71	
2 (A = B)	8.55	7.92	8.44	8.88	7.43	7.45	7.63	
(bpy)	8.53	7.83	8.50	9.14				
3 (bpy)	8.29	7.70	8.17	8.47	7.63	7.82	8.43	8.67
(B)*	8.26	7.91	8.65	9.21	7.80	7.15	7.39	
(C)*	8.21	8.04	8.69	9.15	7.36	7.59	7.70	
4 (bpyA)	8.05	8.13	7.56	8.51	7.72	8.37	7.73	8.65
(bpyC)	8.39	8.39	7.75	8.96	8.02	8.39	7.70	8.99
(azpyB)	8.29	8.44	7.84	9.02	7.18	7.23	7.43	

*pyridine ring B and C cannot be distinguished.

 © 2005 Wiley-VCH Verlag GmbH & Co. KGaA, Weinheim

makes in a beautiful way use of the fact that in the compound *mer*-$[Ru(azpy)_3](PF_6)_2$, the azpy ligands are two-by-two in mutual α, β and ε configurations as shown in the bis(chelate) complexes $[Ru(azpy)_2Cl_2]$ and subsequently these configurations have known[26] interligand NOE cross-peaks. The use of these known geometries of $[Ru(azpy)_2Cl_2]$ complexes plays a key role in the assignment of compound **1.**

NMR Characterization of 1

The ^1H NMR spectrum of **1** (600 MHz) at low temperature and low concentration shows 16 well-resolved resonances some of which appear to be multiplet signals due to overlap of resonances (Figure S1, supporting information, for supporting information see also the footnote on the first page of this article). As **1** has C_1 symmetry, all three azpy ligands are inequivalent, resulting in 21 resonances, which have been fully assigned using 2D COSY and NOESY NMR spectroscopy.

First, from 2D COSY NMR the three sets of azpy pyridine signals and three sets of azpy phenyl signals have been distinguished. As in the NMR spectra only three sets of phenyl signals appear, the phenyl rings are assumed to rotate fast on the NMR time scale. The H6 protons of the azpy ligands were easily recognised from the smaller *J* coupling in comparison to the J coupling of the H3 atoms and appear at δ = 8.51, 8.70 and 9.06 ppm. The NOESY spectrum (Figure 6) shows several NOE cross peaks (Table S1, Supporting Information), i.e. one *o*-*o* coupling, one coupling between two H6 hydrogen atoms and four cross peaks between H6 and *ortho* resonances. The *mer*-$[Ru(azpy)_3]^{2+}$ backbone consists of pairs of azpy ligands of the isomeric bis(ligand) complexes, α-$Ru(azpy)_2$ (in Figure 4 these have been denoted as azpy ligand A and B), β-$Ru(azpy)_2$ (in Figure 4 these have been denoted as B and C) and ε-$Ru(azpy)_2$ (azpy ligands C and A in Figure 4). So because the azpy ligands A and B of **1** actually represent the α configuration, A6-*o*B and B6-*o*A NOEs are expected[24,26] in the 2D NOESY spectrum of **1**. Likewise, ligands B and C in **1** are expected[26] to display B6–C6 and *o*B-*o*C NOEs. The synthesis of the ε isomer, ε-$[Ru(azpy)_2Cl_2]$ has been reported in a short letter,[27] but no NMR spectroscopic data have been presented. Therefore the crystal structure of **1** is used to determine which NOE cross peaks are to be expected for this ε configuration. According to distances in the crystal structure of **1** the unknown ε-$Ru(azpy)_2$ backbone should give rise to 6C-*o*A (average distance of H46–H10 and H44–H14 = 4.0 Å) and 6A-*o*C cross peaks (average distance of H6–H47 and H6–H54 = 3.7 Å).

A close look in the NOESY spectrum shows that one of the H6 resonances (at, 8.70 ppm) gives cross peaks to two *ortho* signals. These NOEs unambiguously assign the resonance at δ = 8.70 ppm to correspond to the H6A atom giving cross peaks to *o*B and *o*C. In fact, the NOE 6A-*o*B is expected, as this is the known cross peak for the α configuration. The 6A-*o*C is a cross peak apparently occurring in the ε configuration, as was also likely from the crystal structure. How to discriminate between the *o*B and *o*C resonances? One of these *ortho* resonances is shifted upfield related to the other. The *o*B hydrogens are positioned within the shielding cone of pyridine ring A. For this reason the high-field resonance at δ = 7.02 ppm can be assigned to the *o*B hydrogens. A cross peak occurs between *o*B and *o*C in agreement with the β configuration. Two H6 resonances remain: the H6 resonances at δ = 8.51 and 9.06 ppm, which present a cross peak between each other. This 6B-6C NOE perfectly agrees with the β-$Ru(azpy)_2$ configuration. The signal at δ = 8.51 ppm is assigned to 6B, as this resonance is within the shielding cone of the pyridine ring of ligand C and so should appear at higher field.

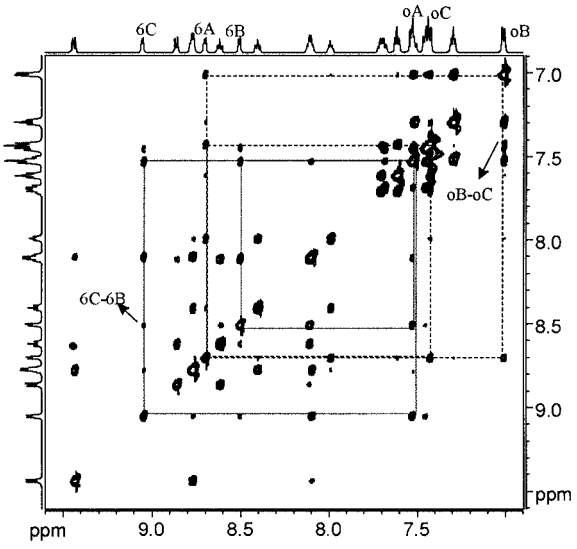

Figure 6. ^1H-^1H NOESY spectrum (600 MHz) and some assignments of the aromatic region of **1** in $[D_6]$acetone, 183 K. The dashed lines indicate the 6A-oB and 6A-oC NOEs. The dotted lines indicate the oA-6C and oA-6B NOEs. Arrows indicate the NOEs 6C-6B and oB-oC.

Two other NOE cross peaks observed in the 2D NOESY spectrum are the 6B-*o*A and 6C-*o*A NOEs. The first one is due to the α configuration of the ligands A and B, the second one is due to the ε configuration of ligands C and A.

NMR Characterization of 2

Interestingly, the ^1H NMR spectrum of **2** at room temperature shows partly sharp and partly broadened resonances (Figure 5). Cooling the NMR sample to 195 K all resonances sharpen. The ^1H NMR spectrum of **2** at 195 K shows only two sets of pyridine rings and one set of phenyl ring signals. Due to the C_2 axis present in this complex, the two azpy ligands are equivalent (A = B) and even the two pyridine rings of the bpy ligand are indistinguishable (see Figure 4). It appears to be difficult to assign the two sets of pyridine rings to either the bpy or the azpy ligand. An indication to assign properly the pyridine rings to either the azpy or the bpy ligand, is that the resonances of one pyridine ring are broadened at room temperature, whereas the other set of pyridine resonances is sharp at room temperature (Figure 5). As less broadening occurs introducing a

 © 2005 Wiley-VCH Verlag GmbH & Co. KGaA, Weinheim

bpy ligand in these $[RuL_2L']^{2+}$ complexes (vide infra) it seems reasonable to assume that the broadened resonances correspond to the azpy ligand. Therefore, from the VT NMR studies (Figure 5) it follows that the sharp (at all temperatures) resonance at around 9.1 ppm corresponds to the H3 of bpy. Using COSY connectivities the other resonances are assigned.

The two most important NOE cross peaks that appear in the spectrum of **2** are (Figure S2, supp. inf.): 1) A NOE between the H6 resonance of one azpy ligand and the *ortho* resonance of the other azpy ligand (H6A–*o*B=H6B–*o*A) as A and B are forming the α configuration, and 2) a NOE between the H6 resonance of the bpy ligand and the *ortho* resonance of azpy (H6C-*o*A) which is a NOE due to the ε configuration (vide supra).

NMR Characterization of 3

The ^{1}H NMR assignment of β-$[Ru(azpy)_2(bpy)](PF_6)_2$ (**3**) is based on almost the same reasonings as used for **1**. The ^{1}H NMR of **3** (600 MHz) at room temperature shows all sharp resonances. However, also for this compound some signal broadening was observed at certain concentrations and temperatures, albeit not as extensively broadened as for example compound **1** (data not shown). Compound **3** consists again of pairs of ligands derived from known bis(ligand) moieties (Figure 3), which again can perfecly be used to assign the resonances properly. Ligand A and B form the α-Ru(azpy)(bpy) moiety. The 1D and 2D NOE data of α-$[Ru(azpy)(bpy)Cl_2]$ are just recently published.[29] Ligand B and C form the β-$[Ru(azpy)_2]$ moiety. Pyridine ring A (without prime) and ligand C form part of the ε-$Ru(azpy)_2$ backbone. In the 2D NOESY NMR spectrum (Figure S3, supp. inf.) one of the H6 resonances gives NOE cross peaks to two *ortho* resonances. These NOEs are assigned as the 6A-*o*B and 6A-*o*C NOEs in correspondence with the known cross peaks (H6-*o*) of the α-Ru(azpy)(bpy) moiety and ε-$Ru(azpy)_2$ configuration. Again the *o*B resonance is at higher field than the *o*C resonance as the *o*B hydrogens are in the shielding cone of pyridine ring A. Using the bpy H3-H3′ NOE, the other bpy pyridine ring can be assigned. The resonance 6A′ couples to two six resonances, i.e. 6B and 6C. As the chemical shifts of the protons 6B and 6C are almost identical they could not be assigned based on (de)shielding effects. Consequently, pyridine rings B and C could not be distinguished.

NMR Characterization of 4

The ^{1}H NMR of **4** shows all sharp resonances at room temperature and they remain sharp in the whole used temperature range. The ^{1}H-^{1}H 2D NOESY spectrum is shown in Figure S4, supp. inf. The H3-H3′ NOE of the bpy ligands has been used to assign the two bpy ligands. A simple ball and stick model shows that one of the bpy ligands has both its H6 hydrogen atoms in the shielding region of a pyridine ring, so the corresponding H6 resonances should both appear at high field. The other bpy ligand should have one H6 resonance at low field and one at high field (one H6 atom is in the shielding cone of a pyridine ring whereas the other H6 atom is above the azo bond, which gives less shielding). This allows the assignment of the resonances at δ = 8.05 and 7.72 ppm as H6A and H6A′ and the resonances at δ = 8.39 and 8.02 ppm as 6C and 6C′. Both H6C and H6A resonances give NOE cross peaks to the *ortho* resonance of the azpy ligand in agreement with the proposed structure of **4**.

Apparently, from the above-mentioned NMR spectroscopic data it is clear that the assignment of these kind of tris(ligand) complexes is quite complicated and the ^{1}H NMR assignment in literature of these kind of complexes is confusing, incomplete and sometimes erroneous.[19,21]

Variable Temperature and Concentration Studies

Although as yet not studied in detail, the concentration and temperature-dependent NMR spectra (300 MHz) show interesting differences between the complexes **1**, **2**, **3** and **4**. The temperature series of **1** at the lower concentration (Figure 5) results in sharper resonances at 193 K than in case of the higher concentration. The series of ^{1}H NMR spectra at various temperatures of **2** show less broadening in comparison to **1** and the differences between the two concentrations of **2** seem smaller. Finally the series of spectra of **3** also do show some signal broadening, which is comparable to **2**; one set of sharp resonances and one set of broadened reasonances (data not shown). In general, the comparison of **1** with **2** and **3** lead to the suggestion that introducing a bpy ligand in such tris(ligand) complexes results in a more rigid structure and consecutively less broadening. This is in agreement with the fact that the complexes $[Ru(azpy)(bpy)_2](PF_6)_2$ and $[Ru(bpy)_3](PF_6)_2$ do not show any signal broadening. Signal broadening in NMR occurring for this type of tris(ligand)ruthenium(II) complexes is not known in literature. For example in case of the related complex $[Ru(abpy)_3]^{2+}$ [(abpy = 2,2-azobis(pyridine)] ^{1}H NMR spectra data are reported, but no broadening has been mentioned.[28]

One mechanism that may be responsible for signal broadening in (azpy)ruthenium complexes is sterically hindered rotations of one or more phenyl rings.[30] In theory this implies that upon cooling the sample during the NMR experiment, the phenyl ring rotation becomes slower on the NMR time scale and at the lowest temperatures it is possible to stop the phenyl ring rotation (on the NMR time scale). This would result in distinct resonances for the *o* and *m* protons on one side of the phenyl ring and the *o* and *m* protons on the other side. However, the fact that such distinct resonances were not observed for any of the azpy-containing (tris)ligand complexes indicates that hindered rotations of phenyl rings are not responsible for the observed signal broadening. However, hindered tolyl-ring rotations might still be present in *mer*-$[Ru(tazpy)_3](PF_6)_2$, since upon cooling and diluting the NMR sample of this compound, no conditions were found which resulted in sharp resonances.

 © 2005 Wiley-VCH Verlag GmbH & Co. KGaA, Weinheim

The fact that the broadening of the resonances of the tris(ligand) complexes is also dependent on concentration might suggest stacking or intermolecular interactions.

The possibility of ligand exchange/decoordination can be ruled out by the fact that no free ligand was observed at low temperatures and the fact that addition of free ligand did not influence the broadening of the signals.

Another explanation for the VT NMR results appears to lie in intramolecular rearrangements, which are known in the literature[31] to be able to result in NMR signal broadening. Nevertheless more research is needed to comprehend this phenomenon of signal broadening.

Cytotoxicity Tests

The complexes **1**, **2**, **3** and **4** have been tested for their cytotoxicity against a series of human tumor cell lines. The data are summarized in Table 6. Compound **1** shows in the cell lines EVSA-T and M19 quite a significant cytotoxicity, but in the other cell lines the IC_{50} values are moderate to low. Compound **2** exhibits in EVSA-T, M19 and MCF-7 a considerable cytotoxicity. Compound **3** displays only in the cell line M19 a considerable cytotoxicity and compound **4** still shows a considerable cytotoxicity in the cell lines EVSA-T and H226. Interesting to mention is that the compound $[Ru(bpy)_3](PF_6)_2$ does not show any cytotoxic effect under these circumstances (data not shown). It is important to note that the activity of these complexes cannot be caused by traces of starting materials, like for example α-$[Ru(tazpy)_2(NO_3)_2]$ or azpy. The former one shows an activity of approximately 8 μM[32] and the ligand azpy shows no cytotoxicity at all.[33] It is quite remarkable that this series of compounds **1**, **2**, **3** and **4** show a moderate cytotoxicity in some cell lines,[33] as these complexes do not have any anionic (chloride) ligands, to allow, after hydrolysis, coordination to DNA bases. This behavior might point to a class of very interesting ruthenium complexes acting by another mechanism than cisplatin and therefore opening the way to a new category of anticancer agents, agents which might be successful against cancer types where the old generation drugs appeared to be inactive. The activity of these tris(chelated) complexes might be caused by an intercalative interaction with DNA rather than a cisplatin-like covalent interaction with DNA. Interestingly just recently a publication appeared[34] concerning a series of tris(ligand) complexes $[Ru(L)_2(Y)]Cl_2$ with L bpy or phen and Y thiosemicarbazone-type of ligands. These complexes show a considerable antitumor activity in mice and therefore strengthening the fact that tris(ligand) complexes are a very important group of potential new ruthenium anticancer drugs.

Conclusions

Tris(ligand)ruthenium(II) azpy-like complexes show in many aspects interesting properties. The NMR spectroscopic data of the series of complexes $[RuL_3](PF_6)_2$ (L = 2-phenylazopyridine or *o*-tolylazopyridine) and $[RuL'_2L''](PF_6)_2$ (L′ and L′′ are 2-phenylazopyridine or 2,2′-bipyridine) show broadening of the resonances for especially the complexes **1**, **2** and **5**. This broadening appears to depend on temperature, concentration and steric hindrance within the complex. Choosing the right conditions, sharp resonances have been obtained and the complicated NMR spectra of these tris(ligand) complexes could be almost completely resolved. Especially the fact that these tris(chelated) complexes are build of pairs of known configurations (e.g. α-, β-, and ε-$Ru(azpy)_2$) with previously determined (2D) NMR spectroscopic data, allowed the assignment of almost all resonances of the tris(ligand) complexes.

The cytotoxicity data show that the complexes *mer*-$[Ru(azpy)_3](PF_6)_2$, α-$[Ru(azpy)_2(bpy)](PF_6)_2$, β-$[Ru(azpy)_2(bpy)](PF_6)_2$, and $[Ru(azpy)(bpy)_2](PF_6)_2$ have a moderate cytotoxicity in some particular cell lines. In general, the fact that these fully coordinated tris(chelated) complexes still show some activity, suggests intercalative properties responsible for eventual cell death. In conclusion, these complexes appear to act through another mechanism than the compound cisplatin, which indicates that in general these ruthenium 2-phenylazopyridine complexes are a very interesting class of anticancer complexes, conceivably being able to lead to a different type of anticancer drugs.

Experimental Section

Syntheses: The syntheses of the tris(ligand)ruthenium(II) complexes mentioned below are modifications of literature syntheses[12,13,22] for *mer*-$[Ru(azpy)_3]^{2+}$, $[Ru(azpy)_2(bpy)]^{2+}$ and $[Ru(azpy)(bpy)_2]^{2+}$ using *cis*-$[Ru(bpy)_2Cl_2]\cdot 2H_2O$ or α- and β-$[Ru(azpy)_2(NO_3)_2]$ as starting materials.[23,24,35]

***mer*-$[Ru(azpy)_3](PF_6)_2$ (1):** α-$[Ru(azpy)_2(NO_3)_2]$ (40.0 mg, $6.76\cdot10^{-5}$ mol) and azpy (37.4 mg, $2.04\cdot10^{-4}$ mol) were dissolved in water (5 mL) and methanol (5 mL). The red solution was refluxed for

Table 6. IC_{50} values [μM] of the tris(chelated) ruthenium complexes **1**, **2**, **3** and **4**.

Tested compound	A498	EVSTA-T	H226	IGROV	M19	MCF-7	WIDR
1	55.4	12.8	45.6	32.1	4.47	25.2	29.2
2	89.8	14.6	46.5	62.6	13.3	17.9	23.2
3	92.0	38.7	65.2	54.6	19.5	52.4	64.4
4	77.8	20.7	17.7	63.8	25.9	40.4	87.0
α-$[Ru(azpy)_2Cl_2]$	0.27	0.063	0.48	0.27	0.064	0.27	0.27
Cisplatin	7.5	1.4	10.9	0.6	1.9	2.3	3.2
5-Fluorouracil	1.1	3.7	2.6	2.3	3.4	5.8	1.7

 © 2005 Wiley-VCH Verlag GmbH & Co. KGaA, Weinheim

one hour, during which time the solution turned red-brown. After cooling to room temperature, a concentrated aqueous solution of NH_4PF_6 (240 mg) was added, which led to the precipitation of a brown product. The brown product was washed with water and dried with diethyl ether, resulting in a yield of 38.0 mg (75%). $C_{33}H_{27}F_{12}N_9P_2Ru$ (940.1): calcd. C 42.1, H 2.9, N 13.4; found C 42.1, H 3.0, N 13.2.

α-[Ru(azpy)$_2$(bpy)](PF$_6$)$_2$ (2): α-[Ru(azpy)$_2$(NO$_3$)$_2$] (30.0 mg, $5.07\cdot10^{-5}$ mol) and bpy (23.8 mg, $1.47\cdot10^{-4}$ mol) were dissolved in water (5 mL) and methanol (5 mL). The purple solution was refluxed for 90 minutes, resulting in a brown solution. After cooling to room temperature, a concentrated aqueous solution NH_4PF_6 was added, which led to the precipitation of a red-brown product. This product was washed with water and diethyl ether and dried in vacuo with P_4O_{10}. Yield: 45.7 mg (99%). $C_{32}H_{26}F_{12}N_8P_2Ru$ (913.1): calcd. C 42.1, H 2.9, N 12.3; found C 43.6 H 3.0, N 12.6.

β-[Ru(azpy)$_2$(bpy)](PF$_6$)$_2$ (3): β-[Ru(azpy)$_2$(NO$_3$)$_2$] (20.0 mg, $3.38\cdot10^{-5}$ mol) and bpy (15.8 mg, $1.0\cdot10^{-4}$ mol) were refluxed for 1.5 hours in a mixture of water (3.5 mL) and of methanol (3.5 mL). During this time a color change from purple to red occurred. The resulting solution was filtered and a concentrated aqueous solution of NH_4PF_6 was added. A brown crystalline material formed within an hour. This product was collected by filtration and washed with water and diethyl ether. Yield: 22.7 mg (74%). $C_{32}H_{26}F_{12}N_8P_2Ru$ (913.1): calcd. C 42.1, H 2.9, N 12.3; found C 41.7, H 3.0, N 13.2.

[Ru(azpy)(bpy)$_2$](PF$_6$)$_2$ (4): *cis*-[Ru(bpy)$_2$Cl$_2$]·2H$_2$O (25.0 mg, $4.80\cdot10^{-5}$ mol) and azpy (44.0 mg, $2.40\cdot10^{-4}$ mol) were refluxed for 3.5 hours in water (5 mL), during which the solution changed color from yellow to red. The reaction mixture was filtered and a concentrated aqueous solution of NH_4PF_6 was added. A red precipitate could be collected, which was subsequently washed with small amounts of water and diethyl ether. Yield: 38.3 mg (90%). $C_{32}H_{25}F_{12}N_7P_2Ru\cdot1.5H_2O$ (925.1): calcd. C 40.8, H 3.1, N 10.8; found C 40.5, H 2.7, 10.9.

***mer*-[Ru(tazpy)$_3$](PF$_6$)$_2$ (5):** The precursor material α-[Ru(tazpy)$_2$(NO$_3$)$_2$] was prepared analogous to the synthesis[24] of α-[Ru(azpy)$_2$(NO$_3$)$_2$] with use of the ligand *o*-tolylazopyridine. α-[Ru(tazpy)$_2$(NO$_3$)$_2$] (20.0 g, $3.23\cdot10^{-5}$ mol) was refluxed with tazpy (19 mg, $9.6\cdot10^{-5}$ mol) in a mixture of methanol (5 mL) and water (5 mL) for one hour. A color change from violet to brown was noted and the solution was cooled to room temperature. A concentrated solution of NH_4PF_6 was then added, resulting in a brown precipitate, which was collected, washed with water, and dried in vacuo with P_4O_{10}. Yield: 24.6 mg (78%). $C_{36}H_{33}F_{12}N_9P_2Ru$ (982.1): calcd. C 44.00, H 3.38, N 12.83; found: C 44.0, H 3.1, N 12.9.

X-ray Crystal Structure Determination of 1 and 5: Crystals of suitable size were placed in the cold nitrogen stream of a Nonius KappaCCD diffractometer on rotating anode. Data were collected at 150 K, using Mo-K_α radiation (graphite monochromator, λ = 0.71073 Å). For **5** an absorption correction based on multiple measurements of symmetry-related reflections was applied (PLATON/MULABS,[36] T-range 0.898–0.950). The structures were solved by direct methods (SHELXS86,[37]) and refined on F^2 using full-matrix least-squares techniques (SHELXL-97-2,[38]). One of the PF_6 counterions in the crystal structure of **1** was refined with a two-site disorder model. Mild distance restraints were applied to enforce a reasonable geometry of the minor disorder component. Hydrogen atoms were included in the model on calculated positions, riding on their carrier atoms. The methyl groups of **5** were rotated along the C–C bond during refinement. All non-hydrogen atoms were refined with anisotropic displacement parameters with exception of the minor component atoms of the disordered counterion in **1**. Hydrogen atom displacement was described with a fixed isotropic parameter linked to the equivalent isotropic parameter of the carrier atom. Pertinent data for each of the structure determinations are given in Table 1. CCDC-251700 contains the supplementary crystallographic data for this paper. These data can be obtained free of charge from The Cambridge Cyrstallographic Data Centre via www.ccdc.cam.ac.uk/data_request/cif.

Physical Measurements: The NMR measurements were performed with a Bruker 300 DPX spectrometer and a 600 DPX spectrometer. Spectra were recorded in [D$_6$]acetone and calibrated on the solvent peak. 2D ^{1}H-^{1}H NOESY spectra were performed using the standard Bruker pulse sequences, with a mixing time of 0.8–1 s.

Cytotoxicity Tests. Determination IC$_{50}$ Values: For the determination of the IC_{50} values of the compounds **1**, **2**, **3** and **4** a panel of human tumor cell lines (MCF-7, EVSA-T, WIDR, IGROV, M19, A498 and H266) has been used. The in vitro cytotoxicity assays using these cell lines were performed at the Dr. Daniel den Hoed kliniek (Rotterdam Cancer Institute), Department of Medical oncology (Rotterdam, The Netherlands).

A stock solution of the test and reference compounds was used, which contained 1 mg compound/200 μL. The compounds were dissolved in DMSO. On the first day 150 μL of trypsinized tumor cells (1500–2000 cells/well) were plated in 96-wells flatbottom microtiter plates. The plates were preincubated 48 h at 37 °C, 8.5% CO_2 to allow the cells to adhere. On day 2, a threefold dilution sequence of ten steps was made in full medium, starting with the 1 mg compound/200 μL stock solution. Every dilution was used in quadruplicate by adding 50 μL to a column of four wells. On day 7 the incubation was terminated by washing the plate twice with PBS. Cytotoxicity was estimated by the microculture sulforhodamine B (SRB) test.[39] The absorbance was read at 540 nm using an automatic microplate reader (labsystems Multiskan MS). Data were used for construction of concentration response curves and determination of the IC_{50} value by use of Deltasoft 3 software.

Supporting Information (see also footnote on the first page of this article): ^{1}H NMR spectrum of **1** (Figure S1), 2D NOESY spectra of **2–4** (Figure S2–S4) and Table S1 showing NOE cross peaks for **1–4** (see also footnote on the first page of this article).

Acknowledgments

This work was supported by the Council for Chemical Sciences of the Netherlands Organization for Scientific Research (CW-NWO). We thank Johnson Matthey Chemicals (Reading, UK) for a generous loan of $RuCl_3\cdot3H_2O$. We thank C. Erkelens and A. W. M. Lefeber for assistance with the NMR pulse techniques. Dr. Dick de Vos is kindly acknowledged for facilitating determination of the IC_{50} values. Additional support from COST Action D20 allowing regular research exchanges to partner laboratories from EU countries is gratefully acknowledged.

[1] A. C. G. Hotze, S. E. Caspers, D. de Vos, H. Kooijman, A. L. Spek, A. Flamigni, M. Bacac, G. Sava, J. G. Haasnoot, J. Reedijk, *J. Biol. Inorg. Chem.* **2004**, *9*, 354–364.
[2] A. H. Velders, H. Kooijman, A. L. Spek, J. G. Haasnoot, D. de Vos, J. Reedijk, *Inorg. Chem.* **2000**, *39*, 2966–2967.
[3] E. Wong, C. M. Giandomenico, *Chem. Rev.* **1999**, *99*, 2451–2466.

 © 2005 Wiley-VCH Verlag GmbH & Co. KGaA, Weinheim

[4] A. M. Pyle, J. K. Barton, *Prog. Inorg. Chem.* **1990**, *38*, 413–475.
[5] Y.-S. Wong, S. J. Lippard, *J. Chem. Soc. Chem. Commun.* **1977**, 824–825.
[6] K. W. Jennette, S. J. Lippard, G. A. Vassiliades, W. R. Bauer, *Proc. Natl. Acad. Sci. USA* **1974**, *71*, 3839–3843.
[7] J. K. Barton, *Science* **1986**, *233*, 727–734.
[8] J. K. Barton, A. T. Danishefsky, J. M. Goldberg, *J. Am. Chem. Soc.* **1984**, *106*, 2172–2176.
[9] J. K. Barton, J. M. Goldberg, C. V. Kumer, N. J. Turro, *J. Am. Chem. Soc.* **1986**, *108*, 2081–2088.
[10] J. G. Liu, B. H. Ye, Q. L. Zhang, X. H. Zou, Q. X. Zhen, X. Tian, L. N. Ji, *J. Biol. Inorg. Chem.* **2000**, *5*, 119–128.
[11] C. Das, A. Saha, C. H. Hung, G. H. Lee, S. M. Peng, S. Goswami, *Inorg. Chem.* **2003**, *42*, 198–204.
[12] S. Goswami, R. Mukherjee, A. Chakravorty, *Inorg. Chem.* **1983**, *22*, 2825–2832.
[13] R. A. Krause, K. Krause, *Inorg. Chem.* **1982**, *21*, 1714–1720.
[14] M. Kakoti, A. K. Deb, S. Goswami, *Inorg. Chem.* **1992**, *31*, 1304–1306.
[15] I. Chakraborty, S. Sengupta, S. Das, S. Banerjee, A. Chakravorty, *Dalton Trans.* **2003**, 134–140.
[16] M. N. Ackermann, J. W. Naylor, E. J. Smith, G. A. Mines, N. S. Amin, M. L. Kerns, C. Woods, *Organometallics* **1992**, *11*, 1919–1926.
[17] S. Sengupta, I. Chakraborty, A. Chakravorty, *Eur. J. Inorg. Chem.* **2003**, 1157–1160.
[18] P. Majumdar, S. M. Peng, S. Goswami, *J Chem. Soc. Dalton Trans.* **1998**, 1569–1574.
[19] P. Byabartta, S. K. Jasimuddin, G. Mostafa, T. H. Lu, C. Sinha, *Polyhedron* **2003**, *22*, 849–859.
[20] S. Pal, T. K. Misra, C. Sinha, A. M. Z. Slawin, J. D. Woollins, *Polyhedron* **2000**, *19*, 1925–1933.
[21] P. Byabartta, J. Dinda, P. K. Santra, C. Sinha, K. Panneerselvam, F. L. Liao, T. H. Lu, *J. Chem. Soc. Dalton Trans.* **2001**, 2825–2832.
[22] S. Goswami, A. R. Chakravarty, A. Chakravorty, *Inorg. Chem.* **1981**, *29*, 2246–2250.
[23] A. H. Velders, PhD Thesis, Leiden University, **2000**, Leiden.
[24] A. C. G. Hotze, A. H. Velders, F. Ugozzoli, M. Biagini-Cingi, A. M. Manotti-Lanfredi, J. G. Haasnoot, J. Reedijk, *Inorg. Chem.* **2000**, *39*, 3838–3844.
[25] A. Seal, S. Ray, *Acta Crystallogr. Sect. C* **1984**, *40*, 929–932.
[26] A. H. Velders, K. van der Schilden, A. C. G. Hotze, J. Reedijk, H. Kooijman, A. L. Spek, *Dalton Trans.* **2004**, 448–455.
[27] A. M. Popov, M. B. Egorova, V. A. Lutovinov, R. I. Dmitrieva, *Zh. Obshch. Khim.* **1990**, *60*, 2169.
[28] M. Krejcík, S. Záliš, J. Klíma, D. Sýkora, W. Matheis, A. Klein, W. Kaim, *Inorg. Chem.* **1993**, *32*, 3362–3368.
[29] A. C. G. Hotze, E. P. L. Van der Geer, S. Caspers, H. Kooijman, A. L. Spek, J. G. Haasnoot, J. Reedijk, *Inorg. Chem.* **2004**, *32*, 4935–4943.
[30] A. H. Velders, A. G. Quiroga, J. G. Haasnoot, J. Reedijk, *Eur. J. Inorg. Chem.* **2003**, 713–719.
[31] J. I. Musher, *Inorg. Chem.* **1972**, *11*, 2335–2340.
[32] A. C. G. Hotze, M. Bacac, A. H. Velders, B. A. J. Jansen, H. Kooijman, A. L. Spek, J. G. Haasnoot, J. Reedijk, *J. Med. Chem.* **2003**, *46*, 1743–1750.
[33] Even if 1% impurity of α-$[Ru(azpy)_2(NO_3)_2]$ would be present (which is the upper limit, as NMR and Elemental Analysis did not have an indication at all), then this impurity can not cause the here presented cytotoxicity of the tris chelate complexes.
[34] U. K. Mazumder, M. Gupta, S. S. Karki, S. Bhattacharya, S. Rathinasamy, S. Thangavel, *Chem. Pharm. Bull.* **2004**, *52*, 178–185.
[35] B. P. Sullivan, D. J. Salmon, T. J. Meyer, *Inorg. Chem.* **1978**, *17*, 3334–3341.
[36] A. L. Spek, *J. Appl. Crystallogr.* **2003**, *36*, 7.
[37] G. M. Sheldrick, shelxs86 Program for crystal structure determination. University of Göttingen, Germany **1986**.
[38] G. M. Sheldrick, shelxl-97–2 Program for crystal structure refinement. University of Götingen, Germany **1997**.
[39] Y. P. Keepers, P. E. Pizao, G. J. Peters, J. Van Ark-Otte, B. Winograd, H. M. Pinedo, *Eur. J. Cancer* **1991**, *27*, 897–900.

Received: February 3, 2005

 © 2005 Wiley-VCH Verlag GmbH & Co. KGaA, Weinheim

Spectroscopy and Redox Behaviour of Dicopper(II) and Dinickel(II) Complexes of Bis(cyclen) and Bis(cyclam) Ligands

Sanae El Ghachtouli,[a] Cyril Cadiou,[a] Isabelle Déchamps-Olivier,[a] Françoise Chuburu,*[a] Michel Aplincourt,[a] Véronique Turcry,[b] Michel Le Baccon,[b] and Henri Handel[b]

Keywords: Copper / Nickel / Bis(cyclen) ligands / Bis(cyclam) ligands / Electrochemistry / EPR spectroscopy

The dinuclear Cu^{II} and Ni^{II} complexes of *meta*-xylyl and pyridyl biscyclen and biscyclam have been prepared and characterised in solution by means of UV/Visible spectra, electrochemical and EPR studies. X-ray structures of copper biscyclen complexes have been obtained. The comparison of all the data shows that the potentially coordinating N(*py*) pyridyl atom promotes the interaction between the two metal centers, whether it is spontaneously coordinated (biscyclen complexes) or not (biscyclam ones).

(© Wiley-VCH Verlag GmbH & Co. KGaA, 69451 Weinheim, Germany, 2005)

Introduction

Tetraazamacrocyclic ligands like cyclen and cyclam are well known for their remarkable capacity to coordinate metallic ions. Their preorganisation, the flexibility of the macrocyclic framework and the soft character of the nitrogen donor atoms make the cyclic tetramines well suited for the complexation of d-block metals.[1] Thus, two of the properties of macrocyclic complexes that set them apart from the acyclic ones are selectivity in binding and kinetic stability with respect to dissociation. These features have been harnessed to develop macrocycles able to transport radioisotopic agents to a tumour site (^{64}Cu and ^{67}Cu for example).[2] Moreover, changes in the nitrogen (or carbon) substitution can determine their potential applications. In particular, functionalisation of cyclen by substituents such as acetate binding arms has led to a new class of ligands which are able to coordinate lanthanide cations especially Gd^{III}.[3] The corresponding complexes are developed and used as MRI contrast agents. Besides these medical applications, transition-metal complexes of tetraazamacrocycles in many respects, can be seen as metalloenzyme models, particularly when the ligand framework exhibits two or even three cavities. The corresponding bis- or tris-macrocycles may then be able to hold two or more metal centres in proximity, mimicking the multinuclear metal arrays at the active sites of the concerned metalloenzymes.[4] Since the length of the bridging groups controls the inter-metal ion distances, these ligands have been studied to examine the strength, more or less pronounced of the interaction between the metal centres. Kaden, Fabbrizzi and co-workers have shown through electrochemical and EPR studies of metallic bistetraazamacrocyclic complexes, that below an intermetallic distance of about 8 Å, metal–metal interactions can be detected.[5] In fact, in these studies the only parameter considered to tune the inter-metal distance is the spacer geometry. However, the flexibility of the macrocycle can induce favoured configurations of the cavity and then modifications of the metal coordination polyhedron. This factor may affect the intermetallic distance as well as topological modification of the ligand occurring during the redox process. Effectively, as recently shown for cyclam complexes the change in the metal redox state can be associated with their geometrical reorganisation.[6] Finally, the introduction of additional donor atoms on the intercycle spacer may interfere in the metal–metal distance due to selective coordination of one of the two metals to the linker.

In order to test the influence of these latter parameters, the preparation of dinuclear copper(II) and nickel(II) complexes based upon cyclen and cyclam cavities (Scheme 1) was improved and their electronic properties studied by means of electrochemical and EPR measurements.

Results and Discussion

Syntheses of Ligands and Complexes

The ligands $\mathbf{L^1}$ to $\mathbf{L^4}$ were synthesised according the bisaminal methodology[7] and the corresponding dinuclear complexes were obtained by addition of equimolar amounts of metallic salts (ClO_4 or BF_4 salts – see experimental section). Monocrystals suitable for an X-ray analysis were obtained for the copper complexes of cyclen ligands $\mathbf{L^1}$ and $\mathbf{L^2}$.

[a] GRECI, Université de Reims Champagne–Ardenne, B. P. 1039, 51687 Reims Cedex 2, France
[b] UMR CNRS 6521, Université de Bretagne Occidentale, B. P. 809, 29285 Brest Cedex, France
E-mail: francoise.chuburu@univ-reims.fr
Supporting information for this article is available on the WWW under http://www.eurjic.org or from the author.

 © 2005 Wiley-VCH Verlag GmbH & Co. KGaA, Weinheim **DOI: 10.1002/ejic.200500120**

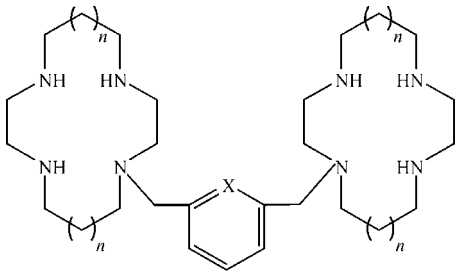

X = **C**, *n* = **0** biscyclen-meta: **L**[1]

X = **N**, *n* = **0** biscyclen-pyridine: **L**[2]

X = **C**, *n* = **1** biscyclam-meta: **L**[3]

X = **N**, *n* = **1** biscyclam-pyridine: **L**[4]

Scheme 1.

Structural Characterisation in the Solid State of Complexes $[Cu_2L^{1,2}]$

POV-ray depiction of $[Cu_2L^1]^{4+}$ complex is provided in Figure 1. The monocrystals were isolated by slow diffusion of a saturated sodium perchlorate solution into an aqueous solution of the complex. They show that two copper ions are coordinated by the four macrocyclic nitrogen atoms of each cyclen cavity and by a water molecule, leading to two pentacoordinate subunits linked together by a metaxylyl bridge. Selected bond lengths and angles are shown in Table 1. The Cu–NH bond lengths [2.016(5)–2.031(5) Å] are close to the ones in bis-*para*xylyl cyclen copper complex[8] while the bonds to the tertiary macrocyclic nitrogens are slightly longer [2.035(5)/2.046(5)] Å. This is certainly the consequence of the *N*-alkylation on these atoms as it is known that the M–N bond lengths are increased by *N*-alkyl substitution.[8–10] The copper coordination spheres are completed by oxygen donors from water molecules (one per copper ion) with Cu–O bond lengths of [2.142(4)/2.160(5)] Å. For each copper ion, the resulting geometry is based on a square planar pyramid, the metal ion being approximately at a distance of 0.50 Å from the base of the pyramid. At last for this complex, the intramolecular Cu–Cu distance is measured at 9.713 Å, while shorter intermolecular Cu–Cu distances are observed (7.333, 8.274, 9.582 Å).

The X-ray structure of the copper(II) complex of **L**[2] is provided in Figure 2 and relevant geometry details in Table 2. Monocrystals were grown by slow diffusion of diethylether in an acetonitrile solution of the tetrafluoroborate copper complex. Crystallographic analysis of $[Cu_2L^2(BF_4)](BF_4)_3$ shows the two copper ions to be pentacoordinate as expected for copper held in a cyclen cavity. The crystal structure underlines that the pyridyl nitrogen atom [N(*py*)] allows the discrimination of the two cavities since this atom is coordinated to only one of the two copper ions. Thus, the Cu(1) atom is bonded to the four nitrogen atoms of the first macrocyclic cavity [Cu–NH: from 2.019(7) to 2.033(7) Å; Cu–NR: 2.041(6) Å] and at a greater distance by the nitrogen atom of the pyridine ring [Cu–N(*py*): 2.266(6) Å]. The coordination of the N(*py*) atom certainly allows the formation of an efficient five-membered chelate ring which geometrically leads to a smaller N(*py*)-Cu–N angle, of 80.4(1)° for the N_1 nitrogen carrying the pyridine linker, compared to values of 95.4(3) to 129.6(3)° for the other three N(*py*)-Cu–N angles. In parallel, the Cu(2) atom is coordinated to the four nitrogen atoms of the second macrocyclic cavity [Cu–NH: from 2.021(7) to 2.038(7) Å; Cu–NR: 2.064(6) Å] and to a tetrafluoroborate anion [Cu–F: 2.135(6) Å]. The distances of the copper ions with regard to their corresponding macrocyclic cavities are about 0.54 Å (CuN_5 chromophore) or 0.51 Å (CuN_4 chromophore). The main consequence of the N(*py*) atom coordination to one of the two copper ions is the significant shortening of the intramolecular Cu–Cu distance since it is

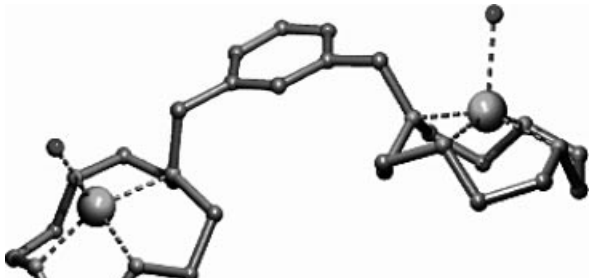

Figure 1. POV-ray diagram of $[Cu_2L^1(H_2O)_2]^{4+}$.

Table 1. Bond lengths [Å] and angles [°] in $[Cu_2L^1]^{4+}$.

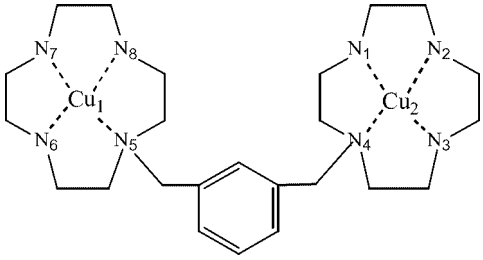

Cu1–O1	2.142(4)	O1–Cu1–N1	104.6(2)
Cu1–N1	2.019(5)	O1–Cu1–N2	104.4(2)
Cu1–N2	2.016(5)	O1–Cu1–N3	105.6(2)
Cu1–N3	2.029(5)	O1–Cu1–N4	103.0(2)
Cu1–N4	2.046(5)	N1–Cu1–N2	86.4(2)
Cu2–O2	2.160(5)	N1–Cu1–N3	149.9(2)
Cu2–N5	2.035(5)	N1–Cu1–N4	87.0(2)
Cu2–N6	2.031(5)	N2–Cu1–N3	86.2(2)
Cu2–N7	2.026(5)	N2–Cu1–N4	152.6(2)
Cu2–N8	2.022(5)	N3–Cu1–N4	86.3(2)
		O2–Cu2–N5	108.6(2)
		O2–Cu2–N6	106.9(2)
		O2–Cu2–N7	98.1(2)
		O2–Cu2–N8	102.3(2)
		N5–Cu2–N6	86.5(2)
		N5–Cu2–N7	153.3(2)
		N5–Cu2–N8	86.0(2)
		N6–Cu2–N7	86.6(2)
		N6–Cu2–N8	150.8(2)
		N7–Cu2–N8	87.6(2)

 © 2005 Wiley-VCH Verlag GmbH & Co. KGaA, Weinheim

decreased to 5.779 Å. This distance is the shortest intermetallic one in the crystal. Compared to the $[Cu_2\mathbf{L^1}]^{4+}$ complex, $[Cu_2\mathbf{L^2}(BF_4)](BF_4)_3$ could be better for the observation of metal–metal interactions.

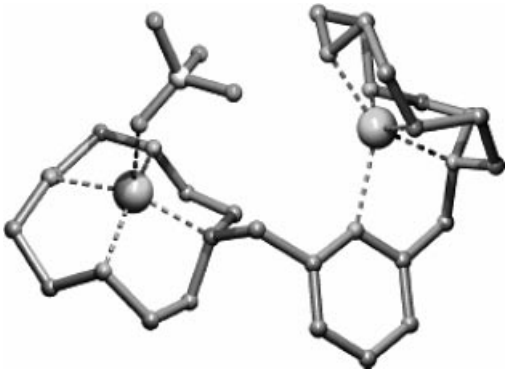

Figure 2. POV-ray diagram of $[Cu_2\mathbf{L^2}(BF_4)]^{3+}$.

Table 2. Bond lengths [Å] and angles [°] in $[Cu_2\mathbf{L^2}]^{4+}$.

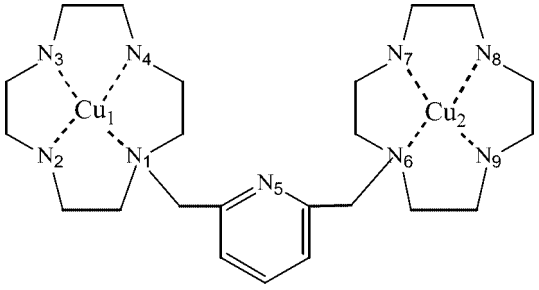

Cu1–N1	2.041(6)	N1–Cu1–N2	86.8(3)
Cu1–N2	2.030(7)	N1–Cu1–N3	149.4(3)
Cu1–N3	2.033(7)	N1–Cu1–N4	85.5(3)
Cu1–N4	2.019(7)	N1–Cu1–N5	80.4(2)
Cu1–N5	2.266(6)	N2–Cu1–N3	85.5(3)
Cu2–N6	2.064(6)	N2–Cu1–N4	148.5(3)
Cu2–N7	2.029(7)	N2–Cu1–N5	113.3(3)
Cu2–N8	2.038(7)	N3–Cu1–N4	85.9(3)
Cu2–N9	2.021(7)	N3–Cu1–N5	129.6(3)
Cu2–F	2.135(6)	N4–Cu1–N5	95.4(3)
		N6–Cu2–N7	86.9(3)
		N6–Cu2–N8	151.7(3)
		N6–Cu2–N9	86.2(3)
		N6–Cu2–F	109.1(3)
		N7–Cu2–N8	86.2(3)
		N7–Cu2–N9	149.4(3)
		N7–Cu2–F	102.7(3)
		N8–Cu2–N9	85.8(3)
		N8–Cu2–F	99.2(3)
		N9–Cu2–F	107.7(3)

Solution Properties

Electronic Absorption Spectroscopy

The UV/Visible absorption maxima of the complexes $[Cu_2\mathbf{L}]^{4+}$ and $[Ni_2\mathbf{L}]^{4+}$ ($\mathbf{L} = \mathbf{L^{1-4}}$) in water and acetonitrile are given as supporting information.

Copper Complexes: As commonly observed for these compounds, the featureless nature of the spectra makes difficult a detailed description of coordination geometries. Nevertheless, the main information resulting from the visible spectra of the copper biscyclen complexes ($[Cu_2\mathbf{L^{1,2}}]^{4+}$) are the following: for $[Cu_2\mathbf{L^1}]^{4+}$ whatever the solvent, the spectrum exhibits a broad band at 594 nm typical of a square based pyramidal copper complex (CuN_4S chromophore, S = solvent).[8] For $[Cu_2\mathbf{L^2}]^{4+}$, the spectrum is dissymmetrical and its deconvolution analysis shows that it is the superimposing of two spectra, the first one characteristic of a CuN_4S chromophore (with a band at 584–594 nm), the second one attributed to a CuN_5 chromophore[11] (shoulder between 684 and 735 nm, according to the solvent). Moreover, the presence of this shoulder indicates that the coordination of the pyridyl nitrogen N(*py*) to the copper ion is maintained in solution, whatever the pH conditions.

For the cyclam copper complexes $[Cu_2\mathbf{L^{3,4}}]^{4+}$, the absorption maxima at about 520 nm are typical of square planar copper complexes.[12] The lack of absorption at about 650 nm[13] is indicative of an absence of interaction between the pyridyl nitrogen atom N(*py*) and a copper ion for the $[Cu_2\mathbf{L^4}]^{4+}$ complex.

Nickel Complexes: For the nickel biscyclen complexes ($[Ni_2\mathbf{L^{1,2}}]^{4+}$) the UV/Visible spectra are indicative of octahedral coordination for the nickel in solution, solvent molecules occupying the free positions of the octahedron (chromophore NiN_4S_2).[14] Two bands are observed for both complexes in water and in acetonitrile corresponding to the predicted $^3A_{2g} \rightarrow {}^3T_{2g}$ (950–800 nm) and $^3A_{2g} \rightarrow {}^3T_{1g}$ (F) (560–500 nm) transitions for a d^8 metal ion under octahedral symmetry, the third transition $^3A_{2g} \rightarrow {}^3T_{1g}$ (P) (300–400 nm) being hidden by the stronger absorbance of the ligand ($\lambda < 300$ nm).

For the nickel cyclam complexes ($[Ni_2\mathbf{L^{3,4}}]^{4+}$), the solution visible spectra show a single band with the maximum in the range 450–470 nm, depending on both the complexes and the solvent. This signal is in accordance with the $[Ni(cyclam)]^{2+}$ spectrum ($\lambda = 459$ nm) and is consistent with the adoption by the metal of a square-planar geometry, the metal being perfectly fitted inside the macrocyclic cavity. In solution, the coexistence for $[Ni(cyclam)]^{2+}$complexes of square planar (low spin) and octahedral (high spin) geometries is well documented leading to a "yellow to blue" equilibrium between these species.[15] For the $[Ni_2\mathbf{L^{3,4}}]^{4+}$ complexes, we were not able to detect any additional peaks corresponding to octahedral nickel(II) ions. Two reasons may be responsible for that: either no octahedral complexes are present in solution or, because of low molar extinction coefficients, the octahedral complexes are difficult to detect. Finally, for $[Ni_2\mathbf{L^4}]^{4+}$, whatever the solvent and the pH conditions, the spectrum is identical and in addition similar to the one of $[Ni_2\mathbf{L^3}]^{4+}$. As for its copper homologue, this is indicative of an absence of interaction between the pyridyl nitrogen atom N(*py*) and the nickel.

Electrochemical Properties of the Bismacrocyclic Complexes

The binuclear $[Cu_2\mathbf{L}]$ and $[Ni_2\mathbf{L}]$ complexes ($\mathbf{L} = \mathbf{L^{1-4}}$) were all investigated by cyclic voltammetry in CH_3CN, the

 © 2005 Wiley-VCH Verlag GmbH & Co. KGaA, Weinheim

working electrode being a glassy carbon disk and the Fc^+/Fc couple being used as a reference in acetonitrile.

Biscyclen Complexes: The cyclen cavity is not well adapted to stabilize +I and +III oxidation states for copper and nickel.[16] Therefore, it was not possible to obtain reproducible voltammograms, mainly because of the degradation of oxidised and reduced forms during the experiment.

Biscyclam Complexes: The copper complexes $[Cu_2\mathbf{L^3}]^{4+}$ and $[Cu_2\mathbf{L^4}]^{4+}$ show two irreversible bielectronic exchanges (one electron per metallic centre) separated by $\approx$ 2.40 V (Table 3). The anodic peaks happen respectively for $[Cu_2\mathbf{L^3}]^{4+}$ and $[Cu_2\mathbf{L^4}]^{4+}$at 1.25 V and 1.15 V while the cathodic ones happen at –1.21 V and –1.22 V. These values are in accordance with the ones measured for the monomeric [Cu(cyclam)]$^{2+}$ (1.02 V and –1.28 V), taking into account the incidence of the *N*-alkylation of the macrocyclic cavity on the redox potentials.[5d,17] In reduction, the two copper complexes exhibit a similar behaviour i.e. the $Cu^{II/I}$ process is irreversible and the reverse process is accompanied by a partial release of the metal, reported by an anodic peak at –0.60 V (Cu^0). In oxidation, the forward and reverse peak heights are inequivalent ($i_a >> i_c$), indicating that the electronic exchange $Cu^{II/III}$ is irreversible too. Moreover, the high anodic current wave detected for the first cycle, the decrease of its intensity when the number of cycles increased, and the apparition of a deposit at the electrode during the experiment show that the oxidated species $[Cu_2\mathbf{L^{3,4}}]^{6+}$ are highly unstable and react rapidly in the medium. This is consistent with observations generally done with copper tetraazamacrocyclic complexes.[18] We have checked that, as demonstrated by Fabbrizzi et al.,[5d] in concentrated perchloric acid solution (70%) at a Pt electrode, the Cu^{III} bistetraazamacrocyclic complexes become stable, at least at the time scale of the voltammetry experiment. In this special medium, the oxidation process is effectively quasi reversible ($i_a = i_c$). In order to have a greatest resolution of the signals associated with the consecutive redox events ($Cu^{II}\ Cu^{II} \rightarrow Cu^{II}\ Cu^{III} \rightarrow Cu^{III}\ Cu^{III}$) whose potentials are not very distant,[5d] differential pulse voltammetry (DPV) was used. The DPV profiles obtained for the two complexes in the oxidation scan are similar and exhibit a single wave peak. The measurements reproduce well the one already done by Fabbrizzi et al.[5d] for the $[Cu_2\mathbf{L^3}]^{4+}$ complex and indicate that for these two complexes the ring-to-ring distance is certainly too long to induce a two consecutive one-electron steps process.

Table 3. Electrochemical parameters for the $Cu_2\mathbf{L^3}$ and $Cu_2\mathbf{L^4}$ complexes.

	Oxidation potential	Reduction potential
$Cu_2\mathbf{L^3}$ (CH_3CN)[a]	E_p = 1.25 V	E_p = –1.21 V
$Cu_2\mathbf{L^4}$ (CH_3CN)[a]	E_p = 1.15 V	E_p = –1.22 V
$Cu_2\mathbf{L^3}$ ($HClO_4$, 70%)[b]	$E_{1/2}$ = 0.98 V (0.10 V)	–
$Cu_2\mathbf{L^4}$ ($HClO_4$, 70%)[b]	$E_{1/2}$ = 1.02 V (0.10 V)	–

[a] Potential values are given vs. Fc^+/Fc. [b] Potential values are expressed vs. SCE.

Cyclic voltammograms recorded for the nickel complexes $[Ni_2\mathbf{L^3}]^{4+}$ and $[Ni_2\mathbf{L^4}]^{4+}$ are reported in Figure 3. In reduction, the behaviour of the two complexes is quasi reversible and the $Ni^{II/I}$ system is electrochemically slow. The oxidation of the two complexes is more complicated since more than one CV wave is observed. Thus, for the complex $[Ni_2\mathbf{L^3}]^{4+}$ two oxidation potentials at 0.80 and 1.12 V are detected while the complex $[Ni_2\mathbf{L^4}]^{4+}$ shows two oxidation processes, the first one at 0.84 V and the second one split into two peaks at 1.03 and 1.18 V. For $[Ni_2\mathbf{L^3}]^{4+}$ the two CV waves are quasi reversible while for $[Ni_2\mathbf{L^4}]^{4+}$, the reversibility of the first system is very poor. It is noticeable that previous voltammetry experiments carried out for $[Ni_2\mathbf{L^3}]^{4+}$ [5d] have shown a simple oxidative behaviour since only the first system (0.80 V) was detected. As the purity of our complexes is satisfactory, one can think that in CH_3CN, two bismacrocyclic Ni^{II} species are successively oxidised. In $[Ni_2\mathbf{L^3}]^{4+}$ complex, the proportion of these two species is largely in favour of the first one while in $[Ni_2\mathbf{L^4}]^{4+}$ the proportion is similar. In CH_3CN, an increase of the temperature (298 K up to 313 K) results in growth of the second system at the expense of the first one (Figure 4a). When the CV waves are recorded at temperatures of 298 K down to 233 K (Figure 4b, Figure 5b), for both complexes the second system tends to disappear. It is also noticeable that for $[Ni_2\mathbf{L^4}]^{4+}$ the first system becomes more reversible. From these observations, it can be assumed that the oxidation of the first species is followed by a rearrangement. A temperature decrease can prevent this isomerisation and the vanishing at lower temperatures of the second oxidative system, would tend to show that the two oxidative processes are dependent on each other. As far as nickel(II) cyclam complexes are concerned, several stereoisomers have to be considered, according to the configuration of the macrocyclic cavity (Figure 6). There are five possible configurational isomers of planar complexes of the macrocyclic ligand cyclam:[19] RSRS (++++) i.e. type I, RSRR (+-++) i.e. type II, RRSS (+--+) i.e. type III, RSSR (++--) i.e. type IV, RRRR (+-+-) i.e. type V, where + indicates that the hydrogen of the NH is above the plane of the macrocycle and - indicates that it is below the plane.

A cluster analysis of Ni-14 membered tetraazamacrocycles found in the Cambridge Structural database[20] shows that the most frequent configurations encountered for these complexes are the type I and type III ones; the amount of these two forms can moreover vary according to the coordination shell geometry of the nickel and the macrocycle substitution. On certain conditions, isomerisation between type I and type III structures have been evidenced: for instance, the oxidatively induced isomerisation of type I [Ni(cyclam)]$^{2+}$ into type III has been reported,[6a] while in bistetraazamacrocyclic series, the isomerisation of the type III [Zn_2 (bis *para*-cyclam)] complex into the type I[21] has been described. Such an isomerisation can be proposed for the $[Ni_2\mathbf{L^3}]^{4+}$ and $[Ni_2\mathbf{L^4}]^{4+}$complexes. Unfortunately, the impossibility to isolate and characterise independently the supposed type III and type I isomers prevents any kinetic quantitative study of the equilibrium between these two

 © 2005 Wiley-VCH Verlag GmbH & Co. KGaA, Weinheim

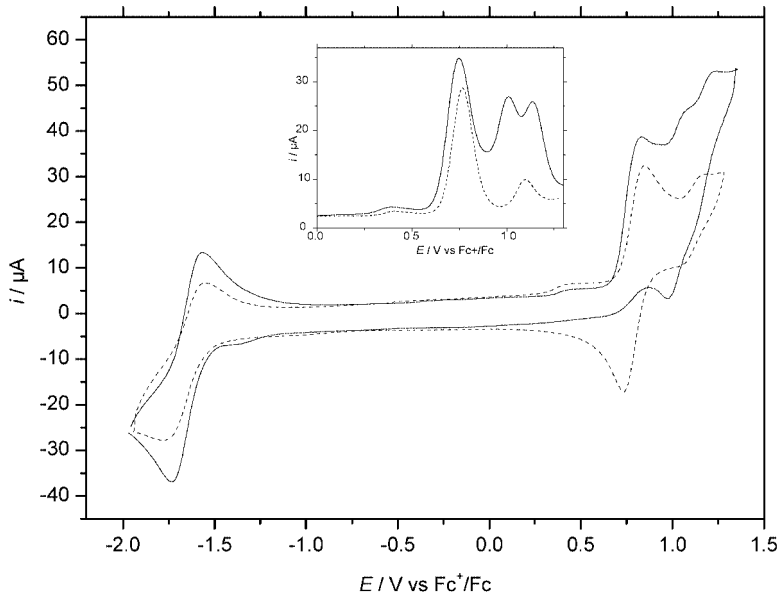

	$E_{½}$ox (ΔE_p)	$E_{½}$red (ΔE_p)
$[Ni_2\mathbf{L^3}]^{4+}$ (CH_3CN)[a]	0.80 V (0.10 V)	-1.66 V (0.19V)
	1.12 V (0.11 V)	
$[Ni_2\mathbf{L^4}]^{4+}$ (CH_3CN)[a]	0.84 V (irrev)	-1.65 V (0.17 V)
	1.03 V (0.11 V)	
	1.18 V (0.10 V)	

Figure 3. Cyclic voltammetry at a glassy carbon disk (CH_3CN/Bu_4NPF_6, c = 0.1 mol L^{-1}; v = 100 mV s^{-1}) of millimolar solutions of $[Ni_2\mathbf{L^3}]^{4+}$ (dashed lines) and $[Ni_2\mathbf{L^4}]^{4+}$ (straight lines) and Differential Pulse Voltammetry of their oxidation system (10 mV step potential).

configurations. However, the variation of the CV traces with the scan sweep rate can be indicative (Figures 4c and 5a). Comparison of the CV traces shows that for $[Ni_2\mathbf{L^4}]^{4+}$ the increase of the sweep rate improves the reversibility of the first system. Moreover, during the same experiments, the second system is affected since it tends to disappear for both complexes. It is interesting to notice that changes observed by increasing the CV sweep rate are similar to the changes previously noted by lowering the temperature (Figure 4b and Figure 5b). It led us to propose a configurational equilibrium in solution, slightly shifted upon electrochemical oxidation between the type III and the type I isomers of $[Ni_2\mathbf{L^3}]^{4+}$ and $[Ni_2\mathbf{L^4}]^{4+}$ biscyclams. Voltammetric data alone cannot bring any geometrical information about the coordination shell and it is difficult to identify the structures formed upon the oxidation. However, by comparison of the gap between redox potentials determined for type III and type I isomers of [Ni(cyclam)]$^{2+}$[6a] one can propose for $[Ni_2\mathbf{L^3}]$ that the first system ($E_{½ox}$ = 0.80 V) corresponds to the oxidation of the two Ni ions held in a type III cavity while the second system ($E_{½ox}$ = 1.12 V) corresponds to the oxidation of the two Ni ions held in a type I cyclam cavity. The oxidative process can then be modelled as a classical square scheme, involving the electron-transfer reactions and the isomerisation processes (Scheme 2): the first oxidation peak corresponds to the electrogeneration of the type III $[Ni_2\mathbf{L^3}]^{6+}$ complex that undergoes a partial rearrangement to form the type I $[Ni_2\mathbf{L^3}]^{6+}$. Since the potential corresponding to the generation of the type I $[Ni_2\mathbf{L^3}]^{6+}$ is more positive than the redox potential of the $Ni^{II/III}$ in the type III complex, type I $[Ni_2\mathbf{L^3}]^{6+}$ species is immediately reduced into type I $[Ni_2\mathbf{L^3}]^{4+}$ species; this species is further oxidised at a more positive potential. This implies that the isomerisation process requires an elongation of the metal–nitrogen bonds of the tetraazamacrocycle, which readily takes place

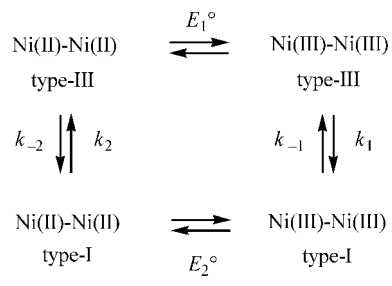

Scheme 2.

 © 2005 Wiley-VCH Verlag GmbH & Co. KGaA, Weinheim

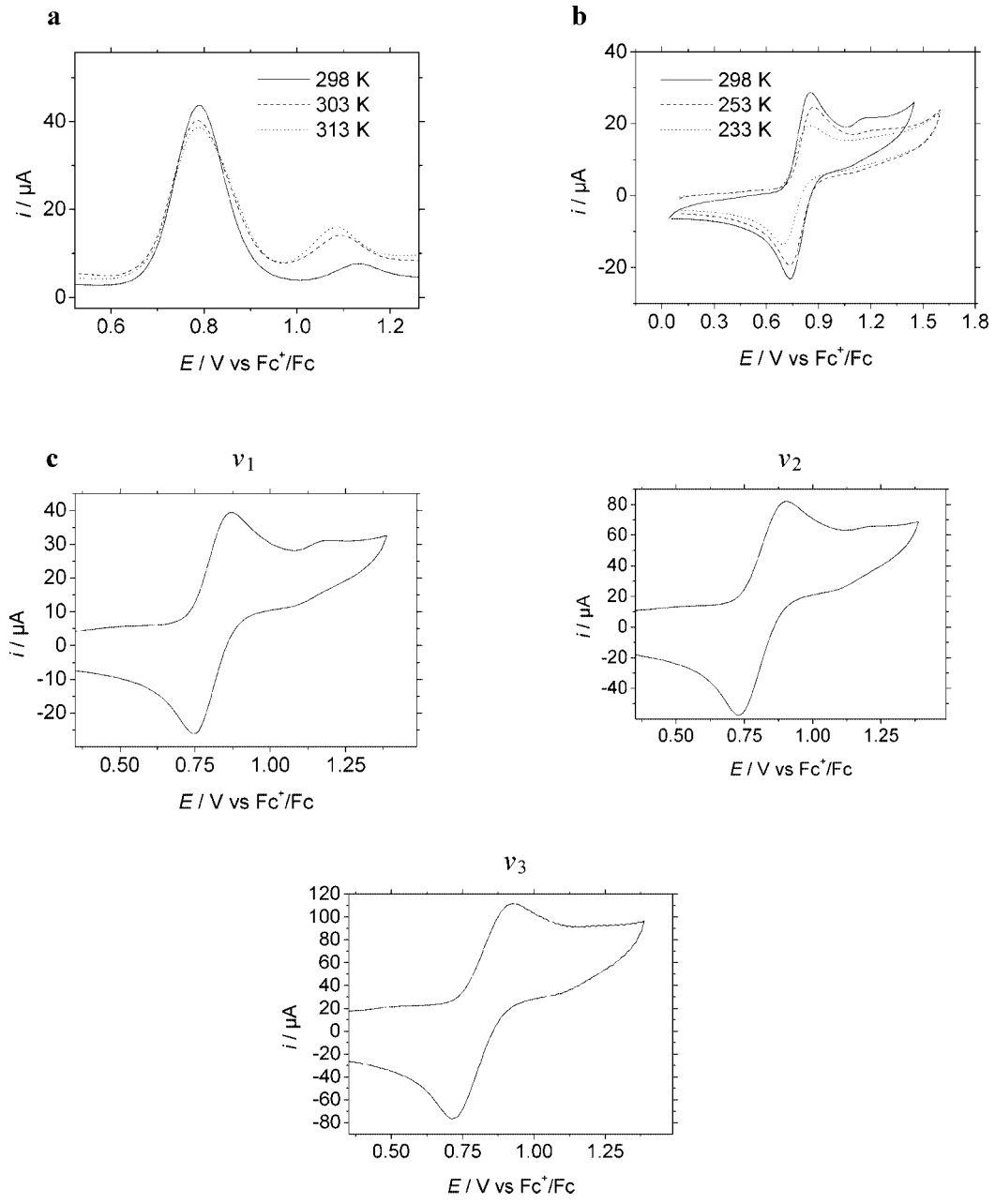

Figure 4. a: DPV profiles. b: CV curves of $[Ni_2\mathbf{L^3}]^{4+}$ at different temperatures. c: CV curves at v_1 = 100 mV s^{-1}, v_2 = 500 mV s^{-1}, v_3 = 1000 mV s^{-1}.

on cyclam derivatives by modification of the electron density on the metal, induced by the electrochemical oxidation $Ni^{II/III}$. Consequently, such isomerisation is negligible in acetonitrile without an electrochemical oxidation-reduction cycle. For complex $[Ni_2\mathbf{L^4}]^{4+}$, the electronic process is certainly more complicated than suggested by the square scheme since the oxidation peak of the supposed type I isomer is split. At this stage, only hypothesis can be formulated to interpret this signal. On the course of the (type III → type I) isomerisation process, a modification of the metal coordination sphere takes place as previously said. At the next step, the coordination of the nitrogen atom of the pyridine linker can occur on one of the two nickel centres, to lead to the oxidable type I $[Ni_2\mathbf{L^4}]^{4+}$ entity. This assumption is supported by the fact that most of the type I Ni^{II} complexes based on cyclam cavities are known to exhibit whether in a square planar or a square pyramidal configuration.[13,20] To test this proposal, modelling of type I $[Ni_2\mathbf{L^4}]^{4+}$ was improved in order to check the preferential equilibrium geometry of the complex. Whatever the type I starting geometry [N(*py*) coordinated or not], the most stable configuration corresponds to a situation where the nitrogen pyridyl atom is coordinated to one of the two nickel metals (Figure 7). Moreover, insofar as we can trust these calculations (because of the system size, the calculation level is restricted) the pyridinic nitrogen atom brings

 © 2005 Wiley-VCH Verlag GmbH & Co. KGaA, Weinheim

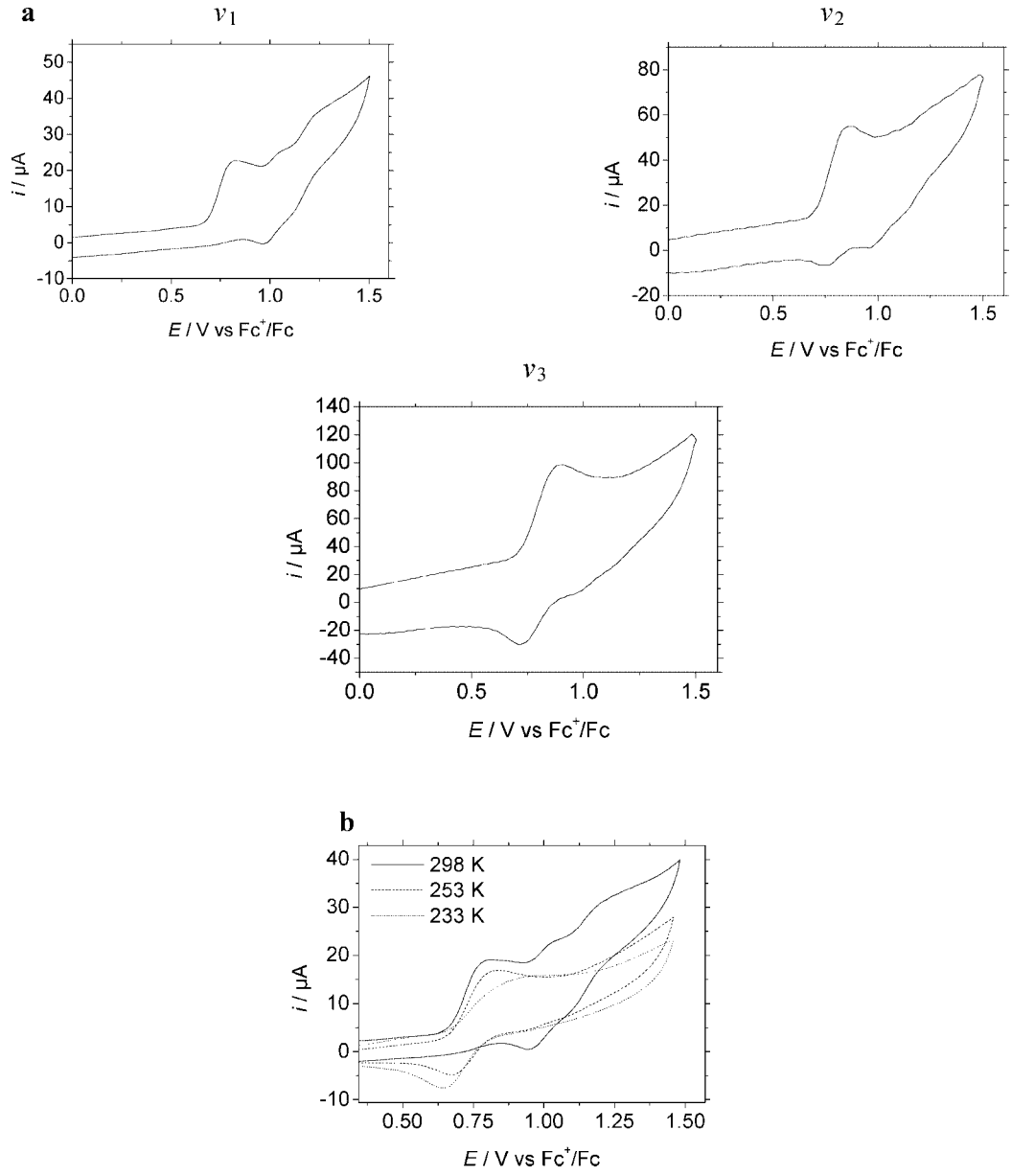

Figure 5. CV curves of $[Ni_2\mathbf{L^4}]^{4+}$. a: v_1 = 100 mV s^{-1}, v_2 = 600 mV s^{-1}, v_3 = 2000 mV s^{-1}. b: at different temperatures.

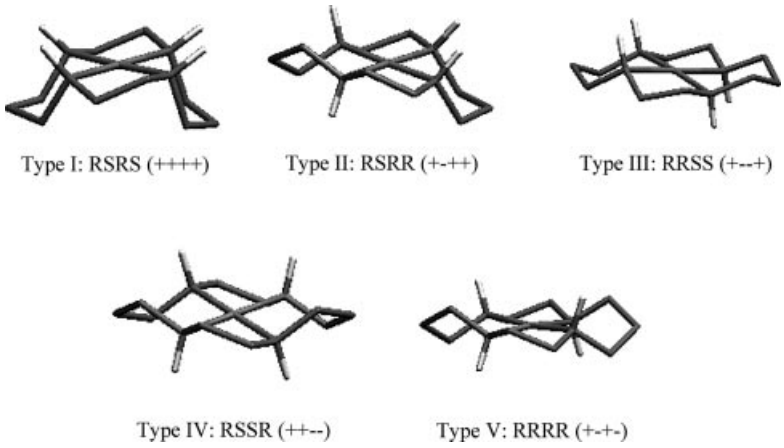

Figure 6. Five possible configurational isomers of planar complexes of the macrocyclic ligand cyclam.

 © 2005 Wiley-VCH Verlag GmbH & Co. KGaA, Weinheim

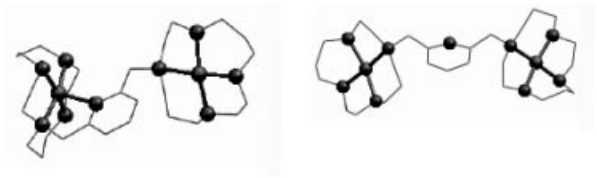

E_F(UHF/LANL2MB)	0	42.47 kcal mol^{-1}
E_F (UB3LYP/LANL2DZ)	0	38.42 kcal mol^{-1}
d (Ni ... N*py*)	2.271Å / 5.419 Å	5.351Å / 5.319 Å
d (Ni ... Ni)	6.865 Å	10.251 Å

Figure 7. Relative energies of formation (kcal mol^{-1}) and main geometrical parameters of type I isomers of $[Ni_2\mathbf{L^4}]^{4+}$ complexes (on the structures, hydrogen atoms are omitted for clarity).

the macrocycles and the metallic ions nearer (6.86 Å). Consequently, the two distinct peaks of the type I oxidation system can be assigned either to two different coordination modes of the two nickel ions (respectively NiN_5 and NiN_4) or to consecutive monoelectronic processes, the first one being assigned to the $Ni^{II/III}$ process at one of the metal centres, the second one to be ascribed to the one-electron oxidation at the other metal centre. Even if this last interpretation was previously proposed for a [Ni_2(biscyclam)] complex[5b] in which the metal centres are separated by 7.09 Å, none of these two propositions can be ruled out on the basis of electrochemical experiments.

EPR Spectroscopy of the Bismacrocyclic Complexes

The EPR spectra of the $[Cu_2\mathbf{L^{1-4}}]^{4+}$ complexes were recorded in DMF solution at 100 K in order to determine their *g* and *A* parameters (Figure 8). The simulated anisotropic EPR parameters are listed in Table 4. By way of comparison, the EPR parameters of the known acetate complexes $[Cu_2\mathbf{L^{1,3}}]^{4+}$[22] are also reported.

The X-band EPR spectra of frozen solutions exhibit a strong absorption at ≈ 3200 G, attributable to the allowed transitions $\Delta M_S = 1$. For the cyclam complexes $[Cu_2\mathbf{L^{3,4}}]^{4+}$ the EPR parameters are similar which means that the copper ions are held in an identical environment. The $g_{\|}$ values are found to be the same for both complexes, namely 2.182. These values are greater than the *g* ones, which is typical of axially symmetric d^9 copper complexes and a $d_{x^2-y^2}$ ground state.[23] The hyperfine coupling constants $A_{\|}$ (100 10^{-4} cm^{-1}) are as expected,[8,22] about half the value of the mononuclear complexes, in which the metal is held in a square planar environment. In the parallel region, the hyperfine system shows seven lines. This signal is typical of copper(II) dimers weakly coupled and can be interpreted as a triplet state spectrum originating from exchange-coupled pairs of copper(II) ions.[22] Thus, two series of seven lines are theoretically expected,[24] one for each allowed ΔM_S = 1 transition; they correspond to the hyperfine coupling between the two copper d^9 ions (I_{Cu} = 3/2). According to the zero-field splitting amplitude, the two septets can either overlap (weak D factor) or be shifted, even if in this case it is difficult to observe all the lines.[4c,5b] The simulation[25] of

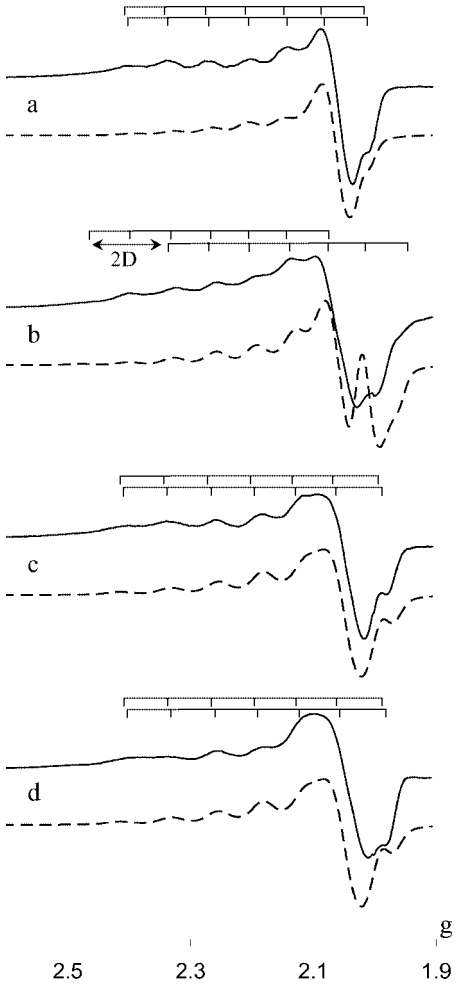

Figure 8. Experimental EPR spectra of biscyclen complexes. a: $[Cu_2\mathbf{L^1}](BF_4)_4$. b: $[Cu_2\mathbf{L^2}](BF_4)_4$ and of biscyclam complexes. c: $[Cu_2\mathbf{L^3}](BF_4)_4$. d: $[Cu_2\mathbf{L^4}](BF_4)$. Dotted spectra: simulated EPR spectra.

the spectrum can then help for the interpretation of the signals: for the complexes $[Cu_2\mathbf{L^{3,4}}]^{4+}$, the simulated spectra tend to demonstrate that the two septets overlap. This means that the exchange interaction between the two copper ions is weak. Nevertheless, the Cu^{II}–Cu^{II} interaction is present as shown by the existence of more than four hyperfine lines in the spectra of the $[Cu_2\mathbf{L^{3,4}}]^{4+}$ complexes and by

 © 2005 Wiley-VCH Verlag GmbH & Co. KGaA, Weinheim

Table 4. EPR parameters of $[Cu_2\mathbf{L^{1-4}}]$ complexes in frozen solution (DMF) at 100 K.

	$g_{\parallel}$	$g_{\perp}$	$A_{\parallel}$ [10^{-4} cm^{-1}]	$D_{\parallel}$ [10^{-4} cm^{-1}][a]
$[Cu_2\mathbf{L^1}]^{4+}$[b]	2.207	2.065	81	8
$[Cu_2\mathbf{L^1}]^{4+}$[c]	2.20	2.07	102	
$[Cu_2\mathbf{L^2}]^{4+}$[b]	2.193	2.03	90	90
$[Cu(cyclen)]^{2+}$[d]	2.198	2.057	184	
$[Cu_2\mathbf{L^3}]^{4+}$[b]	2.182	2.05	100	8
$[Cu_2\mathbf{L^3}]^{4+}$[c]	2.19	2.06	107	
$[Cu_2\mathbf{L^4}]^{4+}$[b]	2.182	2.05	100	8
$[Cu(cyclam)]^{2+}$[d][24]	2.186	2.049	205	

$$r = \sqrt[3]{\frac{0.65\, g_{\parallel}^2}{D_{\parallel}}} \qquad (1)$$

[a] Parameter obtained by simulation (Simfonia).[25] [b] This work. [c] Ref.[22] [d] Ref.[12].

smaller values for $A_{\parallel}$.[4c,5,8,22,24] For an analogous series of xylyl-bismacrocyclic dicopper acetate complexes,[22] a second weak absorption at $\approx$ 1550 G was previously reported and assigned to the forbidden $\Delta M_S = 2$ transition. This transition was claimed as a further proof of intramolecular electron exchange between the two copper ions. Unfortunately, we were not able to highlight this signal for the two complexes $[Cu_2\mathbf{L^{3,4}}]^{4+}$ certainly because in these compounds the presence of a noncoordinating anion (BF_4^-) in solution prevents any strengthening of such interaction between the metal ions.

For the cyclen complexes $[Cu_2\mathbf{L^{1,2}}]^{4+}$, the comparison of the EPR parameters with the ones of the mononuclear $[Cu(cyclen)]^{2+}$ shows that $g_{\parallel}$ and $g_{\perp}$ are similar for all complexes. As already described for the cyclam complexes, the $A_{\parallel}$ values of $[Cu_2\mathbf{L^{1,2}}]^{4+}$ are half that determined for mononuclear $[Cu(cyclen)]^{2+}$. Moreover, the $g_{\parallel}$ parameters of $[Cu_2\mathbf{L^{1,2}}]^{4+}$ are higher than the ones of the cyclam analogues. This indicated that the coordination Scheme of copper ions in cyclen and cyclam is different. It is confirmed by the $A_{\parallel}$ values since, in cyclen complexes, the hyperfine coupling constants are smaller than the cyclam ones. It corresponds to a coordination of the copper ions outside the cyclen cavity, which is consistent with the crystal structure and the UV/Visible spectra of the complexes. Interestingly, the EPR spectrum of the pyridyl $[Cu_2\mathbf{L^2}]^{4+}$ complex exhibits more than seven lines in the parallel region. The simulated spectrum allows the proposal of an hyperfine system of nine lines. In this case, we assumed that the two septets are shifted by zero-field splitting 2D[24] and the simulation of the spectrum allowed the determination of a $D_{\parallel}$ parameter of 90 10^{-4} cm^{-1}. This value is tenfold increased compared to the ones simulated for the other complexes. This means that in the pyridyl $[Cu_2\mathbf{L^2}]^{4+}$ complex, the interaction between the metallic centres is stronger. From the D value, one can estimate the mean distance between the two paramagnetic cations, provided that the zero-field splitting is due to a pure dipole–dipole interaction:[24] from Equation (1) (Table 4), one obtains r_{Cu-Cu} = 7.03 Å for complex $[Cu_2\mathbf{L^2}]^{4+}$ in frozen DMF solution. This would indicate that in solution, the probable coordination of the pyridyl nitrogen shown by UV/Visible spectroscopy, would tend to move the two copper ions closer and then to favour exchange interaction between them.

Conclusions

The dinuclear Cu^{II} and Ni^{II} complexes based on biscyclen $\mathbf{L^{1,2}}$ or biscyclam $\mathbf{L^{3,4}}$ ligands have been studied. X-ray analysis of copper biscyclen complexes have shown that the pyridyl nitrogen atom [N(*py*)] coordinates one of the two copper ions. In solution, the comparison of the UV/Visible spectra of these two complexes indicates that the coordination of the N(*py*) atom is maintained, even upon acidification. The coordination of the N(*py*) atom leads to the shortening of the intermetallic copper–copper distance: as a result, the dipolar intermetallic interaction is promoted. This is underlined by the EPR spectrum of $[Cu_2\mathbf{L^2}]^{4+}$ complex, which exhibits in the parallel region nine equidistant lines (against seven for $[Cu_2\mathbf{L^1}]^{4+}$).

For the cyclam complexes, no evidence of the N(*py*) atom coordination to one of the two metal centres was found. However, EPR spectra of these dinuclear copper complexes show that a weak intermetallic interaction is still present since the parallel region of the spectra present seven equidistant lines. Nevertheless, for the corresponding nickel biscyclam complexes, electrochemical oxidation–reduction cycles, which promote a configurational rearrangement between type III and type I configurations of Ni biscyclam, can induce a coordination of the N(*py*) atom in the type I geometry. In this case, the strengthening of the metal–metal interaction is suggested by the splitting of the corresponding CV traces.

From this study, one can conclude that the existence of a potentially coordinating atom on the intercycle spacer can improve the metal–metal interaction. Consequently, bismacrocycles possessing more than one potentially coordinating atom on the spacer are currently under study.

Experimental Section

Syntheses: The metals salts were purchased from Aldrich. The other reagents were used as highest grade commercially available without further purification.

Ligand Synthesis: The synthesis and the characterisation of ligands $\mathbf{L^1}$ and $\mathbf{L^3}$ have been described previously elsewhere.[7] Ligands $\mathbf{L^2}$ and $\mathbf{L^4}$ have been synthesised according to the same procedure from cyclen or cyclam glyoxal ligands and 2,6-bis(bromomethyl)-pyridine.[26]

Ligand $\mathbf{L^2}$: Yield 69%. ^{13}C NMR ($CDCl_3$): δ = 44.4, 45.6, 46.3, 51.2, 60.5 (CH_2N), 121.1, 136.6, 158.4 (C_{ar}). Elemental analysis calcd. (%) for the hydrochloride salt of L^2: $C_{23}H_{45}N_9 \cdot 6HCl \cdot H_2O$: C 40.36, H 7.81, N 18.42; found: C 40.23, H 7.76, N 18.17.

Ligand $\mathbf{L^4}$: Yield 71%. ^{13}C NMR ($CDCl_3$): δ = 26.2–28.7 (CH_2CH_2N), 47.3, 47.9, 48.8, 49.1, 50.6, 53.2, 55.3, 59.5 (CH_2N), 120.9, 136.3, 158.6 (C_{ar}). Elemental analysis calcd. (%) for the hydrochloride salt of L^4: $C_{27}H_{53}N_9 \cdot HCl \cdot 2H_2O$: C 42.75, H 8.37, N 16.62; found: C 42.99, H 8.11, N 16.45.

 © 2005 Wiley-VCH Verlag GmbH & Co. KGaA, Weinheim

Synthesis of $Cu_2L^1(ClO_4)_4{\cdot}4H_2O$: The neutral ligand ($5.2{\cdot}10^{-5}$ mol) was dissolved in distilled water (10 mL) followed by the addition of an ethanolic solution of the copper(II) perchlorate salt ($1.17{\cdot}10^{-4}$ mol). The blue solution was refluxed for 2 h and the solvents were evaporated under vacuum. The solid was washed twice with absolute ethanol. Elemental analysis calcd. (%) for $C_{24}H_{54}Cl_4Cu_2N_8O_{20}$: C 27.62, H 5.21, N 10.74; found: C 27.99, H 5.14, N 10.45.

This solid was further dissolved in water and the diffusion of an aqueous saturated sodium perchlorate solution produced monocrystals of $[Cu_2L^1(H_2O)_2](ClO_4)_4{\cdot}H_2O$, suitable for X-ray analysis.

Synthesis of $Cu_2L^{1-4}(BF_4)_4$ and $Ni_2L^{1-4}(BF_4)_4$: The neutral ligands ($5.2\ 10^{-5}$ mol) were dissolved in distilled water (10 mL) and aqueous solutions of copper(II) or nickel (II) salts ($1.17\ 10^{-4}$ mol in 5 mL) were added dropwise. The resulting solutions were heated at reflux for 2 h, the solvents were evaporated under vacuum afterwards. The solids were washed twice with absolute ethanol.

Elemental analysis for $Cu_2L^1(BF_4)_4{\cdot}2H_2O$: $C_{24}H_{50}B_4Cu_2N_8F_{16}O_2$ calcd. (%): C 30.12, H 5.27, N 11.71; found: C 29.99, H 5.02, N 12.39. $Cu_2\mathbf{L^2}(BF_4)_4$, $3H_2O$ $C_{23}H_{51}B_4Cu_2N_9F_{16}O_3$ calcd. (%): C 28.30, H 5.27, N 12.92; found: C 28.22, H 4.83, N 12.67. $Cu_2\mathbf{L^3}(BF_4)_4$ $C_{28}H_{54}B_4Cu_2N_8F_{16}$ calcd. (%): C 34.42, H 5.57, N 11.47; found: C 34.78, H 5.60, N 11.53. $Cu_2\mathbf{L^4}(BF_4)_4$, $2H_2O$ $C_{27}H_{57}B_4Cu_2N_9F_{16}O_2$ calcd. (%): C 31.98, H 5.67, N 12.43; found: C 32.17, H 5.32, N 11.90.

$Ni_2\mathbf{L^1}(BF_4)_4{\cdot}1H_2O$: $C_{24}H_{48}B_4Ni_2N_8F_{16}O$ calcd. (%): C 31.02, H 5.21, N 12.06; found: C 30.73, H 5.61, N 12.36. $Ni_2\mathbf{L^2}(BF_4)_4$, $C_{23}H_{45}B_4Ni_2N_9F_{16}$ calcd. (%): C 30.28, H 4.97, N 13.82, found: C 30.61, H 5.34, N 13.69. $Ni_2\mathbf{L^3}(BF_4)_4$, $3H_2O$ $C_{28}H_{60}B_4Ni_2N_8F_{16}O_3$ calcd. (%): C 32.94, H 5.92, N 10.97; found: C 32.85, H 5.58, N 10.34. $Ni_2\mathbf{L^4}(BF_4)_4$, $2H_2O$ $C_{27}H_{57}B_4Ni_2N_9F_{16}O_2$ calcd. (%): C 32.29, H 5.72, N 12.55; found: C 32.34, H 5.08, N 11.99.

Crystals of $Cu_2\mathbf{L^2}(BF_4)_4$ suitable for X-ray crystallography were obtained by slow diffusion of diethyl ether into an acetonitrile solution of the complex.

Spectroscopic Measurements: Electronic spectra in aqueous or acetonitrile solutions (10^{-3} mol L^{-1}) were all measured in the 300–900 nm range with a Lambda 6 Perkin–Elmer spectrophotometer. The acetonitrile solution of trifluoroacetic acid (0.1 mol L^{-1}) was prepared by dilution of trifluoroacetic acid Aldrich product at 99%. The acidification of acetonitrile copper complex solutions was obtained by successive additions of trifluoroacetic acid solution (100 μL).

The X-band EPR spectra (9.40 GHz) were recorded in DMF solutions at 100 K, with a Bruker spectrophotometer ELEXSYS 500. Simulations were carried out using the software Simfonia.[25]

Electrochemical Measurements: Voltammetric data were recorded with an Autolab with a PGSTAT12 potentiostat (ECO Chemie) associated to a conventional three electrodes electrochemical cell, the working electrode being a glassy carbon or platinum disk, a platinum plate being used as a counter electrode and in aqueous medium a saturated calomel electrode was used as the reference while in acetonitrile a silver electrode separated from the complex solution was used as a pseudo reference. In acetonitrile, the potential of the pseudo reference was measured vs. the ferricinium/ferrocene couple. Complexes concentrations were always close to 10^{-3} mol L^{-1} and in acetonitrile tetrabutylammonium hexafluorophosphate 10^{-1} mol L^{-1} was used as the supporting electrolyte. In concentrated perchloric acid solutions no additional electrolyte was employed.

Computational Details: The calculations have been performed using the Gaussian 98[27] program package. Both geometry and energy calculations were performed at the UHF/LANL2 MB level. Each molecular structure has been fully optimised and characterised as minimum by frequency analysis. Single point energy have further been calculated at the UB3LYP/LANL2DZ level [the LANL2DZ basis set as parameterised in Gaussian has been supplemented with polarisation function on nitrogen atoms (d_N = 0.80)].

Crystal Structure Determination: The crystal data were collected at 173 K with a Kappa CCD diffractometer using monochromated Mo-K_α radiation (λ = 0.71073 Å).

Table 5. Crystal data and details of the structure determination for $[Cu_2\mathbf{L^1}](ClO_4)_4$ and $[Cu_2\mathbf{L^2}\ BF_4]\ (BF_4)_3$.

	$[Cu_2\mathbf{L^1}](ClO_4)_4(H_2O)_3$	$[Cu_2\mathbf{L^2}\ BF_4](BF_4)_3$
Empirical formula	$C_{24}\ H_{52}\ N_8\ O_{19}\ Cl_4\ Cu_2$	$C_{23}\ H_{45}\ N_9\ B_4\ F_{16}\ Cu_2$
Formula mass	1025.62	921.97
Temperature [K]	173	173
Crystal system	monoclinic	orthorhombic
Space group	$P12_{1/n}1$	*Pbca*
Color	blue	blue
a [Å]	14.9096(3)	20.1554(2)
b [Å]	8.8632(2)	20.2243(3)
c [Å]	30.7758(6)	17.7403(2)
α [°]	90	90
β [°]	96.913(5)	90
γ [°]	90	90
Volume [Å^3]	4037(1)	7231.5(2)
Z	4	8
$D_{calcd.}$ [g cm^{-3}]	1.69	1.69
Absorption coefficient [mm^{-1}]	1.402	1.292
F(000)	2120	3744
λ (Mo-K_α) [Å]	0.71073	0.71073
No independent reflections	9584	11472
No reflcns. [$I > 3.0\ \sigma(I)$]	4599	4506
*R*1	0.056	0.072
wR_2	0.080	0.085
Goodness-of-fit on F^2	1.442	1.200

 © 2005 Wiley-VCH Verlag GmbH & Co. KGaA, Weinheim

The structures were solved by direct methods. After refinement of the non-hydrogen atoms, difference-Fourier maps revealed maxima of residual electron density close to positions expected for hydrogen atoms. Hydrogen atoms were introduced as fixed contributors at calculated positions [C–H = 0.95 Å, B(H) = 1.3 B_{eqv}]. Final difference maps revealed no significant maxima. All calculations were using the Nonius OpenMoleN package.[28] Neutral atom scattering factor coefficients and anomalous dispersion coefficients were taken from a standard source.

CCDC-261457 (for $[Cu_2\mathbf{L^1}(H_2O)_2]\cdot 4ClO_4\cdot 3H_2O$) and CCDC-261458 (for $[Cu_2\mathbf{L^2}BF_4]\cdot 3BF_4$) contains the supplementary crystallographic data for this paper. These data can be obtained free of charge from The Cambridge Crystallographic Data Centre via www.ccdc.cam.ac.uk/data_request/cif.

Crystal data and details of the structure determination for $[Cu_2\mathbf{L^1}]\cdot(ClO_4)_4$ and $[Cu_2\mathbf{L^2}BF_4]\cdot(BF_4)_3$ are given in the following Table 5.

Acknowledgments

We thank Dr. A. de Cian (Université Louis Pasteur, Strasbourg, France) for the single-crystal X-ray analyses, Dr. Y. Frappart (Université René Descartes, Paris, France) for the EPR spectra. Dr. E. Derat (Université de Reims Champagne Ardenne, France) is gratefully acknowledged for helpful discussions in molecular modelling as well as the computational centre of "Université de Reims Champagne Ardenne" for computational facilities.

[1] A. Bianchi, M. Micheloni, P. Paoletti, *Coord. Chem. Rev.* **1991**, *110*, 17.
[2] a) J. R. Morphy, D. Parker, R. Alexander, A. Bains, M. A. W. Eaton, A. T. Millican, K. Titmas, D. J. Weatherby, *J. Chem. Soc. Chem. Commun.* **1988**, 156; b) J. R. Morphy, D. Parker, R. Kataky, M. A. W. Eaton, A. T. Millican, A. Phipps, C. J. Walker, *J. Chem. Soc. Chem. Commun.* **1989**, 792.
[3] A. E. Merbach, E. Tóth (Eds.), *The Chemistry of Contrast Agents in Medical Magnetic Resonance Imaging*, Wiley, Chichester, **2001**.
[4] a) A. Mc.Auley, S. Subramanian, *Inorg. Chem.* **1997**, *36*, 5376; b) A. McAuley, S. Subramanian, M. J. Zawarotko, K. Biradha, *Inorg. Chem.* **1999**, *38*, 5078; c) M. Lachkar, R. Guilard, A. Atmani, A. De Cian, J. Fischer, R. Weiss, *Inorg. Chem.* **1998**, *37*, 1575; d) P. Comba, Y. D. Lampeka, L. Lötzbeyer, A. I. Prikhod'ko, *Eur. J. Inorg. Chem.* **2003**, 34; e) A. Bencini, E. Berni, A. Bianchi, C. Giorgi, B. Valtancoli, D. K. Chand, H. J. Schneider, *Dalton Trans.* **2003**, 793; f) Y. Dong, L. F. Lindoy, P. Turner, G. Wei, *Dalton Trans.* **2004**, 1264.
[5] a) L. Fabbrizzi, F. Forlini, A. Perotti, B. Seghi, *Inorg. Chem.* **1984**, *23*, 807; b) R. Schneider, A. Riesen, T. A. Kaden, *Helv. Chim. Acta* **1986**, *69*, 53; c) L. Fabbrizzi, L. Montagna, A. Poggi, T. A. Kaden, Siegfried, *Inorg. Chem.* **1986**, *25*, 2672; d) M. Ciampolini, L. Fabbrizzi, A. Perotti, A. Poggi, B. Seghi, F. Zanobini, *Inorg. Chem.* **1987**, *26*, 3527; e) L. Fabbrizzi, L. Montagna, A. Poggi, T. A. Kaden, Siegfried, *J. Chem. Soc., Dalton Trans.* **1987**, 2631; f) T. A. Kaden, *Coord. Chem. Rev.* **1999**, *190–192*, 371.
[6] a) D. T. Pierce, T. L. Hatfield, E. J. Billo, Y. Ping, *Inorg. Chem.* **1997**, *36*, 2950; b) C. Amatore, J. M. Barbe, C. Bucher, E. Duval, R. Guilard, J. N. Verpeaux, *Inorg. Chim. Acta* **2003**, *356*, 267; c) C. Bucher, J. C. Moutet, J. Pécaut, G. Royal, E. Saint-Aman, F. Thomas, *Inorg. Chem.* **2004**, *43*, 3777.
[7] M. Le Baccon, F. Chuburu, L. Toupet, H. Handel, M. Soibinet, I. Déchamps-Olivier, J. P. Barbier, M. Aplincourt, *New J. Chem.* **2001**, *25*, 1168.
[8] M. Soibinet, I. Déchamps-Olivier, E. Guillon, J. P. Barbier, M. Aplincourt, F. Chuburu, M. Le Baccon, H. Handel, *Eur. J. Inorg. Chem.* **2003**, 1984.
[9] A. E. Goeta, J. A. K. Howard, D. Maffeo, H. Puschmann, J. A. Gareth Williams, D. S. Yufit, *J. Chem. Soc., Dalton Trans.* **2000**, 1873.
[10] Y. Dong, G. A. Lawrence, L. F. Lindoy, P. Turner, *Dalton Trans.* **2003**, 1567.
[11] B. J. Hathaway, A. A. G. Tomlinson, *Coord. Chem. Rev.* **1970**, *5*, 1.
[12] K. Miyoshi, T. Tanaka, E. Kimura, S. Tsuboyama, S. Murata, H. Shimizu, K. Ishizu, *Inorg. Chim. Acta* **1983**, *78*, 23.
[13] H. Kurosaki, C. Bucher, E. Espinosa, J. M. Barbe, R. Guilard, *Inorg. Chim. Acta* **2001**, *322*, 145.
[14] T. Yokoyama, H. Kitagawa, H. A. Iwasawa, M. Zenki, *Inorg. Chim. Acta* **1996**, *253*, 1.
[15] L. Sabatini, L. Fabbrizzi, *Inorg. Chem.* **1979**, *18*, 438.
[16] a) A. Bencini, L. Fabbrizzi, A. Poggi, *Inorg. Chem.* **1981**, *20*, 2544; b) A. Buttafava, L. Fabbrizzi, A. Perotti, A. Poggi, G. Poli, B. Seghi, *Inorg. Chem.* **1986**, *25*, 1456.
[17] a) L. Fabbrizzi, *Comments Inorg. Chem.* **1986**, *25*, 4197; b) C. Bisi Castellani, M. Licchelli, A. Perotti, A. Poggi, *J. Chem. Soc., Chem. Commun.* **1984**, 806; c) F. V. Lovecchio, E. S. Gore, D. H. Busch, *J. Am. Chem. Soc.* **1974**, *96*, 3109.
[18] E. Kimura, T. Koike, R. Machida, R. Nagai, M. Kodama, *Inorg. Chem.* **1984**, *23*, 4181.
[19] B. Bonisch, C. K. Poon, M. L. Tobe, *Inorg. Chem.* **1965**, *4*, 1102.
[20] M. A. Donnelly, M. Zimmer, *Inorg. Chem.* **1999**, *38*, 1650.
[21] X. Liang, J. A. Parkinson, M. Weishäupl, R. O. Gould, S. J. Paisey, H. Park, T. M. Hunter, C. A. Blindauer, S. Parsons, P. J. Sadler, *J. Am. Chem. Soc.* **2002**, *124*, 9105.
[22] S. Brandès, C. Gros, F. Denat, P. Pullumbi, R. Guilard, *Bull. Soc. Chim. Fr.* **1996**, *133*, 65.
[23] B. J. Hatthaway, D. E. Billing, *Coord. Chem. Rev.* **1970**, *5*, 143.
[24] E. F. Hasty, L. J. Wilson, D. N. Henrickson, *Inorg. Chem.* **1978**, *17*, 1834.
[25] Simfonia, EPR Data Analysis and Simulation, **1994–96**, Bruker.
[26] M. A. Reppy, M. E. Cooper, J. L. Smithers, D. L. Gin, *J. Org. Chem.* **1999**, *64*, 4191.
[27] M. J. Frisch, G. W. Trucks, H. B. Schlegel, G. E. Scuseria, M. A. Robb, J. R. Cheesemen, V. G. Zakrzewski, J. A. Montgomery, R. E. Stratmann, J. C. Burant, S. Dapprich, J. M. Millam, A. D. Daniels, K. N. Kudin, M. C. Strain, O. Farkas, J. Tomasi, V. Barone, M. Cossi, R. Cammi, M. Mennucci, C. Pomelli, C. Adamo, S. Clifford, J. Ochterski, G. A. Petersson, P. Y. Ayala, Q. Cui, K. Morokuma, D. K. Malik, A. D. Rabuk, K. Raghavachari, J. B. Foresman, J. Cioslowski, J. V. Ortiz, B. B. Stefanov, G. Liu, A. Liashenko, P. Piskorz, I. Komaromi, R. Gomperts, R. L. Martin, D. J. Fox, T. Keith, M. A. Al-Laham, C. Y. Peng, A. Nanayakkara, G. Gonzalez, M. Challacombe, P. M. W. Gill, B. G. Johnson, W. Chen, M. W. Wong, J. L. Andres, M. Head-Gordon, E. S. Replogle, J. A. Pople, *Gaussian 98* (Revision A.1), Gaussian, Inc. Pittsburg PA, **1998**.
[28] *OpenMoleN*, Interactive Structure Solutions, B. V., Nonius Delft, The Netherlands, **1997**.

Received: February 8, 2005

 © 2005 Wiley-VCH Verlag GmbH & Co. KGaA, Weinheim

Sonochemical Synthesis and Characterization of $Ni(C_4H_6N_2)_6(PF_6)_2$, $Fe(C_4H_6N_2)_6(BF_4)_2$, and $Ni(C_4H_6N_2)_6(BF_4)_2$ in 1-Butyl-3-methylimidazole with Hexafluorophosphate and Tetrafluoroborate

David S. Jacob,[a] Shirli Makhluf,[a] Ishay Brukental,[b] Ronit Lavi,[b] Leonid A. Solovyov,[c] Israel Felner,[d] Israel Nowik,[d] Rachel Persky,[a] Hugo E. Gottlieb,[a] and Aharon Gedanken*[a]

Keywords: Ionic liquids / Sonochemistry / Iron / Nickel / Imidazole / X-ray powder diffraction / Structure analysis

This paper reports on the inorganic sonochemical synthesis of crystalline $Ni(C_4H_6N_2)_6(PF_6)_2$, $Fe(C_4H_6N_2)_6(BF_4)_2$, and $Ni(C_4H_6N_2)_6(BF_4)_2$ in the ionic liquids, 1-butyl-3-methylimidazolium hexafluorophosphate $(BMI)^+(PF_6)^-$ and 1-butyl-3-methylimidazolium tetrafluoroborate $(BMI)^+(BF_4)^-$. The structures of the compounds were determined and refined by using powder X-ray diffraction methods. The salts crystallize in the trigonal $P\bar{3}$ space group. IR, Raman and ^{19}F NMR spectroscopic studies confirm that the PF_6^- and BF_4^- anions are not bonded to the metal cations. Magnetic measurements reveal the paramagnetic nature of the complexes. Mössbauer investigations show that the iron atom in $Fe(C_4H_6N_2)_6(BF_4)_2$ is in the oxidation +2 state. The broad EPR signals, which reflect the octahedral symmetry of the nickel complexes, were measured for $Ni(C_4H_6N_2)_6(PF_6)_2$ and $Ni(C_4H_6N_2)_6(BF_4)_2$.
(© Wiley-VCH Verlag GmbH & Co. KGaA, 69451 Weinheim, Germany, 2005)

Introduction

Room-temperature ionic liquids (RTILs) have aroused increasing interest worldwide as solvents, templates, and charge-compensating groups for numerous types of reactions due to their unique physical properties.[1a–1d] There are only very few reports in the area of synthetic coordination chemistry in ionic liquids.[2–5]

Recently, we have presented a report on the inorganic sonochemical synthesis of a $Fe^{II}(1\text{-methylimidazole})_6(PF_6)_2$ in $(BMI)^+(PF_6)^-$ ionic liquid solvents.[6] The product was obtained as a result of the sonochemical decomposition of $Fe(CO)_5$ in $(BMI)^+(PF_6)^-$. The charge on the Fe^{II} ion in the complex is stabilized by the two PF_6^- anions originating from the ionic liquid. We found that the PF_6^- anions enter the final structure, wherein the ionic liquids act as clean and effective solvents for the crystallization of the complex. However, it is usually assumed that the ionic liquids are entirely innocuous and noncoordinating solvents.

[a] Department of Chemistry and Kanbar Laboratory for Nanomaterials at the Bar-Ilan University Center for Advanced Materials and Nanotechnology, Bar-Ilan University, 52900 Ramat-Gan, Israel
E-mail: gedanken@mail.biu.ac.il
[b] Department of Physics, Bar-Ilan University, 52900 Ramat-Gan, Israel
[c] Institute of Chemistry and Chemical Technology, Siberian Branch, Russian Academy of Sciences, 660049 Krasnoyarsk, Russia
[d] The Racah Institute of Physics, The Hebrew University of Jerusalem, 91904 Jerusalem, Israel

In the current study, we have continued to explore inorganic sonochemical reactions in ionic liquids, and in this paper, we report the synthesis of iron and nickel complexes of 1-methylimidazole in two different ionic liquids (as solvents) under sonochemical conditions using carbonylmetal compounds as precursors. The precursors in all these cases are the corresponding carbonyl complexes [$Fe(CO)_5$ and $Ni(CO)_4$], which are not soluble in $(BMI^+)(PF_6^-)$ and $(BMI^+)(BF_4^-)$ ionic liquids. It is well known that pentacarbonyliron and tetracarbonylnickel yield amorphous iron and amorphous nickel when sonicated in decalin (or any other nonvolatile organic solvent) under argon.[7a,7b] On the other hand, the decomposition of $Fe(CO)_5$ and $Ni(CO)_4$ in decalin under oxygen yields amorphous metal oxides.[8] The sonochemical decomposition of these carbonyl complexes in $(BMI^+)(PF_6^-)$ and $(BMI^+)(BF_4^-)$ form crystalline products. The current paper demonstrates the generality of our previous study, and that in none of the four cases (two carbonyl complexes in two solvents) are metal oxides formed.

The sonochemical products of the decomposition of the carbonyl complexes in ionic liquids are crystalline. They differ from the amorphous products formed when the same reactions are performed in nonvolatile organic solvents. In the sonochemical reactions in ionic liquids, we found that the anions of the ionic liquid solvents serve as charge-compensating groups and cause the crystallization of the products.

Powder X-ray diffraction (PXRD) is used to investigate the crystal structure of the metal complexes synthesized un-

 DOI: 10.1002/ejic.200500024 © 2005 Wiley-VCH Verlag GmbH & Co. KGaA, Weinheim

der the sonochemical conditions. The synthesized inorganic complexes are characterized by C, H, N analysis and several spectroscopic methods, such as Mössbauer, IR, Raman, MS, EPR, and ^{19}F NMR. The thermal stability of the (*N*-methylimidazole)metal complexes and of ionic liquid solvents is studied with the help of thermal gravimetric analysis (TGA). The magnetic properties of the synthesized complexes of iron and nickel are also reported in this paper.

Results and Discussion

Powder XRD

The unit cell parameters (Table 1) of (1-methylimidazole)$_6$-Ni$(PF_6)_2$ (**A**), (1-methylimidazole)$_6$Fe$(BF_4)_2$ (**B**) and (1-methylimidazole)$_6$Ni$(BF_4)_2$ (**C**) were determined from PXRD peak positions. The initial atomic coordinates were derived from the structure models of (1-methylimidazole)$_6$-Fe$(PF_6)_2$,[6] (5-methylpyrazole)$_6$Ni$(ClO_4)_2$,[9] and (2-methyltetrazole)$_6$Ni$(BF_4)_2$,[10] whose unit-cell dimensions and PXRD patterns are analogous to those of **A**, **B** and **C**. The crystal structure of **A** was found to be identical to that of (1-methylimidazole)$_6$Fe$(PF_6)_2$.[6] The structure refinement was performed by applying the Derivative Difference Minimization (DDM)[11] method, in which derivatives of the profile difference are minimized, instead of the squared difference, which allows a full-profile refinement independently of the underlying background curve. The calculations were carried out using a computer code package based on a corrected and modified version of the Rietveld[12] refinement program DBWS.[13] The PXRD patterns of both **B** and **C** exhibited very complex background components caused, presumably, by an amorphous admixture and the structural faults discussed below, which made the application of DDM essential.

The PXRD structure refinement and the electron density map analysis of **B** and **C** revealed additional pseudo-positions of metal and fluorine atoms in the unit cell, which are related to the main ones by a mirror plane operation (x, y, $1/2 - z$). The presence of these positions was indicative of structural faults such as twin and/or line defects. The twinning and molecular disorder is known to be a typical phenomenon for structures of this type.[6,9,10,14a,14b] To allow for the presence of the faults, the structure model of **B** and **C** was constructed from two sub-sets of atomic positions related to each other by the mirror plane. The occupancies of the two sub-sets were refined independently for the anions and the cations applying the stoichiometric constraints. Atomic coordinates of methylimidazole were allowed to refine with soft constraints applied to the C–C and the C–N distances. The hydrogen atoms were added geometrically and refined using the riding model.

The structure refinement results are summarized in Tables 1, 2, 3 and 4. The final consistency between the observed and calculated PXRD profiles after the DDM structure refinement is illustrated in Figure 1. The crystal structure and the alternative positions of molecules in the unit cell are shown in Figures 2 and 3. The metal atoms in **A**, **B** and **C** have a typical octahedral coordination of six equivalent nitrogen atoms of the methylimidazole groups. The tetrafluoroborate anion has two alternative orientations with equal probabilities as follows from the occupancies of the respective atomic positions (Tables 2 and 3). The occupancies of the alternative pseudo-positions related to the (methylimidazole)metal complexes indicate a high concentration of the structural faults. The faults, in turn, may be responsible for the atomic disorder reflected in the high isotropic displacement parameters.

Table 1. Crystallographic details.

	A	**B**	**C**
Empirical formula	$Ni(C_4H_6N_2)_6(PF_6)_2$	$Fe(C_4H_6N_2)_6(BF_4)_2$	$Ni(C_4H_6N_2)_6(BF_4)_2$
Formula mass	841.27	722.09	724.95
Crystal system	trigonal	trigonal	trigonal
Space group	$P\bar{3}$	$P\bar{3}$	$P\bar{3}$
a [Å]	11.3758(2)	11.2574(5)	11.1678(3)
c [Å]	7.9948(1)	7.7756(3)	7.7560(2)
V [Å^3]	895.99(2)	853.38(6)	837.73(4)
Z	1	1	1
Radiation type	Cu-K_α	Cu-K_α	Cu-K_α
Wavelength [Å]	1.5418	1.5418	1.5418
Temperature [K]	293	293	293
Data collection method	θ-2θ scan	θ-2θ scan	θ-2θ scan
Increment in 2θ [°]	0.02	0.02	0.02
2θ range [°]	8–90	8–80	8–80
Refinement on	–	I_{net}	I_{net}
R_B	–	0.047	0.040
R_{DDM}	–	0.138	0.129
H-atom treatment	–	H atoms constrained	H atoms constrained
Weighting scheme	–	based on measured s.u. values	based on measured s.u. values
CCDC-	–	271215	271216

 © 2005 Wiley-VCH Verlag GmbH & Co. KGaA, Weinheim

Table 2. Fractional atomic coordinates, occupancies and isotropic displacement parameters [Å^2] for **B**.

	Occupancy	*x*	*y*	*z*	B_{iso}
Fe(1)	0.59(1)	0	0	0	5.7(2)
N(1)	0.59(1)	0.1150(28)	0.1812(26)	0.1618(31)	8.5(3)
N(2)	0.59(1)	0.2849(16)	0.3786(17)	0.2686(30)	8.5(3)
C(1)	0.59(1)	0.2459(23)	0.2819(30)	0.1410(27)	8.5(3)
C(2)	0.59(1)	0.1717(28)	0.3405(27)	0.3575(27)	8.5(3)
C(3)	0.59(1)	0.0730(22)	0.2132(30)	0.3038(46)	8.5(3)
C(4)	0.59(1)	0.4130(13)	0.4992(14)	0.3088(50)	8.5(3)
B(1)	0.50(3)	2/3	1/3	0.2400(41)	18.5(5)
F(1)	0.50(3)	2/3	1/3	0.0714(29)	18.5(5)
F(2)	0.50(3)	0.7275(21)	0.4631(17)	0.3062(36)	18.5(5)
Fe(1A)	0.41	0	0	1/2	5.7
N(1A)	0.41	0.1150	0.1812	0.3382	8.5
N(2A)	0.41	0.2849	0.3786	0.2314	8.5
C(1A)	0.41	0.2459	0.2819	0.3590	8.5
C(2A)	0.41	0.1717	0.3405	0.1425	8.5
C(3A)	0.41	0.0730	0.2132	0.1962	8.5
C(4A)	0.41	0.4130	0.4992	0.1912	8.5
B(1A)	0.50	2/3	1/3	0.2600	18.5
F(1A)	0.50	2/3	1/3	0.4286	18.5
F(2A)	0.50	0.7275	0.4631	0.1938	18.5

Table 3. Fractional atomic coordinates, occupancies and isotropic displacement parameters (Å^2) for **C**.

	Occupancy	*x*	*y*	*z*	B_{iso}
Ni(1)	0.58(1)	0	0	0	5.2(1)
N(1)	0.58(1)	0.1051(21)	0.1731(17)	0.1594(20)	9.4(2)
N(2)	0.58(1)	0.2793(10)	0.3692(11)	0.2558(31)	9.4(2)
C(1)	0.58(1)	0.2353(18)	0.2714(20)	0.1291(20)	9.4(2)
C(2)	0.58(1)	0.1734(20)	0.3396(20)	0.3620(17)	9.4(2)
C(3)	0.58(1)	0.0712(18)	0.2114(22)	0.3016(30)	9.4(2)
C(4)	0.58(1)	0.4071(9)	0.4926(10)	0.2960(24)	9.4(2)
B(1)	0.50(3)	2/3	1/3	0.2550(44)	16.8(4)
F(1)	0.50(3)	2/3	1/3	0.0837(26)	16.8(4)
F(2)	0.50(3)	0.7260(12)	0.4669(10)	0.3166(19)	16.8(4)
Ni(1A)	0.42	0	0	1/2	5.2
N(1A)	0.42	0.10510	0.17310	0.34060	9.4
N(2A)	0.42	0.27930	0.36920	0.24420	9.4
C(1A)	0.42	0.23530	0.27140	0.37090	9.4
C(2A)	0.42	0.17340	0.33960	0.13800	9.4
C(3A)	0.42	0.07120	0.21140	0.19840	9.4
C(4A)	0.42	0.40710	0.49260	0.20400	9.4
B(1A)	0.50	2/3	1/3	0.24500	16.8
F(1A)	0.50	2/3	1/3	0.41630	16.8
F(2A)	0.50	0.72600	0.46690	0.18340	16.8

Mössbauer Spectroscopy and DC Magnetic Measurements

Mössbauer studies performed at room temperature (Figure 4) exhibit a single asymmetric quadrupole doublet [½eqQ = 0.558(5)] with an isomer shift of *IS* = 1.065(5) mm/s and a line width of 0.27 mm/s.[15] This relatively high *IS* value is assigned to Fe^{2+} in the high-spin state. The quadrupole splitting obtained is a result of the small distortion away from octahedral symmetry as discussed above. The narrow line width indicates clearly that, as far as the Fe ions are concerned, the measured sample is a single-phase material. The asymmetry in the doublet lines is due to a texture effect produced on the particles during the Mössbauer study.

Table 4. Selected geometric parameters [Å, °] for **B** and **C**.

B			
Fe(1)–N(1)	2.186(24)	N(1)–Fe(1)–N(1)[a]	89.8(8)
N(1)–C(1)	1.346(31)	Fe(1)–N(1)–C(1)	127.2(20)
C(1)–N(2)	1.373(34)	Fe(1)–N(1)–C(3)	127.6(21)
N(2)–C(2)	1.319(34)	N(1)–C(1)–N(2)	111.3(23)
C(2)–C(3)	1.368(34)	C(1)–N(2)–C(2)	104.3(21)
C(3)–N(1)	1.320(46)	N(2)–C(2)–C(3)	109.1(25)
N(2)–C(4)	1.436(19)	C(2)–C(3)–N(1)	109.1(27)
B(1)–F(1)	1.311(38)	C(3)–N(1)–C(1)	105.2(26)
B(1)–F(2)	1.367(22)	C(4)–N(2)–C(1)	132.8(19)
		C(4)–N(2)–C(2)	122.9(20)
		F(1)–B(1)–F(2)	112.1(11)
		F(2)–B(1)–F(2)[b]	106.7(9)
C			
Ni(1)–N(1)	2.091(15)	N(1)–Ni(1)–N(1)[a]	91.4(5)
N(1)–C(1)	1.334(23)	Ni(1)–N(1)–C(1)	122.3(14)
C(1)–N(2)	1.365(26)	Ni(1)–N(1)–C(3)	132.9(14)
N(2)–C(2)	1.340(26)	C(3)–N(1)–C(1)	104.8(18)
C(2)–C(3)	1.392(24)	N(1)–C(1)–N(2)	109.9(16)
C(3)–N(1)	1.306(31)	C(1)–N(2)–C(2)	109.0(15)
N(2)–C(4)	1.438(13)	N(2)–C(2)–C(3)	102.5(17)
B(1)–F(1)	1.329(40)	C(2)–C(3)–N(1)	113.5(18)
B(1)–F(2)	1.380(16)	C(4)–N(2)–C(1)	135.3(13)
		C(4)–N(2)–C(2)	115.7(13)
		F(1)–B(1)–F(2)	110.3(6)
		F(2)–B(1)–F(2)[b]	108.6(5)

[a] *y*, *x* + *y*, –*z*. [b] 1 – *y*, *x* – *y*, *z*.

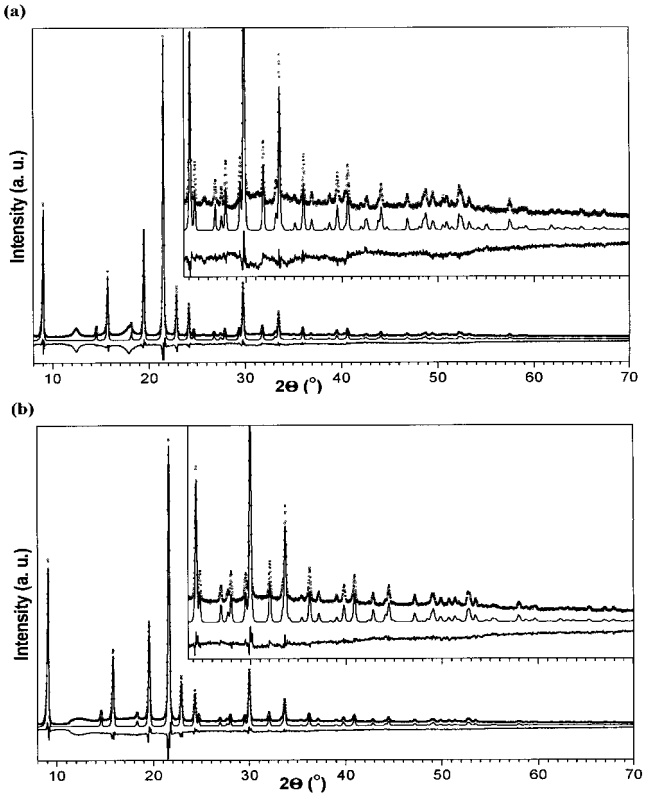

Figure 1. Observed (circles), calculated (solid line), and difference (bottom curve) PXRD profiles for **B** (a) and **C** (b) after the DDM structure refinement.

 © 2005 Wiley-VCH Verlag GmbH & Co. KGaA, Weinheim

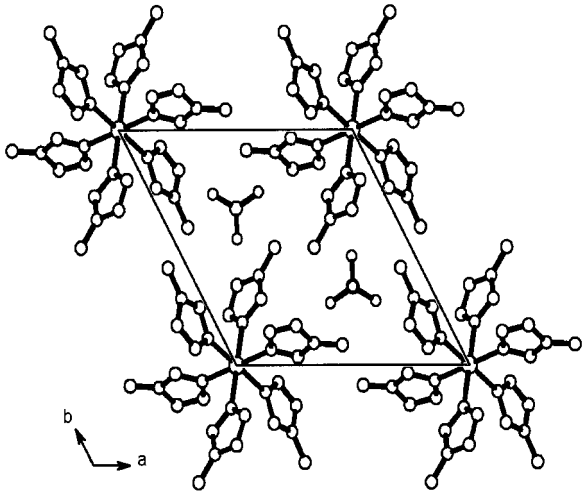

Figure 2. Projection *ab* of the crystal structure of **B** and **C**.

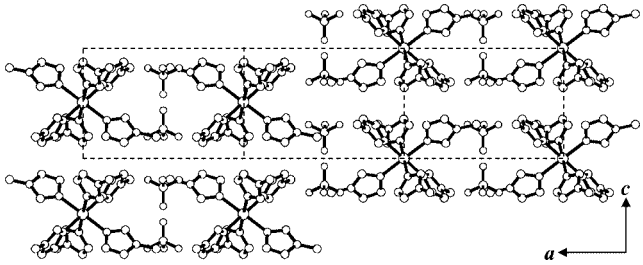

Figure 3. Alternative positions of molecules in the crystals of **B** and **C**. The unit cell boundaries are shown by dashed lines.

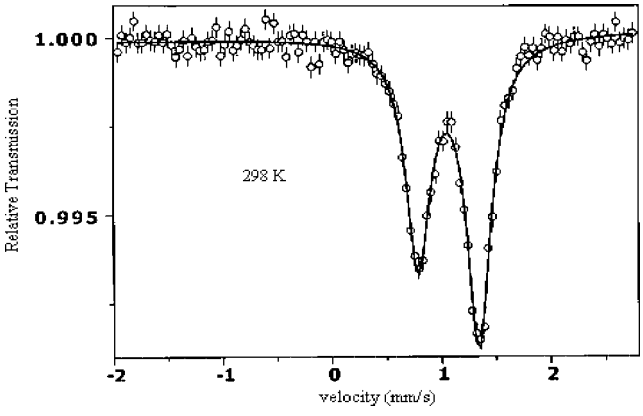

Figure 4. ^{57}Fe Mössbauer spectrum of $(C_4H_6N_2)_6Fe(BF_4)_2$ measured at 298 K.

In order to depict the high-spin state of Fe^{2+} ions in (1-methylimidazole)$_6$Fe(BF$_4$)$_2$, DC magnetic measurements were performed. DC magnetic measurements shown in Figure 5 conclusively confirm the high-spin state of Fe^{2+}, which is similar to the reports of high-spin Fe^{2+} compounds containing imidazole derivatives as ligands.[16a–16c] The temperature dependence of the susceptibility (measured at 1 T) have the typical paramagnetic shape down to 5 K, and adheres to the Curie–Weiss law: $\chi(T) = \chi_0 + C/(T - \theta)$, where χ_0 is the temperature-independent part of χ, C is the Curie constant, and θ is the Curie–Weiss temperature. The fit (solid line) yields: χ_0 = –0.0008 emu/mol Oe, C = 4.21(2) emu K/mol Oe and θ = –3.8(1) K. The linear isothermal magnetization (up to 1 T) shown in the inset confirms the paramagnetic nature at 5 K. The extracted paramagnetic effective moment is P_{eff} = 5.78 μ_B, a value which is midway between the common experimental 5.4 μ_B and the free ion P_{eff} = 6.7 μ_B (no spin-orbit coupling) for the high-spin state of Fe^{2+} ions.[17,18]

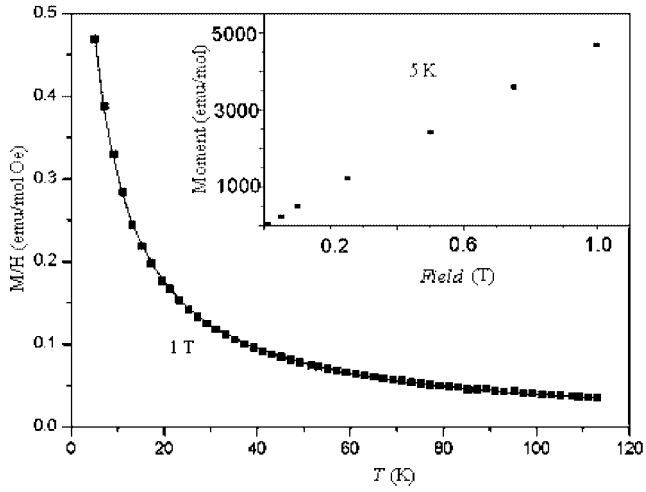

Figure 5. The DC magnetic susceptibility of $(C_4H_6N_2)_6Fe(BF_4)_2$ and linear $M(H)$ curve at 5 K.

Magnetic Measurements

The (imidazole)metal complexes show paramagnetic behavior[18,19] which can be seen in Figure 6. Higher magnetization values are measured for the (imidazole)iron complexes as compared to the (imidazole)nickel complexes, due to the different electronic ground-state configurations of the

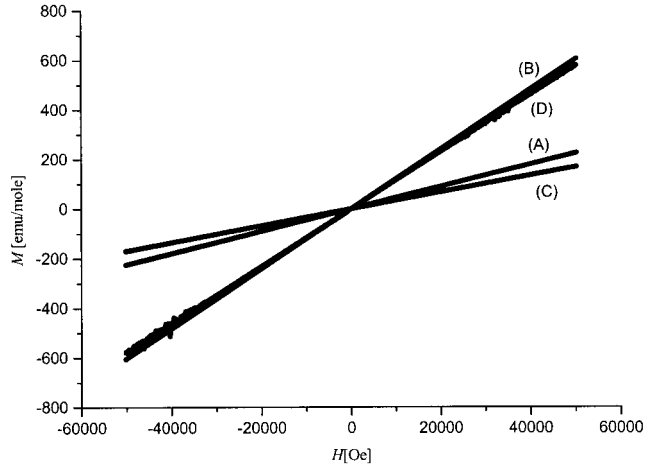

Figure 6. Comparison studies of the magnetization curve at room temperature for $(C_4H_6N_2)_6Ni(PF_6)_2$ (**A**), $(C_4H_6N_2)_6Fe(BF_4)$ (**B**)$_2$, $(C_4H_6N_2)_6Ni(BF_4)_2$ (**C**), and $(C_4H_6N_2)_6Fe(PF_6)$ (**D**).[6]

 © 2005 Wiley-VCH Verlag GmbH & Co. KGaA, Weinheim

$Fe^{2+}(d^6)$ and $Ni^{2+}(d^8)$ ions in the complexes, with the theoretical spin magnetic moment (μ_s) values being d^6 = 4.90 B.M. and d^8 = 2.83 B.M., respectively. The (imidazole)-iron complexes shows similar magnetization properties whereas the (imidazole)nickel complexes are different. The change in magnetization can be observed due to interference of the orbital motion of the electron with the electric fields of the other atoms, ions, and molecules surrounding the metal ions.[20] The magnetizations of the synthesized (imidazole)metal complexes do not saturate in the range of the applied magnetic field.

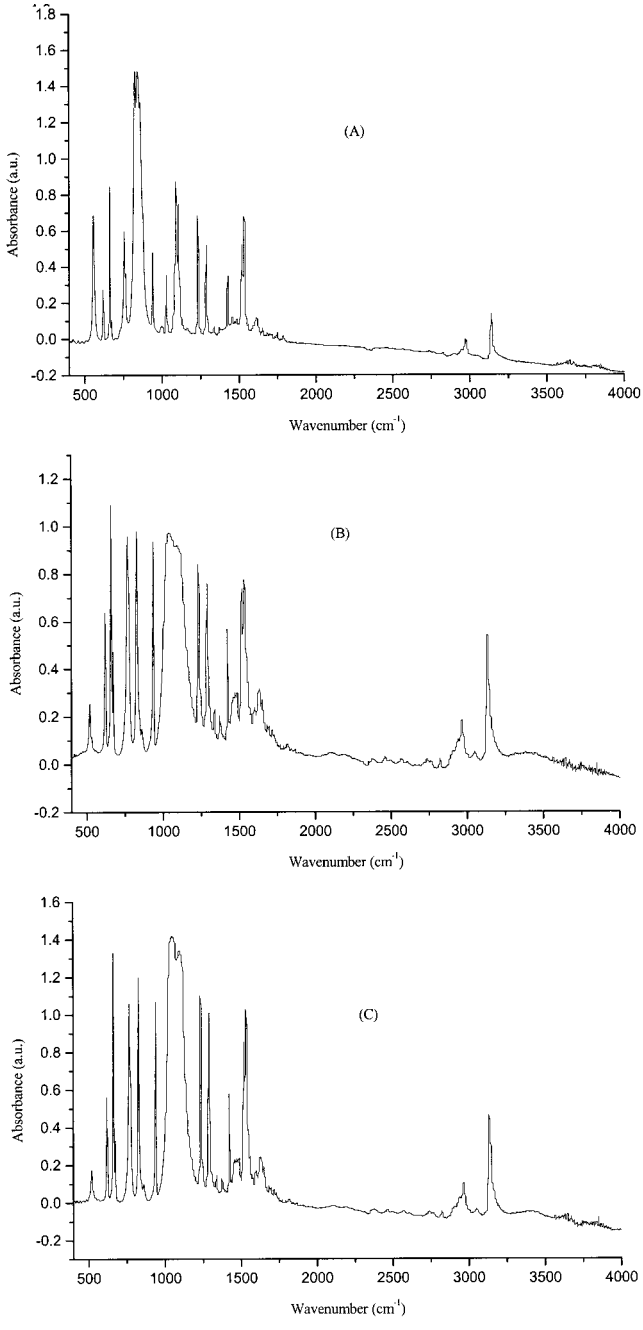

Figure 7. IR absorption spectra of the complexes $(C_4H_6N_2)_6Ni(PF_6)_2$ (**A**), $(C_4H_6N_2)_6Fe(BF_4)_2$ (**B**), and $(C_4H_6N_2)_6Ni(BF_4)_2$ (**C**).

Infrared and Raman Spectroscopy

The IR and Raman spectra are recorded for the iron and nickel complexes. They provide support to the characterization of the product by identifying the vibration of the ligands surrounding the central transition metal ion. The IR absorption spectra for the $(C_4H_6N_2)_6Ni(PF_6)_2$ (**A**), $(C_4H_6N_2)_6Fe(BF_4)_2$ (**B**) and $(C_4H_6N_2)_6Ni(BF_4)_2$ (**C**) are illustrated in Figure 7 (a, b, c). Table 5 shows the comparisons of the proposed assignments with those reported in the literature for the bands observed in the complexes of iron (**B**) and nickel (**A** and **C**).[18,19] The vibrational bands assigned to the organic ligand, $C_4H_6N_2$, are mostly blue-shifted, but some are assigned as shifted to the red. Our conclusion is that on average, the assigned bands illustrated in Table 5 are in good agreement with the interpretation of Reedijk,[18,19] Perchard and Novak.[20] The M–N vibrations are observed in the Raman spectra below 300 cm^{-1} and their locations agree with the literature values.[18,19] The IR and Raman active vibrations due to BF_4^- and PF_6^- anions are present in the spectra and also match the literature values.[21,22] Smaller shifts are observed for these bands, as compared with the literature values. The intense Raman line for the PF_6^- ion assigned to the symmetric mode ν_1 = 742 cm^{-1} is present in the $(C_4H_6N_2)_6Ni(PF_6)_2$ (**A**) spectra.[22] The IR and Raman active vibrations due to the BF_4^- ion for the $(C_4H_6N_2)_6Fe(BF_4)_2$ (**B**) and $(C_4H_6N_2)_6Ni(BF_4)_2$ (**C**) complexes are shown in Table 6. The Raman and IR measurements strengthen our assignment of the ligands surrounding the Fe and Ni ions. The observed vibration bands for the PF_6^- and BF_4^- anions confirm that the anions are not bonded to the metal ions.[19,23]

NMR Spectroscopy

^1H and ^{13}C NMR signals are probably too broad to be observed due to the paramagnetic properties of the iron and nickel complexes. The ^{19}F NMR spectrum [Figure 8 (a)] confirms the presence of PF_6^- in the $(C_4H_6N_2)_6Ni(PF_6)_2$ complex (**A**). The ^{19}F NMR spectra of $(C_4H_6N_2)_6Fe(BF_4)_2$ (**B**) and $(C_4H_6N_2)_6Ni(BF_4)_2$ (**C**) are presented in Figure 8 (b, c). The observed singlets (the coupling constant to boron is known to be very small in this anion[24]) have a shoulder deriving from the minor ^{10}B isotopomer (the isotope effect is 54 ppb). The NMR spectroscopic results reveal relatively narrow ^{19}F peaks. Thus, this demonstrates that the PF_6^- and BF_4^- anions are not bonded to the metal cations; see for instance ref.[25]

EPR Spectroscopy

The continuous wave electron paramagnetic resonance (cwEPR) spectroscopy is used to probe the point symmetry of the nickel complexes.

The EPR powder spectrum of (1-methylimidazole)$_6$-$Ni(PF_6)_2$ (**A**) and (1-methylimidazole)$_6Ni(BF_4)_2$ (**C**) at 3425G are presented in Figure 9 (a, b). These complexes

 © 2005 Wiley-VCH Verlag GmbH & Co. KGaA, Weinheim

Table 5. IR and Raman vibrational bands [cm^{-1}] for the complexes $(C_4H_6N_2)_6Ni(PF_6)_2$ (**A**), $(C_4H_6N_2)_6Fe(BF_4)_2$ (**B**), and $(C_4H_6N_2)_6Ni(BF_4)_2$ (**C**).

Liquid ligand			Vibration frequency					
			$(C_4H_6N_2)_6Ni(PF_6)_2$ (**A**)		$(C_4H_6N_2)_6Fe(BF_4)_2$ (**B**)		$(C_4H_6N_2)_6Ni(BF_4)_2$ (**C**)	
IR	Raman	Assignment	IR	Raman	IR	Raman	IR	Raman
3131 w	3128	C–H stretching	3139 m	3158 s	3134 s	3155 s	3133 s	3160 s
3105 m	3103	C–H stretching	–	–	–	–	–	–
3009 sh	3000		–	–	–	–	–	–
2986 sh	2951	CH_3 stretchings	2972 m	2973 s,b	2966 m,b	2968 s,b	2965 m	2966 s
2952 m			2949 sh	2823 w	2942 sh	2823 w	2941 sh	2822 w
1675 w		combination bands	1652 w	–	1651 w	–	1651 w	–
1589 w			1610 w		1632 w		1620 w	
1518 s	1510	ring stretching (R_1)	1533 s	1532 s	1532 s	1516 s	1532 s	1517 s
1506 sh	1500	ring stretching (R_2)	1518 sh		1515 sh		1518 sh	
1463 w	1472	CH_3 bending	1487–1455 w	–	1485–1456 w	–	1486–1465 w	–
1421 m	1420	CH_3 bending	1425 s	1423 s	1421 s	1421 s	1421 s	1421 s
1361 w	1353	ring stretching (R_3)	1373 w	1350 s,b	1372 w	1350 s	1373 w	
1328 w	1328	ring stretching (R_4)	1337 w		1336 w		1338 w	1338 s,b
1286 s	1288	in-plane C–H bending	1288 s	1287 s	1288 s	1288 s	1289 s	1289 s,b
1232 vs	1230	ring stretching (R_5) + CN stretching	1234 s	1232 w	1233 s	1233 w	1234 s	1234 w
1109 s	1105	in-plane C–H bending	1109 s		1100 s		1111 s,b	
1078 vs	1075	in-plane C–H bending	1092 s	1092 sb	1092 s,b	1095 s,b	1096 s,b	1097 s,b
1029 m	1025	CH_3 deformation	1028 m	1027 s	1036	1028 s	1037 s,b	1028 s
909 s	904	ring stretching (R_6)	939 s	938 w	936 s	936 s	939 s	938 w
860 sh	847	out-of-plane C–H bending	859 s,b	851 w	860 sh	858 w	860 sh	857 w
821 s	818	out-of-plane C–H bending	826 s,b	–	827 s	–	827 s	–
744 s	740	out-of-plane C–H bending	764 sh, 756 s	742 s	767 s	769 s,b	774 sh, 766 s	763 s
665 vs	665	ring stretching and CN stretching	673 sh, 663 s	670 s	673 sh, 660 s	670 s	674 sh, 662 s	671 s
618 s	616	ring deformation	618 m	–	619 s	–	619 s	–
355 w	353	C–N deformation	–	375 s	–	371 s	–	376 s
224 w	220	C–N deformation	–	246 s	–	236 s	–	247 s

Table 6. IR and Raman active vibtational bands of the BF_4^- anion in $(C_4H_6N_2)_6Fe(BF_4)_2$ (**B**) and $(C_4H_6N_2)_6Ni(BF_4)_2$ (**C**).

$[BF_4^-]$	$Fe(C_4H_6N_2)_6(BF_4)_2$ (**B**)				$Ni(C_4H_6N_2)_6(BF_4)_2$ (**C**)			
	ν_1	ν_2	ν_3	ν_4	ν_1	ν_2	ν_3	ν_4
IR [cm^{-1}]	662–664	–	1037–1111	519–532	660–673	–	1036–1092	519–532
Raman [cm^{-1}]	769	371	1028	520	763	376	1028	520

contain Ni^{2+} with $3d^8$ in octahedral symmetry, where the ground-term $^3A_{2g}$ nondegenerate state arises from the $(t_{2g})^6(e_g)^2$ configuration. Distortions from perfect octahedral symmetry result in a zero-field splitting of the three $S = 1A_{2g}$ terms ($m_s = 1$, 0, or –1). Transitional metal systems with $S = 1$ are often "EPR-silent" in the x-band EPR because of large zero-field splitting. The existence of an EPR spectrum Figure 9 (a, b) indicates a high symmetry about the metal atom, with a small zero-field splitting (less than the applied frequency, i.e. 9.7 GHz). The zero-field splitting arises from lowering, to some extent, the point symmetry from O_h, causing unequal magnetic field splitting, $m_s(-1) \leftrightarrow m_s(0)$ and $m_s(0) \leftrightarrow m_s(+1)$ transitions of the $^3A_{2g}$ ground state admixture with components of the nearest excited state, $^3T_{2g}$ [arises from the $(t_{2g})^5(e_g)^3$ configuration $^3T_{2g}$ state]. It is noticable that the two spectrum lines are very broad, which is commonly observed in concentrated paramagnetic samples.[9] Comparing the cwEPR spectrum of (1-methylimidazole)$_6$Ni$(PF_6)_2$ (**A**) with that of (1-methylimidazole)$_6$Ni$(BF_4)_2$ (**C**), we found that complex **C** shows more crystalline properties as complex **A**. The cwEPR spectra of the nickel complexes are consistent with powder spin-triplet systems reported in the literature.[9,18,19]

Thermal Analysis

To probe the mechanism of the reaction, we had to learn more about the thermal stability of the synthesized complexes, the precursors, and the ionic liquids. This was reached by studying the thermogravimetry analysis (TGA) of the products and the ionic liquids between 25 and 1000 °C with a heating rate of 3 °C min^{-1} under an N_2 flow. The TGA curve is shown in Figure 10 (a) for the $(C_4H_6N_2)_6Ni(PF_6)_2$ (**A**), $(C_4H_6N_2)_6Fe(BF_4)_2$ (**B**), $(C_4H_6N_2)_6Ni(BF_4)_2$ (**C**) and $(C_4H_6N_2)_6Fe(PF_6)_2$ (**D**) complexes. The TGA curve reveals that the anions affect the stability of the complexes.[26,27] The weight loss measured at a temperature of 250 °C, determined from the curve in Figure 10 (a), is 6.74% (0.28 mg) for **A**, 2.00% (0.11 mg) for **B**, 5.38% (0.23 mg) for **C** and 27.25% (1.01 mg) for **D**. The TGA curve shows that the BF_4^- anion complexes are more stable

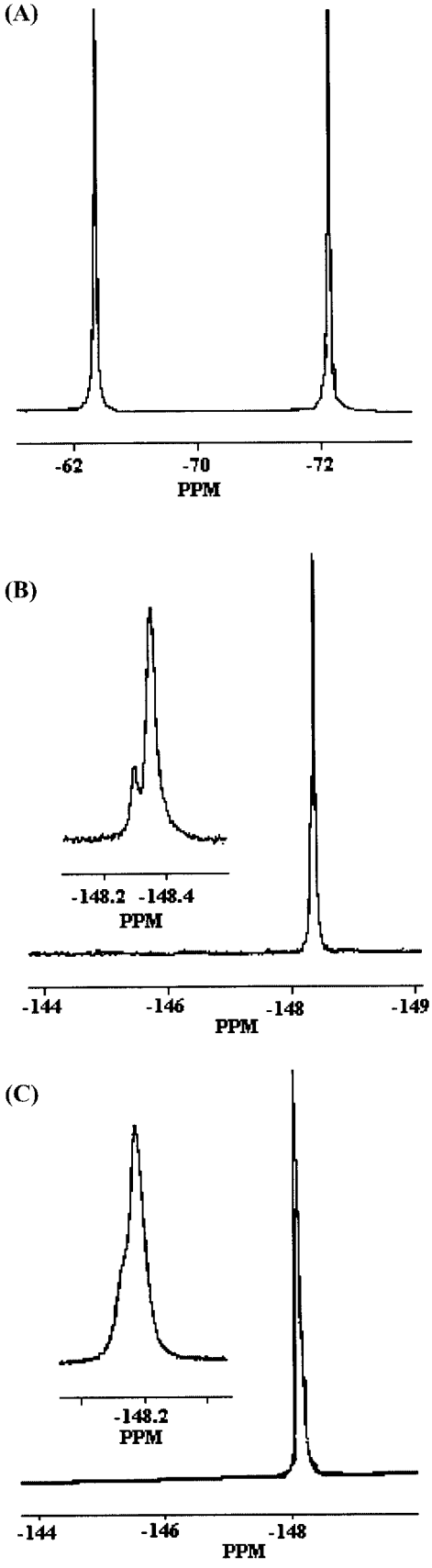

Figure 8. ^{19}F NMR spectra for $(C_4H_6N_2)_6Ni(PF_6)_2$ (**A**), $(C_4H_6N_2)_6Fe(BF_4)_2$ (**B**), and $(C_4H_6N_2)_6Ni(BF_4)_2$ (**C**).

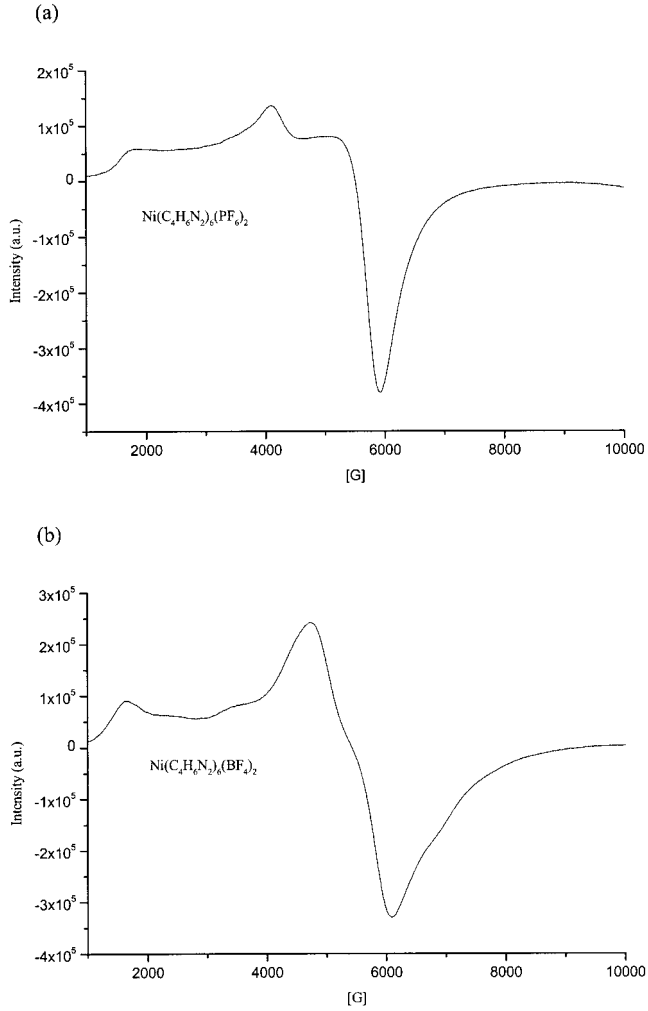

Figure 9. X-band EPR spectra of Ni^{2+} powder complexes at room temperature of $(C_4H_6N_2)_6Ni(PF_6)_2$ (a), and $(C_4H_6N_2)_6Ni(BF_4)_2$ (b).

than the PF_6^- anion complexes for both iron and nickel. The thermal stability of the ionic[28] liquids employed in our reactions, $(BMI^+)(PF_6^-)$ and $(BMI^+)(BF_4^-)$, were also studied using TGA between 25 and 1000 °C at a flow rate of 3 °C min^{-1} under N_2. The TGA graph of the ionic liquids is shown in Figure 10 (b), and the physical properties of the ionic liquid used for our reaction are summarized in Table 7. From Figure 10 (b) we observe at a temperature of 150 °C that there is no weight loss for the $(BMI^+)(PF_6^-)$ and $(BMI^+)(BF_4^-)$ ionic liquids. The decomposition temperature ranges of ionic liquids measured from TGA curves are found to be 332–516 °C $(BMI^+)(PF_6^-)$ and 309–528 °C $(BMI^+)(BF_4^-)$. The TGA curve confirms that the ionic liquids $(BMI^+)(PF_6^-)$ and $(BMI^+)(BF_4^-)$ are stable at the reaction temperature. They do not form a metal fluoride, or undergo any other decomposition at the reaction temperature.[29] It is therefore concluded from the TGA results that the ionic liquids react only as a result of the bubble's collapse.

 © 2005 Wiley-VCH Verlag GmbH & Co. KGaA, Weinheim

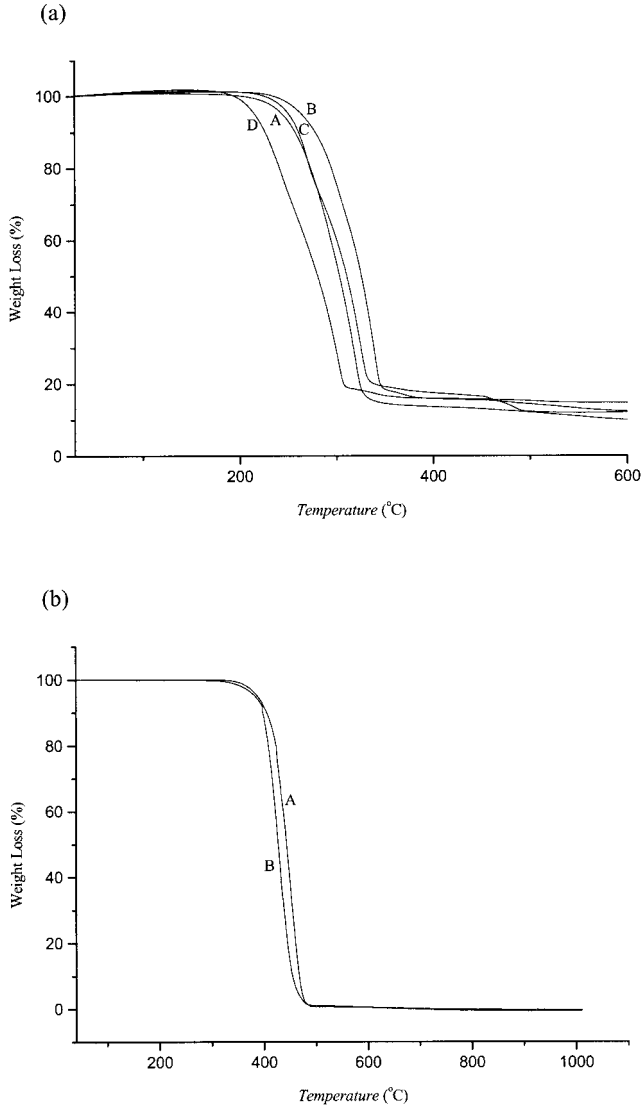

Figure 10. TGA curve (a) of iron and nickel complexes $(C_4H_6N_2)_6Ni(PF_6)_2$ (**A**), $(C_4H_6N_2)_6Fe(BF_4)_2$ (**B**), $(C_4H_6N_2)_6Ni(BF_4)_2$ (**C**), and $(C_4H_6N_2)_6Fe(PF_6)$ (**D**);[6] (b) TGA curve of ionic liquids (A) $(BMI)^+(PF_6)^-$ and (B) $(BMI)^+(BF_4)^-$.

Conclusions

The synthesis of transition metal complexes in ionic liquids under ultrasonic conditions has given a new direction to the chemistry of ionic liquids. In brief, the sonication products of 1-methylimidazole and carbonylmetal complexes in ionic liquids $(BMI^+)(PF_6^-)$ and $(BMI^+)(BF_4^-)$ (which act as solvents) form the complexes $(C_4H_6N_2)_6Fe(PF_6)_2$,[6] $(C_4H_6N_2)_6Ni(PF_6)_2$, $(C_4H_6N_2)_6Fe(BF_4)_2$, and $(C_4H_6N_2)_6Ni(BF_4)_2$ when sonicated in air. The interesting part of this reaction under ultrasound conditions is that there is no hydrolysis of PF_6 in the presence of metals, and there are no reports of metathesis or decomposition of cations to give different products. In these reactions the anions of the ionic liquids contribute to the final structure of the products, as was stated in our previous paper[6] and in ref.[30] The sonochemical products of Fe^{2+} and Ni^{2+} ions are octahedrally coordinated by six 1-methylimidazole molecules. The PF_6^- and BF_4^- anions act as charge-stabilizing agents in the formation of the crystals, which are characterized by the trigonal lattice with the $P\bar{3}$ space group. The PXRD structure analysis revealed a high concentration of twin and/or line defects in the crystals. Thus, ionic liquid solvents are effective as donors of anions for the cation stabilization under ultrasonic conditions. Although a tremendous amount of work has been carried out on applications of ionic liquids, there have been a few reports in recent years where ionic liquids are used in sonochemistry. In particular, much work is still needed to explore and utilize the fundamental chemistry and properties of these interesting liquids in sonochemistry.

Experimental Section

General: 1-Butyl-3-methylimidazolium hexafluorophosphate $(BMI^+)(PF_6^-)$ (96%), 1-butyl-3-methylimidazolium tetrafluoroborate $(BMI^+)(BF_4^-)$ (97%) and 1-methylimidazole were purchased from Aldrich. Pentacarbonyliron (99.5%) and tetracarbonylnickel (100%) were purchased from Strem Chemicals, USA; they were handled very carefully with safety precautions in an effective fume hood; refer to Material Safety Data Sheet (MSDS) for further information and safety measurements. PXRD data were collected with a Bragg–Brentano geometry using a DRON-4 diffractometer with a graphite secondary monochromator (Cu-K_α radiation, λ = 1.5418 Å) and a scintillation counter. The measurements were carried out at room temperature under air. A ^{57}Fe Mössbauer study of (1-methylimidazole)$_6Fe(BF_4)_2$ was performed at ambient temperature using a conventional constant acceleration drive and a 50 mCi ^{57}Co:Rh source. The experimental spectrum was analyzed by a least-squares fitting procedure, and the ^{57}Fe isomer shifts are relative to α-Fe, measured at room temperature. DC magnetic measurements were performed using a commercial (Quantum Design) super-conducting quantum interference device (SQUID) magnetometer. The magnetic measurements were performed with a Quantum Design MPMSXL SQUID magnetometer for $(C_4H_6N_2)_6Ni(PF_6)_2$ (**A**), $(C_4H_6N_2)_6Fe(BF_4)_2$ (**B**), $(C_4H_6N_2)_6Ni(BF_4)_2$ (**C**), and $(C_4H_6N_2)_6Fe(PF_6)_2$ (**D**). The magnetization was measured at room temperature as a function of an external field being swept up from –50 kOe to 50 kOe and down to –50 kOe in steps of 200 Oe. The IR absorption spectra of the complexes were recorded in the range of 400–4000 cm^{-1} by means of a Nicolet (Impact 410) spectrometer with KBr pellets (5 mg of sample in 500 mg of KBr). Raman spectroscopic measurements were carried out at room temperature with a Jobin Yvon Horiba Raman system. The 524 nm line of an Ar^+ laser was used as the excitation source. The Raman spectra were recorded in the range 100–4000 cm^{-1}. Powder samples

Table 7. Physical properties of the ionic liquids.

Ionic liquid	Decomposition temperature range (TGA)	Molecular weight [g/mol]	Density [g/ml]
1-Butyl-3-methylimidazolium hexafluorophoshate (96%)	332–516 °C	284.18	1.510
1-Butyl-3-methylimidazolium tetrafluoroborate (97%)	309–528 °C	226.02	1.320

 © 2005 Wiley-VCH Verlag GmbH & Co. KGaA, Weinheim

were measured at room temperature with a Bruker EPR 100d X-band spectrometer, frequency 9.766 GHz, microwave power 6.34 mW.

Synthesis of the Complexes: The synthetic procedure for the metal complexes of 1-metylimidazole in an ionic liquid under ultrasonic conditions is reported in our previous communication.[6] All the metal complexes of 1-methylimidazole were crystallized from ethanol (due to high solute solubility).[31]

(1-Methylimidazole)$_6$Ni^{II}(PF$_6$)$_2$ (A): $Ni(CO)_4$ (6.18 mmol, 1.056 g) and 1-methylimidazole (24 mmol, 2 g) were dispersed in ionic liquid (BMI^+)(PF_6^-) (17.6 mmol, 5 g) under ultrasonic conditions. Transparent blue needle-shaped crystals (1.35 mmol, 1.141g) were obtained. $C_{24}H_{36}F_{12}N_{12}NiP_2$ (841.27): calcd. C 34.26, H 4.28, N 19.98; found C 34.70, H 4.47, N 19.73. ^{19}F NMR (188.3 MHz in [D$_6$]DMSO): δ = –70.25 (d, J_{PF} = 709 Hz) ppm (confirming the presence of PF_6^-). MS (DCI, FAB): *m*/*z* = 82 [$C_4H_6N_2$], 145 [PF_6].

(1-Methylimidazole)$_6$Fe^{II}(BF$_4$)$_2$ (B): $Fe(CO)_5$ (6.08 mmol, 1.192 g) and 1-methylimidazole (24 mmol, 2 g) were dispersed in ionic liquid (BMI^+)(BF_4^-) (22 mmol, 5 g) under ultrasonic conditions. Transparent needle-shaped crystals (2.16 mmol, 1.560g) were obtained. $C_{24}H_{36}B_2F_8FeN_{12}$ (722.09): calcd. C 39.88, H 4.98, N 23.26; found C 40.33, H 5.39, N 23.69. ^{19}F NMR (188.3 MHz in [D$_6$]-DMSO): δ = –148.35 ppm (confirming the presence of BF_4^-). MS (DCI, FAB): *m*/*z* = 82 [$C_4H_6N_2$], 87 [BF_4].

(1-Methylimidazole)$_6$Ni^{II}(BF$_4$)$_2$ (C): $Ni(CO)_4$ (6.18 mmol, 1.056 g) and 1-methylimidazole (24 mmol, 2 g) were dispersed in ionic liquid (BMI^+)(BF_4^-) (22 mmol, 5 g) under ultrasonic conditions. Transparent blue needle-shaped crystals (1.41 mmol, 1.024g) were obtained. $C_{24}H_{36}B_2F_8N_{12}Ni$ (724.95): calcd. C 39.72, H 4.96, N 23.17; found C 40.44, H 5.35, N 23.31. ^{19}F NMR (188.3 MHz in [D$_6$]DMSO): δ = –148.19 ppm (confirming the presence of BF_4^-). MS (DCI, FAB): *m*/*z* = 82 [$C_4H_6N_2$], 87 [BF_4].

[1] a) T. Welton, *Chem. Rev.* **1999**, *99*, 2071–2083; b) J. Dupont, R. Souza, P. Suarez, *Chem. Rev.* **2002**, *102*, 3667–3692; c) D. Zhao, M. Wu, Y. Kon, E. Min, *Catal. Today* **2002**, *74*, 157–189; d) K. Marsh, A. Deev, A. Wu, E. Tran, A. Klamt, *Korean J. Chem. Eng.* **2002**, *19*, 357–362.

[2] L. Xu, W. Chen, J. Xiao, *Organometallics* **2000**, *19*, 1123–1127.

[3] C. Mathews, P. Smith, T. Welton, A. White, D. Williams, *Organometallics* **2001**, *20*, 3848–3850.

[4] S. Christie, S. Subramanian, L. Wang, M. J. Zaworotko, *Inorg. Chem.* **1993**, *32*, 5415–5417.

[5] K. Jin, X. Huang, L. Pang, J. Li, A. Appel, S. Wherland, *Chem. Commun.* **2002**, 2872–2873.

[6] D. Jacob, V. Kahlenberg, K. Wurst, L. A. Solovyov, I. Felner, L. Shimon, H. Gottlieb, A. Gedanken, *Eur. J. Inorg. Chem.* **2005**, 522–528.

[7] a) K. S. Suslick, S. B. Choe, A. A. Cichowlas, M. W. Grinstaff, *Nature* **1991**, *353*, 414–416; b) Y. Koltypin, G. Kataby, X. Cao, R. Prozorov, A. Gedanken, *J. Non-Cryst. Solids* **1996**, *201*, 159–162.

[8] K. V. P. M. Shafi, Y. Koltypin, A. Gedanken, R. Prozorov, J. Balogh, J. Lendvai, I. Felner, *J. Phys. Chem. B* **1997**, *101*, 6409–6414.

[9] D. Collison, M. Helliwell, V. M. Jones, F. E. Mabbs, E. J. L. McInnes, P. C. Riedi, G. M. Smith, R. G. Pritchard, W. I. Cross, *J. Chem. Soc., Faraday Trans.* **1998**, *94*, 3019–3025.

[10] E. J. Van den Heuvel, P. L. Franke, G. C. Verschoor, A. P. Zuur, *Acta Crystallogr. C* **1983**, *39*, 337–339.

[11] L. A. Solovyov, *J. Appl. Crystallogr.* **2004**, *37*, 743–749.

[12] H. M. Rietveld, *J. Appl. Crystallogr.* **1969**, *2*, 65–71.

[13] D. B. Wiles, R. A. Young, *J. Appl. Crystallogr.* **1981**, *14*, 149–151.

[14] a) I. R. Baird, S. J. Rettig, B. R. James, K. A. Skov, *Can. J. Chem.* **1998**, *76*, 1379–1388; b) E. J. Heuvel, P. L. Franke, G. C. Verschoor, A. P. Zuur, *Acta Crystallogr. C* **1983**, *39*, 337–339.

[15] B. L. Little, G. J. Long, *Inorg. Chem.* **1978**, *17*, 3401–3413.

[16] a) G. Carver, P. L. W. Tregenna-Piggott, A. Barra, A. Neels, J. A. Stride, *Inorg. Chem.* **2003**, *42*, 5771–5777; b) J. A. Garcia'-Va'zquez, J. Romero, A. Sousa-Pedrares, A. Sousa, A. D. Garnovskii, D. A. Garnovskii, *J. Chem. Crystallogr.* **2000**, *30*, 23–26; c) F. Seel, R. Lehnert, E. Bill, A. Trautwein, *Z. Naturforsch. B: Anorg.Chem., Org. Chem.* **1980**, *35B*, 631–638.

[17] M. M. Schieber, *Experimental Magnetochemistry*, North Holland Publishers, Amsterdam, **1967**, p. 23.

[18] J. Reedijk, *Inorg. Chim. Acta* **1969**, *3*, 517–522.

[19] J. Reedijk, *J. Inorg. Nucl. Chem.* **1971**, *33*, 179–188.

[20] F. A. Cotton, G. Wilkinson, *Advanced Inorganic Chemistry*, John Wiley & Sons, Inc., New York, **1962**, pp. 505–508.

[21] C. Perchard, A. Novak, *Spectrochim. Acta* **1967**, *23A*, 1953.

[22] N. Greenwood, *J. Chem. Soc.* **1959**, 3811–3815.

[23] K. Nakamoto, *Infrared Spectra of Inorganic and Coordination Compounds*, Wiley, New York, **1963**.

[24] L. Woodward, L. Anderson, *J. Inorg. Nucl. Chem.* **1956**, *3*, 326–327.

[25] H. Günther, *NMR Spectroscopy*, John Wiley & Sons, Chichester, **1980**, p. 220.

[26] K. Kuhlmann, D. M. Grant, *J. Phys. Chem.* **1964**, *68*, 3208–3213.

[27] J. Dam, G. Hakvoort, J. Jansen, J. Reedijk, *J. Inorg. Nucl. Chem.* **1975**, *37*, 713–718.

[28] a) K. J. Baranyai, G. B. Deacon, D. R. MacFarlane, J. M. Pringle, J. L. Scott, *Aust. J. Chem.* **2004**, *57*, 145–147; b) M. Kosmulski, J. Gustafsson, J. B. Rosenholm, *Thermochim. Acta* **2004**, *412*, 47–53.

[29] G. S. Fonseca, A. P. Umpierre, P. F. P. Fichtner, S. R. Teixeira, J. Dupont, *Chem. Eur. J.* **2003**, *9*, 3263–3269.

[30] K. Jin, X. Huang, L. Pang, J. Li, A. Appel, S. Wherland, *Chem. Commun.* **2002**, 2872–2873.

[31] B. Pamplin, *Crystal Growth*, Pergamon Press, Oxford, **1980**, vol. 16, pp. 395–420.

Received: January 10, 2005
Published Online: May 27, 2005

 © 2005 Wiley-VCH Verlag GmbH & Co. KGaA, Weinheim

1-D Open-Channeled 3-D Supramolecular Self-Assembled Frameworks Encapsulating Unprecedented Cyclic $(H_2O)_8$ Clusters or Solvent Molecules

Dong-sheng Li,[a,b] Yao-yu Wang,*[a] Xin-jun Luan,[a] Ping Liu,[a] Cai-hua Zhou,[a,b] Hai-rui Ma,[a] and Qiz-hen Shi[a]

Keywords: Hydroxybutanedioic acid / Copper / Bipyridine / Phenanthroline / Self-assembly / 1-D open channel

Two novel 1-D coordination polymers, $\{[Cu(Hhbd)(bpy)]\cdot 3H_2O\}_n$ (**1**) and $\{[Cu(Hhbd)(phen)]\cdot H_2O\cdot MeOH\}_n$ (**2**) [Hhbd = α-hydroxybutanedioicate dianion, bpy = 2,2′-bipyridine, phen = 1,10-phenanthroline], were rationally designed and synthesized with an identical construction strategy, using Hhbd ligands as bridges and chelating aromatic ligands as terminal ligands. Interestingly, the chelating aromatic ligand and the –OH groups of the Hhbd ligand play an important role in the self-assembly of the polymeric coordination chain by providing potential supramolecular recognition sites for π–π aromatic stacking and hydrogen-bond interactions, resulting in the self-assembly of the molecular double chains to give a 3-D supramolecular framework with 1-D open channels. More significantly, in **1** the host framework encapsulates unprecedented centrosymmetric cyclic $(H_2O)_8$ clusters that have a chair conformation and are connected into 1-D arrays by supramolecular association along the 1-D open channels. In contrast, the channels of **2** contain lattice water and disordered methanol molecules. TGA and XRPD show that the host frameworks of **1** and **2** are stable when the guest solvent molecules are removed from the channels. Variable-temperature magnetic susceptibility measurements for both complexes indicate the presence of weak antiferromagnetic exchange interactions between adjacent copper(II) ions.

(© Wiley-VCH Verlag GmbH & Co. KGaA, 69451 Weinheim, Germany, 2005)

Introduction

Research into self-assembling processes has recently become a rapidly growing area in supramolecular chemistry, biochemistry, and materials science.[1–4] Indeed, self-assembling processes are utilized by nature in many interesting chemical and biomolecular systems, such as in the folding of proteins and nucleic acids.[5–7] Moreover, the principles of self-assembly provide a new strategy for the rational design and synthesis of new supramolecular architectures, especially for the preparation of extended channel-containing metal-organic frameworks. Such systems are of potential utility for molecular recognition, ion exchange, gas storage, heterogeneous catalysis, and for the development of new magnetic materials.[8–10] Therefore, chemists have made significant efforts to introduce the self-assembling process into artificial systems.[11–13] As a result of this work, the self-assembly of organic, organometallic, and/or inorganic building blocks through metal-ligand binding, hydrogen bonds, or π–π interactions has become a powerful tool for the generation of large cage-like molecules and porous substances with channels.[14–18] Although important progress has been made in the construction of such assemblies by the exploitation of any one of these individual intermolecular interactions, a lot of research dealing with the combination of two or all three of them can still be carried out, allowing for the construction of an almost infinite number of new supramolecular entities.[19]

During the past decades, for materials chemists and especially for inorganic chemists, polycarboxylates have become one of the most used spacers in the synthesis of compounds that have potential applications as molecular-based magnetic materials, and for the preparation of porous materials that show host–guest behavior.[20–25] However, hydroxypolycarboxylic acids, although important as polycarboxylate ligands, have been seldom used to date. The unique features of hydroxypolycarboxylic acids have drawn our attention. First of all, these acids possess terminal carboxylic acid and hydroxyl groups that may be completely or partially deprotonated. This leads to a versatile coordination behavior, and as such, distinct bonding modes towards metal cations, such as nonchelating, chelating, and bridging modes can be realized.[26,27] Secondly, hydroxypolycarboxylic acids can act not only as hydrogen-bond acceptors, but also as hydrogen-bond donors to form new extended structures by means of additional hydrogen-bond interactions. Thirdly, some hy-

[a] Department of Chemistry & Shaanxi Key Laboratory of Physico-inorganic Chemistry, Northwest University, Xi'an 710069, P. R. China
Fax: +86-29-8837-3398
E-mail: wyaoyu@nwu.edu.cn
[b] Department of Chemistry & Chemical Engineering, Yan′an University, Yan'an 716000, P. R. China
Supporting information for this article is available on the WWW under http://www.eurjic.org or from the author.

droxypolycarboxylic acids [*α*-hydroxybutanedioic acid (H_3hbd), 2,3-dihydroxybutanedioic acid (H_4dhbd), and 2-hydroxy-1,2,3-tricarballylic acid (H_4htb), etc.] are present in fruits and living cells, and they also play an important role in biological processes.[28–30]

Currently we are exploring the self-assembly of metal ions with ligands that are capable of forming hydrogen bonds and bringing about π–π interactions, and that behave as directional motifs capable of extending the dimensionality of the channel-containing product materials. In the present work, by using H_3hbd as the bridging ligand, and 2,2′-bipyridine (bpy) or 1,10-phenanthroline (phen) as terminal ligands, we have prepared two similar neutral 1-D coordination polymers, namely $\{[Cu(Hhbd)(bpy)]\cdot 3H_2O\}_n$ (**1**) and $\{[Cu(Hhbd)(phen)]\cdot H_2O\cdot MeOH\}_n$ (**2**) [Hhbd = *α*-hydroxybutanedioicate dianion]. Interestingly, under the direction of supramolecular recognition, and attraction through π–π aromatic stacking, and hydrogen-bond interactions provided by Hhbd and the aromatic chelating ligands, these 1-D chains may self-assemble to form molecular double chains that may also self-assemble to give a final 3-D framework that contains 1-D open channels. Unexpectedly, we found unprecedented cyclic $(H_2O)_8$ clusters encapsulated within the host framework of **1**. These clusters are connected into 1-D arrays along the 1-D open channels by supramolecular association.

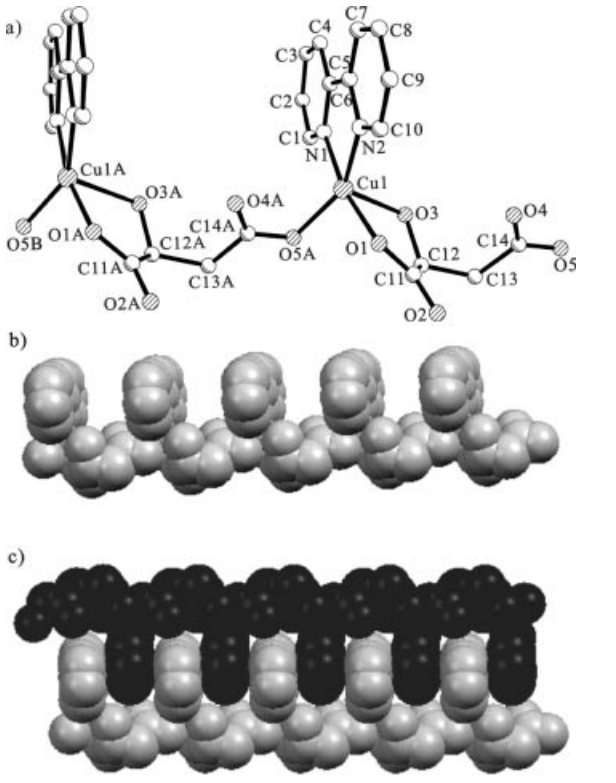

Figure 1. (**a**) View of the coordination environment of the copper atoms in **1**; (**b**) 1-D single-stranded polymeric chain; (**c**) ladder-like, double-stranded chains.

Results and Discussion

Description of the Structures

{[Cu(Hhbd)(bpy)]·3H$_2$O}$_n$ (1)

A single-crystal X-ray structural analysis showed that **1** crystallizes in the monoclinic space group $P2_1/c$, with one copper(II) atom, one tridentate Hhbd ligand, one bpy ligand, and three lattice water molecules in each crystallographic unit. Each copper(II) atom is coordinated to three oxygen atoms from two different Hhbd ligands, and two nitrogen atoms from a chelating bpy ligand to give 3+1+1 distorted trigonal-bipyramidal geometry at the metal centers with a trigonality index $\tau = 0.93$.[31] Copper(II) is approximately coplanar with the equatorial plane defined by atoms O3, O5, N2, and shows a deviation of 0.0375 Å toward O1, as seen in part a of Figure 1. Selected bond lengths and angles are listed in Table 1, and are in close agreement with bond parameters previously reported for carboxylate and bpy containing copper(II) complexes.[32,33] In addition, the fact that the Cu–$O_{carboxyl}$ bonds [av.1.967(2) Å] are significantly shorter than the Cu–$O_{hydroxyl}$ bond [2.209(3) Å] indicates that the hydroxyl group of **1** is protonated; this is also found in many other *α*-hydroxycarboxylate complexes.[27,34]

It is worthwhile to note that the Hhbd dianion adopts an *R* conformation and bridges the copper centers to form 1-D polymeric chains running along the crystallographic *a* axis with an adjacent Cu···Cu distance of 7.013 Å (part b in Figure 1). The bpy ligands lie on one side of this chain in a parallel fashion. Interestingly, a pair of 1-D chains self-assemble to generate a molecular double chain under the direction of strong aromatic π–π interactions between the bpy units with a face-to-face distance of ca.3.375–3.422 Å (part c in Figure 1). There are significant C–H···O hydrogen bonds involving the bpy carbon atoms (C7) and the uncoordinated carboxyl oxygen atoms (O4) (C···O 3.357 Å, C–

Table 1. Selected bond lengths [Å] and angles [°] for **1** and **2**.

1		**2**	
Cu–O(1)	1.943(2)	Cu–O(1)	1.943(2)
Cu–O(5A)	1.992(2)	Cu–O(4A)	1.984(3)
Cu–O(3)	2.209(3)	Cu–O(3)	2.183(3)
Cu–N(1)	1.984(3)	Cu–N(1)	2.008(4)
Cu–N(2)	2.001(3)	Cu–N(2)	2.016(4)
O(1)–Cu–N(1)	168.40(12)	O(1)–Cu–N(1)	170.53(15)
N(1)–Cu–O(5A) [a]	94.26(11)	N(1)–Cu–O(4A)	91.89(11)
N(1)–Cu–N(2)	80.82(12)	N(1)–Cu–N(2)	82.16(16)
O(1)–Cu–O(3)	78.33(10)	O(1)–Cu–O(4A)	95.54(11)
O(5A)–Cu–O(3)	92.31(10)	O(1)–Cu–N(2)	93.69(15)
O(1)–Cu–O(5A)	94.83(11)	O(4A)–Cu–N(2)	153.24(15)
O(1)–Cu–N(2)	94.73(11)	O(1)–Cu–O(3)	78.36(13)
O(5A)–Cu–N(2)	150.15(11)	O(4A)–Cu–O(3)	97.61(14)
N(1)–Cu–O(3)	94.12(11)	N(1)–Cu–O(3)	94.86(14)
N(2)–Cu–O(3)	117.31(11)	N(2)–Cu–O(3)	108.85(15)

[a] Symmetry codes: A: $x - 1$, y, z for **1** and A: $x + 1$, y, z for **2**.

 © 2005 Wiley-VCH Verlag GmbH & Co. KGaA, Weinheim

H···O 164°), and these provide an additional attractive force between the strands.[35] To the best of our knowledge, the double chains represent the first example of perfect molecular double chains formed using hydroxypolycarboxylate ligands. Furthermore, neighboring pairs of double chains interact with each other through strong hydrogen bonds between the uncoordinated carboxyl oxygen atoms (O2) and the coordinated, protonated hydroxyl groups (O3) (O···O 2.676 Å, O–H···O 177°). These interactions form the final 3D framework that feature 1-D open channels when viewed along the crystallographic *a* axis (Figure 2). The approximate dimensions of these channels are 10.41 Å × 6.67 Å, which are large enough to encapsulate guest solvent molecules.

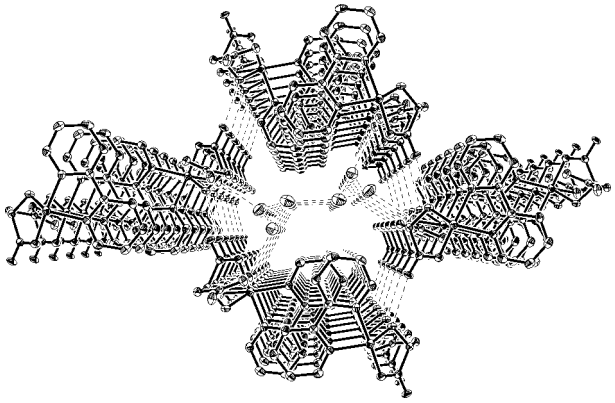

Figure 2. View of the 3-D supramolecular framework of **1** containing 1-D open channels encapsulating arrays of cyclic $(H_2O)_8$ clusters.

The most remarkable feature in **1** is that, in the 1-D open channels, the guest water molecules form a centrosymmetric cyclic $(H_2O)_8$ cluster that adopts a chair conformation (Figure 3). Two closely related isomers of nearly identical low-energy with S_4 and D_{2d} symmetries have been theoretically predicted for the $(H_2O)_8$ cluster.[36] Evidence for the existence of both of these isomers has been obtained from studies of gas-phase $C_6H_6(H_2O)_8$ and molecular beams.[37,38] However, only three kinds of $(H_2O)_8$ clusters, namely, the cubic cage-like $(H_2O)_8$ cluster with *Ci* symmetry, the icelike cyclic $(H_2O)_8$ cluster with –4*m*2 symmetry, and the opened-cube $(H_2O)_8$ cluster with centrosymmetric symmetry, have been found within different crystal hosts,[39–41] but no centrosymmetric cyclic $(H_2O)_8$ clusters have ever been reported.

Within the centrosymmetric cyclic $(H_2O)_8$ cluster only three water molecules are crystallographically unique. The hydrogen bond O···O distances range from 2.772 to 2.850 Å (mean value 2.799 Å), and are slightly longer than the average hydrogen bond length observed in icelike cyclic $(H_2O)_8$ clusters with –4*m*2 symmetry.[40] There is a narrow variation in the O···O···O angles, with an average value of 120.72°. These structural parameters are similar to those of cyclic $(H_2O)_6$ clusters.[42] Each water molecule in the cluster is involved in the formation of two hydrogen bonds with an adjacent water molecule. The water octamers are self-assembled along the channels, and are held together by

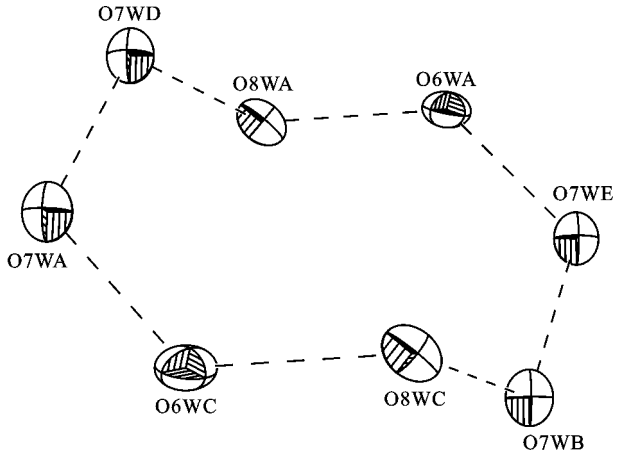

Figure 3. A centrosymmetric cyclic $(H_2O)_8$ cluster in **1** displaying a chair conformation. The view is along the crystallographic *b* axis; hydrogen bond O···O distances [Å] and O···O···O angles [°]: O7WA···O7WD 2.777(3), O7WA···O6WC 2.798(6), O6WC···O8WC 2.850(7), O8WC···O7WB 2.722(8), O6WC···O8WA 5.437(9); O7WD···O7WA···O6WC 118.65(11), O7WA···O6WC···O8WC 127.49(9), O6WC···O8WC···O7WB 125.85(10), O8WC···O7WB···O7WE 110.78(9).

O7W···O6W and O7W···O8W hydrogen bonds to give extended 1-D arrays consisting of eight-membered rings of water,which share a common side formed by an O7W···O7W hydrogen bond (Figure 4). Additionally, atoms O6W and O8W both donate a hydrogen bond towards a carboxyl oxygen atom situated on the Hhbd ligand of the host framework (O4, O5) (av.2.850 Å). These additional interactions play an important role incontributing to the stability of the 1-D cyclic $(H_2O)_8$ cluster arrays. The supramolecular association of water molecules into arrays is presumably enforced by the shape and the condition of the interior of the host's channel. These results further illustrate the structural diversity possible for water clusters and the sensitive dependence of their structures on the nature of their environment.

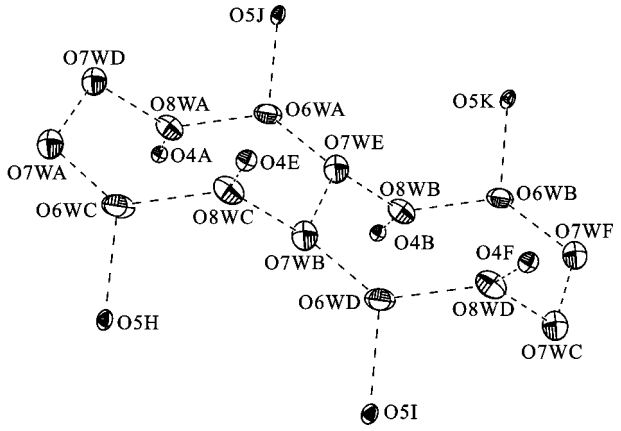

Figure 4. Extended 1-D array consisting of eight-membered rings of water molecules that shared an edge; these arrays are located in the 1-D open channels of **1**. The O···O···O angle for adjacent eight-membered water rings: O6WA···O7WE···O8WB 115.07(8)°.

 © 2005 Wiley-VCH Verlag GmbH & Co. KGaA, Weinheim

{[Cu(Hhbd)(phen)]·H_2O·MeOH}$_n$ (2)

Complexes **1** and **2** have the same space group, $P2_1/c$, and similar crystal data. The central copper(II) atoms in both complexes have the same coordination geometry, and the bond lengths and angles, as shown in Figure 5, part a, Table 1, are also similar. In other dicarboxylate complexes, such as the manganese maleate/diimine systems, and the copper ipa/diimine systems, the replacement of bpy with phen, a chelating aromatic ligand of a larger size, led to a dramatic change in the framework topologies.[33,43] In the study reported in this paper, we used phen instead of bpy, and having used similar reaction conditions, only the analogous neutral polymeric chains were formed in **2** (part b in Figure 5). However, there are some subtle differences between the two complexes; the aromatic π–π stacking interactions between the phen entities are stronger in **2** (the distance between the phen rings is ca.3.27–3.30 Å). Additionally, the 1-D open channels in the final 3-D host framework of **2** (ca. 9.97×4.67 Å),which are also formed through molecular double chains held together by $O_{hydroxyl}$–H···$O_{carboxyl}$ hydrogen bonds, are occupied by water and disordered methanol molecules (Figure 6). As shown above, the most critical factor to note for the two complexes is that their structural identity does not derive from their chemically very similar ancillary ligands, phen and bpy, but from the coordination geometry of their Hhbd ligands, in particular, of the hydroxyl groups bound to the central metal atom.

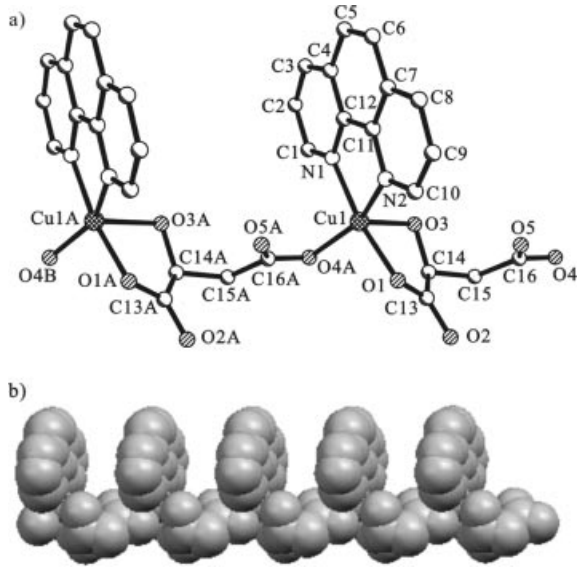

Figure 5. (a) Veiw of the coordination environment of the copper(II) atoms in **2**; (b) a neutral 1-D single-stranded polymeric chain.

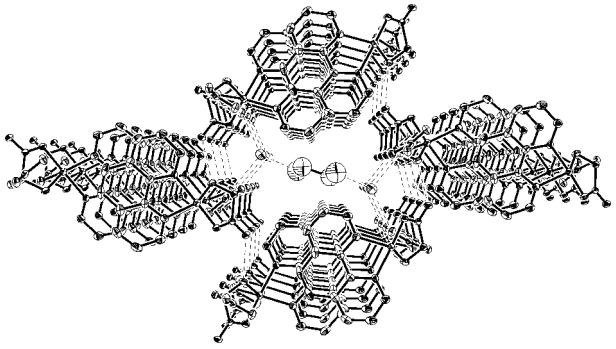

Figure 6. View of the 3-D supramolecular formwork of **2** with 1-D open channels containing the free water and disordered methanol molecules.

IR Spectra and TGA Analysis

The infrared spectra of the two complexes are quite similar, with a broad band centered at ca. 3420–3380 that is due to the –OH stretchingvibration of the water molecules involved in extensive hydrogen-bonding interactions.[44] Furthermore, the spectra exhibit the ν_{as}(OCO) and ν_s(OCO) vibrations of the carboxylate groups that occur at 1608 and 1393 cm^{-1} for **1** and at 1604 and 1403 cm^{-1} for **2**. $\Delta[\nu_{as(OCO)} - \nu_{s(OCO)}] > 200\ cm^{-1}$ for both complexes, a value that suggests that the carboxylate is coordinated in a monodentate fashion, This is in agreement with the crystal structure. Less significant absorption bands occur at 3050–2920 (stretching vibrations of the aromatic C–H groups), 860–720 (out-of-plane motion of the C–H groups of the pyridyl rings) and 570 cm^{-1} ($\nu_{(M-N)}$ vibration).

Thermogravimetric analysis (TGA) showed that the weight of **1** remains almost unchanged from 40 to 210 °C (first stage). The second stage occurs between 210 and 230 °C. A weight loss of 12.86% (calcd. 13.30%) over this range is attributed to the loss of three water molecules. When the temperature is above 235 °C, the product begins to lose the Hhbd and bpy ligands and then starts to decompose. In contrast to **1**, the lattice water and disordered methanol molecules of **2** are lost between 50 and 110 °C; the overall observed loss (11.67%) is in agreement with the calculated value (11.75%). When the temperature is above 240 °C, the complex begins to lose its ligands and then starts to decompose. These data analyses reveal that: (1) The free water and the disordered methanol molecules are removed from the channels of **2** in the range of 50–110 °C, whereas the coordinated phen and Hhbd ligands do not decompose over this temperature range. (2) The water molecules in **1** are involved in strong and extensive hydrogen-bond interactions, leading to the loss of water at higher temperatures. (3) The 1-D neutral polymeric chains of **1** and **2** are stable under 235 °C and 240 °C, respectively. In addition, after heating a sample of **1** at 230 °C, and a sample of **2** at 120 °C, for 2 h the guest solvent molecules are removed (the evacuated frameworks are defined as **1′** and **2′**, respectively). The X-ray power diffraction patterns of **1′** and **2′** are similar to those of **1** and **2**, although minor differences can be seen in the positions, intensities and widths of some peaks, indicating that the frameworks of **1** and **2** are retained after the removal of the guest species. On the other hand, it may also indicate that the 1-D open channels in **1** and **2** have the ability to absorb other hydrophilic small molecules. An investigation of these properties and the synthesis of other metal-Hhbd frameworks are underway.

 © 2005 Wiley-VCH Verlag GmbH & Co. KGaA, Weinheim

Magnetic Properties

Variable-temperature magnetic susceptibility measurements over the 5–300 K range were carried out for **1** and **2**, and the plots of χ_M and $1/\chi_M$ vs. T are shown in Figure 7. Both $1/\chi_M$ vs. T plots are almost linear down to very low temperatures. Fitting the curves to the Curie–Weiss law $[1/\chi_M = (T - \theta)/C]$ gives a Curie–Weiss constant of C = 0.387 $cm^3 K mol^{-1}$ and a Weiss temperature, θ, of –0.431 K for **1** with an agreement factor of $R = 7.13 \times 10^{-4}$, and C = 0.420 $cm^3 K mol^{-1}$ and θ = –0.456 K for **2** with an agreement factor of $R = 4.07 \times 10^{-4}$, where $R = \Sigma[(1/\chi_M)_{obs} - (1/\chi_M)_{calc}]^2/\Sigma[(1/\chi_M)_{obs}]^2$. The θ values for the two complexes are indicative of weak antiferromagnetic interactions.[45,46] In order to evaluate the exchange interaction between neighboring copper(II) atoms, the experimental data were fitted using the expression (see below) obtained from the Bonner–Fisher calculation based on the effective spin Hamiltonian $H = -J\Sigma(S_iS_{i+1})$.[47]

$$\chi_M^{\ J} = \frac{N\beta^2 g^2 S(S+1)}{3kT}\frac{1+u}{1-u}$$

where

$$u = \coth\left[\frac{JS(S+1)}{kT}\right] - \left[\frac{kT}{JS(S+1)}\right]$$

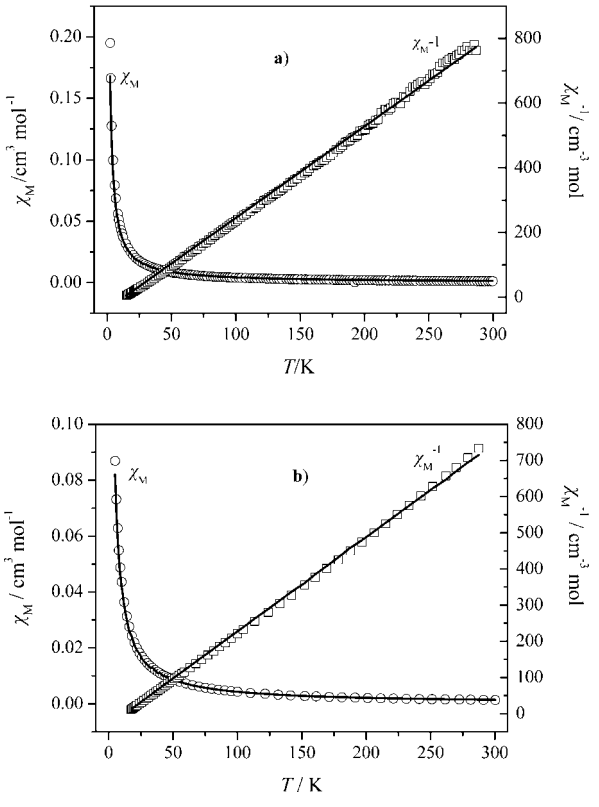

Figure 7. Experimental (○ and □) and fitted (–) curves showing the temperature dependence of χ_M and χ_M^{-1}. (a) for **1**; (b) for **2**.

Finally, this expression fits very well with the experimental susceptibilities of **1** and **2**, giving g = 2.09 and J = –0.487 cm^{-1} for **1** and g = 2.15 and J = –0.517 cm^{-1} for **2**. These very low J values are in agreement with the values of θ reported above. The antiferromagnetic interactions are obviously due to a long-range superexchange pathway between adjacent magnetic centers.[48,49]

Conclusion

In summary, two 3-D supramolecular frameworks with 1-D channels, $\{[Cu(Hhbd)(bpy)]\cdot 3H_2O\}_n$ (**1**) and $\{[Cu(Hhbd)(phen)]\cdot H_2O\cdot MeOH\}_n$ (**2**), were constructed from Hhbd-bridged 1-D chains of copper(II) units and chelating aromatic ligands. The Hhbd ligand adopts a coordination geometry identical to that observed for very similar ancillary chelating ligands. This results in the same structure topologies, in which the aromatic chelating ligand and the –OH groups of the Hhbd ligand play an important role in the self-assembly of the polymeric coordination chains by providing potential supramolecular recognition sites for π–π aromatic stacking and hydrogen-bond interactions. More significantly, in **1** the host framework encapsulates unprecedented centrosymmetric cyclic $(H_2O)_8$ clusters that adopt a chair conformation and are connected into 1-D arrays by supramolecular association.

Experimental Section

Synthesis of $\{[Cu(Hhbd)(bpy)]\cdot 3H_2O\}_n$ (1) and $\{[Cu(Hhbd)(phen)]\cdot H_2O\cdot MeOH\}_n$ (2): Reagents and solvents were purchased from commercial sources (Aldrich) and used as received. The two complexes were prepared in a similar way. Firstly, a sample of copper acetate monohydrate (0.40 g, 2 mmol) was dissolved in deionized water (15 mL). Secondly, *dl*-α-hydroxybutanedioic acid (H_3hbd) (0.29 g, 2.2 mmol) with either 2,2′-bipyridine (bpy) (0.33 g, 2.1 mmol) or 1,10-phenanthroline (phen) (0.42 g, 2.1 mmol) was suspended in MeOH (20 mL) and stirred at ambient temperature for 20 min. Thirdly, the MeOH solution was added slowly drop by drop to the previously prepared copper acetate solution with continuous stirring. The resulting mixture was then stirred for a further 40 min and then filtered. Finally, the blue filtrate solution was transferred to a tube and placed inside a conical flask containing acetone under air. After 13 d, blue crystals of **1** and **2** were manually harvested under the microscope and analyzed using single-crystal X-ray diffraction. Yield: 71% for **1** and 69% for **2**. (**1**) $C_{14}H_{18}CuN_2O_8$ (405.85): calcd. C 41.43, H 4.47, Cu 15.66, N 6.90; found C 41.40, H 4.45, Cu 15.60, N 6.88. (**2**) $C_{17}H_{18}CuN_2O_7$ (425.89): calad. C 47.94, H 4.26, Cu 14.92, N 6.58; found C 47.91, H 4.23, Cu 14.84, N 6.55.

Physical Measurements: Elemental analyses (C,H,N) were determined with a PE 2400 Elemental analyzer, and the analyses of the copper contents were performed on a Perkin–Elmer Optima 3300 DV ICP analyzer. Infrared spectra of KBr pellets were recorded with a BRUKER EQUINOX-55 spectrometer in the range of 4000–400 cm^{-1}. Thermal analyses were performed with a NETZSCH STA 449C microanalyzer with a heating rate of 10 °C min^{-1} under air. The XRPD patterns were recorded with a Rigaku D/Max 3III diffractometer with a scanning rate of 4 deg min^{-1}. Magnetic measurements were carried out on a polycrystalline sample with a SQUID magnetometer operating in the 5–

 © 2005 Wiley-VCH Verlag GmbH & Co. KGaA, Weinheim

300 K temperature range with an applied field of 5 kOe. Diamagnetic corrections were estimated from the Pascal constants.

Crystal Data Collection and Refinement: Diffraction experiments for **1** and **2** were carried out with Mo-K_α radiation using a BRUKER SMART APEX-CCD diffractometer at 293(2) K. A summary of the crystallographic data and structure refinement details are given in Table 2. Both structures were solved by direct methods and refined with the full-matrix least-squares technique on F^2 using SHELXS-97[50] and SHELXL-97.[51] All non-hydrogen atoms were refined anisotropically. CCDC-261630 (for **1**) and CCDC-261631 (for **2**) contain the supplementary crystallographic data for this paper. These data can be obtained free of charge from The Cambridge Crystallographic Data Centre via www.ccdc.cam.ac.uk/data_request/cif.

Table 2. Crystal data and structure refinement details for **1** and **2**.

Compound	**1**	**2**
Empirical formula	$C_{14}H_{18}CuN_2O_8$	$C_{17}H_{18}CuN_2O_7$
Formula mass	405.86	425.89
Temperature [K]	293(2)	293(2)
Crystal system	monoclinic	monoclinic
Space group	$P2_1/c$	$P2_1/c$
a [Å]	7.0132(10)	7.0968(7)
b [Å]	19.730(3)	11.2090(11)
c [Å]	11.8998(16)	20.829(2)
β [°]	94.551(3)	98.302(2)
V [Å^3]	1641.4(4)	1639.5(3)
Z	2	2
$D_{calcd.}$ [g·cm^{-3}]	1.642	1.725
μ [mm^{-1}]	1.377	1.397
F [000]	836	876
θ [°]	2.00–28.26	1.98–28.29
Reflections collected	9894	9802
Independent reflections (R_{int})	3757 (0.0829)	3795 (0.0788)
R_1, wR_2[a] [$I > 2\sigma(I)$]	0.0483, 0.0817	0.0651, 0.1364
Residuals [e·Å^{-3}]	0.632 / –0.477	0.880 / –0.679

[a] $R_1 = \Sigma||F_o| - |F_c||/\Sigma|F_o|$; $wR_2 = [\Sigma w(F_o^2 - F_c^2)^2/\Sigma w(F_o^2)^2]^{1/2}$.

Supporting Information Available: XRPD patterns and the magnetic data for compounds **1** and **2**.

Acknowledgments

This work was supported by the National Natural Science Foundation of China (Grant No. 20471048) and TRAPOYT.

[1] G. F. Swiegers, T. J. Malefetse, *Chem. Rev.* **2000**, *100*, 3483–3493.
[2] M. Fujita, *Molecular Self-Assembly – Organic vs. Inorganic Approaches, Structure and Bonding*, vol. 96, Springer – Verlag, Berlin, Heidelberg, Germany, **2000**.
[3] R. Dultzler, E. B. Campbell, M. Cadene, B. T. Chait, R. Mackinnon, *Nature* **2002**, *415*, 287–289.
[4] R. Kitaura, S. Kitagawa, Y. Kubota, T. C. Kobayashi, K. Kindo, Y. Mita, *Science* **2002**, *298*, 2358–2361.
[5] J. W. Steed, J. L. Atwood (Eds.), *Supramolecular Chemistry*, John Wiley & Sons, West Sussex, UK, **2000**.
[6] J. M. Lehn, *Science* **2002**, *295*, 2400–2402.
[7] R. Dutzler, E. B. Campbell, R. Mackinnon, *Science* **2003**, *300*, 108–110.
[8] S. R. Haiper, S. M. Cohen, *Angew. Chem. Int. Ed.* **2004**, *43*, 2385–2388.
[9] C. Burda, X. Chen, *Chem. Rev.* **2005**, *105*, 1025–1102.
[10] J. S. Seo, D. Whang, H. Lee, S. I. Jun, J. Oh, Y. J. Jeon, K. Kim, *Nature* **2000**, *404*, 982–984.
[11] R. Robson, *J. Chem. Soc., Dalton Trans.* **2000**, 3735–3744.
[12] M. Eddaoudi, D. B. Moler, H. L. Li, B. L. Chen, T. M. Reineke, M. O'Keeffe, O. M. Yaghi, *Acc. Chem. Res.* **2001**, *34*, 319–330.
[13] J. H. Fournier, T. Maris, J. D. Wuest, W. Z. Guo, E. gallopini, *J. Am. Chem. Soc.* **2003**, *125*, 1002–1006.
[14] F. Corbellini, R. Fiammengo, P. Timmerman, M. Crego-Calama, K. Versluis, A. J. R. Heck, I. Luyten, D. N. Reinhoudt, *J. Am. Chem. Soc.* **2002**, *124*, 6569–6575.
[15] L. H. Uppadine, J. M. Lehn, *Angew. Chem. Int. Ed.* **2004**, *43*, 240–245.
[16] V. Arima, E. Fabiano, R. I. R. Blyth, F. D. Sala, F. Matino, J. Thompson, R. Cingolani, R. Rinald, *J. Am. Chem. Soc.* **2004**, *126*, 16951–16958.
[17] R. Kitaura, K. Seki, G. Akiyama, S. Kitagawa, *Angew. Chem. Int. Ed.* **2003**, *42*, 428–433.
[18] B. Q. Ma, P. Coppens, *Chem. Commun.* **2004**, 932–933.
[19] R. García-Zarracino, H. Höpfl, *Angew. Chem. Int. Ed.* **2004**, *43*, 1507–1511.
[20] H. Li, M. Eddaoudi, M. O'Keeffe, O. M. Yaghi, *Nature* **1999**, *402*, 276–279.
[21] S. S. Y. Chui, S. M. F. Lo, J. P. H. Charmant, A. G. Orpen, I. D. Williams, *Science* **1999**, *283*, 1148–1150.
[22] S. I. Noro, S. Kitagawa, M. Kondo, K. Seki, *Angew. Chem. Int. Ed.* **2000**, *39*, 2081–2084.
[23] R. H. Wang, M. C. Hong, D. Q. Yuan, Y. Q. Sun, L. J. Xu, J. H. Luo, R. Cao, A. S. C. Chan, *Eur. J. Inorg. Chem.* **2004**, 37–43.
[24] X. M. Zhang, M. L. Tong, M. L. Gong, X. M. Chen, *Eur. J. Inorg. Chem.* **2003**, 138–142.
[25] C. N. R. Rao, S. Natarajan, R. Vaidhyanathan, *Angew. Chem. Int. Ed.* **2004**, *43*, 1466–1496.
[26] P. Schwendt, P. Švančárek, L. Kuchta, J. Marek, *Polyhedron* **1998**, *17*, 2161–2171.
[27] R. E. Tapscott, *Transition Metal Chemistry*, Vol.8 (Eds.: G. A. Melson, B. N. Figgis), Marcel Dekker Inc., New York, Basel, **1982**.
[28] J. J. Max, C. Chapados, *J. Phys. Chem. A* **2002**, *106*, 6452–6461.
[29] J. Gawroński, K. Gawrońska, *Tartaric and malic acid in synthesis: A source book of building blocks, ligands, auxiliaries, and resolving agents*, Wiley Interscience, New York, NY, **1999**.
[30] N. Kotsakis, C. P. Raptopoulou, V. Tangoulis, A. Terzis, J. Giapintzakis, T. Jakusch, T. Kiss, A. Salifoglou, *Inorg. Chem.* **2003**, *42*, 22–31.
[31] A. W. Addison, T. N. Rao, J. Reedijk, J. Vin Rijin, G. C. Verschoor, *J. Chem. Soc., Dalton Trans.* **1984**, 1439–1456.
[32] S. Dalai, P. S. Mukherjee, G. Rogez, T. Mallah, M. G. B. Drew, N. R. Chaudhuri, *Eur. J. Inorg. Chem.* **2002**, 3292–3297.
[33] X. M. Chen, G. F. Liu, *Chem. Eur. J.* **2002**, *8*, 4811–4817.
[34] Z. H. Zhou, J. J. Ye, Y. Y. Deng, G. Wang, J. X. Gao, H. L. Wan, *Polyhedron* **2002**, *21*, 787–790.
[35] G. R. Desiraju, *Acc. Chem. Res.* **1996**, *29*, 441–452.
[36] J. K. Gregory, D. C. Clary, *J. Phys. Chem.* **1996**, *100*, 18014–18020.
[37] C. J. Gruenloh, J. R. Carney, C. A. Arrington, T. S. Zwier, S. Y. Fredericks, K. D. Jordan, *Science* **1997**, *276*, 1678–1681.
[38] U. Buck, I. Ettischer, M. Melzer, V. Buch, J. Sadlej, *Phys. Rev. Lett.* **1998**, *80*, 2578–2581.
[39] W. B. Blanton, S. W. Gordon-Wylie, G. R. Clark, K. D. Jordan, J. T. Wood, U. Geiser, T. J. Collins, *J. Am. Chem. Soc.* **1999**, *121*, 3551–3552.
[40] J. L. Atwood, L. J. Barbour, T. J. Ness, C. L. Raston, P. L. Raston, *J. Am. Chem. Soc.* **2001**, *123*, 7192–7196.
[41] R. J. Doedens, E. Yohannes, M. I. Khan, *Chem. Commun.* **2002**, 62–63.
[42] R. Custelcean, C. Afloroaei, M. Vlassa, M. Polverejan, *Angew. Chem. Int. Ed.* **2000**, *39*, 3094–3096.
[43] C. Ma, C. Chen, Q. Liu, F. Chen, D. Dai, L. Li, L. Sun, *Eur. J. Inorg. Chem.* **2003**, 2872–2879.

 © 2005 Wiley-VCH Verlag GmbH & Co. KGaA, Weinheim

[44] E. Berti, F. Cecconi, C. A. Ghilardi, S. Midollini, A. Orlandini, E. Pitzalis, *Inorg. Chem. Commun.* **2002**, *5*, 1041–1047.
[45] S. Mukhopadhyay, P. B. Chatterjee, D. Mandal, G. Mostafa, A. Caneschi, J. V. Slageren, T. J. R. Weakley, M. Chaudhury, *Inorg. Chem.* **2004**, *43*, 3413–3426.
[46] L. Y. Wang, L. C. Li, D. Z. Liao, Z. H. Jiang, S. P. Yan, *Eur. J. Inorg. Chem.* **2004**, 2266–2271.
[47] M. E. Fisher, *Am. J. Phys.* **1964**, *32*, 343–346.
[48] P. S. Mukherjee, D. Ghoshal, E. Zangrando, T. Mallah, N. R. Chaudhuri, *Eur. J. Inorg. Chem.* **2004**, 4675–4680.
[49] S. Dalai, P. S. Mukherjee, G. Rogez, T. Mallah, M. G. B. Drew, N. R. Chaudhuri, *Eur. J. Inorg. Chem.* **2002**, 3292–3297.
[50] G. M. Sheldrick, *SHELXS*, University of Göttingen, Germany, **1997**.
[51] G. M. Sheldrick, *SHELXL*, *Program for the Refinement of Crystal Structures*, University of Göttingen, Germany, **1997**.
Received January 27, 2005
Published Online: May 27, 2005

 © 2005 Wiley-VCH Verlag GmbH & Co. KGaA, Weinheim

Ru^{III} Complexes of Edta and Dtpa Polyaminocarboxylate Analogues and Their Use as Nitric Oxide Scavengers

Tim Storr,[a,b] Beth R. Cameron,*[a] Robert A. Gossage,[a,c] Helen Yee,[a] Renato T. Skerlj,[a] Marilyn C. Darkes,[a] Simon P. Fricker,[a] Gary J. Bridger,[a] Nathan A. Davies,[d] Michael T. Wilson,[d] Kevin P. Maresca,[e] and Jon Zubieta[e]

Keywords: Bioinorganic chemistry / Ruthenium / Polyaminocarboxylates / Nitric oxide scavenging

In this study a series of Ru^{III} complexes, chelated by analogues of ethylenediaminetetraacetic acid (edta) and diethylenetriaminepentaacetic acid (dtpa), were produced and tested for NO scavenging ability. Modifications to the edta and dtpa ligand frameworks were made in an effort to alter the reactivity, aqueous stability and pharmacokinetics of the resulting Ru^{III} complexes. The X-ray structure of the nitrosyl complex **38** confirms that the Ru^{III} complex **27** reacts with NO to form a linear {Ru–NO}[6] complex. The nitrosyl complex $[C_{15}H_{15}N_4O_{11}Ru]$ crystallized in the $P2_1/c$ space group with a = 12.731(3) Å, b = 10.894(2) Å, c = 14.241 (3) Å, β = 107.320(4)°, V = 1885.6(7) Å^3, and Z = 4. Kinetic studies on the reactions of **14** ($k = 2.38\times10^6$ M^{-1} s^{-1}) and **27** ($k = 2.30\times10^5$ M^{-1} s^{-1}) with NO exemplify the difference in chemical properties obtained by ligand framework manipulation. Binding constants of **14** ($K_B = 5\times10^6$ M^{-1}) and **27** ($K_B = 2\times10^5$ M^{-1}) with NO were also measured, indicating the tight binding of NO by the Ru^{III} complexes. The activity of the Ru^{III} complexes to scavenge nitric oxide was evaluated using RAW264 murine macrophage cells. Ligand analogues of edta that have a pyridine donor as part of the *N*,*N* chelate such as **20** and **24** exhibit similar scavenging activity to the parent compound. Ligand analogues of dtpa that have R groups at the central amine in place of the carboxylic acid such as **31**, **34**, and **37** are also efficient NO scavengers.

(© Wiley-VCH Verlag GmbH & Co. KGaA, 69451 Weinheim, Germany, 2005)

Introduction

The discovery that nitric oxide (NO) acts as a signaling molecule in the body has led to a significant amount of research concerning its function and also the role this small molecule plays in the physiology and pathophysiology of disease. As a testament to the importance of this work, Robert Furchgott, Ferid Murad, and Louis Ignarro were awarded the Nobel Prize in physiology or medicine for their pioneering work on NO. NO is produced in the body during the conversion of L-arginine to L-citrulline, a process catalyzed by the enzyme nitric oxide synthase (NOS).[1] A dysfunction in NO metabolism has been implicated in many disease states. For example, a decrease in NO production can lead to severe hypertension, a condition that is treated with vasodilators (NO donors) such as nitroprusside.[2] The overproduction of NO has been implicated to play a role in many disease states such as septic shock,[3] rheumatoid arthritis,[4] diabetes,[5] asthma,[6] and cancer.[7,8] One approach to attenuate the overproduction of NO is through the use of NOS inhibitors. There are several isoforms of NOS, and these can be divided into the Ca^{2+}-dependent [constitutive NOS (cNOS): nNOS and eNOS] and Ca^{2+}-independent (inducible NOS: iNOS). NOS inhibitors necessarily need to be specific for iNOS, to prevent any deleterious effects of inhibiting the essential constitutive NOS. An alternative strategy, eliminating the necessity of specific NOS inhibitors, is to use NO scavengers. Transition metal complexes such as pyridoxylated hemoglobin polyethylene (PHP)conjugates,[9] dinuclear copper complexes,[10] Fe dithiocarbamates[11] or Ru-containing[12,13] complexes have shown considerable potential as NO scavengers.

Ruthenium complexes have been investigated as immunosuppressive agents,[14] *anti*-tumour and *anti*-metastatic agents,[15–18] antiangiogenic agents,[19] and as nitric oxide (NO) scavengers.[2,12,20,21] Our research program has focused on the use of ruthenium complexes, and in particular Ru^{III} polyaminocarboxylate (PAC) complexes, as NO scavengers. An effective NO scavenger must meet certain criteria

[a] AnorMED Inc.,
200-20353 64th Ave., Langley, BC, V2Y 1N5, Canada
Fax: +1-604-530-0976
E-mail: Bcameron@anormed.com
[b] Present address: Department of Chemistry, University of British Columbia,
Vancouver, BC, V6T 1Z1, Canada
[c] Present address: Department of Chemistry, Acadia University, Wolfville, Nova Scotia, B4P 2R6, Canada
[d] Department of Biological and Chemical Sciences, University of Essex,
Wivenhoe Park, Colchester, CO4 3SQ, UK
[e] Department of Chemistry, Syracuse University, Center for Science and Technology,
Syracuse, NY 13244-4100, USA
Supporting information for this article is available on the WWW under http://www.eurjic.org or from the author.

including (but not limited to) the following: (1) Fast NO reaction kinetics; (2) activity and stability in in vitro and in vivo biological systems; (3) low toxicity; (4) rapid clearance from the organism. The rich coordination chemistry of ruthenium allows for fine-tuning of all the necessary properties for an effective NO scavenger listed above through manipulation of the ligand framework. We have identified **AMD6245** and **AMD6221** as efficient NO scavengers in several disease models of varying pathophysiological complexity.[21–24] The PAC ligands bind to the ruthenium atom in a pentadentate fashion with the sixth coordination site being occupied by a water molecule or chloride ion.[12,25–27] In aqueous solution, a water molecule rapidly substitutes the chloride ion,[28,29] which in turn is a labile substituent that undergoes substitution with various ligands.[29–32] The Ru^{III}PAC complex reacts with NO to form a relatively inert Ru^{II}-$^{+}$NO species[12,33] making these compounds an attractive class of therapeutic agents. It is possible with the Ru^{III} complexes to control the compartmental localization of the NO scavenger by alteration of the multidentate ligand framework. Fine adjustment of lipophilicity, charge, and steric bulk offer potential avenues for enhancement of the pharmacological activity of these compounds. Indeed, while our two lead compounds **AMD6245** and **AMD6221** have shown significant activity, both exhibit drawbacks such as slow plasma clearance,[34] and nonselective reactivity (dimer formation,[35] and reactivity with thiols,[36–38] and N-heterocycles[29,39]) for the former, and fast plasma clearance[34] for the latter.

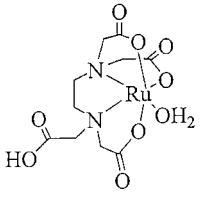

AMD6245

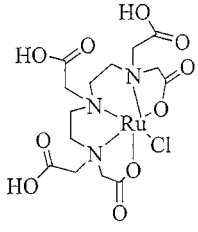

AMD6221

In an aerobic aqueous environment **AMD6245** is rapidly oxidized to form a μ-oxo Ru^{III}–Ru^{IV} dimer.[35] Dimer formation is particularly evident by a color change from yellow to green in solution, which occurs more rapidly under basic conditions. The mechanism is probably through an intermediate involving deprotonation of the coordinated H_2O molecule[35] (pK_a = 7.6). Although the in vitro NO scavenging ability does not appear to be affected by dimer formation, extra care is taken in formulation of **AMD6245** since the bioavailability of this dimer is not known. We therefore sought analogous ruthenium complexes that are less prone to oxidation/dimerization when in a formulated solution. This oxidation/dimerization does not appear to occur with **AMD6221** probably because the pK_a of the coordinated H_2O molecule (pK_a = 8.3)[40] is higher than that observed in **AMD6245**. Previously, we have shown that **AMD6245** has a significantly higher plasma C_{max} than **AMD6221** (74.5 μg/mL vs. 11.6 μg/mL) accompanied by a slower plasma clearance (1.13 mL/h vs. 19.9 mL/h) when administered as a single intravenous injection (20 mg/kg) in rats.[34] These studies suggest that the pharmacokinetic behaviour of Ru^{III} PAC complexes is influenced by the coordination environment of the Ru center as well as groups on the periphery (those not immediately bound to the metal center).

Herein, we report the synthesis and characterization of analogues of **AMD6245** and **AMD6221**. There were essentially two objectives to be achieved in the modification of the lead compounds **AMD6245** and **AMD6221**. First, modification of the ligand framework on **AMD6245** was undertaken to reduce dimer formation[35] and/or nonspecific reactivity.[29,36,37,39] It is this nonspecific reactivity with cellular components that is thought to reduce the NO scavenging ability of **AMD6245** in in vitro studies when compared to kinetic results and when compared to **AMD6221**. Second, modification of the **AMD6221** ligand framework was undertaken to increase lipophilicity, in an effort to prolong the activity of this complex in vivo. In both cases the NO scavenging ability of these compounds as well as the stability of the formulated solutions were evaluated using an in vitro RAW264 murine macrophage assay. Based on these results the most promising compounds will be further evaluated to determine the pharmacokinetic parameters.

Results and Discussion

Ligand Synthesis

The first approach at modification of the edta ligand framework to form symmetric analogs involved changing the number of carboxylate groups as in [{2-[(carboxymethyl)amino]ethyl}amino]acetic acid (**1**), or alternatively changing the ethylenediamine fragment to 1,3-propanediamine as in ({3-[bis(carboxymethyl)amino]propyl}-(carboxymethyl)amino)acetic acid (**3**).[41] (Scheme 1).

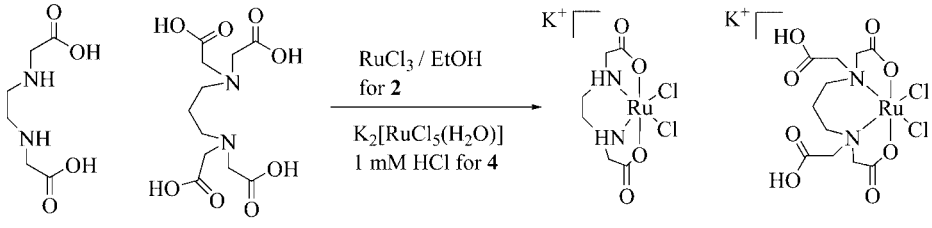

1 **3** **2** 22% **4** 24%

Scheme 1.

 © 2005 Wiley-VCH Verlag GmbH & Co. KGaA, Weinheim

The synthesis of the first two nonsymmetrical edta analogs utilized compound **5**[42] as the starting point (Scheme 2). *N*-Alkylation of **5** with benzyl bromide under standard conditions and subsequent acid hydrolysis with trifluoroacetic acid afforded compound **6** in 45% overall yield. Similarly, *N*-alkylation with 3-bromomethylbenzoate afforded **8**, which was then deprotected over two steps to afford compound **9** in 50% overall yield.

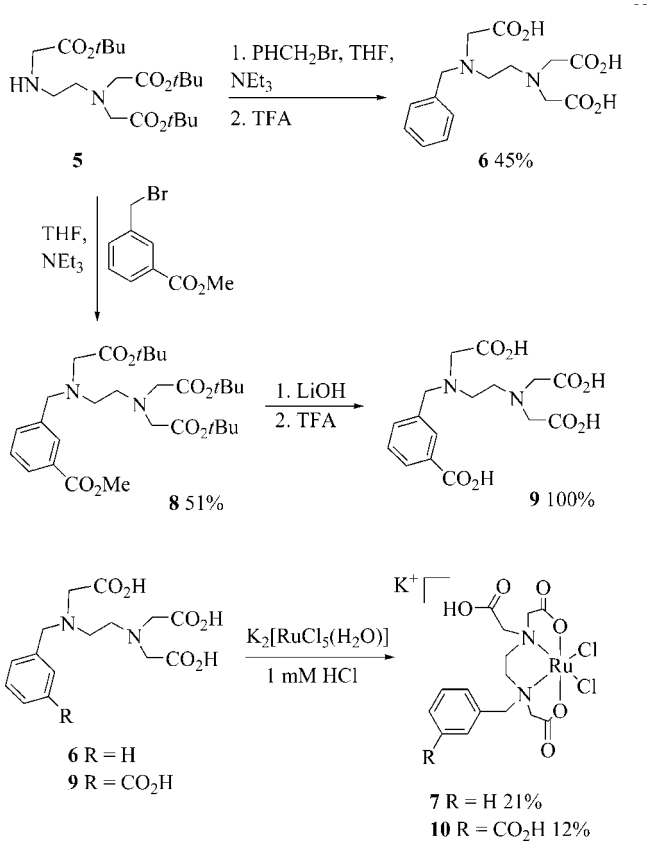

Scheme 2.

A second route, used to prepare the nonsymmetrical edta analog **13** (31% overall yield), which has a pendant pyridyl group, is a five-step procedure from pyridine-2-carbaldehyde (**11**) (Scheme 3). The main advantage of this method is that the starting materials are readily available (intermediate **5** is not required). Schiff-base formation between *N*-BOC ethylenediamine and pyridine-2-carbaldehyde followed sequentially by imine reduction and acid hydrolysis afforded a dark oil which was used without further purification. The three acid moieties were then added to this intermediate by *N*-alkylation with *tert*-butyl bromoacetate to afford compound **12**. Standard acid hydrolysis was then used to produce compound **13**. The symmetric ligand **15**, exhibiting two pendant pyridyl groups for metal binding, was synthesized by a literature method (Scheme 4).[43]

Edta ligand analogues, where one N atom of edta is replaced by a pyridyl N atom (**19, 23**), were prepared by multi-step synthetic routes as shown in Scheme 5. Reaction of methanesulfonyl chloride with methyl 6-(hydroxymethyl)pyridine-2-carboxylate[44] (**17**) afforded compound **18** in

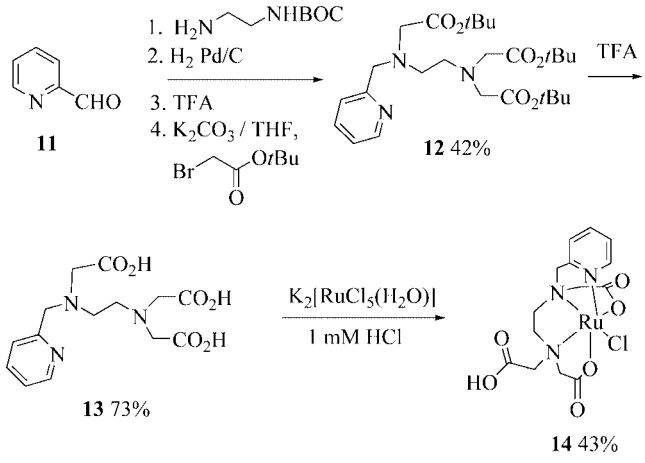

Scheme 3.

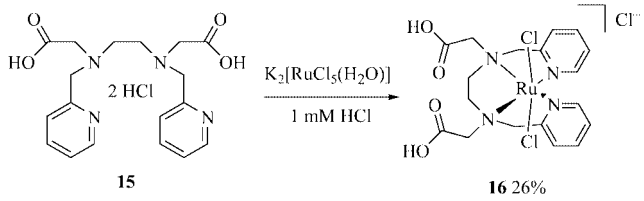

Scheme 4.

near quantitative yield. Nucleophilic substitution of the mesylate group with iminodiacetic acid dimethyl ester followed by base (LiOH) hydrolysis of all three methyl esters to the corresponding carboxylic acid groups afforded the tricarboxylic acid ligand **19** in 39% overall yield**.** Ligand **23** was prepared in 4 steps in an overall yield of 38% from 6-(hydroxymethyl)pyridine-2-carbaldehyde[45] (**21**). Mesylation of the hydroxy group of **21** followed by *N*-alkylation with iminodiacetic acid di-*tert*-butyl ester[46] and subsequent reduction ($NaBH_4$) of the aldehyde group afforded compound **22**. Acid hydrolysis of the *tert*-butyl ester groups with trifluoroacetic acid (TFA) afforded compound **23** in 43% yield.

A significant amount of effort has been dedicated to developing structural analogs of dtpa due to the widespread use of this ligand in medical imaging.[47] Our intention in utilizing dtpa analogs in this study was to add lipophilicity in an effort to increase the plasma half-life and distribution of the Ru^{III} PAC compounds. Structural manipulations focused on removing charge, more specifically eliminating the acid functional group attached to the central N atom. Incorporation of a pyridyl moiety into the dtpa framework was realized with the synthesis of compound **26** (Scheme 6). Reaction of two equivalents of iminodiacetic acid dimethyl ester with 2,6-bis(bromomethyl)pyridine hydrogen bromide[48] **25** under basic conditions afforded the deprotected ligand **26** in one step in 71% yield. Due to the basic nature of the reaction mixture the compound was isolated as the tri-sodium salt. The 4-bromopyridyl-substituted derivative of this ligand has been reported,[46] which may provide a route to extensive structure-activity relationships (SAR) on complexes of this type.

 © 2005 Wiley-VCH Verlag GmbH & Co. KGaA, Weinheim

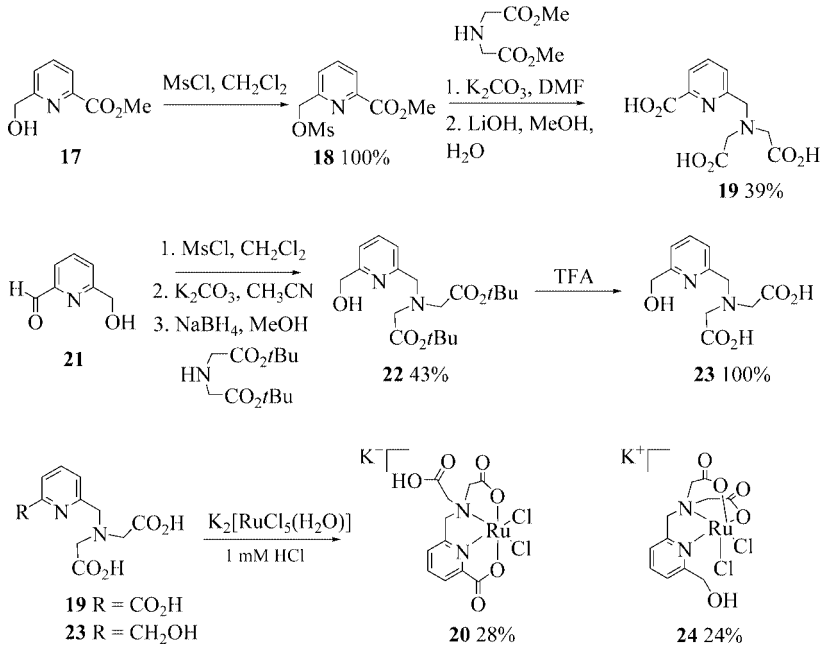

Scheme 5.

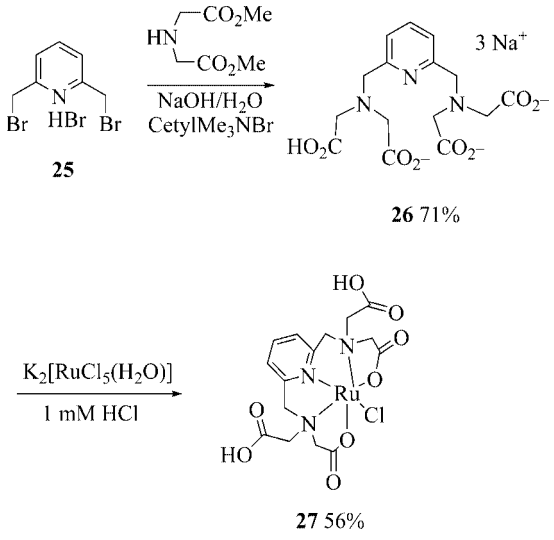

Scheme 6.

Dtpa analogs with various R groups attached to the central amine were also prepared as shown in Scheme 7. Using a similar synthetic strategy to that developed by Williams and Rapoport,[49] compounds **30** (R = ethyl), **33** (R = butyl), and **36** (R = benzyl) were prepared. The synthetic strategy is outlined using compound **30**. Two equivalents of compound **28** were reacted with ethylamine to afford the protected dtpa analog **29**. Standard TFA hydrolysis of the *tert*-butyl ester groups afforded compound **30** in 53% overall yield. The compounds described in this section were characterized by ^{1}H and ^{13}C NMR as well as mass spectrometry. Due to the extremely hygroscopic nature of the synthesized ligands, elemental analysis of the compounds was not carried out. Elemental analysis of the Ru complexes described in the next section was however used as a characterization tool.

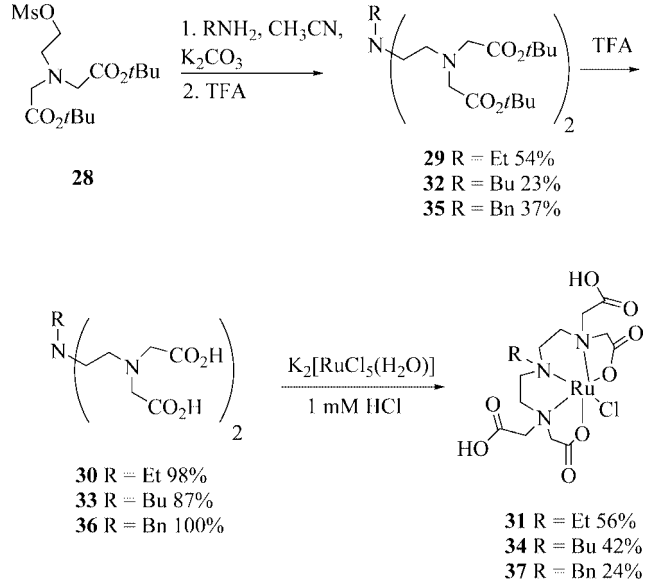

Scheme 7.

Ru^{III} Complexes

The complexation of ruthenium to a PAC ligand was typically performed in 1 mM HCl heated to reflux using $K_2[RuCl_5(OH_2)]$[50] as the source of ruthenium. In only one circumstance (complex **2,** Scheme 1) was an alternate source of ruthenium ($RuCl_3$) used to prepare the complex. The complexes were often obtained by precipitation from the reaction mixture, however in a few instances chromatog-

 © 2005 Wiley-VCH Verlag GmbH & Co. KGaA, Weinheim

raphy was required for purification. The Ru^{III}PAC complexes were isolated as light yellow powders, and were found to be slightly soluble in water. The complexes were characterized by infrared spectroscopy (IR), mass spectroscopy (MS), elemental analysis, and in one case X-ray crystallography.

All edta-type complexes (except **14**) were characterized as the potassium salt with two chlorides bound to the metal center. The driving force for this type of structure is thought to be the mildly acidic (HCl) reaction conditions. The orientation of the two chloride ligands (*cis* or *trans*) is not known from the characterization data, however, the *cis* form is shown in the appropriate schemes. For compound **2**, stretching frequencies assigned to the coordinated carboxylates (CO_2^-; 1640 cm^{-1}), and the Ru–Cl[51] bonds (318 cm^{-1}) were visible. The absence of uncoordinated carboxylates (>1700 cm^{-1}) as well as the intact MS peak at *m/z* 346 $[M]^-$ lead to the structural formulation in Scheme 1. Mass spectroscopic data for all the Ru compounds are shown in Table 1. The calculated isotopic distribution pattern for each fragment matched the observed pattern. Compound **4** is also shown in Scheme 1, and was characterized in a similar fashion to **2** with the major difference being the presence of uncoordinated carboxylates (CO_2H, 1738 cm^{-1}) in the IR spectrum. The mass spectrum of compound **4** was informative; the fragmentation pattern showed the loss of a chloride ligand as well as two free acid moieties consistent with the proposed structure. Whether the two acid functions bound in compound **4** are from opposing N atoms to give a symmetric structure (as shown) or from a single N atom is unclear but exchange processes are most likely to occur in solution. The paramagnetic Ru^{III} center precluded NMR studies on any dynamic processes.

Complexes **7** and **10** are shown in Scheme 2. Strong absorptions in the IR spectrum (>1700 cm^{-1}) confirm the presence of uncoordinated carboxylate moieties in both complexes. For compound **7**, the presence of a $[M]^-$ peak (80% intensity) as well as an $[M - Cl - H]^-$ peak (100% intensity) in the ES-MS spectra confirms the structural interpretation and shows the facile loss of a chloride ion from the complex. This is to be expected as substitution for a chloride by water in aqueous solution would parallel the reactivity observed for **AMD6245**.[12] Only the $[M - Cl - H]^-$ peak (100% intensity) was present in the mass spectrum of compound **10**. The effect of adding another N atom, in the form of a pyridyl moiety, to form compound **14** was investigated as shown in Scheme 3. The structural formulation fits the general trend (vide supra) in that the Ru^{III} center exhibits a higher affinity for N donors over O-donors (acid groups) under the complexation conditions employed. This trend is further borne out with compound **16** (Scheme 4), synthesized from **15**,[43] which was concluded to have four N atoms bound based on the characterization data. The effect of substituting one edta N atom for a pyridyl moiety was also investigated as shown in Scheme 5. Compounds **20** and **24** were produced as their potassium salts. Elemental analysis and mass spectroscopic data are consistent with the proposed structures. An absorption due to an uncoordinated carboxylic acid was present in the IR of **20**, yet absent in **24**. The close proximity of the acid function attached to the pyridine in compound **20** most likely leads to the acid connectivity shown.

The four Ru^{III} dtpa analogs **27**, **31**, **34**, and **37** are shown in Scheme 6 and 7. All four compounds exhibit a Ru–Cl bond, two free acid functional groups, and three coordinated N atoms. The crystal structure of the product of the reaction of **27** with NO (Figure 1) further substantiates the structural interpretation. The mass spectroscopic data for the four Ru^{III} dtpa analogs (Table 1) showed similar molecular ions and fragmentation patterns to the parent complex **AMD6221**.[12] The presence of an $[M - Cl - 2H]^-$ peak with successive loss of carboxylate groups (44 mass units),

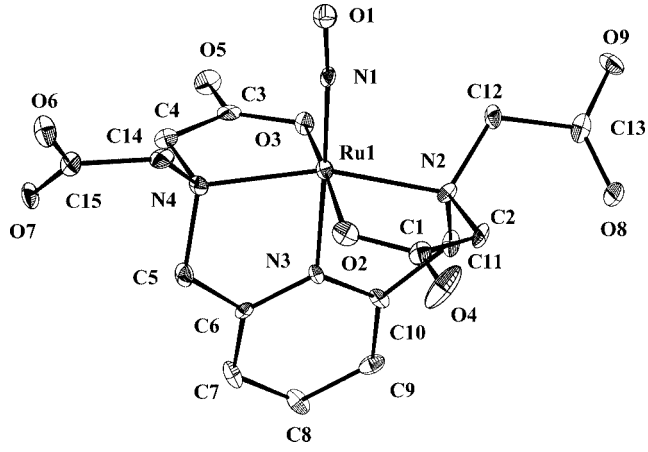

Figure 1. An ORTEP view of the structure of **38**, showing the atom-labelling scheme and 50% thermal ellipsoids.

Table 1. Mass spectral fragmentation patterns for the ruthenium PAC complexes.

	Polarity	MS peaks (intensities) and assignment
1	(–)ES-MS	346 $[M]^-$ (100)
4	(–)ES-MS	440 $[M - Cl - H]^-$ (25), 404 $[M - 2Cl - 2H]^-$ (100), 360 $[M - 2Cl - CO_2H]^-$ (30), 316 $[M - 2Cl - 2(CO_2H)]^-$ (25)
7	(–)ES-MS	494 $[M]^-$ (80), 458 $[M - Cl - H]^-$ (100)
10	(–)ES-MS	502 $[M - Cl - H]^-$ (100)
14	(–)ES-MS	459 $[M - H]^-$ (60), 423 $[M - Cl - H]^-$ (100), 379 $[M - Cl - CO_2H]^-$ (45), 333 $[M - Cl - 2(CO_2H)]^-$ (30)
16	(+)ES-MS	458 $[M - 2Cl - 2H]^+$ (100), 414 $[M - 2Cl - H - CO_2H]^+$ (50), 370 $[M - 2Cl - 2(CO_2H)]^+$ (75)
20	(–)ES-MS	402 $[M - Cl - H]^-$ (100)
24	(–)ES-MS	446 $[M - H + Na]^-$ (100)
27	(–)ES-MS	466 $[M - Cl - 2H]^-$ (40), 423 $[M - Cl - H - CO_2H]^-$ (65), 379 $[M - Cl - 2(CO_2H)]^-$ (45), 334 $[M - Cl - 3(CO_2H)]^-$ (100)
31	(–)ES-MS	461 $[M - Cl - 2H]^-$ (45), 417 $[M - Cl - H - CO_2H]^-$ (100), 373 $[M - Cl - 2(CO_2H)]^-$ (30)
34	(–)ES-MS	489 $[M - Cl - 2H]^-$ (50), 445 $[M - Cl - H - CO_2H]^-$ (100), 401 $[M - Cl - 2(CO_2H)]^-$ (20)
37	(–)ES-MS	523 $[M - Cl - 2H]^-$ (95), 479 $[M - Cl - H - CO_2H]^-$ (80), 433 $[M - Cl - 2(CO_2H)]^-$ (10), 388 $[M - Cl - H - CO_2H - C_7H_7]^-$ (100)

 © 2005 Wiley-VCH Verlag GmbH & Co. KGaA, Weinheim

and in the case of **37** loss of a benzyl moiety (C_7H_7, 91 mass units), supports the proposed structures.

Reaction with NO

It is well documented that Ru^{III}PAC complexes react with small molecules such as NO.[33,52] As an example, compound **27** was treated with sodium nitrite in acid medium to form the Ru–NO complex **38**. Confirmation that compound **27** binds with NO in the proposed manner lies in the crystal structure of the nitrosyl complex (Figure 1). The structure consists of discrete mononuclear units, with the Ru site in a distorted octahedral environment defined by the amine donors N1 and N4 and the carboxylate oxygen donors O2 and O3 in the equatorial plane and the pyridine nitrogen N3 and the nitrosyl N1 occupying the axial positions. Consequently, one carboxylate group at each amine terminus adopts a pendant mode. Selected bond lengths and angles are given in Table 2. The structure clearly demonstrates a linear [∠Ru(1)–N(1)–O(1) = 175.8(4)°] {RuNO}[6] complex, where an electron is formally transferred from NO to Ru^{III}, so a Ru^{II}-$^{+}$NO assignment can be made. This complex coordinates in a similar fashion to the nitrosyl complex of **AMD6221** with the NpyN donor atoms coordinated in a meridonal geometric arrangement about the Ru center.[12] The difference is that the complex described here has one carboxylate from each N atom coordinated to the Ru, whereas with the nitrosyl complex of **AMD6221** one carboxylate from a terminal N atom and the carboxylate on the central N atom coordinate to the Ru center. This type of structure is not possible with **27** as the central carboxylate has been removed.

Table 2. Selected bond lengths [Å] and angles [°] for the nitrosyl complex **38**.

Ru(1)–O(2)	2.028(4)	N(3)–Ru(1)–N(1)	177.3(2)
Ru(1)–O(3)	2.021(3)	N(4)–Ru(1)–N(2)	159.81(16)
Ru(1)–N(1)	1.753(5)	O(2)–Ru(1)–O(3)	170.61(15)
Ru(1)–N(2)	2.116(4)	N(1)–Ru(1)–O(2)	93.75(18)
Ru(1)–N(3)	2.015(4)	N(1)–Ru(1)–O(3)	95.62(18)
Ru(1)–N(4)	2.117(4)	N(1)–Ru(1)–N(2)	102.56(19)
N(1)–O(1)	1.158(5)	N(1)–Ru(1)–N(4)	97.63(18)
		O(1)–N(1)–Ru(1)	175.8(4)

The coordination sphere of Ru affects the rate of reaction with NO and the stability of the resultant nitrosyl complex. Stopped flow techniques similar to those for **AMD6245** and **AMD6221**[12,52] were used in order to investigate the reaction of select Ru^{III}PAC complexes with NO. A saturated nitric oxide aqueous solution was prepared by introducing a degassed buffer solution to a NO atmosphere (generated from sulfuric acid and sodium nitrite) and agitating to ensure saturation. Using this method NO solutions were obtained in a concentration range of 1.6–2.0 mM. UV/Vis spectral changes were monitored upon mixing solutions of candidate Ru compounds and NO. Second-order rate constants (k) and binding affinities (K_B) for complexes **14** and **27** are shown in Table 3 and compared with the parent compounds **AMD6245** and **AMD6221**, respectively. **AMD6245** is by the far the most efficient scavenger of NO in the absence of competing ligands. The extreme lability of this coordinated water molecule has been attributed to hydrogen bonding of the pendant carboxylate group to the water molecule thereby weakening the Ru–OH_2 bond and/or creating an open site for associative attack of the incoming ligand.[28] Alternatively, it has been proposed that the activation for associative attack of the incoming nucleophile is a result of the transient coordination of the pendant carboxylate group.[53,54] Modification of the coordination sphere can drastically change the rate of substitution. For instance, k is reduced at least one order of magnitude when a N_2O_4 coordination environment in **AMD6245** is changed to a N_2pyO_3 coordination environment as in **14**. The second-order rate constant for the reaction of **14** with NO was determined to be $2.38(\pm0.8)\times10^6$ M^{-1} s^{-1} at 20 °C (pH = 7.4; 50 mM phosphate buffer). A slight decrease in k = $2.30(\pm1.0)\times10^5$ M^{-1} s^{-1} at 20 °C (pH = 7.4; 50 mM phosphate buffer) is also observed when the N_3O_3 coordination environment of **AMD6221** is changed to a $NpyNO_3$ coordination sphere as in **27**. The binding constant of **14** (K_B = 5×10^6 M^{-1}) with NO was assessed by means of an UV/Vis titration (see supporting information; for supporting information see also the footnote on the first page of this article) and was found to be considerably lower than that of **AMD6245** and NO ($K_B > 10^8$ M^{-1}). The binding constant of **27** ($K_B = 2\times10^5$ M^{-1}) with NO was found to be identical to **AMD6221**. These results clearly demonstrate that manipulation of the ligand framework provides an opportunity to fine tune the chemical properties of the ruthenium complex to optimize the scavenging characteristics of the Ru^{III}PAC complexes. The stability and performance of the Ru complexes in an in vitro NO scavenging assay is however a much better indication of the potential utility of these compounds for their intended use as NO scavengers in vivo.

Table 3. Kinetic parameters for the reaction of selected Ru^{III}PAC complexes with NO.

Compound	Coordination sphere	k (M^{-1} s^{-1})	K_B (M^{-1})
AMD6245[a]	N_2O_4	$2.24\pm0.05\times10^7$ (7.3 °C)	$>10^8$
14	N_2pyO_3	$2.38\pm0.8\times10^6$ (20 °C)	$5\pm1.7\times10^6$
27	$NpyNO_3$	$2.30\pm1.0\times10^5$ (20 °C)	$2\pm0.75\times10^5$
AMD6221[a]	N_3O_3	3.0×10^5 (20 °C)	2×10^5

[a] Ref.[12]

NO Scavenging

The NO scavenging ability of the ruthenium complexes was evaluated using RAW264 murine macrophage cells. These cells are stimulated to produce NO by the addition of lipopolysaccharide (LPS) and interferon-γ (IFN-γ). In an aqueous biological environment NO reacts with O_2 to form nitrite and nitrate,[55] thus quantification of the

 © 2005 Wiley-VCH Verlag GmbH & Co. KGaA, Weinheim

amount of nitrite produced in the cell media by the Griess assay[1] is an indirect but cost effective measurement of the amount of NO produced by the cells. The difference in the amount of nitrite in the cell media of cells in the presence or absence (control) of a ruthenium complex was used to evaluate the NO scavenging ability of the ruthenium complexes. To confirm the viability of the cells is not affected by the Ru compounds, a cytotoxicity assay was performed prior to the NO scavenging assay. The RAW264 murine macrophage cells (not stimulated to produce NO) were exposed to the Ru complex at concentrations of 12.5–100 μM under the same conditions that were used in the NO scavenging assay and the amount of cytotoxic effect measured by a 3-[4,5-dimethylthiazol-2-yl]-2,5-diphenyltetrazolium bromide (MTT) assay.[21] The Ru complexes were then evaluated for NO scavenging at the highest nontoxic concentration.

The results of the NO scavenging ability of the ruthenium complexes are presented in Table 4. Results for selected compounds are displayed in Figure 2. The change in the rate of NO substitution for selected analogs has been explored in kinetic studies discussed above. The NO scavenging assay using RAW264 murine macrophage cells addresses the activity of the compounds in relation to their NO scavenging ability in a biological milieu. Second, the ability of the formulated solutions to maintain NO scavenging activity upon storage can also be examined and this was addressed by monitoring the activity in the NO scavenging assay of a single stock solution over a two-week period. The observed in vitro NO scavenging ability of **AMD6245** (even at 2 weeks after the preparation of stock solutions) (Table 4) may be due to the presence of endogenous reductants capable of furnishing the monomer.

The results for the edta Ru^{III}PAC analogs clearly demonstrate the peripheral ligand effect on the NO scavenging ability of the metal complex. The limited activity of compound **2** may be due to a lack of a pendant carboxylic group to assist in the substitution reaction of the coordinated water molecule by NO.[31,56] It is not immediately obvious as to why compound **4** with pendant carboxy groups shows lower scavenging ability compared to **2**. Compound **7** was the only compound of the series to show toxicity and was thus tested for NO scavenging activity at a lower concentration. Even at a lower concentration (50 μM) compound **7** displayed suitable activity. Compound **10**, a close analog to **7**, was found to have minimal activity ($\Delta[NO_2^-] \approx 5$ μM). An interesting result is seen with the pyridyl edta analogues, **14, 16, 20,** and **24**. If the pyridine ring is incorporated into the structure such that it is part of the edta chelate where the N atom of the pyridine ring replaces one of the edta N atoms (**20, 24**), the NO scavenging ability is

Table 4. $\Delta[NO_2^-]$ in media from untreated RAW264 macrophage cells using freshly formulated and aged stock solutions of ruthenium complex.

Compound	Conc.[a]	$\Delta[NO_2^-]$[b]	Stability[c] 1 week	Stability[c] 2 weeks
AMD6245	100	12.2±0.8	11.7±0.7	13.5±1.2
AMD6221	100	37.6±0.5	36.2±0.3	42.5±0.4
2	100	7.8±0.62	6.9±0.42	6.0±0.67
4	100	5.1±0.35	–	–
7	50	9.3±1.1	–	–
10	100	5.2±1.3	–	–
14	100	20.6±0	11.7±0	10.8±0.27
16	100	24.7±0	22.5±0	18.8±0.70
20	100	11.1±0.69	10.7±0.12	11.3±0.83
24	100	13.0±0.58	10.17±0.32	11.5±0.85
27	100	29.4±0	25.9±0.09	19.9±0.18
31	100	38.5±0.5	39.3±0.4	37.8±0.3
34	100	26.0±0.5	26.9±0.4	26.6±0.3
37	100	20.4±0.12	19.6±0.07	20.5±0.61
38	100	0.97±0	1.1±0.8	–

[a] The NO scavenging assay was performed at the highest nontoxic concentration (μM). [b] Change in $[NO_2^-]$ between treated and untreated RAW264 cells as measured by the Griess assay. [c] Stock solutions were stored at 4 °C and the NO scavenging experiment was performed at 1 and 2 weeks after the solutions were prepared. The stability assay was performed only on those compounds that had an initial $\Delta[NO_2^-] > 8$ μM.

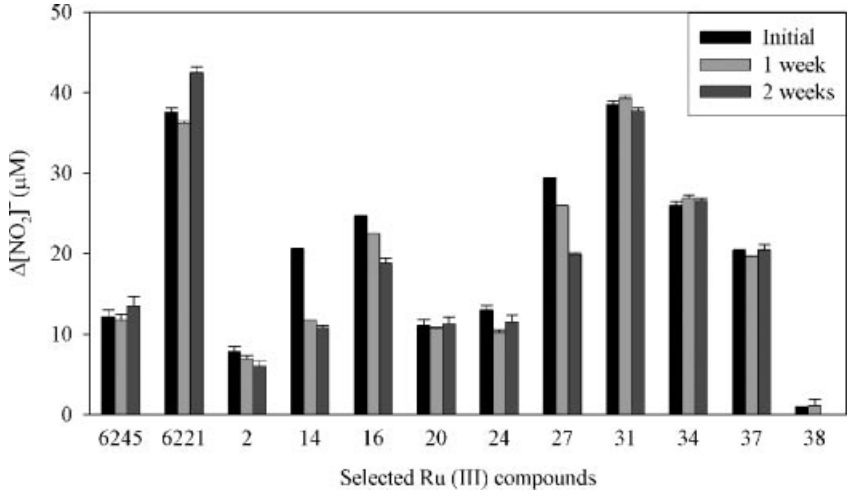

Figure 2. $\Delta[NO_2^-]$ in media from untreated RAW264 macrophage cells using freshly formulated and aged stock solutions of ruthenium complex.

 © 2005 Wiley-VCH Verlag GmbH & Co. KGaA, Weinheim

similar to that of **AMD6245**. However, if the pyridine ring is a pendant coordinating group (**14, 16**) the NO scavenging ability appears to be almost twice that of **AMD6245** in this assay. Further investigation using the stability assay as described demonstrated that the activity of **14** and **16** is not maintained after dissolution for extended periods of time whereas complexes **20** and **24** show no change in their ability to scavenge NO when dissolved in solution over an extended period (see Figure 2).

Incorporation of the pyridine ring to form an analog of **AMD6221** is demonstrated with **27**. The N atom of the pyridyl ring in **27** replaces one of the N atoms of the dtpa ligand. In contrast to the situation with the edta analogues, this compound is less active than its parent and does not appear to maintain its activity when dissolved in solution over extended periods of time. The theory that the Ru complexes act as scavengers of nitric oxide is supported by the fact that compound **38**, the nitrosyl analog of **27**, does not lower the nitrite level from the control. This hypothesis has been demonstrated in detail for **AMD6221**.[20]

The best results were obtained when structural changes were made by replacement of the central carboxylic acid group of the dtpa ligand with alkyl or aromatic moieties as in **31, 34,** and **37**. The complexes were generally nontoxic and were quite effective in the NO scavenging assay ($\Delta[NO_2^-] > 20$ μM), with **31** being the most active ($\Delta[NO_2^-] > 38.5$ μM). This group of complexes also maintained their ability to scavenge NO when dissolved in solution over extended periods of time.

Conclusions

The ligand frameworks of **AMD6245** and **AMD6221** were modified in an effort to develop active alternatives exhibiting both NO scavenging ability and stability in formulated solution. Compounds with a pyridine ring as part of the *N*, *N* chelate of edta (**20**, **24**) are active alternatives to **AMD6245.** Changes to the **AMD6221** ligand framework afforded a group of compounds that have excellent NO scavenging ability and good stability when formulated as aqueous solutions. The compounds substituted with alkyl or aromatic groups at the central N atom (**31, 34, 37**) are good alternatives to **AMD6221** and further testing of these compounds is warranted.

Experimental Section

Materials and Equipment: Chemical reagents were purchased from Aldrich and used without further purification except $RuCl_3 \cdot H_2O$ which was purchased from Johnson Matthey. All solvents (anhydrous grade) were obtained from Aldrich and used as supplied. $K_2[RuCl_5(OH_2)]$,[50] ({3-[bis(carboxymethyl)amino]propyl}(carboxymethyl)amino)acetic acid (**3**),[41] *N*,*N*′-bis(2-pyridylmethyl)-ethylenediamine-*N*,*N*′-diacetic acid (**15**),[43] methyl 6-(hydroxymethyl)pyridine-2-carboxylate (**17**),[44] 6-(hydroxymethyl)pyridine-2-carbaldehyde (**21**),[45] iminodiacetic acid di-*tert*-butyl ester,[46] 2,6-bis(bromomethyl)pyridine hydrogen bromide (**25**),[48] and *N*-(hydroxyethyl)iminodiacetic acid di-*tert*-butyl ester[49] were prepared according to literature procedures. ^1H NMR and ^{13}C NMR spectra were recorded with a Bruker Avance 300 with chemical shifts referenced to $SiMe_4$. IR spectra (as CsI pellets) were recorded with a Mattson Galaxy Series 5000 FTIR spectrophotometer (only the relative intense bands are reported). Electrospray mass spectra (ES-MS) were recorded with a Bruker-HP Esquire-LC Ion Trap mass spectrometer and injected as aqueous solutions. Elemental analyses were performed by Atlantic Microlab, Inc. (Norcross, GA). Rate constants were determined using an Applied Photophysics DX17 stopped-flow spectrometer with a measured deadtime of 1 ms.

X-ray Diffraction Data Collection and Solution and Refinement of 38: Purple crystals of **38** were obtained from slow evaporation of an aqueous solution. The selected crystal of the complex **38** was studied with a Bruker diffractometer equipped with the SMART CCD system,[57] using graphite-monochromated Mo-K_α radiation (λ = 0.71073 Å). The data collection was carried out at 90(5) K. The data were corrected for Lorentz polarization effects and absorption corrections were made using SADABS.[58] All calculations were performed using SHELXTL.[59] The structures were solved by direct methods and all of the non-hydrogen atoms were located from the initial solution. After locating all the non-hydrogen atoms in the structure, the model was refined against F^2, initially using isotropic and later anisotropic thermal displacement parameters until the final value of Δ/σ_{max} was less than 0.001. At this point the hydrogen atoms were located from the electron density difference map and a final cycle of refinements was performed, until the final value of Δ/σ_{max} was again less than 0.001. No anomalies were encountered in the refinement of the structure. The relevant parameters for crystal data, data collection, structure solution and refinement are summarized in Table 5, and important bond lengths and bond angles are presented in Table 2.

Table 5. Crystal data and structure refinement for nitrosyl complex **38**.

Chemical formula	$C_{15}H_{15}N_4O_{11}Ru$	Formula mass	528.38
a	12.731(3) Å	Space group	$P2_1/c$
b	10.894(2) Å	*T*	93 K
c	14.241 (3) Å	λ	0.71073 Å
α	90°	Density (calcd.)	1.861 mg/m^3
β	107.320(4)°	μ(Mo-*Kα*)	0.903 mm^{-1}
γ	90°	R_1[a]	0.0360
Volume	1885.6(7) Å^3	wR_2[b]	0.0757

[a] $R_1 = \Sigma(F_o - F_c)/F_o$. [b] $wR_2 = [\Sigma(F_o^2 - F_c^2)^2/\Sigma wF_o^2]^{1/2}$.

CCDC-251648 (for **38**) contains the supplementary crystallographic data for this paper. These data can be obtained free of charge from The Cambridge Crystallographic Data Centre via www.ccdc.cam.ac.uk/data_request/cif.

Synthesis of Complex 2 {[KRu(1-H$_2$)Cl$_2$]·2H$_2$O}: *N*-{2-[(Carboxymethyl)amino]ethyl}aminoacetic acid (**1**) (0.130 g, 0.74 mmol) was dissolved in EtOH (20 mL) and $RuCl_3 \cdot H_2O$ (0.155 g, 0.74 mmol) added. The mixture was heated to 60 °C during which time a precipitate formed. The solid was collected by filtration and washed with Et_2O to afford the desired product **2** (0.062 g, 22%) as a brown solid. IR (CsI) $\tilde{\nu}$ (cm^{-1}) = 1640 (CO_2^-), 318 (Ru–Cl). ES-MS: *m*/*z* = 346 (100) [M]$^-$. $C_6H_{10}Cl_2KN_2O_4Ru \cdot 2H_2O$ (420.9): calcd. C 17.11, H 3.35, N 6.65, Cl 16.83; found C 17.40, H 3.76, N 6.80, Cl 17.20.

Synthesis of Complex 4 [KRu(3-H$_2$)Cl$_2$]: To a stirred solution of *N*-[{3-[bis(carboxymethyl)amino]propyl}-*N*-(carboxymethyl)aminoacetic acid[41] (**3**) (0.291 g, 0.54 mmol) dissolved in HCl (5 mL,

 © 2005 Wiley-VCH Verlag GmbH & Co. KGaA, Weinheim

1 mM) was added $K_2[RuCl_5(H_2O)]$ (0.203 g, 0.54 mmol) and the reaction mixture was heated to 100 °C for 1.5 h. The solution was then cooled and a yellow powder was collected by filtration. The precipitate was washed with the mother liquor, ice-cold H_2O (2×10 mL), EtOH (3×5 mL), and Et_2O (3×5 mL) and dried in vacuo to afford the product complex **4** (0.075 g, 24%) as a yellow solid. IR (CsI) $\tilde{\nu}$ (cm^{-1}) = 1738 (CO_2H), 1642 (CO_2^-), 316 (Ru–Cl). ES-MS: *m*/*z* = 440 $[M - Cl - H]^-$ (25), 404 $[M - 2Cl - 2H]^-$ (100), 360 (30) $[M - 2Cl - CO_2H]^-$, 316 (25) $[M - 2Cl - 2(CO_2H)]^-$. $C_{11}H_{16}Cl_2KN_2O_8Ru{\cdot}3H_2O$ (568.9): calcd. C 23.20, H 3.89, N 4.92, Cl 12.45; found C 22.97, H 3.67, N 4.80, Cl 12.15.

Synthesis of Complex 7 [KRu(6-H_2)Cl_2] via 5 and 6

***tert*-Butyl {[Bis(*tert*-butoxycarbonylmethyl)aminoethyl]amino}-acetate (5):** Compound **5** was prepared by an alternative method to that reported in the literature.[42] To a stirred solution of ethylenediamine (0.50 g, 8.30 mmol) in THF (70 mL) and triethylamine (3.34 g, 33.00 mmol) was added *tert*-butyl bromoacetate (4.90 g, 25.00 mmol) and the reaction mixture was stirred for 16 h at room temperature. The solvent was removed in vacuo and the residue was partitioned between CH_2Cl_2 (80 mL) and H_2O (50 mL). The separated aqueous phase was extracted with CH_2Cl_2 (2×80 mL) and the combined organic extracts were dried ($MgSO_4$) and the solvents evaporated in vacuo. The crude material was purified by column chromatography on silica gel (CH_2Cl_2/MeOH, 19:1) to afford the product **5** (0.887 g, 27%) as an oil. ^{1}H NMR (300 MHz, $CDCl_3$, 25 °C): δ = 1.43 (s, 27 H), 2.63 (t, *J* = 6.0 Hz, 2 H), 2.84 (t, *J* = 6.0 Hz, 2 H), 3.28 (s, 2 H), 3.42 (s, 4 H) ppm. ^{13}C NMR (300 MHz, $CDCl_3$, 25 °C): δ = 28.46, 28.51, 47.42, 51.84, 54.15, 56.41, 81.31, 81.36, 171.22, 171.68 ppm.

[{2-[Benzyl(carboxymethyl)amino]ethyl}carboxymethylamino]acetic Acid (6): To a stirred solution of compound **5** (0.734 g, 1.80 mmol) and triethylamine (0.382 g, 3.60 mmol) in THF (10 mL) was added benzyl bromide (0.316 g, 1.8 mmol) and the reaction was stirred at 35 °C for 22 h. The solvent was removed in vacuo and the residue was partitioned between CH_2Cl_2 (10 mL) and saturated aqueous $NaHCO_3$ (10 mL). The separated aqueous phase was extracted with CH_2Cl_2 (2×10 mL), and the combined organic extracts were dried ($MgSO_4$) and the solvents evaporated in vacuo. The crude material was purified by column chromatography on silica gel (hexanes/EtOAc, 7:1), to afford the ester-protected precursor (0.496 g, 55%) as a colorless oil. ^{1}H NMR (300 MHz, $CDCl_3$, 25 °C): δ = 1.40 (s, 18 H), 1.42 (s, 9 H), 2.80–2.88 (m, 4 H), 3.24 (s, 2 H), 3.44, (s, 4 H), 3.80 (s, 2 H), 7.21–7.34 (m, 5 H) ppm. The ester-protected precursor (0.496 g, 1.00 mmol) was dissolved in TFA (12.6 g, 100 mmol) and the solution was stirred at room temperature for 16 h. The solvent was removed in vacuo and the residue was lyophilized from an aqueous solution to afford the product **6** (0.454 g, 82%) as a white solid. ^{1}H NMR (300 MHz, CD_3OD, 25 °C): δ = 3.10 (t, *J* = 6.0 Hz, 2 H), 3.39–3.45 (br. s, 6 H), 4.09 (s, 2 H), 4.59 (s, 2 H), 7.47–7.50 (m, 3 H), 7.57–7.60 (m, 2 H) ppm. ^{13}C NMR (300 MHz, CD_3OD, 25 °C): δ = 50.59, 53.04, 56.26, 60.90, 130.66, 131.42, 132.01, 132.78, 169.39, 175.74 ppm.

Preparation of 7: The title compound **7** (0.046 g, 21%) was prepared as a yellow solid from **6** (0.210 g, 0.38 mmol) and $K_2[RuCl_5(H_2O)]$ (0.142 g, 0.38 mmol) by a procedure analogous to that described for **4**. IR (CsI) $\tilde{\nu}$ (cm^{-1}) = 1726 (CO_2H), 1641 (CO_2^-), 391 (Ru–Cl). ES-MS: *m*/*z* = 494 (80) $[M]^-$, 458 (100) $[M - Cl - H]^-$. $C_{15}H_{18}Cl_2KN_2O_6Ru{\cdot}2H_2O$ (568.9): calcd. C 31.64, H 3.89, N 4.92, Cl 12.45; found C 31.63, H 3.96, N 4.77, Cl 13.03.

Synthesis of Complex 10 [KRu(9-H_2)Cl_2] via 8 and 9

Methyl 3-{[{2-[Bis(*tert*-butoxycarbonylmethyl)amino]ethyl}(*tert*-butoxycarbonylmethyl)amino]methyl}benzoate (8): The title compound **8** (0.115 g, 51%) was prepared as a colorless oil from compound **5** (0.165 g, 0.41 mmol) and 3-bromomethylbenzoate (0.094 g, 0.41 mmol) by a procedure analogous to that described for the first step of compound **6**. ^{1}H NMR (300 MHz, $CDCl_3$, 25 °C): δ = 1.40 (s, 18 H), 1.43 (s, 9 H), 2.79–2.86 (m, 4 H), 3.25 (s, 2 H), 3.40 (s, 4 H), 3.83 (s, 2 H), 3.87 (s, 3 H), 7.35 (dd, *J* = 6.0, 9.0 Hz, 1 H), 7.55 (d, *J* = 9.0 Hz, 1 H), 7.89 (d, *J* = 6.0 Hz, 1 H), 7.95 (s, 1 H) ppm.

3-{[{2-[Bis(carboxymethyl)amino]ethyl}(carboxymethyl)amino]-methyl}benzoic Acid (9): To a stirred solution of **8** (0.771 g, 1.40 mmol) in MeOH (19 mL) and H_2O (6 mL) was added lithium hydroxide (0.236 g, 5.60 mmol) and the reaction was stirred at room temperature for 16 h (in the absence of light) and then the solvent was evaporated in vacuo. This intermediate was used directly in the next step without further purification. The residue was dissolved in TFA (8.30 g, 73.00 mmol) and stirred for 16 h then evaporated in vacuo. Ethanol was added to the residue, the resulting suspension was filtered, and the product lyophilized to afford white solid compound **9** (1.04 g, 100%). ^{1}H NMR (300 MHz, CD_3OD, 25 °C): δ = 3.15 (t, *J* = 6 Hz, 2 H), 3.43–3.48 (br. s, 6 H), 4.09 (s, 2 H), 4.64 (s, 2 H), 7.59 (dd, *J* = 6.0, 9.0 Hz, 1 H), 7.85 (d, *J* = 6.0 Hz, 1 H), 8.12 (d, *J* = 9.0 Hz, 1 H), 8.26 (s, 1 H) ppm. ^{13}C NMR (300 MHz, CD_3OD, 25 °C): δ = 50.47, 53.65, 54.16, 60.01, 65.74, 130.65, 132.05, 132.30, 133.13, 133.48, 136.67, 168.93, 169.07, 175.12 ppm. ES-MS: *m*/*z* = 369 $[M + H]^+$.

Preparation of 10: Compound **10** (0.051 g, 12%) was prepared as a yellow solid from **9** (0.377 g, 0.60 mmol) and $K_2[RuCl_5(H_2O)]$ (0.236 g, 0.60 mmol) by a procedure analogous to that described for compound **4**. IR (CsI) $\tilde{\nu}$ (cm^{-1}) = 1709 (CO_2H), 1639 (CO_2^-), 389 (Ru–Cl). ES-MS: *m*/*z* = 502 (100) $[M - Cl - H]^-$. $C_{16}H_{18}Cl_2KN_2O_8Ru{\cdot}5H_2O$ (667.0): calcd. C 28.79, H 4.23, N 4.20, Cl 10.62; found C 28.63, H 3.69, N 4.29, Cl 11.08.

Synthesis of Complex 14 {[Ru(13-H_2)Cl]} via 11 and 12

***tert*-Butyl *N*-(*tert*-Butoxycarbonylmethyl)-*N*-{2-[(*tert*-butoxycarbonylmethyl)(pyridin-2-ylmethyl)amino]ethyl}aminoacetate (12):** To a solution of pyridine-2-carbaldehyde (**11**) (3.20 g, 30.0 mmol) in benzene (50 mL) was added *N*-BOC-ethylenediamine (5.26 g, 33 mmol) and the mixture was heated to reflux with stirring in a Dean–Stark apparatus for 1.5 h. The reaction mixture was evaporated to dryness, dissolved in MeOH (50 mL) and 5% Pd/C was added (0.5 g). The mixture was hydrogenated at 50 psi with a Parr apparatus overnight. The mixture was filtered through celite, and the filtrate was evaporated to give the pyridine intermediate (≈ quantitative). ^{1}H NMR (300 MHz, $CDCl_3$, 25 °C): δ = 1.40 (s, 9 H), 2.75–2.85 (m, 2 H), 3.20–3.35 (m, 2 H), 3.90 (s, 2 H), 5.30 (br. s, 1 H), 7.10–7.20 (m, 1 H), 7.30–7.36 (m, 1 H), 7.60–7.70 (m, 1 H), 8.50–8.60 (m, 1 H) ppm. The pyridine intermediate (5.08 g) was dissolved in CH_2Cl_2 (30 mL) and TFA (30 mL) was added. The mixture was allowed to continue stirring overnight at room temperature and then evaporated to give a dark oil. ^{1}H NMR [300 MHz, $(CD_3)_2SO/D_2O$, 25 °C]: δ = 3.10–3.20 (m, 2 H), 3.20–3.30 (m, 2 H), 4.48 (s, 2 H), 7.40–7.45 (m, 2 H), 7.80–7.90 (m, 1 H), 8.60 (m, 1 H) ppm. This intermediate was used without further purification in the next step. To a solution of the oil from above in DMF (80 mL) was added K_2CO_3 (27.9 g, 10.0 equiv.) followed by *tert*-butyl bromoacetate (8.95 mL, 3.0 equiv.) and the mixture was stirred at room temperature for 48 h. The reaction mixture was filtered through celite and the filtrate was evaporated to give a dark oil. Purification by column chromatography on silica gel (CH_2Cl_2/MeOH, 19:1) gave the tri-*tert*-butyl ester (4.14 g, 42% for two steps) **12** as a light yellow oil. ^{1}H NMR (300 MHz, $CDCl_3$, 25 °C): δ = 1.35–1.50 (m, 27 H), 2.83–2.86 (m, 4 H), 3.37 (s, 2 H), 3.43 (s,

 © 2005 Wiley-VCH Verlag GmbH & Co. KGaA, Weinheim

4 H), 3.95 (s, 2 H), 7.10–7.20 (m, 1 H), 7.52 (d, J = 7.5 Hz, 1 H), 7.64 (dt, J = 7.5, 1.7 Hz, 1 H), 8.51 (d, J = 4.7 Hz, 1 H) ppm.

***N*-Carboxymethyl-*N*-{2-[(carboxymethyl)(pyridin-2-ylmethyl)-amino]ethyl}aminoacetic Acid (13):** The title compound **13** (3.24 g, 73%) was prepared as a yellow solid from **12** (4.14 g, 8.35 mmol) and TFA (30 mL) by a procedure analogous to the hydrolysis step for compound **6**. ^{1}H NMR (300 MHz, D_2O, 25 °C): δ = 3.00–3.15 (m, 2 H), 3.20–3.30 (m, 2 H), 3.59 (s, 4 H), 4.04 (s, 2 H), 4.51 (s, 2 H), 7.50 (m, 1 H), 7.61 (d, J = 7.7 Hz, 1 H), 7.98 (dt, J = 7.7, 1.6 Hz, 1 H) 8.63 (d, J = 5.0 Hz, 1 H). $C_{14}H_{19}N_3O_6$·1.8TFA: calcd. C 39.83, H 3.95, N 7.92; found C 38.85, H 4.19, N 8.06.

Preparation of 14: Complex **14** (0.26 g, 43%) was prepared as a yellow/orange solid from **13** (0.75 g, 1.30 mmol) and $K_2[RuCl_5(OH_2)]$ (0.5 g, 1.3 mmol) by an analogous procedure to that described for compound **4**. IR (CsI) $\tilde{\nu}$ (cm^{-1}): 1730 (CO_2H), 1688, 1618 (CO_2^-), 320 (Ru–Cl). ES-MS: m/z = $C_{14}H_{17}ClN_3O_6Ru$·0.5H_2O (469.0): calcd. C 35.87, H 3.87, N 8.96, Cl 7.56; found C 35.86, H 3.79, N 8.98, Cl 7.58.

Synthesis of Complex 16 {[Ru(15-H_2)Cl_2]Cl}: To a solution of compound **15** (H_2bped·2HCl)[43] (1.0 g, 2.50 mmol) in water (10 mL, pH = 4) was added a solution of $K_2[RuCl_5(OH_2)]$ (0.838 g, 2.50 mmol) in HCl (minimum volume, 1 mM). The reaction mixture was heated to reflux temperature for 1.5 h. The dark green solution was reduced to approximately one half the original volume and on slow evaporation a yellow-orange solid precipitated from the reaction mixture. This was collected by filtration and re-crystallised from H_2O/EtOH to yield orange microcrystalline solid **16** (0.37 g, 26%). IR (CsI) $\tilde{\nu}$ (cm^{-1}) = 1726 (CO_2H). ES-MS: m/z = 458 (100) [M – 2Cl – 2H]$^+$, 414 (50) [M – 2Cl – H – CO_2H]$^+$, 370 (75) [M – 2Cl – 2(CO_2H)]$^+$. $C_{18}H_{22}Cl_3N_4O_4Ru$ (565.0): C 38.21, H 3.92, N 9.90, Cl 18.80; found C 38.21, H 3.96, N 9.90, Cl 18.79.

Synthesis of Complex 20 {[KRu(19-H_2)Cl_2]} via 18 and 19

Methyl 6-(Methylsulfonyloxymethyl)pyridine-2-carboxylate (18): To a stirred solution of compound **17**[44] (0.220 g, 1.30 mmol) and triethylamine (0.400 g, 4.00 mmol) in CH_2Cl_2 (13 mL) cooled in an ice bath was added dropwise methanesulfonyl chloride (0.180 g, 1.60 mmol). After 30 min the reaction was quenched with saturated aqueous $NaHCO_3$ (15 mL) and the aqueous phase was separated and extracted with CH_2Cl_2 (3×15 mL). The combined organic extracts were dried ($MgSO_4$) and the solvent was evaporated in vacuo to afford product **18** (0.347 g, 100%) as a yellow-orange oil. ^{1}H NMR (300 MHz, $CDCl_3$, 25 °C): δ = 3.15 (s, 3 H), 4.01 (s, 3 H), 5.44 (s, 2 H), 7.70 (d, J = 6.0 Hz, 1 H), 7.92 (dd, J = 6.0, 9.0 Hz, 1 H), 8.12 (d, J = 9.0 Hz, 1 H) ppm.

6-{[Bis(carboxymethyl)amino]methyl}pyridine-2-carboxylic Acid (19): To a stirred solution of compound **18** (0.323 g, 1.3 mmol) and iminodiacetic acid dimethyl ester (0.191 g, 1.2 mmol) in DMF was added K_2CO_3 (0.359 g, 2.6 mmol) and the reaction mixture was stirred at 35 °C for 16 h. The solvent was removed in vacuo and partitioned between H_2O (10 mL) and CH_2Cl_2 (15 mL). The aqueous portion was extracted with CH_2Cl_2 (3×15 mL), and the combined organic extracts were dried ($MgSO_4$) and the solvents evaporated in vacuo. The crude material was purified by column chromatography (CH_2Cl_2/MeOH, 19:1) on silica gel to afford the ester-protected precursor (0.200 g, 49%) as a colorless oil. ^{1}H NMR (300 MHz, $CDCl_3$, 25 °C): δ = 3.70 (s, 6 H), 3.97 (s, 3 H), 4.16 (s, 4 H), 5.36 (s, 2 H), 7.51 (d, J = 9.0, 1 H), 7.84 (dd, J = 6.0, 9.0, 1 H), 8.02 (d, J = 6.0 Hz, 1 H) ppm. ^{13}C NMR (300 MHz, $CDCl_3$, 25 °C): δ = 49.48, 52.63, 53.32, 68.46, 124.46, 124.79, 138.25, 155.93, 157.31, 165.88, 170.09 ppm. To a 0 °C solution of the ester-protected precursor (0.200 g, 0.65 mmol) in MeOH (19 mL) and H_2O (6 mL) was added LiOH·H_2O (0.270 g, 6.4 mmol). The mixture was stirred at room temperature for 17 h in the absence of light. The solution was acidified with 2 N HCl and the solvent was removed in vacuo. The crude material was purified on Dowex cation exchange resin (H^+ form, 50W-200 mesh) to afford product **19** (0.172 g, 78%). ^{1}H NMR (300 MHz, D_2O, 25 °C): δ = 4.02 (s, 2 H), 4.15 (s, 2 H), 5.39 (s, 2 H), 7.95 (d, J = 7.5 Hz, 1 H), 8.25 (d, J = 7.2 Hz, 1 H), 8.46 (dd, J = 7.2, 7.5 Hz, 1 H) ppm. ^{13}C NMR (300 MHz, D_2O, 25 °C): δ = 50.27, 50.56, 127.02, 128.74, 147.29, 152.83, 156.73, 173.22, 173.46 ppm. ES-MS: m/z = 313 [M + H]$^+$.

Preparation of 20: Compound **20** (0.064 g, 28%) was prepared as a yellow solid from **19** (0.157 g, 0.48 mmol) and $K_2[RuCl_5(H_2O)]$ (0.172 g, 0.46 mmol) by a procedure analogous to that described for compound **4**. IR (CsI): $\tilde{\nu}$ (cm^{-1}) = 1709 (CO_2H), 1632, 1607 (CO_2^-), 341 (Ru–Cl). ES-MS: m/z = 402 (100) [M – Cl – H]$^-$. $C_{11}H_{10}Cl_2KN_2O_6Ru$·2$H_2O$ (512.9): calcd. C 25.74, H 2.75, N 5.46, Cl 13.81; found C 25.56, H 2.64, N 5.06, Cl 12.97.

Synthesis of Complex 24 [KRu(19-H_2)Cl_2] via 22 and 23

***tert*-Butyl *N*-(*tert*-Butoxycarbonylmethyl)-*N*-{[6-(hydroxymethyl)pyridin-2-yl]methyl}aminoacetate (22):** The mesylate intermediate (3.61 g, 100%) was prepared as a brown oil from 6-(hydroxymethyl)pyridine-2-carbaldehyde (**21**)[45] (2.30 g, 1.7 mmol), methanesulfonyl chloride (2.12 g, 1.8 mmol), and triethylamine (5.08 g, 50 mmol) by an analogous procedure to that described for compound **18**. ^{1}H NMR (300 MHz, $CDCl_3$, 25 °C): δ = 3.15 (s, 3 H), 5.43 (s, 2 H), 7.70 (m, 1 H), 7.97 (m, 2 H), 10.05 (s, 1 H) ppm. Reaction of the mesylate (3.61 g, 1.7 mmol) with di-*tert*-butyl iminodiacetate[46] (3.706 g, 1.5 mmol) following conditions similar to the first step in the synthesis of compound **19** afforded, after column chromatography on silica gel (hexanes/EtOAc, 4:1), the aldehyde as a colorless oil (2.25 g, 45%). ^{1}H NMR (300 MHz, $CDCl_3$, 25 °C): δ = 1.46 (s, 18 H), 3.50 (s, 4 H), 4.14 (s, 2 H), 7.85 (m, 1 H), 7.94 (m, 1 H), 10.05 (s, 1 H) ppm. The aldehyde (2.25 g, 6.2 mmol) was reduced in MeOH (60 mL) under nitrogen with sodium borohydride (0.235 g, 6.2 mmol). The reaction was heated to 60 °C with stirring, and after 1 h the solvent was removed in vacuo and the residue was partitioned between H_2O (30 mL) and CH_2Cl_2 (30 mL). The aqueous phase was separated and extracted with CH_2Cl_2 (3×40 mL) and the combined organic extracts were dried ($MgSO_4$) and the solvents evaporated in vacuo to afford the product **22** (2.16 g, 38% for 3 steps) as a colorless oil. ^{1}H NMR (300 MHz, $CDCl_3$, 25 °C): δ = 1.46 (s, 18 H), 3.48 (s, 4 H), 3.98 (t, J = 4.5 Hz, 1 H), 4.05 (s, 2 H), 4.72 (d, J = 4.5 Hz, 2 H), 7.08 (d, J = 6.0 Hz, 1 H), 7.53 (d, J = 9.0 Hz, 1 H), 7.66 (dd, J = 6.0, 9.0 Hz, 1 H) ppm. ^{13}C NMR (300 MHz, $CDCl_3$, 25 °C): δ = 28.57, 56.22, 59.88, 64.13, 81.47, 119.04, 122.02, 137.64, 158.25, 158.65, 170.90 ppm. ES-MS: m/z = 367 [M + H]$^+$.

***N*-Carboxymethyl-*N*-{[6-(hydroxymethyl)pyridin-2-yl]methyl}aminoacetic Acid (23):** Compound **23** (0.492 g, 100%) was prepared as a white solid from **22** (2.10 g, 5.7 mmol) and TFA (10 mL) by a procedure analogous to the hydrolysis step for compound **6**. ^{1}H NMR (300 MHz, D_2O, 25 °C): δ = 3.64 (s, 4 H), 4.28 (s, 2 H), 4.85 (s, 2 H), 7.69 (br. s, 2 H), 8.27 (t, J = 8.0 Hz, 1 H) ppm. ^{13}C NMR (300 MHz, D_2O, 25 °C): δ = 55.98, 60.07, 123.75, 125.19, 147.02, 152.72, 155.65, 174.85 ppm. ES-MS: m/z 255 [M + H]$^+$.

Preparation of 24: The title compound **24** (0.035 g, 24%) was prepared as a yellow solid from **23** (0.152 g, 0.32 mmol) and $K_2[RuCl_5(H_2O)]$ (0.118 g, 0.32 mmol) by a procedure analogous to compound **4**. IR (CsI) $\tilde{\nu}$ (cm^{-1}) = 1657, 1630 (CO_2^-), 316 (Ru–Cl). ES-MS: m/z = 446 (100) [M – H + Na]$^-$. $C_{11}H_{12}Cl_2KN_2O_5Ru$·

 © 2005 Wiley-VCH Verlag GmbH & Co. KGaA, Weinheim

$2H_2O$ (498.9): calcd. C 28.64, H 3.71, N 6.07, Cl 15.37; found C 28.44, H 3.67, N 6.02, Cl 15.36.

Synthesis of Complex 27 [Ru(26-H_2)Cl] via 26: Trisodium ({6-[bis-(carboxymethyl)amino]methyl}pyridin-2-ylmethyl}carboxymethyl-amino)acetate (**26**). An aqueous solution of sodium hydroxide (30 mL, 10 mM), 2,6-bis(bromomethyl)pyridine hydrogen bromide (**25**)[48] (1.0 g, 2.9 mmol), iminodiacetic acid dimethyl ester (0.934 g, 5.8 mmol), and cetyltrimethylammonium bromide (0.21 g, 0.58 mmol) was stirred at room temperature for 3 days. A white precipitate formed which was removed by filtration and the filtrate was evaporated to give a white solid. This solid was purified by recrystallisation from water and ethanol to give the desired compound **26** as the sodium salt (0.9 g, 71%). ^{1}H NMR (300 MHz, D_2O, 25 °C): δ = 3.27 (s, 8 H), 3.93 (s, 4 H), 7.30 (d, J = 7.5 Hz, 2 H), 7.80 (t, J = 7.8 Hz, 1 H) ppm.

Preparation of 27: The title compound **27** (0.550 g, 56%) was prepared as a yellow solid from **26** (0.781 g, 1.8 mmol) and $K_2[RuCl_5(OH_2)]$ (0.670 g, 1.8 mmol) by a procedure analogous to compound **4**. IR (CsI) $\tilde{\nu}$ (cm^{-1}) = 1734 (CO_2H), 1649 (CO_2^-), 350 (Ru–Cl). ES-MS: m/z = 466 (40) [M – Cl – 2H]$^-$, 423 (65) [M – Cl – H – CO_2H]$^-$, 379 (45) [M – Cl – 2(CO_2H)]$^-$, 334 (100) [M – Cl – 3(CO_2H)]$^-$. $C_{15}H_{17}ClN_3O_8Ru{\cdot}2.5\,H_2O$ (549.0): calcd. C 32.82, H 4.04, N 7.66, Cl 6.46; found C 32.82, H 3.95, N 7.66, Cl 6.47.

Synthesis of Complex 31 ([Ru(29-H_2)Cl] via 28, 29, and 30

***tert*-Butyl *N*-(*tert*-Butoxycarbonylmethyl)-*N*-(2-methylsulfonyloxyethyl)aminoacetate (28):** The title compound **28** (9.490 g, 99%) was prepared as an oil from *N*-(hydroxyethyl)iminodiacetic acid di-*tert*-butyl ester[49] (7.50 g, 30.0 mmol), methanesulfonyl chloride (3.550 g, 30.0 mmol), and triethylamine (14.8 g, 150 mmol) by a procedure analogous to that described for compound **18**. ^{1}H NMR (300 MHz, $CDCl_3$, 25 °C): δ = 1.46 (s, 18 H), 3.08 (m, 5 H), 3.48 (s, 4 H), 4.34 (t, J = 6.0 Hz, 2 H) ppm.

***tert*-Butyl *N*-{2-[{2-[Bis(*tert*-butoxycarbonylmethyl)amino]ethyl}-ethylamino]ethyl}-*N*-(*tert*-butoxycarbonylmethyl)aminoacetate (29):** To a stirred solution of compound **28** (3.169 g, 8.6 mmol) in acetonitrile (50 mL) was added ethylamine (0.130 g, 2.9 mmol). Potassium carbonate (4.70 g, 34.4 mmol) was added and the suspension stirred for 16 h at 45 °C. The solvent was removed in vacuo and the residue partitioned between $CHCl_3$ (100 mL) and saturated aqueous $NaHCO_3$ (100 mL). The aqueous portion was extracted with $CHCl_3$ (3 × 75 mL), and the combined organic extracts were dried ($MgSO_4$), filtered and the solvent was removed in vacuo to afford a brown oil. The crude product was purified by column chromatography on silica gel (98:2:1, CH_2Cl_2:MeOH/NEt_3) to afford a colorless oil of compound **29** (0.701 g, 55%). ^{1}H NMR (300 MHz, $CDCl_3$, 25 °C): δ = 1.00 (t, J = 6.0 Hz, 3 H), 1.46 (s, 36 H), 2.56 (m, 6 H), 2.80 (t, J = 7.5 Hz, 4 H), 3.45 (s, 8 H). ^{13}C NMR (300 MHz, $CDCl_3$, 25 °C): δ = 28.17, 48.16, 52.10, 52.61, 53.44, 56.30, 80.77, 170.70. ES-MS: m/z = 588 [M + H]$^+$.

Preparation of 30: Compound **30** (0.699 g, 98%) was prepared as an off-white solid from **29** (0.591 g, 1.0 mmol) and TFA (10 mL) by a procedure analogous to that described for the second step in the synthesis of compound **6**. ^{1}H NMR (300 MHz, D_2O, 25 °C): δ = 0.92 (t, J = 6.9 Hz, 3 H), 2.96 (d, J = 6.9 Hz, 2 H), 3.24 (s, 8 H), 3.69 (s, 8 H) ppm. ^{13}C NMR (300 MHz, D_2O, 25 °C): δ = 29.59, 49.19, 49.35, 49.95, 55.39, 170.68 ppm. ES-MS: m/z = 420 [M + H]$^+$.

Preparation of 31: Complex **31** (0.037 g, 21%) was prepared as a yellow solid from **30** (0.241 g, 0.34 mmol) and $K_2[RuCl_5(H_2O)]$ (0.128 g, 0.34 mmol) by a procedure analogous to that described for compound **4**. IR (CsI) $\tilde{\nu}$ (cm^{-1}) = 1719 (CO_2H), 1678, 1601 (CO_2^-), 415 (Ru–Cl). ES-MS: m/z = 461 (45) [M – Cl – 2H]$^-$, 417 (100) [M – Cl – H – CO_2H]$^-$, 373 (30) [M – Cl – 2(CO_2H)]$^-$. $C_{14}H_{23}ClN_3O_8Ru{\cdot}H_2O$ (516.0): calcd. C 32.59, H 4.88, N 8.15, Cl 6.87; found C 32.43, H 4.80, N 8.02, Cl 7.81.

Synthesis of Complex 34 [Ru(33-H_2)Cl] via 32 and 33

Preparation of 32: Compound **32** (0.439 g, 27%) was prepared as a colorless oil from **28** (2.97 g, 8.1 mmol), butylamine (0.200 g, 3.0 mmol), and potassium carbonate (4.47 g, 32.4 mmol) by a procedure analogous to that described for compound **29.** ^{1}H NMR (300 MHz, $CDCl_3$, 25 °C): δ = 0.81 (t, J = 6.0 Hz, 3 H), 1.20 (m, 4 H), 1.38 (s, 36 H), 2.38 (t, J = 7.5 Hz, 2 H), 2.54 (t, J = 6.0 Hz, 4 H), 2.71 (t, J = 6.0 Hz, 4 H), 3.37 (s, 8 H) ppm. ^{13}C NMR (300 MHz, $CDCl_3$, 25 °C): δ = 14.36, 20.91, 28.49, 52.43, 53.61, 53.76, 54.92, 56.83, 81.31, 171.02 ppm. ES-MS: m/z = 616 [M + H]$^+$.

Preparation of 33: Compound **33** (0.442 g, 87%) was prepared as an off-white solid from **32** (0.425 g, 0.69 mmol) and TFA (14.8 g, 100 mmol) by a procedure analogous to that described for the second step in the synthesis of compound **6**. ^{1}H NMR (300 MHz, D_2O, 25 °C): δ = 0.672 (br. s, 3 H), 0.81 (br. s, 2 H), 1.15 (br. s, 2 H), 2.71 (br. s, 2 H), 3.12 (br. s, 8 H), 3.56 (s, 8 H). ES-MS: m/z = 448 [M + H]$^+$.

Preparation of 34: Complex **34** (0.083 g, 42%) was prepared as a yellow solid from **33** (0.243 g, 0.33 mmol) and $K_2[RuCl_5(H_2O)]$ (0.123 g, 0.33 mmol) by a procedure analogous to that described for compound **4**. IR (CsI) $\tilde{\nu}$ (cm^{-1}) = 1736 (CO_2H), 1657 (CO_2^-), 411 (Ru–Cl). ES-MS: m/z = 489 (50) [M – Cl – 2H]$^-$, 445 (100) [M – Cl – H – CO_2H]$^-$, 401 (20) [M – Cl – 2(CO_2H)]$^-$. $C_{16}H_{27}ClN_3O_8Ru{\cdot}4\,H_2O$ (598.1): calcd. C 32.14, H 5.90, N 7.03, Cl 5.93; found C 32.23, H 5.60, N 6.94, Cl 6.02.

Synthesis of Complex 37 ([Ru(33-H_2)Cl] via 35 and 36

Preparation of 35: Compound **35** (1.35 g, 37%) was prepared as a colorless oil from **28** (4.86 g, 13.0 mmol), benzylamine (0.47 g, 4.4 mmol), and potassium carbonate (7.18 g, 52.0 mmol) by a procedure analogous to that described for compound **29**. ^{1}H NMR (300 MHz, $CDCl_3$, 25 °C): δ = 1.43 (s, 36 H), 2.59 (t, J = 6.0 Hz, 4 H), 2.82 (t, J = 6.0 Hz, 4 H), 3.40 (s, 8 H), 7.24 (m, 5 H) ppm. ^{13}C NMR (300 MHz, $CDCl_3$, 25 °C): δ = 28.19, 52.08, 52.86, 56.16, 59.17, 80.75, 126.78, 128.14, 128.85, 139.62, 170.74 ppm. ES-MS: m/z = 650 [M + H]$^+$.

Preparation of 36: Ligand **36** was prepared as a white solid from **35** (1.00 g, 1.5 mmol) and TFA (10 mL) by a procedure analogous to that described for the second step in the synthesis of compound **6**. ^{1}H NMR (300 MHz, D_2O, 25 °C): δ = (t, J = 6.0 Hz, 4 H), 3.48 (t, J = 6.0 Hz, 4 H), 3.73 (s, 8 H), 4.43 (s, 4 H), 7.51 (br. s, 5 H) ppm. ^{13}C NMR (300 MHz, D_2O, 25 °C): δ = 50.22, 50.85, 55.43, 59.04, 129.50, 130.05, 130.90, 131.39, 172.64 ppm.

Preparation of 37: Complex **37** (0.078 g, 24%) was prepared as a yellow solid from **36** (0.256 g, 0.3 mmol) and $K_2[RuCl_5(H_2O)]$ (0.124 g, 0.3 mmol) by a procedure analogous to that described for compound **4**. IR (CsI) $\tilde{\nu}$ (cm^{-1}) = 1736 (CO_2H), 1657 (CO_2^-), 401 (Ru–Cl). ES-MS: m/z = 523 (95) [M – Cl – 2H]$^-$, 479 (80) [M – Cl – H – CO_2H]$^-$, 433 (10) [M – Cl – 2(CO_2H)]$^-$, 388 (100) [M – Cl – H – CO_2H – C_7H_7]$^-$. $C_{19}H_{25}ClN_3O_8Ru{\cdot}4\,H_2O$ (632.1): calcd. C 35.60, H 5.35, N 6.56, Cl 5.53; found C 35.62, H 5.22, N 6.47, Cl 5.33.

Preparation of Nitrosyl Complex 38: To a solution of complex **27** (0.10 g, 0.18 mmol) in H_2SO_4 (0.1 M, 5 mL) heated at reflux temperature was added an aqueous solution of 0.1 M $NaNO_2$ (3.6 mL, 0.36 mmol). The reaction mixture was heated at 50 °C for 1 h. Ma-

 © 2005 Wiley-VCH Verlag GmbH & Co. KGaA, Weinheim

terial that had not dissolved was removed by filtration, and the solvent was removed in vacuo from the filtrate. The residue was dissolved in a minimal amount of water and upon slow evaporation at room temperature a solid was formed. The solid was collected by filtration, washed with MeOH and dried in air to afford complex **38** (0.074 g, 82%). Suitable crystals for X-ray diffraction were obtained by slow evaporation of an aqueous solution. IR (CsI) $\tilde{\nu}$ (cm^{-1}) = 1898 (NO), 1736 (CO_2H), 1616 (CO_2^-). ^1H NMR (300 MHz, D_2O/K_2CO_3, 25 °C): δ = 4.23–4.56 (m, 8 H), 5.21 (ABq, 4 H), 7.96 (d, 2 H), 8.41 (t, 1 H) ppm. ES-MS: *m/z* = 498 $[M]^-$. $C_{15}H_{16}N_4O_9Ru\cdot 3.5\,H_2O$ (561.0): calcd. C 32.15, H 4.14, N 10.00; found C 32.15, H 3.97, N 9.91.

Kinetic Studies

Determination of Binding Constants: On addition of an aqueous NO solution to a solution of a complex an absorbance change is observed in the near-UV region of the spectrum which is utilized to determine the binding stoichiometry of NO to Ru^{III} and to obtain an estimate of the binding affinity. The binding constants were determined from plots of the fractional saturation, *Y*, against the total concentration of NO added. *Y* is defined as $Y = (A - A_0)/(A_\infty - A_0)$, where A_0 and A_∞ are absorbances at a selected wavelength (λ) in the absence and presence of saturating NO and A is the absorbance (at λ) after the addition of a sub-saturating concentration of NO. The monitoring wavelength was selected for each complex to ensure the largest change in ΔA on NO binding, this was between 280 and 350 nm depending on the complex under study. All spectra were recorded using a Hewlett–Packard 8451 diode array spectrophotometer (Agilent UK).

Determination of Rate Constants: The kinetics of NO binding to Ru complexes were determined using an Applied Photophysics DX17 stopped-flow spectrometer with a measured dead time of 1 ms. In the stopped flow experiment the temperature was maintained within ±0.1 °C. One syringe was charged with a solution of NO (100 μM)[12] and one with the ruthenium complex (100 μM) so that the final concentration of complex was 50 μM after mixing. Both the NO and complex solutions were prepared in potassium phosphate buffer (100 mM) at pH = 7.4. The calculated rate constants are determined from an average of at least 6 experiments (see supporting information for the spectrophotometric curves, for supporting information see also the footnote on the first page of this article).

RAW 264 Murine Macrophage Assay for NO Scavenging by Ruthenium Complexes: RAW264 cells were cultured on 24 well plates (2×10^6 cells/well) in 2 mL Eagle's minimal essential medium. The cells were activated by the addition of 10 μg/mL *E.coli* 0111:B4 lipopolysaccharide (Sigma L2630) and 100 IU/mL mouse recombinant IFN-γ. The production of nitric oxide was estimated from the amount of nitrite in the medium after 18 h using the Greiss assay as described previously.[21] To estimate the NO scavenging ability of the ruthenium complexes, the nitrite accumulation was measured under the following conditions: 1) Nonactivated cells, 2) LPS/IFN-γ activated cells and 3) LPS/IFN-γ activated cells treated with appropriate amount of Ru complex. The cells were activated to produce NO in the presence of the appropriate ruthenium complex (100 μM or nontoxic concentration) and the results are reported as the change in the amount of nitrite produced between treated cells (condition 3) and nontreated cells (condition 2). The experiment was repeated on stock solutions of the ruthenium complexes that were stored at 4 °C for one and two weeks. Control experiments were performed to show that ruthenium complexes were not cytotoxic at the concentrations used in this study, as determined from an MTT assay.[20]

The **Supporting Information** available (see also the footnote on the first page of this article) includes the UV/Vis plots used to determine the binding constants (K_B) of compounds **14** and **27** with NO.

[1] M. Feelisch, J. Stamler (Eds.), *Methods in Nitric Oxide Research*, John Wiley & Sons Ltd., West Sussex, UK, **1996**.
[2] S. P. Fricker, in: *Nitrogen Monoxide-Related Disease and Nitrogen Monoxide Scavengers as Potential Drugs* (Eds.: A. Sigel, H. Sigel), Marcel Dekker, Inc., New York, **1999**, vol. 36, pp. 665–719.
[3] T. Evans, A. Carpenter, H. Kinderman, J. Cohen, *Circ. Shock* **1993**, *41*, 77–81.
[4] X. Wei, I. G. Charles, A. Smith, J. Ure, G. Feng, F. Huang, D. Xu, W. Muller, S. Moncada, F. Y. Liew, *Nature* **1995**, *375*, 408–411.
[5] J. A. Corbett, M. L. McDaniel, *Diabetes* **1992**, *41*, 897–903.
[6] Q. Hamid, D. R. Springall, V. Riveros-Moreno, P. Chanez, P. Howarth, A. Redington, J. Bousquet, P. Goddard, S. Holgate, J. M. Polak, *Lancet* **1993**, *342*, 1510–1513.
[7] O. Gallo, E. Masini, L. Morbidelli, A. Franchi, I. Fini-Storchi, W. A. Vergari, M. Ziche, *Journal of the National Cancer Institute* **1998**, *90*, 587.
[8] K. Doi, T. Akaike, H. Horie, Y. Noguchi, S. Fujii, T. Beppu, M. Ogawa, H. Maeda, *Cancer* **1996**, *77*, 1598–1604.
[9] K. Murakami, C. Privalle, P. Enkhbaatar, K. Shimoda, F. C. Schmalsteig, J. DeAngelo, S. Lee, L. D. Traber, D. L. Traber, *Clin. Sci.* **2003**, *105*, 629–635.
[10] L. Chiarantini, A. Cerasi, L. Giorgi, M. Formica, M. F. Ottaviani, M. Cangiotti, V. Fusi, *Bioconjugate Chem.* **2003**, *14*, 1165–1170.
[11] C.-S. Lai, in *Methods using a nitric oxide scavenger for in vivo reduction of nitric oxide levels, and compositions useful therefore*, US Patent 5847004, **1998**, p. 20.
[12] B. R. Cameron, M. C. Darkes, H. Yee, M. Olsen, S. P. Fricker, R. T. Skerlj, G. J. Bridger, N. A. Davies, M. T. Wilson, D. J. Rose, J. Zubieta, *Inorg. Chem.* **2003**, *42*, 1868–1876.
[13] B. R. Cameron, M. C. Darkes, I. R. Baird, R. T. Skerlj, Z. L. Santucci, S. P. Fricker, *Inorg. Chem.* **2003**, *42*, 4102–4108.
[14] C. M. Bastos, K. A. Gordon, T. D. Ocain, *Bioorg. Med. Chem. Lett.* **1998**, *8*, 147–150.
[15] F. T. Garzon, M. R. Berger, B. K. Keppler, D. Schmahl, *Cancer Chemother. Pharmacol.* **1987**, *19*, 347–349.
[16] R. Vilaplana, M. A. Romero, M. Quiros, J. M. Salas, F. Gonzalez-Vilchez, *Metal-Based Drugs* **1995**, *2*, 211–219.
[17] G. Sava, E. Alessio, A. Bergamo, G. Mestroni, *Top. Biol. Inorg. Chem.* **1999**, *1*, 143–169.
[18] G. Sava, I. Capozzi, A. Bergamo, R. Gagliardi, M. Cocchietto, L. Masiero, M. Onisto, E. Alessio, G. Mestroni, S. Garbisa, *Int. J. cancer* **1996**, *68*, 60–66.
[19] L. Morbidelli, S. Donnini, S. Filippi, L. Messori, F. Piccioli, P. Orioli, G. Sava, M. Ziche, *British Journal of Cancer* **2003**, *88*, 1484–1491.
[20] R. Mosi, B. Seguin, B. Cameron, L. Amankwa, M. C. Darkes, S. P. Fricker, *Biochem. Biophys. Res. Commun.* **2002**, *292*, 519.
[21] S. P. Fricker, E. Slade, N. A. Powell, O. J. Vaughan, G. R. Henderson, B. A. Murrer, I. L. Megson, S. K. Bisland, F. W. Flitney, *British Journal of Pharmacology* **1997**, *122*, 1441–1449.
[22] A. G. Baggs, S. Fricker, M. Abrams, C. Lee, M. P. Fink, *Surgical Forum* **1997**, *48*, 84–86.
[23] R. Pritchard, F. W. Flitney, M. A. Darkes, S. P. Fricker, *VIIIth International Congress of the Metastasis Research Society* **2000**, p. 776.
[24] G. M. Pieper, A. M. Roxa, M. B. Adams, G. Hilton, M. Johnson, C. C. Felix, B. Kampalath, M. Darkes, Y. Wanggui, B. Cameron, S. P. Fricker, *J. Cardiovasc. Pharmacol.* **2002**, *39*, 441.
[25] B. R. Cameron, S. P. Fricker, M. Darkes, H. Yee, R. Mosi, *J. Inorg. Biochem.* **2001**, *86*, 31.
[26] J. Jolley, C. J. Campbell, A. Castineiras, A. I. Yanovsky, K. B. Nolan, *Polyhedron* **1999**, *18*, 49–55.

 © 2005 Wiley-VCH Verlag GmbH & Co. KGaA, Weinheim

[27] M. M. T. Khan, D. Chatterjee, R. R. Merchant, P. Paul, S. H. R. Abdi, D. Srinivas, M. R. H. Siddiqui, M. A. Moiz, M. M. Bhadbhade, K. Venkatasubramanian, *Inorg. Chem.* **1992**, *31*, 2711–2718.
[28] H. C. Bajaj, R. van Eldik, *Inorg. Chem.* **1988**, *27*, 4052–4055.
[29] T. Matsubara, C. Creutz, *Inorg. Chem.* **1979**, *18*, 1956–1966.
[30] H. C. Bajaj, A. Das, R. van Eldik, *J. Chem. Soc., Dalton Trans.* **1998**, 1563–1568.
[31] H. C. Bajaj, R. van Eldik, *Inorg. Chem.* **1990**, *29*, 2855–2858.
[32] D. Chatterjee, *Coord. Chem. Rev.* **1998**, *168*, 273–293.
[33] A. Wanat, T. Schneppensieper, A. Karocki, G. Stochel, R. van Eldik, *J. Chem. Soc., Dalton Trans.* **2002**, 941.
[34] N. Yasuda, R. MacFarland, M. Darkes, S. Fricker, *21st Annual meeting American College of Toxicology* (San Diego, CA) **1999**.
[35] R. B. Baar, F. C. Anson, *J. Electroanal. Chem.* **1985**, *187*, 265–282.
[36] B. R. Cameron, G. J. Bridger, K. P. Maresca, J. Zubieta, *Inorg. Chem.* **2000**, *39*, 3928–3930.
[37] Y. Yoshino, T. Uehiro, M. Saito, *Bull. Chem. Soc. Jpn.* **1974**, *47*, 1651.
[38] V. G. Povse, J. A. Olabe, *Transition Met. Chem.* **1998**, *23*, 657–662.
[39] T. Matsubara, C. Creutz, *J. Am. Chem. Soc.* **1978**, *100*, 6255.
[40] R. Prakash, G. Ramachandriah, *J. Chem. Soc., Dalton Trans.* **2000**, 85.
[41] J. A. Weyh, R. E. Hamm, *Inorg. Chem.* **1968**, *7*, 2431–2435.
[42] S. Achilefu, R. R. Wilhelm, H. N. Jimerez, M. A. Schmidt, A. Srinivasan, *J. Org. Chem.* **2000**, *65*, 1562–1565.
[43] P. Caravan, S. J. Rettig, C. Orvig, *Inorg. Chem.* **1997**, *36*, 1306.
[44] L. Huang, A. R. Morgan, J. W. Lown, *Bioorg. Med. Chem. Lett.* **1993**, *3*, 1751–1756.
[45] Y. Okuyama, H. Nakano, C. Kabuto, E. Nozawa, K. Takahashi, H. Hongo, *Heterocycles* **2002**, *58*, 457–469.
[46] H. Takalo, P. Pasanen, J. Kankare, *Acta Chem. Scand. B* **1988**, *42*, 373.
[47] P. Caravan, J. J. Ellison, T. J. McMurry, R. B. Lauffer, *Chem. Rev.* **1999**, *99*, 2293–2352.
[48] M. Newcomb, W. Gokel, D. J. Cram, *J. Am. Chem. Soc.* **1974**, *96*, 6810–6811.
[49] M. A. Williams, H. Rapoport, *J. Org. Chem.* **1993**, *58*, 1151–1158.
[50] A. Werner, *Ber. Dtsch. Chem. Ges.* **1907**, *40*, 2614.
[51] K. Nakamoto, Infrared and Raman Spectra of Inorganic and Coordination Compounds, Part B, John Wiley & Sons Ltd, New York, **1997**.
[52] N. A. Davies, M. T. Wilson, E. Slade, S. P. Fricker, B. A. Murrer, N. A. Powell, G. R. Henderson, *Chem. Commun.* **1997**, 47–48.
[53] H. Ogino, M. Shimura, *Advances in Inorganic and Bioinorganic Mechanisms* **1986**, *4*, 107–135.
[54] H. Ogino, T. Katsuyama, S. Ito, *Bull. Chem. Soc. Jpn.* **1990**, *63*, 1370–1373.
[55] H. H. Awad, D. M. Stanbury, *International Journal of Chemical Kinetics* **1993**, *25*, 375–381.
[56] H. C. Bajaj, R. van Eldik, *Inorg. Chem.* **1989**, *28*, 1980–1983.
[57] *Smart Software Reference Manual*; Siemens Analytical X-ray Instruments, Inc. Madison, WI, **1994**.
[58] Sheldrick, G. M. *SADABS: Program for Empirical Absorption Correction*; University of Göttingen: Göttingen, Germany, **1996**.
[59] Sheldrick, G. M. *SHELXL96: Program for Refinement of Crystal Structures*; University of Göttingen: Göttingen, Germany, **1996**.

Received: January 08, 2005
Published Online: May 31, 2005

 © 2005 Wiley-VCH Verlag GmbH & Co. KGaA, Weinheim

Preparation of an $Li_{0.7}Ni_{0.8}Co_{0.2}O_2$ Electrode Material From a New Li–Co–Ni Mixed-Citrate Precursor

Yodalgis Mosqueda,[a] Eduardo Pérez-Cappe,[b] Pilar Aranda,[c] and Eduardo Ruiz-Hitzky*[c]

Keywords: Citrates / Electrode materials / Lithium batteries / Mixed-valent compounds / Oxides

A new chemical route to prepare the mixed oxide $Li_{0.7}Ni_{0.8}Co_{0.2}O_2$, which is a member of the well-known Li-Ni-Co-O family that is of interest as an electrode material for rechargeable lithium batteries, from a mixed citrate is reported. In a first step the new citrate $(NH_4)_3LiNi_{0.8}Co_{0.2}(C_6H_5O_7)_2$, is synthesized, which, after thermal decomposition, gives the layered mixed-oxide phase $Li_{0.7}Ni_{0.8}Co_{0.2}O_2$. This oxide has been characterized by chemical analysis, XRD, FTIR, SEM, and DTA, revealing an "ideal" trigonal α-$NaFeO_2$ type structure with a well-ordered distribution of Li and Ni ions in different lattices. Thermoelectric power and four-point electrical conductivity measurements indicate a nonactivated conductivity mechanism of a small polaron. The $Li_{0.7}Ni_{0.8}Co_{0.2}O_2$ compound prepared by this so-called "citrate route" has a better reversibility of Li-insertion in charge–discharge cycles than related phases reported previously.
(© Wiley-VCH Verlag GmbH & Co. KGaA, 69451 Weinheim, Germany, 2005)

Introduction

Among the $LiMO_2$ (M = V, Cr, Mn, Co, Ni) series, the $Li_x(Ni_{1-y}Co_y)_{1-x}O_2$ family shows structures based on either cubic close packed (fcc) or distorted (fcc) oxygen lattices.[1–3] These families of oxides exhibit very interesting physical and electrochemical properties that have made most of them applicable as positive electrodes in high-energy-density batteries.[4–8] The $Li_x(Ni_{1-y}Co_y)_{1-x}O_2$ system exhibits several advantageous properties in comparison to the $LiNiO_2$ and $LiCoO_2$ end members, such as higher capacity, lower material cost, better thermal stability, and superior rechargeable performance.[9–11] One of the key requirements to obtain a good electrode material within this family of compounds is to reach a good cationic order of Ni and Li ions in different structural sites. However, many authors have reported the presence of divalent nickel ions (r = 0.68 Å) at the lithium sites (r = 0.74 Å) in the nickel-rich phases because this element in its trivalent oxidation state is relatively unstable and, due to its small ionic size (r = 0.56 Å) fits better in the lithium octahedral position.[12–14] This can be seen by XRD and IR spectroscopy. In this way, strong overlap in the (006)/(012) and (018)/(110) couples of diffraction lines, as well as a (003)/(104) integrated intensity ratio lower than 1.2, indicate the presence of cationic disorder.[12,13] Moreover, the characteristic IR pattern in oxides with well-ordered cationic distribution, which consists of the presence of two well-individualized IR characteristic regions for the vibration modes of LiO_6 (300–200 cm^{-1}) and $M^{3+}O_6$ (650–400 cm^{-1}) sites, is lost.[15,16] When the lithium ions surrounding the nickel divalent ions are preferentially deintercalated, the oxidation process of extra nickel ions, i.e. from the divalent (r = 0.68 Å) to the trivalent state (r = 0.56 Å), takes place. On reversing polarity in the charge–discharge cycles, these lithium ions can no longer fit back into their sites due to octahedral distortion, and therefore the electrochemical cyclability is limited.[12,17,18]

Taking into account the above observations, one of the strategies for preparing materials with better cycling properties has been directed towards new routes of synthesis to produce trigonal ($R\bar{3}m$) Ni-rich phases with an ordered distribution of Li^+ and M^{3+} ions in the octahedral sites. Synthetic methods that lead to small-particle-size materials are also of interest because they favor the ionic and electronic diffusion in the cathode material intergrain frontiers, as well as the overpotential decrease of the ionic transfer across the cathode/electrolyte interface.[19,20] Chemical methods involving salts after precipitation and convenient thermal treatments have been the strategies for the preparation of small-particle-size oxides. In this way, the so-called citrate method has been employed in the preparation of multicomponent oxides (perovskites, spinels, ferrites, etc.) to produce materials with a high chemical homogeneity and small particle size.[21–30] This method involves the precipitation of citrate salts at controlled pH and concentration ratio of the involved ions, followed by their thermal decomposition. The Pechini process[26] for the synthesis of mixed oxides is one of the different reported pathways in which polyhydroxy alcohols are used to produce the esterification of

[a] Department of Chemistry, Orient University, Santiago de Cuba, Cuba
[b] Laboratory of Solid State Ionics, IMRE Havana University, Havana, Cuba
[c] Instituto de Ciencia de Materiales de Madrid, Cantoblanco 28049, Madrid, Spain
E-mail: eduardo@icmm.csic.es
Supporting information for this article is available on the WWW under http://www.eurjic.org or from the author.

 © 2005 Wiley-VCH Verlag GmbH & Co. KGaA, Weinheim **DOI: 10.1002/ejic.200400383**

complex mixtures of citrates to give a polymeric resin, which is decomposed above 400 °C.[21,23–26] However, the formation of a dense and rigid resin intermediate of citric acid and ethylene glycol, which leads to crystallite agglomeration during pyrolysis, has been found to be a critical problem of this approach.[25] A modified Pechini method has been reported recently by Julien et al.,[30] in which a gel precursor is prepared by addition of citric acid to a mixture of the metal acetates followed by heating at 800 °C to obtain the micro-sized $LiNi_{0.6}Co_{0.4}O_2$ phase. Alternative routes[27–30] are based on the higher solubility of the citrate salts in ethanol vs. water, as reported by Zhecheva and coworkers[29] for the preparation of $LiCoO_2$ powders with small particle size. These authors showed that the chelating ability of citric acid, and therefore its ability to form complexes with metal ions, is highly dependent on the ions' concentration. Thus, concentrated lithium-cobalt-citrate solutions (1:1:2, Li:Co:citric acid) lead to the formation of a homogeneous $(NH_4)_3LiCo(C_6H_5O_7)_2$ citrate. The thermal decomposition of this amorphous citrate yields a $LiCoO_2$ phase with an "ideal" trigonal α-$NaFeO_2$-type structure.[29]

Although the method employed by Zhecheva et al.[29] is efficient for the preparation of lithium cobalt oxides, there is no evidence of its application to systems involving other metal such as nickel, or when a substitution of cobalt by nickel must take place. The aim of the present work is to extend Zhecheva's method[29] to the synthesis of $LiNi_{0.8}Co_{0.2}O_2$ by using, in this case, a new precursor consisting of a mixed nickel-cobalt citrate of appropriate stoichiometry. We intend to optimize the synthesis conditions to reach a well-defined crystalline phase of the mixed citrate that could produce the ideal trigonal Li-Co-Ni oxide (rich in nickel) by a new chemical route followed by thermal decomposition. As is reported below, the resulting oxide has a $Li_{0.7}Ni_{0.8}Co_{0.2}O_2$ composition whose structural and electrochemical features are studied in comparison with the phase of similar composition ($Li_{0.8}Ni_{0.8}Co_{0.2}O_2$) prepared by a ceramic method.

Results and Discussion

Preparation and Structural Characterization of the Precursor Citrate and the $Li_{0.7}Ni_{0.8}Co_{0.2}O_2$ Phase

During the preparation of the precursors of the Li-Co-Ni mixed oxides we observed that attempts to prepare the mixed citrates of a selected stoichiometry in the presence of lithium salts always resulted in mixtures of amorphous and crystalline Li-Co and Li-Ni phases, except when the pH and the concentration of the solutions were strictly controlled. Therefore, based on the experimental results of Zhecheva et al.[29] applied to lithium–transition metal (Co or Ni) citrate single-phase preparations, we estimated what would be the optimum pH value to obtain the Li-Co-Ni tridentate citrate as a single phase with a 1:1:2 Li:(Co-Ni):citrate ratio. The variation of the concentration of citrate (Cit) species vs. pH (Figure 1) is obtained by solving the three equilibrium equations of citric acid dissociation in water.[31]

$$H_3Cit\ (aq) \rightleftharpoons H_2Cit^-\ (aq) + H^+\ (aq);\ K_a = 8.4\times10^{-4} \quad (1)$$

$$H_2Cit^-\ (aq) \rightleftharpoons HCit^{2-}\ (aq) + H^+\ (aq);\ K_a = 1.8\times10^{-5} \quad (2)$$

$$HCit^{2-}\ (aq) \rightleftharpoons Cit^{3-}\ (aq) + H^+\ (aq);\ K_a = 4\times10^{-6} \quad (3)$$

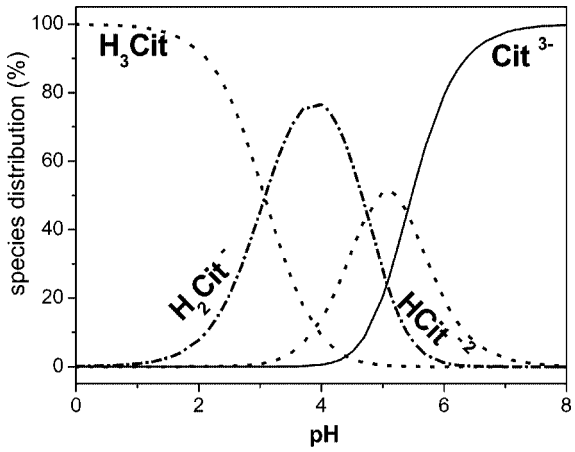

Figure 1. Phase diagram of citric acid species as a function of pH (calculated for a total citric acid concentration of 1 mol L^{-1}).

The distribution diagram of equilibrium species for citric acid shows that the Cit^{3-} species predominate around pH 7. To favor the presence of such species it is necessary to increase the pH, which in our case is achieved by adding the Li^+ ions as carbonate and, finally, aqueous ammonia solution to adjust to pH 7. Under these conditions Cit^{3-}, Li^+, Co^{2+}, Ni^{2+}, and NH_4^+ species are present, thus making possible the precipitation of the mixed citrate containing Li^+ and NH_4^+ ions, which act as counterions as with other reported ammonium metal citrates, such as $(NH_4)_4M(C_6H_5O_7)_2$ (M = Co, Zn, and Cu), studied by Zhecheva,[29] Swanson,[32] and Both,[33] respectively.

The mixed citrate $(NH_4)_3LiNi_{0.8}Co_{0.8}(C_6H_5O_7)_2$ obtained at pH 7 (see Experimental Section) precipitates as a blue-green solid when the resulting solution is dried. The elemental analysis (CHN) of the solid (C 28.40, N 9.19, H 4.12) is in good agreement with the calculated values (C 28.93, N 8.51, H 4.42). The STEM-EDX analysis of this sample for different particles of the solid shows Ni/Co, O/Ni, O/Co, and O/C atomic ratios of about 3.79, 4.56, 18.90, and 1.53, respectively, which indicate good homogeneity of the sample compositions.

The formation of a citrate salt is clearly revealed by IR spectroscopy (Figure 2) as the characteristic vibration bands of the carboxylic groups of the citric acid at 1740 cm^{-1} and 1690 cm^{-1} ($\nu_{C=O}$), 1420 cm^{-1} ($\nu_{CO} + \delta_{OH}$ in plane), and 930 cm^{-1} (δ_{OH} out plane) are replaced by the two characteristic antisymmetric and symmetric stretching vibration bands of carboxylate groups at 1576 cm^{-1} and 1385 cm^{-1}, respectively.[29,34] It is well known that the position and separation between ν_{as} and ν_s stretching vibrations of COO^- can be used to establish the coordination mode of the carboxylate anions around the metal ion.[35–37] The presence of the band assigned to the symmetric vibration

 © 2005 Wiley-VCH Verlag GmbH & Co. KGaA, Weinheim

mode below 1400 cm^{-1} – it appears at 1385 cm^{-1} in the citrate synthesized here – suggests the coordination of the carboxylate as a bidentate ligand. The large band centered at 3190 cm^{-1} (Figure 2) can be assigned to the ν_{OH} stretching vibrations of perturbed 2-hydroxy groups, thus indicating the participation of such hydroxyls in the metal coordination. The bands at 1190 cm^{-1} and 1138 cm^{-1} correspond to the ν_{CO} stretching vibration modes of these tertiary alcohol groups.[34]

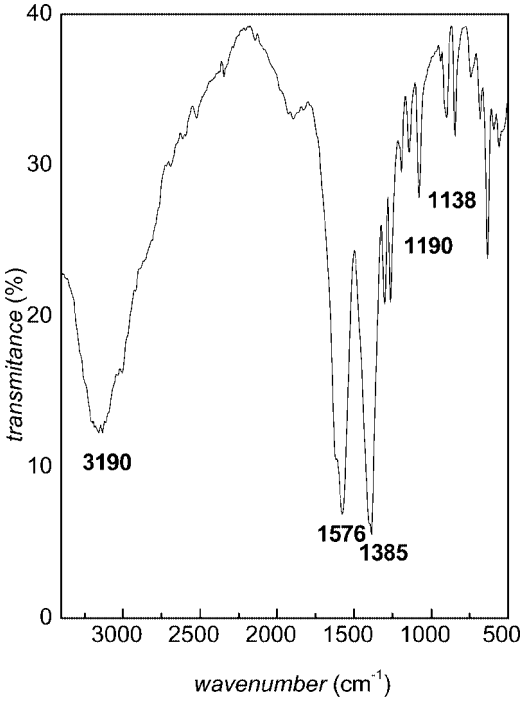

Figure 2. IR spectrum of the citrate $(NH_4)_3LiNi_{0.8}Co_{0.2}(C_6H_5O_7)_2$.

Figure 3 shows the XRD patterns of the mixed Li-Co-Ni citrate obtained at pH 7 (considered as the optimal acidity conditions) and another citrate obtained at pH 6. This latter solid exhibits a poor diffractogram, suggesting the presence of the citrate together with other phases, including amorphous materials. It is important to remark that thermal decomposition of both citrates results in different crystalline Li-Ni-Co mixed oxides with rhombohedral symmetry ($R\bar{3}m$).

The XRD patterns (Figure 3 c and d) are similar to those reported in the literature for $Li_{1-x}[Ni_{(x-y)}Ni_x]Co_{1-y}O_2$,[1–3,7,8,10,12,13] but a clear splitting of the (006) and (012) reflections as well as the (018) and (110) diffraction lines is observed for the oxide obtained from the citrate prepared at pH 7. This observation indicates that the corresponding mixed oxide has an α-$NaFeO_2$-type structure with a better ordered cationic distribution[12,13] than the oxide prepared from the citrate obtained at pH 6. The presence of NiO and Co_3O_4 phases that could take part in the resulting product can be discarded as their more intense XRD diffraction peaks do not appear in the patterns. Some of them could be overlapped by the most intense signals of the $Li_{0.7}Ni_{0.8}Co_{0.2}O_2$ mixed oxide but the other reflections are not detected in the background.

The XRD profiles of the ordered Li-Ni-Co mixed oxide as well as its new citrate precursor (pH 7) were indexed with the CELREF V3 computer program.[38] The unit-cell parameters in the hexagonal system (space Group: $R\bar{3}m$) are a = 0.2841 and c = 1.4070 nm, $\alpha = \gamma = 90°$, $\beta = 120°$ (calculated from the structural data in Table S1 in the Supporting Information). These parameters are not far from those of the $LiNi_{0.8}Co_{0.2}O_2$ oxide prepared by a ceramic route (a = 0.2867, c = 0.1416 nm, $\alpha = \gamma = 90°$, $\beta = 120°$ by Rougier[12] and a = 0.2862, b = 0.1412 nm, $\alpha = \gamma = 90°$, β

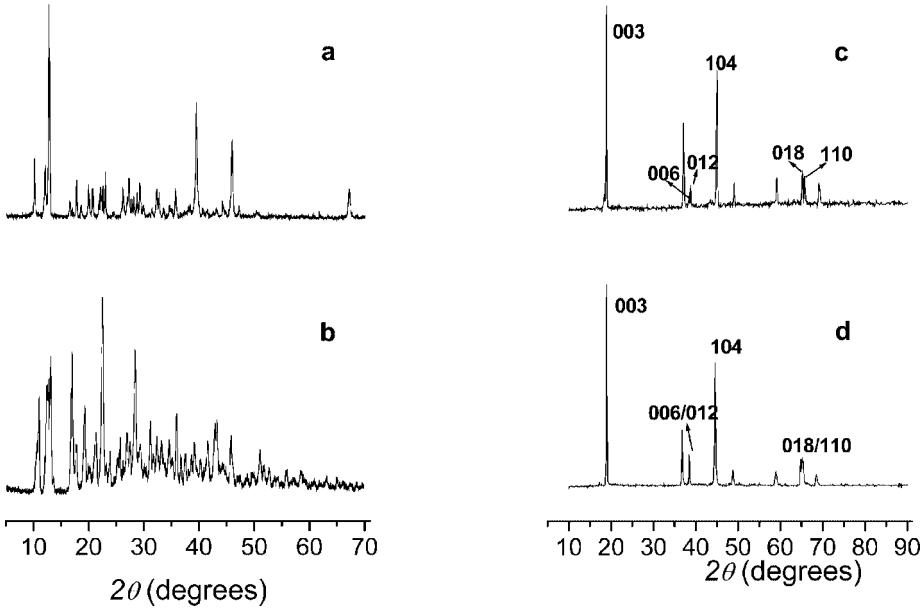

Figure 3. XRD patterns of the Li-Ni-Co citrate precursors obtained in this work at pH 7 (a) and pH 6 (b), and of the mixed Li-Ni-Co oxides obtained by thermal decomposition at 750 °C from the corresponding citrate prepared at pH 7 (c) and pH 6 (d).

 © 2005 Wiley-VCH Verlag GmbH & Co. KGaA, Weinheim

= 120° in this work) or from those of $LiNi_{0.6}Co_{0.4}O_2$ reported by Julen et al.[30] by a sol-gel route (a = 0.2839, c = 0.1409 nm, $\alpha = \gamma = 90°$, $\beta = 120°$). For the precursor (citrate synthesized at pH 7) the unit-cell parameters in the monoclinic system ($P2_1/m$ space group) are a = 0.8839, b = 1.3768, c = 0.9057 nm, $\beta = 114.9°$ (powder X-ray diffraction data given in Table S2 in the Supporting Information).

The DTA and TG curves (Figure 4) of the citrate prepared at pH 7 show an endothermic peak at 140 °C, which is accompanied by a weight loss that was assigned to a first NH_3 loss according to TG/MS results (see Figure 1 in the Supporting Information). The complex endothermic peak observed between 170 °C and 240 °C accompanied by the second weight loss was assigned to loss of the residual NH_3 molecules and also the well known transformation of citrate $(C_6H_5O_7)^{3-}$ into *cis*-aconitate $(C_6H_3O_6)^{3-}$ and a water molecule.[21,25,29] Above 300 °C several exothermic processes take place accompanied by drastic weight losses due to the vigorous combustion reactions of the residual organic matter. The total weight loss for $(NH_4)_3LiNi_{0.8}Co_{0.2}(C_6H_5O_7)_2$ is about 82%, which agrees well with the calculated values for a final product of composition $LiNi_{0.8}Co_{0.2}O_2$ (80.5%).

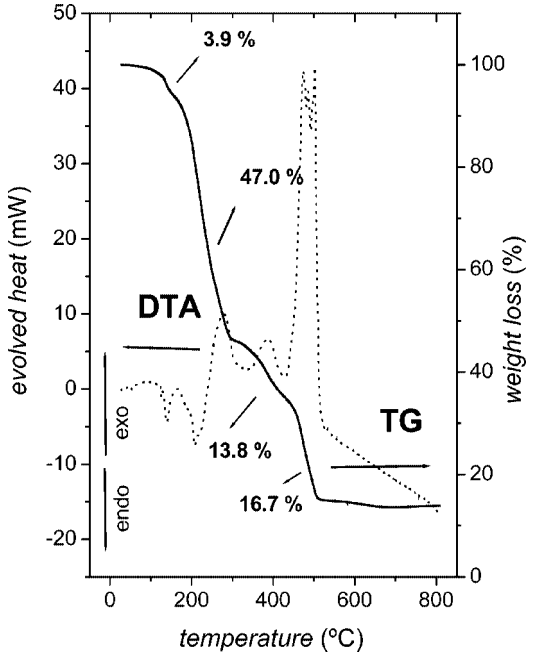

Figure 4. TG and DTA curves of the citrate $(NH_4)_3LiNi_{0.8}Co_{0.2}(C_6H_5O_7)_2$ heated in air.

The thermal evolution of the citrate synthesized at pH 7 was also followed by XRD with the objective to determine at what temperature this precursor is transformed into the lamellar mixed oxide with trigonal structure. Figure 5 shows that the citrate precursor gives the Li-Ni-Co-O-phase at 750 °C.

The citrate thermal decomposition at 750 °C for 30 hours gives a well-ordered $Li_xNi_{0.8}Co_{0.2}O_2$ material of composition 4.98% Li, 47.91% Ni, and 12.16% Co (see analytical data in Table S3 in the Supporting Information) that fits well with the ideal $Li_{0.7}Ni_{0.8}Co_{0.2}O_2$ phase (Li 5.08%, Ni

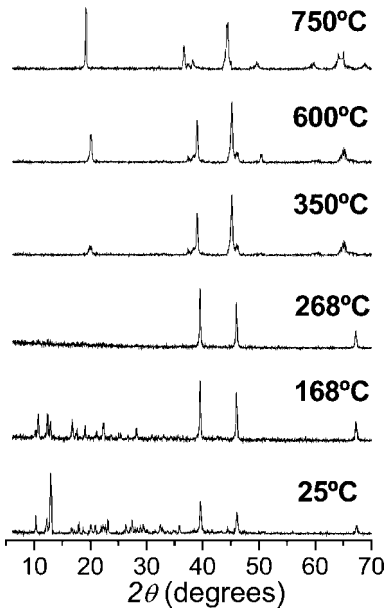

Figure 5. Evolution of the XRD patterns with temperature of the $(NH_4)_3LiNi_{0.8}Co_{0.2}(C_6H_5O_7)_2$ citrate precursor until transformation into the trigonal Li-Ni-Co-O mixed-oxide phase at 750 °C.

49.12%, Co 12.33%). From iodometric titration we deduced a mean oxidation state of +3 for both cobalt and nickel, i.e. Co^{III} and Ni^{III}. This result indicates that the loss of Li^+ does not lead to the formation of Ni^{2+} ions as some authors have proposed.[39] Moreover, in the present case the loss of Li^+ provokes the oxidation of Ni^{3+} and Co^{3+} to the +4 oxidation state, as will be discussed later in relation to the electrical characterization of the mixed oxide. The high temperature used during the citrate–oxide transformations could be responsible for the loss of lithium from the solids.

Figure 6 shows the IR spectrum of the $Li_{0.7}Ni_{0.8}Co_{0.2}O_2$ phase in the 200 to 800 cm^{-1} region. As observed in related Li-Co-Ni mixed oxides, the number of resolved IR bands (4 bands: 2 A_{2U} and 2 E_U) corresponds to that predicted for a rhombohedral structure.[3,15,16] In our case the band at 256 cm^{-1} can be ascribed to the LiO_6 stretching vibrations, and the absorption bands between 500–700 cm^{-1} can be assigned to vibrations of the $M^{3+}O_6$ octahedral species. In addition, that the spectrum may be divided into two parts suggests the occurrence of distinct LiO_6 and $M^{3+}O_6$ vibrational frequencies,[15,16] which agrees well with the existence of an ordered ion distribution in a distorted rock-salt structure which corresponds to the interpretation of the XRD results.

The SEM image of the $Li_{0.7}Ni_{0.8}Co_{0.2}O_2$ phase (Figure 7) shows the agglomeration of fine particles with a homogeneous particle-size distribution (ca. 1 mμ). It is expected that the particle size should diminish with a shorter reaction time, thus favoring the Li ion diffusivity,[30,39,40] which is very important for rechargeable lithium-ion battery applications.[19,20] However, it has been observed that under such conditions the order in the distribution of the ions, for instance Li^+ and M^{3+} ions, may be not reached. So, to achieve good electrochemical properties it is necessary to establish

 © 2005 Wiley-VCH Verlag GmbH & Co. KGaA, Weinheim

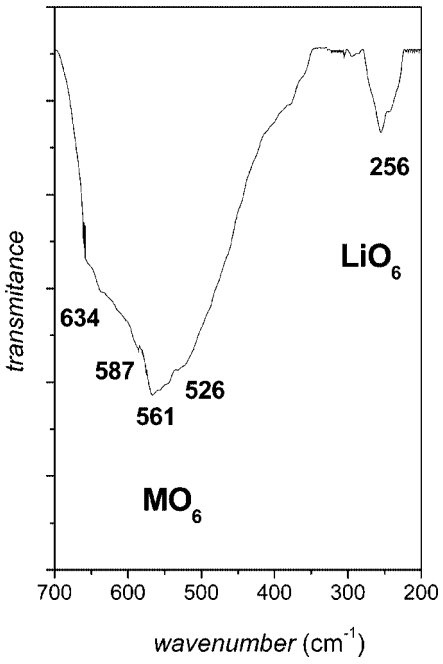

Figure 6. IR spectrum of the $Li_{0.7}Ni_{0.8}Co_{0.2}O_2$ phase obtained after thermal decomposition in air of the $(NH_4)_3LiNi_{0.8}Co_{0.2}(C_6H_5O_7)_2$ citrate precursor at 750 °C for 30 h.

a compromise in the preparation conditions to allow the formation of a well-ordered phase with a relatively small size particle. In the case of the $Li_{0.7}Ni_{0.8}Co_{0.2}O_2$ phase synthesized from the mixed citrate, the particle size is smaller than in the $Li_{0.8}Ni_{0.8}Co_{0.2}O_2$ phase (0.5–20 μm) also obtained in this work by the classical ceramic route. This is also applicable for comparison to other Li-Co-Ni phases obtained from sol-gel precursors followed by calcination at 700–800 °C, such as $LiNi_{0.5}Co_{0.5}O_2$ (3 μm, at 800 °C for 10 h),[9] $LiNi_{0.25}Co_{0.75}O_2$ (1–10 μm at 800 °C for 2 h),[39] and $LiNi_{0.6}Co_{0.4}O_2$ (1 μm, at 700 °C for 4 h).[30]

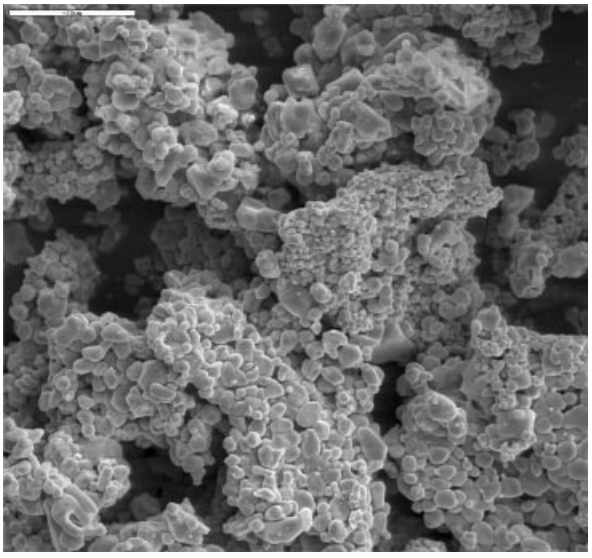

Figure 7. SEM image of the $Li_{0.7}Ni_{0.8}Co_{0.2}O_2$ phase obtained after thermal decomposition in air of the $(NH_4)_3LiNi_{0.8}Co_{0.2}(C_6H_5O_7)_2$ citrate precursor at 750 °C for 30 h.

The study of sample composition carried out by STEM-EDX analysis of different particles shows a high homogeneity in the $Li_{0.7}Ni_{0.8}Co_{0.2}O_2$ phase, with Ni/Co, O/Ni, and O/Co ratios in the 4.09–4.15, 0.70–0.61, and 2.57–2.60 ranges of composition, respectively.

Electrical and Electrochemical Characterization of the $Li_{0.7}Ni_{0.8}Co_{0.2}O_2$ Phase

Figure 8 shows the evolution of the thermoelectric power of the $Li_{0.7}Ni_{0.8}Co_{0.2}O_2$ compound with temperature. All are positive values that are almost independent of the temperature in the studied range. This behavior has been attributed to a small polaron Ni^{3+}-O^{2-}-Ni^{4+}-type transport mechanism, where there is no thermal activation of the number of carriers.[10,40,41] This behavior can be explained by considering the actual lithium content in this sample ($x = 0.7$), hence the loss of the ideal Li^+ stoichiometry may be compensated by the presence of Ni^{4+}/Ni^{3+} couples.[41]

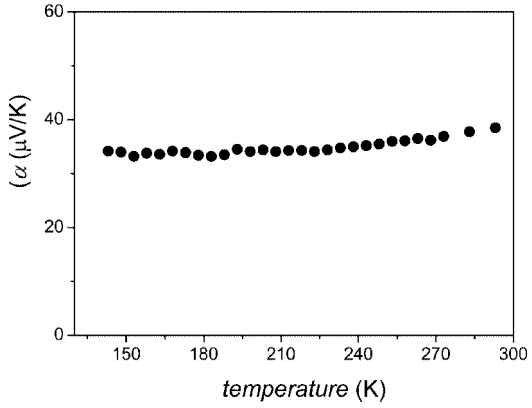

Figure 8. Variation of the thermoelectric power with temperature in the $Li_{0.7}Ni_{0.8}Co_{0.2}O_2$ phase obtained after thermal decomposition in air of the $(NH_4)_3LiNi_{0.8}Co_{0.2}(C_6H_5O_7)_2$ citrate precursor at 750 °C for 30 h.

Previous studies[10,41] have confirmed that, during lithium deintercalation, trivalent nickel ions, rather than trivalent cobalt ions, are preferentially oxidized to the tetravalent state. To unambiguously confirm this behavior a detailed study of the electronic transport properties was carried out during lithium extraction. From a general point of view, nickel oxidation must lead to small polaron-type conductivity, while cobalt oxidation must lead to a tendency to electronic delocalization through the t^2–t^2 overlapping.

Saadoune and Delmas[41] have studied different compositions of $Li_xNi_{0.8}Co_{0.2}O_2$ ($x > 0.5$) and have observed that there is no change in the transport mechanism. Our results for the $Li_{0.7}Ni_{0.8}Co_{0.2}O_2$ phase prepared from the citrate precursor are very similar to theirs and confirm an activated character with an activation energy of 0.17 eV in the electrical conductivity (Figure 9). This result confirms the electronic localization in this phase, which is in good agree-

 © 2005 Wiley-VCH Verlag GmbH & Co. KGaA, Weinheim

ment with the presence of Ni^{4+} ions in the material and therefore the existence of Ni^{4+}-O^{2-}-Ni^{3+} hopping. Considering the actual composition of the $Li_{0.7}Ni_{0.8}Co_{0.2}O_2$ phase, it must be assumed that there are a significant number of Ni^{4+} ions, leading to the presence of holes in the Ni^{4+}/Ni^{3+} narrow band and the respective decrease of the Ni^{4+}-O^{2-}-Ni^{3+} distance as a resulting of the higher valence of Ni^{4+}, which makes the Ni^{3+}-O^{2-}-Ni^{4+} hopping easier. Finally, it should be noted that our $Li_{0.7}Ni_{0.8}Co_{0.2}O_2$ presents a good conductivity value in the 10^{-2} S cm^{-1} range, which is one of the requirements for applications in secondary lithium batteries.

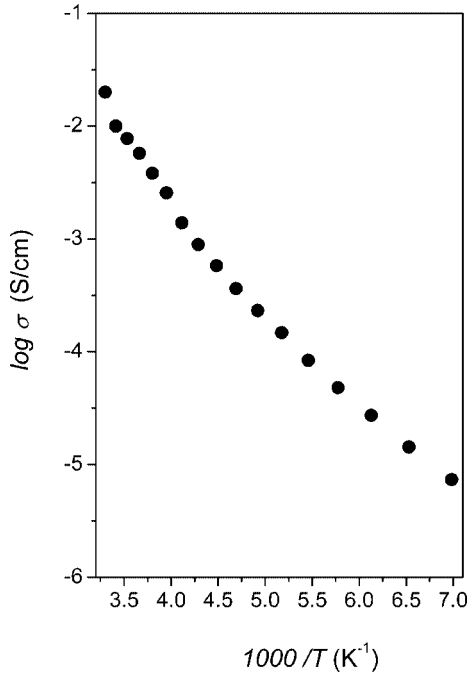

Figure 9. Variation of the electrical conductivity with temperature in the $Li_{0.7}Ni_{0.8}Co_{0.2}O_2$ phase obtained after thermal decomposition in air of the $(NH_4)_3LiNi_{0.8}Co_{0.2}(C_6H_5O_7)_2$ citrate precursor at 750 °C for 30 h.

The first charge and discharge curves of the $Li_{0.7}Ni_{0.8}Co_{0.2}O_2$ phase used as a positive electrode (without any addition of conductive carbon due to its good electrical conductivity) are illustrated in Figure 10, in which the Li content has been varied in the $0.7 \geq x \geq 0.4$ composition domain whilst operating at a 70 μA cm^{-2} current density. This graphic shows that the electrochemical process is well reversible, with the coulombic efficiency of the first discharge process being about 96% of the first charge one. The monotonous increment of the voltage vs. composition curve suggests the occurrence of a monophasic reaction in the charge/discharge process, as has been reported by several authors.[1,7,29,30] On the contrary, for the material obtained by the traditional ceramic method ($Li_{0.8}Ni_{0.8}Co_{0.2}O_2$), the first insertion/deinsertion lithium cycle exhibits a very poor percentage of recovered lithium (about 50%), i.e. a poor reversibility.

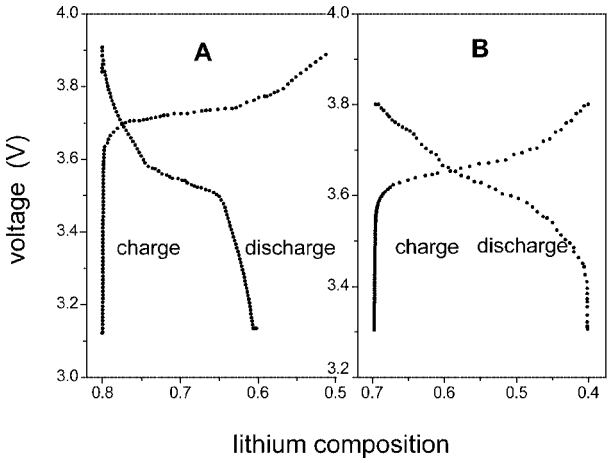

Figure 10. First charge/discharge cycle of (a) the $Li_{0.7}Ni_{0.8}Co_{0.2}O_2$ phase (Li/$LiClO_4$ (PC/EC)/$Li_{0.7}Ni_{0.8}Co_{0.2}O_2$ cell) and (b) the $Li_{0.8}Ni_{0.8}Co_{0.2}O_2$ phase prepared by the ceramic method (Li/$LiClO_4$ (PC/EC)/$Li_{0.8}Ni_{0.8}Co_{0.2}O_2$ cell), both at 70 μA cm^{-2}.

The low polarization effect observed is in good agreement with the lithium content determined from chemical analysis ($x = 0.7$), because it is known that when x becomes close to 1 the ionic conductivity decreases as the number of available sites for Li^+ ion diffusion becomes very small, leading to a strong polarization effect.[41]

Figure 11 shows a plot of the $-dx/dV$ values vs. the potential for the first charge/discharge cycle of the cell prepared from the $Li_{0.7}Ni_{0.8}Co_{0.2}O_2$ phase. The occurrence of a single step of extraction and insertion of lithium from the cathode suggests the existence of a unique phase in our compound, in contrast to the $Li_{0.75}Ni_{0.8}Co_{0.2}O_2$ ceramic phase already reported by Saadone and Delmas.[41] In this last case, the observed minimum in the dx/dV plot is associated with order–disorder transitions during the insertion/deinsertion of the Li^+ ions.

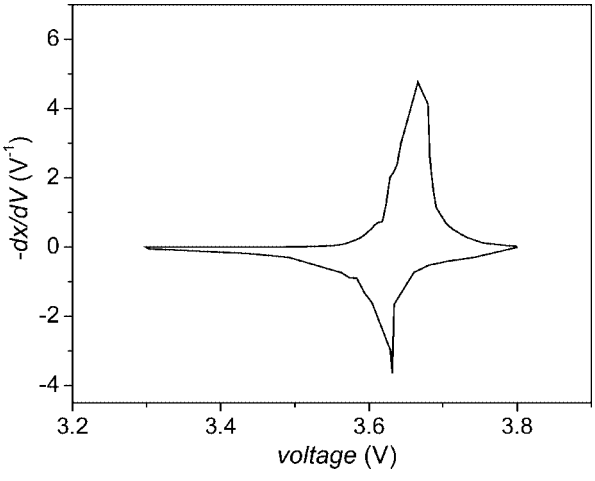

Figure 11. Derivative curve ($-dx/dV$) vs. voltage for the first charge/discharge cycle of the Li/$LiClO_4$(PC/EC)/$Li_{0.7}Ni_{0.8}Co_{0.2}O_2$ cell. In the derivative term, x represents the content of Li.

The excellent cyclability of this cell, at least for the first four charge/discharge processes, is shown in Figure 12. The

 © 2005 Wiley-VCH Verlag GmbH & Co. KGaA, Weinheim

data show a specific capacity of 80 mAh g^{-1}, corresponding to the insertion/extraction of 0.3 Li^+. The experimental conditions were selected in order to ensure that the lithium insertion never goes lower than 0.4 moles to avoid irreversible phase transformations. This limitation implies that the maximum amount in the lithium content was that of the starting oxide, i.e. $x = 0.7$.

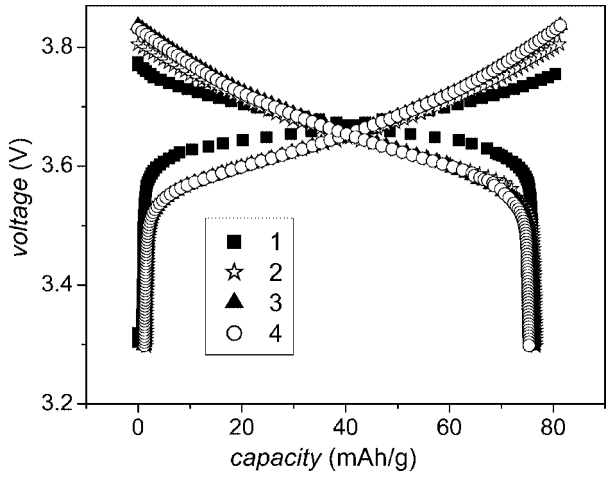

Figure 12. Galvanostatic cycling curves of the Li/$LiClO_4$ (PC/EC)/$Li_{0.7}Ni_{0.8}Co_{0.2}O_2$ cell at a constant current density of 70 μA cm^{-2}. The Li content has been varied in the $0.7 \geq x \geq 0.4$ composition domain.

The theoretical capacity calculated for a variation of $\Delta x = 0.6$ in the lithium content for a similar cell prepared with materials of the same family compounds is about 160 mAh g^{-1},[29,30,41] which is equivalent to the value of 80 mAh g^{-1} obtained by us for $\Delta x = 0.3$ extracted and reinserted.

Concluding Remarks

The main requirement to obtain a Ni-rich phase such as $Li_{0.7}Ni_{0.8}Co_{0.2}O_2$ with well-ordered cationic distribution of Li and Ni from citrate precursors is the pH control in the precursor synthesis to form a unique phase of the mixed citrate. Working at unsuitable pH conditions results in a mixture of citrate phases which, after thermal decomposition, gives rise to mixed oxides presenting a disordered Li/Ni cationic distribution.

The $Li_{0.7}Ni_{0.8}Co_{0.2}O_2$ oxide prepared from the mixed citrate $(NH_4)_3LiNi_{0.8}Co_{0.2}(C_6H_5O_7)_2$ shows good electrical conductivity that is high enough to ensure the required behavior as an electrode material for convenient electrochemical insertion/deinsertion of lithium without addition of conductive carbon.

Comparing the results of electrochemical behavior towards Li insertion/deinsertion of $Li_{0.7}Ni_{0.8}Co_{0.2}O_2$ as an electrode material with that of the already reported $Li_{0.75}Ni_{0.8}Co_{0.2}O_2$ phase prepared by a ceramic method shows that the novel phase presents an enhanced performance in the cyclability properties.

Experimental Section

The Li-Co-Ni citrate with a Li/Co/Ni/citric acid stoichiometry ratio of 1:0.2:0.8:2, respectively, was synthesized by adding Li_2CO_3 (1.92 g; Merck) to a mixture of aqueous solutions of $Co(NO_3)_2 \cdot 6H_2O$ (11.98 g; Riedel-de Haën) and $Ni(NO_3)_2 \cdot 6H_2O$ (2.98 g; Aldrich) to reach the 1:4 Co/Ni stoichiometry selected. A saturated solution of citric acid (Aldrich) was then added dropwise to this mixture, which was stirred rapidly until a clear solution was obtained. Afterwards, the pH was adjusted to 7 with aqueous ammonia (6 M; Merck) and the mixture was heated at 80 °C for 4 h. This thermal treatment produced the formation of a blue-green precipitate, which was isolated, washed with ethanol, and dried at 100 °C in air. The solid was characterized and then used to prepare the mixed oxide by heating at 750 °C for 30 h. For comparative purposes, a $Li_xNi_{0.8}Co_{0.2}O_2$ phase was prepared by a conventional ceramic route based on the thermal decomposition of stoichiometric mixtures of $Ni(NO_3)_2 \cdot 6H_2O$, $Co(NO_3)_2 \cdot 6H_2O$, and $Li(OH) \cdot H_2O$ at 400 °C and subsequent solid-state reaction in air at 750 °C for 30 h.[3]

The elemental analyses (CHN) were performed with a Perkin–Elmer 240C microanalyzer. The Li, Ni, and Co contents were determined with an ICP-AES spectrometer Perkin–Elmer Optima 3300. The mean oxidation state of cobalt and nickel was determined by iodometric titration. The XRD patterns were recorded with a Philips PW1710 diffractometer using Cu-K_α radiation from 10° to 90° (2θ) at 2° min^{-1}. The temperatures for the programmed recording of XRD patterns (5 °C min^{-1}) during the heating of the citrate precursor carried out in the Anton Paar high temperature chamber of the diffractometer, were selected from the DTA and TG curves of the sample obtained in a Seiko SSC/5200 analyzer (5 °C min^{-1} heating rate from room temperature to 900 °C in air). The TG/MS measurement were carried out with a Thermostatar Baltzers Instrument coupled to a Seiko SSC/5200 TG-DTA System using 100 mL min^{-1} He flux, heating from 25 to 600 °C at 2 °C min^{-1}. The Infrared spectra of the citrate precursor (KBr pellets) and mixed oxides (polyethylene pellets) were recorded with an ATI MATTSON Genesis Series FTIR spectrometer in the 400–4000 cm^{-1} region and a Perkin–Elmer FTIR spectrophotometer model 567 in the 200–700 cm^{-1} region, respectively. The morphology, particle-size distribution, and purity of the phases were studied with a SEM Zeiss DSM-960 microscope coupled with an EDX Tacor-Northen Serie Z-II spectrometer operating at 20 kV and a STEM LEO-910 microscope also coupled with an EDX system.

Thermoelectric power and four-point conductivity measurements in the –133 to 20 °C temperature range were carried out simultaneously using a homemade apparatus described elsewhere.[42] Pellets of pressed powder (7 tons cm^{-2}) were sintered at 700 °C for 4 h in air. The electrochemical measurements were carried out in Li/$LiClO_4$(PC/EC)/$Li_xNi_{0.8}Co_{0.2}O_2$ cells. The positive electrode consists of sintered pellets (0.13 cm diameter) pressed at 3 tons cm^{-2} of the pure mixed oxide (i.e., without addition of carbon as electric conductor). The cells, assembled in an argon-filled dry box, were galvanostatically cycled under low current density (70 μA cm^{-2}) in the $0.7 \geq x \geq 0.4$ and $0.8 \geq x \geq 0.4$ lithium composition ranges for the oxides prepared by the chemical and ceramic methods, respectively.

Acknowledgments

Financial support from the CSIC and the Havana University (CITMA) through a Spanish–Cuban cooperation (reference

 © 2005 Wiley-VCH Verlag GmbH & Co. KGaA, Weinheim

2001CU0007) and from the CICYT (Spain, MAT2000-1585-C03-01 and MAT2003-06003-C02-01) is gratefully acknowledged. The authors would like to thank Dr. S. Letaïef and Mr. F. Pinto for helpful technical assistance.

[1] J. N. Reimers, J. R. Dahn, *J. Electrochem. Soc.* **1992**, *139*, 2091–2097.
[2] W. Li, J.-N. Reimers, J. R. Dahn, *Solid State Ionics* **1993**, *67*, 123–130.
[3] R. Alcántara, J. Morales, J. L. Tirado, R. Stoyanova, E. Zhecheva, *J. Electrochem. Soc.* **1995**, *142*, 3997–4005.
[4] T. Ohzuku, A. Ueda, *Solid State Ionics* **1994**, *69*, 201–211.
[5] A. Manthiram, J. Kim, *Chem. Mater.* **1998**, *10*, 2895–2909.
[6] M. Broussely, F. Perton, D. Biensan, J. Bodet, A. Lecerf, C. Delmas, A. Rougier, J. P. Pérès, *J. Power Sources.* **1995**, *54*, 109–114.
[7] I. Saadoune, M. Ménétrier, C. Delmas, *J. Mater. Chem.* **1997**, *7*, 2505–2511.
[8] R. J. Gummow, M. M. Tackeray, W. I. David, S. Hull, *Mater. Res. Bull.* **1992**, *27*, 327–337.
[9] D.-W. Kim, Y.-K. Sun, *Solid State Ionics* **1998**, *111*, 243–252.
[10] C. Delmas, I. Saadoune, *Solid State Ionics* **1992**, *53–56*, 370–375.
[11] J. Molenda, P. Wilk, J. Marzec, *Solid State Ionics* **1999**, *119*, 19–22.
[12] A. Rougier, I. Saadoune, P. Gravereau, P. Willman, C. Delmas, *Solid State Ionics* **1996**, *90*, 83–90.
[13] E. Zhecheva, R. Stoyanova, *Solid State Ionics* **1993**, *66*, 143–145.
[14] J. Morales, C. Pérez, J. L. Tirado, *Mater. Res. Bull.* **1990**, *25*, 623–625.
[15] R. K. Moore, W. B. White, *J. Am. Ceram. Soc.* **1970**, *53*, 679–682.
[16] P. Tarte, J. Prudhomme, *Spectrochim. Acta, Ser. A* **1970**, *26A*, 747–754.
[17] R. Stoyanova, E. Zhecheva, R. Alcántara, P. Labela, J. L. Tirado, *Solid State Commun.* **1997**, *102*, 457–462.
[18] J. P. Pérès, C. Delmas, A. Rougier, M. Broussely, F. Perton, P. Biesan, P. Willmann, *J. Phys. Chem. Solids* **1996**, *57*, 1057–1060.
[19] M. Mizushima, P.-C. Jones, P.-J. Wiseman, J.-B. Goodenough, *Solid State Ionics* **1981**, *3/4*, 171–174.
[20] S. Kikkawa, S. Miyazaki, M. Koizumi, *J. Power Sources* **1985**, *14*, 231–234.
[21] D. Heennings, W. Mayr, *Solid State Chem.* **1978**, *26*, 329–338.
[22] D. J. Anderton, F. R. Sale, *Powder Metall.* **1979**, *22*, 14–18.
[23] M. S. Baythoun, F. R. Sale, *J. Mater. Sci.* **1982**, *17*, 2557–2560.
[24] A. Douy, M. Odier, *Mater. Res. Bull.* **1989**, *24*, 1119–1126.
[25] J.-H. Choy, Y.-S. Han, J.-T. Kim, Y.-H. Kim, *J. Mater. Chem.* **1995**, *5*, 57–63.
[26] M. Pechini, *US Patent.* **1967**, 3,330,697.
[27] V. K. Sankaranarayanan, Q. A. Pankhurst, D. P. Disckon, C. E. Johnson, *J. Magn. Magn. Mater.* **1993**, *120*, 73–75.
[28] V. K. Sankaranarayanan, Q. A. Pankhurst, D. P. Disckon, C. E. Johnson, *J. Magn. Magn. Mater.* **1993**, *125*, 199–208.
[29] E. Zhecheva, R. Stoyanova, M. Gorova, R. Alcántara, J. Morales, J. L. Tirado, *Chem. Mater.* **1996**, *8*, 1429–1440.
[30] C. Julien, L. El-Farh, S. Rangan, M. Massot, *J. Sol-Gel Sci. Technol.* **1999**, *15*, 63–72.
[31] *Handbook of Analytical Chemistry* (Ed.: J. Lurie), MIR Publishers, Moscow, **1971**.
[32] R. Swanson, W. H. Ilsey, A. G. Stanislowski, *J. Inorg. Biochem.* **1983**, *18*, 187–194.
[33] R. C. Bott, D. S. Sagatys, D. E. Lynch, G. Smith, C. H. Kennard, T. C. Mak, *Aust. J. Chem.* **1991**, *44*, 1495–1498.
[34] *Infrared and Raman Spectra of Inorganic and Coordination Compounds* (Ed.: K. Nakamoto), John Wiley & Sons, New York, **1986**, pp. 231–282.
[35] J. Catterick, P. Thornton, *Adv. Inorg. Chem. Radiochem.* **1977**, *19*, 291–296.
[36] G. B. Deacon, R. J. Philips, *Coord. Chem. Rev.* **1980**, *33*, 227–231.
[37] L. P. Battaglia, A. B. Corradi, G. Marcotrigiano, L. Menabue, G. C. Pellacanni, *J. Am. Chem. Soc.* **1995**, *117*, 2663–2669.
[38] U. D. Altermatt, I. D. Brown, *Acta Crystallogr. Sect. A* **1987**, *34*, 125–130.
[39] C. C. Chang, N. Scarr, P. N. Kumta, *Solid State Ionics* **1998**, *112*, 329–344.
[40] M. Thackeray, *J. Electrochem. Soc.* **1995**, *142*, 2558–2563.
[41] I. Saadoune, C. Delmas, *J. Solid State Chem.* **1998**, *136*, 8–15.
[42] E. Pérez-Cappe, A. Villanueva, J. C. Gálvan, G. Pérez-Urrutia, E. Ruiz-Hitzky, *Abstracts VI Reunión Nacional de Materiales*, **1999**, San Sebastián.

Received: May 11, 2004
Published Online: May 31, 2005

 © 2005 Wiley-VCH Verlag GmbH & Co. KGaA, Weinheim

A New Spherical Metallacryptate Compound $[Na\subset\{Cu_6(Thr)_8(H_2O)_2(ClO_4)_4\}]\cdot ClO_4\cdot 5H_2O$: Magnetic Properties and DFT Calculations

Sheng-Chang Xiang,[a] Sheng-Min Hu,[a] Jian-Jun Zhang,[a] Xin-Tao Wu,*[a] and Jun-Qian Li[b]

Keywords: Spherical metallacryptate / Magnetic properties / Density functional calculations / Broken symmetry / Threonine

The hexanuclear copper(II) complex with threoninato acid has been synthesized. Its structure can be described as an octahedron cage with D_{2h} symmetry in which six copper ions are bound by eight threoninato acids with a $[3.1_12_23_10]$ coordination mode and one Na^+ cation being captured within the center of the cage. In contrast with other hexanuclear copper compounds containing amino acids, the title compound has a prolate Cu_6 octahedron with the longest axial distance and a rectangle equatorial plane, as well as special coordinated perchlorate ions. Compared with classic cryptate, hexanuclear copper(II) compounds with amino acids can be regarded as a new topologic type of spherical macrotricyclic metallacryptates [2,2,2,2] whose cages have a high selectivity for sodium ions. The analysis of magnetic susceptibility data shows that the threoninato compound has a ground state with spin $S = 3$. The computing coupling constant between the equatorial Cu centers and the axial ones is 4.4 cm^{-1}, calculated by using DFT methods for a model compound. This is close to three known experimental values of 1.39, 0.56 or 0.43 cm^{-1} for complexes with 4-hydroxy-L-prolinato, L-prolinato or L-threoninato acid as ligands, respectively. The dominant ferromagnetic interactions for these complexes can be essentially attributed to the orthogonality between the magnetic orbitals, d_{xz} or d_{yz} orbitals for the equatorial Cu^{II} centers and $d_{x^2-y^2}$ orbitals for the axial ones.

(© Wiley-VCH Verlag GmbH & Co. KGaA, 69451 Weinheim, Germany, 2005)

Introduction

The crown ether[1] is one of the classic synthetic ionophores, and the discovery of its cation-binding properties launched the rich field of host-guest chemistry.[2] While increasing the denticity of the crowns through construction of three-dimensional cavities, the cryptands[3] increase the binding affinities of the crowns for alkali metals. Using hydroxamic acid [e.g., salicylhydroxamic acid (SHI)] or oxime as ligands to stabilize the metallacrown ring, Pecoraro[4] synthesized a series of metallacrown analogs by introducing the heteroatom substitution approach which incorporates transition metal ions and nitrogen atoms into the methylene positions of the crown ethers. Once transition metals have been incorporated into metallacrowns they tend to have some interesting properties, which are not found in the simple organic crowns, such as redox activity, strong absorption spectra, and paramagnetism. Pecoraro[5] has obtained a cylindrical metallacryptate $Na[(Na(DMF)_3)_2\{[Na_{0.5}[Ga(SHI)]_4]_2(\mu_2\text{-}OH)_4\}]$, whose $[Na_{0.5}[Ga(SHI)]_4]_2$ metal cycles can be fused together through bridging hydroxides to form bicyclic metallacrowns. The cavity thus formed can selectively bind sodium cations. Another type of the inorganic analogs of cryptates,[6] based on a polyoxometalate framework, shows selectivity for lanthanides.

As the basic building units of proteins, amino acids are ubiquitous and indispensable ligands in biology, and it has been proven that amino acids are excellent ligands for the construction of 3d–4f heteronuclear clusters.[7,8] We[9] have also obtained two hexanuclear copper complexes with two amino acids, glycine (Gly) and L-proline (Pro), respectively, which also have a cavity that binds the sodium cation. Another hexanuclear copper analog with 4-hydroxy-L-proline (hpro) has been synthesized by Winpenny,[10] which is ferromagnetically coupled, yielding an $S = 3$ spin ground state. Bu[11] has produced a one-dimension analog $\{Cu_6Na\}_n$ chain by using 1,5-diazacyclooctane-*N*,*N*′-diacetate acid as the ligand. In this paper, we wish to report a new hexanuclear copper complex $[Na\subset\{Cu_6(Thr)_8(H_2O)_2(ClO_4)_4\}]\cdot ClO_4\cdot 5H_2O$ (**1**) with threoninato acid (Thr) as an inorganic analog of cryptands, which binds sodium cations through eight oxygen atoms of the carboxylate groups of eight threoninato acids.

The aims of this work, from a new viewpoint, are to recognize hexanuclear copper compounds with amino acids as a new type of spherical macrotricyclic metallacryptates, and to study the influence of the various ligands on the structure and magnetic properties of this family. Furthermore,

[a] State Key Laboratory of Structural Chemistry, Fujian Institute of Research on the Structure of Matter, Chinese Academy of Sciences,
Fuzhou, Fujian 350002, P. R. China
E-mail: wxt@ fjirsm.ac.cn
[b] Department of Chemistry, Fuzhou University,
Fuzhou, Fujian 350002, P. R. China

the magnetic properties of these complexes are firstly calculated by employing $\{Cu_6(Gly)_8\}^{4+}$ as a model by using the broken-symmetry approach[12] with density functional theory (DFT). Finally the nature of magnetic exchange for these complexes is explained from the scope of orbital interaction.

Results and Discussion

Structural Description

Part (a) of Figure 1 shows the skeleton structure of **1**. Selected interatomic distances and bond angles for compound **1** are collected in Table 1, respectively. As shown in Figure 1, a Na^+ ion is trapped in the center of a $\{Cu_6(Thr)_8\}$ cage, whose structure may be described as a four-blade propeller. The central metal ion is surrounded by eight carboxylate oxygen atoms which link it to the copper atoms of four $[Cu(Thr)_2]$ units with a mean Na–O distance 2.576 Å. The four units then use their spare carboxylate oxygen atoms to coordinate to the two Cu^{II} centers at the axial vertices, respectively (each Cu^{II} center coordinates to four carboxylate oxygen atoms and the mean Cu_a–O distance is about 1.959 Å). The square pyramidal configuration of the axial Cu^{II} atom is completed by the coordination of a water molecule from the apical position (Cu_a–O_w distances are 2.246 and 2.290 Å, respectively). If the weak interaction is not considered, each equatorial Cu^{II} ion of the cluster has a coordination number (CN) of four and its coordination geometry can be described as square planar. The average Cu_e–O and Cu_e–N distances are 1.949 Å and 1.971 Å, respectively. The six Cu^{II} centers of this cluster form an octahedron with idealized D_{2h} symmetry, the sodium ion being therefore approximately octahedrally surrounded by copper. The four equatorial Cu atoms provide a rectangular plane of the octahedron with two side lengths (the nearest Cu_e–Cu_e distances) of 5.162 and 4.789 Å, but not a square plane as in other amino acid compounds.[9,10] The average distance between axial and equatorial copper atoms is 5.012 Å. Although threoninato acid is a tetradentate ligand, it actually acts as a tridentate ligand by utilizing its amino and carboxylate groups to chelate one Cu^{II} ion and bridge another, as shown in part (b) of Figure 1. The coordination mode indicated by the Harris notation[13] is $[3.1_12_23_10]$.

Four of the five perchlorate ions lie between the propellers formed by the four $[Cu(Thr)_2]$ units as shown in Figure 2. Because the structure of the $[Cu_6]$ unit is distorted, these four perchlorate ions, as the linkages, are not symmetrically equivalent, so that the four Cu^{II} atoms located at the equatorial vertices of a non-binding octahedron provide a rectangular plane, not a square one as for other amino acid compounds. Two oxygen atoms from half of these ions are weakly coordinated to two Cu centers from $[Cu(Thr)_2]$ units, occupying the axial positions of their tetragonally

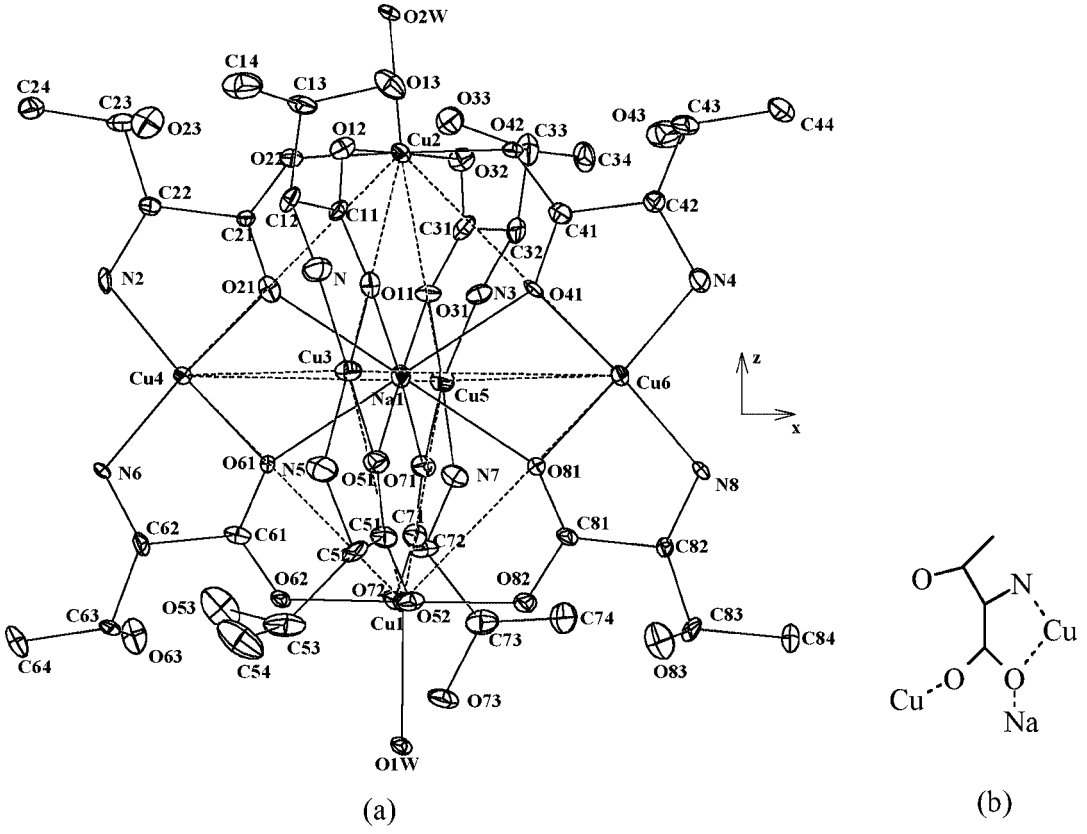

Figure 1. (a) ORTEP view of **1** shows the coordination geometries of Cu^{II} and threoninato acid with vibration ellipsoids at the 30% probability level. Hydrogen atoms are omitted for clarity. (b) The coordination mode $[3.1_12_23_10]$ of threoninato ligand indicated by the Harris notation.

 © 2005 Wiley-VCH Verlag GmbH & Co. KGaA, Weinheim

Table 1. Selected distances between atoms [Å] and bond angles [°].

Cu(1)–O(52)	1.964(3)	Na(1)–O(11)	2.564(3)	O(31)–Cu(5)–O(71)	92.50(11)
Cu(1)–O(62)	1.944(3)	Na(1)–O(21)	2.557(3)	O(31)–Cu(5)–N(3)	83.84(12)
Cu(1)–O(72)	1.979(3)	Na(1)–O(31)	2.597(3)	O(71)–Cu(5)–N(3)	169.93(13)
Cu(1)–O(82)	1.941(3)	Na(1)–O(41)	2.543(3)	O(31)–Cu(5)–N(7)	174.97(13)
Cu(1)–O(1W)	2.290(2)	Na(1)–O(51)	2.588(3)	O(71)–Cu(5)–N(7)	82.47(12)
Cu(2)–O(12)	1.961(3)	Na(1)–O(61)	2.555(3)	N(3)–Cu(5)–N(7)	101.13(13)
Cu(2)–O(22)	1.958(3)	Na(1)–O(71)	2.587(3)	O(41)–Cu(6)–O(81)	92.22(10)
Cu(2)–O(32)	1.961(3)	Na(1)–O(81)	2.616(3)	O(41)–Cu(6)–N(4)	84.71(12)
Cu(2)–O(42)	1.965(3)	O(82)–Cu(1)–O(62)	178.15(11)	O(81)–Cu(6)–N(4)	175.69(15)
Cu(2)–O(2W)	2.246(2)	O(82)–Cu(1)–O(52)	90.30(12)	O(41)–Cu(6)–N(8)	175.07(12)
Cu(3)–O(11)	1.958(3)	O(62)–Cu(1)–O(52)	87.98(11)	O(81)–Cu(6)–N(8)	83.41(12)
Cu(3)–O(51)	1.951(3)	O(82)–Cu(1)–O(72)	90.53(11)	N(4)–Cu(6)–N(8)	99.77(13)
Cu(3)–N(1)	1.965(3)	O(62)–Cu(1)–O(72)	91.19(11)	O(41)–Na(1)–O(61)	178.01(11)
Cu(3)–N(5)	2.005(4)	O(52)–Cu(1)–O(72)	178.79(11)	O(41)–Na(1)–O(21)	114.12(10)
Cu(4)–O(21)	1.952(3)	O(82)–Cu(1)–O(1W)	90.50(10)	O(61)–Na(1)–O(21)	66.23(9)
Cu(4)–O(61)	1.958(2)	O(62)–Cu(1)–O(1W)	89.99(10)	O(41)–Na(1)–O(11)	74.31(9)
Cu(4)–N(2)	1.954(3)	O(52)–Cu(1)–O(1W)	84.43(10)	O(61)–Na(1)–O(11)	104.11(10)
Cu(4)–N(6)	1.981(3)	O(72)–Cu(1)–O(1W)	96.45(10)	O(21)–Na(1)–O(11)	72.40(9)
Cu(5)–O(31)	1.922(2)	O(22)–Cu(2)–O(32)	93.71(12)	O(41)–Na(1)–O(71)	108.04(10)
Cu(5)–O(71)	1.952(3)	O(22)–Cu(2)–O(12)	88.37(12)	O(61)–Na(1)–O(71)	73.56(9)
Cu(5)–N(3)	1.953(3)	O(32)–Cu(2)–O(12)	177.60(12)	O(21)–Na(1)–O(71)	105.63(10)
Cu(5)–N(7)	1.981(3)	O(22)–Cu(2)–O(42)	178.78(11)	O(11)–Na(1)–O(71)	177.50(11)
Cu(6)–O(41)	1.944(2)	O(32)–Cu(2)–O(42)	86.59(11)	O(41)–Na(1)–O(51)	106.06(11)
Cu(6)–O(81)	1.951(3)	O(12)–Cu(2)–O(42)	91.30(11)	O(61)–Na(1)–O(51)	72.07(10)
Cu(6)–N(4)	1.964(3)	O(22)–Cu(2)–O(2W)	86.32(10)	O(21)–Na(1)–O(51)	108.49(10)
Cu(6)–N(8)	1.977(3)	O(32)–Cu(2)–O(2W)	91.96(11)	O(11)–Na(1)–O(51)	64.93(9)
Cu(1)–Cu(2)	7.1331(8)	O(12)–Cu(2)–O(2W)	89.36(11)	O(71)–Na(1)–O(51)	114.74(10)
Cu(1)–Cu(3)	5.0017(7)	O(42)–Cu(2)–O(2W)	94.85(10)	O(41)–Na(1)–O(31)	72.63(9)
Cu(1)–Cu(4)	5.0498(7)	O(51)–Cu(3)–O(11)	90.06(11)	O(61)–Na(1)–O(31)	109.25(10)
Cu(1)–Cu(5)	5.0631(7)	O(51)–Cu(3)–N(1)	174.15(14)	O(21)–Na(1)–O(31)	72.78(9)
Cu(1)–Cu(6)	4.9778(7)	O(11)–Cu(3)–N(1)	84.55(13)	O(11)–Na(1)–O(31)	115.06(10)
Cu(2)–Cu(3)	5.0596(7)	O(51)–Cu(3)–N(5)	85.44(13)	O(71)–Na(1)–O(31)	65.34(9)
Cu(2)–Cu(4)	4.9722(7)	O(11)–Cu(3)–N(5)	174.78(13)	O(51)–Na(1)–O(31)	178.53(11)
Cu(2)–Cu(5)	4.9675(7)	N(1)–Cu(3)–N(5)	99.83(15)	O(41)–Na(1)–O(81)	65.91(8)
Cu(2)–Cu(6)	5.0013(7)	O(21)–Cu(4)–N(2)	84.39(12)	O(61)–Na(1)–O(81)	113.78(9)
Cu(3)–Cu(4)	4.7017(7)	O(21)–Cu(4)–O(61)	91.16(10)	O(21)–Na(1)–O(81)	178.92(12)
Cu(3)–Cu(6)	5.1685(8)	N(2)–Cu(4)–O(61)	173.54(13)	O(11)–Na(1)–O(81)	108.58(10)
Cu(4)–Cu(5)	5.1554(8)	O(21)–Cu(4)–N(6)	174.92(11)	O(71)–Na(1)–O(81)	73.41(9)
Cu(5)–Cu(6)	4.8753(8)	N(2)–Cu(4)–N(6)	100.51(12)	O(51)–Na(1)–O(81)	72.46(9)
		O(61)–Cu(4)–N(6)	84.06(11)	O(31)–Na(1)–O(81)	106.29(10)

elongated octahedral environment, which gives a long side of the rectangle (5.162 Å). The other ClO_4^- ions, however, bind to two Cu^{II} atoms through only one O-donor of its oxygen atoms, which supplies a short side (4.789 Å). As the location barrage, the distances between the Cu_e and O atoms of single-O-donor perchlorate ions are longer than those between the Cu_e and O atoms of two-O-donor ones. The four perchlorate ions act as the fixed interaction of propellers, which makes the skeleton of **1** more stable. The fifth ClO_4^- ion and several water molecules in the periphery have large thermal parameters in contrast with the skeleton atoms.

Some parameters for hexanuclear copper compounds with different amino acids are collected in Table 2. Different ligands lead to the large structural differences, including space group, shape of the octahedron, axial ligand and coordination modes of the perchlorate ions. *catena*-$[Na\subset Cu_2\{Cu(hpro)_2\}_4(ClO_4)_5]\cdot 4H_2O$ is a one-dimensional compound based on the $\{NaCu_6\}$ unit with hydroxyl groups from hpro ligands as the bridge, whereas others are zero-dimensional clusters with solvents, OH^- or perchlorate ions as axial ligands. In glycine complexes, there are two different $\{Cu_6Na\}$ units, one of them with one more Na^+ ion outside the cage. The hpro compound has a compressed octahedron with the shortest axial Cu_a–Cu_a distance forming the chain, while complex **1** has a prolate octahedron with the longest axial distance and a rectangle equatorial plane occurring with the perchlorate ions at the corners. From the Na–O distances, it can be seen that the size and inclusion ability of these octahedron cages are uniform, even though there are many distinctions among the hexanuclear compounds with various amino acids.

New Spherical Metallacryptate [2,2,2,2]

Figure 3 shows that on substituting the Cu_a–O linkage for the bridging N–C units of the classical cryptate [2,2,2] and the O–Cu_e–O linkage for the $[OCH_2CH_2O]$ units, because of their similar O–O distance (2.79 and 2.73 Å,[14] respectively), hexanuclear copper(II) compounds with amino acids can be seen as a new type of spherical macrotricyclic metallacryptate [2,2,2,2]. The four equatorial Cu^{II} ions are a way of bringing the eight oxygen atoms into the

 © 2005 Wiley-VCH Verlag GmbH & Co. KGaA, Weinheim

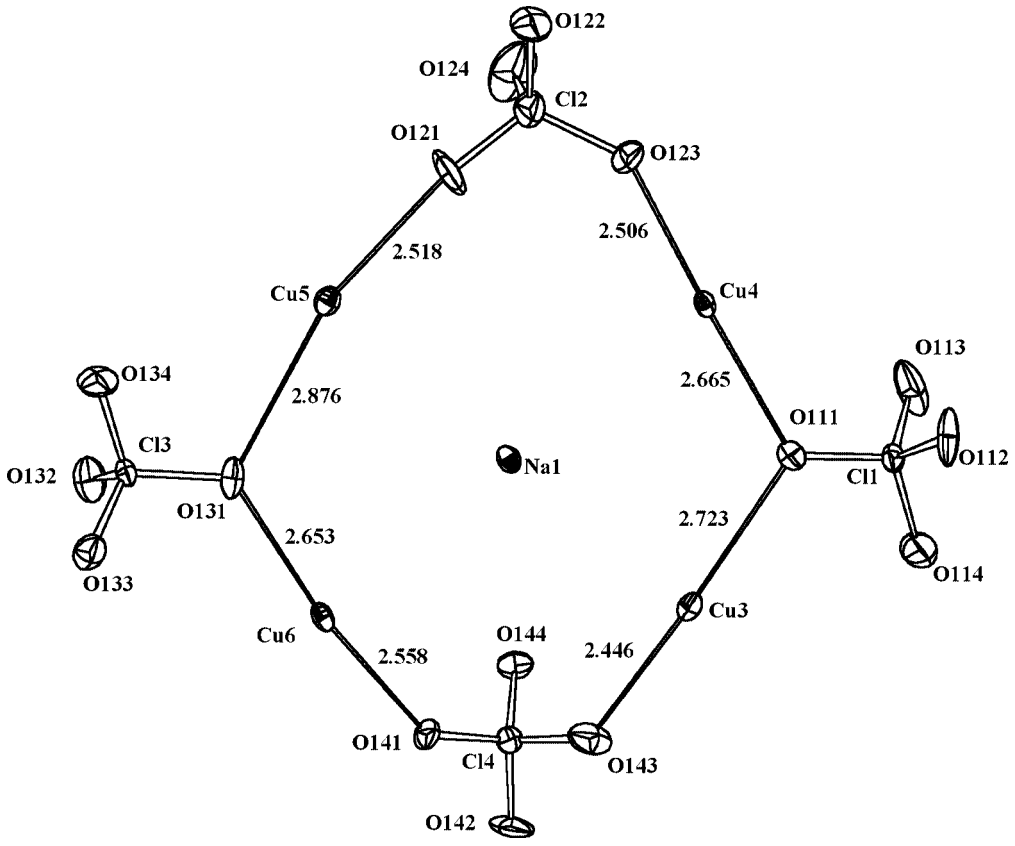

Figure 2. Coordination modes of the four perchlorate ions and the distances [Å] between equatorial Cu^{II} atoms and coordination oxygen atoms of perchlorate ions with vibration ellipsoids at the 30% probability level.

right positions to function as a non-metal cryptate that binds the center sodium cation, while the two axial metal ions use the directionality of the d orbitals to bring the ligands into a definite geometry as the bridging N atoms in the cryptate. The employment of d orbitals results in the enhancement of the connection number of the bridging atoms from three to four. Subtracting the shortest diagonal O–O distance of the cage (O41–O61, 5.098 Å) with the double bonding radii of the oxygen atoms (2 × 1.16 Å),[15] we can estimate that the cavity radius of compound **1** is 1.39 Å, similar to the ionic radius (1.32 Å[16]) of the Na^+ cation with a coordination number (CN) of eight. Winpenny et al.[10] has considered that this kind of cage can selectively bind the Na^+ cation even in the presence of excess Li^+, K^+, Ca^{2+}, La^{3+} or Lu^{3+}, whose ionic radii with a CN of eight are 1.06, 1.65, 1.26, 1.30 and 1.12 Å, respectively.[16] We have still obtained the title compound even in the presence of excess Y^{3+} (1.16 Å)[16] or trivalent rare earth ions. The cryptate [2,2,2], with a cavity size of 1.4 Å, can bind many kinds of metal ions besides alkali or alkaline earth metals to form complexes.[17] The replacement of the bridging N atoms with metal atoms increases the connection number of bridging atoms and thus alters the topological structure of the cryptate, which can further improve the selectivity of the cavity to sodium.

Magnetochemistry

Temperature-dependent magnetic susceptibilities of **1** are measured from ground crystalline samples in the temperature ranges of 4–300 K under a constant magnetic field of 10000 G and are shown in Figure 4 in the forms of χ_m vs. T and $\chi_m T$ vs. T per Cu_6 unit. At room temperature (300 K), the $\chi_m T$ value is 1.7 emu mol^{-1} K for **1**, compared with the expected values 2.25 emu mol^{-1} K for six spin-only Cu^{II} ions (S = 1/2, g = 2). The difference may result from the diamagnetic contribution of the compound. Upon cooling, **1** shows a continuous slight increase in $\chi_m T$, and a subsequent much sharper increase below ca. 25 K, suggesting that overall **1** is ferromagnetic, as confirmed by the positive Weiss constant (10.8 K). In order to investigate the exchange interaction of **1**, a model Heisenberg Spin-Hamiltonian is employed [Equation (1)].

$$H = -2J'(S_1 + S_2)(S_3 + S_4 + S_5 + S_6) \quad (1)$$

J' is the exchange coupling constant between the equatorial Cu atoms and the axial Cu ones, and S_i is the spin operator of each Cu center whose suffix is identical to that shown in Figure 1. From the model and the Van Vleck equation,[18] the molar susceptibilities of **1** can be deduced

 © 2005 Wiley-VCH Verlag GmbH & Co. KGaA, Weinheim

Table 2. Coupling constants and some structural parameters for hexanuclear Cu^{II} complexes with different amino acids (the unit for bond lengths is Å).

Amino Acids	Gly (ref.[9])	Pro (ref.[9])	Pro (ref.[10])	Hpro (ref.[10])	Thr (this work)
Molecular formula	$Na[NaCu_6(Gly)_8(H_2O)_2]$-$(ClO_4)_6\cdot 2H_2O$	$[NaCu_6(Pro)_8(OH)]$-$(ClO_4)_4\cdot H_2O$	$[Na\subset Cu_2\{Cu(Pro)_2\}_4$-$(ClO_4)_5CH_3OH]\cdot H_2O$	*catena*-$[Na\subset Cu_2\{Cu(hpro)_2\}_4$-$(ClO_4)_5]\cdot 4H_2O$	$[Na\subset\{Cu_6(Thr)_8(H_2O)_2\}]$-$(ClO_4)_5\cdot 5H_2O$
Space group	$P\bar{1}$	$I4$	$I4$	$P2_1$	$P2_1$
Symmetry	Pseudocubic O_h	D_{4h}	D_{4h}	Idealized D_{4h}	D_{2h}
Bond lengths					
Cu_e–O	1.952	1.952	1.933	1.942	1.949
Cu_e–N	1.995	1.995	1.994	2.006	1.972
Na–O	2.604	2.552	2.546	2.563	2.576
Cu_a–Cu_a	7.115	7.021	7.011	6.998	7.133
Cu_e–Cu_e	5.052	5.000	4.991	5.041	5.162, 4.789
Cu_a–Cu_e	5.041	4.983	4.974	4.996	5.012
Axial ligand and its mean coordination bond lengths	H_2O (2.353)	OH^- (2.314) H_2O (3.612)	Perchlorate ion (2.390) CH_3OH (2.220)	Hydroxyl groups from hpro (2.312)	H_2O (2.268)
Coordination modes of perchlorate ions	In its cell, there are two different $\{Cu_6Na\}$ units with three kinds of perchlorate ions. Two oxygen atoms from six ions are coordinated to two Cu centers, whereas two ions of the second kind only bind to one Cu center through a single O-donor. The other four ions just bind to the peripheral Na^+ cation.	Four ions are symmetrically equivalent. Two oxygen atoms from each ion are coordinated to two Cu centers, respectively.	Four ions are symmetrically equivalent. Two oxygen atoms from each ion are coordinated to two Cu centers, respectively. The fifth ion is coordinated to an axial Cu atom.	Two oxygen atoms from three ions are coordinated to two Cu centers, whereas the fourth ion binds to one Cu through two of its oxygen atoms, and to another with one O-donor.	Two oxygen atoms from two ions are coordinated to two Cu centers, whereas the others bind to two Cu centers with only single O-donors.
The coupling constant J' [cm^{-1}]			+0.56	+1.39	+0.43

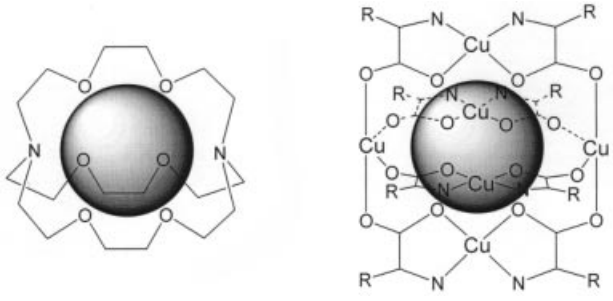

Figure 3. The classic cryptate [2,2,2] (left) and spherically metallacryptate [2,2,2,2] (right). The latter has macrotricycles made up of four blades and the equatorial cycle of perchlorate ions as shown in Figure 2 as an example. The central sphere represents a sodium cation. R is the substitution group of the amino acids or H atom for glycine.

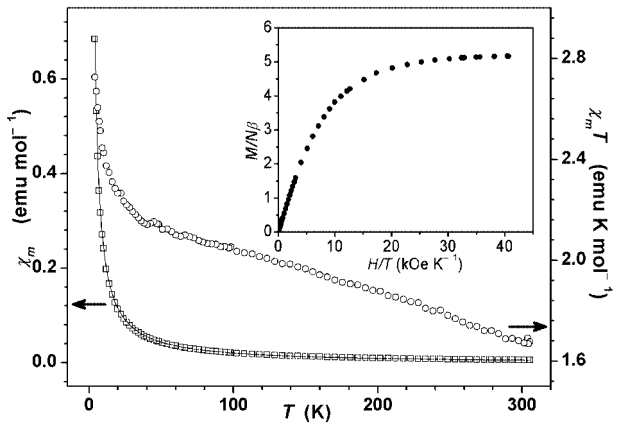

Figure 4. Plot of experimental χ_m vs. T (left) and $\chi_m T$ vs. T (right) for compound **1**. The solid line represents the fitted results. In the inset is a plot of $M/N\beta$ vs. H/T for **1** indicating the spin ground state, $S_T = 3$.

as in Equation (2) with the addition of the sample's diamagnetic contribution χ_{dia} by use of the Kambe vector coupling method,[19] which originates from a total of 20 spin states ranging in spin values from 0 to 3.

$J = J'/k$, and k is the Boltzmann constant, g the Landé factor. After the best least-squares fit to the experimental data, the parameters are given as: $g = 2.01$, $J' = 0.43\ cm^{-1}$ and $\chi_{dia} = -2.60$ (10^{-3} emu mol^{-1}) with a final agreement factor $R = 2.32\times10^{-6}$ [$R = \Sigma(\chi_m^{obsd.} - \chi_m^{calcd.})^2/\Sigma(\chi_m^{obsd.})^2$].

Attempts to fit the data by employing the method proposed by Belorizky[20] for octahedron clusters, which includes the coupling between the equatorial metal ions as

$$\chi_m = \frac{3}{8}\times\frac{g^2[28\exp(4J/T) + 30\exp(2J/T) + 16\exp(-2J/T) + 2\exp(-6J/T) + 20]}{T[7\exp(4J/T) + 15\exp(2J/T) + 14\exp(-2J/T) + 3\exp(-4J/T) + 3\exp(-6J/T) + 22]} + \chi_{dia} \quad (2)$$

 © 2005 Wiley-VCH Verlag GmbH & Co. KGaA, Weinheim

well as the next nearest interactions, gives the same values for g, J' and χ_{dia} as above. But the next nearest interactions and the coupling through the perchlorate ions are so small that they can be regarded as negligible. The coupling constant of **1** agrees with that of the prolinato compound,[10] 0.56 cm^{-1}. The positive J' value indicates that **1** has a ground state with spin $S = 3$, which is also proven by the $M/N\beta$ vs. H/T plot in the inset of Figure 4 with a saturation value for $M_S/N\beta$ of about 5.2.

DFT Studies

The computational strategy adopted in previous theoretical studies[21] for exchange coupling binuclear complexes is adapted to the hexanuclear complexes by using an approach that Ruiz[22] proposed. The approach consists of evaluating the exchange coupling constant J_{ij} between two paramagnetic metal centers i and j in the hexanuclear molecule by calculating the energy difference between the triplet and broken-symmetry states of a model molecule in which metal atoms are substituted by diamagnetic Zn^{2+} cations in all positions but i and j. Then the coupling constant is given below by employing a phenomenological Heisenberg Hamiltonian $H_{ij} = -2J_{ij}\cdot S_i\cdot S_j$;

$$J_{ij} = \frac{E_{BS} - E_{TS}}{S(S+1)} = \frac{E_{BS} - E_{TS}}{2} \quad (3)$$

where the total spin $S = S_1 + S_2 = 1$ for the triplet state, and the energy of the broken-symmetry solution is taken as an approximation to that of the singlet state. The procedure keeps with the proposal of Perdew and co-workers,[23] who suggest that the broken-symmetry single determinant is the correct solution of the Kohn–Sham equations for the singlet state. The triplet energy of the model compounds is gained from the single point energy calculation with the convergence parameter 10^{-8}. The energy of the broken-symmetry states is obtained by investigating the stability of the singlet solution with respect to a symmetry-broken solution, which is carried out by means of the formalism developed by Bauernschmitt and Ahlrichs,[24] as implemented in *Gaussian* 03[25] by the keyword STABLE with the option OPT. If the singlet B3LYP solution is unstable, the program finds the symmetry-broken B3LYP solution, which yields the energy of broken-symmetry states.

In order to simplify the computing work and make the theoretical result representative, the $\{Cu_6(Gly)_8\}^{4+}$ is employed as a model to investigate the magnetic properties of hexanuclear Cu^{II} compounds with amino acids. Its structural data are obtained from CCDC-165331. Because of the symmetry, the coupling constants J_{ij} are only calculated for $i = 1$. After metal atoms are replaced with diamagnetic Zn^{2+} cations in all positions but i and j, the four values of J_{ij} are obtained from equation (c) as shown in Table 3. All of them are positive, indicating that the interaction between the axial copper atoms and the equatorial ones is ferromagnetic. The average value, +4.4 cm^{-1}, is near to three known sets of experimental data, 1.39, 0.56 or 0.43 cm^{-1} for complexes with hpro, Pro or Thr as ligands, respectively.

Table 3. Exchange coupling constants J_{ij} (cm^{-1}) and energies (a.u.) of the triplet (E_{TS}) and broken-symmetry states (E_{BS}) for the $\{Cu_2Zn_4(Gly)_8\}^{4+}$ model compounds. 1 and 2 represent the two axial metal atoms and 3 to 6 the four equatorial ones, respectively.

i,j	E_{BS}	E_{TS}	J_{ij}
1,3	–12665.6168369	–12665.6167647	7.9
1,4	–12665.6186476	–12665.6185943	5.8
1,5	–12665.6181018	–12665.6180721	3.2
1,6	–12665.6168756	–12665.6168696	0.6

Exchange coupling in carboxylate-bridge complexes is largely determined by the conformation of the bridge and the interaction between the d orbitals of the metal and the bridge.[26] As has been shown in the few well-characterized Cu^{II} complexes bridged by *syn-anti* carboxylate groups, a *syn-anti* conformation of the (Cu–O–C–O′–Cu′) bridge is unfavorably oriented to give a strong overlap between the magnetic orbitals of the copper atoms.[27] For dinuclear copper carboxylates, the magnetic orbitals belong to the Cu $d_{x^2-y^2}$ orbital.[28] But for the hexanuclear Cu^{II} complexes with amino acids, the coordination geometry around each equatorial Cu^{II} ion is an elongated octahedron, the Cu^{II} unpaired electron can be mainly described by the d_{xz} or d_{yz} metallic orbital defined by the short bonds of the Cu–amino acid units; the x and z direction is shown in part (a) of Figure 1. Whereas the coordination geometry around each axial copper(II) ion is a square pyramid with their magnetic orbitals primarily being ascribed to the $d_{x^2-y^2}$ metallic orbital. The planes of the magnetic orbitals d_{xz} or d_{yz} of the equatorial Cu^{II} ions are nearly perpendicular to those of the $d_{x^2-y^2}$ planes of the two axial Cu^{II} ions, which provides a favorable orientation for the orthogonality of the magnetic orbitals, thus causing a dominant ferromagnetic interaction. The values of the magnetic coupling for these amino acid compounds are within those observed in the copper complexes[26,29,30] with bridging *syn-anti* carboxylate groups (0.37–14 cm^{-1}).

Experimental Section

General: All starting materials are of reagent grade and used without further purification. Elemental analyses were carried out by the Elemental Analysis Lab of our Institute. Magnetic measurements were carried out with a Quantum Design PPMS model 6000 magnetometer.

Synthesis of 1: $Cu(ClO_4)_2\cdot 5H_2O$ (0.353 g, 1 mmol) was dissolved in 10 mL of H_2O, followed by the addition of threonine (0.119 g, 1 mmol). The pH value of the above solution was then carefully adjusted by slow addition of 0.1 M aqueous NaOH until the precipitate that had formed remained (pH ≈ 5.5). The mixture was then filtered and the filtrate was placed in a desiccator with phosphorus pentoxide. Blue prismatic crystals were obtained several weeks later and isolated by filtration, washed with cold water, and dried in the air. Yield 0.11 g (44.6% based on threonine). $C_{32}H_{78}Cl_5Cu_6N_8NaO_{51}$ (1972.50): calcd. C 19.49, H 3.99, N 5.68; found C 19.26, H 3.83, N 6.09.

Structure Determination and Refinement: A blue prismatic single crystal with approximate dimensions of 0.20 mm × 0.15 mm

 © 2005 Wiley-VCH Verlag GmbH & Co. KGaA, Weinheim

× 0.10 mm was mounted on a glass fiber. X-ray diffraction intensity data were collected on a Rigaku Mercury CCD diffractometer equipped with graphite-monochromated Mo-K_α radiation (λ = 0.71073 Å) by using an ω scan mode at 130.15 K. A total of 22772 reflections were collected within $3.01 \leq \theta \leq 25.03°$, yielding 9896 unique reflections (R_{int} = 0.0621), of which 8718 were considered as observed ($I > 2\sigma(I)$). The crystal structure was solved by direct methods with the Siemens *SHELXTL*^{TM} version 5 package of crystallographic software[15] and refined by full-matrix least-squares refinement on F^2. All non-hydrogen atoms were refined anisotropically. The hydrogen atoms on all carbon and nitrogen atoms were generated symmetrically, allowed to ride on their respective parent atoms and included in the structure factor calculations with assigned isotropic thermal parameters but not refined. The final $R = \Sigma||F_o| - |F_c|| / \Sigma|F_o|$, and $Rw = \{\Sigma[w(F_o^2 - F_c^2)^2] / \Sigma w(F_o^2)^2\}^{1/2}$ ($w = 1/[\sigma^2(F_o^2) + (aP)^2 + bP]$, where $P = (F_o^2 + 2F_c^2)/3$). The crystallographic data are summarized in Table 4.

CCDC-252441 contains the supplementary crystallographic data for this paper. These data can be obtained free of charge from The Cambridge Crystallographic Data Centre via www.ccdc.cam.ac.uk/data_request/cif.

Computational Details: All calculations have been performed by means of the *Gaussian* 03 suite of ab initio programs[25] using the B3LYP DFT method in which Becke's hybrid exchange functional[31] and the correlation functional[32] of Lee, Yang, and Parr are combined. A basis set of triple-ζ quality[33] is used for the Cu and Zn atoms and of double-ζ quality[34] for other atoms in all calculations.

Table 4. Crystal data collection and structural refinement parameters for **1**.

Empirical formula	$C_{32}H_{78}Cl_5Cu_6N_8NaO_{51}$
Formula mass	1972.50
Crystal appearance	blue prism
Crystal size [mm]	0.20 × 0.15 × 0.10
Crystal system	monoclinic
Space group	*P*2(1)
Unit cell dimensions	
a [Å]	11.6818(10)
b [Å]	23.2158(19)
c [Å]	13.0804(12)
β [°]	94.781(5)
V [Å^3]	3535.1(5)
Z	2
μ [mm^{-1}]	2.083
θ range for data collection [°]	3.01 to 25.03
h, *k*, *l* range	–13 to 13, –22 to 27, –15 to 15
Max./min. transmission	0.9183 to 1.0000
D_c [g cm^{-3}]	1.853
F(000)	2008
Measured reflections	22772
Independent reflections	9896
Observed reflections ($I > 2\sigma(I)$)	8718
R_{int}	0.0621
Parameters refined	928
Goodness of fit on F^2	1.073
R[a]	0.0779
Rw[b]	0.1936
Max./mean shift in the final cycle	0.001/0.000
Max./min. $\Delta\rho$ [e Å^3]	2.437/–1.490

[a] $R = \Sigma(||F_o| - |F_c||)/\Sigma|F_o|$, [b] $Rw = \{\Sigma w[(F_o^2 - F_c^2)^2]/\Sigma w[(F_o^2)^2]\}^{1/2}$, $w = 1/[\sigma^2(F_o^2) + (aP)^2 + bP]$, $P = (F_o^2 + 2F_c^2)/3$], a = 0.1110, b = 14.4871.

Acknowledgments

This work is supported by grants from the State Key Laboratory of Structure Chemistry, Fujian Institute of Research on the Structure of Matter, the National Ministry of Science and Technology of China (001CB1089), Chinese Academy of Sciences, the National Science Foundation of China (20273073, 20333070 and 90206040), and Fujian Province (2003J042, 2004HZ01-1). Xiang gratefully acknowledges the support of K. C. Wong Education Foundation, Hong Kong.

[1] a) C. J. Pederson, *J. Am. Chem. Soc.* **1967**, *89*, 7017–7036; b) C. J. Pedersen, *J. Am. Chem. Soc.* **1967**, *89*, 2495–2496; c) C. J. Pedersen, *J. Am. Chem. Soc.* **1970**, *92*, 386–391; d) C. J. Pedersen, *J. Am. Chem. Soc.* **1970**, *92*, 391–394; e) C. J. Pedersen, H. K. Frensdorf, *Angew. Chem. Int. Ed. Engl.* **1972**, *11*, 1–6; f) C. J. Pedersen, *Angew. Chem. Int. Ed. Engl.* **1988**, *27*, 1021–1027.

[2] a) D. J. Cram, J. M. Cram, *Acc. Chem. Res.* **1978**, *11*, 8–14; b) D. J. Cram, G. M. Lein, *J. Am. Chem. Soc.* **1985**, *107*, 3657–3668; c) D. J. Cram, *Angew. Chem. Int. Ed. Engl.* **1988**, *27*, 1009–1020.

[3] a) J.-M. Lehn, J. P. Sauvage, *J. Am. Chem. Soc.* **1975**, *97*, 6700–6707; b) J.-M. Lehn, *Acc. Chem. Res.* **1978**, *11*, 49; c) J.-M. Lehn, *Angew. Chem. Int. Ed. Engl.* **1988**, *27*, 89–112.

[4] A. D. Cutland, J. A. Halfen, J. W. Kampf, V. L. Pecoraro, *J. Am. Chem. Soc.* **2001**, *123*, 6211–6212, and references therein.

[5] M. S. Lah, B. R. Gibney, D. L. Tierney, J. E. Penner-Hahn, V. L. Pecoraro, *J. Am. Chem. Soc.* **1993**, *115*, 5857–5858.

[6] a) J. Fischer, L. Ricard, R. Weiss, *J. Am. Chem. Soc.* **1976**, *98*, 3050–3052; b) I. Creaser, M. C. Heckel, R. J. Neitz, M. T. Pope, *Inorg. Chem.* **1993**, *32*, 1573–1578.

[7] S.-M. Hu, J.-C. Dai, X.-T. Wu, L.-M. Wu, C.-P. Cui, Z.-Y. Fu, M.-C. Hong, Y.-C. Liang, *J. Cluster Sci.* **2002**, *13*, 33–41.

[8] a) J.-J. Zhang, S.-M. Hu, L.-M. Zheng, X.-T. Wu, Z.-Y. Fu, J.-C. Dai, W.-X. Du, H.-H. Zhang, R.-Q. Sun, *Chem. Eur. J.* **2002**, *8*, 5742–5749; b) J.-J. Zhang, S.-Q. Xia, T.-L. Sheng, S.-M. Hu, L. Guido, M. Franc, X.-T. Wu, S.-C. Xiang, R.-B Fu, *Chem. Commun.* **2004**, 1186–1187.

[9] S.-M. Hu, W.-X. Du, J.-C. Dai, L.-M. Wu, C.-P. Cui, Z.-Y. Fu, X.-T. Wu, *J. Chem. Soc. Dalton Trans.* **2001**, 2963–2964.

[10] L. Wang, I. Satoshi, Y. Yasuhiko, H. Yoshimasa, R. Olivier, A. Guillem, R. E. P. Winpenny, *Dalton Trans.* **2003**, 2318–2324.

[11] M. Du, X.-H. Bu, Y.-M. Guo, R. Joan, *Chem. Eur. J.* **2004**, *10*, 1345–1354.

[12] a) E. Ruiz, P. Alemany, S. Alvarez, J. Cano, *J. Am. Chem. Soc.* **1997**, *119*, 1297–1303; b) E. Ruiz, P. Alemany, S. Alvarez, J. Cano, *Inorg. Chem.* **1997**, *36*, 3683–3688; c) L. Noodleman, *J. Chem. Phys.* **1981**, *74*, 5737–5743.

[13] R. A. Coxall, S. G. Harris, D. K. Henderson, S. Parsons, P. A. Tasker, R. E. P. Winpenny, *J. Chem. Soc. Dalton Trans.* **2000**, 2349–2356.

[14] M. Doux, N. Mezailles, L. Ricard, P. Le Floch, *Eur. J. Inorg. Chem.* **2003**, 3878–3894.

[15] G. M. Sheldrick, *SHELXTL*^{TM} *Version 5 Reference Manual*, Siemens Energy & Automation Inc., Madison, WI, **1994**.

[16] a) J. E. Huheey, E. A. Keoter, R. L. Keiter, *Inorganic Chemistry, Principles of Structure and Reactivity, Fourth Edition*, Harper Collins College Publishers, New York, **1993**, pp. 114–117; b) R. D. Shannon, *Acta Crystallogr. Sect. A* **1976**, *32*, 751–767.

[17] J. M. Lehn, J. P. Sauvage, *J. Chem. Soc. D* **1971**, 440–441.

[18] J. H. Van Vleck, *The Theory of Electric and Magnetic Susceptibilities*, Oxford University Press, London, **1932**.

[19] K. Kambe, *J. Phys. Soc. Jpn.* **1950**, *5*, 48–51.

[20] E. Belorizky, P. Fries, *J. Chem. Phys.* **1993**, *90*, 1077–1100.

[21] S.-C. Xiang, J.-Q. Li, Y.-F. Zhang, *Chem. Phys. Lett.* **2003**, *370*, 170–179.

 © 2005 Wiley-VCH Verlag GmbH & Co. KGaA, Weinheim

[22] E. Ruiz, J. Cano, S. Alvarez, A. Caneschi, D. Gatteschi, *J. Am. Chem. Soc.* **2003**, *125*, 6791–6794.
[23] a) J. P. Perdew, A. Savin, K. Burke, *Phys. Rev. A* **1995**, *51*, 4531–4541; b) J. P. Perdew, M. Ernzerhof, K. Burke, A. Savin, *Int. J. Quantum Chem.* **1997**, *61*, 197–205.
[24] R. Bauernschmitt, R. Ahlrichs, *J. Chem. Phys.* **1996**, *104*, 9047–9718.
[25] M. J. Frisch, G. W. Trucks, H. B. Schlegel, G. E. Scuseria, M. A. Robb, J. R. Cheeseman, J. A. Montgomery, Jr., T. Vreven, K. N. Kudin, J. C. Burant, J. M. Millam, S. S. Iyengar, J. Tomasi, V. Barone, B. Mennucci, M. Cossi, G. Scalmani, N. Rega, G. A. Petersson, H. Nakatsuji, M. Hada, M. Ehara, K. Toyota, R. Fukuda, J. Hasegawa, M. Ishida, T. Nakajima, Y. Honda, O. Kitao, H. Nakai, M. Klene, X. Li, J. E. Knox, H. P. Hratchian, J. B. Cross, C. Adamo, J. Jaramillo, R. Gomperts, R. E. Stratmann, O. Yazyev, A. J. Austin, R. Cammi, C. Pomelli, J. W. Ochterski, P. Y. Ayala, K. Morokuma, G. A. Voth, P. Salvador, J. J. Dannenberg, V. G. Zakrzewski, S. Dapprich, A. D. Daniels, M. C. Strain, O. Farkas, D. K. Malick, A. D. Rabuck, K. Raghavachari, J. B. Foresman, J. V. Ortiz, Q. Cui, A. G. Baboul, S. Clifford, J. Cioslowski, B. B. Stefanov, G. Liu, A. Liashenko, P. Piskorz, I. Komaromi, R. L. Martin, D. J. Fox, T. Keith, M. A. Al-Laham, C. Y. Peng, A. Nanayakkara, M. Challacombe, P. M. W. Gill, B. Johnson, W. Chen, M. W. Wong, C. Gonzalez, J. A. Pople, *Gaussian 03*, Gaussian, Inc., Pittsburgh PA, **2003**.
[26] B. Żurowska, J. Mroziński, *Inorg. Chim. Acta* **2003**, *342*, 23–28, and references therein.
[27] C. Ruiz-Perez, J. Sanchiz, M. H. Molina, F. Lloret, M. Julve, *Inorg. Chem.* **2000**, *39*, 1363–1370.
[28] A. Rodríguez-Fortea, P. Alemany, S. Alvarez, E. Ruiz, *Chem. Eur. J.* **2001**, *7*, 627–637.
[29] M. Murugesu, R. Clérac, B. Pilawa, A. Mandel, C. E. Anson, A. Powell, *Inorg. Chim. Acta* **2002**, *337*, 328–336.
[30] M. Inoue, M. Kubo, *Inorg. Chem.* **1970**, *9*, 2310–2314.
[31] A. D. Becke, *J. Chem. Phys.* **1993**, *98*, 5648–5652.
[32] C. Lee, W. Yang, R. G. Parr, *Phys. Rev. B* **1988**, *37*, 785–789.
[33] A. Schaefer, C. Huber, R. Ahlrichs, *J. Chem. Phys.* **1994**, *100*, 5829–5835.
[34] A. Schaefer, H. Horn, R. Ahlrichs, *J. Chem. Phys.* **1992**, *97*, 2571–2577.

Received: October 14, 2004
Published Online: June 1, 2005

 © 2005 Wiley-VCH Verlag GmbH & Co. KGaA, Weinheim

A Study Using X-ray Absorption and Emission Spectroscopy of Dioxygen-Binding Xerogels Incorporating Cyclam Units Complexed with Copper Salts

José Goulon,*[a] Chantal Goulon-Ginet,[a,b] Andrei Rogalev,[a] Fabrice Wilhelm,[a] Nicolas Jaouen,[a] Delphine Cabaret,[c] Yves Joly,[d] Géraud Dubois,[e,f] Robert J. P. Corriu,[g] Gabriel David,[e] Stéphane Brandès,[e] and Roger Guilard*[e]

Keywords: X-ray absorption spectroscopy / Tetraazamacrocyclic ligand / Dioxygen binding / Peroxo ligand / Copper

X-ray absorption spectroscopy was used to elucidate how hybrid xerogels complexed with $CuCl_2$ could reversibly bind molecular dioxygen. Difference EXAFS analyses at the Cu K-edge suggest that dioxygen could bridge two Cu atoms in a μ-η^1:η^1 peroxo-like conformation with unequal Cu···O distances. Only the short distance (R_{Cu-O1} = 1.86 ± 0.01 Å) was unambiguously determined and looks typical of a Cu^{II} site. The Cu···Cu internuclear distances would be rather long: $R_{Cu-Cu} \approx 4.0$ Å (3.9 Å) for the oxygenated (oxygen-free) xerogels. Cl K-edge EXAFS spectra revealed the pre-existence in the oxygen-free xerogels of Cu^{I} sites with short Cl–Cu bonds (2.11 ± 0.03 Å). Pentacoordinate Cu^{II} sites with a longer Cl–Cu bond (2.45 ± 0.03 Å) were also identified. Another signal at a further distance (2.73 ± 0.03 Å) suggests that the Cl ions could bridge mixed-valence $\{Cu^{I},Cu^{II}\}$ sites. In oxygenated xerogels complexed with $CuCl_2$, ca. 75% of the Cu atoms would be singly bound to dioxygen while the signature of the pentacoordinate Cu^{II} sites would totally vanish. Substituting $CuBr_2$ for $CuCl_2$ yields xerogels with a poor capability to bind dioxygen. This is remarkably correlated with a decrease of the signatures at R_{Cu-O1} = 1.86 Å and R_{Cu-Cu} = 4.0 Å. EXAFS spectra of the oxygen-free xerogel complexed with $CuBr_2$ again exhibit signatures assigned to short (2.30 Å)/long (2.49 Å) Cu–Br bonds as expected for mixed-valence $\{Cu^{I},Cu^{II}\}$ systems. Inactive xerogels prepared with metallated cyclams seem to undergo a structural change during hydrolysis and polycondensation. Deconvoluted XANES spectra of the active xerogels exhibit a strong pre-edge resonance which is characteristic of mixed-valence Cu^{I} sites. This interpretation was supported by ab initio XANES simulations carried out beyond the muffin-tin approximation.

(© Wiley-VCH Verlag GmbH & Co. KGaA, 69451 Weinheim, Germany, 2005)

Introduction

In the past decade, nanostructured organic-inorganic hybrid polymers have attracted much attention because these novel materials offer unique combinations of optical, physical[1,2] or chemical[3–5] properties. It was a stimulating challenge for chemists to prepare hybrid polymers chelating metal cations in such a way that the metal would still be accessible for catalytic activity. Starting from the consideration that saturated polyazamacrocycles, especially the 1,4,8,11-tetraazacyclotetradecane (cyclam), had a strong capability to bind transition metal cations,[6–10] two partner groups (located in Dijon and Montpellier) settled upon incorporating cyclam units within silica matrices prepared by a sol-gel process.[11–13] Two strategies illustrated in Scheme 1 were explored:[13]

(A) The hydrolysis and polycondensation of $[Cu(cyclam)]^{2+}$ or $[Co(cyclam)]^{2+}$ alkoxysilylated complexes quantitatively produced hybrid polymers incorporating the metallated cyclam units.

(B) The hydrolysis and polycondensation of the alkoxysilylated (uncomplexed) cyclam precursors was performed first and the metal salt (e.g. $CuCl_2$) was then incorporated into the hybrid xerogel (Scheme 1).

Interestingly, it was found that, in the case of $CuCl_2$, the materials prepared by routes (A) and (B) had different spectrochemical properties reflecting different structures. Typically, xerogels of type (A) had a strong X-band EPR signal at 3200 G with a broad linewidth ($g \approx 2.15$) at room tem-

[a] European Synchrotron Radiation Facility,
B. P. 220, 38043 Grenoble Cedex, France
E-mail: goulon@esrf.fr
[b] Université J. Fourier, Faculté de Pharmacie,
38706 La Tronche, France
[c] Universités Paris VI et VII, Laboratoire de Minéralogie-Cristallographie associé au CNRS,
4 place Jussieu, 75252 Paris Cedex 05, France
[d] Laboratoire de Cristallographie du CNRS, associé à l'Université J. Fourier,
B. P. 166, 38042 Grenoble Cedex 9, France
[e] Laboratoire d'Ingénierie Moléculaire pour la Séparation et les Applications des Gaz, UMR 5633, CNRS, Université de Bourgogne, Faculté des Sciences Gabriel,
Boulevard Gabriel, 21100 Dijon, France
[f] Present address: IBM Almaden Research Center,
650 Harry Road, San Jose, CA 95120, USA
[g] Université de Montpellier II, Laboratoire de Chimie Moléculaire et Organisation du Solide, UMR 5637, CNRS,
Place E. Bataillon, 34095 France
Supporting information for this article is available on the WWW under http://www.eurjic.org or from the author.

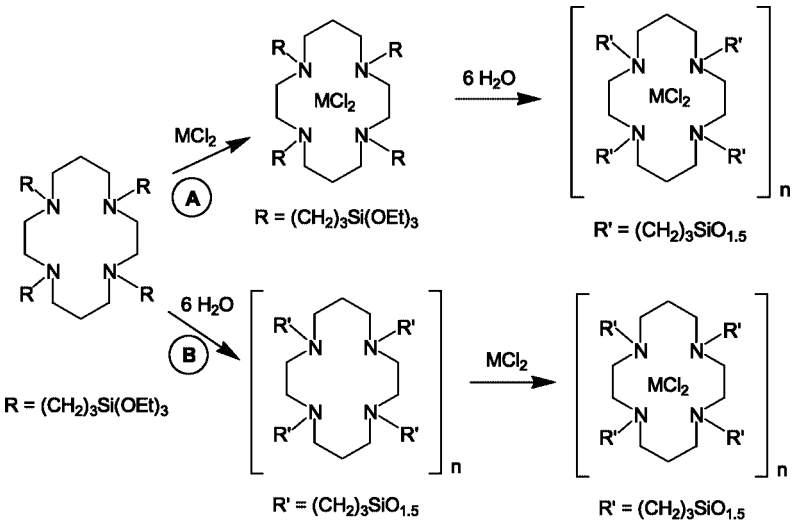

Scheme 1. Alternative routes to yield metallated hybrid xerogels following Route (A) and Route (B).

perature and at 100 K. This signal was assigned to Cu^{II} centers, but this broad signal vanished for xerogels of type (B). In contrast, xerogels of type (B) exhibited a much weaker signal at 1550 G ($g \approx 4.40$), which often characterizes dicopper interactions associated with a dinuclear structure. What made this structural problem even more interesting was the discovery that xerogels prepared by route (B) could bind (and possibly activate) molecular dioxygen whereas xerogels prepared by route (A) were essentially inactive. Recent tests have confirmed that the ability of xerogels of type (B) to bind dioxygen would be as high as for hemocyanin (Hc).

We tried to elucidate the puzzling structure of xerogels of type (B) using X-ray absorption and the XANES spectra were compared with ab initio simulations performed with an advanced code (FDMNES) that offered a double benefit. First, we could control the charge transfer from the ligand toward the metal, this option being useful here to describe the contribution of the neutral cyclam ligands. Second, we were not constrained to using spherically averaged muffin-tin potentials as with standard codes. The latter advantage is particularly sensible for covalent bonding.

Results and Discussion

Coordination Geometry: EXAFS Studies

The structural information contained in EXAFS spectra is often difficult to decipher. Analyses become most delicate when destructive interferences cause major spectral distortions and a loss of information.[14,15] Global fits can be either misleading or simply unreliable due to large correlations. Even with such complicated problems, the strength of EXAFS stems from its very high sensitivity to small structural changes and this is precisely what we tried to exploit with difference analyses. It is indeed recommended that the consistency of the analyses be checked by combining EXAFS spectra collected adifferent absorption edges.

EXAFS analyses of model compounds **1** = Cu(TPP), **3** = $[Cu(tmc)](BF_4)_2$ and **6** = [Cu(tpc)Cl]Cl are detailed only in the supporting information section. This preliminary study was very helpful because it made the limits of a direct data reduction fully transparent even though high quality data were collected over a wide spectral range. Given the highly symmetrical (D_{4h}) geometry of the copper porphyrin, the FT spectra of **1** offer a rich pattern of signatures which justified refined analyses, taking the multiple scattering paths into account. In contrast, the poor rigidity of the 14-membered saturated macrocyclic ligand restricted the information that could be extracted from the EXAFS spectra of complexes **3** and **6**. In the hexacoordinate species **3**, dynamic distortions of the axial and equatorial bonds can be predicted from the Jahn–Teller theorem[16] and were found to cause significant spectral distortions. Compound **6** was initially expected to be pentacoordinate, the copper ion being shifted away from the average plane of the four nitrogens with some trigonal distortion also arising from the ligand field. Published crystal structures of related pentacoordinate Cu complexes[17–19] raised a troublesome question regarding the true chemical formulation of compound **6**. Such pentacoordinate complexes were systematically found to be mixed-valence complexes due to the presence of linear anions $[Cl{-}{-}{-}Cu^{I}{-}{-}{-}Cl]^{-}$. The problem is that EXAFS is critically sensitive to the presence of such anions in which the short Cu^{I}–Cl bond (2.116 Å) is comparable to the Cu^{II}–N bond (2.13 Å). Destructive interferences between these two EXAFS signals are expected, the practical result being a loss of intensity of the Cu---N signature. This is a typical circumstance where, in our experience, analyses based only on fits would dangerously fail because the mathematical problem is poorly defined.[14,15] In combining the EXAFS spectra of species **6** recorded at both the Cu and Cl K-

 © 2005 Wiley-VCH Verlag GmbH & Co. KGaA, Weinheim

edges, we could produce strong evidence of the contributions of the linear anion $[Cl{-}{-}{-}Cu^{I}{-}{-}{-}Cl]^{-}$. This was received as a strong warning that standard fitting procedures may not be suitable to analyze the EXAFS spectra of our xerogels.

Active Xerogels Complexed with $CuCl_2$

In this paper, reactive materials towards dioxygen binding will be considered as "active" systems while unreactive solids in an ambient atmosphere will be called "inactive". Our strategy was first to compare the Cu K-edge FT EXAFS spectra of the oxygenated xerogel **XB2** with the oxygen-free xerogel **XB1**, both xerogels being complexed with $CuCl_2$. The relevant FT spectra $Im\tilde{\chi}_N(R)$ are displayed in Figure 1A. For model compound **3**, the FT spectra exhibit strong signatures which can be assigned unambiguously to the {Cu···N} and {Cu···Cα1} single scattering paths involving the cyclam ring with R_{Cu-N} = 2.02(2) Å and $R_{Cu-C\alpha1}$ = 2.8(8) Å. Since these signatures are nicely superimposed for the two xerogels, we were led to the first conclusion that the coordination geometry of the cyclam macrocycle can hardly be heavily altered in the oxygenated xerogel **XB2**. It thus became attractive to envisage difference analyses. We have reproduced in Figure 1B the FT spectra $Im\tilde{\chi}_N(R)$ and $|\tilde{\chi}_N(R)|$ obtained by Fourier transforming the difference EXAFS signal of a virtual species [**XB2-XB1**].

The most striking feature in Figure 1B is a sharp, nicely resolved peak which we assigned to a short Cu–O1 bond. The corresponding distance would be much too short to reflect any realistic distortion of the cyclam macrocycle. This led us to incorporate the phase shifts and scattering amplitudes of a Cu···O shell, calculated with FEFF8.9 for a cluster that has the structure of a well-characterized Cu–dioxygen model compound, into the optical FT.[20] Then by using a standard single shell fit, we could refine the distance: R_{Cu-O1} = 1.855 ± 0.005 Å, the Debye–Waller factor: $[\sigma_{Cu-O1}]^2$ = 0.00086 Å^2 and the average number density of bound oxygen atoms: N_{Cu-O1} = 0.76 ± 0.06 per copper site. The distance R_{Cu-O1} is much shorter than any Cu^{II}–OH bond length (1.97–2.02 Å) in copper hydroxyhalide minerals[21–25] like atacamite, paratacamite or in active phases of supported catalysts used for oxychlorination of ethylene.[26–28] In contrast, our R_{Cu-O1} distance compares remarkably well with the Cu–O bond lengths of Cu–dioxygen complexes of known crystal structures.[29,30] For instance, it is very close to the distance R_{Cu-O1} = 1.852 Å or R_{Cu-O1} = 1.868 Å found respectively in the end-on dinuclear μ-*trans* peroxo dicopper complex of Karlin[31,32] and Susuki[33] in which the dioxygen molecule is bound to two copper sites. If we accept that this may also be true for xerogel **XB2**, then our fit led us to expect the fraction of bound dioxygen molecules per copper site to be of the order of ca. 38%. It is quite remarkable that this value is nicely consistent with earlier measurements of oxygen adsorption which had established that the fraction of bound dioxygen should be near 40%. Note that the Cu···O1 signal could be seen directly in the FT spectrum of xerogel **XB2** displayed in Figure 1(A). Unfortunately, it interferes with the negative sidelobe of the intense Cu···N signal that makes the assignment problematic.

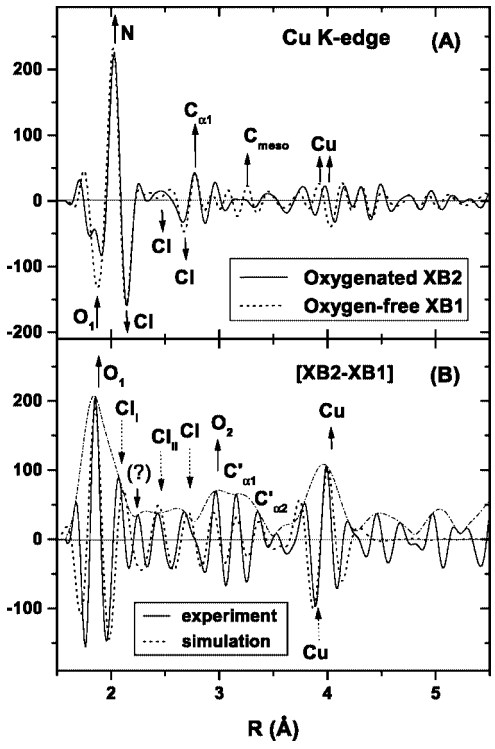

Figure 1. (A) Comparison of the Cu K-edge FT spectra $Im\tilde{\chi}(R)$ of xerogel **XB2**$[CuCl_2]/O_2$ (solid line) and of xerogel **XB1**$[CuCl_2]/N_2$ (dotted line). Arrows indicate where weak contributions of bridging chloride ions may interfere in xerogel **XB1**. (B) Cu K-edge FT spectra $Im\tilde{\chi}(R)$ (solid line) and $|\tilde{\chi}(R)|$ (dot-dashed line) of the difference signal of [**XB2** (oxygenated) – **XB1** (oxygen-free)]. A simulated FT difference EXAFS spectrum $Im\tilde{\chi}(R)$ (dotted line) is also reproduced which was calculated using a structure derived from Figure 3(A).

In the difference FT spectrum $|\tilde{\chi}_N(R)|$ shown in Figure 1B, there is another strong signature peak near 4 Å. We have assigned this signal to the derivative of a single scattering Cu···Cu EXAFS signal, resulting from a small variation of the distance R_{Cu-Cu} when dioxygen is bound to copper. At this stage, we would like to stress that this signal cannot be an experimental artefact since it is present in all difference analyses performed with individual scans. Clearly, the assignment of such a weak Cu···Cu EXAFS signal in the FT spectra displayed in Figure 1(A) would again be problematic because it is feared that this signal could interfere with the intense contributions of multiple-scattering paths involving the nitrogen atoms of the cyclam ligand. This is where a difference analysis can offer a decisive simplification of the spectra. Based on our experience, only a heavy scatterer like a copper atom could give such a strong signature at a long distance in the FT difference spectrum.

A simulation of the difference spectrum that is also reproduced in Figure 1(B) supports our interpretation. Using phase-shifts and scattering amplitudes calculated with

 © 2005 Wiley-VCH Verlag GmbH & Co. KGaA, Weinheim

FEFF8.9 for the same Cu–dioxygen model compound,[20] the best agreement was obtained for $R_{Cu-Cu} = 3.99 \pm 0.03$ Å; $[\sigma_{Cu-Cu}]^2 = 0.0032$ Å^2 in the oxygenated xerogel **XB2**; $R_{Cu-Cu} = 3.89 \pm 0.02$ Å; $[\sigma_{Cu-Cu}]^2 = 0.0032$ Å^2 in the oxygen-free xerogel **XB1**. The number density $N_{Cu-Cu} = 0.76$ was found (within the experimental uncertainty) to be equal to N_{Cu-O1}, which indeed supports the consistency of our assignment. Multiple scattering (MS) paths involving the coordination shell and the central atom are well-known sources of complication in the analyses of the EXAFS spectra at long distances but they should not play a major role here because: (i) the contribution of the MS paths involving copper and the nitrogen atoms of the first shell should cancel out in the difference as well as the contribution of the single scattering (SS) paths; (ii) MS paths involving oxygen or chlorine atoms cannot contribute to a signal that would be as intense or even more intense than the contribution of the first shell SS path. These considerations were supported by many more simulations, which are not reproduced in this paper.

Insight into the dioxygen species that is formed in the oxygenated xerogel **XB2** can also be drawn from solution chemistry of copper(I) complexes or from a systematic review of the crystal structures of Cu–dioxygen complexes.[29,30] The oxygenation of Cu^I complexes can generate three types of 2:1 Cu/O_2 species: an end-on *trans*-1,2-peroxodicopper(II), a side-on μ-η^2:η^2-peroxodicopper(II) and a bis(μ-oxo)dicopper(III) complex. The nature of the species that forms is primarily dictated by the denticity of the ligand.[30] In particular, the oxygenation of Cu^I complexes of sterically unhindered tetradendate tripodal ligands exclusively produces μ-1,2-peroxo complexes. Beyond denticity, other factors such as chelate ring size, nature of the donor atoms, electronic effects, steric demands and geometry are secondary in most cases. It appears that the internuclear distance R_{Cu-Cu} found for xerogel **XB2** would be significantly longer than the Cu···Cu distances in side-on dinuclear μ-η^2:η^2-peroxo copper complexes but shorter than in the end-on dinuclear *trans* μ-η^1:η^1-peroxo copper complex of Karlin et al.[31] ($R_{Cu-Cu} = 4.36$ Å). A side-on conformation should be ruled out for two reasons: (i) each dioxygen molecule would contribute to four equivalent Cu–O1 bonds and the signal at 1.86 Å should thus be twice as intense as what we found; (ii) for a coplanar side-on conformation, there is a limit ($R_{Cu-Cu} \approx 3.6$ Å) beyond which the four equivalent Cu–O1 bonds would split into two groups of unequal distances: $R_{Cu-O1} \leq R_{Cu-O2}$ and the end-on arrangement gains a higher probability.

Because no Cu/O_2 intermediate has been characterized, upon oxygenation in solution, for a tetrasubstitued cyclam copper(I) complex, one has to rely on comparisons with other tetradendate systems. In this regard, the aliphatic tetraamine ligands derived from tris(2-aminoethyl)amine (tren) are considered as good models of the immobilized cyclams although the former are not macrocyclic.[33–35] These ligands form μ-1,2-peroxodicopper(II) species, and accordingly, it is more likely that the reaction of xerogel **XB1** and dioxygen leads to the formation of an end-on μ-1,2-peroxodicopper(II) complex, in conformity with the EXAFS results. Yet, the Cu–Cu distance of 4.0 Å, shorter than in structurally characterized μ-1,2-peroxodicopper(II) complexes, suggests a distorted arrangement of the peroxo moiety.

We may then raise the subsidiary question whether there is any additional information available in the difference spectrum that could give us some indication about R_{Cu-O2}. We wish to underline that the following exercise is far more speculative than the previous assignments of the Cu···O1 and Cu···Cu signatures. We tried to assign the single scattering contribution of the second oxygen to the (next) most intense peak of the FT difference spectrum, i.e. to a signal peak at $R_{Cu-O2} \approx 2.96$ Å. One could find a few arguments supporting this very speculative assignment: (i) the signal had the expected phase for a Cu···O shell; (ii) this signal also shows up in the FT spectrum of xerogel **XB2** displayed in Figure 1(A) and, thus, cannot be an experimental artefact; (iii) to remain consistent with $R_{Cu-Cu} \approx 4$ Å, we have added the constraint: $R_{Cu-O2} \leq 3.02$ Å, but steric hindrance from the carbon atoms of the *N*-propyl groups would make distances $R_{Cu-O2} \leq 2.7$ Å very unlikely. A tentative estimation of the Cu–O1–O2 angle is possible only if we assume that the distance $d_{O1-O2} = 1.432$ Å as in the end-on peroxo structure of Karlin et al.[31] To a first approximation, one would calculate a bent angle Cu–O1–O2 of 127.7° to be compared with 108° in the structure of Karlin et al.[31] Recall that Kitajima et al.[20] predicted that, for pentacoordinate copper sites, the end-on dinuclear μ-η^1:η^1-peroxo-like structure should be the most favorable structure with Cu–O–O angles of the order of 130°. Our speculative assignment of the signal peaking at ca. 2.96 Å to the Cu···O2 single scattering path had another geometrical implication in that the distance Cu···Cu would be too short to enable the sequence of four atoms {Cu1···O1···O2···Cu2} be coplanar. From elementary 3D geometry considerations, we found that the directions of the Cu1–O1 and Cu2–O2 bonds should be rotated by ca. 93° with respect to each other. This would be required to minimize the steric hindrance between the two macrocyclic ligands.

We have implicitly suggested so far that dinuclear sites {Cu1;Cu2} should pre-exist in the oxygen-free xerogel **XB1**. Supporting arguments were found in the EXAFS spectra recorded at the Cl K-edge. The Cl K-edge FT spectra $\mathrm{Im}\tilde{\chi}_N(R)$ of the oxygen-free and oxygenated xerogels **XB1** and **XB2**, respectively, are shown in Figure 2(A) whereas difference FT spectra of the virtual species [**XB1**-**XB2**] are displayed in Figure 2(B). Here, the optical FT spectra were systematically corrected using the phase shifts and scattering amplitudes of a Cl···Cu shell. We carefully checked the consistency of our E_0 value with respect to earlier analyses of other model compounds involving Cl···Metal distances. At short distances, there are unbalanced contributions of Cu^I sites and pentacoordinate Cu^{II} sites with well-resolved signatures peaking at: $R_{Cl-Cu^I} = 2.11 \pm 0.03$ Å, and $R_{Cl-Cu^{II}} = 2.44 \pm 0.03$ Å, respectively. Interestingly, we also found a well-defined signal at a long distance: $R_{Cl-Cu} \geq 2.71 \pm 0.03$ Å which seems to agree with our suspicion

 © 2005 Wiley-VCH Verlag GmbH & Co. KGaA, Weinheim

that the Cl^- ions could asymmetrically bridge the copper sites.

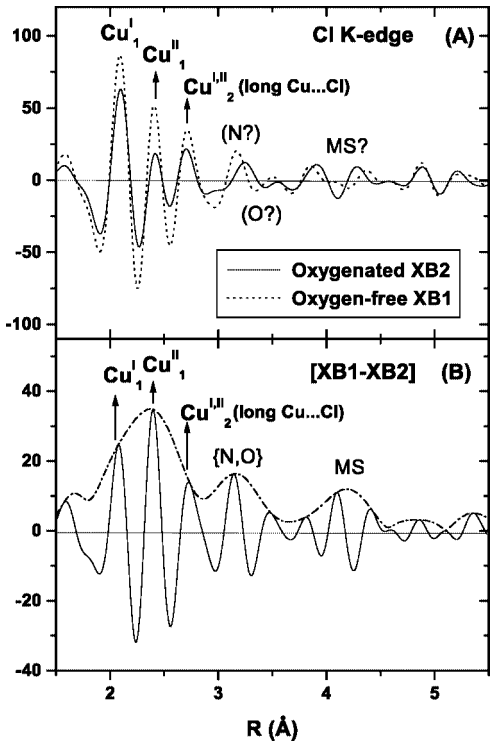

Figure 2. (A) Comparison of the Cl K-edge FT EXAFS spectra $Im\tilde{\chi}(R)$ of xerogel **XB2**[$CuCl_2$]/O_2 (solid line) and of xerogel **XB1**[$CuCl_2$]/N_2 (dotted line). Arrows mark the expected Cl···Cu distances for Cu^I–Cl and Cu^{II}–Cl bonds. The signal at 2.7 Å would be consistent with a Cl anion bridging mixed-valence $\{Cu^I,Cu^{II}\}$ sites. (B) Cl K-edge FT spectra $Im\tilde{\chi}(R)$ (solid line) and $|\tilde{\chi}(R)|$ (dot-dashed line) of the difference EXAFS signal of [**XB1** (oxygen-free) – **XB2** (oxygenated)].

Thus, we were led to seriously consider the existence of mixed-valence Cu^I and Cu^{II} sites. Note that the long distance $R_{Cl–Cu_2}$ looks quite comparable with distances (e.g. 2.674–2.707 Å) reported for chloride ions bridging mixed-valence dinuclear $\{Cu^I,Cu^{II}\}$ sites.[36] Such distances are, however, only slightly shorter than the distances (2.71–2.76 Å) found for chloride ions symmetrically bridging two Cu^{II} sites in copper hydroxychloride minerals[21,23,24] (e.g. atacamite). Cl K-edge EXAFS data are not accurate enough to discriminate between these two structural options. However, from the estimated Cu1···Cu2 distance in the deoxy-xerogel **XB1** ($R_{Cu1–Cu2} \approx 3.89$ Å), one would predict the bridging angle Cu1–Cl–Cu2 to be either 97° or 105° depending on whether Cu1 is taken as a Cu^I or a pentacoordinate Cu^{II} site. This compares rather well with the bridging angle (92°) reported for chloride ions in mixed-valence dinuclear $\{Cu^I,Cu^{II}\}$ sites.[36]

Concentrating on the FT spectrum of the oxygenated xerogel **XB2**, we found [Figure 2(A)–2(B)] only a modest amplitude reduction of the Cu^I–Cl signal while the signature of the pentacoordinate Cu^{II}–Cl site vanished completely. This rather astonishing result was confirmed a posteriori by re-investigating the Cu K-edge FT difference spectra. From Figure 1(B) we identified a positive peak at $R_{Cu^{II}–Cl} \approx 2.44$ Å together with a poorly resolved side-peak at $R_{Cu^I–Cl} \approx 2.10$ Å. There might still be an additional signal correlated with the long Cl··Cu2 distance ($R_{Cu–Cl} \approx 2.7$ Å) but it would be interfering with the signal, which we had previously assigned to the Cu1···O2 signature. These various Cu···Cl signatures are expected to appear as positive peaks in the FT difference spectrum of [**XB2-XB1**] as a consequence of the difference in the phase shifts of oxygen and chlorine scattering atoms. As far as we are concerned, the main interest of this exercise was essentially to probe the self-consistency of our assignments in the difference analyses.

At this stage, we tried to summarize in Figure 3 the possible structures of the Cu sites in the active xerogels. According to our analyses, up to four different Cu sites could coexist in xerogels **XB1** and **XB2**. In Figure 3(A), we sketched what a dinuclear site corresponding to the dioxygen adduct in **XB2** could look like. There is probably a small shift (≈ 0.2 Å ?) of the Cu atoms out of the average nitrogen plane and, most likely, also a trigonal distortion of the Cu^I–N bonds but there is no hope as yet of extracting this information from the EXAFS spectra. Moreover, any distortion of this type referring to the cyclam ligand should already pre-exist in the oxygen-free xerogel. From Figure 3(A), we realized that steric hindrance of the carbons (Cα) located on the same side of the cyclam as the dioxygen adduct should probably define the most stable configuration.

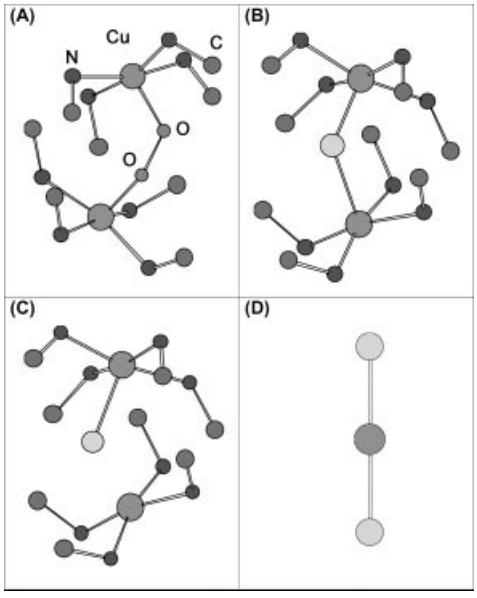

Figure 3. (A) Stereogeometry of the dinuclear μ-η^1:η^1 peroxo-like Cu site consistent with the difference EXAFS analysis with: $R_{Cu–O1}$ = 1.855 Å; $R_{Cu–O2}$ = 2.965 Å; $R_{Cu–Cu}$ = 3.988 Å. The Cu atoms were arbitrarily shifted by 0.2 Å from the average 4-N plane whereas the Cu–O bond had to be tilted by 10° with respect to the cyclam axes in order to minimize the steric hindrance of the carbons. (B) Stereogeometry of the postulated mixed-valence $\{Cu^I,Cu^{II}\}$ dinuclear site in xerogel **XB1**. (C) Stereogeometry of tetra- and pentacoordinate Cu^{II} sites coexisting only in xerogel **XB1**. (D) Linear counterion [Cl---Cu^I---Cl] identified in species **6**.

 © 2005 Wiley-VCH Verlag GmbH & Co. KGaA, Weinheim

With regards to the oxygen-free xerogel, a dinuclear site in which a chloride ion would bridge two pentacoordinate copper atoms with a formal valence of 1.5 would be unstable since the system would spontaneously evolve towards configurations sketched in Figure 3(B) and (C). The dinuclear configuration of Figure 3(B) would be most convincing for a mixed-valence $\{Cu^{I},Cu^{II}\}$ species, i.e. with a pentacoordinate Cu^{I} site, a short Cu^{I}–Cl bond (2.11 Å) and a long distance Cl–Cu^{II} (2.7 Å). In the configuration of Figure 3(C), the Cu^{II} site would be pentacoordinate with the intermediary bond length $R_{Cu^{II}–Cl} \approx 2.44$ Å and the bare, tetracoordinate Cu^{I} site could easily be oxidized. Dynamic exchanges between configurations (B) and (C) would require only a small translation of the bridging chlorine atom. Last but not least, EXAFS cannot rule out at this stage the presence of linear anions $[Cl{-}{-}{-}Cu^{I}{-}{-}{-}Cl]^{-}$ [Figure 3(D)] as discussed for complex **6** (see Supporting Information).

Building on these considerations, we have generated a simulated spectrum, which approaches the experimental Cu K-edge FT difference spectrum of Figure 1(B) reasonably well. Indeed, we do not pretend that the structural problem has been solved but, at least, we come up with a model that is consistent with all EXAFS analyses. For convenience, we assumed that the signals observed at $R \approx 3.15$ Å could be assigned to the shortest intermolecular distance Cu2···C′α3. The parameters defining the scattering paths contributing to the simulated difference spectrum displayed in Figure 1(B) are listed in Table S1 of the supporting information section. The contribution of the MS paths was found to be marginal in this exercise.

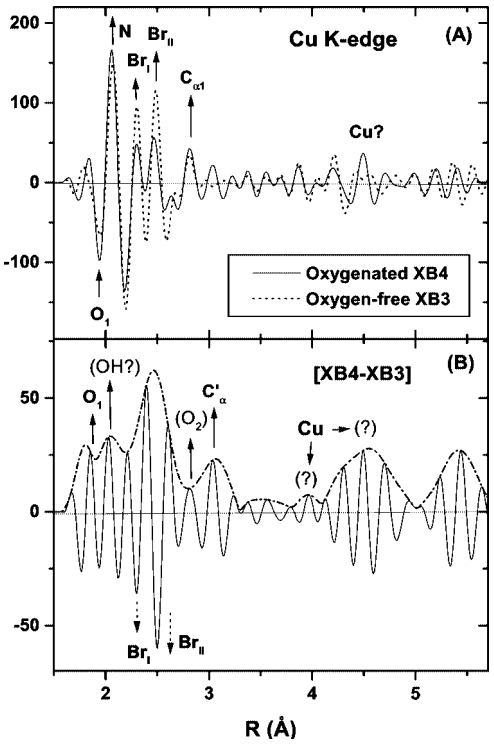

Figure 4. (A) Comparison of the Cu K-edge FT EXAFS spectra $Im\tilde{\chi}(R)$ of xerogel **XB4**$[CuBr_2]/O_2$ (solid line) and xerogel **XB3**$[CuBr_2]/N_2$ (dotted line). The split contributions of the Cu^{I}–Br and Cu^{II}–Br bonds are identified as (Br_I) and (Br_{II}). (B) Cu K-edge FT spectra Im $\tilde{\chi}(R)$ (solid line) and $|\tilde{\chi}(R)|$ (dot-dashed line) of the difference EXAFS signal of [**XB4** (oxygenated) – **XB3** (oxygen-free)]. Note the weaker amplitude of the Cu···O_1 signal.

Xerogels of Type (B) Complexed with $CuBr_2$

The Cu K-edge FT EXAFS spectra $Im\tilde{\chi}_N(R)$ of the oxygenated xerogel **XB4** and of the oxygen-free xerogel **XB3** complexed with $CuBr_2$ are compared in Figure 4(A). The FT difference spectra of the virtual species [**XB4**–**XB3**] is again reproduced in Figure 4(B). On comparing the FT spectra displayed in Figure 1(A) and Figure 4(A), it would appear that the peak assigned to the Cu···N distances is less intense and slightly shifted towards long distances in the xerogels complexed with $CuBr_2$, the average bond length increasing from 2.02Å to ca. 2.06 Å. In the FT spectrum of the oxygen-free xerogel **XB3**, there is clear evidence that bromine atoms are present in the coordination shell of copper and a refined EXAFS analysis suggested that two different Cu–Br bond lengths should be envisaged. The shortest one ($R = 2.30 \pm 0.02$ Å) would again fall very close to the Cu–Br bond length of the linear anion[37] $[Br{-}{-}{-}Cu^{I}{-}{-}{-}Br]^{-}$ and would be shorter than the Cu–Br bond length[38] in $[Cu^{I}–Br_3]^{2-}$; the long distance ($R = 2.49 \pm 0.02$ Å) would be typical of a pentacoordinate Cu^{II} complex.[39] These two resolved signals were identified as Br_I and Br_{II} in Figure 4(A) and Figure 4(B). Thus, there is again a strong indication that mixed-valence $\{Cu^{I},Cu^{II}\}$ sites[40–42] could be present in these xerogels, the signature of the Cu^{I} site being definitively less intense than the signature of the Cu^{II} site.

Independent chemical tests had previously established that the capability of xerogel **XB3** to fix dioxygen was rather poor as compared to xerogel **XB1**. This could be correlated with our observation that the difference FT spectrum of Figure 4(B) exhibits only a very weak signal at the short distance $R_{Cu–O1} = 1.86$ Å where we expect the characteristic signature of the formation of the same end-on dinuclear μ-η^1:η^1-peroxo structure discussed in the previous section.

It should be noted that the difference signals in Figure 4(B) are much less intense than in Figure 1(B). Also, the situation looks more confusing at further distances where the signature at $R_{Cu–Cu} = 3.99$ Å is now very weak whereas new signatures show up at 4.2–4.5 Å. This is not completely unexpected since: (i) the amount of dinuclear peroxo-like complex is certainly heavily reduced; (ii) we would have been suspicious if we had found the same internuclear Cu···Cu distance for the oxygen-free xerogels complexed either with $CuBr_2$ (**XB3**) or with $CuCl_2$ (**XB1**). Anyhow, the signals that show up at 4.2–4.5 Å are weak on the scale of Figure 1(B) and we clearly approach the noise limit of difference analyses.

Nevertheless, one may question why the structural changes between xerogels **XB4** and **XB3** should be so small. One could speculate that, in the presence of trapped water molecules, the dioxygen adduct would be partly and irreversibly decomposed to yield $Cu^{I,II}$–OH bonds (1.87/2.00 Å), with the OH^{-} anions replacing the released bromide anions. This would explain the presence of imperfectly

 © 2005 Wiley-VCH Verlag GmbH & Co. KGaA, Weinheim

resolved signatures at 1.86/1.99 Å in Figure 4(B). Note that one would also expect longer Cu···Cu distances if there is no more bridging Br^- anion.

Inactive Xerogels Complexed with $CuCl_2$

The FT spectra $Im\tilde{\chi}_N(R)$ of the inactive xerogel **XA1** and of the oxygen-free, active xerogel **XB1** are now compared in Figure 5A. The strong signal peaking at 2.002 Å in the FT spectrum of **XA1** is most likely to be assigned once again to Cu···N distances. If one assumes that this peak refers to the average R_{Cu-N} bond length, then the corresponding bond length would be shorter than in the active xerogel **XB1** ($R_{Cu-N} \approx 2.022$ Å) and also much shorter than in model compound **6** or in its silylated precursor ($R_{Cu-N} \approx 2.13$ Å). In EXAFS, a shorter bond length is most often correlated with a stronger intensity but, quite paradoxically, the intensity of the Cu···N signal in the inactive xerogel **XA1** is reduced by ca. 30% with respect to xerogel **XB1**. In fact the intensity of the Cu···N peak is similar to the intensity of the Cu···N peak in **6** in which we pointed out the role of a destructive interference. The FT spectrum of xerogel **XA1** exhibits a well resolved negative signal peaking at 2.28 Å which one might be tempted to assign to a Cu···Cl distance. Unfortunately, such a speculative assignment would not make any sense because all crystal structures reported so far show that in pentacoordinate Cu^{II} complexes the Cu–Cl bond length is of the order of $R_{Cu-Cl} \approx 2.44$–2.47 Å as discussed earlier and illustrated by model compound **6**. There are still signatures in the FT spectrum of **XA1** which could be perfectly assigned to Cu···Cα1 and Cu···Cα2 single scattering paths and would indicate that the copper atoms are coordinated to the cyclam although the conformation of the macrocyclic ligand is certainly not the same as in the active xerogels.

We suspect that, in xerogel **XA1**, the EXAFS signal of the Cu···N distances are heavily distorted by destructive interferences within the coordination polyhedron. The negative side-lobes of the Cu···N peak are anomalously small and distorted which fuelled our suspicions. In a desperate attempt to recover some structural information lost in destructive interferences, we tried to display in Figure 5(B) the difference spectra of the virtual species [**XA1-XB1**] and [**XA1-XB2**]. The rather strong intensity of the signatures found in the FT difference spectrum of [**XA1-XB1**] confirms that the copper environment is fundamentally different in these two xerogels but, at this stage, a detailed interpretation of the difference spectrum is hopeless. If we restrict ourselves to the coordination shell, we may conjecture that there should be at least two additional signatures interfering with the Cu···N signal in the EXAFS spectrum of the inactive xerogel **XA1**: (i) the first one peaking at ca. 1.9 Å looks most typical of Cu···OH distances; (ii) the second one peaking at ca. 2.15 Å might well reflect a distortion of the cyclam macrocycle resulting in two sets of Cu···N bond lengths, e.g. 2.03 Å and 2.15 Å. It has been pointed out a while ago by Barefield and Wagner[6] that macrocycles with tertiary amines such as tetramethylcyclam could accommodate a sixth ligand at short distance with a significant folding of the macrocycle resulting in two pairs of nonequal Cu–N bonds. Such an interpretation could perhaps be consistent with the FT difference spectra of Figure 5(B). However, this is one interpretation amongst several. At a purely speculative level, we also considered the case of a dinuclear copper site now bridged with two OH^- anions. This model would explain why xerogel **XA1** could not bind anymore dioxygen. The present EXAFS study was nevertheless worth the time and effort involved: (i) it gave the experimental proof that xerogels **XA1** and **XB1** have fairly different local structures; (ii) and also that subtle changes in the coordination geometry of the cyclam would yield strong Cu···N residual signatures around 2.0(3) Å in the FT difference spectra. A contrario, the latter point supports the consistency of our difference analysis of xerogels **XB1** and **XB2**.

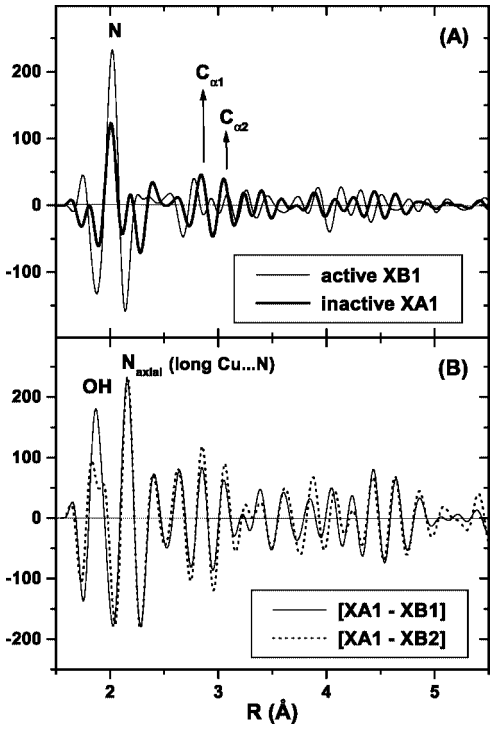

Figure 5. (A) Comparison of the FT spectra $Im\tilde{\chi}(R)$ of the inactive xerogel **XA1**[$CuCl_2$]/air (thick line) and active xerogel **XB1**[$CuCl_2$]/N_2 (solid line). Note the poor intensity of the (distorted) Cu···N signal of the inactive xerogel **XA1**. (B) FT spectra $Im\tilde{\chi}(R)$ of the difference EXAFS of [**XA1** (inactive) – **XB1** (oxygen-free)] (solid line) and of [**XA1** (inactive) – **XB2** (oxygenated)] (dotted line). Note the well-resolved contributions of the interfering signatures assigned to additional Cu···O and Cu···N single scattering paths.

Valence and Ligand Field Information

XANES Spectra as Fingerprints

We have regrouped in Figure 6(A) the deconvoluted Cu K-edge XANES spectra of all active xerogels, i.e the oxygen-free xerogels **XB1**[$CuCl_2$] or **XB3**[$CuBr_2$] and the oxygenated species **XB2**[$CuCl_2$]/O_2 or **XB4**[$CuBr_2$]/O_2. We have also added, on the same plot, the Cu K-edge XANES spectrum of the inactive xerogels **XA1**[$CuCl_2$]/Air. All spectra

 © 2005 Wiley-VCH Verlag GmbH & Co. KGaA, Weinheim

were recorded over the same energy range and were deconvoluted with the same parameters (i.e. ΔE_G; ΔE_L). Therefore, there is no extra difficulty in comparing deconvoluted spectra. Noticeably, the Cu K-edge XANES spectra of all active xerogels have the same morphology. The most characteristic features were labeled from (A) to (F). Quantitative information regarding the peak energy and relative intensity of the near-edge features (A)–(E) are summarized in Table 2S (supporting information section). Most striking is the very sharp "white line" (C) peaking at 8985.33 eV, the intensity of which decreases by only ca. 15% in air or dioxygen. In all XANES spectra, there is a shoulder labeled (D) which peaks at 8987.4 eV. It is particularly well resolved in the spectra of xerogels **XB1**[$CuCl_2$] and **XB2**[$CuCl_2$]. Much weaker but still quite real are the pre-edge structures (A) and (B) found at 8980.4 eV and 8983.3 eV, respectively. In the case of the inactive xerogel **XA1**, the white line (C) is not only shifted towards high energy but its intensity is reduced in the ratio 3:1 whereas the shoulder (D) seems to become progressively smaller.

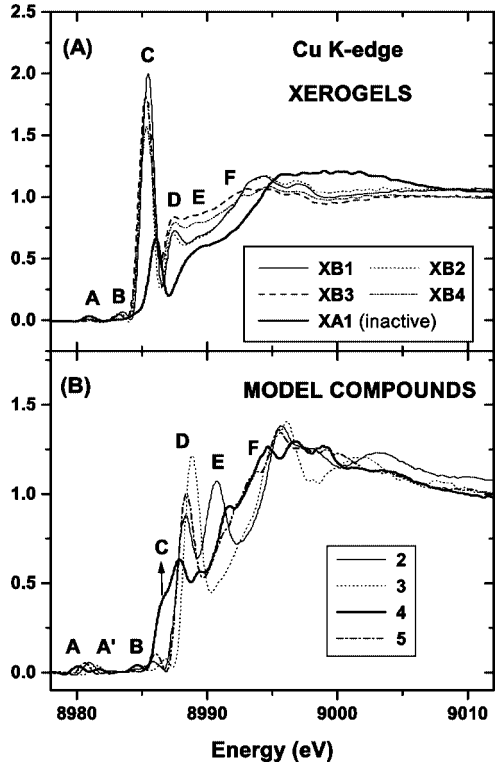

Figure 6. Numerically deconvoluted Cu K-edge XANES spectra. (A) XANES spectra of active xerogels: **XB1**[$CuCl_2$]/N_2; **XB2**[$CuCl_2$]/O_2; **XB3**[$CuBr_2$]/N_2 and **XB4**[$CuBr_2$]/O_2. The XANES spectrum of the inactive xerogel **XA1**[$CuCl_2$]/Air is also shown for comparison. The strong pre-edge resonance (C) is a characteristic feature of all XANES spectra of active xerogels. (B) Note the absence of any sharp resonance (C) in the Cu K-edge XANES spectra of various $[Cu(cyclam)]^{2+}$ complexes with variable coordination geometries: **2** = $Cu(cyclam)(ClO_4)_2{\cdot}0.5H_2O$; **3** = $[Cu(tmc)](BF_4)_2$; **4** = $[Cu(tmc)Cl](BF_4)$; **5** = $[Cu(dmdpc)](BF_4)_2$.

The Cu K-edge XANES spectra of model compounds **2**–**5** were regrouped in Figure 6(B). Clearly, the XANES spectra of tetra-, penta- or hexacoordinate cyclam complexes are quite different. The case of the pentacoordinate complex **4** is particularly relevant here since it was found to exhibit a marked analogy with the XANES spectrum of freshly prepared samples of the silylated precursor. We wish to stress that the sharp white line (C) is very weak in the XANES spectrum of such a pentacoordinate Cu^{II} complex.

The Cl K-edge XANES spectra of the oxygen-free xerogel **XB1** and of the oxygenated sample **XB2** are shown in Figure 7(A). We included on the same plot the Cl K-edge XANES spectrum of **6** which, according to the EXAFS study, should be a pentacoordinate complex of Cu^{II} contaminated with some fraction of the linear anion $[Cl{-}{-}{-}Cu^{I}{-}{-}{-}Cl]^{-}$. It immediately appears from Figure 7(A) that the morphology of the Cl K-edge XANES spectra of xerogels **XB1** and **XB2** is similar. Interestingly, the modest intensity of the pre-edge resonance labeled "A" peaking at 2819 eV in the case of complex **6** is very weak in the case of the active xerogels.

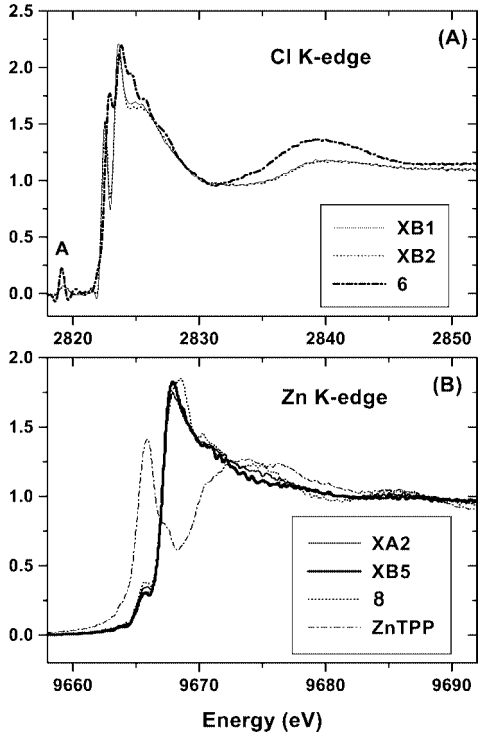

Figure 7. (A) Deconvoluted Cl K-edge XANES spectra of the active xerogels **XB1**[$CuCl_2$]/N_2 and **XB2**[$CuCl_2$]/O_2. The Cl K-edge XANES spectrum of the mixed-valence $\{Cu^{I},Cu^{II}\}$ complex **6** is also shown. It exhibits only a weak pre-edge resonance (A) at 2819 eV that vanishes for Cu^{I} compounds. (B) Deconvoluted Zn K-edge XANES spectra of xerogels **XA2**[$ZnCl_2$]/Air, **XB5**[$ZnCl_2$]/Air and of the zinc complex **8**. The XANES spectrum of Zn(TPP) was added as a reference.

This resonance was reported by Hedman et al.[43] to reflect the amount of ligand character in the antibonding orbital $(1 - \alpha^2)^{1/2}(Cu\ 3d_{x^2-y^2}) - \alpha(Cl\ 3p)$ of Cu^{II} compounds. In Cu^{I} compounds as well as in the linear anion $[Cl{-}{-}{-}Cu^{I}{-}{-}{-}Cl]^{-}$, this resonance should become much weaker because the Cu 3d orbitals should become nearly filled just as in the case of the Zn 3d orbitals of $ZnCl_2$. Figure 7(A) would thus confirm that the copper atoms in xerogels **XB1** or **XB2**

 © 2005 Wiley-VCH Verlag GmbH & Co. KGaA, Weinheim

could hardly be "standard" Cu^{II} sites, as already anticipated from their EXAFS spectra.

The Zn K-edge XANES spectra of xerogels **XA2**[$ZnCl_2$], **XB5**[$ZnCl_2$] and of the silylated zinc complex **8** are displayed in Figure 7(B). The XANES spectrum of the zinc porphyrin Zn(TPP) was included as a reference. Substituting $ZnCl_2$ for $CuCl_2$ yields xerogels of type (A) and (B) that may still be slightly different but the differences in their XANES spectra become much more subtle. Here the XANES spectra of the xerogels are dominated by a single, sharp white line peaking at 9669 eV. The very weak pre-edge shoulder is consistent with a limited contribution of 3d atomic orbitals of Zn to the empty excited states. Obviously there seems to be a much stronger charge transfer from the metal to the porphyrin dianion in the case of Zn(TPP).

Simulation of XANES Spectra

In the previous section, the XANES spectra were used as sensitive fingerprints of the coordination geometry and electronic structure of the Cu sites in the xerogels. One may wonder whether ab initio simulations could help us to correlate quantitatively the observed changes with the electronic structure and the geometrical arrangement of the cyclam units. We will concentrate on two questions: (i) can we reproduce the very sharp, intense resonance (C) peak at 8986.8 eV? (ii) can we find any reliable indication that Cu^{I} sites exist in xerogels of type (B)? This is important because there is no known example of dioxygen reversibly bound to true Cu^{II} sites. We compare in Figure 8(A), Figure 8(B) and Figure 8(C), the deconvoluted experimental XANES spectra of model compounds **1**, **2** and **5** with simulated XANES spectra calculated with the MSW option of the code FDMNES, i.e. using muffin-tin potentials and the Xα functional density for exchange correlation. In each case, the geometry of the molecular cluster is systematically shown.

For the copper porphyrin **1**, we used the same muffin-tin radii as Case and Karplus[44] who already stressed that the ground state, formally written as Cu^{II} ($3d^9$) could easily transform into Cu^{I} ($3d^{10}$) by charge transfer excitation. As illustrated with Figure 8(A), the agreement between the deconvoluted experimental spectrum and our simulation looks encouraging. The simulated spectrum of Figure 8(A) reproduces the strong pre-edge resonance which was found to be highly sensitive to the charge transfer from the aromatic pyrrole towards the copper atom. The best agreement with the experimental results was obtained from the following occupation of the valence atomic orbitals: [Cu $3d^{9.40}$, $4s^{0.20}$; N $(2s2p)^{4.97}$; $C_{pyrrole}$, C_{meso} $(2s2p)^{4.10}$, C_{phenyl} $(2s2p)^{3.98}$] whereas the muffin-tin zero had to be adjusted to $V0_{imp}$ = –16.0 eV. It is not surprising that the MS calculation cannot reproduce the relative amplitudes and linewidths of the various shape resonances (especially beyond the edge) because the deconvolution is not perfect, whereas the FDMNES code takes into account only the real part of the Hedin–Lundqvist exchange-correlation potential but not its imaginary part.

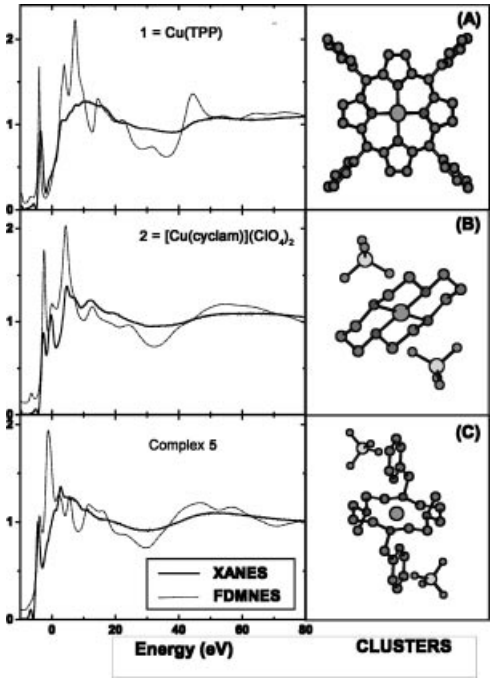

Figure 8. MSW simulations of the XANES spectra of model compounds: (A) **1** = Cu(TPP); (B) **2** = [Cu(cyclam)]$(ClO_4)_2$·0.5H_2O; (C) **5** = [Cu(dmdpc)]$(BF_4)_2$. Deconvoluted experimental spectra are shown again for comparison.

As illustrated with Figure 8(B) and Figure 8(C), our simulations of the XANES spectra of complexes **2** and **5** also look rather encouraging. Here, we expect a different charge delocalization because the cyclam macrocycles are neutral whereas the porphyrin macrocycle is a dianion. We kept the same muffin-tin radii as for the simulation of the copper porphyrin but we changed the occupation of the valence atomic orbitals. Since the crystal structure of species **2** is unknown, we incorporated the crystal structure of **2′** = [Cu(cyclam)]$(ClO_4)_2$, in which the two perchlorate anions are only very weakly bound at long distances, into our calculation. Nevertheless, Figure 8(B) reveals that the simulated XANES spectrum of species **2′** is very similar to the experimental spectrum of complex **2** which implies that **2** is most likely tetracoordinate. We used the following occupancy of the valence atomic orbitals: [Cu $3d^{9.46}$, $4s^{0.26}$; N $(2s2p)^{4.74}$; O_{axial} $(2s2p)^{6.40}$], the muffin-tin zero being now arbitrarily adjusted to $V0_{imp}$ = –18.5 eV. Note that the resonance doublet in the edge is remarkably well reproduced. For the hexacoordinate complex **5**, the best agreement with the experimental spectrum was obtained with the following occupation of the valence atomic orbitals: [Cu $3d^{9.72}$, $4s^{0.22}$; N_{equat} $(2s2p)^{4.64,\ 4.71}$; N_{axial} $(2s2p)^{4.92}$], the muffin-tin zero now being shifted to $V0_{imp}$ = –21.5 eV.

In contrast, we systematically failed to reproduce the XANES spectra of the xerogel **XB1**. In particular, we never succeeded in reproducing the sharp resonance (C) peaking at 8985.4 eV. These negative results led us to envisage that the XANES spectrum of xerogel **XB1** should result from two contributions; the first one being formally associated with a Cu^{I} ($3d^{10}$) site and the second one to a Cu^{II} ($3d^9$)

 © 2005 Wiley-VCH Verlag GmbH & Co. KGaA, Weinheim

site. This required us to perform two consecutive calculations, i.e. one for each individual copper site. The difficulty is that we need a consistent calibration of the energy scale of these two spectra. Unfortunately, standard multiple scattering calculations are not reliable enough for such an exercise because the muffin-tin zero (V0) depends on the different occupation of the valence orbitals for a given copper site. This stimulated us to run the FDM option of the FDMNES code since no muffin-tin approximation is made, V0 will no longer be defined. In order to avoid a prohibitive computing time, we have performed a test calculation with a simplified dinuclear cluster in which the two copper atoms were asymmetrically bridged by one chlorine atom. The macrocyclic ligand surrounding each absorbing site was restricted to four nitrogen atoms and twelve α carbons. For the first calculation, the absorbing atom was the Cu^{I} site ($1s^1$; $3d^{10}$; $4s^{0.1}$; $4p^{0.2}$), the Cu^{II} site ($1s^2$; $3d^9$; $4s^{0.1}$; $4p^{0.2}$) contributing as a scattering atom; for the second calculation, the role of the two sites was exchanged. For simplicity, no screening effect was taken into account for the Cu^{I} site. With regards to the other scattering atoms, we extrapolated the population of the atomic orbitals from previous calculations, i.e. N_{equat} $(2s2p)^{4.58,4.60}$; Cl $(3s3p)^{7.84}$; C $(2s2p)^{4.04}$. The calculated atomic photo-ionization energies of the Cu^{I} and Cu^{II} sites were ε_{ii} = 9071.24 eV and 9059.964 eV, respectively.

The XANES spectra simulating the resolved contributions of equipopulated $\{Cu^{I};Cu^{II}\}$ sites are compared in Figure 9 in which we also reproduced the XANES spectrum of xerogel **XB1**. Since it is a usual trend of FDM calculations to generate sharp resonance lines, we found it preferable to numerically convolute the simulated XANES spectra with Lorentzian lineshapes centered at the Fermi energy E_F (Lorentzian half-width: Γ = 0.1–0.2 eV). The key conclusion is that resonances (A) (B), (C), (D) are most likely to be assigned to Cu^{I} sites, whereas resonances (E), (F) should involve the Cu^{II} site. We would like to emphasize that this is the first simulation in which resonance (C) could be reproduced with a strong intensity and we observed that this line would not depend so much on the internuclear distance $R_{Cu–Cu}$.

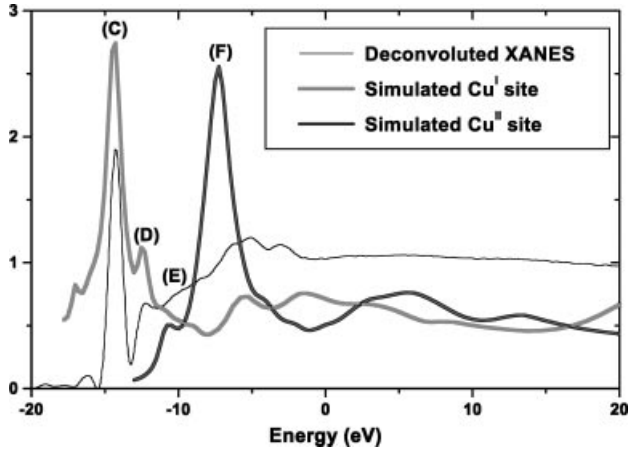

Figure 9. Simulated XANES spectra of mixed-valence $\{Cu^{I};Cu^{II}\}$ sites. The resolved contributions of the Cu^{I} and Cu^{II} sites were simulated using the *Finite Difference* option of the code FDMNES. A deconvoluted XANES spectrum of xerogel **XB1** is reproduced again for comparison. Note that resonance (C) is most likely to be assigned to the Cu^{I} site.

Conclusion

FT difference analyses at the Cu K-edge gave a strong indication that, in the oxygenated xerogel **XB2**, dioxygen would bridge two copper atoms in a kind of end-on μ-η^1:η^1 peroxo-like conformation with a short Cu–O1 distance: $R_{Cu–O1}$ = 1.855 ± 0.005 Å but with a rather long internuclear distance: $R_{Cu–Cu} \approx$ 4.0 Å. The number density $N_{Cu–O1}$ = 0.75 ± 0.1 agrees fairly well with independent measurements of O_2 adsorption (38% per copper site). There is no doubt that in both the oxygenated (**XB2**) and the oxygen-free (**XB1**) xerogels the Cu atoms are still complexed by the cyclam units. This is proved by the presence in the FT spectra of each individual xerogel of characteristic signatures assigned to the Cu···N and Cu···Cα1 single scattering paths at typical distances: $R_{Cu–N}$ = 2.02(2) Å and $R_{Cu–Cα1}$ = 2.8(8) Å, respectively. Interestingly, there is no evidence of a structural rearrangement affecting the coordination of the cyclam macrocycle in the oxygenated xerogel. This may not be so surprising if the substituted macrocycle is totally immobilized within the rigid inorganic polymeric structure of the xerogel. This could explain the reactivity of these xerogels towards dioxygen and why dioxygen is bound almost reversibly.

If we retain the model of an end-on peroxo-like conformation, then one should also observe the weaker signature of a second single scattering path at a longer Cu···O2 distance. The best we could do was to assign, in a purely speculative way, this Cu···O2 signature to a residual signal found in the difference spectrum at $R_{Cu–O2}$ = 2.9(6) Å. If this assignment is correct, then the Cu–O1–O2 angle was estimated to be ca. 128° in noticeable agreement with arguments previously developed by Kitajima et al.[20] However, we wish to underline that the corresponding deductions relative to the stereogeometry of the complex are indirect and remain speculative.

The Cl K-edge EXAFS study turned out to be particularly informative in the case of the active xerogels **XB1** and **XB2**. It established that, in the oxygen-free xerogel **XB1**, we had pentacoordinate Cu sites with both short Cu^{I}–Cl bonds ($R \approx$ 2.11 ± 0.03 Å) and typical Cu^{II}–Cl bonds ($R \approx$ 2.44 ± 0.03 Å). Chloride ions may well asymmetrically bridge dinuclear, mixed-valence copper sites as suggested by the detection in the FT spectra of a characteristic signal at a long distance ($R \geq$ 2.7 Å). We found it somewhat amazing that in the oxygenated xerogel **XB2**, the amplitude of the Cu^{I}–Cl signal decreased by ca. 20% while the signature of the pentacoordinate Cu^{II}–Cl site vanished. This result was confirmed a posteriori by the FT difference analysis at the Cu K-edge once it became possible to identify the Cu···Cl signatures. Note that the released chloride anions are most probably disordered and could hardly contribute to any detectable EXAFS signal.

 © 2005 Wiley-VCH Verlag GmbH & Co. KGaA, Weinheim

Substituting $CuBr_2$ for $CuCl_2$ yields xerogel **XB3**, known to be much less reactive. Such poor activity could be correlated with a cut by ca. 50% in the intensity of the $Cu\cdots O_1$ signal (R = 1.86 Å) in the FT difference spectrum of [**XB4**-**XB3**] where **XB4** denotes the relevant oxygenated xerogel. However, we found an additional signal at $R \approx 1.98$ Å which we assigned tentatively to the Cu^{II}–OH bond of a pentacoordinate mononuclear Cu site. Inactive xerogels prepared with metallated cyclams by route (A) were also found to have a fairly different structure. It seems that a major structural change had occurred during hydrolysis and polycondensation and it was speculated that a folded conformation of the cyclam would allow the copper atom to accommodate the coordination of two OH^- anions at short distances ($R \geq 1.9$ Å) while maintaining two short ($R \approx 2.00$ Å) and two long ($R \approx 2.15$ Å) Cu–N bonds. At this stage, no refined interpretation of the EXAFS spectra of the xerogels prepared by means of route (A) is possible.

Deconvoluted XANES spectra of all xerogels prepared by route (B), i.e. by incorporating $CuCl_2$ into the hybrid xerogel, exhibit a strong pre-edge resonance at 8985.4 eV which seems to be associated with the Cu^I site of a mixed-valence $\{Cu^I,Cu^{II}\}$ structure. Simulations of the XANES spectra of a number of model compounds were carried out with the standard MSW option of the code FDMNES and gave rather encouraging results. In contrast, we systematically failed to reproduce the XANES spectrum of xerogel **XB1** using the standard MSW approach. This is not too surprising since this XANES spectrum is expected to be the superposition of the individual contributions of Cu^I and Cu^{II} sites. Unfortunately, the relative chemical shift of the Cu^I and Cu^{II} pre-edge resonances cannot be reproduced accurately enough with MSW codes relying on the crude muffin-tin approximation. A very encouraging result was nevertheless obtained using the Finite Differences option of the advanced code FDMNES. A preliminary simulation carried out beyond the muffin-tin approximation allowed us to assign unambiguously the strong pre-edge resonance (C) at 8985.4 eV to a Cu^I site.

Experimental Section

Materials: The active/inactive xerogels were complexed with $CuCl_2$, $CuBr_2$ or $ZnCl_2$:

XA1 = Xerogel type (A)[$CuCl_2$]/Air **XA2** = Xerogel type (A)[$ZnCl_2$]/air

XB1 = Xerogel type (B)[$CuCl_2$]/N_2 **XB2** = Xerogel type (B)[$CuCl_2$] + O_2

XB3 = Xerogel type (B)[$CuBr_2$]/N_2 **XB4** = Xerogel type (B)[$CuBr_2$] + O_2

XB5 = Xerogel type (B)[$ZnCl_2$]/air

All details concerning the synthesis of the metallated xerogels can be found elsewhere.[11–13] Samples **XB1**-**XB4** were handled in vacuo in tight cells and filled in glove boxes. Model compounds used as reference for the XANES or EXAFS study included: **1** = Cu(TPP); **2** = Cu(cyclam)$(ClO_4)_2\cdot 0.5H_2O$; **3**[45] = [Cu(tmc)]$(BF_4)_2$; **4**[46] = [Cu(tmc)Cl](BF_4); **5**[46] = [Cu(dmdpc)]$(BF_4)_2$; **6** = [Cu(tpc)Cl]Cl; **7** = [Cu(tpsc)Cl]Cl; **8** = [Zn(tpsc)Cl]Cl. TPP denotes the (*meso*-5,10,15,20-tetraphenylporphyrinato) macrocyclic dianion; cyclam is the 1,4,8,11-tetraazacyclotetradecane ligand; tmc refers to the 1,4,8,11-tetramethyl-1,4,8,11-tetraazacyclotetradecane macrocycle; dmdpc refers to the 1,8-dimethyl-4,11-bis(2-pyridylmethyl)-1,4,8,11-tetraazacyclotetradecane ligand; tpc and tpsc denote the 1,4,8,11-tetrapropyl-1,4,8,11-tetraazacyclotetradecane and the 1,4,8,11-tetrakis(trimethylsilylpropyl)-1,4,8,11-tetraazacyclotetradecane macrocycle, respectively.

Instruments and Methods: X-ray absorption and emission spectra were recorded with the ESRF beamline ID12.[47] The X-ray source is a helical undulator which, for the present project, was operated in the linear polarization mode. In order to scan EXAFS spectra over 2000 eV, we used the so-called "*gap-scan*" technique[48] which consists of optimizing the magnetic gap of the undulator during a scan of the monochromator in such a way that the energy of the monochromatic photons always matches the peak intensity of the undulator spectrum. The monochromator was equipped with a pair of Si (111) crystals cooled down to 152 K. The energy resolution was very close to the intrinsic limits, i.e. $\Delta E \approx 0.40$ eV at the Cl K-edge; $\Delta E \approx 1.56$ eV (1.72 eV) at the Cu (Zn)K-edges. The energy calibration was consistent with the SSRL criterion assigning the first inflexion point of the Cu foil XANES spectrum to 8980.3 eV.[49] Vertically focusing double mirrors (VFM) allowed us to keep the level of unwanted harmonics well below 5 orders of magnitude. EXAFS or XANES spectra were systematically recorded in the (integrated) Fluorescence Yield (FY) mode. Sample pellets were inserted in a vacuum-tight sample holder and were excited by the incident X-ray beam through a 12.5 μm thin Kapton window (5 mm active diameter). The sample holder (cooled down to 80 K) was itself located inside a high vacuum fluorescence chamber equipped with eight low noise photodiodes arranged in the backscattering geometry and collecting the fluorescence photons emitted over a wide solid angle. X-ray emission spectra were recorded in the spectral ranges of the Cu $K\beta_{1,3}$ (and $K\beta_{2,5}$) fluorescence lines using a high resolution spectrometer equipped with a spherically bent Si (220) crystal analyzer operated with the 440 reflection at a Bragg angle of 46.17°. The analyzer energy scale was calibrated against that of the double crystal monochromator by measuring the elastic scattering line of the reference sample **1**.

EXAFS Data Collection and Analyses: High quality Cu K-edge EXAFS spectra were recorded on model compounds **1** = Cu(TPP), **3** = [Cu(tmc)]$(BF_4)_2$ and **6** = [Cu(tpc)Cl]Cl as well as on xerogels **XA1**, **XB1**, **XB2**, **XB3** and **XB4**. For each sample, several long scans (2500 data points) were collected at low temperature (T = 80 K) over a very wide energy range [i.e. 8944–10941 eV]. No radiation damage was detected and all accumulated spectra could be averaged. EXAFS oscillations could be detected up to k = 20–22 $Å^{-1}$ in $k.\chi(k)$ spectra (Figures S1–S3 in the Supporting Information), even for the xerogels in which the metal concentration was rather low. We found a double benefit in collecting EXAFS data over a wide range in the momentum space: (i) the resolution of the FT spectra in the direct space was maximized; (ii) the identification of the signatures of heavy scattering atoms (i.e. Cu, Br or Cl) in the FT spectra by varying k_{max} in the window function was easier.

EXAFS spectra were also recorded at the Cl K-edge for xerogels **XB1** and **XB2**. The presence of a weak potassium K-edge signal at 3610 eV (associated with trace amounts of this element nonuniformly distributed over the Kapton window) in the spectra required us to truncate the $k\cdot\chi(k)$ spectra for $k \geq 14.4$ $Å^{-1}$ (see Figure S4 in the Supporting Information). A very weak argon K edge at

 © 2005 Wiley-VCH Verlag GmbH & Co. KGaA, Weinheim

3200 eV was identified which was treated as a second order perturbation.

The EXAFS analyses followed standard procedures detailed elsewhere.[14] The spectra recorded in FY detection mode were systematically corrected for self-absorption.[14,50] Throughout this paper, phase and amplitude corrected "optical" FT spectra[14] were displayed. Phase shifts and backscattering amplitudes were generated using the code FEFF8.9.[51,52] Numerical fitting methods in both the direct and reciprocal spaces[14] were also available as options in our EXAFS data analysis package.

XANES: Numerical Deconvolution and ab initio Simulations: The convoluted effects of the core hole lifetime and of the finite energy resolution of the monochromator resulted in smooth but broad Voigt lineshapes, which restricted the possibility of resolving and assigning the pre-edge and shape resonances in the experimental XANES spectra. Following a strategy pioneered at the ESRF by Loeffen et al.,[53] the experimental XANES spectra were deconvoluted numerically in order to recover narrow lineshapes. The price to be paid was an artificial increase of the noise level in the XANES spectra. XANES spectra were simulated with the advanced code FDMNES which offers two options:

(i) Multiple Scattered Wave (MSW) calculations can be carried out with muffin-tin potentials spherically averaged in the atomic or outer-sphere regions but only volume-averaged in the interstitial region. In practice, the averaged muffin-tin zero ($V0_{imp}$) is a critical parameter that needs to be carefully adjusted. Muffin-tin radii can be automatically determined from standard prescriptions (e.g. using the Norman criterion[54]). Local electronic densities were obtained by superposition of atomic contributions but the Clementi–Roetti atomic wave functions[55] can be replaced by external wave functions taking into account relativistic effects (as in FEFF8.10). The occupancy of the valence orbitals can be artificially altered in order to simulate charge transfers between atoms that are no longer neutral. The Coulomb potential was then calculated by solving the Poisson equation where the energy dependent exchange-correlation potential was approximated either by a standard Xα functional density or by the real part of a Hedin–Lundqvist functional.[56]

(ii) In the finite-difference method (FDM)[57] the Schrödinger equation was solved over a grid of discrete points in a spherical volume centered at the absorbing atom. There is no need to introduce any artificial spherical symmetry or to define any interstitial region. This is most appreciable in the case of directional covalent bonding. In the present study, the lack of an arbitrarily defined muffin-tin zero was essential in order to accurately determine the contribution of Cu^{I} and Cu^{II} sites. The occupancy of the valence orbitals was artificially altered to simulate charge transfers between atoms just as in the MSW option. Unfortunately, FDM calculations resulted in a dramatic increase in computing time, which required us to perform our calculations on the powerful NEC SX-5 machine of the CNRS in Orsay (IDRIS).

Supporting Information Available (see also footnote on the first page of this article): This includes: (i) selected *raw* experimental EXAFS spectra; (ii) a detailed EXAFS study of model compounds **1**, **3** and **6**; (iii) Figure S7 illustrating the quality of the single shell fit of the Cu–O1 signal in the FT difference spectrum; (iv) Table S1 listing the parameters of scattering paths contributing to the simulated FT difference spectrum displayed in Figure 1(B); (v) a comparison of numerically deconvoluted and raw Cu K-edge XANES spectra for the model compound **1** as well as for all xerogels complexed with $CuCl_2$; (vi) Table S2 listing the peak energy and relative intensities of the resolved resonances (A)–(E).

Acknowledgments

This work is part of a joint collaboration supported by AIR-LIQUIDE and the French C.N.R.S. The allocation of 220 hours of free computing time on the NEC SX-5 machine of the IDRIS computing center in Orsay was greatly appreciated.

[1] C. K. Jørgensen, R. Reisfeld, *Struct. Bonding* **1996**, *85* (251 pages).
[2] Selected Papers on Sol-Gel for Photonics, in *SPIE Milestone Series, Vol. MS 148* (Ed.: S. I. Najafi), **1998**, 522 pages.
[3] R. J. P. Corriu, D. Leclercq, *Angew. Chem. Int. Ed. Engl.* **1996**, *35*, 1420–1436.
[4] R. J. P. Corriu, *Angew. Chem. Int. Ed.* **2000**, *39*, 1376–1398.
[5] B. Boury, R. J. P. Corriu, *Chem. Commun.* **2002**, 795–802.
[6] E. K. Barefield, F. Wagner, *Inorg. Chem.* **1973**, *12*, 2435–2439.
[7] L. Fabbrizzi, A. Poggi, *J. Chem. Soc. Chem. Commun.* **1980**, 646–647.
[8] R. Machida, E. Kimura, M. Kodama, *Inorg. Chem.* **1983**, *22*, 2055–2061.
[9] L. Fabbrizzi, M. Licchelli, P. Pallavicini, L. Parodi, *Angew. Chem. Int. Ed.* **1998**, *37*, 800–802.
[10] M. Meyer, V. Dahaoui-Gindrey, C. Lecomte, R. Guilard, *Coord. Chem. Rev.* **1998**, *178–180*, 1313–1405.
[11] G. Dubois, Ph. D. Thesis, Université de Montpellier-II **1999**.
[12] G. Dubois, R. J. P. Corriu, C. Reyé, S. Brandès, F. Denat, R. Guilard, *Chem. Commun.* **1999**, 2283–2284.
[13] G. Dubois, C. Reyé, R. J. P. Corriu, S. Brandès, F. Denat, R. Guilard, *Angew. Chem. Int. Ed.* **2001**, *40*, 1087–1090.
[14] J. Goulon, C. Goulon-Ginet, V. Gotte, X-ray Absorption Spectroscopy Applied to Porphyrin Chemistry, in: *The Porphyrin Handbook, Vol. 7* (Eds.: K. M. Kadish, K. M. Smith, R. Guilard), **2000**, 79–166.
[15] J. L. Poncet, R. Guilard, P. Friant, C. Goulon-Ginet, J. Goulon, *Nouv. J. Chim.* **1984**, *8*, 583–590.
[16] J. S. Griffith, *The Theory of Transition Metal Ions*, Cambridge University Press, Cambridge, **1961**.
[17] T. Sakurai, K. Kobayashi, H. Masuda, S. Tsuboyama, K. Tsuboyama, *Acta Crystallogr. Sect. C* **1983**, *39*, 334–337.
[18] S. Tsuboyama, K. Kobayashi, T. Sakurai, K. Tsuboyama, *Acta Crystallogr. Sect. C* **1984**, *40*, 1178–1181.
[19] K. Panneerselvam, T.-H. Lu, H. Aneetha, Y.-H. Lai, S.-C. Lin, C.-S. Chung, *Anal. Sci.* **1999**, *15*, 499–500.
[20] N. Kitajima, K. Fujisawa, C. Fujimoto, Y. Morooka, S. Hashimoto, T. Kitagawa, K. Toriumi, K. Tatsumi, A. Nakamura, *J. Am. Chem. Soc.* **1992**, *114*, 1277–1291.
[21] A. F. Wells, *Acta Crystallogr.* **1949**, *2*, 175–180.
[22] A. F. Wells, in: *Structural Inorganic Chemistry*, 4th Edition, The Clarendon Press, Oxford, **1975**, Chapter 25.
[23] A. A. Voronova, B. K. Vainshtein, *Sov. Phys. – Crystallogr.* **1958**, *3*, 445–451.
[24] A. A. Voronova, B. K. Vainshtein, *Sov. Phys. Crystallogr.* **1973**, *18*, 63–66.
[25] H. R. Oswald, Y. Iitaka, S. Locchi, A. Ludi, *Helv. Chim. Acta* **1961**, *44*, 2103–2109.
[26] M. Loos, J. Goulon, M. Bertucci, R. Bachelard, *J. Phys.* **1986**, *47*, 285–288.
[27] M. Loos, J. Goulon, M. Bertucci, R. Bachelard, *Physica B* **1989**, *158*, 188–190.
[28] M. Loos, Ph. D. Thesis, Université de Nancy-I **1990**.
[29] A. G. Blackman, W. B. Tolman, *Struct. Bonding* **2000**, *97*, 179–211.
[30] L. M. Mirica, X. Ottenwaelder, D. Stack, *Chem. Rev.* **2004**, *104*, 1013–1046.
[31] R. R. Jacobson, Z. Tyeklar, A. Farooq, K. D. Karlin, S. Liu, J. Zubieta, *J. Am. Chem. Soc.* **1988**, *110*, 3690–3692.
[32] Z. Tyeklar, R. R. Jacobson, N. Wei, N. N. Murthy, J. Zubieta, K. D. Karlin, *J. Am. Chem. Soc.* **1993**, *115*, 2677–2689.

 © 2005 Wiley-VCH Verlag GmbH & Co. KGaA, Weinheim

[33] K. Komiyama, H. Furutachi, S. Nagatomo, A. Hashimoto, H. Hayashi, S. Fujinami, M. Suzuki, T. Kitagawa, *Bull. Chem. Soc. Jpn.* **2004**, *77*, 59–72.
[34] M. Becker, F. W. Heinemann, S. Schindler, *Chem. Eur. J.* **1999**, *5*, 3124–3129.
[35] M. Weitzer, S. Schindler, G. Brehm, S. Schneider, E. Hörmann, B. Jung, S. Kaderli, A. D. Zuberbühler, *Inorg. Chem.* **2003**, *42*, 1800–1806.
[36] S. R. Breeze, S. Wang, *Inorg. Chem.* **1996**, *35*, 3404–3408.
[37] J. L. Fulton, M. M. Hoffmann, J. G. Darab, B. J. Palmer, E. A. Stern, *J. Phys. Chem. A* **2000**, *104*, 11651–11663.
[38] G. J. A. A. Koolhaas, W. L. Driessen, J. Reedijk, J. L. Van der Plas, R. A. G. De Graaff, *Inorg. Chem.* **1996**, *35*, 1509–1517.
[39] F. Hanic, *Acta Crystallogr.* **1959**, *12*, 739–744.
[40] B. Scott, R. Willett, L. Porter, J. Williams, *Inorg. Chem.* **1992**, *31*, 2483–2492.
[41] J. C. Dyason, P. C. Healy, L. M. Engelhardt, C. Pakawatchai, V. A. Patrick, C. L. Raston, *J. Chem. Soc. Dalton Trans.* **1985**, 831–838.
[42] G. A. Bowmaker, P. D. W. Boyd, C. E. F. Rickard, M. L. Scudder, I. G. Dance, *Inorg. Chem.* **1999**, *38*, 5476–5477.
[43] B. Hedman, K. O. Hodgson, E. I. Solomon, *J. Am. Chem. Soc.* **1990**, *112*, 1643–1645.
[44] D. A. Case, M. Karplus, *J. Am. Chem. Soc.* **1977**, *99*, 6182–6194.
[45] C. Bucher, E. Duval, E. Espinosa, J.-M. Barbe, J.-N. Verpeaux, C. Amatore, R. Guilard, *Eur. J. Inorg. Chem.* **2001**, 1077–1079.
[46] C. Amatore, J.-M. Barbe, C. Bucher, E. Duval, R. Guilard, J.-N. Verpeaux, *Inorg. Chim. Acta* **2003**, *356*, 267–278.
[47] J. Goulon, A. Rogalev, C. Gauthier, C. Goulon-Ginet, S. Pasté, R. Signorato, C. Neumann, L. Varga, C. Malgrange, *J. Synchrotron Rad.* **1998**, *5*, 232–238.
[48] A. Rogalev, V. Gotte, J. Goulon, C. Gauthier, J. Chavanne, P. Elleaume, *J. Synchrotron Rad.* **1998**, *5*, 989–991.
[49] L.-S. Kau, J. Spira-Solomon, J. E. Penner-Hahn, K. O. Hodgson, E. I. Solomon, *J. Am. Chem. Soc.* **1987**, *109*, 6433–6442.
[50] J. Goulon, C. Goulon-Ginet, R. Cortès, J.-M. Dubois, *J. Phys.* **1982**, *43*, 539–548.
[51] J. J. Rehr, J. Mustre de Leon, S. I. Zabinsky, R. C. Albers, *J. Am. Chem. Soc.* **1991**, *113*, 5135–5140.
[52] A. L. Ankudinov, J. J. Rehr, *Phys. Rev. B* **2000**, *62*, 2437–2445.
[53] P. W. Loeffen, R. F. Pettifer, S. Müllender, M. A. Van Veenendaal, J. Röhler, D. S. Sivia, *Phys. Rev. B* **1996**, *54*, 14877–14880.
[54] J. G. Norman, *Mol. Phys.* **1976**, *31*, 1191–1198.
[55] E. Clementi, C. Roetti, *Atom. Data Nucl. Data Tables* **1974**, *14*, 177–478.
[56] L. Hedin, B. I. Lundqvist, *J. Phys. C: Solid State Phys.* **1971**, *4*, 2064–2083.
[57] Y. Joly, *Phys. Rev. B* **2001**, *63*, 125120 (10 pages).

Received: December 14, 2004
Published Online: June 7, 2005

 © 2005 Wiley-VCH Verlag GmbH & Co. KGaA, Weinheim

Trialkoxysilyl-Functionalized Silver(I) Carboxylates: New Building Blocks for the Synthesis of Immobilizable and Immobilized Homogeneous Catalysts

Kati Vehlow,[a,b] Katrin Köhler,*[a][‡] Siegfried Blechert,[b] Sebastian Dechert,[c] and Franc Meyer[c]

Keywords: Silver / Carboxylate ligands / Fluorinated ligands / Immobilization / Silica / Catalysis

Partly fluorinated trialkoxysilyl-substituted carboxylic acids $(RO)_3Si(CH_2)_3N(R')C(O)(CF_2)_3COOH$ (**3a**: R = Et, R′ = H; **3b**: R = R′ = Me) have been prepared in a straightforward synthesis from the respective trialkoxysilyl-substituted primary and secondary amines and hexafluoroglutaric anhydride. Treatment with silver(I) oxide yields the corresponding silver carboxylates **4a**,**b** which have been thoroughly characterized in solution and in the solid state, including an X-ray crystallographic analysis of **4a**. The molecular structure of **4a** consists of archetypal carboxylate-bridged disilver(I) pairs with a strong closed-shell Ag–Ag (d^{10}–d^{10}) interaction and a unique intramolecular bond between a silyl ether group and the metal ion. In addition the amide oxygen atoms are involved in H-bonding and in intermolecular silver coordination, giving rise to an unusual two-dimensional network structure. Silyl-free acid $iPr_2NC(O)(CF_2)_3COOH$ (**5**) and its silver salt **6** have been prepared and structurally characterized for comparison. It is shown that the trialkoxysilyl tail in **4a**,**b** allows for convenient attachment of these silver complexes to silica surfaces, as is corroborated by DRIFT measurements. The immobilized silver carboxylates **7a**,**b** exhibit remarkable stability and are expected to open an easy access to a wide variety of SiO_2-grafted transition metal catalysts via transfer of the carboxylate ligand in simple exchange reactions.
(© Wiley-VCH Verlag GmbH & Co. KGaA, 69451 Weinheim, Germany, 2005)

Introduction

For several decades, the immobilization of homogeneous catalysts has been a major topic and has been pursued in various academic and industrial laboratories.[1] Stimulus for this comes from the great benefits of combining the advantages of homogeneous (high activity, high selectivity, high reproducibility) and heterogeneous (easy separation and recovery of the catalyst from the reaction mixture) catalysis.[2]

One of the major drawbacks of homogeneous catalysts is the need for separation of the relatively expensive catalysts from the reaction mixture at the end of the process. A solution to this separation problem is the use of immobilized homogeneous catalysts, which can be recovered from the reaction mixture by simple filtration or centrifugation and then, potentially, be reused.[3,4] In addition to this separation advantage, the catalytic performance of the immobilized catalysts, e.g. stability and selectivity, are sometimes improved compared to their homogeneous analogs.[5,6] Therefore, there is a growing need to develop more efficient and practical immobilization methods.

The most widely used method of immobilization of homogeneous transition metal catalysts is the binding of at least one of the catalyst ligands to a solid support via a covalent bond. Immobilization can be done either on inorganic or organic polymer support materials. Inorganic materials such as silica have many advantages compared to the organic materials: high chemical stability, high mechanical stability, no swelling properties, excellent thermal stability and an almost unlimited access to tailor-made particles including tailor-made surfaces.[7] A common and easy method for the immobilization of functionalities on SiO_2 surfaces is the reaction of alkoxysilyl-substituted functionalities with the OH groups of silica.[5,7] However, the number of available alkoxysilyl-substituted catalyst ligands is limited – especially alkoxysilyl-substituted anionic ligands are very rare. Thus there is great interest in new and versatile building blocks, which can easily be covalently combined with the support material on one side and with the metal atom of the homogeneous catalyst on the other.

Many homogeneous catalysts based on e.g. ruthenium, rhodium, tungsten, cobalt, palladium or copper contain halogen atoms, which do not participate in the catalytic cycle.[8–10] Replacement of those halogen atoms by other ligands such as anionic carboxylates has recently been explored for several catalyst systems.[11–13] It has often been observed that the catalytic performance of the carboxylate-

[a] Merck KGaA,
Frankfurter Strasse 250, 64293 Darmstadt, Germany
[b] Institut für Chemie, Technische Universität Berlin,
Strasse des 17. Juni 135, 10623 Berlin, Germany
[c] Institut für Anorganische Chemie, Georg-August-Universität Göttingen,
Tammannstrasse 4, 37077 Göttingen, Germany
[‡] New address: Sartorius AG,
Weender Landstrasse 94–108, 37075 Göttingen, Germany
Fax: +49-551-3082510
E-mail: katrin.koehler@sartorius.com

 DOI: 10.1002/ejic.200500082 © 2005 Wiley-VCH Verlag GmbH & Co. KGaA, Weinheim

substituted catalysts is in the same range as the parent halogen-substituted catalysts. Therefore, we were searching for new type **A** building blocks bearing two functionalities (Scheme 1): an immobilizable alkoxysilyl-group and an accessible carboxylic acid group that after deprotonation may act as a ligand towards transition metal ions. Silver salts of these functional carboxylates are sought as suitable synthons that will allow subsequent attachment of the metal complex fragment via halide exchange, forming the respective silver halide.

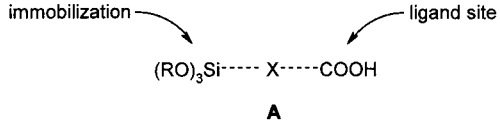

Scheme 1.

With respect to the spacer X, fluorinated moieties are of particular interest, since they may provide favorable solubility and higher stability of the silver salts and of the resulting metal carboxylate complexes. In addition, electron-withdrawing carboxylates have proven superior in various catalytic processes.[12–14]

In this contribution, we report on the synthesis and spectroscopic properties of two new partly fluorinated trialkoxysilyl-substituted silver(I) carboxylates with a type **A** backbone. A related fluorinated silver(I) carboxylate lacking the silyl group has been prepared for comparison, and unusual structural features of these complexes in the solid state are described. It should be noted that silver(I) carboxylates have been intensively studied for their rich and diverse structural chemistry in the solid state,[15–17] and silver(I) complexes with fluorinated carboxylates have previously attracted interest as potential precursors for chemical vapor deposition (CVD) yielding metallic silver layers.[18–20]

Results and Discussion

Synthesis and Spectroscopy

Partly fluorinated trialkoxysilyl-substituted carboxylic acids **3** were prepared in almost quantitative yields by the reaction of the trialkoxysilyl-substituted primary amine **1a** and secondary amine **1b** with hexafluoroglutaric anhydride (**2**) in tetrahydrofuran (Scheme 2). The reactions have to be carried out in the absence of water to avoid hydrolysis of the silyl function, which is catalyzed by acidic protons. Products **3a** and **b** can be isolated as colorless oils or used in situ in the next step of the synthetic sequence. Compound **3a** has been mentioned previously but was not isolated.[13]

IR spectra of acids **3a**,**b** (Table 1) show the characteristic bands for $\tilde{\nu}_{as}$(COO) at 1775 cm^{-1} (**3a**) or 1781 cm^{-1} (**3b**) and for $\tilde{\nu}_{s}$(COO) at 1445 cm^{-1} (**3a**) or 1464 cm^{-1} (**3b**) as well as

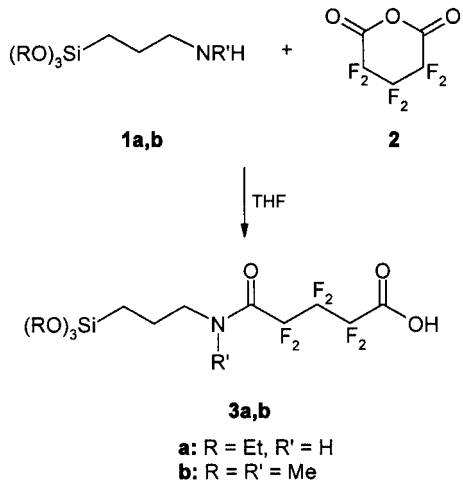

Scheme 2. Synthesis of the trialkoxysilyl-functionalized carboxylic acids **3**.

strong absorptions for the C–F stretches around 1165 cm^{-1}. As expected for an *N*-monosubstituted amide,[21] **3a** features two bands at 1703 and 1549 cm^{-1} (amide I and amide II, respectively), while a single band at 1679 cm^{-1} is observed for *N*,*N*-disubstituted amide **3b**. Distinct ^{1}H, ^{13}C, and ^{19}F NMR signals for the *E* and *Z* amide isomers are detected for **3b**, revealing an *E*/*Z* ratio of 0.62:1 at 297 K.

Table 1. Characteristic IR spectral frequencies in cm^{-1}.

Compound	$\tilde{\nu}_{as}$(COO)	$\tilde{\nu}_{s}$(COO)	$\Delta\tilde{\nu}$[a]	$\tilde{\nu}$(CON)	$\tilde{\nu}$(CF)
3a (film)	1775	1445	330	1703/ 1549	1168
3b (film)	1781	1464	317	1679	1160
5 (film)	1785	1452	333	1654	1172/1158
5 (KBr)	1769	1451	318	1642	1176/1151
4a (THF)	1691	1391	300	1716/1550	1153
4a (MTBE)	1658	1407	251	1722/1541	1169
4a (KBr)	1687	1393	294	1706/1549	1163
4b (THF)	1685[b]	1401	[b]	1658[b]	1164
4b (MTBE)	1685[b]	1407	[b]	1659[b]	1166
4b (film)	1651(br)	1401	250	1651(br)	1160
6 (THF)	1679	1384	295	1679	1151
6 (MTBE)	1681	1386/1369	≈300	1658	1159
6 (KBr)	1687(sh)/1675	1393	≈290	1687(sh)/1675	1150
7a (DRIFT)	1664	n.a.	n.a.	1713/1539	n.a.
7b (DRIFT)	1669(br)	n.a.	n.a.	1669(br)	n.a.

[a] $\Delta\tilde{\nu} = \tilde{\nu}_{as}$(COO) – $\tilde{\nu}_{s}$(COO) for the silver(I) carboxylate. [b] assignment of $\tilde{\nu}_{as}$(COO) and $\tilde{\nu}$(CON) is tentative, hence no value for $\Delta\tilde{\nu}$ is included. n.a. = not assignable because of SiO_2 absorptions.

Conversion of carboxylic acids **3** into the appropriate silver(I) carboxylates **4** can be achieved by reacting the respective acid **3a**,**b** with silver(I) oxide in MTBE. Alternatively, acids **3** generated in situ from the respective amine **1a**,**b** and hexafluoroglutaric anhydride (**2**) can be directly converted into **4a**,**b** by the addition of silver(I) oxide in MTBE (Scheme 3). Following the latter method the reaction mixture was stirred overnight at room temperature in the dark. After filtration and removal of the solvent, complex **4a** was obtained as a colorless solid while **4b** was isolated as a colorless oil.

 © 2005 Wiley-VCH Verlag GmbH & Co. KGaA, Weinheim

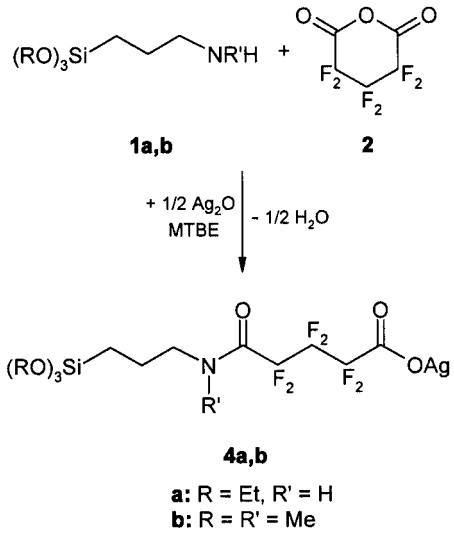

Scheme 3. Synthesis of the trialkoxysilyl-functionalized silver carboxylates **4**.

Formation of the silver carboxylate complexes **4a**,**b** is confirmed by the absence of $\tilde{\nu}_{as}$(COO), $\tilde{\nu}_{s}$(COO) vibrations for the free acids and the appearance of distinct $\tilde{\nu}_{as}$(COO) and $\tilde{\nu}_{s}$(COO) stretches around 1680 and 1395 cm^{-1} (Table 1).[22] In contrast, the characteristic bands for the amide functions in **4a**,**b** are barely shifted from their position in **3a**,**b**.[23] The separation of the $\tilde{\nu}_{as}$(COO) and $\tilde{\nu}_{s}$(COO) stretches of around $\Delta\tilde{\nu}$ = 290 cm^{-1} for **4a** may indicate a bridging carboxylate coordination (compare the crystallographic results, vide infra).[23,24] As noted previously, however, the precise type of carboxylate coordination cannot be proposed on the basis of the $\Delta\tilde{\nu}$ parameter.[19,24] Formation of silver carboxylate complexes is further corroborated by a significant low-field shift of the carboxylic ^{13}C NMR resonance from around 160.8 ppm in the acids **3a**,**b** to around 163.8 ppm in **4a**,**b**. At the same time the ^{13}C NMR resonance for the amide group is almost unchanged at around 158.7 ppm.

Proper solvent selection is critical for the formation of pure products **4**. While the reaction mixture is colorless in MTBE and a colorless product is isolated from this solvent, the reaction mixture turns yellow in THF and a deeply yellow product is obtained in the latter case. The color of the product remains yellow even after complete removal of THF. All attempts to further purify these yellow products or to identify the colored species failed. However, the highly colored impurity can only be present in trace amounts, since X-ray crystallographic analyses of the materials **4a** obtained from both solvents gave identical results (vide infra) and the IR spectra of KBr pellets of both materials are basically identical ($\Delta\tilde{\nu} \approx 294\ cm^{-1}$). In contrast to MTBE, THF appears to coordinate to the silver ions in **4a** in solution, since ^{1}H NMR spectroscopic experiments in CD_2Cl_2 reveal a slight shift of the THF solvent signal to lower field. Furthermore, IR absorptions for the $\tilde{\nu}_{as}$(COO) and $\tilde{\nu}_{s}$(COO) stretches of **4a** measured in either THF or MTBE solution show significant differences (Table 1), with $\Delta\tilde{\nu}$ being 300 cm^{-1} in THF while being 251 cm^{-1} in MTBE (amide I and amide II bands for **4a** are quite similar in the two solvents). If isolated as pure compounds **4a** and **4b** are stable at room temperature and show no significant light sensitivity. Upon heating the color of solid **4a** and **4b** changes from colorless via red to brown, and at 160 °C formation of a silver film occurs. In solution, compounds **4** start to decompose under light at room temperature within several days. No decomposition is observed when keeping the solution at –20 °C under exclusion of light.

In order to investigate the influence of the alkoxysilyl group on the stability and structural features of type **4** compounds, an analog of **4** devoid of the alkoxysilyl group has been synthesized from the route shown in Scheme 4. The alkoxysilyl-free acid **5** can be readily prepared from diisopropylamine and hexafluoroglutaric anhydride in dichloromethane. Crystallization from dichloromethane/hexane at room temperature gave colorless X-ray quality crystals of **5**. Attempts to carry out the synthesis of **5** in MTBE or THF leads to the formation of the diamide $iPr_2NC(O)(CF_2)_3C(O)NiPr_2$.

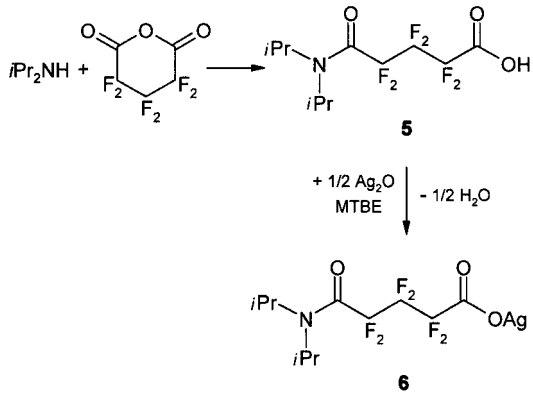

Scheme 4. Synthesis of the silyl-free carboxylic acid **5** and the silver carboxylate **6**.

Addition of **5** to a suspension of silver(I) oxide in MTBE leads to the formation of the silyl-free silver(I) carboxylate **6** (Scheme 4). After stirring the reaction mixture in the dark for 4 h at room temperature, the colorless product is conveniently isolated by filtration followed by removal of the solvent. Crystals of **6** could be obtained by diffusion of hexane into a saturated solution of the crude product in chloroform. If carried out in THF instead of MTBE the color of the reaction solution turned yellow and a yellow product was isolated, just like the observation made with the earlier described silver(I) carboxylates **4a** and **4b**. IR spectral features of **6** are quite similar if measured either in THF or MTBE solution or as KBr pellets, showing a single broad band for $\tilde{\nu}_{as}$(COO) and $\tilde{\nu}(CO)_{amide}$ at ca. 1680 cm^{-1} and a $\tilde{\nu}_{s}$(COO) band at ca. 1380 cm^{-1}. Compared to the alkoxysilyl-containing silver(I) carboxylates **4** the silyl-free silver(I) carboxylate **6** exhibits much lower thermal stability and much higher light sensitivity. **6** cannot be handled in air due to its strong hygroscopic behavior, and it decomposes within minutes under exposure to light in both solution and

 © 2005 Wiley-VCH Verlag GmbH & Co. KGaA, Weinheim

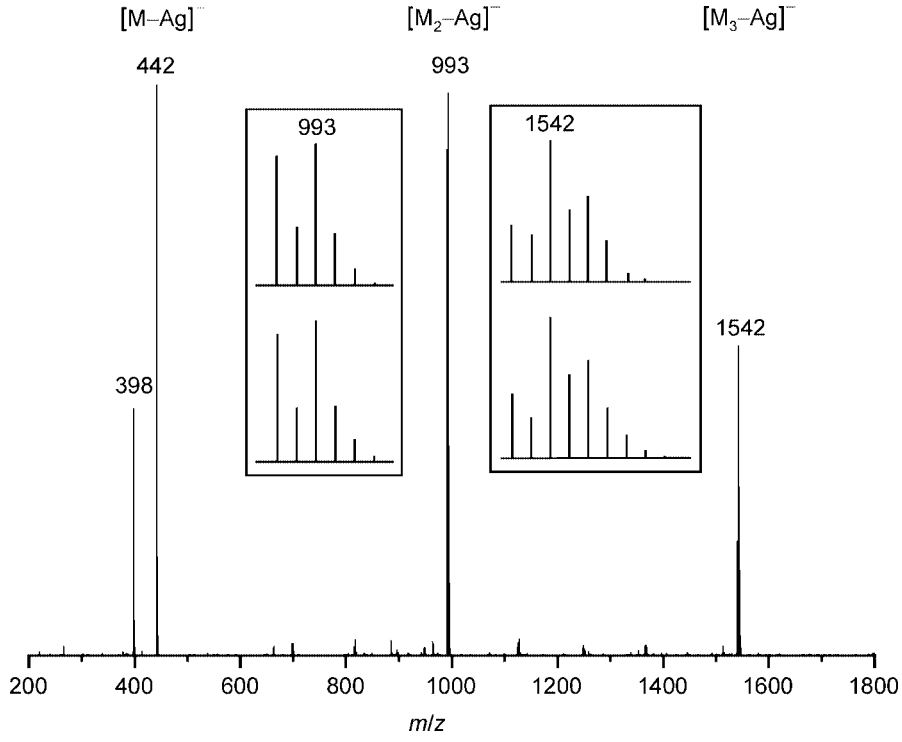

Figure 1. Part of the negative ion ESI mass spectrum of **4a**. The insets show the experimental (upper) and calculated (lower) isotopic distribution pattern for distinct ions $[M_x - Ag]^-$ (x = 2, 3).

as a solid. Upon heating **6** decomposes at around 95 °C turning into a dark colored solid.

Positive ion ESI mass spectra of acetonitrile solutions of all silver carboxylate complexes **4a**, **4b**, and **6** show a prominent peak for simple $[Ag(NCMe)_2]^+$, but minor signals characteristic for various ions $[M_x + Ag]^+$ (x = 1–3) or $[M_x + Na]^+$ (x = 1, 2) are also discernible, thus suggesting the presence of oligomeric aggregates in solution. This is most apparent from the negative ion ESI mass spectrum of **4a** depicted in Figure 1, where all major peaks can be clearly assigned to ions $[M_x - Ag]^-$ (x = 1–3). Aggregation also takes place in the solid state, as is described in the following section.

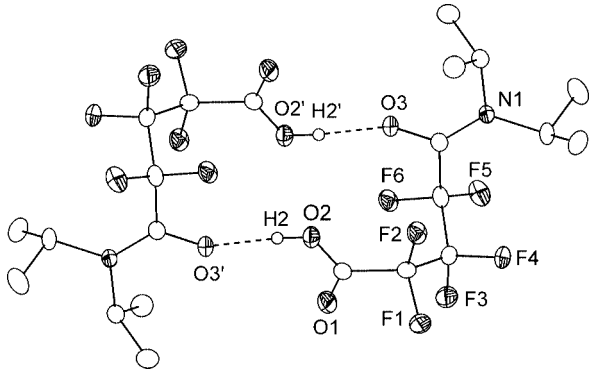

Figure 2. ORTEP plot (30% probability thermal ellipsoids) of the molecular structure of **5**. For the sake of clarity all hydrogen atoms except H2 have been omitted. Selected atom distances [Å] and angles [°]: O2–H2 0.85(3), H2···O3′ 1.75(3), O2···O3′ 2.595(2); O2–H2···O3′ 175(3). Symmetry transformation used to generate equivalent atoms (′): 1 – x, 1 – y, 1 – z.

Crystal Structures

Silver complexes **4a** and **6** have been investigated by X-ray crystallography in order to fully understand their distinct spectroscopic and mass-spectrometric features and to rationalize the different thermal stability and light sensitivity of the alkoxysilyl-substituted and silyl-free silver(I) carboxylates **4** and **6**, respectively. For comparison, the structure of acid **5** has also been determined crystallographically and is shown in Figure 2. Molecular structures of **4** and **6** are depicted in Figure 3, Figure 4 (complex **6**), Figure 5, and Figure 6 (complex **4a**), along with selected atom distances and bond angles.

In the solid state carboxylic acid **5** exists as a dimer composed of two acid molecules that are linked via intermolecular hydrogen bonding (Figure 2). The hydrogen bond occurs between the carboxylic group as an H-donor and the amide-O atom as an H-acceptor, forming an unusual 16-membered ring structure. Though dimer or catemer formation of carboxylic acids via hydrogen bonds between two acid functionalities (**B**; Scheme 5) is an archetypal structural motif and is a mainstay of organic crystal engineering,[25,26] carboxylic acid association involving other groups

 © 2005 Wiley-VCH Verlag GmbH & Co. KGaA, Weinheim

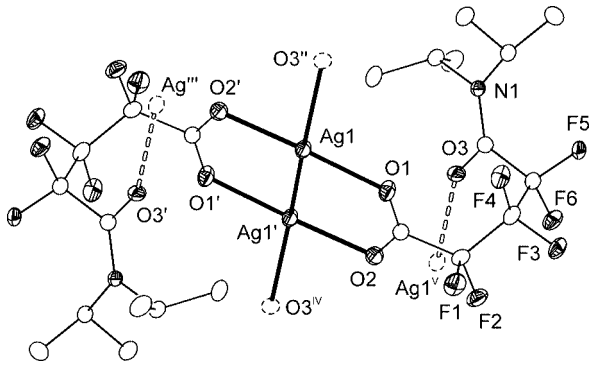

Figure 3. ORTEP plot (30% probability thermal ellipsoids) of the molecular structure of **6**. For the sake of clarity all hydrogen atoms have been omitted. Selected atom distances [Å] and angles [°]: Ag1–O1 2.192(3), Ag1–O2′ 2.219(3), Ag1–O3′′ 2.444(3), Ag1–Ag1 2.9362(8); O1–Ag1–O2′ 159.1(1), O1–Ag1–O3 105.3(1), O1–Ag1–Ag1′ 76.07(7), O2′–Ag1–O3′′ 87.53(9), O2′–Ag1–Ag1′ 85.25(7), O3′′–Ag1–Ag1′ 154.33(7). Symmetry transformations used to generate equivalent atoms (^{I}): 1 – *x*, 1 – *y*, 1 – *z*, (^{II}): 1 + *x*, *y*, *z*, (^{III}): 2 – *x*, 1 – *y*, 1 – *z*, (^{IV}): –*x*, 1 – *y*, 1 – *z*, (^{V}): *x* – 1, *y*, *z*.

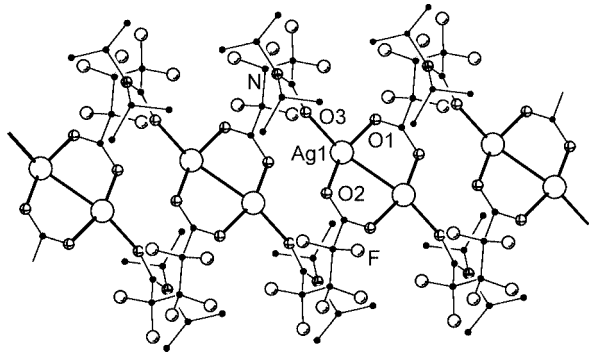

Figure 4. Plot of the chain structure of **6**. For the sake of clarity all hydrogen atoms have been omitted.

such as, e.g., a carbonyl or amide is rather rare if both groups are present in the same molecule.[27]

Reaction of **5** with Ag_2O gives yellow crystals of **6**. The structure consists of carboxylate-bridged metal-pairs **C**, featuring a strong closed-shell interaction that leads to a short Ag–Ag distance of 2.94 Å (Figure 3). Such interactions are quite common for the heavier coinage metals, and metal-metal distances of comparable magnitude have been reported for numerous compounds.[28] Since the coordination sphere of the Ag^+ ions in type **C** dimeric units is generally not satisfied by the two oxygen atoms, coordination of additional donors typically leads to polymeric or oligomeric arrays, and silver carboxylate dimers **C** have thus been exploited as building blocks for the assembly of extended coordination networks.[29] In the present case the Ag–Ag pairs are coated by their two acid molecules, and these pairs constitute subunits of a chain structure that is created through intermolecular coordination of the amide oxygen atoms to next neighbor metal pairs (Figure 4). Taking into account the closed-shell interaction and the coordination of three oxygen atoms, each silver is found in a strongly distorted

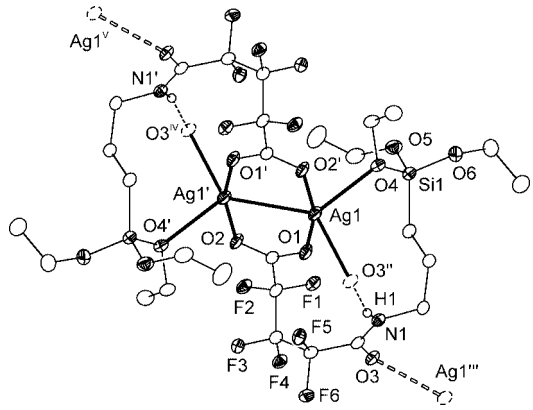

Figure 5. ORTEP plot (30% probability thermal ellipsoids) of the molecular structure of **4a**. For the sake of clarity all hydrogen atoms except H1 have been omitted. Selected atom distances [Å] and angles [°]: Ag1–O1 2.185(3), Ag1–O2′ 2.196(3), Ag1–O3′′ 2.606(2), Ag1–O4 2.606(2), Ag1–Ag1′ 2.9682(6), N1–H1 0.81(4), H1···O3′′ 2.22(4), N1···O3′′ 3.017(4); O1–Ag1–O2′ 161.12(9), O1–Ag1–O3′′ 86.55(8), O1–Ag1–O4 100.13(9), O1–Ag1–Ag1′ 78.42(6), O2′–Ag1–O3′′ 106.47(8), O2′–Ag1–O4 89.67(9), O2′–Ag1–Ag1′ 82.74(6), O3′′–Ag1–O4 105.51(7), O3′′–Ag1–Ag1′ 129.15(6), O4–Ag1–Ag1′ 124.78(5), N1–H1···O3′′ 165(4). Symmetry transformations used to generate equivalent atoms (′): 1 – *x*, 1 – *y*, 1 – *z*, (′′): *x*, ½ – *y*, –½ + *z*, (′′′): *x*, ½ – *y*, ½ + *z*, (^{IV}): 1 –*x*, ½ + *y*, ½ – *z*, (^{V}): 1 – *x*, ½ + *y*, ½ – *z*.

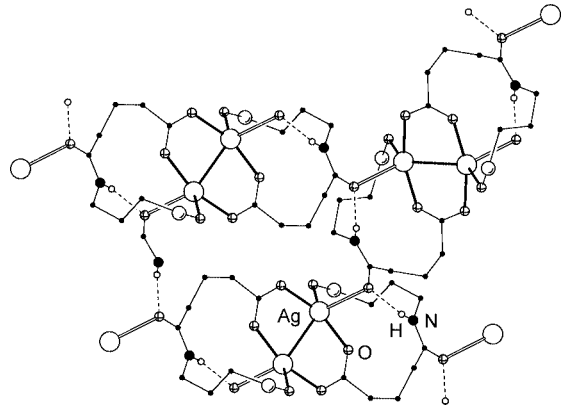

Figure 6. Plot of the network structure of **4a**. For the sake of clarity all hydrogen atoms except H1, all fluorine atoms, two ethoxy groups and the carbon atoms of the coordinating ethoxy group have been omitted.

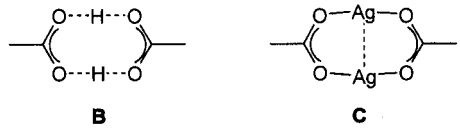

Scheme 5.

square-planar environment [distance to the least-squares planes of the four surrounding atoms is 0.415(1) Å].

A similar type **C** motif with d^{10}–d^{10} interaction and a short Ag–Ag distance of 2.97 Å is also observed for **4a**. In contrast to **6**, however, the silver ions in **4a** show a distorted trigonal-bipyramidal coordination environment, because a silyl ether group is involved in metal ion binding [*d*(Ag1–O4) = 2.606(2) Å, Figure 5]. Oxygen atoms from the car-

 © 2005 Wiley-VCH Verlag GmbH & Co. KGaA, Weinheim

boxylic acid functionalities occupy the axial positions, whereas the adjacent silver ion, an amide oxygen atom and an oxygen atom from the silyl ether group make up the equatorial positions. Direct coordination of silyl ethers to transition metal atoms is quite rare and **4a** is one of the very few structurally characterized examples for the heavier group 11 elements. To the best of our knowledge, **4a** is the only silver compound with a distance between the metal center and the oxygen atom of a Si–O–C fragment which is distinctly below 3 Å.[30] Like in **4a** the Ag–Ag pairs are coated by acid molecules, and additional coordination of oxygen atoms from two adjacent dimeric building blocks results in the formation of a two-dimensional network structure (Figure 6). Each of these amide oxygen atoms at the same time acts as a hydrogen-bond acceptor for the N–H protons of an adjacent amide.

Immobilization

Immobilization of the silver(I) carboxylates **4** onto silica was performed by a pre-treatment step of the silica material followed by the actual immobilization step (Scheme 6). First the silica was successively washed with methanol, dichloromethane and hexane in order to remove any impurities from the SiO_2, and the treated material was dried at 200 °C under high vacuum for 4 h to achieve thermal desorption of physically adsorbed water molecules from the silica gel surface.

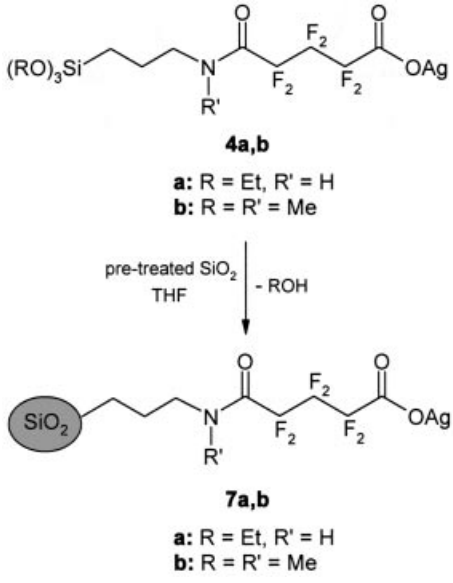

Scheme 6. Immobilization of **4** onto silica gel.

Silver(I) carboxylates **4** were subsequently attached to the silica surface by adding a solution of **4** in THF to a silica/THF suspension and stirring the reaction mixture at room temperature for 21 h in the dark. Immobilized silver(I) carboxylates **7a** and **b** were isolated as white solids by filtration and thoroughly washed with THF and hexane. The combined filtrates were evaporated under vacuum and checked for any remaining starting material. No residual **4** was detected, thus confirming that complete immobilization had occurred. This corresponds to an immobilization ratio of 0.1 mmol of **4** per g of SiO_2 and accordingly 5 wt.-% of **4**, which is a good ligand loading rate for a potential subsequent transformation of the silver(I) carboxylates into powerful immobilized catalysts.[31–33] Immobilized silver(I) salts **7** show remarkable stability when taking into account that stabilization of their homogeneous silver(I) precursors **4** occurred by aggregation, which is necessarily reduced upon covalent immobilization of **4** on the silica surface. The immobilized silver(I) salts **7** start to decompose under light at room temperature within several days; when kept under the exclusion of light they can be stored over a period of a few weeks without decomposition. Upon heating, the color of **7** changes from white to yellow (90 °C) to brown (180 °C).

DRIFT (Diffuse Reflectance Infra-red Fourier Transform) measurements of **7a**,**b** confirm the adsorption of the silver carboxylate compounds onto the silica. The pre-treated silica shows, inter alia, the expected sharp peak at 3747 cm^{-1} for isolated noninteracting silanol groups and broad bands at 1993, 1862, 1625, 1195, 980, and 845 cm^{-1} for the H–O–H (adsorbed water) and Si–O–Si modes of silica itself.[34–36] While these features remain unchanged in **7a**,**b**, additional peaks appear at 1713, 1664 and 1539 cm^{-1} (**7a**) or 1669 cm^{-1} (**7b**). This is close to the position of the $\tilde{\nu}_{as}$(COO) and $\tilde{\nu}$(CON) modes of the respective precursor compounds **4a**,**b** (Table 1), in agreement with nondestructive adsorption of complexes **4a**,**b** onto the silica.

Conclusions and Outlook

A straightforward synthetic approach is reported for some new silver(I) carboxylates that incorporate a partly fluorinated tail with an appended trialkoxysilyl substituent. The silver carboxylate complexes have been thoroughly characterized both in solution and in the solid state and have been found to form oligonuclear or polymeric assemblies that are based on archetypal carboxylate-bridged disilver(I) units with short d^{10}–d^{10} interactions. Inter alia, an unusual coordination of an alkoxysilyl oxygen atom towards silver has been discovered.

The trialkoxysilyl anchor enables a convenient attachment of complexes **4a**,**b** to silica surfaces. The future potential of the newly prepared immobilizable type **4** compounds and immobilized type **7** compounds is summarized in Scheme 7. The development of the flexible fluorinated silver carboxylates reported in this work is expected to open an easy access to a wide variety of SiO_2-grafted transition metal species **E** (M = transition metal complex fragment) via simple exchange reactions. Metal exchange may be carried out either before [route (**a**)] or after [route (**b**)] the immobilization step, depending on the specific requirements of the particular system. Since separation of the insoluble silver halides from the silica-bound catalyst may pose a problem, the former route (**a**) should in most cases be advantageous.

 © 2005 Wiley-VCH Verlag GmbH & Co. KGaA, Weinheim

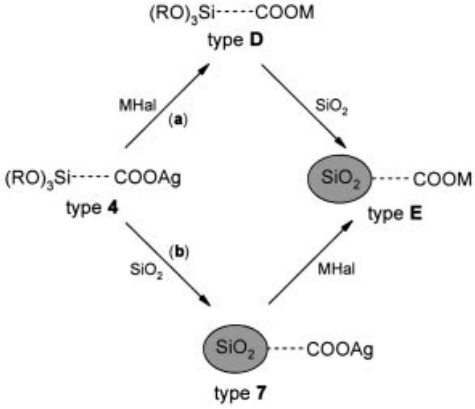

Scheme 7.

A detailed evaluation of various type **E** immobilized transition metal complexes in catalytic reactions will be reported in due course.

Experimental Section

General Remarks: All operations were carried out under argon using standard vacuum and Schlenk techniques or in a glovebox under argon (Labmaster 130, MBraun, Germany). All solvents were dried and purified by passing them through suitable drying columns or by employing standard drying agents.[37,38] 3-(Triethoxysilyl)propylamine (Fluka), 3-(methylamino)propyltrimethoxysilane (ABCR), hexafluoroglutaric anhydride (ABCR), diisopropylamine (Merck) and silver(I) oxide (Merck) were used as received. All stoichiometric calculations involving silica gel (KG 60, Merck) are based on an average surface area of 510 $m^2 g^{-1}$. ^1H and ^{13}C NMR spectra were recorded with a Bruker DPX 250 Advance, Bruker AMX 300 or Bruker DRX 500 Advance at ambient temperature. Data are given in ppm relative to solvent signals for ^1H and ^{13}C NMR spectra or relative to an external standard for ^{19}F NMR experiments ($CFCl_3$ at 0 ppm). IR spectra were recorded with a Bruker Equinox 55 FT-IR instrument as KBr pellets, as films between KBr plates or in solution using a CaF_2 cell. DRIFT measurements (Diffuse Reflectance Infra-red Fourier Transform) were recorded with a Bruker IFS-66 FT-IR instrument; the samples were scanned 256 times. Elemental analyses were measured with a Vario EL. Melting points were obtained with a BÜCHI capillary apparatus B-540. Mass spectra were collected with a Finnigan MAT 8200 (EI, 70 eV) or a Finnigan MAT LCQ (ESI).

$(EtO)_3Si(CH_2)_3N(H)C(O)(CF_2)_3COOH$ (3a):[13] Hexafluoroglutaric anhydride (**2**) (192 μL, 1.40 mmol) dissolved in THF (7.5 mL) was added dropwise to a solution of 3-(triethoxysilyl)propylamine (**1a**) (331 μL, 1.40 mmol) in THF (7.5 mL). The mixture was stirred for 30 min at room temperature, and all volatiles were then removed under reduced pressure at 25 °C. **3a** was isolated as a colorless oil. Yield: 615 mg (99%). $C_{14}H_{23}F_6NO_6Si$ (443.41). ^1H NMR (250 MHz, [D$_8$]THF): δ = 0.58 (t, ^3J = 8.3 Hz, 2 H, SiCH_2), 1.17 (t, ^3J = 7.0 Hz, 9 H, CH_3), 1.63 (pseudo-quint, ^3J = 8.0 Hz, 2 H, SiCH$_2$CH_2), 3.25 (pseudo-q, ^3J = 6.8 Hz, 2 H, CH_2N), 3.78 (q, ^3J = 7.0 Hz, 6 H, OCH_2), 8.32 (br, 1 H, N*H*), 13.53 (s, 1 H, COO*H*) ppm. ^{19}F NMR (235 MHz, [D$_8$]THF): δ = –125.5 (s, 2 F, CF_2), –120.5 (t, $^4J_{F,F}$ = 9.5 Hz, 2 F, CF_2CONH), –119.5 (t, $^4J_{F,F}$ = 9.5 Hz, 2 F, CF_2COOH) ppm. $^{13}C\{^{19}F\}$ NMR (75 MHz, [D$_8$]-THF): δ = 8.4 (SiCH_2), 18.7 (CH_3), 23.5 (SiCH$_2$CH_2), 43.1 (CH_2NH), 58.9 (OCH_2), 109.5 (CF_2COOH), 110.3 (CF_2CON), 111.5 (CF_2), 158.6 (CON), 160.7 (COOH) ppm. MS (EI): *m*/*z* (%) = 425 (47) [M$^+$ – H$_2$O], 352 (100) [M$^+$ – EtOH, – EtO], 220 (33) [(EtO)$_3$SiC$_3$H$_6$NH$^+$], 163 (68) [(EtO)$_3$Si$^+$], 45 (50) [EtO$^+$]. MS (ESI+): *m*/*z* (%) = 1662 (15) [M$_4^+$ – 2 EtOH – H$_2$O], 1634 (13) [M$_4^+$ – 3 EtOH], 1606 (14) [M$_4^+$ – 4 EtOH + H$_2$O], 1578 (7) [M$_4^+$ – 5 EtOH + 2 H$_2$O], 1550 (4) [M$_4^+$ – 6 EtOH + 3 H$_2$O], 1339 (100) [M$_3^+$ + EtOH – 2 H$_2$O], 1311 (72) [M$_3^+$ – H$_2$O], 1283 (26) [M$_3^+$ – EtOH], 1255 (8) [M$_3^+$ – 2 EtOH + H$_2$O], 942 (20) [M$_2^+$ + 2 EtOH – 2 H$_2$O]. IR (film): $\tilde{\nu}$ = 3326 (br), 3088 (w), 2980 (m), 2937 (m), 2896 (m), 1916 (w), 1775 (vs), 1703 (vs), 1549 (m), 1484 (w), 1445 (m), 1412 (w), 1393 (m), 1370 (w), 1350 (w), 1297 (w), 1271 (m), 1246 (m), 1169 (vs), 1081 (s), 1050 (s), 944 (m), 915 (w), 877 (w), 783 (m), 720 (w), 646 (m), 593 (w), 562 (w), 491 (m), 456 (m) cm^{-1}.

$(MeO)_3Si(CH_2)_3N(Me)C(O)(CF_2)_3COOH$ (3b): Analogous to the preparation of **3a**, 3-(methylamino)propyltrimethoxysilane (**1b**) (277 μL, 1.40 mmol) and hexafluoroglutaric anhydride (**2**) (192 μL, 1.40 mmol) were used. **3b** was isolated as a colorless oil. Yield: 575 mg (99%). $C_{12}H_{19}F_6NO_6Si$ (415.36). ^1H NMR (250 MHz, [D$_8$]THF): δ = 0.55 (t, ^3J = 8.3 Hz, 2 H, *Z*-SiCH_2), 0.56 (t, ^3J = 8.4 Hz, 2 H, *E*-SiCH_2), 1.66 (pseudo-quint, ^3J = 8.0 Hz, 2 H, *E*-SiCH$_2$CH_2), 1.80 (pseudo-quint, ^3J = 8.0 Hz, 2 H, *Z*-SiCH$_2$CH_2), 2.95 (s, 3 H, *E*-NCH_3), 3.14 (t, $^5J_{H,F}$ = 2.4 Hz, 3 H, *Z*-NCH_3), 3.37 (t, ^3J = 7.6 Hz, 2 H, *Z*-CH_2N), 3.43 (t, ^3J = 7.7 Hz, 2 H, *E*-CH_2N), 3.52 (s, 9 H, *Z*-OCH_3), 3.53 (s, 9 H, *E*-OCH_3), 13.74 (s, 1 H, COO*H*) ppm. ^{19}F NMR (235 MHz, [D$_8$]THF): δ = –122.5 (s, 2 F, *E*-CF_2), –122.3 (s, 2 F, *Z*-CF_2), –116.4 (t, $^4J_{F,F}$ = 10.0 Hz, 2 F, *Z*-CF_2CON), –116.2 (t, $^4J_{F,F}$ = 10.1 Hz, 2 F, *E*-CF_2CON), –110.5 (t, $^4J_{F,F}$ = 10.0 Hz, 2 F, *Z*-CF_2COOH), –109.9 (t, $^4J_{F,F}$ = 10.0 Hz, 2 F, *E*-CF_2COOH) ppm. $^{13}C\{^{19}F\}$ NMR (75 MHz, [D$_8$]THF: δ = 6.7 (*E*-SiCH_2), 6.9 (*Z*-SiCH_2), 20.6 (*E*-SiCH$_2$CH_2), 22.7 (*Z*-SiCH$_2$CH_2), 34.8 (*E*-NCH_3), 35.0 (*Z*-NCH_3), 50.5 (OCH_3), 52.4 (*E*-CH_2N), 52.9 (*Z*-CH_2N), 109.7 (CF_2COOH), 112.0 (CF_2CON), 112.2 (CF_2), 158.7 (CON), 160.9 (COOH) ppm. MS (ESI+): *m*/*z* = 1680 (25), 1297 (75), 1213 (47) [M$_3^+$ – MeOH], 1299 (14) [M$_3^+$ – 2 MeOH + H$_2$O], 960 (33), 830 (100) [M$_2^+$], 816 (10) [M$_2^+$ – MeOH + H$_2$O]. MS (ESI–): *m*/*z* = 1890 (28) [M$_5^-$ – 4 MeOH – Me$_2$O], 1563 (13) [M$_4^-$ – 3 MeOH], 1517 (100) [M$_4^-$ – 3 MeOH – Me$_2$O], 1180 (93) [M$_3^-$ – 2 MeOH], 1134 (8) [M$_3^-$ – 2 MeOH – Me$_2$O], 797 (18) [M$_2^-$ – MeOH]. IR (film): $\tilde{\nu}$ = 3350 (br), 2950 (m), 2846 (m), 2650 (m), 2514 (m), 1918 (w), 1781 (s), 1679 (s), 1489 (w), 1464 (m), 1414 (m), 1374 (w), 1316 (m), 1271 (m), 1243 (m), 1160 (vs), 1094 (s), 1044 (s), 950 (m), 899 (w), 868 (m), 823 (s), 783 (m), 757 (m), 714 (w), 700 (w), 648 (w), 566 (w), 464 (m) cm^{-1}.

$iPr_2NC(O)(CF_2)_3COOH$ (5): Diisopropylamine (590 μL, 4.2 mmol) was added dropwise to a solution of hexafluoroglutaric anhydride (**2**) (577 μL, 4.2 mmol) in dichloromethane (30 mL) and the reaction mixture was stirred for 1 h at room temperature. Aqueous HCl (6 M, 20 mL) was added and the reaction mixture was stirred for an additional 10 min. The organic layer was separated and dried over $MgSO_4$. This solution was allowed to concentrate slowly under vacuum and small amounts of hexane were added. Large, colorless X-ray quality crystals of **5** were obtained after 2 days. Yield: 767 mg (57%), m.p. 125–126 °C. $C_{11}H_{15}F_6NO_3$ (323.23): calcd. C 40.87, H 4.68, N 4.33; found C 41.0, H 4.6, N 4.2. ^1H NMR (250 MHz, $CDCl_3$): δ = 1.28 (d, ^3J = 6.6 Hz, 12 H, *E*-CH_3), 1.43 (d, ^3J = 6.8 Hz, 12 H, *Z*-CH_3), 3.62 (sept, ^3J = 6.8 Hz, 2 H, *Z*-C*H*), 4.38 (sept, ^3J = 6.6 Hz, 2 H, *E*-C*H*), 10.04 (s, 1 H, COO*H*) ppm. ^{19}F NMR (235 MHz, $CDCl_3$): δ = –121.4 (m, 2 F, CF_2), –114.3 (m, 2 F, CF_2COOH), –109.3 (m, 2 F, CF_2CON) ppm. $^{13}C\{^{19}F\}$ NMR (62.9 MHz, $CDCl_3$): δ = 19.5 (*E*-CH_3), 20.4 (*Z*-CH_3), 48.7 (*Z*-C*H*), 49.7 (*E*-C*H*), 108.6 (CF_2CON), 110.8 (CF_2COOH), 111.3 (CF_2), 158.2 (CONH), 159.5 (COOH). MS (EI): *m*/*z* = 323 (6) [M$^+$], 308 (24) [M$^+$ – CH$_3$], 280 (17) [M$^+$ – *i*Pr],

 © 2005 Wiley-VCH Verlag GmbH & Co. KGaA, Weinheim

266 (100) [M^+ – N*i*Pr], 43 (43) [*i*Pr^+]. IR (KBr): $\tilde{\nu}$ = 3408 (br), 3018 (m), 2986 (s), 2946 (s), 2888 (m), 2831 (m), 2658 (m), 2525 (m), 1769 (vs), 1642 (vs), 1546 (w), 1479 (m), 1451 (m), 1380 (s), 1372 (m), 1359 (m), 1277 (s), 1246 (s), 1176 (vs), 1151 (vs), 1104 (s), 1050 (s), 1020 (s), 941 (s), 927 (m), 904 (m), 896 (m), 877 (m), 820 (m), 774 (m), 740 (m), 718 (s), 637 (m), 626 (m), 589 (m), 560 (m), 516 (w), 488 (w), 414 (w) cm^{-1}. IR (film): $\tilde{\nu}$ = 2981 (s), 2945 (s), 2885 (m), 2831 (m), 2647 (w), 2513 (w), 1785 (s), 1654 (vs), 1477 (m), 1452 (m), 1383 (s), 1353 (m), 1270 (w), 1243 (m), 1172 (vs), 1158 (vs), 1120 (w), 1051 (m), 1026 (m), 942 (m), 927 (w), 895 (m), 874 (m), 815 (m), 801 (m), 780 (w), 755 (w), 719 (m), 653 (w), 619 (m), 572 (w), 495 (w) cm^{-1}.

$(EtO)_3Si(CH_2)_3N(H)C(O)(CF_2)_3COOAg$ (4a): Hexafluoroglutaric anhydride (**2**) (192 μL, 1.40 mmol) dissolved in MTBE (7.5 mL) was added dropwise to a solution of 3-(triethoxysilyl)propylamine (**1a**) (331 μL, 1.40 mmol) in MTBE (7.5 mL). After 10 min the reaction mixture was added to a suspension of silver(I) oxide (324 mg, 1,40 mmol) in MTBE (15 mL). The resulting mixture was stirred for 18 h at room temperature in the dark. After filtration all volatiles were removed under full vacuum and **4a** was obtained as pure colorless crystals. Yield: 674 mg (88%). $C_{14}H_{22}AgF_6NO_6Si$ (550.02): calcd. C 30.39, H 4.01, N 2.53; found C 30.5, H 4.2, N 2.7. ^{1}H NMR (250 MHz, [D$_8$]THF): δ = 0.57 (t, ^3J = 8.3 Hz, 2 H, SiCH_2), 1.16 (t, ^3J = 7.0 Hz, 9 H, CH_3), 1.62 (quint, ^3J = 7.7 Hz, 2 H, $SiCH_2CH_2$), 3.24 (q, ^3J = 6.7 Hz, 2 H, CH_2NH), 3.77 (q, ^3J = 7.0 Hz, 6 H, OCH_2), 8.18 (t, ^3J = 5.5 Hz, 1 H, N*H*) ppm. ^{19}F NMR (235 MHz, [D$_8$]THF): δ = –124.6 (s, 2 F, CF_2), –120.3 (t, $^4J_{F,F}$ = 9.9 Hz, 2 F, CF_2CONH), –115.3 (t, $^4J_{F,F}$ = 9.9 Hz, 2 F, CF_2COOAg). ^{13}C NMR (75 MHz, [D$_8$]THF): δ = 8.2 (SiCH_2), 18.5 (CH_3), 23.3 ($SiCH_2CH_2$), 42.9 (CH_2N), 58.8 (OCH_2), 110.5 (tt, $^1J_{C,F}$ = 264.9, $^2J_{C,F}$ = 31.7 Hz, CF_2CONH), 111.7 (tquint, $^1J_{C,F}$ = 264.9, $^2J_{C,F}$ = 32.2 Hz, CF_2), 112.1 (tt, $^1J_{C,F}$ = 264.4, $^2J_{C,F}$ = 32.8 Hz, CF_2COOAg), 158.9 (t, $^2J_{C,F}$ = 25.8 Hz, CON), 163.8 (t, $^2J_{C,F}$ = 25.5 Hz, COOAg) ppm. MS (ESI+): *m*/*z* = 1757 (6) [M_3^+ + Ag], 1207 (12) [M_2^+ + Ag], 939 (22) [M_2^+ – Si(OEt)$_3$], 699 (41) [M^+ + Ag + MeCN], 388 (15) [M^+ – Si(OEt)$_3$], 189 (100) [Ag(MeCN)$_2^+$]. MS (ESI–): *m*/*z* = 1542 (52) [M_3^+ – Ag], 993 (99) [M_2^+ – Ag], 442 (100) [M^+ – Ag], 398 (40) [M^+ – Ag – CO_2]. IR (KBr): $\tilde{\nu}$ = 3445 (br), 3083 (w), 2977 (m), 2930 (m), 2895 (m), 1706 (vs), 1687 (vs), 1549 (m), 1445 (w), 1393 (m), 1271 (m), 1249 (m), 1163 (vs), 1104 (s), 1079 (s), 958 (m), 944 (m), 811 (m), 790 (m), 761 (m), 488 (br) cm^{-1}. IR (MTBE): $\tilde{\nu}$ = 3303 (br), 3084 (w), 2957 (w), 2929 (w), 2870 (w), 1780 (w), 1722 (s), 1658 (vs), 1541 (m), 1443 (w), 1407 (m), 1392 (m), 1371 (w), 1272 (w), 1247 (m), 1226 (w), 1169 (vs), 1224 (s), 1108 (s), 1077 (vs), 959 (m) cm^{-1}. IR (THF): $\tilde{\nu}$ = 3274 (br), 3068 (w), 2987 (m), 2930 (w), 2884 (m), 1716 (vs), 1691 (vs), 1550 (m), 1445 (w), 1391 (m), 1269 (m), 1245 (m), 1186 (m), 1153 (vs), 1104 (s), 1084 (s), 1059 (m), 959 (m), 941 (m), 898 (w), 807 (m), 791 (m), 759 (m), 679 (w),657 (w), 500 (br) cm^{-1}.

$(MeO)_3Si(CH_2)_3N(Me)C(O)(CF_2)_3COOAg$ (4b): Analogous to the preparation of **4a**, 3-(methylamino)propyltrimethoxysilane (**1b**) (277 μL, 1.40 mmol), hexafluoroglutaric anhydride (**2**) (192 μL, 1.40 mmol), silver(I) oxide (324 mg, 1,40 mmol) and MTBE were used. **4b** was isolated as a pure colorless oil. Yield: 683 mg (93%). $C_{12}H_{18}AgF_6NO_6Si$ (521.99): calcd. C 27.44, H 3.45, N 2.67; found C 27.3, H 3.5, N 2.6. ^{1}H NMR (250 MHz, [D$_8$]THF): δ = 0.56 (t, ^3J = 8.3 Hz, 2 H, SiCH_2), 1.65 (m, 2 H, $SiCH_2CH_2$), 2.96 (s, 3 H, *E*-NCH_3), 3.12 (t, $^5J_{H,F}$ = 2.1 Hz, 3 H, *Z*-NCH_3), 3.38 (t, ^3J = 7.6 Hz, 2 H, *Z*-CH_2N), 3.40 (t, ^3J = 7.5 Hz, 2 H, *E*-CH_2N), 3.51 (s, 9 H, *E*-OCH_3), 3.52 (s, 9 H, *Z*-OCH_3) ppm. ^{19}F NMR (235 MHz, [D$_8$]THF): δ = –121.1 (s, 2 F, *E*-CF_2), –120.9 (s, 2 F, *Z*-CF_2), –112.9 (t, $^4J_{F,F}$ = 10.3 Hz, 2 F, *Z*-CF_2CON), –112.8 (t, $^4J_{F,F}$ = 10.7 Hz, 2 F, *E*-CF_2CON), –109.9 (m, 2 F, *Z*-CF_2COOAg), –109.5 (t, $^4J_{F,F}$ = 10.4 Hz, 2 F, E-CF_2COOAg) ppm. ^{13}C{^{19}F} NMR (75 MHz, [D$_8$]THF: δ = 6.4 (*E*-SiCH_2), 6.6 (*Z*-SiCH_2), 20.3 (*E*-$SiCH_2CH_2$), 22.6 (*Z*-$SiCH_2CH_2$), 34.9 (*E*-NCH_3), 35.0 (*Z*-NCH_3), 50.3 (OCH_3), 52.3 (*E*-CH_2N), 52.9 (*Z*-CH_2N), 111.8 (CF_2), 112.0 (CF_2COOAg and CF_2CON), 158.5 (CON), 163.7 (COOAg) ppm. MS (ESI+): *m*/*z* = 671 (14) [M^+ + Ag + MeCN], 189 (100) [Ag(MeCN)$_2^+$], 148 (21) [Ag(MeCN)$^+$]. IR (film): $\tilde{\nu}$ = 3416 cm^{-1} (br), 3160 (w), 2948 (m), 2892 (w), 2845 (m), 1783 (s), 1651 (vs), 1559 (w), 1490 (w), 1401 (m), 1271 (m), 1242 (m), 1160 (vs), 1091 (s), 1044 (s), 950 (m), 809 (m), 755 (m), 704 (w), 657 (w), 585 (w), 567 (w), 463 (m) cm^{-1}. IR (MTBE): $\tilde{\nu}$ = 3490 (w), 2935 (w), 2902 (w), 2846 (m), 1787 (w), 1685 (s), 1659 (s), 1407 (m), 1371 (w), 1320 (s), 1273 (w), 1244 (w), 1166 (s), 1113 (m), 1069 (m), 1042 (w) cm^{-1}. IR (THF): $\tilde{\nu}$ = 2947 (w), 2865 (w), 1685 (vs), 1658 (vs), 1484 (w), 1401 (m), 1316 (w), 1271 (w), 1164 (vs), 1092 (vs), 1056 (s), 985 (w), 949 (m) cm^{-1}.

***i*Pr_2NC(O)$(CF_2)_3$COOAg (6):** *i*Pr_2NC(O)$(CF_2)_3$COOH **(5)** (71 mg, 0.22 mmol) dissolved in MTBE (1.5 mL) was added at room temperature to a suspension of silver(I) oxide (51 mg, 0.22 mmol) in 3 mL MTBE. The resulting mixture was stirred for 4 h at room temperature in the dark. After filtration all volatiles were removed under full vacuum and the residue was washed three times with hexane and then dried under vacuum yielding **6** as a colorless solid. Crystals of **6** could be obtained by diffusion of hexane into a saturated solution of **6** in chloroform. Yield: 87 mg (92%). $C_{11}H_{14}AgF_6NO_3$ (429.99): calcd. C 30.72, H 3.28, N 3.26; found C 30.7, H 3.3, N 3.3. ^{1}H NMR (250 MHz, [D$_8$]THF): δ = 1.22 (d, ^3J = 6.5 Hz, 12 H, *E*-CH_3), 1.40 (d, ^3J = 6.7 Hz, 12 H, *Z*-CH_3), 3.59 (sept, ^3J = 6.7 Hz, 2 H, *Z*-C*H*), 4.33 (sept, ^3J = 6.5 Hz, 2 H, *E*-C*H*) ppm. ^{19}F NMR (235 MHz, [D$_8$]THF): δ = –118.4 (s, 2 F, CF_2), –110.5 (t, $^4J_{F,F}$ = 10.4 Hz, 2 F, CF_2COOAg), –107.1 (t, $^4J_{F,F}$ = 10.4 Hz, 2 F, CF_2CON) ppm. ^{13}C{^{19}F} NMR (75 MHz, [D$_8$]-THF): δ = 19.9 (*E*-CH_3), 20.5 (*Z*-CH_3), 48.0 (*Z*-CH), 49.2 (*E*-CH), 112.0 (CF_2CON), 112.3 (CF_2), 112.5 (CF_2COOAg), 157.5 (CON), 164.1 (COOAg) ppm. MS (ESI+): *m*/*z* = 948 (24) [M_2^+ + 2 Na + MeCN], 517 (43) [M^+ + 2 Na + MeCN], 493 (23) [M^+ + Na + MeCN], 189 (100) [Ag(MeCN)$_2^+$], 148 (18) [Ag(MeCN)$^+$]. MS (ESI–): *m*/*z* = 322 (100) [M^- – Ag]. IR (KBr): $\tilde{\nu}$ = 3448 (br), 2975 (m), 2941 (m), 2882 (w), 1687 (s), 1675 (vs), 1477 (m), 1449 (m), 1393 (br, m), 1348 (m), 1266 (m), 1241 (m), 1150 (vs), 1120 (m), 1099 (m), 1047 (m), 1032 (m), 1018 (m), 941 (m), 904 (w), 892 (w), 873 (w), 822 (m), 810 (m), 778 (m), 760 (m), 751 (m), 738 (w), 716 (w), 655 (w), 619 (m), 593 (w), 561 (w), 490 (w) cm^{-1}. IR (THF): $\tilde{\nu}$ = 1679 (vs), 1384 (m), 1347 (m), 1269 (m), 1240 (w), 1151 (s), 1086 (m), 1055 (m), 1017 (w), 987 (w), 941 (w), 908 (m), 819 (m), 809 (m), 775 (m), 757 (m), 749 (m), 736 (w), 613 (w), 557 (w) cm^{-1}. IR (MTBE): $\tilde{\nu}$ = 1681 (s), 1658 (s), 1452 (w), 1386 (s), 1369 (s), 1270 (w), 1211 (m), 1193 (m), 1159 (s), 1094 (vs), 1078 (vs), 1023 (m), 942 (w), 857 (w), 822 (m), 805 (m), 756 (w), 746 (w) cm^{-1}.

[KG 60]–$(CH_2)_3$N(H)C(O)$(CF_2)_3$COOAg (7a): Silica gel (KG 60) was washed successively with methanol, dichloromethane and hexane and was dried at 200 °C under full vacuum for 4 h. A solution of $(EtO)_3Si(CH_2)_3N(H)C(O)(CF_2)_3COOAg$ **(4a)** (113.2 mg, 0.2 mmol) in THF (10 mL) was added to a suspension of the pretreated KG 60 (2000 mg) in THF (20 mL). After stirring for 21 h at room temperature in the dark the functionalized silica gel was isolated by filtration with subsequent washing using THF and *n*-hexane. Drying overnight under full vacuum afforded 2089.9 mg of [KG 60]–$(CH_2)_3$N(H)C(O)$(CF_2)_3$COOAg (**7a**). Remaining $(EtO)_3Si(CH_2)_3N(H)C(O)(CF_2)_3COOAg$ **(4a)** was not found in the filtrates. Carbon analysis: found 0.8%, which corresponds to 0.1 mmol **4a** per g KG 60 (5 wt.-%). IR (DRIFT): $\tilde{\nu}$ = 1713 (w), 1664 (w), 1539 (w) cm^{-1}.

 © 2005 Wiley-VCH Verlag GmbH & Co. KGaA, Weinheim

Table 2. Crystal data and refinement details for **4a**, **5**, and **6**.

	4a	**5**	**6**
Empirical formula	$C_{14}H_{22}AgF_6NO_6Si$	$C_{11}H_{15}F_6NO_3$	$C_{11}H_{14}AgF_6NO_3$
Formula mass	550.29	323.24	430.10
Crystal size [mm]	0.32×0.22×0.12	0.37×0.32×0.21	0.18×0.14×0.12
Crystal system	monoclinic	monoclinic	triclinic
Space group	$P2_1/c$ (No. 14)	$P2_1/n$ (No. 14)	$P\bar{1}$ (No. 2)
a [Å]	11.9243(14)	10.0312(12)	6.0029(8)
b [Å]	17.5007(15)	10.4731(9)	9.3849(12)
c [Å]	9.9726(10)	13.8976(15)	13.4770(18)
α [°]	90	90	89.299(10)
β [°]	92.595(9)	104.649(9)	79.890(10)
γ [°]	90	90	77.089(10)
V [Å^3]	2079.0(4)	1412.6(3)	728.27(17)
$\rho_{calcd.}$ [g cm^{-3}]	1.758	1.520	1.961
Z	4	4	2
F(000)	1104	664	424
μ [mm^{-1}]	1.110	0.159	1.461
T_{max}/T_{min}	0.8905/0.7195	0.9736/0.9248	0.8830/0.6586
hkl range	±13, ±20, ±11	±11, ±12, ±16	–7 to 6, ±10, –15 to 14
θ range [°]	1.71–24.65	2.47–24.82	2.23–24.54
Measured reflections	11169	8627	6776
Unique refl. [R_{int}]	3340 [0.0451]	2404 [0.0352]	2408 [0.0411]
Observed refl. $I > 2\sigma(I)$	2472	1711	2023
Refined parameters	269	198	203
Goodness-of-fit	0.926	1.006	1.016
R_1, wR_2 [$I > 2\sigma(I)$]	0.0295, 0.0615	0.0313, 0.0685	0.0311, 0.0641
R_1, wR_2 (all data)	0.0481, 0.0658	0.0512, 0.0727	0.0427, 0.0667
Resid. electron density [e Å^{-3}]	0.294/–0.779	0.219/–0.177	0.767/–0.417

[KG 60]–$(CH_2)_3N(Me)C(O)(CF_2)_3COOAg$ (7b): Analogous to the preparation of **7a**, KG 60 (2030 mg) in THF (20 mL) and $(MeO)_3Si(CH_2)_3N(Me)C(O)(CF_2)_3COOAg$ **(4b)** (106.1 mg, 0.2 mmol) in THF (10 mL) were used. Drying overnight under full vacuum afforded 2127.1 mg of [KG 60]–$(CH_2)_3N(Me)C(O)(CF_2)_3COOAg$ (**7b**). Remaining $(MeO)_3Si(CH_2)_3N(Me)C(O)(CF_2)_3COOAg$ **(4b)** was not found in the filtrates. Carbon analysis: found 1.0%, which corresponds to 0.1 mmol **4b** per g KG 60 (5 wt.-%). IR (DRIFT): $\tilde{\nu}$ = 1669 (m) cm^{-1}.

X-ray Crystallographic Study: X-ray data were collected with a STOE IPDS II diffractometer (graphite monochromated Mo-K_α radiation, λ = 0.71073 Å) by use of ω scans at –140 °C (Table 2). The structures were solved by direct methods and refined on F^2 using all reflections with SHELX-97.[39,40] The non-hydrogen atoms were refined anisotropically. Hydrogen atoms not involved in hydrogen bonding were placed in calculated positions and assigned to an isotropic displacement parameter of 0.08 Å^2. The positional and isotropic thermal parameters of the nitrogen-bonded hydrogen atom H1 in **4a** and the oxygen-bonded H2 in **5** were refined without constraints. Face-indexed absorption corrections were performed numerically with the program X-RED.[41]

CCDC-259720 (for **4a**), -259721 (for **5**) and -259722 (for **6**) contain the supplementary crystallographic data for this paper. These data can be obtained free of charge from The Cambridge Crystallographic Data Centre via www.ccdc.cam.ac.uk/data_request/cif.

Acknowledgments

K. K. and K. V. thank the analytical department of Merck KGaA for NMR and IR spectroscopic measurements and C,H,N analyses.

[1] N. E. Leadbeater, M. Marco, *Chem. Rev.* **2002**, *102*, 3217–3274.
[2] C. Coperet, M. Chabanas, R. P. Saint-Arroman, J.-M. Basset, *Angew. Chem.* **2003**, *115*, 164–191; *Angew. Chem. Int. Ed.* **2003**, *42*, 156–181.
[3] C. A. McNamara, M. J. Dixon, M. Bradley, *Chem. Rev.* **2002**, *102*, 3275–3300.
[4] Q.-H. Fan, Y.-M. Li, A. S. C. Chan, *Chem. Rev.* **2002**, *102*, 3385–3466.
[5] D. Rechavi, M. Lemaire, *Chem. Rev.* **2002**, *102*, 3467–3494.
[6] C. E. Song, S. Lee, *Chem. Rev.* **2002**, *102*, 3495–3524.
[7] D. E. De Vos, M. Dams, B. F. Sels, P. A. Jacobs, *Chem. Rev.* **2002**, *102*, 3615–3640.
[8] W. A. Herrmann, *Kontakte (Darmstadt)* **1991**, *1*, 22–42.
[9] W. A. Herrmann, *Kontakte (Darmstadt)* **1991**, *3*, 29–52.
[10] B. Cornils, W. A. Herrmann, *Journal of Catalysis* **2003**, *216*, 23–31.
[11] W. Buchowicz, F. Ingold, J. C. Mol, M. Lutz, A. L. Spek, *Chem. Eur. J.* **2001**, *7*, 2842–2847.
[12] J. O. Krause, O. Nuyken, M. R. Buchmeiser, *Chem. Eur. J.* **2004**, *10*, 2029–2035.
[13] J.-F. Carpentier, F. Agbossou, A. Mortreux, *Tetrahedron: Asymmetry* **1995**, *6*, 39–42.
[14] K. Takagi, I. Tomita, Y. Nakamura, T. Endo, *Macromolecules* **1998**, *31*, 2779–2783.
[15] S. P. Neo, Z. Y. Zhou, T. C. W. Mak, T. S. A. Hor, *Inorg. Chem.* **1995**, *34*, 520–523.
[16] S.-L. Zheng, M.-L. Tong, S.-D. Tan, Y. Wang, J.-X. Shi, Y.-X. Tong, H. K. Lee, X.-M. Chen, *Organometallics* **2001**, *20*, 5319–5325.
[17] D. R. Whitcomb, R. D. Rogers, *J. Chem. Crystallogr.* **1995**, *25*, 137–142.
[18] T. Haase, K. Kohse-Hoinghaus, B. Atakan, H. Schmidt, H. Lang, *Chem. Vap. Deposition* **2003**, *9*, 144–148.
[19] E. Szłyk, I. Szymańska, A. Surdykowski, T. Głowiak, A. Wojtczak, A. Goliński, *Dalton Trans.* **2003**, 3404–3410.
[20] D. A. Edwards, M. F. Mahon, K. C. Molloy, V. Ogrodnik, *J. Mater. Chem.* **2003**, *13*, 563–570.

 © 2005 Wiley-VCH Verlag GmbH & Co. KGaA, Weinheim

[21] M. Hesse, H. Meier, B. Zeeh, *Spektroskopische Methoden in der Organischen Chemie*, 6th ed.; Thieme Verlag: Stuttgart, **2002**, p. 52 ff.
[22] For Silver trifluoroacetate (CF_3COOAg; KBr pellet) these bands appear at 1682 cm^{-1} [$\tilde{\nu}_{as}(COO)$] and 1440 cm^{-1} [$\tilde{\nu}_{s}(COO)$].
[23] IR spectra of a film of the oily compound **4b** show a single broad band at ca. 1670 cm^{-1} for the $\tilde{\nu}(CO)_{amide}$ and $\tilde{\nu}_{as}(COO)$ stretches, and hence no exact values for these vibrations and for $\Delta\tilde{\nu} = \tilde{\nu}_{as}(COO) - \tilde{\nu}_{s}(COO)$ can be given for **4b**.
[24] G. B. Deacon, R. J. Phillips, *Coord. Chem. Rev.* **1980**, *33*, 227–250.
[25] G. R. Desiraju, *Crystal Engineering: The Design of Organic Solids*, Elsevier: New York, **1989**.
[26] D. Braga, F. Grepioni, G. R. Desiraju, *Chem. Rev.* **1998**, *98*, 1375–1406.
[27] J. M. Newman, M. M. Papadakis, H. W. Thompson, R. A. Lalancette, *Acta Crystallogr. Sect. C* **2002**, *58*, m89–m91.
[28] P. Pyykkö, *Chem. Rev.* **1997**, *97*, 597–636.
[29] See for instance: L. Brammer, M. D. Burgard, C. S. Rodger, J. K. Swearingen, N. P. Rath, *Chem. Commun.* **2001**, 2468–2469.
[30] A Ag–O distance of about 2.9 Å was reported for $[C_6H_4O_2\text{-}(Me_2SiNtBu)_2]_2Ag_4$ in: M. Veith, K. L. Woll, *Chem. Ber.* **1993**, *126*, 2383–2388.
[31] M. R. Buchmeiser, S. Lubbad, M. Mayr, K. Wurst, *Inorg. Chim. Acta* **2003**, *345*, 145–153.
[32] K. Melis, D. De Vos, P. Jacobs, F. Verpoort, *J. Mol. Cat. A* **2001**, *169*, 47–56.
[33] S. J. Connon, A. M. Dunne, S. Blechert, *Angew. Chem.* **2002**, *114*, 3989–3993; *Angew. Chem. Int. Ed.* **2002**, *41*, 3835–3838.
[34] J. Fierro (Ed.), *Spectroscopic Characterization of Heterogeneous Catalysts, Part A*; Studies, in: *Surface Science and Catalysis, 57*; Elsevier: Amsterdam, **1991**.
[35] L. Britcher, H. Rahiala, K. Hakala, P. Mikkola, J. B. Rosenholm, *Chem. Mater.* **2004**, *16*, 5713–5720.
[36] A. Fidalgo, L. M. Ilharco, *Chem. Eur. J.* **2004**, *10*, 392–398.
[37] D. D. Perrin, W. L. F. Armarego, *Purification of Laboratory Chemicals*, 3rd ed.; Pergamon Press: New York, **1988**.
[38] A. B. Pangborn, M. A. Giardello, R. H. Grubbs, R. K. Rosen, F. J. Timmers, *Organometallics* **1996**, *15*, 1518–1520.
[39] G. M. Sheldrick, *SHELXL-97*, *Program for Crystal Structure Refinement*, University of Göttingen, **1997**.
[40] G. M. Sheldrick, *SHELXS-97*, *Program for Crystal Structure Solution*, University of Göttingen, **1997**.
[41] STOE & CIE GmbH, *X-RED*, Darmstadt, **2002**.

Received: January 25, 2005
Published Online: June 2, 2005

 © 2005 Wiley-VCH Verlag GmbH & Co. KGaA, Weinheim

Design, Preparation and Characterization of the Adducts of the Bis-Amido Cobalticinium Complex $[Co^{III}(\eta^5\text{-}C_5H_4CONHC_5H_4N)_2][PF_6]$ with Fumaric and Maleic Acids

Dario Braga,*[a] Stefano L. Giaffreda,[a] Marco Polito,[a] and Fabrizia Grepioni*[a]

Keywords: Organometallic complexes / Amides / Hydrogen bonding / Crystal engineering / Supramolecular chemistry

The supramolecular hydrogen-bonded adducts obtained by treating the cationic bis-amido complex $[Co^{III}(\eta^5\text{-}C_5H_4CONHC_5H_4N)_2]^+$ with fumaric and maleic acid are investigated and their modes of aggregation in the solid state are explored. It is shown that the bis-amido organometallic complex can be mono- and di-protonated in the reaction with the dicarboxylic acids, leading to the formation of complex, mixed-anion supramolecular salts containing either the dication $[Co^{III}(\eta^5\text{-}C_5H_4CONHC_5H_4N)(\eta^5\text{-}C_5H_4CONHC_5H_4NH)]^{2+}$, $[\mathbf{1}H]^{2+}$, or the trication $[Co^{III}(\eta^5\text{-}C_5H_4CONHC_5H_4NH)_2]^{3+}$, $[\mathbf{1}H_2]^{3+}$. The derivatives of the reaction with fumaric acid, namely, $[Co^{III}(\eta^5\text{-}C_5H_4CONHC_5H_4N)(\eta^5\text{-}C_5H_4CONHC_5H_4NH)]^{2+}\cdot[PF_6]^-\cdot 1/2[\text{fumarate}]^{2-}$, $[\mathbf{1}H]^{2+}\cdot PF_6^-\cdot 1/2[\text{fumarate}]^{2-}$, and $[Co^{III}(\eta^5\text{-}C_5H_4CONHC_5H_4NH)_2]^{3+}\cdot[PF_6]^-\cdot[H(\text{fumarate})_2]^{3-}\cdot H_3O^+\cdot H_2O$, $[\mathbf{1}H_2]^{3+}\cdot[PF_6]^-\cdot[H(\text{fumarate})_2]^{3-}\cdot H_3O^+\cdot H_2O$, contain either the dianion $[\text{fumarate}]^{2-}$ or the hydrogen-bridged supramolecular trianion $[H(\text{fumarate})_2]^{3-}$, depending on the amide/acid stoichiometric ratio. In the case of maleic acid, on the other hand, the possibility of intramolecular hydrogen-bond formation generates exclusively salts of the hydrogen maleate anions, namely, $[Co^{III}(\eta^5\text{-}C_5H_4CONHC_5H_4N)(\eta^5\text{-}C_5H_4CONHC_5H_4NH)]^{2+}\cdot 5/2[PF_6]^-\cdot 3/2[\text{Hmaleate}]^-$, $2[\mathbf{1}H]^{2+}\cdot 5/2[PF_6]^-\cdot 3/2[\text{Hmaleate}]^-$, $2[Co^{III}(\eta^5\text{-}C_5H_4CONHC_5H_4NH)_2]^{3+}\cdot 3[PF_6]^-\cdot 3[\text{Hmaleate}]^-\cdot 2H_2O$, $2[\mathbf{1}H_2]^{3+}\cdot 3[PF_6]^-\cdot 3[\text{Hmaleate}]^-\cdot 2H_2O$ and $[Co^{III}(\eta^5\text{-}C_5H_4CONHC_5H_4NH)_2]^{3+}\cdot 2[PF_6]^-\cdot[\text{Hmaleate}]^-\cdot H_2O$, $[\mathbf{1}H_2]^{3+}\cdot 2[PF_6]^-\cdot[\text{Hmaleate}]^-\cdot H_2O$, in which the hydrogen maleate anions act as bridges between the protonated bis-amido organometallic sandwiches.

(© Wiley-VCH Verlag GmbH & Co. KGaA, 69451 Weinheim, Germany, 2005)

Introduction

In the context of crystal engineering,[1] organometallic molecules and ions are beginning to attract an increasing interest since organometallic molecules and molecular ions combine the supramolecular bonding capacity of organic molecules with the presence of metal atoms. The number of possible combinations of the valence, spin and charge states of the metal atoms with the coordination geometries and supramolecular bonding capacity of functionalised organometallic complexes is virtually unlimited.[2] One of the important issues in this area of chemistry is that of being able to design, synthesize and ultimately exploit the topological properties of solid-state materials based on coordination compounds, whether linked together to form supramolecular complexes or joined in extended coordination networks through space.[3] The goal is to achieve an intelligent control of the recognition and assembly processes that lead from molecular or ionic components to superstructures,[4] hence from individual to collective chemical and physical properties.[5]

[a] Dipartimento di Chimica G. Ciamician, Università di Bologna, Via F. Selmi 2, 40126 Bologna, Italy
Fax: +39-051-2099456
E-mail: dario.braga@unibo.it

In recent years, we have directed our efforts,[6] together with others,[7] towards the exploration of the area of organometallic supramolecular solid-state chemistry and crystal engineering. While many organic compounds often utilized by the crystal engineer are commercially available and can be used directly in supramolecular assembly experiments, this is not so with organometallic species, which need, most often, to be synthesized on purpose.

With this idea in mind, we have begun to prepare, also in collaboration with others, novel organometallic building blocks with adequate supramolecular-bonding functionalities for the construction of target architectures.[8] We have focused our strategy on the possibility of adding hydrogen bonding donor/acceptor groups to robust sandwich complexes. The rationale for this choice is that the hydrogen bond is the strongest of the non-covalent interactions and the one that best combines strength and directionality.[9] Strength is synonym of cohesion and stability, while directionality implies topological control and selectivity, which are fundamental prerequisites for a successful control of the aggregation processes.[10]

It is now well demonstrated that coordination ligands functionalised with –COOH and –OH groups form essentially the same type of hydrogen-bonding interactions, whether as part of organic molecules or as part of metal

complexes.[2,7,11] This is not surprising, as hydrogen bonds formed by such strong donor and acceptor groups are at least one order of magnitude stronger than most non-covalent interactions. In terms of topology, dicarboxylic acid molecules allow construction of supramolecular networks because of the twin hydrogen-bonding function. We have extensively exploited this feature by using sandwich organometallic dicarboxylic acids such as $[Fe(\eta^5\text{-}C_5H_4COOH)_2]$, $[Co(\eta^5\text{-}C_5H_4COOH)_2]^+$ and $[Cr(\eta^6\text{-}C_6H_5COOH)_2]$.[12] The cobalt cationic complex, in particular, has proved to be extremely versatile for applications in solid–solid and solid–gas reactions.[13]

Recently, we have expanded this chemistry towards organometallic bis-amido complexes. We have reported the solid-state investigation of the bis-amido cobalticinium complex $[Co^{III}(\eta^5\text{-}C_5H_4CONHC_5H_4N)_2][PF_6]$, $[\mathbf{1}]^+[PF_6]^-$, together with its utilization in the formation of a hydrogen-bonded adduct with ferrocene dicarboxylic acid, namely, $[Co^{III}(\eta^5\text{-}C_5H_4CONHC_5H_4N)_2][Fe(\eta^5\text{-}C_5H_4COOH)_2][PF_6]$.[14] It is worth stressing that $[\mathbf{1}]^+$ possesses, at least in principle, both the capacity of acting as a cationic di-base for protonation and hydrogen-bond formation, as well as that of acting as a coordination ligand. In this study we explore the first of these characteristics. The downside of this is feature is that the counterion (in all cases discussed herein the $[PF_6]^-$ anion) is also "carried through" the acid–base reaction and the subsequent crystallization, thereby decreasing the level of predictability of the supramolecular architectures resulting from acid-base aggregation. As it will be seen in the following section, our compounds can be described as hetero-anionic salts, that is, containing both $[PF_6]^-$ and the anions obtained from deprotonation of fumaric and maleic acids of the protonated bis-amide $[\mathbf{1}]^+$.

In this paper we describe the results obtained from the reactions between $[\mathbf{1}]^+[PF_6]^-$ and the dicarboxylic fumaric and maleic acids. The idea is that of using the –COOH groups of the two acids as a probe of the hydrogen-bonding capacity of the organometallic complex $[Co^{III}(\eta^5\text{-}C_5H_4CONHC_5H_4N)_2]^+$. Our interest stems from the observation that the cationic starting material can, at least in principle, behave both as a mono- and as a di-protonic acceptor at the two N-termini (thus leading to the formation of di- and tri-cationic complexes, see Scheme 1). These protonated forms can form hydrogen bonds with suitable acceptors. Furthermore, the presence of the two –(CO)NH amido groups confers additional hydrogen-bonding capacity to the molecule.

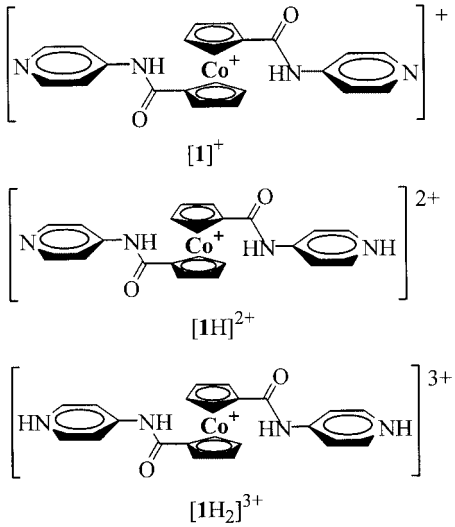

Scheme 1. The cationic bis-amide complex $[Co^{III}(\eta^5\text{-}C_5H_4CONHC_5H_4N)_2]$, $[\mathbf{1}]^+$, together with the di- and tri-cationic species $[\mathbf{1}H]^{2+}$ and $[\mathbf{1}H_2]^{3+}$ obtained by mono- and di-protonation of the two N-termini.

Results and Discussion

As pointed out above, the organometallic amide $[\mathbf{1}]^+$ can exist in solution in three different forms depending on the degree of protonation, that is, $[Co^{III}(\eta^5\text{-}C_5H_4CONHC_5H_4N)_2]^+$, $[\mathbf{1}]^+$, $[Co^{III}(\eta^5\text{-}C_5H_4CONHC_5H_4N)(\eta^5C_5H_4CONHC_5H_4NH)]^{2+}$, $[\mathbf{1}H]^{2+}$, and $[Co^{III}(\eta^5\text{-}C_5H_4CONHC_5H_4NH)_2]^{3+}$, $[\mathbf{1}H_2]^{3+}$. In the reaction with acids, the degree of protonation can be generally "tuned" by varying the base/acid molar ratio. Of the three cations, only the structure of $[\mathbf{1}]^+$ has been reported before and we refer the reader to the previous publication,[14] while the structures of the mono-protonated and di-protonated compounds have not yet been reported. Since the supramolecular structure of $[\mathbf{1}H]^{2+}$ is related to the following discussion, we shall first describe the packing of the dication $[Co^{III}(\eta^5\text{-}C_5H_4CONHC_5H_4N)(\eta^5\text{-}C_5H_4CONHC_5H_4NH)]^{2+}$, $[\mathbf{1}H]^{2+}$, while the tri-cation $[\mathbf{1}H_2]^{3+}$ will be seen in the structure of the adducts discussed below. Selected hydrogen bonding parameters for $[\mathbf{1}H]^{2+}$, as well as for all the other species described herein, are reported in Table 1.

The dication $[Co^{III}(\eta^5\text{-}C_5H_4CONHC_5H_4N)(\eta^5\text{-}C_5H_4CONHC_5H_4NH)]^{2+}$, $[\mathbf{1}H]^{2+}$, has been crystallized as its $[PF_6]^-$ salt in the form $2[Co^{III}(\eta^5\text{-}C_5H_4CONHC_5H_4N)(\eta^5\text{-}C_5H_4CONHC_5H_4NH)]^{2+}\cdot 4[PF_6]^-\cdot H_2O$, $2[\mathbf{1}H]^{2+}\cdot 4[PF_6]^-\cdot H_2O$. The most interesting feature is that the dication forms hydrogen-bonded dimers in the solid state via N–H···N interactions, as shown in Figure 1. The resulting supramolecular aggregate is thus a tetracation "held together" by two N–H···N hydrogen bonds [N(4)···N(3) 2.715(4), N(8)···N(6) 2.738(4) Å, for the two crystallographically independent units shown in Figure 1].

It is worth noting that one of the tetracations is hydrogen-bridged with two water molecules [N···O 2.943(5) Å] and both cations also interact with the $[PF_6]^-$ anions, establishing N–H···F hydrogen-bonding interactions with the amidic N–H units [N···F distances in the range 3.025(4)–3.072(5) Å], as shown in Figure 2.

Reactions with Fumaric Acid

Even though it is possible to envisage several stoichiometric molar ratios between base and acid in the reaction of $[\mathbf{1}]^+$ with acids (see Table 1), our experiments show that

 © 2005 Wiley-VCH Verlag GmbH & Co. KGaA, Weinheim

Table 1. Relevant hydrogen bonding parameters for all species discussed herein.

Compound	Donor···Acceptor	D···A [Å]
$2[\mathbf{1}H]^{2+}\cdot 4[PF_6]^-\cdot H_2O$	N(1)···F(19)	3.037(5)
	N(2)···F(8)	3.025(4)
	N(4)···N(3)	2.715(4)
	N(5)···F(21)	3.072(5)
	N(7)···O(5)	2.943(5)
	N(8)···N(6)	2.738(4)
$[\mathbf{1}H]^{2+}\cdot[PF_6]^-\cdot 1/2[\text{fumarate}]^{2-}$	N(2)···O(4)	2.703(6)
	N(1)···O(3)	2.809(6)
	N(3)···N(4)	2.669(7)
$[\mathbf{1}H_2]^{3+}\cdot[PF_6]^-\cdot[H(\text{fumarate})_2]^{3-}\cdot H_3O^+\cdot H_2O$	N(1)···O(3)	2.763(4)
	N(2)···O(10)	2.965(5)
	N(3)···O(100)	2.690(4)
	N(4)···O(200)	2.743(4)
	O(100)···O(8)	2.739(4)
	O(100)···O(200)	2.829(4)
	O(100)···O(6)	2.703(4)
	O(200)···O(100)	2.829(4)
	O(200)···O(5)	2.976(5)
	O(5)···O(8)	2.466(4)
$2[\mathbf{1}H]^{2+}\cdot 5/2[PF_6]^-\cdot 3/2[\text{Hmaleate}]^-$	N(4)···N(8)	2.688(6)
	N(6)···N(2)	2.686(6)
	N(1)···O(100)	2.832(6)
	N(3)···O(5)	2.923(5)
	N(5)···O(7)	2.916(6)
	N(7)···O(8)	2.836(6)
	O(6)···O(7)	2.460(5)
$2[\mathbf{1}H_2]^{3+}\cdot 3[PF_6]^-\cdot 3[\text{Hmaleate}]^-\cdot 2H_2O$	N1···O13	2.757(5)
	O100···O15	2.798(7)
	O100···O12	2.771(5)
	N2···O100	2.689(5)
	O200···O8	2.936(5)
	O200′···O8	2.838(5)
	N3···O14	3.016(5)
	N4···O8	2.789(5)
	N5···O10	2.822(5)
	N6···O12	2.791(6)
	N7···O6	2.794(4)
	N8···O200	2.702(6)
	O5···O7	2.407(4)
	O9···O11	2.416(4)
	O16···O14	2.477(5)
$[\mathbf{1}H_2]^{3+}\cdot 2[PF_6]^-\cdot[\text{Hmaleate}]^-\cdot H_2O$	O(4)···O(5)	2.411(5)
	N(1)···O(3)	2.884(7)
	N(2)···O(5)	2.923(7)
	N(2)···O(6)	2.873(8)
	N(4)···O(100)	2.787(8)
	O(100)···F(7)	3.1750(8)
	N(3)···F(12)	3.179(7)

only two stoichiometries yield crystalline aggregates, namely, $[Co^{III}(\eta^5\text{-}C_5H_4CONHC_5H_4N)(\eta^5\text{-}C_5H_4CONHC_5H_4NH)]^{2+}\cdot[PF_6]^-\cdot 1/2[\text{fumarate}]^{2-}$, $[\mathbf{1}H]^{2+}\cdot PF_6^-\cdot 1/2[\text{fumarate}]^{2-}$, and $[Co^{III}(\eta^5\text{-}C_5H_4CONHC_5H_4NH)_2]^{3+}\cdot[PF_6]^-\cdot[H(\text{fumarate})_2]^{3-}\cdot H_3O^+\cdot H_2O$, $[\mathbf{1}H_2]^{3+}\cdot[PF_6]^-\cdot[H(\text{fumarate})_2]^{3-}\cdot H_3O^+\cdot H_2O$, obtained from the 2:1 and the reverse 1:2 amide/acid ratios, respectively. Amide/acid ratios 2:1, 1:1 and 1:1.5 all yielded the fumarate derivative $[\mathbf{1}H]^{2+}\cdot[PF_6]^-\cdot 1/2[\text{fumarate}]^{2-}$, while the ratios 1:2 and 1:3 both yielded the hydrogen fumarate derivative $[\mathbf{1}H_2]^{3+}\cdot[PF_6]^-\cdot[H(\text{fumarate})_2]^{3-}\cdot H_3O^+\cdot H_2O$. Why other stoichiometries, in particular the 1:1, are not obtained, is difficult to say. One should keep in mind, however, that the acid/base protonation equilibrium in solution is not the only aspect that may influence the final solid-state product stoichiometry. Solubility equilibria, for example, may favour one species over another, while kinetic aspects may have a role in the formation of long-living crystal nuclei in solution.

In the cases yielding $[Co^{III}(\eta^5\text{-}C_5H_4CONHC_5H_4N)(\eta^5\text{-}C_5H_4CONHC_5H_4NH)]^{2+}\cdot[PF_6]^-\cdot 1/2[\text{fumarate}]^{2-}$, $[\mathbf{1}H]^{2+}\cdot PF_6^-\cdot 1/2[\text{fumarate}]^{2-}$, the diprotic acid is able to protonate two molecules of the amide, raising the charge of the organometallic moiety from +1 to +2. This product is formed with stoichiometric ratios of up to 1:1.5 (which, incidentally, implies that there is unreacted fumaric acid that precipitates together with the crystals of the adduct). Above 1:1.5 the protonation equilibrium changes: the excess of fumaric acid leads to complete protonation of the bis-amido complex, to a total cationic charge of +3 and formation of the complex $[\mathbf{1}H_2]^{3+}$. The resulting material $[\mathbf{1}H_2]^{3+}\cdot[PF_6]^-\cdot[H(\text{fumarate})_2]^{3-}\cdot H_3O^+\cdot H_2O$ is crystallized together with a protonated water molecule (see below). The expected product, $[\mathbf{1}H_2]^{3+}\cdot[PF_6]^-\cdot[\text{fumarate}]^{2-}$, corresponding to the stoichiometric ratio 1:1 was not isolated.

Thus, the two crystals $[\mathbf{1}H]^{2+}\cdot[PF_6]^-\cdot 1/2[\text{fumarate}]^{2-}$ and $[\mathbf{1}H_2]^{3+}\cdot[PF_6]^-\cdot[H(\text{fumarate})_2]^{3-}\cdot H_3O^+$ contain the diprotonated and the triprotonated organometallic complexes, respectively. In spite of this difference, the two complexes show interesting structural relationships in the solid state:

i) The organometallic complexes in both the $[\mathbf{1}H]^{2+}\cdot[PF_6]^-\cdot 1/2[\text{fumarate}]^{2-}$ and the $[\mathbf{1}H_2]^{3+}\cdot[PF_6]^-\cdot[H(\text{fumarate})_2]^{3-}\cdot H_3O^+\cdot H_2O$ crystals adopt a *cisoid* (eclipsed) conformation of the Cp-pyridyl ligands.

ii) In $[\mathbf{1}H]^{2+}\cdot[PF_6]^-\cdot 1/2[\text{fumarate}]^{2-}$ the monoprotonated amide forms a cyclic dimer with another complex through N–H···N hydrogen bonds [N(3)···N(4) 2.669(7) Å], as shown in Figure 3.

iii) The dimers are linked together in a zigzag fashion by the interaction of the deprotonated fumarate dianions and the outer amido N–H groups (see Figure 3) [N(1)···O(3) 2.809(6), N(2)···O(4) 2.703(6) Å]. Each carboxylate unit "pinches" the two N–H groups of one complex; in such a way the organometallic cation and the fumarate dianion interact via four N–H···O bonds.

iv) In the case of $[\mathbf{1}H_2]^{3+}$, on the other hand, a dimer cannot form because both N-termini are protonated, nonetheless the complex retains the eclipsed geometry of the ligands and substituents (see part a of Figure 4). The pyridyl NH groups interact through hydrogen bonding with the $[H_3O]^+$ cation and the water molecule [N(3)···O(100) 2.690(4) and N(4)···O(200) 2.743(4) Å], which in turn interact with each other [O(100)···O(200) 2.829(4) Å]. The $[H_3O]^+$ cation and the water molecule are also hydrogen bonded to the $[H(\text{fumarate})_2]^{3-}$ anions (see part b of Figure 4) [O(100)···O(6) 2.703(4), O(100)···O(8) 2.739(4), O(200)···O(5) 2.976(5) Å].

v) The trications $[\mathbf{1}H_2]^{3+}$ are linked together by a supramolecular anion formed by a hydrogen fumarate unit and a fumarate dianion. Since the proton is mid-way along the

 © 2005 Wiley-VCH Verlag GmbH & Co. KGaA, Weinheim

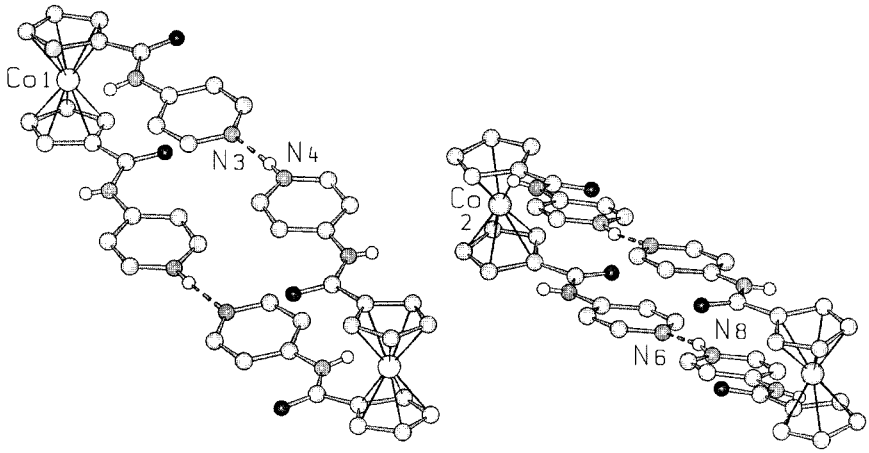

Figure 1. The supramolecular aggregates present in $2[\mathbf{1}H]^{2+}\cdot 4[PF_6]^-\cdot H_2O$. The tetra-cation is "held together" by two N–H···N hydrogen bonds [N(4)···N(3) 2.715(4), N(8)···N(6) 2.738(4) Å for the two crystallographically independent units]. [H_{CH}, H_{water} and $H_{[H_3O]^+}$ atoms not shown for clarity].

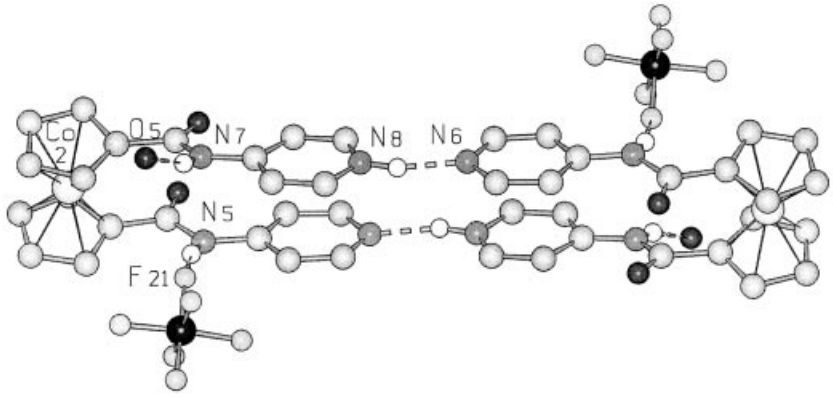

Figure 2. N–H···O and N–H···F hydrogen-bonding interactions between the bis-amide $[Co^{III}(\eta^5\text{-}C_5H_4CONHC_5H_4N)(\eta^5\text{-}C_5H_4CONHC_5H_4NH)]^{2+}$ and the hexafluorophosphate anions and the water molecules. [H_{CH}, H_{water} and $H_{[H_3O]^+}$ atoms not shown for clarity].

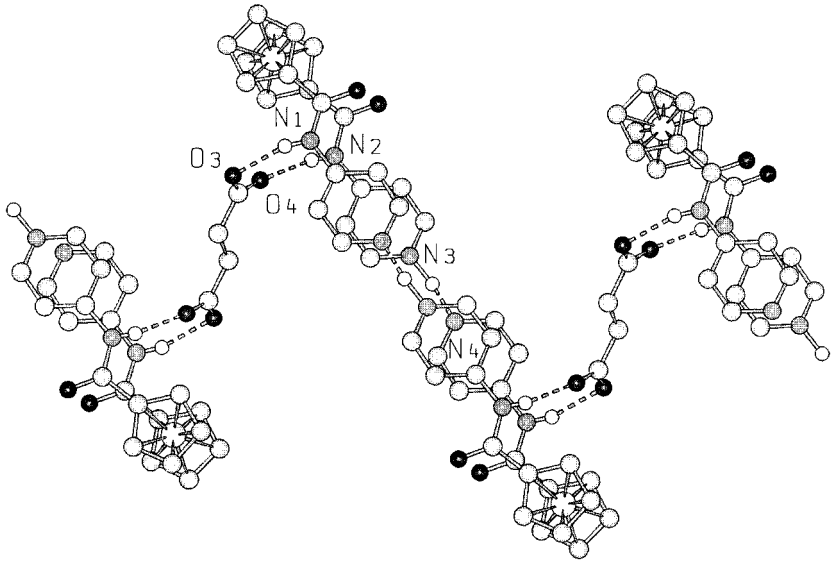

Figure 3. Crystalline $[\mathbf{1}H]^{2+}\cdot[PF_6]^-\cdot 1/2[\text{fumarate}]^{2-}$. The hydrogen-bridged amide dimers [N(3)···N(4) 2.669(7) Å] are linked together in a zigzag fashion through the interaction of the deprotonated fumarate dianions and the outer amido N–H groups, [N(1)···O(3) 2.809(6), N(2)···O(4) 2.703(6) Å]. Each carboxylate unit "pinches" both the amido N–H groups of one complex; in such a way each fumarate dianion interacts with the organometallic cations through four N–H···O bonds. [H_{CH}, H_{water} and $H_{[H_3O]^+}$ atoms not shown for clarity].

 © 2005 Wiley-VCH Verlag GmbH & Co. KGaA, Weinheim

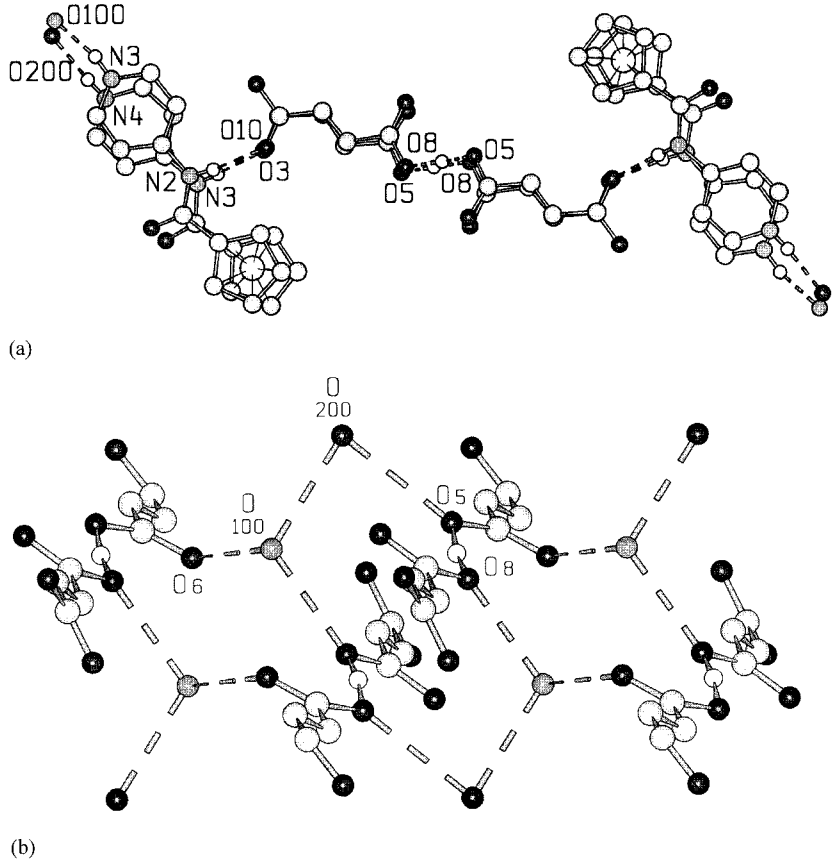

Figure 4. (a) In crystalline $[\mathbf{1}H_2]^{3+}\cdot[PF_6]^-\cdot[H(fumarate)_2]^{3-}\cdot H_3O^+\cdot H_2O$ the trications are linked together by a supramolecular anion formed by a hydrogen fumarate unit and a fumarate dianion. Since the proton is mid-way along the O···O bond in this unit, it is more appropriate to describe the systems as a superanion $[H(fumarate)_2]^{3-}$, with an O(5)···O(8) separation of 2.466(4) Å. (b) The $[H_3O]^+$ cation and the water molecule interact via hydrogen bonding with each other [O(100)···O(200) 2.829(4) Å] and with the $[H(fumarate)_2]^{3-}$ anion [O(100)···O(6) 2.703(4), O(100)···O(8) 2.739(4), O(200)···O(5) 2.976(5) Å]. [H_{CH}, H_{water} and $H_{[H_3O]^+}$ atoms not shown for clarity].

O···O bond [O(5)···O(8) 2.466(4) Å], it is more appropriate to describe the system as a superanion of formula $[H(fumarate)_2]^{3-}$.

vi) On both sides the supramolecular trianion $[H(fumarate)_2]^{3-}$ interacts with the amido N–H groups, as observed in $[\mathbf{1}H]^{2+}$ with N(1)···O(3) and N(2)···O(10) separations of 2.763(4) and 2.965(5) Å, respectively.

Reactions with Maleic Acid

In terms of supramolecular bonding capacity and hydrogen-bond formation, maleic acid differs from fumaric acid-mainly in the fact that mono-deprotonation leads in general to formation of an intramolecular hydrogen bond. As a consequence of the intramolecular hydrogen-bonding formation the carboxylate groups are available only for hydrogen-bonding acceptance.

The structure of $[Co^{III}(\eta^5\text{-}C_5H_4CONHC_5H_4N)(\eta^5\text{-}C_5H_4CONHC_5H_4NH)]^{2+}\cdot 5/2[PF_6]^-\cdot 3/2[Hmaleate]^-$, $2[\mathbf{1}H]^{2+}\cdot 5/2[PF_6]^-\cdot 3/2[Hmaleate]^-$, is reminiscent of those of the mono-protonated amide salt $[Co^{III}(\eta^5\text{-}C_5H_4CONHC_5H_4N)(\eta^5\text{-}C_5H_4CONHC_5H_4NH)]^{2+}\cdot 4[PF_6]^-\cdot H_2O$ and of the hydrogen fumarate salt $[\mathbf{1}H]^{2+}\cdot[PF_6]^-\cdot 1/2[maleate]^{2-}$. These systems have in common the presence of hydrogen bond dimers in the solid state (see Figure 5). The N–H···N

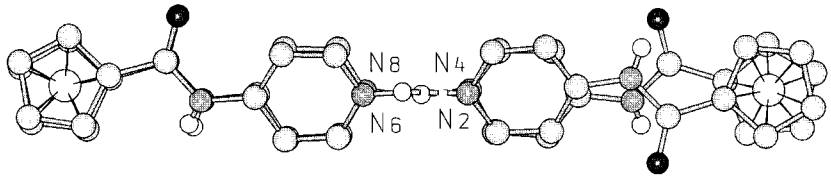

Figure 5. The hydrogen bonded dimer in crystalline $[Co^{III}(\eta^5\text{-}C_5H_4CONHC_5H_4N)(\eta^5\text{-}C_5H_4CONHC_5H_4NH)]^{2+}\cdot 5/2[PF_6]^-\cdot 3/2[Hmaleate]^-$, $2[\mathbf{1}H]^{2+}\cdot 5/2[PF_6]^-\cdot 3/2[Hmaleate]^-$. Note how the amido groups are eclipsed in one of the two dications and staggered in the other. [H_{CH}, H_{water} and $H_{[H_3O]^+}$ atoms not shown for clarity].

 © 2005 Wiley-VCH Verlag GmbH & Co. KGaA, Weinheim

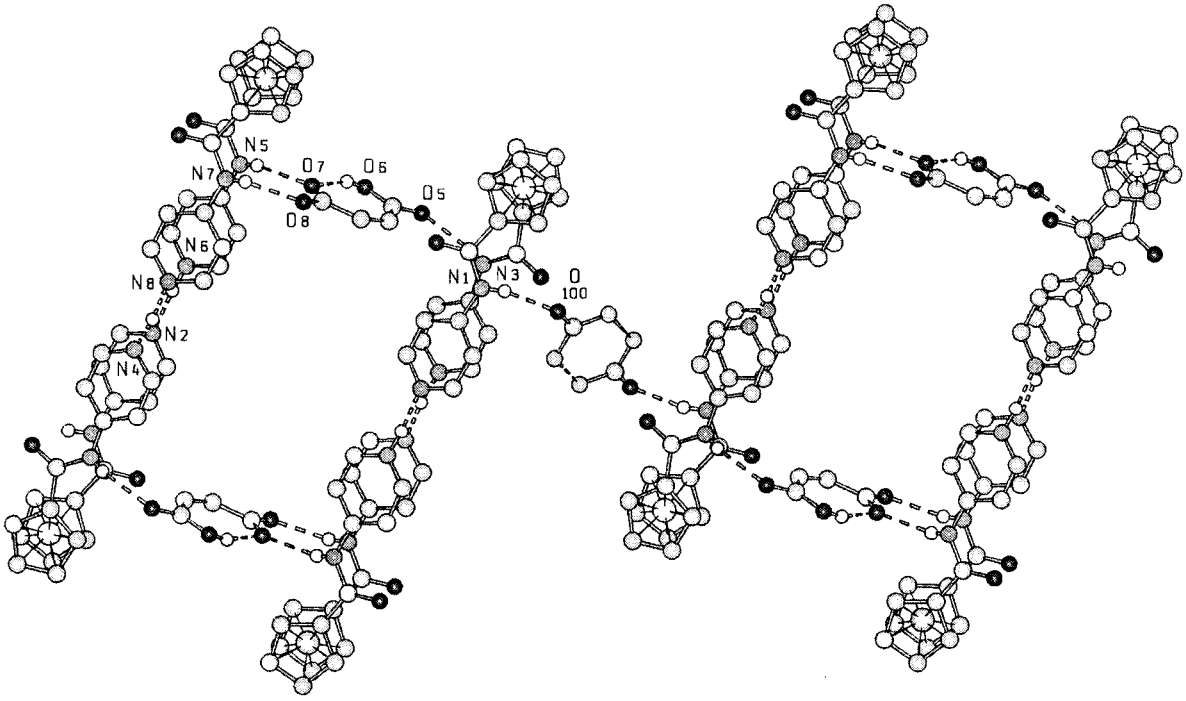

Figure 6. The structure of $2[\mathbf{1}H]^{2+}\cdot 5/2[PF_6]^-\cdot 3/2[Hmaleate]^-$ shows the presence of hydrogen-bonded dimers in the solid state of the type observed for $[Co^{III}(\eta^5\text{-}C_5H_4CONHC_5H_4N)(\eta^5\text{-}C_5H_4CONHC_5H_4NH)]^{2+}\cdot[PF_6^-]_4\cdot H_2O$, as well as the hydrogen fumarate salts $[\mathbf{1}H]^{2+}\cdot[PF_6]^-\cdot 1/2[fumarate]^{2-}$. Note, however, that the amido groups are eclipsed in one of the two di-cations and staggered in the other (see Figure 5). The "dimers of dimers" are held together by a hydrogen oxalate anion, which is disordered over two orientations (only one of the two images is shown here for clarity). [H_{CH}, H_{water} and $H_{[H_3O]^+}$ atoms not shown for clarity].

separations are comparable in length [N(4)···N(8) 2.688(6); N(6)···N(2) 2.686(6) Å]. Note, however, that the amido groups are eclipsed in one of the two dications and staggered in the other. This difference seems to suggest that in solution the complex is present with both, possibly dynamically interconverting conformations, which are frozen out at the stage of crystallization. It is also noteworthy that compound $2[\mathbf{1}H]^{2+}\cdot 5/2[PF_6]^-\cdot 3/2[Hmaleate]^-$ is the only case, in this study, where the Cp-amido ligands show both the staggered and eclipsed relative orientations of the C(=O)NH units. The arrangement of the hydrogen maleate anions provides a possible rationale for the difference. As shown in Figure 6, the hydrogen maleate anions provide two types of bridges between neighbouring dimers.

Because of the mentioned scarcity of hydrogen-bonding donor sites, the interaction links have to utilize the amido N–H groups. The structure can be described as formed of "dimers of dimers" held together by two ordered hydrogen maleate anions, for a total of six N–H···O interactions [N(3)···O(5) 2.923(5), N(5)···O(7) 2.916(6), N(7)···O(8) 2.836(6) Å]. The N(1)–H(100) donor group, which is not involved in the "dimer of dimer" formation, can thus be used to link together the "dimers of dimers" through the disordered hydrogen maleate [N(1)···O(100) 2.832(6) Å] (see Figure 6). This picture also provides a rationale for the disorder observed in the latter hydrogen maleate anion, which is oriented randomly in two positions around the crystallographic inversion centre.

Let us now consider the cases of compounds $2[Co^{III}(\eta^5\text{-}C_5H_4CONHC_5H_4NH)_2]^{3+}\cdot 3[PF_6]^-\cdot 3[Hmaleate]^-\cdot 2H_2O$, $2[\mathbf{1}H_2]^{3+}\cdot 3[PF_6]^-\cdot 3[Hmaleate]^-\cdot 2H_2O$, and $[Co^{III}(\eta^5\text{-}C_5H_4CONHC_5H_4NH)_2]^{3+}\cdot 2[PF_6]^-\cdot[Hmaleate]^-\cdot H_2O$, $[\mathbf{1}H_2]^{3+}\cdot 2[PF_6]^-\cdot[Hmaleate]^-\cdot H_2O$. These two crystalline materials, in spite of the different stoichiometry, bear some close structural relationships. In both systems the intramolecular hydrogen maleate anion acts as a bridge between two trications (compare Figure 7 and Figure 8) by accepting hydrogen-bond donation from the protonated pyridine N-terminus and from the amido N–H system of two distinct cations [N···O distances in the range 2.789(5)–2.923(7) Å]. The hydrogen maleate bridges thus generate an extended network of alternating cations and anions, thanks also to the rotational freedom about the Cp–Co–Cp axis. In addition to this, in compound $2[\mathbf{1}H_2]^{3+}\cdot 3[PF_6]^-\cdot 3[Hmaleate]^-\cdot 2H_2O$ the two hydrogen maleates that do not act as bridges still interact each with an organometallic cation via NH···O hydrogen bonds [N(5)···O(10), N(8)···O(9), N(1)···O(13) Å] (Figure 7) and establish hydrogen-bonding interactions with the water molecules [O···O distances in the range 2.771(5)–2.936(5) Å].

 © 2005 Wiley-VCH Verlag GmbH & Co. KGaA, Weinheim

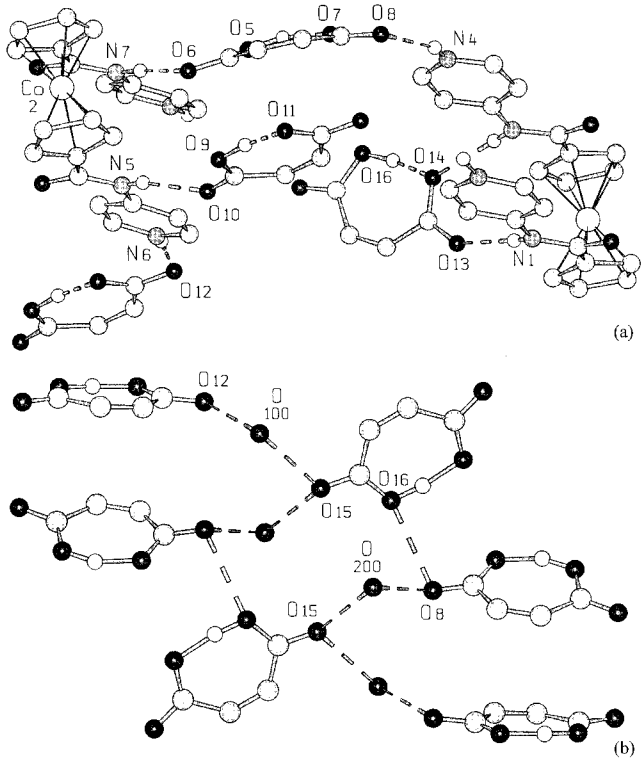

Figure 7. (a) The extended hydrogen-bonded network in crystalline $2[\mathbf{1}H_2]^{3+}\cdot 3[PF_6]^-\cdot 3[Hmaleate]^-\cdot 2H_2O$. Note how one hydrogen maleate anion acts as a bridge between trications while another one establishes hydrogen at the intracation level. (b) The hydrogen bonding interactions between the water molecules and the hydrogen maleates that are not involved in the cation bridging (water hydrogen atoms not shown for clarity). [H_{CH}, H_{water} and $H_{[H_3O]^+}$ atoms not shown for clarity].

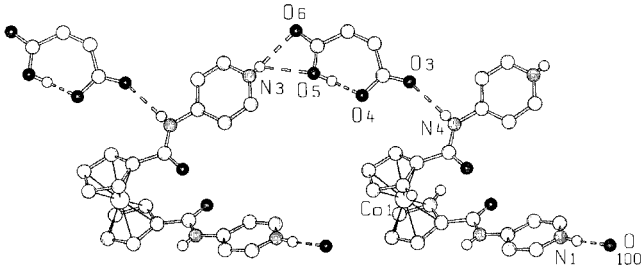

Figure 8. (a) The extended hydrogen-bonded network in crystalline $[\mathbf{1}H_2]^{3+}\cdot 2[PF_6]^-\cdot[Hmaleate]^-\cdot H_2O$. Note how the hydrogen maleate anion acts as a bridge between trications forming an extended network. [H_{CH}, H_{water} and $H_{[H_3O]^+}$ atoms not shown for clarity]

Conclusions

The aim of this study was to explore the supramolecular bonding capacity of the cationic bis-amide complex $[Co^{III}(\eta^5\text{-}C_5H_4CONHC_5H_4N)_2][PF_6]$, $[\mathbf{1}]^+[PF_6]^-$, towards the dicarboxylic fumaric and maleic acids. The idea was to use the –COOH groups as a probe of the hydrogen-bonding capacity of the organometallic complex.

In previous studies we have extensively investigated the behaviour of organometallic dicarboxylic acids, such as, $[Fe(\eta^5\text{-}C_5H_4COOH)_2]$, $[Co(\eta^5\text{-}C_5H_4COOH)_2]^+$ and $[Cr(\eta^6\text{-}C_6H_5COOH)_2]$[12] towards a variety of organic and inorganic acids or bases. The results of these studies have led us to the successful exploitation of the acid/base behaviour of one such species, namely the zwitterionic form $[Co(\eta^5\text{-}C_5H_4COOH)(\eta^5\text{-}C_5H_4COO)]$, obtained by deprotonation of the cobalticinium cationic acid, in heterogeneous reactions with vapours of acids and bases.[13,15] In a parallel investigation we have studied the reactivity of neutral disubstituted pyridyl and pyrimidyl ferrocenyl species towards acids and metal complexes.[16] With the present work we intended to extend these findings to a new class of supramolecular synthons, namely that of cationic bis-amido complexes, of which $[Co^{III}(\eta^5\text{-}C_5H_4CONHC_5H_4N)_2]^+$ is the prototype.[17]

In the course of this investigation we have shown that both fumaric and maleic acids are sufficiently strong as to protonate the pyridine moiety. However, in the case of maleic acid, formation of the intramolecular hydrogen bond yields compounds that contain only the hydrogen maleate monoanion, while in the case of fumaric acid, both the completely deprotonated fumarate dianion and the supramolecular trianion formed by one hydrogen fumarate mono-anion and one fumarate dianion were obtained.

In terms of organometallic moieties, most adducts, but not all, contain the dimer formed by the monoprotonated dication $[\mathbf{1}H]^{2+}$ and are held together by intercation N–H···N hydrogen bonds between a protonated and a free pyridyl N atom, while the O-atom acceptors on the fumarate and hydrogen maleate anions appear to be involvedexclusively in interactions with the amido –(CO)N–H hydrogen-bond donors. Only in the case of $[\mathbf{1}H_2]^{3+}\cdot 2[PF_6]^-\cdot[Hmaleate]^-\cdot H_2O$ an interaction between the N-atom and the acid is observed.

Further studies are in progress to utilize the bis-amido complexes in the formation of complexes of complexes, for applications in coordination chemistry and crystal engineering.

Experimental Section

All reactants were purchased from Aldrich and used without further purification. Reagent grade solvents and bidistilled water were used.

Synthesis of $[\mathbf{1}H]^{2+}\cdot 2[PF_6]^-$: $[\mathbf{1}H]^{2+}$ was synthesized following a procedure, slightly modified, reported by Beer and Stokes.[18]

Synthesis of $[\mathbf{1}]^+\cdot[PF_6]^-$: $[\mathbf{1}H]^{2+}$ was treated with a 0.1 M solution of NH_3, in order to obtain deprotonation of the two pyridine moieties. Elementary analysis: calcd. C 46.01, N 9.55, H 3.16; found C 46.04, N 9.53, H 3.12.

Synthesis of $[\mathbf{1}H]^{2+}\cdot[PF_6]^-\cdot 1/2[fumarate]^{2-}$: $[\mathbf{1}]^+\cdot[PF_6]^-$ (0.11 mmol) and fumaric acid, $C_4H_2O_4$ (0.11 mmol) were dissolved in 5 mL of water. Crystals suitable for single-crystal X-ray diffraction were obtained by slow evaporation of water. The same compound was obtained after reaction of $[\mathbf{1}]^+\cdot[PF_6]^-$ (0.11 mmol) with $C_4H_2O_4$ (0.5 and 1.5 mmol; 2:1 and 1:1.5 reagents ratio, respectively). Elemen-

 © 2005 Wiley-VCH Verlag GmbH & Co. KGaA, Weinheim

tary analysis: calcd. C 45.59, N 8.86, H 3.19; found C 45.57, N 8.85, H 3.20.

Synthesis of $[1H_2]^{3+}\cdot[PF_6]^-\cdot[H(fumarate)_2]^{3-}\cdot H_3O^+\cdot H_2O$: $[1]^+\cdot[PF_6]^-$ (0.11 mmol) and fumaric acid, $C_4H_2O_4$, (0.22 mmol) were dissolved in 5 mL of water. Crystals suitable for single-crystal X-ray diffraction were obtained by slow evaporation of water. The same compound was obtained after reaction of $[1]^+\cdot[PF_6]^-$ (0.11 mmol) with $C_4O_4H_2$ (0.33 mmol; 1:3 reagents ratio). Elementary analysis: calcd. C 42.77, N 6.65, H 3.59; found C 42.78, N 6.63, H 3.60.

Synthesis of $2[1H]^{2+}\cdot 5/2[PF_6]^-\cdot 3/2[maleate]^{2-}$: $[1]^+\cdot[PF_6]^-$ (0.22 mmol) and maleic acid, $C_4H_2O_4$, (0.11 mmol) were dissolved in 5 mL of water. Crystals suitable for single-crystal X-ray diffraction were obtained by slow evaporation of water. Elementary analysis: calcd. C 43.12, N 8.04, H 2.86; found C 42.14, N 80.02, H 2.86.

Synthesis of $2[1H_2]^{3+}\cdot 3[PF_6]^-\cdot 3[Hmaleate]^-\cdot 2H_2O$: $[1]^+\cdot[PF_6]^-$ (0.11 mmol) and maleic acid, $C_4H_2O_4$, (0.22 mmol) were dissolved in 5 mL of water. Crystals suitable for single-crystal X-ray diffraction were obtained by slow evaporation of water. Elementary analysis: calcd. C 40.21, N 6.69, H 2.83; found C 40.22, N 6.70, H 2.83.

Synthesis of $[1H_2]^{3+}\cdot 2[PF_6]^-\cdot[Hmaleate]^-\cdot H_2O$: $[1]^+\cdot[PF_6]^-$ (0.11 mmol)and an excess of maleic acid, $C_4H_2O_4$, were dissolved in 5 mL of water. Crystals suitable for single-crystal X-ray diffraction were obtained by slow evaporation of water. Elementary analysis: calcd. C 36.64, N 6.57, H 2.72; found C 36.62, N 6.55, H 2.72.

Crystal Structure Determination: Crystal data for all compounds were collected on a Bruker ApexII CCD diffractometer. Crystal data and details of measurements are summarised in Table 2. Common to all compounds: Mo-*Kα* radiation, λ = 0.71073 Å, monochromator: graphite. Data for $2[\mathbf{1}H]^{2+}\cdot 5/2[PF_6]^-\cdot 3/2[Hmaleate]^-$ were collected at 293 K, all other data were collected at 273 K. SHELX97[19a] was used for structure solution and refinement based on F^2. Non-hydrogen atoms were refined anisotropically. The $[PF_6]^-$ anion in $[\mathbf{1}H]^{2+}\cdot[PF_6]^-\cdot 1/2[fumarate]^{2-}$ is disordered over two positions (refined with an occupancy ratio of 80:20) around the F1–F5 axis. One of the two $[Hmaleate]^-$ ions in $[\mathbf{1}H]^{2+}\cdot 5/2[PF_6]^-\cdot 3/2[Hmaleate]^-$ is disordered over two equivalent positions around an inver-

Table 2. Crystal data and details of measurements for $2[1H]^{2+}\cdot 4[PF_6]^-\cdot H_2O$, $[1H]^{2+}\cdot[PF_6]^-\cdot 1/2[fumarate]^{2-}$, $[1H_2]^{3+}\cdot[PF_6]^-\cdot[H(fumarate)_2]^{3-}\cdot H_3O^+\cdot H_2O$, $2[1H]^{2+}\cdot 5/2[PF_6]^-\cdot 3/2[Hmaleate]^-$, $2[1H_2]^{3+}\cdot 3[PF_6]^-\cdot 3[Hmaleate]^-\cdot 2H_2O$ and $[1H_2]^{3+}\cdot 2[PF_6]^-\cdot[Hmaleate]^-\cdot H_2O$.

Compound	$2[1H]^{2+}\cdot 4[PF_6]^-\cdot H_2O$	$[1H]^{2+}\cdot[PF_6]^-\cdot 1/2[fumarate]^{2-}$	$[1H_2]^{3+}\cdot[PF_6]^-\cdot[H(fumarate)_2]^{3-}\cdot H_3O^+\cdot H_2O$
Formula	$C_{44}H_{40}Co_2F_{24}N_8O_5P_4$	$C_{24}H_{20}CoF_6N_4O_4P$	$C_{30}H_{30}CoF_6N_4O_{12}P$
M_r	1458.58	632.34	482.48
System	monoclinic	monoclinic	triclinic
Space group	$P2_1/c$	$P2_1/n$	$P\bar{1}$
a [Å]	23.468(2)	7.9833(3)	7.583(7)
b [Å]	15.373(1)	29.284(1)	13.552(5)
c [Å]	15.304(1)	10.5411(4)	16.526(4)
α [°]	90	90	89.38(2)
β [°]	92.714(3)	90.836(1)	84.90(4)
γ [°]	90	90	80.66(5)
V [Å^3]	5515.1(7)	2464.1(2)	1669(2)
Z	4	4	2
T [K]	293	293	293
μ(Mo-K_α) [mm^{-1}]	0.852	0.848	1.676
Measured reflns.	63612	23263	13537
Unique reflns.	16083	5369	5844
Refined parameters	823	372	471
GOF on F^2	1.018	0.885	1.010
R_1 [on F, $I > 2\sigma(I)$]	0.0641	0.0611	0.0648
wR_2 (on F^2,all data)	0.2342	0.1832	0.1392
Compound	$2[1H]^{2+}\cdot 5/2[PF_6]^-\cdot 3/2[Hmaleate]^-$	$2[1H_2]^{3+}\cdot 3[PF_6]^-\cdot 3[Hmaleate]^-\cdot 2H_2O$	$[1H_2]^{3+}\cdot 2[PF_6]^-\cdot[Hmaleate]^-\cdot H_2O$
Formula	$C_{50}H_{41.50}Co_2F_{15}N_8O_{10}P_{2.5}$	$C_{56}H_{53}Co_2F_{18}N_8O_{18}P_3$	$C_{26}H_{25}CoF_{12}N_4O_7P_2$
M_r	1394.70	1678.83	854.37
System	triclinic	triclinic	monoclinic
Space group	$P\bar{1}$	$P\bar{1}$	$P2_1/a$
a [Å]	10.6826(5)	12.7015(8)	13.1655(4)
b [Å]	14.2849(7)	14.6608(9)	12.7040(4)
c [Å]	19.6711(9)	19.758(1)	19.7122(6)
α [°]	95.080(1)	70.667(1)	90
β [°]	104.807(1)	86.814(1)	97.7600(10)
γ [°]	107.763(1)	70.147(1)	90
V [Å^3]	2718.2(2)	3258.7(3)	3266.8(2)
Z	2	2	4
T [K]	273	293	293
μ(Mo-K_α) [mm^{-1}]	0.802	0.712	1.737
Measured reflns	26312	38487	25629
Unique reflns.	9654	15238	5745
Refined parameters	782	970	463
GOF on F^2	1.074	0.823	1.024
R_1 [on F, $I > 2\sigma(I)$]	0.0550	0.0543	0.0656
wR_2 (on F^2,all data)	0.1758	0.1576	0.2010

 © 2005 Wiley-VCH Verlag GmbH & Co. KGaA, Weinheim

sion centre, and was difficult to model; the position of the independent carbon atom and of the oxygen atom involved in the intramolecular hydrogen bond could not be separated well from those of the second, inverted image; the refinement was then done by attributing an average C/O scattering factor to the two atoms. All hydrogen atoms bound to nitrogen and oxygen atoms were located by difference Fourier syntheses. Only the hydrogen atoms bound to the water molecule in $2[\mathbf{1H}]^{2+}\cdot 4[PF_6]^-\cdot H_2O$ and $[\mathbf{1H_2}]^{3+}\cdot 2[PF_6]^-\cdot$ [Hmaleate]$^-\cdot H_2O$, and the H_{COOH} hydrogen in the disordered maleate monoanion in $2[\mathbf{1H}]^{2+}\cdot 5/2[PF_6]^-\cdot 3/2$[Hmaleate]$^-$ could not be located. Hydrogen atoms bound to carbon atoms were added in calculated positions. SCHAKAL99[19b] was used for the graphical representation of the results. The program PLATON[19c] was used to calculate the hydrogen-bonding interactions reported in Table 1.

CCDC-260092 to -260097 contain the supplementary crystallographic data for this paper. These data can be obtained free of charge from The Cambridge Crystallographic Data Centre via www.ccdc.cam.ac.uk/data_request/cif.

Acknowledgments

We thank MIUR (PRIN 2004 and FIRB2001) and the University of Bologna for financial support.

[1] a) G. R. Desiraju, *Crystal Engineering: The Design of Organic Solids*; Elsevier: Amsterdam, **1989**; b) *Crystal Engineering: from Molecules and Crystals to Materials* (Eds.: D. Braga, F. Grepioni, A. G. Orpen), Kluwer Academic Publishers, Dordrecht, **1999**; c) C. B. Aakeröy, A. S. Borovik, *Coord. Chem. Rev.* **1999**, *183*, 1; d) M. D. Hollingsworth, *Science* **2002**, *295*, 2410; e) D. Braga, *Chem. Commun.* **2003**, 1258; f) D. Braga, J. Miller, G. R. Desiraju, A. G. Orpen, S. L. Price, *CrystEngComm* **2002**, *4*, 500; g) L. Brammer, *Chem. Soc. Rev.* **2004**, *33*, 476; h) M. W. Hosseini, *CrystEngComm* **2004**, *6*, 318.

[2] D. Braga, F. Grepioni, G. R. Desiraju, *Chem. Rev.* **1998**, *98*, 1375.

[3] a) C. B. Aakeröy, *Acta Crystallogr. Sect. B* **1997**, *53*, 569; b) D. Braga, F. Grepioni, *Coord. Chem. Rev.* **1999**, *183*, 19; c) L. J. Brammer, *J. Chem. Soc. Dalton Trans.* **2001**, *16*, 3145; d) L. Brammer, *Dalton Trans.* **2003**, *16*, 3145; e) M. W. Hosseini, *Coord. Chem. Rev.* **2003**, *240*, 157; f) M. Eddaouddi, D. B. Moler, H. Li, B. Chen, T. M. Reineke, M. O'Keeffe, O. M. Yaghi, *Acc. Chem. Res.* **2001**, *34*, 319; g) S. R. Batten, *CrystEngComm* **2001**, 28; h) K. T. Holman, A. M. Pivovar, J. A. Swift, M. D. Ward, *Acc. Chem. Res.* **2001**, *34*, 107; i) O. M. Yaghi, G. Li, H. Li, *Nature* **2000**, *378*, 703; j) S.-I. Noro, S. Kitagawa, M. Kondo, K. Seki, *Angew. Chem. Int. Ed.* **2000**, *39*, 2082; k) S. B. Batten, R. Robson, *Angew. Chem. Int. Ed. Engl.* **1998**, *37*, 1460; l) M. Fujita, *Acc. Chem. Res.* **1999**, *32*, 53; m) O. R. Evans, R. G. Xiong, Z. Y. Wang, G. K. Wong, W. B. Lin, *Angew. Chem. Int. Ed.* **1999**, *38*, 536; n) O. R. Evans, W. B. Lin, *Acc. Chem. Res.* **2002**, *35*, 511; o) C. Janiak, *Dalton Trans.* **2003**, *14*, 2781; p) L. Carlucci, G. Ciani, D. M. Proserpio, *CrystEngComm* **2003**, *5*, 269; q) H. W. Roesky, M. Andruh, *Coord. Chem. Rev.* **2003**, *236*, 91; r) O. M. Yaghi, M. O'Keeffe, N. W. Ockwig, H. K. Chae, M. Eddaoudi, J. Kim, *Nature* **2003**, *423*, 705; s) B. Moulton, M. J. Zaworotko, *Chem. Rev.* **2001**, *101*, 1629; t) M. D. Ward, M. J. Horner, *CrystEngComm* **2004**, *6*, 401; u) S. A. Barnett, N. R. Champness, *Coord. Chem. Rev.* **2003**, *246*, 145; v) C. Janiak, *Dalton Trans.* **2003**, 2781.

[4] a) J. M. Lehn, *Supramolecular Chemistry: Concepts and Perspectives*, Wiley-VCH, Weinheim, **1995**; b) I. Haiduc, F. T. Edelmann, *Supramolecular Organometallic Chemistry*, Wiley-VCH, Weinheim, **1999**; c) J. W. Steed, J. L. Atwood, *Supramolecular Chemistry*, John Wiley & Sons, New York, **2000**.

[5] a) *The Crystal as a Supramolecular Entity. Perspectives in Supramolecular Chemistry*, vol. 2 (Ed.: G. R. Desiraju), Wiley, Chichester, UK, **1996**; b) *J. Chem. Soc. Dalton Trans.* **2000**, 3705, the whole issue; c) *Perspectives in Supramolecular Chemistry, vol. 7 – Crystal Design: Structure and Function* (Ed.: G. R. Desiraju), Wiley, Chichester, **2003**.

[6] a) D. Braga, F. Grepioni, *Acc. Chem. Res.* **2000**, *33*, 601; b) D. Braga, L. Maini, F. Grepioni, C. Elschenbroich, F. Paganelli, O. Schiemann, *Organometallics* **2001**, *20*, 1875.

[7] a) A. M. Beatty, *CrystEngComm* **2001**, 51; b) L. Brammer, J. C. Mareque-Rivas, R. Atencio, S. Fang, F. C. Pigge, *J. Chem. Soc. Dalton Trans.* **2000**, 3855; c) C. M. Zakaria, G. Ferguson, A. J. Lough, C. Glidewell, *Acta Crystallogr. Sect. B* **2002**, *58*, 786; d) C. Elschenbroich, F. Lu, K. Harms, *Organometallics* **2002**, *21*, 5152; e) C. Elschenbroich, O. Schiemann, O. Burghaus, K. Harms, *J. Am. Chem. Soc.* **1997**, *119*, 7452; f) M. C. Tse, K. K. Cheung, M. C. W. Chan, C. M. Che, *Chem. Commun.* **1998**, *21*, 2295; g) Y. J. Kim, J. G. Verkade, *Inorg. Chem.* **2003**, *42*, 4262; h) J. C. M. Rivas, L. Brammer, *Coord. Chem. Rev.* **1999**, *183*, 43; i) M. Oh, G. B. Carpenter, D. A. Sweigart, *Organometallics* **2003**, *22*, 2364; j) M. Oh, G. B. Carpenter, D. A. Sweigart, *Angew. Chem. Int. Ed.* **2002**, *41*, 3650; k) M. Oh, G. B. Carpenter, D. A. Sweigart, *Chem. Commun.* **2002**, *18*, 2168; l) M. Oh, G. B. Carpenter, D. A. Sweigart, *Acc. Chem. Res.* **2004**, *37*, 1; m) C. M. Zakaria, G. Ferguson, A. J. Lough, C. Glidewell, *Acta Crystallogr. Sect. B* **2002**, *58*, 786; n) U. Geiger, J. A. Schlueter, *Chem. Rev.* **2004**, *104*, 5203; o) M. Oh, J. A. Reingold, G. B. Carpenter, D. A. Sweigart, *Coord. Chem. Rev.* **2004**, *248*, 561; p) C. Elschenbroich, M. Wolf, J. Pebler, K. Harms, *Organometallics* **2004**, *23*, 454.

[8] a) D. Braga, L. Maini, M. Polito, M. Rossini, F. Grepioni, *Chem. Eur. J.* **2000**, *6*, 4227; b) D. Braga, L. Maini, F. Grepioni, A. DeCian, O. Felix, J. Fisher, M. W. Hosseini, *New J. Chem.* **2000**, *24*, 547; c) D. Braga, F. Grepioni, *J. Chem. Soc. Dalton Trans.* **1999**, 1; d) D. Braga, L. Maini, L. Prodi, A. Caneschi, R. Sessoli, F. Grepioni, *Chem. Eur. J.* **2000**, *6*, 1310; e) D. Braga, L. Maini, M. Polito, F. Grepioni, *Organometallics* **1999**, *18*, 2577.

[9] a) L. J. Prins, D. N. Reinhoudt, P. Timmerman, *Angew. Chem. Int. Ed.* **2001**, *40*, 2382; b) C. B. Aakeröy, K. R. Seddon, *Chem. Soc. Rev.* **1993**, 397; c) M. S. Gordon, J. H. Jensen, *Acc. Chem. Res.* **1996**, *29*, 536; d) D. Braga, F. Grepioni, *Acc. Chem. Res.* **1997**, *30*, 81; e) L. Brammer, D. Zhao, F. T. Ladipo, J. Braddock-Wilking, *Acta Crystallogr. Sect. B* **1995**, *51*, 632; f) J. J. Novoa, I. Nobeli, F. Grepioni, D. Braga, *New J. Chem.* **2000**, *24*, 5.

[10] a) G. R. Desiraju, *Acc. Chem. Res.* **2002**, *35*, 565; b) D. Braga, L. Maini, M. Polito, F. Grepioni, *Struct. Bonding* **2004**, *111*, 1; c) K. Biradha, *CrystEngComm* **2003**, *5*, 374.

[11] See for example, a) A. D. Burrows, *Struct. Bonding* **2004**, *108*, 55; b) L. M. Epstein, E. S. Shubina, *Coord. Chem. Rev.* **2002**, *231*, 165; c) A. M. Beatty, *Coord. Chem. Rev.* **2003**, *246*, 131.

[12] D. Braga, L. Maini, M. Polito, E. Tagliavini, F. Grepioni, *Coord. Chem. Rev.* **2003**, *246*, 53.

[13] a) D. Braga, G. Cojazzi, D. Emiliani, L. Maini, F. Grepioni, *Chem. Commun.* **2001**, 2272; b) D. Braga, G. Cojazzi, D. Emiliani, L. Maini, F. Grepioni, *Organometallics* **2002**, *21*, 1315; c) D. Braga, L. Maini, M. Mazzotti, K. Rubini, A. Masic, R. Gobetto, F. Grepioni, *Chem. Commun.* **2002**, 2296.

[14] D. Braga, M. Polito, F. Grepioni, *Cryst. Growth Des.* **2004**, *4*, 769.

[15] a) D. Braga, L. Maini, M. Polito, F. Grepioni, *Organometallics* **1999**, *18*, 2577; b) D. Braga, L. Maini, M. Mazzotti, K. Rubini, F. Grepioni, *CrystEngComm* **2003**, *29*, 154.

[16] a) D. Braga, D. D′Addario, F. Grepioni, M. Polito, D. M. Proserpio, J. W. Steed, E. Tagliavini, *Organometallics* **2003**, *22*, 4532.

 © 2005 Wiley-VCH Verlag GmbH & Co. KGaA, Weinheim

[17] D. Braga, F. Grepioni, S. Giaffreda, unpublished results.
[18] P. Beer, S. E. Stokes, *Polyhedron* **1995**, *14*, 873.
[19] a) G. M. Sheldrick, SHELXL97, Program for Crystal Structure Determination; University of Göttingen, Göttingen, Germany, **1997**; b) E. Keller, SCHAKAL99, Graphical Representation of Molecular Models; University of Freiburg, Germany, **1999**; c) A. L. Speck, *Acta Crystallogr. Sect. A* **1990**, *46*, 9574.

Received: February 17, 2005
Published Online: June 2, 2005

 © 2005 Wiley-VCH Verlag GmbH & Co. KGaA, Weinheim

Grafting Poly(4-vinylpyridine) with a Second-Order Nonlinear Optically Active Nickel(II) Chromophore

Ugo Caruso,[a] Roberto Centore,*[a] Barbara Panunzi,[b] Antonio Roviello,*[a] and Angela Tuzi[a]

Keywords: N ligands / Nickel / Nonlinear optics / Poly(4-vinylpyridine)

Metal-containing polymers are obtained by grafting commercial poly(4-vinylpyridine) (average molecular weight 60000 or 160000) with a Ni^{II} chromophore complex. The metal-containing chromophore was obtained from a tridentate benzoylhydrazine ligand. Chromophore fragments were grafted onto the polymer by formation of a coordinative bond between the metal and the pyridinic nitrogen. Two acentric mononuclear Ni^{II} complexes containing pyridine as an additional ligand, in a square-planar or in an octahedral environment, have been prepared and characterised also by single-crystal X-ray analysis. The chemical and thermal properties of the model complexes and of the grafted polymers were examined and compared with those of Cu^{II}- and Pd^{II}-based ones, in particular with reference to their NLO properties.
(© Wiley-VCH Verlag GmbH & Co. KGaA, 69451 Weinheim, Germany, 2005)

Introduction

Metallopolymers are a very attractive class of materials because of their widespread applications.[1a–1c] In particular, polymers bearing metallic chromophores are of current interest in the area of nonlinear optically (NLO) active materials.[2a,2b] Considerable effort has been directed toward molecular engineering of second order NLO-active coordination complexes that can be covalently bonded to a polymeric system. There are many examples in the recent literature of polymers with a metal-containing chromophoric moiety in the main chain or as side groups.[3a–3c] In particular, researchers aim to produce materials with high NLO responses that are easy to synthesise and are chemically and thermally stable.

Recently, we have developed a new approach to second-order NLO active metallopolymers based on grafting metallochromophores onto preformed (and commercially available) coordinating polymers, such as poly(4-vinylpyridine).[4a–4c] Metallochromophores are obtained by coordination of suitable metal ions to push-pull *N*-salicylidene-*N′*-aroylhydrazine-type tridentate ligands. An example of a polymer based on this approach is shown in Scheme 1 (M = metal atom).

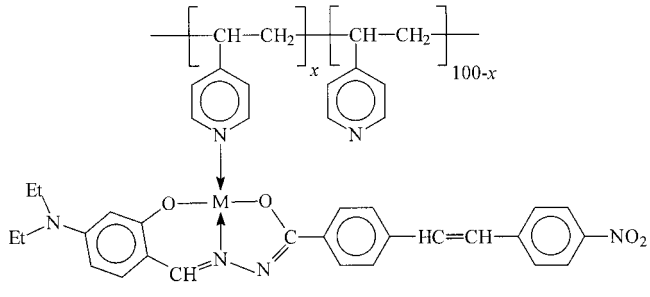

Scheme 1.

It is likely that the coordination properties of the metal have an effect on the properties of the grafted polymer. In fact, in the case of expansion of the coordination sphere of the metal from square planar to penta- or hexacoordinate environments, a partial cross-linking (by coordination) can occur in the polymer system. This, in turn, should affect some polymer properties related to second order NLO applications, such as the glass-transition temperature and the time stability of the orientational order induced during the poling process and its extent. Up to now we have restricted our investigation to Cu^{II}- and Pd^{II}-containing metallopolymers, for which the coordination geometry expected and most frequently found is square planar, so that coordinative cross-linking of the polymers should not be expected. Actually, for model complexes of Cu^{II} with some ligands having a longer conjugation path, crystallographic evidence for weak interaction of the square-planar coordinated metal with an additional pyridine molecule, leading to pseudo-pentacoordinate complexes, has been observed.[4a–4c]

[a] Dipartimento di Chimica, Università degli Studi di Napoli "Federico II",
Via Cinthia, 80126 Napoli, Italy
E-mail: roberto.centore@unina.it
antonio.roviello@unina.it
[b] Dipartimento di Scienza degli Alimenti, Università degli Studi di Napoli "Federico II",
Via Università 100, 80155 Portici, Napoli, Italy

To the best of our knowledge, only a few reports of nickel-based NLO active polymers have appeared,[5a–5c] and some of these deal with host–guest-type systems.[6a,6b] In this paper we report a detailed investigation of the polymer system shown in Scheme 1 and containing Ni^{II} as the metal ion, for which a greater relevance of hexacoordination of the metal can be expected. In addition, the crystal structures of the model complexes (pyridine adducts) shown in Scheme 2 are also reported.

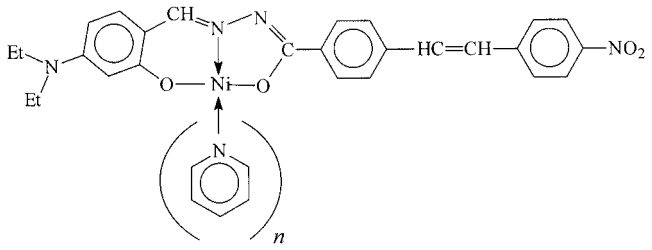

Scheme 2.

Results and Discussion

A general outline of the synthetic route to the new nickel-grafted polymers is shown in Scheme 3.

The model complex [Ni(L)Py] was synthesised as described in the Experimental Section. Its DSC heating curve shows only a broad endothermic signal starting at about 250 °C, corresponding to loss of the coordinated pyridine. No melting was observed under the polarizing microscope up to decomposition (about 345 °C, as detected by TGA analysis). The second-order molecular nonlinearity of [Ni(L)Py] was determined by the EFISH technique. The result obtained, $\mu\beta = 850 \times 10^{-48}$ esu, indicates a moderate activity and is consistent with results we have reported for Cu^{II} and Pd^{II} complexes containing the same ligand or closely related ligands ($\mu\beta$ between 1100×10^{-48} and 1500×10^{-48} esu[4a,4c]).

Recrystallisation of [Ni(L)Py] from THF/hexane gave brick-red prismatic crystals suitable for X-ray analysis that confirmed the square-planar coordination of nickel by the tridentate ligand and one pyridine molecule; a solvent (THF) molecule is also included in the crystal lattice. Remarkably, the same complex, when recrystallised by evaporation from pyridine, gave dark-violet crystals that, in about two hours at room temperature, turned to dark red, undergoing about 33% weight loss. Subsequent structural analysis confirmed that the dark-violet crystals contain the hexacoordinate complex [Ni(L)Py_3], in which two additional pyridine molecules are coordinated to the metal in apical positions, and pointed out the presence of a large amount of solvent of crystallisation in the crystals (2.5 pyridine molecules for each complex molecule). Since the crystals easily lose the solvent at room temperature, and also some coordinated pyridine on heating, as evidenced by the complex TGA pattern, the X-ray structural analysis for this complex was necessarily performed at low temperature (–100 °C).

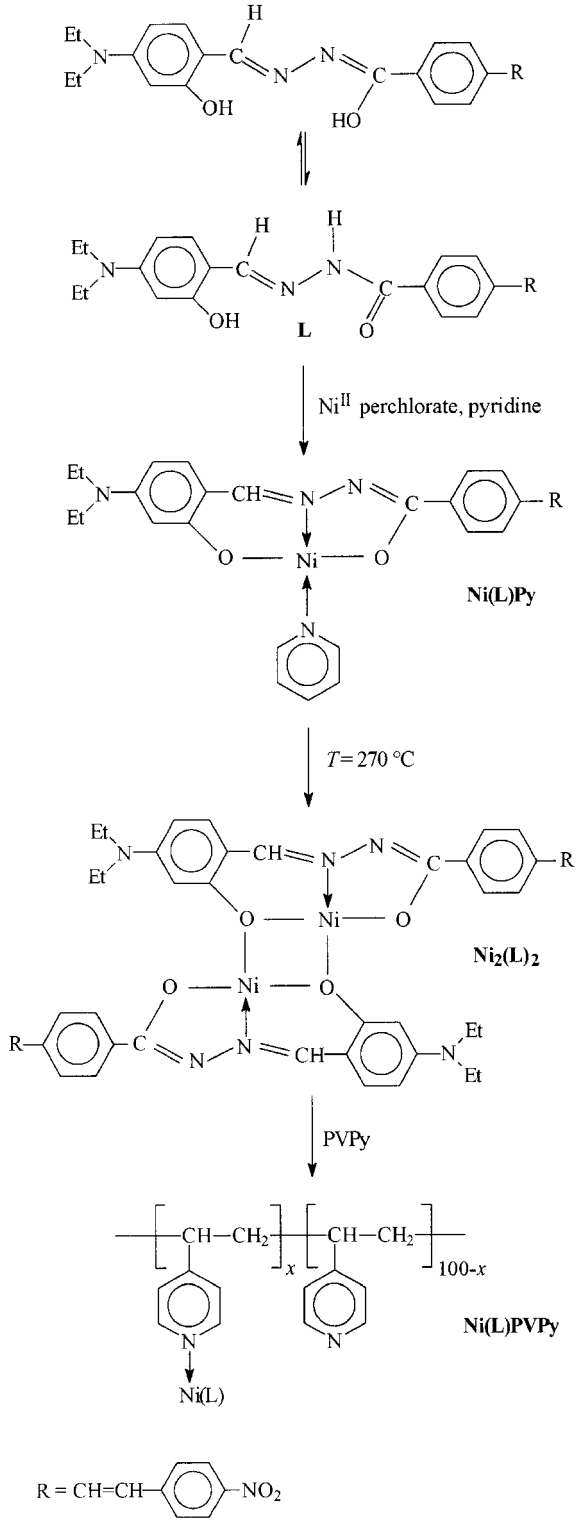

Scheme 3.

 © 2005 Wiley-VCH Verlag GmbH & Co. KGaA, Weinheim

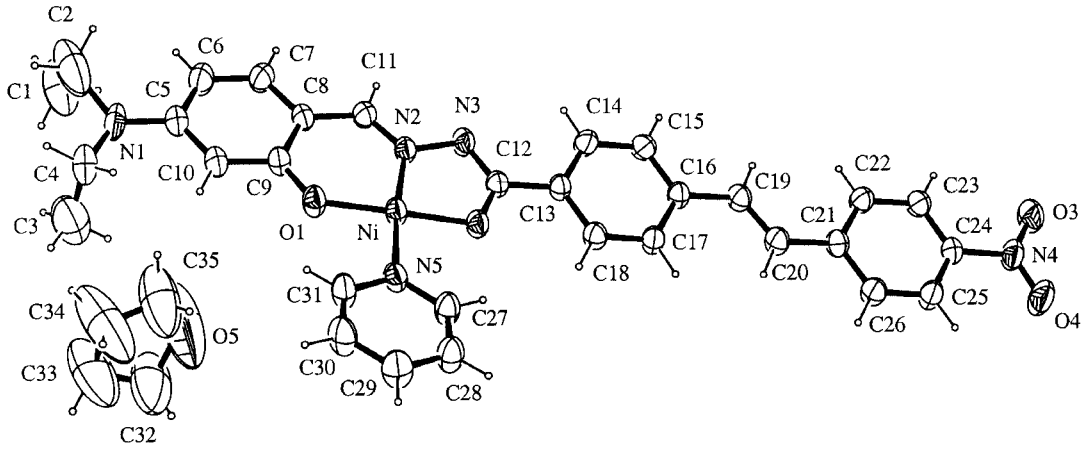

Figure 1. ORTEP view of [Ni(L)Py]. Thermal ellipsoids are at the 30% probability level. The THF solvent molecule is also shown.

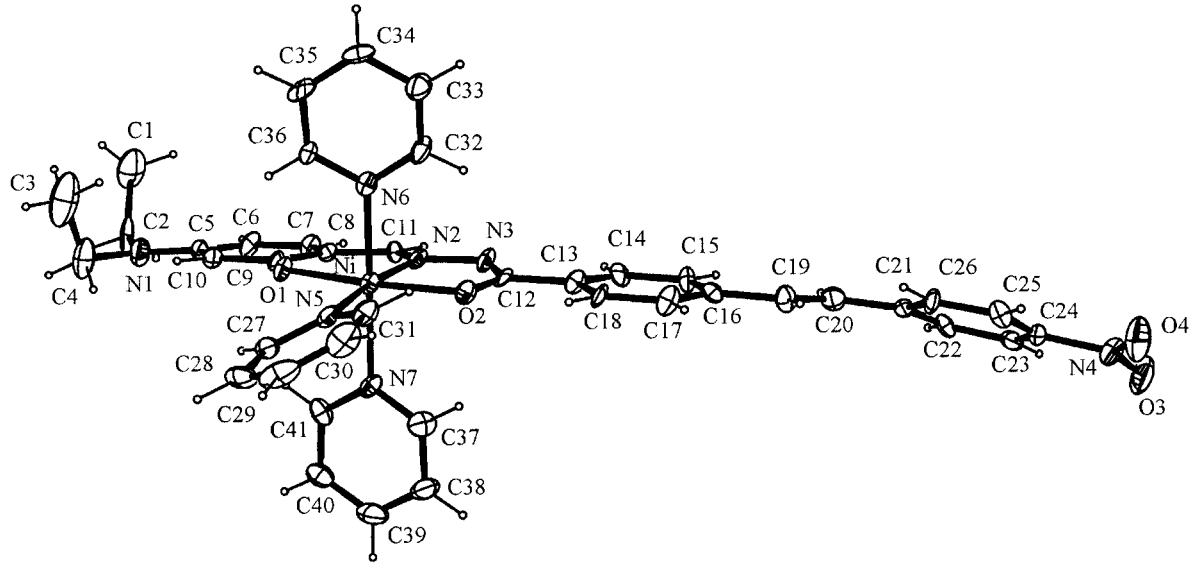

Figure 2. ORTEP view of [Ni(L)Py_3]. Thermal ellipsoids are at the 30% probability level. Pyridine solvent molecules are not shown.

The molecular structures of complexes [Ni(L)Py] and [Ni(L)Py_3] are shown in Figures 1 and 2 respectively. Selected bond lengths and angles are given in Table 1.

As evidenced by the C–O and C–N bond lengths (see Table 1), and in accordance with analogous compounds,[4a–4c] the tridentate ligand is present in its enol form in both complexes. It adopts a substantially planar conformation in the first complex, while a small torsion of the nitrophenyl group around the C20–C21 bond is present in the second (see Table 1). The coordination geometry is different in the two complexes: it is square planar in [Ni(L)Py], with general geometric features very close to those observed for analogous Cu^{II} and Pd^{II} compounds,[4a–4c] whereas in [Ni(L)Py_3] the metal is hexacoordinate with a fairly regular octahedral coordination geometry, with the tridentate ligand and one pyridine in the equatorial positions, while two additional pyridine molecules occupy the axial positions at the same mean distance (shorter than those recorded for analogous pseudo-pentacoordinate Cu^{II} complexes[4a–4c]). As compared to the square-planar complex, the distances between the metal and ligands are slightly longer in the octahedral complex, as expected. The mean plane of the (N5, C27–C31) coordinated pyridine is twisted by about 22° with respect to the equatorial coordination plane, while the mean planes of the two axial pyridines are twisted by about 18° with respect to each other. Solvent molecules are present in the crystal packing of both compounds, and this seems to be necessary in order to get crystallisation. In particular, in [Ni(L)Py_3] the pyridine solvent molecules are placed into channels running parallel to the *c* axis across the crystal, and this could explain why these molecules are easily lost even at room temperature. One pyridine solvent molecule lies on the binary axis along *c*, while the other two are placed near the screw axis parallel to *c*. Although crystals of [Ni(L)Py_3] are acentric (space group *Fdd*2), no relevant NLO activity

 © 2005 Wiley-VCH Verlag GmbH & Co. KGaA, Weinheim

Table 1. Selected bond lengths [Å], bond angles [°] and torsion angles [°] for [Ni(L)Py] and [Ni(L)Py_3] with esd's in parentheses.

	[Ni(L)Py]	[Ni(L)Py_3]
Ni–O1	1.817(4)	2.016(5)
Ni–O2	1.840(3)	2.051(5)
Ni–N2	1.822(4)	1.995(6)
Ni–N5	1.948(5)	2.104(7)
Ni–N6		2.158(6)
Ni–N7		2.195(6)
O1–C9	1.310(6)	1.312(8)
O2–C12	1.298(6)	1.270(9)
N2–C11	1.279(6)	1.277(8)
N3–C12	1.305(6)	1.326(10)
O1–Ni–N2	95.4(2)	91.9(3)
O2–Ni–N2	83.2(2)	79.2(2)
O1–Ni–N5	89.8(2)	95.2(3)
O2–Ni–N5	91.8(2)	93.7(3)
O2–Ni–N6		89.5(2)
N2–Ni–N6		94.6(2)
N5–Ni–N6		87.9(2)
O2–Ni–N7		89.7(2)
N2–Ni–N7		90.5(2)
N5–Ni–N7		86.9(2)
N6–Ni–N7		174.6(2)
C11–N2–N3–C12	–177.2(5)	–170.8(6)
C7–C8–C11–N2	178.1(6)	–178.0(7)
N3–C12–C13–C18	–172.4(5)	175.5(7)
C15–C16–C19–C20	–177.7(5)	–5.6(13)
C19–C20–C21–C26	174.5(5)	–16.5(8)
O1–Ni–N5–C27	178.4(4)	28.5(6)
O1–Ni–N6–C32		–157.2(6)
O1–Ni–N7–C37		175.2(6)

is expected for them because the molecules are elongated perpendicularly to the polar binary axis, which gives rise to an antiparallel arrangement of the push–pull fragments.

As far as the thermal behaviour of the hexacoordinate species is concerned, the TGA curve of [Ni(L)Py_3] above 100 °C (when the crystallisation pyridine molecules and both the axial pyridine molecules are lost) is the same as that of the square-planar complex [Ni(L)Py], as shown in Figure 3. From 220 to 250 °C a weight loss of about 11% is observed due to removal of coordinated pyridine from the square-planar complex and formation of a species that is stable up to 330 °C, which does not melt before decomposition. The elemental analysis of that species (a red crystalline product) is compatible with formation of the dinuclear [$Ni_2(L)_2$] species. Its TGA curve is shown in Figure 4. This behaviour suggests a good way to obtain [$Ni_2(L)_2$] species, since the methods described previously for other M^{II} ions[3c, 4a-4c] do not give products with a satisfactory degree of purity. Thermal treatment of [Ni(L)Py] at 270 °C for 3 min gave the dinuclear species quantitatively, which was then used in the grafting reaction onto the poly(4-vinylpyridine) (PVPy) backbones.

Grafted polymers were obtained by a bridge-splitting reaction of [$Ni_2(L)_2$] and anchoring of the Ni(L) fragments directly onto the pyridine nitrogens of the PVPy chains, as described previously.[4a–4c] Since a suitable choice of the molecular weight of the polymer backbone and of the grafting percentage of chromophoric fragment allows us to tune the spectroscopic, rheological, and thermodynamic properties of the final materials, two different compositions in complex (35% and 60% by weight) and two different molecular weights of PVPy (60000 and 160000) were studied. The latter choice was made in order to gain more viscous systems that are useful in the spin-coating deposition of polymeric thin films.

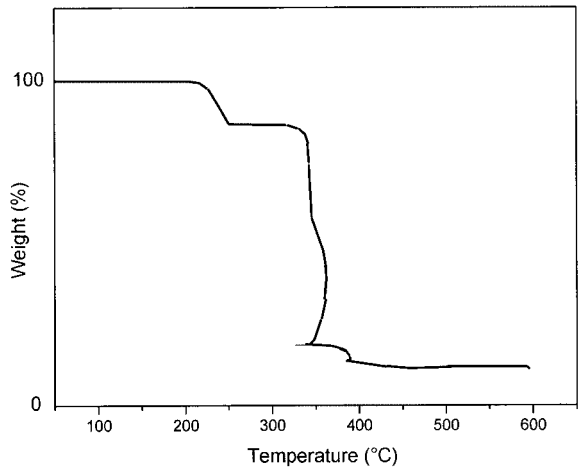

Figure 3. TGA curve of [Ni(L)Py] at a heating rate of 20 °C min^{-1}.

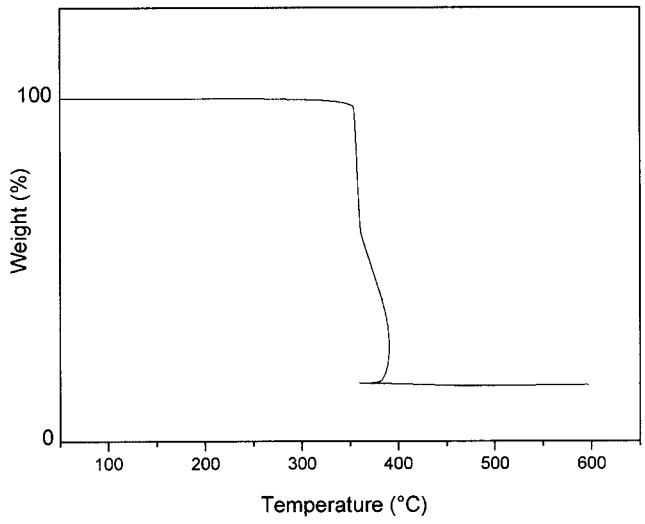

Figure 4. TGA curve of [$Ni_2(L)_2$] at a heating rate of 20 °C min^{-1}.

All the grafted PVPy samples are soluble in DMF and in *N*-methyl-2-pyrrolidinone. The ^{1}H NMR spectra of the four grafted PVPy samples, recorded in DMF solution, show broad peaks due to the high molecular weight of the polymers. No sharp peak pertaining to a free low-molecular-weight complex is detected. The signal at about δ = 8.5 ppm, due to the *ortho* hydrogen of the coordinated pyridine nitrogen, which occurs at about δ = 8.2 ppm in free PVPy and a peak at about δ = 3.4 ppm due to the –CH_2–*N*-φ protons in the chromophore, are the only significant resonances.

 © 2005 Wiley-VCH Verlag GmbH & Co. KGaA, Weinheim

Table 2. Relevant spectroscopic and thermodynamic data for the polymers.

	T_g[a] [°C]	T_d[b] [°C]	η_{inh}[c] [dl/g]	%NiO_{calc}[d]	%NiO_{exp}[e]	ε[f] [L mol^{-1} cm^{-1}]	λ_{max}[g] [nm]	%NiL_{calc}[h]
PVPy60000	146[i]	360	0.27	–	–	–	–	–
[Ni(L)35PVPy60]	200	340	0.29	4.8	5.1	$4.0\cdot10^3$	360, 440	32
[Ni(L)60PVPy60]	243	332	0.37	7.6	8.6	$7.5\cdot10^3$	361, 440	59
PVPy160000	146[i]	360	0.51	–	–	–	–	–
[Ni(L)35PVPy160]	199	338	0.57	5.0	5.1	$4.6\cdot10^3$	360, 441	38
[Ni(L)60PVPy160]	244	335	0.60	7.2	8.6	$9.8\cdot10^3$	360, 442	58

[a] Glass-transition temperature. [b] Decomposition temperature (5% weight loss) in air. [c] Inherent viscosity (c = 50.0 mg mL^{-1}) in NMP at 60 °C. [d] Calculated metal content as NiO. [e] Experimental metal content as NiO. [f] Molar extinction coefficient. [g] Absorption maxima. [h] Coordinated fragment (as NiL) content calculated from absorbance values (on the basis of the absorbance of the dinuclear complex). [i] Dried at 200 °C.

The most relevant UV/Vis and thermodynamic data of the polymers are reported in Table 2. The values of the molar extinction coefficient from the UV/Vis spectra recorded in $CHCl_3$ solutions follow the chromophore content.

The glass-transition temperatures (T_g) increase with the grafting amount, and they are independent of the molecular weight of the polymer backbone. Remarkably, in this case we note a higher increase of the T_g with respect to analogous Cu^{II}- and Pd^{II}-grafted polymers.[4a–4c] In particular, the T_g values for both [Ni(L)35PVPy60] and [Ni(L)35PVPy160] are 53 °C above the value for free PVPy and those of [Ni(L)60PVPy60] and [Ni(L)60PVPy160] 98 °C above this value. For the Cu^{II}- and Pd^{II}-grafted PVPy (same ligand L), increases of 48 °C for both the 35% grafted polymers and only 74 °C for both the 60% ones were observed.[7]

UV/Vis absorption spectra for the mononuclear and the dinuclear species, the ligand and a metallated polymer (the curve for [Ni(L)35PVPy60] is reported as an example) are shown in Figure 5. As expected, the UV/Vis absorption pattern and λ_{max} value for the free ligand L are very different from those pertaining to the species containing L as a tridentate ligand, i.e. the mononuclear square-planar complex, the dinuclear complex and the grafted polymers, which are essentially identical. These spectra are also very similar to those we have recorded for complexes containing the same ligand and Cu^{II} or Pd^{II} metal ions.[4a] The UV/Vis spectra of the octahedral species are complicated by the various equilibria between adducts with different coordination geometry occurring in solution and also depend on the donor capability of the solvent.

The DSC curves for the two commercial PVPy samples and the corresponding grafted polymers are given in Figure 6. It should be noted that the signal due to the glass transition for a sample dried at 200 °C is very sharp (about 30 °C) in all cases. The larger increase in the T_g as compared with Cu^{II} and Pd^{II} systems[4a–4c] may be correlated with the tendency of the Ni^{II} ion to add two other pyridine molecules, thus promoting a stronger interaction between the polymer chains. Other experimental evidence of this behaviour is the observation that the solutions in which the grafting reaction was performed, and also the 10% solutions obtained by dissolving the metallated polymers at 200 °C to prepare spin-coated thin film samples, yield a gel upon quick cooling to room temperature.

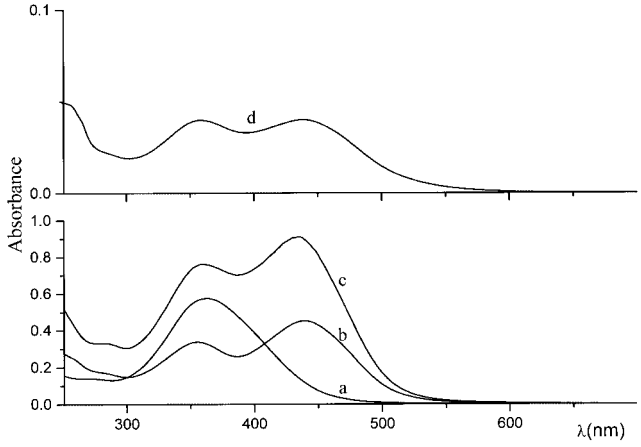

Figure 5. UV/Vis absorption spectra of L (curve a), [Ni(L)Py] (curve b), [$Ni_2(L)_2$] (curve c) and [Ni(L)35PVPy60] (curve d).

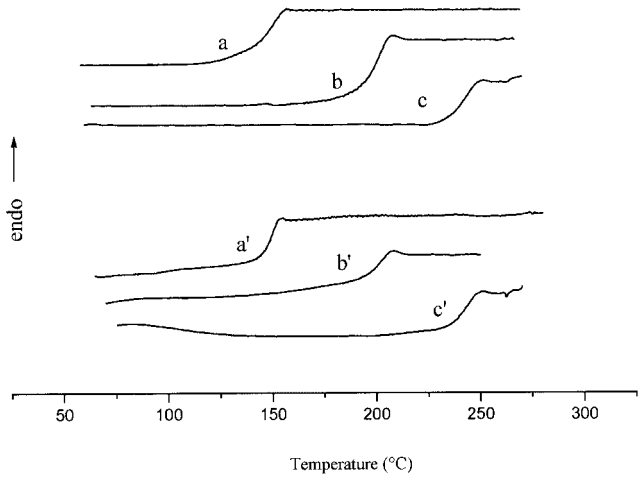

Figure 6. DSC curves (10 °C min^{-1}, N_2 atmosphere) for PVPy 60000 (a), [Ni(L)35PVPy60] (b), and [Ni(L)60PVPy60] (c), and PVPy 160000 (a′), [Ni(L)35PVPy160] (b′) and [Ni(L)60PVPy160] (c′).

Another point that is probably also related to the pyridine–metal interactions is the increase of the inherent viscosities with the grafting percentage with respect to that of free **PVPy**. In contrast, the inherent viscosities of the Cu^{II}-

 © 2005 Wiley-VCH Verlag GmbH & Co. KGaA, Weinheim

and Pd^{II}-grafted PVPy samples decrease with the metal content.[4a–4c]

Thermal treatments of polymer samples simulating poling conditions (i.e. annealing near or above the T_g for 30 min) do not produce appreciable changes in their thermal behaviour. No evidence of crystallinity was detected in the subsequent DSC heating runs or by optical observations under a polarizing microscope. On a sample deposited as a thin film on a glass slide by the spin-coating technique from hot NMP solution, a transparent homogeneous surface was observed. X-ray spectra recorded for the untreated polymer samples show only haloes typical of an amorphous phase.

The high T_g values, the good thermal stability (decomposition temperatures are generally over 330 °C) and the absence of structured phases make these metallated polymers promising as materials for second order NLO applications. Moreover, the ability to establish interactions between the polymer chains (by metal coordination) could be used to obtain a kind of cross-linking at temperatures lower than the T_g, thus providing a stabilisation of the polar order of the chromophore units that is higher than in the analogous Cu^{II}- and Pd^{II}-grafted PVPy samples.

Conclusions

The use of a fragment containing the nickel(II) ion bound to a tridentate ligand in the preparation of grafted poly(4-vinylpyridine) samples for nonlinear optics affords significant improvements in the properties of the final materials. The ability of Ni^{II} to enlarge its coordination sphere is evidenced by the isolation and structural determination of a tetracoordinate square-planar model complex and of the corresponding hexacoordinate octahedral complex (resulting from addition of two other pyridine molecules to the first complex). The crosslinking related to the coordination expansion is reflected in the higher glass-transition temperatures of this series of metallated polymers and in the increase of their inherent viscosities. This should enhance the poling time stability.

Experimental Section

Materials: All solvents, poly(4-vinylpyridine) (PVPy; M_n = 60000 and 160000 uma), 4-diethylamino-2-hydroxybenzaldehyde, 4-nitrocinnamic acid and nickel(II) perchlorate hexahydrate are commercially available (Aldrich) and were used without purification.

Physical Measurements: Phase-transition temperatures and enthalpies were measured using a differential thermal analyzer DSC Perkin–Elmer Pyris (scanning rate 10 °C min^{-1}, nitrogen flow). Optical observations were performed with a Zeiss Axioscop polarizing microscope equipped with an FP90 Mettler temperature heating stage. UV/Vis absorption spectra were recorded at room temperature with a Jasco V-560 Spectrophotometer in DMF. IR spectra were recorded with a JASCO FP-750 apparatus. Thermogravimetric analysis was performed in air with a TA Instruments SDT 2960 with simultaneous DSC-TGA recording. ^1H NMR spectra were recorded by Varian spectrometers operating at 200 MHz or at 300 MHz. X-ray diffraction patterns were recorded on a flat film camera (Ni-filtered Cu-K_α radiation). The inherent viscosities of polymers (NMP solutions at 60.0 °C) were measured with an Ubbelohde viscometer.

Synthesis: Synthetic pathways for the metallated polymers [Ni(L)-PVPy] and for the dinuclear complex $[Ni_2(L)_2]$ and mononuclear complex [Ni(L)Py] are reported in Scheme 3. The synthesis of the ligand L has already been described by us.[4a]

[Ni(L)Py]: A solution of nickel(II) perchlorate hexahydrate (2.5 g, 6.84 mmol) in 20 mL of water was added at about 100 °C to a solution of L (3.0 g, 6.54 mmol) in 100 mL of pyridine. The resulting solution was stirred at 100 °C for about 10 min, after which time a dark-red solid precipitated upon further addition of water (about 80 mL). This solid was recovered by filtration and washed three times with water, then dried at 110 °C. Yield: 3.46 g (89%). Decomposition occurs before melting. $C_{31}H_{29}N_5NiO_4$: calcd. C 62.59, H 5.04, N 11.78; found C 62.58, H 4.98, N 11.68. Recrystallisation from $CHCl_3$/heptane gave brick-red crystals of [Ni(L)Py]. Single crystals for X-ray diffraction analysis were obtained from THF solution. ^1H NMR (200 MHz, $CDCl_3$, Me_4Si): δ = 8.68 (d, 2 H), 8.20 (d, 2 H), 7.92 (d, 2 H), 7.76 (s, 1 H), 7.63 (d, 2 H), 7.48 (m, 4 H), 7.19 (m, 3 H), 6.22 (s, 1 H), 6.17 (s, 2 H), 3.346 (q, 4 H), 1.17 (t, 6 H) ppm.

[Ni(L)Py_3]: Dark-violet crystals of the hexacoordinate complex were obtained by slow evaporation of a pyridine solution of [Ni(L)Py]. The sample was stored at room temperature under pyridine atmosphere for further characterisations.

[$Ni_2(L)_2$]: This dinuclear complex was obtained by thermal treatment of the mononuclear complex [Ni(L)Py] at 270 °C for 3 min. The resulting dark-red crystals were used without further treatment. Yield: quantitative. Decomposition occurs before melting. $C_{52}H_{48}N_8Ni_2O_8$: calcd. C 60.56, H 4.85, N 10.87; found C 60.44, H 4.80, N 10.79.

Ni(L)PVPy: Four polymers {[Ni(L)35PVPy60], [Ni(L)60PVPy60], [Ni(L)35PVPy160] and [Ni(L)60PVPy160]} were obtained by grafting the fragment Ni(L) (at 35% and 60% by weight) onto two PVPy samples (60000 and 160000 average molecular weight). The polymers were prepared following a synthetic procedure already described by the authors,[4b] by dissolving the appropriate amount of PVPy (previously dried at 200 °C) in DMF and the dimeric complex $[Ni_2(L)_2]$ in DMF and blending and stirring the solution for 25 min at 90 °C. The polymer that precipitated upon addition of water was washed twice with vigorous stirring and dried at 120 °C. The yield was quantitative.

[Ni(L)35PVPy160]: Calcd. C 72.37, H 6.02, N 12.46; found C 71.00, H 6.16, N 12.22.

[Ni(L)35PVPy60]: Calcd. C 72.37, H 6.02, N 12.46; found C 70.38, H 6.12, N 12.08.

[Ni(L)60PVPy60]: Calcd. C 68.26, H 5.57, N 11.84; found C 67.80, H 5.60, N 11.85.

[Ni(L)60PVPy160]: Calcd. C 68.26, H 5.57, N 11.84; found C 67.65, H 5.68, N 11.76.

X-ray Analysis: X-ray data collection for [Ni(L)Py] was performed at room temperature on an Enraf–Nonius MACH3 diffractometer in the ω/θ scan mode, using graphite-monochromated Mo-K_α radiation (λ = 0.71069 Å). Cell parameters were obtained from a least-squares fit of the θ angles of 25 reflections in the range 7.04° $\leq \theta \leq$ 8.95°. A semi-empirical absorption correction (ψ scans) was applied.

Data collection for $Ni(L)Py_3$ was performed at low temperature (–100 °C) on a Bruker–Nonius kappa CCD diffractometer (Mo-K_α

 © 2005 Wiley-VCH Verlag GmbH & Co. KGaA, Weinheim

radiation, phi scans + omega scans to fill the asymmetric unit). Cell parameters were obtained from a least-squares fit of the θ angles of 30 reflections in the range $6.02° \leq \theta \leq 9.89°$. A semi-empirical absorption correction (multiscan, SADABS) was applied.

Both structures were solved by direct methods and refined anisotropically by the full-matrix least-squares method on F^2 against all independent measured reflections (SHELXS and SHELXL program of the SHELX 97 package[8]). H atoms were placed in calculated positions as riding on their carriers atoms. Max. residual electron density 0.691 (–0.424) e Å^{-3} for [Ni(L)Py] and 0.315 (–0.333) e Å^{-3} for [Ni(L)Py$_3$]. Some crystal, collection and refinement data are reported in Table 3.

Table 3. Crystallographic data collection and refinement for [Ni(L)Py] and [Ni(L)Py$_3$].

	[Ni(L)Py]	[Ni(L)Py$_3$]
Chemical formula	$C_{31}H_{29}N_5NiO_4{\cdot}C_4H_8O$	$C_{41}H_{39}N_7NiO_4{\cdot}2.5(C_5H_5N)$
Formula mass	666.41	950.25
T [K]	293	173
Crystal system	triclinic	orthorhombic
Space group	$P\bar{1}$	$Fdd2$
a [Å]	9.667(9)	42.992(5)
b [Å]	11.61(1)	50.457(5)
c [Å]	15.83(1)	9.101(3)
α [°]	71.93(6)	90
β [°]	86.04(5)	90
γ [°]	72.70(7)	90
V [Å^3]	1606(2)	19710(7)
Z, $D_{calcd.}$ [g cm^{-3}]	2, 1.373	16, 1.281
μ [mm^{-1}]	0.655	0.449
Theta range	1.36°, 27.93°	3.05°, 25.02°
Data/parameters	7709/415	7671/614
R_1 [$I > 3\sigma(I)$]	0.0631	0.0462
R_1, wR_2 (all data)	0.1904, 0.2346	0.2227, 0.1124

$$R1 = \frac{\sum \left| |F_o| - |F_c| \right|}{\sum |F_o|} \quad ; \quad wR2 = \left\{ \frac{\sum \left[w\left(F_o^2 - F_c^2\right)^2 \right]}{\sum \left[w\left(F_o^2\right)^2 \right]} \right\}^{1/2}$$

CCDC-249658 (for [Ni(L)Py]) and CCDC-249659 (for [Ni(L)Py$_3$]) contain the supplementary crystallographic data for this paper. These data can be obtained free of charge from The Cambridge Crystallographic Data Centre via www.ccdc.cam.ac.uk/data_request/cif.

NLO Characterisation: The second-order optical nonlinearity of [Ni(L)Py] was determined by the EFISH technique, in chloroform, by measuring the $\mu_g\beta$ dot product of the chromophore, where μ_g is the ground state permanent dipole moment and β the (vector) quadratic hyperpolarizabilty of the molecule. The light source was a Q-switched Nd:Yag laser whose emission at 1.06 μm was shifted to 1.907 μm by stimulated Raman scattering in a high-pressure hydrogen cell. The measurements were calibrated relative to a quartz wedge: the experimental value of $d_{11}^{quartz} = 1.2 \times 10^{-9}$ esu at 1.06 μm was extrapolated to 1.1×10^{-9} esu at 1.907 μm. A detailed description of the experimental apparatus is given elsewhere.[9]

Acknowledgments

We thank the CIMCF of the Università di Napoli "Federico II" for X-ray (MACH 3) and NMR facilities and the C.R.d.C. "Nuove Tecnologie per le attività produttive" (Regione Campania, Italy) for the Nonius kappa-CCD diffractometer. Financial support from MIUR (Italy) within FIRB2001 grant is also acknowledged. Thanks are due to Dr. Alain Fort of IPCMS-CNRS GONLO of Strasbourg (France) for help with the EFISH measurements.

[1] a) T. D. Trouts, D. S. Tyson, R. Pohl, D. V. Kozlov, A. G. Waldron, F. N. Castellano, *Adv. Funct. Mater.* **2003**, *13*, 398; b) W.-J. Kuo, G.-H. Hsiue, R.-J. Jeng, *Macromolecules* **2001**, *34*, 2373; c) R. J. Forster, J. G. Vos, *Macromolecules* **1990**, *23*, 4372.

[2] a) S. Di Bella, I. Fragalà, *Synth. Met.* **2000**, *115*, 191; b) X. T. Tao, H. Suzuki, T. Watanabe, S. H. Lee, S. Miyata, H. Sasabe, *Appl. Phys. Lett.* **1997**, *70*, 1503.

[3] a) F. Cariati, U. Caruso, R. Centore, A. De Maria, M. Fusco, B. Panunzi, A. Roviello, A. Tuzi, *Inorg. Chim. Acta* **2004**, *357*, 548; b) I. Aiello, U. Caruso, M. Ghedini, B. Panunzi, A. Quatela, A. Roviello, F. Sarcinelli, *Polymer* **2003**, *44*, 7635; c) Special publication: W. Chiang, M. E. Thompson, D. Van Engen, *Spec. Publ. – R. Soc. Chem.* **1991**, *91* (Org. Mater. Non-linear Opt. 2), 210.

[4] a) F. Cariati, U. Caruso, R. Centore, W. Marcolli, A. De Maria, B. Panunzi, A. Roviello, A. Tuzi, *Inorg. Chem.* **2002**, *41*, 6597; b) U. Caruso, A. De Maria, B. Panunzi, A. Roviello, *J. Polym. Sci., Polym. Chem. Ed.* **2002**, *40*, 2987; c) F. Borbone, U. Caruso, R. Centore, A. De Maria, A. Fort, M. Fusco, B. Panunzi, A. Roviello, A. Tuzi, *Eur. J. Inorg. Chem.* **2004**, 2467.

[5] a) M. Yang, L. Zhang, Z. Lei, P. Ye, J. Si, Q. Yang, Y. Wang, *J. App. Polym. Sci.* **1998**, *70*, 1165; b) M. J. Yang, K. Ding, L. J. Zhang, W. G. Chen, *Synth. Met.* **1995**, *71*, 1739; c) A. Borshch, M. Brodyn, V. Lyakhovetsky, V. Volkov, A. Kutsenko, S. Maloletov, *Mater. Sci.* **2002**, *20*, 29.

[6] a) A. E. Underhill, C. A. S. Hill, *Mol. Cryst. Liq. Cryst. Sect. A* **1992**, *217*, 7; b) C. S. Winter, S. N. Oliver, J. D. Rush, C. A. S. Hill, A. E. Underhill, *J. Appl. Phys.* **1992**, *71*, 512.

[7] A. Roviello and co-workers, unpublished results.

[8] G. M. Sheldrick, SHELX-97, University of Göttingen, Germany, **1997**.

[9] T. Thami, P. Bassoul, M. A. Petit, J. Simon, A. Fort, M. Barzoukas, A. Villaeys, *J. Am. Chem. Soc.* **1992**, *114*, 915.

Received: October 26, 2004
Published Online: June 3, 2005

 © 2005 Wiley-VCH Verlag GmbH & Co. KGaA, Weinheim

[1]Borahafnocenophanes: Synthesis, Structure and Catalytic Activity

Holger Braunschweig,*[a] Mario Kraft,[a] Krzysztof Radacki,[a] and Sascha Stellwag[a]

Keywords: Boron / Hafnium / Metallocenophanes / *ansa*-Metallocenes / Ethylene polymerisation

Various [1]borahafnocenophanes of the general formula $[R_2NB(\eta^5\text{-}C_5H_4)_2HfCl_2]$ [R = CH_3, **13**; R = C_2H_5, **14**; R_2 = $(CH_2)_5$, **15**] were synthesised in high yields by a convenient two-step, one-pot synthesis, and their constitution in solution elucidated from multinuclear NMR spectroscopic data. Suitable single crystals of complexes **13** and **15** were subjected to X-ray diffraction studies, thus providing the first structural data of [1]borahafnocenophanes. The catalytic activity of the new complexes in the Ziegler–Natta polymerisation of ethylene was studied and compared to that of corresponding [1]borazirconocenophanes.

(© Wiley-VCH Verlag GmbH & Co. KGaA, 69451 Weinheim, Germany, 2005)

Introduction

Over the past few decades Group 4 metallocenophanes have been studied intensively due to their potential as Ziegler–Natta-type catalysts for the polymerisation of olefins.[1] By tailoring the ligand framework and the *ansa*-bridge in particular, highly active and, with respect to the polymerisation of propene, highly stereoselective catalysts were designed.[2–4] R_2C, R_4C_2 and R_2Si bridges have been commonly incorporated.[5–7] The introduction of a boranediyl bridge, i.e. a $B{=}NR_2$ moiety, is believed to be of some advantage with respect to the catalytic performance of such *ansa* complexes, since the small boron atom imposes high rigidity, and therefore has a potential to improve the stereoselectivity of the catalyst, especially at higher temperature, where the polymerization is usually performed. In addition, a three coordinate boron atom is to some extent Lewis-acidic, a fact that is believed to enhance the activity of the Group 4 metal centre. Thus, [1]borametallocenophanes and related constrained-geometry complexes (CGC)[8] of Ti and Zr were put into focus very recently.[9,10] Shapiro and Reetz reported the first [1]borazirconocenophanes **1** and **2**,[11] which displayed a phenylboranediyl-moiety linking the two η^5-coordinated ligands. These complexes, however, could only be obtained as adducts with Et_2O, THF, SMe_2 or PMe_3 (Figure 1), therefore cancelling the Lewis acidity of the boron atom. Rufanov et al. reports the isolation of a metallocenophane incorporating a base-free three-coordinate boron bridge,[12] although these results are not reproducible and the complex is poorly characterized. Hence, the validity of this assignment is still in question.[10] Attempts to synthesise analogous zirconocene complexes in the absence of Lewis-bases have so far failed.[11] The reaction of **1** with $Li[C_6F_5]$ was reported by Lancaster to yield the corresponding anionic *ansa*-zirconocene **3**.[13]

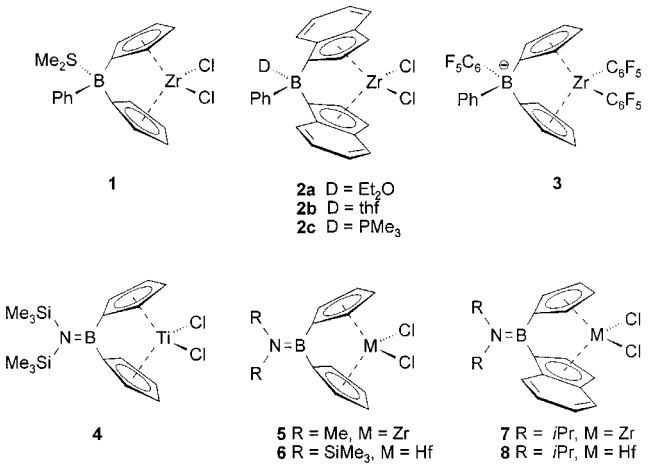

Figure 1. Boron-bridged metallocenes of Ti, Zr, and Hf.

In 1999 we reported on the titanium complex **4** as the first base-free [1]borametallocenophane of Group 4,[14] and in the same year we and Ashe extended the use of the aminoboranediyl-bridge to the synthesis of the corresponding zirconium complexes.[15,16] Subsequently, the chemistry of base-free [1]borazircono- and titanocenophanes was developed to some extent, providing evidence for their enhanced properties as Ziegler–Natta-type catalysts.[8,14–19] In sharp contrast to those Ti- and Zr-based *ansa* complexes, knowledge of corresponding [1]borahafnocenophanes is restricted to the brief spectroscopic characterisation of only two examples, $[(Me_3Si)_2NB(\eta^5\text{-}C_5H_4)_2HfCl_2]$ (**6**) and $[iPr_2NB(\eta^5\text{-}C_5H_4)(\eta^5\text{-}C_9H_6)HfCl_2]$ (**8**).[15] Structural studies, as well as information on their performance as catalysts, however, remained elusive.

[a] Department of Chemistry, Julius Maximilians Universität Würzburg,
Am Hubland, 97074 Würzburg, Germany
Fax: +49-931-888-4623
E-mail: h.braunschweig@mail.uni-wuerzburg.de

In this paper we address this deficiency and report on a series of new [1]borahafnocenophanes, their characterisation in the crystalline state and their use as catalysts for the polymerisation of ethylene.

Results and Discussion

As described earlier the reaction of amino(dihalo)borane R_2NBX_2 (R = Me, *i*Pr, $SiMe_3$; X = Cl, Br) with two equiv. of Na[C_5H_5] leads straightforwardly to the respective amino(biscyclopentadienyl)borane in excellent yields.[17] The reaction of Et_2NBBr_2 (**9**) and $(CH_2)_5NBBr_2$ (**10**) with 2 equiv. Na[C_5H_5] gave, at reaction times of 16 h, $Et_2NB(\eta^1\text{-}C_5H_5)_2$ (**11**) and $(CH_2)_5NB(\eta^1\text{-}C_5H_5)_2$ (**12**), respectively, in almost quantitative yields [Equation (1)]. The constitution in solution of the biscyclopentadienyl ligand precursors has been studied and reported elsewhere.[17] As shown in Equation (1), in the initial product the boron is bound to a sp^3-hybridised carbon, yielding the kinetically favoured product; below room temperature a sigmatropic proton rearrangement takes place to give the thermodynamically favoured product.

The rearrangement process leads to two new isomers per Cp-ring in which boron is bound to sp^2-hybridised carbon atoms. The rearrangement is not reversible, presumably due to interactions between the vinylic π-electrons of the adjacent carbon atoms with the empty p_z-orbital of boron. A nomenclature to distinguish between the three isomers was introduced, describing the positions of the double bonds in the Cp ring with respect to the boron atom: **a**llylic/**a**llylic (aa), **v**inylic/**a**llylic (va) and **v**inylic/**h**omoallylic (vh).[17] In biscyclopentadienylborane systems 6 isomers are theoretically possible (aa/aa, aa/va, aa/vh, va/va, va/vh and vh/vh), however only the three isomers in which boron is bound to a sp^2-hybridised carbon (va/va, va/vh and vh/vh) are expected at ambient temperatures. Due to these isomeric mixtures the resulting ^1H and the ^{13}C NMR spectra of both ligand precursors (**11** and **12**) are complex. A low field shift of around 10 ppm in the ^{11}B NMR was reported for $R_2NB(\eta^1\text{-}C_5H_5)_2$ (R = Me, *i*Pr, $SiMe_3$) compared to the corresponding amino(dihalo)boranes;[15,17] for **11** and **12** similar shifts to lower field compared to the parent boranes were observed.

The hafnium complexes $[Me_2NB(\eta^5\text{-}C_5H_4)_2HfCl_2]$ (**13**), $[Et_2NB(\eta^5\text{-}C_5H_4)_2HfCl_2]$ (**14**) and $[(CH_2)_5NB(\eta^5\text{-}C_5H_4)_2HfCl_2]$ (**15**) are obtained according to Equation (2) in a convenient two-step, one-pot reaction, starting from the ligand precursors $R_2NB(\eta^1\text{-}C_5H_5)_2$ and 2 equiv. BuLi and subsequent treatment with $HfCl_4$. The dimetallation of the ligand precursor is carried out at –80 °C with subsequent warming to ambient temperatures, yielding quantitatively the dilithiated Cp derivative that is treated in situ with $HfCl_4$ at low temperature. Complexes **13**, **14** and **15** are sparingly soluble in toluene but soluble in CH_2Cl_2 and proved to be stable in the solid state towards decomposition over weeks when stored at room temperature.

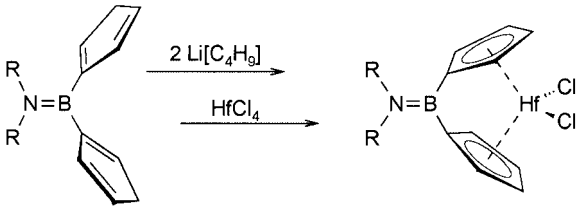

13 R = CH_3
14 R = C_2H_5
15 R,R = $-(CH_2)_5-$ (2)

The structure of **13**–**15** in solution was derived from multinuclear NMR spectra, showing the expected two pseudo triplets in the ^1H NMR spectra for the AA′BB′ spin system of the cyclopentadienyl protons at δ = 5.66, 6.73 (**13**), 5.65, 6.73 (**14**) and 5.31, 6.33 ppm (**15**). The carbon signals for the Cp-rings in the ^{13}C NMR spectra are all in the same range at 110 and 125 ppm, respectively. The signals for the C_{ipso} of the Cp ring could not be detected in the room temperature ^{13}C NMR spectra of **13**–**15** due to quadrupolar $^{13}C\text{-}^{11}B$ coupling.[20] Virtually unaffected by the complexation of the ligand is the ^{11}B NMR signal of **13**–**15**, as reported before.[8]

Pale yellow crystals of **13** and **15** suitable for X-ray diffraction were obtained from toluene at –35 °C (Figure 2). Their crystal structures are compared with those of the complexes $[(\eta^5\text{-}C_5H_5)_2HfCl_2]$[21] (**16**), $[Me_2C(\eta^5\text{-}C_5H_4)_2HfCl_2]$[22] (**17**) and $[Me_2Si(\eta^5\text{-}C_5H_4)_2HfCl_2]$[23] (**18**). All bond lengths and angles discussed here are summarised

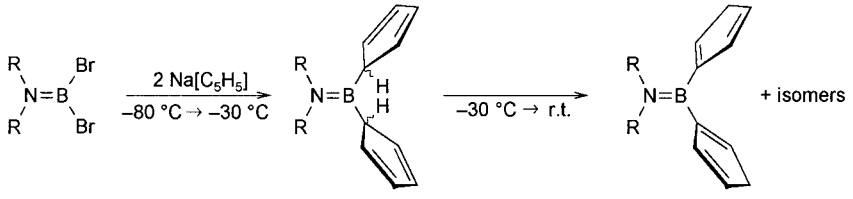

kinetically favoured product thermodynamically favoured product

11 R = C_2H_5
12 R,R = $-(CH_2)_5-$ (1)

 © 2005 Wiley-VCH Verlag GmbH & Co. KGaA, Weinheim

in Table 1, and Figure 3, part a, defines the angles α, δ and θ used in the discussion.

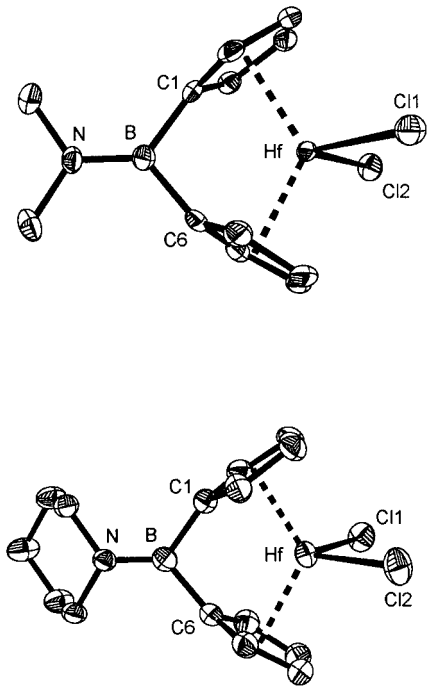

Figure 2. Structure of **13** (left) and **15** (right) in the solid state (ellipsoids at 50% probability); selected distances and angles see Table 1.

Table 1. Selected angles [°] and bond length [Å] of $(CH_3)_2NB(\eta^5\text{-}C_5H_4)_2ZrCl_2$ (**5**), $(CH_3)_2NB(\eta^5\text{-}C_5H_4)_2HfCl_2$ (**13**), $(CH_2)_5NB(\eta^5\text{-}C_5H_4)_2HfCl_2$ (**15**), $(\eta^5\text{-}C_5H_5)_2HfCl_2$ (**16**), $(CH_3)_2C(\eta^5\text{-}C_5H_4)_2HfCl_2$ (**17**) and $(CH_3)_2Si(\eta^5\text{-}C_5H_4)_2HfCl_2$ (**18**).

Complex	**5**	**13**	**15**	**16**	**17**	**18**
tilt angle α	65.5	64.7	64.9	53.5	70.1	57.7
Cl–M–Cl	100.9	99.6(1)	99.2(1)	96.2	98.9	97.6
δ	120.8	121.4	121.7	129.2	117.1	127.6
θ	105.9	105.2(3)	105.5(2)	/	99.4	93.7
M–Cl	2.443	2.404(1)	2.413(1)	2.423	2.409	2.421
M–Cp[c]	2.198	2.178	2.178	2.179	2.173	2.182
N–B	1.384	1.369(5)	1.371(4)	/	/	/
B–C_{ipso}	1.573	1.578(5)	1.581(4)	/	/	/
d	/	1.066	1.061	0.935	1.134	0.964
Reference	[16]	this work		[21]	[22]	[23]

Introducing the bridging unit causes changes in the geometry of the molecule with respect to the parent compound **16**. The *tilt angle* α increases with the incorporation of smaller bridging atoms, according to the trend C > B > Si; an α value of 53.5° is found for **16**, 57.7° for **18**, 64.7° for **13**, 64.9 for **15** and 70.1° for **17**. Virtually the same trend is found for the angle δ, being of 129.2° for **16**, 127.6° for **18**, 121.7° for **15**, 121.4° for **13** and 117.1° for **17**, respectively, highlighting the close relationship between α and δ. Furthermore, it is interesting to consider the values of θ for the four structures. These indicate a smaller deviation from the ideal tetrahedral angular value (109°) in **17** than in **18**, according to the smaller covalent radius of C with respect to Si. This results in a shorter C_{ipso}–E (E = C, **17**; E = Si, **18**) bond and a larger θ value for **17** (99.4°) than **18** (93.7°). The corresponding angles for **13** and **15** are 105.2(3)° and 105.5(2)°, respectively, reflecting the distortion of these complexes (a value of θ = 120° would be expected given the sp^2-hybridization of B). However, a direct comparison of the angle θ for the 4 structures is not possible, due to the different hybridisation of the bridging atoms.

An important factor for the polymerisation activity is the position of the metal centre relative to the Cp-centroids, which is described by the angle δ (Figure 3, part b). The polymerisation activities might increase when the metal protrudes from the wedge created by the Cp-ligands, due to a better accessibility of the metal centre to the incoming olefin. As expected, there is a relationship between the *tilt angle* α and the distance (*d*) of the metal from the vector connecting the Cp-centroids. The differences in the values *d* for the new compounds with respect to the parent complex, expressed in per cent, demonstrate the effect of the bridging moiety.[22] In **16** the distance *d* is 0.935 Å; a similar value is found for **18** (0.964 Å), with a change of 3.1%, while in the carbon bridged complex **17** the metal protrudes 1.134 Å (21.3%) away from the Cp-Cp vector. In both boron bridged complexes **13** and **15** the hafnium centre displays similar deviations with respect to its position in **16**, 1.066 Å (14.0%) and 1.061 Å (13.5%).

The B–N distance is typical for a corresponding double bond [1.369(5) Å for **13** and 1.371(4) Å for **15**] and similar to that found in the Zr complex $[Me_2NB(\eta^5\text{-}C_5H_4)_2ZrCl_2]$ (**5**) (B–N distance 1.384 Å). The angle θ in the compounds **13** and **15** [105.2(3)° and 105.5(2)°] is virtually the same as

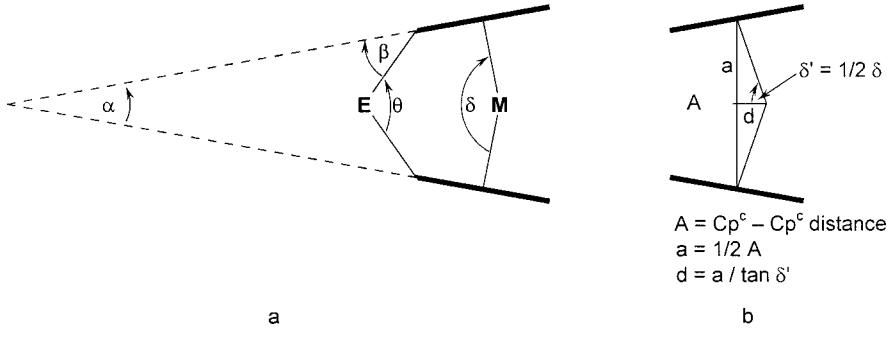

Figure 3. Structural parameter of *ansa*-metallocenes.

 © 2005 Wiley-VCH Verlag GmbH & Co. KGaA, Weinheim

that observed in **5** (105.9°), as is the *tilt angle α* (**13**, 64.7°, **15**, 64.9° and **5**, 65.5°). The remaining structural parameters of **13** and **15**, especially those related to bond length and angles at the metal centre, are similar to those of **5**, reflecting the similar size of Zr and Hf.

The structural changes in the so-called *unstrained* complexes **13** and **15** compared to the parent complex **16**, are less pronounced then those observed in related *strained ansa*-metallocenes.[24] The small boron bridge in [1]boraferrocenophanes causes a more pronounced change in the geometric parameters compared to the parent ferrocene, e.g. *tilt angles* of about 32° are usually observed in [1]boraferrocenophanes.[25]

Polymerisation of Ethylene

The [1]borahafnocenophanes **13** and **14** were studied as catalysts for the polymerisation of ethylene. After activation with a 4500 fold excess of MAO the complexes polymerise ethylene at slightly elevated temperature with an activity of about 260 $kg_{PE}·mol_{Hf}^{-1}·h^{-1}$. As to be expected from studies on various Zr- and Hf-based catalyst systems,[2,26,27] the activity displayed here is lower than that of corresponding [1]borazirconocenophanes by a factor of 7.[28] However, the molecular masses (M_w) of the obtained PE-samples as determined by GPC-methods were found to be 19200 $g·mol^{-1}$ for **13** and 34500 $g·mol^{-1}$ for **14**, thus being significantly higher than in the case of Zr.

Conclusions

The synthetic method described in this paper and previously reported for titanium and zirconium complexes provides a general route to Group 4 [1]borametallocenophanes. Determination of the first crystal structures of [1]borahafnocenophanes **13** and **15** allows for a direct comparison of important structural parameters to those of corresponding complexes of Ti and Zr. It is now demonstrated that [1]borametallocenophane complexes of all three Group 4 metals can act as active catalysts in olefin polymerisation when sufficiently activated. The activity of [1]borahafnocenophanes was found to be lower than that of comparable zirconium complexes, but the resulting polymers are characterised by a higher molecular weight. Studies on the catalytic behaviour of Group 4 [1]borametallocenophanes as a function of the steric and electronic properties of the ligand framework are ongoing.

Experimental Section

All manipulations were carried out under dry argon with common Schlenk techniques. Solvents were dried with a solvent purification system (SPS) from M. Braun columns and stored under argon over molecular sieves; reagents were dried and purified by standard procedures. Dibromo(diethylamino)borane,[29] dibromo(piperidino)borane,[30] Me_2NB-(η^1-C_5H_5)$_2$[17] and Na[C_5H_5][31] were obtained according to literature procedures. Li[C_4H_9] and $HfCl_4$ were obtained commercially and used without further purification. NMR: Bruker Avance 200 at 64.21 MHz (^{11}B, $BF_3·OEt_2$ in C_6D_6 as external standard), Bruker Avance 400 at 400.13 MHz (^{1}H, internal standard TMS), 100.61 MHz (^{13}C{^{1}H}, APT, internal standard TMS).

Mass spectra were recorded with a Thermo Finnigan Trio 1000 and with a Finnigan MAT 8200. Elemental analyses (C, H, N) were obtained from a Carlo–Erba elemental analyzer, model 1160. The polymerisation experiments were carried out in a 500-mL glass autoclave from Büchi.

$Et_2NB(\eta^1\text{-}C_5H_5)_2$ (11): $(C_2H_5)_2NBBr_2$ (1.75 g, 7.20 mmol) is added to a suspension of Na[C_5H_5] (1.21 g, 14.40 mmol) in hexane (40 mL) at –80 °C. The mixture is allowed to come to ambient temperature and is subsequently stirred for 16 h. Insoluble materials are removed by centrifugation and the solvent is removed in vacuo yielding 1.45 g (94%) **11** as a yellow oil. ^{1}H NMR (400 MHz, CD_2Cl_2, 25 °C, isomeric mixture of **va/va**, **va/vh** and **vh/vh**): δ = 1.11, 1.16, 1.20 [t, ^3J(H,H) = 7.02 Hz, 18 H, CH_3], 3.05, 3.09, 3.12 (m, 12 H, CH_{2Cp}), 3.21, 3.26, 3.36 (q, $^3J_{H,H}$ = 7.02 Hz, 12 H, CH_2), 6.3–6.7 (m, 18 H, CH_{Cp}) ppm. ^{11}B NMR (64 MHz, CD_2Cl_2, 25 °C): δ = 37.9 ppm. ^{13}C NMR (100 MHz, CD_2Cl_2, 25 °C, isomeric mixture of **va/va**, **va/vh** and **vh/vh**): δ = 16.23, 16.40, 16.41 (CH_3), 43.23, 43.67, 43.77, 44.17, 46.85, 46.94 (CH_2, CH_{2Cp}); 131.97, 133.21, 133.26, 135.89, 137.13, 137.26, 137.35, 138.95, 141.74 (CH_{Cp}) ppm. MS: *m*/*z* (%) = 213 (75) [M^+], 198 (100) [M^+ – CH_3], 148 (60) [M^+ – C_5H_5], 141 (35) [M^+ – $(C_2H_5)_2$], 77 (92) [$C_5H_6B^+$]. $C_{14}H_{20}BN$ (213.13): calcd. C 78.90, H 9.46, N 6.57; found C 79.32, H 9.57, N 6.37.

$(CH_2)_5NB(\eta^1\text{-}C_5H_5)_2$ (12): As described for **11**, Na[C_5H_5] (1.44 g, 16.20 mmol) is suspended in hexane (40 mL) and reacted with $(CH_2)_5NBBr_2$ (2.07 g, 8.10 mmol) at –80 °C. Insolubles are removed by centrifugation and all volatiles are removed in vacuo, yielding 1.68 g (92%) **12** as a yellow oil. ^{1}H NMR (400 MHz, C_6D_6, 25 °C, isomeric mixture of **va/va**, **va/vh** and **vh/vh**): δ = 1.3–1.5 (m, 18 H, CH_{2pip}), 2.90, 3.00, 3.08 (m, 12 H, CH_{2Cp}), 3.2–3.4 (m, 12 H, CH_{2pip}), 5.5–7.2 (m, 18 H, CH_{Cp}) ppm. ^{11}B NMR (64 MHz, C_6D_6, 25 °C): δ = 36.8 ppm. ^{13}C NMR (100 MHz, C_6D_6, 25 °C, isomeric mixture of **va/va**, **va/vh** and **vh/vh**): δ = 26.14, 26.18, 29.27, 29.32, 29.37, 43.75, 47.17, 47.46, 50.66, 50.99, 51.34 (CH_{2pip}, CH_{2Cp}), 132.36, 132.45, 133.80, 133.84, 136.31, 137.36, 138.02, 138.15, 139.07, 139.63, 141.37, 141.95 (CH) ppm. MS: *m*/*z* (%) = 225 (75) [M^+], 166 (88) [M^+ – C_5H_5], 77 (100) [C_5H_6B], 65 (35) [C_5H_5]. $C_{15}H_{20}BN$ (225.14): calcd. C 80.02, H 8.95, N 6.22; found C 80.38, H 8.73, N 6.48.

$[Me_2NB(\eta^5\text{-}C_5H_4)_2HfCl_2]$ (13): A solution of $Me_2NB(\eta^1\text{-}C_5H_5)_2$ (0.98 g, 5.30 mmol) in hexane (40 mL) is treated at –80 °C with Li[C_4H_9] (4.24 mL, 10.60 mmol). After warming up to ambient temperature the mixture was stirred for further 16 h. The resulting suspension is centrifuged and the solid washed with 40 mL hexane, suspended in toluene, and then treated with $HfCl_4$ (1.70 g, 5.30 mmol) at –80 °C. The pale yellow reaction mixture is allowed to come to room temperature and stirred for 16 h, insolubles are removed by centrifugation and the solution is concentrated and stored at –35 °C. 1.93 g (84%) **13** was isolated as pale yellow crystals. ^{1}H NMR (400 MHz, CD_2Cl_2, 25 °C): δ = 3.11 (s, 6 H, CH_3), 5.66 (pt, 4 H, CH_{Cp}), 6.73 (pt, 4 H, CH_{Cp}) ppm. ^{11}B NMR (64 MHz, CD_2Cl_2, 25 °C): δ = 37.7 ppm. ^{13}C NMR (100 MHz, CD_2Cl_2, 25 °C): δ = 40.33 (CH_3), 110.13, 124.67 (CH_{Cp}) ppm. MS: *m*/*z* (%) = 433 (100) [M^+], 418 (16) [M^+ – CH_3], 397 (11) [M^+ – HCl], 389 (27) [M^+ – $(CH_3)_2N$], 368 (49) [M^+ – C_5H_5], 353 (28) [M^+ – C_5H_5 – CH_3]. $C_{12}H_{14}BCl_2HfN$ (432.46): calcd. C 33.33, H 3.26, N 3.24; found C 33.71, H 3.74, N 3.03.

 © 2005 Wiley-VCH Verlag GmbH & Co. KGaA, Weinheim

[$Et_2NB(\eta^5\text{-}C_5H_4)_2HfCl_2$] (14): As described for **13**, $Et_2NB(\eta^1\text{-}C_5H_5)_2$ (1.08 g, 4.80 mmol) was treated at –80 °C with $Li[C_4H_9]$ (3.84 mL, 9.60 mmol) and subsequently with $HfCl_4$ (1.54 g, 4.80 mmol). Compound **14** was obtained as a pale yellow microcrystalline material (1.53 g, 69%). ^1H NMR (400 MHz, CD_2Cl_2, 25 °C): δ = 1.27 (t, $^3J_{H,H}$ = 7.20 Hz, 6 H, CH_3), 3.45 (q, $^3J_{H,H}$ = 7.20 Hz, 4 H, CH_2), 5.65 (pt, 4 H, CH_{Cp}), 6.73 (pt, 4 H, CH_{Cp}) ppm. ^{11}B NMR (64 MHz, CD_2Cl_2, 25 °C): δ = 38.1 ppm. ^{13}C NMR (100 MHz, CD_2Cl_2, 25 °C): δ = 16.20 (CH_3), 43.72 (CH_2), 109.89, 124.58 (CH) ppm. MS: *m/z* (%) = 461 (100) [M^+], 389 (56) [$M^+ - (C_2H_5)_2N$], 353 (44) [$M^+ - (C_2H_5)_2N - HCl$]. $C_{14}H_{18}BCl_2HfN$ (460.51): calcd. C 36.51, H 3.94, N 3.04; found C 36.84, H 4.29, N 2.78.

[$(CH_2)_5NB(\eta^5\text{-}C_5H_4)_2HfCl_2$] (15): As described for **13**, $(CH_2)_5NB(\eta^1\text{-}C_5H_5)_2$ (0.86 g, 3.80 mmol) was treated at –80 °C with 2.5 M $Li[C_4H_9]$ (2.96 mL, 7.60 mmol) and subsequently with $HfCl_4$ (1.22 g, 3.80 mmol). Compound **15** was obtained as a pale yellow microcrystalline material (1.35 g, 78%). Recrystallisation from toluene yielded single crystals suitable for X-ray diffraction. ^1H NMR (400 MHz, C_6D_6, 25 °C): δ = 1.1–1.3 (m, 6 H, CH_{2pip}), 3.00 (m, 4 H, CH_{2pip}), 5.31 (pt, 4 H, CH_{Cp}), 6.66 (pt, 4 H, CH_{Cp}). ^{11}B NMR (64 MHz, C_6D_6, 25 °C): δ = 36.8. ^{13}C NMR (100 MHz, C_6D_6, 25 °C): δ = 24.76, 28.19, 49.50 (CH_{2pip}), 109.64, 124.48 (CH_{Cp}). MS: *m/z* (%) = 474 (38) [M^+], 438 (100) [$M^+ - HCl$], 351 (55) [$M^+ - HCl - (CH_2)_5N$]. $C_{15}H_{18}BCl_2HfN$ (472.52): calcd. C 38.13, H 3.84, N 2.96; found C 38.51, H 4.19, N 2.63.

Polymerization: A 500-mL glass autoclave equipped with a 15 mL dropping funnel was charged with toluene (200 mL) and methylaluminoxan solution (30 mL, 10 wt.-% in toluene). A solution of the complex (5 mL) in toluene ($2\cdot10^{-3}$ M) was placed in the dropping funnel. The autoclave was pressurized with ethylene until a pressure of 2 bar was reached, simultaneously the temperature was raised to 60 °C. The polymerization was initiated by adding the complex to the toluene/MAO solution. At all times of the polymerization experiment the ethylene pressure was constantly maintained at 2 bar. The polymerization was stopped by ventilation of the autoclave and adding acidic methanol (30 mL) to quench the excess of MAO. The resulting mixture was stirred in methanol (800 mL) for 1 h and then filtered and dried at 90 °C, giving the polyethylene as a white powder, which was analyzed by high temperature gel permeation chromatography.

Crystal Structure Determination: The crystal data of **13** and **15** were collected at Bruker APEX diffractometer with CCD area detector and graphite-monochromated Mo-K_α radiation. The structures were solved by direct methods, refined with the SHELX software package (G. Sheldrick, University of Göttingen, 1997) and expanded using Fourier techniques. All non-hydrogen atoms were refined anisotropically. Hydrogen atoms were assigned idealized positions and were included in structure factor calculations. **Crystal Data for 13:** $C_{12}H_{14}BCl_2HfN$ M_r = 432.44, pale yellow block, 0.28 × 0.18 × 0.17, monoclinic, space group *P*21/*n*, *a* = 11.4561(9) Å, *b* = 10.0071(8) Å, *c* = 12.0774(9) Å, β = 105.013(1)°, *V* = 1337.32(18) Å^3, *Z* = 4, $\rho_{calcd.}$ = 2.148 g·cm^{-3}, μ = 8.174 cm^{-2}, *F*(000) = 816, *T* = 193 K; R_1 = 0.0188, w_R = 0.0491, 2649 independent reflections [$2\theta \leq 52.16°$] and 154 parameters. **Crystal Data for 15:** $C_{22}H_{26}BCl_2HfN$ M_r = 564.64, pale yellow plates, 0.23 × 0.23 × 0.10, triclinic, space group *P*–1, *a* = 9.752(2) Å, *b* = 11.627(3) Å, *c* = 11.884(3) Å, *a* = 118.441(3)°, β = 101.620(3)°, γ = 101.310(3)°, *V* = 1091.8(4) Å^3, *Z* = 2, $\rho_{calcd.}$ = 1.717 g·cm^{-3}, μ = 5.028 cm^{-2}, *F*(000) = 552, *T* = 173 K; R_1 = 0.0191, w_R = 0.0483, 4298 independent reflections [$2\theta \leq 52.1°$] and 244 parameters.

CCDC-260992 and -260993 contain the supplementary crystallographic data for this paper. These data can be obtained free of charge from The Cambridge Crystallographic Data Centre via www.ccdc.cam.ac.uk/data_request/cif.

Acknowledgments

This work was financially supported by the EPSRC. Thanks to Steve Holding (RAPRA Technology Ltd.) for performing the polymer analyses. The experimental assistance of Carina Grimmer and Viktor Weber in performing the polymerization experiments is gratefully acknowledged.

[1] W. Kaminsky, *J. Chem. Soc., Dalton Trans.* **1998**, 1413.
[2] H. H. Brintzinger, D. Fischer, R. Mülhaupt, B. Rieger, R. Waymouth, *Angew. Chem. Int. Ed. Engl.* **1995**, *34*, 1143 (and references cited therein).
[3] G. W. Coates, *Chem. Rev.* **2000**, *100*, 1223.
[4] L. Resconi, L. Cavallo, A. Fait, F. Piemontesi, *Chem. Rev.* **2000**, *100*, 1253.
[5] J. A. Ewen, R. L. Jones, A. Razavi, J. D. Ferrara, *J. Am. Chem. Soc.* **1988**, *110*, 6255.
[6] J. A. Ewen, L. Haspeslach, J. L. Atwood, H. Zhang, *J. Am. Chem. Soc.* **1987**, *109*, 6544.
[7] W. A. Herrmann, J. Rohrmann, E. Herdtweck, W. Spaleck, A. Winter, *Angew. Chem. Int. Ed. Engl.* **1989**, *28*, 1511.
[8] H. Braunschweig, F. M. Breitling, E. Gullo, M. Kraft, *J. Organomet. Chem.* **2003**. *680*, 31.
[9] S. Aldridge, C. Bresner, *Coord. Chem. Rev.* **2003**, *244*, 71.
[10] P. Shapiro, *Eur. J. Inorg. Chem.* **2001**, 321.
[11] a) D. S. Stelck, P. J. Shapiro, N. Basickes, *Organometallics* **1997**, *16*, 4546; b) M. T. Reetz, M. Willuhn, C. Psiorz, R. Goddard, *Chem. Commun.* **1999**, 1105.
[12] K. A. Rufanov, V. V. Kotov, N. B. Kazennova, D. A. Lemenovskii, E. V. Avtomonov, J. Lorberth, *J. Organomet. Chem.* **1996**, *525*, 287.
[13] S. J. Lancaster, M. Bochmann, *Organometallics* **2001**, *20*, 2093.
[14] H. Braunschweig, C. von Koblinski, R. Wang, *Eur. J. Inorg. Chem.* **1999**, 69.
[15] H. Braunschweig, C. von Koblinski, M. Mamuti, U. Englert, R. Wang, *Eur. J. Inorg. Chem.* **1999**, 1899.
[16] A. J. Ashe III, X. Fang, J. W. Kampf, *Organometallics* **1999**. *18*, 2288.
[17] H. Braunschweig, C. von Koblinski, M. Neugebauer, U. Englert, X. Zheng, *J. Organomet. Chem.* **2001**, *619*, 305.
[18] H. Braunschweig, M. O. Kristen, C. von Koblinski, EP 1140955.
[19] A. J. Ashe III, X. Fang, A. Hokky, J. W. Kampf, *Organometallics* **2004**, *23*, 2197.
[20] B. Wrackmeyer, *Prog. NMR Spectrosc.* **1979**, *12*, 227.
[21] G. L. Soloveichik, T. M. Arkhireeva, V. K. Belskii, B. M. Bulychev, *Metalloorg. Khim.* **1988**, *1*, 226.
[22] R. M. Shaltout, J. Y. Corey, N. P. Rath, *J. Organomet. Chem.* **1995**, *503*, 205.
[23] X.-Z. Zhou, Y. Wang, S.-S. Xu, H.-G. Wang, X.-K. Yao, *Chem. Res. Chin. Univ.* **1992**, *8*, 239.
[24] A metallocenophane is regarded to be *unstrained*, if it derives from a metallocene, in which the Cp rings are already tilted due to the presence of other ligands at the metal centre, and *strained* when the parent metallocene displays a parallel orientation of the Cp rings.
[25] a) H. Braunschweig, R. Dirk, M. Müller, P. Nguyen, R. Resendes, D. P. Gates, I. Manners, *Angew. Chem. Int. Ed. Engl.* **1997**, *36*, 2338; b) A. Berenbaum, H. Braunschweig, R. Dirk, U. Englert, J. C. Green, F. Jäkle, A. J. Lough, I. Manners, *J. Am. Chem. Soc.* **2000**, *122*, 5765.
[26] a) W. Kaminsky, R. Engelhausen, K. Zoumis, W. Spaleck, J. Rohrmann, *Makromol. Chem.* **1992**, *193*, 1643; b) W. Kaminsky, *J. Chem. Soc., Dalton Trans.* **1998**, 1413; c) M. W. Kim, E.

Hong, K. Han, S. I. Woo, Y. Do, *J. Organomet. Chem.* **1998**, *564*, 109; d) K. Weiss, U. Neugebauer, S. Blau, H. Lang, *J. Organomet. Chem.* **1996**, *520*, 171; e) G. Jany, M. Gustafsson, T. Repo, E. Aitola, J. A. Dobado, M. Klinga, M. Leskelä, *J. Organomet. Chem.* **1998**, *553*, 173.
[27] R. Togni, R. L. Haltermann, *Metallocenes*, Wiley-VCH, Weinheim **1998**.
[28] H. Braunschweig, unpublished results.
[29] W. Gerrad, H. R. Hudson, E. F. Mooney, *J. Chem. Soc.* **1960**, 5168.
[30] O. C. Musgrave, *J. Chem. Soc.* **1956**, 4305.
[31] T. K. Panda, M. T. Gamer, P. W. Roesky, *Organometallics* **2003**, *22*, 877.

Received: January 21, 2005
Published Online: June 2, 2005

 © 2005 Wiley-VCH Verlag GmbH & Co. KGaA, Weinheim

EurJIC
European Journal of Inorganic Chemistry

Issue 14/2005

Pages 2765–2940

Papers available ahead of print in Early View at www.interscience.wiley.com

Earliest available Table of Contents:
Automatically, free of charge by e-mail through
www.interscience.wiley.com/alerts

COVER PICTURE

The cover picture shows an allegory of bioinorganic chemistry and biomimetic studies. Here, the metalloprotein (human Mn-SOD, PDB-code 1MSD) is posing for the painter. As a bioinorganic chemist, he is designing new molecules that would reproduce this protein activity; he is testing the activity of these molecules and deciphering mechanisms. Here, we show the structure of a small Mn^{II} complex that has been studied for its SOD-like activity by pulsed radiolysis. In the painting, the UV/Vis trace of a multipulse experiment at 300 nm is shown, with successive spikes and plateaus. An overall increase in the absorbance of the successive plateaus is observed. The asterisks indicate irradiations. Simulations of the individual growth of the spikes, of the individual decrease down to the plateau and of the overall increase of the absorbance for the successive plateaus leads to the proposition of a mechanism. This is the triangular cycle shown in the painting, involving an $\{MnOO\}^6$ adduct between Mn^{II} and superoxide. This label, $\{MnOO\}^6$, is proposed by analogy with the nomenclature used for iron–nitroxide adducts. Each event indicated in the cycle has been proven. Moreover, this study shows unambiguously that the Mn^{II} compound displays a catalytic activity for superoxide dismutation. Details are presented in the article by J.-P. Renault, C. Policar et al. on p. 2789ff. In the original picture by Magritte, the inset in the lower right-hand corner, is entitled "La clairvoyance" (clear-sightedness) and was painted in 1936.

SHORT COMMUNICATIONS

Contents

2779 **S. Salameh, M. Abul-Haj, M. Quirós,* J. M. Salas**

A Nonanuclear Ni^{II} Cluster with a 1,2,4-Triazolo[4,3-*a*]pyrimidine Derivative

Keywords: Cluster compounds / Nickel / Triazolopyrimidine / Magnetic properties

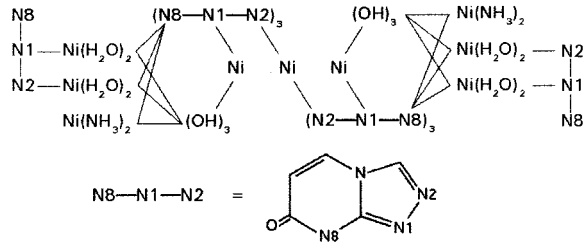

 © 2005 Wiley-VCH Verlag GmbH & Co. KGaA, Weinheim

2783 **M. C. Giménez-López, M. Clemente-León, E. Coronado,* F. M. Romero,* S. Shova, J.-P. Tuchagues**

Structural Transformations and Magnetic Effects Induced by Solvent Exchange in the Spin Crossover Complex $[Fe(bpp)_2][Cr(bpy)(ox)_2]_2$

Keywords: Spin crossover / Iron / Solvent sensing / Hydration / Magnetic properties

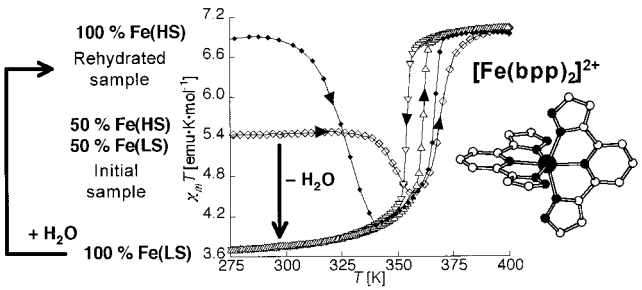

FULL PAPERS

2789 **S. Durot, F. Lambert, J.-P. Renault,* C. Policar***

A Pulse Radiolysis Study of Catalytic Superoxide Radical Dismutation by a Manganese(II) Complex with an N-Tripodal Ligand

Keywords: Bioinorganic chemistry / Enzyme models / Manganese / Superoxide dismutase / SOD mimic / Pulsed radiolysis / MnOO adduct

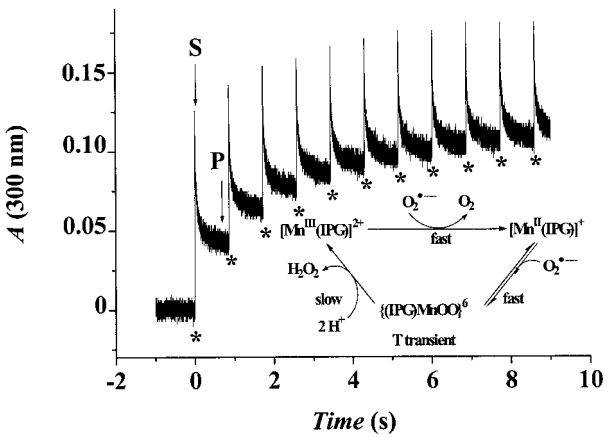

2794 **B. Weber, I. Käpplinger, H. Görls, E.-G. Jäger***

The Relationship between the Structure and Magnetic Properties of Bioinspired Iron(II/III) Complexes with Schiff-Base-Like Chelate Ligands, Part I: Complexes with Dianionic $[N_4]$ Macrocycles

Keywords: Bioinorganic chemistry / Iron / Macrocycles / Magnetic properties / Schiff bases

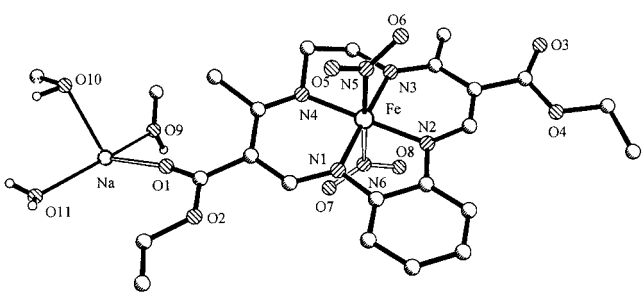

$[Na(MeOH)_2(H_2O)_{0.5}]$ $[Fe^{III}2(NO_2)_2]$

2812 **A. A. Trifonov,* E. A. Fedorova, V. N. Ikorskii, S. Dechert, H. Schumann, M. N. Bochkarev**

Solvent-Mediated Redox Transformations of Ytterbium Bis(indenyl)diazabutadiene Complexes

Keywords: Diazadiene ligands / N ligands / Radical ions / Ytterbium

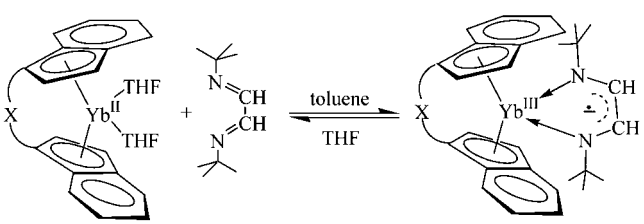

 © 2005 Wiley-VCH Verlag GmbH & Co. KGaA, Weinheim

2819 **K. I. Nättinen, P. E. N. de Bairos, P. J. Seppälä, K. T. Rissanen***

Anion Template Effect and the Polymerization Degree − Diversity through Flexibility

Keywords: Crystal engineering / N ligands / Zeolite analogues / Self-assembly / Transition metals

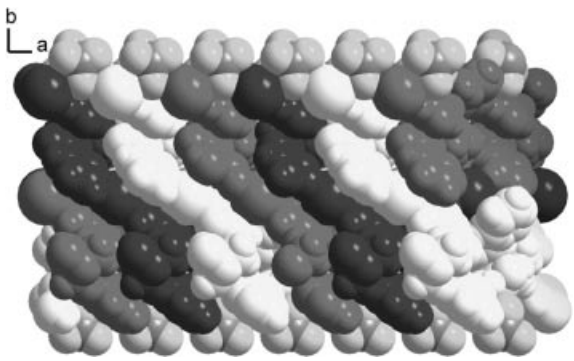

2826 **M. Trani, F. Cannito, G. Natile,* P. A. Marzilli, L. G. Marzilli***

Slowly Exchanging *cis*-PtA_2B_2 Atropisomers with A_2 = Chiral Diamine Ligands and B = 5,6-Dimethylbenzimidazole

Keywords: Cisplatin / Anticancer drug / Platinum complexes / Chiral diamines / 5,6-Dimethylbenzimidazole

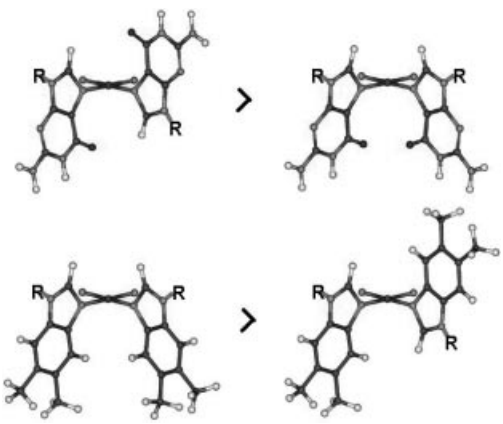

2836 **J. Müller, G. Kehr, R. Fröhlich, G. Erker***

Structural Features of Titanium Complexes of Salicylaldiminato Derivatives of Amino Acids

Keywords: Chelate ligands / Titanium / Tridentate ligands / Metallamacrocycles / Catalytic hydrocyanation

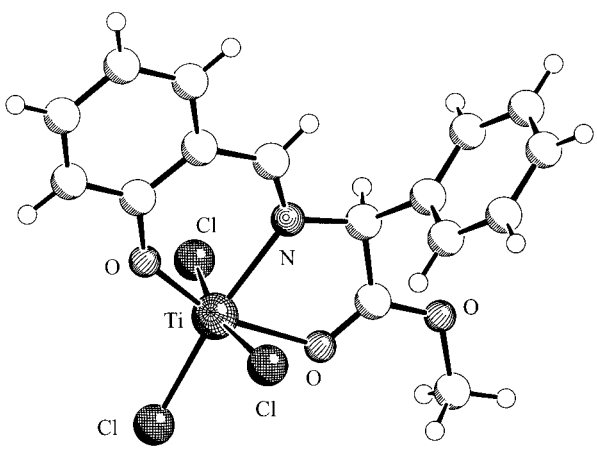

2842 **U. Jäger-Fiedler, P. Arndt, W. Baumann, A. Spannenberg, V. V. Burlakov, U. Rosenthal***

Reactions of Zirconocene Bis(trimethylsilyl)-acetylene Complexes with Fluorinated Pyridines: C−H vs. C−F Bond Activation

Keywords: Zirconocene / C−F bond activation / C−H bond activation / Organometallics / Heterocycles

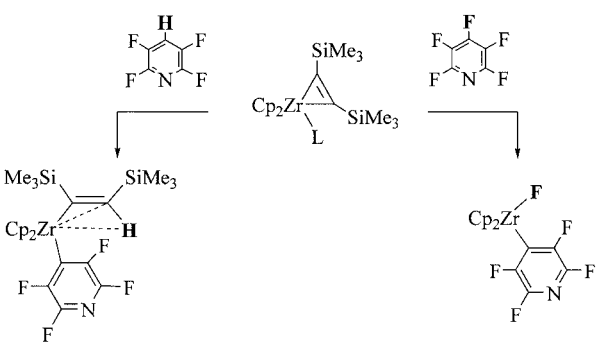

 © 2005 Wiley-VCH Verlag GmbH & Co. KGaA, Weinheim

2850 **C. Lorber,* F. Wolff, R. Choukroun, L. Vendier**

Ethylene Homo- and Copolymerization Activity of a Series of [ONNO]-Type Amine Bis(phenolate) Based Vanadium(II−V) Catalysts

Keywords: Vanadium / Amine (bis)phenolates / Polymerization / Copolymer / Crystal structure / Olefins

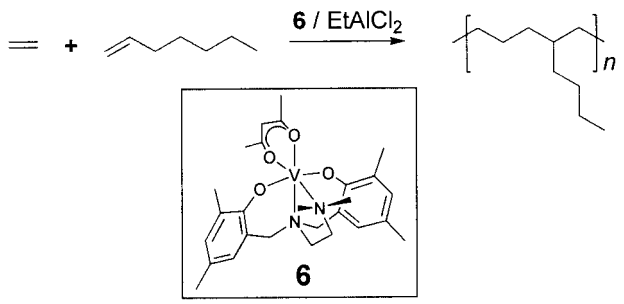

2860 **E. Colacio,* A. Debdoubi, R. Kivekäs, A. Rodríguez**

Multidimensional Cyanide-Bridged Heterometallic $Fe^{II}-Cu^{I}$ and Homometallic Cu^{I} Coordination Polymers from Solvothermal Reactions Involving either $K_3[Fe(CN)_6]$ or KCN as the Source of Cyanide Anions

Keywords: Coordination polymers / Copper / Cyanides / Heterometallic complexes / Solvothermal synthesis

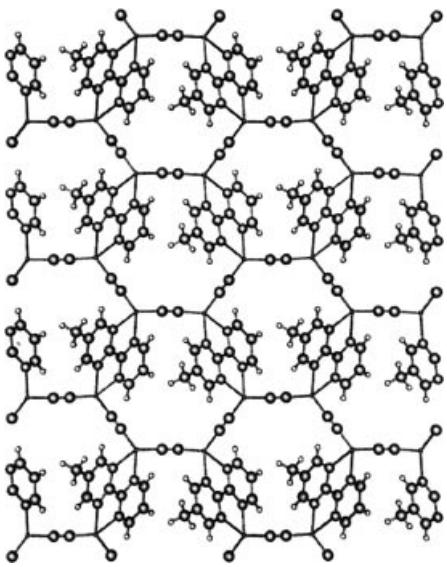

2869 **H. Xu, F.-B. Xu,* Q.-S. Li, W.-G. Duo, H.-B. Song, Z.-Z. Zhang***

Synthesis, Structure and Spectroscopic Properties of Novel 9,10-Bis{[6-(diphenylphosphanyl)-2-pyridylmethyl]propylaminomethyl}anthracene-Bridged Group 11 Metal (M = Cu^{I} and Ag^{I}) Dinuclear Complexes

Keywords: Dinuclear complexes / Phosphanyl-pyridine ligands / Copper / Silver / Charge transfer interaction / Dual emission

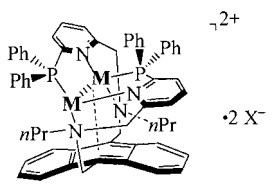

M = Cu^{I} or Ag^{I}, X = ClO_4^- or BF_4^-

2875 **S. Rachmilovich-Calis, A. Masarwa, N. Meyerstein, D. Meyerstein***

The Fenton Reaction in Aerated Aqueous Solutions Revisited

Keywords: Alcohols / Chain reactions / Dioxygen / Oxidation / Fenton reaction / Iron

$Fe(H_2O)_6^{2+} + H_2O_2 \leftrightarrows [(H_2O)_5Fe^{II}H_2O_2] \rightarrow (H_2O)_5Fe^{IV}{=}O^{2+} + H_2O$

$(H_2O)_5Fe^{IV}{=}O^{2+} + R^1R^2CHOH \rightarrow Fe(H_2O)_5(OH)^{2+} + R^1R^2C^{\cdot}OH\ (\equiv R^{\cdot})$

$R^{\cdot} + O_2 \rightarrow RO_2^{\cdot}$

$RO_2^{\cdot} \rightarrow R^1R^2C{=}O + HO_2^{\cdot}$

$RO_2^{\cdot}\backslash HO_2^{\cdot} + Fe(H_2O)_6^{2+} \leftrightarrows (H_2O)_5Fe^{III}\text{-}OOR^{2+}$

$(H_2O)_5Fe^{III}\text{-}OOR^{2+} \xrightarrow{H^+} Fe(H_2O)_6^{3+} + HOOR$

$(H_2O)_5Fe^{III}\text{-}OOR^{2+} + Fe(H_2O)_6^{2+} \xrightarrow{H^+} (H_2O)_5Fe^{IV}{=}O^{2+} + Fe(H_2O)_6^{3+} + ROH$

$(H_2O)_5Fe^{IV}{=}O^{2+} + Fe(H_2O)_6^{2+} \xrightarrow{2H^+} 2Fe(H_2O)_6^{3+}$

 © 2005 Wiley-VCH Verlag GmbH & Co. KGaA, Weinheim

2881 **G. Reeske, M. Schürmann, B. Costisella, K. Jurkschat***

Organotin-Substituted Crown Ethers for Ditopic Complexation of Anions and Cations

Keywords: Ditopic complexation / Host-guest chemistry / NMR spectroscopy / X-ray crystallography / Tin

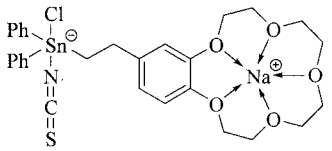

4·NaSCN

2888 **J. Rosdahl, T. F. Fässler, L. Kloo***

On the Structure of Nonastannide Clusters in Liquid and Solid State

Keywords: EXAFS spectroscopy / Cluster compounds / Polyanions / Solid-state structures / Ab initio calculations

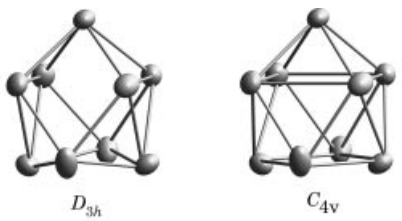

D_{3h} C_{4v}

Which symmetry is most representativ for the structure?

2895 **T. A. Vanderah,* I. Levin, M. W. Lufaso**

An Unexpected Crystal-Chemical Principle for the Pyrochlore Structure

Keywords: Pyrochlore / Displacive disorder / Bismuth zinc niobates / Phase equilibria

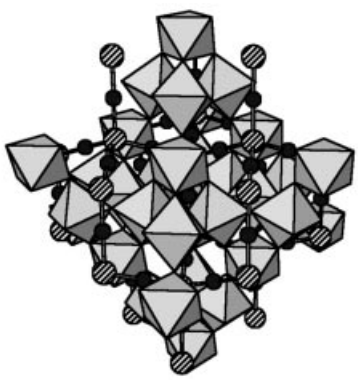

2902 **H. Casellas, C. Massera, P. Gamez,* A. M. Manotti Lanfredi, J. Reedijk***

N-Donor Ligand Coordination Polymers of Cu^{II}, Zn^{II}, and Cd^{II} Obtained at Elevated Temperature and Pressure

Keywords: Coordination polymers / N ligands / Multidirectional ligands / Chain structures / Pi interactions

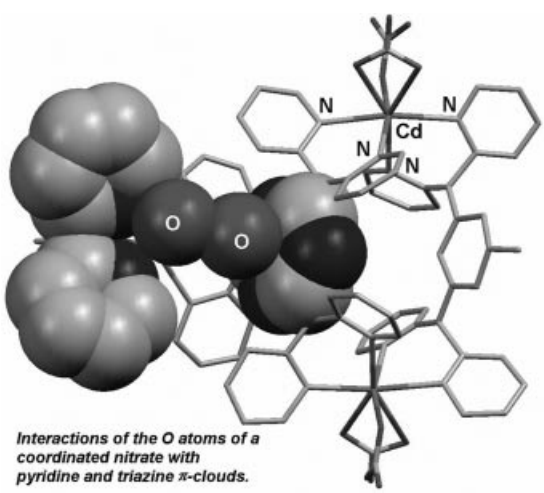

Interactions of the O atoms of a coordinated nitrate with pyridine and triazine π-clouds.

 © 2005 Wiley-VCH Verlag GmbH & Co. KGaA, Weinheim

2909 **X. Li, Z.-Y. Zhang, Y.-Q. Zou***

Synthesis, Structure and Luminescence Properties of Four Novel Terbium 2-Fluorobenzoate Complexes

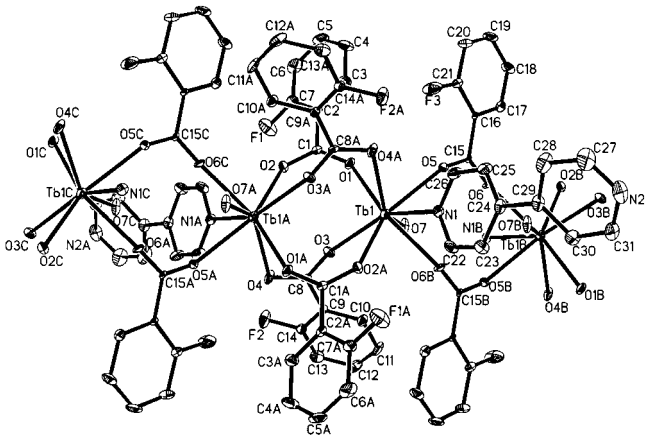

Keywords: Fluorinated ligands / Luminescence / O ligands / Terbium

2919 **M. Kaczorowska, D. Schröder,* H. Schwarz**

Fragmentation of Alkoxo(catecholato)vanadium(V) Complexes $[(C_6H_4O_2)V(OR^1)(OR^2)]^+$ in the Gas Phase

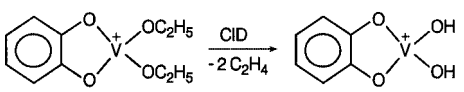

Keywords: Alkoxo complexes / Catecholates / Elimination / Hydrogen migration / Vanadium

2924 **C. Alonso-Moreno, A. Antiñolo, F. Carrillo-Hermosilla, P. Carriòn, I. López-Solera, A. Otero,* S. Prashar, J. Sancho**

Novel Indenylzirconium Complexes as Supported Catalysts in the Polymerization of Ethylene

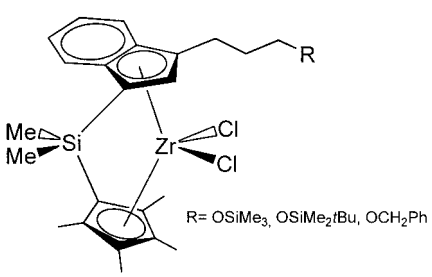

Keywords: Metallocene / Zirconium / Homogeneous catalysis / Supported catalysts / Polymerization / Ethylene

2935 **W. Shi, A. Rothenberger***

Synthetic Applications of Lawesson's Reagent in Reactions with Cu^I Alkoxides

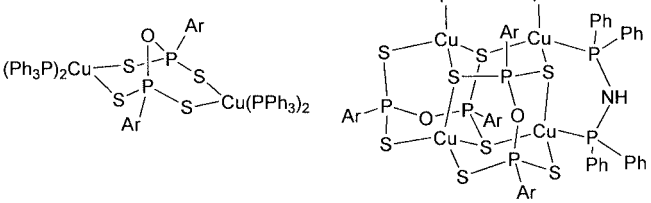

Keywords: Metal alkoxide / P ligands / S ligands / Elimination

 © 2005 Wiley-VCH Verlag GmbH & Co. KGaA, Weinheim

A Nonanuclear Ni^{II} Cluster with a 1,2,4-Triazolo[4,3-*a*]pyrimidine Derivative

Sawsan Salameh,[a] Mohammad Abul-Haj,[a] Miguel Quirós,*[b] and Juan M. Salas[b]

Keywords: Cluster compounds / Nickel / Triazolopyrimidine / Magnetic properties

This article describes the nickel cluster compound $[Ni_9L_8(OH)_6(NH_3)_4(H_2O)_8](NO_3)_4{\cdot}8H_2O$, where **L** represents the anionic form of the ligand 7,8-dihydro-1,2,4-triazolo[4,3-*a*]-pyrimidin-7-one. The structure of the cation of this compound is rather complicated, involving nine metal atoms, eight bridging organic ligands, bridging hydroxyl groups, and terminal ammonia and water molecules. The central nickel atom lies on a crystallographic inversion centre, while the other eight define two disorted "cubane-like" $[Ni_4(OH)_3]^{5+}$ subclusters. Each subcluster is linked to the central atom by three triple bridging organic ligands. Additional **L** ligands bridge two external metal atoms in each subcluster. The variation with temperature of the magnetic susceptibility of the compound indicates the presence of both ferromagnetic and antiferromagnetic interactions; the latter is predominant.
(© Wiley-VCH Verlag GmbH & Co. KGaA, 69451 Weinheim, Germany, 2005)

Introduction

The condensation of a 1,2,4-triazole ring and another of a pyrimidine molecule may give rise to four different families of heterocyclic, bicyclic compounds. Among these, the thermodynamically more stable, and hence the most studied ones, are 1,2,4-triazolo[1,5-*a*]pyrimidines, which bind to metal atoms in a number of different ways to give rise to different structural motifs.[1] More bonding possibilities arise if the positions of the nitrogen atoms in the heterocycle are interchanged, defining the isomeric families 1,2,4-triazolo[1,5-*c*]pyrimidines,[2] 1,2,4-triazolo[4,3-*a*]pyrimidines,[3] and 1,2,4-triazolo[4,3-*c*]pyrimidines.[4] These are far less thermodynamically stable, and isomerisation processes (Dimroth rearrangement) are possible on heating, possibly catalysed by acidic or basic pH conditions,[5] so working with any of these families is potentially more difficult.

Our research group has just started to explore the coordination possibilities of one of these families, namely the 1,2,4-triazolo[4,3-*a*]pyrimidines, which differ from the 1,5-*a* derivatives in the position of one of the nitrogen atoms of the triazole ring, which is separated as far as possible from the pyrimidine ring, is subject to less steric hindrance, and is contiguous to the other external imidazole nitrogen atom. The skeleton of this family of compounds, as well as the numbering scheme used for identifying their atoms, is shown in Scheme 1.

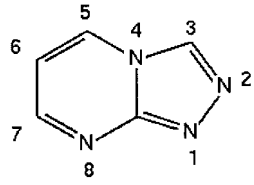

Scheme 1.

The first metal complex of one of these derivatives (with an exocyclic oxo group in position 7) is a silver dimer recently published by us.[6] In this complex the ligand bridges the metal atoms through the two nitrogen atoms of the triazole ring. Following this research line, we have started to explore the behaviour of this ligand towards metal atoms of the first transition series. We used a pH high enough to deprotonate the nitrogen atom of the pyrimidine ring, which usually carries the acidic proton (N8), so that it could become a new binding site, and we have been successful in obtaining a crystalline solid with nickel(II) in ammonia aqueous solution. The solid is a nonanuclear cluster, and the metal atoms are bridged by organic ligands and hydroxyl groups, which transmit both ferromagnetic and antiferromagnetic interactions.

Results and Discussion

The main feature of the crystal structure of the title compound is the presence of centrosymmetric clusters built from nine nickel atoms, eight **L** ligands, six hydroxo groups, four ammonia molecules and eight water molecules. Discrete clusters with nine metal atoms are not very frequently observed, nevertheless, a number of nonanuclear nickel compounds have been described with different bridging li-

[a] Department of Chemistry and Chemical Technology, Al-Quds University,
P. O. Box 20002 Abu Dis, Jerusalem, Palestine
[b] Departamento de Química Inorgánica, Facultad de Ciencias, Universidad de Granada,
18071 Granada, Spain
Fax: +34-958-248526
E-mail: mquiros@ugr.es

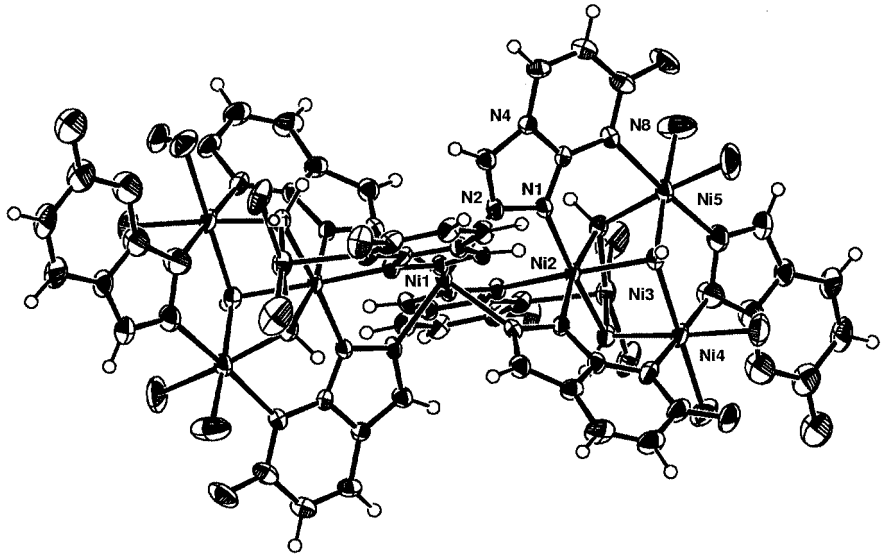

Figure 1. Molecular structure of the $[Ni_9L_8(OH)_6(NH_3)_4(H_2O)_8]^{4+}$ cluster according to X-ray analysis. Both halves are related by a crystallographic inversion centre. Non-hydrogen atoms are represented by ellipsoids at the 50% probability level. Only the metal atoms on one side of the central metal atom, and the nitrogen atoms of one of the organic ligands have been labelled for clarity.

gands and different topologies,[7,8] some of them involving hydroxo groups.[9,10]

Two crystallographically independent clusters are present in the unit cell, but they are chemically equivalent and subsequently will be described jointly. The quality of the crystal data is not high enough for a very accurate structural determination and, in fact, some ambiguity remains in the assignment of the water and ammonia molecules. Additionally, some of the nitrate counteranions and interstitial water molecules are poorly defined and have been introduced into the structural model with partial occupancy (see Exp. Sect.).

A view of one of these clusters is shown in Figure 1. The nickel atom placed at the centre of the cluster (Ni1) lies on a crystallographic inversion centre, and is octahedrally coordinated to by the nitrogen atom in position 2 of the six different **L** moieties. The environment of this atom has approximate D_{3d} symmetry, and the Ni1···N2 distances are in the range of 2.07–2.11 Å.

On each side of this central atom, a $Ni_4(OH)_3$ subcluster is placed. Nickel and oxygen atoms in this subcluster form a cubane-like backbone with one of the vertices missing. Each hydroxyl group bridges three nickel atoms, one of these (Ni2) is close to the centre of the cluster (distance Ni1···Ni2, 3.65–3.66 Å) and is linked to the three hydroxyl groups, whereas the other three (Ni3, Ni4 and Ni5, which we will refer to as the "external" nickel atoms from here onward) are linked to only two hydroxyl groups each. The "cubane" is heavily distorted with the external metal atoms, which are adjacent to the empty vertex,separated outwards from their ideal positions. This is reflected in the bond angles around the hydroxyl oxygen atoms, which are in the 92.0–96.0° range if Ni2 is considered, and in the 113.9–125.5° range if it is not. The distortion of the "cubane" is also seen in the intermetallic distances, 2.97–3.03 Å for Ni2···Ni(external), and 3.36···3.64 Å for Ni(external)··· Ni(external). Nickel···oxygen distances (the edges of the cube) are in the range of 2.04–2.08 Å for Ni2–OH, and 2.00–2.06 Å for Ni(external)–OH bonds.

Several examples of structures containing Ni_4O_4 "cubane-like" clusters can be found in the bibliography; in most of them, the oxygen atoms belong to methoxy groups,[11] or to more complex organic molecules,[12] but surprisingly, very few have bridging hydroxo groups.[13] The Ni–O distances in these species are around 2.0–2.1 Å, and the cubes are usually quite distorted with angles above and below 90° around the oxygen and nickel atoms, respectively; the actual degree of distortion clearly is conditioned by the presence of other ligands. On the other hand, the only examples of "incomplete" Ni_4O_3 cubanes that we have found are those linked by extra oxygen bridges to other metal atoms, thus they are just portions of more complex Ni–O skeletons.[14]

The six organic ligands coordinated to the central metal atom join it to both cubane-like subclusters (three ligands to each), and act as triple bridges through the nitrogen atoms at positions 2, 1 and 8: N2 is linked to Ni1 as previously said, N1 is linked to Ni2 and N8 is linked to Ni3, Ni4 or Ni5. Atom Ni2 is then coordinated to the three hydroxyl oxygen atoms, and the N1 atom of the three organic ligands in an approximate C_{3v} environment.

An additional triazolopyrimidine ligand is present on each side of the cluster bridging two of the "external" metal atoms (namely Ni4 and Ni5) through the two nitrogen atoms of the triazole ring (N1 to Ni4 and N2 to Ni5). The coordination environments of the three external nickel atoms are completed by two water or ammonia molecules: those attached to Ni3 have been assigned as ammonia, and those attached to Ni4 and Ni5 as water, although these as-

 © 2005 Wiley-VCH Verlag GmbH & Co. KGaA, Weinheim

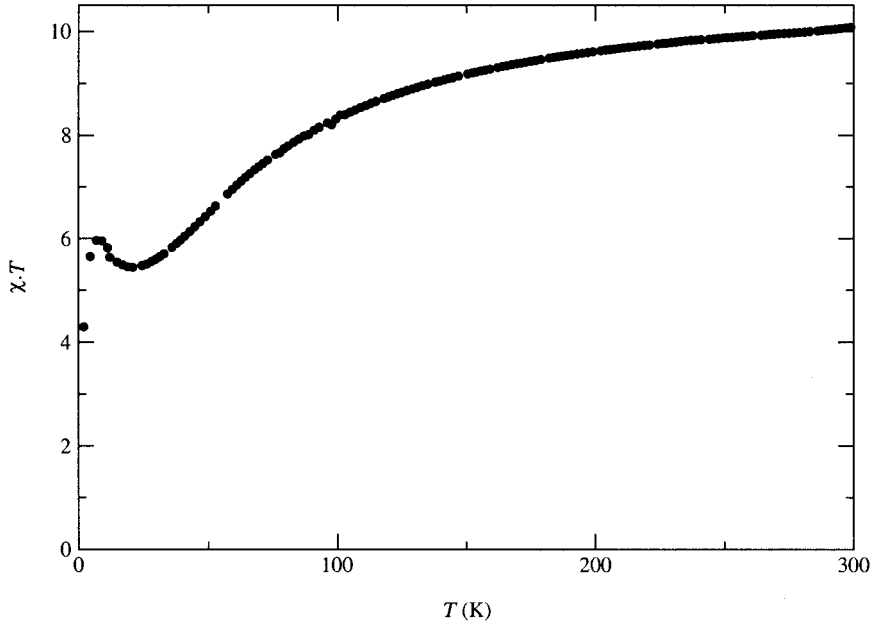

Figure 2. Variation with temperature of the magnetic susceptibility of the title compound, represented as a χT vs. T curve (χ in emu per mol of clusters).

signments are far from being certain (see Exp. Sect.). An octahedral environment is completed in this way for Ni4 and Ni5, whereas a not very frequently observed square-pyramidal environment is found for Ni3. For this atom, the sixth position is not available since the above-mentioned organic ligand attached to Ni4 and Ni5 is orientated in that direction preventing either water or ammonia from occupying that position.

If a comparison is made between the geometries of all the organic ligands in the title compound and those in the previously mentioned silver dimeric complex,[6] in which the ligand is in the neutral form, the most noticeable differences are the lengthening of the C7–O7 bond (from 1.221 to 1.24–1.30 Å) and, probably more significantly, the closing of the C7–N8–C8 angle (from 122.0 to 116–117°), a consequence of the N8 deprotonation. This is true for both triple bridging and double bridging ligands, supporting the idea that all are anionic. The non-coordinated N8 atom of the double bridging ligand forms an intramolecular hydrogen bond with one of the water molecules attached to Ni4 [distances 2.743(9) and 2.862(11) Å].

The magnetic susceptibility of the compound has been measured in the 2–300 K temperature range. The results are shown in Figure 2, in the form of a χT vs. T plot. The product χT steadily decreases with T reaching a minimum at 20 K. It then increases reaching a maximum at 8 K before decreasing sharply at very low temperature. This behaviour indicates that both ferromagnetic and antiferromagnetic interactions are taking place, the latter being predominant. The decrease at very low T may be attributed to antiferromagnetic intermolecular interactions. After normalising the χT value where $T \rightarrow \infty$ to 1, the normalised values at different temperatures are 0.89 (300 K), 0.48 (minimum at 19 K), 0.53 (maximum at 8 K), and 0.38 (at 2 K, the lowest temperature used).

Due to the low symmetry of the cluster, with five structurally different types of metal atoms, a large number of different coupling constants are expected (at least ten, even if those between atoms on different sides of the central metal atom are neglected). Deriving an expression for χ as a function of temperature from the resulting complex spin Hamiltonian, and fitting the many adjustable parameters to the experimental data, would be a very difficult task (if possible at all), so the values of the coupling constants have not been determined, and not even their signs (that indicate which pairs interact ferromagnetically and which antiferromagnetically) have been deduced.

The data above 50 K obey the Curie–Weiss law very well. The linear fitting of $1/\chi$ vs. T yields a value of –35.4(3) K for θ (somehow quantifying the strong antiferromagnetic interactions that prevail in this region), and an effective magnetic moment per nickel atom as $T \rightarrow \infty$ of 3.166(1) B.M. (g = 2.24).

Experimental Section

Reagents were obtained from standard commercial sources; organic reagents were of synthetic grade and inorganic reagents of analytical grade. The ligand 7,8-dihydro-1,2,4-triazolo[4,3-*a*]pyrimidin-7-one hemihydrate was synthesised as described previously.[6,15] Microanalysis of C, H and N were performed with a Fisons Instruments EA-1008 analyser. Magnetic susceptibility measurements were made with a SQUID MPMS-XL Quantum Design magnetometer, at the Universidad Complutense (Madrid), using a magnetic field of 1.00 T. Diamagnetic corrections were applied.

Synthesis of the Nickel Complex: Nickel chloride hexahydrate (0.238 g, 1 mmol) and 7,8-dihydro-1,2,4-triazolo[4,3-*a*]pyrimidin-7-one (LH) hemihydrate (0.145 g, 1 mmol) were dissolved in separate aliquots of 1 M aqueous ammonia (10 mL). Both solutions were mixed, and the resulting blue solution was left to stand so that

 © 2005 Wiley-VCH Verlag GmbH & Co. KGaA, Weinheim

the excess ammonia was eliminated. Deep blue crystals of the title compound, suitable for X-ray work, were obtained. Elemental analysis of $C_{40}H_{74}N_{40}Ni_9O_{42}$ $[Ni_9\mathbf{L}_8(OH)_6(NH_3)_4(H_2O)_8](NO_3)_4 \cdot 8H_2O$ (2315.5): calcd. C 20.75, H 3.22, N 24.20; found C 20.7, H 3.5, N 24.2.

Crystallography: Data for a single crystal of the title complex (dimensions, $0.28 \times 0.15 \times 0.06$ mm) were collected at room temperature with a Bruker SMART APEX CCD system with Mo-K_α radiation (λ = 0.7107 Å). Data were corrected for absorption (multiscan, transmission range, 0.6667–0.8775). The structure was solved by Direct Methods. According to the elemental analysis data, four ammonia molecules are present per cluster, but the quality of the crystal data does not allow us to unambiguously distinguish between water and ammonia molecules. The Fourier peaks attached to the square-pyramidal Ni atom (Ni3) have been assigned as ammonia because of the coordination polyhedron of this atom, and because more favourable thermal parameters are obtained in this way, but of course, this assignment cannot be taken as granted (other assignments or possible disordered situations cannot be discarded). The structure was refined anisotropically (except for hydrogen atoms, disordered water molecules and two poorly defined nitrate anions) on F^2 using SHELXL-97.[16] Hydrogen atoms of the heterocycle and of the hydroxyl groups were placed at ideal positions, and those of the water and ammonia molecules were ignored. Isotropic thermal parameters for all H atoms were fixed to 1.2 times the equivalent isotropic thermal parameter of their parent atoms.

Crystal Data for $[Ni_9L_8(OH)_6(NH_3)_4(H_2O)_8](NO_3)_4 \cdot 8H_2O$: Triclinic, space group $P\bar{1}$, a = 11.0481(5), b = 18.2700(8), c = 21.3860(9) Å, α = 65.966(1) β = 83.287(1), γ = 86.043(1)°, V = 3914.4(3) Å^3, Z = 2, D_{calc} = 1.963 Mg/m^{-3}, μ = 2.237 mm^{-1}, 45862 reflections (17819 unique) collected (θ range 1.25–28.45°), wR_2 = 0.2454, R[12041 data with $I > 2\sigma(I)$] = 0.0808.

CCDC-265692 contains the supplementary crystallographic data for this paper. These data can be obtained free of charge from The Cambridge Crystallographic Data Centre via www.ccdc.cam.ac.uk/data_request/cif.

Acknowledgments

This work was supported by a project of the Ministry of Science and Technology of Spain (BQU, 2001–2955-CO2). M. Abul Haj acknowledges TEMPUS program of the European Community for an individual mobility grant.

[1] J. M. Salas, M. A. Romero, M. P. Sánchez, M. Quirós, *Coord. Chem. Rev.* **1999**, 1119–1142.
[2] M. A. E. Shaban, A. E. A. Morgan, *Adv. Heterocycl. Chem.* **2000**, *77*, 345–394.
[3] M. A. E. Shaban, A. E. A. Morgan, *Adv. Heterocycl. Chem.* **1999**, *73*, 131–176.
[4] M. A. E. Shaban, A. E. A. Morgan, *Adv. Heterocycl. Chem.* **2000**, *75*, 243–281.
[5] H. S. El-Khadem, J. Kawai, D. L. Swartz, *Heterocycles* **1989**, *28*, 239–248.
[6] S. Salameh, M. Abul-Haj, M. Quirós, J. M. Salas, *Inorg. Chim. Acta* **2005**, *358*, 824–827.
[7] S. A. Ivanov, M. A. Kozee, W. A. Merrill, S. Agarwal, L. F. Dahl, *J. Chem. Soc., Dalton Trans.* **2002**, 4105–4115.
[8] F. Meyer, R. F. Winter, E. Kaifer, *Inorg. Chem.* **2001**, *40*, 4597–4603.
[9] E. K. Brechin, S. G. Harris, S. Parsons, R. E. P. Winpenny, *Angew. Chem. Int. Ed. Engl.* **1997**, *36*, 1967–1969.
[10] G. S. Papaefstathiou, A. Escuer, R. Vicente, M. Font-Bardía, X. Solans, S. P. Perlepes, *Chem. Commun.* **2001**, 2414–2415.
[11] T. K. Paine, E. Rentschler, T. Weyhermüller, P. Chaudhuri, *Eur. J. Inorg. Chem.* **2003**, 3167–3178.
[12] G. Aromí, A. S. Batsanov, P. Christian, M. Heliwell, O. Roubeau, G. A. Timco, R. E. P. Winpenny, *J. Chem. Soc., Dalton Trans.* **2003**, 4466–4471.
[13] L. Ballester, E. Coronado, A. Gutiérrez, A. Monge, M. F. Perpiñán, E. Pinilla, T. Rico, *Inorg. Chem.* **1992**, *31*, 2053–2056.
[14] M. Murrie, D. Biner, H. Stœckli-Evans, H. U. Güdel, *Chem. Commun.* **2003**, 230–231.
[15] H. Reimlinger, M. A. Peiren, *Chem. Ber.* **1970**, *103*, 3266–3277.
[16] G. M. Sheldrick, *SHELXL97*, University of Göttingen, Germany, **1997**.

Received: March 9, 2005
Published Online: June 14, 2005

 © 2005 Wiley-VCH Verlag GmbH & Co. KGaA, Weinheim

Structural Transformations and Magnetic Effects Induced by Solvent Exchange in the Spin Crossover Complex $[Fe(bpp)_2][Cr(bpy)(ox)_2]_2$

Mari Carmen Giménez-López,[a] Miguel Clemente-León,[a] Eugenio Coronado,*[a] Francisco M. Romero,*[a] Sergiu Shova,[b][‡] and Jean-Pierre Tuchagues[b]

Keywords: Spin crossover / Iron / Solvent sensing / Hydration / Magnetic properties

Structural, thermal, magnetic and solvent-exchange properties of the spin crossover compound $[Fe(bpp)_2][Cr(bpy)(ox)_2]_2$ containing paramagnetic anions are given. This complex salt **1** crystallises as a dihydrate with two inequivalent (high-spin and low-spin) Fe^{II} sites. The dehydrated compound is a spin-crossover material with $T_{1/2}\uparrow$ = 369 K and $T_{1/2}\downarrow$ = 353 K. Rehydration takes place without loss of crystallinity, yielding a polymorph (**2**) with 100 % high-spin Fe^{II} sites. The different high-spin fractions in **1** and **2** have been correlated to structural changes in the Fe^{II} second coordination sphere. The magnetic response to the presence of different sorbed molecules has also been explored.
(© Wiley-VCH Verlag GmbH & Co. KGaA, 69451 Weinheim, Germany, 2005)

The spin crossover between the diamagnetic low-spin (LS, S = 0) and the paramagnetic high-spin (HS, S = 2) states in iron(II) complexes has attracted much interest.[1] Although the purely molecular origin of the effect is clearly established by its observation in solution, cooperativity plays a key role in the solid state, where the phenomenon may be accompanied by a structural phase transition. The transition is triggered by a given external perturbation (light irradiation, pressure or temperature change) and the response (change of the optical and magnetic properties) may be observed abruptly with a hysteretic behaviour. These materials can then be considered as bistable systems suitable for practical applications.

In the search of increasing cooperativity, high-dimensional structures have been designed in which the functional molecular units are linked by bridging ligands.[2] Using this strategy, some nanoporous frameworks displaying spin crossover effects that are influenced by the reversible exchange of solvate molecules have been obtained.[3] Another approach relies on hydrogen bonding. In this context, the abrupt and hysteretic spin transitions of $[Fe(bpp)_2]X_2$ complex salts [bpp = 2,6-bis(pyrazol-3-yl)pyridine; X = anion] are well documented.[4] The amino groups of the pyrazolyl moieties can set up hydrogen bonds with its environment and this gives rise to a cooperative behaviour and a marked dependence of the spin transition on the nature of the anion and the extent of hydration.[5] This family of compounds may provide good candidates for the study of solvation effects in spin crossover that can lead to interesting applications in molecular sensing. Further, these salts exhibit Light-Induced Excited Spin State Trapping (LIESST) effects at high temperatures with relatively long lifetimes of the photoinduced metastable states.[6] In this report, we give evidence for the strong dependence of the electronic configuration of the Fe^{2+} cations on the exchange of guest solvent molecules in the salt $[Fe(bpp)_2][Cr(bpy)(ox)_2]_2$ (**1**) (bpy = 2,2′-bipyridine; ox = oxalate dianion). The complex anion has been chosen for its ability to form hydrogen bonds and π–π stacking interactions.[7]

Compound **1** crystallises as a dihydrate $[Fe(bpp)_2][Cr(bpy)(ox)_2]_2{\cdot}2H_2O$ and its structure[8] comprises isolated $[Fe(bpp)_2]^{2+}$ and $[Cr(bpy)(ox)_2]^-$ complexes and water molecules. Two crystallographically independent octahedral iron(II) sites, Fe(1A) and Fe(1B), were found (Figure 1a). Both sites have a pseudo C_{2v} symmetry, with the tridentate bpp ligand binding to the iron ion in meridional positions. The Fe(1A) coordination sphere is consistent with high-spin Fe^{II}, with Fe–N bond lengths lying in the range 2.146(2)–2.210(2) Å. In contrast, the Fe–N bond lengths of the Fe(1B) site are typical low-spin values, lying in the range 1.921(2)–1.976(2) Å. Several examples of coexistence of HS and LS species in the same compound have been reported. In these cases, the different iron centres adopt similar ligand-binding geometries but different second coordination spheres.[9] We observed a similar behaviour: the four non-coordinating N–H groups of complex **A** (Figure 1a) are hydrogen-bonded to three $[Cr(bpy)(ox)_2]^-$ anions and one water molecule, whereas complex **B** is connected to four $[Cr(bpy)(ox)_2]^-$ anions. Since the oxalate oxygen atom of the

[a] Institut de Ciència Molecular, Universitat de València
Dr. Moliner, 50, 46100 Burjassot, Spain
Fax: +34-963-544-859
E-mail: fmrm@uv.es
[b] Laboratoire de Chimie de Coordination du CNRS
205 route de Narbonne. 31077 Toulouse cedex, France
Fax: +33-5-61553003
E-mail: tuchague@lcc-toulouse.fr
[‡] On leave from: State University of Moldova,
Mateevici str. 60, 2009 Chisinau, Moldova

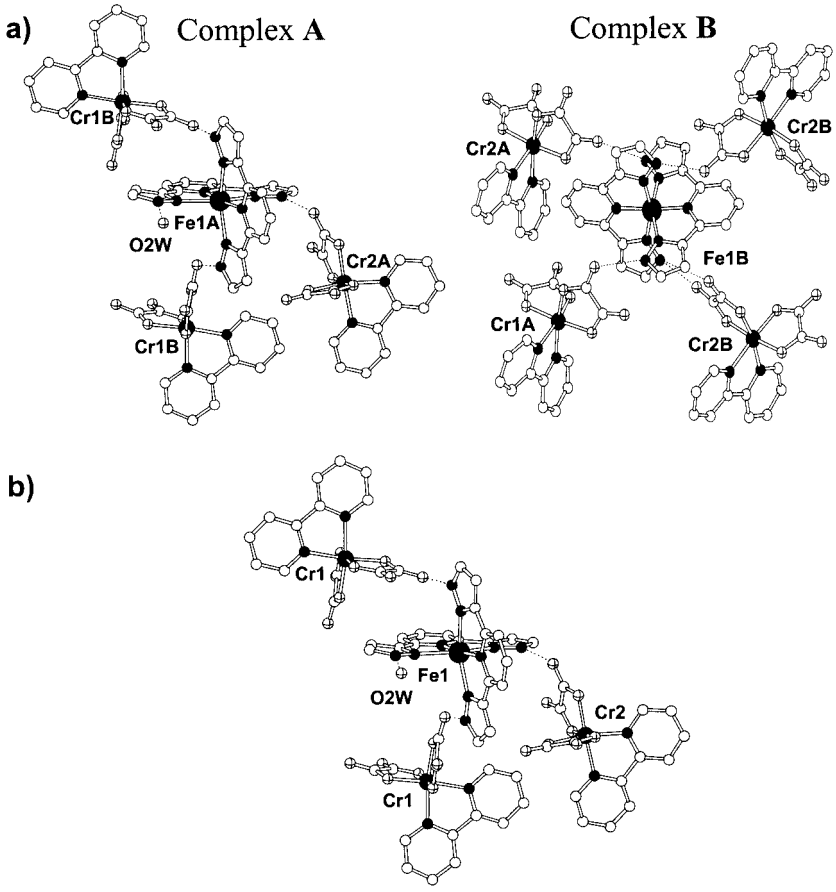

Figure 1. View of the crystal structure of the hydrated salt $[Fe(bpp)_2][Cr(bpy)(ox)_2]_2 \cdot 2H_2O$ showing the first and second coordination spheres of the Fe^{2+} cations; a) original sample (**1**), b) rehydrated sample (**2**).

anion is a better hydrogen-bonding acceptor than water, the electron density of the non-coordinating nitrogen atoms of **B** is increased with respect to **A**. This leads to stronger donor–metal σ-interaction, favouring the LS state for complex **B**.

The magnetic properties of **1** are in agreement with this structural analysis. The product of the molar magnetic susceptibility with the temperature, $\chi_M T$, (Figure 2, curve 1) shows a nearly constant value of 5.5 emu·K·mol^{-1} from 50 K to room temperature, in agreement with the presence of half of the Fe^{2+} ions in the HS state and two Cr^{3+} ions per formula unit. At temperatures above 320 K, $\chi_M T$ decreases and reaches a minimum at 356 K, followed by an increase to a value of 7 emu·K·mol^{-1} at 400 K, indicating that 100% of the Fe sites are HS at this temperature. On cooling now the compound (curve 2) below 300 K, a $\chi_M T$ value of 3.7 emu·K·mol^{-1} is observed, as expected for two uncorrelated Cr^{3+} ions with all the iron(II) centres in the LS configuration. Successive temperature cycles (heating and cooling modes, Figure 2) reveal that the preheated sample displays a spin crossover behaviour with $T_{1/2}\uparrow$ = 369 K and $T_{1/2}\downarrow$ = 353 K.

The thermogravimetric analysis (TGA) of **1** (Figure 3a) indicates a weight loss of about 3% upon heating of the compound in the 300–380 K range. This is clearly a dehydration process that corresponds to the loss of two water molecules. The DSC measurement of the original sample (Figure 3b, curve 1) shows two different endothermic processes that can be attributed to dehydration. In the cooling mode (curve 2), the dried sample exhibits an exothermic feature at 354 K, characteristic of a high-spin to low-spin transition. This process was masked in the measurement of

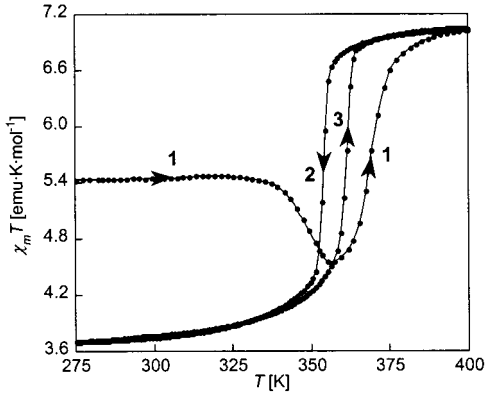

Figure 2. Temperature dependence of $\chi_M T$ for compound **1** in the 275–400 K range. Curve 1: original sample in the heating mode. Curves 2 and 3: subsequent temperature cycle (cooling and heating modes, respectively).

 © 2005 Wiley-VCH Verlag GmbH & Co. KGaA, Weinheim

the original hydrated sample and it can be also characterised by the sharp endothermic peak observed in the heating mode (curve 3) at 358 K.

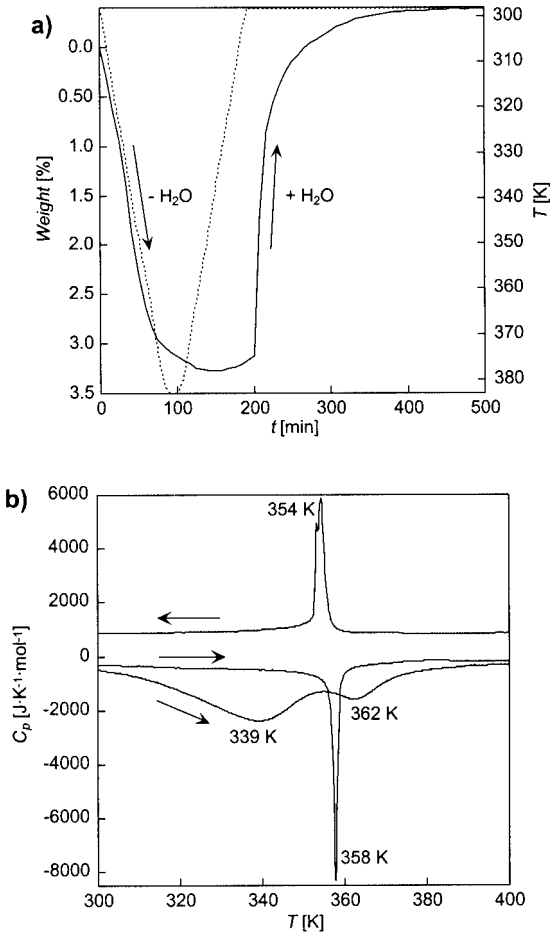

Figure 3. a) Thermogravimetric analysis of compound **1** showing the dehydration-rehydration process. The weight loss of the sample was measured in the 300–380 K range at a constant heating rate of 1 K/min. Then the sample was allowed to cool in an ambient atmosphere. b) Differential scanning calorimetry of **1** in the range of 300–400 K. Curve 1: original sample in the heating mode. Curves 2 and 3: subsequent temperature cycle (cooling and heating modes, respectively).

Based on the thermal and magnetic studies, it is possible to conclude that the initial sweeping-rate-dependent decrease of $\chi_M T$ is due to a change of spin accompanying the dehydration, while the abrupt increase/decrease of $\chi_M T$ observed at higher temperatures is associated to a spin transition of the dehydrated compound. This behaviour is typical of $[Fe(bpp)_2]X_2$ salts.[9] The main difference here is that the spin transition is pushed to very high temperatures as compared to previous examples. Removal of water molecules may allow a fourth $[Cr(bpy)(ox)_2]^-$ anion to be located in the second coordination sphere of Fe(1A), giving rise to a strong stabilisation of the LS state.

Rehydration of a dried sample of **1** proceeds readily and the total weight of the original sample can be recovered in a few minutes (Figure 3a). Surprisingly, the rehydrated sample and the original sample show different magnetic behaviours. Below 50 K, both samples exhibit a continuous increase of $\chi_M T$ with increasing temperature. This can be attributed to zero-field splitting and spin-orbit coupling effects, although intermolecular interactions between the different spin carriers cannot be discarded. From 50 K to room temperature (Figure 4a), the $\chi_M T$ value of the rehydrated sample is equal to 7.5 emu·K·mol^{-1}, suggesting that all the Fe^{2+} cations are in the HS state. As shown for the original sample, loss of water causes a sudden decrease of $\chi_M T$ above room temperature. By further heating, the spin transition characteristic of the dehydrated sample is again observed. TGA and DSC studies confirm again the hypotheses based on the magnetic behaviour. The markedly different magnetic properties of the original and rehydrated samples are very interesting: the magnetic measurements reflect the history of the dehydration-rehydration process.

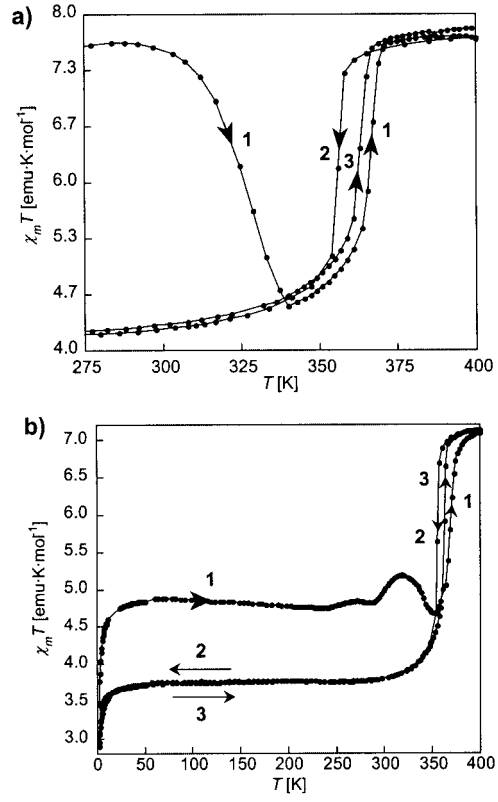

Figure 4. Temperature dependence of $\chi_M T$ for rehydrated (a) and MeOH-solvated (b) samples in the 2–400 K range. Curves 1: first treatment in the heating mode. Curves 2 and 3: subsequent temperature cycles (cooling and heating modes, respectively).

Temperature-dependent X-ray diffraction data suggest that this process occurs without drastic changes in the crystal structure. This prompted us to study the crystal structure of the rehydrated phase. For this purpose, a single crystal of **1** was heated to 343 K under dry nitrogen until constant loss of weight in a TGA instrument. Afterwards, the crystal was kept in ambient atmosphere to allow rehydration and the structure of the rehydrated single crystal

 © 2005 Wiley-VCH Verlag GmbH & Co. KGaA, Weinheim

was solved by X-ray diffraction measurements (Figure 1b). The resulting compound **2** is also a dihydrate and it retains the same crystal symmetry.[10] One of the unit cell parameters is halved and only one independent Fe^{II} site is now present. Its environment is very similar to that observed for the HS site Fe(1A) of the original compound, with Fe–N bond lengths in the 2.145(3)–2.204(3) Å range and the second coordination sphere containing three $[Cr(bpy)(ox)_2]^-$ anions and one water molecule hydrogen-bonded to the pyrazolyl moieties. Hence, after rehydration the two crystallographically independent high-spin Fe(1A) and low-spin Fe(1B) sites become equivalent and a 100% content of HS species is observed.

These findings suggest that spin crossover materials can be very sensitive to exchangeable guest solvent molecules such as alcohols, which are able to form hydrogen bonds. In principle, it could be possible to correlate the nature of the absorbed solvent with the magnetic properties; in such a way that spin crossover could be used as a molecular probe. As an example, **1** has been dehydrated and resolvated with methanol. The solvation process can be easily monitored in a TGA apparatus. An increase of weight corresponding to the absorption of one MeOH molecule was observed. Magnetic measurements of this methanol-solvated sample (Figure 4b) show a distinct behaviour with respect to the rehydrated material. The $\chi_M T$ value at 200 K is 4.8 emu·K·mol^{-1} and corresponds to 33% Fe^{II} centres in the HS state. This value remains nearly constant on increasing the temperature. At 330 K, desolvation starts and $\chi_M T$ decreases to a minimum value at 350 K.[11] Further heating results in a sudden increase of the magnetic signal that corresponds to the spin transition of the desolvated sample. Successive temperature cycles reveal the same magnetic behaviour than that observed for the dehydrated material.

To summarize, the dry material at room temperature exhibits only the paramagnetism of the Cr^{III} centres, with all the Fe^{2+} ions in their LS configuration. Upon exposure to ambient moisture, the compound undergoes a spin crossover to an HS phase. This transition can be correlated to the replacement of a $[Cr(bpy)(ox)_2]^-$ anion by a water molecule in the second coordination sphere of the Fe^{2+} cations. In contrast, treatment of a dry sample with dry methanol vapours yields a material with only 33% of the Fe^{II} sites in the HS configuration.

Clearly, the magnetic properties of this spin crossover compound are very sensitive to the presence of different solvates. This is a well-known effect that has recently drawn special attention in the field of crystal engineering.[12] However, there are only a few qualitative studies on the influence of absorption of solvent molecules in the spin states of dry compounds.[13] These studies lack of any structural evidence. The present work provides a deeper insight into the spin changes associated with different resolvation processes. As compared to previously reported examples based on high-dimensional networks, our approach relies simply on hydrogen bonding. Further work will be devoted to study the influence of the paramagnetic anion on the solvent sensing properties.

Experimental Section

General: All chemicals and solvents were used as received. $Ba[Cr(bpy)(ox)_2]_2\cdot 3H_2O$ and bpp were synthesized according to previously described methods.[14,15]

$[Fe(bpp)_2][Cr(bpy)(ox)_2]_2\cdot 2H_2O$ (1): A solution of bpp (140 mg, 0.66 mmol) and $FeSO_4\cdot 7H_2O$ (92 mg, 0.33 mmol) in 40 mL of MeOH was added to a suspension of $Ba[Cr(bpy)(ox)_2]_2\cdot 3H_2O$ (361 mg, 0.33 mmol) in 30 mL of water. The resulting mixture was stirred for 2 h to promote complete precipitation of $BaSO_4$, which was removed by filtration. After a few days, large red crystals were obtained by slow concentration of the mother liquor. Yield: 199 mg (53%). IR (KBr): $\tilde{\nu}$ = 3544 (w), 3444 (w), 3127 (m), 2921 (m), 1711 (vs), 1679 (vs), 1653 (vs), 1609 (s), 1370 (s), 803 (m), 773 (m), 543 (m), 415 (w) cm^{-1}. $C_{50}H_{38}Cr_2FeN_{14}O_{18}$ (1282.8): calcd. C 46.82, H 2.99, N 15.29; found C 46.82, H 2.93, N 15.08; calcd. Cr/Fe 66.6:33.3, found 65.8/34.2.

Physical Measurements: Dc magnetic susceptibility measurements were performed on polycrystalline samples using a magnetometer (Quantum Design MPMS-XL-5) equipped with a SQUID sensor. Variable-temperature measurements were carried out in the temperature range 2–400 K in a magnetic field of 0.1 T. The temperature sweeping rate was the same for the experiments performed on the original and methanol-solvated samples: 0.5 K·min^{-1} (2–10 K), 1 K·min^{-1} (10–50 K), 5 K·min^{-1} (50–200 K), 2 K·min^{-1} (200–400 K). For the rehydrated sample, the last change in the sweeping rate was set to 340 K. Thermogravimetric measurements were carried out with a Mettler Toledo TGA/SDTA 851 apparatus in the 298–1373 K temperature range under nitrogen and at a scan rate of 5 K·min^{-1}. The dehydration-rehydration process was monitored by heating the ground sample under a stream of nitrogen from 298 to 383 K (1 K·min^{-1}). Then, the system was kept at this temperature during 20 min to allow complete loss of water molecules. Afterwards, the sample was cooled to 298 K. At this point, the stream of nitrogen was replaced by a stream of humid air to allow complete rehydration of the sample. For the solvation experiment, a stream of nitrogen saturated with dry methanol was used. The total flux of nitrogen was constant during the experiments. After saturation (constant weight), the samples were quickly introduced in the SQUID apparatus, protecting them from the environment. Heat capacity measurements under nitrogen were performed in a Mettler Toledo DSC 821e apparatus with warming and cooling rates equal to 4 K·min^{-1} from 253 to 423 K. IR transmission measurements of KBr pellets were recorded at room temperature with a Nicolet Avatar 320 FT-IR spectrophotometer in the range 4000–400 cm^{-1}. C,H,N elemental analyses were carried out in a CE instruments EA 1110 CHNS analyzer. The Cr/Fe ratios were measured with a Philips ESEM X230 scanning electron microscope equipped with an EDAX DX-4 microsonde.

[1] "Spin Crossover in Transition Metal Compounds I–III", in: *Topics in Current Chemistry* (Eds.: P. Gütlich, H. A. Goodwin), **2004**, pp. 233–235, and references therein.
[2] a) J. A. Real, E. Andrés, M. C. Muñoz, M. Julve, T. Granier, A. Bousseksou, F. Varret, *Science* **1995**, *268*, 265; b) V. Niel, A. L. Thompson, M. C. Muñoz, A. Galet, A. E. Goeta, J. A. Real, *Angew. Chem. Int. Ed.* **2003**, *42*, 3759; c) A. Galet, V. Niel, M. C. Muñoz, J. A. Real, *J. Am. Chem. Soc.* **2003**, *125*, 14224; d) V. Niel, M. C. Muñoz, A. B. Gaspar, A. Galet, G. Levchenko, J. A. Real, *Chem. Eur. J.* **2002**, *8*, 2446.
[3] G. J. Halder, C. J. Kepert, B. Moubaraki, K. S. Murray, J. D. Cashion, *Science* **2002**, *298*, 1762.
[4] a) K. H. Sugiyarto, H. A. Goodwin, *Aust. J. Chem.* **1988**, *41*, 1645; b) H. Sugiyarto, K. Weitzner, D. C. Craig, H. A. Good-

 © 2005 Wiley-VCH Verlag GmbH & Co. KGaA, Weinheim

win, *Aust. J. Chem.* **1997**, *50*, 869; c) K. H. Sugiyarto, W. A. McHale, D. C. Craig, D. Rae, M. L. Scudder, H. A. Goodwin, *Dalton Trans.* **2003**, 2443.
[5] K. H. Sugiyarto, D. C. Craig, A. D. Rae, H. A. Goodwin, *Aust. J. Chem.* **1994**, *47*, 869.
[6] a) Th. Buchen, P. Gütlich, K. H. Sugiyarto, H. A. Goodwin, *Chem. Eur. J.* **1996**, *2*, 1134; b) S. Marcen, L. Lecren, L. Capes, H. A. Goodwin, J. F. Létard, *Chem. Phys. Lett.* **2002**, *358*, 87.
[7] M. C. Muñoz, M. Julve, F. Lloret, J. Faus, M. Andruh, *J. Chem. Soc., Dalton Trans.* **1998**, 3125.
[8] Crystal data for **1**: $C_{100}H_{76}Cr_4Fe_2N_{28}O_{36}$, M = 2565.59, crystal dimensions: 0.50×0.45×0.05 mm, triclinic, $P\bar{1}$, a = 15.5434(15), b = 17.723(2), c = 20.985(2) Å, α = 102.002(12), β = 103.291(11), γ = 103.299(12), V = 5263.4(9) Å^3, Z = 2, $\rho_{calcd.}$ = 1.629 Mg m^{-3}, μ(Mo-K_α) = 0.769 mm^{-1}. A dark-red plate-like single crystal of **1** was used for data collection at 180 K with a Stoe Imaging Plate Diffractometer System (IPDS) diffractometer equipped with a graphite-monochromated Mo-K_α radiation source (λ = 0.71073 Å), and an Oxford Cryostream Cooler Device. Data were collected using the φ rotation movement with a crystal-to-detector distance of 70 mm (φ = 0.0–250°, Δφ = 1.4°). Of 52754 measured reflections, 19375 (4.14° < 2θ < 52.20°) were independent (R_{int} = 0.0470) and used to refine 1812 parameters. Semiempirical absorption corrections were made based on equivalent reflections with the program MULTISCAN.[16] The structure was solved by direct methods using SHELXS-97[17] and refined by full-matrix least squares on F_o^2 with SHELXL-97[18] with anisotropic displacement parameters for non-hydrogen atoms. All H atoms attached to carbon atoms were introduced in idealized positions (d_{CH} = 0.96 Å) using the riding model with their isotropic displacement parameters fixed at 120% of their riding atom. Positional parameters of the hydrogen atoms of three solvate water molecules were obtained from difference Fourier syntheses and verified by the geometric parameters of hydrogen bonds. O(4w) molecules, which are positioned in hydrophobic cavities, are disordered among two positions with a 0.6:0.4 ratio of the occupancy factors. There are no short intermolecular contacts from O(4w) which can be characterized as possible H-bonds. The hydrogen atoms for this water molecule were not localized. There is only one short intermolecular contact [O4w···O(2B) = 2.826 Å], which can be characterized as possible H-bond. R_1 = 0.0419 for 14420 reflections with $I \geq 2\sigma(I)$, wR_2 = 0.1071; R_1 = 0.0623, wR_2 = 0.1194, GOF = 0.984 for all data. Max./min. residual peaks in the final difference map: 0.955/–0.482 e·Å^{-3}. CCDC-258048 contains the supplementary crystallographic data for this paper. These data can be obtained free of charge from The Cambridge Crystallographic Data Centre via www.ccdc.cam.ac.uk/data_request/cif.
[9] K. H. Sugiyarto, M. L. Scudder, D. C. Craig, H. A. Goodwin, *Aust. J. Chem.* **2000**, *53*, 755.
[10] Crystal data for **2**: $C_{50}H_{38}Cr_2FeN_{14}O_{18}$, M = 1282.79, crystal dimensions: 0.20×0.12×0.05 mm, triclinic, $P\bar{1}$, a = 9.04700(10), b = 15.6410(2), c = 20.6980(3) Å, α = 102.5530(5), β = 102.0710(5), γ = 103.9340(5), V = 2666.95(6) Å^3, Z = 2, ρ_{calc}d. = 1.597 Mg m^{-3}, μ(Mo-K_α) = 0.758 mm^{-1}. A dark-red plate-like single crystal of **2** was used for data collection with a Nonius Kappa CCD diffractometer (4.34° < 2θ < 55.32°) equipped with a graphite-monochromated Mo-K_α radiation source (λ = 0.71073 Å). Data collection was performed at 180 K. Of 22949 measured reflections, 12198 were independent (R_{int} = 0.0403) and used to refine 793 parameters. The structure was solved by direct methods (SIR97)[19] and refined against F^2 with a full-matrix least-squares algorithm using SHELXL-97[18] and the WinGX (1.64) software package.[20] All non-hydrogen atoms were refined anisotropically. H-atoms were added in calculated positions and refined riding on the corresponding atoms except H atoms of –NH groups and water molecules. H-atoms of –NH groups were located by difference Fourier maps and refined isotropically. H-atoms of water molecules were calculated on the basis of geometry and force-field considerations using the CALC-OH program[21] and refined isotropically fixing the H–H and H–O distances. Final R [$I > 2\sigma(I)$]: R_1 = 0.0538, wR_2 = 0.1505; final R (all data): R_1 = 0.0933, wR_2 = 0.1961. Max./min. residual peaks in the final difference map: 0.700/–1.230 e·Å^{-3}. CCDC-259006 contains the supplementary crystallographic data for this paper. These data can be obtained free of charge from The Cambridge Crystallographic Data Centre via www.ccdc.cam.ac.uk/data_request/cif.
[11] Between 300 and 330 K, a slight increase of the magnetic signal is observed. This behaviour is also observed in a blank measurement performed with a sample dehydrated in the TGA equipment and then transferred to the SQUID instrument. Besides this accident, the magnetic behaviour of this sample is the same as that observed in curves 2 and 3 for dry samples. This accident is most probably due to the presence of humidity within the equipment.
[12] M. Hostettler, K. W. Törnroos, D. Chernyskov, B. Vangdal, H. B. Bürgi, *Angew. Chem. Int. Ed.* **2004**, *43*, 4589.
[13] a) Y. Garcia, P. J. van Koningsbruggen, E. Codjovi, R. Lapouyade, O. Kahn, L. Rabardel, *J. Mater. Chem.* **1997**, *7*, 857; b) Y. Garcia, P. J. van Koningsbruggen, R. Lapouyade, L. Fournès, L. Rabardel, O. Kahn, V. Ksenofontov, G. Levchenko, P. Gütlich, *Chem. Mater.* **1998**, *10*, 2426; c) O. Roubeau, J. G. Haasnoot, E. Codjovi, F. Varret, J. Reedijk, *Chem. Mater.* **2002**, *14*, 2559.
[14] J. A. Broomhead, *Aust. J. Chem.* **1962**, *15*, 228.
[15] Y. Lin, S. A. Lang, *J. Heterocycl. Chem.* **1977**, *14*, 345.
[16] R. H. Blessing, *Acta Crystallogr. A* **1995**, *51*, 33.
[17] G. M. Sheldrick, *SHELXS-97, Program for Crystal Structure Solution*, University of Göttingen, Göttingen, Germany, **1990**.
[18] G. M. Sheldrick, *SHELXL-97, Program for the refinement of crystal structures from diffraction data*, University of Göttingen, Göttingen,Germany, **1997**.
[19] A. Altomare, M. C. Burla, M. Camalli, G. Cascarano, C. Giacovazzo, A. Guagliardi, A. G. G. Moliterni, G. Polidori, R. Spagna, *J. Appl. Crystallogr.* **1999**, *32*, 115.
[20] L. J. Farrugia, *J. Appl. Crystallogr.* **1999**, *32*, 837.
[21] M. Nardelli, *J. Appl. Crystallogr.* **1999**, *32*, 563.

Received March 17, 2005
Published Online: June 14, 2005

 © 2005 Wiley-VCH Verlag GmbH & Co. KGaA, Weinheim

A Pulse Radiolysis Study of Catalytic Superoxide Radical Dismutation by a Manganese(II) Complex with an N-Tripodal Ligand

Stéphanie Durot,[a] François Lambert,[a] Jean-Philippe Renault,*[b] and Clotilde Policar*[a]

Keywords: Bioinorganic chemistry / Enzyme models / Manganese / Superoxide dismutase / SOD mimic / Pulsed radiolysis / MnOO adduct

This article presents a pulse radiolysis study of the reactivity of a SOD-mimic Mn^{II} complex $[Mn^{II}(IPG)]^+$ **1** with superoxide. It uses an improved set-up with a circulating cell. It provides convergent pieces of evidence that **1** catalyses efficiently the dismutation of superoxide. Three sets of experiments are described: (1) Transient formation and decay of an adduct labeled $\{MnOO\}^6$ were studied. (2) A multi-pulse experiment showed a reproducible behaviour upon successive superoxide pulses. (3) Superoxide decay was monitored at 270 nm to provide an overall kinetic constant. A mechanism is proposed.

(© Wiley-VCH Verlag GmbH & Co. KGaA, 69451 Weinheim, Germany, 2005)

The superoxide radical anion ($O_2^{\cdot-}$), produced by the one-electron reduction of dioxygen, has been shown to be a highly toxic species.[1–6] It is known to be involved in oxidative stress.[2,7–9] Superoxide dismutases (SOD) catalyze $O_2^{\cdot-}$ dismutation into dioxygen and hydrogen peroxide and constitute an endogenous protection.[2–5,10] Since superoxide has been shown to play an important role in several diseases, low-molecular-weight SOD mimics have potential use as pharmaceutical agents.[8,9,11] Synzymes[12] can also enlighten the understanding of the natural enzyme catalytic mechanism. A wide range of putative catalysts for superoxide dismutation has been reported.[4,9,13] SOD activity is usually estimated on the basis of indirect activity tests, such as the Mc-Cord Fridovich test.[10] These tests are informative, as they provide a quantification of the activity in conditions close to physiological, but they may lead to errors in the interpretation of results, as previously shown.[9,14,15] According to us and others,[9,14,16] both indirect and direct methods are necessary, as they provide complementary information. In the indirect methods, superoxide is provided at a constant rate and at concentrations close to what is encountered during oxidative stress. This provides a test for the ability of the putative SOD mimic to be useful under physiological situations. However, in most cases it is difficult to distinguish between a catalyst and a scavenger. With direct methods, as superoxide can be used in large excess relative to the putative SOD mimic, unambiguous characterization of the catalyst and the scavenger is accomplished. However, direct methods for the determination of catalytic rate constants, including stopped-flow and pulse radiolysis, are rarely used.[9,13,15–17]

In this work, we provide convergent pieces of evidence by pulse radiolysis that a manganese(II) complex **1**, $[Mn(IPG)(MeOH)]_n(PF_6)_n$ (IPG^- = *N*,*N*-(2-pyridylmethyl[(1-methylimidazol-2-yl)methyl]glycinate, see Figure 1), catalyses the dismutation of superoxide. The crystal structure of complex **1** and its reactivity towards superoxide both in anhydrous DMSO and in aqueous medium have been previously reported.[18,19] It displays a good SOD-like activity, as shown by the McCord–Fridovich test (IC50 = $(2.0 \pm 0.2) \times 10^{-6}$ mol L^{-1} or k_{cat} = $(2.9 \pm 0.3) \times 10^6$ mol^{-1} L s^{-1}).[19,20] In the present article, three sets of experiments are described with different purposes: (a) transient formation and decay of an adduct between Mn and superoxide were studied under conditions for which $[\mathbf{1}]_0 > [O_2^{\cdot-}]_0$. (b) A multi-pulse experiment showed a reproducible behaviour upon successive $O_2^{\cdot-}$ pulses. (c) Superoxide decay was monitored at 270 nm under conditions for which $[\mathbf{1}]_0 < [O_2^{\cdot-}]_0$ to provide an overall kinetic constant.

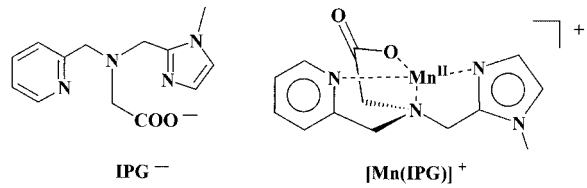

Figure 1. Ligand IPG^- = *N*,*N*-(2-pyridylmethyl[(1-methylimidazol-2-yl)methyl]glycinate and schematic structure for $[Mn(IPG)]^+$.

[a] Laboratoire de Chimie Bio-organique et Bio-inorganique, UMR8124, Bâtiment 420, Université Paris XI,
91405 Orsay Cedex, France
Fax: +33-169157231
E-mail: cpolicar@icmo.u-psud.fr
[b] Laboratoire de Radiolyse (DSM/DRECAM/SCM-URA331) CEA Saclay,
91191 Gif-sur-Yvette, France
E-mail: JRENAULT@drecam.cea.fr
Supporting information for this article is available on the WWW under http://www.eurjic.org or from the author.

The superoxide radical was produced in oxygenated aqueous solutions by pulse radiolysis,[21] and its direct reaction with the putative SOD mimic was monitored by UV/Visible spectrophotometry. High-energy ionizing radiation generates primary radicals ($H^{\cdot}$, e^{-}_{aq}, $HO^{\cdot}$), that are rapidly and quantitatively converted into either superoxide $O_2^{\cdot-}$ or its protonated form hydroperoxyl $HO_2^{\cdot}$, in the presence of either formate or alcohols.[22,23] Propan-2-ol was chosen as formate might coordinate to manganese. The aqueous solution was driven at a constant rate through the UV/Visible microcell, where it was irradiated for a short time period. The irradiation frequency (1 Hz) was chosen so that between two pulses the solution was totally renewed. Absorbance was averaged over 100 pulses. This technique provides an improvement of the signal-to-noise ratio, relative to the single-pulse experiments generally used.[4,16,17,24]

The reaction of **1** with superoxide was studied over a wide range of time scales (from 10^{-6} to 1 s). Experiments were performed at pH 7.8 (5 mM phosphate buffer) in order to allow comparison with the previous indirect test.[19]

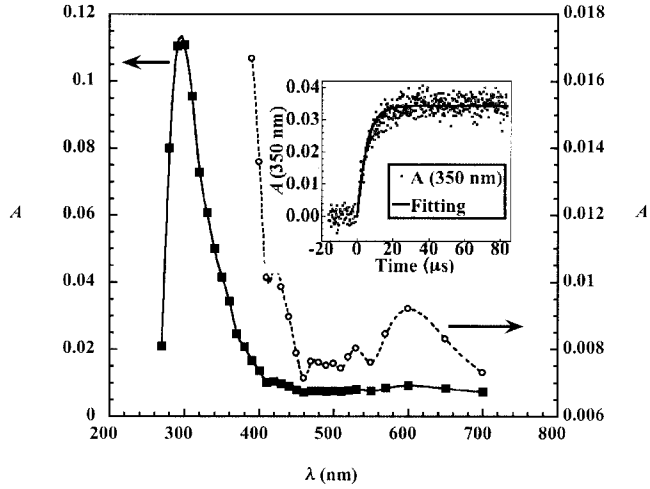

Figure 2. Difference absorption spectrum of the transient T formed during the reaction of **1** with superoxide 40 μs after the pulse. T decays with a half-life of ca. 0.04 s. Squares refer to the left axis and circles to the right axis. [**1**] = 10^{-3} mol L^{-1}; propan-2-ol 0.1 mol L^{-1}; phosphate buffer 5 mmol L^{-1}; irradiation pulse 1 μs; [$O_2^{\cdot-}$] = 7.3×10^{-5} mol L^{-1}; averaging over 100 pulses; flux 1 mL min^{-1}; irradiation frequency 1 Hz. Inset: kinetic trace at 350 nm, fitted by $A = A_0[1 - \exp(-k_{app}t)]$.

1. Self-Decay of Superoxide

First, it was checked that the self-decay of $O_2^{\cdot-}$ followed a second order rate law, as expected for the auto-dismutation of superoxide. The observed rate constant had a value of 1.3×10^5 mol^{-1} L s^{-1}, consistent with that reported in the literature[23] at pH 7.8 (1.0×10^5 mol^{-1} L s^{-1}).

2. Reaction of 1 with Superoxide under Conditions for which $[1]_0 > [O_2^{\cdot-}]_0$: Search for an Intermediate

Absorbance was monitored at different wavelengths during the reaction between **1** and $O_2^{\cdot-}$, under conditions where $[1]_0 > [O_2^{\cdot-}]_0$ [conditions (A): $[1]_0 = 10^{-5}$, 2.5×10^{-5}, 5×10^{-5}, 10^{-4} and 5×10^{-4} mol L^{-1} and $[O_2^{\cdot-}]_0 = 1.3\times10^{-6}$ mol L^{-1} and conditions (B): $[1]_0 = 5\ 10^{-4}$ mol L^{-1} and 10^{-3} mol L^{-1} and $[O_2^{\cdot-}]_0 = 7.3\times10^{-5}$ mol L^{-1}]. The difference absorption spectrum of a transient T, recorded 40 μs after the pulse, showed an intense peak at 300 nm and a smaller peak at 600 nm, as shown in Figure 2. Figure 2 inset shows the kinetic trace of transient formation at 350 nm. A rate constant, k_1, for the formation of the transient T was derived, $(2.2\pm0.3)\times10^8$ mol^{-1} L s^{-1}).

T can reasonably be ascribed to an adduct between $[Mn(IPG)]^+$ and $O_2^{\cdot-}$. No assignment of the oxidation state of manganese and oxygen (neither Mn^{II} and superoxide nor Mn^{III} and peroxide) is made here. We suggest to label it $\{MnOO\}_n$ (with $n = 6$ here), by analogy to Enemark and Feltham $\{FeNO\}_n$ nomenclature: n represents the number of d electrons from the metal center and the π* single electron from superoxide.[1,25] Such adducts have already been described for reactions involving Mn^{II} complexes and superoxide, by pulse radiolysis[16,23,24,26,27] and stopped-flow[28] studies. Complexes with an oxygenated coordination sphere (sulfate, formate, pyrophosphate,[26] phosphate,[24] aqua[27]) form adducts labeled $[MnO_2]^+$ characterised by an absorption maximum at 260–270 nm. The adduct observed with the complex $[Mn^{II}(TPAA)](PF_6)_2$ (TPAA = tris[2-[*N*-(2-pyridylmethyl)amino]ethyl]amine, a heptadentate nitrogen ligand) exhibits absorption maxima at 290 and 310 nm.[16] Although protonated species (MnOOH) have been previously considered,[24,26] we, and others,[24,27] excluded them on the basis of the published pK_a for (MnOOH/MnOO) (2.5 to 5.5).[24,26] Complex **1** shows an N_3O_1 coordination sphere. The absorption maximum for T at 300 nm is thus in the expected range. Furthermore, its formation rate constant is consistent with rate constants reported for similar adducts, ranging from 7.5×10^6 mol^{-1} s L^{-1} to 4.4×10^8 mol^{-1} L s^{-1}.[16,23,24,26–29] In addition, the existence of an intermediate $\{MnOO\}^6$ is consistent with reactivity studies previously performed in anhydrous DMSO. A di-μ-oxo dimer $[(IPG)Mn^{III}(O)_2Mn^{IV}(IPG)]^+$ has been obtained upon addition of 0.5 equiv. of superoxide on the manganese complex, and characterised by using UV/Visible spectroscopy and EPR. Its formation has been rationalised by the reaction of a postulated adduct $\{MnOO\}^6$ with the remaining monomeric manganese(II) complex.[19]

3. Multipulse Experiment on a Noncirculating Solution: Is the Behaviour of the Complex towards Superoxide Reproducible?

Experiments were recorded at different time scales ($t \le 8.4\times10^{-5}$ s, $t \le 8.4\times10^{-4}$ s, $t \le 8.4\times10^{-3}$ s, $t \le 8.4\times10^{-2}$ s), indicating that the transient T decays with a half-life of about 0.04 s.

To obtain more information on the mechanism of the reaction of **1** with $O_2^{\cdot-}$ and check the reproducibility of the

 © 2005 Wiley-VCH Verlag GmbH & Co. KGaA, Weinheim

behaviour of **1** towards $O_2^{\cdot-}$, a multi-pulse experiment[30] was performed. 11 repeated irradiations were applied to a noncirculating complex solution. This solution thus received successive doses of superoxide, approximately 0.75 equiv. each.

The trace recorded at 300 nm is provided in Figure 3. After the superoxide pulse, an absorption peak S (for spike) was observed with a decrease and a stabilisation of the absorbance on a plateau P. This behaviour was reproducibly recorded up to 11 times, and the absorbance reached a higher level on successive plateaus. It should also be noted that the size of the peak was decreasing upon repetitive pulses.

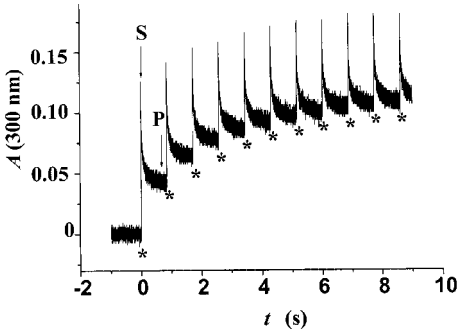

Figure 3. Variation of absorbance with time at 300 nm, during a multipulse experiment. [**1**] = 10^{-4} mol L^{-1}; propan-2-ol 0.1 mol L^{-1}; phosphate buffer 5 mmol L^{-1}; irradiation pulse 1 μs; [$O_2^{\cdot-}$] = 7.3×10^{-5} mol L^{-1}; irradiation frequency 1 Hz. Arrows indicate the first spike S and the plateau P. Stars indicate irradiations.

Difference absorption spectra, obtained at the spike S (2.6 ms ≤ t ≤ 22.6 ms) and at the plateau P (800 ms ≤ t ≤ 820 ms) after the first pulse are shown in Figure 4 and compared to that of the short time transient T. The S and P spectra are both characterised by an intense absorption maximum at 280 nm. It was checked that both S and P spectra are reproducibly obtained after each further pulse. The comparison of spectra labelled S, P and T seems to indicate that at the spike S, the solution is a mixture of the transient T and of the product characterised by the spectrum measured at the plateau P. The absorbance decay after the spike was completed within 0.5 s, and had a half-life (0.02 s) of the same order of magnitude as the half-life of the transient T.

A tentative attempt was made to analyse and simulate the behaviour of the successive plateaus.[31] This behaviour can be described by a catalytic cycle, involving an adduct {MnOO}^{6} as the transient T [ε_T(300 nm)[32] = 1500 L mol^{-1} cm^{-1}] and a species R responsible for the residual absorbance at the plateaus (Scheme 1). Electrochemical oxidation of the manganese(II) complex **1** leads to a yellow solution, whose UV/Visible spectrum is consistent with the main peaks observed at the plateaus.[33] The species R may thus be ascribed to the manganese(III) complex [Mn^{III}(IPG)]$^{2+}$ (a rough estimation from the electrochemical generation leads to an ε_P(300 nm) of about 1800 L mol^{-1} cm^{-1}). A simple ping-pong mechanism cannot reproduce the behaviour of the plateaus upon successive irradiations: as

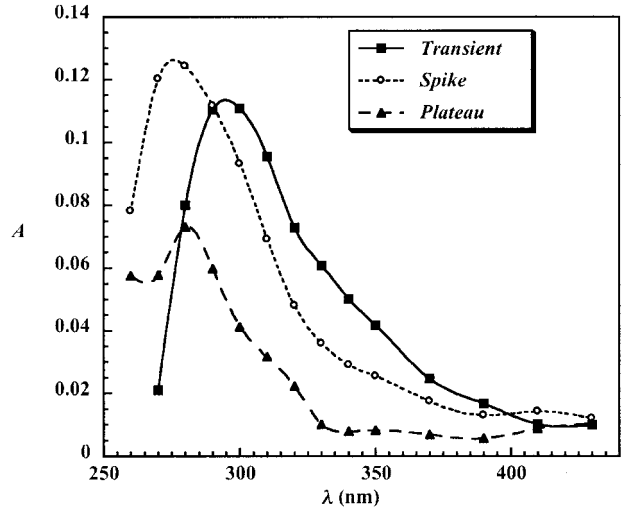

Figure 4. Difference absorption spectra of the solution during the reaction of **1** with superoxide. Absorbance was read at the top of the spike S (2.6 ms ≤ t ≤ 22.6 ms) and at the plateau P (800 ms ≤ t ≤ 820 ms) after the first pulse. The spectrum of transient T is added for the sake of comparison. [**1**] = 10^{-4} mol L^{-1}; propan-2-ol 0.1 mol L^{-1}; phosphate buffer 5 mmol L^{-1}; irradiation pulse 1 μs; [$O_2^{\cdot-}$] = 7.3×10^{-5} mol L^{-1}; irradiation frequency 1 Hz.

ε_P(300 nm) and ε_T(300 nm) are close, the decay in absorbance to reach the plateau P cannot be assigned solely to the formation of [Mn^{III}(IPG)]$^{2+}$. A pathway back to Mn^{II} has to be considered (see Scheme 1).

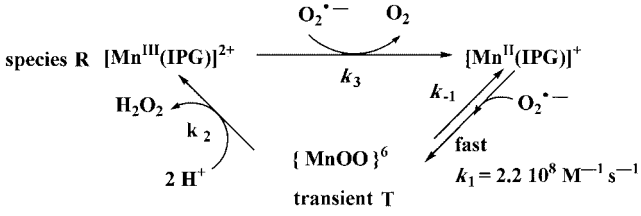

Scheme 1. Proposed reaction scheme for the reaction of **1** with superoxide. It consists of a catalytic cycle involving a manganese(II)–superoxide adduct as a transient and a manganese(III) complex as the species R responsible for the spectrum at the plateau.

From the schematic mechanism in Scheme 1, an iterative formula for X_n, representing the fraction of Mn^{II} at plateau n can be derived, see Equation (1).

$$X_{n+1} = X_n - \frac{k_1 X_n \times 0.75}{k_3(1-X_n)+k_1X_n} \times \frac{k_2}{k_{-1}+k_2} + \frac{k_3(1-X_n)\times 0.75}{k_3(1-X_n)+k_1X_n} \quad (1)$$

The second term stands for the fraction of transient T decaying back to [Mn^{II}(IPG)]$^+$ (k_{-1}), as T may decay either to [Mn^{II}(IPG)]$^+$ (k_{-1}) or to [Mn^{III}(IPG)]$^{2+}$ (R) (k_2). The third term stands for the transformation of [Mn^{III}(IPG)]$^{2+}$ (R) to [Mn^{II}(IPG)]$^+$, which is assumed here to be complete. At each pulse, 0.75 equiv. of superoxide is introduced into the system.

The best fit, up to the sixth iteration, (see Figure 5) was obtained for $k_1 = 3k_3$ and $k_{-1} = 2.2k_2$.[34]

 © 2005 Wiley-VCH Verlag GmbH & Co. KGaA, Weinheim

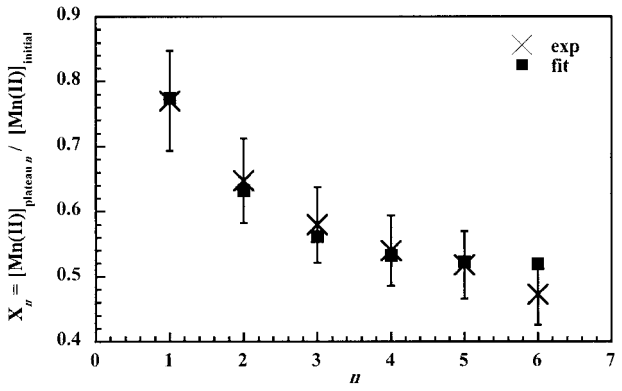

Figure 5. Cross marks: iterative values for the Mn^{II} fraction at plateau *n*, deduced from the absorbance measured at the plateau, assuming only **1** and $[Mn^{III}(IPG)]^{2+}$ are present at the plateau (error arbitrarily fixed at 10%). Square marks: simulation using successive iterations for X_n (see text).

4. Superoxide Decay at 270 nm under Conditions for which $[1]_0 < [O_2^{\cdot-}]_0$: Overall Catalytic Rate Constant

The catalytic nature of the reaction was confirmed by following the decay of the absorbance of superoxide at 270 nm in the presence of **1**, with $[1]_0 < [O_2^{\cdot-}]_0$ ($[1]_0 = 2\times10^{-7}$ mol·L^{-1} and 10^{-5} mol·L^{-1} and $[O_2^{\cdot-}]_0 = 7.3\times10^{-5}$ mol·L^{-1}). It should be noted that only a limited range of concentrations for **1** were informative, as the adduct {MnOO}^{6} itself absorbs at that wavelength.

The decay of superoxide is faster at high concentrations of complex **1** and follows apparent first-order kinetics. The deduced catalytic rate constant $k_{cat} = 3.8\pm0.2\times10^6$ mol^{-1}Ls^{-1} is of the same order of magnitude as that calculated from the indirect xanthine-xanthine oxidase-cytochrome c test ($2.9\pm0.3\times10^6$ mol^{-1}Ls^{-1}).[19]

Conclusions

This pulse radiolysis study allows us to propose a catalytic mechanism involving a transient adduct {MnOO}^{6}, and a manganese(III) complex for the reaction of complex **1** with superoxide. These two species were characterised by their differential absorption spectra. The formation rate of the adduct is among the fastest reported in the literature. The multipulse experiment showed unambiguous reproducible behaviour upon successive superoxide pulses (up to 11). Complex **1** efficiently catalyses the dismutation of superoxide with a rate constant equal to 1% of that of the manganese superoxide-dismutase. The present study provides convergent pieces of evidence for catalytic activity. To complete the mechanistic scheme suggested here for the reactivity of the manganese(II) compounds, further research is now underway on the reactivity of the Mn^{III} species. Moreover, further research to improve the catalytic activity of the manganese SOD mimics is now in progress.

Experimental Section

The pulse radiolysis experiments were carried out with a 10 MeV Titan β linear accelerator at the Laboratory of Radiolysis, CEA Saclay. Pulses from 5 ns to 1 μs are available, and the pulse frequency is adjustable. A 10 ns pulse corresponds to a 20 Gray dose. Solutions saturated with oxygen are driven in a quartz circulating microcell (spectral path length 1 cm, volume 400 μL) at a constant flux (1 mL/min). The spectroscopic and temporal analysis is mediated by an optical fibre, linked to a monochromator, then to a photomultiplicator and lastly to a Tektronix numerical oscilloscope allowing the observation of the temporal evolution of absorbance. Absorbance was averaged over 100 pulses as it provides an improvement of the signal-to-noise ratio, relative to the single-pulse experiments generally used. The amount of superoxide generated during pulse radiolysis was established by the absorbance value at 260 nm, assuming that $\varepsilon_{260} = 1940$ L mol^{-1} cm^{-1}.[23]

Measurements were carried out in a 5 mmol L^{-1} phosphate buffer, propan-2-ol 100 mmol L^{-1} at pH 7.8 and 25 °C at different concentrations of Mn^{II} complex. Solutions were oxygen saturated by bubbling O_2 for at least 60 min. A 1 μs-pulse, generating a 7.3×10^{-5} mol L^{-1} superoxide concentration, was imposed upon the solution. The irradiation frequency was 1 Hz, so that the cell content was totally renewed between two pulses. The disappearance of superoxide was followed at 270 nm (($\varepsilon_{270} = 1479$ L mol^{-1} cm^{-1} at pH 7.8 and 23 °C[21]). Spectra are differential, the reference absorbance being recorded before irradiation.

Rates were derived assuming either second-order kinetics corresponding to the self-dismutation of superoxide ($A = A_0/[1 + k_{obs}A_0t)]$) or pseudo-first-order kinetics in the presence of the complexes ($A = A_0[\exp(-k_{obs}t)] + B$, and $k_{obs} = k_{cat}$ [complex]). Simulations of kinetic traces are performed using Gepasi3 (self-dismutation) or Kaleidagraph (complex catalysed dismutation; see the Supporting Information for a Figure providing k_{obs} = f([**1**]); see also the footnote on the first page of this article).

[1] I. Fridovich, *Arch. Biochem. Biophys.* **1986**, *247*, 1–11.
[2] B. Halliwell, J. M. C. Gutteridge, in *Free radicals in biology and medicine*, 3 ed.; Oxford University Press: New York, **1999**, pp. 1–35.
[3] L. Benov, I. Fridovich, *J. Biol. Chem.* **1999**, *274*, 4202–4206.
[4] D. E. Cabelli, D. P. Riley, J. A. Rodriguez, J. S. Valentine, H. Zhu, in *Biomimetic oxidations catalysed by transition metal complexes* (Ed.: B. Meunier), Imperial College Press: London, **2000**, pp. 461–508.
[5] R. J. Watts, D. Washington, J. Howsawkeng, F. J. Loge, A. L. Teel, *Advances in Environmental Research* **2003**, *7*, 961–968.
[6] C. C. Winterbourn, A. J. Kettle, *BBRC* **2003**, *305*, 729–736.
[7] I. Fridovich, *Ann. Rev. Biochem.* **1995**, *64*, 97–112.
[8] D. Salvemini, C. Muscoli, D. P. Riley, S. Cuzzocrea, *Pulmonary Pharmacology Therapeutics* **2002**, *15*, 439–447.
[9] D. P. Riley, *Chem. Rev.* **1999**, *99*, 2573–2587.
[10] J. M. McCord, I. Fridovich, *J. Biol. Chem.* **1969**, *244*, 6049–6055.
[11] D. Salvemini, Z.-Q. Wang, J. L. Zweiser, A. Samouilov, H. Macarthur, T. P. Misko, M. G. Currie, S. Cuzzocrea, J. A. Sikorski, D. P. Riley, *Science* **1999**, *286*, 304–306.
[12] Synzyme stands for synthetic enzyme[9].
[13] I. Spasojevic, I. Batinic-Haberle, R. D. Stevens, P. Hambright, A. N. Thorpe, J. Grodkowski, P. Neta, I. Fridovich, *Inorg. Chem.* **2001**, *40*, 726–739.
[14] J.-L. Pierre, *Regard sur la Biochimie* **2000**, 17–20.
[15] R. H. Weiss, A. G. Flickinger, W. J. Rivers, M. M. Hardy, K. W. Aston, U. S. Ryan, D. P. Riley, *J. Biol. Chem.* **1993**, *268*, 23049–23054.
[16] A. Deroche, I. Morgenstern-Badarau, M. Cesario, J. Guilhem, B. Keita, L. Nadjo, C. Houée-Levin, *J. Am. Chem. Soc.* **1996**, *118*, 4567–4573.
[17] S. Goldstein, G. Czapski, D. Meyerstein, *J. Am. Chem. Soc.* **1990**, *112*, 6489–6492.

 © 2005 Wiley-VCH Verlag GmbH & Co. KGaA, Weinheim

[18] C. Policar, F. Lambert, M. Cesario, I. Morgenstern-Badarau, *Eur. J. Inorg. Chem.* **1999**, 2201–2207.
[19] C. Policar, S. Durot, M. Cesario, F. Lambert, F. Ramiandrasoa, I. Morgenstern-Badarau, *Eur. J. Inorg. Chem.* **2001**, 1807–1817.
[20] From the measured IC50 values, it is possible to calculate a rate constant value, which is independent of both detector concentration and nature. At the IC50 concentration, superoxide reacts at the same speed with cytochrome c and the putative SOD-mimic. Then, $k = k_{cytc} \times [cytc]/IC50$.[35] In the case of cytochrome c Fe^{III} as detector, k_{cytc}(pH 7.8; 21 °C) = $2.6\ 10^5\ mol^{-1}\ L\ s^{-1}$.[36].
[21] B. H. J. Bielski, *Photochem. Photobiol.* **1978**, *28*, 645–649.
[22] B. H. J. Bielski, R. L. Arudi, *Anal. Biochem.* **1983**, *133*, 170–178.
[23] B. H. J. Bielski, D. E. Cabelli, R. L. Arudi, A. B. Ross, *J. Phys. Chem. Ref. Data* **1985**, *14*, 1041–1100.
[24] D. E. Cabelli, B. H. J. Bielski, *J. Phys. Chem.* **1984**, *88*, 6291–6294.
[25] D. P. Linder, K. R. Rodgers, J. Banister, G. R. A. Wyllie, M. K. Ellison, W. R. Scheidt, *J. Am. Chem. Soc.* **2004**, *126*, 14136–14148.
[26] D. E. Cabelli, B. H. J. Bielski, *J. Phys. Chem.* **1984**, *88*, 3111–3115.
[27] F. Jacobsen, J. Holcman, K. Sehested, *J. Phys. Chem. A* **1997**, *101*, 1324–1328.
[28] J. Stein, J. P. Fackler, G. J. McClune, J. A. Fee, L. T. Chan, *Inorg. Chem.* **1979**, *18*, 3511–3519.
[29] C. Bull, E. C. Niederhoffer, T. Yoshida, J. A. Fee, *J. Am. Chem. Soc.* **1991**, *113*, 4069–4076.
[30] M. E. McAdam, R. A. Fox, F. Lavelle, E. M. Fielden, *Biochem. J.* **1977**, *165*, 81–87.
[31] We thank one of the referees for suggesting such an analysis.
[32] Estimate assuming that 100% of **1** has been converted into the transient over the first 40 ms.
[33] The electrochemical generation of the Mn^{III} species was done in a two-compartment cell, with a three-electrode set up (working electrode: vitreous carbon (15 cm^2), reference electrode: SCE, KCl sat., counter electrode: Pt grid) collidine/collidinium buffer (50 mM, pH 7.5) (collidine: 2,4,6-pyridine) in MeOH, $[Mn(IPG)^+]$ = 2 mM, potential of the electrolysis: 1V/SCE). The Mn^{III} was unstable and the Mn^{II} species was recovered within a few hours.
[34] The quality of the fit was greatly decreased after the sixth iteration (not shown). This could be due to several experimental factors: cumulative doses, bleaching by UV analysis light, accumulation of hydrogen peroxide and the oversimplified description in the scheme of the reactivity of the Mn^{III} species (R).
[35] R. F. Pasternack, B. Halliwell, *J. Am. Chem. Soc.* **1979**, *101*, 1026–1031.
[36] J. Butler, W. H. Koppenol, E. Margoliash, *J. Biol. Chem.* **1982**, *257*, 10747–10750.

Received: October 06, 2004
Published Online: May 24, 2005

 © 2005 Wiley-VCH Verlag GmbH & Co. KGaA, Weinheim

The Relationship between the Structure and Magnetic Properties of Bioinspired Iron(II/III) Complexes with Schiff-Base-Like Chelate Ligands, Part I: Complexes with Dianionic [N_4] Macrocycles

Birgit Weber[a][‡] Indira Käpplinger,[a] Helmar Görls,[a] and Ernst-G. Jäger*[a]

Keywords: Bioinorganic chemistry / Iron / Macrocycles / Magnetic properties / Schiff bases

The molecular structures and the spin ground-state of the iron(II/III) complexes **Fe1**, **Fe2** and **Fe3**, which contain dianionic macrocyclic [N_4] ligands derived from substituted acetylacetaldehydes and 1,2-diamines, have been investigated by X-ray analysis and temperature-dependent susceptibility measurements, respectively. The iron(II) complexes **Fe^{II}1** (which is dimeric by intermolecular coordination of one peripheral carbonyl group), **Fe^{II}1MeOH**, **$(Fe^{II}L)_2$dabco** (L = **1**, **2**, **3**; dabco = 1,4-diazabicyclo[2.2.2]octane) and the iron(III) complex **Fe^{III}1Cl** are pentacoordinate and have an intermediate-spin ground-state at room temperature (S = 1 for Fe^{II}; S = 3/2 for Fe^{III}). The intermediate-spin state was confirmed by DFT-MO calculations for **Fe^{II}1MeOH** and **Fe^{III}1Cl** and is also in agreement with the Mössbauer data of **Fe^{II}1** and ESR measurements of **Fe^{III}1Cl**. The iron centre in **Fe^{II}2** is nearly square-planar and shows a strong decrease of the magnetic moment below $T \approx 250$ K. This is probably due to an S = 0 to S = 1 spin-crossover or, more likely, to intermolecular antiferromagnetic interactions (shortest Fe–Fe distance of 3.4 Å). A new pair of octahedral iron(II/III) complexes with an N-heterocyclic axial ligand, **$Fe^{II}3(Py)_2$**/[**$Fe^{III}3(Py)_2$**]PF_6, could be crystallised. In contrast to the previously described pairs **$Fe^{II}1(Him)_2$**/[**$Fe^{III}1(Him)_2$**]PF_6 and **$Fe^{II}2Py_2$**/[**$Fe^{III}2Py_2$**]ClO_4, the orientation of the planes of the axial ligands is nearly independent of the oxidation step of the central atom. Octahedral derivatives with biologically relevant anions as axial ligands have been crystallised for the first time, namely [$BzEt_3N$][**$Fe^{III}1(NCS)_2$**], [Et_4N][**$Fe^{III}2(CN)_2$**]$(H_2O)_{0.5}$, Na[**$Fe^{III}2(NO_2)_2$**]$(MeOH)_2(H_2O)_{0.5}$ and [**$Fe^{III}2(NO_2)OH_2$**](MeOH). The latter shows a magnetic moment of $\mu_{eff} \approx 2.85\ \mu_B$ at room temperature, which decreases to 1.85 μ_B at lower temperature. This indicates an incomplete S = 1/2 to S = 3/2 spin-crossover, which is probably due to the presence of H_2O as a weak axial ligand.
(© Wiley-VCH Verlag GmbH & Co. KGaA, 69451 Weinheim, Germany, 2005)

Introduction

Iron is known to be a ubiquitous biometal with a great variety of metabolic functions.[1] Many iron-containing proteins are derived from haem with the porphyrinato macrocycle as a typical dianionic equatorial [N_4] ligand. The unique biological role of (porphyrin)iron compounds may be one reason for the unbroken interest in this important class of molecules over nearly a century. This is reflected in the countless number of papers and many extensive reviews, monographs and handbooks.[2] Compared with the porphyrins, including such variations as expanded porphyrins, confused porphyrins etc., there are only a few other examples of similar [N_4] macrocycles that can act as dianionic equatorial ligands. Besides the synthetic porphyrins and their tetrabenzotetraaza derivatives, the phthalocyanines and complexes with tetradentate [N_2O_2]-coordinated dianions of *N*,*N*-bridged salicylaldimines (e.g. "salen") have been investigated extensively, and in part quite successfully, as models for the active sites of haem proteins. For instance, the reversible uptake of dioxygen − the main function of haemoglobin − was realized with simple "(salen)Co" much earlier[3] than with (porphyrin)iron compounds detached from the protein; the first catalysts of technical relevance for cytochrome-P450-like oxygenation reactions were derived from (salen)Mn.[4]

During the last decades we have created a pool of chelate complexes[5] with ligand systems that can be subdivided into the three basic structures given in Scheme 1. All these compounds are structural or functional models of active sites of metalloenzymes: Type **I**, which is formally most related to porphyrins, contains tetradentate twofold negatively charged macrocyclic ligands with an [N_4] donor set and a more or less extended π-system. [The special ligand Me_4TAA, first published in 1969 as its nickel complex (Me_4TAA)Ni[6] and today known in complexes with nearly all transition elements and many main group metals,[7] has been characterised by F. A. Cotton: "The latter bears many similarities to porphyrinato systems, but its chemical behav-

[a] Institute of Inorganic and Analytical Chemistry, University of Jena,
August-Bebel-Strasse 2, 07743 Jena, Germany
Fax: +49-3641-442716
E-mail:cej@uni-jena.de.
[‡] Present address: Ludwig-Maximilians-Universität München, Department Chemie,
Butenandtstraße 5–13 (Haus D), 81377 München, Germany

 DOI: 10.1002/ejic.200400759

iour seems to be even more diverse."[7b]] Type **II** is derived from dianionic open-chain ligands with an [N_2O_2] coordination sphere ("salen" is a special case with a fused benzene ring for $R^1 + R^2$). Type **III** is derived from tridentate dianions; the coordinatively highly unsaturated formula unit promotes the formation of oligonuclear structures[8] similar to those found in biological systems. Previous investigations on cobalt, copper and nickel complexes of types **I**, **II** and **III** have already shown that the variation of the *N*,*N*′-bridges X, Y and the substituents R^{1-3} can be used to control properties such as the electronic state of the central atom,[9] the redox potentials,[10,11a,11d,11e] the affinity of vacant axial coordination sites towards additional ligands,[11] as well as the binding and activation of dioxygen,[5b,12] carbon dioxide[13] or nitric oxide.[14] These results indicated that the macrocycles **I** and, in some respect, also the complexes **II** share many common characteristics with porphyrins, but marginal ligand variations can dramatically change the behaviour. This situation is particularly typical of the chemistry of the iron complexes.

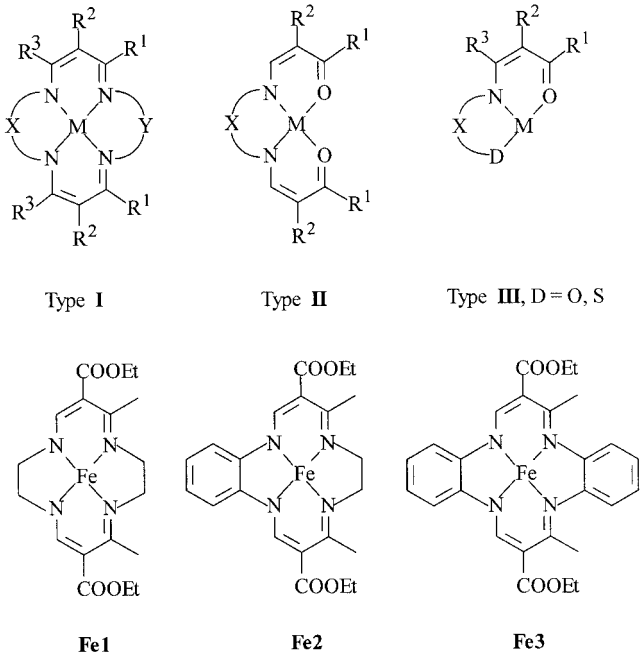

Scheme 1. Formulae of basic chelate complexes studied in our laboratory (**I**–**III**) and formulae of macrocyclic iron complexes used in this work (**Fe1**–**Fe3**). The arabic numbers represent the dianion of the macrocyclic ligand $\mathbf{H_2L}$ ($\mathbf{L^{2-}}$ = **1**, **2**, **3**). **Fe1a** denotes the more hydrophilic variant of **Fe1** with acetyl (COMe) instead of the ester groups COOEt. The abbreviation $\mathbf{Me_4TAA}$ ("tetramethyldibenzo*tetraaza*[14]*annulene*") is used for $\mathbf{L^{2-}}$ in type **I** with X = Y = *o*-phenylene, $R^1 = R^3$ = Me, and R^2 = H. The basic macrocycles **FeL** and the axial ligands [MeOH, dabco (μ-1,4-diazabicyclo[2.2.2]-octane), Py (pyridine), N-MeIm (*N*-methylimidazole), I^- etc.] are given in bold (with the exception of the tables); all other components of the formula units or within the lattice are given in plain characters.

Busch et al.,[15a,15b] Holm et al.[15c,15d] and Goedken et al.[16] have described iron(II/III) complexes of type **I** with R^2 = H or Ph. The parent compound of **Fe1** (R^2 = H) has been characterised as a square-planar intermediate-spin (S = 1) complex[15a] that gives an octahedral diadduct, probably with a high-spin (S = 2) ground state, in pyridine solution. No addition of imidazole − a very characteristic reaction of (porphyrin)iron compounds − could be observed. Even in our earlier reports[17] we accentuated the high tendency of the carbonyl-substituted derivative **Fe1** to give octahedral low-spin diadducts, especially with imidazole. Many such derivatives have been isolated as solids and could be characterised by X-ray structure analysis and susceptibility measurements.[18] The existence of others (also with biologically relevant anions such as nitrite and sulfite[19b]) could be proved in solution by spectrophotometric titration.[19] In this respect, the carbonyl-substituted derivative **Fe1** is more closely related to porphyrins than the parent compound. On the other hand, several pentacoordinate iron(III) halides of type **I** have been described as intermediate-spin (S = 3/2) complexes,[15,20] whereas the derivative $\mathbf{Fe(Me_4TAA)Cl}$ has a high-spin (S = 5/2) ground state, just as most halides of (porphyrin)iron(III) compounds. The formation of various pentacoordinate halides and pseudo-halides **Fe1X** (X = F, Cl, Br, I, N_3^-, SCN^-) has been monitored by spectrophotometric equilibrium studies in two-phase systems,[21] but their spin state is uncertain in some cases. In contrast, all the pentacoordinate nitrosyl derivatives **FeLNO** (**L** = **1**, **2**, **3**) have an S = 1/2 ground state, just as the analogous (porphyrin)iron compounds.[22]

The existence of coordinatively unsaturated species that are able to reversibly bind additional axial ligands, as well as the possibilities of changing the oxidation number and the spin state of the central atom, are key features of many haem proteins. For instance, the iron(II) atom in deoxygenated haemoglobin has an effective coordination number of five as the bonding to the nitrogen atom of the imidazole ring of the "proximal" histidine group causes a strong displacement from the [N_4] plane of the equatorial porphyrin; the ground state is high spin (S = 2). After oxygenation, the central atom is best described as six-coordinate low-spin (S = 1/2) iron(III) in a weakly distorted octahedral environment, antiferromagnetically coupled with the unpaired electron of an axially coordinated superoxide radical ion. For comparison with our macrocycles we are therefore mainly interested in structural and magnetic information as a function of the coordination number and the oxidation state of iron in these complexes.

This paper is focused on (i) the spin state of complexes with coordination number less than 6, (ii) the dependence of the orientation of axial N-heterocycles in octahedral diadducts on the oxidation state of the central atom, and (iii) attempts to isolate adducts with biologically relevant anions as solids for structural and magnetic studies.

Results and Discussion

Syntheses and General Characterisation

In contrast to the analogous nickel and copper compounds, the iron complexes of type **I** cannot be synthesised

 © 2005 Wiley-VCH Verlag GmbH & Co. KGaA, Weinheim

by a direct metal-templated condensation of the precursor complexes of type **II** with diamines. The best synthetic method is the reaction of an iron(II) salt, chiefly the acetate, with the free ligands $\mathbf{H_2 1}$, $\mathbf{H_2 2}$ and $\mathbf{H_2 3}$, respectively, which can be obtained by demetallation of the copper(II) complexes. The synthesis of the basic iron(II) complexes **Fe1**,[17b,17c,21] **Fe2**[10d] and **Fe3**[23] has been described previously. However, since all these publications are in German in mainly non-international, and in part no longer available, journals, and also because some steps of the ligand syntheses have been modified to prevent the use of gaseous hydrogen sulfide, we will give a summary of the syntheses in the Experimental Section.

Adducts of the iron(II) complexes with axial ligands were obtained by adding an excess of the corresponding ligand to the reaction mixture during the synthesis of the iron(II) complex. The products precipitated upon slow cooling of the reaction mixture. In some cases mono- and/or diadducts were formed depending on the concentrations and the temperature regime.[17b,17c] Diffusion procedures are better suited for diadduct formation starting from the isolated parent complexes. The air sensitivity of the iron(II) complexes is strongly dependent on the type of additional axial ligands and decreases in general from **Fe1** to **Fe3**. This sequence is in agreement with the redox potentials of the complexes.[5c,10d]

The iron(III) complexes are best prepared starting from the iron(II) derivatives by in-situ oxidation with iodine in the presence of an excess of sodium iodide to promote the precipitation of the iodide **FeLI**.[20,21] The latter is a good precursor for a large range of iron(III) derivatives with different axial ligands.[5c,18] Carbon tetrachloride is a suitable Cl donor to yield the chloride derivatives **FeLCl**. All the iron(III) complexes are relatively air-stable but water-sensitive, especially in the presence of primary or secondary amines (piperidine!) or phosphonic acid esters as axial ligands. Here, hydrolysis and/or radical redox processes occur. All complexes are therefore best handled under dry argon.

Intermediate-Spin Complexes with Coordination Numbers 4, 4+1 and 5

Crystals suitable for X-ray structure analysis were obtained for the solvent-free iron(II) complexes **Fe1** and **Fe2**. Only one stable solvate with an O-donor, **Fe1MeOH**, could be crystallised. The previously described crystalline 1:1 solvates of **Fe1** with the N-donors ammonia or pyridine[17b] decompose even at room temperature under dry argon. Attempts were made with the alternative N-donor 1,4-diazabicyclo[2.2.2]octane (dabco) and, in all cases, good crystals

Table 1. Spin state (*S*), room-temperature magnetic moment (μ_{eff}) and bond lengths [Å] and angles [°] within the first coordination sphere of macrocyclic iron(II/III) complexes with coordination numbers (*CN*) 4, 4+1 and 5.

Complex	*CN*	*S* μ_{eff} [μ_B]	Fe–$N_{1,2}$[a]	Fe–$N_{3,4}$[a]	Average L_{eq}	Fe–L_{ax}	Fe–pl_{eq}[b]	Average N–Fe–N[c]	Average N–Fe–N[d]	Shortest Fe–Fe
Fe^{II}1	4+1	1	1.877(2)	1.907(2)	1.893	2.702	0.077	93.1(1)	87.0(1)	6.502
		3.7	1.879(3)	1.908(2)						
Fe^{II}1MeOH	5	1	1.879(2)	1.915(2)	1.902	2.329(2)	0.110	92.8(1)	86.8(1)	7.098
		3.3	1.906(2)	1.906(2)						
Fe^{II}2[e] Fe(1)	4	1	1.87	1.90	1.89	–	0.03	94	86	
		ca. 3.0	1.86	1.93						3.345
Fe(2)			1.93	1.95	1.91	–	0.04	93	87	4.503
			1.86	1.92						
$(Fe^{II}1)_2$dabco	5	1	1.886(2)	1.913(2)	1.900	2.338(2)	0.197	92.8(1)	86.1(1)	5.244[f]
		3.3	1.888(2)	1.914(2)						7.285[g]
$(Fe^{II}2)_2$dabco	5	1	1.895(2)	1.917(2)	1.906	2.326(2)	0.158	93.4(1)	85.8(1)	5.279[f]
		3.0	1.899(2)	1.912(2)						7.249[g]
$(Fe^{II}3)_2$dabco	5	1	1.894(5)	1.933(5)	1.913	2.327(5)	0.181	94.3	84.7(2)	4.211[f]
		3.1	1.896(5)	1.927(5)						7.274[g]
Fe^{III}1Cl	5	3/2	1.909(5)	1.920(5)	1.922	2.262(4)	0.405	90.2(2)	85.2(2)	6.217
		3.8	1.912(5)	1.948(5)						
Fe^{III}1I	5	3/2	1.892(3)	1.925(3)	1.906	2.637(1)	0.34	90.8(2)	85.4(2)	7.172
		4.2	1.884(3)	1.924(3)						
Fe^{III}1NO	5	1/2	1,928(2)	1.920(2)	1.924	1.732(2)	0.376			
		1.8	1.895(2)	1.954(2)						
$Fe^{II}Me_4$TAA	4	1	1.916	1.922	1.918	–	–0.114	95.5	84.1	5.909
			1.917	1.916						
$Fe^{II}(Me_4TAA)CO$	5		1.918	1.926	1.927	1.693	0.292	94.8	82.6	5.917
			1.933	1.931						
$Fe^{III}(Me_4TAA)Cl$	5	5/2	2.003	2.006	2.002	2.250	0.596	89.8	80.0	7.485
		6.0	1.995	2.005						

[a] Designation according to Figure 1. [b] Displacement of the iron atom from the main plane of the equatorial N-donor atoms. [c] Five-membered rings. [d] Six-membered rings. [e] The quality of the data is not sufficient and we are only publishing the conformation of the molecule, although distances and angles are similar to those of the other complexes. [f] Shortest distance between dinuclear units in the lattice. [g] Distance between dabco-bridged Fe atoms.

 © 2005 Wiley-VCH Verlag GmbH & Co. KGaA, Weinheim

of the bridged complexes **(FeL)$_2$dabco** (**L** = **1**, **2**, **3**) were obtained. With imidazole and its derivatives the octahedral diadducts **FeL(HIm)$_2$** are strongly favoured. Sub-stoichiometric amounts of imidazole result in the formation of polymeric species.[17b,17c] In contrast, several iron(II) complexes of the general type **II** give mononuclear mono- and diadducts with imidazole.[5a] Additionally to the known pentacoordinate iron(III) complex **Fe^{III}1I** with axial iodide,[20] all the chlorides **Fe^{III}LCl** were isolated as solids, but only **Fe^{III}1Cl** gave crystals of sufficient quality. Selected parameters of the molecular structures and the magnetic moments at room temperature are listed in Table 1. The data of **Fe1I**,[20] **Fe1NO**,[22] **Fe(Me$_4$TAA)**,[16a] **Fe(Me$_4$TAA)CO**[16c] and **Fe(Me$_4$TAA)Cl**[16b] are included for comparison. The atom numbering in the table corresponds to that given in Figure 1. Figure 2 shows the molecular structures of selected examples, if possible approximately in the same projection of the basic chelate ring.

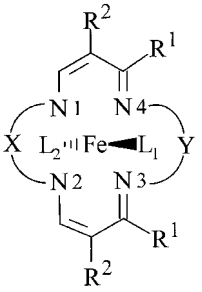

Figure 1. Unified atom numbering scheme used in Tables 1 and 3 for the equatorial donor atoms.

At first sight, the new data show few characteristic differences. The room-temperature magnetic moments are in satisfactory agreement with former measurements using a Gouy balance[17b] for **Fe1** (3.38 μ_B), **Fe1MeOH** (3.37 μ_B), **Fe1NH$_3$** (3.12 μ_B), **Fe1Py** (3.08 μ_B), and **Fe1I** (4.07 μ_B).[17c] These values are all higher to a greater or lesser degree than the spin-only value of 2.83 μ_B for two (S = 1) and 3.87 μ_B for three (S = 3/2) unpaired electrons, but all of them are within the region expected for intermediate-spin iron(II) and iron(III) complexes.[15a] (The reason for the increased values is probably a contribution of an orbital magnetic moment, due to an unsymmetrical population of the d_{xz} and d_{yz} orbitals, see also Figure 7.)

The iron atom has an approximately square-planar coordination sphere in **Fe2**. The central atom in all the other complexes is pentacoordinate with an approximately square-pyramidal geometry − in **Fe1** by intermolecular coordination of one of the peripheral carbonyl groups (*CN* = 4+1).The bond lengths and angles within the first coordina-

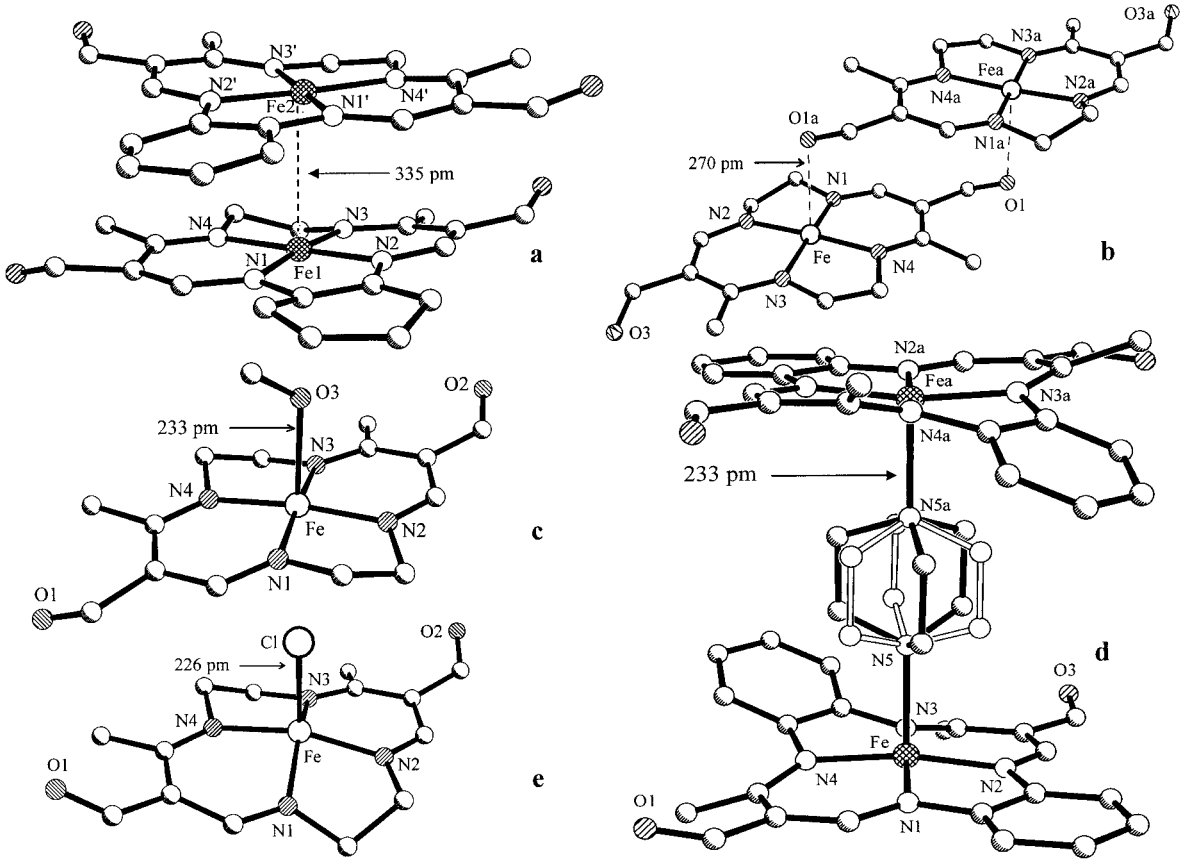

Figure 2. Molecule structures and coordination numbers *CN* of macrocyclic iron complexes: (a) **Fe^{II}2** (*CN* = 4), (b) **Fe^{II}1** (*CN* = 4+1), (c) **Fe^{II}1MeOH** (*CN* = 5), (d) **(Fe^{II}3)$_2$dabco** (*CN* = 5; the open lines represent the bonds of the 1:1 disorder), (e) **Fe^{III}1Cl** (*CN* = 5). Ethoxy groups are omitted for clarity.

 © 2005 Wiley-VCH Verlag GmbH & Co. KGaA, Weinheim

tion sphere, including those of the octahedral complexes described in the next sections (cf. Table 3), reflect the rules formerly elaborated for a large number of our macrocyclic iron complexes:[5a] the Fe–N distances within the equatorial plane are, for low-spin and intermediate-spin complexes, nearly independent of the type of equatorial ligand $\mathbf{L^{2-}}$, the coordination number and the oxidation state of the central atom [average of 16 significant mean values from Tables 1 and 3 of 191(1) pm]. Larger differences exist between the Fe–N distances on the non-methylated side (N1, N2) and the methylated side (N3, N4) of the six-membered chelate rings [average of 32 significant values in each case: 189(1) and 192(1) pm, respectively]. The distances to the axial ligands are always longer than those within the equatorial plane. This is in contrast to the conditions in the case of many derivatives of (porphyrin)iron compounds and is obviously due to the higher effective field strength, which is accompanied by shorter equatorial Fe–N distances, of the ligands $\mathbf{L^{2-}}$ (**L** = **1**, **2**, **3**). The displacement of the central atom from the best equatorial [N_4] plane in pentacoordinate complexes is more obvious in the presence of relatively strong axial ligands with short distances to the iron atom (Cl^- > dabco > MeOH > COOEt) but there is no clear correlation. Interestingly, a small but significant displacement is also observed for the iron atom in $\mathbf{Fe^{II}2}$, which is directed towards the neighbouring iron atom in the asymmetric unit (Fe–Fe distance of 335 pm).

Two selected prototypes of complexes with a quite different behaviour are included in Table 1. The first one, the nitrosyl derivative **Fe1NO**, which we interpreted as $\mathbf{(Fe^{III})^{+}NO^{-}}$,[22a] has a temperature-independent $S = 1/2$ spin ground state. The axial Fe–N distance of 173 pm is shorter than the equatorial Fe–N bonds, which are approximately in the same range as for the other complexes. These deviations can be explained by assuming a very strong ligand field of the axial NO^- ligand. The other one, the pentacoordinate chloride complex **Fe(Me$_4$TAA)Cl**, which has a magnetic moment of 5.95 μ_B,[16b] is undoubtedly a high-spin iron(III) complex and resembles the behaviour of the pentacoordinate halides of (porphyrin)iron compounds. This is also reflected in an average Fe–N distance of over 200 pm that is typical for high-spin iron(II/III) complexes such as those of the general type **II**.[5a,22] Taking into account that the similar complex $\mathbf{Fe3^{III}Cl}$ is clearly an intermediate-spin complex (μ_{eff} = 4.20 μ_B at room temperature; structure data unfortunately not available), the difference indicates a lower field strength of the ligand **Me$_4$TAA**. The reason for this could be the stronger "saddle-shaped" distortion of the macrocycle, caused by the two additional methyl groups in R^3, and/or the absence of the peripheral carbonyl group in R^2, which increases the π-acceptor strength of the ligand and the effective charge of the central atom in the other complexes. In agreement with this idea, **Fe(Me$_4$TAA)** forms derivatives with carbon monoxide and other strong π-acceptors as axial ligand much more easily than **Fe3**.[16c,16d]

On closer inspection, the structural nuances of the complexes are reflected in the temperature dependence of the magnetic behaviour. Selected examples are depicted in Figure 3.

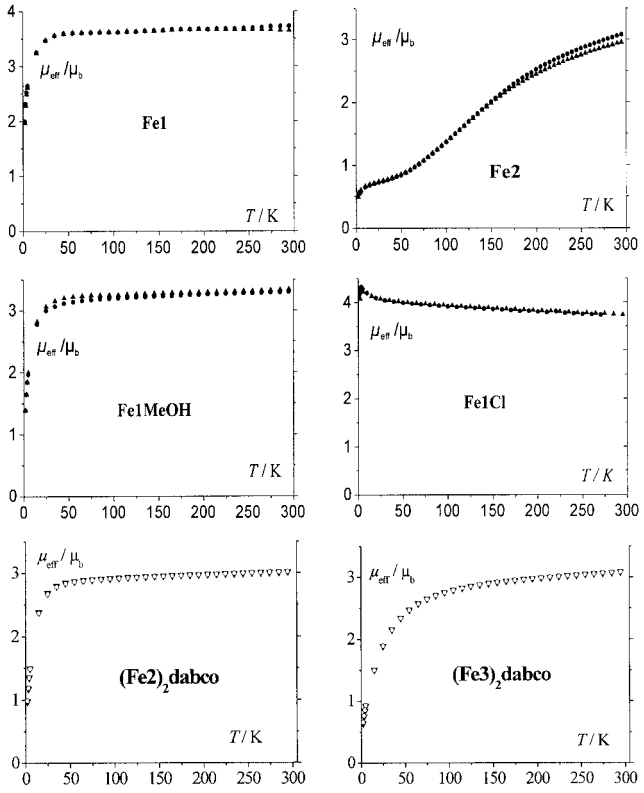

Figure 3. Temperature dependence of the effective magnetic moment of selected macrocyclic iron complexes: **Fe2** (*CN* = 4), **Fe1** (*CN* = 4+1), **Fe1MeOH**, **Fe1Cl**, **(Fe2)$_2$dabco**, **(Fe3)$_2$dabco** (all *CN* = 5). All measurements were carried out at 0.2 and 0.5 T.

With the exception of **Fe1Cl**, the magnetic moment decreases at lower temperature. **Fe2** shows a characteristic sigmoid curve progression which is apparent even at room temperature (Figure 3). This peculiarity can be explained as an incomplete and smooth transition into the low-spin $S = 0$ state, accompanied by antiferromagnetic interactions between two iron atoms (as mentioned above, the lattice of **Fe2** consists of pairs of two molecules with an iron–iron distance of 335 pm, which is short enough for direct interactions). The relatively steep decrease of the magnetic moment of several complexes at $T < 20$ K (left side of Figure 3) is not quite clear because the shortest Fe–Fe distance in the lattice is quite long (for **Fe1** and **Fe1MeOH** > 650 pm). In the case of the dinuclear iron(II) complex **(Fe3)$_2$dabco** the decrease of the magnetic moment starts already at $T < 150$ K. The Fe–Fe distances within the dinuclear unit are nearly identical for all **(FeL)$_2$dabco** derivatives (729, 725, and 727 pm for **L** = **1**, **2**, and **3**, respectively), but the Fe–Fe distances between the dinuclear units in the lattice are significantly shorter, especially for **(Fe3)$_2$dabco** (524, 528, and 421 pm for **L** = **1**, **2**, and **3**, respectively). This could explain the different behaviour of the latter.

The strong influence of the equatorial ligand is reflected in the zero-field Mössbauer spectra of solid samples of the

 © 2005 Wiley-VCH Verlag GmbH & Co. KGaA, Weinheim

solvent-free complex **Fe1**. The spectrum at 4.2 K is given in Figure 4. The observed quadrupole splitting of ΔE_Q = 3.37 mm s^{-1} (isomer shift δ = 0.32 mm s^{-1}) is very large for an iron(II) complex, even if a square-planar coordination sphere is considered. The data for similar complexes are given in Table 2. ΔE_Q appears to increase with increasing σ-donating ability (basicity) of the equatorial ligand. This is in agreement with earlier observations revealing a stronger σ-donor ability of the ligands **1**–**3** in comparison to similar porphyrin ligands.

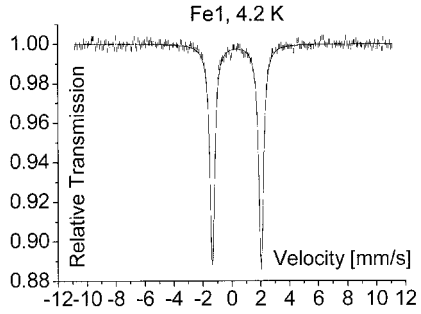

Figure 4. Mössbauer spectrum of **Fe^{II}1** at 4.2 K. Solid line: simulation of the spectrum with Lorentzian doublets.

Table 2. Mössbauer data of square-planar intermediate-spin (S = 1) iron(II) complexes.

Compound	Conditions	δ(Fe) [mm s^{-1}]	ΔE_Q [mm s^{-1}]	μ_{eff} [μ_B][a]	Ref.
Fe^{II}1	solid, 4.2 K	0.32	3.37	3.7	this work
Fe^{II}(TPP)	solid, 77 K	0.50	+1.51	4.4	[24a]
Fe^{II}(OEP)	solid, 83 K	0.59	+1.60	4.7	[24a]

[a] At room temperature.

The ESR spectrum of a frozen solution of **Fe1Cl** in toluene at 10 K is given in Figure 5. The g values (g_y^{eff} = 4.594, g_x^{eff} = 3.486 and g_z^{eff} = 2.039) can be assigned to the population of the ground-state (S = 1/2) Kramers doublet of the S = 3/2 system. The signal at 6.203 is due to small (μ-oxo?) impurities. The signal intensity of the impurity increases with decreasing temperature. The spectrum is similar to those reported for **Fe1I**,[20] although with slightly shifted g values, which can be assigned to a different rhombicity parameter E/D (D = axial, E = rhombic zero-field splitting parameter) of around 0.1 for the chloride complex (0.22 for the iodide adduct). In contrast to **Fe1I**, the chloride complex **Fe1Cl** is not ESR-silent in the solid state. A broad signal is observed at around g = 4.7, which can be explained by differences in the molecular packing in the crystal.

The intermediate-spin state of the iron(III) complexes is also reflected in the characteristic shifts of the resonances in the ^{1}H NMR spectra. As an example, the spectrum of

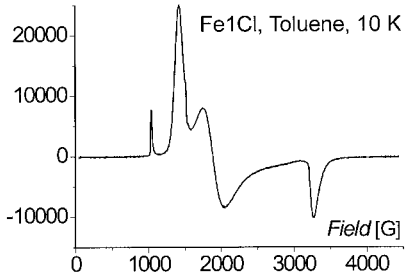

Figure 5. ESR spectrum of **Fe^{III}1Cl** in frozen toluene solution at 10 K.

Fe1Cl in toluene at 45 °C is given in Figure 6. With the help of predictions about the signal shifts based on literature proposals[25] and the signal intensities a clear assignment is possible. The observed paramagnetic shift can be interpreted by taking only the contact shift into account. The temperature dependence of the shifts obeys the Curie law.

Molecular orbital calculations based on the molecular structure were performed for **Fe1MeOH** and **Fe1Cl** to confirm the intermediate-spin ground state. Similar calculations were also performed for **Fe1I** and, for better comparison, the coordinate system was chosen the same way. The z axis of the molecular coordinate system was chosen in the direction of the axial ligand bond with the iron atom located at the origin of the coordinate system. The x and y axes are directed between the equatorial nitrogen atoms so that the σ-bonds with the equatorial ligand are formed by the $3d_{xy}$ orbital of the iron atom. The results of the spin-polarized calculations for **Fe1MeOH** are given in Figure 7.

The MO diagram of **Fe1Cl** is similar to that of **Fe1I** discussed in detail previously,[22] and is therefore not displayed here. Small differences are found in the bonding conditions between the iron atom and the axial ligand. In the case of the iodide adduct, covalent interactions between the $3d_{z^2}$ (σ-bonding) and $3d_{xz,yz}$ (weakly π-antibonding) orbitals of the iron atom and the $5p_z$ orbital of the axial ligand are present, while the $5p_{x,y}$ orbitals of the iodide ion are nearly non-bonding. In case of the chloride adduct π-interactions between the $3p_{x,y}$ orbitals of the chloride ion and the $3d_{xz,yz}$ orbitals of the iron atom are present and are more pronounced than in the case of the iodide adduct. This explains the hypsochromic shift of the typical LTMCT (equatorial *l*igand-*t*o-*m*etal *c*harge *t*ransfer) band in the UV/Vis spectrum of the chloride complex relative to the iodide one.[21]

The intermediate-spin state of **Fe1MeOH** is clearly mirrored in the molecular orbital diagrams. The unoccupied d_{xy} orbital responsible for the σ-bond with the equatorial ligand is clearly separated from the other four d orbitals and the strong interaction with the macrocycle leads to a reduced iron contribution. The interactions with the axial ligand (methanol) are not reflected in the MO diagrams, thereby indicating a very weak bond. The pattern of the MO energies is actually more similar to the typical pattern of a square-planar coordination than a square-pyramidal one, therefore the coordination number of the iron atom can also be described as 4+1.

 © 2005 Wiley-VCH Verlag GmbH & Co. KGaA, Weinheim

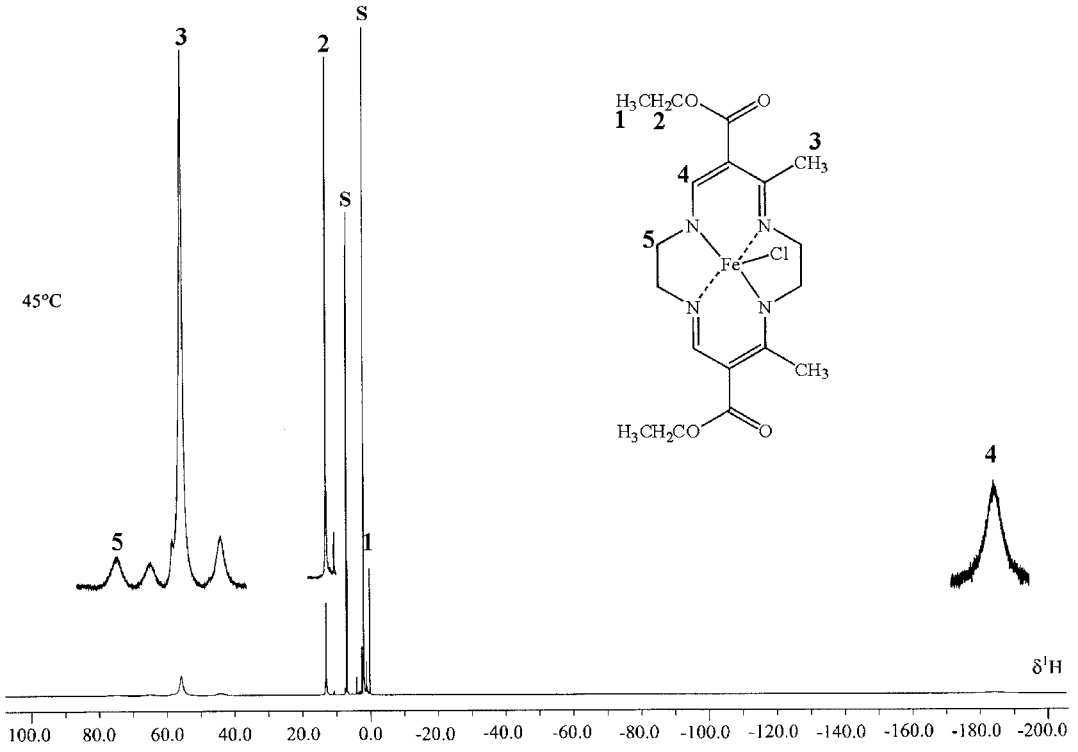

Figure 6. ^{1}H NMR spectrum and signal assignment of **Fe^{III}1Cl** in toluene solution at 45 °C. "S" denotes the solvent.

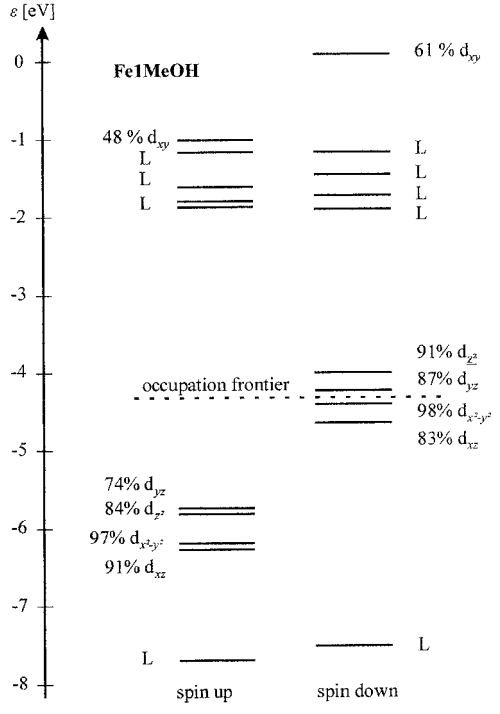

Figure 7. Orbital energies between 0 and –8 eV for the intermediate-spin state of **Fe1MeOH** for spin-polarised calculations. The approximate assignment for each level is given (L donates the equatorial ligand).

Orientation of Axial N-Heterocycles in Octahedral Complexes

One of the biological functions of b-type cytochromes is to switch the direction of charge-transfer processes depending on the potential. The active site contains haem with two axial imidazole rings of histidine. The voltage-dependent change of the orientation of the heterocyclic planes could be a possible mechanism for the switching. Former X-ray studies on the pair **Fe^{II}1(HIm)$_2$** and [**Fe^{III}1(HIm)$_2$**]-PF_6 gave evidence for such a charge-dependent reorientation of the imadazole planes,[18a] but it was not possible to clarify the role of the intermolecular hydrogen bonds in this case. Later on, an overview of the orientation of axial ligand planes in octahedral homo- and heteroligand diadducts of fifteen iron(II/III) complexes was given.[18b] We have now successfully crystallised **Fe^{II}3(Py)$_2$** and **[Fe^{III}3(Py)$_2$]**-PF_6, the first pair of complexes derived from the basic complex **Fe3**. The structures of both complexes are depicted in Figure 8 (right side), together with those of **Fe^{II}2Py$_2$** and [**Fe^{III}2Py$_2$**]ClO_4 (left side) for comparison. The corresponding bond lengths and angles are summarised in Table 3.

Addition of two neutral nitrogen ligands at the axial coordination sites of the macrocyclic iron complexes leads to low-spin complexes. The spin state was confirmed by ESR investigations in the case of the iron(III) complexes.[18b,19c] The iron atom is surrounded by six nitrogen atoms, resulting in a relatively symmetric close coordination sphere with an approximate D_{4h} symmetry. (Porphyrin)iron com-

 © 2005 Wiley-VCH Verlag GmbH & Co. KGaA, Weinheim

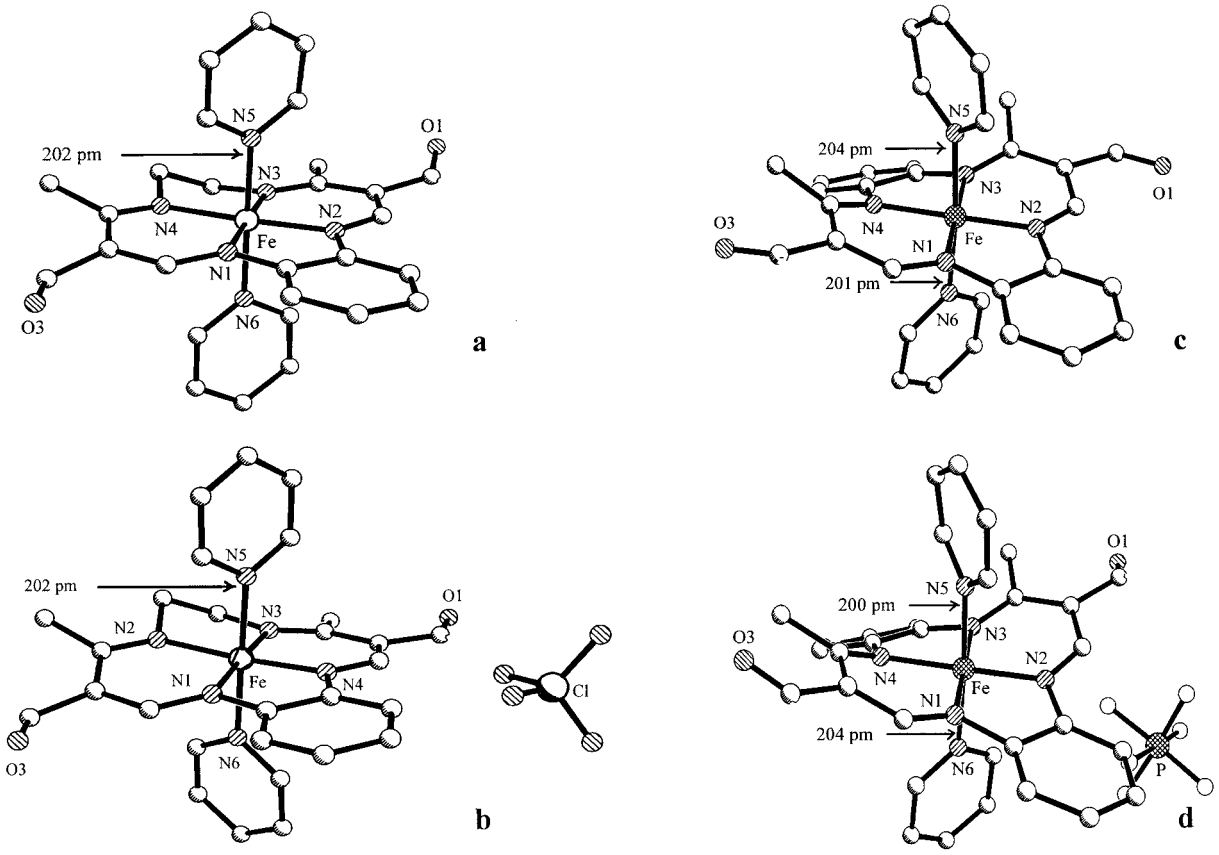

Figure 8. Molecule structures of (a) **$Fe^{II}2(Py)_2$**, (b) **[$Fe^{III}2(Py)_2$]ClO_4**, (c) **$Fe^{II}3(Py)_2$** and (d) **[$Fe^{III}3(Py)_2$]PF_6**. Ethoxy groups are omitted.

Table 3. Bond lengths [Å] and angles [°] within the first coordination sphere of macrocyclic iron(II/III) complexes with coordination number (*CN*) 6 and spin state *S*.

Complex	*CN*	S	Fe–$N_{1,2}$[a]	Fe–$N_{3,4}$[a]	Average FeL_{eq}	Fe–L_{ax}	Fe–pl_{eq}[b]	Angle $[L_{ax}]_{1_2}$[c]
$[Fe^{III}1(Py)_2]PF_6$	6	1/2	1.882(5)	1.926(6)	1.899	2.045(3)	0.000	15
			1.893(6)	1.925(6)		2.063(3)		
$Fe^{II}2(Py)_2$[d]	6	0	1.917(2)	1.925(2)	1.920	2.018(2)	0.017	9
			1.904(2)	1.932(2)		2.037(2)		
$[Fe^{III}2(Py)_2]^+$[d]	6	1/2	1.893(2)	1.909(2)	1.902	2.022(2)	0.015	79
			1.887(2)	1.918(2)		2.040(2)		
$Fe^{II}3(Py)_2$	6	0	1.898(2)	1.934(2)	1.915	2.035(2)	0.010	90
			1.900(2)	1.929(2)		2.006(2)		
$[Fe^{III}3(Py)_2]^+$[e]	6	1/2	1.89	1.93	1.90	2.00	0.010	80
			1.90	1.90		2.04		
$[Fe^{III}1(N\text{-}MeIm)_2]^+$	6	1/2	1.893(6)	1.925(6)	1.907	2.017(7)	–	88
			1.882(5)	1.929(6)		2.001(6)		
$[Fe^{III}1(NCS)_2]^-$	6	1/2	1.896(2)	1.923(2)	1.909	1.947(3)	0.003	
			1.892(2)	1.926(2)		1.954(3)		
$[Fe^{III}2(CN)_2]^-$	6	1/2	1.910(2)	1.931(2)	1.918	2.002(3)	–	
			1.902(2)	1.930(2)		2.004(3)		
$[Fe^{III}2(NO_2)_2]^-$	6	1/2	1.887(3)	1.907(3)	1.901	1.982(3)	–	13
			1.895(2)	1.916(3)		2.000(3)		
$[Fe^{III}2(NO_2)OH_2]$	6	1/2	1.895(2)	1.925(3)	1.913	1.963(3)	0.018	
			1.904(3)	1.927(3)		2.055(4)		
$[Fe^{III}3(NO_2)NO]$ (?)[e,f]	6	0	1.85	1.90	1.89	2.00	0.032	
			1.91	1.91		1.96		

[a] Designation according to Figure 1. [b] Displacement of the iron atom from the main plane of the equatorial donor atoms. [c] Dihedral angle between the planes of the two axial ligands. [d] See ref.[18b] [e] The quality of the data is not sufficient and we are only publishing the conformation of the molecule, although distances and angles are similar to those of the other complexes. [f] Because of the disorder of the second axial NO_x ligand and the diamagnetism of the compound, the correct composition is uncertain.

 © 2005 Wiley-VCH Verlag GmbH & Co. KGaA, Weinheim

pounds with similar axial ligands are also low-spin complexes, while complexes with sterically demanding axial ligands such as benzimidazole or 2-methylimidazole are high spin due to the small energetic splitting of the iron 3d orbitals.[26,27] Similar high-spin diadducts of our macrocycles have not been obtained up to now.

The iron atom is situated in the $[N_4]$ plane of the equatorial ligand. The average $Fe–N_{eq}$ bond lengths (190–192 pm) for both pairs in Figure 8 are in the range typical for all of our low-spin and intermediate-spin complexes, but significantly shorter than in similar (porphyrin)iron complexes (196–200 pm).[28] The change of the oxidation state of the iron atom from +2 to +3 leads to an almost negligible shortening of the equatorial bond lengths. A slight lengthening of these bonds in octahedral complexes of **Fe1** in comparison with the square-planar and pentacoordinate complexes can be explained by the increased electron density at the central atom. The bond lengths between the iron atom and the axial ligands are in the region 200–204 pm, similar to those in low-spin (porphyrin)iron complexes, and are independent of the oxidation state of the central atom.

The most characteristic difference between the structures of both pairs in Figure 8 is the orientation of the planes of the axial pyridine rings. In the case of **Fe^{II}2(Py)$_2$** both pyridine rings are nearly coplanar and are directed at the centre carbon atom of the six-membered chelate rings, similar to the case of **Fe^{II}1(Him)$_2$**. The angle between their planes amounts to only 9°. In the iron(III) derivative [**Fe^{III}2(Py)$_2$**]-ClO_4, however, both planes of the pyridine rings are twisted more in the direction at the equatorial N-atoms and the five-membered rings, and the angle between them is now 79°. This finding suggests that the similar behaviour of the pair **Fe^{II}1(Him)$_2$**/[**Fe^{III}1(Him)$_2$**]PF_6 is not necessarily a result of reorganisation of intermolecular hydrogen bonds. In contrast, the planes of the pyridine rings in the pair **Fe^{II}3(Py)$_2$** and [**Fe^{III}3(Py)$_2$**]PF_6 remain in a nearly unchanged orientation with an angle of 90° and 80°, respectively; they are independent of the oxidation state of the central atom. This is a consequence of the "saddle-shaped" distortion of the twofold phenylene-bridged equatorial ligand that allows only one energetically favoured orientation of the planes of the axial pyridine rings (perpendicular to each other) along the "trough" on each side.

All attempts to crystallise the iron(II) counterparts of [**Fe^{III}1(Py)$_2$**]PF_6 and [**Fe^{III}1(N-Meim)$_2$**]ClO_4 (Table 3) were unsuccessful.

Octahedral Complexes with Biologically Relevant Anions as Axial Ligands

Extended spectrophotometric equilibrium studies of the equilibria (1) and (2),[5a,5c,18b,19] particularly with the more hydrophilic complex **Fe1a**, have provided conclusive proof of the existence of octahedral iron(III) complexes [**Fe^{III}1aXY**] in solution with a large number of axial ligands, including anions as hydroxide, sulfite, nitrite, cyanide, thiocyanate, and even such "exotic" ligands as $[Fe(CN)_6]^{4-}$ and $[Fe(CN)_6]^{3-}$.[19a] In several cases, for example X = HIm, Y = CN^-, strong stabilizing interactions between both axial ligands have been detected.

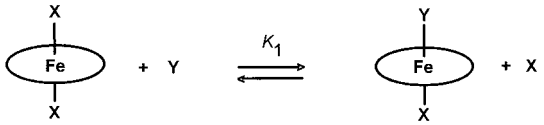

(1)

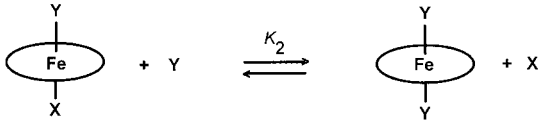

(2)

In view of the fact that anionic and mixed axial ligands play a key role in the chemistry of haem enzymes, we were interested in obtaining structural information for such complexes, especially to determine whether interactions between axial ligands through the central atom are reflected in the structural parameters. Unfortunately, attempts to isolate pure crystals failed in most cases, therefore only a few examples are presented here.

One of the many functions of haem enzymes in biological systems is the activation of small molecules and ions such as nitric oxide (NO), nitrite (NO_2^-) or sulfite (SO_3^{2-}). There has been a renewed interest in the biological nitrogen cycle with the discoveries of the biomedical functions of nitric oxide[29,30] and the clarification of the X-ray structure of the haem enzyme cytochrome c nitrite reductase.[31] This development increased the interest in model compounds with manageable electronic interactions to obtain a better understanding of the coherences of the biological activity of these small molecules. An overview of the properties of nitrosyliron complexes of ligand types **I** and **II** has been published.[22] A dinitrite adduct and several mononitrite adducts (with occupation of the sixth coordination site by other ligands) of "picket-fence" porphyrins have been prepared and several attempts have been made to describe the iron–nitrite bond.[32a–32d] All of these compounds are low-spin iron(III) complexes.

The reaction of our macrocyclic iron(II) complexes with nitrite under inert conditions yields the corresponding nitrosyliron complex as the main product, according to Equation (3), in all three cases. This was proved by ESR spectroscopy and by preparing **Fe1^{15}NO** using ^{15}N-labelled $NaNO_2$.

$$2\,\mathbf{Fe1} + 3\,NO_2^- + H_2O \rightarrow \mathbf{Fe1NO} + [\mathbf{Fe1(NO_2)_2}]^- + 2\,OH^- \quad (3)$$

The reaction of the iron(III) complexes with nitrite in organic solvents is even more complex. Although the spectrophotometric titration of [**Fe^{III}1a**]$^+$ clearly indicates the existence of a dinitrito and a mixed hydroxo-nitrito derivative in alkaline aqueous solution,[19b] all attempts to crystallise such derivatives of **Fe1** failed. Upon exclusion of air, the isolated reaction product of **Fe1Cl** or **Fe1I** in methanol is

 © 2005 Wiley-VCH Verlag GmbH & Co. KGaA, Weinheim

the corresponding nitrosyl complex according to Equation (4). On the other hand, **Fe1NO** reacts in methanol or pyridine with air to give the nitrite adduct [Equation (5)]. The existence of a mono- and dinitrite adduct has been proved by UV/Vis spectroscopy.[22] Similar reactions have been found for ferric porphyrin complexes.[34]

$$\mathbf{Fe1}^{+} + 2\,NO_2^{-} \rightarrow \mathbf{Fe1NO} + NO_3^{-} \quad (4)$$

$$\mathbf{Fe1NO} + 1/2\,O_2 + D \rightarrow \mathbf{Fe1(NO_2)D};\ D = Py,\ MeOH \quad (5)$$

For **Fe2** it was possible, starting from the corresponding iodide or chloride complex, to isolate a nitrite diadduct and a few crystals of a mixed adduct with one nitrite ion and one water molecule as axial ligand *trans* to the nitrite ion. The molecule structures are given in Figure 9a, b. In both complexes the iron atom has a nearly octahedral coordination sphere and is located in the plane of the macrocycle. The Fe–N_{eq} and Fe–N_{NO_2} distances are similar to those of other diadducts. The oxygen atoms of the nitrite ligands point towards the six-membered chelate ring and, in the case of the diadduct, both nitrite groups are coplanar. The coordination of water in the case of the monoadduct is interesting. This has been postulated in many quantum-chemical investigations but has never been described in detail. The relatively large distance of 206 pm between the iron atom and the bound water molecule suggests a weak coordination.

While the nitrite diadduct is a pure low-spin complex over the whole temperature range, the nitrite monoadduct performs a spin transition between the S = 1/2 and S = 3/2 states. Such spin transition behaviour has already been reported for other six-coordinate iron(III) complexes[35a,35b] and is also typical of some nitrosyliron complexes of type **II**.[22,35c,35d] The effective moments plotted against temperature are given for both compounds in Figure 10.

Calculations based on the SCC-Xα method did confirm the S = 1/2 configuration as the ground state for both complexes. The energy difference to the S = 3/2 first excited state of **[Fe2(NO$_2$)OH$_2$]**(MeOH) is, at around 20 kJ mol^{-1}, small for this program. (The expected value at room temperature is significantly lower, but experience with the program used shows that the obtained values are within this region for this program.[40]) Therefore an admixture of this state and the ground state at room temperature is plausible. Another possibility is an interaction between both spin states that would explain the room-temperature effective moment of 2.82 μ_B, which is significantly lower than the expected spin-only value of 3.87 μ_B. Similar effects have been described in the literature for other iron(III) complexes.[36] Measurements of the effective magnetic moment at higher temperatures are not possible as the complex decomposes with loss of water. On the basis of these calculations it could be shown that the overlap population between Fe and O_{H_2O} decreases by 60% during the spin transition. The resulting pentacoordinate complex should be an intermediate-spin complex similar to the corresponding iron(III) halide complexes.

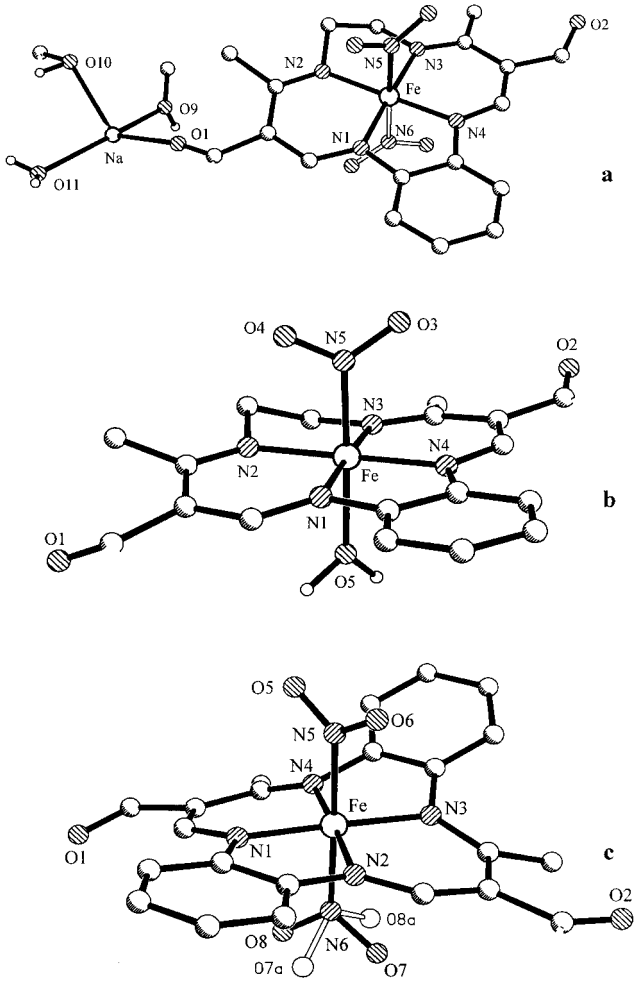

Figure 9. Molecule structures of (a) Na[**Fe^{III}2(NO$_2$)$_2$**](MeOH)$_2$(H$_2$O)$_{0.5}$, (b) [**Fe^{III}2(NO$_2$)OH$_2$**] and (c) [**Fe^{III}3(NO$_2$)NO$_x$**]$^-$. Ethoxy groups are omitted.

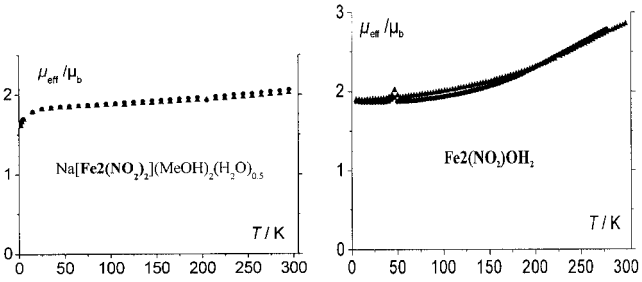

Figure 10. Temperature dependence of the effective magnetic moment of Na[**Fe^{III}2(NO$_2$)$_2$**](MeOH)$_2$(H$_2$O)$_{0.5}$ (left) and [**Fe^{III}2(NO$_2$)OH$_2$**] (right). The measurements were carried out at 0.2 and 0.5 T.

For **Fe3** − the complex most similar to (porphyrin)iron compounds − a derivative with the approximate composition (nBu$_4$N)$_2$[**Fe3(NO$_2$)NO$_x$**](NO$_2$)(H$_2$O), with one axial nitrite and one other axial NO_x ligand has been crystallised. Unfortunately, the latter is disordered in such a manner that it was impossible to decide between an NO_2 with two and an NO with four orientations. Additionally, the presence of

 © 2005 Wiley-VCH Verlag GmbH & Co. KGaA, Weinheim

potential cations and anions in the lattice makes it more difficult to clearly define the charge of the central unit. The diamagnetism of the crystals suggests a neutral complex [**Fe^{III}3(NO$_2$)NO**] with low-spin iron(III), antiferromagnetically coupled with the nitrosyl radical. This interpretation agrees with the distances and angles within the central unit. Mixed axial nitrite-nitrosyl coordination has also been found in iron(II)[32e] and iron(III)[32d] complexes with "picket-fence" porphyrins.

The thiocyanate anion is of interest not only because of its biological relevance but also because it is, along with azide, one of the pseudo-halides that give heterogeneous equilibria with [**Fe^{III}1a**]$^+$ [Equation (6)] between aqueous and lipophilic phases accompanied by a "structural mimicry":

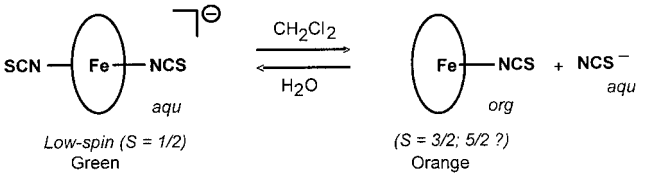

(6)

While the green product, in agreement with its EPR spectrum, is doubtless an octahedral low-spin iron(III) complex, the orange one, which is stable only in lipophilic solvents such as dichloromethane, benzene or toluene, has not been unambiguously characterised to date. Unfortunately, all attempts to obtain pure crystals of this product also failed. Crystals suitable for X-ray structure determination were only obtained for the diadduct [BzEt$_3$N][**Fe^{III}1(NCS)$_2$**].

The only examples of thiocyanato adducts of (porphyrin)-iron compounds described in the literature are a pentacoordinate monoadduct of high-spin iron(III)[37] and a hexacoordinate low-spin complex with pyridine as second axial ligand.[38] Cationic macrocyclic iron(II/III) complexes with neutral equatorial ligands easily form thiocyanato diadducts.[39] Thus, the complex [BzEt$_3$N][**Fe1(NCS)$_2$**] is the first macrocyclic iron complex with an anionic [N$_4$] ligand and two axially bound thiocyanate ligands (Figure 11).

For a proper description, the adduct has to be referred to as a diisothiocyanato complex, which is also the case for the corresponding porphyrin monoadducts. The linear coordination of the thiocyanate ion is confirmed by the Fe–N$_{ax}$–C$_{ax}$ angles of 171° and 179°. The Fe–N distances are comparable with those in cationic complexes described previously. The only conspicuous feature of the complex is the arrangement of the free ester groups of the equatorial ligand, where both carbonyl oxygen atoms point to the unsubstituted site of the ligand. For all other complexes of this ligand type characterised by X-ray structure analysis, at least one, but mostly both, of the terminal carbonyl oxygen atoms are directed towards the methyl group. The low-spin state of the iron(III) atom was confirmed by ESR spectroscopy (*g* values: 1.973, 2.125, 2.162).[18]

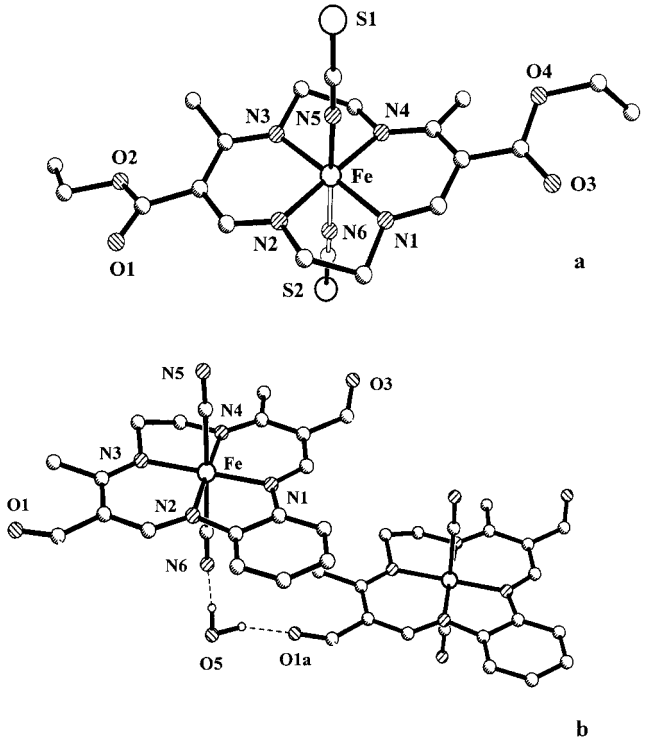

Figure 11. Molecule structures of (a) [**Fe^{III}1(NCS)$_2$**]$^-$ and (b) [**Fe^{III}2(CN)$_2$**]$^-$(H$_2$O)$_{0.5}$ (cations omitted for clarity).

An octahedral anionic complex with two cyanide ions as axial ligands, [Et$_4$N][**Fe^{III}2(CN)$_2$**] could be crystallised with the unsymmmetrically bridged macrocycle.

Dicyanide complexes are well documented and characterised in the literature.[41,42] The question as to whether the cyanide ion is bound to the iron atom through the carbon or the nitrogen atom was decided in favour of the carbon atom (the difference of the *R*1 values, the resulting C–N bond length and the remaining electron density were considered). This result fits with results in the literature. The distances between the iron atom and the equatorial nitrogen atoms are, with an average of 192 pm, slightly longer than those of other octahedral iron(III) complexes and are more comparable with those found for iron(II) complexes. Compared with the isothiocyanate diadduct, the axial bond lengths are also long and more similar to pyridine adducts. These differences in the bond lengths lead to the conclusion that in the case of cyanide as axial ligand, additional negative charge is localised at the iron atom (and therefore delocalised over the macrocyclic ligand), resulting in a lengthening of the bonds. In the case of the larger thiocyanate ion, the negative charge is localised on the easily polarizable sulfur rather than the iron atom, resulting in shorter bond. The low-spin state of the iron(III) atom was confirmed by ESR spectroscopy. In contrast to neutral octahedral complexes the ground-state electron configuration of the cyanide diadduct is $(d_{xz},d_{yz})^4(d_{xy})^1$. The same results can be found for comparable cyanide diadducts in the literature.[41,42]

 © 2005 Wiley-VCH Verlag GmbH & Co. KGaA, Weinheim

Conclusions

The results described above confirm the close relation of our macrocycles with porphyrins, but they also indicate some special features. In general, the anions $\mathbf{L^{2-}}$ (**L** = **1**, **2**, **3**) seem to be stronger ligands for iron than most porphyrinato systems. The reasons for this could be: (i) the stronger basicity and σ-donor ability of the four nitrogen donor atoms, especially in the case of **L** = **1**; (ii) the presence of the electron-withdrawing carbonyl groups in conjugation with the π-system of the six-membered chelate rings, which promote potential π-backbonding and increase the effective charge of the central atom, especially when **L** = **2** and **3**, where the π-system is extended over one phenylene ring (the second phenylene in **3** is hardly included in the conjugation); (iii) the smaller hollow within the cavity of the 14-membered macrocycle, which is better suited for the radii of iron(II/III) in lower spin states.

The pronounced tendency to stabilize the intermediate-spin ground state in iron(II/III) complexes with coordination numbers below six, even when similar compounds are in a high-spin state [e.g. **Fe^{III}(Me$_4$TAA)Cl** or the halides of (porphyrin)iron compounds], is a typical feature of the ligands $\mathbf{L^{2-}}$. Intermediate spin (S = 1) was found in the iron(II) complexes **Fe2** (CN = 4, planar), **Fe1** (CN = 4+1 by weak intermolecular coordination of the ester carbonyl group), **Fe1MeOH** and the bridged complexes **(FeL)$_2$dabco** (**L** = **1**, **2**, **3**; all CN = 5, square-pyramidal). The preference to bind axial O-ligands − MeOH or even such a weak O-donor as COOEt − indicates that the iron atom in **Fe1** is the "hardest" central atom in the series **FeL**. The magnetic behaviour of the iron(II) complexes at lower temperature is often determined by intermolecular interactions in the lattice: **Fe2**, with the shortest Fe–Fe distance of 335 pm, shows a sigmoid decrease of the magnetic moment, whereas **(Fe3)$_2$dabco**, where the *inter*molecular Fe–Fe distance (421 pm) is much shorter than the *intra*molecular distance (727 pm), shows a steep decrease of the moment starting already at around 150 K. The complexes **FeLCl** (**L** = **1**, **2**, **3**) and the iodide **Fe1I** represent the iron(III) case of intermediate-spin (S = 3/2) behaviour. The intermediate-spin state could be confirmed by Mössbauer spectrometry for **Fe1**, by ESR and NMR spectroscopy for **Fe1Cl**, and by DFT-MO calculations for **Fe1MeOH**, **Fe1Cl** and, previously, for **Fe1I** (see refs.[22b,22c] for more calculations).

The pair **Fe^{II}3(Py)$_2$**/[**Fe^{III}3(Py)$_2$**]PF_6 was characterised as a third example of potential "voltage-dependent molecular switches" based on octahedral low-spin iron(II/III) complexes with N-heterocycles as axial ligands. Comparison with the pairs **Fe^{II}1(HIm)$_2$**/[**Fe^{III}1(HIm)$_2$**]PF_6 and **Fe^{II}2(Py)$_2$**/[**Fe^{III}2(Py$_2$)**]ClO_4 resulted in the conclusions that: (i) the charge-dependent change of the orientation of the axial planes is not necessarily accompanied by reorganisation of intermolecular hydrogen bonds, and (ii) the "saddle-shaped" distortion of the ligand **3** allows only orientation of the axial planes perpendicular to each other; no charge-dependent twist of these planes is possible. Other new octahedral low-spin complexes with axial N-heterocycles are [**Fe^{III}1(Py)$_2$**]PF_6 and [**Fe^{III}1(N-MeIm)$_2$**]ClO_4, but unfortunately their iron(II) counterparts could not be obtained as suitable crystals.

Octahedral low-spin derivatives of the macrocyclic iron complexes **FeL** with biologically relevant anions as axial ligands have been crystallised for the first time, although their existence in solution was proved many years ago. Reactions with nitrite resulted in the anionic diadduct [**Fe^{III}2(NO$_2$)$_2$**]$^-$ with pentacoordinate sodium as counterion, and, more interestingly, in the neutral mixed-ligand complex [**Fe^{III}2(NO$_2$)OH$_2$**]. The presence of water as a relatively weak axial ligand results in a temperature-dependent admixing of low-spin (favoured at low temperature) and, possibly, intermediate-spin species. DFT-MO calculations agree with this interpretation. With cyanide and thiocyanate ions the octahedral low-spin diadducts [Et_4N][**Fe2(CN)$_2$**] and [$BzEt_3N$][**Fe1(NCS)$_2$**] could be crystallised. Unfortunately, it was not possible to obtain pure crystals of the pentacoordinate neutral counterpart of the latter, **Fe^{III}1(NCS)**, which exists together with the anionic diadduct in an equilibrium of distribution between a lipophilic and an aqueous phase.

With regard to the existence of high-spin iron(II/III) complexes and to the processes of spin conversion, some of the iron complexes of type **II** are more closely related to (porphyrin)iron compounds than the macrocycles **I**. This will be the subject of a following paper.

Experimental Section

General Procedures and Instrumentation: If not stated differently, all syntheses were carried out under argon using Schlenk tube techniques. All solvents were purified as described in the literature[43] and distilled under argon. Magnetic measurements of pulverized samples were performed with a Quantum Design MPMSR-5s SQUID magnetometer in a temperature range from 1.7 to 400 K, with the exception of **Fe2Cl** and **Fe3Cl**. All measurements were carried out at two field strengths (0.2 and 0.5 T). Diamagnetic corrections were made using values calculated with tabulated Pascal constants (as a rule, suitable values can be estimated as $\chi_{dia} \approx 0.6 \times 10^{-6} M_{complex}$). The measurements of the highly air-sensitive iron(II) compounds were repeated several times under strongly inert conditions to ensure that the samples remain in the iron(II) state during preparation. For comparison, an additional sample was measured after exposure to air. ESR investigations were carried out with an ESP 300E (Bruker) instrument at liquid-nitrogen temperature with the solid or in solution (methanol, toluene) or equipped with an N_2/He-flow cryostat from 4.2 K up to room temperature. Molecular orbital calculations were carried out in a local density approximation (LDA) by the spin-polarized self-consistent-charge (SCC-)Xα method.[44,45]

Syntheses: The syntheses of the free ligands are summarised in Scheme 2 for **H$_2$1** and **H$_2$2** and in Scheme 3 for **H$_2$3**. All steps of the ligand syntheses were carried out in air. From a thermodynamic point of view, the driving force of the complex formation starting from the free ligand, as well as of the reverse protolysis of the complex, depends on the competition between two protons and the divalent metal ion to bind the anion of the deprotonated ligand:

$$M^{2+} + 2HL \rightleftharpoons ML + 2H^+ \quad (7)$$

 © 2005 Wiley-VCH Verlag GmbH & Co. KGaA, Weinheim

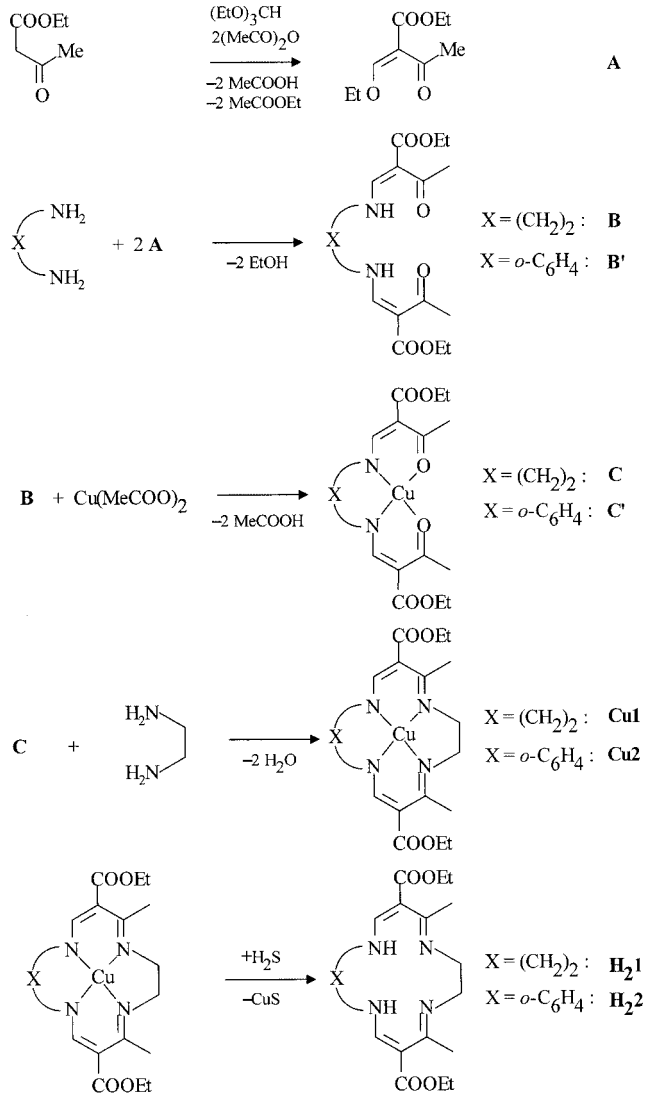

Scheme 2. Syntheses of the free macrocyclic ligands H_2**1** and H_2**2**.

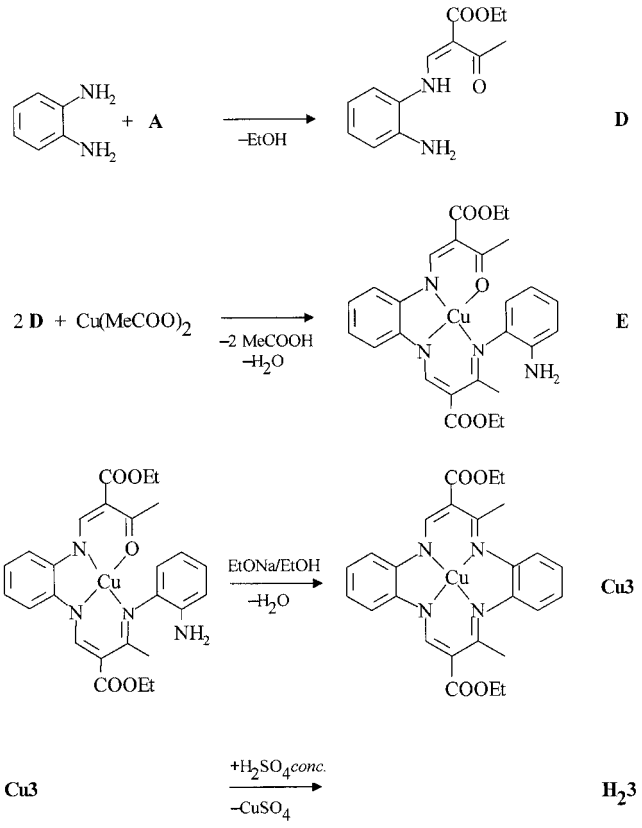

Scheme 3. Synthesis of the free macrocyclic ligand H_2**3**. The Cu-driven condensation of two molecules **D** is expected to give the *anti* isomer of the copper complex **E** with respect to the methyl groups. The X-ray analysis of **E** confirms, however, the depicted *syn* structure.[14b]

The key step of the syntheses of the free ligands is a template reaction using the copper(II) ion as template, followed by the demetallation of the macrocyclic copper complex. The different conditions of the demetallation reflect the different properties of the ligands: the release of the protonated macrocycle H_2**3** from **Cu3** is possible by dissolving it in sulfuric acid without any auxiliary reagent. This is obviously due to the relatively low stability of the copper complex **Cu3**, where the copper(II) ion is too large for the small hollow of the rigid anion $\mathbf{3}^{2-}$. To obtain the ligands H_2**1** and H_2**2**, addition of the auxiliary reagent hydrogen sulfide is necessary to remove the copper ion. Different reaction conditions are also typical for the formation of iron complexes. As in the case of porphyrins, iron(II) is easier to incorporate into the macrocycles than iron(III). The complex **Fe1** was formed nearly quantitatively in a fast reaction using a 1:1 ratio of ligand and iron(II) acetate, even under moderate basic conditions. For the complexes **Fe2** and **Fe3** an excess of the iron(II) salt is necessary to prevent contamination by the free ligand. Additionally, the complex formation requires an increase of the reaction time from a few minutes (**Fe1**) to 2–3 h (**Fe2**) or 10–11 h (**Fe3**). This increase reflects the kinetic effect of the increasing rigidity of the ligand structures.

Syntheses of the Macrocyclic Ligands

6,13-Bis(ethoxycarbonyl)-7,12-dimethyl-1,4,8,11-tetraazacyclotetradeca-5,7,12,14-tetraene ($H_2$1):[17b,46b] The preparation of this ligand by a template synthesis of the copper complex **Cu1**, followed by demetallation with hydrogen sulfide in dilute sulfuric acid and precipitation with sodium hydroxide, gave the free ligand in nearly quantitative yield. However, to prevent the use of gaseous hydrogen sulfide, the latter can be replaced by precipitation from homogeneous solution by in situ hydrolysis with thioacetamide. In this case the yield of the last step drops to about 45%.

Compound A:[47] Ethyl acetoacetate (130 g, 1 mol), acetic anhydride (204 g, 2 mol) and triethyl orthoformate (148 g, 1 mol) were refluxed together for 40 min. The low-boiling side-products were distilled off at normal pressure until foggy clouds appeared in the reaction vessel. The main product was then obtained by fractionatal vacuum distillation (b.p. 145–150 °C at 2 kPa). The purity of the oily, colourless to bright greenish-yellow product was determined by GC analysis. Yield: 140.1 g (75%).

Compound B:[33] Compound **A** (140.1 g, 0.75 mol) was dissolved in methanol (130 mL) and freshly distilled ethylenediamine (22.8 g, 0.379 mol), dissolved in methanol (130 mL), was then slowly added to the solution. The reaction mixture was stirred vigorously and the ligand precipitated immediately. The colourless product was filtered off and recrystallised from ethanol or dioxane. Yield: 94 g (77%).

Compound C:[33] Compound **B** (10 g, 0.029 mol) and copper acetate monohydrate (5.9 g, 0.035 mol, finely pulverized) were mixed and

 © 2005 Wiley-VCH Verlag GmbH & Co. KGaA, Weinheim

heated in DMF or ethanol (500 mL) to reflux for 30 min. After cooling, violet crystals precipitated that were filtered off, washed with methanol and dried. Yield: 10.1 g (85%).

Cu1:[46a] Compound **C** (50 g, 0.12 mol) was dissolved in ethylenediamine (100 mL, dried and freshly distilled from solid potassium hydroxide) and heated to reflux until the colour had changed from deep blue to brownish-violet (15–30 min). After cooling, the product was filtered off and washed with water. Yield: 38.5 g (72%).

$H_2$1:[17b,46b] **Cu1** (2.0 g, 0.0047 mol) was suspended in methanol (10 mL) and stirred for 15 min. Ice-cold (0 °C) dilute sulfuric acid (ca. 2 M, 40 mL) was then added to the suspension. After 1 min, thioacetamide (4.2 g, 0.056 mol) was added to the suspension and the reaction mixture was stirred for a further 3 min. The suspension was filtered through a fluted filter paper into a calculated volume of ice-cold sodium hydroxide solution (ca. 4 M) such that the mixture became neutral or weakly basic after addition of all of the acidic filtrate. The free ligand was filtered off and washed with water until a nearly neutral pH was obtained. The crude material was recrystallised from methanol as fine colourless needles. Yield: 0.8–1 g (47–58%).

6,13-Bis(ethoxycarbonyl)-7,12-dimethylbenzo[*b*]-1,4,8,11-tetraazacyclotetradeca-5,7,12,14-tetraene ($H_2$2): Cu2 was synthesised in analogy to **Cu1** using 1,2-phenylenediamine instead of ethylenediamine in step **B**.[10d,33]

$H_2$2:[10d] **Cu2** (2.0 g, 0.0042 mol) was suspended in methanol (10 mL) and stirred for 15 min. Ice-cold (0 °C) sulfuric acid (5 M, 40 mL) was then added to the suspension. After 1 min, thioacetamide (4.2 g, 0.056 mol) was added to the suspension and the reaction mixture was stirred for a further 3 min. The suspension was then filtered into ice-cold sodium hydroxide (4 M, 100 mL) taking care to ensure that the solution did not warm up. The free ligand was filtered off and washed with water until a nearly neutral pH was obtained. The crude material was dissolved in a little dioxane and reprecipitated with distilled water to obtain yellow crystals. Yield: 0.8–1 g (45–60%).

6,13-Bis(ethoxycarbonyl)-7,12-dimethyldibenzo[*b*,*i*]-1,4,8,11-tetraazacyclotetradeca-5,7,12,14-tetraene ($H_2$3):[23a] In earlier reports, the complexes **M3** (M = Cu, Co)[23c] and the intermediates **E**[23b] were postulated as isomeric structures with an *anti* configuration of the methyl groups attached to the six-membered chelate rings. However, the X-ray structural analysis of the free ligand **$H_2$3** and the nitrosylcobalt complex **Co3NO** proved the *syn* structure.[14b]

Compound D:[23b] A suspension of *o*-phenylenediamine (12 g, 0.11 mol) in ethanol (100 mL) was heated to reflux. Compound **A** (18.6 g, 0.1 mol) was slowly added to the solution and the mixture was refluxed for 20 min. After cooling, compound **D** precipitated as yellow needles that were collected and recrystallised twice from methanol or ethanol. Yield: 13.14 g (53%). M.p. 84 °C.

Compound E:[23b] Compound **D** (24.8 g, 0.1 mol) was heated to reflux in methanol (200 mL) and a suspension of finely ground copper acetate monohydrate (9.98 g, 0.05 mol) in methanol (150 mL) was slowly added to the solution. The suspension was refluxed for approximately 6 h. After cooling, the product was filtered off immediately, washed with methanol and dried. Yield: 23.56 g (87%).

Cu3:[23c] Compound **E** (6.68 g, 0.012 mol) was heated to reflux in dry ethanol (150 mL). Metallic sodium (0.31 g, 0.013 mol), dissolved in dry ethanol (50 mL), was slowly added to the suspension and the mixture refluxed for 6 h. After cooling, the product was filtered off immediately, washed with cold methanol and dried. Yield: 5.99 g (96%).

$H_2$3:[23a] **Cu3** (2 g, 0.0038 mol) was suspended in cooled concentrated H_2SO_4 (50 mL) where it underwent a colour change from brown to yellow. The suspension was added dropwise to a water/ice mixture, taking care to ensure the solution did not warm up. The free ligand precipitated as yellow needles that were collected on a paper filter, washed with water until a neutral pH was obtained, and dried at room temperature. The crude material was dissolved in a little dioxane and reprecipitated with distilled water to obtain yellow crystals. Yield: 1.2–1.4 g (70–80%).

Syntheses of the Iron(II) Complexes

[6,13-Bis(ethoxycarbonyl)-7,12-dimethyl-1,4,8,11-tetraazacyclotetradeca-5,7,12,14-tetraenato(2–)]iron(II) (Fe1):[17b] Iron(II) acetate (2.08 g, 11.9 mmol) and **$H_2$1** (4.30 g, 11.8 mmol) were dissolved in methanol (60 mL) and refluxed for 1 h. After standing overnight, the red precipitate was collected and dried in vacuo. Yield: 2.27 g (46%). $C_{18}H_{26}FeN_4O_4$ (418.27): calcd. C 51.68, H 6.27, N 13.40; found C 48.34, H 6.09, N 12.22; the discrepancy between the calcd. and found values is due to the high air sensitivity of the complex. IR (Nujol): $\nu_{C=O}$ = 1671 cm^{-1}. MS (DEI): *m*/*z* (%) = 418 (100) [M^+], 373 (15) [$M^+ - OC_2H_5$], 344 (5) [M^+ – COOEt].

[6,13-Bis(ethoxycarbonyl)-7,12-dimethylbenzo[*b*]-1,4,8,11-tetraazacyclotetradeca-5,7,12,14-tetraenato(2–)]iron(II) (Fe2):[10d] Iron(II) acetate (0.76 g, 4.4 mmol) and **$H_2$2** (1.27 g, 3.1 mmol) were suspended in methanol (20 mL) and refluxed for 6 h. The black product was collected, washed with a small volume of methanol and dried in vacuo. Yield: 1.14 g (77%). $C_{22}H_{26}FeN_4O_4$ (466.31): calcd. C 56.66, H 5.62, Fe 11.98, N 12.02; found C 55.23, H 5.52, Fe 12.1, N 12.24; the discrepancy between the calcd. and found values is due to the high air sensitivity of the complex. IR (Nujol): $\nu_{C=O}$ = 1676 cm^{-1}. MS (DEI): *m*/*z* (%) = 43 (100), 466 (50) [M^+].

[6,13-Bis(ethoxycarbonyl)-7,12-dimethyldibenzo[*b*,*i*]-1,4,8,11-tetraazacyclotetradeca-5,7,12,14-tetraenato(2–)]iron(II) (Fe3):[23a] Iron(II) acetate (1.33 g, 7.7 mmol) and **$H_2$3** (2.29 g, 5.0 mmol) were suspended in methanol (20 mL) and refluxed for 12 h. The black product was collected, washed with a small volume of methanol and dried in vacuo. Yield: 2.24 g (88%). $C_{26}H_{26}FeN_4O_4$ (514.35): calcd. C 60.71, H 5.09, N 10.89; found C 59.95, H 5.09, N 11.01. IR (Nujol): $\nu_{C=O}$ = 1686 cm^{-1}. MS (DEI): *m*/*z* (%) = 514 (100) [M^+], 486 (20) [$M^+ - C_2H_4$], 468 (15) [$M^+ - OC_2H_5$].

Dinuclear Adducts with Bridging 1,4-Diazabicyclo[2.2.2]octane (dabco)

(Fe1)$_2$dabco: Iron(II) acetate (0.31 g, 1.8 mmol) and 0.65 g of **$H_2$1** were dissolved in 20 mL of methanol and refluxed for 20 min. After cooling, a solution of dabco (0.2 g, 1.8 mmol) in 5 mL of methanol was slowly added to the solution. Slow crystallisation overnight yielded red needles suitable for X-ray structure analysis. The product was collected, washed with a little ice-cold methanol and dried in vacuo. Yield: 0.33 g (39%). $C_{36}H_{52}Fe_2N_8O_8 \cdot C_6H_{12}N_2$ (948.73): calcd. C 53.71, H 6.80, N 14.77; found C 52.48, H 6.59, N 14.78. IR (Nujol): $\nu_{C=O}$ = 1673, 1652 cm^{-1}. MS (DEI): *m*/*z* (%) = 112 (100) [M^+(dabco)], 418 (90) [M^+(**Fe1**)]. DTG: Up to 250 °C loss of 11.3% (calcd. for 1 dabco: 11.8%); decomposition at 300 °C.

(Fe2)$_2$dabco: Fe2 (0.5 g, 1.1 mmol) was suspended in 20 mL of methanol. Then, 1.3 mL of a 1 M solution of dabco in methanol was added to the suspension and left standing for slow crystallisation. After 2 d, red-black needles were obtained. The product was collected, washed with a little methanol and dried in vacuo. Yield: 0.3 g (55%). $C_{44}H_{52}Fe_2N_8O_8 \cdot C_6H_{12}N_2$ (1044.8): calcd. C 57.48, H 6.18, N 13.42; found C 56.60, H 6.12, N 13.41. IR (Nujol): $\nu_{C=O}$ = 1674 cm^{-1}. MS (DEI): *m*/*z* (%) = 112 (100) [M^+(dabco)], 466 (10) [M^+(**Fe2**)]. DTG: Up to 100 °C loss of 11.3% (solvent in the crys-

 © 2005 Wiley-VCH Verlag GmbH & Co. KGaA, Weinheim

tal), up to 300 °C loss of 12.4% (calcd. for 1 dabco: 10.7%); decomposition at 350 °C.

$(Fe3)_2$dabco: Fe3 (0.65 g, 1.3 mmol) was suspended in 40 mL of methanol. Then, 1.8 mL of a 1 M solution of dabco in methanol was added to the suspension and left standing for slow crystallisation. After 2 d, black needles were obtained. The product was collected, washed with a little methanol and dried in vacuo. Yield: 0.45 g (61%). $C_{52}H_{52}Fe_2N_8O_8{\cdot}C_6H_{12}N_2$ (1140.9): calcd. C 61.06, H 5.65, N 12.28; found C 58.96, H 5.90, N 12.03. IR (Nujol): $\nu_{C=O}$ = 1686 cm^{-1}. MS (DEI): *m*/*z* (%) = 42 [fragment], 112 (90) [M^+(dabco)], 514 (10) [M^+(**Fe3**)]. DTG: Up to 250 °C loss of 9.7% (calcd. for 1 dabco: 9.8%); at 350 °C decomposition.

Syntheses of the Iron(III) Complexes: The syntheses of the iron(III) iodide complexes **Fe1I**[19c,21] and **Fe2I**[10d] have been described previously.

[6,13-Bis(ethoxycarbonyl)-7,12-dimethyl-1,4,8,11-tetraazacyclotetradeca-5,7,12,14-tetraenato(2–)]iron(III) Chloride (Fe1Cl): Fe1 (1.36 g, 3.3 mmol) was suspended in tetrachloromethane (20 mL) for 2 d. The CCl_4 was then removed by cold vacuum distillation and the obtained solid was recrystallised from methanol. The precipitate was filtered off and dried in vacuo. The mother solution was allowed to stand overnight to produce single crystals of **Fe1Cl** suitable for X-ray crystallography. Yield: 1.04 g (69%). $C_{18}H_{26}ClFeN_4O_4$ (453.72): calcd. C 47.65, H 5.78, N 12.35; found C 44.81, H 5.37, N 11.50. IR (Nujol): $\nu_{C=O}$ = 1680 cm^{-1}. MS (DEI): *m*/*z* (%) = 28 (100), 453 (10) [M^+], 418 (30) [M^+ – Cl]. DTG: Decomposition at 170 °C.

[6,13-Bis(ethoxycarbonyl)-7,12-dimethylbenzo[*b*]-1,4,8,11-tetraazacyclotetradeca-5,7,12,14-tetraenato(2–)]iron(III) Chloride (Fe2Cl): Fe2 (0.67 g, 1.4 mmol) was suspended in tetrachloromethane (20 mL) for 2 d. The CCl_4 was then removed by cold vacuum distillation and the solid product was recrystallised from methanol. The precipitate was filtered off and dried in vacuo. Yield: 0.59 g (84%). $C_{22}H_{26}ClFeN_4O_4$ (501.764): calcd. C 52.66, H 5.22, N 11.17; found C 52.52, H 4.89, N 11.45. IR (Nujol): $\nu_{C=O}$ = 1685 cm^{-1}. MS (DEI): *m*/*z* (%) = 36 (100), 501 (50) [M^+], 466 (20) [M^+ – Cl].

[6,13-Bis(ethoxycarbonyl)-7,12-dimethyldibenzo[*b*,*i*]-1,4,8,11-tetraazacyclotetradeca-5,7,12,14-tetraenato(2–)]iron(III) Chloride (Fe3Cl): Fe3 (0.96 g, 1.9 mmol) was suspended in tetrachloromethane (30 mL) for 2 d. The CCl_4 was then removed by cold vacuum distillation and the solid was recrystallised from methanol. The precipitate was filtered off and dried in vacuo. Yield: 0.87 g (83%). $C_{26}H_{26}ClFeN_4O_4$ (549.80): calcd. C 56.79, H 4.77, N 10.19; found C 55.60, H 4.61, N 10.48. IR (Nujol): $\nu_{C=O}$ = 1697 cm^{-1}. MS (DEI): *m*/*z* (%) = 31 (100), 549 (90) [M^+], 514 (15) [M^+ – Cl].

Synthesis of Diadducts of Iron(II/III) Complexes

$Fe3(Py)_2$: Fe3 (40 mg) was dissolved in pyridine (7 mL) and a layer of heptane (10 mL) was added over the pyridine solution. After a few days, a fine black-red crystalline precipitate was obtained. $C_{26}H_{26}FeN_4O_4{\cdot}2C_5H_5N$ (672.55): calcd. C 64.3, H 5.4, N 12.5; found C 64.4, H 5.2, N 12.4.

$[Fe3(Py)_2]PF_6$: Fe3I (30 mg) was dissolved in pyridine (15 mL) and then a solution of NH_4PF_6 in methanol (2 M) was added dropwise until a precipitate was obtained. $C_{26}H_{26}FeN_4O_4{\cdot}2C_5H_5N{\cdot}PF_6$ (817.52): calcd. C 52.9, H 4.4, N 10.3; found C 52.8, H 4.6, N 10.1. MS (DEI): *m*/*z* (%) = 79 (100) [pyridine], 514 (<1) [M^+(**Fe3**)].

$[Fe1(Py)_2]PF_6$: Fe1I (30 mg) was dissolved in a solution of pyridine in benzene (1 M, 15 mL) and then a solution of NH_4PF_6 in methanol (2 M) was added dropwise to the solution until a precipitate was obtained. $C_{18}H_{26}FeN_4O_4{\cdot}2C_5H_5N{\cdot}PF_6$ (721.44): calcd. C 46.6, H 5.0, N 11.7; found C 46.6, H 4.9, N 11.5. MS (DEI): *m*/*z* (%) = 79 (100) [pyridine], 418 (19) [M^+(**Fe1**)].

$[Fe1(N\text{-}MeIm)_2]ClO_4(H_2O)$: Fe1I (30 mg) was dissolved in a solution of *N*-methylimidazole in methanol (1.4 M, 15 mL). A solution of $NaClO_4$ in water was added dropwise to the solution until a precipitate was obtained. $C_{18}H_{26}FeN_4O_4{\cdot}2C_4H_6N_2{\cdot}ClO_4{\cdot}H_2O$ (693.90): calcd. C 44.6, H 5.7, N 16.0; found C 61.4, H 5.9, N 13.5. MS (DEI): *m*/*z* (%) = 82 (100) [*N*-methylimidazole], 418 (25) [M^+(**Fe1**)].

$Na[Fe2(NO_2)_2](MeOH)_2(H_2O)_{0.5}$: Fe2Cl (0.032 g, 0.05 mmol) was suspended in methanol (5 mL). A solution of sodium nitrite in methanol/water (1 M, 5 mL) was then added. After a few days, black crystals were obtained. The product was collected, washed with a little methanol and dried in vacuo. Yield: 0.01 g (40%). IR (Nujol): $\nu_{C=O}$ = 1665 cm^{-1}. MS (ESI neg.): *m*/*z* (%) = 512 (100) [M^-(**$Fe2(NO_2)$**)], 558.1 (50) [M^-{**$Fe2(NO_2)_2$**}].

The following procedures were carried out only with the aim of obtaining crystals suitable for X-ray investigations. No yield is given and the main product in the solution may have another identity. Crystal growth was accomplished by using a temperature gradient or different solubility in different solvents. The choice of the counterion may be crucial for crystallisation of the compound. Dropwise addition of nonpolar solvents (*n*-heptane and *n*-hexane are not suitable) can also be used for crystallisation. The addition of water may be used as a last alternative in the case of water-miscible solvents.

$(BzEt_3N)[Fe1(SCN)_2]$: Fe1I (30 mg) was dissolved in 15 mL of a saturated solution of $(BzEt_3N)SCN$ in water/methanol (1:1).

$Et_4N[Fe2(CN)_2](H_2O)_{0.5}$: Fe2I (30 mg) was dissolved in a saturated solution of Et_4NCN in water (15 mL). The mixture was heated and filtered while still hot.

$[Fe2(NO_2)OH_2](MeOH)$: Fe2I (30 mg) was dissolved in methanol (15 mL). The solution was added dropwise to a heated saturated solution of nBu_4NNO_2 in water/methanol (4:1).

$(nBu_4N)_2[Fe3(NO_2)NO_x](NO_2)(H_2O)$: Fe3I (40 mg) was dissolved in dichloromethane (30 mL) and 5 mL of this solution was added to a saturated solution of nBu_4NNO_2 in methanol.

Crystal Structure Determination: The intensity data for the compounds were collected with a Nonius KappaCCD diffractometer, using graphite-monochromated Mo-K_α radiation. Data were corrected for Lorentz and polarisation effects, but not for absorption.[48a,48b] The structures were solved by direct methods (SHELXS[49]) and refined by full-matrix least-squares techniques against F_o^2 (SHELXL-97[50]). The hydrogen atoms were included at calculated positions with fixed thermal parameters. All non-hydrogen atoms were refined anisotropically.[50] Na[**$Fe2(NO_2)_2$**]$(MeOH)_2(H_2O)_{0.5}$ shows a disordered methanol and water molecule with the same oxygen position. This disorder could be solved. The data for compound **Fe1Cl** are not of adequate quality, although the esd's are good enough to be discussed in this paper. For **Fe2**, $[Fe3(Py)_2]PF_6$ and $(nBu_4N)_2$[**$Fe3(NO_2)NO_x$**]$(NO_2)(H_2O)$ we are only publishing the conformation of the central complex unit and the crystallographic data; we will not deposit the data with the Cambridge Crystallographic Data Centre. XP (SIEMENS Analytical X-ray Instruments, Inc.) was used for structure representations.

Crystal Data for Fe1:[51] $C_{18}H_{26}FeN_4O_4$, M_r = 418.28 g mol^{-1}, brown prism, size 0.32×0.20×0.12 mm, monoclinic, space group $P2_1/c$, a = 12.5031(4), b = 11.0732(4), c = 27.4969(6) Å, β = 92.798(2)°, V = 3802.4(2) $Å^3$, T = –90 °C, Z = 8, $\rho_{calcd.}$ =

 © 2005 Wiley-VCH Verlag GmbH & Co. KGaA, Weinheim

1.461 g cm^{-3}, μ(Mo-K_α) = 8.25 cm^{-1}, F(000) = 1760, 11872 reflections in h(–16/16), k(–14/13), l(–34/33), measured in the range 1.63° $\leq \theta \leq$ 27.47°, completeness for θ_{max} 90.8%, 7906 independent reflections, R_{int} = 0.028, 5880 reflections with $F_o > 4\sigma(F_o)$, 508 parameters, 0 restraints, $R1_{obs}$ = 0.050, wR^2_{obs} = 0.127, $R1_{all}$ = 0.075, wR^2_{all} = 0.142, GOOF = 0.988, largest difference peak/hole: 0.446/–0.409 e Å^{-3}.

Crystal Data for Fe1MeOH:[51] $C_{19}H_{30}FeN_4O_5$, M_r = 450.32 g mol^{-1}, brown prism, size 0.10 × 0.09 × 0.08 mm, monoclinic, space group $P2_1/n$, a = 7.3249(2), b = 29.5441(9), c = 9.7511(3) Å, β = 94.912(2)°, V = 2102.46(11) Å^3, T = –90 °C, Z = 4, $\rho_{calcd.}$ = 1.423 g cm^{-3}, μ(Mo-K_α) = 7.55 cm^{-1}, F(000) = 952, 8074 reflections in h(–9/9), k(–38/38), l(–12/12), measured in the range 2.76° $\leq \theta \leq$ 27.49°, completeness for θ_{max} 97.2%, 4694 independent reflections, R_{int} = 0.033, 3559 reflections with $F_o > 4\sigma(F_o)$, 271 parameters, 0 restraints, $R1_{obs}$ = 0.038, wR^2_{obs} = 0.093, $R1_{all}$ = 0.060, wR^2_{all} = 0.105, GOOF = 0.838, largest difference peak/hole: 0.349/–0.283 e Å^{-3}.

Crystal Data for Fe2: $C_{22}H_{26}FeN_4O_4$, triclinic, space group $P\bar{1}$, a = 13.019(3), b = 13.753(3), c = 13.757(3) Å, α = 103.28(3), β = 117.00(3), γ = 97.04(3)°, V = 2061.7(8) Å^3, T = –90 °C, Z = 4, F(000) = 976, 5550 measured reflections, 5192 independent reflections, R_{int} = 0.045, 3598 reflections with $I > 2\sigma(I)$, 535 parameters, 0 restraints, $R1$ = 0.162, wR^2 = 0.338, GOOF = 1.052, largest residual electron density: 1.129 e Å^{-3}. Due to technical problems, the measurement stopped too early and reflections at high θ angles are missing. Therefore, the anisotropy refinement and hydrogen atoms were set aside resulting in a dissatisfactory $R1$ value and a high remaining maximum electron density.

Crystal Data for Fe1Cl:[51] $C_{18}H_{26}ClFeN_4O_4$, M_r = 453.73 g mol^{-1}, brown prism, size 0.20 × 0.18 × 0.12 mm^3, monoclinic, space group $P2_1/n$, a = 13.5466(6), b = 7.8215(4), c = 18.5515(9) Å, β = 96.539(3)°, V = 1952.83(16) Å^3, T = –90 °C, Z = 4, $\rho_{calcd.}$ = 1.543 g cm^{-3}, μ(Mo-K_α) = 9.42 cm^{-1}, F(000) = 948, 7129 reflections in h(–17/15), k(–10/9), l(–23/24), measured in the range 3.42° $\leq \theta \leq$ 27.52°, completeness for θ_{max} 96.2%, 4320 independent reflections, R_{int} = 0.065, 3701 reflections with $F_o > 4\sigma(F_o)$, 257 parameters, 0 restraints, $R1_{obs}$ = 0.130, wR^2_{obs} = 0.207, $R1_{all}$ = 0.156, wR^2_{all} = 0.216, GOOF = 1.248, largest difference peak and hole: 1.009/–1.123 e Å^{-3}.

Crystal Data for Fe3(Py)$_2$:[51] $C_{36}H_{36}FeN_6O_4$, triclinic, space group $P\bar{1}$, a = 10.6327(3), b = 12.0421(4), c = 14.7871(5) Å, α = 66.015(2), β = 71.582(2), γ = 66.368(2)°, V = 1558.09(9) Å^3, T = –90 °C, Z = 2, F(000) = 704, 12217 measured reflections, 7108 independent reflections, R_{int} = 0.028, 6385 reflections with $I > 2\sigma(I)$, 424 parameters, 0 restraints, $R1$ = 0.044, wR^2 = 0.103, GOOF = 1.016, largest residual electron density: 0.421 e Å^{-3}.

Crystal Data for [Fe3(Py)$_2$]PF$_6$: $C_{36}H_{36}F_6FeN_6O_4P$, orthorhombic, space group $Pbca$, a = 16.840(3), b = 20.335(4), c = 20.857(4) Å, V = 7142(3) Å^3, T = –90 °C, Z = 8, μ(Mo-K_α) = 5.65 cm^{-1}, F(000) = 3368. The data are not of the best quality and so we are publishing only the conformation of the molecule, although the distances and angles are of plausible size.

Crystal Data for [Fe1(Py)$_2$]PF$_6$:[51] $C_{28}H_{36}F_6FeN_6O_4P$, monoclinic, space group $P2_1/n$, a = 9.211(2), b = 14.861(3), c = 24.180(5) Å, β = 100.51(3)°, V = 3254.2(11) Å^3, T = 20 °C, Z = 4, F(000) = 1492, 8631 measured reflections, 4697 independent reflections, R_{int} = 0.028, 3596 reflections with $I > 2\sigma(I)$, 442 parameters, 0 restraints, $R1$ = 0.052, wR^2 = 0.138, GOOF = 1.067, largest residual electron density: 0.436 e Å^{-3}.

Crystal Data for [Fe1(N-MeIm)$_2$]ClO$_4$(H$_2$O):[51] $C_{26}H_{40}ClFeN_8O_9$, monoclinic, space group $P2_1/n$, a = 14.897(1), b = 13.613(1), c = 16.096(1) Å, β = 95.950(7)°, V = 3246.6(4) Å^3, T = –90 °C, Z = 4, F(000) = 1468, 12274 measured reflections, 7233 independent reflections, R_{int} = 0.082, 4759 reflections with $I > 2\sigma(I)$, 425 parameters, 0 restraints, $R1$ = 0.131, wR^2 = 0.238, GOOF = 1.140, largest residual electron density: 0.552 e Å^{-3}.

Crystal Data for (BzEt$_3$N)[Fe1(NCS)$_2$]:[51] $C_{33}H_{48}FeN_7O_4S_2$, monoclinic, space group $P2_1/n$, a = 11.7266(2), b = 24.7177(6), c = 12.7940(2) Å, β = 96.551(1)°, V = 3684.19(12) Å^3, T = –90 °C, Z = 4, F(000) = 1540, 7450 measured reflections, 7450 independent reflections, 5659 reflections with $I > 2\sigma(I)$, 487 parameters, 0 restraints, $R1$ = 0.056, wR^2 = 0.118, GOOF = 1.055, largest residual electron density: 0.415 e Å^{-3}.

Crystal Data for Et$_4$N[Fe2(CN)$_2$](H$_2$O):[51] $C_{32}H_{48}FeN_7O_5$, monoclinic, space group $P2_1/n$, a = 11.1860(2), b = 11.8490(4), c = 25.0733(9) Å, β = 92.355(2)°, V = 3320.5(5) Å^3, T = –90 °C, Z = 4, F(000) = 1420, 13220 measured reflections, 7482 independent reflections, R_{int} = 0.062, 4899 reflections with $I > 2\sigma(I)$, 446 parameters, 0 restraints, $R1$ = 0.063, wR^2 = 0.119, GOOF = 1.010, largest residual electron density: 0.436 e Å^{-3}.

Crystal Data for [Fe2(NO$_2$)OH$_2$](MeOH):[51] $C_{23}H_{29}FeN_6O_{10}$, orthorhombic, space group $Pna2_1$, a = 16.273(1), b = 11.6454(7), c = 13.8026(7) Å, V = 2615.7(3) Å^3, T = –90 °C, Z = 4, F(000) = 1180, 5725 measured reflections, 5725 independent reflections, 4004 reflections with $I > 2\sigma(I)$, 344 parameters, 1 restraint (origin of the unit cell), $R1$ = 0.077, wR^2 = 0.138, GOOF = 1.031, largest residual electron density: 0.507 e Å^{-3}.

Crystal Data for Na[Fe2(NO$_2$)$_2$](MeOH)$_2$(H$_2$O)$_{0.5}$:[51] $C_{46.4}H_{67.2}Fe_2N_{12}Na_2O_{22}(CH_4O)_2$, M_r = 1366.89 g mol^{-1}, red-brown prism, size 0.12 × 0.10 × 0.09 mm, monoclinic, space group $P2_1/n$, a = 11.3381(3), b = 13.3795(6), c = 21.1046(8) Å, β = 102.522(2)°, V = 3125.4(2) Å^3, T = –90 °C, Z = 2, $\rho_{calcd.}$ = 1.452 g cm^{-3}, μ(Mo-K_α) = 5.65 cm^{-1}, F(000) = 1431, 11116 reflections in h(–14/14), k(–14/17), l(–27/27), measured in the range 1.89° $\leq \theta \leq$ 27.48°, completeness for θ_{max} 98.8%, 7082 independent reflections, R_{int} = 0.033, 5071 reflections with $F_o > 4\sigma(F_o)$, 419 parameters, 0 restraints, $R1_{obs}$ = 0.0546, wR^2_{obs} = 0.1280, $R1_{all}$ = 0.0886, wR^2_{all} = 0.146, GOOF = 0.962, largest difference peak/hole: 0.845/–0.619 e Å^{-3}.

Crystal Data for (nBu$_4$N)$_2$[Fe3(NO$_2$)NO$_x$](NO$_2$)(H$_2$O): $C_{58}H_{100}FeN_9O_{11}$ (x = 2), M_r = 1161.32 g mol^{-1}, green prism, size 0.34 × 0.32 × 0.20 mm, triclinic, space group $P\bar{1}$, a = 12.961(3), b = 15.203(4), c = 17.985(4) Å, α = 94.779(9), β = 106.047(9), γ = 107.84(1)°, V = 3186.9(13) Å^3, T = –90 °C, measured in the range 3.03° $\leq \theta \leq$ 27.59°.

Crystal Data for (Fe1)$_2$dabco:[51] $C_{42}H_{64}Fe_2N_{10}O_8$, M_r = 948.73 g mol^{-1}, brown prism, size 0.10 × 0.09 × 0.08 mm, triclinic, space group $P\bar{1}$, a = 8.3623(2), b = 11.8244(3), c = 12.6364(3) Å, α = 110.604(2), β = 100.490(2), γ = 100.238(2)°, V = 1109.61(5) Å^3, T = –90 °C, Z = 1, $\rho_{calcd.}$ = 1.420 g cm^{-3}, μ(Mo-K_α) = 7.17 cm^{-1}, F(000) = 502, 8736 reflections in h(–10/10), k(–14/15), l(–16/16), measured in the range 2.03° $\leq \theta \leq$ 27.46°, completeness for θ_{max} 99.6%, 5057 independent reflections, R_{int} = 0.0221, 4346 reflections with $F_o > 4\sigma(F_o)$, 307 parameters, 0 restraints, $R1_{obs}$ = 0.0490, wR^2_{obs} = 0.1398, $R1_{all}$ = 0.0586, wR^2_{all} = 0.1478, GOOF = 1.018, largest difference peak/hole: 1.059/–0.673 e Å^{-3}.

Crystal Data for (Fe2)$_2$dabco:[51] $C_{50}H_{64}Fe_2N_{10}O_8$, M_r = 1044.81 g mol^{-1}, black prism, size 0.10 × 0.09 × 0.08 mm, monoclinic, space group $P2_1/n$, a = 11.8119(2), b = 13.1486(3), c = 16.7867(3) Å, α = 90.00, β = 108.6320(10), γ = 90.00°, V = 2470.50(8) Å^3, T = –90 °C, Z = 2, $\rho_{calcd.}$ = 1.405 g cm^{-3}, μ(Mo-K_α) = 6.52 cm^{-1}, F(000) = 1100, 18857 reflections in h(–14/15), k(–17/

 © 2005 Wiley-VCH Verlag GmbH & Co. KGaA, Weinheim

17), *l*(–21/20), measured in the range 2.39° ≤ θ ≤ 27.47°, completeness for θ_{max} 99.8%, 5644 independent reflections, R_{int} = 0.0422, 4402 reflections with $F_o > 4\sigma(F_o)$, 308 parameters, 0 restraints, $R1_{obs}$ = 0.0516, wR^2_{obs} = 0.1412, $R1_{all}$ = 0.0710, wR^2_{all} = 0.1535, GOOF = 1.026, largest difference peak/hole: 1.094/–0.833 e Å^{-3}.

Crystal Data for (Fe3)$_2$dabco:[51] $C_{58}H_{64}Fe_2N_{10}O_8{\cdot}CH_3OH$, M_r = 1172.93 g mol^{-1}, dark-green prism, size 0.10 × 0.09 × 0.08 mm, triclinic, space group $P\bar{1}$, a = 11.3944(6), b = 12.2186(8), c = 13.1020(8) Å, α = 116.067(4), β = 113.938(3), γ = 93.166(4)°, V = 1435.76(15) Å^3, T = –90 °C, Z = 1, $\rho_{calcd.}$ = 1.357 g cm^{-3}, μ(Mo-K_α) = 5.7 cm^{-1}, F(000) = 616, 10088 reflections in *h*(–14/14), *k*(–15/14), *l*(–16/16), measured in the range 2.04° ≤ θ ≤ 27.40°, completeness for θ_{max} 98.3%, 6431 independent reflections, R_{int} = 0.0396, 5119 reflections with $F_o > 4\sigma(F_o)$, 387 parameters, 0 restraints, $R1_{obs}$ = 0.1018, wR^2_{obs} = 0.2585, $R1_{all}$ = 0.1240, wR^2_{all} = 0.2702, GOOF = 1.160, largest difference peak/hole: 1.090/–0.734 e Å^{-3}.

Acknowledgments

We gratefully acknowledge financial support from the Deutsche Forschungsgemeinschaft and the Fonds der Chemischen Industrie. The authors thank Dr. V. Schünemann and P. Wegner (Lübeck) for the Mössbauer spectrum, Dr. W. Poppitz and S. Schönau for the MS measurements, Dr. M. Friedrich and B. Rambach for measuring the ESR spectra, and Dr. K. Karaghiosoff for measuring the ^{1}H NMR spectrum of **Fe1Cl**.

[1] W. Kaim, B. Schwederski, "Bioinorganic Chemistry: Inorganic Elements", in *The Chemistry of Life*, John Wiley & Sons, Chichester, **1994.**

[2] *The Porphyrin Handbook* (Eds.: K. M. Kadish, K. M. Smith, R. Guilard), Elsevier–Academic Press, **1999**, vol. 1–10 and **2003**, vol. 11–20.

[3] T. Tsumaki, *Bull. Chem. Soc. Jpn.* **1938**, *13*, 252.

[4] a) E. N. Jacobsen, *Comprehensive Organometallic Chemistry II* (Eds.: G. Wilkinson, F. G. A. Stone, E. W. Abel, L. S. Hegedus), Pergamon, New York, **1995**, vol. 12 chapter 11.1; b) T. Katsuki, *Coord. Chem. Rev.* **1995**, *140*, 189.

[5] a) E.-G. Jäger, in *Chemistry at the Beginning of the Third Millennium* (Eds.: L. Fabbrizzi, A. Poggi), Springer-Verlag, Berlin, Heidelberg, New York, **2000**, p. 103; b) E.-G. Jäger, J. Knaudt, K. Schuhmann, A. Guba, in *Peroxide Chemistry – Mechanistic and Preparative Aspects of Oxygen Transfer* (Ed.: W. Adam), Wiley-VCH, Weinheim, **2000**, p. 249; c) E.-G. Jäger, St. Barth, H. Keutel, F. Wiesemann, U. Gaudig, in *Bioinorganic Chemistry – Transition Metals in Biology and their Coordination Chemistry* (Ed.: A. X. Trautwein), Wiley-VCH, Weinheim, **1997**, p. 584.

[6] a) E.-G. Jäger, *Z. Anorg. Allg. Chem.* **1969**, *364*, 177; b) E.-G. Jäger, *Z. Chem.* **1964**, *4*, 437.

[7] a) P. Mountford, *Chem. Soc. Rev.* **1998**, *27*, 105; b) F. A. Cotton, J. Czuchajowska, *Polyhedron* **1990**, *9*, 2553.

[8] a) R. Wegner, M. Gottschaldt, H. Görls, E.-G. Jäger, D. Klemm, *Chem. Eur. J.* **2001**, *7*, 2143; *Angew. Chem.* **2000**, *112*, 608; *Angew. Chem. Int. Ed.* **2000**, *39*, 595; b) H. Keutel, H. Görls, W. Poppitz, A. Schütz, E.-G. Jäger, *J. Prakt. Chem.* **1999**, *341*, 785; c) H. Elias, D. Hess, H. Paulus, E.-G. Jäger, F. Gräfe, *Z. Anorg. Allg. Chem.* **1990**, *101*, 101; d) E.-G. Jäger, K. Müller, *Z. Anorg. Allg. Chem.* **1985**, *526*, 29; e) E.-G. Jäger, K. Müller, *Z. Anorg. Allg. Chem.* **1981**, *482*, 201.

[9] a) Y. Nishida, K. Hayashida, N. Oishi, S. Kida, *Inorg. Chim. Acta* **1980**, *38*, 213; b) V. V. Minin, Yu. V. Rakitin, G. M. Larin, E.-G. Jäger, *Zh. Neorg. Khim.* **1981**, *26*, 650; *Chem. Abstr.* **1981**, *94*, 200292z.

[10] a) D. G. Pillsbury, D. H. Busch, *J. Am. Chem. Soc.* **1976**, *98*, 7836; b) J. A. Streeky, D. G. Pillsbury, D. H. Busch, *Inorg. Chem.* **1980**, *19*, 3148; c) Yu. E. Kovalenko, Ya. D. Lampeka, I. Ya. Levitin, K. B. Yatsimirkii, K. Müller, D. Seidel, E.-G. Jäger, *Russ. Chem. Bull.* **1993**, *42*, 981 (Engl. Transl. from *Izv. Akad. Nauk Ser. Khim.* **1993**, no. 6, 1092); d) E.-G. Jäger, H. Keutel, M. Rudolph, B. Krebs, F. Wiesemann, *Chem. Ber.* **1995**, *128*, 503.

[11] a) E.-G. Jäger, M. Rudolph, R. Müller, *Z. Chem.* **1978**, *18*, 229; b) E.-G. Jäger, P. Renner, R. Schmidt, *Z. Chem.* **1978**, *18*, 193; c) E.-G. Jäger, B. Kirchhof, E. Schmidt, B. Remde, A. Kipke, R. Müller, *Z. Anorg. Allg. Chem.* **1982**, *485*, 141; d) E.-G. Jäger, G. Schlenvoigt, B. Kirchhof, M. Rudolph, R. Müller, *Z. Anorg. Allg. Chem.* **1982**, *485*, 173; e) E.-G. Jäger, K. Schuhmann, H. Görls, *Inorg. Chim. Acta* **1997**, *255*, 295; E.-G. Jäger, K. Schuhmann, H. Görls, *Chem. Ber./Recueil* **1997**, *130*, 1643; f) K. Schuhmann, E.-G. Jäger, *Eur. J. Inorg. Chem.* **1998**, 2051.

[12] a) K. Kubokura, H. Okawa, S. Kida, *Bull. Chem. Soc. Jpn.* **1978**, *51*, 2036; b) G. M. Larin, V. V. Minin, E.-G. Jäger, P. Renner, *Zh. Neorg. Khim.* **1980**, *25*, 183; *Chem. Abstr.* **1980**, *92*, 139940z; c) E.-G. Jäger, K. Müller, *Z. Anorg. Allg. Chem.* **1983**, *501*, 40; d) E.-G. Jäger, J. Knaudt, M. Rudolph, M. Rost, *Chem. Ber.* **1996**, *129*, 1041; e) J. Knaudt, St. Förster, U. Bartsch, A. Rieker, E.-G. Jäger, *Z. Naturforsch., Teil B* **2000**, *55*, 86; f) R. Wegner, M. Gottschaldt, W. Poppitz, E.-G. Jäger, D. Klemm, *J. Mol. Catal. A: Chem.* **2003**, *201*, 91.

[13] M. Rudolph, S. Dautz, E.-G. Jäger, *J. Am. Chem. Soc.* **2000**, *122*, 10821.

[14] a) E.-G. Jäger, D. Seidel, M. Rudolph, A. Schneider, *Z. Chem.* **1986**, *26*, 76; b) H. Görls, G. Reck, E.-G. Jäger, K. Müller, D. Seidel, *Cryst. Res. Technol.* **1990**, *25*, 1277.

[15] a) D. P. Riley, J. A. Stone, D. H. Busch, *J. Am. Chem. Soc.* **1977**, *99*, 767; b) D. P. Riley, D. H. Busch, *Inorg. Chem.* **1984**, *23*, 3235; c) T. J. Truex, R. H. Holm, *J. Am. Chem. Soc.* **1972**, *94*, 4529; d) S. Koch, R. H. Holm, R. B. Frankel, *J. Am. Chem. Soc.* **1975**, *97*, 6714.

[16] a) V. L. Goedken, J. J. Pluth, S.-M. Peng, B. Bursten, *J. Am. Chem. Soc.* **1976**, *98*, 8014; b) M. C. Weiss, B. Bursten, S.-M. Peng, V. L. Goedken, *J. Am. Chem. Soc.* **1976**, *98*, 8021; c) V. L. Goedken, S. M. Peng, J. Molin-Norris, Y. Park, *J. Am. Chem. Soc.* **1976**, *98*, 8391; d) V. L. Goedken, Y.-A. Park, *J. Chem. Soc., Chem. Commun.* **1975**, 214.

[17] a) E.-G. Jäger, *Vortragsberichte zum Symposium "Koordinationschemie der Übergangselemente"*, Sektion C, Jena **1969**, p. 96; b) E.-G. Jäger, E. Stein, F. Gräfe, W. Schade, *Z. Anorg. Allg. Chem.* **1985**, *526*, 15; c) E.-G. Jäger, F. Gräfe, *Z. Anorg. Allg. Chem.* **1988**, *561*, 25.

[18] a) F. Wiesemann, R. Wonnemann, B. Krebs, H. Keutel, E.-G. Jäger, *Angew. Chem. Int. Ed. Engl.* **1994**, *33*, 1363; b) I. Käpplinger, H. Keutel, E.-G. Jäger, *Inorg. Chim. Acta* **1999**, *291*, 190; c) I. Käpplinger, M. Grodzicki, V. Schünemann, H. Görls, A. X. Trautwein, E.-G. Jäger, private communication, Cambridge Crystallographic Data Centre, CSD 408794/5, October **1998**.

[19] a) E.-G. Jäger, *Z. Chem.* **1985**, *25*, 446; b) E.-G. Jäger, B. Schweder, S. Radzuweit, *Z. Chem.* **1988**, *28*, 152; c) E.-G. Jäger, H. Keutel, *Inorg. Chem.* **1997**, *36*, 3512.

[20] H. Keutel, I. Käpplinger, E.-G. Jäger, M. Grodzicki, V. Schünemann, A. X. Trautwein, *Inorg. Chem.* **1999**, *38*, 2320.

[21] E.-G. Jäger, H. Hähnel, H.-F. Klein, A. Schmidt, *J. Prakt. Chem.* **1991**, *333*, 423.

[22] a) B. Weber, H. Görls, M. Rudolf, E.-G. Jäger, *Inorg. Chim. Acta* **2002**, *337*, 247; b) B. Weber, PhD Thesis, University of Jena, **2002**; c) B. Weber, *A Contribution to a Deeper Understanding of the Nature of the Iron–Nitrosyl Bond in Bioanalogue Iron Complexes*, Der Andere Verlag, Osnabrück, **2003**.

[23] a) K. Müller, E.-G. Jäger, *Z. Anorg. Allg. Chem.* **1989**, *577*, 195; b) E.-G. Jäger, D. Seidel, W. Schade, *Z. Chem.* **1983**, *23*, 32; c) E.-G. Jäger, D. Seidel, *Z. Chem.* **1983**, *23*, 261; d) W. Schade, E.-G. Jäger, K. Müller, D. Seidel, *J. Prakt. Chem.* **1989**, *331*, 559.

 © 2005 Wiley-VCH Verlag GmbH & Co. KGaA, Weinheim

[24] a) O. K. Medhi, J. Silver, *J. Chem. Soc., Chem. Commun.* **1989**, 1199; b) A. Hudson, H. J. Whitfield, *Inorg. Chem.* **1967**, *6*, 1120.
[25] A. Walker, *Proton NMR and EPR spectroscopy of Paramagnetic Metalloporphyrins*, in *The Porphyrin Handbook* (Eds.: K. M. Kadish, K. M. Smith, R. Guilard), **2000**, Vol. 5, Ch. 36, p. 81.
[26] K. R. Levan, C. E. Strouse, *Abstract of paper, American Crystallographic Association Summer meeting*, Snowman, **1983**.
[27] a) E. Elkaim, K. Tanaka, P. Coppens, W. R. Scheidt, *Acta Crystallogr., Sect. B.* **1987**, *43*; 457; b) D. K. Geiger, Y. J. Lee, W. R. Scheidt, *J. Am. Chem. Soc.* **1984**, *106*, 6339.
[28] W. R. Scheidt, Y. J. Lee, *Struct. Bonding (Berlin)* **1987**, *64*, 1.
[29] *Nitric Oxide. Principles and Actions* (Ed.: J. Lancaster), Academic Press, San Diego, **1996**.
[30] P. L. Feldman, O. W. Griffith, D. J. Stuehr, *Chem. Eng. News* **1993**, *71*, 26.
[31] O. Einsle, A. Messerschmidt, P. Stach, G. P. Bourenkov, H. D. Bartunik, R. Huber, P. M. H. Kroneck, *Nature* **1999**, *400*, 476.
[32] a) H. Nasri, J. A. Goodwin, W. R. Scheidt, *Inorg. Chem.* **1990**, *29*, 185; b) H. Nasri, Y. Wang, B. H. Huynh, A. F. Walker, W. R. Scheidt, *Inorg. Chem.* **1991**, *30*, 1483; c) H. Nasri, K. J. Haller, Y. Wang, B. H. Huynh, W. R. Scheidt, *Inorg. Chem.* **1992**, *31*, 3459; d) M. K. Ellison, C. E. Schulz, W. R. Scheidt, *Inorg. Chem.* **1999**, *38*, 100; e) H. Nasri, M. K. Ellison, S. Chen, B. H. Huynh, W. R. Scheidt, *J. Am. Chem. Soc.* **1997**, *119*, 6724.
[33] L. Wolf, E.-G. Jäger, *Z. Anorg. Allg. Chem.* **1966**, *346*, 76.
[34] a) A. R. Newman, A. N. French, *Inorg. Chim. Acta* **1987**, *129*, L37; b) M. G. Finnegan, A. G. Lappin, W. R. Scheidt, *Inorg. Chem.* **1990**, *29*, 181; c) M. Frangione, J. Port, M. Baldiwala, A. Judd, J. Galley, M. DeVega, K. Linna, L. Caron, E. Anderson, J. A. Goodwin, *Inorg. Chem.* **1997**, *36*, 1904.
[35] a) T. Ikeue, Y. Ohgo, T. Yamaguchi, M. Takahashi, M. Takeda, M. Nakamura, *Angew. Chem. Int. Ed.* **2001**, *40*, 2617; b) W. O. Koch, V. Schünemann, M. Gerdan, A. X. Trautwein, H.-J. Krüger, *Chem. Eur. J.* **1998**, *4*, 686; c) F. V. Wells, S. W. McCann, H. H. Wickman, S. L. Kessel, D. N. Hendrickson, R. D. Feltham, *Inorg. Chem.* **1982**, *21*, 2306; d) E. König, G. Ritter, J. Dengler, L. F. Larkworthy, *Inorg. Chem.* **1992**, *31*, 1196.
[36] P. Gütlich, A. Hauser, H. Spiering, *Angew. Chem.* **1994**, *106*, 2109; *Angew. Chem. Int. Ed. Engl.* **1994**, *33*, 2024.
[37] a) M. Mylrajan, L. A. Andersson, J. Sun, T. M. Loer, C. S. Thomas, E. P. Sullivan Jr., M. A. Thomson, K. M. Long, O. P. Anderson, S. H. Strauss, *Inorg. Chem.* **1995**, *34*, 3953; b) H. Nasri, M. Debbabi, *Polyhedron* **1998**, *17*, 3607.
[38] a) W. R. Scheidt, Y. J. Lee, D. K. Geiger, K. Taylor, K. Hatano, *J. Am. Chem. Soc.* **1982**, *104*, 3367; b) D. K. Geiger, V. Chumplang, W. R. Scheidt, *Inorg. Chem.* **1985**, *24*, 4736.
[39] a) M. J. Maroney, E. O. Fey, D. A. Baldwin, R. E. Stenkamp, L. H. Jensen, N. J. Rose, *Inorg. Chem.* **1986**, *25*, 1409; b) L. Ballester, A. Gutierrez, M. F. Perpinan, S. Rico, M. T. Azcondo, C. Belletto, *Inorg. Chem.* **1999**, *38*, 4430.
[40] I. Käpplinger, PhD Thesis, University of Jena, **2002**.
[41] a) W. R. Scheidt, K. J. Haller, K. Hatano, *J. Am. Chem. Soc.* **1980**, *102*, 3017; b) M. Schappacher, J. Fischer, R. Weiss, *Inorg. Chem.* **1989**, *28*, 389; c) T. J. Bartczak, S. Wolowiec, L. Latos-Grazynski, *Inorg. Chim. Acta* **1998**, *277*, 242.
[42] M. Nakamura, T. Ikeue, H. Fujii, T. Toshimura, *J. Am. Chem. Soc.* **1997**, *119*, 6284.
[43] Autorenkollektiv, *Organikum*, Johann Ambrosius Barth Verlagsgesellschaft mbH, Leipzig, Berlin, Heidelberg, **1993**.
[44] M. Grodzicki, *J. Phys. B* **1980**, *13*, 2683.
[45] M. Grodzicki, "Theory and Application of the Self-Consistent-Charge Xα Method", habilitation thesis, Hamburg, Germany, **1985**.
[46] a) E.-G. Jäger, *Z. Chem.* **1968**, *8*, 30; b) E.-G. Jäger, *Z. Chem.* **1968**, *8*, 470.
[47] L. Claisen, *Justus Liebigs Ann. Chem.* **1897**, *279*, 1.
[48] a) *COLLECT, Data Collection Software*, B. V. Nonius, The Netherlands, **1998**; b) Z. Otwinowski, W. Minor, *Processing of X-ray Diffraction Data Collected in Oscillation Mode*, in *Methods in Enzymology, Macromolecular Crystallography, Part A* (Eds.: C. W. Carter, R. M. Sweet), Academic Press, San Diego, **1997**, vol. 276, p. 307.
[49] G. M. Sheldrick, *Acta Crystallogr., Sect. A* **1990**, *46*, 467.
[50] G. M. Sheldrick, *SHELXL-97*, University of Göttingen, Germany, **1993**.
[51] CCDC-240934 (**Fe1**), -240945 (**Fe1MeOH**), -240936 (**Fe1Cl**), -240937 {Na[**Fe2(NO$_2$)$_2$**](MeOH)$_2$(H$_2$O)$_{0.5}$}, -241784 [**Fe3(Py)$_2$**], -241781 {[**Fe1(Py)$_2$**]PF$_6$}, -241782 {[**Fe1(N-MeIm)$_2$**]ClO$_4$(H$_2$O)}, -241785 {(BzEt$_3$N)[**Fe1(NCS)$_2$**]}, -241783 {Et$_4$N[**Fe2(CN)$_2$**](H$_2$O)}, -241780 {[**Fe2(NO$_2$)OH$_2$**]MeOH}, -266535 [**(Fe1)$_2$dabco**], -266536 [**(Fe2)$_2$dabco**], and -266537 [**(Fe3)$_2$dabco**·MeOH] contain the supplementary crystallographic data for this paper. These data can be obtained free of charge from The Cambridge Crystallographic Data Centre via www.ccdc.cam.ac.uk/data_request/cif.

Received: September 13, 2004
Published Online: June 14, 2005

 © 2005 Wiley-VCH Verlag GmbH & Co. KGaA, Weinheim

Solvent-Mediated Redox Transformations of Ytterbium Bis(indenyl)-diazabutadiene Complexes

Alexander A. Trifonov,*[a] Elena A. Fedorova,[a] Vladimir N. Ikorskii,[b] Sebastian Dechert,[c][‡] Herbert Schumann,[c] and Mikhail N. Bochkarev[a]

Keywords: Diazadiene ligands / N ligands / Radical ions / Ytterbium

The reactions of diamagnetic $[(C_9H_7)_2Yb(THF)_2]$ (**2**) and [*rac*-$(CH_2\text{-}1\text{-}C_9H_6)_2Yb(THF)_2$] (**3**) with *t*BuN=CH–CH=N*t*Bu (DAD) in toluene result in the formation of the paramagnetic complexes $[(C_9H_7)_2Yb(DAD)]$ (**4**) and [*rac*-$(CH_2\text{-}1\text{-}C_9H_6)_2Yb$(DAD)] (**5**), respectively. The IR, UV/Vis, and ^{1}H NMR spectroscopic data, the magnetic properties, and the single-crystal X-ray diffraction studies of **4** and **5** indicate that in the solid state and in noncoordinating media both complexes are ytterbium(III) derivatives containing the DAD radical-anion, whereas the ^{1}H NMR and UV/Vis spectra of solutions of **4** and **5** in the coordinating solvent THF give evidence for divalent ytterbium. Recrystallization of **4** and **5** from THF/hexane results in the recovery of the starting ytterbium complexes **2** and **3** due to an unusual redox substitution of the radical anion of diazabutadiene by THF in the coordination sphere of ytterbium.
(© Wiley-VCH Verlag GmbH & Co. KGaA, 69451 Weinheim, Germany, 2005)

Introduction

During the past two decades, 1,4-disubstituted diazadienes have attracted considerable attention as useful ligands in transition metal chemistry due to their redox and coordination properties. The lone electron pair at both nitrogen atoms and the π-electrons of the C=N bonds allow theese molecules to act both as an n- and a π-electron donor. They can also coordinate metal atoms both as a neutral ligand[1] and, based on their quite pronounced electron affinity,[2] as a radical anion[3] or dianion[4] by accepting one or two electrons from the metal. Especially the ligand substituted at the nitrogen atoms with the bulky *tert*-butyl group (DAD) has been widely employed for the synthesis of stable complexes of electropositive lanthanides.[5] Considering the reduction state and the coordination mode of the DAD ligand, these compounds can be divided into two main groups. The first group contains homo- and hetero-ligated compounds containing the DAD radical anion coordinated to the lanthanide atom through two nitrogen atoms,[5] while in the second group the doubly reduced enediamido fragment is 2σ:π-bonded to the central metal atom.[6] Due to the low energy of the π*-orbital of diazadiene ligands,[2c] their complexes with ytterbium, a metal which has two stable oxidation states with a low Yb^{II}/Yb^{III} transformation potential,[7] are of particular interest with respect to intramolecular metal–ligand electron transfers. In our previous studies we have synthesized and structurally characterized the homoleptic ytterbium(III) complex $[(DAD)_3Yb]$ (**1**).[5c] In order to explain the results obtained for **1** from variable temperature magnetic measurements, a temperature-induced valence tautomerism has been suggested. Thus, complex **1** is assumed to exist as the divalent ytterbium derivative $[Yb^{II}(DAD^{-\cdot})_2(DAD^0)]$ at temperatures of 5 to 15 K, while in the temperature range 80 to 300 K the complex is transformed into the trivalent ytterbium compound $[Yb^{III}(DAD^{-\cdot})_3]$. Continuing our studies on intramolecular redox processes in DAD ytterbium complexes, we report here on unusual solvent-mediated redox transformations of the bis(indenyl)diazabutadieneytterbium complexes $[(Ind)_2Yb(DAD)]$.

[a] G. A. Razuvaev Institute of Organometallic Chemistry of Russian Academy of Sciences,
Tropinina 49, 603950 Nizhny Novgorod GSP-445, Russia
Fax: +7-8312-127-497
E-mail: trif@imoc.sinn.ru
[b] International Tomography Center of SB RAS,
Institutskaya str. 3a, 630090 Novosibirsk, Russia
E-mail: ikon@tomo.nsc.ru
[c] Institut für Chemie der Technischen Universität Berlin,
Straße des 17. Juni 135, 10623 Berlin, Germany
Fax: +49-30-3142-2168
E-mail: schumann@chem.tu-berlin.de
[‡] Present address: Institut für Anorganische Chemie, Georg August Universität Göttingen,
Tammannstr. 4, 37077 Göttingen, Germany
E-mail: dechert@chemie.uni-goettingen.de

Results and Discussion

The addition of *N*,*N*′-di-*tert*-butyl-1,4-diazabutadiene (DAD) in THF to THF solutions of $[(\eta^5\text{-Ind})_2Yb(THF)_2]$ [Ind = C_9H_7 (**2**), *rac*-$(CH_2\text{-}1\text{-}C_9H_6)$ (**3**)][8] does not cause any change in the color of the reaction mixtures and the ^{1}H NMR spectra of these mixtures show superposition of the spectra of the Yb^{II} complexes and of free DAD. Evapora-

 © 2005 Wiley-VCH Verlag GmbH & Co. KGaA, Weinheim DOI: 10.1002/ejic.200401014

tion of the solvent in vacuo leaves a deep-red solid which, on addition of toluene, dissolves with formation of a brown (for **2**) or greenish-black solution (for **3**). The ^{1}H NMR spectra of these solutions show a set of broadened signals indicative of the presence of paramagnetic Yb^{III} species and radical anionic [DAD]$^{-\cdot}$ (Scheme 1).

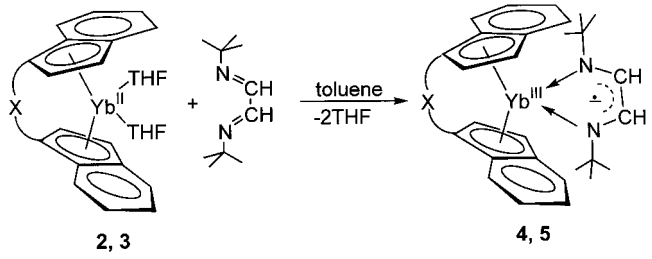

2, 3 **4, 5**

2, 4 X = no bridge; two seperated C_9H_7 ligands
3, 5 X = CH_2-CH_2

Scheme 1.

Cooling of the concentrated toluene solutions causes precipitation of the complexes [(η^5-Ind)$_2$Yb^{III}(DAD$^{-\cdot}$)] [Ind = C_9H_7 (**4**), *rac*-(CH_2-1-C_9H_6) (**5**)], which were isolated as dark-brown (**4**) and greenish-black (**5**) crystalline solids in yields of 74 and 81%, respectively. Both complexes are highly air- and moisture-sensitive, moderately soluble in toluene, and less soluble in hexane.

Crystals suitable for single-crystal X-ray diffraction studies were obtained by slow cooling of toluene solutions of **4** and **5** to –20 °C. Complex **5** crystallizes as a toluene solvate [*rac*-(CH_2-1-C_9H_6)$_2$Yb(DAD)](C_7H_8)$_{0.5}$. The molecular structures of **4** and **5** are depicted in Figures 1 and 2, respectively; crystal and structural refinement data are listed in Table 1.

In both compounds, the ytterbium atom is η^5-coordinated by the two cyclopentadienyl units of the indenyl ligands and the two nitrogen atoms of the radical anionic DAD ligand and adopts the geometry of a distorted tetrahedron. Complex **5** exists in the crystalline state only in the racemic form. The Yb–Cp$_{Centr.}$ distances in **4** [2.376(3) and 2.383(3) Å] as well as in **5** [2.371(2) and 2.383(2) Å] are shorter than those in the starting Yb^{II} complexes **2** [2.457(1) Å][9a,9b] and **3** [2.43(3)–2.45(3) Å][8b] and are close to the values reported for the indenylytterbium(III) derivatives [(1-C_4H_7-4,7-$Me_2C_9H_4$)$_2$Yb(μ-Cl)$_2$Li(THF)$_2$] [2.333(3) and 2.336(4) Å][10a] and [*meso*-(CH_2-1-C_9H_6)$_2$YbN($SiMe_3$)$_2$] [2.328(3) and 2.332(3) Å].[10b] The shortening of the Yb–Cp$_{Centr.}$ distances in **4** and **5** compared to those in **2** and **3** indicates the oxidation of the ytterbium atom from Yb^{II} to Yb^{III}.[11] However, in both cases the magnitude of the shortening is considerably less than would be expected on the basis of the difference in the ionic radii of Yb^{II} and Yb^{III} (0.155 Å). Further, it should be noted that the values of the Yb–Cp$_{Centr.}$ bond lengths in **4** and **5** lie between the corresponding values of [Cp$_2$Yb(DAD)] [2.324(7) and 2.334(4) Å][5g] and [Cp*$_2$Yb(DAD)] [2.401(2) and 2.414(2) Å][5h] and reflect the comparable steric demand of the cyclopentadienyl, pentamethylcyclopentadienyl, and indenyl ligands. Whereas the two Yb–N bond lengths in **4** [2.318(5) and 2.335(5) Å] as well as in **5** [2.321(4) and 2.343(5) Å] differ significantly between each other, the values still lie between the corresponding, almost equal values of [Cp$_2$Yb(DAD)] [2.309(9) and 2.306(9) Å][5g] and [Cp*$_2$Yb(DAD)] [2.385(4) and 2.394(3) Å].[5h] The Yb–N bond lengths in **4** and **5** are comparable to the lengths of the Yb^{III}–N coordination bonds in the compounds [Cp*$_2$Yb(bipy)] (2.32 Å),[12d] [{Cp*$_2$Yb(bipy)}$^+$-{Cp*$_2$YbCl$_2$}$^-$] (2.37 Å),[12d] [{Cp*$_2$Yb(phen)}$^+$(I)$^-$-(CH_2Cl_2)] (2.36 Å),[12d] and [Cp$_2$Yb($PzMe_2$)-($HpzMe_2$)] [2.360(6), 2.414(6) Å],[12e] but are much longer than the covalent Yb^{III}–N bonds in [(η^5-C_9H_7)$_2$YbN-($SiMe_3$)$_2$] [2.160(5), 2.163(5) Å],[12a] [(η^5-MeC_5H_4)$_2$Yb-(NPh_2)] [2.216(5) Å],[12b] [(η^5-MeC_5H_4)$_2$Yb(NPh_2)(THF)] [2.287(6) Å],[12b] and [{Li(THF)$_4$}{Yb(NPh_2)$_4$}] [2.188(9)–2.2401(9) Å].[12c] The bond lengths within the DAD ligand of **4** and **5** should indicate its radical-anionic character since an electron transfer to the LUMO of the ligand is expected to cause delocalization of the charge over the whole conjugated NCCN fragment, which involves changes in the bond lengths. Compared to the N=C [1.267(2) Å][13] and C–C bond lengths [1.467(2) Å][13] in the free DAD molecule, the N=C bonds in the DAD ligands of **4** [1.323(8) and 1.309(8) Å] and **5** [1.324(7) and 1.331(6) Å] are substantially elongated, while the C–C bonds [**4**: 1.412(9), **5**: 1.429(7) Å] are shortened and close to the values of aromatic carbon–carbon bonds.[14] This bonding situation is similar to that described for [Cp*$_2$Sm(DAD)],[5d] [Cp$_2$Yb(DAD)],[5g] and [Cp*$_2$Yb(DAD)],[5h] and proves the radical-anionic character of the DAD ligand in **4** and **5**. In summary, the struc-

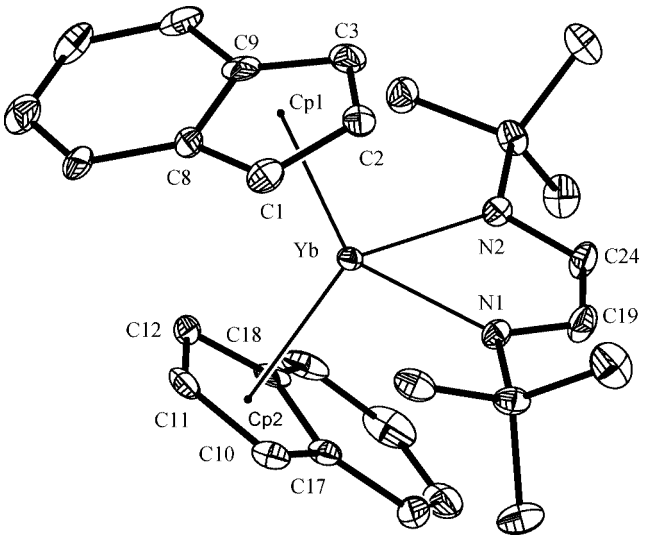

Figure 1. ORTEP diagram (30% probability thermal ellipsoids) of [(C_9H_7)$_2$Yb(DAD)] (**4**) showing the non-hydrogen-atom numbering scheme. Hydrogen atoms have been omitted for clarity. Relevant bond lengths [Å] and angles [°]: Yb–Cp1$_{Cent.}$ 2.383(3), Yb–Cp2$_{Cent.}$ 2.376(3), Yb–C1 2.630(7), Yb–C2 2.578(6), Yb–C3 2.616(6), Yb–C9 2.760(7), Yb–C8 2.770(6), Yb–C11 2.601(7), Yb–C12 2.605(6), Yb–C18 2.724(6), Yb–C17 2.741(6), Yb–C10 2.656(7), Yb–N2 2.318(5), Yb–N1 2.335(5), N1–C19 1.323(8), N2–C24 1.309(8), C19–C24 1.412(9); Cp1$_{Cent.}$–Yb–Cp2$_{Cent.}$ 125.44(11), N1–Yb–N2 74.35(19).

 © 2005 Wiley-VCH Verlag GmbH & Co. KGaA, Weinheim

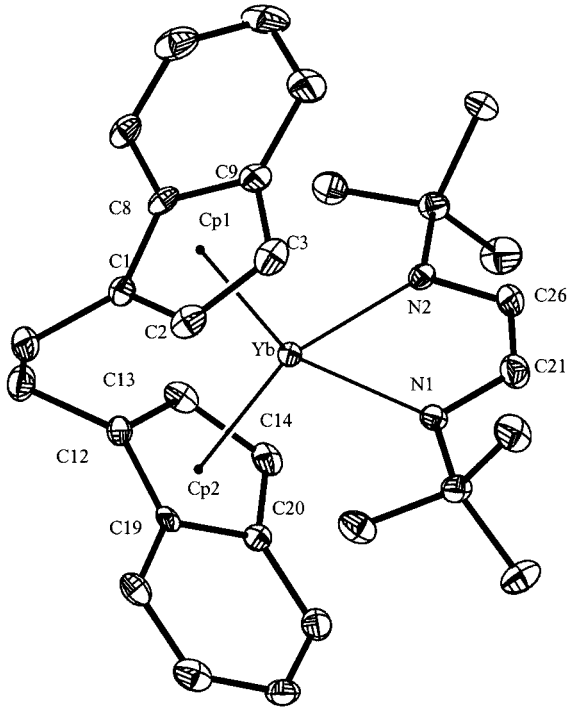

Figure 2. ORTEP diagram (30% probability thermal ellipsoids) of [*rac*-(CH_2-1-C_9H_6)$_2$Yb(DAD)] (**5**) showing the non-hydrogen-atom numbering scheme. Hydrogen atoms have been omitted for clarity. Relevant bond lengths [Å] and angles [°]: Yb–$Cp1_{Cent.}$ 2.371(2), Yb–$Cp2_{Cent.}$ 2.383(2), Yb–C1 2.646(5), Yb–C2 2.605(5), Yb–C3 2.623(5), Yb–C8 2.704(5), Yb–C9 2.719(5), Yb–C12 2.652(5), Yb–C13 2.590(5), Yb–C14 2.632(5), Yb–C19 2.750(5), Yb–C20 2.730(5), Yb–N1 2.321(4), Yb–N2 2.343(5), N1–C21 1.324(7), N2–C26 1.331(6), C21–C26 1.420(7); $Cp1_{Cent.}$–Yb–$Cp2_{Cent}$ 120.05(8), N1–Yb–N2 75.33(15).

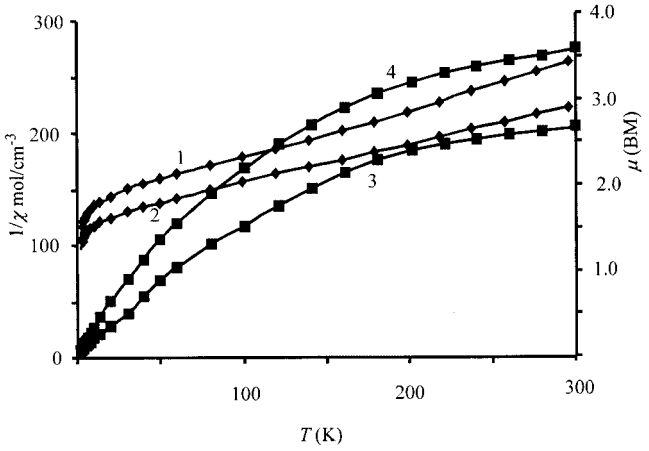

Figure 3. Thermal dependence of $1/\chi$ vs. T [K] and μ vs. T [K] for [(C_9H_7)Yb(DAD)] (**4**; curve 1: μ vs. T; curve 3: $1/\chi$ vs. T) and [*rac*-(CH_2-1-C_9H_6)$_2$Yb(DAD)] (**5**; curve 2: μ vs. T; curve 4: $1/\chi$ vs. T) at 5 kOe.

tural parameters of **4** and **5** are in agreement with the trivalent oxidation state of the ytterbium atom and the radical-anionic character of the DAD ligand. Unexpectedly, **4** and **5** are ESR silent in the temperature range 173 to 300 K in the solid state as well as in toluene solution. This fact is attributable either to a substantial broadening of the signal of the DAD radical anion in the field of the paramagnetic Yb^{III} ion or to antiferromagnetic coupling of the spin carriers.

Magnetic measurements of crystalline samples of **4** and **5** were carried out at 5 kOe in the temperature range 2 to 300 K. Plots of $1/\chi$ vs. T and μ vs. T are shown in Figure 3.

For **4** as well as for **5**, the measurements show a nonlinear dependence of the reciprocal value of the magnetic susceptibility χ as a function of temperature. The effective magnetic moments of the complexes increase from 1.6 μ_B (**4**) and 1.5 μ_B (**5**) at 2 K to 3.4 μ_B (**4**) and 3.0 μ_B (**5**) at 300 K. The values of the effective magnetic moments of **4** and **5** in benzene solution at 300 K, estimated according to the published procedure,[15] are in agreement with the data obtained for the crystalline samples by the SQUID method. The Yb^{III} ion has the electronic configuration $4f^{13}$ and is paramagnetic. The expected magnetic moment of Yb^{III} complexes is 3.8 μ_B at 5–30 K and 4.5 μ_B at 90–300 K;[16] the experimental values range from 3.4 to 4.9 μ_B.[17] An Yb^{III} complex that also contains a radical anion, as is suggested for **4** and **5**, should show a magnetic moment of 4.8 μ_B at room temperature provided that the spins of the two unpaired electrons do not interact. However, the experimental values of the magnetic moments obtained for **4** and **5** are considerably lower than the predicted ones, which could be caused either by redox tautomerism between paramagnetic [$(Ind)_2Yb^{III}(DAD^{\cdot-})$] and diamagnetic [$(Ind)_2Yb^{II}(DAD^0)$] molecules or antiferromagnetic coupling of the two unpaired electrons in [$(Ind)_2Yb^{III}(DAD^{\cdot-})$]. Recently, Andersen and co-workers studied the Yb^{III} complexes [Cp^*_2Yb(bipy)], [{1,3-t-$Bu_2C_5H_3$}$_2$Yb(phen)], and [Cp^*_2Yb(phen)] which contain an organic radical anion similar to **4** and **5**. They found effective magnetic moments at 300 K of 2.4, 3.4, and 4.0 μ_B, respectively. In order to interpret the low magnetic moments of these compounds, antiferromagnetic coupling between the spin carriers was postulated.[12d] Antiferromagnetic coupling between trivalent rare-earth ions and paramagnetic semiquinone ligands has been found also to be dominating for the series of complexes [Ln(DTBSQ)($HBPz_3$)$_2$] [Ln = Er, Tb, Dy, Yb; DTBSQ = 3,5-di-*tert*-butylsemiquinone, $HBPz_3$ = hydrotris(pyrazolyl)borate].[18] Hatfield and co-workers have described a strong exchange coupling between the lanthanide ions and the phthalocyaninato radical in bis(phthalocyaninato)lanthanide sandwich compounds [(Pc^{-2})Ln^{III}(Pc^{-1})] (Ln = Gd, Tb, Dy, Ho, Er, Tm, Yb, Lu). The value of the room-temperature magnetic moment for trivalent ytterbium antiferromagnetically coupled with an organic radical anion was calculated to be 3.46 μ_B.[19] Taking those results into account, the analysis of the $1/\chi$ vs. T and μ vs. T plots suggests that an antiferromagnetic spin interaction is a plausible reason for the low magnetic moments of **4** and **5**; however the available data do not allow us to exclude definitely the existence of redox tautomers.

The IR spectrum of neutral DAD shows two characteristic and strong absorption bands at 1620 and 1200 cm^{-1},

 © 2005 Wiley-VCH Verlag GmbH & Co. KGaA, Weinheim

which are assigned to the ν(C=N) and ν(C–N) vibrations, respectively. In the IR spectra of **4** and **5** the absorption at 1200 cm^{-1} is still very strong, but the band at about 1600 cm^{-1} is very weak, which identifies the DAD ligand as a radical anion. The infrared data of **4** and **5** are consistent with those of [Cp$_2$Yb(DAD)][5g] and [Cp*$_2$Yb(DAD)],[5h] complexes which also contain the radical-anionic DAD ligand.

The UV/Vis spectra of **4** and **5** in hexane show strong absorptions at 318 and 335 nm, respectively, which correspond well with the strong band of (DAD$^{-\cdot}$)Na$^+$ at 325 nm, but differ from that of neutral DAD at 285 nm, thus giving further proof of the radical-anionic character of the DAD ligand (Figure 4). In contrast, the spectra of **4** and **5** recorded in the coordinating solvent THF at room temperature show evidence for the formation of free DAD and the respective THF-coordinated indenylytterbium(II) complexes [(C$_9$H$_7$)$_2$Yb(THF)$_2$] and [*rac*-(CH$_2$-1-C$_9$H$_6$)$_2$Yb(THF)$_2$].

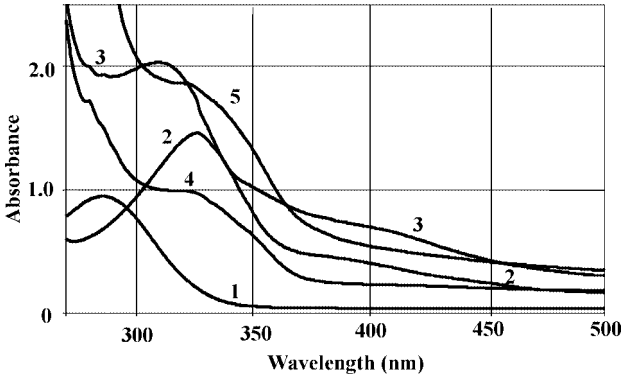

Figure 4. UV/Vis spectra. 1: DAD in hexane; 2: DAD$^{-\cdot}$Na$^+$ in THF; 3: [(C$_9$H$_7$)$_2$Yb(DAD)] (**4**) in hexane; 4: [(C$_9$H$_7$)$_2$Yb(DAD)] (**4**) in THF; 5: [(C$_9$H$_7$)$_2$Yb(THF)$_2$] (**2**) in THF.

According to the paramagnetism of **4** and **5**, their ^{1}H NMR spectra recorded in [D$_6$]benzene at 25 °C show a set of broadened signals that are substantially shifted with respect to those of comparable diamagnetic complexes (Figure 5 and Figure 6). The *tert*-butyl groups and the imino groups of the DAD ligand each gives rise to a singlet at δ = 27.90 (**4**) and 34.21 ppm (**5**) and a broad singlet at δ = –28.74 (**4**) and –18.53 ppm (**5**), respectively. The signals for the protons of the indenyl units appear at δ = 12.16, 10.41, –18.42, and –39.25 ppm in the intensity ratio of 2:2:2:1 for **4**, and at δ = 36.01, 32.74, 23.79, –0.85, –9.90, and –84.34 ppm with equal intensity for **5**. The proton signals of the ansa-ethylene group in **5** appear as two singlets at δ = –21.76 and –23.04 ppm. Variable temperature ^{1}H NMR measurements (–60 to 20 °C) of **4** in [D$_8$]toluene solution reveal a considerable temperature dependence of the chemical shift value of the imino protons (Figure 7), only a slight temperature dependence of the chemical shift value of the *tert*-butyl protons, and no temperature dependence of the chemical shift values of the indenyl protons.

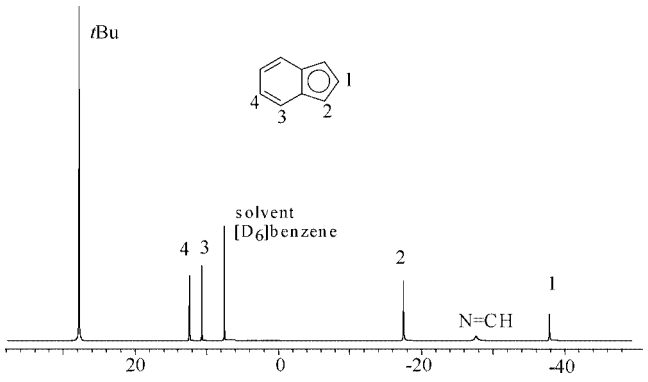

Figure 5. ^{1}H NMR spectrum of [(C$_9$H$_7$)$_2$Yb(DAD)] (**4**) in [D$_6$]benzene at 20 °C.

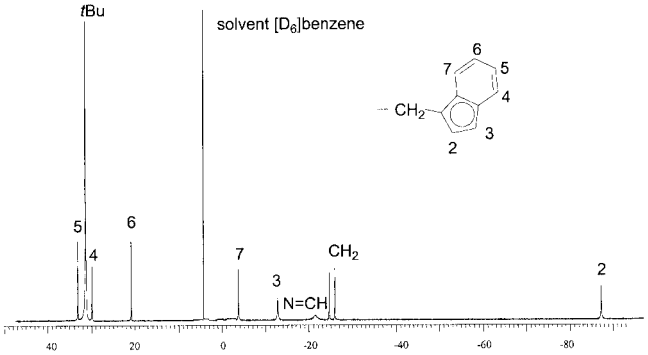

Figure 6. ^{1}H NMR spectrum of [*rac*-(CH$_2$-1-C$_9$H$_6$)$_2$Yb(DAD)] (**5**) in [D$_6$]benzene at 20 °C.

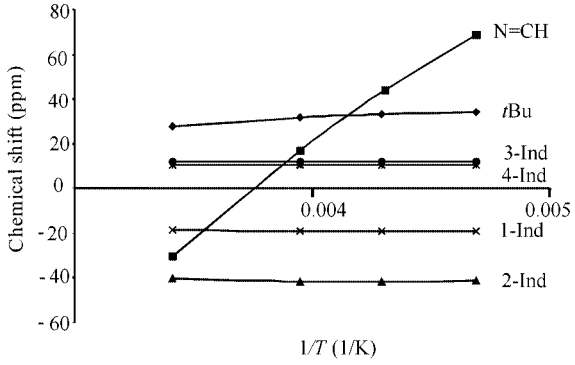

Figure 7. Variable temperature ^{1}H NMR spectroscopic data for [(C$_9$H$_7$)$_2$Yb(DAD)] (**4**) in [D$_8$]toluene: δ vs. 1/*T*.

The nature of the solvent influences the ^{1}H NMR spectra of **4** and **5** dramatically. Thus, in contrast to the ^{1}H NMR spectra of solutions of **4** and **5** in aromatic hydrocarbons, the spectra of solutions in the coordinating solvent [D$_8$]-THF show the sharp signals of DAD^0 and diamagnetic [(C$_9$H$_7$)$_2$Yb^{II}(THF)$_2$] or [*rac*-(CH$_2$-1-C$_9$H$_6$)$_2$Yb^{II}(THF)$_2$], respectively. It is worth noting that in the ^{1}H NMR spectra of solutions of **4** and **5** in [D$_8$]THF at 25 °C, recorded just after the preparation of the samples, the signals assigned to the diamagnetic Yb^{II} metallocenes (δ = 0 to 9 ppm) are still broad; they change to sharp signals with resolved coupling patterns only after about 6 h. The spectra of **4** and **5** in

 © 2005 Wiley-VCH Verlag GmbH & Co. KGaA, Weinheim

CD_2Cl_2 cannot be recorded since the complexes react with this solvent.

In order to isolate the indenylytterbium(II) species that is present in the THF solutions, we added hexane at 20 °C to concentrated THF solutions of **4** and **5** and isolated the starting ytterbium(II) metallocenes $[(C_9H_7)_2Yb^{II}(THF)_2]$ (**2**) and [*rac*-$(CH_2$-1-$C_9H_6)_2Yb^{II}(THF)_2$] (**3**) in high yields (82 and 73%, respectively). *N*,*N*′-Di-*tert*-butyl-1,4-diazabutadiene was identified and isolated from the mother liquor by chromatographic methods in almost quantitative yields (Scheme 2).

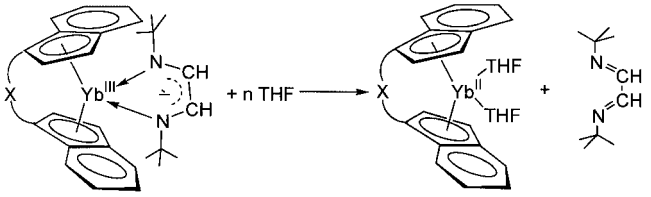

Scheme 2.

The above results allow the conclusion that complexes **4** and **5** exist as indenyl derivatives of trivalent ytterbium coordinated by the *N*,*N*′-di-*tert*-butyl-1,4-diazabutadiene radical anion $[(Ind)_2Yb^{III}(DAD^{-\cdot})]$ in the crystalline state as well as in noncoordinating solvents. Dissolution of **4** or **5** in coordinating solvents like THF causes displacement of the radical-anionic DAD ligand by THF molecules. This process implies an electron transfer from the diazadiene radical anion to the ytterbium(III) ion, resulting in the oxidation of the ligand to neutral DAD and reduction of Yb^{III} to Yb^{II}, followed by substitution of the neutral DAD ligand by two THF molecules. An analogous reductive substitution process has been established for the complex [Cp^*_2Yb-(DAD)], but not for [Cp_2Yb(DAD)] because of its shorter Yb–N distances.[5h] One can suppose that steric repulsion of the bulky indenyl and *N*,*N*′-di-*tert*-butyl-1,4-diazabutadiene ligands will be decisive for the examined reactions and the elongation and weakening of the Yb–N bonds in **4** and **5**. Hence, the energy of the Coulombic interaction between the $[(Ind)_2Yb^{III}]^+$ cationic species and the radical anion of diazadiene $DAD^{-\cdot}$ is comparable with that of the coordination bonds between Ind_2Yb^{II} and THF, and, as a result, the DAD ligand redox substitution becomes feasible. A similar behavior towards THF has been described by Evans and co-workers for decamethylsamarocene complexes with aromatic polycyclic ligands.[20] However, unlike the indenylytterbium complexes **4** and **5**, the samarium derivatives cannot be regenerated by removal of THF and addition of aromatic or aliphatic solvents.

Experimental Section

All experiments were performed in evacuated tubes, using standard Schlenk techniques, with rigorous exclusion of traces of moisture and air. THF, benzene, toluene, and hexane were purified by distillation from sodium/benzophenone ketyl and were condensed in vacuo prior to use. Indene (commercially available) was used after drying over molecular sieves. Commercially available 1,2-bis(indenyl)ethane was used as purchased (Dalchim). IR spectra were recorded as Nujol mulls on a Specord M80 spectrophotometer, and NMR spectra on a Bruker DPX200 spectrometer in [D_6]benzene, [D_8]THF, or [D_5]pyridine at 298 K. Chemical shifts for ^1H and ^{13}C NMR spectra were referenced internally using the residual solvent resonances and are reported relative to TMS. The UV/Vis spectra were recorded in evacuated quartz cuvettes on a Perkin–Elmer Lambda 25 spectrophotometer. The ESR spectra were measured on a Bruker ER 200D-1SRC instrument. GC analyses were performed with a Tzvet 530 gas chromatograph. Magnetic susceptibility measurements of solid samples were carried out on a SQUID magnetometer MPMS-5S from Quantum Design at 5 kOe. Magnetic measurements in benzene solution were performed according to the published procedure[15] on a Bruker DPX200 spectrometer. Lanthanide metal analyses were carried out by complexometric titration.

Synthesis of $[(C_9H_7)_2Yb(THF)_2]$ (2): A solution of indene (1.35 g, 11.68 mmol) in THF (10 mL) was added to a suspension of the naphthalene complex $[(C_{10}H_8)Yb(THF)_2]$ (2.60 g, 5.84 mmol) in THF (40 mL) and the reaction mixture was heated to 60 °C and stirred vigorously for 12 h. The resulting brown solution was filtered, THF was evaporated, and naphthalene was sublimed in vacuo at 60 °C. The solid residue was washed with hexane (2 × 20 mL) and recrystallized from THF/toluene (1:5 v/v). The precipitate was washed with cold toluene and dried in vacuo at room temperature to yield **2** as ruby-red crystals (2.36 g, 74%). $C_{26}H_{30}O_2Yb$ (547.5): calcd. C 57.03, H 5.52; found C 56.59, H 5.99. ^1H NMR (200 MHz, [D_5]pyridine): δ = 1.73 (m, 8 H, THF), 3.59 (m, 8 H, THF), 5.74 (d, $^3J_{H,H}$ = 3.2 Hz, 4 H, Ind), 6.2 (t, $^3J_{H,H}$ = 3.0 Hz, 2 H, Ind), 6.65 (m, 4 H, Ind), 7.31 (m, 4 H, Ind) ppm. $^{13}C\{^1H\}$ NMR (50 MHz, [D_5]pyridine): δ = 25.8 (THF), 67.9 (THF), 95.7 (Ind), 117.7 (Ind), 117.9 (Ind), 121.4 (Ind), 127.5(Ind) ppm. IR (KBr, Nujol): $\tilde{\nu}$ = 3060 cm^{-1} (w), 1320 (s), 1040(s), 860 (s), 760(s), 720 (s).

Synthesis of $[(CH_2$-1-$C_9H_6)_2Yb(THF)_2]$ (3): A solution of 1,2-bis-(indenyl)ethane (1.03 g, 4.02 mmol) in THF (10 mL) was added to a suspension of the naphthalene complex $[(C_{10}H_8)Yb(THF)_2]$ (1.79 g, 4.02 mmol) in THF (30 mL) and the reaction mixture was heated to 60 °C and stirred vigorously for 16 h. The resulting brown solution was filtered, THF was evaporated, and naphthalene was sublimed in vacuo at 60 °C. The solid residue was washed with hexane (2 × 20 mL) and recrystallized from THF/toluene (1:5 v/v). The precipitate was washed with cold toluene and dried in vacuo at room temperature to yield **3** as ruby-red crystals (1.89 g, 82%). $C_{28}H_{32}O_2Yb$ (573.6): calcd. C 58.63, H 5.62; found C 58.97, H 5.31. ^1H NMR (200 MHz, [D_5]pyridine): δ = 1.74 (br. s, 8 H, THF), 2.97 (s, 2 H, CH_2), 3.33 (s, 2 H, CH_2), 3.56 (br. s, 8 H, THF), 5.61 (d, $^3J_{H,H}$ = 4.0 Hz, 1 H, Ind), 5.75 (d, $^3J_{H,H}$ = 4.0 Hz, 1 H, Ind), 6.31 (m, 2 H, Ind), 6.48–6.69 (m, 4 H, Ind), 7.12 (m, 2 H, Ind), 7.55 (d, $^3J_{H,H}$ = 8.0 Hz, 1 H, Ind), 7.66 (d, $^3J_{H,H}$ = 8.0 Hz, 1 H, Ind) ppm. $^{13}C\{^1H\}$ NMR (50 MHz, [D_5]pyridine): δ = 25.8 (THF), 28.6 (CH_2), 28.7 (CH_2), 67.9 (THF), 94.5 (Ind), 94.8 (Ind), 112.4 (Ind), 115.1 (Ind), 117.1 (Ind), 117.3 (Ind), 119.1 (Ind), 119.8 (Ind), 121.0 (Ind), 121.2 (Ind), 123.9 (Ind), 125.3 (Ind), 125.6 (Ind), 127.2 (Ind), 127.8 (Ind) ppm. IR (KBr, Nujol): $\tilde{\nu}$ = 3060 cm^{-1} (w), 1320 (s), 1040(s), 860 (s), 760(s), 720 (s).

Synthesis of $[(C_9H_7)_2Yb(DAD)]$ (4): A solution of DAD (0.15 g, 0.89 mmol) in THF (2 mL) was added to a solution of **2** (0.49 g, 0.89 mmol) in THF (10 mL). The reaction mixture was stirred for

 © 2005 Wiley-VCH Verlag GmbH & Co. KGaA, Weinheim

Table 1. Crystallographic data and structure refinement details for **4** and **5**.

	4	**5**
Empirical formula	$C_{24}H_{34}N_2Yb$	$C_{30}H_{36}N_2Yb{\cdot}0.5(C_7H_8)$
Formula mass	571.61	643.72
Crystal system	orthorhombic	monoclinic
Space group	$P2_12_12_1$ (no. 19)	$P2_1/c$ (no. 14)
a [Å]	9.2626(1)	18.6543(4)
b [Å]	14.3870(2)	8.3894(2)
c [Å]	18.1551(3)	17.9212(3)
β [°]	90	92.898(1)
V [Å^3]	2419.37(6)	2801.05(10)
Z	4	4
Density (calcd.) [g cm^{-3}]	1.569	1.526
μ [mm^{-1}]	3.882	3.363
T_{max}/T_{min}	0.5738/0.3079	0.9504/0.7035
F(000)	1144	1300
Crystal size [mm^3]	0.40 × 0.24 × 0.22	0.46 × 0.10 × 0.02
θ range [°]	1.81–27.50	2.19–27.50
Index ranges	$-12 \le h \le 11$ $-18 \le k \le 18$ $-23 \le l \le 14$	$-24 \le h \le 20$ $-9 \le k \le 10$ $-23 \le l \le 23$
Reflections collected	18803	20977
Independent reflections	5556 [R_{int} = 0.0896]	6425 [R_{int} = 0.0886]
Data/restraints/parameters	5556/0/286	6425/15/333
Goodness-of-fit on F^2	0.970	1.008
R indices [$I > 2\sigma(I)$]	R_1 = 0.0399 wR_2 = 0.0662	R_1 = 0.0434 wR_2 = 0.0619
R indices (all data)	R_1 = 0.0570 wR_2 = 0.0704	R_1 = 0.0834 wR_2 = 0.0710
Abs. struct. parameter	–0.024(15)	–
Largest diff. peak/hole [e Å^{-3}]	0.977/–1.649	0.817/–0.979

0.5 h at 20 °C. After the removal of THF in vacuo, toluene (10 mL) was added and the solution was heated to 60 °C for 1.5 h. The toluene was then evaporated in vacuo. Recrystallization of the solid residue from toluene (–20 °C) gave **4** as dark-brown crystals (0.37 g, 74%). $C_{28}H_{34}N_2Yb$ (571.6): calcd. C 58.83, H 6.00, Yb 30.27; found C 58.30, H 6.27, Yb 30.30. ^{1}H NMR (200 MHz, [D$_6$]benzene, 20 °C): δ = 27.90 (s, 18 H, Me$_3$C), 12.16 (s, 4 H, 3-Ind), 10.41 (s, 4 H, 4-Ind), –18.42 (s, 4 H, 2-Ind), –28.74 (s, 2 H, N=CH), –39.25 (s, 2 H, 1-Ind) ppm. IR (Nujol, KBr): $\tilde{\nu}$ = 3050 cm^{-1} (w), 1580 (w), 1365 (s), 1245 (s), 1200 (s), 770 (s), 740 (s).

Synthesis of [*rac*-(CH$_2$-1-C$_9$H$_6$)$_2$Yb(DAD)](C$_6$H$_5$CH$_3$)$_{0.5}$ (5): Similar to the procedure described for **4**, compound **5** was obtained from DAD (0.25 g, 1.49 mmol) in THF (5 mL) and **3** (0.86 g, 1.49 mmol) in THF (10 mL). Recrystallization from toluene afforded **5** as greenish-black crystals (0.77 g, 81%). $C_{33.5}H_{40}N_2Yb$ (643.7): calcd. C 62.50, H 6.26, Yb 26.88; found C 62.88, H 6.62, Yb 26.34. ^{1}H NMR (200 MHz, [D$_6$]benzene, 20 °C): δ = 36.01 (s, 2 H, 5-Ind), 34.21 (s, 18 H, Me$_3$C), 32.79 (s, 2 H, 4-Ind), 23.79 (s, 2 H, 6-Ind), –0.86 (s, 2 H, 7-Ind), –9.90 (s, 2 H, 3-Ind), –18.53 (s, 2 H, N=CH), –21.76 (s, 2 H, CH$_2$), –23.04 (s, 2 H, CH$_2$), –84.34 (s, 2 H, 2-Ind) ppm. IR (Nujol, KBr): $\tilde{\nu}$ = 3050 cm^{-1} (w), 1585 (w), 1370 (s), 1255 (s), 1200 (s), 780 (s), 7450 (s).

X-ray Crystallographic Study: The crystal data and details of data collection are given in Table 1. X-ray data were collected at –100 °C on a Siemens SMART CCD diffractometer (graphite monochromated Mo-K_α radiation, λ = 0.71073 Å, ω-scan technique) fitted with an area-detector. The structures were solved by direct methods using SHELXS-97[21] and refined on F^2 using all reflections with SHELXL-97.[22] The toluene solvent molecule in **5** is disordered about a crystallographic center of inversion. The C–C distances between ring carbon atoms were restrained to be equal. The atoms of the disordered part in **5** were refined isotropically, all other non-hydrogen atoms were refined anisotropically. The hydrogen atoms were placed in calculated positions and assigned using an isotropic displacement parameter of 0.08 Å^2. SADABS[23] was used to perform area-detector scaling and absorption corrections. The geometrical aspects of the structure were analyzed using the PLATON program.[24]

CCDC-257892 (**4**) and -257893 (**5**) contain the supplementary crystallographic data for this paper. These data can be obtained free of charge from The Cambridge Crystallographic Data Centre via www.ccdc.cam.ac.uk/data_request/cif.

Acknowledgments

This work was supported by the Russian Foundation for Basic Research (grant no. 03-03-32112), a grant of the President of the Russian Federation supporting scientific schools (no. 58.2003.3), the Fonds der Chemischen Industrie, and the Deutsche Forschungsgemeinschaft (Graduiertenkolleg "Synthetische, mechanistische und reaktionstechnische Aspekte von Metallkatalysatoren"). We gratefully acknowledge Dr. Yu. A. Kurskii for recording the NMR spectra and Prof. V. K. Cherkasov for recording the ESR spectra.

[1] a) K. Vrieze, *J. Organomet. Chem.* **1986**, *300*, 307–326; b) H. Bock, H. tom Dieck, *Chem. Ber.* **1967**, *100*, 228–246; c) J. Scholz, B. Richter, R. Goddar, K. Krueger, *Chem. Ber.* **1993**, *126*, 57–61.

[2] a) H. tom Dieck, I. W. Renk, *Chem. Ber.* **1971**, *104*, 110–130; b) H. tom Dieck, K.-D. Franz, F. Hoffmann, *Chem. Ber.* **1975**, *108*, 163–173; c) J. Reinhold, R. Benedix, P. Birner, H. Hennig, *Inorg. Chim. Acta* **1979**, *33*, 209–213.

[3] a) M. G. Gardner, G. R. Hanson, F. C. Lee, C. L. Raston, *Inorg. Chem.* **1994**, *33*, 2456–2461; b) F. G. N. Cloke, C. I. Dalby, M. J. Henderson, P. B. Hitchcock, C. H. L. Kennard, R. N.

 © 2005 Wiley-VCH Verlag GmbH & Co. KGaA, Weinheim

Lamb, C. L. Raston, *J. Chem. Soc., Chem. Commun.* **1990**, 1394–1396; c) K.-H. Thiele, V. Lorenz, G. Thiele, P. Zoennchen, J. Scholz, *Angew. Chem.* **1994**, *106*, 1461–1463; *Angew. Chem. Int. Ed. Engl.* **1994**, *33*, 1372–1373.

[4] a) H. tom Dieck, J. Rieger, G. Fendesack, *Inorg. Chim. Acta* **1990**, *177*, 191–197; b) W. A. Hermann, M. Denk, W. Scherer, F.-R. Klingan, *J. Organomet. Chem.* **1993**, *444*, C21–C24; c) B. Richter, J. Scholz, J. Sieler, K.-H. Thiele, *Angew. Chem.* **1995**, *107*, 2865–2867; *Angew. Chem. Int. Ed. Engl.* **1995**, *34*, 2867–2869; d) F. G. N. Cloke, G. R. Hanson, M. J. Henderson, P. B. Hitchcock, C. L. Raston, *J. Chem. Soc., Chem. Commun.* **1989**, 1002–1003; e) J. Scholz, M. Dlikan, D. Stroehl, A. Dietrich, H. Schumann, K.-H. Thiele, *Chem. Ber.* **1990**, *123*, 2279–2285; f) J. Scholz, A. Dietrich, H. Schumann, K.-H. Thiele, *Chem. Ber.* **1991**, *124*, 1035–1039.

[5] a) F. G. N. Cloke, H. C. de Lemos, A. A. Sameh, *J. Chem. Soc., Chem. Commun.* **1986**, 1344–1345; b) F. G. N. Cloke, *Chem. Soc. Rev.* **1993**, *22*, 17–21; c) M. N. Bochkarev, A. A. Trifonov, F. G. N. Cloke, C. I. Dalby, P. T. Matsunaga, R. A. Andersen, H. Schumann, J. Loebel, H. Hemling, *J. Organomet. Chem.* **1995**, *486*, 177–182; d) A. Recknagel, M. Noltemeyer, F. T. Edelmann, *J. Organomet. Chem.* **1991**, *410*, 53–61; e) A. Scholz, K.-H. Thiele, J. Scholz, R. Weimann, *J. Organomet. Chem.* **1995**, *501*, 195–200; f) P. Poremba, F. T. Edelmann, *J. Organomet. Chem.* **1997**, *549*, 101–104; g) A. A. Trifonov, E. N. Kirillov, M. N. Bochkarev, H. Schumann, S. Muehle, *Russ. Chem. Bull.* **1999**, *48*, 382–384; h) A. A. Trifonov, Yu. A. Kurskii, M. N. Bochkarev, S. Muehle, S. Dechert, H. Schumann, *Russ. Chem. Bull.* **2003**, *52*, 601–606.

[6] a) A. A. Trifonov, L. N. Zakharov, M. N. Bochkarev, Yu. T. Struchkov, *Izv. Akad. Nauk, Ser. Khim.* **1994**, 148–151; b) H. Goerls, B. Neumueller, A. Scholz, J. Scholz, *Angew. Chem.* **1995**, *107*, 372–375; *Angew. Chem. Int. Ed. Engl.* **1995**, *34*, 673–676; c) J. Scholz, H. Goerls, H. Schumann, R. Weimann, *Organometallics* **2001**, *20*, 4394–4402.

[7] a) R. G. Finke, S. R. Keenan, D. A. Shirardi, P. L. Watson, *Organometallics* **1986**, *5*, 598–601; b) L. R. Morss, *Chem. Rev.* **1976**, *76*, 827–841; c) A. M. Bond, G. B. Deacon, R. H. Newnham, *Organometallics* **1986**, *5*, 2312–2316.

[8] The synthesis and characterization of complexes **2**[8a] and **3**[8b] have been previously reported. We describe here a new convenient synthesis for **2** and **3** by reaction of naphthaleneytterbium, $[(C_{10}H_8)Yb(THF)_2]$, with indene or 1,2-bis(indenyl)ethane in THF. a) G. B. Deacon, R. H. Newnham, *Aust. J. Chem.* **1985**, *38*, 1757–1765; b) A. V. Khvostov, B. M. Bulychev, V. K. Belsky, A. I. Sizov, *J. Organomet. Chem.* **1999**, *584*, 164–170.

[9] a) J. Z. Jin, Z. S. Jin, W. Q. Chen, Y. Zhang, *Chinese J. Struct. Chem. (Jiegou Huaxue)* **1993**, *12*, 241–245; b) A. A. Trifonov, M. N. Bochkarev, S. Dechert, H. Schumann, unpublished results.

[10] a) H. Schumann, D. Karasiak, S. Muehle, *Z. Anorg. Allg. Chem.* **2000**, *626*, 1434–1443; b) A. T. Gilbert, B. L. Davis, T. J. Emge, R. D. Broene, *Organometallics* **1999**, *18*, 2125–2132.

[11] R. D. Schannon, *Acta Crystallogr., Sect. A* **1976**, *32*, 751–767.

[12] a) E. Sheng, S. Wang, G. Yang, S. Zhou, L. Cheng, K. Zhang, Z. Huang, *Organometallics* **2003**, *22*, 684–692; b) Y. Wang, Q. Shen, F. Xue, K. Tu, *J. Organomet. Chem.* **2000**, *598*, 359–364; c) W.-K. Wong, L. Zhang, F. Xue, T. C. W. Mak, *Polyhedron* **1997**, *16*, 345–347; d) M. Schulz, J. M. Boncella, D. J. Berg, T. D. Tilley, R. A. Andersen, *Organometallics* **2002**, *21*, 460–472; e) X. Zhou, Z. Huang, R. Cai, L.-B. Zhang, L.-X. Zhang, X. Huang, *Organometallics* **1999**, *18*, 4128–4133.

[13] C. J. M. Huige, A. L. Spek, J. L. de Boer, *Acta Crystallogr., Sect. C* **1985**, *41*, 113–116.

[14] F. A. Allen, O. Konnard, D. G. Watson, L. Brammer, G. Orpen, R. Taylor, *J. Chem. Soc., Perkin Trans.* **1987**, 1–19.

[15] a) D. F. Evans, *J. Chem. Soc.* **1959**, 2003–2005; b) D. F. Evans, G. V. Fazakerley, R. F. Phillips, *J. Chem. Soc. A* **1971**, 1931–1934.

[16] a) M. Gerloch, E. C. Constable, *Transition Metal Chemistry*, VCH, Weinheim, **1995**; b) E. A. Boudreaux, L. N. Mulay, *Theory and Applications of Molecular Paramagnetism*; Wiley Interscience, New York, **1976**.

[17] W. J. Evans, M. A. Hozbor, *J. Organomet. Chem.* **1987**, *326*, 299–306.

[18] A. Caneschi, A. Dei, D. Gatteschi, S. Poussereau, L. Sorace, *Dalton Trans.* **2004**, 1048–1055.

[19] K. L. Trojan, J. L. Kendall, K. D. Kepler, W. E. Hatfield, *Inorg. Chim. Acta* **1992**, *198–200*, 795–803.

[20] a) W. J. Evans, T. A. Ulibarri, J. W. Ziller, *J. Am. Chem. Soc.* **1990**, *112*, 219–223; b) W. J. Evans, S. L. Gonzales, J. W. Ziller, *J. Am. Chem. Soc.* **1994**, *116*, 2200–2608.

[21] G. M. Sheldrick, *SHELXS-97 Program for the Solution of Crystal Structures*, University of Göttingen, **1990**.

[22] G. M. Sheldrick, *SHELXL-97 Program for the Refinement of Crystal Structures*, University of Göttingen, **1997**.

[23] G. M. Sheldrick, *SADABS Program for Empirical Absorption Correction of Area Detector Data*, University of Göttingen, **1996**.

[24] A. L. Spek, *PLATON A Multipurpose Crystallographic Tool*, University of Utrecht, **2000**.

Received: December 10, 2004
Published Online: June 9, 2005

 © 2005 Wiley-VCH Verlag GmbH & Co. KGaA, Weinheim

Anion Template Effect and the Polymerization Degree – Diversity through Flexibility

Kalle I. Nättinen,[a,b] Paulo E. N. de Bairos,[a,c] Petri J. Seppälä,[a] and Kari T. Rissanen*[a]

Keywords: Crystal engineering / N ligands / Zeolite analogues / Self-assembly / Transition metals

Two 2D (**M1** and **M2**) and one 1D (**M3**) metal-organic frameworks (MOFs) have been prepared from pyridine functionalized tetradentate ligand tetrakis(nicotinoxymethyl)methane **TNM** with silver tetrafluoroborate, nickel chloride, and copper hexafluorophosphate. **M1** manifests a previously unpresented mode of 4,4 threefold parallel interpenetration for 2D MOFs. Large channels (vdW diameter 9.4 Å) through eclipsed 2D layers of **M2** were observed. While the open space percentage in the noninterpenetrated **M2** was 38.0 %, the triple interpenetration of the sheets of **M1** reduced the void to 10.8 %. With the same ligand and a similar, weakly coordinating anion as that in **M1**, the structure **M3** was rendered one-dimensional. The result is explained partly by the flexibility of the **TNM** ligand and partly by the lack of a suitable bridging solvent.

(© Wiley-VCH Verlag GmbH & Co. KGaA, 69451 Weinheim, Germany, 2005)

Introduction

Since the beginning of crystal engineering,[1] there has been a search for reliable methods to predict and control the product of crystal syntheses. The study of the crystal structures has a dual focus: the analysis of the obtained structures and the prediction of yet to be formed crystals. Meticulous analysis of the crystal structures together with the growing understanding of weak intermolecular interactions such as the CH···O and π-interactions have made it possible to have some control over the outcome of the crystallizations. With yet another compound, some properties of the crystal – centrosymmetricity and porosity being good examples – can be dictated, although complete control still escapes the chemist in many cases. The efforts made to accumulate this knowledge have been documented to general crystal structure databases such as IUCR[2] for inorganic and CSD[3] for organic structures, as well as more specific databases including the metal-organic framework database of interpenetrated frameworks by S. R. Batten,[4] and the topological analysis of the CSD database of Proserpio et al.[5] etc. Our interests lie within the creation of noninterpenetrated metal-organic structures, MOFs,[6–8] their properties and the control of their dimensionality. The prevention of interpenetration can be achieved by using templates (e.g. solvents), bulky ligands, or as in our case, bulky, weakly coordinating anions such as PF_6^-, BF_4^-, or ClO_4^-.[9] The use of these anions indeed seems to block the formation of interpenetrated 3D frameworks,[10,11] but also often results in a network with lower dimensionality. The lowered dimensionality renders the results less useful for applications since the covalent bonding throughout the framework in 3D structures principally stands for higher thermal stability. In this work we examine the reasons behind the lowered dimensionality and the role of the bulky anions as templates for the frameworks.

Results and Discussion

The tetradentate ligand **TNM** is by nature more chelating than the **TINM** (tetrakis(isonicotinoxymethyl)methane): the pyridyl nitrogens are sterically more hindered, thereby rendering the formation of 3D MOFs more difficult (Scheme 1). We have previously shown the synthesis of 3D MOFs possible using the **TNM** ligand. However, this requires an additional bridging element, the methanol molecules, in order to create the 3D connectivity. The frameworks with lower dimensionality are predominantly achieved when using the **TNM** ligand and the bulky anions BF_4^- and PF_6^-, and also in structures with smaller coordinative anions.[12]

[a] Nanoscience Center, Department of Chemistry, University of Jyväskylä,
P. O. Box 35, 40014 Jyväskylä, Finland
Fax: +358-14-2602501
E-mail: kari.rissanen@jyu.fi
[b] VTT, VTT Processes,
P. O. Box 1607, FIN-33101 VTT, Finland
E-mail: kalle.nattinen@vtt.fi
[c] Departamento de Química da Universidade da Madeira,
Campus da Penteada, 9000-390 Funchal, Portugal
Fax: +351-291-705149
E-mail: p-bairos@sapo.pt
Supporting information for this article is available on the WWW under http://www.eurjic.org or from the author.

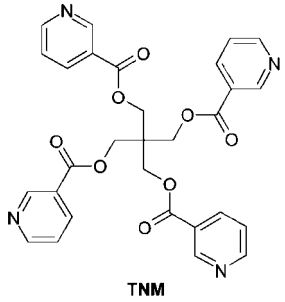

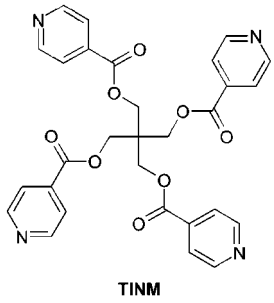

Scheme 1.

The flexibility of the **TNM** ligand allows the enveloping of the anions within the frameworks and the formation of MOFs with anions of different sizes. The result is a variety of topologies differing from those obtained by the small coordinative anions. The use of the Ag^{I} cation resulted in a 2D structure, which was also the case with the use of the Ni^{II} cation. The use of Cu^{I} without the presence of methanol prevented the formation of the Cu–MeOH–Cu bridged structure[12] – a 1D structure was formed instead.

The Threefold Interpenetrated 2D Layer Structure M1

The ligands are located in two sheets, forming the top and bottom of the polymeric layer (Scheme 2). The Ag^{I} cations, being located in the top, bottom, and middle of the layer, bridge the ligand sheets together, resulting in a 1.5 nm layer (Scheme 2 and Figure 1). There are two Ag^{I} cations with different coordination environments. The Ag1 cations bridging the **TNM** ligands in the top and bottom of the layers have a distorted square-planar coordination with the two pyridyl ligands [Ag–N distances of 2.167(1) and 2.174(2) Å] coordinated to opposite sides of the Ag^{I} and two BF_4^- anions [Ag–F distances 2.883(2) and 2.947(2) Å] on the sides of the axis formed by the py-Ag-py coordination. The distortion of the coordination sphere manifests itself by the fluorides of the BF_4^- being positioned above the plane of the Ag^{I} cation and the pyridyl nitrogens. This is explained by the steric repulsion of the layer of threefold interpenetrated frameworks which pushes the anions above the optimum arrangement. Interestingly, the pyridyl ligands are not eclipsed but arranged nearly perpendicularly. The square-planar coordination sphere of the Ag2 cations in the middle of the layer in **M1** is arranged in a similar way to the Ag1 in the top and bottom of the layer: two pyridyl nitrogens [Ag–N distances of 2.101(1) and 2.146(2) Å] and two loosely bound fluorides of the neighboring BF_4^- anions [Ag–F distances 3.029(1) and 3.370(2) Å]. The coordination sphere is nondistorted. The pyridyl ligand conformation is eclipsed, as usual for opposing pyridyl ligands (Figure 2).[12] The Ag2 is "sandwiched" between two neighboring pyridyl rings which are positioned so that an octahedral environment for Ag2 is formed. The Ag2–C distances to the carbons of these pyridyl rings are 3.164 and 3.218 Å. On the basis of molecular modeling calculations (energy minimization)[13] comparing the coordination environments of Ag1 and Ag2 (two pyridyl rings and two BF_4^-) the environment of Ag2 is more stable, even without the added stability of the "sandwich" pyridyl rings. This result is backed up by the obvious distortion from the optimum square-planar geometry of Ag1 and the results of CSD[3] searches showing the predominance of the eclipsed geometry. However, the conformation of the pyridyl ligands around the Ag^{I} cations is primarily dictated by the connectivity of the framework.

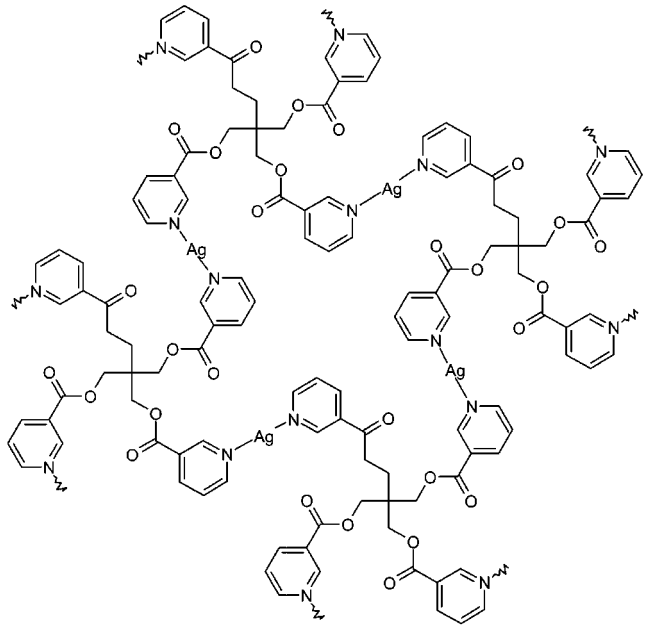

Scheme 2. A schematic presentation of **M1** without the BF_4^- anions.

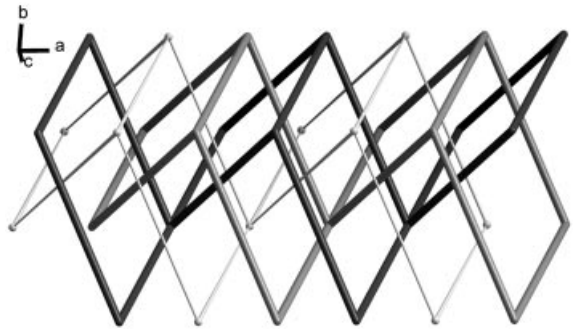

Figure 1. A schematic presentation of the threefold interpenetration of the 4,4 nets of **M1**. Only central carbon atoms and the connections between them are shown.

 © 2005 Wiley-VCH Verlag GmbH & Co. KGaA, Weinheim

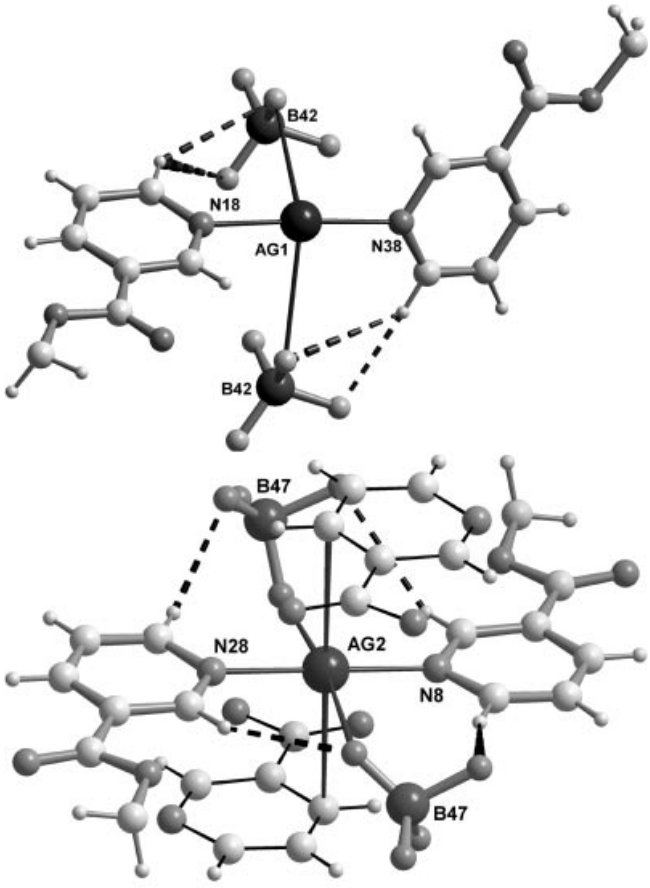

Figure 2. The coordination spheres of Ag1 and Ag2, showing the weak hydrogen bonds between the pyridyl hydrogen atoms and the fluorides of the BF_4^-. The shortest weak CH···F bond for those BF_4^- around the Ag1 is 2.365(2) Å (H39···F44) and for the BF_4^- around the Ag2 2.351(5) Å (H29···F50). The pyridyl rings on top and bottom of the Ag2 and their interactions with the Ag2 are also shown.

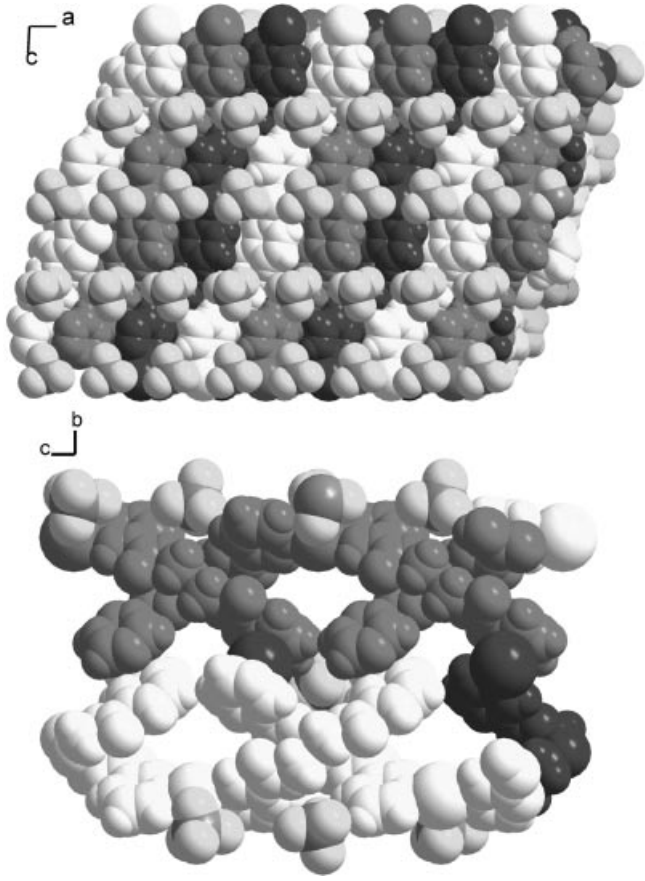

Figure 3. A space-filling presentation of **M1** along the *b* and *a* axis, showing the interpenetration of the layers and the channels along the *a* axis. The BF_4^- anions are shown only in the middle one of the three horizontally adjacent cavities shown in the lower figure. The three separate layers are shown in light, medium, and dark grey.

This explains the unfavored coordination geometry of the Ag1.

The BF_4^- anions are in close vicinity to the Ag^I cations, resulting in sparse anion layers between the polymeric frameworks and also channels (filled with anions) inside the layers. The 4,4 topology 2D sheets are threefold parallel interpenetrated (Figure 1), however, not completely consuming the open space of the framework. Besides the channels containing the BF_4^- anions, an additional set of channels remains along the *a* axis (Figure 3). The disordered solvent that could not be localized from the cavities was treated with SQUEEZE/BYPASS.[14]

The threefold parallel interpenetration of two-dimensional 4,4 nets is already known.[15–18] However, the mode of interpenetration of **M1** is previously unpresented. This mode is due to the use of the flexible tetradentate ligand which provides new geometrical possibilities for the network. In our previous work we presented a noninterpenetrated 2D structure with four **TNM** ligands coordinated to each Cu^{II} cation.[12] The use of Ag^I with two coordination sites for the **TNM** ligand makes the network of **M1** looser: the smallest loop in **M1** consists of eight ligand arms plus the metal coordination (56 bonds), whereas in our previous 2D **TNM** structure, the size of the loop (28 bonds) was half that of the **M1**. The amount of counter anions per metal cation is also halved in **M1**. The larger loops and reduced number of anions are the reasons for the threefold interpenetration in **M1**.

The 2D Layer Structure M2

We have previously synthesized a 3D MOF from **TINM** and $NiCl_2$[12] and respectively shown that the **TNM** ligand is unable to form a 3D MOF with a coordinative anion (and without the aid of an additional bridging component).[12,10] However, the formation of structures with lower dimensionality is possible with these components: 1 and 2D structures have already been obtained.[12,19] Here we present an eclipsed 2D layer structure with large pores (5.0 × 8.1 Å) through the crystal lattice along the *a* axis and smaller pores along the *b* and *c* axes (Scheme 3 and Figure 4). Similarly with the $CoCl_2$ structure reported earlier,[19] the net-

 © 2005 Wiley-VCH Verlag GmbH & Co. KGaA, Weinheim

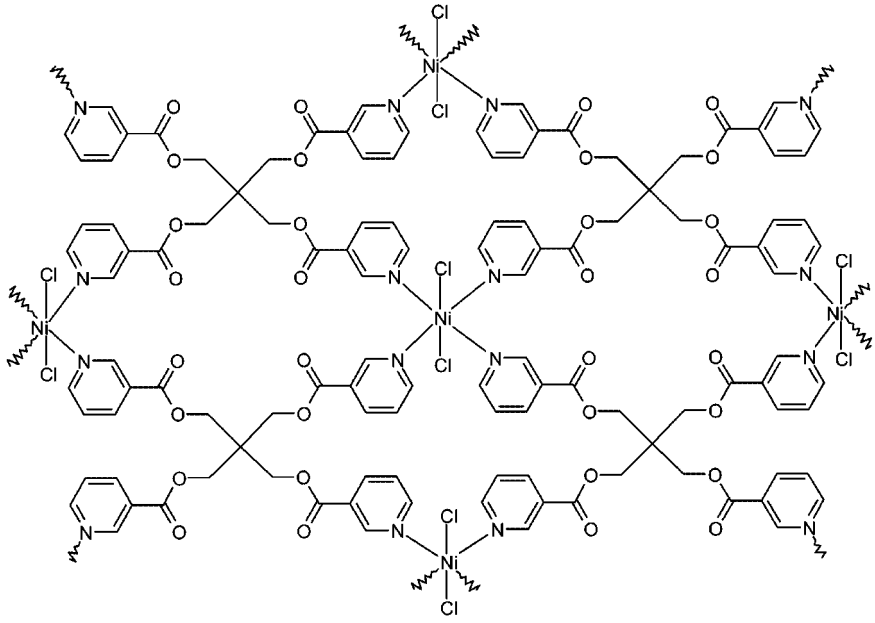

Scheme 3. A schematic presentation of **M2**.

work complies with the 4,4 topology with alternating nodes of the ligand central carbons and the Ni^{II} cations. The angles and distances between the nodes are presented in Figure 5.

The chloride anions are coordinated to the Ni^{II} cations in a 35.6 and 35.8° angle to the normal of the plane formed by the Ni^{II} cations in one layer. The octahedral coordination sphere of the Ni^{II} cations is tilted sideways (see Figure 4 and Figure 5) in order to minimize the repulsion of the chloride anions of neighboring layers. The layers are held together by weak hydrogen bonds between the chloride anions, the carbonyls, and the aromatic hydrogens. The attractive interactions are neither very strong nor numerous, resulting in the disorder of the molecule. The disorder was modeled by splitting the two arms (the carbonyl group and the pyridyl rings) of the independent half of the ligand into two positions. The population parameters of these halves were refined and then fixed to the refined values for the refinement of their temperature factors. The disordered solvent was treated with SQUEEZE/BYPASS.[20] The solvent accessible void for the structure was 30.0%.[20]

The 1D Chain Structure M3

The use of **TNM** together with the $Cu(PF_6)_2$/$Cu(OH)_2$/$CuPF_6$ and in the absence of MeOH resulted in a 1D MOF structure. Each chain is composed of two parallel rows of **TNM** ligands with paired, linear conformation. The pyridyl groups of the parallel rows are superimposed and bridged together by the Cu^{I} cations with the N–Cu–N axis perpendicular to the direction of the polymeric chain (Scheme 4). The PF_6^- and OH^- anions and the coordinated water molecules are enveloped in the wrinkles of the heavily puckered chains. The puckering is due to the linear coordination of the *meta*-isomer pyridyl rings to the Cu^{I} (Figure 6).

The neighboring chains are held together by the CH···O interactions between the aromatic hydrogens and the car-

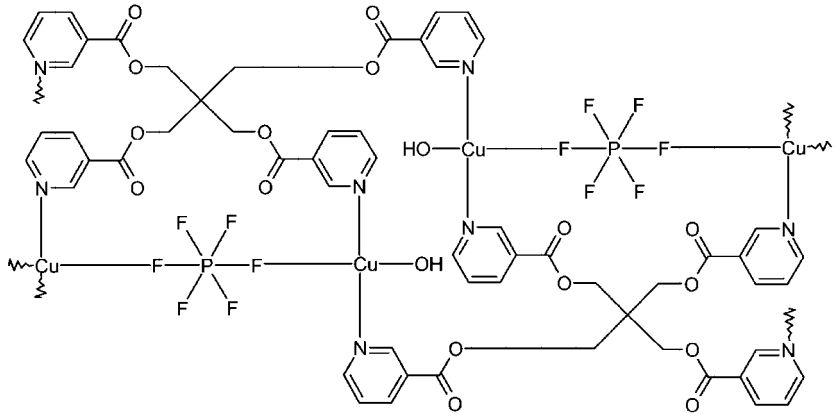

Scheme 4. A schematic presentation of **M3**.

 © 2005 Wiley-VCH Verlag GmbH & Co. KGaA, Weinheim

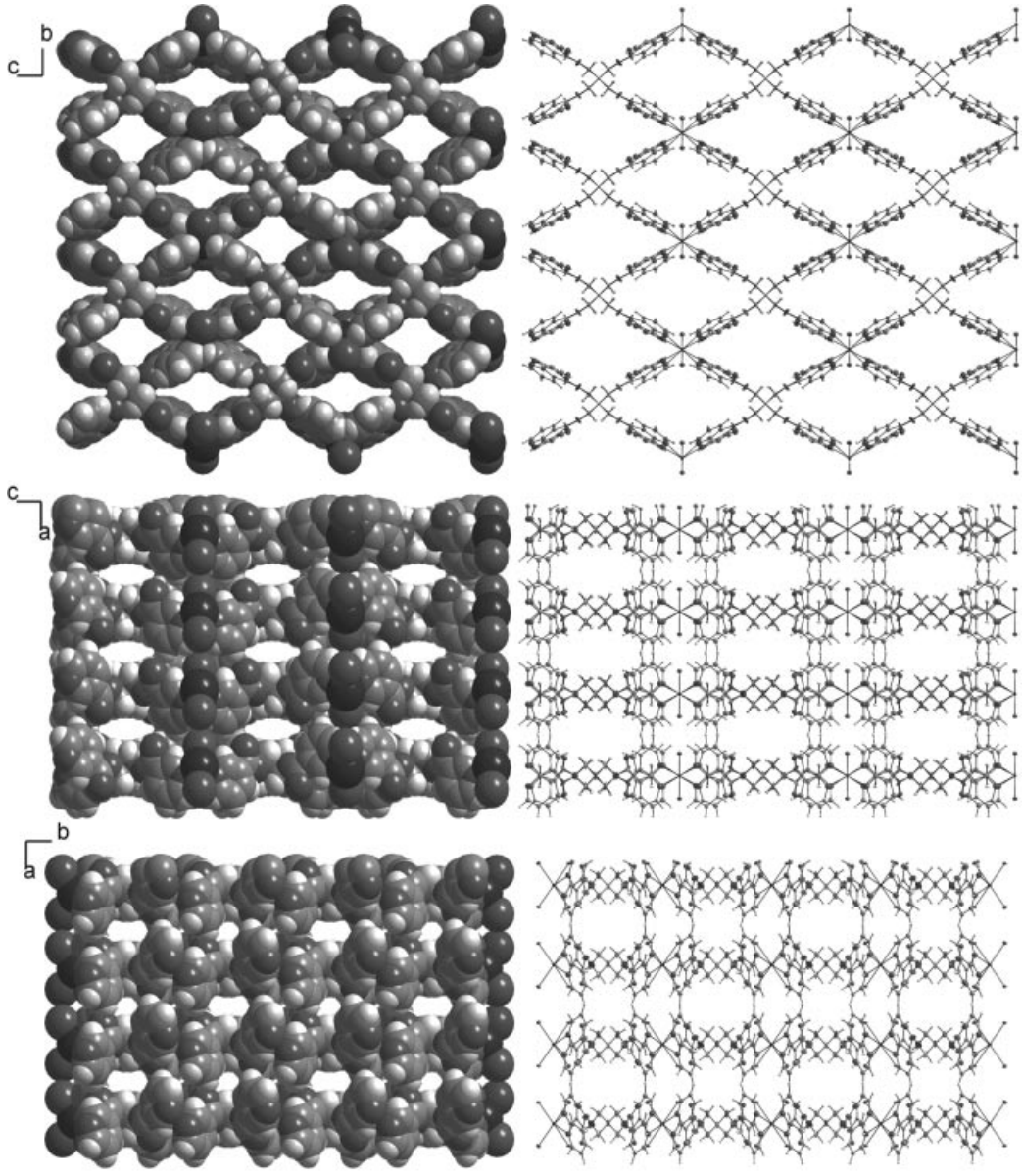

Figure 4. The space-filling and ball and stick plots for **M2**, showing the pores through the lattice along all crystallographic axes.

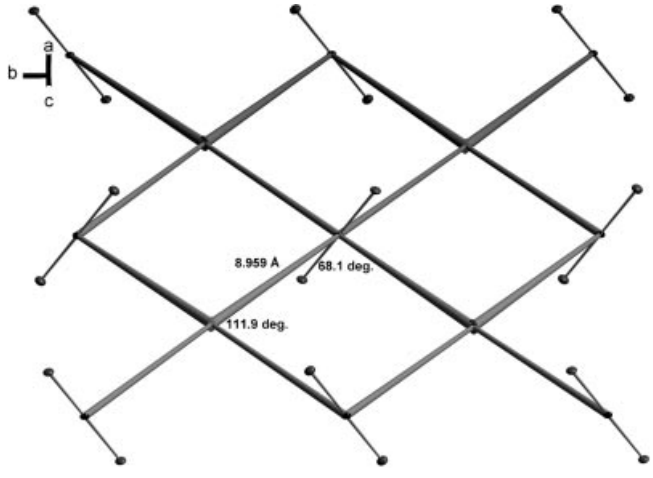

Figure 5. A schematic presentation of **M2**. The angles and distances between the nodes of the network are shown.

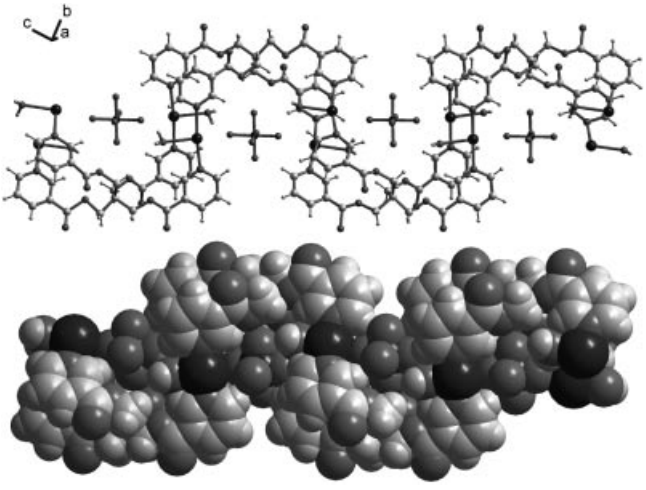

Figure 6. The ball and stick and space-filling plots of four ligands of a chain in **M3** shown along the crystallographic *a* axis.

 © 2005 Wiley-VCH Verlag GmbH & Co. KGaA, Weinheim

bonyl oxygens as well as the π···π and van der Waals interactions. We have previously reported a 3D structure prepared from the same reagents.[10] However, in this previously reported structure the 1D chains were bridged together by the solvent methanol molecules. The absence of an additional bridging component like methanol in the preparation of **M3** prevents the formation of higher dimensionality products. The disorder around the square-planar coordination sphere of the Cu^{I} cations excludes the detailed discussion of the coordination bond lengths. The disorder was treated by setting geometrical restraints on the ligand. Furthermore, the disordered solvent was treated with SQUEEZE/BYPASS.[20]

Conclusions

The choice of the anions is critical for the topology of the resulting framework. In spite and because of the flexibility of the **TNM** and **TINM** ligands, the frameworks obtained with bulky noncoordinative anions are systematically different from those obtained with small coordinative anions. The flexibility of these ligands allows the tight enveloping of the anions within the forming framework or in other words, the templation of the frameworks by the anions. The use of $AgBF_4$ with **TNM** resulted in the formation of a threefold interpenetrated 2D network **M1**. The use of Ni^{II} instead of Co^{II} did not change the topology of the formed 2D frameworks.[19] However, unlike in the previous Co^{II} structure, the layers were eclipsed, which resulted in large channels (vdW diameter 9.4 Å) through the 2D layers of **M2**. The lack of a suitable bridging solvent (to allow polymerization in the 2nd and 3rd dimension) in the **M3** rendered the structure one-dimensional. As usual, the interpenetration was found to consume the available open space in **M1** resulting in a low value of 10.8%. In the noninterpenetrated structure **M2** the open space percentage was 38.0%.

Experimental Section

Materials and Measurements: All commercially available chemicals are of reagent grade and used as received without further purification. **TNM** and $Cu(PF_6)_2/Cu(OH)_2/CuPF_6$ were synthesized as previously reported.[10,21] The purity of **M1**–**2** was confirmed by elemental analysis, whereas the EA of **M3** gave inaccurate results due to the decomposition of the structure in air. Transferring the crystals directly from the mother liquid to the perfluorinated oil used in the single-crystal X-ray diffraction experiments, the decomposition was prevented and the diffraction experiment was enabled.

The Threefold Interpenetrated 2D Layer Structure M1: In a solution of **TNM** (22 mg, 39.5 μmol) dissolved in MeOH (3 mL) was added $AgBF_4$ (16 mg, 82.2 μmol) in water (1.5 mL). The solution was slowly allowed to evaporate, and the crystalline solid was collected from the solution before complete evaporation of the solvents and dried in air. Yield: 29%. $C_{29}H_{24}Ag_2B_2F_8N_4O_8$ + 8 H_2O: calcd. C 32.0, H 3.7, N 5.1; found C 31.9, H 2.9, N 5.0.

The 2D Layer Structure M2: A MeOH solution of **TNM** (1.5 mL, 14.4 mM) was carefully layered on top of a THF solution of $NiCl_2{\cdot}6H_2O$ (1.5 mL, 15 mM). The solutions were slowly allowed to diffuse and the crystalline solid was collected from the interface of the solvents and dried overnight in air. Yield: 57%. $C_{29}H_{24}Cl_2N_4NiO_8$ + 2 MeOH: calcd. C 49.6, H 4.3, N 7.5; found C 49.2, H 4.2, N 7.4.

The 1D Chain Structure M3: To a solution of **TNM** (6 mg, 10.8 μmol) dissolved in MeCN (1.5 mL) was added a saturated

Table 1. Crystallographic parameters for complexes **M1**–**M3**.

	M1	**M2**	**M3**
Empirical formula	$[Ag_2(C_{29}H_{24}N_4O_8)(BF_4)_2]$	$[Ni(C_{29}H_{24}N_4O_8)Cl_2]$	$[Cu_2(C_{29}H_{24}N_4O_8)(PF_6)(OH)(H_2O)]$
Formula mass	945.88	686.13	863.60
Crystal color, shape	colorless, prisms	green, prisms	colorless, prisms
Crystal dimensions [mm]	0.15×0.20×0.30	0.15×0.20×0.35	0.15×0.15×0.15
Crystal system	monoclinic	orthorhombic	triclinic
Space group	$P2_1/c$ (No. 14)	$Cccm$ (No. 66)	$P\bar{1}$ (No. 2)
a [Å]	5.5700(3)	14.2220(8)	6.7490(10)
b [Å]	41.5200(3)	20.0730(12)	15.919(3)
c [Å]	15.5158(2)	29.6847(18)	33.874(6)
α [deg.]	90	90	90.361(6)
β [deg.]	92.711(4)	90	89.682(9)
γ [deg.]	90	90	97.801(9)
V [Å^3]	3584.3(2)	8474.3(9)	3605.5(11)
Calculated density [Mg/m^3]	1.753	1.076	1.591
Temperature of collection [K]	123	123	173
Z	4	8	4
R_{obs}	R_1 = 0.0952, wR_2 = 0.2015	R_1 = 0.0626, wR_2 = 0.1911	R_1 = 0.1399, wR_2 = 0.3563
R_{all}	R_1 = 0.2116, wR_2 = 0.2449	R_1 = 0.1274, wR_2 = 0.2178	R_1 = 0.3321, wR_2 = 0.4291
GooF	0.951	1.060	0.871
θ range for data collection [°]	1.0 to 25.2	3.2 to 27.5	3.0 to 24.7
Scan type	phi / omega, 1°	phi / omega, 1°	phi / omega, 1°
Refl. collected / unique / cell refinement	17569 / 5938 / 3788	20148 / 4947 / 1235	17478 / 8999 / 5136
Refined parameters	478	178	668
Res. electron density [e/Å^3]	1.956 / –1.467	0.966 / –0.471	1.513 / –0.776

 © 2005 Wiley-VCH Verlag GmbH & Co. KGaA, Weinheim

water solution of $Cu(PF_6)_2/Cu(OH)_2/CuPF_6$ (5 mL). The solution was slowly allowed to evaporate, and the crystalline solid was collected from the solution before complete evaporation of the solvents and dried in air. Yield: 54%.

X-ray Crystallographic Study: The single-crystal X-ray diffraction was done with a Nonius–Kappa CCD diffractometer with graphite-monochromatized Mo-K_α (λ = 0.71073 Å) radiation. The Collect software system was used in the measurement and DENZO-SMN[22] in the processing of the data. The structures were solved and refined by full-matrix least squares on F^2 with the WinGX-software package utilizing SHELXS97 and SHELXL97 modules.[23–25] Hydrogen atoms were refined by a riding model. Absorption correction was not performed for any of the complexes. The graphic presentations of the structures were created with the software Diamond.[26] The crystallographic parameters for the structures **M1**–**M3** are presented in Table 1.

CCDC-256787–256789 contain the supplementary crystallographic data for this paper. These data can be obtained free of charge from The Cambridge Crystallographic Data Centre via www.ccdc.cam.ac.uk/data_request/cif.

Acknowledgments

K. N. and K. R. thank the Finnish Academy (proj. no. 777871) for financial support. P. B. thanks Professor Joao Rodrigues and the Socrates program at Universidade da Madeira for the financial support.

[1] G. M. J. Schmidt, *Pure Appl. Chem.* **1971**, *27*, 647–678.
[2] Fachinformationszentrum Karlsruhe (FIZ), 76344 Eggenstein-Leopoldshafen, Germany. WWW: http://www.fiz-karlsruhe.de.
[3] F. H. Allen, O. Kennard, *Chem. Des. Autom. News.* **1993**, *8*, 1.
[4] S. Batten, School of Chemistry, Monash University 3800, Australia. WWW: http://web.chem.monash.edu.au/Department/Staff/Batten/Intptn.rtf.
[5] V. A. Blatov, L. Carlucci, G. Ciani, D. M. Proserpio, *Cryst. Eng. Comm.* **2004**, *6*, 377–395.
[6] B. F. Hoskins, R. Robson, *J. Am. Chem. Soc.* **1990**, *112*, 1546.
[7] T. M. Reineke, M. Eddaoudi, D. Moler, M. O'Keeffe, O. M. Yaghi, *J. Am. Chem. Soc.* **2000**, *122*, 4843.
[8] M. Eddaoudi, J. Kim, N. Rosi, D. Vodak, J. Wachter, M. O'Keefe, O. M. Yaghi, *Science* **2002**, *295*, 469.
[9] S. R. Batten, R. Robson, *Angew. Chem. Int. Ed. Engl.* **1998**, *37*, 1460–1494.
[10] K. I. Nättinen, P. E. N. de Bairos, K. T. Rissanen, unpublished results.
[11] B. F. Hoskins, R. Robson, *J. Am. Chem. Soc.* **1990**, *112*, 1546–1554.
[12] K. Nättinen, J. Linnanto, K. Rissanen, *Eur. J. Inorg. Chem.* **2003**, *22*, 4078–4086.
[13] M. J. Frisch, G. W. Trucks, H. B. Schlegel, G. E. Scuseria, M. A. Robb, J. R. Cheeseman, V. G. Zakrzewski, J. A. Montgomery Jr., R. E. Stratmann, J. C. Burant, S. Dapprich, J. M. Millam, A. D. Daniels, K. N. Kudin, M. C. Strain, O. Farkas, J. Tomasi, V. Barone, M. Cossi, R. Cammi, B. Mennucci, C. Pomelli, C. Adamo, S. Clifford, J. Ochterski, G. A. Petersson, P. Y. Ayala, Q. Cui, K. Morokuma, P. Salvador, J. J. Dannenberg, D. K. Malick, A. D. Rabuck, K. Raghavachari, J. B. Foresman, J. Cioslowski, J. V. Ortiz, A. G. Baboul, B. B. Stefanov, G. Liu, A. Liashenko, P. Piskorz, I. Komaromi, R. Gomperts, R. L. Martin, D. J. Fox, T. Keith, M. A. Al-Laham, C. Y. Peng, A. Nanayakkara, M. Challacombe, P. M. W. Gill, B. Johnson, W. Chen, M. W. Wong, J. L. Andres, C. Gonzalez, M. Head-Gordon, E. S. Replogle, J. A. Pople, *Gaussian98* (Revision A.11), Gaussian, Inc., Pittsburgh, PA, **2001**.
[14] A. L. Spek, PLATON, A Multipurpose Crystallographic Tool, Utrecht University, Utrecht, The Netherlands, **1998**.
[15] W. Lin, O. R. Evans, R.-G. Xiong, Z. Wang, *J. Am. Chem. Soc.* **1998**, *120*, 13272–13273.
[16] D. M. L. Goodgame, D. A. Grachvogel, S. Holland, N. J. Long, A. J. P. White, D. J. Williams, *J. Chem. Soc., Dalton Trans.* **1999**, 3473–3482.
[17] L. Carlucci, G. Ciani, D. M. Proserpio, S. Rizzato, *CrystEngComm* **2002**, *4*, 413–425.
[18] C.-H. Ge, X.-D. Zhang, P. Zhang, W. Guan, F. Guo, Q.-T. Liu, *Polyhedron* **2003**, *22*, 3493–3497.
[19] P. Grosshans, A. Jouaiti, M. W. Hosseini, N. Kyritsakas, *New J. Chem.* **2003**, *27*, 793–793.
[20] A. L. Spek, PLATON, A Multipurpose Crystallographic Tool, Utrecht University, Utrecht, The Netherlands, **1998**.
[21] K. Nättinen, K. Rissanen, *Cryst. Growth Des.* **2003**, *3*, 339–353.
[22] Z. Otwinowski, W. Minor, *Methods in Enzymology, Macromolecular Crystallography, Part A* (Eds.: C. W. Carter Jr., M. Sweet), **1997**, pp. 307–326, Academic Press, New York.
[23] L. J. Farrugia, *J. Appl. Crystallogr.* **1999**, *32*, 837–838.
[24] G. M. Sheldrick, *Acta Crystallogr. Sect. A* **1990**, *46*, 467–473.
[25] G. M. Sheldrick, SHELXL-97 – *A program for crystal structure refinement*, **1997**, University of Göttingen, Germany.
[26] DIAMOND – Visual Crystal Structure Information System, Prof. Dr. G. Bergerhoff, Gerhard-Domagk-Str. 1, 53121 Bonn, Germany.

Received: January 5, 2005
Published Online: June 9, 2005

 © 2005 Wiley-VCH Verlag GmbH & Co. KGaA, Weinheim

Slowly Exchanging *cis*-PtA_2B_2 Atropisomers with A_2 = Chiral Diamine Ligands and B = 5,6-Dimethylbenzimidazole

Manuela Trani,[a] Francesco Cannito,[b] Giovanni Natile,*[c] Patricia A. Marzilli,[d] and Luigi G. Marzilli*[d]

Keywords: Cisplatin / Anticancer drug / Platinum complexes / Chiral diamines / 5,6-Dimethylbenzimidazole

cis-PtA_2G_2 complexes, in which A_2 is a bidentate amine ligand and G is a unidentate guanine derivative bound to platinum through N7, are simple models of the G-G cross-link DNA lesion formed by the anticancer drug cisplatin. Rotation of the G bases about the Pt–N7 bonds is usually rapid except for bulky amine ligand(s). This paper concerns *cis*-$PtA_2(Me_2Bzm)_2$ adducts [A_2 = 2,2′-bipiperidine (Bip) and *N*,*N*,*N*′,*N*′-tetramethyl-2,3-diaminobutane (Me_4DAB); Me_2Bzm = 5,6-dimethylbenzimidazole] for which the interconversion among possible rotamers (one HH and two HT) is slow on the NMR time scale. The amounts of the rarely observed HH conformer were 52 and 37 % at 5 °C for $BipPt(Me_2Bzm)_2$ and $Me_4DABPt(Me_2Bzm)_2$, respectively, and increased to 60 and 44 % at 50 °C. This result represents the first reported clear evidence for the existence of the HH atropisomer in *cis*-PtA_2B_2 adducts (B = G or Me_2Bzm base) with fully substituted diamines, such as Me_4DAB or Me_4EN (Me_4EN = *N*,*N*,*N*′,*N*′-tetramethyl-1,2-diaminoethane). The lack of an O-substituent on the C4 atom of Me_2Bzm (corresponding to C6 of G) undoubtedly allows for a relatively stable HH conformer. Thermodynamic parameters confirm the crucial role of the substituents in positions 4 and 6 of the base systems (for Me_2Bzm and G derivatives, respectively) in determining the stability of different rotamers. The greater abundance of the HH rotamer for $BipPt(Me_2Bzm)_2$ than for $Me_4DABPt(Me_2Bzm)_2$ indicates that an increase in the steric bulk of the carrier ligand favors the HT rotamers over the HH rotamer. For both $BipPt(Me_2Bzm)_2$ and $Me_4DABPt(Me_2Bzm)_2$ adducts, the major HT rotamer has the six-membered ring of each Me_2Bzm ligand on the more crowded side of the *cis* amine with respect to the platinum coordination plane: the N–CH_2– group in Bip and the N–Me_{eq} (N–Me_{eq} = quasi-equatorial N–Me) in Me_4DAB adducts. The latter result is in complete agreement with previous findings from our laboratories concerning $BipPtG_2$ and $Me_4DABPtG_2$ compounds and gives further support to the view that the major HT rotamer is stabilized by the six-membered ring of each base canted toward the *cis* base.
(© Wiley-VCH Verlag GmbH & Co. KGaA, 69451 Weinheim, Germany, 2005)

Introduction

Cisplatin [*cis*-$PtCl_2(NH_3)_2$] is one of the most widely used drugs in the treatment of several cancers.[1,2] Its precise mechanism of action is not completely understood, but it is known to target primarily nuclear DNA, forming a critical lesion by cross-linking two adjacent guanine bases or an adenine and a guanine base of the same strand.[1–6] A serious limitation in studies of adducts between Pt anticancer drugs and DNA is the fluxional character of these adducts. We have called this limitation the "dynamic motion problem."[7]

We have been investigating *cis*-PtA_2G_2 complexes, in which A_2 is a bidentate amine ligand designed to possess steric bulk near the *cis* coordination sites and G is a unidentate guanine derivative bound to platinum through N7.[7–14] In these models the interconversion between rotamers (by rotation around the Pt–N7 bonds) is slow on the NMR time scale,[15] and thus the presence of different rotamers can be detected by NMR spectroscopy. The G bases can be in a head-to-head arrangement (HH), in which both H8 atoms lie on the same side of the coordination plane, or in a head-to-tail arrangement (HT), in which the H8 atoms lie on opposite sides of the coordination plane (ΛHT and ΔHT, Scheme 1).

For $BipPtG_2$ and $Me_2DABPtG_2$ adducts (Bip = 2,2′-bipiperidine, Me_2DAB = *N*,*N*′-dimethyl-2,3-diaminobutane; C_2-symmetrical ligands are obtained for *S*,*R*,*R*,*S* or *R*,*S*,*S*,*R* configurations at the four stereocenters located on the N, C, C, and N atoms of the chelate ring, Scheme 2), the HT conformers typically dominated over the HH conformer.[11,12,16,17] This dominance was attributed to interligand interactions, which were classified as "first-to-first," "first-to-second," and "second-to-second" sphere com-

[a] Department of Chemistry, Emory University, Atlanta, GA 30322, USA
[b] Consorzio Interuniversitario di Ricerca in Chimica dei Metalli nei Sistemi Biologici (C.I.R.C.M.S.B.), Via C. Ulpiani 27, 70126 Bari, Italy
[c] Dipartimento Farmaco-Chimico, Università di Bari, Via E. Orabona 4, 70125 Bari, Italy
[d] Department of Chemistry, Louisiana State University, Baton Rouge, LA 70803, USA
E-mail: lmarzil@lsu.edu
Supporting information for this article is available on the WWW under http://www.eurjic.org or from the author.

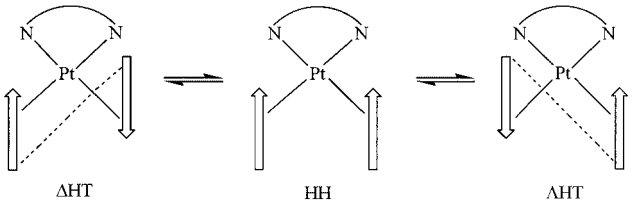

Scheme 1. Schematic representation of HH, ΔHT, and ΛHT atropisomers for *cis*-PtA_2B_2 complexes.

munications.[17,18] The latter two types of interactions involve phosphate groups,[11,12,17,18] and in this study we examine adducts lacking this group in order to focus on first-to-first sphere communications (FFC). FFC are interligand interactions involving portions of the ligands close to the metal center. Base-to-base interactions and H-bonding interactions between G O6 and N–H of a *cis* amine fall into this category. For C_2-symmetrical Bip and Me_2DAB ligands the latter interaction should favor the HT rotamer having the O6 atom of each G near the N–H of the *cis* amine, and on the opposite side of the platinum coordination plane from the N–CH_2– or the N–Me group. One HT rotamer was in fact favored but, contrary to our expectations, the O6 of each guanine of this major rotamer was near the N–CH_2– or the N–Me group of the *cis* amine, not near the N–H group.

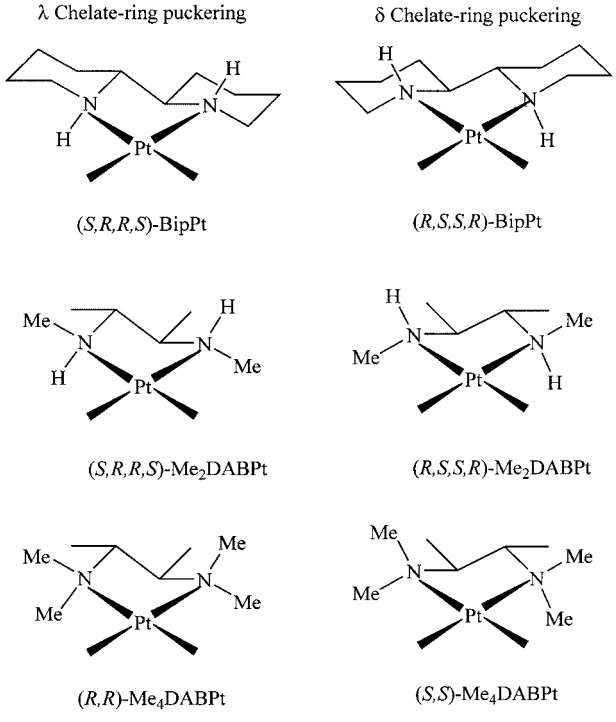

Scheme 2. Schematic representation of Bip, Me_2DAB, and Me_4DAB ligands coordinated to a platinum(II) moiety.

In the NMR spectra of $BipPtG_2$ and $Me_2DABPtG_2$ complexes, the H8 signal of the major HT rotamer is more downfield than the H8 signal of the minor HT rotamer. This result is an indication that in the major HT rotamer the H8 proton of each guanine is pointing farther away from the *cis* G (so that it experiences a smaller shielding effect from the *cis* G) as the six-membered ring of each guanine moves toward the *cis* guanine ("6-in" orientation). The HH rotamer has one H8 signal more downfield than the H8 signal of the major HT form (HH_d base), and the second H8 signal more upfield than the H8 signal of the minor HT conformer (HH_u base). The latter signal must belong to a guanine having H8 pointing toward the *cis* G and embedded in its shielding cone; therefore this guanine must have the "6-out" orientation.

The "6-in" orientation of the *cis* G's in HT conformers of $BipPtG_2$ and $Me_2DABPtG_2$ adducts has implications relevant to the stability of the conformers. For example, the interaction between the H8 atom of each G and the *cis* amine will be smaller when H8 is on the side of the N–H than when it is on the side of the N–CH_2– or the N–Me of the *cis* amine with respect to the platinum coordination plane. Therefore the conformer with H8 near the N–H of the *cis* amine will be favored and will have the six-membered ring of each guanine on the same side as the N–CH_2– or the N–Me group of the *cis* amine. The fact that the "6-in" orientation of *cis* guanines is favored suggests strongly that this orientation allows better base-base, dipole-dipole (the H8 of one guanine closer to the O6 of the second guanine), and stacking interactions.

In the HH rotamer, the "6-out" guanine (with a shielded H8) has the six-membered ring on the same side of the coordination plane as the N–H of the *cis* amine (whereas the second guanine has the six-membered ring near the N–CH_2– or the N–Me of the *cis* amine). The smaller steric interaction of the former guanine with the *cis* amine allows the "6-out" orientation to occur, and as a consequence the negatively charged O6 atom of this "6-out" guanine is farther from the O6 atom of the *cis* G.

More recently, in order to achieve a better understanding of systems lacking N–H groups, studies were conducted on adducts with the carrier ligand, Me_4DACH (Me_4DACH = *N*,*N*,*N*′,*N*′-tetramethyl-1,2-diaminocyclohexane).[19] The dissymmetry of Me_4DACH with respect to the platinum coordination plane is very small (each diamine N-donor has methyls on both sides of the coordination plane), which makes the ligand fundamentally different from the Bip and Me_2DAB ligands previously investigated. As Cramer found in his classic study on Me_4ENPtG_2 adducts (Me_4EN = *N*,*N*,*N*′,*N*′-tetramethyl-1,2-diaminoethane, G = Guo),[15] no HH rotamer was observed at equilibrium in any of the $Me_4DACHPtG_2$ adducts; moreover, the H8 chemical shifts are very similar for the major and the minor HT rotamers. The absence of a significant amount of HH rotamer could be a consequence of the bulk produced on both sides of the coordination plane by the four N–Me groups. This bulk on both sides of the coordination plane does not allow "6-out" canting of at least one G, which is required for minimizing O6···O6 electrostatic repulsions.[20] Moreover, two $Me_4DACHPt(5'\text{-}GMP)_2$ ΔHT rotamers were shown by X-ray crystallography to have a "6-in" orientation of the two G's in spite of the opposite chiralities of the Me_4DACH ligands in the two compounds.[21]

 © 2005 Wiley-VCH Verlag GmbH & Co. KGaA, Weinheim

Despite the many studies conducted on cisplatin models, numerous questions remain unanswered. In an effort to achieve a better understanding of the factors influencing formation and stability of conformers in models of the cisplatin-DNA cross-link, we undertook a study of *cis*-PtA_2-$(Me_2Bzm)_2$ complexes (A_2 = Bip and Me_4DAB; Me_2Bzm = 5,6-dimethylbenzimidazole; Scheme 3). Me_2Bzm lacks the O substituent on the C4 atom (corresponding to C6 of purines); therefore, a comparison between Me_2Bzm and G adducts allows us to unravel the role of such an oxygen atom in the formation and stability of conformers. Moreover, Me_2Bzm has several "probe protons" on its periphery that might help in assessing the ligand canting.[22]

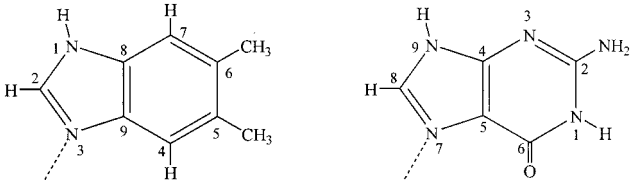

Scheme 3. Shorthand drawings of 5,6-dimethylbenzimidazole and guanine bases.

Results

[*rac*-BipPt($Me_2Bzm)_2$]$^{2+}$ Complex: The lack of chirality in the Me_2Bzm ligands renders indistinguishable the NMR spectroscopic data obtainable for [*rac*-BipPt-$(Me_2Bzm)_2]^{2+}$ and for the single enantiomers [(*R*,*S*,*S*,*R*)-BipPt$(Me_2Bzm)_2]^{2+}$ and [(*S*,*R*,*R*,*S*)-BipPt$(Me_2Bzm)_2]^{2+}$; therefore, only the NMR spectroscopic data concerning the *rac* isomer (used in higher concentration) will be described. The ^{1}H NMR spectrum of [*rac*-BipPt$(Me_2Bzm)_2]^{2+}$ (in D_2O at pH 6 and 5 °C) exhibited four sets of signals for each proton (Figure 1 shows the H2 region), indicating the presence of one HH and two HT conformers. Complete assignment of the signals for each conformer (Table 1) was possible on the basis of a ^{1}H/^{1}H ROESY experiment carried out at 5 °C. In the ^{1}H/^{1}H ROESY spectrum, the H2 signal at δ = 8.57 ppm had an NOE cross-peak to the H2 signal at δ = 8.42 ppm, allowing the assignment of these signals to the HH conformer (HH_d and HH_u denote the HH base having the H2 signal downfield and upfield with respect to the H2 signal of the major HT rotamer, respectively). The other two signals at δ = 8.54 and 8.38 ppm must belong to the major HT (MHT) and minor HT (mHT) rotamers, respectively. The H2 signal of the major HT conformer at δ = 8.54 ppm had an NOE cross-peak to the H4 signal at δ = 8.16 ppm; similarly, the H2 signal of the minor HT conformer at δ = 8.38 ppm had an NOE cross-peak to the H4 signal at δ = 8.18 ppm. Therefore, the H4 signals at δ = 8.16 and 8.18 ppm were assigned to the major and minor HT conformers, respectively. The remaining two H4 signals belonging to the HH rotamer (8.08 and 8.29 ppm) were assigned to the HH_d and HH_u bases of the HH rotamer, respectively, on the basis of the opposite relationship in chemical shift between the H2 and H4 protons.

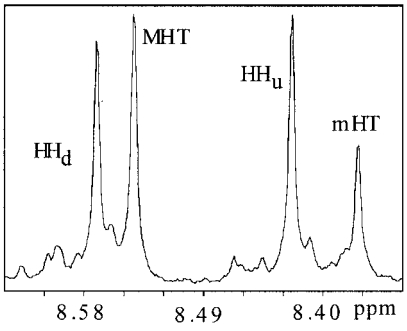

Figure 1. H2 region of the ^{1}H NMR spectrum of [*rac*-BipPt$(Me_2Bzm)_2]^{2+}$ at 5 °C.

Table 1. ^{1}H NMR Shifts (ppm) of Me_2Bzm for [*rac*-BipPt$(Me_2Bzm)_2]^{2+}$ at 5 °C and pH 6.

	MHT[a]	mHT[a]	HH_d[a]	HH_u[a]
H2	8.54	8.38	8.57	8.42
H4	8.16	8.18	8.08	8.29
H7	7.29	7.37	7.21	7.26
Me5	2.42	2.49	2.21	2.47
Me6	2.24	2.34	2.01	2.20

[a] MHT = equivalent bases of the major head-to-tail conformer; mHT = equivalent bases of the minor head-to-tail conformer; HH_d = base of the HH conformer with downfield H2; HH_u = base of the HH conformer with upfield H2.

NOE cross-peaks between H4 and Me5 signals, between Me5 and Me6 signals, and between Me6 and H7 signals were used to complete the assignments of the Me_2Bzm protons (Supporting information; for supporting information see also the footnote on the first page of this article). NOE cross-peaks between the H4 signals of Me_2Bzm and the N–CH_2– signals of Bip allowed us to assign the Δ or Λ conformations to the HT rotamers and to identify the orientation of each base in the HH rotamer. The H4 signal at δ = 8.16 ppm belonging to the major HT conformer had a cross-peak to the N–CH_2– signal of the Bip ligand at δ = 2.78 ppm. Therefore, the major HT rotamer has the Me_2Bzm six-membered rings close to the *cis* N–CH_2– groups of the Bip ligand [this corresponds to the rotamer having the ΔHT conformation in the (*R*,*S*,*S*,*R*) adduct and the ΛHT conformation in the (*S*,*R*,*R*,*S*) adduct]. It follows that the minor HT rotamer must have the six-membered ring of each Me_2Bzm near the N–H of the *cis* amine corresponding to ΛHT and ΔHT conformations for the (*R*,*S*,*S*,*R*) and (*S*,*R*,*R*,*S*) adducts, respectively. The H4 signal at δ = 8.08 ppm belonging to the HH_d base of the HH conformer also had a cross-peak to the N–CH_2– signals of the Bip ligand at δ = 2.78 ppm, therefore the HH_d base of the HH rotamer has the six-membered ring near the *cis* N–CH_2– group of Bip. Thus, the HH_u base of the HH rotamer must have the six-membered ring close to the N–H of the *cis* amine.

 © 2005 Wiley-VCH Verlag GmbH & Co. KGaA, Weinheim

When the temperature was increased from 5 to 50 °C, a change in the ratio of conformers was observed and the HH conformer became more favored. The respective percentages of HH, major HT, and minor HT conformers were 52, 31, and 17, at 5 °C; 57, 30, and 13, at 35 °C; and 60, 28, and 12, at 50 °C.

[(*R*,*S*,*S*,*R*)-BipPt(Me_2Bzm)$_2$]$^{2+}$ and [(*S*,*R*,*R*,*S*)-BipPt(Me_2Bzm)$_2$]$^{2+}$ Complexes: The reason for preparing derivatives with pure enantiomeric Bip ligands was to investigate their CD spectra. The CD spectrum at pH 6 of [(*R*,*S*,*S*,*R*)-BipPt(Me_2Bzm)$_2$]$^{2+}$ exhibits positive bands around 300 and 260 nm and negative bands around 285, 240, and 210 nm. On the other hand, the CD spectrum at pH 6 of [(*S*,*R*,*R*,*S*)-BipPt(Me_2Bzm)$_2$]$^{2+}$ shows negative bands at 300 and 260 nm and positive bands at 285, 240, and 210 nm (Figure 2). The CD spectra of *cis*-Pt(Me_2Bzm)$_2$ adducts are not expected to be similar to those of *cis*-PtG_2 adducts because of the different nature of the $\pi \rightarrow \pi^*$ electron transitions; however, the trends observed for chiral BipPt(Me_2Bzm)$_2$ adducts at long wavelengths (>230 nm) resemble the trends observed for $BipPtG_2$ adducts. For instance, the CD spectrum of (*R*,*S*,*S*,*R*)-BipPt(5′-GMP)$_2$ at neutral pH exhibits a negative band at 288 nm and a positive band at 254 nm (which were identified as characteristic of a ΔHT conformation); conversely, the CD spectrum of (*S*,*R*,*R*,*S*)-BipPt(5′-GMP)$_2$ exhibits a positive band at 288 nm and a negative band at 254 nm (which were identified as characteristic of a ΛHT conformation).[12] Therefore, the CD spectra are in agreement with a dominant ΔHT rotamer for [(*R*,*S*,*S*,*R*)-BipPt(Me_2Bzm)$_2$]$^{2+}$ and a dominant ΛHT rotamer for [(*S*,*R*,*R*,*S*)-BipPt(Me_2Bzm)$_2$]$^{2+}$. This result is in full agreement with the NMR investigation showing that the major rotamer had the ΔHT conformation for [(*R*,*S*,*S*,*R*)-BipPt(Me_2Bzm)$_2$]$^{2+}$ and the ΛHT conformation for [(*S*,*R*,*R*,*S*)-BipPt(Me_2Bzm)$_2$]$^{2+}$.

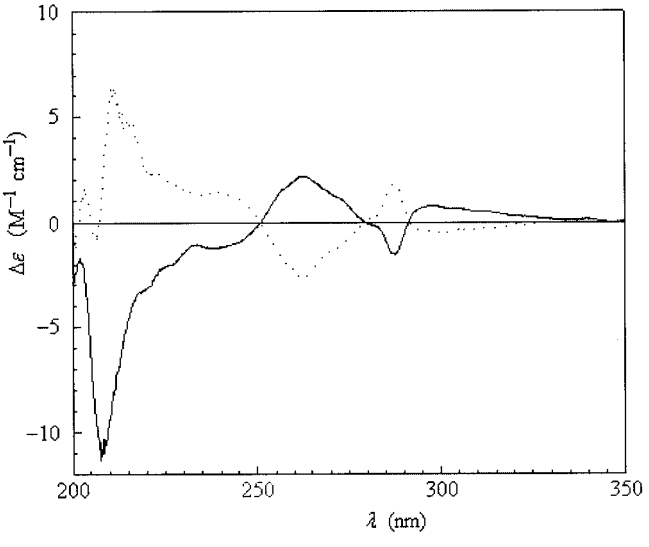

Figure 2. CD spectra of [(*R*,*S*,*S*,*R*)-BipPt(Me_2Bzm)$_2$]$^{2+}$ (solid line) and [(*S*,*R*,*R*,*S*)-BipPt(Me_2Bzm)$_2$]$^{2+}$ (dotted line) collected at room temperature and pH 6.

[*rac*-Me_4DABPt(Me_2Bzm)$_2$]$^{2+}$ Complex: As for the Bip complexes, the lack of chirality in the Me_2Bzm ligand renders the NMR spectroscopic data obtained for [*rac*-Me_4DABPt(Me_2Bzm)$_2$]$^{2+}$ identical to those obtained for complexes with individual Me_4DAB enantiomers. Therefore, only the NMR spectroscopic data concerning the *rac* isomer (used in higher concentration) will be described. The ^{1}H NMR spectrum of [*rac*-Me_4DABPt(Me_2Bzm)$_2$]$^{2+}$ (D_2O, pH 6.5, 5 and 25 °C) had four sets of signals, indicating the presence of one HH (with inequivalent bases) and two HT conformers (each one with equivalent bases) as expected (Figure 3). Complete assignment of signals for each conformer (Table 2 and Table 3) was possible on the basis of ^{1}H/^{1}H NOESY and ^{1}H/^{13}C HMQC experiments, and on the basis of previous results from these laboratories on the (*S*,*S*)-Me_4DABPt(3′-GMP)$_2$ adduct.[23]

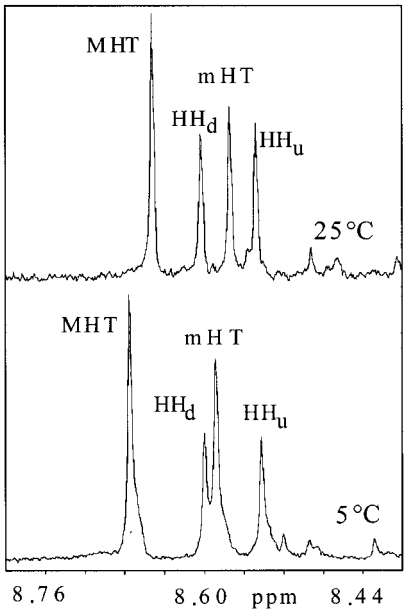

Figure 3. H2 region of the ^{1}H NMR spectra of [*rac*-Me_4DABPt(Me_2Bzm)$_2$]$^{2+}$ at 5 (bottom) and 25 °C (top).

In the ^{1}H/^{1}H NOESY spectrum of [*rac*-Me_4DABPt(Me_2Bzm)$_2$]$^{2+}$ at 5 °C, the intense H2 signal at δ = 8.67 ppm had a cross-peak to the intense H4 signal at δ = 8.17 ppm; thus, these resonances were assigned to the major HT rotamer. The less intense H2 signal at δ = 8.59 ppm had a cross-peak to the less intense H4 signal at δ = 8.19 ppm; thus, these resonances were assigned to the minor HT rotamer. The two H2 signals of equal intensity at δ = 8.60 and 8.54 ppm must belong to the HH rotamer (HH_d and HH_u bases, respectively). The H4 signals at δ = 8.27 and 8.28 ppm must also belong to the HH rotamer. Their assignment to the HH_u and HH_d bases, respectively, was possible on the basis of NOE cross-peaks between the H4 protons and the *cis* amine N–Me's as described in the following paragraph. NOE cross-peaks be-

 © 2005 Wiley-VCH Verlag GmbH & Co. KGaA, Weinheim

Table 2. ^{1}H NMR Shifts (ppm) of Me_2Bzm and Amine N–Me's for [*rac*-$Me_4DABPt(Me_2Bzm)_2]^{2+}$ at 5 and 25 °C and at pH 6.

	5 °C				25 °C			
	MHT[a]	mHT[a]	HH_d[a]	HH_u[a]	MHT	mHT	HH_d	HH_u
H2	8.67[b]	8.59[c]	8.60[b]	8.54[c]	8.65	8.57	8.60	8.54
H4	8.17[c]	8.19[b]	8.28[c]	8.27[b]	8.17	8.19	8.27	8.25
H7	7.25	7.26	7.15	7.16	7.31	7.32	7.23	7.24
Me5	2.41	2.42	2.33	2.37	2.45	2.46	2.41	2.43
Me6	2.22	2.24	2.06	2.09	2.30	2.31	2.20	2.21
N–Me(ax)	2.89	2.73	2.79	2.85	2.91	2.75	2.81	2.88
N–Me(eq.)	2.58	2.78	2.69	2.65	2.60	2.79	2.71	2.67

[a] MHT = equivalent bases of major head-to-tail conformer; mHT = equivalent bases of minor head-to-tail conformer; HH_d = base of the HH conformer with downfield H2; HH_u = base of the HH conformer with upfield H2. [b] Near "quasi-axial" N–Me. [c] Near "quasi-equatorial" N–Me.

Table 3. ^{13}C NMR Shifts (ppm) of Me_2Bzm and Amine N–Me's for [*rac*-$Me_4DABPt(Me_2Bzm)_2]^{2+}$ at 25 °C and pH 6.

	MHT[a]	mHT[a]	HH_d[a]	HH_u[a]
C2	145.0	145.4	144.8	145.0
C4	119.6	119.5	120.8	120.5
C7	116.3	116.3	116.1	116.1
Me5	22.5	22.6	22.5	22.5
Me6	22.4	22.4	22.3	22.3
N–Me(ax)	45.2	47.0	46.3	47.2
N–Me(eq.)[b]	53.6 (14.6)	52.6 (18.2)	53.9 (13.4)	52.8 (18.2)

[a] MHT = equivalent bases of the major head-to-tail conformer; mHT = equivalent bases of the minor head-to-tail conformer; HH_d = base of the HH conformer with downfield H2; HH_u = base of the HH conformer with upfield H2. [b] $^3J(^1H,^{13}C)$ in Hz, given in parentheses.

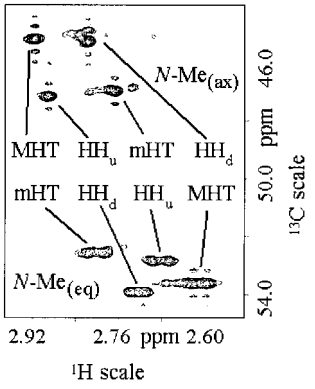

Figure 4. N–Me region of the ^{1}H/^{13}C HMQC spectrum (25 °C) of [*rac*-$Me_4DABPt(Me_2Bzm)_2]^{2+}$.

tween H4 and Me5 signals, between Me5 and Me6 signals, and between Me6 and H7 signals were used to complete the assignments of the Me_2Bzm signals (Supporting Information).

Assignment of the Δ and Λ conformations to the two HT rotamers and of the HH_d and HH_u bases in the HH rotamer was derived from the relative positions of the H2 (five-membered ring) and H4 (six-membered ring) protons with respect to the N–Me_{ax} and N–Me_{eq} (quasi-axial and quasi-equatorial N–Me groups of the carrier ligand, respectively) as revealed by the ^{1}H/^{1}H NOESY spectrum.[24] The latter experiment depends on the assignment of the proton resonances to the axial and equatorial N–Me's of the Me_4DAB ligand. This assignment was made on the basis of a previous investigation carried out in these laboratories on the (*S*,*S*)-$Me_4DABPt(3'\text{-GMP})_2$ adduct,[23] showing that the equatorial N–Me resonances have ^{13}C NMR chemical shifts at ca. 53 ppm, while the axial N–Me resonances have ^{13}C NMR chemical shifts at ca. 46 ppm. Therefore the ^{1}H/^{13}C HMQC experiment reported in Figure 4 was sufficient to distinguish between axial and equatorial N–Me signals.

The strong NOE cross-peaks observed between the H2 and the N–Me_{ax} signals and between the H4 and the N–Me_{eq} signals for the major HT conformer provide evidence that the six-membered ring of each base is near the N–Me_{eq} group of the *cis* amine; thus, the MHT rotamer has the ΔHT conformation for the [(*S*,*S*)-$Me_4DABPt(Me_2Bzm)_2]^{2+}$ adduct and the ΛHT conformation for the [(*R*,*R*)-$Me_4DABPt(Me_2Bzm)_2]^{2+}$ adduct. Likewise, strong NOE cross-peaks between the H2 and the N–Me_{eq} signals and between the H4 and the N–Me_{ax} signals for the minor HT conformer are indications that the six-membered ring is close to the N–Me_{ax} group of the *cis* amine, a situation which corresponds to the mHT atropisomer having the ΛHT conformation in the [(*S*,*S*)-$Me_4DABPt(Me_2Bzm)_2]^{2+}$ adduct and the ΔHT conformation in the [(*R*,*R*)-$Me_4DABPt(Me_2Bzm)_2]^{2+}$ adduct. For the HH rotamer, a strong NOE cross-peak between H2 and N–Me_{ax} signals for the HH_d base indicates that this base has the six-membered ring near the N–Me_{eq} of the *cis* amine. The H4 signal at δ = 8.28 ppm has a NOE cross-peak to an equatorial N–Me signal (δ = 2.69 ppm); thus, it is assigned to the HH_d base. On the other hand, a strong NOE cross-peak between the H2 and the N–Me_{eq} signals for the HH_u base indicates that this base has the six-membered ring close to the N–Me_{ax} of the *cis* amine. The H4 signal at δ = 8.27 ppm has a NOE cross-peak to an axial N–Me signal (δ = 2.85 ppm); thus, it is assigned to the HH_u base. The H2/N–Me and H4/N–Me regions of ^{1}H/^{1}H NOESY spectra for [*rac*-$Me_4DABPt(Me_2Bzm)_2]^{2+}$ are reported in Figure 5 and Figure 6, respectively.

As found also for the [*rac*-$BipPt(Me_2Bzm)_2]^{2+}$ adduct, the percentages of the different [*rac*-$Me_4DABPt(Me_2Bzm)_2]^{2+}$ conformers depend on temperature. The relative abundances of the HH, major HT, and minor HT conformers were 37, 39, and 24, at 5 °C; 42, 35, and 23, at 25 °C; and 44, 35, and 21, at 50 °C.

 © 2005 Wiley-VCH Verlag GmbH & Co. KGaA, Weinheim

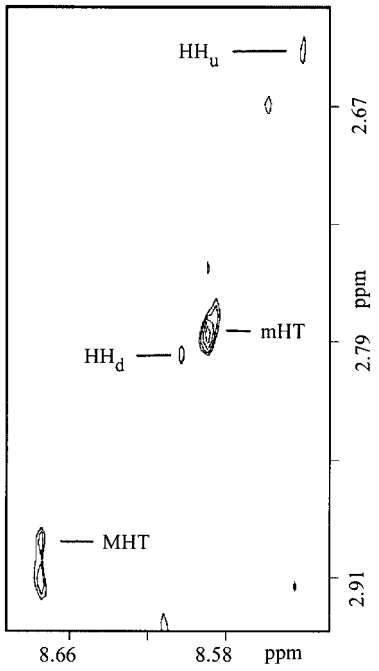

Figure 5. H2/NMe region of the $^1H/^1H$ NOESY spectrum of [*rac*-$Me_4DABPt(Me_2Bzm)_2]^{2+}$ at 5 °C.

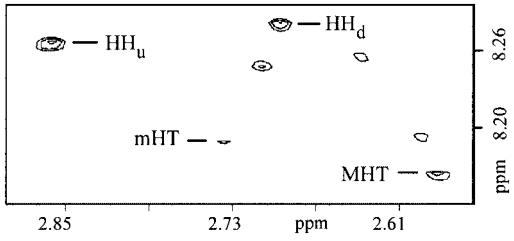

Figure 6. H4/N–Me region of the $^1H/^1H$ NOESY spectrum of [*rac*-$Me_4DABPt(Me_2Bzm)_2]^{2+}$ at 5 °C.

[(*S*,*S*)-$Me_4DABPt(Me_2Bzm)_2]^{2+}$ and [(*R*,*R*)-$Me_4DABPt(Me_2Bzm)_2]^{2+}$ Complexes: CD data for both [(*S*,*S*)-$Me_4DABPt(Me_2Bzm)_2]^{2+}$ and [(*R*,*R*)-$Me_4DABPt(Me_2Bzm)_2]^{2+}$ adducts have been collected. The CD spectrum at pH 6 of [(*S*,*S*)-$Me_4DABPt(Me_2Bzm)_2]^{2+}$ exhibits positive bands around 300, 275, and 210 nm, and a negative band at 240 nm. In contrast, the CD spectrum at pH 6 of [(*R*,*R*)-$Me_4DABPt(Me_2Bzm)_2]^{2+}$ shows negative bands at 300, 275, and 210 nm, and a positive band at 240 nm (Figure 7). Thus, the CD spectra of [(*S*,*S*)-$Me_4DABPt(Me_2Bzm)_2]^{2+}$ and [(*R*,*R*)-$Me_4DABPt(Me_2Bzm)_2]^{2+}$ resemble those observed for [(*R*,*S*,*S*,*R*)-$BipPt(Me_2Bzm)_2]^{2+}$ and [(*S*,*R*,*R*,*S*)-$BipPt(Me_2Bzm)_2]^{2+}$ only for wavelengths above 230 nm, while they are rather different for wavelengths below 230 nm. Moreover, for wavelengths above 230 nm the Cotton effect is dominated by coupling between $\pi \rightarrow \pi^*$ transitions of *cis* bases and can be diagnostic for the Λ or Δ conformation of the dominant HT rotamer.[21] Thus for the Me_4DAB complexes also, as previously observed for the Bip adducts, the CD spectra are in agreement with the dominance of the ΔHT conformation for [(*S*,*S*)-$Me_4DABPt(Me_2Bzm)_2]^{2+}$ and of the ΛHT conformation for [(*R*,*R*)-$Me_4DABPt(Me_2Bzm)_2]^{2+}$. This result is in full agreement with the NMR spectroscopic data showing that the major HT rotamer had the Δ conformation in the [(*S*,*S*)-$Me_4DABPt(Me_2Bzm)_2]^{2+}$ adduct and the Λ conformation in the [(*R*,*R*)-$Me_4DABPt(Me_2Bzm)_2]^{2+}$ adduct.

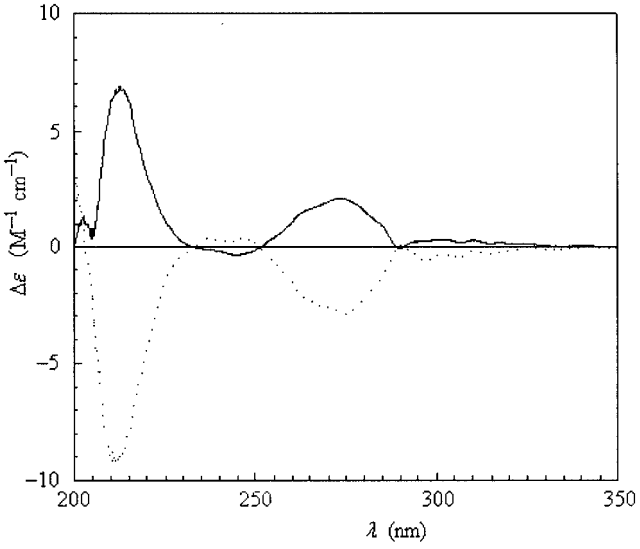

Figure 7. CD spectra of [(*S*,*S*)-$Me_4DABPt(Me_2Bzm)_2]^{2+}$ (solid line) and [(*R*,*R*)-$Me_4DABPt(Me_2Bzm)_2]^{2+}$ (dotted line) collected at room temperature and pH 6.

From the percentages of individual rotamers at different temperatures the activation parameters for the equilibria HH ⇄ MHT and HH ⇄ mHT have been evaluated and the values are reported in Table 4.

Table 4. Enthalpy (ΔH, kJ·mol^{-1}) and Entropy (ΔS, J K^{-1} mol^{-1}) for the Equilibria HH ⇄ MHT and HH ⇄ mHT (K_{MHT} = [MHT]/[HH]; K_{mHT} = [mHT]/[HH]) in *cis*-PtA_2B_2 Complexes.[a]

		ΔH	ΔS
[*rac*-$BipPt(Me_2Bzm)_2]^{2+}$	MHT	–3.9 (0.9)	–18.1 (2.8)
	mHT	–8.2 (0.3)	–38.9 (1.0)
[*rac*-$Me_4DABPt(Me_2Bzm)_2]^{2+}$	MHT	–4.6 (1.9)	–16.5 (6.4)
	mHT	–5.1 (0.4)	–21.9 (1.4)

[a] Figures in parentheses are the root mean square errors.

Discussion

Base Canting in *cis*-PtA_2B_2 Adducts: The G H8 signals are generally used as a probe for assessing the degree and direction ("6-in" or "6-out") of base canting in *cis*-PtA_2G_2 adducts.[25] In the HH conformer of $BipPtG_2$ and $Me_2DABPtG_2$ adducts (with C_2-symmetry of the bidentate ligand), one base generally has low canting, while the other base is strongly canted. For the highly canted base, the six-membered ring moves toward the *cis* amine, and the H8 atom moves toward the *cis* G. Because of the ring-current anisotropy of the *cis* G, the H8 signal of the canted G experiences an upfield shift. The H2 of Me_2Bzm is in a position corresponding to that of H8 of a G base; therefore, the canting can be deduced from the position of the H2 ^1H

 © 2005 Wiley-VCH Verlag GmbH & Co. KGaA, Weinheim

NMR resonance of [*cis*-$PtA_2(Me_2Bzm)]^{2+}$ adducts. Moreover, for the Me_2Bzm ligand, the H4 and Me5 shifts can also be used to confirm the direction and degree of canting.

Of particular significance is the very small difference in H2 chemical shifts of the HH rotamer of [BipPt-$(Me_2Bzm)_2]^{2+}$ (δ = 0.15 ppm) when compared to that of the H8 signals of the HH rotamer of $BipPtG_2$ species (ca. 1.3 ppm). For *cis*-PtG_2 adducts unfavorable electrostatic and steric interactions between O6 atoms of *cis* G's are likely in the HH rotamer, for which the O6···O6 distance can be estimated to be smaller than the sum of the van der Waals radii for guanines orthogonal to the platinum coordination plane.[26] Some relief from unfavorable electrostatic and steric interactions can be achieved if one or both G's can be canted "6-out". Such a canting is possible in $BipPtG_2$ as well as in $Me_2DABPtG_2$ adducts because one G in the HH rotamer has the six-membered ring adjacent to the N–H of the *cis* amine. The "6-out" canting of this guanine will not only be allowed by the small steric interaction between the six-membered ring of the guanine and the N–H of the *cis* amine, but might also be favored by H-bond formation between the G-O6 and the amine N–H.

The main difference between G and Me_2Bzm bases resides in the absence, in the latter case, of the oxygen substituent. The absence of such a substituent greatly reduces the steric and electrostatic interactions between *cis*-bases, which therefore can both be "quasi orthogonal" to the coordination plane.

For $BipPtG_2$ adducts,[12] the H8 signal of the major HT conformer was 0.3 to 0.5 ppm downfield from the H8 signal of the minor HT conformer (depending upon the G base and the pH); in contrast, in $[BipPt(Me_2Bzm)_2]^{2+}$ the difference in chemical shift between the H2 signals of the major and minor HT rotamers is only 0.16 ppm. For HT conformers of *cis*-PtG_2 adducts base canting is driven by dipole-dipole interactions. Calculations show that a "6-in" canting of the two guanines (up to 20° rotation about the Pt–N7 bond, starting from the plane of each guanine orthogonal to the coordination plane) will bring the H8 of each guanine closer to the O6 of the *cis* guanine with consequent increase in stability of the rotamer.[28] This situation is probably attained in the MHT rotamer of $BipPtG_2$ and $Me_2DABPtG_2$ compounds, in which the H8 atom of each guanine is on the same side as the N–H of the *cis* amine with respect to the coordination plane. In contrast, in the minor HT rotamer of $BipPtG_2$ and $Me_2DABPtG_2$ compounds such a "6-in" canting of the two guanines is limited by steric interaction between the H8 of each guanine and the *N*-alkyl substituent on the *cis* amine, both on the same side of the coordination plane. With respect to the MHT rotamer, the smaller "6-in" canting of the two guanines in mHT causes both a lower stability of this rotamer and a greater shielding of the H8 protons, which therefore resonate at higher field.

In the Me_2Bzm adducts there is no strong dipole-dipole interaction of the type just described for the G adducts. Any dipole-dipole interaction should be weak. The absence of a strong driving force to base canting explains why the separation between the H2 resonances of HT rotamers is smaller in Me_2Bzm adducts than in G adducts.

As mentioned, information about canting can also be gained from the H4 and Me5 signals of Me_2Bzm. The H4 and Me5 signals of the major HT rotamer were slightly upfield with respect to the corresponding signals for the minor HT rotamer ($\Delta\delta$ of 0.02 and 0.07 ppm for H4 and Me5, respectively). The differences in chemical shift between the two H4 and between the two Me5 signals of the HH rotamer were 0.21 and 0.26 ppm, respectively (Table 1). As expected, the trend in chemical shifts for H4 and Me5 is opposite to that for H2 because canting that brings H2 closer to the *cis* base will bring H4 and Me5 farther from the *cis* base and vice-versa.

As observed in the case of $[BipPt(Me_2Bzm)_2]^{2+}$, for $[Me_4DABPt(Me_2Bzm)_2]^{2+}$ the separations between the two H2 signals of the HH rotamer (δ = 0.06 ppm) and between the H2 signals of the two HT conformers (δ = 0.08 ppm) are also small (Table 2). The explanation given for the former complex applies also to the latter.

The slightly greater separation between the two H2 resonances of the HH rotamer and between the H2 resonances of the two HT rotamers for the $[BipPt(Me_2Bzm)_2]^{2+}$ vs. the $[Me_4DABPt(Me_2Bzm)_2]^{2+}$ adduct is in agreement with the former complex having a greater canting freedom for one Me_2Bzm ligand of the HH rotamer (the Me_2Bzm having the six-membered ring adjacent to the N–H of the *cis* amine) and for the two Me_2Bzm ligands of one HT rotamer (the rotamer having the H2 of each Me_2Bzm near the N–H of the *cis* amine). However, as already pointed out, the degree of canting observed in the $[BipPt(Me_2Bzm)_2]^{2+}$ adduct is far smaller than that observed in the $BipPtG_2$ adducts because in the latter case the steric and electrostatic repulsion between the O6's of the *cis* G's in the HH conformer or the electrostatic attraction between the O6 of one G and the H8 of the *cis* G in the HT rotamers drives the tilting of the guanine(s).

Comparison with Base Canting in Re or Ru Metal Complexes Containing *cis*-Benzimidazole Ligands: The current work complements our previous studies on Re and Ru complexes containing *cis* Me_3Bzm (Me_3Bzm = 1,5,6-trimethylbenzimidazole) ligands.[22,27] For $[Re_2O_3Cl_4(Me_3Bzm)_4]$,[27] the four Me_3Bzm ligands have an HH-HT-HH arrangement. The central HT arrangement was formed by pseudo-bridging "stacked" Me_3Bzm ligands (designated as Me_3Bzm^s), while the peripheral HH arrangements were formed by one Me_3Bzm^s base and one of the two equivalent "terminal" Me_3Bzm bases (designated as Me_3Bzm^t). The structure showed that the two Me_3Bzm^t bases were highly canted with respect to the two Me_3Bzm^s bases. In the ^1H NMR spectrum the H2 signal of the Me_3Bzm^t bases was ≈ 1.3 ppm downfield from that of the Me_3Bzm^s H2 signal; the H4 and Me5 signals showed the opposite trend. The high degree of canting of the Me_3Bzm^t bases with respect to the Me_3Bzm^s bases was attributed to the electrostatic attraction between the positively charged H2 of Me_3Bzm^t and the negatively charged O and Cl groups in the core of the dimer.

 © 2005 Wiley-VCH Verlag GmbH & Co. KGaA, Weinheim

For *cis*,*cis*,*cis*-[$RuCl_2(Me_2SO)_2(Me_3Bzm)_2$] ($Me_2SO$ = dimethyl sulfoxide)[22] one HT and one HH form were observed in solution. For the HH conformer, the H2 signal of the uncanted Me_3Bzm base that is *cis* to the Cl atoms was 1.5 ppm downfield with respect to the H2 signal of the canted Me_3Bzm base that is *cis* to the Me_2SO groups. Opposite trends were observed for the H4 and Me5 signals. In the X-ray structure of the HH conformer, the Me_3Bzm close to the Me_2SO groups was highly canted, with the H2 atom pointing toward the Me_3Bzm base close to the Cl atoms. The six-membered ring of the canted Me_3Bzm ligand was inserted between the two *cis* Me_2SO ligands so as to avoid steric interaction with the bulky Me_2SO groups. This insertion causes the H2 atom to move toward the *cis* Me_3Bzm. The latter Me_3Bzm is kept in a fixed position because of favorable electrostatic attraction between its H2 and the two *cis* Cl ligands.

The results obtained with the Re and Ru complexes emphasize the role of electrostatic interactions in determining the canting of Me_2Bzm/Me_3Bzm ligands. Electrostatic interactions of this type are not present in the platinum complexes investigated here, which, in fact, show little or negligible canting.

Distribution of Conformers: The HH rotamer, disfavored in most of the previously studied *cis*-PtG_2 adducts,[17] is the most favored conformer for [$BipPt(Me_2Bzm)_2$]$^{2+}$ and [$Me_4DABPt(Me_2Bzm)_2$]$^{2+}$ complexes, and its stability increases with increasing temperature. The HH:HT ratio was 1.1 at 5 °C and 1.5 at 50 °C for [$BipPt(Me_2Bzm)_2$]$^{2+}$, whereas the maximum observed HH:HT ratio was 0.8 for $BipPt(1\text{-Me-}5'\text{-GMP})_2$ complexes and was generally less than 0.3 for N1 unmethylated guanine adducts.[17]

Dipole–dipole interactions appear to play a crucial role in determining the stability of the HT rotamers in G complexes. Such interactions favor the HT rotamers over the HH rotamer because in the former case the positive end of one dipole (near the H8 atom) can approach the negative end of the second dipole (near the O6 atom). Moreover, the H8 and O6 atoms of *cis* guanines can approach each other more closely if each guanine is canted "6-in". The HH rotamer is formed in small yield in $BipPtG_2$ and $Me_2DABPtG_2$ complexes and is practically absent in the $Me_4DACHPtG_2$ adducts. In the former cases, one G (that having the six-membered ring adjacent the N–H of the *cis* amine) can be canted "6-out" so as to bring the O6 atom of one G farther from the O6 atom of the *cis* G. Such a "6-out" canting is not possible in the $Me_4DACHPtG_2$ complex because of steric interaction between the six-membered ring of each guanine and the adjacent Me-substituent on the *cis* amine; therefore, no HH rotamer is formed.

The absence of dipole-dipole interaction in Me_2Bzm adducts makes the HH and the two HT rotamers comparable in stability, with the consequence that the three rotamers are found in comparable amounts.

The slightly greater percentage of the HH rotamer for [$BipPt(Me_2Bzm)_2$]$^{2+}$ than for [$Me_4DABPt(Me_2Bzm)_2$]$^{2+}$ can be explained by the presence in the former case of a smaller steric interaction between the two six-membered rings of the Me_2Bzm ligands: for the HH rotamer these rings are on the same side of the coordination plane. In fact, in the Bip complex one Me_2Bzm has the six-membered ring on the same side of the plane as the N–H of the *cis* amine and thus the Me_2Bzm can be canted "6-out"; in contrast, in the Me_4DAB complex, both Me_2Bzm ligands have the six-membered ring on the side of one N–Me of the *cis* amine, a situation which greatly reduces the possibility of canting. However, even in the Me_4DAB complex, one Me_2Bzm (the one having the six-membered ring on the side of the plane as the "quasi axial" N–Me of the *cis* amine) can be canted "6-out" slightly more than the other Me_2Bzm (the one having the six-membered ring on the same side of the plane as the "quasi equatorial" N–Me). As a consequence, the H2 proton of the former base is more shielded by the *cis* base and resonates at higher field (HH_u) than the other (HH_d).

In both the Bip and Me_4DAB complexes with two *cis* G's or two *cis* Me_2Bzm ligands, one HT rotamer is more abundant than the other. Moreover, the major HT rotamer has the H8 or H2 signals (for G and Me_2Bzm adducts, respectively) downfield from that of the minor HT rotamer, an indication that these protons are less shielded by the *cis* base in the major HT rotamer than in the minor HT rotamer and that the two bases are more canted "6-in" in MHT than in mHT. Why the Me_2Bzm bases tend to be canted "6-in" in the HT rotamers is not clear. One possibility is that a stacking interaction can take place between *cis* Me_2Bzm bases. Therefore, as in the case of *cis* guanines, a "6-in" canting of the two bases is preferred because it ensures better stacking. Moreover, the canting can be greater when H2 is adjacent to the N–H (Bip complex) or to the "quasi axial" N–Me (Me_4DAB complex) of the *cis* amine than when H2 is adjacent to the N–CH_2– or to the "quasi equatorial" N–Me of the *cis* amine.

Thermodynamic Parameters: Both the MHT and mHT rotamers have lower enthalpy and entropy than the HH rotamer (Table 4). Therefore, the higher entropy of the HH rotamer leads to the preference of this isomer over the MHT and mHT forms. The values of ΔH and ΔS for the MHT and mHT rotamers are more dispersed in the Bip than in the Me_4DAB complex. This greater dispersion can be easily understood by keeping in mind that in the former case the two HT rotamers are more different (the six-membered ring of Me_2Bzm is on the side of the N–CH_2– of the *cis* amine in one rotamer and on the side of the N–H of the *cis* amine in the other rotamer) than in the latter case (both rotamers have the six-membered ring of each Me_2Bzm on the side of a N–Me of the *cis* amine).

For both the Bip and Me_4DAB complexes, the MHT rotamer has higher enthalpy and entropy than the mHT rotamer, and this greater entropy makes the former rotamer favored. The opposite trend was observed in the related $Me_2DABPtG_2$ complexes (G = 9-ethylguanine, 3′-GMP, and 5′-GMP)[29] for which the major HT rotamer was always lower in enthalpy and entropy than the minor HT rotamer, and the lower enthalpy was responsible for the greater abundance of the former rotamer with respect to

 © 2005 Wiley-VCH Verlag GmbH & Co. KGaA, Weinheim

the latter. This appears to be a major difference between Me_2Bzm and G derivatives and can be correlated to the presence, in corresponding positions of the base ring-systems, of a proton (H4) in one case and of an oxygen (O6) in the latter case.

Conclusions

Comparisons of analogous complexes containing two *cis* Me_2Bzm or two *cis* guanine ligands have clarified the factors influencing the properties of the guanine complexes. Electrostatic interactions between *cis* G's have been found to be the major driving force in base canting. The repulsion between O6 of *cis* G's is responsible for the "6-out" canting of at least one G in the HH rotamer. On the other hand, electrostatic attraction between the O6 of one G and the H8 of the *cis* G and base stacking are responsible for the preferential "6-in" canting of the two G's in the HT rotamer. The "6-out" canting of a base in the HH rotamer may be impeded by steric interaction between the six-membered ring of this base and a substituent on the *cis* amine. Similarly, the "6-in" canting of each base in the HT rotamer may be limited by steric interaction between the H8 of the base and a substituent on the *cis* amine.

The role of electrostatic interactions is greatly reduced in *cis*-$PtA_2(Me_2Bzm)_2$ complexes, as compared to the *cis*-PtA_2G_2 analogs, because the Me_2Bzm bases lack an oxygen substituent. Nevertheless, for both types of complexes the six-membered rings of the two bases are found on the most crowded side of the *cis* amine with respect to the coordination plane for the major HT rotamer. Also, for both types of complexes the major HT has the signal for the five-membered ring proton (H2 for Me_2Bzm and H8 for G) less shielded than the signal of that proton of the minor HT. As previously concluded for *cis*-PtA_2G_2 analogs, these findings are clear indications that for Me_2Bzm complexes also the major HT rotamer has more canted "6-in" bases than the minor HT rotamer and that such a greater canting is favored by smaller steric interactions between the H2 proton of each base and substituents on the *cis* amine. In the absence of major electrostatic interactions, the driving force for such a "6-in" canting of the two Me_2Bzm bases is likely to be base-stacking.

Thermodynamic parameters confirm the crucial role played by the H4 and O6 substituents (for Me_2Bzm and G derivatives, respectively) in determining the stability of different rotamers.

Experimental Section

Materials: 5,6-Dimethylbenzimidazole was purchased from Aldrich. (*R*,*S*,*S*,*R*)-BipPt$(NO_3)_2$, (*S*,*R*,*R*,*S*)-BipPt$(NO_3)_2$, *rac*-BipPt$(NO_3)_2$,[24] (*S*,*S*)-Me_4DABPt$(NO_3)_2$, (*R*,*R*)-Me_4DABPt$(NO_3)_2$, and *rac*-Me_4DABPt$(NO_3)_2$ were synthesized as described elsewhere.[23]

Preparation of $[Me_4DABPt(Me_2Bzm)_2]^{2+}$ Complexes: Stock solutions of (*R*,*S*,*S*,*R*)-BipPt$(NO_3)_2$, (*S*,*R*,*R*,*S*)-BipPt$(NO_3)_2$, (*S*,*S*)-Me_4DABPt$(NO_3)_2$, and (*R*,*R*)-Me_4DABPt$(NO_3)_2$ (4 mM) and of *rac*-BipPt$(NO_3)_2$ and *rac*-Me_4DABPt$(NO_3)_2$ (ca. 8 mM) were prepared in D_2O. NMR samples were prepared by adding 300 μL of complex solution into an NMR tube containing a suspension of 5,6-Me_2Bzm in 350 μL of H_2O (Me_2Bzm:Pt = 2.3). The pH was adjusted to 6 with 1% DNO_3. The reaction, monitored by ^1H NMR spectroscopy (23 °C), required several days (at, 55 °C) for completion.

NMR Spectroscopy: 1D NMR spectroscopic data were collected with Unity Varian 600 MHz and Inova 600 MHz instruments. A selective presaturation pulse was employed to suppress the HDO resonance, and the residual HDO peak was used as reference. FID's were accumulated for 64 scans.

2D experiments were performed in D_2O with a Unity Varian 600 MHz spectrometer. 2048 × 512 Matrices were collected at 5 °C for rotational nuclear Overhauser (ROESY) and $^1H/^1H$ nuclear Overhauser (NOESY) experiments (spectral window of ca. 6000 Hz in both dimensions), 2048 × 256 Matrices were collected at 25 °C for $^1H/^{13}C$ heteronuclear multiple-quantum coherence experiments (HMQC).

Circular Dichroism (CD) Spectroscopy: Solutions (ca. 0.04 mM) for CD experiments were prepared by diluting 30 μL of the NMR solution into 3 mL of H_2O. CD spectra were recorded at room temperature from 350 to 200 nm on a JASCO J-600 CD spectropolarimeter.

Thermodynamic Parameters: The equilibrium constants (K_{MHT} = [MHT]/[HH] and K_{mHT} = [mHT]/[HH]) were evaluated from the percentages of the different rotamers at different temperatures. The plots of $\ln K_{MHT}$ and $\ln K_{mHT}$ as a function of $1/T$ were linear within the experimental errors, and from their slopes and intercepts the values of ΔH and ΔS for the transformations were evaluated. The estimated thermodynamic parameters are listed in Table 4.

Supporting Information (see footnote on the first page of this article): Assignment of the Me5, Me6, and H7 signals of the Me_2Bzm ligand for $[rac\text{-BipPt}(Me_2Bzm)_2]^{2+}$ and $[rac\text{-}Me_4DABPt(Me_2Bzm)_2]^{2+}$. Equilibrium constants K_{MHT} and K_{mHT} at different temperatures and plots of the logarithm of the equilibrium constants as a function of $1/T$.

Acknowledgments

This work was supported by NIH Grant GM 29222 to LGM. We also acknowledge Dr. J. S. Saad, Prof. R. Cini, and members of COST D20 W.G. 001 and 003 for helpful discussions.

[1] J. Reedijk, *Chem. Commun.* **1996**, 801–806.
[2] M. J. Bloemink, J. Reedijk, in: *Metal Ions in Biological Systems*, vol. 32, **1996**, 641–685.
[3] S. E. Sherman, S. J. Lippard, *Chem. Rev.* **1987**, *87*, 1153–1181.
[4] T. P. Kline, L. G. Marzilli, D. Live, G. Zon, *J. Am. Chem. Soc.* **1989**, *111*, 7057–7068.
[5] C. S. Fouts, L. G. Marzilli, R. A. Byrd, M. F. Summers, G. Zon, K. Shinozuka, *Inorg. Chem.* **1988**, *27*, 366–376.
[6] M. Iwamoto, S. Mukundan Jr., L. G. Marzilli, *J. Am. Chem. Soc.* **1994**, *116*, 6238–6244.
[7] H. C. Wong, R. Coogan, F. P. Intini, G. Natile, L. G. Marzilli, *Inorg. Chem.* **1999**, *38*, 777–787.
[8] Y. Xu, G. Natile, F. P. Intini, L. G. Marzilli, *J. Am. Chem. Soc.* **1990**, *112*, 8177–8179.
[9] D. Kiser, F. P. Intini, Y. Xu, G. Natile, L. G. Marzilli, *Inorg. Chem.* **1994**, *33*, 4149–4158.
[10] S. O. Ano, F. P. Intini, G. Natile, L. G. Marzilli, *J. Am. Chem. Soc.* **1997**, *119*, 8570–8571.
[11] L. G. Marzilli, F. P. Intini, D. Kiser, H. C. Wong, S. O. Ano, P. A. Marzilli, G. Natile, *Inorg. Chem.* **1998**, *37*, 6898–6905.

 © 2005 Wiley-VCH Verlag GmbH & Co. KGaA, Weinheim

[12] S. O. Ano, F. P. Intini, G. Natile, L. G. Marzilli, *Inorg. Chem.* **1999**, *38*, 2989–2999.
[13] S. T. C. Sullivan, A. Ciccarese, F. P. Fanizzi, L. G. Marzilli, *Inorg. Chem.* **2001**, *40*, 455–462.
[14] S. T. Sullivan, A. Ciccarese, F. P. Fanizzi, L. G. Marzilli, *Inorg. Chem.* **2000**, *39*, 836–842.
[15] R. E. Cramer, P. L. Dahlstrom, *J. Am. Chem. Soc.* **1979**, *101*, 3679–3681.
[16] J. Saad, T. Scarcia, G. Natile, L. G. Marzilli, *Inorg. Chem.* **2002**, *41*, 4923–4935.
[17] J. S. Saad, T. Scarcia, K. Shinozuka, G. Natile, L. G. Marzilli, *Inorg. Chem.* **2002**, *41*, 546–557.
[18] H. C. Wong, K. Shinozuka, G. Natile, L. G. Marzilli, *Inorg. Chim. Acta* **2000**, *297*, 36–46.
[19] M. Benedetti, J. S. Saad, L. G. Marzilli, G. Natile, *Dalton Trans.* **2003**, 872–879.
[20] J. D. Orbell, M. R. Taylor, S. L. Birch, S. E. Lawton, L. M. Vilkins, L. J. Keefe, *Inorg. Chim. Acta* **1988**, *152*, 125–134.
[21] M. Benedetti, G. Tamasi, R. Cini, G. Natile, *Chem. Eur. J.* **2003**, *9*, 6122–6132.
[22] E. Alessio, M. Calligaris, M. Iwamoto, L. G. Marzilli, *Inorg. Chem.* **1996**, *35*, 2538–2545.
[23] J. S. Saad, M. Benedetti, G. Natile, L. G. Marzilli, manuscript in preparation.
[24] S. O. Ano, F. P. Intini, G. Natile, L. G. Marzilli, *J. Am. Chem. Soc.* **1998**, *120*, 12017–12022.
[25] In previous related papers from our laboratories the expression "canted G base" was used to mean a G whose H8 experiences an upfield shifting effect caused by the ring-current anisotropy of the *cis* base (J. Kozelka, M. H. Fouchet, J. C. Chottard, *Eur. J. Biochem.* **1992**, *205*, 895–906). Conversely, the expression "uncanted base" was used to mean a G whose H8 is positioned away from the *cis* G and, therefore, is less shielded. In this paper the expression "canting" has been used to mean exclusively the sloping of a guanine plane on the coordination plane.
[26] The calculation has been performed starting from the X-ray structure of $Me_4DACHPtG_2$ ΔHT rotamer (ref.[21]) and rotating the two G's about the Pt–N7 bonds so as to have an HH conformer with guanine bases orthogonal to the coordination plane. Under these conditions the O6···O6 distance was found to be ca. 2.0 Å (sum of the van der Waals radii ca. 3.0 Å).
[27] E. Alessio, L. Hansen, M. Iwamoto, L. G. Marzilli, *J. Am. Chem. Soc.* **1996**, *118*, 7593–7600.
[28] The calculation has been performed starting from the X-ray structure of $Me_4DACHPtG_2$ ΔHT rotamer (ref.[21]) and rotating the two G's about the Pt–N7 bonds so as to reach a given canting angle. For each canting angle the O6···H8 distance between the two G's has been measured.
[29] G. Colonna, N. G. Di Masi, L. G. Marzilli, G. Natile, *Inorg. Chem.* **2003**, *42*, 997–1005.

Received: January 13, 2005
Published Online: June 2, 2005

 © 2005 Wiley-VCH Verlag GmbH & Co. KGaA, Weinheim

Structural Features of Titanium Complexes of Salicylaldiminato Derivatives of Amino Acids

Jens Müller,[a] Gerald Kehr,[a] Roland Fröhlich,[a] and Gerhard Erker*[a]

Keywords: Chelate ligands / Titanium / Tridentate ligands / Metallamacrocycles / Catalytic hydrocyanation

Condensation of salicylaldehyde with amino acid derivatives gave the salicylaldimine derivatives **3** that reacted with $TiCl_4$ with release of HCl to yield the chelate complexes [(SalPhgOMe)$TiCl_3$] (**4a**), [(SalValOMe)$TiCl_3$] (**4b**), and the dipeptide derivative [(SalAlaValOMe)$TiCl_3$] (**4d**). The complex [(Sal*PhgOMe)$TiCl_3$] (**4c**) was prepared analogously starting from 3,5-di-*tert*-butyl-2-hydroxybenzaldehyde and phenylglycine methyl ester. Complex *rac*-**4a** was characterized by X-ray diffraction and shown to feature a typical structure where the monoanionic ligand is tridentate, coordinating to the central titanium atom through both the phenolate oxygen atom and the ester carbonyl oxygen atom as well as through the imine nitrogen atom. A hydrolyzed carboxylate analogue of **4a** exhibits an analogous central structural framework. In this case, however, the overall structure of *rac*-**5a** was found to be a metallacyclic tetramer where four titanium atoms bind four such tridentate ligands.

(© Wiley-VCH Verlag GmbH & Co. KGaA, 69451 Weinheim, Germany, 2005)

Introduction

Group 4 metal complexes of peptide derivatives are receiving an increased interest lately. This section of the field of coordination chemistry[1] has become of increasing importance with regard to a variety of ongoing developments. Thus, titanium–protein complexes may play a role in the cancerostatic potential of some organometallic complexes of this light Group 4 element.[2,3] Titanium as well as zirconium complexes of modified peptide ligands have found some useful applications in enantioselective catalysis.[4,5] Heterogenized oligopeptide–zirconium complexes have been thought to exhibit an enzyme-like behavior in some organophosphate hydrolysis reactions,[6] to mention a few such recent developments and observations in this growing field.[7]

We had recently studied the chemistry and the structural features of the reaction products between [Cp_2TiMe^+] or [Cp_2ZrMe^+] cations with a variety of oligopeptide derivatives.[8,9] Addition and subsequent liberation of methane eventually resulted in a variety of stable products that all showed the structural motif of a tridentate chelate complex framework (see Scheme 1). In some cases a carbonyl group of a protective group (e.g. Boc) was involved (**1**), in other cases it was the C=O group of the next amino acid building block that made up one of the fused chelate ring systems (**2**).

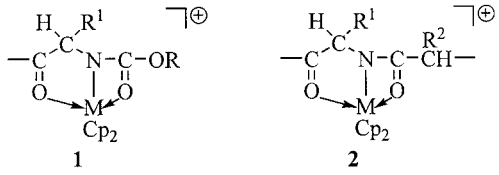

Scheme 1.

It was the question whether we had here observed a special structural feature of a specific class of Group 4 metallocene–peptide complexes or if the observed structural motif in the systems **1/2** was an example of a general structural type in this area of coordination chemistry. For that reason we have investigated a number of remotely related titanium complexes derived from very electrophilic Group 4 metal components. We actually found favoured related structural frameworks in systems that were obtained from the reactions of $TiCl_4$ with salicylaldiminato derivatives of amino acids and dipeptides. Some representative examples are described and discussed in this article.

Results and Discussion

We have prepared a small series of salicylaldimine ligands (**3a**–**d**) by treatment of salicylaldehyde with the hydrochlorides of the respective amino acid methyl esters in dichloromethane with the aid of triethylamine.[10] For this study we have employed the amino acids (L)-phenylglycine and (L)-valine. For the synthesis of **3c** we have used 3,5-di-*tert*-butyl-2-hydroxybenzaldehyde as the coupling component. The chelate ligand **3d** was prepared by condensation

[a] Organisch-Chemisches Institut der Universität Münster, Corrensstr. 40, 48149 Münster, Germany
Fax: +49-251-83 36503
E-mail: erker@uni-muenster.de

Supporting information for this article is available on the WWW under http://www.eurjic.org or from the author.

of salicylaldehyde with the peptide derivative HAlaValOMe (employed as the TFA adduct).

Treatment of the ligand system **3a** with $TiCl_4$ proceeded cleanly in dichloromethane solution with cleavage of HCl (Scheme 2). After a reaction time of ca. 1.5 h, the complex formation was complete. After workup, the product **4a** was isolated as a red solid in ca. 90% yield. The corresponding titanium complexes [(SalValOMe)$TiCl_3$] (**4b**), [(Sal*PhgOMe)$TiCl_3$] (**4c**), and the dipeptide-derived product [(SalAlaValOMe)$TiCl_3$] (**4d**) were synthesized analogously by treatment of the free HO-containing ligands with $TiCl_4$ in dichloromethane with cleavage of 1 equiv. of HCl. The reactions were practically quantitative, and these products were isolated in yields between 85% and 96%.

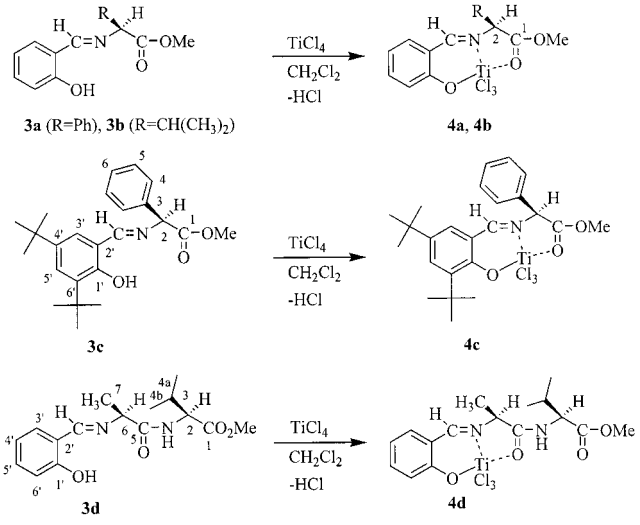

Scheme 2.

The complexes **4a**–**d** were characterized spectroscopically (see below) and by C,H,N elemental analyses. Single crystals of **4a** were obtained from a saturated THF solution at –22 °C, which allowed characterization by an X-ray crystal structure analysis (see Figure 1). The (SalPhgOMe) system is sensitive to racemization, and it seems that the racemate of the corresponding Ti complex (*rac*-**4a**) crystallizes much easier than its pure enantiomers. Therefore, we have only obtained single crystals of *rac*-**4a** (and consequently also of its derivative *rac*-**5a**) for the X-ray crystal structure analyses, despite numerous attempts to crystallize the enantiomerically pure compounds. Therefore, the degree of enantiomeric purity of the complexes **4**, derived from single amino acids, must remain open at this time. In the case of the dipeptide derivative **4d**, we only observed a single diastereoisomer by NMR spectroscopy, which indicates that enantiomerization at the proximal amino acid (Ala) in this (and probably the related **4b**) system, seems not to be a serious problem under the applied conditions. The ligands **3a** (SalPheOMe) and **3b** (SalValOMe) crystallized as the pure enantiomers (for details see the Exp. Sect. and the Supporting Information; for Supporting Information see also the footnote on the first page of this article).

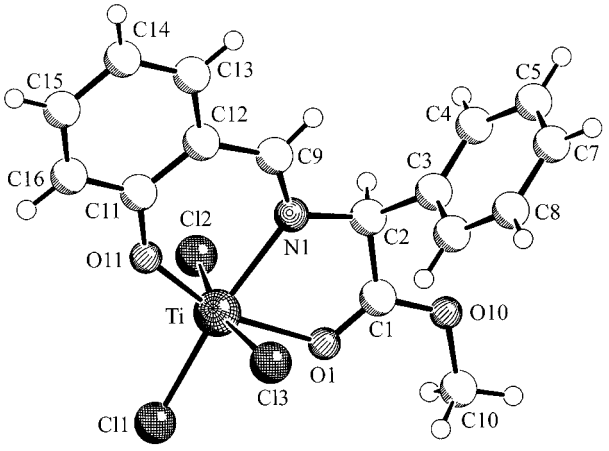

Figure 1. View of the molecular structure of the [(SalPhgOMe)-$TiCl_3$] complex *rac*-**4a**; selected bond lengths [Å] and angles [°]: Ti–Cl1 2.265(1), Ti–Cl2 2.327(1), Ti–Cl3 2.319(1), Ti–N1 2.177(2), Ti–O1 2.111(2), Ti–O11 1.797(2), C1–O10 1.303(3), C1–C2 1.507(3), C2–C3 1.520(3), C2–N1 1.482(3), N1–C9 1.281(3), C9–C12 1.448(3), C11–O11 1.346(3); Cl1–Ti–Cl2 93.9(1), Cl1–Ti–Cl3 94.7(1), Cl1–Ti–N1 171.3(1), Cl1–Ti–O1 96.5(1), Cl1–Ti–O11 104.1(1), Cl2–Ti–Cl3 165.3(1), Cl2–Ti–N1 84.6(1), Cl2–Ti–O1 83.9(1), Cl2–Ti–O11 95.3(1), Cl3–Ti–N1 85.1(1), Cl3–Ti–O1 83.3(1), Cl3–Ti–O11 94.2(1), N1–Ti–O1 74.9(1), N1–Ti–O11 84.5(1), O1–Ti–O11 159.4(1), Ti–O1–C1 119.8(1), O1–C1–O10 123.5(2), O1–C1–C2 121.9(2), O10–C1–C2 114.5(2), C1–C2–N1 106.2(2), C2–N1–C9 118.0(2), Ti–N1–C2 116.1(1), Ti–N1–C9 125.9(1), Ti–O11–C11 141.0(1). For additional values see the text.

In complex *rac*-**4a** the (SalPhgOMe) ligand binds to the titanium atom through the phenolic oxygen atom, the imine nitrogen atom and the ester carbonyl oxygen atom. The core atoms of this tridentate chelate ligands are oriented close to planar. The bond between Ti and the phenolic oxygen atom O11 is short [1.797(2) Å] and the corresponding Ti–O11–C11 angle [141.0(1)°] is substantially enlarged.[11] The Ti–N1 linkage amounts to 2.177(2) Å, with the C9–N1 bond [1.281(3) Å] being in the typical C=N double bond range.[12] The nitrogen atom N1 shows a trigonal-planar coordination geometry [Ti–N1–C9: 125.9(1)°, Ti–N1–C2: 116.1(1)°, C9–N1–C2: 118.0(2)°]. The Ti–O1 distance is 2.111(2) Å, and the corresponding C1–O1–Ti angle was found at 119.8(1)°. The C1–O1 length [1.229(3) Å] is in the typical carbonyl C=O double bond range. The adjacent C1–O10 bond is much longer at 1.303(3) Å.

The coordination geometry at the central titanium atom is distorted octahedral. There is a pronounced *trans* effect: The Ti–Cl1 bond (*trans* to N1) is much shorter [2.265(1) Å] than the Ti–Cl2 [2.327(1) Å] and Ti–Cl3 [2.319(1) Å] bonds. The three *trans* angles amount to 171.3(1)° (Cl1–Ti–N1), 165.3(1)° (Cl2–Ti–Cl3) and 159.4(1)° (O1–Ti–O11). Ten of the twelve *cis* angles are within a narrow range between 83.3(1)° and 96.5(1)°. Only the N1–Ti–O1 angle is markedly smaller at 74.9(1)°, which probably is a typical feature of the five-membered chelate substructure. Consequently, the adjacent O11–Ti–Cl1 angle is widened to 104.1(1)°.

Complex **4a** seems to adopt a similar structure in solution. The ^{13}C NMR spectra clearly indicate the coordina-

 © 2005 Wiley-VCH Verlag GmbH & Co. KGaA, Weinheim

tion of the ester carbonyl group. On going from the ligand (**3a**: δC1 = 171.1 ppm) to the complex **4a** (δC1 = 182.3 ppm) this carbonyl carbon resonance is shifted to larger δ values by $\Delta\delta$ = +11.2 ppm. This is very characteristic for the formation of a Ti–O=C metal coordination.[8,9] The coordination is also evidenced by a similar shifting of the adjacent OCH_3 resonances on going from **3a** to **4a** (^{1}H: $\Delta\delta$ = +0.48 ppm; ^{13}C: $\Delta\delta$ = +6.8 ppm; see Table 1). The evidence for the imine coordination to the titanium atom comes from a comparison of the ^{15}N NMR spectra. Complex **4a** features a ^{15}N NMR imine nitrogen resonance at δ = –104.9 ppm, which is shifted by $\Delta\delta$ = –16.3 ppm relative to the noncoordinated **3a** reference. In contrast, the increased coordination number of the imine nitrogen atom in **4a** does not lead to very characteristic differences in the ^{13}C ($\Delta\delta$ = –1.9 ppm) or ^{1}H NMR spectra. The complexes **4b**–**d** show similar spectroscopic features (see Table 1), so that we must assume analogous solution structures of these compounds featuring tridentate salicylaldimine/amino acid derived chelate ligands.

Table 1. Comparison of selected ^{1}H and ^{13}C NMR spectroscopic data of the ligand systems **3** and their corresponding metal complexes **4** .[a]

	3a	**4a**	**3b**	**4b**	**3c**	**4c**	**3d**	**4d**
C*H*=N	8.40	7.99	8.33	8.35	8.42	8.00	8.44	8.46
*C*H=N	167.1	165.2	167.5	164.2	168.6	166.3	167.4	164.0
N*C*H	75.1	75.6	78.5	78.0	75.0	75.6	68.8	69.2
NC*H*	5.20	5.99	3.77	4.62	5.20	5.97	4.05	5.26
C=O	171.1	182.3	172.2	183.5	171.3	182.4	172.0	179.2
O*C*H$_3$	52.0	58.8	52.7	58.4	52.9	58.8	172.4[b]	171.1[b]
OC*H*$_3$	3.75	4.23	3.74	4.32	3.76	4.24	3.69[c]	3.84[c]

[a] ^{1}H/^{13}C NMR spectra in CD_2Cl_2. [b] Terminal –CO_2CH_3 carbonyl group. [c] Terminal –OCH_3 group.

During an attempt to crystallize complex **4a** from dichloromethane, apparently some of the compound was unintendedly hydrolyzed and single crystals of the Ti–chelate carboxylate complex *rac*-**5a** were isolated (see Scheme 3). In the crystal state this complex attains an interesting tetranuclear structure (see Figures 2 and 3) in which the chelate carboxylates have become connected in a metallacyclic fashion by means of a bridging octahedrally coordinated quartet of titanium atoms. The coordination of each of the four subunits is chemically equivalent, although crystallographically slightly different. Again, we find the same structural framework motif that was already observed in the related monomeric complex **4a** (see above). This shall be illustrated with the subunit A in the tetramer of **5a** in the crystal.

The substructures of *rac*-**5a** feature the typical array of Ti–O/N bonds at their distorted octahedral Ti atom. In the subunit A of *rac*-**5a** the Ti–O3 bond length is 1.803(4) Å, which is almost as short as the respective bond in *rac*-**4a** (see above). The Ti–N1 linkage in *rac*-**5a** amounts to 2.164(5) Å, the adjacent C3–N1 double bond has a length of 1.274(7) Å. The O1–Ti distance in *rac*-**5a** was found at 2.002(4) Å, and the C1–O1 bond [1.267(6) Å] is in the typical carboxylate C=O bond range.[12] The C1–O2 distance in the Ti–carboxylate is in a similar range [1.247(6) Å]. The O2(A)–Ti1(B) bond length amounts to 2.054(4) Å. The Ti1(A)–O2(D) distance is 2.086(4) Å. Together with the pair of remaining chloride ligands [Ti–Cl1: 2.262(2) Å; Ti–Cl2: 2.261(2) Å] this completes the distorted octahedral co-

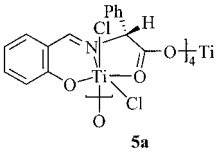

Scheme 3.

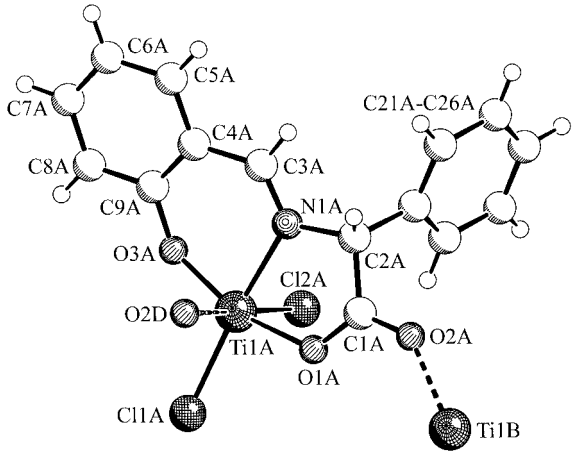

Figure 2. Projection of a typical mononuclear chelate complex subunit of the cyclotetramer *rac*-**5a**.

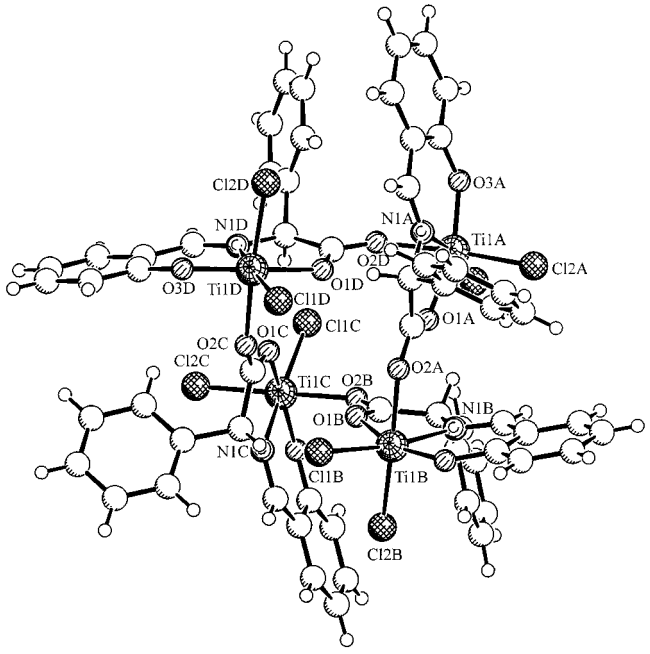

Figure 3. View of the tetrameric cyclic structure of complex *rac*-**5a**.

 © 2005 Wiley-VCH Verlag GmbH & Co. KGaA, Weinheim

ordination geometry around the central titanium atom of this subunit. As expected, the three *trans* angles deviate in a typical manner from the ideal 180° [O3A–Ti1A–O1A: 157.3(2)°; O2D–Ti1A–Cl2A: 173.7(1)°; N1A–Ti1A–Cl1A: 169.4(1)°]. The *cis* angles are in a narrow range between 83.6(2)° and 97.6(2)°, again with the exception of the small O1A–Ti1A–N1A angle inside the five-membered ring substructure of the chelate [75.0(2)°]. As previously observed for the structure of *rac*-**4a**, this also leads to an increased O3A–Ti1A–Cl1A angle [104.2(2)°] in the Ti–carboxylate *rac*-**5a**.

The complexes **4** were briefly checked for their catalytic activity. For this characterization we used the hydrocyanation reaction of **6** to yield **7** (see Scheme 4), a system that was described previously by Hoveyda et al.[5,13] The complexes **4b**–**d** were employed. They all were more active than the in situ catalyst, generated by treatment of **3b** with $Ti(OiPr)_4$. Not unexpectedly, we did not observe any asymmetric induction with any of these simple catalyst systems under the applied reaction conditions at +4 °C.[4,5] However, the conversion of **6** to **7** showed very low *ee* values of ca. 6–9%, when carried out with the **4b** catalyst system at –78 °C.

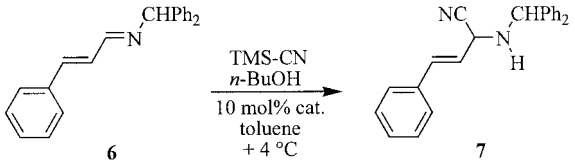

Scheme 4.

Conclusions

This study has shown that $TiCl_4$ reacts with the salicylaldimine derivatives **3** with cleavage of HCl to give tridentate chelate complex structures of a type which is reminiscent of the oligopeptide–metallocene cation complexes that we had obtained and structurally characterized previously (see Scheme 1).[8,9] It seems that the electrophilic Group 4 metals in general favour the formation of such tridentate chelate structures whenever it is possible. In the case of the peptide-derived systems **1** and **2** (see above) tridentate chelate complex frameworks were formed, featuring anellated five- and four-membered ring structures, whereas in the case of the systems **4** the salicylaldimine moiety was involved in the formation of a closely related framework built up of anellated six- and five-membered chelate ring systems. Since these chelate structures form so easily, it can probably be assumed that similar structures are also readily available in the reactions of such ligand precursors with e.g. $Ti(OiPr)_4$. It may be that such structures play an important role in the respective catalyst systems, as proposed,[5] although in the previous studies the catalysts were usually generated in situ and not isolated or structurally characterized. Since the isolated complexes **4** are catalytically active, it may be tempting to actually prepare, isolate and structurally characterize such a catalyst by using an optimized longer oligopeptide-derived ligand system known from the literature[5] to gain direct experimental evidence of the stereochemical features of such active catalyst systems.

Experimental Section

General Remarks: Reactions with air- and moisture-sensitive compounds or reagents were carried out under argon using Schlenk-type glassware or in a glovebox. Solvents were dried and distilled under argon prior to use. For additional general information, including a list of the instruments used for physical characterization of the compounds see refs.[8,9] For the atom numbering scheme used in the NMR listings, see Scheme 2. Most NMR assignments were secured by additional 2D NMR experiments [^1H-^{15}N ghmbc experiment based on an $^nJ(^{15}N,^1H)$ coupling constant of 5 Hz].[14]

X-ray Crystal Structure Analyses: Data sets were collected with Enraf Nonius CAD4 and Nonius KappaCCD diffractometers, in case of Mo radiation, equipped with a rotating anode generator. Programs used: Data collection EXPRESS (Nonius B.V., **1994**) and COLLECT (Nonius B.V., **1998**), data reduction MolEN (K. Fair, Enraf–Nonius B. V., **1990**) and Denzo-SMN (Z. Otwinowski, W. Minor, *Methods in Enzymology*, **1997**, *276*, 307–326), absorption correction for CCD data SORTAV (R. H. Blessing, *Acta Crystallogr.* **1995**, *A51*, 33–37; R.H. Blessing, *J. Appl. Crystallogr.* **1997**, *30*, 421–426) and Denzo (Z. Otwinowski, D. Borek, W. Majewski, W. Minor, *Acta Crystallogr.* **2003**, *A59*, 228–234), structure solution SHELXS-97 (G. M. Sheldrick, *Acta Crystallogr.* **1990**, *A46*, 467–473), structure refinement SHELXL-97 (G. M. Sheldrick, University of Göttingen, **1997**), graphics SCHAKAL (E. Keller, **1997**) and DIAMOND (K. Brandenburg, University of Bonn, **1997**). CCDC-261081, -261082, -261560 and -261561 contain the supplementary crystallographic data for this paper. These data can be obtained free of charge from The Cambridge Crystallographic Data Centre via www.ccdc.cam.ac.uk/data_request/cif.

Preparation of the Salicylaldimines

SalPhgOMe (3a): Triethylamine (2.48 g, 24.6 mmol, 1.05 equiv.) was added to a suspension of HCl·H–Phg–OMe (3.00 g, 24.6 mmol, 1.05 equiv.) in dichloromethane (40 mL). After addition of salicylaldehyde (4.71 g, 23.4 mmol, 1.00 equiv.), the colour of the solution turned yellow and the reaction mixture was stirred at room temperature overnight. The solution was washed twice with water and the organic layer dried with magnesium sulfate. Removal of the solvent (at ca. +5 °C to avoid racemisation) led to a yellow solid (5.36 g, 19.9 mmol, 85%). Single crystals for the X-ray crystal structure analysis were obtained by crystallisation from ethanol at –22 °C. M.p. 65.6 °C. $C_{16}H_{15}NO_3$ (269.3): calcd. C 71.63, H 5.61, N 5.20; found C 71.33, H 5.63, N 5.22. $[\alpha]_D^{20} = -26.8$ ($c = 0.3$, $CHCl_3$). IR (KBr): $\tilde{\nu}$ = 2949, 2743, 2675, 2492, 1749, 1629, 1576, 1496, 1464, 1440, 1405, 1315, 1281, 1258, 1209, 1167, 1150, 1127, 1092, 1060, 1036, 982, 854, 776, 758, 742, 731, 697, 612, 561, 521 cm^{-1}. ^1H NMR (300.1 MHz, CD_2Cl_2, 298 K): δ = 13.06 (s, 1 H, OH), 8.40 (s, 1 H, CH=N), 7.46–7.26 (m, 7 H, H_{phenyl}), 6.98–6.89 (m, 2 H, H_{phenyl}), 5.20 (s, 1 H, 2-H), 3.75 (s, 3 H, OCH_3) ppm. $^{13}C\{^1H\}$ NMR (75.5 MHz, CD_2Cl_2, 298 K): δ = 171.1 (C-1), 167.4 (CH=N), 161.4 (C–OH), 137.7, 133.3, 132.4, 129.3, 128.8, 128.2, 119.6, 117.3 (C_{phenyl}), 75.1 (C-2), 53.0 (OCH_3) ppm. GHMBC (60.8/599.8 MHz, CD_2Cl_2, 298 K): δ (^{15}N)/δ(^1H) = –88.6/13.06, 8.40, 5.20 (CH=*N*/1′-O*H*, C*H*=N, 2-H) ppm.

SalValOMe (3b): According to the preparation of **3a**, HCl·H–ValOMe (3.00 g, 17.9 mmol) was treated with triethylamine (1.81 g,

 © 2005 Wiley-VCH Verlag GmbH & Co. KGaA, Weinheim

17.9 mmol) and salicylaldehyde (2.08 g, 17.0 mmol) to yield **3b** as a yellow solid (3.32 g, 14.1 mmol, 83%). Single crystals for the X-ray crystal structure analysis were obtained by crystallisation from a 1:1 mixture of pentane/diethyl ether at –22 °C. M.p. 34.9 °C. $C_{13}H_{17}NO_3$ (235.3): calcd. C 66.36, H 7.28, N 5.95; found C 66.37, H 7.26, N 5.85. $[\alpha]_D^{20}$ = –38.4 (*c* = 1.0, $CHCl_3$), IR (KBr): $\tilde{\nu}$ = 2955, 2344, 1736, 1625, 1573, 1493, 1455, 1429, 1409, 1338, 1368, 1331, 1305, 1276, 1196, 1173, 1137, 1115, 1060, 1032, 1020, 977, 880, 847, 762, 736, 675, 663, 601, 549, 461 cm^{-1}. ^1H NMR (300.1 MHz, CD_2Cl_2, 298 K): δ = 13.11 (s, 1 H, OH), 8.33 (s, 1 H, CH=N), 7.40–7.30 (m, 2 H, H_{phenyl}), 6.97–6.85 (m, 2 H, H_{phenyl}), 3.77 (d, ^3J = 6.3 Hz, 1 H, 2-H), 3.74 (s, 3 H, OCH_3), 2.38 (m, 1 H, CH_{iPr}), 0.97 (d, ^3J = 6.8 Hz, 6 H, 2 CH_3) ppm. $^{13}C\{^1H\}$ NMR (75.5 MHz, CD_2Cl_2, 298 K): δ = 172.2 (C-1), 167.5 (CH=N), 162.0 (C–OH), 133.5, 132.5, 119.4, 117.7 (C_{phenyl}), 78.5 (C-2), 52.7 (OCH_3), 32.7 (CH_{iPr}), 19.9, 18.7 (2 CH_3) ppm.

Sal*PhgOMe (3c): Triethylamine (173 mg, 1.70 mmol, 1.00 equiv.) was added to a solution of HCl·H–Phg–OMe (344 mg, 1.70 mmol, 1.00 equiv.) in ethanol (20 mL). After addition of 3,5-di-*tert*-butyl-2-hydroxybenzaldehyde (400 mg, 1.70 mmol, 1.00 equiv.), the reaction mixture was stirred at room temperature for 3 d. The solvent was removed and the residue taken up in dichloromethane (20 mL). The yellow solution was washed twice with an aqueous 5% $NaHCO_3$ solution (20 mL) and once with water (20 mL). The organic layer was dried with magnesium sulfate and removal of the solvent led to 532 mg (1.39 mmol, 82%) of a yellow solid. M.p. 93.0 °C. $C_{24}H_{31}NO_3$ (381.5): calcd. C 75.56, H 8.19, N 3.67; found C 75.43, H 8.27, N 3.44. $[\alpha]_D^{20}$ = –6.9 (*c* = 0.16, CH_2Cl_2). IR (KBr): $\tilde{\nu}$ = 3482, 3417, 2961, 2869, 1752, 1630, 1474, 1452, 1439, 1391, 1365, 1322, 1274, 1252, 1200, 1161, 1087, 1065, 835, 726, 696, 504 cm^{-1}. ^1H NMR (599.8 MHz, CD_2Cl_2, 298 K): δ = 13.49 (s, 1 H, OH), 8.42 (s, 1 H, CH=N), 7.48 (m, 2 H, 4-H), 7.43 (AB, ^4J = 2.4 Hz, 1 H, 5′-H), 7.41 (m, 2 H, 5-H), 7.36 (m, 1 H, 6-H), 7.12 (AB, ^4J = 2.4 Hz, 1 H, 3′-H), 5.20 (s, 1 H, 2-H), 3.76 (s, 3 H, OCH_3), 1.46 [s, 9 H, 6′–$C(CH_3)_3$], 1.30 [s, 9 H, 4′-$C(CH_3)_3$] ppm. $^{13}C\{^1H\}$ NMR (150.8 MHz, CD_2Cl_2, 298 K): δ = 171.3 (C-1), 168.6 (CH=N), 158.3 (C-1′), 140.9 (C-4′), 137.9 (C-3), 137.1 (C-6′), 129.3 (C-5), 128.8 (C-6), 128.2 (C-4), 128.2 (C-5′), 127.0 (C-3′), 118.2 (C-2′), 75.0 (C-2), 52.9 (OCH_3), 35.3 [6′-*C*(CH_3)$_3$], 34.4 [4′-*C*(CH_3)$_3$], 31.5 [4′-C(*C*H$_3$)$_3$], 29.5 [6′-C(*C*H$_3$)$_3$] ppm.

SalAlaValOMe (3d): Triethylamine (320 mg, 3.16 mmol, 1.05 equiv.) was added to a solution of TFA·H–Ala–Val–OMe (1.00 mg, 3.16 mmol, 1.05 equiv.) in ethanol (20 mL). After addition of salicylaldehyde (367 mg, 3.01 mmol, 1.00 equiv.), the reaction mixture was stirred at room temperature for 2 d. The solvent was removed and the residue taken up in dichloromethane (20 mL). The yellow solution was washed twice with an aqueous 5% $NaHCO_3$ solution (20 mL) and once with water (20 mL). The organic layer was dried with magnesium sulfate and removal of the solvent led to 692 mg (2.26 mmol, 75%) of a yellow oil. $C_{16}H_{22}N_2O_4$ (306.4): calcd. C 62.73, H 7.24, N 9.14; found C 62.72, H 7.05, N 9.05. $[\alpha]_D^{20}$ = +112.0 (*c* = 0.1, CH_2Cl_2). IR (KBr): $\tilde{\nu}$ = 3426, 2965, 2926, 2869, 2365, 1739, 1669, 1626, 1587, 1517, 1465, 1435, 1369, 1317, 1283, 1204, 1152, 1034, 912, 756, 626 cm^{-1}. ^1H NMR (499.8 MHz, C_6D_6, 298 K): δ = 12.85 (s, 1 H, OH), 7.53 (s, 1H CH=N), 7.02 (m, 1 H, 6′-H), 7.00 (m, 1 H, 4′-H), 6.80 (ABCD, ^3J = 7.7, ^4J = 1.4 Hz, 1 H, 3′-H), 6.64 (ABCD, ^3J = 7.5, ^4J = 1.6 Hz, 1 H, 5′-H), 6.61 (d, ^3J = 8.7 Hz, 1 H, NH), 4.77 (m, 1 H, 2-H), 3.64 (q, ^3J = 6.8 Hz, 1 H, 6-H), 3.17 (s, 3 H, OCH_3), 2.03 (m, 1 H, 3-H), 1.34 (d, ^3J = 6.9 Hz, 3 H, 7-H), 0.85 (d, ^3J = 6.9 Hz, 3 H, 4a-H), 0.77 (d, ^3J = 6.9 Hz, 3-H, 4b-H) ppm. $^{13}C\{^1H\}$ NMR (125.7 MHz, C_6D_6, 298 K): δ = 172.0 (C-1), 171.5 (C-5), 167.1 (CH=N), 161.6 (C-1′), 133.2 (C-4′), 132.3 (C-3′), 119.0 (C-5′), 118.9 (C-2′), 117.5 (C-6′), 68.6 (C-6), 57.1 (C-2), 51.5 (OCH_3), 31.4 (C-3), 20.9 (C-7), 19.0 (C-4a), 17.5 (C-4b) ppm.

Preparation of the Titanium Complexes

[(SalPhgOMe)TiCl$_3$] (4a): $TiCl_4$ (1.10 g, 5.79 mmol, 1.00 equiv.) was added to a solution of SalPhgOMe (**3a**) (1.56 g, 5.79 mmol, 1.00 equiv.) in dichloromethane (20 mL). The colour of the solution immediately turned red. After stirring at room temperature for 1.5 h, the solvent was removed and the red solid (2.75 g, 5.21 mmol, 90%) dried in vacuo. Single crystals for the X-ray crystal structure analysis were obtained by crystallisation from THF at –22 °C. Decomp. 207.4 °C. $C_{16}H_{14}Cl_3NO_3Ti{\cdot}1.25CH_2Cl_2$ (528.7): calcd. C 39.19, H 3.15, N 2.65; found C 39.56, H 3.04, N 2.61. $[\alpha]_D^{20}$ = –43.2 (*c* = 0.25, CH_2Cl_2). IR (KBr): $\tilde{\nu}$ = 3439, 3062, 2960, 2870, 1649, 1616, 1596, 1560, 1496, 1475, 1453, 1370, 1273, 1251, 1228, 1156, 1123, 1051, 1030, 1005, 921, 841, 763, 734, 703, 661, 586, 551, 456, 427 cm^{-1}. ^1H NMR (499.8 MHz, CD_2Cl_2, 298 K): δ = 7.99 (d, ^4J = 2.0 Hz, 1 H, CH=N), 7.66 (ABCD, ^3J = 8.5, ^4J = 2.0 Hz, 1 H, 5′-H), 7.51 (m, 5 H, 4-H, 5-H u. 6-H), 7.39 (ABCD, ^3J = 8.5, ^4J = 1.5 Hz, 1 H, 3′-H), 7.19 (ABCD, ^3J = 8.5, ^4J = 1.0 Hz, 1 H, 4′-H), 6.91 (ABCD, ^3J = 8.5 Hz, 1 H, 6′-H), 5.99 (d, ^4J = 2 Hz, 1 H, 2-H), 4.23 (d, ^5J = 2 Hz, 3 H, OCH_3) ppm. $^{13}C\{^1H\}$ NMR (125.7 MHz, CD_2Cl_2, 298 K): δ = 182.3 (C-1), 165.2 (CH=N), 162.1 (C-1′), 137.8 (C-5′), 135.7 (C-3′), 133.6 (C-3), 130.8 (C-5), 130.4 (C-4 u. C-6), 125.8 (C-2′), 125.6 (C-4′), 114.9 (C-6′), 75.6 (C-2), 58.8 (OCH_3). GHMBC (60.8/599.8 MHz, CD_2Cl_2, 298 K): δ (^{15}N)/δ (^1H) = –104.9/7.99 (CH=*N*/C*H*=N) ppm.

X-ray Crystal Structure Analysis of *rac*-4a: Formula $C_{16}H_{14}Cl_3NO_3Ti{\cdot}3C_4H_8O$, *M* = 638.84, red crystal 0.35 × 0.20 × 0.15 mm, *a* = 10.396(1), *b* = 19.708(1), *c* = 15.139(1) Å, β = 91.83(1)°, *V* = 3100.2(4) $Å^3$, $\rho_{calcd.}$ = 1.369 g cm^{-3}, μ = 5.75 cm^{-1}, empirical absorption correction (0.824 ≤ *T* ≤ 0.919), *Z* = 4, monoclinic, space group $P2_1/c$ (No. 14), λ = 0.71073 Å, *T* = 198 K, ω- and φ-scans, 20865 reflections collected (±*h*, ±*k*, ±*l*), [(sinθ)/λ] = 0.66 $Å^{-1}$, 7378 independent (R_{int} = 0.037) and 5630 observed reflections [$I \geq 2\sigma(I)$], 353 refined parameters, *R* = 0.048, wR_2 = 0.121, max./min. residual electron density 0.46/–0.47 e·$Å^{-3}$, hydrogen atoms calculated and refined as riding atoms.

[(SalValOMe)TiCl$_3$] (4b): According to the preparation of **4a**, SalValOMe (**3b**) (500 mg, 2.13 mmol) was treated with $TiCl_4$ (403 mg, 2.13 mmol) to yield **4b** as a red solid (850 mg, 2.04 mmol, 96%). Decomp. 207.4 °C. $C_{13}H_{16}Cl_3NO_3Ti{\cdot}1/3CH_2Cl_2$ (416.8): calcd. C 38.42, H 4.03, N 3.36; found C 38.48, H 3.93, N 3.50. $[\alpha]_D^{20}$ = +204.4 (*c* = 0.125, CH_2Cl_2). IR (KBr): $\tilde{\nu}$ = 2966, 2934, 2874, 1752, 1643, 1598, 1460, 1399, 1377, 1318, 1273, 1251, 1227, 1155, 1123, 1098, 1055, 984, 920, 844, 759, 663, 558, 456, 416 cm^{-1}. ^1H NMR (599.8 MHz, CD_2Cl_2, 298 K): δ = 8.35 (s, 1 H, CH=N), 7.69 (ABCD, ^3J = 7.8, ^4J = 1.5 Hz, 1 H, 5′-H), 7.63 (ABCD, ^3J = 7.8, ^4J = 1.5 Hz, 1 H, 3′-H), 7.25 (ABCD, ^3J = 7.8, ^4J = 1.2 Hz, 1 H, 4′-H), 6.89 (ABCD, ^3J = 7.8 Hz, 1 H, 6′-H), 4.62 (dd, ^3J = 5.9, ^4J = 0.8 Hz, 1 H, 2-H), 4.32 (s, 3H OCH_3), 2.64 (m, 1 H, 3-H), 1.20 (d, ^3J = 6.8 Hz, 3 H, 4a-H), 1.16 (d, ^3J = 6.8 Hz, 3 H, 4b-H) ppm. $^{13}C\{^1H\}$ NMR (150.8 MHz, CD_2Cl_2, 298 K): δ = 183.5 (C-1), 164.2 (CH=N), 162.0 (C-1′), 137.7 (C-5′), 135.8 (C-3′), 125.8 (C-2′), 125.5 (C-4′), 114.9 (C-6′), 78.0 (C-2), 58.4 (OCH_3), 34.7 (C-3), 20.7 (C-4a), 19.0 (C-4b) ppm.

[(Sal*PhgOMe)TiCl$_3$] (4c): According to the preparation of **4a**, Sal*PhgOMe (**3c**) (200 mg, 0.52 mmol) was treated with $TiCl_4$ (100 mg, 0.52 mmol) to yield **4c** as a red solid (330 mg, 0.44 mmol, 85%). Decomp. 336.5 °C. $C_{24}H_{30}Cl_3NO_3Ti{\cdot}2.5CH_2Cl_2$ (747.1): calcd. C 42.60, H 4.72, N 1.87; found C 42.95, H 4.58, N 2.18. $[\alpha]_D^{20}$ = –27.3 (*c* = 0.08, CH_2Cl_2). IR (KBr): $\tilde{\nu}$ = 3065, 2961, 2907, 2869, 1654, 1613, 1565, 1553, 1454, 1400, 1365, 1325, 1268, 1249,

 © 2005 Wiley-VCH Verlag GmbH & Co. KGaA, Weinheim

1211, 1185, 1051, 1030, 1010, 922, 873, 822, 764, 728, 699, 614, 603, 584, 541, 456 cm^{-1}. ^1H NMR (599.8 MHz, CD_2Cl_2, 298 K): δ = 8.00 (d, ^4J = 1.5 Hz, 1 H, CH=N), 7.72 (d, ^4J = 2.2 Hz, 1 H, 5′-H), 7.52 (m, 5 H, 4-H, 5-H, 6-H), 7.22 (d, ^3J = 2.3 Hz, 1 H, 3′-H), 5.97 (s, 1 H, 2-H), 4.24 (s, 3 H, OCH_3), 1.55 [s, 9 H, 6′-C$(CH_3)_3$], 1.28 [s, 9 H, 4′-C$(CH_3)_3$] ppm. $^{13}C\{^1H\}$ NMR (150.8 MHz, CD_2Cl_2, 298 K): δ = 182.4 (C-1), 166.3 (CH=N), 159.8 (C-1′), 148.7 (C-4′), 136.8 (C-6′), 133.8 (C-3), 133.1 (C-5′), 130.9 (C-3′), 130.8 (C-6), 130.4 (C-5), 130.3 (C-4), 126.7 (C-2′), 75.6 (C-2), 58.8 (OCH_3), 35.8 [6′-*C*$(CH_3)_3$], 35.1 [4′-*C*$(CH_3)_3$], 31.2 [4′-C(*C*$H_3)_3$], 29.9 [6′-C(*C*$H_3)_3$] ppm.

[(SalAlaValOMe)TiCl$_3$] (4d): According to the preparation of **4a**, SalAlaValOMe (**3d**) (250 mg, 0.82 mmol) was treated with $TiCl_4$ (155 mg, 0.82 mmol) to yield **4d** as a red solid (830 mg, 0.75 mmol, 92%). Decomp. 118.2 °C. $C_{16}H_{21}Cl_3N_2O_4Ti{\cdot}7.5CH_2Cl_2$ (1096.6): calcd. C 25.74, H 3.31, N 2.55; found C 25.36, H 2.92, N 3.32. $[\alpha]_D^{20}$ = +60.6 (*c* = 0.18, CH_2Cl_2). IR (KBr): $\tilde{\nu}$ = 3282, 2965, 1743, 1622, 1600, 1556, 1448, 1396, 1274, 1248, 1226, 1143, 930, 826, 756, 657, 552, 426 cm^{-1}. ^1H NMR (499.8 MHz, CD_2Cl_2, 298 K): δ = 8.46 (s, 1 H, CH=N), 7.84 (d, ^3J = 8.3 Hz, 1 H, 2-NH), 7.64 (m, 2 H, 3′-H u. 5′-H), 7.22 (ABCD, ^3J = 7.6, ^4J = 1.0 Hz, 1 H, 4′-H), 6.87 (ABCD, ^3J = 8.6 Hz, 1 H, 6′-H), 5.26 (q, ^3J = 7.2 Hz, 1 H, 6-H), 4.75 (dd, ^3J = 8.6 Hz, 1 H, 2-H), 3.84 (s, 3 H, OCH_3), 2.24 (m, 1 H, 3-H), 1.87 (d, ^3J = 7.5 Hz, 3 H, 7-H), 0.97 (d, ^3J = 6.7 Hz, 3 H, 4a-H), 0.88 (d, ^3J = 6.7 Hz, 3 H, 4b-H) ppm. $^{13}C\{^1H\}$ NMR (125.7 MHz, CD_2Cl_2, 298 K): δ = 179.2 (C-5), 171.1 (C-1), 164.0 (CH=N), 161.7 (C-1′), 137.4 (C-5′), 135.4 (C-3′), 125.6 (C-2′), 125.1 (C-4′), 115.0 (C-6′), 69.2 (C-6), 60.3 (C-2), 53.5 (OCH_3), 31.8 (C-3), 22.8 (C-7), 19.2 (C-4a), 17.8 (C-4b) ppm.

X-ray Crystal Structure Analysis of *rac*-5a: Formula $C_{15}H_{11}Cl_2NO_3Ti{\cdot}CH_2Cl_2$, M = 456.97, red crystal 0.25 × 0.10 × 0.07 mm, a = 14.182(1), b = 14.401(1), c = 19.735(1) Å, α = 75.70(1), β = 89.91(1), γ = 85.97(1)°, V = 3895.5(4) Å^3, $\rho_{calcd.}$ = 1.558 g cm^{-3}, μ = 10.02 cm^{-1}, empirical absorption correction (0.788 ≤ T ≤ 0.933), Z = 8, triclinic, space group $P\bar{1}$ (No. 2), λ = 0.71073 Å, T = 198 K, ω- and φ-scans, 37081 reflections collected (±h, ±k, ±l), [(sinθ)/λ] = 0.62 Å^{-1}, 15775 independent (R_{int} = 0.058) and 10717 observed reflections [$I \geq 2\ \sigma(I)$], 912 refined parameters, R = 0.080, wR_2 = 0.214, max./min. residual electron density 1.84/–0.97 e·Å^{-3} in the region of the solvent molecules, phenyl group C21B–C26B refined with split positions, some of the solvent molecules heavily disordered, refinement with split positions did not improve the model, hydrogen atoms calculated and refined as riding atoms.

Catalytic Hydrocyanation Reactions: The catalyst (0.043 mmol) was dissolved in toluene(2 mL) under argon. After stirring at room temperature for 10 min, imine **6** (0.43 mmol)[13] was added and the mixture was cooled to 4 °C. After an equilibration time of 20 min, trimethylsilyl cyanide (0.85 mmol) was added and a solution of *n*-butanol (0.64 mmol) in toluene (2 mL) was added through a syringe pump over a period of 10 h. After further stirring at 4 °C for 14 h, the reaction was quenched by the addition of diethyl ether (5 mL). Filtration through a plug of silica gel, removal of the solvent and crystallisation from a 1:1 mixture of diethyl ether/pentane at –22 °C yielded the product. Enantiomeric analysis was carried out by HPLC (Kromasil, KR100-5CHI-TBB, 250 × 4.6 mm, flow 0.5 mL/min, *n*-hexane) after a reaction time of 12 and 24 h, respectively. Details are provided with the Supporting Information.

Supporting Information (see also footnote on the first page of this article): Additional spectroscopic data of the compounds **3** and **4**; X-ray crystal structure analyses of the compounds **3a** and **3b**; details of the catalytic hydrocyanation reactions.

Acknowledgments

Financial support from Deutsche Forschungsgemeinschaft and the Fonds der Chemischen Industrie is gratefully acknowledged.

[1] a) A. D. Ryabov, *Angew. Chem.* **1991**, *103*, 945–955; *Angew. Chem. Int. Ed. Engl.* **1991**, *30*, 931–941; b) K. Severin, R. Bergs, W. Beck, *Angew. Chem.* **1998**, *110*, 1722–1743; *Angew. Chem. Int. Ed.* **1998**, *37*, 1653–1654; c) K. Haas, W. Ponikwar, H. Nöth, W. Beck, *Angew. Chem.* **1998**, *110*, 1200–1203; *Angew. Chem. Int. Ed.* **1998**, *37*, 1086–1089; d) R. H. Fish, *Coord. Chem. Rev.* **1999**, *185–186*, 569–584; e) R. Fish, G. Jaouen, *Organometallics* **2003**, *22*, 2166–2177.

[2] a) H. Sun, H. Li, A. Weir, P. J. Sadler, *Angew. Chem.* **1998**, *110*, 1622–1625; *Angew. Chem. Int. Ed.* **1998**, *37*, 1577–1579; b) M. Guo, P. J. Sadler, *J. Chem. Soc., Dalton Trans.* **2000**, 7–9; c) M. Guo, Z. Guo, P. J. Stadler, *J. Biol. Inorg. Chem.* **2001**, *6*, 698–707.

[3] a) H. Köpf, P. Köpf-Maier, *Angew. Chem.* **1979**, *91*, 509; *Angew. Chem. Int. Ed. Engl.* **1979**, *18*, 477–488; b) P. Köpf-Maier, W. Wagner, H. Köpf, *Cancer Chemother. Pharmacol.* **1981**, *5*, 237–241; c) M. M. Harding, G. Mokdsi, *Curr. Med. Chem.* **2000**, *7*, 1289–1303; d) B. K. Keppler, *Metal Complexes in Cancer Chemotherapy*, Wiley-VCH, Weinheim, **1993**, p. 260–323.

[4] a) J. R. Porter, H. F. Traverse, A. H. Hoveyda, M. L. Snapper, *J. Am. Chem. Soc.* **2001**, *123*, 984–985; b) J. R. Porter, W. G. Wirschun, K. W. Kuntz, M. L. Snapper, A. H. Hoveyda, *J. Am. Chem. Soc.* **2000**, *122*, 2657–2658; c) L. C. Akullian, M. L. Snapper, A. H. Hoveyda, *Angew. Chem.* **2003**, *115*, 4376–4379; *Angew. Chem. Int. Ed.* **2003**, *42*, 4244–4247.

[5] N. S. Josephsohn, K. W. Kuntz, M. L. Snapper, A. H. Hoveyda, *J. Am. Chem. Soc.* **2001**, *123*, 11594–11599.

[6] A. Berkessel, D. A. Hérault, *Angew. Chem.* **1999**, *111*, 99–102; *Angew. Chem. Int. Ed.* **1999**, *38*, 102–105.

[7] a) P. D. Hustad, J. Tian, G. W. Coates, *J. Am. Chem. Soc.* **2002**, *124*, 3614–3621; b) S. Matsui, M. Mitani, J. Saito, Y. Tohi, H. Makio, N. Matsukawa, Y. Takagi, K. Tsuru, M. Nitabaru, T. Nakano, H. Tanaka, N. Kashiwa, T. Fujita, *J. Am. Chem. Soc.* **2001**, *123*, 6847–6856; c) M. Mitani, J. Mohri, Y. Yoshida, J. Saito, S. Ishii, K. Tsuru, S. Matsui, R. Furuyama, T. Nakano, H. Tanaka, S. Kojoh, T. Matsugi, N. Kashiwa, T. Fujita, *J. Am. Chem. Soc.* **2002**, *124*, 3327–3336; d) J. Tian, P. D. Hustad, G. W. Coates, *J. Am. Chem. Soc.* **2001**, *123*, 5134–5135.

[8] J. Wonnemann, M. Oberhoff, G. Erker, R. Fröhlich, K. Bergander, *Eur. J. Inorg. Chem.* **1999**, *584*, 318–322.

[9] D. Harmsen, G. Erker, R. Fröhlich, G. Kehr, *Eur. J. Inorg. Chem.* **2002**, *1*, 3156–3171.

[10] H. Brunner, T. Zwack, M. Zabel, W. Beck, A. Boehm, *Organometallics* **2003**, *22*, 1741–1750; and references cited therin.

[11] a) G. Erker, K. Engel, J. L. Atwood, W. E. Hunter, *Angew. Chem.* **1983**, *95*, 506–507; *Angew. Chem. Int. Ed.* **1983**, *22*, 494–495; b) G. Erker, U. Dorf, C. Krüger, Y.-H. Tsay, *Organometallics* **1987**, *6*, 680–682; and references cited therin.

[12] F. H. Allen, O. Kennard, D. G. Watson, L. Brammer, A. G. Orpen, *J. Chem. Soc., Perkin Trans. 2* **1987**, S1–S19.

[13] J. R. Porter, W. G. Wirschun, K. W. Kuntz, M. L. Snapper, A. H. Hoveyda, *J. Am. Chem. Soc.* **2000**, *122*, 2657–2658.

[14] S. Braun, H. O. Kalinowski, S. Berger, *150 and More Basic NMR Experiments*; VCH, Weinheim, **1998**, and references therein.

Received: January 25, 2005
Published Online: June 14, 2005

 © 2005 Wiley-VCH Verlag GmbH & Co. KGaA, Weinheim

Reactions of Zirconocene Bis(trimethylsilyl)acetylene Complexes with Fluorinated Pyridines: C–H vs. C–F Bond Activation

Ulrike Jäger-Fiedler,[a] Perdita Arndt,[a] Wolfgang Baumann,[a] Anke Spannenberg,[a] Vladimir V. Burlakov,[b] and Uwe Rosenthal*[a]

Keywords: Zirconocene / C–F bond activation / C–H bond activation / Organometallics / Heterocycles

The zirconocene complexes $Cp_2Zr(L)(\eta^2\text{-}Me_3SiC_2SiMe_3)$ (**1a**: L = THF; **1b**: L = pyridine) and the ethylene bis(tetrahydroindenyl) complex *rac*-(ebthi)$Zr(\eta^2\text{-}Me_3SiC_2SiMe_3)$ (**2**) react with 2,3,5,6-tetrafluoropyridine with C–H bond activation to produce the 4-substituted pyridyl complexes with agostic alkenyl groups $Cp'_2Zr(4\text{-}C_5NF_4)[\text{–}C(SiMe_3)=CH(SiMe_3)]$ ($Cp'_2 = Cp_2$) (**3**) and (Cp'_2 = ebthi) (**4**). With 2,3,4,6-tetrafluoropyridine, after C–H bond activation, complex **2** yields two isomers of the 5-substituted pyridyl complex *rac*-(ebthi)$Zr(3\text{-}C_5NF_4)[\text{–}C(SiMe_3)=CH(SiMe_3)]$ with agostic alkenyl groups, **5a** and **5b**. With pentafluoropyridine complex **1b** gives, after dissociation of the bis(trimethylsilyl)acetylene (btmsa), C–F bond activation at the 4-position and formation of $Cp_2Zr(4\text{-}C_5NF_4)F$ (**6**). Complex **1b** reacts with 3-chloro-2,4,5,6-tetrafluoropyridine by means of a preferred C–Cl activation to give $Cp_2Zr(3\text{-}C_5NF_4)Cl$ (**7**). These results are in contrast to the reactions of the titanium complex $Cp_2Ti(\eta^2\text{-}Me_3SiC_2SiMe_3)$ which, with 2,3,5,6-tetrafluoropyridine, gave C–F activation in preference to C–H activation. With pentafluoropyridine, C–F bond activation at the 2-position was found rather than at the 4-position.

(© Wiley-VCH Verlag GmbH & Co. KGaA, 69451 Weinheim, Germany, 2005)

Introduction

Among reactions of different titanocene and zirconocene complexes of bis(trimethylsilyl)acetylene $Cp_2M(L)(\eta^2\text{-}Me_3SiC_2SiMe_3)$ (M = Ti, without L; M = Zr, L = THF, pyridine), the activation of seemingly unreactive bonds by the pentamethylcyclopentadienyl complexes $Cp^*_2M(\eta^2\text{-}Me_3SiC_2SiMe_3)$ (M = Ti, Zr) and the ethylene bis(tetrahydroindenyl) complexes *rac*-(ebthi)$M(\eta^2\text{–}Me_3SiC_2SiMe_3)$ (M = Ti, Zr) has been described by us in some reviews.[1–10] For example, cleavage of C–H, C–C (Cp-ring opening, cleavage of butadiynes), Si–C, P–C, N–H, N–C, N–N, Si–O, N–O, C–O, C–S and C–B bonds gave complexes with potential applications in stoichiometric and catalytic reactions.

The inertness of fluorocarbons is a consequence of the great strength of the C–F bond which arises from the small size and the high electronegativity of the fluorine atom. Nevertheless, the activation of several types of carbon–fluorine bonds by transition metal complexes has been summarised in many reviews.[11–16]

Examples of the activation of C–F bonds by electron-deficient group 4 transition-metal species of zirconium and titanium with subsequent C–F bond cleavage are relatively rare. One of the first examples for titanium was reported by Stone et al. who isolated $Cp_2Ti(C_6F_5)F$ upon pyrolysis of $Cp_2Ti(C_6F_5)_2$.[17] Later Burk and coworkers described the elimination of a cyclopropane $(CH_2)_2CR_2$ and the formation of a titanocene-fluoro-dienone complex $Cp_2Ti(F)[(O\text{–}C(CCF_3)_3C=CF_2)]$ by F-abstraction in the reaction of a tetrakis(trifluoromethyl)cyclopentadienone-titanacyclobutane complex $[Cp_2Ti(CH_2)_2CR_2][O=C(CCF_3)_4]$.[18] Beckhaus and coworkers described the complete defluorination of trifluoromethyl-substituted Cp-ligands by titanium amide complexes.[19] More recently similar reactions were described by Deck et al. for the corresponding pentafluorophenyl substituents of cyclopentadienyl and indenyl ligands.[20] Hessen and coworkers reported that the complex $[Cp^*_2Ti(\eta^1\text{-}FC_6H_5)][BPh_4]$ reacts with trifluorotoluene to yield 1,2-diphenyl-1,1,2,2-tetrafluoroethane and $Cp^*_2TiF_2$.[21] Stoichiometric and catalytic C–F bond activations for the aromatisation of cyclic perfluorocarbons were achieved using titanocene and zirconocene, generated from Cp_2MCl_2 (M = Ti, Zr) and $Mg/HgCl_2$ or Cp_2ZrCl_2 and $Al/HgCl_2$.[22]

Zirconocene generating systems such as Cp_2ZrPh_2 or $Cp_2ZrCl_2/2\ n$BuLi can defluorinate perfluorodecalin to perfluoronaphthalene.[23] 2-Fluoro- and 3-fluoropyridine can also be defluorinated by various complexes such as Cp'_2MCl_2 (M = Ti, Zr, Hf; Cp′ = Cp, Cp*) in combination with different aluminium compounds acting as reducing agents.[24] In a series of outstanding papers, Jones and co-

[a] Leibniz-Institut für Organische Katalyse an der Universität Rostock e.V.,
Albert-Einstein-Str. 29a, 18059 Rostock, Germany
Fax: +49-381-1281-5000
E-mail: uwe.rosenthal@ifok-rostock.de
[b] A. N. Nesmeyanov Institute of Organoelement Compounds, Russian Academy of Sciences,
Vavilov St. 28, 117813 Moscow, Russia
Fax: +7-095-1355085

workers described the activation of several types of C–F bonds in alkanes, arenes and olefins using $Cp^*_2ZrH_2$. The published mechanistic investigations showed different pathways depending on the substrate used.[25–31] Caulton et al. showed that Cp_2ZrHCl reacts with fluoroethylene with formation of Cp_2ZrFCl, $Cp_2Zr(CH_2CH_3)Cl$ and Cp_2ZrF_2.[32] In the case of zirconium, hydride complexes were mostly used in C–F bond activation reactions. One exception was the reaction of *rac*-(ebthi)Zr(Me)(NH*t*Bu) with pentafluoropyridine published by Bergman and coworkers. Using the monomeric imidozirconocene complex [*rac*-(ebthi)-Zr=N*t*Bu], they observed activation of the *ortho* C–F bond and the formation of an amininopyridinato complex *rac*-(ebthi)ZrF(-N*t*Bu-2-C_5NF_4).[33]

In the light of the surprising results concerning zirconocene difluorides and alkyl monofluorides in the catalytic polymerisation of olefins,[34–37] we began to question whether the above mentioned alkyne complexes could activate C–F bonds to form the zirconocene fluoro complexes by C–F bond cleavage. These investigations were also extended to cover the question of whether hydride complexes (Zr–H systems, formed by reactions of systems containing Zr–F and Al–H bonds) could cleave the C–F bonds of $B(C_6F_5)_3$.[38,39]

In this work we extended and compared the investigations of Beckhaus and his group concerning reactions of our titanium reagents[1–10] $Cp_2Ti(\eta^2\text{-}Me_3SiC_2SiMe_3)$ and $Cp^*_2Ti(\eta^2\text{–}Me_3SiC_2SiMe_3)$ towards pyridine and fluorinated pyridines with the reactions of the corresponding zirconocene complexes. In this paper we describe the reactions of the zirconocene complexes $Cp_2Zr(L)(\eta^2\text{-}Me_3SiC_2SiMe_3)$ (**1a**: L = THF, **1b**: L = pyridine) and the ethylene bis(tetrahydroindenyl) complex *rac*-(ebthi)$Zr(\eta^2\text{-}Me_3SiC_2SiMe_3)$ towards fluorinated pyridines. These reactions were used to probe any differences in the behaviour between the bis(trimethylsilyl)acetylene complexes of Ti and Zr.

Results and Discussion

Very recently, Beckhaus and coworkers published a series of excellent examples of reactions of titanocene bis(trimethylsilyl)acetylene complexes with different N-heterocyclic compounds.[40–43] In these reactions, the complexes $Cp_2Ti(\eta^2\text{-}Me_3SiC_2SiMe_3)$ and $Cp^*_2Ti(\eta^2\text{-}Me_3SiC_2SiMe_3)$ act as sources of titanocene "Cp_2Ti" and permethyltitanocene "Cp^*_2Ti" after dissociation of the alkyne. They react differently with pyridine and fluorinated pyridines (Scheme 1 and Scheme 2). Under C–H activation, $Cp_2Ti(\eta^2\text{-}Me_3SiC_2SiMe_3)$ and pyridine give an H-bridged binuclear titanium fulvalene derivative. 2-Fluoropyridine reacts with $Cp_2Ti(\eta^2\text{-}Me_3SiC_2SiMe_3)$ by means of C–F activation to give an F-bridged binuclear titanium complex. It is remarkable that no C–H activation product was found in this case. With $Cp_2Ti(\eta^2\text{-}Me_3SiC_2SiMe_3)$, pentafluoropyridine gives a similar perfluorinated product.

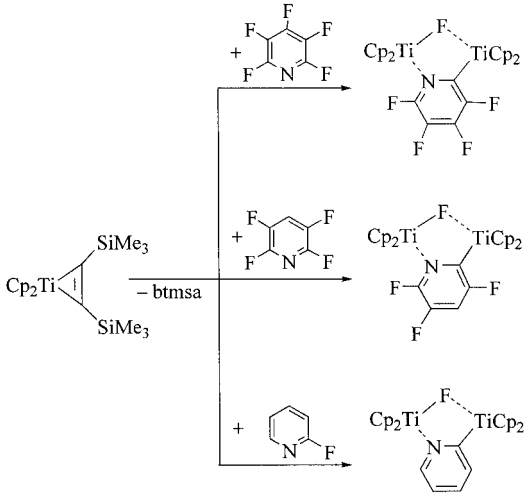

Scheme 1.

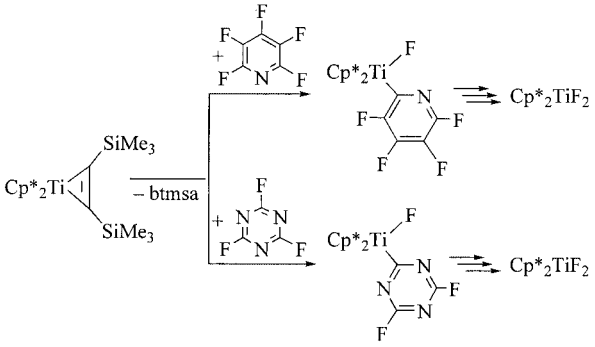

Scheme 2.

With $Cp^*_2Ti(\eta^2\text{-}Me_3SiC_2SiMe_3)$ the pentafluoropyridine forms, after C–F activation, a mononuclear titanium(IV) monofluoro complex $Cp^*_2Ti(2\text{-}C_5NF_4)F$ as an intermediate, as demonstrated by ^1H and ^{19}F NMR spectroscopic measurements. The latter complex reacts with an excess of the substrate to give the difluoride complex $Cp^*_2TiF_2$. A similar reaction was found for the cyanuric fluoride (Scheme 2).

In addition to C–F activation after elimination of the bis(trimethylsilyl)acetylene, there is another pathway for the reactions of the corresponding zirconocene complexes **1** and **2** with fluorinated pyridines. Upon C–H activation and without alkyne elimination, formation of agostic alkenyl complexes was observed. Both possibilities represent the typical reactions of these metallocene bis(trimethylsilyl)-acetylene complexes (Scheme 3).

The zirconocene complex $Cp_2Zr(THF)(\eta^2\text{-}Me_3SiC_2SiMe_3)$ (**1a**) and the ethylene bis(tetrahydroindenyl) complex *rac*-(ebthi)$Zr(\eta^2\text{-}Me_3SiC_2SiMe_3)$ (**2**) react with 2,3,5,6-tetrafluoropyridine by means of C–H bond activation to produce the complexes $Cp'_2Zr(4\text{-}C_5NF_4)$[–C(SiMe$_3$)=CH(SiMe$_3$)] ($Cp'_2 = Cp_2$) (**3**) and ($Cp'_2$ = ebthi) (**4**) (Scheme 3) containing both fluorosubstituted pyridyl groups metallated in the 4-position and agostic alkenyl groups. With 2,3,4,6-tetrafluoropyridine complex **2** yields,

 © 2005 Wiley-VCH Verlag GmbH & Co. KGaA, Weinheim

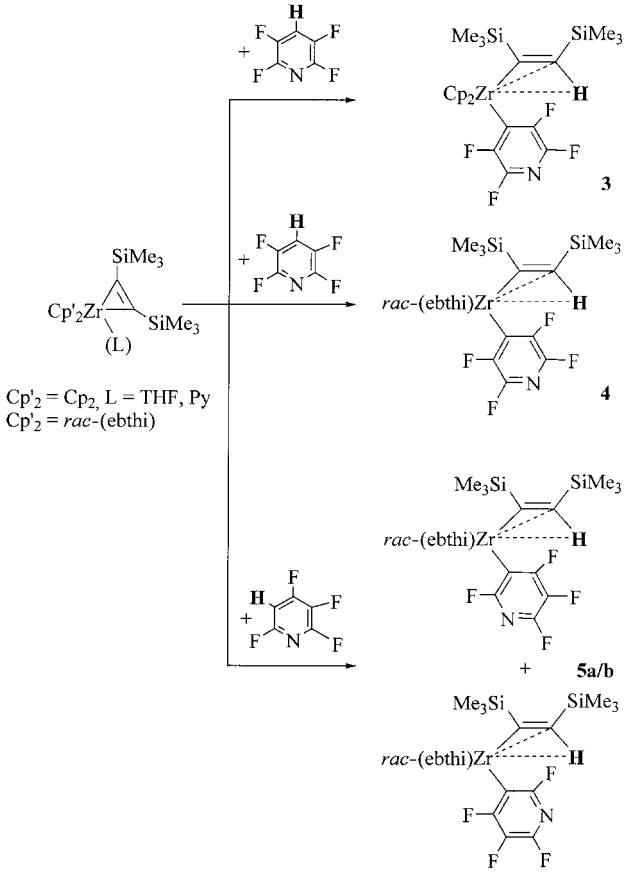

Scheme 3.

after C–H bond activation, two isomers **5a** and **5b** (1 to 2 ratio) of the corresponding complex *rac*-(ebthi)Zr(3-C_5NF_4)[–C($SiMe_3$)=CH($SiMe_3$)] bearing fluorosubstituted pyridyl substituents metallated in the 5-position as well as agostic alkenyl groups (Scheme 3).

With pentafluoropyridine and **1b**, elimination of bis(trimethylsilyl)acetylene and C–F bond activation in the 4-position was observed with subsequent formation of Cp_2Zr(4-C_5NF_4)F (**6**) (Scheme 4). As described in this work, in the case of zirconium such a species was isolated whereas in the above mentioned reaction of $Cp^*_2Ti(\eta^2\text{-}Me_3SiC_2SiMe_3)$ with pentafluoropyridine the respective C–F activation reaction resulted in formation of a similar mononuclear titanium(IV) mono-fluoro complex $Cp^*_2Ti(2\text{-}C_5NF_4)F$ only as an intermediate which reacts to give the difluoride $Cp^*_2TiF_2$ (see Scheme 2).

According to these results, C–H activation is preferable to C–F activation for zirconium. For zirconium, the attack for C–F bond activation occurs in the 4-position and not in the 2-position as described for titanium. Both positions are activated but in the case of zirconium the 4-position is favoured.

It is possible to explain the favoured reaction at the 4-position for zirconium by invoking a bimolecular reaction with precoordination of the pentafluoropyridine as an N-donor and a subsequent attack of a second zirconocene moiety at the 4-position (Scheme 4). Coordination of the

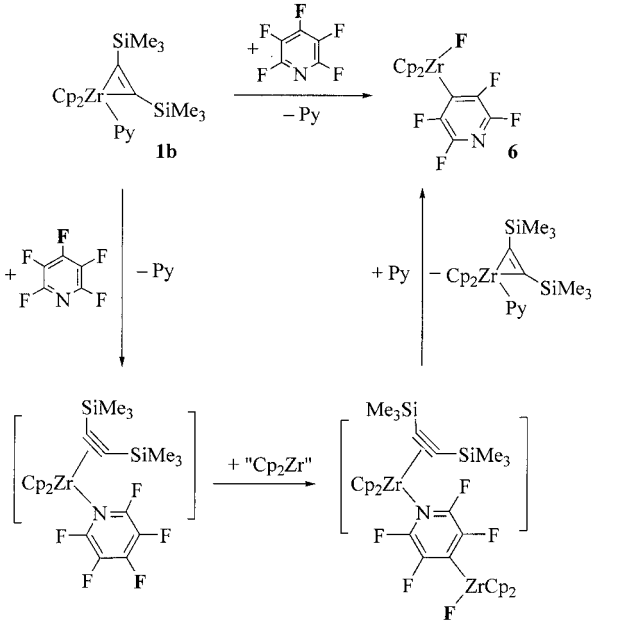

Scheme 4.

pyridine or such a precoordination of the pentafluoropyridine is generally impossible for the complex $Cp_2Ti(\eta^2\text{-}Me_3SiC_2SiMe_3)$ because of the smaller sized titanium atom.

It is reasonable to assume that the above mentioned C–H bond activation of 2,3,5,6-tetrafluoropyridine in complexes containing a fluorosubstituted pyridyl metallated in the 4-position could also proceed via a similar precoordination. In contrast, the unsubstituted pyridine in complex **1b** did not show such reactivity since it has no H-atoms in the 4-position which could be activated.

Another explanation for the favoured reaction at the 4-position follows from suggestions by Jones, Braun and Perutz (Scheme 5).[15,44] The observed preference for C–F bond activation in the 2-position for titanium provides evidence for concerted oxidative addition of the pyridine by means of a three-centred transition state (a). An electron transfer reaction pathway through a tight ion pair (b) or an S_NAr type nucleophilic mechanism via a Meisenheimer intermediate (c) would result in an attack at the 4-position of the pentafluoropyridine as found for zirconium.

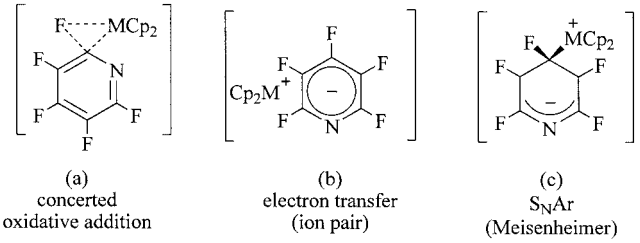

Scheme 5.

These results for the activation in the 4-position are also in contrast to the above mentioned reaction very recently described by Bergman[33] in which *rac*-(ebthi)Zr(Me)(NH*t*Bu) reacts with pentafluoropyridine via the monomeric imidozirconocene complex [*rac*-(ebthi)Zr=N*t*Bu]

 © 2005 Wiley-VCH Verlag GmbH & Co. KGaA, Weinheim

to afford the amininopyridinato complex *rac*-(ebthi)ZrF-(–N*t*Bu-2-C_5NF_4) with activation of the *ortho* C–F bond (Scheme 6).

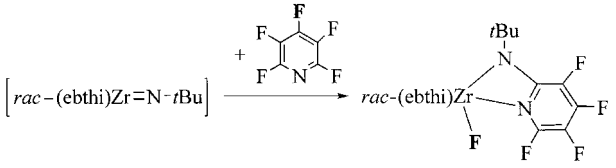

Scheme 6.

On the other hand, Bergman described only N-donor coordination for the unsubstituted pyridine and no C–H bond activation whereas the imidozirconocene complex [*rac*-(ebthi)Zr=N*t*Bu] reacted, for example with benzene, with activation of the C–H bond and formation of the complex *rac*-(ebthi)Zr(Ph)NH*t*Bu.[33]

The activation of pentafluoropyridine in the 4-position with formation of $L_nM(4\text{-}C_5NF_4)F$ complexes was shown by Perutz and Braun to be typical for Ni,[44] Pd,[45] Rh[46] and Pt.[47] An example of reactions of this type is shown in Scheme 7.

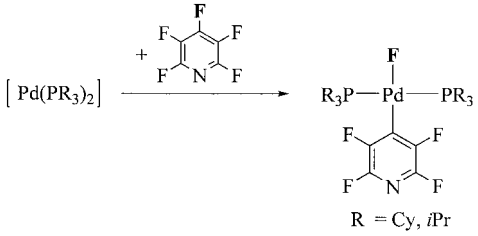

Scheme 7.

One can conclude from these results that the chemo- and regioselectivity of the C–H and C–F bond activations in reactions of fluorinated pyridines depends on the *metals* (C–F for Ti, C–H for Zr; 2-position for Ti, 4-position for Zr and Ni) and the *ligands* (Zr: 2-position for L = imido, 4-position for L = alkyne).

For the purpose of comparing the different reactivities of C–F and C–Cl bonds in halogenated pyridines, we found that complex **1b** reacts with 3-chloro-2,4,5,6-tetrafluoropyridine by means of a preferred C–Cl activation to give $Cp_2Zr(3\text{-}C_5NF_4)Cl$ (**7**) (Scheme 8). This result is very similar to that described by Perutz and Braun for the reaction of Ni^0 complexes with 3-chloro-2,4,5,6-tetrafluoro-pyridine (Scheme 9).[44]

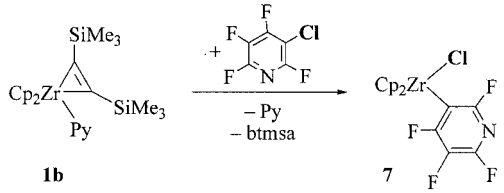

Scheme 8.

In general, the preferred reactivity of C–Cl bonds over C–F bonds is not restricted to the 3-position of the 3-chloro-2,4,5,6-tetrafluoro-pyridine. Traces of 2-chloro-3,4,5,6-tetrafluoro-pyridine contained in our batch of pentafluoro-pyridine also reacted with complex **2** with preferred C–Cl bond activation to give the complex *rac*-(ebthi)-$Zr(2\text{-}C_5NF_4)Cl$.[48]

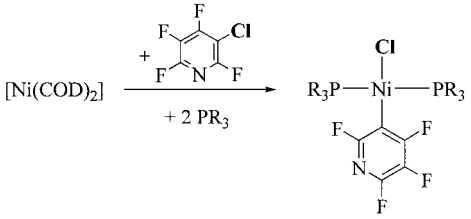

Scheme 9.

NMR-Spectroscopic and Molecular Structure Data

Unfortunately, all of the new compounds are only sparingly soluble in aromatic hydrocarbons so that in most cases the detection of the fluorinated carbon atoms was unsuccessful. However, the presence of the fluorinated pyridines is evident from their ^{19}F NMR signals. The most characteristic NMR spectroscopic and molecular structural feature of compounds **3** and **4** is the agostic interaction of the alkenyl group Zr–Cα=CβH. This alkenyl unit shows ^1H-NMR signals at rather low fields and the ^{13}C-NMR signals of Cα appear at low field whereas the Cβ signals are located upfield of the normal olefinic range. Typical for the additional agostic interaction is the very small coupling constant $^1J_{C\beta\text{-}H}$ (96 Hz in **3**, 97 Hz in **4** and 100 Hz in **5**). In the molecular structure, acute Zr–Cα–Cβ angles and short Zr–Cβ bond lengths reflect this special type of interaction. All these features have been previously observed in similar complexes such as $[Cp_2Zr\{\text{–}C(SiMe_3)=CH(SiMe_3)\}]_2[\mu\text{-}C\equiv C]$ (**A**),[49] [*rac*-(ebthi)Zr(C≡C-2-Py){–C(SiMe$_3$)=CH(SiMe$_3$)}] (**B**)[49] and the β-propiolactamate $[Cp_2Zr(\text{–}NC_3H_4O)\{\text{–}C(SiMe_3)=CH(SiMe_3)\}]$ (**C**)[50] which are all typical zirconocene σ-alkenyl complexes with agostic Cβ–H···Zr interactions (Table 1).

Table 1. Comparison of spectroscopic and structural data of complexes with agostic interactions $Cp'_2Zr(R)[C\alpha(SiMe_3)=C\beta H\text{-}(SiMe_3)]$.

Compound	**3**	**4**	A	B	C
Cp′$_2$	Cp_2	ebthi	Cp_2	ebthi	Cp_2
R	4-C_5NF_4	4-C_5NF_4	[μ-C≡C]	C≡C-2-Py	NC_3H_4O
^1H-NMR [ppm]					
δ(Cβ-H)	6.65	6.27	7.94	7.69	8.04
^{13}C-NMR					
δ(Cα)	218.8	223.6	236.4	227.6	227.0
δ(Cβ)	101.1	115.4	149.1	114.5	106.3
$^1J_{C\beta\text{-}H}$ [Hz]	96	97	125	98	101
Bond lengths [Å]					
d(Zr–Cα)	2.247(2)	2.257(2)	2.235(7)	2.262(3)	2.242(3)
d(Zr–Cβ)	2.554(2)	2.556(2)	2.530(7)	2.530(4)	2.543(3)
d(Cα = Cβ)	1.323(3)	1.331(3)	1.329(9)	1.319(5)	1.330(4)
Angles [°]					
ZrCαCβ	87.3(2)	86.8(2)	86.5(5)	85.6(2)	86.9(2)

 © 2005 Wiley-VCH Verlag GmbH & Co. KGaA, Weinheim

Table 2. Crystallographic data.

	3	4	6	7
Crystal system	triclinic	monoclinic	monoclinic	orthorhombic
Space group	$P\bar{1}$	$P2_1/n$	$P2_1/n$	$P2_12_12_1$
a [Å]	9.961(2)	9.520(2)	9.484(2)	7.716(2)
b [Å]	10.544(2)	25.141(5)	7.845(2)	9.007(2)
c [Å]	13.207(3)	13.741(3)	19.025(4)	20.755(4)
α [°]	108.51(3)			
β [°]	99.85(3)	106.40(3)	101.94(3)	
γ [°]	104.00(3)			
V [Å^3]	1229.1(4)	3155.0(11)	1384.9(5)	1442.4(6)
Z	2	4	4	4
Density [g cm^{-3}]	1.467	1.425	1.873	1.874
μ(Mo-K_α) [mm^{-1}]	0.586	0.472	0.845	0.985
T [K]	200	200	200	200
Reflections (measured)	3658	11391	3952	6273
Reflections (independent)	3658	6180	2142	1843
Reflections (observed)	3165	5116	1834	1620
No. parameters	284	372	183	199
R_1 [$I > 2\sigma(I)$]	0.0248	0.0335	0.0276	0.0266
wR_2 (all data)	0.0606	0.0921	0.0714	0.0552

In the ^{19}F NMR spectra of complexes **3**, **4**, **5**, **6** and **7** the shifts for the fluorine substitutents on the pyridine ring are in the low field region for uncoordinated fluoroaromatics (ca. –100 ppm) and are not shifted to the extreme high field as found for the fluoro bridged Zr–F–C groups (ca. –200 ppm).[51] The signal for the fluoride at zirconium was found at 1.3 ppm for complex **6**. This is in the range typically seen for other zirconocene fluorides (ca. 20–30 ppm).[52]

The increased steric demand of the *rac*-ebthi ligand system is responsible for restricted rotation of the pyridyl group about the Zr–C bond. For the Cp complex **3** only two ^{19}F resonances were found whereas the ebthi complex **4** exhibits four (an exchange between the otherwise equivalent *ortho* or *meta* fluoro substituents by pyridyl rotation does not occur). Therefore, two possible and different orientations of the asymmetric 5-pyridyl substituent are the most probable explanation for the presence of two isomeric forms

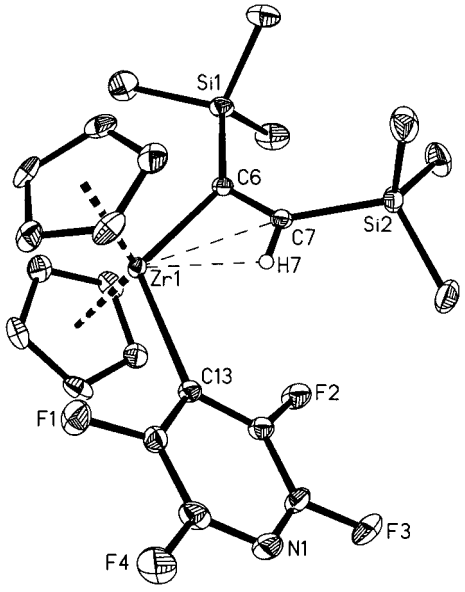

Figure 1. Molecular structure of complex **3**. Hydrogen atoms (except H7) are omitted for clarity. The thermal ellipsoids correspond to the 30% probability level. Selected bond lengths [Å] and angles [°]: Zr1–C6 2.247(2), Zr1–C7 2.554(2), Zr1–H7 2.14(2), Zr1–C13 2.432(2); Zr1–C6–C7 87.3(2), C7–C6–Si1 131.8(2), C6–C7–Si2 137.4 (2).

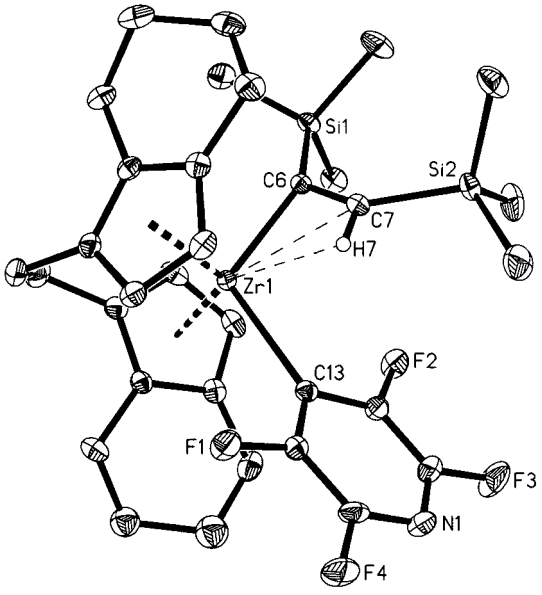

Figure 2. Molecular structure of complex **4**. Hydrogen atoms (except H7) are omitted for clarity. The thermal ellipsoids correspond to the 30% probability level. Selected bond lengths [Å] and angles [°]: Zr1–C6 2.257(2), Zr1–C7 2.556(2), Zr1–H7 2.16(3), Zr1–C13 2.426(2); Zr1–C6–C7 86.8(2), C7–C6–Si1 128.0(2), C6–C7–Si2 137.6 (2).

 © 2005 Wiley-VCH Verlag GmbH & Co. KGaA, Weinheim

of **5** (Scheme 3). Accordingly, differences show up for the proton signal of the agostic CH group: it appears as a *triplet* in **3** (coupling to two fluorine atoms made equivalent by pyridyl rotation) but only as a *doublet* in **4** and **5**.

Complexes **3**, **4**, **6** and **7** were investigated by X-ray crystallography. The crystallographic data are presented in Table 2 and the molecular structures are shown in Figure 1, Figure 2, Figure 3 and Figure 4, respectively. Complexes **3**, **4**, **6** and **7** display the general feature of bent metallocenes and show no interactions between the fluoro substituents of the pyridine ring and the central atom. Complexes **3** and **4** are characterised by a molecular geometry typical for species containing agostic interactions of the alkenyl group Zr–Cα=CβH (Table 1). Notable features are Zr–Cα bonds in the range of a single bond, Cα–Cβ distances in the range typical for double bonds and a very small Zr–Cα–Cβ angle which indicates the additional interaction of the H(Cβ) with the central zirconium atom (Figure 1 and Figure 2). The tetrafluoropyridyl ring σ-bonded at the 4-position exhibits relatively long Zr–C single bond lengths [Zr1–C13 = 2.432(2) Å in **3** and 2.426(2) Å in **4**].

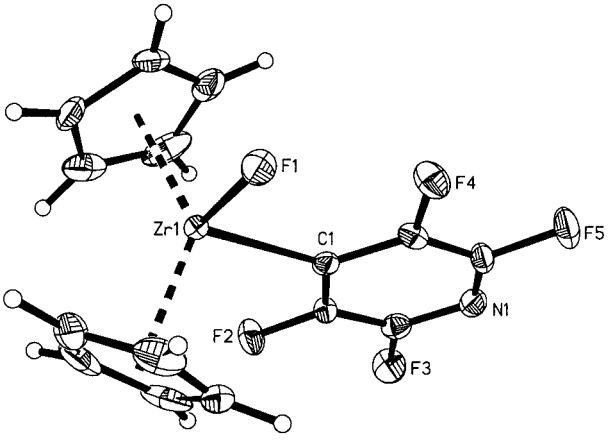

Figure 3. Molecular structure of complex **6**. The thermal ellipsoids correspond to the 30% probability level. Selected bond lengths [Å] and angles [°]: Zr1–C1 2.347(3), Zr1–F1 1.946(2); F1–Zr1–C1 99.38(9).

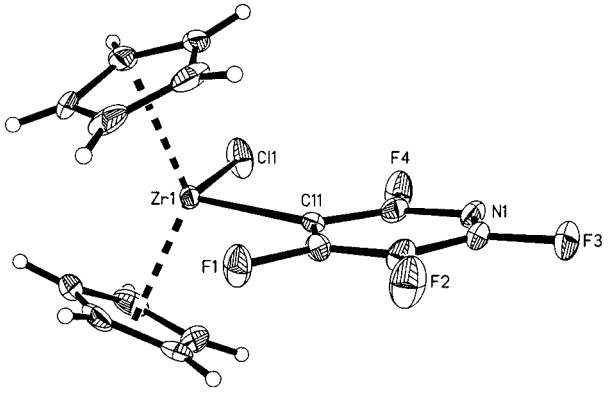

Figure 4. Molecular structure of complex **7**. The thermal ellipsoids correspond to the 30% probability level. Selected bond lengths [Å] and angles [°]: Zr1–C11 2.353(5), Zr1–Cl1 2.422(1); Cl1–Zr1–C11 104.9(1).

The molecular structure of complex **6** is depicted in Figure 3. The tetrafluoropyridyl ring σ-bonded at the 4-position in the molecule has shorter Zr–C bond lengths [Zr1–C13 = 2.347(3) Å] compared with **3** and **4** mentioned above. The observed Zr1–F1 bond length of 1.946(2) Å and the C1–Zr1–F1 angle of 99.38(9)° are in the same range as found in other zirconocene fluoro complexes. For example, some bond lengths were observed in the complex $Cp_2Zr(F)(C_6F_5)$ [Zr–C = 2.346 Å and Zr–F = 1.946 Å].[25] The monofluoride [(η^5-tetrahydroindenyl)$_2$Zr(F)(CH_2CH_2-2-Py)] [Zr–C = 2.377(3) Å] and the difluoride [(η^5-tetrahydroindenyl)$_2ZrF_2$] [Zr–F = 1.946(2) and 1.974(2) Å] exhibit comparable bond lengths.[52]

In the molecular structure of complex **7** (Figure 4), the bond length for Zr1–C11 [2.353(5) Å] is the same as that found for complex **6**. The observed Zr1–Cl1 bond length of 2.422(1) Å corresponds well with that found in other complexes of this type, e.g. Cp*$_2$Zr(Cl)($CH_2CH{=}CH_2$) (Zr–C = 2.324 Å and Zr–Cl =2.436 Å).[53]

Conclusions

Using the reactions presented we have documented that zirconocene bis(trimethylsilyl)acetylene complexes are able to activate C–H, C–F and C–Cl bonds of differently substituted pyridines. Whereas the corresponding titanocene bis(trimethylsilyl)acetylene complexes react with elimination of the alkyne and preferential C–F bond activation with formation of binuclear Ti^{III} complexes, an additional reaction possibility exists for zirconium in which the alkyne can remain part of the complex and form, after C–H bond activation, Zr^{IV} complexes with agostic σ-alkenyl groups. The latter is a typical example of the different reactivity between titanocene and zirconocene bis(trimethylsilyl)acetylene complexes. For titanium, a favourable elimination of the alkyne with formation of Ti^{III} complexes can be observed whereas for zirconium no elimination of the alkyne occurs but, instead, the formation of Zr^{IV} complexes.

Experimental Section

General: All operations were carried out under argon with standard Schlenk techniques. Prior to use, solvents were freshly distilled from sodium tetraethylaluminate and stored under argon. Deuterated solvents were treated with sodium or sodium tetraethylaluminate then distilled and stored under argon. Fluorinated pyridines were dried over molecular sieves and degassed before use. The following spectrometers were used: Mass spectrometry: AMD 402; NMR spectroscopy: Bruker ARX 400 (^{1}H, ^{13}C) and Bruker AC 250 (^{19}F) instruments. Chemical shifts were referenced to signals of the solvents used which were [D_6]benzene (δ_H = 7.16, δ_C = 128.0 ppm) and [D_8]toluene (δ_H = 2.03, δ_C = 20.4 ppm). The ^{19}F NMR spectra were referenced to external $CFCl_3$. The spectra were assigned with the help of DEPT experiments. Melting points were measured in sealed capillaries using a Büchi 535 apparatus. Elemental analyses were performed using a Leco CHNS-932 elemental analyser.

X-ray Crystallographic Study of Complexes 3, 4, 6 and 7: Data were collected with a STOE-IPDS-diffractometer using graphite-mono-

 © 2005 Wiley-VCH Verlag GmbH & Co. KGaA, Weinheim

chromated Mo-K_α radiation. The structures were solved by direct methods (SHELXS-86)[54] and refined by full-matrix least-squares techniques against F^2 (SHELXL-93).[55] XP (BRUKER AXS) was used for structure representations.

CCDC-263968 (for **3**), -263969 (for **4**), -263970 (for **6**) and -263971 (for **7**) contain the supplementary crystallographic data for this paper. These data can be obtained free of charge from The Cambridge Crystallographic Data Centre via www.ccdc.cam.ac.uk/data_request/cif.

Preparation of Complex 3: Complex **1a** (266 mg, 0.5 mmol) was dissolved in THF/*n*-hexane (ca. 1 to 3, 10 mL) and treated with 2,3,5,6-tetrafluoropyridine (115 μL, 1.14 mmol) while stirring. After 2 h at 60 °C the brown solution had become green and a grey precipitate had formed. After filtration, the precipitate was recrystallised from THF/*n*-hexane at –32 °C. Filtration gave a yield of 160 mg of colourless crystals (51%). M.p. 147 °C (dec.). $C_{23}H_{29}F_4NSi_2Zr$ (542.87): calcd. C 50.89, H 5.38, N 2.58; found C 50.98, H 5.30, N 2.55. ^{1}H NMR (C_6D_6): δ = 0.15 (t, $J_{H,F}$ = 0.7 Hz, 9 H, β-$SiMe_3$), 0.25 (s, 9 H, α-$SiMe_3$), 5.34 (s, 10 H, Cp), 6.65 (t, $J_{H,F}$ = 3.9 Hz, 1 H, CH) ppm. ^{13}C{^{1}H} NMR (C_6D_6): δ = 0.2 (t, $J_{C,F}$ = 1.6 Hz, β-$SiMe_3$), 2.0 (α-$SiMe_3$), 101.1 ($^1J_{C,H}$ = 96.2, $J_{C,F}$ = 1.8 Hz, β-CH), 108.1 (Cp), 146.0, 143.6 (2 m, CF), 162.8 (t, $^2J_{C,F}$ = 57 Hz, *p*-C), 218.8 (t, $J_{C,F}$ = 1.5 Hz, α-C) ppm. ^{19}F{^{1}H} NMR (C_6D_6): δ = –96.5 (AA′XX′), –110.5 (AA′XX′) ppm. ^{29}Si NMR (C_6D_6): δ = –3.2 ($^2J_{Si,H}$ = 3 Hz (CH) and 6.6 Hz (Me), β-Si), –6.9 ($^2J_{Si,H}$ = 6.4, $^3J_{Si,H}$ = 19 Hz, α-Si) ppm. MS (70 eV): *m*/*z* 541 $[M]^+$, 391 $[M - C_5F_4N]^+$, 370 $[M - Me_3SiC{=}CHSiMe_3]^+$, 220 $[M - C_5F_4N - Me_3SiC{=}CHSiMe_3]^+$.

Preparation of Complex 4: This was prepared as described above starting from complex **2** (300 mg, 0.57 mmol) and 2,3,5,6-tetrafluoropyridine (230 μL, 2.3 mmol) in *n*-heptane. At 80 °C the solution became red-brown and a yellow precipitate formed which was filtered off to give complex **4**. The yield was 161 mg (42%). M.p. 197 °C (dec.). $C_{33}H_{43}F_4NSi_2Zr$ (675.19): calcd. C 58.54, H 6.40, N 2.07; found C 58.28, H 6.62, N 1.99. ^{1}H NMR (C_6D_6): δ = 0.14 (d, $J_{H,F}$ = 0.7 Hz, 9 H, β-$SiMe_3$), 0.40 (s, 9 H, α-$SiMe_3$), 0.65–2.59 (20 H, CH_2), 5.15 (t, $J_{H,F} \approx {}^3J_{H,H} \approx$ 2.4 Hz, 1 H, CH), 5.87 (t, $J_{H,F} \approx {}^3J_{H,H} \approx$ 3.0 Hz, 1 H, CH), 5.97 (dd, $J_{H,F} \approx$ 1.5, $^3J_{H,H} \approx$ 2.7 Hz, 1 H, CH), 6.27 (d, $J_{H,F}$ = 4.5 Hz, 1 H, =CHβ), 6.45 (d, $^3J_{H,H}$ = 2.7 Hz, 1 H, CH) ppm. ^{13}C{^{1}H} NMR (C_6D_6): δ = 0.9 (β-$SiMe_3$), 3.4 (α-$SiMe_3$), 21.8, 22.1, 22.3, 22.7, 23.3 (2 C), 24.1, 25.6 (d, $J_{C,F} \approx$ 1 Hz), 27.7, 28.5 (10×CH_2), 100.1, 103.3 (d, $J_{C,F}$ = 4.0 Hz), 105.3, 106.4 (d, $J_{C,F}$ = 10.5 Hz) (4×CH), 115.4 ($^1J_{C,H}$ = 96.8, $J_{C,F}$ = 4.4 Hz, β-CH), 120.8, 122.1 (d, $J_{C,F} \approx$ 1 Hz), 122.7 (d, $J_{C,F} \approx$ 1 Hz), 125.7, 129.4, 129.6 (6×quat. C), 223.6 (d, $J_{C,F}$ = 4.4 Hz, α-C) ppm; the C atoms of the pyridine were not found. ^{19}F{^{1}H} NMR (C_6D_6): δ = –95.7 (m), –97.4 (m), –112.6 (m), –114.6 (m) ppm. MS: *m*/*z* 675 $[M]^+$, 524 $[M - C_5F_4N]^+$, 504 $[M - C_8H_{19}Si_2]^+$, 354 $[M - C_5F_4N - C_8H_{19}Si_2]^+$.

Preparation of Complexes 5a/b: These were prepared as described above starting from complex **2** (243 mg, 0.43 mmol) and 2,3,4,6-tetrafluoropyridine (49 μL, 0.48 mmol) in *n*-heptane (10 mL). After 1.5 h at 60 °C the green solution had become red-brown and a yellow precipitate had formed which was filtered off to give a 1:2 mixture of complexes **5a** and 5**b**. Yield 233 mg (75%). M.p. 180–181 °C (dec.). $C_{33}H_{43}F_4NSi_2Zr$ (675.19): calcd. C 58.54, H 6.40, N 2.07; found C 58.30, H 6.28, N 2.01. ^{1}H NMR (C_6D_6): **5a**: δ = 0.15 (s, 9 H, β-$SiMe_3$), 0.40 (s, 9 H, α-$SiMe_3$), 0.6–2.7 (20 H, CH_2), 5.17 (t, $J_{H,F} \approx {}^3J_{H,H} \approx$ 2.6 Hz, 1 H, CH), 5.83 (t, $J_{H,F} \approx {}^3J_{H,H} \approx$ 3.0 Hz, 1 H, CH), 5.99 (dd, $J_{H,F} \approx$ 1.5, $^3J_{H,H} \approx$ 2.9 Hz, 1 H, CH), 6.40 (d, $J_{H,F}$ = 3.7 Hz, 1 H, =CHβ), 6.42 (d, $^3J_{H,H}$ = 2.8 Hz, 1 H, CH) ppm. **5b**: δ = 0.18 (s, 9 H, β-$SiMe_3$), 0.41 (s, 9 H, α-$SiMe_3$), 0.6–2.7 (20 H, CH_2), 5.18 (t, $J_{H,F} \approx {}^3J_{H,H} \approx$ 2.6 Hz, 1 H, CH), 5.80 (t, $J_{H,F} \approx {}^3J_{H,H} \approx$ 3.0 Hz, 1 H, CH), 5.95 (dd, $J_{H,F} \approx$ 1.6, $^3J_{H,H} \approx$ 2.6 Hz, 1 H, CH), 6.39 (d, $J_{H,F}$ = 3.7 Hz, 1 H, =CHβ), 6.45 (d, $^3J_{H,H}$ = 2.8 Hz, 1 H, CH) ppm. ^{13}C{^{1}H} NMR (C_6D_6): **5a**: δ = 0.9 (β-$SiMe_3$), 3.4 (α-$SiMe_3$), 21.9, 22.2, 22.4, 22.8, 23.3 (2 C), 23.9, 25.6, 27.8, 28.3 (10×CH_2), 99.7, 104.2 (d, $J_{C,F}$ = 4.2 Hz), 105.1, 106.7 (d, $J_{C,F}$ = 11.0 Hz) (4×CH), 116.1 (d, $J_{C,F}$ = 3.3 Hz, =CHβ), 120.5, 121.7 (d, $J_{C,F} \approx$ 1 Hz), 122.9 (d, $J_{C,F} \approx$ 1 Hz), 125.7, 129.5, 129.6 (6×quat. C), 225.2 (d, $J_{C,F}$ = 4.0 Hz, α-C) ppm; **5b**: δ = 1.0 (β-$SiMe_3$), 3.4 (α-$SiMe_3$), 21.8, 22.3, 22.4, 22.7, 23.4 (2 C), 24.2, 25.2 (d, $J_{C,F} \approx$ 1 Hz), 27.8, 28.5 (10×CH_2), 99.9, 103.0 (d, $J_{C,F}$ = 3.9 Hz), 105.1, 105.9 (d, $J_{C,F}$ = 10.0 Hz) (4×CH), 116.7 ($^1J_{C,H} \approx$ 100, $J_{C,F}$ = 3.5 Hz, =CHβ), 119.9, 121.8 (d, $J_{C,F} \approx$ 1 Hz), 122.4 (d, $J_{C,F} \approx$ 1 Hz), 125.6, 129.2, 129.6 (6×quat. C), 222.9 (d, $J_{C,F}$ = 4.7 Hz, α-C) ppm; the C-atoms of the pyridine were not found. ^{19}F{^{1}H} NMR (C_6D_6): **5a**: δ = –43.9 (m), –88.0 (m), –92.7 (m), –171.5 (m) ppm. **5b**: δ = –41.9 (m), –90.0 (m), –93.7 (m), –170.3 (m) ppm. The molar ratio **a/b** is about ½. MS: *m*/*z* 675 $[M]^+$, 354 $[M - C_5F_4N - C_8H_{19}Si_2]^+$.

Preparation of Complex 6: This was prepared as described above starting from complex **1b** (553 mg, 1.2 mmol) and pentafluoropyridine (142 μL, 1.3 mmol) in *n*-hexane (15 mL). The violet solution became red-brown after 16 h at 60 °C and a dark precipitate formed which was filtered, washed with *n*-hexane and recrystallised from benzene. Yield 308 mg (67%). M.p. 134 °C (dec.). $C_{15}H_{10}F_5NZr$ (388.98): calcd. C 46.14, H 2.58, N 3.59; found C 45.99, H 2.30, N 3.36. ^{1}H NMR (C_6D_6): δ = 5.67 (s, 10 H, Cp) ppm. ^{13}C{^{1}H} NMR (C_6D_6): δ = 113.59 (Cp) ppm. ^{19}F{^{1}H} NMR (C_6D_6): δ = 1.3 (s, Zr–F), –89.8 (br), –138.4 (m) ppm. MS: *m*/*z* 389 $[M]^+$, 370 $[M - F]^+$, 239 $[M - C_5F_4N]^+$.

Preparation of Complex 7: This was prepared as described above starting from complex **1b** (667 mg, 1.42 mmol) and 3-chloro-2,4,5,6-tetrafluoropyridine (168 μL, 1.48 mmol) in *n*-heptane (20 mL). The violet solution immediately became brown and a beige precipitate formed. The solvent was removed in a vacuum and the residue was recrystallised from benzene. Yield 251 mg (73%). M.p. 162 °C (dec.). $C_{15}H_{10}ClF_4NZr$ (404.95): calcd. C 44.27, H 2.48, N 3.44; found C 44.44, H 2.55, N 3.25. ^{1}H NMR (C_6D_6): δ = 5.73 ppm; ([D$_8$]toluene, 90 °C): δ = 5.84 (s, 10 H, Cp) ppm. ^{13}C{^{1}H} NMR (C_6D_6): δ = 113.9 ppm; ([D$_8$]toluene, 90 °C): δ = 114.3 (Cp), 133.7, 151.0, 157.1, 161.9 (4×d, C–F) ppm; Zr–C atom not found. ^{19}F{^{1}H} NMR (C_6D_6): δ = –43.5 (br), –88.0 (br), –91.4 (m), –169.4 (m) ppm. MS: *m*/*z* 405 $[M]^+$, 370 $[M - Cl]^+$, 255 $[M - C_5F_4N]^+$, 131 $[M - ZrC_5F_4NCl]^+$.

Acknowledgments

This work was supported by the Deutsche Forschungsgemeinschaft (SPP, 1118, Project No. Ro 1269/6), the Land Mecklenburg-Vorpommern and the Russian Foundation for Basic Research (Project No. 05-03-32515). Funding and facilities provided by the Leibniz-Institut für Organische Katalyse an der Universität Rostock are gratefully acknowledged. We thank our technical staff, in particular Petra Bartels and Regina Jesse, for assistance.

[1] A. Ohff, S. Pulst, C. Lefeber, N. Peulecke, P. Arndt, V. V. Burlakov, U. Rosenthal, *Synlett* **1996**, 111–118.
[2] U. Rosenthal, P.-M. Pellny, F. G. Kirchbauer, V. V. Burlakov, *Acc. Chem. Res.* **2000**, *33*, 119–129.
[3] U. Rosenthal, V. V. Burlakov, in *Titanium and Zirconium in Organic Synthesis* (Ed.: I. Marek) Wiley-VCH, Weinheim, **2002**, chapter 10, p. 355–390.

[4] U. Rosenthal, V. V. Burlakov, P. Arndt, W. Baumann, A. Spannenberg, *Organometallics* **2003**, *22*, 884–900.
[5] U. Rosenthal, P. Arndt, W. Baumann, V. V. Burlakov, A. Spannenberg, *J. Organomet. Chem.* **2003**, *670*, 84–96.
[6] U. Rosenthal, *Angew. Chem.* **2003**, *115*, 1838–1842; *Angew. Chem. Int. Ed.* **2003**, *42*, 1794–1798.
[7] A. Spannenberg, P. Arndt, W. Baumann, U. Rosenthal, *J. Organomet. Chem.* **2003**, *683*, 261–266.
[8] U. Rosenthal, *Angew. Chem.* **2004**, *116*, 3972–3977; *Angew. Chem. Int. Ed.* **2004**, *43*, 3882–3887.
[9] A. Spannenberg, P. Arndt, W. Baumann, U. Rosenthal, *J. Organomet. Chem.* **2003**, *683*, 261–266.
[10] U. Rosenthal, in *Acetylene Chemistry II. Chemistry, Biology, and Material Science* (Eds.: F. Diederich, P. J. Stang, R. R. Tykwinski) Wiley-VCH, Weinheim, **2003**, chapter 4, p. 139–171.
[11] J. L. Kiplinger, T. G. Richmond, C. E. Osterberg, *Chem. Rev.* **1994**, *94*, 373–431.
[12] J. Burdeniuc, B. Jedlicka, R. H. Crabtree, *Chem. Ber./Recueil* **1997**, *130*, 145–154.
[13] T. G. Richmond, *Angew. Chem.* **2000**, *112*, 3378–3380; *Angew. Chem. Int. Ed.* **2000**, *39*, 3241–3244.
[14] T. G. Richmond, in *Topics in Organometallic Chemistry*, Vol. 3 (Ed.: S. Murai) Springer, New York, **1999**, p. 243–269.
[15] W. D. Jones, *Dalton Trans.* **2003**, 3991–3995.
[16] U. Mazurek, H. Schwarz, *Chem. Commun.* **2003**, 1321–1326.
[17] P. M. Treichel, M. A. Chaudhari, F. G. A. Stone, *J. Organomet. Chem.* **1963**, *1*, 98–100.
[18] M. J. Burk, D. L. Staley, W. Tumas, *J. Chem. Soc., Chem. Commun.* **1990**, 809–810.
[19] C. Santamaria, R. Beckhaus, D. Haase, W. Saak, R. Koch, *Chem. Eur. J.* **2001**, *7*, 622–655.
[20] P. A. Deck, M. A. Konate, B. V. Kelly, C. Slebodnik, *Organometallics* **2004**, *23*, 1089–1097, and references cited therein.
[21] M. W. Bouwkamp, J. de Wolf, I. d. H. Morales, J. Gercama, A. Meetsma, S. I. Troyanov, B. Hessen, J. H. Teuben, *J. Am. Chem. Soc.* **2002**, *124*, 12956–12957.
[22] J. L. Kiplinger, T. G. Richmond, *Chem. Commun.* **1996**, 1115–1116.
[23] J. L. Kiplinger, T. G. Richmond, *J. Am. Chem. Soc.* **1996**, *118*, 1805–1806.
[24] B.-H. Kim, H.-G. Woo, W.-G. Kim, S.-S. Yun, T.-S. Hwang, *Bull. Korean Chem. Soc.* **2000**, *21*, 211–214.
[25] B. L. Edelbach, A. K. F. Rahman, R. J. Lachicotte, W. D. Jones, *Organometallics* **1999**, *18*, 3170–3177.
[26] B. L. Edelbach, B. M. Kraft, W. D. Jones, *J. Am. Chem. Soc.* **1999**, *121*, 10327–10331.
[27] B. M. Kraft, R. J. Lachicotte, W. D. Jones, *J. Am. Chem. Soc.* **2000**, *122*, 8559–8560.
[28] B. M. Kraft, R. J. Lachicotte, W. D. Jones, *J. Am. Chem. Soc.* **2001**, *123*, 10973–10974.
[29] B. M. Kraft, R. J. Lachicotte, W. D. Jones, *Organometallics* **2002**, *21*, 727–731.
[30] B. M. Kraft, W. D. Jones, *J. Organomet. Chem.* **2002**, *658*, 132–140.
[31] E. Clot, C. Megret, B. M. Kraft, O. Eisenstein, W. D. Jones, *J. Am. Chem. Soc.* **2004**, *126*, 5647–5653.
[32] L. A. Watson, D. V. Yandulov, K. G. Caulton, *J. Am. Chem. Soc.* **2001**, *123*, 603–604.
[33] H. M. Hoyt, F. E. Michael, R. G. Bergman, *J. Am. Chem. Soc.* **2004**, *126*, 1018–1019.
[34] S. Becke, U. Rosenthal (Bayer AG), US 6,303,718 B1 (October 16, 2001).
[35] S. Becke, U. Rosenthal, P. Arndt, W. Baumann, A. Spannenberg (Bayer AG), DE 101 10 227 A1 (September 05, 2002).
[36] A. Spannenberg, P. Arndt, W. Baumann, V. V. Burlakov, U. Rosenthal, S. Becke, T. Weiß, *Organometallics* **2004**, *23*, 3819–3825.
[37] P. Arndt, A. Spannenberg, W. Baumann, V. V. Burlakov, U. Rosenthal, S. Becke, T. Weiß, *Organometallics* **2004**, *23*, 4792–4795.
[38] U. Jäger-Fiedler, P. Arndt, W. Baumann, V. V. Burlakov, A. Spannenberg, U. Rosenthal, *7th North-German Colloquium of PhD Students of Inorganic Institutes,* Hamburg, **2004**, September 29–30, abstracts 4.1.
[39] X. Yang, C. L. Stern, T. J. Marks, *J. Am. Chem. Soc.* **1994**, *116*, 10015–10031.
[40] S. Kraft, R. Beckhaus, D. Haase, W. Saak, *Angew. Chem.* **2004**, *116*, 1609–1614; *Angew. Chem. Int. Ed.* **2004**, *43*, 1583–1587.
[41] I. M. Piglosiewicz, *Diploma Thesis*, University of Oldenburg, **2004**.
[42] I. M. Piglosiewicz, S. Kraft, R. Beckhaus, D. Haase, W. Saak, *Eur. J. Inorg. Chem.* **2005**, in press.
[43] S. Kraft, E. Hanuschek, R. Beckhaus, D. Haase, W. Saak, *Chem. Eur. J.* **2005**, *11*, 969–978.
[44] T. Braun, R. N. Perutz, *Chem. Commun.* **2002**, 2749–2757.
[45] N. A. Jasim, R. N. Perutz, A. C. Whitwood, T. Braun, J. Inzundu, B. Neumann, S. Rothfeld, H.-G. Stammler, *Organometallics* **2004**, *23*, 6140–6149.
[46] D. Noveski, T. Braun, B. Neumann, A. Stammler, H.-G. Stammler, *Dalton Trans.* **2004**, 4106–4119.
[47] M. Reinhold, J. E. McGrady, R. N. Perutz, *J. Am. Chem. Soc.* **2004**, *126*, 5268–5276, and references cited therein.
[48] A. Spannenberg, U. Jäger-Fiedler, P. Arndt, U. Rosenthal, *Z. Krist.* **2005**, in press.
[49] D. Thomas, N. Peulecke, V. V. Burlakov, B. Heller, W. Baumann, A. Spannenberg, R. Kempe, U. Rosenthal, R. Beckhaus, *Z. Anorg. Allg. Chem.* **1998**, *624*, 919–924.
[50] P. Arndt, C. Lefeber, A. Tillack, U. Rosenthal, *Chem. Ber.* **1996**, *129*, 1281–1285.
[51] P. Arndt, W. Baumann, A. Spannenberg, U. Rosenthal, V. V. Burlakov, V. B. Shur, *Angew. Chem.* **2003**, *115*, 1455–1458; *Angew. Chem. Int. Ed.* **2003**, *42*, 1414–1418.
[52] A. Spannenberg, P. Arndt, W. Baumann, V. V. Burlakov, U. Rosenthal, S. Becke, T. Weiß, *Organometallics* **2004**, *23*, 3819–3825.
[53] R. D. Ernst, B. G. Harvey, A. M. Arif, *Z. Kristallogr., New Cryst. Struct.* **2003**, *47*, 218–219.
[54] G. M. Sheldrick, *Acta Crystallogr. Sect. A* **1990**, *46*, 467–473.
[55] G. M. Sheldrick, *SHELXL-93*, University of Göttingen, Germany, **1993**.

Received: February 18, 2005
Published Online: June 9, 2005

 © 2005 Wiley-VCH Verlag GmbH & Co. KGaA, Weinheim

Ethylene Homo- and Copolymerization Activity of a Series of [ONNO]-Type Amine Bis(phenolate) Based Vanadium(II–V) Catalysts

Christian Lorber,*[a] Fabien Wolff,[a] Robert Choukroun,[a] and Laure Vendier[a]

Keywords: Vanadium / Amine (bis)phenolates / Polymerization / Copolymer / Crystal structure / Olefins

The synthesis and structural characterization of new paramagnetic amine bis(phenolate) [ONNO]-vanadium(III) and -vanadium(II) complexes, V^{III}(acac)[ONNO], V^{III}(Cl)(THF)[ONNO], and V^{II}(TMEDA)[ONNO], is described. These compounds complete the family of [ONNO]-vanadium(IV/V) complexes previously reported. The members of the [ONNO]-vanadium family at various oxidation states that range from vanadium(II) to vanadium(V), in association with $EtAlCl_2$ cocatalyst, were studied in the polymerization of ethylene and in the copolymerizations of ethylene-1-hexene and ethylene-norbornene. Poly(ethylene-*co*-1-hexene) and poly(ethylene-*co*-norbornene) were produced with co-monomer content of up to 11 mol-% and 29 mol-% for 1-hexene and norbornene, respectively.
(© Wiley-VCH Verlag GmbH & Co. KGaA, 69451 Weinheim, Germany, 2005)

Introduction

In the past decade, a tremendous amount of effort has been devoted to the design of new "non-metallocene" group 4 transition metal complexes because of their importance as α-olefin polymerization catalysts.[1] Particularly, chelating diamide,[1a,2–4] dialkoxide,[1a,5–6] or phenoxyimine[7,8] ligands have been extensively studied as rigid supporting environments for titanium and zirconium complexes, which has resulted in the emergence of a great deal of novel and useful chemistry, including the discovery of highly active olefin polymerization precatalysts. Among these new ligands, chelating, dianionic [ONNO]-type amine bis(phenolate) ligands associated with group 4 metal complexes[5] have proven to be highly active 1-hexene polymerization catalysts, and in some cases, even isospecific living polymerization was possible.[5a] Recently yttrium-[ONNO] complexes have been reported for their catalytic activity in the ring-opening polymerization of ε-caprolactone.[9]

Vanadium-based catalysts in homogeneous Ziegler–Natta polymerization have been known for about half a century.[10] Although generally less active, their use presents a number of interesting advantages over group 4 metal catalysts:[11] (i) the synthesis of high molecular weight polymers with narrow polydispersity, (ii) the preparation of ethylene/α-olefin copolymers with high α-olefin incorporation, and (iii) the preparation of syndiotactic polypropylene. The major reason for the low activity of these systems is their deactivation during the polymerization process, probably due to reduction of the catalytically active vanadium species to low-valent, less active or inactive species. Nevertheless, $V(acac)_3$ is currently employed in the synthesis of EP (ethylene–propylene) and EPDM (ethylene–propylene–diene monomer) elastomers.

As part of an ongoing study of vanadium chemistry with various supporting ligands,[12] and in particular of vanadium complexes for olefin polymerization, we have recently used ancillary diamido ligands with sterically demanding protecting groups[13] or imido ligands[14] on vanadium(IV) complexes as a way to overcome the problem of catalyst deactivation by stabilization of the formal oxidation state of the vanadium center. Following this approach, we recently described the synthesis of a series of oxo-vanadium(V)[15] and vanadium(IV)[16] complexes with the ancillary amine bis(phenolate) [ONNO]-type ligand (Figure 1) that are of the type V^{V}(=O)(X)[ONNO] {X = O*i*Pr (**1**), N_3 (**2**), Cl (**3**) and V^{IV}(Y)[ONNO] (Y = O*i*Pr (**4**), Cl (**5**)}, and we demonstrated interesting features in the solution and the solid-state structure of these unprecedented complexes. To complete our study on this new family of complexes, we wish to report here on the synthesis, and structural characterization, of new vanadium(III) and vanadium(II) complexes supported by [ONNO]-type bis(phenoxy)amine ligand, and to compare their ethylene homo- and copolymerization activity with other members of the vanadium(II–V) complex family.

Results and Discussion

In previous articles we have described the synthesis of [ONNO]-type amine bis(phenolate) complexes of oxo-vanadium(V) [**1**–**3**] and vanadium(IV) [**4**–**5**].[15,16] Although vanadium complexes with oxidation numbers from +3 to +5 are known to catalyze ethylene polymerization, the active spe-

[a] Laboratoire de Chimie de Coordination du CNRS, UPR 8241, 205 route de Narbonne, 31077 Toulouse Cedex 04, France
Fax: +33-5-61-55-30-03
E-mail: lorber@lcc-toulouse.fr

 © 2005 Wiley-VCH Verlag GmbH & Co. KGaA, Weinheim **DOI: 10.1002/ejic.200500149**

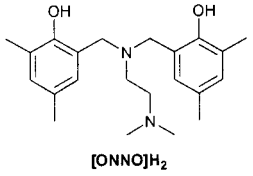

V^{V}(=O)(O*i*Pr)[ONNO]	**1**
V^{V}(=O)(N_3)[ONNO]	**2**
V^{V}(=O)(Cl)[ONNO]	**3**
V^{IV}(O*i*Pr)$_2$[ONNO]	**4**
V^{IV}(Cl)$_2$[ONNO]	**5**
V^{III}(acac)[ONNO]	**6**
V^{III}(Cl)(THF)[ONNO]	**7**
V^{II}(TMEDA)[ONNO]	**8**

Figure 1. Structure of [ONNO]-type bis(phenoxy)amine ligand and designation of Vanadium-[ONNO] complexes used in this study.

cies is probably a vanadium(III) complex. Vanadium(II) species are generally considered inactive. To verify this point, we decided to prepare vanadium(III) and vanadium(II) compounds containing the [ONNO] ligand and to test the whole family of [ONNO]-vanadium complexes as olefin polymerization catalysts.

Synthesis of the Vanadium(III) and Vanadium(II) Complexes

Reacting V(acac)$_3$ with 1 equiv. of [ONNO]H$_2$ in toluene at 80 °C for 14 h afforded, after workup, the desired vanadium(III) complex V(acac)[ONNO] (**6**) as an orange solid with 87% yield (Scheme 1). Accordingly, **6** is a d^2-paramagnetic, NMR-silent compound with an effective magnetic moment μ_{eff} of 2.91 μ_B at 20 °C.

$$V(acac)_3 + [ONNO]H_2 \xrightarrow[-\ 2\ acacH]{toluene,\ 80\,°C} \underset{\mathbf{6}}{V(acac)[ONNO]}$$

Scheme 1. Synthesis of trivalent complex V(acac)[ONNO].

When 1 equiv. of K$_2$[ONNO] was slowly added to a THF solution of VCl$_3$(THF)$_3$ at ambient temperature there was an immediate reaction (Scheme 2). After careful workup and recrystallization in THF/toluene–pentane, yellow crystals of V(Cl)(THF)[ONNO] (**7**) were obtained (yield 31%). As for **6**, complex **7** is NMR-silent, and room temperature magnetic susceptibility measurements gave a μ_{eff} of 2.87 μ_B.

$$VCl_3(THF)_3 + K_2[ONNO] \xrightarrow[-\ 2\ KCl]{THF,\ r.t.} \underset{\mathbf{7}}{V(Cl)(THF)[ONNO]}$$

Scheme 2. Synthesis of trivalent complex V(Cl)(THF)[ONNO].

An entry to the [ONNO]-vanadium(II) chemistry was successfully achieved by reacting the vanadium(II) precursor VCl$_2$(tmeda)$_2$ [tmeda *N*,*N*,*N*′,*N*′-tetramethylethylenediamine] with 1 equiv. of K$_2$[ONNO] at room temperature whilst stirring in THF for 2 h to give red crystals of complex V(tmeda)[ONNO] (**8**) (Scheme 3). Complex **8** is a high-spin d^3-paramagnetic, NMR-silent compound with a μ_{eff} of 3.90 μ_B at 20 °C.

$$VCl_2(tmeda)_2 + K_2[ONNO] \xrightarrow[-\ 2\ KCl\ -\ tmeda]{THF,\ r.t.} \underset{\mathbf{8}}{V(tmeda)[ONNO]}$$

Scheme 3. Synthesis of divalent complex V(tmeda)[ONNO].

X-ray Structure Determination

During the course of our investigation, crystals of [ONNO]H$_2$ were obtained from a cold dichloromethane/pentane solution (–20 °C), and we report its molecular structure with an ORTEP diagram shown in Figure 2.[17] The main features of the solid-state structure is the tripodal configuration that adopts the ligand framework; this arrangement seems to arise from three intramolecular hydrogen-bond interactions between O1–HO1···N1 (2.05 Å, 146.0°), O1–HO1···O2 (2.54 Å, 130.4°), and O2–HO2···N2 (2.03 Å, 151.6°).

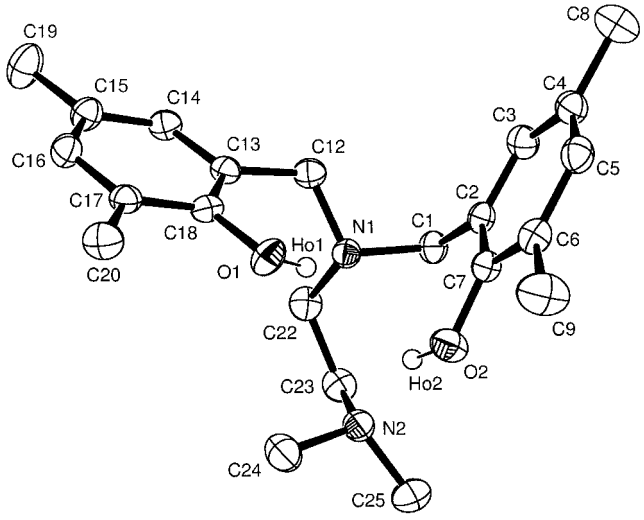

Figure 2. Ortep drawing of the molecular structure of [ONNO]H$_2$ showing 50% probability ellipsoids. Hydrogen atoms are omitted for clarity. Selected parameters (bonds, Å; angles, °): N1–C12 1.467(3), N1–C1 1.482(3), N1–C22 1.473(3), C18–O1 1.371(2), C7–O2 1.367(2), N2–C23 1.462(3), N2–C24 1.467(3), N2–C25 1.465(3), O1–H···N1 2.05, O1–H1···O2 2.54, O2–H2···N2 2.03, O1–H–N1 146.0, O1–H1–O2 130.4, O2–H2–N2 151.6.

Crystals of all three complexes (**6**–**8**) were obtained: red-orange crystals of **6** were obtained by careful layering a toluene solution of **6** with pentane, yellow crystals of **7** by low-temperature crystallization in THF/toluene–pentane solution, and red crystals of **8** by layering a toluene solution of **8** with pentane. The thermal ellipsoid plots are depicted in Figure 3, Figure 4, and Figure 5, with a comparison of selected bond lengths and angles in Table 1. Complex **8** presents two independent molecules in the cell with very similar structural parameters; therefore only one of these molecules will be described here. The solid-state structures confirm our first formulations: complexes **6**–**8** are mononuclear complexes, containing an octahedrally coordinated vanadium(III) center surrounded by a tetradentate [ONNO] ligand and one acac ligand (**6**), a chlorine atom and a THF solvate

 © 2005 Wiley-VCH Verlag GmbH & Co. KGaA, Weinheim

molecule (**7**), and tmeda ligand (**8**). With regard to the [ONNO] ligand, in all complexes, the two phenolate rings have a *trans* configuration, and both amino-nitrogen donor atoms are coordinated to the metal center; these features are ones that they share with their group 4- and other vanadium-[ONNO] analogues.[5b,5d–f,15,16] Bonding distances between the metal center and the O and N donors of [ONNO] are in the range typically observed for such complexes: (i) V–O(phenoxide) distances are ca. 1.9–2.0 Å, which is slightly longer than those of higher oxidation state [ONNO]-vanadium(v/iv) analogues by about 0.1 Å,[14,15] (ii) the two vanadium–nitrogen bonds formed between the metal center and the tripodal amino-N atom and the dimethylamino sidearm N atom have distances that range from 2.13 to 2.32 Å. Bonds formed by vanadium and the additional ligands are typical: V–O(acac) approximately 2.00 Å (in **6**), V–Cl1 = 2.377(2) Å (in **7**), V–O(THF) = 2.131(4) Å (in **7**), and V–N(TMEDA) = 2.302(8) and 2.383(8) Å (in **8**).

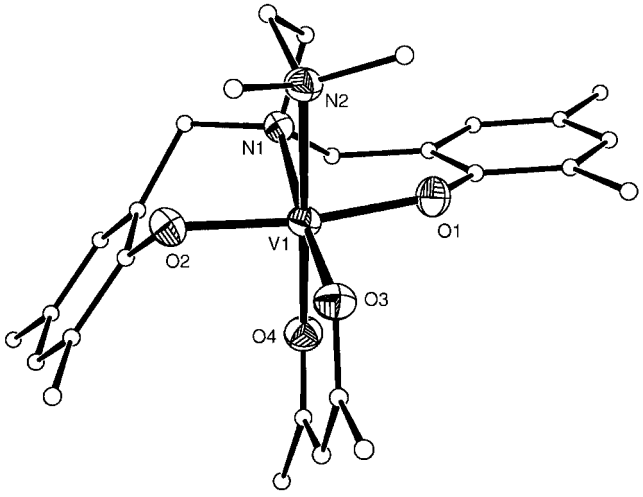

Figure 3. Ortep drawing of the molecular structure of **6** showing 50% probability ellipsoids (except on C atoms for clarity) and partial atom-labeling schemes. Hydrogen atoms are omitted for clarity.

The crystals of **7** contain the isomer with the chlorine atom *trans* to the dimethylaminoethyl sidearm and the THF ligand *trans* to the tripodal nitrogen atom of [ONNO]. However, because of the paramagnetism of the complex and the impossibility of recording its NMR spectrum we cannot exclude the presence of the other isomer (with the Cl atom *trans* to the tripodal N atom) in solution.

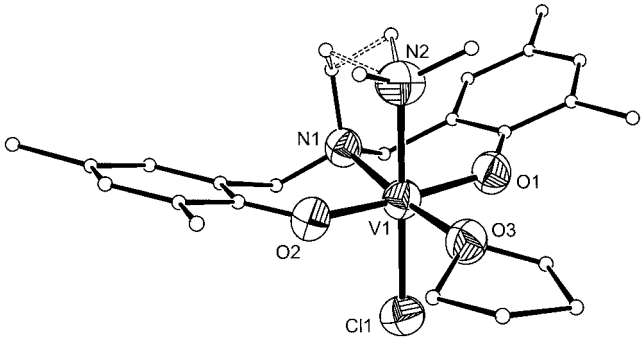

Figure 4. Ortep drawing of the molecular structure of **7** showing 50% probability ellipsoids (except on C atoms for clarity) and partial atom-labeling schemes. Hydrogen atoms are omitted for clarity.

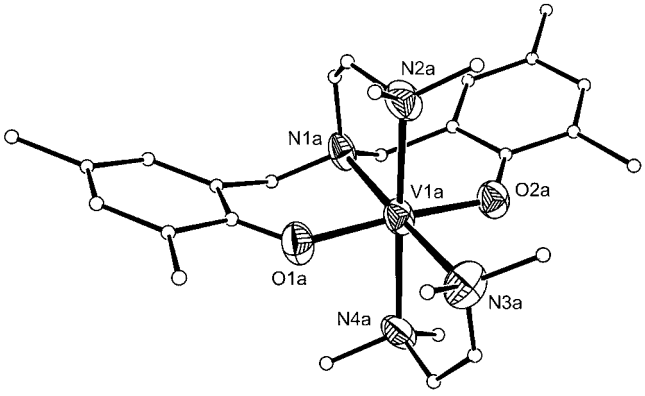

Figure 5. Ortep drawing of the molecular structure of molecule A of **8** showing 50% probability ellipsoids (except on C atoms for clarity) and partial atom-labeling schemes. Hydrogen atoms are omitted for clarity.

Interestingly, the configuration of the [ONNO] fragment in the crystal structure of **6** is very different from that of **7** and **8**. The configuration of the [ONNO] ligand in **7** and **8**

Table 1. Selected structural parameters for complexes **6**–**8** (distances are given in Å and angles in °).[a]

	V(acac)[ONNO] (**6**)	V(Cl)(THF)[ONNO] (**7**)	V(tmeda)[ONNO] (**8**)[b]
V–O1	1.9179(12)	1.895(4)	2.060(7)
V–O2	1.9317(12)	1.906(4)	2.065(7)
V–N1	2.2020(14)	2.126(4)	2.215(8)
V–N2	2.2147(14)	2.233(5)	2.322(8)
V–X1	1.9761(13) (*O3*)	2.377(2) (*Cl1*)	2.302(8) (*N3*)
V–X2	1.9979(12) (*O4*)	2.131(4) (*O3*)	2.383(8) (*N4*)
O1–V–O2	170.15(5)	173.90(18)	174.1(3)
N1–V–N2	82.62(5)	82.29(17)	79.3(3)
X1–V–X2	90.34(5)	91.73(12)	80.5(3)
V–O1–$C_{phenolate}$	135.4(1)	132.7(4)	130.3(7)
V–O2–$C_{phenolate}$	116.2(1)	132.9(3)	130.1(6)
δ[c]	+132	–142	–150

[a] X1 = X2 = O_{acac} (**6**) or N_{tmeda} (**8**); X1 = Cl, X2 = O_{THF} (**7**). [b] For independent molecule A. [c] Angle defined by the two planes containing the two phenolate aromatic rings; the + sign refers to a folding away from the NMe_2 sidearm, whereas the – sign refers to a folding towards the NMe_2 sidearm.

 © 2005 Wiley-VCH Verlag GmbH & Co. KGaA, Weinheim

is symmetry related [the two aromatic rings of the bis(phenolate) framework (without the sidearm)]; the phenolate groups of the [ONNO] framework fold in towards the pendant (dimethylamino)ethyl sidearm, and the angle between the two planes of the aromatic rings are approximately –142° (**7**) and –151° (**8**) [the minus sign refers to a folding towards the NMe_2 sidearm; in contrast, the folding away from the NMe_2 sidearm has a positive sign]. In contrast, the phenolate groups of the [ONNO] ligand of **6** fold back away from the pendant (dimethylamino)ethyl sidearm; the angle δ between the two planes of the aromatic rings is now about +116° with a molecular structure that has two non-symmetry-related phenolate rings. Such a helicoidal distortion of the tripodal amino nitrogen donor atom induces a lower symmetry in the ligand framework of **6**, as already observed in the solid-state structure of two other [ONNO]-vanadium complexes,[15,16] and seems to arise from the presence of an O-ligated anionic ligand (alkoxo, oxo, acac) in a *trans* position to the (dimethylamino)ethyl sidearm nitrogen donor atom. Figure 6 presents a summary of the geometry of all the [ONNO]-vanadium compounds that we have prepared.

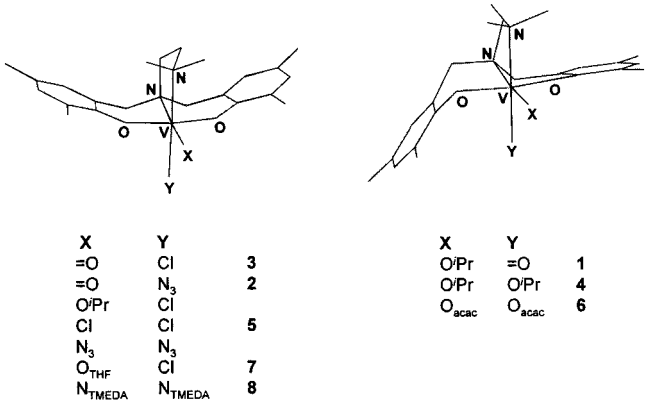

Figure 6. Symmetrical and non-symmetrical geometry in [ONNO]-Vanadium(II–IV) complexes.

Homopolymerization Studies

Together with the [ONNO]-vanadium complexes that present oxidation states of +5 and +4 reported by us in previous articles,[15,16] we are now introducing a family of vanadium complexes that are supported by the same ancillary ligand and that stabilize four oxidation states of the metal center (from +2 to +5), which allows us the opportunity to evaluate their activity toward the homopolymerization of ethylene, propene, and 1-hexene.

Ethylene Polymerization

Preliminary studies conducted on **6** with MAO cocatalyst (500 equiv.) under 1 bar of ethylene failed to produce polyethylene. We had already observed such behavior with other vanadium catalysts that do not possess V–Cl bonds.[14] Moreover, it is well known that vanadium catalysts give higher polymerization activities or polymers with lower polydispersity indices upon activation with simple chloroalkylaluminum reagents (such as $EtAlCl_2$ or Et_2AlCl) rather than MAO.[11b,11c,14,18,19] As a result, all of our further studies were conducted with $EtAlCl_2$ as cocatalyst.

The catalyst activity of the vanadium(II–V) complexes **1**–**8** of the [ONNO] ligand for the polymerization of ethylene has been evaluated under the same set of conditions of 10 equiv. of $EtAlCl_2$ under 1 atm of ethylene at 20 °C in toluene (except for catalysts **2** and **3** that are not soluble in toluene, and these reactions were thus conducted in dichloromethane). The results are summarized in Table 2 and are classified by the oxidation states of the catalysts; a comparison with standard V-based catalysts VCl_4, VCl_4·DME, and $V(acac)_3$ tested in our hands under the same experimental conditions is also presented.

Under these conditions, [ONNO]-vanadium(V) complexes **2** and **3** exhibit modest activities ranging from 17 to 22 $kg_{PE}\,mol^{-1}{}_{[V]}\,h^{-1}$, a number comparable to other vanadium systems described in the literature.[1a,11,14,18] This modest activity may be attributable to the use of dichloromethane as solvent; catalyst **1** gives a much higher produc-

Table 2. Ethylene polymerization promoted by various vanadium catalysts [conditions: catalyst (about 10 mg, ca. 0.01 mmol) in 10 mL of solvent; $EtAlCl_2$ cocatalyst (10 equiv.); ethylene (1 bar); time of polymerization 15 min run, except when the solution solidifies to give a polymer gel, the asterix (*) denotes such a reaction].

Catalyst	Solvent	Time [min]	Yield [mg]	Activity[a]	T_m [°C][b]	M_w [g/mol × 10^{-3}][c]	M_n [g/mol × 10^{-3}][c]	M_w/M_n[c]
$V^{V}O(O^iPr)$[ONNO] (**1**)	toluene	5*	227	272	134.0	118	44	2.65
$V^{V}O(N_3)$[ONNO] (**2**)	CH_2Cl_2	15	55	22	138.7	146	32	4.60
$V^{V}O(Cl)$[ONNO] (**3**)	CH_2Cl_2	15	42	17	136.4	716	190	3.76
$V^{IV}(O^iPr)_2$[ONNO] (**4**)	toluene	3*	237	474	138.7	677	338	2.00
$V^{IV}(Cl)_2$[ONNO] (**5**)	toluene	15	156	62	139.0	889	438	2.03
VCl_4	toluene	10*	373	22	135.1	152	19	8.13
VCl_4·DME	toluene	4*	250	200	137.5	152	48	3.19
V^{III}(acac)[ONNO] (**6**)	toluene	3*	218	436	133.4	673	202	3.33
V^{III}(acac)[ONNO] (**6**)	pentane	5*	268	322	128.5	1003	381	2.63
V^{III}(Cl)(THF)[ONNO] (**7**)	toluene	15	129	52	135.2	458	204	2.24
$V(acac)_3$	toluene	10*	141	85	135.8	176	72	2.43
V^{II}(tmeda)[ONNO] (**8**)	toluene	15	4	1	–	2259	745	3.03

[a] In $kg_{PE}\,mol^{-1}\,h^{-1}\,atm^{-1}$. [b] Determined by DSC. [c] Determined by SEC in 1,2,4-trichlorobenzene at 140 °C versus polystyrene standards.

 © 2005 Wiley-VCH Verlag GmbH & Co. KGaA, Weinheim

tivity of 272 $kg_{PE}\,mol^{-1}_{[V]}\,h^{-1}$. Polymer properties are typical of high molecular weight (M_w = 1.18–7.16 × 10^5 $g\,mol^{-1}$), high density polyethylenes [HDPE] (T_m = 134–139 °C), and a reasonably narrow, unimodal polydispersity indice, M_w/M_n = 2.65, is observed with **1**.

Under the above conditions, the activities of the vanadium(IV)-[ONNO] catalysts **4** and **5** are much higher; 474 $kg_{PE}\,mol^{-1}_{[V]}\,h^{-1}$ (**4**) and 62 $kg_{PE}\,mol^{-1}_{[V]}\,h^{-1}$ (**5**). Meanwhile, polydispersity indices are very low (2.00 and 2.03, respectively), which suggests that the active species is well defined, and the [ONNO] ligand remains coordinated to the metal during the catalytic process. Melting temperatures are again very high (ca. 139 °C) corresponding to HDPE.

Vanadium(III)-[ONNO] catalyst **6** is a particularly efficient catalyst; as with **4**, a rapid initial polymerization occurs, which results in the solidification of the solution with formation of a gel of PE in less than 2 min (activity = 436 $kg_{PE}\,mol^{-1}_{[V]}\,h^{-1}$). This problem could be partly resolved by conducting the reaction in pentane. We then observe a slightly lower productivity, but a gain in the polydispersity (3.33 in toluene versus 2.63 in pentane), and a high molecular weight polymer (M_w = 1.00 × 10^6 $g\,mol^{-1}$). Interestingly, ethylene polymerization with the other vanadium(III) catalyst **7** is a little bit slower than with **6**, although the low polydispersity (2.24) suggests again a well-defined active species.

Finally, vanadium(II) complex **8** gives poor yields of PE. As expected, this confirms that this reduced oxidation state of the vanadium center gives only inactive or less active polymerization catalysts. Nevertheless, one cannot exclude that the absence of activity is due to the presence of the chelating TMEDA ligand at the metal center, and additional polymerization experiments with vanadium(III–V) catalysts in the presence of TMEDA will be necessary to address this point.

Although clear trends are not easily apparent (except for the V^{II} state that is inactive), the following conclusion can be drawn: (i) catalysts **2**, **3**, **5**, and **7** with V–Cl or V–N_3 bonds give lower activities relative to catalysts **1**, **4**, and **6** that have alkoxide or acac ligands, (ii) the activities and quality of the polyethylenes obtained with catalysts **1**, **4**, and **6** (with oxidation states +5 to +3) are very similar. This could suggest that these different systems involve a similar catalytically active species that is most probably a [ONNO]-vanadium(III) complex (in the case of **1** and **4**, resulting from the reduction of the V^V or V^{IV} center by the aluminum cocatalyst). Clearly, further studies will be needed to clarify these points.

Propene and 1-Hexene Homopolymerization

Unfortunately, none of the [ONNO]-vanadium complexes could catalyze propene polymerization at 20 °C, even under 4 bar propene, using $EtAlCl_2$ as cocatalyst (V/Al = 1:10). This is surprising as the $V(acac)_3/EtAlCl_2$ system is known to initiate living propene polymerization,[20] but this may result from the strong steric hindrance of the tetradentate dianionic [ONNO] ligand.

Less surprisingly, we were unable to polymerize 1-hexene with our catalysts, even at high temperatures (70 and 135 °C). To the best of our knowledge, V-based catalysts reported for such a reaction are very rare.[21]

Ethylene Copolymerization Studies

The copolymerization of ethylene with α-olefins is a common means of generating polyethylenes with controlled crystallinity and density. These polymers are known as linear low-density polyethylenes (LLDPE). The introduction of short-chain branches originating from the co-monomer decreases the crystallinity and melting temperature of the copolymer as the co-units interfere with crystallization and reduce the size of crystallites. Preliminary studies of the copolymerization of ethylene with 1-hexene and norbonene with our new vanadium compounds are described below.

The copolymerization of ethylene with 1-hexene was conducted at ambient temperature in toluene with complexes **1** and **4**–**7** in the presence of $EtAlCl_2$ cocatalyst (V/Al = 1:10), under 2 bar ethylene with a ratio of 1:800 for catalyst/1-hexene, and was compared to that of $V(acac)_3$ (see Table 3).

Although **7** did not produce any polymer, a white polymeric material was obtained with the other catalysts **1** and **4**–**6**. The ^{13}C NMR spectra (370 K) of the resulting polymers reveals that these catalysts produced poly(ethylene-*co*-hexene)s (EH) typical of EH block copolymers, and the polyethylene sequences are separated by isolated hexene units (no HH dyads are observed; Figure 7 shows a

Table 3. Results of ethylene–1-hexene copolymerization [conditions: catalyst (0.01 mmol) in 10 mL of toluene; $EtAlCl_2$ cocatalyst (10 equiv.); ethylene (2 bar); 1-hexene (8 mmol); time of polymerization 30 min run].

Catalyst	Yield [mg]	Activity[a]	T_m [°C][b]	1-Hexene content [mol%][c]	M_w [g/mol × 10^{-3}][d]	M_n [g/mol × 10^{-3}][d]	M_w/M_n[d]
1	354	78	73.5, 83.6, 92.7, 96.8, 104.2, 120.7	4.0	32	7.6	4.26[e]
4	60	12	62.5, 72.1, 81.1, 91.6, 102.2, 111.2	3.5	73	21	3.53
5	192	38	63.0, 72.6, 82.8, 92.5, 96.1, 105.6, 117.9	4.2	–	–	–
6	600	120	63.5, 73.0, 83.0, 93.1, 107.3	7.4	71	41	1.70
6[f]	702	140	63.3, 72.9, 82.4, 92.6, 103.0, 109.6	3.6	149	72	2.07
6[g]	303	61	62.3, 72.2, 81.9, 91.3, 102.5, 107.1	10.6	33	17	1.90
$V(acac)_3$	838	167	63.6, 73.2, 83.2, 92.9, 103.1, 119.8	7.5	2882	13	225.52

[a] In $kg_{PE}\,mol^{-1}\,h^{-1}$. [b] Determined by DSC. [c] Determined by ^{13}C NMR spectroscopy (370 K). [d] Determined by SEC in 1,2,4-trichlorobenzene at 140 °C versus polystyrene standards. [e] Bimodal distribution. [f] Ethylene (4 bar). [g] Ethylene (1 bar).

 © 2005 Wiley-VCH Verlag GmbH & Co. KGaA, Weinheim

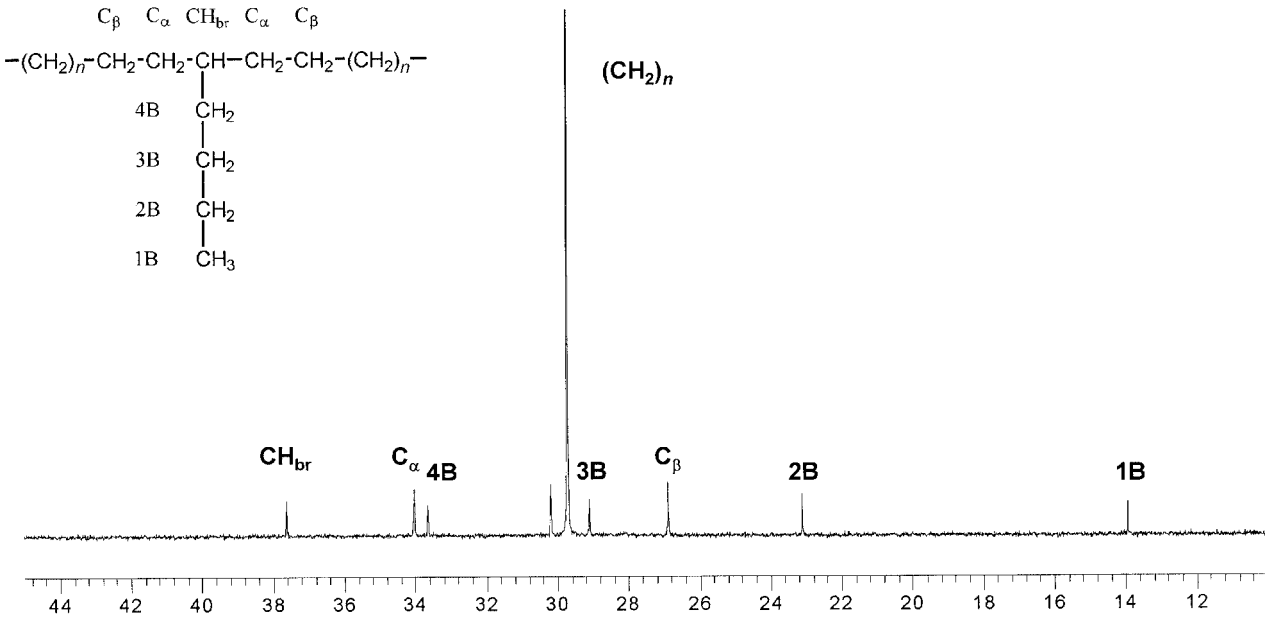

Figure 7. ^{13}C NMR spectrum [370 K, 1,2,4-trichlorobenzene/[D_2]tetrachloroethane] of the ethylene–*co*-1-hexene polymer made using **6**/$EtAlCl_2$.

$^{13}C\{^1H\}$ NMR spectrum of an EH copolymer obtained using **6**/$EtAlCl_2$).

The integration of the signals of 1-hexene versus ethylene in the ^{13}C NMR spectra of these EH copolymers allowed us to determine the 1-hexene incorporation ratio into the copolymers.[22] This value was found to be relatively modest, ca. 4 mol%, with catalysts **1**, **4** and **5**, and slightly higher with **6** (7.4 mol%). Increasing the ethylene pressure to 4 bar (with catalyst **6**) resulted in a decrease in catalyst productivity, whereas (logically) the 1-hexene content diminished to 8.8 mol%. Conversely, lowering the ethylene pressure to 1 bar decreased the activity with incorporation of more 1-hexene units (10.6%). These conditions have not been optimized; in particular, we have also noticed an increase in the 1-hexene content and productivity of **6** by working in a pentane solution.

In all cases, the EH copolymers have a low molecular weight M_w of 32×10^3 (with **1**), 73×10^3 (with **4**) and 71×10^3 (with **6**), but with different molecular weight distributions; the EH copolymers produced by **1** and **4** have a broad molecular weight distribution [PDI = 4.26 (bimodal), and 3.53 for **1**, and **4**, respectively], whereas narrow unimodal polydispersity indices are obtained with **6** at various ethylene pressures [PDI = 1.90 (1 bar), 1.70 (2 bar), and 2.07 (4 bars)].

The effect of the incorporation of 1-hexene into the copolymer on the melting behavior of the EH copolymer is illustrated in Figure 8, which shows the DSC endotherms obtained after step-crystallization of the copolymers made using **6**/$EtAlCl_2$. Furthermore, it has been established that 1-hexene does not enter the crystal lattice of PE, therefore, a DSC analysis can give an idea of the heterogeneity in the co-monomer distribution.[23,24] The DSC thermograms of the EH copolymers show five to six melting temperature values ranging from ca. 63 °C to ca. 111 °C. According to these endotherms, and those found in the literature,[23,24] separations based on different populations of crystalline lamellae have occurred, depending on the amount and distribution of 1-hexene units in the molecular chain ("intrachain heterogeneity"). Long polymer segments recrystallize into larger crystals, which melt at higher temperatures, whereas short segments form small crystals, which melt at lower temperatures. Each peak of the DSC curve corresponds to one type of polymer fraction, which could have a different amount and distribution of short-chain branching in the PE chain.

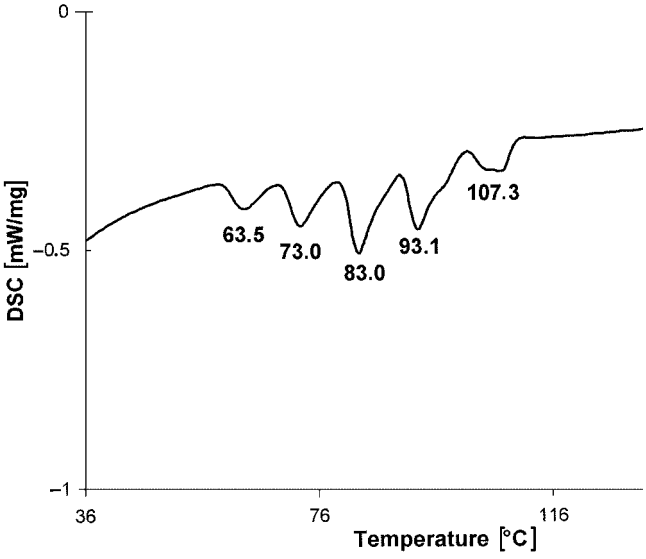

Figure 8. DSC thermogram obtained for an ethylene–*co*-1-hexene polymer made using **6**/$EtAlCl_2$.

 © 2005 Wiley-VCH Verlag GmbH & Co. KGaA, Weinheim

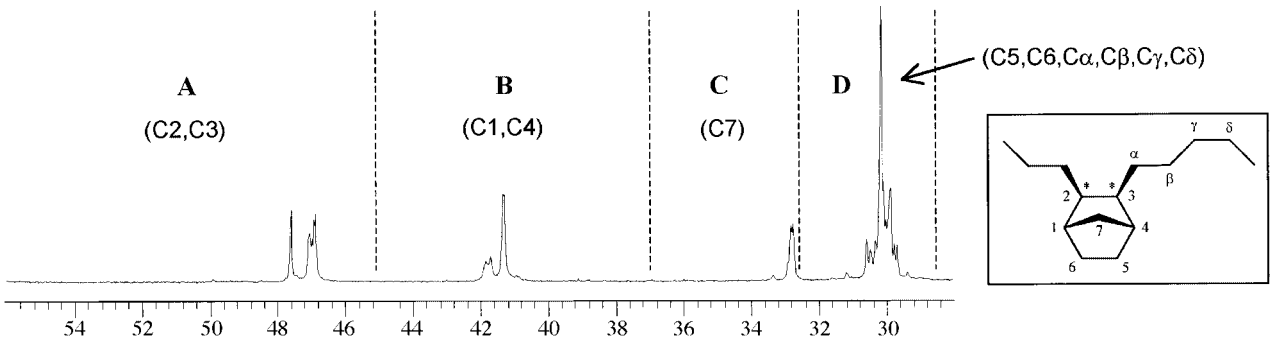

Figure 9. ^{13}C NMR spectrum [370 K, 1,2,4-trichlorobenzene–[D_2]tetrachloroethane] of the ethylene–*co*-norbornene polymer made using **6**/$EtAlCl_2$ (ethylene 1 bar).

As materials, poly(ethylene-*co*-norbornene)s possess rather interesting properties (high glass transitions, good chemical and heat resistance, and excellent transparency) that make them promising, in particular, for their potential applications in optoelectronics. Under the above conditions used to produce the poly(ethylene-*co*-hexene) [room temperature, and 1–4 bar ethylene, in the presence of norbornene], preliminary studies show that **6** associated with $EtAlCl_2$ (V/Al = 1:10) presents an interesting catalytic activity for ethylene–norbornene copolymerization (Table 4): activity = 292 $kg_{copolymer}\,mol^{-1}\,h^{-1}$ at 2 bar ethylene. The resultant polymer was poly(ethylene-*co*-norbornene) with a similar overall ^{13}C NMR spectrum (see Figure 9), high norbornene content (14–29 mol%),[25] and a microstructure that possesses no norbornene repeat units and contains both *meso* and *racemo* alternating ethylene–norbornene sequences as well as isolated norbornene units. More details on the copolymerization behavior of these systems will be described elsewhere.

Table 4. Results of ethylene–norbornene copolymerization [conditions: catalyst (0.01 mmol) in 10 mL of toluene; $EtAlCl_2$ cocatalyst (10 equiv.); ethylene (1–4 bar); 1-hexene (8 mmol); time of polymerization 15 or 30 min run].

Catalyst	*P* [bar]	Time [min]	Yield [mg]	Activity[a]	Norbornene content [mol%][b]
6	1	30	329	66	29
6	2	15	730	292	18
6[c]	4	15	868	347	14

[a] In $kg_{PE}\,mol^{-1}\,h^{-1}$. [b] Norbornene content in mol% determined by ^{13}C NMR spectroscopy (370 K). [c] Toluene (20 mL).

Conclusions

We described the synthesis and molecular structure of three new amine(bisphenolate) complexes of vanadium(II) and (III). We used the whole family of [ONNO]-vanadium complexes, from vanadium(II) to vanadium(V), as ethylene polymerization catalysts in association with the $EtAlCl_2$ cocatalyst. To the best of our knowledge, this is the first comprehensive study of a catalytic polymerization system with a single ancillary ligand set to stabilize such a broad scale of oxidation states of the metal center.

Preliminary studies show that some of these new complexes are efficient catalysts for ethylene-α-olefin copolymerization, producing poly(ethylene-*co*-1-hexene) and poly(ethylene-*co*-norbornene) with high α-olefin content. These promising results still need to be optimized, and future studies are in progress to determine the best catalytic conditions (temperature, ethylene pressure, co-monomer and cocatalyst concentration), as well as the effect of halogenated compounds as activity enhancers.[26] These studies will appear in due course. From our preliminary polymerization results, and because it is easily prepared from commercially available $V(acac)_3$, $V^{III}(acac)$[ONNO] appears as the most interesting complex for further studies. Our study also confirms the importance of the vanadium(III) as the active species in V-based catalytic systems.

Experimental Section

General Remarks: Starting materials for ligand synthesis were purchased from Aldrich Inc. or Fluka Inc. and used as received. All experiments requiring a dry atmosphere were performed using standard Schlenk line or drybox techniques under argon. Solvents were refluxed and dried over appropriate drying agents under argon, collected by distillation, and stored in the drybox over 4 Å molecular sieves. The ligand [ONNO]H_2 was prepared according to a known synthesis.[5e] K_2[ONNO] was prepared by adding excess K into a THF solution of [ONNO]H_2, filtering and evaporating to dryness. $V(acac)_3$ was purchased from Fluka. $EtAlCl_2$ (25 mol-% in toluene) was purchased from Aldrich. All vanadium precursors $VCl_3(THF)_3$ and $VCl_2(tmeda)_2$ were prepared as published previously.[27,28] [ONNO]-vanadium(V) and -vanadium(IV) complexes were prepared according to published syntheses.[15,16] NMR spectroscopic data were recorded with a AMX-400 spectrometer, and referenced internally to residual protonated-solvent (^1H) resonances and are reported relative to tetramethylsilane (δ = 0 ppm). Pseudo-quantitative ^{13}C NMR spectra of the copolymers were obtained at 370 K in 1,2,4-trichlorobenzene/[D_2]tetrachloroethane containing approximately 3 mg of $Cr(acac)_3$ to reduce T_1 (inverse-gated, $d1$ = 5 s). Co-monomer incorporation was measured by integration of characteristic signals. Elemental analyses were performed at the Laboratoire de Chimie de Coordination (Toulouse, France). Magnetic susceptibility data were collected on powdered samples of the different compounds with use of a homemade Faraday-type automatic magnetometer with mercury tetra(thiocyanato) cobaltate susceptibility at 20 °C, $16.44 \times 10^{-6}\,cm^3\,mol^{-1}$). Diamag-

 © 2005 Wiley-VCH Verlag GmbH & Co. KGaA, Weinheim

netic corrections were applied by using Pascal's constants as described previously.[12b] Size exclusion chromatography (SEC) analyses were carried out at the CNRS-LCPO laboratory (Bordeaux-Pessac, France) and at Polimeri Europa (Milan, Italy) in 1,2,4-trichlorobenzene at 140 °C relative to polystyrene standards. DSC thermograms of the polymers were measured on a DSC 204 Netzsch apparatus using a modified method.[29] The polymer sample was melted in a DSC crucible at 170 °C under nitrogen (10 °C/min). It was then successively annealed under nitrogen at descending temperature stages, starting from the melt by steps of 10 °C to reach 20 °C (with isotherms of 2 h between 110 and 60 °C). The cooled sample was then heated at 5 °C/min from 20 to 200 °C (the melting temperature values T_m and the heat of fusion (ΔH_f) were taken from the second heating curve).

Synthesis of V^{III}(acac)[ONNO] (6): To a solution of V(acac)$_3$ (100 mg, 0.29 mmol) in toluene (2 mL) was added [ONNO]H$_2$ (102 mg, 0.29 mmol) in portions at room temperature. The reaction mixture was heated at 80 °C for 14 h, after which the volatiles were removed under vacuum. The resulting orange solid was washed with pentane (3 × 5 mL) and dried under vacuum. Yield: 128 mg, 87%. μ_{eff} (20 °C) = 2.91 μ_B. $C_{27}H_{37}N_2O_4V$ (504.54): calcd. C 64.27, H 7.39, N 5.55; found C 64.02, H 7.24, N 5.69.

Synthesis of V^{III}(Cl)(THF)[ONNO] (7): K$_2$[ONNO] (174 mg) was slowly added in portions to a solution of VCl$_3$(THF)$_3$ (150 mg, 0.41 mmol) in THF (2 mL). The solution was left at ambient temperature whilst stirring overnight. Volatiles were removed under vacuum. The resulting solid was extracted with toluene, the solution was filtered through Celite and dried in vacuo. The solid was washed with pentane and dried under vacuum. Crystallization from a THF/toluene–pentane solution (room temperature and then at –20 °C) afforded yellow crystals of **7**. Yield: 65 mg, 31%. μ_{eff} (20 °C) = 2.87 μ_B. $C_{26}H_{38}ClN_2O_3V$ (512.99): calcd. C 61.87, H 7.47, N 5.46; found C 62.07, H 7.15, N 5.11.

Synthesis of V^{II}(tmeda)[ONNO] (8): K$_2$[ONNO] (366 mg) was slowly added in portions to a solution of VCl$_2$(TMEDA)$_2$ (300 mg, 0.84 mmol) in THF (4 mL), whilst stirring. After 2 h at room temperature, the volatiles were removed under vacuum. The resulting solid was extracted with toluene (5 mL), the solution was filtered through Celite and slowly layered with pentane (7 mL). Red crystals of **8** were obtained and dried under vacuum. Yield: 200 mg, 46%. μ_{eff} (20 °C) = 3.90 μ_B. $C_{28}H_{46}N_4O_2V$ (521.63): calcd. C 63.47, H 8.89, N 10.74; found: C 63.40, H 8.70, N 10.66.

Typical Ethylene Polymerization Catalyses: A 10 mL toluene solution of catalyst (5 mg) was flushed under 1 bar ethylene. The AlEtCl$_2$ (10 equiv. of a 1 M solution in toluene) cocatalyst dissolved in toluene (1.5 mL) was added to initiate the polymerization, and the ethylene pressure was maintained constant during the polymerization. The polymerization was stopped by adding methanol (5 mL), and the polyethylenes were filtered, washed with methanol, water and acetone, and dried for 48 h at 80 °C.

Typical Ethylene-α-olefin Copolymerization Catalyses: A 10 mL toluene solution of catalyst (5 mg) and 1-hexene (680 mg) [or norbornene (760 mg)] was flushed under 2 bar ethylene. The AlEtCl$_2$ (10 equiv. of a 1 M solution in toluene) cocatalyst dissolved in toluene (1.5 mL) was added to initiate the polymerization, and the ethylene pressure was maintained constant during the polymerization. The polymerization was stopped by adding methanol (5 mL), and the polyethylenes were filtered, washed with methanol, water and acetone, and dried for 48 h at 80 °C.

Crystal Structure Determination of [ONNO]H$_2$ and 6–8: (Table 5) For the four compounds, data were collected at low temperature (T = 180 K) with a Stoe Imaging Plate Diffraction System (IPDS), equipped with an Oxford Cryosystems Cryostream Cooler Device and using a graphite-monochromated Mo-K_α radiation (λ = 0.71073 Å). Final unit cell parameters were obtained by means of a least-squares refinement of a set of 8000 well-measured reflections, and the crystal decay was monitored during data collection by measuring 200 reflections by image; no significant fluctuation of intensities was observed. Structures were solved by means of

Table 5. Crystal data and structure refinement parameters for [ONNO]H$_2$ and **6**–**8**.

	[ONNO]H$_2$	**6**	**7**	**8**
Chemical formula	$C_{22}H_{32}N_2O_2$	$C_{27}H_{37}N_2O_4V$	$C_{26}H_{38}ClN_2O_3V$	$C_{56}H_{92}N_8O_4V_2$
Formula weight	356.50	504.53	512.97	1043.26
Crystal system	orthorhombic	monoclinic	monoclinic	monoclinic
Space group	$P2_12_12_1$	$P2_1$	$P2_1/c$	$P2_1/c$
a [Å]	8.457(5)	7.780(2)	11.660(5)	13.135(5)
b [Å]	14.127(5)	20.859(4)	20.125(5)	13.516(5)
c [Å]	17.023(5)	8.596(2)	11.737(5)	32.246(5)
α [°]	90	90	90	90
β [°]	90	112.780(3)	102.444(5)	91.517(1)
γ [°]	90	90	90	90
V [Å]^3	2033.7(15)	1286.2(5)	2689.5(18)	5724(3)
Z	4	2	4	8
$D_{calcd.}$ [g cm^{-3}]	1.164	1.303	1.267	1.201
μ (Mo-K_α) [mm^{-1}]	0.074	0.420	0.496	0.377
F(000)	776	536	1088	2248
2θ range [°]	5.6–52.6	5.1–51.8	4.0–46.5	4.00–46.6
Measured reflections	15550	11887	15570	30871
Unique reflections/R_{int}	2371/0.0715	4747/0.0209	3849/0.0967	7893/0.1393
Parameters/restraints	243/0	315/1	313/3	648/21
Final R indices [$I>\sigma 2(I)$]	R_1 = 0.0409, wR_2 = 0.0929	R_1 = 0.0238, wR_2 = 0.0621	R_1 = 0.0576, wR_2 = 0.1328	R_1 = 0.1391, wR_2 = 0.3381
Final R indices all data	R_1 = 0.0524, wR_2 = 0.0981	R_1 = 0.0246, wR_2 = 0.0626	R_1 = 0.1135, wR_2 = 0.1581	R_1 = 0.1587, wR_2 = 0.3518
Flack parameter	–	–0.003(11)	–	
Goodness of fit	1.025	1.025	0.920	1.141
$\Delta\rho_{max} - \Delta\rho_{min}$ [e Å^3]	0.150 and –0.170	0.177 and –0.203	0.468 and –0.327	0.750 and –0.919

 © 2005 Wiley-VCH Verlag GmbH & Co. KGaA, Weinheim

direct methods with the programs SIR92/97,[30] and subsequent difference Fourier maps and models were refined by least-squares procedures on F^2 by using SHELXL-97[31] integrated in the package WINGX version 1.64,[32] and empirical absorption corrections were applied to the data.[33] All hydrogen atoms were located on differences Fourier maps and introduced in the refinement as fixed contributors using a riding model with an isotropic thermal parameter fixed at 20% higher than those of the C sp^2 atoms and 50% for the C sp^3 atoms to which they were connected. Methyl groups they were refined with the torsion angle as a free variable. For the three compounds, all non-hydrogen atoms were anisotropically refined, and in the last cycles of refinement, weighting schemes were used, where weights are calculated from the following formula: $w = 1/[\sigma^2(F_o^2) + (aP)^2 + bP]$, where $P = (F_o^2 + 2F_c^2)/3$. In the case of compound **6**, with a polar space group ($P2_1$), SHELXL automatically generates floating origin restraints to fix the X-ray 'centre of gravity' of the structure in the polar axis direction (in the case of $P2_1$, with unique axis *b*, the polar axis is *Y*). Complex **8** presents two independent molecules in the cell with very similar structural parameters. The crystal structure of **8** refined to a high *R* factor because of poor quality, probably as a result of multilayer-type crystals (considering the reciprocal), which could not be treated as twin crystals. The resulting R_{int} was very high (13.93%), which explains the poor final *R* value. The final residues (with low values $+0.90 < Q < -0.95$) are all located close to the metal centers.

CCDC-263761, –263762, –263763 and CCDC-263764 contain the supplementary crystallographic data for this paper. These data can be obtained free of charge from The Cambridge Crystallographic Data Centre via www.ccdc.cam.ac.uk/data_request/cif.

Acknowledgments

This research was supported by the Centre National de la Recherche Scientifique (CNRS). Prof. H. Cramail (Bordeaux, France) and Dr. G. Conti (Polimeri Europa, Milan, Italy) are thanked for the SEC.

[1] For recent reviews see: a) S. K. Spitzmesser. V. C. Gibson, *Chem. Rev.* **2003**, *103*, 283–315; b) G. J. P. Britovsek, V. C. Gibson, D. F. Wass, *Angew. Chem. Int. Ed.* **1999**, *38*, 429–447.

[2] a) J. D. Scollard, D. H. McConville, *J. Am. Chem. Soc.* **1996**, *118*, 10008–10009; b) J. D. Scollard, D. H. McConville, N. C. Payne, J. J. Vittal, *Macromolecules* **1996**, *29*, 5241–5243.

[3] a) R. Baumann, W. M. Davis, R. R. Schrock, *J. Am. Chem. Soc.* **1997**, *119*, 3830–3831; b) R. R. Schrock, F. Schattenmann, M. Aizenberg, W. M. Davis, *Chem. Commun.* **1998**, 1999–2000; c) R. Baumann, R. R. Schrock, *J. Organomet. Chem.* **1998**, *557*, 69–75; d) R. R. Schrock, R. Baumann, S. M. Reid, J. T. Goodman, R. Stumpf, D. M. Davis, *Organometallics* **1999**, *18*, 3649–3670; e) J. T. Goodman, R. R. Schrock, *Organometallics* **2001**, *20*, 5205–5211.

[4] a) A. Shafir, M. P. Power, G. D. Whitener, J. Arnold, *Organometallics* **2001**, *20*, 1365–1369; b) R. M. Gauvin, C. Lorber, R. Choukroun, B. Donnadieu, J. Kress, *Eur. J. Inorg. Chem.* **2001**, 2337–2346; c) Y. M. Jeon, S. J. Park, J. Heo, K. Kim, *Organometallics* **1998**, *17*, 3161–3163; d) S. Tinkler, R. J. Deeth, D. J. Duncalf, A. McCamley, *J. Chem. Soc. Chem. Commun.* **1996**, 2633–2634; e) , F. G. N. Clocke, T. J. Geldbach, P. B. Hitchcock, J. B. Love, *J. Organomet. Chem.* **1996**, *506*, 343–345; f) N. A. H. Male, M. Thornton-Pett, M. Bochmann, *J. Chem. Soc. Dalton Trans.* **1997**, 2487–2494; g) V. C. Gibson, B. S. Kimberley, A. J. P. White, D. J. Williams, P. Howard, *J. Chem. Soc. Chem. Commun.* **1998**, 313–314; h) C. H. Lee, Y.-H. La, S. J. Park, J. W. Park, *Organometallics* **1998**, *17*, 3648–3655.

[5] a) E. Y. Tshuva, I. Goldberg, M. Kol, *J. Am. Chem. Soc.* **2000**, *122*, 10706–10707; b) E. Y. Tshuva, I. Goldberg, M. Kol, H. Weitman, Z. Goldschmidt, *Chem. Commun.* **2000**, 379–380; c) E. Y. Tshuva, I. Goldberg, M. Kol, Z. Goldschmidt, *Chem. Commun.* **2001**, 2120–2121; d) E. Y. Tshuva, S. Groysman, I. Goldberg, M. Kol, Z. Goldschmidt, *Organometallics* **2002**, *21*, 662–670; e) E. Y. Tshuva, I. Goldberg, M. Kol, Z. Goldschmidt, *Organometallics* **2001**, *20*, 3017–3028; f) E. Y. Tshuva, Goldberg I., M. Kol, Z. Goldschmidt, *Inorg. Chem.* **2001**, *40*, 4263–4270.

[6] a) Y. Nakayama, K. Watanabe, N. Ueyama, A. Nakamura, A. Harada, J. Okuda, *Organometallics* **2000**, *19*, 2498–2503; b) R. M. Gauvin, J. A. Osborn, J. Kress, *Organometallics* **2000**, *19*, 2944–2946; c) H. Mack, M. S. Eisen, *J. Chem. Soc. Dalton Trans.* **1998**, 917–921; d) M. G. Thorn, Z. C. Etheridge, P. E. Fanwick, I. P. Rothwell, *Organometallics* **1998**, *17*, 3636–3638; e) X. Bei, D. C. Swenson, R. F. Jordan, *Organometallics* **1997**, *16*, 3282–3302.

[7] See for example: a) M. Mitani, R. Furuyama, J-I. Mohri, J. Saito, S. Ishii, H. Terao, H. Tanaka, T. Fujita, *J. Am. Chem. Soc.* **2003**, *125*, 4293–4305; b) S. Matsui, Y. Tohi, M. Mitani, J. Saito, H. Makio, H. Tanaka, M. Nitabaru, T. Nakano, T. Fujita, *Chem. Lett.* **1999**, 1065–1066; c) S. Matsui, T. Fujita, *Catal. Today* **2001**, *66*, 63–73; d) J. Saito, M. Mitani, S. Matsui, J-I. Mohri, S. Kojoh, N. Kashiwa, T. Fujita, *Angew. Chem. Int. Ed.* **2001**, *40*, 2918–2920; e) Y. Susuki, N. Kashiwa, T. Fujita, *Chem. Lett.* **2002**, 358–359; f) M. Mitami, T. Nakano, T. Fujita, *Chem. Eur. J.* **2003**, *9*, 2396–2402.

[8] a) J. Tian, G. W. Coates, *Angew. Chem. Int. Ed.* **2000**, *39*, 3626–3629; b) M. Fujita, G. W. Coates, *Macromolecules* **2002**, *35*, 9640–9647; c) J. Tian, P. D. Hustad, G. W. Coates, *J. Am. Chem. Soc.* **2002**, *124*, 3614–3621.

[9] C.-X. Cai, L. Toupet, C. W. Lehmann, J.-F. Carpentier, *J. Organomet. Chem.* **2003**, *683*, 44–55.

[10] a) K. Ziegler, E. Holzkamp, H. Breil, H. Martin, *Angew. Chem.* **1955**, *67*, 426; b) G. Natta, P. Pino, P. Corradini, F. Danusso, E. Mantica, G. Mazzanti, G. Moraglio, *J. Am. Chem. Soc.* **1955**, *77*, 1708–1710.

[11] For recent reviews see: a) G. W. Coates, P. D. Hustad, S. Reinartz, *Angew. Chem. Int. Ed.* **2002**, *41*, 2236–2257; b) H. Hagen, J. Boersma, G. van Koten, *Chem. Soc. Rev.* **2002**, *31*, 357–364; c) S. Gambarotta, *Coord. Chem. Rev.* **2003**, *237*, 229–243.

[12] a) C. Lorber, R. Choukroun, B. Donnadieu, *Inorg. Chem.* **2003**, *42*, 673–675; b) C. Lorber, R. Choukroun, B. Donnadieu, *Inorg. Chem.* **2002**, *41*, 4217–4226; c) R. Choukroun, B. Donnadieu, C. Lorber, P.-M. Pellny, W. Baumann, U. Rosenthal, *Chem. Eur. J.* **2000**, *6*, 4505–4509; d) R. Choukroun, B. Donnadieu, C. Lorber, *Chem. Eur. J.* **2002**, *8*, 2700–2704; e) R. Choukroun, C. Lorber, B. Donnadieu, *Organometallics* **2002**, *21* 1124–1126; f) F. Wolff, R. Choukroun, C. Lorber, B. Donnadieu, *Eur. J. Inorg. Chem.* **2003**, 628–632; g) R. Choukroun, C. Lorber, L. Vendier, B. Donnadieu, *Organometallics* **2004**, *23*, 5488–5492; h) R. Choukroun, C. Lorber, L. Vendier, B. Donnadieu, *Organometallics* **2004**, *23*, 1434–1437; i) C. Lorber, R. Choukroun, L. Vendier, *Organometallics* **2004**, *23*, 1845–1850.

[13] C. Lorber, B. Donnadieu, R. Choukroun, *Organometallics* **2000**, *19*, 1963–1966.

[14] C. Lorber, B. Donnadieu, R. Choukroun, *J. Chem. Soc., Dalton Trans.* **2000**, 4497–4498.

[15] F. Wolff, C. Lorber, R. Choukroun, B. Donnadieu, *Inorg. Chem.* **2003**, *42*, 7839–7845.

[16] F. Wolff, C. Lorber, R. Choukroun, B. Donnadieu, *Eur. J. Inorg. Chem.* **2004**, 2861–2867.

[17] During the course of our study, the crystal structure of $[ONNO]H_2$ was reported, but its structural parameters have not been discussed: M. Velusamy, M. Palaniandavar, R. S. Gopalan, G. U. Kulkarni, *Inorg. Chem.* **2003**, *42*, 8283–8293.

[18] N. Desmangles, S. Gambarotta, C. Bensimon, S. Davis, H. Zahalka, *J. Organomet. Chem.* **1998**, *562*, 53–60.

[19] A. K. Atanov, V. C. Gibson, D. Zaher, M. R. J. Elsegood, S. H. Dale, *Chem. Commun.* **2004**, 1956–1957.
[20] a) Y. Doi, S. Ueki, T. Keii, *Macromolecules* **1979**, *12*, 814–819; b) Y. Doi, T. Keii, *Adv. Polymer Sci.* **1986**, *73/74*, 201–209; c) Y. Doi, N. Nomura, K. Ohgizawa, K. Soga, *Makromol. Chem. Rapid Commun.* **1991**, *12*, 245–246.
[21] K. Nomura, A. Sagara, Y. Imanishi, *Macromolecules* **2002**, *35*, 1583–1590.
[22] Pseudo-quantitative ^{13}C NMR spectroscopy allowed us to determined the 1-hexene incorporation ratio into the copolymers by integration of 1-hexene versus ethylene signals, according to Equation (1).

$$\%\ 1\text{-hexene} = \frac{1}{1+\frac{1}{2}[(CH_2)_n+\frac{1}{2}C_\alpha+C_\beta]} \quad (1)$$

[23] M. R. Ribeiro, A. Deffieux, M. Fontanille, M. F. Portela, *Macromol. Chem. Phys.* **1995**, *196*, 3833–3844.
[24] a) K. Jokela, A. Väänänen, M. Torkkeli, P. Starck, R. Serimaa, J. Seppälä, *J. Polymer Sci.: Part B: Polym. Phys.* **2001**, *39*, 1860–1875; b) E. Adison, M. Ribeiro, A. Deffieux, M. Fontanille, *Polymer* **1992**, *33*, 4337–4342; c) P. Starck, *Polymer International* **1996**, *40*, 111–122; d) P. Starck, P. Lehmus, J. V. Seppälä, *Polymer Eng. Sci.* **1999**, *39*, 1444–1455; e) M. L. Arnal, V. Balsamo, G. Ronca, A. Sanchez, A. J. Müller, E. Canizales, C. Urbina de Navarro, *J. Thermal Anal. Cal.* **2000**, *59*, 451–470; f) A. Alizadeh, L. Richardson, J. Xu, S. McCartney, H. Marand, Y. W. Cheung, S. Chum, *Macromolecules* **1999**, *32*, 6221–6235; g) K. Czaja, B. Sacher, M. Bialek, *J. Thermal Anal. Cal.* **2002**, *67*, 547–555; h) F. M. Mirabella, *J. polym. Sci. Part B: Polym. Phys.* **2001**, *39*, 2800–2818; i) P. Starck, B. Löfgren, *Eur. Polym. J.* **2002**, *38*, 97–107.
[25] The norbornene content in the copolymers is calculated in a straightforward manner from the four peak groups in the ^{13}C NMR spectrum and by application of the formula in Equation (2), according to: M. Arndt-Rosenau, I. Beulich, *Macromolecules* **1999**, *32*, 7335–7343.

$$\%Norbornene = \frac{\frac{1}{2}[I(C2,C3)+I(C1,C4)+I(C7)]}{\frac{1}{2}[I(C5,C6)+I(C\alpha,C\beta,C\gamma,C\delta)]} = \frac{2}{5}\frac{5N}{2N+2E} = \frac{I(A)+I(B)+I(C)}{2{,}5I(D)} \quad (2)$$

[26] It is known that the activity of homogeneous vanadium catalysts generally used in the preparation of EPDM (ethylene/propylene/diene terpolymer) can be noticeably increased by means of certain organic halogenated compounds, often called "activators" or "promoters" (such as CCl_4, $CHCl_3$, CH_3CCl_3), that act as oxidizing agent allowing the reoxidation of vanadium(II)-deactivated species into potentially reactivated vanadium(III) ones [see for examples: a) K. Bujadoux. E. Adisson, A. Deffieux, M. Fontanille, *J. Polym. Sci.* **1994**, *32*, 1033–1042; b) S. C. Kao, F. J. Karol (Union Carbide), U. S. Patent 5030605, **1991** [*Chem. Abstr. 115*: 160022e]; c) Ref.[30]
[27] L. E. Manzer, *Inorganic Syntheses* **1982**, *21*, 135–140.
[28] J. J. H. Edema, W. Stauthamer, F. van Bolhuis, S. Gambarotta, W. J. J. Smeets, A. L. Spek, *Inorg. Chem.* **1990**, *29*, 1302–1306.
[29] E. Addison, M. R. Ribeiro, A. Deffieux, M. Fontanille, *Polymer* **1992**, *33*, 4337–4342.
[30] a) A. Altomare, G. Cascarano, C. Giacovazzo, A. Guagliardi, *J. Appl. Cryst.* **1993**, *26*, 343–350; b) A. Altomare, M. C. Burla, M. Camalli, G. L. Cascarano, G. Giacovazzo, A. Guagliardi, A. G. G. Moliterni, G. Polidori, R. Spagna, *J. Appl. Crystallogr.* **1999**, *32*, 115–119.
[31] G. M. Sheldrick, *SHELX97 [includes SHELXS97, SHELXL97, CIFTAB]*, *Programs for Crystal Structure Analysis (Release 97–2)*, Institüt für Anorganische Chemie, Universität Göttingen, **1998**.
[32] L. J. Farrugia, *J. Appl. Crystallogr.* **1999**, *32*, 837–838.
[33] N. Walker, D. Stuart, *Acta Crystallogr. A* **1983**, *39*, 158–166.

Received: February 18, 2005
Published Online: June 14, 2005

 © 2005 Wiley-VCH Verlag GmbH & Co. KGaA, Weinheim

Multidimensional Cyanide-Bridged Heterometallic Fe^{II}–Cu^{I} and Homometallic Cu^{I} Coordination Polymers from Solvothermal Reactions Involving either $K_3[Fe(CN)_6]$ or KCN as the Source of Cyanide Anions

Enrique Colacio,*[a] Ahderrahmane Debdoubi,[b] Raikko Kivekäs,[c] and Antonio Rodríguez[a]

Keywords: Coordination polymers / Copper / Cyanides / Heterometallic complexes / Solvothermal synthesis

The reaction between $K_3[Fe(CN)_6]$, $CuCl_2{\cdot}2H_2O$ and 1,10-phenanthroline (phen) under hydrothermal conditions gives rise to the formation of the 3D cyanide-bridged heterometallic Fe^{II}–Cu^{I} complex $[Fe(CN)_4(phen)_2Cu_2]$ (**1**). Its 3D network structure is constructed from two types of fused cyanide-bridged 10- and 14-metal-membered centrosymmetric rings (Fe_2Cu_8 and Fe_2Cu_{12}), which are defined by the general sequences $\{(Cu^I)_4\text{-}Fe^{II}\text{-}(Cu^I)_4\text{-}Fe^{II}\}$ and $\{(Cu^I)_6\text{-}Fe^{II}\text{-}(Cu^I)_6\text{-}Fe^{II}\}$, respectively. The copper(I) and iron(II) atoms exhibit distorted triangular planar and distorted octahedral coordination environments, respectively. Complex **1** is the first example of a 3D cyanide-bridged bimetallic complex prepared by hydrothermal methods. The use of methanol as solvent, KCN as source of cyanide anions and 2,2′,6,6′-bipyrimidine as the bridging ligand results in the isolation of the 2D homometallic copper(I) complex $[Cu_2(CN)_2(bpym)]{\cdot}H_2O$ (**2**). Its structure consists of neutral 2D (6,3) honeycomb layers in the *ab* plane made of fused $Cu_6(CN)_4(bpym)_2$ rings, in which the copper(I) atoms exhibit a distorted tetrahedral geometry. The layers are interdigitated in such a way that the bpym ligands lie above and below the ring cavities of neighbouring networks, with an ABCD repeat sequence of layers. Water molecules are located in the free space between the A/D and B/C layers. Under the same conditions as used for **1**, but with 4-methyl-2,2′,6,6′-bipyrimidine 2-oxide instead of phen, the 3D complex $[Cu_2(CN)_2(mbpym]$ (**3**) was obtained (mbpym = 4-methyl-2,2′,6,6′-bipyrimidine). During the reaction the oxygen atom of the *N*-oxide group is eliminated and the novel ligand mpym formed. Its structure consists of distorted tetrahedral copper(I) atoms connected by cyanide and mpym bridging ligands to give rise to a 3D chiral network.

(© Wiley-VCH Verlag GmbH & Co. KGaA, 69451 Weinheim, Germany, 2005)

Introduction

Research on multidimensional polymetallic coordination polymers is currently of great interest because of their fascinating structural diversity and potential applications as functional materials in fields such as electrical conductivity, molecule-based magnets, molecular absorption, ion-exchange, heterogeneous catalysis, etc.[1] Among these materials, cyanide-bridged bimetallic complexes deserve special attention as they exhibit, among others, interesting electrochemical, zeolitic, magnetic and photomagnetic properties.[2] These compounds can be prepared either by assembling cyanometallates and metal complexes or by multicomponent self-assembly of cyanide, metal ions and multidentate ligands. Although the majority of these systems are still being prepared by conventional solution routes, attention has recently turned to solvothermal techniques. In this regard, we and others have recently reported homo- and heterometallic cyanide-bridged complexes, which were assembled through hydrothermal reactions with azine and diazine ligands and either CuCN or hexacyanometallate anions as sources of cyanide anions.[3–8] As an extension of our work in this field, in this paper we report three novel coordination polymers that have been constructed from simple phenanthroline and bipyrimidine ligands, namely $[Fe(CN)_4(phen)_2Cu_2]$ (**1**; phen = 1,10-phenanthroline), $[Cu_2(CN)_2(bpym]{\cdot}H_2O$ (**2**; bpym = 2,2′-bipyrimidine) and $[Cu_2(CN)_2$ (mbpym)] (**3**; mbpym = 4-methyl-2,2′-bipyrimidine).

[a] Departamento de Química Inorgánica, Facultad de Ciencias, Universidad de Granada,
18071 Granada, Spain
Fax: +34-958-248526
E-mail: ecolacio@ugr.es
[b] Unité de Calorimétrie et Materiaux, Université Abdelmalek Essaadi, Faculté des Sciences,
P. O. Box 2121, Tétouan 93002, Morocco
[c] Department of Chemistry, Laboratory of Inorganic Chemistry, P. O. Box 55, 00014, University of Helsinki, Finland
E-mail: raikkok@saunalahti.fi

Results and Discussion

Solvothermal reactions are typically carried out in the 100–260 °C temperature range under autogenous pressure. Under these conditions, the reduced viscosity of the solvent enhances diffusion processes, thus favouring the solvent extraction of solids, the self-assembly of the precursors and the crystal growth from the solution. In fact, a rich variety of 1D to 3D polymetallic systems with intriguing structures and topologies have been recently prepared by solvothermal

 DOI: 10.1002/ejic.200401000

reactions, the great majority of them being hometallic in nature. The complexity of these reactions, in principle, prevents the control and prediction of crystal structures. Nevertheless, it is clear from empirical observations that the architecture of these multidimensional materials depends strongly on the subtle interplay between the characteristics of the metal ion (oxidation state, coordination preferences, plasticity of the coordination sphere, available coordination positions, redox capability, etc.), ligand (type and number of donor groups, bridging capability, connectivity, steric constraints, etc.) and reaction conditions (temperature, heating time, solvent, etc.). In this regard, Zubieta's group has prepared in the last few years a variety of multidimensional cyano-bridged complexes with simple diimine ligands. For these systems both changes of the ligand and the steric constraints imposed by the ligand substituents often give rise to the formation of quite different architectures.[4] As expected, a change in the reaction stoichiometry and/or counterion may also have a direct influence on the structure of the final product. For instance, the hydrothermal reaction of $Cu(CH_3COO)_2{\cdot}H_2O$, $K_3[Fe(CN)_6]$ and phen in a 2:1:1.5 molar ratio give rise to the 1D homometallic compound $[Cu_6(CN)_6(phen)_4]$.[5] However, the use of $CuCl_2{\cdot}2H_2O$ instead of $Cu(CH_3COO)_2{\cdot}H_2O$ and a 1:1:1 molar ratio allowed us to isolate $[Fe(CN)_4(phen)_2Cu_2]$ (**1**), an interesting 3D bimetallic complex. As far as we know, this compound is only the second example of a cyano-bridged bimetallic complex prepared by solvothermal techniques, and the first example of such a compound exhibiting a 3D structure.

While chelating donor ligands, such as phen, act as passivating agents by blocking metal coordination sites, bridging ligands are expected to favour the propagation of the structure. In a previous paper,[3] we reported that the solvothermal reaction of $K_3[Fe(CN)_6]$, $CuCl_2{\cdot}2H_2O$ and bpym, a bisdidentate ligand, in methanol leads to a 2D material made of honeycomb layers with alternating bpym and cyanide bridges. However, under the same solvothermal conditions, the use of KCN instead of $K_3[Fe(CN)_6]$ as a source of cyanide anions resulted in the formation of a different 2D homometallic compound $[Cu_2(CN)_2(bpym)]{\cdot}H_2O$ (**2**).

Recently, we have prepared the compound 4-methyl-2,2′-bipyrimidine 2-oxide (mbpymo, see Scheme 1), which, in principle, might bridge two metal ions to produce polynuclear complexes. However, all attempts to obtain this kind of compound were unsuccessful.[9] In view of this, we decided to use hydrothermal methods to force their preparation. Thus, by following the same synthetic procedure as that for **2**, but using $K_3[Fe(CN)_6]$ instead of KCN, the 3D complex $[Cu_2(CN)_2(mbpym)]$ (**3**), which contains cyanide and 4-methyl-2,2′-bipyrimidine (mbpym) bridging ligands was obtained (when KCN is used as a source of cyanide anions no definite compound could be isolated). During the hydrothermal reaction the *N*-oxide group of the ligand is lost and mbpym formed. This fact, and the reduction of iron(III) and copper(II) ions to iron(II) and copper(I), respectively, are a consequence of the high pressure and temperature used in the hydrothermal reactions for preparing complexes **1**–**3**. Cyanide groups, from either KCN or the dissociation of $[Fe(CN)_6]^{3-}$, are probably responsible for the reduction process, yielding cyanogen as the oxidation product. Moreover, it is well known that copper(I) cyanide species are more stable at elevated temperatures and pressures than those of copper(II).[4]

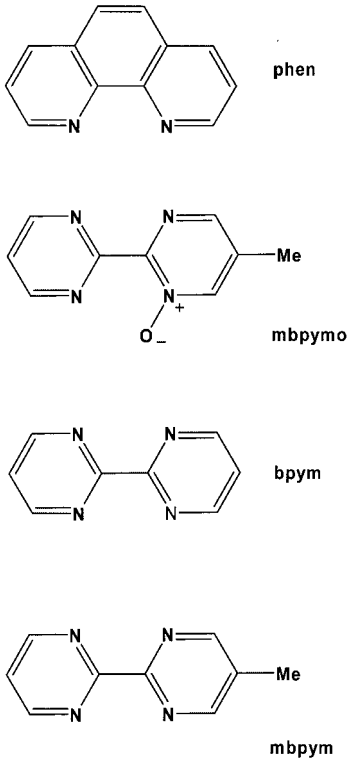

Scheme 1.

X-ray Structures

The asymmetric unit of the structure of **1**, together with the atomic labelling scheme, is given in Figure 1; selected bond lengths and angles are gathered in Table 1. The structure is constructed from two types of 10-metal-membered (Fe_2Cu_8) and two types of 14-metal-membered (Fe_2Cu_{12}) centrosymmetric rings, which fuse out of plane into an intricate 3D network. Within these rings, which are defined by the general sequences $\{(Cu^I)_4\text{-}Fe^{II}\text{-}(Cu^I)_4\text{-}Fe^{II}\}$ and $\{(Cu^I)_6\text{-}Fe^{II}\text{-}(Cu^I)_6\text{-}Fe^{II}\}$, respectively, the metal centres are bridged by cyanide groups (Figure 1, middle). The Fe_2Cu_8 rings are similar to those observed in the 2D Fe^{II}–Cu^I compound $[Fe(bipy)_2(CN)_4Cu_2]$.[3] There are four independent Cu^I atoms in the structure, all of which exhibit a distorted trigonal-planar geometry with Cu–X bond lengths and X–Cu–X angles (X = C or N) in the ranges 1.872–1.975 Å and 104.49(12)–140.68(13)°, respectively. Each of these Cu^I atoms is connected by cyanide groups to two Cu^I atoms and one Fe^{II} atom, with Cu···Cu and Cu···Fe distances in the ranges 4.8736(6)–4.9456(6) Å and 4.7773(8)–4.9683(6) Å, respectively. There are two crystallographically independent Fe^{II} atoms in the structure (Fe1 and Fe2),

 © 2005 Wiley-VCH Verlag GmbH & Co. KGaA, Weinheim

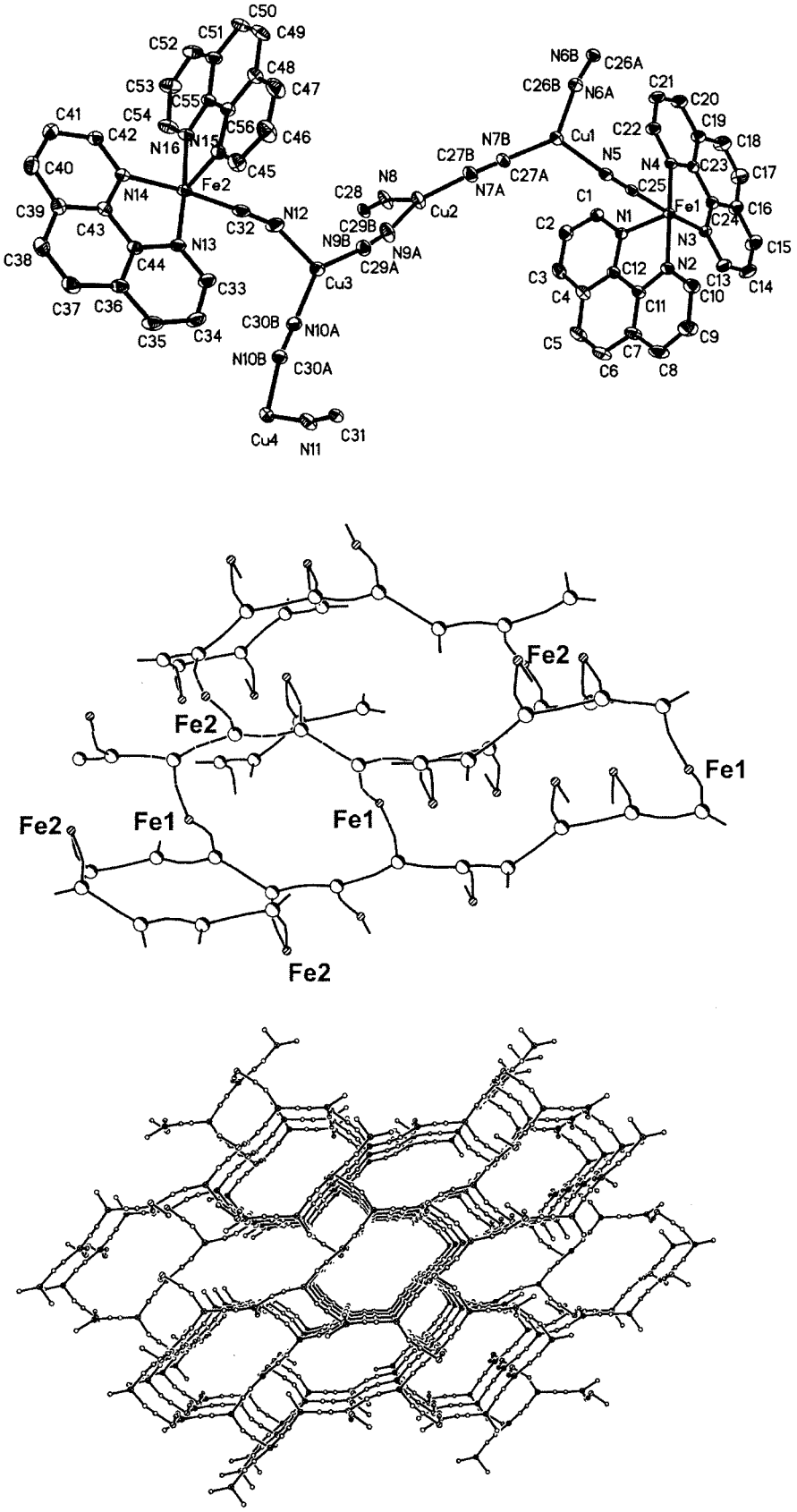

Figure 1. Asymmetric unit of **1** with the disordered CN bridging groups labelled as X (top). A fragment of the structure showing the two types of fused Fe_2Cu_8 and Fe_2Cu_{12} rings (middle); grey and black balls represent Cu and Fe atoms, respectively. View down the *b* axis of the 3D network of **1** (bottom). In the two latter views phen ligands have been omitted for clarity.

 © 2005 Wiley-VCH Verlag GmbH & Co. KGaA, Weinheim

which exhibit a distorted octahedral FeN_4O_2 coordination environment. Each Fe^{II} atom is coordinated by four nitrogen atoms belonging to two bidentate phen ligands and to two carbon atoms from cyanide groups, these latter bridging each Fe^{II} atom to two Cu^{I} atoms and displaying a *cis* orientation. As expected for the Fe–CN–Cu coordination, the Fe–C–N angles [171.3(3)–177.3(3)°] are closer to linearity than the Cu–N–C angles [148.5(3)–165.3(2)°]. This is due to the stronger covalent interaction between C and Fe^{II} atoms. The bond lengths and angles in the Fe(CN)(phen) unit are similar to those found for the $Fe(bipy)(CN)_2$ unit in the 2D compound $[Fe(bipy)_2(CN)_4Cu_2]$ and the molecular squares $[Fe_2Cu_2(\mu\text{-}CN)_4(bipy)_6](PF_6)_4\cdot 2H_2O$ and $[Fe_2Co_2(\mu\text{-}CN)_4(bipy)_6]\cdot 2CHCl_3\cdot CH_3NO_2$.[10]

Table 1. Selected bond lengths [Å] and angles [°] for **1**.

Cu1–X1	1.918(4)	X3–Cu1–X1	132.38(13)
Cu1–X3	1.872(3)	X1–Cu1–N5	106.52(12)
Cu1–N5	1.974(3)	X3–Cu1–N5	120.65(12)
Cu2–X4	1.883(3)	X4–Cu2–X5	131.25(13)
Cu2–X5	1.930(4)	X7–Cu3–X6	139.99(14)
Cu2–N8	1.936(3)	X5–Cu2–N8	105.92(12)
Cu3–X6	1.878(4)	X6–Cu3–N12	115.50(13)
Cu3–X7	1.913(3)	X7–Cu3–N12	104.49(12)
Cu3–N12	1.951(3)	X2[a]-Cu4–X8	140.68(13)
Cu4–X2[a]	1.878(3)	X2[a]-Cu4–N11	113.46(12)
Cu4–X8	1.907(3)	X8–Cu4–N11	105.84(11)
Cu4–N11	1.975(3)	N2–Fe1–N1	81.96(10)
Fe1–N1	1.996(2)	N4–Fe1–N3	81.68(10)
Fe1–N2	1.978(2)	N14–Fe2–N13	82.12(10)
Fe1–N3	2.011(3)	N16–Fe2–N15	82.03(10)
Fe1–N4	1.982(2)		
Fe1–C25	1.910(4)		
Fe1–C31[b]	1.891(3)		
Fe2–N13	1.987(2)		
Fe2–N14	1.990(2)		
Fe2–N15	1.991(2)		
Fe2–N16	1.982(2)		
Fe2–C28[c]	1.891(4)		
Fe2–C32	1.894(4)		

[a] Equivalent positions: $x - 1/2, -y + 3/2, z + 1/2$. [b] $-x + 1, -y + 2, -z + 1$. [c] $-x + 3/2, y - 1/2, -z + 3/2$.

The Fe1 and Fe2 centres are chiral and display opposite absolute configurations, therefore the crystal as a whole is racemic. One of the Fe_2Cu_8 rings contains two Fe1 atoms and the other one two Fe2 atoms, with approximate dimensions 11×18 Å^2 and 8×18 Å^2, respectively. The Fe_2Cu_{12} rings containing Fe1 and Fe2 have approximate dimensions 8×23 Å^2 and 13×25 Å^2. Cavities created by the out-of-plane fusion of the rings are filled by the coordinated phen ligands. Within the rings the maximum deviation from the mean plane corresponds to the iron(II) atoms. It should be noted that **1** is the first example of a 3D cyanide-bridged bimetallic complex prepared by hydrothermal methods.

We have shown that the related 2D Fe^{II}–Cu^{I} bimetallic compound $[Fe(bipy)_2(CN)_4Cu_2]$[3] exhibits a high spin:low spin equilibrium with 96% of the Fe^{II} atoms in the low-spin state ($S = 0$) at room temperature. Likewise, it has been shown recently that a series of cyanide-bridged Fe^{II}–M systems (M = Pd^{II}, Pt^{II}, Ni^{II}, Au^{I}, Ag^{I}) exhibit thermal-, pressure-, and light-induced spin crossover transitions.[11] In the case of **1**, however, the magnetic measurements reveal that the compound is diamagnetic at room temperature, thus indicating that the ligand field is strong enough to force all the Fe^{II} atoms to be in the low-spin state.

The structure of **2** (Figure 2) is very similar to that previously reported by us for the dehydrated compound $[Cu_2(CN)_2(bpym)]$[3] and consists of neutral 2D(6,3) honeycomb layers in the *ab* plane made of fused $Cu_6(CN)_4(bpym)_2$ rings and water molecules. The structure can be alternatively described as constructed from zig-zag $\{Cu(CN)\}_4$ chains linked by bisdidentate bridging bpym ligands generating the (6,3) net topology. Selected bond lengths and angles are given in Table 2. Two major differences between the structure of **2** and its dehydrated complex are observed: a) in **2**, the mean plane of the bpym ligand is almost perpendicular to the layers, with a dihedral angle of 90.2° (or 89.8°), whereas in the dehydrated complex this dihedral angles is only 73°; b) in **2**, the layers are stacked in such a way that bpym ligands are interdigitated and aligned above and below one sheet with the cavities in neighbouring layers, giving rise to an ABCD repeat pattern of layers (Figure 3). The bpym ligands of layers A and B are parallel.

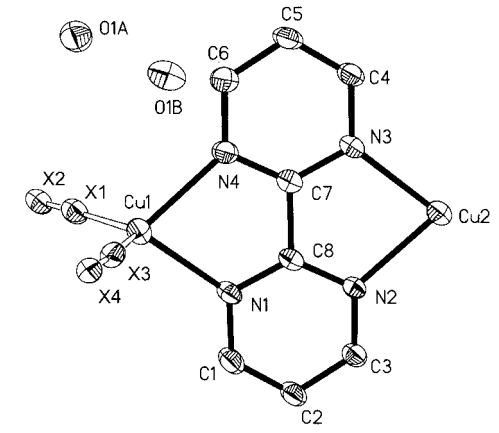

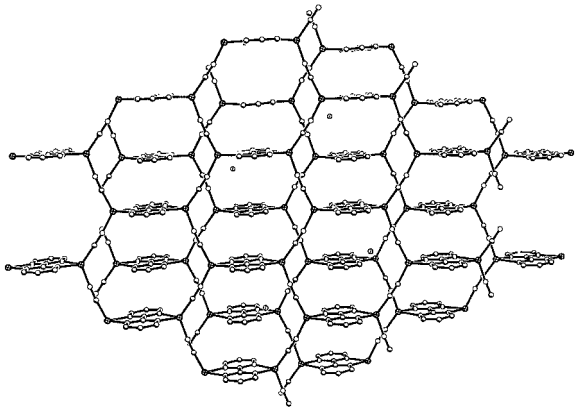

Figure 2. Perspective view of the asymmetric unit of **2** with the disordered CN bridging groups labelled as X (top). View down the *c* axis of two neighbouring layers with the same orientation of the bpym ligands (bottom).

 © 2005 Wiley-VCH Verlag GmbH & Co. KGaA, Weinheim

Table 2. Selected bond lengths [Å] and angles [°] for **2**.

Cu1–N1	2.102(4)
Cu1–N4	2.140(4)
Cu1–X1	1.888(7)
Cu1–X3	1.909(7)
Cu2–N2	2.129(4)
Cu2–N3	2.131(4)
Cu2–X2[a]	1.899(7)
Cu2–X4[b]	1.873(7)
X1–Cu1–N1	117.22(19)
X3–Cu1–N1	107.52(17)
N4–Cu1–N1	78.04(15)
X3–Cu1–X1	125.7(2)
X1–Cu1–N4	111.89(19)
X3–Cu1–N4	105.85(18)
X4[b]-Cu2–X2[a]	126.0(2)
N2–Cu2–N3	78.14(15)
X2[a]–Cu2–N2	113.33(18)
X4[b]–Cu2–N2	109.68(17)
X2[a]–Cu2–N3	110.08(18)
X4[b]–Cu2–N3	109.33(17)

[a] Equivalent positions: x, $y + 1$, z. [b] $x - 1/2$, $y + 1/2$, z.

Likewise, the mean planes of the layers C and D are also parallel but form a dihedral angle of 47.5° with those of layers A and B. Thus, layers are arranged in couples, with interlayer distances of about 4 Å and 6 Å for layers of the same couple (AB and CD) and different couples (BC and DA), respectively. In **2**, however, the repeat pattern of layers is of the ABAB type. Water molecules are located in the free space between the layers of different couples.

In **2**, Cu1 and Cu2 exhibit distorted tetrahedral coordination environments, which are formed by the coordination of two bridging cyano groups and one bridging bisdidentate bpym ligand, with Cu–X(cyano) (X = C or N) and Cu–N(bpym) bond lengths in the ranges 1.873(7)–1.909(7) Å and 2.102(4)–2.140(4) Å, respectively. As expected, the small bite of the bpym ligands leads to distorted tetrahedral coordination geometries with bond angles in the range 78.04(15)–125.7(2)°. The Cu···Cu distances across the cyanide ligands are 4.9431(12) Å and 4.9614(12) Å, whereas that across the bpy ligand is 5.6686(11) Å. The Cu_6 ring

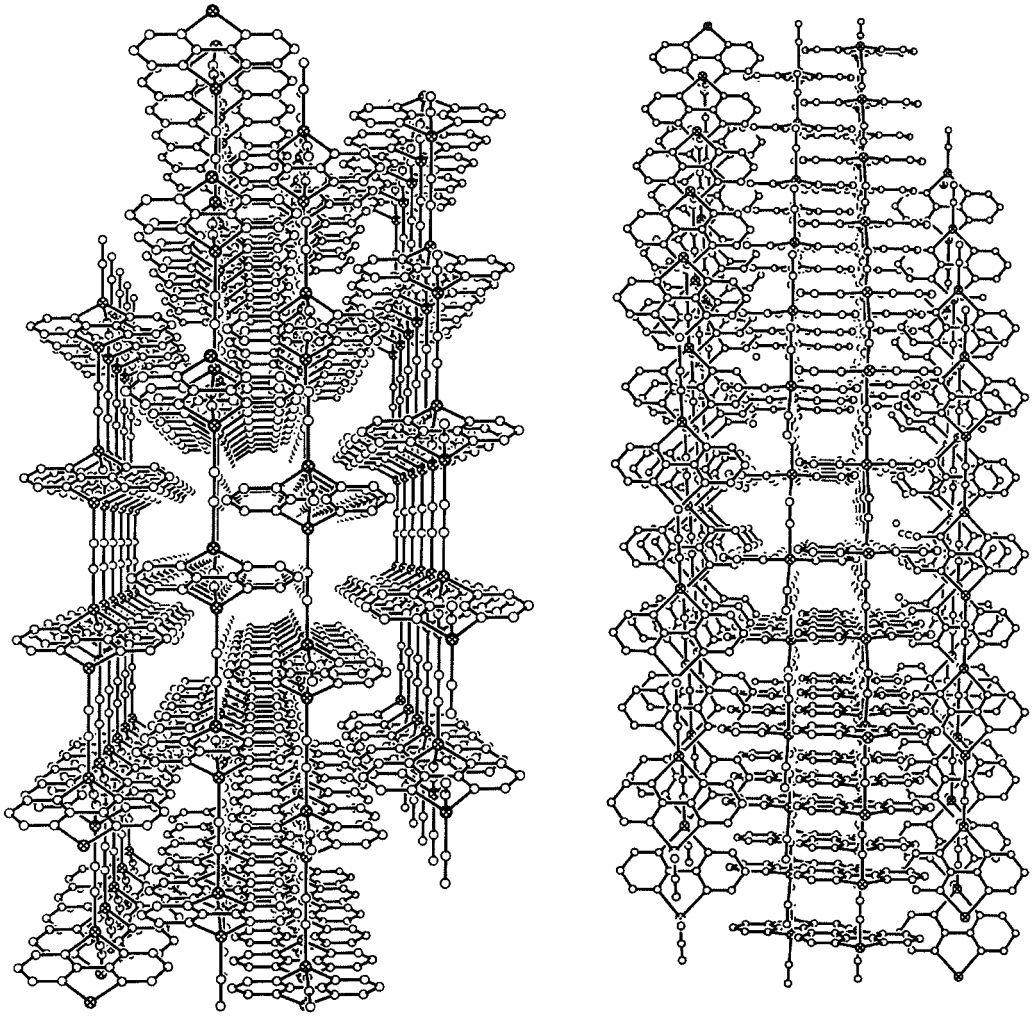

Figure 3. Two perspective views of the stacking of layers of **2** showing the interdigitation of bpym ligands in the *ac* plane (left) and the two different orientations of the bpym ligands (right).

 © 2005 Wiley-VCH Verlag GmbH & Co. KGaA, Weinheim

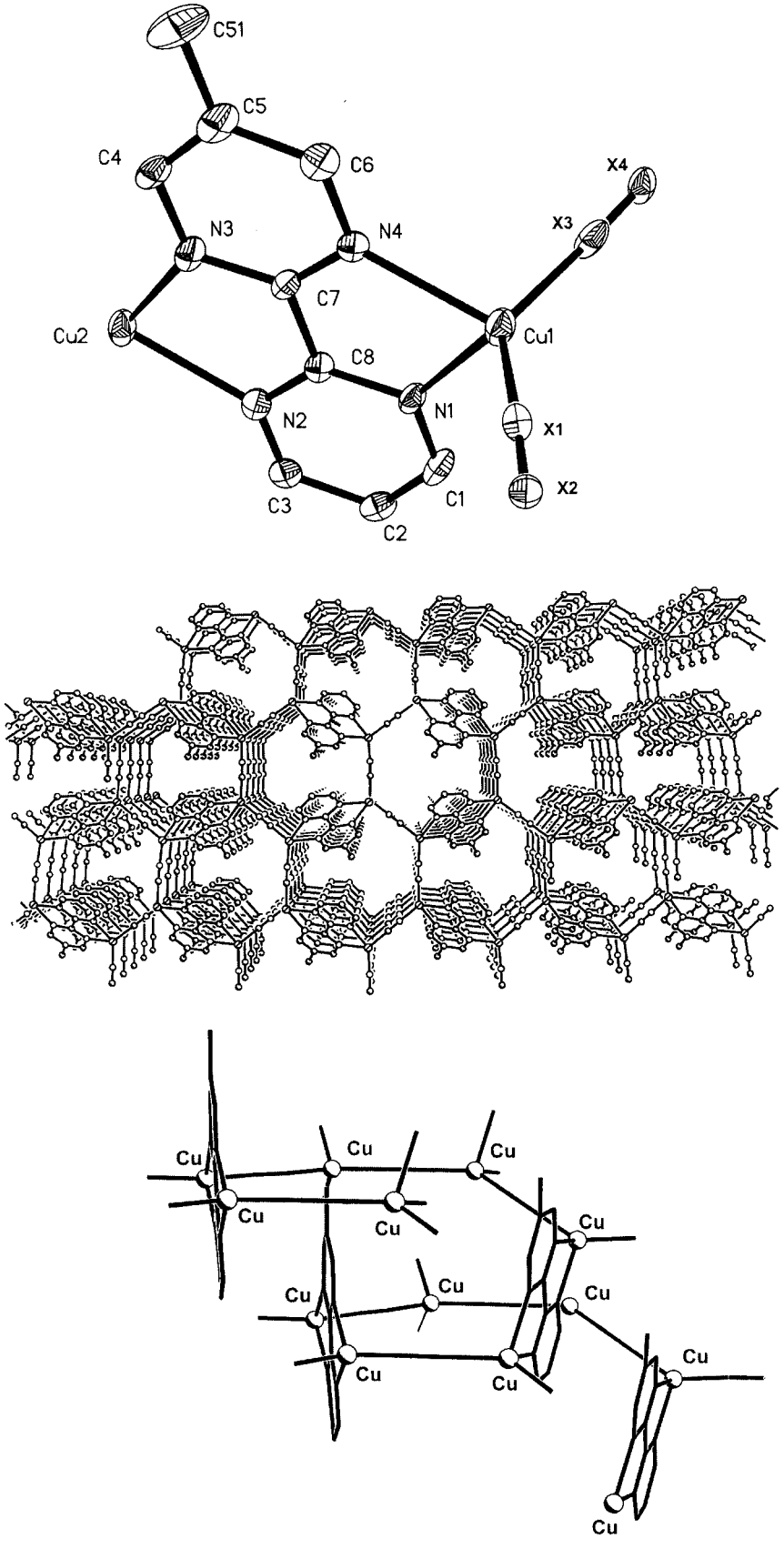

Figure 4. Asymmetric unit of **3** with the disordered CN bridging groups labelled as X (top). View of the 3D network down the *a* axis (middle). Spiral distribution of Cu^{I} atoms along the *a* axis (bottom).

 © 2005 Wiley-VCH Verlag GmbH & Co. KGaA, Weinheim

has approximate dimensions of 8.8×11 Å^2, with Cu···Cu distances across the ring in the range 9.917(17)–10.9254(16) Å.

The asymmetric unit of the structure of $[Cu_2(mbpym)(CN)_2]$ (**3**) is given in Figure 4; selected bond lengths and angles are listed in Table 3. There are two crystallographically independent distorted tetrahedral copper(I) atoms in the structure, which are coordinated, as in **2**, by two bridging cyano groups and one bisdidentate bridging mbpym ligand. In contrast to **2**, the join of the Cu^I atoms does not take place in the same plane, therefore the structure is 3D. When viewed down the *a* axis, the structure seems to be made of fused hexagonal rings (Figure 4, middle). However, a closer examination reveals that these rings are not closed (Figure 4, bottom), and the Cu atoms are distributed in the *a* direction in a spiral manner leading to a 3D chiral network with hexagonal channels of approximate dimensions 9×9.5 Å^2. The space filling is achieved by orientation of the mbpym ligands in such a way that the methyl groups lie on the channels. The bond lengths and angles are similar to those observed in **2**. The Cu···Cu distance across the mbpym is 5.7311(10) Å, whereas the Cu···Cu distances across the cyanide ligands are 4.9526(9) Å and 4.9590 (9) Å.

Table 3. Selected interatomic distances [Å] and angles [°] for **3**.

Cu1–N1	2.154(6)
Cu1–X1	1.874(10)
Cu1–X3	1.903(8)
Cu1–N4	2.143(5)
Cu2–N2	2.166(6)
Cu2–X2[a]	1.915(9)
Cu2–N3	2.150(7)
Cu2–X4[b]	1.900(7)
X1–Cu1–N1	109.5(3)
X3–Cu1–N1	107.2(3)
X3–Cu1–X1	132.5(3)
N4–Cu1–N1	76.9(2)
X1–Cu1–N4	109.7(2)
X3–Cu1–N4	107.1(2)
X2[a]–Cu2–N2	109.1(2)
N3–Cu2–N2	78.1(2)
X4[b]–Cu2–N2	106.0(3)
X4[b]–Cu2–X2[a]	135.0(2)
X2[a]–Cu2–N3	105.9(3)
X4[b]–Cu2–N3	108.1(3)

[a] Equivalent positions: $x - 1/2, -y + 3/2, z - 1/2$. [b] $x + 1/2, y - 1/2, z$.

Concluding Remarks

From the above results the following conclusions can be drawn: (i) The use of hexacyanoferrate(III) as a precursor together with $CuCl_2 \cdot 2H_2O$ and polydentate ligands in simple hydrothermal reactions allows the isolation of homo- and heterometallic cyanide-bridged complexes with intriguing 3D architectures. (ii) The introduction of sterically demanding substituents in the bisdidentate ligand bpym leads to the formation of different structures (compound **2** vs. compound **3**). (iii) Solvothermal chemistry is a versatile and useful synthetic tool to prepare cyanide-bridged polymers.

Solvothermal reactions between other cyanometallate precursors, metal salts and a wide variety of polydentate ligands are currently under examination in our laboratory.

Experimental Section

4-Methyl-2,2′-bipyrimidine was prepared by condensation of 2-cyanopyrimidine with hydroxylamine·HCl and further condensation with 3-ethoxy-2-methylpropenal.[9] The rest of the reagents are commercially available and were used without further purification.

$[Fe(CN)_4(phen)_2Cu_2]$ (1): A mixture of $CuCl_2 \cdot 2H_2O$ (0.21 g, 1.22 mmol), phen (0.22 g, 1.22 mmol), $K_3[Fe(CN)_6]$ (0.4 g, 1.22 mmol) and water (8 mL) was added to a Teflon-lined stainless steel Parr acid digestion vessel and heated at 180 °C for 2 d under autogenous pressure. Slow cooling of the resulting solution to room temperature afforded dark red crystals of **1**. Yield: 0.22g (55%). IR (KBr): ν_{CN} = 2090, 2096 and 2119 cm^{-1}. $C_{28}H_{16}Cu_2N_8Fe$: calcd. C 51.90, H 2.49, N 17.31; found C 51.55, H 2.56, N 17.09. A Fe/Cu ratio of 0.51 was determined by SEM (scanning electron microscopy).

$[Cu_2(CN)_2(bpym] \cdot H_2O$ (2): Dark red crystals of **2** were grown from the hydrothermal treatment of $CuCl_2 \cdot 2H_2O$ (0.054 g, 0.32 mmol), 2,2′-bipyrimidine (0.050 g, 0.32 mmol), KCN (0.123 g, 1.92 mmol) and methanol (8 mL) in the same conditions as for **1**. Yield: 0.026g (47%). IR (KBr): ν_{CN} = 2116 cm^{-1}. $C_{10}H_8Cu_2N_6O$: calcd. C 33.78, H 2.27, N 23.65; found C 33.75, H 2.09, N 23.75.

$[Cu_2(CN)_2(mbpym]$ (3): This compound was prepared as dark red crystals under the same hydrothermal conditions as above with $CuCl_2 \cdot 2H_2O$ (0.098 g, 0.57 mmol), 4-methyl-2,2′-bipyrimidine 2-oxide (0.1 g, 0.57 mmol), $K_3[Fe(CN)_6]$ (0.189 g, 0.57 mmol) and methanol (8 mL). Yield: 0.032g (32%). IR (KBr): ν_{CN} = 2071 cm^{-1}. $C_{11}H_8Cu_2N_6$: calcd. C 37.58, H 2.30, N 23.92; found C 37.51, H 2.36, N 23.52.

Physical Measurements: Elemental analyses were carried out at the Instrumentation Scientific Centre of the University of Granada on a Fisons–Carlo–Erba analyser model EA 1108. IR spectra were recorded on a MIDAC progress IR spectrometer using KBr pellets.

X-ray Crystallography: Single-crystal diffraction data for **1**–**3** were measured on a Bruker Smart Apex diffractometer using graphite-monochromated Mo-K_α radiation (λ = 0.71069 Å). All data sets were corrected for Lorentz and polarisation effects, and absorption corrections were made with SADABS.[12] A total of 45034, 7827 and 7832 reflections giving 7791, 2902 and 3101 unique reflections were collected (R_{int} = 0.0402, 0.0359 and 0.0260) for **1**, **2** and **3**, respectively.

The structures were solved by direct methods and refined on F^2 with the SHELXL97 program.[13] For each compound, refinement of each CN bridge between two Cu^I atoms indicated disordering with respect to the C and N termini. When site occupation parameters of the bridging CN atom positions did not differ markedly from the ratio 50:50 the parameters were fixed to 50% C and 50% N. The disordered CN atom positions are labelled in tables and drawings with X1, X2, X3 etc. For example, in compound **1** the first atom position: 0.5 N6a + 0.5 C26b = X1; second 0.5 N6b + 0.5 C26a = X2; third 0.5 N7a + 0.5 C27b = X3, etc. For all structures, the non-hydrogen atoms were refined with anisotropic displacement parameters and the hydrogen atoms were treated as riding atoms using the SHELX97 default parameters.

 © 2005 Wiley-VCH Verlag GmbH & Co. KGaA, Weinheim

For **1**, the asymmetric unit of the structure consists of four Cu^{I} atoms, two Fe^{II} atoms, eight cyanide ions and four phen ligands. Four of the cyanide ions bridging the copper atoms are disordered.

For **2**, in addition to the disordered bridging cyanide groups, the oxygen atom of the water molecule is disordered over two sites. Site occupation parameters for the atoms were refined, but the hydrogen atom of the disordered water molecule could not be reliably located.

Complex **3** has a lot of pseudo-symmetry and the structure can be solved and refined both in centrosymmetric space group *C*2/*c* and in non-centrosymmetric space group *Cc*. Site occupation parameters for each disordered CN atom position were fixed to 50% C and 50% N for both space groups. Refinement in the centrosymmetric space group resulted in a partly disordered mbpym ligand, whereas refinement in the non-centrosymmetric space group gave a fully ordered ligand. As the *R*1 value of 0.0732 in the centrosymmetric space group is markedly higher than that of 0.0477 in the non-centrosymmetric space group we report here the structure in the lower symmetry space group *Cc*. The structure of **2** was refined as a racemic mixture. The crystal data for **1** to **3** are summarised in Table 4.

Table 4. Crystallographic data and structural refinement details for **1**–**3**.

	1	**2**	**3**
Empirical formula	$C_{28}H_{16}Cu_2FeN_8$	$C_{10}H_8Cu_2N_6O$	$C_{11}H_8Cu_2N_6$
Formula mass	647.42	355.30	351.31
Crystal system	monoclinic	monoclinic	monoclinic
Space group	$P2_1/n$ (no. 14)	*C*2/*c* (no. 15)	*Cc* (no. 9)
a [Å]	19.2111(19)	14.927(2)	6.0928(6)
b [Å]	12.6738(13)	9.3301(12)	16.8890(16)
c [Å]	23.607(2)	19.464(3)	13.4625(13)
β [°]	110.041(2)	97.491(2)	96.174(2)
V [Å^3]	5399.7(9)	2687.6(6)	1377.3(2)
Z	8	8	4
T [°C]	25	–173	–173
λ [Å]	0.71069	0.71069	0.71069
ρ [g cm^{-3}]	1.593	1.756	1.694
μ [cm^{-1}]	21.24	31.64	30.81
Goodness-of-fit	1.043	1.076	1.060
$R1^{[a]}[I > 2\sigma(I)]$	0.0307	0.0572	0.0477
$wR2^{[b]}$ $[I > 2\sigma(I)]$	0.0739	0.1173	0.1168
Flack parameter *x*	–	–	0.47(3)

[a] $R1 = \Sigma||F_o| - |F_c||/\Sigma|F_o|$. [b] $wR2 = \{[\Sigma w(F_o^2 - F_c^2)^2]/[\Sigma w(F_o^2)^2]\}^{1/2}$.

CCDC-250057 (for **1**), -250058 (for **2**) and -250059 (for **3**) contain the supplementary crystallographic data for this paper. These data can be obtained free of charge from The Cambridge Crystallographic Data Centre via www.ccdc.cam.ac.uk/data_request/cif.

Acknowledgments

This work was supported by the Spanish Ministerio de Ciencia y Tecnología through the project BQU2001/3221 and Junta de Andalucía. A. R. thanks the Ministerio de Ciencia y Tecnología for a predoctoral fellowship.

[1] a) R. Robson, in *Comprehensive Supramolecular Chemistry* (Eds.: D. D. MacNicol, F. Toda, R. Bishop), Pergamon Press, Oxford, **1996**, chapter 22, p. 733; M. J. Zaworotko, *Angew. Chem. Int. Ed.* **2000**, *39*, 3052; b) A. J. Blake, N. R. Champness, P. Hubberstey, W. S. Li, M. A. Withersby, M. Schröder, *Coord. Chem. Rev.* **1999**, *183*, 117; c) S. A. Oxtoby, N. R. Champness, *Coord. Chem. Rev.* **2003**, *246*, 145; d) S. R. Batten, *Curr. Opin. Solid State Mater. Sci.* **2001**, *5*, 107; e) H. Li, M. Eddaoudi, M. M. O'Keefe, O. M. Yaghi, *Nature* **1999**, *402*, 276 and references cited therein; f) H. K. Chae, D. Y. Siberio-Pérez, J. Kim, Y. Go, M. Eddaoudi, A. J. Matzger, M. O'Keeffe, O. M. Yaghi, *Nature* **2004**, *427*, 523; g) M. Fujita, Y. J. Kwon, S. Washizu, K. Ogura, *J. Am. Chem. Soc.* **1994**, *116*, 1151; h) S. Noro, S. Kitagawa, M. Kondo, K. Seki, *Angew. Chem. Int. Ed.* **2000**, *39*, 2082 and references cited therein; i) S. Kitagawa, R. Kitaura, S.-I. Noro, *Angew. Chem. Int. Ed.* **2004**, *43*, 2334; j) L. C. Tabares, J. A. R. Navarro, J. M. Salas, *J. Am. Chem. Soc.* **2001**, *123*, 383; k) *Magnetism: A Supramolecular Function* (Ed.: O. Kahn), NATO ASI Series C484, Kluwer Academic Publishers, Dordrecht, The Netherlands, **1996**; l) *Molecular Magnetism: From Molecular Assemblies to Devices* (Eds.: E. Coronado, P. Delhaés, D. Gatteschi, J. S. Miller), NATO ASI Series E321, Kluwer Academic Publishers, Dordrecht, The Netherlands, **1996**; m) E. Coronado, J. R. Galán-Mascarós, C. J. Gómez-García, V. Laukhin, *Nature* **2000**, *408*, 447; n) *Magnetism: Molecules to Materials* (Eds.: J. S. Miller, M. Drillon), Wiley-VCH, Weinheim, **2001**–**2004**; C. Janiak, *Dalton Trans.* **2003**, 2781; o) D. Luneau, *Curr. Opin. Solid State Mater. Sci.* **2001**, *5*, 123.

[2] a) K. R. Dunbar, R. A. Heintz, *Prog. Inorg. Chem.* **1997**, *45*, 283; b) M. Verdaguer, *Science* **1996**, *272*, 698; W. Entley, G. S. Girolami, *Science* **1995**, *268*, 397; S. Ferlay, T. Mallah, R. Ouahes, P. Veillet, M. Verdaguer, *Nature* **1995**, *378*, 701; c) M. Verdaguer, A. Bleuzen, V. Marvaud, J. Vaissermann, M. Seuleiman, C. Desplanches, A. Scuiller, C. Train, R. Garde, G. Gelly, C. Lomenech, I. Rosenman, P. Veillet, C. Cartier, F. Villain, *Coord. Chem. Rev.* **1999**, *190*, 1023; d) W. P. Fehlhammer, M. Fritz, *Chem. Rev.* **1993**, *93*, 1243; e) M. Ohba, K. Okawa, *Coord. Chem. Rev.* **2000**, *198*, 313; f) A. Marvilliers, S. Parsons, E. Rivière, J. P. Audière, M. Kurmoo, T. Mallah, *Eur. J. Inorg. Chem.* **2001**, 1287 and references cited therein; g) R. J. Parker, K. D. Lu, S. R. Batten, B. Moubaraki, K. S. Murray, L. Spiccia, J. D. Cashion, A. D. Rae, A. Willis, *J. Chem. Soc., Dalton Trans.* **2002**, 3723 and references cited therein; h) J. Černák, M. Orendáč, I. Potočňák, J. Chomič, A. Orendáčová, J. Skoršepa, A. Feher, *Coord. Chem. Rev.* **2002**, *224*, 51 and references cited therein; i) H.-Z. Kou, B. C. Zhou, D.-Z. Liao, R.-J. Wang, Y. Li, *Inorg. Chem.* **2002**, *41*, 25 and references cited therein; j) D. J. Chesnut, D. Hagrman, P. J. Zapf, R. P. Hammond, R. LaDuca, R. C. Haushalter, J. Zubieta, *Coord. Chem. Rev.* **1999**, *190*, 757 and references cited therein; k) D. J. Chesnut, D. Plewak, J. Zubieta, *J. Chem. Soc., Dalton Trans.* **2001**, 2567; l) J. S. Miller, J. L. Manson, *Acc. Chem. Res.* **2001**, *34*, 563; m) R. Lescouëzec, J. Vaissermann, C. Ruiz-Pérez, F. Lloret, R. Carrasco, M. Julve, M. Verdaguer, Y. Dromzée, D. Gatteschi, W. Wernsdorfer, *Angew. Chem. Int. Ed.* **2001**, *40*, 1760; n) M. L. Toma, R. Lescouëzec, F. Lloret, M. Julve, J. Vaissermann, M. Verdaguer, *Chem. Commun.* **2003**, 1850; o) M. Pilkington, S. Decurtins, *Comprehensive Coordination Chemistry II* **2004**, *7*, 177–229; p) A. Figuerola, C. Díaz, J. Ribas, V. Tangoulis, J. Granell, F. Lloret, J. Mahía, M. Maestro, *Inorg. Chem.* **2003**, *42*, 641; q) I. Muga, J. M. Gutiérrez-Zorrilla, P. Vitoria, P. Román, L. Lezama, J. I. Beitia, *Eur. J. Inorg. Chem.* **2004**, 1886.

[3] E. Colacio, J. M. Domínguez-Vera, F. Lloret, J. M. Moreno-Sánchez, R. Kivekäs, A. Rodríguez, R. Sillanpää, *Inorg. Chem.* **2003**, *42*, 4209.

[4] a) D. J. Chesnut, D. Hagrman, P. J. Zapf, R. P. Hammond, R. LaDuca, R. C. Haushalter, J. Zubieta, *Coord. Chem. Rev.* **1999**, *190*, 757 and references cited therein; b) D. J. Chesnut, D. Plewak, J. Zubieta, *J. Chem. Soc., Dalton Trans.* **2001**, 2567; c) D. J. Chesnut, A. Kusnetzow, R. Birge, J. Zubieta, *J. Chem. Soc., Dalton Trans.* **2001**, 2581; d) D. J. Chesnut, A. Kusnetzow, R. Birge, J. Zubieta, *Inorg. Chem.* **1999**, *38*, 5484; e) D. J. Ches-

 © 2005 Wiley-VCH Verlag GmbH & Co. KGaA, Weinheim

nut, A. Kusnetzow, J. Zubieta, *J. Chem. Soc., Dalton Trans.* **1998**, 4081; f) D. J. Chesnut, J. Zubieta, *J. Chem. Soc., Chem. Commun.* **1998**, 1707.
[5] J.-H. Yu, J.-Q. Xu, Q.-X. Yang, L.-Y. Pan, T.-G. Wang, C.-H. Lü, T.-H. Ma, *J. Mol. Struct.* **2003**, *658*, 1.
[6] D.-Q. Chu, L.-M. Wang, J.-Q. Xu, *Mend. Commun.* **2004**, *1*, 25–27.
[7] T. Pretsch, I. Bridgam, H. Hans, *Z. Anorg. Allg. Chem.* **2004**, *630*, 353–360.
[8] Y. Kang, Y.-G. Yao, Y.-Y. Qin, J. Zhang, Y.-B. Chen, Z. J. Li, Y.-H. Wen, J.-K. Cheng, R.-F. Hu, *Chem. Commun.* **2004**, *9*, 1046.
[9] E. Colacio, A. Debdouibi, A. Romerosa, unpublished results.
[10] a) H. Oshio, H. Onodera, O. Tamada, H. Mizutani, T. Hikichi, T. Ito, *Chem. Eur. J.* **2000**, *6*, 2523; b) H. Oshio, O. Tamada, H. Onodera, T. Ito, T. Ikoma, S. Tero-Kubota, *Inorg. Chem.* **1999**, *38*, 5686.
[11] a) J. A. Real, A. B. Gaspar, V. Niel, M. C. Muñoz, *Coord. Chem. Rev.* **2003**, *236*, 121; b) Y. García, V. Niel, M. C. Muñoz, J. A. Real, *Top. Curr. Chem.* **2004**, *233*, 229.
[12] G. M. Sheldrick, SADABS, a program for empirical absorption corrections, University of Göttingen, Germany, **1996**.
[13] G. M. Sheldrick, SHELX97, University of Göttingen, Germany, **1997**.

Received: December 03, 2004
Published Online: June 14, 2005

 © 2005 Wiley-VCH Verlag GmbH & Co. KGaA, Weinheim

Synthesis, Structure and Spectroscopic Properties of Novel 9,10-Bis{[6-(diphenylphosphanyl)-2-pyridylmethyl]propylaminomethyl}anthracene-Bridged Group 11 Metal (M = Cu^I and Ag^I) Dinuclear Complexes

Hu Xu,[a] Feng-Bo Xu,*[a] Qing-Shan Li,[a] Wei-Guo Duo,[a] Hai-Bin Song,[a] and Zheng-Zhi Zhang*[a]

Keywords: Dinuclear complexes / Phosphanyl-pyridine ligands / Copper / Silver / Charge transfer interaction / Dual emission

Dinuclear complexes $[M_2(\mu\text{-BPNNAn})]X_2$ (M = Cu^I, X = ClO_4^- **1**, X = BF_4^- **2**; M = Ag^I, X = BF_4^- **3**, X = ClO_4^- **4**) have been prepared by treating 9,10-bis{[6-(diphenylphosphanyl)-2-pyridylmethyl]propylaminomethyl}anthracene (BPNNAn) with $M(CH_3CN)_4X$ in CH_2Cl_2. The structures of complexes **1**, **2** and **3** have been determined by single-crystal X-ray diffraction studies. In the complexes, BPNNAn acts as a chelating ligand and two metal ions riding on two bridgehead carbon atoms in the anthracene group leads to the deformation of the anthracenyl ring. The Cu–Arene charge transfer interaction is observed from the nonfluorescent emission of Cu complex **1**, while the Ag complex **3** exhibits dual emission at high concentrations in a CH_2Cl_2 solution.

(© Wiley-VCH Verlag GmbH & Co. KGaA, 69451 Weinheim, Germany, 2005)

Introduction

In recent years increasing interest, focused on phosphanyl-pyridine ligands as building blocks, stems from its ability to form hetero- or homonuclear metal complexes.[1] The typical representative 2-(diphenylphosphanyl)pyridine (dppy) has been widely used to synthesize dppy-bridged dinuclear species because of the short bite between the two donor atoms and the poor flexibility.[2] On the other hand, anthracenyl rings exist in a great deal of organic compounds as a good fluorophore. These types of compounds have been applied as a fluorescence chemosensor for small molecules or metal ions.[3] Therefore, we wish to associate two dppy units with an anthracenyl group through long chain spacers to form a polydentate ligand and to explore the change in fluorescence after the bonding to metal atoms. Herein we report the novel dinuclear complexes $[M_2(\mu\text{-BPNNAn})]X_2$ (M = Cu, X = ClO_4^- **1**, X = BF_4^- **2**; M = Ag, X = BF_4^- **3**, X = ClO_4^- **4**) constructed from the polydentate phosphanyl-pyridyl ligand 9,10-bis{[6-(diphenylphosphanyl)-2-pyridylmethyl]propylaminomethyl}-anthracene (BPNNAn) and Group 11 metals. The Cu complexes are formed through charge transfer interactions and Ag complexes give dual fluorescence emission at high concentrations in CH_2Cl_2 solution.

[a] State Key Laboratory of Element-Organic Chemistry, Nankai University,
Tianjin 300071, People's Republic of China
E-mail: zzzhang@public.tpt.tj.cn
xfbo@eyou.com

Results and Discussion

BPNNAn was prepared from 9,10-bis(propylaminomethyl)anthracene, 6-(bromomethyl)-2-chloropyridine and lithium diphenylphosphide by two-step reactions. In the ligand molecule, two dppy units are linked together through an eight atom chain. Meanwhile, there are two lone-pair electrons belonging to two tertiary N atoms associated with the dppy units by a methylene spacer. Hence, it is potentially a polydentate ligand. Its Group 11 dinuclear complexes $[M_2(\mu\text{-BPNNAn})]X_2$ (M = Cu, X = ClO_4^- **1**, X = BF_4^- **2**; M = Ag, X = BF_4^- **3**, X = ClO_4^- **4**) were obtained by the reaction of BPNNAn with $M(CH_3CN)_4X$ (M = Cu or Ag; X = ClO_4^- or BF_4^-) in a 1:2 mol ratio and are stable in air and moisture in the solid state, and soluble in dichloromethane and acetone (Scheme 1).

Slow evaporation of a solution of complex **1** in acetone and ethyl acetate yields bright yellow crystalline material, which has been determined as **1**·2CH_3COCH_3 (Figure 1a) by a single-crystal X-ray diffraction study. Using similar methods, bright yellow crystalline **2**·1.5$ClCH_2CH_2Cl$ and pale green crystalline **3**·2CH_3OH (Figure 1b, only one of the two independent molecules is shown) can be obtained. The detailed crystallographic data and structural refinements for **1**, **2** and **3** are summarized in Table 1.

It can be envisaged that two dppy units contained in BPNNAn occur at a relatively extended distance to relieve their mutual repulsion. However, after coordination with the group 11 metals (M = Cu, Ag) a great conformational change of the ligand takes place. BPNNAn acts as a chelating ligand, in which the dppy-N and tertiary N atoms from

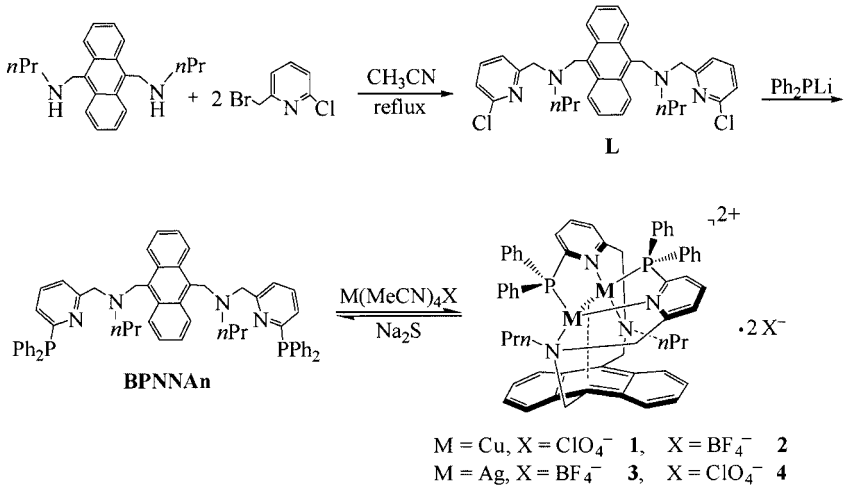

Scheme 1. Synthesis of $[M_2(\mu\text{-BPNNAn})]X_2$.

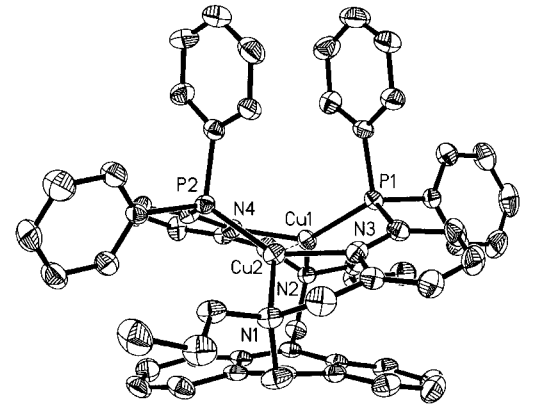

1a

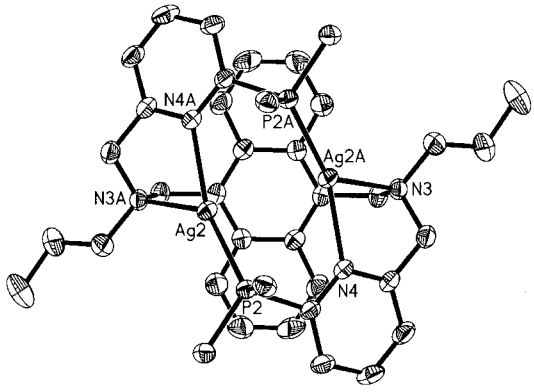

1b

Figure 1. (1a) Perspective view (35% thermal ellipsoids) of the $[Cu_2(\mu\text{-BPNNAn})]^{2+}$ cation in **1**·2CH_3COCH_3. (1b) Perspective view (35% thermal ellipsoids) of eight-membered ring $M_2P_2N_2C_2$ from the anthracene plane in **3**·2CH_3OH. Only the ipso carbons of the phenyl groups of the P atoms are shown, and the hydrogen atoms have been omitted for clarity.

one arm and the P atom from the other simultaneously capture one of the M atoms. Each metal center exhibits a three coordinated trigonal pyramidal geometry. The two metal atoms ride on the two bridgehead carbon atoms in the anthracene group as shown in Figure 2 (only displaying complex **1**). Such a coordination mode leads to a remarkable structural change in the anthracenyl ring. To relieve the steric repulsion, the 9,10-carbon atoms of the anthracenyl ring are markedly bent towards the two metal cores, out of the coplanar configuration, and form dihedral angles of 20.1° (**1**) and 9.3° (10.8°) (**3**) between the side benzene rings in the anthracenyl units. The values are larger than that of 7.7° in our mono-Cu–η^6–arene complex.[4] For the same reason *n*-propyl groups on the tertiary N atoms and two phenyl rings on the P atoms stretch away from the M cores in a linear direction as much as possible. The dinuclear cations of **1** (Figure 1a), and **3** (Figure 1b) possess the C_2-symmetric structures. No interaction is observed between cations and anions. Selected bond lengths [Å] and angles [°] for complexes **1**, **2** and **3** are summarized in Table 2.

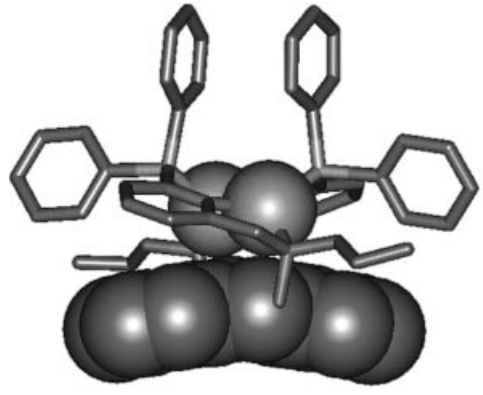

Figure 2. Space filling view of the Cu···Cu cores riding on 9,10-bridgehead carbon atoms of anthracene unit in complex **1**.

 © 2005 Wiley-VCH Verlag GmbH & Co. KGaA, Weinheim

Table 1. Crystal data and structure refinement for **1**, **2** and **3**.

	1·2 CH_3COCH_3	**2**·1.5 $ClCH_2CH_2Cl$	**3**·2 CH_3OH
Chemical formula	$C_{60}H_{68}Cl_2Cu_2N_4O_{10}P_2$	$C_{30.50}H_{31}BCl_{1.50}CuF_4N_2P$	$C_{60}H_{64}Ag_2B_2F_8N_4O_2P_2$
Formula mass	1313.14	660.07	1324.45
Crystal system	triclinic	triclinic	monoclinic
Space group	*P*-1	*P*-1	*C*2/*c*
a [Å]	12.706(6)	13.252(7)	28.330(18)
b [Å]	13.390(6)	13.596(7)	25.547(17)
c [Å]	18.865(8)	17.908(9)	21.349(14)
α [°]	83.765(8)	79.657(9)	90
β [°]	82.941(8)	77.676(9)	131.005(8)
γ [°]	77.030(8)	76.604(9)	90
V [Å^3]	3093(2)	3037(3)	11660(13)
Z	2	4	8
$D_{calcd.}$ [mg m^{-3}]	1.410	1.443	1.509
μ [mm^{-1}]	0.887	0.952	0.798
F(000)	1364	1354	5392
T [K]	293(2)	293(2)	293(2)
No. of data collected	16067	15927	33453
No. of unique data	10821	10666	11903
No. of refined parameters	790	833	810
Goodness-of-fit on F^2 [a]	1.065	1.030	1.015
R_1 [b]	0.0708	0.0621	0.0406
wR_2	0.1533	0.1546	0.0851
R_1 [b]	0.1517	0.1182	0.0959
wR_2	0.1974	0.2030	0.1083

[a] GOF = $\{\Sigma[w(F_o^2 - F_c^2)^2/(n-p)]\}^{1/2}$, where *n* is the number of reflections and *p* is the number of parameters refined. [b] $R_1 = \Sigma(||F_o| - |F_c||)/\Sigma|F_o|$; w$R_2 = 1/[\sigma^2(F_o^2) + (0.0691P) + 1.4100P]$ where $P = (F_o^2 + 2F_c^2)/3$.

Table 2. Selected bond lengths [Å] and angles [°] for complexes **1**, **2** and **3**.[a]

1·2 CH_3COCH_3		**2**·1.5 $ClCH_2CH_2Cl$		**3**·2 CH_3OH	
Cu(1)–Cu(2)	2.9734(16)	Cu(1)–N(4)	2.034(5)	Ag(2)–Ag(2)#2	3.0874(19)
Cu(1)–P(1)	2.177(2)	Cu(1)–N(2)	2.132(5)	Ag(2)–N(4)#2	2.287(3)
Cu(1)–N(2)	2.150(5)	Cu(1)–P(1)	2.1836(19)	Ag(2)–P(2)	2.3699(18)
Cu(1)–N(4)	2.007(5)			Ag(2)–N(3)#2	2.434(4)
N(2)–Cu(1)–P(1)	126.76(15)	N(4)–Cu(1)–N(2)	84.01(19)	N(4)#2–Ag(2)–P(2)	150.32(10)
N(4)–Cu(1)–P(1)	140.09(16)	N(4)–Cu(1)–P(1)	139.16(14)	N(4)#2–Ag(2)–N(3)#2	74.55(13)
P(1)–Cu(1)–Cu(2)	79.91(6)	N(2)–Cu(1)–P(1)	130.08(14)	P(2)–Ag(2)–N(3)#2	133.76(9)
N(2)–Cu(1)–Cu(2)	144.70(14)			N(4)#2–Ag(2)–Ag(2)#2	84.67(10)
N(4)–Cu(1)–N(2)	83.5(2)			P(2)–Ag(2)–Ag(2)#2	78.51(5)
N(4)–Cu(1)–Cu(2)	87.28(16)			N(3)#2–Ag(2)–Ag(2)#2	135.22(9)

[a] Symmetry transformations used to generate equivalent atoms: #2 $-x + 1, y, -z + 3/2$.

Apart from the two tertiary N atoms, two dppy units in a head-to-tail mode forming an eight-membered ring $M_2P_2N_2C_2$, which has an eclipsed conformation, bridge the metal atoms. The torsion angle P(1)–Cu(1)–Cu(2)–P(2) of 117.8° for **1** is much smaller than that of 125.2°(128.3°) for **3**. While in $[Ag_2(\mu\text{-}L^1)_2(MeCN)_2]^{2+}$ [L^1 = 2-(diphenylphosphanyl)-6-(pyrazol-1-yl)pyridine],[5] $[Cu_2(\mu\text{-}L)_2(MeCN)_2]^{2+}$ (L = 6-(diphenylphosphanyl)-2,2′-bipyridine)[6] and $[Cu_2(\mu\text{-}L^1)_2(MeCN)_2]^{2+}$ [L^1 = 2-(diphenylphosphanyl)-6-(pyrazol-1-yl)pyridine],[7] the similar eight-membered rings are staggered conformations.

The Cu···Cu distance 2.9734(16) Å for **1** is close to the sum of the van der Waals radii of Cu^I centers and lies towards the longer distances of the known Cu–Cu bonds [2.639(2)–2.938(2) Å] for dinuclear Cu^I complexes.[8] The value is slightly longer than that of 2.721(3) Å in $[Cu_2(\mu\text{-dppy})_3(MeCN)]^+$[9] and much shorter than those of 3.584(1) Å, 3.625(1) Å and 3.941(2) Å in $[Cu_2(\mu\text{-dppy})_2(MeCN)]^+$,[10] $[Cu_2(\mu\text{-}L^1)_2(MeCN)_2]^{2+}$ [L^1 = 2-(diphenylphosphanyl)-6-(pyrazol-1-yl)pyridine][7] and $[Cu_2(\mu\text{-}L)_2(MeCN)_2]^{2+}$ (L = 6-(diphenylphosphanyl)-2,2′-bipyridine),[6] respectively.

The Ag···Ag separation of 3.0874(19) Å [3.0963(16) Å] in **3** is slightly shorter than that of 3.145 Å in $[Ag_2(dppy)_2]^{2+}$[11] and 3.162(1)–3.223(1) Å in $[Ag_3\{HC(PPh_2)_3\}_2]^{3+}$.[12] And the value compares with those found in $[Ag_2(\eta^1\text{-dppy})(\mu\text{-dppy})_2]^{2+}$ [3.072(1) Å],[13] $[Ag_2Cl_2(dppy)_3]$ [3.074(2) Å][14] and $[Ag_2(dpm)_2(NO_3)_2]$ (3.085 Å) [dpm = bis(diphenylphosphanyl)methane].[15] But the Ag···Ag distance of **3** is slightly longer than that of 2.964(1) Å reported in $[Ag_2(\mu\text{-}L^1)_2(MeCN)_2]^{2+}$ [L^1 = 2-(diphenylphosphanyl)-6-(pyrazol-1-yl)pyridine],[5] which indicates the possibility of a weak Ag···Ag bond. Since the value of 3.30 Å represents the upper limit for the Ag···Ag interactions in coordination compounds,[16] it can be concluded that Ag···Ag interactions are present in complex **3**.

 © 2005 Wiley-VCH Verlag GmbH & Co. KGaA, Weinheim

In addition, there is an intramolecular π-π stacking interaction between two phenyl rings on two P atoms that are nearly orthogonal to the anthracene mean plane. They stack partially with separations of 3.33 Å and 3.47 Å (3.39 Å) for **1** and **3**, respectively. The π-π stacking interactions may be one of the reasons for drawing two metal atoms together that are located close to one another. The distance of the center of the M···M to the anthracene central ring in **1** is 2.9 Å, while the corresponding value in **3** is 3.2 Å. When $[M_2(\mu\text{-BPNNAn})]X_2$ react with Na_2S, the free ligand BPNNAn can be recovered quantitatively by removing the coordinated Cu or Ag atoms from the polydentate complexes (Scheme 1).

Compared with the free ligand, the fluorescence emission intensity of $[M_2(\mu\text{-BPNNAn})]X_2$ changes dramatically. The spectrum of BPNNAn in CH_2Cl_2 solution (1.0×10^{-5} M) at room temperature displays the expected strong emission peak for the anthracenyl fluorophore centered at 431 nm. Complex **1** in CH_2Cl_2 gives a feeble emission, while **3** gives a moderately strong peak (Figure 3). What is more interesting is that a broad new emission peak, centered at 460 nm, emerges, except for the anthracenic emission of **3**. The new emission for **3** is dependent on concentration and is ascribable to the formation of excimer type intermolecular complexes resulting from the interaction between the two anthracenyl rings. When the concentration is very low, the emission peak results mainly from the anthracenyl ring. With the increase of the concentration, the excimer emission gradually appears and becomes dominant (Figure 4). Therefore, we propose that there is a series of conversion processes for **3** in the CH_2Cl_2 solution. Firstly, the Ag···Ag bond separates away from the anthracenyl unit and the deformation of the anthracenyl ring forms **3′**. Then the combining of two **3′** forms the dimer. But in the low concentration range, **3′** cannot efficiently form the dimer, which generates a new emission. At high concentration, the dimer occurs in larger quantities than both **3** and **3′**. So the new emission dominates in the emission spectrum in Ag complexes at high concentration (Scheme 2). As for **1** the feeble emission shows the formation of a charge transfer complex in the Cu complex,[17] in which the charge transfer interaction is fairly strong and prevents **1** from forming the analogs of **3′**. On the other hand, complex **1** does not generate the dual emission as **3** does, which also further proves the presence of the aforementioned Cu–Arene charge transfer interaction in Cu complexes. Besides, we also observe the fluorescence emission intensity change process for the solution of BPNNAn in CH_2Cl_2 containing $Cu(CH_3CN)_4ClO_4$ of different concentrations (Figure 5). With the increasing concentration of Cu^I, the fluorescence emission intensity of the solution descends gradually until the emission becomes weak. Recording the fluorescence intensity against the ratio

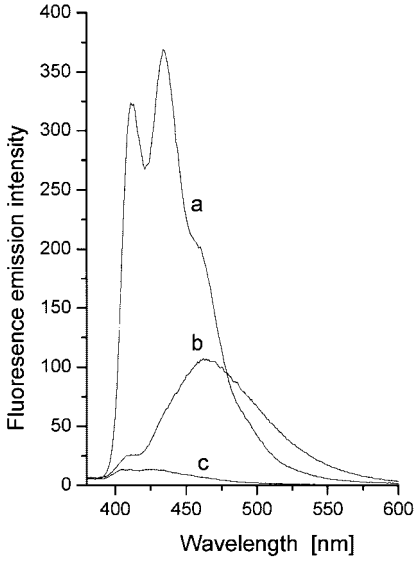

Figure 3. Fluoresence emission spectra of **a** (BPNNAn), **b** (**3**) and **c** (**1**) (λ_{ex} = 360 nm) at 298 K in CH_2Cl_2 (1.0×10^{-5} M).

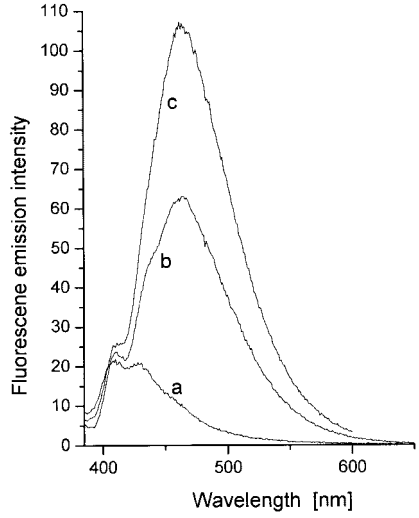

Figure 4. Fluorescene emission intensity of **3** in different concentrations of a CH_2Cl_2 solution: (a) 1.0×10^{-6} M, (b) 5.0×10^{-6} M, (c) 1.0×10^{-5} M.

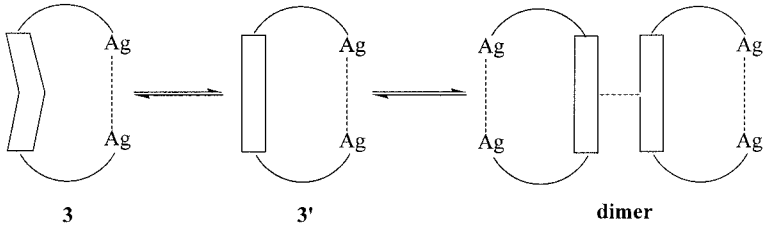

Scheme 2. Conversion process of **3** in CH_2Cl_2 solution.

 © 2005 Wiley-VCH Verlag GmbH & Co. KGaA, Weinheim

[Cu^I] to [**1**], we get a corresponding curve, which indicates that a compound like **1** will only be formed in the end if sufficient Cu^I exists in solution (Figure 6).

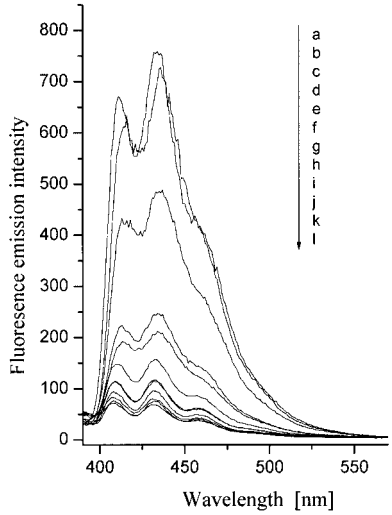

Figure 5. Fluorescence emission spectra (λ_{ex} = 360 nm) of solutions containing $Cu(CH_3CN)_4ClO_4$ of different concentrations in a CH_2Cl_2 solution of BPNNAn (1.0×10^{-5} M) (a = 0×10^{-5} M, b = 0.2×10^{-5} M, c = 0.4×10^{-5} M, d = 0.6×10^{-5} M, e = 0.8×10^{-5} M, f = 1.0×10^{-5} M, g = 1.2×10^{-5} M, h = 1.4×10^{-5} M, i = 1.6×10^{-5} M, j = 1.8×10^{-5} M, k = 2.0×10^{-5} M, l = 2.2×10^{-5} M).

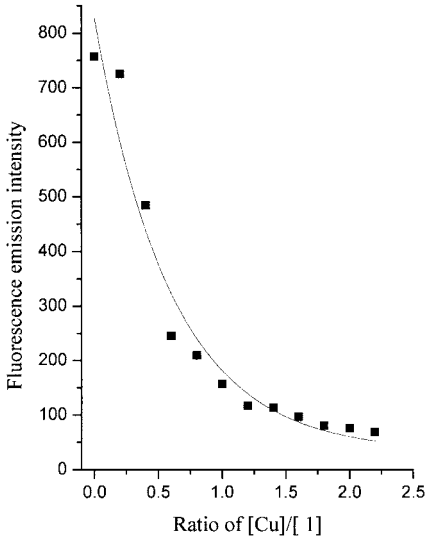

Figure 6. Plot of the recorded relation of fluorescence intensity at 431 nm against the ratio of [Cu^I] to [**1**] (1.0×10^{-5} M) in CH_2Cl_2.

There is a hemilabile coordination mode in these structures, which makes the study of the catalytic activity of these BPNNAn systems with the late transition metals highly feasible. The work in this field is presently under way.

Conclusions

We have prepared a new polydentate phosphane ligand BPNNAn and obtained its Group 11 dinuclear complexes **1**, **2**, **3** and **4**, in which anthracene planes are remarkably bent. Complexes [M_2(μ-BPNNAn)]X_2 react with Na_2S to release quantitatively the free ligand BPNNAn. Cu···Arene charge transfer interactions in the Cu complexes exist, which leads to nonfluorescence emission of the complexes, while Ag complexes, which possess Ag···Ag bonds, generate dual fluorescence emission under the same conditions.

Experimental Section

General Procedures: All reactions were carried out under prepurified argon using standard Schlenk or vacuum line techniques unless stated otherwise. The solvents were purified by standard methods. ^1H and ^{31}P NMR spectra were recorded on a Bruker AC-300 NMR spectrometer. Elemental analyses were measured by using a Perkin–Elmer 2400C Elemental Analyzer. The fluorescence spectroscopy was measured with a Cary Eclipse fluorescence spectrophotometer.

CAUTION: Metal perchlorates are potentially explosive in reactions with organic compounds and proper care should always be taken.

Preparation of 9,10-Bis[(6-chloro-2-pyridylmethyl)propylaminomethyl]anthracene (L): 6-(bromomethyl)-2-chloropyridine (4.54 g, 22 mmol) and K_2CO_3 (5.52 g, 40 mmol) were added to a solution containing 9,10-bis(propylaminomethyl)anthracene (3.0 g, 10 mmol) in MeCN (80 mL). The resulting mixture was stirred at refluxing temperature for 3 days while being exposed to air. This solution was cooled and then filtered through Celite. The solvent was removed in vacuo and water (50 mL) was added. The aqueous phase was extracted with CH_2Cl_2 (3×40 mL) and the organic phase dried with anhydrous Na_2SO_4 overnight. Most of the CH_2Cl_2 was removed under vacuum and ether was added. Cooling to –10 °C yielded a pale yellow solid, which was recrystallized with dichloromethane-haxane to afford **L**. Yield: 2.64 g (46.2%). ^1H NMR (300 MHz, $CDCl_3$): δ = 8.48–8.51(q, 4 H, An*H*) (An = Anthracene), 7.42–7.46(q, 4 H, An*H*), 7.19–7.24(t, 2 H, Py*H*) (Py = Pyridine), 6.99–7.02(d, 2 H, Py*H*), 6.86–6.89(d, 2 H, Py*H*), 4.55(s, 4 H, AnCH_2), 3.61(s, 4 H, NCH_2Py), 2.54–2.59(t, 4 H, CH_2CH$_2$CH$_3$), 1.57–1.69(m, 4 H, CH$_2$CH_2CH$_3$), 0.76–0.81(t, 6 H, CH$_2$CH$_2$CH_3) ppm. Elemental analysis for $C_{34}H_{36}Cl_2N_4$ (571.6 g): calcd. C 71.45, H 6.30, N 9.81; found: C 71.44, H 6.42, N 9.72.

Preparation of BPNNAn: A solution of *n*BuLi in hexane (4 mL, 1.88 M) was added dropwise to a solution of Ph_2PH (1.29 g, 6.94 mmol) in THF (15 mL) at 0 °C with stirring and the resulting solution was stirred for half an hour at this temperature. Then the mixture was added dropwise to a solution of **L** (1.80 g, 3.15 mmol) in THF (20 mL) at –78 °C and the mixture was allowed to warm slowly to room temperature and continuously stirred for 5 h, after which the solution was refluxed for 2 h. After cooling, the solvent was removed in vacuo and water (50 mL) was added. The aqueous phase was extracted with CH_2Cl_2 (3×30 mL) and the organic phase dried with anhydrous Na_2SO_4 overnight. Most of the CH_2Cl_2 was removed under vacuum and the residue was cooled to 0 °C for 8 h to afford a light yellow solid BPNNAn. Yield: 1.6 g (57.4%). ^1H NMR(300 MHz, $CDCl_3$): δ = 8.52–8.55 (q, 4 H, An*H*), 7.43–7.46 (q, 4 H, An*H*), 7.23–7.35 (m, 22 H, Ph*H* and Py*H*), 7.04–7.07(d, 2 H, Py*H*), 6.75–6.78(d, 2 H, Py*H*), 4.60(s, 4 H, AnCH_2), 3.76(s, 4 H, NCH_2Py), 2.54–2.59(t, 4 H, CH_2CH$_2$CH$_3$), 1.57–1.68(m, 4 H, CH$_2$CH_2CH$_3$), 0.73–0.78 (t, 6 H, CH$_2$CH$_2$CH_3) ppm. ^{31}P NMR (300 MHz, $CDCl_3$): δ = –4.42 (s) ppm. Elemental analysis for $C_{58}H_{56}N_4P_2$ (871.1 g): calcd. C 79.90, H 6.43, N 6.43; found: C 79.81, H 6.22, N 6.55.

 © 2005 Wiley-VCH Verlag GmbH & Co. KGaA, Weinheim

Preparation of Complex $[Cu_2(\mu\text{-BPNNAn})](ClO_4)_2$ (1): Solid $[Cu(MeCN)_4][ClO_4]$ (0.107 g, 0.328 mmol) was added to a solution of BPNNAn (0.143 g, 0.164 mmol) in CH_2Cl_2 (20 mL) with stirring at –30 °C. The resulting solution was allowed to warm slowly to room temperature and stirred continuously for 2 h at this temperature. Subsequent diffusion of diethyl ether into the concentrated solution gave complex **1** as a yellow powder. Yield: 0.09 g (45.69%). ^{31}P NMR (300 MHz, $[D_6]$DMSO): δ = 12.80(s) ppm. Elemental analysis for $C_{58}H_{56}Cl_2Cu_2N_4O_8P_2 \cdot 2CH_3C(O)CH_3$ (1313.1 g): calcd. C 58.49, H 5.18, N 4.26; found: C 58.18, H 5.45, N 4.25.

Preparation of Complex $[Cu_2(\mu\text{-BPNNAn})](BF_4)_2$ (2): Complex **2**, as a bright yellow powder, was synthesized by BPNNAn (0.110 g, 0.126 mmol) and $[Cu(MeCN)_4][BF_4]$ (0.079 g, 0.251 mmol) by the same procedure as used for **1**. Yield: 0.112 g (74.67%). ^{31}P NMR (300 MHz, $[D_6]$DMSO): δ = 12.82(s) ppm. Elemental analysis for $C_{58}H_{56}Cu_2B_2N_4F_8P_2 \cdot 1.5ClCH_2CH_2Cl$ (1320.1 g): calcd. C 55.45, H 4.70, N 4.24; found: C 55.05, H 4.91, N 4.47.

Preparation of Complex $[Ag_2(\mu\text{-BPNNAn})](BF_4)_2$ (3): Complex **3**, as a pale yellow powder, was synthesized by BPNNAn (0.143 g, 0.164 mmol) and $[Ag(MeCN)_4][BF_4]$ (0.118 g, 0.328 mmol) by the same procedure as used for **1**, but in darkness. Yield: 0.120 g (57.97%). ^{31}P NMR (300 MHz, $[D_6]$DMSO): δ = 21.97 ppm. Elemental analysis for $C_{58}H_{56}Ag_2B_2N_4F_8P_2 \cdot 2CH_3OH$ (1324.5 g): calcd. C 54.36, H 4.83, N 4.23; found: C 54.30, H 4.74, N 4.07.

Preparation of Complex $[Ag_2(\mu\text{-BPNNAn})](ClO_4)_2$ (4): Complex **4**, as a pale yellow powder, was synthesized by BPNNAn (0.143 g, 0.164 mmol) and $[Ag(MeCN)_4][ClO_4]$ (0.122 g, 0.328 mmol) by the same procedure as used for **1**, but in darkness. Yield: 0.150 g (71.09%). ^{31}P NMR (300 MHz, $[D_6]$DMSO): δ = 22.04 ppm. Elemental analysis for $C_{58}H_{56}Ag_2Cl_2N_4O_8P_2$ (1285.8 g): calcd. C 54.12, H 4.35, N 4.35; found: C 53.76, H 4.43, N 4.03.

Reaction of Complexes with Na_2S: A solution of excess $Na_2S \cdot 9H_2O$ in distilled water (5 mL) was added to a solution of **1** (58 mg, 0.048 mmol) in acetone (15 mL) with stirring and a black precipitate was immediately produced. Stirring was continued for 30 min and a white solid was generated. CH_2Cl_2 (15 mL) was added to the solution and stirring continued until the white solid disappeared. The black precipitate was filtered and the solvent was removed under vacuum. The residue was recrystallized from CH_2Cl_2-diethyl ether to give BPNNAn. Yield: 30 mg (71.4%).

Similar reactions for complex **2**, **3** and **4** can be undertaken to give BPNNAn quantitatively.

X-ray Crystallography: The structures of **1**, **2** and **3** were solved by direct methods and all non-hydrogen atoms were subjected to anisotropic refinement by full-matrix least-squares on F^2 using the SHELXTL package. Data collection was performed at room temperature with a Bruker SMART 1000 CCD diffractometer operating at 50 kV and 20 mA using Mo-K_α radiation (0.71073 Å). An empirical absorption correction was applied using the SADABS program. All hydrogen atoms were generated geometrically (C–H bond lengths fixed at 0.96 Å), assigned appropriate isotropic thermal parameters and included in structure factor calculations.

CCDC-244084, -258486 and -258487 contain the supplementary crystallographic data for this paper. These data can be obtained free of charge from The Cambridge Crystallographic Data Centre via www.ccdc.cam.ac.uk/data_request/cif.

Ackowledgments

We thank the National Natural Science Foundation for financial support of this work through grant 20472036.

[1] See for example: a) J. P. Farr, M. M. Olmstead, A. L. Balch, *J. Am. Chem. Soc.* **1980**, *102*, 6654–6656; b) T. J. Barder, F. A. Cotton, G. L. Powell, S. M. Tetrick, R. A. Walton, *J. Am. Chem. Soc.* **1984**, *106*, 1323–1332; c) C. G. Arena, E. Rotondo, F. Faraone, M. Lanfranchi, A. Tiripicchio, *Organometallics* **1991**, *10*, 3877–3885; d) L. Costella, A. Del Zotto, A. Mezzetti, E. Zangrando, P. Rigo, *J. Chem. Soc. Dalton Trans.* **1993**, 3001–3008; e) W.-H. Chan, Z.-Z. Zhang, T. C. W. Mak, C. M. Che, *J. Chem. Soc. Dalton Trans.* **1998**, 803–810; f) L. Barloy, S. Ramdeehul, J. A. Osborn, C. Carlotti, F. Taulelle, A. D. Cian, J. Fisher, *Eur. J. Inorg. Chem.* **2000**, 2523–2532; g) V. J. Catalano, B. L. Bennett, S. Muratidis, B. C. Noll, *J. Am. Chem. Soc.* **2001**, *123*, 173–174.

[2] a) Z.-Z. Zhang, H. Cheng, *Coord. Chem. Rev.* **1996**, *147*, 1–39; b) S.-M. Kuang, H. Cheng, L.-J. Sun, Z.-Z. Zhang, Z.-Y. Zhou, B.-M. Wu, T. C. W. Mak, *Polyhedron* **1996**, *15*, 3417–3426; c) Z.-Z. Zhang, H. Cheng, S.-M. Kuang, Y.-Q. Zhou, Z.-X. Liu, J.-K. Zhang, H.-G. Wang, *J. Organomet. Chem.* **1996**, *516*, 1–10; d) S.-M. Kuang, F. Xue, C.-Y. Duan, T. C. W. Mak, Z.-Z. Zhang, *J. Organomet. Chem.* **1997**, *534*, 15–21; e) S.-M. Kuang, Z.-Z. Zhang, B.-M. Wu, T. C. W. Mak, *J. Organomet. Chem.* **1997**, *540*, 55–60; f) S.-M. Kuang, F. Xue, T. C. W. Mak, Z.-Z. Zhang, *Inorg. Chim. Acta* **1999**, *284*, 119–123.

[3] a) R. Martinez-Manez, F. Sancenon, *Chem. Rev.* **2003**, *103*, 4419–4476; b) F.-B. Xu, Q.-S. Li, X.-S. Zeng, X.-B. Leng, Z.-Z. Zhang, *Organometallics* **2002**, *21*, 4894–4896; c) F.-B. Xu, Q.-S. Li, X.-B. Leng, Z.-Z. Zhang, *Organometallics* **2004**, *23*, 632–634.

[4] F.-B. Xu, Q.-X. Liu, L.-Z. Wu, X.-B. Leng, Z.-C. Li, X.-S. Zeng, Y.-L. Chow, Z.-Z. Zhang, *Organometallics* **2003**, *22*, 633–640.

[5] S.-M. Kuang, Z.-Z. Zhang, Q.-G. Wang, T. C. W. Mak, *J. Chem. Soc. Dalton Trans.* **1998**, 2927–2930.

[6] J. S. Field, R. J. Haines, C. J. Parry, S. H. Sookraj, *Polyhedron* **1993**, *12*, 2425–2428.

[7] S.-M. Kuang, Z.-Z. Zhang, Q.-G. Wang, T. C. W. Mak, *J. Chem. Soc. Dalton Trans.* **1998**, 1115–1119.

[8] C. M. Che, Z. Mao, V. M. Mikowski, M. C. Tse, C. K. Chan, K. K. Cheng, D. L. Phillips, K. H. Leung, *Angew. Chem. Int. Ed.* **2000**, *39*, 4084–4088.

[9] E. Lastra, M. P. Gamasa, J. Gimeno, M. Lanfranchi, A. Tiripicchio, *J. Chem. Soc. Dalton Trans.* **1989**, 1499–1506.

[10] M. P. Gamasa, J. Gimeno, E. Lastra, X. Solans, *J. Organomet. Chem.* **1988**, *346*, 277–286.

[11] H.-F. Liu, W. Liu, P. Zhang, M.-S. Huang, L.-X. Zhen, *Xiamen Daxue Xuebao Ziran Kexueban* **1992**, *31*, 57–60.

[12] C. M. Che, H. K. Yip, V. W.-W. Yam, P. Y. Cheung, T. F. Lai, S. J. Shieh, S. M. Peng, *J. Chem. Soc. Dalton Trans.* **1992**, 427–433.

[13] A. Del Zotto, E. Zangrando, *Inorg. Chim. Acta* **1998**, *277*, 111–117.

[14] N. W. Alcock, P. Moore, P. A. Lampe, K. F. Mok, *J. Chem. Soc. Dalton Trans.* **1982**, 207–210.

[15] D. M. Ho, R. Bau, *Inorg. Chem.* **1983**, *22*, 4073–4079.

[16] M. Jansen, *Angew. Chem. Int. Ed. Engl.* **1987**, *26*, 1098–1110.

[17] F. Fages, J. P. Desvergne, H. Bouas-Laurent, P. Marsau, J. M. Lehn, F. Kotzyba-Hibert, A. M. Albrecht-Gary, M. Al-Joubbeh, *J. Am. Chem. Soc.* **1989**, *111*, 8672–8680.

Received: January 17, 2005
Published Online: June 14, 2005

 © 2005 Wiley-VCH Verlag GmbH & Co. KGaA, Weinheim

The Fenton Reaction in Aerated Aqueous Solutions Revisited

Sandra Rachmilovich-Calis,[a] Alexandra Masarwa,[a] Naomi Meyerstein,[b] and Dan Meyerstein*[a,c]

Keywords: Alcohols / Chain reactions / Dioxygen / Oxidation / Fenton reaction / Iron

The oxidation of alcohols in aerated acidic aqueous solutions by the Fenton reagent is a chain reaction. The length of the chain depends linearly on the number of CH_nOR (n = 1 or 2) groups in the alcohol. The reaction is accelerated by increasing the concentration of $Fe(H_2O)_6^{2+}$, but this cation is also active in at least one of the termination steps of the chain reaction. Addition of ethanol to a solution containing sucrose shortens the chain length. Saturation with dioxygen, instead of air, increases the chain length. An increase in alcohol concentration increases the chain length up to a limiting value. A complicated mechanism, which is in agreement with all these observations, is proposed. However, efforts to simulate the mechanism succeed only in simulating the $Fe(H_2O)_6^{3+}$ yield, but indicate that the observed process is considerably faster than the predicted one. In the latter the rate-determining step is the Fenton reaction, the rate constant of which is well known.

(© Wiley-VCH Verlag GmbH & Co. KGaA, 69451 Weinheim, Germany, 2005)

Introduction

In 1894 Fenton reported that alcohols are oxidized in the presence of H_2O_2 and $Fe(H_2O)_6^{2+}$.[1] After more than 110 years of further research the active intermediate in, and detailed mechanism of, this kind of reactions are still ambiguous and repeatedly discussed in many publications and reviews.[2–9] In 1934 Haber and Weiss[10] suggested that the key step in this process is:

$$H_2O_2 + Fe(H_2O)_6^{2+} \rightarrow {}^{\cdot}OH + OH^- + Fe(H_2O)_6^{3+} \quad (1)$$

This reaction and its analogous reactions

$$H_2O_2 + M^nL_m \rightarrow {}^{\cdot}OH + OH^- + M^{n+1}L_m \quad (2)$$

the "Fenton-like" reactions, play an important role in a variety of catalytic and biological processes. In biology this reaction is believed to be the main source of the ROS (Reactive Oxygen Species) in the cell[11–13] that cause a variety of diseases, for example cancer, arteriosclerosis, essential hypertension, Alzheimer's disease, amyloidosis, osteoarthritis, etc.[14,15]

However, detailed kinetic studies indicate that hydroxyl radicals are not formed in all these reactions.[3,4,16–23] The detailed mechanism seems to involve one of the following routes:[19]

$$H_2O_2 + M^nL_m \leftrightharpoons L_mM^n{\cdot}H_2O_2 \text{ or } L_{m-1}M^n{\cdot}H_2O_2 + L \quad (3)$$

followed by:

$$L_{m-1}M^n \cdot H_2O_2 \xrightarrow{+L} M^{n+1}L_m + {}^{\cdot}OH + OH^- \quad (4a)$$

$$L_{m-1}M^n \cdot H_2O_2 \rightarrow L_{m-1}M^{n+2}{=}O + H_2O \quad (4b)$$

$$L_{m-1}M^n \cdot H_2O_2 \xrightarrow{+RH} M^{n+1}L_m + R^{\cdot} + H_2O + OH^- \quad (4c)$$

$${}^{\cdot}OH + RH \rightarrow R^{\cdot} + H_2O \quad (5)$$

$$L_{m-1}M^{n+2}{=}O + {>}RH \xrightarrow{+L} M^{n+1}L_m + R^{\cdot} + OH^- \quad (6)$$

Thus, in the presence of an organic substrate, RH, ultimately the same radicals $R^{\cdot}$ are formed. The results point out that the choice of the route to $R^{\cdot}$ depends on the nature of M, L, RH and its concentration, and on the medium, for example the pH.[3,4,19,24,25] Recent results indicate that for $M_nL_m = Fe(H_2O)_6^{2+}$ reaction (4b) is the dominant pathway.[16–18,26]

We decided recently to use the Fox assay[27] to determine the concentrations of H_2O_2 and hydroperoxides in biological samples. In this assay, the yield of Fe^{III} is measured by the absorption of its complex with xylenol orange. The addition of alcohols to the aerated reaction mixture increases the Fe^{III} yield. Thus, for example, in solutions containing 0.1 M sorbitol the yield is $[Fe(H_2O)_6^{3+}]/[H_2O_2] = 14$. This result clearly points out that the $[Fe(H_2O)_6^{3+}]$ is formed in a chain reaction. Two mechanisms have been suggested in the literature for this process. The first, suggested by Wolff,[27] is as follows:

[a] Department of Chemistry, Ben-Gurion University of the Negev, Beer-Sheva, Israel
[b] Department of Physiology, Faculty of Health Sciences, Ben-Gurion University of the Negev, Beer-Sheva, Israel
[c] Department of Biological Chemistry, College of Judea and Samaria, Ariel, Israel
E-mail: danmeyer@bgumail.bgu.ac.il
Fax: +972-3-906-7440
Tel: +972-3-906-6153

$$H_2O_2 + Fe(H_2O)_6^{2+} \rightarrow HO^{\cdot} + OH^- + Fe(H_2O)_6^{3+} \quad (7)$$

$$HO^{\cdot} + R_2CHOH \rightarrow H_2O + R_2C^{\cdot}OH \quad (8)$$

$$R_2C^{\cdot}OH + O_2 \rightarrow R_2C(OO^{\cdot})OH \quad (9)$$

$$R_2C(OO^{\cdot})OH \rightarrow R_2C{=}O + HO^{\cdot}_2 \quad (10)$$

$$HO^{\cdot}_2 + Fe(H_2O)_6^{2+} \rightarrow H_2O_2 + Fe(H_2O)_6^{3+} \quad (11)$$

However, it is difficult to suggest which reaction terminates this chain process as the rates of reactions (8), (9), (10), and (11) are known and are high. Thus, second-order reactions between the radicals are not expected to compete with these reactions.

The second mechanism, proposed by Gebicki,[28] has reaction (12) instead of (11) in the reaction mechanism [reactions (7)–(10) are analogous to Wolff]:

$$2\ HO^{\cdot}_2 \rightarrow H_2O_2 + O_2 \quad (12)$$

This mechanism is clearly wrong as it predicts a yield of $[Fe(H_2O)_6^{3+}]/[H_2O_2]$ of 2.

We decided, therefore, to investigate the mechanism of this reaction in detail. The results indeed point out that the mechanism is considerably more complicated, although some of its aspects remain unresolved.

Results and Discussion

Initially, the effect of $Fe(H_2O)_6^{2+}$ concentration on the kinetics of the FOX assay with the substrate sucrose was studied. The results (Figure 1) are quite surprising. As expected, the rate of the process increases with $Fe(H_2O)_6^{2+}$ concentration. However the yield of $Fe(H_2O)_6^{3+}$ clearly decreases with the increase of $Fe(H_2O)_6^{2+}$ concentration, in other words the results point out that $Fe(H_2O)_6^{2+}$ is involved in at least one of the chain-termination steps. This termination step cannot be due to the competition between reactions (13) and (8a).

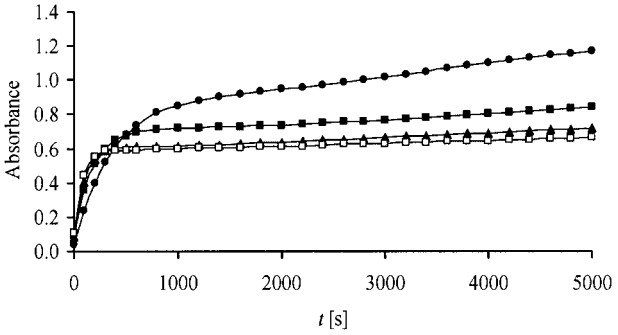

Figure 1. Kinetic measurements for different concentrations of iron(II) ammonium sulfate. The test solutions contained 10 mM sucrose, 2 μM H_2O_2, and the FOX reagent at a concentration of 250 μM (●), 400 μM (■), 600 μM (▲), and 800 μM (□) of iron(II) ion in air-saturated solutions.

$$^{\cdot}OH + Fe(H_2O)_6^{2+} \xrightarrow{H^+} H_2O + Fe(H_2O)_6^{3+} \quad (13)$$

with $k_{13} = 3.0 \times 10^8\ M^{-1}s^{-1}$,[29]

$$R_2CHOH + HO^{\cdot} \rightarrow R_2C^{\cdot}OH + H_2O \quad (8a)$$

with $k_{8a} = 2.3 \times 10^9\ M^{-1}s^{-1}$,[30] as even at the highest $[Fe(H_2O)_6^{2+}]$, $k_{13}[Fe(H_2O)_6^{2+}]$ is only 1.5% of k_{8a}[sucrose].

In the second set of experiments the effect of the nature of the organic solute on the yield of $Fe(H_2O)_6^{3+}$ was studied. The yield of Fe^{III} increases with the number of CH_nOX groups. The results are summarized in Table 1 and Figure 2. These results again clearly demonstrate that a competition between reactions (13) and (8) cannot determine the chain length. As recent results[16–18] point out that the Fenton reaction in acidic solutions proceeds via:

$$Fe(H_2O)_6^{2+} + H_2O_2 \rightarrow (H_2O)_5Fe^{IV}{=}O^{2+} + H_2O \quad (4b')$$

it seemed reasonable to suggest that the chain length is determined by the competition between reactions (14) and (15):

$$(H_2O)_5Fe^{IV}{=}O^{2+} + Fe(H_2O)_6^{2+} \xrightarrow{2\ H^+} 2\ Fe(H_2O)_6^{3+} \quad (14)$$

$$(H_2O)_5Fe^{IV}{=}O^{2+} + R^1R^2HCOH \rightarrow 2\ Fe(H_2O)_6^{3+} + {}^{\cdot}CR^1R^2(OH) \quad (15)$$

The specific rates of these reactions are unknown, although it is reasonable to suggest that reaction (14) proceeds via an inner-sphere mechanism and, as the specific rate of water exchange of $Fe(H_2O)_6^{2+}$, reaction (16), is $3.2 \times 10^6\ M^{-1}s^{-1}$,[31]

$$Fe(H_2O)_6^{2+} + H_2O^* \rightarrow Fe(H_2O)_5(H_2O^*)^{2+} + H_2O \quad (16)$$

it is estimated that $k_{14} \leq 3 \times 10^6\ M^{-1}s^{-1}$.

It is not unreasonable to suggest that k_{15} increases linearly with the number of CH_nOX groups. Therefore, the simplest mechanism that explains the results is that outlined in reactions (4b′)–(14) below. All the reactions in this group, with the exception of reactions (15) and (14), are known reactions. Furthermore, reaction (14) has been proposed in the literature[16] and reactions analogous to reaction (15) have also been proposed.[16,36]

$$Fe(H_2O)_6^{2+} + H_2O_2 \leftrightharpoons [(H_2O)_5Fe^{II}{\cdot}H_2O_2] \rightarrow (H_2O)_5Fe^{IV}{=}O^{2+} + H_2O \quad (4b')$$

with $k = 56\ M^{-1}s^{-1}$ [16]

$$(H_2O)_5Fe^{IV}{=}O^{2+} + R^1R^2CHOH \rightarrow Fe(H_2O)_5(OH)^{2+} + R^1R^2C^{\cdot}OH\ (\equiv R^{\cdot}) \quad (15)$$

$$R^{\cdot} + O_2 \rightarrow RO_2^{\cdot} \quad (9')$$

with $k \geq 1 \times 10^9\ M^{-1}s^{-1}$ [32]

$$RO_2^{\cdot} \rightarrow R^1R^2C{=}O + HO^{\cdot}_2 \quad (10')$$

with $400\ s^{-1} < k < 2600\ s^{-1}$ [33,34]

$$RO_2^{\cdot}\backslash HO^{\cdot}_2 + Fe(H_2O)_6^{2+} \leftrightharpoons (H_2O)_5Fe^{III}{-}OOR^{2+} \quad (17)$$

with $k > 2 \times 10^6\ M^{-1}s^{-1}$, $K \approx 200\ M^{-1}$ [35]

$$(H_2O)_5Fe^{III}{-}OOR^{2+} \xrightarrow{H^+} Fe(H_2O)_6^{3+} + HOOR \quad (18)$$

with $k \approx 1500\ M^{-1}s^{-1}$ [35]

 © 2005 Wiley-VCH Verlag GmbH & Co. KGaA, Weinheim

Table 1. The influence of substrate structure on the chain length in the FOX assay. The test solutions contained 2–7 μM H_2O_2, the FOX assay, and 100 mM organic substrate in air-saturated solutions.

Substrate	CH_nOX groups	k(·OH+ alcohol) [$M^{-1}s^{-1}$][54]	$[Fe^{III}]/[H_2O_2]$[a]	$[Fe^{III}]/[H_2O_2]$[a] without XO
None	0		1.9	1.9
Methanol	1	1.0×10^9	3.6	4.4
Ethanol	1	1.9×109	4.8	6.6
Ethylene glycol	2	2.4×10^9	5.7	6.4
Glycerol	3	2.0×10^9	8.3	9.0
Pentaerythritol	4[b]	3.3×10^9	9.6	
Sorbitol	6		13.7	14.5
Glucose	6	1.5×10^9	14.5	18.7
Sucrose	11	2.3×10^9	24.4	
Diethyl ether	1	3.6×10^9	4.6	
Dioxane	2[b]	2.8×10^9	4.9	

[a] Average of several determinations, error limit ±10%. [b] The CH_2OX groups are not adjacent.

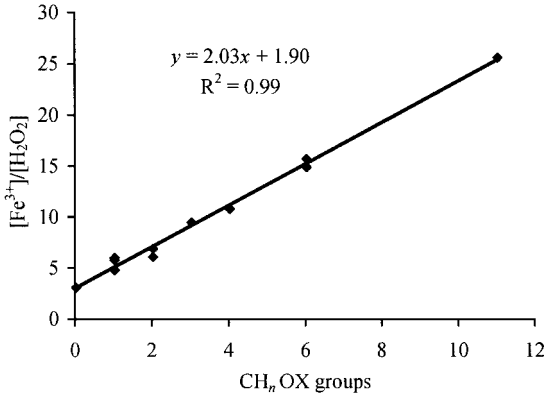

Figure 2. The influence of substrate structure [number of CH_nOX (n = 1 or 2) groups] on the chain length in the FOX assay. The test solutions contained 2–7 μM H_2O_2, 100 mM organic substrate, and the FOX reagent in air-saturated solutions.

$$(H_2O)_5Fe^{III}–OOR^{2+} + Fe(H_2O)_6^{2+} \rightarrow (H_2O)_5Fe^{IV}=O^{2+} + Fe(H_2O)_6^{3+} + ROH \quad (19)$$

with $k \approx 5\times10^5$ $M^{-1}s^{-1}$ [35]

$$(H_2O)_5Fe^{IV}=O^{2+} + Fe(H_2O)_6^{2+} \xrightarrow{2\,H^+} 2\,Fe(H_2O)_6^{3+} \quad (14)$$

with $k < 3\times10^6$ $M^{-1}s^{-1}$.

In order to check the validity of this mechanism, the effect of the concentration of the organic substrate on the yield of $Fe(H_2O)_6^{3+}$ was measured; the results for ethanol and sucrose are presented in Figure 3. The results point out that the yield of $Fe(H_2O)_6^{3+}$ initially increases with $[R^1R^2HCOH]$, as expected, but surprisingly reaches a limiting value at high substrate concentrations. These results indicate that at low $[R^1R^2HCOH]$ the competition between reactions (14) and (15) influences the chain length, but this competition has no effect at high concentrations. Indeed, a careful analysis of Figure 1 shows that the effect of $[Fe(H_2O)_6^{2+}]$ on the yield of $Fe(H_2O)_6^{3+}$ is large at low $[Fe(H_2O)_6^{2+}]$ and reaches a limiting value at higher concentrations. These results suggest that another termination step contributes to the mechanism. This conclusion is supported by the effect of adding C_2H_5OH to reaction mixtures containing sucrose (Figure 4). The results clearly demonstrate that the addition of ethanol shortens the chain length rather than extending it as predicted in reactions (4b′)–(14). This effect might be due to the fact that, in principle, two types of radicals R· are formed: a) a terminal α,ω radical ·CH(CHR′OH)OH (≡ $^{\cdot}R^1$), b) a β radical ·C(CHR′OH)(CHR′′OH)OH (≡ $^{\cdot}R^2$).

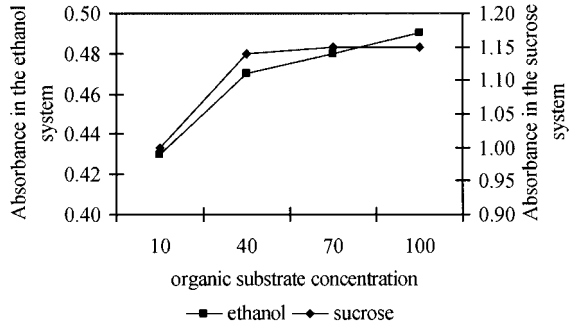

Figure 3. The influence of increasing concentrations of ethanol and sucrose on the absorbance of $Fe^{III}XO$ formed. The test solutions contained 5 μM H_2O_2 with 10–100 mM ethanol and 2 μM H_2O_2 with 10–100 mM sucrose and the FOX reagent in air-saturated solutions.

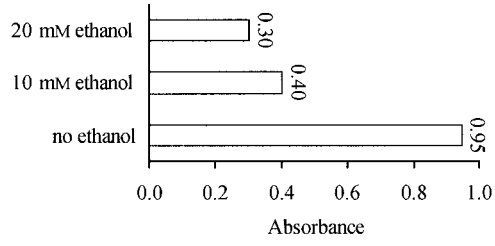

Figure 4. The absorbance of $Fe^{III}XO$ formed in sucrose-containing solutions in the presence of different concentrations of ethanol. The test solutions contained 10 mM sucrose, 2 μM H_2O_2, the FOX reagent, and 0–20 mM of ethanol in air-saturated solutions.

Both these radicals react with dioxygen to yield the $R^iO_2^{\cdot}$ radicals. However, these eliminate $HO_2^{\cdot}$ at considerably different rates

$$^{\cdot}O_2CH(CHR'OH)OH \rightarrow HO_2^{\cdot} + CH(O)(CHR'OH) \quad (10'a)$$

with k = 400 s^{-1} [33,34]

$$^{\cdot}O_2C(CHR'OH)(CHR''OH)OH \rightarrow HO_2^{\cdot} + C(O)(CHR'OH)(CHR''OH) \quad (10'b)$$

 © 2005 Wiley-VCH Verlag GmbH & Co. KGaA, Weinheim

with $k = 2600\ s^{-1}$ [33,34]

For sugars, there is an additional, faster elimination step for the group next to the ether linkage ($k > 7000\ s^{-1}$).[33,34]

All the $HO_2^{\cdot}$ radicals contribute to the chain process via reactions (17), (18), and (19). However the $RO_2^{\cdot}$ radicals, which are longer lived for the $^{\cdot}O_2CH(CHR'OH)OH$ radicals (α,ω-attack), yield some $HO_2CH(CHR'OH)OH$ via reaction (18). The latter product is usually unstable and might decompose by reaction (20)[37]

$$HO_2CH(CHR'OH)OH \rightarrow C(O)(CHR'OH)OH + H_2O \text{ or } HC(O)(CHR'OH) + H_2O_2 \quad (20)$$

The decomposition into the acid is acid catalyzed, whereas the aldehyde analog preferably forms in more basic solutions and at higher temperatures.[37] Thus, part of reaction (20), which competes with reaction (4b′), is clearly a termination step. This mechanism also explains the role of $Fe(H_2O)_6^{2+}$ in shortening the chain length at high $[HCR^1R^2OH]$. Under these conditions the competition between reaction (10) and reaction (17) is clearly a function of $[Fe(H_2O)_6^{2+}]$ and, as reaction (17) is partially followed by reactions (18) and (20), reaction (17) contributes to a termination step. This contribution of $Fe(H_2O)_6^{2+}$ to the termination step is limited by the fact that reaction (19) competes with reaction (18) and reaction (4b′) with reaction (20).

This reaction scheme also explains the effect of the number of CH_nOX groups on the $Fe(H_2O)_6^{3+}$ yield: clearly, with more CH_nOX groups the ratio $[R^{2\cdot}]/[R^{1\cdot}]$ increases. This decreases the contribution of reaction (20), which is partially a termination step. In order to check this hypothesis the effect of pentaerythritol was checked. The result, Table 1, clearly demonstrates that the chain length corresponds to four CH_nOH groups, even though they are not adjacent. However, it should be noted that the rate of $HO_2^{\cdot}$ elimination from $^{\cdot}O_2CH(OH)C(CH_2OH)_3$ is not known and might be considerably higher than that of $R'O_2^{\cdot}$ radicals. It should be noted that there is a large variety in the rates of $HO_2^{\cdot}$ elimination reactions;[33,34,38,39] the source of these differences is not yet fully understood.[33,34,38,39]

When the solutions were saturated with O_2, instead of air, the yield of $Fe(H_2O)_6^{3+}$ increased (Table 2). In these experiments, only the yield was measured as they were performed in sealed syringes. The effect is small, though significant, for one CH_nOX group, and increases somewhat for a larger number of CH_nOX groups. The effect of differing oxygen concentrations on a system containing ethanol was noted previously.[40] As reaction (9′) is very fast, and as $k[^{\cdot}R+Fe(H_2O)_6^{2+}]$ is about three orders of magnitude slower[41] and $[O_2]$ is at least two orders of magnitude larger than that of any of the intermediates, the dioxygen effect cannot be attributed to an acceleration of reaction (9′). Thus, one has to conclude that the dioxygen effect in the ethanol system is due to the reaction of dioxygen with one of the reactive intermediates. No such reaction is known and a plausible one is:

Table 2. The effect of oxygen on the yields in the FOX assay for different substrates (comparison of air- and oxygen-saturated solutions). The test solutions contained 2 μM H_2O_2, the FOX assay, and 100 mM organic substrate (ethanol, glycerol, sorbitol, and sucrose).

Increase on oxygen saturation	$[Fe^{III}]/[H_2O_2]$ (oxygen)[a]	$[Fe^{III}]/[H_2O_2]$ (air)[a]	CH_nOX groups	Substrate
None	–	1.9	1.9	0
Ethanol	+26%	6.2	4.9	1
+56%	12.2	7.8	3	glycerol
+50%	24.2	16.1	6	sorbitol
+48%	42.4	28.6	11	sucrose

[a] Single determination, error limit ±15%.

$$(H_2O)_5Fe^{III}–OOR^{2+} + O_2 \underset{H^+}{\rightarrow} (H_2O)_5Fe^{IV}–OOR^{3+} + HO_2^{\cdot} \quad (21)$$

followed by:

$$(H_2O)_5Fe^{IV}–OOR^{3+} \overset{H_2O}{\rightarrow} Fe(H_2O)_6^{3+} + RO_2^{\cdot} \quad (22)$$

or by:

$$(H_2O)_5Fe^{IV}–OOR^{3+} \overset{H^+}{\rightarrow} (H_2O)_5Fe^{VI}=O^{4+} + ROH \quad (23)$$

Reaction (21) might compete with reaction (18) and thus elongate the chain length. Alternatively, the reaction occurring could be:

$$Fe^{IV} + O_2 \rightarrow Fe^{V} + O_2^{\cdot-} \quad (24)$$

although the relative redox potentials do not support this possibility. Oxidation of $PFe^{IV}=O$ by H_2O_2 to $PFe^{III}–O_2^{\cdot-}$ has been suggested in the literature.[42–44]

The larger dioxygen effect for systems with more than or equal to two CH_nOX groups is attributed to the competition between reactions (9) and reactions (25) (β-elimination of water from 1,2-diol-type radicals):[38]

$$^{\cdot}CH(CHR'OH)OH \rightarrow O=CH(C^{\cdot}HR') + H_2O \quad (25a)$$

$$^{\cdot}C(CHR'OH)(CHR''OH)OH \rightarrow O=C(C^{\cdot}HR')(CHR''OH) + H_2O \quad (25b)$$

Reactions (25) are acid catalyzed and, at pH 1.8, the experimental pH, the rate for the glycol radical, for example, is $2.5 \times 10^3\ s^{-1}$.[45] Reaction (25) competes slightly with reactions (9), the rate of which in air saturated solutions is around $7 \times 10^5\ s^{-1}$.[32] The radicals formed in reactions (25) form peroxyl radicals, which do not eliminate $HO_2^{\cdot}$ radicals. Clearly, reactions (25) do not occur for radicals derived from alcohols with one CH_nOX group or nonadjacent CH_nOX groups.

In kinetic simulations the general trend of the reactions ($[Fe^{II}]$, [substrate] effect) could be modeled reasonably well by including only the group of reactions (4b′)–(14) outlined above. Reactions for α,ω and β radicals were differentiated and the option included that part of the formed ROOH leads to a termination reaction instead of being returned to the cycle. These reactions do not include any explanations for the [dioxygen] effect and therefore this effect could not be modeled. The reactions (21–25) could not be incorpo-

 © 2005 Wiley-VCH Verlag GmbH & Co. KGaA, Weinheim

rated in the simulations as the calculations proved to be too complicated. The simulations could be fitted to the $Fe(H_2O)_6^{3+}$ yields but the kinetics were always considerably slower than the observed ones. This stems from the fact that reaction (4b) is the rate-determining step and the rate constant of this reaction is well known.

Finally, it should be noted that when ROOH peroxides other than H_2O_2 are used, the yield of $Fe(H_2O)_6^{3+}$ is considerably lower.[27,46] This suggests that in these reactions the yield of $(H_2O)_5Fe^{IV}=O^{2+}$ is considerably lower than in the H_2O_2 system. This suggests that either $R^3O^{\cdot}$ radicals are formed in these reactions, which might be true also for reaction (19), or that reaction (4c) takes place in these systems to produce another mixture of $R^{\cdot}$ radicals than reaction (15). $R^3O^{\cdot}$ radicals might decompose via:[47]

$$CHR'R''O^{\cdot} \xrightarrow{\text{fast}} {}^{\cdot}CR'R''OH \quad (26)$$

This is, for example, expected to happen for fatty acid hydroperoxides, which are formed biologically, or for the radical formed from $(CH_3)_3COOH$ via:

$$C(CH_3)_3O^{\cdot} \rightarrow C(CH_3)_2O + {}^{\cdot}CH_3 \quad (27)$$

with $k = 2.0 \times 10^3\ s^{-1}$,[48] etc.

Concluding Remarks

This study clearly demonstrates that the mechanism of the Fenton reaction and Fenton-like reactions, in aerated aqueous solutions containing organic substrates, is considerably more complex than assumed so far. It seems reasonable to propose that reactions analogous to reaction (17) occur also in nonaqueous media. Therefore, also in these media the mechanisms of the Fenton process are probably considerably more complicated than proposed.[6,49–52]

The results point out that the yield of Fe^{III} depends on the nature of the peroxide and the nature of all the organic compounds present in the solution. Thus, the use of the FOX assay for the determination of the total peroxides in biological samples is difficult if at all feasible.

Finally, it is tempting to speculate that analogous reactions in biological systems might lead to considerable deleterious biological processes by damaging sugars bound to the membranes of cells[13] and/or to the sugar moieties in RNA and DNA.

Experimental Section

Materials: All the chemicals purchased from Sigma or Aldrich were of A.R. grade and therefore used without further purification. The water used was deionized and was further purified with a Millipore Milli-Q setup with a final resistivity of >10 MΩ

Preparation of the FOX Reagent: The FOX reagent containing iron(II) ammonium sulfate, H_2SO_4, xylenol orange, and an organic substrate was mixed with hydrogen peroxide to give final concentrations of 2–9 μM hydrogen peroxide, 250–800 μM iron(II) ion, 25 mM H_2SO_4, 100 μM xylenol orange (XO), and 10–100 mM organic substrate. The solutions were incubated for 40 min at room temperature. The absorbance was read at 560 nm. All spectra were run against blanks containing the FOX reagent. In some experiments, the XO was added only after 40 min for the analytical determination of the Fe^{III} yield.

UV/Vis measurements were carried out with a Hewlett–Packard Diode Array spectrophotometer model 8452A, which enables measurements in the range of 190–820 nm at a resolution of ±2 nm.

Determination of the H_2O_2 Concentration: The concentration of H_2O_2 was determined using the iodide method.[53] A stock solution containing KI, NaOH, and ammonium heptamolybdate was mixed with a second stock solution containing potassium hydrogenphthalate to give final concentrations of 0.08 M KI, 3.2×10^{-5} M ammonium heptamolybdate, and 0.02 M potassium hydrogen phthalate (final pH 4.0). The final solution was then mixed with H_2O_2 at concentrations ranging between 1×10^{-6} and 1×10^{-5} M. Addition of H_2O_2 leads to the production of I_3^- via the following reactions:

$$2\ I^- + H_2O_2 + 2\ H^+ \rightarrow I_2 + 2\ H_2O \quad (28)$$

$$I_2 + I^- \rightleftharpoons I_3^- \quad (29)$$

The absorbance of I_3^- was measured at 352 nm (ε = 26500 $M^{-1}\,cm^{-1}$).

Rate Simulations: Kinetic simulations were performed in order to evaluate the effects of H_2O_2, Fe^{II}, and organic substrate concentrations and the input rates and pattern of the mechanism. The simulations explored the formation kinetics of Fe^{III} and were compared to the experimental results. The kinetic calculations were performed with the Pro-Kineticist II program by Applied Photophysics.

Acknowledgments

This study was supported in part by grants from the Israel Science Foundation and from the Budgeting and Planning Committee of The Council of Higher Education and the Israel Atomic Energy Commission. D. M. wishes to express his thanks to Mrs. Irene Evens for her ongoing interest and support.

[1] H. J. H. Fenton, *J. Chem. Soc.* **1894**, *65*, 899–910.
[2] H. B. Dunford, *Coord. Chem. Rev.* **2002**, *233*, 311–318.
[3] S. Goldstein, D. Meyerstein, G. Czapski, *Free Radical Biol. Med.* **1993**, *15*, 435–445.
[4] S. Goldstein, D. Meyerstein, *Acc. Chem. Res.* **1999**, *32*, 547–550.
[5] F. Gozzo, *J. Mol. Catal. A, Chem.* **2001**, *171*, 1–22.
[6] D. T. Sawyer, A. Sobkowiak, T. Matsushita, *Acc. Chem. Res.* **1996**, *29*, 409–416.
[7] A. Y. Sychev, *Russ. Chem. Rev.* **1995**, *64*, 1105–1129.
[8] C. Walling, *Acc. Chem. Res.* **1975**, *8*, 125–131.
[9] C. Walling, *Acc. Chem. Res.* **1998**, *31*, 155–157.
[10] F. Haber, J. J. Weiss, *Proc. R. Soc. London A* **1934**, *147*, 332–351.
[11] M. C. Gutteridge, T. Westermarck, B. Halliwell, *Free Radicals, Aging and Degenerative Diseases*, Alan R. Liss, Inc., New York, **1986**, p. 99–139.
[12] D. Chiu, F. Kuypers, B. Lubin, *Semin. Hematol.* **1989**, *26*, 257–276.
[13] B. Halliwell, J. M. C. Gutteridge, *Free Radicals in Biology and Medicine*, Oxford University Press, **1999**.
[14] D. Harman, in *Modern Aging Research*, vol. 8 (Eds.: J. E. Johnson, Jr., R. Walford, D. Harman, J. Miquel), Alan R. Liss, Inc., New York, **1986**, p. 3.
[15] D. Harman, *Antioxid. Redox Signaling* **2003**, *5*, 557–561.
[16] M. L. Kremer, *Phys. Chem. Chem. Phys.* **1999**, *1*, 3595–3605.
[17] M. L. Kremer, *J. Inorg. Biochem.* **2000**, *78*, 255–257.

 © 2005 Wiley-VCH Verlag GmbH & Co. KGaA, Weinheim

[18] M. L. Kremer, *J. Phys. Chem. A* **2003**, *107*, 1734–1741.
[19] M. Masarwa, H. Cohen, D. Meyerstein, D. L. Hickman, A. Bakac, J. H. Espenson, *J. Am. Chem. Soc.* **1988**, *110*, 4293–4297.
[20] H. C. Sutton, C. C. Winterbourn, *Free Radical Biol. Med.* **1989**, *6*, 53–60.
[21] W. C. Bray, M. H. Gorin, *J. Am. Chem. Soc.* **1932**, *54*, 2124–2125.
[22] A. E. Cahill, H. Taube, *J. Am. Chem. Soc.* **1952**, *74*, 2312–2318.
[23] X. Zhang, D. Zhang, D. H. Busch, R. Van Eldik, *J. Chem. Soc., Dalton Trans.* **1999**, 2751–2758.
[24] E. Luzzatto, H. Cohen, C. Stockheim, K. Wieghardt, D. Meyerstein, *Free Radical Res.* **1995**, *23*, 453–463.
[25] H. Bamnolker, H. Cohen, D. Meyerstein, *Free Radical Res. Commun.* **1991**, *15*, 231–241.
[26] D. A. Wink, C. B. Wink, R. W. Nims, P. C. Ford, *Environ. Health Perspect.* **1994**, *102*, 11–15.
[27] S. P. Wolff, *Methods Enzymol.* **1972**, *233*, 182–189.
[28] J. M. Gebicki, *Redox Rep.* **2000**, *5*, 15–16.
[29] Z. Stuglik, Z. P. Zargorski, *Radiat. Phys. Chem.* **1981**, *17*, 229–233.
[30] J. S. Moore, K. G. Kemsley, J. V. Davies, G. O. Phillips, *Radiation Biology and Chemistry. Research Developments*, Elsevier, New York, **1979**, p. 99–113.
[31] T. J. Swift, R. E. Connick, *J. Chem. Phys.* **1962**, *37*, 307–320.
[32] P. Neta, J. Grodkowski, A. B. Ross, *J. Phys. Chem. Ref. Data* **1996**, *25*, 709–1050.
[33] E. Bothe, M. N. Schuchmann, D. Schultefrohlinde, C. Von Sonntag, *Photochem. Photobiol.* **1978**, *28*, 639–644.
[34] E. Bothe, D. Schultefrohlinde, C. Von Sonntag, *J. Chem. Soc., Perkin Trans. 2* **1978**, 416–420.
[35] C. Mansano-Weiss, H. Cohen, D. Meyerstein, *J. Inorg. Biochem.* **2002**, *91*, 199–204.
[36] B. H. J. Bielski, *Free Radical Res. Commun.* **1991**, *12*, 469–477.
[37] H. Schultze, D. Schultefrohlinde, *J. Chem. Soc., Faraday Trans. 1* **1975**, *71*, 1099–1105.
[38] C. Von Sonntag, H. P. Schuchmann, in *Radiation Chemistry: Present Status and Future Trends* (Eds.: C. D. Jonah, B. S. M. Rao), Elsevier Science, **2001**, pp. 481–511.
[39] C. Von Sonntag, H. P. Schuchmann, in *Peroxyl Radicals in Aqueous Solution* (Ed.: Z. B. Alfassi), Wiley, Chichester, **1997**, pp. 173–234.
[40] D. L. Ingles, *Aust. J. Chem.* **1972**, *25*, 97–104.
[41] H. Cohen, D. Meyerstein, *Inorg. Chem.* **1988**, *27*, 3429–3431.
[42] D. C. Ulmer, M. S. A. Leisola, R. Fiechter, *J. Biotechnol.* **1984**, *1*, 13–24.
[43] M. S. A. Leisola, D. C. Ulmer, R. Waldner, R. Fiechter, *J. Biotechnol.* **1984**, *1*, 331–339.
[44] C. Crestini, A. Pastorini, P. Tagliatesta, *Eur. J. Inorg. Chem.* **2004**, 4477–4483.
[45] K. M. Bansal, M. Gratzel, A. Henglein, E. Janata, *J. Phys. Chem.* **1973**, *77*, 16–19.
[46] C. Gay, J. M. Gebicki, *Anal. Biochem.* **2000**, *284*, 217–220.
[47] K. G. Konya, T. Paul, S. Lin, J. Lusztyk, K. U. Ingold, *J. Am. Chem. Soc.* **2000**, *122*, 7518–7527.
[48] D. Johnson, P. Cassanelli, R. A. Cox, *Atmos. Environ.* **2004**, *38*, 1755–1765.
[49] M. J. Perkins, *Chem. Soc. Rev.* **1996**, *25*, 229–236.
[50] D. H. R. Barton, *Chem. Soc. Rev.* **1996**, *25*, 237–239.
[51] D. T. Sawyer, *Coord. Chem. Rev.* **1997**, *165*, 297–313.
[52] G. B. Shulpin, G. V. Nizova, Y. N. Kozlov, L. Gonzalez Cuervo, G. Suess-Fink, *Adv. Synth. Catal.* **2004**, *346*, 317–332.
[53] D. Meyerstein, A. Treinin, *Trans. Faraday Soc.* **1963**, *59*, 1114–1120.
[54] G. V. Buxton, C. V. Greenstock, W. P. Helman, A. R. Ross, *J. Phys. Chem. Ref. Data* **1988**, *17*, 513–886.

Received: January 31, 2005
Published Online: June 14, 2005

 © 2005 Wiley-VCH Verlag GmbH & Co. KGaA, Weinheim

Organotin-Substituted Crown Ethers for Ditopic Complexation of Anions and Cations[‡]

Gregor Reeske,[a] Markus Schürmann,[a] Burkhard Costisella,[a] and Klaus Jurkschat*[a]

Dedicated to Prof. W.-W. Du Mont on the occasion of his 60th birthday

Keywords: Ditopic complexation / Host-guest chemistry / NMR spectroscopy / X-ray crystallography / Tin

The syntheses of the organotin-substituted crown ethers *m*-($Ph_2XSnCH_2CH_2$)-15-benzocrown-5 (**2**, X = Ph; **3**, X = I; **4**, X = Cl; **5**, X = NCS) and the salt [*m*-($Ph_3SnCH_2CH_2$)-15-benzocrown-5·Na]$^+SCN^-$ (**2a**) are reported. Compounds **2a** and **4** (as its aqua complex **4**·H_2O) are characterized by single-crystal X-ray diffraction sudies. Multinuclear NMR spectroscopy and electrospray mass spectrometry reveal the triorganotin chloride **4** to be a ditopic host towards sodium rhodanide. This statement is further supported by the ability of compound **4** to transport sodium rhodanide through an organic membrane.

(© Wiley-VCH Verlag GmbH & Co. KGaA, 69451 Weinheim, Germany, 2005)

Introduction

The simultaneous recognition and sensing of anions and cations is a new area of increasing research activities.[1,2] Practical applications of ion-pair recognition range from complexation of zwitterionic amino acids and peptides,[3,4] the transport of ion pairs across biological membranes[5–12] to solubility enhancement of ion pairs in nonpolar solvents for ion extraction.[13] Ion-pair receptors known so far are based on the combination of crown compounds or calixarenes with (i) ammonium groups exploiting hydrogen bonding[14,15] or (ii) Lewis acidic groups.[16–20] Straightforward examples of the latter case involve the work of Reetz et al.[18a] on an organoboron-substituted crown ether, and Willem et al.[18b] who reported the sodium rhodanide complex of triorganotin carboxylates containing the [18]crown-6 and [15]crown-5 substituents. However, an essential shortcoming of the latter compounds is the kinetic lability of the tin–carboxylate bond, which makes the corresponding zwitterionic complexes unstable in solution.[18b]

In continuation of our own studies on organotin halides as Lewis acids for selective complexation of anions[21–23] we report here the synthesis and structures of kinetically more stable carbon-bonded organotin-functionalized crown ethers and demonstrate that such compounds are able to complex and transport sodium rhodanide in nonpolar organic solvents.

Results and Discussion

Synthetic Aspects and Molecular Structures in the Solid State

The reaction of 4-vinylbenzo-15-crown-5[24,25] (**1**) with triphenyltin hydride provided [2-(6,7,9,10,12,13,15,16-octahydro-5,8,11,14,17-pentaoxabenzocyclopentadec-2-yl)ethyl]-triphenylstannane (**2**) as a colorless oil (Scheme 1).

Treatment of the tetraorganostannane **2** with 1 molequiv. of iodine gave the triorganotin iodide **3**. The latter was quantitatively converted into its chloride derivative **4** by reaction with AgCl in acetonitrile over a period of 14 d. The reaction of triorganotin iodide **3** with AgSCN in CH_3CN gave the triorganotin rhodanide **5** in quantitative yield.

The treatment of **2** with NaSCN in ethanol provided the corresponding sodium rhodanide complex **2a** as a colorless solid. Single crystals of **2a** suitable for X-ray diffraction analyses were obtained by recrystallization from dichloromethane/*n*-hexane.

The molecular structure of **2a** is shown in Figure 1 and selected geometric parameters are collected in Table 1.

The sodium cation is coordinated by five oxygen atoms with Na–O distances ranging between 2.317(7) and 2.469(6) Å. These values are in line with those reported for similar compounds.[18] The rhodanide anion is located close

[‡] This work contains part of the PhD Thesis of G. R., Dortmund University, **2004**. Parts of this work were first presented at the XI. International Conference on the Coordination and Organometallic Chemistry of Germanium, Tin, and Lead, Santa Fe, NM, USA, June 27–July 2, **2004**, Book of Abstracts, p26.

[a] Lehrstuhl für Anorganische Chemie II der Universität Dortmund,
44221 Dortmund, Germany
Fax: +49-231-7555048
E-mail: klaus.jurkschat@uni-dortmund.de

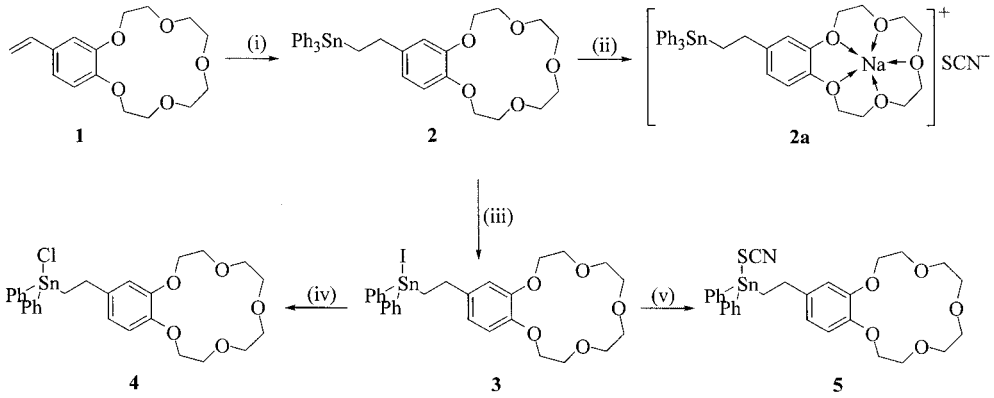

Scheme 1. Synthesis of the organotin-substituted crown ethers. i) Ph_3SnH, AIBN; ii) NaSCN, EtOH; iii) I_2, CH_2Cl_2, – PhI; iv) AgCl, CH_3CN, – AgI; v) AgSCN, CH_3CN, – AgI.

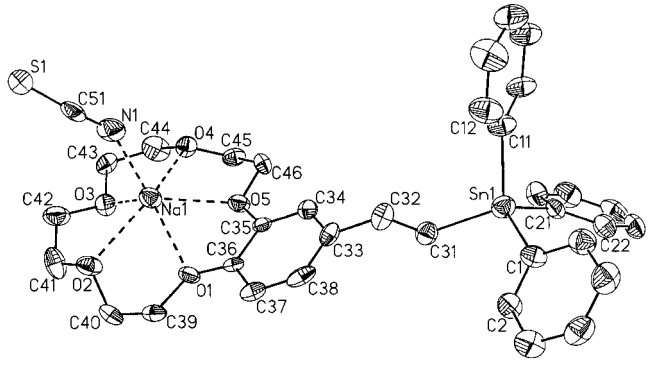

Figure 1. Molecular structure of the sodium rhodanide complex **2a**. Atomic displacement parameters are drawn at 30% probability level.

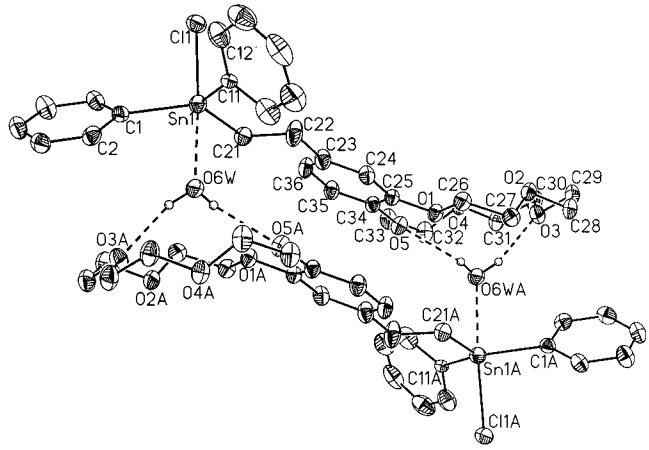

Figure 2. Molecular structure of $4 \cdot H_2O$. Atomic displacement parameters are drawn at 30% probability level.

Table 1. Selected bond lengths [Å] and angles [°] for **2a**.

Sn–C(11)	2.141(9)	Na–N	2.344(9)
Sn–C(21)	2.125(9)	Na–O(1)	2.453(5)
Sn–C(31)	2.141(7)	Na–O(2)	2.438(6)
S–C(51)	1.625(11)	Na–O(3)	2.313(7)
N–C(51)	1.164(10)	Na–O(4)	2.469(6)
		Na–O(5)	2.375(6)
C(1)–Sn–C(11)	108.0(4)	O(1)–Na-(O3)	117.0(2)
C(1)–Sn–C(21)	110.5(4)	O(2)–Na–O(4)	141.0(3)
C(1)–Sn–C(31)	108.0(4)	O(3)–Na-(O2)	71.5(2)
C(21)–Sn–C(11)	105.5(4)	O(3)–Na-(O4)	70.5(3)
C(21)–Sn–C(31)	112.0(4)	O(3)–Na-(O5)	120.0(3)
C(31)–Sn–C(11)	111.0(3)	O(5)–Na-(O1)	62.75(20)
O(1)–Na–O(4)	125.5(2)	O(5)–Na-(O2)	127.5(2)
O(1)–Na–O(2)	66.5(2)	O(5)–Na-(O4)	67.5(2)

to the sodium cation with an Na–N distance of 2.344(9) Å. The tin atom shows the expected tetrahedral configuration.

Crystallization of the triorganotin chloride **4** at –5 °C from CH_2Cl_2/Et_2O (1:2) in the presence of air moisture afforded single crystals of the aqua complex $4 \cdot H_2O$ as its CH_2Cl_2 solvate.

The molecular structure of $4 \cdot H_2O$ is shown in Figure 2, selected geometric parameters are collected in Table 2.

Table 2. Selected bond lengths [Å] and angles [°] for $4 \cdot H_2O$.

Sn–C(1)	2.125(4)	O(1)–C(26)	1.430(5)
Sn–C(11)	2.109(4)	O(2)–C(27)	1.406(5)
Sn–C(21)	2.125(4)	O(5)–C(33)	1.430(5)
Sn–Cl(1)	2.453(1)		
Sn–O(6W)	2.469(4)		
O(1)–C(25)	1.359(5)		
C(1)–Sn–Cl(1)	95.0(12)	C(11)–Sn–Cl(1)	96.5(11)
C(1)–Sn–O(6W)	81.0(16)	C(11)–Sn–O(6W)	86.5(14)
Cl(1)–Sn–O(6W)	176.0(11)	C(21)–Sn–C(1)	121.5(17)
C(11)–Sn–C(1)	116.0(16)	C(21)–Sn–Cl(1)	96.0(13)
C(11)–Sn–C(21)	118.5(17)	C(21)–Sn–O(6W)	83.5(16)

The compound crystallizes monoclinically with one molecule in the unit cell. The tin atom in $4 \cdot H_2O$ is pentacoordinate and adopts a distorted trigonal-bipyramidal configuration [geometrical goodness $\Delta(\Sigma\vartheta) = 68.5°$].[26,27] The equatorial positions are occupied by C(1), C(11), C(21) and the axial positions by Cl(1) and the water oxygen atom. The tin atom is displaced by 0.22 Å from the plane defined by C(1), C(11), C(21) in the direction of Cl(1). The Sn(1)–Cl(1) and Sn–O(6W) distances of 2.453(1) and 2.469(4) Å, respectively, are comparable with those of other aqua complexes of organotin chlorides.[28,29] In CH_2Cl_2 solution, compound

 © 2005 Wiley-VCH Verlag GmbH & Co. KGaA, Weinheim

4·H_2O shows a dissociation equilibrium between **4**·H_2O and **4** + H_2O. The equilibrium is fast on the NMR time-scale with the population of **4** + H_2O dominating at room temperature (δ^{119}Sn = 2 ppm). However, at –70 °C the aqua complex **4**·H_2O dominates (δ^{119}Sn = –155 ppm). These results are supported by NOE decoupling experiments at different temperatures. At room temperature the water proton resonance shows a large NOE to the resonances of the crown ether ring suggesting hydrogen bonding to the oxygen atoms of the latter. Upon lowering of the temperature, this NOE becomes smaller, which implies a larger distance between the crown ether protons and the water protons.

Complexation Studies

In comparison to the organotin-substituted crown ether **2**, the ^{13}C NMR spectrum of its sodium complex **2a** shows low-field shifts of approximately 2 ppm for the crown ether carbon resonances. The same effect was observed for the ^{13}C NMR spectrum ($CDCl_3/CD_3CN$, 4:1) of the chlorodiphenylstannyl-substituted crown ether **4** to which 1 mol-equiv. of sodium tetraphenylborate ($NaBPh_4$) had been added. This clearly indicates complexation of the sodium cation by the crown ether. The ^{119}Sn NMR spectrum of the same solution showed a single resonance at δ = –9.2 ppm indicating, as expected, no coordination of the tetraphenylborate anion.

The ^{119}Sn NMR spectrum at –70 °C of a CD_2Cl_2 solution of the triorganotin chloride **4,** to which 1 mol-equiv. of $[(Ph_3P)_2N]Cl$ had been added, showed a single resonance at δ = –198 ppm indicating the in situ formation of the dichlorotriorganostannate [**4**·Cl][$(Ph_3P)_2N$] (**4a**). In a similar manner, addition of $n$$Bu_4NSCN$ to a solution of the triorganotin rhodanide **5** afforded, in situ, the complex [**5**·SCN][$n$$Bu_4N$] (**5a**). Its ^{119}Sn NMR spectrum at –70 °C showed a single resonance at δ = –253 ppm. The ^{119}Sn NMR spectrum at –70 °C of a solution of the chlorodiphenylstannyl-substituted crown ether **4**, to which 1 mol-equiv. of Bu_4NSCN had been added, showed three resonances at δ = –198 ppm (signal a, integral 18), –216 ppm (signal b, integral 69) and –253 ppm (signal c, integral 13). Addition of a further 3 mol-equiv. of Bu_4NSCN changed the integral ratios of signals (a), (b) and (c) to 9, 69, and 21, respectively. Signals (a) and (c) are assigned to **4a** and **5a**, respectively, whereas signal (b) is tentatively assigned to [**4**·SCN][$n$$Bu_4N$] (**4b**). The latter assignment is supported by the observation of the same ^{119}Sn chemical shift of a CD_2Cl_2 solution of the triorganotin rhodanide **5** to which 1 mol-equiv. of $[(Ph_3P)_2N]Cl$ had been added, and by the fact that organostannate complexes of type $[R_3SnXY]^-$ are more stable than their corresponding symmetrically substituted derivatives $[R_3SnX_2]^-$ and $[R_3SnY_2]^-$.[30] The ^{119}Sn NMR spectra at room temperature of all the solutions mentioned above showed no resonances, indicating fast exchange between the species present in the corresponding samples.

The ^{119}Sn NMR spectrum at room temperature of a solution of the triorganotin chloride **4** in CD_2Cl_2 to which 1 mol-equiv. of NaSCN had been added showed in comparison to compound **4** a low-frequency-shifted single broad resonance at δ = –225 ppm ($\nu_{1/2}$ = 2013 Hz) which at –60 °C shifted to δ = –248 ppm ($\nu_{1/2}$ = 937 Hz). The ^{13}C NMR spectrum of the same solution showed $^1J(^{13}C\text{-}^{117/119}Sn)$ coupling constants of 595/621 and 716/751 Hz to the Sn–CH_2 and Sn–C_i carbon atoms, respectively, that are larger than the corresponding couplings of 426/446 and 540/566 Hz measured for compound **4**. Both the ^{119}Sn chemical shifts and the $^1J(^{13}C\text{-}^{117/119}Sn)$ coupling constants clearly indicate the tin atom in the complex [**4**·NaSCN] to be pentacoordinate. The ultimate evidence for the coordination of the rhodanide anion to the tin atom stems (i) from the observation of a $^2J(^{13}C\text{-}^{117/119}Sn)$ coupling of 59 Hz to the rhodanide carbon atom and (ii) from an HMBC correlation experiment showing a ^5J coupling of the *o*-phenyl protons to the rhodanide carbon atom. The binding of the sodium cation to the crown ether oxygen atoms is clearly evidenced by similar high-frequency shifts of the ^{13}C resonances for the crown ether carbon atoms as observed for the sodium complex **2a** (see above).

These results unambiguously prove that the chlorodiphenylstannyl-substituted crown ether **4** is a ditopic receptor simultaneously binding the sodium cation and rhodanide anion.

This statement obtains further support from electrospray mass spectrometry (ESMS) and transport experiments. Thus, the ESMS spectrum (negative mode) of a solution of the triorganotin chloride **4** to which NaSCN had been added showed mass clusters at m/z = 685.14 and 766.22 which are assigned to $[\mathbf{5} + SCN]^-$ and $[\mathbf{5} + 2\ SCN + Na]^-$, respectively. In the positive mode the spectrum showed a major mass cluster at m/z = 650.05 which is assigned to $[\mathbf{5}\cdot Na]^+$. Minor mass clusters at m/z = 569.07 and 609.06 were also present which were assigned to $[\mathbf{4} - Cl]^+$ and $[\mathbf{4} - Cl + OH + Na]^+$, respectively.

The transport properties of the chlorodiphenylstannyl-substituted crown ether **4** were investigated by a U-tube experiment (Figure 3).

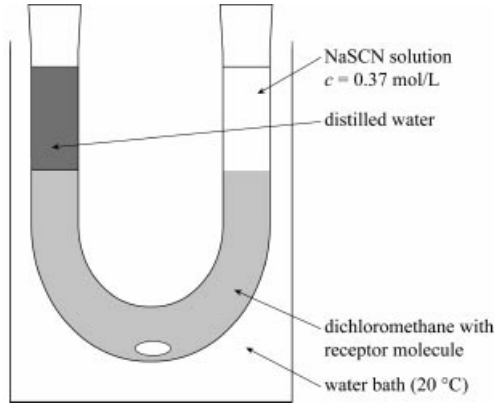

Figure 3. Schematic presentation of the U-tube experiment.

Figure 4 demonstrates the superior capability of compound **4** over triphenyltin chloride and the unsubstituted 15-benzocrown-5 to transport NaSCN from an aqueous

 © 2005 Wiley-VCH Verlag GmbH & Co. KGaA, Weinheim

phase through a dichloromethane layer into another aqueous phase. This apparently becomes possible by the simultaneous complexation of the sodium cation and the rhodanide anion by the ditopic host **4**.

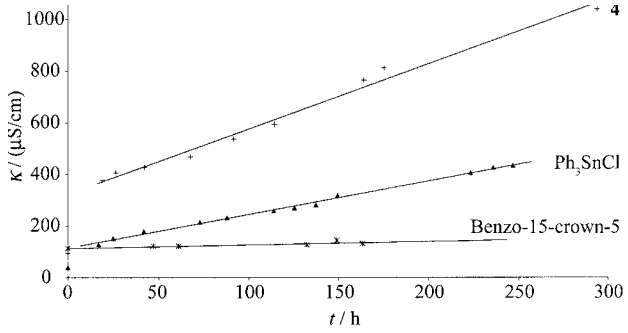

Figure 4. Plot of the electric conductivity vs. time illustrating the different ability of the triorganotin chloride **4**, triphenyltin chloride, and the unsubstituted crown ether benzo-15-crown-5 to transport sodium rhodanide through a dichloromethane layer. The concentration of **4**, Ph_3SnCl as well as that of the crown ether was 0.0268 mol/L.

Conclusions

Linking a chlorodiorganostannyl moiety via a dimethylene spacer with a crown ether was shown to provide the robust ditopic host **4** for the complexation of sodium rhodanide. It even serves for the efficient extraction of the latter from an aqueous solution. Given the large variety of crown ethers and related compounds such as azacrowns and cryptands on the one hand and the experience with mono- bi- and multicentered organometal-based Lewis acids on the other, the concept of combining representatives of these classes of compounds in one molecule appears to be promising for designing tailor-made hosts for the complexation of any salt.

Experimental Section

General Methods: All solvents were purified by distillation under nitrogen from appropriate drying agents. The hydrostannylation was carried out under nitrogen. 4-Vinylbenzo-15-crown-5[24,25] and triphenyltin hydride[31] were synthesized as described in the literature. The NMR experiments were carried out with Bruker DRX 500, Bruker DRX 400, DPX 300, Varian Nova 600 and Varian Mercury 200 spectrometers. Chemical shifts δ are given in ppm and are referenced to the solvent peaks with the usual values calibrated against tetramethylsilane (^1H, ^{13}C) and tetramethylstannane (^{119}Sn). The numbering of the carbon atoms applied for the assignment of the ^{13}C resonances is shown in Scheme 2.

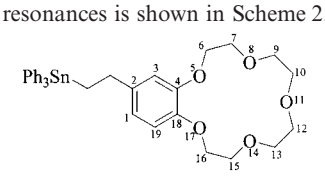

Scheme 2.Numbering scheme for the assignment of the ^{13}C NMR resonances.

The ability of compound **4** to transport the rhodanide anion through an organic phase was investigated by U-tube experiments as shown in Figure 3. The conductivity was determined with an apparatus of the type LF530 from the company Wissenschaftlich-Technische Werkstätten. The cell was calibrated at 20 °C with an NaCl standard solution. The rhodanide transported to the aqueous layer was identified by reaction with iron(III).

Complexation Studies: The samples for ^1H, ^{13}C and ^{119}Sn NMR spectroscopy were prepared by dissolving the triorganotin chloride **4** (ca. 80 mg) and the corresponding amounts of $NaBPh_4$, nBu_4NSCN and NaSCN in deuterated solvents. The ^1H (400.1 MHz) and ^{13}C (100.6 MHz) spectra were recorded at 303 K whereas the ^{119}Sn (149.4 MHz) NMR spectra were recorded at both 303 and 208 K. NaSCN was dried in vacuo (10^{-3} Torr) at 100 °C for several days and stored under nitrogen. $NaBPh_4$ and nBu_4NSCN were stored in a desiccator.

Crystallography: Crystals of **2a** were grown from ethanol and of **4**·H_2O from a CH_2Cl_2/Et_2O solution at –5 °C. Crystallographic data are collected in Table 3. Intensity data for the colorless crystals were collected with a Nonius KappaCCD diffractometer with graphite-monochromated Mo-K_α radiation. The data collections covered almost the whole sphere of the reciprocal space with 2 (**2a**), 4 (**4**·H_2O) sets at different κ angles and 203 (**2a**), 424 (**4**·H_2O) frames by ω-rotation (Δ/ω = 1°) at 2×90 s (**2a**), 70 s (**4**·H_2O) per frame. Crystal decay was monitored by repeating the initial frames at the end of the data collection. After analysis of the duplicate reflections, there was no indication of any decay. The structures were solved by direct methods (SHELXS97[32]) and successive difference Fourier syntheses. Refinement applied full-matrix least-squares methods (SHELXL97[33]). The H atoms were placed in geometrically calculated positions using a riding model with U_{iso} constrained at 1.2 times U_{eq} of the carrier C atom, whereas the H atoms [H(6W1), H(6W1)] (**4**·H_2O) bonded to the water molecule O(6W) were located in the difference Fourier map and refined isotropically. In **2a** there are two C atoms disordered over two sites with occupancies of 0.5 [C(42), C(43), C(43′), C(44′)], whereas C(43′) is refined isotropically. In **4**·H_2O one Cl atom of the solvent molecule CH_2Cl_2 is disordered over two sites with occupancies of 0.9 [Cl(3) and 0.1 Cl(3′)]. Atomic scattering factors for neutral atoms and real and imaginary dispersion terms were taken from ref.[34] The figures were created by SHELXTL.[35] CCDC-248340 (**2a**) and -248341 (**4**·H_2O) contain the supplementary crystallographic data for this paper. These data can be obtained free of charge from The Cambridge Crystallographic Data Centre via www.ccdc.cam.ac.uk/data_request/cif.

[2-(6,7,9,10,12,13,15,16-Octahydro-5,8,11,14,17-pentaoxabenzocyclopentadec-2-yl)ethyl]triphenylstannane (2): 4-Vinylbenzo-15-crown-5 (12.8 g, 44 mmol) and AIBN (115 mg) were added to Ph_3SnH (26.7 g, 41 mmol). The mixture was stirred at 70 °C for 12 h. After cooling to room temperature, CH_2Cl_2 (40 mL) was added and the solution was filtered through Celite. The filtrate was concentrated to give a yellow oil. The latter was purified by column chromatography (silica gel, CH_2Cl_2). Elution with ethanol gave 16.9 g (60%) of **2** as a slightly yellow oil. ^1H NMR (400.1 MHz, $CDCl_3$, 300 K): δ = 1.80 [t, $^3J(^1H\text{-}^1H)$ = 7.7, $^3J(^1H\text{-}^{117/119}Sn)$ = 54.5 Hz, 3 H, Sn–CH_2], 2.93 [t, $^3J(^1H\text{-}^1H)$ = 7.7, $^2J(^1H\text{-}^{117/119}Sn)$ = 56.9 Hz, 2 H, CH_2–Ar], 3.72–3.79 [m, 8 H, H(9)–H(13)], 3.82–3.85 [m, 2 H, H(7)], 3.87–3.93 [m, 2 H, H(15)], 3.94–3.98 [m, 2 H, H(6)], 4.07–4.10 [m, 2 H, H(16)], 6.62 {d, ^3J[H(1)-H(19)] = 2.0 Hz, 1 H, H(19)}, 6.66 {dd, ^3J[H(1)-H(19)] = 2.0, ^4J[H(1)-H(3)] = 8.2 Hz, 1 H, H(1)}, 6.73 {d, ^4J[H(1)-H(3)] = 8.2 Hz, 1 H, H(3)}, 7.32–7.45 (m, 15 H, $SnPh_3$) ppm. $^{13}C\{^1H\}$ NMR (100.6 MHz, $CDCl_3$, 300 K): δ = 13.1 [$^1J(^{13}C\text{-}^{117/119}Sn)$ = 383 Hz, Sn–CH_2], 32.0 [$^2J(^{13}C\text{-}^{117/119}Sn)$ = 18 Hz, CH_2–Ar], 69.1 [C(6)], 69.7 [C(16)], 69.8 [C(7)],

 © 2005 Wiley-VCH Verlag GmbH & Co. KGaA, Weinheim

Table 3. Crystallographic data of **2a** and **4**·H_2O.

	2·NaSCN	**4**·H_2O
Empirical formula	$C_{34}H_{38}O_5Sn$·NaSCN	$C_{29}H_{35}Cl_3O_5Sn$·H_2O
Formula mass [g/mol]	726.40	706.63
Crystal system	monoclinic	triclinic
Crystal size	0.08 × 0.04 × 0.04	0.15 × 0.13 × 0.13
Space group	$P2_1/b$	$P\bar{1}$
a [Å]	22.0800(17)	10.6889(3)
b [Å]	9.9015(7)	12.1158(3)
c [Å]	16.0185(9)	13.1338(4)
α [°]	90.00	84.0147(10)
β [°]	103.277(3)	76.4871(11)
γ [°]	90.00	69.7220(12)
V [Å^3]	3408.4(4)	1550.80(7)
Z	4	2
$\rho_{calcd.}$ [mg/m^3]	1.416	1.513
μ [mm^{-1}]	0.864	1.121
F(000)	1488	720
θ range [°]	2.98–25.04	3.17–25.36
Index ranges	$-26 \le h \le 25$	$-12 \le h \le 12$
	$-11 \le k \le 11$	$-13 \le k \le 14$
	$-17 \le l \le 17$	$-15 \le l \le 15$
No. of reflections collected	18544	19140
Completeness of θ_{max} (%)	89.0	99.8
No. of independent reflections/$R_{int.}$	5367/0.085	5680/0.037
No. of reflections observed with [$I > 2\sigma(I)$]	1522	3606
No. of refined parameters	410	369
GoF(F^2)	0.597	0.920
$R_1(F)$ [$I > 2\sigma(I)$]	0.0399	0.0427
$wR_2(F^2)$ (all data)	0.0944	0.1006
$(\Delta/\sigma)_{max.}$	0.001	0.001
Largest difference peak/hole [e/Å^3]	0.259/–0.219	0.826/–0.779

69.9 [C(15)], 70.8–71.3 [C(9)–C(13)], 114.1 [C(19)], 114.5 [C(3)], 120.4 [C(1)], 128.4 [^3J(^{13}C-$^{117/119}$Sn) = 47 Hz, Sn–Ph C(*m*)], 128.8 [^4J(^{13}C-$^{117/119}$Sn) = 10 Hz Sn–Ph, C(*p*)], 137.0 [^2J(^{13}C-$^{117/119}$Sn) = 36 Hz, Sn–Ph C(*o*)], 138.1 [^3J(^{13}C-$^{117/119}$Sn) = 55 Hz, C(2)], 138.7 [Sn–Ph C(*i*)], 147.3 [C(18)], 149.1 [C(4)] ppm. ^{119}Sn{^{1}H} NMR (149.2 MHz, CH_2Cl_2, D_2O capillary, 300 K): δ = –103 ppm. $C_{34}H_{38}O_5Sn$ (645.37): calcd. C 63.3, H 5.9; found C 63.0, H 5.9.

Iodo[2-(6,7,9,10,12,13,15,16-octahydro-5,8,11,14,17-pentaoxabenzocyclopentadec-2-yl)ethyl]diphenylstannane (3): Iodine (2.78 g, 10.97 mmol) was added in small portions to a magnetically stirred solution of **2** (7.07 g, 10.97 mmol) in CH_2Cl_2 (50 mL) in an ice bath. The reaction mixture was stirred overnight. The solvent and the iodobenzene were removed in vacuo. Addition of CH_2Cl_2 (20 mL), filtration and evaporation of the solvent afforded 7.46 g (97%) of **2** as a slightly yellow oil. ^{1}H NMR (500.13 MHz, $CDCl_3$): δ = 2.09 [t, ^3J(^{1}H-^{1}H) = 8.0, ^2J(^{1}H-$^{117/119}$Sn) = 52.6 Hz, 2 H, Sn–CH_2], 2.30 [t, ^3J(^{1}H-^{1}H) = 8.0, ^3J(^{1}H-$^{117/119}$Sn) = 88.5 Hz, 2 H, Ar-CH_2], 3.68–3.75 (m, 8 H, OCH_2), 3.77–3.82 (m, 4 H, OCH_2), 3.83–3.88 (m, 4 H, OCH_2), 3.91–3.96 (m, 4 H, OCH_2), 4.01–4.07 (m, 4 H, OCH_2), 6.65 (s, 1 H, Ar-H), 6.68 (s, 2 H, Ar-H), 7.30–7.50 (m, 10 H, Sn–Ph) ppm. ^{13}C{^{1}H} NMR (125.77 MHz, $CDCl_3$, 300 K): δ = 19.9 (Sn–CH_2), 31.8 (CH_2–Ar), 68.6–70.7 [C(6)–C(16)], 114.1 [C(3)], 114.5 [C(19)], 120.5 [C(1)], 128.6 [^3J(^{13}C-$^{117/119}$Sn) = 58 Hz, Sn–Ph C(*m*)], 129.7 [Sn–Ph C(*p*)], 135.8 [^2J(^{13}C-$^{117/119}$Sn) = 47 Hz, Sn–Ph C(*o*)], 136.3 [C(2)], 137.2 [Sn–Ph C(*i*)], 147.4 [C(18)], 148.9 [C(4)] ppm. ^{119}Sn{^{1}H} NMR (111.91 MHz, CH_2Cl_2, D_2O capillary): δ = –130 ppm. $C_{24}H_{33}IO_5Sn$ (695.17): calcd. C 48.4, H 4.8; found C 48.3, H 4.9.

Aqua Complex of Chloro[2-(6,7,9,10,12,13,15,16-octahydro-5,8,11,14,17-pentaoxabenzocyclopentadec-2-yl)ethyl]diphenylstannane (4·H_2O): AgCl (3.08 g, 21.48 mmol) was added to a solution of **3** (7.46 g, 10.47 mmol) in CH_3CN (100 mL). After stirring in darkness for 14 d, the solution was filtered. The solvent was evaporated to give a light yellow oil. The latter was dissolved in CH_2Cl_2/Et_2O (2:1) and cooled to –5 °C for several days to give 3 g (73%) of **4** as colorless crystals. ^{1}H NMR (400.13 MHz, CD_2Cl_2, 300 K): δ = 2.08 [t, ^3J(^{1}H-^{1}H) = 7.8, ^2J(^{1}H-$^{117/119}$Sn) = 59.2 Hz, 2 H, Sn–CH_2], 3.08 [t, ^3J(^{1}H-^{1}H) = 7.8, ^3J(^{1}H-$^{117/119}$Sn) = 87.8 Hz, 2 H, CH_2–Ar], 3.62–3.67 [m, 8 H, H(9)–H(13)], 3.74–3.77 [m, 2 H, H(7)], 3.78–3.83 [m, 2 H, H(15)], 3.87–3.91 [m, 2 H, H(6)], 3.99–4.04 [m, 2 H, H(16)], 6.67–6.75 (m, 3 H, Ar), 7.39–7.78 (m, 10 H, Sn–Ph) ppm. ^{13}C{^{1}H} NMR (100.63 MHz, CD_2Cl_2 300 K): δ = 20.9 [^1J(^{13}C-^{117}Sn) = 426, ^1J(^{13}C-^{119}Sn) = 446 Hz, Sn–CH_2], 31.0 [^2J(^{13}C-$^{117/119}$Sn) = 23 Hz, CH_2–Ar], 68.4 [C(6)], 68.8 [C(16)], 69.3 [C(7)], 69.4 [C(15)], 70.1–70.6 [C(9)–C(13)], 113.6 [C(19)], 114.0 [C(3)], 120.3 [C(1)], 128.8 [^3J(^{13}C-$^{117/119}$Sn) = 59 Hz, Sn–Ph C(*m*)], 129.9 [^4J(^{13}C-$^{117/119}$Sn) = 13 Hz Sn–Ph C(*p*)], 135.8 [^2J(^{13}C-$^{117/119}$Sn) = 47 Hz, Sn–Ph C(*o*)], 137.3 [^3J(^{13}C-$^{117/119}$Sn) = 61 Hz, C(2)], 139.6 [^1J(^{13}C-^{117}Sn = 540, ^1J(^{13}C-^{119}Sn) = 566 Hz, Sn–Ph C(*i*)], 146.6 [C(18)], 148.3 [C(4)] ppm. ^{119}Sn{^{1}H} NMR (111.9 MHz, CD_2Cl_2, 298 K): δ = 2 ppm. ^{119}Sn{^{1}H} NMR (111.9 MHz, CD_2Cl_2, 193 K): δ = –155 ppm. $C_{28}H_{33}ClO_5Sn$·H_2O (621.74): calcd. C 54.1, H 5.7; found C 53.7, H 5.7.

[2-(6,7,9,10,12,13,15,16-Octahydro-5,8,11,14,17-pentaoxabenzocyclopentadec-2-yl)ethyl]diphenyl(thiocyanato)stannane (5): AgSCN (8.30 g, 50.04 mmol) was added to a solution of **3** (3.50 g, 5.04 mmol) in CH_3CN (150 mL). The reaction mixture was stirred in darkness for 12 h followed by filtration from AgI and unreacted AgSCN. The filtrate was concentrated to give a light yellow solid. The latter was recrystallized from methanol to give 3.0 g (98%) of **5** as a colorless solid. ^{1}H NMR (400.13 MHz, CD_3OD, 300 K): δ = 1.93 [t, ^3J(^{1}H-^{1}H) = 7.5, ^2J(^{1}H-$^{117/119}$Sn) = 67.3 Hz, 2 H, Sn–

 © 2005 Wiley-VCH Verlag GmbH & Co. KGaA, Weinheim

CH_2], 3.12 [t, $^3J(^1H\text{-}^1H)$ = 7.8, $^3J(^1H\text{-}^{117/119}Sn)$ = 102.4 Hz, 2 H, CH_2–Ar], 3.55–4.00 (m, 16 H, CH_2O), 6.65–6.90 (m, 3 H, Ar), 7.29–7.64 (m, 10 H, Sn–Ph) ppm. $^{13}C\{^1H\}$ NMR (150.84 MHz, CD_2Cl_2, 300 K): δ = 23.3 (Sn–CH_2), 31.6 [$^2J(^{13}C\text{-}^{117/119}Sn)$ = 28 Hz, CH_2–Ar], 66.6–68.7 (CH_2O), 113.1 [C(19)/C(3)], 120.8 [C(1)], 128.6 [$^3J(^{13}C\text{-}^{117/119}Sn)$ = 64 Hz, $SnPh_2$ C(*m*)], 129.3 [$SnPh_2$ C(*p*)], 135.4 [SCN, determined by HMBC experiment], 136.4 [$^2J(^{13}C\text{-}^{117/119}Sn)$ = 46 Hz, $SnPh_2$ C(*o*)], 138.2 [$SnPh_2$ C(*i*)], 138.4 [C(2)], 141.9 [C(18)], 145.6 [C(4)] ppm. $^{119}Sn\{^1H\}$ NMR (111.9 MHz, $CDCl_3$): δ = –180 ($\nu_{1/2}$ = 1930 Hz) ppm.

Sodium Rhodanide Complex 2a: The triorganotin chloride **2** (1 g, 1.55 mmol) and NaSCN (0.170 g, 1.55 mmol) were dissolved in ethanol (5 mL) and the mixture was heated at reflux for 1 h. The reaction mixture was cooled to room temperature providing 700 mg (62%) of **2a** as colorless crystals. ^1H NMR (400.1 MHz, $CDCl_3$, 300 K): δ = 1.77 [t, $^3J(^1H\text{-}^1H)$ = 8.28, $^2J(^1H\text{-}^{117/119}Sn)$ = 52.2 Hz, 2 H, $SnCH_2$], 2.93 [t, $^3J(^1H\text{-}^1H)$ = 8.28, $^3J(^1H\text{-}^{117/119}Sn)$ = 56.5 Hz, 2 H, CH_2–Ar], 3.71 (m, 4 H, OCH_2), 3.79 (m, 4 H, OCH_2), 3.86 (m, 2 H, OCH_2), 3.93 (m, 4 H, OCH_2), 4.11 (m, 2 H, OCH_2), 6.58 [s, 1 H, H(3)], 6.70 [s, 2 H, H(1), H(19)], 7.43–7.33 (m, 15 H, Sn–Ph) ppm. $^{13}C\{^1H\}$ NMR (100.6 MHz, $CDCl_3$ 300 K): δ = 13.0 (Sn–CH_2), 31.8 (CH_2–Ar), 69.0–66.5 [C(6)–C(16)], 112.3 [C(19)], 112.4 [C(3)], 121.0 [C(1)], 128.4 [$^3J(^{13}C\text{-}^{117/119}Sn)$ = 49 Hz, Sn–Ph C(*m*)], 128.8 [$^4J(^{13}C\text{-}^{117/119}Sn)$ = 11 Hz, Sn–Ph C(*p*)], 136.8 [$^2J(^{13}C\text{-}^{117/119}Sn)$ = 35 Hz, Sn–Ph C(*o*)], 138.5 [C(2)], 138.7 [Sn–Ph C(*i*)], 144.6 [C(4)], 146.3 [C(18)] ppm. $^{119}Sn\{^1H\}$ NMR (149.2 MHz, $CDCl_3$): δ = –104 ppm. $C_{35}H_{38}NNaO_5SSn$ (726.45): calcd. C 57.7, H 5.3, N 1.9; found C 58.0, H 5.3, N 1.9.

Complex [4·Na][BPh_4]: ^1H NMR (400.1 MHz, $CDCl_3/CD_3CN$, 4:1, 300 K): δ = 2.08 [t, $^3J(^1H\text{-}^1H)$ = 7.9, $^2J(^1H\text{-}^{117/119}Sn)$ = 56.8 Hz, 2 H, Sn–CH_2], 3.12 [t, $^3J(^1H\text{-}^1H)$ = 7.8, $^3J(^1H\text{-}^{117/119}Sn)$ = 52.0 Hz, 2 H, CH_2–Ar], 3.58–3.67 [m, 8 H, H(9)–H(13)], 3.68–3.77 [m, 2 H, H(7)], 3.78–3.82 [m, 2 H, H(15)], 3.88–3.92 [m, 2 H, H(6)], 3.98–4.04 [m, 2 H, H(16)], 6.76–6.80 (m, 3 H, Ar), 6.87 (m, BPh_4^-), 7.02 [t, $^3J(^1H\text{-}^1H)$ = 7.2 Hz, BPh_4^-], 7.37–7.60 (m, 10 H, Sn–Ph) ppm. $^{13}C\{^1H\}$ NMR (100.63 MHz, $CDCl_3/CD_3CN$, 4:1, 300 K): δ = 20.5 (Sn–CH_2), 30.3 (CH_2–Ar), 66.3 [C(6)], 66.7 [C(16)], 67.2 [C(7)], 67.3 [C(15)], 67.8–68.1 [C(9)–C(13)], 112.9 [C(19)], 113.1 [C(3)], 116.3 (BPh_4^-), 121.1 [C(1)], 121.3 (BPh_4^-), 124.1 (BPh_4^-), 128.2 [$^3J(^{13}C\text{-}^{117/119}Sn)$ = 59 Hz, Sn–Ph, C(*m*)], 129.3 [$^4J(^{13}C\text{-}^{117/119}Sn)$ = 14 Hz, Sn–Ph C(*p*)], 135.2 [$^2J(^{13}C\text{-}^{117/119}Sn)$ = 43 Hz, Sn–Ph C(*o*)], 135.4 (BPh_4^-), 137.5 [C(2)], 139.2 [Sn–Ph C(*i*)], 144.6 [C(18)], 146.1 [C(4)], 162.7–164.2 (q, BPh_4^-) ppm. $^{119}Sn\{^1H\}$ NMR (149.2 MHz, $CDCl_3/CD_3CN$, 4:1, 300 K): δ = –9 ppm.

Complex [$n$$Bu_4N$][4·SCN]: ^1H NMR (400.1 MHz, CD_2Cl_2, 300 K): δ = 0.93 [t, $^3J(^1H\text{-}^1H)$ = 8 Hz, 12 H, $n$$Bu_4N^+$ CH_3], 1.29 [q, $^3J(^1H\text{-}^1H)$ = 7.3 Hz, 8 H, $n$$Bu_4N^+$ CH_2], 1.45 (m, 8 H, $n$$Bu_4N^+$ CH_2), 1.91 [t, $^3J(^1H\text{-}^1H)$ = 8.8, $^2J(^1H\text{-}^{117/119}Sn)$ = 74.8 Hz, 2 H, Sn–CH_2], 2.93 (m, 8 H, $n$$Bu_4N^+$ N–CH_2), 3.0 [t, $^3J(^1H\text{-}^1H)$ = 8.8, $^3J(^1H\text{-}^{117/119}Sn)$ = 52.3 Hz, 2 H, CH_2–Ar], 3.65 [s, 8 H, H(9)–H(13)], 3.75–3.84 [m, 4 H, H(7) H(15)], 3.98–4.05 [m, 4 H, H(6) H(15)], 6.72–6.84 (m, 3 H, Ar), 7.25–7.40 [m, 6 H, Sn–Ph H(*m*), H(*p*)], 7.84–8.20 [m, $^3J(^1H\text{-}^{117/119}Sn)$ = 30.6 Hz, 4 H, Sn–Ph H(*o*)]. $^{13}C\{^1H\}$ NMR (100.63 MHz, CD_2Cl_2, 300 K): δ = 13.3 ($n$$Bu_4N^+$), 19.5 ($n$$Bu_4N^+$), 23.6 ($n$$Bu_4N^+$), 31.5 ($CH_2$–Ar), 58.5 ($n$$Bu_4N^+$), 68.4 [C(6)], 69.0 [C(16)], 69.3 [C(7)], 69.4 [C(15)], 70.1–70.5 [C(9)–C(13)], 113.9 [C(19)], 114.1 [C(3)], 120.2 [C(1)], 127.6 [$^3J(^{13}C\text{-}^{117/119}Sn)$ = 64 Hz, Sn–Ph, C(*m*)], 128.1 [Sn–Ph C(*p*)], 136.7 [$^2J(^{13}C\text{-}^{117/119}Sn)$ = 47 Hz, Sn–Ph C(*o*)], 138.9 [C(2)], 146.8 [C(18)], 148.8 [C(4)] ppm. $^{119}Sn\{^1H\}$ NMR (149.2 MHz, CD_2Cl_2, 300 K): no resonance found. $^{119}Sn\{^1H\}$ NMR (149.2 MHz, CD_2Cl_2, 208 K): δ = –253 (13%), –217 (69%), –198 (18%) ppm.

Complex [$n$$Bu_4N$][5·SNC]: $^{119}Sn\{^1H\}$ NMR (149.2 MHz, CD_2Cl_2, 203 K): δ = 308 (3%), –252 (97%) ppm.

Complex [$(Ph_3P)_2N$][5·Cl]: $^{119}Sn\{^1H\}$ NMR (149.2 MHz, CD_2Cl_2, 203 K): δ = –250 (19%), –214 (64%), –197 (17%) ppm.

Complex 4·NaSCN: ^1H NMR (400.1 MHz, CD_2Cl_2, 300 K): δ = 1.96 [t, $^3J(^1H\text{-}^1H)$ = 8.3, $^2J(^1H\text{-}^{119/117}Sn)$ = 66.0 Hz, 2 H, Sn–CH_2], 3.10 [t, $^3J(^1H\text{-}^1H)$ = 8.0, $^3J(^1H\text{-}^{117/119}Sn)$ = 84.8 Hz, 2 H, CH_2–Ar], 3.47–3.60 [m, 8 H, H(9)–H(13)], 3.61–3.70 [m, 4 H, H(7), H(15)], 3.80–3.92 [m, 4 H, H(6), H(16)], 6.61–6.80 (m, 3 H, Ar), 7.30–7.79 (m, 10 H, Sn–Ph) ppm. $^{13}C\{^1H\}$ NMR (150.84 MHz, CD_2Cl_2, 300 K): δ = 24.8 [$^1J(^{13}C\text{-}^{117}Sn)$ = 595, $^1J(^{13}C\text{-}^{119}Sn)$ = 621 Hz, Sn–CH_2], 31.5 [$^2J(^{13}C\text{-}^{117/119}Sn)$ = 32 Hz, CH_2–Ar], 67.2–69.2 [C(6)–C(16)], 113.5 [C(19)], 113.6 [C(3)], 121.8 [C(1)], 128.3 [$^3J(^{13}C\text{-}^{117/119}Sn)$ = 66 Hz, Sn–Ph, C(*m*)], 129.1 [$^4J(^{13}C\text{-}^{117/119}Sn)$ = 13 Hz, Sn–Ph C(*p*)], 135.6 [N=C=S, $^2J(^{13}C\text{-}^{117/119}Sn)$ = 59 Hz], 136.5 [$^2J(^{13}C\text{-}^{117/119}Sn)$ = 45 Hz, Sn–Ph C(*o*)], 139.2 [$^3J(^{13}C\text{-}^{117/119}Sn)$ = 68 Hz, C(2)], 142.7 [$^1J(^{13}C\text{-}^{117}Sn)$ = 716, $^1J(^{13}C\text{-}^{119}Sn)$ = 751 Hz, Sn–Ph C(*i*)], 144.9 [C(18)], 146.7 [C(4)] ppm. $^{119}Sn\{^1H\}$ NMR (149.2 MHz, CD_2Cl_2, 298 K): δ = –225 ($\nu_{1/2}$ = 2013 Hz) ppm. $^{119}Sn\{^1H\}$ NMR (149.2 MHz, CD_2Cl_2, 203 K): δ = –248 ($\nu_{1/2}$ = 937 Hz) ppm. ESMS (+p): *m*/z = 650.1 [$Ph_2Sn(SCN) - C_{16}H_{23}O_5$]·$Na^+$. ESMS (–p): *m*/*z* = 685.1 [$Ph_2Sn(SCN)_2 - C_{16}H_{23}O_5$]$^-$, 766.2 [$Ph_2Sn(SCN)_2 - C_{16}H_{23}O_5$·NaSCN]$^-$.

Acknowledgments

We are grateful to the Deutsche Forschungsgemeinschaft and the Fonds der Chemischen Industrie for financial support.

[1] P. A. Gale, *Coord. Chem. Rev.* **2003**, *240*, 191.
[2] G. J. Kirkovits, J. A. Shriver, P. A. Gale, J. L. Sessler, *J. Inclusion Phenom. Macrocyclic Chem.* **2001**, *41*, 69.
[3] H. Tsukube, M. Wada, S. Shinoda, H. Tamiaki, *Chem. Commun.* **1999**, 1007.
[4] M. A. Hossain, H. J. Schneider, *J. Am. Chem. Soc.* **1998**, *120*, 11208.
[5] A. V. Koulov, J. M. Mahoney, B. D. Smith, *Org. Biomol. Chem.* **2003**, *1*, 27.
[6] D. T. Rosa, V. G. Young, D. Coucouvanis, *Inorg. Chem.* **1998**, *37*, 5042.
[7] S. Kubik, R. Goddard, *J. Org. Chem.* **1999**, *64*, 9475.
[8] B. R. Cameron, S. J. Loeb, *Chem. Commun.* **1997**, 573.
[9] K. Tanigaki, T. Sato, Y. Tanaka, T. Ochi, A. Nishikawa, K. Nagai, H. Kawashima, S. Ohkuma, *FEBS Lett.* **2002**, *524*, 37.
[10] D. M. Rudkevich, J. D. Mercerchalmers, W. Verboom, R. Ungaro, F. Dejong, D. N. Reinhoudt, *J. Am. Chem. Soc.* **1995**, *117*, 6124.
[11] M. A. S. Hossain, H. J. Schneider, *Chem. Eur. J.* **1999**, *5*, 1284.
[12] J. M. Mahoney, A. M. Beatty, B. D. Smith, *J. Am. Chem. Soc.* **2001**, *123*, 5847.
[13] D. J. White, N. Laing, H. Miller, S. Parsons, S. Coles, P. A. Tasker, *Chem. Commun.* **1999**, 2077.
[14] A. J. Evans, P. D. Beer, *Dalton Trans.* **2003**, 4451.
[15] P. R. A. Webber, P. D. Beer, *Dalton Trans.* **2003**, 2249.
[16] M. T. Blanda, J. Frels, J. Lewicki, *Supramol. Chem.* **1998**, *9*, 255.
[17] M. T. Blanda, M. A. Herren, *Chem. Commun.* **2000**, 343.
[18] a) M. T. Reetz, C. Niemeyer, K. Harms, *Angew. Chem.* **1991**, *103*, 1515; *Angew. Chem. Int. Ed. Engl.* **1991**, *30*, 1472; b) M. Kemmer, M. Biesemans, M. Gielen, J. C. Martins, V. Gramlich, R. Willem, *Chem. Eur. J.* **2001**, *7*, 4686.
[19] T. Sakurai, Y. Takeuchi, *Appl. Organomet. Chem.* **2004**, *18*, 23.
[20] T. Sakurai, Y. Takeuchi, *Heteroatom Chem.* **2003**, *14*, 365.
[21] M. Schulte, G. Gabriele, M. Schürmann, K. Jurkschat, D. Dakternieks, A. Duthie, *Organometallics* **2003**, *22*, 328.

 © 2005 Wiley-VCH Verlag GmbH & Co. KGaA, Weinheim

[22] D. Dakternieks, K. Jurkschat, H. J. Zhu, E. R. T. Tiekink, *Organometallics* **1995**, *14*, 2512.
[23] N. A. Chaniotakis, K. Jurkschat, D. Müller, K. Perdikaki, G. Reeske, *Eur. J. Inorg. Chem.* **2004**, 2283.
[24] J. Smid, B. El Haj, T. Majewicz, A. Nonni, R. Sinta, *Org. Prep. Proced. Int.* **1976**, *8*, 193.
[25] A. G. Talma, H. Van Vossen, E. J. R. Sudhoelter, J. Van Eerden, D. N. Reinhoudt, *Synthesis* **1986**, 680.
[26] M. Beuter, U. Kolb, A. Zickgraf, E. Brau, M. Bletz, M. Drager, *Polyhedron* **1997**, *16*, 4005.
[27] U. Kolb, M. Beuter, M. Dräger, *Inorg. Chem.* **1994**, *33*, 4522.
[28] J. Beckmann, M. Henn, K. Jurkschat, M. Schürmann, D. Dakternieks, A. Duthie, *Organometallics* **2002**, *21*, 192.
[29] S. E. Johnson, C. B. Knobler, *Organometallics* **1994**, *13*, 4928.
[30] M. Suzuki, I.-H. Son, R. Noyori, *Organometallics* **1990**, *9*, 3043.
[31] H. G. Kuivila, O. F. Beumel, *J. Am. Chem. Soc.* **1961**, *83*, 1246.
[32] G. M. Sheldrick, *Acta Crystallogr. Sect. A* **1990**, *46*, 467.
[33] G. M. Sheldrick, University of Göttingen, **1997**.
[34] *International Tables for X-ray Crystallography* Kluwer Academic Publishers, Dordrecht, **1992**, vol. C.
[35] G. M. Sheldrick, *SHELXTL* (Release 5.1, Software Reference Manual), Bruker AXS, Inc., Madison, Wisconsin, USA, **1997**.
Received: March 2, 2005
Published Online: June 14, 2005

 © 2005 Wiley-VCH Verlag GmbH & Co. KGaA, Weinheim

On the Structure of Nonastannide Clusters in Liquid and Solid State

Jan Rosdahl,[a] Thomas F. Fässler,[b] and Lars Kloo*[a]

Keywords: EXAFS spectroscopy / Cluster compounds / Polyanions / Solid-state structures / Ab initio calculations

The nonastannide clusters have been investigated using EXAFS, NMR and Raman spectroscopy as well as quantum chemical calculations explicitly considering a model cationic field and solid-state statistics. NMR spectroscopic and EXAFS results are basically identical to those previously published and consistent with a fluctional model of the cluster. The quantum chemical calculations show that there is no significant difference in energy between the two model geometries, C_{4v} and D_{3h}, and that the vibrational frequencies are very low, clearly indicating that the cluster is expected to be fluctional. The solid-state statistics show that both model geometries can be used to describe all known nonastannide structures with reasonable success, illustrating that the classification of the nonastannide clusters in terms of specific symmetries is entirely arbitrary.

(© Wiley-VCH Verlag GmbH & Co. KGaA, 69451 Weinheim, Germany, 2005)

Introduction

Homoatomic clusters of the main-group elements, E_n, is a group of molecules that have attracted some interest over the last decades.[1–3] This is partly due to the fact that these clusters are considered to form one of many extensions to the exciting borane chemistry. However, when using heavier atoms the bonds become more flexible with regards to acceptable bond lengths and angles, as compared to the lighter elements. Good candidates for investigating such flexibility effects are the nine-vertex clusters with C_{4v} or D_{3h} symmetry, such as E_9^{4-} or E_9^{3-} (E = Ge, Sn or Pb), due to their highly related geometries. In order to simplify the matter somewhat, we will mainly focus on the nonastannide clusters.

Over the last three decades, several crystallographic structures containing Sn_9^{4-} or Sn_9^{3-} have been reported.[4–15] Several of these have been classified as having a C_{4v} geometry, as expected according to Wade's rules for a *nido* cluster such as Sn_9^{4-}.[16] However, some appear to adopt a D_{3h} geometry, which is typical for a *closo* geometry and expected for Sn_9^{2-}, but it is most certainly not the correct geometry for a *nido* cluster such as Sn_9^{4-}. The same has been observed for other elements and is not considered to be unusual, yet unexplained. Many of the structure determinations indicate that there is some "disorder" in the structure and sometimes the structure is described in terms of going from C_{4v} geometry towards D_{3h}, or vice versa. The description is, nevertheless, still very static and often neglects the information contained in the anisotropic displacement parameters (ADPs), which we will show is unfortunate.

The prediction of the dynamic behavior of Sn_9^{4-} is at least as old as one of the first structures and was later complemented by a NMR spectroscopic investigation in solution.[5,17] However, the energy barrier for the fluctional behavior of the cluster was never determined, despite the low temperatures used during the experiments. This fluctional behaviour can even be retained when incorporating $Pt_2(PPh_3)$ into the cluster,[18] while other additions are more questionable with regards to the fluctional behaviour.[19,20]

Many of the early theoretical results for nonastannide clusters are based on extended Hückel calculations and they all report that the C_{4v} geometry is more stable than D_{3h}.[21,22] This is in good agreement with both earlier and more recent results,[5,20] but the opposite result can also be obtained, indicating that the difference in energy is very small.[23]

Since the description of the behaviour of nonastannide clusters in solution and solid state is so inconsistent, we believe that one of them can not be entirely correct. In order to get a more coherent description of the nature of these clusters, we have conducted an investigation involving EXAFS, NMR and Raman spectroscopy as well as quantum chemical calculations explicitly considering the effect of the cationic field and solid-state statistics.

Results and Discussion

Spectroscopy

The NMR spectroscopic results for the nonastannide cluster in ethylenediamine (en) solution are essentially the

[a] Department of Chemistry, Inorganic Chemistry, Royal Institute of Technology,
10044 Stockholm, Sweden
[b] Lehrstuhl für Anorganische Chemie mit Schwerpunkt Neue Materialien, Technische Universität München,
Lichtenbergstr. 4, 85747 Garching, Germany

 © 2005 Wiley-VCH Verlag GmbH & Co. KGaA, Weinheim DOI: 10.1002/ejic.200500043

same as those previous obtained, showing a heptet at a chemical shift of +1208 ppm and J = 264 Hz for the tin-potassium system in ethylenediamine, thus confirming the fluctional behaviour of the clusters in solution.[17,24] The integrated satellite peak intensities also confirm this interpretation, since the number of neighbours in the cluster is determined to be between four and five, as expected for a fluctional nine-atomic cluster that is close to both C_{4v} and D_{3h} symmetry.

The Raman spectroscopic results for the nonastannide cluster in en solution are also similar to previous results, displaying a peak at 155 cm^{-1} for the sample containing K and Sn with a ratio of 1:1.[25] This peak is assigned to the symmetrical breathing mode of vibration. Similar spectra were observed for the Na:Sn system. Furthermore, the position of the peak and the number of observed bands are not conclusive for either geometry.

EXAFS measurements have been conducted for three different samples corresponding to an en solution with Sn_9^{4-}, a solid with Sn_9^{4-} and a solid with Sn_9^{3-}. The expected result would be that all three samples should exhibit significantly different EXAFS patterns, since these three systems were chosen to represent three different classes, a fluctional cluster, a cluster with rigid C_{2v} geometry and a cluster with rigid D_{3h} geometry. However, all three samples give rise to very similar EXAFS traces, as can be seen in Figure 1 and Figure 2. The EXAFS pattern for the solution is somewhat more limited in resolution than those of the solids. Despite this, the similarities are hard to ignore. Furthermore, the EXAFS results for the two solids are almost identical to each other and thus consistent with a fluctional cluster model also in solid state (see Figure 1).

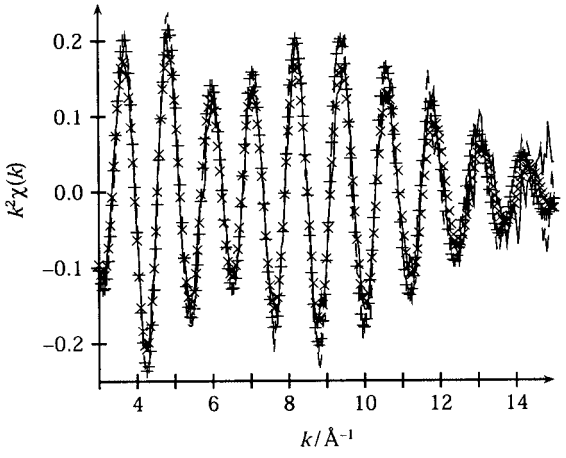

Figure 1. The reduced EXAFS data for the two solid model compounds. The solid line corresponds a solid with Sn_9^{3-}, while the dashed line corresponds to a solid with Sn_9^{4-}. The fitted models for the two samples are shown as × and +, respectively.

All three EXAFS traces can be fitted with a single Sn–Sn path, with a Sn–Sn distance of 3.06(4), 2.974(5)and 2.987(8) Å for the solution with Sn_9^{4-}, the solid with Sn_9^{4-} and the solid with Sn_9^{3-}, respectively. The problem with detecting longer distances is also consistent with a fluctional cluster model, since the largest variations are obtained for

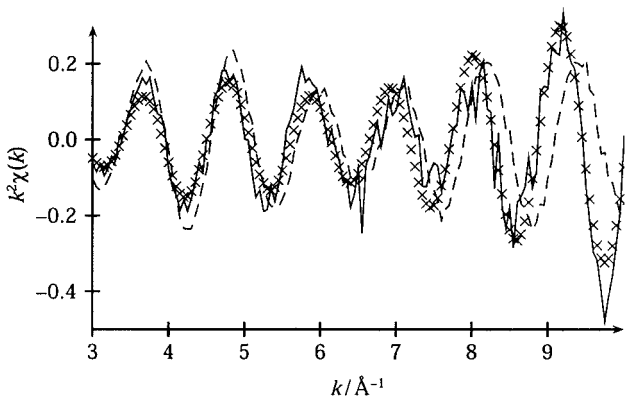

Figure 2. The reduced EXAFS data for the solution with Sn_9^{4-} (solid line) and fitted model (×). For comparison, the dashed line shows the solid with Sn_9^{4-}.

the longest Sn–Sn distances, thus dampening them below the level of noise. However, the longer Sn–Sn distances are present when calculating theoretical EXAFS spectra with rigid models of Sn_9^{4-}, both C_{4v} and D_{3h} geometries, and this is the only difference between experiment and theory (see Figure 3).

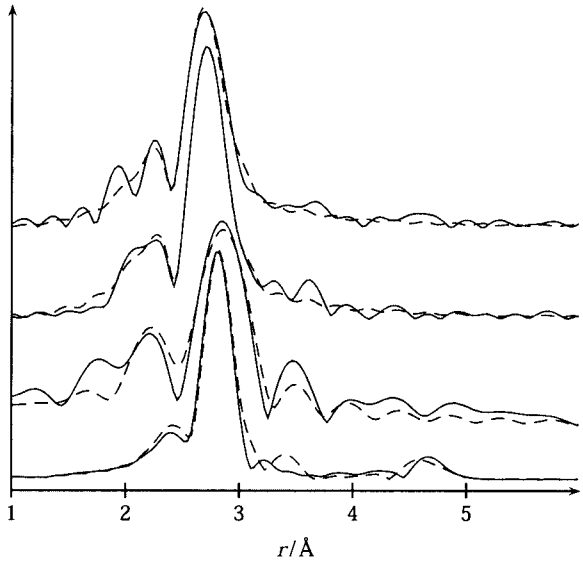

Figure 3. The radial distribution functions of the EXAFS data, fitted models and theoretical models. They are from top to bottom: solid sample with Sn_9^{3-} (solid line) and fitted model (dashed line); solid sample with Sn_9^{4-} (solid line) and fitted model (dashed line); solution with Sn_9^{4-} (solid line) and fitted model (dashed line); theoretical Sn_9^{4-} cluster with C_{4v} (solid line) and D_{3h} geometry (dashed line).

Solid-State Statistics

Several crystal structures of nonastannides are known, obtained at various temperatures and with different compositions.[4–15] The most common way to determine the symmetry of a cluster, when it is not very obvious, is to compare the angle and distance ratios with the idealised geometries.[26,9] A more blunt approach is to simply investigate the

 © 2005 Wiley-VCH Verlag GmbH & Co. KGaA, Weinheim

histogram of intramolecular Sn–Sn distances, which exhibits some of the expected similarities with the EXAFS results, see Figure 3 and Figure 4. If the ratio between the number of distances that fall in the two regions $2.55 \leq d_{Sn-Sn} < 3.95$ and $3.95 \leq d_{Sn-Sn} \leq 5.15$, where d_{Sn-Sn} is the Sn–Sn distance in Å, is 7:5 (21:15) the cluster is classified as being more of D_{3h} type, while a ratio of 5:4 (20:16) is obtained for clusters being more of C_{4v} type. A naive explanation for the above ratios would be that a D_{3h} structure is expected to have 21 shorter distances; 12 between the capping atoms and the closest atoms in the prism, 6 within the triangles in the prism and 3 for the edges in the prism, and 15 longer distances. A similar reasoning for C_{4v} results in 20 shorter distances; 4 between the capping atom and the upper square, 4 within the lower square, 8 between the squares and 4 within the upper square, and 16 longer distances. However, both these approaches only consider the static positional information from the crystal structure determination and totally neglects the information in ADPs, which often constitute a large portion of the information of a crystallographic study.

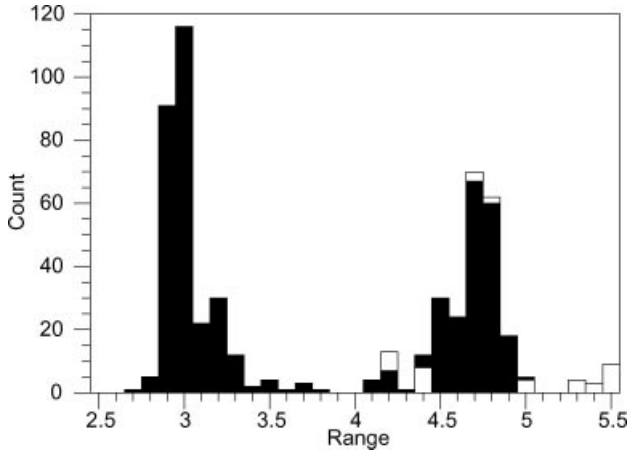

Figure 4. Histogram over intra (filled) and inter (open) molecular Sn–Sn distances.

We believe that the ADPs must be considered in order to get a more complete and dynamic picture of a solid-state structure. Therefore, we suggest that the symmetry of a cluster should be examined and possibly determined by fitting the idealised models to the crystallographic data, while considering the anisotropic displacement parameters. A nice feature with this approach is that the size of the ellipsoids needed to enclose the model using the experimental data will give an unbiased value of how good the fit is.

Since it is only necessary, more or less, to displace four of the nine atoms in order to change the symmetry from C_{4v} to D_{3h} or vice versa, it is evident that the remaining five atoms ought to fit both models reasonably well, which is clearly seen in Table 1, where the median of the fit never is worse than 30%. Moreover, ellipsoids with 80% probability is sufficient to include any of the two models in any of the structures, and ellipsoids with 50% probability will do the same for nearly half of the structures. This is also the level of the probability surfaces presented in most articles reporting solid-state structures.

The fit is generally better for the C_{4v} geometry compared to the D_{3h} one, mainly due to the extra parameter in the fit which is absent in the latter case. Furthermore, it can be seen that structures containing Sn_9^{3-} are better described in terms of a D_{3h} geometry than a C_{4v}, as expected, while structures containing Sn_9^{4-} often are better described in terms of a C_{4v} geometry. However, there are exceptions. Both models can be used, with reasonable success, to describe any of the nonastannide structures reported so far,

Table 1. Part of the statistical data for the various fits. The size of the ellipsoid needed to include the model is given in % and the distance between the experimental and the corresponding model position is given as d [Å].

	C_{4v}				D_{3h}				Combined						
	Max		Median		Max		Median		Max		Median				
System	%	d/Å	%	d/Å	%	d/Å	%	d/Å	%	d/Å	%	d/Å	Ratio	T/K	Ref.
$[K^+\text{-}([2,2,2]crypt)]_3[Sn_9]^{3-}(en)_{0.5}$	24.7	0.35	0.4	0.06	2.9	0.16	0.4	0.08	0.3	0.05	0.1	0.03	0.30	243	[10]
$[K^+\text{-}([2,2,2]crypt)]_3[Sn_9]^{3-}(en)_{1.5}$	60.2	0.46	3.3	0.12	0.2	0.04	0.1	0.02	0.2	0.04	0.1	0.02	0.01[a]	213	[6]
$[Na^+\text{-}([2,2,2]crypt)]_4[Sn_9]^{4-}$	0.4	0.07	0.1	0.03	39.9	0.38	10.3	0.20	0.3	0.06	0.1	0.03	0.96	278	[5]
$[K^+\text{-}([2,2,2]crypt)]_3[K^+][Sn_9]^{4-}$	0.4	0.06	0.2	0.04	51.2	0.38	24.8	0.23	0.2	0.04	0.1	0.03	0.92	173	[7]
$[K^+\text{-}([2,2,2]crypt)][Cs^+]_7([Sn_9]^{4-})_2(en)_3$	0.1	0.04	0.1	0.03	55.6	0.37	15.2	0.21	0.1	0.03	0.1	0.02	0.96	293	[12]
$[K^+\text{-}(18\text{-crown-}6)]_4[Sn_9]^{4-}(en)$	46.3	0.42	8.1	0.18	1.2	0.10	0.4	0.06	0.5	0.07	0.2	0.05	0.14[a]	193	[9]
$[K^+\text{-}(18\text{-crown-}6)]_3[K^+][Sn_9]^{4-}(en)$	17.5	0.27	3.6	0.14	5.2	0.16	1.6	0.12	0.5	0.06	0.1	0.04	0.36	243	[9]
$[Rb^+\text{-}(18\text{-crown-}6)]_2[Rb^+]_2[Sn_9]^{4-}(en)_{1.5}$	1.2	0.08	0.2	0.04	63.6	0.39	16.4	0.18	0.4	0.05	0.2	0.04	0.89	293	[13]
$[Na^+]_4[Sn_9]^{4-}(en)_7$	7.4	0.33	1.7	0.20	5.0	0.22	0.7	0.18	2.1	0.25	1.2	0.14	0.40[a]	293	[4]
$[Li^+\text{-}(NH_3)_4]_4[Sn_9]^{4-}(NH_3)$	0.4	0.04	0.1	0.02	80.2	0.37	25.1	0.17	0.2	0.02	0.1	0.01	0.93	123	[11]
$[K^+]_4[Sn_9]^{4-}$	3.1	0.10	0.4	0.06	51.8	0.35	17.6	0.19	1.5	0.08	0.4	0.05	0.87	293	[14]
$[Rb^+]_{12}[Sn_4]_2^{8-}[Sn_9]^{4-}$	5.7	0.15	1.5	0.08	58.8	0.42	28.7	0.23	5.3	0.15	2.0	0.08	0.95[b]	293	[15]
$[Rb^+]_{12}[Sn_4]_2^{8-}[Sn_9]^{4-}$	16.8	0.29	4.3	0.14	20.9	0.24	4.1	0.13	4.0	0.16	0.9	0.08	0.49[c]	293	[15]

[a] Better solutions exist for the combined model, $x\ C_{4v} + (1 - x)\ D_{3h}$, when x adopts a negative value. However, these were discarded since the fit was considered to be good enough even when x was limited to $0 \leq x \leq 1$. [b] This is for the structure where six of the atoms are labeled by an extra A and refined isotropically. [c] This is for the structure where six of the atoms are labeled by an extra B and refined.

 © 2005 Wiley-VCH Verlag GmbH & Co. KGaA, Weinheim

clearly showing that the clusters are fluctional also in solid state and not only in solution (see Figure 5).

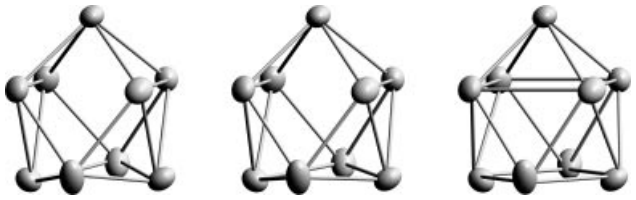

Figure 5. The three different models fitted to the same experimental data. They are from left to right; D_{3h}, C_{2v} and C_{4v}. The three-fold rotation axis in the case of D_{3h} is aligned horizontally. The crystallographic data being illustrated corresponds to $(K^+$-[18-crown-6]$)_3$-$[K^+][Sn_9]^{4-}$(en).[9]

An interesting feature of all the structures is that all tin atoms are located at general positions. This shows that all the clusters have unique geometries that are not directly enforced by the symmetry of the space group and that the different geometries most likely reflects the true nature of the clusters.

Theory

The calculational results clearly show that there is essentially no difference in energy between the two model symmetries, C_{4v} and D_{3h}, regardless the choice of basis set or theoretical method. The difference in energy between C_{4v} and D_{3h} being –3.5, –0.8 and +4.7 kJ·mol^{-1} at HF, B3LYP and MP2 levels, respectively, with the smallest basis set. The difference in energy is even smaller using larger basis sets, indicating that larger basis sets are required in order to properly describe the electron delocalisation in the cluster. Moreover, the preferred geometry appears to be dependent of the level of the calculation, illustrating the delicate balance between the different geometries in question. In addition, the vibrational frequencies are very low, highlighting that the potential energy surface is extremely flat for the two models (Table 2). Similar results have previously been reported, including the lead cluster congener.[20,27]

The obtained vibrational frequencies are lower than the experimentally observed ones, indicating that the harmonic oscillator approximation is not optimal.[25,20] Assuming that frequencies are reasonably correct, it immediately follows that the molecule will have several vibrational states occupied even at quite low temperatures. The most important vibrational mode is the lowest mode, the B_1 or E′, depending on the symmetry, whose vibrating motion is in the direction towards the alternative symmetry, see Figure 6. This shows that regardless of which of the two symmetries the cluster adopts it will always, as lowest vibrational mode, be vibrating in a manner that is directed towards the other symmetry. In this context it is noteworthy to remember that vibrational excitations correspond to larger oscillation amplitudes.

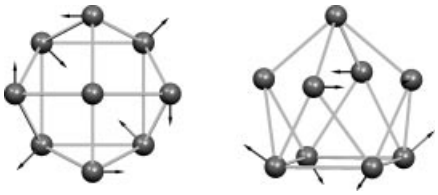

Figure 6. The displacement vectors for the lowest vibration mode of the theoretical model with C_{4v} geometry. In the left figure, the cluster is viewed upon along the C_4 axis, while in the right figure it is viewed almost perpendicularly to the C_4 axis.

The obtained vibrational frequencies are not particularly dependent on the choice of basis set, but the intensities are. This wouldn't be a problem if the relative intensities were

Table 2. Vibrational frequencies for the two model compounds at different levels of theory. Imaginary frequencies are shown as negative numbers and correspond to transition states (saddle points).

	HF		B3LYP		MP2	
Vibration	C_{4v}	D_{3h}	C_{4v}	D_{3h}	C_{4v}	D_{3h}
B_1:E'	26	–21	12	–7	–28	31
E:E′	51		44		51	
E:A_1'		82		74		78
B_1:E"	87	64	77	64	79	82
A_1:E"	82		81		89	
A_2:A_1"	70	95	71	87	93	98
B_2:E'	93	93	87	90	95	98
E:E'	90		85		98	
E:E"		94		90		101
B_2:E"	96		91		102	
E:A_2"	96	91	92	86	106	103
E:A_2'		96		91		109
A_1:E'	118	115	104	104	111	111
E:E'	125		113		120	
E:A_1'		128		115		120
B_1:E"	125	138	114	124	120	131
B_2:E"	140		127		135	
A_1:A_2"	139	141	130	129	140	137
E:A_1'	143	141	132	131	143	142
E:E'		147		134		146
A_1:E'	151		137		150	

 © 2005 Wiley-VCH Verlag GmbH & Co. KGaA, Weinheim

left almost intact, but this is unfortunately not the case. However, a general trend is that the intensities increase with increasing number of diffuse functions in the basis set, which easily can be explained with the increased flexibility of the electron cloud.

The cationic field, introduced in an attempt to mimic more normal solid-state conditions for the cluster, leaves the vibrational frequencies almost unaffected, while having a significant impact on the total energy by mainly shifting the potential energies for the nuclei and electrons, resulting in a bound HOMO in a majority of the cases, see Figure 7 and Figure 8.

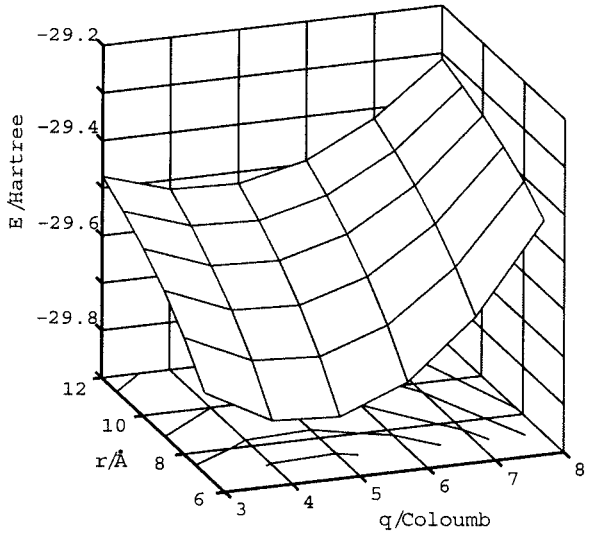

Figure 7. The variation of the total energy with respect to the radius and the charge of the cationic field for a Sn_9^{4-} cluster with C_{4v} geometry. The corresponding Figure for the D_{3h} geometry is virtually identical and thus not explicitly shown.

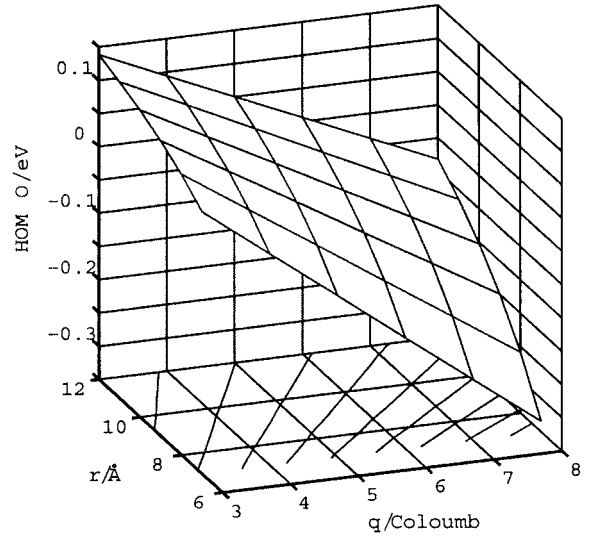

Figure 8. The variation of the HOMO energy level with respect to the radius and the charge of the cationic field for a Sn_9^{4-} cluster with C_{4v} geometry. The corresponding Figure for the D_{3h} geometry is virtually identical and thus not explicitly shown.

The ELF results are also practically unaffected by the field, and the differences are well within the expected accuracy of calculation.[28] Moreover, the iso-surfaces exhibit the same size, shape and location for the different cationic fields considered within the model geometries. This shows that the skeletal electrons are almost unaffected by the cationic field, thus leaving the polyhedral framework practically intact. When comparing iso-surfaces for the two model geometries, it becomes evident that they do not differ much at all, the largest difference in the enclosed iso-surface volumes is never larger than 2.2 Å^3 and this is less than 5% of the total volume in question (see Figure 9 and Figure 10).

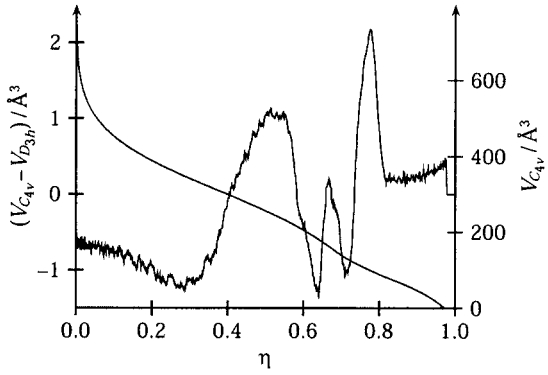

Figure 9. The difference in the enclosed iso-surface volumes between the C_{4v} and D_{3h} models together with the enclosed surface volume for the C_{4v} model at various η.

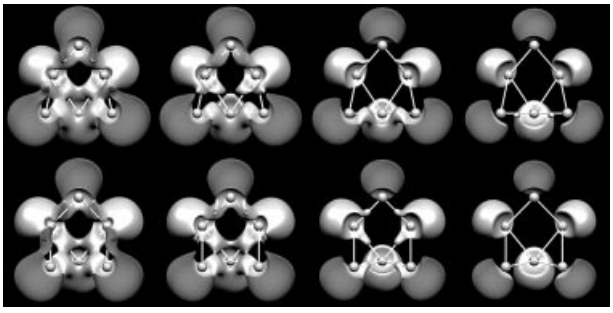

Figure 10. The iso-surfaces at η = 0.66, 0.69, 0.76 and 0.81, from left to right, for the optimised C_{4v} (upper) and D_{3h} geometry (lower). The surfaces are sliced through a σ_v mirror plane coinciding with the plane of the paper, i.e. the four-fold rotation axis for the C_{4v} model is aligned vertically in the plane of the paper and the three-fold rotation axis for the D_{3h} model is aligned horizontally in the plane of the paper.

Moreover, the preferred total charge for the field is about +5, slightly higher than the corresponding charge of the anionic cluster.

Conclusions

The nonstannide clusters are probably best viewed upon as highly fluctional, almost liquid-like drops that retain their fluctional behavior even in solid state and at low temperatures. Due to this fluctionality of the cluster it becomes superficial to discuss the symmetry of the cluster, since the only information known so far is the vibrational average and not the static ideal that is so vital for the discussion.

 © 2005 Wiley-VCH Verlag GmbH & Co. KGaA, Weinheim

Experimental Section

Chemicals: Ethylenediamine (en, Merck, for synthesis, 99%) was refluxed with sodium for several hours, distilled under nitrogen and stored with molecular sieves before being used. Potassium metal (Alpha, 99.95%), sodium metal (Alpha, 99.95%) and tin metal (Baker, 99.98%) was used as purchased. The two solid samples, $(K^+$-[2,2,2]crypt$)_3[Sn_9]^{3-}$ and $(K^+$-[18-crown-6]$)_3[K^+][Sn_9]^{4-}$(en), were prepared as described elsewhere.[10,9]

Syntheses: The alloys were made by fusing the elements in a dry pyrex tube at 250 °C and with the molar ratios 10:1, 5:1, 1:1, 1:5 and 1:10 between potassium or sodium and tin. Ethylenediamine was added to the tube after the reaction was completed and the reaction mixture was allowed to equilibrate for 24 hours before further analysis of the solution. All work was carried out in a glove box with a dry nitrogen atmospehere (< 1 ppm O_2, < 1 ppm H_2O) due to the alloys sensitivety to oxygen.

NMR Spectroscopy: NMR spectra were recorded with a Varian Unity 300 MHz spectrometer operating at 111.87 MHz for ^{119}Sn. Chemical shifts are given with respect to $SnCl_4$ at +150 ppm.

Raman Spectroscopy: Raman spectra were obtained with a Bio-Rad Fourier Transform Raman system, employing the 1024 nm radiation of an infrared Nd:YAG laser. 4 cm^{-1} resolution was used.

EXAFS: X-ray absorption (EXAFS) data were recorded at the Stanford Synchrotron Radiation Laboratory (SSRL), using beam line 4 at 3.0 GeV and 50–90 mA. Monochromatic radiation was obtained from a Si(220) double crystal monochromator. High-order harmonics were rejected by 50% detuning. Incident and transmitted X-rays were monitored with argon-filled ion chambers. Six scans were made for all samples. The solid samples were contained in a cell of 1 mm thickness with Kapton film as windows, internally referenced by the K-edge of a tin foil to 29.2 keV. The liquid sample was contained in a cell of 2 mm thickness with Kapton film as windows and the fluorescence was detected with a Ge-detector after passing through an Ag filter. The FEFF program was employed to calculate the Sn–Sn phase shift and amplitude functions, which were used in the non-linear, least-squares fit of the k^3-weighted EXAFS data.[29,30]

Solid-State Statistics: The models were fitted to the crystallographic data with an in-house developed program, using the least-squares method minimising:

$$\sum_i \Delta X_i^T U_i^{-1} \Delta X_i$$

where ΔX_i is the positional difference between the model and the crystallographic data and U_i is the anisotropic displacement parameter for the i:th atom. Three different models were considered, C_{4v}, D_{3h} and a mixture of the two, $x\ C_{4v} + (1 - x)\ D_{3h}$. The last model was mainly used for determining the ratio between the two other ones, when the two models are oriented in such way that the combined model will have C_{2v} symmetry. Both models were fitted simultaneously to the data in order to limit the possibility of obtaining unrealistic results.

Common for all models is that there are three parameters related to the orientation of the model relative to the data. In addition, there are four and three parameters related to the size and shape of the C_{4v} and D_{3h} models, respectively. The combined model has an additional parameter related to the mixing of the two previous models. Thus, in total there are 7, 6 and 11 parameters that are fitted for the C_{4v}, D_{3h} and $x\ C_{4v} + (1 - x)\ D_{3h}$ models, respectively.

Calculations: All quantum chemical calculations, except the Electron Localisation Functions (ELF), were performed using Gaussian98 (rev. A7) with a variety of computers.[31] ECP-based basis sets were used for tin, employing the Stuttgart group, quasi-relativistic ECP's (46 and 28 core electrons) and slightly modified valence spaces;[32] (14s10p2d1f)/[3s3p2d1f] and (14s10p3d2f)/[4s4p3d2f] for the 46 core electron ECP, and (12s12p8d2f1g)/[6s6p3d2f1g] for the 28 core electron ECP.[33,34] Calculations were performed at Hartree–Fock (HF), B3LYP and 2nd-order Møller–Plesset perturbation theory (MP2) level and vibrational frequency calculations were performed.

The ELF calculations were performed using the TopMod program package.[28,35] The grid was chosen so that the distance between the borders and the closest atom was at least 6.0 a.u., and the step size was never larger than 0.1 a.u. The ELF iso-surfaces were visualised with the program Molekel.[36,37]

The cationic field was entered as point charges located at the vertices of a truncated icosahedron, more known as a buckyball or a football. The radius was varied between 7.0 and 12.0 Å at 1.0 Å interval and the point charges were uniformly assigned so that the total charge was varied between 3.0 and 8.0 Coulomb at 1.0 Coulomb interval. The center of the truncated icosahedron was aligned with the center of the molecule and a five-fold rotation axis was aligned with the rotational axis of the highest order of the molecule and another five-fold rotation axis was aligned with a suitable mirror plane, thus assuring that both symmetries are broken by the cationic field.

Acknowledgments

We are grateful to The Swedish Research Council and EU RTN for supporting this work. The authors thank Per Persson, Umeå University, for helpful discussions. Portions of this research were carried out at the Stanford Synchrotron Radiation Laboratory, a national user facility operated by Stanford University on behalf of the U.S. Department of Energy, Office of Basic Energy Sciences.

[1] J. D. Corbett, *Chem. Rev.* **1985**, *85*, 383–397.
[2] J. D. Corbett, *Angew. Chem. Int. Ed.* **2000**, *39*, 670–690.
[3] T. F. Fässler, *Coord. Chem. Rev.* **2001**, *215*, 347–377.
[4] L. Diehl, K. Khodadadeh, D. Kummer, J. Strähle, *Chem. Ber.* **1976**, *109*, 3404–3418.
[5] J. D. Corbett, P. A. Edwards, *J. Am. Chem. Soc.* **1977**, *99*, 3313–3317.
[6] S. C. Critchlow, J. D. Corbett, *J. Am. Chem. Soc.* **1983**, *105*, 5715–5716.
[7] R. C. Burns, J. D. Corbett, *Inorg. Chem.* **1985**, *24*, 1489–1492.
[8] T. F. Fässler, M. Hunziker, *Z. Anorg. Allg. Chem.* **1996**, *622*, 837–844.
[9] T. F. Fässler, R. Hoffmann, *Angew. Chem. Int. Ed. Angew. Chem. Int. Ed. Engl.* **1999**, *38*, 543–546.
[10] T. F. Fässler, R. Hoffmann, *Z. Kristallogr.-New Crystal Structures* **2000**, *215*, 139–142.
[11] N. Korber, A. Fleischmann, *J. Chem. Soc., Dalton Trans.* **2001**, 383–385.
[12] R. Hauptmann, R. Hoffmann, T. F. Fässler, *Z. Anorg. Allg. Chem.* **2001**, *627*, 2220–2224.
[13] R. Hauptmann, T. F. Fässler, *Z. Anorg. Allg. Chem.* **2002**, *628*, 1500–1504.
[14] C. Hoch, M. Wendorff, C. Röhr, *Acta Crystallogr., Sect. C* **2002**, *58*, 45–46.
[15] C. Hoch, M. Wendorff, C. Röhr, *J. Alloys Compd.* **2003**, *361*, 206–221.
[16] K. Wade, *Adv. Inorg. Chem. Radiochem.* **1976**, *18*, 1–66.

 © 2005 Wiley-VCH Verlag GmbH & Co. KGaA, Weinheim

[17] R. W. Rudolph, W. L. Wilson, F. Parker, R. C. Taylor, D. C. Young, *J. Am. Chem. Soc.* **1978**, *100*, 4629–4630.
[18] B. Kesanli, J. Fettinger, D. R. Gardner, B. Eichhorn, *J. Am. Chem. Soc.* **2002**, *124*, 4779–4786.
[19] B. Kesanli, J. Fettinger, B. Eichhorn, *Chem. Eur. J.* **2001**, *7*, 5277–5285.
[20] J. Campbell, H. P. A. Mercier, H. Franke, D. P. Santry, D. A. Dixon, G. J. Schrobilgen, *Inorg. Chem.* **2002**, *41*, 86–107.
[21] L. L. Lohr Jr., *Inorg. Chem.* **1981**, *20*, 4229–4235.
[22] R. C. Burns, R. J. Gillespie, J. A. Barnes, M. J. McGlinchey, *Inorg. Chem.* **1982**, *21*, 799–807.
[23] A. Hirsch, Z. Chen, H. Jao, *Angew. Chem. Int. Ed.* **2001**, *40*, 2834–2838.
[24] W. L. Wilson, *Preparation and NMR Characterization of tin and lead Anionc Clusters*, Ph. D. thesis, The University of Michigan, **1982**.
[25] H. G. von Schnering, M. Baitinger, U. Bolle, W. Carrillo-Cabrera, J. Curda, Y. Grin, F. Heinemann, J. Llanos, K. Peters, A. Schmeding, M. Somer, *Z. Anorg. Allg. Chem.* **1997**, *623*, 1037–1039.
[26] L. J. Guggenberger, E. L. Muetterties, *J. Am. Chem. Soc.* **1976**, *98*, 7221–7225.
[27] J. Campbell, D. A. Dixon, H. P. A. Mercier, G. J. Schrobilgen, *Inorg. Chem.* **1995**, *34*, 5798–5809.
[28] S. Noury, X. Krokidis, F. Fuster, B. Silvi, *Computers & Chemistry* **1999**, *23*, 597–604.
[29] A. L. Ankudinov, B. Ravel, J. J. Rehr, S. D. Conradson, *Phys. Rev. B.* **1998**, *58*, 7565–7576.
[30] M. Newville, *J. Synchrotron Radiat.* **2001**, *8*, 322–324.
[31] M. J. Frisch, G. W. Trucks, H. B. Schlegel, G. E. Scuseria, M. A. Robb, J. R. Cheeseman, V. G. Zakrzewski, J. A. Montgomery, Jr., R. E. Stratmann, J. C. Burant, S. Dapprich, J. M. Millam, A. D. Daniels, K. N. Kudin, M. C. Strain, O. Farkas, J. Tomasi, V. Barone, M. Cossi, R. Cammi, B. Mennucci, C. Pomelli, C. Adamo, S. Clifford, J. Ochterski, G. A. Petersson, P. Y. Ayala, Q. Cui, K. Morokuma, D. K. Malick, A. D. Rabuck, K. Raghavachari, J. B. Foresman, J. Cioslowski, J. V. Ortiz, A. G. Baboul, B. B. Stefanov, G. Liu, A. Liashenko, P. Piskorz, I. Komaromi, R. Gomperts, R. L. Martin, D. J. Fox, T. Keith, M. A. Al-Laham, C. Y. Peng, A. Nanayakkara, C. Gonzalez, M. Challacombe, P. M. W. Gill, B. Johnson, W. Chen, M. W. Wong, J. L. Andres, C. Gonzalez, M. Head-Gordon, E. S. Replogle, J. A. Pople, *Gaussian 98, Revision A.7*. Gaussian, Inc., Pittsburgh PA, **1998**.
[32] The most diffuse functions were removed from the contracted part of the basis set.
[33] A. Bergner, M. Dolg, W. Kuechle, H. Stoll, H. Preuss, *Mol. Phys.* **1993**, *80*, 1431–1441.
[34] J. M. L. Martin, A. Sundermann, *J. Chem. Phys.* **2001**, *114*, 3408–3420.
[35] S. Noury, X. Krokidis, F. Fuster, B. Silvi, *TopMod package*, **1997**.
[36] P. Flükiger, H. P. Lüthi, S. Portmann, J. Weber, *MOLEKEL 4.3*, **2000–2002**.
[37] S. Portmann, H. P. Lüthi, *Chimia* **2000**, *54*, 766–770.

Received: January 13, 2005
Published Online: June 17, 2005

 © 2005 Wiley-VCH Verlag GmbH & Co. KGaA, Weinheim

An Unexpected Crystal-Chemical Principle for the Pyrochlore Structure

Terrell A. Vanderah,*[a] Igor Levin,[a] and Michael W. Lufaso[a]

Keywords: Pyrochlore / Displacive disorder / Bismuth zinc niobates / Phase equilibria

Phase equilibrium studies of the Bi–Zn–Nb–O system show that pyrochlore does not form at chemical compositions predicted by the traditional formula for this crystal structure, $A_2B_2O_6O'$, where A denotes large (8-coordinated, e.g. Bi^{3+}) and B small (6-coordinated, e.g. Zn^{2+}, Nb^{5+}) cation sites. Instead, pyrochlore forms only at compositions with excess B cations which, surprisingly, occupy the large A-cation sites. Reports of similar behavior in other pyrochlores suggest a previously unrecognized inherent structural feature (displacive disorder) which allows the formation of a large family of cubic pyrochlores with small B cations occupying up to ca. 25 % of the large A-cation sites. Many pyrochlores can now be synthesized by deliberately combining large and small metal ions on the A sites.
(© Wiley-VCH Verlag GmbH & Co. KGaA, 69451 Weinheim, Germany, 2005)

Introduction

The mineral pyrochlore, $(Na,Ca)_2Nb_2O_6(OH,F)$, was named in 1826 from the Greek for *fire* and *green* because some specimens turned green upon ignition.[1] *Pyrochlore* also denotes a large group of 22 crystallographically similar minerals that are highly diverse chemically[2] and widely distributed geologically. The general formula is $\mathbf{A_{1\rightarrow2}B_2O_6(O,OH,F)\cdot}\boldsymbol{n}\mathbf{H_2O}$, where, in geological specimens, **A** is a relatively large cation (Ca, K, Ba, Y, Ce, Pb, U, Sr, Cs, Na, Sb^{3+}, Bi, and/or Th; radii larger than or equal to ca. 1.0 Å) and **B** is a smaller cation (Nb, Ta, Ti, Sn, Fe, and/or W); the seventh anion position in the crystal structure can be occupied by O^{2-}, OH^-, and/or F^-.[1]

A large number of pyrochlore analogs have been synthesized with an amazing variety of chemical compositions and exploitable properties.[3–9] These include ferroelectricity,[4,10,11] temperature-stable high-permittivity properties,[12,13] fast-ion oxygen conductivity,[6–8] and a wide variety of electrical properties including metallic conductivity, semiconductivity, superconductivity, and electronic phase transitions.[4,5,14–18] The threefold symmetry of the metal arrangement in the crystal structure leads to interesting and diverse magnetic-ordering properties such as ferromagnetism, antiferromagnetism, and spin-glass behavior;[19–21] colossal magnetoresistance (CMR) has also been observed.[22,23] Pyrochlores are known to exhibit catalytic properties,[6] optical properties of interest for pigments and luminescent materials,[6,24] and refractory properties resulting in their consideration as host ceramics for nuclear waste immobilization.[4,25]

The remarkable variety of properties obtainable with the pyrochlore crystal structure reflects its inherent chemical and structural versatility. This non-molecular arrangement[4,5,26,27] is unusual in that it can be considered as two relatively independent, interpenetrating three-dimensional frameworks (Figure 1). The $A_2B_2O_7$ overall formula for ideal oxide pyrochlores is often written as $A_2B_2O_6O'$ (or $A_2B_2O_6X$) to distinguish the oxygen atoms (or anions) in the two different networks. The ideal cubic structure is highly symmetrical, crystallizing in space group $Fd\bar{3}m$ (No. 227), with four crystallographically distinct sites occupied by the A (site 16*d*), B (site 16*c*), O (site 48*f*), and O′ (site 8*b*) ions. Symmetry fixes the positions of all ions except those in 48*f*, which have a single variable parameter along the *x*-direction. The extensive compositional ranges known for pyrochlore compounds reflect the versatility of the A_2O' substructure: "defect" pyrochlores form readily since this network can be partially occupied or even completely absent, as in the pyrochlore-type polymorph of WO_3 (W_2O_6).[29] In addition, the O′ position can be occupied by anions other than O^{2-} such as OH^-, F^-,[30] and S^{2-},[31] forming oxyhydroxide, oxyfluoride, and oxysulfide pyrochlores. A number of non-oxide pyrochlores are known[27,32] including chlorides[33] and fluorides.[34,35] The pyrochlore structure is therefore highly "tailorable"; e.g., the identities and oxidation states of the B-cations, which play a leading role in electronic properties, can be controlled by achieving electroneutrality through deliberate choices of the A and O′ ions and their concentrations.

Although solid-state chemists realize that ions are not hard spheres with fixed sizes, the use of *structure field maps*[36] to predict the crystalline arrangement of new complex oxides has been moderately successful, especially given the scarcity of theoretical tools. For a given crystal structure, the map is constructed empirically from known com-

[a] National Institute of Standards and Technology, Ceramics Division,
Gaithersburg, MD 20899, USA

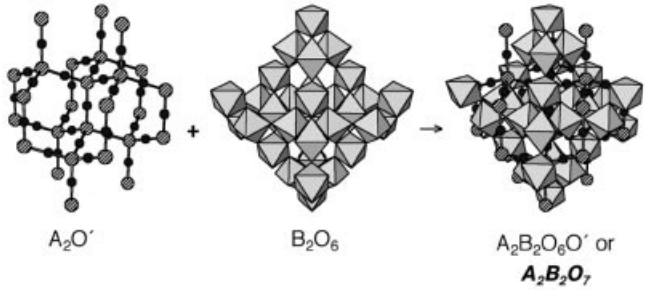

Figure 1. The ideal crystal structure of pyrochlore represented as two interpenetrating networks. Small black spheres denote A cations, large hatched spheres represent O′ oxygen anions, and gray octahedra contain B cations with oxygen atoms located at the six vertices. The A_2O' network corresponds to that of anticristobalite-type[28] Cu_2O, featuring four-coordinate O′ ions and two-coordinate A cations. The B_2O_6 framework consists of $[BO_6]$ octahedra sharing all vertices to form large cavities. The structures are interwoven such that the O′ ions of the A_2O' network occupy the centers of these cavities, while the A cations reside in puckered hexagons formed by oxygen atoms in the B_2O_6 framework. The final coordination number of the A cations is eight including the two oxygen atoms in the A_2O' network, which cap the puckered hexagonal ring above and below.

pounds by plotting the ionic radii[37] of the A vs. the B cations; new compounds may form the same structure if the radii of the proposed A and B cations correspond to a point in the observed stability field. The use of structure field maps and cation radius ratios to predict the formation of pyrochlores has been somewhat successful for ideal formulations.[4,8,38–41] For example, for $A^{3+}{}_2B^{4+}{}_2O_7$ pyrochlores, the A cation can be as small as Lu^{3+} (0.977 Å) or as large as Bi^{3+} (1.17 Å), while the radii of the B cations fall between ca. 0.58 and 0.72 Å.[4] The approach has been less useful for pyrochlores with substitutions on the A and B sites;[6,42] nevertheless, there is general agreement that the A cation must be appreciably larger than the B cation for the structure to form.

In the late 1990s, pyrochlore-containing Bi–Zn–Nb–O materials attracted considerable attention as they were found to exhibit properties suitable for embedded (miniaturized) temperature-stable capacitors and filters.[12,43] The composition of the pyrochlore phase was given in numerous reports as $Bi_{1.5}Zn_{1.0}Nb_{1.5}O_7$, which incited considerable controversy since this would require half of the small Zn^{2+} cations (radius 0.74 Å) to be mixed with the much larger Bi^{3+} ions on the A sites of the structure [i.e., $Bi_{1.5}Zn_{0.5}(Zn_{0.5}Nb_{1.5})O_7$, B-site cations in parentheses]. The size of Zn^{2+}, which is rarely observed with coordination numbers higher than 6, falls well outside the structure field maps for the A site cations in ideal pyrochlores.[4,40] Subsequently, the composition $Bi_{1.5}Zn_{1.0}Nb_{1.5}O_7$ was shown to be a two-phase mixture of pyrochlore and ZnO; however, a pure single-phase cubic pyrochlore was indeed obtained at the composition $Bi_{1.5}Zn_{0.92}Nb_{1.5}O_{6.92}$,[44] which also requires a considerable concentration of Zn^{2+} on the A sites.

A structural determination of $Bi_{1.5}Zn_{0.92}Nb_{1.5}O_{6.92}$[44] revealed static displacive disorder in the A_2O' portion of the structure and concluded a structural formula of $Bi_{1.5}Zn_{0.42}\square_{0.08}(Zn_{0.50}Nb_{1.5})O_{6.92}$. The A sites were assumed to be occupied by a (disordered) mixture of Bi^{3+}, Zn^{2+}, and vacancies (□); observation of reflections with Miller indices 442, forbidden for an ideal pyrochlore, required lower-symmetry positions for the A and O′ ions, even though the average structure retains cubic symmetry [$Fd\bar{3}m$, a = 10.5616(1) Å] The combined displacements (Figure 2) of the A (0.39 Å) and O′ (0.46 Å) ions change the coordination number of the A cations from 8 to (5 + 3), thus permitting the smaller Zn^{2+} ion to achieve a chemically reasonable environment, with fewer nearest oxygen neighbors, by local correlations of the displaced ions, as

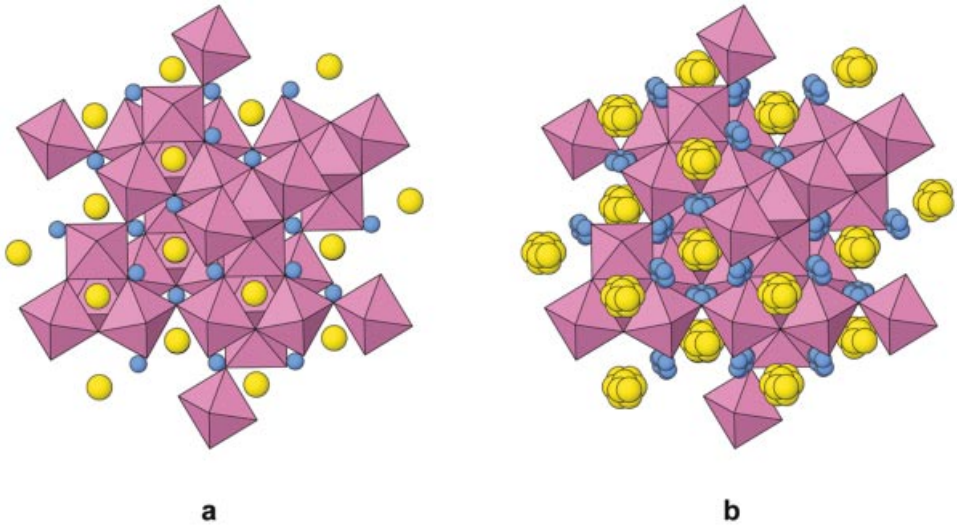

Figure 2. Comparison of the ideal (**a**) pyrochlore structure (Figure 1) and actual (**b**) structure determined for $Bi_{1.5}Zn_{0.92}Nb_{1.5}O_{6.92}$, with displacive disorder in the A_2O' network.[44] Blue spheres represent A cation sites, yellow spheres represent the O′ oxygen sites (bonds in the A_2O' network have been omitted for clarity), and red octahedra denote the B_2O_6 framework. In part **b**, a disordered mixture of Bi^{3+}, Zn^{2+}, and vacancies is distributed randomly among the six equivalent sites represented by each toroid of blue spheres; cuboctahedral clusters of yellow spheres denote the 12 possible displaced positions for the O′ ions.

 © 2005 Wiley-VCH Verlag GmbH & Co. KGaA, Weinheim

subsequently confirmed by a detailed study of diffuse scattering.[45] Single-crystal X-ray diffraction analysis[46] also confirmed the displacively disordered structural model for $Bi_{1.5}Zn_{0.92}Nb_{1.5}O_{6.92}$. Interestingly, vibrational spectroscopic studies suggest that the glass-like dielectric behavior observed for $Bi_{1.5}Zn_{0.92}Nb_{1.5}O_{6.92}$ is caused by this displacive disorder.[44,47] The present study of the equilibrium phase diagram for the Bi_2O_3–ZnO–Nb_2O_5 system was carried out to elucidate the compositional range of this highly unusual pyrochlore as well as its thermodynamic compatibility with other phases in the system.

Results and Discussion

Subsolidus phase relations obtained for the Bi_2O_3–ZnO–Nb_2O_5 system are shown in Figure 3. The previously reported binary phase equilibria for the perimeter systems (Bi_2O_3–Nb_2O_5,[48–50] Bi_2O_3–ZnO,[51] ZnO–Nb_2O_5[52,53]) were confirmed in the present study, with the exception of the Bi_2O_3–Nb_2O_5 system above 0.75 Bi_2O_3 (represented here as a solid solution extending to Bi_2O_3) which we did not investigate in detail. This region apparently forms a series of modulated fluorite superstructures;[49] differences in the reported diagrams likely arise from variations in cooling methods and whether specimens were examined by X-ray or electron diffraction methods.

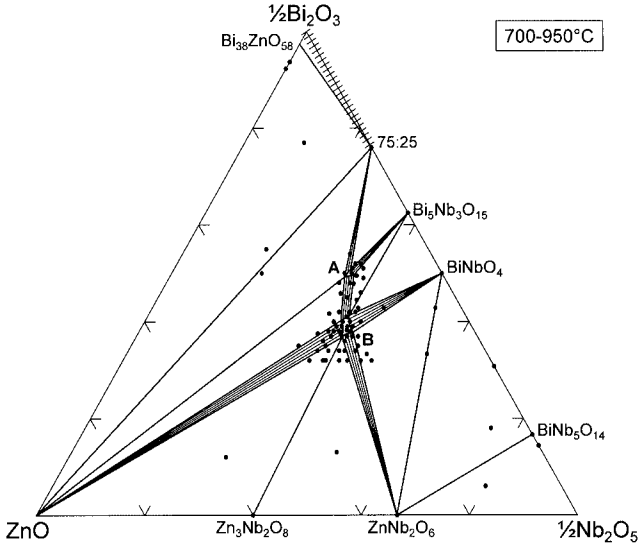

Figure 3. Subsolidus phase equilibrium diagram in air for the Bi_2O_3–ZnO–Nb_2O_5 system. Black dots denote the compositions of specimens prepared in the study; concentrations are on a molar fraction basis. Ternary phase formation is limited to zirconolite (A) and pyrochlore (B), both of which form single-phase solid solution regions. As shown, zirconolite forms thermodynamically stable mixtures with pyrochlore, ZnO, the 75:25 Bi_2O_3:Nb_2O_5 solid solution, and $Bi_5Nb_3O_{15}$. Bi–Zn–Nb–O pyrochlores will form stable mixtures with zirconolite, $Bi_5Nb_3O_{15}$, $BiNbO_4$, $ZnNb_2O_6$, $Zn_3Nb_2O_8$, and ZnO. Temperature-stable dielectric ceramics are processed in the two-phase region indicated between zirconolite (A) and pyrochlore (B).

Only two ternary phases were found to form in the Bi_2O_3–ZnO–Nb_2O_5 system, monoclinic zirconolite[54,55] (A) and cubic pyrochlore (B) (Figure 3). Observable shifts in their X-ray powder diffraction patterns indicated that both compounds are nonstoichiometric and form solid solution regions. Pyrochlore does not form at the conventionally predicted composition $Bi_2Zn_{2/3}Nb_{4/3}O_7$, which falls in the zirconolite region A. Instead, pyrochlore forms at substantially lower Bi concentrations in this chemical system. The present results indicate, in fact, that the single-phase field for the pyrochlore structure falls *completely outside* compositions predicted for conventional pyrochlores, i.e., those with Bi^{3+} on the A sites and a Zn^{2+}/Nb^{5+} mixture on the B sites, as shown in Figure 4. We conclude that the unconventional placement of small B-type cations such as Zn^{2+} on the large A-cation sites, accompanied by displacive disorder in the A_2O' network, is *required* for stabilization of the pyrochlore structure in the Bi–Zn–Nb–O system.

A number of reports found in the literature suggest that displacive disorder in the A_2O' network is an inherent feature of the pyrochlore structure. Nearly thirty years ago, a detailed structural study of $Sn^{2+}{}_{1.76}(Ta_{1.56}Sn^{4+}{}_{0.44})O_{6.54}$[56] found that Sn^{2+} was displaced 0.38 Å from the ideal A-cation positions, nearly the same as in $Bi_{1.5}Zn_{0.92}Nb_{1.5}O_{6.92}$. These authors mention observation of the "forbidden" 442 reflection as "glaring" evidence of deviation from the ideal pyrochlore structure. Similar behavior was found for $Bi_{1.74}Ti_2O_{6.62}$, again with Bi^{3+} displacements of 0.38 Å,[57] and also for the stoichiometric compound $Bi_2Ti_2O_7$.[58] Pyrochlore-type $Tl_2Nb_2O_{6+x}$ compounds were also found to exhibit Tl ion displacements, apparently dynamic at room temperature.[59] Numerous titanate and zirconate pyrochlores with rare earth A-cations are known to exhibit characteristic diffuse intensity distributions[60] analogous to those observed for β-cristobalite (SiO_2), which features atoms in the same positions as the A_2O' network of pyrochlore. A study of $La_2Zr_2O_7$ concluded that the La^{3+} ions do not occupy the ideal A sites, but are dynamically disordered around an annulus perpendicular to the O′–La–O′ linear unit.[60] This behavior is analogous to the orientational disorder of the [SiO_4] tetrahedra in β-cristobalite, which results in typical Si–O bond lengths and angles as opposed to the chemically unreasonable values in the average structure. Similar improvements in bond lengths are achieved for La^{3+} in the pyrochlore $La_2Zr_2O_7$ by this mechanism;[60] the annulus containing the La positions occurs in the same plane as the toroids of six possible A sites in $Bi_{1.5}Zn_{0.92}Nb_{1.5}O_{6.92}$ (Figure 2, part b).

The unconventional substitution of small B-type cations on the A sites of pyrochlore has also been previously observed; the present results as well as several other reports suggest that up to about 25% of the A sites in the $A_2B_2O_6O'$ structure can be substituted with small, typically B-site cations. Examples include the ferroelectric oxysulfide pyrochlore $Cd_{2-x}Zn_xNb_2O_6S$,[31] and the series $Bi_{2-x}B_xRu_2O_{7-y}$ (B = Mn, Co, Ni, Cu, Zn, Mg), with x-values as high as 0.5.[16] Similar cubic pyrochlores have been reported with Nb instead of Ru; i.e., $Bi_{1.5}MNb_{1.5}O_7$ (M = Cu, Mg, Mn, Ni), which would require half of the small M cations to be mixed with Bi^{3+} on the A sites.[61] These re-

 © 2005 Wiley-VCH Verlag GmbH & Co. KGaA, Weinheim

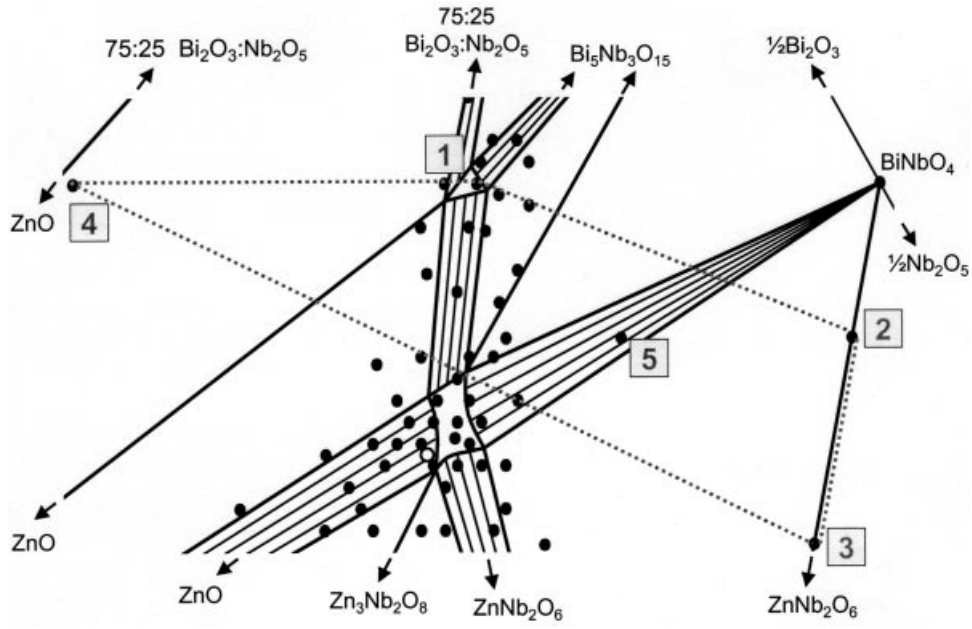

Figure 4. Magnified portion of the Bi_2O_3–ZnO–Nb_2O_5 phase equilibrium diagram (Figure 3), emphasizing the regions of zirconolite and pyrochlore phase formation. The zirconolite structure forms at compositions within the small triangle containing the composition $Bi_2Zn_{2/3}Nb_{4/3}O_7$ (1). The cubic pyrochlore phase forms within the four-sided region below zirconolite. Joins (lines) emanate from the curved sides and vertices of this region to compounds that form thermodynamically stable two-phase mixtures with pyrochlore. The dotted line connects compositions 1 ($Bi_2Zn_{2/3}Nb_{4/3}O_7$), 2 ($Bi_{1.5}Zn_{0.166}Nb_{1.833}O_7$), 3 ($BiZn_{1/3}Nb_{5/3}O_6$), and 4 ($Bi_2Zn_{4/3}Nb_{2/3}O_6$) to outline the compositional field in which conventional pyrochlores and/or defect pyrochlores are expected to form (5 = $Bi_{1.5}Zn_{0.5}Nb_{1.5}O_{6.5}$); i.e., with no Zn^{2+} ions on the A sites. The single-phase region found for pyrochlore is seen to fall *completely outside* this field, indicating that the structure only forms at compositions with excess B cations that are accommodated on A sites. The open circle in the two-phase ZnO-pyrochlore field corresponds to the composition $Bi_{1.5}Zn_{1.0}Nb_{1.5}O_7$, given in numerous reports as the stoichiometry of the pyrochlore phase, but which actually lies outside the single-phase region.

ports do not include detailed X-ray powder diffraction data; however, all of these cubic pyrochlores should exhibit displacive disorder in the A_2O' network to provide chemical accommodation of the small B-type cations – their X-ray powder diffraction patterns should exhibit weak forbidden reflections such as the 442, which can be indexed using the reported $Fd\bar{3}m$ cubic unit cells, but which serve as (easily overlooked) diagnostic flags for the displacement of atoms to lower-symmetry positions in the space group.

The present study confirmed observation of weak peaks at the positions of the diagnostic 442 reflections in the powder diffraction patterns for pyrochlore phases forming in the systems Bi–M–Nb–O with M = Co, Fe, Ni, Mn, Cu, and Cr, as shown in Figure 5. As in the Bi–Zn–Nb–O system, the pyrochlore phase in these systems does *not* form as a pure compound at conventional formulations (i.e. $Bi_2Co_{2/3}Nb_{4/3}O_7$, $Bi_2Ni_{2/3}Nb_{4/3}O_7$, Bi_2FeNbO_7, Bi_2MnNbO_7, $Bi_2Cu_{2/3}Nb_{4/3}O_7$, or Bi_2CrNbO_7). Recent phase equilibrium studies of the Bi_2O_3–Mn_2O_3–Nb_2O_5 and Bi_2O_3–Fe_2O_3–Nb_2O_5 systems[62] found that, similar to the Bi_2O_3–ZnO–Nb_2O_5 system (Figure 3), the pyrochlore single-phase fields occur at substantially lower Bi concentrations than the conventional formulas, and at compositions requiring the mixing of B-type Mn and Fe cations on the A-sites with Bi^{3+}. Furthermore, *all* X-ray powder diffraction patterns for pyrochlore and pyrochlore-containing specimens in these studies exhibited clearly observable 442 reflections. We conclude that, as for the Bi–Zn–Nb–O system, the occurrence of displacive disorder in the A_2O' network is *required* for the formation of pyrochlore in the Bi–Mn–Nb–O and Bi–Fe–Nb–O chemical systems. We refer to these as misplaced-displacive cubic pyrochlores – pyrochlores which exhibit misplacement of traditionally octahedral B-site cations onto the larger A-sites, accompanied by displacive disorder in the A_2O' substructure to facilitate lower coordination numbers for the smaller species.

A structural study of the cubic pyrochlores $Bi_2Ru_2O_7$, $Bi_{1.6}Cu_{0.4}Ru_2O_7$, and $Bi_{1.6}Co_{0.4}Ru_2O_7$[14] confirmed static displacive disorder in both the A and O′ sites for all three compounds, and proposed that this was a common feature of $A_2B_2O_7$ pyrochlores having a lone electronic pair on the A-site cation (e.g. Bi^{3+}, Pb^{2+}, Tl^+). Similar conclusions were drawn for the series $Bi_{2-y}Yb_yRu_2O_{7-\delta}$[18] and $Bi_{2-x}(CrTa)O_{7-y}$[63] More generally, we suggest that this is an inherent feature of the chemically versatile pyrochlore structure which occurs to accommodate cations with shapes (i.e. lone pairs) or sizes (i.e. typical B-type cations) that are non-ideal for the coordination environment provided by the rigid B_2O_6 framework. This more general principle is demonstrated in the Ca-Ti–Nb–O system, which forms a cubic pyrochlore near the composition $Ca_{1.5}Ti_{1.5}NbO_7$ [=$Ca_{1.5}Ti_{0.5}(TiNb)O_7$].[64] Structural studies of single crystals of $Ca_{1.5}Ti_{1.5}NbO_7$ and also isostructural $Ca_{1.5}Ti_{1.5}TaO_7$[65] revealed displacive disorder in both the A and O′ positions

 © 2005 Wiley-VCH Verlag GmbH & Co. KGaA, Weinheim

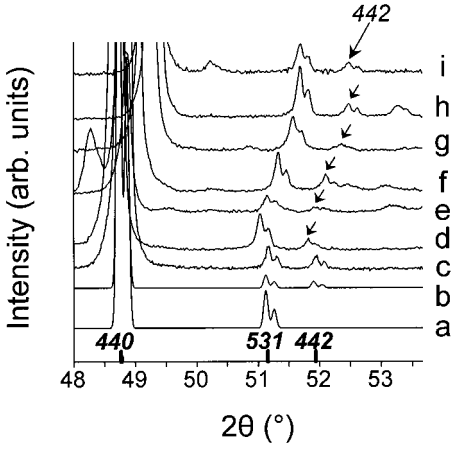

Figure 5. Selected regions of X-ray powder diffraction patterns showing that pyrochlore phases in the Bi–M–Nb–O systems (M = Zn, Co, Fe, Ni, Mn, Cu, and Cr) all exhibit weak peaks at the positions of the 442 reflections, diagnostic for displacive disorder in the A_2O' network. Patterns a) and b) are calculated for $Bi_{1.5}Zn_{0.92}Nb_{1.5}O_{6.92}$ assuming the ideal (a) pyrochlore structure (shown in part **a** of Figure 2), and (b) using the refinement results with static disordered displacements in the A and O′ sites[42] (see part **b** of Figure 2); the latter calculated pattern matches the experimentally observed pattern for $Bi_{1.5}Zn_{0.92}Nb_{1.5}O_{6.92}$ (c). The 442 reflection occurs just below 52° 2θ for the Zn compound and is forbidden in the ideal pyrochlore structure (a). This reflection is seen in all of the other patterns (at slightly shifted 2θ-values reflecting different unit cell volumes) for equilibrated specimens with nominal compositions (d) $Bi_2Co_{2/3}Nb_{4/3}O_7$, (e) $Bi_2Ni_{2/3}Nb_{4/3}O_7$, (f) Bi_2FeNbO_7, (g) Bi_2MnNbO_7, (h) $Bi_2Cu_{2/3}Nb_{4/3}O_7$, and (i) $Bi_{4/3}CrNbO_6$. Although pyrochlore is the major phase in these specimens, it does not form as a single phase at these conventional formulations.

of the cubic pyrochlore structures; the Ti^{4+} ions in the A_2O' network were displaced 0.7 Å from the ideal A sites, resulting in chemically reasonable bond lengths to five oxygen atoms, while Ca^{2+} ions remained in the ideal positions. Interestingly, the $Ca_{1.5}Ti_{1.5}NbO_7$ pyrochlore was found to exhibit dielectric relaxation similar to that of $Bi_{1.5}Zn_{0.92}Nb_{1.5}O_{6.92}$,[47] suggesting that displacive disorder, not the presence of Bi^{3+}, gives rise to this phenomenon.

Conclusions

Realizing that the pyrochlore structure can accommodate small B-type metals on up to 25% of the large A-sites by displacive disorder, solid state chemists are no longer restricted to the formula $A_2B_2O_6O'$ in the preparation of pyrochlore-type compounds with yet unknown, potentially useful properties. Many compounds can now be synthesized and/or modified by deliberate combinations of large and small metal ions on the A-sites. Since large A cations and smaller B-type cations tend to be electronically dissimilar, electrical and magnetic properties should be strongly affected by mixing them in the A_2O' network.[14] Ionic conductivity properties should also depend strongly on the occurrence of B cations, vacancies, and displacive disorder in the A_2O' network. For the theoretical community, the challenge remains to understand why some chemical systems *only* form so-called misplaced-displacive cubic pyrochlore phases, even though conventional crystal chemistry suggests that normal pyrochlores should form.

Experimental Section

Approximately 80 polycrystalline specimens (3–4 g each) were prepared in air by solid-state reactions using Bi_2O_3 (99.999%), ZnO (99.99%), and Nb_2O_5 (99.999%). Prior to each heating, each sample was mixed by grinding with an agate mortar and pestle for 15 min, pelletized, and placed on sacrificial powder of the same composition on Pt foil supported by alumina ceramic. After an initial overnight calcine at 800 °C (below the m.p. of Bi_2O_3, 825 °C) multiple 4-hour heatings (with intermediate grinding and re-pelletizing) were carried out at 950–980 °C. (Exceptions were low-melting specimens with Bi contents above 90 mol-% $BiO_{1.5}$, which were not heated above 700 °C). Samples were furnace-cooled to ca. 700 °C and then air-quenched on the bench-top. Typically, three to five heatings were required to attain equilibrium, which was presumed when no further changes could be detected in the weakest peaks observed in the X-ray powder diffraction patterns. Thermogravimetric analyses (TGA) of pure ZnO and Bi_2O_3 in flowing air indicated no significant weight loss below 1000 °C for Bi_2O_3 and about 1200 °C for ZnO. For the pyrochlore phase of composition $Bi_{1.5}Zn_{0.92}Nb_{1.5}O_{6.92}$, TGA under flowing oxygen indicated congruent-like melting at ca. 1185 °C coinciding with the onset of appreciable volatility. Single pyrochlore-type crystals were easily obtained by heating $Bi_{1.5}Zn_{0.92}Nb_{1.5}O_{6.92}$ powder in a Pt capsule (sealed by welding) to 1275 °C, followed by slow-cooling (5 °C/h) to below the freezing point.

Polycrystalline pyrochlore-containing specimens in the Bi–M–Nb–O systems (M = Co, Ni, Fe, Mn, Cu, and Cr) were synthesized as above at the following chemical compositions, with reagents and final soak temperatures in parentheses: $Bi_2Co_{2/3}Nb_{4/3}O_7$ (Co_3O_4, spectroscopic grade, pre-analyzed by TGA, 925 °C), $Bi_2Ni_{2/3}Nb_{4/3}O_7$ (NiO, 99.998%, 925 °C), Bi_2FeNbO_7 (Fe_2O_3, reagent grade, 925 °C), Bi_2MnNbO_7, ($MnCO_3$, reagent grade, pre-analyzed by TGA, 885 °C), $Bi_2Cu_{2/3}Nb_{4/3}O_7$ (CuO, reagent grade, 825 °C), and $Bi_{4/3}CrNbO_6$ (Cr_2O_3, reagent grade, 975 °C). All specimens, when equilibrated, were mixtures containing pyrochlore as the major phase.

Phase assemblages in the Bi_2O_3–ZnO–Nb_2O_5 system were ascertained using the disappearing phase method[66,67] and X-ray powder diffraction data obtained with a Philips[68] diffractometer equipped with incident Soller slits, a theta-compensating slit and graphite monochromator, and a scintillation detector. Samples were mounted in welled glass slides. Patterns were collected at ambient temperatures using Cu-K_α radiation over the range 3–70° 2θ with a 0.02° 2θ step size and a 2 s count time. Intensity data measured as relative peak heights above background were obtained using the DATASCAN software package, and processed using JADE. For unit cell refinements, observed 2θ line positions were first corrected using SRM 660, LaB_6,[69] as an external calibrant. Lattice parameters were refined using JADE (2θ values, Cu-$K_{\alpha1}$ = 1.540593 Å).

Unit cell parameters and compositions for several single-phase pyrochlore specimens are given in Table 1. The present data suggest that the limiting compositions of the pyrochlore phase field, located at the four cusps (corners) in Figure 4, are approximately $Bi_{1.64}Zn_{0.33}(Zn_{0.52}Nb_{1.48})O_7$ (highest Bi-content), $Bi_{1.61}Zn_{0.39}(Zn_{0.55}Nb_{1.46})O_7$, $Bi_{1.48}Zn_{0.44}(Zn_{0.44}Nb_{1.56})O_7$ (highest Nb-content), and $Bi_{1.47}Zn_{0.52}(Zn_{0.48}Nb_{1.52})O_7$ (lowest Bi-content,

 © 2005 Wiley-VCH Verlag GmbH & Co. KGaA, Weinheim

highest Zn-content). During synthesis, the pyrochlore phase formed early in partially reacted samples and was readily purified within the single-phase region, suggesting high thermodynamic stability.

Table 1. Compositions, cubic unit cell parameters (***a***, space group $Fd\bar{3}m$, #227), and structural formulas for single-phase pyrochlore specimens. These compositions correspond to the points within the four-sided pyrochlore region shown in Figure 4. The structural formulas have been normalized to seven oxygen atoms (full occupancy of the O′ site) for purposes of comparison. Parentheses denote cations in the octahedral B-sites.

Composition	*A* [Å]	Structural formula
$Bi_{1.50}Zn_{0.91}Nb_{1.54}O_7$	10.551(1)	$Bi_{1.50}Zn_{0.45}(Zn_{0.46}Nb_{1.54})O_7$
$Bi_{1.52}Zn_{0.93}Nb_{1.52}O_7$	10.555(1)	$Bi_{1.50}Zn_{0.45}(Zn_{0.48}Nb_{1.52})O_7$
$Bi_{1.55}Zn_{0.91}Nb_{1.51}O_7$	10.553(1)	$Bi_{1.55}Zn_{0.42}(Zn_{0.49}Nb_{1.51})O_7$
$Bi_{1.60}Zn_{0.93}Nb_{1.47}O_7$	10.564(1)	$Bi_{1.60}Zn_{0.40}(Zn_{0.53}Nb_{1.47})O_7$
$Bi_{1.63}Zn_{0.88}Nb_{1.47}O_7$	10.571(1)	$Bi_{1.63}Zn_{0.35}(Zn_{0.53}Nb_{1.47})O_7$

Acknowledgments

We thank R. S. Roth for helpful discussions, L. P. Cook for thermogravimetric analyses, J. Suh for technical assistance, and P. K. Schenk and N. Swanson for graphical representation of the phase diagram data.

[1] R. V. Gaines, H. C. W. Skinner, E. E. Foord, B. Mason, A. Rosenzweig (Eds.), *Dana's New Mineralogy*, Wiley: New York, **1997**, pp. 341–352, 8th edition.
[2] So diverse that geologists have referred to the pyrochlore structure as a "chemical garbage can".
[3] A *Web of Science* search (1975 to present) for articles containing the term *pyrochlore* in the title returned 837 hits.
[4] M. A. Subramanian, G. Aravamudan, G. V. Subba Rao, *Prog. Solid State Chem.* **1983**, *15*, 55 an extensive pyrochlore review covering literature up to ca. 1981.
[5] B. J. Kennedy, *Physica B* **1998**, *241–243*, 303.
[6] L. Minervini, R. W. Grimes, *J. Am. Ceram. Soc.* **2000**, *83*, 1873, and references therein.
[7] B. J. Wuensch, K. W. Eberman, C. Heremans, E. M. Ku, P. Onnerud, E. M. E. Yeo, S. M. Haile, J. K. Stalick, J. D. Jorgensen, *Solid State Ionics* **2000**, *129*, 111.
[8] M. Pirzada, R. W. Grimes, J. F. Maguire, *Solid State Ionics* **2003**, *161*, 81, and references therein.
[9] G. D. Blundred, C. A. Bridges, M. J. Rosseinsky, *Angew. Chem. Int. Ed.* **2004**, *43*, 3562, and references therein.
[10] G. Jeanne, G. Desgardin, G. Allais, B. Raveau, *J. Solid State Chem.* **1975**, *15*, 193, and references therein.
[11] D. Bernard, J. Pannetier, J. Lucas, *Ferroelectrics* **1978**, *21*, 429.
[12] C. A. Randall, J. C. Nino, A. Baker, H.-J. Youn, A. Hitomi, R. Thayer, L. F. Edge, T. Sogabe, D. Anderson, T. R. Shrout, S. Trolier-McKinstry, M. Lanagan, *Bull. Am. Ceram. Soc.* **2003**, *82*, 9101, and references therein.
[13] R. J. Cava, W. F. Peck, J. J. Krajewski, *J. Appl. Phys.* **1995**, *78*, 7231, and references therein.
[14] M. Avdeev, M. K. Haas, J. D. Jorgensen, R. J. Cava, *J. Solid State Chem.* **2002**, *169*, 24.
[15] S. Yonezawa, Y. Muraoka, Y. Matsushita, Z. Hiroi, *J. Phys. Soc. Japan* **2004**, *73*, 819.
[16] E. Beck, A. Ehmann, B. Krutzsch, S. Kemmler-Sack, H. R. Khan, C. J. Raub, *J. Less-Common Met.* **1989**, *147*, L17.
[17] G. Mayer-Von Kuerthy, W. Wischert, R. Kiemel, S. Kemmler-Sack, *J. Solid State Chem.* **1989**, *79*, 34.
[18] L. Li, B. J. Kennedy, *Chem. Mater.* **2003**, *15*, 4060, and references therein.
[19] A. P. Ramirez, A. P. Hayashi, A. R. J. Cava, R. Siddharthan, B. S. Shastry, *Nature* **1999**, *399*, 333.
[20] J. E. Greedan, J. Avelar, M. A. Subramanian, *Solid State Commun.* **1992**, *82*, 797, and references therein.
[21] M. A. Subramanian, C. C. Torardi, D. C. Johnson, J. Pannetier, A. W. Sleight, *J. Solid State Chem.* **1988**, *72*, 24.
[22] Y. Shimakawa, Y. Kubo, T. Manako, *Nature* **1996**, *379*, 53.
[23] M. A. Subramanian, B. H. Toby, A. P. Ramirez, W. J. Marshall, A. W. Sleight, G. H. Kwei, *Science* **1996**, *273*, 81.
[24] M. Hamoumi, M. Wiegel, G. Blasse, *J. Solid State Chem.* **1994**, *108*, 410.
[25] R. C. Ewing, W. J. Weber, J. Lian, *J. Appl. Physics* **2004**, *95*, 5949, an extensive review.
[26] A. F. Wells, *Structural Inorganic Chemistry*, Clarendon: Oxford, **1975**, pp. 209, 499, 4th edition.
[27] B. G. Hyde, S. Andersson, *Inorganic Crystal Structures*, Wiley: New York, **1989**, pp. 344–349.
[28] The prefix "*anti-*" refers to switching of the cation and anion positions. Compared to the β-cristobalite (SiO_2) structure, the A cations occupy the oxygen positions and the O′ oxygen atoms occupy the Si positions.
[29] R. Nedjar, M. M. Borel, M. Hervieu, B. Raveau, *Mater. Res. Bull.* **1988**, *23*, 91.
[30] J. Miranday, G. Gauthier, R. DePape, *C. R. Acad. Sci., Ser. B* **1971**, *273*, 970.
[31] D. Bernard, J. Pannetier, J. Y. Moisan, J. Lucas, *J. Solid State Chem.* **1973**, *8*, 31.
[32] H. Nyman, S. Andersson, B. G. Hyde, M. O'Keeffe, *J. Solid State Chem.* **1978**, *26*, 123.
[33] M. Ledesert, B. Raveau, *J. Solid State Chem.* **1987**, *67*, 340.
[34] N. Ruchard, J. Grannec, A. Tressaud, P. Gravereau, *C. R. Acad. Sci. II, Ser. B* **1995**, *321*, 507.
[35] Y. Calage, M. Zemirli, J. M. Greneche, F. Varret, R. DePape, G. Ferey, *J. Solid State Chem.* **1987**, *69*, 197.
[36] O. Muller, R. Roy, *The Major Ternary Structural Families*, Springer-Verlag: New York, **1974**, pp. 4–14.
[37] As determined from observed bond lengths, values are from R. D. Shannon, *Acta Crystallogr., Sect. B* **1976**, *32*, 751.
[38] R. S. Roth, *J. Res. NBS* **1956**, *56*, 17.
[39] E. Aleshin, R. Roy, *J. Am. Ceram. Soc.* **1962**, *45*, 18.
[40] B. C. Chakoumakos, *J. Solid State Chem.* **1984**, *53*, 120.
[41] N. Wakiya, A. Saiki, N. Kieda, K. Shinozaki, N. Mizutani, *J. Solid State Chem.* **1992**, *101*, 71.
[42] V. S. Darshane, *J. Indian Chem. Soc.* **1980**, *57*, 108.
[43] M. Valant, P. K. Davies, *J. Am. Ceram. Soc.* **2000**, *83*, 147, and references therein.
[44] I. Levin, T. G. Amos, J. C. Nino, T. A. Vanderah, C. A. Randall, M. T. Lanagan, *J. Solid State Chem.* **2002**, *168*, 69.
[45] R. L. Withers, T. R. Welberry, A.-K. Larsson, Y. Liu, L. Norén, H. Rundlöf, F. J. Brink, *J. Solid State Chem.* **2004**, *177*, 231.
[46] W. G. Mumme, I. E. Grey, R. S. Roth, personal communication (with permission) that the model was refined to an *R* factor of 4%.
[47] S. Kamba, V. Porokhonskyy, A. Pashkin, V. Bovtun, J. Petzelt, J. C. Nino, S. Trolier-McKinstry, M. T. Lanagan, C. A. Randall, *Phys. Rev. B* **2002**, *66*, 54106.
[48] R. S. Roth, J. L. Waring, *J. Res. NBS* **1962**, *66A*, 451.
[49] C. D. Ling, R. L. Withers, S. Schmid, J. G. Thompson, *J. Solid State Chem.* **1998**, *137*, 42.
[50] M. Valant, D. Suvorov, *J. Am. Ceram. Soc.* **2003**, *86*, 939.
[51] J. P. Guha, S. Kunej, D. Suvorov, *J. Mater. Sci.* **2004**, *39*, 911.
[52] A. A. Ballman, H. Brown, *J. Cryst. Growth* **1977**, *41*, 36.
[53] R. R. Dayal, *J. Less-Common Met.* **1972**, *26*, 381.
[54] I. Levin, T. G. Amos, J. C. Nino, T. A. Vanderah, I. M. Reaney, C. A. Randall, M. T. Lanagan, *J. Mater. Res.* **2002**, *17*, 1406.
[55] The zirconolite and pyrochlore structures are related but distinctly different. In zirconolite-type $Bi_2Zn_{2/3}Nb_{4/3}O_7$, Zn^{2+} ions are also displacively disordered near the centers of six-membered rings of $[(Nb,Zn)O_6]$ octahedra, resulting in a (5 + 1) co-

 © 2005 Wiley-VCH Verlag GmbH & Co. KGaA, Weinheim

ordination environment similar to that of the A-site Zn^{2+} ions in pyrochlore-type $Bi_{1.5}Zn_{0.92}Nb_{1.5}O_{6.92}$[42].
[56] T. Birchall, A. W. Sleight, *J. Solid State Chem.* **1975**, *13*, 118.
[57] I. Radosavljevic, J. S. O. Evans, A. W. Sleight, *J. Solid State Chem.* **1998**, *136*, 63.
[58] A. L. Hector, S. B. Wiggin, *J. Solid State Chem.* **2004**, *177*, 139, and references therein.
[59] S. Uma, S. Kodialam, A. Yokochi, N. Khosrovani, M. A. Subramanian, A. W. Sleight, *J. Solid State Chem.* **2000**, *155*, 225, and references therein.
[60] Y. Tabira, R. L. Withers, T. Yamada, N. Ishizawa, *Z. Kristallogr.* **2001**, *216*, 92, and references therein.
[61] V. P. Sirotinkin, A. A. Bush, *Inorg. Materials* **2003**, *39*, 974.
[62] I. Pazos, A. Adler, M. Lufaso, T. Vanderah, results presented at the Summer Undergraduate Research Fellowship Symposium, National Institute of Standards and Technology, Gaithersburg, MD, August 10–11, **2004**, manuscripts in preparation.
[63] U. Ismunandar, T. Kamiyama, K. Oikawa, A. Hoshikawa, B. J. Kennedy, Y. Kubota, K. Kato, *Mater. Res. Bull.* **2004**, *39*, 553.
[64] A. Jongejan, A. L. Wilkins, *J. Less-Common Met.* **1970**, *21*, 225.
[65] P. Bordet, L. Cranswick, W. G. Mumme, R. S. Roth, I. E. Grey, (with permission), manuscript in preparation.
[66] C. G. Bergeron, S. H. Risbud, *Introduction to Phase Equilibria in Ceramics*, American Ceramic Society: Westerville, **1984**.
[67] C. S. Barrett, *Structure of Metals*, McGraw-Hill: New York, **1943**, chapter X, 1st edition.
[68] Certain commercial equipment and software are identified in order to adequately specify the experimental procedure; recommendation or endorsement by the National Institute of Standards and Technology is not therein implied.
[69] C. R. Hubbard, Y. Zhang, R. L. McKenzie, *Certificate of Analysis, SRM 660*, National Institute of Standards and Technology, Gaithersburg, MD, 20899, **1989**.

Received: March 18, 2005
Published Online: June 17, 2005

 © 2005 Wiley-VCH Verlag GmbH & Co. KGaA, Weinheim

N-Donor Ligand Coordination Polymers of Cu^{II}, Zn^{II}, and Cd^{II} Obtained at Elevated Temperature and Pressure

Hélène Casellas,[a] Chiara Massera,[b] Patrick Gamez*[a] Anna Maria Manotti Lanfredi,[b] and Jan Reedijk*[a]

Keywords: Coordination polymers / N ligands / Multidirectional ligands / Chain structures / Pi interactions

Reactions of Copper(II), Zinc(II), and Cadmium(II) nitrate with 2,4,6-tris(dipyridin-2-ylamino)-1,3,5-triazine (dpyatriz) at elevated temperature and pressure lead to new 1D coordination polymers which exhibit solid-state structures significantly different from those obtained at room temperature and atmospheric pressure. In addition, these coordination compounds exhibit unusual anion–π interactions.

(© Wiley-VCH Verlag GmbH & Co. KGaA, 69451 Weinheim, Germany, 2005)

Introduction

Supramolecular interactions are important in several fields of contemporary chemistry. Supramolecules are often self-assembled systems by means of a variety of interactions which may interplay. In crystal engineering, synergistic effects between intermolecular non-covalent interactions are of great importance and must be regarded as a single interrelated entity. The targeted molecular self-assembly of coordination architectures from tailored molecular components is a potential route to novel one-, two-, and three-dimensional networks.[1,2] The preparation of polymeric complexes can be accomplished by using rationally designed polydentate ligands. Many advanced 2D and 3D metallosupramolecular structures[3] have been generated in this way with encouraging applications in catalysis,[4] drug design,[5] separation studies,[6] gas storage,[7] and molecular recognition.[8] Furthermore, their preparation has highlighted another consideration: it is not only the building blocks that are important, but also the experimental parameters such as solvent, temperature, pressure, etc. used during the synthesis may lead to different species.[9] For example, the reaction of $Cu^{I}Br$ with 2,2′-dipyridyl under ambient conditions leads to a 1:1 adduct, while a polymeric structure is formed at 170 °C and autogenous pressure.[10]

In the course of research investigations to prepare triazine-based coordination polymers and study their physical and catalytic properties,[11–13] the ligand 2,4,6-tris(dipyridin-2-ylamino)-1,3,5-triazine (dpyatriz) has been synthesized (Figure 1).[14,15] Coordination compounds of Cu^{II} and Zn^{II} nitrate with dpyatriz obtained at room temperature and normal pressure in acetonitrile have been recently reported.[11,16] In this paper, new coordination polymers obtained from dpyatriz and various metal nitrates in acetonitrile at 105 °C in a closed pressure tube are described, showing significantly different coordination networks, as well as uncommon supramolecular interactions.

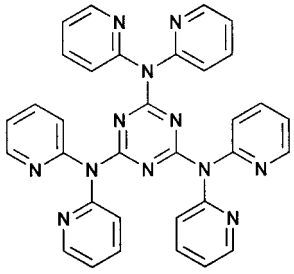

Figure 1. 2,4,6-Tris(dipyridin-2-ylamino)-1,3,5-triazine (dpyatriz).

Results and Discussion

Reaction of $Cu(NO_3)_2{\cdot}3H_2O$ in acetonitrile with dpyatriz yields light-blue parallelepipeds of $[Cu_2(dpyatriz)(NO_3)_4](H_2O)$ (**1**), whose crystal structure was determined by X-ray diffraction (Figure 2). The dinuclear building blocks consist of one pentacoordinate copper ion Cu(1) involved in the self-assembly of the coordination polymer and one isolated pentacoordinate copper ion Cu(2). Cu(1) is in a square-pyramidal geometry ($\tau = 0.167$)[17] with N(6) in an axial position (Table 1). The basal plane is formed by three N-coordinating 2-pyridyl moieties [N(5), N(11), and N(12)] from two didentate dipyridylamine units belonging to a symmetry-related dpyatriz ligand. The in-plane Cu–N dis-

[a] Leiden Institute of Chemistry, Gorlaeus Laboratories, Leiden University,
P. O. Box 9502, 2300 RA Leiden, The Netherlands.
Fax: +31 71 5274671
E-mail: p.gamez@chem.leidenuniv.nl
reedijk@chem.leidenuniv.nl
[b] Dipartimento di Chimica Generale ed Inorganica, Chimica Analitica, Chimica Fisica, Universita' degli Studi di Parma, Parco Area delle Scienze 17/A, 43100 Parma, Italy

tances can be regarded as normal (Table 1). The fourth position is occupied by the oxygen atom O(1) of a nitrate counter-anion. The angles around Cu(1) in the basal plane are close to 90°, varying from 83.7(3) to 93.5(3)° (Table 2). Cu(2) is also in a square-pyramidal geometry ($\tau = 0.137$).[17]

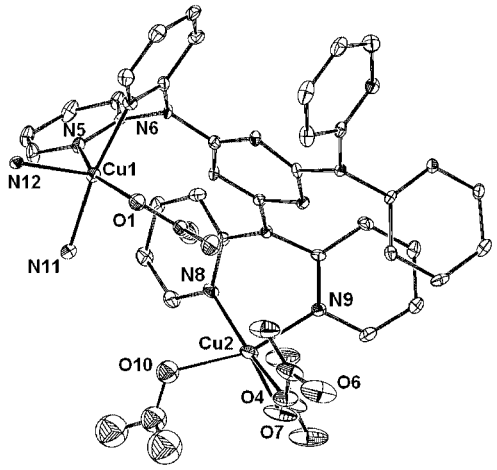

Figure 2. ORTEP plot of the repeating unit of **1**, where the N11 and N12 atoms belong to a symmetry-related unit. The water molecule and the hydrogen atoms are omitted for clarity; thermal ellipsoids are at the 20% probability level.

The basal plane around Cu(2) is constituted of two nitrogen atoms N(8) and N(9), from a dipyridylamine group, and two oxygen atoms O(7) and O(10), from two nitrate anions (one of these oxygen atoms is statistically distributed over two different positions indicated with O10 and O10′). The in-plane Cu–N distances are in the usual range, as well as the Cu–O distances (Table 1).[18] The axial position is occupied by the oxygen atom O(4) from a third coordinated nitrate ion, at a somewhat longer distance. The angles around Cu(2) in the basal plane vary from 86.1(5) to 95.9(4)° (Table 2). In addition, a water molecule O(18) is present in the crystal lattice (not depicted in Figure 2). This water molecule is hydrogen-bonded to the oxygen atom O(6a) of a nitrate group coordinated to Cu(2a) of an adjacent polymer chain [O(1S)–H···O(6a) 2.931(8) Å] (Figure 3).

This dinuclear copper complex makes up a 1D zigzag polymer through the coordination of Cu(1) by a dipyridylamine moiety from an adjacent repeating unit (Figure 3). Most interestingly, a quite different 1D ladder coordination polymer has been obtained from $Cu(NO_3)_2 \cdot 3H_2O$ and dpyatriz in acetonitrile, at room temperature and atmospheric pressure.[11] The different crystal packing observed in the present study is obviously due to the higher temperature and pressure used during the crystallisation process. This result illustrates the difficulty to predict a crystal structure. Indeed, crystal growth involves several intermolecular synergistic noncovalent interactions between all synthons,[19] i.e. ligands, metal ions, anions and solvents, which have certainly to be considered for a better crystal structure prediction. In addition, the temperature and the pressure applied during the crystallisation are clearly important and should also be taken into account.

Table 1. Selected bond lengths [Å] for $[Cu_2(dpyatriz)(NO_3)_4](H_2O)$ (**1**), $[Zn_2(dpyatriz)(NO_3)_4](H_2O)$ (**2**), and $[Cd_3(dpyatriz)_2(NO_3)_6]$ (**3**).

1	**2**	**3**
Cu(1)–N(6) 2.136(7)	Zn(1)–N(6) 2.083(14)	Cd(1)–N(6) 2.402(5)
Cu(1)–N(5) 2.011(8)	Zn(1)–N(11) 2.085(14)	Cd(1)–N(11′) 2.474(4)
Cu(1)–N(11) 1.995(7)	Zn(1)–O(1) 2.257(13)	Cd(1)–N(12′) 2.379(5)
Cu(1)–N(12) 2.025(7)	Zn(1)–O(2) 2.409(17)	Cd(1)–N(5) 2.450(5)
Cu(1)–O(1) 2.022(6)	Zn(1)–N(5) 2.155(17)	Cd(1)–O(5) 2.568(5)
	Zn(1)–N(12) 2.145(17)	Cd(1)–O(4) 2.646(7)
Cu(2)–N(8) 1.978(7)		
Cu(2)–N(9) 1.981(7)	Zn(2)–N(8) 2.128(18)	Cd(2)–N(9) 2.348(5)
Cu(2)–O(7) 1.975(7)	Zn(2)–N(9) 2.134(13)	Cd(2)–N(8) 2.435(7)
Cu(2)–O(10′) 1.942(12)	Zn(2)–O(4) 2.026(15)	Cd(2)–O(7) 2.400(9)
Cu(2)–O(4) 2.270(9)	Zn(2)–O(10) 2.296(19)	
	Zn(2)–O(11) 2.133(18)	
	Zn(2)–O(7) 2.131(22)	

Table 2. Selected angles [°] for $[Cu_2(dpyatriz)(NO_3)_4](H_2O)$ (**1**), $[Zn_2(dpyatriz)(NO_3)_4](H_2O)$ (**2**), and $[Cd_3(dpyatriz)_2(NO_3)_6]$ (**3**).

1	**2**	**3**
N(5)–Cu(1)–O(1) 91.7(3)	N(6)–Zn(1)–N(11) 107.7(6)	N(6)–Cd(1)–(N11′) 82.65(15)
N(11)–Cu(1)–O(1) 83.7(3)	N(11)–Zn(1)–O(2) 102.3(6)	N(12′)–Cd(1)–N(11′) 80.91(14)
N(11)–Cu(1)–N(12) 88.0(3)	O(1)–Zn(1)–O(2) 56.6(6)	N(12′)–Cd(1)–O(5) 74.17(15)
N(5)–Cu(1)–N(12) 93.5(3)	N(6)–Zn(1)–O(1) 96.3(6)	O(5)–Cd(1)–O(4) 49.77(15)
	N(12)–Zn(1)–N(5) 171.1(6)	N(6)–Cd(1)–O(4) 73.24(15)
N(8)–Cu(2)–N(9) 88.0(3)		O(1)–Cd(1)–N(5) 165.92(15)
O(7)–Cu(2)–N(9) 87.9(3)	O(4)–Zn(2)–N(8) 118.0(7)	
O(7)–Cu(2)–O(10) 90.4(5)	O(4)–Zn(2)–O(10) 86.0(7)	N(9)–Cd(2)–N(8) 83.57(19)
O(10′)–Cu(2)–O(7) 95.9(4)	O(11)–Zn(2)–O(10) 61.2(7)	N(9)–Cd(2)–N(8′) 96.43(19)
N(8)–Cu(2)–O(10) 86.1(5)	N(8)–Zn(2)–O(11) 96.3(7)	O(7′)–Cd(2)–O(7) 180.000(1)
O(10′)–Cu(2)–N(8) 92.7(4)	O(7)–Zn(2)–N(9) 168.9(7)	

 © 2005 Wiley-VCH Verlag GmbH & Co. KGaA, Weinheim

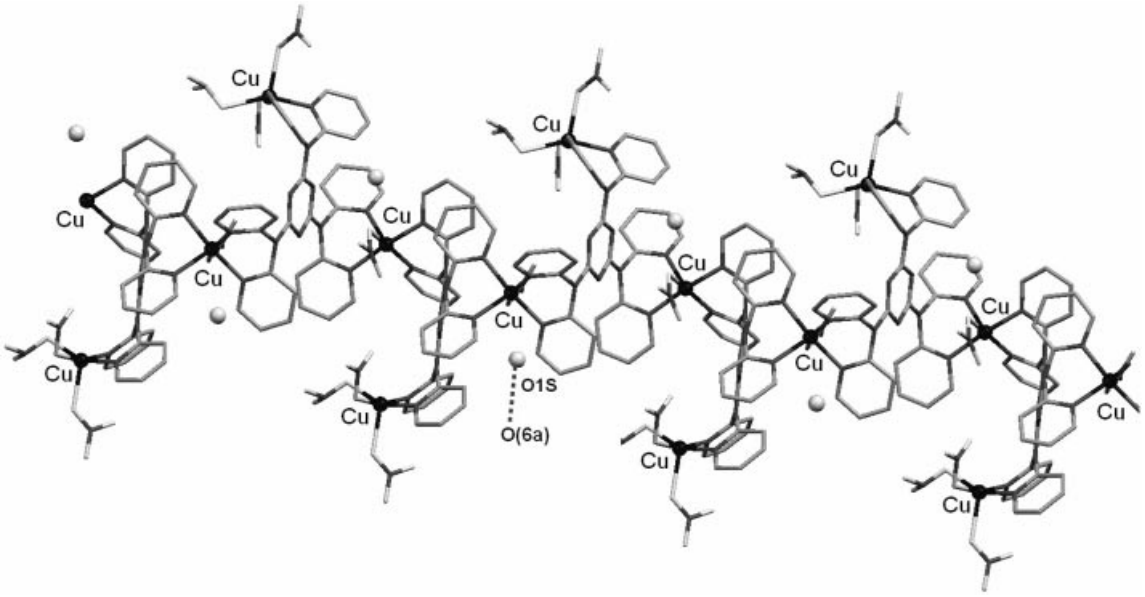

Figure 3. Representation of the copper(II) 1D zigzag coordination polymer.

Another very interesting feature of this high-temperature-prepared supramolecular species is the interaction between the oxygen atom O(2) of the nitrate anion coordinated to Cu(1) and the π-cloud of a 1,3,5-triazine ring, with a centroid···O(2) distance of 3.67(1) Å and an angle of the centroid···O(2) axis to the plane of 67.7(3)° (Figure 4). Noncovalent anion–π interactions are quite uncommon and have only recently been discovered, owing to the electron-donating character of an anion which is expected to lead to repulsive interactions with aromatic π-clouds.[20,21] This type of interactions has been first demonstrated by NMR studies.[22–24] Several recent articles have reported theoretical calculations on the binding of uncoordinated anions with electron-deficient triazine derivatives, indicating energetically favorable noncovalent interactions.[21,25,26] Very recently, first crystallographic evidences of such interactions has been described between 1,3,5-triazine groups and free anions.[27,28] The present compound reveals the possible interaction between a nitrate and an electron-poor aromatic ring.

A different, but related coordination polymer has been obtained by reaction of $Zn(NO_3)_2{\cdot}6H_2O$ and dpyatriz in

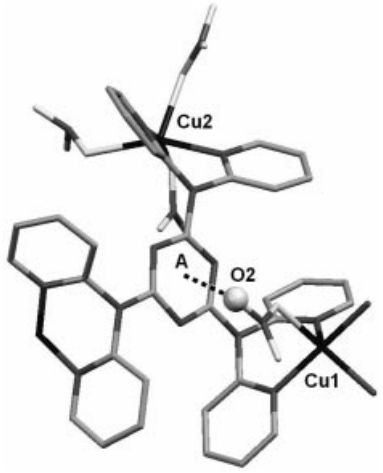

Figure 4. Oxygen–π interaction in **1** between a nitrate anion and an *s*-triazine ring. A···O(2) = 3.67(1) Å; triazine plane–A–O(2) axis = 67.7(3)°.

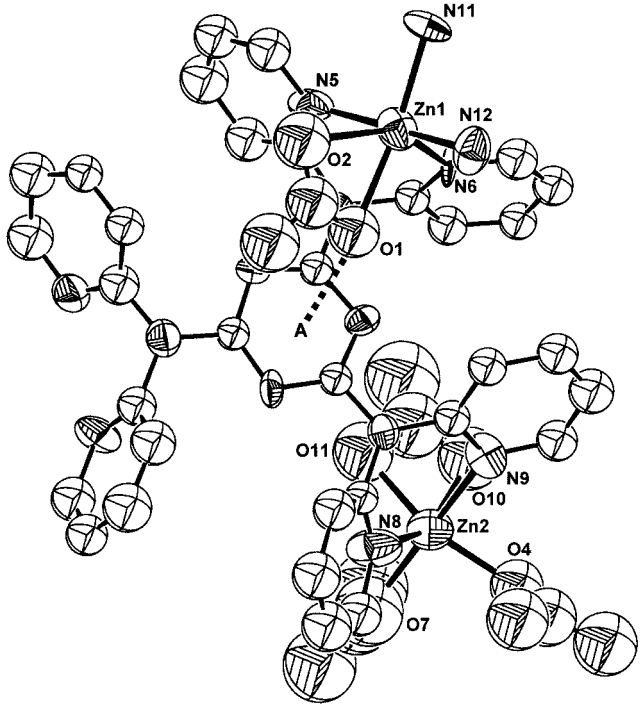

Figure 5. ORTEP plot of the repeating unit of **2** where the N11 and N12 atoms belong to a symmetry-related unit. The water molecule and the hydrogen atoms are omitted for clarity; thermal ellipsoids are at the 50% probability level. A···O(1) = 3.11(3) Å; triazine plane–A–O(2) axis = 67.2(5)°.

 © 2005 Wiley-VCH Verlag GmbH & Co. KGaA, Weinheim

acetonitrile at the same temperature. The dinuclear repeating unit of the zig-zag polymer present in the compound $[Zn_2(dpyatriz)(NO_3)_4](H_2O)$ (**2**) is depicted in Figure 5.

Zn(1), which is involved in the self-assembly of the coordination polymer, is in a highly distorted octahedral environment, due to the coordination of the nitrate anion in a didentate fashion. The basal plane of the octahedron is formed by two N-coordinating pyridine rings [N(6) and N(11)] of two symmetry-related dpyatriz ligands, and by two oxygen atoms, O(1) and O(2), of a nitrate ion. The in-plane Zn–N distances can be regarded as normal (Table 1).[29] The large in-plane Zn–O distances stem from the didentate coordination mode of the anion which induces a great distortion. The axial positions are taken up by two N-donors, N(5) and N(12), of two symmetry-related dipyatriz ligands. The angles around Zn(1) in the basal plane vary from 56.6(6) to 107.7(6)°, showing once again the important distortion resulting from the particular coordination of the nitrate ion (Table 2). Zn(2) is in a distorted octahedral geometry as well. The basal plane is constituted of one N-atom N(8) from a pyridine group at a normal distance (Table 1). The remaining positions are occupied by three O-atoms, O(4), O(10), and O(11), of two nitrate ions. The axial positions are occupied by one N-atom, N(9), of a pyridine group and by the O-atom O(7) of a third nitrate ion. The angles around Zn(2) in the basal plane are far from 90°, varying from 61.2(7) to 118.0(6)°, due to the didentate binding mode of one nitrate ion (Table 2). In addition, a water molecule is present in the crystal lattice.

This dinuclear zinc complex represents the repeating unit of a 1D zigzag polymer closely related to the one obtained with copper(II) nitrate (Figure 3). A completely different coordination compound, i.e a tetranuclear zinc(II) complex, has been reported as obtained at room temperature and ambient pressure from the same reactants,[16] just like in the case of the copper polymer.

Like the copper coordination polymer, the zinc polymer exhibits anion–π interactions. Indeed, anion–π interactions are realised between the oxygen atom O(1) of the didentate nitrate anion coordinated to Zn(1) and the 1,3,5-triazine ring with a centroid···O(1) distance of 3.11(3) Å and an angle of the centroid···O(1) axis to the plane of 67.2(5)° (Figure 5).

Finally, the reaction of $Cd(NO_3)_2{\cdot}4H_2O$ in acetonitrile at 105 °C with dpyatriz yields colorless diamond-shaped crys-

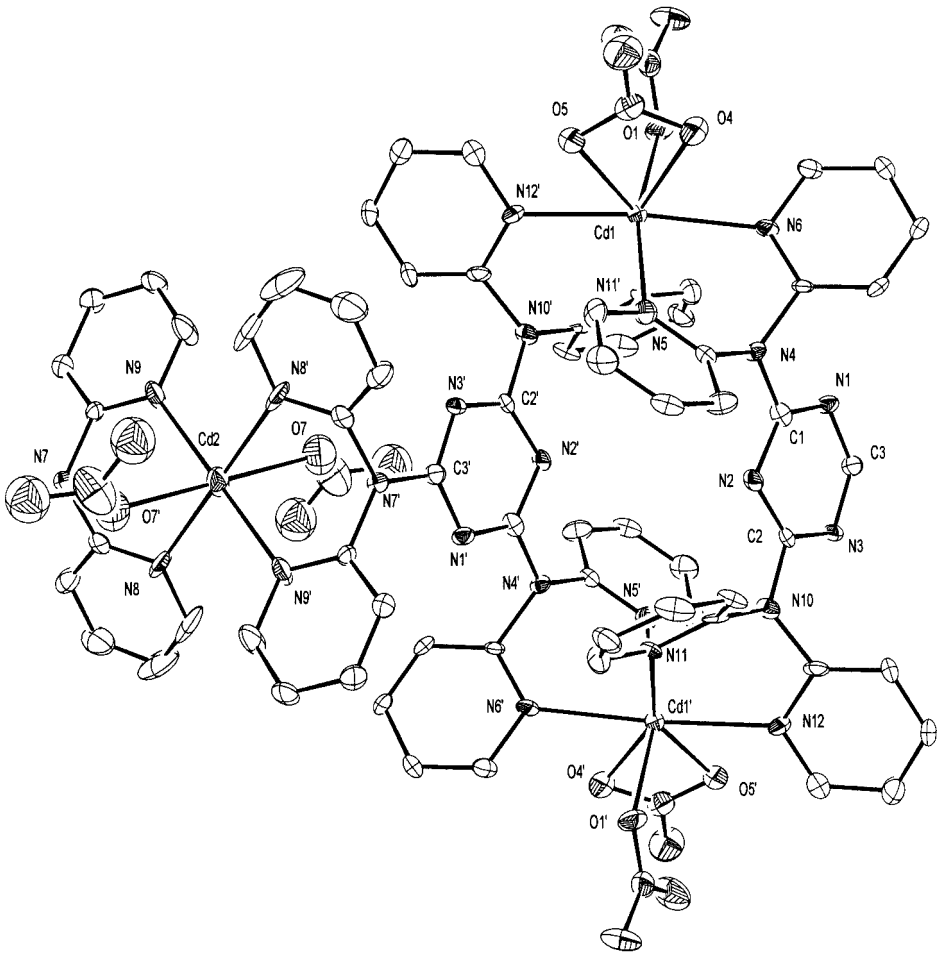

Figure 6. ORTEP view of the building block (containing two asymmetric units) forming the polymeric chain. Hydrogen atoms are omitted for clarity; thermal ellipsoids are at the 20% probability level.

 © 2005 Wiley-VCH Verlag GmbH & Co. KGaA, Weinheim

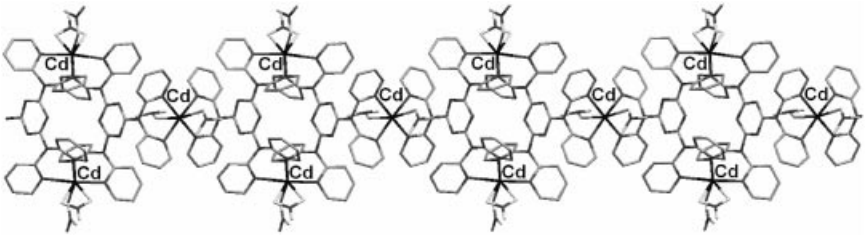

Figure 7. Representation of the cadmium(II) 1D linear coordination polymer.

tals of $[Cd_3(dpyatriz)_2(NO_3)_6]$ (**3**) whose crystal structure was determined by X-ray diffraction (Figure 6).

Cd(1) shows a pentagonal bypiramid configuration due to the coordination of a nitrate ion acting as a chelating ligand. The basal plane of the bipyramid is constituted by three *N*-pyridyl donor atoms, N(6), N(11′), and N(12′), of two didentate dipyridylamine groups belonging to different dpyatriz ligands and by two oxygen atoms, O(4) and O(5), of the chelating anion (Table 1). The in-plane Cd–N distances are normal; the large in-plane Cd–O distances are due to the chelating nitrate ion. The axial positions are occupied by one N-donor atom, N(5), of a dipyridylamino group and by an oxygen atom, O(1), of a monodentate nitrate ion. The angles around the cadmium(II) ion in the basal plane vary from 73.2(2) to 82.7(2)° with the exception of the O(4)–Cd(1)–O(5) angle of 49.8(2)°, distorted because of the chelating behaviour of the nitrate ion (Table 2). Cd(2), which lies on an inversion center, is in an octahedral environment constituted of four N-coordinating 2-pyridyl groups located in the basal plane [N(8) and N(9)], and two axially coordinated O-atoms of two monodentate nitrate ions [O(7)]. The in-plane Cd–N distances are typical as well as the axial Cd–O bond length (Table 1).[30] The angles around Cd(2) in the basal plane vary from 83.6(2) to 96.9(3)° (Table 2).

This trinuclear cadmium unit represents the building block of a 1D linear polymer through the coordination of Cd(2) by a dipyridylamino moiety of an neighbouring repeating unit (Figure 7).

Electron–π interactions further stabilize the polymer chains. Indeed, the symmetrically related oxygen atoms O(8) and O(8′) of the monodentate nitrate ions coordinated to Cd(2) are strongly interacting with electron-poor triazine rings with a short centroid···O distance[21] of 3.26(1) Å (Figure 8, A and A′). The angle of the centroid···O axis to the plane is 79.9(2)°. In addition, the remaining oxygen atoms of the anions, O(9) and O(9′), are interacting with pyridine groups of dipyridylamino units, probably due to the fact that the pyridine rings involved are coordinated to a cadmium ion, thus enhancing their electron-poor character (Figure 8, B and B′). The centroid···O distance is 3.58(2) Å and the centroid···O axis to the plane angle is 49.0(3)°. To the best of our knowledge, this is the first crystallographic example of such nitrate–pyridine π-cloud interactions. The distances and angles observed are far from the theoretical calculated values for the extensively studied model system *s*-triazine anion.[21,26] Unfortunately, no theoretical investigations have been yet performed on the *less electron-deficient, dissymmetric* pyridine ring, but one would rationally anticipate *longer ring–anion bonds* as well as an *optimal plane–axis angle inferior to 90°*.

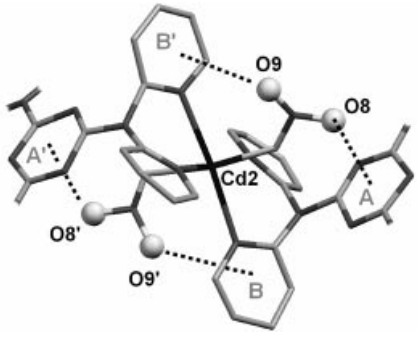

Figure 8. π interactions in **3** between the oxygen atoms of nitrate anions and electron-deficient 1,3,5-triazine and pyridine rings. A···O(8) = 3.26(1) Å; triazine plane–A–O(8) axis = 79.9(2)°. B′···O(9) = 3.58(2) Å; pyridine plane–B′–O(9) axis = 49.0(3)°.

Conclusions

In conclusion, the supramolecular molecules **1**, **2**, and **3** have been obtained at elevated temperature and pressure. The polymeric complexes show anion–π interactions, and experimental evidence of coordinated nitrate anions interacting with triazine or pyridine rings is described, demonstrating the possible existence of anion–π interactions. In addition, the high temperature and pressure applied during their synthesis resulted in notably different crystal structures when compared to those of the coordination compounds prepared from the same reactants, at room temperature and atmospheric pressure.

Experimental Section

General Remarks: Infrared spectra were collected with a Perkin–Elmer Paragon 1000 spectrophotometer equipped with a Golden Gate Diamond ATR as a sample support. Vis/NIR spectra were measured with a Perkin–Elmer Lambda 900 spectrophotometer using the diffuse reflectance technique, with MgO as a reference. Elemental analyses were performed at the Microanalytical Laboratory of the Leiden Institute of Chemistry, The Netherlands. X-band EPR spectra were recorded with a JEOL electron spin resonance spectrometer, equipped with an Esprit 330 data system, at room temperature and at 77 K, with dpph as an internal reference (g = 2.0036).

 © 2005 Wiley-VCH Verlag GmbH & Co. KGaA, Weinheim

Table 3. Summary of crystal data and refinement parameters for complexes **1**, **2**, and **3**.

	1	**2**	**3**
Empirical formula	$C_{33}H_{26}Cu_2N_{16}O_{13}$	$C_{33}H_{26}Zn_2N_{16}O_{13}$	$C_{66}H_{48}Cd_3N_{30}O_{18}$
Formula mass	981.78	985.44	1886.54
Crystal system	orthorhombic	orthorhombic	triclinic
Space group	$P2_12_12_1$ (No. 19)	$P2_12_12_1$ (No. 19)	$P\bar{1}$ (No. 1)
a [Å]	13.749(5)	13.912(5)	11.063(5)
b [Å]	14.762(5)	14.458(5)	12.468(5)
c [Å]	19.432(5)	19.890(5)	15.891(5)
α [°]	90	90	110.315(5)
β [°]	90	90	105.067(5)
γ [°]	90	90	92.877(5)
V [Å^3]	3944(2)	4001(2)	1961(2)
Z	4	4	1
ρ(calcd.) [g·cm^{-3}]	1.653	1.636	1.598
μ [mm^{-1}]	1.165	1.285	0.893
Measured reflections	17662	17748	16660
Unique reflections	5684	2529	7564
Observed reflections	2650	1429	5940
R_{int}	0.0895	0.1694	0.0251
R [$I > 2\sigma(I)$]	0.0479	0.0551	0.0596
wR [$I > 2\sigma(I)$]a	0.0831	0.1000	0.1223

Preparation of $[Cu_2(dpyatriz)(NO_3)_4](H_2O)$ (1): $Cu(NO_3)_2{\cdot}3H_2O$ (7.1 mg, 0.0293 mmol) was added to a suspension of dpyatriz (11.5 mg, 0.0195 mmol) in acetonitrile (6 mL). After dissolving the copper salt, the closed pressure tube was placed in an oven at 105 °C. Single crystals of **1** suitable for X-ray analysis were obtained as light-blue needles at 105 °C after 2 d. Yield: 16 mg (83%). $C_{33}H_{26}Cu_2N_{16}O_{13}$ (981.78): calcd. C 40.37, H 2.67, N 22.83; found C 39.85, H 2.21, N 22.17. IR (neat): $\tilde{\nu}$ = 1607, 1558, 1471, 1374, 1278, 1005, 772, 668 cm^{-1}. UV/Vis (reflectance): λ = 262 (LMCT), 643 and 975 (d–d transitions) nm. Solid-state EPR: g = 2.12 (room temp.), 2.11 (77 K).

Preparation of $[Zn_2(dpyatriz)(NO_3)_4](H_2O)$ (2): $Zn(NO_3)_2{\cdot}6H_2O$ (8.1 mg, 0.0273 mmol) was added to a suspension of dpyatriz (10.7 mg, 0.0182 mmol) in acetonitrile (6 mL). After dissolving the zinc salt, the closed pressure tube was placed in an oven at 105 °C. Single crystals of **2** suitable for X-ray analysis were obtained as colorless parallelepipeds at this temperature after 2 d. Yield: 14 mg (77%). $C_{33}H_{26}Zn_2N_{16}O_{13}$ (985.44): calcd. C 40.22, H 2.66, N 22.74; found C 39.98, H 2.28, N 22.62. IR (neat): $\tilde{\nu}$ = 3080, 1608, 1558, 1378, 1286, 1022, 771, 667 cm^{-1}. UV/Vis (reflectance): λ = 269 (LMCT) nm.

Preparation of $[Cd_3(dpyatriz)_2(NO_3)_6]$ (3): $Cd(NO_3)_2{\cdot}4H_2O$ (9.3 mg, 0.0301 mmol) was added to a suspension of dpyatriz (11.8 mg, 0.0200 mmol) in acetonitrile (12 mL). After dissolving the cadmium salt, the closed pressure tube was placed in an oven at 105 °C. Colorless diamond-shaped single crystals of **3** suitable for X-ray analysis were obtained at 105 °C in a pressure tube after 3 d. Yield: 17 mg (91%). $C_{66}H_{48}Cd_3N_{30}O_{18}$ (1886.54): calcd. C 42.01, H 2.54, N 22.26; found C 41.89, H 2.28, N 21.64. IR (neat): $\tilde{\nu}$ = 3082, 1603, 1550, 1378, 1292, 1014, 768, 664 cm^{-1}. UV/Vis (reflectance): λ = 288 (LMCT) nm.

X-ray Crystallographic Study: The molecular structures were determined by single-crystal X-ray diffraction methods. Crystallographic and experimental details for the different structures are summarized in Table 3. Intensity data and cell parameters were recorded at room temperature (293 K) with a Bruker AXS Smart 1000 single-crystal diffractometer (Mo-K_α radiation), equipped with a CCD area detector. The data reductions were performed using the SAINT[31] and SADABS[32] programs. The structures were solved by direct methods using the SIR97 program[33] and refined on F_o^2 by full-matrix least-squares procedures, using the SHELXL-97 program.[34] Most of the non-hydrogen atoms were refined with anisotropic atomic displacements. The hydrogen atoms were included in the refinement at idealized geometries (C–H 0.95 Å) and refined "riding" on the corresponding parent atoms. The weighting scheme used in the last cycle of refinement was $w = 1/[\sigma^2(F_o^2) + (0.0347P)^2]$ (**1**), $w = 1/[\sigma^2(F_o^2) + (0.0411P)^2]$ (**2**) and $w = 1/[\sigma^2(F_o^2) + (0.0400P)^2 + 6.1257P]$ (**3**), where $P = (F_o^2 + 2F_c^2)/3$. Molecular geometry calculations were carried out using the PARST97 program.[35] All calculations were carried out with a DIGITAL Alpha Station 255 computer. CCDC-255636 (**1**), -255637 (**2**), and -255638 (**3**) contain the supplementary crystallographic data for this paper. These data can be obtained free of charge at www.ccdc.cam.ac.uk/conts/retrieving.html [or from the Cambridge Crystallographic Data Centre, 12 Union Road, Cambridge CB2 1EZ, UK; Fax: +44-1223/336-033; E-mail: deposit@ccdc.cam.ac.uk].

Acknowledgments

The authors thank COST Action D21/003/2001 for allowing regular exchange of preliminary results within a European network before publication and the Dutch National Research School Combination Catalysis (HRSMC and NIOK) for financial support. Exchange visits with the groups of Profs. E. Hahn and B. Krebs (Westfälische Wilhelms-Universität, Münster) through an NWO and DFG grant in the framework of the joint Graduierten-Kolleg are thankfully acknowledged.

[1] G. J. McManus, Z. Q. Wang, M. J. Zaworotko, *Cryst. Growth Des.* **2004**, *4*, 11–13.
[2] M. Eddaoudi, D. B. Moler, H. L. Li, B. L. Chen, T. M. Reineke, M. O'Keeffe, O. M. Yaghi, *Acc Chem. Res.* **2001**, *34*, 319–330.
[3] O. M. Yaghi, M. O'Keeffe, N. W. Ockwig, H. K. Chae, M. Eddaoudi, J. Kim, *Nature* **2003**, *423*, 705–714.
[4] O. Ohmori, M. Fujita, *Chem. Commun.* **2004**, 1586–1587.
[5] O. Almarsson, M. J. Zaworotko, *Chem. Commun.* **2004**, 1889–1896.
[6] J. Y. Lu, A. M. Babb, *Chem. Commun.* **2002**, 1340–1341.
[7] J. L. C. Rowsell, A. R. Millward, K. S. Park, O. M. Yaghi, *J. Am. Chem. Soc.* **2004**, *126*, 5666–5667.

 © 2005 Wiley-VCH Verlag GmbH & Co. KGaA, Weinheim

[8] Y. Ishii, Y. Takenaka, K. Konishi, *Angew. Chem. Int. Ed.* **2004**, *43*, 2702–2705.
[9] J. L. C. Rowsell, O. M. Yaghi, *Microporous Mesoporous Mater.* **2004**, *73*, 3–14.
[10] R. P. Hammond, M. Cavaluzzi, R. C. Haushalter, J. A. Zubieta, *Inorg. Chem.* **1999**, *38*, 1288–1292.
[11] P. Gamez, P. de Hoog, O. Roubeau, M. Lutz, W. L. Driessen, A. L. Spek, J. Reedijk, *Chem. Commun.* **2002**, 1488–1489.
[12] P. Gamez, P. de Hoog, M. Lutz, A. L. Spek, J. Reedijk, *Inorg. Chim. Acta* **2003**, *351*, 319–325.
[13] P. de Hoog, P. Gamez, O. Roubeau, M. Lutz, W. L. Driessen, A. L. Spek, J. Reedijk, *New J. Chem.* **2003**, *27*, 18–21.
[14] P. de Hoog, P. Gamez, W. L. Driessen, J. Reedijk, *Tetrahedron Lett.* **2002**, *43*, 6783–6786.
[15] J. Pang, Y. Tao, S. Freiberg, X. P. Yang, M. D′Iorio, S. N. Wang, *J. Mater. Chem.* **2002**, *12*, 206–212.
[16] P. Gamez, P. de Hoog, M. Lutz, W. L. Driessen, A. L. Spek, J. Reedijk, *Polyhedron* **2003**, *22*, 205–210.
[17] A. W. Addison, T. N. Rao, J. Reedijk, J. Vanrijn, G. C. Verschoor, *J. Chem. Soc., Dalton Trans.* **1984**, 1349–1356.
[18] D. Huang, H. B. Song, M. Du, S. T. Chen, X. H. Bu, *Inorg. Chem.* **2004**, *43*, 931–944.
[19] G. R. Desiraju, *Comprehensive Supramolecular Chemistry*, Pergamon, Oxford, **1996**, vol. 6.
[20] D. Quinonero, C. Garau, C. Rotger, A. Frontera, P. Ballester, A. Costa, P. M. Deya, *Angew. Chem. Int. Ed.* **2002**, *41*, 3389–3392.
[21] M. Mascal, A. Armstrong, M. D. Bartberger, *J. Am. Chem. Soc.* **2002**, *124*, 6274–6276.
[22] H. J. Schneider, *Angew. Chem. Int. Ed. Engl.* **1991**, *30*, 1417–1436.
[23] H. J. Schneider, T. Blatter, B. Palm, U. Pfingstag, V. Rudiger, I. Theis, *J. Am. Chem. Soc.* **1992**, *114*, 7704–7708.
[24] H. J. Schneider, F. Werner, T. Blatter, *J. Phys Org Chem.* **1993**, *6*, 590–594.
[25] C. Garau, A. Frontera, D. Quinonero, P. Ballester, A. Costa, P. M. Deya, *ChemPhysChem* **2003**, *4*, 1344–1348.
[26] D. Kim, P. Tarakeshwar, K. S. Kim, *J. Phys Chem. A* **2004**, *108*, 1250–1258.
[27] P. de Hoog, P. Gamez, H. Mutikainen, U. Turpeinen, J. Reedijk, *Angew. Chem. Int. Ed.* **2004**, *43*, 5815–5817.
[28] S. Demeshko, S. Dechert, F. Meyer, *J. Am. Chem. Soc.* **2004**, *126*, 4508–4509.
[29] H. D. Bian, Q. Yu, H. Liang, S. P. Yan, D. Z. Liao, P. Cheng, Z. H. Jiang, *Appl. Organomet. Chem.* **2004**, *18*, 416–417.
[30] R. Q. Zou, X. H. Bu, R. H. Zhang, *Inorg. Chem.* **2004**, *43*, 5382–5386.
[31] *SAINT, Software Users Guide, Version 6.0*, Bruker Analytical X-ray Systems, **1999**.
[32] G. M. Sheldrick, *SADABS v2.03: Area-Detector Absorption Correction*, University of Göttingen, **1999**.
[33] A. Altomare, M. C. Burla, M. Camalli, G. L. Cascarano, C. Giacovazzo, A. Guagliardi, A. G. G. Moliterni, G. Polidori, R. Spagna, *J. Appl. Crystallogr.* **1999**, *32*, 115–119.
[34] G. M. Sheldrick, *SHELXL-97, Program for Crystal Structure Refinement*, University of Göttingen, **1997**.
[35] M. Nardelli, *J. Appl. Crystallogr.* **1996**, *29*, 296–300.

Received: February 16, 2005
Published Online: June 17, 2005

 © 2005 Wiley-VCH Verlag GmbH & Co. KGaA, Weinheim

Synthesis, Structure and Luminescence Properties of Four Novel Terbium 2-Fluorobenzoate Complexes

Xia Li,[a] Zhuo-Yong Zhang,[a] and Ying-Quan Zou*[b]

Keywords: Fluorinated ligands / Luminescence / O ligands / Terbium

Four new complexes $[Tb(2\text{-}FBA)_3\cdot(2\text{-}HFBA)\cdot H_2O]_2$ (**1**), $\{[Tb(2\text{-}FBA)_3\cdot(4,4'\text{-}bpy)\cdot H_2O]_3\}_n$ (**2**), $[Tb(2\text{-}FBA)_3\cdot(2,2'\text{-}bpy)]_2$ (**3**), and $[Tb(2\text{-}FBA)_3\cdot phen\cdot CH_3CH_2OH]_2\cdot[Tb(2\text{-}FBA)_3\cdot phen]_2$ (**4**) (2-HFBA: 2-fluorobenzoic acid; 4,4′-bpy: 4,4′-bipyridine; 2,2′-bpy: 2,2′-bipyridine; phen: 1,10-phenanthroline) have been synthesized and characterized by X-ray diffraction analysis. Complex **1** is a dimeric molecule with a one-dimensional supramolecular structure formed by hydrogen bonds. Complex **2** is an infinite one-dimensional polymer chain formed by bridging carboxylato groups; its 2D framework structure is formed by hydrogen bonds. The structure of complex **3** contains three independent binuclear molecules in the asymmetric unit. In two of them, two Tb^{3+} ions are held together by four 2-FBA groups, with two of them in a bidentate-bridging mode and the other two in a chelating-bridging mode. In the third, two Tb^{3+} ions are held together by four 2-FBA groups, all of which are in the bidentate-bridging mode. One 2-FBA group and one 2,2′-bpy chelate to one Tb^{3+} ion, resulting in coordination numbers of the central terbium ion of nine and eight, respectively. The structure of complex **4** contains two nonequivalent binuclear molecules in the asymmetric unit – $[Tb(2\text{-}FBA)_3\cdot phen\cdot CH_3CH_2OH]_2$ and $[Tb(2\text{-}FBA)_3\cdot phen]_2$. In the former, the Tb^{3+} ion is surrounded by eight atoms, five O atoms from five 2-FBA groups, one O atom from one ethanol molecule and two N atoms from phen, and the 2-FBA groups act in monodentate and bridging coordination modes. In the latter, the Tb^{3+} ion is coordinated by nine atoms, seven O atoms from five 2-FBA groups and two N atoms of phen, and the 2-FBA groups link the Tb^{3+} ion in chelating, bridging, and chelating-bridging coordination modes. Complexes **1**, **3**, and **4** emit a bright green light under UV light in the solid state. There are four emission peaks in the luminescence spectra at 488, 543, 584, and 618 nm, corresponding to the $^5D_4\rightarrow{}^7F_6$, $^5D_4\rightarrow{}^7F_5$, $^5D_4\rightarrow{}^7F_4$, and $^5D_4\rightarrow{}^7F_3$ transitions, respectively, of the Tb^{3+} ion.

(© Wiley-VCH Verlag GmbH & Co. KGaA, 69451 Weinheim, Germany, 2005)

Introduction

Most terbium complexes emit intense green fluorescence and have potential applications in fluorescent probes and in electroluminescent devices.[1,2] The luminescent intensities of lanthanide complexes depend on their ligands, and some lanthanide carboxylate complexes have good luminescent properties. This kind of lanthanide complex has been studied in recent years due to the variety of structural types and potential applications in catalysis and luminescent probes, etc.[1–4] We are interested in the structural chemistry of these complexes. Many structural studies on lanthanide carboxylate complexes have been reported. In lanthanide monocarboxylate complexes, the carboxylate groups are coordinated simultaneously to the lanthanide ion in different modes, namely monodentate, chelating, bridging, and bridging-chelating modes. Consequently, the complexes are often mononuclear, dinuclear dimers, polymeric chains, or network structures. Generally, lanthanide complexes with only a monoacid form coordination polymers with bridging carboxylato groups, such as $[Nd(3\text{-}CH_3C_6H_4COO)_3]$ and $[Tb(3\text{-}CH_3C_6H_4COO)_3]$,[5] $[Nd(2\text{-}CH_3OC_6H_4COO)_3\cdot 4H_2O]$,[6] $[Eu(4\text{-}CH_3C_6H_4COO)_3]$,[7] and $[Eu(2,3\text{-}DMOBA)_3]_n$ (2,3-DMOBA = 2,3-dimethoxybenzoate).[8] However, lanthanide complexes with a monoacid and 1,10-phenanthroline (phen) or 2,2′-bipyridine (2,2′-bpy) are commonly dimeric molecules with a bridging linkage of the carboxylato groups, such as in $[Eu(4\text{-}CH_3C_6H_4COO)_3(phen)]$,[9] $[Sm_2(4\text{-}CH_3C_6H_4COO)_6(2,2'\text{-}bpy)_2]$,[10] $[Eu(m\text{-}CH_3C_6H_4COO)_3(phen)](H_2O)$,[11] and $[Eu_2(3,4\text{-}DMBA)_6\cdot(phen)_2]$ (3,4-DMBA = 3,4-dimethylbenzoate).[12] In these complexes, the phen or 2,2′-bpy ligand coordinates to the metal in a chelating mode to form a stable five-membered ring. Lanthanide carboxylate complexes containing 2,2′-bpy or phen have interesting structures, with both high stability and intense fluorescence.[9–12] 4,4′-Bipyridine (4,4′-bpy), however, coordinates to the metal with one or two N atoms, and is weaker than phen or 2,2′-bpy. In this paper terbium and 2-fluorobenzoic acid (2-HFBA) have been used to synthesize a new complex $[Tb(2\text{-}FBA)_3\cdot(2\text{-}HFBA)\cdot$

[a] Department of Chemistry Capital Normal University, Beijing 100037, People's Republic of China
[b] Department of Chemistry Beijing Normal University, Beijing 100875, People's Republic of China
Fax: +86-1062208564
E-mail: zouyq@263.net

 DOI: 10.1002/ejic.200500001 © 2005 Wiley-VCH Verlag GmbH & Co. KGaA, Weinheim

$H_2O]_2$ (**1**). When 4,4′-bpy, 2,2′-bpy, or phen was added to the complexes, new mixed-ligand terbium complexes with interesting structures were obtained, namely $\{[Tb(2\text{-}FBA)_3 \cdot (4,4'\text{-}bpy) \cdot H_2O]_3\}_n$ (**2**), $[Tb(2\text{-}FBA)_3 \cdot (2,2'\text{-}bpy)]_2$ (**3**), and $[Tb(2\text{-}FBA)_3 \cdot phen \cdot CH_3CH_2OH]_2 \cdot [Tb(2\text{-}FBA)_3 \cdot phen]_2$ (**4**). Crystal analysis showed that complex **1** is a dimeric molecule, whereas complex **2** is a polymer in which 4,4′-bpy coordinates to Tb^{3+} ion and the 2-FBA groups coordinate to the Tb^{3+} ion in only one bidentate-bridging mode. The structure of complex **3** contains three independent binuclear molecules, and the structure of complex **4** contains two nonequivalent binuclear molecules. These structural features are rare in lanthanide carboxylate complexes. Complexes **1**, **3**, and **4** emit intense green fluorescence.

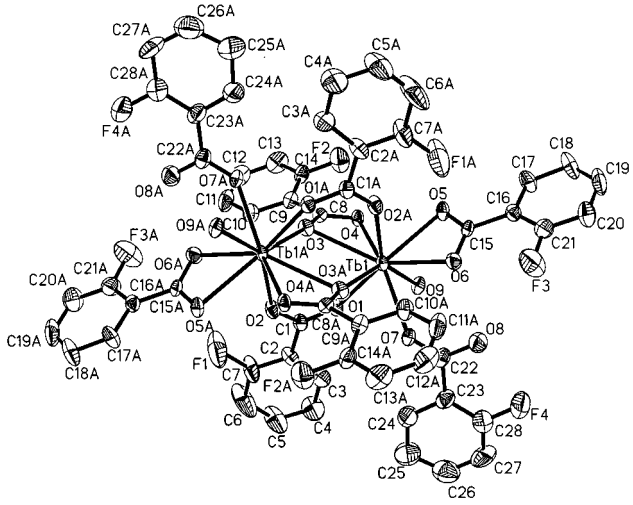

a

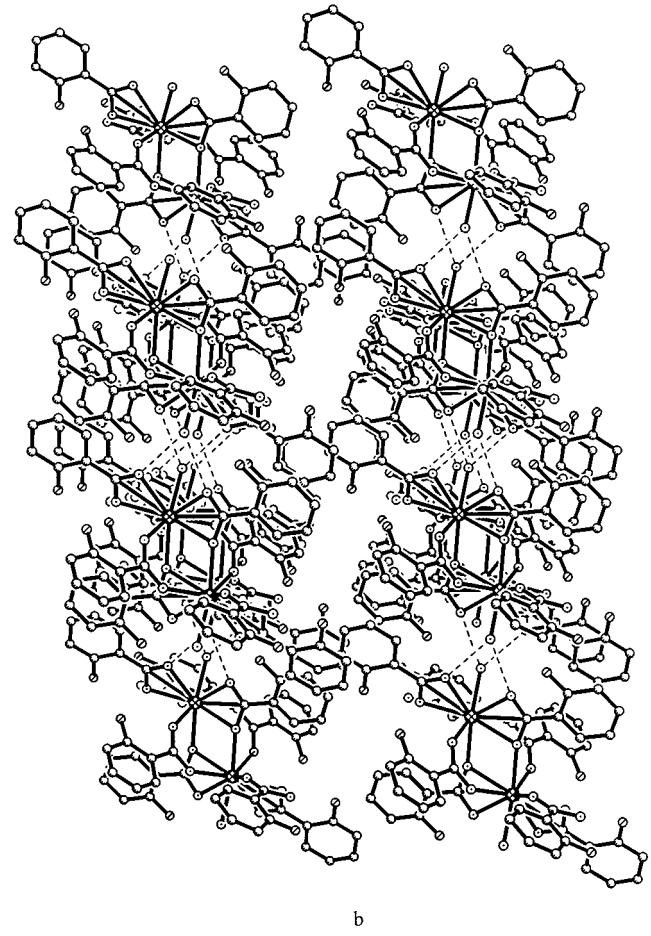

b

Figure 1. Molecular structure of complex **1** (a) and the packing diagram viewed along the *b*-axis (b). All hydrogen atoms have been omitted for clarity; the thermal ellipsoids are shown at the 30% probability level.

Results and Discussion

Structural Description of $[Tb(2\text{-}FBA)_3 \cdot (2\text{-}HFBA) \cdot H_2O]_2$ (1)

The structure of complex **1** is shown in Figure 1 (part a), which shows that the Tb^{3+} ion is coordinated by seven oxygen atoms from 2-FBA groups, one oxygen atom from one 2-HFBA ligand, and one oxygen atom from water, giving a coordination number of nine. The two Tb^{3+} ions are linked together by four bridging carboxylato groups to form a centrosymmetric dimeric unit, which is rare for lanthanide carboxylate complexes. The majority of known lanthanide complexes containing a monoacid display a one-dimensional polymer chain, such as in $[Tb(3\text{-}CH_3C_6H_4COO)_3]$,[5] $[Nd(2\text{-}CH_3OC_6H_4COO)_3 \cdot 4H_2O]$,[6] and $[Eu(2,3\text{-}DMOBA)_3]_n$.[8] The distance between two Tb^{3+} ions is 3.951(3) Å (Table 1). All the 2-FBA groups are coordinated to the Tb^{3+} ion and can be classified into three different coordination modes: the carboxylato groups O5–C15–O6 are in a chelating mode, in which two O atoms coordinate to the same Tb^{3+} ion, the carboxylato groups O1–C1–O2 are in a bridging mode, in which two O atoms coordinate to two different Tb^{3+} ions to form a bidentate bridge, and the carboxylato groups O3–C8–O4 are in a chelating-bridging mode, in which two O atoms chelate one Tb^{3+} ion and one of them also simultaneously links to another Tb^{3+} ion, forming a tridentate bridge. The 2-HFBA ligand binds in a monodentate mode through a single oxygen atom to the Tb^{3+} ion. It is not common to observe a monodentate carboxylic acid ligand coordinated to a lanthanide center. The Tb–O bonds have an average length of 2.436 Å and the O–Tb–O bond angles lie in the range 50.2(2)–148.7(3)°. There is a bonding water molecule (O9) at a distance of 2.410(7) Å to the Tb^{3+} ion, which takes part in hydrogen bonds with the coordinated oxygen of carboxylato groups and the fluorine atoms in the benzene ring [O9–H9A···O5 ($-x + 1$, $-y$, $-z + 2$) with d(O9···O5) = 2.754 Å and ∠O9–H9A–O5 = 166.16°; O9–H9B···F2 ($-x + 1$, $-y$, $-z + 2$) with d(O9···F2) = 3.047 Å and ∠O9–H9B–F2 = 153.38°] to form a one-dimensional supramolecular chain (Figure 1, part b). This case is different from the three complexes with a one-dimensional polymeric structure mentioned above.

 © 2005 Wiley-VCH Verlag GmbH & Co. KGaA, Weinheim

Table 1. Bond lengths [Å] and angles [°] for complex **1**.

Tb(1)–O(3)#1[a]	2.316(8)	Tb(1)–O(1)	2.329(8)
Tb(1)–O(2)#1	2.333(8)	Tb(1)–O(6)	2.409(8)
Tb(1)–O(9)	2.410(7)	Tb(1)–O(4)	2.426(8)
Tb(1)–O(7)	2.462(9)	Tb(1)–O(5)	2.546(8)
Tb(1)–O(3)	2.668(8)		
O(3)#1–Tb(1)–O(1)	78.1(3)	O(3)#1–Tb(1)–O(2)#1	73.6(3)
O(1)–Tb(1)–O(2)#1	135.3(3)	O(3)#1–Tb(1)–O(6)	100.3(3)
O(1)–Tb(1)–O(6)	142.0(3)	O(2)#1–Tb(1)–O(6)	77.6(3)
O(3)#1–Tb(1)–O(9)	141.5(3)	O(1)–Tb(1)–O(9)	74.6(3)
O(2)#1–Tb(1)–O(9)	143.9(3)	O(6)–Tb(1)–O(9)	85.6(3)
O(3)#1–Tb(1)–O(4)	125.5(3)	O(1)–Tb(1)–O(4)	79.5(3)
O(2)#1–Tb(1)–O(4)	89.5(3)	O(6)–Tb(1)–O(4)	126.6(3)
O(9)–Tb(1)–O(4)	75.3(3)	O(3)#1–Tb(1)–O(7)	73.9(3)
O(1)–Tb(1)–O(7)	73.7(3)	O(2)#1–Tb(1)–O(7)	128.0(3)
O(6)–Tb(1)–O(7)	69.6(3)	O(9)–Tb(1)–O(7)	72.7(3)
O(4)–Tb(1)–O(7)	142.5(3)	O(3)#1–Tb(1)–O(5)	139.9(3)
O(1)–Tb(1)–O(5)	141.9(3)	O(2)#1–Tb(1)–O(5)	72.4(3)
O(6)–Tb(1)–O(5)	52.0(3)	O(9)–Tb(1)–O(5)	72.1(3)
O(4)–Tb(1)–O(5)	74.7(3)	O(7)–Tb(1)–O(5)	112.4(3)
O(3)#1–Tb(1)–O(3)	75.3(3)	O(1)–Tb(1)–O(3)	68.4(3)
O(2)#1–Tb(1)–O(3)	71.4(3)	O(6)–Tb(1)–O(3)	148.7(3)
O(9)–Tb(1)–O(3)	117.5(3)	O(4)–Tb(1)–O(3)	50.2(2)
O(7)–Tb(1)–O(3)	134.9(3)	O(5)–Tb(1)–O(3)	112.3(3)

[a] Symmetry transformations used to generate equivalent atoms: #1 $-x + 2$, $-y$, $-z + 2$.

Structural Description of $\{[Tb(2\text{-}FBA)_3\cdot(4,4'\text{-bpy})\cdot H_2O]_3\}_n$ (2)

The structure of complex **2** is shown in Figure 2 (part a), which shows that each terbium ion is connected by six oxygen atoms from six 2-FBA groups, one oxygen atom from water, and one nitrogen atom from a 4,4′-bpy molecule. The 2-FBA groups coordinate the terbium ion in only a bidentate-bridging mode. Complexes in which carboxylato groups coordinate a metal in only one coordination mode, such as $[Nd(3\text{-}CH_3C_6H_4CO_2)_3]$[5] and $[Eu(4\text{-}CH_3C_6H_4COO)_3]$.[7] in which the carboxylato groups adopt only one bridging-chelating mode, are not common. Two adjacent Tb^{3+} ions are connected by four bridging O1–C1–O2 and O3–C8–O4 groups to form a dimeric unit. These dimeric units are linked by two simple bridging carboxylato groups (O5–C15–O6) to form a one-dimensional polymer chain along the [1,0,0] direction. The distances between two adjacent Tb^{3+} ions in the polymer chain are 4.269 Å (Tb1···Tb1A) within the dimeric unit and 5.637 Å between the dimeric units (Table 2). The Tb1A···Tb1···Tb1B angle is 159.1°, and the $Tb–O_{carboxyl}$ distances range from 2.470(4) Å to 2.513(4) Å, with a mean value of 2.492 Å. The O–Tb–O bond angles are in the range 71.70(14)–143.71(14)°, and the $Tb–O_{water}$ bond length is 2.566(4) Å. The 4,4′-bpy ligand coordinates to Tb^{3+} ion through one N atom. There is a bonding nitrogen atom (N1) of 4,4′-bpy at a distance of 2.851(5) Å to the Tb^{3+} ions. The two pyridyl rings are not coplanar, and have a dihedral angle of 146.0°. The uncoordinated N atom of 4,4′-bpy forms a hydrogen bond with coordinated water [O7–H7A···N2B, with d(O7···N2B) = 2.857 Å and ∠O7–H7A–N2B = 170.0°]. Adjacent 1D chains are interlinked by these hydrogen bonds to form a two-dimensional supramolecular network structure along the [1,0,1] direction (Figure 2, part b). Complex **2** is different from the complex $[Tb_2(O_2CPh)_6(4,4'\text{-bpy})]_n$,[1] in which 4,4′-bpy bridges two different metals with two N atoms. Complex **2** is also different from the complexes $\{[Eu(m\text{-MOBA})_3\cdot 2H_2O]1/2(4,4'\text{-bpy})\}_\infty$ (*m*-MOBA = *m*-methoxybenzoate)[13] and $\{[Eu(\alpha\text{-FURA})_3\cdot 2H_2O]\cdot NO_3\cdot(4,4'\text{-Hbpy})\}_\infty$ (α-FURA = α-furoate),[14] in which the 4,4′-bpy molecule does not coordinate to the metal. Lanthanide carboxylate complexes containing coordinated 4,4′-bpy are less common due to the weak coordination of 4,4′-bpy in this kind of complex.

Table 2. Bond lengths [Å] and angles [°] for complex **2**.

Tb(1)–O(6)#1[a]	2.470(4)	Tb(1)–O(3)	2.476(4)
Tb(1)–O(5)	2.487(4)	Tb(1)–O(1)	2.504(4)
Tb(1)–O(2)#2	2.504(4)	Tb(1)–O(4)#2	2.513(4)
Tb(1)–O(7)	2.566(4)	Tb(1)–N(1)	2.851(5)
O(6)#1–Tb(1)–O(3)	99.78(15)	O(6)#1–Tb(1)–O(5)	83.05(14)
O(3)–Tb(1)–O(5)	143.71(14)	O(6)#1–Tb(1)–O(1)	142.84(14)
O(3)–Tb(1)–O(1)	75.50(15)	O(5)–Tb(1)–O(1)	80.72(14)
O(6)#1–Tb(1)–O(2)#2	78.13(14)	O(3)–Tb(1)–O(2)#2	71.70(14)
O(5)–Tb(1)–O(2)#2	142.85(14)	O(1)–Tb(1)–O(2)#2	131.55(14)
O(6)#1–Tb(1)–O(4)#2	133.69(15)	O(3)–Tb(1)–O(4)#2	122.08(14)
O(5)–Tb(1)–O(4)#2	74.71(15)	O(1)–Tb(1)–O(4)#2	72.77(16)
O(2)#2–Tb(1)–O(4)#2	95.84(16)	O(6)#1–Tb(1)–O(7)	71.31(15)
O(3)–Tb(1)–O(7)	72.88(14)	O(5)–Tb(1)–O(7)	73.95(15)
O(1)–Tb(1)–O(7)	72.15(15)	O(2)#2–Tb(1)–O(7)	127.62(16)
O(4)#2–Tb(1)–O(7)	135.85(17)	O(6)#1–Tb(1)–N(1)	68.34(15)
O(3)–Tb(1)–N(1)	142.93(15)	O(5)–Tb(1)–N(1)	71.85(15)
O(1)–Tb(1)–N(1)	135.20(15)	O(2)#2–Tb(1)–N(1)	71.50(15)
O(4)#2–Tb(1)–N(1)	66.29(15)	O(7)–Tb(1)–N(1)	129.25(15)

[a] Symmetry transformations used to generate equivalent atoms: #1 $-x + 1$, $-y + 1$, $-z + 1$; #2 $-x$, $-y + 1$, $-z + 1$.

Structural Description of $[Tb(2\text{-}FBA)_3\cdot(2,2'\text{-bpy})]_2$ (3)

The structure of complex **3** is shown in Figure 3 (a, b and c). It is dimeric and, interestingly, there are three independent molecules in the asymmetric unit, in which each molecular unit is dimeric with an inversion center. Each $Tb1^{3+}$ ion is coordinated by nine atoms, seven oxygen atoms from five 2-FBA groups and two nitrogen atoms of one 2,2′-bpy ligand (Figure 3, part a). They adopt a distorted monocapped square-antiprism arrangement, with atoms O3, O5, O4A, and O6A forming the upper and O1, O2, N1, and N2 the lower square-planes with a dihedral angle between them of 4.4°; atom O4 caps the upper plane. The 2-FBA ligands act in chelating, bridging, and chelating-bridging modes. Two Tb1 ions are held together by four 2-FBA groups, with two of them in a bidentate bridging mode, and the other two in a chelating-bridging mode. In addition, each terbium ion is also chelated by one 2-FBA group and one 2,2′-bpy ligand. The Tb1···Tb1A distance is 4.137 Å (Table 3). The Tb1–O bond lengths range from 2.28(8) to 2.91(9) Å, with an average length of 2.459 Å. It is reasonable that the Tb1–O4 distance, 2.91 Å, of the tridentate bridging carboxylato group is the largest due to O3–C18–O4–Tb1 being an unstable four-membered ring. This feature has been observed in other lanthanide carboxylate complexes. The O–Tb1–O angles vary considerably in the range 53.00(3)–150.00(3)°, but they are not uncommon

 © 2005 Wiley-VCH Verlag GmbH & Co. KGaA, Weinheim

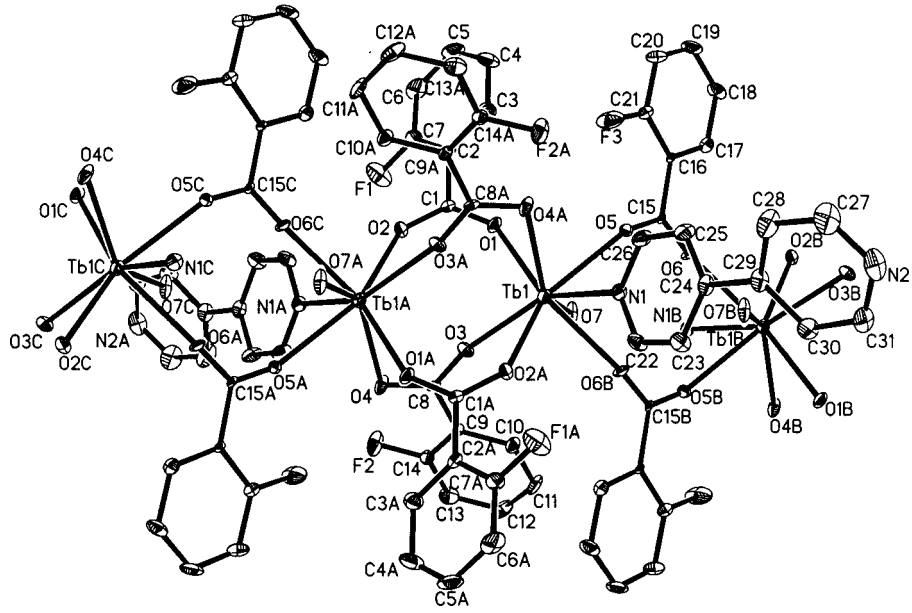

a

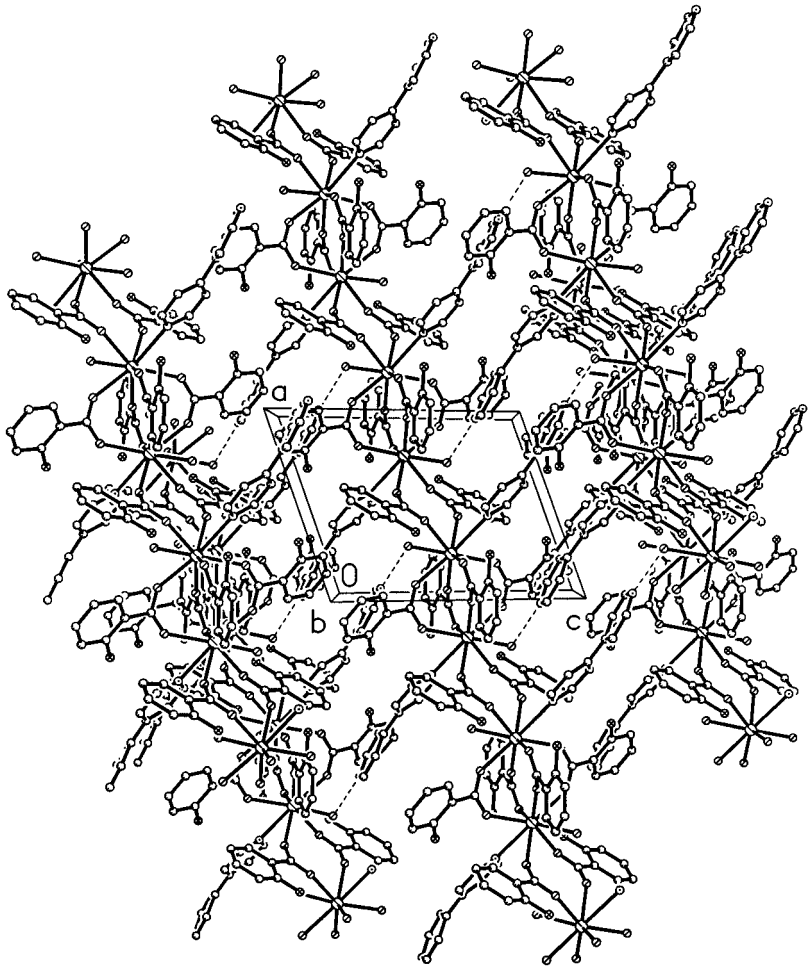

b

Figure 2. Molecular structure of complex **2** (a) and the packing diagram (b). All hydrogen atoms have been omitted for clarity; the thermal ellipsoids are shown at the 30% probability level.

 © 2005 Wiley-VCH Verlag GmbH & Co. KGaA, Weinheim

for lanthanide carboxylate complexes. The 2,2′-bpy ligand coordinates to the Tb^{3+} ion in a conventional chelation mode with two N atoms, forming a five-membered ring. The two pyridyl rings of the 2,2′-bpy ligand are not coplanar and form a dihedral angle of 12.2° in the dimer. The Tb1–N bond lengths are similar, with an average value of 2.56 Å, and the N–Tb1–N bond angle is 62(3)°.

Each $Tb2^{3+}$ ion is eight-coordinate, with six oxygen atoms from five 2-FBA groups and two nitrogen atoms from one chelating 2,2′-bpy ligand (Figure 3, part b). The two terbiums in the dimer are held together by four 2-FBA groups, all with a bidentate-bridging coordination mode, and each terbium ion is further bonded to one chelating 2-FBA group and one 2,2′-bpy molecule. Thus, each terbium ion has a distorted square-antiprism coordination geometry with O7, O8, N3, and N4 forming one square face and O9, O11, O10A, and O12A the other. The dihedral angle between the two faces is 4.6°. The 2-FBA ligands coordinate the terbium ion in chelating and bidentate-bridging coordination modes. Obviously, the structures given in Figure 3 (part b) and Figure 3 (part a) are different with respect to the different linking modes of the four 2-FBA groups to the two terbium ions. The Tb2···Tb2A distance is 4.260 Å. The Tb2–O distances vary in the range 2.35(7) to 2.48(8) Å, with an average value of 2.372 Å, and the O–Tb2–O angles range from 53.00(3) to 149.00(3)°. The average Tb2–N distance is 2.53 Å and the N–Tb2–N angle is 62(4)°. The dihedral angle between the two pyridyl rings of the 2,2′-bpy molecule is 6.0°.

As shown in Figure 3 (part c), the $Tb3^{3+}$ ion is coordinated by nine atoms, seven oxygen atoms from five 2-FBA groups and two nitrogen atoms of one 2,2′-bpy ligand. The coordination polyhedron of the $Tb3^{3+}$ ion is a distorted monocapped square-antiprism, which is quite similar to that of the $Tb1^{3+}$ ion in Figure 3 (part a) but differs from that of the Tb2 ion in Figure 3 (part b). The distance be-

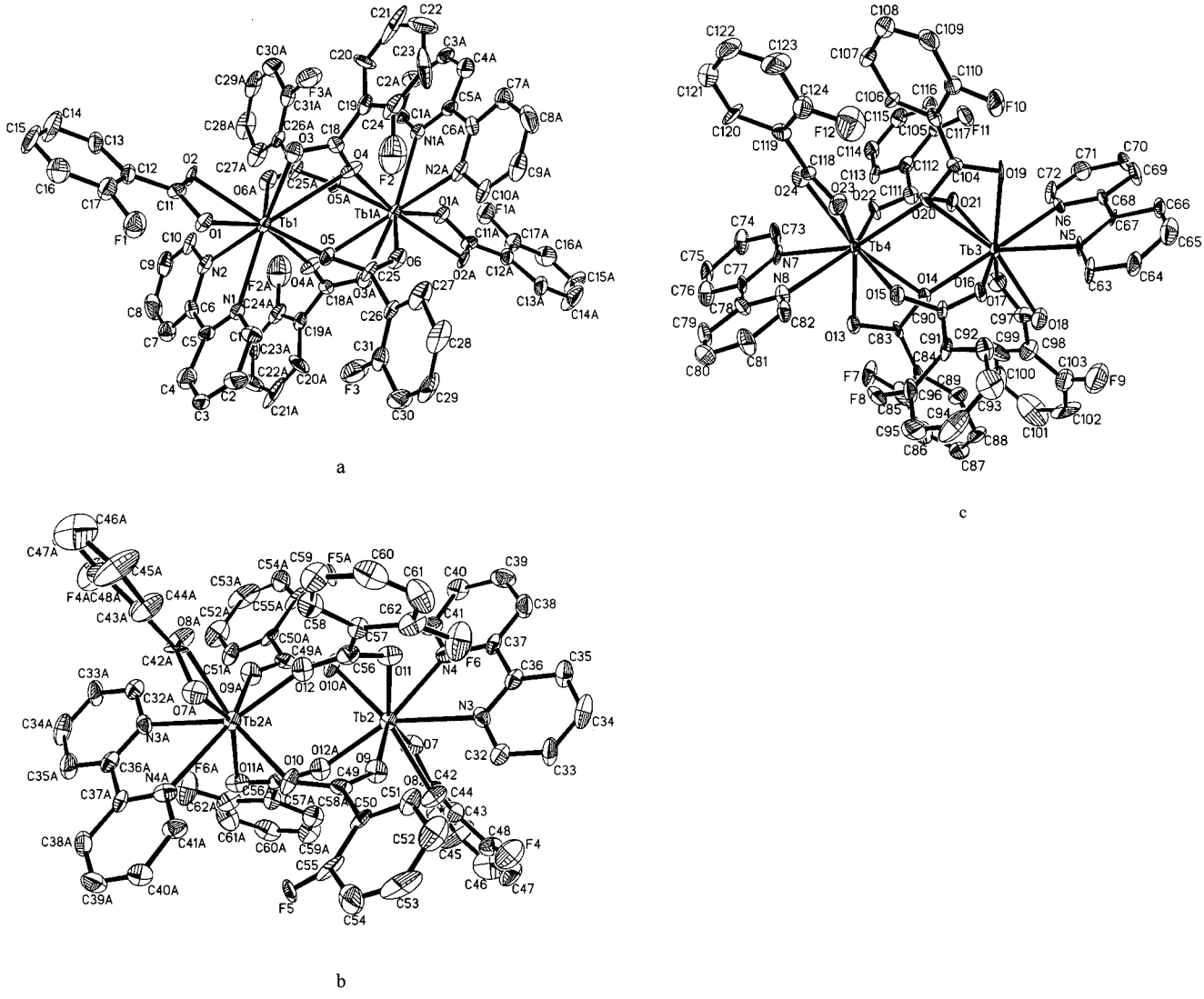

Figure 3. Molecular structures of the complex **3**. (a), (b), and (c) show three different structures. All hydrogen atoms have been omitted for clarity; the thermal ellipsoids are shown at the 30% probability level.

 © 2005 Wiley-VCH Verlag GmbH & Co. KGaA, Weinheim

Table 3. Bond lengths [Å] and angles [°] for complex **3**.

Tb(1)–O(4)#1[a]	2.28(8)	Tb(1)–O(6)#1	2.36(8)
Tb(1)–O(5)	2.37(7)	Tb(1)–O(3)	2.41(9)
Tb(1)–O(1)	2.42(7)	Tb(1)–O(2)	2.46(7)
Tb(1)–N(2)	2.55(11)	Tb(1)–N(1)	2.58(9)
Tb(1)–O(4)	2.91(9)	Tb(2)–O(12)#2	2.27(9)
Tb(2)–O(10)#2	2.32(8)	Tb(2)–O(9)	2.35(8)
Tb(2)–O(11)	2.37(8)	Tb(2)–O(8)	2.44(8)
Tb(2)–O(7)	2.48(7)	Tb(2)–N(4)	2.52(11)
Tb(2)–N(3)	2.54(10)	Tb(3)–O(21)	2.35(7)
Tb(3)–O(16)	2.36(7)	Tb(3)–O(14)	2.37(7)
Tb(3)–O(18)	2.44(9)	Tb(3)–O(17)	2.45(8)
Tb(3)–O(19)	2.48(8)	Tb(3)–N(6)	2.56(8)
Tb(3)–N(5)	2.57(8)	Tb(3)–O(20)	2.60(8)
Tb(4)–O(22)	2.34(7)	Tb(4)–O(15)	2.35(8)
Tb(4)–O(20)	2.37(7)	Tb(4)–O(23)	2.43(8)
Tb(4)–O(24)	2.44(8)	Tb(4)–O(13)	2.48(8)
Tb(4)–N(8)	2.56(9)	Tb(4)–N(7)	2.58(8)
Tb(4)–O(14)	2.58(7)		
O(4)#1–Tb(1)–O(6)#1	76(3)	O(4)#1–Tb(1)–O(5)	75(3)
O(6)#1–Tb(1)–O(5)	131(3)	O(4)#1–Tb(1)–O(3)	121(3)
O(6)#1–Tb(1)–O(3)	85(3)	O(5)–Tb(1)–O(3)	77(3)
O(4)#1–Tb(1)–O(1)	150(3)	O(6)#1–Tb(1)–O(1)	129(3)
O(5)–Tb(1)–O(1)	93(3)	O(3)–Tb(1)–O(1)	82(3)
O(4)#1–Tb(1)–O(2)	144(3)	O(6)#1–Tb(1)–O(2)	77(3)
O(5)–Tb(1)–O(2)	140(3)	O(3)–Tb(1)–O(2)	79(3)
O(1)–Tb(1)–O(2)	53(3)	O(4)#1–Tb(1)–N(2)	79(3)
O(6)#1–Tb(1)–N(2)	78(3)	O(5)–Tb(1)–N(2)	132(3)
O(3)–Tb(1)–N(2)	150(3)	O(1)–Tb(1)–N(2)	90(3)
O(2)–Tb(1)–N(2)	74(3)	O(4)#1–Tb(1)–N(1)	81(3)
O(6)#1–Tb(1)–N(1)	137(3)	O(5)–Tb(1)–N(1)	74(3)
O(3)–Tb(1)–N(1)	138(3)	O(1)–Tb(1)–N(1)	70(3)
O(2)–Tb(1)–N(1)	105(3)	N(2)–Tb(1)–N(1)	62(3)
O(4)#1–Tb(1)–O(4)	75(3)	O(6)#1–Tb(1)–O(4)	68(3)
O(5)–Tb(1)–O(4)	68(2)	O(3)–Tb(1)–O(4)	46(2)
O(1)–Tb(1)–O(4)	126(3)	O(2)–Tb(1)–O(4)	114(2)
N(2)–Tb(1)–O(4)	141(3)	N(1)–Tb(1)–O(4)	139(3)
O(12)#2–Tb(2)–O(10)#2	76(3)	O(12)#2–Tb(2)–O(9)	78(3)
O(10)#2–Tb(2)–O(9)	127(3)	O(12)#2–Tb(2)–O(11)	125(3)
O(10)#2–Tb(2)–O(11)	82(3)	O(9)–Tb(2)–O(11)	76(3)
O(12)#2–Tb(2)–O(8)	82(3)	O(10)#2–Tb(2)–O(8)	138(3)
O(9)–Tb(2)–O(8)	81(3)	O(11)–Tb(2)–O(8)	139(3)
O(12)#2–Tb(2)–O(7)	81(3)	O(10)#2–Tb(2)–O(7)	88(3)
O(9)–Tb(2)–O(7)	132(3)	O(11)–Tb(2)–O(7)	149(3)
O(8)–Tb(2)–O(7)	53(3)	O(12)#2–Tb(2)–N(4)	144(3)
O(10)#2–Tb(2)–N(4)	79(3)	O(9)–Tb(2)–N(4)	138(3)
O(11)–Tb(2)–N(4)	75(3)	O(8)–Tb(2)–N(4)	101(3)
O(7)–Tb(2)–N(4)	74(3)	O(12)#2–Tb(2)–N(3)	147(3)
O(10)#2–Tb(2)–N(3)	136(3)	O(9)–Tb(2)–N(3)	80(3)
O(11)–Tb(2)–N(3)	72(3)	O(8)–Tb(2)–N(3)	71(3)
O(7)–Tb(2)–N(3)	97(3)	N(4)–Tb(2)–N(3)	62(4)
O(21)–Tb(3)–O(16)	137(3)	O(21)–Tb(3)–O(14)	80(3)
O(16)–Tb(3)–O(14)	72(2)	O(21)–Tb(3)–O(18)	124(3)
O(16)–Tb(3)–O(18)	88(3)	O(14)–Tb(3)–O(18)	88(3)
O(21)–Tb(3)–O(17)	71(3)	O(16)–Tb(3)–O(17)	128(3)
O(14)–Tb(3)–O(17)	74(3)	O(18)–Tb(3)–O(17)	53(3)
O(21)–Tb(3)–O(19)	80(3)	O(16)–Tb(3)–O(19)	90(3)
O(14)–Tb(3)–O(19)	125(2)	O(18)–Tb(3)–O(19)	144(3)
O(17)–Tb(3)–O(19)	142(3)	O(21)–Tb(3)–N(6)	78(3)
O(16)–Tb(3)–N(6)	140(3)	O(14)–Tb(3)–N(6)	145(3)
O(18)–Tb(3)–N(6)	83(3)	O(17)–Tb(3)–N(6)	74(3)
O(19)–Tb(3)–N(6)	76(3)	O(21)–Tb(3)–N(5)	136(3)
O(16)–Tb(3)–N(5)	77(3)	O(14)–Tb(3)–N(5)	145(3)
O(18)–Tb(3)–N(5)	73(3)	O(17)–Tb(3)–N(5)	114(3)
O(19)–Tb(3)–N(5)	71(3)	N(6)–Tb(3)–N(5)	63(3)
O(21)–Tb(3)–O(20)	66(3)	O(16)–Tb(3)–O(20)	74(3)
O(14)–Tb(3)–O(20)	74(2)	O(18)–Tb(3)–O(20)	158(3)
O(17)–Tb(3)–O(20)	130(3)	O(19)–Tb(3)–O(20)	51(2)
N(6)–Tb(3)–O(20)	119(3)	N(5)–Tb(3)–O(20)	114(3)
O(22)–Tb(4)–O(15)	137(3)	O(22)–Tb(4)–O(20)	74(3)
O(15)–Tb(4)–O(20)	76(3)	O(22)–Tb(4)–O(23)	126(3)
O(15)–Tb(4)–O(23)	74(3)	O(20)–Tb(4)–O(23)	74(3)
O(22)–Tb(4)–O(24)	85(3)	O(15)–Tb(4)–O(24)	128(3)
O(20)–Tb(4)–O(24)	92(3)	O(23)–Tb(4)–O(24)	54(3)
O(22)–Tb(4)–O(13)	90(3)	O(15)–Tb(4)–O(13)	81(3)
O(20)–Tb(4)–O(13)	125(3)	O(23)–Tb(4)–O(13)	144(3)
O(24)–Tb(4)–O(13)	139(3)	O(22)–Tb(4)–N(8)	141(3)
O(15)–Tb(4)–N(8)	78(3)	O(20)–Tb(4)–N(8)	143(3)
O(23)–Tb(4)–N(8)	74(3)	O(24)–Tb(4)–N(8)	84(3)
O(13)–Tb(4)–N(8)	75(3)	O(22)–Tb(4)–N(7)	78(3)
O(15)–Tb(4)–N(7)	136(3)	O(20)–Tb(4)–N(7)	147(3)
O(23)–Tb(4)–N(7)	110(3)	O(24)–Tb(4)–N(7)	68(3)
O(13)–Tb(4)–N(7)	70(3)	N(8)–Tb(4)–N(7)	63(3)
O(22)–Tb(4)–O(14)	74(3)	O(15)–Tb(4)–O(14)	67(3)
O(20)–Tb(4)–O(14)	75(3)	O(23)–Tb(4)–O(14)	135(3)
O(24)–Tb(4)–O(14)	158(3)	O(13)–Tb(4)–O(14)	51(2)
N(8)–Tb(4)–O(14)	117(3)	N(7)–Tb(4)–O(14)	113(3)

[a] Symmetry transformations used to generate equivalent atoms: #1 $-x, -y + 1, -z$; #2 $-x + 1, -y + 1, -z + 1$.

tween the two central terbium ions (Tb3···Tb4) is 3.951 Å. The average Tb3–O and Tb3–N bond lengths are 2.436 Å and 2.56 Å, respectively. The O–Tb3–O angles range from 53.00(3) to 144.00(3)°; the N–Tb3–N angle is 63(3)°. The two pyridyl rings of 2,2′-bpy in the dimer are not coplanar, and have a dihedral angle of 10.1°.

The structure of complex **3** contains three independent centrosymmetric units [Figure 3, parts a–c]. Figure 3 (part b) is different from Figure 3 (part a) or Figure 3 (part c) owing to the different bonding mode of the carboxyl groups, similar to the previously reported complex [Eu_2(*p*-$CH_3C_6H_4COO$)(phen)$_2$], which contains two nonequivalent binuclear molecules.[9] The mean Tb1–O distance (2.459 Å) in Figure 3 (part a) is longer than that of Tb2–O (2.372 Å) in Figure 3 (part b), and the distance between the central metal ions Tb1···Tb1A (4.137 Å) in Figure 3 (part a) is shorter than that of Tb2···Tb2A (4.260 Å) in Figure 3 (part b). A similar feature in the following discussion for complex **4** can be found due to the different bonding mode of the carboxyl groups. The Tb1–O mean distance in Figure 3 (part a) is close to that of Tb3–O (2.436 Å) in Figure 3 (part c), and the distance between the central metal ions Tb1···Tb1A in Figure 3 (part a) is close to that of Tb3···Tb4 (3.951 Å) in Figure 3 (part c) due to the similar coordination environments of $Tb1^{3+}$ and $Tb3^{3+}$. The corresponding O–Tb–O bond angles for the three molecules are in agreement with each other. For coordinated 2,2′-bpy, the two pyridyl rings are not coplanar in the complex, although the Tb–N bond lengths and the N–Tb–N bond angles for the three molecules are in good agreement.

Structural Description of a phen-Containing Terbium 2-Fluorobenzoate Complex with Two Different Compositions, [Tb(2-FBA)$_3$·phen·CH_3CH_2OH]$_2$ and [Tb(2-FBA)$_3$·phen]$_2$ (4)

The structure of complex **4** is shown in Figure 4 (parts a and b). Obviously, the structure of complex **4** contains two nonequivalent binuclear molecules, namely [Tb(2-FBA)$_3$·phen·CH_3CH_2OH]$_2$ (Figure 4, part a) and [Tb(2-FBA)$_3$·phen]$_2$ (Figure 4, part b); both dimers are centrosymmetric.

Figure 4 (part a) shows that four 2-FBA groups function as a bridge and connect two terbium ions to form a dimeric molecule with a Tb1···Tb1A separation of 4.423 Å. Each $Tb1^{3+}$ ion is further bonded to a monodentate 2-FBA group, one chelated phen, and one ethanol molecule to give a coordination number of eight. The $Tb1^{3+}$ ion is in a distorted square-antiprism arrangement in which the dihedral angle between the top (atoms O1, O5, O2A, O6A) and bottom (atoms O3, O7, N1, N2) planes is 3.0°. The 2-FBA groups link the $Tb1^{3+}$ ion in monodentate and bidentate-bridging coordination modes. The Tb1–O(carboxyl) distances are in the range 2.30(4) to 2.43(4) Å, with an average distance of 2.348 Å, and the O–Tb1–O(carboxyl) angles range from 72.90(13) to 144.9(13)° (Table 4). The bond length for the oxygen atom of the ethanol molecule to the terbium ion is 2.575 Å. The coordinated ethanol molecules

 © 2005 Wiley-VCH Verlag GmbH & Co. KGaA, Weinheim

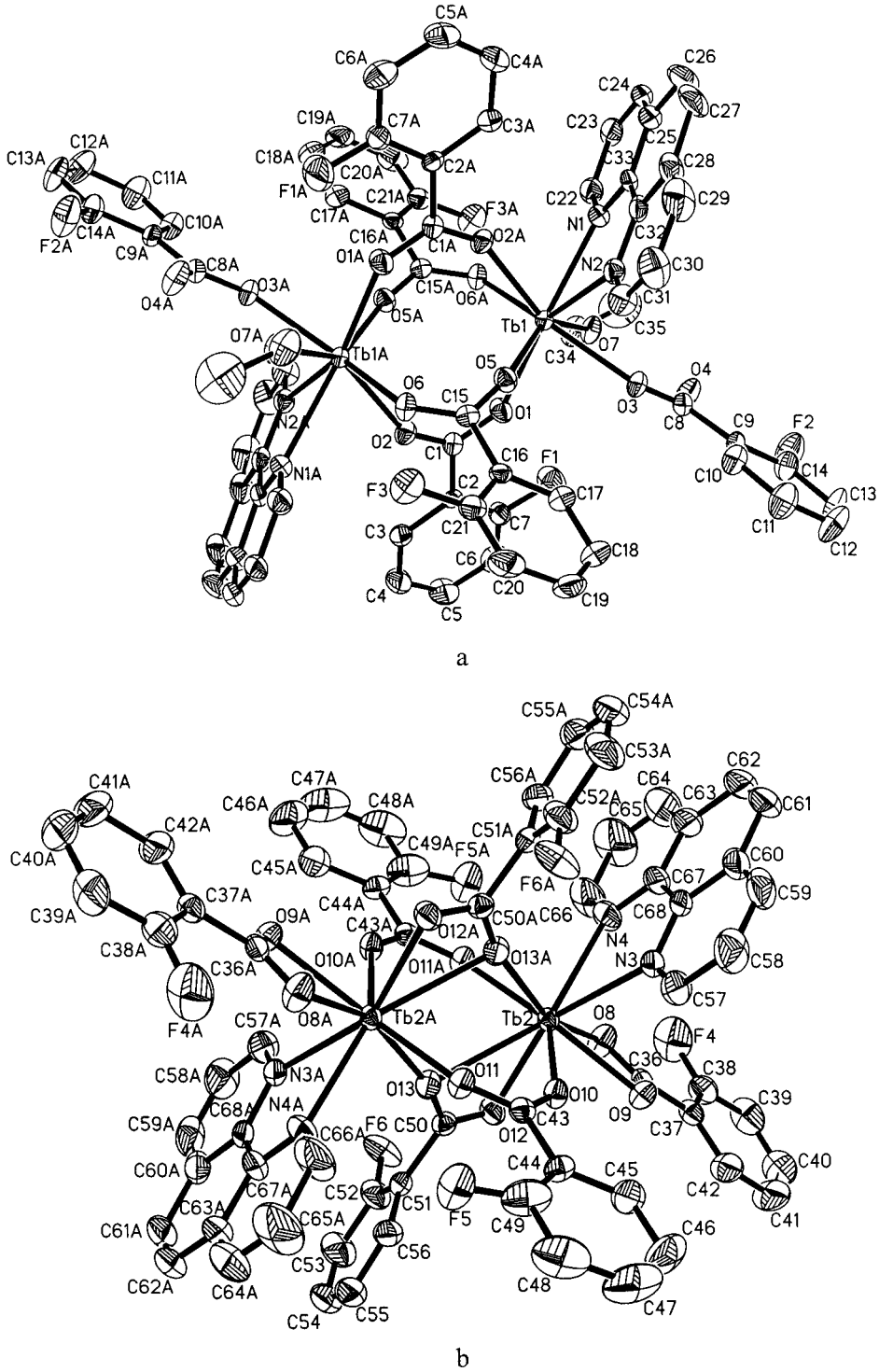

Figure 4. Molecular structures of complex **4**. (a) and (b) show two different structures. All hydrogen atoms have been omitted for clarity; the thermal ellipsoids are shown at the 30% probability level.

form hydrogen bonds with uncoordinated carboxyl oxygen atoms (O7–H7···O4, with an O7···O4 distance of 2.578 Å and O7–H7···O4 angle of 136.18°). The phen ligand acts as a typical chelating ligand coordinating to the terbium ion, with an average Tb1–N distance of 2.43 Å and N–Tb1–N angle of 63.7(16)°.

Figure 4 (part b) shows that the $Tb2^{3+}$ ion is surrounded by nine atoms, seven oxygen atoms from five 2-FBA groups and two nitrogen atoms from one phen molecule. The $Tb2^{3+}$ ion is in a distorted monocapped square-antiprism configuration. Atoms O10, O12, O11A, and O13A and O8, O9, N3, and N4 form the upper and lower square-planes,

 © 2005 Wiley-VCH Verlag GmbH & Co. KGaA, Weinheim

Table 4. Bond lengths [Å] and angles [°] for complex **4**.

Tb(1)–O(5)	2.30(4)	Tb(1)–O(1)	2.34(4)
Tb(1)–O(6)#1[a]	2.36(4)	Tb(1)–O(2)#1	2.37(4)
Tb(1)–O(3)	2.37(4)	Tb(1)–O(7)	2.43(4)
Tb(1)–N(1)	2.55(5)	Tb(1)–N(2)	2.60(5)
Tb(2)–O(13)#2	2.30(4)	Tb(2)–O(10)	2.34(4)
Tb(2)–O(11)#2	2.36(4)	Tb(2)–O(9)	2.42(4)
Tb(2)–O(12)	2.44(4)	Tb(2)–O(8)	2.50(4)
Tb(2)–N(4)	2.55(5)	Tb(2)–N(3)	2.65(5)
Tb(2)–O(13)	2.71(4)		
O(5)–Tb(1)–O(1)	74.5(14)	O(5)–Tb(1)–O(6)#1	121.5(13)
O(1)–Tb(1)–O(6)#1	80.2(14)	O(5)–Tb(1)–O(2)#1	78.3(13)
O(1)–Tb(1)–O(2)#1	122.9(14)	O(6)#1–Tb(1)–O(2)#1	72.9(13)
O(5)–Tb(1)–O(3)	83.6(13)	O(1)–Tb(1)–O(3)	84.3(14)
O(6)#1–Tb(1)–O(3)	144.9(13)	O(2)#1–Tb(1)–O(3)	140.6(13)
O(5)–Tb(1)–O(7)	143.4(14)	O(1)–Tb(1)–O(7)	75.3(14)
O(6)#1–Tb(1)–O(7)	72.5(13)	O(2)#1–Tb(1)–O(7)	136.6(13)
O(3)–Tb(1)–O(7)	73.2(13)	O(5)–Tb(1)–N(1)	138.6(15)
O(1)–Tb(1)–N(1)	146.9(15)	O(6)#1–Tb(1)–N(1)	79.0(15)
O(2)#1–Tb(1)–N(1)	74.4(14)	O(3)–Tb(1)–N(1)	98.4(14)
O(7)–Tb(1)–N(1)	73.9(15)	O(5)–Tb(1)–N(2)	78.2(15)
O(1)–Tb(1)–N(2)	145.2(15)	O(6)#1–Tb(1)–N(2)	133.3(15)
O(2)#1–Tb(1)–N(2)	70.7(14)	O(3)–Tb(1)–N(2)	71.5(14)
O(7)–Tb(1)–N(2)	118.6(14)	N(1)–Tb(1)–N(2)	63.7(16)
O(13)#2–Tb(2)–O(10)	77.7(14)	O(13)#2–Tb(2)–O(11)#2	74.3(14)
O(10)–Tb(2)–O(11)#2	135.2(13)	O(13)#2–Tb(2)–O(9)	143.5(14)
O(10)–Tb(2)–O(9)	75.0(13)	O(11)#2–Tb(2)–O(9)	141.9(13)
O(13)#2–Tb(2)–O(12)	123.9(14)	O(10)–Tb(2)–O(12)	87.5(15)
O(11)#2–Tb(2)–O(12)	80.2(15)	O(9)–Tb(2)–O(12)	78.7(14)
O(13)#2–Tb(2)–O(8)	155.7(16)	O(10)–Tb(2)–O(8)	125.3(15)
O(11)#2–Tb(2)–O(8)	90.5(14)	O(9)–Tb(2)–O(8)	52.5(14)
O(12)–Tb(2)–O(8)	70.1(15)	O(13)#2–Tb(2)–N(4)	90.0(18)
O(10)–Tb(2)–N(4)	138.1(18)	O(11)#2–Tb(2)–N(4)	76.2(17)
O(9)–Tb(2)–N(4)	94.4(17)	O(12)–Tb(2)–N(4)	130.9(19)
O(8)–Tb(2)–N(4)	67.7(19)	O(13)#2–Tb(2)–N(3)	72.9(15)
O(10)–Tb(2)–N(3)	75.7(16)	O(11)#2–Tb(2)–N(3)	126.2(16)
O(9)–Tb(2)–N(3)	77.2(15)	O(12)–Tb(2)–N(3)	153.5(16)
O(8)–Tb(2)–N(3)	103.1(16)	N(4)–Tb(2)–N(3)	62(2)
O(13)#2–Tb(2)–O(13)	74.7(14)	O(10)–Tb(2)–O(13)	66.3(13)
O(11)#2–Tb(2)–O(13)	73.0(13)	O(9)–Tb(2)–O(13)	114.5(13)
O(12)–Tb(2)–O(13)	50.0(13)	O(8)–Tb(2)–O(13)	119.4(14)
N(4)–Tb(2)–O(13)	148.3(17)	N(3)–Tb(2)–O(13)	134.1(15)

[a] Symmetry transformations used to generate equivalent atoms: #1 $-x + 2, -y + 2, -z$; #2 $-x + 1, -y, -z + 1$.

respectively, with a dihedral angle between them of 8.2°; atom O13 caps the upper plane. The 2-FBA ligands act in chelating, bidentate-bridging, and chelating-bridging modes. Two terbium ions are connected by four 2-FBA groups − two bidentate-bridging and two chelating-bridging − to give a Tb2···Tb2A distance of 3.985 Å. In addition, each terbium ion is chelated by one 2-FBA group and one phen ligand. Obviously, Figure 4 (part b) is unlike Figure 4 (part a) but quite similar to Figure 3 (part a) and Figure 3 (part c). The Tb2–O bond lengths range from 2.30(4) to 2.71(4) Å, with an average distance of 2.439 Å, and the O–Tb2–O angles range from 52.5(14) to 155.7(16)°. The phen molecule chelates the terbium ion with an average Tb2–N bond length of 2.60 Å and N–Tb2–N angle of 62(2)°.

However, there are very few cases where two molecules with two different compositions and structures exist in an asymmetric unit. By comparing Figure 4 (part b) with Figure 4 (part a), their formulas, the coordination environment of central ion and coordination mode of carboxylato groups are different. The differences result in different distances of Tb–O(carboxyl) and Tb···Tb. The mean Tb2–O(carboxyl) distance of 2.439 Å in Figure 4 (part b) is longer than that of Tb1–O(carboxyl) (2.348 Å) in Figure 4 (part a), and the distance between the central metal ions (Tb2···Tb2A) (3.985 Å) in Figure 4 (part b) is shorter than that between Tb1 and Tb1A (4.423 Å) in Figure 4 (part a). A similar feature was observed in complex **3**. The fact that Ln^{3+} ions are bridged by chelating-bridging carboxylato groups results in a larger Ln–O distance and a smaller Ln–Ln distance.

Figure 3 (parts a, b and c) and Figure 4 (part b) exhibit common structures of lanthanide carboxylate complexes with 2,2′-bpy or phen, in which the carboxylate groups coordinate to lanthanide in different modes, such as monodentate, chelating-bidentate, bidentate-bridging, and tridentate-bridging. Generally, ternary lanthanide complexes containing a monoacid and 2,2′-bpy or phen are centrosymmetric dimers with a coordination number at the metal of eight or nine. The structure of eight-coordinate complexes is the same as that in Figure 3b, where two metal ions are linked together by four carboxylato groups with a bidentate-bridging coordination mode, and each metal ion is also chelated by one carboxylato group and one 2,2′-bpy or phen molecule, such as in $[Sm_2(4\text{-}CH_3C_6H_4COO)_6(2,2'\text{-}bpy)_2]$,[10] $[Eu(m\text{-}CH_3C_6H_4COO)_3(phen)](H_2O)$,[11] and $[Eu_2(3,4\text{-}DMBA)_6(phen)_2]$.[12] The structure of nine-coordinate complexes is the same as those in Figure 3 (parts a and c) and Figure 4 (part b), where two metal ions are linked together by four carboxylato groups with bidentate-bridging and chelating-bridging modes, and each metal ion is also chelated by one carboxylato group and one 2,2′-bpy or phen ligand, such as in $[Eu(2,3\text{-}DMOBA)_3{\cdot}bpy]_2$ (2,3-DMOBA = 2,3-dimethoxybenzoate),[15] $[Ln_2(O_2CCH_3)_6(phen)_2]$ (Ln = Ce, Gd),[16] and $[La_2(propionato)_6(2,2'\text{-}bpy)_2]$.[17] Eight- or nine-coordinate complexes are formed depending on the different bridges over the two central metal ions of the four carboxyl groups, namely whether the four carboxylato groups are all in a bidentate-bridging mode or two of them are in a bidentate-bridging mode and the other two in a chelating-bridging mode. The phen or 2,2′-bpy molecule coordinates to the metal in conventional chelation through two N atoms to form a five-membered ring. However, although the two phenyl rings are coplanar in the phen complexes since this molecule is rigid, the two pyridyl rings are not coplanar in 2,2′-bpy complexes since this is a flexible ligand.

Fluorescence Spectra

The complexes **1**, **3**, and **4** emit a bright-green light in the solid state under UV light. Fluorescence was observed in the range of 400–700 nm by selective excitation at 353 nm, as shown in Figure 5 (parts a, b, and c). There are four main emission peaks in the luminescence spectra at

 © 2005 Wiley-VCH Verlag GmbH & Co. KGaA, Weinheim

488, 543, 584, and 618 nm, corresponding to the transition between the first excited state ($^5D_4$) and the ground-state multiplet ($^7F_{6-3}$) of the Tb^{3+} ion, namely $^5D_4 \rightarrow {}^7F_6$, $^5D_4 \rightarrow {}^7F_5$, $^5D_4 \rightarrow {}^7F_4$, and $^5D_4 \rightarrow {}^7F_3$, respectively. The most intense emission band is at 543 nm. The luminescence spectra of complexes **1** and **3** are similar to that of complex **4**. The splits observed in the emission bands correspond to $^5D_4 \rightarrow {}^7F_6$, $^5D_4 \rightarrow {}^7F_5$. Shoulder peaks at 486 nm, 542 and 548 nm were observed. The nonluminescence of complex **2** may be due to 4,4′-bpy coordinating in a monodentate manner, which means that the ligand-to-metal energy transfer processes are not effective.

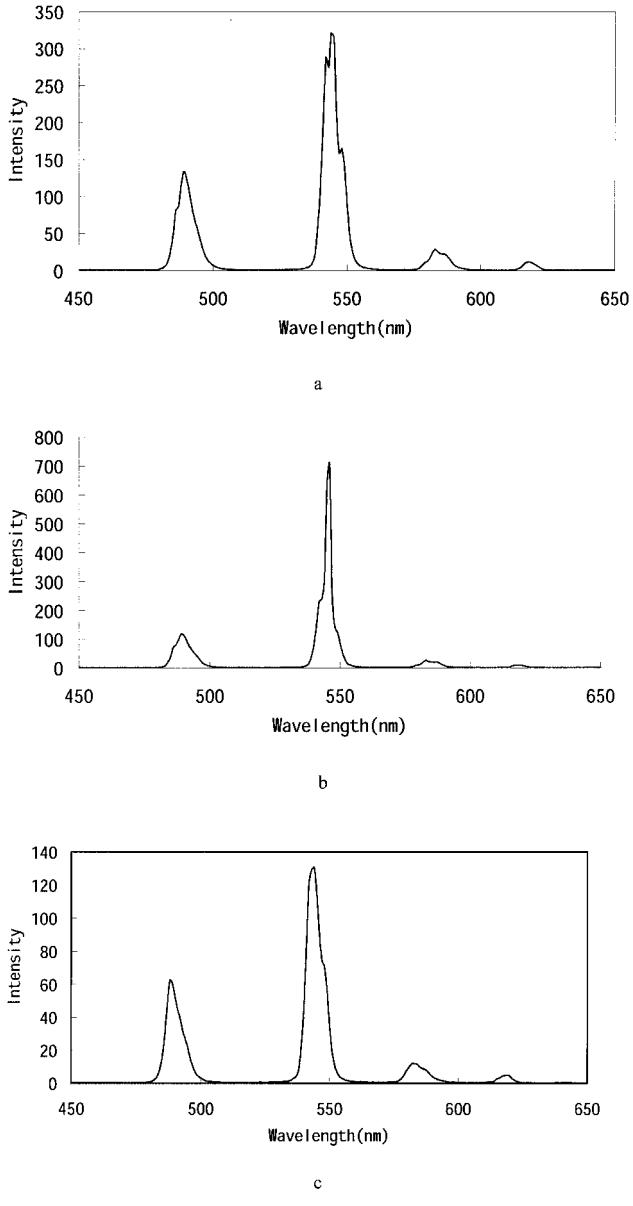

Figure 5. The fluorescence spectra of complexes **1** (a; λ_{exc} = 353 nm), **3** (b; λ_{exc} = 353 nm), and **4** (c; λ_{exc} = 353 nm).

Conclusion

The complexes discussed above were constructed based on terbium and 2-fluorobenzoic acid, with 4,4′-bpy, 2,2′-bpy, or phen acting as co-ligands to generate terbium complexes with various structures. Complex **1** is a dimeric molecule, unlike the majority of known lanthanide complexes containing a monoacid, which are one-dimensional polymers. Complex **2** is one of the very few lanthanide complexes containing a coordinated 4,4′-bpy molecule, complex **3** contains three independent binuclear molecules, and complex **4** contains two different binuclear molecules. Several other structural features of these complexes are of particular importance. In particular, complexes **1**, **3**, and **4** exhibit good fluorescence properties.

Experimental Section

Fluorescence Spectroscopy: Fluorescence spectra were measured on an F-4500 FL spectrophotometer in the solid state at room temperature.

$[Tb(2\text{-}FBA)_3 \cdot (2\text{-}HFBA) \cdot H_2O]_2$ (1): 2-Fluorobenzoic acid (1.5 mmol) was dissolved in the appropriate amount of ethanol. The pH of the solution was controlled in the range 6–7 by addition of 2 M NaOH solution. An ethanolic solution of $TbCl_3 \cdot 6H_2O$ (0.5 mmol) was then added dropwise. The mixture was heated under reflux with stirring for 3 h. Single crystals were obtained from the mother liquor after a month at room temperature. Yield: 0.0969 g (26.39%). $C_{56}H_{38}F_8O_{18}Tb_2$ (1468.7): calcd. C 45.80, H 2.61; found C 45.39, H 3.00.

$[Tb(2\text{-}FBA)_3 \cdot (4,4'\text{-}bpy) \cdot H_2O]_n$ (2): 2-Fluorobenzoic acid (1.5 mmol) was dissolved in the appropriate amount of ethanol. The pH of the solution was controlled in the range 6–7 by addition of 2 M NaOH solution. An ethanolic solution of 4,4′-bipyridine (0.5 mmol) and an ethanolic solution of $TbCl_3 \cdot 6H_2O$ (0.5 mmol) were then added dropwise, successively. The mixture was heated under reflux with stirring for 2 h. Single crystals were obtained from the mother liquor after seven weeks at room temperature. Yield: 0.1200 g (31.98%). $C_{62}H_{44}F_6N_4O_{14}Tb_2$ (1500.9): calcd. C 49.62, H 2.96, N 3.73; fC 51.18, H 3.06, N 4.32.

$[Tb(2\text{-}FBA)_3 \cdot (2,2'\text{-}bpy)]_2$ (3): When 2,2′-bpy was used instead of 4,4′-bpy, complex **3** was obtained. Yield: 0.1959 g (53.50%). $C_{124}H_{80}F_{12}N_8O_{24}Tb_4$ (2929.64): calcd. C 50.84, H 2.75, N 3.82; found C 50.82, H 3.06 N, 3.80.

$[Tb(2\text{-}FBA)_3 \cdot phen]_2$ and $[Tb(2\text{-}FBA)_3 \cdot phen \cdot CH_3CH_2OH]_2$ (4): When phen was used instead of 4,4′-bpy, complex **4** was obtained. Yield: 0.1983 g (50.89%). $C_{136}H_{92}F_{12}N_8O_{26}Tb_4$ (3117.9): calcd. C 52.39, H 2.97, N 3.59; found C 52.75, H 2.69, N 3.61.

X-ray Crystallographic Study: X-ray crystal data collection for the complexes was performed on a Bruker Smart 1000 CCD diffractometer with monochromated Mo-K_α radiation (λ = 0.71073 Å) at 293 K (Table 5). Semi-empirical absorption corrections were applied using the SADABS program. All calculations were carried out with SHELXS-97 and SHELXL-97.[18,19] The structures were solved by direct methods and refined on $|F|^2$ by full-matrix least-squares methods.

CCDC-250512, -250511, -250513, and -250514 (for **1**–**4**, respectively) contain the supplementary crystallographic data for this paper. These data can be obtained free of charge from The Cambridge Crystallographic Data Centre via www.ccdc.cam.ac.uk/data_request/cif.

 © 2005 Wiley-VCH Verlag GmbH & Co. KGaA, Weinheim

Table 5. Crystal data and structure refinement for complexes **1**–**4**.

Compound	**1**	**2**	**3**	**4**
Empirical formula	$C_{56}H_{38}F_8O_{18}Tb_2$	$C_{62}H_{44}F_6N_4O_{14}Tb_2$	$C_{124}H_{80}F_{12}N_8O_{24}Tb_4$	$C_{136}H_{92}F_{12}N_8O_{26}Tb_4$
Formula mass	1468.70	1500.85	2929.64	3117.86
Crystal system	triclinic	triclinic	triclinic	triclinic
Space group	$P\bar{1}$	$P\bar{1}$	$P\bar{1}$	$P\bar{1}$
Unit-cell dimensions	1	2	1	2
a [Å]	9.100(7)	9.745(3)	11.281(4)	11.261(3)
b [Å]	11.548(9)	12.770(4)	21.845(7)	12.627(4)
c [Å]	13.600(11)	13.312(4)	22.213(7)	22.746(7)
α [°]	110.625(12)	113.134(4)	93.142(6)	81.154(5)
β [°]	92.949(13)	104.747(5)	90.885(6)	78.244(5)
γ [°]	91.065(13)	97.008(5)	91.585(6)	80.697(5)
Volume [Å^3]	1334.8(18)	1426.6(8)	5463(3)	3100.3(16)
Z	1	1	2	1
$d_{calcd.}$ [g cm^{-3}]	1.827	1.747	1.781	1.670
T [K]	293(2)	293(2)	293(2)	293(2)
λ [Å]	0.71073	0.71073	0.71073	0.71073
μ [mm^{-1}]	2.732	2.550	2.659	2.350
F(000)	720	740	2880	1540
Limiting indices	$-7 \le h \le 10$ $-13 \le k \le 13$ $-15 \le l \le 16$	$-7 \le h \le 11$ $-14 \le k \le 15$ $-15 \le l \le 15$	$-12 \le h \le 13$ $-25 \le k \le 25$ $-20 \le l \le 26$	$-7 \le h \le 13$ $-14 \le k \le 15$ $-25 \le l \le 27$
Reflections collected/unique	6908/4692 R(int.) = 0.0547	7414/4992 R(int.) = 0.0191	28575/19190 R(int.) = 0.173	16241/10893 R(int.) = 0.0283
Final R indices [$I > 2\sigma(I)$]	R_1 = 0.0688 wR_2 = 0.1678	R_1 = 0.0377 wR_2 = 0.1123	R_1 = 0.0790 wR_2 = 0.1671	R_1 = 0.0382 wR_2 = 0.0778
R indices (all data)	R_1 = 0.0980 wR_2 = 0.1919	R_1 = 0.0455 wR_2 = 0.1223	R_1 = 0.1686 wR_2 = 0.2039	R_1 = 0.0685 wR_2 = 0.0982
Largest diff. peak and hole [e Å^{-3}]	2.576 and –2.742	0.939 and –0.736	2.692 and –3.145	0.833 and –0.649

Acknowledgments

We are grateful to the Natural Science Foundation of Beijing (No. 2022007). This project was also sponsored by the Science and Technology Program of the Beijing Municipal Education Commission (KM200510028007) and the Scientific Research Foundation for Returned Overseas Chinese Scholars, Beijing Municipal Government.

[1] C. Seward, N. X. Hu, S. Wang, *J. Chem. Soc., Dalton Trans.* **2001**, 134–137.
[2] T. M. Reineke, M. Eddaoudi, M. Fehr, D. Kelley, O. M. Yaghi, *J. Am. Chem. Soc.* **1999**, *121*, 1651–1657.
[3] L. Pan, K. M. Adams, H. E. Hernandez, X. Wang, C. Zheng, Y. Hattori, K. Kaneko, *J. Am. Chem. Soc.* **2003**, *125*, 3062–3067.
[4] Y. Wang, X. J. Zheng, W. J. Zhuang, L. P. Jin, *Eur. J. Inorg. Chem.* **2003**, 3572–3582.
[5] J. F. Ma, Z. S. Jin, J. Z. Ni, *Acta Chim. Sinica* **1993**, *51*, 265–272.
[6] T. N. Polynova, B. B. Smolyar, T. F. Filippova, M. A. Porai-Koshits, S. B. Pirkes, *Koord. Khim.* **1987**, *13*, 130–135.
[7] Q. H. Jin, X. Li, Y. Q. Zou, *Acta Crystallogr., Sect. C* **2001**, *57*, 676–677.
[8] X. Li, Y. Q. Zou, B. Zheng, H. M. Hu, *Acta Crystallogr., Sect. C* **2004**, *60*, m197–m199.
[9] L. P. Jin, M. Z. Wang, G. L. Cai, *Sci. China, Ser. B* **1994**, *24*, 577–583.
[10] X. Li, Y. Q. Zou, *Z. Kristallogr.* **2003**, *218*, 448–450.
[11] L. P. Jin, R. F. Wang, M. Z. Wang, G. L. Cai, S. X. Liu, J. L. Huang, *Chem. J. Chin. Univ.* **1993**, *14*, 1195–1200.
[12] L. Y. Wang, X. J. Zheng, L. P. Jin, S. Z. Lu, *Chem. J. Chin. Univ.* **1999**, *20*, 1110–1114.
[13] X. Li, X. Zheng, L. Jin, S. Lu, W. Qin, *J. Mol. Struct.* **2000**, *519*, 85–91.
[14] X. Li, X. Zheng, L. Jin, S. Lu, J. Zhang, *J. Mol. Struct.* **2001**, *559*, 341–346.
[15] X. Li, L. P. Jin, X. J. Zheng, S. Z. Lu, J. H. Zhang, *J. Mol. Struct.* **2002**, *607*, 59–67.
[16] A. Panagiotopoulos, T. F. Zafiropoulos, S. P. Perlepes, E. Bakalbassis, I. Masson-Ramade, O. Kahn, A. Terzis, C. P. Raptopoulou, *Inorg. Chem.* **1995**, *34*, 4918–4920.
[17] J. S. Brodkin, B. M. Foxman, W. Clegg, J. T. Cressey, D. R. Harbron, P. A. Hunt, B. P. Straughan, *Chem. Mater.* **1996**, *8*, 242–247.
[18] *Phase Annealing in SHELX-90: Direct Methods for Larger Structures*: G. M. Sheldrick, *Acta Crystallogr., Sect. A* **1990**, *46*, 467–473.
[19] G. M. Sheldrick, *SHELXL97, Program for X-ray Crystal Structure Solution*, University of Göttingen, Germany, **1997**.

Received January 2, 2005
Published Online: June 21, 2005

 © 2005 Wiley-VCH Verlag GmbH & Co. KGaA, Weinheim

Fragmentation of Alkoxo(catecholato)vanadium(V) Complexes $[(C_6H_4O_2)V(OR^1)(OR^2)]^+$ in the Gas Phase

Malgorzata Kaczorowska[a] Detlef Schröder,*[a] and Helmut Schwarz[a]

Keywords: Alkoxo complexes / Catecholates / Elimination / Hydrogen migration / Vanadium

Electrospray ionization (ESI) mass spectrometry is used to investigate the gas-phase dissociation behavior of vanadium(V) complexes $[(C_6H_4O_2)V(OR^1)(OR^2)]^+$ containing two identical or different alkoxy groups (R^1, R^2 = CH_3, C_2H_5, *n*-C_3H_7, *i*-C_3H_7 and *t*-C_4H_9) and a catecholato ligand ($C_6H_4O_2$). The fragmentation reactions of the complexes are studied by collision-induced dissociation (CID) and labeling experiments. For $[(C_6H_4O_2)V(OR^1)(OR^2)]^+$ cations with alkoxo groups larger than methyl, a trend for preferential evaporation of hydrocarbon fragments is observed, followed by expulsion of neutral alcohols. Further, the CID spectra of all complexes show a signal which can be assigned to the complex $[(C_6H_4O_2)VO]^+$.

(© Wiley-VCH Verlag GmbH & Co. KGaA, 69451 Weinheim, Germany, 2005)

Introduction

Over the past years, interest in transition-metal oxides has grown steadily, due to the promising role which these compounds play in heterogeneous catalysis.[1] Metal oxides often serve as catalysts which are characterized by high selectivities and activities in many processes.[2] An important group of transition-metal catalysts are vanadium oxides,[3] used, for example, in the oxidation of sulfur dioxide in the industrial production of sulfuric acid and for the oxidation of hydrocarbons, e.g. propane and *n*-butane, to valuable products such as maleic acid and its anhydride. With respect to the oxidation of saturated hydrocarbons, mixed vanadium oxide/vanadium phosphate oxide (VPO) is of particular interest as a catalyst.[4]

Interest in transition-metal alkoxides arises from their potential role in metal-mediated oxidation reactions. High-valent transition-metal oxo complexes have been recognized to enable activations of C–H or O–H bonds in many important chemical and biological processes.[5] In general, C–H bond activation of alkanes by a transition-metal oxide [M]=O can occur in two different ways (Scheme 1). The first conceivable route (a) is transfer of a hydrogen atom from a C–H bond to the oxygen atom concomitant with bonding of the alkyl residue to the metal atom. The alternative reaction (b) involves C–O bond formation which yields a metal alkoxide concomitant with an additional metal–hydrogen bond.

For many reactions of transition-metal oxides with alkanes it is not easy to predict a clear preference for one of these routes. Experimental data needed for such a prediction are often not available because many of the relevant species are either difficult to isolate or elusive. Theoretical approaches are an attractive alternative under these circumstances, although application of quantum mechanical calculations to coordinatively unsaturated transition-metal compounds is all but trivial. In particular, many reactions of transition-metal oxides involve many low-lying excited electronic states.[6–9] Theoretical investigations of the activation of methane by the bare metal oxide cation FeO^+, which serves as a prototype for C–H bond activation of alkanes by transition-metal oxides in the gas phase,[6,10] predict preference of reaction (a), but route (b) is also not too energy-demanding and is conceivable as well.[11] Further, the formation of alkoxometal complexes has been proposed in the reactions of oxides of group V–VIII transition metals with methanol.[12] Metal alkoxides are also important intermediates in the dihydroxylation of olefins by OsO_4,[13] and reactions of the chromium dioxide cation with hydrocarbons in the gas phase.[14] With respect to our particular interest in vanadium alkoxides, the presence of $VOCH_3$ units has been considered essential for the selective oxidation of methanol to formaldehyde.[15,16]

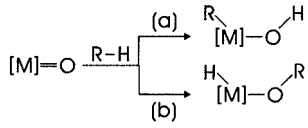

Scheme 1.

In this article, we present an experimental study of composite vanadium(V) cations in the gas phase, which contain two identical or different alkoxy groups. The interest is focused on the examination of the effects of the substituents on the dissociation behavior of the complexes. More simple vanadium complexes like trimethylvanadate have been suc-

[a] Institut für Chemie der Technischen Universität Berlin, Strasse des 17. Juni 135, 10623 Berlin, Germany

cessfully examined before by various spectrometric means.[17] For our investigation, we aimed at producing vanadium(v) complexes of the type $[(L)V(OR^1)(OR^2)]^+$ in the gas phase, where R^1, R^2 = CH_3, C_2H_5, *n*-C_3H_7, *i*-C_3H_7, and *t*-C_4H_9. Our first choice for the ligand L to which the vanadium atom is connected by two single bonds through oxygen atoms was $[(C_2H_4O_2)V(OR^1)(OR^2)]^+$, where $C_2H_4O_2$ corresponds to glycolate. In this case, however, the fragmentations were not unequivocal, because several of the fragment ions observed can be assigned to dissociation of alkoxy groups as well as to the dissociation of the glycolate unit. Therefore, we switched to the more robust catechol ligand, for which such a problem does not exist (see below). Our focus lies on alkoxovanadium(v) complexes, which might be formed as transient intermediates in the oxidation of alkanes by vanadium oxides, because low-valent vanadium oxide cations and clusters cannot oxidize alkanes.[18–21]

In the experiments, electrospray ionization (ESI) mass spectrometry is employed, a technique which permits transfer of ionic complexes into the gas phase directly from solution, with a variable degree of desolvation or fragmentation. The possibility of analyzing the complexes in the gas phase in the absence of solvent provides essential information about ion structures and stoichiometries. Understanding of the gas-phase chemistry of transition-metal alkoxides can therefore provide insight into their fundamental properties at a molecular level and might thereby help to explain their behavior in the condensed phase.

Results

ESI of $VOCl_3$,dissolved in different alcohols and mixtures of alcohols with a small amount of catechol, leads to the formation of the desired vanadium(v) complexes $[(C_6H_4O_2)V(OR^1)(OR^2)]^+$. The abundances of the ions of interest critically depend on the concentration of catechol as well as the mixing ratio of the alcohols. If the concentration of catechol in the solution is too high, complexes with a $[(C_6H_4O_2)V(C_6H_4O_2)]^+$ core prevail. Likewise, the yields of the mixed alkoxy complexes are poor, when the concentration of the second alcohol is too small, as formation of $[(C_6H_4O_2)V(OR^1)_2]^+$ prevails.

In the cation ESI spectra of $VOCl_3$ in methanol with catechol under soft ionization conditions, the monocationic vanadium(v) complexes shown in Scheme 2 are observed. In structure **I**, the metal center V^V is connected with the aromatic ring through the oxygen atoms of catechol and forms an additional double bond with the vanadyl oxygen atom. This cation appears in the mass spectra of all mixtures examined.

The CID spectrum of mass-selected **I** (*m*/*z* = 175) shows a mass difference of Δ*m* = –28 (Table 1), which may be assigned to expulsion of CO or C_2H_4; given the $VC_6H_4O_3^+$ stoichiometry of **I**, loss of C_2H_4 appears unlikely, however. By analogy, Δ*m* = –44 is assigned to loss of CO_2. The CID spectra of **I** recorded at higher collision energies are dominated by VO^+ with additional signals corresponding to Δ*m* = –28, –44, –56, and –72, which can be assigned to CO, CO_2, two molecules of CO, and possibly CO + CO_2, respectively. For the cation **II** (*m*/*z* = 193), containing two hydroxy groups, the main process upon CID is loss of a water molecule (Δ*m* = –18), which formally leads to **I**. Likewise the strong signal for Δ*m* = –32 evolving in the case of complex **III** (*m*/*z* = 207) can be assigned to the loss of methanol. Similar to cation **III**, the CID spectra of complex **IV** containing two methoxy groups bound to a vanadium(v) center are characterized by the elimination of methanol (Δ*m* = –32), which can be explained by the mechanism depicted in Scheme 3. The key step corresponds to a hydrogen migration from the carbon atom of one to the oxygen atom of the second methoxy group. This scenario also accounts for the experimentally observed loss of formaldehyde (Δ*m* = –30). The CID spectrum is dominated, however, by the expulsion of a CH_3 radical (Δ*m* = –15), a process which is unique for the complex with R^1 = R^2 = CH_3; the fragment with Δ*m* = –45 is assigned to a combined loss of CH_3 + CH_2O. The CID spectra of mass-selected $[(C_6H_4O_2)V(OCD_3)_2]^+$ fully confirm theses conclusions in that preferential eliminations of CD_3 (Δ*m* = –18), CD_2O (Δ*m* = –32), and CD_3OD (Δ*m* = –36) are observed.

Table 1. Neutral losses (given as mass differences, Δ*m*) observed upon CID of the mass-selected cations **I–IV**, generated by ESI of $VOCl_3$ with catechol in methanol. Data given relative to the base peak (100) of the CID products at E_{lab} = 3 eV.

	–15	–18	–28	–30	–32	–44	–45
I			100			60	
II		100	96				
III					100		
IV	100			55	45		27

The CID spectra of the mixed methoxy complexes $[(C_6H_4O_2)V(OCH_3)(OC_2H_5)]^+$, $[(C_6H_4O_2)V(OCH_3)(OC_3H_7)]^+$ and $[(C_6H_4O_2)V(OCH_3)\{OC(CH_3)_3\}]^+$ are dominated by losses of corresponding alkenes generated from the larger alkoxy group, i.e. C_2H_4, C_3H_6, and C_4H_8, respectively (Table 2). Alkene elimination leads to the formation of **III**, prior to further degradation to structure **I** (Scheme 4). Minor dissociation pathways correspond to the expulsion of alcohols: methanol and ethanol from $[(C_6H_4O_2)V(OCH_3)(OC_2H_5)]^+$, methanol and propanol for the $[(C_6H_4O_2)V(OCH_3)(OC_3H_7)]^+$ complex, and finally,

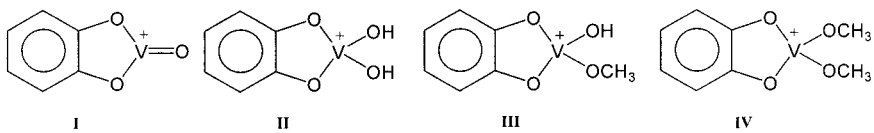

I II III IV

Scheme 2.

Table 2. Neutral losses observed upon of CID (collision gas: xenon) of mass-selected $[(C_6H_4O_2)V(OR^1)(OR^2)]^+$ complexes generated by ESI of $VOCl_3$ with $C_6H_4(OH)_2$ in methanol, ethanol, *n*-propanol, isopropyl alcohol, *tert*-butyl alcohol, and in mixtures of these alcohols. Data given relative to the base peak (100) of the CID products at E_{lab} = 3 eV.

R^1/R^2	–15	–18	–28	–30	–32	–42	–46	–56	–60	–74	–84	–88	–98	(c)/(d)[a]
CH_3/CH_3[b]	100			65	37									100:0
CH_3/C_2H_5			100		15		14		11					21:79
$CH_3/n\text{-}C_3H_7$					6	100			11	7				14:86
$CH_3/i\text{-}C_3H_7$					100	62			77	15				70:30
$CH_3/t\text{-}C_4H_9$		44			19			100		13		13		22:78
C_2H_5/C_2H_5			100				80	30		3				37:63
$C_2H_5/n\text{-}C_3H_7$			1			100	15		6					17:83
$C_2H_5/i\text{-}C_3H_7$						100	78		33					53:47
$C_2H_5/t\text{-}C_4H_9$							33	100		7				28:72
$n\text{-}C_3H_7/n\text{-}C_3H_7$						100			1		70			1:99
$n\text{-}C_3H_7/t\text{-}C_4H_9$						6		100					3	3:97
$i\text{-}C_3H_7/i\text{-}C_3H_7$						100			<5[c]		75			<3:>97
$i\text{-}C_3H_7/t\text{-}C_4H_9$						1		100	22				3	21:79
$t\text{-}C_4H_9/t\text{-}C_4H_9$								100		32				24:76

[a] Ratio of hydrogen transfer according to routes (c) and (d), see Scheme 6 and text for details. [b] In addition, a consecutive loss of CH_3 and CH_2O is observed [Δm (%) = –45 (30)]. [c] Poor abundances of $[M^+]$ formed upon ESI; the value given is an upper limit derived from the noise level.

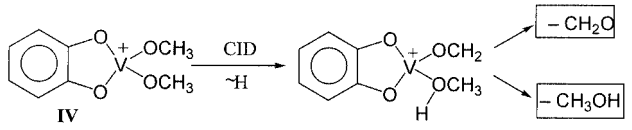

Scheme 3.

methanol and *tert*-butyl alcohol for the cation-$[(C_6H_4O_2)V(OCH_3)(OC(CH_3)_3)]^+$, respectively. For the latter complex, also loss of water is observed (Δm = –18). The CID spectra of mass-selected $[(C_6H_4O_2)V(OCH_3)(OCH_2CD_3)]^+$ generated from [2,2,2-D_3]ethanol reveal a preferential combined elimination of $C_2H_2D_2$ (Δm = –30) and CH_3OD (Δm = –63). The labeling experiments thereby confirm that the key reactions under CID of mixed methoxy complexes correspond to losses of alkenes according to Scheme 4.

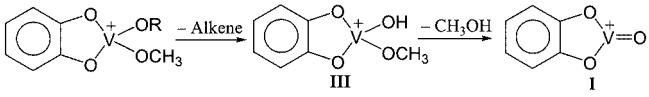

Scheme 4.

The CID spectra of mass-selected $[(C_6H_4O_2)V(OCH_3)\{OCH(CH_3)_2\}]^+$ are also characterized by the elimination of C_3H_6, but the reaction does not dominate in this case. Instead, the major fragmentation is associated with an expulsion of methanol (Δm = –32), along with smaller amounts of $(CH_3)_2CHOH$ (Δm = 60).

Similar to the complexes containing one methoxy group and another larger alkoxy group, expulsion of ethene (Δm = –28) predominates upon CID of mass-selected $[(C_6H_4O_2)V(OC_2H_5)_2]^+$; expulsion of ethanol is observed also (Δm = –46). Possible pathways for the neutral losses upon CID of $[(C_6H_4O_2)V(OC_2H_5)_2]^+$ are presented in Scheme 5, which also suggest the formation of **II** by a consecutive loss of a second C_2H_4 unit followed by the elimination of H_2O to finally yield **I**. Note that the route via **II** is impossible for the complexes with a methoxy ligand as shown in Scheme 4, because alkene elimination is not feasible for R = CH_3. Upon CID of mass-selected $[(C_6H_4O_2)V(OC_2H_5)(OC_2D_5)]^+$, eliminations of C_2H_4 (Δm = –28) and C_2D_4 (Δm = –32) compete with each other with an apparent kinetic isotope effect (KIE) of 2.3 ± 0.1 associated with H-migration from the β-carbon atom in the course of alkene elimination. The significant magnitude of the KIE implies that C–H bond activation is rate-determining, as expected.[22,23]

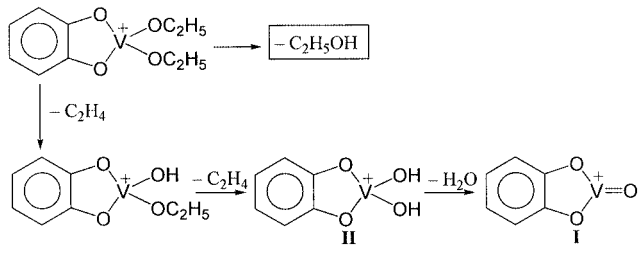

Scheme 5.

The CID spectra of mixed complexes containing one ethoxy group are dominated by expulsion of alkenes from the larger alkoxy group: C_3H_6 for $[(C_6H_4O_2)V(OC_2H_5)(OC_3H_7)]^+$ as well as $[(C_6H_4O_2)V(OC_2H_5)\{OCH(CH_3)_2\}]^+$ cations and C_4H_8 for $[(C_6H_4O_2)V(OC_2H_5)\{OC(CH_3)_3\}]^+$, respectively, along with smaller amounts of corresponding alcohols (Table 2).

The fragmentations of $[(C_6H_4O_2)V(OC_3H_7)_2]^+$ and $[(C_6H_4O_2)V\{OCH(CH_3)_2\}]^+$ are very similar to each other. In both cases, the major CID signal corresponds to the loss of C_3H_6 (Δm = –42). As a result, cations containing one hydroxy group $[(C_6H_4O_2)V(OH)(OC_3H_7)]^+$ and $[(C_6H_4O_2)V(OH)\{OCH(CH_3)_2\}]^+$ are formed. These ions undergo a second loss of C_3H_6 (Δm = –84) to yield structure **II**, which can then expel water to finally afford **I**. Likewise, the CID spectra of $[(C_6H_4O_2)V(OC_3H_7)\{OC(CH_3)_3\}]^+$ and $[(C_6H_4O_2)V\{OCH(CH_3)_2\}\{OC(CH_3)_3\}]^+$ are quite similar and characterized by the elimination of C_4H_8 fragments

 © 2005 Wiley-VCH Verlag GmbH & Co. KGaA, Weinheim

(*m*/*z* = 235) along with small amounts of neutral *tert*-butyl alcohol. For $[(C_6H_4O_2)V(OC_3H_7)\{OC(CH_3)_3\}]^+$ an additional signal is present at *m*/*z* = 249, which can be assigned to the expulsion of C_3H_6 (Table 2). The fragmentation of the vanadium(V) complex with two *tert*-butoxy groups under CID conditions leads to predominant formation of the $[(C_6H_4O_2)V\{OC(CH_3)_3\}(OH)]^+$ concomitant with neutral butene. Also in this case, formation of complex **I** is observed at elevated collision energies.

Discussion

The comparison of the CID patterns of the various alkoxovanadium(V) complexes described above allows some general trends in reactivity to be derived. As a first and obvious conclusion, the dimethoxy complex $[(C_6H_4O_2)V(OCH_3)_2]^+$ is considered as being unique in that it cannot undergo olefin loss and instead expels a methyl radical which is only observed for this particular complex. Formally, the expulsion of $CH_3^{\cdot}$ affords a free valence at the remaining oxygen atom, thus formally leading to a hypervalent vanadium compound or an oxygen-centered radical. However, catechol can be considered to act as a redox-active ligand[24] in that electronic rearrangement may lead to an $OV(OCH_3)^+$ cation coordinated to an *ortho*-quinone ligand, i.e. a formal vanadium(IV) complex. For the other complexes, a clear trend for the preferential evaporation of hydrocarbon fragments from the larger alkoxy group is observed, followed by evaporation of neutral alcohol ligands (R^1OH and R^2OH).

In recursion to the above results, it is interesting to consider the fragmentation processes occurring upon CID in terms of one of two possible routes. Quite obviously, the trends among the various alkoxovanadium cations depend on the structure of the alkoxy groups. For a more detailed consideration, some kind of categorization of the reactions observed is required. Let us therefore distinguish between β-hydrogen transfer to afford a ketone [route (c)] and γ-hydrogen transfer to afford an alkene [route (d)] (Scheme 6). By analogy to ample previous findings on gaseous transition-metal alkoxides,[14,25–28] a hydridometal species is proposed in route (d); note, however, that in the particular case of the $[(C_6H_4O_2)V(OR)(OR')]^+$ complexes studied here, a metal hydride does not need to be involved as an intermediate because hydrogen transfer can directly occur to the other alkoxo group.[17] Within this framework for classification of the fragmentations observed experimentally, the reactions which lead to expulsions of neutral alcohols as well as carbonyl compounds are considered as belonging to route (c). Likewise, alkene losses are assigned to route (d). Similarly, the resulting consecutive products are attributed to the corresponding primary reactions of either routes, e.g. $\Delta m = -84$ in the case of R^1, $R^2 = OC_3H_7$ corresponds to the sequential elimination of two propene units. The last column of Table 2 shows the (normalized) ratio of the routes (c) and (d); other fragmentations, such as the loss of CH_3 from the dimethoxy derivative, are neglected in this comparison. For almost all complexes studied here, the contribution of route (d) is much higher than that of route (c). Exceptions are R^1, $R^2 = CH_3$, of course, for which route (d) is impossible, and the ions containing an *isopropyl* unit for which the amount of route (c) is enhanced. When the competition among the substituents is considered, the β-hydrogen-transfer steps according to route (c) show a small discrimination between R^1 and R^2 with a slight preference for the elimination of the smaller alcohol. In contrast, route (d) is much more specific in that a high preference for the elimination of the larger alkene is observed. These differential substituent effects can be understood on the basis of the mechanisms proposed above. Thus, in route (c), one substituent must serve as hydrogen donor while the other one acts as hydrogen acceptor and is then lost as an alcohol. By such, the substituent effects counterbalance each other. In the olefin elimination according to route (d), however, only one alkoxo group is involved and formation of the more substituted alkene is favored, as expected.

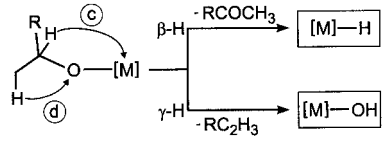

Scheme 6.

Conclusion

Electrospray mass spectrometry allows the generation of cationic alkoxovanadium(V) complexes $[(C_6H_4O_2)V(OR^1)(OR^2)]^+$, bearing a catecholate unit ($C_6H_4O_2$) as ligand. For all vanadium(V) complexes described above, a trend for the preferential evaporation of hydrocarbon fragments from alkoxy groups larger than CH_3 is observed, followed by evaporation of neutral alcohol ligands (R^1OH and R^2OH). The subsequent fragments formed at elevated collision energies still contain the catecholato ligand, suggesting a common $[(C_6H_4O_2)VO]^+$ core. The results demonstrate that the bond between vanadium(V) and catechol is much stronger than those between the metal center and the alkoxo groups.

With respect to the role of vanadium in oxidation catalysis, the mass-spectrometric studies reported in this work suggest mononuclear vanadium(V) centers to be of limited use for the conversion of alcohols with β-H atoms into the corresponding carbonyl compounds because alkene elimination can obviously compete quite efficiently.

Experimental Section

The experiments were performed using a commercial VG BIO-Q mass spectrometer equipped with an ESI source followed by a tandem mass spectrometer of QHQ configuration (Q = quadrupole, H = hexapole).[29] All examined ionized vanadium(V) complexes were generated by ESI of dilute methanolic solutions of $VOCl_3$, the appropriate alcohol(s), and catechol. All solutions were introduced

 © 2005 Wiley-VCH Verlag GmbH & Co. KGaA, Weinheim

into the ESI source through a silica capillary with a syringe pump (3 μL/min). For each ion studied, the instrument parameters were optimized for maximum ion abundances. Nitrogen was used as a nebulizer and drying gas at a source temperature of 80 °C. Collision induced dissociation (CID) experiments were performed with xenon as a collision gas at a pressure of approximately $3 \cdot 10^{-4}$ mbar, and several collision energies (E_{lab} from 0 to 30 eV). For the CID experiments, the ions were mass-selected using Q1, allowed to interact with the collision gas in the hexapole collision cell, and the ionic products were then analyzed by scanning Q2. The cations observed in all solvents used can be divided into two major categories: vanadium-containing cations and metal-free cations; the latter are of no interest in this study, except that they were tried to be kept minimal in order to increase the yields of metal-containing ions. For all species, the number of ligands of the formed solvated cations depends on the cone voltage in the ESI source which determines the softness or hardness of the ionization conditions. All vanadium(v) complexes presented here are formed at a cone voltage of U_c = 20 eV, which corresponds to gentle ionization conditions where multiply ligated ions prevail. At $U_c > 80$ V, diatomic VO^+ prevails for all mixtures studied.

Acknowledgments

This work was supported by the Deutsche Forschungsgemeinschaft (SFB 546), the Fonds der Chemischen Industrie, and the Gesellschaft von Freunden der Technischen Universität Berlin.

[1] C. N. R. Rao, *Transition Metal Oxides*, VCH, New York, **1995**.
[2] K. Liu, A. Wagner (Eds.), *The chemical dynamics and kinetics of small radicals* World Scientific, Singapore, **1995**, parts I and II,.
[3] *Appl. Catal. A* **1997**, 157; the entire volume deals with this topic.
[4] J. Haber, *Handbook of Heterogeneous Catalysis* (Eds.: G. Ertl, H. Knözinger, J. Weitkamp)Wiley-VCH, Weinheim, **1997**, p. 2253.
[5] J. A. Davies, P. L. Watson, J. F. Liebman. A. Greenberg (Eds.), *Selective Hydrocarbon Activation, Principles and Progress*, VCH, New York, **1990**.
[6] D. Schröder, H. Schwarz, S. Shaik, in: "Metal-Oxo and Metal-Peroxo Species in Catalytic Oxidations" (Ed.: B. Meunier), *Structure and Bonding*, Springer, Berlin, **2000**, vol. 97, pp. 91–123.
[7] J. N. Harvey, R. Poli, *Chem. Soc. Rev.* **2003**, *32*, 1–8.
[8] H. Schwarz, *Int. J. Mass Spectrom.* **2004**, *237*, 75–105.
[9] J. M. Mercero, J. M. Matxain, X. Lopez, D. M. York, A. Largo, L. A. Eriksson, J. M. Ugalde, *Int. J. Mass Spectrom.* **2005**, *240*, 37–99.
[10] D. Schröder, H. Schwarz, *Angew. Chem.* **1995**, *107*, 2176–2179.
[11] K. Yoshizawa, Y. Shiota, T. Yamabe, *Chem. Eur. J.* **1997**, *3*, 1160–1169.
[12] L. Deng, T. Ziegler, *Organometallics* **1996**, *15*, 3011–3021.
[13] M. B. Smith, J. March, *March's Advanced Organic Chemistry*, Wiley, New York, **2001**, p. 1048.
[14] A. Fiedler, I. Kretzschmar, D. Schröder, H. Schwarz, *J. Am. Chem. Soc.* **1996**, *118*, 9941–9952.
[15] B. M. Weckhuysen, D. E. Keller, *Catal. Today* **2003**, *78*, 25–46.
[16] M. Engeser, D. Schröder, H. Schwarz, *Chem. Eur. J.*, in press.
[17] D. Schröder, J. Loos, M. Engeser, H. Schwarz, H.-C. Jankowiak, R. Berger, R. Thissen, O. Dutuit, J. Döbler, J. Sauer, *Inorg. Chem.* **2004**, *43*, 1976–1985.
[18] R. C. Bell, A. W. Castleman, *J. Phys. Chem. A* **2002**, *106*, 9893–9899, and references therein.
[19] D. Schröder, M. Engeser, M. Brönstrup, C. Daniel, J. Spandl, H. Hartl, *Int. J. Mass Spectrom.* **2003**, *228*, 743–751.
[20] J. N. Harvey, M. Diefenbach, D. Schröder, H. Schwarz, *Int. J. Mass Spectrom.* **1999**, *182/183*, 85–87.
[21] M. Engeser, M. Schlangen, D. Schröder, H. Schwarz, *Organometallics* **2003**, *22*, 3933–3943.
[22] D. Schröder, H. Schwarz, *Top. Curr. Chem.* **2003**, *225*, 133–152.
[23] J. Loos, D. Schröder, H. Schwarz, *Encyclopedia of Mass Spectrometry*, vol. 4 (Ed.: N. M. M. Nibbering), Elsevier, Amsterdam, **2005**, pp. 659–666.
[24] W. O. Koch, V. Schunemann, M. Gerdan, A. X. Trautwein, H.-J. Kruger, *Chem. Eur. J.* **1998**, *4*, 1255–1265.
[25] C. J. Cassady, B. S. Freiser, S. W. McElvany, J. Allison, *J. Am. Chem. Soc.* **1984**, *106*, 6125–6126.
[26] C. J. Cassady, B. S. Freiser, *J. Am. Chem. Soc.* **1985**, *107*, 1566–1572.
[27] C. J. Cassady, B. S. Freiser, *J. Am. Chem. Soc.* **1985**, *107*, 1573–1579.
[28] D. Schröder, H. Schwarz, *Angew. Chem.* **1990**, *102*, 925–927; *Angew. Chem. Int. Ed. Engl.* **1990**, *29*, 910–912.
[29] D. Schröder, T. Weiske, H. Schwarz, *Int. J. Mass Spectrom.* **2002**, *219*, 729–738.

Received February 21, 2005
Published Online: June 21, 2005

 © 2005 Wiley-VCH Verlag GmbH & Co. KGaA, Weinheim

Novel Indenylzirconium Complexes as Supported Catalysts in the Polymerization of Ethylene

Carlos Alonso-Moreno,[a] Antonio Antiñolo,[a] Fernando Carrillo-Hermosilla,[a] Pedro Carrión,[a] Isabel López-Solera,[a] Antonio Otero,*[a] Sanjiv Prashar,[b] and José Sancho[c]

Keywords: Metallocene / Zirconium / Homogeneous catalysis / Supported catalysts / Polymerization / Ethylene

A series of substituted indene {C_9H_7R-3 [R = $CH_2CH_2CH_2OSiMe_3$ (**1**), $CH_2CH_2CH_2OCH_2C_6H_5$ (**2**), $CH_2CH_2CH_2OSiMe_2tBu$ (**3**)]}, and *ansa*-indene compounds {$Me_2Si(C_9H_6R\text{-}3)_2$-1 [R = $CH_2CH_2CH_2OSiMe_3$ (**4**)], $Me_2Si(C_9H_6R\text{-}3)$-1(C_5HMe_4) [R = $CH_2CH_2CH_2OSiMe_3$ (**5**), $CH_2CH_2CH_2OCH_2C_6H_5$ (**6**), $CH_2CH{=}CH_2$ (**7**), $CH_2CH_2CH_2OSiMe_2tBu$ (**8**)]} have been prepared. The lithium derivatives of **1**–**8** were employed in the synthesis of the indenylzirconium complexes [$Zr(\eta^5\text{-}C_9H_6R\text{-}1)_2Cl_2$] [R = $CH_2CH_2CH_2OSiMe_3$ (**17**), $CH_2CH_2CH_2OCH_2C_6H_5$ (**18**), $CH_2CH_2CH_2OSiMe_2tBu$ (**19**)], *rac*-[$Zr\{Me_2Si(\eta^5\text{-}C_9H_5R\text{-}3)_2\text{-}1\}Cl_2$] [R = $CH_2CH_2CH_2OSiMe_3$ (**20**)], [$Zr\{Me_2Si(\eta^5\text{-}C_9H_5R\text{-}3)\text{-}1(\eta^5\text{-}C_5Me_4)\}Cl_2$] [R = $CH_2CH_2CH_2OSiMe_3$ (**21**), $CH_2CH_2CH_2OCH_2C_6H_5$ (**22**), $CH_2CH{=}CH_2$ (**23**), $CH_2CH_2CH_2OSiMe_2tBu$ (**24**)] and [$Zr(Me_2Si\{\eta^5\text{-}C_9H_5(CH_2CH_2CH_2O)\text{-}3\}\text{-}1\{\eta^5\text{-}C_5Me_4\})Cl$] (**21a**). The alkyl complexes [$Zr(Me_2Si\{\eta^5\text{-}C_9H_5(CH_2CH_2CH_2O)\text{-}3\}\text{-}1\{\eta^5\text{-}C_5Me_4\})Me$] (**25**) and [$Zr\{Me_2Si(\eta^5\text{-}C_9H_5R\text{-}3)\text{-}1(\eta^5\text{-}C_5Me_4)\}Me_2$] [R = $CH_2CH_2CH_2OSiMe_2tBu$ (**26**)] have been synthesized by the reaction of the corresponding *ansa*-zirconocene derivative with the alkyl Grignard reagent. The molecular structure of [$(Zr\{C_9H_6(CH_2CH_2CH_2O)\text{-}1\}Cl_2)_2(Zr\text{–}O)$] (**17a**), a subproduct in the formation of **17** has been determined by single-crystal X-ray diffraction studies. The indenylzirconium complexes **17–24** have been immobilized on partially dehydroxylated SiO_2, and these supported systems used to polymerize ethylene in the presence of methylaluminoxane. The catalytic activity of these compounds in both homogeneous and heterogeneous polymerization is reported.
(© Wiley-VCH Verlag GmbH & Co. KGaA, 69451 Weinheim, Germany, 2005)

Introduction

On the basis of production data for 2000, 85–95 million tons of polyolefins (essentially homopolymers and copolymers of ethylene and propylene) were produced globally. The worldwide polypropylene capacity is approximately 34 million tons, all of which is made with supported catalysts. Sixty percent of polyethylene is made with supported catalysts, bringing the current market for polyolefins produced on supported catalysts to a total of 65–70 million tons per year. This already impressive market is still in full growth.[1,2]

Metallocene/MAO catalytic systems are highly efficient in producing polyolefins with defined microstructures and narrow molecular weight distributions,[3,4] although to date, these systems have generally been applied in solution. However, for most industrial applications, it is desirable to employ these catalysts in gas-phase reactions in order to take advantage of existing heterogeneous polymerization plant infrastructure and thus avoiding the costly modification needed for incorporating homogeneous systems. The single-site catalysts therefore need to be immobilized on a solid support in order to be active in gas-phase processes. Supported single-site catalysts are presently being used worldwide in the annual production of 1 billion kg of polyethylene.

The most common method of applying metallocene compounds to heterogeneous polymerization is to support the complexes on inorganic solids (in most cases silica gel).[5–7] There are four different routes to supported catalysts: (i) Direct adsorption of the metallocene on the carrier surface leading to physisorption or chemisorption of the metallocene (direct heterogenization). (ii) Direct adsorption of the metallocene/MAO adduct on the support. (iii) Initial adsorption of MAO to the support followed by adsorption of the metallocene (indirect heterogenization). (iv) Covalent bonding between the ligands of the metallocene complex and the carrier surface followed by activation with external MAO.

Several metallocene compounds containing functional groups linked to cyclopentadienyl or indenyl ligands have

[a] Departamento de Química Inorgánica, Orgánica y Bioquímica, Facultad de Ciencias Químicas, Universidad de Castilla–La Mancha, Campus Universitario,
13071 Ciudad Real, Spain
Fax: +34-926-295-318
E-mail: Antonio.Otero@uclm.es
[b] Departamento de Tecnología Química, Ambiental y de los Materiales, E.S.C.E.T., Universidad Rey Juan Carlos,
28933 Móstoles, Madrid, Spain
Fax: +34-91-488-8143
E-mail: S.Prashar@escet.urjc.es
[c] Centro Tecnológico de Repsol-YPF, Carretera de Extremadura, Km. 18, 28931 Móstoles, Madrid, Spain

 © 2005 Wiley-VCH Verlag GmbH & Co. KGaA, Weinheim **DOI: 10.1002/ejic.200500165**

been described.[8] One of the most promising methods to obtain supported catalysts comes from the reaction between the functional group of these metallocene complexes and another functional group on the solid surface (route iv). This option was applied to obtain some supported mono- or bis(cyclopentadienyl) derivatives.[8b,9–11] When silica is employed as a support, the surface hydroxy groups have frequently been used for immobilizing the catalyst although they can also cause some decomposition of the metallocene complex. A strained siloxane group generated by dehydroxylation has been shown to react with alkoxysilane groups,[12] and this reactivity opens up the possibility of supporting metallocene complexes with pendant alkoxy or silyloxy groups on dehydroxylated silica.

In this paper we describe the synthesis and characterization of a series of alkoxy- and silyloxy-substituted indene compounds and their zirconium(IV) derivatives, and the successful immobilization of the metallocene catalysts on dehydroxylated silica.

Results and Discussion

The preparation of the substituted indene precursors C_9H_7R-3 [R = $CH_2CH_2CH_2OSiMe_3$ (**1**), $CH_2CH_2CH_2OCH_2C_6H_5$ (**2**), $CH_2CH_2CH_2OSiMe_2tBu$ (**3**)] was achieved by the reaction of $BrCH_2CH_2CH_2OR$ (R = $SiMe_3$, $CH_2C_6H_5$, $SiMe_2tBu$) and indenyllithium [Equation (1)]. ^1H NMR spectroscopy showed the isolated product of **1–3** to be virtually exclusively the 3-isomer (>98%). The 1-H signal for **1–3** was observed as a doublet, at $\delta \approx 3.2$ ppm, corresponding to two protons and 2-H as a triplet, at $\delta \approx 6.1$ ppm, corresponding to one proton. In addition, **1–3** were characterized by electron impact mass spectrometry (see Exp. Sect.).

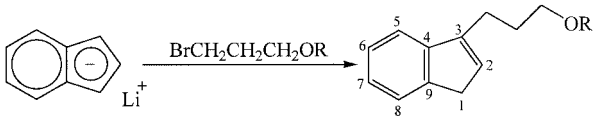

R = $SiMe_3$ (**1**), CH_2Ph (**2**), $SiMe_2tBu$ (**3**) (1)

Compounds **1–3** were lithiated in the normal manner with *n*-butyllithium giving the lithium derivatives $Li(C_9H_6R$-1) [R = $CH_2CH_2CH_2OSiMe_3$ (**9**), $CH_2CH_2CH_2OCH_2C_6H_5$ (**10**), $CH_2CH_2CH_2OSiMe_2tBu$ (**11**)]. Compounds **9–11** were treated with $ZrCl_4$ to yield the zirconocene complexes $[Zr(\eta^5$-C_9H_6R-1$)_2Cl_2]$ [R = $CH_2CH_2CH_2OSiMe_3$ (**17**), $CH_2CH_2CH_2OCH_2Ph$ (**18**), $CH_2CH_2CH_2OSiMe_2tBu$ (**19**)] [Equation (2)].

The substituted indenyl ligands are prochiral and can yield two diastereomers for the zirconocene complexes. A *re*,*re* or *si*,*si* attachment gives rise to the two enantiomers of the *rac* diastereomer, whereas a *re*,*si* attachment leads to the *meso* diastereomer.[13–15] The synthetic approach employed in this study gave, as shown by NMR spectroscopy, a 1:1 *rac*/*meso* isomer ratio.

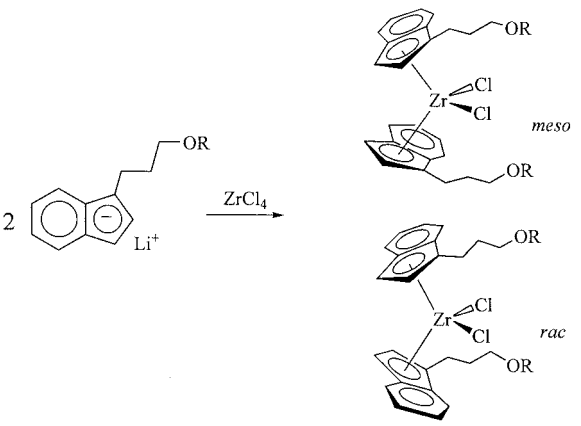

R = $SiMe_3$(**17**), CH_2Ph (**18**), $SiMe_2tBu$ (**19**) (2)

^1H and ^{13}C NMR spectra of **17–19** exhibit two sets of signals in a 1:1 ratio, corresponding to the presence of both distereomers (see Exp. Sect.). The characterization was simplified by the fact that the *rac* isomer has C_2 symmetry which makes the two indenyl rings equivalent. This is also true for the *meso* isomer because of a mirror plane. In the ^1H NMR spectra of **17–19**, the protons in position 2 and 3 of the indenyl ligand showed only vicinal coupling and were thus observed as doublets in the ^1H NMR spectra. It was possible to assign the 2-H and 3-H signals to their respective diastereomers using NOE experiments. An interesting observation is that for a sample containing a mixture of the diastereomers, the "inner-pair" of 2-H and 3-H doublets were assigned to the *rac* isomer, whereas for the *meso* isomer the two doublets were the "outer-pair". Because of the complex nature caused by overlapping signals we were not able to assign the multiplet systems observed for the protons of both the pendant chain and the indenyl C_6 fragment to their respective diasteromers.

During the preparation of **17**, a minor product was, at times, detected. We were able to isolate this subproduct, $[(Zr\{C_9H_6(CH_2CH_2CH_2O)-1\}Cl_2)_2(Zr$–$O)]$ (**17a**), by fractional recrystallization and characterize it by single-crystal X-ray diffraction studies. The molecular structure and atomic numbering scheme are shown in Figure 1. Selected bond lengths and angles for **17a** are given in Table 1.

The structure consists of a dinuclear complex of zirconium. The metal atoms are bound to the indenyl ligand in an η^5 mode, to the oxygen atoms of the pendant chains which bridge the two zirconium atoms, and to two chlorine atoms in a four-legged piano-stool conformation. The indenyl ligands are in a *trans* disposition.

During the preparation of **9** it is possible that a second lithiation occurs at the oxygen atom of the pendant chain with the elimination of $nBuSiMe_3$ to give $Li[C_9H_6(CH_2CH_2CH_2OLi)$-1]. If this subproduct is present when the reaction of **9** is carried out with $ZrCl_4$, the presence of **17a** may be detected in the isolated product [Equation (3)].

The bridged bis(indene) compound, $\{Me_2Si[(C_9H_6$-R-3$)$-1$]_2\}$ (**4**) (R = $CH_2CH_2CH_2OSiMe_3$), was prepared by

 © 2005 Wiley-VCH Verlag GmbH & Co. KGaA, Weinheim

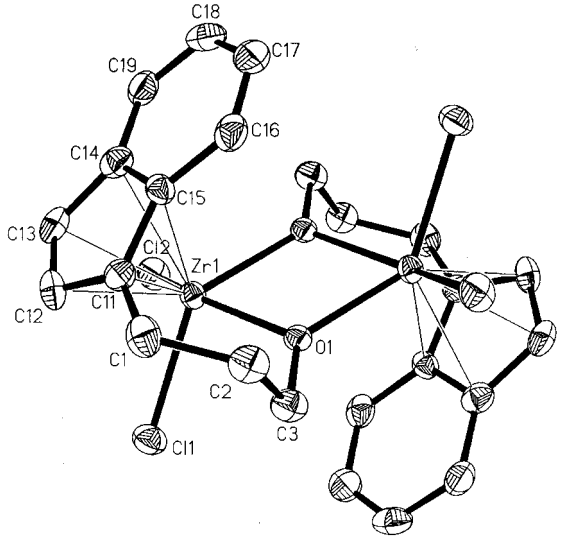

Figure 1. Molecular structure and atom labelling scheme for [(Zr{$C_9H_6(CH_2CH_2CH_2O)$-1}$Cl_2)_2$(*Zr–O*)] (**17a**) with thermal ellipsoids at 30% probability.

Table 1. Selected bond lengths [Å] and angles [°] for **17a**; Cent(1) is the centroid of C(11)–C(15); * refers to the average bond length between Zr(1) and the carbon atoms of the C_5 ring of the indenyl moiety.

Zr(1)–Cent(1)	2.188
av Zr(1)–C[Cent(1)]*	2.486(9)
Zr(1)–Cl(1)	2.415(2)
Zr(1)–Cl(2)	2.447(2)
Zr(1)–O(1)	2.131(5)
Cent(1)–Zr(1)–O(1)	105.2
Cent(1)–Zr(1)–Cl(1)	109.0
Cent(1)–Zr(1)–Cl(2)	109.7
O(1)–Zr(1)–Cl(1)	88.13(15)
O(1)–Zr(1)–Cl(2)	143.8(2)
O(1)–Zr(1)–O(1)′	70.1(2)
Cl(1)–Zr(1)–Cl(2)	88.90(3)
Zr(1)–O(1)–C(3)	122.08(5)

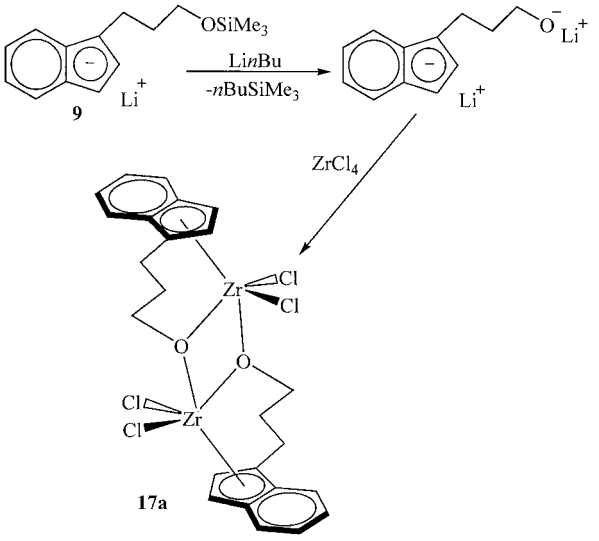

(3)

the reaction of 2 equiv. of $BrCH_2CH_2CH_2OSiMe_3$, with $Li_2[Me_2Si(C_9H_6)_2$-1] and isolated as a mixture of its *meso* and *rac* isomers [Equation (4)].

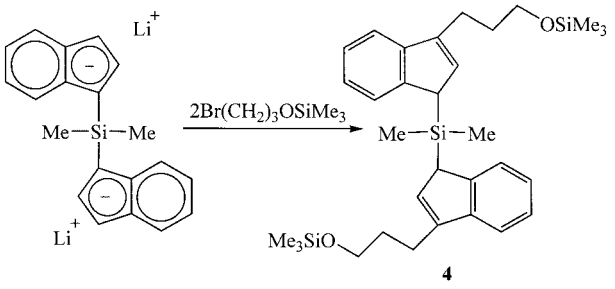

(4)

^{1}H NMR spectroscopy showed the isolated product of **4** to be virtually exclusively (>98%) the symmetrically substituted indene isomer. In addition, **4** was characterized by electron impact mass spectrometry (see Exp. Sect.). Double deprotonation of **4** with2 equiv. of *n*-butyllithium gave the corresponding dilithium derivative, $Li_2[Me_2Si(C_9H_5R\text{-}3)_2$-1] (**12**) (R = $CH_2CH_2CH_2OSiMe_3$), whose reaction with $[ZrCl_4(THF)_2]$ in toluene gave the *ansa*-indenyl complex, [Zr{$Me_2Si(\eta^5$-C_9H_5R-3)$_2$-1}Cl_2] [R = $CH_2CH_2CH_2OSiMe_3$ (**20**)], exclusively as the *rac* isomer [Equation (5)]. Use of $[ZrCl_4(THF)_2]$ as the zirconium source has been suggested to modify the ratio of the diastereomers formed.[14] This proposal is reinforced by the observation that the reaction of **12** with $ZrCl_4$ gave **20** as a 3:2 *rac*/*meso* mixture.

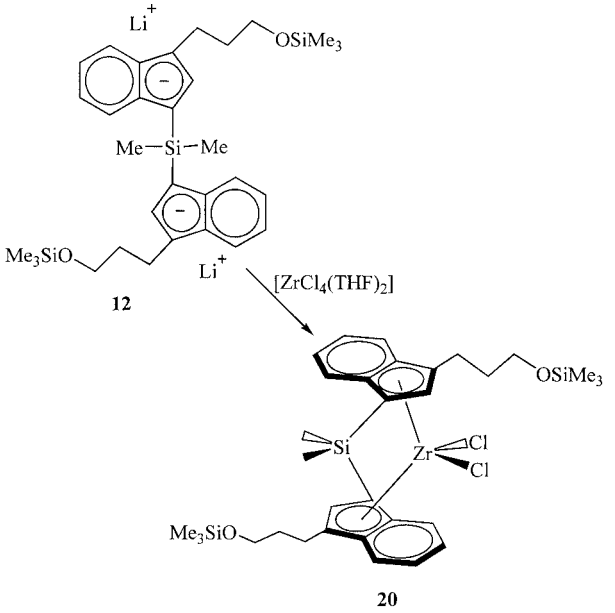

(5)

Compound **20** was characterized by NMR spectroscopy. The proton signal assignments were made according to a procedure using ^{1}H and ^{13}C NMR correlated spectroscopy (HETCOR) (see Exp. Sect.).

The preparation of the asymmetrically substituted *ansa* ligand precursors [$Me_2Si(C_9H_6R$-3)-1(C_5HMe_4)] [R = $CH_2CH_2CH_2OSiMe_3$ (**5**), $CH_2CH_2CH_2OCH_2C_6H_5$ (**6**),

$CH_2CH_2CH_2OSiMe_2tBu$ (**8**)] was achieved by the reaction of $Me_2Si(C_5Me_4H)Cl$ and the corresponding lithium derivatives **9**–**12** [Equation (6)].

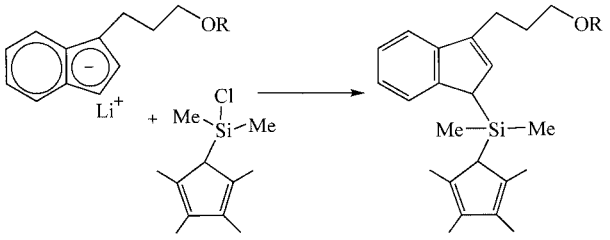

R = $SiMe_3$ (**5**), CH_2Ph (**6**), $SiMe_2tBu$ (**8**) (6)

The reaction of **2** with an excess of *n*BuLi gave the lithium derivative $Li[C_9H_6(CH_2CH{=}CH_2)\text{-}1]$ (**10a**) by a bimolecular elimination [Equation (7)]. The subsequent reaction of **10a** with $Me_2Si(C_5Me_4H)Cl$ yielded the asymmetrically substituted *ansa* ligand precursor, $\{Me_2Si[C_9H_6(CH_2CH{=}CH_2)\text{-}3]\text{-}1(C_5HMe_4)\}$ (**7**). ^1H NMR spectroscopy showed the isolated products **5**–**8** to be virtually exclusively (>98%) the regioisomer where the $SiMe_2$ *ansa* bridge is situated in position 1 in both the indenyl and cyclopentadienyl moieties. In addition, **5**–**8** were characterized by electron impact mass spectrometry (see Exp. Sect.).

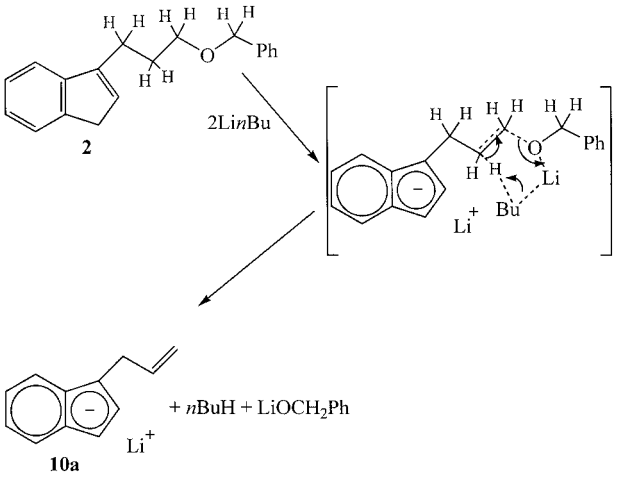

(7)

Compounds **5**–**8** were then lithiated in the normal way with *n*-butyllithium to give the corresponding dilithium derivatives, $Li_2[Me_2Si(C_9H_5R\text{-}3)\text{-}1(C_5Me_4)]$ [R = $CH_2CH_2CH_2OSiMe_3$ (**13**), $CH_2CH_2CH_2OCH_2C_6H_5$ (**14**), $CH_2CH{=}CH_2$ (**15**), $CH_2CH_2CH_2OSiMe_2tBu$ (**16**)] whose reaction with $[ZrCl_4(THF)_2]$ gave the *ansa*-zirconocene complexes $[Zr\{Me_2Si(\eta^5\text{-}C_9H_5R\text{-}3)\text{-}1(\eta^5\text{-}C_5Me_4)\}Cl_2]$ [R = $CH_2CH_2CH_2OSiMe_3$ (**21**), $CH_2CH_2CH_2OCH_2C_6H_5$ (**22**), CH_2CHCH_2 (**23**), $CH_2CH_2CH_2OSiMe_2tBu$ (**24**)] [Equation (8)].

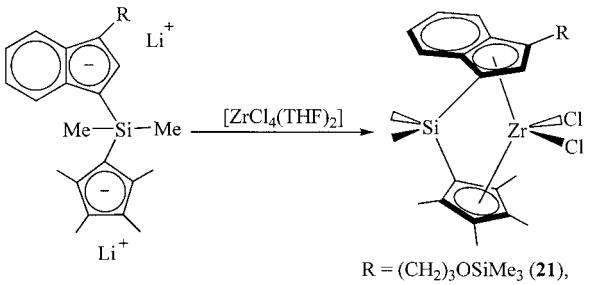

R = $(CH_2)_3OSiMe_3$ (**21**), $(CH_2)_3OCH_2Ph$ (**22**), $CH_2CH{=}CH_2$ (**23**), $(CH_2)_3OSiMe_2tBu$ (**24**) (8)

When the lithiation reaction of **5** was carried out in the presence of excess of *n*-butyllithium, the trilithium derivative, $Li_2\{Me_2Si[C_9H_5(CH_2CH_2CH_2OLi)\text{-}3]\text{-}1(C_5Me_4)\}$ (**13a**) was formed through the elimination of the $SiMe_3$ moiety [Equation (9)]. Compound **13a** was characterized by ^1H NMR spectroscopy which confirmed the loss of the $SiMe_3$ group. The reaction of **13a** with $[ZrCl_4(THF)_2]$ gave the *ansa*-zirconocene complex $[Zr(Me_2Si\{\eta^5\text{-}C_9H_5(CH_2CH_2CH_2O)\text{-}3\}\text{-}1\{\eta^5\text{-}C_5Me_4\})Cl(Zr\text{–}O)]$ (**21a**), where the oxygen atom of the pendant chain is directly bonded to the metal center [Equation (9)].

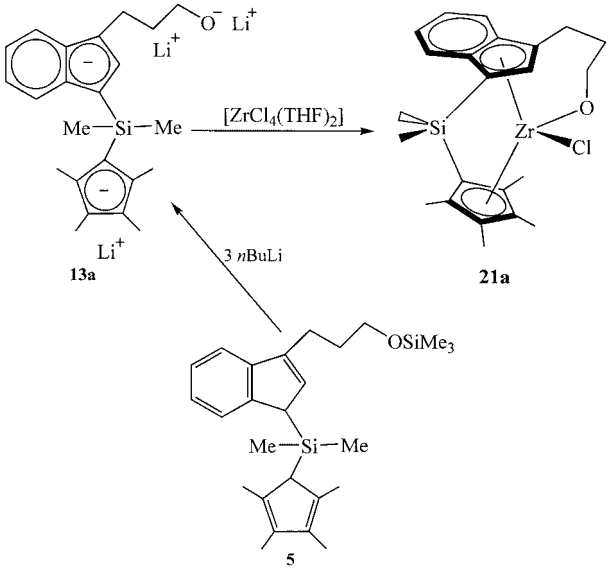

(9)

Compounds **21**–**24** were characterized spectroscopically (see Exp. Sect.). The ^1H NMR spectra show the lack of symmetry in these chiral complexes, with four singlets being observed for the cyclopentadienyl methyl groups, two singlets for the *ansa*-bridge methyl groups, a singlet for the proton of the indenyl C_5 ring and four multiplets corresponding to the protons of the C_6 ring of the indenyl moiety. In addition signals were observed for the pendant alkyl chain.

The alkyl derivatives, $[Zr(Me_2Si\{\eta^5\text{-}C_9H_5(CH_2CH_2CH_2O)\text{-}3\}\text{-}1\{\eta^5\text{-}C_5Me_4\})Me(Zr\text{–}O)]$ (**25**) and $[Zr\{Me_2Si(\eta^5\text{-}C_9H_5R\text{-}3)\text{-}1(\eta^5\text{-}C_5Me_4)\}Me_2]$ [R = $CH_2CH_2CH_2OSi$-

 © 2005 Wiley-VCH Verlag GmbH & Co. KGaA, Weinheim

Me_2tBu (**26**)] were prepared by the reaction of the Grignard reagent MeMgBr with the corresponding mono- or dihalo *ansa*-zirconocene complexes **21a** and **24**, respectively [Equations (10) and (11)]. Compounds **25** and **26** were characterized by spectroscopic methods (see Exp. Sect.). The ^1H NMR spectrum for **25** is similar to that recorded for its parent compound **21a** but in addition a singlet for the metal-bonded methyl group is observed. For **26**, two signals, assigned to the inequivalent metal-bonded methyl groups, were recorded.

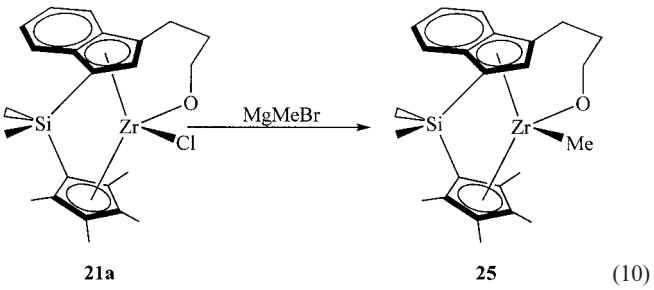

21a **25** (10)

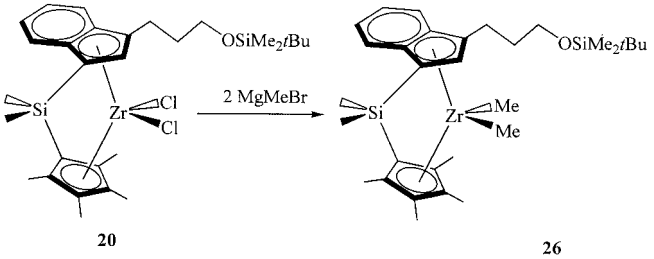

20 **26** (11)

Figure 2 shows IR spectra corresponding to the reaction between a toluene solution of [Zr{$Me_2Si(\eta^5$-C_9H_5R-3)-1(η^5-C_5Me_4)}Cl_2] [R = $CH_2CH_2CH_2OSiMe_2tBu$ (**17**)] and the surface of a partially dehydroxilated silica, after removal of solvent (see Exp. Sect.). The spectrum of silica preheated at 773 K has a sharp band at 3747 cm^{-1} (assigned to isolated OH groups) with a small broad shoulder at 3670 cm^{-1}, which can be attributed to silanols that are perturbed due to interparticle contact[16] or to OH groups retained deep within the pores[17] (Figure 2a). The magnitude of the silanol number, which is independent of the origin and structural characteristics of amorphous silica, is considered to be ca. 1.8 OH nm^{-2} for a silica dehydroxylated at 733 K.[18] Bands at 1866 cm^{-1} and 1640 cm^{-1} are combination and overtone bands of Si–O network bonds. After contact with the metallocene solution and removal of the solvent (Figure 2b), new bands can be seen in the 2900 and 1400 cm^{-1} regions and these correspond to stretching and bending modes of the cyclopentadienyl ligands. The OH groups that were initially isolated are now partially perturbed, generating broad ν(OH) bands at lower frequencies due to an interaction with the cyclopentadienyl π-electron system through

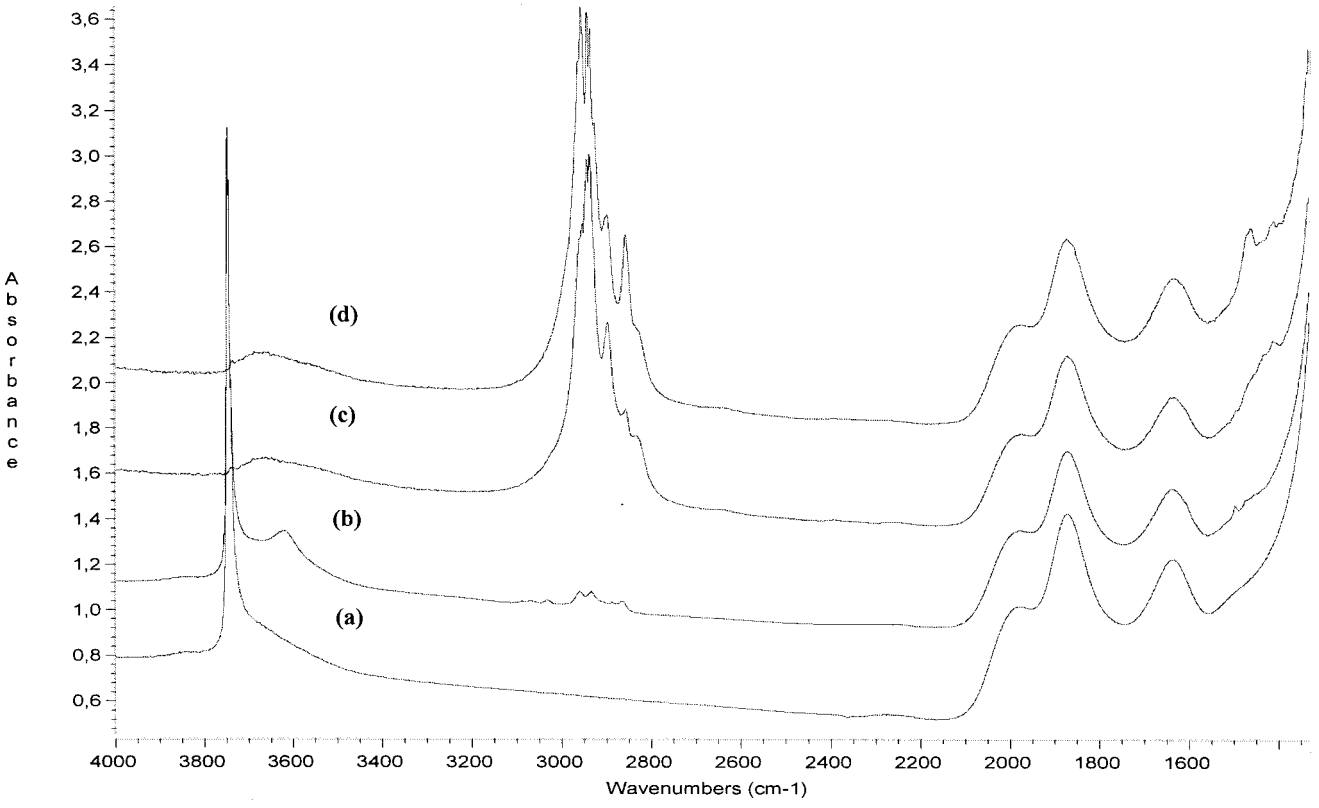

Figure 2. (a) SiO_2 dehydroxylated; (b) after grafting of **17**; (c) after addition of MAO; (d) after contact with C_2H_4.

 © 2005 Wiley-VCH Verlag GmbH & Co. KGaA, Weinheim

hydrogen bonding.[19] The total intensity of the band due to the hydroxy groups was slightly modified after the addition of an excess of metallocene solution, a situation also observed by dos Santos and co-workers in the reaction between partially dehydroxylated silica and [Zr(η^5-C_5H_4-*n*Bu)$_2$Cl$_2$].[20]

It is well established that the surface hydroxy group density on silica decreases with thermal activation as a result of an increase in the number of siloxane reactive bridges. These strained groups can activate covalent bonds such as the Si–O bond in silicon ethers or N–H in ammonia.[21] We could propose a similar behavior with our silicon ether metallocene derivatives. Similar results were found in the reaction of [Zr(η^5-C_5H_5)$_2$Cl$_2$] and dehydroxylated silica.[22]

The behavior of the catalyst system after the addition of the MAO cocatalyst was also studied by FT-IR spectroscopy. The IR spectrum of a sample of **17**-SiO_2 treated with MAO (Al/Zr = 100) is shown in Figure 2c. After addition of MAO at room temperature, the infrared band attributed to the isolated silanol groups (at 3747 cm^{-1}) disappeared completely, indicating a reaction between some basic methyl groups of MAO and the acidic silanol moieties of the silica. New infrared bands were observed in the ν(CH) region (one intense band at 2940 cm^{-1} and three weak bands at 2898, 2856 and 2838 cm^{-1}). These signals were assigned to stretching vibrations of the C–H bonds of the methyl groups in MAO. The grafted MAO should be able to activate neighboring surface zirconocene molecules.[23] The catalytic activity of **17**-SiO_2, after treatment with MAO, towards ethylene polymerization was confirmed, using FT-IR spectroscopy, by monitoring the appearance of vibrations due to polyethylene in the regions 3000–2800 and 1500–1300 cm^{-1} (Figure 2d). Intense bands were observed at 2970, 2850 and 1380 cm^{-1}, which correspond to the ν(CH) and δ(CH) vibrations of polyethylene, respectively.

The polymerization of ethylene, under homogeneous conditions and using **9**–**13** and **15**–**17** as the catalyst, with metal/MAO catalyst ratios of 1:100 (in order to compare with supported catalysts) or 1:500, has been carried out. The polymerization experiments were carried out at 70 °C and at an olefin pressure of 1.5 bar. The results of the experiments are given in Table 2.

In all the cases, as expected, higher activities were found for the 500:1 Al/Zr ratio. The highest catalytic activities were recorded for **19**, **22** and **23**. In comparison, **20** gave a notably low catalytic activity. The activities recorded for the *ansa*-zirconocene complexes **22** and **23** are higher than their unsubstituted analogue, [Zr{Me_2Si(η^5-C_9H_6)(η^5-C_5Me_4)}-Cl_2], although **24** gave a similar value. Only compound **19** shows a higher value than its corresponding unsubstituted reference complex.

The complexes **17**–**24** were supported on dehydroxylated silica and, in the presence of MAO (Zr/Al 1:100), were employed as heterogeneous catalysts in the polymerization of ethylene. The experiments were carried out at 70 °C and at an olefin pressure of 1.5 bar and the results are given in Table 3.

The amount of supported metallocene was verified by surface elemental analyses (Zr). The average results of several samples are summarized in Table 3.

Supported substituted complexes **17**, **21**, and **24** show similar or higher activities than their reference unsubstituted complexes. We could propose that, at least in these cases, more active surface species were obtained than those obtained from "conventional" unsubstituted complexes. Later complexes could be fixed on the surface by reaction between Zr–Cl moieties and Si–OH acidic groups, to give strong Zr–O–Si bonding, hard to activate by MAO. In contrast, the new complexes could be fixed by the reaction be-

Table 2. Homogeneous ethylene polymerization results for **17**–**24**, [Zr(η^5-C_9H_7)$_2$Cl$_2$], [Zr{Me_2Si(η^5-C_9H_6)$_2$-1,1′}Cl$_2$] and [Zr{Me_2Si(η^5-C_9H_6)(η^5-C_5Me_4)}Cl$_2$] as references. Polymerization conditions: 70 °C, 1.5 bar monomer pressure, 33 μmol Zr, 250 mL toluene, t_{Pol} = 30 min.

Complex	Activity[a,c]	Activity[a,b]
[Zr(η^5-C_9H_7)$_2$Cl$_2$]	598	352
[Zr(η^5-C_9H_6R-1)$_2$Cl$_2$] R = $CH_2CH_2CH_2OSiMe_3$ (**17**)	287	21
[Zr(η^5-C_9H_6R-1)$_2$Cl$_2$] R = $CH_2CH_2CH_2OCH_2Ph$ (**18**)	388	145
[Zr(η^5-C_9H_6R-1)$_2$Cl$_2$] R = $CH_2CH_2CH_2OSiMe_2t$Bu (**19**)	725	76
[Zr{Me_2Si(η^5-C_9H_6)$_2$-1,1′}Cl$_2$]	485	280
rac-[Zr{Me_2Si(η^5-C_9H_5R-3)$_2$-1,1′}Cl$_2$] R = $CH_2CH_2CH_2OSiMe_3$ (**20**)	88	26
[Zr{Me_2Si(η^5-C_9H_6)(η^5-C_5Me_4)}Cl$_2$]	558	180
[Zr{Me_2Si(η^5-C_9H_5R-3)-1(η^5-C_5Me_4}Cl$_2$] R = $CH_2CH_2CH_2OSiMe_3$ (**21**)	212	114
[Zr{Me_2Si(η^5-C_9H_5R-3)-1(η^5-C_5Me_4}Cl$_2$] R = $CH_2CH_2CH_2OCH_2Ph$ (**22**)	831	115
[Zr{Me_2Si(η^5-C_9H_5R-3)-1(η^5-C_5Me_4}Cl$_2$] R = CH_2CHCH_2 (**23**)	787	387
[Zr{Me_2Si(η^5-C_9H_5R-3)-1(η^5-C_5Me_4}Cl$_2$] R = $CH_2CH_2CH_2OSiMe_2t$Bu (**24**)	525	259

[a] In kg PE (mol Zr) h^{-1}. [b] Al/Zr 100:1. [c] Al/Zr 500:1.

Table 3. Heterogeneous ethylene polymerization results. Polymerization conditions: 70 °C, 1.5 bar monomer pressure, 250 mL toluene, 33 μmol Zr (approx. 300 mg of supported catalyst), Al/Zr 100:1, t_{Pol} = 30 min.

Complex	% Zr	Activity[a]
[Zr(η^5-C_9H_7)$_2$Cl$_2$]	0.60	96
[Zr(η^5-C_9H_6R-1)$_2$Cl$_2$] R = $CH_2CH_2CH_2OSiMe_3$ (**17**)	0.81	85
[Zr(η^5-C_9H_6R-1)$_2$Cl$_2$] R = $CH_2CH_2CH_2OCH_2Ph$ (**18**)	0.67	15
[Zr(η^5-C_9H_6R-1)$_2$Cl$_2$] R = $CH_2CH_2CH_2OSiMe_2t$Bu (**19**)	0.72	32
[Zr{Me_2Si(η^5-C_9H_6)$_2$-1,1′}Cl$_2$]	0.84	104
rac-[Zr{Me_2Si(η^5-C_9H_5R-3)$_2$-1,1′}Cl$_2$] R = $CH_2CH_2CH_2OSiMe_3$ (**20**)	0.85	19
[Zr{Me_2Si(η^5-C_9H_6)(η^5-C_5Me_4)}Cl$_2$]	0.94	97
[Zr{Me_2Si(η^5-C_9H_5R-3)-1(η^5-C_5Me_4}Cl$_2$] R = $CH_2CH_2CH_2OSiMe_3$ (**21**)	0.76	122
[Zr{Me_2Si(η^5-C_9H_5R-3)-1(η^5-C_5Me_4}Cl$_2$] R = $CH_2CH_2CH_2OCH_2Ph$ (**22**)	0.89	35
[Zr{Me_2Si(η^5-C_9H_5R-3)-1(η^5-C_5Me_4}Cl$_2$] R = $CH_2CH_2CH_2OSiMe_2t$Bu (**24**)	0.82	199

[a] In kg PE (mol Zr) h^{-1}.

 © 2005 Wiley-VCH Verlag GmbH & Co. KGaA, Weinheim

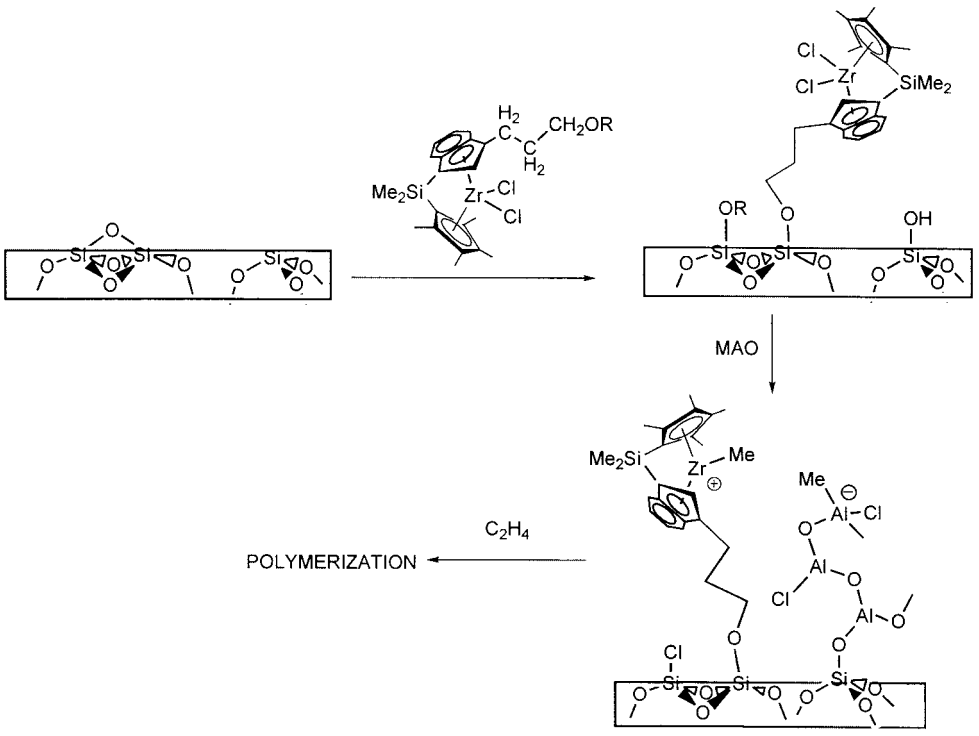

Scheme 1. Proposed mechanism in the immobilization of the catalyst at the siloxane bridge and its subsequent activation with MAO.

tween the $(CH_2)_2OR$ group and the siloxane bridges, to give surface species, which remember the structure of the analogous molecular complexes, to give more active catalysts (Scheme 1).

In addition, it is noteworthy that supported complexes **17**, **21** and **24** show similar or higher activities than their corresponding homogeneous catalysts, with a 100:1 Al/Zr ratio, showing both the advantages of supporting the complexes (reduced MAO addition to activate), and the use of pendant reactive chains (more active species).

Conclusions

We have carried out the synthesis of indenyl-containing zirconium complexes with pendant chains capable of interacting with dehydroxylated silica. We have successfully immobilized the complexes on silica and tested the activity of these supported catalysts in the polymerization of ethylene and compared the results with the reference unsubstituted complexes.

Experimental Section

General Remarks: All reactions were prepared using standard Schlenk tube techniques under dry nitrogen. Solvents were distilled from appropriate drying agents and degassed before use. $[ZrCl_4(THF)_2]$, $ZrCl_4$, C_9H_8, $Me_2Si(C_5HMe_4)Cl$, $SiMe_2Cl_2$, $BrCH_2CH_2CH_2OH$ and $(Me_3Si)_2NH$ were purchased from Aldrich and used directly. Grace Davison XPO 2407 silica (200 m^2/g, according to data from supplier) was dehydroxylated under vacuum (10^{-2} Torr) at 773 K for 16 h, cooled and stored under dry nitrogen. Ethylene (Alphagaz), iBu_3Al (TIBA, Aldrich) and MAO (EURECENE, 10, Crompton) were used without further purification. ^1H and ^{13}C spectra were recorded with Varian UNITY FT-300, Varian GEMINY FT-400 and Varian INNOVA FT-500 spectrometers and referenced to the residual deuterated solvent. Microanalyses were carried out with a Perkin–Elmer 2400 microanalyzer. Mass spectrometric analyses were performed with a Vg Autospec instrument or a Hewlett–Packard 5988A (m/z = 50–1000) (electron impact). Infrared spectra were recorded with a Nicolet Magna 550-FT spectrophotometer using an infrared cell equipped with CaF_2 or KBr windows; this setup allowed in situ studies. A total of 32 scans were typically accumulated for each spectrum (resolution 2 cm^{-1}). The samples consisted of ca. 20 mg of silica pressed into a self-supported disc of 1 cm diameter. The samples were dehydroxylated at 773 K for 16 h. Zirconocene grafting was performed using a 10^{-2} M solution of the metallocene in toluene to give approximately 1% Zr/SiO_2. The samples were warmed at 333 K for 1 h, washed with toluene and dried in vacuo at 343 K until no further change was observed (sublimation of the excess complex was observed).

Preparation of $C_9H_7(CH_2CH_2CH_2OSiMe_3)$-3 (1): $BrCH_2CH_2CH_2OSiMe_3$ (9.04 g, 43.04 mmol) was added to a solution of $Li(C_9H_7)$ (5.25 g, 43.04 mmol) in Et_2O at –78 °C. The reaction mixture was allowed to warm to room temperature and stirred for 15 h. The solvent was removed in vacuo and hexane (100 mL) was added. The mixture was filtered and the solvent removed from the filtrate under reduced pressure to yield the title compound as a yellow oil. Compound **1** was purified by flash distillation (8.47 g, 80%). ^1H NMR (400 MHz, $CDCl_3$, 25 °C): δ = 0.20 (s, 9 H, $OSiMe_3$), 1.65 and 2.08 (2 m, each 2 H, $CH_2CH_2CH_2O$), 3.40 (m, 2 H, 1-H), 3.82 (t, J = 6.3 Hz, 2 H, CH_2OSiMe_3), 6.32 (m, 1 H, 2-H), 7.26 and 7.33 (2 t, J = 7.3 Hz, each 1 H, 5-H and 8-H), 7.50 and 7.58 (2 d, J = 7.3 Hz, each 1 H, 6-H and 7-H) ppm. EI MS: m/z (%) = 246 (30) [M^+, $C_9H_7(CH_2CH_2CH_2OSiMe_3)^+$], 130 (100) [$M^+ - C_9H_7$], 115 (24) [$M^+ - CH_2CH_2CH_2OSiMe_3$].

 © 2005 Wiley-VCH Verlag GmbH & Co. KGaA, Weinheim

Preparation of $C_9H_7(CH_2CH_2CH_2OCH_2Ph)$-3 (2): The synthesis of **2** was carried out in an identical manner to **1**: $Li(C_9H_7)$ (5.25 g, 43.04 mmol) and $BrCH_2CH_2CH_2OCH_2Ph$ (12.87 g, 43.04 mmol). Yield (7.39 g, 65%). ^1H NMR (400 MHz, $CDCl_3$, 25 °C): δ = 2.43 and 2.76 (2 m, each 2 H, $CH_2CH_2CH_2O$), 3.41 (m, 2 H, 1-H), 3.66 (t, J = 6.3 Hz, 2 H, CH_2OCH_2Ph), 4.62 (s, 2 H, CH_2OCH_2Ph), 6.29 (m, 1 H, 2-H), 7.29–7.56 (m, 9 H, 5-H–8-H and OCH_2Ph) ppm. EI MS: *m*/*z* (%) = 264 (27) [M^+, $C_9H_7(CH_2CH_2CH_2OCH_2Ph)^+$], 173 (100) [$M^+ - CH_2Ph$], 91 (40) [$M^+ - C_9H_7CH_2CH_2CH_2O$].

Preparation of $C_9H_7(CH_2CH_2CH_2OSiMe_2\,tBu)$-3 (3): The synthesis of **3** was carried out in an identical manner to **1**: $Li(C_9H_7)$ (5.25 g, 43.04 mmol) and $BrCH_2CH_2CH_2OSiMe_2tBu$ (10.90 g, 43.04 mmol). Yield (7.81 g, 63%). ^1H NMR (400 MHz, $CDCl_3$, 25 °C): δ = 0.18 (s, 6 H, $OSiMe_2tBu$), 1.00 (s, 9 H, $OSiMe_2tBu$), 2.01 and 2.68 (2 m, each 2 H, $CH_2CH_2CH_2O$), 3.38 (m, 2 H, 1-H), 3.79 (t, J = 6.3 Hz, 2 H, CH_2OSiMe_2tBu), 6.28 (m, 1 H, 2-H), 7.58 and 7.65 (2 t, J = 7.3 Hz, each 1 H, 5-H and 8-H), 7.80 and 7.86 (2 d, J = 7.3 Hz, each 1 H, 6-H and 7-H) ppm. EI MS: *m*/*z* (%) = 287 (7) [M^+, $C_9H_7(CH_2CH_2CH_2OSiMe_2tBu)^+$], 231 (100) [$M^+$ – *t*Bu], 115 (45) [$M^+ - CH_2CH_2CH_2OSiMe_2tBu$].

Preparation of {$Me_2Si([C_9H_6(CH_2CH_2CH_2OSiMe_3)$-3]$_2$-1,1′} (4): $BrCH_2CH_2CH_2OSiMe_3$ (8.37 g, 38.14 mmol) was added to a solution of $Li_2[Me_2Si(C_9H_6)_2]$ (5.73 g, 19.07 mmol) in Et_2O (50 mL) at –78 °C. The mixture was allowed to warm to 25 °C and stirred for 15 h. The solvent was removed in vacuo and hexane (100 mL) was added. The mixture was filtered and the solvent removed from the filtrate under reduced pressure to yield the title compound as a yellow oil. Compound **4** was purified by flash distillation (6.28 g, 60%). ^1H NMR (400 MHz, $CDCl_3$, 25 °C, two isomers): δ = 0.06 and 0.07 (2 s, each 18 H, 4×$OSiMe_3$), –0.64 and –0.22 [2 s, each 3 H, $SiMe_2$ (*meso*)], –0.49 [s, 6 H, $SiMe_2$ (*rac*)], 1.75 and 2.50 (2 m, each 8 H, 4×$CH_2CH_2CH_2O$), 3.24 and 3.35 (2 d, J = 1.6 Hz, each 2 H, 4×1-H), 3.54 (m, 8 H, 4×CH_2OSiMe_3), 5.97 and 6.17 (2 d, J = 1.6 Hz, each 2 H, 4×2-H), 7.14–7.46 (m, 16 H, 4×5-H, 6-H, 7-H and 8-H) ppm. EI MS: *m*/*z* (%) = 548 (17) [M^+, $Me_2Si(C_9H_6CH_2CH_2CH_2OSiMe_3)_2^+$], 230 (70) [$M^+ - C_9H_6CH_2CH_2CH_2OSiMe_3 - SiMe_3$], 130 (100) [$M^+ - Me_2Si(C_9H_6CH_2CH_2CH_2OSiMe_3)(C_9H_6)$].

Preparation of {$Me_2Si[C_9H_6(CH_2CH_2CH_2OSiMe_3)$-3]-1($C_5HMe_4$)} (5): $ClMe_2Si(C_5HMe_4)$ (4.43 g, 20.8 mmol) in Et_2O (50 mL) was added to a solution of $Li[C_9H_6(CH_2CH_2CH_2OSiMe_3)$-1] (**9**) (5.25 g, 20.80 mmol) in Et_2O (50 mL) at –78 °C. The reaction mixture was allowed to warm to room temperature and stirred for 15 h. The solvent was removed in vacuo and hexane (100 mL) was added to the resulting yellow oil. The mixture was filtered and the solvent removed from the filtrate under reduced pressure to yield the title compound as a yellow oil (6.19 g, 70%). ^1H NMR (400 MHz, $CDCl_3$, 25 °C): δ = –0.31 and –0.59 (2 s, each 3 H, $SiMe_2$), 0.01 (s, 9 H, $OSiMe_3$), 1.68, 1.73, 1.86 and 1.88 (4 s, each 3 H, C_5Me_4), 1.80 and 2.50 (2 m, each 2 H, $CH_2CH_2CH_2O$), 2.91 and 3.39 (2 m, each 1 H, C_5HMe_4 and 1-H), 3.56 (t, J = 6.3 Hz, 2 H, CH_2OSiMe_3), 6.10 (d, J = 1.6 Hz, 1 H, 2-H), 7.04–7.34 (m, 4 H, 5-H–8-H) ppm. EI MS: *m*/*z* (%) = 424 (14) [M^+, $\{Me_2Si[C_9H_6(CH_2CH_2CH_2OSiMe_3)](C_5HMe_4)\}^+$], 303 (24) [$M^+ - C_5HMe_4$], 179 (100) [$M^+ - C_9H_6CH_2CH_2CH_2OSiMe_3$].

Preparation of {$Me_2Si[C_9H_6(CH_2CH_2CH_2OCH_2Ph)$-3]-1($C_5HMe_4$)} (6): The synthesis of **6** was carried out in an identical manner to **5**. $ClMe_2Si(C_5HMe_4)$ (4.33 g, 20.30 mmol) and $Li[C_9H_6(CH_2CH_2CH_2OCH_2Ph)$-1] (5.12 g, 20.30 mmol). Yield 5.39 g, 60%. ^1H NMR (400 MHz, $CDCl_3$, 25 °C): δ = –0.55 and –0.27 (2 s, each 3 H, $SiMe_2$), 1.77, 1.89, 1.91 and 1.92 (4 s, each 3 H, C_5Me_4), 1.82 and 2.56 (2 m, each 2 H, $CH_2CH_2CH_2O$), 2.94 and 3.22 (2 m, each 1 H, C_5HMe_4 and 1-H), 3.49 (t, J = 6.3 Hz, 2 H, CH_2OCH_2Ph), 4.44 (m, 2 H, OCH_2Ph), 6.13 (d, J = 1.6 Hz, 1 H, 2-H), 7.02–7.33 (m, 9 H, 5-H–8-H and OCH_2Ph) ppm. EI MS: *m*/*z* (%) = 442 (26) [M^+, $\{Me_2Si[C_9H_6(CH_2CH_2CH_2OCH_2Ph)](C_5HMe_4)\}^+$], 321 (15) [$M^+ - C_5HMe_4$], 179 (100) [$M^+ - C_9H_6CH_2CH_2CH_2OCH_2Ph$].

Preparation of {$Me_2Si(C_9H_6(CH_2CH=CH_2)$-3)-1($C_5HMe_4$)} (7): The synthesis of **7** was carried out in an identical manner to **5**. $ClMe_2Si(C_5HMe_4)$ (3.97 g, 10.15 mmol) and $Li[C_9H_6(CH_2CH=CH_2)$-1] (**10a**) (1.64 g, 10.15 mmol). Yield 2.55 g, 75%. ^1H NMR (400 MHz, $CDCl_3$, 25 °C): δ = –0.59 and –0.28 (2 s, each 3 H, $SiMe_2$), 1.67, 1.72, 1.84 and 1.88 (4 s, each 3 H, C_5Me_4), 2.88 and 3.20 (2 m, each 1 H, C_5HMe_4 and 1-H), 3.22 (m, 2 H, $CH_2CH=CH_2$), 5.06 (m, 2 H, $CH_2CH=CH_2$), 5.87 (m, 1 H, $CH_2CH=CH_2$), 6.08 (d, J = 1.6 Hz, 1 H, 2-H), 7.00–7.27 (m, 4 H, 5-H–8-H) ppm. EI MS: *m*/*z* (%) = 334 (12) [M^+, $\{Me_2Si[C_9H_6(CH_2CH=CH_2)](C_5HMe_4)\}^+$], 213 (41) [$M^+ - C_5HMe_4$], 179 (100) [$M^+ - C_9H_6CH_2CH=CH_2$].

Preparation of {$Me_2Si[C_9H_6(CH_2CH_2CH_2OSiMe_2tBu)$-3]-1($C_5HMe_4$)} (8): The synthesis of **8** was carried out in an identical manner to **5**. $ClMe_2Si(C_5HMe_4)$ (4.11 g, 16.98 mmol) and $Li[C_9H_6(CH_2CH_2CH_2OSiMe_2tBu)$-1] (5.10 g, 16.98 mmol). Yield 5.35 g, 60%. ^1H NMR (400 MHz, $CDCl_3$, 25 °C): δ = –0.58 and –0.28 (2 s, each 3 H, $SiMe_2$), –0.05 (s, 6 H, $OSiMe_2tBu$), 0.80 (s, 9 H, $OSiMe_2tBu$), 1.74, 1.78, 1.87 and 1.89 (4 s, each 3 H, C_5Me_4), 1.82 and 2.54 (2 m, each 2 H, $CH_2CH_2CH_2O$), 2.93 and 3.39 (2 m, each 1 H, C_5HMe_4 and 1-H), 3.60 (t, J = 6.3 Hz, 2 H, CH_2OSiMe_2tBu), 6.10 (d, J = 1.6 Hz, 1 H, 2-H), 7.05–7.31 (m, 4 H, 5-H–8-H) ppm. EI MS: *m*/*z* (%) = 467 (25) [M^+, $\{Me_2Si[C_9H_6(CH_2CH_2CH_2OSiMe_2tBu)](C_5HMe_4)\}^+$], 345 (35) [$M^+ - C_5HMe_4$], 179 (100) [$M^+ - C_9H_6CH_2CH_2CH_2OSiMe_2tBu$].

Preparation of Li[$C_9H_6(CH_2CH_2CH_2OSiMe_3)$-1] (9): *n*BuLi (1.60 M in hexane) (15.22 mL, 24.35 mmol) was added to a solution of **1** (5.00 g, 20.29 mmol) in Et_2O (100 mL) at –78 °C. The mixture was allowed to warm to 25 °C and stirred for 15 h. The solvent was removed in vacuo to give a yellow solid which was washed with hexane (2×50 mL) and dried under vacuum to yield a yellow solid of the title complex (4.35 g, 85%). $C_{15}H_{21}LiOSi$ (252.4): calcd. C 71.39, H 8.39; found C 71.03, H 8.30.

Preparation of Li[$C_9H_6(CH_2CH_2CH_2OCH_2Ph)$-1] (10): The synthesis of **10** was carried out in an identical manner to **9**: **2** (5.25 g, 19.86 mmol) and *n*BuLi (1.60 M in hexane) (14.90 mL, 23.83 mmol). Yield (3.49 g, 65%). ^1H NMR (400 MHz, C_6D_6/[D_8]-THF, 25 °C): δ = 2.01 and 3.05 (2 m, each 2 H, $CH_2CH_2CH_2O$), 3.45 (t, J = 6.3 Hz, 2 H, CH_2OCH_2Ph), 4.19 (s, 2 H, CH_2OCH_2Ph), 6.08 and 6.58 (2 m, each 1 H, 3-H and 2-H), 6.77–7.62 (m, 9 H, 5-H–8-H and OCH_2Ph) ppm. $C_{19}H_{19}LiO$ (270.29): calcd. C 84.43, H 7.09; found C 84.63, H 7.07.

Preparation of Li[$C_9H_6(CH_2CH=CH_2)$-1] (10a): The synthesis of **10a** was carried out in an identical manner to **9**: **2** (5.25 g, 33.60 mmol) and *n*BuLi (1.60 M in hexane) (63.00 mL, 100.80 mmol). Yield (4.08 g, 75%).^1H NMR (400 MHz, C_6D_6/[D_8]-THF, 25 °C): δ = 3.75 (m, 2 H, $CH_2CH=CH_2$), 4.92 (m, 2 H, $CH_2CH=CH_2$), 6.20 (m, 1 H, CH_2CHCH_2), 6.13 and 6.60 (2 m, each 1 H, 3-H and 2-H), 6.81–7.64 (m, 4 H, 5-H–8-H) ppm. $C_{12}H_{11}Li$ (162.2): calcd. C 88.88, H 6.84; found C 88.52, H 6.75.

Preparation of Li[$C_9H_6(CH_2CH_2CH_2OSiMe_2tBu)$-1] (11): The synthesis of **11** was carried out in an identical manner to **9**: **3** (5.00 g, 17.33 mmol) and *n*BuLi (1.60 M in hexane) (13.00 mL, 20.80 mmol). Yield (3.67 g, 72%). $C_{18}H_{27}LiOSi$ (294.4): calcd. C 73.43, H 9.24; found C 73.11, H 9.27.

 © 2005 Wiley-VCH Verlag GmbH & Co. KGaA, Weinheim

Preparation of $Li_2[Me_2Si(C_9H_5R\text{-}3)_2\text{-}1]$ (R = $CH_2CH_2CH_2OSiMe_3$) (12): The synthesis of **12** was carried out in an identical manner to **9**: **4** (5.00 g, 9.11 mmol) and *n*BuLi (1.60 M in hexane) (13.67 mL, 21.86 mmol). Yield (4.00 g, 78%). $C_{32}H_{46}Li_2O_2Si_3$ (560.8): calcd. C 68.53, H 8.27; found C 68.21, H 8.24.

Preparation of $Li_2[Me_2Si(C_9H_5R\text{-}3)\text{-}1(C_5Me_4)]$ (R = $CH_2CH_2CH_2OSiMe_3$) (13): The synthesis of **13** was carried out in an identical manner to **9**: **5** (5.00 g, 11.77 mmol) and *n*BuLi (1.60 M in hexane) (17.65 mL, 28.25 mmol). Yield (4.16 g, 81%). $C_{26}H_{38}Li_2OSi_2$ (436.6): calcd. C 71.52, H 8.77; found C 71.33, H 8.71.

Preparation of $Li_2\{Me_2Si[C_9H_5(CH_2CH_2CH_2OLi)\text{-}3]\text{-}1(C_5Me_4)\}$ (13a): The synthesis of **13a** was carried out in an identical manner to **9**: **5** (5.00 g, 11.77 mmol) and *n*BuLi (1.60 M in hexane) (22.10 mL, 35.31 mmol). Yield (3.13 g, 72%).^{1}H NMR (400 MHz, C_6D_6/[D$_8$]THF, 25 °C): δ = –0.30 and –0.58 (2 s, each 3 H, SiMe_2), 1.68, 1.70, 1.82 and 1.86 (4 s, each 3 H, C_5Me_4), 1.76 and 2.59 (2 m, each 2 H, CH_2CH_2CH$_2$O), 3.53 (t, J = 6.3 Hz, 2 H, CH_2OSiMe$_3$), 6.14 (s, 1 H, 2-H), 6.98 (m, 2 H, 5-H, 8-H), 7.29 (m, 2 H, 6-H, 7-H) ppm. $C_{23}H_{29}Li_3OSi$ (370.40): calcd. C 74.58, H 7.89; found C 74.12, H 7.92.

Preparation of $Li_2[Me_2Si(C_9H_5R\text{-}3)\text{-}1(C_5Me_4)]$ (R = $CH_2CH_2CH_2OCH_2Ph$) (14): The synthesis of **14** was carried out in an identical manner to **9**: **6** (5.00 g, 10.57 mmol) and *n*BuLi (1.60 M in hexane) (15.85 mL, 25.36 mmol). Yield (3.27 g, 68%). $C_{30}H_{36}Li_2OSi$ (454.6): calcd. C 79.27, H 7.98; found C 79.34, H 7.96.

Preparation of $Li_2[Me_2Si(C_9H_5R\text{-}3)\text{-}1(C_5Me_4)]$ (R = $CH_2CH{=}CH_2$) (15): The synthesis of **14** was carried out in an identical manner to **9**: **7** (5.00 g, 14.95 mmol) and *n*BuLi (1.60 M in hexane) (22.43 mL, 35.88 mmol). Yield (4.14 g, 80%). $C_{23}H_{28}Li_2Si$ (346.4): calcd. C 79.74, H 8.15; found C 79.29, H 8.11.

Preparation of $Li_2[Me_2Si(C_9H_5R\text{-}3)\text{-}1(C_5Me_4)]$ (R = $CH_2CH_2CH_2OSiMe_2tBu$) (16): The synthesis of **13** was carried out in an identical manner to **9**: **8** (5.00 g, 10.71 mmol) and *n*BuLi (1.60 M in hexane) (16.10 mL, 25.70 mmol). Yield (4.00 g, 78%). $C_{29}H_{44}Li_2OSi_2$ (478.7): calcd. C 72.76, H 9.26; found C 72.54, H 9.17.

Preparation of $[Zr\{\eta^5\text{-}C_9H_6(CH_2CH_2CH_2OSiMe_3)\text{-}1\}_2Cl_2]$ (17): Toluene (100 mL) was added to a solid mixture of $ZrCl_4$ (1.15 g, 4.95 mmol) and Li[$C_9H_6(CH_2CH_2CH_2OSiMe_3)$-1] (**9**) (2.50 g, 9.90 mmol). The resulting pale yellow solution was stirred for 15 h. The mixture was filtered and the solvent removed in vacuo to yield a yellow oil of the title complex (1.87 g, 58%). ^{1}H NMR (300 MHz, $CDCl_3$, 25 °C, two isomers): δ = 0.15, 0.18 (2 s, each 18 H, 4×OSiMe_3), 1.60–2.00 and 2.60–3.15 (2 m, each 8 H, 4×CH_2CH_2CH$_2$O), 3.45–3.80 (2 m, each 4 H, 4×CH_2OSiMe$_3$), 5.75 (d, J = 3 Hz, 2 H, *meso*-3-H), 5.88 (d, J = 3 Hz, 2 H, *rac*-3-H), 6.13 (d, J = 3 Hz, 2 H, *rac*-2-H), 6.37 (d, J = 3 Hz, 2 H, *meso*-2-H), 7.20–7.70 (m, 16 H, 4×5-H–8-H) ppm. ^{13}C{^{1}H} (75 MHz, $CDCl_3$, 25 °C, two isomers): δ = –0.3 (OSiMe_3), 24.3 and 24.6 (*C*H$_2$CH$_2$CH$_2$O), 30.5 (CH$_2$*C*H$_2$CH$_2$O), 61.9 (*C*H$_2$OSiMe$_3$), 99.1 (*meso*-C-3), 99.29 (*rac*-C-3), 120.2 (*meso*-C-2), 121.8 (*rac*-C-2), 118.8–139.0 (C-5–C-8) (C-4, C-9 not observed) ppm. EI MS: *m*/*z* (%) = 652 (13) [M$^+$, Zr($C_9H_6CH_2CH_2CH_2OSiMe_3)_2Cl_2^+$], 297 (100) [M$^+$ – $C_9H_6CH_2CH_2CH_2OSiMe_3$ – Cl]. $C_{30}H_{42}Cl_2O_2Si_2Zr$ (652.95): calcd. C 55.18, H 6.48; found C 55.36, H 6.45.

Preparation of $[Zr\{\eta^5\text{-}C_9H_6(CH_2CH_2CH_2OCH_2Ph)\text{-}1\}_2Cl_2]$ (18): The synthesis of **18** was carried out in identical manner to **17**. $ZrCl_4$ (1.16 g, 4.96 mmol) and Li[$C_9H_6(CH_2CH_2CH_2OCH_2Ph)$-1] **10** (2.50 g, 9.91 mmol). Yield: 2.33 g, 68%. ^{1}H NMR (300 MHz, $CDCl_3$, 25 °C, two isomers): δ = 1.84–2.07 and 2.40–3.13 (2 m, each 8 H, 4×CH_2CH_2CH$_2$O), 3.36–3.62 (m, 8 H, 4×CH_2OCH$_2$Ph), 4.03–4.58 (2 m, each 4 H, 4×OCH_2Ph), 5.68 (d, J = 3 Hz, 2 H, *meso*-3-H), 5.88 (d, J = 3 Hz, 2 H, *rac*-3-H), 6.10 (d, J = 3 Hz, 2 H, *rac*-2-H), 6.33 (d, J = 3 Hz, 2 H, *meso*-2-H), 7.14–7.68 (m, 36 H, 4×5-H–8-H and 4×OCH$_2$*Ph*) ppm. ^{13}C{^{1}H} (75 MHz, $CDCl_3$, 25 °C, two isomers): δ = 24.4 and 24.7 (*C*H$_2$CH$_2$CH$_2$O), 29.9 (CH$_2$*C*H$_2$CH$_2$O), 69.4 (*C*H$_2$OCH$_2$Ph), 72.9 (OC*H*$_2$Ph), 99.1 (*meso*-C-3), 99.3 (*rac*-C-3), 120.4 (*meso*-C-2), 122.0 (*rac*-C-2), 117.9–144.4 (C-5–C-8 and OCH$_2$*Ph*) (C-4, C-9 not observed) ppm. EI MS: *m*/*z* (%) = 688 (15) [M$^+$, Zr($C_9H_6CH_2CH_2CH_2OCH_2Ph)_2Cl_2^+$], 388 (73) [M$^+$ – $C_9H_6CH_2CH_2CH_2OCH_2Ph$ – Cl], 261 (100) [M$^+$ – $C_9H_6CH_2CH_2CH_2OCH_2Ph$ – 2 Cl – CH$_2$Ph]. $C_{38}H_{38}Cl_2O_2Zr$ (688.84): calcd. C 66.26, H 5.56; found C 66.46, H 5.52.

Preparation of $[Zr\{\eta^5\text{-}C_9H_6(CH_2CH_2CH_2OSiMe_2tBu)\text{-}1\}_2Cl_2]$ (19): The synthesis of **19** was carried out in identical manner to **17**. $ZrCl_4$ (0.99 g, 4.25 mmol) and Li[$C_9H_6(CH_2CH_2CH_2OSiMe_2tBu)$-1] (**11**) (2.50 g, 8.49 mmol). Yield: 1.66 g, 53%. ^{1}H NMR (300 MHz, $CDCl_3$, 25 °C, two isomers): δ = 0.03, 0.05 (2 s, each 12 H, OSiMe_2), 0.89, 0.91 (2 s, each 18 H, OSiMe$_2$*tBu*), 1.57–1.87 and 2.62–3.04 (2 m, each 8 H, 4×CH_2CH_2CH$_2$O), 3.57–3.71 (m, 8 H, 4×CH_2OSiMe$_2$*t*Bu), 5.68 (d, J = 3 Hz, 2 H, *meso*-3-H), 5.84 (d, J = 3 Hz, 2 H, *rac*-3-H), 6.07 (d, J = 3 Hz, 2 H, *rac*-2-H), 6.30 (d, J = 3 Hz, H, *meso*-2-H), 7.16–7.63 (m, 16 H, 4×5-H–8-H) ppm. ^{13}C{^{1}H} (75 MHz, $CDCl_3$, 25 °C, two isomers): δ = –5.2 (OSi*Me*$_2$*t*Bu), 24.1 and 24.4 (*C*H$_2$CH$_2$CH$_2$O), 26.0 (OSiMe$_2$*tBu*), 32.3 (CH$_2$*C*H$_2$CH$_2$O), 62.3 (*C*H$_2$OSiMe$_2$*t*Bu), 99.0 (*meso*-C-3), 99.2 (*rac*-C-3), 120.39 (*meso*-C-2), 212.89 (*rac*-C-2), 120.5–139.3 (C-5–C-8) (C-4, C-9 not observed) ppm. EI MS: *m*/*z* (%) = 737 (15) [M$^+$ Zr($C_9H_6CH_2CH_2CH_2OSiMe_2tBu)_2Cl_2^+$], 699 (14) [M$^+$ – Cl], 261 (100) [M$^+$ – $C_9H_6CH_2CH_2CH_2OSiMe_2tBu$ – Cl – SiMe$_2$*t*Bu]. $C_{36}H_{54}Cl_2O_2Si_2Zr$ (773.11): calcd. C 58.66, H 7.38; found C 58.39, H 7.33.

Preparation of *rac*-$[Zr(Me_2Si\{\eta^5\text{-}C_9H_5(CH_2CH_2CH_2OSiMe_3)\text{-}3\}_2\text{-}1,1')Cl_2]$ (20): Toluene (100 mL) was added to a solid mixture of [$ZrCl_4(THF)_2$] (2.06 g, 5.47 mmol) and Li$_2$\{Me$_2$Si[C_9H_5-(CH$_2$CH$_2$CH$_2$OSiMe$_3$)-3]$_2$-1,1′\} (**12**) (3.09 g, 5.47 mmol). The resulting pale yellow solution was stirred for 15 h. The mixture was filtered and the filtrate concentrated (10 mL) and cooled to –30 °C to yield an orange solid of the title complex (1.16 g, 30%). ^{1}H NMR (500 MHz, $CDCl_3$, 25 °C): δ = 0.09 (s, 18 H, 2×OSiMe_3), 1.12 (s, 6 H, SiMe_2), 1.77 and 2.86 (2 m, each 4 H, 4×CH_2CH_2CH$_2$O), 3.55 (m, 4 H, 2×CH_2OSiMe$_3$), 5.81 (s, 2 H, 2×2-H), 7.05 and 7.30 (2 t, J = 8.6 Hz, each 2 H, 2×6-H and 7-H), 7.40 and 7.53 (2 d, J = 8.6 Hz, each 2 H, 2×5-H and 8-H) ppm. ^{13}C{^{1}H} (75 MHz, $CDCl_3$, 25 °C): δ = –1.2 (SiMe_2), –0.2 (OSiMe_3), 24.7, (*C*H$_2$CH$_2$CH$_2$O), 32.9 (CH$_2$*C*H$_2$CH$_2$O), 62.3 (*C*H$_2$OSiMe$_3$), 77.4 and 85.4 (C-1 and C-3) (C-4, C-9 not observed), 117.2 (C-2), 124.5, 124.9, 126.7 and 126.8 (C-5–C-8) ppm. $C_{32}H_{46}Cl_2O_2SiZr$ (709.1): calcd. C 54.20, H 6.54; found C 54.35, H 6.57.

Preparation of $[Zr(Me_2Si\{\eta^5\text{-}C_9H_5(CH_2CH_2CH_2OSiMe_3)\text{-}3\}\text{-}1\{\eta^5\text{-}C_5Me_4\})Cl_2]$ (21): Toluene (100 mL) was added to a solid mixture of [$ZrCl_4(THF)_2$] (2.46 g, 6.53 mmol) and Li$_2$\{Me$_2$Si[C_9H_5-(CH$_2$CH$_2$CH$_2$OSiMe$_3$)-3]-1(C_5Me_4\} (**13**) (2.57 g, 6.53 mmol). The resulting pale yellow solution was stirred for 15 h. The mixture was filtered and the filtrate concentrated to 10 mL and cooled to –30 °C to yield yellow solid of the title complex (0.76 g, 20%). ^{1}H NMR (500 MHz, $CDCl_3$, 25 °C): δ = 0.08 (s, 9 H, OSiMe_3), 0.94 and 1.17 (2 s, each 3 H, SiMe_2), 1.90, 1.94, 1.95 and 2.00 (4 s, each 3 H, C_5Me_4), 1.98 and 3.00 (2 m, each 2 H, CH_2CH_2CH$_2$O), 3.63 (m, 2

 © 2005 Wiley-VCH Verlag GmbH & Co. KGaA, Weinheim

H, CH_2OSiMe$_3$), 5.59 (s, 1 H, 2-H), 7.06 and 7.33 (2 t, J = 8.6 Hz, each 1 H, 6-H and 7-H), 7.45 and 7.57 (2 d, J = 8.6 Hz, each 1 H, 5-H and 8-H) ppm. ^{13}C{^{1}H} (125 MHz, $CDCl_3$, 25 °C): δ = –0.5 (OSiMe_3), 1.0 and 1.1 (SiMe_2), 12.1, 12.6, 14.6, 15.3 (C$_5Me_4$), 24.9 ($CH_2CH_2CH_2O$), 32.7 ($CH_2CH_2CH_2O$), 62.1 (CH_2OSiMe_3), 116.3 (C-2), 124.3 and 125.4 (C-5 and C-8), 126.1 and 126.3 (C-6 and C-7), 84.3, 95.6, (C-1, C-3) (C-4, C-9 not observed), 124.0–135.3 (C_5Me$_4$) ppm. $C_{26}H_{38}Cl_2OSi_2Zr$ (584.9): calcd. C 53.39, H 6.55; found C 53.22, H 6.52.

Preparation of [Zr(Me$_2$Si{η^5-C$_9$H$_5$(CH$_2$CH$_2$CH$_2$O)-3}-1{η^5-C$_5$Me$_4$})Cl(*Zr–O*)] (21a): The synthesis of **21a** was carried out in identical manner to **21**. Li$_2${Me$_2$Si[C$_9$H$_5$(CH$_2$CH$_2$CH$_2$OSiMe$_3$)-3]-1(C$_5$HMe$_4$)} (**13a**) (2.42 g, 6.53 mmol) and [ZrCl$_4$(THF)$_2$] (2.46 g, 6.53 mmol). Yield: 0.29 g, 29%. ^{1}H NMR (500 MHz, $CDCl_3$, 25 °C): δ = 0.86 and 1.00 (2 s, each 3 H, SiMe_2), 1.64, 1.82, 1.86 and 2.01 (4 s, each 3 H, C$_5Me_4$), 1.82 and 2.96 (2 m, each 2 H, CH_2CH_2CH$_2$O), 3.95 (m, 2 H, CH_2O), 5.91 (s, 1 H, 2-H), 6.94 and 7.18 (2 t, J = 8.6 Hz, each 1 H, 6-H and 7-H), 7.34 and 7.41 (2 d, J = 8.6 Hz, each 1 H, 5-H and 8-H) ppm. ^{13}C{^{1}H} (125 MHz, $CDCl_3$, 25 °C): δ = 0.0 and 0.6 (SiMe_2), 9.8, 10.9, 13.2 and 13.3 (C$_5Me_4$), 24.5 ($CH_2CH_2CH_2O$), 29.6 ($CH_2CH_2CH_2O$), 68.9 (CH_2O), 114.4 (C-2), 122.4 and 123.6 (C-5 and C-8), 124.2 and 124.3 (C-6 and C-7), 89.2, 98.4 (C-1, C-3) (C-4, C-9 not observed), 120.0–130.9 (C_5Me$_4$) ppm. $C_{23}H_{29}ClOSiZr$ (476.2): calcd. C 58.01, H 6.14; found C 58.31, H 6.12.

Preparation of [Zr(Me$_2$Si{η^5-C$_9$H$_5$(CH$_2$CH$_2$CH$_2$OCH$_2$Ph)-3}-1{η^5-C$_5$Me$_4$})Cl$_2$] (22): The synthesis of **22** was carried out in identical manner to **21**. Li$_2${Me$_2$Si[C$_9$H$_5$(CH$_2$CH$_2$CH$_2$OCH$_2$Ph)-3]-1(C$_5$HMe$_4$)} (**14**) (1.96 g, 5.65 mmol) and [ZrCl$_4$(THF)$_2$] (2.13 g, 5.65 mmol). Yield: 0.86 g, 26%. ^{1}H NMR (500 MHz, $CDCl_3$, 25 °C): δ = 0.89 and 1.09 (2 s, each 3 H, SiMe_2), 1.80, 1.87, 1.90 and 1.94 (4 s, each 3 H, C$_5Me_4$), 1.89 and 2.98 (2 m, each 2 H, CH_2CH_2CH$_2$O), 3.44 (m, 2 H, CH_2OCH$_2$Ph), δ_A = 4.50, δ_B = 4.48 (AB, J_{AB} = 12.3 Hz, 2 H, OCH_2Ph), 5.50 (s, 1 H, 2-H), 6.98 and 7.25 (2 t, J = 8.6 Hz, each 1 H, 6-H and 7-H), 7.41 and 7.52 (2 d, J = 8.6 Hz, each 1 H, 5-H and 8-H), 7.21–7.30 (m, 5 H, OCH$_2$*Ph*) ppm. ^{13}C{^{1}H} (125 MHz, $CDCl_3$, 25 °C): δ = 1.1 and 1.4 (SiMe_2), 12.3, 12.5, 14.7, 15.3 (C$_5Me_4$), 25.2 ($CH_2CH_2CH_2O$), 29.9 ($CH_2CH_2CH_2O$), 72.9 (CH_2OCH_2Ph), 77.4 (OCH_2Ph), 116.4 (C-2), 124.3 and 125.4 (C-5 and C-8), 126.2 and 126.3 (C-6 and C-7), 84.5, 95.6 (C-1, C-3) (C-4, C-9 not observed), 124.0–138.5 (C_5Me$_4$) ppm. $C_{30}H_{36}Cl_2OSiZr$ (602.8): calcd. C 59.77, H 6.02; found C 59.51, H 5.95.

Preparation of [Zr(Me$_2$Si{η^5-C$_9$H$_5$(CH$_2$CH=CH$_2$)-3}-1{η^5-C$_5$Me$_4$})Cl$_2$] (23): The synthesis of **23** was carried out in identical manner to **21**. Li$_2${Me$_2$Si[C$_9$H$_5$(CH$_2$CH=CH$_2$)-3]-1(C$_5$HMe$_4$)} (**15**) (2.59 g, 7.47 mmol) and [ZrCl$_4$(THF)$_2$] (2.82 g, 7.47 mmol). Yield: 0.85 g, 23%. ^{1}H NMR (500 MHz, $CDCl_3$, 25 °C): δ = 0.93 and 1.17 (2 s, each 3 H, SiMe_2), 1.84, 1.93, 1.94 and 2.00 (4 s, each 3 H, C$_5Me_4$), δ_A = 3.72, $\delta_{A'}$ = 3.68 (AA′BB′C, $J_{AA'}$ = 16.4 Hz, 2 H, CH_2CH=CH$_2$), δ_B = 5.06, $\delta_{B'}$ = 5.09 (AA′BB′C, $J_{BB'}$ = 1.1, J_{BC} = 2.4, $J_{BC'}$ = 10 Hz, 2 H, CH$_2$CH=CH_2), 5.61 (s, 1 H, 2-H), δ_C = 5.98 (AA′BB′C, J_{AC} = $J_{A'C}$ = 6.3 Hz, 1 H, CH$_2$CH=CH$_2$), 7.05 and 7.34 (2 t, J = 8.6 Hz, each 1 H, 6-H and 7-H), 7.47 and 7.57 (2 d, J = 8.6 Hz, each 1 H, 5-H and 8-H) ppm. ^{13}C{^{1}H} (125 MHz, $CDCl_3$, 25 °C): δ = 1.1 and 1.4 (SiMe_2), 12.1, 12.5, 14.9, 15.3 (C$_5Me_4$), 33.4 (CH_2CH=CH$_2$), 116.3 (CH$_2$CH=CH_2), 136.0 (CH$_2$CH=CH$_2$), 117.1 (C-2), 124.3 and 125.5 (C-5 and C-8), 126.4 and 126.5 (C-6 and C-7), 84.5, 98.3 (C-1, C-3) (C-4, C-9 not observed), 124.1–137.0 (C_5Me$_4$) ppm. $C_{23}H_{28}Cl_2SiZr$ (494.7): calcd. C 55.84, H 5.71; found C 55.92, H 5.73.

Preparation of [Zr(Me$_2$Si{η^5-C$_9$H$_5$(CH$_2$CH$_2$CH$_2$OSiMe$_2$*t*Bu)-3}-1{η^5-C$_5$Me$_4$})Cl$_2$] (24): The synthesis of **24** was carried out in identical manner to **21**. Li$_2${Me$_2$Si[C$_9$H$_5$(CH$_2$CH$_2$CH$_2$OSiMe$_2$*t*Bu)-3]-1(C$_5$HMe$_4$)} (**16**) (2.56 g, 5.36 mmol) and [ZrCl$_4$(THF)$_2$] (2.02 g, 5.36 mmol). Yield 1.00 g, 30%. ^{1}H NMR (500 MHz, $CDCl_3$, 25 °C): δ = 0.08 (s, 6 H, OSiMe_2*t*Bu), 0.96 and 1.18 (2 s, each 3 H, SiMe_2), 0.90 (s, 9 H, OSiMe_2*tBu*), 1.90, 1.93, 1.94 and 2.00 (4 s, each 3 H, C$_5Me_4$), 1.85 and 3.02 (2 m, each 2 H, CH_2CH_2CH$_2$O), 3.64 (m, 2 H, CH_2OSiMe$_2$*t*Bu), 5.61 (s, 1 H, 2-H), 7.05 and 7.33 (2 t, J = 8.6 Hz, each 1 H, 6-H and 7-H), 7.48 and 7.60 (2 d, J = 8.6 Hz, each 1 H, 5-H and 8-H) ppm. ^{13}C{^{1}H} (125 MHz, $CDCl_3$, 25 °C): δ = –5.0 (OSiMe_2*t*Bu), 1.4 and 1.7 (SiMe_2), 12.4, 12.7, 14.9, 15.5 (C$_5Me_4$), 25.1 ($CH_2CH_2CH_2O$), 26.2 and 18.6 (OSiMe$_2$*tBu*), 33.1 ($CH_2CH_2CH_2O$), 62.8 (CH_2OSiMe$_2$*tBu*), 116.7 (C-2), 124.6 and 125.7 (C-5 and C-8), 126.3 and 126.5 (C-6 and C-7), 84.6, 95.9 (C-1, C-3) (C-4, C-9 not observed), 119.2–138.1 (C_5Me$_4$) ppm. $C_{29}H_{44}Cl_2OSi_2Zr$ (627.0): calcd. C 55.56, H 7.07; found C 55.61, H 7.08.

Preparation of [Zr(Me$_2$Si{η^5-C$_9$H$_5$(CH$_2$CH$_2$CH$_2$O)-3}-1{η^5-C$_5$Me$_4$})Me(*Zr–O*)] (25): The synthesis of **25** was carried out in identical manner to **26**. MgMeBr (3 M in THF) (0.21 mL, 0.63 mmol) and **21a** (0.30 g, 0.63 mmol). Yield: 0.24 g, 83%. ^{1}H NMR (500 MHz, C_6D_6, 25 °C): δ = –1.13 (s, 3 H, Zr–*Me*), 0.67 and 0.71 (2 s, each 3 H, SiMe_2), 1.70, 1.84, 1.87 and 2.03 (4 s, each 3 H, C$_5Me_4$), 1.56 and 2.65 (2 m, each 2 H, CH_2CH_2CH$_2$O), 3.89 (m, 2 H, CH_2O), 5.97 (s, 1 H, 2-H), 6.91 and 7.14 (2 t, J = 8.6 Hz, each 1 H, 6-H and 7-H), 7.32 and 7.36 (2 d, J = 8.6 Hz, each 1 H, 5-H and 8-H) ppm. ^{13}C{^{1}H} (125 MHz, C_6D_6, 25 °C): δ = –3.1 and –3.0 (SiMe_2), 10.7, 11.8, 14.0 and 14.6 (C$_5Me_4$), 24.5 (Zr–*Me*), 25.9 ($CH_2CH_2CH_2O$), 32.0 ($CH_2CH_2CH_2O$), 68.3 (CH_2O), 115.7 (C-2), 123.9 and 124.0 (C-5 and C-8), 126.1 and 126.2 (C-6 and C-7), 82.20, 93.11 (C-1, C-3) (C-4, C-9 not observed), 117.66–128.74 (C_5Me$_4$) ppm. $C_{24}H_{32}OSiZr$ (455.8): calcd. C 63.24, H 7.08; found C 63.34, H 7.09.

Preparation of [Zr(Me$_2$Si{η^5-C$_9$H$_5$(CH$_2$CH$_2$CH$_2$OSiMe$_2$*t*Bu)-3}-1{η^5-C$_5$Me$_4$})Me$_2$] (26): MgMeBr (3 M in THF) (0.38 mL, 1.15 mmol) was added to a solution of **24** (0.30 g, 0.48 mmol) in THF (50 mL) at –78 °C. The reaction mixture was allowed to warm to room temperature and stirred for 4 h. The solvent was removed in vacuo and hexane (25 mL) added. The mixture was filtered and the solvent was removed from the filtrate in vacuo to yield the title complex (0.24 g, 87%). ^{1}H NMR (500 MHz, C_6D_6, 25 °C): δ = –1.42 and –0.36 (2 s, each 3 H, Zr–*Me*), 0.04 (s, 6 H, OSiMe_2*t*Bu), 0.98 and 1.83 (2 s, each 3 H, SiMe_2), 0.97 (s, 9 H, OSiMe_2*tBu*), 1.61, 0.50, 0.67 and 1.74 (4 s, each 3 H, C$_5Me_4$), 1.80 and 3.00 (2 m, each 2 H, CH_2CH_2CH$_2$O), 3.55 (m, 2 H, CH_2OSiMe$_2$*t*Bu), 5.45 (s, 1 H, 2-H), 6.88 and 7.16 (2 t, J = 8.6 Hz, each 1 H, 6-H and 7-H), 7.26 and 7.57 (2 d, J = 8.6 Hz, each 1 H, 5-H and 8-H) ppm. ^{13}C{^{1}H} (125 MHz, C_6D_6, 25 °C): δ = –5.0 (OSiMe_2*t*Bu), 11.5 and 25.5 (SiMe_2), 1.0, 1.3, 14.9, 18.4 (C$_5Me_4$), 24.6 ($CH_2CH_2CH_2O$), 25.5 and 21.4 (OSiMe$_2$*tBu*), 33.7 ($CH_2CH_2CH_2O$), 36.5 and 36.7 (Zr–*Me*), 62.3 (CH_2OSiMe$_2$*tBu*), 117.5 (C-2), 126.3 and 124.2 (C-5 and C-8), 124.0 and 127.7 (C-6 and C-7), 80.11, 90.38 (C-1, C-3) (C-4, C-9 not observed), 120.8–129.5 (C_5Me$_4$) ppm. $C_{31}H_{50}OSi_2Zr$ (586.1): calcd. C 63.52, H 8.60; found C 63.68, H 8.64.

X-ray Crystal-Structure Determination of [(Zr{C$_9$H$_6$-(CH$_2$CH$_2$CH$_2$O)-1}Cl$_2$)$_2$(*Zr–O*)] (17a): Intensity data were collected with a NONIUS-MACH3 diffractometer equipped with a graphite monochromator and a Mo-K_α radiation source (λ = 0.71073 Å) using an $\omega/2\theta$-scan technique. The final unit-cell parameters were determined from 25 well-centered reflections and refined by least-squares methods. Data were corrected for Lorentz and polarization effects but not for absorption. The structure was solved by direct methods using the SHELXS computer program[24]

 © 2005 Wiley-VCH Verlag GmbH & Co. KGaA, Weinheim

and refined on F^2 by full-matrix least squares (SHELXL-97).[25] All non-hydrogen atoms were refined with anisotropic thermal parameters. The hydrogen atoms were included in calculated positions and were refined with an overall isotropic temperature factor using a riding model. Weights were optimized in the final cycles. Crystallographic data are given in Table 4. CCDC-259059 contains the supplementary crystallographic data for this paper. These data can be obtained free of charge from The Cambridge Crystallographic Data Centre via www.ccdc.cam.ac.uk/data_request/cif.

Table 4. Crystal data and structure refinement for **17a**.

Emprical formula	$C_{12}H_{12}Cl_2OZr$
Formula mass	334.34
T [K]	293(2)
Crystal system	orthorombic
Space group	P_{bca}
a [Å]	12.2690(10)
b [Å]	13.4540(10)
c [Å]	14.4320(10)
V [Å^3]	2382.2(3)
Z	8
D_c [g cm^{-3}]	1.864
μ [mm^{-1}]	1.345
F(000)	1328
Crystal dimensions [mm]	0.3×0.2×0.1
θ range [°]	2.65 to 24.27
hkl ranges	$0 \le h \le 14$, $0 \le k \le 15$, $0 \le l \le 17$
No. of reflections measured	2096
Reflections observed	1084
Goodness-of-fit on F^2	0.965
Final R indices [$I > 2\sigma(I)$][a]	$R_1 = 0.0522$, $wR_2 = 0.1015$
Largest difference peak [e/Å^3]	0.509/–0.502

[a] $R_1 = \Sigma||F_o| - |F_c||/\Sigma|F_o|$; $wR_2 = [\Sigma[w(F_o^2 - F_c^2)^2]/\Sigma[w(F_o^2)^2]^{0.5}$.

Homogeneous Polymerization Experiments: Polymerizations were carried out in a 1-L glass reactor using toluene as a solvent (250 mL). Catalysts (33 μmol) were treated with the appropriate quantity of a solution of MAO in toluene (10% Al) for 15 min. Toluene (230 mL), TIBA scavenger (2 mL) and activated catalyst were introduced, in this order, into the reactor and the temperature was fixed at 343 K. The nitrogen was removed and a continuous flow of ethylene (1.5 bar) was introduced over 30 min. The reaction mixture was then quenched by the addition of acidified methanol. The polymer was collected by filtration, washed with methanol and dried under vacuum at room temperature for 24 h.

Heterogeneous Polymerization Experiments: The supported catalysts were prepared under an inert gas using Schlenk techniques and a glove-box. A solution of the zirconocene complex (quantity needed to obtain a theoretical level of 1% Zr/SiO_2) in toluene (30 mL) was added to partially dehydroxylated silica (1.00 g) and the mixture was stirred at 333 K for 16 h. The slurries were filtered through fritted discs and washed with toluene (10×20 mL). The resultant solids were carefully washed with toluene and dried under vacuum. Polymerizations were carried out in a 1-L glass reactor using toluene as a solvent (250 mL). The supported catalysts (approx. 300 mg) were treated with the appropriate quantity of a solution of MAO in toluene (10% Al) for 15 min. The solvent and the volatiles were removed in vacuo. Toluene (230 mL), TIBA scavenger (2 mL) and activated catalyst in freshly distilled toluene (20 mL) were introduced, in this order, into the reactor and the temperature was fixed at 343 K. The nitrogen was removed and a continuous flow of ethylene (1.5 bar) was introduced over 30 min. The reaction mixture was then quenched by the addition of acidified methanol. The polymer was collected by filtration, washed with methanol and dried under vacuum at room temperature for 24 h.

Acknowledgments

We gratefully acknowledge financial support from the Ministerio de Educación y Ciencia, Spain (grant nos. BQU2002-04638-C02-01 and MAT2003-05345), the Junta de Comunidades de Castilla–La Mancha (grant nos. PAC-02-003 PAI-02-010), and the Universidad Rey Juan Carlos (GVC-2004-165). P. C. and C. A. acknowledge fellowships from REPSOL-YPF-UCLM (contracts CTR-01-165 and CTR-00-084).

[1] A. Razavi, *Metallocene catalyst technology and environment*, Clean Processes and Environment: the Catalytic Evolution, Feluy, Belgium, **1999**.
[2] D. J. B. Potter, L. Tattum, "Polypropylene Annual Review", *Chem. Week* **1999**, *30*, 4–11, supplement.
[3] W. Kaminsky, *Macromol. Chem. Phys.* **1996**, *197*, 3907–3945.
[4] W. Kaminsky, M. Arndt, *Adv. Polym. Sci.* **1997**, *127*, 143–187.
[5] W. Kaminsky, D. Arrowsmith, C. Strübel, *J. Polym. Sci., Part A: Polym. Chem.* **1999**, *37*, 2959–2968.
[6] R. Goertzki, G. Fink, B. Tesche, B. Steinmetz, R. Rieger, W. Uzick, *J. Polym. Sci., Part A: Polym. Chem.* **1999**, *37*, 677–682.
[7] P. Roos, G. B. Meier, J. J. C. Samson, G. Weicker, K. R. Westerterp, *Macromol. Rapid Commun.* **1997**, *18*, 319–324.
[8] See, for example: a) U. Siemeling, *Chem. Rev.* **2000**, *100*, 1495–1526; b) P. Jutzi, T. Redeker, *Eur. J. Inorg. Chem.* **1998**, 663–674; c) R. Leino, P. Lehmus, A. Lehtonen, *Eur. J. Inorg. Chem.* **2004**, 3201–3222; d) B. Y. Lee, J. S. Oh, *J. Organomet. Chem.* **1998**, *552*, 313–317.
[9] a) M. Galan-Fereres, T. Koch, E. Hey-Hawkins, M. S. Eisen, *J. Organomet. Chem.* **1999**, *580*, 145; b) M. Antberg, H. Lüker, L. Böhm, *Eur. Pat. 293815*, **1988**.
[10] J. Sancho-Royo, G. Hidalgo-Llinas, A. Muñoz-Escalona-Lafuente, F. Martínez-Nuñez, C. Martín-Marcos, P. Lafuente-Cañas, B. Peña-Garcia, *Eur. Pat. Appl. 839836*, 1998.
[11] B. Y. Lee, J. S. Oh, *Macromolecules* **2000**, *33*, 3194–3195.
[12] J. Blümel, *J. Am. Chem. Soc.* **1995**, *117*, 2112–2113.
[13] C. Krüger, F. Lutz, M. Nolte, G. Erker, M. Aulbac, *J. Organomet. Chem.* **1993**, *452*, 79.
[14] G. Erker, M. Aulbach, M. Knickmeier, D. Winbermühle, C. Krüger, S. Werner, *J. Am. Chem. Soc.* **1993**, *115*, 4590–4601.
[15] W. Kaminsky, A. Laban, *Appl. Catal., A* **2001**, *222*, 47–61.
[16] B. A. Morrow, *Stud. Surf. Sci. Catal.* **1990**, *57*, 161.
[17] M. C. Haag, C. Krug, J. Dupont, G. Barrera, J. H. Z. dos Santos, T. Uozumi, T. Sano, K. Soga, *J. Mol. Cat. A: Chem.* **2001**, *169*, 275–281.
[18] P. Hoffman, E. Knoezinger, *Surf. Sci.* **1987**, *188*, 181.
[19] L. T. Zhuraviev, *Colloids Surf., A* **1993**, *74*, 71.
[20] J. H. Z. dos Santos, C. Drug, M. Barbosa, F. C. Stedile, J. Dupont, M. de Camargo, *J. Mol. Catal. A: Chem.* **1999**, *139*, 199–207.
[21] B. A. Morrow, I. A. Cody, *J. Phys. Chem.* **1976**, *80*, 1998.
[22] C. Alonso, A. Antiñolo, F. Carrillo-Hermosilla, P. Carrión, A. Otero, E. Villaseñor, J. Sancho, *J. Mol. Cat. A: Chem.* **2004**, *220*, 286.
[23] J. C. W. Chien, *Top. Catal.* **1999**, *7*, 23–26.
[24] G. M. Sheldrick, *Acta Crystallogr., Sect. A* **1990**, *46*, 467.
[25] G. M. Sheldrick, *Program for the Refinement of Crystal Structures from Diffraction Data*, University of Göttingen, Göttingen, Germany, **1997**.

Received: February 24, 2005
Published Online: June 21, 2005

Synthetic Applications of Lawesson's Reagent in Reactions with Cu^{I} Alkoxides

Weifeng Shi[a] and Alexander Rothenberger*[a]

Dedicated to Prof. Reinhart Ahlrichs on the occasion of his 65th birthday

Keywords: Metal alkoxide / P ligands / S ligands / Elimination

The reaction of Lawesson's reagent with CuO*t*Bu and tertiary phosphanes produced the complexes $[Cu_2(\mu_2\text{-}ArS_2P\text{–}O\text{–}PS_2Ar)(PPh_3)_4]$ (**1**) (Ar = *p*-C_6H_4OMe) and $[Cu_4\{Ar(\mu_2\text{-}S)_2P\text{–}O\text{–}P(\mu_2\text{-}S)_2Ar\}_2(dppa)_2]$ (**2**) (dppa = $Ph_2PNHPPh_2$) in high yields. The ligand $[ArS_2P\text{–}O\text{–}PS_2Ar]^{2-}$ is the first of a new family of dianionic P/S ligands.
(© Wiley-VCH Verlag GmbH & Co. KGaA, 69451 Weinheim, Germany, 2005)

Introduction

Coordination chemistry with phosphorus- and sulfur-containing ligands is still an active area of research.[1] The motivation for research in this field is diverse and includes the use of thio-functionalised organophosphorus compounds as additives to vulcanisation processes, as precursors for CVD processes and as insecticides.[2–4] Recent activities in this field made use of silyl esters of diphenylphosphanyldithioic and phenyltrithiophosphonic acid as starting materials for coinage metal clusters.[5] Also the coordination chemistry of other P/S-containing anions, e.g., phosphorodithioato and -selenolato anions $[(RO)_2PE_2]^-$ (R = organic group; E = S, Se), with transition metal cations has received much attention.[6] Lawesson's reagent,[7] widely known as a powerful thionation reagent in organic synthesis, offers another route to complexes containing P/S-based anionic ligands (Scheme 1).[8]

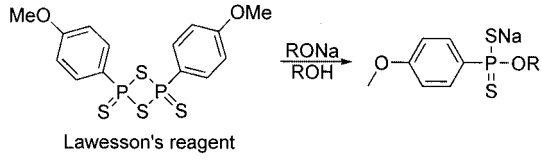

Scheme 1. Synthesis of sodium phosphonodithioate salts (R = Me, Et, *i*Pr).

Metathesis of the sodium phosphonodithioate salts (Scheme 1) gave rise to several metal complexes.[8] The generated *O*-alkyl (4-methoxyphenyl)phosphonodithioato ligands are bidentate and chelate metal atoms via the S atoms, whilst the introduced alkoxide group is not involved in coordination. As part of a wider study of the reactivity of late transition metal alkoxides, we have studied reactions of CuO*t*Bu with Lawesson's reagent in aprotic solvents and report here the first results.

Results and Discussion

When Lawesson's reagent was heated with 2 equiv. of CuO*t*Bu in toluene, a yellow precipitate was formed which dissolved upon addition of PPh_3. Crystallization from a mixture of dichloromethane and pentane gave, to our surprise, no phosphane-stabilised copper(I) phosphonodithioate, which could have been regarded as analogous compound to the sodium phosphonodithioate salts prepared by Woollins et al. (Scheme 1).[8] Instead, the Cu^{I} pyrophosphonodithioate $[Cu_2(\mu_2\text{-}ArS_2P\text{–}O\text{–}PS_2Ar)(PPh_3)_4]$ (**1**) (Ar = *p*-C_6H_4OMe) was obtained in 80% yield (Scheme 2).

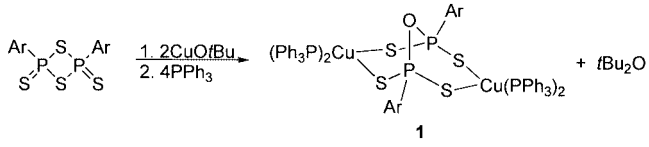

Scheme 2. Synthesis of **1** (Ar = *p*-C_6H_4OMe).

The structure of **1** was initially determined by X-ray analysis (Figure 1). The dianionic ligand $[ArS_2P\text{–}O\text{–}PS_2Ar]^{2-}$ generated in the reaction of CuO*t*Bu with Lawesson's reagent bridges two $[Cu(PPh_3)_2]^+$ ions. Compound **1** is consists of two puckered annulated six-membered $[CuS_2P_2O]$ rings and an organic shell of phenyl rings of the PPh_3

[a] Institut für Anorganische Chemie, Universität Karlsruhe, Engesserstraße 15, 76131 Karlsruhe, Germany
E-mail: ar252@chemie.uni-karlsruhe.de
Supporting information for this article is available on the WWW under http://www.eurjic.org or from the author.

 DOI: 10.1002/ejic.200500220 © 2005 Wiley-VCH Verlag GmbH & Co. KGaA, Weinheim

ligands (each one disordered over two positions; 50:50) and *p*-C_6H_4OMe groups from Lawesson's reagent. The Cu^I centres show a distorted tetrahedral coordination environment.

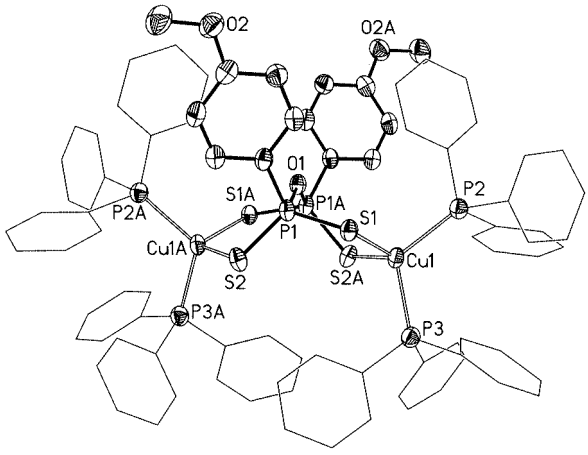

Figure 1. Molecular structure of **1** in the solid state (ellipsoids at 50% probability level; hydrogen atoms are omitted for clarity; label A denotes symmetry operation $-x + 1, y, -z - 1/2$). Selected bond lengths [Å] and angles [°]: Cu(1)–P(3) 2.3181(15), Cu(1)–P(2) 2.3193(14), Cu(1)–S(1) 2.3643(14), Cu(1)–S(2A) 2.3749(15), P(1)–O(1) 1.640(2), P(1)–S(2) 1.9909(17), P(1)–S(1) 1.9927(16); O(1)–P(1)–S(2) 110.33(12), O(1)–P(1)–S(1) 110.01(7), S(2)–P(1)–S(1) 117.41(8), P(1A)–O(1)–P(1) 130.3(3).

The P–O and P–S distances in **1** are in good agreement with values observed in $[K_2(C_{10}H_6)PS_2(\mu\text{-}O)PS_2]$, which is the closest related compound to **1**.[9] The $^{31}P\{H\}$ NMR spectrum was recorded from crystals of **1** dissolved in $CDCl_3$ (verified by redetermination of the unit cell). Resonances at $\delta = 91.5$ ppm for the generated $[ArS_2P\text{–}O\text{–}PS_2Ar]^{2-}$ dianion and at $\delta = -3.6$ ppm for coordinated PPh_3 ligands were observed and the IR spectrum showed a strong band at $\tilde{\nu}_{as}(P\text{–}O\text{–}P) = 841\ cm^{-1}$. The detailed mechanism of the formation of the $[ArS_2P\text{–}O\text{–}PS_2Ar]^{2-}$ dianion in **1** is difficult to confirm. We propose the initial formation of an intermediate Cu^I phosphonodithioate salt $[ArP(OtBu)S_2Cu]$, which instantly decomposes to form tBu_2O and **1**. It was impossible to isolate and characterize intermediate complexes. The separation of tBu_2O from the solvent toluene cannot be achieved by distillation, and in GC/MS experiments tBu_2O was not detected due to large solvent excess. The reaction was therefore performed in C_6D_6 and all volatile products were distilled off. Redistillation into an NMR tube afforded a sample containing tBu_2O formed in the reaction (Supporting Information; for Supporting Informations see also the footnote on the first page of this article). Reactions of CuO*t*Bu with Lawesson's reagent in the presence of several different phosphane ligands were also performed. Addition of dppa (dppa = $Ph_2PNHPPh_2$) afforded the tetranuclear complex $[Cu_4\{Ar(\mu_2\text{-}S)_2P\text{–}O\text{–}P(\mu_2\text{-}S)_2Ar\}_2(dppa)_2]$ (**2**) (Scheme 3, Figure 2).

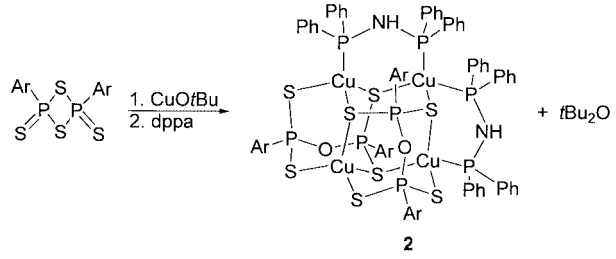

Scheme 3. Synthesis of **2** (Ar = *p*-C_6H_4OMe; dppa = $Ph_2PNHPPh_2$).

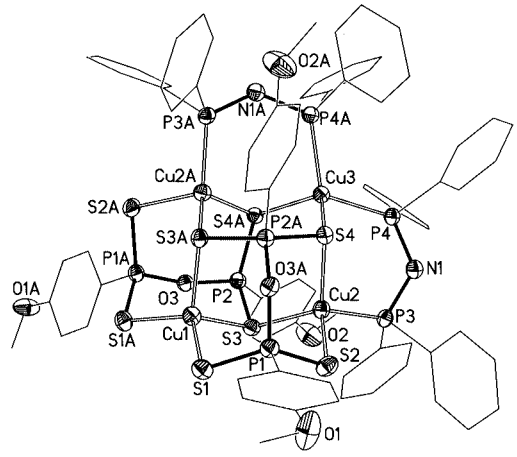

Figure 2. Molecular structure of **2** in the solid state (ellipsoids at 50% probability level; hydrogen atoms are omitted for clarity). Label A denotes symmetry operation $-x - 1, y, -z + 3/2$. Selected bond lengths [Å] and angles [°]: Cu(1)–S(1) 2.2958(16), Cu(1)–S(3) 2.3394(19), Cu(2)–P(3) 2.2209(19), Cu(2)–S(3) 2.3178(16), Cu(2)–S(4) 2.337(2), Cu(2)–S(2) 2.3570(17), Cu(3)–P(4) 2.3318(18), Cu(3)–S(4) 2.3641(16), S(1)–P(1) 1.994(2), S(2)–P(1) 1.990(3), S(3)–P(2) 2.011(2), S(4)–P(2A) 2.027(2), P(1)–O(3A) 1.662(5), P(2)–O(3) 1.613(4), P(2)–S(4A) 2.027(2), P(3)–N(1) 1.707(6), P(4)–N(1) 1.709(5); O(3A)–P(1)–S(2) 109.66(19), O(3A)–P(1)–S(1) 110.14(17), S(2)–P(1)–S(1) 118.99(12), O(3)–P(2)–S(3) 108.20(18), S(3)–P(2)–S(4A) 119.43(10), P(3)–N(1)–P(4) 127.3(3), P(2)–O(3)–P(1A) 136.3(3).

In the solid state **2** consists of two fused adamantane cage frameworks in which two $[ArS_2P\text{–}O\text{–}PS_2Ar]^{2-}$ dianions coordinate the Cu atoms Cu(1,2,2A). Cu(3) is located in the periphery of the cluster and two dppa ligands complete the remaining coordination sites of Cu(2,2A,3). Like in **1**, Cu atoms in **2** exhibit distorted tetrahedral coordination environments but the new ligand $[Ar(S)_2P\text{–}O\text{–}PS_2Ar]^{2-}$ now bridges two Cu atoms via the S atoms S(3,3A,4,4A), whilst the remaining S atoms S(1,1A,2,2A) are coordinated to one Cu atom each. Spectroscopic data and observed bond lengths in **2** verify the uniform composition of crystals of **2** and can be compared with **1** or $[K_2(C_{10}H_6)PS_2(\mu\text{-}O)PS_2]$.[9]

Conclusions

The results presented here show that the reaction of the Cu^I alkoxide CuO*t*Bu and Lawesson's reagent in toluene produces Cu^I complexes containing the new dianionic ligand

 © 2005 Wiley-VCH Verlag GmbH & Co. KGaA, Weinheim

$[ArS_2P–O–PS_2Ar]^{2–}$ in high yield. Currently, investigations in this area are extended to different Lawesson-type reagents, metal alkoxides and phosphane ligands. Studies of the influence of organic substituents of transition metal alkoxides on the fragmentation of Lawesson-type reagents will be the subject of future work in this area. Compounds **1** and **2** are the first representatives of a range of metal complexes currently prepared using these ligands and illustrate that a variety of coordination modes is to be expected.

Experimental Section

General Remarks: All operations were carried out under purified dinitrogen. Toluene was dried with sodium, dichloromethane was dried with CaH_2, pentane was dried with $LiAlH_4$ and freshly distilled. Chemicals were purchased from Aldrich. Cu*O*t*Bu and dppa were prepared according to published procedures.[10,11]

1: To a solution of Lawesson's reagent (202 mg, 0.50 mmol) in toluene (12 mL) was added dropwise a solution of Cu*O*t*Bu (136 mg, 1.00 mmol) in toluene (10 mL). The resulting yellow solution was refluxed for about 5 h during which time a color change to brown and the formation of a yellow precipitate was observed. The precipitate was dissolved by addition of a solution of PPh_3 (524 mg, 2.0 mmol) in toluene (10 mL). The solvent was removed under reduced pressure. Addition of CH_2Cl_2 (3 mL) and pentane (5 mL) and storage of the solution at room temp. for 1 d produced colorless crystals; yield 0.68 g (81%); m.p. 194 °C. ^{1}H NMR (400 MHz, $CDCl_3$, 25 °C): δ = 7.9–6.7 (m., 19 H, ar. H), 3.8 (s, 3 H, OCH_3) ppm. ^{13}C NMR (100 MHz, $CDCl_3$, 25 °C): δ = 161.5–113.1 (ar. C), 55.3 (s, OCH_3) ppm. ^{31}P NMR (162 MHz, $CDCl_3$, 25 °C, 65% H_3PO_4): δ = 91.2 (s, $ArPS_2O$), –3.6 (s, $CuPPh_3$) ppm. IR (KBr): $\tilde{\nu}$ = 3046 w, 1593 s, 1431 (P–C), 1250 s, 1105 s, 841 s (P–O–P), 657 s (P=S) cm^{-1}. $C_{86}H_{74}Cu_2O_3P_6S_4$ (1594.2): calcd. C 64.6, H 4.6; found C 64.4, H 4.6.

2: To a solution of Lawesson's reagent (202 mg, 0.50 mmol) in toluene (12 mL) was added dropwise a solution of Cu*O*t*Bu (136 mg, 1.00 mmol) in toluene (10 mL). The resulting yellow solution was refluxed for about 5 h during which time a colour change to brown and the formation of a yellow precipitate was observed. The precipitate was dissolved by addition of a solution of dppa (385 mg, 1.00 mmol) in toluene (10 mL). The solvent was removed under reduced pressure. Addition of CH_2Cl_2 (3 mL) and pentane (5 mL) and storage of the solution at room temp. for 1 d produced colorless crystals of **2**; yield 0.42 g (79%); m.p. 201 °C. ^{1}H NMR (400 MHz, CD_2Cl_2, 25 °C): δ = 8.1–6.9 (m., 24 H, ar. H), 5.4 (s, 1 H, NH, next to peak of CH_2Cl_2), 3.9–3.8 (s, 3 H, OCH_3) ppm. ^{13}C NMR (100 MHz, CD_2Cl_2, 25 °C): δ = 162.2–113.5 (10 C, ar. C), 55.8 (s, 1 C, OCH_3) ppm. ^{31}P NMR (162 MHz, CD_2Cl_2, 25 °C, 65% H_3PO_4): δ = 89.1 (s, $ArPS_2O$), 38.3 (br. s, $NPPh_2$) ppm. IR (KBr): $\tilde{\nu}$ = 3297 w (N–H), 3051 w, 1596 s, 1435 s (P–C), 1258 s, 1107 s, 880 bs (P–O–P), 694 s (P=S) cm^{-1}. $C_{76}H_{68}Cu_4N_2O_6P_8S_8$ (1859.8): calcd.C 48.9, H 3.7; found C 49.3, H 3.8.

X-ray Crystallographic Study: Data for **1** and **2** were collected with a STOE IPDS II diffractometer using graphite-monochromated Mo-K_α radiation (λ = 0.71073 Å). The structures were solved by direct methods and refined by full-matrix least squares on F^2 (all data) using the SHELXTL program package.[12] Hydrogen atoms were placed in calculated positions, non-hydrogen atoms were assigned anisotropic thermal parameters. Disordered components were refined with isotropic thermal parameters. Crystal data for **1**: $C_{86}H_{74}Cu_2O_3P_6S_4CH_2Cl_2$; M = 1681.52; monoclinic, space group $C2/c$; Z = 4; a = 22.431(5), b = 13.711(3), c = 26.435(5) Å, β = 104.20(3)°; V = 7882(3) Å^3; T = 100(2) K; $F(000)$ = 3472; $D_{calcd.}$ = 1.417 g·cm^{-3}. 29604 reflections measured, of which 8548 were unique (R_{int} = 0.0485); 238 parameters; final wR_2 = 0.2063 (all data); R_1 = 0.0742 [$I > 2\sigma(I)$]; largest difference peak/hole 2.446/–1.145 e·Å^{-3}. Crystal data for **2**: $C_{76}H_{68}Cu_4N_2O_6P_8S_83CH_2Cl_2$ M = 2130.51; monoclinic, space group $C2/c$, Z = 4; a = 18.457(4), b = 19.747(4), c = 24.311(5) Å, β = 93.66(3)°; V = 8843(3) Å^3; T = 100(2) K; $F(000)$ = 4328; $D_{calcd.}$ = 1.600 g cm^{-3}. 13293 reflections measured, of which 7876 were unique (R_{int} = 0.0460); 509 parameters; final wR_2 = 0.2042 (all data); R_1 = 0.0682 [$I > 2\sigma(I)$]; largest difference peak/hole 0.995/–1.633 e·Å^{-3}. CCDC-263199 and -263200 contain the supplementary crystallographic data for this paper. These data can be obtained free of charge from The Cambridge Crystallographic Data Centre via www.ccdc.cam.ac.uk/data_request/cif.

Supporting Information (see footnote on the first page of this article): NMR spectra of tBu_2O formed during the reaction.

Acknowledgments

The authors thank the DFG Centre for Functional Nanostructures and the Forschungszentrum Karlsruhe for financial support. A. R. thanks Professor Fenske for his support.

[1] a) T. Cantat, N. Mezailles, L. Ricard, Y. Jean, P. Le Floch, *Angew. Chem.* **2004**, *116*, 6542–6545; *Angew. Chem. Int. Ed.* **2004**, *46*, 6382–6385; b) M.-A. Munoz-Hernandez, V. Montiel-Palma, E. Huitron-Rattinger, S. Cortes-Llamas, N. Tiempos-Flores, J.-M. Grevy, C. Silvestru, P. P. Power, *Dalton Trans.* **2005**, 193–199; c) M. C. Aragoni, M. Arca, F. Demartin, F. A. Devillanova, F. Isaia, V. Lippolis, G. Verani, *Inorg. Chim. Acta* **2005**, *358*, 213–216; d) C. Silvestru, J. E. Drake, *Coord. Chem. Rev.* **2001**, *223*, 117–216.

[2] J. A. McCleverty, R. S. Z. Kowalski, N. A. Bailey, R. Mulvaney, D. A. Ocleirigh, *Dalton Trans.* **1983**, 627–634.

[3] M. Gianni, W. R. Caseri, V. Gramlich, U. W. Suter, *Inorg. Chim. Acta* **2000**, *299*, 199–208.

[4] J. H. Wilson Jr., Mobil Oil Corp., US Patent no. 3366536, **1968**.

[5] a) D. Fenske, A. Rothenberger, M. Shafaei Fallah, *Eur. J. Inorg. Chem.* **2005**, 59–62; b) D. Fenske, A. Rothenberger, M. Shafaei Fallah, *Z. Anorg. Allg. Chem.* **2004**, *630*, 943–947 and references cited therein.

[6] a) H. Keck, A. Kruse, W. Kuchen, J. Mathow, H. Wunderlich, *Z. Naturforsch., B* **1987**, *42*, 1373–1378; b) G. Thiele, G. Liehr, E. Lindner, *Chem. Ber.* **1974**, *107*, 442–447; c) S. Chaudhury, V. K. Jain, V. S. Jakkal, K. Venkatasubramanian, *J. Organomet. Chem.* **1992**, *424*, 115–125; d) W. Kuchen, H. Mayatepek, *Chem. Ber.* **1968**, *101*, 3454; e) A. Silvestru, A. Rotar, J. E. Drake, M. B. Hursthouse, M. E. Light, S. I. Farcas, R. Rösler, C. Silvestru, *Can. J. Chem.* **2001**, *79*, 983–991; f) M. Azad Malik, C. Byrom, P. O'Brien, M. Motevalli, *Inorg. Chim. Acta* **2002**, *338*, 245–248; g) C. W. Liu, C.-M. Hung, B. K. Santra, Y.-H. Chu, J.-C. Wang, Z. Lin, *Inorg. Chem.* **2004**, *43*, 4306–4314.

[7] B. S. Pedersen, S. Scheibye, K. Clausen, S. O. Lawesson, *Bull. Soc. Chim. Belg.* **1978**, *87*, 293–297.

[8] I. P. Gray, A. M. Z. Slawin, J. D. Woollins, *Dalton Trans.* **2004**, 2477–2486.

[9] P. Kilian, A. M. Z. Slawin, J. D. Woollins, *Eur. J. Inorg. Chem.* **1999**, 2327–2333.

[10] T. Greiser, E. Weiss, *Chem. Ber.* **1976**, *109*, 3142–3146.

[11] H. Nöth, E. Fluck, *Z. Naturforsch., B* **1984**, *39*, 744–753.

[12] G. M. Sheldrick, *SHELXTL-97*, University of Göttingen, **1997**.

Received: March 15, 2005
Published Online: June 21, 2005

 © 2005 Wiley-VCH Verlag GmbH & Co. KGaA, Weinheim

EurJIC
European Journal of Inorganic Chemistry

Issue 15/2005

Pages 2941–3180

Papers available ahead of print in Early View at www.interscience.wiley.com

Earliest available Table of Contents: Automatically, free of charge by e-mail through www.interscience.wiley.com/alerts

COVER PICTURE

The cover picture shows the potential energy curves for a generic valence tautomeric complex with a schematic representation emphasizing the intramolecular electron transfer between the metal ion and the ligand, which can be induced by different external stimuli such as temperature, pressure or irradiation. The diagram is accompanied by a representation of the different redox-active ligands involved in valence tautomerism that are presented in the Microreview by E. Evangelio and D. Ruiz-Molina on p. 2957 ff.

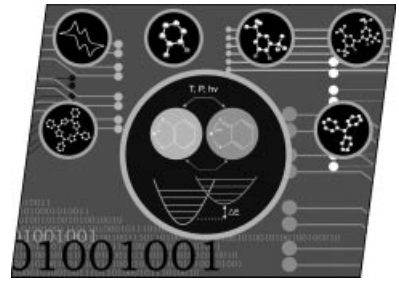

MICROREVIEW

Contents

2957 **E. Evangelio, D. Ruiz-Molina***

Valence Tautomerism: New Challenges for Electroactive Ligands

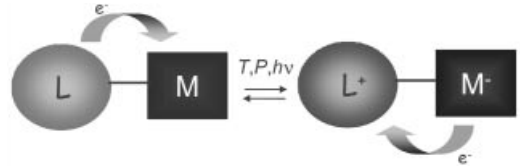

Keywords: Valence tautomerism / Electroactive / Intramolecular electron transfer / Bistability / Switch

 © 2005 Wiley-VCH Verlag GmbH & Co. KGaA, Weinheim

SHORT COMMUNICATIONS

2973 **S. K. Schneider, P. Roembke, G. R. Julius, C. Loschen, H. G. Raubenheimer,* G. Frenking,* W. A. Herrmann***

Extending the NHC Concept: C−C Coupling Catalysis by a Pd^{II} Carbene (*r*NHC) Complex with Remote Heteroatoms

Keywords: Carbene ligands / C−C Coupling / Density functional calculations / Homogeneous catalysis

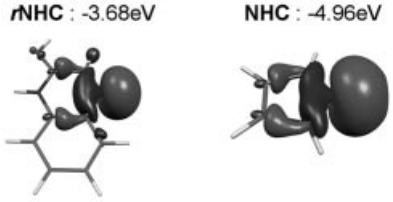

2978 **Z. Ma, Z. Chen, R. Cao***

Two Novel Cadmium Polymeric Metallamacrocyclic Complexes Constructed from a Pyridylmethyl-Functionalized Tetraaza Ligand

Keywords: Cadmium complexes / Crystal structures / Macrocyclic compounds / Hydrothermal method

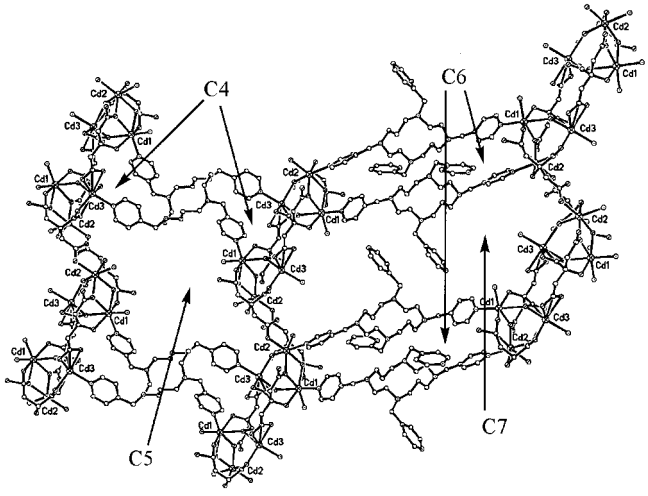

FULL PAPERS

2983 **K. Kromm, S. Eichenseher, M. Prommesberger, F. Hampel, J. A. Gladysz***

Synthesis and Reactivity of 1,2- and 1,3-Diphosphanes that Contain Four Chiral Rhenium Fragments: Architecturally Novel Tetrametallo-DMPE and -DMPP Species that are Unprivileged Ligands for Enantioselective Catalysis

Keywords: Rhenium / Chiral diphosphane / Phosphane oxide / Rhodium / Hydrogenation / Hydrosilylation

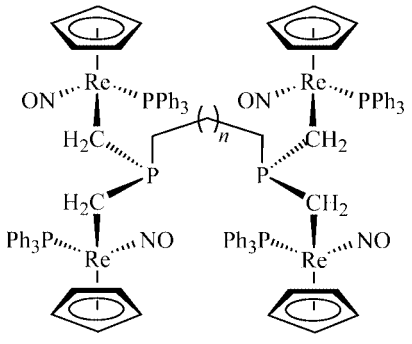

 © 2005 Wiley-VCH Verlag GmbH & Co. KGaA, Weinheim

2999 **J.-L. Carreón-Macedo, J. N. Harvey,* R. Poli***

The Reductive Elimination of Methane from *ansa*-Hydrido(methyl)metallocenes of Molybdenum and Tungsten: Application of Hammond's Postulate to Two-State Reactions

Keywords: Density functional theory / Metallocenes / Minimum energy crossing points / Hammond's postulate / Spin crossover reactivity

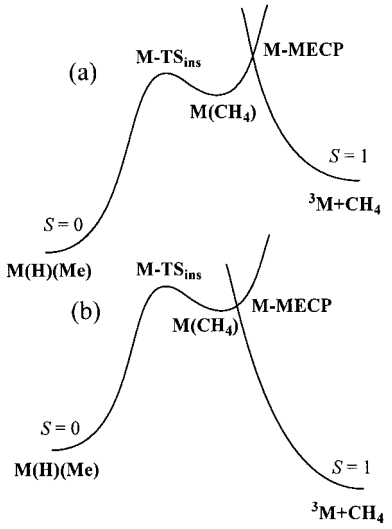

3009 **A. Dolbecq,* C. Mellot-Draznieks, P. Mialane, J. Marrot, G. Férey, F. Sécheresse**

Hybrid 2D and 3D Frameworks Based on ε-Keggin Polyoxometallates: Experiment and Simulation

Keywords: Molybdenum / Organic−inorganic hybrid materials / Polyoxometallates / Simulation

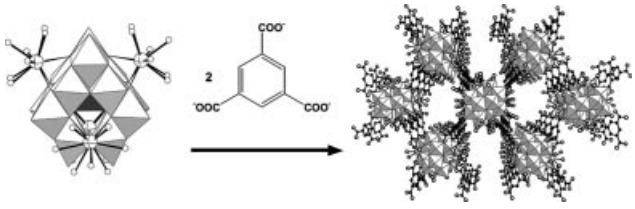

3019 **N. E. Katz,* F. Fagalde, N. D. Lis de Katz, M. G. Mellace, I. Romero, A. Llobet, J. Benet-Buchholz**

Synthesis, Properties and Molecular Structure of $[Ru(tpm)(bpy)(CH_3CN)](PF_6)_2$ (tpm = tris(1-pyrazolyl)methane, bpy = 2,2′-bipyridine) − Another Example of Nitrile Hydrolysis Promoted by Ruthenium(II)

Keywords: Scorpionate ligands / Ruthenium / Bipyridines / Hydrolysis / Acetonitrile complexes

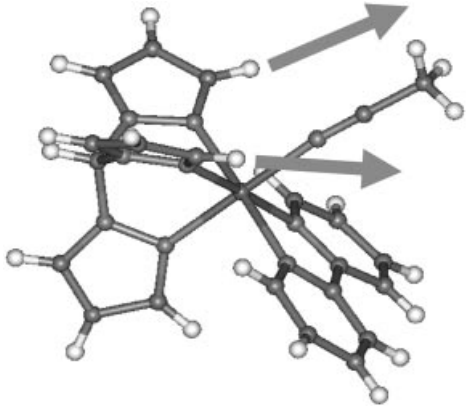

3024 **C. Ma,* Y. Han, R. Zhang, D. Wang**

Self-Assembled Triorganotin(IV) Moieties with 1,3,5-Benzenetricarboxylic Acid: Syntheses and Crystal Structures of Monomeric, Helical, and Network Triorganotin(IV) Complexes

Keywords: Crystal engineering / Helical structures / Networks / Self-assembly / Tin

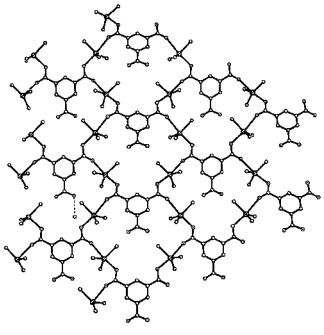

Novel triorganotin(IV) complexes of the type $(R_3Sn)_3(TMA)\cdot Y\cdot L$

R = CH_3, Y = $3CH_3OH$, L = 0	**1**
R = CH_3, Y = $2CH_3OH$, L = 0	**2**
R = $C_6H_5CH_2$, Y = 0, L = 0	**3**
R = *o*-F-$C_6H_4CH_2$, Y = 0, L = 0	**4**
R = *o*-Cl-$C_6H_4CH_2$, Y = 0, L = 0	**5**
R = C_6H_5, Y = 0, L = CH_2Cl_2	**6**
R = C_6H_5, Y = 0, L = $EtOH\cdot 2H_2O$	**7**
R = C_6H_5, Y = 0, L = $Et_2O\cdot CH_2Cl_2$	**8**
$[(CH_3)_3Sn]_2(HTMA)\cdot H_2O$	**9**

H_3TMA = 1,3,5-benzenetricarboxylic acid

 © 2005 Wiley-VCH Verlag GmbH & Co. KGaA, Weinheim

3034 **L.-H. Bi, U. Kortz,* B. Keita, L. Nadjo, L. Daniels**

The Palladium(II)-Substituted, Lone Pair Containing Tungstoarsenates(III) $[Na_2(H_2O)_2PdWO(H_2O)(\alpha\text{-}AsW_9O_{33})_2]^{10-}$ and $[Cs_2Na(H_2O)_8Pd_3(\alpha\text{-}AsW_9O_{33})_2]^{9-}$

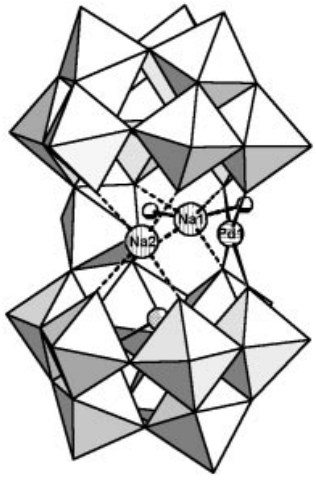

Keywords: Arsenic / Crystal structure / Electrochemistry / Palladium / Polyoxometalates / Tungsten

3042 **N. A. Bokach, A. A. Krokhin, A. A. Nazarov, V. Y. Kukushkin,* M. Haukka, J. J. R. Fraústo da Silva, A. J. L. Pombeiro***

Interplay between Nitrones and (Nitrile)Pd^{II} Complexes: Cycloaddition vs. Complexation Followed by Cyclopalladation and Deoxygenation Reactions

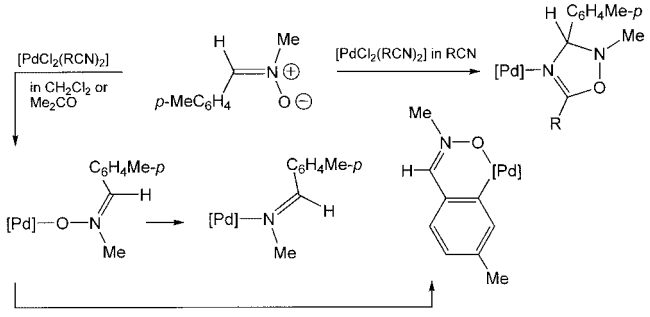

Keywords: Palladium / Nitrone complexes / Nitrile complexes / 1,3-Dipolar cycloaddition / Cyclometalation

3049 **J. Ruiz,* M. D. Santana,* A. Lozano, C. Vicente, G. García, G. López, J. Pérez, L. García**

Synthesis and Characterization of Heterotrinuclear Complexes of Nickel and Palladium with Pyridinecarboxylate as Bridging Ligands

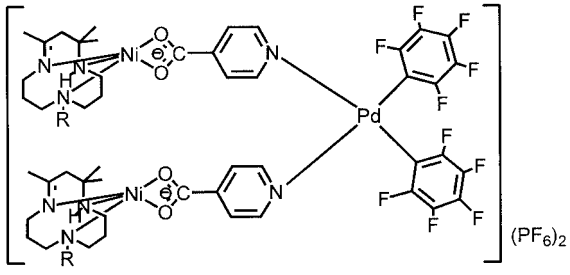

Keywords: Palladium / Nickel / Pyridinecarboxylate / Heterotrinuclear complexes / Mononuclear complexes

3057 **S. Singh, S. S. Kumar, V. Jancik, H. W. Roesky,* H.-G. Schmidt, M. Noltemeyer**

A Facile One-Step Synthesis of a Lipophilic Gold(I) Carbene Complex − X-ray Crystal Structures of LAuCl and LAuC≡CH (L = 1,3-di-*tert*-Butyl imidazol-2-ylidene)

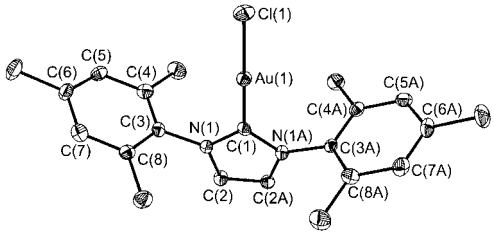

Keywords: Adduct / Gold(I) / Carbene / Acetylide

 © 2005 Wiley-VCH Verlag GmbH & Co. KGaA, Weinheim

3063 **M. Jeżowska-Bojczuk,* W. Szczepanik, S. Mangani, E. Gaggelli, N. Gaggelli, G. Valensin**

Identification of Copper(II) Binding Sites in the Aminoglycosidic Antibiotic Neomycin B

Keywords: Bioinorganic chemistry / Aminoglycoside antibiotics / Neomycin B / N,O ligands / Copper

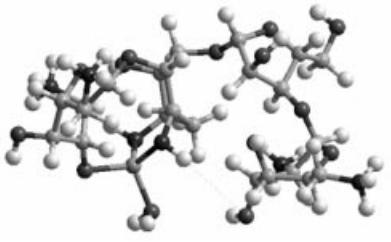

3072 **Y. Guo, R. Weiss, M. Epple***

A Straightforward Route to Copper/Zinc Oxide Nanocomposites: The Controlled Thermolysis of $Zn[Cu(CN)_3]$

Keywords: Cyanides / Copper / Zinc / Thermochemistry / EXAFS spectroscopy

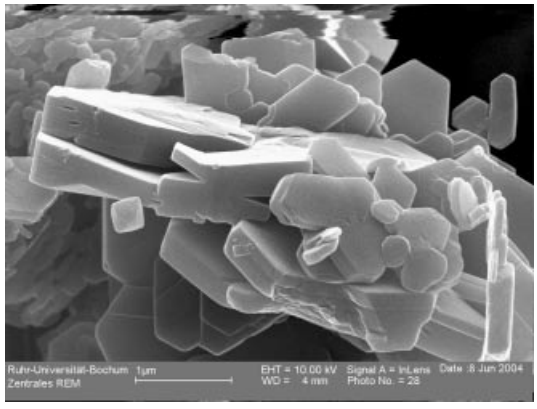

3080 **K. Pavani, A. Ramanan***

Influence of 2-Aminopyridine on the Formation of Molybdates under Hydrothermal Conditions

Keywords: Hydrothermal synthesis / N ligands / Molybdenum / Crystal structure

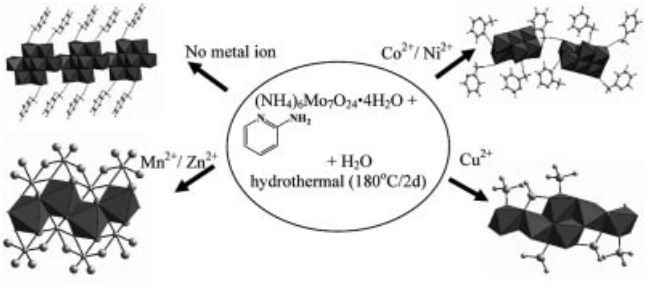

3088 **H. Sugimoto,* Y. Furukawa, M. Tarumizu, H. Miyake, K. Tanaka, H. Tsukube**

Synthesis and Crystal Structures of $[W(3,6\text{-dichloro-1,2-benzenedithiolate})_3]^{n-}$ (n = 1, 2) and $[Mo(3,6\text{-dichloro-1,2-benzenedithiolate})_3]^{2-}$: Dependence of the Coordination Geometry on the Oxidation Number and Counter-Cation in Trigonal-Prismatic and Octahedral Structures

Keywords: Coordination modes / Molybdenum / S ligands / Salt effects / Tungsten

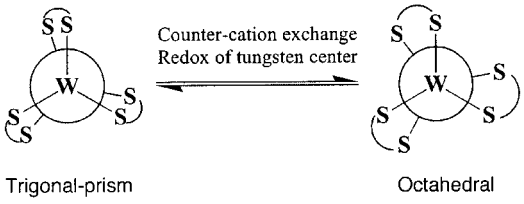

 © 2005 Wiley-VCH Verlag GmbH & Co. KGaA, Weinheim

3093 **J. García-Martín, R. López-Garzón,* M. L. Godino-Salido, R. Cuesta-Martos, M. D. Gutiérrez-Valero, P. Arranz-Mascarós, H. Stoeckli-Evans**

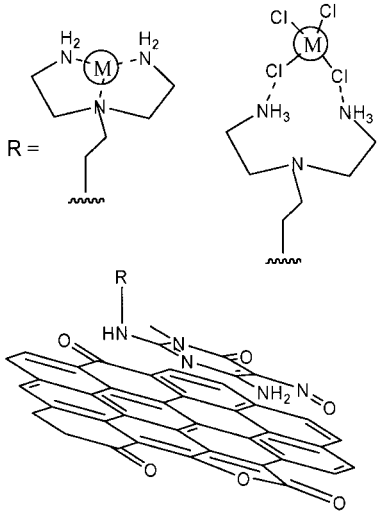

Adsorption of Zn^{2+} and Cd^{2+} from Aqueous Solution onto a Carbon Sorbent Containing a Pyrimidine−Polyamine Conjugate as Ion Receptor

Keywords: Adsorption / Cadmium / Ligand design / N ligands / Zinc

3104 **M.-L. Fu, G.-C. Guo,* A.-Q. Wu, B. Liu, L.-Z. Cai, J.-S. Huang**

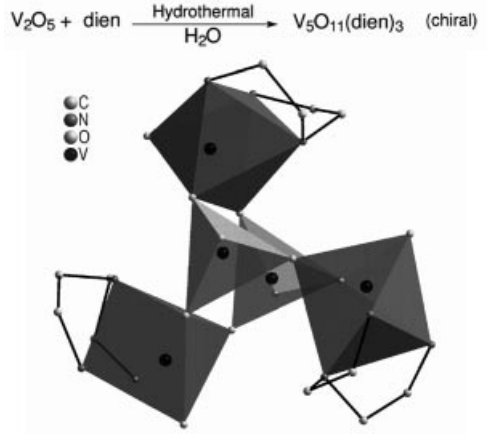

Synthesis, Crystal Structure and Characterisation of a Novel Chiral Mixed-Valence Vanadium Oxide Hybrid, $[V_5O_{11}(dien)_3]$

Keywords: Chirality / dien ligand / Magnetism / Mixed-valence compounds / Vanadium

3109 **K. Matlawska,* U. Kalinowska, A. Erxleben, R. Osiecka, J. Ochocki**

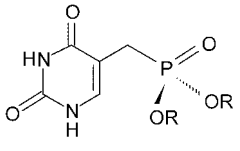

Novel Analogues of 5-Fluorouracil − Synthesis, X-ray Crystallography, and Cytotoxic Effects in Normal Human Peripheral Blood Lymphocytes and Colon Adenocarcinoma HT 29

Keywords: Alkali metals / Phosphonate ligands / X-ray diffraction / Antitumor agents / Uracil derivatives

 © 2005 Wiley-VCH Verlag GmbH & Co. KGaA, Weinheim

3118 **S. G. Baca,* I. G. Filippova, C. Ambrus, M. Gdaniec, Y. A. Simonov, N. Gerbeleu, O. A. Gherco, S. Decurtins**

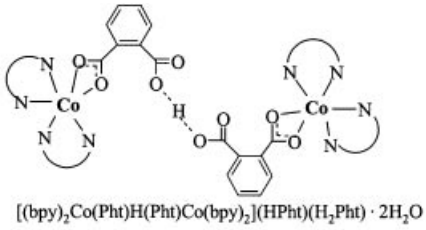

From Mono- and Dinuclear to Polynuclear Cobalt(II) and Cobalt(III) Coordination Compounds Based on *o*-Phthalic Acid and 2,2′-Bipyridine: Synthesis, Crystal Structures, and Properties

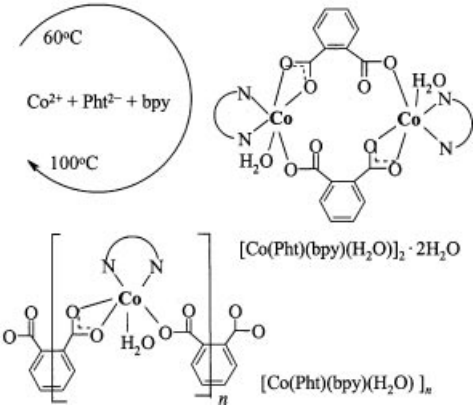

Keywords: Carboxylate ligands / Cobalt / Magnetic properties / N ligands

3131 **Y. H. Ding,* S. Inagaki***

Silanes/Oxygen/(Water): Green High-Energy-Density Materials

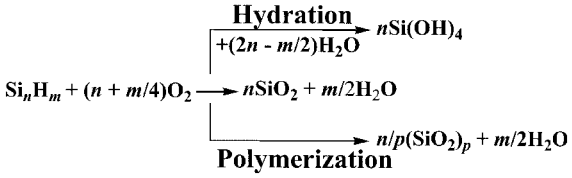

Keywords: Silanes / Green high-energy-density materials / Ab initio calculations / Bond energy

3135 **M. Ortiz, A. Penabad, A. Díaz, R. Cao,* A. Otero, A. Antiñolo, A. Lara**

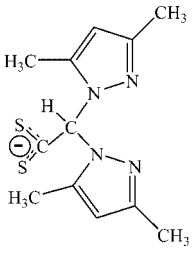

Ruthenium Complexes of the Scorpionate Ligand Bis(3,5-dimethylpyrazol-1-yl)dithioacetate and the Effect of Nitric Oxide Coordination

Keywords: N ligands / Nitric oxide / Ruthenium / S ligands / Scorpionate ligands

3141 **H. Chen, P. Yang,* C. Yuan, X. Pu**

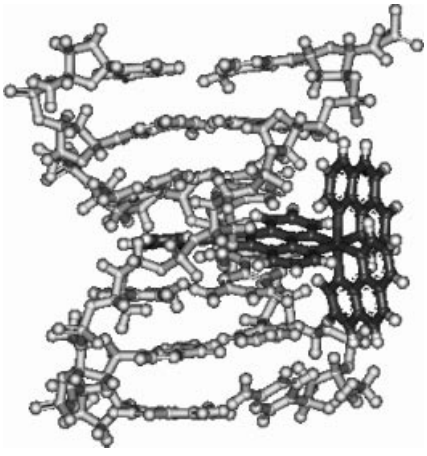

Study on the Binding of Base-Mismatched Oligonucleotide $d(GCGAGC)_2$ by Cobalt(III) Complexes

Keywords: Mismatched DNA / Cobalt / Binding / Oligonucleotides

 © 2005 Wiley-VCH Verlag GmbH & Co. KGaA, Weinheim

3149 **J. Widoniak, S. Eiden-Assmann,* G. Maret**

Synthesis and Characterisation of Monodisperse Zirconia Particles

Keywords: Zirconia / Monodisperse / Colloids / Particles / Sol−gel processes

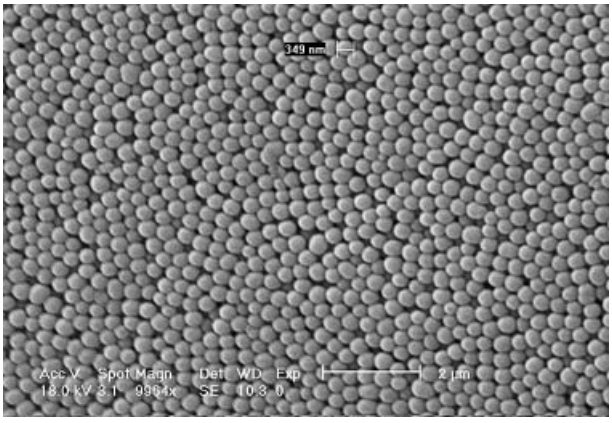

3156 **X. Li, R. Cao,* W. Bi, D. Yuan, D. Sun**

Self-Assembly of 1D to 3D Cadmium Complexes: Structural Characterization and Properties

Keywords: Cadmiun / Hydrothermal synthesis / Layered compounds / O ligands / Self-assembly

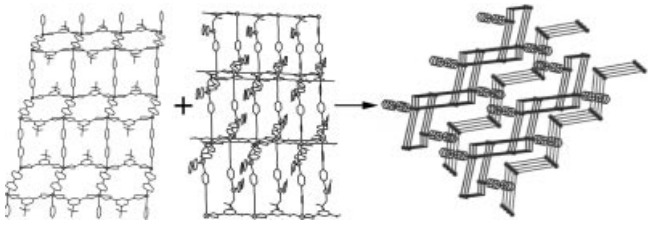

3167 **V. Pawlowski, G. Knör, C. Lennartz,* A. Vogler***

Luminescence and Theoretical Studies of Cu(tripod)X [tripod = 1,1,1-Tris(diphenylphosphanylmethyl)ethane; X^- = Halide, Thiophenolate, Phenylacetylide]

Keywords: Electronic spectra / Luminescence / Copper complexes / Phosphane ligands / Quantumchemical calculations

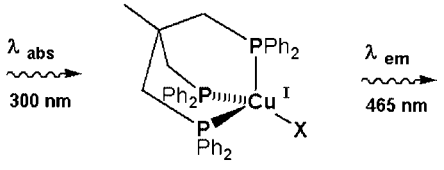

3172 **Dj. U. Miodragović,* Ž. J. Vitnik, S. M. Milosavljević, M. J. Malinar, I. O. Juranić**

NH···π Interactions Stabilize the Most-Hindered Rotamer of the (*S*)-Tyrosinato Side Group in Bis[(*S*)-tyrosinato](diamine)cobalt(III) Complexes: An NMR Spectroscopic and DFT Study

Keywords: Amino acids / Cobalt / Conformational analysis / Density functional calculations / NMR spectroscopy / Pi interactions

 © 2005 Wiley-VCH Verlag GmbH & Co. KGaA, Weinheim

Valence Tautomerism: New Challenges for Electroactive Ligands

Emilia Evangelio[a] and Daniel Ruiz-Molina*[a]

Keywords: Valence tautomerism / Electroactive / Intramolecular electron transfer / Bistability / Switch

Valence tautomeric complexes combine redox-active ligands and transition metal ions with two or more accessible oxidation states, exhibiting two nearly degenerated electronic states with localized electronic structures. Charge distribution in such electronic isomers has an appreciable sensitivity to the environment so an external perturbation, like photons, temperature and/or pressure, may lead to an intramolecular electron transfer between both redox active units and therefore to a reversible interconversion between the two degenerated electronic states. Moreover, since each electronic isomer exhibits different optical, electronic and/or magnetic properties, these complexes are being proposed as candidates for future use in molecular electronic devices and switches. Most of the valence tautomeric complexes reported thus far are based on quinone or quinone-type ligands with a series of transition metal ions such as Co, Cu, Ni and Mn. Nevertheless, in the last few years, the number of electroactive ligands identified to be active in valence tautomeric complexes is being expanded by including new radical ligands such as polychlorotriphenylmethyl, phenoxyl or tetraphenylporphyrin radicals.

(© Wiley-VCH Verlag GmbH & Co. KGaA, 69451 Weinheim, Germany, 2005)

Introduction

Development of molecular-scale systems that exhibit intramolecular electron-transfer phenomena induced by external stimuli has attracted considerable attention.[1] The interest is twofold. First, the possibility of inducing a reversible change in the electronic distribution of a molecular system opens the door to their potential use in information storage and integrated molecular-sized devices. And second, from a theoretical point of view, to study the role of various parameters governing the intramolecular electron transfer (IET) rates. Mixed-valence systems are excellent candidates for such studies since they contain at least two redox sites with different oxidation states linked by a bridge that medi-

[a] Institut de Ciència dels Materials de Barcelona (CSIC), Esfera UAB, 08193, Cerdanyola, Catalonia, Spain
Fax: +34-935801853
E-mail: dani@icmab.es

Emi Evangelio was born in Barcelona, Spain, in 1977. She studied Chemistry at the University of Barcelona where she received her laureate degree in 2002 and Masters degree in 2004 with the work "Organometallic Compounds of Platinum(II) and Platinum(IV) Derivatives from Phenanthrene and Anthracene". She is currently busy with a PhD at the Institut de Ciència de Materials de Barcelona. Her research is devoted to structural, magnetic and optical properties of catechol compounds and derivatives.

Daniel Ruiz-Molina obtained his PhD in 1996 at the Institut of Materials Science of Barcelona (ICMAB) working with Prof. J. Veciana. His work focused on the controlled synthesis of dendrimers and magnetic organic materials. In 1997, he joined Hendrickson's Group at UCSD as a postdoctoral research fellow for three years. His project involved the synthesis and characterization of new molecular switches and single-molecule magnets. Since July 2001, he holds a permanent position at the ICMAB. His main interests are the preparation and characterization of multifunctional molecular materials and switches (optical, magnetic and electric properties) and the preparation of molecular ordered arrays on surfaces (2D) for molecular electronics.

MICROREVIEWS: This feature introduces the readers to the authors' research through a concise overview of the selected topic. Reference to important work from others in the field is included.

ates the transfer of electrons from one site to the other.[2] Depending on the strength of the interaction between the redox centers, Robin and Day[3] classified the mixed-valence systems into three main groups. The potential energy curves for the three types of mixed-valence compounds, which represent the systems for any geometry along the nuclear coordinate, are shown in Figure 1.

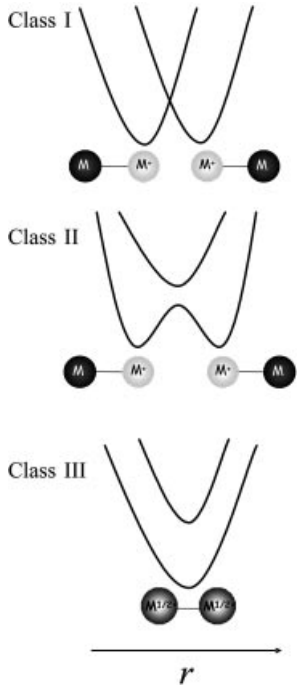

Figure 1. Potential energy curves for mixed-valence systems. The curves are arranged into three main groups according to the Robin and Day classification. In Class I the interaction between the redox centers is negligible; in Class II the interaction between the redox centers is weak or moderate and in Class III the electronic interaction is so intense that the electron is completely delocalized over the molecule.

In the Class I mixed-valence systems the interaction between the redox centers is zero or extremely weak and, therefore, the system only exhibits the properties of the isolated redox units. Even if the molecule acquires sufficient activation energy to reach the intersection region, the probability of electron exchange would be negligible. On the contrary, in Class III mixed-valence systems the electronic interaction is so intense that the electron is completely delocalized over the entire molecule. Then, the properties of each isolated unit are no longer observed and new properties associated with the delocalized species appear. Finally, for Class II systems the interaction between the redox centers is moderate. The electronic interaction has almost no effect on the potential energy curves in the vicinity of the equilibrium geometries but causes mixing in the vicinity of the crossing point. In other words, the electron is vibrationally localized in one of the redox centers due to the presence of an activation energy barrier (ΔG), although such a barrier may be overcome by an external optical or thermal stimulus, to promote an IET process.

The study of molecular mixed-valence class II systems was initiated by Taube's seminal work on compounds such as $[(NH_3)_5Ru\text{-bridge-}Ru(NH_3)_5]^{5+}$. Since then, most of the mixed-valence complexes that have been shown to exhibit intramolecular electron-transfer phenomena are homo- and heteronuclear metallic complexes where the two metal atoms with different oxidation states are connected through an organic bridging ligand.[4] From them, ruthenium complexes and ferrocene moieties have been widely used thanks to their great stability, ease of oxidation and their kinetic inertness.[5] Mixed-valence molecular systems where the electro-active units are pure organic groups have so far received less attention, probably due to their high instability,[6] although for these systems electron transfer could be fine-tuned in a far more precise manner thanks to the flexibility of organic synthesis. The different types of electroactive organic units used thus far are: i) anion radicals derived from conjugated diquinones and diimides,[7] ii) cation radicals derived from bis(tetrathiafulvalenes),[8] iii) cation radicals derived from bis(hydrazines),[9] iv) quinoid groups[10] and v) ion radicals derived from π-conjugated polyarylmethyl/polyarylamines[11] and polychlorotriphenylmethyl radicals.[12] In most of these cases the intramolecular electron transfer is mediated through an organic bridge and only in a few cases does it take place through a bridging metal ion.[13]

Finally, a third type of class II mixed-valence systems is the heterogeneous complexes combining both redox-active ligands and transition metal ions. Some complexes with non-innocent electro-active ligands exhibit a reversible intramolecular electron transfer between the metal ion and the ligand, leading to an internal charge redistribution and therefore to the existence of two different electronic isomers. This family of complexes, termed Valence Tautomeric (VT), is of considerable interest. First, they are unique model systems, which provide insight into the basic factors affecting intramolecular electron transfer in coordination complexes. And second, from an applied perspective, the large changes in the optical, structural, and magnetic properties that often accompany the valence tautomeric interconversion have potential applications in bistable molecular switching materials and devices. In this review, we will first give a brief introduction to the concepts of valence tautomerism, its origin, physical properties and interconversion mechanisms. In a subsequent section, we will make a compendium of the different redox-active ligands used thus far in valence tautomeric complexes, and we will finally mention some new ideas based on the combination of valence tautomeric equilibrium with additional redox reactions involved with the redox-active ligand.

Valence Tautomerism

Valence tautomeric metal complexes with at least two redox-active centers, the metal ion and an electro-active ligand, are characterized by the existence of two electronic isomers (valence tautomers) with different charge distribu-

 © 2005 Wiley-VCH Verlag GmbH & Co. KGaA, Weinheim

tions, and consequently, different optical, electric and magnetic properties. The interconversion between the different electronic isomers is accomplished by a reversible intramolecular electron transfer involving the metal ion and the redox active ligand, analogous with that observed for Prussian blue analogs.[14] A schematic representation of valence tautomerism together with the corresponding potential energy curve plotted as a function of the nuclear coordinate, is shown in Figure 2.

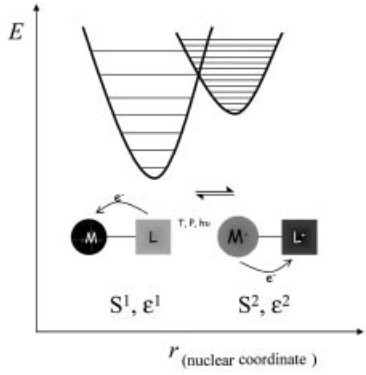

Figure 2. Potential energy curves for a valence tautomeric complex with a schematic representation emphasizing the intramolecular electron transfer between the metal ion and the ligand.

One of the first descriptions of valence tautomerism and an excellent example of the above mentioned charge distribution sensitivity is exhibited by the cobalt bis(quinone) complex [Co^{III}(3,5-DTBCat)(3,5-DTBSQ)(bpy)] (**1**), where 3,5-$DTBCat^{2-}$ and 3,5-$DTBSQ^{-}$ refer, respectively, to the catecholate (Cat^{2-}) and semiquinonate (SQ^{-}) forms of 3,5-di-*tert*-butyl-o-quinone, and bpy is 2,2′-bipyridine.[15] In solution, the equilibrium in Equation (1) can be induced by variations of temperature and monitored by magnetic measurements and spectroscopic techniques such as UV/Vis, NMR and/or EPR spectroscopy.[16]

$$[Co^{III}(3,5\text{-DTBCat})(3,5\text{-DTBSQ})(bpy)]\ (\mathbf{1},\ ls\text{-}Co^{III}) \rightleftharpoons [Co^{II}(3,5\text{-DTBSQ})_2(bpy)]\ (\mathbf{1},\ hs\text{-}Co^{II}) \quad (1)$$

For instance, a solution of complex **1** in toluene at low temperatures shows a band at 600 nm characteristic of the **1**, *ls*-Co^{III} tautomer. An increase of temperature promotes an intramolecular electron transfer so the **1**, *ls*-Co^{III} converts into the **1**, *hs*-Co^{II} tautomer as one of the ligands is oxidized by one electron from a Cat^{2-} to an SQ^{-} ligand. As a consequence, the intensity of the 600 nm band decreases and a band at 770 nm characteristic of the **1**, *hs*-Co^{II} tautomer increases in intensity (see Figure 3). Accompanying the optical changes, variations in the magnetic response are also observed. The **1**, *ls*-Co^{III} isomer has an $S = 1/2$ ground state whereas the **1**, *hs*-Co^{II} isomer has an $S = 2$ ground state.

This interconversion is an entropy-driven process, analogous with the extensively studied low-spin to high-spin crossover phenomena. The large entropy gain arises from: 1) a gain in electronic entropy due to the higher spin state degeneracy of the *hs*-Co^{II} form and 2) the higher density of vibrational states of the *hs*-Co^{II} form due its longer metal-ligand bond lengths. Thus thermal population of tautomeric states is dictated by the Gibbs free energy expression shown in Equation (2). At low temperatures, $T\Delta S$ is negligible compared to ΔH, and consequently if $\Delta H > kT$ only the *ls*-Co^{III} state is populated. An increase in the temperature will increase the $T\Delta S$ contribution, making it non-negligible and favoring the population of the *hs*-Co^{II} state, up to a critical temperature T_c where $\Delta G = 0$ and $\Delta H = T\Delta S$. A further increase in the temperature will change the sign of ΔG.

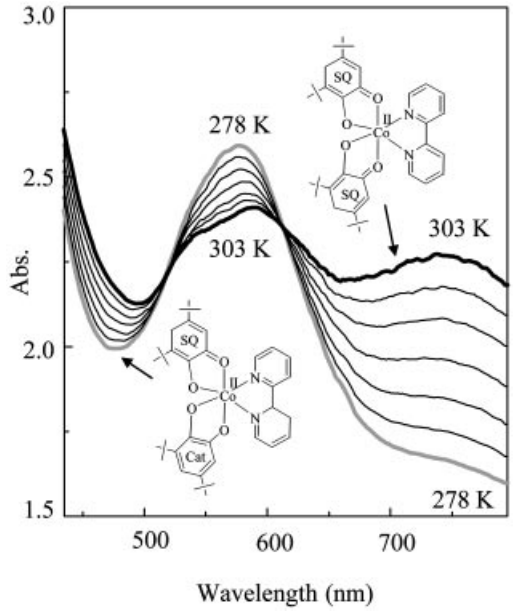

Figure 3. Temperature dependence of the electronic absorption spectrum of a CH_2Cl_2 solution of complex **1**.

$$\Delta G = \Delta G_{hs\text{-}Co^{II}} - \Delta G_{ls\text{-}Co^{III}} = \Delta H - T\Delta S \quad (2)$$

It is important to emphasize that whereas most of the valence tautomeric complexes reported thus far exhibit a temperature-dependent interconversion in solution, the number of examples exhibiting a valence-tautomeric interconversion in the solid state is rather limited. For this, the presence of solvate molecules within the crystalline network and their effects on the phonon relaxation, play a critical role. For instance, a plot of the magnetic susceptibility vs. temperature for a sample of complex **2** recrystallized from four different solvents is shown in Figure 4. In this figure it is shown that for complex [Co^{III}(3,5-DTBSQ)(3,5-DTBCAT)(phen)]·$C_6H_5CH_3$ (**2**), the tautomeric interconversion between the **2**, *ls*-Co^{III} and **2**, *hs*-Co^{II} isomers can be reversibly driven with temperature and monitored by large changes in the magnetic susceptibilities, with an interconversion that occurs abruptly within a narrow temperature range of ca. 30 °C. On the contrary, a polycrystalline sample recrystallized from ethanol has a μ_{eff} value essentially independent of the temperature and close to the value of 1.7 μ_B expected for the low-spin isomer. For samples recrystallized from acetonitrile and dichloromethane, incomplete transitions were observed (see Figure 4).[17]

 © 2005 Wiley-VCH Verlag GmbH & Co. KGaA, Weinheim

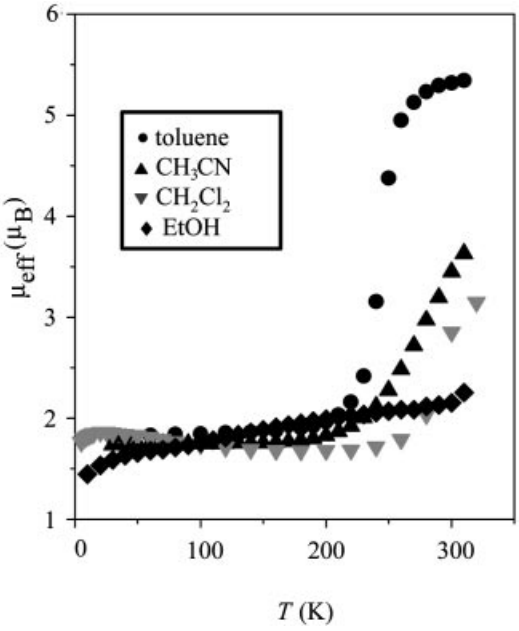

Figure 4. Plots of the effective magnetic moment (μ_{eff}) vs. temperature for complex **2** in different solvents: toluene, acetonitrile, dichloromethane, and ethanol.

Moreover, since valence tautomeric complexes are electronically labile, they exhibit significant vibronic interactions and therefore an appreciable sensitivity to the environment. As a consequence, intramolecular electron transfer can be induced not only by temperature variations but also by irradiation or pressure.

Light-Induced Tautomerism

Adams et al. reported results of the first picosecond time-resolved optical experiments on valence tautomeric complexes in solution.[18] In such work, pulsed laser photolysis, both on the picosecond (90 ps pulse) and the nanosecond (24 ns pulse) time-scales, were carried out for a series of complexes with the general formula [Co(3,5-DTBSQ)$_2$-(N-N)]. The authors showed that when the complex is in the *ls*-Co^{III} form, a laser pulse could it excite it to a LMCT excited state. Such excited states experience a rapid intersystem crossing to the *hs*-Co^{II} state with a subsequent electron recombination to finally yield the *ls*-Co^{III} isomer. At room temperature, the rate of *hs*-Co^{II} to *ls*-Co^{III} conversion (k_{bvt}) ranges from 6.1×10^7 to 6.7×10^8 s^{-1} and its temperature dependence follows an Arrhenius-like behavior in the 140–300 K range. However, below 140 K, deviations from linearity are seen, most likely due to the involvement of quantum mechanical tunneling. Valence tautomerism for this family of complexes was also shown to take place in the solid state after illumination at low temperatures.[19] For instance, variations on the μ_{eff} vs. T plot of [Co^{III}(3,5-DTBSQ)(3,5-DTBCAT)(phen)]·C_6H_5Cl (**2**) before and after illumination are shown in Figure 5.[20] Similar interconversion in the solid state has been reported by Dei et al. for the new dinuclear complex [{Co(cth)}$_2$(dhbq)](PF$_6$)$_3$ (**3**), both by irradiation with a laser connected to the SQUID magnetometer and by reflectivity spectra.[21] Their results showed that the light-induced phenomenon is perfectly reversible although the photoinduced population rate corresponds to only 43% of the sample, most likely due to opacity phenomena.

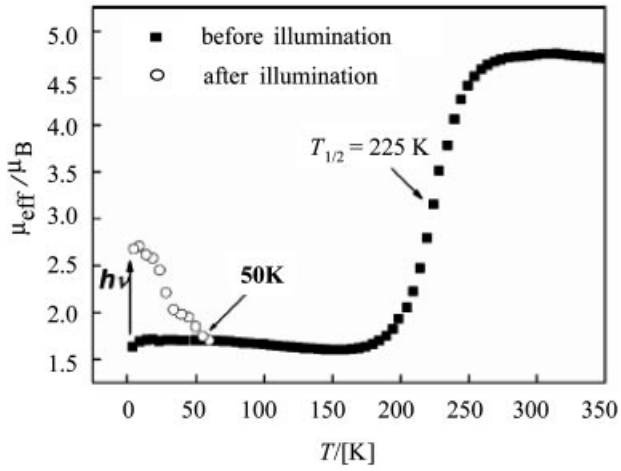

Figure 5. Plot of the χT product as a function of temperature T for complex **3** measured before and after irradiation at 647 nm. The bump at 45 K on the irradiation curve is a result of a small amount of oxygen.

Finally, additional femtosecond spectroscopic experiments by Neuwahl et al. in a simple cobalt-dioxolene derivative in solution demonstrated the involvement of not two but at least three states in a two-step process for a valence tautomeric interconversion in solution.[22] Besides the Co^{III}-Cat and Co^{II}-Sq pairs involved in the tautomerism, the third species may originate from several possible electronic isomers, such as a Co^{III}-Cat species with divergent electronic congurations or a low-spin Co^{II}-Sq isomer, which is expected to be characterized by a triplet electronic ground state.

Pressure-Induced Tautomerism

The X-ray structure analysis of complex **2** at three different temperatures (137, 238 and 295 K) revealed an average metal-ligand bond length increase of 0.18 Å on passing from the **2**, *ls*-Co^{III} to the **2**, *hs*-Co^{II} tautomer. As shown in Figure 6, such a change is due to a drastic change in the population of the antibonding e_g* orbitals.

Such increase of the molecular size when passing from the low-spin to the high-spin isomer has also been used to modulate valence tautomerism by pressure effects.[23] Verdaguer et al.[24] studied the nonsolvated complex **2** and its related solvated form [Co^{II}(3,5DTBSQ)$_2$(phen)]·$C_6H_5CH_3$ by EXAFS and XANES. EXAFS data indicated that the **2**, *hs*-Co^{II} tautomer has bond lengths of Co–O = 2.08 Å and Co–N = 2.13 Å whereas the **2**, *ls*-Co^{III} tautomeric complex is smaller with Co–O = 1.91 Å and Co–N = 1.93 Å. Both complexes could be reversibly driven from the larger **2**, *hs*-Co^{II} tautomer to the smaller **2**, *ls*-Co^{III} tautomeric form upon application of pressure, within the 0.075–0.700 GPa

 © 2005 Wiley-VCH Verlag GmbH & Co. KGaA, Weinheim

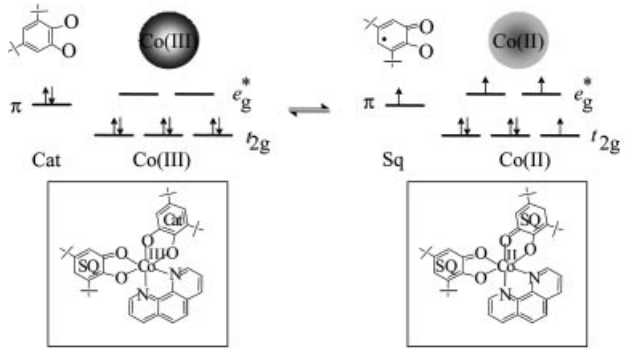

Figure 6. Representation of the orbital occupancy, both metal and ligand based, on the two different tautomeric forms for complex **2**.

range for the solvated form and 0.10–2.5 GPa for the non-solvated form. In addition to EXAFS and XANES, pressure-induced valence tautomerism has also been recently monitored by changes in the magnetic response.[25]

Redox-Active Ligands

So far, many different types of redox-active ligands have been described in the literature. Among them are π-conjugated molecules with coordinating capabilities such as quinone-types,[26] crown-ethers,[27] ferrocene,[28] tetrathiafulvalenes derivatives,[29] and polymers/oligomers,[30] such as polyanilines and polythiophenes.[31] However, we must emphasize that even though the number of metal complexes based on redox-active ligands is considerable, those exhibiting valence tautomerism are rather limited since they must simultaneously satisfy two conditions: 1) the degree of covalency in the interaction between metal ion and electroactive ligand must be low, and 2) the energy of their frontier orbitals must be similar.[32] In other words, it is necessary that these complexes exhibit localized electronic structures, low orbital mixing, and a small energy difference between the two electronic tautomers. Most of the valence tautomeric complexes reported thus far are based on quinone or quinone-type ligands with a series of transition metal ions. Nevertheless, in the last few years the number of electroactive ligands inducing valence tautomerism is being expanded by including new electroactive ligands such as schiff-base, phenoxyl, tetraphenylporphyrin and polychlorotriphenylmethyl radicals. Examples of each case are revised below.

Quinone Ligands

Metal dioxolene complexes have been the subject of a vigorously growing and fascinating research field for a long time due to their rich structural, physical and chemical properties.[33] In addition to exhibiting valence tautomerism, the subject of the present review, several other interesting features such as the design of paramagnetic molecules with predetermined spin topologies[34] and activation of small molecules like O_2 and N_2 have also been described.[35] Most of these interesting features are related to their rich redox activity, since they are "noninnocent" electroactive ligands that may exist as neutral quinones (Q), radical semiquinones (SQ^{-}) or dianionic catecholates (Cat^{2-}) (Scheme 1), although in valence tautomeric complexes they are only found in the SQ^{-} and Cat^{2-} forms due to the limiting binding ability of the quinone ligand.[36] Charge localization within the metal-quinone chelate ring has been observed for different transition metal complexes (cobalt, manganese, nickel and copper among them),[37] allowing the observation in some cases of valence tautomerism. However, in other cases such as for ruthenium complexes, charge distribution is less clear and a delocalized electronic structure may be an appropriate description.[16]

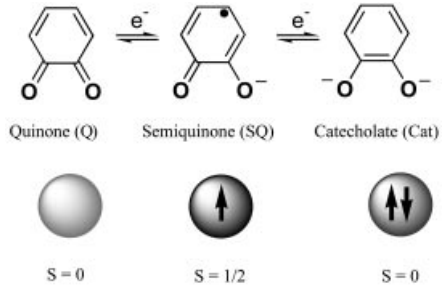

Scheme 1.

Cobalt Complexes

The best investigated family of quinone-based valence tautomeric complexes is that of cobalt-dioxolene molecules, where the valence tautomeric interconversion involves an intramolecular electron transfer between a six-coordinate cobalt ion and a coordinated dioxolene ligand. The simplest cobalt-quinone complexes undergoing valence tautomerism belong to the family of ionic complexes with the general formula [ML(diox)]Y, where L = tetraazamacrocycle ancillary ligand, diox = 9,10-dioxophenantrene and Y = PF_6, BPh_4, I.[25] Such complexes undergo a temperature- and pressure-induced intramolecular electron-transfer equilibrium with a transition temperature that varies with the volume and coulombic interaction of the counterion Y. Moreover, substitution of CH_2Cl_2 solvent molecules with their deuterated analogs drastically modifies its magnetic properties giving rise to a thermal hysteresis, an important issue if future technological applications are envisaged for these molecular systems.[38]

Before the previous monodioxolene complexes were reported, most cobalt complexes shown to exhibit valence tautomerism were of the general formula [Co(N-N)$(Q)_2$], where N-N is a diazine ligand, Q = 3,5- and 3,6-di-*tert*-butylcatecholato or semiquinone form. Several interesting features have been observed for this family of complexes, among them a marked effect of the nature of the quinone and ancillary ligands on the tautomerism. For instance, whereas in complex [Co(bpy)(3,6-DBSQ)(3,6-DBCat)] bipyridine ligands of adjacent molecules stack to form a one-dimensional lattice resulting in a remarkable photomechanical effect upon irradiation, replacement by the 3,5-di-*tert*-

 © 2005 Wiley-VCH Verlag GmbH & Co. KGaA, Weinheim

butylcatecholato induces a dimerization. As far as the ancillary ligand is concerned, Hendrickson et al.[39] and Pierpont et al.[40] have also concluded that it is possible to systematically control valence tautomerism by changing the counterligand chelate ring flexibility and their donor abilities. Another interesting example has been described by Awaga et al., who reported valence tautomerism in the spin-labeled complex [Co(nnbpy)(3,5-DTBSQ)$_2$] (**4**), where nnbpy is a bipyridine substituted nitronyl nitroxide radical. Even though the temperature dependence of the magnetic susceptibility indicates a tautomeric interconversion above 250 K, the radical ligand behaves as a Curie spin over the whole temperature region.[41] A schematic representation of the valence tautomerism observed for complex **4** is shown in Scheme 2.

In addition to variations in the number and nature of the electroactive and counter ligands, different polynuclear tautomeric complexes have also been reported (see Scheme 3). For instance, Dei et al. reported the dinuclear complex [{Co(cth)}$_2$(dhbq)](PF$_6$)$_3$ (**3**) that undergoes a gradual thermal tautomeric transition at around 175 K and quantitative photoconversion.[21] Pierpont et al. followed this approach to establish the photomechanical polymer [Co(pyz)(3,6-DBQ)$_2$]$_n$ (**5**). This coordination polymer exhibited a temperature-induced tautomeric interconversion in the solid state that is derived from a mechanical process

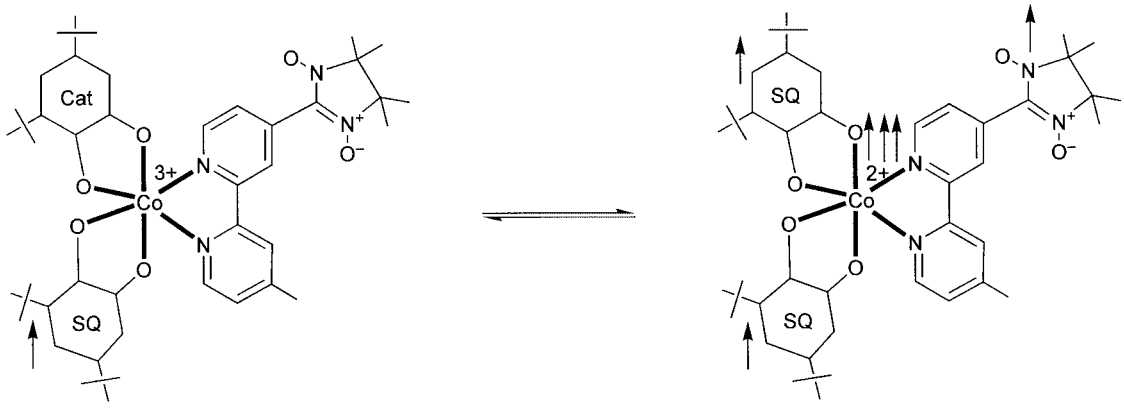

Scheme 2.

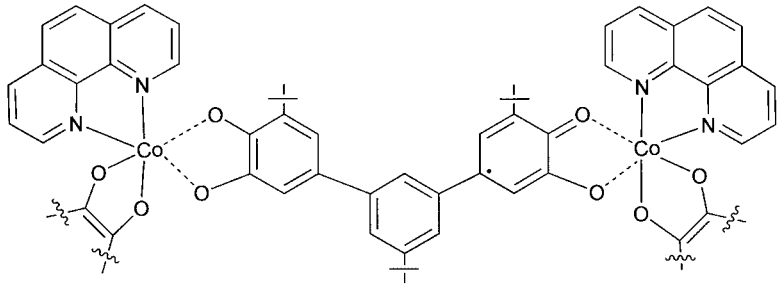

6

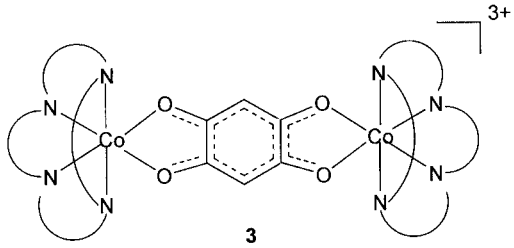

3

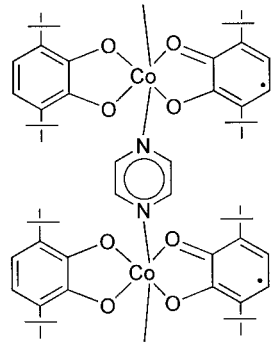

5

Scheme 3.

 © 2005 Wiley-VCH Verlag GmbH & Co. KGaA, Weinheim

due to variations on the bond lengths although no hysteresis effects were observed.[42] On the contrary, such hysteresis was observed more recently by Schultz et al., who used a bis-bidentate ligand to obtain the coordination polymer $[Co(phen)L]\cdot 0.5CH_2Cl_2$ (**6**). This cobalt-dioxolene polymer exhibits the necessary cooperative properties that lead to thermal hysteresis in a valence tautomeric equilibrium, even though the transition could be classified as gradual.[43]

Copper Complexes

Some copper complexes containing dioxolene ligands may yield, under the right conditions, the valence tautomeric interconversion shown in Equation (3) and Figure 7.[44]

$$[Cu^{II}(DTBCat)(L)] \rightleftharpoons [Cu^{I}(DTBSQ)(L)] \quad (3)$$

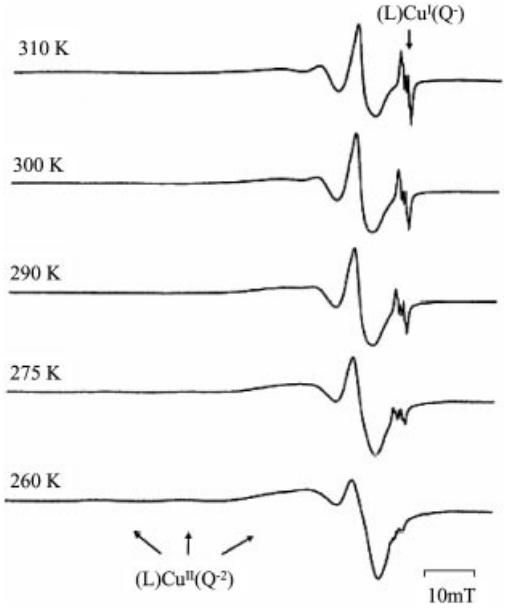

Figure 7. EPR spectra illustrating the temperature-dependent redox isomerism (**3**), with L = mtb and Q = 3,5-di-*tert*-butyl-*o*-quinone, in THF solution.

One of the first examples of valence tautomerism involving the Cu^{II}/Cu^{I} pair was reported in a copper containing amine oxidase enzyme that catalyzes the oxidation of amines to aldehydes,[45] an important process involved in relevant biological functions such as growth regulation and tissue maturation. Indeed, the oxidation of primary amines to aldehydes takes place through a two-electron reduction of O_2 to H_2O_2 catalyzed by the active copper center of the homodimeric enzyme. For this to be achieved and to circumvent spin conservation problems an interconversion from its initial Cu^{II}-catecholate form to the Cu^{I}-semiquinone form, mediated by an intramolecular electron transfer between both units, takes place. Dooley et al. presented evidence for the generation of such a Cu^{I}-semiquinone natural form on several amine oxidases under anaerobic conditions by taking advantage of the very different EPR characteristics (*g* factor and hyperfine-coupling constants) between the pairs Cu^{II}/diamagnetic ligand and Cu^{I}/radical ligand.[45] These studies suggested that the Cu^{I}-semiquinone and the Cu^{II}-catecholate forms are in equilibrium; the Cu^{II}-catecholate form being more stable at low temperatures and the Cu^{I}-semiquinone form at high temperatures.

These exciting results and other biological and commercial processes have motivated the synthesis and characterization of different copper-quinone synthetic models. These studies have shown that the electronic distribution in a series of complexes with the general formula $[(Q^{n-})Cu^{n+}L]$ depends on the donor or acceptor characteristics of the ligand L. With strong π-acceptor ligands, such as L = CO, CNR, PR_3 or AsR_3, the Cu^{I}-semiquinone form is favored, whereas the use of non π-acceptor ligands, such as amine ligands, favors the Cu^{II}-semiquinone form.[46] For instance, Kaim et al. have reported the use of a thioether ligand that favors the Cu^{I}-semiquinone form to induce sensitive valence tautomerism in paramagnetic copper complexes related to amine oxidase enzymes.[47] Similar studies have also been done by Speier et al., who described the existence of valence tautomerism for the species $[Cu(py)_2(PhenQ)_2]$ (**7**).[48] The temperature dependence of the isotropic ESR spectrum of complex **7** in a pyridine solution indicates that at 373 K the complex is in the form $[Cu^{I}(PhenSQ)]$ whereas at 233 K the $[Cu^{II}(PhenCat)]$ tautomer is present, exclusively.

Manganese Complexes

A few years after the first report on cobalt tautomerism, similar temperature-dependent shifts in electronic spectra were observed for a related complex of manganese.[49] The main difference is that valence tautomerism in this case involves three different tautomeric forms associated with three different oxidation states where the manganese ions can be found. Complex $[Mn(py)_2(3,5\text{-}DBCat)_2]$ (**8**) experienced a reversible change in color from the intense purple of the Mn^{IV} form to the pale green-brown characteristic color of the Mn^{II} form. The interconversion takes place through a Mn^{III} form, which usually exhibits similar colors to that of the Mn^{IV} form, as confirmed later in the solid state[50] and in solution.[51] More recently, valence tautomerism in an adduct of a tetrazamacrocycle complex of manganese with a single *o*-benzoquinone ligand has also been reported.[52] The tautomeric interconversion involves two species with nearly degenerate electronic states and a strong sensitivity to variations of the counterion.

Iron and Nickel Complexes

Very recently, two new examples of nickel and iron-quinone complexes have been reported to exhibit valence tautomerism. Tanaka et al. reported complexes $[Ni(PyBz_2)(tBu_2SQ)]PF_6$ (**9**) and $[Ni(MePyBz_2)(tBu_2Cat)]PF_6$ (**10**) as the first examples for the successful control of valence tautomerism between the Ni^{II}-SQ and Ni^{III}-Cat frameworks.[53] Moreover, drastic differences in the electronic states of both complexes are observed due to the steric effects induced by the *o*-methyl group in the $MePyBz_2$ ligand, which weakens the coordination of the pyridine moiety to the nickel ion compared with the unsubstituted $PyBz_2$ ligand. On the other hand, Banerjee et al. reported a semiquinone-cate-

 © 2005 Wiley-VCH Verlag GmbH & Co. KGaA, Weinheim

cholate based mixed valence complex [Fe(bispicen)-(Cl_4Cat)(Cl_4SQ)]·DMF (**11**), for which valence tautomerism has been followed by electronic absorption spectroscopy. The tautomer Fe^{III}-(Cl_4Cat)(Cl_4SQ) is favored at low temperatures, while at an elevated temperature, the Fe^{II}-(Cl_4SQ)$_2$ tautomeric form dominates. This is the first example where a mixed valence semiquinone/catecholate iron(III) complex undergoes intramolecular electron transfer.[54]

Phenoxyl Ligands

Transition metal complexes in which one or more of the ligands is present as a phenoxyl radical have attracted much interest due to their broad occurrence in technical processes[55] and enzymatic metalloproteins such as galactose oxidase (GAO)[56] or glyoxal oxidase (GLO).[57] Phenoxyl radicals are monovalent oxygen radical species that exhibit delocalization of the unpaired electron over the aromatic ring and in most cases *ortho* and *para* substituents that give steric protection.[58] For instance, it has been shown that *tert*-butyl substituents at the *ortho* and *para* positions of the phenolates facilitate one-electron oxidation to the corresponding phenoxyl radicals, because these substituents decrease the oxidation potential of the phenolates and provide enough steric bulk to suppress bimolecular decay reactions of the generated phenoxyl radicals.[59] Several groups have prepared metal-phenoxyl complexes giving new insights into the chemical factors that govern the generation and stability of this type of radicals,[60] among those worth mentioning are the ones produced by Wieghardt et al. They have established that bidentate *O,N*-coordinated *o*-aminophenolato ligands can be found in one of the following different protonation and oxidation levels: *o*-imidophenolate(2$^-$) anions, *o*-iminobenzosemiquinonate(1$^-$) radical monoanions or even *o*-iminobenzoquinone. All these forms can exist in coordination compounds as confirmed by low-temperature X-ray crystallography.[61] In addition, *o*-iminobenzosemiquinonate(1$^-$) anions are paramagnetic (S = 1/2) ligands that couple either ferro- or antiferromagnetically when coordinated to a paramagnetic transition metal ion, depending on the symmetry of the magnetic d orbital of the metal ion.

A further step has been the study and characterization of *O,N*-coordinated type ligands containing two phenolate donor groups. These ligands, in addition to producing phenoxyl radicals in the presence of air, exhibit better chelating capabilities and good π-donor atoms that stabilize higher oxidation states,[62] which has allowed the observation of valence tautomerism in some of their complexes. The advantages of valence tautomeric Schiff-base complexes over transition metal complexes with *o*-quinone ligands are considerable. First, valence tautomeric Schiff-base complexes display higher stabilities relative to atmospheric oxygen in solution and in the solid state. Second, the differences between the optical properties of isomers involved in the valence tautomerism of the cobalt Schiff-base complex are enhanced when compared to those observed for cobalt complexes with *o*-quinone ligands. Third, the Schiff-base ligand exhibits a richer electrochemical behavior since it can exist in different oxidation forms, ranging from +1 to –3, which may lead to stable coordination complexes with several metal ions in a variety of oxidation states. For instance, the tridentate ligand [(2-hydroxy-3,5-di-*tert*-butyl-1-phenyl)imino]-3,5-di-*tert*-butyl-1,2-benzoquinone ligand (Cat-N-BQ), may in principle exist in different oxidation states although it usually coordinates in the mononegative Cat-N-BQ or dinegative Cat-N-SQ radical forms (see Scheme 4).[63]

Using such a ligand, in 1988 Pierpont et al. reported the new complex [Co^{III}(Cat-N-BQ)(Cat-N-SQ)] (**12**), although at that time no evidence for tautomeric interconversion was shown to take place.[64] A few years later, the temperature

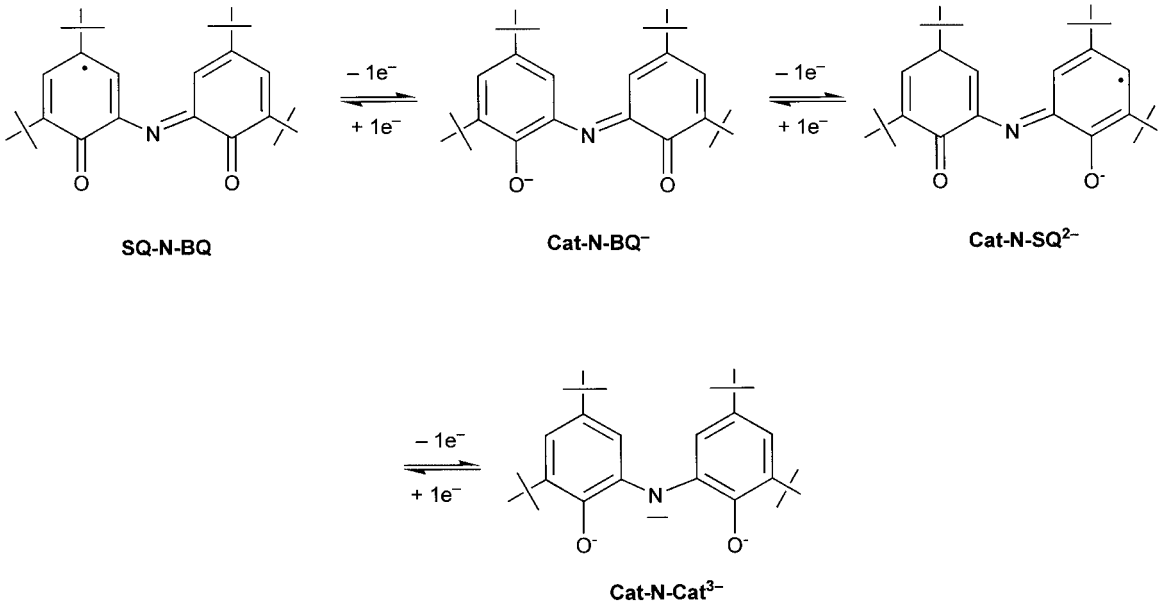

Scheme 4.

dependence of the spectral and magnetic properties of solutions of this compound in nonpolar solvents suggested the existence of the valence tautomeric equilibrium shown in Equation (4). The temperature dependence of the ^{1}H NMR spectrum of a [D_8]toluene solution of complex [Co^{III}(Cat-N-BQ)(Cat-N-SQ)] is shown in Figure 8.[65]

$$[Co^{III}(Cat\text{-}N\text{-}BQ)(Cat\text{-}N\text{-}SQ)] \rightleftharpoons [Co^{II}(Cat\text{-}N\text{-}BQ)_2] \quad (4)$$

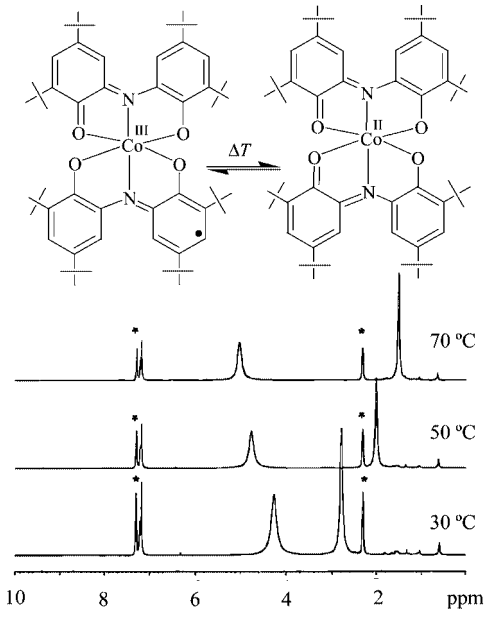

Figure 8. Temperature dependence of the ^{1}H NMR spectrum of a [D_8]toluene solution of [Co(Cat-N-BQ)(Cat-N-SQ)]. The observed signals are due to the *tert*-butyl groups of the ligand. Resonances associated with ring protons are not shown.

The interconversion temperature (T_c) was determined to be close to 300 K by the ratio between the enthalpy and the entropy changes in solution but no tautomerism was observed in the solid state, as evidenced by the lack of changes in the variable-temperature magnetic susceptibility data. This fact was initially attributed to the lack of solvate molecules within the crystalline network, which are assumed to impart a "softness" to the lattice that makes it possible to appreciate the dimensional change in the complex. However, in subsequent work, the same authors showed that complex **12** exhibits a tautomeric interconversion in the solid state but at much higher temperatures than in solution.[66] The large difference between the interconversion T_c in the solid state and in solution is suggested to come from the entropy changes associated with the modifications of vibronic interactions.

Valence tautomerism has also been reported for the related manganese complex [Mn^{IV}(Cat-N-SQ)$_2$] (**13**). In this case, valence tautomerism involves three different tautomeric isomers associated with the three different oxidation states in which the manganese ion can be found: Mn^{IV}, Mn^{III} and Mn^{II}.[67] Variable-temperature magnetic susceptibility data for a crystalline sample of complex **13** is characterized by a constant μ_{eff} value of 1.9 μ_B consistent with the formulation [Mn^{IV}(Cat-N-SQ)$_2$] (**13**, Mn^{IV}). This fact evidenced the lack of valence tautomerism for complex **13** in the solid state, at least in the temperature range studied. For this reason, variable-temperature magnetic susceptibility data for a [D_8]toluene solution of complex **13** were recorded. From 5 to 270 K complex **13** exhibits a constant μ_{eff} value of 1.8–1.9 μ_B in solution, characteristic of the **13**, Mn^{IV} tautomer. Then, from 270 to 360 K the value of μ_{eff} increases gradually to a value of 4.8 μ_B, which is over the spin-only value of 3.9 μ_B (g = 2) expected for the **13**, Mn^{III} isomer but below that expected for the **13**, Mn^{II} tautomer (5.9 μ_B). Since the tautomeric interconversion in solution usually occurs gradually over a large temperature range (>80–100 °C) it was impossible to completely shift the tautomeric equilibrium to the [Mn^{II}(Cat-N-Q)$_2$] isomer. Further support of the existence of the valence tautomerism shown in Scheme 4 was provided by variable temperature electronic absorption spectra for a toluene solution of complex **13** in the 293–353 K temperature range.

In addition to the Schiff-base ligands previously described and in the course of studies on metal-phenoxyl radical complexes, Shimazaki et al. have recently reported that the one-electron oxidized form of a new mononuclear nickel(II)-bis(salicylidene)diamine complex exhibits valence tautomerism. Indeed, the one-electron oxidation of **14** has been found to be temperature dependent in CH_2Cl_2 yielding the corresponding Ni^{III}-phenolate complex at $T < -120$ °C and the Ni^{II}-phenoxyl radical species at $T > -100$ °C, which is regarded as a tautomerism of the oxidation states governed by temperature.[68] A schematic representation for the tautomeric equilibrium of this species in solution is shown in Scheme 5.

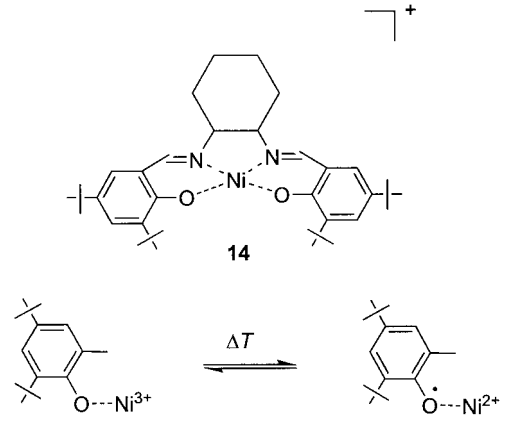

Scheme 5.

Polychlorotriphenylmethyl Radicals

Perchlorotriphenylmethyl radicals (PTM) have their central carbon atom, where most of the spin density is localized, sterically shielded by an encapsulation with six bulky chlorine atoms that increases its life expectancy and thermal and chemical stability.[69] Moreover, the cyclic voltammetry of perchlorotriphenylmethyl radicals shows the formation of two different stable ionic species that correspond

 © 2005 Wiley-VCH Verlag GmbH & Co. KGaA, Weinheim

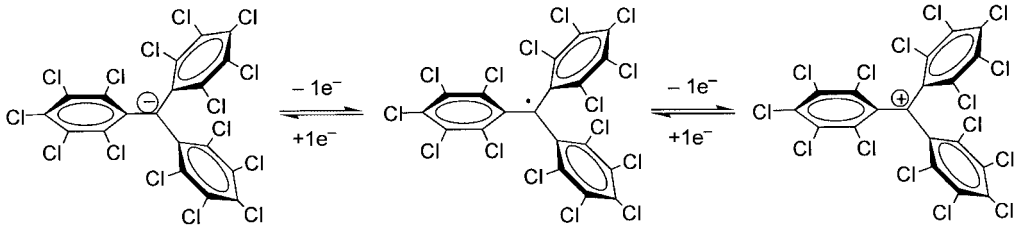

Scheme 6.

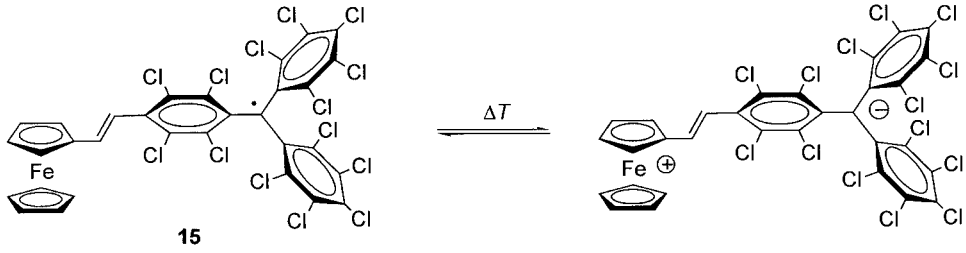

Scheme 7.

to the oxidation and reduction of this radical (see Scheme 6). This allows the corresponding anions and cations to be obtained, either chemically or electrochemically, both in solution and in solid state, which also show considerable stabilities in accordance with the steric shielding of their central carbon atoms. Such persistence as well as the particular structural and conformational characteristics of radicals of this family, has enabled them to be functionalized in order to build pure organic open-shell dendrimers with high-spin ground states[70] and pure-organic mixed-valence molecular wires exhibiting intramolecular electron-transfer phenomena.[71]

More recently, Veciana et al. have described the use of perchlorotriphenylmethyl radicals, properly functionalized with carboxylic groups, to obtain complexes combining paramagnetic metal ions and pure organic radicals as ligating sites. Even though this approach has been successfully used to obtain novel mononuclear[72] and extended transition metal complexes exhibiting nonconventional structural motifs, such as nanoporous frameworks with exotic magnetic behavior,[73] no valence tautomerism has been reported on such complexes so far. Nevertheless, the same authors did report valence tautomerism on a new family of molecular systems comprising PTM radicals and ferrocene

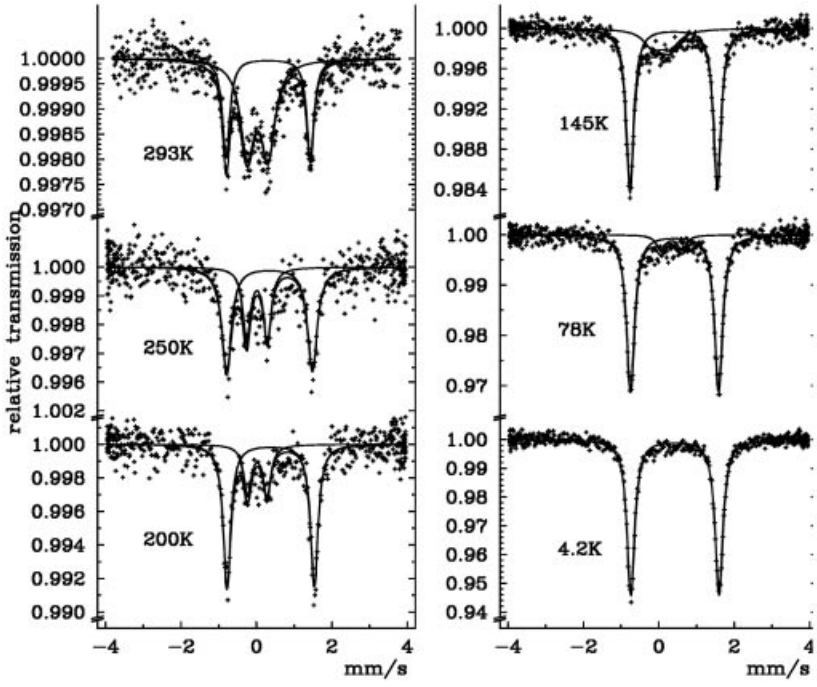

Figure 9. ^{57}Fe Mössbauer spectra of radical **15** as a function of temperature, showing the interconversion between the Fe^{III} and Fe^{II} redox states.

 © 2005 Wiley-VCH Verlag GmbH & Co. KGaA, Weinheim

units (see Scheme 7).[74] Ferrocene chromophores are interesting not only because of their electron donor capacities and rich electrochemistry but also because they are electroactive species whose oxidation state can be controlled by means of a chemical or electrochemical stimulus, with their oxidized states being of open-shell character.

As far as we know, this is the only example described, so far, where valence tautomerism was followed by variable-temperature Mössbauer experiments. The ^{57}Fe Mössbauer spectra of radical **15** as a function of temperature are shown in Figure 9. As can be seen in this figure, the Mössbauer spectrum of **15** exhibited a temperature-dependent behavior, in solid state, that is in agreement with the observation of a temperature-dependent intramolecular electron transfer from the ferrocene center to the radical as shown from left to right in Scheme 7. The conversion appears to be gradual up to room temperature and fully reversible as confirmed by repetitive temperature-variable Mössbauer experiments.

Metalloporphyrins

The cation radicals of metalloporphyrins have been extensively studied because they serve as model systems for biological-redox intermediates. In these systems, the formation of a ring vs. a metal centered cation is determined by factors such as the intrinsic redox potentials of the porphyrin ring and metal center, the number and type of ligands on the metal ion and the nature of the solvent. Thanks to such electronic lability, some metalloporphyrins are susceptible to exhibiting valence tautomerism. A well-recognized case is the heme system, in which the porphinoid macrocyclic ligand can participate directly in the electron-transfer process, or nickel complexes of porphinoid ligands related to the function of factor F430 in the methane-releasing coenzyme M reductase.[75] A drawing of the heme and coenzyme F430 are shown in Scheme 8.

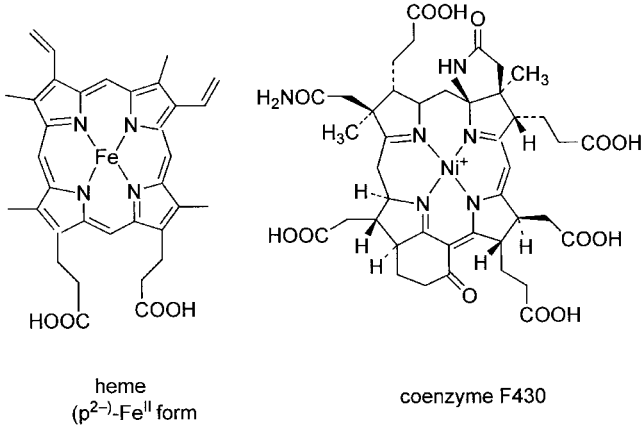

Scheme 8.

In addition to the occurrence in natural systems, in 1975 Dolphin et al. showed the existence of a reversible intramolecular electron transfer in an oxidized nickel tetraphenylporphyrin (TPP).[76] The reversible temperature-dependent transformation can be described as shown in Equation (5).

$$[Ni^{II}(TPP)]^{\cdot+}\ ClO_4^- \rightleftharpoons [Ni^{III}(TPP)]^+\ ClO_4^- \quad (5)$$

At room temperature, oxidation of complex Ni(TPP) (where TPP = tetraphenylporphyrin) yields a green solution associated with the electronic form $[Ni^{II}(TPP^{\cdot})^+]$ with a π-cation radical. Upon freezing at 77 K, the green solution becomes orange. These spectral changes are consistent with conversion to a low-spin $[Ni^{III}(TPP)]^+$ (S = 1/2) in which the unpaired electron resides in a metal ion orbital, as confirmed by temperature-dependent ESR spectroscopy. Kadish et al. also studied electron-transfer mechanisms of five different nickel(II) porphyrins by replacing the phenyl groups with alkyl groups, all of them exhibiting a temperature-dependent valence tautomerism.[77] In addition to variations on the porphyrin ring, it has been proposed that axial ligation also plays a significant role in mediating the tautomerism. For instance, Bocian et al.[78] have shown based on spectroscopic data that relatively stable $[Ni^{III}(TPP)]^+$ can be obtained, even at ambient temperatures, when coordinating ligands such as THF, py and CH_3CN, are present. The spectroscopic data indicate that the conversion to Ni^{III} species is facilitated by mixing of the metal ion and porphyrin ring orbitals, the latter of which contains the hole in the π-cation form.

Redox-Tuned Valence Tautomerism

The redox activity of the ligands not only allows for the existence of valence tautomerism but also for additional switching capacities resulting from an electrochemical process. Such a strategy has been shown to be very useful for the systematic tuning of the critical temperature (T_c), at which there are equal amounts of both tautomers, as well as of the net magnetic moments and optical properties of the tautomeric isomers. Different examples of redox-tuned valence tautomerism are revised below.

Quinone Ligands

A study of the influence of the temperature on the cyclic voltammetric behavior of complex $[Co^{III}$(3,5-DTBCat)(3,5-DTBSQ)(bpy)] (**1**, *ls*-Co^{III}) revealed interesting features. This was the first time that changes in the redox properties of both isomers were followed.[79] As shown in Figure 10, at 273 K the **1**, *ls*-Co^{III} tautomer shows two well-defined processes at $E_{1/2}$ of –0.34 and +0.25 V vs. Ag wire. The redox couple observed at $E_{1/2}$ = –0.34 V is associated with the reduction of the semiquinone ligand to the catecholate form, whereas the second redox process is characteristic of the oxidation of the catecholate ligand to the semiquinone form. As the temperature is increased, slight shifts of the redox processes into the direction of more positive potentials and the apparition of new redox processes at approximately $E_{1/2}$ = –0.75 and +0.40 V, are observed. Since the tautomeric interconversion in solution occurs gradually

 © 2005 Wiley-VCH Verlag GmbH & Co. KGaA, Weinheim

over a large temperature range, it was impossible to completely shift the tautomeric equilibrium to the **1**, *hs*-Co^{II} isomer. For this reason, the voltammetric response of complex [Co^{III}(3,5-DTBCat)(3,5-DTBSQ)(phen)] (**2**) at different temperatures was also studied (see Figure 10). The cyclic voltammogram of **2** in CH_2Cl_2 at 273 K shows a similar pattern to that observed for **1** at 303 K with a mixture of **2**, *ls*-Co^{III} and **2**, *hs*-Co^{II} since it exhibits a lower temperature interconversion. As the temperature is increased, **2**, *ls*-Co^{III} converts completely into the **2**, *hs*-Co^{II} tautomer, whose cyclic voltammogram shows a one-reduction process at $E_{1/2}$ = –0.20 V vs. Ag wire, and two irreversible one-electron oxidation processes. The reduction process is associated with the reduction of the two semiquinone ligands to the catecholate form whereas the oxidation processes are mostly associated with the irreversible oxidation of the semiquinone ligand to the quinone form and to the oxidation of the metal center.

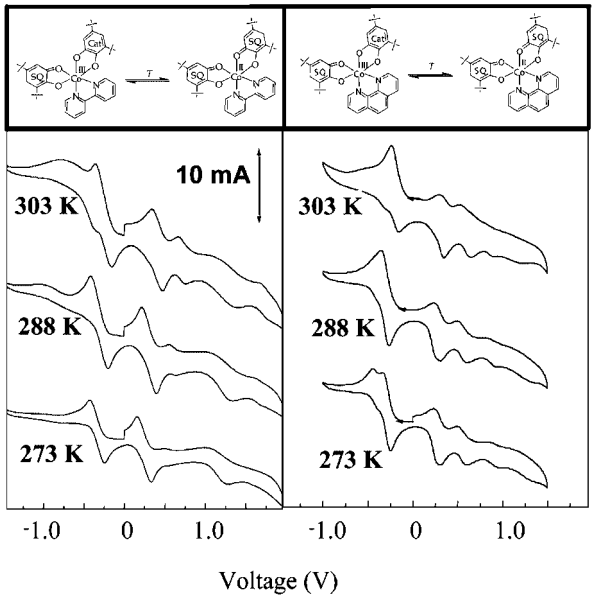

Figure 10. Variable-temperature electrochemical experiments for complexes **1** and **2** in CH_2Cl_2.

Such temperature-dependent redox behavior was also used to selectively oxidize or reduce each one of the tautomeric isomers.[80] Reduction of [Co^{III}(3,5-DTBCat)(3,5-DTBSQ)(bpy)] in CH_2Cl_2 at 273 K with 1 equivalent of $CoCp_2$ yielded [Co^{III}(3,5-DTBCat)$_2$(bpy)][$CoCp_2$] (**1**$^-$, *ls*-Co^{III}) as a dark-green microcrystalline material, whereas reduction of the corresponding high-spin isomer [Co^{II}(3,5-DTBSQ)$_2$(bpy)] (**1**, *hs*-Co^{II}) yielded a purple microcrystalline material characterized as [Co^{II}(3,5-DTBCat)(3,5-DTBSQ)(bpy)][$CoCp_2$] (**1**$^-$, *hs*-Co^{II}). Moreover, the electronic absorption spectra of **1**$^-$, *ls*-Co^{II} and **1**$^-$, *hs*-Co^{II} in acetone exhibited a temperature dependence consistent with the valence-tautomeric equilibrium shown in Scheme 9. This allowed the establishment of an array of four states showing different optical and magnetic ground states, controlled by two temperature-controlled valence-tautomeric equilibria and two reversible redox processes. The possibility of entering the cycle at each state and advancing through the square array in a clockwise and counter-clockwise direction was also established.

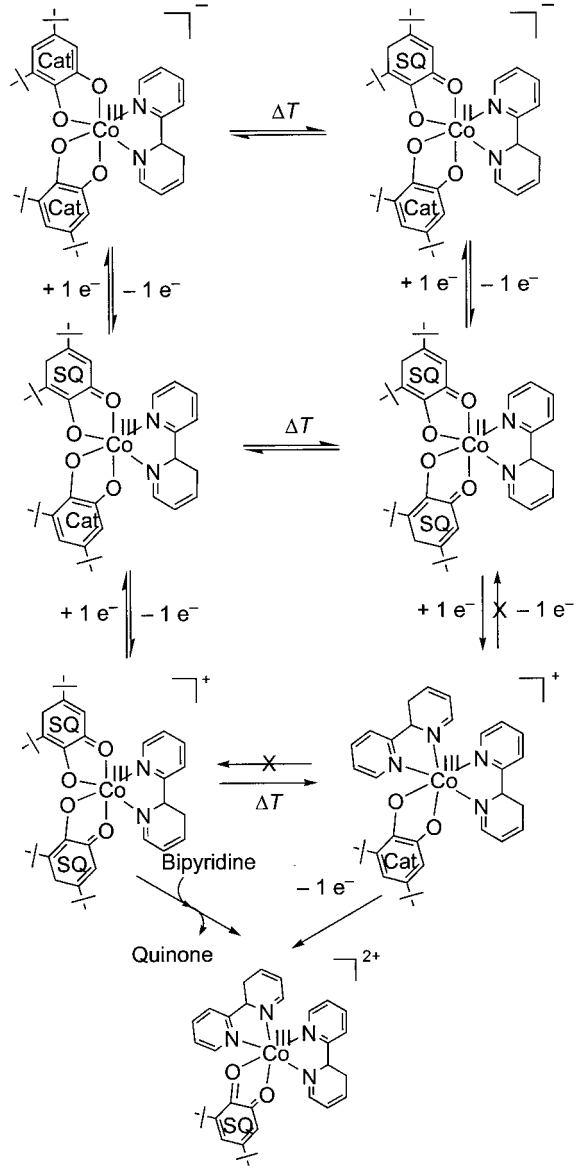

Scheme 9.

Such an array was not obtained for the corresponding oxidized species. Indeed, complex **1**, *ls*-Co^{III} was oxidized by a H_2O_2/HCl mixture yielding an olive-green microcrystalline material characterized as [Co^{III}(3,5-DTBSQ)$_2$(bpy)]·Cl (**1**$^+$, *ls*-Co^{III}). However, oxidation of complex **1**, *hs*-Co^{II} with 1 equivalent of $AgBF_4$ surprisingly yielded [Co(3,5-DTBCat)(bpy)$_2$](BF_4)·2CH_2Cl_2 (**16**). A feasible mechanism for obtaining complex **16** is shown in Scheme 9. Single oxidation of one semiquinone to the quinone form occurs, but the resulting quinone ligand is not basic enough to interact with first-row transition metal ions and therefore the ligand is lost to introduce a new bipyridine ligand that keeps the octahedral coordination around the cobalt ion. A similar mechanism was found for the double oxidation of **1**, *ls*-Co^{III} by $AgBF_4$ and **1**, *hs*-Co^{II} by a mixture of $HClO_4/H_2O_2$ to

 © 2005 Wiley-VCH Verlag GmbH & Co. KGaA, Weinheim

yield in both cases $[Co^{III}(3,5\text{-DTBSQ})(bpy)_2]\cdot X_2$, where X = BF_4 or ClO_4, respectively.[81]

Phenol Ligands

To avoid the low donor capabilities of quinone ligands, Rovira et al. established an array of four states based on the oxidation of the tautomeric complex $[Co^{III}(Cat\text{-}N\text{-}BQ)(Cat\text{-}N\text{-}SQ)]$ (**12**).[82] The advantage of this complex lies in the rich electrochemical behavior of the Schiff-base ligand, which can exist in up to five different oxidation forms, ranging from +1 to –3. Its cyclic voltammogram shows a one-electron oxidation process at $E_{1/2}$ = +0.18 V and a reversible one-electron reduction at $E_{1/2}$ = –0.38 V, both being associated with electrochemical processes occurring at ligand-based orbitals. Potential controlled electrolysis experiments demonstrated the reversibility of both redox processes, indicating no structural changes such as ligand loss or decomposition on the time-scale of the experiment. Therefore, the charged species formed from partial oxidation of complex **12** was generated chemically. Interestingly, the variable-temperature absorption spectra of a toluene solution of complex $[Co^{III}(Cat\text{-}N\text{-}BQ)_2]^+$ (**12**$^+$) shows the existence of an equilibrium consistent with the existence of a temperature-induced valence tautomerism [Equation (6)].

$$[Co^{III}(Cat\text{-}N\text{-}BQ)_2]^+ \rightleftharpoons [Co^{II}(Cat\text{-}N\text{-}BQ)(SQ\text{-}N\text{-}BQ)]^+ \quad (6)$$

This allowed the establishment of an array of four states showing different optical and magnetic ground states by using a reversible oxidation process as an additional stimulus. In a further step, to expand the number of states within the array, Ruiz-Molina et al. converted the valence tautomeric equilibrium of complex $[Mn^{IV}(Cat\text{-}N\text{-}SQ)_2]$ (**13**, Mn^{IV}) by an additional reversible oxidation process to an array of six states. The cyclic voltammogram of complex **13** shows two oxidation processes at $E_{1/2}$ = +0.68 V and $E_{1/2}$ = +0.15 V and a reversible reduction at $E_{1/2}$ = –0.46 V (vs. Ag wire), which have been identified as electrochemical processes involving ligand-based orbitals. Therefore, the charged species **13**$^+$ formed from partial oxidation of complex **13** was generated chemically. Moreover, the variable-temperature magnetic susceptibility data and electronic spectroscopy for a [D_8]toluene solution of a toluene solution was consistent with the valence tautomerism shown in Equation (7).

$$[Mn^{IV}(Cat\text{-}N\text{-}Q)(Cat\text{-}N\text{-}SQ)]^+ \rightleftharpoons [Mn^{III}(Cat\text{-}N\text{-}Q)_2]^+ \rightleftharpoons [Mn^{II}(Cat\text{-}N\text{-}Q)(SQ\text{-}N\text{-}Q)]^+ \quad (7)$$

Polychlorotriphenylmethyl Radicals

The polychlorotriphenylmethyl radical **17**, derived from the valence tautomeric complex **15**, by replacing the ferrocene unit by a permethylated ferrocene, has been converted into an array of three redox states that exhibit distinct physical properties by reduction into their diamagnetic anionic form **17**$^-$ and/or oxidation into the ferrocenium radical derivative **17**$^+$.[83] Interest in these molecular systems is considerable since they not only exhibit variations in color and magnetic properties but also show nonlinear optical responses due to their octupolar nature and their donor-acceptor dyad topology. Indeed, the color of the [K([18]-crown-6)]$^+$**17**$^-$ salt is deep purple, radical **17** is brown, the **17**$^+$$BF_4^-$ salt is yellow, and the hydrocarbon **17**-H is pale pink. In accordance with their distinct colors, the optical absorption spectra of the three species **17**, **17**$^+$, **17**$^-$ show striking differences. Among them, is a remarkable broad intervalence charge-transfer (IVCT) absorption band in the NIR region observed for radical **17**, centered at 1520 nm which is associated with an intramolecular electron transfer from the ferrocene donor unit to the radical acceptor unit (the PTM unit). On the other hand the IVCT band is absent, in agreement with the lack of electron-donor character of the organometallic unit when it is oxidized or reduced. The dynamic hyperpolarizabilities of these three species were measured by hyper-Rayleigh scattering (HRS) experiments. In accordance with the presence of an intense IVCT band, radical **17** gives a large nonlinear optical response with a dynamic hyperpolarizability value β = $545(\pm 30)\times 10^{-30}$ esu. This value is reduced almost ninefold to $66(\pm 7)\times 10^{-30}$ esu for **17**$^+$, and even more for the carbanion **17**$^-$ which has a β = $30(\pm 3)\times 10^{-30}$ esu. The magnetic properties of the three species that have been studied are also different. Thus, while [K([18]crown-6)]$^+$**17**$^-$ is diamagnetic, the paramagnetic susceptibility of compounds **17** and **17**$^+$BF4$^-$ in the solid state between 4–300 K showed quasi-ideal paramagnetic behavior with effective magnetic moments of 1.72 for **17** and 2.50 μ_B for **17**$^+$BF4$^-$ at 300 K; as expected for systems with S = 1/2 and S = 2×1/2 units.

To demonstrate the complete reversibility of the redox reactions of radical **17**, several oxidation and reduction cycles were performed. As shown in Figure 11, the optical

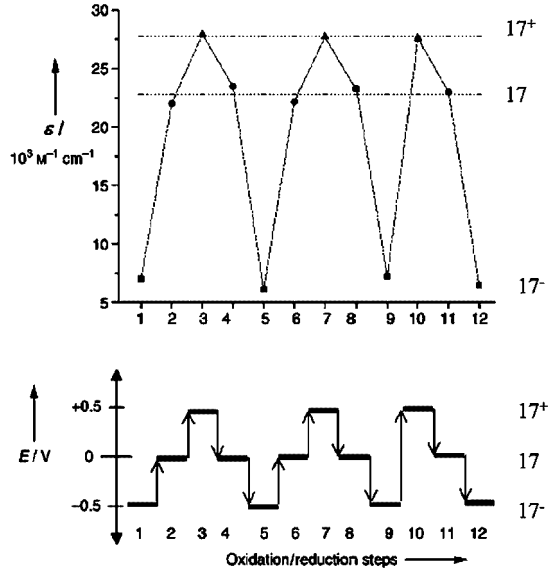

Figure 11. Cyclic stepwise oxidations and reductions carried out in THF with a chronoamperometric technique monitoring the changes in the visible spectrum for **17**-H, [K([18]crown-6)]$^+$**17**$^-$, **17**, and **17**$^+$$BF_4^-$.

 © 2005 Wiley-VCH Verlag GmbH & Co. KGaA, Weinheim

spectrum was recorded, after each step, and could be fully recovered after each cycle. Analogous switching behavior was also detected with EPR spectroscopy by studying the magnetic response in solution of the redox-switchable molecular array. Such chemical transformations along with the conversions by electrical stimuli led us to expect a plethora of signal transduction mechanisms should this molecular switchable array be used as a molecular logic gate. Therefore, radical **17** appeared as an ideal candidate for developing a multiproperty three-state switching molecular device governed by electrical and/or thermal inputs.

Acknowledgments

Authors are grateful to the Spanish Ministry of Education for financial support from the DGI (Spain), project MAT2003–04699 and COST Chemistry D14 Action "Functional Materials". D. R. M. would also like to thank Prof. A. Dei and Prof. D. N. Hendrickson for fruitful discussions and sharing their knowledge.

[1] a) P. Gütlich, Y. Garcia, T. Woike, *Coord. Chem. Rev.* **2001**, *219–221*, 839–879; b) O. Kahn, J. P. Launay, *Chemtronics* **1988**, *3*, 140–151; c) A. Hauser, *Coord. Chem. Rev.* **1991**, *111*, 275–290.
[2] N. Sutin, *Acc. Chem. Res.* **1982**, *15*, 275–282.
[3] M. B. Robin, P. Day, *Adv. Inorg. Chem. Radiochem.* **1967**, *10*, 247–422.
[4] a) M. D. Ward, *Chem. Ind.* **1996**, 568–573; b) R. Ziessel, M. Hissler, A. El-Ghayoury, A. Harriman, *Coord. Chem. Rev.* **1998**, *178–180*, 1251–1298; c) M. N. Paddon-Row, *Acc. Chem. Res.* **1994**, *27*, 18–25; d) M. R. Wasielewski, *Chem. Rev.* **1992**, *92*, 435–461.
[5] J. P. Launay, *Chem. Soc., Rev.* **2001**, *30*, 386–397.
[6] For a general review on pure organic mixed-valence systems, see: D. Ruiz-Molina, J. Sedó, C. Rovira, J. Veciana, in: *Handbook of Advanced Electronic Materials and Devices* (Ed.: H. S. Nalwa) **2001**, 303–327 and references cited therein.
[7] a) S. F. Rak, L. L. J. Miller, *J. Am. Chem. Soc.* **1992**, *114*, 1388–1394; b) L. L. Miller, C. A. Liberko, *Chem. Mater.* **1990**, *2*, 339–340 and references cited therein.
[8] a) K. Lahlil, A. Moradpour, C. Bowlas, F. Menou, P. Cassoux, J. Bonvoisin, J. P. Launay, G. Dive, D. Dehareng, *J. Am. Chem. Soc.* **1995**, *117*, 9995–10002.
[9] a) S. F. Nelsen, H. Q. Tran, M. A. Nagy, *J. Am. Chem. Soc.* **1998**, *120*, 298–304; b) S. F. Nelsen, R. F. Ismagilov, Y. Teki, *J. Am. Chem. Soc.* **1998**, *120*, 2200–2201.
[10] A. Dei, D. Gatteschi, C. Sangregorio, L. Sorace, *Acc. Chem. Res.* **2004**, *37*, 827–835.
[11] a) J. Bonvoisin, J. P. Launay, M. Van der Auweraer, F. C. De Schryver, *J. Phys. Chem.* **1994**, *98*, 5052–5057; b) C. Lambert, G. Nöll, *J. Am. Chem. Soc.* **1999**, *121*, 8434–8442; c) S. Utamapanya, A. Rajca, *J. Am. Chem. Soc.* **1991**, *113*, 9242–9251.
[12] a) J. Bonvoisin, J. P. Launay, C. Rovira, J. Veciana, *Angew. Chem. Int. Ed.* **1994**, *33*, 2106–2109; b) J. Sedo, D. Ruiz, J. Vidal-Gancedo, C. Rovira, J. Bonvoisin, J. P. Launay, J. Veciana, *Adv. Mater.* **1997**, *8*, 748–752.
[13] D. M. Adams, L. Noodleman, D. N. Hendrickson, *Inorg. Chem.* **1997**, *36*, 3966–3984.
[14] a) J. S. Miller, *Adv. Mater.* **1994**, *6*, 217–221; b) W. R. Entley, G. S. Girolami, *Science* **1995**, *268*, 397–400; c) S. Ferlay, T. Mallah, R. Ouahes, P. Veillet, M. Verdaguer, *Nature* **1995**, *378*, 701–702; d) T. Mallah, S. Thiebaut, M. Verdaguer, P. Veillet, *Science* **1993**, *262*, 1554–1557; e) O. Sato, T. Iyoda, A. Fujishima, K. Hashimoto, *Science* **1996**, *271*, 49–51.
[15] R. M. Buchanan, C. G. Pierpont, *J. Am. Chem. Soc.* **1980**, *102*, 4951–4957.
[16] C. G. Pierpont, *Coord. Chem. Rev.* **2001**, *217*, 99–125.
[17] Similar differential behavior has been observed for a series of Co(CTH)(Phendiox)Y·solvent complexes: A. Bencini, A. Caneschi, C. Carbonera, A. Dei, D. Gatteschi, R. Righini, C. Sangregorio, J. Van Slageren, *J. Mol. Struct.* **2003**, *656*, 141–154.
[18] a) D. M. Adams, B. Li, J. D. Simon, D. N. Hendrickson, *Angew. Chem. Int. Ed. Engl.* **1995**, *34*, 1481–1483; b) D. M. Adams, D. N. Hendrickson, *J. Am. Chem. Soc.* **1996**, *118*, 11515–11528.
[19] a) O. Sato, S. Hayami, Z.-Z. Gu, K. Takahashi, R. Nakajima, A. Fujishima, *Chem. Phys. Lett.* **2002**, *355*, 169–174; b) O. Sato, S. Hayami, Z.-Z. Gu, R. Saki, R. Nakajima, A. Fujishima, *Chem. Lett.* **2001**, 874–875.
[20] A. Cui, K. Takahashi, A. Fujishima, O. Sato, *J. Photochem. Photobio. A: Chem.* **2004**, *167*, 69–73.
[21] C. Carbonara, A. Dei, J.-F. Letard, C. Sangregorio, L. Sorace, *Angew. Chem. Int. Ed.* **2004**, *43*, 3136–3138.
[22] F. V. R. Neuwahl, R. Righini, A. Dei, *Chemical Physics Letters* **2002**, *352*, 408–414.
[23] For the analogous spin crossover systems, studies using hydrostatic cells adapted to magnetic susceptibility, Mössbauer, optical absorption and reflectivity methods in conjuction with methods of detection such as IR, EXAFS and X-ray diffraction techniques, have been successfully used in the last years: P. Gütlich, A. B. Gaspar, V. Ksenofontov, Y. Garcia, *J. Phys.: Condens. Matter.* **2004**, *16*, S1087–S1108.
[24] C. Roux, D. M. Adams, J. P. Itie′, A. Polian, D. N. Hendrickson, M. Verdaguer, *Inorg. Chem.* **1996**, *35*, 2846–2852.
[25] A. Caneschi, A. Dei, F. F. De Biani, P. Gütlich, V. Ksenofontov, G. Levchenko, A. Hoefer, F. Renz, *Chem. Eur. J.* **2001**, *7*, 3926–3930.
[26] C. G. Pierpont, C. W. Lange, *Prog. Inorg. Chem.* **1994**, *41*, 331.
[27] A. M. Costero, C. Andreu, R. Martínez-Mañez, J. Soto, L. E. Ochando, J. M. Amigó, *Tetrahedron* **1998**, *54*, 8159–8170.
[28] W. R. Cullen, J. D. Woollins, *Coord. Chem. Rev.* **1981**, *39*, 1–30.
[29] C. Rovira, *Chem. Rev.* **2004**, *104*, 5289–5318.
[30] T. Hirao, *Coord. Chem. Rev.* **2002**, *226*, 81–91.
[31] J. L. Reddinger, J. R. Reynolds, *Macromolecules* **1997**, *30*, 673–675.
[32] P. Gütlich, A. Dei, *Angew. Chem. Int. Ed. Engl.* **1997**, *36*, 2734–2736.
[33] A. Vlcek, *Comments, Inorg. Chem.* **1994**, *16*, 207–228.
[34] a) A. Bencini, A. Caneschi, A. Dei, D. Gatteschi, C. Sangregorio, D. Shultz, L. Sorace, M. G. F. Vaz, *C. R. Chimie* **2003**, *6*, 663–676; b) A. Dei, D. Gatteschi, *Inorg. Chim. Acta* **1992**, *198–200*, 813–822.
[35] C. G. Pierpont, C. W. Lange, *Prog. Inorg. Chem.* **1994**, *41*, 331–443.
[36] a) C. G. Pierpont, R. M. Buchanan, *Coord. Chem. Rev.* **1981**, *38*, 45–87.
[37] The solution behavior of some nickel, rhodium and iridium complexes can also be correctly explained by valence tautomeric equilibria: a) R. R. Rakhimov, P. M. Solozhenkin, N. N. Kopitaya, V. S. Pupkov, A. I. Prokofiev, *Dokl. Akad. Nauk. SSSR* **1988**, *300*, 1177; b) G. A. Abakumov, G. A. Razuvaev, V. I. Nevodchikov, V. K. Cherkasov, *J. Organomet. Chem.* **1988**, *341*, 485–494; c) C. W. Lange, M. Foldeaki, V. I. Nevodchikov, V. K. Cherkasov, G. A. Abakumov, C. G. Pierpont, *J. Am. Chem. Soc.* **1992**, *114*, 4220–4222.
[38] O. Cador, A. Dei, C. Sangregorio, *Chem. Commun.* **2004**, 652–653.
[39] a) D. M. Adams, A. Dei, A. L. Rheingold, D. N. Hendrickson, *Angew. Chem. Int. Ed. Engl.* **1993**, *32*, 880–882; b) D. M. Adams, A. Dei, A. L. Rheingold, D. N. Hendrickson, *J. Am. Chem. Soc.* **1993**, *115*, 8221–8229.

 © 2005 Wiley-VCH Verlag GmbH & Co. KGaA, Weinheim

[40] a) O.-S. Jung, D. H. Lee, Y. S. Sohn, C. G. Pierpont, *Inorg. Chem.* **1998**, *37*, 5875–5880; b) O.-S. Jung, D. H. Jo, Y. A. Lee, B. J. Conklin, C. G. Pierpont, *Inorg. Chem.* **1997**, *36*, 19–24; c) O.-S. Jung, C. G. Pierpont, *J. Am. Chem. Soc.* **1994**, *116*, 2229–2230.
[41] A. Yamaguchi, K. Awaga, *J. Mater. Chem.* **2001**, *11*, 2142–2145.
[42] O.-S. Jung, C. G. Pierpont, *J. Am. Chem. Soc.* **1994**, *116*, 2229–2230.
[43] S. H. Bodnar, A. Caneschi, A. Dei, D. A. Shultz, L. Sorace, *Chem. Commun.* **2001**, 2150–2151.
[44] W. Kaim, *Dalton Trans.* **2003**, 761–768.
[45] M. S. Dooley, M. A. McGuirl, D. E. Brown, P. N. Turowski, W. S. McIntire, P. F. Knowles, *Nature* **1991**, *349*, 262–264.
[46] a) J. Rall, W. Kaim, *J. Chem. Soc., Faraday Trans.* **1994**, *90*, 2905–2908; b) G. Speier, S. Tisza, Z. Tyeklar, C. W. Lange, C. G. Pierpont, *Inorg. Chem.* **1994**, *33*, 2041–2045.
[47] a) W. Kaim, M. Wanner, A. Knödler, S. Zalis, *Inorg. Chim. Acta* **2002**, *337*, 163–172; b) J. Rall, M. Wanner, M. Albrecht, F. M. Hornung, W. Kaim, *Chem. Eur. J.* **1999**, *5*, 2802–2809.
[48] G. Speier, Z. Tyeklar, P. Toth, E. Speier, S. Tisza, A. Rochenbauer, A. M. Whalen, N. Alkire, C. G. Pierpont, *Inorg. Chem.* **2001**, *40*, 5653–5659.
[49] M. W. Lynch, D. N. Hendrickson, B. J. Fitzgerald, C. G. Pierpont, *J. Am. Chem. Soc.* **1981**, *103*, 3961–3963.
[50] A. S. Attia, O.-S. Jung, C. G. Pierpont, *Inorg. Chim. Acta* **1994**, *226*, 91–98.
[51] a) A. S. Attia, C. G. Pierpont, *Inorg. Chem.* **1998**, *37*, 3051–3056; b) A. S. Attia, C. G. Pierpont, *Inorg. Chem.* **1997**, *36*, 6184–6187.
[52] A. Caneschi, A. Dei, *Angew. Chem. Int. Ed.* **1998**, *37*, 3005–3007.
[53] H. Ohtsu, K. Tanaka, *Angew. Chem. Int. Ed.* **2004**, *43*, 6301–6303.
[54] N. Shaikh, S. Goswami, A. Panja, X.-Y. Wang, S. Gao, R. J. Butchler, P. Banerjee, *Inorg. Chem.* **2004**, *43*, 5908–5918.
[55] B. A. Jazdzewski, W. B. Tolman, *Coord. Chem. Rev.* **2000**, *200–202*, 633–685.
[56] J. W. Whittaker, *Chem. Rev.* **2003**, *103*, 2347–2363.
[57] M. M. Whittaker, P. J. Kersten, D. Cullen, J. W. Whittaker, *J. Biol. Chem.* **1999**, *274*, 36226–36232.
[58] E. R. Altwicker, *Chem. Rev.* **1967**, *67*, 475–531.
[59] P. Chaudhuri, K. Wieghardt, *Prog. Inorg. Chem.* **2002**, *50*, 151.
[60] A. K. Nairn, R. Bhalla, S. P. Foxon, X. Liu, L. J. Yellowlees, B. C. Gilbert, P. H. Walton, *J. Chem. Soc., Dalton Trans.* **2002**, 1253–1255 and references cited therein.
[61] K. S. Min, T. Weyhermüller, K. Wieghardt, *Dalton Trans.* **2004**, 178–186 and references cited therein.
[62] T. K. Paine, T. Weyhermüller, L. D. Slep, F. Neewe, E. Bill, E. Bothe, K. Wieghardt, P. Chaudhuri, *Inorg. Chem.* **2004**, *43*, 7324–7338.
[63] This ligand may sometimes exhibit a more complicated behavior: P. Chauduri, M. Hess, K. Hildebrand, E. Bill, T. Weyhermüller, K. Wieghardt, *Inorg. Chem.* **1999**, *38*, 2781.
[64] S. K. Larsen, C. G. Pierpont, *J. Am. Chem. Soc.* **1988**, *110*, 1827.
[65] A. Caneschi, A. Cornia, A. Dei, *Inorg. Chem.* **1998**, *37*, 3419–3452.
[66] O. Cador, F. Chabre, A. Dei, C. Sangregorio, J. Van Slageren, M. G. F. Vaz, *Inorg. Chem.* **2003**, *42*, 6432–6440.
[67] D. Ruiz-Molina, K. Wurst, D. Hendrickson, C. Rovira, J. Veciana, *Adv. Funct. Mater.* **2002**, *12*, 347–351.
[68] Y. Shimazaki, F. Tani, K. Fukui, Y. Naruta, O. Yamauchi, *J. Am. Chem. Soc.* **2003**, *125*, 10512–10513.
[69] M. Ballester, *Acc. Chem. Res.* **1985**, *18*, 380–387.
[70] D. Ruiz-Molina, J. Veciana, F. Palacio, C. Rovira, *J. Org. Chem.* **1997**, *62*, 9009–9017.
[71] a) C. Rovira, D. Ruiz-Molina, O. Elsner, J. Vidal-Gancedo, J. Bonvoisin, J.-P. Launay, J. Veciana, *Chem. Eur. J.* **2001**, *7*, 240–250; b) O. Elsner, D. Ruiz-Molina, J. Vidal-Gancedo, C. Rovira, J. Veciana, *Nano Letters* **2001**, *1*, 117–120.
[72] a) D. Maspoch, D. Ruiz-Molina, K. Wurst, C. Rovira, J. Veciana, *Chem. Commun.* **2002**, 2958–2959; b) D. Maspoch, D. Ruiz-Molina, K. Wurst, J. Vidal-Gancedo, C. Rovira, J. Veciana, *Dalton Transactions* **2004**, 1073.
[73] D. Maspoch, D. Ruiz-Molina, K. Wurst, N. Domingo, J. Tejada, C. Rovira, J. Veciana, *Nature Materials* **2003**, *3*, 190–195.
[74] I. Ratera, D. Ruiz-Molina, F. Renz, J. Ensling, K. Wurst, C. Rovira, P. Gütlich, J. Veciana, *J. Am. Chem. Soc.* **2003**, *125*, 1462–1463.
[75] W. Kaim, B. Schwederski, *Pure Appl. Chem.* **2004**, *76*, 351–364 and references cited therein.
[76] D. Dolphin, T. Niem, R. H. Felton, I. Fujita, *J. Am. Chem. Soc.* **1975**, *97*, 5288–5290.
[77] D. Chang, T. Malinski, A. Ulman, K. M. Kadish, *Inorg. Chem.* **1984**, *23*, 817–824.
[78] J. Seth, V. Palaniappan, D. F. Bocian, *Inorg. Chem.* **1995**, *34*, 2201–2206.
[79] D. Ruiz-Molina, D. N. Hendrickson, *Submitted for Publication*.
[80] D. Ruiz, J. Yoo, I. Guzei, A. L. Rheingold, D. N. Hendrickson, *Chem. Commun.* **1998**, 2089–2090.
[81] D. Ruiz-Molina, L. N. Zakharov, A. L. Rheingold, D. N. Hendrickson, *J. Phys. Chem. Sol* **2004**, *65*, 831–837.
[82] D. Ruiz-Molina, J. Veciana, K. Wurst, D. N. Hendrickson, C. Rovira, *Inorg. Chem.* **2000**, *39*, 617–619.
[83] C. Sporer, I. Ratera, D. Ruiz-Molina, Y. Zhao, J. Vidal-Gancedo, K. Wurst, P. Jaitner, K. Clays, A. Persoons, C. Rovira, J. Veciana, *Angew. Chem. Int. Ed.* **2004**, *43*, 5266 –5268.

Received: April 19, 2005
Published Online: June 28, 2005

 © 2005 Wiley-VCH Verlag GmbH & Co. KGaA, Weinheim

Extending the NHC Concept: C–C Coupling Catalysis by a Pd^{II} Carbene (*r*NHC) Complex with Remote Heteroatoms

Sabine K. Schneider,[a] Patric Roembke,[b] Gerrit R. Julius,[b] Christoph Loschen,[c] Helgard G. Raubenheimer,*[b] Gernot Frenking,*[c] and Wolfgang A. Herrmann*[a]

Keywords: Carbene ligands / C–C Coupling / Density functional calculations / Homogeneous catalysis

A palladium complex, *trans*-Cl(PPh_3)$_2$Pd{C^a-*cyclo*-C_6H_4-*o*-N(Me)C=C^bH}(C^a–C^b), that contains a carbene ligand with remote heteroatoms (*r*NHC) is much more active in certain C–C coupling reactions than comparably simple NHC- and phosphane-containing precatalysts. The *r*NHC ligand binds strongly by electrostatic as well as orbital interaction to the metal.

(© Wiley-VCH Verlag GmbH & Co. KGaA, 69451 Weinheim, Germany, 2005)

Carbon–carbon bond formation with palladium complexes as catalysts is a key step in the synthesis of organic chemicals, natural products as well as in a variety of industrial processes.[1–3] Important examples of such catalysis are found in the Suzuki and Heck reaction types.[4,5] Activity in this area is presently characterized by a search for new ligands and, not independent thereof, the collection of mechanistic information.[6] Phosphanes have been the ligands of choice and are still further investigated.[1,7] However, numerous studies have been undertaken in the recent past to overcome their limitations and replace them by ligands that afford stable compounds while avoiding unwanted side reactions and aiming at even increased activities.[8] Recent successes include the use of N-heterocyclic carbenes (NHC's) as ligands in the precursor complexes.[9–11]

Very few N-heterocyclic-coordinated carbene ligands with remote heteroatoms (*r*NHC's) are known[12] (related, but without remote heteroatoms are α-N carbenes derived from pyridine[13] or azoles[14]). The recent discovery of the exceptional stability and complex dynamics of such Pd^{II} and Pt^{II} compounds[15] encouraged a study to establish their potential use as precatalysts in coupling reactions. Herein we report on a series of comparative Mizoroki–Heck (M–H) and Suzuki–Miyaura (S–M) couplings that involve a number of phosphane and NHC complexes, and the cationic complex chloro(2-methoxy-*N*-methylquinolin-4-yl)-bis(triphenylphosphane)palladium(II) (**1**), that has been described in detail before.[15] A more meaningful comparison of competitive activities with the most effective systems in the literature, will only be possible after steric effects have been incorporated into **1** and other *r*NHC ligands. In this preliminary report we show that such ligand types certainly have potential as precatalysts and also describe a quantum mechanical comparison between NHC and *r*NHC model ligands and complexes. Descriptions of the ligand electronic structures as well as the metal–ligand bonding in NHC and the "newcomer" *r*NHC complex types are extracted from DFT calculations at the RI-BP86/SVP level.[16]

The catalyst precursors, all prepared according to standard procedures and screened for their activity and efficiency in well-known M–H and S–M reactions, are shown in Figure 1 and the results obtained in Table 1 and Table 2. These reactions do not represent troublesome couplings but

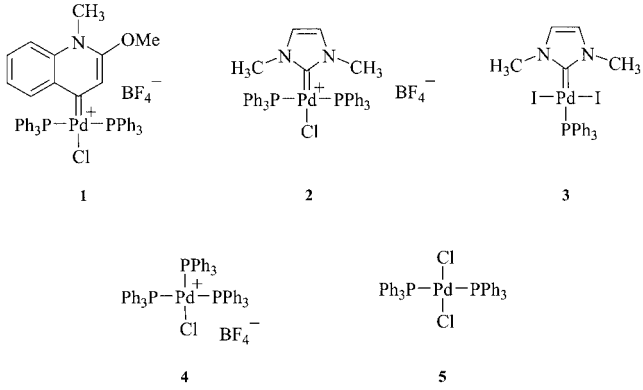

Figure 1. Precatalysts employed in C–C coupling reactions.

[a] Department of Chemistry, Technische Universität München, Lichtenbergstr. 4, 85747 Garching, Germany
E-mail: wolfgang.herrmann@ch.tum.de
Fax: +49-89-289-13473
[b] Department of Chemistry and Polymer Science, Private Bag X1, Matieland, Stellenbosch, South Africa
E-mail: hgr@sun.ac.za
Fax: +27-21-808-3849
[c] Fachbereich Chemie, Philips-Universität, Hans-Meerweinstr, 35043 Marburg, Germany
E-mail: frenking@chemie.uni-marburg.de
Fax: +49-6421-282 5566

Supporting information for this article is available on the WWW under http://www.eurjic.org or from the author.

Table 1. Mizoroki–Heck reaction.

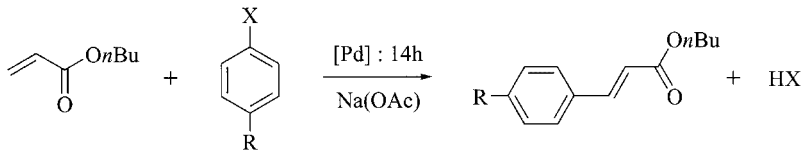

Entry[a]	R	mol-% Pd	Temp. [°C]	Catalyst	Conversion [%][b]	Yield [%][b]	TON [mol product (mol cat)$^{-1}$]
1	$C(O)CH_3$	0.01	130	**1**	>99.99	94	9400
2	$C(O)CH_3$	0.01	130	**3**	45	41	4100
3	$C(O)CH_3$	0.001	145	**1**	>99.99	94	94000
4	$C(O)CH_3$	0.0001	145	**1**	92	91	910000
5	$C(O)CH_3$	0.0001	145	**3**	8	6	60000
6	$C(O)CH_3$	0.5[c]	150	**1**	85	81	162
7	OCH_3	0.5	145	**1**	84	80	160
8[d]	H	0.1	145	**1**	>99.99	95	950
9	H	0.1	145	**2**	68	66	660
10	H	0.1	145	**3**	20	17	170
11	H	0.1	145	**4**	38	34	340
12	H	0.1	145	**5**	39	37	370
13	H	0.5[c]	150	**1**	64	55	110

[a] X = Br, except for **6** and **13**; ratio of aryl halide/olefin/NaOAc = 1:1.5:1.5; solvent: DMAc (dimethylacetamide). [b] GC yield and conversion using diethylene glycol/di-*n*-butyl ether as internal standard. [c] X = Cl; 0.2 mol-equiv. of $[R_4N]Br$ added to the reaction mixture. [d] For Entries 8–12 compare also Figure 2.

simple ones using relatively simple catalytic systems to allow a comparison on an electronic (and not steric) basis and to show that *r*NHC ligands deserve further attention. The data indicate clearly the superiority of the stable *r*NHC complex which gives relatively high conversions even at low concentration. Under the reported conditions TON's of 9.1×10^5 in the M–H and 3.2×10^6 in the S–M coupling are reached. Catalyst loading in the latter situation, however, is too low and affects the efficiency of the process. Arylchlorides couple successfully at 0.5% loading level of the *r*NHC complex according to M–H, and at 1.0% in the S–M reaction without any evidence of palladium black formation, even after stirring for 24 hours.

An even better picture of the relative catalyst activities emerged from the time-conversion curves in Figure 2 and Figure 3 determined under similar conditions for the two types of C–C coupling respectively.

The two sets of curves are remarkably similar,[10] and the *r*NHC complex, which requires no induction period, comes out on top of the chosen series again. Cationic charge (or alternatively, the number of phosphane ligands present) on the complex is not an important parameter for the halophosphane compounds **4** and **5**, but differentiate clearly between NHC complexes **2** and **3**.

To better understand from a chemical viewpoint the reasons behind the relatively high activity of the *r*NHC complex in comparison with a simple cationic NHC complex, we theoretically analyzed their metal–carbene bonds. First, the geometries of the model compounds **1M** and **2M** with phenyl (on P) and methyl (on N and O) substituents replaced by hydrogen atoms, were optimized at the RI-BP86/SVP level.[16]

For this study the crystal and molecular structures of **2** – prepared similarly to **1**[15] (compare also ref.[17]) – were determined. Crystal data and calculated geometries are given as Supporting Information (for details see also the footnote on the first page of this article). The agreement between calculated and experimental bond lengths is quite good. Both methods indicate similar Pd–C(carbene) bond lengths, but a significantly larger *trans* influence is exhibited by the *r*NHC ligand (experimental Pd–Cl bond length 0.044 Å longer in **1** than in **2**)

We used different methods for extracting chemical bonding information in **1M** and **2M**. Figure 4 shows the most important frontier orbitals of the two simplified free carbene ligands *r*NHC and NHC. The σ-donor HOMO orbital in *r*NHC is 1.28 eV higher in energy than in NHC. HOMO-1, the highest-lying occupied π-orbital, has a much larger coefficient at the carbene C-atom in NHC than in *r*NHC affording a higher electron population at the C(carbene) p(π) AO in NHC (0.66) than in *r*NHC (0.53) which is disadvantageous for M–L π back donation in the former complex. The LUMO of NHC (not shown) is a π* orbital of the C=C double bond which has a node at the C(carbene) atom. The next low-lying π-acceptor orbital, LUMO+1, has a large coefficient at the C(carbene) p(π) AO. The π-acceptor LUMO of *r*NHC is lower in energy than the LUMO+1 of NHC but it is much more delocalized. The increase in the p(π) AO population on the carbene carbon atom of *r*NHC after formation of the complex **1M** ($\Delta q\pi$ = 0.28 e) is larger than in NHC ($\Delta q\pi$ = 0.20 e) and suggests that this ligand may also be a somewhat stronger π-acceptor than the latter species.

A deeper insight into the metal–carbene bonding situation results from an energy decomposition analysis (EDA)[17,19] of **1M** and **2M** (Table 3). The metal–carbene interactions in the *r*NHC carbene complex, **1M**, are significantly stronger (ΔE_{int} = –107.6 kcal/mol) than in **2M** (ΔE_{int} =

 © 2005 Wiley-VCH Verlag GmbH & Co. KGaA, Weinheim

Table 2. Suzuki–Miyaura coupling.

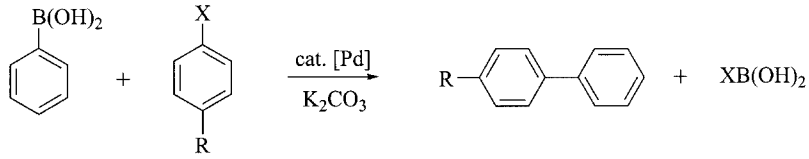

Entry[a]	R	X	mol-% Pd	Catalyst	Time	Yield (%)[b]	TON [mol product. mol cat^{-1}]
1	$C(O)CH_3$	Br	0.0001	**1**	13 h	>99.99	1000000
2	$C(O)CH_3$	Br	10^{-5}	**1**	13 h	32	3200000
3	$C(O)CH_3$	Cl	1.0[c]	**1**	14 h	46	460
4	H	Br	0.01	**1**	13 h	>99.99	10000
5	H	Br	0.001	**1**	13 h	98	98000
6	H	Br	0.1	**1**	10 min	95	950
7	H	Br	0.1	**3**	10 min	16	160
8[d]	OCH_3	Br	0.1	**1**	13 h	>99.99	1000
9	OCH_3	Br	0.1	**2**	13 h	85	850
10	OCH_3	Br	0.1	**3**	13 h	32	320
11	OCH_3	Br	0.1	**4**	13 h	72	720
12	OCH_3	Br	0.1	**5**	13 h	77	770
13	OCH_3	Br	0.01	**1**	13 h	54	5400

[a] Ratio of aryl halide/phenylboronic acid/K_2CO_3 = 1:1.2:1.5; solvent: xylene; T = 130 °C. [b] GC yield using diethylene glycol/di-*n*-butyl ether as internal standard. [c] Cs_2CO_3 was used as base. [d] For Entries 8–12 compare also Figure 3.

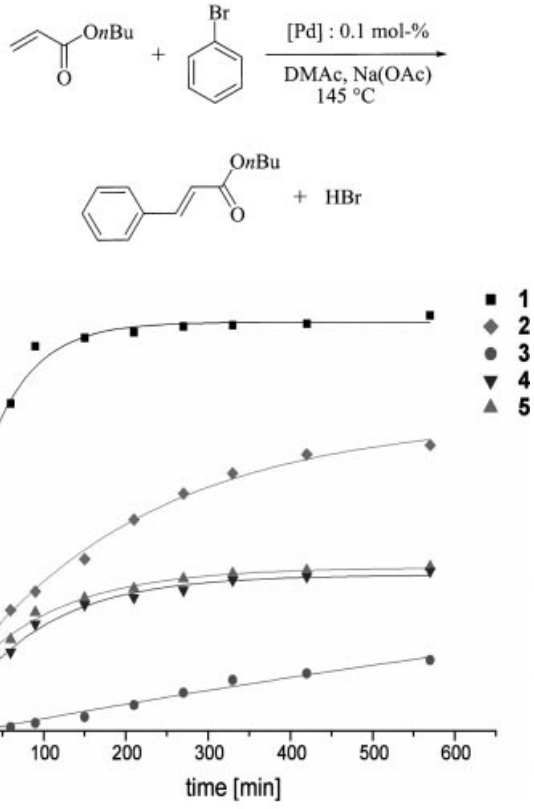

Figure 2. Time-conversion-curves: Mizoroki–Heck reaction.

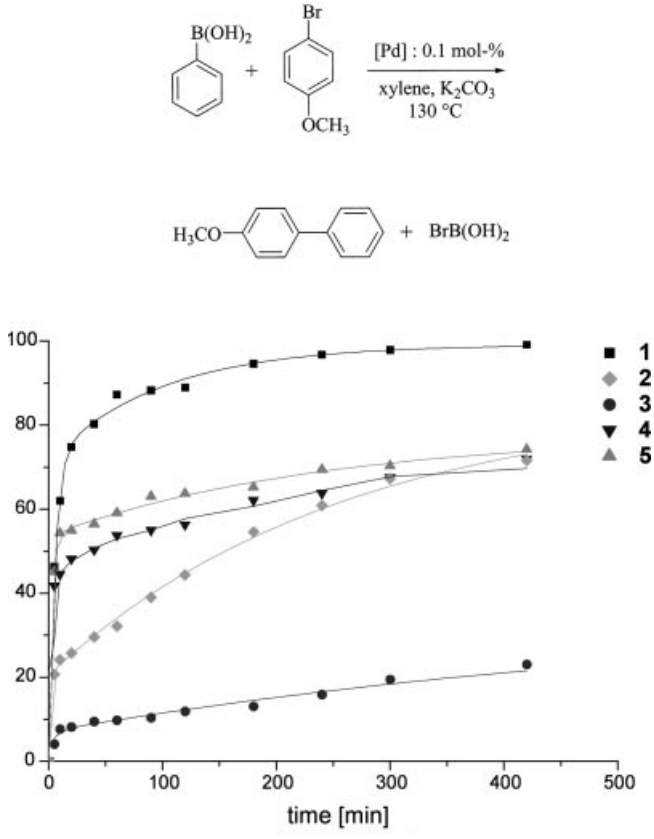

Figure 3. Time-conversion-curves: Suzuki–Miyaura reaction.

–85.5 kcal/mol). The rather small calculated geometry relaxation of the fragments (ΔE_{prep}) indicates that the former complex also has a bond dissociation energy of ca. 20 kcal/mol higher than the latter (also compare a related discussion involving other carbene complexes by one of us[20]).

The metal–carbene bonding in both complexes comes mainly from classical electrostatic interactions, ΔE_{elstat}, which contribute ca. 70% to the attractive forces.

 © 2005 Wiley-VCH Verlag GmbH & Co. KGaA, Weinheim

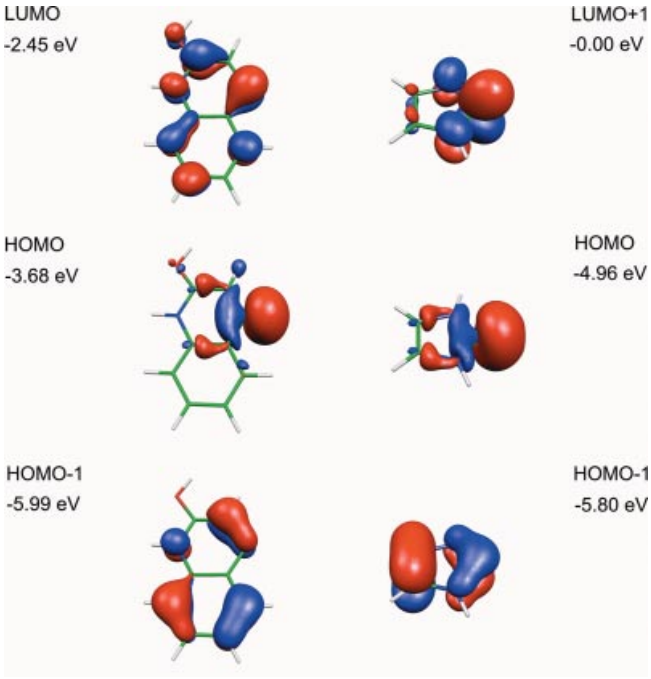

Figure 4. Frontier orbitals of the free model carbenes *r*NHC (left) and NHC (right).

Table 3. Energy decomposition analyses of **1M** and **2M**.[a]

	1M		**2M**	
ΔE_{int}	–107.6		–85.5	
ΔE_{Pauli}	184.9		157.9	
ΔE_{elstat}	–204.6	(69.9%)	–171.8	(70.6%)
ΔE_{orb}	–87.9	(30.1%)	–71.5	(29.4%)
a′	–72.8	(82.8%)	–60.4	(84.5%)
a′′	–15.1	(17.2%)	–11.1	(15.5%)
ΔE_{prep}	3.6		2.4	
$\Delta E = -D_e$	–104.0		–83.1	

[a] Energy given in kcal mol^{-1}.

The most interesting part of the EDA is the breakdown of the total orbital interaction term, $\Delta E_{orb,}$ into orbital contributions of different symmetry (Table 3). The EDA calculations of complexes **1M** and **2M** were carried out with C_s symmetry, which means that the strength of the σ-bonding is given by the a′ orbitals while π-bonding is given by the a′′ orbitals. The former contribution is clearly more important [72.8 kcal/mol (82.8%) in **1M** and 60.4 kcal/mol (84.5%) in **2M**] than π-bonding [15.1 kcal/mol (17.2%) in **1M** and 11.1 kcal/mol (15.5%) in **2M**].

In conclusion, this study, using palladium as central metal, has shown that a carbene-type ligand with no heteroatom in the immediate vicinity of the carbon donor atom activates the metal centre significally more than comparable simple N-heterocyclic carbenes. No serious dichotomy arises when Heck- and Suzuki-type conversions are compared. The exceptionally strong metal–carbene bond in such a complex – as determined by quantum chemical DFT calculations – is mainly due to very strong metal–ligand electrostatic attraction as well as an energetically higher-lying σ-HOMO on the ligand that overlaps well and donates electrons readily.

All our results are in accordance with an *r*NHC ligand that remains attached to the central metal during the catalytic cycle and indicate that catalytic activity could be increased by further ligand tailoring, especially an increase in steric bulk.[11,21] Finally we anticipate that this work will provide an impetus for further study and that the new class of ligands will find application in other important catalytic processes and should, individually, be considered as useful alternatives to NHC′s as we shall show in future reports.

Experimental Section

The preparation of the catalyst precursor complex **2** is described in the Supporting Information, **3**[11a] as well as **4**[22] were prepared according to literature procedures and **5** is commercially available.

Heck Reaction: A constant ratio of sodium acetate (3.00 mmol, 246 mg) and aryl halide (2.00 mmol, e. g. 315 mg bromobenzene) as well as 100 mg diethylene glycol/di-*n*-butyl ether were placed in a Schlenk tube equipped with a stirring bar under argon. Then 3.00 mmol of *n*-butyl acrylate (0.43 mL) and 2 mL degassed DMAc were added. After 10 min at the desired temperature, the catalyst solution was added against a positive stream of argon. To terminate the reaction the mixture was allowed to cool to room temperature and 3 mL of aqueous HCl added. The water phase was extracted thrice with 2 mL of dichloromethane and the organic fraction dried with $MgSO_4$. Conversions and yields were determined by GC-MS using diethylene glycol/di-*n*-butyl ether as internal standard.

Suzuki Reaction: Phenylboronic acid (2.40 mmol, 293 mg) and potassium carbonate (3.00 mmol, 415 mg) were placed in a Schlenk tube equipped with a stirring bar under argon. Aryl halide (2.00 mmol; e. g. 374 mg bromoanisole), 100 mg diethylene glycol/di-*n*-butyl ether and 2 mL degassed xylene were added. After thermostating at 130 °C for 10 min, the catalyst solution was added against a positive stream of argon. To end the reaction, the mixture was cooled to room temperature and 3 mL of water added. The water phase was extracted three times with 2 mL of diethyl ether and the organic phases dried with $MgSO_4$.

Acknowledgments

This work was supported by the Fonds der Chemischen Industrie (SKS), the NRF (PR) and Sasol Technologies (GRJ).

[1] W. A. Herrmann, in: *Applied Homogenous Catalysis with Organometallic Compounds*, (Eds.: B. Cornils, W. A. Herrmann), Wiley-VCH, Weinheim, **1996**, vol. 1 and 2, p. 712.
[2] a) H. Geisler, in *Transition Metals for Organic Synthesis*, vol. 1 (Eds.: M. Beller, C. Bolm), Wiley-VCH, Weinheim, **1998**, vol. 1, p. 158; b) F. Diederich, P. J. Stang (Eds.), *Metal-catalyzed Cross-coupling Reactions*, Wiley-VCH, Weinheim, **1998**.
[3] a) J. Tsuji, *Palladium Reagents and Catalysts*, Wiley, Chichester, **1995**; b) L. Brandsma, S. F. Vasilevsky, H. D. Verkruijsse, *Application of Transition Metal Catalysts in Organic Synthesis*, Springer, Berlin, **1998**.
[4] a) N. Miyaura, A. Suzuki, *J. Chem. Soc., Chem. Commun.* **1979**, 866; b) N. Miyaura, T. Yanagi, A. Suzuki, *Synth. Commun.* **1981**, *11*, 513; c) A. Suzuki, *J. Organomet. Chem.* **1999**, *576*, 147; d) N. Miyaura, A. Suzuki, *Chem. Rev.* **1995**, *95*, 2457.
[5] a) T. Mizoroki, K. Mori, A. Ozaki, *Bull. Chem. Soc. Jpn.* **1971**, *44*, 581; b) R. F. Heck, J. P. Nolley Jr., *J. Org. Chem.* **1972**, *37*,

 © 2005 Wiley-VCH Verlag GmbH & Co. KGaA, Weinheim

2320; c) A. de Meijere, F. E. Meyer, *Angew. Chem.* **1994**, *106*, 2473; *Angew. Chem. Int. Ed. Engl.* **1994**, *33*, 2473; d) M. Shibasaki, E. M. Vogl, *J. Organomet. Chem.* **1999**, *576*, 1.
[6] U. Christmann, R. Vilar, *Angew. Chem. Int. Ed.* **2005**, *44*, 366 and references cited therein.
[7] a) F. Ozawa, in: S. Komiya (Ed.), *Synthesis of Organometallic Compounds*, Wiley, Sussex, **1997**, p. 249; b) S. D. Walker, T. E. Barder, J. R. Martinelli, S. L. Buchwald, *Angew. Chem. Int. Ed.* **2004**, *43*, 1871.
[8] V. Farina, *Adv. Synth. Catal.* **2004**, *346*, 1553.
[9] a) J. Huang, S. P. Nolan, *J. Am. Chem. Soc.* **1999**, *121*, 9889; b) L. Xu, W. Chen, J. Xiao, *Organometallics* **2000**, *19*, 1123; c) W. A. Herrmann, *Angew. Chem.* **2002**, *114*, 1342; *Angew. Chem. Int. Ed.* **2002**, *41*, 1290 and references therein; d) W. A. Herrmann, K. Öfele, D. v. Preysing, S. K. Schneider, *J. Organomet. Chem.* **2003**, *687*, 229 and references cited therein.
[10] a) I. D. Hills, G. C. Fu, *J. Am. Chem. Soc.* **2004**, *126*, 13178; b) P. W. N. van Leeuwen, *Homogenous Catalysis Understanding the Art*, Kluwer Academic Publishers, Dordrecht, **2004**, p. 271 and references cited therein.
[11] a) W. A. Herrmann, V. P. W. Böhm, C. W. K. Gstöttmayr, M. Grosche, C.-P. Reisinger, T. Weskamp, *J. Organomet. Chem.* **2001**, *617*, 616; b) H. Palencia, F. Garcia-Jimenez, J. M. Takacs, *Tetrahedron Lett.* **2004**, *45*, 3849.
[12] H. G. Raubenheimer, M. Desmet, P. J. Olivier, G. J. Kruger, *J. Chem. Soc. Dalton Trans.* **1996**, 4431.
[13] a) H. G. Raubenheimer, J. G. Toerien, G. J. Kruger, R. Otte, W. van Zyl, P. Olivier, *J. Organomet. Chem.* **1994**, *466*, 291; b) J. S. Owen, J. A. Labinger, J. E. Bercaw, *J. Am. Chem. Soc.* **2004**, *126*, 8247.
[14] X. Li, L. N. Appelhans, J. W. Faller, R. H. Crabtree, *Organometallics* **2004**, *23*, 3378.
[15] a) W. H. Meyer, M. Deetlefs, M. Pohlmann, R. Scholz, M. W. Esterhuysen, G. R. Julius, H. G. Raubenheimer, *Dalton Trans.* **2004**, 413.
[16] The calculations were carried out using the program package TURBOMOLE: a) R. Ahlrichs, M. Bär, M. Häser, H. Horn, C. Kölmel, *Chem. Phys. Lett.* **1989**, *162*, 165; b) O. Treutler, R. Ahlrichs, *J. Chem. Phys.* **1995**, *102*, 346; c) Becke–Perdew (BP86) exchange-correlation functional and Resolution-of-the-Identity-Approximation (RI): S. H. Vosko, L. Wilk, M. Nusair, *Can. J. Phys.* **1980**, *58*, 1200; d) J. P. Perdew, *Phys. Rev. B* **1986**, *33*, 8822; e) D. Becke, *Phys. Rev. A* **1988**, *38*, 3098; Erratum:J. P. Perdew, *Phys. Rev. B* **1986**, *34*, 7406; f) K. Eichkorn, O. Treutler, H. Öhm, M. Häser, R. Ahlrichs, *Chem. Phys. Lett.* **1995**, *242*, 652; g) For the calculations an SVP basis set was used:A. Schäfer, H. Horn, R. Ahlrichs, *J. Chem. Phys.* **1992**, *97*, 2571.
[17] A. Fürstner, G. Seidel, D. Kremzow, C. W. Lehmann, *Organometallics* **2003**, *22*, 907.
[18] The EDA calculations have been performed using the program package ADF: a) F. M. Bickelhaupt, E. J. Baerends, *Rev. Comput. Chem.* (Eds.: K. B. Lipkowitz, D. B. Boyd), Wiley-VCH, New York, **2000,** vol. 15, p. 1; b) G. te Velde, F. M. Bickelhaupt, E. J. Baerends, S. J. A. van Gisbergen, C. Fonseca Guerra, J. G. Snijders, T. Ziegler, *J. Comput. Chem.* **2001**, *22*, 931. The calculations have been carried out at the BP86 level [16c–e] using uncontracted Slater-type orbitals (STOs) as basis functions: c) J. G. Snijders, E. J. Baerends, P. Vernooijs, *At. Nucl. Data Tables* **1982**, *26*, 483; The basis sets have TZP quality. An auxiliary set of s, p, d, f and g STOs was used to fit the molecular densities and to represent the Coulomb and exchange potentials accurately in each SCF cycle; d) J. Krijn, E.J. Baerends, *Fit Functions in the HFS-Method*, Internal Report (in Dutch), Vrije Universiteit Amsterdam, The Netherlands, **1984**.
[19] For a review of EDA results on bonding in transition metal complexes see: G. Frenking, K. Wichmann, N. Fröhlich, C. Loschen, M. Lein, J. Frunzke, V. M. Rayón, *Coord. Chem. Rev.* **2003**, *238*, 55.
[20] M. Lein, A. Szabó, A. Kovács, G. Frenking, *Faraday Discuss.* **2003**, 365.
[21] a) T. Weskamp, V. P. W. Böhm, W. A. Herrmann, *J. Organomet. Chem.* **1999**, *585*, 348; b) A. F. Littke, G. C. Fu, *Angew. Chem. Int. Ed.* **1999**, *38*, 2411; c) J. P. Wolfe, S. L. Buchwald, *Angew. Chem. Int. Ed. Angew. Chem. Int. Ed. Engl.* **1999**, *38*, 2413; d) A. F. Littke, C. Dai, G. C. Fu, *J. Am. Chem. Soc.* **2000**, *122*, 4020; e) T. Hundertmark, A. F. Littke, S. L. Buchwald, G. C. Fu, *Org. Lett.* **2000**, *2*, 1729.
[22] E. P. Urriolabeita, *J. Chem. Educ.* **1997**, *74*, 325.

Received: April 14, 2005
Published Online: June 28, 2005

 © 2005 Wiley-VCH Verlag GmbH & Co. KGaA, Weinheim

Two Novel Cadmium Polymeric Metallamacrocyclic Complexes Constructed from a Pyridylmethyl-Functionalized Tetraaza Ligand

Zhen Ma,[a,b] Zhongning Chen,[a] and Rong Cao*[a]

Keywords: Cadmium complexes / Crystal structures / Macrocyclic compounds / Hydrothermal method

A new octadentate ligand L was synthesized by tetrafunctionalization of 1,4,8,11-tetraazacyclotetradecane (L^1, cyclam) with 4-pyridylmethyl groups and its two novel cadmium polymeric metallamacrocyclic complexes, $[Cd_3L_{1.5}(C_6H_5O_7)_2{\cdot}6H_2O]_n$ (**1**) and $[CdCl_2L_2{\cdot}2.5H_2O]_n$ (**2**), were obtained by hydrothermal methods.
(© Wiley-VCH Verlag GmbH & Co. KGaA, 69451 Weinheim, Germany, 2005)

Macrocyclic and macrobicyclic compounds attract increasing interests of chemists owing to their interesting structures, properties and important roles in coordination chemistry and many other fields, such as material chemistry and medicinal chemistry.[1–6] Unlike polyoxa macrocyclic and macrobicyclic compounds, polyaza compounds can be functionalized by several groups, such as alkynyl,[7] phosphanylmethyl,[8] carboxyl,[9] and heterocyclic groups[10] on their secondary N-sites and thereby show some novel properties in coordination, electro-, photoluminescent and catalytic chemistry. Hence, we recently started the investigation on the complexes constructed from functionalized polyaza ligands, in order to prepare some novel structures and study their applications in material and medicinal chemistry. In this communication, we will report a new tetrafunctionalized octadentate ligand L and its two novel cadmium polymeric metallamacrocyclic complexes, $[Cd_3L_{1.5}(C_6H_5O_7)_2{\cdot}6H_2O]_n$ (**1**) and $[CdCl_2L_2{\cdot}2.5H_2O]_n$ (**2**), which were obtained by hydrothermal methods.

The ligand (L) was synthesized by the reaction of 1,4,8,11-tetraazacyclotetradecane (cyclam, L^1) with 4-pyridylmethyl chloride according to a previously reported procedure (Figure 1).[10] Complex **1** was obtained from the hydrothermal reaction of cadmium nitrate, L and sodium citrate. Single-crystal X-ray analysis illustrates that **1** is an interesting polymeric metallamacrocyclic complex. There are three crystallographic independent Cd^{2+} ions: Cd(1) is coordinated by five oxygen and two nitrogen atoms in a pentagonal-bipyrimidal geometry, Cd(2) is coordinated by five oxygen and one nitrogen atoms in an octahedral geometry, while Cd(3) is coordinated by six oxygen and one nitrogen atoms in a pentagonal-bipyrimidal geometry. The citrate ligand shows an η^1-η^2-η^2-η^3-μ_4 coordination mode to connect four central metal ions by its six oxygen donors of three carboxylic groups and a hydroxy group (Supporting Information, Figure S1). One oxygen atom of it is uncoordinated and two oxygen donors coordinate to two central ions. The ligand L adopts two coordination modes: one acts as tetradentate ligand to coordinate four cadmium ions by its four pyridyl nitrogen atoms (η^1-μ_4, L^a), the other as bidentate ligand to two cadmium ions by its two *para*-pyridyl nitrogen atoms (η^1-μ_2, L^b) (Figure 1). The most striking feature of **1** is that its structure is built from seven interesting metallacycle units. The three Cd^{2+} ions form a novel M_3O_3 trinuclear heterocyclohexane-like metallacycle by the connection of citrate ligands (first metallacycle unit, C1; Figure 2). Every two of such trinuclear units are bridged by two citrate ligands to form a hexanuclear unit with a dinuclear 14-membered metallamacrocycle (C2; Figure 2). Every hexanuclear unit is connected with two other neighboring hexanuclear units by two citrate ligands to form columns of the structure with a dinuclear 12-membered metallamacrocycle (C3; Figure 2). Although several similar examples[11–16] of structures of the Cd_3O_3 unit have been reported, the major conformation is a heterocubane,[12,14,15] different from that in **1**. The fourth metallamacrocycle is a dinuclear 21-membered one formed by the linkage of two trinuclear Cd_3O_3 units through the two neighboring pyridyl

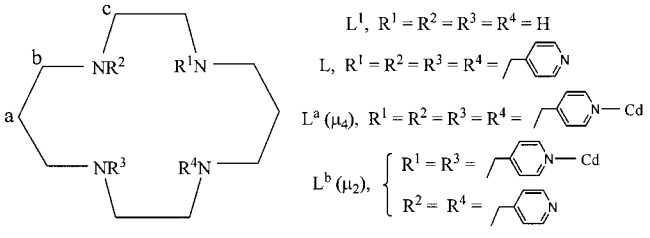

Figure 1. Schematic diagram of the ligands.

[a] State Key Laboratory, Fujian Institute of Research on the Structure of Matter,
Fuzhou, Fujian 350002, P. R.China
E-mail: rcao@ms.fjirsm.ac.cn
[b] Central Laboratory, Fuzhou University,
Fuzhou, Fujian 350002, P. R.China
Supporting information for this article is available on the WWW under http://www.eurjic.org or from the author.

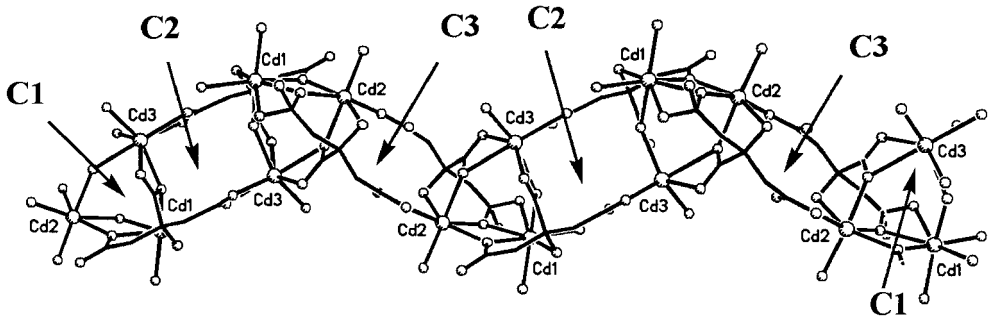

Figure 2. Structure of the two hexanuclear units linked by two citrate units in complex **1**. Selected bond lengths [Å]: Cd(1)–O(3) 2.289(3), Cd(1)–N(7) 2.290(4), Cd(1)–O(8) 2.301(4), Cd(1)–N(13A) 2.303(4), Cd(1)–O(12) 2.376(3), Cd(1)–O(10) 2.463(3), Cd(1)–O(7) 2.556(6), Cd(2)–O(10) 2.216(3), Cd(2)–N(12B) 2.249(4), Cd(2)–O(13) 2.253(4), Cd(2)–O(5) 2.272(3), Cd(2)–O(8) 2.441(4), Cd(2)–O(11) 2.461(3), Cd(3)–N(11) 2.254(4), Cd(3)–O(2) 2.288(5), Cd(3)–O(3) 2.310(3), Cd(3)–O(6) 2.356(4), Cd(3)–O(4) 2.461(4), Cd(3)–O(1) 2.484(4), Cd(3)–O(5), 2.570(3).

arms of an L^a ligand with the distance between the two Cd ions [Cd(1) and Cd(3)] being 6.546 Å (C4; Figure 3). The fifth macrocycle is a hexanuclear 50-membered metallamacrocycle (C5) formed by the linkage of four trinuclear units through four pyridyl arms from two L^a ligands in a parallelogram-type geometry as shown in Figure 3. The four corners of the parallelogram are occupied by cadmium ions, the side lengths are 15.293 and 11.092 Å, while the diagonals are 13.584 and 23.006 Å. The sixth macrocycle is a tetranuclear 42-membered parallelogram metallamacrocycle formed by the linkage of two trinuclear units through two L^b ligands (C6; Figure 3), the sides of the parallelogram are 3.761 and 20.160 Å and the diagonals are 20.434 and 20.582 Å. The seventh macrocycle is an octanuclear 68-membered parallelogram metallamacrocycle formed by the linkage of six trinuclear Cd_3O_3 units through two L^b ligands (C7), the sides of the parallelogram are16.448 and 20.161 Å and the diagonals are 21.343 and 29.974 Å. The columns formed by the hexanuclear units are linked by L^a and L^b ligands to result in a three-dimensional conforma-

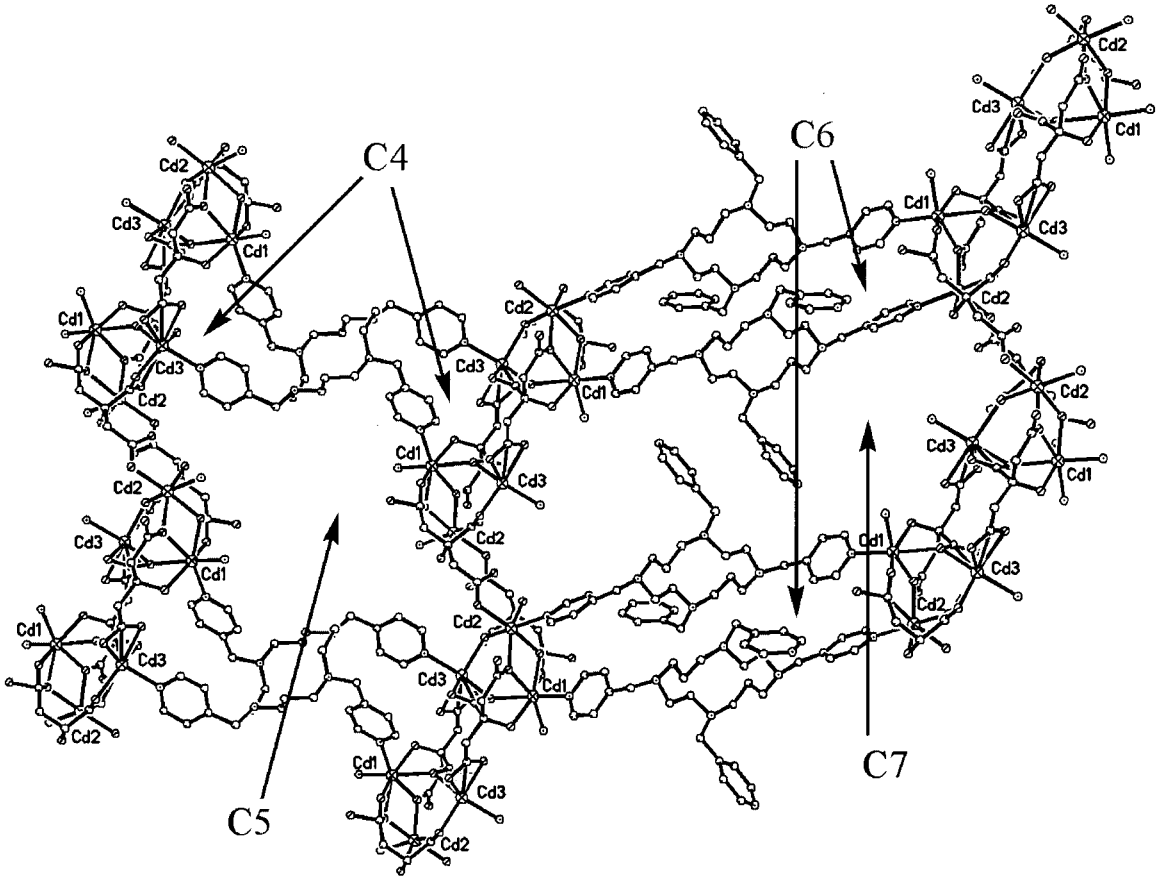

Figure 3. Molecular structure of complex **1**. Some molecules of L are omitted for clarity. There are four types of metallamacrocycles shown in this Figure: C4 and C5 (left) and C6 and C7 (right).

 © 2005 Wiley-VCH Verlag GmbH & Co. KGaA, Weinheim

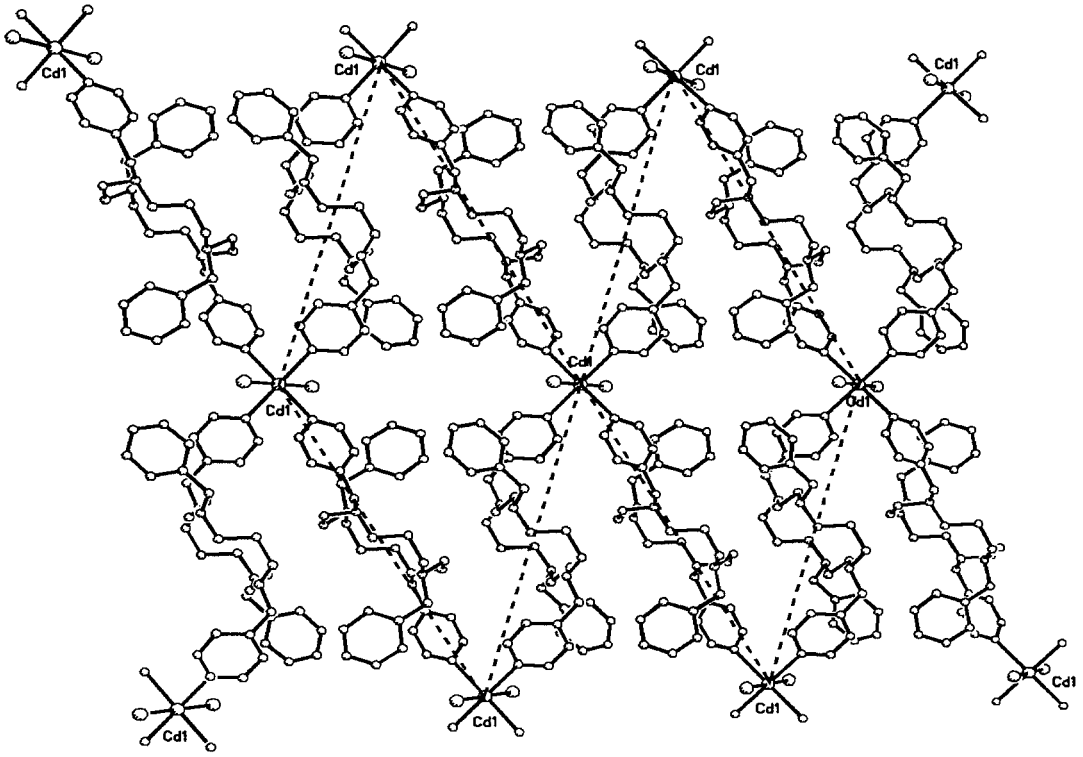

Figure 4. Molecular structure of complex **2**. Selected bond lengths [Å]: Cd(1)–N(6) 2.355(3), Cd(1)–N(5) 2.441(3), Cd(1)–Cl(1) 2.6145(9).

tion. Water molecules as guests exist in the structure and there are intermolecular hydrogen bonds O–H···O between neighboring water molecules.

Interestingly, when $CdCl_2$ was used as reactant, complex **2** was isolated, where no citrate ligands are observed because of the strong coordination ability of chloride ions to cadmium ions. A similar reaction without citrate ligand also resulted in **2**. This means that no substitution reaction between chloride ions and citrate ligands occurred under these hydrothermal conditions, and the citrate ligand did not play an important role in the formation of **2**. Compound **2** is a two-dimensional polymeric structure composed of $CdCl_2$ and ligand L (Figure 4). The ligand L shows only one conformation with two pendant pyridyl groups coordinated to cadmium ions and the other two being free (η^1-μ_2, L^b; Figure 1). In this structure, the cadmium ions are coordinated by four nitrogen atoms from four pyridyl groups of L^b and two chloride ions in a distorted octahedral geometry. The two chloride ions occupy the two apical positions and the basal plane consists of the four nitrogen atoms. The basic unit of this structure is a tetranuclear 76-membered metallamacrocycle in which four $CdCl_2$ units are connected by four L^b units in a parallelogram geometry with the two sides being 18.739 and 16.728 Å and the two diagonals being 13.508 and 32.856 Å. The metallamacrocycles are further extended into a planar structure by sharing cadmium ions. In both complexes **1** and **2**, the ligand L functions as a bridging ligand with the cyclam unit being uncoordinated, similar to the observation in the gold complex of *N*-phosphanylmethyl-functionalized cyclam reported by Che et al.[17]

In summary, two novel cadmium polymeric metallamacrocyclic complexes have been prepared from pyridyl-functionallized 1,4,8,11-tetraazacyclotetradecane by a hydrothermal method; different cadmium reactants influence the structures of the complexes dramatically. Further studies are underway and will be reported in a full paper.

Experimental Section

Synthesis of the Free Ligands L^1 and L: L^1 was prepared according to a reported procedure.[18] Free ligand L was prepared by tetrafunctionalization of L^1 with 4-pyridylmethyl chrolide according to a revised reported procedure.[10] Yield 41%; M.p. 152–153 °C. $C_{34}H_{44}N_8$ (564.77): calcd. C 72.30, H 7.85, N 19.84; found C 72.33, H 7.96, N 19.50. ^{1}H NMR (500 MHz, $CDCl_3$, 25 °C): δ =1.77 (s, 4 H, a), 2.53 (s, 8 H, b), 2.61 (s, 8 H, c), 3.41 (s, 8 H, –CH_2–pyr), 7.24 (d, J = 3.5 Hz, 8 H, aryl), 8.47 (d, J = 4.0 Hz, 8 H, aryl) ppm. EI-MS: *m/z* (%) = 567.2, 566.3, 565.2 (100), 356.8, 256.4, 242.2, 178.7. IR (KBr disk): $\tilde{\nu}$ = 3073 (w), 3020 (w), 2958 (s, br.), 2797(m), 1596 (s), 1559 (m), 1467 (m), 1414 (s), 1366 (m), 1248 (m), 1155 (m), 1121 (m), 1103 (m), 1041 (m), 799 (s) cm^{-1}.

Synthesis of Complex 1: A mixture of $Cd(NO_3)_2{\cdot}4H_2O$ (0.044 g, 0.14 mmol), L (0.040 g, 0.071 mmol), $Na_3C_6H_5O_7{\cdot}2H_2O$ (0.021 g, 0.071 mmol), and distilled water (20 mL) was sealed in a 25-mL stainless steel reactor with Teflon liner and heated at 110 °C for 3 d. Colorless crystals of **1** were isolated by mechanical separation from the mixture of **1** and unidentified white powder. The yield of **1** was 12% based on Cd^{2+}. $C_{63}H_{88}Cd_3N_{12}O_{20}$ (1670.65): calcd. C 45.29, H 5.31, N 10.06; found C 45.32, H 5.29, N 10.02.

Synthesis of Complex 2: A mixture of $CdCl_2{\cdot}2.5H_2O$ (0.032 g, 0.14 mmol), L (0.040 g, 0.071 mmol), $Na_3C_6H_5O_7{\cdot}2H_2O$ (0.021 g, 0.071 mmol), and distilled water (20 mL) was sealed in a 25-mL

 © 2005 Wiley-VCH Verlag GmbH & Co. KGaA, Weinheim

stainless steel reactor with Teflon liner and heated at 110 °C for 3 d. Colorless crystals of **2** were isolated by mechanical separation from a mixture of **2** and unidentified white powder. The yield of **2** was ca. 35% based on $CdCl_2$. $C_{68}H_{93}CdCl_2N_{16}O_{2.50}$ (1357.88): calcd. C 60.14, H 6.90, N 16.51; found C 60.23, H 6.85, N 16.26.

X-ray Crystallography: Crystal data for L: $C_{34}H_{44}N_8$ (564.77), monoclinic, space group $P2_1/n$, T = 130(2) K, a = 5.9649(4), b = 11.7400(7), c = 21.839(2) Å, β = 96.586(4)°, V = 1519.3(2) Å^3, Z = 2, $D_{calcd.}$ = 1.235 g·cm^{-3}, $F(000)$ = 608, μ(Mo-K_α) = 0.076 mm^{-1}, colorless from methanol, 0.75 × 0.50 × 0.25 mm, θ range for data collection 3.31–27.48°, 11320 collected, 3462 unique and 3150 observed (R_{int} = 0.0265) reflections, 190 parameters, R = 0.0435 and wR = 0.1049 for observed reflections with $I > 2\sigma(I)$, GOF = 1.058, $(\Delta\rho)_{max}$ = 0.262, $(\Delta\rho)_{min}$ = –0.205 e/Å^{-3}. Crystal data for **1**: $C_{63}H_{88}Cd_3N_{12}O_{20}$ (1670.65), triclinic, space group $P\bar{1}$, T = 130(2) K, a = 13.104(4), b = 16.448(5), c = 18.682(6) Å, α = 104.619(3), β = 102.754(1), γ = 106.923(2)°, V = 3534.2(18) Å^3, Z = 2, $D_{calcd.}$ = 1.570 g·cm^{-3}, $F(000)$ = 1708, μ = 0.974 mm^{-1}, colorless from water, 0.50 × 0.25 × 0.15 mm, θ range 3.02–25.00°, 22192 collected, 12317 unique and 10957 observed (R_{int} = 0.0220) reflections, 904 parameters, R = 0.0507 and wR = 0.1143 for observed reflections with $I > 2\sigma(I)$, GOF = 1.051, $(\Delta\rho)_{max}$ = 1.720, $(\Delta\rho)_{min}$ = –0.870 e/Å^{-3}. Crystal data for **2**: $C_{68}H_{93}CdCl_2N_{16}O_{2.50}$ (1357.88), triclinic, space group $P\bar{1}$, T = 130(2) K, a = 9.469(3), b = 13.271(4), c = 13.508(4) Å, α = 80.028(7), β = 78.940(8), γ = 86.796(7)°, V = 1640.3(8) Å^3, Z = 1, $D_{calcd.}$ = 1.375 g·cm^{-3}, $F(000)$ = 715, μ = 0.474 mm^{-1}, colorless, 0.30 × 0.25 × 0.05 mm, θ range 2.38–25.00°, 10544 collected, 5735 unique and 4813 observed (R_{int} = 0.0393) reflections, 411 parameters, R = 0.0483 and wR = 0.1013 for observed reflections with $I > 2\sigma(I)$, GOF = 1.093, $(\Delta\rho)_{max}$ = 0.873, $(\Delta\rho)_{min}$ = –0.472 e/Å^{-3}. Data collections for the three compounds were performed with a Rigaku Mercury-CCD diffractometer with graphite-monochromated Mo-K_α radiation (λ = 0.71073 Å). The data sets were collected at 130 K (ω-scan mode). The structures of the three compounds were solved by direct methods, the metal atoms were located from the E-maps, and other non-hydrogen atoms were derived from the successive difference Fourier syntheses and refined anisotropically. All hydrogen atoms were theoretically located. The structures were refined on F^2 by full-matrix least squares using the SHELXTL-97 program package. CCDC-262561, -262562, and -262563 (for L, **1**, and **2**, respectively) contain the supplementary crystallographic data for this paper. These data can be obtained free of charge at www.ccdc.cam.ac.uk/conts/retrieving.html [or from the Cambridge Crystallographic Data Center, 12 Union Road, Cambridge CB2 1EZ, UK; Fax: +44-1223-336-033; E-mail: deposit@ccdc.cam.ac.uk].

Supporting Information: Coordination modes of the citrate ligand (Figure S1); structural figures of the two complexes (Figures S2–S10); molecular structure (Figure S11), ^{1}H NMR spectrum (Figure S12), and EI mass spectrum (Figure S13) of ligand L.

Acknowledgments

The authors are grateful for financial support from the NSF of China (90206040, 20325106, 20333070), the innovation fund of Fujian Province (2003J044) and "One Hundred Talent Project" from CAS.

[1] P. D. Beer, N. G. Berry, A. R. Cowley, E. J. Hayes, E. C. Oates, W. W. H. Wong, *Chem. Commun.* **2003**, 2408–2409.
[2] C. Bucher, R. S. Zimmerman, V. Lynch, J. L. Sessler, *Chem. Commun.* **2003**, 1646–1647.
[3] M. Albrecht, S. Schmid, M. deGroot, P. Weis, R. Fröhlich, *Chem. Commun.* **2003**, 2526–2527.
[4] J. Farkas, Jr., S. J. Stoudt, E. M. Hanawalt, A. D. Pajerski, H. G. Richey, Jr., *Organometallics* **2004**, *23*, 423–427.
[5] J. Nelson, M. Nieuwenhuyzen, I. Pál, R. M. Town, *J. Chem. Soc., Dalton Trans.* **2004**, 229–235.
[6] B. Bag, P. K. Bharadwaj, *Inorg. Chem.* **2004**, *43*, 4626–4630.
[7] M. V. Baker, D. H. Brown, B. W. Skelton, A. H. White, *J. Chem. Soc., Dalton Trans.* **2000**, 4607–4616.
[8] B.-C. Tzeng, W.-C. Lo, C.-M. Che, S.-M. Peng, *Chem. Commun.* **1996**, 181–182; P. Planinic, D. Matkovic-Calogovic, H. Meider, *J. Chem. Soc., Dalton Trans.* **1997**, 3445–3451.
[9] L. Burai, É. Tóth, G. Moreau, A. Sour, R. Scopelliti, A. E. Merbach, *Chem. Eur. J.* **2003**, *9*, 1394–1404.
[10] M. E. Padilla-Tosta, J. M. Lloris, R. Martonez-Manez, A. Benito, J. Soto, T. Pardo, M. A. Miranda, M. D. Marcos, *Eur. J. Inorg. Chem.* **2000**, 741–748; N. W. Alcock, K. P. Balakrishnan, P. Moore, *J. Chem. Soc., Dalton Trans.* **1986**, 743–749.
[11] J. Tao, X. Yin, Z.-B. Wei, R.-B. Huang, L.-S. Zheng, *Eur. J. Inorg. Chem.* **2004**, 125–133.
[12] I. Busching, H. Strasdeit, *Chem. Commun.* **1994**, 2789–2790.
[13] X. Liang, J. A. Parkinson, S. Parsons, M. Weishaupl, P. J. Sadler, *Inorg. Chem.* **2002**, *41*, 4539–4547.
[14] M.-L. Tong, S.-L. Zheng, J.-X. Shi, Y.-X. Tong, H. K. Lee, X. M. Chen, *J. Chem. Soc., Dalton Trans.* **2002**, 1727–1734.
[15] S. Lulinski, I. Madura, J. Serwatowski, J. Zachara, *Inorg. Chem.* **1999**, *38*, 4937–4941.
[16] E. A. Vinogradova, O. Yu. Vassilyeva, V. N. Kokozay, B. W. Skelton, J. K. Bjernemose, P. R. Raithby, *J. Chem. Soc., Dalton Trans.* **2002**, 4248–4252.
[17] B.-C. Tzeng, K.-K. Cheung, C.-M. Che, *Chem. Commun.* **1996**, 1681–1682.
[18] E. K. Barefield, *Inorg. Chem.* **1972**, *11*, 2273–2274.

Received April 5, 2005
Published Online: June 17, 2005

 © 2005 Wiley-VCH Verlag GmbH & Co. KGaA, Weinheim

Synthesis and Reactivity of 1,2- and 1,3-Diphosphanes that Contain Four Chiral Rhenium Fragments: Architecturally Novel Tetrametallo-DMPE and -DMPP Species that are Unprivileged Ligands for Enantioselective Catalysis

Klemenz Kromm,[a] Sandra Eichenseher,[a] Markus Prommesberger,[a] Frank Hampel,[a] and J. A. Gladysz*[a]

Keywords: Rhenium / Chiral diphosphane / Phosphane oxide / Rhodium / Hydrogenation / Hydrosilylation

Reactions of enantiopure (*S*)-[(η^5-C_5H_5)Re(NO)(PPh_3)(=CH_2)]$^+$ PF_6^- [(*S*)-**2**] and $PH_2CH_2(CH_2)_nCH_2PH_2$ (0.5 equiv.) give ($S_{Re}S_{Re}$)-[(η^5-C_5H_5)Re(NO)(PPh_3){$CH_2PH_2CH_2(CH_2)_n$-$CH_2PH_2CH_2$}(Ph_3P)(ON)Re(η^5-C_5H_5)]$^{2+}$ $2PF_6^-$ [*n* = 0/1, ($S_{Re}S_{Re}$)-**3/4**; 65–62/77–58 %]. Reaction of racemic **2** (BF_4^- salt) and $PH_2(CH_2)_2PH_2$ (0.5 equiv.) gives the *meso* and *rac* diastereomers of **3** (BF_4^- salts) in 28 % and 38 % yields after crystallization. Treatments of ($S_{Re}S_{Re}$)-**3/4** with *t*BuOK and then (*S*)-**2** give the tetrarhenium complexes ($S_{Re}S_{Re}S_{Re}S_{Re}$)[{(η^5-C_5H_5)Re(NO)(PPh_3)(CH_2)}$_2${$PHCH_2(CH_2)_n$-CH_2PH}{(CH_2)(Ph_3P)(ON)Re(η^5-C_5H_5)}$_2$]$^{2+}$ $2PF_6^-$ [*n* = 0/1, ($S_{Re}S_{Re}S_{Re}S_{Re}$)-**7/8**; 89–88/98–87 %]. The crystal structure of ($S_{Re}S_{Re}S_{Re}S_{Re}$)-**7** is determined and its conformation analyzed. Reactions of ($S_{Re}S_{Re}S_{Re}S_{Re}$)-**7/8** and *t*BuOK give air-sensitive diphosphanes ($S_{Re}S_{Re}S_{Re}S_{Re}$)-{(η^5-C_5H_5)Re(NO)(PPh_3)(CH_2)}$_2${$PCH_2(CH_2)_nCH_2P$}{(CH_2)(Ph_3P)(ON)Re(η^5-C_5H_5)}$_2$ [*n* = 0/1, ($S_{Re}S_{Re}S_{Re}S_{Re}$)-**9/10**; 92/62 %]. Additions of (a) PhIO give the corresponding dioxides (72/62 %), and (b) [$Rh(NBD)_2$]$^+$ PF_6^- give the corresponding chelates [(P–P)Rh(NBD)]$^+$ PF_6^- (75/82 %) (NBD = norbornadiene). These catalyze hydrogenations of protected dehydroamino acids and hydrosilylations of propiophenone with only modest enantioselectivities. Similar results are obtained when ($S_{Re}S_{Re}S_{Re}S_{Re}$)-**9/10** are applied in rhodium-catalyzed conjugate additions of aryl boronic acids, or palladium-catalyzed allylic alkylations.
(© Wiley-VCH Verlag GmbH & Co. KGaA, 69451 Weinheim, Germany, 2005)

Introduction

For some time, we have been interested in incorporating metal fragments into donor ligands that can be used in metal-catalyzed reactions – in other words, bimetallic catalysts in which one metal remains a "spectator" with respect to bond-breaking and bond-making.[1–4] This has in part been inspired by the immensely useful ferrocene-containing ligands, many of which are chiral and regularly applied in a variety of enantioselective catalytic transformations.[5] It would seem logical that other chiral metal fragments could also possess suitable – and perhaps superior – architectures for asymmetric induction. Furthermore, as described in several recent papers,[1,4b,6] eighteen-valence-electron complexes that feature a donor atom in the α or β position (e. g., L_nMPR_2: or $L_nMCH_2PR_2$:) are much more basic and nucleophilic than organic analogs that lack the metal (:PR_3). This is largely due to repulsive interactions involving the lone pair and occupied metal-based orbitals.[7] Hence, there are also opportunities for unusual electronic effects that may aid bond activation.

In previous papers, we have exploited these steric and electronic phenomena in reactions that result in new stereocenters,[2] and those that do not.[4] Other groups are also making important contributions to the design and application of non-ferrocenyl metal-containing ligands in catalysis.[8] We have often but not exclusively[4b] used the easily resolved[9] chiral rhenium fragment [(η^5-C_5H_5)Re(NO)(PPh_3)]$^+$ (**I**). Two types of bidentate ligands have been prepared, as illustrated by the diphosphanes **II** and diamine **IIIa** in Figure 1. In the first, the rhenium is part of the chelate backbone. In the second, two rhenium fragments are positioned exocyclic to the chelate backbone. The former gives rhodium complexes that catalyze hydrogenations and hydrosilylations with good to excellent enantioselectivities.[2a,2b,2e] The latter also gives metal complexes,[3] but these were not extensively investigated as catalysts, in part because the nitrogen atoms are configurationally labile stereocenters that can lead to multiple diastereomers upon chelation.

This situation – which can be desirable for some purposes but undesirable for others – is easily circumvented, as shown in ligand **IV**. Now four rhenium fragments are present, arrayed such that the donor atoms are no longer stereocenters. Accordingly, in this paper we describe (1) an

[a] Institut für Organische Chemie, Friedrich-Alexander-Universität Erlangen-Nürnberg,
Henkestraße 42, 91054 Erlangen, Germany
Fax: +49-9131-8526865
E-mail: gladysz@organik.uni-erlangen.de
Supporting information for this article is available on the WWW under http://www.eurjic.org or from the author.

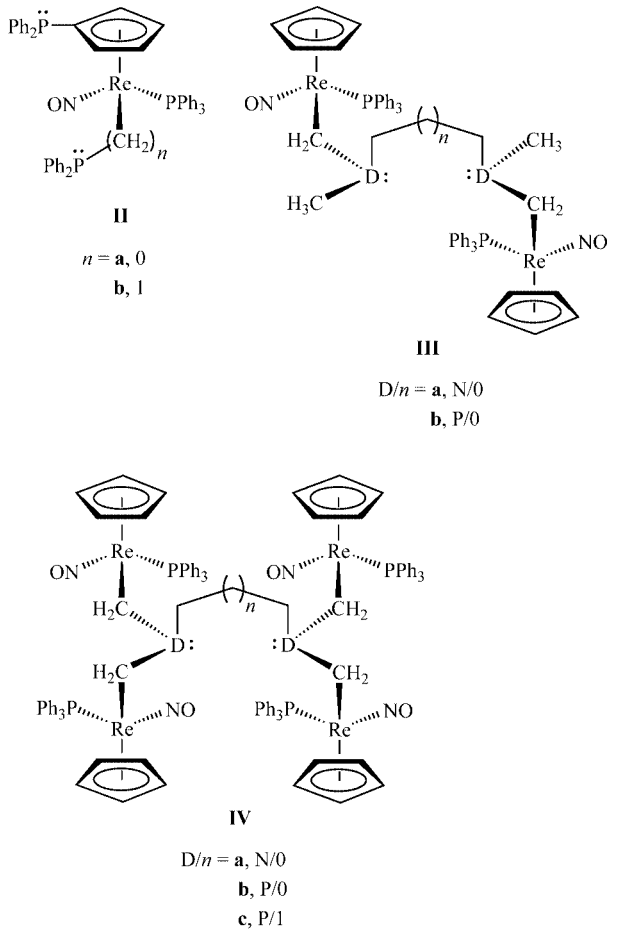

Figure 1. Evolution of families of chiral chelating ligands based upon the chiral rhenium fragment $[(\eta^5\text{-}C_5H_5)Re(NO)(PPh_3)]^+$ (**I**).

efficient and convenient route to diphosphanes of the type **IVb**,**c**, (2) the structural characterization of a diprotonated derivative, (3) the formation of dioxide and rhodium derivatives, and (4) exploratory catalytic reactions. These ligands can be regarded as derivatives of 1,2-bis(dimethylphosphanyl)ethane (DMPE) and 1,3-bis(dimethylphosphanyl)-propane (DMPP), the prototypical electron-rich 1,2- and 1,3-diphosphanes in coordination chemistry.[10]

Results

1. Dirhenium Complexes: The diprimary diphosphanes $PH_2CH_2(CH_2)_nCH_2PH_2$ (n = 0, 1) were purchased or prepared from the corresponding dibromides by published Arbuzov/reduction sequences.[11] As shown in Scheme 1, the enantiopure methyl complex (*S*)-$(\eta^5\text{-}C_5H_5)Re(NO)(PPh_3)(CH_3)$ [(*S*)-**1**][12,13] and trityl salt Ph_3C^+ PF_6^- were reacted in CH_2Cl_2 at –60 °C to generate the methylidene complex (*S*)-$[(\eta^5\text{-}C_5H_5)Re(NO)(PPh_3)(=CH_2)]^+$ PF_6^- [(*S*)-**2**].[14] Then a half-equivalent of $PH_2CH_2(CH_2)_nCH_2PH_2$ was added. Workups gave the diphosphonium salts $(S_{Re}S_{Re})$-$[(\eta^5\text{-}C_5H_5)Re(NO)(PPh_3)\{CH_2PH_2CH_2(CH_2)_n\text{-}CH_2PH_2CH_2\}(Ph_3P)(ON)Re(\eta^5\text{-}C_5H_5)]^{2+}$ $2PF_6^-$ [n = 0/1, $(S_{Re}S_{Re})$-**3/4**][13] as yellow needles or powders in 65–62% and 77–58% yields. Both products were thermally stable and tolerated several hours in air. They were soluble in most polar organic solvents (CH_2Cl_2, DMF, ethanol, THF, dioxane) and insoluble in aliphatic or aromatic hydrocarbons.

Complexes $(S_{Re}S_{Re})$-**3/4** and all other new compounds below were characterized by IR and NMR (^1H, ^{13}C, ^{31}P) spectroscopy, mass spectrometry, and microanalysis, as summarized in the experimental section. The two rhenium moieties gave a single set of NMR signals. The ^1H NMR spectra showed two doublets of multiplets for the diastereotopic PHH′ protons, each with distinct ^1J(H,P) values. The ^{13}C NMR spectra exhibited P*C*H_2C signals (18.9/24.0 ppm) that were coupled to both protonated phosphorus atoms; that in $(S_{Re}S_{Re})$-**4** was particularly well-resolved [dd, ^1J(C,P) = 39, ^3J(C,P) = 15 Hz]. A number of chemical shift trends were evident, as analyzed elsewhere.[10a]

As shown in Scheme 2, a similar sequence was conducted with $PH_2(CH_2)_2PH_2$ and the *tetrafluoroborate* salt of the *racemic* methylidene complex, $[(\eta^5\text{-}C_5H_5)Re(NO)(PPh_3)\text{-}(=CH_2)]^+$ BF_4^- (**2′**). The less soluble *meso* diastereomer $(S_{Re}R_{Re})$-$[(\eta^5\text{-}C_5H_5)Re(NO)(PPh_3)\{CH_2PH_2(CH_2)_2PH_2\text{-}CH_2\}(Ph_3P)(ON)Re(\eta^5\text{-}C_5H_5)]^{2+}$ $2BF_4^-$ [$(S_{Re}R_{Re})$-**3′**] precipitated from the reaction mixture and was isolated in 28% yield. This material was insoluble in all common solvents except DMSO. The *rac* diastereomer $(S_{Re}S_{Re},R_{Re}R_{Re})$-**3′** was isolated from the supernatant in 38% yield. The configurational assignments followed from the close similarity of the NMR and IR data for the latter diastereomer (especially the ^{13}C $ReCH_2$ signals) with those of non-racemic $(S_{Re}S_{Re})$-**3**.

As shown in Scheme 1, $(S_{Re}S_{Re})$-**3/4** were treated with *t*BuOK in THF. This gave bright orange solutions of the disecondary diphosphanes $(S_{Re}R_{Re})$-$(\eta^5\text{-}C_5H_5)Re(NO)\text{-}(PPh_3)\{CH_2PHCH_2(CH_2)_nCH_2PHCH_2\}(Ph_3P)(ON)Re(\eta^5\text{-}C_5H_5)$ [n = 0/1, $(S_{Re}S_{Re})$-**5/6**]. Since two phosphorus stereocenters are generated, ^{31}P NMR spectra of $(S_{Re}S_{Re})$-**5** were recorded in situ. In the absence of special kinetic or thermodynamic phenomena,[15] three diastereomers would be expected: $S_{Re}S_PS_PS_{Re}$, $S_{Re}R_PR_PS_{Re}$, and $S_{Re}S_PR_PS_{Re}$ (identical with $S_{Re}R_PS_PS_{Re}$). The last should exhibit two *P*CH_2 signals; the others, which have a C_2 axis, should give only one. The ^{31}P NMR spectrum showed four signals {δ [^1J(P,H)]: –29.6 (189), –32.3 (189), –36.1 (201), –36.4 (201) ppm} in an area ratio of 21:21:40:18. If it is assumed that the two peaks of equal intensity arise from $(S_{Re}S_PR_PS_{Re})$-**5**, a 42:40:18 mixture of diastereomers is obtained. Given this poor selectivity, no attempts were made to deconvolute the other NMR signals, and the mixtures were used directly for subsequent chemistry. The phosphorus inversion barriers are believed to be high, as supported by data for related compounds below.

2. Tetrarhenium Complexes: Following an extraction/filtration step, crude $(S_{Re}S_{Re})$-**5/6** were added to a cold solution of enantiopure (*S*)-**2** in CH_2Cl_2. As shown in Scheme 1, workups gave the ditertiary diphosphonium salts $(S_{Re}S_{Re}S_{Re}S_{Re})$-$[\{(\eta^5\text{-}C_5H_5)Re(NO)(PPh_3)(CH_2)\}_2\text{-}\{PHCH_2(CH_2)_nCH_2PH\}\{(CH_2)(Ph_3P)(ON)Re(\eta^5\text{-}C_5H_5)\}_2]^{2+}$

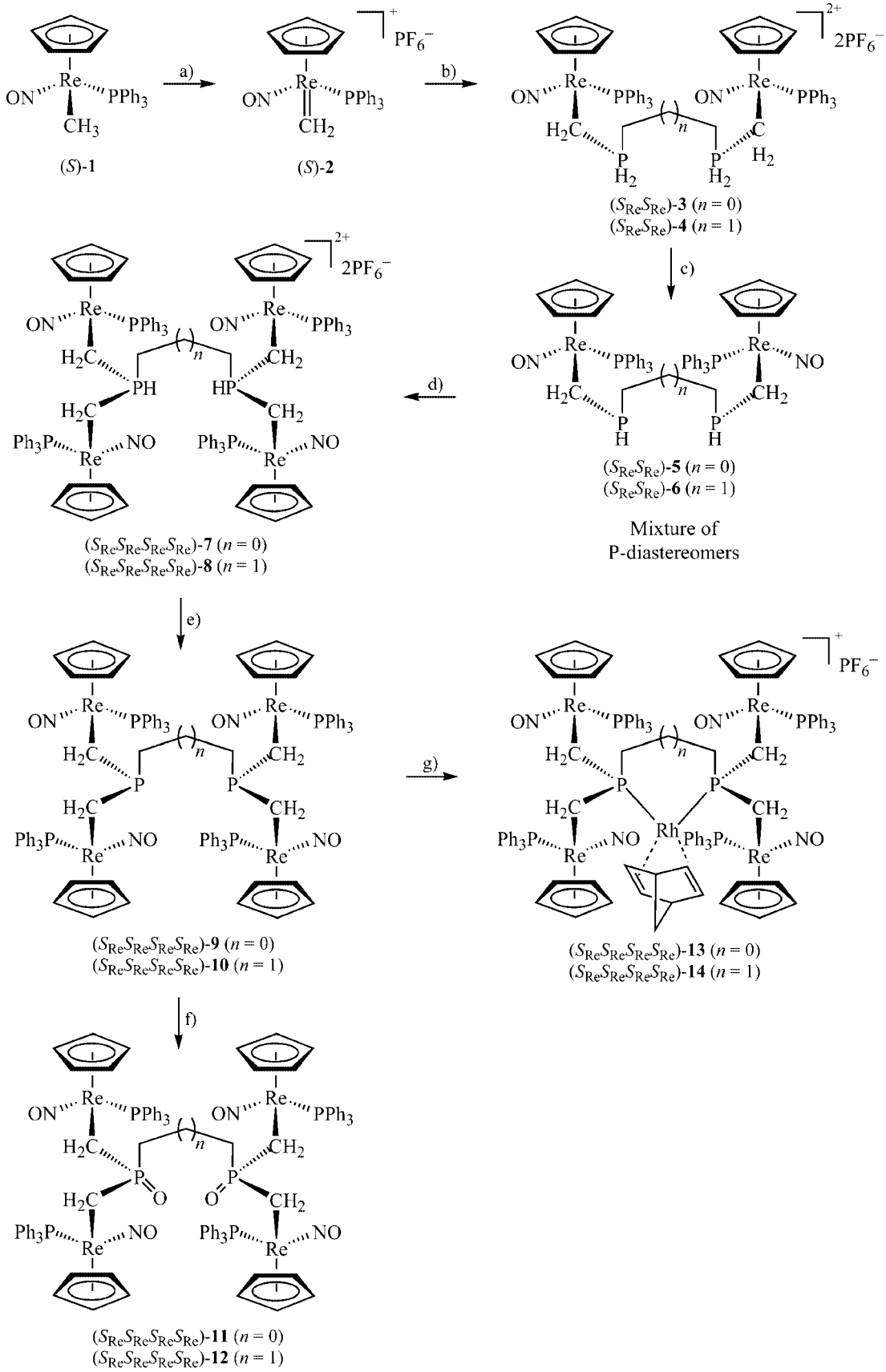

Scheme 1. Syntheses of tetrarhenium complexes; a) Ph_3C^+ PF_6^-, CH_2Cl_2, –60 °C; b) $PH_2CH_2(CH_2)_nCH_2PH_2$ (n = 0, 1), CH_2Cl_2, –60 to 25 °C; c) *t*BuOK, THF or CH_2Cl_2, 25 °C; d) (*S*)-**2**, CH_2Cl_2, –60 to 25 °C; e) *t*BuOK, THF, 25 °C; f) air or PhIO, CH_2Cl_2 or THF, 25 °C; g) $[Rh(NBD)_2]^+$ PF_6^-, THF, 25 °C.

 © 2005 Wiley-VCH Verlag GmbH & Co. KGaA, Weinheim

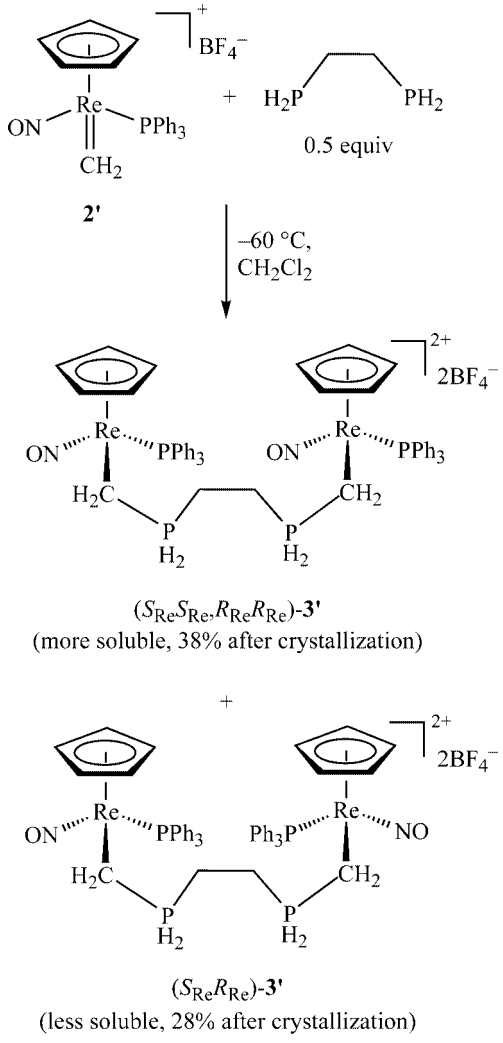

Scheme 2. Syntheses of the racemic and *meso* diphosphonium salt **3′**.

$2PF_6^-$ [n = 0/1, ($S_{Re}S_{Re}S_{Re}S_{Re}$)-**7/8**].[13] These lack the phosphorus stereocenters of the precursors. The former was isolated as red prisms in 89–88% yields, and the latter as a yellow-orange powder in 98–87% yields. Both could be stored for months under ambient conditions, and were characterized analogously to the dirhenium analogs. They were soluble in CH_2Cl_2, acetone, THF, and 1,2-difluorobenzene, and insoluble in alcohols, ether, benzene, and alkanes.

The two L_nReCH_2 groups on each phosphorus atom of ($S_{Re}S_{Re}S_{Re}S_{Re}$)-**7/8** are diastereotopic, and related to those on the other phosphorus atom by a C_2 axis. Thus, two sets of NMR signals were observed. For example, ^{13}C NMR spectra showed two signals for the Re*C*H_2P*C*H_2Re carbons, and ^1H NMR spectra four multiplets for the ReC*HH′*PC*H′′H′′′*Re protons. As illustrated with ($S_{Re}S_{Re}S_{Re}S_{Re}$)-**7** in Figure 2 (top), ^{31}P NMR spectra exhibited two PPh_3 signals. For all tetrarhenium complexes, the ^{31}P NMR coupling patterns are best approximated by non-first-order AA′BB′ CC′ spin systems, with CC′ representing the phosphorus atoms of the $PCH_2(CH_2)_nCH_2P$ moiety. The apparent triplets of the PPh_3 groups of ($S_{Re}S_{Re}S_{Re}S_{Re}$)-**7** could be duplicated in simulations, and the broad singlet of the PCH_2 group is interpreted as an unresolved triplet. Various chemical shift trends are analyzed elsewhere.[10a]

Complexes ($S_{Re}S_{Re}S_{Re}S_{Re}$)-**7/8** were reacted with *t*BuOK under rigorous oxygen-free conditions. Workups gave the title ditertiary diphosphanes ($S_{Re}S_{Re}S_{Re}S_{Re}$)-{(η^5-C_5H_5)Re(NO)(PPh_3)(CH_2)}$_2${$PCH_2(CH_2)_nCH_2P$}{(CH_2)-(Ph_3P)(ON)Re(η^5-C_5H_5)}$_2$ [n = 0/1, ($S_{Re}S_{Re}S_{Re}S_{Re}$)-**9/10**][13] as highly air sensitive, analytically pure red powders in 92% and 62% yields. Solutions could be kept for several hours at room temperature under argon. In contrast, the related monorhenium monophosphanes (η^5-C_5H_5)Re-(NO)(PPh_3)(CH_2PR_2) are stable in air for several hours, with even solutions showing only minor decomposition.[4a] Complexes ($S_{Re}S_{Re}S_{Re}S_{Re}$)-**9/10** were characterized similarly to the others described above. The diastereotopic L_nReCH_2 groups gave separate NMR signals, as exemplified by the ^{31}P NMR spectrum of ($S_{Re}S_{Re}S_{Re}S_{Re}$)-**9** in Figure 2. Mass spectra showed only oxidation products.

In principle, the diastereotopic L_nReCH_2 groups can be exchanged via a phosphorus inversion/bond rotation sequence. Inversion barriers for tertiary organophosphanes are typically 28–36 kcal mol^{-1} (120–150 kJ·mol^{-1}).[16] Thus, NMR spectra of ($S_{Re}S_{Re}S_{Re}S_{Re}$)-**9** were recorded at elevated temperatures. However, no coalescence phenomena were observed in [D_8]toluene at 110 °C, conditions under which the complex has a half-life of ca. 10 min. From the frequency differences of the diastereotopic cyclopentadienyl (^1H, ^{13}C) and PPh_3 (^{31}P) groups, lower limits of 19.0–20.4 kcal mol^{-1} (79.4–85.5 kJ·mol^{-1}) could be calculated for the phosphorus inversion barrier ($\Delta G^{\ddagger}_{383\ K}$). This is much higher than the 14–16 kcal mol^{-1} typically found for analogous pyramidal metal phosphido complexes, L_nMPR_2.[17,18]

3. Derivatives of Tetrarhenium Diphosphanes and other Reactions: As shown in Scheme 1, when ($S_{Re}S_{Re}S_{Re}S_{Re}$)-**9** was worked up in air, the diphosphane dioxide ($S_{Re}S_{Re}S_{Re}S_{Re}$)-{(η^5-C_5H_5)Re(NO)(PPh_3)(CH_2)}$_2$-{$PO(CH_2)_2PO$}{$(CH_2)(Ph_3P)(ON)$Re(η^5-C_5H_5)}$_2$ [($S_{Re}S_{Re}S_{Re}S_{Re}$)-**11**] was isolated in 95% yield. Alternatively, ($S_{Re}S_{Re}S_{Re}S_{Re}$)-**7/8** were sequentially treated with *t*BuOK and the oxygen atom donor PhIO. Workups gave ($S_{Re}S_{Re}S_{Re}S_{Re}$)-**11/12** in 72% and 62% yields, with the latter containing small amounts of Ph_3PO. Both complexes were yellow-orange powders that could be stored under ambient conditions for months without decomposition. As shown in Figure 2, the ^{31}P NMR signal of the PO group of ($S_{Re}S_{Re}S_{Re}S_{Re}$)-**11** was 53 ppm downfield of the corresponding signal in ($S_{Re}S_{Re}S_{Re}S_{Re}$)-**9**, and coupled to the phosphorus atoms of the PPh_3 groups [^3J(P,P) = 17 Hz].

Next, the preparation of rhodium chelate complexes of the tetrarhenium diphosphanes was investigated. Thus, ($S_{Re}S_{Re}S_{Re}S_{Re}$)-**7/8** were sequentially treated with *t*BuOK and $[Rh(NBD)_2]^+$ PF_6^- under rigorous inert atmosphere conditions (NBD = norbornadiene). As shown in Scheme 1, workups gave the target complexes ($S_{Re}S_{Re}S_{Re}S_{Re}$)-[({(η^5-

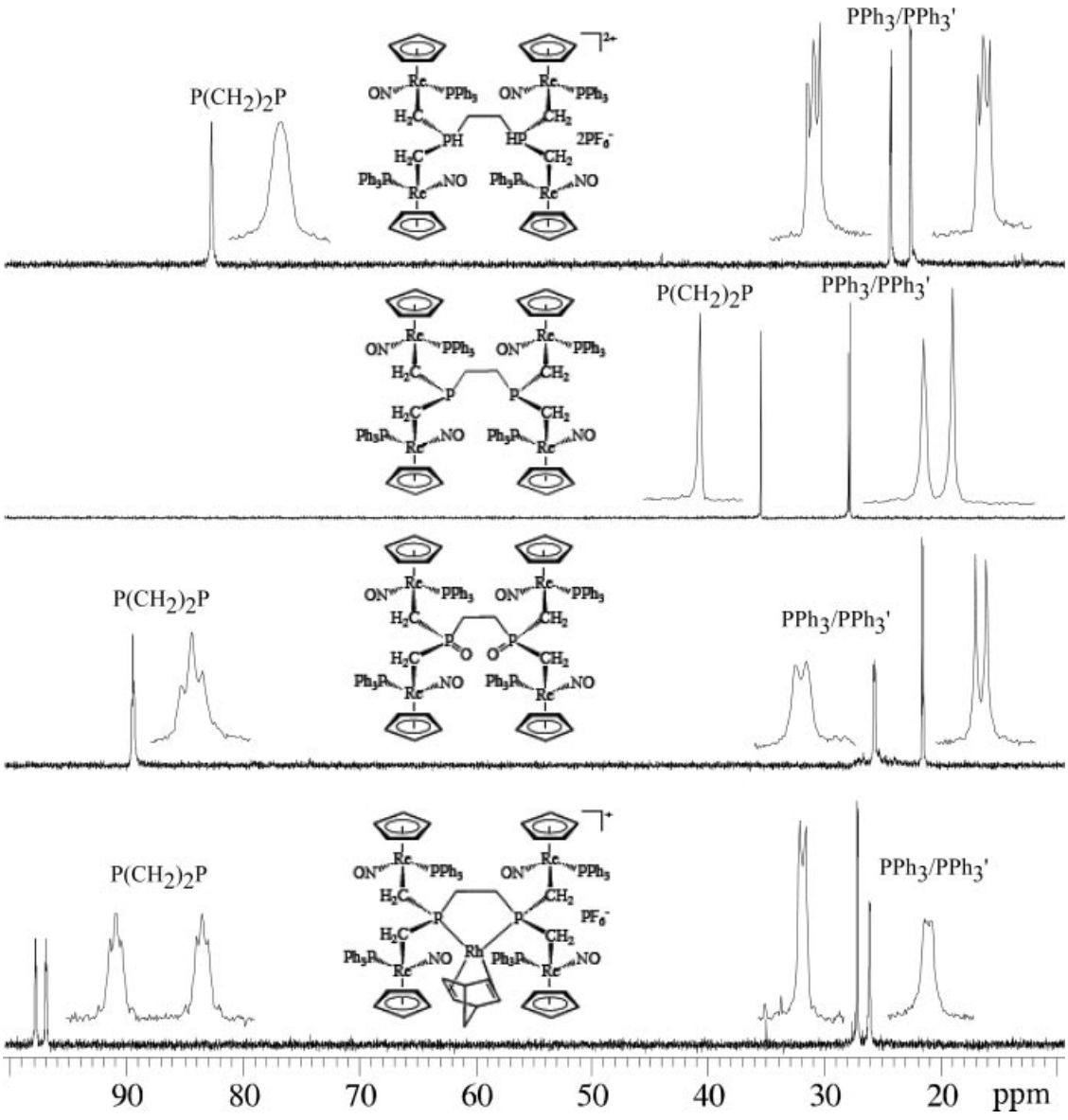

Figure 2. $^{31}P\{^{1}H\}$ NMR spectra of tetrarhenium complexes ($S_{Re}S_{Re}S_{Re}S_{Re}$)-**7**, -**9**, -**11**, and -**13** (from top to bottom).

C_5H_5)Re(NO)(PPh_3)$(CH_2)\}_2\{PCH_2(CH_2)_nCH_2P\}\{(CH_2)$-$(Ph_3P)(ON)Re(\eta^5$-$C_5H_5)\}_2)Rh(NBD)]^+$ PF_6^- [n = 0/1, ($S_{Re}S_{Re}S_{Re}S_{Re}$)-**13/14**] as analytically pure red-brown powders in 75% and 82% yields. The mass spectra exhibited molecular ions with the correct isotope distributions. The ^1H and ^{13}C NMR spectra showed diagnostic signals for the NBD ligand. As illustrated in Figure 2, ^{31}P spectra displayed rhodium couplings [^1J(P,Rh) = 150–142 Hz] that confirmed the P–Rh–P chelate. Chemical shift trends, including ^{31}P NMR ring size effects, are analyzed elsewhere.[10a]

Finally, we sought to probe the Brønsted basicities of ($S_{Re}S_{Re}S_{Re}S_{Re}$)-**9/10** with respect to related monorhenium complexes. Thus, ($S_{Re}S_{Re}S_{Re}S_{Re}$)-**7**, the monorhenium phosphonium salt $[(\eta^5$-$C_5H_5)Re(NO)(PPh_3)(CH_2PPh_2H)]^+$ PF_6^-,[4a] and *t*BuOK were combined in a 1:2:2 mol ratio in an NMR tube. After 1 h, all of the ($S_{Re}S_{Re}S_{Re}S_{Re}$)-**7** remained. However, the monorhenium complex had been completely converted into the conjugate base (η^5-C_5H_5)Re-(NO)(PPh_3)(CH_2PPh_2). These data strongly suggest that the second L_nReCH_2 moiety on each phosphorus atom in ($S_{Re}S_{Re}S_{Re}S_{Re}$)-**9/10** further enhances the Brønsted basicity, and the equilibrium sketched in Scheme 3 can be formulated.

4. Catalysis: The tetrarhenium diphosphanes **9/10** were evaluated as ligands in several metal catalyzed transformations. Reactions previously examined with rhodium chelates of the monorhenium diphosphanes **II** (Figure 1)[2a,2b,2e] were studied first. Thus, the protected dehydroamino acids **15a**–**c** shown in Equation (1) of Scheme 4 were hydrogenated in the presence of ($S_{Re}S_{Re}S_{Re}S_{Re}$)-**13** or -**14** that had been generated in situ from ($S_{Re}S_{Re}S_{Re}S_{Re}$)-**7** or -**8**, *t*BuOK, and $[Rh(NBD)_2]^+$ PF_6^-. Reactions were complete over the course of 1–2 days at 75 °C under 8 bar of H_2. However, rhodium adducts of **II** were active at room temperature and under 1 bar of H_2. Furthermore, the enantioselectivities were poor, with the DMPP-type complex ($S_{Re}S_{Re}S_{Re}S_{Re}$)-

 © 2005 Wiley-VCH Verlag GmbH & Co. KGaA, Weinheim

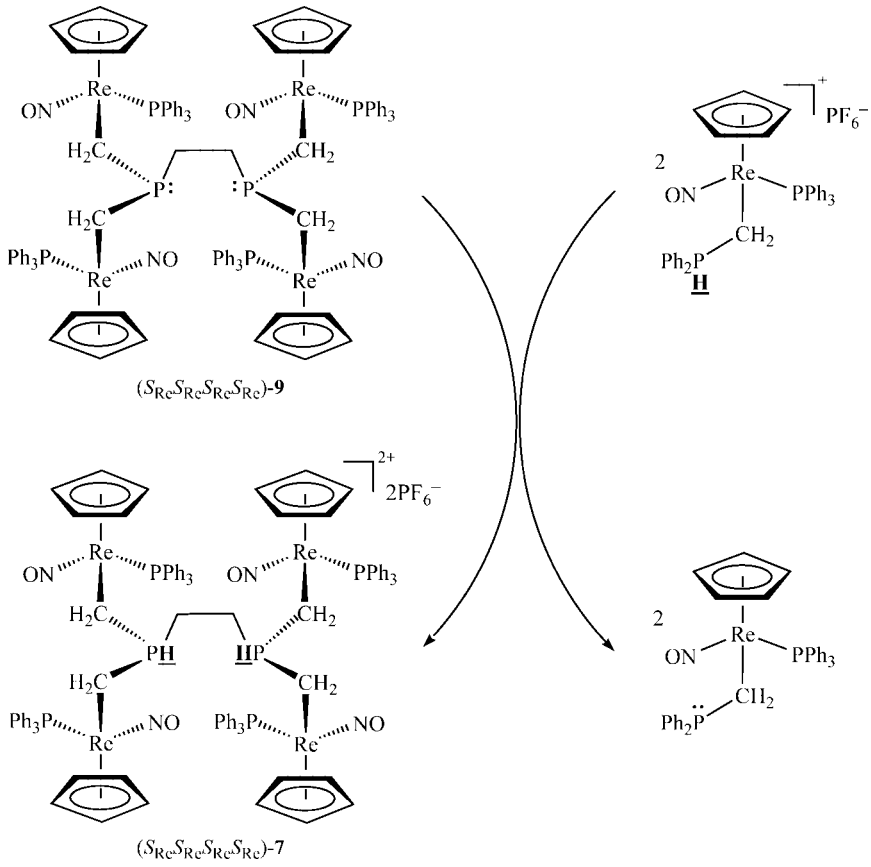

Scheme 3. Relative Brønsted basicities.

14 slightly better than the DMPE-type complex ($S_{Re}S_{Re}$-$S_{Re}S_{Re}$)-**13** (33–30% vs. 12% *ee*).

As shown in Equation (2) of Scheme 4, ($S_{Re}S_{Re}S_{Re}S_{Re}$)-**13** was next evaluated as a catalyst for the hydrosilylation of propiophenone (**17**). Reactions with Ph_2SiH_2 were monitored by NMR, and required 6–14 days to reach 85–75% conversions. The silyl ether **18** was deprotected to the alcohol, which was racemic by chiral GC analysis. Under similar conditions, rhodium adducts of **II** gave complete reactions within 12 h, and *ee* values of 62–38%.[2e] Interestingly, ($S_{Re}S_{Re}S_{Re}S_{Re}$)-**13** that had been isolated was less active than that generated in situ. Parallel experiments with Mes_2SiH_2 gave analogous results. This suggests that some of the activity associated with the catalysts generated in situ may arise from by-products, as opposed to ($S_{Re}S_{Re}S_{Re}S_{Re}$)-**13/14**.

Equation (3) of Scheme 4 shows another type of rhodium-catalyzed reaction, the conjugate addition of an arylboronic acid to an enone.[19] These are commonly carried out in dioxane/water mixtures at 100 °C with catalysts generated in situ from Rh(acac)($H_2C{=}CH_2$)$_2$ and a chelating diphosphorus donor ligand. We first verified earlier reports that (*S*)-BINAP is an effective ligand for the addition of phenylboronic acid to 2-cyclohexen-1-one (**19**).[20] GC and HPLC analysis indicated the formation of 3-phenylcyclohexanone (**20**) in >99% yield and >99% *ee*. However, under analogous conditions, ($S_{Re}S_{Re}S_{Re}S_{Re}$)-**9** and ($R_{Re}R_{Re}R_{Re}R_{Re}$)-**10** (generated in situ) gave **20** in only 8–7% yields (48–41% conversions) and 38–2% *ee*. The ligand (*R*)-**IIb** (Figure 1) was therefore tested, and afforded **20** in 30% yield (65% conversion) and 40% *ee*.

Many chiral chelating ligands have proven effective in palladium-catalyzed enantioselective allylic alkylations.[21] As shown in Equation (4) of Scheme 4, the condensation of dimethyl malonate with the allylic acetate **21** was probed using a standard set of conditions. Control experiments with racemic BINAP and (*S*)-BINAP gave the substitution product **22** in 61–47% yields (unoptimized) after flash chromatography. Analysis of the latter by chiral HPLC indicated a 94% *ee*. Analogous reactions with ($S_{Re}S_{Re}S_{Re}S_{Re}$)-**9** and ($R_{Re}R_{Re}R_{Re}R_{Re}$)-**10** gave **22** in 47–37% yields but *ee* values of only 2%. The ligand (*R*)-**IIb** afforded a 16% *ee*. Hence, the title ligands give disappointing *ee* values in all reactions assayed, as further detailed elsewhere.[10b] They can therefore be regarded as *un*privileged ligands,[22] and possible factors are analyzed below.

5. Structural Data: The crystal structure of a CH_2Cl_2 disolvate of ($S_{Re}S_{Re}S_{Re}S_{Re}$)-**7** was determined as summarized in Table 2 and the experimental section. The unit cell was tetragonal, with four molecules of ($S_{Re}S_{Re}S_{Re}S_{Re}$)-**7** and belonging to the space group $P4_22_12$. Key metrical parameters are summarized in Table 1. The structure of the dication is depicted in Figure 3, together with *one* of the two PF_6^- anions. The dication features a C_2 axis at the midpoint of the C3/C3A bond and perpendicular to the idealized P–C3–C3A–P plane. This exchanges pairs of atoms such as

 © 2005 Wiley-VCH Verlag GmbH & Co. KGaA, Weinheim

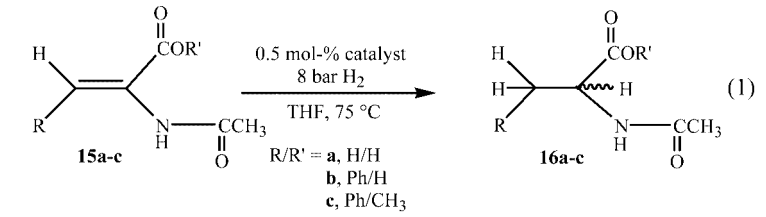

Catalyst	Starting material	Conversion [%]	*ee* [%]
($S_{Re}S_{Re}S_{Re}S_{Re}$)-**13** (in situ)	**15b,c**	92-90	12
($S_{Re}S_{Re}S_{Re}S_{Re}$)-**14** (in situ)	**15a-c**	>99-94	33-30

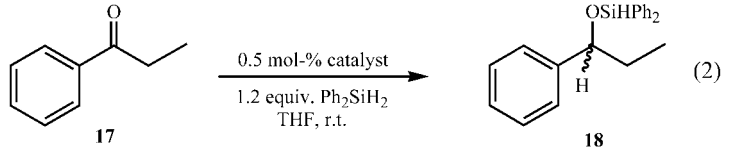

Catalyst	Conversion [%]	*ee* [%]
($S_{Re}S_{Re}S_{Re}S_{Re}$)-**13** (in situ)	86	0
($S_{Re}S_{Re}S_{Re}S_{Re}$)-**13** (isolated)	32	0

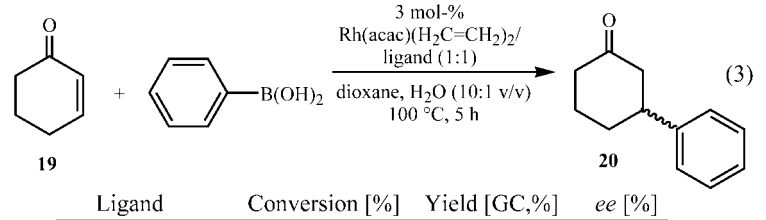

Ligand	Conversion [%]	Yield [GC,%]	*ee* [%]
(*S*)-BINAP	100	>99	>99(*S*)
($S_{Re}S_{Re}S_{Re}S_{Re}$)-**9**	41	7	2(*S*)
($R_{Re}R_{Re}R_{Re}R_{Re}$)-**10**	48	8	38(*R*)
(*R*)-**IIb**	65	30	40(*R*)

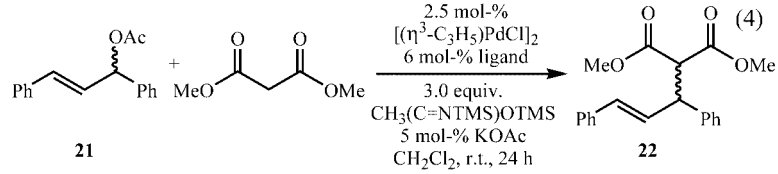

Ligand	Yield [isolated,%]	*ee* [%]
rac-BINAP	61	0
(*S*)-BINAP	47	94(*R*)
($S_{Re}S_{Re}S_{Re}S_{Re}$)-**9**	37	2(*S*)
($R_{Re}R_{Re}R_{Re}R_{Re}$)-**10**	47	2(*R*)
(*R*)-**IIb**	45	16(*R*)

Scheme 4. Summary of catalytic reactions.

Re1/Re1A, Re2/Re2A, P3/P3A, and C3/C3A. Three of the fluorine atoms of the PF_6^- ion in Figure 3 are disordered (F33, F34, F35), but only the average positions are shown.

The most striking feature of the dication is the grouping of the bulky PPh_3 ligands in the same hemisphere. An up/down motif that would minimize steric interactions might have been intuitively expected. Consequently, a cavity is defined by the four cyclopentadienyl rings in the opposite hemisphere. This provides a pocket for the disordered PF_6^- anion. The P30–F34 bond is directed towards the PCH_2CH_2P bridge, and forms F–H–P hydrogen bonds with both PH groups (2.55 Å from the average position for F34 to the calculated hydrogen positions). The non-disordered fluorine atoms F31 and F31A form very slightly longer F–H–P hydrogen bonds with H3 and H3A, respectively.

The structures of many related molecules with $ReCH_2X$ linkages have been studied in solution and the solid state.[3,14,23–26] The Re–CH_2 and CH_2–X conformations often have an important bearing upon diastereomer equilibria and reaction stereoselectivity. Thus, Newman-type pro-

 © 2005 Wiley-VCH Verlag GmbH & Co. KGaA, Weinheim

Table 1. Key distances [Å] and angles [°] of ($S_{Re}S_{Re}S_{Re}S_{Re}$)-**7**·$(CH_2Cl_2)_2$.

Re1–C1	2.195(8)
Re1–N1	1.744(6)
Re1–P1	2.352(2)
C1–P3	1.777(7)
N1–O1	1.208(7)
Re1–Cp1(centr)	1.964
Re2–C2	2.183(7)
Re2–N2	1.747(6)
Re2–P2	2.347(2)
C2–P3	1.764(7)
N2–O2	1.219(8)
Re2–Cp2(centr)	1.969
H3–F34/H3A–F34	2.55[a]
H3–F31A/H3A–F31	2.64
Re1–N1–O1	174.5(6)
N1–Re1–P1	90.8(2)
N1–Re1–C1	101.6(3)
C1–Re1–P1	88.2(2)
Re1–C1–P3	111.2(4)
Re2–N2–O2	173.6(6)
N2–Re2–P2	92.0(2)
N2–Re2–C2	100.0(3)
C2–Re2–P2	86.4(2)
Re2–C2–P3	111.6(4)
C1–P3–C2	116.6(4)
C1–P3–C3	106.8(4)
C2–P3–C3	111.5(4)
P3–C3–C3A	112.9(6)
N1–Re1–C1–P3	–54.8(4)
P1–Re1–C1–P3	–145.2(4)
N2–Re2–C2–P3	–56.1(5)
P2–Re2–C2–P3	–147.5(4)
Re1–C1–P3–C2	–165.5(4)
Re1–C1–P3–C3	69.1(5)
Re2–C2–P3–C1	74.0(5)
Re2–C2–P3–C3	–162.0(4)
C1–P3–C3–C3A	159.8(3)
C2–P3–C3–C3A	31.3(4)
P3–C3–C3A–P3A	157.0(4)

[a] Average involving two disordered positions of F34.

jections down the C1–Re1 and C2–Re2 bonds of the dication are depicted in Figure 4. In accord with all previous findings,[3,14,23–25] the X group (P3) is *roughly anti* to the bulky PPh_3 ligand, as quantified by the Ph_3P–Re–CH_2–P

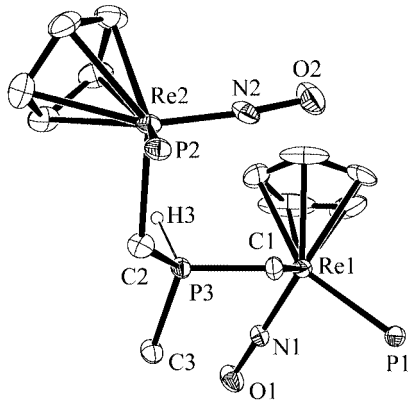

V

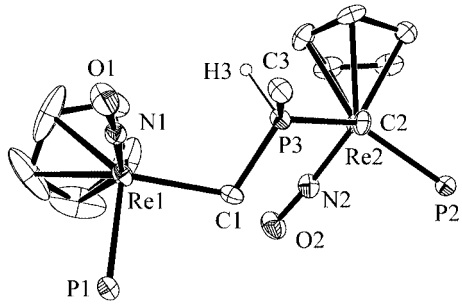

VI

Figure 4. Partial views of the dication of ($S_{Re}S_{Re}S_{Re}S_{Re}$)-**7** down the C1–Re1 (**V**) and C2–Re2 (**VI**) bonds.

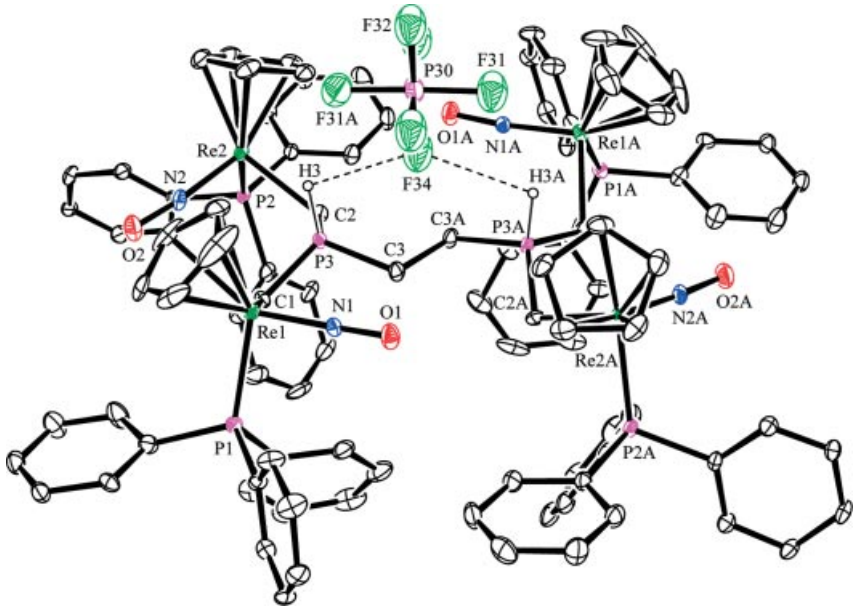

Figure 3. Molecular structure of ($S_{Re}S_{Re}S_{Re}S_{Re}$)-**7**·$(CH_2Cl_2)_2$ with solvate molecules and one PF_6^- anion omitted.

 © 2005 Wiley-VCH Verlag GmbH & Co. KGaA, Weinheim

torsion angles (**V**, –145.2°; **VI**, –147.5°). This places the X group between the smaller cyclopentadienyl and nitrosyl ligands, which is the least congested interstice on rhenium.

Complexes are also known in which the X group bears three sterically differentiated substituents (L/M/S). Typically, the largest group (L) exhibits a torsion angle near 180°, such that the Re–CH_2 and X–L bonds are *anti*.[3,23–25] This is evident in the partial structure **V**, where there is a large CH_2Re substituent and a Re1–C1–P3–C2 torsion angle of –165.5. The overall result is a "*W*"-shaped five-atom Ph_3P–*Re*–CH_2–*P*–CH_2Re conformation. However, the situation in **VI** is different. Now the medium CH_2CH_2 group occupies the terminus of the "*W*"-segment (P2–Re2–C2–P3–C3). The large CH_2Re substituent is roughly gauche to the Re2–C2 bond, as reflected by a Re2–C2–P3–C1 torsion angle of 74.0°. Possible implications are analyzed below.

In efforts to better understand the modest enantioselectivities in Scheme 4, crystal structures of ($S_{Re}S_{Re}S_{Re}S_{Re}$)-**13/14** were sought. All attempts to grow suitable single crystals were unsuccessful. Racemates are often easier to crystallize than enantiopure compounds. However, as easily seen from Scheme 2, the use of racemic rhenium building blocks would give intractable mixtures of diastereomers. Thus, the enantiomers ($S_{Re}S_{Re}S_{Re}S_{Re}$)- and ($R_{Re}R_{Re}R_{Re}R_{Re}$)-**7** were independently synthesized, mixed in a 1:1 ratio, and treated with *t*BuOK and then $[Rh(NBD)_2]^+$ PF_6^-. However, no crystals of racemic **13** could be obtained, even after adding a 10-fold excess of the BAr_F^- anion.

Discussion

1. Design Elements: Scheme 1 establishes the ready availability of a novel new class of diphosphane ligands that contain four symmetrically-disposed chiral-at-rhenium substituents and are based upon 1,ω-bis(dimethylphosphanyl)-alkane carbon skeletons. This methodology can likely be extrapolated to many types of derivatives, such as pentamethylcyclopentadienyl analogs or species with still longer methylene bridges. The overall yields of the ditertiary diphosphonium salts ($S_{Re}S_{Re}S_{Re}S_{Re}$)-**7/8** from commercially available $Re_2(CO)_{10}$ (25%/22%) are similar to those of **II-a**,**b**,[2b] which compares well with most of the widely applied chiral ferrocene-based ligands.[5] Since ($S_{Re}S_{Re}S_{Re}S_{Re}$)-**7/8** can be stored for indefinite periods, they represent convenient depots for the very air sensitive title diphosphanes ($S_{Re}S_{Re}S_{Re}S_{Re}$)-**9/10**.

The title diphosphanes can also be viewed in the evolutionary context of Figure 5. The structure **VII** embodies the essential features of DIOP, the classic chiral diphosphane introduced by Kagan in 1971.[27] The stereocenters can be moved closer to the phosphorus atoms as in **VIII**, a well-known example of which is CHIRAPHOS.[28] In **IX**, the phosphorus atoms become stereocenters, as exemplified by DIPAMP, another very early chiral diphosphane.[29] In later efforts, stereocenters were introduced exocyclic to the chelate backbone. Structure **X** corresponds to the DuPHOS ligand family,[30] in which the phosphorus atoms are no longer stereogenic. Motif **XI** can be viewed as a hybrid with both phosphorus and exocyclic stereocenters, and corresponds to **IIIb** in Figure 1. Finally, **XII** represents our new family of chiral diphosphanes.

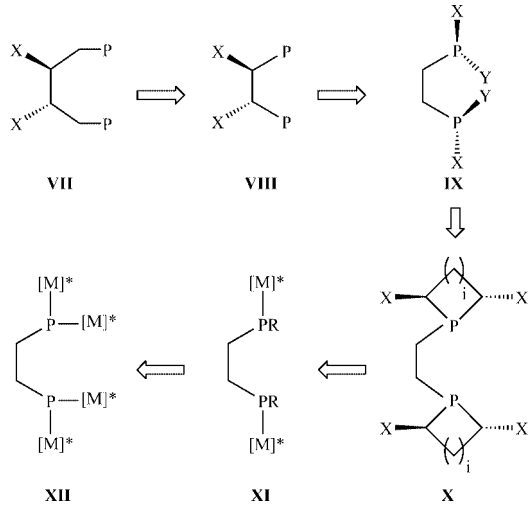

Figure 5. Motifs for chiral chelating diphosphanes. [M]* = "chiral-at-metal" group.

Surprisingly, we have not been able to locate any reports of diphosphanes with analogous arrays of four homochiral substituents. The most readily envisioned cases would involve substituents derived from the chiral pool. Unlike most chiral pool compounds, both enantiomers of the chiral rhenium building blocks are equally available. Therefore, both enantiomers of our ligands are easily accessed. There are also possibilities for other diastereomers, all of which are depicted schematically in Figure 6 using standard formalisms for systems with constitutionally equal stereocenters.[31] The shaded and unshaded circles in formulae **i**–**vii** denote mirror images of the chiral fragments. There are six chiral stereoisomers (**i**–**iii** with enantiomers a/b) and four *meso*-stereoisomers (**iv**–**vii**). Of the latter, **iv** and **v** possess a center of inversion (*i*) and two mirror planes, whereas **vi** and **vii** have only one mirror plane.

In seven of the ten isomers, at least one phosphorus atom is pseudoasymmetric.[32] These are designated with P_r and P_s chirality descriptors in Figure 6.[31] The many consequences of pseudoasymmetric atoms have been analyzed in detail. One requirement is that the configurations, here at phosphorus, remain invariant upon reflection through a mirror plane (e. g., **iia** vs. **iib**; **iiia** vs. **iiib**). Those in *meso* **iv**–**vi** are stereogenic but achirotopic since they lie on a local symmetry plane and permuting two rhenium fragments generates another *meso* form. Formula **ia** corresponds to the isomers synthesized in Scheme 1, ($S_{Re}S_{Re}S_{Re}S_{Re}$)-**9/10**. For illustration purposes, **v** would correspond to the structure shown in Figure 6.

Practical syntheses of these other diastereomers will require some serendipity, but should be possible. Consider the diastereomers ($S_{Re}S_{Re}$,$R_{Re}R_{Re}$)-**3′** and ($S_{Re}R_{Re}$)-**3′** in Scheme 2, which are easily separated. Subsequent reaction of the diphosphane corresponding to ($S_{Re}R_{Re}$)-**3′** with

 © 2005 Wiley-VCH Verlag GmbH & Co. KGaA, Weinheim

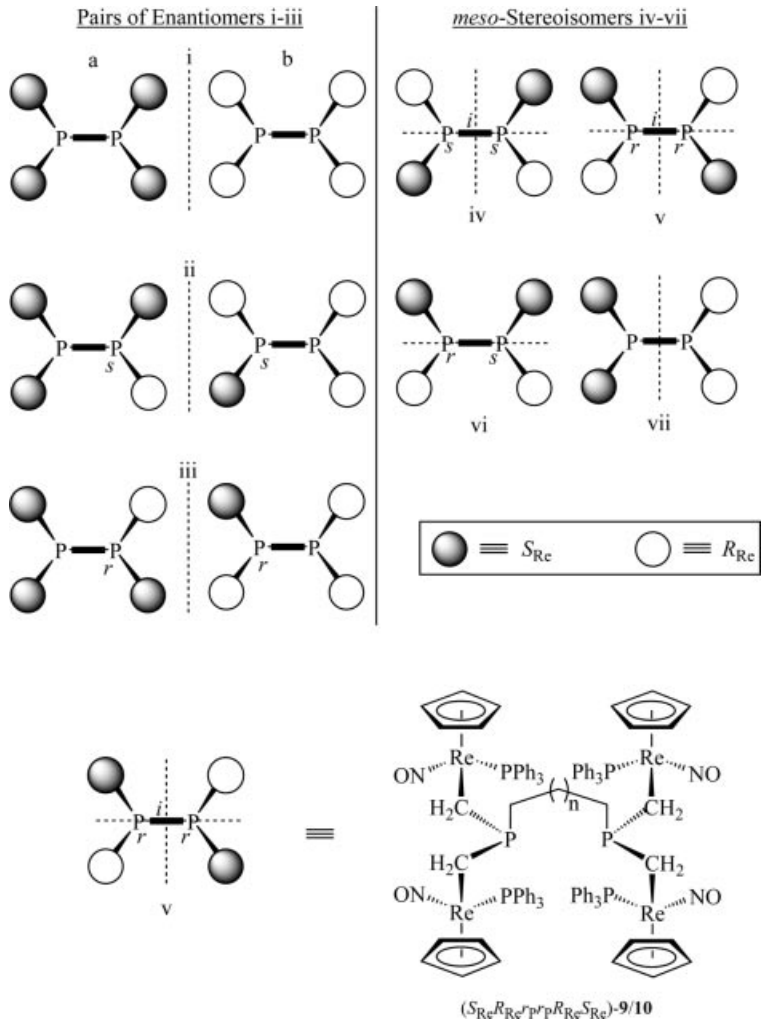

Figure 6. Possible stereoisomers of tetrarhenium diphosphanes. The descriptors *r* and *s* denote pseudoasymmetric phosphorus atoms, and *i* a center of inversion.

enantiopure rhenium methylidene complex **2** would yield only two non-racemic diastereomers, one of the type **ii** and the other of the type **iii**. This likely represents a tractable separation, and would allow all chiral stereoisomers to be secured. On the other hand, an analogous sequence with ($S_{Re}S_{Re}$,$R_{Re}R_{Re}$)-**3′** would be less useful, resulting in the known diastereomer **i**, and as many as three *meso* diastereomers (**iv**–**vi**).

2. Structure and Catalysis: The congested nature of the tetrarhenium systems is obvious in the crystal structure of ($S_{Re}S_{Re}S_{Re}S_{Re}$)-**7** (Figure 3). Despite this, the diphosphane ligands ($S_{Re}S_{Re}S_{Re}S_{Re}$)-**9/10** and $[Rh(NBD)_2]^+$ PF_6^- react to form the stable rhodium chelates ($S_{Re}S_{Re}S_{Re}S_{Re}$)-**13/14**. Bulky ligands and/or sterically restricted binding pockets can be favorable for asymmetric catalysis. However, the rates and *ee* values for enantioselective hydrogenations and hydrosilylations (Scheme 4) are much lower than those with analogous rhodium chelates of the diphosphanes **IIa**,**b** (Figure 1). One possible explanation is that the ligands in ($S_{Re}S_{Re}S_{Re}S_{Re}$)-**13/14** are simply too voluminous to allow effective catalysis. The residual activities might be due in part to achiral rhodium-containing decomposition products, which would be consistent with the modest *ee* values. One probe would be to test related complexes with only two chiral rhenium fragments, such as could be derived from **IIIb** (Figure 1). However, as noted above, multiple diastereomers are possible due to the phosphorus stereocenters.

The performances of ($S_{Re}S_{Re}S_{Re}S_{Re}$)-**9** and ($R_{Re}R_{Re}R_{Re}R_{Re}$)-**10** in rhodium-catalyzed conjugate additions of aryl boronic acids and palladium-catalyzed allylic alkylations are also disappointing (Scheme 4). In both reactions, catalysts are commonly generated in situ, and there is the question whether analogous species are formed from ($S_{Re}S_{Re}S_{Re}S_{Re}$)-**9** and ($R_{Re}R_{Re}R_{Re}R_{Re}$)-**10**. The aqueous conditions associated with the former reaction are a possible complicating factor. The diphosphane **IIb**, which we view as sterically less congested, also gives *ee* values distinctly lower than those of benchmark ligands. This leads us to believe that both classes of ligands are simply not

 © 2005 Wiley-VCH Verlag GmbH & Co. KGaA, Weinheim

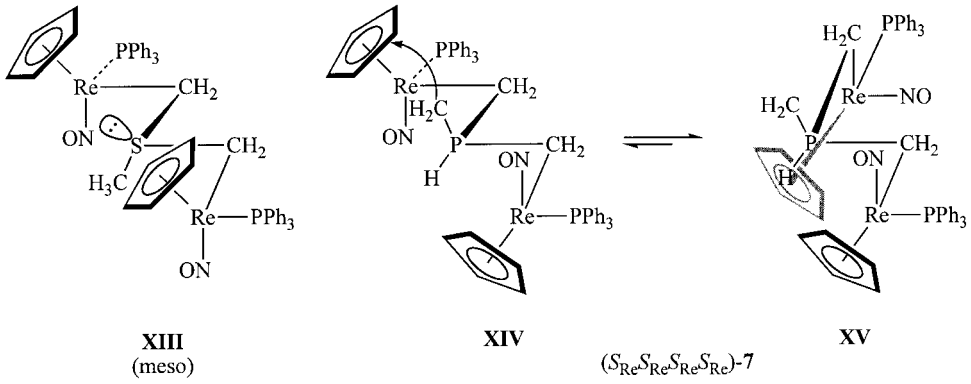

XIII (meso) **XIV** **XV** ($S_{Re}S_{Re}S_{Re}S_{Re}$)-**7**

Figure 7. Conformations of compounds with Ph_3P–Re–CH_2–X–CH_2–Re–PPh_3 linkages.

competitive with existing systems. However, we note in passing that a DIOP derivative has been prepared with four P-ferrocenyl substituents.[33] The rhodium chelate catalyzes the hydrogenation of itaconic acid with reasonable enantioselectivities (40% *ee*).

The conformational features of ($S_{Re}S_{Re}S_{Re}S_{Re}$)-**7** highlighted in Figure 4 can be compared to those in related complexes. The crystal structure of the *meso* sulfonium salt ($S_{Re}R_{Re}$)-[{(η^5-C_5H_5)Re(NO)(PPh_3)(CH_2)}$_2$(SCH_3)]$^+$ I^- has been determined, and the conformation of the cation is depicted in **XIII** in Figure 7.[23] The seven-atom P–Re–CH_2–S–CH_2–Re–P linkage adopts an extended "*VVV*"-shape, with *anti* relationships between the bulkiest groups (*Ph*$_3$*P*–Re vs. CH_2–*S* and *Re*–CH_2 vs. S–*C*H_2*Re*). The sulfur atom is a pseudoasymmetric, and can assume a "matched" configuration such that the small lone pair is *syn* to both larger cyclopentadienyl ligands, and the medium CH_3 substituent is *syn* to both smaller nitrosyl ligands.

Since the rhenium atoms in ($S_{Re}S_{Re}S_{Re}S_{Re}$)-**7** have the same configuration, a conformation analogous to that in **XIII** is not possible. The conformation **XIV** would maintain *anti* relationships between the bulkiest groups (*Ph*$_3$*P*–Re vs. CH_2–*P* and *Re*–CH_2 vs. P–*C*H_2*Re*) and a "*VVV*" shape. However, now the medium *C*H_2CH_2 substituent on phosphorus is forced into a *syn* relationship with one of the larger cyclopentadienyl ligands. This unavoidable "mismatch" raises the steric energy, and the alternative conformation **XV** is found in the crystal instead. Here, the ReCH_2–P bond has been rotated to bring the *Re*–CH_2 group *anti* to the P–*C*H_2CH_2 group, as in the partial structure **VI** (Figure 4). We therefore speculate that diastereomers of **7/8** of the types **ii** or **iii** (Figure 6), in which the type of "matched" relationship in **XIII** can be maintained on one of the two phosphorus atoms, may afford less congested and therefore superior catalysts.

Despite the inauspicious beginning in Scheme 4, we continue to believe that the tetrarhenium complexes in Scheme 1 should have useful applications in enantioselective catalysis, especially for reactions that involve fundamentally different mechanisms. For example, chiral phosphane oxides, diphosphane dioxides, and related species are very useful nucleophilic catalysts for enantioselective condensations of appropriate allylsilanes with carbonyl compounds.[34] High *ee* values can be obtained, and ($S_{Re}S_{Re}S_{Re}S_{Re}$)-**11/12** represent attractive candidates for such chemistry. Furthermore, we have recently found that the rhenium-containing monophosphane (η^5-C_5H_5)Re(NO)(PPh_3)(CH_2PPh_2) effects enantioselective Baylis–Hillman reactions.[35] Thus, this general class of complexes has a promising future in catalysis, as will be detailed in future reports from this laboratory.

3. Conclusion

The types of chelating ligands available that contain the chiral rhenium fragment **I** have been significantly augmented by the new 1,2- and 1,3-diphosphanes ($S_{Re}S_{Re}S_{Re}S_{Re}$)-**9/10**. These electron-rich, DMPE/DMPP derivatives are efficiently synthesized as outlined in Scheme 1, and are readily converted to diphosphane dioxides and rhodium chelate complexes. However, they have not proved to be effective ligands for metal-catalyzed enantioselective reactions in the cases examined to date. This may be due to their considerable bulk, as reflected by the crystal structure of a diprotonated derivative. Nonetheless, metal-containing ligands continue to make a major impact in enantioselective catalysis,[1,5] and additional applications of the compounds reported herein remain under investigation.

Experimental Section

General: Most general procedures, chemical purifications, and instruments were identical with those in a recent full paper.[4a] Further information is provided elsewhere.[10] HPLC was conducted using a ThermoQuest instrument package (pump/autosampler/detector P4000/AS 3000/UV 6000LP). Solvents were freshly dried before use, as detailed in the supporting information; for supporting information see also the footnote on the first page of this article. Purification steps new to this study: 2-cyclohexen-1-one (95+%, Aldrich), vacuum-distilled; H_2O (reaction cosolvent), freeze-pump-thaw degassed (3 cycles); KOAc (Merck), dried 24 h at 120 °C.

[(η^5-C_5H_5)Re(NO)(PPh_3){$CH_2PH_2CH_2(CH_2)_nCH_2PH_2CH_2$}-($Ph_3P$)(ON)Re($\eta^5$-$C_5H_5$)]$^{2+}$ 2X$^-$ (*n*/X = 0/PF_6, 3; 0/BF_4, 3′; 1/PF_6, 4): (**A**) A Schlenk flask was charged with (*S*)-**1** (0.327 g,

 © 2005 Wiley-VCH Verlag GmbH & Co. KGaA, Weinheim

0.585 mmol)[9,36,37] and CH_2Cl_2 (15 mL), and was cooled to –60 °C. Then Ph_3C^+ PF_6^- (0.250 g, 0.644 mmol) was added with stirring. After 30 min, $PH_2(CH_2)_2PH_2$ (0.0275 g, 0.293 mmol) was added by syringe to the yellow solution, which turned orange. After 30 min, the cold bath was removed. Some precipitate formed. The suspension was concentrated by oil pump vacuum to ca. 10 mL. After 5 h, the precipitate was collected by filtration and dried by oil pump vacuum. The product was dissolved in a minimum of boiling CH_2Cl_2 and stored at –32 °C. After 24 h, the fine yellow needles were collected by filtration and dried by oil pump vacuum to give ($S_{Re}S_{Re}$)-**3** (0.286 g, 0.191 mmol, 65%). M. p. 160–162 °C (dec). $C_{50}H_{52}F_{12}N_2O_2P_6Re_2$ (1499.2): calcd. C 40.05, H 3.50, N 1.87; found C 40.06, H 3.50, N 1.87. IR (thin film [cm^{-1}]): $\tilde{\nu}$ = 1650 (s, NO), 830 (s, PF). ^1H NMR (400 MHz, CD_3NO_2): PPh_3 at δ = 7.57–7.40 (m, 30 H); 6.63/6.09 [2 dm, ^1J(H,P) = 480/496 Hz, 4 H, PHH′], 5.36 (s, 10 H, C_5H_5), 2.27 (m, 4 H, PCH_2C), 2.03 (m, 2 H, ReC*H*H′), 1.86 (m, 2 H, ReCH*H*′). $^{13}C\{^1H\}$ NMR (100.5 MHz, CD_3NO_2): PPh_3 at δ = 135.2 [d, ^1J(C,P) = 53 Hz, *i*], 134.8 [d, ^2J(C,P) = 11 Hz, *o*], 132.5 (s, *p*), 130.3 [d, ^3J(C,P) = 9 Hz, *m*]; 92.2 (s, C_5H_5), 18.9 (m, P*C*H_2C), –43.5 (m, $ReCH_2$). $^{31}P\{^1H\}$ NMR (161.8 MHz, CD_3NO_2): δ = 21.0 [d, ^3J(P,P) = 18 Hz, PPh_3], 1.5 {br. s [t, ^1J(P,H) = 488 Hz without ^1H decoupling], PCH_2}, –143.0 [sept, ^1J(P,F) = 705 Hz, PF_6]. MS (FAB, 3-NBA): *m*/*z* (%) = 1353 (2) $[M + PF_6]^+$, 1207 (6) $[M – H]^+$, 558 (100) $[(\eta^5\text{-}C_5H_5)Re(NO)(PPh_3)(CH_2)]^+$.

(**B**) Complex **1** (0.551 g, 0.987 mmol),[9,36,37] CH_2Cl_2 (20 mL), Ph_3C^+ BF_4^- (0.363 g, 1.10 mmol), and $PH_2(CH_2)_2PH_2$ (0.050 g, 0.53 mmol) were combined in a procedure analogous to **A**. After 30 min, the cold bath was removed. Some precipitate formed. After 2 h, the yellow powder was collected by filtration, washed with CH_3CN (2×5 mL), and dried by oil pump vacuum to give ($S_{Re}R_{Re}$)-**3′** (0.191 g, 0.138 mmol, 28%). The volatiles were removed from the filtrate by oil pump vacuum. The residue was dissolved in a minimum of CH_2Cl_2 and a layer of ether (30 mL) was gently added. After 2 days, the supernatant was decanted and the orange powder dried by oil pump vacuum to give ($S_{Re}S_{Re}$,$R_{Re}R_{Re}$)-**3′** (0.259 g, 0.188 mmol, 38%).

Data for ($S_{Re}R_{Re}$)-3′: M. p. 152–154 °C (dec). $C_{50}H_{52}B_2F_8N_2O_2P_4Re_2$ (1382.9): calcd. C 44.43, H 3.79, N 2.03; found C 43.20, H 3.68, N 2.05. IR (thin film [cm^{-1}]): $\tilde{\nu}$ = 1638 (s, NO). ^1H NMR (400 MHz, [D$_6$]DMSO): PPh_3 at δ = 7.50–7.48 (m, 18 H), 7.28–7.24 (m, 12 H); 5.35 (s, 10 H, C_5H_5), 3.95 (br. s, 4 H, PH_2), 2.08 (m, 4 H, PCH_2C), 1.64 (m, 4 H, $ReCH_2$). $^{13}C\{^1H\}$ NMR (100.5 MHz, [D$_6$]DMSO): PPh_3 at δ = 133.8 [d, ^1J(C,P) = 53 Hz, *i*], 133.0 [d, ^2J(C,P) = 11 Hz, *o*], 130.9 (s, *p*), 129.0 [d, ^3J(C,P) = 9 Hz, *m*]; 90.7 (s, C_5H_5), 17.5 (m, P*C*H_2C), –37.1 (m, $ReCH_2$). $^{31}P\{^1H\}$ NMR (161.8 MHz, [D$_6$]DMSO): δ = 21.5 (br. s, PPh_3), 3.4 (br. m, PCH_2), –143.2 [sept, ^1J(P,F) = 705 Hz, PF_6].

Data for ($S_{Re}S_{Re}$,$R_{Re}R_{Re}$)-3′: M. p. 171–174 °C (dec). $C_{50}H_{52}B_2F_8N_2O_2P_4Re_2$ (1382.9): calcd. C 43.43, H 3.79, N 2.03; found C 43.50, H 3.75, N 1.92. IR (thin film [cm^{-1}]): $\tilde{\nu}$ = 1652 (s, NO). ^1H NMR (400 MHz, CD_3CN): PPh_3 at δ = 7.52–7.47 (m, 30 H); 6.60/6.02 [2 dm, ^1J(H,P) = 480/492 Hz, 4 H, PHH′], 5.30 (s, 10 H, C_5H_5), 2.08 (m, 4 H, PCH_2C), 1.80 (m, 2 H, ReC*H*H′), 1.65 (m, 2 H, ReCH*H*′). $^{13}C\{^1H\}$ NMR (100.5 MHz, CD_3CN): PPh_3 at δ = 135.1 [d, ^1J(C,P) = 53 Hz, *i*], 134.5 [d, ^2J(C,P) = 9 Hz, *o*], 132.0 (s, *p*), 130.0 [d, ^3J(C,P) = 9 Hz, *m*]; 91.9 (s, C_5H_5), 18.4 (m, P*C*H_2C), –43.5 (m, $ReCH_2$). $^{31}P\{^1H\}$ NMR (161.8 MHz, CD_3CN): δ = 21.0 (br. s, PPh_3), 3.1 (br. s, PCH_2), –143.2 [sept, ^1J(P,F) = 705 Hz, PF_6].

(**C**) Complex (*R*)-**1** (0.871 g, 1.56 mmol),[9,36,37] CH_2Cl_2 (35 mL), Ph_3C^+ PF_6^- (0.666 g, 1.72 mmol), and $PH_2(CH_2)_3PH_2$ (0.0926 g, 0.857 mmol)[11] were combined in a procedure analogous to **A**. A similar workup gave ($R_{Re}R_{Re}$)-**4** as a yellow microcrystalline powder (1.368 g, 0.904 mmol, 58%). M. p. 154–155 °C (dec). $C_{51}H_{54}F_{12}N_2O_2P_6Re_2$ (1513.2): calcd. C 40.48, H 3.60, N 1.85; found C 40.24, H 3.41, N 1.68. IR (thin film [cm^{-1}]): $\tilde{\nu}$ = 1652 (s, NO), 836 (s, PF). ^1H NMR (400 MHz, CD_3NO_2): PPh_3 at δ = 7.57–7.39 (m, 30 H); 6.59/6.04 [2 dm, ^1J(H,P) = 476/468 Hz, 4 H, PHH′], 5.36 (s, 10 H, C_5H_5), 2.25 (m, 6 H, $CH_2CH_2CH_2$), 2.02 (m, 2 H, ReC*H*H′), 1.89 (m, 2 H, ReCH*H*′). $^{13}C\{^1H\}$ NMR (100.5 MHz, CD_3NO_2): PPh_3 at δ = 135.4 [d, ^1J(C,P) = 53 Hz, *i*], 134.9 [d, ^2J(C,P) = 9 Hz, *o*], 132.5 (s, *p*), 130.3 [d, ^3J(C,P) = 10 Hz, *m*]; 92.3 (s, C_5H_5), 24.1 [dd, ^1J(C,P) = 39, ^3J(C,P) = 15 Hz, P*C*H_2C], 18.9 (s, C*C*H_2C), –43.3 (m, $ReCH_2$). $^{31}P\{^1H\}$ NMR (161.8 MHz, CD_3NO_2): δ = 21.1 [d, ^3J(P,P) = 16 Hz, PPh_3], 0.1 [d, ^3J(P,P) = 16 Hz, PCH_2], –143.2 [sept, ^1J(P,F) = 706 Hz, PF_6]. MS (FAB, 3-NBA): *m*/*z* (%) = 1367 (10) $[M + PF_6]^+$, 1221 (10) $[M – H]^+$, 558 (100) $[(\eta^5\text{-}C_5H_5)Re(NO)(PPh_3)(CH_2)]^+$.

$[\{(\eta^5\text{-}C_5H_5)Re(NO)(PPh_3)(CH_2)\}_2\{PHCH_2(CH_2)_nCH_2PH\}\text{-}\{(CH_2)(Ph_3P)(ON)Re(\eta^5\text{-}C_5H_5)\}_2]^{2+}$ $2PF_6^-$ (n = 0/1, 7/8): (**A**) A Schlenk flask was charged with ($S_{Re}S_{Re}$)-**3** (0.831 g, 0.554 mmol) and THF (50 mL). Then *t*BuOK (1.0 M in THF; 1.39 mL, 1.39 mmol) was added dropwise with stirring. After 30 min, the solvent was removed by oil pump vacuum. The residue was extracted with CH_2Cl_2 (30 mL). The extract was filtered through a Celite plug (2×3 cm, CH_2Cl_2 rinses). A Schlenk tube was charged with (*S*)-**1** (0.650 g, 1.16 mmol)[9,36,37] and CH_2Cl_2 (30 mL), and was cooled to –60 °C. Then Ph_3C^+ PF_6^- (0.497 g, 1.28 mmol) was added with stirring. After 30 min, the Celite filtrate was added via cannula along the wall of the tube, such that it cooled before reaching the solution. The cold bath was then removed. After 3 h, the mixture was filtered through a Celite plug (4×5 cm). The filtrate was concentrated by oil pump vacuum to ca. 15 mL and a layer of ether (ca. 50 mL) was added. After 48 h, the red prisms were isolated by decantation of the supernatant and dried under a N_2 stream to give ($S_{Re}S_{Re}S_{Re}S_{Re}$)-**7**·$(CH_2Cl_2)_2$ (1.352 g, 0.486 mmol, 88%).[38] M. p. 288 °C (dec). $C_{98}H_{94}F_{12}N_4O_4P_8Re_4\cdot(CH_2Cl_2)_2$ (2782.3): calcd. C 43.17, H 3.55, N 2.01; found C 43.38, H 3.70, N 2.01. IR (thin film [cm^{-1}]): $\tilde{\nu}$ = 2015 (w, PH), 1633 (s, NO), 830 (s, PF). ^1H NMR (400 MHz, CD_3NO_2): PPh_3 at δ = 7.66–7.14 (m, 60 H); 6.35 [dt, ^1J(H,P) = 472, ^3J(P,P) = 13 Hz, 2 H, PH], 5.34 (s, 10 H, C_5H_5), 5.32 (s, 4 H, CH_2Cl_2), 5.21 (s, 10 H, $C_5H'_5$), CH_2 at 2.61, 2.38, 1.98, 1.78, 1.64, 1.52 (6 m, 12 H). $^{13}C\{^1H\}$ NMR (100.5 MHz, CD_3NO_2): PPh_3 at δ = 135.8 [d, ^1J(C,P) = 54 Hz, *i*], 134.9 [d, ^2J(C,P) = 10 Hz, *o*], 134.7 [d, ^2J(C,P) = 10 Hz, *o′*], 132.6 (s, *p*), 132.4 (s, *p′*), 130.4 [d, ^3J(C,P) = 10 Hz, *m*], 130.2 [d, ^3J(C,P) = 10 Hz, *m′*]; 92.8 (s, C_5H_5), 92.5 (s, C′$_5H_5$), 53.8 (s, CH_2Cl_2), 21.7 [d, ^1J(C,P) = 34 Hz, P*C*H_2C], –27.4 (m, $ReCH_2$), –31.5 [d, ^1J(C,P) = 34 Hz, ReC′H_2]. $^{31}P\{^1H\}$ NMR (161.8 MHz, CD_3NO_2): δ = 80.0 {br. s [d, ^1J(P,H) = 472 Hz without ^1H decoupling], PCH_2}, 23.3 [apparent t, ^3J(P,P) = 12 Hz, PPh_3], 21.6 [apparent t, ^3J(P,P) = 10 Hz, P′Ph_3], –142.8 [sept, ^1J(P,F) = 705 Hz, PF_6]. MS (FAB, 3-NBA): *m*/*z* (%) = 2467 (12) $[M + PF_6]^+$, 2321 (2) $[M – H]^+$, 558 (100) $[(\eta^5\text{-}C_5H_5)Re(NO)(PPh_3)(CH_2)]^+$.

(**B**) Complex ($R_{Re}R_{Re}$)-**4** (1.311 g, 0.866 mmol), THF (60 mL), *t*BuOK (1.0 M in THF; 2.17 mL, 2.2 mmol), (*R*)-**1** (1.016 g, 1.82 mmol),[9,36,37] CH_2Cl_2 (50 mL), and Ph_3C^+ PF_6^- (0.740 g, 1.91 mmol) were combined in a procedure analogous to **A**. A similar workup in which the product was collected by filtration, washed with ether (2×10 mL), and dried by oil pump vacuum gave ($R_{Re}R_{Re}R_{Re}R_{Re}$)-**8**·$(CH_2Cl_2)_2$ as a yellow-orange powder (1.976 g, 0.752 mmol, 87%).[38] M. p. 242 °C (dec). $C_{99}H_{96}F_{12}N_4O_4P_8Re_4\cdot(CH_2Cl_2)_2$ (2796.3): calcd. C 43.38, H 3.63, N 2.00; found C 42.94, H 3.58, N 1.90. IR (thin film [cm^{-1}]): $\tilde{\nu}$ = 2015 (w, PH), 1633 (s,

 © 2005 Wiley-VCH Verlag GmbH & Co. KGaA, Weinheim

NO), 830 (s, PF). ^{1}H NMR (400 MHz, $CDCl_3$): PPh_3 at δ = 7.41–7.20 (m, 60 H); 6.08 [dm, ^1J(H,P) = 460 Hz, 2 H, PH], 5.32 (s, 4 H, CH_2Cl_2), 5.19 (s, 10 H, C_5H_5), 5.15 (s, 10 H, $C_5H'_5$), CH_2 at 2.15–1.91 (m, 8 H), 1.52–1.38 (m, 6 H). $^{13}C\{^1H\}$ NMR (100.5 MHz, CD_3NO_2): δ = PPh_3 at 135.1 [d, ^1J(C,P) = 46 Hz, *i*], 134.5 [d, ^1J(C,P) = 47 Hz, *i'*], 134.0 [d, ^2J(C,P) = 10 Hz, *o*], 139 [d, ^2J(C,P) = 11 Hz, *o'*], 131.3 [d, ^4J(C,P) = 2 Hz, *p*], 131.2 [d, ^4J(C,P) = 2 Hz, *p'*], 129.4 [d, ^3J(C,P) = 10 Hz, *m*], 129.2 [d, ^3J(C,P) = 10 Hz, *m'*]; 91.4 (s, C_5H_5), 91.1 (s, C'_5H_5), 53.8 (s, CH_2Cl_2), 28.9 [d, ^1J(C,P) = 14 Hz, P*C*H$_2$C], 28.5 [d, ^2J(C,P) = 9 Hz, C*C*H$_2$C], –27.3 [d, ^1J(C,P) = 21 Hz, ReCH$_2$], –32.6 [d, ^1J(C,P) = 39 Hz, ReC′H$_2$]. $^{31}P\{^1H\}$ NMR (161.8 MHz, CD_3NO_2): δ = 72.1 [apparent t, ^3J(P,P) = 16 Hz, PCH$_2$], 23.3 [d, ^3J(P,P) = 14 Hz, PPh_3], 22.6 [d, ^3J(P,P) = 18 Hz, P′Ph$_3$], –142.3 [sept, ^1J(P,F) = 718 Hz]. MS (FAB, 3-NBA): *m/z* (%) = 2337 (2) $[M - H]^+$, 558 (100) $[(\eta^5\text{-}C_5H_5)Re(NO)(PPh_3)(CH_2)]^+$.

{(η^5-C$_5$H$_5$)Re(NO)(PPh$_3$)(CH$_2$)}$_2${PCH$_2$(CH$_2$)$_n$CH$_2$P}{(CH$_2$)(Ph$_3$P)(ON)Re(η^5-C$_5$H$_5$)}$_2$ (*n* = 0/1, 9/10): (**A**) A glass vial was charged with ($S_{Re}S_{Re}S_{Re}S_{Re}$)-**7**·$(CH_2Cl_2)_2$ (0.180 g, 0.0647 mmol) and THF (5 mL) in a glove box. Then *t*BuOK (1.0 M in THF; 0.142 mL, 0.14 mmol) was added dropwise with stirring, and the vial sealed with a screw cap. After 30 min, the solvent was removed by oil pump vacuum. [D$_8$]Toluene (2 mL) was added with stirring. After 10 min, the sample was passed through a PTFE syringe filter. An aliquot of the orange filtrate was assayed by NMR (^{1}H, ^{13}C, ^{31}P). The aliquot was readded and the solvent removed by oil pump vacuum to give ($S_{Re}S_{Re}S_{Re}S_{Re}$)-**9** as an orange powder (0.138 g, 0.0595 mmol, 92%). M. p. 178–180 °C (dec). $C_{98}H_{92}N_4O_4P_6Re_4$ (2320.5): calcd. C 50.73, H 4.00, N 2.41; found C 51.12, H 3.88, N 2.25. IR (thin film [cm^{-1}]): $\tilde{\nu}$ = 1610 (s, NO). ^{1}H NMR (400 MHz, [D$_8$]toluene): PPh_3 at δ = 7.61–7.49 (m, 24 H), 6.93–6.91 (m, 36 H); 5.14 (s, 10 H, C_5H_5), 5.09 (s, 10 H, $C_5H'_5$), CH_2 at 2.60–2.50 (m, 8 H), 1.73–1.56 (m, 4 H). $^{13}C\{^1H\}$ NMR (75.5 MHz, [D$_8$]toluene): PPh_3 at δ = 138.5 (d, ^1J(C,P) = 50 Hz, *i*), 134.5 (d, ^2J(C,P) = 10 Hz, *o*), 134.3 (d, ^2J(C,P) = 10 Hz, *o'*), 129.8 (d, ^3J(C,P) = 10 Hz, *m*), 128.5 (s, *p*), 128.4 (s, *p'*); 91.7 (s, C_5H_5), 91.6 (s, C'_5H_5), 31.8 [dd, *J*(C,P) = 14, *J*(C,P) = 7 Hz, P*C*H$_2$C], –8.1 (m, ReCH$_2$), –11.8 (m, ReC′H$_2$). $^{31}P\{^1H\}$ NMR (121.5 MHz, [D$_8$]toluene or [D$_8$]THF): δ = 37.5 or 34.9 (br. s, PCH$_2$), 27.9 or 27.6 (br. s, PPh_3), 27.4 or 27.4 (br. s, P′Ph$_3$).

(**B**) Complex ($R_{Re}R_{Re}R_{Re}R_{Re}$)-**8**·$(CH_2Cl_2)_2$ (0.150 g, 0.0536 mmol), THF (10 mL) and *t*BuOK (1.0 M *in* THF; 0.161 mL, 0.16 mmol) were combined in a procedure analogous to **A**. The toluene filtrate was concentrated to ca. 3 mL and layered with pentane (10 mL). After 3 days, the supernatant was decanted from an orange powder, which was dried by oil pump vacuum to give ($R_{Re}R_{Re}R_{Re}R_{Re}$)-**10** (0.078 g, 0.033 mmol, 62%). M. p. 164–166 °C (dec). $C_{99}H_{94}N_4O_4P_6Re_4$ (2334.5): calcd. C 50.93, H 4.06, N 2.40; found C 50.29, H 4.35, N 2.03. IR (thin film [cm^{-1}]): $\tilde{\nu}$ = 1617 (s, NO). ^{1}H NMR (400 MHz, C_6D_6 or [D$_8$]toluene): PPh_3 at δ = 7.74–7.70 or 7.64–7.61 (m, 10 H), 7.56–7.51 or 7.47–7.40 (m, 12 H), 7.11–7.08 or 7.04–7.02 (m, 12 H), 7.03–6.95 or 6.97–6.89 (m, 26 H); 5.15 or 5.04 (s, 10 H, C_5H_5), 4.92 or 4.84 (s, 10 H, $C_5H'_5$), CH_2 at 2.69–2.61 or 2.57–2.52 (m, 6 H), 1.98–1.69 or 1.80–1.72 (m, 8 H). $^{13}C\{^1H\}$ NMR (100.5 MHz, C_6D_6): PPh_3 at δ = 138.0 [d, ^1J(C,P) = 50 Hz, *i*], 137.4 (d, ^1J(C,P) = 50 Hz, *i'*), 134.4 (d, ^2J(C,P) = 10 Hz, *o*), 134.2 (d, ^2J(C,P) = 11 Hz, *o'*), 129.8 (s, *p*), 131.1 (s, *p'*), 129.7 [d, ^3J(C,P) = 10 Hz, *m*], 129.3 [d, ^3J(C,P) = 10 Hz, *m'*]; 91.5 (s, C_5H_5), 91.1 (s, C'_5H_5), 39.7 [dd, ^1J(C,P) = 22, ^3J(C,P) = 8 Hz, P*C*H$_2$C], 24.6 [t, ^2J(C,P) = 13 Hz, C*C*H$_2$C], –5.6 [dd, ^1J(C,P) = 41, ^2J(C,P) = 5 Hz, ReCH$_2$], –12.9 [dd, ^1J(C,P) = 32, ^2J(C,P) = 5 Hz, ReC′H$_2$]. $^{31}P\{^1H\}$ NMR (161.8 MHz, C_6D_6): δ = 31.4 (s, PCH$_2$), 27.3 (s, PPh_3), 26.8 (s, P′Ph$_3$).

{(η^5-C$_5$H$_5$)Re(NO)(PPh$_3$)(CH$_2$)}$_2${POCH$_2$(CH$_2$)$_n$CH$_2$PO}{(CH$_2$)(Ph$_3$P)(ON)Re(η^5-C$_5$H$_5$)}$_2$ (*n* = 0/1, 11/12): (**A**) A Schlenk tube was charged with ($S_{Re}S_{Re}S_{Re}S_{Re}$)-**7**·$(CH_2Cl_2)_2$ (0.120 g, 0.0431 mmol) and THF (10 mL). Then *t*BuOK (1.0 M *in* THF; 0.134 mL, 0.13 mmol) was added dropwise with stirring. After 30 min, the solvent was removed by oil pump vacuum. The remaining workup was conducted in air. The residue was extracted with CH_2Cl_2 (20 mL), and the extract filtered through Celite (2×2 cm). The filtrate was concentrated to ca. 5 mL and layered with ether (10 mL). After 2 days, the supernatant was decanted from a yellow powder, which was dried by oil pump vacuum to give ($S_{Re}S_{Re}S_{Re}S_{Re}$)-**11** (0.0963 g, 0.0409 mmol, 95%). M. p. 195–198 °C (dec). $C_{98}H_{92}N_4O_6P_6Re_4$ (2352.5): calcd. C 50.04, H 3.94, N 2.38; found C 49.81, H 3.63, N 2.09. IR (thin film [cm^{-1}]): $\tilde{\nu}$ = 1637 (s, NO), 1181 (m, PO). ^{1}H NMR (400 MHz, [D$_8$]THF): PPh_3 at δ = 7.53–7.22 (m, 60 H); 5.45 (br. s, 10 H, C_5H_5), 5.29 (br. s, 10 H, $C_5H'_5$), CH_2 at 3.12 (br. s, 2 H), 2.64 (m, 2 H), 2.46 (m, 2 H), 2.24 (m, 4 H), 2.05 (m, 2 H). $^{13}C\{^1H\}$ NMR (100.5 MHz, [D$_8$]THF): PPh_3 at δ = 134.8 [d, ^1J(C,P) = 53 Hz, *i*], 134.4 [d, ^2J(C,P) = 11 Hz, *o*], 132.1 (s, *p*), 131.7 (s, *p'*), 129.8 [d, ^3J(C,P) = 11 Hz, *m*], 129.6 [d, ^3J(C,P) = 9 Hz, *m'*]; 92.4 (s, C_5H_5), 91.0 (s, C'_5H_5), 28.7 [d, ^1J(C,P) = 56 Hz, P*C*H$_2$C], –18.3 [d, ^1J(C,P) = 22 Hz, ReCH$_2$], –22.8 [d, ^1J(C,P) = 39 Hz, ReC′H$_2$]. $^{31}P\{^1H\}$ NMR (161.8 MHz, [D$_8$]THF or $CDCl_3$): δ = 88.2 or 80.5 [apparent t, ^3J(P,P) = 17 Hz, or br. s, PO], 25.6 or 28.3 [d, ^3J(P,P) = 16 Hz, or br. s, PPh_3], 21.2 or 26.4 [d, ^3J(P,P) = 18 Hz, or br. s, P′Ph$_3$]. MS (FAB, 3-NBA): *m/z* (%) = 2353 (5) $[M]^+$, 2337 (4) $[M - O]^+$, 558 (100) $[(\eta^5\text{-}C_5H_5)Re(NO)(PPh_3)(CH_2)]^+$.

(**B**) A Schlenk flask was charged with ($S_{Re}S_{Re}S_{Re}S_{Re}$)-**7** (0.131 g, 0.0501 mmol) and THF (10 mL). Then *t*BuOK (1.0 M in THF; 0.16 mL, 0.16 mmol) was added dropwise with stirring. After 10 min, PhIO (0.034 g, 0.16 mmol)[39] was added. The mixture turned orange. After 2.5 h, the solvent was removed by rotary evaporation. The residue was extracted with benzene (6×5 mL). The extracts were filtered through Celite (2×4 cm). The orange filtrate was concentrated by rotary evaporation to ca. 2 mL, and hexanes (80 mL) were added with vigorous stirring. The yellow-orange precipitate was collected by filtration, washed with hexanes (5 mL), and dried by oil pump vacuum to give ($S_{Re}S_{Re}S_{Re}S_{Re}$)-**11** (0.085 g, 0.036 mmol, 72%). M. p. 200–203 °C (dec). $C_{98}H_{92}N_4O_6P_6Re_4$ (2352.5): calcd. C 50.04, H 3.94, N 2.38; found C 50.41, H 4.23, N 2.08.

(**C**) Complex ($S_{Re}S_{Re}S_{Re}S_{Re}$)-**8** (0.131 g, 0.0499 mmol), THF (10 mL), *t*BuOK (1.0 M *in* THF; 0.16 mL, 0.16 mmol), and PhIO (0.034 g, 0.16 mmol)[39] were combined in a procedure analogous to **B**. A similar workup (precipitation with 50 mL of hexanes; washing with 2 mL) gave ($S_{Re}S_{Re}S_{Re}S_{Re}$)-**12** (0.074 g, 0.0031 mmol, 62%) that typically contained ca. 5% of Ph_3PO. M. p. 190–192 °C (dec). IR (thin film [cm^{-1}]): $\tilde{\nu}$ = 1629 (s, NO), 1183 (w, PO). ^{1}H NMR (500 MHz, $CDCl_3$): PPh_3 at δ = 7.69–7.06 (m, 60 H); 5.17 (s, 10 H, C_5H_5), 5.09 (s, 10 H, $C_5H'_5$), CH_2 at 2.18, 2.08, 1.78, 1.63, 1.48, 1.11 (6 m, 12 H). $^{13}C\{^1H\}$ NMR (125.7 MHz, $CDCl_3$): PPh_3 at δ = 136.5 [d, ^1J(C,P) = 51 Hz, *i*], 136.1 [d, ^1J(C,P) = 52 Hz, *i'*], 133.7 [d, ^2J(C,P) = 12 Hz, *o*], 133.6 [d, ^2J(C,P) = 10 Hz, *o'*], 129.9 (s, *p*), 128.3 [d, ^3J(C,P) = 9 Hz, *m*], 128.3 [d, ^3J(C,P) = 9 Hz, *m'*]; 90.6 (s, C_5H_5), 90.5 (s, C'_5H_5), 35.2 [d, ^1J(C,P) = 12 Hz, P*C*H$_2$C], 34.7 [d, ^2J(C,P) = 13 Hz, C*C*H$_2$C], –13.0 [d, ^1J(C,P) = 57 Hz, ReCH$_2$], –13.5 [d, ^1J(C,P) = 72 Hz, ReC′H$_2$]. $^{31}P\{^1H\}$ NMR (202.4 MHz, $CDCl_3$): δ = 78.8 [apparent t, ^3J(P,P) = 13 Hz, PO], 26.7 [d, ^3J(P,P) = 15 Hz, PPh_3], 26.5 [d, ^3J(P,P) = 13 Hz, P′Ph$_3$]. MS (FAB, 3-NBA): *m/z* (%) = 2367 (9) $[M]^+$, 544 (100) $[(\eta^5\text{-}C_5H_5)Re(NO)(PPh_3)]^+$.

 © 2005 Wiley-VCH Verlag GmbH & Co. KGaA, Weinheim

[({(η^5-C_5H_5)Re(NO)(PPh_3)(CH_2)}$_2${$PCH_2(CH_2)_nCH_2P$}{(CH_2)-(Ph_3P)(ON)Re(η^5-C_5H_5)}$_2$)Rh(NBD)]$^+$ PF_6^- [*n* = 0/1, 13/14 (see Scheme 1)**]:** (**A**) A glass vial was charged with ($S_{Re}S_{Re}S_{Re}S_{Re}$)-**7**·(CH_2Cl_2)$_2$ (0.124 g, 0.0447 mmol) and THF (5 mL) in a glove box. Then *t*BuOK (1.0 M *in* THF; 0.107 mL, 0.11 mmol) was added dropwise with stirring. The vial was sealed with a screw cap. After 30 min, the solvent was removed by oil pump vacuum. The orange powder was extracted with toluene (5 mL) in a glove box. The extract was passed through a PTFE syringe filter. Then [Rh(NBD)$_2$]$^+$ PF_6^- (0.0193 g, 0.0447 mmol)[40] was added with stirring. After 1 h, pentane (20 mL) was added dropwise. After 30 min, the precipitate was collected by filtration and dissolved in $CHCl_3$ (5 mL). A layer of pentane was gently added. After 2 days, the supernatant was decanted and the red-brown powder dried by oil pump vacuum to give ($S_{Re}S_{Re}S_{Re}S_{Re}$)-**13**·($CHCl_3$)$_2$ (0.093 g, 0.032 mmol, 75%). M. p. 230–235 °C (dec). $C_{105}H_{100}F_6N_4O_4P_8Re_4Rh$·($CHCl_3$)$_2$ (2899.3): calcd. C 44.33, H 3.55, N 1.93; found C 44.26, H 3.86, N 1.72. IR (thin film [cm^{-1}]): ṽ = 1630 (s, NO), 834 (s, PF). ^{1}H NMR (400 MHz, [D$_8$]THF): PPh_3 at δ = 7.38–7.36 (m, 32 H), 7.29–7.24 (m, 18 H), 7.14–7.11 (m, 10 H); 7.27 (s, 2 H, $CHCl_3$), 5.20 (s, 10 H, C_5H_5), 5.14 (s, 10 H, $C_5H'_5$), NBD at 5.45 (br. s, 4 H, =CH),[41] 3.16 (br. s, 2 H, bridgehead CH),[41] 1.68 (br. s, 2 H, CH_2); CH_2 at 2.48–2.42 (m, 2 H), 2.20–2.01 (m, 10 H). ^{13}C{^{1}H} NMR (100.5 MHz, [D$_8$]THF): PPh_3 at δ = 136.2 [d, ^1J(C,P) = 53 Hz, *i*], 136.0 [d, ^1J(C,P) = 51 Hz, *i'*], 135.1 [d, ^2J(C,P) = 11 Hz, *o*], 134.9 [d, ^2J(C,P) = 10 Hz, *o'*], 131.1 (s, *p*), 130.9 (s, *p'*), 129.5 [d, ^3J(C,P) = 10 Hz, *m*], 129.3 [d, ^3J(C,P) = 10 Hz, *m'*]; 91.3 (s, C_5H_5), 90.0 (s, C'_5H_5), 77.0 (s, $CHCl_3$), NBD at 91.2/91.0 (2 br. s, =CH),[41] 81.6/80.0 (2 m, bridgehead CH),[41] 54.8 (br. s, CH_2); 31.9 (m, P*C*H$_2$C), –16.3 (m, Re*C*H$_2$), –21.5 (m, Re*C'*H$_2$). ^{31}P{^{1}H} NMR (161.8 MHz, [D$_8$]THF): δ = 97.3 [dt, ^1J(P,Rh) = 150, ^3J(P,P) = 9 Hz, P*C*H$_2$], 27.1 [d, ^3J(P,P) = 9 Hz, PPh_3], 26.0 [d, ^3J(P,P) = 9 Hz, P'Ph$_3$], –143.5 [sept, ^1J(P,F) = 709 Hz, PF_6]. MS (FAB, 3-NBA): *m*/*z* (%) = 2516 (8) [M]$^+$, 558 (100) [(η^5-C_5H_5)Re(NO)(PPh_3)(CH_2)]$^+$.

(**B**) Complex ($R_{Re}R_{Re}R_{Re}R_{Re}$)-**8**·(CH_2Cl_2)$_2$ (0.120 g, 0.0428 mmol), THF (5 mL), *t*BuOK (1.0 M in THF; 0.094 mL, 0.094 mmol), and [Rh(NBD)$_2$]$^+$ PF_6^- (0.0185 g, 0.0428 mmol)[40] were combined in a procedure analogous to **A**. The crude product was dissolved in THF (5 mL) and pentane (20 mL) was added with stirring. The brown powder was collected by filtration and dried by oil pump vacuum to give ($R_{Re}R_{Re}R_{Re}R_{Re}$)-**14** (0.094 g, 0.035 mmol, 82%). M. p. 223–226 °C (dec). $C_{106}H_{102}F_6N_4O_4P_7Re_4Rh$ (2674.6): calcd. C 47.60, H 3.84, N 2.09; found C 47.19, H 4.09, N 2.05. IR (thin film [cm^{-1}]): ṽ = 1640 (vs, NO), 842 (s, PF). ^{1}H NMR (400 MHz, [D$_8$]THF): PPh_3 at δ = 7.46–7.40 (m, 60 H); 5.28 (s, 10 H, C_5H_5), 4.39 (br. s, 10 H, $C_5H'_5$), NBD at 5.23/5.20 (2 br. s, 4 H, =CH),[41] 3.89/3.75 (2 br. s, 2 H, bridgehead CH),[41] 1.49 (br. s, 2 H, CH_2); CH_2 at 2.65–2.55 (m, 4 H), 1.98–1.92 (m, 2 H), 1.62–1.55 (m, 8 H). ^{13}C{^{1}H} NMR (100.5 MHz, [D$_8$]THF): PPh_3 at δ = 137.2 [d, ^1J(C,P) = 52 Hz, *i*], 136.9 [d, ^1J(C,P) = 50 Hz, *i'*], 134.6 [d, ^2J(C,P) = 12 Hz, *o*], 134.4 [d, ^2J(C,P) = 12 Hz, *o'*], 131.3 (s, *p*), 131.1 (s, *p'*), 129.7 [d, ^3J(C,P) = 10 Hz, *m*], 129.3 [d, ^3J(C,P) = 10 Hz, *m'*]; 91.7 (s, C_5H_5), 91.5 (s, C'_5H_5), NBD at 91.9/91.8 (2 br. s, =CH),[41] 77.7/73.5 (2 m, bridgehead CH),[41] 53.7 (br. s, CH_2); 29.1 [dd, J(C,P) = 16, J(C,P) = 4 Hz, P*C*H$_2$C], 23.5 [t, ^2J(C,P) = 6 Hz, C*C*H$_2$C], –13.2 (m, Re*C*H$_2$), –14.1 (m, Re*C'*H$_2$). ^{31}P{^{1}H} NMR (161.8 MHz, [D$_8$]THF): δ = 53.7 [d, ^1J(P,Rh) = 141 Hz, P*C*H$_2$], 24.3 (br. s, PPh_3), 21.7 (br. s, P'Ph$_3$), –143.5 [sept, ^1J(P,F) = 709 Hz, PF_6]. MS (FAB, 3-NBA): *m*/*z* (%) = 2529 (6) [M]$^+$, 558 (100) [(η^5-C_5H_5)Re(NO)(PPh_3)(CH_2)]$^+$.

Relative Brønsted Basicities: A 5-mm NMR tube was charged with ($S_{Re}S_{Re}S_{Re}S_{Re}$)-**7** (0.0196 g, 0.0075 mmol), [(η^5-C_5H_5)Re(NO)(PPh_3)(CH_2PPh_2H)]$^+$ PF_6^- (0.0133 g, 0.015 mmol),[4a] and CD_2Cl_2 (0.60 mL) in a glove box. A reference ^{31}P{^{1}H} NMR spectrum was recorded. Then *t*BuOK (1.0 M in THF; 0.015 mL, 0.015 mmol) was added. The orange solution became darker. After 1 h, a ^{31}P{^{1}H} NMR spectrum showed complete conversion of [(η^5-C_5H_5)Re(NO)(PPh_3)(CH_2PPh_2H)]$^+$ PF_6^- to (η^5-C_5H_5)Re(NO)(PPh_3)(CH_2PPh_2) and no reaction of ($S_{Re}S_{Re}S_{Re}S_{Re}$)-**7**.

Hydrogenations: A Fisher–Porter bottle was charged with **7** or **8** (0.012 mmol) and THF (10 mL) in a glove box, and *t*BuOK (1.0 M in THF; 0.028 mL, 0.028 mmol) was added with stirring. After 5 min, [Rh(NBD)$_2$]$^+$ PF_6^- (0.0043 g, 0.010 mmol)[40] was added, giving an orange solution. After 30 min, **15** (2.00 mmol; Scheme 4) and THF (10 mL) were added. The bottle was closed under argon and purged with H_2 (75 psi, 3 ×). The mixture was vigorously stirred under H_2 (120 psi, 8 bar, 75 °C). After 1–2 h, **16** was isolated by a standard workup.[2b,2e] Configurations and enantiomeric purities were determined as described previously.[2b,2e]

Hydrosilylations: A glass vial was charged with **7** or **8** (0.0052 mmol) and THF (5 mL) in a glove box, and *t*BuOK (1.0 M *in* THF; 0.0125 mL, 0.012 mmol) was added with stirring. After 5 min, [Rh(NBD)$_2$]$^+$ PF_6^- (0.0022 g, 0.0050 mmol)[40] was added. After 30 min, **17** (0.184 g, 1.00 mmol; Scheme 4), and Ar_2SiH_2 (1.2 mmol) were added, and the vial sealed with a screw cap. The sample was stirred (24–26 °C, glove box). Aliquots were dissolved in $CDCl_3$ and the ^{1}H NMR signals of **17** integrated against those of **18**.[2e] After 14 days, a saturated solution of K_2CO_3 in methanol was added (1 mL). After 1 h, the solvents were removed by oil pump vacuum and the residue filtered through a silica gel column (4 × 1 cm) using hexanes. This gave crude 1-phenyl-1-propanol, the enantiomeric purity of which was assayed by GC (Lipodex-E).

Conjugate Additions: A Schlenk tube was charged with **7** or **8** (0.0144 mmol) and dioxane (1 mL) in a glove box, and *t*BuOK (1.0 M in THF, 0.03 mL, 0.03 mmol) was added with stirring. After 30 min, Rh(acac)(H_2C=CH_2)$_2$ (0.0031 g, 0.012 mmol)[42] was added, giving a brown mixture. After 30 min, phenylboronic acid (0.244 g, 2.00 mmol) and **19** (0.039 mL, 0.039 g, 0.40 mmol; Scheme 3) were added. After 15 min, H_2O (0.100 mL) was added, giving a brown solution. The sample was stirred under argon at 100 °C. After 5 h, the dark brown solution was cooled to room temperature. Saturated aqueous $NaHCO_3$ (5 mL) was added. The organic layer was separated. The aqueous layer was extracted with CH_2Cl_2 (3 × 5 mL). The combined organic phases were dried ($MgSO_4$). Hexanes (10 mL) were added, and the solution was filtered through a silica gel pad (2 × 3 cm) using hexanes/EtOAc (5:1 v/v, 2 × 5 mL; this removes rhodium complex). Decane (0.039 mL, 0.029 g, 0.20 mmol; internal standard) was added to the filtrate. The yield of **20** was assayed by GC (OPTIMA-5). The solution was filtered through a silica gel column using hexanes/EtOAc (5:1 v/v) and the enantiomeric purity was assayed by HPLC (Chiralcel OD). NMR: See Supporting Information.

Allylic Alkylations: A Schlenk tube was charged with **7** or **8** (0.0180 mmol) and CH_2Cl_2 (1 mL) in a glove box, and *t*BuOK (1.0 M in THF, 0.054 mL, 0.054 mmol) was added with stirring. After 5 min, [Pd(η^3-C_3H_5)Cl]$_2$ (0.0027 g, 0.0074 mmol) was added, followed by a solution of **21** (0.0757 g, 0.300 mmol; Scheme 4)[43] in CH_2Cl_2 (1 mL). A vial was charged with dimethyl malonate (0.103 mL, 0.119 g, 0.901 mmol), CH_3(C=NTMS)OTMS (0.220 mL, 0.183 g, 0.900 mmol), KOAc (0.0015 g, 0.015 mmol), and CH_2Cl_2 (1 mL). This mixture was added dropwise to the Schlenk tube with stirring. After 24 h, ether (15 mL) was added. The mixture was washed with cold, saturated aqueous NH_4Cl (2 × 7.5 mL), dried (Na_2SO_4), and concentrated by rotary evaporation. Flash chromatography on silica gel (1.5 × 17 cm, 3:1 v/v, hex-

 © 2005 Wiley-VCH Verlag GmbH & Co. KGaA, Weinheim

anes/EtOAc, R_f = 0.68) gave a slightly yellow oil that when dried by oil pump vacuum afforded **22** as white solid. The enantiomeric purity was analyzed by HPLC (Chiralcel OD). NMR: See Supporting Information.

X-ray Crystallography: Data were collected on ($S_{Re}S_{Re}S_{Re}S_{Re}$)-**7**·$(CH_2Cl_2)_2$ (see above) as outlined in Table 2. Cell parameters were obtained from 10 frames using a 10° scan and refined with 12270 reflections. Lorentz, polarization and absorption corrections were applied.[44] The space group was determined from systematic absences and subsequent least-squares refinement. The structure was solved by direct methods. The parameters were refined with all data by full-matrix-least-squares on F^2 using SHELXL-97.[45] Non-hydrogen atoms were refined with anisotropic thermal parameters. The hydrogen atoms were fixed in idealized positions using a riding model. Scattering factors were taken from the literature.[46] The asymmetric unit contained a half molecule of the tetrarhenium complex. Three fluorine atoms of one PF_6^- anion (F33, F34, and F35) were disordered about a symmetry axis and were refined with an occupancy ratio of 50:50. The rhenium configuration was established by Flack's *x* parameter [found: –0.018(7); theory for correct and inverted structures: 0 and 1].[47]

Table 2. Crystallographic data for ($S_{Re}S_{Re}S_{Re}S_{Re}$)-**7**·$(CH_2Cl_2)_2$.

Molecular formula	$C_{100}H_{98}Cl_4F_{12}N_4O_4P_8Re_4$
Molecular mass	2782.18
Temp. of collection [°C]	–100(2)
Diffractometer	KappaCCD
Radiation [Å]	Mo-K_α
Crystal system	tetragonal
Space group	$P4_22_12$
Unit cell dimensions:	
a [Å]	20.5410(2)
b [Å]	20.5410(2)
c [Å]	24.5424(3)
V [Å^3]	10355.2(2)
Z	4
$\rho_{calcd.}$ [Mg·m^{-3}]	1.785
μ [mm^{-1}]	4.961
Crystal dimensions, mm	0.30 × 0.30 × 0.25
Θ Range [°]	1.29 ≤ Θ ≤ 27.88
Range/indices (*h*,*k*,*l*)	–27,27; –19,19; –32,32
No. of reflections	24377
No. of unique data	12348
No. of observed data	8896 [$I > 2\sigma(I)$]
No. refined parameters	608
Refinement	least-squares on F^2
R_{int}	0.0598
R indices [$I > 2\sigma(I)$]	R_1 = 0.0380
	wR_2 = 0.0757
R indices (all data)	R_1 = 0.0751
	wR_2 = 0.0952
Goodness of fit	1.007
Largest diff. peak/hole [e·Å^{-3}]	1.451/–0.926

CCDC-265274 contains the supplementary crystallographic data for this paper. These data can be obtained free of charge at www.ccdc.cam.ac.uk/conts/retrieving.html [or from the Cambridge Crystallographic Data Centre, 12 Union Road, Cambridge CB2 1EZ, UK; Fax: +44-1223-336-033; E-mail: deposit@ccdc.cam.ac.uk].

Supporting Information: Sources and purification of starting materials; independent characterization of enantiomeric complexes, NMR spectroscopic data for known compounds, and polarimetric data.

Acknowledgments

We thank the Deutsche Forschungsgemeinschaft (DFG; GL 300–4/1) and Johnson Matthey PMC (rhodium and palladium loans) for support.

[1] Review of non-ferrocene-based metal-containing bidentate ligands: O. Delacroix, J. A. Gladysz, *Chem. Commun.* **2003**, 665.
[2] a) B. D. Zwick, A. M. Arif, A. T. Patton, J. A. Gladysz, *Angew. Chem. Int. Ed. Engl.* **1987**, *26*, 910; *Angew. Chem.* **1987**, *99*. 921; b) K. Kromm, B. D. Zwick, O. Meyer, F. Hampel, J. A. Gladysz, *Chem. Eur. J.* **2001**, *7*, 2015; c) K. Kromm, F. Hampel, J. A. Gladysz, *Helv. Chim. Acta* **2002**, *85*, 1778; d) K. Kromm, F. Hampel, J. A. Gladysz, *Organometallics* **2002**, *21*, 4264; e) K. Kromm, P. L. Osburn, J. A. Gladysz, *Organometallics* **2002**, *21*, 4275.
[3] L. J. Alvey, O. Delacroix, C. Wallner, O. Meyer, F. Hampel, S. Szafert, T. Lis, J. A. Gladysz, *Organometallics* **2001**, *20*, 3087.
[4] a) S. Eichenseher, O. Delacroix, K. Kromm, F. Hampel, J. A. Gladysz, *Organometallics* **2005**, *24*, 245; b) J. Giner Planas, F. Hampel, J. A. Gladysz, *Chem. Eur. J.* **2005**, *11*, 1402; c) F. K. Friedlein, F. Hampel, J. A. Gladysz submitted for publication.
[5] Reviews since 2003: a) L.-X. Dai, T. Tu, S.-L. You, W.-P. Deng, X.-L. Hou, *Acc. Chem. Res.* **2003**, *36*, 659; b) T. J. Colacot, *Chem. Rev.* **2003**, *103*, 3101; c) R. C. J. Atkinson, V. C. Gibson, N. J. Long, *Chem. Soc. Rev.* **2004**, *33*, 313; d) P. Barbaro, C. Bianchini, G. Giambastiani, S. L. Parisel, *Coord. Chem. Rev.* **2004**, *248*, 2131.
[6] D. Rais, R. G. Bergman, *Chem. Eur. J.* **2004**, *10*, 3970, and earlier papers cited therein.
[7] For other possible contributing factors, see: P. L. Holland, R. A. Andersen, R. G. Bergman, *Comments Inorg. Chem.* **1999**, *21*, 115.
[8] Lead references from 2004 and 2005: a) C. Bolm, L. Xiao, L. Hintermann, T. Focken, G. Raabe, *Organometallics* **2004**, *23*, 2363; b) S. E. Gibson, H. Ibrahim, C. Pasquier, V. M. Swamy, *Tetrahedron: Asymmetry* **2004**, *15*, 465; c) R. G. Arrayás, O. G. Mancheño, J. C. Carretero, *Chem. Commun.* **2004**, 1654; d) R. S. Prasad, C. E. Anderson, C. J. Richards, L. E. Overman, *Organometallics* **2005**, *24*, 77; e) F.-E. Hong, Y.-J. Ho, Y.-C. Chang, Y.-L. Huang, *J. Organomet. Chem.* **2005**, *690*, 1249.
[9] F. Agbossou, E. J. O'Connor, C. M. Garner, N. Quirós Méndez, J. M. Fernández, A. T. Patton, J. A. Ramsden, J. A. Gladysz, *Inorg. Synth.* **1992**, *29*, 211.
[10] Additional details of this study can be found as follows: a) K. Kromm, Doctoral Thesis, University of Erlangen-Nürnberg, **2002**; b) S. Eichenseher, Doctoral Thesis, University of Erlangen-Nürnberg, **2005**.
[11] R. W. Alder, C. Ganter, M. Gil, R. Gleiter, C. J. Harris, S. E. Harris, H. Lange, A. G. Orpen, P. N. Taylor, *J. Chem. Soc. Perkin Trans. 1* **1988**, 1643.
[12] Chiral compounds not preceded by *R*/*S* descriptors are racemic. Rhenium configurations are designated by a modified Cahn–Ingold–Prelog system: a) K. Stanley, M. C. Baird, *J. Am. Chem. Soc.* **1975**, *97*, 6598; b) T. E. Sloan, *Top. Stereochem.* **1981**, *12*, 1; c) The priority sequence for ligands in this study is (η^5-C_5H_5) > PPh_3 > NO > CH_2P > CH_3 > CH_2.
[13] Both enantiomers of all compounds derived from $PH_2CH_2(CH_2)_nCH_2PH_2$ were prepared. For clarity of presentation, the configurations of the lead series with *n* = 1 have been inverted in sections 1 and 2 of the results section. Data for enantiomers that were independently characterized are collected in the supporting information.
[14] J. H. Merrifield, C. E. Strouse, J. A. Gladysz, *Organometallics* **1982**, *1*, 1204.
[15] A low temperature deprotonation of a chiral $[FePPhH_2]^+$ species shows a 4:1 selectivity for the two diastereotopic protons: G. T. Crisp, G. Salem, F. S. Stephens, S. B. Wild, *J. Chem. Soc. Chem. Commun.* **1987**, 600.

 © 2005 Wiley-VCH Verlag GmbH & Co. KGaA, Weinheim

[16] a) A. Rauk, L. C. Allen, K. Mislow, *Angew. Chem. Int. Ed. Engl.* **1970**, *9*, 400; *Angew. Chem.* **1970**, *82*, 453; b) R. D. Baechler, K. Mislow, *J. Am. Chem. Soc.* **1970**, *92*, 3090.
[17] W. E. Buhro, B. D. Zwick, S. Georgiou, J. P. Hutchinson, J. A. Gladysz, *J. Am. Chem. Soc.* **1988**, *110*, 2427.
[18] a) G. T. Crisp, G. Salem, S. B. Wild, F. S. Stephens, *Organometallics* **1989**, *8*, 2360; b) E. Hey-Hawkins, S. Kurz, *J. Organomet. Chem.* **1994**, *479*, 125; c) W. Malisch, N. Gunzelmann, K. Thirase, M. Neumayer, *J. Organomet. Chem.* **1998**, *571*, 215.
[19] T. Hayashi, K. Yamasaki, *Chem. Rev.* **2003**, *103*, 2829.
[20] a) Y. Takaya, M. Ogasawara, T. Hayashi, M. Sakai, N. Miyaura, *J. Am. Chem. Soc.* **1998**, *120*, 5579; b) For the conditions employed, see: M. T. Reetz, D. Moulin, A. Gosberg, *Org. Lett.* **2001**, *3*, 4083.
[21] Recent reviews: a) B. M. Trost, *Chem. Pharm. Bull.* **2002**, *50*, 1; b) B. M. Trost, C. Lee, In: *Catalytic Asymmetric Synthesis*, 2nd ed.; (Ed.: I. Ojima); Wiley-VCH: New York, **2000**, p. 593; c) G. Helmchen, *J. Organomet. Chem.* **1999**, *576*, 203; d) A. Pfaltz, M. Lautens, In: *Comprehensive Asymmetric Catalysis*, vol. II (Eds.: E. N. Jacobsen, A. Pfaltz, H. Yamamoto); Springer: Berlin, **1999**, Chapter 24; e) B. M. Trost, D. L. van Vranken, *Chem. Rev.* **1996**, *96*, 395.
[22] T. P. Yoon, E. N. Jacobsen, *Science* **2003**, *299*, 1691.
[23] F. B. McCormick, W. B. Gleason, X. Zhao, P. C. Heah, J. A. Gladysz, *Organometallics* **1986**, *5*, 1778.
[24] O. Meyer, A. M. Arif, J. A. Gladysz, *Organometallics* **1995**, *14*, 1844.
[25] T.-S. Peng, A. M. Arif, J. A. Gladysz, *J. Chem. Soc. Dalton Trans.* **1995**, 1857.
[26] See also: a) I. Saura-Llamas, J. A. Gladysz, *J. Am. Chem. Soc.* **1992**, *114*, 2136; b) M. A. Dewey, G. A. Stark, J. A. Gladysz, *Organometallics* **1996**, *15*, 4798.
[27] a) T. P. Dang, H. B. Kagan, *J. Chem. Soc. D* **1971**, 481; b) H. B. Kagan, T. P. Dang, *J. Am. Chem. Soc.* **1972**, *94*, 6429.
[28] M. D. Fryzuck, B. Bosnich, *J. Am. Chem. Soc.* **1977**, *99*, 6262.
[29] a) O. Korpiun, R. A. Lewis, J. Chickos, K. Mislow, *J. Am. Chem. Soc.* **1968**, *90*, 4842; b) B. D. Vineyard, W. S. Knowles, M. J. Sabacky, G. L. Bachman, D. J. Weinkauff, *J. Am. Chem. Soc.* **1977**, *99*, 5946; c) W. S. Knowles, *Angew. Chem. Int. Ed.* **2002**, *41*, 1998; *Angew. Chem.* **2002**, *114*, 2096.
[30] M. J. Burk, *Acc. Chem. Res.* **2000**, *33*, 363.
[31] V. Prelog, G. Helmchen, *Helv. Chim. Acta* **1972**, *55*, 2581.
[32] A pseudoasymmetric atom has four distinct ligands, two of which are enantiomorphic: E. L. Eliel, S. H. Wilen, *Stereochemistry of Organic Compounds*, Wiley-Interscience: New York, **1994**, p. 66 and 1204.
[33] D. Guillaneux, L. Martiny, H. B. Kagan, *Collect. Czech. Chem. Commun.* **2000**, *65*, 717.
[34] a) S. E. Denmark, J. Fu, *Chem. Rev.* **2003**, *103*, 2763; b) Yanagisawa, A., In: *Comprehensive Asymmetric Catalysis*, vol. II (Eds.: E. N. Jacobsen, A. Pfaltz, H. Yamamoto), Springer: Berlin, **1999**, Chapter 27.
[35] F. Seidel, Diplom Thesis, University of Erlangen-Nürnberg, **2004**.
[36] Y. Zhou, M. A. Dewey, Y. Liu, J. A. Gladysz, *Organometallics* **1993**, *12*, 3918.
[37] If the (*S*)-**1** is more than a few days old, it is best to first dissolve it in CH_2Cl_2, and filter the solution through a silica gel plug directly into the Schlenk flask.
[38] The complexes ($S_{Re}S_{Re}S_{Re}S_{Re}$)-**7** and ($R_{Re}R_{Re}R_{Re}R_{Re}$)-**8** were reproducibly obtained as crystalline or microcrystalline dichloromethane disolvates. However, using similar conditions, other co-workers reproducibly obtained the enantiomers ($R_{Re}R_{Re}R_{Re}R_{Re}$)-**7** and ($S_{Re}S_{Re}S_{Re}S_{Re}$)-**8** as unsolvated powders (supporting information). Subtle aspects of the workup are believed to control the outcome.
[39] H. Saltzman, J. G. Sharefkin, *Organic Syntheses*, Collect. vol. V, Wiley: New York, **1973**, p. 658.
[40] a) N. J. O'Reilly, W. S. Derwin, H. C. Lin, *Synthesis* **1990**, 550; b) Our own independent data for $[Rh(NBD)_2]^+$ PF_6^- are given in the supporting information.
[41] Tentative assignment; this broad signal is consistent with dynamic behavior observed with other chiral rhodium NBD complexes. See: a) H. Berger, R. Nesper, P. S. Pregosin, H. Rüegger, M. Wörle, *Helv. Chim. Acta* **1993**, *76*, 1520; b) M. Valentini, K. Selvakumar, M. Wörle, P. S. Pregosin, *J. Organomet. Chem.* **1999**, *587*, 244; c) B. Crociani, S. Antonaroli, M. L. Di Vona, S. Licoccia, *J. Organomet. Chem.* **2001**, *631*, 117.
[42] R. Cramer, *Inorg. Synth.* **1974**, *15*, 14.
[43] W. Leung, S. Cosway, R. H. V. Jones, H. McCann, M. Wills, *J. Chem. Soc. Perkin Trans. 1* **2001**, 2588.
[44] a) "Collect" data collection software, Nonius B.V., **1998**; b) "Scalepack" data processing software: Z. Otwinowski, W. Minor, *Methods Enzymol.* **1997**, *276*, 307 (Macromolecular Crystallography, part A).
[45] G. M. Sheldrick, *SHELX-97*, Program for refinement of crystal structures, University of Göttingen, **1997**.
[46] D. T. Cromer, J. T. Waber, In: *International Tables for X-ray Crystallography* (Eds.: J. A. Ibers, W. C. Hamilton), Kynoch: Birmingham, England, **1974**.
[47] H. D. Flack, *Acta Cryst., Sect. A* **1983**, *39*, 876.

Received: March 23, 2005
Published Online: July 4, 2005

 © 2005 Wiley-VCH Verlag GmbH & Co. KGaA, Weinheim

The Reductive Elimination of Methane from *ansa*-Hydrido(methyl)metallocenes of Molybdenum and Tungsten: Application of Hammond's Postulate to Two-State Reactions

José-Luis Carreón-Macedo,[a] Jeremy N. Harvey,*[a] and Rinaldo Poli*[b]

Keywords: Density functional theory / Metallocenes / Minimum energy crossing points / Hammond's postulate / Spin crossover reactivity

The energetic profile of the methane reductive elimination from a selected number of hydrido(methyl)molybdenocene and -tungstenocene derivatives has been calculated by DFT methods. The calculations were carried out for the $CH_2(C_5H_4)_2M$ (*a*-M), $SiH_2(C_5H_4)_2M$ (*a*-H_2Si–M), and Si$Me_2(C_5Me_4)_2M$ (*a*-Me_2Si–M*) *ansa*-metallocene systems for M = Mo, W. They include the full optimization of minima [the hydrido(methyl) starting complexes, M(H)(CH_3), the intermediate methane complexes, M(CH_4), and the metallocene products in the singlet and triplet configurations, (^{3}M and ^{1}M)], transition states (for the methyl hydride reductive elimination, M–TS_{ins}, and for the hydrogen exchange, M–TS_{exch}), and the minimum energy crossing point (M–MECP) leading from the singlet methane complexes to the corresponding triplet metallocenes. The results are compared with those previously obtained for the simpler $(C_5H_5)_2M$ (Cp_2M) systems (J. C. Green, J. N. Harvey, and R. Poli, *J. Chem. Soc., Dalton Trans.* **2002**, 1861). The calculated energy profiles, notably the relative energies of M–TS_{ins} and M–MECP, are in agreement with available experimental observations for the *a*-Me_2Si–M* systems. The comparison of the energies and geometries of the rate-determining M–TS_{ins} and M–MECP structures with those of the thermodynamically relevant minima for the various systems show the applicability of Hammond's postulate to two-state reactions. However, one notable exception serves to show that the principle is only quantitatively reliable when all the potential energy surfaces for the set of analogous reactions have similar shapes.
(© Wiley-VCH Verlag GmbH & Co. KGaA, 69451 Weinheim, Germany, 2005)

Introduction

The reductive elimination of alkyl hydride complexes to liberate a molecule of saturated alkane is a fundamental step in catalytic hydrogenation,[1,2] whereas the reverse process is relevant for the functionalization of hydrocarbons.[3,4] Both have been topics of intense investigation.[5–7] A particular class of compounds that has attracted considerable attention is the family of the Group 6 metallocenes, Cp′$_2$M(H)(R) (M = Mo, W; Cp′ = any cyclopentadienyl ligand),[8–13] in particular with R = CH_3, involving the formation and/or activation of methane. An interesting feature of this family (shared with other systems) is that the 16-electron complex Cp′$_2$M has a different spin state – a triplet – from that of the diamagnetic Cp′$_2$M(H)(R).[14–17] Thus, the process that interconverts the two complexes is a two-state reaction.[18] Experimental work suggests that the elimination of methane from Cp′$_2$M(H)(CH_3) proceeds via σ-CH_4 intermediates, Cp′$_2$M(η^2-CH_4) where the CH_4 ligand coordinates through the electrons of one σ-C–H bond, because scrambling processes between the hydride and the methyl H atoms have sometimes been found by deuterium labeling experiments to be competitive or faster than the elimination process. Theoretical studies have addressed this issue and confirmed the existence of such intermediates, which possess a singlet ground state like the alkyl(hydrido) reagent.[15,17] In addition, these studies have identified the transition states leading to the H exchange and the oxidative addition.

However, to fully understand the reaction coordinate leading to the elimination products, it is also necessary to explicitly determine the minimum energy crossing point (MECP) between the singlet and triplet surfaces. As shown schematically in Figure 1, crossing occurs during the elimination process of the CH_4 ligand from the coordination sphere of the intermediate σ-CH_4 complex, M(CH_4), leading to the triplet metallocene, ^{3}M.[17] There are two possible limiting scenarios. In the first one (part a of Figure 1), the insertion transition state (M–TS_{ins}) leading from the M(CH_4) intermediate to the hydrido(methyl) complex, M(H)(Me), has a lower energy than the MECP (M–MECP). When this is the case, provided the exchange of the coordinated C–H bond for the methane ligand also occurs through a lower energy transition state (M–TS_{exch}) than the M–MECP, the hydrogen scrambling process is faster than

[a] School of Chemistry, University of Bristol, Cantock's Close, Bristol BS8 1TS, UK
[b] Laboratoire de Chimie de Coordination, CNRS, 205 Route de Narbonne, 31077 Toulouse cedex, France
Fax: +33-561553003
E-mail: poli@lcc-toulouse.fr

the methane elimination. This situation can be kinetically defined as a pre-equilibrium between the starting M(H)(Me) complex and the intermediate M(CH_4) complex, followed by rate-limiting methane dissociation, in which the overall rate is controlled by the M–MECP energy. In the second scenario (part b of Figure 1), the energy of M–TS_{ins} is higher than the M–MECP. In this case, the methane elimination is kinetically a one-step process determined by the M–TS_{ins} energy, and no H scrambling is observed. In our previous computational study of this phenomenon for the simple metallocenes of Mo and W, Cp_2M,[17] which included the explicit calculation of M–TS_{ins} and M–MECP geometries and energies, we found that E(M–TS_{ins}) > E(M–MECP) for Cp_2Mo [31.0 and 4.3 kJ mol^{-1}, respectively, relative to the M(CH_4) intermediate], whereas the two energies are comparable for Cp_2W (9.8 and 9.1 kJ mol^{-1}). Thus, the Mo system corresponds to the situation (b) whereas the W analogue shows an intermediate behavior. Analogous calculations on the *ansa* system [$CH_2(C_5H_4)_2$]W (*a*-W), on the other hand, resulted in situation (a): E(M–TS_{ins}) = 4.4 kJ mol^{-1} and E(M–MECP) = 17.3 kJ mol^{-1}. The corresponding *ansa*-molybdenum system (*a*-Mo) was not explored in detail.

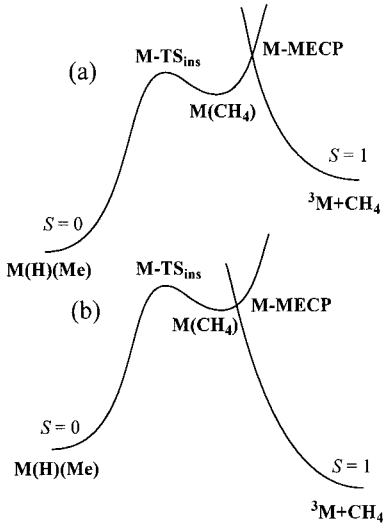

Figure 1. Reaction coordinate leading from $Cp'_2M(H)(CH_3)$ to Cp'_2M + CH_4. (a) E(M–TS_{ins}) < E(MECP); (b) E(M–TS_{ins}) > E(M–MECP).

Recent elegant work by Parkin et al. has provided experimental evidence, through the determination of kinetic isotope effects (KIE), for the occurrence of these two limiting situations with the methane or benzene reductive eliminations of [$Me_2Si(C_5Me_4)_2$]Mo(H)(Ph) and [$Me_2Si(C_5Me_4)_2$]-W(H)(R) where R = Me, Ph. Whereas the molybdenum system is characterized by a normal KIE, i.e. $k_H/k_D > 1$, the tungsten systems exhibit an overall inverse KIE which derives from a combination of an inverse equilibrium isotope effect (EIE) for the reductive-elimination step, and a near-zero KIE for the spin-forbidden methane dissociation step. The KIE for the reductive-elimination step is, like for the Mo case, normal, but it does not determine the overall KIE because it is not the rate-limiting step.[13] This can be expressed in other terms; the nature of the bonding of the key hydrogen (or deuterium) atom at the different stationary points along the reaction coordinate is qualitatively the same in the Mo and W cases. Bonding is fairly tight for the starting metal hydride (in the M–H or M–D bond), then becomes looser at the elimination TS, where H (D) is only partly bonded to M and C, then is at its tightest in the strong C–H (or C–D) bond which is present in the intermediate, the MECP and the products. This difference in bonding leads to differences in zero-point energies, which together with the fact that the overall bottleneck to the reaction is different in the two cases, explains the isotopic effects. Thus, the normal KIE for the decomposition of the Mo complex corresponds to the situation illustrated in Figure 1(b), whereas the overall inverse KIE observed for the W complexes results from an energetic profile as shown in Figure 1(a).

This difference was attributed by Parkin et al. to the relative stability of the starting [$Me_2Si(C_5Me_4)_2$]M(H)(R) and final [$Me_2Si(C_5Me_4)_2$]M complexes (here represented as *a*-Me_2Si–W* or *a*-Me_2Si–Mo*), implicitly invoking Hammond's principle for the relative energy of the two critical points. However, this hypothesis was not accompanied by a computational verification. In a separate contribution, Parkin et al. have reported calculations of the relative energy of the TS and crossing point for the W system, the crossing point having a marginally higher energy (ca. 33 kcal mol^{-1}) than the TS (30.1 kcal mol^{-1}).[19] The study, however, does not report similar calculations for the Mo system. In addition, the crossing point was estimated by a procedure that

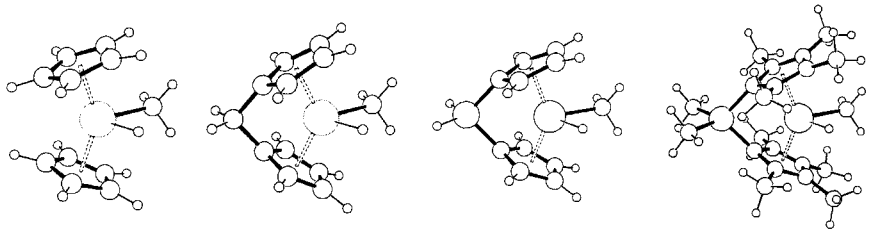

Scheme 1.

 © 2005 Wiley-VCH Verlag GmbH & Co. KGaA, Weinheim

we have termed the "partial optimization method",[20] which is more approximate than the explicit calculation of the MECP. The purpose of the present study is to complete the comparison of the *ansa*-[$CH_2(C_5H_4)_2$]M (M = Mo, W) systems, to compare these systems with the simpler metallocenes that we have previously described,[17] and to analyze the TS and MECP energies and geometries in more detail, in light of Hammond's postulate. In addition, we extend and apply the same analysis to the simplified systems [$H_2Si(C_5H_4)_2$]Mo (*a*-H_2Si–Mo), [$H_2Si(C_5H_4)_2$]W (*a*-H_2Si–W), and finally to the experimentally reported systems *a*-Me_2Si–W* and *a*-Me_2Si–Mo*. The labels used throughout this contribution contain a first part to identify the metallocene core (the generic M in Figure 1), and a second part to identify the way in which this interacts with the methane molecule, following the pattern shown in Figure 1. Views of the hydrido(methyl) derivatives for all systems investigated in this study, and the corresponding labels, are given in Scheme 1.

Results and Discussion

Cp_2M and *a*-M Systems

The new results reported here complete a previous study of ours, dealing with the reductive-elimination process of CH_4 from hydrido(methyl) derivatives of Cp'_2M, where Cp′ = Cp (Cp_2M) or Cp'_2 = $CH_2(C_5H_4)_2$ (*a*-M) and M = Mo and W.[17] In that study, DFT calculations were carried out with the B3LYP functional and two different basis sets. The complete set of critical points along the reaction pathway (including M–TS_{ins} and M–MECP) was determined only with the simpler LANL2DZ basis set, whereas a more sophisticated basis set, where the C and H atoms were described by polarized 6-31G** basis functions, was used only to recalculate all local minima. In addition, all the calculations were carried out using the standard B3LYP level of density functional theory. In recent work, we have found that relative energetics obtained for organometallic species, especially the spin-state splitting between high- and low-spin states, can depend quite strongly on the functional used.[21–23] We therefore decided to validate the method used in our previous work by considering larger basis sets and other DFT functionals, for one of the systems under consideration, i.e. [$CH_2(C_5H_4)_2$]W (*a*-W). These results are summarized in Table 1.

As can be seen, the four sets of calculations using the B3LYP and B3PW91 hybrid functionals yield very similar results. The binding energy of the *a*-W(CH_4) intermediate is slightly lower with the small basis set, and slightly larger with the B3PW91 functional, but the differences are smaller than the expected error levels in both cases. Somewhat larger differences are noted between the hybrid functionals and the gradient-corrected BP86 functional. These differences can all be interpreted in terms of a relatively larger stabilization of the triplet fragment with the hybrid functionals than with BP86. This type of behavior is fairly general[21] and can be attributed to the admixture of Hartree–Fock exchange in hybrid functionals which favors the high-spin state. Even here, though, the differences between methods are only of the order of 10–15 kJ mol^{-1}, and would be unlikely to affect the qualitative conclusions. We have therefore carried out the rest of this work using the simpler B3LYP/LANL2DZ and B3LYP/6-31G** calculations.

In our earlier work, as well as locating some of the stationary points only with the smaller LANL2DZ basis, no TS and MECPs were calculated, with either basis, for the *ansa*-Mo system, [$CH_2(C_5H_4)_2$]Mo (*a*-Mo). We have now completed the study of these four systems by calculating all missing TS and MECPs at both levels, see Table 2.

Table 1. Energies [kJ mol^{-1}] relative to ^{3}[M]+CH_4 of various points on the relevant singlet and triplet potential energy surfaces for the [$CH_2(C_5H_4)_2$]W (*a*-W) system.[a]

	B3LYP			B3PW91[b]	BP86[b]
	LANL2DZ	6-31G**	SDD/6-311+G**		
^{1}*a*-W + CH_4	*35.4*	*33.4*	31.5	32.1	19.5
^{3}*a*-W + CH_4	*0.0*	*0.0*	0.0	0.0	0.0
a-W(CH_4)	*9.7*	*4.5*	5.4	–0.4	–16.9
a-W(H)(Me)	*–121.9*	*–123.3*	–118.4	–120.8	–134.5

[a] Values in *italics* are taken from our previous contribution.[17] [b] Single-point energies at the B3LYP/SDD,6-311++G** geometries.

Table 2. Energies [kJ mol^{-1}] relative to ^{3}M + CH_4 of various points on the relevant singlet and triplet potential energy surfaces for the Cp_2M and *a*-M (M = Mo, W) metallocenes.[a]

	M = Cp_2Mo		M = Cp_2W		M = *a*-Mo		M = *a*-W	
	LANL2DZ	6-31G**	LANL2DZ	6-31G**	LANL2DZ	6-31G**	LANL2DZ	6-31G**
^{1}M + CH_4	*100.9*	*96.1*	*79.8*	*81.9*	*40.6*	*33.9*	*35.4*	*33.4*
^{3}M + CH_4	*0.0*	*0.0*	*0.0*	*0.0*	*0.0*	*0.0*	*0.0*	*0.0*
M(CH_4)	*86.7*	*80.5*	*65.5*	*64.9*	*21.9*	*13.4*	*9.7*	*4.5*
M–MECP	*91.0*	85.7	*74.6*	76.7	29.6	24.4	*27.0*	25.2
M–TS_{exch}	*86.9*	81.1	*66.2*	66.4	23.4	15.8	*14.9*	10.8
M–TS_{ins}	*117.7*	108.2	*75.3*	72.0	49.3	40.0	*14.1*	7.8
M(H)(Me)	*40.8*	*34.2*	*–46.0*	*–45.0*	*–35.3*	*–41.8*	*–121.9*	*–123.3*

[a] Values in *italics* are taken from our previous contribution.[17]

 © 2005 Wiley-VCH Verlag GmbH & Co. KGaA, Weinheim

We shall discuss here only the relevant new points. For the more basic features of this system, we refer the reader to our previous contribution.[17] The relative energies at the two computational levels are in relatively good agreement within the singlet state. The 6-31G** basis set leads to somewhat lower triplet-singlet gaps for the 16-electron Mo systems, whereas nearly identical gaps are found at the two levels for the two W systems. The 6-31G** calculations lead, for all systems, to significantly lower M–TS_{ins} energies relative to the M(CH_4) complex, whereas the relative energy of the M–MECP is less affected. We shall provide a more detailed discussion of the relative energetics and geometries only on the basis of the 6-31G** results. These are given in Figures 2 and 3. However, the considerations would be the same on the basis of the LANL2DZ results.

For all systems, M–TS_{exch} is very low, leading to fast scrambling of the C–H bonds in the M(CH_4) intermediate. Only for the *a*-W system, is the H exchange barrier higher

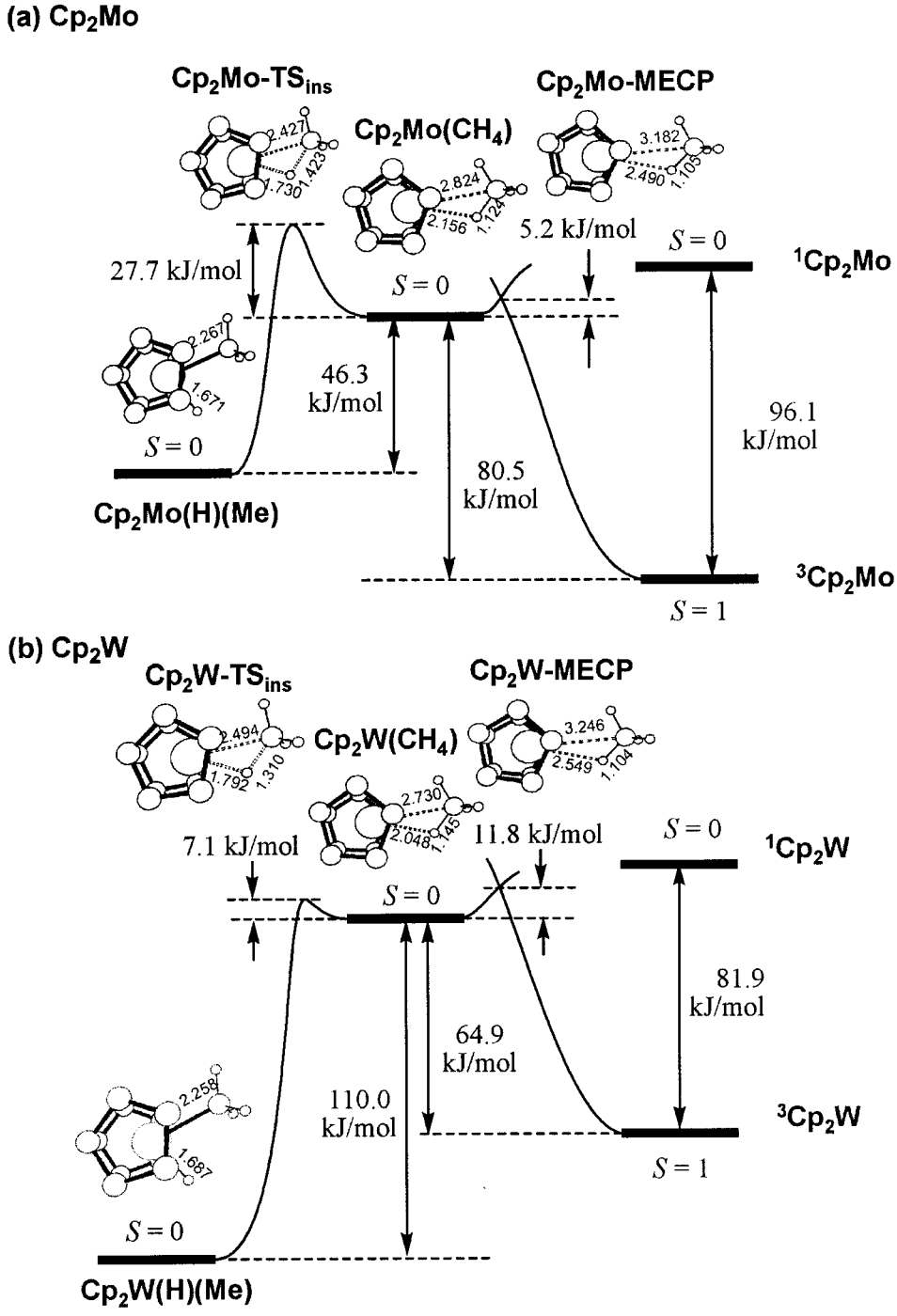

Figure 2. Reaction coordinate for the CH_4 oxidative addition to Cp_2M, with simplified views and selected bonding parameters [Å] for the relevant optimized structures. The H atoms on the cyclopentadienyl rings have been omitted for clarity. All energies are at the B3LYP/6-31G** level.

 © 2005 Wiley-VCH Verlag GmbH & Co. KGaA, Weinheim

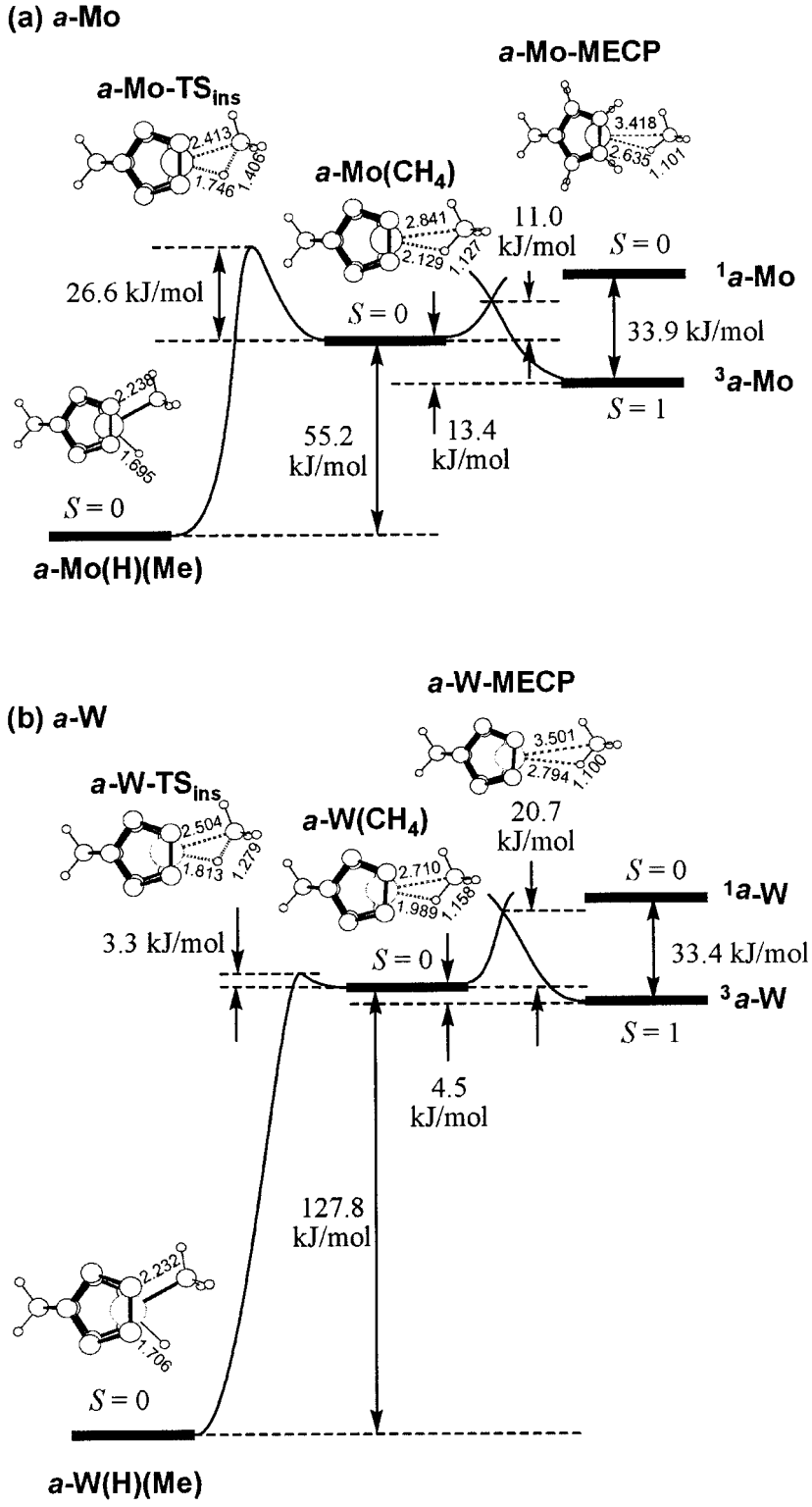

Figure 3. Reaction coordinate for the CH_4 oxidative addition to *a*-M, with simplified views and selected bonding parameters [Å] for the relevant optimized structures. The H atoms on the cyclopentadienyl rings have been omitted for clarity. All energies are at the B3LYP/6-31G** level.

than the insertion barrier (6.4 vs. 3.3 kJ mol^{-1}), but scrambling is still favorable relative to CH_4 dissociation, as experimentally verified for the $Me_2C(C_5H_4)_2W$ system.[12] As we will discuss further on, this is concordant in terms of the high barrier induced by the M–MECP. The M–TS$_{exch}$ geometry is in all cases symmetrical with identical M–H distances and a planar MH_2C arrangement with overall C_{2v} symmetry, in agreement with a previous report.[15]

 © 2005 Wiley-VCH Verlag GmbH & Co. KGaA, Weinheim

For the Cp_2M systems (Figure 2), the qualitative picture remains the same as previously shown on the basis of the LANL2DZ calculations. For the Mo system, the oxidative addition barrier (TS) is much higher than the M–MECP [27.7 vs. 5.2 kJ mol^{-1}, relative to the M(CH_4) intermediate]. For the W system, the M–TS_{ins} is slightly lower than the M–MECP (7.1 vs. 11.8 kJ mol^{-1}), whereas these two energies are closer at the LANL2DZ level. Experimentally, H exchange and CH_4 elimination were found to be competitive, the H exchange barrier being slightly lower.[9] No experimental data is available to be compared with the Mo system. For the *ansa* systems (Figure 3), the CH_4 elimination is again more favorable than the oxidative addition for Mo, whereas oxidative addition is now strongly preferred for the W system. This picture is in qualitative agreement with the experimental observation of H-scrambling processes for $Me_2C(C_5H_4)_2W(H)(CH_3)$, whereas no methane elimination occurs under the same conditions.[12]

a-H_2Si–M and *a*-Me_2Si–M* Systems

The calculations on these two systems were only carried out at the B3LYP/6-31G** level. The energy results are reported in Table 3, while selected geometrical parameters are given in Figures 4 and 5 for the *a*-H_2Si–M and *a*-Me_2Si–M* systems, respectively, together with a representation of the reaction coordinates for the reductive elimination and dissociation processes. Qualitatively, the picture does not differ too much from that of the *a*-M system for either metal.

Both *ansa*-silylene systems display similar energetics to the corresponding *a*-M system for the reductive elimination step leading to the σ-methane complex, but with greater energy gains upon methane dissociation. This fact can be related to the greater facility, for the silylene systems, to better relax the metallocene scaffold, because of the greater size of the silicon atom. This is particularly notable in the triplet state, because this benefits more than does the singlet state, from an energetic point of view, from a parallel geometry. The *a*-M system, on the other hand, is constrained by the smaller C atom to remain in a more strained, and therefore energetically less favorable geometry. The M–TS_{exch} energy is lower than the M–TS_{ins} energy for the two Mo systems and higher for the two W systems. In all cases, however, it is lower than the M–MECP energy. This is in agreement with the occurrence of H-scrambling processes between the hydride and the methyl ligands for the W system.

Comparison of Energies and Geometries for the MECP and Insertion TS

A full comparison of the four systems leads to a satisfactory rationalization of the relative barriers on the basis of Hammond's postulate concerning the relation between exothermicity and barrier height. The metal insertion into the C–H bond (C–H oxidative addition), starting from the M(CH_4) intermediate, has a smaller barrier for the group of W metallocenes (1.8–7.1 kJ mol^{-1} range), for which the process is more exothermic, and a greater one for the Mo group (22.9–27.7 kJ mol^{-1} range), for which the thermodynamics is less favorable. Within each group, the M–TS_{ins} barrier follows approximately the expected trend, for the W group, it decreases steadily from Cp_2W (7.1 kJ mol^{-1}) to *a*-Me_2Si–W* (1.8 kJ mol^{-1}) following the increase of energy gain, then it increases again for *a*-W. For the Mo group, it is highest for Cp_2Mo, which has the smallest energy gain, and lowest for *a*-Me_2Si–Mo* with the greatest energy gain. There is a small inversion of trend between the *a*-H_2Si–Mo and *a*-Mo systems.

The M–TS_{ins} geometry becomes more and more reactant-like (shorter C–H, longer M–C and M–H distances) as the barrier decreases, as expected on the basis of Hammond's postulate. The trend is quite clear within the W group, the only inversion being witnessed for the W–C distance between Cp_2W and *a*-H_2Si–W. Within the Mo series, the C–H bond length follows the order of the energy gain (1.423 Å for Cp_2Mo > 1.414 Å for *a*-H_2Si–Mo > 1.406 Å for *a*-Mo > 1.388 Å for *a*-Me_2Si–Mo*), rather than the order of the insertion barriers. On the other hand, the Mo–C distance is unexpectedly longer for Cp_2Mo–TS_{ins} (2.427 Å), whereas the Mo–H distance is anomalously long, relative to the rest of the series, in *a*-Mo–TS_{ins}. Overall, the energetic and structural trends are very much in line with expectations, on the basis of the oxidative addition thermodynamics and Hammond's postulate.

The same considerations hold true for the CH_4 dissociation process, which involves the spin-inversion phenomenon. For any pair of metallocenes containing the same ligand, the process is slightly more exothermic for Mo and the dissociation barrier (determined by the spin-inversion pro-

Table 3. Energies [kJ mol^{-1}] relative to $^3M + CH_4$ of various points on the relevant singlet and triplet potential energy surfaces for the *a*-H_2Si–M and *a*-Me_2Si–M* (M = Mo, W) metallocenes.

	M = *a*-H_2Si–Mo 6-31G**	M = *a*-H_2Si–W 6-31G**	M = *a*-Me_2Si–Mo* 6-31G**	M = *a*-Me_2Si–W* 6-31G**
$^1M + CH_4$	53.8	47.5	52.4	55.9
$^3M + CH_4$	0.0	0.0	0.0	0.0
M(CH_4)	36.8	24.2	41.4	37.4
M–MECP	43.2	39.1	46.6	49.2
M–TS_{exch}	40.4	33.5	44.1	44.0
M–TS_{ins}	62.5	28.6	64.3	39.2
M(H)(Me)	–13.2	–92.7	–17.1	–90.1

 © 2005 Wiley-VCH Verlag GmbH & Co. KGaA, Weinheim

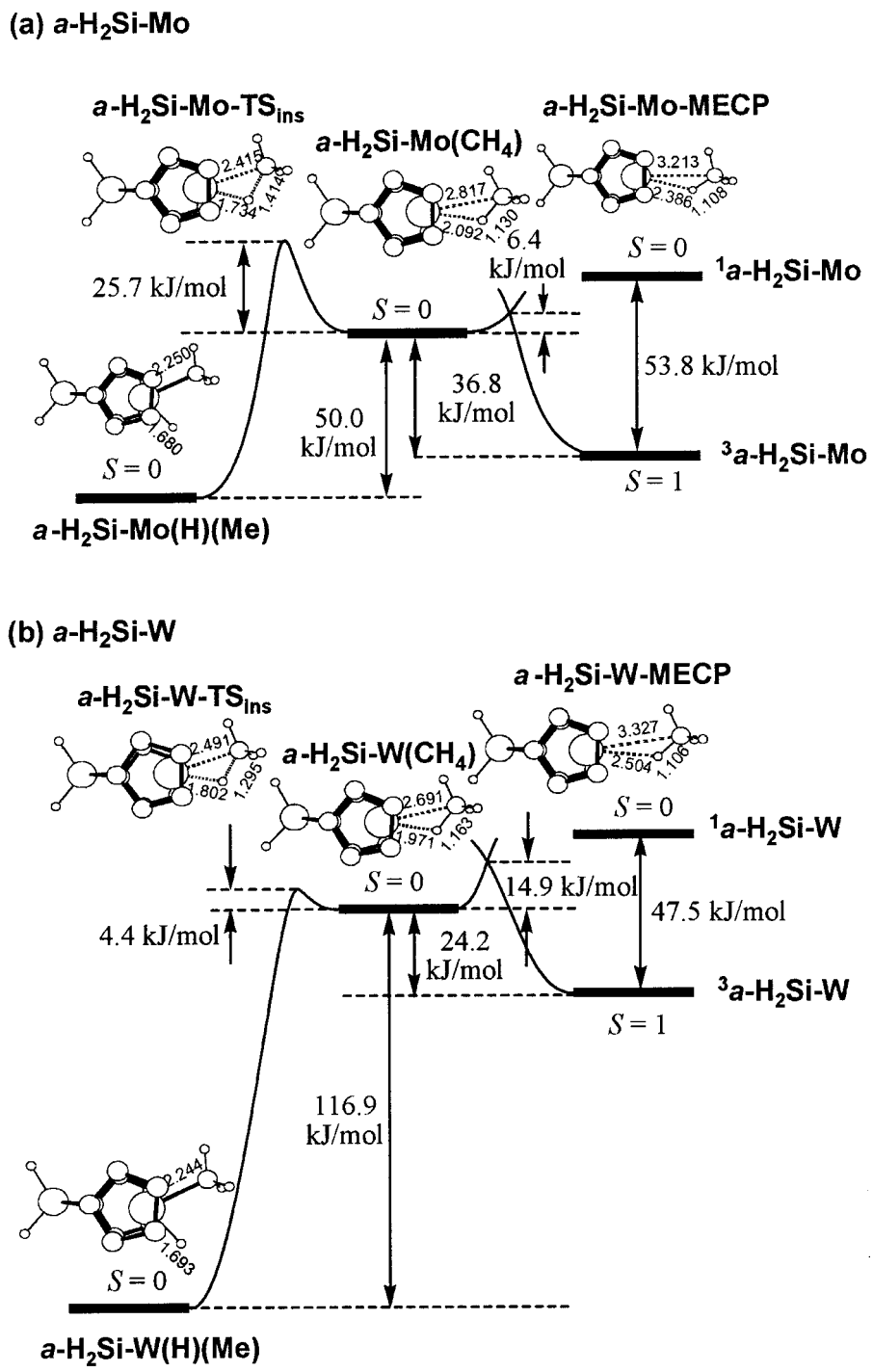

Figure 4. Reaction coordinate for the CH_4 oxidative addition to *a*-H_2Si–M, with simplified views and selected bonding parameters [Å] for the relevant optimized structures. The H atoms on the cyclopentadienyl rings have been omitted for clarity. All energies are at the B3LYP/6-31G** level.

cess) is correspondingly smaller. Within each group of metallocenes containing the same metal, the barrier steadily decreases with an increase of energy gain for the *ansa* systems in the order *a*-M > *a*-H_2Si–M > *a*-Me_2Si–M* (W: 20.7, 14.9 and 11.8 kJ mol^{-1} vs. 4.5, 24.2 and 37.4 kJ mol^{-1}; Mo: 11.0, 6.4 and 5.2 kJ mol^{-1} vs. 13.4, 36.8 and 41.4 kJ mol^{-1}). On going further to the Cp_2M system, at first sight surprisingly, the further increase in the methane dissociation energy is not accompanied by a further decrease in the dissociation barrier, which takes exactly the same values as for the corresponding *a*-Me_2Si–M* system for each metal. This is due to the fact that methane dissociation is anomalously exothermic for this system, due to the relaxation energy associated with moving the two Cp rings parallel to one another. In the MECP region, the presence of the methane molecule prevents both singlet and triplet states from adopting this parallel configura-

 © 2005 Wiley-VCH Verlag GmbH & Co. KGaA, Weinheim

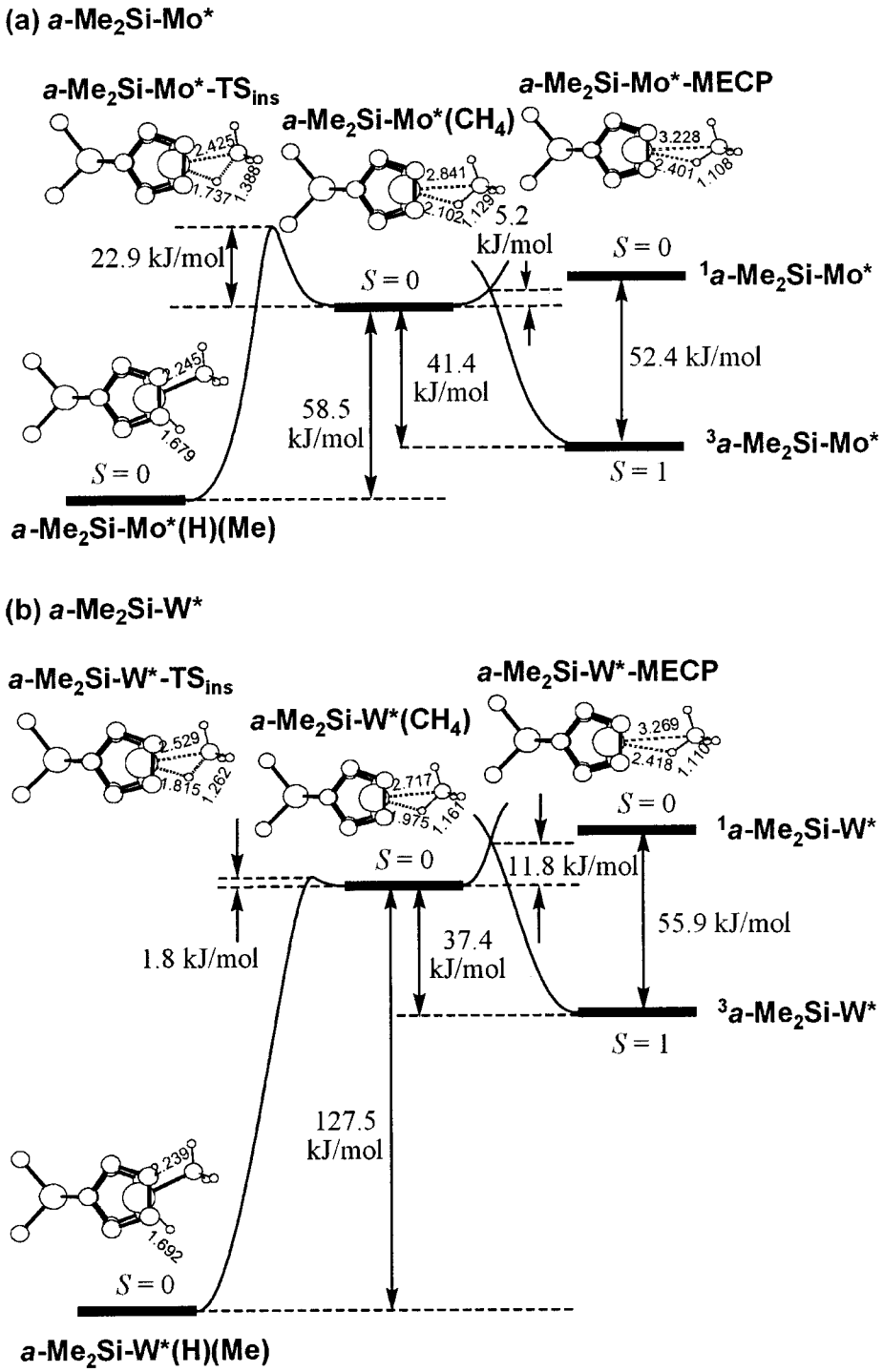

Figure 5. Reaction coordinate for the CH_4 oxidative addition to *a*-Me_2Si–M*, with simplified views and selected bonding parameters [Å] for the relevant optimized structures. The H atoms on the silylene Me groups and the Me groups on the cyclopentadienyl rings have been omitted for clarity. All energies are at the B3LYP/6-31G** level.

tion, so that the local slope and curvature of the potential energy surfaces resemble those for the constrained *ansa*-C and -Si systems. The additional stabilization of the triplet only intervenes well beyond the MECP, and hence has no effect on the relative energy of the latter. The MECP geometry becomes correspondingly more reactant-like as the barrier decreases. As for the oxidative addition TS examined above, there are a few exceptions, but the general trend is well respected. In particular, the trends of C–H, M–C and M–H distances are as expected within the *ansa*-W series. Particularly notable are the trends between the methylene- and the silylene-bridged systems for both metals.

This comparison shows that Hammond's principle can successfully be applied as an approximate guide to predic-

 © 2005 Wiley-VCH Verlag GmbH & Co. KGaA, Weinheim

ting barrier heights and geometries for reaction steps involving a change in spin state. Although there are, a priori, no reasons why the principle should not apply in such cases, this does not appear to be a generally appreciated phenomenon. We previously discussed Hammond's postulate to rationalize trends in spin-isomerization barriers for a series of *para*-substituted phenyl cations,[24] but there do not appear to have been other mentions in the context of spin-forbidden processes.

The exception mentioned above for the Cp_2M systems shows that, as for the more usual application to adiabatic reactions, the principle is only quantitatively reliable when all the potential energy surfaces for the set of analogous reactions have similar shapes. Where the endo- or exothermicity of one of the reactions considered is due to a feature of the potential energy surface which is not present in the other cases, and is not situated in the TS_{ins} or MECP region, deviations from the Hammond's principle predictions can be expected so some care should be taken when applying it to novel situations.

Conclusions

This study completes a previous one[17] in terms of the relative barriers to oxidative addition and elimination from (σ-CH_4)metallocene complexes, and extends it to silylene-bridged *ansa* systems that have been the subject of recent experimental studies.[13] The comparison of the reaction barriers for the various systems considered in this study has shown that the relative barriers for both one-state and two-state processes can be generally related to the reaction energetics through the application of Hammond's postulate. Though minor differences can be related to changes in the ligand system (*ansa* vs. non-*ansa*, methylene- vs. silylene-bridged), a major effect on the energetic profile and on the related kinetic response is that of the nature of the metal center. The calculation shows that the change of kinetic behavior for the same methane reductive elimination process from a hydrido(methyl) complex (i.e. from normal to inverse KIE from an Mo complex to the W analog)[13] is regulated not only by changes in the energy of the reductive elimination TS, but also by changes, quantitatively as important, in the energy of the methane dissociation MECP.

Computational Methods

The bulk of the computations were carried out using the well-established B3LYP hybrid density functional level of theory, as implemented in the Gaussian03[25] program package. The calculations were carried out using two different basis sets: (i) with the standard LANL2DZ basis set for all atoms, which includes an ECP on the W and Mo atoms; (ii) with a similar basis which includes polarization functions. Specifically, the LANL2DZ ECP and basis were retained on the metal atoms, but the standard 6-31G** basis was used on C and H (referred to as "6-31G**" henceforth). All structures were fully optimized, with the optimization of the MECPs being carried out by a combination of Gaussian and the shell script/Fortran code of one of the authors.[26,27] Geometry optimizations without symmetry constraints, backed up in several cases by computation of vibrational frequencies, showed all structures studied here to have at least C_S symmetry, with some belonging to higher point groups. Accordingly, the MECP optimizations were carried out within C_S symmetry. To further test the accuracy of the chosen method, we carried out additional calculations on the $[CH_2(C_5H_4)_2]W$ system only. Specifically, we characterized the singlet and triplet fragment, the σ-CH_4 intermediate and the methyl hydride product, using a larger basis set, with the SDD pseudopotential and associated basis set on W, and the 6-311++G** basis sets for the C and H atoms. Full geometry optimization was carried out with these basis set combinations and the B3LYP functional was used in the main body of the work, with additional single-point energies calculated using the same basis set, at the B3LYP geometries, with the B3PW91 and BP86 density functionals. None of the reported energies include a correction for zero-point energy, as this is difficult to obtain at the MECPs. Nevertheless, frequencies have been calculated for all other stationary points, and used to identify them as minima or transition states.

Acknowledgments

R. P. thanks CINES and CICT (program CALMIP) for granting free CPU time. J.-L. C. M. acknowledges support from Mexico's National Council for Science and Technology (CONACYT). J. N. H. is an EPSRC Advanced Research Fellow.

[1] J. P. Collman, L. S. Hegedus, J. R. Norton, R. G. Finke, *Principles and Applications of Organotransition Metal Chemistry*, University Science Books, Mill Valley, CA, **1987**.
[2] R. H. Crabtree, *The Organometallic Chemistry of the Transition Metals*, 3rd ed., Wiley-Interscience, New York, **2001**.
[3] C. L. Hill, *Activation and Functionalization of Alkanes*, John Wiley and Sons, New York, **1989**.
[4] A. Shilov, G. B. Shul'pin, *Chem. Rev.* **1997**, *97*, 2879–2932.
[5] R. H. Crabtree, *J. Chem. Soc., Dalton Trans.* **2001**, 2437–2450.
[6] W. D. Jones, F. J. Feher, *Acc. Chem. Res.* **1989**, *22*, 91–100.
[7] B. A. Arndtsen, R. G. Bergman, T. A. Mobley, T. H. Peterson, *Acc. Chem. Res.* **1995**, *28*, 154–162.
[8] N. J. Cooper, M. L. H. Green, R. Mahtab, *J. Chem. Soc., Dalton Trans.* **1979**, 1557–1562.
[9] R. M. Bullock, C. E. L. Headford, K. M. Hennessy, S. E. Kegley, J. R. Norton, *J. Am. Chem. Soc.* **1989**, *111*, 3897–3908.
[10] G. Parkin, J. E. Bercaw, *Organometallics* **1989**, *8*, 1172–1179.
[11] L. Labella, A. Chernega, M. L. H. Green, *J. Chem. Soc., Dalton Trans.* **1995**, 395–402.
[12] A. Chernega, J. Cook, M. L. H. Green, L. Labella, S. J. Simpson, J. Souter, A. H. H. Stephens, *J. Chem. Soc., Dalton Trans.* **1997**, 3225–3243.
[13] D. Churchill, K. Janak, J. Wittenberg, G. Parkin, *J. Am. Chem. Soc.* **2003**, *125*, 1403–1420.
[14] P. A. Cox, P. Grebenik, R. N. Perutz, M. D. Robinson, R. Grinter, D. R. Stern, *Inorg. Chem.* **1983**, *22*, 3614–3620.
[15] J. C. Green, C. N. Jardine, *J. Chem. Soc., Dalton Trans.* **1998**, 1057–1061.
[16] M. D. Su, S. Y. Chu, *J. Phys. Chem. A* **2001**, *105*, 3591–3597.
[17] J. C. Green, J. N. Harvey, R. Poli, *J. Chem. Soc., Dalton Trans.* **2002**, 1861–1866.
[18] S. Shaik, D. Danovich, A. Fiedler, D. Schröder, H. Schwarz, *Helv. Chim. Acta* **1995**, *78*, 1393–1407.
[19] K. Janak, D. Churchill, G. Parkin, *Chem. Commun.* **2003**, 22–23.
[20] R. Poli, J. N. Harvey, *Chem. Soc. Rev.* **2003**, *32*, 1–8.
[21] J. N. Harvey, *Struct. Bonding* **2004**, *112*, 151–184.
[22] J.-L. Carreón-Macedo, J. N. Harvey, *J. Am. Chem. Soc.* **2004**, *126*, 5789–5797.

 © 2005 Wiley-VCH Verlag GmbH & Co. KGaA, Weinheim

[23] R. Poli, I. Cacelli, *Eur. J. Inorg. Chem.* **2005**, 2324–2331.
[24] M. Aschi, J. N. Harvey, *J. Chem. Soc. Perkin Trans. 2* **1999**, 1059–1062.
[25] M. J. Frisch, G. W. Trucks, H. B. Schlegel, G. E. Scuseria, M. A. Robb, J. R. Cheeseman, J. Montgomery, J. A. T. Vreven, K. N. Kudin, J. C. Burant, J. M. Millam, S. S. Iyengar, J. Tomasi, V. Barone, B. Mennucci, M. Cossi, G. Scalmani, N. Rega, G. A. Petersson, H. Nakatsuji, M. Hada, M. Ehara, K. Toyota, R. Fukuda, J. Hasegawa, M. Ishida, T. Nakajima, Y. Honda, O. Kitao, H. Nakai, M. Klene, X. Li, J. E. Knox, H. P. Hratchian, J. B. Cross, C. Adamo, J. Jaramillo, R. Gomperts, R. E. Stratmann, O. Yazyev, A. J. Austin, R. Cammi, C. Pomelli, J. W. Ochterski, P. Y. Ayala, K. Morokuma, G. A. Voth, P. Salvador, J. J. Dannenberg, V. G. Zakrzewski, S. Dapprich, A. D. Daniels, M. C. Strain, O. Farkas, D. K. Malick, A. D. Rabuck, K. Raghavachari, J. B. Foresman, J. V. Ortiz, Q. Cui, A. G. Baboul, S. Clifford, J. Cioslowski, B. B. Stefanov, G. Liu, A. Liashenko, P. Piskorz, I. Komaromi, R. L. Martin, D. J. Fox, T. Keith, M. A. Al-Laham, C. Y. Peng, A. Nanayakkara, M. Challacombe, P. M. W. Gill, B. Johnson, W. Chen, M. W. Wong, C. Gonzalez, J. A. Pople, *Gaussian 03 Revision B.04*, Gaussian, Inc., Pittsburgh PA, **2003**.
[26] J. N. Harvey, M. Aschi, H. Schwarz, W. Koch, *Theor. Chem. Acc.* **1998**, *99*, 95–99.
[27] J. N. Harvey, M. Aschi, *Phys. Chem. Chem. Phys.* **1999**, *1*, 5555–5563.

Received: March 18, 2005
Published Online: July 4, 2005

 © 2005 Wiley-VCH Verlag GmbH & Co. KGaA, Weinheim

Hybrid 2D and 3D Frameworks Based on ε-Keggin Polyoxometallates: Experiment and Simulation

Anne Dolbecq,*[a] Caroline Mellot-Draznieks,[a] Pierre Mialane,[a] Jérôme Marrot,[a] Gérard Férey,[a] and Francis Sécheresse[a]

Keywords: Molybdenum / Organic–inorganic hybrid materials / Polyoxometallates / Simulation

The ε-Keggin polyoxomolybdate {ε-$PMo^{V}_{8}Mo^{VI}_{4}O_{40-x}(OH)_x$-$M_4$} is a versatile building unit, with M being either a Zn^{II} or a La^{III} capping ion located at the vertices of a slightly distorted tetrahedron. The charge of the Keggin unit depends on the number of protonated oxo bridging ligands, which has been shown to vary from 0 to 5. The Keggin entity can thus be either an anion (M = Zn, x = 0) or a cation (M = La, x = 3–5). The Zn derivative has been generated in situ by hydrothermal synthesis and forms a 2D material built from the connection of the cations by 4,4′-bipyridine ligands linked to the capping Zn^{II} ions. The reaction of the chloride salt of the La derivative with di-, tri- and tetrasubstituted benzenecarboxylate ligands has allowed us to isolate 2D and 3D materials. The 3D materials seem to be the first examples of hybrid open frameworks based on Keggin building blocks. The 3D framework built from the connection of ε-Keggin units by trimesate ions exhibits tunnels filled only by water molecules, which can be partly removed and reintroduced at room temperature. Besides these experimental results, simulation has allowed us to generate two virtual hybrid structures derived from those of known silicates by replacing the Si ions by hypothetical ε-Keggin cations and the *O*-bridging ligands by terephthalate ions, thus showing that 3D frameworks with large pores can be envisioned in the chemistry of hybrid organic–inorganic materials based on ε-Keggin units and motivating further experimental investigations.
(© Wiley-VCH Verlag GmbH & Co. KGaA, 69451 Weinheim, Germany, 2005)

Introduction

Metal–organic frameworks[1] constitute a recent class of materials with open architectures built from metal ions linked together by organic bridging ligands, most of the time carboxylate ions.[2] These compounds have attracted much interest because of their potential applications in catalysis, gas storage and separation. Their structures can be classified according to the dimensionality of the inorganic network.[3] The largest family contains metal–organic frameworks with discrete inorganic building blocks. Two factors determine the geometry and the size of the cavities, namely the symmetry and size of the molecular units and the nature of the organic ligand. For example, Yaghi et al. have shown that the volume of the cavities increases dramatically when the bridging organic ligand is lengthened.[4] Another way to expand the lattice, known as "scale chemistry",[5] is to increase the size of the inorganic building blocks, which are so far limited to a small number of metal ions. We have recently reported the synthesis of a novel polyoxocation, $[\varepsilon\text{-}PMo^{V}_{8}Mo^{VI}_{4}O_{36}(OH)_4\{La(H_2O)_4\}_4]^{5+}$, which is a mixed-valence ε-Keggin-type polyoxometallate (POM) core capped by four lanthanum ions located at the vertices of a slightly distorted tetrahedron.[6] The La^{III} ions are connected to the molybdenum ions by three triply bridging oxygen atoms and their coordination sphere is completed by disordered water molecules. The overall symmetry of the polyoxocation is tetrahedral. Two examples of transition metal cations (Zn^{II}, Ni^{II}) capping reduced ε-Keggin cores have also been reported.[7] The water molecules bound to transition metal or rare-earth cations capping the POM core can be potentially substituted by N- or O-donor ligands, which opens the way to the design of a new family of hybrid organic–inorganic materials. We have recently obtained the first members of this family, namely two 1D materials formed by the connection of the POMs by squarate or glutarate ligands, respectively.[8] Nevertheless, owing to the overall tetrahedral symmetry of the inorganic cation, 3D materials can be envisioned, which can lead eventually to porous frameworks. We describe in this paper our first results in the synthesis of 2D and 3D frameworks with the ε-Keggin building unit, synthesised by two different ways, namely hydrothermal techniques, which have led to $Na(C_{10}H_{10}N_2)[\varepsilon\text{-}PMo_{12}O_{40}Zn_4(H_2O)_2(C_{10}H_8N_2)_3]\cdot 10H_2O$ (**1**), and standard bench conditions, which have allowed us to isolate $[\varepsilon\text{-}PMo_{12}O_{35}(OH)_5La_4(C_8H_4O_4)_3]\cdot 41H_2O$ (**2**), $[\varepsilon\text{-}PMo_{12}O_{35}(OH)_5\{La(H_2O)_3\}_4(C_9H_3O_6)_2]\cdot 44H_2O$ (**3**) and [ε-

[a] Institut Lavoisier, IREM, UMR 8637, Université de Versailles Saint-Quentin,
45 Avenue des Etats-Unis, 78035 Versailles cedex, France
Fax: +33-139254381
E-mail:dolbecq@chimie.uvsq.fr
Supporting information for this article is available on the WWW under http://www.eurjic.org or from the author.

$PMo_{12}O_{37}(OH)_3\{La(H_2O)_4\}_4(C_{10}H_2O_8)]\cdot 24H_2O$ (**4**). The synthetic routes to obtain the different compounds described in this paper are summarised in Figure 1. Besides these experimental results, we also report here the simulation of two phases built from the connection of a hypothetical ε-Keggin core, capped by pentacoordinate transition metal ions, by a rigid dicarboxylate ligand − the terephthalate ligand − in order to demonstrate the potentiality of this molecular building block for the design of hybrid organic–inorganic materials with large pores.

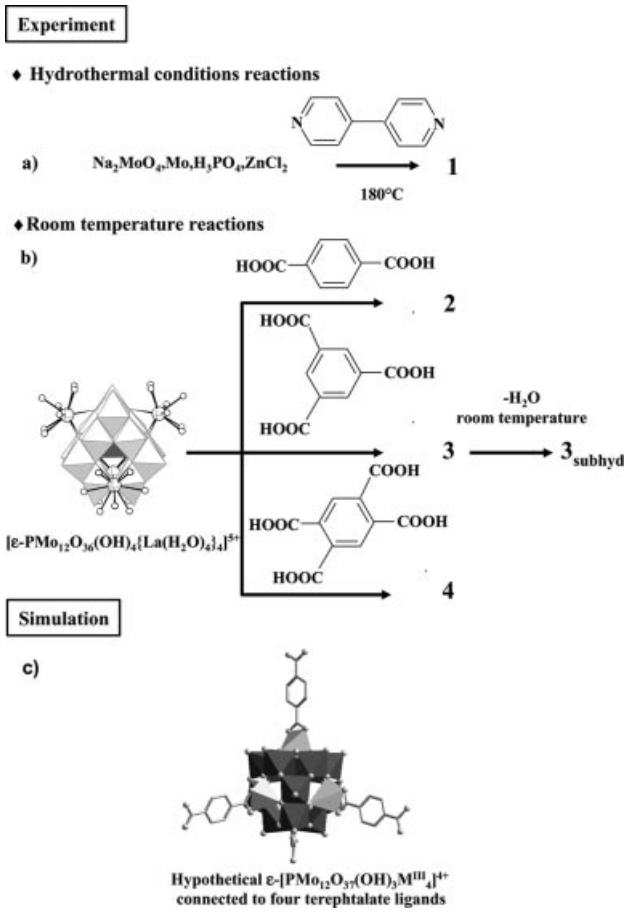

Figure 1. The synthetic conditions used to obtain a) **1** in a hydrothermal "one-pot" synthesis and b) **2**, **3** and **4** from the $[\varepsilon\text{-}PMo_{12}O_{36}(OH)_4\{La(H_2O)_4\}_4]^{5+}$ precursor. Note that for $[\varepsilon\text{-}PMo_{12}O_{36}(OH)_4\{La(H_2O)_4\}_4]^{5+}$ the four water molecules are disordered on the lanthanum ions; c) polyhedral representation of the hypothetical ε-Keggin ion with pentahedral capping transition ions used for the simulation.

Results and Discussion

Synthesis

The synthesis of the hybrid materials with ε-Keggin building units was performed according to two different procedures: the first one exploits hydrothermal conditions and the second one is based on the substitution of water molecules bound to the lanthanum ions of the inorganic precursor by carboxylate groups of the organic ligand (Figure 1). We first chose Zn^{II} ions as capping transition metal ions in hydrothermal reactions because of their ability to adopt low coordination numbers and thus favour the 1:2 POM:ligand stoichiometry. 4,4′-Bipyridine was selected as ligand because it is neutral and thus it should have a greater affinity for the most probable anionic ε-Keggin core capped with divalent Zn ions than the terephthalate ligand. Single crystals of $Na(C_{10}H_{10}N_2)[\varepsilon\text{-}PMo_{12}O_{40}Zn_4(H_2O)_2(C_{10}H_8N_2)_3]\cdot 10H_2O$ (**1**) were obtained from the reaction of a mixture of Na_2MoO_4, Mo as reducing agent, H_3PO_4, $Zn(CH_3COO)_2$ and 4,4′-bipyridine in water adjusted to pH 6.5, and heated at 180 °C. The ε-Keggin core capped with Zn^{II} ions is generated in situ and connects three different neutral bidentate ligands to generate a 2D material. Although the synthetic conditions are quite different, especially the Zn:ligand ratio and the nature of the precursors, the structure of **1** (see below) is close to that of a 2D material reported recently.[7b]

Despite numerous attempts, single crystals of $[\varepsilon\text{-}PMo_{12}O_{35}(OH)_5La_4(C_8H_4O_4)_3]\cdot 41H_2O$ (**2**) of suitable quality for X-ray diffraction could not be obtained, and only microcrystalline powders were formed by slow addition of an aqueous solution of terephthalic acid to a methanolic solution of $[\varepsilon\text{-}PMo_{12}O_{36}(OH)_4\{La(H_2O)_{2.5}Cl_{1.25}\}_4]\cdot 27H_2O$.[6] Elemental analysis indicates that the stoichiometry of the hybrid compound is one ε-Keggin ion for three terephthalate ligands. The structure of **2** is thus certainly very close to that of **1**, with terephthalate ligands in place of bipyridine and La^{III} ions replacing Zn^{II} ions, as also suggested by the similarity of their experimental powder diffraction patterns (Figure 3, b). However, the poor quality of the experimental diagram of **2** prevents any further investigation of the structure.

Single crystals of $[\varepsilon\text{-}PMo_{12}O_{35}(OH)_5\{La(H_2O)_3\}_4(C_9H_3O_6)_2]\cdot 44H_2O$ (**3**) were grown by slow evaporation, at room temperature, of a CH_3OH/H_2O solution containing the chloride salt of the ε-Keggin precursor and a stoichiometric amount of trimesate ions. The determining factors for the crystallisation process are the CH_3OH/H_2O ratio, the pH of the trimesate solution and the stoichiometry of the reaction. Compound **3** rapidly loses water at room temperature to give $\mathbf{3_{subhyd}}$. Single crystals of $[\varepsilon\text{-}PMo_{12}O_{37}(OH)_3\{La(H_2O)_4\}_4(C_{10}H_2O_8)]\cdot 24H_2O$ (**4**) were obtained in a similar manner except that a pure water solution was used instead of a mixture of CH_3OH and H_2O. In the presence of an excess of ligand, and/or if the pH is too high, only microcrystalline powders precipitate.

The infrared spectra of **1**, **2**, $\mathbf{3_{subhyd}}$ and **4** are very similar in the 970–500 cm^{-1} region, where characteristic Mo=O and Mo–O vibrations are found. The bands of **2**, $\mathbf{3_{subhyd}}$ and **4** in the 1650–1350 cm^{-1} domain are characteristic of the O–C–O vibrations of the coordinated ligand.

Structure of $Na(C_{10}H_{10}N_2)[\varepsilon\text{-}PMo_{12}O_{40}Zn_4(H_2O)_2(C_{10}H_8N_2)_3]\cdot 10H_2O$ (1)

The ε-Keggin unit is similar to the building unit encountered in the 1D solids with glutarate and squarate ligands,[8]

Table 1. Ranges and mean bond lengths [Å] within the POM core in **1**, **3** and **4**.

	1	**3**	**4**
P–O	1.529(15)–1.541(10) [1.534]	1.551(6)–1.555(6) [1.553][a]	1.540(6)–1.576(6) [1.559]
Mo–O_a[b]	2.515(14)–2.586(14) [2.528]	2.473(6)–2.647(6) [2.553]	2.434(5)–2.682(5) [2.541]
Mo–$O_{b,c}$[b] *Short*	1.872(11)–2.043(10) [1.956]	1.824(7)–2.027(6) [1.951]	1.794(5)–2.032(5) [1.948]
Long[c]		2.062(7)–2.083(6) [2.074]	2.014(6)–2.094(5) [2.049]
Mo–O_d[b]	1.643(12)–1.683(13) [1.665]	1.676(7)–1.688(7) [1.681]	1.651(6)–1.708(6) [1.675]
Mo^V–Mo^V	2.573(3)–2.614(3) [2.593]	2.5774(12)–2.5983(19) [2.585]	2.5637(11)–2.6215(11) [2.589]
Mo···Mo[d]	2.882(3)–2.869(3) [2.875]	3.1326(13) [3.133]	3.1476(11)–3.1501(10) [3.149]

[a] Mean values are indicated in square brackets. [b] O_a refers to an oxygen atom of the central cavity bound to the phosphorus atom; O_b and O_c refer to bridging oxygen atoms; O_d refers to a terminal oxygen atom. [c] Mo–O distances for O atoms bridging two Mo atoms of the Keggin core with two corresponding Mo–O distances longer than 2.0 Å. [d] Mo···Mo distances between 2.80 and 3.20 Å.

and in the 3D materials **3** and **4** (see below) except that the Mo^V and Mo^{VI} ions are not all localised, as observed previously. Indeed, while valence bond calculations[9] (Table S1, Supporting Information) indicate clearly that Mo1, Mo6 and Mo7 are Mo^V ions, in agreement also with their short intermetallic Mo–Mo bonds (Table 1), the four Mo^{VI} ions and four Mo^V ions remaining are delocalised over eight centres. The Mo–Mo distances for these ions (Table 1) are intermediate between Mo^V–Mo^V (ca. 2.6 Å) and Mo^{VI}···Mo^{VI} bonds (ca. 3.2 Å). The $[\varepsilon\text{-}PMo^V_8Mo^{VI}_4O_{40}]^{11-}$ core is stabilized by four Zn^{II} capping ions and this entity is thus formally anionic. Due to the smaller ionic radii of the Zn^{II} ions compared to the La^{III} ions, and consequently shorter Zn–O distances (Table 2 and Table S2 in the Supporting Information), the volume occupied by the ε-Keggin core is far smaller when it is capped by Zn^{II} ions. A rough estimation, using the mean distance between the central phosphorus atom and the atoms of the ligands L coordinated to the Zn^{II} or La^{III} ions as the radius of a sphere, leads to a volume of 775 $Å^3$ for the Zn derivative ($d_{P\cdots L} \approx 5.7$ Å) and 1630 $Å^3$ for the La derivative ($d_{P\cdots L} \approx 7.3$ Å).

Table 2. Ranges and mean bond lengths [Å] for the Zn–O, Zn–N bonds in **1** and the La–O and C–O bonds in **3** and **4**.

	1
Zn–O[a]	1.897(14)–2.268(18) [2.036]
Zn–N	2.014(11)–2.150(16)(2) [2.068]
	3
La–O(POM)	2.442(7)–2.625(8) [2.551]
La–O(H_2O)	2.500(11)–2.598(8) [2.563]
C–O	1.249(13)–1.308(14) [1.270]
	4
La–O(POM)	2.452(5)–2.676(5) [2.556]
La–O(H_2O)	2.499(6)–2.758(12) [2.610]
C–O	1.207(10)–1.293(10) [1.254]

[a] Mean values are indicated in square brackets.

Three different coordination modes are encountered in **1**. Thus, Zn1 is pentacoordinate, being bound to three oxygen atoms of the ε-Keggin core and two nitrogen atoms of two 4,4′-bipyridine ligands (Figure 2), Zn2 is bound to three oxygen atoms of the Keggin core, one nitrogen atom of a bipyridine ligand and two additional water molecules, and is thus hexacoordinate, and Zn3 only bears one extra ligand, i.e. a bypiridine molecule, and is tetracoordinate (Figure 2). In the (*a*,*b*) plane, one ε-Keggin unit is connected to four adjacent units through four bipyridine molecules linked to Zn1 ions, thus forming a double chain (Figure 3, a). These double chains stack along the *c* axis and are connected to neighbouring ones by bipyridine ligands linked to the Zn2 and Zn3 ions, thus forming a double plane. Intersecting tunnels along the *b* and *c* directions are generated, however the adjacent planes interpenetrate (Figure 3, a) and the material does not exhibit any porosity. Furthermore, disordered sodium ions and free protonated bipyridine ions are found as counterbalancing cations.

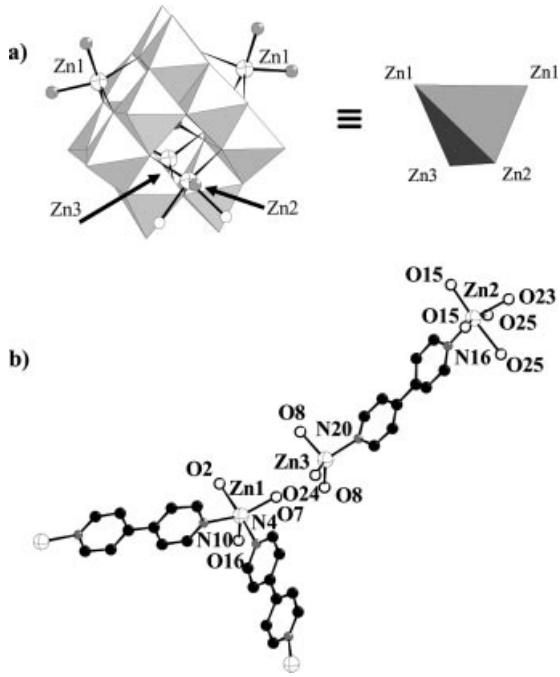

Figure 2. a) Representation of the building unit in **1**, showing the three different coordination modes of the Zn^{II} capping ions and its overall tetrahedral symmetry; b) labelling scheme of the Zn^{II} centres and their ligands.

 © 2005 Wiley-VCH Verlag GmbH & Co. KGaA, Weinheim

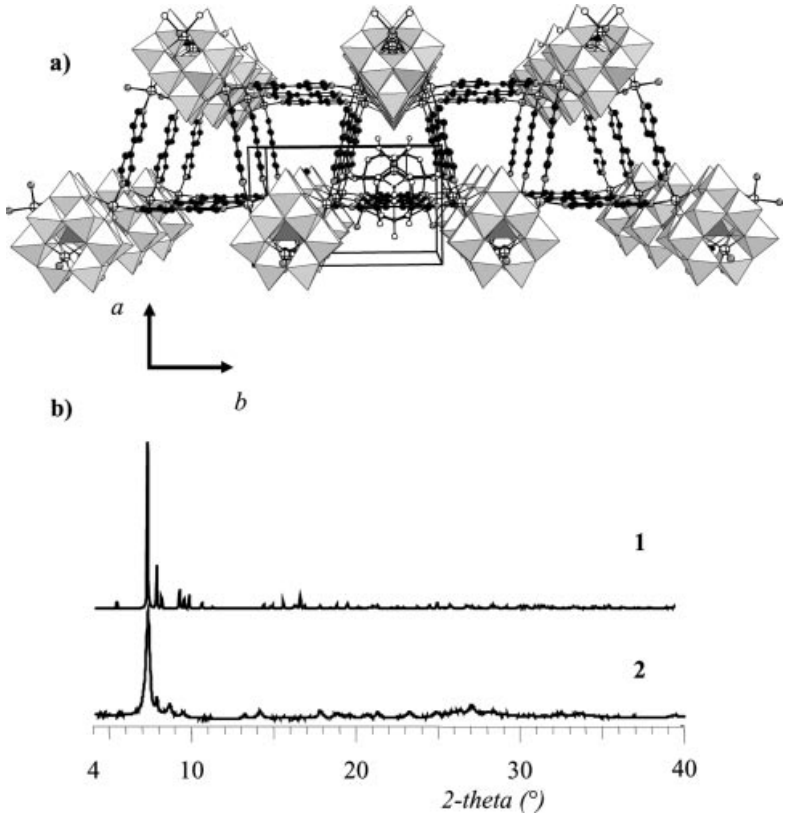

Figure 3. a) View of the double chains in the (*a*,*b*) plane formed by the connection of ε-Keggin units by bipyridine ligands; the connection along the *c* axis ensure the formation of planes. The position of an ε-Keggin cation (ball and stick representation) belonging to an adjacent double plane is also shown. Non-coordinated water molecules and bipyridinium counterions have been omitted for clarity. b) Comparison of the simulated powder pattern of **1** and the experimental powder pattern of **2**.

Structure of $[\varepsilon\text{-}PMo_{12}O_{35}(OH)_5\{La(H_2O)_3(C_9H_3O_6)_2\}]\cdot 44H_2O$ (3)

Crystals of **3** rapidly become amorphous when left in air. X-ray analysis was therefore performed on a single crystal of **3** sealed in a capillary tube. Compound **3**, which exhibits a three-dimensional structure, crystallises in the non-centrosymmetric space group $P2_12_12$. One organic ligand connects three different polyoxocations through La–O bonds, two carboxylate groups adopt a chelating mode while one pendent oxygen atom (O26) remains in the third one (Figure 4, a). The quite short C–O distance [C9–O26 = 1.258(14) Å] of the pendent group indicates that this group is non-protonated. This bonding mode of the trimesate ligand has been encountered a few times.[10] Each lanthanum ion bears three additional water molecules, and the lanthanum ion connected to the bridging carboxylate group (La1) is also connected to another trimesate ligand, therefore the La1 ions are enneacoordinate whereas the La2 ions are only octacoordinate. The geometrical features within the polyoxometallate core are slightly affected by the coordination to organic ligands. As observed for the polymeric structure with squarate and glutarate ions,[8] among the twelve Mo ions, eight Mo^V ions form Mo–Mo bonds ($d_{Mo-Mo} \approx 2.6$ Å, Table 1) while the remaining four are Mo^{VI} centres ($d_{Mo\cdots Mo} \approx 3.2$ Å). Valence bond calculations (Table S1, Supporting Information) confirmed the oxidation state of the Mo ions

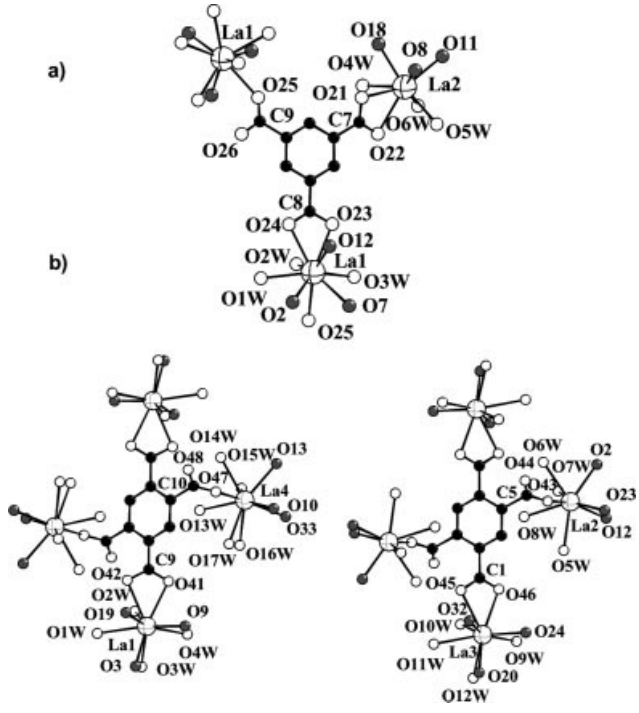

Figure 4. Bonding mode of a) the trimesate ligand in **3** and b) the pyromellitic ligands in **4**; the oxygen atoms bound to the POM core are represented as grey spheres.

 © 2005 Wiley-VCH Verlag GmbH & Co. KGaA, Weinheim

and allowed us to localise four protons on bridging oxygen atoms of the POM core. In order to respect the electroneutrality, one additional proton is assumed to be delocalised over the four remaining μ_2-oxygen atoms of the POM. Indeed, it is well known that the basicity of a Keggin polyoxomolybdate increases when it is reduced, and the doubly bridging oxygen atoms are the preferred protonation sites.[11] The connection of the polyoxocations by the tridentate ligands generates a neutral 3D framework with 1D channels running along the *c* axis (Figure 5). The channels have rectangular free apertures of 6.1 × 7.2 Å, as estimated from the interatomic distances between atoms delimiting the channels and taking into account their van der Waals radii. These channels are filled with clusters of disordered water molecules that form intricate hydrogen bonds with other water molecules of the clusters and the oxygen atoms of the polyoxocation.

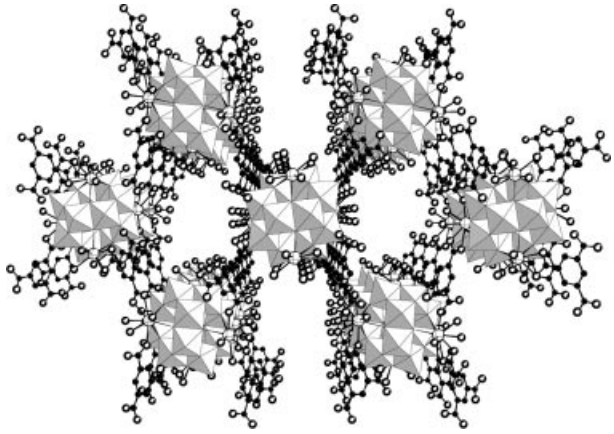

Figure 5. Perspective view of the 3D structure of **3** showing the channels along the *c* direction. Non-coordinated water molecules have been omitted for clarity.

Structure of $[\varepsilon\text{-}PMo_{12}O_{35}(OH)_5\{La(H_2O)_3\}_4(C_{10}H_2O_8)]\cdot 24H_2O$ (4)

Compound **4** crystallises in the centrosymmetric $P\bar{1}$ space group. The asymmetric unit contains a POM polyoxocation and two halves of the organic ligand, in agreement with the 1:1 stoichiometry. Each ligand is bound to four lanthanum ions from four distinct POMs (Figure 4, b). Like in **3**, there are two different connecting modes of the carboxylate groups: two are chelating and two are only monodentate C–O groups. The O–C–O groups are almost perpendicular to the plane of the organic molecule. La2 and La1 are connected to monodentate C–O groups, and La2 bears four additional water molecules in addition to the three oxygen atoms of the POM and is thus octacoordinate while La1 has a supplementary water molecule and is nonacoordinate. La3 and La4 are bound to chelating carboxylate groups and are both nonacoordinated. The geometrical features within the POM are similar to those in **3** (Table 1). The connection of one POM to the organic ligands by La–O–C bonds generates a 3D material that contains small channels running along the *b* axis that are filled, as in **3**, by disordered water molecules (Figure 6).

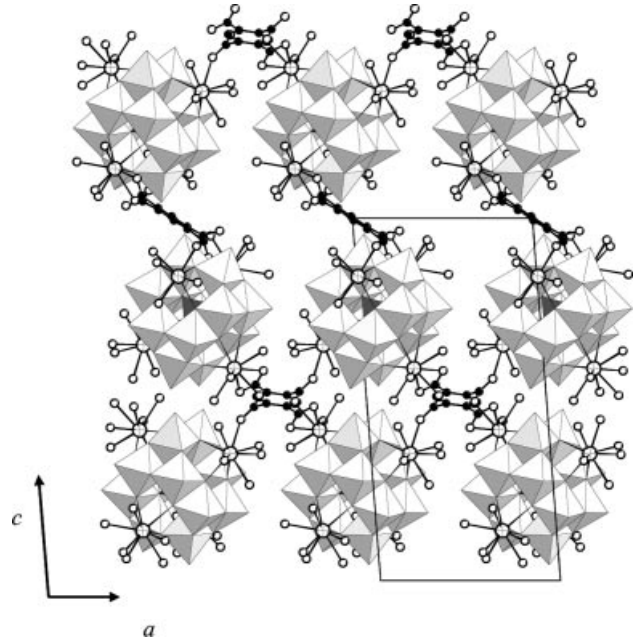

Figure 6. View of the 3D structure of **4** along the *b* axis. Non-coordinated water molecules have been omitted for clarity.

Subhydrate of 3

The stability of **3** was investigated first by a simple treatment at room temperature. The X-ray powder diffraction pattern of freshly filtered, ground crystals of **3** does not exactly fit the calculated powder pattern obtained from the single-crystal X-ray diffraction experiment (Figure 7). Indeed, the first peak is observed for a 2θ value of 6.10° (Figure 7, d), while the first peak in the calculated powder pattern is obtained for a 2θ value of 5.93° (Figure 7, b). This powder pattern progressively evolves with time; the first peak broadens and shifts toward higher 2θ values, while the position of the other ones remains approximately unchanged (Figures 7, e and f). No further change is observed after a few hours at room temperature, indicating that the partial dehydration of **3** is achieved to give $\mathbf{3_{subhyd}}$. When a drop of water is added to the powder sample of $\mathbf{3_{subhyd}}$, the X-ray powder pattern changes and the position of the first peak (Figure 7, c) now matches the position of the first peak in the calculated powder pattern (Figure 7, a). This experiment shows that the dehydration at room temperature is reversible.

Despite the poor quality of the experimental X-ray powder pattern, we tried to simulate the structure of the dehydrated sample $\mathbf{3_{subhyd}}$ by lattice energy minimisations[20] to reproduce the positions of the experimental diffraction peaks. This simulation allowed us to calculate the cell parameters of the dehydrated sample and showed that the contraction mainly affects the *a* parameter.[12] The channels shrink upon dehydration, in agreement with a hydrophobic

 © 2005 Wiley-VCH Verlag GmbH & Co. KGaA, Weinheim

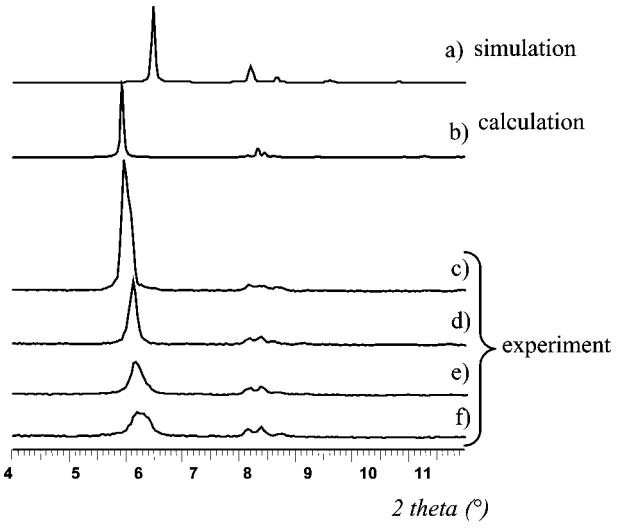

Figure 7. a) Simulated diffraction powder pattern of $\mathbf{3}_{\mathbf{subhyd}}$; b) calculated diffraction powder pattern from the single-crystal X-ray diffraction structure of **3**. Experimental diffraction powder pattern: c) $\mathbf{3}_{\mathbf{subhyd}}$ to which a drop of water has been added, d) **3** freshly filtered (t = 5 min), e) t = 30 min, f) t = 2 h.

character, as a consequence of the presence of aromatic rings on the channel walls. The difference between the volumes of **3** and $\mathbf{3}_{\mathbf{subhyd}}$ (reduction of 12%) leads to an estimated number of water molecules lost by the dehydration at room temperature of 17, assuming that a hydrogen-bonded water molecule occupies a volume of 40 Å^3. The thermogravimetric analysis (TGA) curve performed on $\mathbf{3}_{\mathbf{subhyd}}$ (Figure S1) shows an initial weight loss of 16.0% (calcd. 16.1) attributable to the loss of 32 water molecules trapped within the channels. The second weight loss of 9.6% (calcd. 9.4) corresponds to the loss of water molecules bound to the lanthanum ions and to the formation of oxides. This is in agreement with the following formula [ε-$PMo_{12}O_{35}(OH)_5$-$\{La(H_2O)_3\}_4(C_9H_3O_6)_2$]·$32H_2O$ for $\mathbf{3}_{\mathbf{subhyd}}$, while elemental analysis is more in favour of 27 hydration water molecules (see Experimental Section).

The presence of tunnels filled only with water molecules motivated a measurement of the surface area. Nevertheless, after activation of the sample at 70 °C a BET nitrogen adsorption measurement performed on $\mathbf{3}_{\mathbf{subhyd}}$ revealed a low surface area (ca. 14 $m^2 g^{-1}$), thus confirming the X-ray thermodiffractometry experiment, which shows that the structure collapses. At variance with the dehydration at room temperature and ambient pressure, the dehydration under vacuum is therefore irreversible.

The description of the four hybrid organic–inorganic materials **1**–**4** based on the ε-Keggin unit shows the complexity of these systems. However, an important feature arises from this study: Keggin ions can be used as inorganic bricks to build up hybrid open frameworks. To the best of our knowledge, it indeed seems that this has been found here for the first time. This is probably due to the possibility for ε-Keggin ions to be tetrahedrally decorated by four cations, which act as points of anchorage for linking organic species, and also means that the serendipity which often governs the POM:ligand stoichiometry can be surpassed by the introduction of computer prediction of possible Keggin-based hybrid frameworks. In order to tentatively rationalise what family of open frameworks compounds could be envisioned, the following section describes our first simulation results.

Computational Section

In the current search for new and interesting hybrid open frameworks, the predictability of the framework architecture and its resulting dimensionality are essential. It is highly valuable to consider how systematic approaches may be computationally developed for producing new hybrid frameworks, with the desire of developing virtual libraries that might be accessible through synthesis. With this in mind, some of us (C.M-D, G.F.), have made important efforts to introduce a computational prediction of crystal structures using the concept of building units.[5] The resulting AASBU method (Automated Assembly of Secondary Building Units)[13] was initially devoted to inorganic structures, but the applicability of the method in the realm of hybrid solids has been demonstrated recently.[14] The key feature of the method lies in the use of pre-defined organic and inorganic building units together with pre-defined connection points on each type of unit. The simulations explore their assembly in 3D space through a cascade of simulated annealing and minimisation steps. Indeed, this simulation approach focuses on the capacity of the organic and inorganic sub-units to generate infinite networks, resulting in a list of candidate periodic crystalline arrangements and their respective space group, cell parameters and atomic coordinates.

One of the key points for the success of the method is the knowledge of the chemical conditions associated with the existence of a given building block in the solution. In the same way as we demonstrated the existence of Cr_3–μ_3-O clusters,[14c] the [ε-$PMo^{V}_8Mo^{VI}_4O_{36}(OH)_4$-$\{La(H_2O)_4\}_4$]$^{5+}$ Keggin ion has been characterised in solution.[6] Its recurrence in experimental crystal structures is a clear evidence that the Keggin ion may be regarded as a building unit, the condensation of which with an appropriate organic linker might lead to a whole series of hybrid infinite networks. This section presents an attempt to produce hybrid infinite networks computationally by assembling Keggin inorganic units with a carefully chosen organic counterpart and to demonstrate the capacity of the simulation approach for generating hybrid open-framework candidates that are all built from the same pre-defined Keggin ion and organic ligand, in other words hybrid polymorphs.

In the present computational work, we selected terephthalic acid as a good candidate to generate hypothetical Keggin-based hybrid structures owing to its rigid carbon skeleton and its simple bidentate character. The use of 4,4′-bipyridine would have led to similar results. The isolated Keggin ion offers four anchorage points to the carboxylate function through its four capping M ions, which are placed

 © 2005 Wiley-VCH Verlag GmbH & Co. KGaA, Weinheim

at the corners of a virtual tetrahedron (M is chosen here as a trivalent M^{III} ion). The Keggin–terephthalic acid linkages therefore lead to pentacoordinate M^{III} cations, where each M cation is coordinated to three oxygen atoms of the Keggin ion and two oxygen atoms of the carboxylate ligand. This ε-Keggin cation, with four pentacoordinate capping transition metal ions, is currently a hypothetical ion which has never been isolated but which is chosen here in order to simplify the calculations. Interestingly, considering that each Keggin ion may connect to four terephthalic acids in the four directions of a tetrahedron (Figure 1), the infinite connection of alternating Keggin ions and terephthalic acids is deemed to lead to four-connected networks similar to those observed in dense silicates such as quartz or microporous silicates such as zeolites,[15] all of which contain corner-sharing SiO_4 tetrahedra.

In the present work, the simulation of two candidate hybrid structures is presented. Using the above analogy with silicates, we assembled the Keggin ion and terephthalate ligands in 3D space to simulate two upper hybrid analogues which correspond to the quartz-α and LTA augmented nets.[16] Indeed, according to O'Keeffe et al., each augmented net possesses the same topology as two existing silicates or aluminosilicates: quartz-α ($P3_22_1$, a = 4.90 Å, c = 5.40 Å) and zeolite LTA ($Fm\bar{3}c$, a = 24.61 Å). Both frameworks result from the corner-sharing arrangement of SiO_4 tetrahedra. The crystallographic position of the Si atoms of the silicate structures is indicative of the required positioning of each Keggin ion centre, while the crystallographic position of the oxygen atoms is indicative of the required positioning of the centre of the organic molecule ensuring the linkage between two adjacent Keggin ions. Indeed, this construction process fully uses the analogy between the Si–O–Si linkages typically found in silicates and the metal–ligand–metal linkages found in metal–organic frameworks. The important size of the Keggin ion and of the organic molecule in comparison with that of Si and O atoms requires an extension of the size of each unit cell. The cell size of quartz-α increases to $a \approx 30$ Å, while that of zeolite LTA to more than 130 Å, keeping the Si and O atoms at the same crystallographic positions. In a subsequent step, the replacement of each independent Si and O atom by a Keggin ion and an organic ligand, respectively, was performed in each unit cell, resulting in two hybrid crystal structures with the same chemical composition [ε-$PMo_{12}O_{37}(OH)_3(M^{III})_4](O_2C\text{-}C_6H_4\text{-}CO_2)_2$. In some cases, these steps required a lowering of the initial symmetry. As a final step, the two hybrid crystal structures were submitted to lattice energy minimisations by allowing the atomic positions and the cell parameters to relax. Short-range interactions were calculated with the UFF forcefield.[17] The electrostatic contribution was calculated with an Ewald summation by using partial charges obtained from the charge equilibration method.[18] The simulations were performed using the Cerius2 suite of software[19] on an Octane SGI R12000 workstation operating at 300 MHz.

Energy-minimised structures of the quartz-type and of the LTA-type are shown in Figures 8 and 9, respectively, together with their simulated X-ray powder diffraction pattern (Cu-K_α respectively). The hybrid LTA-type Keggin dicarboxylate converged with cell parameters of a = 119.25 Å, while that of the minimised quartz-type Keggin-dicarboxylate possesses cell parameters of a = 25.93 Å and c = 24.20 Å. The quartz-type structure (Figure 8) can be described as a 3D network of Keggin cations connected by terephthalate ligands to form exclusively distorted 6-rings, directly emanating from the quartz topology. Hence it is a

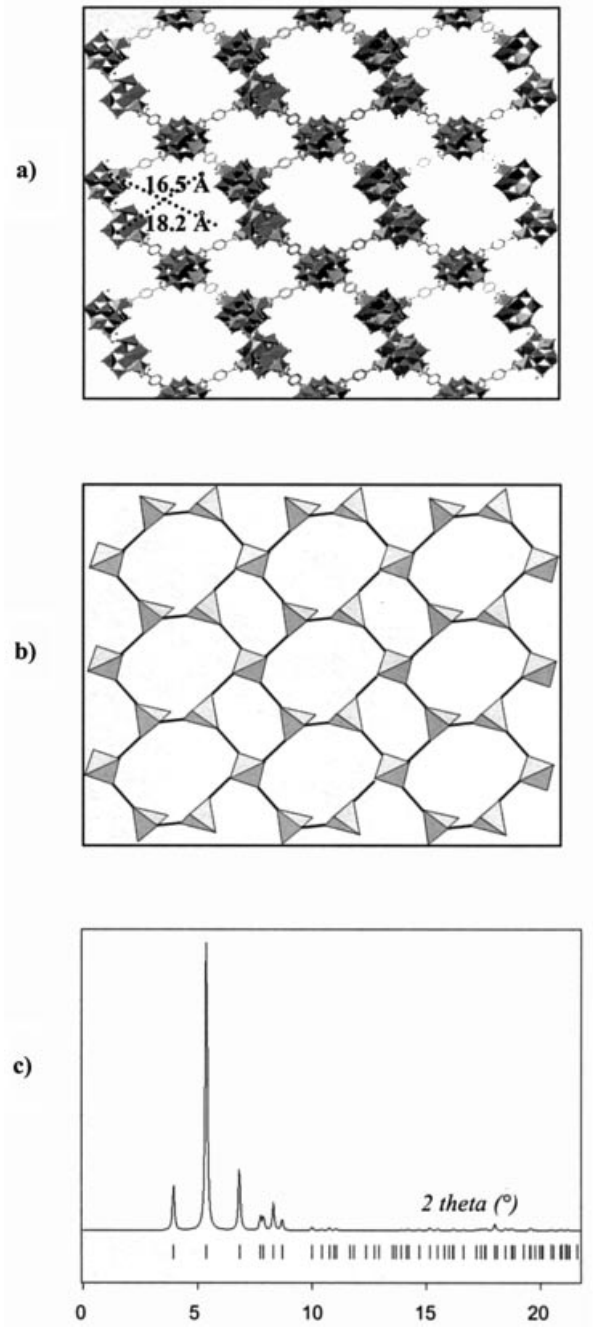

Figure 8. a) Projection along the a axis of the energy minimised structure of the quartz-α type; b) schematic view with ε-Keggin units represented by tetrahedra and terephthalate ligands by rods; c) simulated X-ray powder diffraction pattern (Cu-K_α).

 © 2005 Wiley-VCH Verlag GmbH & Co. KGaA, Weinheim

porous hypothetical structure which forms channels delimited by six Keggin ions with accessible diameters of 16.5×18.3 Å. The LTA-type structure (Figure 9) contains small cages (sodalite-type cages) made of 6-rings of Keggin ions and 4-rings, visible at the centre of Figure 9. Their assembly along each direction generates a bigger cage (here called supercage), made of 4-, 6- and 8-rings, four of which are visible at each corner of Figure 9. These supercages communicate with one another through 8-rings, the connection of which generates channels with larget dimensions (ca. 40 Å of diameter from one terephthalate to the opposite one). The inner diameter of the supercage is around 84 Å. These lattice energy calculations are a preliminary study to a more extended work on the relative stabilities of Keggin-containing hybrid frameworks. We believe that these two hypothetical structures are indicative of the viability of such open-framework architectures.

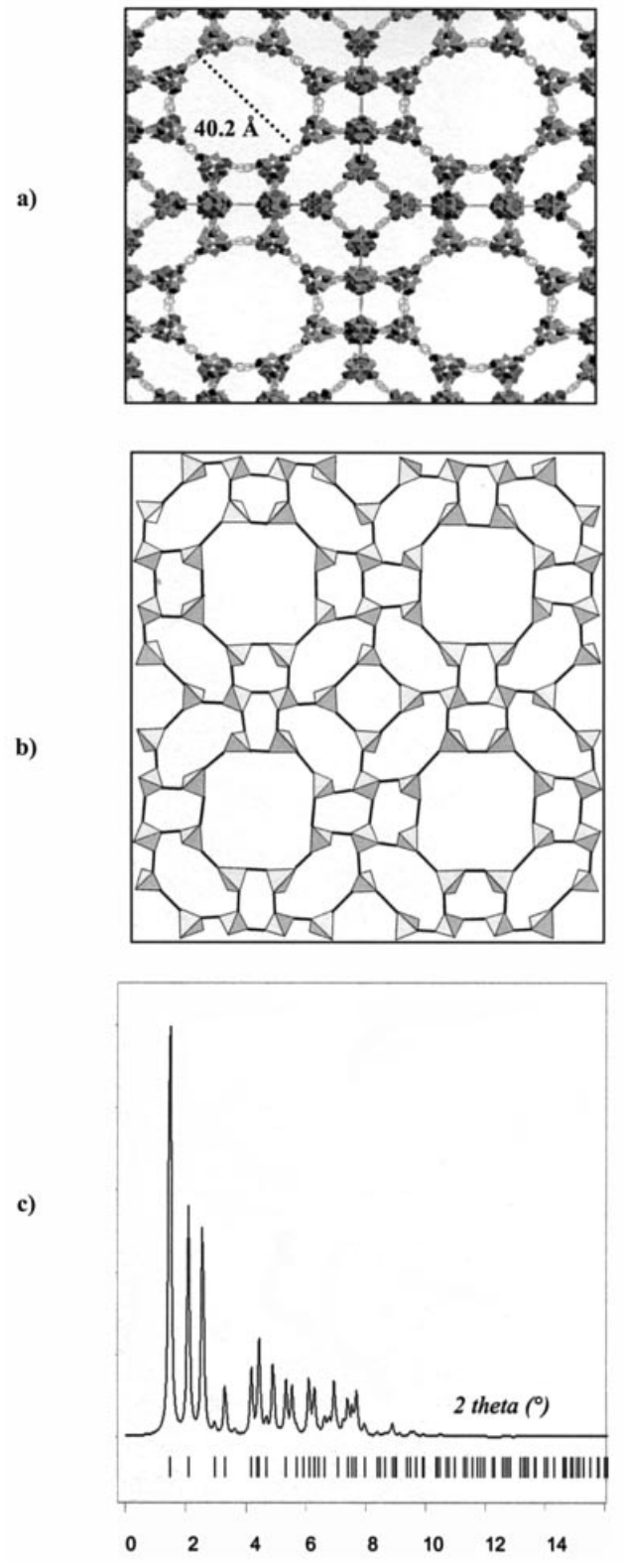

Figure 9. a) Projection along the *c* axis of the energy minimised structure of the zeolite LTA type, b) schematic view with ε-Keggin units represented by tetrahedra and terephthalate ligands by rods, c) simulated X-ray powder diffraction pattern (Cu-K_α).

Conclusions

This study demonstrates that it is possible to build extended frameworks containing a polyoxomolybdate building unit, under mild or hydrothermal conditions, with POM:ligand ratios ranging from 1:3 to 1:1. Two important features of the Keggin core dictate the nature of the final product: its charge related to the valence of the capping ion and the protonation states and also the coordination adopted by the capping ion. The synthesis of the materials described in this paper proves that a large family of original extended frameworks can be isolated, even though no stable porous materials have been obtained so far, and the simulation results show that the materials built from the connection of an ε-Keggin inorganic building unit and rigid linkers can potentially exhibit very large pores. It is now the chemist's role to investigate the synthesis of such phases. We will adopt two strategies: at room temperature we will continue to develop the reactions of the $[\varepsilon\text{-}PMo_{12}O_{36}(OH)_4\text{-}\{La(H_2O)_4\}_4]^{5+}$ polyoxocation with rigid polycarboxylates. We also are planning to investigate the replacement of lanthanum ions by rare-earth cations with smaller coordination numbers, such as Yb^{3+}. These rare-earth centres would be bound to a lower number of water molecules and the stability of the framework could therefore be improved. The second strategy will take advantage of hydrothermal conditions for the synthesis of porous materials with the aim of obtaining phases close to the simulated ones. The ε-Keggin core capped with transition metal cations (Fe^{III}, Ru^{III}, Mn^{III},...) will be generated in situ in the presence of O- or N-donor ligands. Furthermore, as demonstrated by recent results from our group, even if no single crystals are isolated and provided the X-ray powder pattern is of suitable quality, simulation combined with X-ray powder diffraction could allow us to determine the structure of these hybrids. Finally, the incorporation of POMs into hybrid organic–inorganic materials could lead to interesting applications. Indeed, these solids could combine the properties of POMs with those of porous materials, thereby opening-up a new perspective in the field of catalysis by POM-based compounds.

 © 2005 Wiley-VCH Verlag GmbH & Co. KGaA, Weinheim

Experimental Section

General: All chemicals were used as purchased without purification. Elemental analysis was performed by the Service Central d'Analyse of CNRS 69390 Vernaison France. Infrared spectra were recorded with an IRFT Magna 550 Nicolet spectrophotometer at 0.5 cm^{-1} resolution, using the technique of pressed KBr pellets. X-ray powder diffraction data were collected with a Siemens D5000 diffractometer equipped with Cu-K_α radiation. The BET surface area analysis was performed with a Micrometrics ASP200 porosimeter. TGA experiments were performed under air (5°C/min) using a TA Instrument type 2050 analyzer apparatus.

Synthesis of $Na(C_{10}H_{10}N_2)[\varepsilon\text{-}PMo_{12}O_{40}Zn_4(H_2O)_2(C_{10}H_8N_2)_3]\cdot 10H_2O$ (1): A mixture of $Na_2MoO_4\cdot 2H_2O$ (0.47 g, 1.94 mmol), Mo (0.030 g, 0.31 mmol), $Zn(OOCCH_3)_2$ (0.16 g, 0.73 mmol), 4 M H_3PO_4 (46 μL, 0.18 mmol), 4,4′-bipyridine (0.06 g, 0.38 mmol) and water (5 mL; pH adjusted to 6.5 with 1 M NaOH) was sealed in a Teflon-lined reactor which was kept at 180 °C for 60 h. Black parallelepipedic crystals for single-crystal X-ray diffraction were hand selected from a product mixture. Crystals for elemental analysis were isolated by decantation after sonication and washed with EtOH (0.200 g, 36% yield in crystals, based on Mo). IR (KBr pellets): $\tilde{\nu}$ = 1541 s, 1505 s, 1409 s, 1299 w, 1018 w, 961 m, 934 s, 838 w, 815 m, 772 s, 754 s, 699 w, 599 s, 514 w cm^{-1}. $C_{40}H_{58}Mo_{12}N_8NaO_{52}PZn_4$ (2949.7): calcd. C 16.29, Mo 39.03, N 3.80, Na 0.78, P 1.05, Zn 8.87; found C 13.26, Mo 38.93, N 3.06, Na 1.04, P 1.05, Zn 10.75.

Synthesis of $[\varepsilon\text{-}PMo_{12}O_{35}(OH)_5La_4(C_8H_4O_4)_3]\cdot 41H_2O$ (2): $[\varepsilon\text{-}PMo_{12}O_{36}(OH)_4\{La(H_2O)_{2.5}Cl_{1.25}\}_4]\cdot 27H_2O$ (0.100 g, 3.2×10^{-5} mol) was dissolved in CH_3OH (5 mL). A solution of 6×10^{-3} M terephthalic acid (16 mL, 9.6 10^{-5} mol) adjusted to pH 6.0 was then added dropwise. The resulting microcrystalline burgundy powder (0.100 g, yield 86.5% based on molybdenum) was filtered and washed with H_2O and EtOH. IR (KBr pellets): $\tilde{\nu}$ = 1639 s, 1541 s, 1505 m, 1409 s, 1299 w, 961 m, 934 s, 838 w, 815 m, 772 m, 754 s, 699 w, 599 m, 514 m cm^{-1}. $C_{24}H_{99}La_4Mo_{12}O_{93}P$ (3613.88): calcd. C 7.98, La 15.37, Mo 31.85, P 0.86; found C 8.41, La 15.25, Mo 31.37, P 0.90.

Synthesis of $[\varepsilon\text{-}PMo_{12}O_{35}(OH)_5\{La(H_2O)_3(C_9H_3O_6)_{0.5}\}_4]\cdot 44H_2O$ (3): Crystals were obtained by slow evaporation of a solution of $[\varepsilon\text{-}PMo_{12}O_{36}(OH)_4\{La(H_2O)_{2.5}Cl_{1.25}\}_4]\cdot 27H_2O$ (0.050 g, 1.6×10^{-5} mol) dissolved in CH_3OH (5 mL) to which a 10^{-2} M trimesic acid solution (1.6 mL, 1.6×10^{-5} mol), adjusted to pH 3.9 with 1 M NaOH, was added. After two days red parallelepipedic single crystals of **3** (14 mg, yield 28% based on Mo) were filtered off. The crystals were left for two days in air in an open beaker to give **3** $_{subhyd}$. IR (KBr pellets): $\tilde{\nu}$ = 1611 s, 1554 s, 1435 s, 1369 s, 1263 w, 1113 w, 966 m, 932 s, 812 m, 758 s, 685 m, 602 m, 529 s cm^{-1}. $[\varepsilon\text{-}PMo_{12}O_{35}(OH)_5\{La(H_2O)_3(C_9H_3O_6)_{0.5}\}_4]\cdot 27H_2O$ ($C_{18}H_{89}La_4Mo_{12}O_{91}P$, 3499.7): calcd. C 6.17, La 15.88, Mo 32.90, P 0.89; found C 6.32, La 15.90, Mo 32.75, P 0.87.

Synthesis of $[\varepsilon\text{-}PMo_{12}O_{37}(OH)_3\{La(H_2O)_4\}_4(C_{10}H_2O_8)]\cdot 24H_2O$ (4): Single crystals were obtained by slow evaporation of a 4 mL solution of $[\varepsilon\text{-}PMo_{12}O_{36}(OH)_4\{La(H_2O)_{2.5}Cl_{1.25}\}_4]\cdot 27H_2O$ (0.020 g, 0.65×10^{-5} mol) to which a 5×10^{-3} M pyromellitic acid solution (1.3 mL, 0.65×10^{-5} mol) was added. After a few days red parallelepipedic crystals were collected by filtration (0.016 g, yield 75% based on molybdenum). IR (KBr pellets): $\tilde{\nu}$ = 1625 s, 1545 s, 1492 m, 1433 m, 1385 s, 1328 w, 1141 w, 966 m, 932 s, 812 m, 758 s, 685 m, 602 m, 529 s cm^{-1}. $C_{10}H_{77}La_4Mo_{12}O_{84}P$ (3279.6): calcd. C 3.66, La 16.94, Mo 35.10, P 0.94; found C 4.09, La 16.61, Mo 34.95, P 0.91.

X-ray Crystallography: Intensity data collection was carried out with a Siemens SMART three-circle diffractometer equipped with a CCD detector using monochromatic Mo-K_α radiation (λ = 0.71073 Å). The absorption correction was based on multiple and symmetry-equivalent reflections in the data set using the SADABS program[20] based on the method of Blessing.[21] The structure was solved by direct methods and refined by full-matrix least-squares

Table 3. X-ray crystallographic data.

	1	**3**	**4**
Formula	$C_{40}H_{58}Mo_{12}N_8NaO_{52}PZn_4$	$C_{18}H_{123}La_4Mo_{12}O_{108}P$	$C_{10}H_{77}La_4Mo_{12}O_{84}P$
Mol. mass	2949.74	3806.00	3279.56
Crystal system	monoclinic	orthorhombic	triclinic
Space group	$P2_1/m$	$P2_12_12$	$P\bar{1}$
Flack parameter		–0.020(17)	
Z	2	2	2
T [K]	296	296	296
λ [Å]	0.71073	0.71073	0.71073
a [Å]	11.6693(2)	20.5144(3)	12.3192(2)
b [Å]	17.7590(4)	21.7012(4)	12.3654(2)
c [Å]	17.2028(1)	12.1655(1)	25.1114(4)
V [Å^3]	3421.1(1)	5415.9(1)	3774.4(1)
$\rho_{calcd.}$ [g cm^{-3}]	2.724	2.346	2.866
μ [mm^{-1}]	3.624	3.021	4.287
Reflections collected	18313	38147	17178
Unique reflections (R_{int})	6235 (0.1425)	14089 (0.0656)	10642 (0.0784)
Refined parameters	432	584	985
$R_1(F_o)$[a]	0.0815	0.0544	0.0663
$wR_2(F_o^2)$[a]	0.1810	0.1037	0.1434

[a] $R_1 = \frac{\Sigma||F_o|-|F_c||}{\Sigma|F_c|}$; [b] $wR_2 = \sqrt{\frac{\Sigma w(F_o^2-F_c^2)^2}{\Sigma w(F_o^2)^2}}$ with $\frac{1}{w} = \sigma^2F_o^2 + aP^2 + bP$ and $P = \frac{F_o^2+2F_c^2}{3}$,

a = 0.0983, b = 0 for **1**; a = 0.0528, b = 0 for **3**; a = 0.0732, b = 0 for **4**.

 © 2005 Wiley-VCH Verlag GmbH & Co. KGaA, Weinheim

using the SHELX-TL package.[22] Crystallographic data are given in Table 3. Selected bond lengths are listed in Tables 1 and 2.

CCDC-262218, -244419 and -262219 contain the crystallographic data for **1**, **3** and **4**, respectively. These data can be obtained free of charge from The Crystallographic Data Centre via www.ccdc.cam.ac.uk/data_request/cif.

[1] a) S. Kitagawa, R. Kitaura, S.-I. Noro, *Angew. Chem. Int. Ed.* **2004**, *43*, 2334; b) S. L. James, *Chem. Soc. Rev.* **2003**, *32*, 276.

[2] C. N. R. Rao, S. Natarajan, R. Vaidhyanathan, *Angew. Chem. Int. Ed.* **2004**, *43*, 1466.

[3] G. Férey, *Chem. Mater.* **2001**, *13*, 3084.

[4] M. Eddaoudi, J. Kim, N. L. Rosi, D. Vodak, J. B. Watcher, M. O'Keeffe, O. M. Yaghi, *Science* **2002**, *295*, 469.

[5] a) G. Férey, *J. Solid State Chem.* **2000**, *152*, 37; b) L. Beitone, C. Huguenard, M. Henry, F. Taulelle, T. Loiseau, G. Férey, *J. Am. Chem. Soc.* **2003**, *125*, 9102.

[6] P. Mialane, A. Dolbecq, L. Lisnard, A. Mallard, J. Marrot, F. Sécheresse, *Angew. Chem. Int. Ed.* **2002**, *41*, 2398.

[7] a) A. Müller, C. Beugholt, P. Kögerler, H. Bögge, S. Bud'ko, M. Luban, *Inorg. Chem.* **2000**, *39*, 5176; b) C. Lei, J.-G. Mao, Y.-Q. Sun, J.-L. Song, *Inorg. Chem.* **2004**, *43*, 1964.

[8] A. Dolbecq, P. Mialane, L. Lisnard, J. Marrot, F. Sécheresse, *Chem. Eur. J.* **2003**, *9*, 2914.

[9] N. E. Brese, M. O'Keeffe, *Acta Crystallogr. Sect. B* **1991**, *47*, 192.

[10] a) T. J. Prior, M. J. Rosseinsky, *Chem. Commun.* **2001**, 495; b) J.-C. Dai, X.-T. Wu, Z.-Y. Fu, C.-P. Cui, S.-M. Hu, N.-X. Du, L.-M. Wu, H.-H. Zhang, R.-Q. Sun, *Inorg. Chem.* **2002**, *41*, 1391.

[11] J. M. Poblet, X. López, C. Bo, *Chem. Soc. Rev.* **2003**, *32*, 297.

[12] Crystal data of $\mathbf{3}_{\mathbf{subhyd}}$ determined by simulation: orthorhombic space group $P2_12_12$ with a = 17.69, b = 21.48, c = 12.50 Å; V = 4750.4 Å^3.

[13] a) C. Mellot-Draznieks, J. M. Newsam, A. M. Gorman, C. M. Freeman, G. Férey, *Angew. Chem. Int. Ed.* **2000**, *39*, 2270; b) C. Mellot-Draznieks, S. Girard, G. Férey, *J. Am. Chem. Soc.* **2002**, *124*, 15326; c) C. Mellot-Draznieks, G. Férey, C. Schön, Z. Cancarevic, M. Jansen, *Chem. Eur. J.* **2002**, *8*, 4102.

[14] a) C. Mellot-Draznieks, J. Dutour, G. Férey, *Angew. Chem. Int. Ed.* **2004**, *43*, 6290; b) G. Férey, C. Serre, C. Mellot-Draznieks, F. Millange, S. Surblé, J. Dutour, I. Margiolaki, *Angew. Chem. Int. Ed.* **2004**, *43*, 6296; c) C. Serre, F. Millange, S. Surblé, G. Férey, *Angew. Chem. Int. Ed.* **2004**, *43*, 6285.

[15] C. Baerlocher, W. M. Meier, D. H. Olson, *Atlas of Zeolite Framework Types*, *5th revised edition*, Elsevier, Amsterdam, **2001**, and http://www.iza-structure.org/databases/.

[16] M. O'Keeffe, M. Eddaoudi, H. Li, T. Reineke, O. M. Yaghi, *J. Solid State Chem.* **2000**, *152*, 3.

[17] A. K. Rappé, C. J. Casewit, K. S. Colwell, W. A. Goddart III, W. M. Skiff, *J. Am. Chem. Soc.* **1992**, *114*, 10024.

[18] A. K. Rappé, W. A. Goddart III, *J. Phys. Chem. B* **1991**, *95*, 3358.

[19] Cerius2 Program suite from Accelrys, San Diego, USA, and Cambridge, UK.

[20] G. M. Sheldrick, *SADABS*; *program for scaling and correction of area detector data*, University of Göttingen, Göttingen, Germany, **1997**.

[21] R. Blessing, *Acta Crystallogr. Sect. A* **1995**, *51*, 33.

[22] a) G. M. Sheldrick, *Acta Crystallogr. Sect. A* **1990**, *46*, 467; G. M. Sheldrick, SHELX-TL version 5.03, Software Package for the Crystal Structure Determination, Siemens Analytical X-ray Instrument Division: Madison, WI (USA), **1994**.

Received: March 17, 2005
Published Online: June 28, 2005

 © 2005 Wiley-VCH Verlag GmbH & Co. KGaA, Weinheim

Synthesis, Properties and Molecular Structure of [Ru(tpm)(bpy)(CH_3CN)](PF_6)$_2$ (tpm = tris(1-pyrazolyl)methane, bpy = 2,2′-bipyridine) – Another Example of Nitrile Hydrolysis Promoted by Ruthenium(II)[‡]

Néstor E. Katz,*[a] Florencia Fagalde,[a] Noemí D. Lis de Katz,[a] María G. Mellace,[a] Isabel Romero,[b] Antoni Llobet,*[c] and Jordi Benet-Buchholz[d]

Keywords: Scorpionate ligands / Ruthenium / Bipyridines / Hydrolysis / Acetonitrile complexes

The synthesis and isolation of [Ru(tpm)(bpy)(CH_3CN)](PF_6)$_2$ (tpm = tris(1-pyrazolyl)methane; bpy = 2,2′-bipyridine) in good yield is described. This new Ru^{II} complex has been spectroscopically (IR, UV/Vis, emission) and electrochemically (cyclic voltammetry) characterized. Its solid-state structure has been solved by means of X-ray diffraction analysis and shows a distorted octahedral geometry where, as expected, the tpm ligand occupies three facial coordination sites, the bpy ligand chelates two further sites, and the CH_3CN ligand saturates the coordination sphere of the Ru metal center. Electrochemical and spectroscopic results indicate that the CH_3CN ligand acts as a moderately strong π-acceptor. The capacity of the coordinated CH_3CN ligand to undergo basic hydrolysis is also described. A second-order rate constant $k_{obs} = 1.3 \times 10^{-3}$ M^{-1} s^{-1} (T = 25 °C) has been obtained by following the UV/Vis absorption changes over time; the activation parameters obtained over the temperature range 17.0–40.0 °C are: $\Delta H^{\ddagger} = 74 \pm 4$ kJ mol^{-1} and $\Delta S^{\ddagger} = -54 \pm 12$ J mol^{-1} K^{-1}. These results are compared and discussed with regard to related complexes described in the literature that are also capable of carrying out this reaction. The results presented here make it possible to characterize the electronic and steric factors further and understand how they influence the basic hydrolysis of the coordinated CH_3CN ligand.
(© Wiley-VCH Verlag GmbH & Co. KGaA, 69451 Weinheim, Germany, 2005)

Introduction

The hydrolysis of nitriles to amides promoted by transition metals is a subject of interest with industrial and pharmacological applications.[1] Coordination of nitriles to transition metals in high or medium oxidation states normally increases the electrophilicity of the unsaturated nitrile C atom, thus promoting the addition of a great variety of nucleophiles.[1c] When the metal ion is in a low oxidation state, promotion is usually not observed. Thus, Ru^{III} is a much better mediator than Ru^{II} for nitrile hydrolysis.[2,3] The selective hydrolysis of nitriles to amides can also be achieved electrochemically.[4]

When the coligands coordinated to Ru^{II} are strong π-acceptors, such as polypyridines, one would expect an enhancement of the rate constant for nitrile hydrolysis. We could demonstrate[5] a quite unusual effect for a transition metal in oxidation state +2: the Ru^{II}(trpy)(bpy) moiety (trpy = 2,2′:6′:2″-terpyridine; bpy = 2,2′-bipyridine) can accelerate the hydrolysis of acetonitrile to acetamide in basic solutions by a factor of ca. 3×10^3. This result was accounted for by the extensive π-backbonding from Ru^{II} to the polypyridyl ligands.

We describe in this work the synthesis and physicochemical properties of the PF_6^- salt of the new complex [Ru(tpm)(bpy)(CH_3CN)]$^{2+}$ (tpm = tris(1-pyrazolyl)methane). In order to extend our knowledge of the enhancement effect of Ru^{II}, we also report on the hydrolysis of coordinated acetonitrile in this species. The structural and kinetic results obtained can be compared to those determined before for the complex [Ru(trpy)(bpy)(CH_3CN)]$^{2+}$[5,6] in order to understand how the different electronic and geometric constraints influence their reactivity.

The structures of the bpy, tpm and trpy ligands are shown in Scheme 1.

[‡] Presented in part at the XXXVIth International Conference on Coordination Chemistry, Mérida, México, July 18, 2004.
[a] Instituto de Química Física, Facultad de Bioquímica, Química y Farmacia, Universidad Nacional de Tucumán
Ayacucho 491, (T4000INI) San Miguel de Tucumán, Argentina
Fax: +543-814-248-169
E-mail: nkatz@arnet.com.ar
[b] Departament de Química, Universitat de Girona,
Campus de Montilivi, 17071 Girona, Spain
Fax: +34-972-418-150
E-mail: antoni.llobet@udg.es
[c] Departament de Química, Universitat Autònoma de Barcelona,
Bellaterra, 08193, Barcelona, Spain
Fax: +34-935-813-101
E-mail: antoni.llobet@uab.es
[d] Institut Català d′Investigació Química (ICIQ),
43007 Tarragona, Spain
Fax: +34-977-920-224
E-mail: jbenet@iciq.es
Supporting information for this article is available on the WWW under http://www.eurjic.org or from the author.

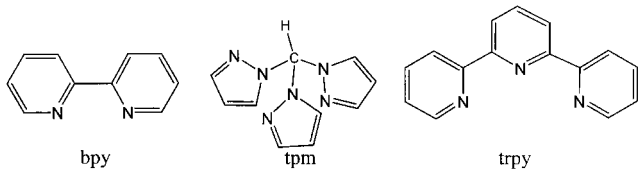

Scheme 1.

Results and Discussion

Synthesis

The synthetic route to $[Ru(tpm)(bpy)(CH_3CN)](PF_6)_2$ involves the substitution of the labile H_2O ligand in the known complex $[Ru(tpm)(bpy)(H_2O)](PF_6)_2$. In order to investigate the hydrolysis in basic solutions, the PF_6^- salt was metastasized to a Br^- salt, so that a higher solubility could be achieved.

UV/Vis and IR spectra

Figure 1 shows the electronic spectrum of $[Ru(tpm)(bpy)(CH_3CN)]^{2+}$. The UV spectrum in CH_3CN shows intraligand $\pi\rightarrow\pi^*$ absorption bands between 200 and 300 nm. In the visible region, bands due to MLCT (metal-to-ligand charge transfer) transitions $d_\pi(Ru)\rightarrow\pi^*$ (bpy) are observed at λ_{max} = 397 nm ($\varepsilon = 3.8\times10^3$ M^{-1}cm^{-1}) and 440 nm ($\varepsilon = 2.7\times10^3$ M^{-1}cm^{-1}). These values are lower than those corresponding to $[Ru(tpm)(bpy)(py)]^{2+}$ (py = pyridine; λ_{max} = 416 and 466 nm),[7] but similar to those of $[Ru(tpm)(py)(4,4'\text{-}(C(O)OC_2H_5)_2\text{-}bpy)]^{2+}$ (λ_{max} = 393 and 446 nm),[7] which leads to the conclusion that introducing a nitrile group into the coordination sphere of the $Ru(tpm)(bpy)^{2+}$ moiety has the same effect as introducing strong π-electron-withdrawing substituents into the 4,4′-positions of bpy. The higher π-acceptor capacity of CH_3CN relative to py has also been encountered when comparing the properties of Ru^{II} complexes containing 1,4,7-trithiacyclonane and 1,10-phenanthroline.[8]

On the other hand, the nitrile stretching frequency in the IR spectrum (of a KBr pellet) of $[Ru(tpm)(bpy)(CH_3CN)](PF_6)_2$ ($\tilde{\nu}_{C\equiv N}$ = 2282 cm^{-1}) is shifted to a higher frequency relative to the free ligand ($\tilde{\nu}_{C\equiv N}$ = 2254 cm^{-1}; $\Delta\tilde{\nu}_{C\equiv N}$ = 28 cm^{-1}). If we compare this result to the decrease in $\tilde{\nu}_{C\equiv N}$ observed in the IR spectrum of $[Ru(NH_3)_5(CH_3CN)](ClO_4)_2$, with respect to the free ligand ($\Delta\tilde{\nu}_{C\equiv N}$ = –15 cm^{-1}),[9] a strongly diminished π-back-bonding effect from Ru^{II} to the nitrile group caused by competition with 2,2′- bpy is inferred for the complex studied here.

Electrochemical Measurements

The cyclic voltammetry in CH_3CN, with 0.1 M TBAH [tetrakis(*n*-butyl)ammonium hexafluorophosphate] as a supporting electrolyte shows in the oxidative range of potential a reversible redox wave for the Ru^{III}/Ru^{II} couple at $E_{1/2}$ = 1.28 V (vs. SCE). Figure S1 shows the cyclic voltammogram. The values of λ_{max} and $E_{1/2}$ are consistent with those of similar complexes with strong π-accepting ligands, such as $[Ru(tpm)(bpy)(pz)]^{2+}$ (pz = pyrazine; λ_{max} = 392 and 457 nm; $E_{1/2}$ = 1.26 V).[10]

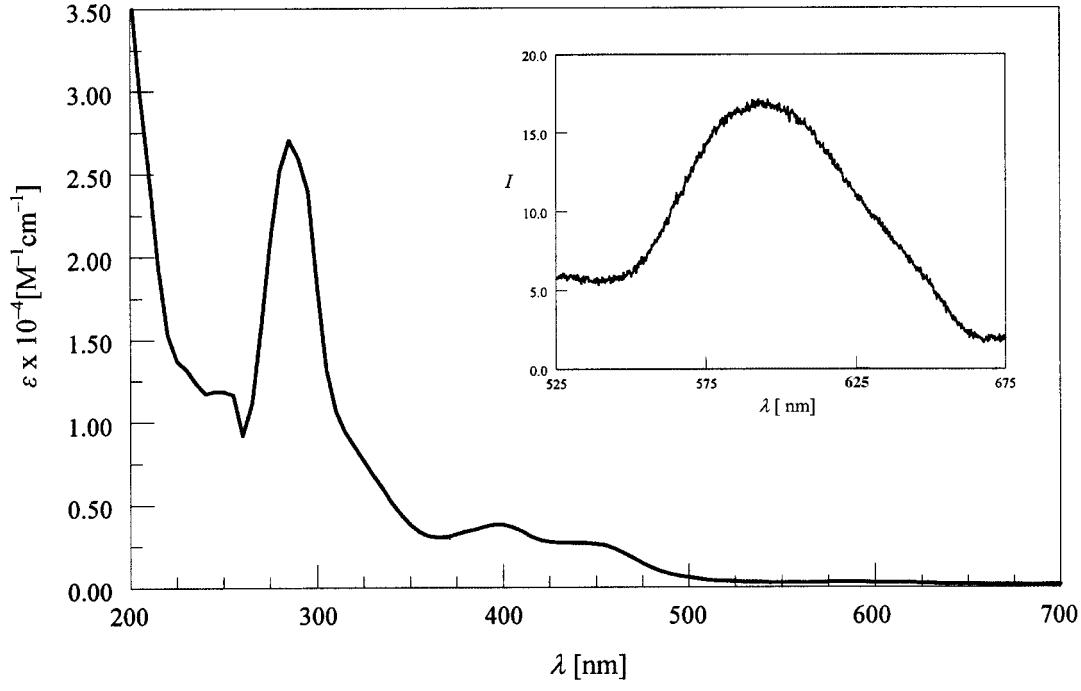

Figure 1. UV/Visible spectrum of $[Ru(tpm)(bpy)(CH_3CN)]^{2+}$, in CH_3CN, at room temperature. The inset shows the emission spectrum of $[Ru(tpm)(bpy)(CH_3CN)]^{2+}$ in CH_3CN, at room temperature (λ_{exc} = 440 nm).

 © 2005 Wiley-VCH Verlag GmbH & Co. KGaA, Weinheim

Luminescence Properties

The inset in Figure 1 shows the emission spectrum of $[Ru(tpm)(bpy)(CH_3CN)]^{2+}$ at room temperature in CH_3CN. The value of λ_{em} = 591 nm (at λ_{exc} = 440 nm) is similar to that determined for $[Ru(tpm)(bpy)(BPE)]^{2+}$ [BPE = *trans*-1,2-bis(4-pyridyl)-ethylene]: λ_{em} = 606 nm at λ_{exc} = 400 nm in CH_3CN[10] providing additional evidence of the behavior of CH_3CN as a stronger π-electron-accepting group than py.[8]

X-ray Structure

Figure 2 shows the ORTEP diagram for the cation $[Ru(tpm)(bpy)(CH_3CN)]^{2+}$. The crystal data are presented in the Supporting Information. The metal center adopts a pseudo-octahedral geometry with 3 N atoms (N1, N3, N5) from the tpm ligand coordinated in a facial manner. The 2,2′-bpy (N7, N8) acts as a chelating ligand, while the sixth position is occupied by the nitrogen atom (N9) of CH_3CN.

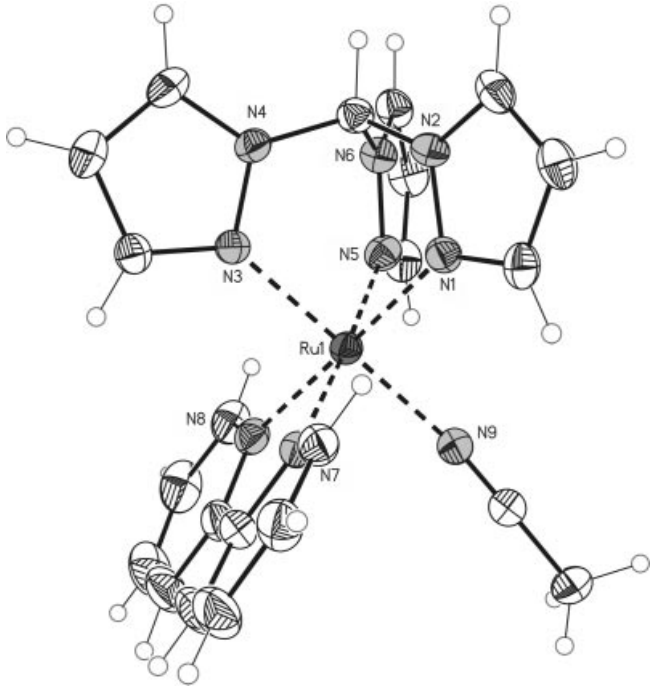

Figure 2. ORTEP-plot view (ellipsoids drawn at 50% probability) of $[Ru(tpm)(bpy)(CH_3CN)]^{2+}$, together with its labeling scheme. Selected bond lengths [Å] and angles [°]: Ru(1)–N(9), 2.0295(18); Ru(1)–N(7), 2.044(2); Ru(1)–N(3), 2.0500(17); Ru(1)–N(8), 2.053(2); Ru(1)–N(5), 2.068(2); Ru(1)–N(1), 2.069(2); N(9)–Ru(1)–N(7), 89.03(8); N(9)–Ru(1)–N(3), 179.65(7); N(7)–Ru(1)–N(3), 90.73(8); N(9)–Ru(1)–N(8), 87.00(8); N(7)–Ru(1)–N(8), 78.64(8); N(3)–Ru(1)–N(8), 92.70(7); N(9)–Ru(1)–N(5), 93.45(8); N(7)–Ru(1)–N(5), 176.51(8); N(3)–Ru(1)–N(5), 86.78(8); N(8)–Ru(1)–N(5), 99.03(8); N(9)–Ru(1)–N(1), 94.24(8); N(7)–Ru(1)–N(1), 98.86(8); N(3)–Ru(1)–N(1), 86.05(8); N(8)–Ru(1)–N(1), 177.20(9); N(5)–Ru(1)–N(1), 83.42(8).

The Ru–N bond lengths, as well as the bonding angles, are within the range found for similar complexes.[10] The Ru^{II}–N9 bond length, 2.029(18) Å, is closer to a Ru^{III}–N bond length (2.025Å in $[Ru(NH_3)_5(PhCN)]^{3+}$)[11] than to a Ru^{II}–N bond length (1.954 Å in $[Ru(NH_3)_5(PhCN)]^{2+}$).[11] The competition of bpy and CH_3CN for the electron density of Ru^{II} makes this metal more electropositive than in the corresponding ammine complexes.

Kinetics of Nitrile Hydrolysis

Figure 3 shows the consecutive spectra obtained at pH = 13.0, I = 0.1 M and T = 25 °C of an aqueous solution of $[Ru(tpm)(bpy)(CH_3CN)]^{2+}$. The MLCT absorption bands at λ_{max} = 397 and 440 nm are shifted to 440 and 510 nm, respectively. Isosbestic points are observed at 410 and 320 nm. These changes are indicative of a hydrolysis process followed by a ligand-substitution reaction. In effect, the observed rate constant is several orders of magnitude higher than that expected for a simple substitution of CH_3CN. As shown in Figure 3, the process is completed in less than 2 hours, while ligand replacements in Ru^{II} polypyridyl complexes normally take several days at room temperature.[5] The final product is coincident with that of the ion $[Ru(tpm)(bpy)(OH)]^{+}$; in effect, when 1 drop of concentrated HCl was added to this complex, two bands developed at λ_{max} = 427 and 494 nm, values identical to those expected for $[Ru(tpm)(bpy)(OH_2)]^{2+}$.[12] The process is not catalytic, since the substitution rate of H_2O for CH_3CN in $[Ru(tpm)(bpy)(OH_2)]^{2+}$ is expected to be very slow.[13] It is well known[4] that coordinated amides are rapidly released from the coordination sphere of Ru^{II} and that they undergo further hydrolysis to carboxylic acids and ammonia in basic solutions.[1c,3] It should be noted, however, that the lifetime of amido-bonded complexes can be increased by using polydentate ligands such as cyclam.[14]

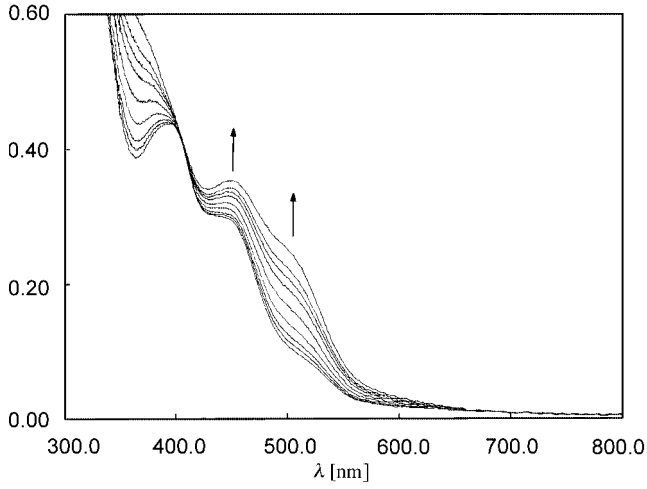

Figure 3. Spectra obtained in aqueous basic solutions of $[Ru(tpm)(bpy)(CH_3CN)]^{2+}$ at times t = 0, 3, 7, 15, 27, 41, 50, 60 and 81 min ([Ru] = 1.2×10^{-4} M; pH = 13; I = 0.1 M; T = 25 °C).

The pseudo-first-order rate constants k_{obs} depend linearly on the concentration of OH^-: $k_{obs} = k_{OH}[OH^-]$ (Figure S2). Table 1 shows the second-order rate constants for acetonitrile hydrolysis (k_{OH}) in several Ru complexes (including that of the free ligand). As shown in Table 1, the

 © 2005 Wiley-VCH Verlag GmbH & Co. KGaA, Weinheim

rate constant for the basic hydrolysis of $[Ru(tpm)(bpy)(CH_3CN)](PF_6)_2$ is 1.3×10^{-3} M^{-1} s^{-1} at 25 °C. Therefore, the Ru^{II}(tpm)(bpy) group accelerates the reaction by a factor of 10^3 with respect to the free ligand, an enhancement effect that is lower than that of $Ru^{III}(NH_3)_5$, but higher than that of $Ru^{II}(NH_3)_5$. The value is also ca. 4 times lower than that of the corresponding Ru^{II}(trpy)(bpy) complex, although the values are within the same order of magnitude and intermediate in the wide range of hydrolysis rate constants reported in the literature.[1b]

Table 1. Rate constants for basic hydrolyses of CH_3CN in several ruthenated species, at 25 °C.

Complex	k_{OH}[M^{-1} s^{-1}]	Reference
CH_3CN	1.6×10^{-6}	[2]
$[Ru(NH_3)_5(CH_3CN)]^{2+}$	$<6\times10^{-5}$	[2]
$[Ru(tpm)(bpy)(CH_3CN)]^{2+}$	1.3×10^{-3}	This work
$[Ru(trpy)(bpy)(CH_3CN)]^{2+}$	4.6×10^{-3}	[4]
$[Ru(NH_3)_5(CH_3CN)]^{3+}$	2.2×10^{2}	[2]

The variation of $\ln(k_{OH}/T)$ with $1/T$ is displayed in Figure 4. From Eyring's rate equation,[15] values of $\Delta H^{\ddagger}$ = (74 ± 4) kJ mol^{-1} and $\Delta S^{\ddagger}$ = (–54 ± 12) J mol^{-1} K^{-1} are determined, which are typical for an associative mechanism. Metal-catalyzed nitrile hydrolyses normally have negative activation entropies, since bimolecular processes are involved.[16]

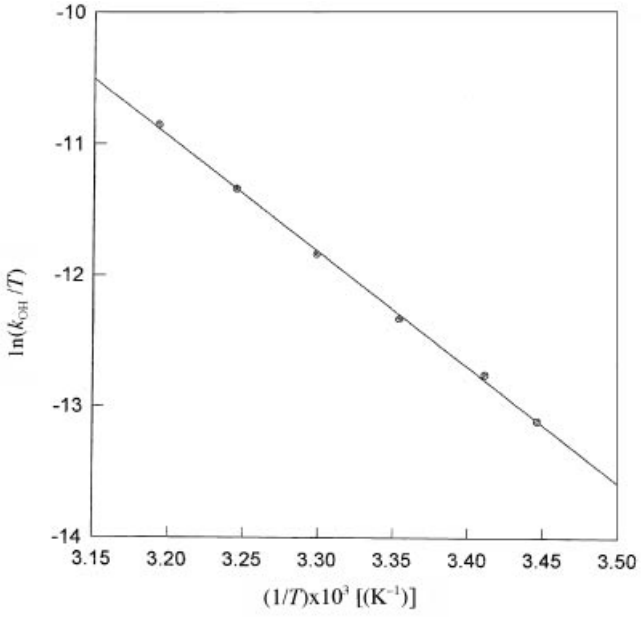

Figure 4. Eyring's plot for the basic hydrolysis of CH_3CN in $[Ru(tpm)(bpy)(CH_3CN)]^{2+}$.

Since trpy is a better π-acceptor than tpm, as evidenced by the higher $E_{1/2}$ values of $[Ru(trpy)(bpy)(L)]^{2+}$ complexes than those of $[Ru(tpm)(bpy)(L)]^{2+}$ complexes,[17,10] one would expect a more energy-demanding hydrolysis process for the latter species, when L = CH_3CN. However, the measured activation enthalpy is the same as that of the trpy species ($\Delta H^{\ddagger}$ = 74 kJ mol^{-1}).[5] On the other hand, the activation entropy is highly negative and much lower than that of the trpy species ($\Delta S^{\ddagger}$ = –42 J mol^{-1} K^{-1}),[5] thus accounting for its lower reaction rate. These entropy differences can be explained by considering the steric constraints imposed by the facial geometry of coordinated tpm. In contrast to the meridional geometry of trpy in $[Ru(trpy)(bpy)(CH_3CN)]^{2+}$,[6] the structure of $[Ru(tpm)(bpy)(CH_3CN)]^{2+}$ (see Figure 2) shows that two of the tpm rings protrude out of the metal-coordinated plane containing the N1, N5, N7, and N8 atoms, thus making the attachment of the hydroxide group to the coordinated nitrile group more entropy-demanding.

Conclusion

The new complex $[Ru(tpm)(bpy)(CH_3CN)]^{2+}$ presents spectral, electrochemical, and photophysical properties similar to analogous species with strong π-electron-accepting groups. Although the Ru^{II}(tpm)(bpy) moiety can also promote the hydrolysis of coordinated CH_3CN by a factor of 10^3 relative to free CH_3CN, the effect is less than that previously observed with the Ru^{II}(trpy)(bpy) moiety, because of the steric constrains imposed by the facial geometry of tpm.

Experimental Section

Materials: All reagents were obtained from Aldrich Chemical Co. and used without further purification. CH_3CN was freshly distilled for electrochemical measurements.

Preparations: All synthetic manipulations were routinely performed under nitrogen using Schlenk tubes and vacuum line techniques. Electrochemical experiments were performed in the dark under N_2 or Ar with degassed solvents.

Synthesis of $[Ru(tpm)(bpy)(CH_3CN)](PF_6)_2$: $[Ru(tpm)(bpy)(H_2O)](PF_6)_2$ (55 mg) prepared as described before,[12] was dissolved in CH_3CN (15 mL) and refluxed for 3 h. The solution was cooled to room temperature, and diethyl ether (100 mL) was added. The orange precipitate that formed was collected on a frit, washed with cold ether, and dried in vacuo over P_4O_{10}. Yield: 36 mg (64%). Elemental analysis: calcd. C 32.9, H 2.6, N 15.7; found C 33.1, H 2.7, N 15.0. IR: $\tilde{\nu}_{C\equiv N}$ = 2282 cm^{-1}. UV/Vis in CH_3CN: λ_{max}, nm (ε, M^{-1} cm^{-1}) = 397(3.8×10^3), 440 (2.7×10^3), 520 (7.2×10^2). $E_{1/2}$ = 1.28 V (vs. SCE).

The Br^- salt of the ion $[Ru(tpm)(bpy)(CH_3CN)]^{2+}$ was obtained by dissolving the PF_6^- salt (25 mg) in acetone (2 mL) and adding nBu$_4$NBr (500 mg) previously dissolved in acetone (2 mL). The precipitate was collected by filtration, washed with cold acetone, and dried in vacuo over P_4O_{10}. Yield: 17 mg (80%).

Equipment: All chemicals were reagent grade and used as received. UV/Visible spectra were recorded with a Shimadzu UV-160A spectrophotometer, equipped with a thermostatted cell compartment. IR spectra (of KBr pellets) were measured using a double-beam Perkin–Elmer 983G spectrophotometer. Chemical analyses were done at INQUIMAE, University of Buenos Aires, Argentina. Fluorescence measurements were determined with a Shimadzu RF-5301 PC spectrofluorometer in CH_3CN at room temperature. Cyclic voltammetry experiments were carried out in CH_3CN, 0.1 M TBAH [tetrakis(*n*-butyl)ammonium hexafluorophosphate] on a

 © 2005 Wiley-VCH Verlag GmbH & Co. KGaA, Weinheim

BAS Epsilon EC apparatus with a conventional three-electrode array, consisting of vitreous C as the working electrode, platinum wire as the auxiliary electrode and Ag/AgCl (3 M KCl) as the reference electrode. Ar was bubbled through the solutions prior to photophysical and electrochemical measurements.

Doubly distilled water was used for all kinetic determinations. pH measurements were carried out with a precision of ± 0.05 pH units, using a Metrohm 744 pH meter. The hydrolysis reactions were studied under pseudo-first-order conditions at temperatures between 17 °C and 40 °C, and pH values between 12.1 and 13.1 (NaOH). The ionic strength was fixed at I = 0.1 M (KCl). A fresh solution of $[Ru(tpm)(bpy)(CH_3CN)](Br)_2$ in water was used for each set of experiments. Absorbance (A) vs. time (t) data were recorded at λ = 510 nm. Duplicate or triplicate runs were made at each value of pH and temperature. The pseudo-first-order rate constants were determined by least-squares fits of $\ln(A_t - A_\infty)$ vs. t, which were linear for more than 3 half-lives. The estimated error in the base hydrolysis rate constants (k_{OH}) is ± 5%.

X-ray Structure Determination: Crystals of $[Ru(tpm)(bpy)(CH_3CN)](PF_6)_2$ were grown by slow diffusion of diethyl ether into a concentrated solution of $[Ru(tpm)(bpy)(pz)](PF_6)_2$[10] in CH_3CN at room temperature. Molecular formula $C_{22}H_{21}F_{12}N_9P_2Ru$, M = 802.49, orthorhombic, a = 12.88244(6), b = 13.4952(5), c = 16.3986(7) Å, V = 2850.9(2) Å^3, space group $P2_12_12_1$, Z = 4, μ = 0.775 mm^{-1}, $d_{calcd.}$ = 1.870 g cm^{-3}. The measurement was made with a Siemens P4 diffractometer equipped with a SMART-CCD-1000 area detector, a MACScience Co. rotating anode with Mo-K_α radiation, a graphite monochromator and a Siemens low temperature device LT2 (T = –120 °C). The measurements were made in the range 1.95 to 31.52°. 44178 reflections were collected, of which 9061 are unique (R_{int} = 0.0726). Full sphere data collection ω and φ scans. Programs used: Data collection Smart V. 5.060 (Bruker AXS, 1999), data reduction Saint + Version 6.02 (Bruker AXS 1999) and absorption correction SADABS (max/min transmission: 1.000000/0.578248, Bruker AXS 1999). Structure solution and refinement was performed using SHELXTL Version 5.10 (Sheldrick, Universtität Göttingen, Göttingen, Germany, 1998). The structure was solved by direct methods and refined by full-matrix least-squares against F^2. All calculated hydrogen positions are free refined. Final R_1 [$I > 2\sigma(I)$] = 0.0331 and $wR(F^2)$ [$I > 2\sigma(I)$] = 0.0719. The number or refined parameters was 472.

CCDC-264142 contains the supplementary crystallographic data for this paper. These data can be obtained free of charge from The Cambridge Crystallographic Data Centre via www.ccdc.cam.ac.uk/data_request/cif.

Supporting Information Available: CIF magnetic files together with additional electrochemical (Figure S1. Cyclic voltammogram of $[Ru(tpm)(bpy)(CH_3CN)]^{2+}$, in CH_3CN, 0.1 M TBAH, v = 200 mV/s) and kinetic (Figure S2. Dependence of the hydrolysis rate constants k_{obs} on [OH^-], at 25 °C) data (See footnote on the first page of this article.).

Acknowledgments

To CONICET, UNT, ANPCyT and Fundación Antorchas for financial support. N.E.K and F.F. are Members of the Research Career (CONICET). M.G. Mellace thanks CONICET for a graduate fellowship. N. E.K. thanks DAAD for the donation of BAS equipment. This research has also been financed by MCYT of Spain through project BQU2003–02884 and by the CIRIT Generalitat de Catalunya (Spain) by the Distinction award and the aid SGR2001-UG-291.

[1] a) A. J. Pombeiro, V. Yu Kukushkin, *Comprehensive Coordination Chemistry* (Eds.: J. A. McCleverty, T. J. Meyer), **2003**, ch. 1–34, 639–660; b) V. Yu. Kukushkin, A. J. L. Pombeiro, *Inorg. Chim. Acta* **2005**, *358*, 1–21; c) V. Yu. Kukushkin, A. J. L. Pombeiro, *Chem. Rev.* **2002**, *102*, 1771–1802.
[2] A. W. Zanella, P. C. Ford, *Inorg. Chem.* **1975**, *14*, 42–47.
[3] Z. N. da Rocha, G. Chiericato Jr., E. Tfouni, *Adv. Chem. Ser.* **1997**, *253*, 297–313.
[4] Z. Naal, E. Tfouni, A. V. Benedetti, *Polyhedron* **1994**, *13*, 133–142.
[5] F. Fagalde, N. D. Lis de Katz, N. E. Katz, *Polyhedron* **1997**, *16*, 1921–1923.
[6] S. C. Rasmussen, S. E. Ronco, D. A. Mlsna, M. A. Billadeau, W. T. Pennington, J. W. Kolis, J. D. Petersen, *Inorg. Chem.* **1995**, *34*, 821–829.
[7] K. A. Barqawi, A. Llobet, T. J. Meyer, *J. Am. Chem. Soc.* **1988**, *110*, 7751–7759.
[8] X. Sala, I. Romero, M. Rodríguez, A. Llobet, G. Gonzalez, M. Martínez, J. Benet-Buchholz, *Inorg. Chem.* **2004**, *43*, 5403–5409.
[9] R. E. Clarke, P. C. Ford, *Inorg. Chem.* **1970**, *9*, 227–235.
[10] N. E. Katz, I. Romero, A. Llobet, T. Parella, J. Benet-Buchholz, *Eur. J. Inorg. Chem.* **2005**, 272–277.
[11] Y. K. Shin, D. J. Szalda, B. S. Brunschwig, C. Creutz, N. Sutin, *Inorg. Chem.* **1997**, *36*, 3190–3197.
[12] A. Llobet, P. Doppelt, T. J. Meyer, *Inorg. Chem.* **1988**, *27*, 514–520.
[13] C. A. Bessel, J. A. Margarucci, J. H. Acquaye, R. S. Rubino, J. Crandall, A. J. Jircitano, D. J. Takeuchi, *Inorg. Chem.* **1993**, *32*, 5779–5784.
[14] Z. N. da Rocha, K. Queiroz Ferreira, M. Silva, E. C. de Oliveira, G. Chiericato Jr., E. Tfouni, *Inorg. Chem.* **2001**, *40*, 5385–5392.
[15] R. G. Wilkins, *Kinetics, Mechanism of Reactions of Transition Metal Complexes*, 2nd ed., VCH, Weinheim, **1991**.
[16] R. Breslow, R. Fairweather, J. Keana, *J. Am. Chem. Soc.* **1967**, *89*, 2135–2138.
[17] F. Fagalde, N. E. Katz, *Polyhedron* **1995**, *14*, 1213–1220.

Received: February 23, 2005
Published Online: July 4, 2005

 © 2005 Wiley-VCH Verlag GmbH & Co. KGaA, Weinheim

Self-Assembled Triorganotin(IV) Moieties with 1,3,5-Benzenetricarboxylic Acid: Syntheses and Crystal Structures of Monomeric, Helical, and Network Triorganotin(IV) Complexes

Chunlin Ma,*[a,b] Yinfeng Han,[a] Rufen Zhang,[a] and Daqi Wang[a]

Keywords: Crystal engineering / Helical structures / Networks / Self-assembly / Tin

A series of novel triorganotin(IV) complexes of the type $[(R_3Sn)_3(TMA)]\cdot Y\cdot L$ [R = CH_3, Y = $3CH_3OH$ (**1**); R = CH_3, Y = $2CH_3OH$ (**2**); R = $C_6H_5CH_2$ (**3**); R = *o*-F-$C_6H_4CH_2$ (**4**); R = *o*-Cl-$C_6H_4CH_2$ (**5**); R = C_6H_5, L = CH_2Cl_2 (**6**); R = C_6H_5, L = $EtOH\cdot 2H_2O$ (**7**); R = C_6H_5, L = $Et_2O\cdot CH_2Cl_2$ (**8**); H_3TMA = 1,3,5-benzenetricarboxylic acid] and $[(CH_3)_3Sn]_2(HTMA)\cdot H_2O$ (**9**) have been synthesized. All complexes were characterized by elemental analysis and by IR, ^1H, ^{13}C, and ^{119}Sn NMR spectroscopy. Except for **4** and **5**, all complexes were also characterized by X-ray crystallography. Complex **1** possesses a network structure where TMA acts as a tridentate ligand coordinated to three trimethyltin(IV) moieties and three methanol molecules that are involved in a hydrogen-bond system, whereas **2** possesses a helical structure where TMA acts as a tetradentate ligand coordinated to three trimethyltin(IV) ions and two methanol molecules that bend into the helical turn in the intra-helix hydrogen-bond system. Complexes **3**–**8** are monomeric structures where TMA acts as a hexadentate ligand coordinated to triorganotin(IV) ions and **9** possesses a network structure where TMA acts as a tetradentate ligand coordinated to trimethyltin(IV) ions and water molecules in the hydrogen-bond system that links the neighboring layers into a 3D network.

(© Wiley-VCH Verlag GmbH & Co. KGaA, 69451 Weinheim, Germany, 2005)

Introduction

In the last years, metal-directed self-assembly[1] has produced fascinating results in two topical areas dealing respectively with the deliberate construction of molecular interlocked/intertwined species, like rotaxanes, catenanes, knots, and helicates,[2,3] and the crystal engineering of extended 2D and 3D networks.[4,5] Conformationally flexible ligands are typical building elements in the former area, while in the latter essentially rigid rod-like organic units are usually employed to connect the metal centers. In particular, multi-benzenecarboxylate ligands have been shown to be good building blocks in the design of self-assembly complexes with desired topologies owing to their rich coordination modes.[6–10] In spite of the rich coordination chemistry exhibited by transition metals with these ligands,[11–17] relatively little is known with respect to the synthesis and the formal coordination of discrete organotin(IV) complexes with these ligands. Therefore, exploring whether organotin(IV) complexes with these ligands can help the construction of novel structure is of interest.

[a] Department of Chemistry, Liaocheng University, Liaocheng 252059, People's Republic of China
Fax: +86-538-6715521
E-mail: macl@lctu.edu.cn
[b] Taishan University, Taian 271021, People's Republic of China

In this work, we selected H_3TMA and the triorganotin(IV) ion on the basis of the following considerations: (a) it has three carboxylic acid groups that may be completely or partially deprotonated, inducing rich coordination modes and allowing interesting structures with higher dimensions; (b) it can act not only as a hydrogen-bond acceptor but also as a hydrogen-bond donor, depending upon the number of deprotonated carboxyl groups; (c) some of the carboxyl groups may not lie in the phenyl ring plane upon complexation to metal ions owing to space hindrance, thus it may connect metal ions in different directions; (d) it possesses high symmetry that may be helpful for the crystal growth of the product formed; (e) triorganotin(IV) ions have a high affinity for hard donor atoms, and ligands containing oxygen atoms, especially carboxylic ligands, are usually employed in the architectures for polymeric complexes. Recently, we began to assemble H_3TMA and triorganotin(IV) ions and hope the rich information stored in H_3TMA will induce novel polymeric structures constructed by tin(IV) centers. Herein we report the syntheses and characterizations of nine triorganotin(IV) complexes constructed from H_3TMA. With a 1:3:3 molar ratio of H_3TMA:EtONa:R_3SnCl we obtained eight trinuclear complexes (**1**–**8**) of the type $[(R_3Sn)_3(TMA)]\cdot Y\cdot L$ [R = CH_3, Y = $3CH_3OH$ (**1**); R = CH_3, Y = $2CH_3OH$ (**2**); R = $C_6H_5CH_2$ (**3**); R = *o*-F-$C_6H_4CH_2$ (**4**); R = *o*-Cl-$C_6H_4CH_2$ (**5**); R = C_6H_5, L = CH_2Cl_2 (**6**); R = C_6H_5, L = $EtOH\cdot 2H_2O$ (**7**); R = C_6H_5, L

 DOI: 10.1002/ejic.200500152

= $Et_2O{\cdot}CH_2Cl_2$ (**8**)], and with a 1:2:2 ratio a 3D network **9** was obtained with the formula $[(CH_3)_3Sn]_2(HTMA){\cdot}H_2O$.

Results and Discussion

Reactions of H_3TMA and sodium ethoxide with triorganotin(IV) chlorides in a 1:3:3 or 1:2:2 stoichiometry afford the air-stable complexes **1**–**8** or **9**, respectively. The synthetic procedures are shown in Scheme 1.

Spectroscopic Studies

IR Spectroscopy

The stretching frequencies of interest are those associated with the C(O)O, Sn–C, and Sn–O groups. The strong absorption in the region 468–496 cm^{-1}, which is absent in the spectrum of the free ligand, is assigned to the Sn–O stretching mode. All these values are consistent with those detected in a number of organotin(IV)–oxygen derivatives.[18,19]

In organotin carboxylate complexes, IR spectroscopy can provide useful information concerning the coordination mode of the carboxyl group. When the carboxylic group coordinates the tin atom in a monodentate manner, the difference between the wavenumbers of the asymmetric and symmetric carboxylic stretching bonds (mode I), $\Delta\nu[\nu_{asC(O)O^-} - \nu_{sC(O)O^-})$ is greater than that observed for ionic complexes. When the ligand chelates (mode II), $\Delta\nu$ is considerably smaller than that for ionic complexes, while for asymmetric bidentate coordination the value is in the

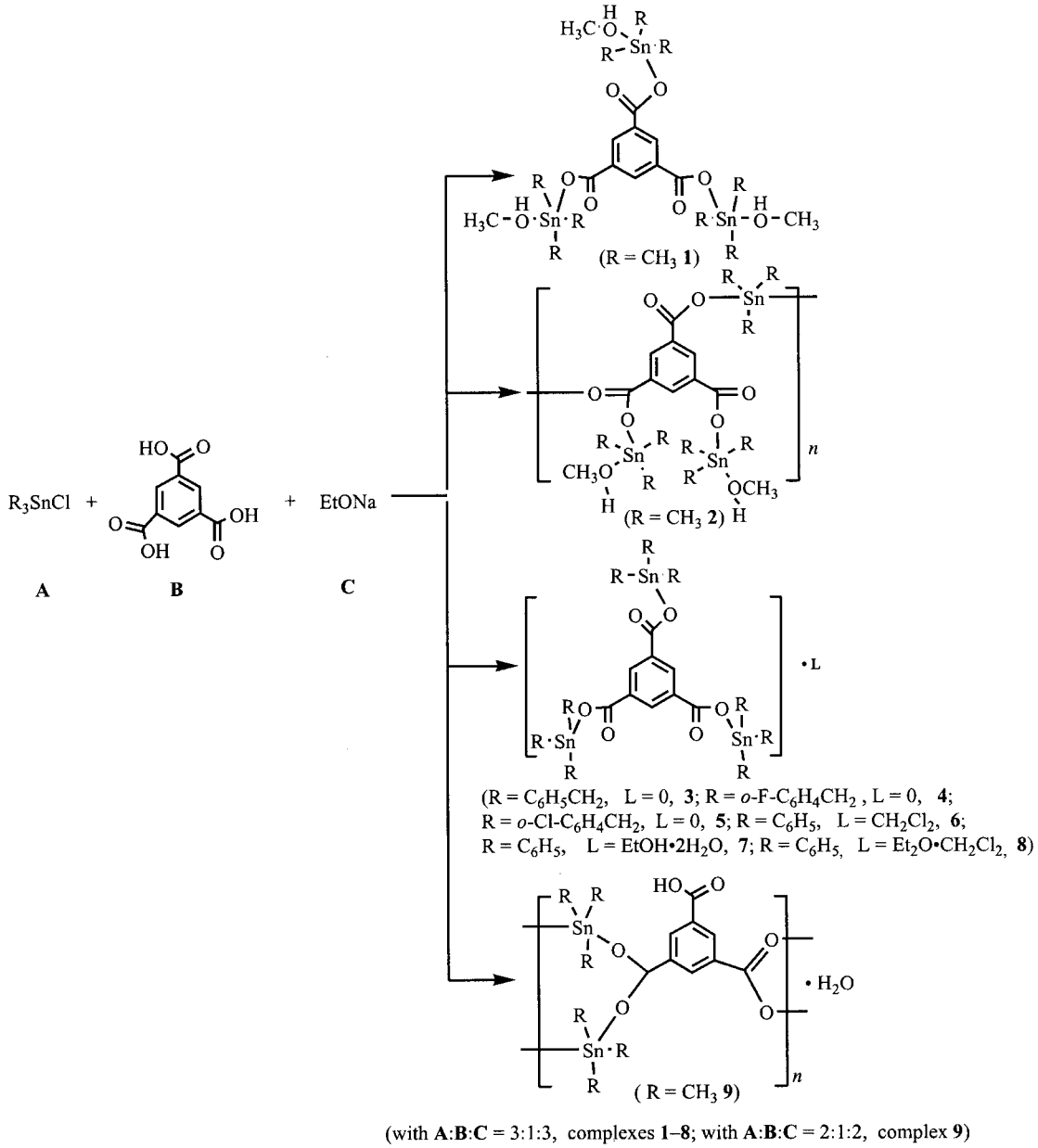

Scheme 1.

 © 2005 Wiley-VCH Verlag GmbH & Co. KGaA, Weinheim

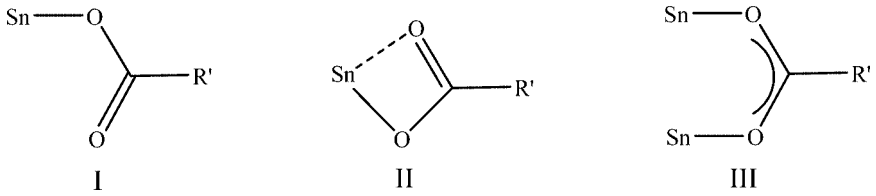

Scheme 2. Different coordination modes of the carboxylate group.

range characteristic of monodentate coordination.[20] The characteristic wavenumber difference for mode III is larger than that for chelated ions and nearly the same as observed for ionic complexes (Scheme 2).

Based on the above results, it was possible to distinguish the coordination mode of the $C(O)O^-$ group. The magnitude of $\Delta\nu$ of about 170 cm^{-1}, compared with those for the corresponding sodium salts, reveals that the carboxylate ligands function as bidentate ligands under the conditions employed.[21,22] This is also consistent with the X-ray diffraction study (see below).

NMR Spectroscopy

The ^1H NMR spectra show the expected integration and peak multiplicities. In the spectrum of the free ligand, the resonance observed at about δ = 10.51 ppm, which is absent in the spectra of the complexes, indicates the replacement of the carboxylic acid proton on complex formation. The chemical shifts of the signals for the methyl groups (δ = 0.81–1.01 ppm) and the phenyl group (δ = 7.21–7.76 ppm) appear at the same position as in the ligands. The $^2J_{Sn,H}$ values of trimethyltin derivatives **1** and **2** (68.6 and 69.4 Hz, respectively) are similar to those previously reported for five-coordinate trigonal bipyramidal tin(IV) adducts.[23]

The ^{13}C NMR spectra of all complexes show a significant downfield shift of all carbon resonances compared with the free ligand because of an electron density transfer from the ligand to the acceptor. Although at least two different types of carboxyl groups are present, only a single resonance is observed for the COO group in the ^{13}C NMR spectra. A possible reason for this is that either accidental magnetic equivalence of the carbonyl carbon atoms occurs or the separations between the sets of resonance are too small to be resolved.

The ^{119}Sn NMR spectra of **1** and **2** show only one signal, typical of a five-coordinate species, which is in accordance with their structures in the solid state.[24] However, the chemical shift for **9** (δ = –55.0 ppm) is within the range corresponding to a coordination number of 4 (δ = –60 to +200 ppm),[24] so it can reasonably be assumed that the structure of **9** in solution is probably different from that observed in the solid state.

Crystal Structure of $[(Me_3Sn)_3(TMA)]\cdot 3CH_3OH$ (1)

The molecular structure is illustrated in Figures 1 and 2 and selected bond lengths and bond angles are given in Table 1. Complex **1** is a two-dimensional polymer in the crystalline state. All the Sn atoms are five-coordinate with a trigonal bipyramidal structure by coordinating an additional methanol group. The axial ligand–tin–axial ligand angles [O(1)–Sn(1)–O(3) = 172.60(18)°, O(4)–Sn(2)–O(6) = 174.97(19)°, and O(7)–Sn(3)–O(9) = 174.7(2)°] suggest that the structures are near to a normal trigonal bipyramid. Intermolecular hydrogen-bond interactions between the methanol and the oxygen atom of an adjacent molecule [O(3A)–H···O(2) = 2.703 Å, O(6B)–H···O(8) = 2.694 Å, and O(9C)–H···O(5) = 2.608 Å] result in the formation of a two-dimensional network.

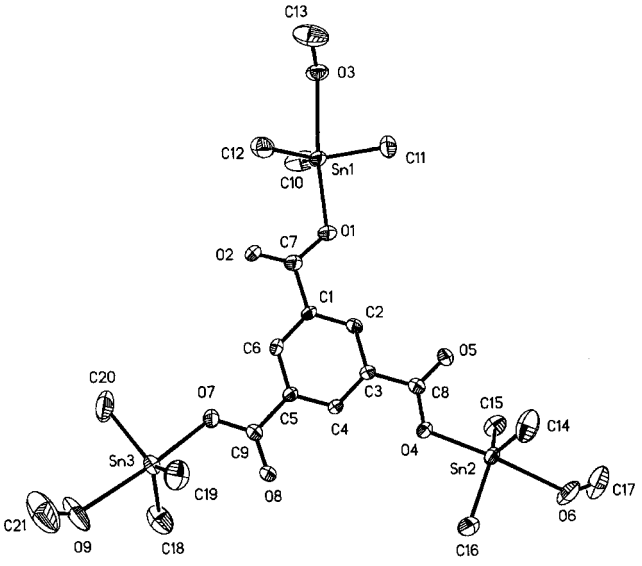

Figure 1. The molecular structure of **1**.

Crystal Structure of $[(Me_3Sn)_3(TMA)]\cdot 2CH_3OH$ (2)

The molecular structure of complex **2** is illustrated in Figures 3 and 4 and selected bond lengths and bond angles are given in Table 1. The asymmetric unit of **2** consists of $[(Me_3Sn)_3(TMA)]\cdot 2CH_3OH$ as the building block. There are two types of independent Sn atoms: the geometry at Sn(1) atom is trigonal bipyramidal with a bridging carboxyl group (O1 and O6A) and the geometries at Sn(2) and Sn(3) are trigonal bipyramidal with coordinating methanol group. The O(1)–Sn(1)–O(6)#1 [$-x$, $-y$, z + 1/2; 168.7(3)°], O(3)–Sn(2)–O(7)#2 [x, y – 1, z; 175.1(3)°], and O(5)–Sn(3)–O(8) [171.0(3)°] angles suggest that the structures are near to an ideal trigonal bipyramid. There are also two types of carboxylate groups, one of which is bidentate and the other monodentate. Due to the anisobidentate coordination mode of the carboxylate groups to the tin atoms, two groups of

 © 2005 Wiley-VCH Verlag GmbH & Co. KGaA, Weinheim

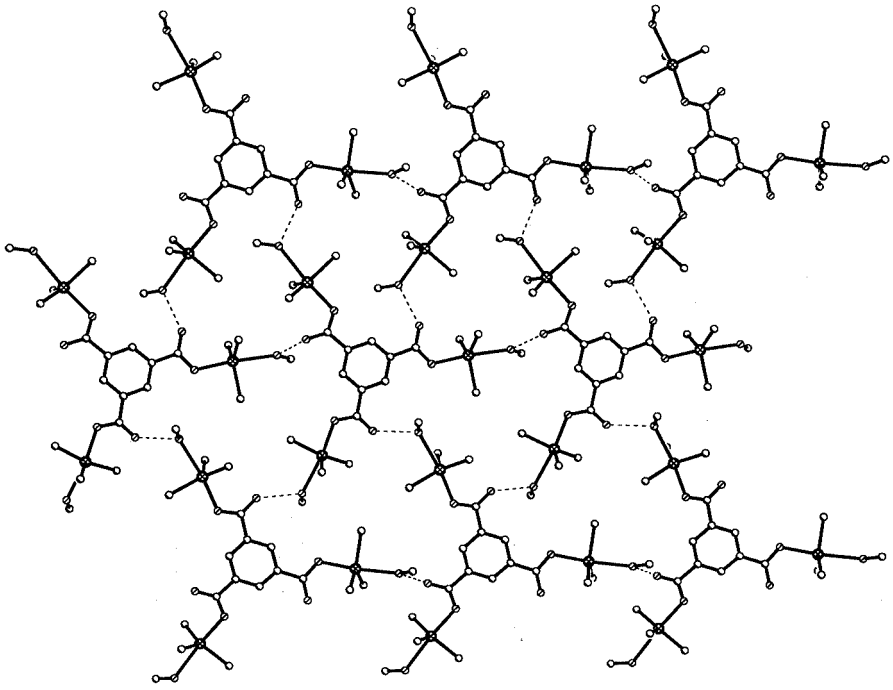

Figure 2. Polymeric network formed through intermolecular OH···O hydrogen-bond interactions in **1**.

Table 1. Selected bond lengths [Å] and bond angles [°] for **1** and **2**. #1: 1 – *x*, –*y*, *z* + 1/2: #2: *x*, *y* – 1, *z*; #3: –*x*, –*y*, *z* – 1/2.

1		**2**	
Sn(1)–O(1)	2.149(5)	Sn(1)–O(1)	2.160(7)
Sn(1)–O(3)	2.493(5)	Sn(1)–O(6)#1	2.549(8)
Sn(1)–C(11)	2.111(9)	Sn(1)–C(11)	2.107(17)
Sn(1)–C(10)	2.096(9)	Sn(1)–C(10)	2.125(13)
Sn(1)–C(12)	2.096(7)	Sn(1)–C(12)	2.135(13)
Sn(2)–C(14)	2.094(9)	Sn(2)–C(14)	2.084(16)
Sn(2)–C(15)	2.118(8)	Sn(2)–C(15)	2.108(12)
Sn(2)–C(16)	2.118(9)	Sn(2)–C(13)	2.158(12)
Sn(2)–O(4)	2.145(5)	Sn(2)–O(3)	2.160(7)
Sn(2)–O(6)	2.509(6)	Sn(2)–O(7)#2	2.569(9)
Sn(3)–C(19)	2.094(8)	Sn(3)–C(16)	2.059(15)
Sn(3)–C(18)	2.100(8)	Sn(3)–C(18)	2.102(14)
Sn(3)–C(20)	2.125(10)	Sn(3)–C(17)	2.118(16)
Sn(3)–O(7)	2.154(5)	Sn(3)–O(5)	2.156(9)
Sn(3)–O(9)	2.477(6)	Sn(3)–O(8)	2.462(9)
		Sn(1)#3–O(6)	2.549(8)
C(11)–Sn(1)–C(10)	120.2(5)	C(11)–Sn(1)–C(10)	115.2(7)
C(11)–Sn(1)–C(12)	118.8(4)	C(11)–Sn(1)–C(12)	127.0(6)
C(10)–Sn(1)–C(12)	118.3(4)	C(10)–Sn(1)–C(12)	114.2(8)
O(1)–Sn(1)–O(3)	172.60(18)	O(1)–Sn(1)–O(6)#1	168.7(3)
C(14)–Sn(2)–C(15)	121.4(4)	C(14)–Sn(2)–C(15)	120.1(6)
C(14)–Sn(2)–C(16)	118.7(4)	C(14)–Sn(2)–C(13)	120.8(6)
C(15)–Sn(2)–C(16)	118.0(4)	C(15)–Sn(2)–C(13)	116.2(6)
O(4)–Sn(2)–O(6)	174.97(19)	O(3)–Sn(2)–O(7)#2	175.1(3)
C(19)–Sn(3)–C(18)	120.9(4)	C(16)–Sn(3)–C(18)	119.3(9)
C(19)–Sn(3)–C(20)	117.8(4)	C(16)–Sn(3)–C(17)	119.1(9)
C(18)–Sn(3)–C(20)	119.6(5)	C(17)–Sn(3)–C(18)	119.2(9)
O(7)–Sn(3)–O(9)	174.7(2)	O(5)–Sn(3)–O(8)	171.0(3)

different Sn–O bond lengths are found, one group corresponding to Sn–O bonds of covalent character [2.156(9)–2.160(7) Å] and the other group corresponding to Sn–O bonds of coordinative character (2.548 Å). Bond lengths of 2.114(3)–2.208(2) Å and 2.381(2)–2.57(1) Å, respectively, have been measured in related trimethyltin carboxylates.[25] Also, there are two methanol molecules in the coordination sphere, with Sn–O bond lengths of 2.462 Å and 2.568 Å, respectively, which are comparable in strength to the intramolecular tin–oxygen bonds and close in length to the sum of the covalent radii of tin and oxygen (2.13 Å),[26] which is recognized as a coordinative bond.

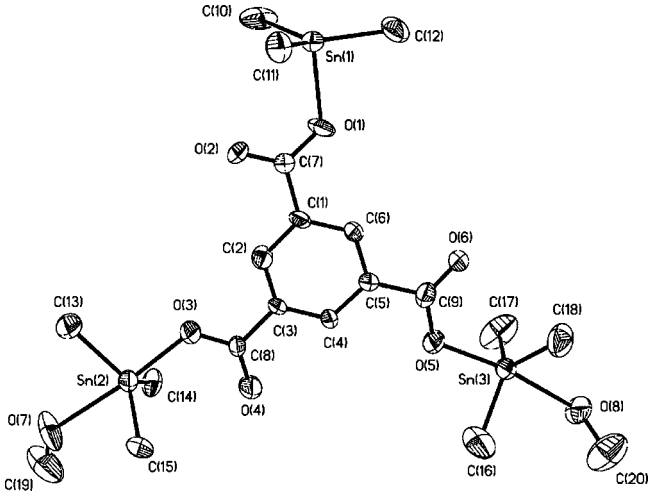

Figure 3. The molecular structure of **2**.

The structure shows that the Sn(1) ion is arranged in an infinite single helix with intervening TMA^{3-} ligands even though the ligand has no intrinsic tendency to form helical structures. The helical structure of **2** is a result of metal–organic ligand interactions coupled with the stereoelectronic characteristics of the ligand and the conditions prevailing during the synthesis. The helix has two distinct

 © 2005 Wiley-VCH Verlag GmbH & Co. KGaA, Weinheim

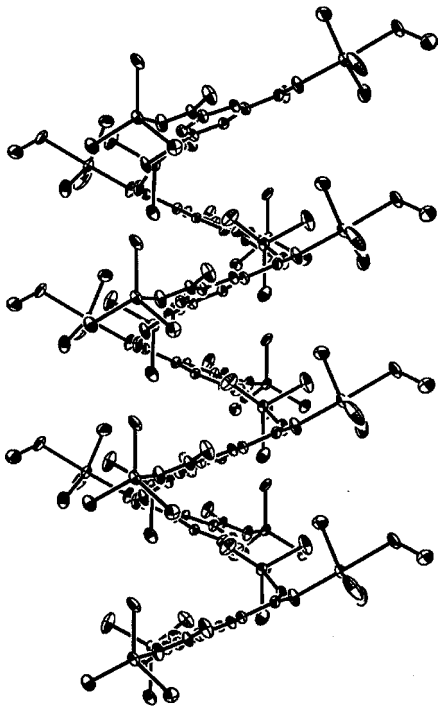

Figure 4. The helical structure of **2**.

Sn···Sn distances of 5.810 and 6.771 Å. The stability of the final helical structure relies on the coordinative bonds that each metal makes with the ligand. The helix is further organized into a metal–organic framework structure through inter-helix hydrogen bonding interactions to form a curved three-dimensional network.

The oxygen–oxygen distances in the crystal are also within the hydrogen-bonding range.[27] Hydrogen bonding is one of the main factors in the construction of supramolecular systems, and there are a variety of such linkages between the oxygen atoms of the carboxylic and coordinated methanol molecules. The packing is such that the oxygen of the coordinated methanol molecule forms two hydrogen bonds with the carboxylic oxygen atom of an adjacent molecule, which means that in the crystal there are a series of parallel helical chains that are linked by hydrogen bonds between coordinated CH_3OH and carboxylic oxygen atoms, which run through each other.

Crystal Structures of $[\{(C_6H_5CH_2)_3Sn\}_3(TMA)]$ (3), $[\{(C_6H_5)_3Sn\}_3(TMA)]\cdot CH_2Cl_2$ (6), $[\{(C_6H_5)_3Sn\}_3(TMA)]\cdot EtOH\cdot 2H_2O$ (7), and $[\{(C_6H_5)_3Sn\}_3(TMA)]\cdot Et_2O\cdot CH_2Cl_2$ (8)

The molecular structures of complexes **3**, **6**, **7**, and **8** are illustrated in Figures 5, 6, 7, and 8, respectively, and se-

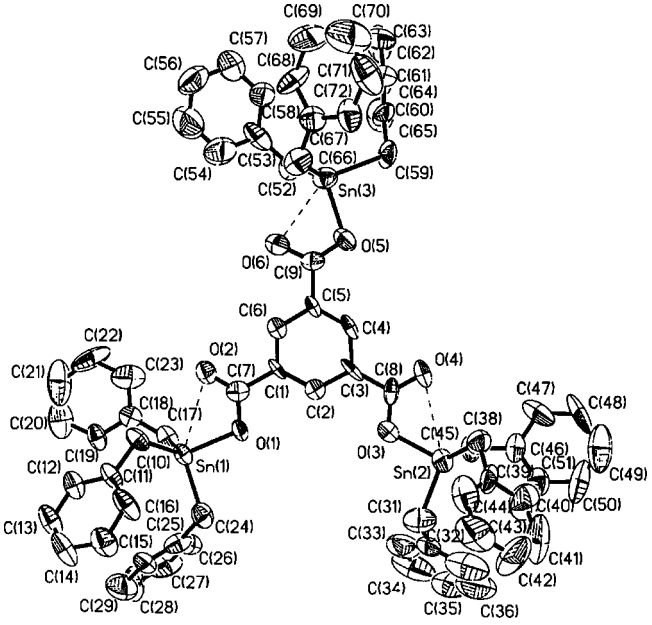

Figure 5. The molecular structure of **3**.

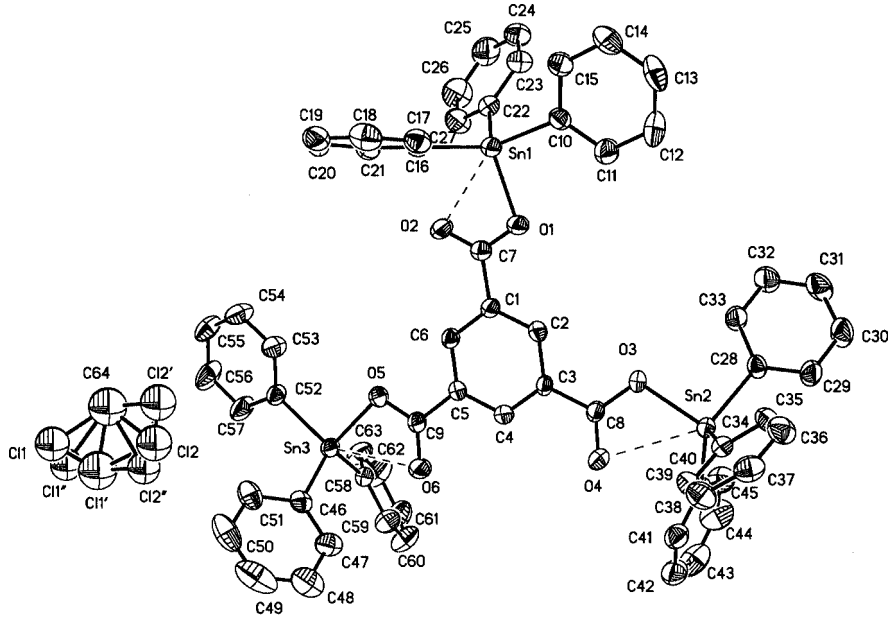

Figure 6. The molecular structure of **6**.

lected bond lengths [Å] and angles [°] are listed in Table 2. Trinuclear triphenyltin or tribenzyltin carboxylate of H_3TMA possesses a monomeric structure. For the complexes, it can be seen that the Sn(1)–O(1), Sn(2)–O(3), and Sn(3)–O(5) bond lengths (2.052–2.097 Å) lie in the range of 2.038(9)–2.115(6) Å that has been reported as the Sn–O covalent bond length, which proves that the oxygen atoms are coordinated to the tin atoms by a strong chemical bond. The intramolecular distances Sn(1)···O(2), Sn(2)···O(4), and Sn(3)···O(6) are in the range 2.634–2.916 Å. Although these distance are considerably longer than the normal Sn–O covalent bond length, they lie in the range of Sn···O distances of 2.61–3.02 Å which have been confidently reported for intramolecular bonds.[28,29] As the oxygen atoms of the carboxylate are involved in a weak coordinative interaction with tin along one of the tetrahedral faces, the structure distortion for the tin atoms in **3** and **6**–**8** is best described as a capped tetrahedron.

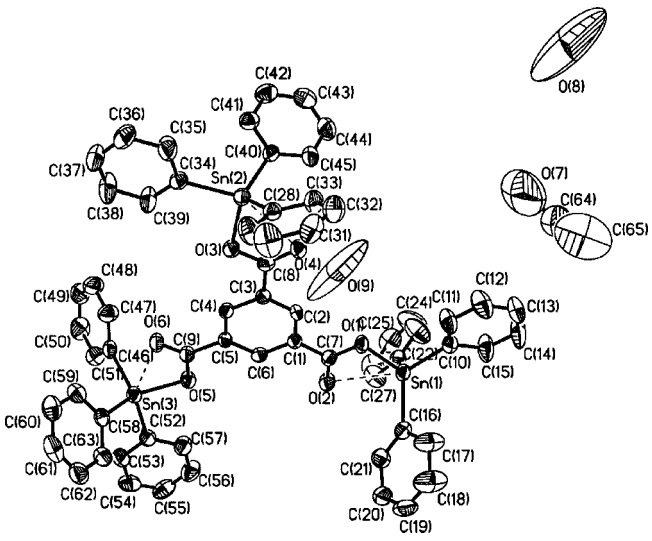

Figure 7. The molecular structure of **7**.

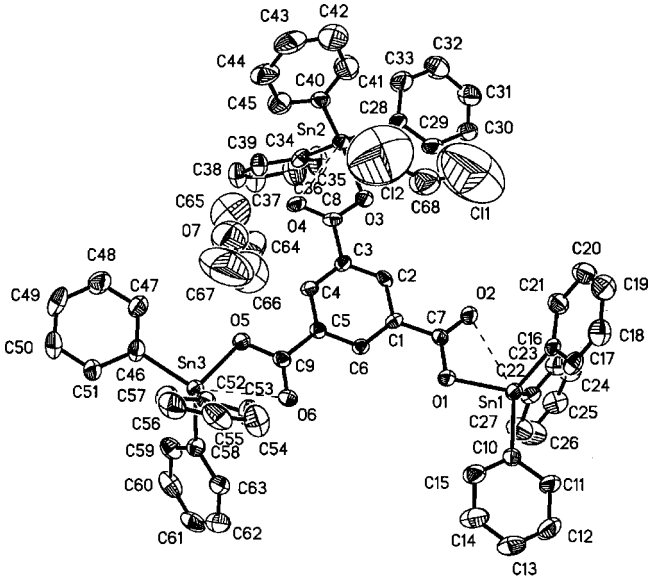

Figure 8. The molecular structure of **8**.

Table 2. Selected bond lengths [Å] and bond angles [°] for **3** and **6**.

3		**6**		**7**		**8**	
Sn(1)–O(1)	2.079(7)	Sn(1)–O(1)	2.070(3)	Sn(1)–O(1)	2.084(3)	Sn(1)–O(1)	2.066(5)
Sn(1)–O(2)	2.855(8)	Sn(1)–O(2)	2.745(3)	Sn(1)–O(2)	2.745(4)	Sn(1)–O(2)	2.783(6)
Sn(1)–C(10)	2.108(11)	Sn(1)–C(10)	2.120(5)	Sn(1)–C(10)	2.120(5)	Sn(1)–C(10)	2.119(8)
Sn(1)–C(24)	2.108(11)	Sn(1)–C(16)	2.122(5)	Sn(1)–C(16)	2.121(6)	Sn(1)–C(16)	2.114(9)
Sn(1)–C(17)	2.133(10)	Sn(1)–C(22)	2.118(5)	Sn(1)–C(22)	2.136(6)	Sn(1)–C(22)	2.115(9)
Sn(2)–O(3)	2.015(9)	Sn(2)–O(3)	2.068(3)	Sn(2)–O(3)	2.068(3)	Sn(2)–O(3)	2.052(5)
Sn(2)–C(38)	2.125(12)	Sn(2)–O(4)	2.801(3)	Sn(2)–O(4)	2.812(4)	Sn(2)–O(4)	2.729(6)
Sn(2)–O(4)	2.916(9)	Sn(2)–C(28)	2.132(5)	Sn(2)–C(28)	2.130(5)	Sn(2)–C(28)	2.112(8)
Sn(2)–C(31)	2.068(14)	Sn(2)–C(34)	2.119(5)	Sn(2)–C(34)	2.136(5)	Sn(2)–C(34)	2.115(9)
Sn(2)–C(45)	2.125(11)	Sn(2)–C(40)	2.120(5)	Sn(2)–C(40)	2.120(6)	Sn(2)–C(40)	2.103(10)
Sn(3)–C(52)	2.052(15)	Sn(3)–O(5)	2.070(3)	Sn(3)–O(5)	2.070(3)	Sn(3)–O(5)	2.058(5)
Sn(3)–C(59)	2.174(10)	Sn(3)–O(6)	2.745(3)	Sn(3)–O(6)	2.769(4)	Sn(3)–O(6)	2.751(6)
Sn(3)–O(5)	2.091(9)	Sn(3)–C(46)	2.122(5)	Sn(3)–C(46)	2.129(6)	Sn(3)–C(46)	2.115(8)
Sn(3)–O(6)	2.633(8)	Sn(3)–C(52)	2.127(5)	Sn(3)–C(52)	2.136(5)	Sn(3)–C(52)	2.125(9)
Sn(3)–C(66)	2.112(12)	Sn(3)–C(58)	2.130(5)	Sn(3)–C(58)	2.134(6)	Sn(3)–C(58)	2.124(9)
C(10)–Sn(1)–C(24)	114.7(4)	C(10)–Sn(1)–C(16)	111.75(19)	C(10)–Sn(1)–C(16)	109.2(2)	C(10)–Sn(1)–C(16)	110.9(3)
C(24)–Sn(1)–C(17)	110.4(5)	C(10)–Sn(1)–C(22)	109.14(19)	C(10)–Sn(1)–C(22)	110.8(2)	C(10)–Sn(1)–C(22)	110.6(3)
C(10)–Sn(1)–C(17)	113.4(5)	C(16)–Sn(1)–C(22)	116.48(18)	C(16)–Sn(1)–C(22)	120.5(2)	C(16)–Sn(1)–C(22)	116.5(3)
O(1)–Sn(1)–O(2)	50.7(3)	O(1)–Sn(1)–O(2)	52.05(11)	O(1)–Sn(1)–O(2)	52.74(11)	O(1)–Sn(1)–O(2)	51.67(18)
C(31)–Sn(2)–C(38)	112.0(5)	C(40)–Sn(2)–C(28)	110.3(2)	C(40)–Sn(2)–C(28)	116.4(2)	C(40)–Sn(2)–C(28)	110.5(4)
C(31)–Sn(2)–C(45)	114.8(5)	C(40)–Sn(2)–C(34)	120.07(19)	C(40)–Sn(2)–C(34)	111.0(2)	C(40)–Sn(2)–C(34)	120.8(3)
C(38)–Sn(2)–C(45)	113.9(4)	C(28)–Sn(2)–C(34)	111.45(18)	C(28)–Sn(2)–C(34)	110.0(2)	C(28)–Sn(2)–(34)	108.7(4)
O(3)–Sn(2)–O(4)	49.4(3)	O(3)–Sn(2)–O(4)	51.43(11)	O(3)–Sn(2)–O(4)	51.61(12)	O(3)–Sn(2)–O(4)	52.33(19)
C(52)–Sn(3)–C(66)	117.1(6)	C(46)–Sn(3)–C(58)	116.61(19)	C(46)–Sn(3)–C(58)	115.5(2)	C(46)–Sn(3)–C(58)	111.1(4)
C(52)–Sn(3)–C(59)	109.5(6)	C(46)–Sn(3)–C(52)	111.9(2)	C(46)–Sn(3)–C(52)	111.2(2)	C(46)–Sn(3)–C(52)	110.6(3)
C(59)–Sn(3)–C(66)	113.8(5)	C(58)–Sn(3)–C(52)	109.92(19)	C(58)–Sn(3)–C(52)	110.4(2)	C(58)–Sn(3)–C(52)	115.7(3)
O(5)–Sn(3)–O(6)	53.6(3)	O(5)–Sn(3)–O(6)	52.22(11)	O(5)–Sn(3)–O(6)	52.13(12)	O(5)–Sn(3)–O(6)	51.74(19)

 © 2005 Wiley-VCH Verlag GmbH & Co. KGaA, Weinheim

Crystal Structure of $[\{(CH_3)_3Sn\}_2(HTMA)]\cdot H_2O$ (9)

The molecular structure of **9** is illustrated in Figure 9. It consists of infinite ribbons extending through the cell in the *b* direction, as indicated in Figure 10. Bond lengths and bond angles are given in Table 3. The trimethyltin(IV) groups are situated in special positions in the crystallographic mirror planes and are linked by a carboxylate; each TMA ligand in **9**, in turn, employs its two bidentate carboxylic groups to coordinate to four metal centers. Thus, four ligands are linked by four metal centers into a 24-membered macrocycle, which is further linked to eight nearest-neighbor Sn centers by four independent TMA ligands to give rise to a lattice plane with a cavity of 10.441–10.445 Å. All the tin atoms possess the same coordination environment. The coordination about the tin atom is only slightly distorted from a regular trigonal bipyramidal geometry. The angles O(3)#1–Sn(1)–O(1) 169.62(15)° and O(2)–Sn(2)–O(4)#2 171.48(16)° are close to a linear arrangement. The sum of the angles subtended at the tin atom in the trigonal plane is 358.3° for Sn(1) and 359.9° for Sn(2), so that the atoms Sn(1), C(10), C(11), and C(12) and Sn(2), C(13), C(14), and C(15) are almost in the same plane. The Sn–C distances [2.100(6)–2.118(7) Å] are equal within experimental error and close to the single-bond value for trigonal bipyramidal tin.[30]

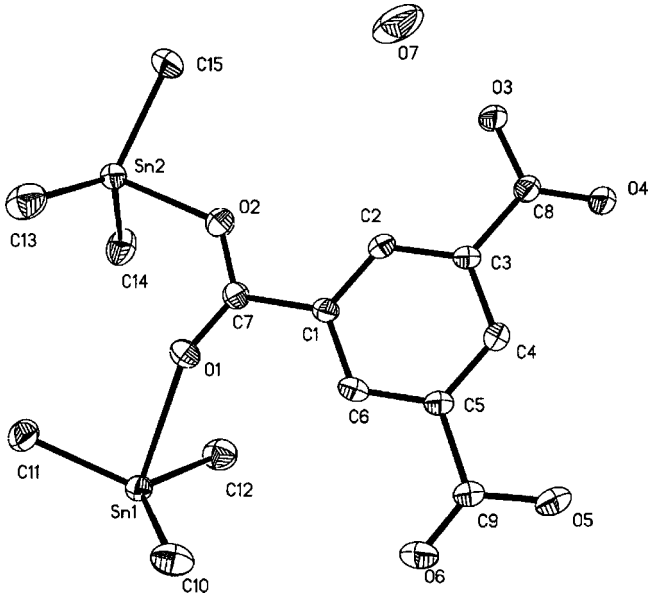

Figure 9. The molecular structure of **9**.

Interestingly, the $[\{(CH_3)_3Sn\}_2(HTMA)]\cdot H_2O$ groups are joined together by hydrogen bonds to form a three-dimensional network. The crystallization water molecule is linked to the O(3) atom to form a hydrogen bond [O(7)–H···O(3)] and to the O(5) and O(6) atoms from the neighboring $[(CH_3)_3Sn]_2(HTMA)\cdot H_2O$ group to form a further two hydrogen bonds [O(7)–H···O(6A) and O(7)···O(5A)–H(5A), respectively]. Viewed along the *a* axis, each layer $[(CH_3)_3Sn]_2(HTMA)\cdot H_2O$ is linked to an adjacent $[(CH_3)_3Sn]_2(HTMA)\cdot H_2O$ unit leading to an infinite network of intermolecular O···H–O hydrogen bonds. Thus, these networks are further organized into metal–organic framework structures through inter-network hydrogen bonding interactions that form a curved three-dimensional network.

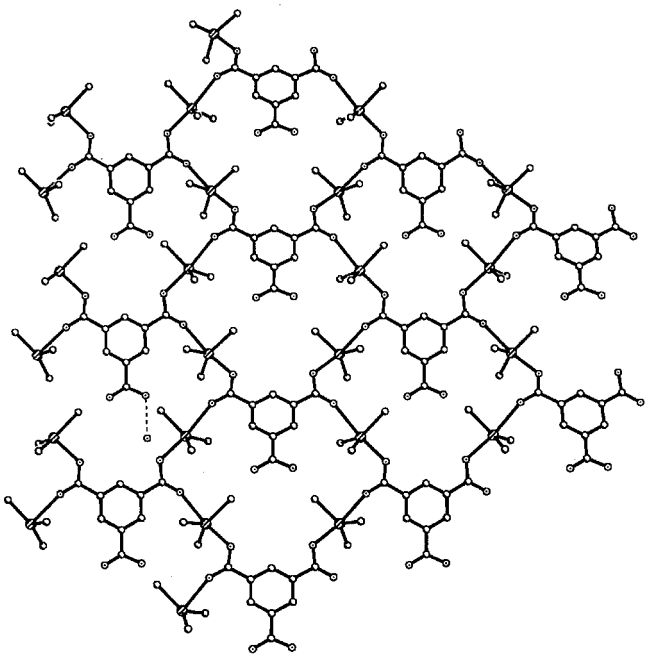

Figure 10. The network structure of **9**.

Table 3. Selected bond lengths [Å] and bond angles [°] for **9**. #1: *x* + 1/2, –*y* + 3/2, *z* – 1/2; #2: *x* – 1/2, –*y* + 3/2, *z*– 1/2; #3: *x* – 1/2, –*y* + 3/2, *z* + 1/2.

Sn(1)–C(11)	2.100(6)	Sn(2)–C(13)	2.106(7)
Sn(1)–C(10)	2.107(7)	Sn(2)–C(15)	2.108(7)
Sn(1)–C(12)	2.118(7)	Sn(2)–C(14)	2.114(7)
Sn(1)–O(3)#1	2.199(4)	Sn(2)–O(2)	2.128(4)
Sn(1)–O(1)	2.515(4)	Sn(2)–O(4)#2	2.569(4)
O(3)–Sn(1)#3	2.199(4)		
C(11)–Sn(1)–C(10)	113.5(3)	C(13)–Sn(2)–C(15)	122.3(3)
C(11)–Sn(1)–C(12)	122.6(3)	C(13)–Sn(2)–C(14)	121.2(3)
C(10)–Sn(1)–C(12)	122.2(3)	C(15)–Sn(2)–C(14)	114.4(4)
O(3)#1–Sn(1)–O(1)	169.62(15)	O(2)–Sn(2)–O(4)#2	171.48(16)

Conclusions

In summary, by carefully controlling the reaction conditions we have found that H_3TMA is a versatile building block for the construction of metal–organic complexes by complete or partial deprotonation of its carboxyl groups. Despite using a 1:3:3 molar ratio of H_3TMA, EtONa, and $(PhCH_2)_3SnCl$ (or Ph_3SnCl), we couldn't obtain a product similar to the polymeric structure of complex **2**. In general, in the crystalline state these complexes generally adopt either a polymeric structure with a five-coordinate tin atom or a discrete five-coordinate form.[21,31] Trimethyltin benzoates mainly assume one-dimensional associated arrangements, whereas triphenyltin benzoates generally exist in a discrete five-coordinate form. A delicate energy balance is

 © 2005 Wiley-VCH Verlag GmbH & Co. KGaA, Weinheim

present between the two forms, although the greater electronegativity of a phenyl group than a methyl group has been cited as a factor influencing the formation of the discrete form, as it gives more access to an axial position of a trigonal bipyramid.[31] A polymeric structure for tribenzyl or triphenyl carboxylates is associated with an electron-withdrawing R group. The contribution of either steric or electronic factors has been discussed by Holmes et al.[31] From structural data accumulated so far, the relative ligand electronegativity appears to be an important factor in determining whether the discrete structural form or the chain form is observed.[32] The axial tin–ligand bond lengths in both forms are subject to variations depending on the substitute electronegativity, ring strain, hydrogen bonds, and steric interactions.

Experimental Section

Materials and Measurements: Trimethyltin chloride, triphenyltin chloride, and 1,3,5-benzenetricarboxylic acid are commercially available and were used without further purification. Tribenzyltin chloride, tri(*o*-chlorobenzyl)tin chloride, and tri(*o*-fluorobenzyl)-tin chloride were prepared by a standard method reported in the literature.[33] The melting points were obtained with Kofler micro-melting point apparatus and are uncorrected. IR spectra were recorded on a Nicolet-460 spectrophotometer using KBr discs and sodium chloride optics. ^{1}H, ^{13}C, and ^{119}Sn NMR spectra were recorded on Varian Mercury Plus 400 spectrometer operating at 400, 100.6, and 149.2 MHz, respectively. The spectra were acquired at room temperature (298 K) unless otherwise specified; ^{13}C spectra are broadband proton decoupled. The chemical shifts are reported in ppm with respect to the references and are stated relative to external tetramethylsilane (TMS) for ^{1}H and ^{13}C NMR, and to neat tetramethyltin for ^{119}Sn NMR spectroscopy. Elemental analyses were performed with a PE-2400II apparatus.

Synthesis of [{(CH$_3$)$_3$Sn}$_3$(TMA)]·3CH$_3$OH (1) and [{(CH$_3$)$_3$Sn}$_3$(TMA)]·2CH$_3$OH (2): The reaction was carried out under nitrogen. H_3TMA (0.210 g, 1 mmol) and sodium ethoxide (0.204 g, 3 mmol) were added to a Schlenk flask and stirred for 0.5 h. Trimethyltin chloride (0.600 g, 3 mmol) was then added and the reaction mixture was stirred for 10 h at 40 °C. After filtration, the solvent was evaporated in vacuo. Yield: 78%. Rhombic crystals of **1** and block crystals of **2** were obtained from methanol solution.
1: M.p. 198–200 °C (dec.). $C_{21}H_{42}O_9Sn_3$ (794.62): calcd. C 31.74, H 5.33; found C 31.57, H 5.06. IR (KBr): $\tilde{\nu}$ = 3227, 1618, 1554, 1537, 1475, 1464, 1418, 583, 472 cm^{-1}. ^{1}H NMR ($CDCl_3/D_2O$): δ = 0.81–0.92 (s, $^2J_{Sn,H}$ = 68.6 Hz, 36 H), 1.78 (s, 3 H), 7.17 (s, 3 H) ppm. ^{13}C NMR ($CDCl_3$): δ = 11.7 [$^1J_{^{119}Sn-^{13}C}$) = 471 Hz], 135.9, 136.4, 170.7 ppm. ^{119}Sn NMR ($CDCl_3$): δ = –111.2 ppm.
2: M.p. > 220 °C (dec.). $C_{20}H_{38}O_8Sn_3$ (762.57): calcd. C 31.50, H 5.02; found C 31.31, H 4.87. IR (KBr): $\tilde{\nu}$ = 3204, 1626, 1565, 1532, 1481, 1479, 1440, 581, 476 cm^{-1}. ^{1}H NMR ($CDCl_3/D_2O$): δ = 0.85–0.88 (s, $^2J_{Sn,H}$ = 69.4 Hz, 27 H), 1.56 (s, 2 H), 3.37 (m, 6 H), 7.26 (s, 3 H) ppm. ^{13}C NMR ($CDCl_3$): δ = 12.3 [$^1J_{^{119}Sn-^{13}C}$) = 492 Hz], 136.2, 136.6, 170.4 ppm. ^{119}Sn NMR ($CDCl_3$): δ = –92.4 ppm.

Synthesis of [{(C$_6$H$_5$CH$_2$)$_3$Sn}$_3$(TMA)] (3): Yield: 84%. M.p. 130–132 °C. $C_{72}H_{66}O_6Sn_3$ (1383.32): calcd. C 62.51, H 4.81; found C 62.26, H 4.87. IR (KBr): $\tilde{\nu}$ = 1627, 1551, 1512, 1461, 1432, 580, 479 cm^{-1}. ^{1}H NMR ($CDCl_3$): δ = 3.24 (s, 18 H), 7.25–8.05 (m, 45 H) ppm. ^{13}C NMR ($CDCl_3$): δ = 34.8, 126.6, 128.7, 129.7, 134.2, 135.0, 171.5 ppm. ^{119}Sn NMR ($CDCl_3$): δ = –54.8 ppm.

Synthesis of [{(*o*-F-C$_6$H$_4$CH$_2$)$_3$Sn}$_3$(TMA)] (4): Yield: 81%. M.p. 142–144 °C. $C_{72}H_{57}F_9O_6Sn_3$ (1545.33): calcd. C 55.96, H 3.72; found C 60.16, H 3.87. IR (KBr): $\tilde{\nu}$ = 1614, 1543, 1509, 1432, 1411, 576, 464 cm^{-1}. ^{1}H NMR ($CDCl_3$): δ = 3.04 (s, 18 H), 6.64–7.58 (m, 36 H) ppm. ^{13}C NMR ($CDCl_3$): δ = 34.6, 126.5, 128.1, 129.2, 134.1, 134.9, 171.0 ppm. ^{119}Sn NMR ($CDCl_3$): δ = –55.6 ppm.

Synthesis of [{(*o*-Cl-C$_6$H$_4$)$_3$Sn}$_3$(TMA)] (5): Yield: 78%. M.p. 150–154 °C. $C_{72}H_{57}Cl_9O_6Sn_3$ (1693.44): calcd. C 51.07, H 3.39; found C 51.26, H 3.21. IR (KBr): $\tilde{\nu}$ = 1621, 1549, 1512, 1439, 1408, 575, 470 cm^{-1}. ^{1}H NMR ($CDCl_3$): δ = 3.24 (s, 18 H), 6.86–7.74 (m, 36 H) ppm. ^{13}C NMR ($CDCl_3$): δ = 34.5, 126.6, 128.3, 129.4, 134.4, 135.2, 171.3 ppm. ^{119}Sn NMR ($CDCl_3$): δ = –55.1 ppm.

Syntheses of [{(C$_6$H$_5$)$_3$Sn}$_3$(TMA)]·CH$_2$Cl$_2$ (6), [{(C$_6$H$_5$)$_3$-Sn}$_3$(TMA)]·Et$_2$OH·2H$_2$O (7), and [{(C$_6$H$_5$)$_3$Sn}$_3$(TMA)]·Et$_2$O·CH$_2$Cl$_2$ (8): A white powder was obtained, which was then recrystallized from different solvents. Colorless crystals of complex **6** were obtained from CH_2Cl_2, while colorless crystals of complexes **7** and **8** grew from 95% EtOH and Et_2O/CH_2Cl_2, respectively.
6: Yield: 81%. M.p. 112–114 °C. $C_{64}H_{50}Cl_2O_6Sn_3$ (1342.01): calcd. C 57.27, H 3.76; found C 57.06, H 3.89. IR (KBr): $\tilde{\nu}$ = 1634, 1587, 1530, 1479, 1450, 587, 496 cm^{-1}. ^{1}H NMR ($CDCl_3$): δ = 5.33 (s, 2 H), 7.21–7.59 (m, 45 H) ppm. ^{13}C NMR ($CDCl_3$): δ = 53.4, 128.6, 130.3, 132.1, 136.7, 136.7, 170.9 ppm. ^{119}Sn NMR ($CDCl_3$): δ = –57.0 ppm.
7: Yield: 72%. M.p. 125–127 °C. $C_{65}H_{58}O_9Sn_3$ (1839.18): calcd. C 58.29, H 4.37; found C 58.27, H 4.12. IR (KBr): $\tilde{\nu}$ = 1612, 1561, 1537, 1476, 1451, 593, 491 cm^{-1}. ^{1}H NMR ($CDCl_3/D_2O$): δ = 1.20 (t, 3 H), 2.61 (t, $J_{H,H}$ = 4.8 Hz, 1 H), 3.12 (s, 4 H), 3.59 (m, 2 H), 7.24–7.56 (m, 45 H) ppm. ^{13}C NMR ($CDCl_3$): δ = 16.4, 58.3, 128.3, 130.5, 131.7, 136.8, 136.9, 171.1 ppm. ^{119}Sn NMR ($CDCl_3$): δ = –57.1 ppm.
8: Yield: 77%. M.p. 131–133 °C. $C_{68}H_{60}O_7Sn_3$ 1416.13): calcd. C 57.67, H 4.27; found C 57.44, H 4.35. IR (KBr): $\tilde{\nu}$ = 1634, 1577, 1542, 1480, 1459, 593, 485. ^{1}H NMR ($CDCl_3/D_2O$): δ = 1.21 (t, $J_{H,H}$ = 7.0 Hz, 6 H), 3.48 (m, 4 H), 5.28 (s, 2 H), 7.23–7.76 (m, 45 H) ppm. ^{13}C NMR ($CDCl_3$): δ = 16.7, 53.4, 67.9, 128.9, 130.4, 131.5, 136.4, 136.8, 171.2 ppm. ^{119}Sn NMR ($CDCl_3$): δ = –57.1 ppm.

Synthesis of [{(CH$_3$)$_3$Sn}$_2$(HTMA)]·H$_2$O (9): Yield: 75%. M.p. >220 °C (dec.). $C_{15}H_{24}O_7Sn_2$ (553.72): calcd. C 32.53, H 4.37; found C 32.37, H 4.34. IR (KBr): $\tilde{\nu}$ = 1702, 1627, 1595, 1521, 1469, 1440, 1359, 567, 472. ^{1}H NMR ($CDCl_3/D_2O$): δ = 1.01 (s, $^2J_{Sn,H}$ = 65.1 Hz, 18 H), 3.24 (s, 2 H), 7.28 (s, 3 H) ppm. ^{13}C NMR ($CDCl_3$): δ = 14.1 [$^1J_{^{119}Sn-^{13}C}$ = 456 Hz], 136.4, 136.7, 171.0, 172.0 ppm. ^{119}Sn NMR ($CDCl_3$): δ = –55.0 ppm.

X-ray Crystallographic Studies: Crystals were mounted in Lindemann capillaries under nitrogen. Diffraction data were collected on a Smart CCD area-detector with graphite monochromated Mo-K_α radiation (λ = 0.71073 Å). A semi-empirical absorption correction was applied to the data. The structures were solved by direct methods using SHELXS-97 and refined against F^2 by full-matrix least-squares using SHELXL-97. Hydrogen atoms were placed in calculated positions. Crystal data and experimental details of the structure determinations are listed in Table 4.
CCDC-256334 (for **1**), -249847 (for **2**), -226854 (for **3**), -248292 (for **6**), -230982 (for **7**), -236567 (for **8**), and -252043 (for **9**) contain the supplementary crystallographic data for this paper. These data can be obtained free of charge from The Cambridge Crystallographic Data Centre via www.ccdc.cam.ac.uk/data_request/cif.

 © 2005 Wiley-VCH Verlag GmbH & Co. KGaA, Weinheim

Table 4. Crystal, data-collection, and structure-refinement parameters for **1**–**3** and **6**–**9**.

Complex	**1**	**2**	**3**	**6**	**7**	**8**	**9**
Empirical formula	$C_{21}H_{42}O_9Sn_3$	$C_{20}H_{38}O_8Sn_3$	$C_{72}H_{66}O_6Sn_3$	$C_{64}H_{50}Cl_2O_6Sn_3$	$C_{65}H_{58}O_9Sn_3$	$C_{68}H_{60}Cl_2O_7Sn_3$	$C_{15}H_{24}O_7Sn_2$
Formula mass	794.62	762.57	1383.32	1342.01	1339.18	1416.13	553.72
Crystal system	monoclinic	orthorhombic	triclinic	triclinic	triclinic	triclinic	monoclinic
Space group	$Pna2_1$	$Pna2_1$	$P\bar{1}$	$P\bar{1}$	$P\bar{1}$	$P\bar{1}$	$P2_1/n$
a [Å]	19.215(8)	41.14(3)	40.08(4)	13.061(6)	12.859(13)	12.759(6)	10.1357(13)
b [Å]	13.024(5)	10.815(7)	11.519(11)	13.913(7)	14.755(14)	14.716(7)	13.013(3)
c [Å]	13.420(6)	6.771(4)	28.12(3)	18.156(9)	19.617(19)	19.513(9)	18.227(4)
α [°]	90	90	90	111.607(6)	110.565(13)	110.923(6)	90
β [°]	97.298(6)	90	91.617(19)	104.883(7)	105.626(13)	105.558(6)	90.160(4)
γ [°]	90	90	90	91.009(7)	93.453(14)	93.646(7)	90
Z	4	4	8	2	2	2	2
Absorption coefficient [mm^{-1}]	2.268	2.502	1.196	1.404	1.174	1.278	2.102
θ range for data collection [°]	1.89 to 25.03	1.95 to 25.03	1.45 to 25.03	1.60 to 25.03	1.50 to 25.03	1.18 to 25.03	2.30 to 25.06
Reflections collected	16796	14435	32303	15452	17262	16263	11946
Unique reflections	5864 (R_{int} = 0.0825)	5236 (R_{int} = 0.0330)	11461 (R_{int} = 0.1832)	10237 (R_{int} = 0.0180)	11385 (R_{int} = 0.0334)	10841 (R_{int} = 0.0434)	4135 (R_{int} = 0.0386)
Data/restraints/parameters	5864/3/307	5236/5/288	11461/38/730	10237/4/677	11385/9/703	10841/50/721	4135/3/223
Final R indices [$I > 2\sigma(I)$]	R_1 = 0.0429 wR_2 = 0.0915	R_1 = 0.0535 wR_2 = 0.1513	R_1 = 0.0540 wR_2 = 0.0873	R_1 = 0.0357 wR_2 = 0.0968	R_1 = 0.0405 wR_2 = 0.0770	R_1 = 0.0631 wR_2 = 0.1532	R_1 = 0.0398 wR_2 = 0.1004
R indices (all data)	R_1 = 0.0775 wR_2 = 0.1120	R_1 = 0.0552 wR_2 = 0.1528	R_1 = 0.2750 wR_2 = 0.1286	R_1 = 0.0572 wR_2 = 0.1095	R_1 = 0.0846 wR_2 = 0.0903	R_1 = 0.1097 wR_2 = 0.1091	R_1 = 0.0575 wR_2 = 0.1113

Acknowledgments

We thank the National Nature Science Foundation of China (20271025) and the National Nature Science Foundation of Shandong Province for financial support.

[1] *Comprehensive Supramolecular Chemistry* (Ed.: J.-M. Lehn), Pergamon Press, Oxford, U. K., **1996**.
[2] a) C. Dietrich-Buchecker, J.-P. Sauvage, *Bull. Soc. Chem. Fr.* **1992**, *129*, 113; b) R. Krärmer, J.-M. Lehn, A. Marquis-Rigault, *Proc. Natl. Acad. Sci. USA* **1993**, *90*, 5394.
[3] M. Fujita, K. Ogura, *Bull. Chem. Soc. Jpn.* **1996**, *69*, 1471 and references cited therein.
[4] a) B. F. Hoskins, R. Robson, *J. Am. Chem. Soc.* **1990**, *112*, 1546; b) R. Robson, B. F. Abrahams, S. R. Batten, R. W. Gable, B. F. Hoskins, J. Liu, *Supramolecular Architecture*, American Chemical Society, Washington, DC, **1992**, Chapter 19.
[5] C. L. Bowes, G. A. Ozin, *Adv. Mater.* **1996**, *8*, 13.
[6] a) M. Sabat, J. A. Ibers, *J. Am. Chem. Soc.* **1982**, *104*, 3715; b) S. A. Bourne, J. Lu, B. Moulton, M. J. Zaworotko, *Chem. Commun.* **2001**, 861; c) A. D. Burrows, D. M. P. Mingos, S. E. Lawrence, A. J. P. White, D. J. Williams, *J. Chem. Soc., Dalton Trans.* **1997**, 1295.
[7] S. S.-Y. Chui, S. M.-F. Lo, J. P. H. Charmant, A. G. Orpen, I. D. Williams, *Science* **1999**, *283*, 1148.
[8] a) O. M. Yaghi, G. Li, H. Li, *Chem. Mater.* **1997**, *9*, 1074; b) C. J. Kepert, M. J. Rosseinsky, *Chem. Commun.* **1998**, 31; c) K.-Y. Choi, K. M. Chun, I.-H. Suh, *Polyhedron* **2001**, *20*, 57.
[9] R. Pech, J. Pickardt, *Acta Crystallogr., Sect. C* **1998**, *44*, 992.
[10] a) T. J. Prior, M. J. Rosseinsky, *CrystEngComm* **2000**, 24; b) M. J. Plater, M. R. S. J. Foreman, E. Coronado, C. J. Gomez-Garcia, A. M. Z. Slawin, *J. Chem. Soc., Dalton Trans.* **1999**, 4209.
[11] a) O. M. Yaghi, C. Davis, G. Hi, H. Li, *J. Am. Chem. Soc.* **1997**, *119*, 2861; b) F. A. A. Paz, J. Klinowski, *Inorg. Chem.* **2004**, *43*, 3882; c) F. A. A. Paz, J. Klinowski, *Inorg. Chem.* **2004**, *43*, 3948.
[12] C. J. Kepert, T. J. Prior, M. J. Rosseinsky, *J. Solid State Chem.* **2000**, *152*, 261.
[13] H. J. Choi, M. P. Suh, *J. Am. Chem. Soc.* **1998**, *120*, 10622.
[14] G. Smith, A. N. Reddy, K. A. Byriel, C. H. L. Kennard, *J. Chem. Soc., Dalton Trans.* **1995**, 3565.
[15] J. Utko, M. Wroblewska, T. Lis, P. Sobota, *J. Organomet. Chem.* **1993**, *447*, 159.
[16] P. Sobota, J. Utko, T. Lis, *J. Organomet. Chem.* **1993**, *447*, 213.
[17] a) O. M. Yaghi, H. Li, T. L. Groy, *J. Am. Chem. Soc.* **1996**, *118*, 9096; b) C. J. Kepert, T. J. Prior, M. J. Rosseinsky, *J. Am. Chem. Soc.* **2000**, *122*, 5158.
[18] R. R. Holmes, C. G. Schmid, V. Chandrasekhar, R. O. Day, J. M. Homels, *J. Am. Chem. Soc.* **1987**, *109*, 1408.
[19] G. K. Sandhu, R. Hundal, *J. Organomet. Chem.* **1991**, *412*, 31.
[20] N. W. Alcock, J. Culver, S. M. Roe, *J. Chem. Soc., Dalton Trans.* **1992**, 1477.
[21] G. K. Saudhu, R. Gupta, S. S. Sandhu, R. V. Parish, *Polyhedron* **1985**, *4*, 81.
[22] G. K. Saudhu, R. Gupta, S. S. Sandhu, R. V. Parish, K. Brown, *J. Organomet. Chem.* **1985**, *279*, 373.
[23] W. D. Honnick, J. J. Zuckerman, *J. Organomet. Chem.* **1979**, *178*, 133.
[24] a) J. Otera, *J. Organomet. Chem.* **1981**, *221*, 57; b) J. Holeček, A. Lyčka, K. Handlír, M. Nádvorník, *Collect. Czech. Chem. Commun.* **1990**, *55*, 1193.
[25] a) V. Chandrasekhar, S. Nagendran, V. Baskar, *Coord. Chem. Rev.* **2002**, *235*, 1; b) R. García-Zarracino, J. Ramos-Quiñoes, H. Höpfl, *Inorg. Chem.* **2003**, *42*, 3835; c) D. Dakternieks, D. J. Clarke, E. R. T. Tiekink, *Z. Kristallogr.* **2002**, *217*, 622.
[26] J. E. Huheey, *Inorganic Chemistry*, 3rd. ed., Harper and Row, New York, **1983**.
[27] G. A. Jeffrey, W. Saenger, *Hydrogen Bonding in Biological Structures*, Springer, Berlin, **1991**.
[28] K. C. Molloy, T. G. Purcell, K. Quill, I. W. Nowell, *J. Organomet. Chem.* **1984**, *267*, 237.
[29] A. R. Forrester, S. J. Garden, R. A. Howie, J. L. Wardell, *J. Chem. Soc., Dalton Trans.* **1992**, 2615.
[30] A. Bondi, *J. Phys. Chem.* **1964**, *68*, 441.

 © 2005 Wiley-VCH Verlag GmbH & Co. KGaA, Weinheim

[31] a) R. G. Swisher, J. F. Vollano, V. Chandrasekgar, R. O. Day, R. R. Holmes, *Inorg. Chem.* **1984**, *23*, 3147; b) J. F. Vollano, R. O. Day, D. N. Rau, V. Chandrasekgar, R. R. Holmes, *Inorg. Chem.* **1984**, *23*, 3153; c) R. R. Holmes, R. O. Day, V. Chandrasekgar, J. F. Vollano, J. M. Holmes, *Inorg. Chem.* **1986**, *25*, 2490; d) P. J. Smith, R. O. Day, V. Chandrasekgar, J. M. Holmes, R. R. Holmes, *Inorg. Chem.* **1986**, *25*, 2495.

[32] K. D. Dimitra, D. Vaso, C. Zbigniew, K. Nikolaos, A. D. Mavroudis, *Appl. Organomet. Chem.* **2002**, *16*, 360.

[33] K. A. Kozeschkow, *Ber. Dtsch. Chem. Ges.* **1935**, *66*, 1961.

Received: February 21, 2005
Published Online: June 28, 2005

 © 2005 Wiley-VCH Verlag GmbH & Co. KGaA, Weinheim

The Palladium(II)-Substituted, Lone Pair Containing Tungstoarsenates(III) $[Na_2(H_2O)_2PdWO(H_2O)(\alpha\text{-}AsW_9O_{33})_2]^{10-}$ and $[Cs_2Na(H_2O)_8Pd_3(\alpha\text{-}AsW_9O_{33})_2]^{9-}$

Li-Hua Bi,[a] Ulrich Kortz,*[a] Bineta Keita,[b] Louis Nadjo,[b] and Lee Daniels[c]

Keywords: Arsenic / Crystal structure / Electrochemistry / Palladium / Polyoxometalates / Tungsten

The monopalladium(II)-substituted $[Na_2(H_2O)_2PdWO(H_2O)(\alpha\text{-}AsW_9O_{33})_2]^{10-}$ (**1**) and the tripalladium(II)-substituted $[Cs_2Na(H_2O)_8Pd_3(\alpha\text{-}AsW_9O_{33})_2]^{9-}$ (**2**) were synthesized in aqueous acidic medium (pH 4.8) by reaction of Pd^{2+} ions with $[As_2W_{19}O_{67}(H_2O)]^{14-}$ and $[\alpha\text{-}AsW_9O_{33}]^{9-}$, respectively. The dimeric polyanions **1** and **2** were characterized by complete elemental analysis, FTIR, and electrochemistry. Single-crystal X-ray analysis was carried out on $Cs_3Na_7[Na_2(H_2O)_2PdWO(H_2O)(\alpha\text{-}AsW_9O_{33})_2]\cdot 1.5NaCl\cdot 22H_2O$ (**1a**), which crystallizes in the triclinic system, space group $P\bar{1}$, with a = 13.2465(16) Å, b = 16.873(2) Å, c = 23.080(3) Å, α = 107.315(2)°, β = 95.025(3)°, γ = 98.040(3)°, and Z = 2; $Cs_3Na_6[Cs_2Na(H_2O)_8Pd_3(\alpha\text{-}AsW_9O_{33})_2]\cdot NaCl\cdot 15H_2O$ (**2a**) crystallizes in the monoclinic system, space group $P2_1/m$, with a = 13.1842(5) Å, b = 19.6584(7) Å, c = 18.2377(6) Å, β = 100.7660(10)°, and Z = 2. Polyanion **1** is composed of two $[\alpha\text{-}AsW_9O_{33}]^{9-}$ fragments connected by a $WO(H_2O)$ unit, one square-planar palladium atom and two sodium ions, leading to a sandwich-type structure with C_s symmetry. Polyanion **2** also consists of two $[\alpha\text{-}AsW_9O_{33}]^{9-}$ moieties, but these are linked by three equivalent, square-planar Pd^{2+} ions, one sodium ion and two cesium ions, leading to a sandwich-type structure with C_{2v} symmetry. A cyclic voltammetric study of polyanion **2** in a pH 5 medium shows a Pd^0 deposition process on the glassy carbon electrode surface. The corresponding wave and the waves for the tungsten redox processes could be separated clearly. The thickness of the film increases with the number of potential cycles or the duration of potentiostatic electrolysis. The deposited film proved to be very stable and efficient in the electrocatalytic reduction of dioxygen. Polyanion **1** was not sufficiently stable in solution to warrant electrochemical characterization.
(© Wiley-VCH Verlag GmbH & Co. KGaA, 69451 Weinheim, Germany, 2005)

Introduction

Polyoxometalates (POMs) are a well-known class of metal–oxygen cluster species with a diverse compositional range and structural variety, and therefore, they attract increasing attention worldwide.[1] Although POMs have been known for about 200 years, a large number of novel polyoxoanions with different size, composition and structure are still being discovered.[2–4] The fascinating properties of POMs allow to envisage applications in different fields including catalysis, medicine and materials science.[5–7] Therefore, systematic structural design of novel POMs and derivatization of known POMs continue to be a considerable focus in the ongoing research in POM chemistry. Most POMs are composed of early transition metal MO_6 ($M = W^{6+}$, Mo^{6+}, etc.) octahedra and main group XO_4 ($X = P^V$, Si^{IV}, etc.) tetrahedra. The most famous POMs are probably the Keggin (e.g. $PW_{12}O_{40}^{3-}$) and the Wells–Dawson (e.g. $P_2W_{18}O_{62}^{6-}$) ions.[2]

The existence of As^{III}-containing POMs has been known for several years.[8] The lone pair of electrons on the heteroatom does not allow the closed Keggin unit to form, which has resulted in some unexpected structures, e.g. $[NH_4As_4W_{40}O_{140}Co_2(H_2O)_2]^{23-}$, $[As_4W_{20}O_{72}(H_2O)_2]^{12-}$, $[H_2AsW_{18}O_{60}]^{7-}$, and $[AsW_8O_{30}AsOH]^{7-}$.[9] A few years ago, Pope et al. reported on $[As_{12}Ce_{16}(H_2O)_{36}W_{148}O_{524}]^{76-}$, which also is the largest polyoxotungstate known to date.[10] This supramolecular polyanion is composed of 12 (α-AsW_9O_{33}) and four (W_5O_{18}) units. More recently, Kortz et al. reported on the second largest tungstoarsenate known to date, $[As_6W_{65}O_{217}(H_2O)_7]^{26-}$.[11] This species consists of four inner (β-AsW_9O_{33}) and two outer (α-AsW_9O_{33}) fragments that are linked by a total of 11 corner-sharing WO_6 octahedra.

The nonatungstoarsenate(III) $[\alpha\text{-}AsW_9O_{33}]^{9-}$ was discovered by Tourné et al. in 1973,[8a] and since then, the interaction of this trivacant ligand with transition-metal ions has been studied. Such work has resulted predominantly in di-

[a] International University Bremen, School of Engineering and Science,
P. O. Box 750 561, 28725 Bremen, Germany
Fax: +49-421-200-3229
E-mail: u.kortz@iu-bremen.de
[b] Laboratoire de Chimie Physique, UMR 8000,
CNRS, Equipe d'Electrochimie et Photoélectrochimie, Université Paris-Sud, Bâtiment 420,
91405 Orsay Cedex, France
[c] Rigaku/MSC,
9009 New Trails Drive, The Woodlands, Texas 77381-5209, USA

 © 2005 Wiley-VCH Verlag GmbH & Co. KGaA, Weinheim **DOI: 10.1002/ejic.200500128**

meric, sandwich-type structures, and the first member of this class ($[Cu_3(H_2O)_2(\alpha\text{-}AsW_9O_{33})_2]^{12-}$) was reported by Hervé et al. in 1982.[12] Since then a number of isostructural derivatives have been characterized: $[M_3(H_2O)_3(\alpha\text{-}AsW_9O_{33})_2]^{12-}$ (M = Mn^{2+}, Co^{2+}, Ni^{2+}, Cu^{2+}, Zn^{2+}) and $[(VO)_3(\alpha\text{-}AsW_9O_{33})_2]^{11-}$.[13] Very recently, Kortz et al. described the first example of a sandwich-type species with four transition metals, $[Cu_4K_2(H_2O)_8(\alpha\text{-}AsW_9O_{33})_2]^{8-}$.[14] Recently, tetrasubstituted sandwich-type POMs based on the $[\beta\text{-}AsW_9O_{33}]^{9-}$ fragment have also been reported, e.g. $[M_4(H_2O)_{10}(\beta\text{-}AsW_9O_{33})_2]^{6-}$ (M = Fe^{3+}, Cr^{3+}).[15]

The 19-tungstodiarsenate(III) $[As_2W_{19}O_{67}(H_2O)]^{14-}$ was also reported by Tourné et al. in 1973,[8a] and its structure was recently confirmed by Kortz and coworkers.[11] This polyanion consists of two $[\alpha\text{-}AsW_9O_{33}]^{9-}$ fragments, which are linked by an additional tungsten center, resulting in a dilacunary species. The interaction of $[As_2W_{19}O_{67}(H_2O)]^{14-}$ with di- and trivalent transition-metal and main-group elements has been investigated by different groups and has resulted in disubstituted products $[M_2As_2W_{19}O_{67}(H_2O)_3]^{n-}$ (n = 10, M = Mn^{2+}, Co^{2+}, Ni^{2+}, Cu^{2+}, Zn^{2+}, VO^{2+}; n = 8, M = Mn^{3+}, Fe^{3+}, Ga^{3+}).[13a, 16]

The 20-tungstodiarsenate(III) $[As_2W_{20}O_{68}(H_2O)]^{10-}$ was first reported by Hervé et al. who synthesized this as a monolacunary species from the dilacunary precursor $[As_2W_{19}O_{67}(H_2O)]^{14-}$.[17] The same authors also studied the interaction of $[As_2W_{20}O_{68}(H_2O)]^{10-}$ with first-row transition-metal ions, which leads to the monosubstituted products $[MAs_2W_{20}O_{68}(H_2O)_2]^{8-}$ (M = Mn^{2+}, Co^{2+}, Ni^{2+}, Cu^{2+}, Zn^{2+}, VO^{2+}).[17] Recently, Kortz et al. reported on the ytterbium derivative $[YbAs_2W_{20}O_{68}(H_2O)_3]^{7-}$.[18]

All of the above sandwich-type structures can be considered to be derivatives of Jeannin's 21-tungstodiarsenate(III) $[As_2W_{21}O_{69}(H_2O)]^{6-}$, which consists of two $[\alpha\text{-}AsW_9O_{33}]^{9-}$ fragments linked by a belt of three tungsten atoms.[19]

Organotin-substituted tungstoarsenates(III) of this structural type have also been prepared. Pope et al. reported on tetrasubstituted $[\{C_6H_5Sn)_2O\}_2H(AsW_9O_{33})_2]^{9-}$,[20] and later, Kortz et al. prepared disubstituted $[(C_6H_5Sn)_2As_2W_{19}O_{67}(H_2O)]^{8-}$.[21] Very recently, Kortz et al. synthesized the first diorganotin-substituted tungstoarsenate(III), $[\{Sn(CH_3)_2(H_2O)_2\}_3(\beta\text{-}AsW_9O_{33})]^{3-}$, which self-condenses in the solid state leading to the hybrid organic–inorganic 2D material $(CsNa_2[\{Sn(CH_3)_2\}_3(\beta\text{-}AsW_9O_{33})]\cdot 7H_2O)_\infty$.[22]

For many years, POM researchers have attempted to incorporate 4d and 5d elements, in general, and Pd, in particular, in lacunary POMs because of the highly interesting catalytic properties of such species. For a long time the two Pd^{II}-containing polyoxotungstates $[Pd_3(A\text{-}PW_9O_{34})_2]^{12-}$ [23] and $[WZnPd_2(H_2O)_2(B\text{-}\alpha\text{-}ZnW_9O_{34})_2]^{12-}$ [24] have been the only known members of this class, and both were not structurally characterized by X-ray diffraction. Nevertheless, it has been demonstrated that these POMs have excellent catalytic properties for the selective and efficient transformation of organic substrates.[25] In 1994, Angus–Dunne et al. reported on the synthesis and structure of $[Pd_2W_{10}O_{36}]^{8-}$, which represents the first palladium(II)-substituted isopolytungstate.[26] In 2001, Krebs et al. reported on the structure of the tripalladium-substituted tungstotellurate $[Pd_3(TeW_9O_{33})_2]^{10-}$, but without providing any synthetic or crystallographic details.[6]

Recently, we also engaged in the synthesis of polyoxotungstates substituted by noble metals (e.g. Pd, Ru). We already reported on the two novel $Ru^{II}(dmso)_3$-supported polyanions $[HW_9O_{33}Ru^{II}_2(dmso)_6]^{7-}$ and $[Ru(dmso)_3(H_2O)XW_{11}O_{39}]^{6-}$ (X = Ge, Si).[27] Furthermore, we investigated the possibility of forming the Pd^{II} analogs of our tricopper(II)-substituted derivatives $[Cu_3(H_2O)_3(\alpha\text{-}XW_9O_{33})_2]^{12-}$ (X = As^{III}, Sb^{III}).[13a] This proved to be possible, and very recently, we reported on the synthesis and electrochemistry of the first structurally characterized palladium(II)-substituted heteropolyanion $[Cs_2Na(H_2O)_{10}Pd_3(\alpha\text{-}SbW_9O_{33})_2]^{9-}$.[28] We have also already reported on the structure and electrochemistry of the Pd^{II}-substituted tungstosilicate $[Cs_2K(H_2O)_7Pd_2WO(H_2O)(A\text{-}\alpha\text{-}SiW_9O_{34})_2]^{9-}$.[29]

Here we report on two novel palladium(II)-substituted tungstoarsenates(III).

Results and Discussion

Synthesis and Structure

The novel palladium(II)-substituted, dimeric tungstoarsenate(III) $[Na_2(H_2O)_2PdWO(H_2O)(\alpha\text{-}AsW_9O_{33})_2]^{10-}$ (**1**) has been synthesized by reaction of $PdCl_2$ with $K_{14}[As_2W_{19}O_{67}(H_2O)]$ in aqueous acidic medium and isolated as a mixed cesium–sodium salt. Polyanion **1** represents only the third example of a structurally characterized palladium-substituted heteropolytungstate.[28,29] The sandwich-type **1** consists of two lacunary B-α-$[AsW_9O_{33}]^{9-}$ Keggin fragments linked by a Pd atom and a $WO(H_2O)^{4+}$ moiety, which leads to a structure with nominal C_s symmetry (see Figure 1 and Figure 2). Alternatively, **1** can be described as a $[As_2W_{19}O_{67}(H_2O)]^{14-}$ fragment that has taken up a palladium atom. We originally expected incorporation of two palladium atoms in dilacunary $[As_2W_{19}O_{67}(H_2O)]^{14-}$. However, it is not clear why this precursor picks up only one rather than the expected two palladium centers. Surprisingly, the third addenda atom position in the central belt of **1** is occupied by a sodium ion (Na2). Interestingly, Na2 is five-coordinate and is bonded by four terminal oxo groups [Na2···O 2.24–2.34(2) Å] of the two Keggin units in **1** and another terminal oxo group [Na2···O 2.42(3) Å] of W19, resulting in a square-pyramidal coordination sphere. Only one of the resulting three vacancies between W19, Na2 and the palladium atom is occupied by an additional sodium ion Na1. This Na1 is six-coordinate and is bonded by four bridging oxo groups [Na1···O 2.50–2.52(2) Å] of **1** and two terminal water molecules [Na1···O 2.41–2.48(3) Å] resulting in an octahedral coordination sphere. The orientation of Na1 in the belt of **1** is not all that surprising, as crystal structures of several 3d transition-metal derivatives have also revealed the presence of sodium ions in analogous positions. In the di- and tri-transition-metal-substituted derivatives $[M_2(H_2O)_2WO(H_2O)Na_3(H_2O)_6(\alpha\text{-}AsW_9O_{33})_2]^{7-}$ (M = Co^{2+}, Zn^{2+}, Mn^{2+}) and $[M_3(H_2O)_3Na_3(H_2O)_6(\alpha$-

 © 2005 Wiley-VCH Verlag GmbH & Co. KGaA, Weinheim

$AsW_9O_{33})_2]^{9-}$ (M = Mn^{2+}, Co^{2+}, Cu^{2+}, Zn^{2+}), three sodium ions were observed in the central belt in equivalent positions.[13] In the monophenyltin derivative $[(C_6H_5Sn)_2Na(H_2O)_2As_2W_{19}O_{67}(H_2O)]^{7-}$, a sodium ion was found between the two tin atoms.[21] Finally, in Pope's $[(C_6H_5Sn)_3Na_3(H_2O)_6(\alpha\text{-}SbW_9O_{33})_2]^{6-}$, three sodium ions are located in the central belt in addition to the three C_6H_5Sn groups.[20]

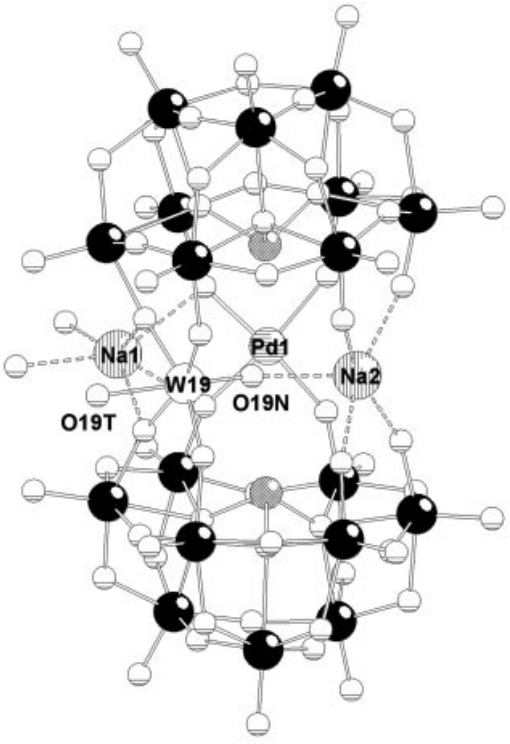

Figure 1. Ball and stick representation of $[Na_2(H_2O)_2PdWO(H_2O)(\alpha\text{-}AsW_9O_{33})_2]^{10-}$ (**1**) showing labels for some selected atoms in the central belt. The shading of the remaining atoms is as follows: tungsten (black), arsenic (cross-hatched), and oxygen (white).

Bond valence sum analysis[30] reveals that in polyanion **1** the *trans*-related terminal ligands of the unique tungsten linker are arranged so that the water molecule is *external* [W19–O19T 2.27(2) Å] and the oxo ligand is *internal* [W19–O19N 1.72(2) Å], see Figure 1. This is in complete agreement with all other compounds containing the $[As_2W_{19}O_{67}(H_2O)]$ fragment, including the precursor itself.[11,13a,16] Interestingly, the situation is reversed for the dipalladium(II)-substituted $[Cs_2K(H_2O)_7Pd_2WO(H_2O)(A\text{-}\alpha\text{-}SiW_9O_{34})_2]^{9-}$ ($Pd_2Si_2W_{19}$) which our group reported very recently.[29] This species is composed of two (A-α-SiW_9O_{34}) Keggin moieties linked by a $WO(H_2O)$ group and two equivalent, square-planar Pd^{2+} ions, leading to a sandwich-type structure with C_{2v} symmetry. In $Pd_2Si_2W_{19}$, the central tungsten atom has the terminal oxo group in the *external* position, and the *trans*-related water molecule is pointing towards the inside of the central polyanion cavity. This observation allows for the conclusion that the two lone pairs of electrons associated with the As^{III} heteroatoms in **1** and **2** exhibit steric and electronic constraints which do not allow the existence of a long, *internal* $W–OH_2$ bond.

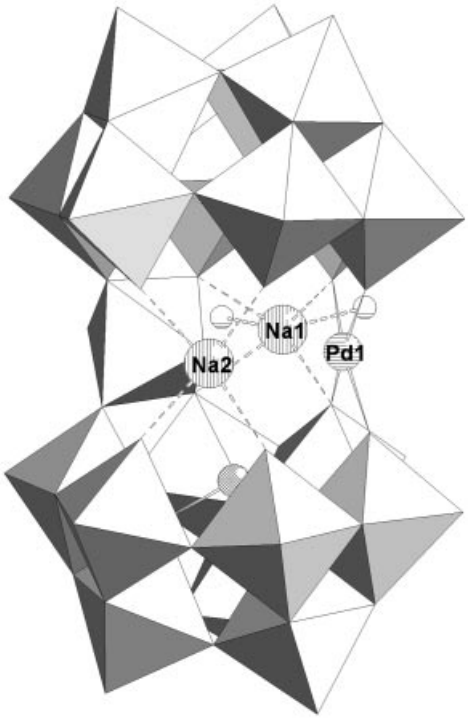

Figure 2. Combined polyhedral/ball and stick representation of **1**. The polyhedra represent WO_6 and the shading of the balls is as follows: arsenic (cross-hatched) and oxygen (white).

We also report on the tripalladium(II)-substituted, dimeric tungstoarsenate(III) $[Cs_2Na(H_2O)_8Pd_3(\alpha\text{-}AsW_9O_{33})_2]^{9-}$ (**2**), which has been synthesized by reaction of $PdCl_2$ with $Na_9[\alpha\text{-}AsW_9O_{33}]$ in aqueous acidic medium and isolated as a mixed cesium–sodium salt. Polyanion **2** is composed of two ($\alpha\text{-}AsW_9O_{33}$) units linked by three square-planar Pd^{2+} ions (see Figure 3). Therefore, **2** represents the arsenic(III) analog of $[Cs_2Na(H_2O)_{10}Pd_3(\alpha\text{-}SbW_9O_{33})_2]^{9-}$ ($Pd_3Sb_2W_{18}$), which we reported very recently.[28] Both of these tripalladium-substituted, sandwich-type species exhibit the same kind of bonding of the palladium atoms to the two Keggin fragments. Specifically, each palladium atom is bound to two oxo groups of the same W_3O_{13} triad of each Keggin unit. Interestingly, this is very different from the structurally related 3d transition-metal derivatives $[(M(H_2O)_3(\alpha\text{-}AsW_9O_{33})_2]^{9-}$ (M = Mn^{2+}, Co^{2+}, Ni^{2+}, Cu^{2+} and Zn^{2+}).[13] The latter exhibit transition-metal centers which are bound by two oxo groups of two different W_3O_{13} triads of each Keggin unit. We believe that the difference in the coordination geometry of the incorporated transition-metal center (square-planar for Pd^{II} versus square pyramidal for Cu^{II} or Zn^{II}) determines which bonding mode is preferred. It must be re-emphasized that this conclusion applies to tungstoarsenates(III). Interestingly, Krebs et al. observed a "non-eclipsed" bonding mode of the three palladium centers in $[Pd_3(TeW_9O_{33})_2]^{10-}$, which indicates that the type of heteroatom may also influence the bonding mode of the palladium ions to the two Keggin caps.[6]

 © 2005 Wiley-VCH Verlag GmbH & Co. KGaA, Weinheim

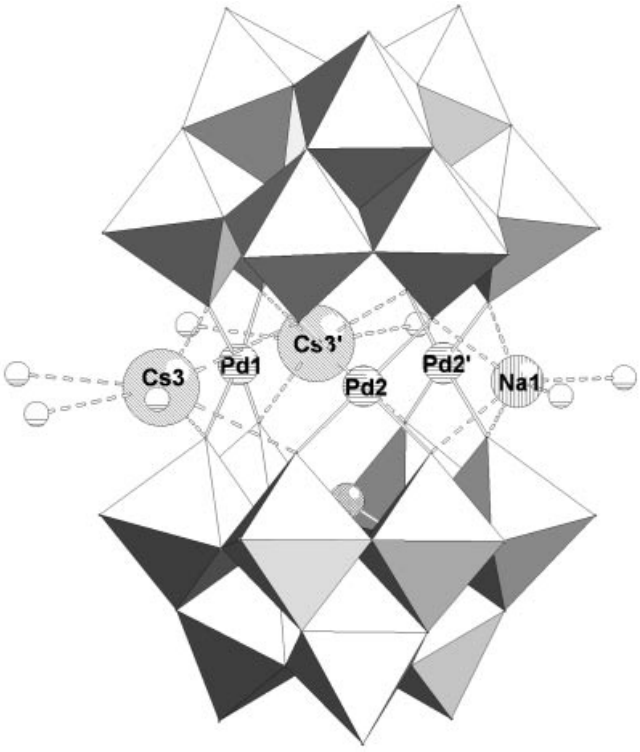

Figure 3. Combined polyhedral/ball and stick representation of $[Cs_2Na(H_2O)_8Pd_3(\alpha\text{-}AsW_9O_{33})_2]^{9-}$ (**2**) showing labels for the heavy atoms in the central belt. The polyhedra represent WO_6 and the shading of the remaining atoms is as follows: arsenic (cross-hatched) and oxygen (white).

The central belt of **2** is completed by two Cs^+ and a Na^+ ion, which occupy the vacancies between the adjacent palladium centers, resulting in a polyanion with idealized C_{2v} symmetry (see Figure 3). The two symmetry-equivalent cesium ions Cs3 and Cs3′ are coordinated to four oxo groups of **2** [Cs···O 3.065–3.168(13) Å] and three oxo groups of a neighboring polyanion [Cs···O 3.069–3.245(13) Å]. As expected, the sodium ion Na1 is six-coordinate and is bonded by four bridging oxo groups [Na1···O 2.448–2.449(16) Å] of **2** and two terminal water molecules [Na1···O 2.40(3) Å], resulting in an octahedral coordination sphere.

The synthetic procedure for **2** is very similar to that of $Pd_3Sb_2W_{18}$, which was prepared by interaction of $Pd(CH_3COO)_2$ with $Na_9[\alpha\text{-}SbW_9O_{33}]$.[28] Polyanion **2** was synthesized in good yield in a simple one-pot procedure by interaction of $PdCl_2$ with $Na_9[\alpha\text{-}AsW_9O_{33}]$ in aqueous acidic medium (pH 4.8). Interestingly, we have not been able to synthesize **2** using $Pd(CH_3COO)_2$ as a palladium source. In fact, reaction of $Pd(CH_3COO)_2$ with $Na_9[\alpha\text{-}AsW_9O_{33}]$ in aqueous acidic medium (pH 4.8) resulted in **1**. As described above, we were eventually able to identify a more rational synthetic procedure for **1** using the dilacunary precursor $[As_2W_{19}O_{67}(H_2O)]^{14-}$ (see also Experimental Section).

Nevertheless, it is somewhat surprising that the two pure, water soluble, commercially available palladium(II) salts $PdCl_2$ and $Pd(CH_3COO)_2$ react differently with the same lacunary polyoxoanion precursor $[\alpha\text{-}AsW_9O_{33}]^{9-}$, resulting in two different products **1** and **2**.

Electrochemistry

The instability of **1** precludes any interesting study of its electrochemical behavior on a well-defined species.

In contrast, **2** will increase the steadily expanding series of the very few Pd-containing heteropolyanions characterized by cyclic voltammetry. With the exception of $K_{12}[WZnPd^{II}_2(H_2O)_2(ZnW_9O_{34})_2]\cdot 38H_2O$, which was studied by Neumann et al.,[25a] and an allusion to the electrochemistry of $K_2Na_6[Pd_2W_{10}O_{36}]\cdot 22H_2O$,[26] only two polyanions $[Cs_2Na(H_2O)_{10}Pd_3(\alpha\text{-}SbW_9O_{33})_2]^{9-}$ ($Pd_3Sb_2W_{18}$)[28] and $[Cs_2K(H_2O)_7Pd_2WO(H_2O)(A\text{-}\alpha\text{-}SiW_9O_{34})_2]^{9-}$ ($Pd_2Si_2W_{19}$)[29] have been characterized to date by cyclic voltammetry. In the latter two examples, cyclic voltammetric studies show deposition of Pd^0 on the glassy carbon electrode surface, giving a film with a particularly well-behaved hydrogen sorption/desorption pattern.

In anticipation of future comparisons, essentially with its Sb-analog $Pd_3Sb_2W_{18}$,[28] polyanion **2** was studied by cyclic voltammetry in 0.4 M (CH_3COO^- + CH_3COOH) pH 5 buffer. Figure 4 shows the pattern observed for a 2×10^{-4} M solution of **2**. For a sequential description of the voltammogram in Figure 4, the potential domain can be divided into two parts. In the domain from –0.1 V to –0.520 V, the first broad cathodic peak observed roughly between –0.300 V and –0.360 V vs. SCE features the Pd^0 deposition process, which is ill-separated from the reduction of the W centers. This behavior is much the same as observed previously for the closely related $Pd_3Sb_2W_{18}$, but differs from that obtained for $PdSO_4$ solutions. With the present complex **2**, the second potential domain starting from –0.1 V to + 1.0 V in the positive potential direction and back to –0.1 V represents unambiguously the oxidation of the deposited Pd surface, followed by the reduction of the oxide. With $PdSO_4$, a broad drawn-out deposition wave was obtained, which is in agreement with the usual observation that the deposition can be performed in a large potential domain.[31] Whatever the Pd-containing compound, the subsequent, sharp cathodic peak with a sharp and narrow anodic counterpart features the hydrogen sorption/desorption processes. It is noteworthy that the film built from **2** shows the same remarkable hydrogen sorption/desorption characteristics obtained previously with $Pd_3Sb_2W_{18}$,[28] thus underscoring the excellent quality of the deposited film, compared with direct deposition from $PdSO_4$.

Typically, the potential cycling program in Figure 4 ensured that the deposition of Pd^0 on the electrode surface was restricted to the potential domain between + 0.2 V and –0.52 V. Alternatively, film deposition can be realized by potentiostatic electrolysis at –0.5 V. The rate at which the film became thicker increases with the more negative value of the potential selected for the cathodic end of the cyclic potential scan or, alternatively, with the more negative value chosen for controlled potential electrolysis. As expected, the

 © 2005 Wiley-VCH Verlag GmbH & Co. KGaA, Weinheim

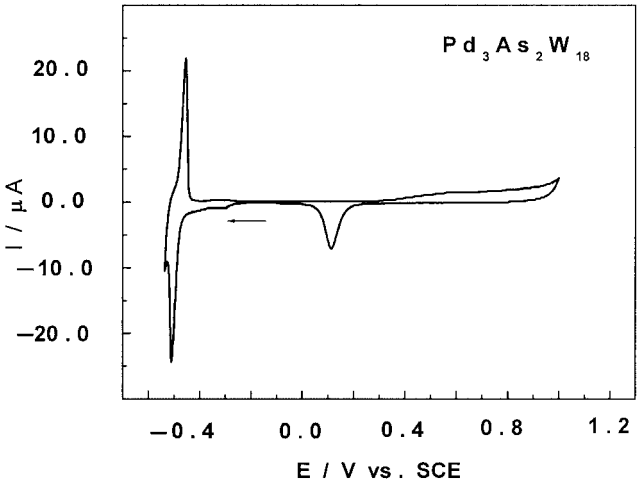

Figure 4. Representative cyclic voltammogram observed upon continuous cycling at a glassy carbon electrode of a 2×10^{-4} M solution of **2** in 0.4 M (CH_3COO^- + CH_3COOH) pH = 5 buffer. The potential variation was between –0.520 V and + 1.0 V. The arrow indicates the direction of the first scan, which starts at –0.1 V. Working electrode: glassy carbon; reference electrode: SCE; scan rate: 2 mV s^{-1}.

thickness increases also with the number of cycles or the duration of potentiostatic electrolysis. These observations parallel the literature results for Pd^0 deposition from ions in solution.[31] The domain starting from –0.1 V to + 1.0 V in the positive potential direction and back to –0.1 V represents unambiguously the oxidation of the deposited Pd surface, followed by reduction of the oxide. This part of the pattern is exactly the same as that obtained previously with $Pd_3Sb_2W_{18}$.[28]

The stability and robustness of the film deposited from **2** was tested in the following way. After deposition of a film on the glassy carbon surface, the electrode was taken out of the solution, copiously rinsed with Millipore water, left for some time in the open air, and then soaked in pure supporting electrolyte (pH = 5). The pattern obtained in Figure 4 is exactly reproduced, except for the broad "first" deposition wave which is missing. This pattern could be cycled several times without observing any changes. This experiment demonstrates the perfect stability of the film. A rough estimate of the film thickness in Figure 4 can be calculated. Typically, the building of the film shown in Figure 4 necessitates 263×10^{-6} C, which corresponds to about 1.3×10^{15} Pd atoms. With an atomic radius of 140 pm for Pd,[32] a monolayer of these atoms would cover an area of 8.1×10^{-5} m^2. With an electrode surface area of 7.07×10^{-6} m^2, the deposited film corresponds to about eleven monolayers.

In short, results gathered from the pertinent literature[31] suggest that Figure 4 features the characteristics of the deposition behavior of Pd^0 on the glassy carbon electrode surface. As a complementary cross-check, we were interested in verifying whether these surfaces display the electrocatalytic behavior that is usually expected for Pd^0 films. The electrocatalytic reduction of dioxygen was studied for this purpose. Figure 5 shows the superposition of the voltammograms obtained with the deposited Pd^0 film in the pure pH 5 electrolyte, and after bubbling air and pure dioxygen, separately, through the solution. It must be noted that no reduction of dioxygen occurred on the glassy carbon surface alone in the potential domain explored.[33] In contrast, a very efficient reduction of dioxygen was observed on the Pd^0-modified surface as can be inferred from the relatively positive potential location of the process. The catalytic process was efficient enough for the voltammograms to be polarogram-shaped. Furthermore, the plateau currents scale up roughly with the concentration of dioxygen in solution. Typically, a thin Pd^0 film comprising roughly six monolayers was used for the experiments shown in Figure 5. Actually, several film thicknesses were used, and a very efficient dioxygen reduction process was observed no matter what the film thickness. Finally, prolonged cycling of these electrodes in the presence of dioxygen did not induce any deactivation of the surfaces.

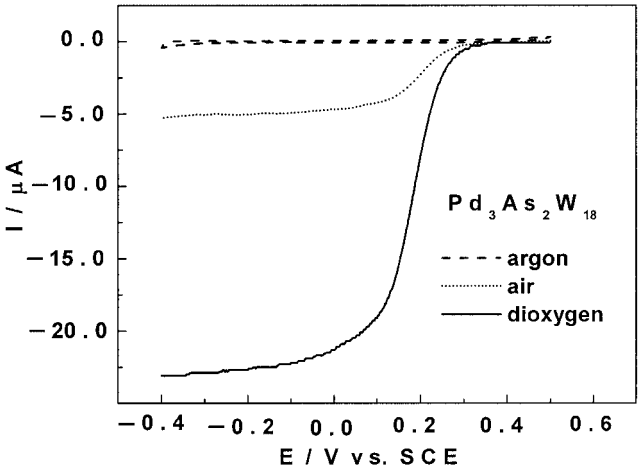

Figure 5. Cyclic voltammetry characterization, in 0.4 M (CH_3COO^- + CH_3COOH) pH = 5 buffer, of the electrocatalytic reduction of dioxygen on a thin film of Pd^0 (6 monolayers) deposited by **2** on a glassy carbon electrode; reference electrode: SCE; scan rate: 2 mV s^{-1}. The polarogram-shaped cyclic voltammograms were obtained with the Pd^0 film in pure supporting electrolyte deaerated with argon after air and pure dioxygen were bubbled, separately, through the solution.

Conclusions

We have synthesized the novel monopalladium(II)-substituted $[Na_2(H_2O)_2PdWO(H_2O)(\alpha\text{-}AsW_9O_{33})_2]^{10-}$ (**1**) and the tripalladium(II)-substituted $[Cs_2Na(H_2O)_8Pd_3(\alpha\text{-}AsW_9O_{33})_2]^{9-}$ (**2**). These polyanions represent the first examples of structurally characterized palladium(II)-substituted tungstoarsenates(III). Both **1** and **2** were prepared in simple, one-pot procedures by reaction of Pd^{2+} ions with $[As_2W_{19}O_{67}(H_2O)]^{14-}$ and $[\alpha\text{-}AsW_9O_{33}]^{9-}$, respectively, in aqueous acidic medium (pH 4.8). Polyanion **2** represents the arsenic(III) analog of $[Cs_2Na(H_2O)_{10}Pd_3(\alpha\text{-}SbW_9O_{33})_2]^{9-}$ ($Pd_3Sb_2W_{18}$), and it is also stable in a large pH domain (pH 0–5). Polyanion **1** is much less stable in solution, which can be rationally explained by structural considerations. The

 © 2005 Wiley-VCH Verlag GmbH & Co. KGaA, Weinheim

backbone of **1** is composed of two $[\alpha\text{-}AsW_9O_{33}]^{9-}$ fragments connected by a $WO(H_2O)^{4+}$ unit, which represents the well-known $[As_2W_{19}O_{67}(H_2O)]^{14-}$ fragment. However, **1** has only one palladium(II) center incorporated rather than the expected two, and furthermore, this polyanion exhibits an additional, highly unusual feature: the third addenda atom position in the central belt of **1** is occupied by a sodium ion. This is completely unprecedented for this structural subclass of polyanions and probably explains the low stability of **1** in solution. In fact, polyanion **1** could be considered as a monolacunary species, and it also appears like an intermediate in the formation of the hypothetical dipalladium(II)-substituted $[Pd_2WO(H_2O)(\alpha\text{-}AsW_9O_{33})_2]^{10-}$, which we have not been able to isolate to date. Furthermore, our synthetic work in this direction is aimed at the synthesis of the antimony(III) analog of **1** with the suggested formula $[Na_2(H_2O)_2PdWO(H_2O)(\alpha\text{-}SbW_9O_{33})_2]^{10-}$and of the dipalladium tungstoantimonate(III) $[Pd_2WO(H_2O)(\alpha\text{-}SbW_9O_{33})_2]^{10-}$.

Both polyanions **1** and **2** were electrochemically investigated, but the low stability of **1** in the aqueous solutions tested in this work precluded a reliable study. On the other hand, cyclic voltammetry of **2** in a pH 5 medium resulted in the deposition of a Pd^0 film on the glassy carbon electrode surface. The voltammogram showed a particularly sharp hydrogen sorption/desorption as observed previously with the closely related $Pd_3Sb_2W_{18}$. The glassy carbon surface modified by deposition of Pd^0 from **2** proved to be stable and remarkably efficient for the electrocatalytic reduction of dioxygen, at least in the pH 5 medium used here.

Experimental Section

Synthesis

The polyanion precursors $Na_9[\alpha\text{-}AsW_9O_{33}]$ and $K_{14}[As_2W_{19}O_{67}(H_2O)]$ were synthesized according to the published procedures.[8a,11] The identity of the products was confirmed by infrared spectroscopy. All other reagents were used as purchased without further purification.

$Cs_3Na_7[Na_2(H_2O)_2PdWO(H_2O)(\alpha\text{-}AsW_9O_{33})_2]\cdot 1.5NaCl\cdot 22H_2O$ (1a): A sample of $PdCl_2$ (0.040 g, 0.23 mmol) was dissolved in NaAc buffer (20 mL of 0.5 M solution, pH 4.8) while stirring. $K_{14}[As_2W_{19}O_{67}(H_2O)]$ (0.50 g, 0.095 mmol) was then added. The solution was heated to 80 °C for about 1 h and filtered after it had cooled, and then CsCl (0.5 mL of 1.0 M solution) was added to the red filtrate. Slow evaporation at room temperature led to 0.34 g (yield 60%) of a red crystalline product after about two weeks. IR: 944 (m), 893 (s), 796 (s), 746 (vs), 608 (w), 503 (w), 462 (w), 435 (w) cm^{-1}. **1a**: calcd. As 2.5, Cl 0.9, Cs 6.7, Na 4.1, Pd 1.8, W 58.6; found As 2.3, Cl 0.6, Cs 6.7, Na 3.8, Pd 1.5, W 57.7.

$Cs_3Na_6[Cs_2Na(H_2O)_8Pd_3(\alpha\text{-}AsW_9O_{33})_2]\cdot NaCl\cdot 15H_2O$ (2a): A sample of $PdCl_2$ (0.06 g, 0.34 mmol) was dissolved in NaAc buffer (20 mL of 0.5 M solution, pH 4.8) while stirring. $Na_9[\alpha\text{-}AsW_9O_{33}]$ (0.50 g, 0.20 mmol) was then added. The solution was heated to 80 °C for about 1 h and filtered after it had cooled, and then CsCl (0.5 mL of 1.0 M solution) was added to the red filtrate. Slow evaporation at room temperature led to 0.30 g (yield 49%) of a brown crystalline product after about two weeks. IR: 955 (sh), 938 (m), 897 (m), 860 (sh), 782 (vs), 730 (m), 685 (m), 516 (w), 483 (w), 448 (w) cm^{-1}. **2a**: calcd. As 2.4, Cl 0.6, Cs 10.8, Na 3.0, Pd 5.2, W 54.0; found As 2.5, Cl 0.5, Cs 10.4, Na 2.8, Pd 4.7, W 54.9.

All elemental analyses were performed by Kanti Labs Ltd. in Mississauga, Canada. The IR spectra were recorded with a Nicolet Avatar FTIR spectrophotometer in KBr pellets.

X-ray Crystallography

A crystal of **1a** was mounted on a glass fiber for indexing and to collect intensity data at 200 K on a Bruker D8 SMART APEX CCD single-crystal diffractometer using Mo-K_α radiation (λ = 0.71073 Å). Direct methods were used to solve the structure and to locate the heavy atoms (SHELXS97). The remaining atoms were then found from successive difference maps (SHELXL97). The final cycle of refinement, including the atomic coordinates, anisotropic thermal parameters (all W, Pd, Cs, Na, As, Cl atoms) and isotropic thermal parameters (all O atoms) converged at $R = 0.102$ and $R_w = 0.230$ [$I > 2\sigma(I)$]. No hydrogen atoms were included in the refinement. In the final difference map, the deepest hole was –10.945 e Å^{-3} and the highest peak 9.592 e Å^{-3}. The residual electron density is located exclusively near the tungsten atoms. Routine Lorentz and polarization corrections were applied and an absorption correction was performed using the SADABS program.[34]

A crystal of compound **2a** was mounted on a glass fiber for indexing and to collect intensity data at 150 K on a Rigaku Saturn 70 CCD single-crystal diffractometer using Mo-K_α radiation (λ = 0.71070 Å). Direct methods were used to solve the structure and to locate the heavy atoms (SHELXS97). The remaining atoms were then found from successive difference maps (SHELXL97). The final cycle of refinement, including the atomic coordinates, anisotropic thermal parameters (all W, Pd, Cs, Na, As, Cl atoms) and isotropic thermal parameters (all O atoms) converged at $R = 0.080$ and $R_w = 0.216$ [$I > 2\sigma(I)$]. No hydrogen atoms were included in the refinement. In the final difference map, the deepest hole was –7.319 e Å^{-3} and the highest peak 5.813 e Å^{-3}. Routine Lorentz and polarization corrections were applied and an absorption correction was performed using the MULTISCAN program.[35] Crystallographic data for **1a** and **2a** are summarized in Table 1.

Further details of the crystal-structure investigations may be obtained from the Fachinformationszentrum Karlsruhe, 76344 Eggenstein-Leopoldshafen, Germany, on quoting the depository numbers CSD-415125 (**1a**) and CSD-415128 (**2a**).

Electrochemistry

General Methods and Materials: Pure water was used throughout. It was obtained by passing through a RiOs 8 unit followed by a Millipore-Q Academic purification set. All reagents were of high-purity grade and were used as purchased without further purification. The UV/Visible spectra were recorded on a Perkin–Elmer Lambda 19 spectrophotometer with 2×10^{-5} M solutions of the relevant polyanion. Matched 1.000 cm optical path quartz cuvettes were used. The compositions of the various media were as follows: for pH 0: HCl or H_2SO_4; for pH 1 to 3: 0.2 M Na_2SO_4 + H_2SO_4; for pH 4 and 5: 0.4 M CH_3COONa + CH_3COOH; for pH 6 and 7: 0.4 M NaH_2PO_4 + NaOH.

Electrochemical Experiments: The same media as those used for UV/Visible spectroscopy were used for the electrochemical investigation, but the polyanion concentration was 2×10^{-4} M. The solutions were deaerated thoroughly for at least 30 min with pure argon and kept under a positive pressure of this gas during the experiments. All cyclic voltammograms were recorded at a scan rate of 2 mV s^{-1}, unless otherwise stated. The source, mounting, and polishing of the glassy carbon (GC, Tokai, Japan) electrodes has been

 © 2005 Wiley-VCH Verlag GmbH & Co. KGaA, Weinheim

Table 1. Crystal data and structure refinement for $Cs_3Na_7[Na_2(H_2O)_2PdWO(H_2O)(\alpha\text{-}AsW_9O_{33})_2]\cdot 1.5NaCl\cdot 22H_2O$ (**1a**) and $Cs_3Na_6[Cs_2Na(H_2O)_8Pd_3(\alpha\text{-}AsW_9O_{33})_2]\cdot NaCl\cdot 15H_2O$ (**2a**).

	1a	**2a**
Formula	$As_2Cl_{1.5}Cs_3H_{50}Na_{10.5}O_{92}PdW_{19}$	$As_2ClCs_5H_{46}Na_8O_{89}Pd_3W_{18}$
M_w [g mol^{-1}]	5965.2	6132.7
Crystal color	Red-brown	Brown
Crystal system	Triclinic	Monoclinic
Crystal size [mm]	0.20 × 0.04 × 0.02	0.18 × 0.06 × 0.03
Space group (No.)	$P\bar{1}$ (2)	$P2_1/m$ (11)
a [Å]	13.2465(16)	13.1842(5)
b [Å]	16.873(2)	19.6584(7)
c [Å]	23.080(3)	18.2377(6)
α [°]	107.315(2)	
β [°]	95.025(3)	100.7660(10)
γ [°]	98.040(3)	
Volume [Å^3]	4830.6(10)	4643.7(3)
Z	2	2
$d_{calcd.}$ [mg m^{-3}]	4.02	4.22
abs. coeff. [mm^{-1}]	24.677	25.353
Reflections (unique)	23941	22880
Reflections (obs.)	18754	17760
R [$I > 2\sigma(I)$][a]	0.102	0.080
R_w (all data)[b]	0.230	0.216
Diff. Peak [e Å^{-3}]	9.592	5.813
Diff. Hole [e Å^{-3}]	–10.945	–7.319

[a] $R = \Sigma||F_o| - |F_c||/\Sigma|F_o|$. [b] $R_w = [\Sigma w(F_o^2 - F_c^2)^2/\Sigma w(F_o^2)^2]^{1/2}$.

described before.[36] The glassy carbon samples had a diameter of 3 mm. The electrochemical set-up was an EG & G 273 A driven by a PC with the M270 software. Potentials are quoted against a saturated calomel electrode (SCE). The counter electrode was platinum gauze with a large surface area. All experiments were performed at room temperature.

Stability Studies: We tried to identify conditions at which polyanions **1** and **2** were stable enough to allow for electrochemical studies. For this purpose, the UV/Vis spectrum of each compound was monitored as a function of pH over a period of at least 24 h at room temperature. This delay was selected as a compromise between the time needed for electrochemical characterization of the complexes and that for eventual long-lasting or preparative-scale catalytic or electrocatalytic processes. Only spectra reproducible with respect to shape, absorbance, and wavelength location over this period of time were considered to indicate complete stability. At these conditions, **2** shows complete stability from pH 0 through to 5. It is interesting to compare this stability domain to that of the closely related polyanion $Pd_3Sb_2W_{18}$, which is stable from pH 0 to 7.[28] Provisionally, this difference might be attributed to the different heteroatoms Sb versus As. A complementary cross-check of these suggested stabilities was obtained by electrochemical experiments: the complete voltammetric study for each pH value lasts, typically, between 8 and 10 h. Perfect reproducibility of the voltammogram obtained for a selected potential scan rate was observed and taken as a complementary criterion of stability. In contrast to the behavior of **2**, no satisfactory stability domain could be determined for **1** in aqueous solution, despite efforts to modify the composition of the supporting electrolytes.

Acknowledgments

U.K. thanks the International University Bremen for research support and the Florida State University Chemistry Department for unlimited access to the single-crystal X-ray diffractometer. B.K. and L.N. thank the University Paris Sud XI and the CNRS (UMR 8000) for research support. Figures 1–3 were generated by Diamond Version 3.0d (copyright Crystal Impact GbR).

[1] *Chemical Reviews, Polyoxometalates* (Ed.: C. L. Hill), **1998**.
[2] M. T. Pope, *Heteropoly and Isopoly Oxometalates*, Springer-Verlag: Berlin, **1983**.
[3] M. T. Pope, A. Müller, *Angew. Chem. Int. Ed.* **1991**, *30*, 34–48.
[4] M. T. Pope, *Comp. Coord. Chem. II* **2003**, *4*, 635–677.
[5] *Polyoxometalates: From Platonic Solids to Anti-Retroviral Activity* (Eds.: M. T. Pope, A. Müller), Kluwer, Dordrecht, The Netherlands, **1994**.
[6] *Polyoxometalate Chemistry: From Topology via Self-Assembly to Applications* (Eds.: M. T. Pope, A. Müller), Kluwer, Dordrecht, The Netherlands, **2001**.
[7] *Polyoxometalate Chemistry for Nano-Composite Design* (Eds.: T. Yamase, M. T. Pope), Kluwer, Dordrecht, The Netherlands, **2002**.
[8] a) C. Tourné, A. Revel, G. Tourné, M. Vendrell, *C. R. Hebd. Seances Acad. Sci. Ser. C* **1973**, *277*, 643–645; b) M. Leyrie, J. Martin-Frére, G. Hervé, *C. R. Hebd. Seances Acad. Sci. Ser. C* **1974**, *279*, 895–897; c) M. Leyrie, G. Hervé, *Nouv. J. Chim.* **1978**, *2*, 233–237.
[9] a) F. Robert, M. Leyrie, G. Hervé, A. Tézé, Y. Jeannin, *Inorg. Chem.* **1980**, *19*, 1746–1752; b) Y. Jeannin, *C. R. Acad. Sci. Ser. IIc* **2000**, *3*, 295–299; c) Y. Jeannin, J. Martin-Frère, *Inorg. Chem.* **1979**, *18*, 3010–3014; d) M. Leyrie, A. Tézé, G. Hervé, *Inorg. Chem.* **1985**, *24*, 1275–1277.
[10] K. Wassermann, M. H. Dickman, M. T. Pope, *Angew. Chem. Int. Ed.* **1997**, *36*, 1445–1448.
[11] U. Kortz, M. G. Savelieff, B. S. Bassil, M. H. Dickman, *Angew. Chem. Int. Ed.* **2001**, *40*, 3384–3386.
[12] F. Robert, M. Leyrie, G. Hervé, *Acta Crystallogr. Sect. B* **1982**, *38*, 358–362.
[13] a) U. Kortz, N. K. Al-Kassem, M. G. Savelieff, N. A. Al Kadi, M. Sadakane, *Inorg. Chem.* **2001**, *40*, 4742–4749; b) P. Mialane, J. Marrot, E. Rivière, J. Nebout, G. Hervé, *Inorg. Chem.* **2001**, *40*, 44–48.
[14] U. Kortz, S. Nellutla, A. C. Stowe, N. S. Dalal, J. van Tol, B. S. Bassil, *Inorg. Chem.* **2004**, *43*, 144–154.

 © 2005 Wiley-VCH Verlag GmbH & Co. KGaA, Weinheim

[15] U. Kortz, M. G. Savelieff, B. S. Bassil, B. Keita, L. Nadjo, *Inorg. Chem.* **2002**, *41*, 783–789.
[16] a) C. Tourné, G. Tourné, *C. R. Acad. Sci. Paris Ser. C* **1975**, *281*, 933–936; b) L. G. Detusheva, L. I. Kuznetsova, V. A. Likholobov, A. A. Vlasov, N. N. Boldyreva, S. G. Poryvaev, V. V. Malakhov, *Russ. J. Coord. Chem.* **1999**, *25*, 569–575; c) P. Mialane, J. Marrot, A. Mallard, G. Hervé, *Inorg. Chim. Acta* **2002**, *328*, 81–86.
[17] F. Lefebvre, M. Leyrie, G. Hervé, C. Sanchez, J. Livage, *Inorg. Chim. Acta* **1983**, *73*, 173–178.
[18] U. Kortz, C. Holzapfel, M. Reicke, *J. Mol. Struct.* **2003**, *656*, 93–100.
[19] Y. Jeannin, J. Martin-Frère, *J. Am. Chem. Soc.* **1981**, *103*, 1664–1667.
[20] G. Sazani, M. H. Dickman, M. T. Pope, *Inorg. Chem.* **2000**, *39*, 939–943.
[21] F. Hussain, U. Kortz, R. J. Clark, *Inorg. Chem.* **2004**, *43*, 3237–3241.
[22] F. Hussain, M. Reicke, U. Kortz, *Eur. J. Inorg. Chem.* **2004**, 2733–2738.
[23] W. H. Knoth, P. J. Domaille, R. L. Harlow, *Inorg. Chem.* **1986**, *25*, 1577–1584.
[24] C. M. Tourné, G. F. Tourné, F. Zonnevijlle, *J. Chem. Soc. Dalton Trans.* **1991**, 143–155.
[25] a) R. Neumann, A. M. Khenkin, *Inorg. Chem.* **1995**, *34*, 5753–5760; b) R. Neumann, A. M. Khenkin, D. Juwiler, H. Miller, M. Gara, *J. Mol. Catal A-Chem.* **1997**, *117*, 169–183; c) U. Schuchardt, D. Cardoso, R. Sercheli, R. Pereira, R. S. da Cruz, M. C. Guerreiro, D. Mandelli, E. V. Spinace, E. L. Fires, *Appl. Catal. A-Gen.* **2001**, *211*, 1–17; d) V. Kogan, Z. Aizenshtat, R. Neumann, *New J. Chem.* **2002**, *26*, 272–274; e) W. Adam, P. L. Alsters, R. Neumann, C. R. Saha-Moller, D. Seebach, A. K. Beck, R. Zhang, *J. Org. Chem.* **2003**, *68*, 8222–8231; f) W. Adam, P. L. Alsters, R. Neumann, C. R. Saha-Moller, D. Sloboda-Rozner, R. Zhang, *J. Org. Chem.* **2003**, *68*, 1721–1728.
[26] S. J. Angus-Dunne, R. C. Burns, D. C. Craig, G. A. Lawrance, *J. Chem. Soc. Chem. Commun.* **1994**, 523–524.
[27] a) L. Bi, F. Hussain, U. Kortz, M. Sadakane, M. H. Dickman, *Chem. Commun.* **2004**, 1420–1421; b) L.-H. Bi, U. Kortz, B. Keita, L. Nadjo, *Dalton Trans.* **2004**, 3184–3190.
[28] L.-H. Bi, M. Reicke, U. Kortz, B. Keita, L. Nadjo, R. J. Clark, *Inorg. Chem.* **2004**, *43*, 3915–3920.
[29] L.-H. Bi, U. Kortz, B. Keita, L. Nadjo, H. Borrmann, *Inorg. Chem.* **2004**, *43*, 8367–8372.
[30] I. D. Brown, D. Altermatt, *Acta Crystallogr. Sect. B* **1985**, *41*, 244–247.
[31] Representative papers on Pd^0 deposition from Pd^{2+} solutions and its electrochemical behaviour include: a) K.-H. Lubert, M. Guttmann, L. Beyer, *J. Electroanal. Chem.* **1999**, *462*, 174–180; b) K.-H. Lubert, M. Guttmann, L. Beyer, K. Kalcher, *Electrochem. Commun.* **2001**, *3*, 102–106; c) X.-G. Zhang, T. Arikawa, Y. Murakami, K. Yahikozawa, Y. Takasu, *Electrochimica Acta* **1995**, *40*, 1889–1897; d) M. J. Ball, C. A. Lucas, N. M. Markovic, V. Stamenkovic, P. N. Ross, *Surface Sci.* **2002**, *518*, 201–209; e) X.-Q. Tong, M. Aindow, J. P. G. Farr, *J. Electroanal. Chem.* **1995**, *395*, 117–126; f) N. Tateishi, K. Yahikozawa, K. Nashimura, M. Suzuki, Y. Iwanaga, M. Watanabe, E. Enami, Y. Matsuda, Y. Takasu, *Electrochimica Acta* **1991**, *36*, 1235–1240; g) X-G. Zhang, Y. Murakami, K. Yahikozawa, Y. Takasu, *Electrochimica Acta* **1997**, *42*, 223–227; h) N. M. Markovic, C. A. Lucas, V. Climent, V. Stamenkovic, P. N. Ross, *Surface Sci.* **2000**, *465*, 103–114; i) L-J. Wan, T. Suzuki, K. Sashikata, J. Okada, J. Inukai, K. Itaya, *J. Electroanal. Chem.* **2000**, *484*, 189–193; j) A. M. El-Aziz, L. A. Kibler, D. M. Kolb, *Electrochem. Commun.* **2002**, *4*, 535–539; k) M. Arenz, V. Stamenkovic, T. J. Schmidt, K. Wandelt, P. N. Ross, N. M. Markovic, *Surface Sci.* **2003**, *523*, 199–209; l) A. Hernandez Creus, Y. Gimeno, P. Diaz, L. Vazquez, S. Gonzalez, R. C. Salvarezza, A. J. Arvia, *J. Phys. Chem. B* **2004**, *108*, 10785–10795.
[32] Landoldt-Börnstein, I. Band, *Atom- und Molekularphysik, 4. Teil: Kristalle*, 6th ed., Springer, Berlin, **1955**, p. 527.
[33] B. Keita, M. Benaïssa, L. Nadjo, R. Contant, *Electrochem. Commun.* **2002**, *4*, 663–668.
[34] G. M. Sheldrick, *SADABS*; University of Göttingen, **1996**.
[35] R. H. Blessing, *Acta Crystallogr. Sect. A* **1995**, *51*, 33–38.
[36] B. Keita, F. Girard, L. Nadjo, R. Contant, R. Belghiche, M. Abbessi, *J. Electroanal. Chem.* **2001**, *508*, 70–80.

Received: February 11, 2005
Published Online: June 21, 2005

 © 2005 Wiley-VCH Verlag GmbH & Co. KGaA, Weinheim

Interplay between Nitrones and (Nitrile)Pd^{II} Complexes: Cycloaddition vs. Complexation Followed by Cyclopalladation and Deoxygenation Reactions

Nadezhda A. Bokach,[a,b] Artem A. Krokhin,[b,c] Alexey A. Nazarov,[c] Vadim Yu. Kukushkin*[b] Matti Haukka,[d] João J. R. Fraústo da Silva,[a] and Armando J. L. Pombeiro*[a]

Keywords: Palladium / Nitrone complexes / Nitrile complexes / 1,3-Dipolar cycloaddition / Cyclometalation

The reaction between the nitrone *p*-MeC$_6$H$_4$CH=N(Me)O and *trans*-[PdCl$_2$(RCN)$_2$] (R = Ph, Me) in the corresponding RCN (or of the nitrone in neat RCN in the presence of PdCl$_2$) proceeds at 45 °C (R = Ph) or reflux (R = Me) for 1 d and allows the isolation of the Δ^4-1,2,4-oxadiazoline complexes [PdCl$_2$\{N^a=C(R)ON(Me)C^{b}H(C$_6$H$_4$Me-*p*)\}$_2$(N^a–C^b)] (R = Ph **1**; R = Me **2**) in ca. 50 and ca. 15 % yields, respectively. The reaction time can be drastically reduced by focused microwave irradiation of the reaction mixture. In CH$_2$Cl$_2$ or acetone, this reaction proceeds in another direction to achieve the unstable nitrone complex [PdCl$_2$\{ON(Me)=CH(C$_6$H$_4$Me-*p*)\}$_2$] (**3**), which was characterized by electrospray mass spectrometry, IR and ^{1}H NMR spectroscopy. Complex **3** is the first representative of (nitrone)Pd^{II} compounds and is the key intermediate in at least two further reactions, i.e. cyclopalladation to give the dimeric complex [Pd$_2$(μ-Cl)$_2$\{ON(Me)=C(H)C$_6$H$_3$Me-*p*\}$_2$] (**5**; 30 % isolated yield) and deoxygenation of the nitrone to furnish the imine compound [PdCl$_2$\{N(Me)=CH(C$_6$H$_4$Me-*p*)\}$_2$] (**4**). The palladium complexes **1**, **2**, **4** and **5** were characterized by C, H, and N analyses, FAB-MS, IR, ^{1}H and ^{13}C\{^{1}H\} spectroscopy, while **4** and **5** additionally by X-ray crystallography.
(© Wiley-VCH Verlag GmbH & Co. KGaA, 69451 Weinheim, Germany, 2005)

Introduction

In organic chemistry, 1,3-dipolar cycloadditions are reactions of paramount importance for the synthesis of a great variety of heterocycles.[1–5] One of the most promising subdirections of research in this area includes metal control of the interplay between various dipolarophiles and dipoles. Indeed, metal-mediated cycloadditions have been the object of extensive investigations in the past decade and substantial progress has been achieved in both stoichiometric and catalytic approaches.[5–8] In the overwhelming majority of these works, *alkenes* have been employed as dipolarophiles, whereas application of *organonitriles* for these purposes was investigated to an incomparably lesser degree.[6,7] Recently we found that significant activation of nitriles−even typically unreactive ones bearing an electron-donor R group in RCN−toward cycloadditions of both allyl anion (i.e., nitrones,[8–11] route *i* in Scheme 1) and propargyl/allenyl anion type (i.e., nitrile oxide,[12,13] route *ii*) dipoles[1,2] can be reached by their ligation to a Pt^{IV} center, while Pt^{II} displays little effect[10] on the reaction. Subsequent liberation of the ligands allowed the metal-mediated synthesis of these two classes of heterocycles.

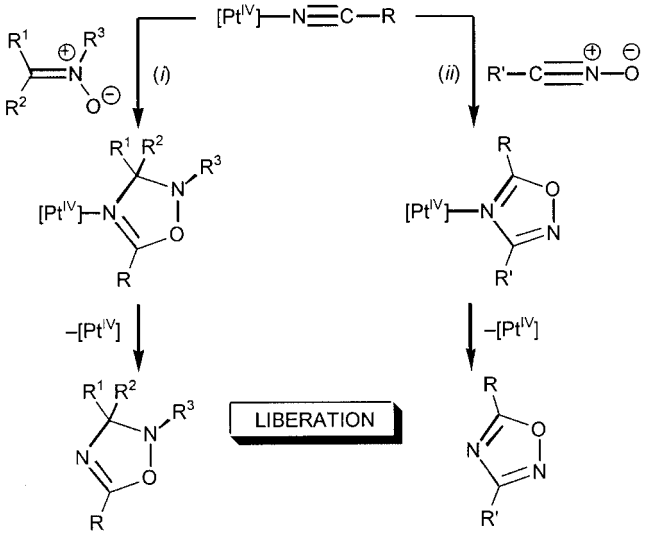

Scheme 1.

As a continuation of our project on reactions of metal-activated nitriles in general[6,14] and 1,3-cycloadditions[8–13] in particular, we have chosen (nitrile)Pd^{II} complexes as di-

[a] Centro de Química Estrutural, Complexo I, Instituto Superior Técnico,
Av. Rovisco Pais, 1049-001 Lisboa, Portugal
E-mail: pombeiro@ist.utl.pt
[b] Department of Chemistry, St. Petersburg State University, 198504, Stary Petergof, Russian Federation
E-mail: kukushkin@VK2100.spb.edu
[c] Institute of Inorganic Chemistry – Bioinorganic, Environmental and Radiochemistry,
Faculty of Chemistry, University of Vienna,
Währinger Str. 42, 1090 Vienna, Austria
[d] Department of Chemistry, University of Joensuu,
P. O. Box 111, 80101 Joensuu, Finland

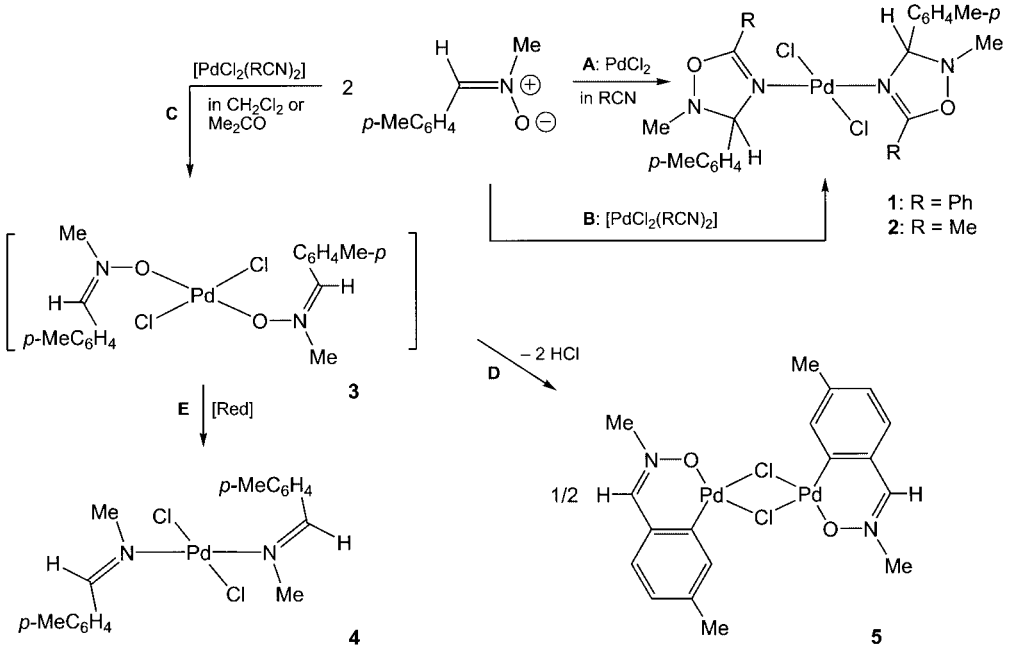

Scheme 2.

polarophiles and observed a palladium-mediated [2 + 3] cycloaddition of a nitrone to achieve (Δ^4-1,2,4-oxadiazoline)-Pd^{II} complexes. A recent brief report[15] on the occurrence of this type of reaction for the benzonitrile complex [$PdCl_2(PhCN)_2$], including an indication that the analogous acetonitrile compound is unreactive, prompted us to display our own results in this field. In contrast to that work, we have observed not only that the [2 + 3] cycloaddition proceeds for [$PdCl_2(MeCN)_2$] but also that other types of reactions, i.e. cyclopalladation and nitrone deoxygenation, take place in these systems. The occurrence of the latter two processes, which were not previously observed in the chemistry of nitrones, explains the lack of selectivity of the cycloaddition and provides further insight into understanding the effect of the metal center upon the cycloaddition.

Results and Discussions

We chose to study the reaction of palladium(II) complexes *trans*-[$PdCl_2(RCN)_2$], bearing nitriles with acceptor (R = Ph) and donor (R = Me) substituents, with a stable nitrone, *p*-$MeC_6H_4CH{=}N(Me)O$, as the dipole/ligand.

Palladium(II)-Mediated 1,3-Dipolar Cycloaddition

The reaction between the nitrone *p*-$MeC_6H_4CH{=}N(Me)O$ and PhCN mediated by a Pd^{II} center was performed by two similar, although technically distinct, routes (Scheme 2, routes **A** and **B**).

In the first route (**A**), both $PdCl_2$ and the nitrone *p*-$MeC_6H_4CH{=}N(Me)O$ were reacted in a suspension of neat PhCN, while in the second route (**B**) the nitrile complex *trans*-[$PdCl_2(PhCN)_2$],[16] dissolved in the corresponding nitrile, was treated with the nitrone. In both routes, the reaction proceeds at 45 °C for 1 d (or for 4 h under 20 W microwave irradiation) and the isolated yield of the Δ^4-1,2,4-oxadiazoline complex [$PdCl_2\{N^a{=}C(Ph)ON(Me)C^bH(C_6H_4\text{-}Me\text{-}p)\}_2(N^a\text{–}C^b)$] (**1**), prepared by the two methods, is almost the same (ca. 50%) irrespective of whether conventional or microwave conditions are applied.

The reaction of $PdCl_2$ with neat PhCN is well known and it constitutes a method for the preparation of *trans*-[$PdCl_2(PhCN)_2$].[16] Hence, it is not surprising that the reaction rates and the isolated yields are similar for both routes, because the first route conceivably includes the formation of [$PdCl_2(PhCN)_2$] (upon dissolution of $PdCl_2$ in PhCN) followed by the cycloaddition of the nitrone. Despite the similarity of the synthetic approaches **A** and **B**, the obvious advantage of the former method is that it allows us to obtain complex **1** starting directly from $PdCl_2$ and omitting the unnecessary step of the isolation of *trans*-[$PdCl_2(PhCN)_2$].

The complex **1** gave satisfactory microanalysis for the PhCN solvate and the expected fragmentation/isotopic pattern in FAB-MS$^+$ ([M – Cl]$^+$ and [M – 2 HCl]$^+$). In the IR spectrum, the complex exhibits a strong band at 1649 cm^{-1} from ν(C=N) of the heterocycle and 2231 cm^{-1} from ν(C≡N) of the solvate. In the ^{1}H NMR spectrum, the Δ^4-1,2,4-oxadiazoline ring displays signals in the aromatic range from 8.62 to 7.32 ppm, two Me groups appear at 2.90 and 2.43, and the C*H* signal emerges at δ = 5.82 ppm. Excess of Ph's from the solvated PhCN were detected in the spectrum by integration. All our data agree well with the previously reported formulation.[15] In addition, we performed an X-ray analysis of **1** and it is indicated that the *R*,*R*- and *S*,*S*-Δ^4-1,2,4-oxadiazoline ligands are in the mutu-

 © 2005 Wiley-VCH Verlag GmbH & Co. KGaA, Weinheim

ally *trans*-positions (see Figure 1 and deposited data). Unfortunately, the rather poor quality of crystals precluded a detailed comparison of the geometrical parameters.

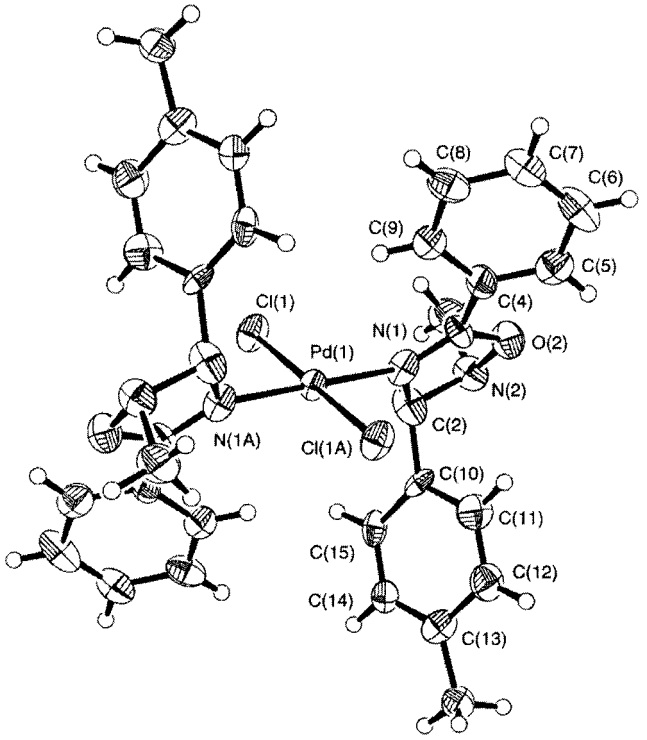

Figure 1. ORTEP view of **1**.

Previously, it has been reported that the acetonitrile complex $[PdCl_2(MeCN)_2]$ is unreactive toward the nitrone *p*-$MeC_6H_4CH=N(O)Me$ even under relatively harsh conditions (80 °C, 1 week).[15] In contrast to that report, in our hands, an interplay between the nitrone *p*-$MeC_6H_4CH=N(O)Me$ and $[PdCl_2(MeCN)_2]$ (or with $PdCl_2$) in MeCN (Scheme 2, **A** and **B**) upon reflux for 1 d (or, 20 min at ca. 80 °C under 70 W microwave irradiation) results in the formation of a broad mixture of products, where the complex **2**, derived from the 1,3-dipolar cycloaddition is formed in 10–15% ^{1}H NMR yield [integration is based on the C*H*(R) proton of the ring which usually emerges in a very specific region from 5.0 to 6.0 ppm]. The complex $[PdCl_2\{N^a=C(Me)ON(Me)C^bH(C_6H_4Me\text{-}p)\}_2$-$(N^a–C^b)]$ (**2**) was isolated as a solid and characterized as the bis-hydrate (see Exp. Sect.). Microwave irradiation of the reaction mixture did not improve the selectivity of the cycloaddition but allowed the dramatic reduction of the reaction time.

Coordination of the Nitrone and Subsequent Reactions

In general, dissociation of RCN from (nitrile)Pd^{II} complexes in non-nitrile solutions (vs. nitrile ones), similar to that described for weak electrolytes by the Ostwald dilution law, increases and consequently the amount of ligated RCN decreases thus favouring the substitution via the expected dissociative mechanism. Thus, to increase the fraction of reactions other than the cycloaddition and to understand the lack of selectivity, indicated in the previous section, we studied the reaction between $[PdCl_2(RCN)_2]$ complexes and the nitrone *p*-$MeC_6H_4CH=N(O)Me$ in dichloromethane and acetone. Indeed, in these experiments we did not detect complexes **1** and **2** but the complex $[PdCl_2\{\underline{O}N(Me)=CH(C_6H_4Me\text{-}p)\}_2]$ (**3**) (Scheme 2, route **C**), which originates from the substitution, was isolated. Although **3** is unstable even in the solid state and undergoes further reactions in solutions (see later) we succeeded to characterize this product by electrospray mass spectrometry ($[M - HCl]^+$ and $[M - 2HCl]^+$ ions were observed). In the IR spectrum of **3**, the ν(C=N) stretching vibration is shifted to a higher frequency (by, 14 cm^{-1}), while the ν(N–O) stretch is shifted to a lower frequency (by 10 cm^{-1}) vs. those signals in the free nitrone and these observations favour *O*-coordination of the nitrone to a Pd^{II} center.

Complexes with *O*-bound nitrones as ligands are known although scarce. These species can be formed (*i*) in the direct reaction of a nitrone and a metal complex at various metal centers such as *hard* (U^{VI},[17] Zn^{II},[18,19] Sn^{IV},[20] Ti^{IV},[15,21] Zr^{IV}),[15] *soft* (Au^{I},[22] Au^{III},[22] Ag^{I})[19] and *borderline* (Ni^{II},[23] Cu^{II}, Mn^{II}, Co^{II}, Fe^{II}, Fe^{III},[24,25] and Ru^{II}- and Os^{II}-[26] porphyrines) Lewis acids and (*ii*) in a metal-mediated process, e.g. by reaction of a carbene ligand with nitrosoarenes at an Fe^{II} center[27] or by addition of 2-methyl-2-nitrosopropane to coordinated ethylene[28] at a Pt^{II} center. To the best of our knowledge, the complex **3** is the first representative of a (nitrone)Pd^{II} compound.

We believe that the nitrone complex **3** can be the key intermediate in at least two further reactions, which are observed in this work, i.e. cyclopalladation to give the dimeric complex $[Pd_2(\mu\text{-}Cl)_2\{\underline{O}N(Me)=C(H)C_6H_3Me\text{-}p\}_2]$ **5** (Scheme 2, route **D**) and deoxygenation of the nitrone to furnish the imine compound $[PdCl_2\{N(Me)=CH(C_6H_4Me\text{-}p)\}_2]$ **4** (Scheme 2, route **E**). Thus, **5** is released as crystals (yield is 30%) when the reaction mixture is kept in CH_2Cl_2 for 3 d at room temperature (Figure 2).

The dimer **5** was characterized by X-ray crystallography. Both palladium atoms form a square-planar arrangement with two mutually *trans* cyclometalated nitrones. The deviation of the metallacycle planes Pd(1)C(1)C(7)C(8)N(1)O(1) from the Pd(1)Cl(1)Pd(1A)Cl(1A) plane is 22.36°. The bond lengths Pd–Cl (*trans* to O) [2.3234(6) Å] and Pd–Cl (*trans* to C) [2.4712(6) Å] are normal and agree well with other palladium(II) halogen-bridged complexes.[29] The difference in the Pd–Cl bond lengths *trans* to O or *trans* to C are due to a strong ground state *trans*-influence of C-bonded ligands.[30] The bond length C(8)–N(1) [1.289(3) Å] is a double one[31] and the bond length N(1)–O(1) [1.331(2) Å] has a value that falls in the range of typical N–O bond lengths in *N*-oxides.[31]

The data on stability of nitrone metal complexes are quite limited in the literature and the only relevant information so far reported is for the iron complexes $[Cp(CO)_2Fe\{\underline{O}N(Ar)=CH(Ar')\}]^+$ which are light- and moisture-sensitive and decompose to the imine ArN=CH(Ar′) (by *deoxygenation*; the reducing agent was not verified[27]) and

 © 2005 Wiley-VCH Verlag GmbH & Co. KGaA, Weinheim

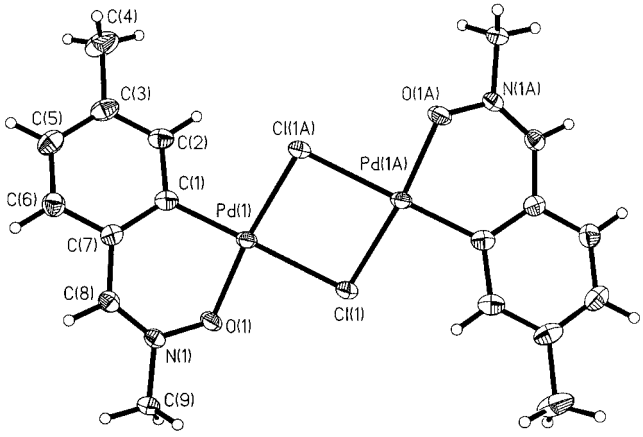

Figure 2. Thermal ellipsoid view of complex **4** with atomic numbering scheme. Thermal ellipsoids are drawn with 50% probability. Selected bond lengths [Å] and angles [°]: Pd(1)–N(1) 2.024(5), Pd(1)–Cl(1) 2.3058(16), N(1)–C(1) 1.250(8), N(1)–C(9) 1.469(8), C(1)–C(2) 1.473(10), N(1)–Pd(1)–Cl(1) 90.53(15), Pd(1)–N(1)–C(1) 126.7(5), Pd(1)–N(1)–C(9) 113.3(4), N(1)–C(1)–C(2) 126.8(6).

to aldehyde O=CH(Ar′) (by *hydration*) along with some unidentified iron-containing products.[27] In accord with this report, we isolated (by mechanical separation of crystals obtained from evaporation of a CH_2Cl_2/Et_2O solution of the residue of the reaction mixture $PdCl_2$–*p*-MeC_6H_4CH=N(O)Me–PhCN) the aldimine compound $[PdCl_2\{N(Me)=CH(C_6H_4Me\text{-}p)\}_2]$ (**4**) (Scheme 2, route **E**; Figure 3) which was characterized by X-ray diffraction study. In complex **4**, the palladium atom is in a square-planar arrangement and two aldimine ligands are mutually *trans*. The value of the C(1)–N(1) [1.250(8) Å] bond length is in the typical double bond range[31] and the Pd–Cl [2.3057(16) Å] bonds are normal.[31]

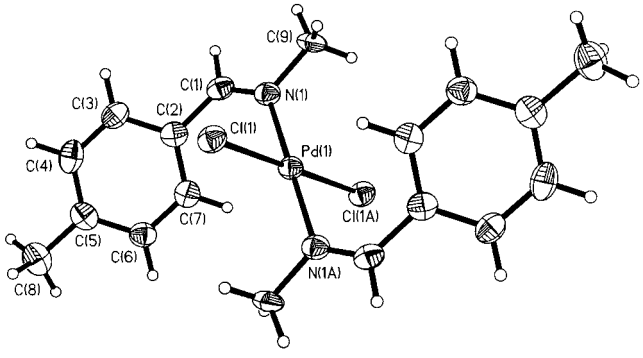

Figure 3. Thermal ellipsoid view of complex **5** with atomic numbering scheme. Thermal ellipsoids are drawn with 50% probability. Selected bond lengths [Å] and angles [°]: Pd(1)–C(1) 1.973(4), Pd(1)–O(1) 1.996(3), Pd(1)–Cl(1) 2.4696(12), N(1)–O(1) 1.333(4), C(1)–Pd(1)–O(1) 92.21(15), C(1)–Pd(1)–Cl(1A) 94.65(13), O(1)–Pd(1)–Cl(1) 87.82(8), Pd(1)–Cl(1)–Pd(1A) 94.73(4).

A possible rationale for the formation of **4** is deoxygenation of the parent nitrone, whereupon the appropriate aldimine MeN=CH(C_6H_4Me-*p*) coordinates to a Pd^{II} center. Indeed, the deoxygenation of nitrones involving metal centers is known and includes $CoCl_2{\cdot}6H_2O$/Sm,[32] $AlCl_3{\cdot}6H_2O$–THF/Zn,[33] $TiCl_4$/NaI,[34] $(CF_3CO)_2O$/NaI[35] reductive systems, or $TiCl_3$.[36] In the first four cases, these systems are believed to involve initial activation of the N–O group of nitrone by an electrophilic reagent followed by the reduction. In the latter case, $TiCl_3$ plays the role of both activator and reducing reagent. Our palladium(II) systems could, in principle, reduce nitrones in a similar way insofar as they contain an activating center, i.e. Pd^{II} (Scheme 2, **C**), and a reducing reagent, e.g. the aldehyde O=(H)-C(C_6H_4Me-*p*), detected in the reaction mixture by NMR method, formed upon metal-mediated hydrolysis of the nitrone.

Final Remarks

The results obtained in this work could be considered from at least two perspectives. From the viewpoint of 1,3-dipolar cycloaddition it is worthwhile to note that (*i*) even the rather electron-deficient nitrile PhCN in the free state does not react with the nitrone (allyl anion type dipole[2]) under the reaction conditions described above. Furthermore, a structurally similar nitrone, i.e. PhCH=N(O)Me, reacts with PhCN under harsh conditions (110 °C, 10 d) giving the corresponding oxadiazoline in 57% yield;[37] (*ii*) in the synthetic experiments we did not observe a significant difference in reactivities toward the cycloaddition between the corresponding palladium(II)- (this work) and platinum(II) (ref.[9]) complexes $[MCl_2(PhCN)_2]$, albeit conditions are not strictly similar (1 d, 40 °C, in PhCN for the Pd^{II} complex and 1 d, 20–25 °C, in CH_2Cl_2 for the Pt^{II} complex). The opposite holds true for the cycloaddition of nitrile oxides (a propargyl/allenyl anion type dipole[2]) to nitriles in $[MCl_2(RCN)_2]$ complexes where the activation of RCN species, toward the cycloaddition, is higher at a Pd^{II} center. A similar trend has been observed by Lippert et al.[38] for nucleophilic addition of water to nitriles ligated to $[M(en)_2]^{2+}$ moieties; the rate of the hydrolysis found for M = Pd^{II} was substantially larger than for M = Pt^{II}. This *difference* in activation between the two metal centers toward nitrile oxides and *similarity* toward nitrones deserves further investigations directed to the understanding of such relative behaviors and the development of a strategy for the metal-mediated 1,3-dipolar cycloaddition.

From the viewpoint of coordination of nitrones, we observed that the more labile Pd^{II} center (vs. the kinetically inert Pt^{II} and Pt^{IV} centers) reacts to a comparable degree with both dipolarophile and dipole and the latter interaction, i.e. ligation of the nitrone to a Pd^{II} center (observed in this work for the first time), inhibits the 1,3-dipolar cycloaddition by coordination of the oxygen atom of the dipole.

In general, the directing of the reaction of nitriles with nitrones to a cycloaddition or a complexation route depends on a delicate balance between donor/acceptor properties of substituents at both dipolarophile and dipole, activating power of the metal center toward cycloaddition and its substitution inertness/lability toward interaction with the reactants. From this perspective the Pd^{II} center occupies an

 © 2005 Wiley-VCH Verlag GmbH & Co. KGaA, Weinheim

intermediate position between such a substitutionally inert strong RCN activator as a Pt^{IV} center (where only efficient cycloaddition of both nitrones and nitrile oxides[8] was observed) and kinetically labile (nitrile)Ti^{IV} and (nitrile)Zr^{IV} systems (where only displacement of nitriles by nitrones was reported[15]).

Experimental Section

Materials and Instrumentation: Solvents and the nitriles were obtained from commercial sources and used as received. The complexes $[PdCl_2(RCN)_2]$ (R = Me,[39] Ph[16]) and the nitrone[40] were prepared as described previously. Positive-ion FAB mass spectra were obtained on a Trio 2000 instrument by bombarding 3-nitrobenzyl alcohol (NBA) matrices of the samples with 8 keV (ca. $1.28\,10^{15}$ J) Xe atoms. Mass calibration for data system acquisition was achieved using CsI. Electrospray ionization mass spectra were recorded with a Bruker Esquire 3000 in positive ion mode. Infrared spectra (4000–400 cm^{-1}) were recorded with a JASCO FT/IR-430 instrument in KBr pellets. ^1H and $^{13}C\{^1H\}$ NMR spectra were measured on Bruker DPX 300 and Varian UNITY 300 spectrometers at ambient temperature.

X-ray Crystal Structure Determinations: Crystals were immersed in cryo-oil, mounted in a Nylon loop and measured at a temperature of 100 K or 120 K. The X-ray diffraction data was collected by a Nonius KappaCCD diffractometer using Mo-K_α radiation (λ = 0.71073 Å). The Denzo-Scalepack[41] program package was used for cell refinements and data reduction. The structures were solved by direct methods using the SHELXS-97 or SIR2000 programs.[42,43] A multiscan absorption correction based on equiv. reflections (XPREP in SHELXTL v. 6.14)[44] was applied to all of the data (the $T_{min.}/T_{max.}$ values were 0.7887/0.9215, 0.10130/0.16564, and 0.8169/0.9055 for **1**, **4**, and **5**, respectively). Structural refinements were carried out using SHELXL-97 with the WinGX graphical user interface.[45,46] All of the hydrogens were placed in idealized positions and constrained to ride on their parent atom. The crystallographic data of **4** and **5** are summarized in Table 1. The selected bond lengths and angles of **4** and **5** are shown in Figure captions. The structure solution of **1** is not satisfactory and therefore the crystallographic details are only given as supplementary material (for details see below).

Table 1. Crystallographic data for complexes **4** and **5**.

	4	**5**
Empirical formula	$C_{18}H_{22}Cl_2N_2Pd$	$C_{18}H_{20}Cl_2N_2O_2Pd_2$
fw	443.68	580.06
Temp. [K]	100(2)	120(2)
λ [Å]	0.71073	0.71073
Crystal system	monoclinic	monoclinic
Space group	$P2_1/c$	$P2_1/c$
a [Å]	6.4998(8)	10.4223(6)
b [Å]	19.8669(16)	12.0034(12)
c [Å]	7.2611(8)	8.0925(11)
α [°]	90	90
β [°]	90.734(6)	96.125(6)
γ [°]	90	90
V [Å^3]	937.56(17)	1006.6(2)
Z	2	2
$\rho_{calcd.}$ [Mg/m^3]	1.572	1.914
μ(Mo-*Kα*) [mm^{-1}]	1.275	2.066
R_1[a] ($I \geq 2\sigma$)	0.0497	0.0339
wR_2[b] ($I \geq 2\ \sigma$)	0.1097	0.0636

[a] $R_1 = \Sigma||F_o| - |F_c||/\Sigma|F_o|$. [b] $wR_2 = \{\Sigma[w(F_o^2 - F_c^2)^2]/\Sigma[w(F_o^2)^2]\}^{1/2}$.

CCDC-262709 to -262711 contain the supplementary crystallographic data for this paper. These data can be obtained free of charge from The Cambridge Crystallographic Data Centre via www.ccdc.cam.ac.uk/data_request/cif.

Synthetic Work and Characterization

Reaction of $PdCl_2$ with *p*-$MeC_6H_4CH=N(O)Me$ in PhCN: Nitrile (0.5 mL) was added to a mixture of $PdCl_2$ (12 mg, 0.068 mmol) and the nitrone *p*-$MeC_6H_4CH=N(O)Me$ (22.4 mg, 0.150 mmol) and the suspension formed left to stand for 1 d at 45 °C. During this time the solid $PdCl_2$ was completely dissolved to give a yellow solution. Then the solvent was removed under vacuum at 50 °C and the oily residue was crystallized under Et_2O (five 2-mL portions) and dried under a stream of nitrogen at room temperature. The reaction can be performed starting from $[PdCl_2(PhCN)_2]$ under the same reaction conditions. The reaction between $PdCl_2$ and *p*-$MeC_6H_4CH=N(O)Me$ in PhCN is complete after 4 h under microwave irradiation (20 W, 50 °C).

$[PdCl_2\{N^a=C(Ph)ON(Me)C^bH(C_6H_4Me\text{-}p)\}_2(N^a–C^b)]$ (1): Yield 50%. $C_{32}H_{32}Cl_2N_4O_2Pd$ (682.0): calcd. C 56.36, H 4.73, N 8.22; found C 58.75, H 5.03, N 8.37%. Calcd. for $C_{32}H_{32}Cl_2N_4O_2Pd\cdot 2/3PhCN$: C 58.68, H 4.74, N 8.71. FAB-MS: *m*/*z* = 647 [M – Cl]$^+$, 609 [M – 2HCl]$^+$. FT-IR (KBr, selected bands): $\tilde{\nu}$ = 1649 (s) ν(C=N) cm^{-1} (ref.[15] 1632 vs. in KBr). ^1H NMR ($CDCl_3$): δ = 8.62 (d, 2 H, *m*-Ar), 7.55 (m, 5 H, Ph), 7.32 (d, 2 H, *o*-Ar), 5.82 (br. s, 1 H, CH), 2.90 (br. s, 3 H, NMe), 2.43 (s, 3 H, *p*-Me) ppm. (ref.[15] 8.68, 7.63, 7.48, 7.40, 7.30, 5.87, 2.95, 2.44 ppm. $CDCl_3$). $^{13}C\{^1H\}$ NMR ($CDCl_3$): δ = 164.74 (C=N), 133.43, 130.46, 129.40, 128.84 and 128.41 (Ph and Ar), 93.76 (CH), 45.75 (NMe), 21.45 (*p*-Me) ppm (ref.[15] 164.3, 139.4, 133.0, 130.4, 129.3, 129.1, 128.7, 128.6, 128.1, 122.5, 93.8, 46.0, 21.5 ppm; $CDCl_3$).

Among other compounds formed in the mixture we succeeded in identifying the aldehyde *p*-$MeC_6H_4C(H)=O$ [^1H NMR ($CDCl_3$): δ = 9.94 (s), 7.76 (d), 7.30 (d), and 2.42 (s)]. In addition, crystals of $[PdCl_2\{N(Me)=CH(C_6H_4Me\text{-}p)\}_2]$ (**4**) suitable for an X-ray study were obtained by slow evaporation of a CH_2Cl_2/Et_2O solution of the residue obtained from the reaction mixture PhCN–$PdCl_2$–*p*-$MeC_6H_4CH=N(O)Me$.

Reaction of $PdCl_2$ (or $[PdCl_2(MeCN)_2]$) and *p*-$MeC_6H_4CH=N(O)Me$ in MeCN: MeCN (5 mL) was added to a mixture of $PdCl_2$ (12.4 mg, 0.07 mmol) (or $[PdCl_2(MeCN)_2]$, 18.1 mg, 0.070 mmol) and *p*-$MeC_6H_4CH=N(O)Me$ (21.0 mg, 0.14 mmol) and it was refluxed on stirring for 1 d, whereupon the solvent was removed in vacuo at room temperature to give a brown powder. ^1H NMR monitoring of the latter shows that the cycloaddition product is formed in 10–15% yield. The powder was treated with two 2-mL portions of Et_2O, the yellow solution was separated from the brown powder by filtration and then the filtrate was evaporated under vacuum at room temperature to give a yellow oily residue that was rapidly washed with cold Et_2O (0.5 mL) and dried again under vacuum at room temperature to give **2**. The reaction can also be performed under focused microwave irradiation (15–20 min, 100 W) and the oxadiazoline complex is formed also in ca. 10–20% yield.

$[PdCl_2\{N^a=C(Me)ON(Me)C^bH(C_6H_4Me\text{-}p)\}_2(N^a–C^b)]\cdot 2H_2O$ (2): Isolated yield is 12%. $C_{22}H_{32}Cl_2N_4O_4Pd$ (557.8): calcd. C 44.50, H 5.43, N 9.43; found C 44.60, H 5.30, N 9.71. FAB-MS: *m*/*z* = 521 [M – HCl]$^+$. FT-IR (KBr, selected bands): $\tilde{\nu}$ = 1650 (s) ν(C=N) cm^{-1}; water of crystallization was observed in the IR spectrum in well-dried KBr (3460 br). ^1H NMR ($CDCl_3$): δ = 7.47 (d, 2 H, *m*-Ar), 7.21 (d, 2 H, *o*-Ar), 5.62 (br. s, 1 H, CH), 2.82 (br. s, 3 H, NMe), 2.45 (s, 3 H, Me), 2.40 (s, 3 H, *p*-Me) ppm. $^{13}C\{^1H\}$ NMR ($CDCl_3$): δ = 166.53 (C=N), 139.19 (*p*-), 130.08 (C_{ipso}), 129.26 and

128.14 (*o*- and *m*-), 91.51 (br., CH), 46.09 (NMe), 21.36 (*p*-Me), 13.78 (Me) ppm.

Reaction of $[PdCl_2(MeCN)_2]$ with *p*-$MeC_6H_4CH=N(O)Me$ in CH_2Cl_2 and Acetone: The nitrone *p*-$MeC_6H_4CH=N(O)Me$ (0.21 mmol) was added to a solution of $[PdCl_2(MeCN)_2]$ (26 mg, 0.10 mmol) in CH_2Cl_2 or acetone (1 mL) at room temperature. The reaction mixture became dark orange within several min, then it was allowed to stay for 2–3 h without stirring. A dark-red solution was formed, the solvent was evaporated under a stream of N_2 and the dark residue washed with Et_2O (two 2-mL portions) and dried in air and then under vacuum at room temperature. In the NMR spectrum of the residue, signals that can be attributed to the nitrone complex $[PdCl_2\{\underline{O}N(Me)=C(H)C_6H_4Me\text{-}p\}_2]$ and the corresponding aldehyde *p*-$MeC_6H_4C(H)O$ were detected. No traces of acetamide or acetic acid, corresponding to MeCN, were detected. Satisfactory elemental analyses can not be obtained because of hydrolytic and redox decomposition of the nitrone complex $[PdCl_2\{\underline{O}N(Me)=C(H)C_6H_4Me\text{-}p\}_2]$. If the reaction mixture is left standing at room temperature for 3 d, the solution becomes slightly lighter and orange-yellow crystals of $[Pd_2(\mu\text{-}Cl)_2\{\underline{O}N(Me)=C(H)C_6H_3Me\text{-}p\}_2]$ are released on the top of the flask. The yield of the cyclometalated product **5** is ca. 30%.

$[PdCl_2\{\underline{O}N(Me)=CH(C_6H_4Me\text{-}p)\}_2]$ (3): MS (ESI+): *m*/*z* = 441 [M – Cl], 403 [M – 2Cl – H]. FT-IR (KBr, selected bands): $\tilde{\nu}$ = 3012, 2944 (w) ν(C–H), 1601 (s) ν(C=N), 1159 (*m*-s) ν(N–O) cm^{-1}; in the free nitrone 1587 (s) ν(C=N), 1167 (*m*-s) ν(N–O) cm^{-1}. ^1H NMR ([D$_6$]acetone): δ = 8.20 (d, 7.8 Hz, 2 H, *m*-Ar), 8.08 (s, 1 H, CH), 7.33 (d, 7.8 Hz, 2 H, *o*-Ar), 3.99 (s, 3 H, NMe), 2.39 (s, 3 H, *p*-Me) ppm. Complex **3** was also detected, by ^1H NMR method, in the reaction between the nitrone and $[PdCl_2(PhCN)_2]$.

$[Pd_2(\mu\text{-}Cl)_2\{\underline{O}N(Me)=C(H)C_6H_3Me\text{-}p\}_2]$ (5): $C_{18}H_{20}Cl_2N_2O_2Pd_2$ (580.1): calcd. C 37.27, H 3.48, N 4.83; found C 37.48, H 3.60, N 4.61. FT-IR (KBr, selected bands): $\tilde{\nu}$ = 1628 (m) ν(C=N), 1582 (s) ν(C=C), 1155 (*m*-s) ν(N–O) cm^{-1}; in the free nitrone 1587 (s) ν(C=N), 1167 (*m*-s) ν(N–O) cm^{-1}. The solid complex is insoluble in the most common deuterated solvents and it reacts with [D$_6$]DMSO to give a solution with the following spectrum, i.e. ^1H NMR ([D$_6$]DMSO): δ = 8.39 (s, 1 H, CH); 7.75 (d, *m*-Ar); 7.14 (d, *o*-Ar); 6.97 (s, *m*-Ar); 3.81 (s, 3 H, NMe); 2.21 (s, 3 H, *p*-Me) ppm.

Acknowledgments

This work has been supported by the Fundação para a Ciência e a Tecnologia (FCT), Portugal, and its POCTI program (POCTI/QUI/43415/2001 project) (FEDER funded) and the Russian Fund for Basic Research (grants 03–03–32363 and 05–03–32140). N.A.B. and V.Yu.K. express gratitude to the POCTI program, Portugal for the grant SFRH/BPD/11448/2002 (N.A.B.) and a grant for Cientista Convidado/Professor at the Instituto Superior Técnico (V.Yu.K.). N.A.B., M.H., and V.Yu.K. would like to thank the Academy of Finland for financial support. V.Yu.K. is very much obliged to ISSEP for the Soros Professorship (2001–2004) and the Royal Society of Chemistry for a Grant for International Authors. The authors also thank NATO for the Collaborative Linkage Grant PST.CLG.979289.

[1] S. Kobayashi, K. A. Jørgensen, *Cycloaddition Reactions in Organic Synthesis*, VCH, Weinheim, **2002**.
[2] a) K. V. Gothelf, K. A. Jørgensen, *Chem. Commun.* **2000**, 1449; b) K. V. Gothelf, K. B. Jensen, K. A. Jørgensen, *Sci. Prog.* **1999**, *82*, 327; c) K. V. Gothelf, K. A. Jørgensen, *Chem. Rev.* **1998**, *98*, 863.
[3] a) S. Karlsson, H.-E. Hogberg, *Org. Prep. Proced. Int.* **2001**, *33*, 103; b) L. Raimondi, M. Benaglia, *Eur. J. Org. Chem.* **2001**, 1033; c) P. De March, M. Figueredo, J. Font, *Heterocycles* **1999**, *50*, 1213.
[4] a) W. Carruthers, *Cycloaddition Reactions in Organic Synthesis*, Pergamon, Oxford, **1990**; b) *1,3-Dipolar Cycloaddition Chemistry* (Ed.: A. Padwa), Wiley-Interscience, New York, **1984**, vol. 1–2.
[5] For a review on metal-mediated 1,3-dipolar cycloadditions see: G. Broggini, G. Molteni, A. Terraneo, G. Zecchi, *Heterocycles* **2003**, *59*, 823.
[6] a) V. Yu. Kukushkin, A. J. L. Pombeiro, *Chem. Rev.* **2002**, *102*, 1771–1802 and references cited therein; b) A. J. L. Pombeiro, V. Yu. Kukushkin, in *Comprehensive Coordination Chemistry*, 2nd ed., Elsevier, Amsterdam, **2003**, vol. 1, pp. 639–660.
[7] a) F. Himo, Z. P. Demko, L. Noodleman, K. B. Sharpless, *J. Am. Chem. Soc.* **2003**, *125*, 9983; b) F. Himo, Z. P. Demko, L. Noodleman, K. B. Sharpless, *J. Am. Chem. Soc.* **2002**, *124*, 12210; c) Z. P. Demko, K. B. Sharpless, *Org. Lett.* **2001**, *3*, 4091; d) Z. P. Demko, K. B. Sharpless, *J. Org. Chem.* **2001**, *66*, 7945.
[8] G. Wagner, A. J. L. Pombeiro, V. Yu. Kukushkin, *J. Am. Chem. Soc.* **2000**, *122*, 3106.
[9] G. Wagner, M. Haukka, J. J. R. Fraústo da Silva, A. J. L. Pombeiro, V. Yu. Kukushkin, *Inorg. Chem.* **2001**, *40*, 264.
[10] M. A. J. Charmier, V. Yu. Kukushkin, A. J. L. Pombeiro, *J. Chem. Soc., Dalton Trans.* **2003**, 2540.
[11] M. L. Kuznetsov, V. Yu. Kukushkin, A. I. Dement′ev, A. J. L. Pombeiro, *J. Phys. Chem. A* **2003**, *107*, 6108.
[12] N. A. Bokach, A. V. Khripoun, V. Yu. Kukushkin, M. Haukka, A. J. L. Pombeiro, *Inorg. Chem.* **2003**, *42*, 896.
[13] N. A. Bokach, V. Yu. Kukushkin, M. Haukka, A. J. L. Pombeiro, *Eur. J. Inorg. Chem.* **2005**, 845.
[14] V. Yu. Kukushkin, A. J. L. Pombeiro, *Inorg. Chim. Acta* **2005**, *358*, 1.
[15] G. Wagner, *Inorg. Chim. Acta* **2004**, *357*, 1320.
[16] G. A. Anderson, M. Lin, *Inorg. Synth.* **1990**, *28*, 60.
[17] S. Kannan, A. Usman, H. K. Fun, *Polyhedron* **2002**, *21*, 2403.
[18] P. Merino, S. Anoro, E. Cerrada, M. Laguna, A. Moreno, T. Tejero, *Molecules* **2001**, *6*, 208.
[19] P. Merino, T. Tejero, M. Laguna, E. Cerrada, A. Moreno, J. A. Lopez, *Org. Biomol. Chem.* **2003**, *1*, 2336.
[20] T. A. K. Alallaf, A. Abdulrahman, *Synth. React. Inorg. Metal-Org. Comp.* **1997**, *27*, 985.
[21] W. W. Ellis, A. Gavrilova, L. Liable-Sands, A. L. Rheingold, B. Bosnich, *Organometallics* **1999**, *18*, 332.
[22] A. Ade, E. Cerrada, M. Contel, M. Laguna, P. Merino, T. Tejero, *J. Organomet. Chem.* **2004**, *689*, 1788.
[23] E. G. Petkova, R. D. Lampeka, M. V. Gorichko, K. V. Domasevitch, *Polyhedron* **2001**, *20*, 747.
[24] F. A. Villamena, R. D. Crist, *J. Chem. Soc., Dalton Trans.* **1998**, 4055.
[25] F. A. Villamena, M.-H. Dickman, D. R. Crist, *Inorg. Chem.* **1998**, *37*, 1446.
[26] J. Lee, B. Twamley, G. B. Richter-Addo, *Chem. Commun.* **2002**, 380.
[27] C. Mukai, W. J. Cho, I. J. Kim, M. Hanaoka, *Tetrahedron Lett.* **1990**, *31*, 6893.
[28] D. Mansuy, M. Dreme, J. C. Chottard, J. P. Girault, J. Guilhem, *J. Am. Chem. Soc.* **1980**, *102*, 844.
[29] For recent works see: a) C. L. Chen, Y. H. Liu, S. M. Peng, S. T. Liu, *J. Organomet. Chem.* **2004**, *689*, 1806; b) R. Zurawinski, B. Donnadieu, M. Mikolajczyk, R. Chauvin, *J. Organomet. Chem.* **2004**, *689*, 380; c) R. Ares, M. Lopez-Torres, A. Fernandez, S. Castro-Juiz, A. Suarez, G. Alberdi, J. J. Fernandez, J. M. Vila, *Polyhedron* **2002**, *21*, 2309.
[30] a) A. D. Ryabov, G. M. Kazankov, A. K. Yatsimirsky, L. G. Kuz'mina, O. Y. Burtseva, N. V. Dvortsova, V. A. Polyakov, *Inorg. Chem.* **1992**, *31*, 3083; b) A. D. Ryabov, R. Le Lagadec, H.

 © 2005 Wiley-VCH Verlag GmbH & Co. KGaA, Weinheim

Estevez, S. Hernandez, L. Alexandrova, V. S. Kurova, A. Fischer, M. Pfeffer, *Inorg. Chem.* **2005**, *44*, 1626.
[31] F. A. Allen, O. Kennard, D. G. Watson, *J. Chem. Soc., Perkin Trans. 2* **1987**, S1.
[32] J. M. Zhang, Y. M. Zhang, *Chinese Chem. Lett.* **2001**, *12*, 945; *Chem. Abstr.* **2001**, 136:279154.
[33] D. K. Dutta, D. J. Konwar, *Chem. Res., Synopses* **1998**, 266.
[34] R. Balicki, *Chem. Ber.* **1990**, *123*, 647.
[35] R. Balicki, *Gazz. Chim. Ital.* **1990**, *120*, 67.
[36] S. V. Kuz′min, M. D. Mizhiritskii, L. M. Kogan, *Zh. Org. Khim.* **1989**, *25*, 663; *Chem. Abstr.* **1989**, 111:173182.
[37] a) Y. Yu, N. Watanabe, M. Ohno, S. Eguchi, *J. Chem. Soc., Perkin Trans. 1* **1995**, 1417; b) Y. Yu, H. Fujita, M. Ohno, S. Eguchi, *Synthesis* **1995**, 498; c) P. H. H. Hermkens, J. H. van Maarseveen, C. G. Kruse, H. W. Scheeren, *Tetrahedron* **1988**, *44*, 6491.
[38] A. Erxleben, I. Mutikainen, B. Lippert, *J. Chem. Soc., Dalton Trans.* **1994**, 3667.
[39] a) F. L. Wimmer, S. Wimmer, P. Castan, R. J. Puddephatt, *Inorg. Synth.* **1992**, *29*, 185; b) I. E. Bekk, E. V. Gusevskaya, V. A. Likholobov, Yu. I. Ermakov, *Reaction Kinetics and Catalysis Letters* **1987**, *33*, 209; c) M. A. Andrews, T. C. T. Chang, C. W. F. Cheng, T. J. Emge, K. P. Kelly, T. F. Koetzle, *J. Am. Chem. Soc.* **1984**, *106*, 5913; d) B. B. Wayland, R. F. Schramm, *Inorg. Chem.* **1969**, *8*, 971.
[40] *Methoden der Organischen Chemie* (*Houben-Weyl*), Georg Thieme Verlag, Stuttgart, New York, **2001**, 4th ed., vol. E 14b.
[41] Z. Otwinowski, W. Minor, "Processing of X-ray Diffraction Data Collected in Oscillation Mode", in *Methods in Enzymology*, *Macromolecular Crystallography*, *Part A* (Eds.: C. W. Carter, Jr., R. M. Sweet), Academic Press, New York, **1997**, vol. 276, pp. 307–326.
[42] G. M. Sheldrick, *SHELXS-97*, Program for Crystal Structure Determination, University of Göttingen, **1997**.
[43] M. C. Burla, M. Camalli, B. Carrozzini, G. L. Cascarano, C. Giacovazzo, G. Polidori, R. J. Spagna, *Appl. Cryst.* **2003**, *36*, 1103.
[44] G. M. Sheldrick, *SHELXTL* Version 6.14, Bruker Analytical X-ray Systems, Bruker AXS, Inc., Madison, Wisconsin**2003**.
[45] G. M. Sheldrick, *SHELXL-97*, Program for Crystal Structure Refinement, University of Göttingen, **1997**.
[46] L. J. Farrugia, *J. Appl. Cryst.* **1999**, *32*, 837.

Received: February 10, 2005
Published Online: June 22, 2005

 © 2005 Wiley-VCH Verlag GmbH & Co. KGaA, Weinheim

Synthesis and Characterization of Heterotrinuclear Complexes of Nickel and Palladium with Pyridinecarboxylate as Bridging Ligands

José Ruiz,*[a] María Dolores Santana,*[a] Abel Lozano,[a] Consuelo Vicente,[a] Gabriel García,[a] Gregorio López,[a] José Pérez,[b] and Luis García[b]

Keywords: Palladium / Nickel / Pyridinecarboxylate / Heterotrinuclear complexes / Mononuclear complexes

Heterotrinuclear pyridinecarboxylate complexes of nickel(II) and palladium(II) of the types [Ni(mcN$_3$)(pyridinecarboxylate)]$_2${μ-[Pd(C$_6$F$_5$)$_2$]}(PF$_6$)$_2$ [mcN$_3$ = 2,4,4-trimethyl-1,5,9-triazacyclododec-1-ene (Me$_3$-mcN$_3$) or 2,4,4,9-tetramethyl-1,5,9-triazacyclododec-1-ene (Me$_4$-mcN$_3$)] have been prepared by two different routes. The corresponding monomeric pyridinecarboxylate complexes of nickel and the monomeric pyridinecarboxylic acid/ester complexes of palladium have also been prepared. The crystal structures of two precursors [Ni(Me$_4$-mcN$_3$)(NC$_5$H$_4$-3-COO)]PF$_6$ and *cis*-[Pd(C$_6$F$_5$)$_2$(NC$_5$H$_4$-4-CH$_2$COOCH$_3$)$_2$] have been established by X-ray diffraction.
(© Wiley-VCH Verlag GmbH & Co. KGaA, 69451 Weinheim, Germany, 2005)

Introduction

Pyridinecarboxylate ligands tend to bind metal ions with both, pyridine and carboxylate groups to form extended networks, where the carboxylate groups balance the metal charges.[1–6] The deliberate, stepwise and controlled synthesis of molecular squares and dinuclear macrocycles using pyridinecarboxylates as spacers has been recently reported by Hor et al.[7]

The versatile carboxylate anion can adopt a wide range of bonding modes including monodentate, symmetric and asymmetric chelating and bidentate and monodentate bridging.[8] It is generally agreed that the carboxylate complexes of the 3d elements, including several examples of nickel derivatives, play an important role in biochemistry.[9]

In this paper we report the preparation by two different routes and the spectroscopic behavior of heterotrinuclear pyridinecarboxylate complexes of nickel and palladium in which the two nickel(II) ions are in a pentacoordinate environment. The corresponding monomeric pyridinecarboxylate complexes of nickel and the monomeric pyridinecarboxylic acid/ester complexes of palladium have also been prepared.

[a] Departamento de Química Inorgánica, Universidad de Murcia, 30071 Murcia, Spain
Fax: +34-968-364-148
E-mail: jruiz@um.es
dsl@um.es
[b] Departamento de Ingeniería Minera, Geológica y Cartográfica. Área de Química Inorgánica, Universidad Politécnica de Cartagena, 30203 Cartagena, Spain

Results and Discussion

Synthesis and Characterization of Monomeric Pyridinecarboxylate Complexes of Nickel(II)

The reaction between [Ni(mcN$_3$)(μ-OH)]$_2$(PF$_6$)$_2$ [mcN$_3$ = 2,4,4-trimethyl-1,5,9-triazacyclododec-1-ene (Me$_3$-mcN$_3$) or 2,4,4,9-tetramethyl-1,5,9-triazacyclododec-1-ene (Me$_4$-mcN$_3$)] and carboxylic acids [HA = isonicotinic (Hisonic) or nicotinic (Hnic) acid] leads to the formation of the carboxylate complexes [Ni(mcN$_3$)(A)](PF$_6$) **1**–**4** shown in Scheme 1.

The acid-base reaction occurs at room temperature in acetone with the concomitant liberation of water. This synthetic method has previously been used for the preparation of pentacoordinate nickel(II) complexes containing N,S-donor,[10] oxamidate,[11] hydroxamate,[12] and pyridonate ligands,[13] as well as phosphate esters and phosphinate derivatives.[14]

Complexes **1**–**4** are air-stable both in the solid state and in solution. They have been characterized by partial elemental analyses, FAB$^+$ mass spectrometry and spectroscopic (IR, UV/Vis, and ^{1}H NMR) methods. The IR spectra of complexes **1**–**4** show characteristic absorptions for the mcN$_3$ ligands:[12,14] 3287–3121 cm^{-1} for $\tilde{\nu}$(N–H), ca. 1660 cm^{-1} for $\tilde{\nu}$(C=N), and two strong bands as a result of the PF$_6^-$ ion at 840 and 560 cm^{-1}. The κ^2-coordination mode in compounds **1**–**4** is revealed by the IR spectra, which contain symmetric OCO stretching bands at ca. 1550 cm^{-1}.[15,16] The κ^2-coordination mode in **4** was authenticated by an X-ray crystal structure determination (vide infra). The electronic spectra of **1**–**4** are quite similar and show two d-d transitions in acetone solution with $\lambda_{max} \approx$

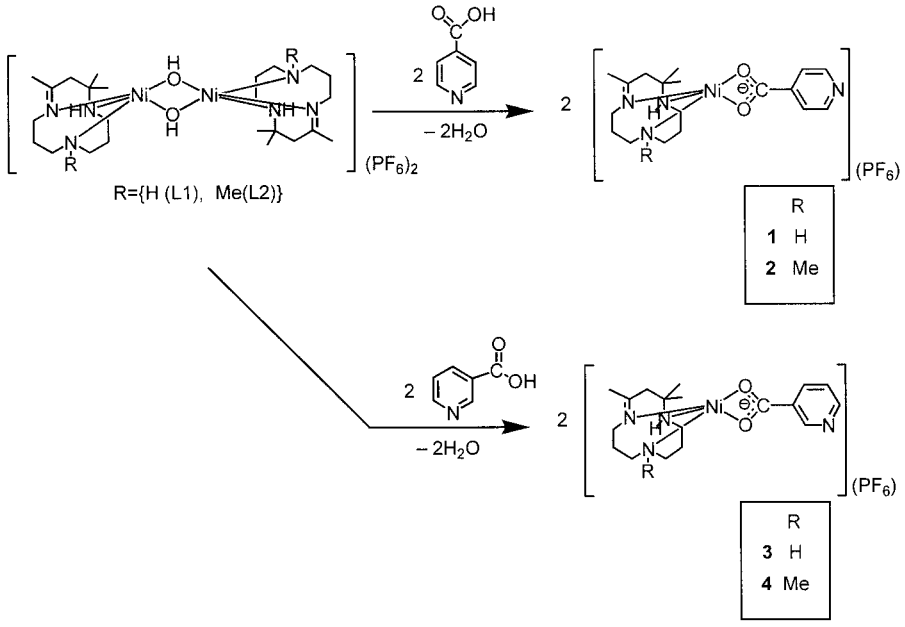

Scheme 1. Monomeric nickel complexes.

63 (ca. 80 $M^{-1}cm^{-1}$) and 390 nm (ca. 200 $M^{-1}cm^{-1}$) which could be assigned to $^3B_1(F) \rightarrow {}^3E(F)$ and $^3B_1(F) \rightarrow {}^3A_2, {}^3E(P)$ transitions, respectively. Both λ_{max} values and molar absorptivities are consistent with a pentacoordinate environment around the nickel(II) center.[17]

NMR Spectroscopic Study of Complexes 1–4

All of the complexes exhibit sharp hyperfine-shifted ^1H NMR signals in acetone solution in the 370 to –35 ppm chemical shift range. The ^1H NMR spectra of complexes **1**–**4** show the resonance line pattern observed for the mcN_3 ligands that was assigned on the basis of previous studies of (macrocycle)nickel complexes[10–14] and from the temperature dependence of the resonances. A representative ^1H NMR spectrum for complex **4** is shown in Figure 1. The α-methylene proton signals shift downfield whereas the β-methylene proton signals shift upfield with regard to the diamagnetic position.[18] Moreover, the signals of the equatorial protons are expected to experience larger contact shifts than those of the axial protons[19] and therefore the most downfield resonances are due to α-CH_{eq} and the most upfield ones to β-CH_{eq}. The isotropically shifted ^1H NMR signals observed for the methyl groups [2-Me, 4-Me(a,b), and 9-Me-N] and phenyl groups of carboxylates can be initially assigned by inspection of their peak areas. All the resonances of the phenyl rings are downfield to TMS in accordance with a dominant σ-delocalization pattern of spin density, consistent with the ground state of nickel(II), although the unpaired electrons could polarize the net spin density in the d_π orbitals. A similar behavior has been observed elsewhere.[20] Curie plots of proton resonances of complex **4** in [D_6]acetone are shown in Figure 2. These plots illustrate the general tendency for the contact shifts to increase more rapidly at lower temperatures and exhibit a temperature dependence closely proportional to T^{-1}.

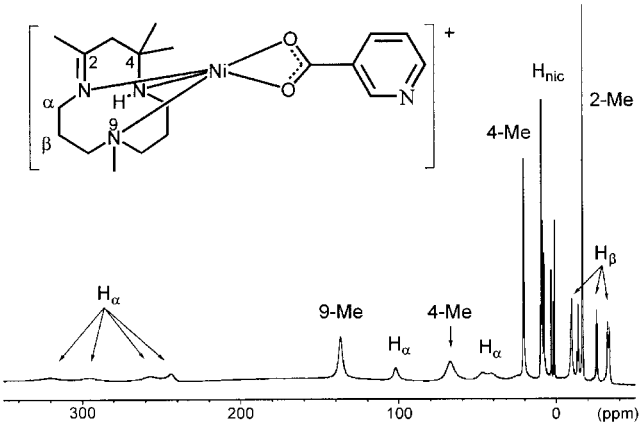

Figure 1. ^1H NMR spectra (in [D_6]acetone solution at room temperature) of complex **4**.

Description of the Crystal Structure of Complex 4

The crystal structure of the cation of complex **4** is shown in Figure 3. Selected geometric data are given in Table 1. In each crystallized cation of complex **4**, the nickel atom is five-coordinate, with a square-pyramid arrangement of the chelating atoms. The Reedijk τ parameter[21] (τ = 0 and 1 for square-pyramidal and trigonal-bipyramidal structures, respectively) shows a value of 0.005. The three nitrogen atoms of the N_3 macrocycle are found at the apical position and two adjacent basal ones, whereas the other two basal positions correspond to the *O,O′*-carboxylate group. The basal plane is formed by N(1), N(2), O(1), and O(2), with an r.m.s. deviation of fitted atoms of 0.0108 Å. The Ni atom is 0.3054(13) Å above the corresponding basal plane towards the apical N(3) atom. The coordinated macrocycle exhibits a chairlike conformation for the two six-membered rings that do not contain the C=N bond. This is the most

 © 2005 Wiley-VCH Verlag GmbH & Co. KGaA, Weinheim

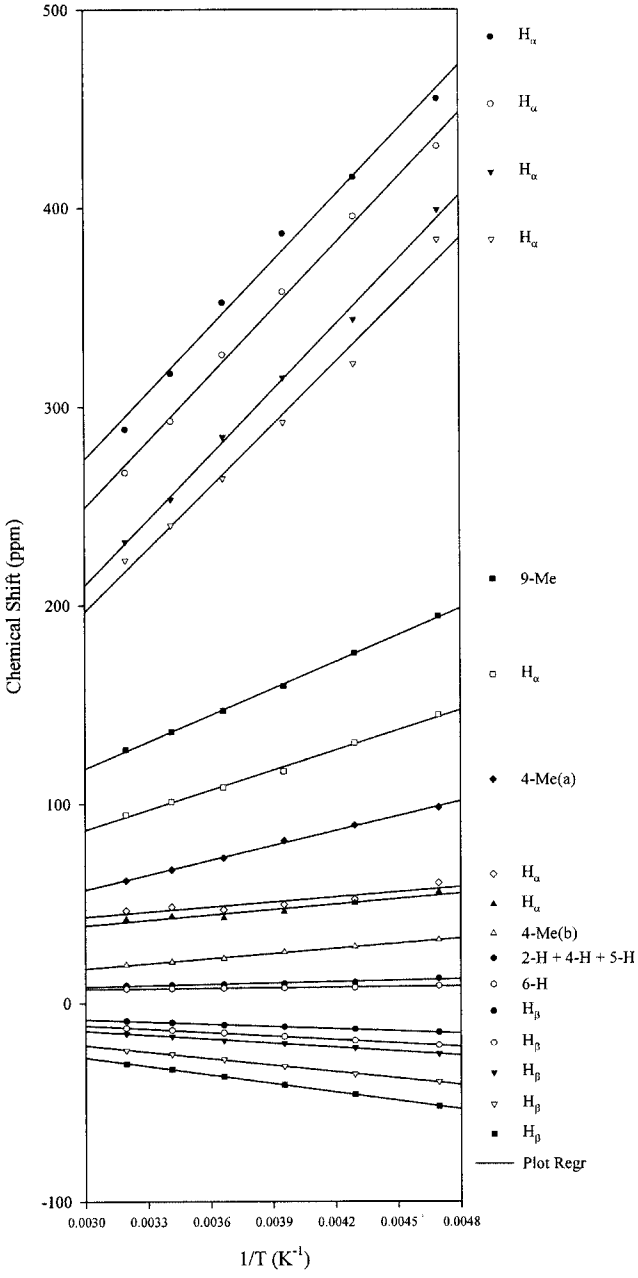

Figure 2. Curie plots of proton resonances of complex **4**.

frequent conformation in complexes having these macrocycles.[13] The Ni–O bond lengths in **4** are close to each other [2.085(2)–2.129(2) Å]. The carboxylate ligands are bonded in a symmetric (or almost) chelating mode with a $\Delta O = \{[Ni–O(2)] – [Ni–O(1)]\}$ value of 0.034 Å. There is a classical intermolecular hydrogen bonding between N(2)–H(2) and N(4) of a neighbor cation generated by ($–x + 2$, $–y + 2$, $–z$) symmetry operation, and a "non-classical" hydrogen bonding between C(16)–H(16) and O(2), generated by the same symmetry operation. The hydrogen bonds of complex **4** are summarised in Table 2 (see Figure 4). These bond lengths are comparable to those reported for other crystallographically characterized nickel carboxylate complexes with a distorted square-pyramidal[22] or octahedral[22–24] geometry. The bite angle of the carboxylate anion shows a value of 62.76(8)°. The torsion angle between the pyridine ring and the nickel-bound carboxylate group is 2.27(8)°. This is the first crystal structure of a pentacoordinate (nicotinato)nickel(II) complex (3D search using the Cambridge Structural Database, CSD version 5.25, July 2004 release).

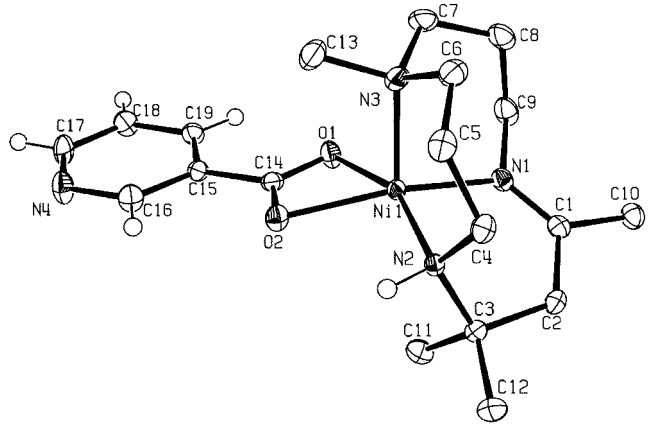

Figure 3. ORTEP drawing of complex **4** showing the atom numbering scheme. Displacement ellipsoids are drawn at the 50% probability level. For clarity hydrogen atoms of the macrocycle are omitted.

Table 1. Selected bond lengths [Å] and angles [°] for complex **4**.

Bond lengths		Bond angles	
Ni(1)–N(1)	1.988(2)	N(1)–Ni(1)–N(2)	92.37(10)
Ni(1)–N(2)	2.008(2)	N(1)–Ni(1)–N(3)	94.91(11)
Ni(1)–N(3)	2.044(3)	N(1)–Ni(1)–O(1)	100.87(9)
Ni(1)–O(1)	2.129(2)	N(1)–Ni(1)–O(2)	157.29(9)
Ni(1)–O(2)	2.085(2)	N(2)–Ni(1)–N(3)	102.68(10)
		N(2)–Ni(1)–O(1)	156.97(9)
		N(2)–Ni(1)–O(2)	98.73(9)
		N(3)–Ni(1)–O(1)	94.93(10)
		N(3)–Ni(1)–O(2)	101.82(10)
		O(2)–Ni(1)–O(1)	62.76(8)

Table 2. Hydrogen bonds for complex **4** [Å and °].

D–H···A	*d*(D–H)	*d*(H···A)	*d*(D···A)	<(DHA)
N(2)–H(2)···N(4)#1	0.93	2.08	2.991(4)	166.3
C(16)–H(16)···O(2)#1	0.95	2.44	3.284(4)	147.6

Symmetry transformations used to generate equivalent atoms:
#1: $–x + 2$, $–y + 2$, $–z$

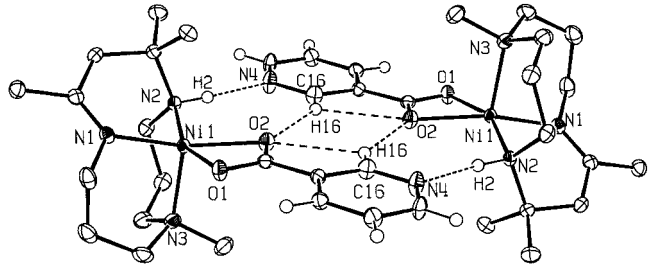

Figure 4. Hydrogen bonding in complex **4**. ORTEP drawing (ellipsoids at 50% probability level) with atom labeling scheme.

 © 2005 Wiley-VCH Verlag GmbH & Co. KGaA, Weinheim

Synthesis and Characterization of Monomeric Pyridinecarboxylic Acid/Ester Complexes of Palladium(II)

The labile complex *cis*-$[Pd(C_6F_5)_2(PhCN)_2]$ has been used as starting material for the preparation of several palladium complexes.[25–28] When *cis*-$[Pd(C_6F_5)_2(PhCN)_2]$[29] was treated with the pyridinecarboxylic acids NC_5H_4-4-COOH (isonicotinic), NC_5H_4-3-COOH (nicotinic) or NC_5H_4-4-CH_2COOH (in methanol), complexes **5**–**7** were obtained in high yields (Scheme 2). Complexes **5**–**7** are all white, air-stable solids. Their IR spectra show the characteristic absorptions of the C_6F_5 group ($\tilde{\nu}$ = 1630 m, 1490 vs, 1050 s, 950 vs cm^{-1})[30] and a split band at $\tilde{\nu} \approx 800\ cm^{-1}$ assigned to the *cis*-$Pd(C_6F_5)_2$ moiety.[31,32] The IR spectra of **5** and **6** show the expected strong ν(C=O) band at $\tilde{\nu} \approx 1720\ cm^{-1}$, a frequency that is typical for aromatic carboxylic acids.[33,34] In complex **7** the ν(C=O) band is observed at $\tilde{\nu} = 1744\ cm^{-1}$. The ^{19}F NMR spectra of complexes **5**–**7** show the presence of two equivalent freely rotating C_6F_5 rings giving three resonances with relative intensities of 4:2:4 due to the *ortho*-, *para*-, and *meta*-F atoms, respectively. The ^1H NMR spectrum of complex **7** shows the methoxy resonance of the pyridinecarboxylic ester ligands at δ = 3.66 ppm.

Description of the Crystal Structure of Complex 7

Figure 5 depicts the structure of the neutral palladium complex. Selected bond lengths and angles are given in Table 3. The coordination around Pd is square-planar. The N1, N2, C1, and C7 atoms form a perfect plane with the Pd atom 0.0037(7) Å above this plane. The angle between the two C_6F_5 rings is 90.72(7)° and the angle between the two N-donor ligands is 90.16(5)°. The Pd–N distances lie within the range reported in complexes containing the $\{Pd(C_6F_5)_2N_2\}$ moiety, such as $[Pd(C_6F_5)_2\{NH{=}CMe_2\}_2]$,[25] $[Pd(C_6F_5)_2\{NH{=}C(OMe)Me\}_2]$[35] and $[Pd(C_6F_5)_2(pz\cdots H\cdots pz)]$ (pz = pyrazolate).[27] The Pd–C_6F_5 bond lengths are in the range found in the literature for (pentafluorophenyl)palladium complexes.[36–38] In addition, there are some interconnections by hydrogen bonds involv-

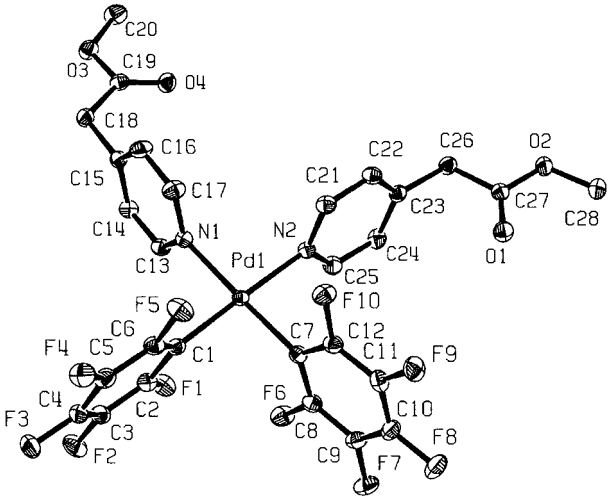

Figure 5. ORTEP drawing of complex **7** showing the atom numbering scheme. Displacement ellipsoids are drawn at the 50% probability level.

Table 3. Selected bond lengths [Å] and angles [°] for complex **7**.

Bond lengths		Bond angles	
Pd(1)–C(1)	2.0012(17)	C(1)–Pd(1)–C(7)	90.72(7)
Pd(1)–C(7)	2.0031(17)	C(1)–Pd(1)–N(2)	178.78(6)
Pd(1)–N(2)	2.0866(14)	C(7)–Pd(1)–N(2)	88.08(6)
Pd(1)–N(1)	2.0897(14)	C(1)–Pd(1)–N(1)	91.04(6)
		C(7)–Pd(1)–N(1)	178.15(6)
		N(2)–Pd(1)–N(1)	90.16(5)

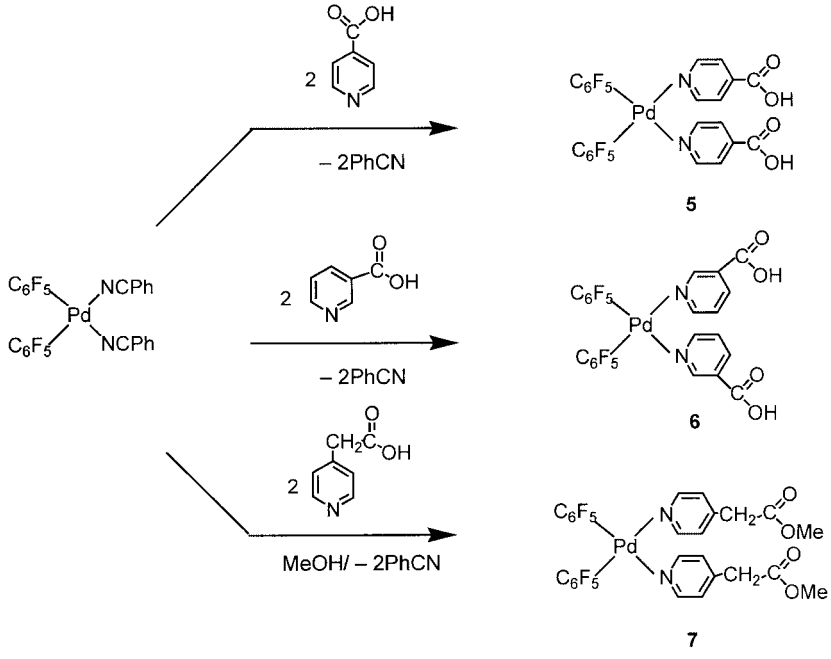

Scheme 2. Monomeric palladium complexes.

 © 2005 Wiley-VCH Verlag GmbH & Co. KGaA, Weinheim

ing some of the *para*-, *meta*-, and *ortho*-fluorine atoms as proton acceptors, with short intermolecular C–H···F distances (Table 4).[25,39]

Table 4. Selection of the shorter intermolecular F···H distances [Å] in complex 7.

F_8H_{25}(i)	2.600
$F_{10}H_{13}$(iii)	2.568
F_9H_{28A}(ii)	2.565
F_6H_{17}(iv)	2.586
F_1H_{21}(iv)	2.546
F_2H_{22}(iv)	2.577

i: 2 – *x*, 2 – *y*, 2 – *z*; ii: 0.5 + *x*, 1.5 – *y*, –0.5 + *z*; iii: 1.5 – *x*, –0.5 + *y*, 1.5 – *z*; iv: 1.5 – *x*, 0.5 + *y*, 1.5 – *z*

Synthesis and Characterization of Heterotrinuclear Pyridinecarboxylate Complexes of Nickel(II) and Palladium(II)

Heterotrinuclear pyridinecarboxylate complexes of nickel(II) and palladium(II) of the types $[Ni(mcN_3)(pyridinecarboxylate)]_2\{\mu\text{-}[Pd(C_6F_5)_2]\}(PF_6)_2$ (mcN_3 = Me_3-mcN_3 or Me_4-mcN_3) **8**–**12** have been prepared by two different routes (Scheme 3). The first method is based on the reaction of the monomeric pyridinecarboxylate complexes of nickel(II) $[Ni(mcN_3)(A)](PF_6)$ **1**–**4** with the labile complex *cis*-$[Pd(C_6F_5)_2(PhCN)_2]$, which takes place with the concomitant release of PhCN. The second method is based on the treatment of the monomeric pyridinecarboxylic derivatives of palladium(II) **5**–**7** with the hydroxo complex $[Ni(mcN_3)(\mu\text{-}OH)]_2(PF_6)_2$ (mcN_3 = Me_3-mcN_3 or Me_4-mcN_3). Complexes **8**–**12** are air-stable both in the solid state and in solution. They were characterized by partial elemental analyses, FAB^+ mass spectrometry and spectroscopic (IR and ^1H NMR) methods. The IR spectra of complexes **8**–**12** show characteristic absorptions for the mcN_3 ligands,[12,14] the absorption of the pyridinecarboxylate ligands, the characteristic absorptions of the C_6F_5 group[30] and a split band at $\tilde{\nu} \approx 800\ cm^{-1}$ assigned to the *cis*-$Pd(C_6F_5)_2$ moiety.[31,32] Two strong bands as a result of the PF_6^- ion at $\tilde{\nu}$ = 840 and 560 cm^{-1} are also observed.

NMR Study of Complexes 8–12

The ^{19}F NMR spectra of complexes **8**–**12** show the presence of two equivalent freely rotating C_6F_5 rings giving three resonances with relative intensities of 4:2:4 due to the *ortho*-, *para*-, and *meta*-F atoms, respectively. The ^1H NMR spectra of the complexes **8**–**12** also show relatively sharp and well-resolved resonances for the macrocyclic protons as well as the expected resonance line pattern. The magnitudes of these shifts are also similar to those observed for the

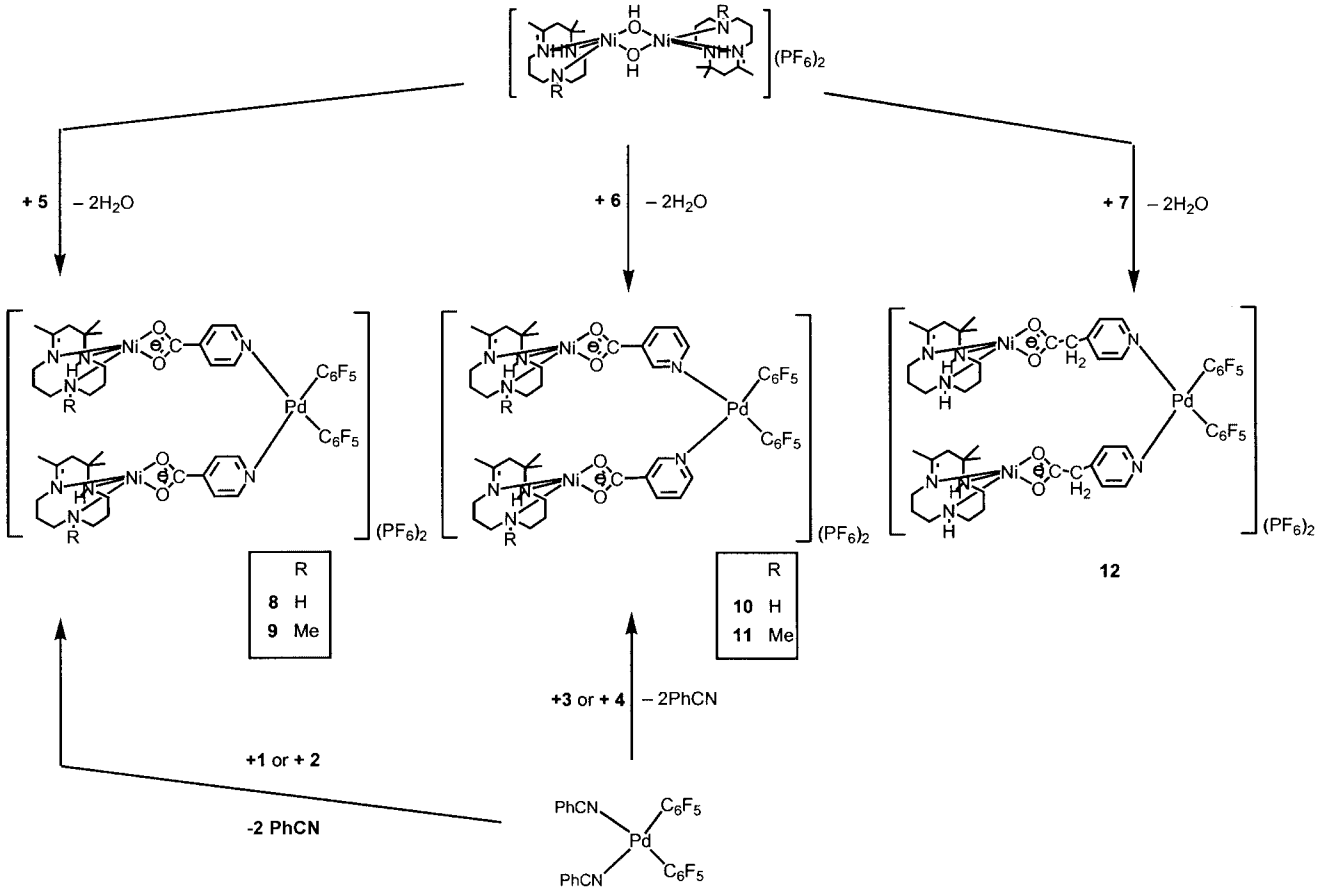

Scheme 3. Heterotrinuclear complexes.

 © 2005 Wiley-VCH Verlag GmbH & Co. KGaA, Weinheim

corresponding monomeric pyridinecarboxylate derivatives of nickel (**1**–**4**). However, the coordination to the *cis*-$Pd(C_6F_5)_2$ moiety through the nitrogen atom of pyridinecarboxylate disturbs the spin density into the pyridine ring and the shifts of pyridinecarboxylate in heterotrinuclear derivatives are in general larger than in monomeric complexes. The temperature dependence of the shifts of **11** in Figure 6 follows the established pattern, with the shifts moving away from the diamagnetic position and increasing with T^{-1}.

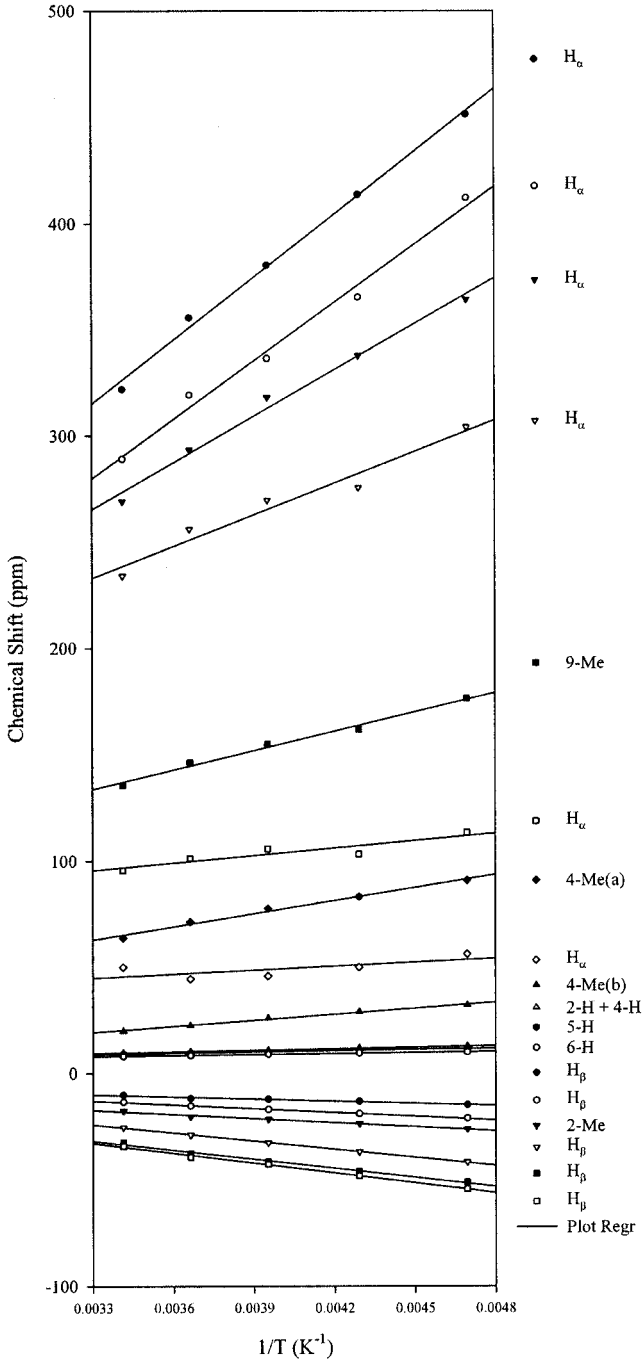

Figure 6. Curie plots of proton resonances of complex **11**.

Experimental Section

General Methods: The C, H, N analyses were performed with a Carlo Erba model EA 1108 microanalyzer. The ^1H and ^{19}F NMR spectra were recorded with a Bruker AC 200E, Bruker AC 300E or Bruker AV-400 spectrometer, using $SiMe_4$ or $CFCl_3$ as standards, respectively. IR spectra were recorded with a Perkin–Elmer 16F PC FT-IR spectrophotometer using Nujol mulls between polyethylene sheets. Fast-atom bombardment (FAB) mass spectra were run with a Fisons VG Autospec spectrometer operating in the FAB^+ mode. The UV/Vis spectra (in acetone) were recorded with a UNICAM 520 spectrophotometer equipped with matched quartz cells in the 300–800 nm range. The chemicals were purchased from Aldrich and were used without further purification. Solvents were dried and distilled by general methods before use. The starting compound $[\{Ni(Me_3\text{-}mcN_3)(\mu\text{-}OH)\}_2](PF_6)_2$ and its 9-methyl derivative,[40,41] as well as *cis*-$[Pd(C_6F_5)_2(PhCN)_2]$[29] were prepared by procedures described elsewhere.

Preparation of Complexes

Complexes 1 and 3: NC_5H_4-4-COOH or NC_5H_4-3-COOH (0.30 mmol) was added to a solution of $[Ni(Me_3\text{-}mcN_3)(\mu\text{-}OH)]_2(PF_6)_2$ (100 mg, 0.15 mmol) in acetone (25 mL). The mixture was stirred overnight at room temperature and the solvent was partially evaporated under reduced pressure. On addition of diethyl ether, the blue-green complexes precipitated and were filtered off, washed with diethyl ether and air-dried. **1:** Yield: 115 mg (92%). $C_{18}H_{29}F_6N_4NiO_2P$ (537): calcd. C 40.25, H 5.44, N 10.43; found C 39.96, H 5.71, N 10.14. MS (FAB^+): *m*/*z* (%) = 391 (100) $[M^+]$. IR (nujol): $\tilde{\nu}$ = 3286, 3268 (NH), 1650 (C=N), 1548 (OCO) cm^{-1}. ^1H NMR [$(CD_3)_2CO$, TMS]: δ = 290.8 (H_α), 263.0 (H_α), 192.3 (H_α, 2 H), 161.4 (H_α), 85.0 (H_α, 2 H), 57.3 (H_α), 38.7 (4-Me, 3 H), 22.7 (4-Me, 3 H), 9.6 (Hisonic, 4 H), –11.0 (H_β), –13.3 (H_β, 2 H), –15.2 (H_β), –17.3 (H_β), –20.3 (2-Me, 3 H), –33.0 (H_β) ppm. **3:** Yield: 117 mg (94%). $C_{18}H_{29}F_6N_4NiO_2P$ (537): calcd. C 40.25, H 5.44, N 10.43; found C 40.03, H 5.61, N 10.14. MS (FAB^+): *m*/*z* (%) = 391 (100) $[M^+]$. IR (nujol): $\tilde{\nu}$ = 3287, 3269 (NH), 1659 (C=N), 1552 (OCO) cm^{-1}. ^1H NMR [$(CD_3)_2CO$, TMS]: δ = 366.8 (H_α), 321.9 (H_α), 226.8 (H_α, 2 H), 207.8 (H_α), 99.7 (H_α, 2 H), 65.5 (H_α), 53.1 (4-Me, 3 H), 16.3 (4-Me, 3 H), 13.4 (2-H + 4-H, 2 H), 9.4 (5-H + 6-H, 2 H), –11.8 (H_β, 2 H), –13.2 (H_β), –16.8 (2-Me, 3 H), –24.0 (H_β), –27.9 (H_β), –30.2 (H_β) ppm.

Complexes 2 and 4: NC_5H_4-4-COOH or NC_5H_4-3-COOH (0.30 mmol) was added to a solution of $[Ni(Me_4\text{-}mcN_3)(\mu\text{-}OH)]_2(PF_6)_2$ (100 mg, 0.12 mmol) in acetone (25 mL). The mixture was stirred overnight at room temperature and the solvent was partially evaporated under reduced pressure. On addition of diethyl ether, the blue-green complexes precipitated and were filtered off, washed with diethyl ether and air-dried. **2:** Yield: 103 mg (83%). $C_{19}H_{31}F_6N_4NiO_2P$ (551): calcd. C 41.41, H 5.67, N 10.17; found C 41.64, H 6.04, N 10.15. MS (FAB^+): *m*/*z* (%) = 405 (100) $[M^+]$. IR (nujol): $\tilde{\nu}$ = 3270 (NH), 1659 (C=N), 1552 (OCO) cm^{-1}. ^1H NMR [$(CD_3)_2CO$, TMS]: δ = 315.0 (H_α), 290.7 (H_α), 252.3 (H_α), 236.9 (H_α, 2 H), 135.6 (9-Me, 3 H), 98.3 (H_α, 2 H), 65.0 (4-Me, 3 H), 48.5 (H_α), 20.2 (4-Me, 3 H), 11.1 (3-H + 5-H, 2 H), 9.1 (2-H + 6-H, 2 H), –9.8 (H_β, 2 H), –13.4 (H_β), –16.9 (2-Me, 3 H), –25.2 (H_β), –32.7 (H_β, 2 H) ppm. **4:** Yield: 113 mg (91%). $C_{19}H_{31}F_6N_4NiO_2P$ (551): calcd. C 41.41, H 5.67, N 10.17; found C 41.27, H 5.94, N 9.97. MS (FAB^+): *m*/*z* (%) = 405 (100) $[M^+]$. IR (nujol): $\tilde{\nu}$ = 3121 (NH), 1661 (C=N), 1530 (OCO) cm^{-1}. ^1H NMR [$(CD_3)_2CO$, TMS]: δ = 320.0 (H_α), 296.0 (H_α), 257.1 (H_α), 243.8 (H_α), 136.8 (9-Me, 3 H), 101.9 (H_α, 2 H), 67.4 (4-Me, 3 H), 46.7 (H_α), 41.5 (H_α), 20.8 (4-Me, 3 H), 9.2 (2-H + 4-H + 5-H, 3

 © 2005 Wiley-VCH Verlag GmbH & Co. KGaA, Weinheim

H), 7.4 (6-H), –9.7 (H_β, 2 H), –13.7 (H_β), –16.5 (2-Me, 3 H), –25.7 (H_β), –32.7 (H_β), –33.7 (H_β) ppm.

Complexes 5–7: NC_5H_4-4-COOH, NC_5H_4-3-COOH, or NC_5H_4-4-CH_2COOH (0.31 mmol) was added to a solution of *cis*-[Pd-$(C_6F_5)_2(PhCN)_2$] (100 mg, 0.15 mmol) in methanol (10 mL), the solution was stirred for 24 h, and the solvent was partially evaporated under reduced pressure. On addition of water, the white complexes precipitated and were filtered off and air-dried. **5:** Yield: 80 mg (75%). $C_{24}H_{10}F_{10}N_2O_4Pd$ (687): calcd. C 41.9, H 1.5, N 4.1; found C 41.6, H 1.4, N 4.1. MS (FAB^+): *m/z* (%) = 519 (100) [$M^+ – C_6F_5$]. IR (nujol): $\tilde{\nu}$ = 1720 (C=O), 798, 787 (Pd–C_6F_5) cm^{-1}. ^1H NMR [$(CD_3)_2CO$, TMS]: δ = 9.27 (d, J_{HH} = 6 Hz, 4 H, $H^{2,6}$), 8.34 (d, J_{HH} = 6 Hz, 4 H, $H^{3,5}$) ppm. ^{19}F NMR [$(CD_3)_2CO$, TMS]: δ = –117.2 (d, 4 F_o, J_{om} = 24.0 Hz), –163.5 (t, 2 F_p, J_{mp} = 19.0 Hz), –165.8 (m, 4 F_m) ppm. **6:** Yield: 85 mg (80%). $C_{24}H_{10}F_{10}N_2O_4Pd$ (687): C 41.9, H 1.5, N 4.1; found C 41.7, H 1.5, N 4.0. IR (nujol): $\tilde{\nu}$ = 1705 (C=O), 796, 784 (Pd–C_6F_5) cm^{-1}. ^{1}HNMR [$(CD_3)_2CO$, TMS]: δ = 9.21 (s, 2 H, 2-H), 8.99 (d, J_{HH} = 5 Hz, 2 H, 6-H), 8.48 (d, J_{HH} = 7 Hz, 2 H, 4-H), 7.72 (dd, J_{HH} = 5 Hz, 2 H, 5-H) ppm. ^{19}F NMR [$(CD_3)_2CO$, TMS]: δ = –117.0 (d, 4 F_o, J_{om} = 28.0 Hz), –163.2 (t, 2 F_p, J_{mp} = 17.0 Hz), –165.5 (m, 4 F_m). **7:** Yield: 85 mg (74%). $C_{28}H_{18}F_{10}N_2O_4Pd$ (743): C 45.3, H 2.4, N 3.8; found C 44.9, H 2.5, N 3.8. MS (FAB^+): *m/z* (%) = 575 (100) [$M^+ – C_6F_5$]. IR (nujol): $\tilde{\nu}$ = 1744 (C=O), 795, 783 (Pd–C_6F_5) cm^{-1}. ^1H NMR [$(CD_3)_2CO$, TMS]: δ = 8.64 (d, J_{HH} = 6 Hz, 4 H, 2,6-H), 7.47 (d, J_{HH} = 6 Hz, 4 H, 3,5-H), 3.79 (s, 4 H, $PhCH_2$), 3.66 (s, 6 H, CH_3) ppm. ^{19}F NMR [$(CD_3)_2CO$, TMS]: δ = –116.8 (d, 4 F_o, J_{om} = 28.0 Hz), –163.7 (t, 2 F_p, J_{mp} = 20.0 Hz), –165.8 (m, 4 F_m) ppm.

Complexes 8 and 10. Method 1: $Pd(C_6F_5)_2(PhCN)_2$ (45.3 mg, 0.07 mmol) was added to a solution of complex **1** or **3** (0.14 mmol) in acetone (25 mL). The mixture was stirred at room temperature for 24 h. The solution was concentrated under reduced pressure and the addition of diethyl ether caused the precipitation of a pale blue solid, which was collected by filtration, washed with diethyl ether and air-dried. Yields: 100 mg (94%) (for **8**) and 97 mg (91%) (for **10**). **Method 2:** $[Ni(Me_3\text{-}mcN_3)(\mu\text{-}OH)]_2(PF_6)_2$ (63.1 mg, 0.073 mmol) was added to a solution of complex **5** or **6** (50.1 mg, 0.073 mmol) in acetone (15 mL) and the resulting solution was refluxed for 5 h. The solvent was partially evaporated under reduced pressure. On addition of Et_2O, the blue complexes precipitated and were filtered off and air-dried. Yields: 81 mg (73%) (for **8**) and 78 mg (70%) (for **10**). **8:** $C_{48}H_{58}F_{22}N_8Ni_2O_4P_2Pd$ (1515): calcd. C 38.1, H 3.9, N 7.4; found C 37.7, H 3.9, N 7.4. MS (FAB^+): *m/z* (%) = 391 (100) $[Ni(Me_3\text{-}mcN_3)(isonic)]^+$. IR (nujol): $\tilde{\nu}$ = 3285, 3271 (NH), 1658 (C=N), 1548 (OCO), 795, 778 (Pd–C_6F_5) cm^{-1}. ^1H NMR [$(CD_3)_2CO$, TMS]: δ = 254.0 (H_α), 236.3 (H_α, 2 H), 168.5 (H_α), 156.3 (H_α), 101.3 (H_α, 2 H), 72.8 (H_α), 54.5 (4-Me, 3 H), 16.3 (4-Me, 3 H), 10.7 (2-H + 6-H, 2 H), 8.8 (3-H + 5-H, 2 H), –12.3 (H_β, 2 H), –14.2 (H_β), –17.3 (H_β), –17.6 (2-Me, 3 H), –24.6 (H_β), 28.8 (H_β), –31.5 (H_β) ppm. ^{19}F NMR [$(CD_3)_2CO$, TMS]: δ = –72.0 (d, 12 F, PF_6^-, J_{FP} = 708 Hz), –116.8 (d, 4 F_o, J_{om} = 24.5 Hz), –163.5 (t, 2 F_p, J_{mp}= 20.7 Hz), –165.7 (m, 4 F_m) ppm. ^{31}P NMR ([D_6]acetone, H_3PO_4): δ = –143.5 (sept, 2 P, J_{PF} = 707 Hz) ppm. **10:** $C_{48}H_{58}F_{22}N_8Ni_2O_4P_2Pd$ (1515): calcd. C 38.1, H 3.9, N 7.4; found C 37.8, H 3.9, N 7.4. MS (FAB^+): *m/z* (%) = 391 (100) $[Ni(Me_3\text{-}mcN_3)(nic)]^+$, 1367 (2) [$M^+$]. IR (nujol): $\tilde{\nu}$ = 3288, 3275 (NH), 1658 (C=N), 1556 (OCO), 795, 778 (Pd–C_6F_5) cm^{-1}. ^1H NMR [$(CD_3)_2CO$, TMS]: δ = 224.1 (H_α, 2 H), 207.1 (H_α), 96.2 (H_α, 2 H), 73.8 (H_α), 52.1 (4-Me, 3 H), 22.8 (H_α), 16.4 (4-Me, 3 H), 12.3 (H_α), 9.7 (2-H + 4-H, 2 H), 9.4 (5-H), 8.6 (6-H), –11.9 (H_β, 2 H), –14.3 (H_β), –17.9 (2-Me, 3 H), –24.6 (H_β), –28.9 (H_β), –32.1 (H_β) ppm. ^{19}F NMR [$(CD_3)_2CO$, TMS]: δ = –71.9 (d, 12 F, PF_6^-, J_{FP} = 712 Hz), –116.2 (d, 4 F_o, J_{om} = 22.5 Hz), –162.7 (t, 2 F_p, J_{mp} = 25.4 Hz), –164.8 (m, 4 F_m) ppm. ^{31}P NMR ([D_6]acetone, H_3PO_4): δ = –143.6 (sept, 2 P, J_{PF} = 709 Hz) ppm.

Complexes 9 and 11. Method 1: $Pd(C_6F_5)_2(PhCN)_2$ (45.3 mg, 0.07 mmol) was added to a solution of complex **2** or **4** (0.14 mmol) in acetone (25 mL). The mixture was stirred at room temperature for 24 h. The solution was concentrated under reduced pressure and the addition of diethyl ether caused the precipitation of a pale blue solid, which was collected by filtration, washed with diethyl ether and air-dried. Yields: 105 mg (97%) (for **9**) and 96 mg (89%) (for **11**). **Method 2:** $[Ni(Me_4\text{-}mcN_3)(\mu\text{-}OH)]_2(PF_6)_2$ (65.3 mg, 0.073 mmol) was added to a solution of complex **5** or **6** (50.1 mg, 0.073 mmol) in acetone (15 mL) and the resulting solution was refluxed for 5 h. The solvent was partially evaporated under reduced pressure. On addition of Et_2O, the blue complexes precipitated and were filtered off and air-dried. Yields: 79 mg (70%) (for **9**) and 86 mg (76%) (for **11**). **9:** $C_{50}H_{62}F_{22}N_8Ni_2O_4P_2Pd$ (1542): calcd. C 38.9, H 4.2, N 7.3; found C 38.5, H 4.4, N 7.3. MS (FAB^+): *m/z* (%) = 405 (100) $[Ni(Me_4\text{-}mcN_3)(isonic)^+]$, 1395 (1) [$M^+$]. IR (nujol): $\tilde{\nu}$ = 3269 (N–H), 1657 (C=N), 1547 (OCO), 797, 780 (Pd–C_6F_5) cm^{-1}. ^1H NMR [$(CD_3)_2CO$, TMS]: δ = 317.7 (H_α), 259.8 (H_α), 242.9 (H_α), 210.5 (H_α, 2 H), 128.9 (9-Me, 3 H), 92.5 (H_α), 87.8 (H_α, 2 H), 56.9 (4-Me, 3 H), 19.0 (4-Me, 3 H), 11.4 (2-H + 6-H, 2 H), 10.4 (3-H + 5-H, 2 H), –10.4 (H_β, 2 H), –12.9 (H_β), –18.3 (2-Me, 3 H), –25.0 (H_β), –30.4 (H_β), –35.2 (H_β) ppm. ^{19}F NMR [$(CD_3)_2CO$, TMS]: δ = –71.6 (d, 12 F, PF_6^-, J_{FP} = 708 Hz), –116.7 (d, 4 F_o, J_{om} = 24.5 Hz), –163.4 (t, 2 F_p, J_{mp} = 20.7 Hz), –165.6 (m, 4 F_m) ppm. ^{31}P NMR ([D_6]acetone, H_3PO_4): δ = –143.3 (sept, 2 P, J_{PF} = 708 Hz) ppm. **11:** $C_{50}H_{64}F_{22}N_8Ni_2O_4P_2Pd$ (1542): calcd. C 38.9, H 4.2, N 7.3; found C 38.4, H 4.2, N 7.1. MS (FAB^+): *m/z* (%) = 405 (100) $[Ni(Me_4\text{-}mcN_3)(nic)^+]$, 1394 (1) [$M$]$^+$. IR (nujol): $\tilde{\nu}$ = 3270 (NH), 1657 (C=N), 1547 (OCO), 797, 785 (Pd–C_6F_5) cm^{-1}. ^1H NMR [$(CD_3)_2CO$, TMS]: δ = 310.6 (H_α), 287.5 (H_α), 249.7 (H_α), 233.5 (H_α), 134.4 (9-Me, 3 H), 95.6 (H_α, 2 H), 63.5 (4-Me, 3 H), 48.8 (H_α, 2 H), 19.8 (4-Me, 3 H), 9.7 (2-H + 4-H, 2 H), 9.3 (5-H), 8.2 (6-H), –9.8 (H_β, 2 H), –13.3 (H_β), –17.1 (2-Me, 3 H), –25.0 (H_β), –32.2 (H_β), –33.4 (H_β) ppm. ^{19}F NMR [$(CD_3)_2CO$, TMS]: δ = –71.2 (d, 12 F, PF_6^-, J_{FP} = 712 Hz), –116.2 (d, 4 F_o, J_{om} = 26.4 Hz), –162.3 (t, 2 F_p, J_{mp} = 16.9 Hz), –164.6 (m, 4 F_m) ppm. ^{31}P NMR ([D_6]-acetone, H_3PO_4): δ = –143.3 (sept, 2 P, J_{PF} = 691 Hz) ppm.

Complex 12: $[Ni(Me_3\text{-}mcN_3)(\mu\text{-}OH)]_2(PF_6)_2$ (63.1 mg, 0.073 mmol) was added to a solution of complex **7** (54.2 mg, 0.073 mmol) in acetone (15 mL) and the resulting solution was refluxed for 5 h. The solvent was partially evaporated under reduced pressure. On addition of Et_2O, the blue complexes precipitated and were filtered off and air-dried. **12:** Yield: 96 mg (85%). $C_{50}H_{62}F_{22}N_8Ni_2O_4P_2Pd$ (1543): calcd. C 38.9, H 4.1, N 7.3; found C 38.5, H 4.3, N 7.0. MS (FAB^+): *m/z* (%) = 405 (100) $[Ni(Me_3\text{-}mcN_3)(PyOAc)]^+$, 1397 (15) [$M^+ + 1 + PF_6$]. IR (nujol): $\tilde{\nu}$ = 3289, 3266 (NH), 1661 (C=N), 1558 (OCO), 795, 783 (Pd–C_6F_5) cm^{-1}. ^1H NMR [$(CD_3)_2CO$, TMS]: δ = 230.2 (H_α, 2 H), 207.4 (H_α), 196.4 (H_α), 185.5 (H_α), 174.3 (H_α), 103.2 (H_α, 2 H), 56.3 (4-Me, 3 H), 19.7(–CH_2–, 2 H), 16.8 (4-Me, 3 H), 8.8 (2-H + 6-H, 2 H), 7.4 (3-H + 5-H, 2 H), –12.0 (H_β, 2 H), –15.1 (H_β), –16.4 (2-Me, 3 H), –23.9 (H_β), 28.8 (H_β, 2 H). ^{19}F NMR [$(CD_3)_2CO$, TMS]: δ = –72.0 (d, 12 F, PF_6^-, J_{FP} = 709 Hz), –116.2 (d, 4 F_o, J_{om} = 25.4 Hz), –163.1 (t, 2 F_p, J_{mp} = 16.9 Hz), –164.8 (m, 4 F_m) ppm. ^{31}P NMR ([D_6]acetone, H_3PO_4): δ = –143.6 (sept, 2 P, J_{PF} = 708 Hz) ppm.

X-ray Data Collection and Structure Determination: Data collection was performed with a Bruker Smart CCD diffractometer with a nominal crystal–detector distance of 4.5 cm. Diffraction data were collected based on an ω-scan. A total of 1371 (**7**) and 2524 (**4**) frames were collected at 0.3° intervals and 10 s per frame. The diffraction

 © 2005 Wiley-VCH Verlag GmbH & Co. KGaA, Weinheim

frames were integrated using the SAINT package[42] and corrected for absorption with SADABS.[43] The crystallographic data are shown in Table 5. The structures were solved by direct methods[44] and refined anisotropically on F^2.[44] Hydrogen atoms were introduced in calculated positions. CCDC-256615 (**4**) and -256616 (**7**) contain the supplementary crystallographic data for this paper. These data can be obtained free of charge from The Cambridge Crystallographic Data Centre via www.ccdc.cam.ac.uk/data_request/cif.

Table 5. Crystal data and summary of data collection and refinement for 4 and 7.

	4·MeCN	**7**
Empirical formula	$C_{21}H_{34}F_6N_5NiO_2P$	$C_{28}H_{18}F_{10}N_2O_4Pd$
Formula mass	592.21	742.84
Crystal system	triclinic	monoclinic
Unit cell dimensions:		
a [Å]	8.1682(5)	14.1830(6)
b [Å]	13.0538(8)	12.7318(6)
c [Å]	13.4683(8)	15.6193(7)
α [°]	110.329(1)	90
β [°]	98.568(1)	91.6980(10)
γ [°]	96.192(1)	90
Unit cell volume [Å^3]	1311.72(14)	2819.2(2)
Temperature [K]	100(2)	100(2)
Space group	$P\bar{1}$	$P2_1/n$
Z	2	4
μ [mm^{-1}]	0.871	0.763
Reflections collected	15437	17361
Independent reflections	5901	6309
R(int)	0.0233	0.0152
R_1 [$I > 2\sigma(I)$][a]	0.0626	0.0241
wR_2 (all data)[b]	0.1314	0.0609

Acknowledgments

This work was supported by the Dirección General de Investigación del Ministerio de Ciencia y Tecnología (Project No. BQU2001-0979-C02-01), Spain, and the Fundación Séneca de la Comunidad Autónoma de la Región de Murcia (Projects No. 00448/PI/04 and 00484/PI/04). A. A. L. thanks the Fundación Séneca for an FPI grant.

[1] J. Y. Lu, E. E. Kohler, *Inorg. Chem. Commun.* **2002**, *5*, 196.
[2] W. Lin, O. R. Evans, R.-G. Xiong, Z. Wang, *J. Am. Chem. Soc.* **1998**, *120*, 13272.
[3] B. Rather, B. Moulton, R. D. B. Walsh, M. J. Zaworotko, *Chem. Commun.* **2002**, 694.
[4] J. Y. Lu, A. M. Babb, *Inorg. Chem.* **2001**, *40*, 3261.
[5] J. Y. Lu, A. M. Babb, *Chem. Commun.* **2001**, 821.
[6] P.-O. Käll, J. G. M. Fahlman, F. Söderlind, *Polyhedron* **2001**, *20*, 2747.
[7] P. Teo, D. M. J. Foo, L. L. Koh, T. S. A. Hor, *Dalton Trans.* **2004**, 3389.
[8] H. Adams, S. Clunas, D. E. Fenton, S. E. Spey, *J. Chem. Soc., Dalton Trans.* **2002**, 441.
[9] I. G. Eremenko, S. E. Nefedov, A. A. Sidorov, M. A. Golubnichaya, P. V. Danilov, V. N. Ikorskii, Y. G. Shevedenkov, V. M. Novotortsev, I. I. Moiseev, *Inorg. Chem.* **1999**, *38*, 3764 and references cited therein.
[10] M. D. Santana, G. García, A. Rufete, M. C. Ramírez de Arellano, G. López, *J. Chem. Soc., Dalton Trans.* **2000**, 619.
[11] M. D. Santana, G. García, M. Julve, F. Lloret, J. Pérez, M. Liu, F. Sanz, J. Cano, G. López, *Inorg. Chem.* **2004**, *43*, 2132.
[12] M. D. Santana, G. García, J. Pérez, E. Molins, G. López, *Inorg. Chem.* **2001**, *40*, 5701.
[13] J. Pérez, L. García, A. G. Orpen, M. D. Santana, P. Saez, G. García, *New J. Chem.* **2002**, *26*, 726.
[14] M. D. Santana, G. García, A. A. Lozano, G. López, J. Tudela, J. Pérez, L. García, L. Lezama, T. Rojo, *Chem. Eur. J.* **2004**, *10*, 1738.
[15] K. Nakamoto, *Infrared and Raman Spectra of Inorganic and Coordination Compounds*,, 4th ed., John Wiley & Sons, New York, **1986**.
[16] R. F. R. Jazzar, P. H. Bhatia, M. F. Mahon, M. K. Whittlesey, *Organometallics* **2003**, *22*, 670.
[17] A. B. P. Lever, *Inorganic Electronic Spectroscopy*, Elsevier, Amsterdam, **1984**, pp. 513–520.
[18] R. H. Holm, C. J. Hawkins, *NMR of Paramagnetic Molecules: Principles and Applications* (Eds.: G. N. La Mar, W. Horrocks, Jr., R. H. Holm), Academic Press, New York, **1973**, pp. 243–332.
[19] A. Dei, M. Wicholas, *Inorg. Chim. Acta* **1989**, *166*, 151.
[20] M. D. Santana, A. Rufete, G. García, G. López, J. Casabó, A. Cabrero, E. Molins, C. Miravitlles, *Polyhedron* **1997**, *16*, 3713.
[21] A. W. Addison, T. N. Rao, J. Reedijk, J. V. Rijn, G. C. Verschoor, *J. Chem. Soc., Dalton Trans.* **1984**, 1349.
[22] D. D. LeCloux, M. C. Keyes, M. Osawa, V. Reynolds, W. B. Tolman, *Inorg. Chem.* **1994**, *33*, 6361.
[23] B. S. Hammes, C. J. Carrano, *Inorg. Chem.* **1999**, *38*, 3562.
[24] A. J. Blake, J. P. Danks, I. A. Fallis, A. Harrison, W.-S. Li, S. Parsons, S. A. Ross, G. Whittaker, M. Schröder, *J. Chem. Soc., Dalton Trans.* **1998**, 3969.
[25] J. Ruiz, V. Rodríguez, N. Cutillas, G. López, J. Pérez, *Organometallics* **2002**, *21*, 412.
[26] J. Ruiz, F. Florenciano, V. Rodríguez, C. de Haro, G. López, J. Pérez, *Eur. J. Inorg. Chem.* **2002**, 2736.
[27] G. López, J. Ruiz, C. Vicente, J. M. Martí, G. García, P. A. Chaloner, P. B. Hitchcock, R. M. Harrison, *Organometallics* **1992**, *11*, 1417.
[28] G. López, J. Ruiz, G. García, C. Vicente, J. Casabó, E. Molins, C. Miravitlles, *Inorg. Chem.* **1991**, *30*, 2605.
[29] C. De Haro, G. García, G. Sánchez, G. López, *J. Chem. Res. Synop.* **1986**, 11; *J. Chem. Res. (M)* **1986**, 1128.
[30] D. A. Long, D. Steele, *Spectrochim. Acta* **1963**, *19*, 1955.
[31] E. Maslowski, *Vibrational Spectra of Organometallic Compounds*, Wiley, New York, **1977**, p. 437.
[32] E. Alonso, J. Forniés, C. Fortuño, M. Tomás, *J. Chem. Soc., Dalton Trans.* **1995**, 3777.
[33] Z. Qin, M. C. Jennings, R. J. Puddephatt, *Inorg. Chem.* **2002**, *41*, 5174.
[34] M. G. Crisp, E. R. T. Tiekink, L. M. Rendina, *Inorg. Chem.* **2003**, *42*, 1057.
[35] J. Ruiz, N. Cutillas, V. Rodríguez, J. Sampedro, G. López, P. A. Chaloner, P. B. Hitchcock, *J. Chem. Soc., Dalton Trans.* **1999**, 2939.
[36] J. Forniés, F. Martínez, R. Navarro, E. P. Urriolabeitia, *J. Organomet. Chem.* **1995**, *495*, 185.
[37] J. Ruiz, M. T. Martínez, F. Florenciano, V. Rodríguez, G. López, J. Pérez, P. A. Chaloner, P. B. Hitchcock, *Inorg. Chem.* **2003**, *42*, 3650.
[38] J. Ruiz, M. T. Martínez, F. Florenciano, V. Rodríguez, G. López, J. Pérez, P. A. Chaloner, P. B. Hitchcock, *Dalton Trans.* **2004**, 929.
[39] J. M. Casas, B. E. Diosdado, L. R. Falvello, J. Forniés, A. Martín, A. J. Rueda, *Dalton Trans.* **2004**, 2733.
[40] J. W. L. Martin, J. H. Johnston, N. F. Curtis, *J. Chem. Soc., Dalton Trans.* **1978**, 68.
[41] A. Escuer, R. Vicente, J. Ribas, *Polyhedron* **1992**, *11*, 453.
[42] *SAINT*, Version 6.22, Bruker AXS Inc.
[43] G. M. Sheldrick, *SADABS*, University of Göttingen, **1996**.
[44] G. M. Sheldrick, *SHELX-97, Programs for Crystal Structure Analysis*, release 97-2, University of Göttingen, Germany, **1998**.

Received: February 9, 2005
Published Online: June 22, 2005

 © 2005 Wiley-VCH Verlag GmbH & Co. KGaA, Weinheim

A Facile One-Step Synthesis of a Lipophilic Gold(I) Carbene Complex – X-ray Crystal Structures of LAuCl and LAuC≡CH (L = 1,3-di-*tert*-Butyl imidazol-2-ylidene)

Sanjay Singh,[a] S. Shravan Kumar,[a] Vojtech Jancik,[a] Herbert W. Roesky,*[a] Hans-Georg Schmidt,[a] and Mathias Noltemeyer[a]

Keywords: Adduct / Gold(I) / Carbene / Acetylide

The reaction of Au(CO)Cl with 1,3-di-*tert*-butylimidazol-2-ylidene and 1,3-dimesitylimidazol-2-ylidene in toluene at room temperature results in CO evolution and readily affords in high yield the adducts **1a** and **1b**, respectively. The reaction of **1a** and **1b** with ethynylmagnesium chloride in THF yields **2a** and **2b**, respectively. The crystal structures of **1a**, **1b**, and **2a** were determined.

(© Wiley-VCH Verlag GmbH & Co. KGaA, 69451 Weinheim, Germany, 2005)

Introduction

Recently there has been a resurgence of interest in the chemistry of gold compounds in general and that of gold(I) compounds in particular. A major driving force for this interest has been the utility of soluble gold compounds in various applications ranging from precursor for gold nanoparticles[1,2] to drugs,[3] and catalysts.[4–6] Among Au^I compounds, there has been considerable success in the preparation of alkynyl gold complexes. These are among the most stable organogold complexes.[7] Although dinuclear complexes such as $R_3PAuC{\equiv}CAuPR_3$ have been known for some time,[8,9] Schmidbaur and co-workers have recently isolated terminal acetylides of gold in the form of gold ethynyl complexes $RAuC{\equiv}CH$ (R = $MePH_2$, Me_3P).[10] A key factor in this successful assembly is the utility of appropriate phosphane ligands in stabilizing such compounds. It has also been shown that these compounds can be used as reliable synthons in crystal engineering owing to strong and predictable aurophilic [Au^I–Au^I] interactions.[11] Another interesting aspect of these complexes has been the ability to exhibit rich photophysical and photochemical behaviour.[12–15]

One of the key challenges in Au^I chemistry remains the availability of reasonably stable synthons, which would allow simple substitution reactions. The use of sterically hindered N-heterocyclic carbenes[16] for such a purpose was regarded as ideal.[17,18] Accordingly, in this paper we describe a facile one-step, high yield synthesis of a lipophilic gold(I)-N-heterocyclic carbene complex LAuCl. We also demonstrate the synthetic utility of the latter by preparing the terminal acetylide $LAuC{\equiv}CH$. The X-ray crystal structures of LAuCl and $LAuC{\equiv}CH$ are described. During the preparation of this manuscript Baker and co-workers reported the synthesis of LAuCl **1a** complex by transmetallation of LAgCl and $(Me_2S)AuCl$.[19]

Results and Discussion

The reaction of Au(CO)Cl with a stoichiometric amount of N-heterocyclic carbene (1,3-di-*tert*-butylimidazol-2-ylidene or 1,3-dimesitylimidazol-2-ylidene) in toluene at room temperature results in a vigorous evolution of carbon monoxide and the formation of the corresponding carbene adducts **1a** and **1b**, respectively (Scheme 1). Thus this synthetic method represents a viable and rational route for the preparation of N-heterocyclic carbene adducts of Au^I.

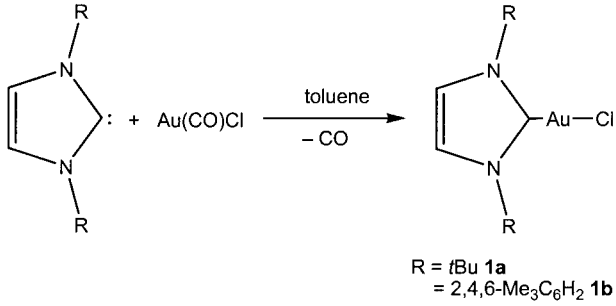

Scheme 1. Synthesis of Au^I N-heterocyclic carbene complexes.

Compounds **1a** and **1b** have been unambiguously characterized by means of spectroscopic, spectrometric, and crystallographic techniques. Both **1a** and **1b** are colorless crystalline solids and are thermally stable. They decompose

[a] Institut für Anorganische Chemie der Georg-August-Universität Göttingen,
Tammannstrasse 4, 37077 Göttingen, Germany
Fax: +49-551-393373
E-mail: hroesky@gwdg.de

with melting at 170 °C and 210 °C respectively. The EI mass spectrum of **1a** revealed that the most intense peak appears at *m*/*z* 320 and corresponds to the loss of one *tert*-butyl group and the chlorine atom from the molecular ion. A similar peak at *m*/*z* 303 in **1b** is due to [M^+ – Cl – Au – H]. The ^{1}H NMR spectrum of **1a** exhibits two singlets (δ = 1.83 and 7.26 ppm) for the protons of the *tert*-butyl groups and (HC=CH) of the carbene. They are shifted downfield relative to the 1,3-di-*tert*-butylimidazol-2-ylidene (δ = 1.51 and 7.06 ppm). The resonances of *o*-Me and *p*-Me in **1b** (δ = 1.75 and 2.13 ppm) are observed upfield relative to the carbene (δ = 2.08 and 2.31 ppm) whereas the (HC=CH) protons in **1b** (δ = 7.46 ppm) are found downfield relative to the carbene (δ = 7.07 ppm). A weak ^{13}C NMR resonance (δ = 167.6 ppm for **1a**) can be assigned to the carbene carbon atom. However, in case of **1b** no resonance downfield to 150 ppm was detected which could be assigned to the carbene carbon.

Single crystals of **1a** and **1b** suitable for X-ray structural analysis were obtained from their toluene solutions. Compound **1a** crystallizes with one molecule of toluene. The molecular structures of **1a** and **1b** are shown in Figure 1 and Figure 2, respectively, and selected metric parameters are given in Table 1. Compound **1a** crystallizes in the monoclinic space group $P2_1/c$ whereas compound **1b** in the orthorhombic space group *Fdd*2, respectively. The X-ray crystal structures of **1a** and **1b** reveal that the compounds are monomeric adducts of the N-heterocyclic carbene Au^I chloride, no Au^I–Au^I interactions were observed.

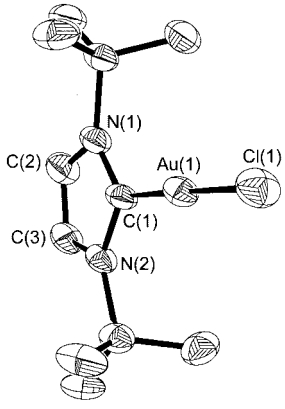

Figure 1. Molecular structure of **1a**. Toluene molecule and hydrogen atoms are omitted for clarity, thermal ellipsoids are shown with 50% probability.

The Au–Cl distances 2.290(2) Å in **1a** and 2.281(4) Å in **1b** are shorter than the Au–Cl distance in [Au(Me$_2$-bimy)Cl] [2.338(2) Å][17] but comparable to that in {PhCH$_2$N(CH)$_2$N(COPh)C}AuCl [2.286(2) Å][18] and [Au(Me$_2$-imyl)Cl] [2.288(3) Å].[20] The Au–C bond lengths 1.983(8) Å in **1a** and 1.933(1) Å in **1b** are similar to those found in [Au(Me$_2$-bimy)Cl][17] [1.985(1) Å], {PhCH$_2$N(CH)$_2$N(COPh)C}AuCl[18] [1.970(1) Å] and in [Au(Me$_2$-imyl)Cl][20] [1.98(1) Å]. The average N–C(1) distance of the ligand in **1a** 1.369 Å and 1.377 Å in **1b** are similar to those observed in [Au(Me$_2$-bimy)Cl] (1.371 Å)[17] and in

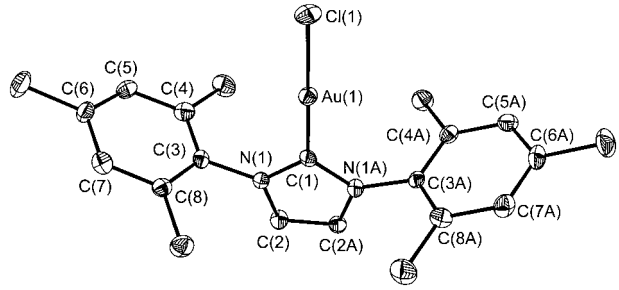

Figure 2. Molecular structure of **1b**. Hydrogen atoms are omitted for clarity, thermal ellipsoids are shown with 50% probability.

Table 1. Selected bond lengths [Å] and angles [°] of **1a**, **1b**, and **2a**.

	1a	**1b**	**2a**
Au(1)–C(1)	1.983(8)	1.933(1)	2.05(1)
Au(1)–Cl(1)	2.290(2)	2.281(4)	
N(1)–C(1)	1.376(9)	1.377(9)	1.37(2)
N(2)–C(1)*	1.362(1)	1.377(9)	1.34(2)
C(2)–C(3)*	1.315(1)	1.372(8)	1.34(2)
Au(1)–C(12)			2.04(2)
C(12)–C(13)			1.11(2)
C(1)–Au(1)–Cl(1)	178.9(2)	180.0(1)	
N(2)–C(1)–N(1)*	104.5(7)	102.6(9)	107(1)
N(1)–C(1)–Au(1)	128.4(5)	128.7(4)	125(2)
N(2)–C(1)–Au(1)*	127.1(5)	128.7(4)	128(1)
C(1)–Au(1)–C(12)			178.7(6)
Au(1)–C(12)–C(13)			171.3(2)

* N(2) corresponds to N(1A) and C(3) corresponds to C(2A) in case of **1b**.

{PhCH$_2$N(CH)$_2$N(COPh)C}AuCl (1.355 Å).[18] The N(1)–C(1)–N(2) angles within the N_2C_3 five-membered ring of the carbene ligand in **1a** 104.5(7)° and 102.6(9)° in **1b** are similar to that in {PhCH$_2$N(CH)$_2$N(COPh)C}AuCl 104.4(1)° but are slightly smaller than those in [Au(Me$_2$-bimy)Cl][17] 108(1)° and in [Au(Me$_2$-imyl)Cl][20] [106(10)°]. In the crystal lattice **1a** forms an extended network through agostic interaction of Au with one proton of the *t*Bu group from neighbouring molecule (2.96 Å) and also interacts with one *o*-H of the solvating toluene molecule (3.06 Å) present in the crystal lattice (Figure 3). These are in the range 1.95–3.20 Å reported for similar H···Au interactions.[21] In the case of **1b** all aromatic hydrogens are involved in hydrogen bonds. Hydrogen atoms on C(7) and C(7A) are bonded by agostic interactions to Au from two different neighbouring molecules with a H···Au distance of 3.18 Å which is comparable to the values in the range 1.95–3.20 Å reported for similar H···Au interactions[21] but slightly longer than those in **1a**. Hydrogen atoms present on C(5), C(5A), C(2) and C(2A) are bonded to Cl atoms of neighbouring molecules in a symmetrical manner as shown in Figure 4. The corresponding H···Cl distances are 2.88 Å and 2.90 Å which agrees with the reported values of intermediate to long range intermolecular interactions.[21,22]

Reaction of the adducts **1a** and **1b** with ethynylmagnesium chloride in THF smoothly affords the corresponding gold(I) ethynyls **2a** and **2b** in good yields (Scheme 2). Compounds **2a** and **2b** decompose with melting at 155 °C and

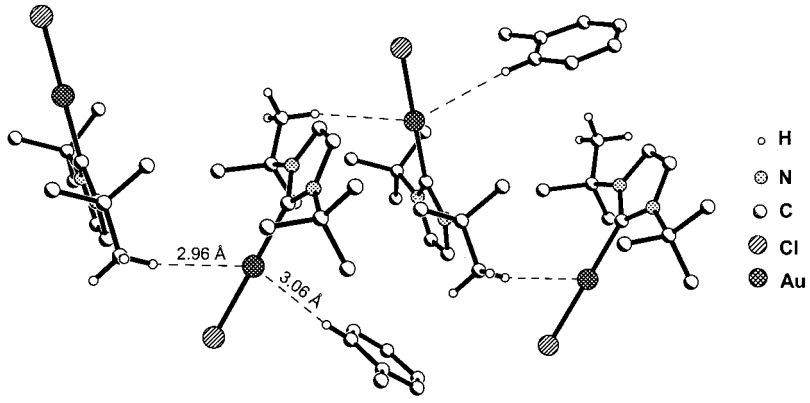

Figure 3. Perspective view of the agostic interactions of Au with *o*-H of the toluene molecule and with H atom of *t*Bu of the carbene ligand in the crystal state of **1a**, forming a zig-zag chain.

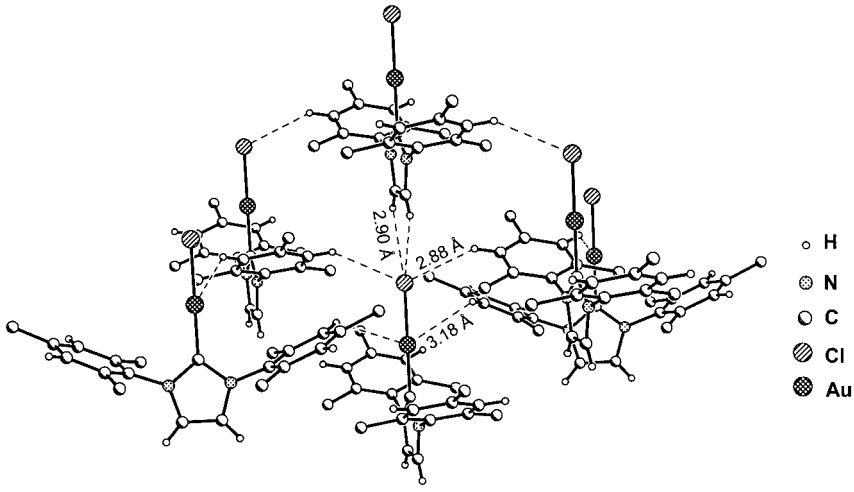

Figure 4. Perspective view of the chain formation through the agostic interaction of the aromatic protons of the carbene ligand with Au and Cl atoms in **1b**.

240 °C respectively. The EI mass spectrum of **2a** revealed the molecular ion peak as the most intense one (*m*/*z* 402), whereas the ion at *m*/*z* 303 in **2b** is the most intense peak and corresponds to the loss of Au and C_2H_2 units from the molecular ion. The IR spectrum of **2a** shows a sharp band (1979 cm^{-1}) which can be attributed to the ethynyl stretching frequency. The corresponding stretching mode for **2b** appears at 1982 cm^{-1}. The ^1H NMR spectrum of **2a** shows the ethynyl proton to resonate at δ = 1.22 ppm whereas the same proton in **2b** resonates at δ = 0.86 ppm. The resonances of the carbene ligand in **2a** and **2b** are shifted downfield relative to the free carbenes. The ^1H NMR spectrum of **2a** shows two singlets (δ = 1.84 and 7.29 ppm) for the protons of the *tert*-butyl groups and (HC=CH) of the carbene. They are shifted downfield relative to the free carbene, (δ = 1.51 and 7.06 ppm). The resonances of *o*-Me and *p*-Me in **2b** (δ = 2.13 and 2.34 ppm) are observed downfield (δ = 2.08 and 2.31 ppm) as well as the (HC=CH) protons

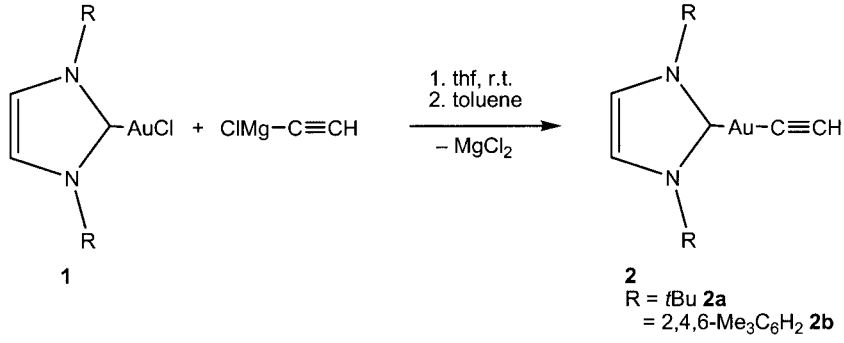

Scheme 2. Synthesis of the monomeric terminal ethynyl Au^I complexes **2a** and **2b**.

 © 2005 Wiley-VCH Verlag GmbH & Co. KGaA, Weinheim

in **2b** (δ = 7.38 ppm) relative to the free carbene (δ = 7.07 ppm). A weak ^{13}C NMR resonance (δ = 187.9 ppm for **2a**) can be assigned to the N–C–N carbon atom and it is shifted downfield relative to **1a** (δ = 167.6 ppm).

Single crystals of **2a** suitable for X-ray structural analysis were obtained from its toluene solution. Repeated efforts to obtain a better data set for **2a** were not successful due to the fast crystal decomposition caused by liberation of the solvating toluene molecules. The most optimistic dataset is reported here. The molecular structure of **2a** is shown in Figure 5 and selected metric parameters are given in Table 1. Compound **2a** is isomorphous to **1a**. The X-ray crystal structure of **2a** reveals that the compound is a monomeric adduct of the N-heterocyclic carbene Au^I acetylide with no Au^I–Au^I interactions. The Au(1)–C(12) distance of 2.04(2) Å in **2a** is similar to that of [($MePh_2P$)AuC≡CH] 2.008(4) Å.[10] The C(12)–C(13) distance of the ethynyl moiety in **2a** [1.11(2) Å] is comparable to that in [($MePh_2P$)AuC≡CH] [1.187(6) Å].[10] The Au(1)–C(12)–C(13) angle of 171.3(2)° in **2a** is comparable to that in [($MePh_2P$)AuC≡CH] [178.9(4)°].[10] The C(1)–Au(1)–C(12) angle in **2a** is close to linearity. The N(1)–C(1)–N(2) angle [107(1)°] is slightly wider than that of the parent compound **1a** [104.5(7)°]. The H····Au agostic interactions observed in the crystal of **2a** are analogous to that of **1a** (Figure 6). Thus the contacts are 2.97 Å and 3.12 Å corresponding to the *o*-H of toluene and H atom of *t*Bu group of the carbene. Due to the disordered toluene molecule in **2a** in two positions with occupancy ratio 87:13 the 2.97 Å distance is attributed to the major 87% part and 3.04 Å distance is attributed to the minor 13% part.

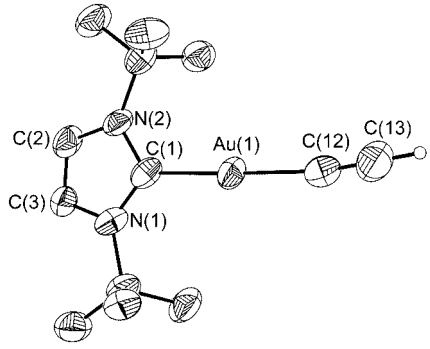

Figure 5. Molecular structure for **2a**. Only the hydrogen atom on the ethynyl group is shown. The toluene molecule is omitted for clarity, thermal ellipsoids are shown with 50% probability.

In summary, we have demonstrated a single step synthesis of N-heterocyclic carbene adducts of gold(I) chloride. The utility of complexes thus synthesized stems from the stability of these complexes which have been used to prepare the first N-heterocyclic carbene gold(I) ethynyl which contains a terminal –C≡CH group.

Experimental Section

All manipulations were performed under a dry and oxygen free atmosphere (N_2 or Ar) using Schlenk line and glove box techniques. Solvents were purified according to conventional procedures and were freshly distilled prior to use. Au(CO)Cl,[23] 1,3-di-*tert*-butylimidazol-2-ylidene and 1,3-dimesitylimidazol-2-ylidene[24] were synthesized according to literature.

Synthesis of (1,3-Di-*tert*-butylimidazol-2-ylidene)gold(I) Chloride (1a): In a glove box a 100 mL Schlenk flask was charged with Au(CO)Cl (1.90 g, 7.30 mmol) and topped with a dropping funnel containing 1,3-di-*tert*-butylimidazol-2-ylidene (1.31 g, 7.25 mmol). Toluene (50 mL) was added to the dropping funnel and the resulting solution was added dropwise to the flask at room temperature. The mixture was stirred until the CO evolution had ceased. It was filtered and the residue was washed with toluene (30 mL). The combined filtrate was concentrated until the compound begins to crystallize and then kept at 0 °C for two days to afford colorless crystals of (1,3-di-*tert*-butylimidazol-2-ylidene)gold(I) chloride **1a** (1.8 g), the mother liquor afforded another crop (0.6 g), combined yield 2.48 g, 83%, m.p. 170 °C (decomp.). $C_{11}H_{20}AuClN_2$ (412): calcd. C 32.04, H, 4.84, N, 6.79; found C 32.27, H, 5.01, N, 6.80. EI-MS: *m/z* (%) 412 (44) [M^+], 376 (14) [M^+ – H – Cl], 356 (14) [M^+ – *t*Bu – H], 320 (100) [M^+ – Cl – *t*Bu], 264 (36) [M^+ – 2 *t*Bu –

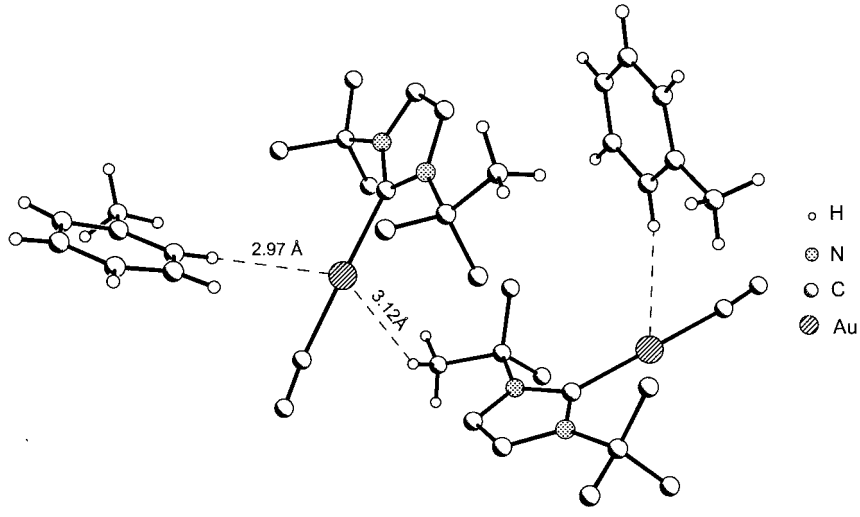

Figure 6. Perspective view of the agostic interactions of Au with *o*-H of the toluene molecule and with H atom of *t*Bu of the carbene ligand in the crystal leading to the formation of a zig-zag chain in the crystal lattice in **2a**.

 © 2005 Wiley-VCH Verlag GmbH & Co. KGaA, Weinheim

Cl – H]. ^{1}H NMR (200 MHz, CD_3CN): δ = 1.83 (s, 18 H, *tBu*), 7.26 (s, 2 H, *HC*=C*H*) ppm. ^{13}C NMR (50 MHz, CD_3CN): δ = 31.2 (s, C*Me*$_3$), 59.0 (s, *C*Me$_3$), 117.7 (s, H*C*=*C*H), 167.6 (s, N*C*N) ppm. IR (KBr, Nujol): $\tilde{\nu}$ = 1646, 1543, 1515, 1406, 1387, 1304, 1262, 1236, 1209, 1183, 1097, 1021, 865, 801, 720, 693, 626 cm^{-1}.

Synthesis of (1,3-Dimesitylimidazol-2-ylidene)gold(I) Chloride (1b): The preparation of **1b** was carried out by using a similar procedure as that for **1a**. The quantities of the reactants used are Au(CO)Cl (1.72 g, 6.60 mmol) and 1,3-dimesitylimidazol-2-ylidene (1.97 g, 6.50 mmol). Yield 2.3 g, 67%, m.p. 210 °C (decomp.). $C_{21}H_{24}AuClN_2$ (536): calcd. C 47.01, H, 4.47, N, 5.22; found C 46.63, H, 4.51, N, 4.95. EI-MS: *m/z* (%) 536 (28) [M$^+$], 500 (92) [M$^+$ – Cl – H], 303 (100) [M$^+$ – Cl – Au – H]. ^{1}H NMR (300 MHz, [D$_8$]THF): δ = 1.75 (s, 12 H, *o*-C*H*$_3$), 2.13 (s, 6 H, *p*-C*H*$_3$), 6.99 (s, 4 H, *m*-*H*), 7.46 (s, 2 H, *HC*=C*H*) ppm. ^{13}C NMR (126 MHz, [D$_8$]-THF): δ = 17.4 (s, *o*-*C*H$_3$), 21.3 (s, *p*-*C*H$_3$), 123.6 (s, H*C*=*C*H), 124.3 (s, mesityl C^{3,5}), 130.0 (s, mesityl C^1), 135.6 (s, mesityl C^{2,6}), 140.2 (s, mesityl C^4).

Synthesis of (1,3-Di-*tert*-butylimidazol-2-ylidene)(ethynyl)gold(I) (2a): (1,3-Di-*tert*-butylimidazol-2-ylidene)gold(I) chloride (1.0 g, 2.43 mmol) was dissolved in THF (30 mL). To this solution was added 5.1 mL (2.55 mmol, 1.05 equiv.) of 0.5 M, THF solution of ethynylmagnesium chloride. The solution was stirred overnight at room temperature and after the removal of all the volatiles, the crude product was extracted with toluene (45 mL). Crude yield (0.72 g, 72%), m.p. 155 °C (decomp.). $C_{13}H_{21}AuN_2$ (402): calcd. C 38.80, H, 5.22, N, 6.96; found C 38.79, H, 5.10, N, 6.85. EI-MS: *m/z* (%) 402 (100) [M$^+$], 376 (20) [M$^+$ –H – HC=CH], 320 (60) [M$^+$ – *t*Bu – HC=CH], 290 (80) [M$^+$ – *t*Bu – HC=CH – 2 Me]. ^{1}H NMR (500 MHz, [D$_8$]THF) 1.22 (s, 1 H, –C≡C*H*), 1.84 (s, 18 H, *t*Bu) 7.29 (d, 2 H, *HC*=C*H*) ppm. ^{13}C NMR (126 MHz, [D$_8$]THF): δ = 32.0 (s, C*Me*$_3$), 59.2 (s, *C*Me$_3$), 89.6 (s, –*C*≡CH), 117.3 (s, H*C*=*C*H), 120.0 (s, –C≡*C*H),187.9 (s, N*C*N) ppm. IR (KBr, Nujol): $\tilde{\nu}$ = 1979, 1665, 1567, 1456, 1407, 1375, 1301, 1261, 1234, 1219, 1194, 1094, 1025, 933, 865, 801, 726, 696, 661, 627, 601 cm^{-1}.

Synthesis of (1,3-Dimesitylimidazol-2-ylidene)(ethynyl)gold(I) (2b): The preparation of **2b** was carried out by using a similar procedure as that for **2a**. The quantities of the reactants used are (1,3-dimesitylimidazol-2-ylidene)gold(I) chloride (1.0 g, 1.86 mmol) and 4.0 mL (2.0 mmol, 1.07 equiv.) of 0.5 M, THF solution of ethynylmagnesium chloride. Yield 0.67 g, 72%, m.p. 240 °C (decomp.). $C_{23}H_{25}AuN_2$ (526.5): calcd. C 52.42, H, 4.74, N, 5.32; found C 51.87, H, 4.82, N, 5.43. EI-MS: *m/z* (%) 526 (64) [M$^+$], 500 (60) [M$^+$ – C_2H – H], 303 (100) [M$^+$ – C_2H – Au – H]. ^{1}H NMR (300 MHz, [D$_8$]THF): δ = 0.86 (s, 1 H, –C≡C*H*), 2.13 (s, 12 H, *o*-C*H*$_3$), 2.34 (s, 6 H, *p*-C*H*$_3$), 7.04 (s, 4 H, *m*-*H*), 7.38 (s, 2 H, *HC*=C*H*) ppm. ^{13}C NMR (75 MHz, [D$_8$]THF): δ = 18.0 (s, *o*-*C*H$_3$), 21.0 (s, *p*-*C*H$_3$), 88.0 (s, –*C*≡CH), 123.5 (s, H*C*=*C*H), 124.4 (s, –C≡*C*H), 130.0 (s, mesityl C^{3,5}), 135.6 (s, mesityl C^1), 136.4 (s, mesityl C^{2,6}), 139.9 (s, mesityl C^4), 190.6 (s, N*C*N) ppm. IR (KBr, Nujol): $\tilde{\nu}$ = 1982, 1730, 1606, 1559, 1484, 1409, 1376, 1339, 1290, 1234, 1164, 1028, 926, 852, 755, 705, 629, 574 cm^{-1}.

X-ray Structure Determinations for 1a, 1b, and 2a: A suitable crystal of each compound was mounted on a glass fiber and coated with paraffin oil. Diffraction data for **1a** and **2a** were collected on a Siemens-Stoe AED2 four-circle instrument and the measurements were made with graphite-monochromated Mo-*K*α radiation (λ = 0.71073 Å). Data for **1b** was obtained on Bruker three circle diffractometer equipped with a SMART 6000 CCD detector using

Table 2. Crystallographic data for the structural analyses of compounds **1a, 1b**, and **2a**.

Compound	**1a**·C_7H_8	**1b**	**2a**·C_7H_8
Formula	$C_{18}H_{28}AuClN_2$	$C_{21}H_{24}AuClN_2$	$C_{20}H_{29}AuN_2$
Fw	504.84	536.84	494.42
T [K]	200(2)	100(2)	200(2)
λ [Å]	0.71073	1.54178	0.71073
Crystal system	monoclinic	orthorhombic	monoclinic
Space group	$P2_1/c$	*Fdd*2	$P2_1/c$
a [Å]	9.355(3)	14.715(3)	9.459(4)
b [Å]	10.291(3)	28.748(6)	10.350(6)
c [Å]	20.56(3)	9.678(2)	20.714(12)
α [deg]	90.00	90.00	90.00
β [deg]	97.84(7)	90.00	98.25(6)
γ [deg]	90.00	90.00	90.00
V [Å^3]	1961(3)	4094(2)	2007(2)
Z	4	8	4
D(calcd.) [g·cm^{-3}]	1.710	1.742	1.636
μ(Mo-*K*α) [mm^{-1}]	7.637	–	7.322
μ(Cu-*K*α) [mm^{-1}]	–	14.732	–
F(000)	984	2080	968
θ Range [deg]	3.59 to 24.98	5.68 to 59.04	3.57 to 24.92
Index range	$-11 \le h \le 11$	$-16 \le h \le 16$	$-11 \le h \le 11$
	$-10 \le k \le 12$	$-31 \le k \le 31$	$-12 \le k \le 12$
	$-23 \le l \le 24$	$-10 \le l \le 10$	$-24 \le l \le 24$
Reflections collected	5093	7611	5214
Independent reflections	3416	1454	3471
Refinement method	Full-matrix least-squares on F^2	Full-matrix least-squares on F^2	Full-matrix least-squares on F^2
Data/restraints/parameters	3416/0/206	1454/1/122	3471/263/278
R_1, R_2 [$I > 2\sigma(I)$][a]	0.0489, 0.1296	0.0127, 0.0299	0.0777, 0.1839
R_1, R_2 (all data)[a]	0.0532, 0.1348	0.0128, 0.0300	0.1021, 0.2084
S	1.092	1.106	1.075
Δρ(min.), Δρ(max.)/e·Å^3	2.660, –2.084	0.487, –0.422	2.814, –3.564

[a] $R_1 = \Sigma||F_o| - |F_c||/\Sigma|F_o|$. $R_2 = [\Sigma w(|F_o^2| - |F_c^2|)^2/\Sigma w|F_o^2|^2]^{1/2}$.

 © 2005 Wiley-VCH Verlag GmbH & Co. KGaA, Weinheim

mirror monochromated Cu-$K\alpha$ radiation (λ = 1.54178 Å) (Table 2). Compound **1b** was refined as a recemic twin with ratio of the components 35.3:64.7. The structures were solved by direct methods using SHELXS-97[25] and refined against F^2 on all data by full-matrix least-squares with SHELXL-97[26]. All non-hydrogen atoms were refined anisotropically. The disordered toluene molecule in **2a** was refined with distance and geometry restrains and restrains for anisotropic displacement parameters. Neutral-atom scattering factors (including anomalous scattering) were taken from the International Tables for X-ray Crystallography. Hydrogen atoms were included at geometrically calculated positions except for protons of the methyl group of disordered toluene molecule in **2a** and refined using a riding model.

Acknowledgments

This work was supported by the Deutsche Forschungsgemeinschaft and the Göttinger Akademie der Wissenschaften. S. S. thanks the Graduiertenkolleg 782 for a fellowship.

[1] K. G. Thomas, P. V. Kamat, *Acc. Chem. Res.* **2003**, *36*, 888–898.
[2] M.-C. Daniel, D. Astruc, *Chem. Rev.* **2004**, *104*, 293–346.
[3] D. H. Brown, W. E. Smith, *Chem. Soc. Rev.* **1980**, *9*, 217–240.
[4] W. A. Herrmann, M. Elison, J. Fischer, C. Kocher, G. R. J. Artus, *Angew. Chem.* **1995**, *107*, 2602–2605; *Angew. Chem. Int. Ed. Engl.* **1995**, *34*, 2371–2374.
[5] S. T. Staben, J. J. Kennedy-Smith, F. D. Toste, *Angew. Chem.* **2004**, *116*, 5464–5466; *Angew. Chem. Int. Ed.* **2004**, *43*, 5350–5352.
[6] C. Nieto-Oberhuber, M. P. Muñoz, E. Buñuel, C. Nevado, D. J. Cárdenas, A. M. Echavarren, *Angew. Chem.* **2004**, *116*, 2456–2460; *Angew. Chem. Int. Ed.* **2004**, *43*, 2402–2406.
[7] G. K. Anderson, *Adv. Organomet. Chem.* **1982**, *20*, 39–114.
[8] R. J. Cross, M. F. Davidson, *J. Chem. Soc., Dalton Trans.* **1986**, 411–414.
[9] J. Vicente, M.-T. Chicote, M.-D. Abrisqueta, P. G. Jones, *Organometallics* **2000**, *19*, 2629–2632.
[10] R.-Y. Liau, A. Schier, H. Schmidbaur, *Organometallics* **2003**, *22*, 3199–3204.
[11] M. J. Irwin, J. J. Vittal, R. J. Puddephatt, *Organometallics* **1997**, *16*, 3541–3547 and references cited therein.
[12] W. Lu, N. Zhu, C.-M. Che, *J. Organomet. Chem.* **2003**, *670*, 11–16.
[13] B.-C. Tzeng, W.-C. Lo, C.-M. Che, S.-M. Peng, *Chem. Commun.* **1996**, 181–182.
[14] H. Xiao, K.-K. Cheung, C.-M. Che, *J. Chem. Soc., Dalton Trans.* **1996**, 3699–3707.
[15] V. W.-W. Yam, S. W.-K. Choi, *J. Chem. Soc., Dalton Trans.* **1996**, 4227–4232.
[16] Stable Carbenes: D. Bourissou, O. Guerret, F. P. Gabbaï, G. Bertrand, *Chem. Rev.* **2000**, *100*, 39–91.
[17] H. M. J. Wang, C. Y. L. Chen, I. J. B. Lin, *Organometallics* **1999**, *18*, 1216–1223.
[18] B. Bovio, A. Burini, B. R. Pietroni, *J. Organomet. Chem.* **1993**, *452*, 287–291.
[19] M. V. Baker, P. J. Barnard, S. K. Brayshaw, J. L. Hickey, B. W. Skelton, A. H. White, *Dalton Trans.* **2005**, 37–43.
[20] H. M. J. Wang, C. S. Vasam, T. Y. R. Tsai, S.-H. Chen, A. H. H. Chang, I. J. B. Lin, *Organometallics* **2005**, *24*, 486–493.
[21] S. Friedrichs, P. G. Jones, *Z. Naturforsch., Teil B* **2004**, *59*, 793–801.
[22] G. Aullón, D. Bellamy, L. Brammer, E. A. Bruton, A. G. Orpen, *Chem. Commun.* **1998**, 653–654.
[23] D. B. Dell'amico, F. Calderazzo, *Gazz. Chim. Ital.* **1973**, *103*, 1099–1104.
[24] A. J. Arduengo, U. S. Patent, **1991**, 5077414.
[25] *SHELXS*-97, *Program for Structure Solution*, G. M. Sheldrick, *Acta Crystallogr. Sec. A* **1990**, *46*, 467–473.
[26] G. M. Sheldrick, *SHELXL-97, Program for Crystal Structure Refinement*, University of Göttingen, Göttingen, Germany, **1997**.

Received February 2, 2005
Published Online: June 22, 2005

 © 2005 Wiley-VCH Verlag GmbH & Co. KGaA, Weinheim

Identification of Copper(II) Binding Sites in the Aminoglycosidic Antibiotic Neomycin B

Małgorzata Jeżowska-Bojczuk,*[a] Wojciech Szczepanik,[a][‡] Stefano Mangani,[b] Elena Gaggelli,[b] Nicola Gaggelli,[b] and Gianni Valensin[b]

Keywords: Bioinorganic chemistry / Aminoglycoside antibiotics / Neomycin B / N,O ligands / Copper

Protonation and copper(II) coordination properties of neomycin B were studied in solution by potentiometry, NMR, UV/Vis, CD, and EPR spectroscopy, XAS and mass spectrometry. Mono- and dinuclear complexes were found depending on the metal-to-ligand molar ratio. Neomycin B anchors Cu^{II} ions above pH 5.0 with an NH_2 group from ring B. Simultaneously, the second amino group of the same ring and the hydroxyl group of ring A complete the binding set of donors. With an increase in pH the remaining $-NH_3^+$ functional groups in the neomycin B molecule are deprotonated without affecting the complexation pattern. However, these groups, particularly the ones located in the D-ring of the antibiotic, may coordinate the second copper(II) ion when the metal is present in excess. We have proved this process with the use of potentiometry, CD and especially mass spectrometry.

(© Wiley-VCH Verlag GmbH & Co. KGaA, 69451 Weinheim, Germany, 2005)

Introduction

Neomycins are aminoglycoside antibiotics produced by *Streptomyces fradiae* as a mixture of three analogues A, B and C. Only neomycin B is used in therapy and it is active against gram-negative aerobic bacteria and *Staphylococcus.* It is topically or orally applied, mainly prior to surgical interventions of the intestine. Parenteral administration of the drug may result in oto- and nephrotoxic effects much more acute than for any other aminoglycoside.[1] A possible explanation was recently provided in our studies,[2] showing that (i) neomycin has the highest potency in cleaving $tRNA^{Phe}$ and (ii) the Cu^{II}-neomycin complex disproportionates H_2O_2 to hydroxyl radicals, as well as oxidizes plasmid DNA with the highest efficiency.

Coordination of aminoglycosides by Cu^{II} ions was extensively investigated[3–6] and evidence was reached for copper selectively yielding high stability complexes over other transition metal ions.[7] Although not present at very high levels intracellularly, the amount of copper(II) in the plasma reflects the state of health of the organism. Under circumstances when antibiotics are applied (e.g. inflammation), the serum level of copper may drastically increase,[8] probably as a result of leukocyte activation that releases even micromolar amounts of copper and iron as well.[9] Increased concentrations of Cu^{II} ions in selected tissues are also observed during the appearance of cancer, anemia[10] or hyperthyroidism.[11] Thus chelation of the metal by xenobiotics, e.g. drugs, may occur in vivo.

The coordination abilities of neomycin B (Figure 1) have not been thoroughly investigated to date. Formation of solid polymeric complexes has been observed with selected transition metal ions but without any evidence of amino groups being involved in binding.[12] The characteristics of the Cu^{II} complex of neomycin B in solution have also been delineated, but the final determined structure concerns only the coordination of neamine,[13] a subunit of neomycin B

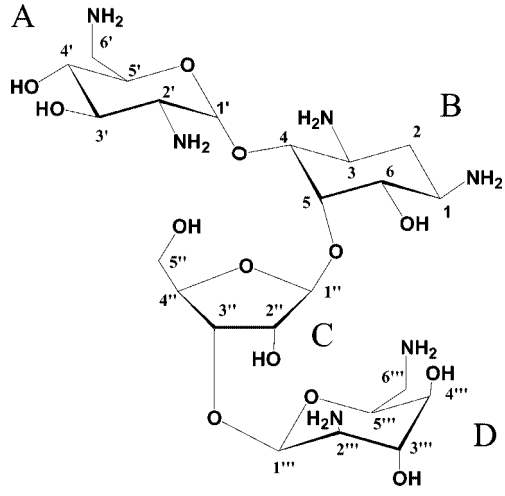

Figure 1. Molecular structure of neomycin B.

[a] Faculty of Chemistry, University of Wrocław,
F. Joliot-Curie 14, 50-383 Wrocław, Poland
Fax: +48-71-3282-348
E-mail: mjb@wchuwr.chem.uni.wroc.pl
[b] Department of Chemistry, University of Siena,
Via Aldo Moro, 53100 Siena, Italy
[‡] Supported by the Foundation for Polish Science (FNP) with the Annual Stipend for Young Scientists.
Supporting information for this article is available on the WWW under http://www.eurjic.org or from the author.

(see rings A and B, Figure 1). The aim of the current study is to gain deeper insight into the Cu^{II}-neomycin binding equilibria depending upon pH and metal ion-to-antibiotic molar ratio.

Results and Discussion

Protonation of Neomycin B

The protonation constants calculated on the basis of potentiometric titrations are presented in Table 1. They correspond to six amino groups present in this hexaprotic antibiotic molecule. Both amino sugar rings (A and D) and the 2-deoxystreptamine ring (B) contain two amino group substituents. Only the pentose ring (C) has no protonating function (Figure 1). The location of the amino groups causes equal distribution of the positive charge within the neomycin B molecule.

Table 1. Protonation and stability constants of neomycin B and its copper(II) complexes.

Protonation constants of neomycin B			Stability constants of Cu^{II}-neomycin B		
species	log β	pK	species	log β	pK
LH_6	46.575(2)	5.69	CuH_3L	31.80(4)	–
LH_5	40.885(2)	7.02	CuH_2L	26.24(1)	5.56
LH_4	33.865(2)	7.603	CuHL	19.02(1)	7.22
LH_3	26.262(3)	8.147	CuL	10.94(1)	8.08
LH_2	18.115(2)	8.745	$CuH_{-1}L$	1.97(1)	8.97
LH	9.370(2)	9.370	$CuH_{-2}L$	–7.99(1)	9.96

Almost all pK_a values are typical for amino functions and fit the characteristic range 7–9 (Table 1), except the first one which is much lower (pK_a = 5.69) in agreement with previous ^{15}N NMR spectroscopic measurements.[14] Such low values of the first deprotonation constant were also found for all other aminoglycosides studied so far: 6.0 for geneticin[3] and kanamycin A[4] that have a +4 charge at low pH, and 5.7 for the +5 charged kanamycin B[5] and tobramycin.[6] Neomycin with its six amines has an almost identical value for this constant as do the pentaprotic antibiotics. Therefore, the decrease in the first pK_a of the aminoglycosides is likely to arise from a local electrostatic interaction between neighboring NH_3^+ groups within the same ring,[4,5,14] rather than from the overall charge of the entire molecule.

All the successive deprotonations are separated from one another by only ca. 0.6 log units (Table 1). The statistics on the deprotonation of bifunctional molecules indicate that each of the two processes is almost parallel (the "ideal" statistical log value is 0.6[15]). ^{15}N NMR spectroscopy allowed us to calculate the pK values and assign them to each amino group of the antibiotic molecule.[14] In spite of diverse experimental conditions, the calculated constants agree with our determinations.

Copper(II) Complexation by Neomycin B

Neomycin B offers more potential possibilities for copper(II) chelation when compared with previously investigated aminoglycoside antibiotics.[3–6] This antibiotic forms six complexes with cupric ion in the pH range 5.5 to 10. At a 1:1 molar ratio or at an excess of the antibiotic, only monomeric complexes are formed in solution, as confirmed by potentiometry and mass spectrometry measurements (Table 1 and Table 2). The first minor species, which starts to occur at pH ca. 5, has CuH_3L stoichiometry (H_6L represents the fully protonated ligand). It is a common feature of the Cu^{II}-aminoglycoside complexes that the binding process is accompanied by a two-proton loss, which results from chelate ring formation by the amine nitrogen and a neighboring hydroxyl oxygen with simultaneous deprotonation of the latter. Cu^{II} anchoring then proceeds at the 3 amino group of the deoxystreptamine ring B due to its lowest deprotonation constant value.[14] In the case of neomycin B there is an additional deprotonation of another amine function. This event is very likely to occur at one of the bisaminated rings (A or D) due to the mentioned electrostatic interaction, but not in ring (B), where Cu^{II} is already bound. A {N,O} type chelation therefore occurs, with deprotonation of another amine, without its involvement in coordination. However, the CuH_3L species exists at too low

Table 2. Summary of the observed ESI-MS ions (m/z) at pH 8.0 {$(NH_4)_2CO_3$, 5 mM} for neomycin B (L) and its Cu^{II} complex. Concentrations: Cu^{II} 0.25 or 0.5 mM and L 0.25 mM.

Components	$m/z_{obsd.}$	$m/z_{calcd.}$	Assignment
neomycin B	308.5[w]	308.4	L – rings C and D + H^+
	456.3[w]	455.5	L – ring A or D + H^+
	616.5[s]	615.6	L + H^+
Cu^{II}-neomycin, 1:1	371.4[s]	370.9	Cu^{II}–L – rings C and D – OH + H^+
	388.3[i]	387.9	Cu^{II}–L – rings C and D + H + H^+
	503.4[w]	503.0	Cu^{II}–L – ring A or D – OH + H^+
	677.7[i]	677.3	Cu^{II}–L + H^+
			and all peaks seen for neomycin B
Cu^{II}-neomycin, 2:1	446.4[w]	446.1	Cu^{II}_2–L – rings C and D + H + H^+
	738.9[i]	738.2	Cu^{II}_2–L + H+
			and all peaks seen for neomycin B
			and Cu^{II}-neomycin B, 1:1

w – weak, i – intermediate, s – strong signal.

 © 2005 Wiley-VCH Verlag GmbH & Co. KGaA, Weinheim

a fraction (12% of total Cu^{II} amount, Figure 2) to allow unambiguous delineation of its characteristics.

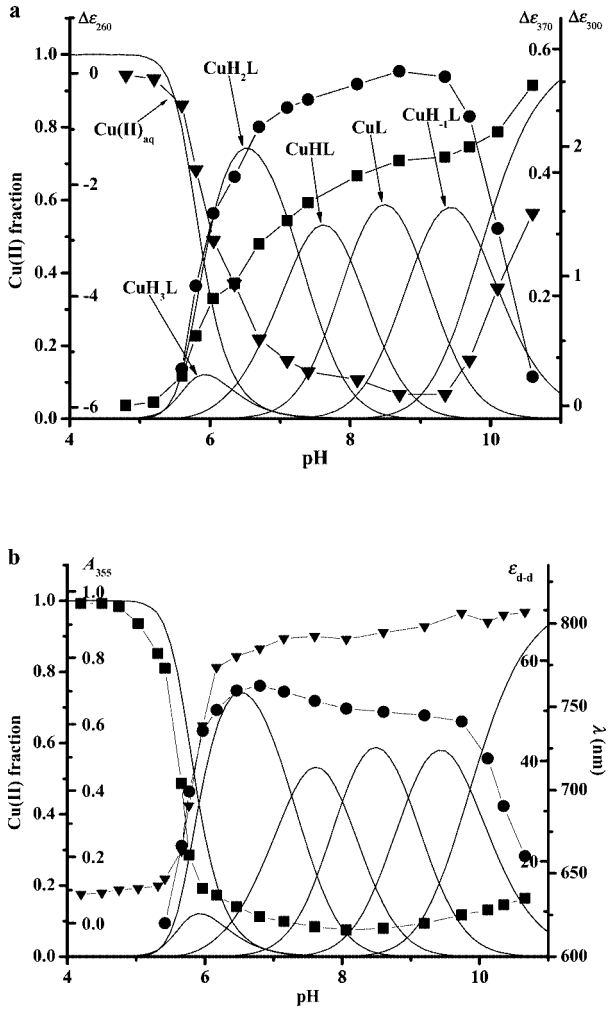

Figure 2. The speciation diagram for the Cu^{II}-neomycin B system with CD spectral parameters overlaid (a): $\Delta\varepsilon$ of CT bands at: 260 nm (▼), 300 nm (■) and 370 nm (●), as well as UV/Vis spectra parameters overlaid (b): ε (▼) and λ (■) of d-d band and shoulder at 355 nm (●). $\Delta\varepsilon$ and ε are in M^{-1} cm^{-1}.

This form is followed by a major species, CuH_2L complex, which prevails over the first at almost the same pH range. The stability constants of both complexes differ by ca. 5.6 log units, in agreement with the deprotonation of another amine nitrogen. However, this value is too low for a spontaneous proton loss and seems to be forced by another electron pair acceptor. If this further deprotonation proceeds at the same ring, where Cu^{II} is already bound, then another deprotonated nitrogen will also be engaged in the coordination process and {N,N,O} type chelation will occur. The results, obtained from spectroscopic measurements confirm that the CuH_2L species involves two nitrogen atoms coordinated to the central metal ion.

In order to establish the coordination pattern of this species unambiguously, ^1H and ^{13}C NMR spectroscopic methods were applied. The chemical shifts (ppm) of neomycin B are summarized in Table 3. Spectral assignment was achieved by COSY and ROESY experiments, by ^{13}C ^1H 2D shift correlated maps and by comparison with reference data.[16,17] Addition of copper to the solution of neomycin and pH adjustment to 6.8, where the CuH_2L complex reaches its maximum concentration, were not very effective in enhancing the nuclear relaxation rates. This fact is reflected by the relatively small values of R_{1p} (Table 4), where R_{1p}, the paramagnetic contribution to the spin-lattice relaxation is defined by Equation (1).

Table 3. ^1H and ^{13}C NMR chemical shift (ppm) of neomycin B 9.9 mM in D_2O at pH 6.8 (value uncorrected for the isotopic effect), T = 298 K and with TSP-d_4 as internal reference standard.

Ring	Proton	δ (ppm)	Carbon	δ (ppm)
B	1	3.31	1	54.04
	2_{ax}, 2_{eq}	1.73, 2.33	2	34.32
	3	3.28	3	51.87
	4	3.70	4	81.92
	5	3.90	5	88.24
	6	3.70	6	76.30
A	1′	5.97	1′	98.72
	2′	3.43	2′	56.98
	3′	3.99	3′	72.24
	4′	3.25	4′	73.95
	5′	4.06	5′	71.87
	$6'_{a,b}$	3.49, 3.28	6′	43.27
C	1′′	5.42	1′′	113.00
	2′′	4.45	2′′	76.39
	3′′	4.57	3′′	78.07
	4′′	4.24	4′′	84.09
	$5''_{a,b}$	3.93, 3.77	5′′	63.40
D	1′′′	5.31	1′′′	98.64
	2′′′	3.60	2′′′	53.44
	3′′′	4.26	3′′′	71.04
	4′′′	3.84	4′′′	70.38
	5′′′	4.35	5′′′	73.37
	$6'''_{a,b}$	3.45, 3.40	6′′′	43.39

$$R_{1p} = R_{1obs} - R_{1f} = \frac{p_b}{R_{1M}^{-1} + \tau_M} \quad (1)$$

where: R_{1obs} and R_{1f} are the spin-lattice relaxation rates measured in the presence and in the absence of the metal respectively, τ_M is the exchange lifetime from the bound to the free state, p_b is the molar fraction of the bound ligand, and R_{1M} is the spin-lattice relaxation rate of the copper-bound ligand. R_{1M} is accounted for by the following simplified equation [Equation (2)] reporting the dipole-dipole interaction, as provided by the Solomon–Bloembergen–Morgan theory.[18]

$$R_{1M} = \frac{1}{10}\left(\frac{\mu_0}{4\pi}\right)^2 \frac{\hbar^2\gamma_I^2\gamma_S^2}{r^6}\left\{\frac{\tau_c}{1+(\omega_I-\omega_S)^2\tau_c^2} + \frac{3\tau_c}{1+\omega_I^2\tau_c^2} + \frac{6\tau_c}{1+(\omega_I+\omega_S)^2\tau_c^2}\right\} \quad (2)$$

where: μ_0 is the vacuum permeability, γ_I and γ_S are the nuclear and electron magnetogyric ratios, ω_I and ω_S are the proton and electron Larmor frequencies, respectively, r is the proton–Cu^{II} distance and τ_c is the effective correlation time.

The proton spin-lattice relaxation rates were selectively affected, as also reported in Table 4, while no sizeable

 © 2005 Wiley-VCH Verlag GmbH & Co. KGaA, Weinheim

change in chemical shift was detected. The relatively larger R_{1p} values experienced by the 2_{ax}, 2_{eq}, 5 and 1′ protons suggest that rings A and B of neomycin B are directly involved in the coordination of the Cu^{II} ion. ^{13}C paramagnetic relaxation rates, together with potentiometric data (Table 1 and Table 5), moreover suggest the 1 and 3 deprotonated amino groups (ring B) and 4′ deprotonated hydroxyl group (ring A) as the possible donor set.

Table 4. Paramagnetic contributions to proton longitudinal relaxation rates (R_{1p}, s^{-1}) of neomycin B, 9.9 mM in D_2O at pH 6.8 (value uncorrected for the isotopic effect), T = 298 K. Contributions were calculated as the difference between the R_1 values in the presence (R_{1obs}) and in the absence (R_{1f}) of $Cu(NO_3)_2$ [ratio Cu^{II}-neomycin: 1:100] and converted into copper-proton distances r_{Cu-H} through Equations (1) and (2) using $\tau_C = 2.73 \times 10^{-10}$ s and $\tau_M = 6.00 \times 10^{-4}$ s. Missing values are due to overlap among protons of the same ring.

Proton	R_{1f}	R_{1obs}	R_{1p}	R_{1M}	r_{Cu-H} [nm]
1, 3, 4, 6	–	–	–	–	–
2_{ax}	2.297	3.569	1.272	–18962	very near
2_{eq}	2.456	3.532	1.076	21564	0.276
5	1.337	2.276	0.939	7101	0.332
1′	1.165	2.336	1.171	–186079	very near
2′–6′	–	–	–	–	–
1″	0.976	1.596	0.620	2017	0.412
2″	0.826	1.207	0.381	835	0.475
3″	1.104	1.510	0.406	922	0.468
4″	0.865	1.432	0.567	1665	0.425
5″a	1.842	2.787	0.945	9019	0.330
5″b	1.974	2.772	0.798	4069	0.370
1‴	1.146	1.768	0.622	2032	0.412
2‴	0.818	1.799	0.981	11836	0.318
3‴	0.772	1.874	1.102	145752	0.259
4‴	1.058	1.687	0.629	2084	0.410
5‴	1.194	1.817	0.623	2039	0.328
6‴ab	1.771	2.721	0.95	9341	0.317

The correlation time in Equation (2) is generally determined by rotation of the metal complex. The reorientational dynamics of the complex was approximated by evaluating the motional correlation time of the free antibiotic in a water solution. This was accomplished by measuring the value of the cross-relaxation rate, σ, of the 2_{ax} and $2_{equiv.}$ protons of the ring B by means of Equation (3).[19]

$$\sigma = R^{bsel} - R^{sel} = \frac{1}{10}\left(\frac{\mu_0}{4\pi}\right)^2 \frac{\gamma_H^4 \hbar^2}{r^6}\left(\frac{6\tau_c}{1+4\omega_H^2\tau_c^2} - \tau_c\right) \quad (3)$$

where: r is the distance between vicinal protons (0.177 nm), and R^{bsel} and R^{sel} are the double- and single-selective spin-lattice relaxation rates, respectively. The value obtained was $\tau_c = 0.27 \pm 0.05$ ns at 298 K.

As stated in Equation (1), exchange of the ligand between free and bound states must be considered. In fact

Table 5. Paramagnetic contributions to carbon longitudinal relaxation rates (R_{1p}, s^{-1}) of neomycin B 9.9 mM in D_2O at pH 6.8 (value uncorrected for the isotopic effect), T = 298 K. Contributions were calculated as the difference between the R_1 values in the presence (R_{1obs}) and in the absence (R_{1f}) of $Cu(NO_3)_2$ [ratio Cu^{II}-neomycin B: 1:100] and converted into copper-carbon distances r_{C-Cu} [nm].

Carbon	R_{1f}	R_{1obs}	R_{1p}	r_{C-Cu} [nm]
1	2.196	3.812	1.616	0.337
2	2.669	2.900	0.231	0.465
3	3.417	6.716	3.299	0.293
4	2.463	3.223	0.760	0.384
5	2.611	3.401	0.790	0.382
6	2.313	2.477	0.164	0.491
1′	2.402	4.014	1.612	0.337
2′	3.004	4.954	1.950	0.325
3′	2.562	3.222	0.640	0.393
4′	2.487	3.401	0.914	0.372
5′	2.687	2.959	0.272	0.454
6′	3.994	4.009	0.015	0.603
1″	2.285	2.703	0.418	0.425
2″	2.462	3.206	0.744	0.386
3″	2.702	2.724	0.022	0.615
4″	2.569	3.175	0.606	0.399
5″	4.887	4.147	–0.740	–
1‴	2.976	4.022	1.046	0.363
2‴	2.405	3.262	0.857	0.377
3‴	2.287	3.160	0.873	0.375
4‴	2.451	3.406	0.955	0.370
5‴	2.163	3.175	1.012	0.366
6‴	3.702	4.156	0.454	0.417

R_{1M}, the structure-sensitive parameter, can be directly obtained from Equation (2) only in cases where fast exchange conditions ($R^{-1}_{1M} >> \tau_M$) prevail. The unusually small, although diverse, R_{1p} values suggest, by themselves, occurrence of a slow-intermediate exchange region, where R^{-1}_{1M} is equal or slightly smaller than τ_M. This being the case, both R^{-1}_{1M} and τ_M would contribute to R_{1p}. The contribution of exchange was measured by the temperature dependence of R_{1p}, which is well known in the literature.[20]

The temperature dependencies of the R_{1p} values of some protons are shown in Figure 3. The plots suggest that slow exchange conditions prevail (this justifies the relatively small paramagnetic effects), but that R_{1p} is close to its maximum where intermediate exchange conditions dominate. The exchange rates were calculated by fitting the initial part of the temperature dependent R_{1p} data (where $R_{1p} \approx p_b k_{off} = p_b/\tau_M$, τ_M being the exchange lifetime) with the Eyring equation [Equation (4)].[20]

$$\tau_M^{-1} = \frac{kT}{h} e^{-\frac{\Delta G^\#}{RT}}$$

$$\ln[R_{1p}] = \ln\left[p_b \frac{kT}{h}\right] - \frac{\Delta G^\#}{RT} \quad (4)$$

where: $\Delta G^\#$ is the free energy of activation for the dissociation process and p_b is approximated to the [Cu^{II}]/[neomycin B] ratio. An average value of $\tau_M = 0.60 \pm 0.03$ ms could be calculated.

 © 2005 Wiley-VCH Verlag GmbH & Co. KGaA, Weinheim

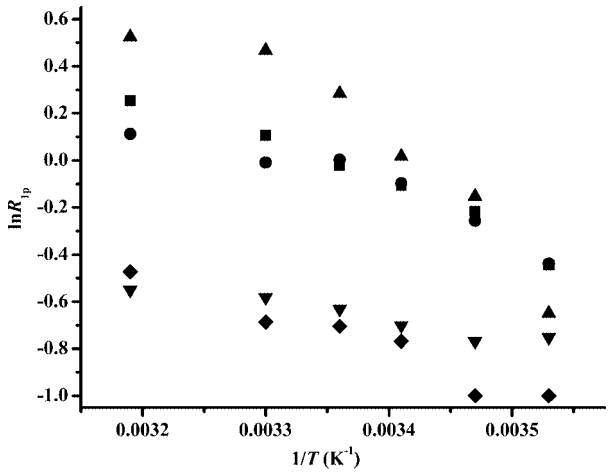

Figure 3. Temperature dependencies of paramagnetic relaxation rates (R_{1p}) of selected protons of neomycin B (9.9 mM) in D_2O (pH 6.8), in the presence of Cu^{II} ions at a concentration of 0.099 mM: 2_{ax} of ring B (■); 2_{eq} of ring B (●); 1′ of ring A (▲); 1″ of ring C (▼); 1‴ of ring D (♦).

Introducing the exchange time value into Equation (1) allowed us to extract all R_{1M} values from the R_{1p} ones. Since Equation (2) provides R_{1M} as a function of τ_c/r^6, taking the value of τ_c for the free ligand to be 0.27 ± 0.05 ns at 298 K, allowed us to calculate all copper–proton and copper–carbon distances, also shown in Table 4 and Table 5. The approximation used is not expected to introduce large errors in the calculated distances because the r^6 dependence minimizes even large errors (up to 50%) in the motional correlation time. The distances were then used as restraints in order to calculate the structure of the Cu^{II}-neomycin B complex in aqueous solution at pH 6.8. The suggested structure was supported by molecular mechanics and dynamics: an energy-minimized molecular model of Cu^{II}-neomycin B complex (Figure 4) was obtained by using the HYPERCHEM graphics package. The stick model of the complex shows the Cu^{II} ion bound to the two deprotonated amino groups of ring B, the 4′ deprotonated hydroxyl group of ring A and a water molecule added to reach the minimum set of donors. The 3‴-OH (ring D) and the 3-NH_2 (ring B) were found at a typical hydrogen bonding distance, such that further stabilization of the complex may be hypothesized. The obtained structure suggests that neomycin B wraps around Cu^{II} in a way that leaves the metal ion exposed to the water medium.

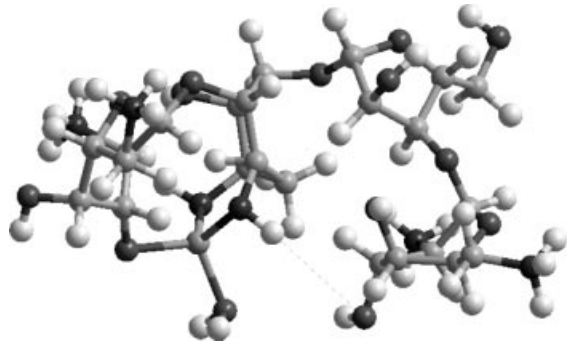

Figure 4. Structural model of the Cu^{II}-neomycin B 1:1 complex in water solution. The dashed line represents the hydrogen bond.

The above coordination model of CuH_2L is also supported by other spectroscopic methods (Table 6). The values of the A_{II} and g_{II} parameters calculated from the EPR spectra confirm the number of nitrogen donors around the metal ion. Moreover, the parameters of charge-transfer bands (CD, UV/Vis) and d-d bands (UV/Vis) change significantly with an increase in the concentration of this species (see Figure 2). The formation of two positive and one negative Cotton effects in the CD spectra (Figure 2, part a, Table 6) is observed. The effects at 260 and 300 nm most probably correspond to $NH_2 \rightarrow Cu^{II}$ CT transitions and those at 370 nm to the $O^- \rightarrow Cu^{II}$ one. The distinct shoulder on electronic absorption spectra around 355 nm suddenly appears around pH 5.5 and its intensity also increases with the rise of the CuH_2L fraction (Figure 2, part b). The d-d band parameters obtained from UV/Vis spectra reflect these changes, while the intensity of this band in the CD spectra is very low and remains at this level until about pH 10 (Figure 2, part b). It is worth stressing that all applied spectroscopic methods show persistence of spectral parameters with the appearance of the following three species. With an increase of pH to 9 solutions containing CuHL, CuL and $CuH_{-1}L$ complexes give very similar spectra. All these species differ from each other by the proton contents only. The values of their deprotonations fit the range 7–9, characteristic for amine group deprotonation.

Table 6. Spectroscopic parameters of particular complex forms of Cu^{II}-neomycin B, 1:1 system.

Species	UV/Vis[a]		CD[a]		EPR[b]	
	λ	ε	λ	$\Delta\varepsilon$	$A_{\parallel}$	$g_{\parallel}$
			700[c]	–0.23		
CuH_2L + CuHL +	616	65	370[d]	+0.54	184	2.24
CuL + $CuH_{-1}L$	356[sh]	270	300[e]	+1.77		
			261[e]	–5.51		

[a] λ [nm], ε and $\Delta\varepsilon$ [M^{-1} cm^{-1}]. [b] A_{II} [Gs]. [c] d-d transition band. [d] CT: $O^- \rightarrow Cu^{II}$. [e] CT: $NH_2 \rightarrow Cu^{II}$, [sh] shoulder.

At about pH 10, the solution of the Cu^{II}-neomycin complex changes its color from deep blue to violet. CD spectra obtained under these conditions present a total disappearance of the charge-transfer band at 370 nm and a distinct decrease of the band intensity at around 260 nm, probably suggesting the stepwise hydrolysis of the bound neomycin molecule, as already reported.[13] Mass spectra recognize this process already at pH 8.0, though to a very low extent (Table 2).

Two-Centered Cu^{II}-Neomycin B Complexes

A unique feature of the copper(II)-neomycin system is the formation of two-centered complexes, occurring at excess concentrations of the metal ion. Such complexes appear below pH 6, although in the pH range 4–6 mononuclear species also occur (Figure 5). However, their concentration

 © 2005 Wiley-VCH Verlag GmbH & Co. KGaA, Weinheim

does not exceed 15% of the total amount of Cu^{II}. It is worth noting that species having the stoichiometry CuH_5L and CuH_4L, present in this system, do not appear in potentiometric titrations for the equimolar Cu^{II}-antibiotic system. It therefore seems likely that either the double excess of Cu^{II} ions over neomycin favors its deprotonation, and subsequent coordination to the metal, or the concentration of both complexes in the 1:1 system is too low for pH-metric detection. Table 7 shows the stability constants for dinuclear species, while Figure 5 presents the course of CD spectral parameters depending on the pH of the solution. The $\Delta\varepsilon$ values of d-d transition bands both for 1:1 and 2:1 systems are overlaid on the speciation diagram for the dinuclear Cu^{II}-neomycin complexes. Apparently, with an excess of the metal ion, an increase of the d-d band intensity follows the formation of the two-centered complexes. Around pH 7.5, where only the 2:1 complexes exist in solution, the CD parameters are stable (Figure 5).

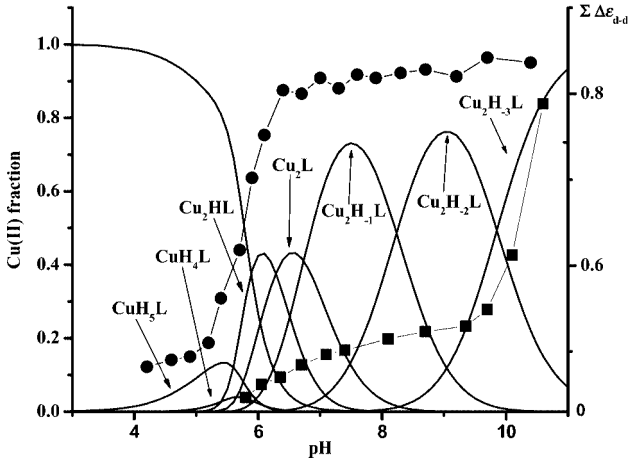

Figure 5. The speciation diagram for Cu^{II}-neomycin B complex at 2:1 molar ratio with $\Delta\varepsilon$ of d-d bands on CD spectra obtained for the 1:1 (■) and 2:1 (●) systems overlaid.

Table 7. The stability constants calculated for the system containing Cu^{II} ions and neomycin B at the molar ratio 2:1.

CuH_5L	43.73(3)
CuH_4L	37.64(6)
Cu_2HL	23.90(3)
Cu_2L	17.62(2)
$Cu_2H_{-1}L$	10.89(1)
$Cu_2H_{-2}L$	2.65(6)
$Cu_2H_{-3}L$	–7.19(2)

In order to ascertain the possibility of a Cu–Cu interaction, XAS spectra were obtained. Figure 6 shows the edge region of the spectra of the studied samples indicating different copper environments while keeping the edge energy values characteristic of Cu^{II} constant, as judged by the position of the main transition at about 8990 eV. The edge shape is characteristic for Cu^{II} complexed to nitrogen or oxygen donors.[21] The 1s-3d pre-edge absorption at ca. 8980 eV are all extremely small and indicate centrosymmetric Cu^{II} binding sites as present in Jahn–Teller distorted tetragonal or square-planar copper complexes.[22] Hence we conclude that the concentrated samples (1 and 2), regardless of the molar ratio, show similar edges resembling that of the free Cu^{II}_{aq}, while the 2 mM sample (3) displays 1s-4p transitions at about 8988 eV and more complex white line transitions (see Figure 6).

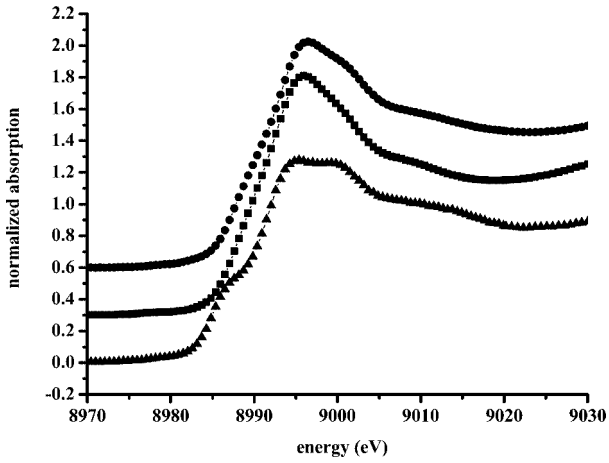

Figure 6. Comparison of the X-ray absorption edges for the Cu^{II}-neomycin B 2:1 complex, Cu^{II} 100 mM (■), Cu^{II}-neomycin B 2:1 complex, Cu^{II} 2 mM (▲) and Cu^{II}-neomycin B 1:1 complex, Cu^{II} 100 mM (●).

The EXAFS spectrum of the Cu^{II}-neomycin B complex 2:1, (100 mM, sample 1) together with its Fourier transform is reported in Figure 7, parts a,b. The spectrum is characteristic of all light O/N type scatterers and, despite the presence of slight distortions due to multiple scattering effects from outer shell atoms, it can be well simulated without introducing multiple scattering contributions into the calculations. The contribution to the total EXAFS of the first shell ligand can be evaluated in four O/N divided into two shells of two donors at 1.94(1) Å and two donors at 2.02(1) Å (see Table 8). Adding a further shell of two N/O atoms at 2.74(2) Å significantly improves the fit leading to a classical Jahn–Teller distorted elongated octahedron for the Cu^{II} coordination. As already indicated by the edge shape the EXAFS spectrum of sample 2 (Cu^{II}-neomycin B 1:1 complex, 100 mM) as with the previous one, can be simulated by a 4+2 type of Cu^{II} coordination consisting of four N/O atoms at 1.98(1) Å and two N/O atoms at 2.32 Å and 2.83 Å, respectively.

Due to the low copper concentration the spectrum of sample 3 (Cu^{II}-neomycin B 2:1 complex, 2 mM) is much noisier than the others. However, the EXAFS (Figure 8, a) displays features, which can be reproduced only by introducing multiple scattering (MS) path contributions from atoms lying in a rigid scaffold containing almost colinear arrangements of atoms. Together with the shape of the edge region, this evidences a significantly different Cu^{II} coordination with respect to the same complex in a more concentrated solution (sample 2). Here Cu^{II} is bound to two N/O atoms at 1.96(1) and 2.00(1) Å and two N/O atoms at 1.91(1) and 1.96(1) Å. The outer shell features evident in the spectrum Fourier transform (Figure 8, b) can be adequately modeled by the MS from outer shell atoms bound

 © 2005 Wiley-VCH Verlag GmbH & Co. KGaA, Weinheim

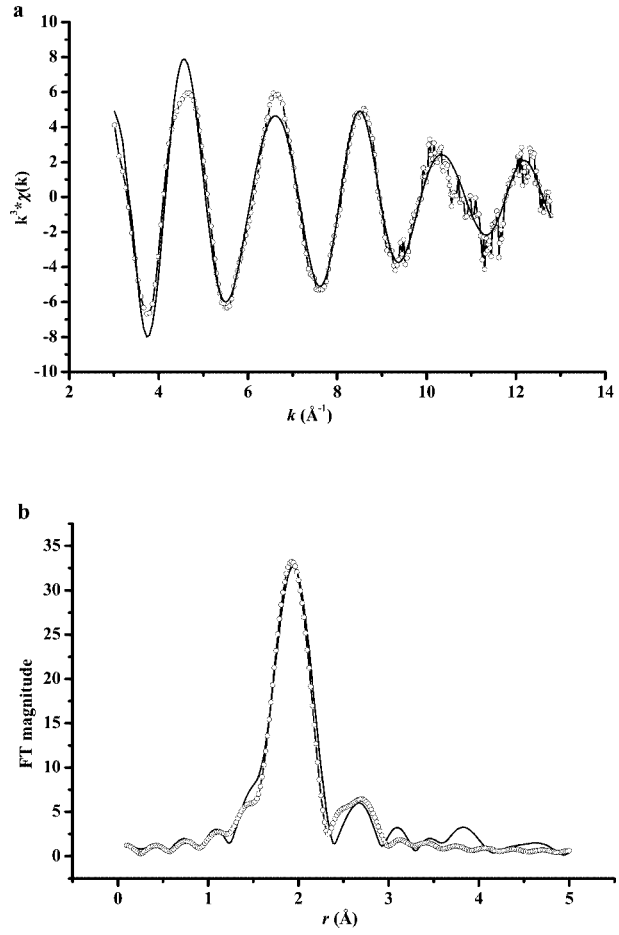

Figure 7. Comparison of experimental (open circles) and theoretical (continuous line) EXAFS data (a) and of their Fourier transform (b) for the Cu^{II}-neomycin B 2:1 complex at 100 mM concentration.

Table 8. Results of data analysis of the full EXAFS spectra for the Cu^{II}-neomycin B, 1:1 and 2:1 systems.

Sample	Shell	Distance [Å]	DWF[a] $2\sigma^2$ [Å^2]	R_{exafs}[b] (%)	FI[b]
1	2N/O	1.93(1)	0.004(1)	24.5	0.39
	2N/O	2.01(1)	0.004(1)		
	2N/O	2.74(2)	0.016(2)		
2	4N/O	1.98(1)	0.008(2)	27.0	0.42
	1N/O	2.32(1)	0.003(2)		
	1N/O	2.83(2)	0.008(3)		
3 (MS)	1N/O	1.96(1)	0.004(2)	42.1	0.69
	1N/O	2.00(1)	0.005(1)		
	1N/O	1.91(1)	0.002(1)		
	1N/O	1.96(1)	0.002(2)		
	1C	2.78(2)	0.009(2)		
	1C	2.75(2)	0.002(2)		
	1N	4.04(2)	0.009(3)		
	1O	3.98(1)	0.014(4)		

[a] DWF is the Debye–Waller factor. [b] R_{exafs} and the fit index (FI) are indicators of the fit quality as reported in the Experimental Section.

to a rigid, bidentate, N/O type ligand. The presence of MS effects makes it impossible to detect the probable presence of two axial O/N ligands between 2.3–2.8 Å as seen in samples 1–2.

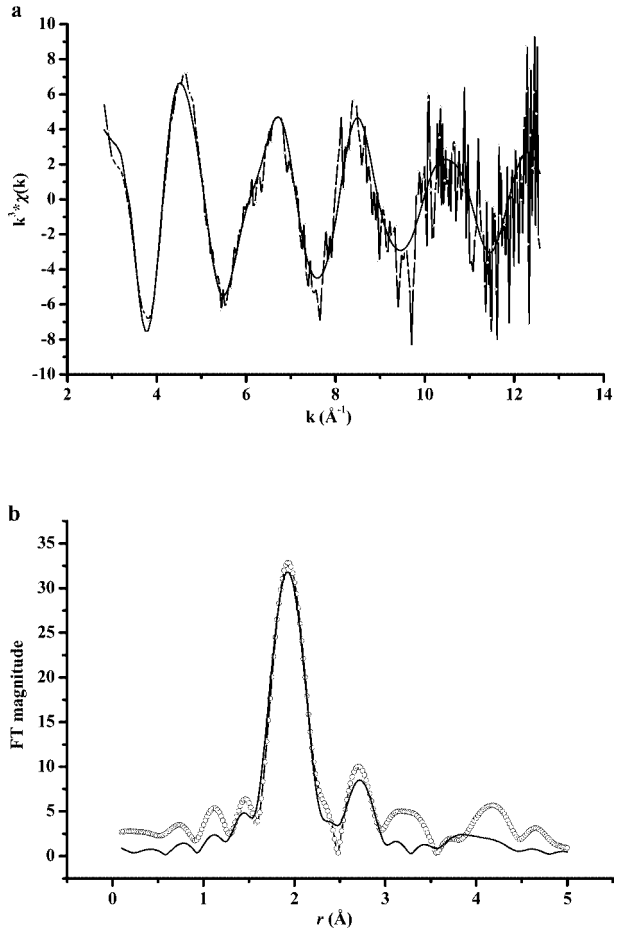

Figure 8. Comparison of experimental (open circles) and theoretical (continuous line) EXAFS data (a) and of their Fourier transform (b) for the Cu^{II}-neomycin B 2:1 complex at 2 mM concentration. The fitting parameters are reported in Table 8.

EXAFS is able to detect metal-metal distances when they are in the 3.5–4.0 Å range. Furthermore, at longer distances the Cu–Cu scattering in nonordered systems like solutions is very weak and can be hidden in the background due to the scattering of light atoms (C, N, O), lying at about the same distance from the metal.[23] However, there is no evidence of Cu–Cu scattering in the case of the neomycin complexes. If there are two Cu atoms bound per neomycin molecule, they should be located at distances larger than 3.5 Å. Lack of the spin relaxation on the EPR spectra, which were obtained under the same conditions, confirms that both metal ions are separated and are most probably located at different rings of the antibiotic.

Mass spectrometry brings additional evidence for the Cu^{II}_2-neomycin complex formation. The distinct peak at *m*/*z* of ca. 739 is observed (Table 2). Its intensity is intermediate but several further peaks originating from the variety of adducts occur at higher values of *m*/*z*. The peaks with

 © 2005 Wiley-VCH Verlag GmbH & Co. KGaA, Weinheim

m/*z* ca. 788, 820, 840, 857 and 918 correspond with adducts formed by two Na, two K, perchlorate, Na + sulfate and three carbonate ions, respectively (data not shown in Table 2).

Conclusions

The results obtained indicate that neomycin B, compared with the other previously investigated aminoglycosides, binds copper(II) ions with the highest affinity. The reason that it happens may be found within the binding pattern. Three-ring aminoglycosides, i.e. kanamycin A and B, tobramycin or geneticin, coordinate Cu^{II} ion mostly by their terminal amino sugar donors and not by the amines of the deoxystreptamine residue, in contrast with what has been presently demonstrated in the case of the four-ring neomycin. Cu^{II} coordination by the donors of this ring not only leads to an increase in stability of the complexes but also leaves the amino groups of the A and D rings uninvolved in any interaction with the metal ion. As a consequence, at excess copper(II) concentrations, a second metal ion may be bound by neomycin B, most probably at a site provided by ring D. In fact, none of its donor groups is directly involved in the coordination process of the first Cu^{II}, while ring A donates a hydroxyl group for axial complex stabilization. Formation of dinuclear species is a unique feature of neomycin B within all of the Cu^{II}-aminoglycoside systems investigated so far.

Experimental Section

Materials: Neomycin B, $CuCl_2$, $Cu(ClO_4)_2$, $Cu(NO_3)_2$, KNO_3, $NaClO_4$, 1,2-ethanediol, DCl, NaOD, TSP-d_4, 3-(trimethylsilyl)-[2,2,3,3-d_4] propionate sodium salt and all other simple chemicals were purchased from Sigma Chemical Co. (St. Louis, MO). Deuterium oxide (99.95%) was obtained from Spectra2000 s.r.l.

Potentiometry: Potentiometric titrations of neomycin B and its complexes with Cu^{II} in the presence of 0.1 M KNO_3 were performed at 25 °C using pH-metric titrations over the pH range 3–12 (Molspin automatic titrator, Molspin Ltd, Newcastle upon Tyne, UK) with 0.1 M NaOH as titrant. Changes in pH were monitored with a combined glass-Ag/AgCl electrode (ATI Russell pH Ltd, Fife, Scotland) calibrated daily in hydrogen ion concentrations by HNO_3 titrations.[24] Samples contained 1 mM neomycin B and Cu^{II}: antibiotic molar ratios of 1:1, 1:2 and 2:1 were used. The data were analyzed using the SUPERQUAD program.[25] Standard deviations computed by the SUPERQUAD program refer to random errors only.

Electronic Absorption (UV/Vis): The electronic absorption spectra were recorded at 25 °C with a Beckman DU-650 (Beckman, Palo Alto, CA) spectrophotometer over the spectral range of 200–900 nm, in a 1 cm cell. The samples contained a 2.5 mM Cu^{II}-neomycin B complex at a 1:1 molar ratio. The experiments were performed in 0.1 M $NaClO_4$ to keep a constant ionic strength, analogous to that used in the potentiometric titrations.

CD Spectroscopy: The spectra were recorded at 25 °C with a Jasco J-715 spectropolarimeter (JASCO, Japan Spectroscopic Co., Hiroshima, Japan), over the range of 200–800 nm, using a 0.5-cm cell. Samples contained a 1:1 or 2:1 Cu^{II}-to-neomycin B ratio at complex concentration of 2.5 mM. For the electronic absorption spectroscopic measurements a 0.1 M aqueous $NaClO_4$ solution was used. The spectra are expressed in terms of $\Delta\varepsilon = \varepsilon_l - \varepsilon_r$, where ε_l and ε_r are molar absorption coefficients for left and right circularly polarized light, respectively.

EPR Spectroscopy: The spectra of the Cu^{II} complex with neomycin B were recorded at 77 K with a Bruker ESP 300E spectrometer (Karlsruhe, Germany) at the X-band frequency (9.3 GHz). 1,2-ethanediol: water (1:2) was used as solvent in the low-temperature experiments to obtain homogeneity of the frozen samples. The concentrations of Cu^{II} in the samples were of 5 mM and Cu^{II}-to-neomycin B molar ratios were 1:1 and 2:1.

NMR Spectroscopy: Neomycin B solutions were made in deuterium oxide (99.95%), adjusted to a 0.1 M ionic strength with KNO_3 and carefully deoxygenated through a freezing-vacuum pumping-sealing-thawing procedure. The desired concentration of copper ions was achieved by using a stock solution of copper nitrate in deuterium oxide (molar ratio Cu^{II}-neomycin: 1:100). The pH was adjusted with either DCl or NaOD. NMR spectroscopic experiments were carried out at 14.1 T and at a controlled temperature (±0.1 K) with a Bruker Avance 600 spectrometer equipped with a Silicon Graphics workstation. TSP-d_4 was used as the internal reference standard. The proton resonance assignment was obtained by COSY and ROESY experiments. Rotating frame Overhauser enhancement spectroscopy (ROESY) was performed at a mixing time of 300 ms and the radio-frequency strength for the spin-lock field was 1.9 KHz. 2D ^1H ^{13}C HSQC shift correlation spectra were obtained in order to detect and assign ^{13}C NMR spectra at relatively low concentrations. Proton spin-lattice relaxation rates ($R_1 = 1/T_1$) were measured with the inversion recovery pulse sequence or with a combination of it with 2D TOCSY, when imposed by resolution limits. This was obtained by introducing a ^1H 180° pulse followed by a variable delay in front of the TOCSY sequence. Relaxation rates were calculated with regression analysis of the initial recovery curves of longitudinal magnetization components, leading to errors in the range of ±3%. A DANTE pulse train was used to measure selective proton spin-lattice relaxation rates.[26]

Molecular Mechanics and Dynamics Calculations: Molecular structures were generated by the HYPERCHEM software package [HYPERCHEM, Hypercube release 7.5 for Windows; Hypercube Inc.: Waterloo, ON, 2002], implemented on a Pentium 120 MHz PC. Charges were calculated by ZINDO-1 semi-empirical methods, and the model was then subjected to 25 ps unrestrained molecular dynamics at 300 K with the MM+ force field. The H–Cu and C–Cu distances, as obtained by NMR spectroscopic experiments, were introduced as restraints for the final 25 ps MD run at 300 K.

XAS Data Collection and Analysis: XAS data at the copper edge were collected at DESY (Hamburg, Germany) with the EMBL bending magnet beam line D2 equipped with a Si(111) double crystal monochromator with an energy resolution of 1.6 eV at 8980 eV. The DORIS-III storage ring was operated under normal conditions (4.5 GeV, 90–140 mA). The second monochromator crystal was detuned to 50% of its peak intensity in order to reject higher harmonics. Ionization chambers in front of and behind the sample were used to monitor the beam intensity. The sample cells were mounted in a 2-stage Displex cryostat (modified Oxford instruments) and kept at 20 K during data collection.

The samples used for data collection are as follows:

1. Cu^{II}-neomycin B complex at a 2:1 molar ratio, Cu^{II} conc. 100 mM

 © 2005 Wiley-VCH Verlag GmbH & Co. KGaA, Weinheim

2. Cu^{II}-neomycin B complex at a 1:1 molar ratio, Cu^{II} conc. 100 mM

3. Cu^{II}-neomycin B complex at a 2:1 molar ratio, Cu^{II} conc. 2 mM

For samples 1 and 2 the data were collected at the copper edge (ca. 8990.0 eV at the edge jump inflection point) by monitoring the sample absorption, while for the more dilute sample 3 the Cu-K_α fluorescence was detected with an energy discriminating 13 element Ge solid state detector (Canberra). The Bragg reflections of a static Si(220) crystal in back-reflection geometry have been used for the absolute energy calibration of the copper spectra.[22] For samples 1 and 2 three to eight spectra were collected for each sample from 8410 to 9810 eV with variable step widths. In the XANES and EXAFS regions steps of 0.3 and 0.6–1.5 eV were used, respectively. For sample 3 only two scans could be collected and the final spectrum resulted from the averaging. The scans spanned the 8500–9810 eV energy range with variable steps in the different regions of the spectrum. After inspection of each scan for edge consistency, the data were normalized by the edge jump and averaged. The EXAFS was then extracted by subtracting the slowly varying atomic background fitted with a cubic spline. Data reduction to extract the EXAFS spectrum was based on standard procedures and performed with the EXPROG software package.[27] The full, k^3 weighted, EXAFS spectra have been compared with theoretical simulations obtained by utilizing the rapid curved multiple scattering theory implemented in the set of programs EXCURVE 9.20.[28] The whole spectrum was analyzed by simulation by varying the atom types and the coordination numbers and iteratively refining the distance (R) and the Debye–Waller factor ($2\sigma^2$) for each atomic shell. The quality of the fit was assessed by the goodness of fit function through the parameter ε^2 which accounts for the degree of over determinacy[29] and by the R factor as defined within EXCURVE 9.20.[28] The pre-edge peak (1s-3d electronic transition at ca. 8980 eV) areas were calculated by subtracting an arctangent function from the normalized edge spectra and integrating over the range 8975–8985 eV.

Mass Spectrometry: The mass spectra were obtained with a Finnigan Mat TSQ 700 instrument (Thermo-Finnigan, Bremen, Germany), using the ESI (electro-spray ionization) technique with N_2 as carrier gas, and flow-rate of 2 μL/min. Three kinds of samples were investigated at pH 8.0 (adjusted with acetic acid and ammonium carbonate): free neomycin B and Cu^{II}-neomycin B complex at 1:1 and 2:1 ratios. All samples were prepared as water solutions. Then methanol was added to a final concentration of 50%, in order to decrease surface tension during sample evaporation. Final sample concentrations were: neomycin B, 0.25 mM and Cu^{II}, 0.25 or 0.5 mM.

Acknowledgments

The authors wish to thank Dr. Wolfram Meyer-Klaucke from EMBL Outstation in Hamburg for collecting XAS data. W. Szczepanik thanks the Foundation for Polish Science (FNP) for the Annual Stipend for Young Scientists. This work was supported by the Polish State Committee for Scientific Research (KBN), grant no. 4 T09A 179 25, for the period 2003–2006.

[1] W. G. Barnes, *Aminoglycoside Antibiotics: A Guide to Therapy*, CRC Press, Inc., Boca Raton, Florida, **1984**.
[2] W. Szczepanik, J. Ciesiołka, J. Wrzesiński, J. Skała, M. Jeżowska-Bojczuk, *Dalton Trans.* **2003**, 1488–1494.
[3] M. Jeżowska-Bojczuk, A. Karaczyn, W. Bal, *J. Inorg. Biochem.* **1998**, *71*, 129–134.
[4] W. Szczepanik, P. Kaczmarek, J. Sobczak, W. Bal, K. Gatner, M. Jeżowska-Bojczuk, *New J. Chem.* **2002**, *26*, 1507–1514.
[5] M. Jeżowska-Bojczuk, W. Bal, H. Kozłowski, *Inorg. Chim. Acta* **1998**, *275–276*, 541–545.
[6] M. Jeżowska-Bojczuk, A. Karaczyn, H. Kozłowski, *Carbohydr. Res.* **1998**, *313*, 265–269.
[7] W. Szczepanik, E. Dworniczek, J. Ciesiołka, J. Wrzesiński, J. Skała, M. Jeżowska-Bojczuk, *J. Inorg. Biochem.* **2003**, *94*, 355–364.
[8] M. C. Linder, *Copper Metabolism*, Plenum Press, New York, **1991**.
[9] N. E. Moat, T. E. Evans, G. J. Quinlan, J. M. Gutteridge, *FEBS Lett.* **1993**, *328*, 103–106.
[10] M. C. Linder, M. Hazegh-Azam, *Am. J. Clin. Nutr.* **1996**, *63*, 797–811.
[11] K. Aihara, Y. Nishi, S. Hatano, M. Kihara, K. Yoshimitsu, N. Takeichi, T. Ito, H. Ezaki, T. Usui, *Am. J. Clin. Nutr.* **1984**, *40*, 26–35.
[12] S. M. Abu-El-Wafa, M. A. El-Ries, F. M. Abou-Attia, R. M. Issa, *Anal. Lett.* **1989**, *22*, 2703–2716.
[13] A. Sreedhara, J. D. Freed, J. A. Cowan, *J. Am. Chem. Soc.* **2000**, *122*, 8814–8824.
[14] R. E. Botto, B. Coxon, *J. Am. Chem. Soc.* **1983**, *105*, 1021–1028.
[15] B. Noszal, in *Biocoordination C: Coordination Equilibria in Biological Active Systems* (Ed.: K. Burger), Ellis Harwood Ltd, London, **1990**.
[16] D. G. Reid, K. Gajjar, *J. Biol. Chem.* **1987**, *262*, 7967–7972.
[17] R. E. Botto, B. Coxon, *J. Carbohydr. Chem.* **1984**, *3*, 545–563.
[18] I. Solomon, *Phys. Rev.* **1955**, *99*, 559–565.
[19] L. D. Hall, H. D. W. Hill, *J. Am. Chem. Soc.* **1976**, *98*, 1269–1270.
[20] I. Bertini, C. Luchinat, *NMR of Paramagnetic Substances*, *Coord. Chem. Rev.* 150, ed.1, Elsevier, Amsterdam, **1996**, pp. 1–300.
[21] R. F. Pettifer, C. Hermes, *J. Appl. Crystallogr.* **1985**, *18*, 404–412.
[22] L. S. Kau, D. J. Spira-Solomon, J. E. Penner-Hahn, K. O. Hodgson, E. I. Solomon, *J. Am. Chem. Soc.* **1987**, *109*, 6433–6442.
[23] P. J. Riggs-Gelasco, T. L. Stemmler, J. E. Penner-Hahn, *Coord. Chem. Rev.* **1995**, *144*, 245–286.
[24] H. Irving, M. G. Miles, L. D. Pettit, *Anal. Chim. Acta* **1967**, *38*, 475–488.
[25] P. Gans, A. Sabatini, A. Vacca, *J. Chem. Soc. Dalton Trans.* **1985**, 1195–1200.
[26] G. A. Morris, R. Freeman, *J. Magn. Reson.* **1978**, *29*, 433–462.
[27] H. F. Nolting, C. Hermes, EXPROG: EMBL EXAFS data analysis and evaluation program package for PC/AT. European Molecular Biology Laboratory, c/o DESY, Hamburg, **1993**.
[28] N. Binsted, S. S. Hasnain, *J. Synchrotron Radiat.* **1996**, *3*, 185–196.
[29] P. A. Lee, J. B. Pendry, *Phys. Rev. B* **1975**, *11*, 2795–2811.

Received: February 1, 2005
Published Online: July 4, 2005

 © 2005 Wiley-VCH Verlag GmbH & Co. KGaA, Weinheim

A Straightforward Route to Copper/Zinc Oxide Nanocomposites: The Controlled Thermolysis of $Zn[Cu(CN)_3]$

Yanzhi Guo,[a] Rainer Weiss,[a] and Matthias Epple*[a]

Keywords: Cyanides / Copper / Zinc / Thermochemistry / EXAFS spectroscopy

Copper–zinc nanocomposites were prepared by thermolysis of copper–zinc cyanides under mild conditions. Two different routes were used for the preparation of the cyanide complex: A batch precipitation method and the continuous overflow precipitation method. The thermolysis of the cyanides was studied in-situ by thermogravimetry coupled with infrared spectroscopy (TG-IR) and by thermogravimetry coupled with mass spectroscopy (TG-MS). The structure of the nanocomposites was investigated by X-ray powder diffraction (XRD) and extended X-ray absorption fine structure (EXAFS). Geometric models were suggested on the atomic scale based on EXAFS results for the precursor, the mixed oxides (CuO/ZnO), and the reduced copper–zinc samples (Cu/ZnO, i.e. catalyst for methanol synthesis). In the batch precipitation method, the influence of temperature on the morphology of the thermolysis products was explored. In the continuous overflow method, the morphology of the Cu–Zn cyanide complex was investigated as a function of concentration and residence time. A high solution concentration and a short residence time (equivalent to a high flow rate) led to smaller particles.

(© Wiley-VCH Verlag GmbH & Co. KGaA, 69451 Weinheim, Germany, 2005)

Introduction

Copper–zinc oxide nanocomposites can be obtained in a variety of morphologies, including thin films,[1] nanowires[2] and nanoparticles.[3] High surface area copper/zinc oxide is an active catalyst for methanol synthesis, for water-gas shift reactions, and for various hydrogenations.[4] It is widely accepted that zinc oxide can improve the dispersion of copper and thereby the catalytic activities.[5] Copper–zinc oxide nanocomposites are usually prepared by co-precipitation from aqueous solutions. Typically, a mixed solution of copper and zinc salts (usually nitrates or acetates) is prepared and the precipitation of both carbonates is induced by addition of sodium or ammonium carbonate whilst stirring, followed by drying and calcination.[6–9] The particle size and crystallinity of the products can be adjusted by the pH, the concentration, the stirring rate, the duration of precipitation and aging, and the calcination conditions.[10] Pollard et al.[4] used the minerals georgeite $[Cu_5(CO_3)_3(OH)_4{\cdot}6H_2O]$ and azurite $[Cu_3(CO_3)_2(OH)_2]$ as precursors for copper–zinc mixed oxides. Recently, a nonaqueous organometallic route was developed by Hambrock et al.[11] and uniform copper–zinc nanoparticles were obtained. They used $Cu[OCH(Me)CH_2NMe_2]$ and Et_2Zn as precursors. The thermolysis was carried out in the coordinating solvent hexadecylamine at elevated temperatures and nano-scale colloidal copper–zinc systems with different zinc contents were obtained. Zhou et al.[2] prepared copper–zinc nanowires by heating CuI_2 and ZnI_2 in a dynamic oxygen atmosphere. A self-catalysed vapour-liquid-solid growth mechanism was suggested.

Polymeric metal cyanides represent a homogeneous mixture of the individual metals on the atomic length scale. The heterogeneous mixing of individual compounds is therefore avoided. The controlled thermolysis of these compounds can be carried out at comparatively low temperature due to the presence of a suitable organic leaving group, i.e. the cyanide in the precursors. A higher temperature is usually required in conventional syntheses to achieve a sufficiently fast diffusion. We have shown that the composition as well as the crystal structure of the bimetallic Fe–Sn and Ru–Sn composites can be fine-tuned by the thermolysis conditions such as time, temperature and the atmosphere.[12–14] Such systems are suitable precursors for the preparation of bimetallic nanocomposites that incorporate the initially blended metals.

Recently we adopted the continuous overflow method for the preparation of calcium phosphate nanoparticles from solution.[15] The particle size, morphology and crystallinity can be adjusted by the process parameters, mainly the residence time (the flow rate of the solutions), and the concentration of the solutions. It was therefore the aim of this work to prepare a suitable cyanide precursor for the Cu/ZnO system and to control its morphology by different crystallisation methods. Thereby, the properties of the final product should be adjustable.[16–18]

[a] Inorganic Chemistry, University of Duisburg-Essen, Universitätsstr. 5–7, 45117 Essen, Germany
Fax: +49-201-183-2621
E-mail: matthias.epple@uni-due.de

Result and Discussion

For the preparation of the Cu–Zn cyanide complex, there are two possible routes as shown in Equations (1), (2) and (3). In both cases, tetrahedral $[Zn(CN)_4]^{2-}$ is formed in the first step (1). Subsequently, both reactions (2) and (3) are likely to occur. Because the stability constant of $[Zn(CN)_4]^{2-}$ (4×10^{19} M^{-4})[19] is smaller than that of $[Cu(CN)_4]^{2-}$ (1×10^{27} M^{-4}),[20] the latter compound is preferred in equilibrium. However, the oxidation state of $[Cu(CN)_4]^{2-}$ is not stable leading to a reduction of Cu^{II} to Cu^{I}. Thus, a transient state of $[Cu(CN)_3]^{2-}$ can be assumed, followed by the formation of $Zn[Cu(CN)_3]$ as precipitate and the release of $(CN)_2$ into the gas phase.

$$4\ CN^- + Zn^{2+} \rightarrow [Zn(CN)_4]^{2-} \quad (1)$$

$$[Zn(CN)_4]^{2-} + Cu^{2+} \rightarrow Cu[Zn(CN)_4]\ \downarrow \quad (2)$$

$$[Zn(CN)_4]^{2-} + Cu^{2+} \rightarrow Zn[Cu(CN)_4] \rightarrow Zn[Cu(CN)_3]\downarrow + \tfrac{1}{2}\ (CN)_2\ \uparrow \quad (3)$$

Batch-Wise Preparation and Thermolysis

For the Cu–Zn cyanide complex prepared by the batch precipitation method, elemental analysis gave 17.5 wt.-% C, 20.2 wt.-% N, 30.3 wt.-% Cu and 31.2 wt.-% Zn. This corresponds to a Cu/Zn/CN molar ratio of 1:1:3.1. We conclude that $Zn[Cu(CN)_3]$ (calcd. 17.4 wt.-% C, 20.3 wt.-% N, 30.7 wt.-% Cu and 31.6 wt.-% Zn) is the main component of the precipitates and a small amount of $Cu[Zn(CN)_4]$ (calcd. 20.6 wt.-% C, 24.0 wt.-% N, 27.3 wt.-% Cu and 28.1 wt.-% Zn) is also present. The infrared spectra of this complex support this assumption (Figure 1). The strong peak at 2155 cm^{-1} is the contribution of CN groups bound (via carbon) to Cu^{I}.[21] An additional contribution at 2217 cm^{-1} is attributed to CN bound (via carbon) to Zn.[22] It is obvious that $Zn[Cu(CN)_3]$ is dominating in the prepared cyanides due to its high peak intensity in the spectra.

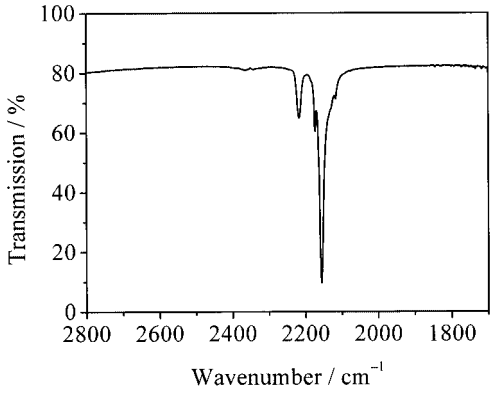

Figure 1. Infrared spectra of $Zn[Cu(CN)_3]$, prepared by the batch precipitation method.

The thermolysis of the copper–zinc complex was studied by thermogravimetric analysis coupled with infrared spectroscopy (TG-IR). When heated up under oxygen, the decomposition of the copper–zinc complex started at about 300 °C (Figure 2, part a). Two steps at about 440 °C and 510 °C can be derived from the TG weight loss curve. The weight loss ceased at about 530 °C. At 1000 °C, only CuO/ZnO was present, as shown by XRD. The total weight loss was about 23%. From the weight loss it can be deduced that the precursor consists of $Zn[Cu(CN)_3]$ (a theoretical weight loss of 22.2% for a complete transformation to CuO/ZnO) rather than $Cu[Zn(CN)_4]$ (a theoretical weight loss of 30.9%). This is in good agreement with the elemental analysis. Two exothermal peaks in the DTA curve correspond to the two steps in the weight loss curve, indicating oxidative combustion.

The infrared spectra in Figure 2 (part b) correspond to the evolved gas phase during heating. The contribution of

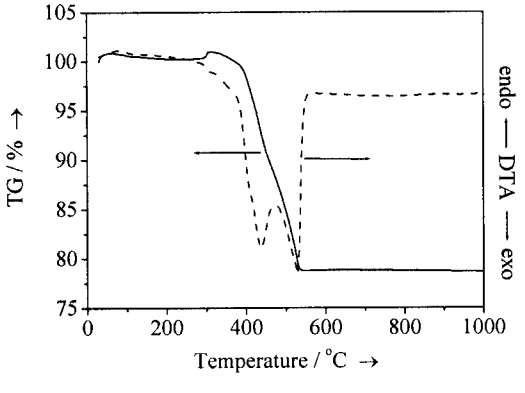

(a)

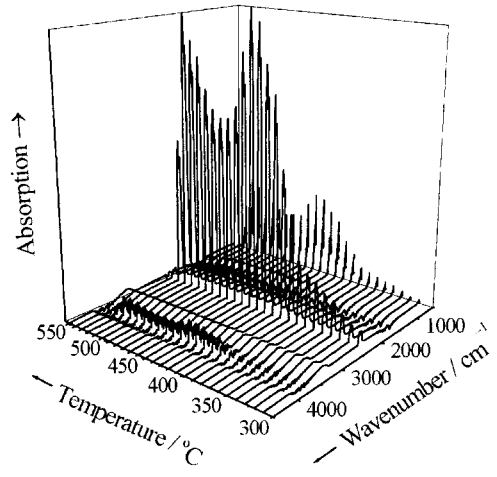

(b)

Figure 2. Thermogravimetric analysis of $Zn[Cu(CN)_3]$ under oxygen (a) and the corresponding time-resolved infrared spectra of the released gases during heating (b) (heating rate 5 K min^{-1}).

 © 2005 Wiley-VCH Verlag GmbH & Co. KGaA, Weinheim

cyanides (CN, at 2343 cm^{-1}) appeared first. Carbon dioxide (C=O, 2360/2312/671 cm^{-1}) was subsequently released at elevated temperature, showing again the two steps at about 440 °C and 510 °C, indicated by the two maxima in the time-resolved spectra.

Another experiment was carried out with thermogravimetric analysis coupled with mass spectroscopy (TG-MS). Air was used as oxidizing gas and the copper–zinc complex was heated from room temperature to 1000 °C. The weight loss started at about 300 °C and stopped at around 620 °C (Figure 3, part a). The thermolysis was shifted to higher temperature compared with the TG-IR results because oxygen was replaced by air and the heating rate was increased from 5 K min^{-1} to 10 K min^{-1}. The total weight loss was

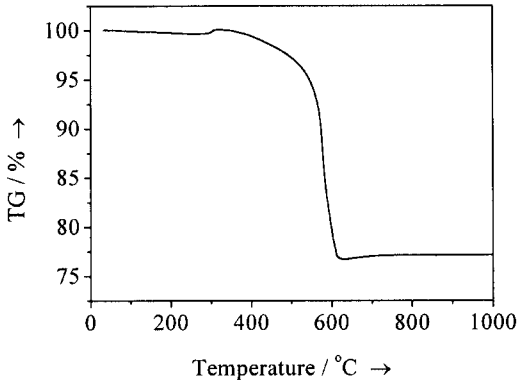

(a)

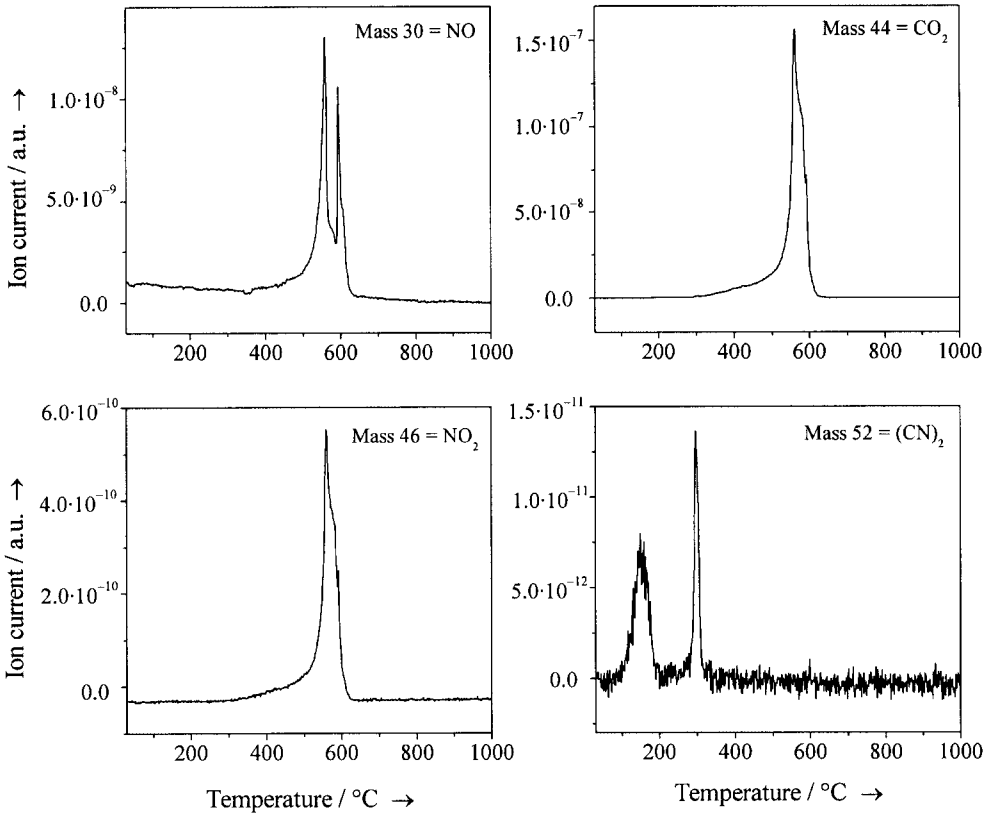

(b)

Figure 3. (a) Thermogravimetric analysis of $Zn[Cu(CN)_3]$ under air, (b) the corresponding time-resolved mass spectra of four different masses in the released gases (heating rate 10 K min^{-1}).

 © 2005 Wiley-VCH Verlag GmbH & Co. KGaA, Weinheim

about 24 wt.-%. The mass spectra in Figure 3 (part b) clearly show the release of gaseous species. Cyanogen [$(CN)_2$: mass 52] was released at low temperatures in two steps, corresponding to the low intensity of the cyanide peak in the IR spectra. The initial "dip" in the TG curve at around 300 °C can be related to a non-oxidative elimination of cyanogen. The release of carbon dioxide, nitrogen monoxide and nitrogen dioxide at higher temperatures occurred in two steps, indicated by two peaks or a broad peak with a shoulder.

The XRD patterns of the thermolysis products under air at different temperatures are shown in Figure 4, part a. Copper oxide and zinc oxide are present. With rising thermolysis temperature, the height of the peaks increased and their width decreased, indicating an increasing particle size (a better crystallinity). The three oxides samples of Figure 4, (part a) were then reduced at 250 °C in H_2/N_2 to Cu/ZnO. The effects of the initial thermolysis temperatures under air are also represented in the XRD patterns of the reduced samples (Figure 4, part b).

EXAFS analysis was performed to investigate the crystal structure of the copper zinc cyanide complex (no single crystals could be obtained so far), of the oxide mixtures (CuO/ZnO), and of the reduced samples (Cu/ZnO). Figure 5 (part a) shows the Cu *K*-edge EXAFS Fourier transform magnitudes (FTs) of the complex $Zn[Cu(CN)_3]$. The nearest neighbours derived from the FTs were fit as 3 carbon atoms at 1.92 Å (Table 1, part a). Another carbon atom appeared at a larger distance, at 2.37 Å. This can be ascribed to different Cu–CN bonds.[21] In this case the coordination polyhedron around Cu can be described as deformed trigonal pyramid with one CN group at a larger distance. The corresponding nitrogen atoms in cyanide appear at 3.12 Å (3 N) and 3.71 Å (1 N), respectively. The Zn *K*-edge EXAFS Fourier transform magnitude of the complex is shown in Figure 5, part b. As nearest neighbours of zinc, 4 nitrogen atoms are present in a distance of 1.93 Å (Table 1, part b). The second peak indicates the corresponding carbon atoms of the cyanide group at 3.22 Å. In both EXAFS spectra (Cu and Zn), a metallic neighbour can be fit in a

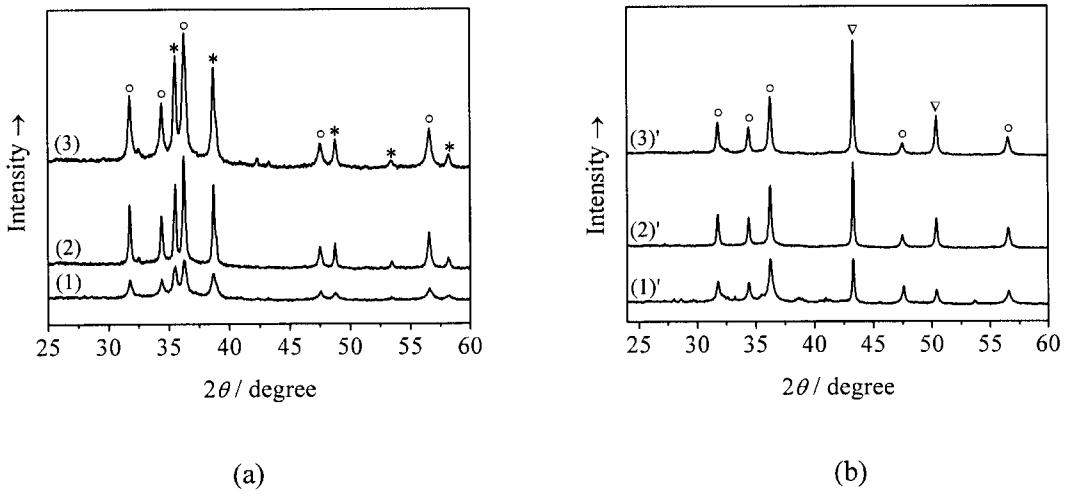

Figure 4. (a) XRD patterns of CuO/ZnO obtained by oxidation of $Zn[Cu(CN)_3]$ at 300 °C (1), 400 °C (2) and 500 °C (3) for 3 hours; (b) XRD patterns of Cu/ZnO obtained by reduction of the corresponding oxide mixtures under H_2/N_2 for 3 hours at 250 °C. The marked peaks correspond to ZnO (o), CuO (*) and Cu (∇).

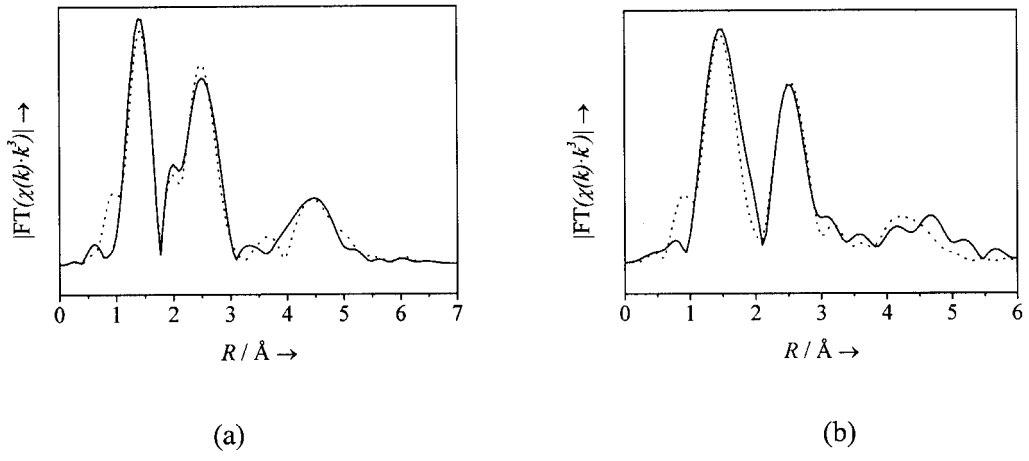

Figure 5. EXAFS Fourier transform magnitudes of the $Zn[Cu(CN)_3]$ prepared by the batch precipitation method. Solid line: experimental data, dot line: fit data. Cu *K*-edge (a) and Zn *K*-edge (b).

 © 2005 Wiley-VCH Verlag GmbH & Co. KGaA, Weinheim

distance of 5.1 to 5.2 Å. By EXAFS, we cannot distinguish between a copper neighbour and a zinc neighbour, but the given stoichiometry suggests a network which consists of Cu–C–N–Zn units that connect fourfold-coordinated Cu and Zn centres.

Table 1. Fit parameters for the Cu *K*-edge (a) and Zn *K*-edge (b) EXAFS spectra of $Zn[Cu(CN)_3]$ prepared by the batch precipitation method.

(a) $Zn[Cu(CN)_3]$	*R* [Å]	Coordination number	$\sigma^2 \cdot 10^3$ [Å^2]
Cu – 3 C	1.92	3.1	3.3
Cu – C	2.37	1.0	2.8
Cu – 3 N	3.12	3.2	0.1
Cu – N	3.71	1.4	4.2
Cu – 4 Zn	5.12	4.2	5.9
(b) $Zn[Cu(CN)_3]$	*R* [Å]	Coordination number	$\sigma^2 \cdot 10^3$ [Å^2]
Zn – 4 N	1.93	4.4	6.6
Zn – 4 C	3.22	4.3	3.0
Zn – 4 Cu	5.20	4.3	5.8

In the Cu *K*-edge FTs of the CuO/ZnO mixture (Figure 6, part a), the shells of Cu–O and Cu–Cu in CuO are clearly present, supporting the X-ray diffraction data (Table 2, part a).[23] Figure 6 (part b) shows the Cu *K*-edge FTs of the reduced samples (Cu/ZnO). The Cu–Cu distances of the first shell are in the range of 2.69–2.74 Å (Table 2, part b), and compare well to that of the bulk metal (2.56 Å). The coordination numbers were about 12, also in agreement with the cubic close packing of the bulk metal. The second shell of copper was at a distance of about 3.5 Å with a coordination number of 6. The weak peaks at about 1.5 Å may result from CuO or Cu_2O (in bulk Cu_2O the first coordination number is 2 and the Cu–O distance is 1.84 Å; see also the results for CuO).[24] Possibly, this is the result of an oxidation of the copper surface due to exposure to air before the EXAFS measurement.

The morphology of the Cu–Zn cyanide complex and the thermolysis products were studied by scanning electron microscopy (Figure 7, parts a–d). The initial complex crystallized as micrometer-scale platelets which were destroyed

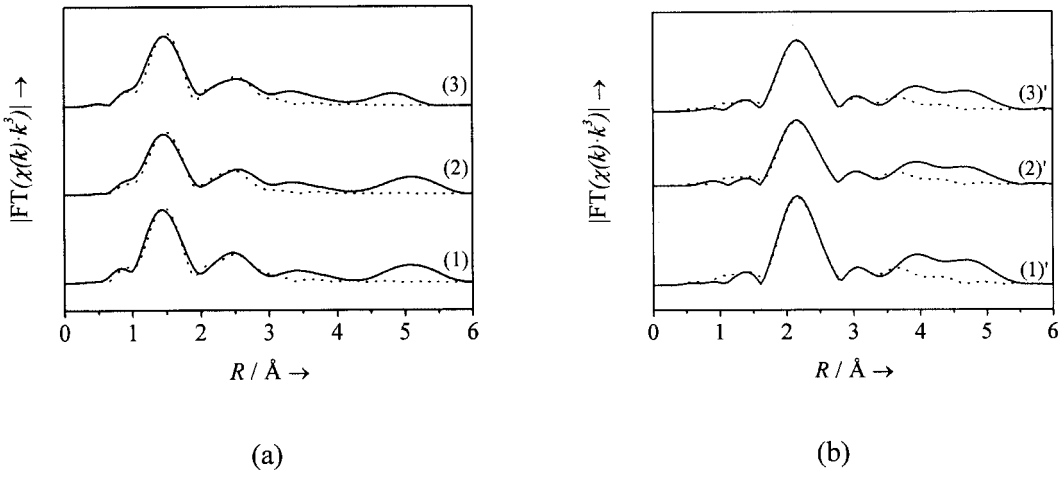

Figure 6. Cu *K*-edge EXAFS Fourier transform magnitudes of (a) CuO/ZnO obtained by thermolysis of $Zn[Cu(CN)_3]$ at 300 °C (1), 400 °C (2) and 500 °C (3) under air for 3 h; (b) Cu/ZnO reduced from the above-mentioned thermolysis products under H_2/N_2 at 250 °C for 3 h. Solid line: experimental data, dot line: fit data.

Table 2. Fit parameters for the Cu *K*-edge EXAFS spectra of CuO/ZnO obtained by thermolysis of $Zn[Cu(CN)_3]$ at 300 °C, 400 °C and 500 °C under air for 3 h (a); and Cu/ZnO reduced from the corresponding thermolysis products under H_2/N_2 at 250 °C for 3 h (b).

(a) CuO/ZnO	Cu – 4 O *R* [Å]	Coordination number	$\sigma^2 \cdot 10^3$ [Å]^2	Cu – 8 Cu *R* [Å]	Coordination number	$\sigma^2 \cdot 10^3$ [Å^2]
300 °C	1.94	3.9	5.5	2.91	8.4	19.9
400 °C	1.96	3.9	4.0	2.93	8.2	22.9
500 °C	1.96	3.8	5.5	2.94	8.1	23.2
(b) Cu/ZnO	Cu – 12 Cu *R* [Å]	Coordination number	$\sigma^2 \cdot 10^3$ [Å]^2	Cu – 6 Cu *R* [Å]	Coordination number	$\sigma^2 \cdot 10^3$ [Å^2]
300 °C/250 °C	2.74	11.9	6.5	3.48	6.8	17.9
400 °C/250 °C	2.69	11.9	7.1	3.41	6.5	13.0
500 °C/250 °C	2.74	12.2	6.9	3.49	6.6	17.1

 © 2005 Wiley-VCH Verlag GmbH & Co. KGaA, Weinheim

by the following thermolysis. The diameter of the agglomerates decreased at higher thermolysis temperatures, in contrast to the crystallite size determined by XRD, which increased with increasing temperatures. However, the macroscopic morphology is not directly related to the internal domain size.

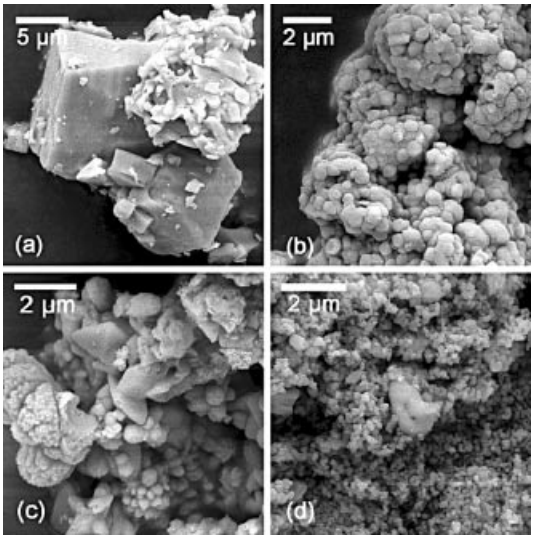

Figure 7. SEM images of $Zn[Cu(CN)_3]$ from batch preparation (a) and its thermolysis products (CuO/ZnO) obtained under air for 3 h at 300 °C (b), 400 °C (c), 500 °C (d), respectively.

Continuous Overflow Preparation

In the continuous overflow precipitation method, the properties of the product can be better controlled in comparison to the simple batch-wise crystallisation. Main variation parameters are the residence time and the concentrations.

We studied the morphology of the Cu–Zn cyanide complex as a function of the solution concentration and the average residence time (related to the flow rate), respectively. First, the concentration was varied at a constant flow rate. It can be seen in Figure 8 parts a–c) that with increasing concentrations of Cu^{2+} and $[Zn(CN)_4]^{2-}$, the complex morphology changed from platelets to spherical particles and the size decreased. Second, the residence time was varied at a constant concentration. This effect is obvious (Figure 8, parts d–f): A shorter residence time led to smaller particles. Hence, we can conclude that higher concentration and low residence time (or high flow rate) both lead to smaller spherical (nano-)particles instead of well-crystalline microcrystals (platelets). Elemental analysis of the sample in Figure 8 (part f) gave a Cu/Zn/CN ratio of 1:1:3.04 (16.8 wt.-% C, 19.6 wt.-% N, 29.0 wt.-% Cu, and 30.6 wt.-% Zn), which indicates that $Zn[Cu(CN)_3]$ was still the main component of the precipitates obtained by continuous overflow method, even at the highest concentration and the shortest residence time.

Conclusions

In summary, a batch-wise and a continuous synthesis method were applied to the precipitation of the copper–zinc coordination compound $Zn[Cu(CN)_3]$. Structurally, this compound consists of Cu–C–N–Zn units that bridge Cu and Zn centres (both in fourfold coordination). With the continuous overflow precipitation method, fine spherical particles are obtained at high solution concentration and short residence time (or a high flow rate). The thermolysis of the cyanides was studied in-situ by TG-IR and TG-MS. Under oxidizing conditions, cyanogen is lost only at lower temperature whereas at higher temperature, thermal decomposition to carbon and nitrogen oxides occurs. The product is a 1:1 mixture of CuO and ZnO which can be reduced to Cu/ZnO, a well-known catalyst.

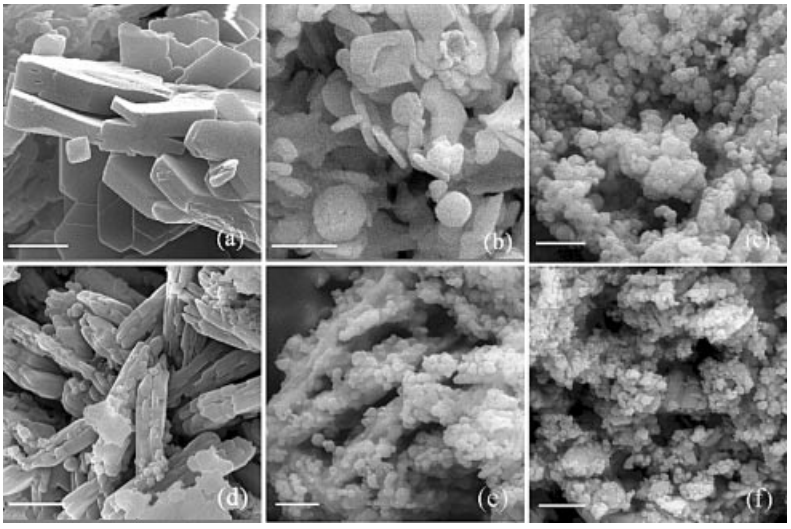

Figure 8. SEM images of $Zn[Cu(CN)_3]$ prepared by continuous overflow method with different $[Zn(CN)_4]^{2-}$ concentrations (residence time of 30 s), i.e., 0.05 mol L^{-1} (a), 0.3 mol L^{-1} (b), 0.4 mol L^{-1} (c) and different residence time (constant concentration of 0.4 mol L^{-1}), i.e., 140 s (d), 30 s (e), 15 s (f). Cu^{2+} and $[Zn(CN)_4]^{2-}$ were always present in stoichiometric ratios (1:1). Scale bar: 1 µm.

 © 2005 Wiley-VCH Verlag GmbH & Co. KGaA, Weinheim

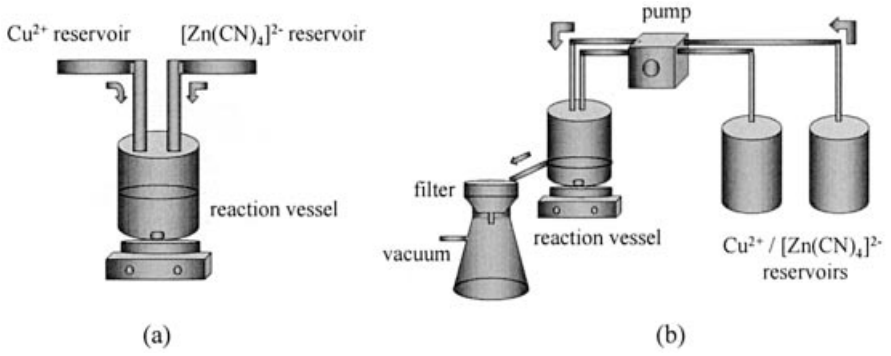

Figure 9. Schematic setups of the batch precipitation method (a) and the continuous overflow method (b).

Experimental Section

In the batch precipitation method (Figure 9, part a), $[Zn(CN)_4]^{2-}$ was prepared by mixing aqueous solutions of zinc sulfate and potassium cyanide. Copper(II) sulfate was then added whilst stirring and copper zinc cyanide was obtained as precipitate. In the continuous overflow precipitation method (Figure 9, part b), the aqueous solutions of $K_2[Zn(CN)_4]$ and $CuSO_4$ were pumped at different flow rates (giving different residence time) into a stirred precipitation vessel at room temperature. The overflowing suspension was immediately filtered. The precipitate was dried overnight under air at room temperature and stored in sealed vials until further characterization. All reagents were used in stoichiometric amounts, i.e. $n(Cu) = n(Zn)$.

The controlled thermolysis of the cyanides was carried out in a horizontal quartz tube reactor with an inner diameter of 30 mm. The thermal decomposition was carried out under air at 300, 400 and 500 °C for 3 hours. The mixed oxides were then reduced under hydrogen/nitrogen (5:95, *v*:*v*) at 250 °C for 3 hours.

Combined thermogravimetry-infrared spectroscopy (TG-IR) was carried out with a Netzsch STA 409 TG-DTA/DSC apparatus connected to a Bruker Vertex 70 infrared system for in-situ gas analysis. Samples were heated from room temperature to 1000 °C at a rate of 5 K min^{-1} under O_2 at a flow rate of 50 mL min^{-1}. The evolved gases were monitored in-situ by infrared spectroscopy (IR). The infrared spectra were all corrected for background absorption. Background spectra were recorded at room temperature before the start of the experiment with the cavity filled by flow gas. Thermogravimetry-mass spectroscopy (TG-MS) was carried out with a TGA 7 Perkin–Elmer thermobalance coupled to a quadrupole mass spectrometer (OmniStar™, Pfeiffer). The sample was heated up with 10 K min^{-1} under synthetic air (20.5% oxygen in nitrogen) at a flow rate of 100 mL min^{-1}.

X-ray diffraction was carried out at room temperature at beamline B2 at the Hamburger Synchrotronstrahlungslabor (HASYLAB) at Deutsches Elektronen Synchrotron (DESY), Hamburg, Germany.

The morphology of the thermolysis products was studied by scanning electron microscopy (LEO Gemini 1530). Extended X-ray absorption fine structure (EXAFS) spectroscopy was carried out at beamline E4 at HASYLAB/DESY. The programs SPLINE and XFIT[25] were used for quantitative data evaluation. Theoretical standards were computed with the program FEFF 6.01a.[26] The amplitude reduction factor S_o^2 was fixed to 1. Variation parameters were the bond lengths, the coordination numbers, the Debye-Waller factors (σ^2), and the zero-energy correction (E_o).

Acknowledgments

This work was supported by the Deutsche Forschungsgemeinschaft within the scope of the Collaborative Research Center SFB 558: Metal–substrate interactions in heterogeneous catalysis. We are grateful for Prof. M. Muhler for TG-MS measurements. We thank J. Gering for experimental assistance. Synchrotron beamtime by HASYLAB at DESY was generously provided.

[1] O. Vazquez Cuchillo, U. Pal, C. Vazquez Lopez, *Modern Phys. Lett. B* **2001**, *15*, 675–678.
[2] S. M. Zhou, X. H. Zhang, X. M. Meng, K. Zou, X. Fan, S. K. Wu, S. T. Lee, *Nanotechnology* **2004**, *15*, 1152–1155.
[3] L. Guo, S. Yang, *Chem. Mater.* **2000**, *12*, 2268–2274.
[4] A. M. Pollard, M. S. Spencer, R. G. Thomas, P. A. Williams, J. Holt, J. R. Jennings, *Appl. Catal. A* **1992**, *85*, 1–11.
[5] Y. Choi, K. Futagami, F. Fijitani, J. Nakamura, *Appl. Catal. A* **2001**, *208*, 163–167.
[6] K. D. Jung, O. S. Joo, *Catal. Lett.* **2002**, *84*, 21–25.
[7] H. Wilmer, T. Genger, O. Hinrichsen, *J. Catal.* **2003**, *215*, 188–198.
[8] R. Naumann d′Alnoncourt, M. Kurtz, H. Wilmer, E. Loeffler, V. Hagen, J. Shen, M. Muhler, *J. Catal.* **2003**, *220*, 249–253.
[9] B. L. Kniep, T. Ressler, A. Rabis, F. Girgsdies, M. Baenitz, F. Steglich, R. Schlögl, *Angew. Chem.* **2004**, *116*, 114–117; *Angew. Chem. Int. Ed.* **2004**, *43*, 112–115.
[10] M. Kurtz, H. Wilmer, T. Genger, O. Hinrichsen, M. Muhler, *Catal. Lett.* **2003**, *86*, 77–80.
[11] J. Hambrock, M. K. Schroeter, A. Birkner, C. Woell, R. A. Fischer, *Chem. Mater.* **2003**, *15*, 4217–4222.
[12] M. Rehbein, M. Epple, R. D. Fischer, *Solid State Sci.* **2000**, *2*, 473–488.
[13] M. Rehbein, R. D. Fischer, M. Epple, *Thermochim. Acta* **2002**, *382*, 143–149.
[14] Y. Guo, R. Weiss, M. Epple, *J. Mater. Chem.* **2005**, *15*, 424–429.
[15] T. Welzel, W. Meyer-Zaika, M. Epple, *Chem. Commun.* **2004**, 1204–1205.
[16] M. M. Günter, T. Ressler, B. Bems, C. Büscher, T. Genger, O. Hinrichsen, M. Muhler, R. Schlögl, *Catal. Lett.* **2001**, *71*, 37–44.
[17] B. Bems, M. Schur, A. Dassenoy, H. Junkes, D. Herein, R. Schlögl, *Chem. Eur. J.* **2003**, *9*, 2039–2052.
[18] M. Schur, B. Bems, A. Dassenoy, I. Kassatkine, J. Urban, H. Wilmes, O. Hinrichsen, M. Muhler, R. Schlögl, *Angew. Chem.* **2003**, *115*, 3945–3947; *Angew. Chem. Int. Ed.* **2003**, *42*, 3815–3817.
[19] R. M. Izatt, J. J. Christensen, J. W. Hansen, G. D. Watt, *Inorg. Chem.* **1965**, *4*, 718–721.
[20] R. Paterson, J. Bjerrum, *Acta Chim. Scand.* **1965**, *19*, 729–734.

 © 2005 Wiley-VCH Verlag GmbH & Co. KGaA, Weinheim

[21] J. Cernak, Z. Zak, J. Chomic, C. Kappenstein, *Acta Crystallogr. C* **1998**, *54*, 1551–1553.
[22] A. G. Sharpe, *The Chemistry of cyano complexes of the transition metals*, Academic Press, London, **1976**.
[23] W. Grünert, N. W. Hayes, R. W. Joyner, E. S. Shapiro, M. R. H. Siddiqui, G. N. Baeva, *J. Phys. Chem. A* **1994**, *98*, 10832–10846.
[24] G. U. Kulkarni, C. N. R. Rao, *Top. Catal.* **2003**, *22*, 183–189.
[25] P. J. Ellis, H. C. Freeman, *J. Synchrotron Radiat.* **1995**, *2*, 190–195.
[26] E. A. Stern, M. Newville, B. Ravel, Y. Yacoby, D. Haskel, *Physica B* **1995**, *208–209*, 117–120.

Received: February 2, 2005
Published Online: June 22, 2005

 © 2005 Wiley-VCH Verlag GmbH & Co. KGaA, Weinheim

Influence of 2-Aminopyridine on the Formation of Molybdates under Hydrothermal Conditions

Katikaneani Pavani[a] and Arunachalam Ramanan*[a]

Keywords: Hydrothermal synthesis / N ligands / Molybdenum / Crystal structure

The hydrothermal reaction of an aqueous ammonium heptamolybdate solution with first-row transition metal salts in the presence of 2-aminopyridine at around 180 °C and under autogenous pressure yields several molybdates, such as the 1D chains in $(C_5N_2H_7)_4Mo_8O_{26}$ (**1**), zero-dimensional $(C_5N_2H_7)_6Mo_7O_{24}\cdot 3H_2O$ (**2**), and the first synthesis of Lindgrenite $[Cu_3Mo_2O_8(OH)_2$ (**3**)] The structures of these materials were established by single-crystal and powder X-ray diffraction techniques. The crystal structures of wolframite-based $MnMoO_4$ (**4**) and $ZnMoO_4$ (**5**) were established by powder X-ray diffraction. The role of 2-aminopyridine (2-ampy) in the formation of the different solids under hydrothermal conditions is discussed.

(© Wiley-VCH Verlag GmbH & Co. KGaA, 69451 Weinheim, Germany, 2005)

Introduction

Molybdenum oxide based materials are of contemporary interest due to their promising applications in the area of catalysis, sorption, electrical conductivity, magnetism, photochemistry, sensors, and energy storage.[1–5] Among these, transition-metal-containing molybdates are attractive candidates due to their structural, electronic, and catalytic properties.[6–10] For example, β-$FeMoO_4$ and $Fe_2(MoO_4)_3$ have been employed in the synthesis of formaldehyde from methanol on a commercial scale, and Fe–Mo–O catalysts exhibit good activity for the oxidation of toluene to benzaldehyde.[11] In addition, it has been found that β-$FeMoO_4$ is a very good precursor of catalysts for hydrodesulfurization (HDS) processes,[12] and cobalt and nickel molybdates are important components of industrial catalysts for the partial oxidation of hydrocarbons and precursors in the synthesis of catalysts for hydrodesulfurization (HDS). Manganese- and nickel-containing molybdates are also potential electrode materials in rechargeable lithium batteries.[13] In recent times, soft chemistry routes, including hydrothermal reactions, have been commonly employed for the manipulation of hybrid molybdates in the presence of organic molecules as structure directors. The role of organic amines has been extensively investigated in the formation of discrete polyoxometalate clusters to three-dimensional networks of molybdenum oxide based materials.[14–20] It is well known that when polyoxomolybdate(POM)-based solids are crystallized from aqueous solution (either under ambient or hydrothermal conditions) in the presence of organic amines, organic/inorganic hybrid salts are invariably formed. These may be salts between organic cations and discrete polyoxomolybdate anions or composite solids with extended POM anions incorporated with organic cations. If an additional transition metal ion is present, the metal complex can either be present as a countercation or as part of the extended network linking POM cluster anions. An examination of the synthetic methodologies reported in the literature suggests that there have been very few attempts to rationalize the reactivity pattern in the formation of these solids. It is important to examine the role of organic amines in a systematic fashion to understand the critical issues involved in controlling the reaction and hence the structure of molybdates, even though hydrothermal reactions are commonly termed as "black-box" in nature. This paper is an attempt in this direction to identify the phases formed in the presence of an organic amine by employing identical reaction conditions and varying only the nature of the metal. We preferred the aromatic diamine 2-aminopyridine ($pK_a \approx 6.9$) as it forms weak complexes with transition metals and hence is readily labile in the presence of hydroxy ligands (Scheme 1) during hydrolysis and condensation reactions to produce an –M–O–Mo–O–M– network. Also, the amine has good solubility in aqueous solution and is hydrothermally stable. This paper describes the synthesis and characterization of several molybdates and proposes a rational model to explain the influence of 2-aminopyridine on their formation under hydrothermal conditions.

Results and Discussion

Powder X-ray diffraction analysis showed that single-phase crystalline molybdates were obtained only from the reactions containing manganese, cobalt, nickel, copper, or

[a] Department of Chemistry, Indian Institute of Technology, New Delhi 110016, India
Fax: +91-11-26582037
E-mail: aramanan@chemistry.iitd.ac.in

 DOI: 10.1002/ejic.200500092

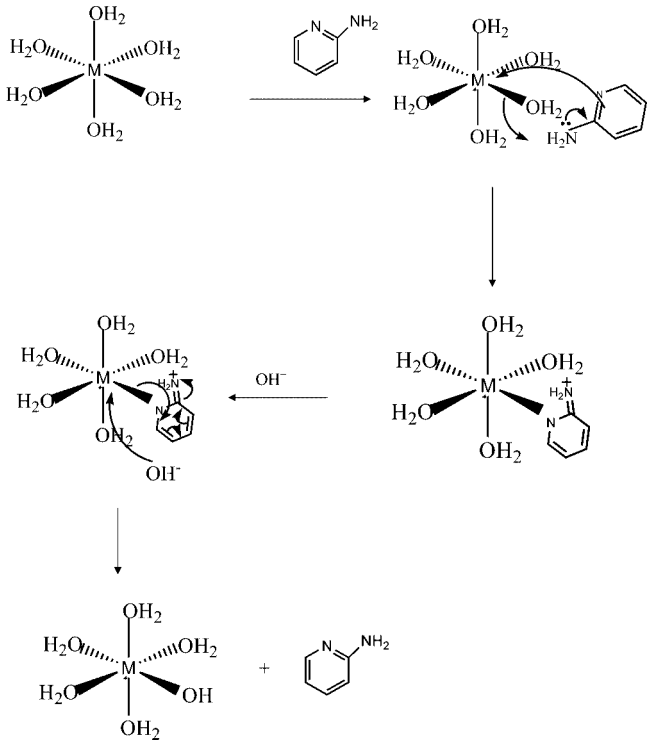

Scheme 1. Role of 2-ampy as a labile group in the hydrolysis condensation of a metal complex.

zinc. In the case of iron(II) chloride, hydrothermal treatment led to amorphous products. Table 1 lists the experimental conditions applied for the hydrothermal synthesis of molybdates, along with phase identification as established by powder and single-crystal X-ray diffraction. Scheme 2 shows the molybdates that were crystallized under hydrothermal conditions in the presence of 2-ampy. In all cases the yields were much higher than 70% (based on molybdenum) and the compounds were isolated as single phases, as determined by thermal studies and powder XRD. The powder X-ray diffraction patterns of $MnMoO_4$ (**4**) and $ZnMoO_4$ (**5**) are similar and the cell parameters and intensities correspond to the Wolframite structure reported in the literature.[21–23] In the case of cobalt and nickel, we obtained a polyoxometalate-based solid **2** that does not contain cobalt or nickel. Hydrothermal treatment of ammonium heptamolybdate and 2-ampy in the absence of a transition metal led to another new solid **1**. The crystal structures of solids **1** and **2** were further established by single-crystal X-ray diffraction. The hydrothermal reaction of ammonium molybdate solution with copper(II) ions in the presence of 2-ampy resulted in the formation of the pure Lindgrenite phase $Cu_3Mo_2O_8(OH)_2$ (**3**). Interestingly, this is the first laboratory synthesis and characterization of the mineral Lindgrenite. Both powder and single-crystal X-ray diffraction data of the product are consistent with the previously reported

Table 1. Experimental details.

Reactants, molar ratio, initial pH	Phase	Space group	Cell parameters	Colour/Morphology
$(NH_4)_6Mo_7O_{24}{\cdot}4H_2O$/2-ampy/$H_2O$, 1:12:1600, pH ≈ 6	$(C_5N_2H_7)_4Mo_8O_{26}$ (**1**) one-dimensional chains	$P2_1/c$ $Z = 2$	$a = 8.243(1)$ Å $b = 20.623(3)$ Å $c = 11.602(1)$ Å $\beta = 93.948(2)°$ $V = 1967.9(5)$ Å^3	White rods
$(NH_4)_6Mo_7O_{24}{\cdot}4H_2O$/$MnCl_2{\cdot}4H_2O$/2-ampy/$H_2O$, 1:8:12:1600, pH ≈ 6	$MnMoO_4$ (**4**) Wolframite	$P2/c$ $Z = 2$	$a = 4.8064$ (4) Å $b = 5.7482$ (4) Å $c = 4.9606$ (5) Å $\beta = 90.831(5)°$ $V = 137.7(1)$ Å^3	Brown rods
$(NH_4)_6Mo_7O_{24}{\cdot}4H_2O$/$Co(CH_3COO)_2{\cdot}6H_2O$ or $NiSO_4{\cdot}6H_2O$/2-ampy/H_2O, 1:8:12:1600, pH ≈ 6	$(C_5N_2H_7)_6Mo_7O_{24}{\cdot}3H_2O$ (**2**) zero-dimensional cluster	$P2_1/n$ $Z = 4$	$a = 14.828(1)$ Å $b = 17.5145(1)$ Å $c = 20.863(1)$ Å $\beta = 107.500(1)°$ $V = 5167.5(6)$ Å^3	Brown blocks
$(NH_4)_6Mo_7O_{24}{\cdot}4H_2O$/$CuCl_2{\cdot}2H_2O$/2-ampy/$H_2O$, 1:8:12:1600, pH ≈ 6	$Cu_3Mo_2O_8(OH)_2$ (**3**) Lindgrenite	$P2_1/n$ $Z = 2$	$a = 5.3928(9)$ Å $b = 14.022(2)$ Å $c = 5.607(1)$ Å $\beta = 98.473$ (3)° $V = 419.43(1)$ Å^3	Green rods
$(NH_4)_6Mo_7O_{24}{\cdot}4H_2O$/$CuCl_2{\cdot}2H_2O$/$H_2O$, 1:8:1600, pH ≈ 6	$(NH_4)_xMo_6O_{18}.yH_2O$ (**6**)	$P\bar{3}$ $Z = 1$	$a = 10.5388(7)$ Å $c = 3.7242(5)$ Å $V = 358.22(6)$ Å^3	White, hexagonal rods
$(NH_4)_6Mo_7O_{24}{\cdot}4H_2O$/$ZnSO_4{\cdot}7H_2O$/2-ampy/$H_2O$, 1:8:12:1600, pH ≈ 6	$ZnMoO_4$ (**5**) Wolframite	$P2/c$ $Z = 2$	$a = 4.668(5)()$ Å $b = 5.7194(6)$ Å $c = 4.8719(6)$ Å $\beta = 89.72(1)°$ $V = 130.07$ Å^3	Black blocks

 © 2005 Wiley-VCH Verlag GmbH & Co. KGaA, Weinheim

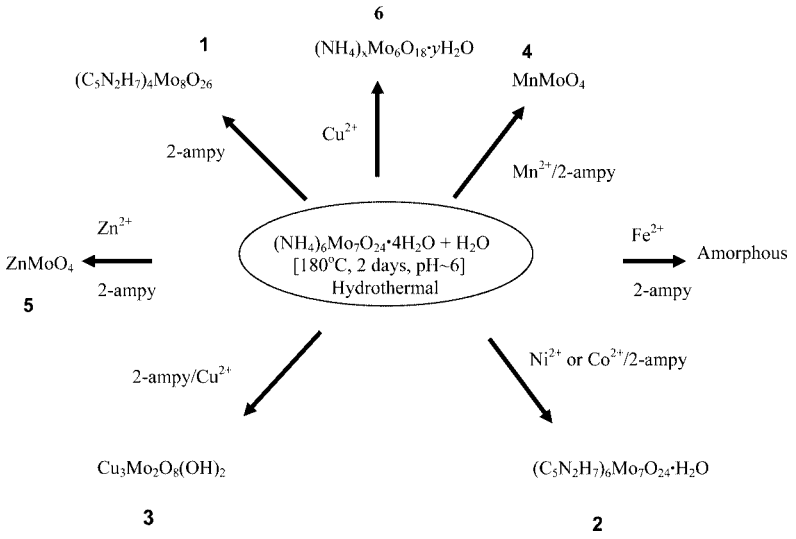

Scheme 2. Experimental details.

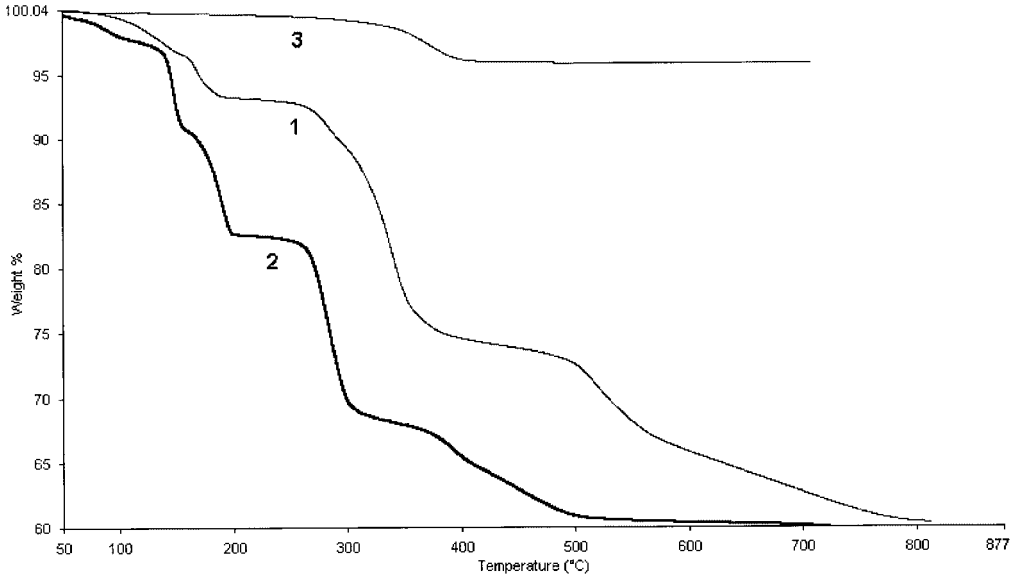

Figure 1. TGA data of compounds **1**–**3**.

crystal structure of the mineral.[24] This solid does not contain 2-ampy and, in its absence, the hydrothermal reaction yields the well-known hexagonal molybdate $(NH_4)_x$-$Mo_6O_{18}{\cdot}yH_2O$ (**6**).[25,26] However when the reaction was carried out with MoO_3 as a starting precursor it resulted in the formation of compound **2**, which is based on a heptamolybdate cluster**.** This indicates that the heptamolybdate phase is stable under these conditions. Thermal analysis of the solids was carried out under nitrogen (Figure 1). $MnMoO_4$(**4**) and $ZnMoO_4$(**5**) do not show any significant weight loss, thus confirming that they are anhydrous substances. In case of **3**, a broad weight loss in the temperature range 175–400 °C shows the loss of one water molecule to give a final composition of $Cu_3Mo_2O_9$. Both **1** and **2** lose their water molecules and organic groups in multiple steps. Weight loss up to 500 °C is probably due to the loss of water and organic groups and corresponds to the composition determined from single-crystal X-ray analysis.

Crystal Structure of 1

The crystal structure of **1** consists of 2-ampy cations and infinite anionic molybdenum oxide chains that are built from edge-sharing octamolybdate clusters $[Mo_8O_{28}]$ (Figure 2a). The $\{Mo_8O_{26}\}_\infty$ chains propagate along the *a*-axis (Figure 2d). Each chain is surrounded by six others (Figure 3). The interchain regions are filled with 2-ampy cations that participate in extensive, strong hydrogen bonding with cluster oxygen atoms. Each Mo_8O_{28} cluster is hydrogen-bonded to four 2-ampy cations through the terminal oxygen atoms O3 and O10 of the cluster. The crystal data are pro-

 © 2005 Wiley-VCH Verlag GmbH & Co. KGaA, Weinheim

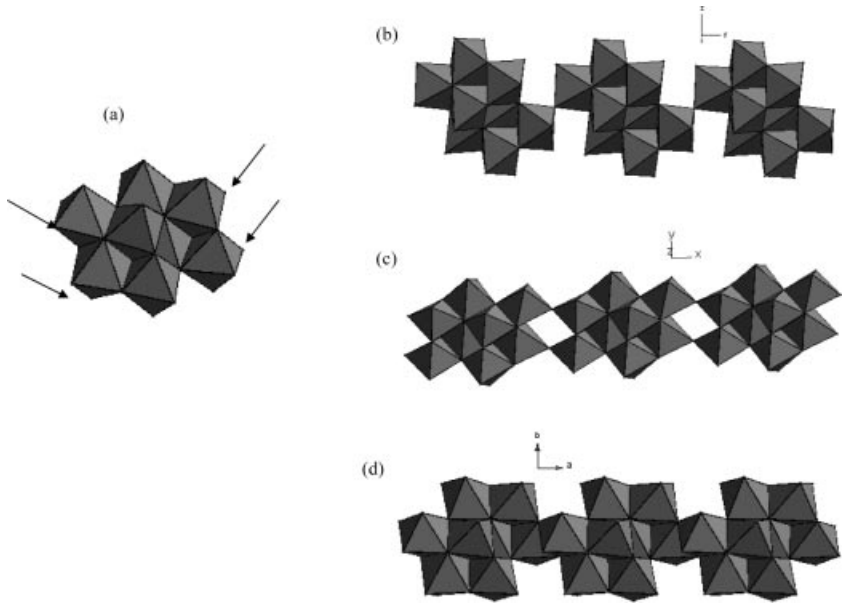

Figure 2. (a) Polyhedral representation of the octamolybdate. Sites through which the subunits are linked into infinite chains in **1** are denoted with arrows. (b) The linkage of octamolybdates through common corners to form chains with the $(Mo_8O_{27})_n^{6n-}$ composition. (c) The linkage of octamolybdates is through pairs of Mo–O–Mo bridges to form a molybdenum oxide chain with the $(Mo_8O_{26})_n^{4n-}$ composition. (d) The linkage of octamolybdates through common edges to form chains with the $(Mo_8O_{26})_n^{4n-}$ composition as in the case of **1**.

vided in Table 2. The Mo–O distances are significantly different due to multiple bonding character and range from 1.687(3) to 2.504 (3) Å. The octamolybdate chains found in **1** are similar to those in two other tetramolybdates, namely $K_2Mo_4O_{13}$[27] and $(NH_4)_2Mo_4O_{13}$.[28] Two other octamolybdates with a slightly different composition, namely $(NH_4)_6Mo_8O_{27}\cdot 4H_2O$ and $(C_4H_{12}N_2)_3Mo_8O_{27}$ ($C_4H_{12}N_2$ = piperazinium ion),[29] and a polymeric octamolybdate [$(MeNC_5H_5)_4Mo_8O_{26}$] reported by Zubieta et al.[30] are also known. The composition of the polymeric solid depends upon the connectivity pattern between the basic octamolybdate fragments. In $(MeNC_5H_5)_4Mo_8O_{26}$, the octamolybdate subunits are connected by linear and symmetrical Mo–O–Mo bridges into infinite chains (Figure 2c), while in $(NH_4)_6Mo_8O_{27}\cdot 4H_2O$ and $(C_4H_{12}N_2)_3Mo_8O_{27}$, the octamolybdate subunits share common corners (Figure 2b). The linkage of octamolybdate blocks through common edges, i.e., the connectivity mode encountered in $(C_5N_2H_7)_4[Mo_8O_{26}]$ (**1**), again results in an $[Mo_8O_{26}]^{4-}$ stoichiometry for the chains (Figure 2d).

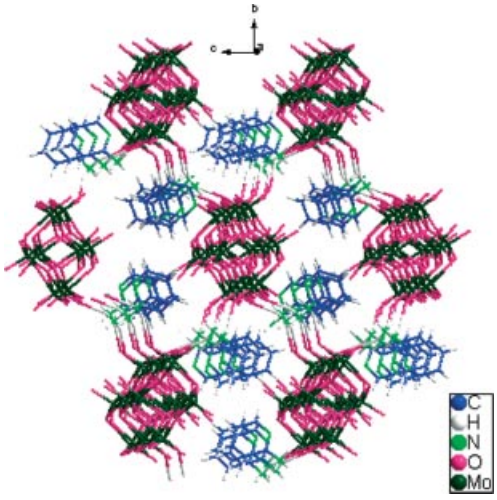

Figure 3. Projection of the unit cell of **1** along the *a*-axis showing the H-bonding between the octamolybdate chain and 2-aminopyridine.

Table 2. Crystal data of compounds **1**–**3**.

Empirical formula	**1**	**2**	**3**
Crystal system	monoclinic	monoclinic	monoclinic
Space group	$P2_1/c$	$P2_1/n$	$P2_1/n$
T [K]	300(2)	300(2)	300(2)
a [Å]	8.243(1)	14.8280(10)	5.3928(9)
b [Å]	20.623(3)	17.5145(12)	14.023(2)
c [Å]	11.602(1)	20.8632(14)	5.6076(10)
α [°]	90	90	90
β [°]	93.94	107.5	98.473
γ [°]	90	90	90
V [Å^3]	1967.9(5)	5167.5(6)	419.43(13)
Z	2	4	2
Collected reflections	16770	58670	4313
Unique reflections	4618	12265	988
Observed reflections	4431	11149	984
R [$I > 2\sigma(I)$]	0.0227	0.032	0.0467
wR_2 (all)	0.06042	0.0957	0.1271

Crystal Structure of 2

The crystal structure of $(C_5N_2H_7)_6Mo_7O_{24}\cdot 3H_2O$ (**2**) is that of a heptamolybdate $[Mo_7O_{24}]^{6-}$ based solid. The Mo_7O_{24} cluster anion contains a central $\{Mo_3O_8\}$ core

 © 2005 Wiley-VCH Verlag GmbH & Co. KGaA, Weinheim

built of three edge-shared MoO_6 octahedral units arranged in a 1×3 rectangular array; two MoO_6 units from above and two from below share the equatorial oxygen atoms at the apices of the octahedra in the rectangle. Each Mo^{VI} atom in the Mo_7O_{24} cluster has a distorted octahedral geometry with an Mo–O bond length in the range of 1.702(3)–2.298(2) Å for terminal and bridging oxygen atoms. Each $Mo_7O_{24}^{6-}$ anion is surrounded by six 2-ampy cations (Figure 4). Each cluster anion exhibits strong H-bonding with six of the 2-ampy cations and only terminal oxygen atoms participate in this H-bonding. Although all six 2-ampy cations are involved in H-bonding, only two of them connect the clusters into an extended 1D chain (Figure 5). The water molecules present also form strong H-bonds among themselves as well as with cluster oxygen atoms. This solid is identical to that reported in the literature, except that we have grown it under hydrothermal conditions.[31] All the bond angles and distances are consistent with Mo_7O_{24} clusters observed in previous reports.[32–34]

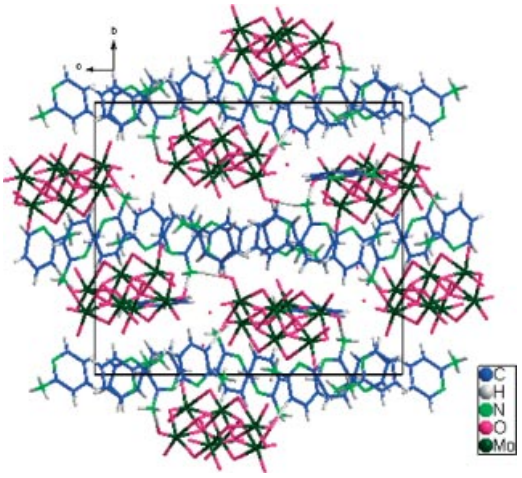

Figure 4. $\{Mo_7O_{24}\}^{6-}$ cluster anions exhibiting H-bonding with water and 2-aminopyridinium cations in **2**.

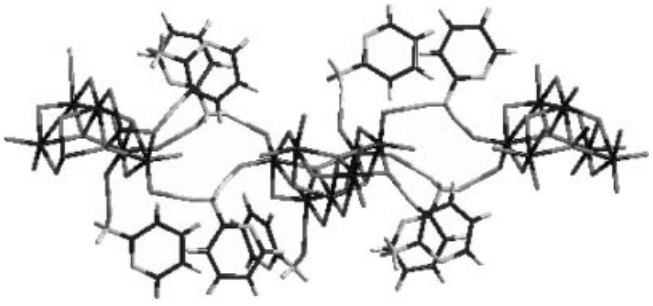

Figure 5. View showing the infinite 1D chain formation of $\{Mo_7O_{24}\}^{6-}$ clusters via the strong H-bonding with 2-aminopyridium cations in **2**.

Crystal Structure of 3

The single-crystal structural analysis of **3** is very similar to that of the naturally occurring mineral Lindgrenite solved by Hawthorne et al.[24] The vanadium analog of **3** has also been reported recently.[35] There are two asymmetric copper atoms in the crystal structure of the synthetic analog of Lindgrenite $[Cu_3Mo_2O_8(OH)_2]$, one of which occurs at the special position, as well as one asymmetric molybdenum and five asymmetric oxygen atoms which all occupy the general position (4e). While the molybdenum atoms are coordinated by four oxygen atoms in a pseudo-tetrahedral arrangement, the copper atoms are pseudo-octahedrally coordinated by oxygen atoms. There is a strong Jahn–Teller distortion around both copper centers, with considerable extension of the apical bonds when compared with the equatorial bonds. The two hydrogen atoms are bonded to O1 and O4. A prominent feature of the Lindgrenite structure is the strips of edge-sharing CuO_6 octahedra that run parallel to the *c*-axis (Figure 6). These strips are cross-linked by MoO_4 tetrahedra that share corners with the CuO_6 octahedra; each MoO_4 tetrahedron links three strips together, with the fourth linkage occurring along the length of one of the strips (Figure 7).

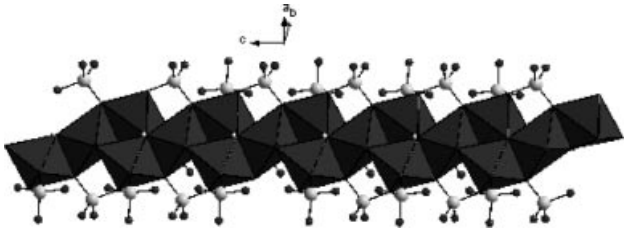

Figure 6. Strips of edge-sharing CuO_6 octahedra running parallel to the *c*-axis in **3**.

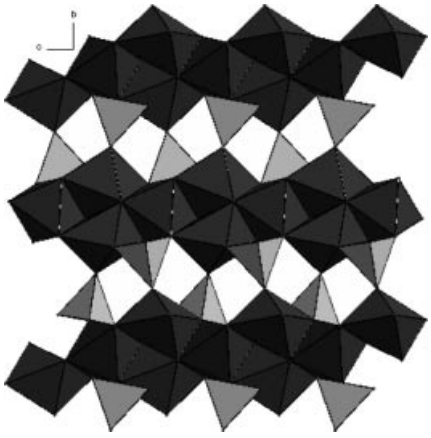

Figure 7. Crystal structure of Lindgrenite (**3**) viewed along the *c*-axis.

Crystal Structures of 4 and 5

The powder X-ray diffraction patterns of $MnMoO_4$ (**4**) and $ZnMoO_4$ (**5**) are isostructural and suggest a Wolframite structure based on the cell parameters and intensities. We did not succeed in obtaining suitable single crystals under our reaction conditions. Both the molybdenum and manganese or zinc atoms in the Wolframite structure are octahedrally coordinated. Each octahedron has two short, two

 © 2005 Wiley-VCH Verlag GmbH & Co. KGaA, Weinheim

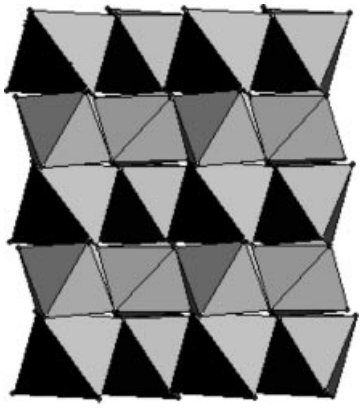

Figure 8. Crystal structural of $MMoO_4$ (M = Mn and Zn).

medium, and two long metal–oxygen bonds (Figure 8). The metal atoms occupy special positions while the oxygen atoms are at general positions. The octahedra are highly distorted with angles ranging from 72.9 (1) to 101.7 (1)° in the molybdenum-containing octahedron and from 75.7(1) to 110.6(2)° in the manganese one. Compounds **4** and **5** have also been synthesized earlier by other groups.[21–23] To the best of our knowledge, however, this is the first report of a low-temperature hydrothermal method for the synthesis of $MnMoO_4$ and $ZnMoO_4$.

Chemistry of the Formation of Molybdates by Hydrothermal Treatment

When heptamolybdates are dissolved in aqueous solution in the presence of 2-ampy (pH ≈ 6.0), other molybdate species such as $[MoO_3(OH)]^-$, $MoO_2(OH)_2(H_2O)_2$, $[Mo_8O_{26}]^{4-}$, and $[H_2Mo_8O_{28}]^{6-}$ may form due to a slight change in the pH and ionic strength of the medium, although heptamolybdate is the predominant cluster at equilibrium. The equilibrium species will change considerably when the aqueous molybdate solution is subjected to hydrothermal treatment.

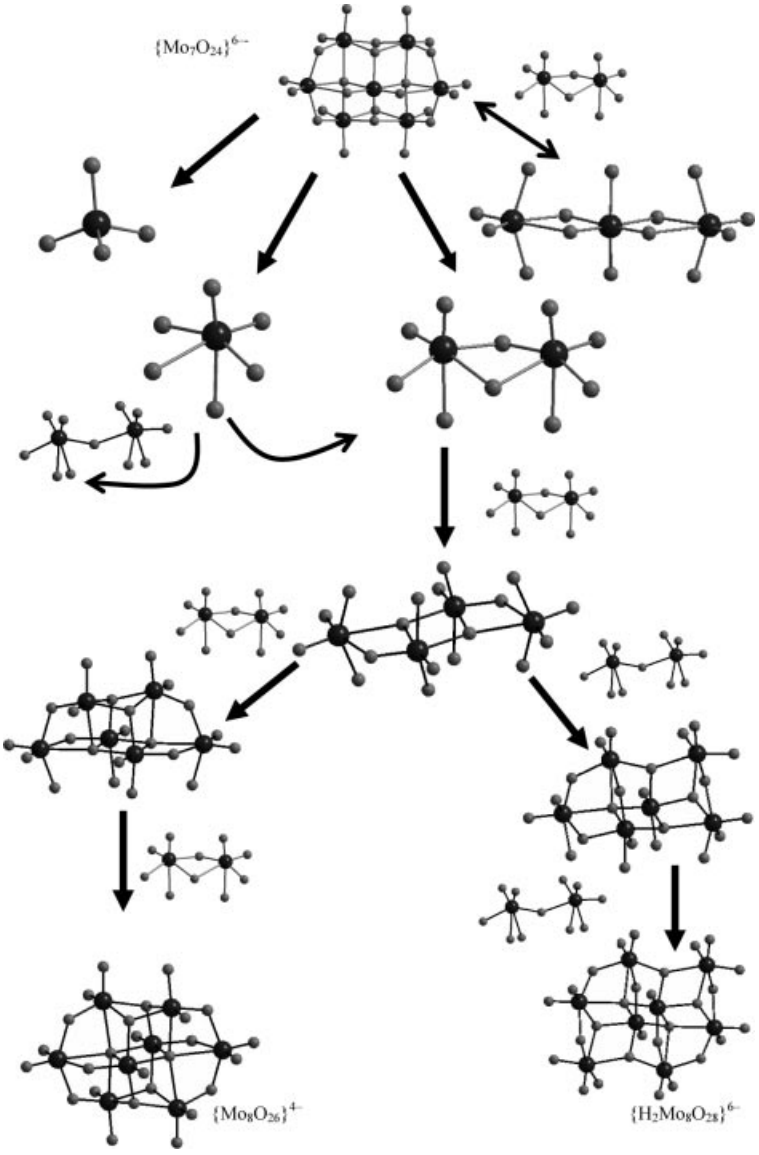

Figure 9. Hypothetical pathway for the self-assembly of polyoxomolybdate cluster anions from heptamolybdates.

 © 2005 Wiley-VCH Verlag GmbH & Co. KGaA, Weinheim

Under these conditions, crystallization of a salt or a solid will be dominated by the electrostatic interactions between the polyoxomolybdate anions and the organic cations; secondary interactions taking place between the hydrated metal ions and other minor molybdate cluster anions, along with noncovalent interactions such as hydrogen bonding, may also influence the structure. On the basis of the solids obtained in this study, it is reasonable to assume that the heptamolybdate cluster anion dominates the equilibrium as long as the reaction is carried out under self-assembly conditions at room temperature without the addition of acid or hydrothermal treatment. In addition, other metal ions in the medium (such as cobalt or nickel) do not compete with the organic ligand (2-ampy in our case). As the larger anion prefers a larger cation, we invariably obtain a salt based on heptamolybdate $[Mo_7O_{24}]^{6-}$ along with the organic cation as in **2**. Since heptamolybdates are hardly protonated, the packing of the final solids is influenced by the hydrogen-bonding interaction between the anions, cations and water molecules, as demonstrated in the structure of **2**. The presence of weakly acidic cobalt or nickel hydrates is responsible for keeping the heptamolybdate clusters stable in solution. The reaction carried out in the absence of these metal ions results in the formation of **1**. Under slightly acidic conditions, the heptamolybdate undergoes fragmentation into smaller units, including MoO_4 and MoO_6 units. A few of these smaller fragments of oxomolybdenum clusters can reassemble to form larger clusters such as $[Mo_8O_{26}]^{4-}$, $[H_2Mo_8O_{28}]^{6-}$, etc. (Figure 9). The cluster $[H_2Mo_8O_{28}]^{6-}$, with its large negative charge, is not completely stable in aqueous solution and under hydrothermal conditions tends to condense to form 1D polymeric chains of the composition $[Mo_8O_{26}]^{4-}{}_\infty$; in the presence of 2-ampy, the solid **1** crystallizes out. A similar framework is also known with K^+ and NH_4^+ cations. When we carried out a hydrothermal reaction of MoO_3 rather than ammonium heptamolybdate with 2-ampy, we obtained only the heptamolybdate cluster based solid **2**. Incidentally, **2** was also obtained when a hydrothermal reaction was carried out in the presence of nickel and cobalt ions. This suggests that the formation of POM clusters such as $[H_2Mo_8O_{28}]^{6-}$ and $[Mo_7O_{24}]^{6-}$ depends on the nature of the starting molybdenum precursor. The reactions occurring in the presence of manganese, copper, and zinc favor a shift in equilibrium towards MoO_x^{n-} species. In the case of Mn and Zn, a Wolframite-based $MMoO_4$ structure is stabilized. Unlike other metal ions, copper(II) ions tend to form polymeric chains[36–38] at around this pH, and these readily react with MoO_4^{2-} ions to give Lindgrenite (**3**). However, hydrothermal treatment of ammonium heptamolybdate with copper(II) ions in the absence of 2-ampy results in ammonium-intercalated hexagonal molybdates. We have previously shown that hexagonal molybdates are the most stable phases formed under hydrothermal conditions in the presence of monovalent alkali metal or ammonium ions.[26] Since we also obtained the Lindgrenite phase from the hydrothermal reaction of sodium molybdate and copper chloride solution (pH ≈ 6), 2-ampy provides a suitable pH for the fragmentation of heptamolybdates into tetrahedral MoO_4. The results reported here suggest that 2-ampy has a major influence on the formation of transition metal molybdates.

Conclusions

The hydrothermal reaction of aqueous ammonium heptamolybdate with manganese, cobalt, nickel, copper, or zinc ions in the presence of 2-aminopyridine results in the formation of several crystalline molybdates. A weak base such as 2-aminopyridine can act as a buffer and form weaker complexes with the transition metal, thus preventing its hydrolysis in aqueous solution. The hydrothermal medium can further influence the condensation of the protonated oxomolybdate clusters or the formation of metal molybdates.

Experimental Section

Syntheses: All chemicals were obtained from Aldrich and used without further purification. $(NH_4)_6Mo_7O_{24}{\cdot}4H_2O$ (0.625 mmol) was mixed with an appropriate amount of transition metal M^{2+} salts (M = Mn, Fe, Co, Ni, Cu, Zn; 5 mmol) and 2-ampy (7.5 mmol) in 18 mL of distilled water (1000 mmol). In order to rationalize the influence of 2-ampy, we also carried out a blank reaction as above without the transition metal chloride. The mixture was transferred into a 30-mL Teflon-lined acid digestion reactor and heated at 180 °C for 2 d and then cooled slowly to room temperature. The pH of the reaction before and after was found to be about 6 in all cases. To investigate the influence of 2-ampy when the molybdenum source is MoO_3, the reaction was carried out by heating the mixture of MoO_3 and 2-ampy in the molar ratio 1:1.5 under the same conditions. In all the cases, the products were washed with water and dried in air at room temperature. All the solids were analyzed by powder X-ray diffraction (Bruker AXS diffractometer with Cu-K_α radiation) for crystallinity and phase identification. TG analyses were carried out with a Perkin–Elmer TGA7 system on well-ground samples under a nitrogen flow with a heating rate of 10 °C min^{-1}. In all cases the phase purity of the samples was established by simulating powder X-ray diffraction patterns on the basis of the single-crystal structure data.

X-ray Crystallography: Single-crystal diffraction studies were carried out with a Bruker SMART CCD diffractometer with Mo-K_α (λ = 0.71073Å) radiation at 28 °C for **1**–**3**. Table 1 lists the experimental parameters used for the single-crystal structure analyses. The software SADABS was used for absorption correction and SHELXTL for space-group and structure determination and refinements.[39,40] The molybdenum atoms were located first and then the remaining atoms were deduced from subsequent difference Fourier syntheses. The hydrogen atoms were located using geometrical constraints. All the atoms except H were refined anisotropically. Least-squares refinement cycles on F^2 were performed until the model converged. Experimental and crystal data are provided in Tables 1 and 2, respectively. CCDC-245096 (**1**) and -249182 (**2**) contain the supplementary crystallographic data for this paper. These data can be obtained free of charge from The Cambridge Crystallographic Data Centre via www.ccdc.cam.ac.uk/data_request/cif. Further details of the crystal-structure investigation for **3** may be obtained from the Fachinformationzentrum Karlsruhe, 76344 Eggenstein-Leopoldshafen, Germany, on quoting the depository number ICSD-415059.

 © 2005 Wiley-VCH Verlag GmbH & Co. KGaA, Weinheim

Acknowledgments

K. P. thanks the CSIR for a research fellowship and A. R. acknowledges the DST, Government of India, for financial support. We thank Dr. N. G. Ramesh for helpful discussions. A. R. also thanks the DST for funding a powder X-ray diffractometer under IRHPA and a Smart Apex CCD single-crystal X-ray diffractometer under FIST for the Department of Chemistry at IIT, Delhi.

[1] A. M. Chippindale, A. K. Cheetham, in: *Studies in Inorgonic Chemistry*, Elsevier, Amsterdam, **1994**, vol. 19, p. 146–184, and references cited therein.
[2] L. F. Johnson, G. D. Boyd, K. Nassau, R. R. Soden, *Phys. Rev.* **1962**, *126*, 1406.
[3] D. W. Bruce, D. O.Hare, *Inorganic Materials*, Wiley, Chichester, **1992**.
[4] T. Bein, "Supramolecular Architecture", *ACS Symp. Ser.* **1992**, p. 499.
[5] A. K. Cheetham, *Science* **1994**, *264*, 794, and references cited therein.
[6] S. Soo Kim, S. Ogura, H. Ikuta, Y. Uchimoto, M. Wakihara, *Solid State Ionics* **2002**, *146*, 249–256.
[7] J. L. Brito, A. L. Barbosa, *J. Catal.* **1997**, *171*, 467–475.
[8] J. Miller, A. G. Sault, N. B. Jackson, L. Evans, M. Gonzales, *Catal. Lett.* **1999**, *58*, 147–152.
[9] L. M. Madeira, M. F. Portela, C. Mazzochia, A. Kaddouri, R. Anouchinsky, *Catal. Today* **1998**, *40*, 229–243.
[10] G. E. Vrieland, C. B. Murchison, *Appl. Catal. A* **1996**, *134*, 101–121.
[11] H. Zhang, J. Shen, X. Ge, *J. Solid State Chem.* **1995**, *117*, 127–135.
[12] J. A. Rodriguez, J. C. Hanson, S. Chaturvedi, A. Maiti, J. L. Brito, *J. Phys. Chem. B* **2000**, *104*, 8145–8152.
[13] Y. Idemoto, H. Sekine, K. Ui, N. Koura, *Solid State Ionics* **2005**, *176*, 299–306.
[14] A. Briceno, R. Atencio, *Acta Crystallogr., Sect. E* **2004**, *60*, i47–i49.
[15] J. B. Strong, G. P. A. Yap, R. Ostrander, L. M. Liable-Sands, A. L. Rheingold, R. Thouvenot, P. Gouzerh, E. A. Maatta, *J. Am. Chem. Soc.* **2000**, *122*, 639–649.
[16] D. G. Allis, R. S. Rarig, E. Burkholder, J. Zubieta, *J. Mol. Struct.* **2004**, *688*, 11–31.
[17] P. J. Hagrman, D. Hagrman, J. Zubieta, *Angew. Chem. Int. Ed.* **1999**, *38*, 2639–2684.
[18] P. Q. Zheng, Y. P. Ren, L. S. Long, R. B. Huang, L. S. Zheng, *Inorg. Chem.* **2005**, *44*, 1190–1192.
[19] T. Duraisamy, A. Ramanan, J. J. Vittal, *J. Mater. Chem.* **1999**, *9*, 763–767.
[20] S. Upreti, A. Ramanan, *Inorg. Chim. Acta* **2005**, *358*, 1241–1246.
[21] A. W. Sleight, B. L. Chamberland, *Inorg. Chem.* **1968**, *7*, 1672–1675.
[22] A. P. Young, C. M. Schwartz, *Science* **1963**, *141*, 348–349.
[23] A. Clearfield, A. Moini, P. R. Rudolf, *Inorg. Chem.* **1985**, *24*, 4606–4609.
[24] F. C. Hawthorne, R. K. Eby, *Neues Jahrb. Mineral., Monatsh.* **1985**, *5*, 234–240.
[25] N. Sotani, *Bull. Chem. Soc. Jpn.* **1975**, *48*, 1820–1825.
[26] S. Upreti, A. Ramanan, *Proc. Indian Acad. Sci. (Chem. Sci.)* **2003**, *115*, 411–417.
[27] B. M. Gatehouse, P. Leverette, *J. Chem. Soc., A* **1971**, 2107–2112.
[28] R. Benchrifa, M. Leblanc, R. de Pape, *Eur. J. Solid State Inorg. Chem.* **1989**, *26*, 593–601.
[29] W. T. A. Harrison, L. L. Dussack, A. J. Jacobson, *Acta Crystallogr., Sect. C* **1996**, *52*, 1075–1077.
[30] B. Modec, J. V. Brencic, J. Zubieta, *Inorg. Chem. Commun.* **2003**, *6*, 506–512.
[31] P. Roman, J. M. Gutierrez Zorrilla, R. M. Martinez, S. G. Blanco, *Transition Met. Chem.* **1986**, *11*, 143–150.
[32] Z. Han, H. Ma, J. Peng, Y. Chen, E. Wang, N. Hu, *Inorg. Chem. Commun.* **2004**, *7*, 182–185.
[33] H. A. Hashmi, *Solid State Ionics* **1997**, *96*, 209–214.
[34] P. Gili, P. A. Lorenzo Luis, A. Mederos, J. M. Arrieta, G. Germain, A. Castineiras, R. Carballo, *Inorg. Chim. Acta* **1996**, *295*, 106–114.
[35] C. D. Wu, C. Z. Lu, H. H. Zhuang, J. S. Huang, *Eur. J. Inorg. Chem.* **2003**, 2867–2871.
[36] S. Vilminot, M. R. Plouet, G. Andre, D. Swierezynski, M. Guillot, F. B. Vigneron, M. Drillon, *J. Solid State Chem.* **2003**, *170*, 255–264.
[37] R. Baies, V. Caignaert, V. Pralong, B. Raveau, *Inorg. Chem.* **2005**, *44*, 2376–2380.
[38] Y. Xu, J. Lu, N. K. Goh, *J. Mater. Chem.* **1999**, *9*, 1599–1602.
[39] G. M. Sheldrick, *Acta Crystallogr., Sect. A* **1990**, *46*, 467–473.
[40] G. M. Sheldrick, *SHELXTL-NT2000*, version 6.12, reference manual, University of Göttingen, Germany.

Received: January 28, 2005
Published Online: July 4, 2005

 © 2005 Wiley-VCH Verlag GmbH & Co. KGaA, Weinheim

Synthesis and Crystal Structures of $[W(3,6\text{-dichloro-1,2-benzenedithiolate})_3]^{n-}$ (n = 1, 2) and $[Mo(3,6\text{-dichloro-1,2-benzenedithiolate})_3]^{2-}$: Dependence of the Coordination Geometry on the Oxidation Number and Counter-Cation in Trigonal-Prismatic and Octahedral Structures

Hideki Sugimoto,*[a] Yuuki Furukawa,[a] Makoto Tarumizu,[a] Hiroyuki Miyake,[a] Koji Tanaka,[b] and Hiroshi Tsukube[a]

Keywords: Coordination modes / Molybdenum / S ligands / Salt effects / Tungsten

The novel complexes $(Et_4N)_2[W(bdtCl_2)_3]$ (**1a**), $(Ph_4P)_2[W(bdtCl_2)_3]$ (**1b**), $(Et_4N)[W(bdtCl_2)_3]$ (**2a**), $(Ph_4P)[W(bdtCl_2)_3]$ (**2b**), $(C_5NH_6)[W(bdtCl_2)_3]$ (**2c**), and $(Et_3NH)_2[Mo(bdtCl_2)_3]$ (**3a**) ($bdtCl_2$ = 3,6-dichloro-1,2-benzenedithiolate) were prepared and characterized by X-ray crystallographic, UV/Vis spectroscopic, and electrochemical methods. Versatile geometrical changes around the tungsten centers were observed. The trigonal-prismatic structure of the tungsten center in $(Et_4N)_2[W(bdtCl_2)_3]$ (**1a**) is changed to an intermediate structure between trigonal prismatic and octahedral upon solid-state oxidation of the complex to $(Et_4N)[W(bdtCl_2)_3]$ (**2a**). Replacement of the counter-cation of $(Et_4N)_2[W(bdtCl_2)_3]$ (**1a**) with Ph_4P^+ also resulted in geometrical changes and somewhat of an octahedral contribution is included in $(Ph_4P)_2[W(bdtCl_2)_3]$ (**1b**). However, almost the same coordination structures are present in the series of structures $(Et_4N)[W(bdtCl_2)_3]$ (**2a**), $(Ph_4P)[W(bdtCl_2)_3]$ (**2b**), and $(C_5NH_6)[W(bdtCl_2)_3]$ (**2c**), with an oxidation number of +5. These structures adopt an intermediate geometry between trigonal prismatic and octahedral. No geometrical change was observed upon changing the metal center from tungsten to molybdenum in $[M(bdtCl_2)_3]^{2-}$ (M = W and Mo).
(© Wiley-VCH Verlag GmbH & Co. KGaA, 69451 Weinheim, Germany, 2005)

Introduction

In recent years, much attention has been directed toward the synthesis of metal complexes containing dithiolene ligands. This interest is primarily due to their utility in magnetic materials, superconductors, nonlinear optical materials, luminescent sensors, and enzyme catalytic centers.[1–4] The synthetic routes to tungsten and molybdenum complexes with dithiolene ligands have been extensively developed,[5,6] and their tris(dithiolene) complexes have been well characterized.[7] These tris(dithiolene) complexes show interesting characteristics in terms of both reversible electron-transfer reactions and geometrical variations around the metal centers. Although six-coordinate metal complexes generally exhibit an octahedral coordination geometry to minimize ligand interactions, it is well known that tris(dithiolene) complexes of molybdenum and tungsten can adopt both octahedral (OCT) and trigonal-prismatic (TP) structures (Scheme S1 in the Supporting Information).[7]

According to the classification of Beswick et al., the coordination geometries are found to largely depend on the nature of the coordinated dithiolene ligands.[7] $[M(mnt)_3]^{2-}$ (M = W and Mo; mnt = 1,2-dicyano-1,2-ethylenedithiolate) complexes[8] adopt intermediate structures between OCT and TP [OCT/TP = average of the values for θ/60 and (90 – φ)/(90 – 55) = 53% for M = Mo and W],[7] whereas $[M(S_2C_2Me_2)_3]^{2-}$ (M = W and Mo; $S_2C_2Me_2$ = 1,2-dimethylethylene-1,2-dithiolate) complexes[9] primarily adopt TP structures (OCT/TP = 1% for M = W and 2% for Mo).[7] When the bdt ligand is employed (bdt = benzene-1,2-dithiolate), $[W(bdt)_3]^{2-}$ structures largely depend on these counter-cations. The $(Ph_4As)_2[W(bdt)_3]$ structure[10] is intermediate between TP and OCT (OCT/TP = 44%),[7] whereas $(Et_4N)_2[W(bdt)_3]$[11] adopts a TP structure (OCT/TP = 2%).[7] The oxidation numbers of the metal centers also have an effect on the geometries. Examples of structurally characterized M^{IV}, M^{V}, and M^{VI} complexes with the same dithiolene ligands and counter-cations are limited to $(Et_4N)_n[M(S_2C_2Me_2)_3]^{0/-/2-}$ (M = W and Mo, n = 0, 1, and 2),[9,12] but all the six complexes adopt near TP geometries.[7] On the other hand, $[W(bdt)_3]^{0/-/2-}$ [10–14] and $[W(S_2C_2Ph_2)_3]^{0/-}$ ($S_2C_2Ph_2$ = 1,2-phenylethylene-1,2-dithiolate)[15] structures adopt variable geometries ranging from OCT/TP = 0% to OCT/TP = 62% (former), and from 39% to 2% (latter).[7] Because these complexes have different

[a] Department of Chemistry, Graduate School of Science, Osaka City University,
Sumiyoshi-ku 3-3-138, Osaka 558-8585, Japan
Fax: +81-6-6605-2522
E-mail: sugimoto@sci.osaka-cu.ac.jp
[b] Institute for Molecular Science,
Higashiyama, Okazaki, 444–8787, Japan
Supporting information for this article is available on the WWW under http://www.eurjic.org or from the author.

 © 2005 Wiley-VCH Verlag GmbH & Co. KGaA, Weinheim **DOI: 10.1002/ejic.200500074**

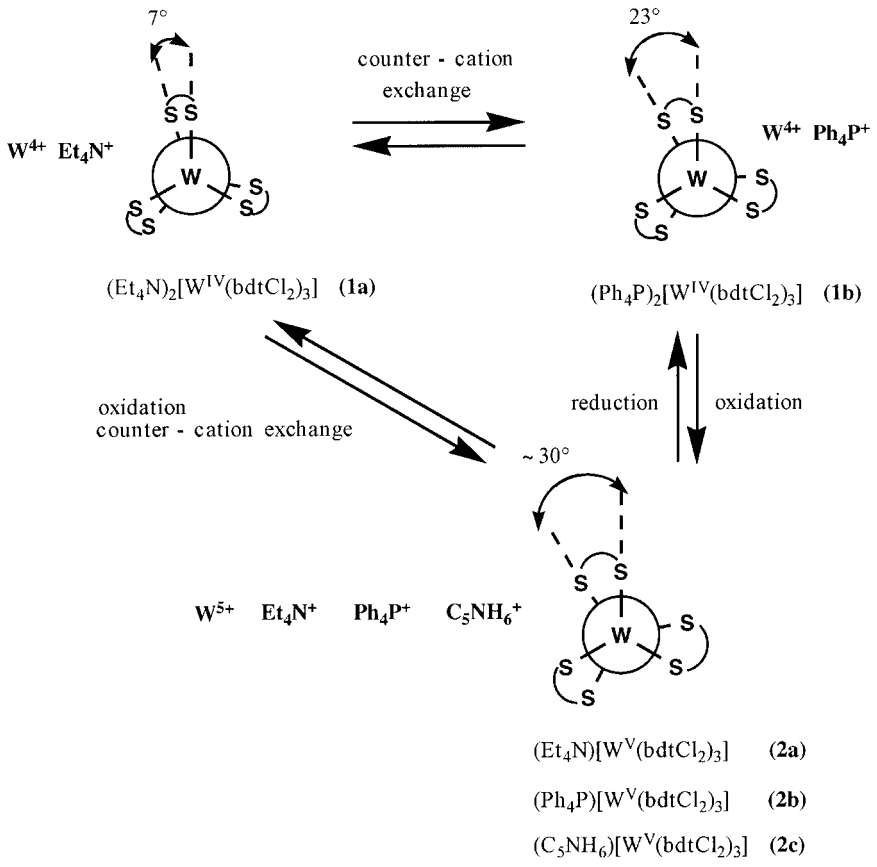

Scheme 1. Diagram showing geometrical changes.

counter-cations, including $Me_2Ph_2P^+$, Me_4N^+, Et_4N^+, Ph_4As^+, and $PhCH_2(Et)_3N^+$, and the effects of the oxidation number and counter-cation on the geometry still remain unclear, we have systematically characterized a series of $[M(dithiolene)_3]^{-/2-}$ (M = W and Mo) complexes containing the same counter-cations but weaker electron-donating dithiolene ligands than $S_2C_2Me_2$. The structural comparison between the tris($bdtCl_2$) complexes of tungsten and molybdenum ($bdtCl_2$ = 3,6-dichloro-1,2-benzenedithiolate) $(Et_4N)_2[W(bdtCl_2)_3]$ (**1a**), $(Ph_4P)_2[W(bdtCl_2)_3]$ (**1b**), $(Et_4N)[W(bdtCl_2)_3]$ (**2a**), $(Ph_4P)[W(bdtCl_2)_3]$ (**2b**), $(C_5NH_6)[W(bdtCl_2)_3]$ (**2c**), and $(Et_3HN)_2[Mo(bdtCl_2)_3]$ (**3a**) reveals new insights into the factors governing the structures of tris(dithiolene) complexes (Scheme 1).

Results and Discussion

Structural Characterization

Figures 1, 2, and 3 show the crystal structures of the anionic tungsten(IV) complexes **1a** and **1b**, and the molybdenum(IV) complex **3a**, respectively, and Figures 4, 5, and 6 show those of the tungsten(V) complexes **2a**–**2c**, respectively. The metal centers of all anions are coordinated to six sulfur atoms from three $bdtCl_2$ ligands, and all the anions interact with the counter-cations through C–H···S bonds (3–3.6 Å). The crystal structure of **2c** reveals that the pyridinium cation stacks between the aromatic phenyls of two anions (ca. 3.5 Å) to form a chain structure (not shown). The θ and φ values (see Experimental Section) given in Scheme S1 are good indications for a geometry between TP (θ = 0° and φ = 90°) and OCT (θ = 60° and $\varphi \approx$ 55°). The values of our new complexes and related complexes taken from the literature are listed in Table 1.

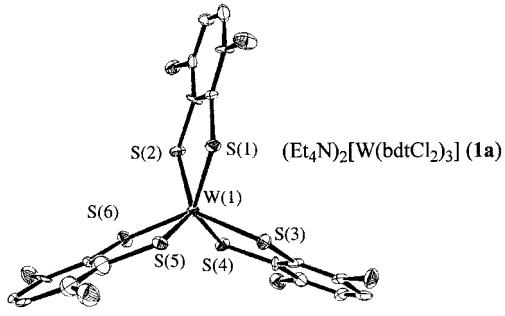

Figure 1. Structure of anion part of **1a** with 50% probability thermal ellipsoids. Selected bond lengths [Å] and angles [°]: W(1)–S(1) 2.374(5), W(1)–S(2) 2.381(5), W(1)–S(3) 2.382(4), W(1)–S(4) 2.358(5), W(1)–S(5) 2.372(4), W(1)–S(6), 2.378(5); S(2)–W(1)–S(1) 81.2(2), S(4)–W(1)–S(1) 141.3(2), S(6)–W(1)–S(1) 131.1(2), S(3)–W(1)–S(2) 128.4(2), S(4)–W(1)–S(2) 82.9(2), S(5)–W(1)–S(2) 139.5(2),S(4)–W(1)–S(3) 81.4(2), S(6)–W(1)–S(3) 141.2(2), S(5)–W(1)–S(4) 130.6(2), S(6)–W(1)–S(5) 81.3(2).

The tungsten(IV) center in **1a** adopts an almost TP structure (θ = 7°, φ = 86°, and OCT/TP = 12%; Scheme S1).

 © 2005 Wiley-VCH Verlag GmbH & Co. KGaA, Weinheim

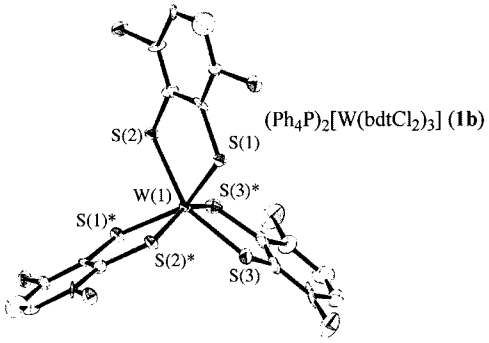

Figure 2. Structures of anion part of **1b** with 50% probability thermal ellipsoids. Selected bond lengths [Å] and angles [°]: W(1)–S(1) 2.380(1), W(1)–S(2) 2.393(1), W(1)–S(3) 2.379(2); S(1)–W(1)–S(1)* 150.63(6), S(2)–W(1)–S(1) 82.62(4), S(3)*–W(1)–S(1) 119.00(5), S(3)*–W(1)–S(2) 153.02(5), S(3)–W(1)–S(2)* 153.02(5), S(3)*–W(1)–S(3) 82.01(6).

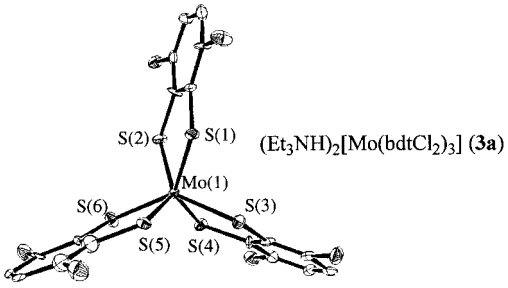

Figure 3. Structure of anion part of **3a** with 50% probability thermal ellipsoids. Selected bond lengths [Å] and angles [°]: Mo(1)–S(1) 2.383(5), Mo(1)–S(2) 2.384(4), Mo(1)–S(3) 2.394(4), Mo(1)–S(4) 2.380(5),Mo(1)–S(5) 2.409(4), Mo(1)–S(6), 2.378(5); S(2)–Mo(1)–S(1) 81.7(2), S(4)–Mo(1)–S(1) 131.7(2), S(6)–Mo(1)–S(1) 136.7(2), S(3)–Mo(1)–S(2) 137.1(2), S(4)–Mo(1)–S(2) 81.7(2), S(5)–Mo(1)–S(2) 134.4(2),S(4)–Mo(1)–S(3) 80.5(2), S(6)–Mo(1)–S(3) 133.6(2), S(5)–Mo(1)–S(4) 137.8(2), S(6)–Mo(1)–S(5) 80.2(2).

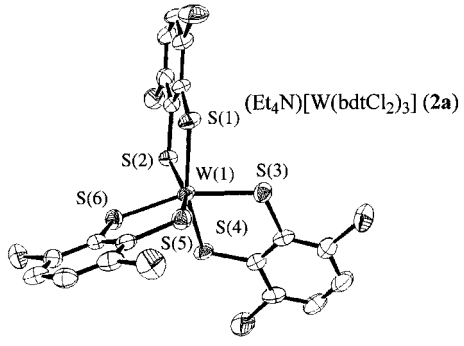

Figure 4. Structure of anion part of **2a** with 50% probability thermal ellipsoids. Selected bond lengths [Å] and angles [°]: W(1)–S(1) 2.369(3), W(1)–S(2) 2.382(3), W(1)–S(3) 2.382(3), W(1)–S(4) 2.382(3), W(1)–S(5) 2.390(3), W(1)–S(6), 2.382(3); S(2)–W(1)–S(1) 82.69(9), S(4)–W(1)–S(1) 110.7(1), S(6)–W(1)–S(1) 157.6(1), S(3)–W(1)–S(2) 159.0(1), S(4)–W(1)–S(2) 84.51(9), S(5)–W(1)–S(2) 111.8(1),S(4)–W(1)–S(3) 82.38(9), S(6)–W(1)–S(3) 109.6(1), S(5)–W(1)–S(4)160.0(1), S(6)–W(1)–S(5) 82.5(1).

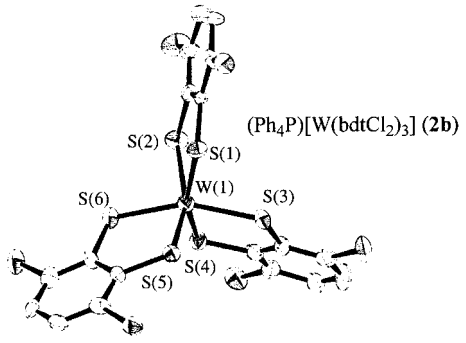

Figure 5. Structure of anion part of **2b** with 50% probability thermal ellipsoids. Selected bond lengths [Å] and angles [°]: W(1)–S(1) 2.389(3), W(1)–S(2) 2.367(2), W(1)–S(3) 2.382(2), W(1)–S(4) 2.382(2), W(1)–S(5) 2.366(2), W(1)–S(6), 2.391(2); S(2)–W(1)–S(1) 82.29(9), S(4)–W(1)–S(1) 111.27(9), S(6)–W(1)–S(1) 154.75(9), S(3)–W(1)–S(2) 155.6(1), S(4)–W(1)–S(2) 82.26(9), S(5)–W(1)–S(2) 114.62(9), S(4)–W(1)–S(3) 82.67(8), S(6)–W(1)–S(3) 113.16(9), S(5)–W(1)–S(4) 155.62(8), S(6)–W(1)–S(5) 85.12(8).

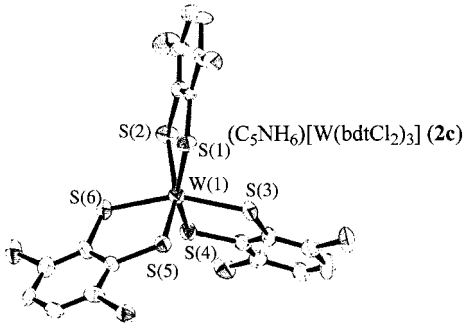

Figure 6. Structure of anion part of **2c** with 50% probability thermal ellipsoids. Selected bond lengths [Å] and angles [°]: W(1)–S(1) 2.385(3), W(1)–S(2) 2.385(3), W(1)–S(3) 2.378(3), W(1)–S(4) 2.379(3), W(1)–S(5) 2.388(3), W(1)–S(6), 2.375(3); S(2)–W(1)–S(1) 82.3(1), S(4)–W(1)–S(1) 114.4(1), S(6)–W(1)–S(1) 157.0(1), S(3)–W(1)–S(2) 157.6(1), S(4)–W(1)–S(2) 84.9(1), S(5)–W(1)–S(2) 110.6(1), S(4)–W(1)–S(3) 82.3(1), S(6)–W(1)–S(3) 111.9(1), S(5)–W(1)–S(4) 157.0(1), S(6)–W(1)–S(5) 81.8(1).

Table 1. Comparison of θ [°], φ [°], and OCT/Tp [%][a] values of **1a**, **1b**, **2a**–**2c**, **3a**, and related complexes.

	θ	φ	OCT/Tp[a]	Ref.
Trigonal prism	0	90	0	
Octahedral	60	≈55	100	
$(Et_4N)_2[W(bdtCl_2)_3]$ (**1a**)	7	86	12	[b]
$(Ph_4P)_2[W(bdtCl_2)_3]$ (**1b**)	23	76	39	[b]
$(Et_4N)[W(bdtCl_2)_3]$ (**2a**)	33	70	56	[b]
$(Ph_4P)[W(bdtCl_2)_3]$ (**2b**)	27	73	45	[b]
$(C_5NH_6)[W(bdtCl_2)_3]$ (**2c**)	30	72	50	[b]
$(Et_3NH)_2[Mo(bdtCl_2)_3]$ (**3a**)	2	88	5	[b]
$(Et_4N)_2[W(bdt)_3]$	4	87	2	[7,11]
$(Ph_4As)_2[W(bdt)_3]$	23	76	44	[7,10]
$(Me_2Ph_2P)[W(bdt)_3]$	30	72	62	[7,13]
$(Ph_4As)_2[W(mnt)_3]$	28	73	53	[7,8]

[a] Average of the values for θ/60 and $(90 - \varphi)/(90 - 55)$. [b] This work.

Interestingly, the coordination geometry of TP changes to an intermediate structure between TP and OCT upon replacing the Et_4N^+ cations of **1a** with the larger Ph_4P^+ cations in **1b** (θ = 23°, φ = 76°, and OCT/TP = 39%), despite the two metal centers having the same oxidation number. Similar geometrical changes were observed between $(Et_4N)_2[W(bdt)_3]$[11] (θ = 4°, φ = 87°, and OCT/TP = 2%)[7] and $(Ph_4As)_2[W(bdt)_3]$[10] (θ = 23°, φ = 76°, and OCT/

 © 2005 Wiley-VCH Verlag GmbH & Co. KGaA, Weinheim

TP = 44%).[7] In both series of $bdtCl_2$ and bdt complexes the smaller counter-cation favors a near TP structure, whereas the larger counter-cation results in an intermediate structure between TP and OCT. Furthermore, when the tungsten(IV) is oxidized (see **1a** vs. **2a**) the coordination geometry changes considerably from an almost TP structure to an intermediate structure between TP and OCT (θ = 33°, φ = 70°, and OCT/TP = 56%). However, in complexes having the larger PPh_4^+ cation, oxidation from **1b** to **2b** (θ = 27°, φ = 73°, and OCT/TP = 45%) results in only slight changes in the coordination geometry.

The θ and φ values of **2c** (θ = 30°, φ = 72°, and OCT/TP = 50%) are similar to those for **2a** and **2b**, indicating that, in tungsten(V) $bdtCl_2$ complexes, geometrical changes rarely occur upon changing the counter-cations. Although $(Me_2Ph_2P)[W(bdt)_3]$[13] was found to adopt an intermediate structure between TP and OCT (θ = 30°, φ = 72°, and OCT/TP = 62%),[7] the structures of $(Me_2Ph_2P)_2[W(bdt)_3]$ and $[W(bdt)_3]^-$, which have different counter-cations from $Me_2Ph_2P^+$, have not been reported. The present results indicate that counter-cations significantly influence the coordination geometries in tungsten(IV) complexes, while little effect is observed in tungsten(V) complexes. Further, the geometries of complexes with small cations such as Et_4N^+ are sensitive to the oxidation state of the metal. The factors governing those geometrical changes have not been identified at this stage, but both packing forces in the crystals and matching of ligand orbitals and metal d orbitals in energies may be important for this series of tungsten $bdtCl_2$ complexes. The molybdenum center in **3a** takes an almost TP structure (θ = 2°, φ = 88°, and OCT/TP = 5%), suggesting that replacement of tungsten with molybdenum in $[M(bdtCl_2)_3]^{2-}$ complexes does not influence the coordination geometry around the metal centers.

Conclusions

A series of tungsten(IV) and -(V) tris(3,6-dichloro-1,2-benzenedithiolate) complexes with Et_4N^+, Ph_4P^+, and pyridinium cations as well as a molybdenum(IV) derivative with an Et_4N^+ cation have been presented. Solid-state crystallographic analysis reveals that the coordination geometries of the six-coordinate tungsten(IV) centers depend significantly on the sizes of the counter-cations, with a trigonal-prismatic geometry for the smaller Et_4N^+ (**1a**) and an intermediate structure between a trigonal prism and an octahedral geometry for the larger Ph_4P^+ (**1b**). On the other hand, tungsten(V) complexes including Et_4N^+, Ph_4P^+, and pyridinium cations (**2a**–**2c**) adopt almost the same intermediate structures. Furthermore, the coordination geometries around tungsten in Et_4N^+ complexes are dependent on the oxidation state of the metal (trigonal prism for W^{IV} and intermediate for W^{V}), except in the case of Ph_4P^+ complexes.

Experimental Section

$(Et_4N)_2[W(bdtCl_2)_3]$ (1a) and $(Et_4N)[W(bdtCl_2)_3]$ (2a): A CH_3CN solution (10 mL) containing H_2bdtCl_2 (0.50 g, 0.0025 mol) and Et_3N (0.75 mL, 0.0047 mol) was added slowly to a suspension of $[WOCl_3(THF)_2]$ (0.45 g, 0.001 mol) in CH_3CN (10 mL) at –40 °C. The solution was warmed to room temperature and stirred for 30 min. The obtained purple suspension was filtered and the filtrate was concentrated to about 6 mL. Addition of Et_4NI (0.38 g, 0.0015 mol) in CH_3OH (15 mL) to the solution gave a purple precipitate. The purple solid was dissolved in the minimum amount of acetone and purified by passing through an alumina column using acetone/CH_3OH as the eluent. A red component of $(Et_4N)_2[W(bdtCl_2)_3]$ was eluted first and then a purple component of $(Et_4N)[W(bdtCl_2)_3]$ was separated. Each solution was evaporated to dryness.

1a: Yield: 0.38 g (35%). $C_{34}H_{46}Cl_6N_2S_6W$ (1071.7): calcd. C 38.11, H 4.33, N 2.61. found C 37.76, H 4.08, N 2.56. UV/Vis (CH_3CN): λ_{max} (ε) = 470 nm (8300 $M^{-1}cm^{-1}$), 535 (4700).

2a: Yield 0.14 g (15%). $C_{26}H_{26}Cl_6NS_6W$ (941.46): calcd. C 33.17, H 2.78, N 1.49; found C 33.41, H 2.70, N 1.54. UV/Vis (CH_3CN): λ_{max} (ε) = 360 nm (9400 $M^{-1}cm^{-1}$), 540 (5200), 650 (sh). ESI-MS: m/z = 811.5 $[M]^-$. CV (V vs. SCE in CH_3CN): –0.19 (reversible), +0.47 (reversible).

$(Ph_4P)_2[W(bdtCl_2)_3]$ (1b): The complex was prepared in the same way as **1a** except that PPh_4Br was employed instead of Et_4NI. Yield: 0.58 g (39%). $C_{66}H_{46}Cl_6P_2S_6W$ (1490.0): calcd. C 53.20, H 3.11; found C 53.46, H 3.41.

$(Ph_4P)[W(bdtCl_2)_3]$ (2b): A methanolic solution (10 mL) of H_2bdtCl_2 (0.07 g, 0.0003 mol) was added to WO_2Cl_2 (0.03 g, 0.0001 mol) and a purple solution was obtained after 24 h. After filtration, Ph_4PBr (0.042 g, 0.0001 mol) was added to the obtained purple solution to give deep-purple microcrystals. The precipitate was collected by filtration and dried in air. Yield: 0.07 g (61%). $C_{42}H_{26}Cl_6PS_6W$ (1150.6): calcd. C 43.84, H 2.28; found C 43.98, H 2.51.

$(C_5NH_6)[W(bdtCl_2)_3]\cdot 2CH_3OH$ (2c)·$2CH_3OH$: This complex was prepared in the same way as **2b** except that pyridinium trifluoromethanesulfonate was used instead of Ph_4PBr. Yield: 0.05 g (54%). $C_{25}H_{20}Cl_6NO_2S_6W$ (955.37): calcd. C 31.43, H 2.11, N 1.47; found C 31.59, H 2.38, N 1.51.

$(Et_4N)_2[Mo(bdtCl_2)_3]$ (3): $[MoO_2Cl_2]$ (0.04 g, 0.2 mmol) was added to a THF solution (10 mL) of H_2bdtCl_2 (0.13 g, 0.6 mmol) and the solution was stirred for 3 h. The obtained green solution was concentrated to 5 mL and purified by passing through a neutral alumina column using acetone/CH_3OH (1:4) as an eluent. A blue band was collected and concentrated to 5 mL, and addition of Et_4NI (0.05 g, 0.19 mmol) gave a blue microcrystalline powder, which was collected by filtration and dried in vacuo. Yield: 0.004 g (21%). $C_{34}H_{46}Cl_6MoNS_6$ (983.80): calcd. C 41.51, H 4.71, N 2.85; found C 41.39, H 4.65, N 2.87. UV/Vis (CH_3CN): λ_{max} (ε) = 284 nm (46800 $M^{-1}cm^{-1}$), 352 (20500), 574 (11000). CV (V vs. SCE in CH_3CN): +0.03 (reversible), +0.62 (reversible).

Calculation of θ and φ Angles (°) in Crystal Structures: The θ angle was calculated as the torsion angle between the two S atoms of $bdtCl_2$ with respect to the aligned centers of gravity between the S1, S3, and S5, and S2, S4, and S6 atoms, respectively. The φ angle was calculated as the dihedral angle between the SMS groupings of the bound ligands (S1MS2, S3MS4, S5MS6; M = Mo and W) and the trigonal planes S1S3S5 and S2S4S6, according to ref.[7] S1–S6 are labeled in Scheme S1 (see Supporting Information). Averaged values are employed in this paper. The percentage (OCT/TP) used for the OCT and TP is the average of the values θ/60 and $(90 - \varphi)/(90 - 55)$, respectively.

 © 2005 Wiley-VCH Verlag GmbH & Co. KGaA, Weinheim

Other Measurements: Cyclic voltammograms were recorded at 100 mV s^{-1} with a Hokuto HZ-3000. The working and counter electrodes were a glassy-carbon disk and a platinum wire, respectively. The sample solutions were deoxygenated with a stream of N_2. The reference electrode used was an SCE. Electronic spectra were recorded with a Shimazu-U2550 spectrometer at 20 °C.

X-ray Crystallographic Study: Single crystals of **1a**, **1b**, **2a**, **2b**, and **2c** were recrystallized from acetone, hexane, acetonitrile/diethyl ether, and methanol, respectively. Although a single crystal of **3** was not obtained by recrystallization, a single crystal of **3a** was obtained by adding Et_3NHBr to a solution of **3** in CH_3CN. Each single crystal obtained was mounted on top of a glass fiber. X-ray data of the complexes were collected with graphite-monochromated Mo-K_α radiation on a Rigaku/MSC Mercury CCD diffractometer. The structures were solved by direct methods (SIR-97)[16] and expanded using DIRDIF 99.[17] The structures were refined anisotropically by full-matrix least-squares on F^2. The non-hydrogen atoms in all structures were attached at idealized positions on the carbon atoms and not refined. All structures converted in the final stages of refinement showed no movement in the atom positions. All calculations were performed with Single Crystal Structure Analysis Software, Ver. 3.6.0.[18] Further crystal data and agreement factors are listed in Tables 2 and 3.

CCDC-261315–261320 (for **1a**, **1b**, **2a**, **2b**, **2c**, and **3a**, respectively) contain the supplementary crystallographic data for this paper. These data can be obtained free of charge from The Cambridge Crystallographic Data Center via www.ccdc.cam.ac.uk/data_request/cif.

Supporting Information: Description of the θ and φ angles (Scheme S1), and detailed bond lengths [Å] and angles [°] around the metal centers (Tables S1–S6).

Table 2. Crystallographic data for **1a**, **1b**, and **3a**.

	1a	**1b**	**3a**
Formula	$C_{34}H_{46}Cl_6N_2S_6W$	$C_{66}H_{46}Cl_6P_2S_6W$	$C_{30}H_{38}Cl_6N_2MoS_6$
Molecular mass	1071.68	1489.96	927.66
Temp. [°C]	–130	–150	–150
Crystal system	orthorhombic	orthorhombic	orthorhombic
Space group	$P2_12_12_1$	$Fdd2$	$P2_12_12_1$
a [Å]	14.580(2)	24.051(1)	14.363(3)
b [Å]	15.283(2)	32.358(2)	15.971(5)
c [Å]	19.227(2)	15.3131(9)	16.641(4)
α [°]	90	90	90
β [°]	90	90	90
γ [°]	90	90	90
V [Å^3]	4284.3(8)	11917.2(12)	3799.0(17)
Z	4	8	4
$D_{calcd.}$ [g cm^{-3}]	1.661	1.660	1.622
Unique data	9244	8320	2743
Observed data	5908	7321	2310
R [%]	7.5	4.0	8.1
wR [%]	17.2	9.8	21.9
GOF	1.062	1.00	1.084

Table 3. Crystallographic data for **2a**–**2c**.

	2a	**2b**	**2c**
Formula	$C_{26}H_{26}Cl_6NS_6W$	$C_{39}H_{42}Cl_6PS_6W$	$C_{25}H_{20}Cl_6NS_6W$
Molecular mass	941.43	1135.67	955.37
Temp. [°C]	–120	–160	–160
Crystal system	monoclinic	monoclinic	monoclinic
Space group	$C2/c$	$P2_1/c$	$P2_1/n$
a [Å]	17.15(8)	22.850(2)	10.391(5)
b [Å]	19.31(8)	13.6306(9)	20.941(10)
c [Å]	20.22(10)	27.388(2)	15.497(8)
α [°]	90	90	90
β [°]	92.57(8)	94.297(4)	106.349(6)
γ [°]	90	90	90
V [Å^3]	6688.1(52)	8506.4(11)	3235.9(27)
Z	8	4	4
$D_{calcd.}$ [g cm^{-3}]	1.870	1.766	1.961
Unique data	7564	23578	7383
Observed data	5893	10962	4491
R [%]	7.2	4.9	6.5
wR [%]	19.2	12.7	14.7
GOF	1.346	0.931	0.992

Acknowledgments

This work was partly supported by a Grant for Scientific Research (no. 16750052 to H.S.) from the Japan Society for Promotion of Science and by CREST of the Japan Science and Technology Agency (JST).

[1] C. Faulmann, P. Cassoux, *Progress in Inorganic Chemistry: Solid-State Properties (Electronic, Magnetic, Optical) of Dithiolene Complex-Based Compounds* (Ed.: E. I. Stiefel), John Wiley & Sons, New Jersey, **2004**, *52*, 399–489.
[2] S. D. Cummings, R. Eisenberg, *Progress in Inorganic Chemistry: Luminescence and Photochemistry of Metal Dithiolene Complexes* (Ed.: E. I. Stiefel), John Wiley & Sons, New Jersey, **2004**, *52*, 315–367.
[3] S. J. N. Burgmayer, *Progress in Inorganic Chemistry: Dithiolene in Biology* (Ed.: E. I. Stiefel), John Wiley & Sons, New Jersey, **2004**, *52*, 491–537.
[4] J. McMaster, J. M. Tunney, C. D. Garner, *Progress in Inorganic Chemistry: Chemical Analogs of the Catalytic Centers of Molybdenum and Tungsten Dithiolene Containing Enzymes* (Ed.: E. I. Stiefel), John Wiley & Sons, New Jersey, **2004**, *52*, 539–583.
[5] J. A. McCleverty, *Prog. Inorg. Chem.* **1968**, *10*, 49–221.
[6] A. Davison, R. H. Holm, *Inorg. Synth.* **1967**, *10*, 8–26.
[7] C. L. Beswick, J. M. Schulman, E. I. Stiefel, *Progress in Inorganic Chemistry: Structures and Structural Trends in Homoleptic Dithiolene Complexes* (Ed.: E. I. Stiefel), John Wiley & Sons, New Jersey, **2004**, *52*, 55–110.
[8] G. F. Brown, E. I. Stiefel, *Inorg. Chem.* **1973**, *12*, 2140–2147.
[9] D. V. Fomitchev, B. S. Lim, R. H. Holm, *Inorg. Chem.* **2001**, *40*, 645–654.
[10] F. Knoch, D. Sellmann, W. Kem, *Z. Kristallogr.* **1993**, *250*, 300–302.
[11] C. Lorber, J. P. Donahue, C. A. Goddard, E. Nordlander, R. H. Holm, *J. Am. Chem. Soc.* **1998**, *120*, 8102–8112.
[12] B. S. Lim, J. P. Donahue, R. H. Holm, *Inorg. Chem.* **2000**, *39*, 263–273.
[13] T. E. Burrow, R. H. Morris, A. Hills, D. L. Hughes, R. L. Richards, *Acta Crystallogr., Sect. C* **1993**, *49*, 1591–1594.
[14] H. Huynh, T. Lugger, F. E. Hahn, *Eur. J. Inorg. Chem.* **2002**, 3007–3009.
[15] C. A. Goddard, R. H. Holm, *Inorg. Chem.* **1999**, *38*, 5389–5398.
[16] A. Altomare, M. Burla, M. Camalli, G. Cascarano, C. Giacovazzo, A. Guagliardi, A. Moliterni, G. Polidori, R. Spagna, *J. Appl. Crystallogr.* **1999**, *32*, 115–119.
[17] P. T. Beurskens, G. Admiraal, G. Beurskens, W. P. Bosman, R. de Gelder, R. Israel, J. M. M. Smits, **1999**. *The DIRDIF-99 program system*, Technical Report of the Crystallography Laboratory, University of Nijmegen, The Netherlands.
[18] *Crystal Structure Analysis Package*, Rigaku and Rigaku/MSC, **2000**–**2004**, 9009 New Trails Dr., The Woodlands, TX 77381, USA.

Received January 24, 2005
Published Online: June 28, 2005

 © 2005 Wiley-VCH Verlag GmbH & Co. KGaA, Weinheim

Adsorption of Zn^{2+} and Cd^{2+} from Aqueous Solution onto a Carbon Sorbent Containing a Pyrimidine–Polyamine Conjugate as Ion Receptor

Javier García-Martín,[a] Rafael López-Garzón,*[a] Mari Luz Godino-Salido,[a] Rafael Cuesta-Martos,[a] Maria Dolores Gutiérrez-Valero,[a] Paloma Arranz-Mascarós,[a] and Helen Stoeckli-Evans[b]

Keywords: Adsorption / Cadmium / Ligand design / N ligands / Zinc

The compound *N*-(4-amino-1-methyl-5-nitroso-6-oxo-1,6-dihydropyrimidin-2-yl)-*N′*-[bis(2-aminoethyl)]ethylenediamine (HL) was synthesised and structurally characterised by analytical methods and ^{1}H, ^{13}C and ^{15}N NMR spectroscopy. The protonation of HL and its coordinating ability towards Zn^{2+} and Cd^{2+} ions in water solution were also studied by potentiometric methods and UV/Visible and ^{1}H-^{13}C NMR spectroscopy. The molecular structures of $[H_3L]^{2+}[CdI_4]^{2-}\cdot 2H_2O$ and $[(Cl_3Zn)(\mu\text{-}Cl)\{Zn(\mu_2\text{-}HL)\}]_2\cdot 2.5H_2O$ were solved by single-crystal X-ray diffraction methods. On the basis of these data, the performance of HL anchored to activated carbon (AC) was evaluated as a molecular receptor for Zn^{2+} and Cd^{2+} metal ions in aqueous solution. This was done by a comparative study of the adsorption capacity of the adsorbents AC alone and HL anchored on the AC (AC-HL) for these metal ions and by a structural study of the AC-HL, AC-HL-Zn^{2+} and AC-HL-Cd^{2+} solid phases by XPS and IR spectroscopy.
(© Wiley-VCH Verlag GmbH & Co. KGaA, 69451 Weinheim, Germany, 2005)

Introduction

Substitution reactions at the C(2) atom of the 4-amino-1-methyl-5-nitroso-6-oxo-1,6-dihydropyrimidin-2-yl moiety with an α-amino acid residue result in molecular compounds containing a rigid, flat pyrimidine moiety and a pendant amino-acidic residue[1] (Scheme 1).

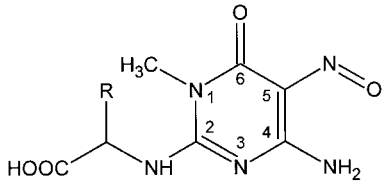

Scheme 1.

These compounds have two Lewis base-type environments that control their coordinating behaviour: one is constituted by the neighbouring C(5)–NO and C(6)=O substituents in the pyrimidine ring, and the other by the characteristic basic functions existing at the amino acid residue linked to the C(2) position of the pyrimidine nucleus. Steric factors prevent co-operative binding of both pyrimidine and amino acid functions, to a single metal centre, and this favours the formation of 1D, 2D and 3D polynuclear solid complexes. In fact, the structures of some of the crystalline polynuclear complexes of these ligands with alkali and alkaline-earth metal ions have been solved[2] and show interesting features similar to those of metal–organic compounds with non-linear optical properties.[3]

The molecules depicted in Scheme 1 are characterised by a strong electronic polarisation at the pyrimidine nucleus as a result of the co-operative effect of the marked electron-withdrawing character of the C(5) nitroso function and the electron-donating character of the amino function at C(2). This fact is consistent with the non-basic character of the N(3) atom which, in our studies, has never been found to be a metal-binding centre of these ligands.[2] The strong polarisation of the pyrimidine π-electron cloud[1b] suggests the existence of low-energy LUMO orbitals that are able to interact with high-energy HOMO orbitals provided by electron-rich aromatic centres. Accordingly, in a recent work[4] we have explained the observed irreversible adsorption of two of these nitrosopyrimidine-amino acid conjugates onto an activated carbon (AC) as being due to π–π donor–acceptor interactions between the pyrimidine moiety of the ligands (acting as acceptor) and the arene centres of the AC[5] (acting as donor). These results suggest that, after adsorption of these molecules on the AC, their pyrimidine moieties remain attached to the carbon surface, coplanar with the graphene sheets, thus losing their ability to bind to metal ions. On the other hand, the amino acid residue linked to C(2) of the pyrimidine ring is projected outside of the carbon surface and becomes the only potential reactive centre for metal ions in the ligand–AC adducts. Hence, although the interactions between metal ions and free ligands

[a] Dpto. Química Inorgánica y Orgánica, Universidad de Jaén, 23071 Jaén, Spain
[b] Institute of Chemistry, University of Nêuchatel, 2007 Nêuchatel, Switzerland

are rather non-specific in aqueous solution, it is expected that the carbon-anchored ligands would behave as monofunctional ligands to metal ions by using only the basic function linked to C(2) of the pyrimidine ring as binding site.

Activated carbons have been extensively used to remove metals from industrial and municipal wastewater as they are cheap and accessible materials. Nevertheless, their efficiencies are strongly limited due to the non-specific nature of the basic functions which are usually added by the activation processes.[6] Moreover, the functionalisation by activation is limited to the edges of the graphene layers and to the entrance of the pores. For these reasons, although advantageous textural (e.g. adequate surface area and specific pore size distribution) and functional properties (both easily achievable by adequate activation processes) are important, the development of specific chemical properties at the carbon surface[7] to improve its metal-capturing properties, which is more difficult to attain, is also vital.

The adducts resulting from the irreversible adsorption of a monolayer of the C(2)-functionalised nitrosopyrimidines on the AC graphitic surface can be regarded as new selectively functionalised activated carbons whose mechanical and textural properties are provided by the carbon skeleton while the chemical functionalisation is provided by the functionality introduced as the C(2)-substituent at the nitrosopyrimidine derivative. Moreover, whenever the basic functions existing at the C(2) substituent of the pyrimidine moiety can be tailored, the adsorption of these compounds becomes an easy and suitable method to develop the desired functionality at the carbon surface. Of course, the efficacy of the proposed method is conditioned to maintaining the heteroaromatic moiety unaltered on changing the substituents at the C(2) position of the pyrimidine moiety.

As already commented, in a recent paper[4] we studied the adsorption of a new molecular receptor of this class, *N*-(4-amino-1-methyl-5-nitroso-6-oxo-1,6-dihydropyrimidin-2-yl)-*N′*-(bis-2-aminoethyl)ethylenediamine (HL), at several pHs, on a basic AC. We found that HL is irreversibly anchored at the arene centres of the carbon surface through the pyrimidine moiety, by strong π–π interactions,[4] thus providing functionalisation of the AC with a triamine grouping. The aim of this work was to gain insight into the performance of the proposed model by comparison of the capacity of an activated carbon and the above ligand previously adsorbed on it (AC-HL) to capture metal ions. For this, the adsorption data of $ZnCl_2$ and $CdCl_2$ in aqueous solution on an AC and AC-HL adsorbent were analysed in the light of the structural data of HL, which was characterised by X-ray diffraction methods, and also the coordination chemistry behaviour of Zn^{II}/HL and Cd^{II}/HL systems in aqueous solution.

Results and Discussion

Characterisation of the Ligand

HL was prepared by a procedure consisting of the nucleophilic attack of one of the amino primary groups of tris(2-aminoethyl)amine to the C(2) position of the pyrimidine precursor 4-amino-2-methoxy-1-methyl-5-nitroso-6-oxo-1,6-dihydropyrimidine (Scheme 2). For this, the pH of the reaction mixture was adjusted such that one of the three amino primary groups remained unprotonated.[8]

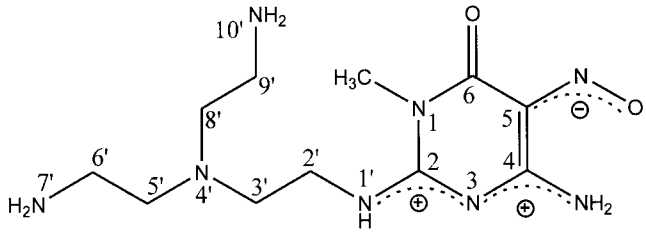

Scheme 2.

N projections in the ^{1}H-^{15}N HMBC spectrum of HL·2HCl exhibit the same signals as the pyrimidine precursor (see Experimental Section) along with another two signals attributable to the secondary and tertiary N atoms of the polyamine residue, with the former at lower field than the latter. The lack of signals for two of the primary amino groups means that they have been protonated and thus confirms the monosubstitution of the polyamine. The carbon atoms were assigned in the ^{1}H-^{13}C HSQC spectrum after the methylene protons of the polyamine moiety had been assigned in the ^{1}H-^{15}N HMBC spectrum.

The structure of compound $[H_3L]^{2+}[CdI_4]^{2-}\cdot 2H_2O$ was solved by single-crystal X-ray diffraction analysis. The molecular structure consists of protonated cations $[H_3L]^{2+}$, tetraiodocadmiate(II) anions and water solvent molecules (Figure 1). This allowed an analysis of the $[H_3L]^{2+}$ unit in which, as expected, the two protons attached to HL are at the primary amino groups of the polyamine.

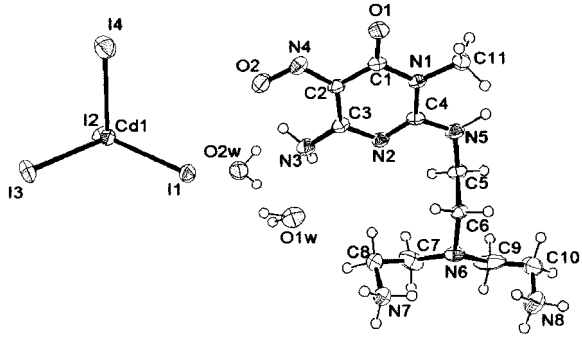

Figure 1. ORTEP drawing of $[H_3L]^{2+}[CdI_4]^{2-}\cdot 2H_2O$.

The structure of $[H_3L]^{2+}$ exhibits a planar conformation of the heterocyclic moiety [including the pyrimidine substituents labelled in Scheme 2 as C(6)O, C(5)NO, C(4)NH_2 and C(2)NH], whereas the C(2) substituent deviates from the aromatic plane. This suggests π electronic delocalisation in the pyrimidine and precludes the C(2)NH and C(4)NH_2 exocyclic substituents from acting as metal ion acceptors. The C(5)-nitroso group is oriented *trans* to C(6), which allows the formation of an intramolecular N–H···O hydrogen bond in an S(6) motif. An intramolecular hydrogen bond also exists between the N(7′) atom of a primary amino

group as donor and the N(4′) atom as acceptor. This description resembles the structure of analogous α-amino acid derivatives.[1,9]

The similarity between the C(5)–NO and N–O bond lengths, (1.320 Å and 1.302 Å, respectively), which are in the range of those observed in oximate anions [RR′C–N–O]$^-$, suggests the existence of a delocalised double bond in the C(5)NO grouping.[10,11] All of the C–N bonds lengths in the HN^2–C(2)–N(3)–C(4)–N^4H_2 fragment are rather similar [C(2)–N^2H = 1.33 Å; C(2)–N(3) = 1.30 Å; N(3)–C(4) = 1.353 Å and C(4)–N^4H_2 = 1.314 Å] and it is not possible to distinguish between single and double bonds. All of these parameters taken together suggest that the representation of Scheme 2 is the most appropriate for HL.

Ligand Protonation

The protonation constants of HL obtained by potentiometric methods in aqueous medium are reported in Table 1. The monoanion L$^-$, which exists at high pH values, binds four protons in the pH range investigated (2.5–10.5). The first three protonations are markedly grouped, and their log *K* values indicate a strongly basic character of the corresponding protonation positions, i.e. they take place at strongly basic atoms. On the contrary, the fourth protonation constant (log *K* = 2.12) indicates a far lower basicity for this position.

Table 1. Protonation constants (log *K*) of HL (0.1 M KCl, 298.1 K).

Reaction	log *K*
$L^- + H^+ \leftrightharpoons HL$	10.94
$HL + H^+ \leftrightharpoons [H_2L]^+$	9.70
$[H_2L]^+ + H^+ \leftrightharpoons [H_3L]^{2+}$	8.75
$[H_3L]^{2+} + H^+ \leftrightharpoons [H_4L]^{3+}$	2.12

The UV/Visible adsorption spectra of HL at various pH values is given in Figure 2. The spectrum at pH 5 is similar to that of the pyrimidine chromophore[2f] and consists of two UV bands due to π–π* transitions at λ_1 = 328 nm (ε_1 = 2.23×10^4 cm^{-1} mol^{-1} L) and λ_2 = 230 nm (ε_2 = 8.85×10^3 cm^{-1} mol^{-1} L). The visible band with a maximum at λ_3 = 524 nm (ε_3 = 76.50 cm^{-1} mol^{-1} L), is assigned to a forbidden n→π* transition of the non-bonding O electron pair of the C(5)NO group.[2f]

The spectra are unchanged in the pH range 4.1 to 10.0, thus indicating that the second and third protonations do not affect the pyrimidine chromophore, i.e. they take place on the primary amino groups of the polyamine. On the contrary, the small red-shift of the 328 nm band as the pH increases above about 10 indicates that the first protonation step takes place either at the -N$^-$-C(2) or NH$^-$-C(4) anions. To gain further insight into this protonation step we studied the ^{1}H and ^{13}C NMR spectroscopic data obtained from HL in D_2O at different pH values; the results are summarised in Figure 3. The significant upfield shifts of the methylene protons at pH values up to 10 suggest that the process

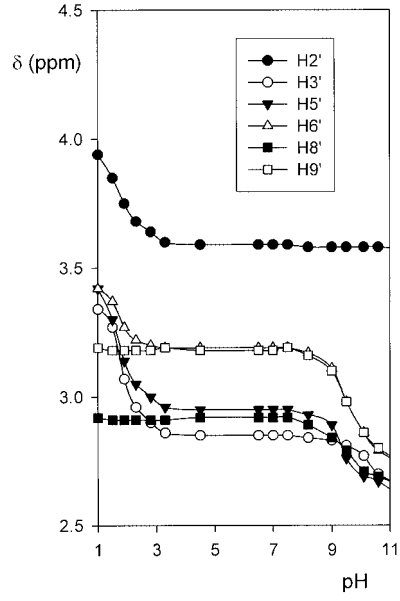

Figure 3. ^{1}H NMR chemical shifts of the HL signals as a function of pH.

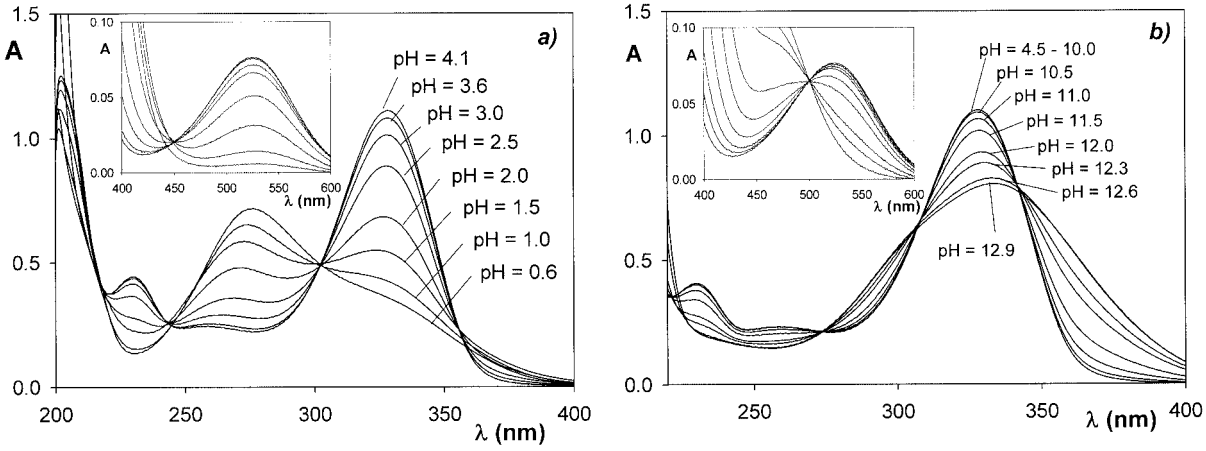

Figure 2. pH-Dependence of the absorption spectra of HL in the UV ([HL] = 5×10^{-5} M, 0.1 M KCl), and visible (inset, [HL] = 10^{-3} M, 0.1 M KCl) regions, a) in acidic media and b) in basic media.

 © 2005 Wiley-VCH Verlag GmbH & Co. KGaA, Weinheim

studied occurs at –N⁻-C(2). Moreover, the deshielding of such protons in the pH range 10–7 indicates the protonation of the two primary amino groups in this pH range.

In the pH range 1–4, where the fourth protonation step occurs (see Figure 2), a blue-shift of the 328 nm band and quenching of the absorption at 524 nm are observed with decreasing pH values. The latter indicates that the σ nonbonding pair on C(5)NO is used in binding this proton, thus hindering the n→π transition (band at 524 nm, see above). Protonation of the NO group instead of the $N(3)_{ring}$ atom is consistent with the above-described polar character of HL, according to which the electron density is higher at NO than at $N(3)_{ring}$.

In addition, in a ^{1}H NMR titration experiment of HL during this protonation (pH range 1–4) a deshielding of the protons at the 2′, 3′, 5′ and 6′ carbon atoms of the polyamine was observed (Figure 3). The non-chemical equivalence of the H5′ and H8′ and H6′ and H9′ signals in the polyamine residue indicates a conformational change accompanying this process, which is probably induced by the formation of an intramolecular hydrogen bond of the $H_2N\cdots HN$–C(2) type (Scheme 3).

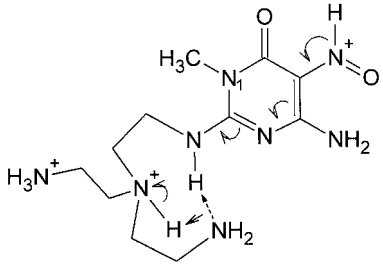

Scheme 3.

Complex Formation in Aqueous Solution

Complex formation in the HL/Zn^{II} and HL/Cd^{II} systems in an aqueous medium was studied by a potentiometric method at [ligand]/[metal] = 1. The complex species formed, together with their stability constants, are listed in Table 2, and the species distribution plots are given in Figure 4.

Table 2. Stability constants of Zn^{II} and Cd^{II} complexes (log K) with HL (0.1 M KCl, 298.1 K).

Reaction	log K Zn^{II}	Cd^{II}
$M^{2+} + H_3L^{2+} \rightleftharpoons [MH_3L]^{4+}$	3.96	2.80
$M^{2+} + [MH_3L]^{4+} \rightleftharpoons [M_2H_2L]^{5+} + H^+$	6.33	
$M^{2+} + H_2L^+ \rightleftharpoons [MH_2L]^{3+}$		4.85
$M^{2+} + HL \rightleftharpoons [MHL]^{2+}$	9.56	7.45
$M^{2+} + 2HL \rightleftharpoons [M(HL)_2]^{2+}$	17.33	13.88
$M^{2+} + [MHL]^{2+} \rightleftharpoons [M_2HL]^{4+}$	3.84	2.94
$M^{2+} + L^- \rightleftharpoons [ML]^+$		9.82
$[ML]^+ + L^- \rightleftharpoons ML_2$		7.59
$M^{2+} + L^- + OH^- \rightleftharpoons MLOH$	3.00	
$M^{2+} + OH^- \rightleftharpoons [MOH]^+$		–8.35
$M^{2+} + 2OH^- \rightleftharpoons M(OH)_2$	–14.60	

Zn^{II} forms mono- and dinuclear complexes with HL in aqueous solution. At low pH values only the complex $[Zn(H_3L)]^{4+}$, with the metal bonded through the pyrimidine moiety, exists. The stability constant (log K = 3.96) is similar to the five-membered metal chelates formed by Zn^{II} with N,O donor ligands, such as the single amino acids glycine (log K = 5.16), methionine (log K = 4.38), ornithine (log K = 4.10) and valine (log K = 5.00) and the nucleoside guanosine (log K = 4.6).[8] This suggests that in the $[Zn(H_3L)]^{4+}$ complex the coordination to the metal ion takes place through the nitrogen atom of the C(5)NO group and the oxygen of C(6)O. This coordinating behaviour of the pyrimidine residue is the only one observed in the tetranuclear complex $[Zn_2(HL)_2][ZnCl_4]_2$ (see below) and also in the polynuclear complexes formed by Zn^{II} with pyrimidine analogues derived from L-valine and L-methionine.[12]

Figure 4 (a) shows that mono-deprotonation of $[Zn(H_3L)]^{4+}$ starts at a pH of around 3.5. The resulting $[Zn(H_2L)]^{3+}$ species is able to bind a second Zn^{II} through the two unprotonated amino groups of the polyamine residue to form the binuclear complex $[Zn_2(H_2L)]^{5+}$. The log K value calculated for the association of a Zn^{2+} ion to the

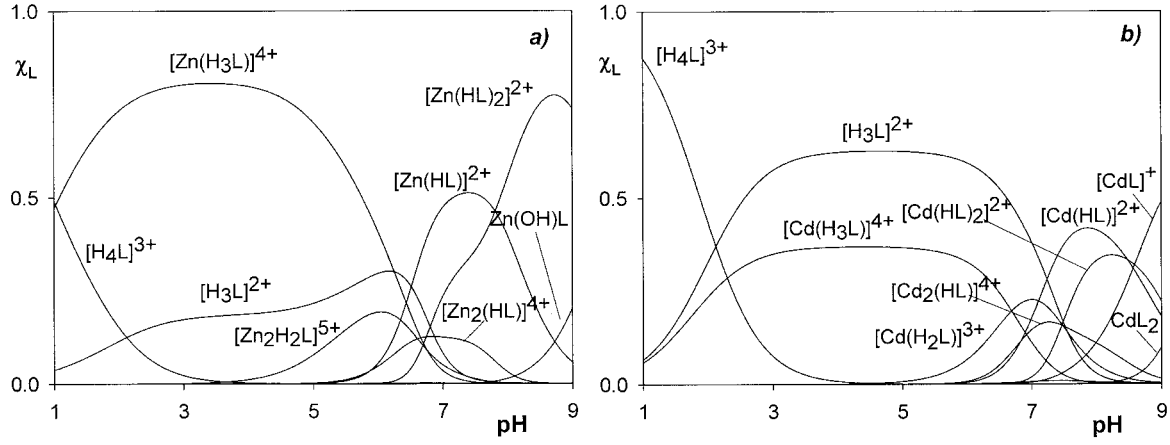

Figure 4. Species distribution plot for a) the HL/Zn^{II} system and b) the HL/Cd^{II} system in aqueous solution (1:1 molar ratio) as a function of pH ([HL] = [Zn^{II}] or [Cd^{II}] = 10^{-3} M, 0.1 M KCl, 298.1 K).

 © 2005 Wiley-VCH Verlag GmbH & Co. KGaA, Weinheim

polyamine moiety, $Zn^{2+} + [ZnH_3L]^{4+} \rightleftharpoons [Zn_2H_2L]^{5+} + H^+$, is 6.33. This suggests the coordination of Zn^{2+} by two of the nitrogen atoms of this moiety. The amount of $[Zn_2(H_2L)]^{5+}$ decreases sharply at slightly alkaline pH due to the formation of $Zn(OH)_2$ (not included in Figure 4 (a) for simplicity), but an additional increase of pH produces the complete deprotonation of the polyamine, and this favours the formation of $[Zn(HL)_2]^{2+}$ rather than the hydroxide species. The stability constant for $[Zn(HL)_2]^{2+}$ ($\log K = 17.33$) is consistent with that found for the 1:1 complex $[Zn(TrenH)]^{3+}$ ($\log K = 7.95$), where $TrenH^+$ is the N-tridentate ligand analogous to HL.[8,13] Finally, at a pH of about 8 deprotonation of the C(2)NH group is promoted by Zn^{II}, resulting in the formation of the complex [ZnL(OH)]. The calculated stability constant for the addition of a hydroxy plus an L anion to a Zn^{II} metal ion is $\log K = 16.70$. This value is similar to the Zn^{II} complex with the analogous *N*,*N*,*N*,*N* tetradentate ligand tris(2-aminoethyl)amine (Tren)[13] and suggests a similar coordinating behaviour.

With the aim of getting further information about the structures of the complexes formed in solution, the ^1H and ^{13}C NMR spectra were recorded of a 1:1 HL/Zn^{II} mixture and HL in aqueous solution at various pH values. Figure 5 displays the differences between the chemical shift values ($\Delta\delta$) of proton and carbon atoms vs. pH obtained from these experiments.

In the pH range 1–5, the $\Delta\delta$ values are significant for the C(5) and C(6) atoms of the pyrimidine and negligible for the remainder (see Figure 5, a1). This indicates that in the main species existing in this pH range, $[Zn(H_3L)]^{5+}$, the ligand is coordinated through the C(5)NO and C(6)O groups. This is also supported by the negligible $\Delta\delta$ values found for all of the methylene protons, which indicates that the polyamine unit is not involved in metal coordination.

In the pH range 4–6, non-zero $\Delta\delta$ values for the 5′, 6′, 8′ and 9′ methylene protons indicate that the formation of $[Zn_2(H_2L)]^{5+}$ by addition of a Zn^{II} ion to $[Zn(H_3L)]^{4+}$, which occurs at this pH, takes place at the monoprotonated

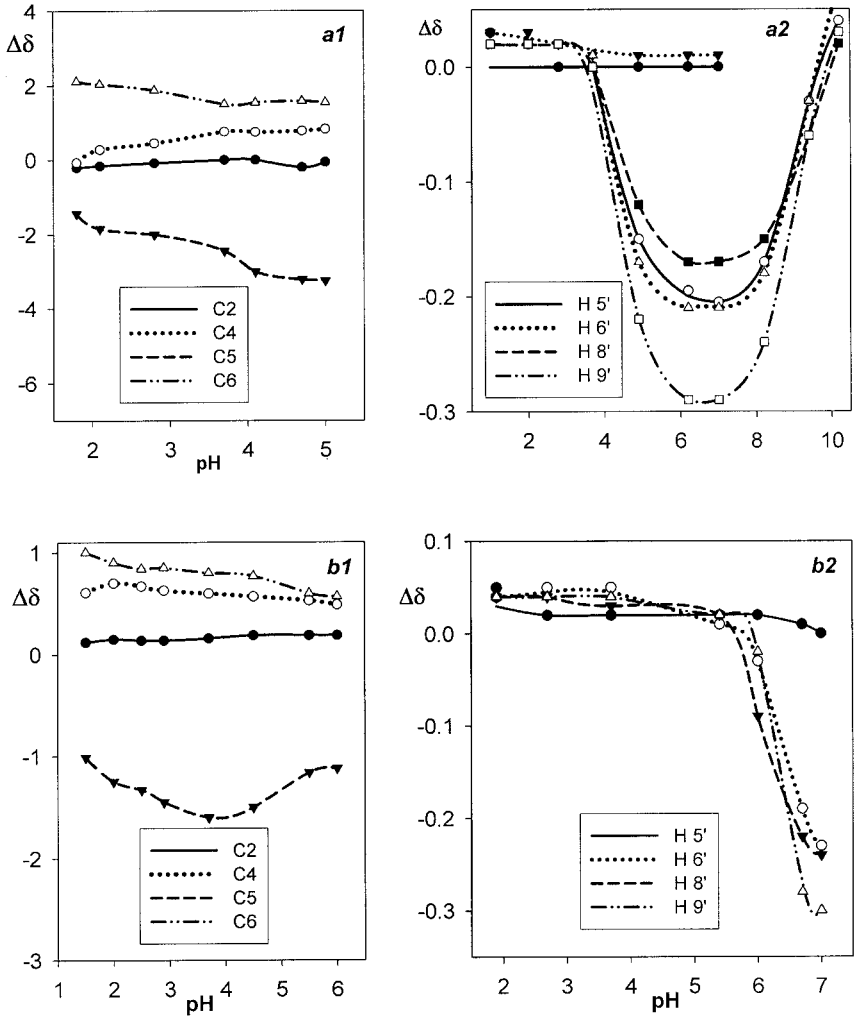

Figure 5. a1: Chemical shift differences between HL/Zn^{II} mixtures (1:1 molar ratio) and HL, at different pHs, for the ring-carbon signals. a2: Chemical shift differences for the polyamine methylenic protons. b1 and b2: Chemical shift differences for Cd^{II}.

 © 2005 Wiley-VCH Verlag GmbH & Co. KGaA, Weinheim

polyamine. Figure 5 (a2) also shows the non-equivalence of the analogous methylene groups of each of the two terminal arms of the polyamine residue. This clearly indicates the involvement of only one of the two primary amine groups in the coordination.

The formation of [ZnLOH] species above pH 8 is accompanied by an increasing deshielding of all of the methylene protons (see Figure 5a2) except that of 2′ (not included in this figure for simplicity), which suffers a small opposite effect. This accounts for the involvement of the deprotonated C(2)-NH group of the polyamine in metal coordination and confirms that L acts as a tetradentate *N*,*N*,*N*,*N* ligand.

The complexation equilibria for HL/Cd^{II} system are given in Table 2, with the speciation plots in Figure 4 (b). These highlight that the coordination chemistry of Cd^{II} is similar to that of Zn^{II} as regards the stoichiometries of most of the complex species formed. The structures of the Cd^{II} complexes are also similar to the analogous Zn^{II} complexes described above. This was proved by an analysis of the data obtained from a NMR pH titration experiment of a 1:1 [Cd^{II}]/[HL] mixture (Figures 5, b1 and b2), which shows similar features to those discussed above for the Zn^{II}/HL system.

The stability constants of $[CdH_2L]^{3+}$ and $[CdHL]^{2+}$ complexes are similar to those of the analogous *N*,*N* bidentate 3-phenylpropane-1,2-diamine (log K = 4.1), pentane-1,2-diamine (log K = 5.5) and hexane-1,2-diamine (log K = 5.4)[14] and *N*,*N*,*N* tridentate, 1,4,7-triazaheptanediene (log K = 8.3)[15] ligands, respectively, thus indicating that the polyamine moiety acts either as a bidentate or tridentate chelating ligand, depending on the pH of the medium.

The main difference between the Zn^{II} and Cd^{II} complexes is that the Zn^{II} complexes are more stable than their Cd^{II} analogues. Hence, the speciation diagrams (Figures 4a and 4b) show that each of the Zn^{II} complexes is formed at significantly lower pHs than the analogous Cd^{II} ones. The higher affinity of Zn^{II} for nitrogen donors[15] than the softer acid Cd^{II} accounts for the lower stability constants of mononuclear complexes of Cd^{II} with the polyamine moiety compared to the analogous Zn^{II} complexes. This agrees with the structural differences observed between $[Zn_2(HL)_2]^{4+}$ and $[H_3L]^{2+}[CdI_4]^{2-}\cdot 2H_2O$ (see below), even when both of them are obtained at the same pH of 6 (Figures 1 and 6): whereas Zn^{II} is bonded to the polyamine in the former, in the latter the Cd^{II} is coordinated to the soft basic iodide ions and the tri-amine remains doubly protonated.

Crystal Structures of $[H_3L]^{2+}[CdI_4]^{2-}\cdot 2H_2O$ and $[(Cl_3Zn)(\mu\text{-}Cl)\{Zn(\mu_2\text{-}HL)\}]_2\cdot 2.5H_2O$

The crystal structures of $[H_3L]^{2+}[CdI_4]^{2-}\cdot 2H_2O$ and $[(Cl_3Zn)(\mu\text{-}Cl)\{Zn(\mu_2\text{-}HL)\}]_2\cdot 2.5H_2O$ were solved by single-crystal X-ray diffraction methods. The crystal and structure refinement data are summarised in Table 3. The molecular structure of $[H_3L]^{2+}[CdI_4]^{2-}\cdot 2H_2O$ consists of $[H_3L]^{2+}$ (whose structure was discussed above), tetraiodocadmiate(II) anions and water molecules (Figure 1). It is interesting to note that the Cd^{II} ion is not coordinated either to the pyrimidine or to the polyamine, but is bonded to four iodide ions. The structure of the CdI_4^{2-} anion corresponds to a deformed tetrahedron due to the involvement of two of the iodide anions in hydrogen bonding as hydrogen acceptors, with two amine primary groups of adjacent $[H_3L]^{2+}$ units acting as hydrogen donors.

The molecular structure of $[(Cl_3Zn)(\mu\text{-}Cl)\{Zn(\mu_2\text{-}HL)\}]_2\cdot 2.5H_2O$ consists of a neutral $[(Cl_3Zn)(\mu\text{-}Cl)\{Zn(\mu_2\text{-}HL)\}]_2$ complex and 2.5 water molecules. Figure 6 shows an ORTEP[16] drawing of the tetranuclear Zn^{II} complex, which contains two HL molecules and eight chloride ions as ligands. Each of the two HL molecules binds to the same

Table 3. Crystal data and structure refinement for $[H_3L]^{2+}[CdI_4]^{2-}\cdot 2H_2O$ and $[(Cl_3Zn)(\mu\text{-}Cl)\{Zn(\mu_2\text{-}HL)\}]_2\cdot 2.5H_2O$.

	$[H_3L]^{2+}[CdI_4]^{2-}\cdot 2H_2O$	$[(Cl_3Zn)(\mu\text{-}Cl)\{Zn(\mu_2\text{-}HL)\}]_2\cdot 2.5H_2O$
Empirical formula	$C_{11}H_{28}CdI_4N_8O_4$	$C_{22}H_{49}Cl_8N_{16}O_{6.50}Zn_4$
Formula mass	956.41	1186.85
Temperature [K]	153(2)	153(2)
Wavelength [Å]	0.71073	0.71073
Space group	$P\bar{1}$	$P2_1/c$
a [Å]	8.1007(8)	16.2932(7)
b [Å]	8.9842(9)	20.6708(7)
c [Å]	17.6145(17)	13.8365(6)
α [°]	86.726(8)	90
β, [°]	83.389(8)	111.885(3)
γ [°]	83,432(8)	90
V [Å^3]	1263.8(2)	4324.2(3)
Z	2	4
Calcd. density [Mg m^{-3}]	2.513	1.823
Absorption coeff. [mm^{-1}]	5.781	2.745
Crystal size [mm]	0.39 × 0.33 × 0.05	0.50 × 0.12 × 0.11
Final R indices [$I > 2\sigma(I)$][a]	R_1 = 0.0616	R_1 = 0.0321
	wR_2 = 0.1855	wR_2 = 0.0800
R indices (all data)[a]	R_1 = 0.0635	R_1 = 0.0413
	wR_2 = 0.1876	wR_2 = 0.0842

[a] $R_1 = \Sigma||F_o| - |F_c||/\Sigma|F_o|$; $wR_2 = [\Sigma w(F_o^2 - F_c^2)^2/\Sigma wF_o^4]^{1/2}$.

 © 2005 Wiley-VCH Verlag GmbH & Co. KGaA, Weinheim

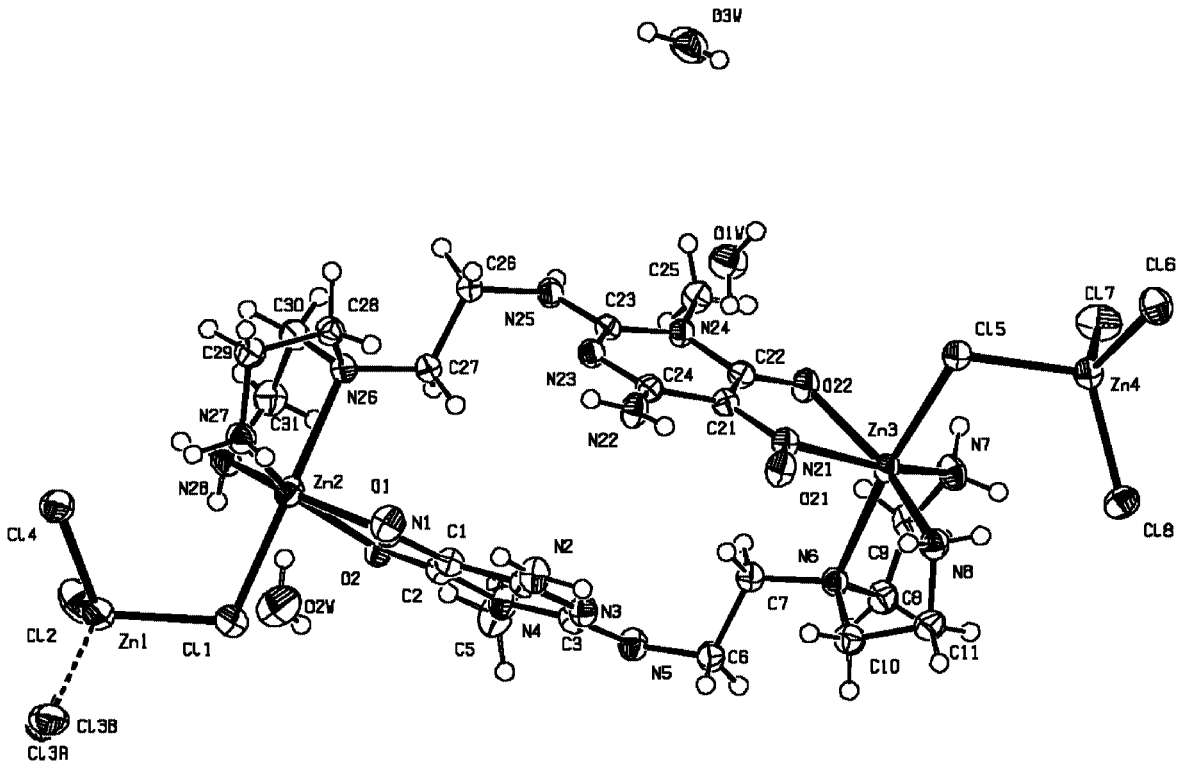

Figure 6. ORTEP drawing of $[(Cl_3Zn)(\mu\text{-}Cl)\{Zn(\mu_2\text{-}HL)\}]_2 \cdot 2.5H_2O$.

two Zn^{II} centres as a bridging ligand. The polyamine moiety acts as an *N*,*N*,*N* tridentate chelating ligand binding to a single Zn^{II} ion, whereas the pyrimidine acts as a didentate chelating ligand to a second Zn^{II} centre through the nitrogen of the NO group and the oxygen of C(6)O. Each of these Zn^{II} centres does is bound to a tetrachlorozincate(II) unit through a bridging chloride ligand. Therefore, the two zinc centres linked to HL have similar hexacoordinate environments consisting of the three nitrogen atoms of the polyamine from one HL molecule, the NO and C(6)O pyrimidine substituents from another HL unit and a chloride anion. The resulting coordination geometry can be described as tetragonal bipyramidal due to the fact that the bond lengths in the equatorial plane are notably shorter than those between the metal centre and the atoms in the apical positions.

The two remaining zinc atoms of the tetranuclear unit are placed in similar tetrahedral environments, with the Zn–μ-chloride bond significantly longer than the three terminal ones. It is noteworthy that none of the N_{cyclic} atoms of the HL units take part either in coordination to zinc or in hydrogen bonding, which points out the poor basicity character of this atom.

The main structural features highlighted for the pyrimidine moiety in $[H_3L]^{2+}$ $[CdI_4]^{2-} \cdot 2H_2O$ above are also exhibited by the HL molecules of the Zn^{II} complex. With this in mind, the opposed orientation of the pyrimidine planes of the two HL molecules in the $[(Cl_3Zn)(\mu\text{-}Cl)\{Zn(\mu_2\text{-}HL)\}]_2$ unit (Figure 6) is probably induced by the attractive dipole–dipole interactions between planes, which would stabilize the formed tetranuclear cyclic unit. This trend to the inverse orientation of the pyrimidine planes in the stacking of analogous pyrimidine compounds has been widely observed.[17]

Adsorption of $Zn^{2+}$and Cd^{2+}

As was mentioned above, a pH study of the adsorption/desorption of water-solved HL on a granular activated carbon (AC) showed the existence of π–π donor–acceptor interactions between the arene centres of the AC and the pyrimidine moiety of HL as the cause of the irreversible character of the adsorption process.[4] Further insight on this is obtained by comparison of the N_{1s} signals of the XPS spectra of the HL and AC-HL systems (Figure 7). This was done by assuming that the low nitrogen content of the AC (0.75%) implies negligible contribution (less than 1/10) to these signals compared to the HL nitrogen. Each of the N_{1s} signals is composed of two overlapping peaks corresponding to the five heterocyclic nitrogen atoms, i.e. the nuclear heterocyclic nitrogen atoms plus those directly bonded to the pyrimidine ring (at 400.02 eV for HL and 400.91 eV for AC-HL), and the three sp^3-type nitrogens of the tetraamine residue (at 398.40 eV for HL and 399.60 eV for AC-HL).

Both of these peaks are significantly shifted in the AC-HL spectrum relative to the HL spectrum. However, this fact is not relevant in the case of the peaks of the nitrogen atoms of the triamine due to the full involvement of these in the supramolecular assembling of solid HL by hydrogen bonds. On the contrary, the shifting of the peak of the heterocyclic nitrogens in AC-HL to higher energies relative to

 © 2005 Wiley-VCH Verlag GmbH & Co. KGaA, Weinheim

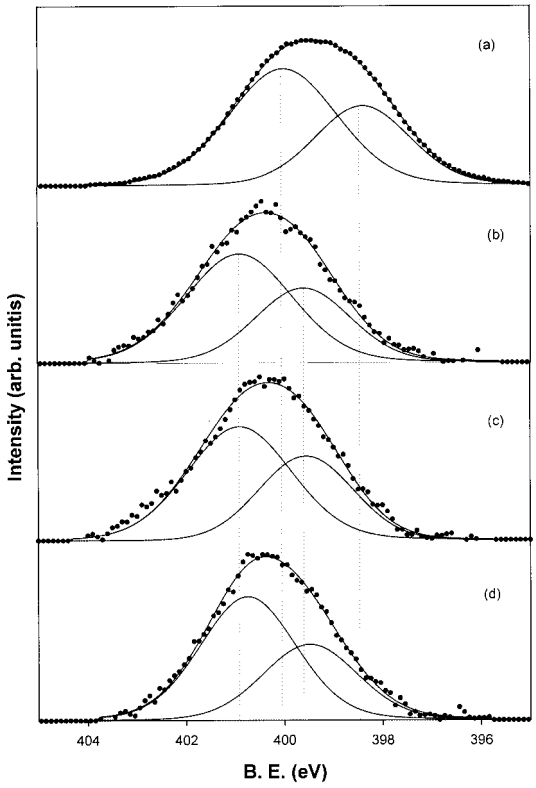

Figure 7. N_{1s} XPS spectra of (a) HL, (b) AC-HL, (c) AC-HL-Zn and (d) AC-HL-Cd.

HL is consistent with electron donation from the arene centres of the AC to the HL aromatic residue, which accompanies the adsorption process.

The anchorage of HL to the arene centres provides functionalisation of the AC with a potential tridentate *N,N,N* ligand that should enhance its capacity for the capture of metal ions. The shapes of the adsorption isotherms of $ZnCl_2$ and $CdCl_2$ on AC and AC-HL in aqueous solution, obtained at pH 5, show a significant improvement of the adsorption capacity relative to unfunctionalised AC, as shown in Figure 8. A pH of 5 was chosen as a compromise value to avoid the precipitation of metal hydroxides whilst ensuring the existence of a non-negligible amount of the partially or totally unprotonated polyamine function, which is available for metal ion–polyamine interaction, as deduced from the solution studies (see Figure 4).

Each of the final solutions obtained in the study of the adsorption of the metals on AC-HL was analysed by UV/visible spectroscopy to prove that no HL was desorbed. The XPS spectra of AC-HL-Zn^{II} and AC-HL-Cd samples, including the N_{1s} peaks, are similar to that of the non-metallated adsorbent, except for a new peak in the former due to the metals ($Zn_{2p3/2}$ at 1022 eV and $Cd_{3d5/2}$ at 406 eV). This indicates that the improvement in the adsorptivity on AC-HL relative to AC alone is due to the presence of HL on the carbon surface. Moreover, further evidence of interactions between the metal ions and HL was obtained by comparison of the IR spectra of the AC-HL adsorbent and AC-HL-metal solid phases, which show the appearance of new bands in the second cases at 488 cm^{-1} and 482 cm^{-1} for Zn^{II} and Cd^{II}, respectively, which are assignable to ν(M–N). In these spectra relatively strong bands assignable to ν(M–O) (at around 420 cm^{-1} in both cases) due to metal atoms bonded to the oxygen functional groups of the AC also appear.[18] These bands were assigned previously by comparing the IR spectrum of an AC sample with those of the AC-Zn and AC-Cd solid phases obtained from the adsorption experiments carried out to obtain the corresponding isotherms.

Both isotherms in Figure 8 fit the Langmuir equation. This allowed us to calculate the maximum adsorption capacity values of 0.042 and 0.097 mmol g^{-1} for AC and AC-HL adsorbents, respectively, in the case of Zn^{II}, and 0.040 and 0.143 mmol g^{-1} for AC and AC-HL in the case of Cd^{II}. These values show that binding of HL to AC enhances the adsorption capacity of AC by a factor of 2.5 in the case of Zn^{II} and 3.5 for Cd^{II}. Nevertheless, these results disagree with the relative values found for the association constants of HL with Zn^{II} and Cd^{II} (see above), which suggest a

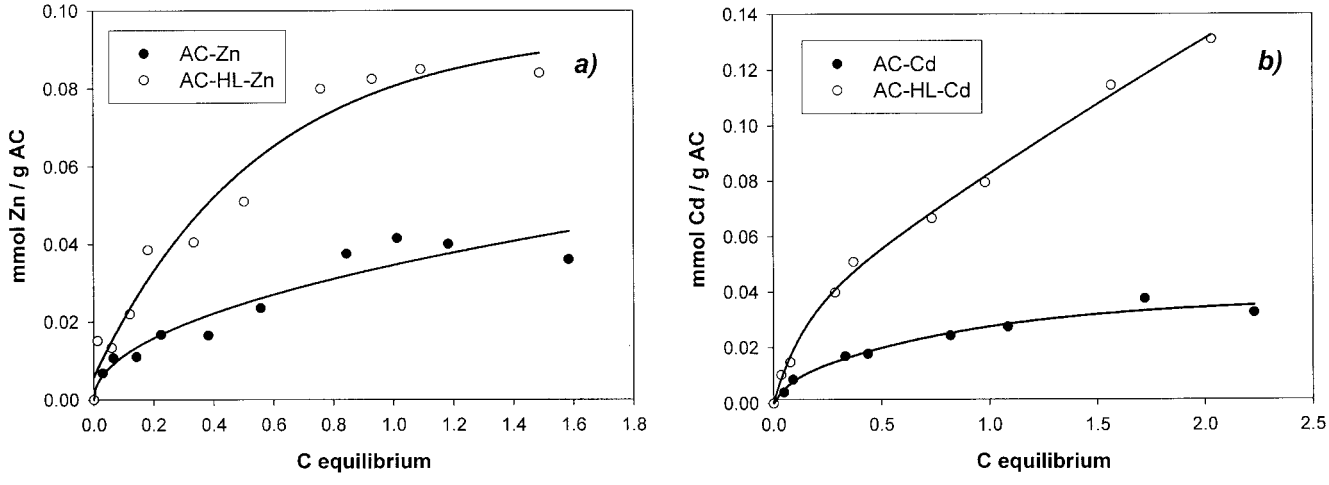

Figure 8. Adsorption isotherms of (a) Zn^{II} and (b) Cd^{II}.

 © 2005 Wiley-VCH Verlag GmbH & Co. KGaA, Weinheim

higher affinity of the triamine function for Zn^{II} than for Cd^{II}. This finding can be explained by assuming that the metals can be adsorbed either as single metal ions, when the triamine is unprotonated, or as MCl_4^{2-} when the triamine group is doubly protonated.

Considering these aspects, the two adsorption mechanisms in the case of Cd^{II} are plausible due to a non-negligible co-existence of $CdCl_4^{2-}$ and Cd^{2+} species in the medium, (log K = 6.63 for $CdCl_4^{2-}$) at the Cl^- concentrations used in the adsorption experiments. On the contrary, in the case of Zn^{2+} only the adsorption of the single metal ion on the unprotonated triamine is expected due to the lack of the more labile $ZnCl_4^{2-}$ species (log K = –0.18).[19] These findings agree with the isolation of the tetraiodocadmiate salt of the doubly protonated ligand from HL/Cd^{II} mixtures at pH 6, and the binuclear Zn^{II} complex of neutral HL from HL/Zn^{II} mixtures at the same pH. These are in accordance with the softer Lewis acid character of Cd^{II} than Zn^{II}.

Some of the chemical pollutants existing in the environment, such as arsenate, phosphate, sulfate, pertechnate, chromate, etc., are water-soluble tetrahedral anionic species. Thus, the above results suggest a possible interest in wastewater detoxification for this class of anions. In fact, the assembling of tetrahedral anions with polyamine receptors has been described in some recent monographs.[20] With this in mind, the observed affinity of the AC-HL adsorbent containing a triamine as available functional group to $CdCl_4^{2-}$ anion is not surprising and suggests the usefulness of the model compound described in this work as a host for tetrahedral anions. It has been suggested[21a] that the specificity of a polyamine receptor to a tetrahedral anion would be determined by the binding affinity, i.e. the nature of the ion-pair interaction. In the case of some macrocyclic polyamines, the strong binding of polyphosphates was found to be due to the existence of both electrostatic and hydrogen-bonding interactions.

The adsorption of a CrO_4^{2-} solution at pH 7 by the AC-HL receptor has been studied by us previously.[4] In that study, the IR spectra of a $[CrO_4]^{2-}[H_3L]^{2+}$ solid compound isolated from aqueous solution prove the existence of strong hydrogen-bonding interactions in the formation of the ion pair. These hydrogen-bonding interactions are likely responsible for the high maximum adsorption capacity of the adsorbent found (up to 0.14 mmol of CrO_4^{2-} per gram of carbon).

These results, together with other previous ones, highlight the versatile behaviour of HL-type receptors anchored on activated carbons, which makes them useful for the capture of both single metal ions and tetrahedral anions. They also encourage further studies with other single and tetrahedral ions for a better comprehension of the factors (topological, chemical, ...) that control the chemical affinity between the model receptor developed and the ions.

Conclusions

HL is characterised by a polarized aromatic moiety and a polyamine function linked by a soft bis-methylene spacer. The compound behaves as bifunctional ligand for Zn^{2+} and Cd^{2+} metal ions in aqueous solution. At low pH values it forms mononuclear complexes with these ions, which are coordinated through the C(5)NO-C(6)O grouping, and acts as a bidentate chelating ligand. The availability of the polyamine function for complex formation with metal ions occurs at slightly acidic pH values and depends on the polarizing character of the metal ion. This is reflected in the fact that the formation of bi- and mononuclear complexes with a metal ion linked through the polyamine moiety takes place at lower pH values with Zn^{2+} than with Cd^{2+} ion. In these complexes, the *N*,*N*,*N* coordinated triamine gives rise to stable metal–amine bonds.

HL is anchored on AC with the pyrimidine ring flat to the arene centres. This process, which is irreversible in water, seems to be due to π–π donor–acceptor interactions between the two aromatic moieties. Moreover, it is favoured by the electron-withdrawing character of the C(5)NO substituent of the pyrimidine moiety of HL. HL adsorption provides functionalisation of the arene centres with NH_2–$(CH_2)_2$–NH–$(CH_2)_2$ functions and this explains the improvement of the capacity of the AC for the adsorption of Zn^{2+} and Cd^{2+} metal ions. Moreover, in the case of Cd^{II}, the amphoteric character of the polyamine function allows it to adsorb Cd^{2+} and $[CdCl_4]^{2-}$ ions. All these results suggest the feasibility of the model proposed for specific functionalisation of the AC based on the topological and electronic properties of HL-type ligands. All these results have been discussed in the light of the coordination chemistry of the polyamine groups existing at the AC modified surface, which highlights the relevance of the solution and crystallographic data obtained in the coordination chemistry study of the ligand.

Experimental Section

Synthesis of 4-Amino-2-methoxy-1-methyl-5-nitroso-6-oxo-1,6-dihydropyrimidine (1): Compound **1**, which is a precursor of the ligand HL, was obtained by a previously reported method.[21]

***N*-(4-Amino-1-methyl-5-nitroso-6-oxo-1,6-dihydropyrimidin-2-yl)-*N*′-[bis(2-aminoethyl)]ethylenediamine Dihydrochloride (HL·2HCl; 2):** A solution of monohydrated **1** (5.5 g, 27.2 mmol) in CH_3CN (100 mL) was added slowly to a refluxing and stirred solution of tris(2-aminoethyl)amine dihydrochloride (6.5 g, 29.7 mmol). After the addition, the solution was refluxed for an additional 2 h, after which time a pink powdery solid appeared. The suspension was then filtered. The solid was washed with ethanol and diethyl ether and used without further purification. Yield: 9.5 g (90%). $C_{11}H_{24}Cl_2N_8O_2{\cdot}1/2H_2O$ (380.01): calcd. C 34.73, H 6.58, N 29.47; found C 34.68, H 6.46, N 29.43. ^{1}H-^{15}N HMBC ([D$_6$]DMSO): δ = 25, 68, 103, 137 ppm. ^{1}H NMR ([D$_6$]DMSO): δ = 2.67 (t, 2 H), 2.71 (t, 4 H), 2.91 (t, 4 H), 3.39 (s, 3 H), 3.53 (t, 2 H) ppm. ^{13}C NMR ([D$_6$]DMSO): δ = 27.8, 36.8, 40.2, 51.1, 52.5, 142.0, 149.8, 154.5, 161.6 ppm.

$[ZnCl_4]_2[Zn_2(HL)_2]{\cdot}2.5H_2O$ (3): A water solution (10 mL) of $ZnCl_2$ (90 mg, 0.66 mmol) was added, whilst stirring, to a solution of **2** (190 mg, 0.5 mmol) in water (10 mL). The pH of the resulting mix-

 © 2005 Wiley-VCH Verlag GmbH & Co. KGaA, Weinheim

ture was adjusted to 6 by adding 2 N KOH. Orange crystals of **3** suitable for X-ray analysis were obtained by slow evaporation of this solution. $C_{11}H_{24.5}Cl_4N_8O_{3.25}Zn_2$ (593.08): calcd. C 22.25, H 4.13, N 18.88; found C 21.76, H 4.67, N 18.42.

$[H_3L][CdI_4]\cdot 2H_2O$ (4): An aqueous solution (10 mL) of $CdCl_2\cdot 2.5H_2O$ (0.15 g, 0.66 mmol) was added to a solution of **2** (0.19 g, 0.5 mmol) and NaI (0.15 g, 1 mmol) in water (30 mL). The pH was then adjusted at 6 by adding 2 N KOH. Orange crystals of **4** were obtained by slow evaporation of the solution. $C_{11}H_{28}CdI_4N_8O_4$ (956.01): calcd. C 13.81, H 2.93, N 11.72; found C 14.60, H 2.99, N 12.35.

Potentiometric Measurements: The potentiometric titrations were carried out at 298.1 ± 0.1 K in 0.1 M KCl with a 713 Metrohm pH-mV meter, equipped with a combined glass electrode and connected to a Metrohm 765 Dosimat autoburette (1 ± 0.001 mL). The experimental procedure used was the same as that described elsewhere.[22] The system was calibrated as a hydrogen concentration probe by titrating known amounts of HCl with CO_2-free KOH solutions and determining the equivalent point by Gran's method,[23] which allows the determination of the standard potential, E^0, and the ionic product of water (pK_w = 13.76 in 0.1 M KCl at 298.1 ± 0.1 K). Ligand concentrations of $1–1.5\times10^{-3}$ M and 1:1 ligand-to-metal molar ratios were employed in the potentiometric measurements. At least four titration experiments (about 150 data points for each one) were performed in the pH ranges 2.5–10. The computer program HYPERQUAD[24] was used to calculate equilibrium constants from emf data.

Spectrophotometric Measurements: Absorption spectra of HL solutions were recorded with a Perkin–Elmer Lambda 19 spectrophotometer. HCl and KOH were used to adjust the pH values, which were measured with a Crison 2002 micropH meter.

X-ray Crystallography: Suitable crystals of **3** and **4** were obtained as orange plates and orange rods, respectively. The intensity data were collected at 153 K (–120 °C) on a Stoe Mark II-Image Plate Diffraction System[25] equipped with a two-circle goniometer and using graphite-monochromated Mo-K_α radiation. The structures were solved by direct methods using the programme SHELXS-97.[26] The refinement and all further calculations were carried out using SHELXL-97.[27] In the case of compound **4** the H-atoms were either located from Fourier difference maps and refined isotropically or included in calculated positions and treated as riding atoms using the SHELXL default parameters. For compound **3**, the majority of the H-atoms were located from Fourier difference maps and refined isotropically. The water H-atoms were located from difference maps but then either refined isotropically or constrained to be 0.83(1) Å and U_{iso} = 1.5·U_{eq}(O-atom) Å^2. The non-H atoms were refined anisotropically by weighted full-matrix least-squares procedures on F^2.

CCDC-259715 (for **3**) and -259716 (for **4**) contain the supplementary crystallographic data for this paper. These data can be obtained free of charge from The Cambridge Crystallographic Data Centre via www.ccdc.cam.ac.uk/data_request/cif.

NMR Spectroscopy: ^{1}H (300.13 MHz), ^{13}C (75.48 MHz) and two dimensional spectra in [D_6]DMSO and in D_2O solutions at different pH values were recorded at 300 K with a Bruker DPX300 spectrometer. The pD values of HL and HL–metal ion solutions were adjusted by adding small amounts of NaOD and DCl solutions. The pH was calculated from the measured pD values using the relationship pH = pD – 0.40.[28]

XPS and IR Data: XPS measurements were performed with an Escalab 200R system (VG Scientific Co.) equipped with an Mg-K_α X-ray source ($h\nu$ = 1253.6 eV) and hemispherical electron analyzer. Prior to the analysis, the samples were pretreated in situ at 623 K for 6 h in He, dry air, or wet air. The IR spectra of AC, AC-metal, AC-HL and AC-HL-metal solid samples, were obtained from KBr pellets of the samples in the 650–400 cm^{-1} range with a Bruker Tensor 27 TGA-IR spectrometer

Adsorption of Zn^{2+} and Cd^{2+}: Adsorption experiments of Zn^{2+} and Cd^{2+} ions on an activated carbon (Merck K24504014; AC) and AC-HL as adsorbent materials, respectively, at pH 5, were carried out. Typically, amounts of 0.0500 g of the adsorbent were added to a 100-mL plastic flask containing 50 mL of the appropriate aqueous solution of the adsorbate ($ZnCl_2$ or $CdCl_2$ salts). For the adsorption experiments of the metals on AC-HL, the adsorbent was obtained from a previous experiment consisting of the adsorption of an HL solution on the AC, at pH 5, by fixing conditions at which the overall HL was irreversibly adsorbed (100 ppm of HL in 100 mL of water and 0.500 g AC[4]). The pH was adjusted in each of the experiments with KOH or HCl. The suspensions were shaken at 25 ± 0.1 °C for two days until equilibrium was reached. After the adsorption experiments, the adsorbents were carefully filtered and the residual metal concentration in the solutions was measured by ICP mass spectroscopy with an AGILENT 7500 Series (Shield Torch System).

Acknowledgments

The authors thank the Spanish Ministerio de Ciencia y Tecnología for financial support (Proyecto PPQ 2000/1667). J. G.-M. acknowledges the Junta de Andalucía for a grant.

[1] a) J. N. Low, M. L. Godino, R. López, A. Pérez-Cadenas, M. Melguizo, J. Cobo, *Acta Crystallogr., Sect. C* **1999**, *55*, 1727–1730; b) J. N. Low, M. López, P. Arranz, J. Cobo, M. L. Godino, R. López, M. D. Gutierrez, M. Melguizo, G. Ferguson, C. Glidewell, *Acta Crystallogr., Sect. B* **2000**, *56*, 882–892; c) J. N. Low, A. Quesada, C. Glidewell, M. A. Fontecha, P. Arranz, M. L. Godino, R. López, *Acta Crystallogr., Sect. E* **2002**, *58*, 942–945.

[2] a) J. M. Moreno, P. Arranz, R. López, M. D. Gutierrez, M. L. Godino, J. Cobo, *Polyhedron* **1999**, *18*, 1635–1640; b) R. López, P. Arranz, M. L. Godino, M. D. Gutierrez, A. Pérez, J. Cobo, J. M. Moreno, *Inorg. Chim. Acta* **2000**, *308*, 59–64; c) P. Arranz, R. López, M. D. Gutierrez, M. L. Godino, J. M. Moreno, *Inorg. Chim. Acta* **2000**, *304*, 137–143; d) J. N. Low, J. M. Moreno, P. Arranz, M. L. Godino, R. López, J. Cobo, C. Glidewell, *Acta Crystallogr., Sect. B* **2001**, *57*, 317–328; e) J. N. Low, P. Arranz, J. Cobo, M. A. Fontecha, M. L. Godino, R. López, C. Glidewell, *Acta Crystallogr., Sect. C* **2001**, *57*, 534–537; f) R. López, P. Arranz, M. L. Godino, M. D. Gutierrez, R. Cuesta, J. M. Moreno, *Inorg. Chim. Acta* **2003**, *355*, 41–48; g) R. Cuesta, C. Glidewell, R. López, J. N. Low, *Acta Crystallogr., Sect. C* **2003**, *59*, 315–318.

[3] a) H. Minemoto, Y. Ozaki, N. Sonoda, *Appl. Phys. Lett.* **1993**, *63*, 3565–3567; b) H. Minemoto, Y. Ozaki, N. Sonoda, *J. Appl. Phys.* **1994**, *76*, 3975–3980; c) R. P. Sharma, S. Kumar, K. K. Bashin, E. R. T. Tiekink, *Z. Kristallogr.* **1997**, *212*, 742–744; d) S. Brahadeeswaran, V. Venkataramanan, J. N. Shewood, H. L. Bhat, *J. Mater. Chem.* **1998**, *8*, 613–618; e) M. Muthuraman, M. Bagieu-Beucher, R. Masse, J. F. Nicoud, R. J. Desiraju, *J. Mater. Chem.* **1999**, *9*, 1471–1474, references cited therein.

[4] J. García-Martín, R. López-Garzón, M. L. Godino-Salido, M. D. Gutiérrez-Valero, P. Arranz-Mascarós, R. Cuesta, F. Carrasco-Marín, *Langmuir*, in press.

[5] a) J. S. Mattson, H. B. Mark, *Activated Carbon Surface Chemistry and Adsorption from Solution*, Marcel Dekker, New York,

1971; b) R. W. Coughlin, F. S. Ezra, R. N. Tan, *J. Colloid Interface Sci.* **1968**, *28*, 386–396; c) C. A. Leon y Leon, J. M. Solar, V. Calemma, L. R. Radovic, *Carbon* **1992**, *30*, 797–811; d) H. Tamon, M. Okazaki, *J. Colloid Interface Sci.* **1996**, *179*, 181–187.
[6] a) L. Radovic, C. Moreno-Castilla, J. Rivera-Utrilla, in *Chemistry and Physics of Carbon* (Ed.: L. Radovic), Marcel Dekker, New York, **2000**, vol. 27, p. 241–283; b) S. D. Faust, O. M. Aly, *Chemistry of Water Treatment*, Ann Arbor Press, Chelsea, **1998**; c) S. D. Faust, O. M. Aly, A*dsorption Processes for Water Treatment*, Butterworths, Boston, **1987.**
[7] L. R. Radovic, I. F. Silva, J. I. Ume, J. A. Menéndez, C. A. Leon y Leon, A. W. Scaroni, *Carbon* **1997**, *35*, 1339–1348.
[8] A. E. Martell, R. M. Smith, R. J. Motekaitis, *NIST Critical Stability Constants of Metal Complexes Database*, Version 7, Texas A & M University, College Station, TX, **2003**.
[9] M. L. Godino, P. Arranz, R. López, M. D. Gutiérrez, J. N. Low, J. F. Gallagher, C. Glidewell, *Acta Crystallogr., Sect. B* **2004**, *60*, 46–64.
[10] a) H. J. Talberg, *Acta Chem. Scand., Ser. A* **1977**, *31*, 485–491; b) E. O. Schlemper, R. K. Murmann, M. S. Hussain, *Acta Crystallogr., Sect. C* **1986**, *42*, 1739–1743.
[11] a) M. J. Davis, J. E. Boggs, D. Coffey, H. P. Hanson, *J. Phys. Chem.* **1965**, *69*, 3727–3730; b) S. H. Bauer, A. L. Andreassen, *J. Phys. Chem.* **1972**, *76*, 3099–3108 (see also ref.[10]).
[12] a) R. López-Garzón, P. Arranz-Mascarós, M. L. Godino-Salido, M. Gutierrez-Valero, A. Perez-Cadenas, J. M. Moreno, *Inorg. Chim. Acta* **2000**, *308*, 59–64; b) R. López-Garzón, M. L. Godino-Salido, P. Arranz-Mascarós, M. A. Fontecha-Cámara, M. D. Gutiérrez-Valero, R. Cuesta, J. M. Moreno, H. Stoeckli-Evans, *Inorg. Chim. Acta* **2004**, *357*, 2007–2014.
[13] M. M. Ibrahim, N. Shimomura, K. Ichikawa, M. Shiro, *Inorg. Chim. Acta* **2001**, *313*, 125–136.
[14] M. J. Robertson, G. N. De Iuliis, M. Maeder, G. A. Lawrence, *Inorg. Chim. Acta* **2004**, *357*, 557–570.
[15] P. Jiang, Z. Guo, *Coord. Chem. Rev.* **2004**, *248*, 205–229.
[16] PLATON/PLUTON version Jan. **1999**: A. L. Spek, *Acta Crystallogr., Sect. A* **1999**, *46*, C-34.
[17] a) A. Quesada, A. Marchal, M. Melguizo, M. Nogueras, A. Sánchez, J. N. Low, D. Cannon, D. M. M. Farell, C. Glidewell, *Acta Crystallogr., Sect. B* **2002**, *58*, 300–315; b) E. J. MacLean, J. N. Low, A. Quesada, M. Melguizo, M. Nogueras, C. Glidewell, *Acta Crystallogr., Sect. C* **2002**, *58*, o442–o444; c) M. Melguizo, A. Quesada, J. N. Low, C. Glidewell, *Acta Crystallogr., Sect. B* **2003**, *59*, 263–276; d) A. Quesada, A. Marchal, M. Melguizo, J. N. Low, C. Glidewel, *Acta Crystallogr., Sect. B* **2004**, *60*, 76–89.
[18] a) J. R. Ferraro, *Low Frequency Vibrations of Inorganic and Coordination Compounds*, Plenum Press, New York, **1971**, pp. 220, 65–75; b) G. Sócrates, *Infrared Characteristic Group Frequencies*, John Wiley & Sons, Chichester, **1994**, p. 233.
[19] *Comprehensive Inorganic Chemistry* (Ed.: J. C. Bailar), vol. 3, Pergamon Press, New York, **1973**.
[20] a) *Supramolecular Chemistry of Anions* (Eds.: A. Bianchi, K. Bowman-James, E. García-España), Wiley, New York, **1997**, chapter 2; b) M. W. Hosseini, J. M. Lehn, *Helv. Chim. Acta* **1987**, *70*, 1312–1319; c) C. Seel, J. de Mendoza, in *Comprehensive Supramolecular Chemistry*, Pergamon, New York, **1996**, vol. 2, chapter 17..
[21] a) M. Engelman, *Ber. Dtsch. Chem. Ges.* **1909**, *42*, 177; b) J. Lifschitz, *Ber. Dtsch. Chem. Ges.* **1922**, *55*, 1619.
[22] M. L. Godino, M. D. Gutiérrez, R. López, J. M. Moreno, *Inorg. Chim. Acta* **1994**, *221*, 127–181.
[23] a) G. Gran, *Analyst* **1952**, *77*, 661–671; b) A. Liberti, T. S. Light, *J. Chem. Educ.* **1962**, *39*, 236–239.
[24] P. Gans, A. Sabatini, A. Vacca, *Talanta* **1996**, *43*, 1739–1753.
[25] Stoe & Cie. *X-Area V1.17 & X-RED32 V1.04 Software*, Stoe & Cie GmbH, Darmstadt, Germany, **2002**.
[26] SHELXS-97, Program for Crystal Structure Determination: G. M. Sheldrick, *Acta Crystallogr., Sect. A* **1990**, *46*, 467–473.
[27] G. Sheldrick, "SHELXL-97", University of Göttingen, Göttingen, Germany, **1999**.
[28] A. K. Covington, M. Paabo, R. A. Robinson, R. G. Bates, *Anal. Chem.* **1968**, *40*, 700–706.

Received: January 21, 2005
Published Online: July 4, 2005

 © 2005 Wiley-VCH Verlag GmbH & Co. KGaA, Weinheim

Synthesis, Crystal Structure and Characterisation of a Novel Chiral Mixed-Valence Vanadium Oxide Hybrid, $[V_5O_{11}(dien)_3]$

Ming-Lai Fu,[a,b] Guo-Cong Guo,*[a] A-Qing Wu,[a] Bin Liu,[a] Li-Zhen Cai,[a] and Jin-Shun Huang[a]

Keywords: Chirality / dien ligand / Magnetism / Mixed-valence compounds / Vanadium

The novel chiral mixed-valence vanadium oxide hybrid $[V_5O_{11}(dien)_3]$ (**1**) (dien = $NH_2C_2H_4NHC_2H_4NH_2$) has been synthesised by a hydrothermal reaction of V_2O_5 and dien in aqueous solution and characterised by elemental analysis, IR spectroscopy, TG-DSC analysis, magnetism, EPR spectroscopy, single-crystal X-ray diffraction and powder XRD. The X-ray diffraction analysis revealed that the structure of **1** can be regarded as being constructed from two $[V^{V}O_4]^{3-}$ groups bicapping three $[V^{IV}O(dien)]^{2+}$ units to form a discrete asymmetric pentanuclear vanadium complex with the dien ligands coordinating directly to the vanadium(IV) centres. Compound **1** exhibits an interesting tube-like 3D supramolecular structure due to abundant hydrogen-bonding interactions between the oxygen atoms of the inorganic backbone and the hydrogen atoms of the dien ligands from adjacent molecules. The variable-temperature magnetic susceptibility data of **1** suggest a weak ferromagnetic interaction among V^{4+} ions in the cluster.
(© Wiley-VCH Verlag GmbH & Co. KGaA, 69451 Weinheim, Germany, 2005)

Introduction

Increasing attention has been paid to inorganic oxides due to their structural diversity and applications in the fields of catalysis, sorption, electrical conductivity, magnetism and photochemistry[1] and the synthesis of new materials possessing unique structures and properties based on inorganic oxides remains a challenge. The role of organic components on the structural modification of inorganic oxides has been well recognised in recent years.[2] Generally, the organic components act as structural directors to tune inorganic frameworks, compensate charges and fill space. On the other hand, they may also function as ligands coordinated directly to the oxide scaffolding or to the secondary metal centres.[3] Recently, the introduction of the hydrothermal technique and the use of organic structure-directing agents has led to the production of various vanadium oxide discrete clusters with 1D, 2D and 3D structures.[4] A large family of inorganic-organic hybrids based on the vanadium oxides has been investigated using organic amines as organic components in which the amines are usually protonated and intercalated between the anionic vanadium oxide layers.[5] However, the investigations of amines as ligands coordinated directly to vanadium centres has been limited.[6] We are interested in introducing transition metal–amine complexes into the inorganic framework and understanding the role of metal complexes on the modification of inorganic framework structures.[7] Herein, we report a novel chiral mixed-valence vanadium oxide, $[V_5O_{11}(dien)_3]$ (**1**), with the achiral tridentate dien ligands coordinated directly to the vanadium(IV) centres.

[a] State Key Laboratory of Structural Chemistry, Fujian Institute of Research on the Structure of Matter, Chinese Academy of Sciences,
Fuzhou, Fujian 350002, P. R. China
E-mail: gcguo@ms.fjirsm.ac.cn
[b] Graduate School of Chinese Academy of Sciences,
Beijing 100039, P. R. China
Supporting information for this article is available on the WWW under http://www.eurjic.org or from the author.

Results and Discussion

The title hybrid was prepared from V_2O_5 (0.182 g, 1 mmol), dien (4 mL) and H_2O (6 mL) under hydrothermal conditions in a 25-mL capacity Teflon-lined steel autoclave at 160 °C for 6 d. The dien in the reaction acts not only as an agent for reducing V^{5+} to V^{4+} but also as a ligand coordinated to V^{4+}. Furthermore, it is an organic base to adjust the pH value of the aqueous solution in order to maintain strongly basic conditions during the whole synthesis which plays a significant role in the formation of **1**. Detailed experiments suggest that excess dien is necessary to yield **1** using V_2O_5 as a starting material and it failed to form if the amount of dien was less than 3.5 mL or if NH_4VO_3 was used as a staring material instead (Table S1; see supporting information, for supporting information see also the footnote on the first page of this article).

A single-crystal X-ray analysis reveals that **1** consists of a chiral mixed-valence vanadium oxide hybrid $[V_5O_{11}(dien)_3]$ (Figure 1). The asymmetric pentanuclear vanadium cluster exhibits two types of vanadium coordination envi-

ronments in which the V(4) and V(5) atoms are in distorted VO_4 tetrahedra and the V(1), V(2) and V(3) atoms exhibit distorted VO_3N_3 octahedral geometries. In the VO_4 tetrahedron, the vanadium centre is coordinated by three bridging oxygen atoms (O_b) and one terminal oxygen atom (O_t). The V–O_b bond lengths are in the range of 1.708(1)–1.743(1) Å, the V–O_t bond lengths are 1.658(2) and 1.662(2) Å and the O–V–O bond angles range from 107.9(1) to 113.0(1)°. In the VO_3N_3 octahedron, each V atom is chelated by one dien ligand in a tridentate manner and in a facial configuration with the V–N bond lengths ranging from 2.137(2) to 2.339(2) Å and coordinated by one O_t atom and two O_b atoms from two VO_4 tetrahedra. The V–O_b bond lengths range from 1.925(1) to 1.966(1) Å and the V–O_t bond lengths are in the range of 1.611(2)–1.621(2) Å thereby form a distorted octahedron with a π configuration[8] in which the three dien ligands coordinated to V1, V2 and V3 exhibit *δδ*, *λλ* and *δδ* conformations, respectively. The significantly distorted V octahedra are evident from the axial angles which range from 158.3(1) to 164.5(1)°. Bond-valence sum (BVS) calculations[9] [V(1) = 4.066, V(2) = 4.057, V(3) = 3.999, V(4) = 5.179, V(5) = 5.160] show that the V octahedra are occupied by V^{4+} ions and the V tetrahedra by V^{5+} ions which is consistent with the overall charge balance of the compound. Magnetic measurements support the BVS calculations for the valence assignment of V atoms (see below). The five vanadium atoms in the pentanuclear cluster can be described as a giant trigonal bipyramid with three V^{4+} atoms lying on the equatorial plane and two V^{5+} atoms occupying the axial positions in which two $[VO_4]^{3-}$ groups are bicapping the $[VO(dien)]^{2+}$ unit through corner-sharing their polyhedra (Figure S1). The present mixed-valence pentanuclear vanadium hybrid has been found for the first time in the neutral form, although mixed-valence pentanuclear vanadium compounds have been previously characterised as anions in $[Et_4N]_2[V_5O_9X(O_2CR)_4]$ salts (X = Cl^-, Br^-; R = Ph, CH_3).[10]

An interesting feature is that the space group of **1** is $P6_3$ which results in its chiral nature. In recent years, much effort has been devoted to the controlled construction of inorganic coordination compounds with enantiopure topologies, stimulated by their potential impact on important areas of research such as enantioselective catalysis and molecular recognition. Achiral molecules[11] as well as chiral species[12] can be used to synthesise chiral coordination compounds. However, the achiral approach almost always leads to a racemic mixture[13] and it is not well understood how homochiral packing in crystals can be induced.[14] Although the inorganic V_5O_{11} backbone and the dien ligand in **1** are achiral, the homochiral structure of **1** is induced by the different twist of the organic ligand chelating to the vanadium(IV) centres. The powder XRD pattern of **1** and the pattern simulated on the basis of the single-crystal structure are presented in Figure 2. The diffraction peaks in both patterns correspond well in their positions, indicating the phase purity of the prepared sample. In the IR spectrum of **1** (Figure S2, supporting information), the strong bands at 967, 867, 832, 735 and 675 cm^{-1} are due to the terminal V=O stretch and the V–O–V stretch. Bands in the 1107–1619 cm^{-1} region can be attributed to characteristic peaks of the dien ligand.

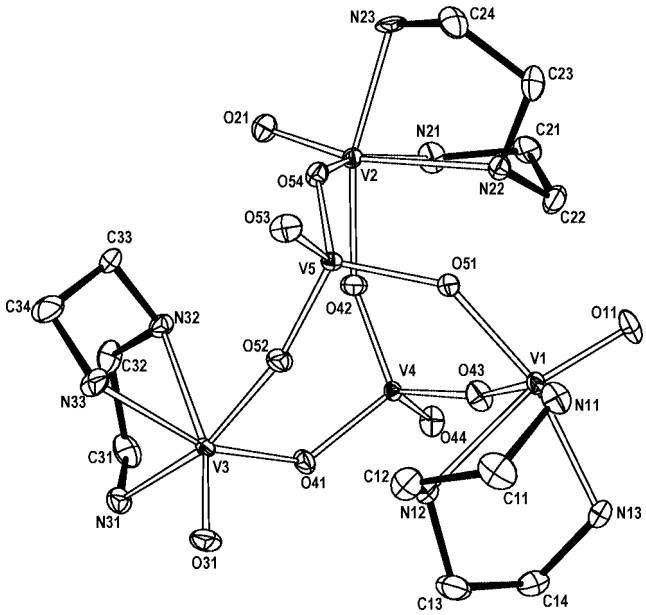

Figure 1. Molecular structure of **1** with 30% thermal ellipsoids. Hydrogen atoms are omitted for clarity.

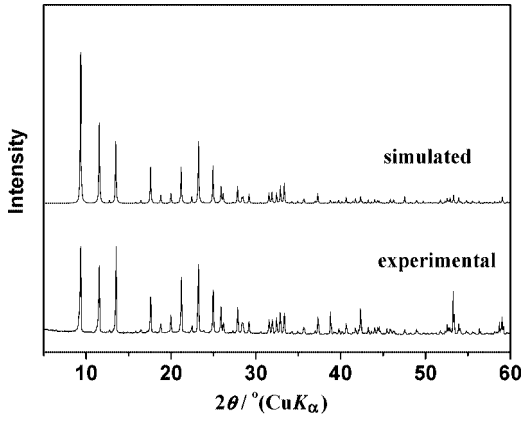

Figure 2. Experimental and simulated powder X-ray diffraction pattern of **1**.

As shown in Figure 3, the $[V_5O_{11}(dien)_3]$ molecules are stably packed together to exhibit an interesting tube-like 3D supramolecular array with 1D channels (about 2.4 Å in free diameter, Figure S3, supporting information) along the *c* direction by means of abundant hydrogen-bonding interactions between the oxygen atoms of vanadium oxides and the hydrogen atoms of dien ligands from adjacent molecules (Table 1; Figures S4 and S5, supporting information). It is of note that the hydrogen-bonding interactions play a significant role in the stabilisation of the structure of **1** which is consistent with the thermal analysis experiments. The TGA and DSC data, recorded from 30 to 1000 °C under flowing N_2, show that the weight of **1** is almost unchanged

 © 2005 Wiley-VCH Verlag GmbH & Co. KGaA, Weinheim

Table 1. Hydrogen bond lengths [Å] and angles [°] of complex **1**.

Atom involved	Distance (N···O)	Angles N–H···O	Symmetry-equivalent operations
N11–H11D···O41_$1	3.040(2)	139.1	$1: *y*, –*x* + *y*
N11–H11C···O44_$1	2.944(2)	112.7	
N13–H13D···O31_$2	3.001(2)	159.2	$2: –*x* + *y*, –*x*, *z*
N13–H13C···O53_$3	2.940(2)	150.9	$3: *y*, –*x* + *y*, –0.5 + *z*
N21–H21D···O53_$4	2.938(2)	167.9	$4: –*x*, 1 – *y*, –0.5 + *z*
N23–H23D···O11_$5	2.913(2)	160.9	$5: –*x* + *y*, 1 – *x*, *z*
N23–H23C···O44_$6	2.876(2)	157.6	$6: –*x*, 1 – *y*, 0.5 + *z*
N31–H31D···O21_$7	2.984(2)	161.0	$7: –1 – *x* + *y*, –*x*, *z*
N31–H31C···O53_$8	2.969(2)	152.5	$8: *x* – *y*, *x*, –0.5 + *z*
N33–H33C···O44_$9	2.904(2)	142.0	$9: *x* – *y*, *x*, 0.5 + *z*

from 30 to 260 °C (Figure S7). In the range of 260–400 °C the main weight loss occurs which is associated with two endothermic peaks and should be due to the loss of organic molecules. The endothermic peaks in this weight-loss stage imply that there exist strong coordination bonds between the V centre and the dien ligand and abundant hydrogen bonds in **1**. The observed weight loss (42.15%) is close to that which would result from losing three dien molecules per empirical formula unit (41.81%). The TGA chart shows that the next weight loss (7.99%) in the range of 400–800 °C may be due to the emission of oxygen to yield V_2O_3 as a residue (calcd. 7.57%).

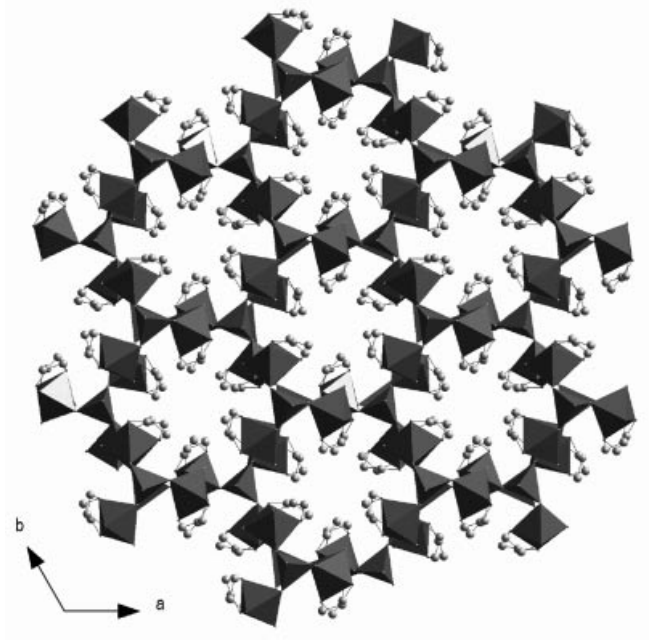

Figure 3. Polyhedral representation of **1** as a packed view along the *c* direction showing the tube-like structure.

The variable-temperature magnetic susceptibility data of **1** were recorded on a crystalline sample in a field of 1 T and in the 2–300 K temperature range as shown in Figure 4 in the χ_M and μ_{eff} vs. *T* plots. The data were fitted using the Curie-Weiss equation above 75 K: $\chi_M = C/(T - \theta) + \chi_0$, $\chi_0 = -3.6(1) \times 10^{-4}$ emu mol^{-1}, $C = 0.970(3)$ emuK mol^{-1} and $\theta = 1.6(2)$ K. The effective magnetic moment, calculated from the equation $\mu_{eff} = 2.828\ C^{1/2}$ is 2.8(2) μ_B which is close to the value of 3 μ_B for three independent unpaired electrons per formula unit. The slow increases in the μ_{eff} value with the decreasing temperature of **1** and a small positive θ clearly indicate the presence of weak ferromagnetic interactions among the V^{4+} ions in **1**. To simulate the experimental magnetic behaviour, we used the analytical experimental expression deduced for trinuclear magnetic metal atoms in compounds with classical spins.[15]

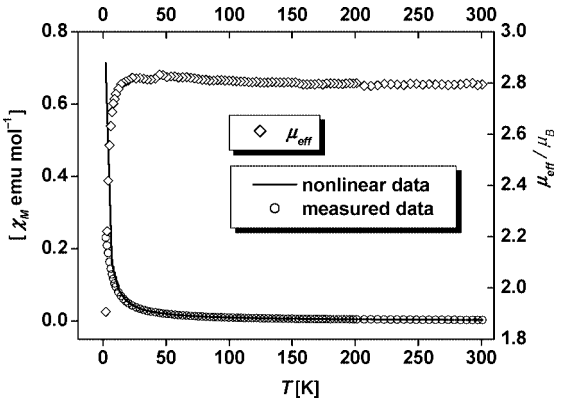

Figure 4. χ_M vs. *T* and μ_{eff} vs. *T* plots for **1**. The solid lines represent the nonlinear curve fit of the experimental data.

$$\chi_M = \frac{N\beta^2 g^2}{4kT} \frac{1 + 5\exp(3J/2kT)}{1 + \exp(3J/2kT)}$$

In this expression, *N* is Avogadro's number, β is Bohr's magneton and *k* is Boltzmann's constant. The best least-squares fit of the theoretical equation to experimental data leads to $g = 1.8570(6)$, $J/k = 3.3(1)$ K and the agreement factor $R = 1.02 \times 10^{-5}$ $\{R = \Sigma\ [(\chi_M T)_{obsd.} - (\chi_M T)_{calcd.}]^2 / \Sigma[(\chi_M T)_{obsd.}]^2\}$. The positive *J* value suggests that a weak ferromagnetic interaction exists in **1** which is in agreement with the result of the fit obtained from the Curie-Weiss law. Unlike the vast majority of known polynuclear vanadium(IV) or -(IV/V) compounds which exhibit antiferromagnetic coupling between V^{IV} magnetic ions,[16] the present chiral pentanuclear vanadium(IV/V) compound shows ferromagnetic behaviour. The EPR spectrum of **1** (Figure 5) at room temperature shows a V^{4+} signal with $g = 1.9543$ which is consistent with the value obtained from the fitting of the magnetic susceptibility data.

 © 2005 Wiley-VCH Verlag GmbH & Co. KGaA, Weinheim

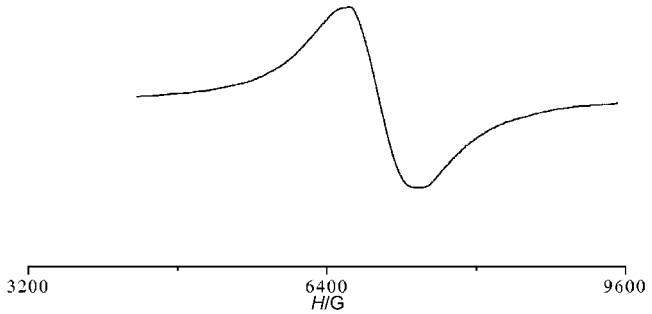

Figure 5. Powder X-band EPR spectrum of **1**.

Conclusions

In conclusion, a novel chiral mixed-valence vanadium oxide hybrid, $[V_5O_{11}(dien)_3]$, in which the dien ligands are chelated to vanadium(IV) centres in a tridentate manner has been successfully synthesised by a hydrothermal process. This result shows that the chiral hybrid can be constructed from achiral starting materials which are induced by the different twist of the organic ligands chelating to the vanadium(IV) centres. The material exhibits an interesting tube-like channel structure resulting from abundant intermolecular hydrogen bonding interactions and shows weak ferromagnetic interactions.

Experimental Section

General Remarks: All reagents were purchased from commercial sources and used without further purification. Elemental analyses (C, H, N and O) were performed with an Elementar Vario EL III microanalyser. The infrared spectrum was recorded as a KBr pellet in the range of 4000–400 cm^{-1} with a Nicolet FTIR Magna 750 spectrophotometer. The powder X-ray diffraction pattern was collected with a Rigaku DMAX2500 diffractometer at 40 kV and 100 mA for Cu-K_α (λ = 1.5406 Å), with a scan speed of 5° min^{-1} at room temperature. The simulated pattern was produced using the Platon program and single-crystal reflection data. A Netzsch STA 449C thermogravimetric analyser was used to obtain TGA and DSC curves under N_2 with a temperature increment of 10 °C min^{-1} in the temperature range 30–1000 °C. An empty Al_2O_3 crucible was used as a reference.

$[V_5O_{11}(dien)_3]$ (1): Powdery V_2O_5 (0.182 g, 1 mmol) was added to a solution of dien (4 mL) in H_2O (6 mL). The mixture was stirred at room temperature for 1 h then transferred into a 25-mL teflon-lined stainless steel autoclave and heated at 160 °C under autogeneous pressure for 6 d. After cooling, the brown crystals obtained by filtration were washed with water and ethanol. Yield: 80% (based on V_2O_5). $C_{12}H_{39}N_9O_{11}V_5$ (740.2): calcd. C 19.47, H 5.31, N 17.03, O 23.78; found C 19.33, H 5.06, N 17.08, O 23.70.

Table 2. Crystal data and structural refinements details for complex **1**.

Empirical formula	$C_{12}H_{39}N_9O_{11}V_5$
Formula mass [g mol^{-1}]	740.22
Crystal colour	brown
Crystal habit	chip
Crystal size [mm]	0.30 × 0.30 × 0.22
Crystal system	hexagonal
Space group	$P6_3$
a [Å]	18.8426(5)
c [Å]	13.0627(7)
V [$Å^3$]	4016.5(3)
Z	6
λ (Mo-K_α) [Å]	0.71073
$D_{calcd.}$ [g cm^{-3}]	1.836
μ (Mo-K_α) [mm^{-1}]	1.747
F(000)	2262
Flack parameter	0.0(2)
2θ range [°]	3.30 to 25
Reflections collected	29579
Independent reflections	4349
Observed data [$I > 2\sigma(I)$]	4084
R_{int}	0.0377
R indexes [$I > 2\sigma(I)$]	R_1 = 0.0334, wR_2 = 0.0831
R indexes (for all reflections)	R_1 = 0.0372, wR_2 = 0.0851
Goodness of fit	0.997
Largest difference peak and hole [e $Å^{-3}$]	0.306, –0.284

Table 3. Selected bond lengths [Å] for compound **1**.

V(1)–O(11)	1.6188(12)	V(3)–O(52)	1.9349(13)
V(1)–O(43)	1.9245(14)	V(3)–O(41)	1.9559(13)
V(1)–O(51)	1.9569(15)	V(3)–N(31)	2.1374(16)
V(1)–N(13)	2.1456(18)	V(3)–N(33)	2.1940(18)
V(1)–N(11)	2.1668(18)	V(3)–N(32)	2.3385(18)
V(1)–N(12)	2.3096(13)	V(4)–O(44)	1.6583(17)
V(2)–O(21)	1.6112(15)	V(4)–O(42)	1.7172(15)
V(2)–O(42)	1.9372(14)	V(4)–O(43)	1.7172(13)
V(2)–O(54)	1.9560(14)	V(4)–O(41)	1.7427(11)
V(2)–N(23)	2.1490(15)	V(5)–O(53)	1.6622(16)
V(2)–N(21)	2.1695(17)	V(5)–O(52)	1.7077(12)
V(2)–N(22)	2.3305(17)	V(5)–O(54)	1.7321(13)
V(3)–O(31)	1.6208(16)	V(5)–O(51)	1.7380(12)

Table 4. Selected bond angles [°] for compound **1**.

O(11)–V(1)–O(43)	105.93(7)	N(21)–V(2)–N(22)	74.93(6)
O(11)–V(1)–O(51)	102.47(7)	O(31)–V(3)–O(52)	105.42(7)
O(43)–V(1)–O(51)	91.26(6)	O(31)–V(3)–O(41)	104.93(7)
O(11)–V(1)–N(13)	93.61(7)	O(52)–V(3)–O(41)	88.33(6)
O(43)–V(1)–N(13)	88.16(7)	O(31)–V(3)–N(31)	94.66(7)
O(51)–V(1)–N(13)	163.41(5)	O(52)–V(3)–N(31)	159.86(7)
O(11)–V(1)–N(11)	95.78(7)	O(41)–V(3)–N(31)	87.98(6)
O(43)–V(1)–N(11)	158.29(5)	O(31)–V(3)–N(33)	94.14(7)
O(51)–V(1)–N(11)	83.85(7)	O(52)–V(3)–N(33)	81.71(6)
N(13)–V(1)–N(11)	90.58(7)	O(41)–V(3)–N(33)	160.29(6)
O(11)–V(1)–N(12)	164.54(8)	N(31)–V(3)–N(33)	95.52(7)
O(43)–V(1)–N(12)	83.65(5)	O(31)–V(3)–N(32)	163.37(6)
O(51)–V(1)–N(12)	89.18(5)	O(52)–V(3)–N(32)	85.76(6)
N(13)–V(1)–N(12)	74.27(6)	O(41)–V(3)–N(32)	87.37(6)
N(11)–V(1)–N(12)	75.17(6)	N(31)–V(3)–N(32)	74.30(6)
O(21)–V(2)–O(42)	103.22(7)	N(33)–V(3)–N(32)	75.02(6)
O(21)–V(2)–O(54)	105.48(7)	O(44)–V(4)–O(42)	109.16(7)
O(42)–V(2)–O(54)	90.22(6)	O(44)–V(4)–O(43)	107.86(7)
O(21)–V(2)–N(23)	94.48(7)	O(42)–V(4)–O(43)	109.92(7)
O(42)–V(2)–N(23)	162.18(6)	O(44)–V(4)–O(41)	108.12(6)
O(54)–V(2)–N(23)	87.08(6)	O(42)–V(4)–O(41)	108.74(6)
O(21)–V(2)–N(21)	94.16(7)	O(43)–V(4)–O(41)	112.97(6)
O(42)–V(2)–N(21)	84.42(6)	O(53)–V(5)–O(52)	108.72(6)
O(54)–V(2)–N(21)	160.34(6)	O(53)–V(5)–O(54)	108.26(7)
N(23)–V(2)–N(21)	92.26(6)	O(52)–V(5)–O(54)	111.94(7)
O(21)–V(2)–N(22)	163.41(6)	O(53)–V(5)–O(51)	109.63(7)
O(42)–V(2)–N(22)	88.37(6)	O(52)–V(5)–O(51)	107.92(7)
O(54)–V(2)–N(22)	86.04(5)	O(54)–V(5)–O(51)	110.33(6)
N(23)–V(2)–N(22)	73.88(6)		

© 2005 Wiley-VCH Verlag GmbH & Co. KGaA, Weinheim

X-ray Crystallographic Study: The single-crystal X-ray data for **1** were collected with a Rigaku Mercury CCD diffractometer with graphite-monochromated Mo-K_α radiation using the ω-scan technique at 293 K and CrystalClear[17] software was used for data reduction. The structure was solved by direct methods using the Siemens SHELXTL™ Version 5 crystallographic software package.[18] The difference Fourier maps based on these atomic positions yielded the other non-hydrogen atoms and the hydrogen atoms bound to nitrogen atoms. The structure was refined using a full-matrix least-squares refinement on F^2. All non-hydrogen atoms were refined anisotropically. The positions of hydrogen atoms bound to carbon atoms were generated symmetrically, allowed to ride on their respective parent atoms and included in the structure factor calculations with assigned isotropic thermal parameters but were not refined. Crystallographic data are summarised in Table 2 and selected bond lengths and angles are listed in Tables 3 and 4. CCDC-260926 contains the supplementary crystallographic data for this paper. These data can be obtained free of charge from the Cambridge Crystallographic Data Centre via www.ccdc.cam.ac.uk/data_request/cif.

Supporting Information (see also footnote on the first page of this article): Details of the compositions of reactants for the preparation of **1**, DSC and TG curves, IR spectra and crystal structural diagrams indicating hydrogen bonds.

Acknowledgments

We gratefully acknowledge the financial support of the NSF of China (20131020), the NSF for Distinguished Young Scientist of China (20425104) and the NSF of Fujian Province (2003I031).

[1] a) A. K. Cheetham, *Science* **1994**, *264*, 794 and references cited therein; b) P. A. Cox, *Transition Metal Oxides*, Clarendon Press, Oxford, **1995**; c) A. Müller, H. Reuter, S. Dillinger, *Angew. Chem. Int. Ed. Engl.* **1995**, *34*, 2328; d) M. T. Pope, A. Müller, *Angew. Chem. Int. Ed. Engl.* **1991**, *30*, 34; e) M. T. Pope, *Heteropoly and Isopoly Oxometalates*, Springer, New York, **1983**; f) A. Müller, F. Peters, M. T. Pope, D. Gatteschi, *Chem. Rev.* **1998**, *98*, 239; g) A. Clearfield, *Chem. Rev.* **1988**, *88*, 125; h) P. J. Hagrman, D. Hagrman, J. Zubieta, *Angew. Chem. Int. Ed.* **1999**, *38*, 2638.

[2] a) S. I. Stupp, P. V. Braun, *Science* **1997**, *277*, 1242; b) O. M. Yaghi, H. Li, C. Davis, D. Richardson, T. L. Groy, *Acc. Chem. Res.* **1998**, *31*, 474; c) S. R. Batten, R. Robson, *Angew. Chem. Int. Ed.* **1998**, *37*, 1460; d) P. V. Braun, P. Osenar, V. Tohver, S. B. Kennedy, S. I. Stupp, *J. Am. Chem. Soc.* **1999**, *121*, 7302.

[3] P. J. Hagrman, J. Zubieta, *Inorg. Chem.* **2000**, *39*, 3260.

[4] a) Y. Zhang, P. J. Zapf, L. M. Meyer, R. C. Haushalter, J. Zubieta, *Inorg. Chem.* **1997**, *36*, 2159; b) L. M. Zheng, J. S. Zhao, K. H. Li, L. Y. Zhang, Y. Liu, X. Q. Xin, *J. Chem. Soc. Dalton Trans.* **1999**, 939; c) L. R. Zhang, Z. Shi, G. Y. Yang, X. M. Chen, S. H. Feng, *J. Chem. Soc. Dalton Trans.* **2000**, 275; d) X. M. Zhang, M. L. Tong, X. M. Chen, *Chem. Commun.* **2000**, 1817; e) J. Tao, X. M. Zhang, M. L. Tong, X. M. Chen, *J. Chem. Soc. Dalton Trans.* **2001**, 770; f) C. M. Liu, S. Gao, H. Z. Kou, *Chem. Commun.* **2001**, 1670; g) J. Do, A. J. Jacobson, *Inorg. Chem.* **2001**, *40*, 2468; h) P. J. Hagrman, J. Zubieta, *Inorg. Chem.* **2001**, *40*, 2800; i) C. M. Liu, Y. L. Hou, J. Zhang, S. Gao, *Inorg. Chem.* **2002**, *41*, 140; j) Y. Lu, E. B. Wang, M. Yuan, G. Y. Luan, Y. G. Li, H. Zhang, C. W. Hu, Y. G. Yao, Y. G. Qin, Y. B. Chen, *J. Chem. Soc. Dalton Trans.* **2002**, 3029.

[5] a) D. Riou, G. Férey, *J. Solid State Chem.* **1995**, *120*, 137; b) L. F. Nazar, B. E. Koene, J. F. Britten, *Chem. Mater.* **1996**, *8*, 327; c) Y. P. Zhang, C. J. O'Connor, A. Clearfield, R. C. Haushalter, *Chem. Mater.* **1996**, *8*, 595; d) Y. P. Zhang, R. C. Haushalter, A. Clearfield, *Chem. Commun.* **1996**, 1055; e) J. Livage, *Coord. Chem. Rev.* **1998**, *178*, 999; f) T. Chirayil, P. Y. Zavalij, M. S. Whittingham, *Chem. Mater.* **1998**, *10*, 2629; g) P. Zavalij, M. S. Whittingham, *Acta Crystallogr. Sect. B* **1999**, *55*, 627.

[6] a) K. Wieghardt, M. Koppen, B. Nuber, J. Weiss, *J. Chem. Soc. Chem. Commun.* **1986**, 1530; b) R. Hotzelmann, K. Wieghardt, U. Florke, H.-J. Haupt, *Angew. Chem. Int. Ed. Engl.* **1990**, *29*, 645; c) J. G. Reynolds, S. C. Sendlinger, A. M. Murray, J. C. Huffman, G. Christou, *Angew. Chem. Int. Ed. Engl.* **1992**, *31*, 1253; d) W. Plass, J. G. Verkade, *J. Am. Chem. Soc.* **1992**, *114*, 2275; e) D. Reardon, J. Guan, S. Gambarotta, G. P. A. Yap, D. R. Wilson, *Organometallics* **2002**, *21*, 4390; f) M. P. Shores, J. R. Long, *J. Am. Chem. Soc.* **2002**, *124*, 3512.

[7] a) M.-L. Fu, G.-C. Guo, X. Liu, B. Liu, L.-Z. Cai, J.-S. Huang, *Inorg. Chem. Commun.* **2005**, *8*, 18; b) M.-L. Fu, G.-C. Guo, L. Z. Cai, Z.-J. Zhang, J.-S. Huang, *Inorg. Chem.* **2005**, *44*, 184.

[8] a) A. R. Gainsford, D. A. House, *Inorg. Chim. Acta* **1969**, *3*, 367; b) A. R. Gainsford, D. A. House, W. T. Robinson, *Inorg. Chim. Acta* **1971**, *5*, 595.

[9] a) I. D. Brown, D. Altermatt, *Acta Crystallogr. Sect. B* **1985**, *41*, 244; b) N. E. Brese, M. O. Keeffe, *Acta Crystallogr. Sect. B* **1991**, *47*, 192.

[10] a) G. B. Karet, Z. Sun, D. D. Heinrich, J. K. McCusker, K. Folting, W. E. Streib, J. C. Huffman, D. N. Hendrickson, G. Christou, *Inorg. Chem.* **1996**, *35*, 6450; b) G. B. Karet, Z. Sun, W. E. Streib, J. C. Bollinger, D. N. Hendrichson, G. Christou, *Chem. Commun.* **1999**, 2249.

[11] a) D. Rabinovich, B. S. Green, M. Lahav, *Acc. Chem. Res.* **1979**, *12*, 191; b) T. Ezuhara, K. Endo, Y. Aoyama, *J. Am. Chem. Soc.* **1999**, *121*, 3279; c) M. A. Withersby, A. J. Blake, N. R. Champness, P. Hubberstey, W.-S. Li, M. Schröder, *Angew. Chem. Int. Ed. Engl.* **1997**, *36*, 2327; d) S. R. Batten, B. F. Hoskins, R. Robson, *Angew. Chem. Int. Ed. Engl.* **1997**, *36*, 636; e) R. Krämer, J.-M. Lehn, A. De Cian, J. Fischer, *Angew. Chem. Int. Ed. Engl.* **1993**, *32*, 703.

[12] a) F. R. Keene, *Coord. Chem. Rev.* **1997**, *166*, 121; b) U. Knof, A. von Zelewsky, *Angew. Chem. Int. Ed.* **1999**, *38*, 302.

[13] O. J. Gelling, F. Van Bolhuis, B. L. Feringa, *J. Chem. Soc. Chem. Commun.* **1991**, 917.

[14] a) H. Koshima, E. Hayashi, K. Matsuura, K. Tanaka, F. Toda, M. Kato, M. Kiguchi, *Tetrahedron Lett.* **1997**, *38*, 5009; b) D. K. Kondepudi, R. J. Kaufman, N. Singh, *J. Am. Chem. Soc.* **1993**, *115*, 10211; c) J. M. McBride, R. L. Carter, *Angew. Chem. Int. Ed. Engl.* **1991**, *30*, 293; d) D. K. Kondepudi, R. J. Kaufman, N. Singh, *Science* **1990**, *250*, 975.

[15] O. Kahn, *Molecular Magnetism*, VCH, Weinheim, Germany, **1993**.

[16] a) J. M. Clemente-Juan, E. Coronado, *Coord. Chem. Rev.* **1999**, *193–195*, 361 and references cited therein; b) A. Müller, F. Peters, M. T. Pope, D. Gatteschi, *Chem. Rev.* **1998**, *98*, 239and references cited therein.

[17] Rigaku, *CrystalClear Version 1.35*, Rigaku Corporation, **2002**.

[18] Siemens, *SHELXTL™ Version 5 Reference Manual*, Siemens Energy & Automation Inc., Madison, Wisconsin, USA, **1994**.

Received: January 19, 2005
Published Online: June 22, 2005

 © 2005 Wiley-VCH Verlag GmbH & Co. KGaA, Weinheim

Novel Analogues of 5-Fluorouracil – Synthesis, X-ray Crystallography, and Cytotoxic Effects in Normal Human Peripheral Blood Lymphocytes and Colon Adenocarcinoma HT 29

Ksenia Matlawska,*[a] Urszula Kalinowska,[b] Andrea Erxleben,[c] Regina Osiecka,[a] and Justyn Ochocki[b]

Keywords: Alkali metals / Phosphonate ligands / X-ray diffraction / Antitumor agents / Uracil derivatives

The aim of many studies is to discover new chemicals as potential antitumor agents. We have prepared novel analogues of 5-fluorouracil (5-Fu): 5-uracilmethylphosphonic acid (5-umpa), dimethyl 5-uracilmethylphosphonate (5-umpm), diethyl 5-uracilmethylphosphonate (5-umpe) and a K^+ (K^+/5-umpa, **1**) and Na^+ (Na^+/5-umpa, **2**) complex of 5-umpa. Complexes **1** and **2** have infinite chain structures built up by H-bonded pairs of 5-umpa$^-$ and $\{(H_2O)K(\mu\text{-}OH_2)_3K(OH_2)\}^{2+}$ and $\{(H_2O)_2Na(\mu\text{-}OH_2)_2Na(OH_2)_2\}^{2+}$ entities. The alkali metal ions bind directly to the exocyclic oxygen atoms O(2) and O(4) of the nucleobase moiety and indirectly, i.e. through hydrogen-bond interactions involving metal-coordinated water molecules, to the phosphonate group. The new derivatives were tested for their antiproliferative and cytotoxic effects on normal human peripheral blood lymphocytes and HT 29 cancer lines in vitro using the tetrazolium salt (MTT) assay. The IC_{50} values were evaluated (the drug concentration inhibiting 50 % of the cell growth after 72 h exposure of cells to the drug). The results indicate that 5-umpa, 5-umpm, 5-umpe, and the K^+ and Na^+ complexes of 5-umpa do not exert toxic effects on regular lymphocytes and on the colon adenocarcinoma HT 29 cell line ($IC_{50} > 1$ mM), in comparison with 5-Fu. However, an atypical course of survival curves was observed after treatment of HT 29 cells with 5-umpa, 5-umpm and the Na^+ complex of 5-umpa. These observations suggest that it is very important to continue the studies in different biological systems in vitro and in vivo using various experimental protocols.
(© Wiley-VCH Verlag GmbH & Co. KGaA, 69451 Weinheim, Germany, 2005)

Introduction

For many years 5-fluorouracil (5-Fu) has been widely used in cancer chemotherapy, especially in the treatment of colorectal, liver, ovarian, head and neck, and lung and breast carcinomas.[1–4] This fluorinated analogue of the natural pyrimidine base uracil can be used alone in monotherapy or in combination with other cytotoxic drugs (e.g. methotrexate, cisplatin) or with agents that are themselves not toxic but that modulate antitumor activity of 5-Fu (e.g. leucovorin).[3,5–10] Unfortunately, clinical application of this drug is limited by many undesirable effects, such as myelosuppresion (leucopenia, thrombocytopenia), gastrointestinal symptoms (nausea, vomiting, stomatitis, diarrhea), neurotoxicity (ataxia of trunk or extremities, unsteady gait, slurred speech, nystagmus), cardiotoxicity, and hyperpigmentation of skin.[1] Due to this scientists continually search for new less toxic and more effective compounds.

We have discovered novel phosphonate derivatives of uracil: 5-umpa (5-uracilmethylphosphonic acid), 5-umpm (dimethyl 5-uracilmethylphosphonate), 5-umpe (diethyl 5-uracilmethylphosphonate), and a K^+ and Na^+ complex of 5-umpa (Scheme 1).[11]

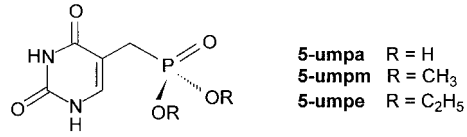

Scheme 1. Schematic structures of the uracil phosphonate derivatives.

Recently, the first three compounds 5-umpa, 5-umpm, and 5-umpe have been shown to prolong the survival time of mice with lymphoid leukemia 1210 when used in combination with cisplatin and as individual agents.[12] These findings prompted studies on the complexing properties with respect to platinum[13] and biologically relevant metal ions.[14,15]

[a] Department of Cytogenetics and Plant Molecular Biology, University of Lodz,
Banacha 12/16, 90-237 Lodz, Poland
Fax: +48-426354423
E-mail: ksenmat@biol.uni.lodz.pl
regos@biol.uni.lodz.pl
[b] Department of Bioinorganic Chemistry, Medical University, Muszynskiego 1, 90-151 Lodz, Poland
Fax: +48-426788398
E-mail: uk@ich.pharm.am.lodz.pl
ochocki@ich.pharm.am.lodz.pl
[c] Department of Chemistry, University of Dortmund, Otto-Hahn-Strasse 6, 44227 Dortmund, Germany
Fax: +49-2317553797
E-mail: andrea.erxleben@uni-dortmund.de

The spectroscopic investigation and X-ray structure determination of 5-umpa, 5-umpm, and 5-umpe were described previously.[11,16] Solution studies on complex formation between the uracil derivative 5-umpa and alkaline earth metal ions have been reported recently and showed that Ca^{2+} and Mg^{2+} interacted directly with the phosphonate oxygen atom, while the neutral nucleobase residue did not participate in complex formation.[15] In the present study, two complexes of 5-umpa with Na^+ and K^+ ions are described. Coordination of alkali metal ions to nucleobase derivatives having negatively charged phosphonate groups also has some relevance to the interaction of alkali metal ions with nucleic acids in biological systems. Due to their function as counterions for the charge neutralization of the sugar-phosphate backbone of DNA and RNA, alkali metal ions are essential for the stability of nucleic acids. In principle, they can interact with nucleic acids through direct coordination or through hydrogen bonding through aqua ligands; the potential binding sites are the negatively charged phosphate groups and the nucleobase donor atoms, in particular, exocyclic carbonyl oxygen atoms. Recently, direct binding of Na^+ ions in the minor groove of DNA, e.g. to N(3) of adenine, O(2) of thymine or cytosine, has been proposed on the basis of high-resolution X-ray analyses of B-DNA fragments.[17] Furthermore, coordination of Na^+ and K^+ to the exocyclic oxygen atoms of nucleobases, such as O(6) of guanine and O(4) of thymine or uracil, has been found to be crucial for the formation of multistranded nucleic acid arrangements, e.g. guanine, uracil or thymine quartets.[18–22] Several studies have been devoted to the preparation of models for alkali-metal-ion–nucleic-acid interactions. These mostly involve the use of neutral model nucleobases that lack phosphate groups as alternative binding sites for the alkali metal ions.[14,15,23–25] Although 5-umpa differs from the natural uracil nucleotide, it can nevertheless give some further insight into the coordination mode in complexes of alkali metal ions and nucleic acids.

Here we report on the solid-state structures of $[\{K(H_2O)(\mu\text{-}OH_2)_{1.5}\}_2(5\text{-umpa}^-)_2]_n$ (**1**) and $[\{Na(H_2O)_2(\mu\text{-}OH_2)\}_2(5\text{-umpa}^-)_2]_n$ (**2**), where Na^+ and K^+ bind directly to the exocyclic oxygen atoms O(2) and O(4) of the nucleobase part and interact indirectly, i.e. through hydrogen-bond interactions involving metal-coordinated water molecules, with the phosphonate group.

The first step in estimating biological activity of new chemical compounds is to study their cytotoxicity in vitro. In view of this, we used the ability of viable cells to convert the yellow dye MTT [3-(4,5-dimethylthiazol-2-yl)-2,5-diphentyltetrazolium bromide] to purple crystals of formazan by mitochondrial dehydrogenases.[26]

Results and Discussion

X-ray suitable crystals of the potassium and sodium complexes of 5-umpa were obtained from aqueous solutions of 5-umpa upon adjusting the pH to 8.9 with KOH or NaOH. Single-crystal X-ray analysis (Table 5) of the potassium complex **1** reveals an infinite chain structure built up by H-bonded pairs of 5-umpa$^-$ and $\{(H_2O)K(\mu\text{-}OH_2)_3\text{-}K(OH_2)\}^{2+}$ entities, in which two K^+ ions are triply bridged by water molecules (Figure 1 and Table 1, Scheme 2).

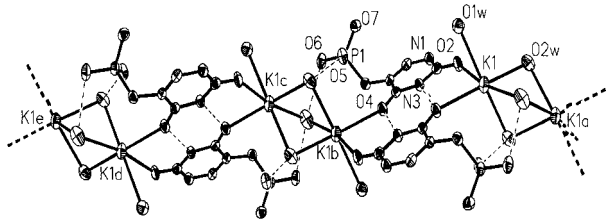

Figure 1. Infinite chain observed in the K^+ complex of 5-umpa showing H-bonding interactions.

Table 1. Bond lengths [Å] and angles [°] in **1** and **2**.

	1	**2**
M(1)–O(2)	2.719(3)	2.429(2)[d]
M(1)–O(4)	2.761(2)[a]	2.423(2)
M(1)–O(1w)	2.873(3)	2.470(2)
M(1)–O(2w)	2.710(3)	2.463(2)
M(1)–O(2w)	2.813(3)[b]	2.405(2)[c]
M(1)–O(3w)	2.801(3)	2.376(3)
O(2)–M(1)–O(4)	81.78(7)[a]	88.92(7)[d]
O(2)–M(1)–O(2w)	90.02(7)	81.81(7)[c,d]
O(2)–M(1)–O(3w)	167.38(6)	101.31(8)[d]
O(1w)–M(1)–O(4)	81.99(7)[a]	96.40(8)
O(2w)–M(1)–O(3w)	77.75(7)	89.95 (8)
O(2w)–M(1)–O(2w)	75.52(9)[b]	88.25(7)[c]
O(2w)–M(1)–O(4)	169.58(8)[a]	170.38(7)[c]
O(3w)–M(1)–O(4)	110.72(6)[a]	93.83(8)

[a] –1/2 –*x*, –1/2 – *y*, 1 – *z*. [b] –1 – *x*, *y*, 1/2 – *z*. [c] –*x*, 1 – *y*, 2 – *z*. [d] –*x*, 1 – *y*, 1 – *z*.

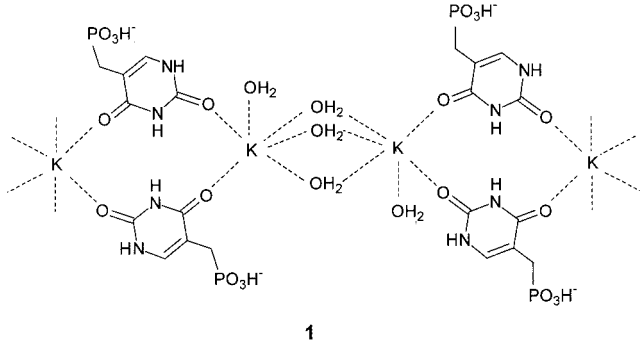

Scheme 2. Formula diagram of **1**. H-bonding interactions are omitted for clarity.

The phosphonate group of the uracil derivative is monodeprotonated as expected on the basis of the pK_a value of 5-umpa (7.15 ± 0.01) and as evident from the P–O bond lengths.[15] Two P–O bonds [P(1)–O(5) and P(1)–O(6)] are of equal length within the standard deviations [1.499(2) and 1.506(2) Å], and these bond lengths are slightly longer than those found for P=O double bonds (1.449–1.489 Å).[30] The P(1)–O(7) bond of 1.576(2) Å is significantly longer and compares well with the average bond length of a P–O single bond, so that the proton can be assumed to be bound to

 © 2005 Wiley-VCH Verlag GmbH & Co. KGaA, Weinheim

O(7).[30] This interpretation is also consistent with the H-bonding pattern described below. Direct binding of K^+ ions to the nucleobase moiety through the exocyclic carbonyl oxygen atoms O(2) and O(4), as well as hydrogen bonding between K^+-bound water and the phosphonate group is observed. Each K^+ is coordinated in a distorted octahedral manner to four water molecules, three of which form bridges to the neighboring K^+ ion, and two carbonyl oxygen atoms; the latter are *cis* to each other. The pairs of 5-umpa$^-$ ligands are connected through direct interaction with K^+ and through two H-bonds of normal length that involve N(3) and O(4) [O(4)···N(3) 2.864(4) Å, –1/2 – *x*, –1/2 – *y*, 1 – *z*]. The H-bonded umpa$^-$ ligands that are located around a twofold axis of symmetry are exactly coplanar. Bond lengths and angles in the uracil ring show no unusual features for this heterocyclic system. Additional H bonding occurs through the bridging water ligands O(2w) and O(3w) and the phosphonate oxygen atoms O(5) and O(6); the O(2w)···O(5) and O(3w)···O(6) distances are 2.707(3) and 2.931(3) Å, respectively. These intrastrand hydrogen-bond formations give rise to eight-membered macrochelates, as indicated in Figure 1. Besides the intrastrand interactions, interstrand H bonding, i.e. between neighboring chains, through the terminal and bridging aqua ligands is observed. This involves phosphonate groups as well as exocyclic carbonyl oxygen atoms [O(2)] (Table 2). Thus, extensive hydrogen bonding is realized in the crystal packing. The shortest H-bond [2.614(3) Å] is formed between two mono-deprotonated phosphonate groups of adjacent chains [O(5)···O(7), –*x*, –*y*, 1 – *z*].

Table 2. Hydrogen-bonding interactions [Å] in **1**.

O(2w)···O(5)[a]	2.707(3)	O(3w)···O(6)[a]	2.931(3)
O(4)···N(3)[b]	2.864(4)	O(1w)···O(2)[c]	2.819(3)
O(1w)···N(1)[d]	2.833(3)	O(2w)···O(6)[e]	2.826(3)
O(1w)···O(6)[f]	2.823(4)	O(5)···O(7)[f]	2.614(3)

[a] –1/2 + *x*, –1/2 – *y*, –1/2 + *z*. [b] –1/2 – *x*, –1/2 – *y*, 1 – *z*. [c] –1/2 – *x*, –1/2 + *y*, 1/2 – *z*. [d] *x*, –1 + *y*, *z*. [e] –1/2 + *x*, 1/2 – *y*, –1/2 + *z*. [f] –*x*, –*y*, 1 – *z*.

The basic structure of the sodium complex of 5-umpa **2** is identical to that of **1**. Figure 2 shows a section of the infinite chain formed by pairs of 5-umpa$^-$ ligands connected through two N(3)···O(4) H-bonds and $\{(H_2O)_2Na(\mu\text{-}OH_2)_2Na(OH_2)_2\}^{2+}$ moieties. For the P–O bond lengths, the same trend is observed as in the case for **1** [P(1)=O(7) 1.507(2) Å, P(1)=O(5) 1.524(2) Å and P(1)–O(6)H 1.559(2) Å]. Again, the alkali metal ions bind directly to the exocyclic carbonyl oxygen atoms O(2) and O(4) and interact indirectly through aqua ligands with the phosphonate oxygen atoms (Table 1 and Table 3) leading to eight-membered macrochelates as shown in Figure 2 and Scheme 3.

However, in contrast to **1**, only one intramolecular hydrogen bond is formed between a terminal water ligand and O(6) of the phosphonate group [2.931(3) Å]. Interestingly, this H-bond involves the phosphonate oxygen atom that is likely to be protonated, considering the P(1)–O(6) bond length of 1.559(2) Å. Compared with the conformation of the phosphonate group observed in **1**, the phosphonate

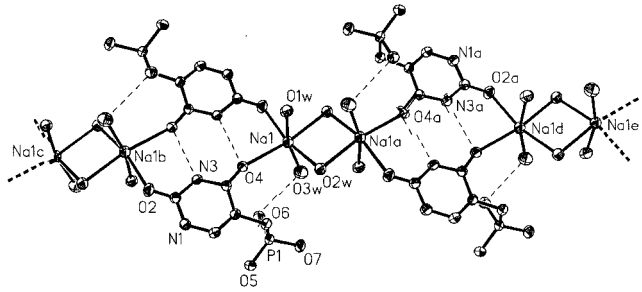

Figure 2. Infinite chain observed in the Na^+ complex of 5-umpa showing H-bonding interactions.

Table 3. Hydrogen-bonding interactions [Å] in **2**.

O(1w)···O(7)[a]	2.701(3)	O(3w)···O(6)	2.936(3)
O(4)···N(3)[b]	2.845(3)	O(1w)···O(2w)[c]	3.167(3)
O(1w)···O(3w)[c]	2.876(3)	O(1w)···N(1)[d]	2.781(3)
O(2w)···O(2)[d]	2.841(3)	O(2w)···O(4w)	2.858(3)
O(3w)···O(4w)[e]	2.785(3)	O(4w)···O(7)	2.735(3)
O(4w)···O(7)[f]	2.834(3)	O(5)···O(6)[g]	2.551(3)

[a] *x*, –1 + *y*, *z*. [b] –*x*, 1 – *y*, 1 – *z*. [c] –*x*, 1 – *y*, 2 – *z*. [d] 1 – *x*, 1 – *y*, 1 – *z*. [e] –1 + *x*, *y*, *z*. [f] –*x*, 2 – *y*, 2 – *z*. [g] –*x*, 2 – *y*, 1 – *z*.

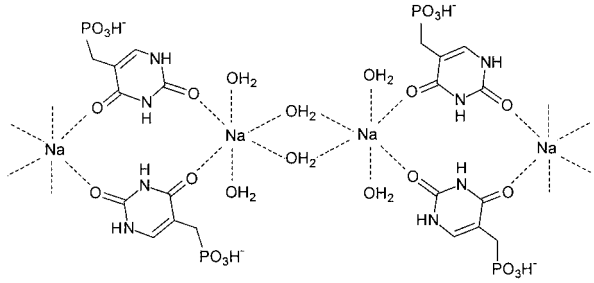

2

Scheme 3. Formula diagram of **2**. H-bonding interactions are omitted for clarity.

group seems to be pointed away from the $\{(H_2O)_2Na(\mu\text{-}OH_2)_2Na(OH_2)_2\}^{2+}$ entity. This allows a short interstrand H-bond between O(7) and O(1w) at *x*, –1 + *y*, *z*. The differences in the H-bonding details (i.e. intra- versus interstrand) in **1** and **2** may be connected to the fact that the average K–O bond length (2.78 Å) in **1** is 0.35 Å longer than the average length of a Na–O bond in **2** (2.43 Å). Furthermore, the different number of bridging and terminal water ligands, as well as the presence of further uncoordinated, interstitial water molecules in **2**, lead to major differences in the crystal packing of **1** and **2**. In particular, the uncoordinated water molecule O(4w) generates an extended network of H-bonding interactions, as depicted in Figure 3. Adjacent chains are stacked along the *x* axis, however, the distance of approximately 5 Å rules out any significant stacking interactions between the uracil rings. The stacks are stabilized by hydrogen bonding between the bridging water ligand O(2w) and the carbonyl oxygen atom O(2) at 1 – *x*, 1 – *y*, 1 – *z*. Neighboring stacks are connected through hydrogen-bonding interactions between terminal O(1w) and the phosphonate group [O(1w)···O(7) 2.701(3) Å, *x*, –1 + *y*, *z*]. In addition, strong H-bonds with a length of 2.551(3) Å

 © 2005 Wiley-VCH Verlag GmbH & Co. KGaA, Weinheim

are formed between adjacent mono-deprotonated phosphonate groups, these are even shorter than the analogous ones in **1**.

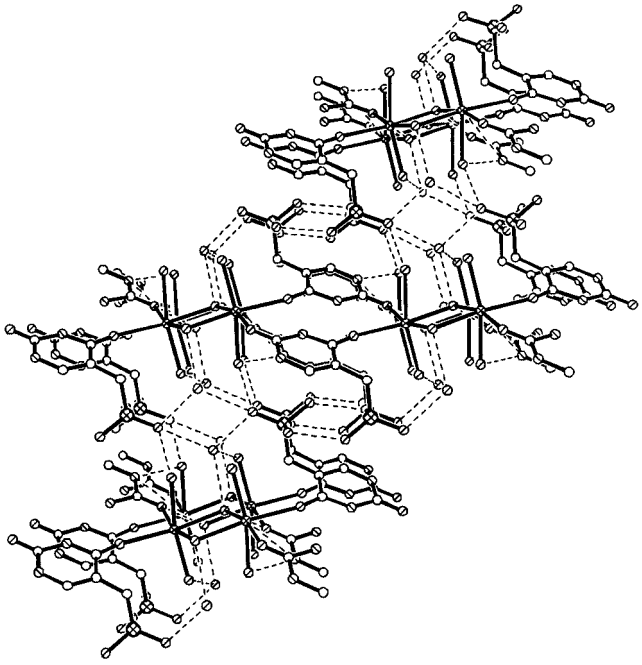

Figure 3. Hydrogen-bonding pattern in the crystal packing of **2**.

Recent solution studies have shown that the phosphonate oxygen atoms were the primary target for alkaline earth metal ions, while the uracil residue did not participate in complex formation when it was in its neutral form.[16] Likewise – although with some exceptions[31] – cocrystallization of Mg^{2+} with neutral nucleobases usually gives structures in which the $[Mg(H_2O)_6]^{2+}$ cation interacts indirectly through the aqua ligands with the nucleobase.[32] By contrast, the nucleobase residue seems to be the primary target of alkali metal ions as evident from the direct binding observed in **1** and **2**, and in other examples with neutral nucleobases.[25]

The observation of direct binding to the carbonyl oxygen atoms of uracil and indirect binding to the phosphonate oxygen atoms can be considered relevant to the interaction of alkali metal ions with natural nucleotides that contain nucleobase residues and negatively charged phosphate groups as alternative binding sites.

Survival curves for regular lymphocytes and HT 29 cells exposed to different concentrations of 5-Fu, 5-umpa, 5-umpm, 5-umpe, Na^+/5-umpa, K^+/5-umpa – and IC_{50} values calculated on grounds of the mathematical analysis of these curves– are presented in Figure 4A–4F (lymphocytes), Figure 5A–5F (HT 29), and in Table 4.

Data for 5-umpe and 5-umpm are not presented in Table 4 due to the fact that the concentrations used (1–10 mM) only caused the growth of the lymphocytes to slow down up to 85% (Figure 4C, Figure 4D). Likewise, in cells treated with Na^+/5-umpa, only the highest concentration caused an evident viability decrease to about 50%; however, this value was never exceeded (Figure 4E). Thus, it was impossible to establish IC_{50} from these survival curves.

The IC_{50} values for-5 Fu, 5-umpa, and K^+/5-umpa are 1.72 mM, 5 mM, and 4.15 mM, respectively, and their relation is as follows: 5-Fu < K^+/5-umpa < 5-umpa (Figure 4A, 4B, 4F).

The IC_{50} values are similar for K^+/5-umpa and 5-umpa, but they are nearly twice that obtained for 5-Fu. All IC_{50} values obtained after treatment of regular lymphocytes with 5-Fu and its novel analogues are higher than 1 mM, which suggests the almost lack of cytotoxic effects of these compounds – this is the most relevant and desired feature of every compound that is considered as a new tumor chemotherapeutic drug.[3,36]

However, the data given in Table 4 show that new analogues of 5-Fu also exhibited no activity in killing HT 29 tumor cells. Only model 5-Fu was very effective against HT 29 tumor cells; the IC_{50} factor was 2.9 μM.

In fact, we would like to point out that it is difficult to establish mutual relationships between the new 5-Fu analogues with respect to their effect on HT 29 tumor cells due to the atypical course of each survival curve. Therefore, it seems reasonable to separately analyze the effects exerted by each particular compound. As mentioned above, 5-Fu is very active against HT 29 tumor cells (Figure 5A). However, even small (0.5 μM) doses of 5-umpa and 5-umpm induced a rapid decrease in the viability of the HT 29 cells to 60–65%. A further increase in the dose slowly diminished the HT 29 cells viability, and finally IC_{50} was reached at 2.16 mM for 5-umpa and 1.58 mM for 5-umpm (Figure 5B, Figure 5C). It was impossible to establish IC_{50} for Na^+/5-umpa. The survival curve for this compound was very atypical. Low concentrations of Na^+/5-umpa, 0.2 μM and 1 μM, caused a rapid loss of the viability of the HT 29 tumor cells to 65% and 51%, respectively. A further dose increase did not affect the viability of the HT 29 cells, which was oscillating near 50% (Figure 5E). The survival curve for K^+/5-umpa was more typical, IC_{50} was 3.31 mM, whereas a dose of 1 μM diminished the viability to 75% (Figure 5F). Compound 5-umpe appeared to be ineffective against the HT 29 cells. Only at the highest concentration did the cell viability decrease to 55% (Figure 5D).

Anticancer chemotherapy usually involves the administration of various chemical compounds, which immediately kill, or take control of transformed cells. Unfortunately, the success of chemotherapy strongly depends on evoked, undesirable effects. The majority of currently used chemotherapeutics do not display particular anticancer specificity, and affect both tumor and nontumor tissues. Present in vitro and in vivo studies point out that many presently applied compounds exhibit mutagenic, teratogenic, and carcinogenic activity.[33]

Our study suggests that 5-Fu and its new analogues show insignificant cytotoxic effects on regular human peripheral blood lymphocytes. These findings might be of help in applying the drugs characterized below as potential anticancer compounds in chemotherapy. According to the cytotoxic and genotoxic studies of Tice et al.,[34] the compounds

 © 2005 Wiley-VCH Verlag GmbH & Co. KGaA, Weinheim

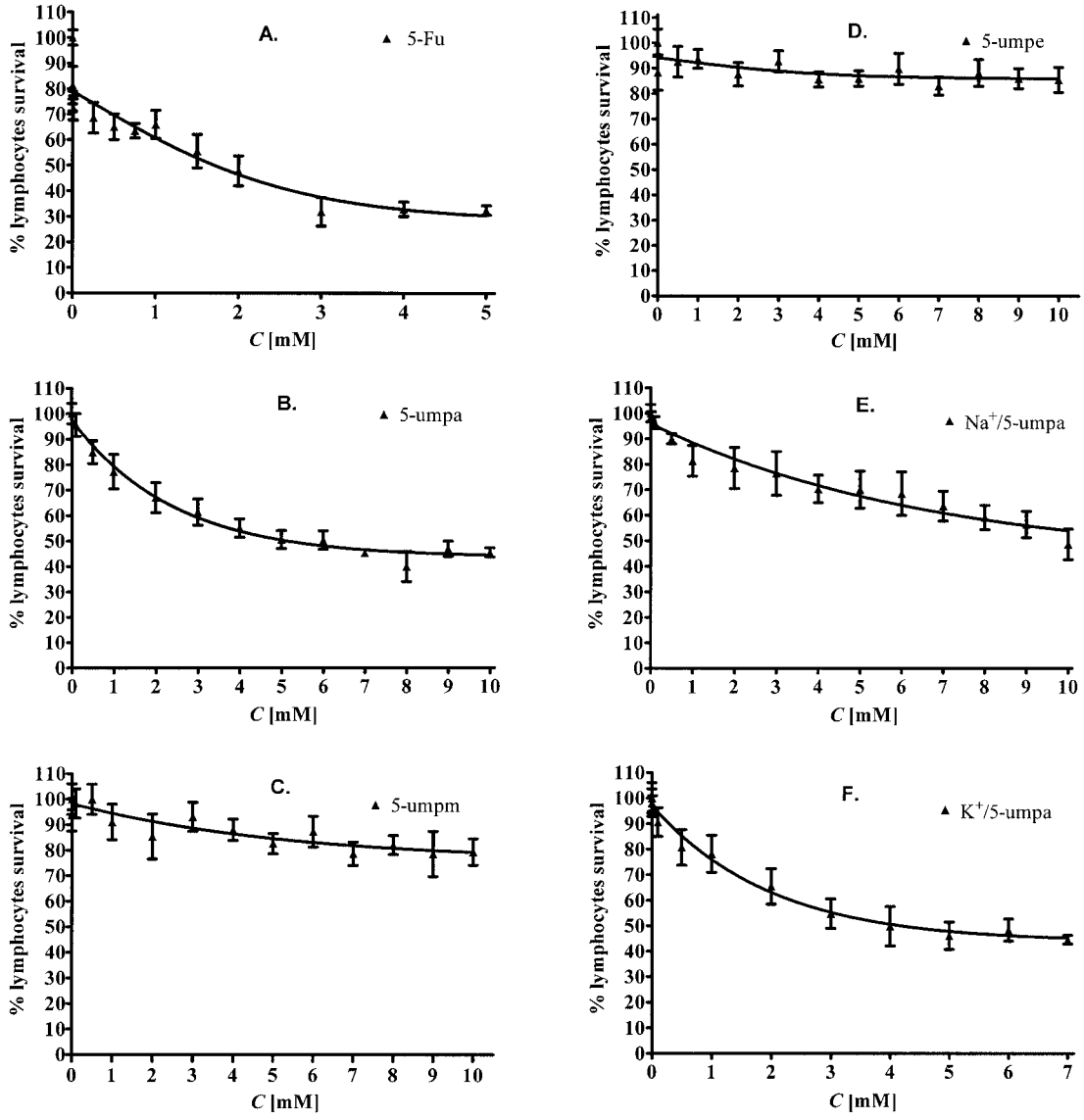

Figure 4. Dose-dependent growth inhibition curves for human peripheral blood lymphocytes after exposure to: 5-Fu **(A)**, 5-umpa **(B)**, 5-umpm **(C)**, 5-umpe **(D)**, Na^+/5-umpa **(E)**, K^+/5-umpa **(F)**. Lymphocytes were treated with various concentrations of the tested compounds for 72 h (37 °C, 5% CO_2). After incubation, the antiproliferative effects of these compounds were examined by MTT assay. These results represent the mean ± s.d. of three replicates from at least six separate experiments.

showing noticeable effects with a concentration of over 10 mM can be recognized as nontoxic; thus, we postulate that Na^+/5-umpa, 5-umpm and 5-umpe remain harmless for human lymphocytes.

The results obtained after exposure of HT 29 colorectal adenocarcinoma cell lines to new 5-Fu analogues seem to be interesting despite the fact that 5-Fu exerts the strongest aversive activity. These results are similar to those reported by Mader et al.[35] and Wiebke et al.[10]

IC_{50} was not assessed for each compound, however, we would like to point out that, in particular, after the treatment with 5-umpa, 5-umpm or Na^+/5-umpa, rapid loss of viability of the HT 29 cells was observed already after small doses of up to 1 μM. A further increase in the dose did not significantly affect the viability decrease. We cannot forget that DNA repair is an accomplice in cancer therapy resistance. It influences the chemosensitivity of tumor cells toward DNA-reactive cytotoxic drugs.[37] Probably, the effectiveness of the repair mechanisms in HT 29 cells strongly contributed to this phenomenon, and results in the limited tolerance to toxic activity of the applied compounds. However, these mechanisms were not fully successful, which may be in favor of the new 5-Fu analogues. It may be assumed that not only the dose but also the expose time should be taken into consideration in toxicity assessment of the new analogues of 5-Fu. Further studies are needed to confirm this hypothesis. In summary, the above results seem to be incredibly interesting because a question can be put forward: is the key element in searching for efficient chemotherapeutics the high toxicity of the compound examined

 © 2005 Wiley-VCH Verlag GmbH & Co. KGaA, Weinheim

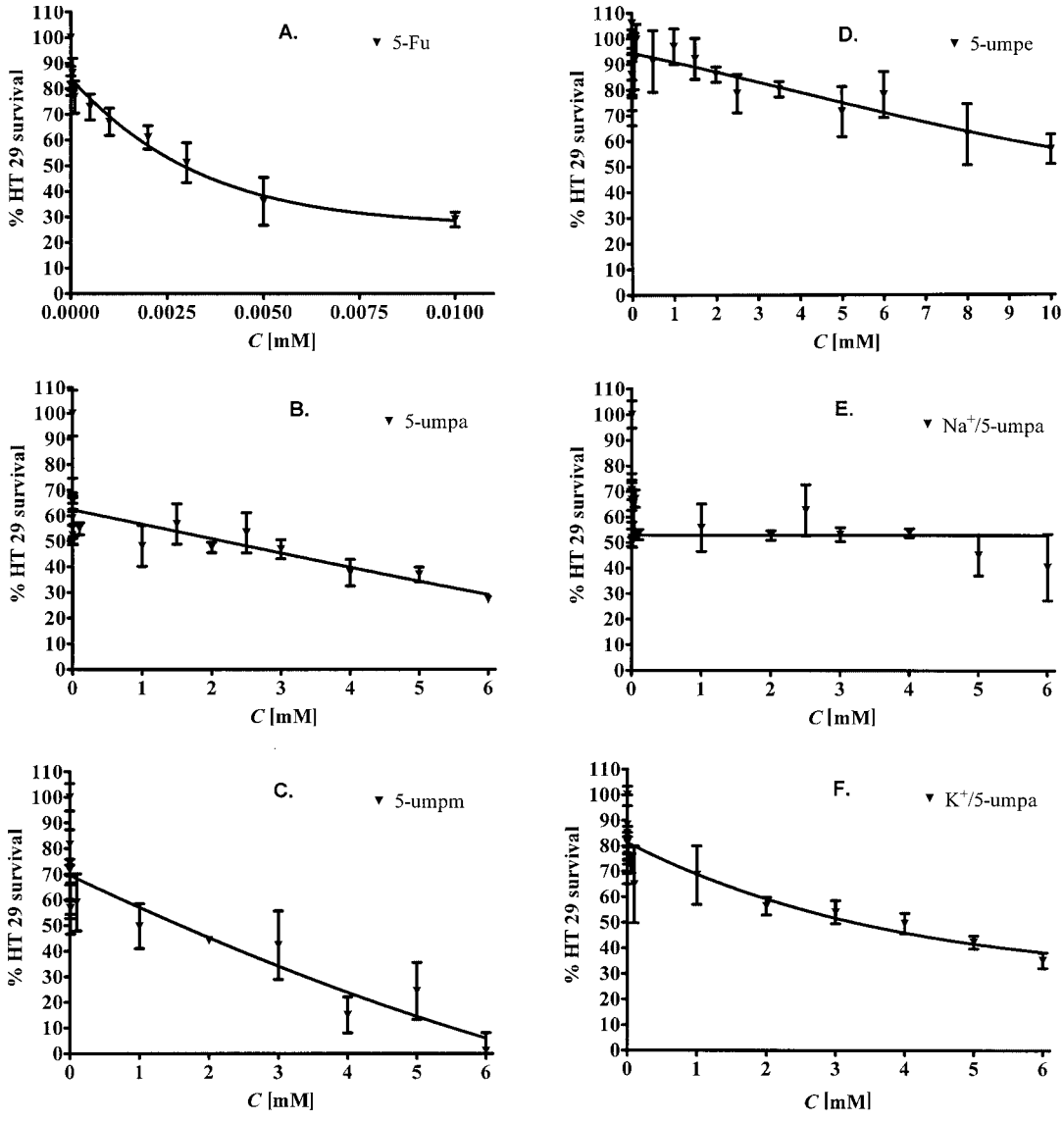

Figure 5. Dose-dependent growth inhibition curves for colon adenocarcinoma cell lines HT 29 after exposure to: 5-Fu **(A)**, 5-umpa **(B)**, 5-umpm **(C)**, 5-umpe **(D)**, Na^+/5-umpa **(E)**, K^+/5-umpa **(F)**. Treatment with various concentrations of the tested compounds for 72 h (37 °C, 5% CO_2). After incubation of HT 29 in 96-well plates, the antiproliferative effects of these compounds were examined by MTT assay. These results represent the mean ± s.d. of three replicates from at least six separate experiments.

Table 4. Cytotoxicity of 5-Fu and its new analogues in normal human peripheral blood lymphocytes and colon adenocarcinoma cells HT 29 in vitro after exposure for 72 h. IC_{50} values were established as drug concentrations that cause 50% inhibition of cell growth after 72 h incubation.

Drug	IC_{50}	
	Lymphocytes	HT 29
5-Fu	1.72 mM	0.0029 mM
5-umpa	5 mM	2.16 mM
5-umpm	–[a]	1.58 mM
5-umpe	–[a]	–[a]
Na^+/5-umpa	–[a]	–[b]

[a] Decrease in the viability of the cells to 80% for 5-umpm and 5-umpe, but to nearly 50% after exposure to the highest concentration of Na^+/5-umpa. [b] Rapid loss of cells viability at low concentrations (0.5–1 μM) to 50–65%, higher concentrations did not further decrease cell viability.

with respect to tumor cells, or the low toxicity towards healthy cells after application of small doses? We opt for the latter, especially, since it promotes searching for adjuvants that exhibit a synergistic effect in the efficient extermination of tumor cells.

Our results are of significance if the studies undertaken by Ochocki and Graczyk,[12] who investigated synergism of new analogues of 5-Fu and cisplatin in vivo in leukemia mouse 1210 (so-called "*platinum pyrimidine blues*"), are referred to. The authors demonstrated that 5-umpe did not exert any cytotoxic effect, whereas umpm, in conjunction with cisplatin, was very effective against L1210 leukemia cells. Our in vitro studies carried out recently confirmed the results of our antecedents with respect to 5-umpe; however, the same studies revealed a nontoxic character of 5-umpm and confirmed its efficiency in the elimination of tumor cells.

 © 2005 Wiley-VCH Verlag GmbH & Co. KGaA, Weinheim

5-umpa seems to deserve more attention. Its carcinotoxicity towards colorectal adenocarcinoma cells was observed already at low concentrations. In vivo studies demonstrated the lethal effect of this compound. It is strongly recommended that the synergism of 5-umpa with cisplatin is investigated, with the use of lower doses for more accurate cytotoxic and genotoxic assessment.

The lack of experimental data for Na^+/5-umpa and K^+/5-umpa results from the fact that these analogues have been prepared recently. Notwithstanding the fact that further studies have to be carried out, our first results demonstrate that these compounds, especially Na^+/5-umpa, display a certain ability to destroy HT 29 colorectal adenocarcinoma cells.

Conclusions

In conclusion, the results of our in vitro experiments conducted with the use of 5-umpa, Na^+/5-umpa, and 5-umpm are very interesting and provide evidence for their potential practical application as anticancer drugs. The results obtained are the basis for further studies to establish, for example, their mechanism of action, genotoxicity, and synergism with other drugs. The results will be useful for the selection of compounds that are the most effective chemotherapeutics whilst simultaneously exhibiting the lowest toxicity to healthy cells, and they can be used during the process of their registration as anticancer drugs. They may also indicate new approaches in searching for novel ways of synthesizing analogues for already existing drugs.

Experimental Section

General Remarks: The peripheral blood was obtained from the Blood Bank in Lodz, Poland, whereas the colon adenocarcinoma HT 29 cell line was purchased from the Centre of Oncology in Gliwice, Poland.

Compound 5-Fu was purchased from Sigma–Aldrich CO (St. Louis, MO, U.S.A). The new phosphonate derivatives: 5-umpa, 5-umpm, 5-umpe, or K^+/5-umpa and Na^+/5-umpa were obtained from the Department of Bioinorganic Chemistry, Medical University, Lodz, Poland.

5-uracilmethylphosphonic acid, dimethyl 5-uracilmethylphosphonate, and diethyl 5-uracilmethylphosphonate were prepared as described previously.[11] Infrared spectra of KBr pellets were measured with an ATI MATTSOM IFS FT spectrometer.

$K(C_5H_6N_2O_5P)(H_2O)_{2.5}$ (1): 5-umpa (103 mg, 0.5 mmol) was dissolved in water (20 mL) and adjusted to pH 8.9 with 1 N KOH. Slow evaporation of the solvent at room temperature gave colorless needles of **1** for X-ray analysis. Yield: 116 mg (90%). Drying of **1** in vacuo gave $K(C_5H_6N_2O_5P)\cdot(H_2O)_{0.75}$. Selected IR data: 3553 (br), 3070 (br), 2923 (br), 2847 (br), 1710 (vs), 1460 (br), (m), 1440 (m), 1327 (m), 1134 (m), 997 (m), 913 (s), 503 (s) cm^{-1}. $K(C_5H_6N_2O_5P)\cdot(H_2O)_{0.75}$: calcd. C 23.42, H 3.29, N 10.93; found C 23.31, H 2.93, N 10.87.

$Na(C_5H_6N_2O_5P)(H_2O)_4$ (2): 5-umpa (103 mg, 0.5 mmol) was dissolved in water (20 mL) and adjusted to pH 8.9 with 1 N NaOH. Slow evaporation of the solvent at room temperature gave colorless plates of 2. Yield: 108 mg (92%). Drying of **2** in vacuo gave $Na(C_5H_6N_2O_5P)\cdot(H_2O)_{0.33}$. Selected IR data: 3512 (br), 3060 (br), 2923 (br), 2852 (br), 1685 (vs), 1460 (br), (m), 1421 (m), 1245 (s), 1143 (m), 1022 (m), 908 (s), 517 (s) cm^{-1}. $Na(C_5H_6N_2O_5P)\cdot(H_2O)_{0.33}$: calcd. C 25.43, H 2.71, N 12.04; found C 25.66, H 2.87, N 11.97.

Fresh stock solutions of all compounds were prepared in water [Sigma–Aldrich CO (St. Louis, MO, U.S.A)] and were heated at 37 °C until the compounds dissolved. Before use, the stock solutions were cooled and diluted in a culture medium; they were then used to investigate the cytotoxicity effects in vitro.

PBS (phosphate buffered saline) MTT, SDS (lauryl sulfate), DMF (*N*,*N*-dimethylformamide), DMSO (dimethyl sulfoxide) were purchased from Sigma–Aldrich CO (St. Louis, MO, U.S.A). The culture medium for lymphocytes consisted of RPMI 1640 medium supplemented with 15% FBS (fetal bovine serum), 1% penicillin–streptomicin solution stabilized, 1% L-glutamine, and 1% PHA (phytohemagglutinin), whereas the culture medium for the HT 29 cell line contained of RPMI 1640 with Glutamax, 10% FBS, 1% penicillin–streptomicin solution stabilized, and 1% MEM non-essential amino acid solution. For trypsinization of adherent HT 29 cells, trypsin-EDTA was used. PHA, RPMI with Glutamax, FBS, and trypsin-EDTA were purchased from Gibco Laboratories Life Technologies, INC (Grand Island, New York, U.S.A.); the remaining reagents were purchased from Sigma–Aldrich CO (St. Louis, MO, U.S.A).

X-ray Crystallographic Study: Crystal data for compounds **1** and **2** were collected at room temperature with an Enraf–Nonius-KappaCCD diffractometer (KappaCCD package, Nonius, Delft, The Netherlands, 1997) using graphite-monochromated Mo-K_α radiation (λ = 0.71069 Å) (Table 5). For data reduction and cell refinement, the programs DENZO and SCALEPACK were used.[27] The structures were solved by direct methods and subsequent Fourier syntheses, and refined by full-matrix least-squares on F^2 with the SHELXTL PLUS and SHELXL-93 programs.[28] All non-hydrogen atoms were refined anisotropically. Carbon- and nitrogen-bound hydrogen atoms were placed at calculated positions and given isotropic thermal parameters equivalent to 1.2 times those of the atom to which they are attached. CCDC-251795 for **1** and CCDC-251794 for **2** contain the supplementary crystallographic data for this paper. These data can be obtained free of charge from The Cambridge Crystallographic Data Centre via www.ccdc.cam.ac.uk/data_request/cif.′

Cell Culture and MTT Assay: The peripheral blood was obtained from six healthy, nonsmoking donors of both sexes. Lymphocytes were isolated by centrifugation in gradient of density of Histopaque 1077 (Sigma–Aldrich CO, St. Louis, MO, U.S.A) (15 min, 100×*g*). Mitogen PHA was used for stimulation of proliferation of lymphocytes which exhibit a doubling time of approximately 30 h. Lymphocytes were counted and then seeded in 96-well microtitre plates (Nunc Brandt Products, U.S.A.) at a density of 10^5cells/well with a final volume of 100 μL. The monolayer of colon adenocarcinoma HT 29 cells in 25 cm^2 flasks was treated with trypsin-EDTA, and then the cells were seeded in 96-well microtitre plates at a density of 6×10^3 cells/well with a final volume 200 μL. The cultures of the HT 29 tumor cells show a doubling time of about 30–40 h.

After a 24-h incubation in a 5% humidified incubator at 37 °C, the cells were treated with different concentrations of 5-Fu and its new analogues. After a 72-h incubation, 20 μL of MTT solution (5 mg/mL in sterile PBS) was added to each well, and the plates were incubated for a further 2 h.

 © 2005 Wiley-VCH Verlag GmbH & Co. KGaA, Weinheim

Table 5. Crystallographic data for **1** and **2**.

	1	**2**
Formula	$K(C_5H_6N_2O_5P)(H_2O)_{2.5}$	$Na(C_5H_6N_2O_5P)(H_2O)_4$
Molecular mass	289.23	300.14
Crystal system	monoclinic	triclinic
Space group	*C*2/*c*	$P\bar{1}$
a [Å]	16.906(1)	6.385(1)
b [Å]	6.626(1)	9.404(1)
c [Å]	20.654(1)	10.841(1)
α [°]	–	83.01(1)
β [°]	104.89(1)	78.46(1)
γ [°]	–	71.74(1)
V [Å^3]	2236.0(4)	604.5(1)
Z	8	2
$\rho_{calcd.}$ [g cm^{-3}]	1.718	1.649
Independent reflections	2048	2403
Observed reflections [$I > 2\sigma(I)$]	1453	1876
R_1, wR_2 [$I > 2\sigma(I)$][a,b]	0.043, 0.131	0.047, 0.151
R_1, wR_2 (all data)	0.066, 0.151	0.079, 0.211

[a] $R_1 = \Sigma||F_o| - |F_c||/\Sigma|F_o|$. [b] $wR_2 = [\Sigma w(F_o^2 - F_c^2)^2/\Sigma w(F_o^2)^2]^{1/2}$; $w^{-1} = \sigma^2(F_o^2) + (aP)^2 + bP$; $P = (F_o^2 + 2F_c^2)/3$ with $a = 0.0898$ for **1**, 0.1074 for **2**, $b = 0.0000$ for **1** and 0.0600 for **2**.

The purple formazan crystals produced were dissolved in a mixture of 20%SDS/50%DMF (120 µL/well, 24 h) in the case of the lymphocytes, and in DMSO in the case of the HT 29 cell line (100 µL/well, 5 min).

The plates were agitated on a plate shaker for 5 min, and the absorbance of each well was measured at 580 nm using a Stat Fax–2100 Awareness Technology Inc. microplate reader.[29]

The sensitivity of the cells to the tested compounds was shown as percentage of the survival of the cells (an untreated control value – 100% in relation to drugs concentration values). The cytotoxic effects were expressed as the IC_{50} value, which is the concentration of the drug required to reduce cell growth to 50% relative to the control. Those parameters were estimated on the basis of the analysis of the cell growth curves using the GraphPad Prism 4 computer program. All results were presented as mean ± s.d. of three replicates from six to twelve independent experiments.

Acknowledgments

The authors would like to thank Professor Bernhard Lippert from the University of Dortmund, Germany for his critical review of this manuscript, which is greatly appreciated. The authors also thank Prof. Stanislaw Szala from the Oncology Centre, Maria Curie-Sklodowska Institute in Gliwice, Poland, for providing the HT 29 colon adenocarcinoma cell line used in this investigation. This study was supported by the German–Polish programme grant No. 503-100-3 and by grant No. 502-13-849 of the Medical University of Łódź. J.O. gratefully acknowledges a fellowship from Deutscher Akademischer Austauschdienst (DAAD).

[1] W. B. Pratt, R. W. Ruddon, W. D. Ensminger, J. Maybaum, *The Anticancer Drugs, 5. Antimetabolites*, Oxford University Press, **1994**, p. 81–86.
[2] K. Ghosal, S. T. Jacob, *Biochem. Pharmacol.* **1997**, *53*, 1569–1575.
[3] S. Garattini, C. LaVecchia, *Eur. J. Cancer.* **2001**, *37*, S128–S147.
[4] B. Bichlarska, T. Kupka, *J. Mol. Struct.* **2002**, *613*, 153–166.
[5] T. Esaki, S. Nakano, T. Tastumoto, M. Karolki-Migita, K. Mitsugi, M. Nakamura, Y. Niho, *Cancer Res.* **1992**, *52*, 6501–6506.
[6] P. G. Johnston, F. Geoffrey, J. Drake, D. Voeller, J. L. Grem, C. J. Allegra, *Eur. J. Cancer.* **1996**, *12*, 2148–2154.
[7] K. Mineura, M. Kowada, *Cell Biol. Intern.* **1996**, *5*, 355–357.
[8] J. L. Fischel, P. Formento, M.-C. Etienne, T. Spector, N. Renee, G. Milano, *Biochem. Pharmacol.* **1997**, *53*, 1703–1709.
[9] J. Taieb, P. Artru, M. Mabro, E. Carola, F. Maindrault, C. Tournigand, M. Krulik, C. Louvet, A. De Gramont, *Eur. J. Cancer* **2002**, *38*, 661–666.
[10] E. A. Wiebke, N. A. Grieshop, P. J. Loehrer, G. J. Eckert, R. A. Sinder, *J. Surg. Res.* **2003**, *111*, 63–69.
[11] J. Ochocki, A. Erxleben, B. Lippert, *J. Heterocycl. Chem.* **1997**, *34*, 1179–1184.
[12] J. Ochocki, J. Graczyk, *Pharmazie* **1998**, *53*, 884–885.
[13] T. Klenner, T. P. Valenzuela-Paz, F. Amelung, H. Münch, H. Zahn, B. K. Keppler (Ed.), H. Blum, *Metal Complexes in Cancer Chemotherapy*, VCH, Weinheim, Germany, **1993**, pp. 87–127.
[14] M. J. Bloemink, J. Dorenbos, R. J. Pheeterbrij, B. K. Keppler, J. Reedijk, H. Zahn, *Inorg. Chem.* **1994**, *33*, 1127–1132.
[15] C. F. Moreno-Luque, R. Grieesser, J. Ochocki, *Z. Anorg. Allg. Chem.* **2001**, *627*, 1882–1887.
[16] C. F. Moreno-Luque, E. Freisinger, B. Costisella, R. Griesser, J. Ochocki, B. Lippert, H. Sigel, *J. Chem. Soc., Perkin Trans.* **2001**, *2*, 2005–2011.
[17] X. Shui, L. McFail-Isom, G. G. Hu, L. D. Williams, *Biochemistry* **1998**, *37*, 8341–8355.
[18] C. Cheung, B. Moore, *Biochemistry* **1992**, *31*, 8406–8414.
[19] C. Kang, X. Zhang, R. Ratliff, R. Moyzis, A. Rich, *Nature* **1992**, *356*, 126–131.
[20] N. H. Sarma, J. Luo, K. Umemoto, R. Yuan, R. H. Sarma, *J. Biomol. Struct. Dyn.* **1992**, *9*, 1131–1141.
[21] G. Gupta, A. E. Garcia, Q. Guo, M. Lu, N. R. Kallenbach, *Biochemistry* **1993**, *32*, 7098–7103.
[22] G. Laughlan, A. I. H. Murchie, D. G. Norman, M. H. Moore, P. C. E. Moody, D. M. Lilley, B. Luisi, *Science* **1994**, *265*, 520–524.
[23] B. Fischer, H. Preut, B. Lippert, H. Schollhorn, U. Thewalt, *Polyhedron* **1990**, *9*, 2199–2204.
[24] H. Witkowski, E. Freisinger, B. Lippert, *Chem. Commun.* **1997**, 1315–1316.
[25] E. Freisinger, A. Schimanski, B. Lippert, *J. Biol. Inorg. Chem.* **2001**, *6*, 378–389.
[26] J. Carmichael, W. DeGraff, A. F. Gazdar, J. D. Minna, J. B. Mitchel, *Cancer Res.* **1987**, *47*, 936–942.
[27] Z. Otwinowsky, W. Minor, *Methods Enzymol.* **1996**, *276*, 307–326.

 © 2005 Wiley-VCH Verlag GmbH & Co. KGaA, Weinheim

[28] G. M. Sheldrick, *SHELXTL-PLUS (VMS)*, Siemens Analitycal X-ray Instruments, Inc. Madison, WI, **1990**; *SHELXL-93*, Program for crystal structure refinement, **1993**, University of Göttingen, Germany.
[29] Z. Machoń, Z. Wieczorek, M. Zimecki, *Pol. J. Pharmacol.* **2001**, *53*, 377–383.
[30] F. H. Allen, O. Kennard, D. G. Watson, L. Brammer, A. G. Orpen, R. Taylor, *J. Chem. Soc., Perkin Trans. 2* **1987**, S1–S19.
[31] M. A. Geday, G. DeMunno, M. Medaglia, J. Anastassopolou, T. Theophanides, *Angew. Chem. Int. Ed. Engl.* **1997**, *36*, 511–513.
[32] C. B. Black, H.-W. Huan, J. A. Cowan, *Coord. Chem. Rev.* **1994**, *135–136*, 165–202.
[33] M. Sorsa, D. Anderson, *Mutat. Res.* **1996**, *355*, 253–261.
[34] R. R. Tice, E. Agurel, D. Anderson, B. Burlinson, A. Hartmann, H. Kobayashi, Y. Miyamae, E. Rojas, J.-C. Ryn, Y. F. Sasaki, *Environ. Mol. Mutagen.* **2000**, *35*, 206–221.
[35] R. M. Mader, A. E. Sieder, J. Braun, B. Rizovski, M. Kalipciyan, M. W. Mueller, R. Jakesz, H. Rainer, G. G. Steger, *Biochem. Pharmacol.* **1997**, *54*, 1233–1242.
[36] S. Feng, S. Chien, *Chem. Eng. Science* **2003**, *58*, 4087–4114.
[37] R. Rosell, R. V. N. Lord, M. Taron, N. Reguart, *Lung Cancer.* **2002**, *38*, 217–227.

Received: January 7, 2005
Published Online: June 21, 2005

 © 2005 Wiley-VCH Verlag GmbH & Co. KGaA, Weinheim

From Mono- and Dinuclear to Polynuclear Cobalt(II) and Cobalt(III) Coordination Compounds Based on *o*-Phthalic Acid and 2,2′-Bipyridine: Synthesis, Crystal Structures, and Properties

Svetlana G. Baca,*[a] Irina G. Filippova,[b] Christina Ambrus,[c] Maria Gdaniec,[d] Yurii A. Simonov,[b] Nicolae Gerbeleu,[a] Olesea A. Gherco,[b] and Silvio Decurtins[c]

Keywords: Carboxylate ligands / Cobalt / Magnetic properties / N ligands

The reaction of *o*-phthalic acid (H_2Pht) and 2,2′-bipyridine (bpy) with cobalt(II) carbonate at different temperatures results in the isolation of three types of new cobalt(II) and cobalt(III) compounds. The mononuclear cobalt(III) complex $[Co(CO_3)(bpy)_2]_2(Pht)\cdot16H_2O$ (**1**) is obtained when the reaction is run at 60 °C. Crystallographic analysis revealed that **1** contains two crystallographically independent $[Co(CO_3)(bpy)_2]^+$ cations, a Pht^{2-} anion, and sixteen solvate water molecules. The latter form a wall of channels with the oxygen atoms of the carboxylate groups of the Pht^{2-} anions, which are occupied by pairs of cations. Increasing the temperature of the reaction to 80 °C leads to the formation of the open dinuclear cobalt(II) complex $[(bpy)_2Co(Pht)H(Pht)Co(bpy)_2](HPht)(H_2Pht)\cdot2H_2O$ (**2**), which crystallizes in two polymorphic modifications **2a** and **2b**. Compound **2a** consists of a centrosymmetric dinuclear $[(bpy)_2Co(Pht)H(Pht)Co(bpy)_2]^+$ cation, an $HPht^-$ anion, an H_2Pht molecule, and two solvate H_2O molecules. In **2b**, a small alteration in the crystal structure leads to an increase of the unit-cell volume. The asymmetric unit of **2b** contains six crystallographically independent Co^{II} complexes, which combine into four $[(bpy)_2Co(Pht)H(Pht)Co(bpy)_2]^+$ units. The main structural unit of the cyclic dinuclear complex $[Co(Pht)(bpy)(H_2O)]_2\cdot2H_2O$ (**4**) is neutral and cenrosymmetric, with the two Co^{II} atoms linked by two phthalate ligands to form a 14-membered cycle. A further temperature increase results in the isolation of both the mononuclear complex $[Co(Pht)(bpy)(H_2O)_3]\cdot3H_2O$ (**3**) and the polynuclear helical coordination polymer $[Co(Pht)(bpy)(H_2O)]_n$ (**5**). Extended hydrogen bonding networks as well as aromatic π–π stacking interactions stabilize multidimensional supramolecular architectures in all compounds. Magnetic susceptibility measurements have been performed for complexes **1**, **2**, **3**, and **5**. Simulations gave the following parameter sets: for complex **2** $|D| = 70\ cm^{-1}$, $g = 2.55$ and $J = -0.1\ cm^{-1}$; for complex **3** $|D| = 80\ cm^{-1}$, $g = 2.6$, and for complex **5** $|D| = 65\ cm^{-1}$, $g = 2.45$. Complex **1** is diamagnetic.
(© Wiley-VCH Verlag GmbH & Co. KGaA, 69451 Weinheim, Germany, 2005)

Introduction

Carboxylate complexes have received a great deal of attention over the last few years due to their interesting coordination chemistry, unusual structural features, remarkable physical and chemical properties, and extensive practical applications as dyes, extractants, drugs, pesticides, magnetic devices, etc.[1] Metal carboxylates with a high stability are also efficient catalysts in a vast range of chemical and biochemical processes.[2] Although a great number of metal carboxylates have been obtained to date, the rational design and synthesis of novel metal carboxylates by employing new synthetic tools or by varying the nature of the reactants and synthetic conditions are currently under active investigation. In this context, *o*-phthalic acid (H_2Pht), which can exhibit a variety of coordination abilities[3] and has a tendency to form large metal cluster aggregates[4–9] or architectures with multi-dimensional frameworks, has been extensively explored. We have recently reported a series of nickel(II), copper(II), and zinc(II) phthalate compounds[3,10–16] that show a great structural diversity, ranging from monomeric to polymeric assemblies. Herein we extend these studies to investigate the interactions of this universal ligand with cobalt ions in the presence of aromatic amines. In this respect, several cobalt phthalate compounds that are already known should be mentioned here. A very interesting example of a three-dimensional cobalt(II) polymer, namely $[Co(Pht)_2(bipy)]_n$ (bipy = 4,4′-bipyridine), which consists of interlinked Co–Pht–Co and Co–bpy–Co linear chains, has been reported by Lightfoot et al.[17] Several dimers linked by *o*-phthalate $[Co_2(Pht)(L)(H_2O)](ClO_4)_2$ (L = 2,2′-bipyridine, 1,10-phenanthroline, and 5-ni-

[a] Institute of Chemistry, Academy of Sciences of Moldova, Academiei 3 str., 2028 Chisinau, R. Moldova
Fax: +373-22-739611
E-mail: sbaca_md@yahoo.com
[b] Institute of Applied Physics, Academy of Sciences of Moldova, Academiei 5 str., 2028 Chisinau, R. Moldova
[c] Department of Chemistry and Biochemistry, University of Berne, 3012 Berne, Switzerland
[d] Faculty of Chemistry, A. Mickiewicz University, 60-780 Poznan, Poland
Supporting information for this article is available on the WWW under http://www.eurjic.org or from the author.

 © 2005 Wiley-VCH Verlag GmbH & Co. KGaA, Weinheim **DOI: 10.1002/ejic.200500008**

tro-1,10-phenanthroline) have also been isolated.[18] Finally, the monomeric complexes $[Co(Pht)(phen)(H_2O)_3]\cdot H_2O$ and [Co(Pht)(dipya)] (phen = 1,10-phenanthroline, dipya = 2,2′-dipyridylamine) have been synthesized.[19] Recently, we have also described the synthesis and structural characterization of cobalt(II) phthalate coordination polymers with derivatives of imidazole, for example 1-methylimidazole (1-MeIm),[3] 2-methylimidazole (2-MeIm),[12] and 4-methylimidazole (4-MeIm).[15] In this paper we report on the synthesis, characterization, and crystal structures of three types of new cobalt(II) and cobalt(III) compounds with *o*-phthalic acid and 2,2′-bipyridine (bpy), namely the mononuclear cobalt(III) and cobalt(II) complexes $[Co(CO_3)(bpy)_2]_2(Pht)\cdot 16H_2O$ (**1**) and $[Co(Pht)(bpy)(H_2O)_3]\cdot 3H_2O$ (**3**), respectively, the open dinuclear complex $[(bpy)_2Co(Pht)H(Pht)Co(bpy)_2](HPht)(H_2Pht)\cdot 2H_2O$ (**2**) and the cyclic dinuclear complex $[Co(Pht)(bpy)(H_2O)]_2\cdot 2H_2O$ (**4**), as well as the polynuclear helical coordination polymer $[Co(Pht)(bpy)(H_2O)]_n$ (**5**).

Results and Discussion

Synthesis

The reaction of *o*-phthalic acid with cobalt(II) carbonate in the presence of amine at different temperatures affords four new coordination compounds, as shown in Scheme 1. An oxidation of cobalt(II) ions to cobalt(III) was observed when the reaction was carried out at 60 °C in the presence of the base K_2CO_3, and the reaction mixture was left in contact with air. This resulted in the formation of crystals of the cobalt(III) complex $[Co(CO_3)(bpy)_2]_2(Pht)\cdot 16H_2O$ (**1**) in two weeks. To the best of our knowledge, **1** is the first example of a trivalent cobalt compound with *o*-phthalic acid, although in **1** the phthalate dianion is acting only as a counterion. It is interesting to note that similar bis(bipyridine)(carbonato)cobalt(III) nitrate and iodide complexes have also been obtained from the initial cobalt(II) salts but only under O_2 or CO_2.[20] It seems that the presence of aromatic amines such as bpy or phen facilitates the oxidation of the initial cobalt(II) species. Increasing the temperature of the reaction to 80 °C leads to the formation of the dimeric complex $[(bpy)_2Co(Pht)H(Pht)Co(bpy)_2](HPht)(H_2Pht)\cdot 2H_2O$ (**2**), the identity of which was confirmed by X-ray crystallography. The two $[Co(bpy)_2]^{2+}$ units in **2** are connected by a symmetric O···H···O hydrogen bond between the carboxylate groups of two different coordinated phthalate ligands. A similar Zn compound has recently been reported.[14] Compound **2** crystallizes from hot H_2O solution in two polymorphic modifications (**2a** and **2b**), which consist of similar structural units and differ in the crystal structure organization. Further increasing the reaction tempera-

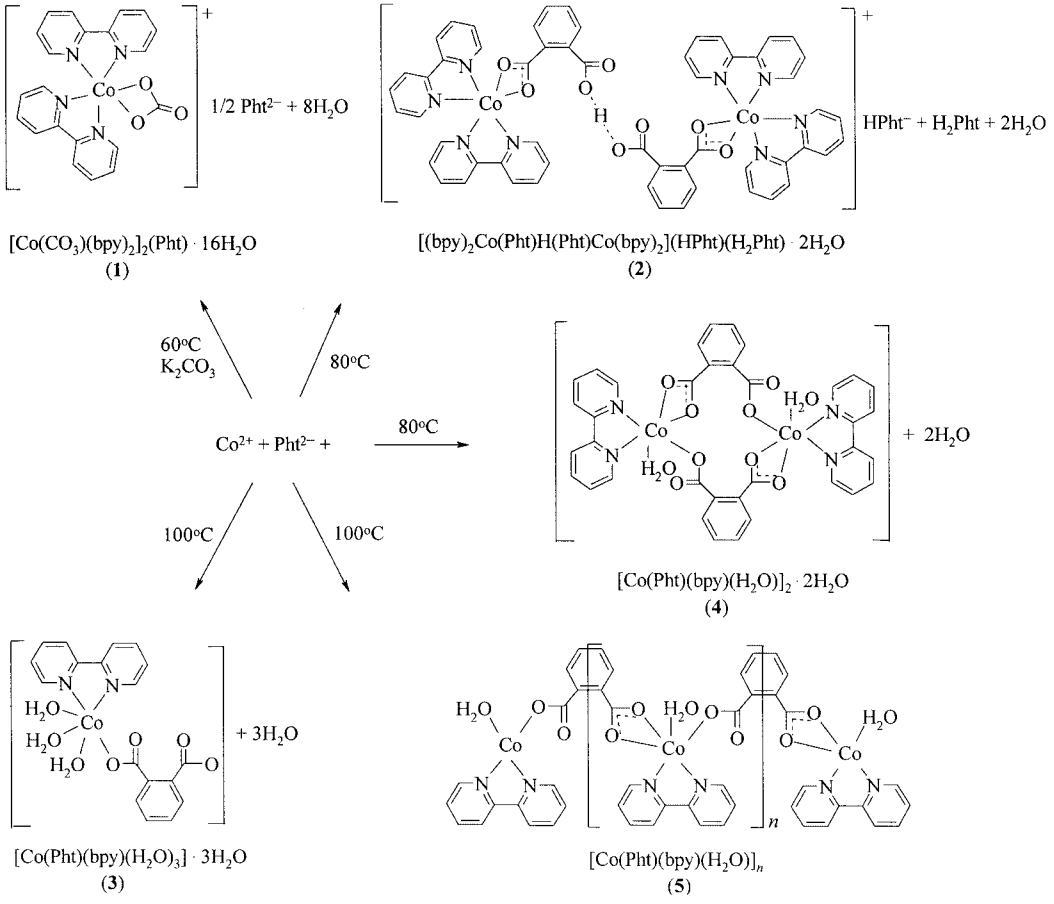

Scheme 1.

 © 2005 Wiley-VCH Verlag GmbH & Co. KGaA, Weinheim

ture resulted in the isolation of two new products, namely the coordination polymer $[Co(Pht)(bpy)(H_2O)]_n$ (**5**) and the mononuclear complex $[Co(Pht)(bpy)(H_2O)_3]\cdot 3H_2O$ (**3**), which were obtained in around 20% and 12% yields, respectively. One needs to mention here that the cyclic dimer **4** (Scheme 1) was obtained from the reaction of cobalt(II) acetate with H_2Pht and bpy in MeOH in a very low yield, therefore the sample was only suitable for X-ray studies. All attempts to optimize the yield of **4** were unsuccessful.

Spectroscopic Studies

The most relevant features of the IR spectra of compounds **1**–**3** and **5** are the absorptions due to the stretching of the dicarboxylate groups. The positions of these bands and the separations ($\Delta\nu$) between $\nu_{asym}(CO_2)$ and $\nu_{sym}(CO_2)$ indicate that the phthalate carboxylate groups function in different coordination modes. For complex **1**, in which the *o*-phthalic acid is fully deprotonated but acts only as a counterion, the characteristic bands of the uncoordinated carboxylate groups of Pht^{2-} appear at 1678 and 1564 cm^{-1} for asymmetric stretching, and at 1403 and 1382 cm^{-1} for symmetric stretching. In the IR spectrum of complex **2**, the medium-intensity peaks at 1717 and 1366 cm^{-1} also indicate the presence of uncoordinated *o*-phthalic acid [$\nu_{asym}(CO_2)$ for *o*-phthalic acid of 1690 and 1678 cm^{-1}].[21] The absorptions at lower frequencies (1579 and 1411 cm^{-1}) can be attributed to deformation vibrations of the chelating carboxylate groups ($\Delta\nu$ = 168 cm^{-1}).[22] The IR spectrum of **3** shows a broad $\nu_{asym}(CO_2)$ absorption with a maximum at 1568 cm^{-1} and a $\nu_{sym}(CO_2)$ absorption at 1404 cm^{-1}, which can be assigned to the chelating carboxylate group ($\Delta\nu$ = 164 cm^{-1}). For polymer **5**, the bands of the dicarboxylate groups appear at 1578 and 1543 cm^{-1} for the asymmetric stretching and at 1420 and 1385 cm^{-1} for the symmetric stretching. The $\Delta\nu$ values are 193 and 123 cm^{-1} and are attributed to the existence of both monodentate and chelating modes of the carboxylate groups, respectively. The infrared spectra of **1**–**3** and **5** also show broad bands in the 3634–3230 cm^{-1} region, which can be assigned to water molecules. Additionally, complex **1** has a strong band at 1638 cm^{-1} and a medium band at 1202 cm^{-1}, which are absent in the IR spectra of other complexes and are indicative of a chelating carbonate group.[23]

Thermogravimetric Studies

Compounds **1**–**3**, and **5** were heated in the temperature range 25–600 °C. The TGA data show that the first weight loss corresponds to the removal of water molecules in all compounds. Complex **1** loses eleven water molecules in two steps from 30 to 150 °C (the total weight loss is 15.40%, calculated 15.07%). On further heating, **1** loses 43.88% of its weight between 160 and 270 °C, which corresponds to the release of the five remaining water molecules, the uncoordinated phthalate dianion (Pht^{2-}), and two bpy molecules (calculated 43.08%). Complex **1** decomposes to the final product Co_2O_3, with a remaining percentage of 13.22% (calculated 12.61%), when heated from 270 to 360 °C. For dimer **2**, the first weight loss is observed from 70 to 150 °C and is due to the loss of two water molecules (observed 2.51%, calculated 2.50%). In the temperature range of 170–510 °C the decomposition of the organic ligands takes place in four unidentified steps with a total weight loss of 85.91% to the final product CoO (found 11.39%, calculated 10.41%). For complex **3**, the first weight loss corresponding to both three uncoordinated and three coordinated water molecules (found 21.91%, calculated 22.17%) is found in the temperature range 30–150 °C. The second weight loss is observed from 150 to 320 °C and corresponds to the dissociation of the bpy ligand (found 30.31%, calculated 32.05%). The third weight loss of 19.58%, from 320 to 450 °C, is due to the loss of phenyl radical.[24,25] A further weight loss of 11.49%, corresponding to the elimination of two molecules of CO[26] (calculated 12.15%), occurs between 450 and 540 °C. The final product is CoO, with a remaining percentage of 16.70% (calculated 15.37%). In contrast to **1**–**3**, the coordination polymer **5** is stable up to approximately 180 °C and then it loses 4.42% of its weight, which corresponds to the loss of a coordinated water molecule (calculated 4.53%). A further mass decrease is observed between 230 and 320 °C and corresponds to the loss of the bpy molecule (found 38.05%, calculated 39.32%). The decomposition of the Pht ligand is observed above 320 °C in two steps, with the weight loss of 18.65 and 14.10% each, by the removal of phenyl radical (calculated 20.28%) and two molecules of CO (calculated 15.93%), respectively, and is completed below 440 °C to give the expected oxide (found 20.15%, calculated 18.86%).

Description of the Crystal Structures

$[Co(bpy)_2(CO_3)]_2(Pht)\cdot 16H_2O$ (1)

X-ray analysis indicates that the asymmetric unit of **1** contains two crystallographically independent $[Co(CO_3)(bpy)_2]^+$ cations, a Pht^{2-} anion, and sixteen solvate water molecules (Figure 1). The structure of the cations is similar to that in the related compounds $[Co(CO_3)(bpy)_2]NO_3\cdot 5H_2O$[20] and $[Co(CO_3)(bpy)_2]Cl\cdot 3H_2O$.[27] Each Co^{III} atom in **1** is coordinated by four nitrogen atoms of two chelating bpy molecules and two oxygen atoms of the chelating CO_3^- group, and thus adopts a distorted octahedral N_4O_2 environment. The average Co–N distances are 1.930 for Co(1) and 1.932 Å for Co(2), while the Co(1)–O bonds are 1.901(2) and 1.893(2) Å, with 1.895(2) and 1.898(2) Å for the Co(2)–O bonds (Table 1). The observed distortion from an octahedral geometry could be caused by the small bite angle of the chelating carbonate group [the O–Co–O angles are 69.42(8)° and 69.31(8)° for Co(1) and Co(2), respectively]. The O–Co–O bite angle of the chelating carbonate ligand agrees well with other bis(bipyridine)(carbonato)cobalt(III) [69.9(2)°][20] and (carbonato)bis(phenanthroline)cobalt(III) complexes [varies from 68.4(5)° to

 © 2005 Wiley-VCH Verlag GmbH & Co. KGaA, Weinheim

69.8(2)°].[20,28] The dihedral angles between the four-membered chelate ring of the carbonate group and two five-membered chelate rings of the bpy ligands are 94.6(1)° and 87.0(1)° for Co(1), and 87.0(1)° and 96.5(1)° for Co(2).

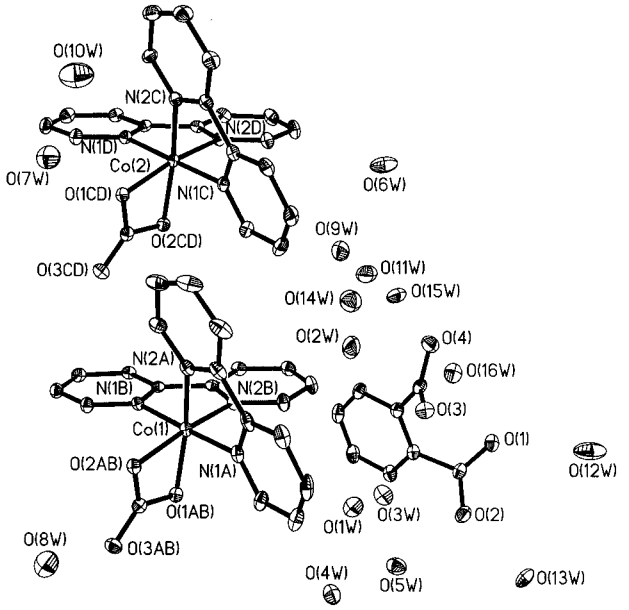

Figure 1. Crystallographically independent structure fragment with numbering scheme and displacement ellipsoids drawn at the 30% probability level in compound **1**. Two water molecules are disordered over two positions: O(13w) and O(13*), O(14w) and O(14*). Hydrogen atoms have been omitted for clarity.

Table 1. Selected bond lengths [Å] and angles [°] for compound **1**.

Co(1)–O(1AB)	1.901(2)	Co(2)–O(1CD)	1.895(2)
Co(1)–O(2AB)	1.893(2)	Co(2)–O(2CD)	1.898(2)
Co(1)–N(1A)	1.920(2)	Co(2)–N(1C)	1.922(2)
Co(1)–N(1B)	1.926(2)	Co(2)–N(1D)	1.934(2)
Co(1)–N(2A)	1.927(2)	Co(2)–N(2C)	1.933(2)
Co(1)–N(2B)	1.947(2)	Co(2)–N(2D)	1.937(2)
O(1AB)–Co(1)–O(2AB)	69.42(8)	O(1CD)–Co(2)–O(2CD)	69.31(8)
O(1AB)–Co(1)–N(1A)	92.76(9)	O(1CD)–Co(2)–N(1C)	89.20(9)
O(1AB)–Co(1)–N(1B)	88.65(9)	O(1CD)–Co(2)–N(1D)	91.59(9)
O(1AB)–Co(1)–N(2A)	165.96(8)	O(1CD)–Co(2)–N(2C)	97.66(9)
O(1AB)–Co(1)–N(2B)	99.21(9)	O(1CD)–Co(2)–N(2D)	165.43(8)
O(2AB)–Co(1)–N(1A)	88.91(8)	O(2CD)–Co(2)–N(1C)	92.41(9)
O(2AB)–Co(1)–N(1B)	92.53(8)	O(2CD)–Co(2)–N(1D)	87.95(9)
O(2AB)–Co(1)–N(2A)	96.95(9)	O(2CD)–Co(2)–N(2C)	166.34(9)
O(2AB)–Co(1)–N(2B)	167.92(9)	O(2CD)–Co(2)–N(2D)	96.85(9)
N(1A)–Co(1)–N(1B)	178.26(9)	N(1C)–Co(2)–N(1D)	179.21(9)
N(1A)–Co(1)–N(2B)	95.92(9)	N(1C)–Co(2)–N(2C)	83.04(9)
N(1A)–Co(1)–N(2A)	83.36(10)	N(1C)–Co(2)–N(2D)	96.13(9)
N(1B)–Co(1)–N(2A)	95.50(10)	N(2C)–Co(2)–N(1D)	96.77(10)
N(1B)–Co(1)–N(2B)	82.85(9)	N(1D)–Co(2)–N(2D)	83.13(9)
N(2A)–Co(1)–N(2B)	94.61(9)	N(2C)–Co(2)–N(2D)	96.44(9)

Pht^{2-} acts as a fully deprotonated counterion. The average dihedral angle between the planes of its carboxylate groups is 60.6°, and the angles between the planes of the carboxylate groups and the aromatic ring are 48.8° and 52.1°. The sixteen solvent water molecules and the uncoordinated oxygen atoms of the carboxylate groups of the Pht^{2-} anion form a system of hydrogen bonds that generate a wall of channels. These channels are extended along the *b* axis (Figure 2) and are occupied by pairs of $[Co(CO_3)(bpy)_2]^+$ cations. The latter are attached to the channels' walls by hydrogen bonds [O(4w)–H···O(3CD) = 2.800(3), O(8w)–H···O(3AB) = 2.814(3), and O(7w)–H···O(1CD) = 2.811(3) Å], as well as by π–π interactions between the Pht ring and the pyridine ring from the Co(1) complex [the centroid–centroid distance is 3.562(2) Å].

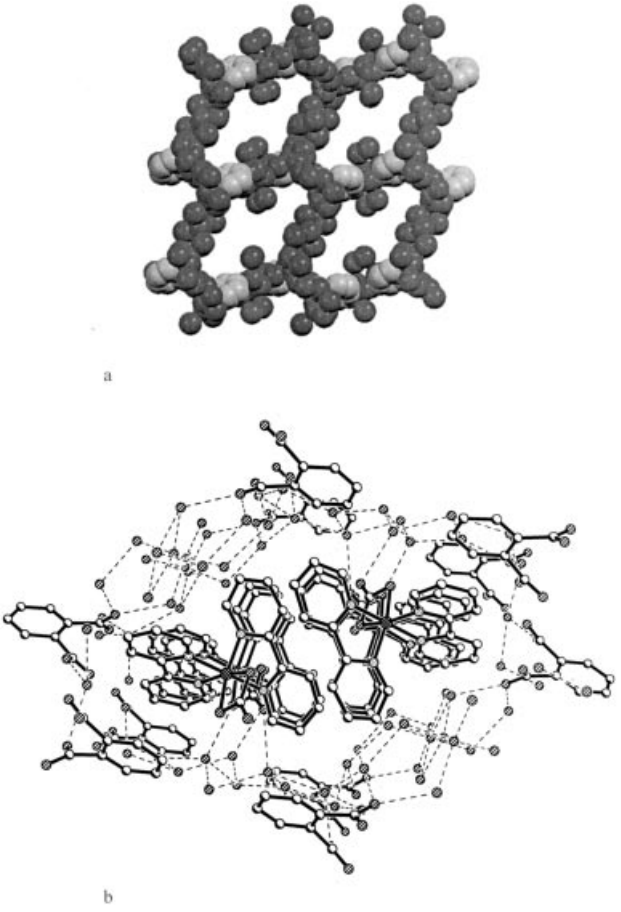

Figure 2. (a) Space-filling representation of channels in the structure of compound **1**. Cations $[Co(bpy)_2(CO_3)]^+$ have been omitted for clarity. (b) One channel with a pair of columns formed by $[Co(bpy)_2(CO_3)]^+$ cations in **1**. Hydrogen atoms have been omitted for clarity and hydrogen bonds are indicated by dotted lines.

The cations are arranged in pairs of columns due to π–π stacking interactions between the antiparallel aromatic rings belonging to two Co(1) complexes and related by a symmetrical center at the (1/2, 1/2, 0) site (Figure 2b). The average contact distance of the adjacent aromatic rings is about 3.52 Å and the centroid–centroid distance is 3.780(2) Å. The corresponding distances for analogous pyridine rings of two Co(2) complexes are about 3.77 and 3.987(1) Å, respectively, and are slightly longer than those for typical aromatic-aromatic π–stacking interactions.[29] Weak C–H···O hydrogen bonds between the CH groups of the pyridine rings and the uncoordinated oxygen atoms of the CO_3 ligands join Co(1) and Co(2) complexes within the column [C(11C)–H···O(3AB) = 3.226 Å, C(11A)–H···O(3CD) = 3.215 Å].

 © 2005 Wiley-VCH Verlag GmbH & Co. KGaA, Weinheim

[(bpy)$_2$Co(Pht)H(Pht)Co(bpy)$_2$](HPht)(H$_2$Pht)·2H$_2$O (2a, 2b)

X-ray diffraction analysis revealed that compound **2** crystallizes in two polymorphic forms: **2a** and **2b** (Table 2). The unit-cell parameters of **2a** and **2b** are related as follows: $a_{2b} \approx -(a_{2a} + c_{2a})$; $b_{2b} \approx b_{2a} + c_{2a} - a_{2a}$; $c_{2b} \approx 2(a_{2a} + b_{2a})$.

The former (**2a**) is isostructural with the analogous Zn complex[14] and also consists of a centrosymmetric dinuclear $[(bpy)_2Co(Pht)H(Pht)Co(bpy)_2]^+$ cation, an $HPht^-$ anion, an H_2Pht molecule, as well as two solvate H_2O molecules (Figure 3). Each Co atom has a distorted octahedral geometry containing four nitrogen atoms of two bpy ligands (the average Co–N bond length is 2.107 Å) and two oxygen atoms from one chelating carboxylate group of the Pht ligand [Co–O 2.112(2) and 2.225(2) Å]. The angle of the chelating carboxylate group O(3)–Co(1)–O(4) is 60.85(6)°. This value is in good agreement with those of similar 3d-metal complexes with a 1,3-chelating bidentate function of the Pht ligand.[10–15] It should be noted that the coordinated carboxylate group of the Pht residue in **2a** is almost coplanar with the aromatic ring − the dihedral angle between them is 10.2(1)°; for the second carboxyl group this angle is equal to 74.1(1)°. The two mononuclear structural units consisting of one metal ion, two bpy molecules, and one residue of *o*-phthalic acid are linked by a very short symmetric O···H···O hydrogen bond of 2.447(3) Å between the carboxylate oxygen atoms O(1) and O(1A) into a dimer. Consequently, the metal-containing backbone can be considered as a $[(bpy)_2Co(Pht)H(Pht)Co(bpy)_2]^+$ unit.

The dinuclear aggregate forms a hydrogen-bonded network with water molecules and the uncoordinated molecule of *o*-phthalic acid. The position of the hydrogen atoms of the carboxylic groups in the uncoordinated phthalate molecules could not be located because of disorder of oxygen atoms over two orientations with 50% probability. Therefore, we propose a model in which the crystal of **2a** contains

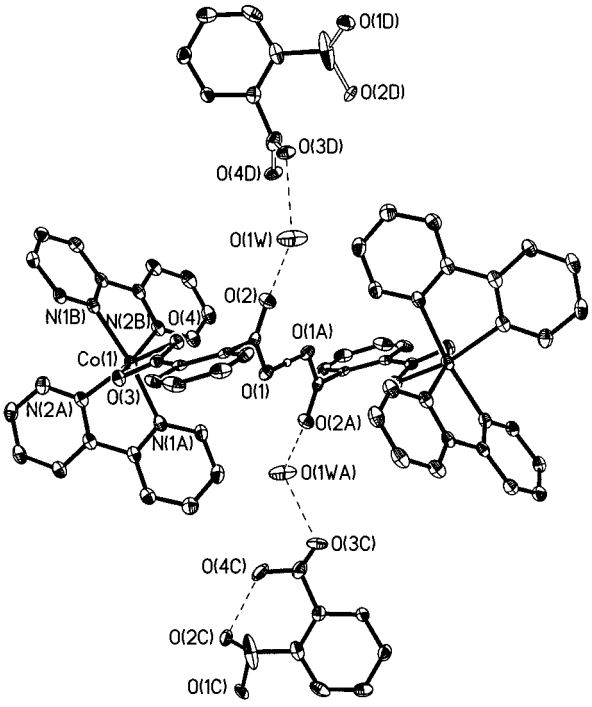

Figure 3. Dimeric aggregate in compound **2a**. Two configurations of the uncoordinated molecule of *o*-phthalic acid with C and D index are shown. All hydrogen atoms except a symmetric O(1)···H···O(1A) bond in the dimer have been omitted for clarity.

chains formed by an alternation of neutral H_2Pht molecules, water molecules, and monodeprotonated hydrogen phthalate anions ($HPht^-$), as shown in Figure 4. In this case, the inversion centers between two disordered carboxylic groups of the neighboring uncoordinated phthalate moieties in the chains have a statistical character (Figure 4). Variations of analogous chains have been observed in $\{[(\eta^6\text{-}C_6H_6)_2Cr]^+[HPht]^-[H_2Pht]\}$ as well as in $\{([(\eta^5\text{-}C_5H_5)_2$-

Table 2. Selected bond lengths [Å] and angles [°] of the two polymorphic forms of **2** (**2a** and **2b**).

2a		**2b**	Min value, max value	Average
Co(1)–O(3)	2.225(2)	Co–O(3)	2.213(2), 2.259(3)	2.233
Co(1)–O(4)	2.112(2)	Co–O(4)	2.099(2), 2.132(2)	2.116
Co(1)–N(1A)	2.119(2)	Co–N(1A)	2.105(3), 2.142(3)	2.121
Co(1)–N(1B)	2.105(1)	Co–N(1B)	2.096(3), 2.117(3)	2.106
Co(1)–N(2A)	2.119(2)	Co–N(2A)	2.108(3), 2.144(3)	2.127
Co(1)–N(2B)	2.086(2)	Co–N(2B)	2.088(3), 2.103(3)	2.095
O(4)–Co(1)–O(3)	60.85(6)	O(4)–Co–O(3)	60.0(1), 60.8(1)	60.4
N(1B)–Co(1)–O(4)	96.25(7)	O(4)–Co–N(1B)	96.4(1), 97.4(1)	96.5
N(2B)–Co(1)–O(4)	93.64(7)	N(2B)–Co–O(4)	93.5(1), 94.3(1)	93.9
N(1A)–Co(1)–O(3)	88.83(7)	N(1A)–Co–O(3)	88.1(1), 90.0(1)	89.1
O(4)–Co(1)–N(1A)	92.82(7)	O(4)–Co–N(1A)	92.4(1), 93.6(1)	93.0
N(1B)–Co(1)–N(1A)	170.88(7)	N(1B)–Co–N(1A)	170.0(1), 171.0(1)	170.5
N(2B)–Co(1)–N(1A)	102.29(8)	N(2B)–Co–N(1A)	100.8(1), 102.4(1)	101.7
N(1B)–Co(1)–O(3)	94.73(7)	N(1B)–Co–O(3)	95.0(1), 96.0(1)	95.6
N(2B)–Co(1)–N(1B)	78.14(8)	N(2B)–Co–N(1B)	77.2(1), 78.3(1)	77.7
N(2A)–Co(1)–O(3)	99.90(7)	N(2A)–Co–O(3)	98.5(1), 101.5(1)	100.1
O(4)–Co(1)–N(2A)	159.02(7)	O(4)–Co–N(2A)	157.2(1), 159.7(1)	158.6
N(1A)–Co(1)–N(2A)	77.61(8)	N(1A)–Co–N(2A)	76.7(1), 77.6(1)	77.1
N(1B)–Co(1)–N(2A)	93.49(8)	N(1B)–Co–N(2A)	93.0(1), 94.8(1)	93.9
N(2B)–Co(1)–N(2A)	106.55(8)	N(2B)–Co–N(2A)	105.2(1), 107.7(1)	106.6
N(2B)–Co(1)–O(3)	152.91(7)	N(2B)–Co–O(3)	152.1(1), 153.6(1)	152.8

 © 2005 Wiley-VCH Verlag GmbH & Co. KGaA, Weinheim

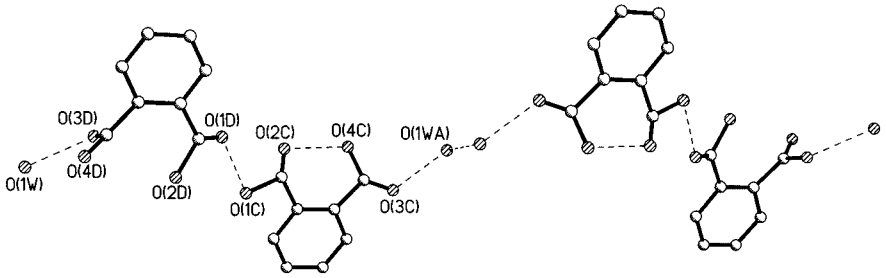

Figure 4. One version of a chain in **2a**. The molecule of Pht with D index is neutral and another one with C index is monodeprotonated.

$Co]^{+})_4([HPht]^{-})_2[Pht]^{2-}\}$.[30] The neutral molecule of *o*-phthalic acid forms two hydrogen bonds: O(1D)···O(1C) = 2.588(6) Å and O(3D)···O(1w) = 2.582(6) Å. Another conformer acts as a monoanion with only one short intramolecular hydrogen bond [O(4C)···O(2C) = 2.390(6) Å]. Two water molecules join pairs of H_2Pht–$HPht^-$ units into zigzag chains through O–H···O hydrogen bonds: O(1w)···O(1wA) ($-x + 1, -y + 2, -z$) = 2.690(4) Å, or O(1w)···O(3C) = 2.702(6) Å. The dinuclear aggregates are attached on both sides of the chains due to hydrogen bonds [O(1w)–H···O(2) = 2.795(3) Å].

Other noncovalent forces that contribute significantly to the 3D structural organization of **2a** should be mentioned, namely aromatic π–π interactions between the uncoordinated phthalate moieties and one of the coordinated bpy molecules (with A indexes), with a centroid–centroid distance of 3.754 Å. The angle between the overlapping aromatic system is 8.3(1)°. There are also π–π stacking interactions between the antiparallel bpy ligands from different dinuclear aggregates (the dihedral angle between the bpy planes being 0°, with a distance between the centroids of the bpy rings of 3.748 Å for the A molecules of bpy and 3.697 Å for B). The uncoordinated phthalate moieties also take part in a C–H···π interaction with the B bpy molecule [the distance between H(5C) and the centroid of the surrounding B ring is 2.646 Å]. Weak C–H···O hydrogen bonds involving the bpy carbon atoms and both the coordinated carboxylate oxygen atom (3.273 Å) and the oxygen atoms of the uncoordinated phthalate molecules (3.059 and 3.275 Å for two possible orientations) are also worthy of mention.

In compound **2b**, a small alteration in the crystal structure increases the unit cell's volume six times compared with that of **2a**. The asymmetric unit of **2b** contains six crystallographically independent Co^{II} complexes, which combine in the crystal structure into four $[(bpy)_2Co(Pht)H(Pht)Co(bpy)_2]^+$ units, as shown in Figure 5. Two of them, namely Co(5)–Co(5A) and Co(6)–Co(6A), are centrosymmetric, while the others [Co(1)–Co(2) and Co(3)–Co(4)] are noncentrosymmetric. A comparison of the main bond lengths and angles in all six Co complexes shows a close similarity between them. The average structural parameters of the coordination environment of the Co atoms are listed in Table 2. The maximum dispersion of distances in Co distorted octahedrons was observed for the Co–O(3) bond lengths, which are in the range 2.259(3)–2.213(2) Å. The Co–O(4) bond lengths vary from 2.099(2) to 2.132(3) Å. In the case of Co–N distances, their values are in the range 2.088(3)–2.144(3) Å, but the interval of bond lengths for each bpy molecule is not more than 0.037 Å.

The crystal structure of **2b** is organized in an analogous manner to **2a**. Every Co complex has satellite uncoordinated phthalate moieties connected to a bpy molecule by a π−π stacking interaction (the distance between the overlap-

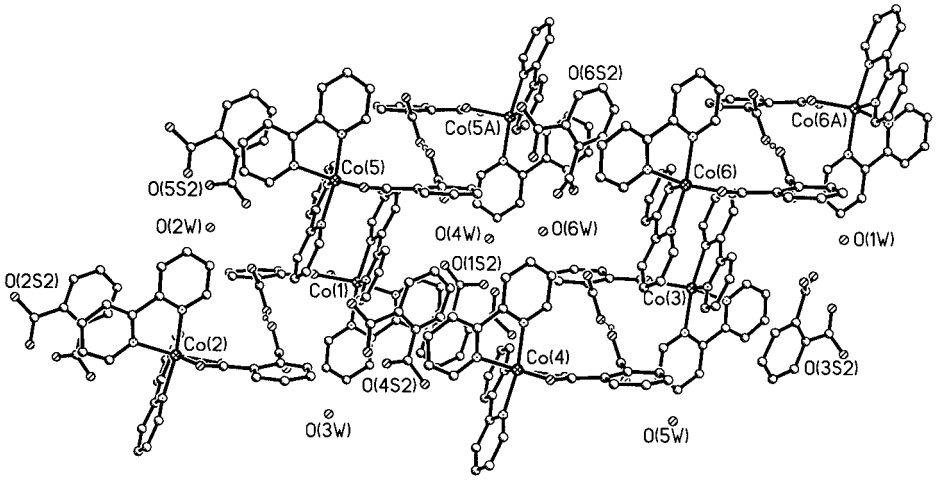

Figure 5. Six crystallographically independent Co complexes, which form four $[(bpy)_2Co(Pht)H(Pht)Co(bpy)_2]^+$ units in compound **2b**. Hydrogen atoms have been omitted for clarity.

 © 2005 Wiley-VCH Verlag GmbH & Co. KGaA, Weinheim

ping aromatic rings is about 3.76 Å). Six Pht^{2-} anions compensate the charge of the dimeric units and take part in the formation of H-bonded chains that are similar to those in **2a** (Figure 4). There are four crystallographically independent chains in **2b**. The quality and volume of experimental data, as well as the disorder of some carboxylate groups of the Pht moieties and water molecules, did not permit the localization of all the hydrogen atoms in the structure. However, the possibility to distinguish both the neutral H_2Pht and monodeprotonated $HPht^-$ anion exists for the four molecules. Molecules with indexes 1S and 5S are neutral H_2Pht, while 3S and 6S molecules are $HPht^-$ anions, and the chains may be described as –O(1S)–H···O(4w){or O(4w′)}–H···O(6w){or O(6w′)}–H···O(6S)– and –O(5S)–H···O(2w){or O(2w′)}–H···O(1w){or O(1w′)}–H···O(3S)–. The distribution of the carboxylic H atom for the two remaining disordered phthalate moieties (2S and 4S) has statistical character as in **2a**. The dinuclear aggregates are attached on both sides of the chains due to O(w)–H···O_{carb} hydrogen bonds that are in the range 2.79(1)–2.98(1) Å. An additional π–π interaction occurs between the bpy molecules of adjacent Co complexes: Co(3) and Co(6), Co(1) and Co(5), Co(2) and Co(4).

An analysis of the charges on the four different supramolecular aggregates consisting of a $[(bpy)_2Co(Pht)H(Pht)Co(bpy)_2]^+$ unit and two satellite uncoordinated phthalate moieties (monodeprotonated or neutral) shows that the structure of **2b** has four types of supramolecular fragments. Two of them are formed around the centrosymmetric dimers Co(5)–Co(5A) and Co(6)–Co(6A) and have a positive charge $\{(H_2Pht)[(bpy)_2Co(5)(Pht)H(Pht)Co(5A)(bpy)_2](H_2Pht)\}^+$ and negative charge $\{(HPht)[(bpy)_2Co(6)(Pht)H(Pht)Co(6A)(bpy)_2](HPht)\}^-$, respectively. The supramolecular aggregate around Co(1)–Co(2) is statistically neutral or has charge +1, and the one around Co(3)–Co(4) has a 0 or –1 charge. This effect could explain the increase of the cell volume in **2b**.

[Co(Pht)(bpy)(H$_2$O)$_3$]·3H$_2$O (3)

Compound **3** (Figure 6) may be subsumed to the structural type $[M(Pht)(Amin)(H_2O)_3]\cdot nH_2O$ [M = Co, Ni; Amin = one bidentate ligand (bpy, dipya, phen)[19,31] or two monodentate ligands (Py, β-Pic, 1-MeIm);[32] n = 0, 1, 3]. In all these compounds, the *o*-phthalic acid residue is fully deprotonated and acts as a monodentate ligand. The Co atom in **3** is in a distorted octahedral environment, being coordinated by two nitrogen atoms from the bpy molecule, with a Co–N(1) distance of 2.126(1) Å and a Co–N(2) distance of 2.134(1) Å, the O(4) atom of the monocoordinated phthalate ligand [2.145(1) Å], and three oxygen atoms of water molecules [O(1w), O(2w), and O(3w) distances of 2.115(1), 2.112(1), and 2.056(1) Å, respectively] (Table 3). The water molecules O(1w) and O(2w) are *trans* to N(1) and N(2), respectively, whereas O(3w) lies *trans* to O(4). Thus, three coordinated water molecules make one edge of the octahedron, whereas the same coordinated water molecules lie in a meridian place in the related compounds.[19,30,31] However, the main features of the crystal packing in compound **3** are maintained. In all these compounds the coordinated and uncoordinated water molecules form both intramolecular and intermolecular hydrogen bonds leading to the organization of double-chains.[32] The arrangement of these chains mainly depends on the nature of the aromatic amine. The presence of supplementary out-of-sphere water molecules in compound **3** generates a 3D network held together by O–H···O hydrogen bonds. The water molecule O(2w) and the carboxylate oxygen atom O(3) are involved in intramolecular H-bonding [O(2w)–H···O(3) = 2.831(2) Å] forming a six-membered hydrogen-bonded Co(1)–O(2w)–H···O(3)–C(22)–O(4)–Co(1) ring (Figure 6). Individual molecules are joined into centrosymmetric dimers by the hydrogen bonds O(2w)–H···O(2) [2.678(2) Å] and O(3w)–H···O(1) [2.713(2) Å] (symmetry code for O(2) and O(3): $-x + 1, -y + 1, -z$). The Co···Co distance within the dimer is 7.368(1) Å. These dimeric units are further connected by O(w)–H···O(carb.) and O(w)–H···O(w) hydrogen bonds into double-chains running along the *a* axis of the unit cell of **3** (Figure 7). The distance between the metal centers of the adjacent dimers is 6.698(1) Å. The hydrogen bond O(4w)–H···O(6w) ($x, -y + 1/2, z - 1/2$) of 2.775(2) Å and possible π–π interactions between antiparallel molecules of bpy (the average distances

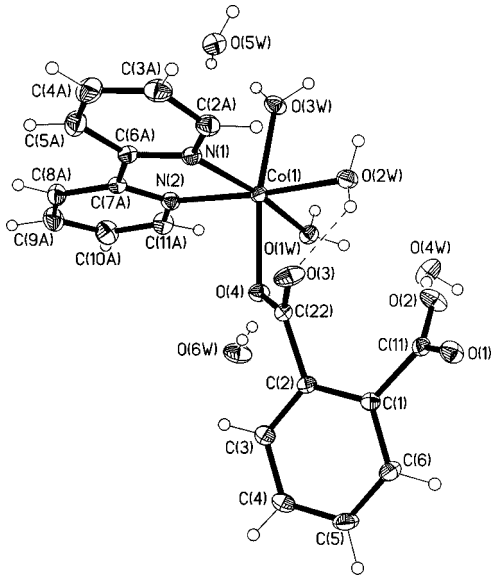

Figure 6. Molecular structure of compound **3**.

Table 3. Selected bond lengths [Å] and angles [°] for compound **3**.

Co(1)–O(4)	2.145(1)	Co(1)–O(1w)	2.115(1)
Co(1)–N(1)	2.126(1)	Co(1)–O(2w)	2.112(1)
Co(1)–N(2)	2.134(1)	Co(1)–O(3w)	2.056(1)
N(1)–Co(1)–O(4)	96.46(5)	O(2w)–Co(1)–O(4)	87.79(5)
N(1)–Co(1)–N(2)	77.36(5)	O(2w)–Co(1)–N(1)	97.29(5)
N(2)–Co(1)–O(4)	95.16(5)	O(2w)–Co(1)–N(2)	174.13(5)
O(3w)–Co(1)–O(4)	170.06(4)	O(2w)–Co(1)–O(3w)	91.17(5)
O(3w)–Co(1)–N(1)	91.36(5)	O(1w)–Co(1)–O(4)	81.87(5)
O(3w)–Co(1)–N(2)	92.53(5)	O(1w)–Co(1)–N(1)	171.32(5)
O(3w)–Co(1)–O(2w)	85.13(5)	O(1w)–Co(1)–N(2)	94.27(5)
O(3w)–Co(1)–O(1w)	91.29(5)		

 © 2005 Wiley-VCH Verlag GmbH & Co. KGaA, Weinheim

between the overlapping rings are 3.56 and 3.23 Å) link the double chains into a 3D network (Figure 8).

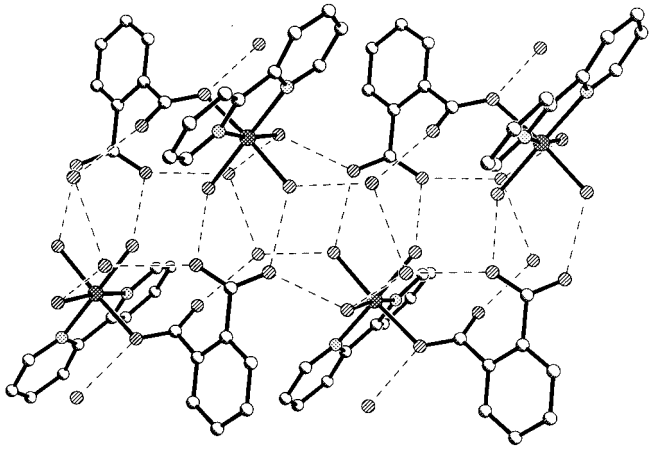

Figure 7. View of a double-chain in compound **3**. Hydrogen atoms have been omitted for clarity and hydrogen bonds are indicated by dotted lines.

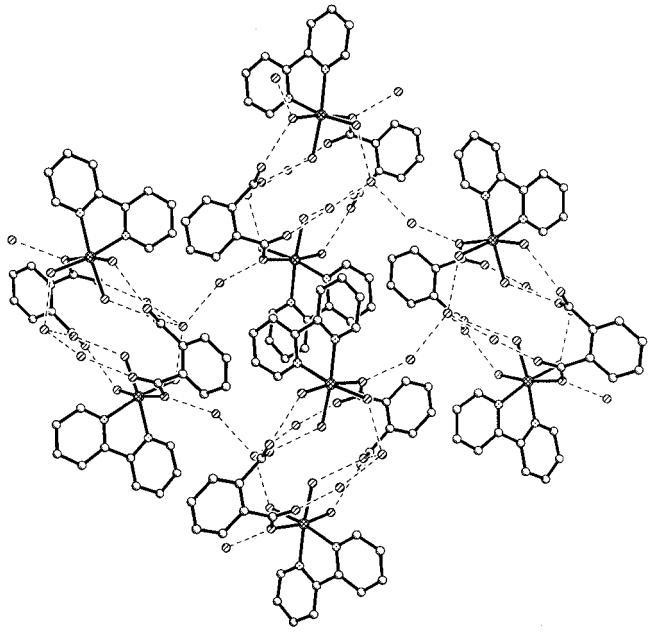

Figure 8. Packing diagram of compound **3**. Hydrogen atoms have been omitted for clarity and hydrogen bonds are indicated by dotted lines.

[Co(Pht)(bpy)(H$_2$O)]$_2$·2H$_2$O (4)

A neutral centrosymmetric dinuclear aggregate [Co(Pht)(bpy)(H$_2$O)]$_2$ is the main structural unit of compound **4**, in which two Co^{II} atoms are linked by two phthalate ligands to form a 14-membered cycle (Figure 9). The coordination modes of the two deprotonated carboxylate groups in the Pht residue are different. One carboxylate group is bidentate to a Co atom, while the other one is monocoordinated to the adjacent Co atom. The Co atoms are in a distorted octahedral environment. Deformation of the Co^{II} coordination polyhedron is observed both in bond lengths [range from 2.076(1) to 2.235(2) Å] and angles [O(3)–Co–O(4) = 60.15°; Table 4]. The Co atom is coordinated by three oxygen atoms [O(1*), O(3), O(4)] from two Pht residues [2.141(1), 2.235(2), and 2.076(1) Å], one water molecule [O(1w) 2.118(1) Å], and two nitrogen atoms [N(1), N(2)] of a bpy molecule [2.097(1) and 2.127(1) Å]. The Co···Co distance in this dimer is 5.034(1) Å. Similar dimers have been described recently in [Zn(Pht)(Im)(H$_2$O)]$_2$,[13] although in this latter complex the Pht ligands exhibit a 1,6-bridging function and the Zn atoms have a tetrahedral environment. A 14-membered cycle is formed in both compounds, but alteration of the structural function of the Pht residue leads to a shorter transannular distance in **4** [O(4)–O(4*) = 3.448(2) Å] compared to that in the Zn dimer [3.964(2) Å].[13]

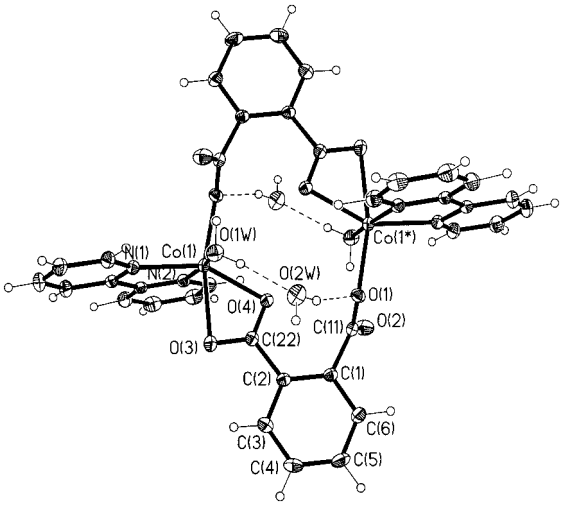

Figure 9. Discrete dinuclear molecule in compound **4**.

Table 4. Selected bond lengths [Å] and angles [°] for compounds **4** and **5**.[a]

4		**5**	
Co(1)–O(1)^1	2.076(1)	Co(1)–O(1)^2	2.054(6)
Co(1)–O(3)	2.235(2)	Co(1)–O(3)	2.196(5)
Co(1)–O(4)	2.141(1)	Co(1)–O(4)	2.181(5)
Co(1)–N(1)	2.097(1)	Co(1)–N(1)	2.151(7)
Co(1)–N(2)	2.127(1)	Co(1)–N(2)	2.108(6)
Co(1)–O(1w)	2.118(1)	Co(1)–O(1w)	2.095(5)
O(1)^1–Co(1)–O(3)	165.32(5)	O(1)^2–Co(1)–O(3)	154.8(2)
O(1)^1–Co(1)–O(4)	105.44(5)	O(1)^2–Co(1)–O(4)	96.9(2)
O(1)^1–Co(1)–N(1)	102.49(5)	O(1)^2–Co(1)–N(1)	85.2(2)
O(1)^1–Co(1)–N(2)	91.56(5)	O(1)^2–Co(1)–N(2)	117.8(2)
O(1)^1–Co(1)–O(1w)	93.04(5)	O(1)^2–Co(1)–O(1w)	89.3(2)
O(3)–Co(1)–O(4)	60.15(5)	O(3)–Co(1)–O(4)	60.3(2)
N(1)–Co(1)–O(3)	92.18(5)	N(1)–Co(1)–O(3)	102.7(2)
N(1)–Co(1)–O(4)	150.90(5)	N(1)–Co(1)–O(4)	86.7(2)
N(1)–Co(1)–N(2)	77.37(5)	N(2)–Co(1)–O(4)	139.0(2)
N(1)–Co(1)–O(1w)	93.63(6)	N(2)–Co(1)–O(3)	87.3(2)
N(2)–Co(1)–O(3)	92.23(5)	N(2)–Co(1)–N(1)	76.0(2)
N(2)–Co(1)–O(4)	93.76(5)	O(1w)–Co(1)–O(4)	111.1(2)
O(1w)–Co(1)–O(3)	85.35(5)	O(1w)–Co(1)–O(3)	89.5(2)
O(1w)–Co(1)–O(4)	92.89(5)	O(1w)–Co(1)–N(1)	161.9(2)
O(1w)–Co(1)–N(2)	170.61(5)	O(1w)–Co(1)–N(2)	91.4(2)

[a] Symmetry transformations used to generate equivalent atoms: ^{1}: $-x + 1, -y, -z + 1$; ^{2}: $-x + 2, -y + 1, z + 1/2$.

 © 2005 Wiley-VCH Verlag GmbH & Co. KGaA, Weinheim

Both the coordinated and solvate water molecules generate an extensive hydrogen-bonding network in **4**. The coordinated water molecule O(1w) is involved in intermolecular H-bonding [O(1w)–H···O(2) (–*x* + 1, –*y*, –*z* + 1) = 2.695(2) Å]. A pair of identical H_2O molecules [O(2w)], one above and the other below the plane of the 14-membered cycle, which additionally constrict the dimer, form hydrogen bonds as donors with the O(1) atoms of the monocoordinated carboxylate groups [O(2w)–H···O(1) = 2.871(2) Å] and as acceptors with the coordinated water molecules [O(1w)–H···O(2w) = 2.722(2) Å]. The second donor function of the O(2w) molecule reduces the organization of layers of dimers (Figure 10) parallel to the (101) plane. These layers are held together by π–π interactions between antiparallel bpy molecules with an average deviation of the bpy atoms from the adjacent ring of 3.41(3) Å.

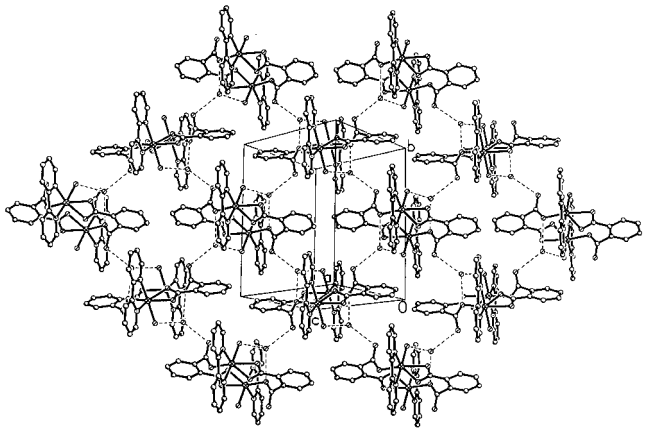

Figure 10. Packing diagram of compound **4**. Hydrogen atoms have been omitted for clarity and hydrogen bonds are indicated by dotted lines.

[Co(Pht)(bpy)(H$_2$O)]$_n$ (5)

The crystal structure of **5** consists of [Co(Pht)(bpy)(H_2O)] entities (Figure 11) as in **4,** but they are joined into a helical polymeric chain (Figure 12). It is necessary to note that **5** is isostructural with [Zn(Pht)(bpy)(H_2O)]$_n$.[33] The coordination polyhedron of the Co atom is composed of the same donor atoms as in **4** and is also distorted. The bond lengths range from 2.054(1) to 2.196(5) Å and the bond angles from 60.3(2)° to 117.8(2)° (Table 4). The Co–O(3) and Co–O(4) bond lengths for the bidentate carboxylate group are similar [2.196(5) and 2.181(5) Å], and that is a rather surprising result in light of the 1,3-chelating function of the Pht ligand.[11,14,15] There is a principal difference in the dihedral

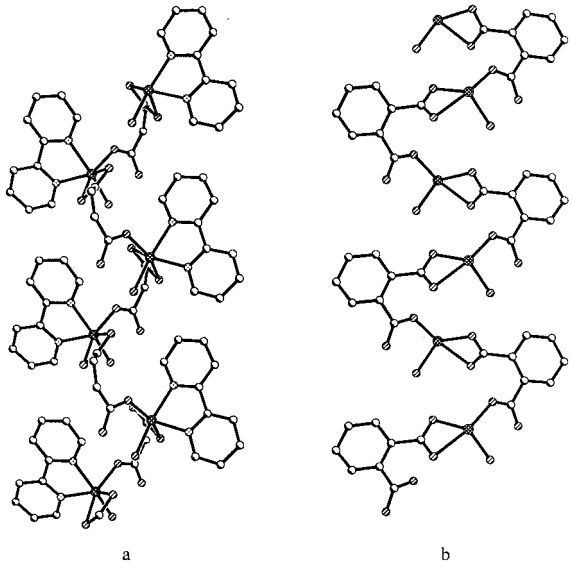

Figure 12. View along the *c*-axis of the single helical chain in compound **5** with bpy wings (a) and Pht wings (b).

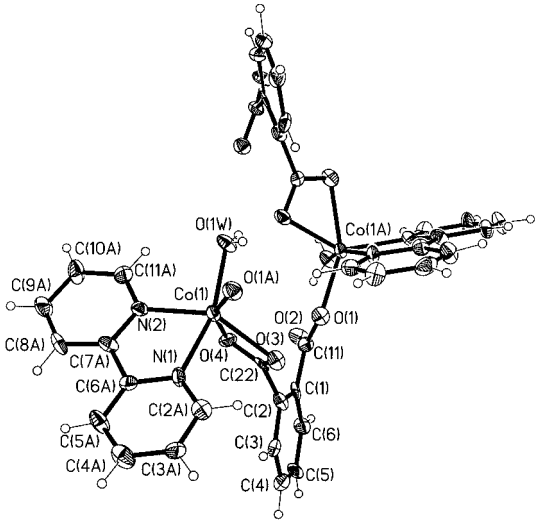

Figure 11. A fragment of the helical polymeric chain in compound **5** with the numbering scheme.

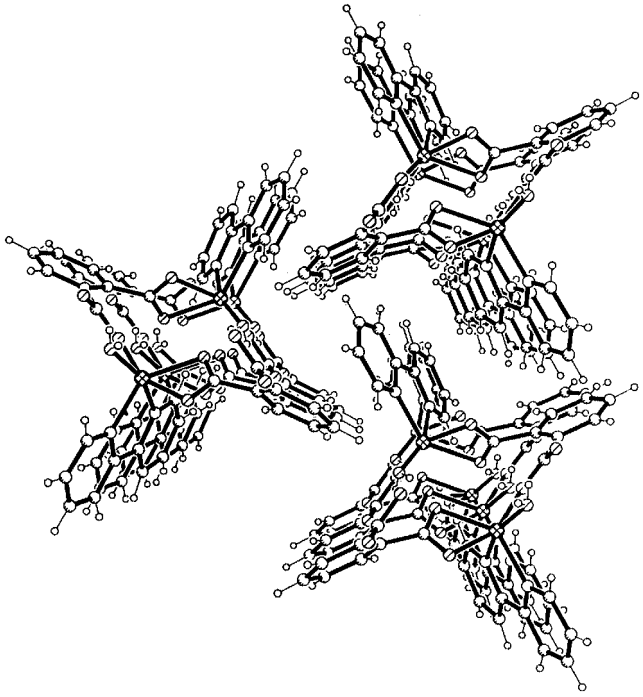

Figure 13. Crystal packing of the helical chains in compound **5**.

 © 2005 Wiley-VCH Verlag GmbH & Co. KGaA, Weinheim

angles between the planes of the coordinated carboxylate group and the aromatic ring in compounds **5** and **4**. In the former, this angle is equal to 61.5°, whereas in the latter the coordinated carboxylate group lies almost in the plane of the aromatic ring (the dihedral angle is 8°). The second carboxylate group of the phthalate dianion is monocoordinated to its adjacent Co atom [Co–O(1) = 2.054(6) Å]. The tridentate chelate-bridging function of the Pht ligand leads to the organization of the infinitive helical chain along the *c*-axis with a pitch of 8.432 Å (Figure 12). The neighboring Co···Co distance is 5.546(1) Å, slightly shorter than the Zn···Zn distance in $[Zn(Pht)(bpy)(H_2O)]_n$ (5.633 Å)[33] and much shorter than that in the helix of $[Co(Pht)(4\text{-MeIm})_2]_n$ [6.247(1) Å].[15] The adjacent complexes within the chain are joined additionally through two O–H···O hydrogen bonds between the coordinated water molecule and carboxylate oxygen atoms O(2) and O(4) of 2.570(8) and 2.760(8) Å, respectively. The chains are held together by van der Waals interactions (Figure 13).

Magnetic Studies

The temperature dependence of the molar magnetic susceptibility, χ_M, of complex **1** indicates a diamagnetic behavior. This corresponds to low-spin Co^{III} ($S = 0$) ions.

The thermal dependence of $\chi_M T$ ($\chi_M T$ being the product of the molar magnetic susceptibility and the temperature) and the simulated curve for a powdered sample of the dinuclear complex **2** are shown in Figure 14. The room-temperature $\chi_M T$ value of 6.0 emu K mol^{-1} agrees well with the calculated value of 6.0 emu K mol^{-1} for a high-spin Co^{II} compound ($S = 3/2$) with $g = 2.55$.[34] The gradual decrease of $\chi_M T$ upon lowering the temperature is typical for high-spin Co^{II}. This decrease of $\chi_M T$ is mainly due to zero-field splitting. Below 100 K, a possible weak antiferromagnetic interaction between neighboring Co^{II} ions provokes a further decrease of the $\chi_M T$ values. A simulation within the temperature range 5–300 K with a *g*-value of 2.55, an axial zero-field splitting parameter[34,35] of $|D| = 70$ cm^{-1}, and an exchange parameter, *J*, of –0.1 cm^{-1} gives the best agreement with the experimental data.

The room-temperature $\chi_M T$ value of 3.05 emu K mol^{-1} for compound **3** (Figure 15) agrees quite well with the calculated value of 3.17 emu K mol^{-1} for a high-spin Co^{II} compound ($S = 3/2$) with $g = 2.6$.[34] The gradual decrease of $\chi_M T$ upon lowering the temperature is typical for high-spin Co^{II}. This decrease of $\chi_M T$ is mainly due to zero-field splitting. A simulation within the temperature range 25–300 K with the parameters $|D| = 80$ cm^{-1} and $g = 2.6$ reproduces the experimental data quite well. At lower temperatures, the measured susceptibility shows a steeper decrease. This is probably due to weak antiferromagnetic intermolecular interactions between the Co^{II} complexes.

The thermal dependence of $\chi_M T$ of complex **5** is depicted in Figure 16. Attempts to obtain a satisfactory simulation for this linear-chain compound of Co^{II} ions were not successful. However, only to give an impression of the deviation from a single ion behavior, a simulation[36] within the temperature range of 100 K to 300 K, with a typical parameter set of $|D| = 65$ cm^{-1} and $g = 2.45$, is depicted in Figure 16. Obviously, intrachain magnetic-exchange interactions have a pronounced effect.

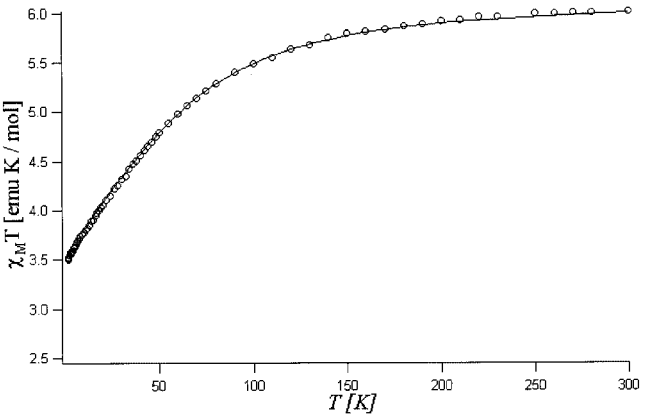

Figure 14. The circles correspond to the temperature dependence $\chi_M T$ for $[(bpy)_2Co(Pht)H(Pht)Co(bpy)_2](HPht)(H_2Pht)\cdot 2H_2O$ (**2**). A simulation from 5 to 300 K with the parameters[34–36] $|D| = 70$ cm^{-1}, $g = 2.55$, and $J = -0.1$ cm^{-1} is depicted as a line.

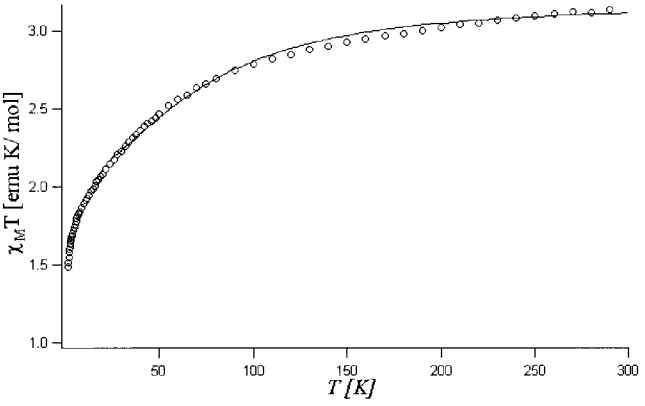

Figure 15. The temperature dependence, $\chi_M T$, for $[Co(Pht)(bpy)(H_2O)_3]\cdot 3H_2O$ (**3**) is depicted as circles. The line corresponds to a simulation from 25 to 300 K with the parameters $|D| = 80$ cm^{-1} and $g = 2.6$.

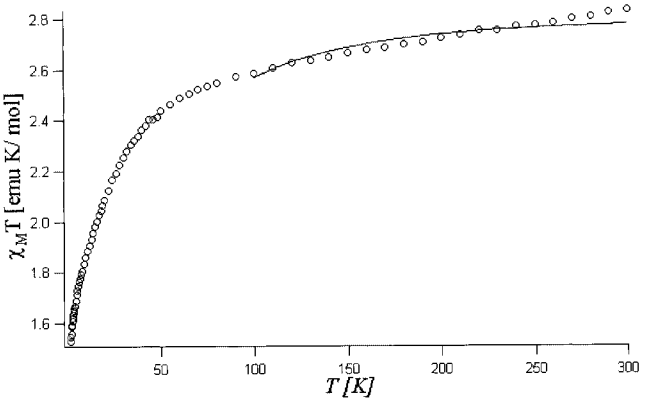

Figure 16. The temperature dependence, $\chi_M T$, for the chain complex $[Co(Pht)(bpy)(H_2O)]_n$ (**5**) is depicted as circles. A simulation for a single-ion behavior within the temperature range of 100 K to 300 K by using a typical parameter set of $|D| = 65$ cm^{-1} and $g = 2.45$ is shown as a line.

 © 2005 Wiley-VCH Verlag GmbH & Co. KGaA, Weinheim

Conclusions

The reaction of cobalt(II) anions with *o*-phthalic acid and bidentate bipyridine ligands has produced some intriguing complexes. Complexes of different nuclearity are obtained depending on the temperature of the reaction: the mononuclear $[Co^{III}(CO_3)(bpy)_2]_2(Pht)\cdot 16H_2O$ (**1**) and $[Co(Pht)(bpy)(H_2O)_3]\cdot 3H_2O$ (**3**) complexes, the open $[(bpy)_2Co(Pht)H(Pht)Co(bpy)_2](HPht)(H_2Pht)\cdot 2H_2O$ (**2**) and cyclic dinuclear $[Co(Pht)(bpy)(H_2O)]_2\cdot 2H_2O$ (**4**), and polynuclear $[Co(Pht)(bpy)(H_2O)]_n$ (**5**). Moreover, in complex **1** the oxidation of cobalt(II) to cobalt(III) ions has occurred. The structural trends displayed in **1**–**5** illustrate the extraordinarily rich binding abilities of the carboxylate groups of the *o*-phthalate ligand and their ability to form extensive hydrogen-bonding interactions and build supramolecular architectures. The variable-temperature magnetic data indicate a weak antiferromagnetic interaction between neighboring Co^{II} centers in both the open dinuclear complex **2** and mononuclear complex **3**, whereas complex **1** is a rare example containing low-spin Co^{III} ($S = 0$) ions.

Experimental Section

General: All reagents were purchased from commercial sources and used as received. IR spectra were recorded with a Perkin–Elmer Spectrum One spectrometer in the region 4000–400 cm^{-1} using KBr pellets. TG analyses were carried out with a Mettler-Toledo TA 50 in dry dinitrogen (60 mL min^{-1}) at a heating rate of 5 °C min^{-1}. Magnetic susceptibility data of powdered samples were collected with an MPMS Quantum Design SQUID magnetometer (XL-5) in the temperature range 300–1.8 K and at a field of 1000 G. The samples were placed in a Saran foil bag and a straw was used as the sample holder. The output data were corrected for the experimentally determined diamagnetism of the sample holder and the diamagnetism of the sample calculated from Pascal's constants. The program MAGPACK[36] was used to model the experimental magnetic susceptibility data.

Synthesis of $[Co(CO_3)(bpy)_2]_2(Pht)\cdot 16H_2O$ (1): A warm solution of H_2Pht (1.66 g, 10 mmol) and bpy (1.56 g, 10 mmol) in water (20 mL) was added to a suspension of $CoCO_3\cdot Co(OH)_2\cdot nH_2O$ (1.18 g) and K_2CO_3 (1.38 g, 10 mmol) in water (30 mL). The resulting mixture was stirred at 60 °C for 30 min. The precipitated solid was removed immediately and the filtrate allowed to cool to room temp. Dark-red crystals of **1** suitable for X-ray diffraction studies were filtered off after two weeks, and washed with water, EtOH, and dried in air. Yield: 1.00 g (30.4% based on bpy). $C_{50}H_{68}Co_2N_8O_{26}$ (1315.0): calcd. C 45.67, H 5.21, N 8.52; found C 45.71, H 5.15, N 8.48. IR (KBr): $\tilde{\nu}$ = 3384 br, 3116 m, 3086 m, 3061 m, 3032 m, 1678 vs, 1639 s, 1606 s, 1563 s, 1501 m, 1472 s, 1449 s, 1403 s, 1382 s, 1318 m, 1282 w, 1247 m, 1202 s, 1157 m, 1123 w, 1109 w, 1075 w, 1037 w, 1025 w, 1004 w, 822 m, 773 vs, 751 sh, 729 s, 692 w, 676 w, 652 m, 509 m, 484 w cm^{-1}.

Synthesis of $[(bpy)_2Co(Pht)H(Pht)Co(bpy)_2](HPht)(H_2Pht)\cdot 2H_2O$ (2): H_2Pht (3.32 g, 20 mmol) and bpy (3.12 g, 20 mmol) were added to a suspension of $CoCO_3\cdot Co(OH)_2\cdot nH_2O$ (2.3 g) in water (50 mL). The resulting mixture was stirred at 80 °C for 10 min. The precipitated solid containing unreacted cobalt(II) carbonate was removed immediately and the filtrate allowed to cool to room temp. Large red crystals were filtered off after a week, washed with water, and dried in air. Yield: 4.52 g (62.87% based on bpy). $C_{72}H_{56}Co_2N_8O_{18}$ (1439.1): calcd. C 60.09, H 3.92, N 7.79; found C 59.90, H 3.86, N 7.59. IR (KBr): $\tilde{\nu}$ = 3428 br, 3073 m, 3035 sh, 1717 s, 1600 vs, 1579 vs, 1564 sh, 1538 s, 1493 sh, 1475 vs, 1444 vs, 1411 vs, 1366 s, 1315 m, 1293 m, 1251 m, 1177 m, 1159 m, 1075 m, 1059 m, 1022 s, 796 m, 773 vs, 736 s, 715 m, 683 w, 650 m, 576 m cm^{-1}. Single crystals suitable for diffraction studies were obtained by recrystallization of **2** from a hot aqueous solution.

Synthesis of $[Co(Pht)(bpy)(H_2O)_3]\cdot 3H_2O$ (3) and $[Co(Pht)(bpy)(H_2O)]_n$ (5). Method A: Cobalt(II) carbonate (1.18 g) was added to a hot solution of H_2Pht (1.69 g, 10 mmol) and bpy (1.56 g, 10 mmol) in water (50 mL). The resulting mixture was heated at reflux for 45 min. The precipitated solid was removed by filtration from the hot solution, and the filtrate allowed to cool to room temp. Cherry-colored crystalline **5** and large, rose-colored crystals of **3** suitable for X-ray investigation were collected by filtration after a week, washed with water and dried in air. The crystals of **3** and **5** were separated by hand. The yields of compounds **5** and **3** were 0.78 g (19.65%) and 0.3 g (12.1%), respectively. An additional batch of **3** was obtained by keeping the mother filtrate in air for 2 weeks. **3:** $C_{18}H_{24}CoN_2O_{10}$ (487.32): calcd. C 44.36, H 4.96, N 5.75; found C 44.28, H 4.68, N 5.67. IR (KBr): $\tilde{\nu}$ = 3230 br, 1652 sh, 1602 vs, 1568 vs, 1484 s, 1444 vs, 1404 vs, 1315 m, 1250 m, 1172 m, 1159 m, 1104 w, 1087 m, 1060 m, 1023 s, 840 s, 820 s, 764 vs, 736 vs, 701 s, 652 s, 632 m cm^{-1}. The identity of **5** was established by comparison of IR data with the crystallographically characterized precipitate from Method B, and by elemental analysis (found for compound **5**: C 54.11, H 3.45, N 6.84). **Method B:** A solution of KHPht (2.04 g, 10 mmol) in 20 mL of water was added to a hot solution of $Co(O_2CMe)_2\cdot 4H_2O$ (2.49 g, 10 mmol) and bpy (1.56 g, 10 mmol) in 20 mL of MeOH. The resulting cherry-colored solution was stirred and heated for 1 h. Crystals of compound **5** suitable for X-ray diffraction studies crystallized after several days, and they were then filtered off, washed with MeOH, and dried in air. Yield: 3.00 g (75.6%). $C_{18}H_{14}CoN_2O_5$ (397.24): calcd. C 54.43, H 3.55, N 7.05, Co 14.84; found C 54.43, H 3.61, N 6.99, Co 14.80. IR (KBr): $\tilde{\nu}$ = 3274 br, 3119 m, 3078 m, 1610 s, 1600 s, 1578 s, 1542 vs, 1492 s, 1474 s, 1446 vs, 1420 vs, 1384 s, 1314 m, 1262 w, 1252 m, 1175 m, 1152 m, 1085 m, 1057 m, 1041 w, 973 w, 921 w, 869 m, 824 m, 815 m, 763 vs, 737 s, 721 m, 692 s, 651 s, 631 m, 576 w, 456 m cm^{-1}. **Method C:** $Co(O_2CMe)_2\cdot 4H_2O$ (0.25 g, 1 mmol) in 10 mL of MeOH was added to a hot solution of H_2Pht (0.17 g, 1 mmol) and bpy (0.16 g, 1 mmol) in 15 mL of MeOH. The resulting cherry-colored solution was heated at reflux for 1 h. Water (1 mL) was then added to the solution and it was allowed to slowly evaporate at room temp. over 3 weeks to give a crystalline precipitate of **5** and several crystals of **4** suitable for diffraction studies. The yield of **5** was 0.25 g (62.5%). It was further identified by comparison of its IR spectrum with the crystallographically characterized precipitate from Method B, and by elemental analysis; found for the title compound **5**: C 54.30, H 3.48, Co 14.90, N 7.01.

X-ray Crystallographic Study: Experimental data for **2a** were collected with an Enraf–Nonius CAD4 single-crystal diffractometer with Cu-K_α radiation at 140 K and were processed using a locally written program.[37] Experimental data for all other crystals were obtained with a KUMA KM4CCD-κ-axis diffractometer with graphite-monochromated Mo-K_α radiation at 130 K for **1**, 293 K for **2b** and **4**, 130 K for **3**, and at 170 K for **5**. The data were processed using the KUMA diffraction (Wroclaw, Poland) program. Crystal data and details of data collection and refinement for **1**–**5** are given in Table 5. The structures were solved by direct methods (SHELXS-97)[38] and refined by the full-matrix least-squares method on F^2 (SHELXL-97)[39] with an anisotropic approach for

Table 5. Crystal data and structure refinements of compounds **1**–**5**.

	1	**2a**	**2b**	**3**	**4**	**5**
Empirical formula	$C_{50}H_{68}Co_2N_8O_{26}$	$C_{72}H_{56}Co_2N_8O_{18}$	$C_{72}H_{56}Co_2N_8O_{18}$	$C_{18}H_{24}CoN_2O_{10}$	$C_{18}H_{16}CoN_2O_6$	$C_{18}H_{14}CoN_2O_5$
Formula mass	1314.98	1439.10	1439.11	487.32	415.26	397.24
Temperature [K]	130(2)	140(2)	293(2)	130(2)	293(2)	170(2)
Wavelength [Å]	0.71073	1.54178	0.71073	0.71073	0.71073	0.71073
Crystal size [mm]	0.7×0.7×0.3	0.3×0.4×0.3	0.6×0.6×0.3	0.8×0.4×0.4	0.5×0.5×0.3	0.25×0.1×0.05
Crystal system	monoclinic	triclinic	triclinic	monoclinic	monoclinic	orthorhombic
Space group	$P2_1/c$	$P\bar{1}$	$P\bar{1}$	$P2_1/c$	$P2_1/n$	$Pna2_1$
a [Å]	14.046(3)	10.901(2)	15.324(3)	8.959(2)	11.520(2)	10.077(2)
b [Å]	14.693(3)	11.690(2)	20.702(4)	18.711(4)	13.072(3)	19.098(4)
c [Å]	28.904(6)	14.022(3)	31.835(6)	12.757(3)	11.957(2)	8.432(2)
α [°]	90.	111.16(3)	104.79(3)	90	90	90
β [°]	91.94(3)	105.79(3).	93.45(3)	102.57(3)	107.25(3)	90
γ [°]	90	91.40(3)	92.95(3)	90.	90	90
Z, D_c [g cm^{-3}]	4, 1.465	1, 1.504	6, 1.475	4, 1.551	4, 1.604	4, 1.626
μ [mm^{-1}]	0.647	4.795	0.594	0.881	1.038	1.091
F(000)	2744	742	4452	1012	852	812
θ range for data coll. [°]	3.41–25.03	3.54–69.98	3.40–25.03	3.45–29.82	3.57–26.37	3.79–25.02
Limiting indices	$-16 \le h \le 16$ $-17 \le k \le 13$ $-34 \le l \le 34$	$0 \le h \le 13$ $-14 \le k \le 14$ $-17 \le l \le 16$	$-9 \le h \le 18$ $-24 \le k \le 24$ $-37 \le l \le 37$	$-12 \le h \le 12$ $-16 \le k \le 25$ $-17 \le l \le 16$	$-11 \le h \le 1\ 4$ $-16 \le k \le 16$ $-14 \le l \le 14$	$-11 \le h \le 5$ $-20 \le k \le 22$ $-10 \le l \le 6$
Reflections collected/unique	61380/10503	5951/5951	83789/33922	23547/5496	9325/3507	4658/2064
Completeness to θ_{max}	[R(int) = 0.0552] 99.6%	[R(int) = 0] 99.0%	[R(int) = 0.0389] 98.7%	[R(int) = 0.0395] 91.8%	[R(int) = 0.0189] 99.6%	[R(int) = 0.0704] 98.8%
Data/restraints/parameters	10503/52/903	5951/6/481	33922/8/2771	5496/0/376	3507/0/309	2064/1/236
Goodness-of-fit on F^2	1.021	1.023	1.116	1.079	1.058	1.033
Final R indices [$I > 2\sigma(I)$]	R_1 = 0.0491, wR_2 = 0.1389	R_1 = 0.0401, wR_2 = 0.1058	R_1 = 0.0644, wR_2 = 0.1956	R_1 = 0.0346, wR_2 = 0.0831	R_1 = 0.0271, wR_2 = 0.0690	R_1 = 0.0568, wR_2 = 0.1089
R indices (all data)	R_1 = 0.0599, wR_2 = 0.1488	R_1 = 0.0489, wR_2 = 0.1102	R_1 = 0.1250, wR_2 = 0.2312	R_1 = 0.0384, wR_2 = 0.0858	R_1 = 0.0301, wR_2 = 0.0714	R_1 = 0.0770, wR_2 = 0.1183
Largest diff. peak/hole [e Å^{-3}]	0.821/–0.667	0.349/–0.661	0.465/–0.836	0.558/–0.695	0.276/–0.270	0.459/–0.473

the non-hydrogen atoms for **1**, **2a**, **3**, **4**, and **5**. The crystals of **2b** have a substructure: $I_{exp.}$ for *hkl* reflections with $l = 2n >> I_{exp}$ for *hkl* with $l = 2n + 1$. The structure of **2b** was refined by using the Konnert–Hendrickson conjugate-gradient algorithm (CGLS) at the early stages, and then the blocked full-matrix refinement was performed. Hydrogen atoms were located from the difference syntheses of electronic density, except for H of disordered phthalate moieties and water molecules. Localized hydrogen atoms were included in the subsequent refinement in the riding-model approximation for **1**, **2a**, **2b**, and **5**. For **3** and **4**, H-atoms were refined in an isotropic approximation. CCDC-258617 (**1**), -258618 (**2a**), -258619 (**2b**), -258939 (**3**), -258620 (**4**), and -258621 (**5**) contain the supplementary crystallographic data for this paper. These data can be obtained free of charge from The Cambridge Crystallographic Data Center via www.ccdc.cam.ac.uk/data_request/cif.

Supporting Information (see footnote on the first page of this article): Figure S1 shows the correlation between the two unit cells of **2a** and **2b**. Hydrogen-bonding interactions in compound **1** (Table S1) and compound **3** (Table S2).

Acknowledgments

This work was supported by the Swiss National Science Foundation (SCOPES 7MDPJ065712.01/1). The authors gratefully acknowledge the assistance of Professor Bocelli, Centro di Studio per la Strutturistica Diffrattometrica del CNR, Parma, Italy, in the collection of crystallographic data sets for compound **2b**.

[1] a) R. C. Mehrotra, R. Bohra, *Metal Carboxylates*, Academic Press, New York, **1983**; b) C. N. R. Rao, S. Natarajan, R. Vaidhyanathan, *Angew. Chem. Int. Ed.* **2004**, *43*, 1466–1496 and references cited therein.

[2] a) *Catalysis in Organic Synthesis* (Ed.: W. H. Jones), Academic Press, New York, **1980**; b) R. A. Sheldon, J. K. Kochi, *Metal Catalyzed Oxidations of Organic Compounds*, Academic Press, New York, **1981**; c) V. V. Goncharuk, G. L. Kamalov, G. A. Kovtun, E. S. Rudakov, V. K. Yatsimirsky *Catalysis. Mechanisms of Homogeneous and Heterogeneous Catalysis, Cluster Approaches*, Naukova Dumka, Kiev, **2002**, p. 541 (in Russian); d) T. Szymanska-Buzar, J. J. Ziolkowski, *Koord. Khim.* **1976**, *2*, 1172–1191 (in Russian); *Chem. Abstr.* **1977**, *86*, 79306m. e) T. Szymanska-Buzar, J. J. Ziolkowski, *J. Mol. Catal.* **1981**, *11*, 371–381; f) S. Uemura, S. R. Patil, *Chem. Lett.* **1982**, *11*, 1743–1746; g) G. Rousselet, C. Chassagnard, P. Capdevielle, M. Maumy, *Tetrahedron Lett.* **1996**, *37*, 8497–8500; h) U. Schuchardt, M. C. Guerreiro, G. B. Shul'pin, *Russ. Chem. Bull.* **1998**, *107*, 247–252; i) E. D. Park, Y.-S. Hwang, J. S. Lee, *Catal. Commun.* **2001**, *2*, 187–190; j) G. Blay, I. Fernandez, T. Gimenez, J. R. Pedro, R. Ruiz, E. Pardo, F. Lloret, M. C. Munoz, *Chem. Commun.* **2001**, 2102–2103; k) G. Suss-Fink, L. G. Cuervo, B. Therrien, H. Stoeckli-Evans, G. B. Shul'pin, *Inorg. Chim. Acta* **2004**, *357*, 475–484; l) P.-G. Lassahn, V. Lozan, G. A. Timco, P. Christian, C. Janiak, R. E. P. Winpenny, *J. Catal.* **2004**, *222*, 260–267.

[3] S. G. Baca, I. G. Filippova, O. A. Gherco, M. Gdaniec, Yu. A. Simonov, N. V. Gerbeleu, P. Franz, R. Basler, S. Decurtins, *Inorg. Chim. Acta* **2004**, *357*, 3419–3429.

[4] R. C. Squire, S. M. J. Aubin, K. Folting, W. E. Streib, D. N. Hendrickson, G. Christou, *Angew. Chem. Int. Ed. Engl.* **1995**, *34*, 887–889.

 © 2005 Wiley-VCH Verlag GmbH & Co. KGaA, Weinheim

[5] R. C. Squire, S. M. J. Aubin, K. Folting, W. E. Streib, G. Christou, D. N. Hendrickson, *Inorg. Chem.* **1995**, *34*, 6463–6471.
[6] E. K. Brechin, R. O. Gould, S. G. Harris, S. Parsons, R. E. P. Winpenny, *J. Am. Chem. Soc.* **1996**, *118*, 11293–11294.
[7] E. K. Brechin, S. G. Harris, S. Parsons, R. E. P. Winpenny, *Chem. Commun.* **1996**, 1439–1440.
[8] E. K. Brechin, A. Graham, A. Parkin, S. Parson, A. M. Seddon, R. E. P. Winpenny, *J. Chem. Soc., Dalton Trans.* **2000**, 3242–3252.
[9] C. Cañada-Vilalta, M. Pink, G. Christou, *Dalton Trans.* **2003**, 1121–1125.
[10] N. V. Gerbeleu, Yu. A. Simonov, G. A. Timko, P. N. Bourosh, J. Lipkowski, S. G. Baka, D. I. Saburov, M. D. Mazus, *Russ. J. Inorg. Chem.* **1999**, *44*, 1191–1204.
[11] S. G. Baca, Yu. A. Simonov, N. V. Gerbeleu, M. Gdaniec, P. N. Bourosh, G. A. Timco, *Polyhedron* **2001**, *20*, 831–837.
[12] Yu. A. Simonov, M. Gdaniec, I. G. Filippova, S. G. Baca, G. A. Timco, N. V. Gerbeleu, *Russ. J. Coord. Chem.* **2001**, *27*, 353–359.
[13] S. G. Baca, I. G. Filippova, N. V. Gerbeleu, Yu. A. Simonov, M. Gdaniec, G. A. Timco, O. A. Gherco, Yu. L. Malaestean, *Inorg. Chim. Acta* **2003**, *344*, 109–116.
[14] S. G. Baca, Yu. A. Simonov, M. Gdaniec, N. V. Gerbeleu, I. G. Filippova, G. A. Timco, *Inorg. Chem. Commun.* **2003**, *6*, 685–689.
[15] S. G. Baca, S. T. Malinovskii, P. Franz, Ch. Ambrus, H. Stoeckli-Evans, N. Gerbeleu, S. Decurtins, *J. Solid State Chem.* **2004**, *177*, 2841–2849.
[16] Yu. A. Simonov, S. G. Baca, I. G. Filippova, M. Gdaniec, O. A. Gherco, N. V. Gerbeleu, *Russ. J. Coord. Chem.* **2004**, *30*, 727–732.
[17] P. Lightfoot, A. Snedden, *J. Chem. Soc., Dalton Trans.* **1999**, 3549–3551.
[18] S.-L. Ma, D.-Z. Liao, Z.-H. Jiang, S.-P. Yan, F.-C. Xue, G.-L. Wang, *Synth. React. Inorg. Met.-Org. Chem.* **1994**, *24*, 137–146.
[19] a) D. Poleti, D. R. Stojakovic, B. V. Prelesnik, Lj. Manojlovic-Muir, *Acta Crystallogr.* **1990**, *46*, 399–402; b) D. Poleti, D. R. Stojakovic, *Thermochim. Acta* **1992**, *205*, 225–233.
[20] E. C. Niederhoffer, A. E. Martell, P. Rudolf, A. Clearfield, *Inorg. Chem.* **1982**, *21*, 3734–3741.
[21] J. E. Arenas, J. I. Marcos, *Spectrochim. Acta* **1980**, *36*, 1075–1081.
[22] G. B. Deacon, R. J. Phillips, *Coord. Chem. Rev.* **1980**, *33*, 227–250.
[23] D. M. Palade, E. S. Il'ina, G. V. Chudaeva, *Zh. Neorg. Khim.* **1972**, *17*, 2480–2485; *Chem. Abstr.* **1973**, *78*, 51908v.
[24] J. Kitchen, J. L. Bear, *Thermochim. Acta* **1970**, *1*, 537–544.
[25] J. Sun, L. Yuan, K. Zhang, D. Wang, *Thermochim. Acta* **2000**, *343*, 105–109.
[26] E. M. Abd Alla, M. I. Abdel-Hamid, *J. Therm. Anal. Calorim.* **2000**, *62*, 769–780.
[27] K. Das, U. C. Sinha, C. Chaterjee, A. Mishnev, *Z. Kristallogr.* **1993**, *205*, 316–318.
[28] E. D. Mckenzie, *J. Chem. Soc. A* **1969**, 1655–1667.
[29] Ch. Janiak, *J. Chem. Soc., Dalton Trans.* **2000**, 3885–3896.
[30] D. Braga, A. Angeloni, L. Maini, A. W. Gotz, F. Grepioni, *New J. Chem.* **1999**, *23*, 17–24.
[31] D. Poleti, L. Karanovic, B. V. Prelesnik, *Acta Crystallogr., Sect. C* **1990**, *46*, 2465–2467.
[32] S. G. Baca, I. G. Filippova, P. Franz, Ch. Ambrus, M. Gdaniec, H. Stoeckli-Evans, Yu. A. Simonov, O. A. Gherco, T. Bejan, N. Gerbeleu, S. Decurtins, *Inorg. Chim. Acta* **2005**, *358*, 1762–1770.
[33] J.-C. Yao, W. Huang, B. Li, S. Gou, Y. Xu, *Inorg. Chem. Commun.* **2002**, *5*, 711–714.
[34] S. M. Ostrovsky, R. Werner, D. A. Brown, W. Haase, *Chem. Phys. Lett.* **2002**, *353*, 290–294.
[35] O. Kahn, *Molecular Magnetism*, Wiley-VCH, New York, **1993**, p. 42.
[36] J. J. Borrás-Almenar, J. M. Clemente-Juan, E. Coronado, B. S. Tsukerblatt, *Inorg. Chem.* **1999**, *38*, 6081–6088.
[37] D. Belletti, *A new hardware and software system for Controlling an Enraf Nonius CAD4 single crystal diffractometer*; Centro di Studio per la Strutturistica Diffrattometrica del CNR, Parma, Italy; Interna Report 1-97, **1997**.
[38] G. M. Sheldrick, *SHELXS-97*, Universität Göttingen, Germany, **1997**.
[39] G. M. Sheldrick, *SHELXL-97*, Universität Göttingen, Germany, **1997**.

Received: January 5, 2005
Published Online: June 22, 2005

 © 2005 Wiley-VCH Verlag GmbH & Co. KGaA, Weinheim

Silanes/Oxygen/(Water): Green High-Energy-Density Materials

Yi Hong Ding*[a] and Satoshi Inagaki*[b]

Keywords: Silanes / Green high-energy-density materials / Ab initio calculations / Bond energy

Design of green high-energy-density materials as powerful as the well-known H_2/O_2 and N_2H_4/O_2 systems is a never-ending goal. Here, we study the energetic properties of reactions of silanes with oxygen (and gaseous water) by the bond energy procedure and high-level quantum chemistry calculations. The silanes/oxygen/(water) reactions finally lead to the green products, namely silica and water or silicic acids that exist in nature. The energy densities of these systems with respect to silica and water are higher than those of the conventional H_2/O_2 and N_2H_4/O_2 systems. Their energy densities with respect to silicic acids are also higher than or comparable to that of the N_2H_4/O_2 system. We propose that silanes/oxygen/(water) could be powerful green high-energy-density materials.
(© Wiley-VCH Verlag GmbH & Co. KGaA, 69451 Weinheim, Germany, 2005)

Introduction

Recently, high-energy-density materials (HEDM) have received considerable attention as energetic carriers and fuels in various fields.[1] On the other hand, green chemistry is actively seeking ways to produce materials benign to human health and the environment.[2] We proposed[3] green high-energy-density materials (green HEDM), which should satisfy four conditions: (i) they should have high energy densities; (ii) they should have considerable kinetic stability; (iii) the predominant products of the reactions should be green compounds, i.e., species benign to human health and environment, especially ones, e.g., N_2, H_2O, silica, etc., which exist in nature; and (iv) the possibility to actually synthesize them for practical use should be high. We previously designed seven N_2H_2O isomers as potential "green HEDMs" that might produce the green exhausts N_2 and H_2O.[3] In fact, the greenness of energetic materials has received recent attention.[4,5]

The bimolecular H_2/O_2 and N_2H_4/O_2 systems are conventional HEDMs, which can produce green exhausts (H_2O and N_2) from the reactions $H_2 + ½\ O_2 \rightarrow H_2O$ and $N_2H_4 + O_2 \rightarrow N_2 + 2\ H_2O$. Here we report a new type of bi- or termolecular green HEDMs: silanes/oxygen/(water) systems. By means of the bond energy procedure and high-level theoretical computations, we find that the energy densities of all the systems are higher than or comparable to those of the conventional H_2/O_2 and N_2H_4/O_2 systems. To the best of our knowledge, this represents the first consideration of the silanes as "**green HEDMs**", although the self-ignition and explosiveness of monosilane (SiH_4) in air has long been known, and SiH_4 has been widely used in the semiconductor industries.[6,7]

[a] State Key Laboratory of Theoretical and Computational Chemistry, Institute of Theoretical Chemistry, Jilin University, Changchun 130023, People's Republic of China
[b] Department of Chemistry, Faculty of Engineering, Gifu University, Yanagido, Gifu 501–1193, Japan

Results and Discussion

In the present work, we investigate the energetic properties of the reactions (Scheme 1) of silanes (Si_nH_m) (Figure 1) including acyclic silanes (1 Si_nH_{2n+2}), cyclic silanes (2 Si_nH_{2n}), ladder silanes (3 $Si_{2n}H_{2n+4}$), and cage silanes (4 $Si_{2n}H_{2n}$).

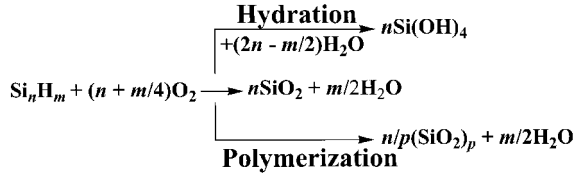

Scheme 1.

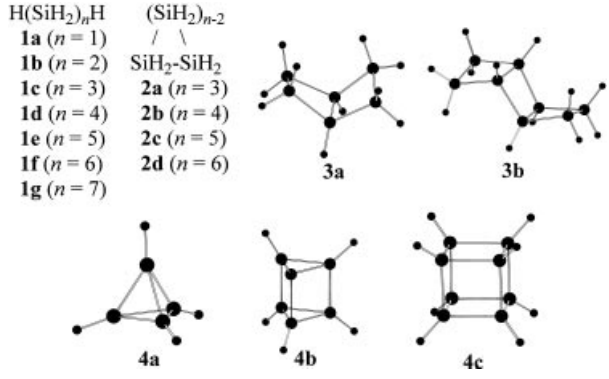

Figure 1.

 DOI: 10.1002/ejic.200500007 © 2005 Wiley-VCH Verlag GmbH & Co. KGaA, Weinheim

The combustion of SiH_4 ($SiH_4 + 2\ O_2 \rightarrow SiO_2 + 2\ H_2O$) releases energy (190.31 kcal/mol at the CBS-QB3 level). The energy density (ED in cal/g) for a reaction system is defined as the released energy (ΔE in cal/mol) divided by the mollar mass (M in g/mol). The molar masses of the elements H, N, O and Si are taken as 1, 14, 16 and 28 g/mol, respectively. The energy density of the SiH_4/O_2 system was calculated to be 1982 cal/g with respect to the products SiO_2 and H_2O. This value is close to that (2191 cal/g) of the known N_2H_4/O_2 system with respect to N_2 and H_2O. Yet, it is still lower than that (3108 cal/g) of the H_2/O_2 system with respect to H_2O. The products SiO_2 and H_2O can further undergo a hydration reaction and increase the energy density of the SiH_4/O_2 system. Two H_2O molecules were found to undergo a stepwise, barrierless addition to the Si=O double bonds of SiO_2, producing monosilicic acid $Si(OH)_4$.[8] The heat of the hydration, $SiO_2 + 2\ H_2O \rightarrow Si(OH)_4$, is 135.73 kcal/mol. The total released energy for $SiH_4 + 2\ O_2 \rightarrow Si(OH)_4$ is thus 326.04 kcal/mol (190.31 + 135.73). The hydration increases the energy density by 1414 cal/g ($135.73 \times 1000/96$). The energy density of the SiH_4/O_2 system with respect to the product $Si(OH)_4$ was calculated to be surprisingly high (3396 cal/g), as high as that (3108 cal/g) of the H_2/O_2 system and much higher than that (2191 cal/g) of the N_2H_4/O_2 system.

Higher silanes need water to be fully converted to $Si(OH)_4$ (see Scheme 1, $n \geq 2$). As listed in Table 1, the energy densities of the seven acyclic silane $(Si_nH_{2n+2})/O_2/H_2O$ systems with respect to $Si(OH)_4$ lie between 3396 ($n = 1$) and 2904 cal/g ($n = 7$) at the CBS-QB3 level. For the four cyclic silane $(Si_nH_{2n})/O_2/H_2O$ systems, the energy densities are between 2944 ($n = 3$) and 2819 cal/g ($n = 6$). The two ladder silane $(Si_{2n}H_{2n+4})/O_2/H_2O$ systems have the energy densities 2760 ($n = 3$) and 2709 cal/g ($n = 4$). The three cage silanes $(Si_{2n}H_{2n})/O_2/H_2O$ have the energy densities 2826, 2672 and 2606 cal/g for $n = 2$–4, respectively. The silanes/oxygen/water examined here by the high-level CBS-QB3 calculations are as powerful HEDMs as the H_2/O_2 or N_2H_4/O_2 systems. The energy densities of SiH_4/O_2 and $Si_2H_6/O_2/H_2O$ are even higher than that of H_2/O_2.

The high-level CBS-QB3 calculations are rather expensive for much larger silanes/oxygen/(water) systems. We employed a semiquantitative bond energy procedure on the assumption of the locality of chemical bonds. The bond energy (BE) is usually defined as the energy required to break a covalent bond in a gaseous substance. Computationally, for a diatomic molecule AB, the A–B bond energy is defined as $BE(A–B) = E(AB) – E(A) – E(B)$, in which $E(X)$ means the total energy of an atom or a molecule X. Then, the bond energy differences between the reactants and products in a chemical reaction are used to estimate the reaction heat. In more detail, for a typical reaction between two diatomic molecules: A–A + B–B → 2 A–B, the reaction heat is described as $\Delta E = 2BE(A–B) – BE(A–A) – BE(B–B)$. At the CBS-QB3 level, the bond energies are calculated to be 109.87 (O–H), 118.71 (O=O), 76.43 (Si–H), 107.42 (Si–O), 146.98 (Si=O), and 45.49 (Si–Si) kcal/mol.[9] The reaction heats (ΔE in kcal/mol) and energy densities (ED in cal/g) of the $Si_nH_m/O_2/H_2O$ systems with respect to $Si(OH)_4$ can be expressed[10,11] by Equation (1)

$$\Delta E = 219.99n + 26.507m \quad (1)$$

and Equation (2)

$$ED = 2291.563 + 276.115/(n/m) \quad (2)$$

As shown in Table 1, the energy densities of the 16 silane $(Si_nH_m)/O_2/H_2O$ systems with respect to $Si(OH)_4$ estimated from the bond energies are very close to the values predicted by the fully geometry-optimized CBS-QB3 calculations. The relatively large errors (100, 258 and 104 cal/g for **1a**, **4a** and **4b**) are caused by the high strain of the three-membered rings. The generally good agreement of the energy densities between the bond energy procedure and high-

Table 1. The energy density (in cal/g) of silanes (Si_nH_m)/oxygen/(water) with respect to silic acid based on the CSB-QB3 (ED1//CBS-QB3) and bond energy (ED1//bond energy) calculations, and with respect to silica based on bond energy (ED2//bond energy) calculations.

Si_nH_m Species	ED1//CBS-QB3	ED1//Bond energy	ED2//Bond energy
SiH_4 (**1a**)	3396	3396	3396
Si_2H_6 (**1b**)	3120	3120	3443
Si_3H_8 (**1c**)	3020	3028	3460
Si_4H_{10} (**1d**)	2970	2982	3470
Si_5H_{12} (**1e**)	2939	2954	3476
Si_6H_{14} (**1f**)	2918	2936	3480
Si_7H_{16} (**1g**)	2904	2923	3482
Si_3H_6 (**2a**)	2944	2844	3500
Si_4H_8 (**2b**)	2858	2844	3500
Si_5H_{10} (**2c**)	2828	2844	3500
Si_6H_{12} (**2d**)	2819	2844	3500
Si_6H_{10} (**3a**)	2760	2752	3522
Si_8H_{12} (**3b**)	2709	2706	3534
Si_4H_4 (**4a**)	2826	2568	3572
Si_6H_6 (**4b**)	2672	2568	3572
Si_8H_8 (**4c**)	2606	2568	3572

 © 2005 Wiley-VCH Verlag GmbH & Co. KGaA, Weinheim

level CBS-QB3 calculations suggests the reliability and usefulness of the bond energy procedure.

Gaseous silicon dioxide can also polymerize to silica $(SiO_2)_p$ to increase the energy density of the Si_nH_m/O_2 systems. Similar accurate evaluation of the reaction heats and energy densities with respect to silica is surely impossible because of the infinite structure of silica. We applied the bond energy procedure. The heat of the reaction: $SiO_2 \rightarrow 1/p(SiO_2)_p$ is calculated from the bond energies to be 135.72 kcal/mol ($107.42 \times 4 - 146.98 \times 2$).[12] This is the same value as that estimated for the hydration because the same numbers of each kind of bonds are broken or formed in the polymerization and the hydration. The reaction heats and energy densities of the $(Si_nH_m)/O_2$ systems with respect to silica and water can be generally expressed by Equation (3)[12,13]

$$\Delta E = 219.99n + 26.507m \quad (3)$$

and Equation (4)

$$ED = 3666.500 - 108.192/(n/m + 0.15) \quad (4)$$

The heat (326.02 kcal/mol) of the reaction $SiH_4 + 2\ O_2 \rightarrow$ silica$[1/p(SiO_2)_p] + 2\ H_2O$ estimated from the bond energy procedure is in excellent agreement with the experimental value of 325.2 ± 1.2 kcal/mol.[14] The estimated reaction heats for the transformation of other silanes (599.02 for Si_2H_6, 872.03 for Si_3H_8, and 1145.03 kcal/mol for Si_4H_{10}) in the gas phase to silica are a little larger than those (573.3, 835.1 ± 0.7 and 1092.4 kcal/mol, respectively[14]) observed for liquid Si_2H_6, Si_3H_8 and Si_4H_{10}; this discrepancy is due to the latent heat of vaporization. With respect to the products silica and water, all of the 16 silanes have energy densities equal to or higher than that (3396 cal/g) of SiH_4 (Table 1), which is higher than that of the H_2/O_2 system. When the increment caused by strain is taken into account, the energy densities of Si_3H_6, Si_4H_4, and $Si_6H_6/O_2/H_2O$ with respect to silica and water are expected to be as high as 3600, 3830, and 3676 cal/g, respectively.

The bond energy procedure shows that the energy densities of the $Si_nH_m/O_2/H_2O$ systems depend on the Si/H ratio (n/m). The energy density with respect to silicic acid increases as the Si/H ratio decreases: 2292 ($n/m \rightarrow \infty$) $<$ ED $\leq$ 3396 (n/m = ¼), while that with respect to silica and water increases with the Si/H ratio: 3396 (n/m = ¼) $\leq$ ED $\leq$ 3667 ($n/m \rightarrow \infty$). The upper limit (3396 cal/g) of the energy density with respect to silicic acid is identical to the lower limit with respect to silica and water. This clearly shows that the polymerization is preferable to the hydration because stable water is needed to complete the hydration. A high Si/H ratio is unfavorable for the energy density with respect to silicic acid, yet it is desirable for the energy density with respect to silica and water. The largest energy density (3667 cal/g) is expected for the combustion of the silane Si_nH_m ($n/m \rightarrow \infty$) followed by the polymerization to silica. The limit "$n/m \rightarrow \infty$" means pure silicon. The bond energy procedure also shows that the silanes with the same Si/H ratio (n/m) have the same energy densities. The cage silanes $(Si_{2n}H_{2n})/O_2/H_2O$ (n/m = 1) have higher energy densities than the cyclic silanes $(Si_nH_{2n})/O_2/H_2O$ (n/m = 0.5) with respect to silica and water, while the opposite is the case with the energy with respect to silicic acid.

The final products of the silane/oxygen/(water) systems, i.e., monosilicic acid $Si(OH)_4$, silica and water, all exist in nature and do no harm to the environment or humans. Monosilicic acid $Si(OH)_4$ is known to be "the dominant form of silicon in natural waters."[15] Silica is abundant[16] and "green"! Monosilane (**1a**) and disilane (**1b**) are now readily available commercially. The acyclic (**1c**,[17] **1d**[17] and **1e**[18]) and cyclic (**2c**[19] and **2d**[20]) silanes have already been synthesized in laboratory. The substituted species of cyclic (**2a**[21] and **2b**[22]), ladder (**3a**[23] and **3b**[24]), and cage (**4a**,[25] **4b**[26] and **4c**[27]) silanes have also been synthesized. Surely, here we only present a limited number of silanes (**1**–**4**) as examples. Given the molecular formula Si_mH_n, silanes could have various structural forms ranging from chainlike, cyclic, ladder, and even cage-type species. The green HEDMs with higher Si/H ratios have larger power. From a synthetic viewpoint, silyl (Si_pH_{2p+1}) derivatives of cyclic and cage silanes are also expected to be promising as green HEDMs.[28] Thus, silanes satisfy the green HEDM conditions (ii) considerable kinetic stability and (iv) high possibility of synthesis.

We are aware that the simplest SiH_4/O_2 system has already been utilized in a microengine for explosive combustion.[6] From the preceding discussions, we know that with respect to the green products $SiO_2 + H_2O$, the power of Si_nH_m/O_2 is between 3396 (n/m = 1/4) $\leq$ ED $\leq$ 3667 ($n/m \rightarrow \infty$). Surely, the power of SiH_4/O_2 is just the lower limit. So there is great hope to design various types of silane systems more powerful than the SiH_4/O_2 system. We optimistically hope that many kinds of interesting and powerful silanes could be synthesized in future as green HEDMs because only the Si/H ratio and strain determines the power. The systems are not only powerful but also "green". We also know that alkenyl silanes such as tetraallylsilane[29] and triallylsilane[30] and alkynyl silanes have been used as igniters. But such systems are surely much less powerful than our designed Si_nH_m systems because they have much lower Si/H ratios.

Conclusion

In summary, silanes/oxygen/(water) systems are green HEDMs. The energy densities of these systems are higher than or comparable to the conventional H_2/O_2 and N_2H_4/O_2 systems. The Si/H ratio together with ring strain is important for the HEDM power of silanes.

Computational Section

For the small and medium-sized silanes/oxygen/(water) systems producing silicic acid, ab initio calculations are performed to obtain the heat of reaction using the composite CBS-QB3 method that is incorporated in the Gaussian program package.[32] This method follows the complete basis set, CBS-Q, model chemistry

 © 2005 Wiley-VCH Verlag GmbH & Co. KGaA, Weinheim

using B3LYP hybrid density functional geometries and frequencies, and has been demonstrated to have high accuracy on a variety of thermochemical properties.[33]

We apply the bond energy procedure for the larger reaction systems producing silicic acid and all the reaction systems producing silica. The bond energies are calculated by the CBS-QB3 method, which is known to give the atomic energies through inclusion of the atomic spin-orbit interactions (readily available from experiment) consistent with the experimental heats of formation of the atoms, although no relativistic corrections are made.[33]

The less computationally expensive B3LYP method underestimates the energy density of the silanes/oxygen/(water) systems. In fact, the energy densities of the SiH_4, Si_2H_6, Si_3H_8, and $Si_7H_{16}/O_2/(H_2O)$ reaction systems with respect to $Si(OH)_4$ are 2782, 2591, 2524, and 2446 cal/g,[31] which are significantly lower than the CBS-QB3 values (3396, 3120, 3020, and 2904 cal/g, respectively).

Acknowledgments

This work was supported by a Grant-in-Aid from the Japanese Society for the Promotion of Science (JSPS). One of the authors (YHD) thanks JSPS for a postdoctoral fellowship for foreign researchers (No. P01272). YHD is also grateful for the support of the National Natural Science Foundation of China (20103003) and the Excellent Young Teacher Foundation of the Ministry of Education of China.

[1] R. J. Bartlett, *Chemistry and Industry* **2000**, *4*, 140–143.
[2] M. Poliakoff, P. Anastas, *Nature* **2001**, *413*, 257.
[3] Y. H. Ding, S. Inagaki, *Chem. Lett.* **2003**, *32*, 304–305.
[4] T. M. Klapotke, G. Holl, *Green Chemistry* **2001**, G75, 3.
[5] J. Giles, *Nature* **2004**, *427*, 580–581.
[6] A. Mehra, X. Zhang, A. A. Ayon, I. A. Waitz, M. A. Schmidt, C. M. Spadaccini, *J. Microelectromech. S.* **2000**, *9*, 517–527.
[7] C. Ennis, *Chemistry Review* **2002**, *12(2)*, 2–6.
[8] All the intermediates and transition states involved in the addition reaction of two H_2O molecules to SiO_2 lie energetically lower than $SiO_2 + 2H_2O$.
[9] The following reactions: $H_2O \rightarrow 2H + {}^3O$, ${}^3O_2 \rightarrow 2\,{}^3O$, $SiH_4 \rightarrow {}^3Si + 4H$, $Si(OH)_4 \rightarrow {}^3Si + 4^3O + 4H$, $SiO_2 \rightarrow {}^3Si + 2^3O$ and $Si_2H_6 \rightarrow 2^3Si + 6H$ are used to calculate the bond energies of the O–H, O=O, Si–H, Si–O, Si=O, and Si–Si bonds that are involved in the reaction systems. Take the reaction $H_2O \rightarrow 2H + {}^3O$ as an example. The CBS-QB3 total energies of H_2O, H, and ${}^3O$ are –76.337462, –0.499818, and –74.987638 a. u., respectively. The energy required to break all the bonds of H_2O is $\Delta E = |2\times(-0.499818) + (-74.987638) - (-76.337462)|$ a. u. = 219.746 kcal/mol. Then the average O–H bond energy is BE(O–H) = 219.746/2 = 109.87 kcal/mol.
[10] In silanes, each Si atom is bonded to four Si or H atoms and each H atom to one Si atom. So there are $(4n - m)/2$ Si–Si and m Si–H bonds in one Si_nH_m.
[11] The calculation details of the reaction heats (ΔE) and energy densities (ED) of $Si_nH_m + (n + m/4)\,O_2 + (2n - m/2)H_2O \rightarrow n\mathrm{Si(OH)_4}$ are as follows: $\Delta E = [4n\times\mathrm{BE(Si–O)} + 4n\times\mathrm{BE(O–H)}] - [(4n - m)/2\times\mathrm{BE(Si–Si)} + \mathrm{m}\times\mathrm{BE(Si–H)} + (n + m/4)\times\mathrm{BE(O{=}O)} + (2n - m/2)\times 2\times\mathrm{BE(O–H)}] = [4\times\mathrm{BE(Si–O)} - 2\times\mathrm{BE(Si–Si)} - \mathrm{BE(O{=}O)}]n + [\tfrac{1}{2}\times\mathrm{BE(Si–Si)} - \mathrm{BE(Si–H)} - \tfrac{1}{4}\times\mathrm{BE(O{=}O)} + \mathrm{BE(O–H)}]m = 219.99n + 26.507m$ kcal/mol. The molar mass of $n\mathrm{Si(OH)_4}$ is $M = 96n$ g/mol. So $\mathrm{ED} = 1000\times\Delta E/M = 2291.563 + 276.115/(n/m)$.
[12] Suppose the polymerization: $SiO_2 \rightarrow 1/p(SiO_2)_p$. In silica [$1/p(SiO_2)_p$], each Si atom in the center of a tetrahedron is bonded to four O atoms. Each O-atom is bonded to two Si atoms. There are 2×2 Si–O bonds around the two O atoms. The total Si–O number is 8 (4 + 2×2). Because each bond is shared by two atoms, the exact number of the Si–O bonds in $1/p(SiO_2)_p$ is 8/2 = 4. As a result, in the polymerization process, two Si=O bonds in each SiO_2 molecule are transformed into four Si–O bonds in silica.
[13] For the $Si_nH_m + (n + m/4)\,O_2 \rightarrow n/p(SiO_2)_p + m/2H_2O$ process, the reaction heats are $\Delta E = 219.99\,n + 26.507m$ kcal/mol, the same as those for the $Si_nH_m + (n + m/4)O_2 + (2n - m/2)H_2O \rightarrow n\mathrm{Si(OH)_4}$ process. The molar mass of $n/p(SiO_2)_p + m/2H_2O$ is $M = 60n + 9m$ g/mol. So $\mathrm{ED} = 1000\times\Delta E/M = 3666.500 - 108.192/(n/m + 0.15)$ cal/g.
[14] F. Feher, G. Jansen, H. Rohmer, *Angew. Chem.* **1963**, *75*, 859; *Angew. Chem. Int. Ed. Engl.* **1963**, *2*, 617–618.
[15] M. Freemantle, *Chem. Eng. News* **2002**, *80*, 27.
[16] R. K. Iler, *The Chemistry of Silica*, John Wiley & Sons, New York, **1979**.
[17] E. D. Spanier, A. G. MacDiarmid, *Inorg. Chem.* **1962**, *1*, 432–433.
[18] H. Bock, W. Ensslin, F. Feher, R. Freund, *J. Am. Chem. Soc.* **1996**, *98*, 668–674.
[19] E. Hengge, G. Bauer, *Angew. Chem.* **1973**, *85*, 304–305; *Angew. Chem. Int. Ed. Engl.* **1973**, *12*, 316.
[20] E. Hengge, K. Dieter, *Angew. Chem.* **1977**, *89*, 417–418; *Angew. Chem. Int. Ed. Engl.* **1977**, *16*, 403.
[21] S. Masamune, Y. Hanzawa, S. Murakami, T. Bally, J. F. Blount, *J. Am. Chem. Soc.* **1982**, *104*, 1150–1153.
[22] E. Hengge, K. Dieter, *Angew. Chem.* **1981**, *93*, 698–701; *Angew. Chem. Int. Ed. Engl.* **1981**, *20*, 678.
[23] H. Matsumoto, H. Miyamoto, N. Kojima, Y. Nagai, *J. Chem. Soc., Chem. Commun.* **1987**, *17*, 1316–1317.
[24] S. Kyushin, M. Kawabata, Y. Yagihashi, H. Matsumoto, M. Goto, *Chem. Lett.* **1994**, *6*, 997–1000.
[25] N. Wiberg, C. M. M. Finger, K. Polborn, *Angew. Chem. Int. Ed. Engl.* **1993**, *32*, 1054–1056.
[26] A. Sekiguchi, T. Yatabe, C. Kabuto, H. Sakurai, *J. Am. Chem. Soc.* **1993**, *115*, 5853–5854.
[27] H. Matsumoto, K. Higuchi, Y. Hitoshi, H., Koike, Y. Naoi, Y. Nagai, *J. Chem. Soc., Chem. Commun.* **1988**, *16*, 1083–1084.
[28] On the basis of Equation (2) and Equation (4), the energy densities of silyl derivatives $Si_n(Si_pH_{2p+1})_m$ ($p \geq 1$) are $\mathrm{ED^*} = 2291.563 + 276.115/[(n + pm)/(2\,pm + m)]$ with respect to silicic acid, and $\mathrm{ED^{**}} = 3666.500–108.192/[(n + pm)/(2\,pm + m) + 0.15]$ with respect to silica and water.
[29] R. A. Fernandes, Y. Yamamoto, *J. Org. Chem.* **2004**, *69*, 735–738.
[30] C. Drohmann, M. Moller, O. B. Gorbatsevich, A. M. Muzafarov, *J. Polym. Sci. Pol. Chem.* **2000**, *38*, 741–751.
[31] At the B3LYP/6-31G(d) level with zero-point energy correction, the total energies are –291.852380 a. u. for SiH_4, –582.533442 a. u. for Si_2H_6, –873.216264 a. u. for Si_3H_8, –2035.948702 a. u. for Si_7H_{16}, –150.316262 a. u. for O_2, –76.387799 a. u. for H_2O and –592.910478 a. u. for $Si(OH)_4$.
[32] M. J. Frisch, G. W. Trucks, H. B. Schlegel, G. E. Scuseria, M. A. Robb, J. R. Cheeseman, V. G. Zakrzewski, J. A. Montgomery, R. E. Stratmann, J. C. Burant, S. Dapprich, J. M. Millam, A. D. Daniels, K. N. Kudin, M. C. Strain, O. Farkas, J. Tomasi, V. Barone, M. Cossi, R. Cammi, B. Mennucci, C. Pomelli, C. Adamo, S. Clifford, J. Ochterski, G. A. Petersson, P. Y. Ayala, Q. Cui, K. Morokuma, D. K. Malick, A. D. Rabuck, K. Raghavachari, J. B. Foresman, J. Cioslowski, J. V. Ortiz, B. B. Stefanov, G. Liu, A. Liashenko, P. Piskorz, I. Komaromi, R. Gomperts, R. L. Martin, D. J. Fox, T. Keith, M. A. Al-Laham, C. Y. Peng, A. Nanayakkara, C. Gonzalez, M. Challacombe, P. M. W. Gill, B. G. Johnson, W. Chen, M. W. Wong, J. L. Andres, M. Head-Gordon, E. S. Replogle, J. A. Pople, *Gaussian 98* (Revision A.7), Gaussian, Inc., Pittsburgh, PA, **1998**..
[33] J. A. Montgomery, Jr., M. Frisch, J. W. Ochterski, G. A. Petersson, *J. Chem. Phys.* **1999**, *110*, 2822–2827.

Received: January 05, 2005
Published Online: June 22, 2005

 © 2005 Wiley-VCH Verlag GmbH & Co. KGaA, Weinheim

Ruthenium Complexes of the Scorpionate Ligand Bis(3,5-dimethylpyrazol-1-yl)-dithioacetate and the Effect of Nitric Oxide Coordination

Mayreli Ortiz,[a] Ariadna Penabad,[a] Alicia Díaz,[a] Roberto Cao,*[a] Antonio Otero,[b] Antonio Antiñolo,[b] and Agustín Lara[b]

Keywords: N ligands / Nitric oxide / Ruthenium / S ligands / Scorpionate ligands

Six new ruthenium(II) complexes with the scorpionate ligand bis(3,5-dimethylpyrazol-1-yl)dithio-κ^3N,N,S-acetate (bdmpzdta) were obtained by treatment of the ligand with $RuCl_3$ or $[RuCl_3(NO)]$ in 1:1 or 2:1 molar ratios in the presence or absence of ethylenediamine. In all six complexes the pyrazolic rings lie in the equatorial plane. The mononitrosyl complexes present a sharp ν(NO) band in the range 1864–1859 cm^{-1} for samples prepared either as KBr tablets or dichloromethane solutions. In the case of $[Ru(NO)(bdmpzdta)_2]Cl$ (**7**), the dithiocarboxylate group of one of the ligands is not coordinated (κ^2N,N). In the other five complexes, however, bdmpzdta behaves as a κ^3N,N,S scorpionate ligand. When the complexes obtained from $RuCl_3$ were dissolved in dichloromethane and NO was bubbled through the solution, a high degree of coordination of NO^+ was observed, according to IR, UV and voltammetric studies.
(© Wiley-VCH Verlag GmbH & Co. KGaA, 69451 Weinheim, Germany, 2005)

Introduction

The physiological functions of nitric oxide (NO) have been widely studied in the past decade as dysfunction in NO metabolism has been associated with a great number of diseases.[1,2] When a patient has a severe infection, as in so-called septic shock, the body generates such a large amount of nitric oxide that the patient's blood pressure practically collapses. A specific inhibitor for induced nitric oxide synthase, iNOS, has yet to be found. An alternative to save patients' lives in cases of septic shock involves finding NO scavengers that can be used when NO is produced in relatively large amounts.

Ru^{III} complexes are known to coordinate NO to form stable Ru^{II} mononitrosyl complexes and these can therefore act as efficient NO scavengers. A number of different Ru^{III} complexes with polyaminocarboxylic acids have been studied as NO scavengers.[3–5]

Recently, we reported different ruthenium(II) complexes with the bis(3,5-dimethylpyrazol-1-yl)methane derivatives bis(3,5-dimethylpyrazol-1-yl)methanesulfonate (bdmpzsa) and bis(3,5-dimethylpyrazol-1-yl)acetate (bdmpza).[6,7] Both ligands lie in the equatorial plane and coordinate as κ^3N,N,O scorpionates, but with a weak interaction through the oxyanionic moiety. Mononitrosyl complexes of Ru^{II} were also obtained from the same ligands with NO coordinated in the apical position.[7] NO was found to have a strong *trans* influence on the oxyanionic moiety. As a consequence, the mononitrosyl bis(bis-pyrazolic) complexes of Ru^{II} show an on/off switching process of the oxyanionic moiety *trans* to the coordinated NO.

We report here the main results obtained on Ru^{II} complexes with a similar ligand: bis(3,5-dimethylpyrazol-1-yl)-dithioacetate (bdmpzdta; **1**), which is depicted in Figure 1. This ligand is expected to behave as a κ^3N,N,S scorpionate, but with a softer anionic moiety. For this reason, a higher scorpionate affinity for Ru^{II} than the previously studied bdmpza and bdmpzsa ligands is to be expected.

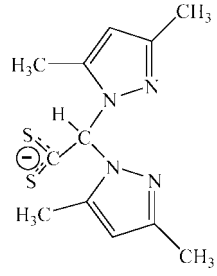

Figure 1. Schematic representation of ligand **1**.

Results and Discussion

In a previous paper,[6] we reported a kinetic study of the interaction of $RuCl_3$ with bis(3,5-dimethylpyrazol-1-yl)ace-

[a] Laboratorio de Bioinorgánica, Facultad de Química, Universidad de La Habana,
La Habana 10400, Cuba
Fax: +537-873-3502
E-mail: cao@fq.uh.cu
[b] Departamento de Química Inorgánica, Orgánica y Bioquímica, Facultad de Ciencias Químicas, Universidad de Castilla-La Mancha,
13071 Ciudad Real, Spain
Supporting information for this article is available on the WWW under http://www.eurjic.org or from the author.

tate (bdmpza; $k = 1.1 \times 10^{-3}$ s^{-1}), and bis(3,5-dimethylpyrazol-1-yl)methanesulfonate (bdmpzsa; $k = 1.6 \times 10^{-3}$ s^{-1}), in a 1:1 molar ratio in methanol. Coordination of the ligand involves the reduction of Ru^{III} to Ru^{II}. We assumed that the reducing agent was methanol, but could not detect the corresponding oxidation product. After this study was published, a signal at δ = 9.2–9.4 ppm, corresponding to methanal, was detected in the ^{1}H NMR spectra when the reaction was carried out in an NMR tube.

The interaction of $RuCl_3$ with bis(3,5-dimethylpyrazol-1-yl)dithioacetate (bdmpzdta; **1**) was studied spectrophotometrically in methanol in an effort to confirm the reduction of Ru^{III}, as observed previously with similar ligands. A decrease in the absorbance of the bdmpzdta band at 350 nm and the appearance and increase in the absorbance of the MLCT band at approximately 300 nm were observed (see Figure 2).

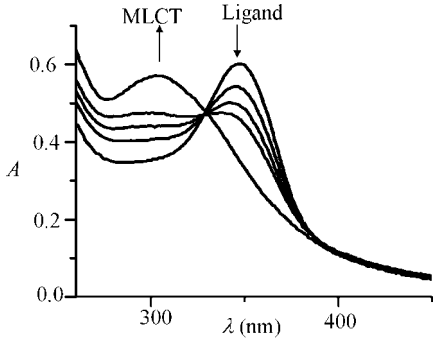

Figure 2. Variations in the UV/Visible spectra with time for the interaction of $RuCl_3$ with bdmpzdta (1:1 molar ratio) in methanol.

This MLCT band corresponds to the transition from Ru^{II} to **1**. A signal at δ = 9.35 ppm (due to methanal) was detected in the ^{1}H NMR spectra when the reaction was carried out in an NMR tube. From the variations observed in the MLCT band, pseudo first-order rate constants of $k = 1.2 \times 10^{-4}$ s^{-1} and 3.4×10^{-4} s^{-1} were obtained for 1:1 and 1:2 Ru^{III}:bdmpzdta molar ratios, respectively. Both values are ten times smaller than those reported previously for similar ligands (bdmpza and bdmpzsa).[6] Furthermore, with these latter ligands the rate constants for 1:2 molar ratios could not be detected using the same procedure.

The complete reduction of Ru^{III} was confirmed by EPR spectroscopy − all the complexes are silent. As one would expect, all NMR spectra contained sharp signals.

The interaction of ligand **1** with $RuCl_3$ gave the complexes $[\{Ru(H_2O)(bdmpzdta)(Cl)\}]_2$ (**2**), [Ru(bdmpzdta)(en)Cl] (**3**) and $[Ru(bdmpzdta)_2]$ (**4**) using procedures similar to those reported for bdmpza and bdmpzsa.[6] Similarly, $[RuNO(bdmpzdta)(Cl)_2]$ (**5**), $[RuNO(bdmpzdta)(en)]Cl_2$ (**6**) and $[RuNO(bdmpzdta)_2]Cl$ (**7**) were synthesised by the interaction of **1** with $[RuCl_3(NO)]$.

The ^{1}H and ^{13}C NMR spectra of **2**, **3**, **4**, **5** and **6** gave only one set of signals for the pyrazolic rings and ethylenediamine (**3**, **6**). In the case of compound **7** (Figure 3) this statement is not completely accurate since the signals of some of the atoms show a slight (or moderate) splitting. The observed equivalence in the NMR signals indicates that the pyrazolic rings of ligand **1** lie in the equatorial plane, as does the ethylenediamine unit in complexes **3** and **6** (Figure 3).

The composition and low solubility of complex **2** in polar organic solvents suggests a dimeric form in which the two chloride ions in the equatorial plane form bridges between the two Ru^{II} centres (Figure 3), similar to a previously reported structure.[8] Under such conditions, and with the water molecule (from $RuCl_3 \cdot xH_2O$) at the apical position *trans* to the coordinated dithiocarboxylate group, the two pyrazolic rings remain equivalent. Each of the two chloride anions in the equatorial plane of compound **5** is coordinated to one Ru^{II} (Figure 3) and the octahedral structure is achieved without the need for bridge formation.

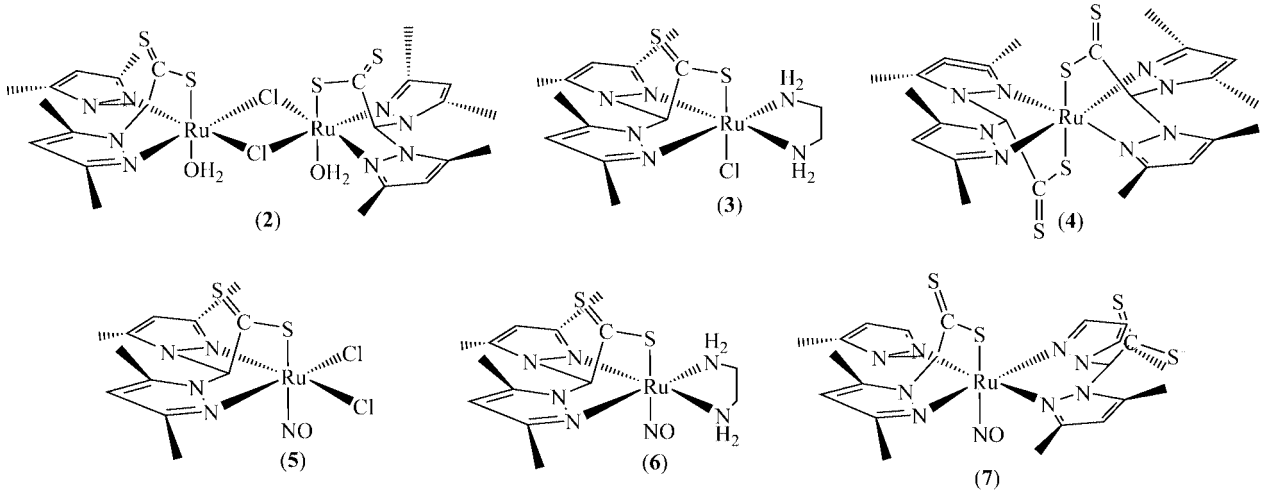

Figure 3. Schematic representation of the synthesised complexes **2**–**7**.

 © 2005 Wiley-VCH Verlag GmbH & Co. KGaA, Weinheim

As expected, the dithiocarboxylate group (a soft base) is very strongly coordinated at an apical position to Ru^{II} (soft acid) through a sulfur atom (Figure 3). Evidence for this structure is provided by the significant shift to higher field of the CS_2^- and aliphatic CH signals in the ^{13}C NMR spectra. Moreover, a significant shift in the $\nu_{C=S}$ and ν_{C-S} stretching bands is observed with respect to the IR spectrum of the free ligand. Coordination of the CS_2^- moiety to Ru^{II} is appreciably stronger than that observed for the CO_2^- moiety of bdmpza and the SO_3^- moiety of bdmpzsa, as reported previously.[6,7,9] Consequently, ligand **1** behaves as a κ^3N,N,S scorpionate ligand.

The strong coordination of the CS_2^- moiety should cause a slight distortion of the two pyrazolic rings in **1**. This distortion takes the rings out of the equatorial plane, although the effect is the same for both rings. This could be the reason why only one set of signals is observed even in the presence of this distortion. In this sense, it is interesting to point out that Otero et al. have investigated Ti^{IV}-bdmpzdta complexes and reported a distortion in the planarity of the pyrazolic rings.[10] In this latter case the soft CS_2^- moiety was coordinated to a hard acid (Ti^{IV}).

The interaction of ligand **1** with Ru^{II} should initially pass through the coordination mode κ^2N,N. The coordination of the CSS^- group should require additional energy and time in order to achieve the formation of the stable Ru^{II}–S bond. This process involves a distortion in the equatorial plane of the pyrazolic rings. Such a situation could explain the kinetically slow coordination of ligand **1** (ten times slower than for bdmpza and bdmpzsa).[6]

The coordination of NO in compounds **5**, **6** and **7** was fully characterised by IR spectroscopy. A sharp and intense band is observed at around 1860 cm^{-1} for all the mononitrosyl complexes, whether the samples were prepared as KBr tablets or CH_2Cl_2 solutions. This band was assigned to the ν(NO) stretching vibration and indicates that in these complexes NO is coordinated in a linear mode, as a $\{RuNO\}^6$ unit according to the Enemark–Feltham formalism.[11] As expected, these ν(NO) values are lower than that for the $[RuCl_3(NO)]$ starting material.

A single set of signals was observed for ligand **1** in the NMR spectra of compounds **5** and **6**, indicating that in the nitrosyl complexes NO is coordinated at the apical position *trans* to the bonded dithiocarboxylate moiety. It is worth pointing out that a single set of signals was also observed for ethylenediamine in compound **6**.

An interesting situation was found for $[Ru(bdmpzdta)_2NO]Cl$ (**7**) as the ^{13}C NMR spectrum (Figure 4) contains two signals for the CS_2^- group (δ = 211.0 and 243.2 ppm). The latter value corresponds to the free CS_2^- group that does not replace NO. In this complex one bdmpzdta is therefore coordinated as a bidentate ligand (κ^2N,N) and the other as a κ^3N,N,S scorpionate ligand. The difference between the two coordinated ligands in compound **7** is that the bidentate one is not distorted from the equatorial plane, while the scorpionate κ^3N,N,S ligand should be. This arrangement explains the observed splitting of the signals in the NMR spectra of **7**, an effect that is particularly significant for the aliphatic CH signal (Figure 4). The signal at δ = 70.3 ppm was assigned to the CH aliphatic group bound to the coordinated CS_2^-, while the signal at δ = 83.4 ppm corresponds to the free CS_2^-.

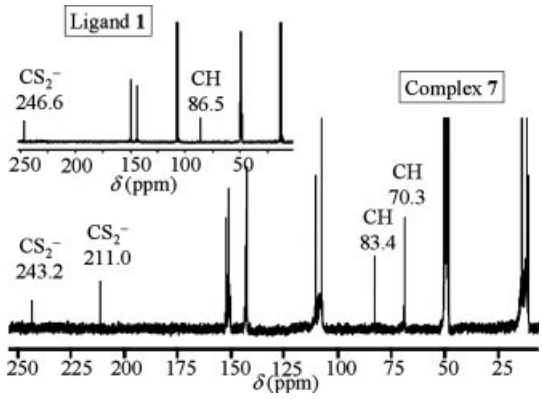

Figure 4. ^{13}C NMR spectra of ligand **1** (inset) and complex **7** in CD_3OD.

In the nitrosyl complexes $[Ru(NO)(L)_2]Cl$ (where L = bdmpza or bdmpzsa), a dynamic on/off switching exchange between the two oxyanionic groups was found to take place in the coordination to Ru^{II} at the only remaining vacant position (*trans* to NO).[7] This process is favoured by the powerful NO *trans* influence over the oxyanionic moiety. In contrast, such an exchange was not observed in complex **7** and the only Ru^{II}–S bond formed was not dissociated by NO in the *trans* position.

The *trans* influence of NO on the dithiocarboxylate group is evidenced by the marked shift observed (about 20 ppm) in the ^{13}C NMR signal relative to that in the corresponding NO-free complex. It appears that the ionic character of this bond is increased when coordinated NO weakens the Ru^{II}–S bond and increases the positive charge on the metal. In this way, the coordinated sulfur atom could increase its electron density with the consequent shielding of the CS_2 carbon atom. The coordination of NO appears to cause a strong electronic shift along the S–Ru^{II}–NO axis, which is also seen in the MLCT band as a hypsochromic shift (by about 10 nm). This change is observed in the UV/Vis spectra when comparing compounds **2**, **3** and **4** with the corresponding mononitrosyl complexes **5**, **6** and **7**, respectively. The mononitrosyl complexes (**5**, **6** and **7**) do not liberate NO under a strong vacuum and in compound **7** the second CS_2^- moiety does not substitute NO. These observations demonstrate the high stability of the Ru^{II}–NO bond. Taking this into consideration, we decided to study the possible interaction of compounds **2**, **3** and **4** with NO in an attempt to obtain the corresponding complexes with coordinated NO^+ ligand. In order to achieve this aim, NO was bubbled through dichloromethane solutions of these complexes under an oxygen-free inert atmosphere. The solutions, which were initially brown, became reddish after 15–20 min. These compounds were isolated and characterised by UV/Vis and IR spectroscopy. The UV/Vis spectra

 © 2005 Wiley-VCH Verlag GmbH & Co. KGaA, Weinheim

Table 1. Spectroscopic properties of the compounds obtained after bubbling NO through CH_2Cl_2 solutions of **2**–**4**.

Compounds	IR ($\tilde{\nu}$, cm^{-1})			UV (λ, nm)
	ν(NO)	ν(C=S)	ν(C–S)	
[{Ru(bdmpzdta)(Cl)(H_2O)}]$_2$ (**2**) + NO(g)	1866	1028	784	286
[Ru(bdmpzdta)(Cl)(en)] (**3**) + NO(g)	1862	1032	782	290
[Ru(bdmpzdta)$_2$] (**4**) + NO(g)	1857	1034	786	292

are very similar (Table 1) to those of complexes obtained from [$RuCl_3$(NO)] (compounds **5**, **6** and **7**). A strong sharp band is observed in the IR spectra of these complexes at around 1860 cm^{-1} and this is assigned to ν(NO). This band was seen when the samples were prepared either as KBr tablets or CH_2Cl_2 solutions (Figure 5 for complex **3** with NO bubbled through). The positions of the ν(NO) bands are very similar to those in **5**, **6** and **7**, respectively, as depicted in Figure 5 for compound **3** (after NO bubbled through) and mononitrosyl complex **6**.

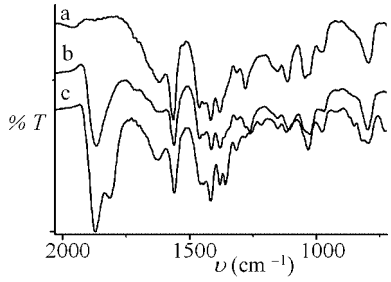

Figure 5. IR spectra of a) compound **3**, b) compound **3** with NO bubbled through and c) compound **6**.

The areas of the ν(NO) bands of the compounds after bubbling NO through were compared with those obtained from [$RuCl_3$(NO)], with the ν(C=S) and ν(C–S) stretching bands taken as references. The areas of the ν(NO) bands of the former compounds correspond to 75–90% of those of the latter. This indicates that a high percentage of Ru^{II} coordinates NO. Possible explanations for the incomplete coordination of NO include unavoidable partial oxidation of NO and its relatively low solubility in CH_2Cl_2. The fact that 100% NO coordination was not achieved in any of these compounds means that they are not pure. Purification of the nitrosyl compound by bubbling NO through solutions of the complexes was not successful.

The ^1H NMR spectra gave an overlap of signals that was not possible to interpret. The ^{13}C NMR spectra of the compounds obtained after bubbling NO through show a double set of signals that are not well resolved in most cases. A well-defined ^{13}C NMR spectrum was obtained only for the product of bubbling NO through a solution of complex **2** (Supporting Information, Figure S1). The differences between the chemical shifts of both set of signals, one of which is much more intense than the other, mainly lie in the range 0.1–1.1 ppm. For the CSS^- signal the observed difference was about 20 ppm. The set of signals with highest intensity is very similar to that of the spectra of the compounds obtained from [$RuCl_3$(NO)] (**5**–**7**), whereas the other set of signals is similar to that of the spectra of the corresponding NO-free complexes (**2**–**4**). Evidently, the compounds obtained by bubbling NO through solutions of complexes **2**–**4** show very similar characteristics (Table 1) to those found for compounds **5**–**7**, respectively, and should therefore be considered as equivalent. This fact should be attributed to the coordination of NO^+ by the bubbled complexes that is assumed to be present in this type of solution.[12]

DMSO solutions of the compounds obtained by bubbling NO through solutions of complexes **2**, **3** and **4** in dichloromethane were studied by voltammetry. The results of these experiments were also similar to those found for compounds **5**, **6** and **7**, respectively. The irreversible cathodic wave assigned to the Ru^{II}–$NO^+ + e^- \rightarrow Ru^{II}$–$NO^0$ reduction[13] is observed in the voltammograms of these six complexes between –700 and –720 mV, as depicted in Figure 6 for complexes **5** and (**2** + NO).

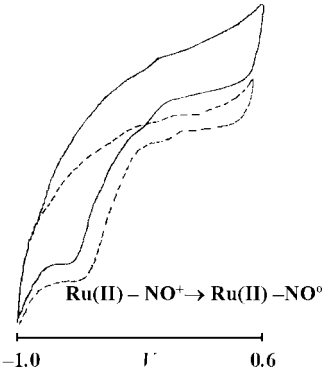

Figure 6. Cyclic voltammograms of complexes **5** (---) and (**2** + NO) (—).

Although the interaction of complexes **2**, **3** and **4** with NO was studied in dichloromethane, it is reasonable to consider the possibility that they could behave as NO scavengers in a biological system. This possibility is currently under investigation.

Conclusions

The interaction of $RuCl_3$ with bis(3,5-dimethylpyrazol-1-yl)dithioacetate (bdmpzdta; **1**) in methanol leads to the reduction of Ru^{III} to Ru^{II} with the stabilisation of the latter species. Reaction of compound **1** with [$RuCl_3$(NO)] gives new, stable nitrosyl complexes. In all six complexes the pyrazolic rings of ligand **1** lie in the equatorial plane with the CS_2^- group also coordinated. The ligand therefore behaves as a κ^3N,N,S scorpionate system. One exception to this trend was observed in complex **7**, where the second ligand

 © 2005 Wiley-VCH Verlag GmbH & Co. KGaA, Weinheim

is coordinated in a κ^2N,N manner with its dithiocarboxylate moiety free.

When NO was bubbled through solutions of complexes **2**, **3** and **4** in dichloromethane, a high level of coordination of NO^+ took place to give compounds that are apparently equivalent to complexes **5**, **6** and **7**, respectively. For example, the ν(NO) band of the latter lies in the range 1864–1859 cm^{-1}, while for the former complex the band appears at 1866–1857 cm^{-1}. The irreversible voltammetric wave corresponding to the Ru^{II}–$NO^+ + e^- \rightarrow Ru^{II}$–NO° reduction is observed in the same range (–700 and –720 mV) for both sets of compounds.

Experimental Section

General Remarks: All chemicals used were of high quality and purchased from Aldrich. The solvents were dried and distilled before use.

Spectroscopy: The electronic spectra were recorded with an Ultrospec III spectrophotometer (Pharmacia-LKB) interfaced with a microcomputer for data acquisition. IR spectra were recorded with a Perkin–Elmer 883 FT-IR spectrometer, with samples prepared as KBr tablets or as CH_2Cl_2 solutions in CaF_2 cells. NMR spectra were obtained with a Bruker AC 250 (62.89 MHz for ^{13}C) spectrometer equipped with an ASPECT 3000 computer. All samples were dissolved in CD_3OD (30 mg/0.4 mL) and recorded at 300 K. The reported chemical shifts (δ) are expressed in ppm and referenced to tetramethylsilane (TMS). The nature of each carbon atom was determined using the DEPT technique with proton pulses at θ = 135°. X-band EPR spectra of nitrosylruthenium complexes at 120 K were obtained on a Bruker EMX-300 X-band spectrometer operating at a frequency of 9.5 GHz or aBruker ESP 300 spectrometer operating at 100 KHz field modulation for dichloromethane solutions and polycrystalline samples, respectively. The frequencies were measured with a Hewlett–Packard 5352B frequency counter. The temperature was regulated with an Oxford Instruments ESR 900 continuous flow helium cryostate (low temperature) and Bruker RS-232 continuous flow nitrogen thermostat (room temperature).

Techniques for Kinetic Determinations: The UV/Vis kinetic determinations were performed spectrophotometrically at 300 K with the appropriate software. Methanolic solutions containing 5.8×10^{-4} M $RuCl_3$ and corresponding amounts of **1** were studied in 1-cm quartz optical cells.

Electrochemical Measurements: Electrochemical measurements were carried out with a Yanaco P-900 cyclic polarograph coupled to a Graphted WX1000 X-Y recorder using a standard three-holder cell. Glassy carbon, Pt and Ag/AgCl (saturated) were used as working, counter and reference electrodes, respectively. The cyclic voltammograms of the complexes (0.01 M) in DMSO solution, which had been previously deoxygenized, were recorded with tetra-*n*-butylammonium tetrafluoroborate (0.2 M) as supporting electrolyte.

[{Li(bdmpzdta)(H_2O)}$_4$] (1): This ligand was prepared as reported previously.[10,14]

[{Ru(bdmpzdta)(Cl)(H_2O)}]$_2$ (2): $RuCl_3$ (0.050 g, 0.24 mmol) was dissolved in methanol (20 mL) and ligand **1** (0.069 g, 0.24 mmol) was added in two portions. The mixture was stirred for 4 h in an inert atmosphere. The solvent was removed from the resulting brownish suspension, the product was dissolved in dichloromethane, and the LiCl filtered off. The solvent was removed from the filtrate under vacuum to give a brown, hygroscopic solid. Yield: 0.166 g (80%). $C_{12}H_{17}ClN_4ORuS_2$ (433.7): calcd. C 33.21, H 3.92, N 12.92; found C 33.23, H 3.94, N 12.90. IR (KBr): $\tilde{\nu}$ = 1562 ν(C=N), 1027 ν_{as}(C=S), 791 cm^{-1} ν_s(C–S). UV/Vis: λ (log ε) = 295 nm (3.36, MLCT). ^1H NMR (250 MHz, CD_3OD, 298 K): δ = 2.12 (s, 6 H, Me^3), 2.40 (s, 6 H, Me^5), 5.95 (s, 2 H, H^4), 7.34 (s, 1 H, CH) ppm. $^{13}C\{^1H\}$ NMR/DEPT-135 (62.89 MHz, CD_3OD, 298 K): δ = 12.4 (+, Me^5), 13.8 (+, Me^3), 76.4 (+, CH), 105.1 (+, C^4), 143.2 (0, C^5), 152.5 (0, C^3), 240.5 (0, CS_2^-) ppm.

[Ru(bdmpzdta)(Cl)(en)] (3): A procedure similar to that described for **2** was used, but with the addition of ethylenediamine (16 μL, 0.24 mmol) before ligand **1**. A brown crystalline solid was obtained. Yield: 0.097 mg (84%). $C_{14}H_{23}ClN_6RuS_2$ (475.7): calcd. C 35.33, H 4.84, N 17.66; found C 35.36, H 4.87, N 17.64. IR (KBr): $\tilde{\nu}$ = 1562 ν(C=N), 1030 ν_{as}(C=S), 792 ν_s(C–S), 3233 $\nu_{as}(NH_2)$, 3127 cm^{-1} $\nu_s(NH_2)$. UV/Vis: λ (log ε) = 297 nm (3.53, MLCT). ^1H NMR (250 MHz, CD_3OD, 298 K): δ = 2.10 (s, 6 H, Me^3), 2.31 (s, 6 H, Me^5), 5.86 (s, 2 H, H^4), 7.12 (s, 1 H, CH), 2.24/2.33 [t, 4 H, CH_2(en)] ppm. $^{13}C\{^1H\}$ NMR/DEPT-135 (62.89 MHz, CD_3OD, 298 K): δ = 12.4 (+, Me^5), 13.8 (+, Me^3), 76.3 (+, CH), 105.1 (+, C^4), 143.2 (0, C^5), 152.5 (0, C^3), 239.6 (0, CS_2^-) ppm.

[Ru(bdmpzdta)$_2$] (4): A procedure similar to that described for **2** was used, but with the addition of a double quantity of ligand **1** (0.138 g, 0.48 mmol) in four portions. A brown crystalline solid was obtained. Yield: 0.141 g (90%). $C_{24}H_{30}N_8RuS_4$ (659.2): calcd. C 43.70, H 4.55, N 16.99; found C 43.73, H 4.58, N 16.97. IR (KBr): $\tilde{\nu}$ = 1562 ν(C=N), 1029 ν_{as}(C=S), 790 cm^{-1} ν_s(C–S). UV/Vis: λ (log ε) = 298 nm (3.14, MLCT). ^1H NMR (250 MHz, CD_3OD, 298 K): δ = 2.15 (s, 12 H, Me^3), 2.35 (s, 12 H, Me^5), 6.06 (s, 4 H, H^4), 7.05 (s, 2 H, CH) ppm. $^{13}C\{^1H\}$ NMR/DEPT-135 (62.89 MHz, CD_3OD, 298 K): δ = 13.4 (+, Me^5), 12.2 (+, Me^3), 75.7 (+, CH), 103.5 (+, C^4), 144.9 (0, C^5), 157.9 (0, C^3), 230.5 (0, CS_2^-) ppm.

[Ru(bdmpzdta)(Cl)$_2$(NO)] (5): [$RuCl_3$(NO)] (0.050 g, 0.21 mmol) was dissolved in methanol (20 mL) and ligand **1** (0.060 g, 0.21 mmol) was added in two portions. The reaction mixture was stirred for 4 h under an inert atmosphere. The solvent was removed from the resulting reddish suspension, the product was dissolved in dichloromethane, and the LiCl was filtered off. The solvent was removed from the filtrate under vacuum to give a brown hygroscopic solid. Yield: 0.071 mg (70%). $C_{12}H_{15}Cl_2N_5ORuS_2$ (481.2): calcd. C 29.93, H 3.12, N 14.55; found C 29.96, H 3.16, N 14.52. IR (KBr): $\tilde{\nu}$ = 1864 ν(NO), 1560 ν(C=N), 1031 ν_{as}(C=S), 785 cm^{-1} ν_s(C–S). IR (CH_2Cl_2): ν(NO) = 1860 cm^{-1}. UV/Vis: λ (log ε) = 284 nm (3.14, MLCT). ^1H NMR (250 MHz, CD_3OD, 298 K): δ = 2.11 (s, 6 H, Me^3), 2.42 (s, 6 H, Me^5), 5.93 (s, 2 H, H^4), 7.32 (s, 1 H, CH) ppm. $^{13}C\{^1H\}$ NMR/DEPT-135 (62.89 MHz, CD_3OD, 298 K): δ = 10.3 (+, Me^5), 13.0 (+, Me^3), 76.4 (+, CH), 105.2 (+, C^4), 140.4 (0, C^5), 146.8 (0, C^3), 218.1 (0, CS_2^-) ppm.

[Ru(bdmpzdta)(en)(NO)]Cl$_2$ (6): A procedure similar to that described for **5** was used, but with the addition of ethylenediamine (14 μL, 0.21 mmol) before ligand **1**. A brown crystalline solid was obtained. Yield: 0.085 g (75%). $C_{14}H_{23}Cl_2N_7ORuS_2$ (541.2): calcd. C 31.05, H 4.25, N 18.11; found C 31.08, H 4.29, N 18.13. IR (KBr): $\tilde{\nu}$ = 1860 ν(NO), 1562 ν(C=N), 1033 ν_{as}(C=S), 785 ν_s(C–S), 3232 $\nu_{as}(NH_2)$, 3130 cm^{-1} $\nu_s(NH_2)$. IR (CH_2Cl_2): ν(NO) = 1860 cm^{-1}. UV/Vis: λ (log ε) = 288 nm (3.34, MLCT). ^1H NMR (250 MHz, CD_3OD, 298 K): δ = 2.31 (s, 6 H, Me^3), 2.10 (s, 6 H, Me^5), 5.85 (s, 2 H, H^4), 7.15 (s, 1 H, CH), 2.20/2.40 [t, 4 H, CH_2(en)] ppm. $^{13}C\{^1H\}$ NMR/DEPT-135 (62.89 MHz, CD_3OD, 298 K): δ = 10.7 (+, Me^5), 13.5 (+, Me^3), 75.2 (+, CH), 106.0 (+, C^4), 140.3 (0, C^5), 147.7 (0, C^3), 220.3 (0, CS_2^-) ppm.

 © 2005 Wiley-VCH Verlag GmbH & Co. KGaA, Weinheim

[Ru(bdmpzdta)$_2$(NO)]Cl (7): A procedure similar to that described for **5** was used, but with the addition of a double quantity of ligand **1** (0.120 g, 0.42 mmol) in four portions. A brown crystalline solid was obtained. Yield: 0.137 g (90%). $C_{24}H_{30}RuN_9OS_4Cl$ (724.7): calcd. C 39.75, H 4.14, N 17.39; found C 39.77, H 4.16, N 17.36. IR (KBr): $\tilde{\nu}$ = 1859 ν(NO), 1560 ν(C=N), 1033 ν_{as}(C=S), 786 cm^{-1} ν_s(C–S). IR (CH_2Cl_2): ν(NO) = 1862 cm^{-1}. UV/Vis: λ (log ε) = 289 nm (3.20, MLCT). ^{1}H NMR (250 MHz, CD_3OD, 298 K): δ = 2.15 (s, 12 H, Me^3), 2.30 (s, 12 H, Me^5), 6.08 (s, 4 H, H^4), 7.07 (s, 2 H, CH) ppm. $^{13}C\{^1H\}$ NMR/DEPT-135 (62.89 MHz, CD_3OD, 298 K): δ = 10.5 (+, Me^5), 13.2 (+, Me^3), 70.3 (+, aliphatic CH of CS_2^- coordinated moiety), 83.4 (+, aliphatic CH of CS_2^- uncoordinated moiety), 105.6/106.2 (+, C^4), 142.8 (0, C^5), 145.7 (0, C^3), 211.0 (0, coordinated CS_2^-), 243.2 (0, uncoordinated CS_2^-) ppm.

Interaction of 2, 3 or 4 with NO in Solution: Nitric oxide was obtained from the reaction between copper and nitric acid (5 M) under a nitrogen atmosphere using Schlenk techniques at 293 K. The gaseous product(s) of this reaction were passed through NaOH(conc) traps to remove nitrogen oxides other than nitric oxide. Compounds **2**, **3** and **4** (0.08–0.11 mmol) were each dissolved in 20 mL of dichloromethane in a Schlenk flask and deoxygenated with oxygen-free nitrogen. These 10^{-3} M solutions had nitric oxide bubbled through them for 20 min and were then stirred for 6 h whilst maintaining anaerobic conditions under nitrogen. The solutions, which were initially brown, became reddish. The corresponding products were isolated by evaporating the solvent under vacuum.

Acknowledgments

This research was supported by the Universidad de Castilla-La Mancha, Spain.

[1] S. Moncada, R. M. J. Palmer, E. A. Higgs, *Biochem. Pharmacol.* **1989**, *38*, 1709–1715.
[2] A. R. Buttler, D. L. H. Williams, *Chem. Soc. Rev.* **1993**, *22*, 233–241.
[3] S. P. Fricker, E. Salde, N. A. Powell, O. J. Vaughan, G. R. Henderson, S. A. Murrer, I. C. Megson, S. K. Bisland, F. W. Flitney, *Br. J. Pharmacol.* **1997**, *122*, 1441–1448.
[4] Y. Chen, F. T. Lin, R. E. Shepherd, *Inorg. Chem.* **1999**, *38*, 973–983.
[5] J. M. Slocik, M. S. Ward, K. V. Somayajula, R. E. Shepherd, *Transition Met. Chem.* **2001**, *26*, 351–364.
[6] M. Ortiz, A. Díaz, R. Cao, A. Otero, J. Fernández-Baeza, *Inorg. Chim. Acta* **2004**, *357*, 19–24.
[7] M. Ortiz, A. Díaz, R. Cao, R. Suardíaz, A. Antiñolo, A. Otero, J. Fernández-Baeza, *Eur. J. Inorg. Chem.* **2004**, 3353–3357.
[8] L. D. Field, B. A. Messerle, L. Soler, I. E. Buys, T. W. Hambley, *J. Chem. Soc., Dalton Trans.* **2001**, 1959–1965.
[9] A. López-Hernández, R. Müller, H. Kopf, N. Burzlaf, *Eur. J. Inorg. Chem.* **2002**, 671–677.
[10] A. Otero, J. Fernández-Baeza, A. Antiñolo, F. Carrillo-Hermosilla, J. Tejeda, A. Lara-Sánchez, L. F. Sánchez-Barba, M. Fernández-López, A. M. Rodríguez, I. López-Solera, *Inorg. Chem.* **2002**, *41*, 5193–5202.
[11] a) J. H. Enemark, R. D. Feltham, *J. Am. Chem. Soc.* **1974**, *96*, 5002–5010; b) R. D. Feltham, J. H. Enemark, *Top. Stereochem.* **1981**, *12*, 155–163.
[12] a) K. Y. Lee, D. J. Kuchynka, K. Kochi, *Inorg. Chem.* **1990**, *29*, 4196–4204; b) K. Mauthner, K. Mereiter, R. Schmid, K. Kirchner, *Inorg. Chim. Acta* **1995**, *236*, 95–100.
[13] B. Serli, E. Zangrando, T. Gianferrara, L. Yellowless, E. Alessio, *Coord. Chem. Rev.* **2003**, *245*, 73–83.
[14] A. Otero, J. Fernández-Baeza, A. Antiñolo, J. Tejeda, A. Lara-Sánchez, *Dalton Trans.* **2004**, 1499–1510.

Received: December 30, 2004
Published Online: June 28, 2005

 © 2005 Wiley-VCH Verlag GmbH & Co. KGaA, Weinheim

Study on the Binding of Base-Mismatched Oligonucleotide d(GCGAGC)$_2$ by Cobalt(III) Complexes

Huili Chen,[a] Pin Yang,*[a] Caixia Yuan,[a] and Xiaohua Pu[a]

Keywords: Mismatched DNA / Cobalt / Binding /Oligonucleotides

The binding of [Co(phen)$_2$(HPIP)]Cl$_3$ and [Co(phen)$_2$(DPQ)]Cl$_3$ to the oligonucleotide d(GCGAGC)$_2$ containing two sheared G:A mispairs has been studied by NMR spectroscopy for the first time. For both the complexes, a considerable number of intermolecular NOEs were observed in NOESY spectra of the cobalt-complex-bound hexanucleotide. The results suggest that [Co(phen)$_2$(HPIP)]Cl$_3$, with HPIP, intercalates between the G$_3$:A$_4$ base pairs from the minor groove and extends to the major groove, and [Co(phen)$_2$ (DPQ)]$^{3+}$ binds to the terminal G$_5$:C$_6$ region from two directions. ^{31}P NMR spectroscopy indicates that [Co(phen)$_2$(HPIP)]Cl$_3$ binding induces a change in the phosphate backbone in the region of the mismatched base pairs, while [Co(phen)$_2$ (DPQ)]$^{3+}$ does not cause obvious changes in the backbone. Melting experiments indicate that [Co(phen)$_2$(HPIP)]Cl$_3$ stabilizes the double-strand structure, while [Co(phen)$_2$(DPQ)]Cl$_3$ cause the duplex to untwist.

(© Wiley-VCH Verlag GmbH & Co. KGaA, 69451 Weinheim, Germany, 2005)

Introduction

Base mismatches arise naturally in the life cycle of a cell as a result of either polymerase error or DNA damage. Under most circumstances the cell corrects these mispairs by using a complex repair system to prevent mutations in the genetic code. Experimental systems for the recognition of mismatches are of particular interest in cases where this repair system is not functioning efficiently and allows errors in the DNA sequence to persist. However, the efficiency of mismatch error recognition and repair depends both on the nature of the mispair and on the flanking DNA sequence.[1–5] For example, the type of GA pairs depends entirely on the context, i.e. the proceeding base pair,[6] head-to-head GA pairing in a (NAGATN)$_2$ sequence switches to the more stable sheared side-by-side GA pairing when the context is changed to (NCGAGN)$_2$ or (NTGAAN)$_2$, while no duplex is formed (or only G:A bulges occur) in a (NGGACN)$_2$ context. Recognizing these "abnormal" structures at the atomic level presents new challenges. The sheared side-by-side G:A pairing has similar stabilities to the standard Watson–Crick base pairs.[7] Up to now, specific recognition of this mispair has not been reported. According to the reported paper,[8–12] the GpA phosphodiester link converts a B$_I$ conformation of normal B-form DNA into a B$_{II}$ conformation, which results in a downfield shift of the GpA ^{31}P resonance. Furthermore, the adenosine swings away from intrastrand stacking on the preceding guanine and participates in cross-strand stacking with the adenine of the opposite strand (Scheme 1). Molecular modeling shows the two stacking guanines lie in the major groove, and the two stacking adenines lie in the minor groove.

Metallocomplexes of the general form [M(phen)$_2$L]$^{n+}$ have contributed to our understanding of fundamental nucleic acid recognition. So far, most studies are limited to spectroscopic methods.[13–17] However, it is difficult to clarify the details of the interaction by the phenomenological information, such as red shift, blue shift, hyperchromicity and hypochromicity etc. Hence, more accurate methods, such as two-dimensional NMR spectroscopy, are needed to describe the interaction between DNA and the metallocomplex.

In this paper, we report on a NMR spectroscopic study of two Co complexes that bind to d(GCGAGC)$_2$ which contains two sheared G:A mispairs. The results indicate that [Co(phen)$_2$(HPIP)]$^{3+}$ indeed can selectively bind to the specific mispairs, and probably has the potential to repair the backbone in the region of the mispairs (Scheme 1 and Figure 1).

We tried to separate the racemic cobalt complex into the enantiomers using potassium antimonyl tartrate, but each isomer racemized in less than 24 hours; however, most of the important experiments could not be accomplished in such a short time. Further, it has been reported that the cobalt complex racemized rapidly in the presence of an oligonucleotide to generate a stable mixture of enantiomers

[a] Institute of Molecular Science,
Key Laboratory of Chemical Biology and Molecular Engineering of Ministry of Education, Shanxi University,
Taiyuan 030006, China
Fax: +86-351-701-1022
E-mail address: yangpin@sxu.edu.cn

Supporting information for this article is available on the WWW under http://www.eurjic.org or from the author.

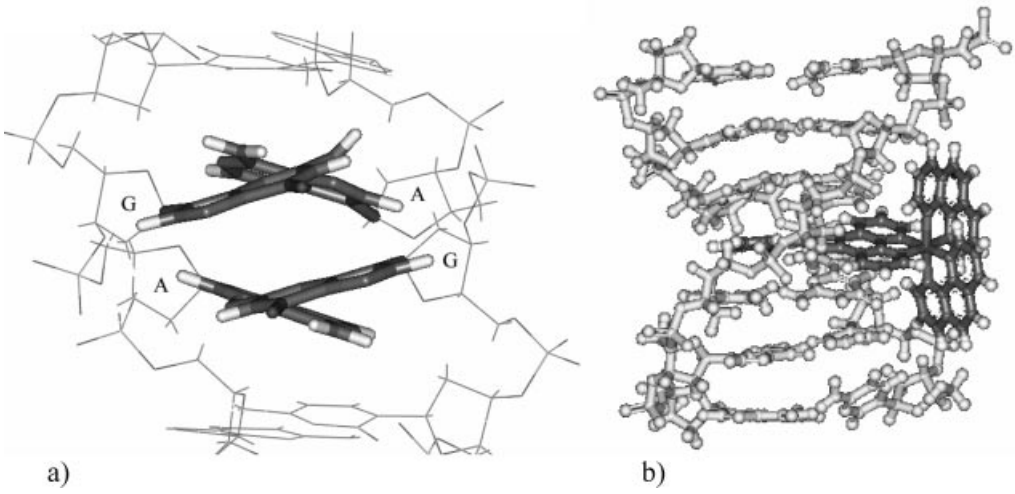

Scheme 1. (a) $d(GCGAGC)_2$; (b) $[Co(phen)_2(HPIP)]^{3+}$-$d(GCGAGC)_2$.

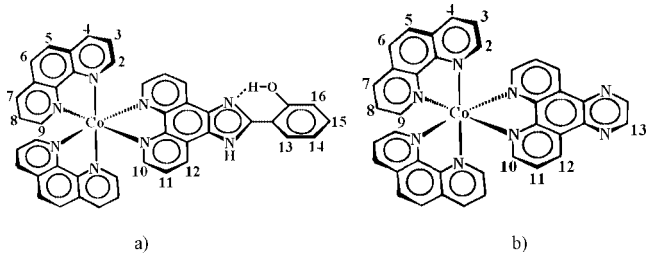

Figure 1. Structure and atom numbering of (a) $[Co(phen)_2(HPIP)]^{3+}$ and (b) $[Co(phen)_2(DPQ)]^{3+}$.

that is enriched in the isomer that interacts most favorably with the oligonucleotide.[18] In addition, molecular modeling suggests[19] that sheared G:A pairs cause a severe twisting of the DNA backbone, so that the right-hand duplex conformation close to the mispair is not very apparent, which weakens the enantiomer selectivity of the complex to DNA. Hence the use of the racemic complexes does not materially affect the conclusions reached from our experiments. We also present the results of the binding of $[Co(phen)_2(DPQ)]^{3+}$ to $d(GCGAGC)_2$ for comparison.

Results and Discussion

Assignment of the Proton Resonances of $d(GCGAGC)_2$

The ^1H NMR resonances of the free oligonucleotide were assigned with the use of both NOESY and TOCSY experiments, according to well-established methods.[21–23] The imino resonances in the NMR spectrum of the oligonucleotide dissolved in H_2O/D_2O (9:1) were examined to determine the extent of nucleotide base pairing. The spectrum indicates that only the terminal residue does not form a stable base pair, and two well-resolved imino resonances are observed. Hence, we believe that the oligonucleotide exists as double strands in our experiments. The imino proton at 10.36 ppm (Figure 2a) and the downfield ^{31}P resonance (Figure 2b) indicates that the sheared G:A base pairs exist in $d(GCGAGC)_2$.[8–12]

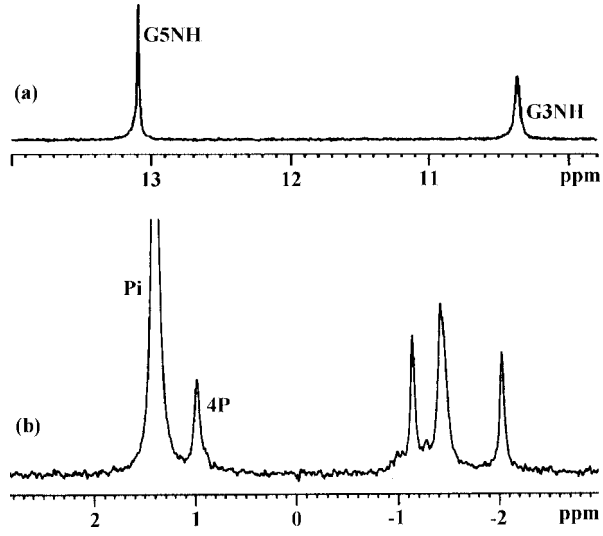

Figure 2. NMR spectra of $d(GCGAGC)_2$, (a) imino region; (b) ^{31}P NMR spectrum.

DNA Binding by $[Co(phen)_2(HPIP)]^{3+}$

The resonance signals of the free complex are assigned by using a combination of NMR experiments. The resonances from phen are easily distinguished from HPIP by the integral of each resonance. Within each ring system, the resonances are then assigned to particular protons with the use of the COSY spectrum. Because of the symmetrical structure of phen, on the NMR time scale, it is not possible to unambiguously distinguish the resonances of protons 5, 4, 3, 2 from 6, 7, 8, 9, respectively. We marked these protons

 © 2005 Wiley-VCH Verlag GmbH & Co. KGaA, Weinheim

as H5/6, H4/7, H3/8, and H2/9. H2/9 is coupled with H3/8 by vicinal $^3J_{H,H}$, while it is coupled with H4/7 by long-range $^4J_{H,H}$, so the coupling constant of H2/9–H3/8 is bigger than that of H2/9–H4/7, and the cross-peak for H2/9–H3/8 is stronger than that for H2/9–H4/7. The resonance for H4/7 has been assigned by its downfield chemical shift,[24,25] hence, the resonance for H2/9 and H3/8 can also been confirmed from the COSY spectrum. The resonances for HPIP were assigned similarly.

The assignment of d(GCGAGC)$_2$-bound [Co(phen)$_2$(HPIP)]$^{3+}$ was also carried out with the help of COSY and NOESY spectra and previously reported hexanucleotide-bound [Ru(phen)$_2$(DPPZ)]$^{2+}$[24] and [Ru(phen)$_2$(DPQ)]$^{2+}$.[25] Further, the possible chemical shifts for intercalated metal-ligand protons are restricted to within 0–1.6 ppm upfield from the location of the resonances for the free metal-ligand.[26,27]

Addition of [Co(phen)$_2$(HPIP)]$^{3+}$ to d(GCGAGC)$_2$ induces large perturbations for the HPIP resonances (especially for H12, 13, 14, 15, 16), and much smaller perturbations for the ancillary phen ligand (Table 1 and Figure 3). This behavior is consistent with the fact that the ligand HPIP preferentially participates in binding with d(GCGAGC)$_2$. The magnitude and direction of the chemical shift change for the HPIP ligand protons are indicative of selective intercalation of this ligand.[28,29] The interaction between the complex and d(GCGAGC)$_2$ leads to two sets of resonances from the ligand phen and one set of resonances from HPIP, which might be caused by the different spatial surrounding of the two ancillary ligands after HPIP intercalates with the oligonucleotide. Molecular modeling shows that after the complex intercalates into the sheared G:A region, the protons H13, 14, 15, and 16 from HPIP are all located in the ring plane formed by the two stacking adenines, and H12 lies in the ring plane formed by the two stacking guanines. The strong shielding from the purine rings causes these resonances to shift upfield to a different extent, the H8 and H2 protons of A4 and H8 of G3 are located in the side face of the aromatic ring of HPIP. In previous work,[16] we observed that, after intercalation, the distance between the neighboring base pairs is doubled and the distances from the intercalating ligand plane to the two neighboring bases are similar to that between the neighboring base pairs before intercalation, so the ring current from HPIP has little effect on the resonances of these protons.

Table 1. ^{1}H NMR chemical shift data for [Co(phen)$_2$(HPIP)]$^{3+}$ bound to d(GCGAGC)$_2$.

Ligand proton	δ(free) [ppm]	δ(bound) [ppm]	$\Delta(\delta)$ [ppm]
HPIP			
H16	8.22	7.82	–0.40
H15	7.21	6.89	–0.30
H14	7.53	7.20	–0.33
H13	7.18	6.95	–0.23
H12	9.45	8.71	–0.74
H11	7.95	7.88	–0.07
H10	7.57	7.65	+0.08
Phen			
H5/6	8.48	8.34–8.51	–0.14 to +0.03
H4/7	9.07	8.93–9.13	–0.14 to +0.06
H3/8	7.92	8.10–8.18	+0.18 to +0.26
		7.85–7.90	–0.07 to –0.02
H2/9	7.65,7.70	7.50–7.70	–

Addition of the metal complex to the hexanucleotide also induces significant broadening of the resonances of d(GCGAGC)$_2$ due to intermediate exchange on the NMR time scale (Figure 3B); this is, again, consistent with intercalation.[24,29] In one- and two-dimensional spectra of this complex bound to the oligonucleotide, two G_3H1' and G_1H1' protons are evident, which were assigned to be the free form in the lower field and the bound form in the higher field according to previously published results,[25] and the exchange between the two forms is slow on the NMR time scale.

The NOESY spectrum of d(GCGAGC)$_2$ with added [Co(phen)$_2$(HPIP)]$^{3+}$ (1:1) was recorded at 20 °C with a mixing time of 300 ms.[24,25] For the nucleotide helix, in addition to the expected intraduplex sequential NOEs, a number of intermolecular NOE cross peaks between [Co(phen)$_2$(HPIP)]$^{3+}$ and d(GCGAGC)$_2$ are observed (Table 2). Of note are the strong NOE cross peaks between the HPIP H14 and H16 protons and G_3H2', G_3H2'', and G_3H8, and the NOE cross peaks between H16 and G_3H3' (see Figure 4 and Figure S1). The medium-intensity NOEs between H10–A_4H2', H10–A_4H2'', H10–A_4H3' are also observed. Molecular modeling indicates that $G_3H2'/H2''$, G_3H8, G_3H3', $A_4H2'/H2''$, and A_4H3' are all located in the DNA major groove, and the distance between the protons from the intercalated ligand to the neighboring nucleotide may be less than 5 Å, therefore some additional NOEs also appear, such as H16–C_2H2'', between H15 and C_2H5, C_2H6, $C_2H2'/H2''$, $G_5H2'/H2''$, and between H13 and $C_2H2'/H2''$ and $G_5H2'/H2''$. In addition, the NOEs between phen and the protons located in the DNA minor groove are also clear, such as H3/8–A_4H4', H3/8–$A_4H5'/H5''$, and H2/9–G_3H1'. All of these data strongly suggest that the complex inserts into the sheared G_3A_4 region from the minor groove A_4 region, and the HPIP system spans the stacked base pairs and extends into the major groove G_3 region. As the metal complex binds by intercalation, a selective loss in intensity of the sequential NOEs might be expected because the distance between the stacked bases at the intercalation site will significantly increase. Obviously, the disappearance of the intrastrand sequential NOEs in the sheared G:A region was detected (Figure 4), such as A_4H8–$G_3H2'/H2''$, A_4H8–G_3H3', $G_3H2'/H2''$–$A_4H2'/H2''$, and simultaneously, the intensity of the sequential A_4H8–G_3H4' NOE apparently diminished. However, the binding of the complex might result in a change in the DNA backbone, and some unexpected NOEs also appeared, such as A_4H1'–G_3H4', A_4H1'–$G_3H2'/H2''$, G_3H1'–$A_4H2'/H2''$, and between A_4H2 and G_3H1', G_5H1', C_6H5, G_5H2', and $A_4H2'/H2''$.

The two imino resonances in the NMR spectrum recorded in H_2O/D_2O (9:1) indicate that the double-strand structure of the hexanucleotide is maintained after [Co(phen)$_2$(HPIP)]$^{3+}$ binding. Only small shifts (<0.05ppm)

 © 2005 Wiley-VCH Verlag GmbH & Co. KGaA, Weinheim

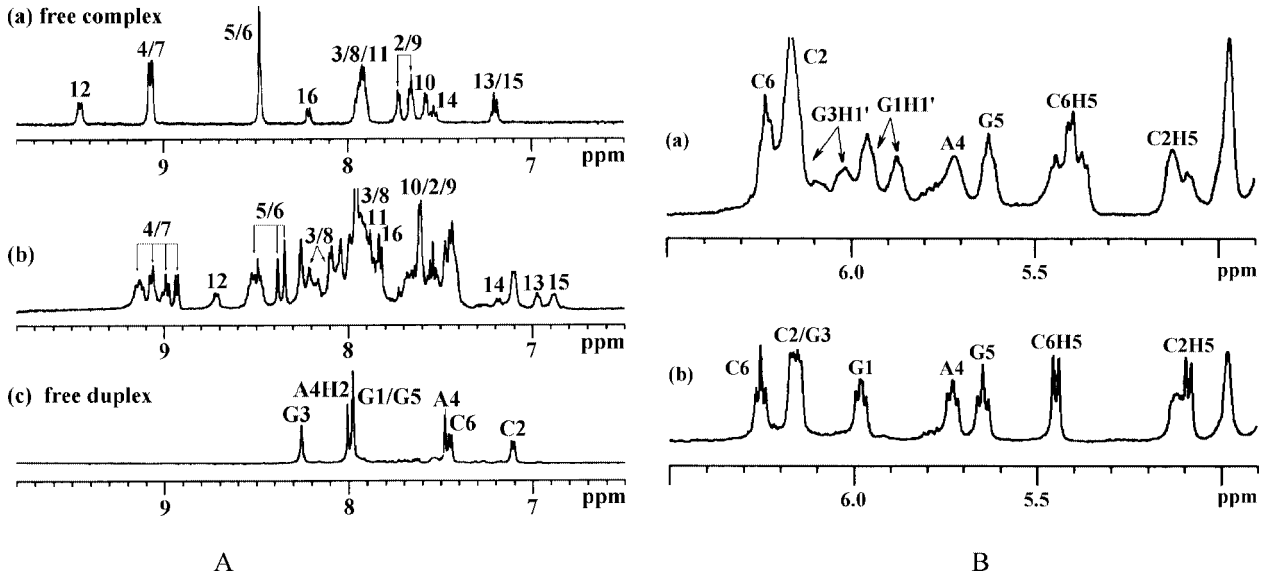

Figure 3. 500 MHz ^{1}H NMR spectra of $[Co(phen)_2(HPIP)]^{3+}$-d(GCGAGC)$_2$ with a metal complex to duplex ratio (R) of 1 (0.98 mM duplex) in 10 mM phosphate (pH 7) containing 20 mM NaCl. (A) aromatic region: (a) $[Co(phen)_2(HPIP)]^{3+}$, (b) $[Co(phen)_2(HPIP)]^{3+}$-d(GCGAGC)$_2$, (c) d(GCGAGC)$_2$; (B) sugar H1′ region: (a) $[Co(phen)_2(HPIP)]^{3+}$-d(GCGAGC)$_2$, (b) d(GCGAGC)$_2$.

Table 2. The NOE peaks between the complex and the oligonucleotide.

Metal-complex protons	Hexanucleotide protons
H16	G_3H8, G_3H3′, G_3H2′/H2′′, C_2H2′′
H15	G_3H8,[a] C_2H1′, C_2H5, G_5H2′/H2′′, C_2H6, C_2H2′/H2′′
H14	G_3H8, G_3H2′/H2′′
H13	G_5H2′/H2′′, C_2H2′/H2′′
H10	A_4H2′/H2′′, A_4H3′
H3/8	A_4H4′, A_4H5′/H5′′
H2/9	G_3H1′

[a] The NOE is very weak.

and a little broadening were observed upon the addition of the complex (Figure S2).

DNA Binding by $[Co(phen)_2(DPQ)]^{3+}$

The resonance assignment of the free- and bound $[Co(phen)_2(DPQ)]^{3+}$ was similar to that of $[Co(phen)_2(HPIP)]^{3+}$ (Figure 5A). The two resonances from the DPQ H12 proton indicate at least two binding orientations for the binding of the metal complex to the helix, and the exchange rate between the two forms is slow. It was not possible to assign unambiguously the H13 resonance because of the overlap with the H4/7 resonances. For the same reason as for $[Co(phen)_2(HPIP)]^{3+}$, we marked phen protons as H5/6, H4/7, H3/8, and H2/9.

Addition of $[Co(phen)_2(DPQ)]^{3+}$ to d(GCGAGC)$_2$ also induces a large upfield chemical shift of the resonance for the DPQ H12 proton. By contrast, resonances from phen exhibit only a small shift, suggesting that the DPQ preferentially binds.

Addition of the metal complex also induces a significant broadening and selective shifts of the hexanucleotide resonances (Figure 5). Especially, significant upfield shifts are observed for the protons located in the major groove in the terminal G_1C_2/G_5C_6 region, such as H8 of G_1 and G_5, H2′ of G_1, and H5 and H2′ of C_6. Similarly, H1′ protons of G_1 and G_5, which are located in the DNA minor groove, also show upfield shifts.

The NOESY spectrum of d(GCGAGC)$_2$ with added $[Co(phen)_2(HPIP)]^{3+}$ (1:1) was recorded at 20 °C with a mixing time of 300 ms. Figure 6 shows the aromatic to the sugar H1′, H3′region (a) and the sugar H2′/2′′region (b). In addition to the expected intraduplex sequential NOE cross peaks, a number of intermolecular NOE cross peaks between the metal complex and the duplex are also observed (Table 3). Of note are the NOE cross peaks between the complex and the terminal protons located in the major groove, such as H13–C_6/C_2H2′, H13–C_6H3′, H12–C_6/C_2H2′, H12–C_6H5, H11–G_5H2′/H2′′, H10–C_6/C_2H2′, and H10–C_6H5. Further, the NOE cross peaks between the phen H4/7 protons and the minor groove H1′ protons of C_6/C_2 are also observed. It was not possible to assign unambiguously the NOE cross peaks between the protons of the complex and the minor groove protons H4′/H5′/5′′ of C_6, C_2, G_1, and G_5 (a-g) because of the overlap of these resonances. These data strongly suggest that the cobalt complex binds to the DNA in the terminal G_1C_2/G_5C_6 region from two directions, one from the minor and the other from the major groove. The intensity of the sequential NOEs from C_6H6–G_5H3′ and G_1H8–C_2H3′ decrease with the binding of the metal complex. Additionally, the different degrees of broadening of the hexanucleotide resonances, induced by the addition of $[Co(phen)_2(DPQ)]^{3+}$, hinders the observation of a selective partial loss of the sequential NOE.

From the imino resonances, we confirm that the bound oligonucleotide still has a duplex conformation (Figure S2).

 © 2005 Wiley-VCH Verlag GmbH & Co. KGaA, Weinheim

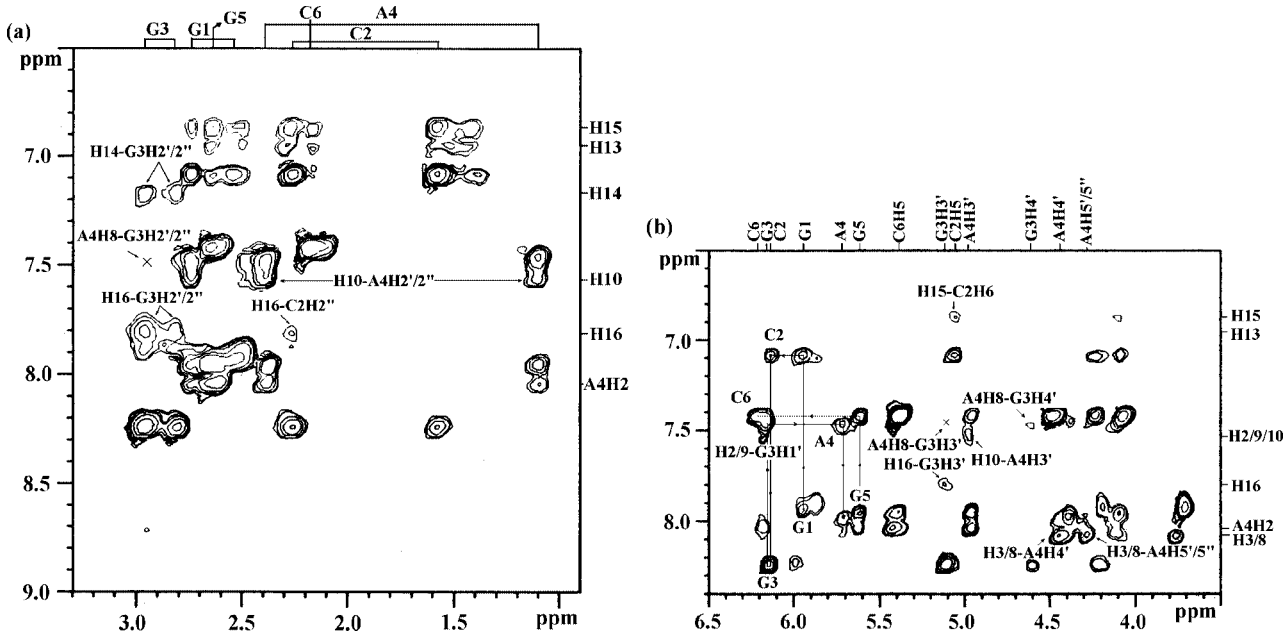

Figure 4. Expansion of the NOESY spectrum (300 ms mixing time) of [Co(phen)$_2$(HPIP)]$^{3+}$ and d(GCGAGC)$_2$ (1 mM) with a metal complex to duplex ratio of 1. It shows the peaks for the hexanucleotide and metal complex from the aromatic (6.5–9.0 ppm) to the sugar (a) H2′/H2′′ region, and (b) H1′, H3′, H4′ and H5′/H5′′region. The NOEs between the cobalt complex and the hexanucleotide are labeled. × indicates the disappearance of the intrastrand sequential NOEs in the sheared G:A region.

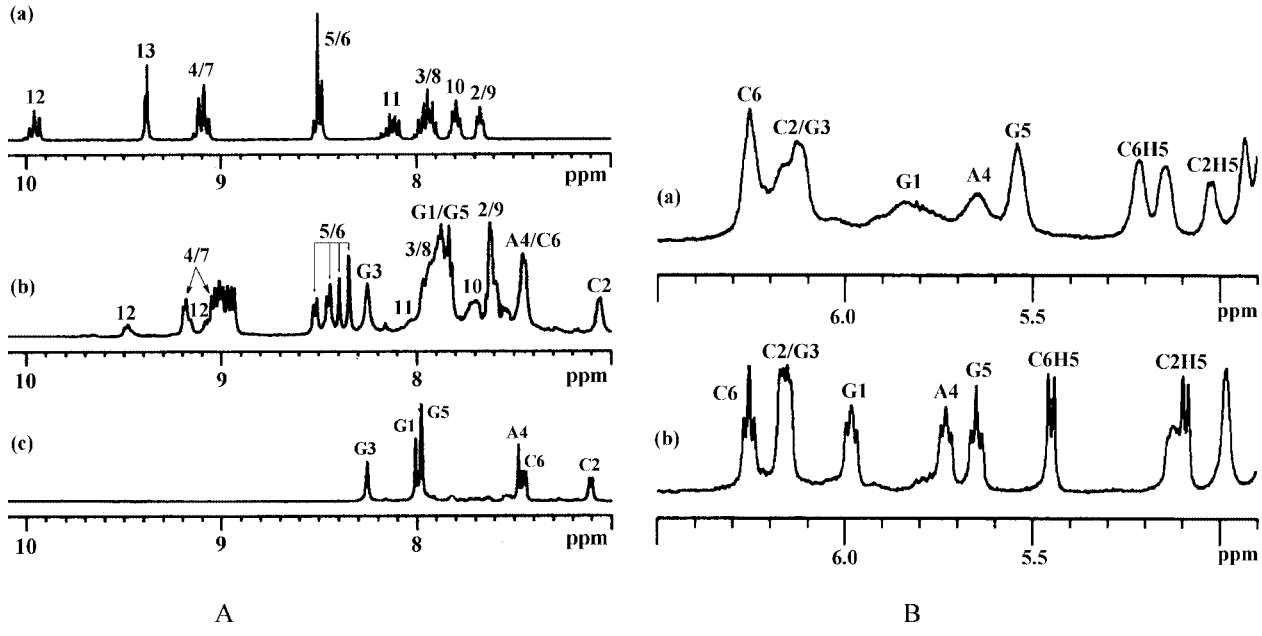

Figure 5. 500 MHz ^{1}H NMR spectra of [Co(phen)$_2$(DPQ)]$^{3+}$-d(GCGAGC)$_2$ with a metal complex to duplex ratio (R) of 1 (0.98 mM duplex) in 10 mM phosphate (pH 7) containing 20 mM NaCl. (A) aromatic region: (a) [Co(phen)$_2$(DPQ)]$^{3+}$, (b) [Co(phen)$_2$(DPQ)]$^{3+}$-d(GCGAGC)$_2$, (c) d(GCGAGC)$_2$; (B) sugar H1′ region: (a) [Co(phen)$_2$(DPQ)]$^{3+}$-d(GCGAGC)$_2$, (b) d(GCGAGC)$_2$.

^{31}P NMR Spectroscopy

^{31}P NMR spectroscopic studies of oligonucleotide bound by intercalators provide direct information on any backbone distortion which accompanies any interaction.[30] Unlike ^{1}H nuclei, for which upfield movement of the ligand resonances is caused by increases in shielding due to penetration into the ring currents of the base stack, the movement of ^{31}P nuclei in oligonucleotides is governed by changes in the torsion angles about the phosphate linkage.[31–33] As shown in Figure 7, the free oligonucleotide exhibits a sharp peak at 1.1 ppm, far away from the other resonances, which is typical for sheared G:A base pairs with a B_{II} conformation.[8–12] When the oligonucleotide is bound by [Co(phen)$_2$(HPIP)]$^{3+}$, the peak shifts upfield, and a new

 © 2005 Wiley-VCH Verlag GmbH & Co. KGaA, Weinheim

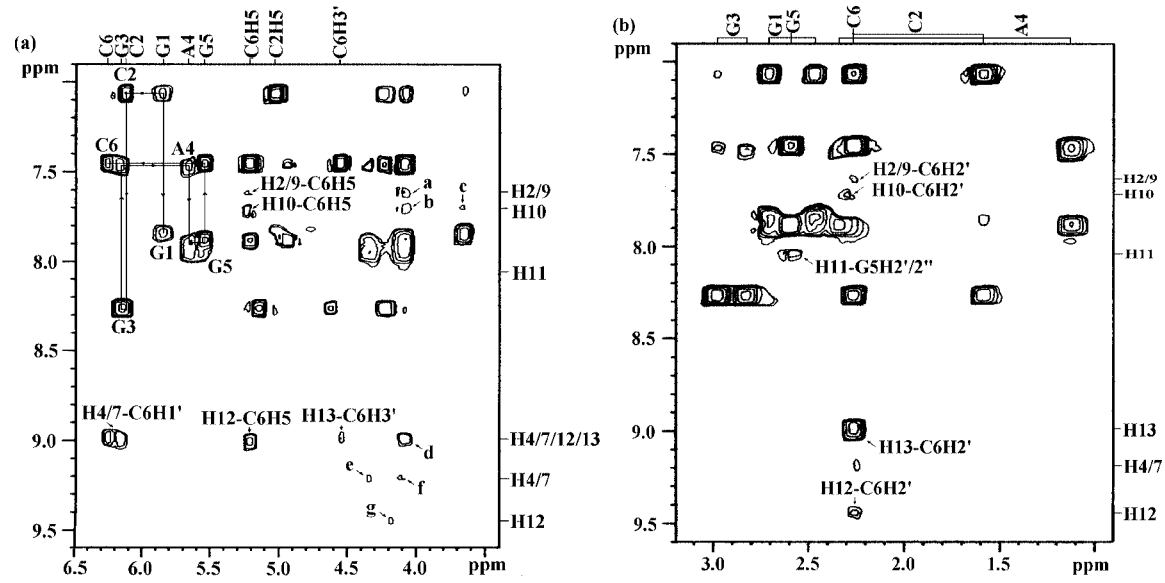

Figure 6. Expansion of the NOESY spectrum (300 ms mixing time) of $[Co(phen)_2(DPQ)]^{3+}$ and d(GCGAGC)$_2$ (0.98 mM) with a metal complex to duplex ratio of 1, showing the peaks from the aromatic to hexanucleotide sugar (a) H1′, H3′ region, and (b) H2′/H2′′ region. The NOEs between the cobalt complex and the hexanucleotide are indicated.

Table 3. The NOE peaks between $[Co(phen)_2(DPQ)]^{3+}$ and the oligonucleotide.

Metal-complex protons	Hexanucleotide protons
H13	C_6H2′,[a] C_6H3′
H12	C_6/C_2H2′, C_6H5
H11	G_5H2′/H2′′
H10	C_2H2′/C_6H2′, C_6H5
H4/7	C_6H1′
H2/9	C_6H5, C_2H2′/C_6H2′

[a] C_2H2′ cannot be distinguished from C_6H2′.

little peak appears on the right of it. We speculate that it belongs to another resonance from 4P. The upfield shift indicates the change in the B_{II} conformation of the phosphate backbone in the G_3A_4 region. In combination with the ^{1}H NMR spectroscopy, we conclude that HPIP selectively inserts into the sheared G:A region. A few new peaks also appear in the upfield region; this occurs as a result of the intercalation of the complex into the G:A region, which causes the distortion of the neighborhood phosphate backbone. The addition of $[Co(phen)_2(dpq)]^{3+}$ shows no obvious change in the ^{31}P NMR resonances of the duplex.

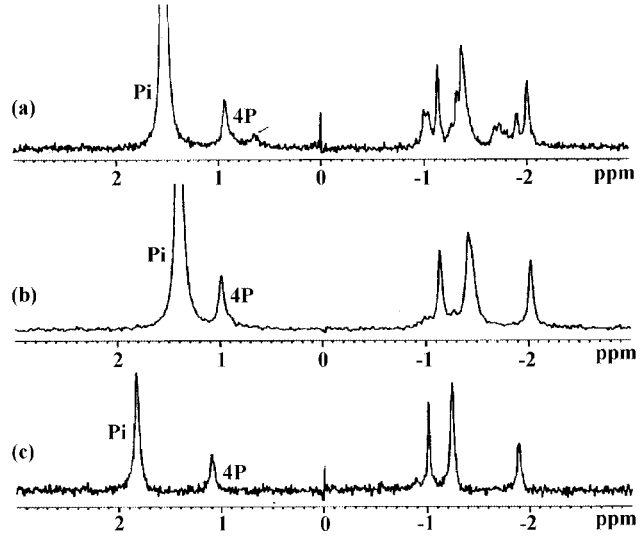

Figure 7. 121.8 MHz ^{31}P NMR spectra of (a) $[Co(phen)_2(HPIP)]^{3+}$-d(GCGAGC)$_2$, (b) $[Co(phen)_2(DPQ)]^{3+}$-d(GCGAGC)$_2$, and (c) free d(GCGAGC)$_2$.

Melting Experiments

Other strong evidence for the binding of the complexes to the duplex was obtained from DNA melting studies.[34] Intercalation of small molecules into the double helix is known to increase the helix melting temperature (T_m), the temperature at which the double helix is denatured into single-stranded DNA. For d(GCGAGC)$_2$, the transition tem-

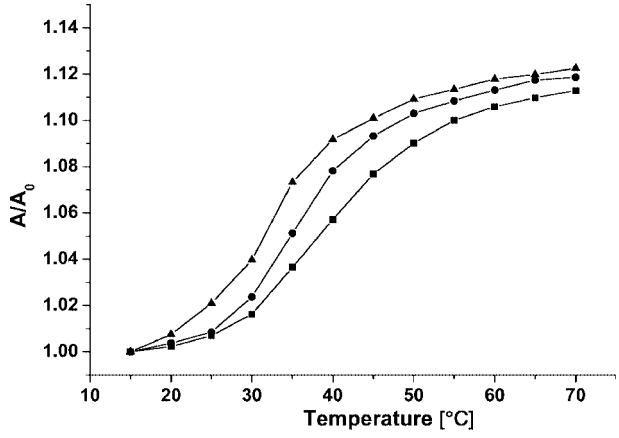

Figure 8. Effect of the Co complexes on the melting temperature of d(GCGAGC)$_2$ (15 μM) with a complex to duplex ratio of 2:1. d(GCGAGC)$_2$ (circle); $[Co(phen)_2(HPIP)]^{3+}$+ d(GCGAGC)$_2$ (square); $[Co(phen)_2(DPQ)]^{3+}$ + d(GCGAGC)$_2$ (triangle).

 © 2005 Wiley-VCH Verlag GmbH & Co. KGaA, Weinheim

perature can be determined by monitoring the absorbance at 254 nm as a function of temperature. As shown in Figure 8, both the Co complexes have a significant effect on T_m. The melting temperature of d(GCGAGC)$_2$ increases from 35 °C to 40 °C with [Co(phen)$_2$(HPIP)]$^{3+}$, whereas it decreases to about 30 °C with [Co(phen)$_2$(DPQ)]$^{3+}$. The increase in T_m provides strong support for the intercalation of [Co(phen)$_2$(HPIP)]$^{3+}$ into the duplex, while [Co(phen)$_2$(DPQ)]$^{3+}$ binds to the duplex but does not intercalate.

Conclusion

The study on the site selective interaction between an octahedral metal complex and the mismatched oligonucleotide by NMR spectroscopy has not been reported up until now. Considering that the distortion of the backbone of DNA with sheared G:A mispairs weakens the selective binding of the enantiomer, we have attempted to study the interaction of an oligonucleotide d(GCGAGC)$_2$ with a racemic cobalt complex and have obtained some significant results.

In the NOESY experiments with d(GCGAGC)$_2$, many NOEs are observed between the metal complexes and the hexanucleotide. For [Co(phen)$_2$(HPIP)]$^{3+}$, as these NOEs are predominantly between HPIP and the major groove protons and between phen and the minor groove protons in the sheared G:A region, we conclude that the ligand HPIP inserts into the adenine base stacking from the minor groove, and extends to the guanine stacking in the major groove. The result of ^{31}P NMR spectroscopic study indicates that the binding of the complex induces a change in the B_{II} conformation of the phosphate backbone in the G_3A_4 region to a B_I conformation. In this sense, the complex has the potential to repair the phosphate backbone in the sheared G:A region. For [Co(phen)$_2$(DPQ)]$^{3+}$, as the NOEs are predominantly from the terminal G_1C_2/G_5C_6 sequence, it is concluded that the complex binds to the oligonucleotide by two modes, one is from the major and the other is from minor groove in the G:C region. The ^{31}P NMR spectroscopic study indicates that addition of the complex does not induce an obvious change in the conformation of the DNA. Melting experiments indicate that [Co(phen)$_2$(HPIP)]Cl$_3$ stabilizes the double-strand structure, while [Co(phen)$_2$(DPQ)]Cl$_3$ causes the duplex to untwist.

The difference in the binding properties between the two complexes could be because of the width of the ligand. The wider minor groove and the narrower major groove in the mispair region is exactly suitable for HPIP to insert between the sheared G:A base pairs.

Overall, the results of this study demonstrate that the octahedral metallointercalator [Co(phen)$_2$(HPIP)]$^{3+}$ can intercalate into the oligonucleotide d(GCGAGC)$_2$ in the sheared G:A region, which could have potential application in the design of mismatch-specific chemical agents.

Experimental Section

Materials: The oligonucleotide d(GCGAGC)$_2$ was purchased from AuGCT Biotechnology Co. Ltd, Beijing. The concentration was determined from the absorbance at 254 nm, and the single strand extinction coefficients were calculated from mononucleotide and dinucleotide data of a nearest-neighbor approximation.[20] The oligonucleotide was dissolved in phosphate buffer (pH 7.0, 0.50 ml of a 10 mM solution), containing NaCl (20 mM) and TMSP (0.05 mM). For the imino proton studies, the sample was dissolved into H_2O/D_2O (9:1). For the non-exchangeable proton studies, the sample was dissolved into the phosphate buffer and repeatedly lyophilized from 99.8% D_2O in a speed vacuum, and then dissolved in D_2O (0.50 ml of a 99.996% solution), with a concentration of 1 mM. The complexes were synthesized as previously reported.[17] Stock solutions of the metal complexes were prepared in D_2O (unbuffered) and added to the hexanucleotide in 10ul aliquots until a metal complex to hexanucleotide duplex ratio of 1 was achieved.

The absorbance spectra were recorded with a Hewlett Packard HP-843 chemstation spectrometer. The DNA melting experiments were carried out by controlling the temperature of the sample cell with a Shimadzu circulating bath while monitoring the absorbance at 254 nm.

NMR Spectroscopic Measurements: NMR measurements were made with Bruker DRX-500 and DRX-300 spectrometers and analyzed with a silicon graphics workstation running Xwin-nmr. Proton chemical shifts were referenced to an internal TMSP standard. Phosphate chemical shifts were referenced to an external 85% H_3PO_4 standard.

All NMR spectra were recorded at approximately 20 °C. Spectra recorded in H_2O/D_2O (9:1) were collected by using a binomial 1:3:3:1 pulse sequence for solvent suppression. Two-dimensional phase-sensitive NOESY spectra in 99.996% D_2O were recorded by the TPPI method, using 2048 data points in t_2 (over a spectral width of 5000 Hz) for 256 t_1 values with a pulse repetition delay 2 s. Suppression of the residual HDO resonance was achieved by low-power presaturation during the relaxation delay. Phase-sensitive TOCSY spectra were accumulated with 2048 data points in t_2 for 256 t_1 values with a pulse repetition delay 2 s.

Acknowledgments

The authors gratefully acknowledge the financial support of this work by the National Natural Science Foundation of China (No.: 30470408) and the Shanxi Provincial Natural Science Foundation for Youth (No.: 20011007).

[1] B. Kramer, W. Kramer, H. J. Fritz, *Cell* **1984**, *38*, 879.
[2] G. V. Fazakerley, E. Quignard, A. Woisard, W. Guschlbauer, G. A. van der Marel, J. H. van Boon, M. Jones, M. Radman, *EMBO J.* **1986**, *13*, 3697.
[3] B. A. Jackson, J. K. Barton, *Inorg. Chem.* **2004**, *43*, 4570.
[4] B. A. Jackson, V. Y. Alekseyev, J. K. Barton, *Biochemistry* **1999**, *38*, 4655.
[5] B. A. Jackson, J. K. Barton, *J. Am. Chem. Soc.* **1997**, *119*, 12986.
[6] J. W. Cheng, S. H. Chou, B. R. Reid, *J. Mol. Biol.* **1992**, *228*, 1037.
[7] W. D. Wilson, M. H. Dotrong, E. T. Zuo, G. Zon, *Nucleic Acids Res.* **1988**, *16*, 5137.
[8] R. Wing, H. Drew, T. Takano, C. Broka, S. Tanaka, K. Itakura, R. E. Dickerson, *Nature* **1980**, *287*, 755.
[9] S. H. Chou, J. W. Cheng, O. Y. Fedoroff, B. R. Reid, *J. Mol. Biol.* **1994**, *241*, 467.
[10] S. H. Chou, J. W. Cheng, O. Y. Fedoroff, V. P. Chuprina, B. R. Reid, *J. Am. Chem. Soc.* **1992**, *114*, 3114.
[11] S. H. Chou, J. W. Cheng, B. R. Reid, *J. Mol. Biol.* **1992**, *228*, 138.

 © 2005 Wiley-VCH Verlag GmbH & Co. KGaA, Weinheim

[12] Y. Li, G. Zon, W. D. Wilson, *Proc. Nat. Acad. Sci. U. S. A.* **1991**, *88*, 26.
[13] Q. L. Zhang, J. G. Liu, H. Chao, G. Q. Xue, L. N. Ji, *J. Inorg. Biochem.* **2001**, *83*, 49.
[14] Q. X. Zhen, Q. L. Zhang, J. G. Liu, B. H. Ye, L. N. Ji, L. Wang, *J. Inorg. Biochem.* **2000**, *78*, 293.
[15] J. G. Liu, B. H. Ye, H. Li, Q. X. Zhen, L. N. Ji, Y. H. Fu, *J. Inorg. Biochem.* **1999**, *76*, 265.
[16] Y. F. Song, P. Yang, *Polyhedron* **2001**, *20*, 501.
[17] H. L. Chen, P. Yang, *Chin. J. Chem.* **2002**, *20*, 1529.
[18] J. P. Rehmann, J. K. Barton, *Biochemistry* **1990**, *29*, 1701.
[19] Z. H. Xiong, P. Yang, *J. Mol. Struct. (Theochem)* **2002**, *582*, 107.
[20] E. G. Richards, *Handbook of Biochemistry and Molecular Biology: Nucleic Acids*, 3rd ed., CRC Press, Cleveland, **1975**, vol. 1, p. 597.
[21] R. M. Scheek, R. Boelens, N. Russo, J. H. van Boom, R. Kaptein, *Biochemistry* **1984**, *23*, 1371.
[22] J. Feigon, W. Leupin, W. A. Denny, D. R. Kearns, *Biochemistry* **1983**, *22*, 5943.
[23] D. J. Patel, L. Shapiro, D. J. Hare, *Biol. Chem.* **1986**, *261*, 1223.
[24] C. M. Dupureur, J. K. Barton, *Inorg. Chem.* **1997**, *36*, 33.
[25] a) J. G. Collins, A. D. Sleeman, J. R. Aldrich-Wright, I. Greguric, T. W. Hambley, *Inorg. Chem.* **1998**, *37*, 3133; b) J. G. Collins, J. R. Aldrich-Wright, I. D. Greguric, P. A. Pellegrint, *Inorg. Chem.* **1999**, *38*, 5502.
[26] C. Giessner-Prettre, B. Q. Pullman, *Rev. Biophys.* **1987**, *20*, 13.
[27] C. Giessner-Prettre, B. Pullman, *Rev. Biophys. Res. Commun.* **1986**, *70*, 578.
[28] a) C. M. Dupureur, J. K. Barton, *J. Am. Chem. Soc.* **1994**, *116*, 10286; b) M. Eriksson, M. Leijon, C. Hiort, B. Norden, A. Graslund, *J. Am. Chem. Soc.* **1992**, *114*, 4933.
[29] J. Feigon, W. A. Denny, W. Leupin, D. R. Kearns, *J. Med. Chem.* **1984**, 450.
[30] D. G. Gorenstein, *Methods Enzymol.* **1992**, *211*, 254.
[31] E. P. Nikonowiez, D. G. Gorenstein, *Biochemistry* **1990**, *29*, 8845.
[32] D. G. Gorenstein, S. A. Schroeder, J. M. Fu, J. T. Metz, V. Roongta, C. R. Jones, *Biochemistry* **1988**, *27*, 7223.
[33] G. G. Prive, U. Heinemann, S. Chandrasegaran, L. S. Kan, M. L. Kopka, R. E. Dickerson, *Science* **1987**, *238*, 498.
[34] D. J. Patel, *Acc. Chem. Res.* **1979**, *12*, 118.

Received: December 21, 2004
Published Online: July 4, 2005

 © 2005 Wiley-VCH Verlag GmbH & Co. KGaA, Weinheim

Synthesis and Characterisation of Monodisperse Zirconia Particles

Johanna Widoniak,[a] Stefanie Eiden-Assmann,*[a] and Georg Maret[a]

Keywords: Zirconia / Monodisperse / Colloids / Particles / Sol–gel processes

Monodisperse spherical ZrO_2 particles were prepared by controlled hydrolysis of zirconium tetraalkoxide in alcoholic solution. Ageing the reaction solution at 60 °C for 4 h yields particles with sizes in the range between 200 and 2000 nm. The influence of various ions and surfactants on the final product was investigated. Stable suspensions of coated, monodisperse, zirconia particles were prepared by hydrolysis and subsequent polymerisation of tetraethoxysilane in an alkaline ethanol solution. Thermal analysis revealed that the weight loss of bound water occurred below 400 °C and is about 35 %. The phase transition from amorphous zirconia to the tetragonal phase proceeded at approximately 450 °C, the transition to the monoclinic phase began at about 600 °C and was completed at about 800 °C. The crystallinity of the powders was investigated by X-ray diffraction. Electrophoretic measurements were carried out to determine the charges on the particle surface. Elementary analyses were used for further investigations. On the basis of the results obtained, the mechanism of particle formation was discussed.

(© Wiley-VCH Verlag GmbH & Co. KGaA, 69451 Weinheim, Germany, 2005)

Introduction

Mesoscale spheres of metal oxides, like zirconia particles, are of particular interest for applications as ceramics. To advance the sintering kinetics, i.e. to obtain shorter sintering times and lower sintering temperatures, elimination of agglomerates and control of the particle size distribution is required. Controlled hydrolysis of metal alkoxides seems to be a promising method for obtaining particles with well-defined sintering properties during the powder synthesis. Zirconia particles are widely used as high-performance ceramics, catalysts or in cosmetics. New applications for zirconia powders are high-temperature fuel cells, lambda probes or bioceramics such as dental prostheses.[1]

The preparation of zirconia powders was described in a number of publications.[2–6] Sada et al.[3] reported the preparation of zirconia particles by hydrolysis of zirconium tetrabutoxide in 1-propanol. The average diameter of particles obtained range from 140 to 380 nm. A decrease in the particle size with increasing reaction ratio was observed. Kato et al.[2] prepared various sizes of particles by the seeded-growth method. Mizutani et al.[5] reported the influence of chain length and branching, and the molecular structure of the alcoholic solvent on the hydrolysis behaviour of zirconium tetrabutoxide. The goal of our research was to establish a controlled and reproducible synthesis of zirconia particles with a narrow size distribution and of various sizes. Additionally, we investigated the influence of ions and polymers and of different ratios of precursors on the synthesis of zirconia particles. In order to change the surface properties of the zirconia particles and to make the particles visible for confocal scanning laser microscopy (CSLM), the particles were coated with a silica shell into which dye molecules could be incorporated.

[a] Fachbereich Physik, Universität Konstanz, 78457 Konstanz, Germany

Results and Discussion

Zirconia particles with a narrow size distribution were obtained in a precipitation reaction from zirconium alkoxide and water in an alcoholic solution. Depending on the reaction conditions, particles in the range between 200 and 2000 nm were obtained (Figure 1). The scanning electron micrographs reveal the perfectly uniform shape and high monodispersity of our particles (Figure 2 and Figure 3). The synthesis proceeds in two steps. During the first step, the hydrolysis, zirconium hydroxide molecules and primary particles are generated. In the second step, the primary particles aggregate (see Figure 1).[5]

$$Zr(OR)_4 + H_2O \rightarrow Zr(OH)_4 + 4\ ROH$$

$$Zr(OH)_4 \rightarrow ZrO_2 + 2H_2O$$

The zirconia particles are formed by a stepwise hydrolysis of zirconium tetraalkoxides, as described above, and polymerisation of hydrolysed zirconium alkoxide.[3] In addition to hydrous zirconia, hydrated polymeric species with a number of Zr–O–Zr bridges are formed. A macromolecular oxide network is then obtained through hydrolysis and condensation.[2,10]

$$Zr(OR)_4 + H_2O \rightarrow (OR)_3Zr(OH) + ROH$$

$$(OR)_3Zr(OH) + (OR)_3Zr(OR) \rightarrow (OR)_3Zr–O–Zr(OR)_3 + ROH$$

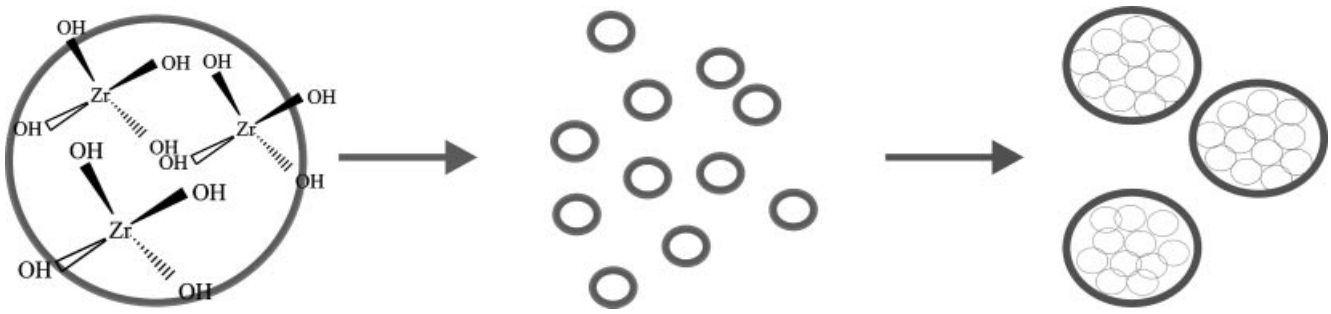

Figure 1. Primary particles formed by the hydrolysis of the metal alkoxide coalesce fast and grow into spheres. Residual primary particles do not form secondary particles but promote the growth of the spheres.

Variation of Precursors and Their Concentrations

To obtain spherical and monodisperse zirconia particles, various zirconium tetraalkoxides and alcohol solvents were tested. Among zirconium tetraethoxide, tetrapropoxide and tetrabutoxide, the best results were obtained with zirconium tetrabutoxide. When ethanol, 1-propanol and 1-butanol were tested as solvents, particularly uniform and monodisperse particles were obtained with ethanol for a wide range of precursor concentrations. 1-Propanol and 1-butanol provided only narrow ranges of concentration where spherical and monodispersed particles were obtained. In the case of ethanol, the induction time for the formation of particles optimally fell between 1 and 5 min. When the induction time was shorter than the optimum, hydrolysis occurred more quickly, and the nuclei formed polydisperse aggregates. In the case of a prolonged induction period, nucleus formation and particle growth proceeded simultaneously and polydisperse particles were formed.[5] An ethanol volume of 100 mL, mixed with 0.2–0.6 mL of Millipore water, aqueous salt or polymer solution, followed by the addition of 3.25–5.00 mL of zirconium tetrabutoxide was found to be the best condition for obtaining uniformly spherical and monodisperse zirconia particles.

The uniformity in size and spherical shape of the resulting particles decreased as the initial amount of water became higher than 0.6 mL or lower than 0.2 mL. The higher the water concentration in the reaction solution, the faster the hydrolysis, and the smaller the particles obtained (Figure 2). For zirconia particles synthesised with NaCl, the

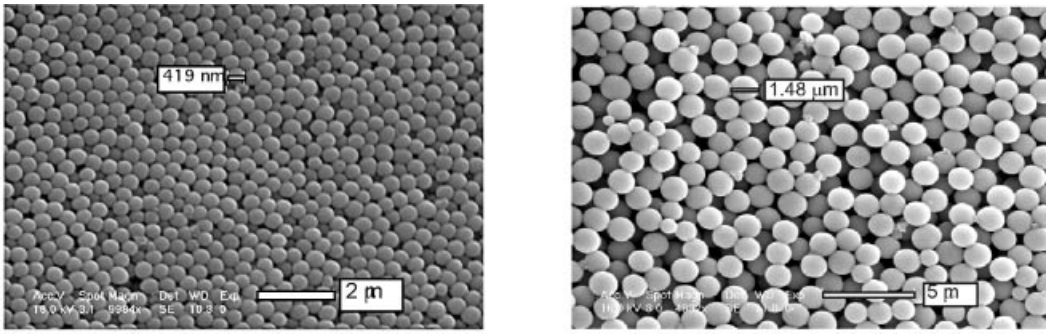

Figure 2. Zirconia particles synthesised with 0.40 mL (l) and 0.20 mL (r) of a 0.1 M NaCl solution, with addition of 3.25 mL $Zr(OBu)_4$ in 100 mL ethanol.

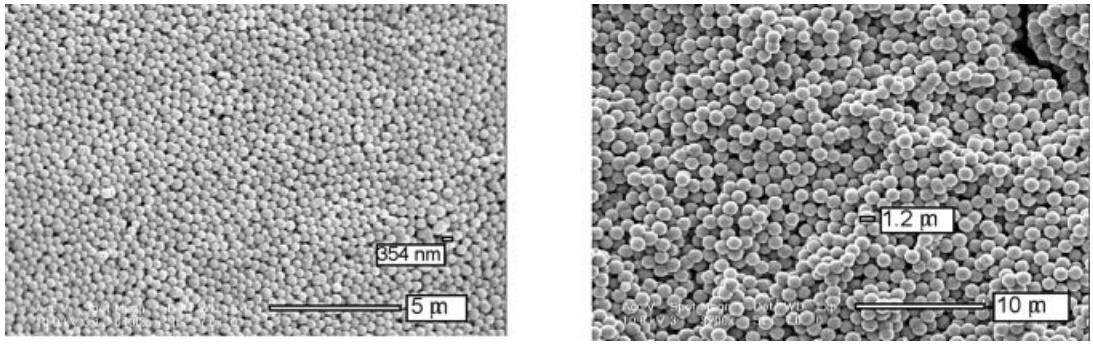

Figure 3. Zirconia particles synthesised with 3.25 mL (l) and 5.00 mL (r) of $Zr(OBu)_4$, with addition of 0.40 mL of a 0.1 M NaCl solution in 100 mL ethanol.

 © 2005 Wiley-VCH Verlag GmbH & Co. KGaA, Weinheim

particle sizes decreased from 1500 to 400 nm when the amount of water in the solution increased from 0.2 to 0.4 mL per 100 mL ethanol. Analogous results were observed for particles synthesised with polymers such as Lutensol ON 50 (Table 1). With a large amount of water, the induction time of hydrolysis was very short; the hydrolysis was fast enough to generate a lot of primary particles. Because of the high density of primary particles, these particles agglomerated in an uncontrolled manner and became polydisperse. No precipitate was observed when the amount of water was below 0.1 mL. The average size increased depending on the initial concentration of $Zr(OBu)_4$. The sizes of the particles synthesised with Lutensol ON 50 increased from 300 to 1200 nm when the amount of zirconium tetrabutoxide increased from 1.25 to 5 mL per 100 mL ethanol (Figure 3, Table 2).

Table 1. Sizes of zirconia particles synthesised with various amounts of 0.1 M Lutensol ON 50 solution with addition of 5.00 mL zirconium butoxide in 100 mL ethanol.

Lutensol ON 50 (0.1 M solution in H_2O, mp) [mL]	Particle size [nm]
0.20	no precipitation
0.40	1200 ± 10%
0.50	1000 ± 10%
0.60	900 ± 10%
0.80	600–800
1.00	400–600

Table 2. Sizes of zirconia particles synthesised with various amounts of zirconium butoxide with addition of 0.40 mL of a 0.1 M NaCl solution in 100 mL ethanol.

$Zr(OBu)_4$ (80% solution in BuOH) [mL]	Particle size [nm]
1.25	300 ± 10%
2.50	450 ± 10%
3.25	550 ± 10%
2.75	700 ± 10%
4.25	1000 ± 10%
5.00	1200 ± 10%

Variation of Salts and Polymers

The stability of dispersion depends inter alia on the magnitude of the electric charge of the particles. Oxide surfaces in an aqueous medium are generally charged positively under acidic conditions and negatively under basic conditions. Similar to the measurements carried out by Kato et al.,[6] zeta potential values between 20 and 30 mV were detected in ethanol solution at pH 6 for our particles. For particles prepared with various salts, no significant differences were observed. In contrast, the zeta potential values obtained for titania particles synthesised with alkali halides increased from lithium chloride to caesium chloride, from 9 to 27 mV. The sizes and size distributions were very sensitive to the type of salt added.[8] The influence of alkali halides on the particles was not as strong as in the case of titania. The smallest particles were obtained, however, by addition of CsCl, the largest with LiCl (Table 3). Particles synthesised with pure Millipore water ranged between 300 and 1400 nm in size. We assume that interactions between the zirconium alkoxide, hydroxide and dioxide molecules and the salt ions are much weaker than those between the titanium compounds and salt ions.

Table 3. Sizes of zirconia particles synthesised with 0.40 mL of 0.1 M various salt or polymer solutions with addition of 3.25 mL zirconium butoxide in 100 mL ethanol.

Added salt or polymer	Particle size [nm]
CsCl	200 ± 10%
KCl	350 ± 10%
NaCl	550 ± 10%
LiCl	700 ± 10%
–	1000 ± 10%
Lutensol ON 50	600 ± 15%
Pluronic PE 6400	2000 ± 15%

The influence of polymers on the size and the size distribution of the colloidal particles was investigated in the next step. Two different types of polymers, diblock-copolymer Lutensol ON [$RO(CH_2CH_2O)_xH$] and triblock-copolymer Pluronic [PEO_n-PPO_m-PEO_n], were used for steric stabilisation. Depending on the amounts of water and zirconium tetrabutoxide, it was possible to obtain particles of up to 1200 nm with Lutensol ON 50 and of up to 2000 nm with Pluronic PE 6400. The hydrophilic part of Lutensol ON is likely to interact with the nanoparticle surface, while the hydrophobic part extends into the medium, thus providing additional steric stabilisation. In the case of Pluronic PE, the presence of two hydrophilic parts can be assumed to lead to a coating of the nanoparticle surfaces. The stabilisation by Pluronic polymers is not as effective and resulted in a broader size distribution of the titania particles. The same effect, but not as strongly pronounced, was observed for zirconia particles. The monodispersity of zirconia particles synthesised with Lutensol ON 50 was higher than that of particles prepared with Pluronic PE 6400.

In order to determine whether polymer molecules were built into the colloidal particles during the aggregation process, we carried out elementary analyses of as-synthesised zirconia powders. Elementary analyses showed carbon values of under 2%, which originated probably from untreated butoxide groups. Therefore, we assume that the polymer was not (or only in very small amounts) built into the final particles during the aggregation process. In the case of titania particles, higher amounts of carbon were observed. The interaction between polymer molecules and titanium alkoxide, hydroxide or dioxide was much stronger, so that polymer molecules were built into the particles. This resulted in porous titania particles with a specific surface area of a_s = 300 m^2/g in average, determined by the Brunauer–Emmett–Teller method. For zirconia particles, the values for the specific surface area were always below 10 m^2/g. Apparently, interactions between zirconium compounds and

 © 2005 Wiley-VCH Verlag GmbH & Co. KGaA, Weinheim

polymer molecules are too weak to prevent a compact aggregation of the primary particles.

X-ray Diffraction and Thermal Analysis

X-ray diffraction patterns showed that the as-prepared ZrO_2 powders were amorphous. The DTA plot of ZrO_2 particles synthesised with salts showed a very broad exothermic peak from 30 to 360 °C due to dehydration (Figure 4). For samples synthesised with polymers, a sharp exothermic peak was observed, probably corresponding to the spontaneous thermal decomposition of untreated alkoxy groups. Bound water and untreated alkoxy groups, lost below 400 °C, make up 40% of the total weight. That means, the synthesised zirconia particles, after storing for 7 d in an oven at 100 °C, contain 4 mol water and hydroxide groups per mol of zirconium dioxide. The total formula can be specified as $ZrO_x(OH)_{2-x}n\ H_2O$ with $(x + n = 4)$. The amount of untreated alkoxy groups should be very low. Elementary analysis exhibited carbon values of under 2%.

For particles synthesised with polymers, the transformation into the tetragonal phase proceeded by heating to 450 °C, and for particles synthesised with addition of salts, to 510 °C. The transition to the monoclinic phase (Baddeleyte) occurred between 600 and 800 °C. A shift to higher transition temperatures was observed for zirconia particles prepared with addition of salt (Figure 4 and Figure 5). High-temperature X-ray diffraction patterns support these results.

X-ray diffraction provided evidence for the existence of small crystalline domains of approximately 5 to 10 nm, so that the particle growth seems to be controlled by the aggregation of primary nuclei (Figure 1). The sizes of crystalline domains were calculated with the Scherrer Formula. The TEM picture clearly showed the rough surface of a zirconia particle and supports the aggregation growth mechanism for the formation of our colloids (Figure 6). The same growth mechanism was found for the titanium dioxide particles synthesised by a hydrolysis process with titanium alkoxide in ethanol.[8] Bogush and Zukowski proposed nucleation followed by aggregation as a model that would confer monodispersity of precipitates.[9] The model is based on the premise that nucleation proceeds for a substantial fraction of the reaction period and that nuclei, as well as small clusters of nuclei, aggregate faster with large particles than they do with each other. Mizutani et al.[5] also described the aggregation model as the best suitable model for the growth of zirconia particles. They specified that the primary particles are formed by the hydrolysis of alkoxides during the induction time. In the second step, these particles aggregate to form larger particles. The growth can be followed by light scattering and hence reduction of light intensity transmitting trough the solution, according to the Tyndall phenomenon. Kato et al.[2,6] investigated the initial growth step of zirconia particles. They observed the growth of nuclei to primary particles of about 10–20 nm by electron microscopy. In the next step, the aggregation to larger particles proceeded because of excess surface energy because of a small radius. Furthermore, they assumed that residual primary particles do not form secondary particles but promote the growth of the spheres. The aggregation mechanism was also described by Sada et al.[3] to be best suitable for the growth of zirconia particles. These authors summarised, according to the reaction kinetics, that if the reaction is very slow, the particle growth takes place through polycondensation of nuclei on the particle surface. In fast reactions, an aggregation process of nuclei grown to primary particles takes place. The clarification of the formation mechanism of hydroxide particles is not trivial, inter alia due to the amorphous state of the precipitated solids. On the basis of

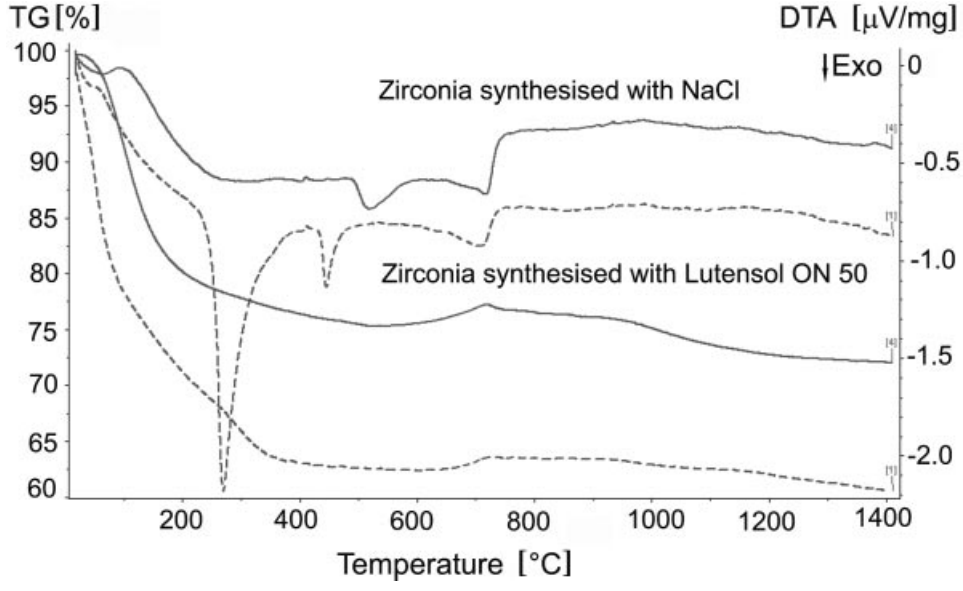

Figure 4. Thermal analysis of zirconia particles synthesised with addition of polymer molecules and with addition of salt ions.

 © 2005 Wiley-VCH Verlag GmbH & Co. KGaA, Weinheim

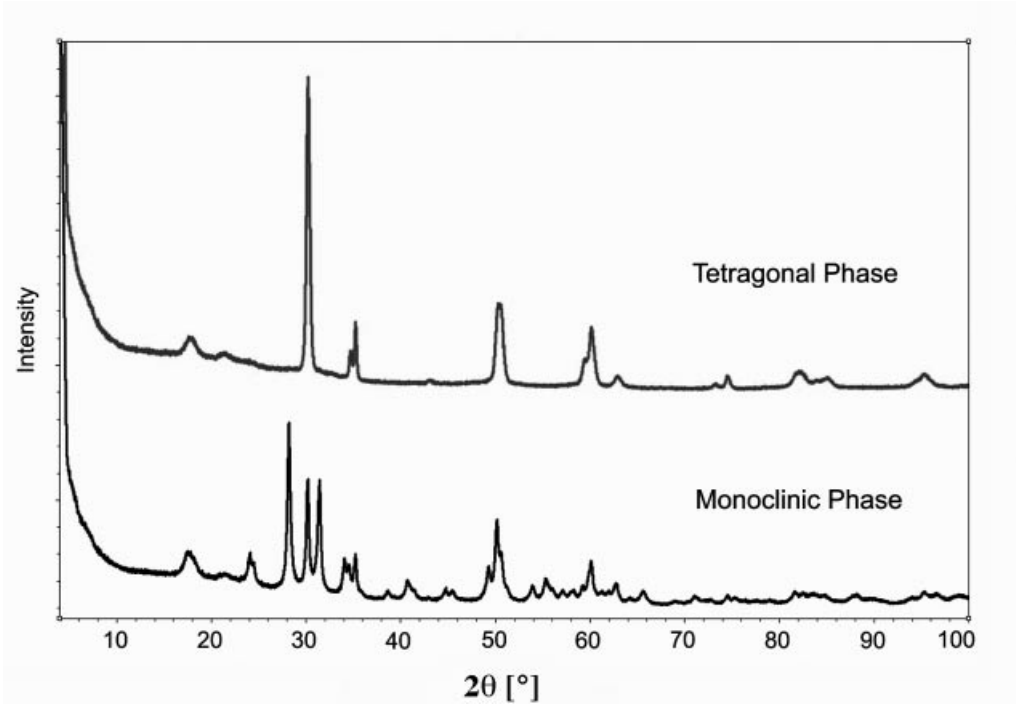

Figure 5. X-ray diffraction patterns of crystalline zirconia particles.

our results and on the literature, we assumed that the aggregation model describes the formation of our zirconia particles very well.

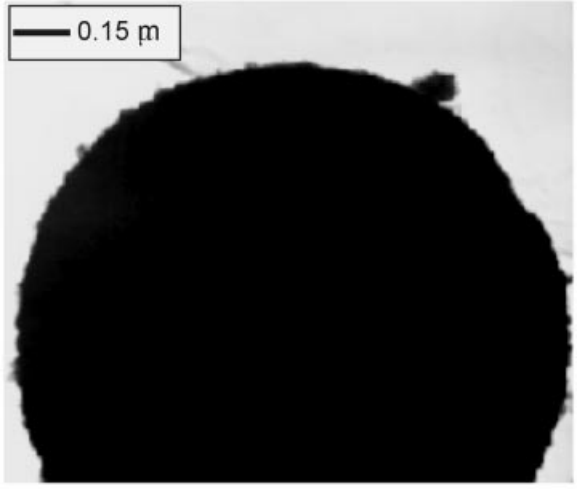

Figure 6. TEM picture illustrating the rough surface of a zirconia particle.

Silica-Coated Zirconia Particles

The surface properties of zirconia particles were controlled by coating with a silica layer. This was achieved by hydrolysis and condensation of TEOS in an ethanol/water/ammonia mixture. In the presence of ammonia as catalyst, the TEOS molecules were able to form bonds with the hydroxide groups of zirconia (Figure 7). The thermal and elementary analyses provided evidence for the existence of hydroxide groups and water at the particle surface. The total formula of zirconia particles was specified as ZrO_x-$(OH)_{2-x}$·nH_2O. The coat was formed according to the silica particle synthesis developed by Stöber et al.[11] Large zirconia spheres coated with fluorescent silica were visible in the CSLM. Therefore, fluorescein (APS-FITC) was added to the reaction solution. The dye molecules were incorporated into the shell. Figure 8 shows zirconia particles coated with a 50-nm thick shell of silica and APS-FITC in a one-step seeded growth process.

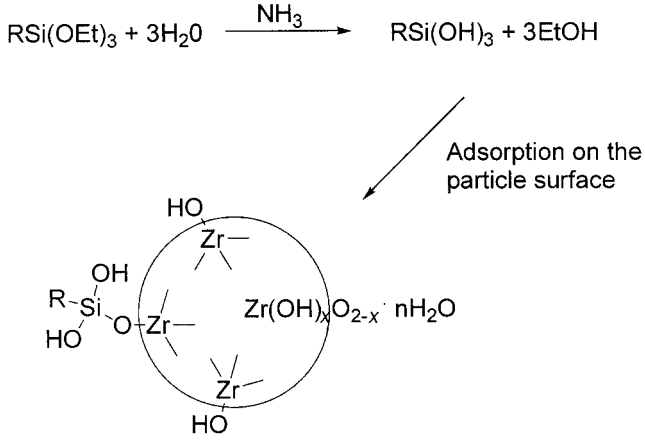

Figure 7. Coating of zirconia particles with TEOS.

 © 2005 Wiley-VCH Verlag GmbH & Co. KGaA, Weinheim

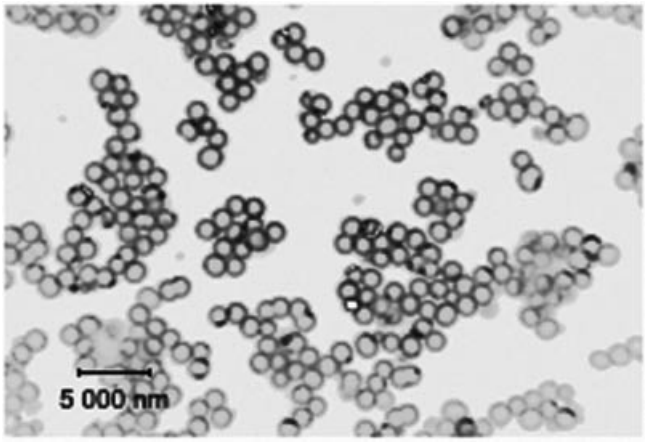

Figure 8. Confocal scanning laser micrograph of 1400 nm big zirconia particles coated with TEOS and fluorescein isothiocyanate acting as dye. The shell thickness is about 50 nm.

Conclusions

The controlled hydrolysis of alkoxides is a simple and powerful method to synthesise particles with well-defined sizes and narrow size distributions. Monodisperse, spherical ZrO_2 particles with sizes between 100 and 2000 nm were synthesised by hydrolysis. The size of the particles decreased with increasing reaction rate or with rising reaction temperature. Smaller particles were obtained with higher water concentration and larger particles with higher concentrations of zirconium butoxide. In contrast to the preparation of TiO_2 particles, in which salt ions and surfactant molecules were able to control the size of the particles and the porosity, the influence of such additives on the final zirconia particles is low. The surface properties of the zirconia particles were controlled by coating with a silica layer. The as-prepared powders were amorphous; a transition to crystalline forms was possible. The phase transition to the tetragonal phase occurred at about 450 °C, while the transition to the monoclinic phase began at 600 °C and was complete at about 800 °C.

Experimental Section

Materials: All reagents and solvents were used as received without further purification. Ethanol p.a., 1-propanol p.a., 1-butanol p.a. and alkali halide salts were purchased from Roth, zirconium alkoxides from Aldrich. Fluorescein isothiocyanate (FITC, isomer I) was purchased from Fluka, (3-aminopropyl)-triethoxysilane (APS) from Aldrich. Lutensol ON 50 and Pluronic PE 6400 were donated by BASF.

Synthesis of Zirconia Particles: In the synthesis of zirconia particles ethanol, 1-propanol and 1-butanol were used as solvents. Zirconium alkoxides like zirconium tetraethoxide, tetrapropoxide and tetrabutoxide were tested as precursors. Monodisperse spherical zirconia particles were synthesised by controlled hydrolysis of zirconium tetrabutoxide (80% solution in butanol) in ethanol. An ethanol volume of 100 mL was mixed with 0.2–0.6 mL of Millipore water, aqueous salt or polymer solution, followed by the addition of 3.25–5.00 mL zirconium tetrabutoxide at 60 °C under inert gas atmosphere, using a magnetic stirrer. Reagents had to be mixed completely, so that nucleation occurred uniformly throughout the solution. Depending on the concentration, visible particle formation started after several seconds or minutes and gave a uniform suspension of ZrO_2 beads. After 4 h, the reaction was finished, and the spheres were collected on a Millipore filter and washed with ethanol, or separated by centrifugation.

Coating of Zirconia Particles with Silica: A silica shell was formed around the zirconia particles by the following process: An aqueous ammonia solution (0.18 mL of a 25% solution) was added to a suspension of zirconia particles (100 mg) in ethanol (10 mL) whilst stirring. Subsequently, TEOS (0.2 mL) was added. To make the particles visible for CSLM, APS-FITC (0.01 mL) was added to the reaction solution. The reaction solution was stirred for 24 h, and the resulting particles were separated by filtration.

APS-FITC was synthesised in the following way: The dye FITC was covalently attached to the coupling agent APS by an addition reaction of the amine group with the thioisocyanate group. The reactants were slowly stirred for 12 h in ethanol, water was excluded to prevent hydrolysis and polymerisation of the APS molecules. 1 mL of ethanol p.a. was used per 0.1 g of APS.[7]

Characterisation of Zirconia Particles: The water content of the ZrO_2 beads was determined thermogravimetrically using a Netzsch-thermoanalyser STA 429 (under O_2, heating rate 10 K/min), combining thermogravimetry (TG), differential thermogravimetry (DTG) and differential thermal analysis (DTA). The crystallinity and phase-purity of the products were monitored by powder X-ray diffraction (XRD) using a Guinier-Huber camera 600 with Cu-$K_{\alpha 1}$ radiation. Scanning electron micrographs (SEM) were obtained with a Philips raster electron microscope (XL Series). Confocal scanning laser micrographs (CSLM) were obtained with a Zeiss Axiovert 200 with a Yokogawa confocal scanner. Electrophoretic mobility was measured with a Brookhaven Zetasizer. Particles were centrifuged out of suspension, and a small fraction of sedimented particles was resuspended in the supernatant again for use in mobility determinations. Nitrogen absorption isotherms were measured at 77 K with a Quantachrome Nova 3000 with samples which were degassed at 475 K and 1 mPa for 12 h.

Acknowledgments

We kindly acknowledge access to characterisation techniques in the groups of Prof. Dr. J. Felsche and Prof. Dr. E. Scheer. This work was performed with the financial support from the Deutsche Forschungsgemeinschaft (SPP, 1113 Ei488/2–1, University of Konstanz).

[1] U. Volz, *Zahnärztl. Implantol.* **2003**, *19*, 176.
[2] T. Ogihara, N. Mitzutani, M. Kato, *J. Am. Ceram. Soc.* **1989**, *72*, 421–426.
[3] H. Kumazawa, Y. Hori, E. Sada, *Chem. Eng. J.* **1993**, *51*, 129–133.
[4] B. Fegley, P. White, H. K. Bowen, *Am. Ceram. Soc. Bull.* **1985**, *64*, 1115–1120.
[5] L. Seok-Keun, M. Ikeda, N. Mizutani, *J. Ceram. Soc. Jpn, Int. Ed.*, *99*, 290–294.
[6] T. Ogihara, N. Mizutani, K. Kato, *Ceram. Int.* **1987**, *13*, 35–40.
[7] A. v. Blaaderen, A. Vrij, *Langmuir* **1992**, *8*, 2921.

 © 2005 Wiley-VCH Verlag GmbH & Co. KGaA, Weinheim

[8] S. Eiden-Assmann, J. Widoniak, G. Maret, *Chem. Mater.* **2004**, *16*, 6.
[9] G. H. Bogush, C. F. Zukoski, *Ultrastructure Processing of Advanced Ceramics* **1988**, 477.
[10] C. Sanchez, J. Livage, M. Henry, F. Babonneau, *J. Non-Cryst. Solids* **1988**, *100*, 65–76.
[11] W. Stöber, A. Fink, E. Bohn, *J. Colloid Interface Sci.* **1968**, *26*, 62–69.

Received: December 14, 2004
Published Online: July 4, 2005

 © 2005 Wiley-VCH Verlag GmbH & Co. KGaA, Weinheim

Self-Assembly of 1D to 3D Cadmium Complexes: Structural Characterization and Properties

Xing Li,[a] Rong Cao,*[a] Wenhua Bi,[a] Daqiang Yuan,[a] and Daofeng Sun[a]

Keywords: Cadmiun / Hydrothermal synthesis / Layered compounds / O ligands / Self-assembly

Self-assembly reactions of 5-sulfoisophthalic monosodium salt (NaH_2sipa), $Cd(NO_3)_2 \cdot 4H_2O$ and 2,2′-bipyridine (or 4,4′-bipyridine) under hydrothermal condition give rise to four polymeric complexes, namely $\{[Cd_3(sipa)_2(2,2'\text{-bpy})_4(H_2O)_2] \cdot 6H_2O\}_n$ (**1**), $\{[Cd(sipa)(H\text{-}4,4'\text{-bpy})(H_2O)] \cdot 2H_2O\}_n$ (**2**); $\{[Cd_2(sipa)(4,4'\text{-bpy})_3(H_2O)_3] \cdot [Cd(sipa)(4,4'\text{-bpy})(H_2O)] \cdot 8H_2O\}_n$ (**3**), and $\{[Cd_3(sipa)_2(4,4'\text{-bpy})_4(H_2O)_2] \cdot 3H_2O\}_n$ (**4**), respectively. X-ray diffraction analyses reveal that complex **1** possesses a 1D rail-like chain structure, **2** is a 1D double chain, **3** has a 2D network consisting of an independent $[Cd_2(sipa)(4,4'\text{-bpy})_3(H_2O)_3]_n^{n+}$ cationic layer and a $[Cd(sipa)(4,4'\text{-bpy})(H_2O)]_n^{n-}$ anionic layer, and **4** is a novel 3D self-penetrating network constructed from two mixed bridging ligands. Thermogravimetric analyses (TGA) and fluorescent measurements of complexes **1**–**4** have also been performed.

(© Wiley-VCH Verlag GmbH & Co. KGaA, 69451 Weinheim, Germany, 2005)

Introduction

The rational design and synthesis of metal–organic coordination polymers with different dimensional topological structures is of great current interest because these complexes are potential candidates as new materials with uses in fluorescence, magnetism, catalysis, nonlinear optics, gas absorption, as semiconductors, and so on.[1] In recent decades, these studies have been developed rapidly and have produced delightful outcomes in which the structures or properties of a great number of reported compounds have been finely tuned by controlling the inorganic/organic component properties such as size, coordination geometries of the metal ions, flexibility, symmetry, and functionality of the organic ligands.[2] However, there are many seemingly insurmountable challenges regarding the preparation of polymeric complexes with directed dimensional networks containing inorganic or organic components exhibiting distinct physical and/or chemical properties. One of the key steps to assemble unusual architectures is to select appropriate organic ligands containing functional coordinating groups, and rigid multidentate ligands are a good choice.[3] The carboxylate groups have a strong ability to bond various metal ions and afford abundant coordination modes, thus rigid multi-carboxylate ligands have been widely used for the design and synthesis of a great variety of structures.[4] Introduction of a sulfonate group into rigid multi-carboxylate ligands may result in the formation of unexpected frameworks as the sulfonic group has a different shape and properties in terms of its coordination ability compared to the carboxylate group. Studies on the coordination chemistry of multi-carboxylate-sulfonic ligands are not very common. 5-Sulfoisophthalic acid (H_3sipa) has three distinct properties: (1) it has multiple coordination sites that may lead to high dimensional structures; (2) it possesses a symmetric geometry and rigidity that may yield novel topological structures; (3) it contains two kinds of coordinating functional groups that may form diverse supramolecular networks. However, only a few coordination polymers containing this ligand have been reported in the past few decades.[5] By employing 5-sulfoisophthalic acid as an organic ligand, we have successfully prepared two unusual planar tetracopper(II) SBUs that were further extended into an infinite metal–organic framework by the bridging carboxylates of the $sipa^{3-}$ ligand, as well as two new zeolite-like supramolecular compounds.[6] Our previous work spurred us on to systematically study metal–sipa coordination chemistry and to investigate the correlation between structures and properties. It has been well-documented that the introduction of terminal ligands into a reaction system can result in the formation of low-dimensional networks as the terminal ligands reduce the available metal binding sites and restrict the polymer's growth in this direction,[7] and that long bridging ligands can induce a single unit to grow into high dimensional frameworks.[8] Thus, the terminal ligand 2,2′-pyridine (2,2′-bpy) or the rigid bridging ligand 4,4′-bipyridine (4,4′-bpy) were introduced into a reaction system containing Cd^{II} ions and the $sipa^{3-}$ ligand with the hope of isolating polymeric complexes with different dimensional structures. Here we report the syntheses, structural

[a] State Key Laboratory of Structural Chemistry, Fujian Institute of Research on the Structure of Matter, Chinese Academy of Sciences,
Fujian, Fuzhou, 350002, China
E-mail: rcao@ms.fjirsm.ac.cn

Supporting information for this article is available on the WWW under http://www.eurjic.org or from the author.

 © 2005 Wiley-VCH Verlag GmbH & Co. KGaA, Weinheim **DOI: 10.1002/ejic.200400983**

characterizations, and fluorescent properties of four novel cadmium complexes $\{[Cd_3(sipa)_2(2,2'\text{-bpy})_4(H_2O)_2]\cdot 6H_2O\}_n$ (**1**), $\{[Cd(sipa)(H\text{-}4,4'\text{-bpy})(H_2O)]\cdot 2H_2O\}_n$ (**2**), $\{[Cd_2(sipa)(4,4'\text{-bpy})_3(H_2O)_3]\cdot[Cd(sipa)(4,4'\text{-bpy})(H_2O)]\cdot 8H_2O\}_n$ (**3**), and $\{[Cd_3(sipa)_2(4,4'\text{-bpy})_4(H_2O)_2]\cdot 3H_2O\}_n$ (**4**). Complexes **1** and **2** possess one-dimensional structures, **3** contains a two-dimensional network consisting of independent cationic and anionic layers, and **4** assumes a novel self-penetrating three-dimension framework and has been briefly reported by us.[9]

Results and Discussion

Preparation of the Complexes

Coordination complexes of $sipa^{3-}$ with transition metals have been reported by our group and others recently,[5,6] but systematic studies on the coordination chemistry of $sipa^{3-}$ have been ignored. Our aim is to employ the hydrothermal method, which has been proven to be a very effective way for the synthesis of zeolite frameworks and high dimensional polymers, and to obtain novel structures by utilizing the $sipa^{3-}$ ligand's abundant coordination modes. It is well known that reaction parameters such as temperature, pH, and the ratio of reactants, as well as the addition of other ligands, can exert a profound influence on the final products under supercritical conditions. In this work, we focus on the influence of a second ligand and the molar ratio of the starting reactants. We started our work by using 2,2′-bpy as second ligand in the hydrothermal reaction of H_2sipa^-, Cd^{2+}, EtOH, and H_2O. Complex **1**, which possesses a 1D rail-like structure was prepared and no influence of the molar ratio of the reactants was observed. 2,2′-Bpy usually acts as a terminal ligand that chelates a metal ion to give low-dimensional structures, whereas 4,4′-bpy can assume different coordination modes (Scheme 1) and may generate 1D to 3D structures. Thus, 4,4′-bpy was employed instead of 2,2′-bpy with the hope of isolating different structures with varied coordination modes of 4,4′-bpy. When 4,4′-bpy replaces 2,2′-bpy in the hydrothermal reaction of H_2sipa^-, Cd^{2+}, and H_2O (H_2sipa^-/Cd^{2+}/4,4′-bpy = 1:1:1), complex **2**, with 1D double-chain, was isolated, which contains a protonated pyridine nitrogen atom with the 4,4′-bpy ligand acting as a monodentate ligand to a metal ion (Scheme 1b). When the molar ratio H_2sipa^-/Cd^{2+}/4,4′-bpy was changed to 2:3:5, the reaction yielded complex **3** with a 2D layer structure. In **3**, the 4,4′-bpy ligand displays two kinds of coordination modes: monodentate to coordinate a single metal ion and bidentate to bridge two metal ions (Scheme 1c and d). When the molar ratio H_2sipa^-/Cd^{2+}/4,4′-bpy was 4:3:4, complex **4**, which contains a 3D self-penetrating framework, was obtained, where the 4,4′-bpy acts as bidentate ligand to link two metal ions (Scheme 1, part d). Hence, by changing the molar ratio of reactants and utilizing a terminal or bridging secondary ligand, we have prepared 1D to 3D cadmium coordination complexes. In this reaction system the bpy ligands not only play the role of chelating or linking metal ions but also control the base/acid balance by protonating/deprotonating reactions between the pyridine nitrogen atoms and carboxylate groups.[5b] To confirm the purity, X-ray powder diffraction analyses (XRPD) were performed for all four complexes (see Supporting Information). These results show that the purity of the complexes is good enough to support our conclusions.

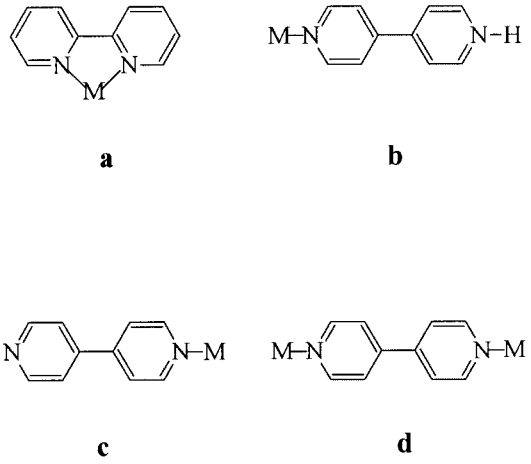

Scheme 1.

Description of Crystal Structures

$\{[Cd_3(sipa)_2(2,2'\text{-bpy})_4(H_2O)_2]\cdot 6H_2O\}_n$ (1)

Single crystal X-ray diffraction reveals that complex **1** possesses a one-dimensional structure constructed from Cd ions and $sipa^{3-}$ and 2,2′-bpy ligands, in which there are two types of coordination environments around the Cd ions. As shown in Figure 1, Cd1 is coordinated by two oxygen atoms from two SO_3 groups of $sipa^{3-}$ ligands and four nitrogen atoms from two 2,2′-bpy ligands. The two oxygen atoms occupy the axial positions, with an O1–Cd1–O1A bond angle of 180°, while the four nitrogen atoms are located in the equatorial plane, with the bond angles N1–Cd1–N1A and N2–Cd1–N2A being 180° and N1–Cd1–O1 and N2–Cd1–O1 being 87.6° and 89.7°, respectively, thus forming a slightly distorted octahedral geometry). The 2,2′-bpy ligand

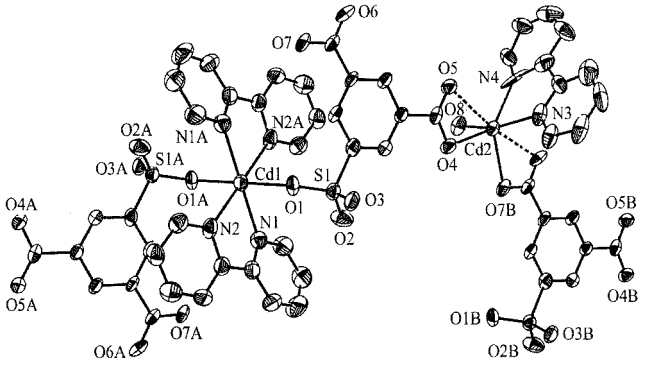

Figure 1. Ortep drawing of the coordination environments around the Cd ions in **1** with thermal ellipsoids at 30% probability. The isolated water molecules have been omitted for clarity.

 © 2005 Wiley-VCH Verlag GmbH & Co. KGaA, Weinheim

binds in a chelate fashion to the metal ion and its two pyridine rings suffer from distortion, with a dihedral angle of 21°. Cd2 is in a distorted pentagonal-bipyramidal coordination environment and is coordinated by two nitrogen atoms (N3 and N4) from the bpy ligand, four oxygen atoms (O4–O7) from chelating carboxylates, and one oxygen atom (O8) (Table 1) from a water molecule, with the four carboxylate oxygen atoms and a nitrogen atom (N4) being located in the equatorial plane with Cd–O distances ranging from 2.292 to 2.616 Å and Cd2–N4 being 2.112 Å; O8 and N3 occupy the axial positions with bond lengths of 2.269 and 2.313 Å, respectively. Here, the long distances of Cd2···O6B (2.560 Å) and Cd2···O5 (2.616 Å) indicate a weak chelating interaction with the metal ions, which may be regarded as a semi-chelate coordination mode.[10] Therefore, Cd2 can also be described as having a pseudo pentagonal bipyramidal coordination geometry. The average bond lengths around Cd1 (2.317 Å) are somewhat shorter than those of Cd2 (2.354 Å), which is understandable due to the weak chelate interaction of the carboxylates in Cd2. The bond lengths S1–O1 (1.452 Å), S1–O2 (1.441 Å), and S1–O3 (1.449 Å) fall within the typical range of S–O bond lengths in a sulfonate ion (1.40–1.50 Å), and the distance C1–S1 (1.788 Å) is also as expected for a $sipa^{3-}$ ligand.[11] Due to the chelating carboxylate and the monodentate sulfonate, the $sipa^{3-}$ unit acts as three-armed connector that links a

Table 1. Selected bond lengths [Å] and angles [°] for **1**.[a]

Cd(1)–N(2)	2.284(9)	Cd(2)–O(4)	2.314(7)
Cd(1)–N(1)	2.327(10)	Cd(2)–O(6)#2	2.560(7)
Cd(1)–O(1)	2.341(7)	Cd(2)–O(5)	2.616(7)
Cd(2)–N(4)	2.112(17)	S(1)–O(2)	1.441(8)
Cd(2)–O(8)	2.269(8)	S(1)–O(3)	1.449(8)
Cd(2)–O(7)#2	2.292(8)	S(1)–O(1)	1.452(7)
Cd(2)–N(3)	2.313(10)	S(1)–C(1)	1.788(11)
N(2)–Cd(1)–N(2)#1	180.000(2)	N(3)–Cd(2)–O(4)	99.2(3)
N(2)–Cd(1)–N(1)	72.3(4)	N(4)–Cd(2)–O(6)#2	90.6(4)
N(2)#1–Cd(1)–N(1)	107.7(4)	O(8)–Cd(2)–O(6)#2	88.1(3)
N(1)#1–Cd(1)–N(1)	180.000(1)	O(7)#2–Cd(2)–O(6)#2	53.1(3)
N(2)–Cd(1)–O(1)#1	90.3(3)	N(3)–Cd(2)–O(6)#2	87.6(3)
N(1)–Cd(1)–O(1)#1	92.4(3)	O(4)–Cd(2)–O(6)#2	136.7(3)
N(2)–Cd(1)–O(1)	89.7(3)	N(4)–Cd(2)–O(5)	80.0(4)
N(1)–Cd(1)–O(1)	87.6(3)	O(8)–Cd(2)–O(5)	91.7(3)
O(1)#1–Cd(1)–O(1)	180.000(1)	O(7)#2–Cd(2)–O(5)	136.1(3)
N(4)–Cd(2)–O(8)	89.9(4)	N(3)–Cd(2)–O(5)	89.5(3)
N(4)–Cd(2)–O(7)#2	142.9(4)	O(4)–Cd(2)–O(5)	52.6(2)
O(8)–Cd(2)–O(7)#2	96.0(3)	O(6)#2–Cd(2)–O(5)	170.7(3)
N(4)–Cd(2)–N(3)	71.0(4)	O(2)–S(1)–O(3)	111.9(6)
O(8)–Cd(2)–N(3)	160.4(4)	O(2)–S(1)–O(1)	113.8(5)
O(7)#2–Cd(2)–N(3)	96.7(4)	O(3)–S(1)–O(1)	110.8(4)
N(4)–Cd(2)–O(4)	132.1(4)	O(2)–S(1)–C(1)	106.3(5)
O(8)–Cd(2)–O(4)	97.0(3)	O(3)–S(1)–C(1)	106.2(5)
O(7)#2–Cd(2)–O(4)	83.6(3)	O(1)–S(1)–C(1)	107.5(5)

[a] Symmetry transformations used to generate equivalent atoms: #1 $-x, -y, -z + 1$; #2 $x, y + 1, z$.

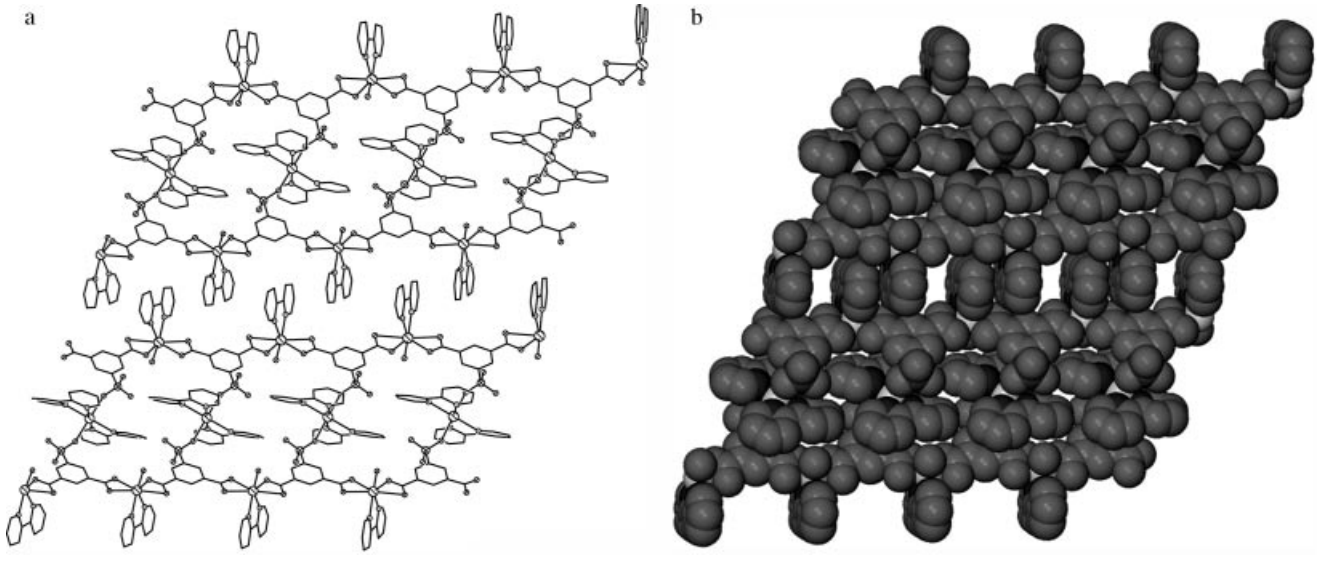

Figure 2. (a) Two-dimensional layer structure of **1**. (b) Space-filling diagram.

 © 2005 Wiley-VCH Verlag GmbH & Co. KGaA, Weinheim

Cd1 and two Cd2. Two Cd1 and four Cd2 centers form a grid unit $[Cd_6(sipa)_4]$ with the shortest Cd2–Cd2A and Cd1–Cd2 distances being 10.211 Å and 9.997 Å, respectively. Such units are extended into a 1D rail-like sheet by connection with a $sipa^{3-}$ ligand, with all metal ions located in the same plane. As expected, the presence of 2,2′-bipy and the coordinated water molecules around Cd2 prevents the one-dimensional chain from being further extended into a higher-dimensional network by covalent bonding (e.g. 2D or 3D), similar to those found in other metal/carboxylate/bpy reaction systems.[12] All pyridine rings of the 2,2′-bpy linking Cd2 orientate toward the outside of the one-dimensional sheet. The nearest distance of a pyridine ring to the adjacent sheet (3.383 Å) suggests a strongly offset face-to-face π···π stacking interaction and results in a 2D network (Figure 2). Complex **1** finally forms a 3D packing structure by hydrogen bonding and off-set face-to-face π···π stacking interactions.

{[Cd(sipa)(H-4,4′-bpy)(H$_2$O)]·2H$_2$O}$_n$ (2)

Compared with that in **1**, the $sipa^{3-}$ ligand in **2** shows different coordination modes: one carboxylate group chelates a Cd ion and the other bridges two Cd ions; the sulfonate group remains uncoordinated. In complex **2**, the 4,4′-bpy ligand is protonated at one end and acts as a monodentate ligand to coordinate to the metal ion; H_2sipa^- transfers its proton to a pyridine nitrogen atom for charge balance, which may be regarded as an acid-base reaction similar to those in previous reports.[5b,13] The Cd ion in **2** adopts a distorted octahedral geometry (Figure 3) and is coordinated in the equatorial plane by one monodentate carboxylate oxygen (O3A–Cd1 = 2.278 Å), one chelating carboxylate group (O1–Cd1 = 2.261 Å; O2···Cd1 = 2.535 Å), and one pyridine nitrogen (N1–Cd1 = 2.287 Å). The axial positions are occupied by one carboxylate oxygen (O4B–Cd1 = 2.389 Å) and one coordinated water molecule (O8–Cd1 = 2.324 Å; Table 2). Each two Cd ions are bridged by two carboxylate groups to form a binuclear cluster unit with a Cd–Cd distance of 3.877 Å. Each binuclear unit is interconnected by two $sipa^{3-}$ ligands to form a one-dimensional double chain along the diagonal of the *a*- and *b*-axes (Figure 4). Although 4,4′-bpy has replaced 2,2′-bpy, one of its nitrogen atoms is protonated and the sulfonate group remains uncoordinated, which results in the one-dimensional chain structure of **2**. The 1D double chain is extended into a 2D layer by hydrogen-bonding interactions, and a three dimensional framework is finally formed by hydrogen bonding and off-set face-to-face π···π stacking interactions between the benzene rings and the pyridine rings of adjacent 2D layers, with distance of about 3.40 Å.

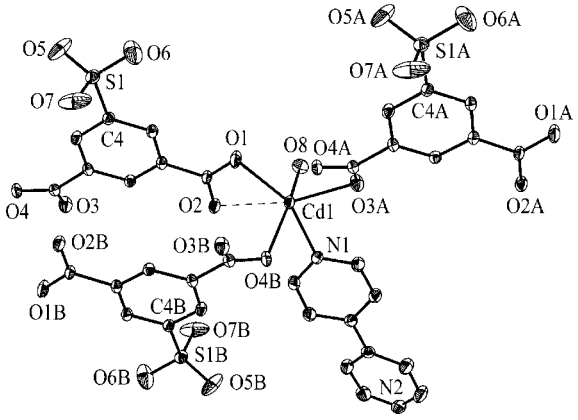

Figure 3. Ortep view of the coordination environment around the Cd ion in **2** with thermal ellipsoids at 30% probability. The isolated water molecules have been omitted for clarity.

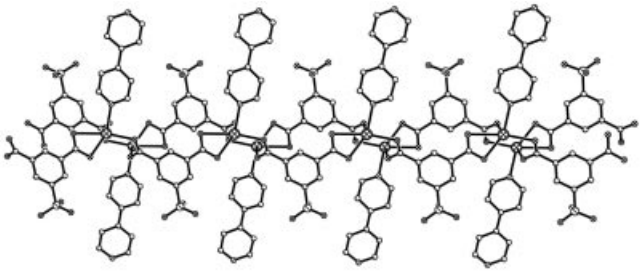

Figure 4. The 1D double-chain along the diagonal of the *a*- and *b*-axes in **2**.

Table 2. Selected bond lengths [Å] and angles [°] for **2**.[a]

Cd(1)–O(1)	2.261(4)	Cd(1)–O(2)	2.535(3)
Cd(1)–O(3)#1	2.278(4)	S(1)–O(6)	1.417(5)
Cd(1)–N(1)	2.287(4)	S(1)–O(5)	1.418(5)
Cd(1)–O(8)	2.324(4)	S(1)–O(7)	1.425(5)
Cd(1)–O(4)#2	2.389(3)	S(1)–C(4)	1.779(5)
O(1)–Cd(1)–O(3)#1	116.89(13)	O(1)–Cd(1)–O(8)	94.29(16)
O(1)–Cd(1)–N(1)	154.97(14)	O(3)#1–Cd(1)–O(8)	86.79(15)
O(3)#1–Cd(1)–N(1)	88.13(14)	N(1)–Cd(1)–O(8)	85.95(15)
O(1)–Cd(1)–O(4)#2	90.96(14)	O(4)#2–Cd(1)–O(2)	82.26(12)
O(3)#1–Cd(1)–O(4)#2	107.93(14)	O(6)–S(1)–O(5)	113.0(4)
O(8)–Cd(1)–O(4)#2	160.02(13)	O(6)–S(1)–O(7)	110.7(4)
O(1)–Cd(1)–O(2)	53.87(12)	O(5)–S(1)–O(7)	112.8(4)
O(3)#1–Cd(1)–O(2)	167.21(14)	O(6)–S(1)–C(4)	107.4(3)
N(1).–Cd(1)–O(2)	101.32(13)	O(5)–S(1)–C(4)	107.0(3)
O(8)–Cd(1)–O(2)	85.32(13)	O(7)–S(1)–C(4)	105.4(2)

[a] Symmetry transformations used to generate equivalent atoms: #1 $x + 1$, $y + 1$, z; #2 $-x$, $-y$, $-z + 1$.

 © 2005 Wiley-VCH Verlag GmbH & Co. KGaA, Weinheim

{[Cd_2(sipa)(4,4′-bpy)$_3$(H_2O)$_3$]·[Cd(sipa)(4,4′-bpy)-(H_2O)]·8H_2O}$_n$ (3)

X-ray diffraction analysis shows that complex **3** has a two-dimensional structure that is different from those in a great number of 2D complexes previously reported[14] – it consists of independent cationic [Cd_2(sipa)(4,4′-bpy)$_3$-(H_2O)$_3$]$_n^{n+}$ and anionic [Cd(sipa)(4,4′-bpy)(H_2O)]$_n^{n-}$ layers. In the cationic layer, two crystallographically different coordinatio environments are observed around Cd1 and Cd2 (Figure 5). Cd1 is six-coordinate, with three carboxylate oxygen atoms and one nitrogen atom in the equatorial plane and one water molecule and one nitrogen atom occupying the axial positions to form a distorted octahedral coordination geometry. Cd2 also adopts a distorted octahedral coordination geometry and is coordinated in the equatorial plane by three nitrogen atoms from pyridine rings and one oxygen atom from a sulfonate group, with two coordinated water molecules located in the axial positions. However, Cd3 in the anionic layer has a slightly distorted pentagonal-bipyramidal coordination environment, with

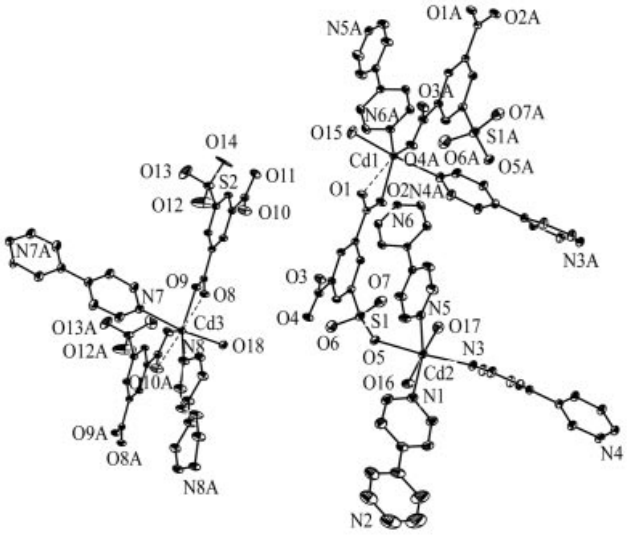

Figure 5. Ortep views of the coordination environments around the Cd ions in **3** with thermal ellipsoids at 30% probability. The isolated water molecules have been omitted for clarity.

Table 3. Selected bond lengths [Å] and angles [°] for **3**.[a]

Cd(1)–O(4)#1	2.296(10)	Cd(3)–O(10)#4	2.559(13)
Cd(1)–O(15)	2.298(11)	Cd(3)–O(8)	2.583(13)
Cd(1)–N(6)#2	2.314(11)	S(1)–O(6)	1.445(8)
Cd(1)–O(2)	2.345(9)	S(1)–O(7)	1.447(7)
Cd(1)–N(4)#3	2.354(12)	S(1)–O(5)	1.465(7)
Cd(1)–O(1)	2.504(12)	S(1)–C(4)	1.776(9)
Cd(2)–N(3)	2.299(11)	S(2)–O(12′)	1.409(12)
Cd(2)–O(5)	2.323(11)	S(2)–O(13)	1.411(9)
Cd(2)–N(5)	2.327(11)	S(2)–O(14)	1.415(10)
Cd(2)–O(16)	2.330(12)	S(2)–O(12)	1.422(12)
Cd(2)–O(17)	2.363(12)	S(2)–O(14′)	1.422(8)
Cd(2)–N(1)	2.368(10)	S(2)–O(13′)	1.460(9)
Cd(3)–N(8)	2.317(11)	S(2)–C(12)	1.780(9)
Cd(3)–O(18)	2.319(11)	N(8)–C(56)	1.372(11)
Cd(3)–O(11)#4	2.344(10)	N(8)–C(56′)	1.430(9)
Cd(3)–O(9)	2.356(9)	C(54)–C(55)	1.408(11)
Cd(3)–N(7)	2.368(12)	C(54)–C(55′)	1.485(11)
O(4)#1–Cd(1)–O(15)	82.1(4)	O(5)–Cd(2)–N(5)	86.8(5)
O(4)#1–Cd(1)–N(6)#2	133.6(2)	N(3)–Cd(2)–O(16)	93.9(3)
O(15)–Cd(1)–N(6)#2	89.5(5)	O(5)–Cd(2)–O(16)	96.1(3)
O(4)#1–Cd(1)–O(2)	84.0(4)	N(5)–Cd(2)–O(16)	86.6(3)
O(15)–Cd(1)–O(2)	94.2(4)	N(3)–Cd(2)–O(17)	86.3(3)
N(6)#2–Cd(1)–O(2)	142.3(2)	O(5)–Cd(2)–O(17)	83.4(3)
O(2)–Cd(1)–N(4)#3	85.3(4)	N(5)–Cd(2)–O(17)	99.0(3)
O(4)#1–Cd(1)–O(1)	136.0(3)	O(16)–Cd(2)–O(17)	174.34(11)
O(15)–Cd(1)–O(1)	90.0(3)	N(3)–Cd(2)–N(1)	94.7(5)
N(6)#2–Cd(1)–O(1)	89.1(3)	O(5)–Cd(2)–N(1)	82.8(5)
O(2)–Cd(1)–O(1)	53.4(2)	N(5)–Cd(2)–N(1)	165.44(13)
N(4)#3–Cd(1)–O(1)	98.6(3)	O(16)–Cd(2)–N(1)	84.5(3)
N(3)–Cd(2)–O(5)	169.38(12)	O(17)–Cd(2)–N(1)	89.8(3)
N(3)–Cd(2)–N(5)	97.4(5)	N(8)–Cd(3)–O(18)	92.4(5)
N(8)–Cd(3)–O(11)#4	137.9(2)	O(18)–Cd(3)–O(10)#4	92.5(3)
O(18)–Cd(3)–O(11)#4	85.4(4)	O(11)#4–Cd(3)–O(10)#4	52.7(3)
N(8)–Cd(3)–O(9)	139.4(2)	O(9)–Cd(3)–O(10)#4	135.1(2)
O(18)–Cd(3)–O(9)	85.8(4)	N(7)–Cd(3)–O(10)#4	89.7(3)
O(11)#4–Cd(3)–O(9)	82.5(4)	N(8)–Cd(3)–O(8)	87.1(2)
N(8)–Cd(3)–N(7)	100.4(5)	O(18)–Cd(3)–O(8)	92.4(3)
O(18)–Cd(3)–N(7)	167.18(10)	O(11)#4–Cd(3)–O(8)	135.0(2)
O(11)#4–Cd(3)–N(7)	85.9(4)	O(9)–Cd(3)–O(8)	52.5(2)
O(9)–Cd(3)–N(7)	83.7(4)	N(7)–Cd(3)–O(8)	87.1(3)
N(8)–Cd(3)–O(10)#4	85.5(3)	O(10)#4–Cd(3)–O(8)	171.34(11)

[a] Symmetry transformations used to generate equivalent atoms: #1 $x + 1$, y, z; #2 $-x + 2$, $-y + 1$, $-z + 1$; #3 $-x + 2$, $-y + 1$, $-z$; #4 $x - 1$, y, z.

 © 2005 Wiley-VCH Verlag GmbH & Co. KGaA, Weinheim

one pyridine nitrogen and a water molecule in the axial positions and two chelating carboxylate groups and one nitrogen atom in the equatorial plane (Figure 5). The distances Cd3···O10A, Cd3···O8, and Cd1···O1 are 2.559, 2.584, and 2.504 Å, respectively, indicating a weak chelate interaction similar to that in **1**.[5,6] C55 and C56 of the 4,4′-bipyridine ring and O12, O13, and O14 of the SO_3 group of the sipa^{3-} ligand are disordered over two positions with bond length C55–C54 = 1.408 Å, C55′–C54 = 1.485 Å and C56–N8 = 1.372 Å, C56′–N8 = 1.430 Å (Table 3).

In the anionic layer each 4,4′-bpy ligand bridges two cadmium ions to yield a zigzag chain along the *c* axis. This chain forms a two dimensional step-like network by the linkage of the sipa^{3-} ligand through its two chelating carboxylate groups in the *ac* plane; the sulfonate groups do not engage in coordination and stand at the zygomorphic sides of the layer (Figure 6, part a). The layer contains two kinds of grids with different dimensions: side lengths 10.237 × 11.813 Å and diagonal distances 15.342 × 15.916 Å based on the metal–metal interval for **A**, and side 10.237 × 11.731 Å and diagonal 15.286 × 15.865 Å for **B**. The dihedral angle between **A** and **B** is 105.50°. On the other hand, the parallelogram 34-membered $Cd_4(sipa)_2(4,4'\text{-bpy})_2$ macro grid can be regarded as a basic building block for the whole 2D step-like structure. Each two $Cd_4(sipa)_2(4,4'\text{-bpy})_2$ units are linked together to form a ladder-like chain by sharing a Cd-bpy-Cd side, and the adjacent ladders are connected by 4,4′-bpy ligands to generate the final 2D step-like layer (Figure 6, part b).

In the cationic layer the sipa^{3-} acting as a three-armed ligand utilizes its monodentate and chelating carboxylate groups to link Cd1 to produce a one-dimensional cationic chain. Each two such chains are connected together by bridges formed by monodentate sulfonate, 4,4′-bpy, and Cd2 to yield a double chain along the *a* axis (Figure 7, part a). In fact, the double chain is an infinite brick-like sheet with a width of about 17.204 Å and height of about 3.710 Å from the closest pyridine ring center to the benzene ring center (the height is almost equal to the sum of the S–O and O–Cd distances). The uncoordinated end of 4,4′-bpy points outside of the brick-like sheet. On the other hand, the cadmium ions and the 4,4′-bpy ligands propagate into a zigzag chain along the *c* axis, and two such chains are fastened together by a sipa^{3-} ligand through its chelating carboxylates and monodentate sulfonate groups to yield a double zigzag cationic chain (Figure 7, part b). The infinite brick-like sheets (Figure 7, part a) and the double zigzag chains (Figure 7, part b) are connected by the sipa^{3-} ligands as linkers and the cadmium ions as nodes to form a two-dimensional cationic step-like network; the uncoordinated pyridine ends of 4,4′-bpy ligands fall on different sides of the step-like plane (Figure 7, part c).

The step-like cationic layer and the step-like anionic layer have an alternate arrangement, where the uncoordinated end of 4,4′-pyridine from the cationic layer penetrates into the cavities of the anionic layer to form a tightly stacked neutral structure through electrostatic forces as well as hydrogen-bonding interactions between carboxylate oxygen atoms, pyridine nitrogen atoms, and free water molecules that are present between the cationic and anionic layers (Figure 8).

It's interesting that the 4,4′-bpy ligands in **3** play different roles in the cationic layer: one acts as a bridging ligand results in the formation of the two dimensional structure,

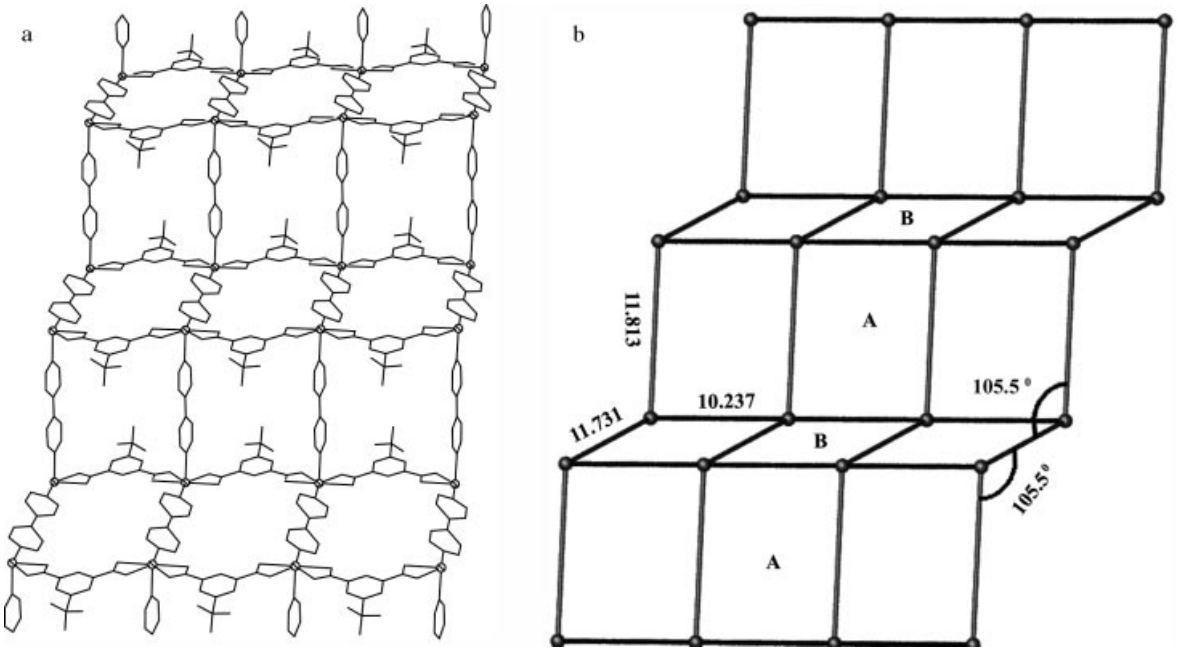

Figure 6. (a) The 2D step-like structure along the *a* axis of **3**. (b) Schematic plot of the 2D step-like structure.

 © 2005 Wiley-VCH Verlag GmbH & Co. KGaA, Weinheim

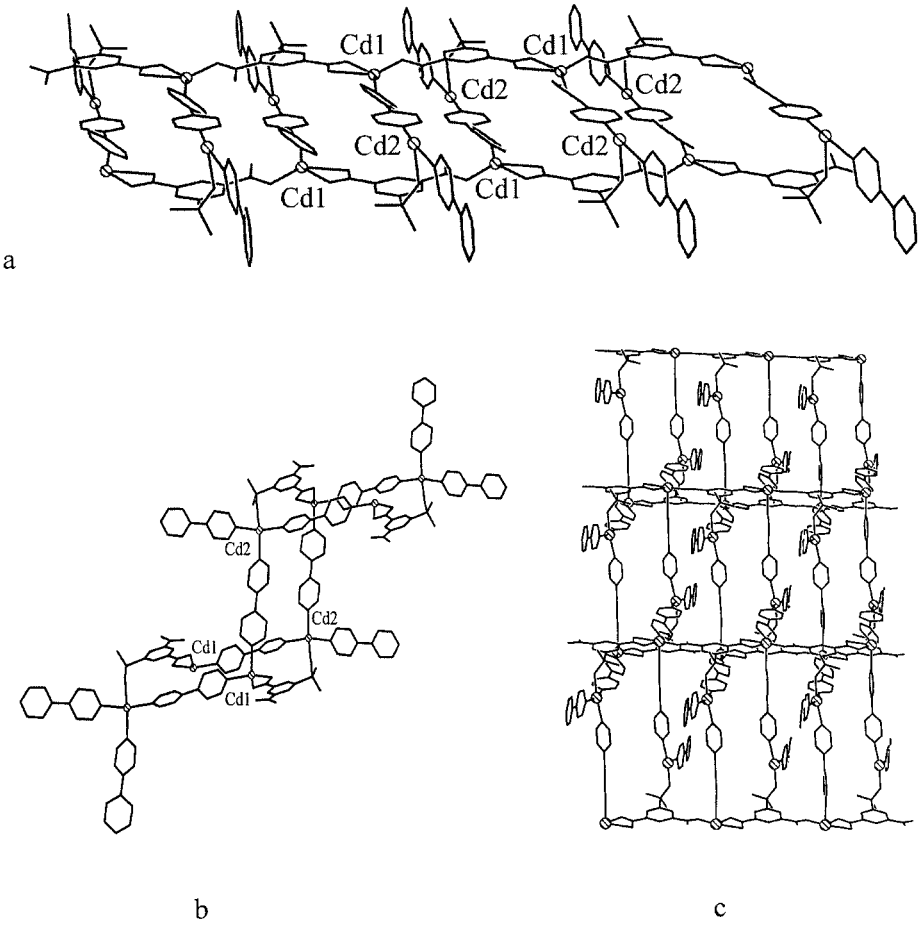

Figure 7. (a) The infinite brick-like sheet along the *c* axis of **3**. (b) The double zigzag chain along the *a* axis. (c) The step-like network.

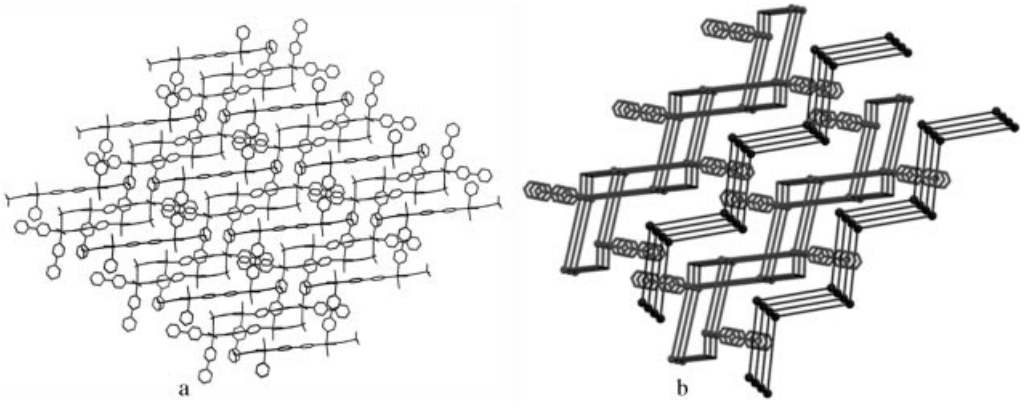

Figure 8. (a) Profile of the stacking structure along the *a* axis of **3**. (b) The stacking structure of **3**, with red representing the step-like cationic layer and blue representing the step-like anionic layer.

whereas the other, in which one nitrogen remains free and does not engage in coordination to the metal ion, acts as a terminal ligand that prevents the formation of three dimensional networks, although the $sipa^{3-}$ ligands employ all their coordination functional groups. In the anionic layer, one 4,4′-bpy bridges two metal ions and two carboxylate groups of $sipa^{3-}$ chelate one metal ion, leading to the formation of a two-dimensional structure; the sulfonate group remains uncoordinated to prevent the formation of three-dimensional frameworks. To the best of our knowledge, **3** is the first example of independent cationic and anionic layers in the structural framework of cadmium sulfonate-carboxylate complexes, which have only rarely been reported in other metal–organic compounds.[15]

 © 2005 Wiley-VCH Verlag GmbH & Co. KGaA, Weinheim

{[Cd_3(sipa)$_2$(4,4′-bpy)$_4$(H_2O)$_2$]·3H_2O}$_n$ (4)

The structure of **4** has already been described in our previous report[9] and a detailed discussion will not be made here. In **4**, four $sipa^{3-}$ ligands and four cadmium ions form a 32-membered-ring $Cd_4(sipa)_4$ unit, which then propagates into a one-dimensional ladder-like double chain by sharing the $sipa^{3-}$ ligands as sides. Four cadmium ions and four bpy ligands encircle a $Cd_4(bpy)_4$ unit[16,17] and the $Cd_4(bpy)_4$ units are further extended into a one-dimensional twisted 8-like chain by sharing vertex cadmium ions. The two types of one-dimensional chains are interlocked and interwoven into a two-dimensional framework by sharing cadmium ions in the *ab* plane (Figure 9 and Table 4). The most intriguing feature is that the two kinds of $Cd_4(sipa)_4$ and $Cd_4(bpy)_4$ units interlock and interconnect each other to produce a pseudocatenate structure. Each $Cd_4(bpy)_4$ unit interlocks two $Cd_4(sipa)_4$ units and each $Cd_4(sipa)_4$ interlocks two $Cd_4(bpy)_4$ through cadmium ion nodes to yield an interwoven structure that is further magnified in different directions into a new three-dimensional, self-penetrating topological network (Figure 10).[18]

Both $sipa^{3-}$ and 4,4′-bpy ligands in **4** take full advantage of their coordination functional groups to link metal ions and generate a new self-penetrating three-dimensional framework, whereas in **1** the presence of the 2,2′-bipy ligand prevents the one-dimensional chain from being further extended into a 2D or 3D network even though the $sipa^{3-}$ ligands employ all their functional groups in coordination. In **2** and **3**, although 4,4′-bpy replaces 2,2′-bpy, one nitrogen atom of the pyridine ligand does not engage in coordination or the sulfonate group remains uncoordinated, which results in preventing the formation of a 3D structure. Thus, the design and syntheses of coordination complexes with different dimensional structures may be carried out by the control or modification of the properties of e coordinating functional groups and/or introduction of a second organic ligand.

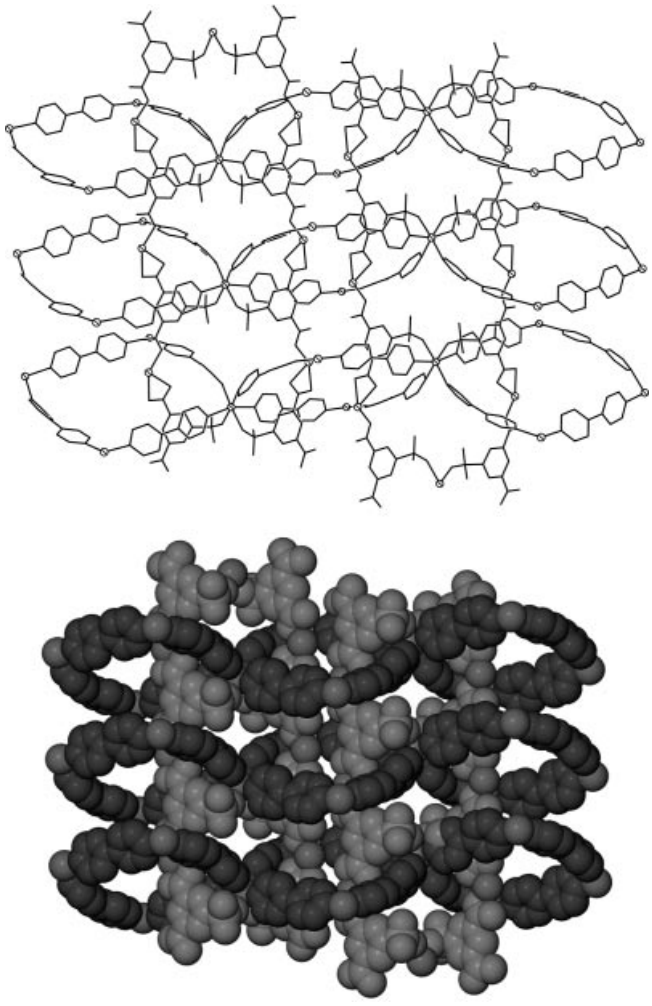

Figure 9. (a) 2D view showing the interlocking and interweaving of two kinds of units [$Cd_4(sipa)_4$ and $Cd_4(bpy)_4$] in the *ab* plane of **4**. (b) Space-filling diagram.

Table 4. Selected bond lengths [Å] and angles [°] for **4**.[a]

Cd(1)–O(5)	2.300(5)	Cd(2)–N(4)#3	2.335(5)
Cd(1)–O(5)#1	2.300(5)	Cd(2)–O(2)	2.355(4)
Cd(1)–N(1)#1	2.358(5)	Cd(2)–N(2)#4	2.375(5)
Cd(1)–N(1)	2.358(5)	Cd(2)–O(1)	2.464(4)
Cd(1)–N(3)	2.397(5)	S(1)–O(7)	1.437(5)
Cd(1)–N(3)#1	2.397(5)	S(1)–O(6)	1.438(5)
Cd(2)–O(4)#2	2.250(4)	S(1)–O(5)	1.466(5)
Cd(2)–O(8)	2.327(4)	S(1)–C(1)	1.775(6)
O(5)–Cd(1)–O(5)#1	86.0(2)	O(8)–Cd(2)–N(4)#3	91.93(17)
O(5)–Cd(1)–N(1)#1	174.27(16)	O(4)#2–Cd(2)–O(2)	136.18(16)
O(5)–Cd(1)–N(1)	93.39(17)	O(8)–Cd(2)–O(2)	87.98(16)
O(5)#1–Cd(1)–N(1)	174.27(16)	N(4)#3–Cd(2)–O(2)	93.03(17)
N(1)#1–Cd(1)–N(1)	87.8(3)	O(8)–Cd(2)–N(2)#4	164.27(17)
O(5)–Cd(1)–N(3)	84.51(16)	O(2)–Cd(2)–N(2)#4	104.00(17)
O(5)#1–Cd(1)–N(3)	81.92(16)	O(4)#2–Cd(2)–O(1)	84.08(16)
N(1)#1–Cd(1)–N(3)	89.75(17)	O(8)–Cd(2)–O(1)	91.98(16)
N(1)–Cd(1)–N(3)	103.70(17)	N(4)#3–Cd(2)–O(1)	146.66(17)
N(3)–Cd(1)–N(3)#1	161.4(2)	O(2)–Cd(2)–O(1)	54.05(14)
O(4)#2–Cd(2)–O(8)	80.44(16)	N(2)#4–Cd(2)–O(1)	87.07(18)

[a] Symmetry transformations used to generate equivalent atoms: #1 $-x$, y, $-z + 1/2$; #2 x, $y - 1$, z; #3 $-x + 1/2$, $y - 1/2$, $-z + 1/2$; #4 x, $-y$, $z - 1/2$.

 © 2005 Wiley-VCH Verlag GmbH & Co. KGaA, Weinheim

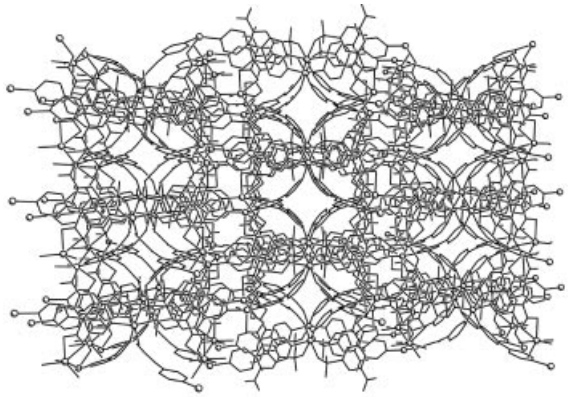

Figure 10. The three-dimensional self-penetrating structure along the *c* axis of **4**. Isolated water molecules are located in the channels.

Thermogravimetric Analysis (TGA)

Thermogravimetric analyses for complexes **1**–**4** were performed under a flow of nitrogen gas from room temperature to 1000 °C at a heating rate of 15 °C min^{-1}. Complex **1** begins to lose free water molecules at 184 °C and then loses further weight with increasing temperature. Differential thermal analysis (DTA) studies show two strongly endothermic reactions at 395 and 440 °C, respectively, which indicates that the framework collapses at 395 °C. For **2**, the first weight loss of 6.87% (calcd.: 6.36%) from 111 to 154 °C corresponds to the loss of two guest water molecules per formula unit ($2H_2O$/[Cd(sipa)(Hbpy)(H_2O)]·$2H_2O$ along with a strong absorption heat reaction; the coordination water molecules are slowly lost over the range 154–375 °C. DTA shows that one strong heat-absorption reaction takes place at 417 °C because of the collapse of the framework of **2**. Complex **3** starts losing weight at 50 °C and loses further weight with increasing temperature. DTA shows that a strongly endothermic reaction occurs at 436 °C, which indicates that the framework of **3** collapses. For **4**, the first weight loss of 5.75% (calcd. 5.86%) from 63 to 144 °C, which is accompanied by heat absorption, corresponds to the loss of three free waters and coordination water molecules per formula unit ($5H_2O$/{[Cd_3(sipa)$_2$-(bpy)$_4$(H_2O)$_2$]·$3H_2O$}). Strong heat absorption takes place in the range 340–420 °C, indicating the collapse of the structural framework at 340 °C.

Fluorescence Measurements

Previous studies have shown that polymeric compounds containing cadmium exhibit photoluminescent properties.[18] Hence, we also investigated the photoluminescent properties of complexes **1**–**4** (Figure 11). In the solid state, complex **1** displays two intense broadband fluorescent emissions at 335 and 351 nm, respectively, upon photoexcitation at 310 nm. Since NaH_2sipa exhibits photoluminescence emission at 355 nm, and free 2,2′-bipyridine exhibits emission at 362 nm, the emission bands at 351 and 335 nm of **1** can be attributed to the ligand donation. Strong photoluminescence emission bands at 510, 458, and 455 nm are observed for complexes **2**, **3**, and **4**, respectively, while free 4,4′-pyridine ligand presents weak photoluminescence emission at 486 nm. The photoluminescent emission of **2**–**4** may therefore be assigned to the nonradiative decay of the intraligand (π–π*) excited state and/or to ligand-to-metal charge transition, similar to previous reports.[5,19,20]

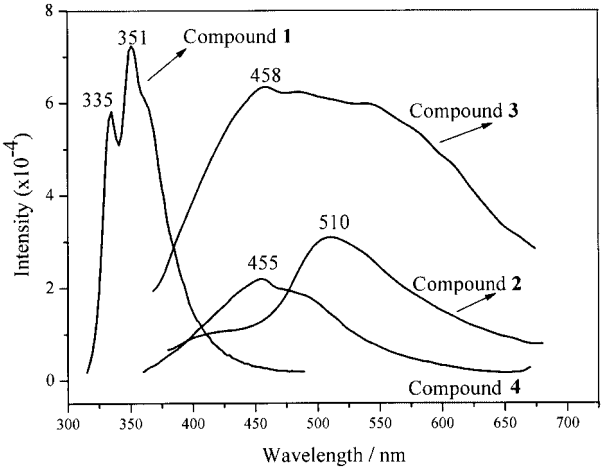

Figure 11. The photoluminescent spectra of **1**–**4** in the solid state at room temperature.

Conclusions

In conclusion, by selecting H_2sipa$^-$, 2,2′-bpy, and 4,4′-bpy as organic ligands, and the cadmium ion as knots, four polymeric complexes have been successfully isolated under hydrothermal conditions. Complex **1** possesses a 1D rail-like chain structure, **2** is a 1D double chain, **3** has a 2D network consisting of independent cationic [Cd_2(sipa)(4,4′-bpy)$_3$(H_2O)$_3$]$_n^{n+}$ and anionic [Cd(sipa)(4,4′-bpy) (H_2O)]$_n^{n-}$ layers, and **4** is a novel 3D self-penetrating network constructed from two mixed bridging ligands. The present work shows that a novel structure can be designed and assembled by combining the topology of organic ligands and the coordination geometry of metal ions.

Experimental Section

General: All chemicals were used as purchased without purification. The IR spectra were recorded as KBr pellets in the 4000–400 cm^{-1} region on a Magna 750 FT-IR spectrophotometer. The C, H, and N microanalyses were carried out with a Perkin–Elmer 240-element analyzer at this institute. Thermogravimetric analyses (TGA) were carried out on a Netzsch STA449C instrument. Fluorescent properties of **1**–**4** were measured on an Edinburgh Instruments analyzer model FL920.

{[Cd_3(sipa)$_2$(2,2′-bpy)$_4$(H_2O)$_2$]·$6H_2O$}$_n$ (1): A mixture of NaH_2sipa (0.053 g, 0.2 mmol), $Cd(NO_3)_2$·$4H_2O$ (0.092 g, 0.3 mmol), 2,2′-bipyridine (0.047 g, 0.3 mmol), EtOH (1.0 mL), and water (15 mL) was placed in a 25-mL Teflon-lined stainless autoclave and heated under autogenous pressure at 160 °C for 3 d. It was then cooled

 © 2005 Wiley-VCH Verlag GmbH & Co. KGaA, Weinheim

Table 5. Summary of crystal data for **1**–**4**.

	1	**2**	**3**	**4**
Empirical formula	$C_{56}H_{54}Cd_3N_8O_{22}S_2$	$C_{18}H_{18}CdN_2O_{10}S$	$C_{56}H_{62}Cd_3N_8O_{26}S_2$	$C_{56}H_{48}Cd_3N_8O_{19}S_2$
Formula mass	1592.39	566.80	1664.46	1538.34
Crystal system	triclinic	triclinic	triclinic	monoclinic
Space group	$P\bar{1}$	$P\bar{1}$	$P\bar{1}$	$C2/c$
a [Å]	8.0333(3)	8.8014(6)	10.24(5)	35.578(4)
b [Å]	10.2111(2)	9.2140(7)	17.97(10)	10.2327(10)
c [Å]	20.2010(7)	13.9886(10)	18.74(12)	16.2118(17)
α [°]	95.68	97.4200(10)	77.71(13)	90
β [°]	94.43	94.5960(10)	87.3(2)	108.913(2)
γ [°]	109.62	113.97	77.4(2)	90
V [Å^3]	1542.38(8)	1016.81	3287(33)	5583.5(10)
Z	1	2	2	4
D_c [g cm^{-3}]	1.714	1.851	1.682	1.830
μ [mm^{-1}]	1.177	1.238	1.113	1.293
λ (Mo-K_α) [Å]	0.71073	0.71073	0.71073	0.71073
F(000)	798	568	1676	3072
θ range [°]	2.71–25.09	1.48–25.09	3.02–25.03	1.21–25.04
R_1 [$I > 2\sigma(I)$]	0.0769	0.0387	0.0357	0.0469
R_1 (all data)	0.1407	0.0461	0.0407	0.0850
S (F^2)	1.022	1.228	1.032	1.077

to room temperature over 24 h. The resulting colorless block-like crystals of **1** were separated from the reaction mixture in about 47% yield (0.15 g) based on NaH_2sipa. $C_{56}H_{54}Cd_3N_8O_{22}S_2$ (1592.4): calcd. C 42.24, H 3.42, N 7.04; found C 42.16, H 3.27, N 7.19. IR (KBr): $\tilde{\nu}$ = 3460 cm^{-1} m, 3088 w, 1668 vs, 1593 m, 1489 w, 1473 m, 1443 s, 1387 m, 1315 m, 1269 s, 1161 vs, 1101 m, 1049 s, 1018 m, 906 w, 864 w, 760 s, 735 m, 708 w, 634 s, 577 w, 411 w.

{[Cd(sipa)(H-4,4′-bpy)(H_2O)]·2H_2O}$_n$ (2): A mixture of NaH_2sipa (0.133 g, 0.5 mmol), $Cd(NO_3)_2$·4H_2O (0.154 g, 0.5 mmol), 4,4′-bipyridine dihydrate (0.096 g, 0.5 mmol), and water (15 mL) was placed in a 25-mL Teflon-lined stainless autoclave and heated under autogenous pressure at 160 °C for 3 d. It was then cooled to room temperature over 24 h. Colorless sheet-like crystals of **2** were separated from the reaction mixture in about 35% yield (0.10 g) based on NaH_2sipa. $C_{18}H_{18}CdN_2O_{10}S$ (566.80): calcd. C 38.14, H 3.20, N 4.94; found C 38.26, H 3.11, N 4.90. IR (KBr): $\tilde{\nu}$ = 3419 cm^{-1} m, 3089 m, 3055 m, 2567 w, 2156 w, 1603 s, 1552 s, 1495 m, 1437 m, 1373 s, 1308 w, 1221 s, 1103 m, 1036 s, 933 w, 877 w, 820 m, 769 w, 731 m, 675 w, 631 s, 580 w, 523 w, 447 w.

{[Cd_2(sipa)(4,4′-bpy)$_3$(H_2O)$_3$]·[Cd(sipa)(4,4′-bpy)(H_2O)]·8H_2O}n (3): A mixture of NaH_2sipa (0.053 g, 0.2 mmol), $Cd(NO_3)_2$·4H_2O (0.092 g, 0.3 mmol), 4,4′-bipyridine dihydrate (0.096 g, 0.5 mmol), EtOH (1.0 mL), and water (15 mL) was placed in a 25-mL Teflon-lined stainless autoclave and heated under autogenous pressure at 160 °C for 5 d. It was then slowly cooled to room temperature over 24 h. Colorless sheet-like crystals of **3** were separated from the reaction mixture in about 54% yield (0.18 g). $C_{56}H_{62}Cd_3N_8O_{26}S_2$ (1664.5): calcd. C 40.41, H 3.75, N 6.73; found C 40.29, H 3.64, N 6.61. IR (KBr): $\tilde{\nu}$ = 3417 cm^{-1} m, 3088 m, 3051 m, 2565 w, 2141 w, 1942 w, 1603 vs, 1556 s, 1491 w, 1414 m, 1363 s, 1308 w, 1221 s, 1198 s, 1147 m, 1103 m, 1043 s, 874 w, 825 m, 806 s, 769 m, 731 m, 631 s, 580 w, 492 w, 447 w.

{[Cd_3(sipa)$_2$(4,4′-bpy)$_4$(H_2O)$_2$]·3H_2O}$_n$ (4): A mixture of NaH_2sipa (0.266 g, 1.0 mmol), $Cd(NO_3)_2$·4H_2O (0.231 g, 0.75 mmol), 4,4′-bipyridine dihydrate (0.192 g, 1.0 mmol), and water (10 mL) was placed in a 25-mL Teflon-lined stainless autoclave and heated under autogenous pressure at 160 °C for 3 d. It was then slowly cooled to room temperature over 24 h. The light-yellow block-like crystals of **4** were separated from the reaction mixture in about 23% yield (0.35 g). $C_{56}H_{48}Cd_3N_8O_{19}S_2$ (1538.3): calcd. C 43.72, H 3.14, N 7.28; found C 43.60, H 2.94, N 7.31. IR (KBr): $\tilde{\nu}$ = 3377 cm^{-1} w, 3211 w, 3055 w, 1942 w, 1605 vs, 1556 s, 1491 w, 1416 m, 1363 s, 1230 s, 1198 s, 1105 w, 1043 m, 1007 w, 922 w, 806 m, 783 w, 719 w, 629 m, 582 m, 492 w, 432 w.

X-ray Crystallography: Single crystals of complexes **1**–**4** with dimensions 0.24 × 0.18 × 0.12 (**1**), 0.36 × 0.24 × 0.10 (**2**), 0.24 × 0.18 × 0.06 (**3**), and 0.28 × 0.22 × 0.18 mm (**4**) were mounted on glass fibers for crystal structure analyses. For **1**, **2**, and **4** the data collections were performed on a Siemens Smart CCD diffractometer and for **3** on a Rigaku CCD diffractometer with graphite-monochromated Mo-K_a radiation (λ = 0.71073 Å) at 293 K. Empirical absorption corrections were applied using the SADABS program for **1**, **2**, and **4** and the CrystalClear program for **3**. All structures were solved by direct methods and the heavy atoms were located from the E-maps. Other non-hydrogen atoms were derived from the successive difference Fourier syntheses. The structures were refined by full-matrix, least-squares minimizations of $\Sigma(F_o - F_c)^2$ with anisotropic thermal parameters for all non-hydrogen atoms. All calculations were performed with the SHELXTL-97 program package.[21] The positions of hydrogen atoms were generated geometrically and treated isotropically. In complex **3**, C55 and C56 of the 4,4′-bipyridine ring and O12, O13, and O14 of the SO_3^- group from $sipa^{3-}$ ligand were disordered over two sets of positions and were refined with restraints. Table 5 summarizes the important crystal data for **1**–**4**.

CCDC-246223 (for **1**), -246224 (for **2**), -246225 (for **3**), and -221212 (for **4**) contain the supplementary crystallographic data for this paper. These data can be obtained free of charge from The Cambridge Crystallographic Data Centre via www.ccdc.cam.ac.uk/data_request/cif.

Acknowledgments

The authors are grateful for financial support from the National Natural Science Foundation of China (90206040, 20325106 and 20333070), the Natural Science Foundation of Fujian Province (B982003), and the "One-hundred Talent" Projects from CAS.

[1] a) W. B. Lin, O. R. Evans, R. G. Xiong, Z. Y. Wang, *J. Am. Chem. Soc.* **1998**, *120*, 13272–13273; b) P. Ayyappan, O. R. Ev-

 © 2005 Wiley-VCH Verlag GmbH & Co. KGaA, Weinheim

ans, Y. Cui, K. A. Wheeler, W. B. Lin, *Inorg. Chem.* **2002**, *41*, 4978–4980; c) O. R. Evans, R. G. Xiong, Z. Y. Wang, G. K. Wong, W. B. Lin, *Angew. Chem. Int. Ed.* **1999**, *38*, 536–538; d) S. R. Batten, R. Robson, *Angew. Chem. Int. Ed.* **1998**, *37*, 1461; e) C. J. Kepert, T. J. Prior, M. J. Rosseinsky, *J. Am. Chem. Soc.* **2000**, *122*, 5158; f) M. Fujita, Y. Kwon, S. Washizu, K. Ogura, *J. Am. Chem. Soc.* **1994**, *116*, 1151; g) C. Chen, K. S. Suslick, *Coord. Chem. Rev.* **1993**, *128*, 293–322; h) J. Nishida, T. Suzuki, M. Ohkita, T. Tsuji, *Angew. Chem. Int. Ed.* **2001**, *40*, 3251–3254; i) R. A. Van Delden, B. L. Feringa, *Angew. Chem. Int. Ed.* **2001**, *40*, 3198–3200; j) G. W. Gokel, A. Mukhopadhyay, *Chem. Soc. Rev.* **2001**, *30*, 274–286.

[2] a) L. Pan, X. Y. Huang, J. Li, Y. G. Wu, N. W. Zheng, *Angew. Chem. Int. Ed.* **2000**, *39*, 527; b) O. M. Yaghi, H. Li, C. Davis, D. Richardson, T. L. Groy, *Acc. Chem. Res.* **1998**, *31*, 474; c) M. Eddaoudi, D. B. Moler, H. Li, B. Chen, T. M. Reineke, M. O'Keeffe, O. M. Yaghi, *Acc. Chem. Res.* **2001**, *34*, 319–330; d) L. Ma, O. R. Evans, B. M. Foxman, W. B. Lin, *Inorg. Chem.* **1999**, *38*, 5837–5840; e) W. B. Lin, O. R. Evans, Y. Cui, *Cryst. Growth Des.* **2002**, *2*, 409–414.

[3] a) X. Li, R. Cao, D. F. Sun, Q. Shi, M. H. Hong, Y. C. Liang, *Inorg. Chem. Commun.* **2002**, *5*, 589–591; b) T. M. Reineke, M. Eddaoudi, D. Moler, M. O'Keeffe, O. M. Yaghi, *J. Am. Chem. Soc.* **2000**, *122*, 4843–4844; c) J. C. Dai, X. T. Wu, Z. Y. Fu, S. M. Hu, W. X. Du, C. P. Cui, L. M. Wu, H. H. Zhang, R. Q. Sun, *Chem. Commun.* **2000**, 12–13.

[4] a) O. M. Yaghi, C. E. Davis, G. M. Li, H. L. Li, *J. Am. Chem. Soc.* **1997**, *119*, 2861–2862; b) H. J. Chio, M. P. Suh, *J. Am. Chem. Soc.* **1998**, *120*, 10622–10623; c) R. Cao, D. F. Sun, Y. C. Liang, M. C. Hong, K. Tatsumi, Q. Shi, *Inorg. Chem.* **2002**, *41*, 2087–2094; d) D. F. Sun, R. Cao, Y. C. Liang, Q. Shi, M. C. Hong, *J. Chem. Soc., Dalton Trans.* **2002**, 1847–1851; e) C. J. Kepert, M. J. Rosseinsky, *Chem. Commun.* **1998**, 31–32; f) K. Y. Choi, K. M. Chun, H. Suh, *Polyhedron* **2001**, *20*, 57–65; g) D. P. Cheng, M. A. Khan, R. P. Houser, *Inorg. Chem.* **2001**, *40* 6858–6859; h) J. Zhu, X. H. Bu, P. Y. Feng, G. D. Stucky, *J. Am. Chem. Soc.* **2000**, *122* 11563–11564.

[5] a) J. Tao, X. Yin, Z. B. Wei, R. B. Huang, L. S. Zheng, *Eur. J. Inorg. Chem.* **2004**, 125–133; b) Z. M. Sun, J. G. Mao, Y. Sun, H. Y. Zeng, A. Clearfield, *Inorg. Chem.* **2004**, *43*, 336–341; c) Z. Wang, M. Ströbele, K. L. Zhang, H. Meyer, X. Z. You, Z. Yu, *Inorg. Chem. Commun.* **2002**, *5*, 230–234; d) A. D. Kulynych, G. K. H. Shimizu, *Cryst. Eng. Commun.* **2002**, *4*, 102–105; e) J. Tao, X. Yin, R. B. Huang, L. S. Zheng, S. W. Ngb, *Acta Crystallogr., Sect. E* **2003**, *59*, m473–m475; f) J. Tao, X. Yin, R. B. Huang, L. S. Zheng, S. W. Ngb, *Acta Crystallogr., Sect. E* **2003**, *59*, m611–m613.

[6] a) D. F. Sun, R. Cao, Y. Q. Sun, W. H. Bi, D. Q. Yuan, Q. Qian, X. Li, *Chem. Commun.* **2003**, 1528–1529; b) D. F. Sun, R. Cao, Y. Q. Sun, X. Li, W. H. Bi, M. C. Hong, Y. J. Zhao, *Eur. J. Inorg. Chem.* **2003**, 94–98.

[7] a) F. A. Cotton, L. M. Daniels, C. Lin, C. A. Murillo, *Inorg. Chem. Commun.* **2001**, *4*, 130–132; b) M. J. Plater, M. R. Foreman, R. A. Howie, J. M. S. Skakle, M. B. Hursthouse, *Inorg. Chim. Acta* **2001**, *319*, 159–175.

[8] a) O. M. Yaghi, G. M. Li, *Angew. Chem. Int. Engl.* **1995**, *34*, 207–209; b) S. Subramanian, M. J. Zaworotko, *Angew. Chem. Int. Engl.* **1995**, *34*, 2127–2129.

[9] X. Li, R. Cao, D. F. Sun, W. H. Bi, D. Q. Yuan, *Eur. J. Inorg. Chem.* **2004**, 2228–2231.

[10] a) J. Tao, M. L. Tong, X. M. Chen, *J. Chem. Soc., Dalton Trans.* **2000**, 3669–3674; b) G. Guilera, J. W. Steed, *Chem. Commun.* **1999**, 1563–1564; c) K. Kimura, T. Kimura, I. Kinoshita, N. Nakashima, K. Kitano, T. Nishioka, K. Isobe, *Chem. Commun.* **1999**, 497–498; d) T. Brandsch, F. A. Schell, K. Weis, M. Ruf, B. Muller, H. Vahrenkamp, *Chem. Ber./Recueil* **1997**, *130*, 283–287.

[11] a) A. Onoda, Y. Yamada, M. Doi, T. Okamura, N. Ueyama, *Inorg. Chem.* **2001**, *40*, 516–521; b) M. Alexiou, C. Dendrinou-Samara, C. P. Raptopoulou, A. Terzis, D. P. Kessissoglou, *Inorg. Chem.* **2002**, *41*, 4732–4738.

[12] M. J. Plater, M. R. S. J. Foreman, E. Coronado, C. J. Cómez-García, *J. Chem. Soc., Dalton Trans.* **1999**, 4209–4216.

[13] M. J. Domasevitch, K. V. Enright, G. D. Moulton, B. Zaworotko, *J. Solid State Chem.* **2000**, *152*, 280–285.

[14] a) X. Li, R. Cao, Y. Q. Sun, Q. Shi, D. Q. Yuan, D. F. Sun, W. H. Bi, M. C. Hong, *Cryst. Growth Design* **2004**, *4*, 255–261; b) P. Ayyappan, O. R. Evans, W. B. Lin, *Inorg. Chem.* **2002**, *41*, 3328–3330; c) T. Reuter, O. Vidoni, V. Torma, G. Schmid, L. Nan, M. Gleiche, L. Chi, H. Fuchs, *Nano. Lett.* **2002**, *2*, 709–711; d) B. Gong, C. Zheng, E. S. Jankun, J. Zhu, *Org. Lett.* **2000**, *2*, 3273–3275; e) K. Suto, S. Yoshimoto, K. Itaya, *J. Am. Chem. Soc.* **2003**, *125*, 14976–14977; f) L. Carlucci, G. Ciani, D. M. Proserpio, *Coord. Chem. Rev.* **2003**, *246*, 247–289; g) S. R. Batten, has summed up the reported interpenetrating structure. For detailed information see: http://web.chem.monash.edu.au/Department/Staff/Batten/Intptn.htm.

[15] a) X. J. Li, D. F. Sun, R. Cao, Y. Q. Sun, Y. Q. Wang, W. H. Bi, S. Y. Gao, M. C. Hong, *Inorg. Chem. Commun.* **2003**, *6*, 908–911; b) S. Haddad, F. Awwadi, R. D. Willett, *Cryst. Growth Design* **2003**, *3*, 501–505; c) N. D. Draper, R. J. Batchelor, B. C. Sih, Z. G. Ye, D. B. Leznoff, *Chem. Mater.* **2003**, *15*, 1612–1616; d) H. Miyasaka, H. Okawa, A. Miyazaki, T. Enoki, *Inorg. Chem.* **1998**, *37*, 4878–4883.

[16] L. Pan, H. M. Liu, S. P. Kelly, X. Y. Huang, D. H. Olson, J. Li, *Chem. Commun.* **2003**, 845–846.

[17] a) T. J. Prior, D. Bradshaw, S. J. Teat, M. J. Rosseinsky, *Chem. Commun.* **2003**, 500–501; b) S. M. Lo, S. Y. Chui, L. Y. Shek, Z. Lin, X. X. Zhang, G. H. Wen, I. D. Williams, *J. Am. Chem. Soc.* **2000**, *122*, 6293–6294.

[18] a) X. Xue, X. S. Wang, L. Z. Wang, R. G. Xiong, B. F. Abrahams, X. Z. You, Z. L. Xue, C. C. Che, *Inorg. Chem.* **2002**, *41*, 6544–6546; b) J. Tao, M. L. Tong, J. X. Shi, X. M. Chen, S. W. Ng, *Chem. Commun.* **2000**, 2043–2044; c) J. Tao, J. X. Shi, M. L. Tong, X. X. Zhang, X. M. Chen, *Inorg. Chem.* **2001**, *40*, 6328–6330.

[19] a) C. M. Che, C. W. Wan, K. Y. Ho, Z. Y. Zhou, *New J. Chem.* **2001**, *25*, 63–65; b) R. X. Yuan, R. G. Xiong, Y. L. Xie, X. Z. You, S. M. Peng, G. H. Lee, *Inorg. Chem. Commun.* **2001**, *4*, 384–385.

[20] a) A. Meijerink, G. Blasse, M. Glasbeek, *J. Phys. Condens. Matter* **1990**, *2*, 6303–6307; b) R. Bertoncello, M. Bettinelli, M. Cassrin, A. Gulino, E. Tondello, A. Vittadini, *Inorg. Chem.* **1992**, *31*, 1558–1565; c) S. L. Zheng, J. H. Yang, X. L. Yu, X. M. Chen, W. T. Wong, *Inorg. Chem.* **2004**, *43*, 830–838.

[21] G. M. Sheldrick, SHELX97, University of Göttingen, Göttingen, Germany, **1997**.

Received: November 27, 2004
Published Online: June 28, 2005

Luminescence and Theoretical Studies of Cu(tripod)X [tripod = 1,1,1-Tris(diphenylphosphanylmethyl)ethane; X^- = Halide, Thiophenolate, Phenylacetylide]

Valeri Pawlowski,[a][‡] Günther Knör,[a] Christian Lennartz,*[b] and Arnd Vogler*[a]

Keywords: Electronic spectra / Luminescence / Copper complexes / Phosphane ligands / Quantumchemical calculations

Complexes of the type Cu^I(tripod)X [tripod = 1,1,1-tris(diphenylphosphanylmethyl)ethane; X^- = Br^-, I^-, PhS^-, $PhC{\equiv}C^-$] are phosphorescent in solution and in the solid state ($\lambda_{max} \approx$ 465 nm). Calculations show that the emissive triplet is of mixed MLCT/LLCT character. The emission is facilitated by the rigid tetrahedral structure, which is imposed by the tripod ligand. Accordingly, a distortion towards a square-planar geometry, which should occur upon MLCT excitation, is prevented. On the other hand, in the triplet state the phenyl substituents of the phosphane ligands undergo a rotation which favours radiationless deactivation. As a result, the emission efficiency is relatively small in solution, but much higher in the solid state owing to the rigidity of the lattice.

(© Wiley-VCH Verlag GmbH & Co. KGaA, 69451 Weinheim, Germany, 2005)

Introduction

The luminescence of transition metal complexes is a rapidly expanding research field.[1,2] Potential applications such as optical sensors or OLEDs (organic light-emitting diodes) have stimulated many studies in this area.[3,4] The appearance of a luminescence at room temperature is largely restricted to complexes of metals which belong to the second and third transition row, while complexes of first-row transition metals are frequently not emissive under ambient conditions. However, there is one notable exception. A variety of mononuclear and polynuclear Cu^I complexes are luminescent at room temperature in solution or in the solid state.[5–8] In particular, mononuclear complexes with polypyridine ligands have attracted much interest.[8,9] These compounds are characterized by emissive low-energy MLCT (metal-to-ligand charge transfer) states. (Phosphane)Cu^I complexes constitute another group of luminescent compounds[5] which, however, have not been investigated to the same extent as (polypyridine)Cu^I complexes. In particular, the nature of the emitting excited states of (phosphane)Cu^I complexes is not clear at all. The present study was undertaken to gain more insight into the excited-state properties of (phosphane)Cu^I complexes and to define structural requirements for potential applications. Complexes of the type Cu^I(tripod)X [tripod = 1,1,1-tris(diphenylphosphanylmethyl)ethane; X^- = Br^-, I^-, PhS^-, $PhC{\equiv}C^-$] were expected to serve this purpose (Scheme 1).

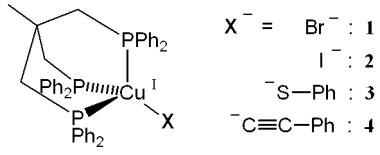

Scheme 1.

The rigid structure of these complexes,[10] which is imposed by the tripod ligand, should facilitate this work. These complexes are kinetically stable, soluble in a variety of organic solvents and volatile at higher temperatures without decomposition. Moreover, the rigidity of the compounds prevents extensive excited-state distortions. Accordingly, calculations of the frontier orbitals may be sufficient to characterize the lowest-energy excited state. In addition, the lack of flexibility could block radiationless deactivations and increase the luminescence efficiency. Finally, the rigidity should reduce the Stokes shift. As a result, the emission is expected to undergo a blue-shift. In this context, it should be mentioned that for certain applications such as OLEDs blue triplet emitters are requested, but are not yet available to the same extent as green and red molecular phosphors.

Results and Discussion

Experimental Results

The neutral compounds Cu(tripod)X [X^- = Br^-, I^-, PhS^-, $PhC{\equiv}C^-$] were readily obtained as white or slightly yellow-

[a] Institut für Anorganische Chemie, Universität Regensburg, 93040 Regensburg, Germany
E-mail: arnd.vogler@chemie.uni-regensburg.de
[b] BASF AG, Computational Chemistry and Biology, GVC/C-A30, 67057 Ludwigshafen, Germany
E-mail: christian.lennartz@basf-ag.de
[‡] Present address: Institute of Molecular and Atomic Physics, National Academy of Science of Belarus, 220072 Minsk, Belarus

ish solids by reaction of the corresponding copper(I) precursors CuX with the tridentate phosphane ligand tripod (Scheme 1). Their monomeric composition was confirmed by elemental analysis, and in the case of the halide derivatives **1** and **2** also by conductivity and molecular weight measurements.[11]

While the electronic spectrum of the tripod ligand in CH_2Cl_2 exhibits a featureless ultraviolet band at λ_{max} = 251 nm, the absorption spectra of the corresponding copper complexes display their maxima in the 300 nm spectral region (Figure 1). These bands are rather intense (ε = 13650 M^{-1} cm^{-1} at λ_{max} = 298 nm for **2** in CH_2Cl_2) and significantly red-shifted in the order of 4000–6500 cm^{-1} from the absorption of free tripod. In the case of the thiophenolate derivative **3**, an additional splitting of the main absorption band occurs with two well-resolved peaks at 270 and 290 nm.

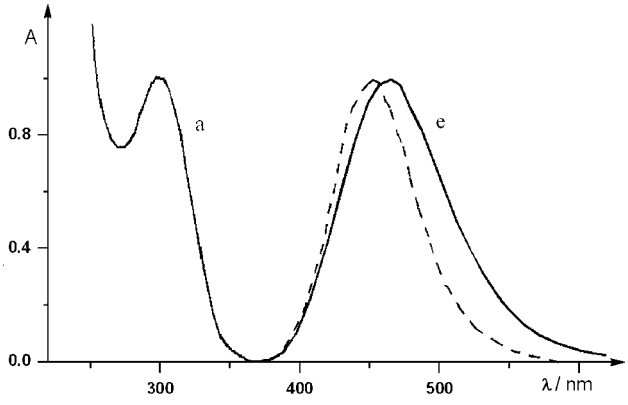

Figure 1. Electronic absorption (a) and emission (e) spectra of Cu(tripod)I (**2**) at room temperature and at 77 K (dashed curve). Absorption: 7.36×10^{-5} M in CH_2Cl_2, 1-cm cell. Emission: λ_{exc} = 300 nm, solid and in toluene matrix, intensity in arbitrary units.

All of the Cu(tripod)X complexes **1**–**4** exhibit an intense blue emission with peaks around 465 nm when excited with ultraviolet light in the solid state. This feature is shown in Figure 1 for Cu(tripod)I (**2**) with λ_{max} = 462 nm. At 77 K in a low-temperature toluene matrix, the luminescence maximum of **2** is blue-shifted to λ_{max} = 453 nm and the spectrum is slightly narrowed, while no significant structuring or larger change of shape of the emission band is observed (Figure 1). In argon-saturated dichloromethane solution, the luminescence of compound **2** shows a broad maximum with λ_{max} = 465 nm. A rather low quantum yield of $\varphi = 8 \times 10^{-4}$ is obtained in CH_2Cl_2 relative to quinine sulfate as a standard, and the luminescence in solution is found to be only moderately quenched by dioxygen. A quite similar behaviour is observed for the corresponding bromide derivative **1**.

The thiophenolate complex **3** also shows a blue emission at λ_{max} = 465 nm in the solid state, but in contrast to the halide derivatives **1** and **2**, a green luminescence with a significantly shifted, structureless band at λ_{max} = 508 nm is dominant in dichloromethane solution (Figure 2). As a solid compound, the luminescence spectrum of the phenylacetylide complex **4** displays a conspicuous structuring with a rather sharp maximum at 465 nm and a clearly resolved shoulder in the region of 510 nm. The peak separation of about 2000 cm^{-1} approximately matches the C≡C stretching frequency of the ligand X. In solution, however, a broad and nearly structureless band with λ_{max} = 475 nm is present in the organometallic derivative **4** as well. The spectroscopic data for all of the copper(I) complexes **1**–**4** in the solid state and in dichloromethane solution are summarized in Table 1.

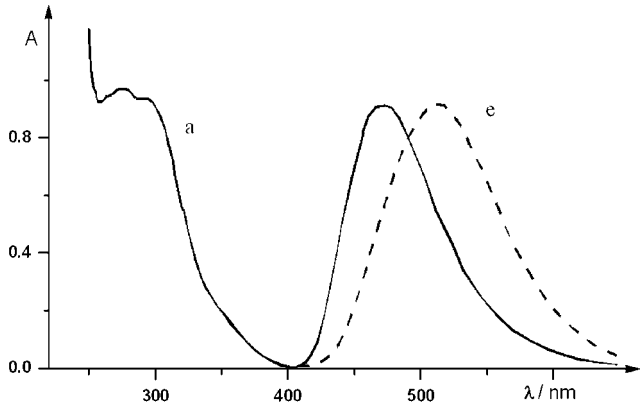

Figure 2. Electronic absorption (a) and emission (e) spectrum of Cu(tripod)SPh (**3**) at room temperature. Absorption: CH_2Cl_2, 1-cm cell. Emission: λ_{exc} = 300 nm, solid and in CH_2Cl_2 solution (dashed curve), intensity in arbitrary units.

Table 1. Absorption and emission maxima of Cu(tripod)X at room temperature.

X	λ_{max} [nm] (CH_2Cl_2)	λ_{em} [nm] (solid)	λ_{em} [nm] (CH_2Cl_2)
Br	296	462	462
I	298	461	465
SPh	270, 290	465	508
C≡CPh	297	465, 510	475

Discussion

The compounds Cu(tripod)X are monomeric and tetrahedral.[10,11] They are kinetically stable in distinction to other Cu^I complexes with monodentate or bidentate phosphane ligands, which undergo dissociation and dimerization in solution.[12,13] The electronic spectra of various (arylphosphane)Cu^I complexes have been reported.[5] However, assignments for the lowest-energy excited states seem to be controversial. In most cases it has been suggested that these states are of the phosphane IL (intraligand) type. This excitation involves the promotion of an electron from the Cu–P σ-bond into π*-orbitals, which are partially delocalized over the aryl substituents. Since the lone-pair of the free phosphane is stabilized by coordination, a blue-shift of this transition should take place. However, this has been frequently not observed. Generally, the lowest-energy transitions of such (arylphosphane)Cu^I complexes are very close to those of the free ligands, sometimes at somewhat higher

 © 2005 Wiley-VCH Verlag GmbH & Co. KGaA, Weinheim

and sometimes at slightly lower energies. The longest-wavelength absorptions of Cu(tripod)X (Table 1) are assigned to spin-allowed transitions in agreement with their high intensities.

Generally, the luminescence of Cu^{I} complexes is a phosphorescence, but occasionally a delayed fluorescence at shorter wavelengths has also been observed.[14–17] In the case of Cu(tripod)X complexes, the emission is certainly a phosphorescence, since it does not overlap with the absorption spectrum. Moreover, at low temperatures Cu(tripod)X complexes do not show a new long-wavelength emission, although the appearance of a phosphorescence should be favoured under these conditions.

Quantum chemical calculations were carried out for all complexes to determine the electronic character of the emission. TD-DFT calculations of the T_1-state at the T_1-geometry based on the singlet orbitals showed that the electronic character of the state is dominated by a one-electron transition from HOMO to LUMO (weight of the leading configurations > 0.95). Therefore the interpretation is based on HOMO and LUMO taken from the singlet wave function calculated at the T_1-state geometry (Figure 3).

The character of the HOMO is dominated by the d-p-π-antibonding interaction between Cu and X. Additionally, there is an antibonding interaction between the phosphane lone pair and the copper d-orbital. The LUMO is mainly localized on the phenyl rings and displays π* character (e_{2u} benzene-type). Accordingly, the electronic character of the transition is best described as MLCT(Cu^{I} → phosphane) + LLCT(X^{-} → phosphane). This is shown in Figure 4 for X = I, but is qualitatively very similar for the other Cu(tripod)-X complexes.

Comparison of the calculated geometries of the singlet ground state and triplet state (Table 2) shows that the main geometrical changes are due to rotations of the phenyl groups in the case of X = Br, I. The maximum rotation angles found among the phenyl groups amount to 50° and 35° for Br^{-} and I^{-}, respectively. The rms distances of all atoms add up to 68 pm and 49 pm, respectively. The Cu–Br/Cu–I bond length is slightly shortened (2.9/3.7 pm) in the triplet state due to the depopulation of the Cu–Br/Cu–I antibonding orbital. Distortions are substantially lower in the case of X = SPh. The maximum rotation is found on the thiophenyl group and amounts to 12° (rms *d* = 26 pm).

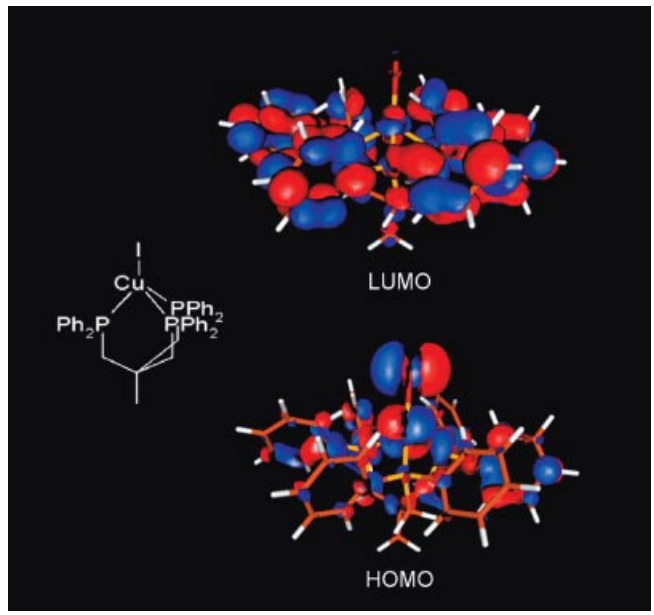

Figure 3. Frontier orbitals of Cu(tripod)I (**2**): HOMO (bottom) and LUMO (top).

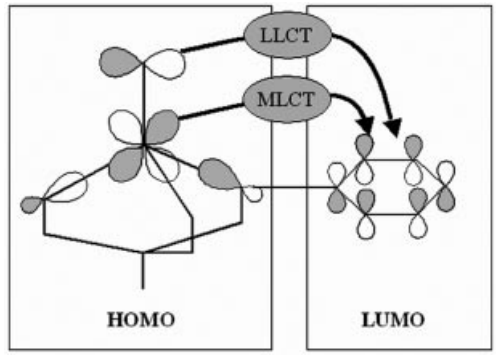

Figure 4. Schematic representation of the electronic transition. Only one of the six phenyl groups is shown.

The Cu–S bond is shortened by 4.7 pm in the triplet state. Nearly no distortions are found for X = C≡C–Ph (rms *d* = 11 pm; elongation of the Cu–C bond: 3.9 pm). In all cases

Table 2. Calculated geometries of the singlet ground states and triplet states of Cu(tripod)X.

Parameter	X = I		X = Br		X = SPh		X = CCPh	
	singlet	triplet	singlet	triplet	singlet	triplet	singlet	triplet
Cu–X[a]	2.584	2.547	2.380	2.351	2.283	2.236	1.909	1.870
Cu–P1[b]	2.307	2.310	2.301	2.358	2.323	2.306	2.319	2.317
Cu–P2[b]	2.303	2.322	2.301	2.298	2.305	2.346	2.322	2.325
Cu–P3[b]	2.304	2.372	2.229	2.344	2.342	2.370	2.324	2.372
max ($C_{ph}C_{ph}$)[c]	1.416	1.425	1.416	1.416	1.414	1.420	1.413	1.415
max (phtor)[d]	35		50		12[e]		2	
rms *d*[f]	0.49		0.68		0.26		0.11	

[a] Distance in Å. [b] Distance between Cu and P atoms of the tripod ligand in Å. [c] Maximum C–C distance in Å observed in the phenyl rings. [d] Maximum changes in torsional angles [°] of phenyl groups found on comparison of singlet and triplet geometry. [e] Thiophenyl group. [f] Root-mean-square distance variation in Å of all atoms in an alignment of singlet and triplet structure.

 © 2005 Wiley-VCH Verlag GmbH & Co. KGaA, Weinheim

Table 3. Emission maxima, orbital energies and calculated dipole moments of Cu(tripod)X.

X	λ_{em} [eV] (exp.)		λ_{em} [eV] (calcd.)[a]		Orbital energy [eV]		Dipole [D]	
	solid	CH_2Cl_2	unshifted	shifted[b]	HOMO	LUMO	S_0	T_1
Br	2.68	2.68	1.53	2.68	–3.78	–2.21	7.30	6.50
I	2.69	2.67	1.62	2.78	–3.88	–2.22	8.50	6.96
SPh	2.67	2.44	1.31	2.46	–3.46	–2.14	8.70	2.50
C≡CPh	2.67	2.61	2.00	3.16	–3.91	–1.90	8.03	5.83

[a] TD-DFT/TZVP. [b] Energies shifted by 1.16 eV to fit the emission energy of X = Br, since this method is known to yield systematical red-shifts.

there is a slight increase of the P–Cu bond length in the triplet state.

The calculated emission energies of Cu(tripod)X with X = I, Br and SPh were found to be systematically red-shifted. Therefore, we added a constant shift of 1.16 eV to facilitate a comparison with the experimental values (Table 3). This shifting behaviour may be understood by the fact that standard approximate exchange-correlation functionals suffer from an artificial stabilization of CT states due to the wrong asymptotic behaviour of the corresponding exchange-correlation functionals.[18] We performed additional single-CI calculations (TZVP basis set) in order to determine the character of the lowest excited state for X = Br. Although this method only gives qualitative results for energies, it does not suffer from the artificial stabilization of charge-transfer states. We found that the CT state actually is the lowest-lying state in Cu(tripod)Br. Therefore, the relative TD-DFT energies should reflect the right trend. Indeed, the shifted TD-DFT energies nicely correlate with the observed phosphorescence energies of of Cu(tripod)X with X = I, Br and SPh (Table 3). The red-shift observed for the thiophenolate complex is caused by a greater destabilization of the HOMO which contains a rather large sulfur contribution.

For the phenylacetylide complex, there is a distinct discrepancy between the calculated and the observed phosphorescence energies. While in comparison to other Cu(tripod)-X complexes a blue-shift is calculated, a red-shift is indeed observed. Probably, here the TD-DFT calculation fails to describe the first excited state correctly due to the problems already mentioned above. For phenylacetylide complexes, such as $(PR_3)Au(C{\equiv}C–Ph)$,[19] an IL (phenylacetylide) phosphorescence occurs at energies which are comparable to the calculated transition energies (Table 3). It is conceivable that contrary to the calculation, the emission of Cu(tripod)(C≡C–Ph) now originates from the phenylacetylide IL triplet, which in reality is located below the MLCT/LLCT triplet. Therefore, the artificial stabilization of the CT states may result in a qualitatively wrong picture here.

The mixed MLCT/LLCT character of the lowest-energy excited state of Cu(tripod)I does not only follow from the present calculations; it is also supported by previous calculations on related systems.[20] Moreover, similar conclusions have been drawn for the assignment of the lowest-energy electronic transition in tetranuclear copper(I) clusters.[6,7] In this context it should be kept in mind that the structures of Cu^I complexes in their MLCT states are planar and not tetrahedral as in their ground states.[21–26] The rigidity of Cu(tripod)X is expected to facilitate the emission since radiationless transitions are hampered when the flexibility including excited-state distortions is restricted. Indeed, all four Cu(tripod)X complexes are luminescent in solution and at room temperature (Table 1). However, in solution at room temperature the efficiency is still rather low. We suggest that the rotations of the phenyl groups at the phosphane ligand, which take place in the lowest triplet state, favour radiationless deactivations. In the solid state the phosphorescence of Cu(tripod)X is much more intense and shifts to shorter wavelengths. This is certainly a consequence of a diminished flexibility in the lattice of the solid compound. However, since the extent of structural changes in the solid state is not well defined, the calculations should be better compared with the emission spectrum in solution. While the formal assignments of MLCT/LLCT transitions are certainly appropriate, the actual amount of charge redistribution seems to be rather small as indicated by the dipole moments (Table 3). Accordingly, a distinct solvent-dependent shift is neither expected nor observed.

In conclusion, the complexes Cu(tripod)X are characterized by a blue emission, which originates from a mixed MLCT ($Cu^I \rightarrow$ tripod)/LLCT ($X^- \rightarrow$ tripod) triplet. Owing to the rigid structure imposed by the tripod ligand, this phosphorescence appears not only in the solid state, but also at room temperature in solution.

Experimental Section

Materials: All solvents used for spectroscopic measurements were of spectrograde quality. CuBr, CuI, CuSPh, CuC≡CPh and the tripodal ligand 1,1,1-tris(diphenylphosphanylmethyl)ethane were commercially available (Aldrich and Strem) and used without further purification. The title compounds were obtained by the following synthetic routes.

Cu(tripod)Br (1): In a procedure different from the published route,[11,27] a solution of CuBr (0.16 g, 1.1 mmol) and tripod (0.71 g, 1.1 mmol) in 40 mL of acetonitrile was refluxed for 20 min, and then cooled to room temperature. The resulting white precipitate was collected by filtration, washed with acetonitrile and diethyl ether, and dried yielding 0.77 g (88%). $C_{41}H_{39}BrCuP_3$ (768.12): calcd. C 64.11, H 5.12, Br 10.40; found C 64.02, H 5.06, Br 9.61.

Cu(tripod)I (2): Similar to the bromide complex **1**, a solution of CuI (0.10 g, 0.5 mmol) and tripod (0.32 g, 0.5 mmol) in 20 mL of acetonitrile was refluxed for 20 min, and then cooled to room temperature. The resulting white precipitate was collected by filtration, washed with acetonitrile and diethyl ether, and dried yielding 0.32 g (73%). $C_{41}H_{39}CuIP_3$ (815.12): calcd. C 60.41, H 4.82, I 15.57; found C 60.23, H 4.57, I 15.23.

 © 2005 Wiley-VCH Verlag GmbH & Co. KGaA, Weinheim

Cu(tripod)SPh (3): A suspension of CuSPh (0.26 g, 1.5 mmol) and tripod (0.96 g, 1.5 mmol) in 60 mL of acetonitrile was stirred at room temperature for 10 min and then kept under reflux for 90 min. After filtration of the hot, yellowish mixture, the solution was reduced to a small volume and cooled to room temperature. The resulting white precipitate was collected by filtration, washed with ethanol, and dried to yield 0.77 g (64%). $C_{47}H_{44}CuP_3S$ (797.39): calcd. C 70.79, H 5.56, S 4.02; found C 70.26, H 4.79, S 3.38.

Cu(tripod)C≡CPh (4): According to the published procedure,[28] a suspension of CuC≡CPh (0.25 g, 1.5 mmol) and tripod (0.96 g, 1.5 mmol) in 60 mL of benzene was stirred at ambient temperature for 24 h. After filtration from a dark green material, the pale yellow solution was concentrated to dryness. The residue was dissolved in toluene and petroleum ether was added. The resulting slightly yellowish precipitate was isolated by filtration, washed with petroleum ether and diethyl ether, and then dried to yield 0.96 g (81%). $C_{49}H_{44}CuP_3$ (789.34): calcd. C 74.56, H 5.62; found C 74.74, H 5.64.

Instrumentation: Absorption spectra were measured with a Shimadzu 2100 spectrophotometer. Emission spectra were recorded with a Hitachi 850 spectrofluorometer equipped with a Hamamatsu 928 photomultiplier for measurements up to 900 nm.

Calculations: Geometries and energies were calculated according to the density functional theory involving the BP86 functional[29] in combination with a split-valence basis set with polarisation functions on all heavy atoms [SV(P)[30]]. Triplet states were optimized according to the unrestricted KS approach. Time-dependent density functional calculations were performed with the same functional in combination with a valence triple zeta basis set (TZVP[31]). For iodine an effective core potential with relativistic corrections (ecp-46-mwb: derived from a multi-electron fit to the quasirelativistic Wood-Boring total valence energies) was employed[32]. Resolution of identity techniques[33] were used throughout. All calculations were carried out with the TURBOMOLE software package.[34]

Acknowledgments

Financial support of the Regensburg group by BASF is gratefully acknowledged.

[1] A. Vogler, H. Kunkely, *Top. Curr. Chem.* **2001**, *213*, 143.
[2] D. M. Roundhill, *Photochemistry and Photophysics of Metal Complexes*, Plenum, New York, **1994**.
[3] J. N. Demas, B. A. DeGraff, *Coord. Chem. Rev.* **2001**, *211*, 317.
[4] H. Yersin, *Top. Curr. Chem.* **2004**, *241*, 1.
[5] C. Kutal, *Coord. Chem. Rev.* **1990**, *99*, 213.
[6] P. C. Ford, A. Vogler, *Acc. Chem. Res.* **1993**, *26*, 220.
[7] P. C. Ford, E. Cariati, J. Bourassa, *Chem. Rev.* **1999**, *99*, 3625.
[8] D. R. McMillin, K. M. McNett, *Chem. Rev.* **1998**, *98*, 1201.
[9] K. Kalyanasundaram, *Photochemistry of Polypyridine and Porphyrin Complexes*, Academic Press, London, **1992**, p. 293.
[10] D. J. Fife, H. J. Mueh, C. F. Campana, K. W. Morse, *Acta Crystallogr., Sect. C* **1993**, *49*, 1714.
[11] L. Sacconi, S. Midollini, *J. Chem. Soc., Dalton Trans.* **1972**, 1213.
[12] D. J. Fife, W. M. Moore, K. W. Morse, *Inorg. Chem.* **1984**, *23*, 1684.
[13] P. Comba, C. Katsichtis, B. Nuber, H. Pritzkow, *Eur. J. Inorg. Chem.* **1999**, 777.
[14] M. T. Buckner, D. R. McMillin, *J. Chem. Soc., Chem. Commun.* **1978**, 759.
[15] M. T. Buckner, T. G. Matthews, F. E. Lytle, D. R. McMillin, *J. Am. Chem. Soc.* **1979**, *101*, 5846.
[16] J. R. Kirchhoff, R. E. Gamache, M. W. Blaskie, A. A. Del Paggio, R. K. Lengel, D. R. McMillin, *Inorg. Chem.* **1983**, *22*, 2380.
[17] Z. A. Siddique, Y. Yamamoto, T. Ohno, K. Nozaki, *Inorg. Chem.* **2003**, *42*, 6366.
[18] A. Dreuw, M. Head-Gordon, *J. Am. Chem. Soc.* **2004**, *126*, 4007.
[19] H.-Y. Chao, W. Lu, Y. Li, M. C. W. Chan, C.-M. Che, K.-K. Cheung, N. Zhu, *J. Am. Chem. Soc.* **2002**, *124*, 14696.
[20] P. Aslanidis, P. J. Cox, S. Divanidis, A. C. Tsipis, *Inorg. Chem.* **2002**, *41*, 6875.
[21] D. Felder, J. F. Nierengarten, F. Barigeletti, B. Ventura, N. Armaroli, *J. Am. Chem. Soc.* **2001**, *123*, 6291.
[22] C. T. Cunningham, J. J. Moore, K. L. H. Cunningham, P. E. Fanwick, D. R. McMillin, *Inorg. Chem.* **2000**, *39*, 3638.
[23] M. T. Miller, P. K. Gantzel, T. P. Karpishin, *Inorg. Chem.* **1999**, *38*, 3414.
[24] K. Shinozaki, Y. Kaizu, *Bull. Chem. Soc. Jpn.* **1994**, *67*, 2435.
[25] S. Sakaki, H. Mitzuani, Y. Kase, *Inorg. Chem.* **1992**, *31*, 4375.
[26] L. X. Chen, G. Jennings, T. Liu, D. J. Gosztola, J. P. Hessler, D. V. Scaltrito, G. J. Meyer, *J. Am. Chem. Soc.* **2002**, *124*, 10861.
[27] M. I. García-Seijo, P. Sevillano, R. O. Gould, D. Fernández-Anca, M. E. García-Fernández, *Inorg. Chim. Acta* **2003**, *535*, 206.
[28] K. Hiraki, Y. Fuchita, Y. Morita, *Bull. Chem. Soc. Jpn.* **1978**, *51*, 2012.
[29] J. P. Perdew, *Phys. Rev. B* **1986**, *33*, 8822; A. D. Becke, *Phys. Rev. A* **1988**, *36*, 3098.
[30] A. Schäfer, H. Horn, R. Ahlrichs, *J. Chem. Phys.* **1992**, *97*, 2571.
[31] A. Schäfer, C. Huber, R. Ahlrichs, *J. Chem. Phys.* **1994**, *100*, 5829.
[32] P. Schwerdtfeger, M. Dolg, W. H. E. Schwarz, G. A. Bowmaker, P. D. W. Boyd, *J. Chem. Phys.* **1989**, *91*, 1762.
[33] K. Eichkorn, F. Weigend, O. Treutler, R. Ahlrichs, *Theor. Chem. Acc.* **1997**, *97*, 119.
[34] R. Ahlrichs, M. Bär, M. Häser, H. Horn, C. Cölmel, *Chem. Phys. Lett.* **1989**, *162*, 165.

Received: November 17, 2004
Published Online: June 22, 2005

 © 2005 Wiley-VCH Verlag GmbH & Co. KGaA, Weinheim

NH···π Interactions Stabilize the Most-Hindered Rotamer of the (*S*)-Tyrosinato Side Group in Bis[(*S*)-tyrosinato](diamine)cobalt(III) Complexes: An NMR Spectroscopic and DFT Study[‡]

Djenana U. Miodragović,*[a] Željko J. Vitnik,[a] Slobodan M. Milosavljević,[a] Mijat J. Malinar,[a] and Ivan O. Juranić[a]

Dedicated to the memory of Professor Milenko B. Ćelap[‡‡]

Keywords: Amino acids / Cobalt / Conformational analysis / Density functional calculations / NMR spectroscopy / Pi interactions

Conformational analysis based on an analysis of the vicinal α- and β-proton coupling constants of (*S*)-tyrosinato ligands in diastereomers of a bis[(*S*)-tyrosinato](1,3-diaminopropane)-cobalt(III) complex is used to calculate the mol fractions of the three most stable rotamers (***t***, ***g***, ***h***) of the (*S*)-tyrosinato ligand's side groups in D_2O solution. The results of this conformational analysis indicate a population increase in the sterically least favorable rotamer ***h*** in diastereomers of C_1-molecular symmetry (complexes **5** and **6**). The TOCSY spectrum of complex **6** in aqueous solution shows an exceptionally small chemical shift of one NH_2 proton from the coordinated diamine, which is explained by an interligand NH···π interaction. These findings demonstrate the persistence of this weak, noncovalent interaction in water solution. DFT calculations for complex **6**, whose diamine ring is in a chair conformation, indicate that the complex with an ***h*** conformation in both its (*S*)-tyrosinato ligand side-residues, which yields the most frequent NH···π interactions, represents an energy minimum. The fact that coordinated 1,3-diaminopropane in the examined complex **6** is in a chair conformation in aqueous solution is proved by the NMR analysis.

(© Wiley-VCH Verlag GmbH & Co. KGaA, 69451 Weinheim, Germany, 2005)

Introduction

The side-residues of aromatic amino acids participate in many in vivo molecular recognitions, such as antibody–antigen,[1–3] enzyme–substrate,[4–7] protein–nucleic acid bases[8,9] etc. Molecular recognition is brought about by various forms of noncovalent interactions in which the side-residues of aromatic amino acids take part, such as hydrogen bonding (Tyr, Trp), stacking interactions, hydrophobic interactions, cation–π interactions, and various forms of XH···π interactions (X = C, N, O). During the past decade the importance of NH···π interactions in molecular recognition in biochemical systems and in maintaining the native protein structure has emerged,[10–14] although such systems are very complex to study because of the multiple weak interactions which act in synergy. This gives rise to a need for simple model systems suitable for studying these interactions.

Although NH···π interactions in proteins have been known since 1984,[15] in complexes of transition metals they have been discovered only recently[16] as, because of their low interaction energy,[17,18] they are difficult to detect in solution. One of the best ways to identify the presence of NH···π interactions in aqueous solution is the anomalous chemical shift of the NH protons involved in the interaction.[19–25]

We recently reported that complexes of cobalt(III) with (*S*)-tyrosinato and (*S*)-phenylalaninato ligands can serve as simple model systems for studing NH···π and π···π interactions.[26,27] In our previous paper,[27] conformational analysis based on an analysis of the vicinal α- and β-proton coupling constants was used to calculate the mol fractions of the three most stable rotamers of (*S*)-tyrosinato and (*S*)-phenylalaninato side-groups in diastereomers of $[Co\{(S)\text{-tyr}\}_2en]^+$ and $[Co\{(S)\text{-phe}\}_2en]^+$ in D_2O solution. The results of this analysis indicated a population increase in the sterically least favorable rotamer ***h*** in C_1-molecular symmetry diastereomers, which for complex **5 tyr** is proved to be due to the intra- and interligand NH···π interactions.[27]

[‡] Mixed-Ligand Cobalt(III) Complexes with Aromatic Amino Acids and a Diamine, 6. Part 5: D. U. Miodragović, Z. M. Miodragović, D. Skala, M. J. Malinar, D. M. Minić, K. Andjelković, *Thermochim. Acta*, in press.

[a] Faculty of Chemistry, University of Belgrade, Studentski trg 12–16, P. O. Box 158, 11000 Belgrade, Serbia and Montenegro
Fax: +381-11-184330
E-mail: dmiodrag@chem.bg.ac.yu

[‡‡] Founder of coordination chemistry in Serbia

 © 2005 Wiley-VCH Verlag GmbH & Co. KGaA, Weinheim **DOI: 10.1002/ejic.200400873**

In this paper, on the basis of conformational analysis, our aim was to obtain the data on the rotamer population of the (*S*)-tyrosinato ligand side-groups in diastereomers of the previously synthesized $[Co\{(S)\text{-tyr}\}_2tn]^+$ complex[28] and to establish whether a population increase of rotamer ***h*** in C_1-molecular symmetry diastereomers of the complex exist, and if so, whether that is due to NH···π interactions as well. We also used ab initio DFT molecular orbital calculations in our study.

Results and Discussion

Rotamer Distribution − NMR Study

The complex bis[(*S*)-tyrosinato](1,3-diaminopropane)cobalt(III) chloride was synthesized by treatment of the alkali metal salt of (*S*)-tyrosine with bis(1,3-diaminopropane)(carbonato)cobalt(III) and then separated into its diastereomers (Figure 1) on an optically active Sephadex QAE column.[28]

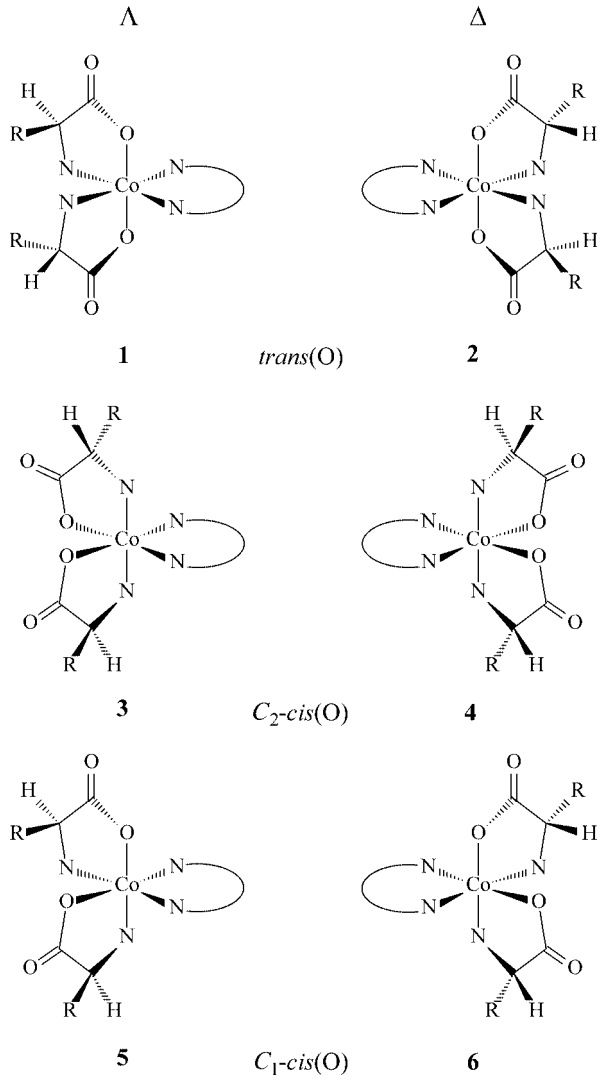

Figure 1. Theoretically possible diastereomers of $[Co\{(S)\text{-tyr}\}_2tn]$ (R = $CH_2C_6H_4OH$).

According to symmetry rules, the diastereomers can be divided into two groups: those having a C_2-molecular axis and higher degree of molecular symmetry [*trans*(O)- and *trans*(N) isomers, complexes **1**–**4**] and those having no symmetry elements [C_1-*cis*(O) isomers, complexes **5** and **6**].

Newman projections for the three most stable rotamers of the (*S*)-tyrosinato ligand side-group in the complex are shown in Figure 2. The mol fractions of the ***t***, ***g***, and ***h*** rotamers of the (*S*)-tyrosinato ligand side-groups in D_2O solution were calculated on the basis of the vicinal coupling constants of the α- and β-protons (J_{AX} and J_{BX})[29–31] as in our previous paper[27] (Table 1).

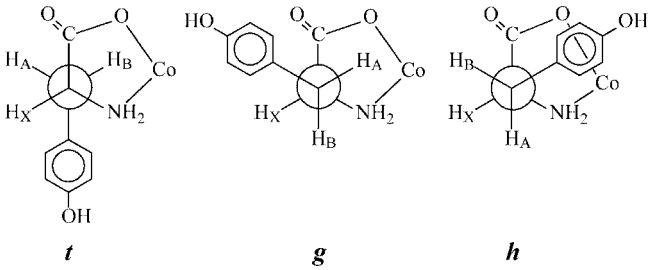

Figure 2. Newman projections of the three staggered rotamers of the (*S*)-tyrosinato side group in the cobalt(III) complex (the β carbon is in front and the α carbon is in the rear).

Table 1. Coupling constants and calculated rotamer mol fractions[31] of the (*S*)-tyrosinato side-groups in noncoordinated (*S*)-tyrosine, and in diastereomers of $[Co\{(S)\text{-tyr}\}_2tn]^+$ (bold), and $[Co\{(S)\text{-tyr}\}_2en]^+$[27] (*) in D_2O solution.

	J_{AX}	J_{BX}	*t*	*g*	*h*
(*S*)-tyrosine	5.4	7.4	45	24	31
Λ-C_2-*cis*(O) (**3**)	4.7	8.1	**53**	**16**	**31**
(**3***)	4.3	10.3	77	12	11
Δ-C_2-*cis*(O) (**4**)	4.6	9.0	**63**	**15**	**22**
(**4***)[a]	5.0	9.4	67	19	14
Λ-C_1-*cis*(O) (**5**)					
tyr I	5.3	8.3	**55**	**22**	**23**
tyr I*	5.3	8.5	57	23	20
tyr II	5.7	5.7	***t*** **+** ***g*** **= 54**		**46**
tyr II*	5.6	5.6	***t*** **+** ***g*** = 51		49
Δ-C_1-*cis*(O) (**6**)					
tyr I	5.2	6.2	**32**	**21**	**47**
tyr I*	4.9	7.2	43	18	39
tyr II	4.6	8.6	**59**	**15**	**26**
tyr II*	4.3	7.8	50	11	39

[a] These results have not been published to date.

With regard to the differences in symmetry, in diastereomers of C_2-molecular symmetry the two (*S*)-tyrosinato ligands have the same chemical environment in solution, and hence the α-and β-protons of both (*S*)-tyrosinato ligands show the same chemical shift as well as the same value for J_{AX} and J_{BX}. Therefore, the side-residues of the (*S*)-tyrosinato ligands have the same mol fractions of rotamers in solution (Table 1, complexes **3** and **4**). In the unsymmetrical complexes, the side-residues of the (*S*)-tyrosin-

 © 2005 Wiley-VCH Verlag GmbH & Co. KGaA, Weinheim

ato ligands have different chemical environments and hence different mol fractions of rotamers ***t***, ***g***, and ***h*** in solution (Table 1, complexes **5** and **6**). As is well known, the α-proton of an aminocarboxylate ligand whose NH_2 group is *trans* to an NH_2 group resonates at lower field (in this paper **tyr I**) than the α-proton of an aminocarboxylate ligand whose NH_2 group is *trans* to oxygen (in this paper **tyr II**).[32,33]

The population analysis of the side-group rotamers of the (*S*)-tyrosinato ligands in diastereomers of $[Co\{(S)\text{-tyr}\}_2tn]^+$ in D_2O solution indicates that the (*S*)-tyrosinato coordination increases the population of the sterically most favorable rotamer ***t*** relative to the population of this rotamer in the noncoordinated amino acid (Table 1). On the other hand, rotamer ***g*** is the least favorable rotamer energy-wise (from the MO calculations) because the phenyl group is closest to the coordinated carboxylic group. Therefore, rotamer ***g*** is the least abundant rotamer. These results are analogous to the results obtained from an examination of the rotamer population of the side-group of (*S*)-phenylalaninato and (*S*)-tyrosinato ligands in diastereomers of $[Co\{(S)\text{-tyr}\}_2en]^+$ and $[Co\{(S)\text{-phe}\}_2en]^+$in D_2O solution.[27] At the same time, it has been noticed[27] that in diastereomers of these complexes with C_1-molecular symmetry, the population of rotamer ***h*** increases due to intra- and interligand NH···π interactions.

In this context, in this paper we intended to examine whether, in the diastereomers of C_1-molecular symmetry of $[Co\{(S)\text{-tyr}\}_2tn]^+$, the population of rotamer ***h*** also increases and whether this increase is caused by NH···π interactions. In order to allow this comparison, the results of the mol fraction abundance of the side-group rotamers of (*S*)-tyrosinato ligands in diastereomers of $[Co\{(S)\text{-tyr}\}_2tn]^+$ and $[Co\{(S)\text{-tyr}\}_2en]^+$[27] in D_2O solution are given in Table 1. A considerable increase can seen in the population of rotamer ***h*** in one residue of the (*S*)-tyrosinato ligand in complexes of C_1-molecular symmetry (**5 tyr II** and **6 tyr I**) relative to the population of this rotamer in noncoordinated (*S*)-tyrosine (mol fractions of rotamer ***h*** are 46 and 47% respectively). As the first result is in agreement with the result obtained in an analogous diastereomer with 1,2-diaminoethane, the population increase of rotamer ***h*** in the side-residue **tyr I** in complex **6** was investigated more closely.

If NH···π interactions lead to a population increase of rotamer ***h*** in complex **6** as well, then the NMR spectrum should show a small chemical shift of the NH proton that takes part in this interaction. A molecular model of the complex with the side-residues of the (*S*)-tyrosinato ligands in conformation ***h*** indicates the possibility of three different NH···π interactions in the molecule (Figure 3, a), namely an NH···π interaction within (*S*)-tyrosinato itself, an NH···π interaction between two coordinated (*S*)-tyrosinato ligands (one is a donor and the other an acceptor of the hydrogen atom), and an NH···π interaction between a partially positively charged hydrogen atom from the coordinated 1,3-diaminopropane and the aromatic ring of the (*S*)-tyrosinato ligand.

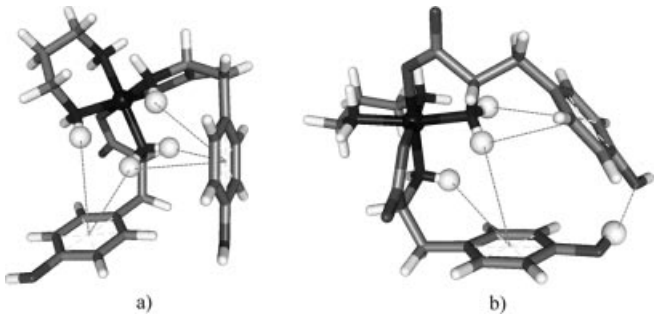

Figure 3. a) Calculated geometry of the Δ-C_1-*cis*(O)-$[Co\{(S)\text{-tyr}\}_2tn]^+$ complex (**6**) [both (*S*)-tyrosinato ligand side-groups adopt an ***h*** conformation and the diamine adopts a chair **A** conformation]. All possible NH···π interactions in the molecule are shown. b) Calculated geometry of complex **6** (**tyr I** adopts a ***t*** and **tyr II** an ***h*** conformation; the diamine adopts an $\mathbf{A}_{tw}$ conformation). Intramolecular NH···π interactions and H-bonds in the molecule are shown.

Since the mol fraction of rotamer ***h*** in the solution is small for the side-residue of **tyr II** (26%), the assumption of an NH···π interaction between two coordinated (*S*)-tyrosinato ligands can be rejected. In order to assign the NH protons, a TOCSY spectrum of complex **6** in H_2O solution was recorded (Figure 4). A small chemical shift of one NH proton at δ = 3.7 ppm (overlaps the signal of the α-proton), originating from coordinated 1,3-diaminopropane, can be seen in the spectrum. The chemical shift of this proton is indicative of strong shielding effects associated with the ring current of the aromatic ring.[23] In the 1,3-diaminopropane ligand, the difference in chemical shift between NH proton involved in the NH···π interaction and its geminal partner is –1.3 ppm. Thus we can conclude that the population increase of rotamer ***h*** of the side-residue **tyr I** in complex **6** is the result of an interligand NH···π interaction, i.e., an NH···π interaction between the partially positively charged hydrogen atom of the 1,3-diaminopropane ligand and the aromatic ring in the (*S*)-tyrosinato ligand.

A significant increase of the population of rotamer ***h*** is not found in analogous diastereomers of the (*S*)-phenylalanine complex. Williams and co-authors[23,34] have recently reported the existence of NH···π interactions in complexes of Co^{III} with (*S*)- and (*R*)-tryptophan and its derivatives. Our results, and those published by Williams,[23,34] are in accordance with the observation of Steiner and Koellner,[14] who noted that Trp and Tyr are the aromatic amino acids most frequently involved in NH···π interactions in proteins. The order efficacy of an aromatic acceptor for hydrogen bonding is Trp >> Tyr > Phe >> His.

DFT Study

DFT calculations were carried out for different conformations of the side-residues of (*S*)-tyrosinato ligands in complex **6** and for two different diamine chair conformations **A** and **B** because this isomer has no symmetry elements (Table 2). In the case of the diamine chair conformation in which the axial protons of the terminal methylene

 © 2005 Wiley-VCH Verlag GmbH & Co. KGaA, Weinheim

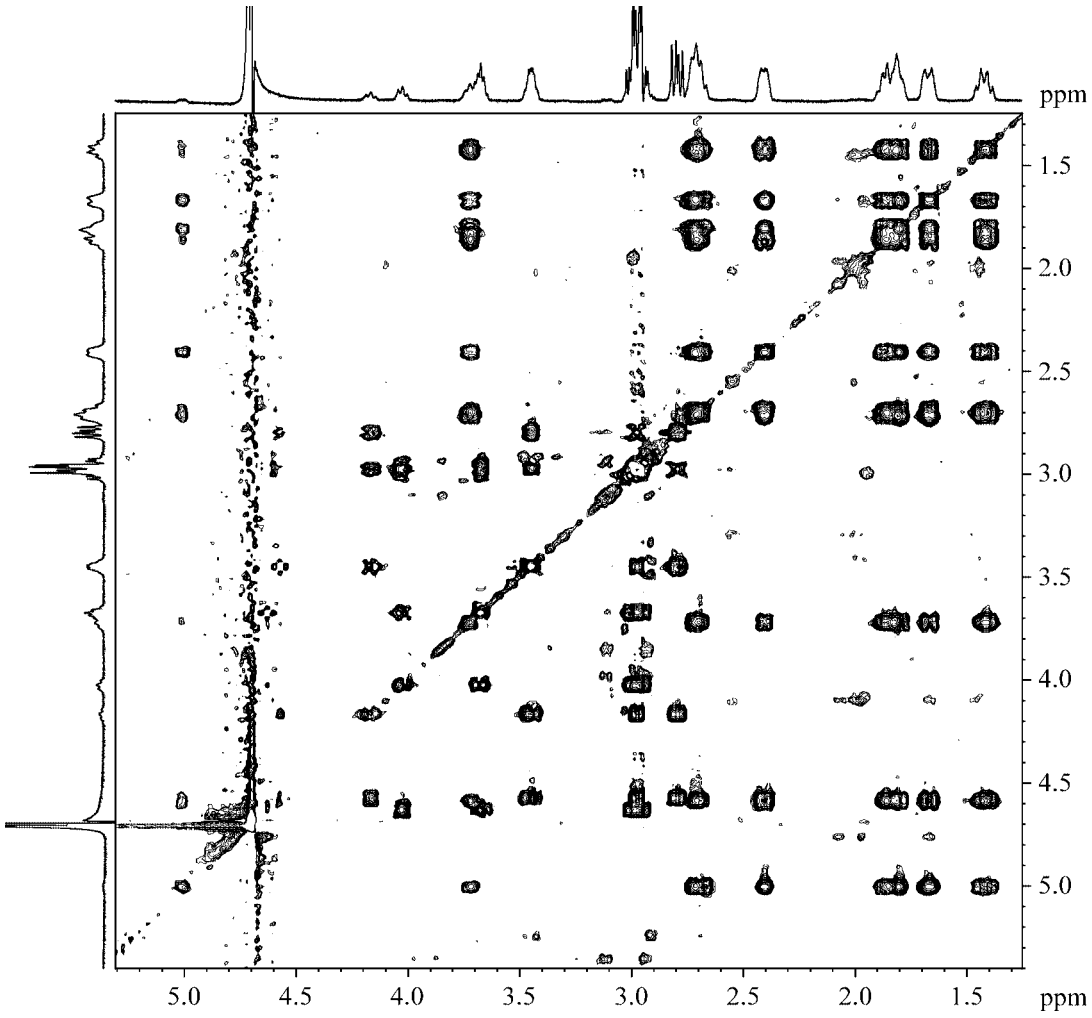

Figure 4. Partial TOCSY (500 MHz; mixing time 60 ms) spectrum of complex **6** in water solution.

groups are pointing toward the coordinated carboxylic group (conformation **A**, Table 2), the complex with two side-residues in conformation ***h*** represents an energy minimum. In this ***h*** conformation, the greatest number of NH···π interactions exist in the molecule (Figure 3, a), and it is followed, energy-wise, by the complexes in which one side-residue assumes an ***h*** and the second a ***t*** conformation. The least stable complex is that with both side-residues in conformation ***g*** (Figure 2). Here, the aromatic ring and the exocyclic oxygen of the coordinated carboxylic group are at the shortest distance, hence the repulsive forces are the greatest. The complexes in which only one side-residue takes conformation ***g*** are less stable energy-wise.

In the case of the diamine chair conformation, in which the axial protons of the terminal methylene groups point towards the α- and NH_2 protons of the coordinated (*S*)-tyrosinato ligand (conformation **B**, Table 2), the same order of stability of the conformers was obtained, but it is obvious that all complexes with the chair conformation **B** of the diamine are less stable than the corresponding complexes with conformation **A**. This is not surprising because in the chair conformation large steric hindrances are present between the axial protons of the terminal methylene groups of the diamine and the α- and NH_2 protons of the coordinated (*S*)-tyrosinato ligand.

Table 2. The relative energies of conformers[a] of complex **6**. The diamine adopts a chair (**A** and **B**) or twisted chair ($\mathbf{A}_{tw}$ and $\mathbf{B}_{tw}$) conformation.

	E_{rel}[b]			
tyr I, **tyr II**	Chair **A**	Chair **B**	$\mathbf{A}_{tw}$	$\mathbf{B}_{tw}$
h, ***g***	33.811	45.837	47.297	49.706
h, ***h***	0.000	12.041	14.080	15.418
h, ***t***	22.204	32.146	35.832	38.605
t, ***g***	42.126	56.878	57.415	66.742
t, ***h***	10.302	20.978	9.549	9.718
t, ***t***	30.766	44.833	49.982	57.887

[a] All energies [kJ mol^{-1}] are calculated relative to the energy of complex **6** (data obtained by a B3LYP/LANL2DZ//B3LYP/6-31G* calculation using an Onsager model) with chair conformation **A** and ***h*** conformations of the (*S*)-tyrosinato ligand side-chains, which represents an energy minimum. [b] In kJ mol^{-1}.

DFT calculations were also carried out for the case where the diamine adopts a twisted chair conformation ($\mathbf{A}_{tw}$ and $\mathbf{B}_{tw}$, Table 2). The most stable geometry of the complex is obtained when **tyr I** adopts a ***t*** and **tyr II** an ***h*** conformation. The molecular model of the complex (Fig-

 © 2005 Wiley-VCH Verlag GmbH & Co. KGaA, Weinheim

ure 3, b) indicates the possibility of forming an intramolecular H-bond only for these conformations of the (*S*)-tyrosinato side-chains.

A full optimization was performed for the most stable conformers of complex **6** (Table 3). The Boltzmann distribution indicates that complex **6** with a chair **A** conformation of the diamine and with both (*S*)-tyrosinato ligands side-chains in the ***h*** conformation is present at about 90%.

Table 3. Relative energies of the fully optimized[a] conformers of complex **6** and Boltzman distribution of the conformers.

		E_{rel}[b]		Population[c]	
tyr I, **tyr II**	Diamine	Chair	$Chair_{tw}$	Chair	$Chair_{tw}$
h, ***h***	**B**	12.754	15.304	0.531	0.191
h, ***h***	**A**	0.000	14.261	88.369	0.290
h, ***t***	**B**	32.125	37.831	0.000	0.000
h, ***t***	**A**	21.496	35.227	0.016	0.000
t, ***h***	**B**	19.594	8.595	0.034	2.817
t, ***h***	**A**	7.218	8.568	4.892	2.847

[a] Obtained by a B3LYP/LANL2DZ calculation using an Onsager solvation model. [b] In kJ mol^{-1}. [c] Percentage at 298 K.

The results obtained on the basis of the NMR spectroscopic data for the rotamer population in complex **6** indicate that **tyr I** in D_2O solution prefers an ***h*** conformation and **tyr II** a ***t*** conformation. On the other hand, the DFT calculations have shown that both (*S*)-tyrosinato side-chains prefer an ***h*** conformation (this complex is energetically the most stable). Because of this discrepancy we included in our DFT calculations two water molecules that are bonded to the hydroxyl groups of the (*S*)-tyrosinato side-chains by hydrogen bonds. The calculation (Table 4) was performed for conformation **A** of the diamine, which in all cases investigated was more stable than conformation **B** (Table 2). One significant difference can be seen in comparison with the data in Table 2, namely that the complex in which **tyr I** adopts an ***h*** and **tyr II** a ***t*** conformation, which is in accordance with experimental results, is now more stable than the complex with the opposite conformation of the side-chains. As mentioned above, the only combination of (*S*)-tyrosinato side-chain rotamers that can form intramolecular H-bonds is when **tyr I** adopts a ***t*** and **tyr II** an ***h*** conformation (Figure 3, b). Incorporation of two water molecules disrupts the intramolecular H-bonds by forming solute–solvent H-bonds, and these intermolecular solute–solvent interactions could enhance or compete with the forces responsible for the stabilization of a particular rotamer in solution.[23,24] Complex solute–solvent interactions and bulk entropy effects cannot be modeled at the MO level, and this could be the reason for the slight difference between the theoretical and experimental results.

Table 4. Relative energies of the fully optimized[a] conformers of complex **6** (diamine adopts a more stable **A** conformation).

tyr I, **tyr II**	E_{rel}[b]
h, ***h***	0.000
h, ***t***	21.310
t, ***h***	23.914
g, ***h***	35.290
t, ***t***	37.468
h, ***g***	41.366
g, ***g***	62.894
t, ***g***	67.219
g, ***t***	70.064

[a] Data obtained by a B3LYP/LANL2DZ calculation using an Onsager model and two water molecules. [b] In kJ mol^{-1}.

Conformation of the 1,3-Diaminopropane Chelate Ring in Solution

The data obtained from the analysis of the vicinal coupling constants of the methylene protons indicate that the 1,3-diaminopropane in complex **6** in D_2O (and H_2O) solution has a chair conformation. Thus, according to the Karplus equation,[35] which describes the dependence of vicinal coupling constant on the dihedral angle of the coupling protons, for the chair conformation the following values of the vicinal coupling constants are expected: $^3J_{aa}$ (10–16 Hz) and $^3J_{ae}$ and $^3J_{ee}$ (3–5 Hz).[36] By extracting the data from the NMR spectrum for complex **6** (at 500 MHz) in D_2O solution, the following data were obtained: the methylene protons bonded to the NH_2 group positioned *trans* to the nitrogen atom, resonate at δ = 2.7 (^3J = 10.6 and 2.7 Hz) and 2.4 ppm (^3J = 5.9 and 2.9 Hz), the methylene group protons bonded to the NH_2 group positioned *trans* to the oxygen atom resonate at δ = 1.9 (^3J = 10.3 and 2.7 Hz) and = 1.8 ppm (^3J = 5.8 and 3.0 Hz), while the protons of the central methylene group resonate at δ = 1.4 ppm. The existence of one vicinal coupling constant greater than 10 Hz indicates that the coordinated 1,3-diaminopropane adopts a chair conformation in D_2O (and H_2O) solution. It is worth mentioning that the relative chemical shifts of the axial and equatorial protons in terminal (bearing NH_2) methylene groups are opposite to the chemical shifts of these protons in a saturated cyclohexane ring, i.e. the axial protons resonate at higher δ values. The molecular model of complex **6** indicates that in the case of a chair conformation of the diamine ring the equatorial protons are found in the region of diamagnetic shielding of the aromatic ring in the tyrosinato ligand, which could explain the anomalous chemical shifts of the axial and equatorial protons of the terminal methylene groups.

Conclusions

The results of a conformational analysis indicate a population increase of the sterically least favorable ***h*** rotamer of the (*S*)-tyrosinato ligand side-group in diastereomers of C_1-molecular symmetry of $[Co\{(S)\text{-tyr}\}_2(diamine)]^+$-type complexes (diamine = 1,2-diaminoethane or 1,3-diaminopropane) in D_2O (and H_2O) solution that is caused by attractive intra- and/or interligand NH···π interactions.

DFT calculations for complex **6**, where the diamine adopts a chair conformation (as supported by NMR spectroscopic data), indicate that the complex with an ***h*** conformation of both the (*S*)-tyrosinato side-residues, which yields

 © 2005 Wiley-VCH Verlag GmbH & Co. KGaA, Weinheim

the most efficient NH···π interactions, represents an energy minimum.

The results obtained on the basis of ^{1}H NMR spectroscopy indicate that intramolecular NH···π interactions persist in aqueous solution, regardless of the energy-wise favored interactions with water molecules. This is in agreement with the results obtained by the investigation of amino–aromatic interactions in peptides.[21] Our results indicate the significance of noncovalent NH···π interactions involving (*S*)-tyrosinato side-chains and highlight the suitability of these simple cobalt(III) complexes to serve as models for studying these relatively poorly understood attractive forces.

Experimental Section

Synthesis: Diastereomers of the bis[(*S*)-tyrosinato](1,3-diaminopropane)cobalt(III) complex were synthesized by a previously described procedure.[28]

NMR Spectroscopy: ^{1}H NMR spectra were recorded on a GEMINI 2000 spectrometer at 200 MHz in D_2O solution (complexes **3**–**6**). The TOCSY spectrum of complex **6** in H_2O solution was recorded at 500 MHz on a Bruker ABX-500 spectrometer (mixing time 60 ms).

Computational Details: The optimized geometries and energies of conformers of Δ-C_1-*cis*(O)-[Co{(*S*)-tyr}$_2$tn]$^+$ (**6**) were obtained using the density functional theory (DFT) with the Becke three-parameter exchange functional (B3),[37] and the Lee–Yang–Parr (LYP) correlation functional.[38] The DFT method was used as it gives good results for all transition metal complexes of the first row.[39,40] These B3LYP calculations were carried out with the GAUSSIAN 98 program.[41] The geometries of all conformers of the complex were fully optimized using 6-31G* basis sets, and for these optimized geometries the energy was calculated with LANL2DZ basis set in the presence of a solvent (H_2O), using an Onsager model.[42–47] Full optimization for the most stable conformers was performed with the LANL2DZ basis set in the presence of a solvent, using an Onsager model and with explicit inclusion of two water molecules.

Acknowledgments

NMR spectra were recorded at the Mayo Clinic NMR Facility, Rochester, USA, by Prof. Nenad Juranić. The ab initio MO calculations were performed by Prof. Walter Knapp at the Free University in Berlin. The authors are grateful to the Ministry of Science and Environmental Protection of the Republic of Serbia (project nos. 1318, 1235, and 1755).

[1] K. Hofstädter, F. Stuart, L. Jiang, J. W. Vrijbloed, J. A. Robinson, *J. Mol. Biol.* **1999**, *285*, 805–815.
[2] D. R. Davies, G. H. Cohen, *Proc. Natl. Acad. Sci. USA* **1996**, *93*, 7–12.
[3] K. Tsumoto, K. Ogasahara, Y. Ueda, K. Watanabe, K. Yutani, I. Kumagai, *J. Biol. Chem.* **1995**, *270*, 18551–18557.
[4] M. Fontecave, J.-L. Pierre, *Bull. Soc. Chim. Fr.* **1996**, *133*, 653–660.
[5] A. Ordentlich, D. Barak, C. Kronman, N. Ariel, Y. Segall, B. Velan, A. Shafferman, *J. Biol. Chem.* **1995**, *270*, 2082–2091.
[6] A. S. Saribas, H. Ding, P. L. Dutton, F. Daldal, *Biochemistry* **1995**, *34*, 16004–16012.
[7] W. W. Johnson, S. Liu, X. Ji, G. L. Gilliland, R. N. Armstrong, *J. Biol. Chem.* **1993**, *268*, 11508–11511.
[8] H. Kawai, M. Tarui, M. Doi, T. Ishida, *FEBS Lett.* **1995**, *370*, 193–196.
[9] T. Ishida, M. Shibata, K. Fujii, M. Inoue, *Biochemistry* **1983**, *22*, 3571–3581.
[10] N. S. Scrutton, A. R. C. Raine, *Biochem. J.* **1996**, *319*, 1–8.
[11] J. B. O. Mitchell, C. L. Nandi, I. K. McDonald, J. M. Thornton, S. L. Price, *J. Mol. Biol.* **1994**, *239*, 315–331.
[12] M. M. Flocco, S. L. Mowbray, *J. Mol. Biol.* **1994**, *235*, 709–717.
[13] J. B. O. Mitchell, C. L. Nandi, S. Ali, I. K. McDonald, J. M. Thornton, S. L. Price, J. Singh, *Nature* **1993**, *366*, 413–413.
[14] T. Steiner, G. Koellner, *J. Mol. Biol.* **2001**, *305*, 535–557.
[15] A. Wlodaver, J. Walter, R. Huber, L. Sjölin, *J. Mol. Biol.* **1984**, *180*, 301–329.
[16] H. Kumita, T. Kato, K. Jitsukawa, H. Einaga, H. Masuda, *Inorg. Chem.* **2001**, *40*, 3936–3942.
[17] M. Levitt, M. F. Perutz, *J. Mol. Biol.* **1988**, *201*, 751–754.
[18] M. Milčić, S. D. Zarić, *Eur. J. Inorg. Chem.* **2001**, 2143–2150.
[19] J. Kemmink, T. E. Creighton, *J. Mol. Biol.* **1993**, *234*, 861–878.
[20] J. Kemmink, C. P. M. van Mierlo, R. M. Scheek, T. E. Creighton, *J. Mol. Biol.* **1993**, *230*, 312–322.
[21] G. A. Worth, R. C. Wade, *J. Phys. Chem.* **1995**, *99*, 17473–17482.
[22] E. Tüchsen, C. Woodward, *Biochemistry* **1987**, *26*, 1918–1925.
[23] P. Emseis, T. W. Failes, D. E. Hibbs, P. Leverett, P. A. Williams, *Polyhedron* **2004**, *23*, 1749–1767.
[24] P. Emseis, D. E. Hibbs, P. Leverett, N. Reddy, P. A. Williams, *Inorg. Chim. Acta* **2004**, *357*, 3251–3263.
[25] P. Emseis, D. E. Hibbs, P. Leverett, N. Reddy, P. A. Williams, *Inorg. Chim. Acta* **2004**, *357*, 2669–2676.
[26] G. A. Bogdanović, D. U. Miodragović, M. J. Malinar, *Acta Crystallogr., Sect. C* **2002**, *58*, 338–340.
[27] D. U. Miodragović, S. M. Milosavljević, M. J. Malinar, M. B. Ćelap, N. Todorović, N. Juranić, *Enantiomer* **2002**, *7*, 375–382.
[28] M. J. Malinar, D. U. Miodragović, S. Milosavljević, M. B. Ćelap, D. Vučelić, *Enantiomer* **1998**, *3*, 349–356.
[29] A. D. Becke, *J. Chem. Phys.* **1993**, *98*, 5648–5652.
[30] C. Lee, W. Yang, R. G. Parr, *J. Chem. Phys. Rev. B* **1988**, *37*, 785–789.
[31] S. Niu, M. B. Hall, *J. Am. Chem. Soc.* **1998**, *120*, 6169–6170.
[32] S. D. Zarić, *Chem. Phys. Lett.* **1999**, *311*, 77–80.
[33] M. J. Frisch, G. W. Trucks, H. B. Schlegel, G. E. Scuseria, M. A. Robb, J. R. Cheeseman, V. G. Zakrzewski, J. A. Montgomery, Jr., R. E. Stratmann, J. C. Burant, S. Dapprich, J. M. Millam, A. D. Daniels, K. N. Kudin, M. C. Strain, O. Farkas, J. Tomasi, V. Barone, M. Cossi, R. Cammi, B. Mennucci, C. Pomelli, C. Adamo, S. Clifford, J. Ochterski, G. A. Petersson, P. Y. Ayala, Q. Cui, K. Morokuma, D. K. Malick, A. D. Rabuck, K. Raghavachari, J. B. Foresman, J. Cioslowski, J. V. Ortiz, A. G. Baboul, B. B. Stefanov, G. Liu, A. Liashenko, P. Piskorz, I. Komaromi, R. Gomperts, R. L. Martin, D. J. Fox, T. Keith, M. A. Al-Laham, C. Y. Peng, A. Nanayakkara, C. Gonzalez, M. Challacombe, P. M. W. Gill, B. Johnson, W. Chen, M. W. Wong, J. L. Andres, C. Gonzalez, M. Head-Gordon, E. S. Replogle, J. A. Pople, *Gaussian 98, Revision A.7*, Gaussian, Inc., Pittsburgh PA, **1998**.
[34] M. W. Wong, M. J. Frisch, K. B. Wiberg, *J. Am. Chem. Soc.* **1991**, *113*, 4776–4782.
[35] M. W. Wong, K. B. Wiberg, M. J. Frisch, *J. Am. Chem. Soc.* **1992**, *114*, 523–529.
[36] M. W. Wong, K. B. Wiberg, M. J. Frisch, *J. Chem. Phys.* **1991**, *95*, 8991–8998.
[37] M. W. Wong, K. B. Wiberg, M. J. Frisch, *J. Am. Chem. Soc.* **1992**, *114*, 1645–1652.
[38] J. G. Kirkwood, *J. Chem. Phys.* **1934**, *2*, 351–361.
[39] L. Onsager, *J. Am. Chem. Soc.* **1936**, *58*, 1486–1493.

 © 2005 Wiley-VCH Verlag GmbH & Co. KGaA, Weinheim

[40] R. B. Martin, *J. Phys. Chem.* **1979**, *83*, 2404–2407.
[41] S. Kim, R. B. Martin, *J. Am. Chem. Soc.* **1984**, *106*, 1707–1712.
[42] K. D. Kopple, G. R. Wiley, R. Tanki, *Biopolymers* **1973**, *12*, 627–636.
[43] M. Watabe, M. Zama, S. Yoshikawa, *Bull. Chem. Soc. Jpn.* **1978**, *51*, 1354–1357.
[44] H. Yoneda, U. Sakaguchi, Y. Nakashima, *Bull. Chem. Soc. Jpn.* **1975**, *48*, 209–213.
[45] P. Emseis, P. Leverett, N. Reddy, P. A. Williams, *Inorg. Chim. Acta* **2003**, *355*, 144–150.
[46] M. Karplus, *J. Chem. Phys.* **1959**, *30*, 11–15.
[47] H. Friebolin, *Basic One- and Two-Dimensional NMR Spectroscopy*, Wiley-VCH, **1998**, p. 90–93.

Received: October 15, 2004
Published Online: July 4, 2005

 © 2005 Wiley-VCH Verlag GmbH & Co. KGaA, Weinheim

EurJIC
European Journal of Inorganic Chemistry

Issue 16/2005

Pages 3181–3376

Papers available ahead of print in Early View at www.interscience.wiley.com

Earliest available Table of Contents:
Automatically, free of charge by e-mail through
www.interscience.wiley.com/alerts

COVER PICTURE

The cover picture shows the first crystallographically characterized cationic triazacyclohexane complex of titanium. The hydrogen atoms of the ring-CH_2 groups engage in C−H···Cl interactions with the anion (only the shortest shown) and give rise to two characteristic doublets in the ^{1}H NMR spectrum with shifts that are highly dependent on the *N*-substituents, solvent and anion. The cationic complex is readily formed by the treatment of triazacyclohexanes with excess $TiCl_4$ which often results in large crystals containing the Ti_2Cl_9 anion. Details are discussed in the article by R. D. Köhn et al. on p. 3217 ff.

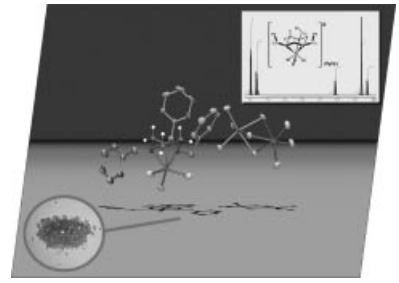

MICROREVIEW

Contents

3197 **R. Fernández, E. Carmona***

Recent Developments in the Chemistry of Beryllocenes

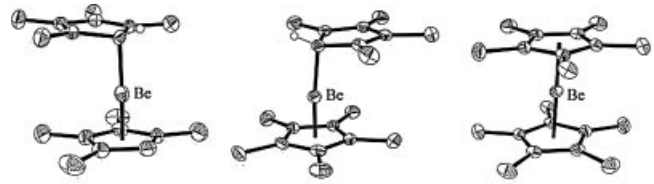

Keywords: Beryllium / Cyclopentadienyl ligands / Half-sandwich complexes / Metallocenes

 © 2005 Wiley-VCH Verlag GmbH & Co. KGaA, Weinheim

SHORT COMMUNICATIONS

3207 **A. Maurer, H.-B. Kraatz, N. Metzler-Nolte***

Synthesis and Electrochemical Characterization of Metallocene−PNA Oligomers

Keywords: Electrochemical DNA detection / Ferrocene / Metallocenes / Peptide nucleic acids

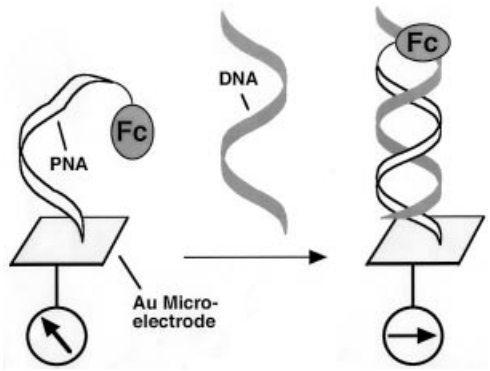

3211 **R. Fu, H. Zhang, L. Wang, S. Hu, Y. Li, X. Huang, X. Wu***

Nonlinear Optical Activity and High Thermal Stability of a New 3D Open-Framework with Interconnected 24-, 16-, and 8-Atom Channels: $(NH_4)Zn[O_3PCH(OH)CO_2]$

Keywords: Zinc / Hydroxy(phosphonoato)acetate / Nonlinear optical activity / Hydrothermal synthesis / Open-framework

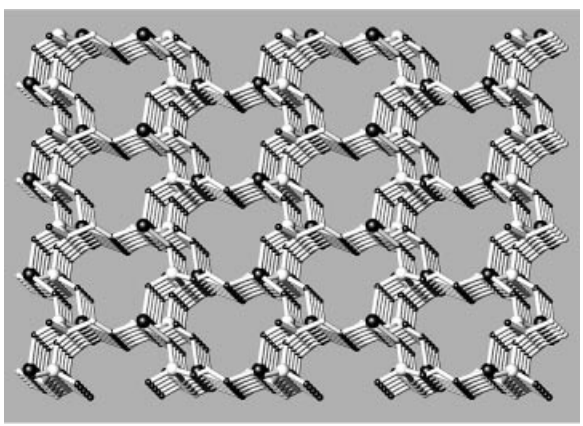

3214 **B. Lou, F. Jiang, D. Yuan, B. Wu, M. Hong***

Synthesis and Characterization of a 3D H-Bonded Supramolecular Complex with Chiral Channels Encapsulating 1D Left-Handed Helical Water Chains

Keywords: Chiral channels / Water chains / Amino acids

FULL PAPERS

3217 **R. D. Köhn,* P. Kampe, G. Kociok-Köhn**

Reaction of 1,3,5-Triazacyclohexanes with $TiCl_4$: Formation of Cationic Complexes

Keywords: N ligands / Tridentate ligands / Titanium

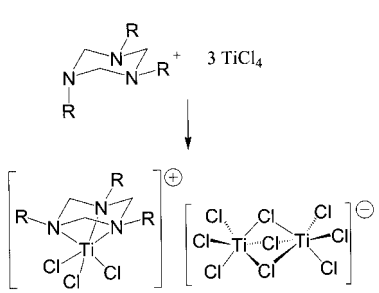

3224 **B. Modec,* D. Dolenc, J. V. Brenčič, J. Koller, J. Zubieta**

Dinuclear Oxomolybdate(v) Species with Oxalato and Pyridine Ligands Revisited: *cis*/*trans* Isomerization of $[Mo_2O_4(\eta^2\text{-}C_2O_4)_2(R\text{-}Py)_2]^{2-}$ (R-Py = Pyridine, Alkyl-Substituted Pyridine) in Water Evidenced by NMR Spectroscopy

Keywords: Isomerization / Molybdenum / N ligands / NMR spectroscopy / Polyoxometalates

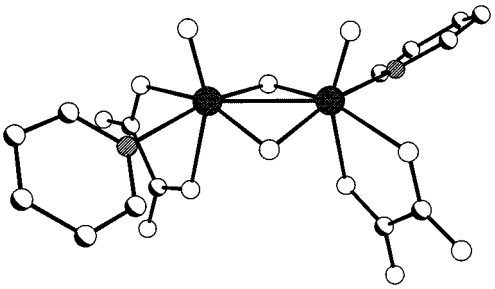

3238 **L. K. Li, Y. L. Song, H. W. Hou,* Y. T. Fan, Y. Zhu**

Syntheses, Structures, and Optical Properties of β-Ferrocenylacrylate Metal Polymers

Keywords: Cadmium / Lead / Nonlinear optics / Organic−inorganic hybrid composites / Polymers

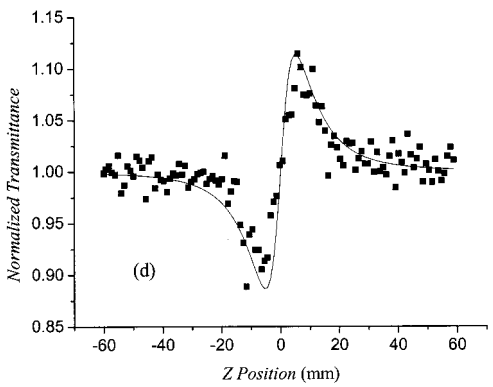

3250 **L. Busetto,* F. Marchetti, S. Zacchini, V. Zanotti**

Formation of C−C Bonds in Diiron Complexes by Addition of Carbanions to Alkynyl(methoxy)carbene Ligands

Keywords: Carbanions / Carbene ligands / C−C coupling

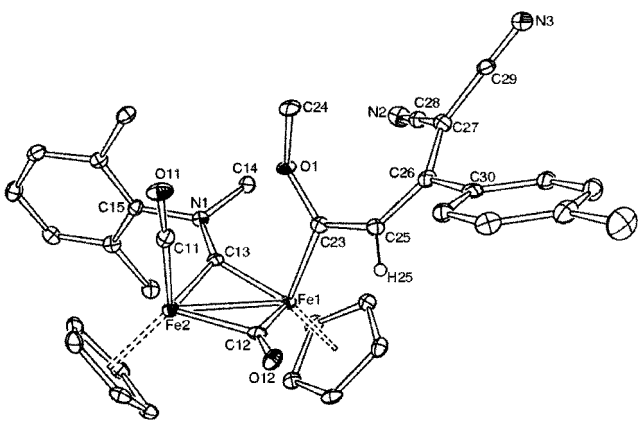

3261 **C. Faulmann,* S. Dorbes, B. Garreau de Bonneval, G. Molnár, A. Bousseksou, C. J. Gomez-Garcia, E. Coronado, L. Valade**

Towards Molecular Conductors with a Spin-Crossover Phenomenon: Crystal structures, Magnetic properties and Mössbauer Spectra of [Fe(salten)Mepepy][M(dmit)$_2$] complexes

Keywords: Conducting materials / Magnetic properties / Moessbauer spectroscopy / Spin crossover / X-ray diffraction

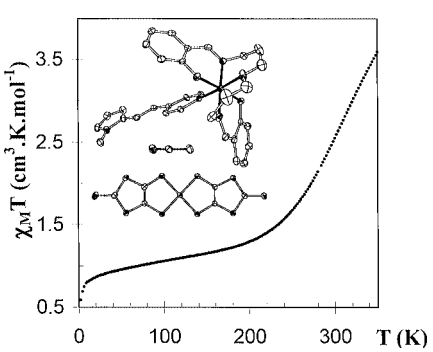

 © 2005 Wiley-VCH Verlag GmbH & Co. KGaA, Weinheim

3271 **T. Akutagawa,* K. Matsuura, S. Nishihara, S.-i. Noro, T. Nakamura***

Supramolecular Cations of (*S*)-, (*R*)-, and (*RS*)-Indan-1-aminium(dibenzo[18]crown-6) in Magnetic $[Ni(dmit)_2]^-$ Salts

Keywords: Crown compounds / Magnetic properties / Supramolecular chemistry / Chirality / S ligands

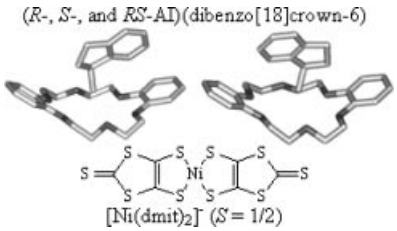

3277 **X.-Y. Wang, B.-L. Li*, X. Zhu, S. Gao***

Extended Networks of Co^{2+} and Mn^{2+} Bridged by NCS^-/N_3^- Anions and Flexible Long Spacers: Syntheses, Structures, and Magnetic Properties

Keywords: Thiocyanate / Azide / Cobalt / Manganese / 1,2-Bis(imidazol-1-yl)ethane / 1,2-Bis(1,2,4-triazol-1-yl)ethane / Magnetic properties

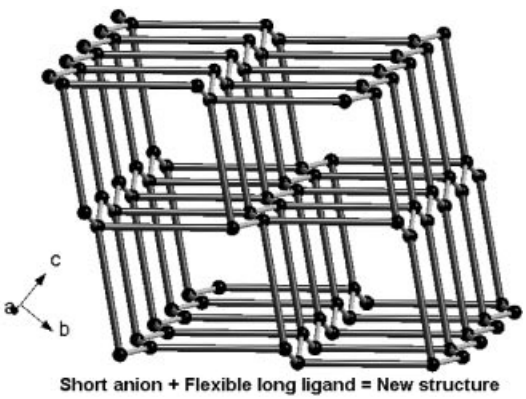

3287 **R. P. Feazell, C. E. Carson, K. K. Klausmeyer***

Variability in the Structures of Luminescent [2-(Aminomethyl)pyridine]silver(I) Complexes: Effect of Ligand Ratio, Anion, Hydrogen Bonding, and π-Stacking

Keywords: Silver / N ligands / X-ray diffraction / Coordination modes

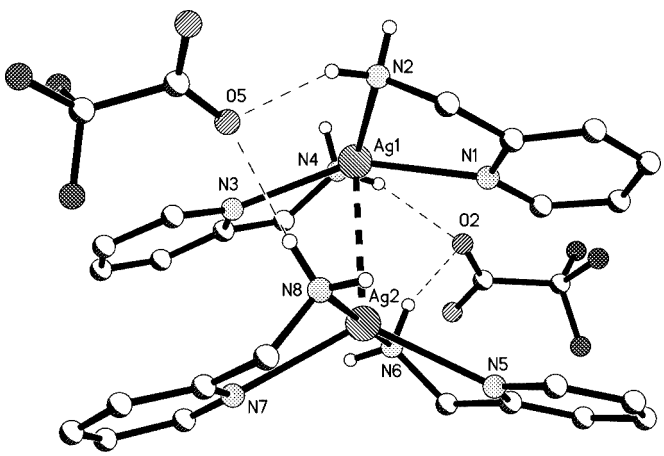

3298 **J. Zhang,* R. Cai, M. Chen, L. Weng, X. Zhou***

Synthesis and Crystal Structure of a Cocrystalline Compound of a Rare Earth Metalloporphyrin with Fullerene $\{[TPPYb(\mu\text{-}OH)_2Yb(THF)\text{-}TPP]\cdot C_{60}\}_n$

Keywords: Metalloporphyrin / Fullerenes / Cocrystal / Ytterbium

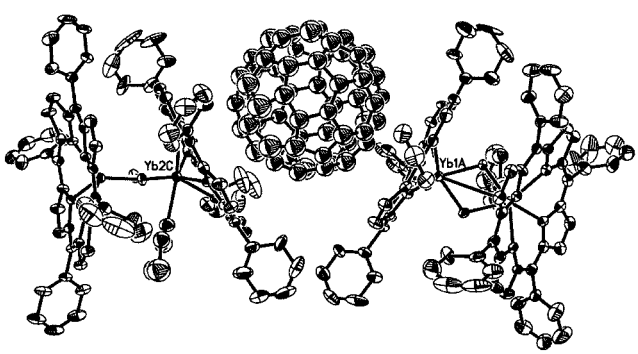

 © 2005 Wiley-VCH Verlag GmbH & Co. KGaA, Weinheim

3303 **A. Pacco, T. N. Parac-Vogt, E. van Besien, K. Pierloot, C. Görller-Walrand, K. Binnemans***

Lanthanide(III)-Induced Conversion of 12-Metallacrown-4 to 5-Metallacrown-5 Complexes in Solution

Keywords: Lanthanides / Hydroxamic acids / Metallacrowns / N,O ligands / Rare earths

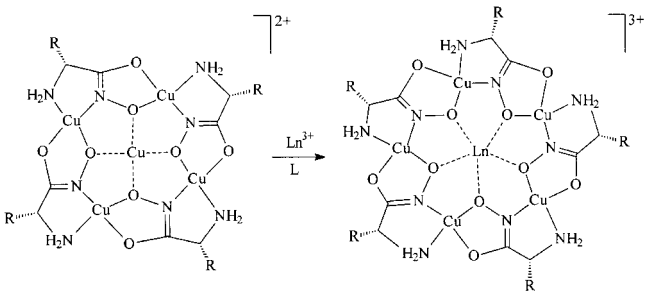

3311 **K. N. Gavrilov, V. N. Tsarev,* S. I. Konkin, S. E. Lyubimov, A. A. Korlyukov, M. Y. Antipin, V. A. Davankov**

Imino- and Oxazolino-Functionalised Pyrrolylphosphanes and Pyrrolylphosphinites: An Unexploited Class of Chiral *P,N*-Bidentate Ligands with Unusual Electronic Properties

Keywords: Allylic substitution / Asymmetric catalysis / Palladium / *P,N*-bidentate ligands / Rhodium

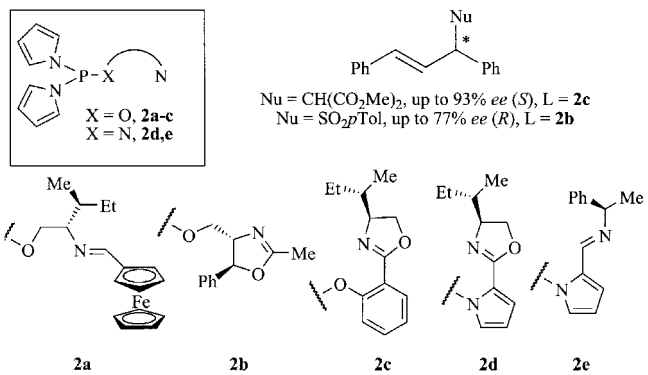

3320 **J. Lombard, S. Romain, S. Dumas, J. Chauvin, M.-N. Collomb, D. Daveloose, A. Deronzier,* J.-C. Leprêtre***

Tetranuclear Polypyridyl Complexes of Ru^{II} and Fe^{II}: Synthesis, Electrochemical, Photophysical and Photochemical Behaviour

Keywords: Bridging ligands / Electrochemistry / Iron / Photochemistry / Ruthenium

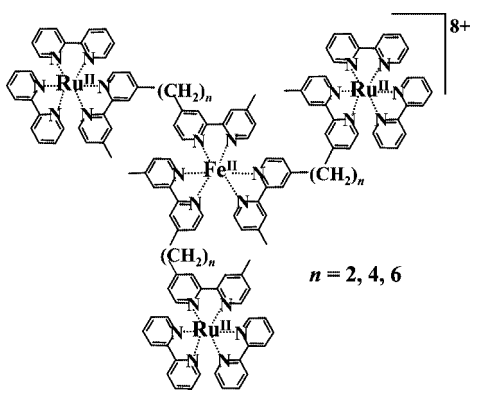

3331 **D. Wandschneider, M. Michalik, H. Oehme, A. Heintz***

Ab initio Study of Some Intramolecularly Donor-Stabilized Silenes

Keywords: Silenes / Ab initio calculation / Donor-acceptor systems

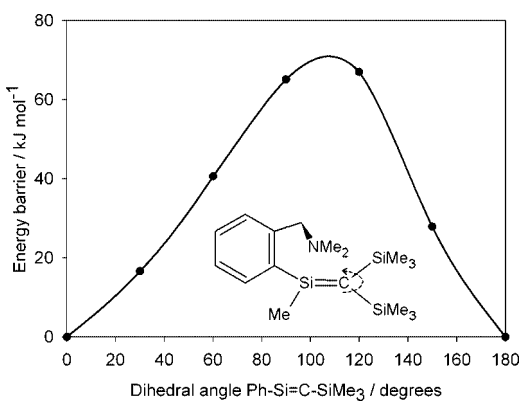

 © 2005 Wiley-VCH Verlag GmbH & Co. KGaA, Weinheim

3337 **D. Belo, M. J. Figueira, J. Mendonca, I. C. Santos, M. Almeida,* R. T. Henriques, M. T. Duarte, C. Rovira, J. Veciana**

Copper, Cobalt and Platinum Complexes with Dithiothiophene-Based Ligands

Keywords: S ligands / Coordination chemistry / Copper / Cobalt / Platinum

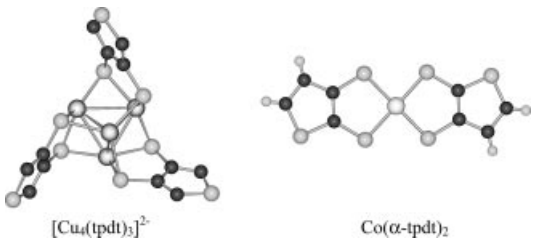

3346 **D. K. Chand,* R. Manivannan, H. S. Sahoo, K. Jeyakumar**

Self-Assembly by Ligand-Exchange Reactions

Keywords: Cage compounds / NMR spectroscopy / Metallacycles / Palladium / Ligand exchange

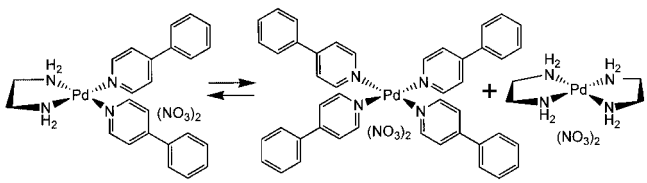

3353 **L. Quebatte, R. Scopelliti, K. Severin***

Atom Transfer Radical Additions with the Cationic Half-Sandwich Complex [Cp*Ru-$(PPh_3)_2(CH_3CN)$]OTf

Keywords: ATRA reaction / Homogeneous catalysis / Radical reaction / Ruthenium

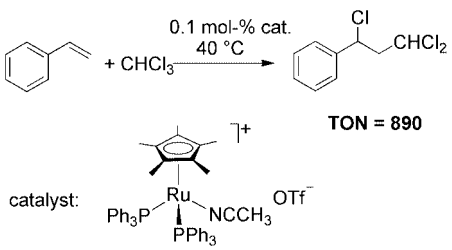

3359 **Y. Fan, G. H. Li, L. Yang, Z. M. Zhang, Y. Chen, T. Y. Song,* S. H. Feng***

Synthesis, Crystal Structure, and Magnetic Properties of a Three-Dimensional Hydroxide Sulfate: $Mn_5(OH)_8SO_4$

Keywords: Hydroxy sulfate / Hydrothermal synthesis / Magnetic properties / Thermodiffractometry / Structure elucidation

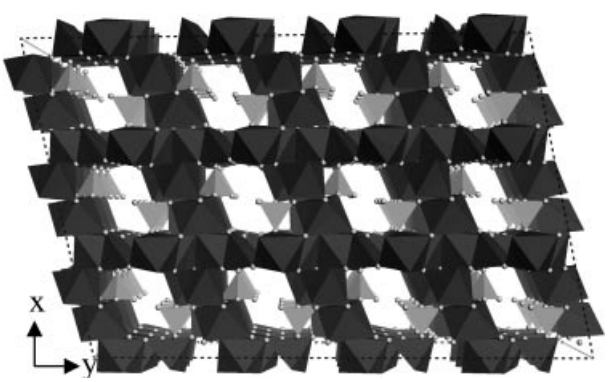

3365 **A. L. Hector,* W. Levason**

Periodates of Tetravalent Titanium, Zirconium, Hafnium and Thorium: Synthesis, Characterisation and EXAFS Study

Keywords: Periodates / Polyoxometalates / EXAFS spectroscopy / Group 4 elements / Thorium

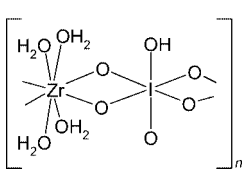

 © 2005 Wiley-VCH Verlag GmbH & Co. KGaA, Weinheim

CORRECTIONS

3371 **U. Braun, T. Habereder, H. Nöth***

Lithium *tert*-Butyl[phenyl(2,2,6,6-tetramethylpiperidino)boryl]amide: A Versatile Reagent

Keywords: Lithium *tert*-butyl[phenyl(2,2,6,6-tetramethylpiperidino)boryl]amide / *N*−Metal borylamides

3372 **M. Bera, W. T. Wong, G. Aromí, D. Ray***

μ-η^1:η^1-*N*,*N*′-Imidazolidine-Bridged Dicopper(II/II) Complexes of a New Dinucleating μ-Bis(tetradentate) Schiff Base Ligand: Synthesis, Structural Characterization, ^{1}H NMR Spectroscopy, and Magnetic Coupling

Keywords: N,O ligand / Imidazolidine / Copper complexes / Magnetic properties

© 2005 Wiley-VCH Verlag GmbH & Co. KGaA, Weinheim

Recent Developments in the Chemistry of Beryllocenes

Rafael Fernández[a] and Ernesto Carmona*[a]

Keywords: Beryllium / Cyclopentadienyl ligands / Half-sandwich complexes / Metallocenes

Synthetic studies on substituted beryllocenes have provided new representatives of this family of compounds. Knowledge of their structures gives a better understanding of the long-standing problem of the structure of the parent beryllocene, $Be(C_5H_5)_2$. Theoretical calculations offer a clear picture of their bonding properties, while spectroscopic and reactivity investigations have clarified their dynamic behaviour. Beryllocenes of the type $BeCp'_2$ (Cp′ = methyl-substituted cyclopentadienyl group) and half-sandwich cyclopentadienylberyllium compounds are considered.
(© Wiley-VCH Verlag GmbH & Co. KGaA, 69451 Weinheim, Germany, 2005)

Introduction

The chemistry of metallocenes started in the early 1950s with the preparation of ferrocene and the recognition of its correct structural and bonding properties.[1] The first main-group metallocenes − the tin and lead compounds $M(C_5H_5)_2$ − were synthesised shortly afterwards.[2] In 1959, $[Be(C_5H_5)_2]$, the lightest member of the alkaline-earth metallocenes and of the general bis(metallocene) series of compounds MCp'_2, was obtained as a volatile, sublimable solid from the reaction of $BeCl_2$ and NaC_5H_5.[3] Over the years, introduction of the pentamethylcyclopentadienyl and other substituted cyclopentadienyl ligands (from now on generally represented by Cp′), including those with bulky substituents, has converted the metallocenes of the alkaline-earth elements into an attractive family of compounds that are characterised by a rich variety of structures.[4]

Beryllocene and some substituted beryllocenes possess a slipped-sandwich structure, whereas the magnesocenes feature parallel (i.e. ferrocene-like) sandwich arrangements.[4] Calcocene adopts an unexpected nonparallel polymeric structure but $[Ca(C_5Me_5)_2]$ is monomeric, although also with nonparallel rings, and this is the structure found in

[a] Instituto de Investigaciones Químicas, Departamento de Química Inorgánica, Consejo Superior de Investigaciones Científicas, Universidad de Sevilla
Avenida de Américo Vespucio, s/n, 41092 Sevilla, Spain
Fax: +34-95-446-0565
E-mail: guzman@us.es

Rafael Fernández was born in 1969 in Sevilla, Spain, where he received both his undergraduate and PhD (2000 under Prof. E. Carmona) degrees. He was awarded a Marie Curie postdoctoral fellowship at the University of Edinburgh, U.K., with Prof. Peter J. Sadler (2001–2003), where he started research in bioinorganic chemistry. At present, he enjoys a Ramón y Cajal fellowship and his current research interests include the design and synthesis of organometallic complexes as anticancer drugs.

Ernesto Carmona (PhD University of Sevilla, 1974 under the late Prof. F. González) is a Professor of Inorganic Chemistry at the University of Sevilla, Spain. He did postdoctoral work at Imperial College, London, with (the late) Prof. Sir G. Wilkinson (1974–77) where he started research in organometallic chemistry. His present research interests comprise C–H and C–C bond-activation reactions, transition metal alkyl and carbene complexes and metallocene chemistry of the main group and the transition elements. He has delivered the Seaborg Lectures (1994), the Pacific Northwest Inorganic Chemistry Lectures (2000), the Goldsmidt–Hermanos Elhúyar Lectures (2000–2001), the Arthur D. Little Lectures (2000–2001) and the Catalán–Sabatier Lecture (2005).

MICROREVIEWS: This feature introduces the readers to the authors′ research through a concise overview of the selected topic. Reference to important work from others in the field is included.

most MCp'_2 compounds of the heavier group 2 elements Ca, Sr and Ba.[4] Interestingly, this structural diversity appears to emerge from a simple, predominantly electrostatic, $M^{2+}\cdots 2Cp'^{-}$ bonding model. Theory predicts[5] that in the unsubstituted metallocenes of Mg to Ba [$M(C_5H_5)_2$] electrostatic forces account for approximately 70–85% of the total interaction energy. As expected, [$Be(C_5H_5)_2$] is more covalent,[5] and replacement of C_5H_5 by C_5Me_5 (viz. in [$Be(C_5Me_5)_2$]) results in further reduction of the ionicity by almost 10%. Numerous quantum chemical calculations on main-group metallocenes have been published in recent years, and the theoretical knowledge gained from these studies has been reviewed recently by Kwon and McKee, who concluded that "there is not enough data from high-level theoretical calculations to have a quantitative understanding of the factors involving covalent or ionic bonding between the Cp ligand and the main-group element".[6]

As already mentioned, the use of Cp′ ligands with different substituents and degrees of substitution has permitted the synthesis and characterisation of many MCp'_2 derivatives of the alkaline-earth elements. The chemistry of these complexes has been compiled in several review articles,[4] usually as part of larger overviews of main-group organometallic compounds. In this Microreview we concentrate on beryllocenes. We revise the longstanding problem of the structure of the parent [$Be(C_5H_5)_2$] and focus on the latest advances in this field. In particular, we discuss the structure and bonding properties of the recently reported beryllocenes with C_5Me_5 and C_5Me_4H rings. Chemical, spectroscopic (NMR) and theoretical studies have provided useful information on their dynamic behaviour. Both bis(cyclopentadienyl) and half-sandwich mono(cyclopentadienyl) beryllium derivatives are examined.

Bis(cyclopentadienyl)beryllium [$Be(C_5H_5)_2$] (1)

Since the preparation of beryllocene by Fisher and Hofmann in 1959,[3] its structure has provoked a long and controversial debate. Structures **I**–**IV** are some of the proposed models.

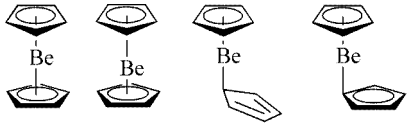

I **II** **III** **IV**

The symmetrical ferrocene-like structure **I** was ruled out because the complex has a permanent dipolar moment in solution[3] (2.24 D in cyclohexane at 25 °C). The first gas-phase electron diffraction study carried out in 1964[7] suggested a non-symmetrical structure **II**, with the Be atom unsymmetrically disposed between the two Cp rings,[8] while molecular orbital calculations[9] were in favour of a non-symmetrical structure of type **III**, in which there is an ionic η^5-Cp ring and a covalently bonded η^1-Cp ring.

Three X-ray studies were carried out between 1972 and 1984. The first, at –120 °C,[10] showed a slipped-sandwich structure **IV**, which was unprecedented at that time. The two Cp rings were found to be parallel and separated by 3.33 Å. The Be atom was disordered between two sites, being η^5-coordinated to one Cp ring ($Be–Cp_{centr}$ = 1.53 Å), and η^1-coordinated to the other, with a Be–C separation of 1.81(5) Å. This is longer than the Be–Me distance found in the complex [$Be(\eta^5\text{-}C_5H_5)Me$][11] (1.706 Å). The same authors carried out a second X-ray investigation, this time at room temperature, that showed similar results, but with the two Cp rings partially eclipsed.[12] A new electron diffraction study provided data compatible with the slipped-sandwich structure.[13]

The third X-ray diffraction determination was carried out in 1984 at –145 °C[14] and also showed a slipped-sandwich structure with disorder at the beryllium atom that alternates its position between two points separated by 1.303 Å. The Be–C–C angles between the metal and the η^1-ring were close to 90° and an important electronic delocalisation of the π-system of this ring was ascertained, with the negative charge being only partially localised on the carbon atom bonded to beryllium. Very recently, a new X-ray crystallographic analysis of [$Be(C_5H_5)_2$] was performed at 20 °C and at –100 °C. At the lower temperature the structure is of the reported η^5/η^1 type but at 20 °C it appears closer to η^5/η^2 coordination.[15]

The slipped-sandwich structure **IV** explains the microwave spectroscopic data of **1**.[16] Moreover, the IR spectrum of [$Be(C_5H_5)_2$] shows little variation between the solid, solution and vapour states.[17] Similarly, the Raman spectrum of solid beryllocene recorded between 160 and 25 °C, and of the liquid at 65 °C, shows no significant differences.[18] Hence, it is clear that the solid-state structure is maintained in all phases.

Adoption of a slipped-sandwich geometry by [$Be(C_5H_5)_2$] has been rationalised by Beattie and Nugent.[19] A variety of structures found for main-group metal cyclopentadienyls, ranging from the centrally bound ferrocene-type to peripherally bonded structures, were discussed. The energy of the $M–C_5H_5$ interaction can be considered as resulting from two effects, namely the strength of the M–C bond and the π-system delocalisation energy. The latter is a minimum for η^5-coordination whereas the η^1/σ binding mode provides the strongest M–C interaction. For an element like beryllium, which forms Be–C bonds of intermediate bond-heterolysis energy, neither of the two forces predominates and the compromise slipped-sandwich structure becomes the most favourable.[19]

Beryllocene is a highly fluxional molecule both in solution[20] and in the condensed phase,[15] according to ^1H, ^9Be and ^{13}C variable temperature NMR studies. The ^1H and the ^{13}C nuclei of the two C_5H_5 rings are magnetically equivalent down to –125 °C, which implies that their exchange is rapid even at these low temperatures. Molecular dynamics calculations[21] have identified two very facile rearrangements, namely a 1,5-sigmatropic shift of the Be(η^5-C_5H_5) unit around the periphery of the η^1-C_5H_5 ring and a "molecular inversion" process that interchanges the η^5 and η^1 ligands. The first is proposed to occur through an η^5/η^2

 © 2005 Wiley-VCH Verlag GmbH & Co. KGaA, Weinheim

transition state, with an activation barrier of 5 kJ mol^{-1}, while for the second an activation energy of 8 kJ mol^{-1} associated with an η^3/η^3 transition state was calculated.[21] Very recently Hung, Macdonald and Schurko[15] have made an important contribution to our understanding of the solid-state structure and dynamics of different beryllocenes and have provided, among other relevant information, an experimentally determined value of 36.9 kJ mol^{-1} for the activation energy of the "molecular inversion" in $[Be(C_5H_5)_2]$ in the solid state.

Numerous theoretical studies have attempted to explain the structure and other properties of $[Be(C_5H_5)_2]$.[21,22] Among the most recent ones, Rayón and Frenking found that at the BP86/6-31G(d) level the η^5/η^1 structure of C_s symmetry is a minimum on the potential energy surface, although with similar energy to the η^5/η^5 D_{5d} structure. The calculations indicate that the potential energy surface around the C_s/D_{5d} forms is very flat, in agreement with the fluxional structure of $[Be(C_5H_5)_2]$. Moreover, a significant covalent contribution (about 40%) to the bonding interaction was calculated. Similar structural conclusions were obtained by Budzelaar and co-workers, who found that the minimum energy structure for beryllocene has η^5 and η^1 rings[5c] that exchange via the η^3/η^3 structure with a barrier of around 7.5 kJ mol^{-1}.

Before closing the discussion on $[Be(C_5H_5)_2]$, two additional comments are appropriate. Firstly, dihydro-1*H*-azaboroyl (Ab) species of composition $[Be(Ab)_2]$ and $[Be(C_5H_5)(Ab)]$ have been prepared as possible models for **1**, as this heterocyclic ligand is isostructural and isoelectronic with C_5H_5.[23] X-ray studies at –150 °C show that $[Be(Ab)_2]$ has η^5 and η^1 ligands that are not parallel but instead form an angle of 14.5°. Secondly, following the report from our group on the synthesis and structure of $[Zn_2(\eta^5\text{-}C_5Me_5)_2]$, an unprecedented dimetallocene that features a metal–metal bonded dizinc unit unsupported by bridging ligands,[24] a theoretical study of the analogous model compounds $[M_2(C_5H_5)_2]$ (M = Be, Mg, Ca) has been reported. The calculations predict that in diberyllocene, $[Be_2(C_5H_5)_2]$, each metal forms a covalent bond with the other, with a Be–Be distance of 2.06 Å, and a predominantly ionic linkage to the adjacent cyclopentadienyl ring.[25]

The Substituted Beryllocenes $[Be(C_5Me_4H)_2]$ (2), $[Be(C_5Me_5)_2]$ (3) and $[Be(C_5Me_5)(C_5Me_4H)]$ (4)

As already mentioned, in the last few years a large number of MCp'_2 compounds of the alkaline-earth metals from Mg to Ba have been prepared using Cp′ ligands with different substituents and degrees of substitution, and their solid-state structures have been determined by X-ray methods.[4] It was therefore surprising to find that, prior to our work, $[Be(C_5H_5)_2]$ was the only structurally characterised beryllocene, although the mixed-ring compound $[Be(C_5Me_5)(C_5H_5)]$ had been obtained when $[Be(\eta^5\text{-}C_5H_5)Cl]$ and $[Li(C_5Me_5)]$ were heated together in a melted mixture (60 °C).[26] It is possible that attempts to make other $[BeCp'_2]$ compounds may have been deterred by the general belief that the small Be^{2+} ion (ionic radius of 0.27 Å in coordination number 4; 0.45 Å estimated value for six-coordination environments)[27] could not accommodate two bulky cyclopentadienyl ligands. This would explain the formation of only the half-sandwich complex $[Be(\eta^5\text{-}C_5Me_5)Cl]$ from the treatment of $BeCl_2$ with C_5Me_5 transfer agents.[28] Nevertheless, the successful isolation of $[Be(C_5Me_5)_2]$ when $BeCl_2$ and $[K(C_5Me_5)]$ react in a diethyl ether/toluene mixture at 115 °C over 3.5 days (vide infra)[29] has revealed that $[Be(C_5Me_5)_2]$ is a stable complex and that it had not been generated before only because coordination of the second C_5Me_5 ring is a slow process with a high kinetic barrier. Recent attempts to synthesise $[Be(Cp^{3Si})_2]$, containing the bulky cyclopentadienyl Cp^{3Si} [1,2,4-$C_5H_2(SiMe_3)_3$], under conditions similar to those used to prepare $[Be(C_5Me_5)_2]$, led only to decomposition products.[30] Since theory predicts an η^5/η^1 structure for the molecules of this compound, failure to generate it is probably due to kinetic difficulties and not to steric overcrowding.[30]

Octamethylberyllocene, $[Be(C_5Me_4H)_2]$ (**2**), and decamethylberyllocene, $[Be(C_5Me_5)_2]$ (**3**), have been synthesised by the reaction of $BeCl_2$ with $[K(C_5Me_4H)]$ and $[K(C_5Me_5)]$, respectively (Scheme 1, a). However, whereas compound **2** requires stirring at room temperature for about 12 h, the synthesis of **3** demands higher reaction temperatures (ca. 115 °C) and times (between 3 and 4 days) and even under these conditions the crude reaction mixture always contains small amounts of the half-sandwich complex $[Be(\eta^5\text{-}C_5Me_5)Cl]$.[29] Clearly, replacement of the chloride ligand by C_5Me_5 in the latter complex is difficult due to steric hindrance. In marked contrast, attempts to isolate the analogous $[Be(\eta^5\text{-}C_5Me_4H)Cl]$ derivative have proved fruitless – the use of stoichiometric amounts of $[K(C_5Me_4H)]$ leads only to $[Be(C_5Me_4H)_2]$ (**2**) and unreacted $BeCl_2$. In accordance with this, extended heating at high temperatures (Scheme 1, b) is also needed for the mixed-ring beryllocene $[Be(C_5Me_5)(C_5Me_4H)]$ (**4**), although the synthesis proceeds in high yield (isolated yields of crystalline **4** of around 70%). The three compounds are volatile, sublimable solids that are very soluble in common non-polar organic solvents. They are very reactive towards O_2 and H_2O and de-

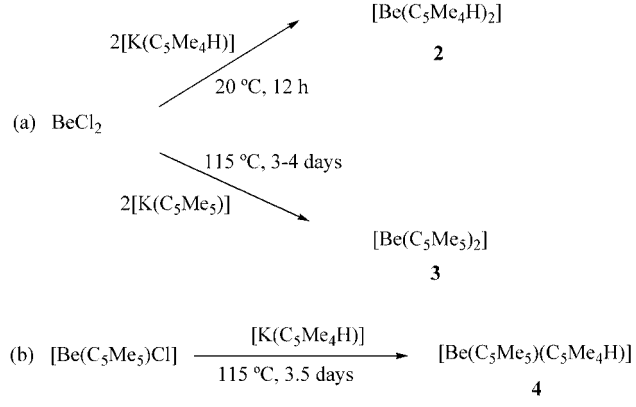

Scheme 1. Synthesis of the beryllocenes **2**–**4**.

 © 2005 Wiley-VCH Verlag GmbH & Co. KGaA, Weinheim

compose immediately upon exposure to air. Compounds **2** and **3** enlarge the beryllocenes series of complexes significantly, while the mixed-ring compound **4** finds precedent only in the related $[Be(C_5Me_5)(C_5H_5)]$ derivative, formulated as $[Be(\eta^5\text{-}C_5Me_5)(\eta^1\text{-}C_5H_5)]$ on the basis of solution IR and NMR spectroscopic studies.[26] Solid-state characterisation of this species by X-ray methods has not been reported.

Compounds **2**–**4** were characterised by X-ray crystallography at low temperatures (100–300 K); the corresponding ORTEP diagrams are given in Figure 1. Recently the structures of **2** and **3** have also been re-determined at low temperature, with similar results.[15]

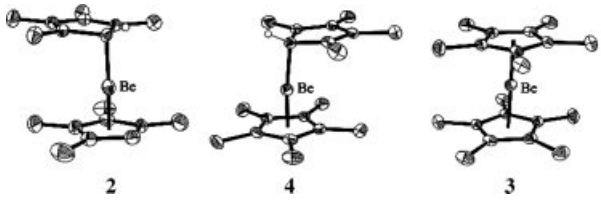

Figure 1. ORTEP perspectives of beryllocenes **2**, **3** and **4**.

Both $[Be(C_5Me_4H)_2]$ (**2**) and $[Be(C_5Me_5)(C_5Me_4H)]$ (**4**) exhibit η^5/η^1 geometries of the kind found for the parent beryllocene. Not unexpectedly, the structure of the mixed-ring beryllocene **4** consists of η^5-C_5Me_5 and η^1-C_5Me_4H binding. In the two compounds the η^1-C_5Me_4H ring bonds to the metal through the unique CH carbon, possibly to form a stronger Be–C bond.[29] The Be–CH bond lengths are identical within experimental error (1.77 Å) and compare well with the corresponding distance in $[Be(C_5H_5)_2]$ [1.826(6) Å].[10,12,14] These Be–CH distances are in the middle of the range of Be–C bonds (1.70–1.85 Å).[29]

The coordination of the η^5-Cp′ ring is highly symmetrical, and for either compound the five Be–C separations are almost identical and cluster around 1.90 Å. Considering that the Be–C(η^5) bond lengths in $[Be(C_5H_5)_2]$ have comparable values (average about 1.92 Å), it is evident that substitution of H by Me within the η^5-Cp′ ligand does not significantly alter the strength of the Be–C(η^5) bonds. The distances from beryllium to the η^5-C_5Me_5 ring centroids of **2** and **4** are also identical within experimental error (1.47 Å) and very similar to the corresponding separation in $[Be(C_5H_5)_2]$ (1.50 Å).[10,12,14]

The Be–C(η^1)–ring plane angle in the two complexes **2** and **4** is close to 100–102°, far from the 125° value which would be expected for η^1-bonding to a tetrahedral ring carbon atom.[31] Similarly, the Be–C(η^1)–C angles to the adjacent carbon atoms are smaller (ca. 99°) than the ideal 109.5° value that would correspond to a tetrahedral geometry. Additionally, the η^5- and η^1-rings are almost planar and nearly parallel, the angles between the rings being 6.6(1)° and 4.9(1)° for **2** and **4**, respectively. In the three compounds **1**, **2** and **4** there is an alternation in the bond lengths within the η^1 ring which is characteristic of the slipped-sandwich structural type. As shown in Figure 2, the difference in the lengths of the $C_{\alpha\beta}$ and $C_{\beta\beta}$ bonds (C_α is the carbon atom adjacent to the beryllium-bound carbon) is only 0.06–0.07 Å. This reveals some diene character for the η^1 rings. Nevertheless, partial delocalisation of the π-system exists, as the differences in the C–C bonds are significantly smaller than in cyclopentadiene (0.12 Å) and in cyclopentadienyl rings bonded in the common η^1/σ fashion. Thus, in $[B(\eta^5\text{-}C_5Me_5)(\eta^1\text{-}C_5Me_5)]^+$[32] and $[\{Hg(\eta^1\text{-}C_5Me_4SiMe_2tBu)Cl\}_4]$[33] the C–C bonds are dissimilar by about 0.14 Å.

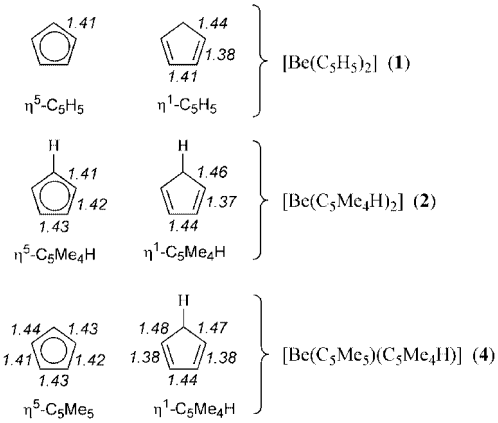

Figure 2. Lengths [Å] of the $C_{\beta\beta}$ and $C_{\alpha\beta}$ bonds in the Cp′ rings of **1**, **2** and **4**.

In contrast with beryllocenes **1**, **2** and **4**, $[Be(C_5Me_5)_2]$ (**3**) exhibits an almost regular, ferrocene-like, sandwich structure in the solid state (Figure 1). The two C_5Me_5 rings are perfectly parallel and planar (the average deviation from the mean plane is 0.01 Å) and are separated by 3.310(1) Å, a distance comparable to the 3.35 Å interlayer gap in graphite.[34] The Be–C_5Me_5 centroid distance of 1.655(1) Å is noticeably longer than the Be–Cp′ centroid separations in **2** and **4** (ca. 1.47 Å), thus revealing a significantly weaker Be–C_5Me_5 bonding interaction. This is not unexpected, however, in view of the existence of two π-C_5Me_5 rings in the molecules of **3** (formal coordination number of six) and of only four valence orbitals on beryllium. The relatively long Be–C_5Me_5 centroid and Be–C distances in **3** are not abnormal. As a matter of fact, they are comparable to those found in the known compounds $[Mg(C_5Me_5)_2]$[35] and $[Al(C_5Me_5)_2]^+$[36] if the differences in the ionic radii of the three metal ions are taken into account. Be^{2+}, when six coordinate, has an (estimated) effective ionic radius[27] of 0.45 Å, Al^{3+} of 0.535 Å and Mg^{2+} of 0.72 Å. Using an estimated value of 1.63 Å for the "ionic radius" of the ring carbon atoms[37] of the $C_5Me_5^-$ group in these compounds,[29] M–C(η^5) distances of 2.08 Å (Be), 2.16 Å (Al) and 2.35 Å (Mg) can be calculated that are in excellent agreement with the experimental values (2.05 Å in the Be, 2.16 Å in the Al and 2.34 Å in the Mg metallocenes).

Solid-state ^9Be and ^{13}C NMR studies have also been employed to elucidate the structure and dynamics of the methyl-substituted beryllocenes **2** and **3**, as well as the parent beryllocene.[15] Interestingly, within the relatively small

 © 2005 Wiley-VCH Verlag GmbH & Co. KGaA, Weinheim

chemical-shift range of ^{9}Be (ca. +25 to –25 ppm) the isotropic chemical shift has been found to vary with the coordination of the Cp′ rings from, for instance, δ = –19.8 ppm in the η^5/η^1 beryllocene **2** to δ = –24.4 ppm in the η^5/η^5 compound **3**. It was also found that the Cp′ rings of **2** feature relatively little motion in the temperature interval from –100 to 80 °C, while in the case of **3** the rate of reorientation of the C_5Me_5 rings decreases substantially at low temperatures.[15]

The bonding in decamethylberyllocene (**3**) has been analysed at different levels of theory and the geometry of its molecules optimised enforcing the η^5/η^5 D_{5d} and the η^5/η^1 C_s symmetries. The B3LYP functional predicts the C_s structure to be the lower energy one by about 3 kcal mol^{-1}, whereas calculations with the PW91 functional lead to a difference of only 1 kcal mol^{-1}. This is consistent with the very fluxional structures of beryllocenes. The very low energy difference between the two geometries suggests that the compression implied by crystal packing may distort the molecules toward the observed η^5/η^5 geometry. The calculations also showed that the electrostatic contribution to the bonding ($Be^{2+}\cdots 2\ C_5Me_5^-$) for the D_{5d} structures of $[Be(C_5H_5)_2]$ and $[Be(C_5Me_5)_2]$ amounts to around 65 and 58%, respectively. Thus, it is clear that the bonding in **1** and **3** has a high covalent character and that the covalency is larger in $[Be(C_5Me_5)_2]$ than in $[Be(C_5H_5)_2]$.[29]

Variable temperature ^{1}H and ^{13}C NMR spectroscopy and reactivity studies are in agreement with the expected fluxionality for these molecules, consisting of two very low-energy processes: a 1,5-sigmatropic shift of the Be(η^5-Cp′) fragment around the periphery of the η^1 ring and the "molecular inversion" that results in the exchange of the two rings.[21] For the parent beryllocene the rates of molecular redistribution in solution[20] (300 K) and in the gas phase (400 K) are of the order of 10^{10}–10^{12} s^{-1} and therefore the processes cannot be detected by NMR methods.

In accordance with this, the two rings of $[Be(C_5Me_4H)_2]$ are equivalent (from –90 to +80 °C) and experience very little chemical-shift variation. Decamethylberyllocene shows a singlet in the ^{1}H NMR spectrum (δ = 1.9–2.0 ppm between –90 and +80 °C) and a unique ^{13}C resonance for the ring carbon nuclei (δ = 109.7 ppm at –90 °C). Naturally, this cannot be taken as being suggestive of fluxionality, but by similarity with the other beryllocenes it is reasonable to assume that the η^5/η^5 and η^5/η^1 structures exist in equilibrium in solution. For the mixed-ring beryllocene **4**, an important contribution of the η^5-C_5Me_5/η^1-C_5Me_4H solid-state structure to the solution structure has been proposed from the variable temperature ^{1}H and ^{13}C{^{1}H} chemical shifts and also from the observation of a well-resolved coupling (10 Hz) between the quadrupolar ^{9}Be and the ^{13}*C*H nuclei in the ^{13}C{^{1}H} NMR spectrum recorded at +95 °C.

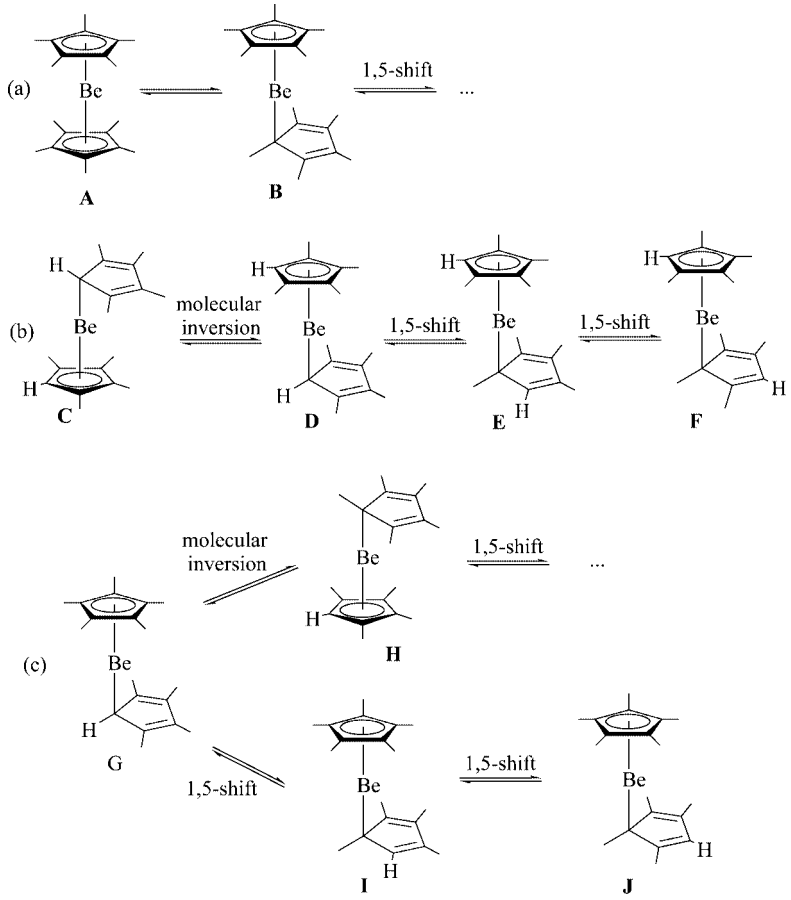

Scheme 2. Rearrangements of substituted beryllocenes: a) $[Be(C_5Me_5)_2]$; b) $[Be(C_5Me_4H)_2]$; c) $[Be(C_5Me_5)(C_5Me_4H)]$.

 © 2005 Wiley-VCH Verlag GmbH & Co. KGaA, Weinheim

Reactions of $[Be(C_5Me_4H)_2]$, $[Be(C_5Me_5)_2]$ and $[Be(C_5Me_5)(C_5Me_4H)]$ with CNXyl: The Half-Sandwich Beryllocenes $[Be(\eta^5\text{-}Cp')\{C(NXyl)Cp''\}]$

The above-mentioned dynamic processes that account for the fluxionality of the beryllocenes should give rise to different isomeric structures (Scheme 2) in the solutions of **2**, **3** and **4**. Interestingly, the study of the reactions of these compounds with CNXyl (Xyl = C_6H_3-2,6-Me_2) could be taken to support the existence of most of these structures in solution and has therefore been employed as a chemical probe for both the sigmatropic shift and the molecular-inversion rearrangements that form them.[38] This relies on the assumption that formation of the iminoacyl complexes (see below) occurs by direct attack of CNXyl on a Be–η^1-Cp′ bond, without a change in the coordination of the η^5-Cp′ ring.

The permethylated beryllocene **3** and CNXyl react at room temperature to form the iminoacyl complex **5** (Scheme 3a). The reaction is reversible and the equilibrium is characterised by $\Delta H°$ and $\Delta S°$ values of 18(0.4) kcal mol^{-1} and 35(1) cal mol^{-1} K^{-1}, respectively. The reaction of $[Be(C_5Me_4H)_2]$ (**2**) and CNXyl is also reversible (Scheme 3b). However, due to the lower symmetry of the C_5Me_4H group, this system is somewhat more complex and three iminoacyl isomers are possible. Two of them, **6a** and **6b**, have been isolated and characterised. Even though variable temperature ^{1}H NMR monitoring of the reaction suggested the formation of another product, its characterisation was not possible. Mechanistically, CNXyl attack on a Be–η^1-Cp′ bond was suggested to explain iminoacyl formation rather than a migratory insertion reaction on the basis of steric crowding around the metal and the availability of only four valence orbitals. Regardless of this, since a Be–η^1-Cp′ bond participates in the C–C coupling, the formation of iminoacyls **5** and **6** (Scheme 3a and b) suggests the existence in solution of the η^5/η^1 structures **B** (in the case of **3**) and **D** and **F** (for **2**) resulting from the 1,5-sigmatropic shift (Scheme 2a and b).

Naturally, the identity of the two Cp′ rings of **2** and **3** does not permit detection of the "molecular inversion" rearrangement that interchanges the two rings. Nonamethylberyllocene (**4**) is therefore unique in this regard. As shown in Scheme 3c, four isomeric iminoacyl complexes are possible and, indeed, the treatment of **4** with CNXyl has allowed the isolation of three of them. As could be antici-

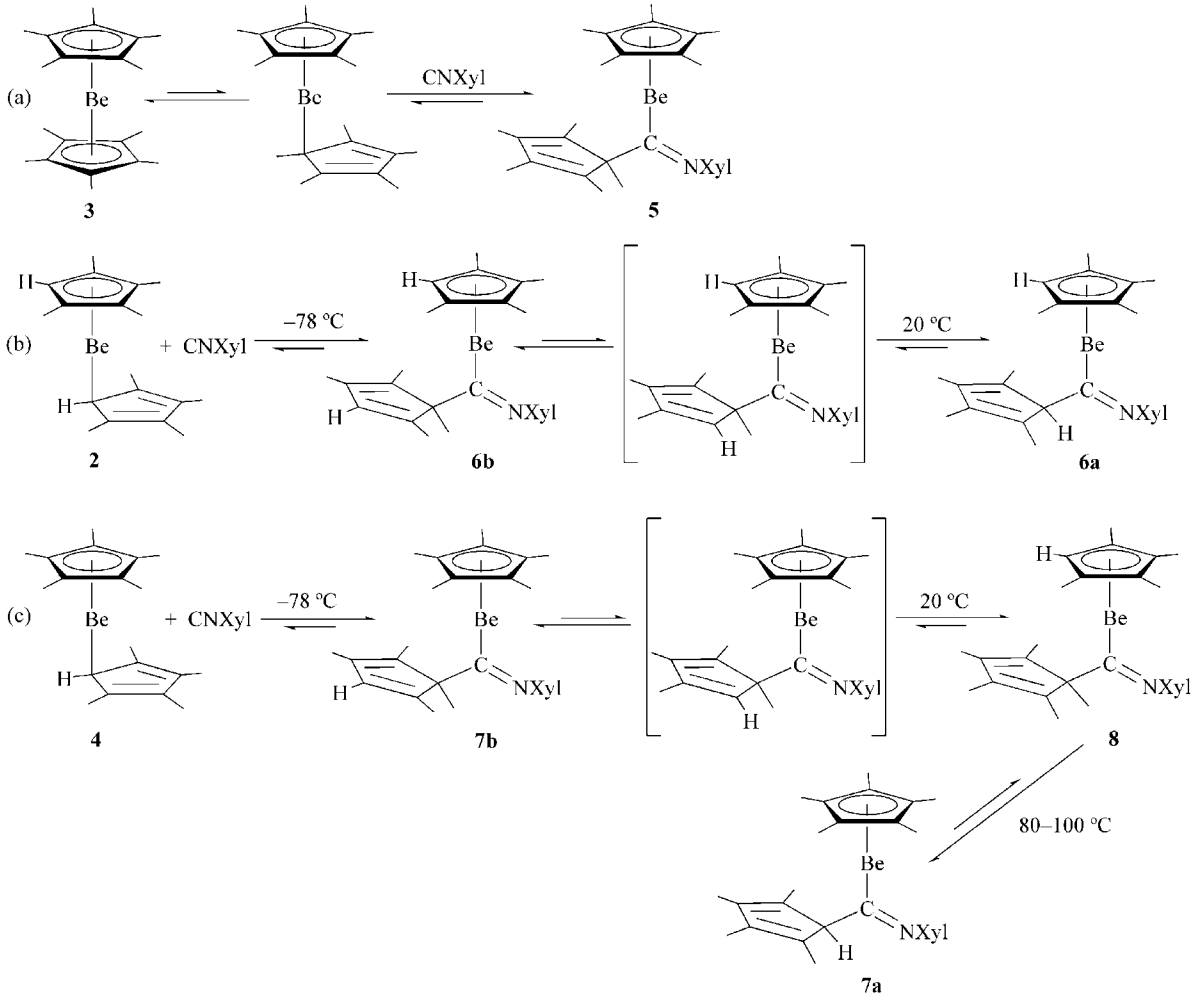

Scheme 3. Reaction of $[Be(C_5Me_5)_2]$ (**3**), $[Be(C_5Me_4H)_2]$ (**2**) and $[Be(C_5Me_5)(C_5Me_4H)]$ (**4**) with CNXyl.

 © 2005 Wiley-VCH Verlag GmbH & Co. KGaA, Weinheim

pated, the thermodynamic isomer **7a** contains an η^5-C_5Me_5 ligand and an iminoacyl fragment that results from C–C coupling between the CH unit of C_5Me_4H and CNXyl. Most interestingly, however, compound **8**, which is generated in the room temperature reaction, has an η^5-C_5Me_4H ring and a C(NXyl)C_5Me_5 iminoacyl ligand, thus indicating that the "inverted" beryllocene structure **H** of Scheme 2c is attainable in solution.

Summarizing the reactivity of beryllocenes represented in Schemes 2 and 3, the formation of iminoacyls **5**–**8** can be accounted for by assuming that iminoacyl formation is a reversible process, as has been convincingly demonstrated. The generation of the different isomers may be explained in relatively simple terms with the aid of Scheme 4 for the particular example of the reaction of **4** with CNXyl. It can be proposed that the different η^5/η^1 beryllocene isomers that may exist in solution (**G**, **H**, **I** and **J**) compete for the isocyanide, so that at a certain temperature the outcome of the reaction depends upon: i) the accessibility of the particular isomer, i.e. its population, and the activation barrier of its C–C coupling reaction, and ii) the thermodynamic stability of the resulting iminoacyl relative to that of the other isomers. For instance, the seemingly exclusive formation of **7b** at –78 °C suggests that its η^5/η^1 beryllocene precursor **J** is accessible at this temperature and, moreover, that it features the lowest barrier of all C–C couplings. Since the formation of **7b** is reversible, other less-facile C–C couplings may occur at higher temperature, for instance that leading to the "inverted" compound **8**. Finally, since the formation of **7a** requires heating at 80–100 °C, it appears that the strongest Be–CH bond of those possible for the Be–η^1-C_5Me_4H unit is the most reluctant to participate in the C–C coupling with CNXyl.

Other Half-Sandwich Cyclopentadienylberyllium Compounds

A large number of beryllium compounds containing only one cyclopentadienyl ligand have been described, mainly by the groups of Morgan, Coates and Gaines, and they have been considered in previous review articles.[4] Therefore, only a brief, non-comprehensive coverage is presented here. Most of these compounds have been prepared by the reaction between beryllocene and the corresponding disubstituted beryllium compound BeR_2, leading to the mixed products [BeCpR] with R = H,[39] Cl,[40] Br,[41] I,[42] CH_3,[11,39b] *t*Bu,[43] C_6F_5,[43] C_6H_5,[44] C≡CH,[45] and C≡C–CH_3.[45] Other half-sandwich beryllium complexes containing different borate ligands have been synthesised by other routes. For example, reaction of [BeCpCl] with $LiBH_4$ and KB_5H_8 leads to the complexes [BeCp(BH_4)][46] and [BeCp(B_5H_8)],[47] respectively. The synthesis of compounds [BeCp(B_3H_8)][48] and [BeCp(B_5H_{10})][49] has been achieved by the reaction of NaCp with [Be(B_3H_8)$_2$] and [BeBr(B_5H_{10})], respectively. The amide complexes [BeCp(NMe_2)], [BeCp(NEt_2)], [BeCp(NPh_2)] and [BeCp{N($SiMe_3$)$_2$}] have been prepared by mixing equimolar amounts of the corresponding Li or Na amide and [BeCpX] (X = Cl, Br). They can also be prepared by stirring an equimolar mixture of beryllocene and the corresponding beryllium bis(amide) complex.[50] Recently, the complex [BeCp($SiMe_3$)] has been synthesised[51] by the base-free reaction of [$LiSiMe_3$] with [BeCpCl]. It constitutes the first example of a compound with a direct Be–Si bond[51] and it is characterised by an Si–Be distance of 2.18 Å, which is significantly longer than the sum of the covalent radii (2.01 Å).

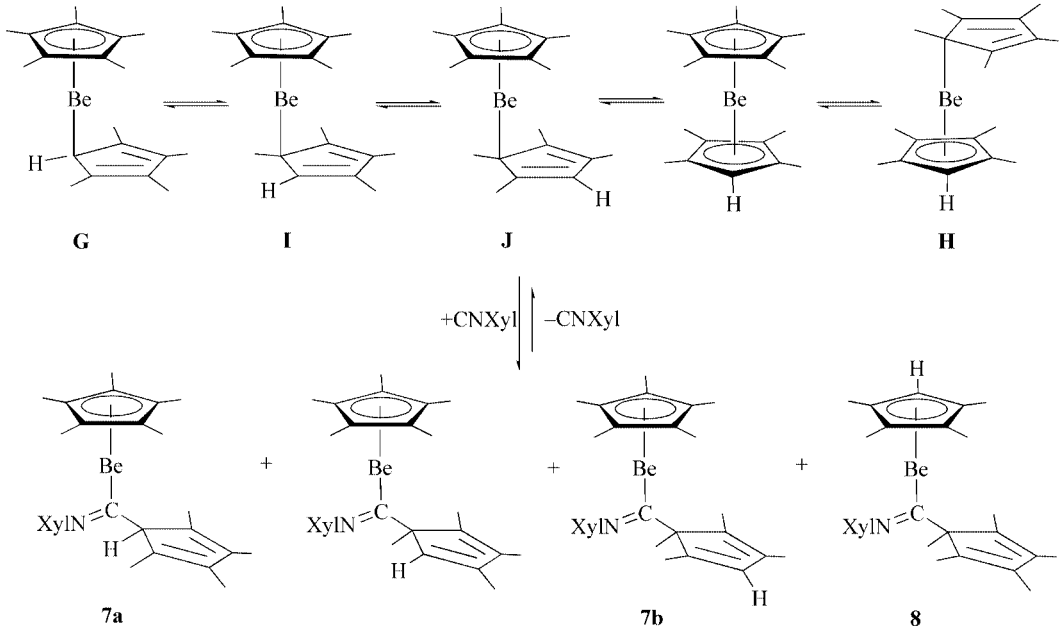

Scheme 4. Reaction of the possible isomers of **4** with CNXyl.

 © 2005 Wiley-VCH Verlag GmbH & Co. KGaA, Weinheim

All these cyclopentadienyl half-sandwich complexes are air-sensitive, colourless solids or liquids whose structural parameters are available mainly from X-ray structural data[47,51,52] and from electron diffraction and microwave studies.[39a,40–42,53] In nearly all cases the molecules are monomeric in the solid state, in solution, and in the gas phase, with pentahapto coordination of the cyclopentadienyl ligand. The beryllium to ring centroid distances (e.g. $[BeCpCl]_{(g)}$ 1.48 Å;[39a] $[BeCpCl]_{(s)}$ 1.45 Å;[52] $[BeCpBr]_{(g)}$ 1.53 Å;[40] $[BeCpMe]_{(g)}$ 1.50 Å;[11] $[BeCpCCH]_{(g)}$ 1.49 Å;[40] $[BeCpB_5H_8]_{(s)}$ 1.47 Å[46]) are all similar to that to the nearest ring in beryllocene[14] (1.505 Å). The Be–CH_3 bond length in [BeCpMe] is not significantly different from the Be–C bond length in dimethylberyllium [1.698(5) Å], but the Be–Cl bond length in [BeCpCl] is significantly longer in the gas phase [1.837(6) Å] and in the solid state [1.869(3) Å] than in monomeric beryllium dichloride (1.75 Å). It seems reasonable to assume that the dative Cl–Be π-bonding interaction is weaker in [BeCpCl] than in $BeCl_2$.

The most notable feature of the NMR spectrum of these compounds is that in the ^{13}C NMR spectrum of [BeCpBr], a ^{13}C–^{9}Be coupling of 1.1 Hz has been observed.[54] $[BeCpBH_4]$ is unique in exhibiting a very well-resolved ^{9}Be NMR multiplet spectrum and is the only known example of ^{9}Be–^{11}B coupling (3.6 Hz), as a 1:1:1:1 quartet and an unresolved ^{9}Be–^{10}B septet of equal intensity of 1.2 Hz are also observed.[57b] The ^{9}Be and ^{29}Si NMR spectra[51] of $[BeCp(SiMe_3)]$ exhibit a large J(Be–Si) coupling constant of 51 Hz, and the ^{9}Be chemical shift of $\delta = -27.70$ ppm is the highest-field value recorded to date, in accordance with the calculated bond-polarity pattern as well as a bond to Si.

Theoretical calculations at different levels have been performed for monocyclopentadienylberyllium compounds, especially for [BeCpH].[9c] It has been shown that [BeCpH] strongly prefers C_{5v} symmetry and pentahapto bonding with a high degree of covalent character. Bonding between beryllium and the monodentate ligand involves one sp hybrid orbital on the metal while the other sp hybrid interacts with the $a_1\pi$ orbital of the ring. The remaining 2p orbitals on beryllium overlap with filled $e_1\pi$ orbitals to form degenerate bonding orbitals. Beryllium is therefore surrounded by an octet of electrons and since these compounds are not electron deficient, there is relatively little tendency for association or complex formation.[11,39a,40,55]

In contrast to the many known organoberyllium compounds that contain a Be(η^5-C_5H_5) fragment,[4] there are only a few in which the cyclopentadienyl ligand is substituted. The half-sandwich species Be(η^5-C_5Me_5)Cl (**9a**) was first isolated by Burns and Andersen in 1987,[28] and later used by Pratten, Cooper and Aroney, to prepare the mixed-ring beryllocene $[Be(C_5Me_5)(C_5H_5)]$, which they characterised by solution IR and NMR studies.[26] The organometallic beryllium compounds Be(η^5-C_5Me_5)Me],[28] [Be(η^5-C_5Me_5)(P*t*Bu_2)][56a] and [Be(η^5-C_5Me_5)(As*t*Bu_2)][56b] were subsequently prepared from **9a**.

The complexes [Be(η^5-C_5Me_5)X] [X = Cl (**9a**), Br (**9b**)] are obtained in high yields when $[BeX_2(OEt_2)_2]$ (X = Cl, Br) are allowed to react with $[M(C_5Me_5)]$ salts (M = Na, K). The alkyl derivatives [Be(η^5-C_5Me_5)R] [R = Me (**10a**), CMe_3 (**10b**), CH_2CMe_3 (**10c**), CH_2Ph (**10d**)] can then be obtained by metathetical exchange with an alkyllithium reagent in Et_2O.[38] Compounds **9** and **10** are crystalline solids, which may be crystallised by cooling their concentrated pentane solutions.

The NMR spectroscopic data for compounds **9** and **10** (^1H, ^{13}C and ^{9}Be)[38] compare well with those reported for other Cp′–Be derivatives. The ^{13}C chemical shift of the Me group of [Be(η^5-C_5Me_5)Me] (**5a**) is $\delta = -25.4$ ppm and the signal appears as a well-resolved 1:1:1:1 pattern due to coupling to ^{9}Be ($I = 3/2$), with a ^1J(Be–C) coupling constant of 30 Hz. In all of the other alkyls this resonance was not observed, presumably due to quadrupolar relaxation by the beryllium nucleus. The ring carbon atoms are not affected by the quadrupolar nucleus since the singlet resonances are sharp and no coupling is detected. The chemical shift value of $\delta = 108$–109 ppm is almost the same as that found for structurally characterised Be(η^5-C_5Me_5) compounds.[28] The ^{9}Be chemical shifts also have normal values. The signals are relatively sharp (half-height width of 3.5 Hz for **9b** and 16 Hz for **10a**) and, due to paramagnetic ring-current effects,[41,57] they are located in the higher-field region of the ^{9}Be chemical shift range (from approximately $\delta = -25$ to +25 ppm).[20,41,57–59]

Both the halides **9** and the alkyls **10** are stable toward disproportionation. In an attempt to obtain the hydride [Be(η^5-C_5Me_5)H], which is isolobal with the alkyls **10**, Andersen et al. treated [Be(η^5-C_5Me_5)Br] with LiAlH. IR studies on the crude reaction product revealed the existence of absorptions at 1950–1985 cm^{-1} that could be due to a Be–H group.[38] However, no hydride resonance could be found by ^1H NMR spectroscopy. Instead, the ^1H, ^{9}Be and $^{13}C\{^1H\}$ NMR spectra of the mixture confirmed the existence of $[Be(C_5Me_5)_2]$ and [Be(C_5Me_5)Br]. Thus, it is possible that [Be(η^5-C_5Me_5)H] forms but it is not stable at room temperature and disproportionates to $[Be(C_5Me_5)_2]$ and BeH_2.

Summary and Outlook

Since 1959, and for a period of over forty years, beryllocene $[Be(C_5H_5)_2]$ (**1**) has been the only member of the beryllocene family of compounds. This singularity, and above all its unusual structure, has motivated an astonishingly large number of both experimental and theoretical investigations.

The preliminary studies reported by our group in 2000 constituted a major turn-about of this situation since synthetic and structural data for two new beryllocenes were provided.[29b] Like **1**, the new beryllocenes, viz. $[Be(C_5Me_4H)_2]$ (**2**) and $[Be(C_5Me_5)_2]$ (**3**), contain two Cp′ rings of the same kind. Shortly afterwards, preliminary information on the structure and chemical behaviour of the mixed-ring compound [Be(η^5-C_5Me_5)(η^1-C_5Me_4H)] (**4**) was also provided by our group.[38b]

The beryllocenes that possess one or two C_5Me_4H rings, i.e. **2** and **4**, feature η^5/η^1 geometries of the slipped-sand-

 © 2005 Wiley-VCH Verlag GmbH & Co. KGaA, Weinheim

wich type, with the η^1-C_5Me_4H ligand bonded to beryllium through the unique CH carbon atom.[29,38] At variance with the parent beryllocene **1**, the structures of **2** and **4** exhibit no positional or thermal disorder. The calculated geometries are in agreement with experimentally observed structures and the calculations reveal that the preference of beryllium for CH binding is due to larger charge localisation on this part of the η^1 ring.

In contrast with this situation, the long sought-after decamethylberyllocene [$Be(C_5Me_5)_2$] (**3**) has an almost regular sandwich structure in the solid state.[29] Possibly, crystal packing effects may originate steric repulsions between the methyl ring substituents that force the molecules of **3** to adopt the η^5/η^5 geometry in the condensed state. This distortion would be energetically facile as the calculated energy difference between the two geometries is very low.

The half-sandwich chloride derivative [$Be(\eta^5$-$C_5Me_5)Cl$] reported by Burns and Andersen[28] in 1987, and the bromide analogue,[38a] are key reagents for Be(η^5-C_5Me_5) chemistry. These compounds have been used as precursors for the synthesis of a number of Be(η^5-C_5Me_5) organometallics, including the alkyls [$Be(\eta^5$-$C_5Me_5)R$] and the beryllocenes [$Be(C_5Me_5)_2$], [$Be(C_5Me_5)(C_5Me_4H)$] and [$Be(C_5Me_5)(C_5H_5)$]. It is foreseeable that they will continue to play a major role in future Be(η^5-C_5Me_5) chemistry.

Acknowledgments

Financial support from the Junta de Andalucía and the Ministry of Science and Technology of Spain (to E.C., Project BQU2001-1995; and to R.F. for a Ramón y Cajal fellowship) is gratefully acknowledged.

[1] a) T. J. Kealy, P. L. Pauson, *Nature* **1951**, *168*, 1039–1040; b) E. O. Fischer, W. Pfab, *Z. Naturforsch. Teil B* **1952**, *7*, 377–379; c) G. Wilkinson, M. Rosenblum, M. C. Whiting, R. B. Woodward, *J. Am. Chem. Soc.* **1952**, *74*, 2125–2126; d) R. B. Woodward, M. Rosenblum, M. C. Whiting, *J. Am. Chem. Soc.* **1952**, *74*, 3458–3459.

[2] a) E. O. Fischer, H. Z. Grubert, *Z. Naturforsch. Teil B* **1956**, *11*, 423; b) E. O. Fischer, H. Z. Grubert, *Z. Anorg. Allg. Chem.* **1956**, *286*, 237.

[3] E. O. Fischer, H. P. Hofmann, *Chem. Ber.* **1959**, *92*, 482–486.

[4] a) T. P. Hanusa, *Organometallics* **2002**, 2559–2571; b) P. Jutzi, N. Burford, *Chem. Rev.* **1999**, *99*, 969–990; c) P. Jutzi, N. Burford, in *Metallocenes*, vol. 1 (Eds: A. Togni, R. L. Halterman), Wiley-VCH, **1998**, chapter 2; d) N. A. Bell, in *Comprehensive Organometallic Chemistry II*, vol. 1 (Eds.: G. Wilkinson, F. G. A. Stone, W. Abel), Pergamon, Oxford, **1995**, chapter 2; e) M. L. Hays, T. P. Hanusa, *Adv. Organomet. Chem.* **1996**, *40*, 117; f) D. Stalke, *Angew. Chem. Int. Ed. Engl.* **1994**, *33*, 2168.

[5] a) V. M. Rayón, G. Frenking, *Chem. Eur. J.* **2002**, *8*, 4693–4707; b) O. Kwon, M. L. McKee, in *Computational Organometallic Chemistry* (Ed.: T. R. Cundari), Marcel Dekker, New York, **2001**, 397; c) P. H. M. Budzelaar, J. J. Engelberts, J. H. van Lenthe, *Organometallics* **2003**, *22*, 1562–1576.

[6] O. Kwon, M. L. McKee, in *Computational Organometallic Chemistry* (Ed.: T. R. Cundari), Marcel Dekker, New York, **2001**, 403.

[7] A. Almenningen, O. Bastiansen, A. Haaland, *J. Chem. Phys.* **1964**, *40*, 3434–3437.

[8] A. Haaland, *Acta Chem. Scand.* **1968**, *22*, 3030–3032.

[9] a) D. S. Marinyk, *J. Am. Chem. Soc.* **1977**, *99*, 1436–1441; b) N. S. Chiu, L. Schäfer, *J. Am. Chem. Soc.* **1978**, *100*, 2604–2607; c) E. D. Jemmis, S. Alexandratos, P. R. Schleyer, A. Streitwieser, H. F. Schaefer, *J. Am. Chem. Soc.* **1978**, *100*, 5695–5700; d) R. Gleiter, M. Böhm, A. Haaland, R. Johansen, J. Lusztyk, *J. Organomet. Chem.* **1979**, *170*, 285–292.

[10] C. H. Wong, T. Y. Lee, K. J. Chao, S. Lee, *Acta Crystallogr., Sect. B* **1972**, *28*, 1662–1665.

[11] D. A. Drew, A. Haaland, *Acta Chem. Scand.* **1972**, *26*, 3079.

[12] C. H. Wong, T. Y. Lee, T. J. Lee, T. W. Chang, C. S. Liu, *Inorg. Nucl. Chem. Lett.* **1973**, *9*, 667–673.

[13] A. Almenningen, A. Haaland, J. Lusztyk, *J. Organomet. Chem.* **1979**, *170*, 271–284.

[14] K. W. Nugent, J. K. Beattie, T. W. Hambley, M. R. Snow, *Aust. J. Chem.* **1984**, *37*, 1601–1606.

[15] I. Hung, C. L. B. Macdonald, R. W. Schurko, *Chem. Eur. J.* **2004**, *10*, 5923–5935.

[16] S. J. Pratten, M. K. Cooper, M. J. Aroney, S. W. Filipazuk, *J. Chem. Soc., Dalton Trans.* **1985**, 1761–1765.

[17] a) K. W. Nugent, J. K. Beattie, *Inorg. Chem.* **1988**, *27*, 4269–4273; b) S. J. Pratten, M. K. Cooper, M. J. Aroney, *Polyhedron* **1984**, *3*, 1347–1350.

[18] J. Lusztyk, K. B. Starowieyski, *J. Organomet. Chem.* **1979**, *170*, 293–297.

[19] J. K. Beattie, K. W. Nugent, *Inorg. Chim. Acta* **1992**, *198–200*, 309.

[20] K. W. Nugent, J. K. Beattie, L. D. Field, *J. Phys. Chem.* **1989**, *93*, 5371–5377.

[21] P. Margl, K. Schwarz, P. Blöchl, *J. Chem. Phys.* **1995**, *103*, 683–690.

[22] L. W. Mire, S. D. Wheeler, E. Wagenseller, D. S. Marynick, *Inorg. Chem.* **1998**, *37*, 3099–3106.

[23] G. Schmid, O. Boltsch, R. Boese, *Organometallics* **1987**, *6*, 435–439.

[24] I. Resa, E. Carmona, E. Gutierrez-Puebla, A. Monge, *Science* **2004**, *305*, 1136–1138.

[25] Y. Xie, H. F. Schaefer III, E. D. Jemmis, *Chem. Phys. Lett.* **2005**, *402*, 414–421.

[26] S. J. Pratten, M. K. Cooper, M. J. Aroney, *J. Organomet. Chem.* **1990**, *381*, 147–153.

[27] R. D. Shannon, *Acta Crystallogr., Sect. A* **1976**, *32*, 751–767.

[28] C. J. Burns, R. A. Andersen, *J. Organomet. Chem.* **1987**, *325*, 31–37.

[29] a) M. M. Conejo, R. Fernández, D. Del Rio, E. Carmona, A. Monge, C. Ruiz, A. M. Márquez, J. F. Sanz, *Chem. Eur. J.* **2003**, *9*, 4452–4461; b) M. M. Conejo, R. Fernández, E. Gutiérrez-Puebla, A. Monge, E. Carmona, *Angew. Chem. Int. Ed.* **2000**, *39*, 1949–1951.

[30] M. J. Harvey, K. T. Quisenberry, T. P. Hanusa, V. G. Young Jr., *Eur. J. Inorg. Chem.* **2003**, 3383–3390.

[31] J. K. Beattie, K. W. Nugent, *Inorg. Chim. Acta* **1992**, *198–200*, 309–318.

[32] A. Voigt, S. Filipponi, C. L. B. Macdonald, J. D. Gorden, A. H. Cowley, *Chem. Commun.* **2000**, 911.

[33] P. B. Hitchcock, J. M. Keates, G. A. Lawless, *J. Am. Chem. Soc.* **1998**, *120*, 599.

[34] F. A. Cotton, G. Wilkinson, C. A. Murillo, M. Bochmann, *Advanced Inorganic Chemistry*, 6th ed., Wiley, New York, **1999**.

[35] R. Fernández, PhD Thesis **2000**, University of Sevilla.

[36] C. Dohmeier, H. Schnöckel, C. Robl, U. Schneider, R. Ahlrichs, *Angew. Chem. Int. Ed. Engl.* **1993**, *32*, 1655.

[37] S. C. Sockwell, T. P. Hanusa, *Inorg. Chem.* **1990**, *29*, 76–80.

[38] a) M. M. Conejo, R. Fernández, E. Carmona, R. A. Andersen, E. Gutiérrez-Puebla, A. Monge, *Chem. Eur. J.* **2003**, *9*, 4462–4471; b) M. M. Conejo, R. Fernández, D. Del Rio, E. Carmona, A. Monge, C. Ruiz, *Chem. Commun.* **2002**, *23*, 2916–2917; c) M. M. Conejo, R. Fernández, E. Carmona, E. Gutiérrez-Puebla, A. Monge, *Organometallics* **2001**, *20*, 2434–2436.

 © 2005 Wiley-VCH Verlag GmbH & Co. KGaA, Weinheim

[39] a) D. A. Drew, A. Haaland, *Acta Chem. Scand.* **1972**, *26*, 3351–3356; b) J. Bicerano, W. N. Lipscomb, *Inorg. Chem.* **1979**, *18*, 1565.
[40] A. Haaland, D. P. Novak, *Acta Chem. Scand. Ser. A* **1974**, *28*, 153–156.
[41] D. A. Drew, G. L. Morgan, *Inorg. Chem.* **1977**, *16*, 1704–1708.
[42] G. E. Coates, D. L. Smith, R. C. Srivastava, *J. Chem. Soc., Dalton Trans.* **1973**, 618.
[43] W. E. Stewart, T. H. Siddal, *Chem. Rev.* **1970**, *70*, 517.
[44] M. C. Böhm, R. Gleiter, G. L. Morgan, J. Lusztyk, K. B. Starowieyski, *J. Organomet. Chem.* **1980**, *194*, 257.
[45] D. A. Coe, J. W. Nibler, T. H. Cook, D. A. Drew, G. L. Morgan, *J. Chem. Phys.* **1975**, *63*, 4842.
[46] D. F. Gaines, K. M. Coleson, J. C. Calabrese, *J. Am. Chem. Soc.* **1979**, *101*, 3979.
[47] D. F. Gaines, J. L. Walsh, J. H. Morris, D. F. Hillenbrand, *Inorg. Chem.* **1978**, *17*, 1516.
[48] D. F. Gaines, J. L. Walsh, *Inorg. Chem.* **1978**, *17*, 1238.
[49] D. A. Drew, G. Gundersen, A. Haaland, *Acta Chem. Scand.* **1972**, *26*, 2147.
[50] T. C. Bartke, Diss. Univ. of Wyoming **1975**; *Diss. Abstr. Intern. B* **1976**, *36*, 6141.
[51] D. A. Saulys, D. R. Powell, *Organometallics* **2003**, *22*, 407–413.
[52] R. Goddard, J. Akhtar, K. Starowieyski, *J. Organomet. Chem.* **1985**, *282*, 149–154.
[53] a) D. A. Drew, A. Haaland, *J. Chem. Soc., Chem. Commun.* **1971**, 1551; b) E. M. Marlett, R. N. Saunders, *U.S. Patent 3,783,054* (**1974**); *Chem. Abstr.* **1974**, *80*, 122953.
[54] a) P. Fisher, J. Stadelhofer, J. Weidlein, *J. Organomet. Chem.* **1976**, *116*, 65; b) K. Wade, *Adv. Inorg. Radiochem.* **1976**, *18*, 1.
[55] K. B. Starowieyski, J. Lusztyk, *J. Organomet. Chem.* **1977**, *133*, 281.
[56] a) J. L. Atwood, S. G. Bott, R. A. Jones, S. U. Koschmieder, *J. Chem. Soc., Chem. Commun.* **1990**, 692–693; b) S. L. Battle, A. H. Cowley, A. Decken, R. A. Jones, S. U. Koschmieder, *J. Organomet. Chem.* **1999**, *582*, 66–69.
[57] a) R. A. Kovar, G. L. Morgan, *J. Am. Chem. Soc.* **1970**, *92*, 5067; b) D. F. Gaines, K. M. Coleson, D. F. Hillenbrand, *J. Magn. Reson.* **1981**, *44*, 84.
[58] M. Niemeyer, P. P. Power, *Inorg. Chem.* **1997**, *36*, 4688–4696.
[59] a) R. Han, G. Parkin, *Inorg. Chem.* **1992**, *31*, 983–988; b) R. Han, G. Parkin, *Inorg. Chem.* **1993**, *32*, 4968–4970.

Received: April 20, 2005
Published Online: July 14, 2005

 © 2005 Wiley-VCH Verlag GmbH & Co. KGaA, Weinheim

Synthesis and Electrochemical Characterization of Metallocene–PNA Oligomers

Andrea Maurer,[a] Heinz-Bernhard Kraatz,[b] and Nils Metzler-Nolte*[a]

Keywords: Electrochemical DNA detection / Ferrocene / Metallocenes / Peptide nucleic acids

The synthesis of ferrocene- and cobaltocenium–PNA conjugates with *C*-terminal cysteine residues by solid phase methods is described. Melting points with complementary DNA reveal that both metallocenes stabilize the duplex, although to a different extent. The effect is more pronounced when there is an overhang of the DNA at the PNA amino terminus. The conjugates were studied by electrochemical methods in solution. They were also immobilized on Au microelectrodes in self-assembled monolayers (SAMs) and further characterized electrochemically on the surface.
(© Wiley-VCH Verlag GmbH & Co. KGaA, 69451 Weinheim, Germany, 2005)

Introduction

Peptide Nucleic Acid (PNA) oligomers are synthetic DNA analogues which have gained considerable attention because of their favourable properties, such as high stability in biological media and sequence-selective binding to RNA and DNA.[1–3] In addition to medicinal applications as a lead structure for antisense agents, analytical applications in molecular biology have been suggested for PNA.[4] In the sequence-specific detection of RNA or ss-DNA, PNA oligomers are superior to ss-DNA because of their higher binding affinity which allows for detection of shorter oligomer sequences.[5,6] At the same time, mismatch sensitivity is improved for PNA·DNA duplexes compared to homologous ds-DNA. In addition, the stability of PNA·DNA duplexes is far less dependent on factors such as salt concentration and impurities than a purely DNA-based detection system would be.[7,8]

Electrochemical systems for DNA detection are potentially cheaper and more reliable than the conventional fluorescence spectroscopy. Ferrocene and its derivatives are often used in such devices because of their favourable electrochemical properties.[9,10] The electrochemically active metal complex is covalently linked to a DNA oligomer which is readily immobilized on an electrode surface,[11,12] making this scheme also suitable for DNA arrays.[13,14] Because of the advantageous properties of PNA, it seems ideal to construct electrochemical DNA sensors using metal-PNA probes. Wang and coworkers have explored PNA-based DNA sensors.[15,16] These workers used freely diffusing metal complexes or so-called reagentless detection. No PNA oligomers with covalently bound electrochemically active metal complexes were known at the time. Our group has subsequently reported the first organometallic PNA monomers and oligomers,[17–19,10] followed by other groups.[20,21] No attempt has been made so far to exploit the favourable combination of properties in metallocene–PNA conjugates for electrochemical DNA detection. In fact, no metallocene conjugates with PNA oligomers were comprehensively characterized so far.

In this paper, we report the synthesis of metallocene–PNA oligomers with thiol groups for immobilization on Au microelectrodes. Ferrocene PNA oligomers are compared to the isostructural but positively charged cobaltocenium derivatives to avoid solubility problems associated with the lipophilic ferrocene group. The metallocene–PNA oligomers are characterized in their interaction with complementary DNA. They were deposited in self-assembled monolayers (SAMs) on Au microelectrodes. The two metallocenes are compared in terms of their suitability for an electrochemical DNA detection system.

Results and Discussion

For this study, a 10-mer PNA sequence was synthesized by standard solid phase techniques on TentaGel R PHB-Cys(Trt)-Fmoc resin. After synthesis of the PNA oligomer, the last Fmoc group was cleaved, and activated ferrocene carboxylic acid (**1**) or cobaltocenium carboxylic acid (**2**) was added. After cleavage from the resin by concentrated TFA, precipitation from cold ether and lyophilization, two PNA oligomers were obtained with sequences $CpFeC_5H_4$-

[a] Institut für Pharmazie und Molekulare Biotechnologie, Universität Heidelberg,
Im Neuenheimer Feld 364, 69120 Heidelberg, Germany
Fax: +49-6221-546441
E-mail: Nils.Metzler-Nolte@urz.uni-heidelberg.de
[b] Department of Chemistry, University of Saskatchewan, 110 Science Place, Saskatoon, S7N 5C9, Canada
Supporting information for this article is available on the WWW under http://www.eurjic.org or from the author.

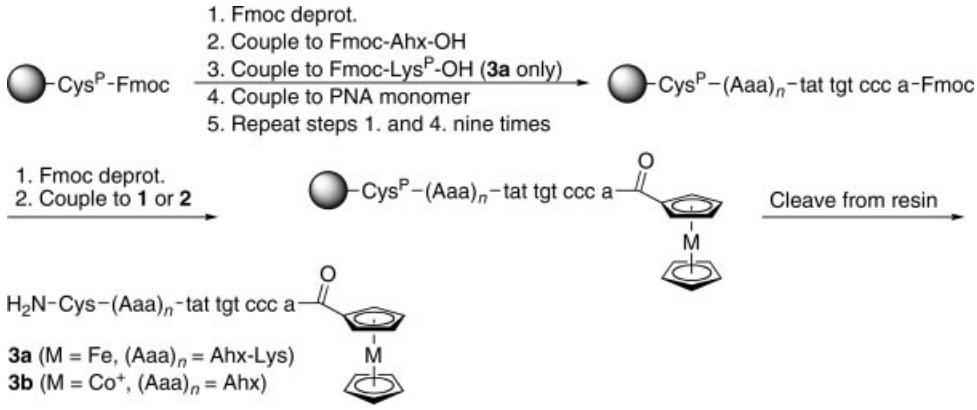

Scheme 1. Synthesis of metallocene–PNA oligomers **3**. See Supporting Information for details.

CO-a-ccc-tgt-tat-Lys-Ahx-Cys-NH_2 (**3a**) and [$CpCoC_5H_4$-CO-a-ccc-tgt-tat-Ahx-Cys-NH_2]$^+$ (**3b**, Ahx denotes ω-aminohexanoic acid). An *N*-acetylated oligomer Ac-a-ccc-tgt-tat-Lys-NH_2 (**3c**) was prepared for comparison (Scheme 1).

Purification and characterization of the PNAs was performed by RP-HPLC and MALDI-TOF mass spectrometry, respectively. The MS for **3a** shows a signal at *m*/*z* = 3233.8, which matches exactly the calculated value of 3233.3 for [M + H]$^+$. Spectra of similar quality were obtained for **3b** and **3c** (see Supporting Information). It should be noted that **3b** carries a positive charge already. The presence of the covalently attached metallocene group is also immediately apparent from the orange-brown or yellow colour of the resin for **3a** or **3b**, respectively, in comparison to white **3c**. A similar colour change was observed for a Mo organometallic complex attached to the pentapeptide enkephalin.[22] We recently found that attaching a cobaltocenium group to peptides significantly enhances the cellular uptake and nuclear localization of such conjugates.[23]

The metal–PNA conjugates were hybridized to complementary DNA in buffered aqueous solution in order to study the influence of the metal complexes on duplex stability. The melting curves for **3**·DNA were recorded in a temperature range of 20–80 °C (see Figure 1 and Table 1), using exactly matching DNA (**I**) and a complementary DNA strand which has three bases overhang at the metallocene PNA end (**II**). Several conclusions can be drawn from the melting temperature data: (1) the uncharged ferrocene influences duplex stability even if the PNA and DNA match exactly [Δ*T* (**3a·I**–**3c·I**) = 4.3 °C], (2) overhanging DNA stabilizes a PNA·DNA duplex [Δ*T* (**3a·II**–**3a·I**) = 1.5 °C], and (3) a positively charged metallocene further stabilizes the PNA·DNA duplex only if the DNA, which is formally a polyanion, overlaps the PNA to make an interaction with the metallocenium cation possible. In effect, the increase in melting temperatures is 5.1 °C in going from **3b·I** to **3b·II**, whereas it is only 1.5 °C in the ferrocene system. The second observation is in agreement with previous results.[5] The third observation has been suggested in work with coordination compounds but could not be proven independently of other factors.[24]

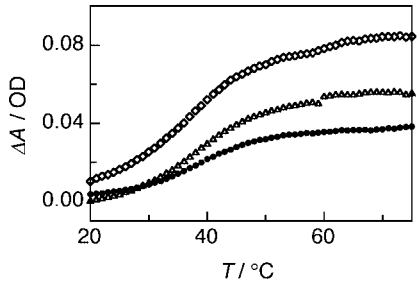

Figure 1. Melting profiles of **3a·I** (open triangles), **3b·I** (open squares), and **3c·I** (filled circles). See Supporting Information for experimental details.

Table 1. PNA·DNA UV melting temperatures (°C). DNA sequences are 5′-ATA-ACA-GGG-T-3′ (**I**) and 5′-ATA-ACA-GGG-TAA-T-3′ (**II**). See Supporting Information for experimental details.

PNA/DNA	I	II
3a	42.8 ± 0.5	44.3 ± 0.5
3b	37.6 ± 0.5	42.6 ± 0.5
3c	38.5 ± 0.5	n. d.

Solution electrochemistry of the metallocene PNAs **3a** and **3b** alone shows a quasireversible wave at E^0 = 0.20 V (**3a**, see Figure 2) and E^0 = –1.51 V (**3b**) vs. Fc/Fc^+ in acetonitrile/H_2O (1:1) solution for the one-electron transitions of the metallocenes. Electron-transfer properties of a ferrocene–PNA monomer and dimer were studied by Baldoli, Maiorana and coworkers.[25] The metal-free conjugate **3c** does not show any signal at comparable concentration. En route to the design of a device for electrochemical DNA analysis, we investigated the electrochemistry of ferrocene–PNA conjugates immobilized on Au electrode surfaces.

Gold microelectrodes were prepared from Au wire (50 μm diameter) sealed into glass capillaries as described before.[26] After polishing on alumina and electrochemical preparation, the thiolated PNAs were immobilized on the Au microelectrodes as a duplex with DNA **II**. For those electrodes, an electrochemical signal can be recorded at *E* = 0.44 V for the ferrocene–PNA–DNA duplex (**3a·II**, see Figure 2) vs. Ag/AgCl in aqueous KCl (3 M) in cyclic vol-

 © 2005 Wiley-VCH Verlag GmbH & Co. KGaA, Weinheim

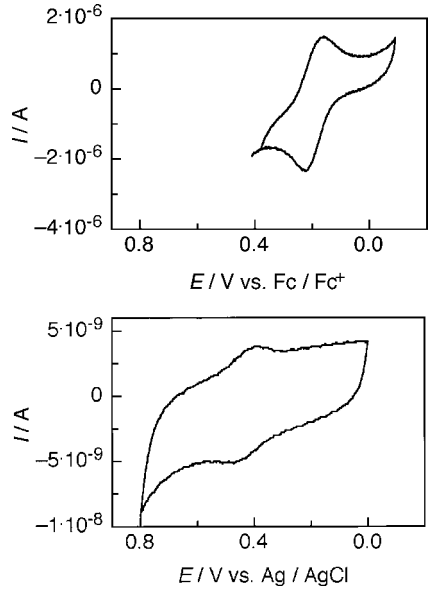

Figure 2. Cyclic voltammograms of **3a** in solution (top, CH_3CN/H_2O solution with 0.1 M $NaClO_4$, ca. 1 mM, platinum electrode with 2 mm diameter, vs. Fc/Fc^+, scan rate 0.5 Vs^{-1}) and of **3a·II** immobilized on the Au surface (bottom, aq. phosphate buffer at pH = 7, Au microelectrode, vs. Ag/AgCl, scan rate 2 Vs^{-1}). See Supporting Information for details.

tammetry (CV) as well as square wave voltammetry (SWV). Under identical conditions, no signal could be observed for the cobaltocenium–PNA conjugate **3b·II**. Ferrocene–DNA conjugates on Au electrodes are known to stand aligned at an angle around 45°. We suspected that the charged cobaltocenium–PNA conjugate might flip to the surface because of the flexible Ahx linker. Indeed, we were able to record a SWV for a cobaltocenium–PNA·DNA duplex that had no Ahx linker and was therefore more rigid (H_2N-Cys-tat-tgt-ccc-a-Cc·5′-ATA-ACA-GGG-T-3′; Cc: $CpCoC_5H_4$-CO-). In this case, a signal at $E = -0.92$ V was observed in the SWV.

From the electrochemical experiment, the surface concentration Γ_0* of **3a·I** was calculated from the oxidative peak current, the known scan rate and the surface area to be $\Gamma_0^* = 4\times10^{-11}$ mol cm^{-2}. This corresponds to roughly 7.3×10^8 molecules on an effective electrode surface of 2.8×10^{-5} cm^{-2}. For this calculation, the roughness factor for the surface area was experimentally determined by Cu-UPD to be 1.43. Under the assumption of complete electrode coverage by a self-assembled monolayer (SAM) this results in a footprint of 384 Å^2 per molecule, which is in agreement with previous measurements on Au-immobilized DNA and simple molecular geometry considerations.

Conclusions

In conclusion, we have presented the synthesis of metallocene PNA conjugates with thiol linkers for immobilization on Au microelectrodes. The synthesis of the first comprehensively characterized metallocene–PNA oligomers by solid phase peptide synthesis (SPPS) is described. Given the ubiquitous use of ferrocene in electrochemical sensors, the easy accessibility of the ferrocene–PNA system along with its favourable properties are worth mentioning. The use of a cobaltocenium–PNA conjugate is reported for the first time. Because ferrocene and cobaltocenium groups are almost isostructural but differ in charge as well as redox properties, subtle effects can be studied in detail as exemplified for the thermal stability of the metallocene bioconjugates in interaction with complementary DNA. The cobaltocenium–PNA conjugate shows excellent chemical stability upon storage and in solution. On the other hand, only the ferrocene–PNA shows clean electrochemical behaviour in the surface-immobilized duplex with complementary DNA. Taking together the ease of synthesis, chemical stability of the conjugates and favourable electrochemical properties, the metallocene–PNA system seems ideally suited for the development of electrochemical DNA arrays. Such devices are currently being developed in our groups.

Supporting Information is available online for this manuscript, including all experimental details as well as HPLC and MS data for PNA oligomers **3a**–**c**. Standard abbreviations are used for DNA bases (capital letters). The same small letters are used to denote PNA bases. Cys^P and Lys^P denotes protected cysteine (S-Trt) and lysine residue (N_ε-Boc-Lys).

Acknowledgments

This work was supported by the German Science Foundation (Deutsche Forschungsgemeinschaft DFG) as part of the Graduiertenkolleg "Molekulare Biotechnologie" and the Max-Buchner-Foundation.

[1] P. E. Nielsen, M. Egholm, R. H. Berg, O. Buchardt, *Science* **1991**, *254*, 1497–1500.
[2] M. Egholm, O. Buchardt, L. Christensen, C. Behrens, S. M. Freier, D. A. Driver, R. H. Berg, S. K. Kim, B. Norden, P. E. Nielsen, *Nature* **1993**, *365*, 566–568.
[3] V. Demidov, V. N. Potaman, M. D. Frank-Kamenetskii, O. Buchardt, M. Egholm, P. E. Nielsen, *Biochem. Pharmacol.* **1994**, *48*, 1309–1313.
[4] S. Matysiak, S. Würtz, N. C. Hauser, H. Gausepohl, J. D. Hoheisel in *Peptide Nucleic Acids*, 1st ed. (Eds.: P. E. Nielsen, M. Egholm), Horizon Scientific Press, Wymondham, **1999**, pp. 119–128.
[5] T. Ratilainen, A. Holmén, E. Tuite, G. Haaima, L. Christensen, P. E. Nielsen, B. Nordén, *Biochemistry* **1998**, *37*, 12331–12342.
[6] H. J. Larsen, T. Bentin, P. E. Nielsen, *Biochim. Biophys. Acta* **1999**, *1489*, 159–166.
[7] A. Holmén, B. Nordénin *Peptide Nucleic Acids*, 1st ed. (Eds.: P. E. Nielsen, M. Egholm), Horizon Scientific Press, Wymondham, **1999**, pp. 87–97.
[8] T. Ratilainen, A. Holmén, E. Tuite, P. E. Nielsen, B. Nordén, *Biochemistry* **2000**, *39*, 7781–7791.
[9] T. S. Zatsepin, S. Y. Andreev, T. Hianik, T. S. Oretskaya, *Russ. Chem. Rev.* **2003**, *72*, 537–554.
[10] D. R. van Staveren, N. Metzler-Nolte, *Chem. Rev.* **2004**, *104*, 5931–5985.
[11] R. C. Mucic, M. K. Herrlein, C. A. Mirkin, R. L. Letsinger, *Chem. Commun.* **1996**, 555–557.
[12] S. Takenaka, *Bull. Chem. Soc. Jpn.* **2001**, *74*, 217–224.
[13] D. H. Farkas, *Clinical Chem.* **2001**, *47*, 1871–1872.
[14] R. M. Umek, S. W. Lin, J. Vielmetter, R. H. Terbrueggen, B. Irvine, C. J. Yu, J. F. Kayyem, H. Yowanto, G. F. Blackburn, D. H. Farkas, Y.-P. Chen, *J. Mol. Diagn.* **2001**, *3*, 74–84.

 © 2005 Wiley-VCH Verlag GmbH & Co. KGaA, Weinheim

[15] J. Wang, E. Palecek, P. E. Nielsen, G. Rivas, X. H. Cai, H. Shiraishi, N. Dontha, D. B. Luo, P. A. M. Farias, *J. Am. Chem. Soc.* **1996**, *118*, 7667–7670.
[16] J. Wang, *Biosens. Bioelectron.* **1998**, *13*, 757–762.
[17] A. Hess, N. Metzler-Nolte, *J. Chem. Soc., Chem. Commun.* **1999**, 885–886.
[18] J. C. Verheijen, G. A. van der Marel, J. H. van Boom, N. Metzler-Nolte, *Bioconjugate Chem.* **2000**, *11*, 741–743.
[19] R. Hamzavi, T. Happ, K. Weitershaus, N. Metzler-Nolte, *J. Organomet. Chem.* **2004**, *689*, 4745–4750.
[20] C. Baldoli, S. Maiorana, E. Licandro, G. Zinzalla, D. Perdicchia, *Org. Lett.* **2002**, *4*, 4341–4344.
[21] S. Maiorana, E. Licandro, D. Perdicchia, C. Baldoli, B. Vandoni, C. Giannini, M. Salmain, *J. Mol. Catal. A* **2003**, *204–205*, 165–175.
[22] D. R. van Staveren, N. Metzler-Nolte, *J. Chem. Soc., Chem. Commun.* **2002**, 1406–1407.
[23] F. Noor, A. Wüstholz, R. Kinscherf, N. Metzler-Nolte, *Angew. Chem. Int. Ed.* **2005**, *44*, 2429–2432; *Angew. Chem.* **2005**, *117*, 2481–2485.
[24] A. A. Mokhir, R. Stiebing, R. Krämer, *Bioorg. Med. Chem. Lett.* **2003**, *13*, 1399–1401.
[25] C. Baldoli, L. Falciola, E. Licandro, S. Maiorana, P. Mussini, P. Ramani, C. Rigamonti, G. Zinzalla, *J. Organomet. Chem.* **2004**, *689*, 4791–4802.
[26] I. Bediako-Amoa, T. C. Sutherland, C.-Z. Li, R. Silerova, H.-B. Kraatz, *J. Phys. Chem.* **2004**, *B108*, 704–714.

Received: April 15, 2005
Published Online: July 6, 2005

 © 2005 Wiley-VCH Verlag GmbH & Co. KGaA, Weinheim

Nonlinear Optical Activity and High Thermal Stability of a New 3D Open-Framework with Interconnected 24-, 16-, and 8-Atom Channels: $(NH_4)Zn[O_3PCH(OH)CO_2]$

Ruibiao Fu,[a] Huishuang Zhang,[a] Longsheng Wang,[a] Shengmin Hu,[a] Yaming Li,[a] Xihe Huang,[a] and Xintao Wu*[a]

Keywords: Zinc / Hydroxy(phosphonoato)acetate / Nonlinear optical activity / Hydrothermal synthesis / Open-framework

Hydrothermal reaction of hydroxy(phosphono)acetic acid, $H_2O_3PCH(OH)CO_2H$, with zinc(II) acetate resulted in a new ammonium zinc hydroxy(phosphonato)acetate, $(NH_4)Zn[O_3PCH(OH)CO_2]$ (**1**). The structure of **1** contains a 3D open-framework consisting of interconnected 24-, 16-, and 8-atom channels. TGA and XRD reveal that the framework is stable up to 350 °C in air. Its powder SHG intensity is about 0.8 times that of potassium dihydrogen phosphate KDP.
(© Wiley-VCH Verlag GmbH & Co. KGaA, 69451 Weinheim, Germany, 2005)

Introduction

Noncentrosymmetric metal-organic coordination polymers have been extensively studied due to their intriguing second-order nonlinear optical (NLO) properties and high thermal stabilities. These properties make them particularly attractive candidates for NLO applications.[1–11] A general strategy to synthesise these nonlinear optically active materials is to use asymmetric ligands as bridging units as well as Zn^{2+} and Cd^{2+}. There are three reasons: (i) asymmetric ligands can serve as asymmetric building blocks to increase the probability of compounds crystallizing in a non-central space group; (ii) asymmetric ligands usually contain push-and-pull functional groups which results in a high efficiency of second harmonic generation (SHG); (iii) Zn^{2+} and Cd^{2+} have the advantage of optical transparency. In this communication, hydroxy(phosphono)acetic acid, containing a chiral carbon atom and three functional groups (OH, COOH and PO_3H_2), has been introduced as a bridging ligand and Zn^{2+} to synthesize a new 3D open-framework with intersected 24-, 16-, and 8-atom channels, $(NH_4)Zn[O_3PCH(OH)CO_2]$ (**1**), possessing nonlinear optical activity and high thermal stability.

Results and Discussion

X-ray single crystal diffraction reveals that 24-, 16-, and 8-atom rings exist in the 3D open-framework within compound **1** (Figure S-1, Supporting information). The Zn^{II} atom is in a slightly distorted $[ZnO_4]$ tetrahedral coordination geometry; it is surrounded by three phosphonate oxygen atoms (O1b, O2a, and O3) and one carboxylate oxygen donor (O5) from four equivalent hydroxy(phosphonato)-acetate groups. The values of the Zn–O bond lengths and O–Zn–O angles are in the range of 1.934(8)–1.967(7) Å and 107.1(3)–113.0(3)°, respectively. On the other hand, the hydroxy(phosphonato)acetate group is in a tetradentate mode. It connects four Zn^{II} atoms (Zn1b, Zn1c, Zn1d, and Zn1e) through three phosphonate oxygen atoms (O1c, O2c, and O3c) and one carboxylate oxygen donor (O5b).

There are three attractive structural features of the 3D open-framework: (i) One left- and one right-helical chain co-exist in an infinite ladder-like double chain (Figure 1). In the double chain, two $[ZnO_4]$ and two $[PCO_3]$ tetrahedrons form an 8-atom ring by sharing four corners (O1, O2, O1b, and O3b). The 8-atom rings interact with each other by sharing corners. (ii) As shown in Figure 2, the double chain connects 16- and 24-atom 1D channels along the crystallographic *a* and *c* axis, respectively. The 16-atom channel is occupied by NH_4^+ ions and assembled by 16-atom rings, which consist of three Zn^{II}, three P, four C and six O atoms with the sequences –Zn–O–P–C–C–O–Zn–O–P–O–Zn–O–C–C–P–O– (Figure S-1, Supporting information), while the 24-atom channel looks like the figure "8", constructed by 24-atom rings containing four hydroxy-(phosphonoato)acetate groups and four Zn^{II} atoms with the sequence –Zn–O–C–C–P–O–Zn–O–C–C–P–O–Zn–O–C–C–P–O–Zn–O–C–C–P–O– (Figure S-1, Supporting information). (iii) The 16-atom channels are parallel to the *c* axis.

Powder XRD patterns confirm that polycrystalline **1** is stable upon heating at 300 °C in air for 2 h (Figure 3). The

[a] Fujian Ins. Res. Struct. Matter, Chinese Academy of Sciences
Fuzhou, Fujian 350002, P. R. China
Fax: +86-591-83794946
E-mail: wxt@fjirsm.ac.cn
Supporting information for this article is available on the WWW under http://www.eurjic.org or from the author.

 DOI: 10.1002/ejic.200500347 © 2005 Wiley-VCH Verlag GmbH & Co. KGaA, Weinheim

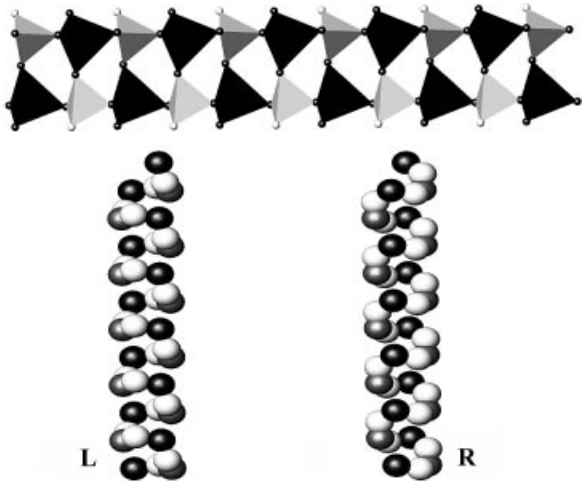

Figure 1. Polyhedral views of the double chain (top); black tetrathedra: ZnO_4; gray tetrahedra: PCO_3; black spheres: O; white spheres: C. Ball representations exhibit the left- and right-helical chains (bottom); black spheres: Zn; gray spheres: P; white spheres: O. Unrelated atoms are omitted for clarity.

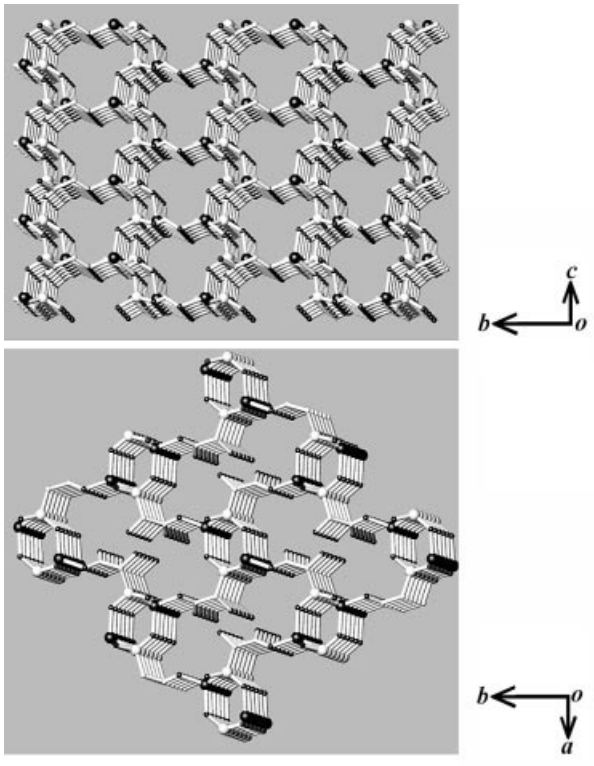

Figure 2. Packing views ofthe the 16- (top) and 24-atom (bottom) channels along the *a* and *c* axis, respectively; Large black spheres: Zn; large white sphere: P; small black spheres: O; small white spheres: C. Unrelated atoms are omitted for clarity.

main peaks of powder XRD still exist after a similar treatment at 350 °C, which indicates that the framework does not collapse. This is in agreement with the result of TGA measurements, which show that there is only little weight loss up to 350 °C (Figure 4). When a beam at λ = 1064 nm fundamental wavelength from a *Q*-switched Nd:YAG laser falls onto some powder of **1**, green light can be seen with naked eyes, confirming its acentricity. In order to evaluate its potential as second-order NLO material, powder second harmonic generation (SHG) measurements of **1** were performed according to a method previously reported by Kurtz.[12] The preliminary experimental result is that the powder SHG intensity of **1** is about 0.8 times that of potassium dihydrogen phosphate (KDP). Compound **1** is transparent in the visible region and insoluble in common solvents. Its remarkable thermal stability makes it an attractive candidate for NLO applications.

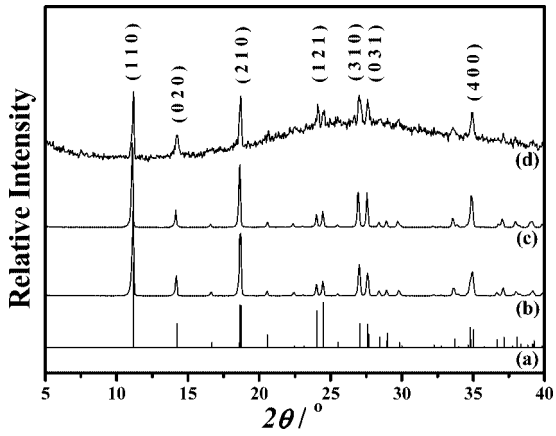

Figure 3. XRD patterns of **1** simulated from X-ray single crystal data (a); polycrystalline without being heated (b); polycrystalline, heated at 300 °C in air for 2 h (c); polycrystalline, heated at 350 °C in air for 2 h (d).

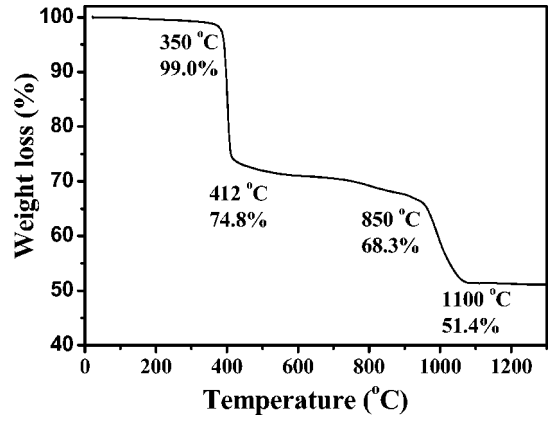

Figure 4. TGA curve of **1**.

Conclusions

In conclusion, we have described a new 3D open-framework with interconnected 24-, 16-, and 8-atom channels, $(NH_4)Zn[O_3PCH(OH)CO_2]$, possessing nonlinear optical activity and high thermal stability. The compound was hydrothermally synthesized by using a bridging ligand with a chiral carbon atom and three functional groups. This result may provide a new way to synthesize attractive hybrid materials of high thermal stability for NLO applications.

 © 2005 Wiley-VCH Verlag GmbH & Co. KGaA, Weinheim

Experimental Section

General Remarks: Reagents were obtained from commercial sources and used as received without further purification. C, H, N analyses were carried out with a Vario EL III element analyzer. Infrared spectra were obtained from KBr pellets in the range 4000–400 cm^{-1} with a Nicolet Magna 750 FT-IR spectrometer. Thermogravimetric analysis (TGA) was performed with a NETZSCH STA 449C under nitrogen at a heating rate of 10 °C·min^{-1} from room temperature to 1300 °C. Powder X-ray diffraction (XRD) patterns were acquired with a DMAX-2500 diffractometer using Cu-K_α radiation under ambient conditions.

Synthesis of $(NH_4)Zn[O_3PCH(OH)CO_2]$ (1): A mixture of $Zn(CH_3COO)_2{\cdot}2H_2O$ (1.0 mmol), NH_4Cl (25 mmol), NaF (4 mmol), hydroxy(phosphono)acetic acid (2 mmol), acetic acid (35 mmol) and water (444 mmol) was heated at 140 °C for 96 h. After the mixture was cooled slowly to room temperature, needle-shaped colorless crystals were obtained in about 10% yield (22.2 mg) based on $Zn(CH_3COO)_2{\cdot}2H_2O$. The pH value of the final mixture was 4.12. The purity of the product was checked by powder X-ray diffraction. $C_2H_6NO_6PZn$ (236.42): calcd. C 10.16, H 2.56, N 5.92; found C 10.06, H 2.62, N 5.96. IR (KBr pellet): $\tilde{\nu}$ = 3345 s (ν_{O-H}), 3215 vs (ν_{N-H}), 3072 s (ν_{N-H}), 2930 w (ν_{C-H}), 2856 m (ν_{C-H}), 2362 w, 1614 vs ($\nu_{C=O}$), 1433 vs (δ_{C-H}), 1279 m (ν_{C-O}), 1202 m (ν_{P-O}), 1126 s (ν_{P-O}), 1082 s (ν_{P-O}), 993 s (ν_{P-O}), 835 m, 766 m, 685 m, 600 m, 559 m, 521 m, 478 m cm^{-1}.

X-ray Crystallography Study: X-ray data on a suitable single crystal were collected at 293 ± 2 K with a Siemens SMART-CCD diffractometer using graphite-monochromated Mo-K_α radiation [λ(Mo-K_α) = 0.71073 Å]. Data were reduced and absorption-corrected with SMART and SADABS software, respectively. The structure was solved by direct methods and refined by full-matrix least-squares techniques on F^2 using SHELXTL-97.[13] All non-hydrogen atoms of **1** were treated anisotropically. Hydrogen atoms of OH and CH were generated geometrically. Idealized positions of H atoms of the NH_4^+ cation were fixed with N–H = 1.0 Å and H···H = 1.63 Å. Crystal data: orthorhombic, space group *Pna*2(1) (no. 33), a = 10.245(2), b = 12.447(3), c = 5.1538(11) Å, V = 657.2(2) $Å^3$, Z = 4, D_c = 2.389 g·cm^{-3}, μ = 3.963 mm^{-1}, F (000) = 472, T = 293(2) K, 1495 reflections were measured in the range of 5.14° ≤ 2θ ≤ 50.14°, 933 independent reflections (R_{int} = 0.0226), 863 observed reflections [$I > 2\sigma(I)$] with R_1 = 0.0518 and wR_2 = 0.1172; R_1 = 0.0562 and wR_2 = 0.1215 (all data) and GOOF on F^2 of 1.191. CCDC-234887 contains the supplementary crystallographic data for this paper. These data can be obtained free of charge from The Cambridge Crystallographic Data Centre via www.ccdc.cam.ac.uk/data_request/cif.

Acknowledgments

This research was supported by grants from the State Key Laboratory of Structure Chemistry, Fujian Institute of Research on the Structure of Matter, the National Ministry of Science and Technology of China (001CB1089), the Chinese Academy of Sciences (CAS), the National Science Foundation of China (20273073, 20333070, and 90206040), and the Science Foundation of CAS and Fujian Province for research funding support (2004HZ01-1, 2003J042, and 2004J041).

[1] O. R. Evans, R.-G. Xiong, Z. Wang, G. K. Wong, W. Lin, *Angew. Chem. Int. Ed.* **1999**, *38*, 536–538.
[2] W. Lin, L. Ma, O. R. Evans, *Chem. Commun.* **2000**, 2263–2264.
[3] R.-G. Xiong, J.-L. Zuo, X.-Z. You, B. F. Albrahams, Z.-P. Bai, C.-M. Che, H.-K. Fun, *Chem. Commun.* **2000**, 2061–2062.
[4] O. R. Evans, Z. Wang, W. Lin, *Chem. Commun.* **1999**, 1903–1904.
[5] O. R. Evans, W. Lin, *Acc. Chem. Res.* **2002**, *35*, 511–522.
[6] O. R. Evans, W. Lin, *Chem. Mater.* **2001**, *13*, 2705–2712.
[7] W. Lin, O. R. Evans, R.-G. Xiong, Z. Wang, *J. Am. Chem. Soc.* **1998**, *120*, 13272–13273.
[8] W. Lin, Z. Wang, L. Ma, *J. Am. Chem. Soc.* **1999**, *121*, 11249–11250.
[9] O. R. Evans, W. Lin, *Chem. Mater.* **2001**, *13*, 3009–3017.
[10] L. Han, M. C. Hong, R. H. Wang, J. H. Luo, Z. Z. Lin, D. Q. Yuan, *Chem. Commun.* **2003**, 2580–2581.
[11] Y. Kang, Y. G. Yao, Y. Y. Qin, J. Zhang, Y. B. Chen, Z. J. Li, Y. H. Wen, J. K. Cheng, R. F. Hu, *Chem. Commun.* **2004**, 1046–1047.
[12] S. K. Kurtz, T. T. Perry, *J. Appl. Phys.* **1986**, *39*, 3798–3813.
[13] G. M. Sheldrick, *SHELXT 97*, *Program for Crystal Structure Refinement*, University of Göttingen, Germany, **1997**.

Received April 22, 2005
Published Online: July 6, 2005

 © 2005 Wiley-VCH Verlag GmbH & Co. KGaA, Weinheim

Synthesis and Characterization of a 3D H-Bonded Supramolecular Complex with Chiral Channels Encapsulating 1D Left-Handed Helical Water Chains

Benyong Lou,[a] Feilong Jiang,[a] Daqiang Yuan,[a] Benlai Wu,[a] and Maochun Hong*[a]

Keywords: Chiral channels / Water chains / Amino acids

A chiral Cu^{II} dinuclear complex $[Cu_2(L\text{-shis})_2]\cdot 4H_2O$ (H_2shis = *N*-salicylidenylhistidine) has been synthesized. The dinuclear units are assembled into a 3D hydrogen-bonded supramolecular structure with 1D chiral channels through hydrogen bonds between imidazole N–H groups and carboxylate oxygen atoms. 1D left-handed helical water chains in an AABB fashion, anchored through weak hydrogen-bonding interactions with the host complex, are embodied in the chiral channels. X-ray powder diffraction shows the porous structure is destroyed when the lattice water molecules are removed thermally from the channels.

(© Wiley-VCH Verlag GmbH & Co. KGaA, 69451 Weinheim, Germany, 2005)

Introduction

Metal-organic frameworks containing channels or pores with various sizes and shapes have attracted much attention because of their potential applications in catalysis, separation and gas sorption and storage.[1–3] Chiral porous materials have great advantages over achiral ones in enantioselective separation and catalysis.[4] A direct and effective method for such materials is to ultilize enantioselective ligands.[5–7] Therein, using natural amino acids as chiral precursors is a simple and practical alternative.[8–10] Moreover, amino acids can afford different kinds of hydrogen bonds, which has an important effect on the structures of metal-organic materials.[11–13] Our interest has been focused on the employment of natural amino acids for synthesizing chiral ligands to direct the assembly of chiral metal-organic porous materials.

One-dimensional (1D) chain arrangement of water molecules has attracted much interest due to its occurrence in many fundamental biological processes which depend on the unique properties of water chains.[14–16] Such water chains could model the biological systems for transport of water or ions across membrane proteins with aquapores, and several examples of 1D water chains anchored by organic compounds or complexes have been reported.[17–22] Chakravarty described an unprecedented 1D helical chain of water in a dicopper(II) complex with a helical porous supramolecular structure-[20] and Vittal reported a staircase-like helical coordination polymeric architecture of a nickel(II) complex that hosts a 1D helical chain of lattice water molecules in a helical pore.[21] In these two cases, the 1D helical water chains are anchored by helical host complexes through weak hydrogen-bonding interactions and exhibit an alternate arrangement of two water molecules in the chains. While trying to construct chiral porous materials using a simple Schiff-base ligand derived from L-histidine, we obtained complex $[Cu_2(L\text{-shis})_2]\cdot 4H_2O$ (**1**) (H_2shis = *N*-salicylidenylhistidine), in which lattice water molecules are well ordered and arrayed in an AABB fashion to form 1D left-handed helical water chains encapsulated in the channels of the H-bonded supramolecular complex.

Results and Discussion

Complex **1** was obtained by the reaction of $Cu(NO_3)_2\cdot 3H_2O$ and a mixture of L-histidine and salicylaldehyde in basic ethanol/aqueous solution. The single-crystal X-ray analysis reveals that complex **1** crystallizes in the chiral space group $C222_1$ and consists of the neutral dinuclear unit $[Cu_2(L\text{-shis})_2]$ and four lattice water molecules, as shown in Figure 1. Cu1 is in a four-coordinate environment in which the shis anion as a tridentate ligand chelates Cu1 through the phenolato oxygen atom O3, the nitrogen atom N1 and the carboxylate oxygen atom O1, and the remaining site is occupied by an imidazole nitrogen atom N3A (A: $x, -y, 1-z$) from another shis ligand. Two Cu^{II} centers are connected by imidazole "arms" from two shis ligands to form a boat-shaped dinuclear unit. There exist H-bond donors (imidazole N–H groups) and acceptors (carboxylate oxygen atoms) on the top and bottom rims of each dinuclear unit, respectively, and this makes it a good building block for a hydrogen-bonded network. In fact, four such dimers are linked through hydrogen bonds [N2···O2B =

[a] State Key Laboratory of Structural Chemistry, Fujian Institute of the Research on the Structure of Matter, Chinese Academy of Sciences,
Fuzhou, Fujian 350002, China
E-mail: hmc@ms.fjirsm.ac.cn

Supporting information for this article is available on the WWW under http://www.eurjic.org or from the author.

 © 2005 Wiley-VCH Verlag GmbH & Co. KGaA, Weinheim **DOI: 10.1002/ejic.200500324**

2.699(5) Å, B: $x + 1/2, 1/2 - y, 1 - z$] to give a large cycle containing eight Cu^{II} centers. The eight-membered rings are further linked to each other through the same hydrogen bonds, generating a two-dimensional supramolecular grid layer.

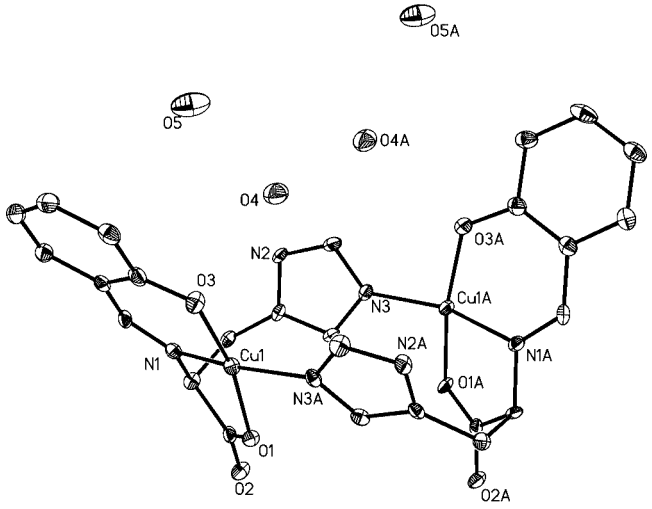

Figure 1. ORTEP view of the dinuclear complex. Selected bond lengths [Å] and angles [°]: Cu1–O1, 1.960(3); Cu1–N1, 1.922(4); Cu1–O3, 1.908(3); Cu1–N3A, 1.959(3); O3–Cu1–N1, 93.29(15); O3–Cu1–O1, 167.32(13); N1–Cu1–N3A, 162.34(13). Symmetry code: A: $x, -y, 1 - z$.

The asymmetric unit contains two water molecules which are bonded to each other through hydrogen bonding [O4···O5 = 2.813(5) Å]. The dinuclear unit anchors one water molecule through hydrogen bonding [O4···O3 = 2.983(5) Å] between coordinated phenolato oxygen atom O3 and atom O4 of water molecules. Atoms O4 and O4A (A: $x, -y, 1 - z$) of anchored water molecules are bonded to each other through hydrogen bonding [O4···O4A = 2.821(7) Å, A: $x, -y, 1 - z$]. Another water molecule is also anchored by a dinuclear unit of another asymmetric unit through hydrogen bonding [O5···O2H = 2.943(5) Å, H: $1 + x, y, z$] between uncoordinated carboxylate oxygen atom O2 and atom O5 of a water molecule. Thus, H-bonded O5–O4–O4A–O5A tetramers are filled with the grids of the 2D layer. Interestingly, the O5 atoms are also bonded to the same water molecules in symmetry through hydrogen bonds [O5···O5C = 2.869(8) Å, C: $3 - x, y, 3/2 - z$] which connect the 2D layers into a 3D structure with 1D chiral channels along the *c*-axis. Moreover, 1D helical water chains with a pitch of 16.9 Å along the *c*-axis are formed in the chiral channels, in which two water molecules are arranged by an AABB fashion (Figure 2). Such weak interactions upon the chiral host induce a homochiral left-handed helicity of water chains (Figure 3). In a sense, the formation of the helical water chain depends on the chemical information and structure of the dinuclear unit which anchors O4 and O4A within an H-bonded distance. Moreover, the H-bonded acceptors in **1** (phenolato and carboxylate oxygen atoms) are in favorable positions for anchoring different water molecules into an extended array.

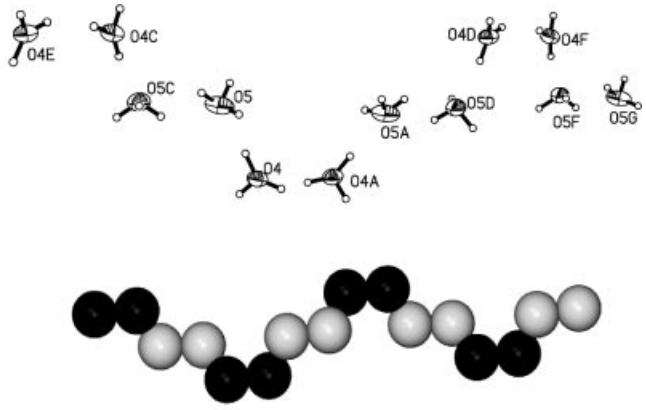

Figure 2. ORTEP view of the helical water chain along the *c*-axis (top) and view of the left-handed helix (bottom) containing water O4 (black) and water O5 (grey) in an AABB fashion. Symmetry codes: A: $x, -y, 1 - z$; C: $3 - x, y, 3/2 - z$; D: $3 - x, -y, z - 1/2$; E: $3 - x, -y, 1/2 + z$; F: $3 - x, y, 1/2 - z$; G: $x, y, z - 1$.

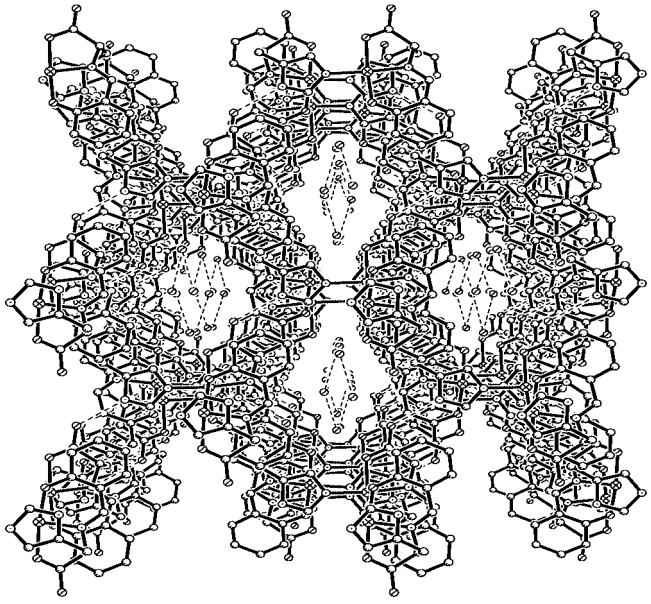

Figure 3. Helical water chains in the 1D channels of the host structure.

The thermogravimetric analysis (TGA) of **1** shows a weight loss of 10.4% in the temperature range 30–150 °C, which agrees with the calculated value (10.1%) for the loss of two water molecules per asymmetric unit. The DSC measurement at 20–150 °C at a rate of 5 °C·min^{-1} shows a single endothermal peak centered at 56.2 °C. The enthalpy per water molecule is ca. 16 kJ·mol^{-1}, which is similar to that observed in another infinite water chain.[19]

To investigate the influence of water molecules on the porous structure, we heated complex **1** at 150 °C for 2 h to remove water molecules (taking a cue from TGA). The elemental analysis of the dehydrated sample is consistent with the formula [Cu_2(L-shis)$_2$]. However, X-ray powder diffraction shows the porous structure of the host complex has been destroyed after the helical water chains being removed (Figure S3). It agrees well with interactions among the 2D

 © 2005 Wiley-VCH Verlag GmbH & Co. KGaA, Weinheim

layers by weak hydrogen bonds between water molecules [O5···O5C = 2.869(8) Å, C: 3 – *x*, *y*, 3/2 – *z*]. When the water molecules are removed, the 2D layers are no longer as well ordered as in $[Cu_2(L\text{-shis})_2]\cdot 4H_2O$.

Conclusions

In conclusion, we have observed left-handed helical water chains in the chiral channels of the H-bonded chiral 3D supramolecular structure based on the dinuclear Cu^{II} complex of a Schiff base derived from L-histidine. The crystal structure of **1** exemplifies a synthetic host model anchoring the homochiral helical water chains in which water molecules are arranged in an AABB fashion.

Experimental Section

General Remarks: All reagents were analytical grade and used without further purification. The IR spectra as KBr disks were recorded with a Magna 750 FT-IR spectrophotometer. C, H, N elemental analyses were carried out with an Elementary Vario ELIII elemental analyzer. Thermogravimetric analysis was performed with a NETZSCH STA 449C instrument. The DSC curve was obtained with a NETZSCH DTA 404PC analyzer at a scan rate of 5 °C·min^{-1}. X-ray powder diffraction was performed with a Rigaku DMAX2500PC diffractometer.

Synthesis of Complex 1: To an aqueous solution (20 mL) of L-histidine (0.155 g, 1 mmol) and NaOH (0.040 g, 1 mmol), salicylaldehyde (0.122 g, 1 mmol) in ethanol (10 mL) was added slowly. The solution was stirred for 30 min and then $Cu(NO_3)_2\cdot 3H_2O$ (0.240 g, 1 mmol) in water (10 mL) was added. After stirring for 1 h, the filtered solution was allowed to stand in air for several days, and blue crystals were obtained in a yield of 60% (210 mg). $C_{26}H_{30}Cu_2N_6O_{10}$ (713.65): calcd. C 43.72, H 4.24, N 11.77; found C 43.47, H 4.38, N 11.55. IR (KBr): $\tilde{\nu}$ = 3416 br. [ν(OH)], 3151 m [ν(NH)], 1637 s [ν_{as}(COO)], 1603 s [ν(C=N)], 1369 m [ν_s(COO)] cm^{-1}.

X-ray Structure Determination: Single-crystal data were collected with a Rigaku Mercury-CCD diffractometer at 130 K, using graphite-monochromated Mo-K_α radiation (λ = 0.7107 Å). The structure was solved by direct methods and refined on F^2 by full-matrix least-squares procedures using the SHELXTL program package.[23] Crystal data: orthorhombic, space group $C222_1$ (no. 20), a = 11.8642(10), b = 14.6000(13), c = 16.9029(17) Å, V = 2927.9(5) Å^3, Z = 4, D_c = 1.619 g/cm^3, 9341 reflections collected, 2583 unique (R_{int} = 0.0468). Final *GooF* = 1.125, $R1$ = 0.0388, $wR2$ = 0.0860, R indices based on 2392 reflections with $I > 2\sigma(I)$ (refinement on F^2). Absolute structure parameter 0.038(19).[24] All non-hydrogen atoms were refined anisotropically and the organic hydrogen atoms were generated geometrically. The hydrogen atoms of water molecules are disordered. Full-occupancy hydrogen atoms H4B, H5B, and half-occupancy hydrogen atoms H4A, H4C, H5A, H5C were located by difference maps and constrained to ride on their parent O atoms in a trigonal arrangement. CCDC-268811 contains the supplementary crystallographic data for this paper. These data can be obtained free of charge from The Cambridge Crystallographic Data Centre via www.ccdc.cam.ac.uk/data_request/cif.

Supporting Information (see footnote on the first page of this article): TGA and DSC curves of **1** (Figures S1 and S2); XRD patterns of **1** and the dehydrated product (Figure S3).

Acknowledgments

This work was supported by grants of the Nation Natural Science Foundation of China and the Natural Science Foundation of Fujian Province.

[1] a) M. Eddaoudi, D. B. Moler, H. Li, B. Chen, T. M. Reineke, M. O'Keeffe, O. M. Yaghi, *Acc. Chem. Res.* **2001**, *34*, 319–330; b) M. Eddaoudi, J. Kim, N. Rosi, D. Vodak, J. Wachter, M. O'Keeffe, O. M. Yaghi, *Science* **2002**, *295*, 469–472.
[2] a) S. Kitagawa, R. Kitaura, S. Noro, *Angew. Chem. Int. Ed.* **2004**,*43*, 2334–2375; b) R. Kitaura, S. Kitagawa, Y. Kubota, T. C. Kobayashi, K. Kindo, Y. Mita, A. Matsuo, M. Kobayashi, H. C. Chang, T. C. Ozawa, M. Suzuki, M. Sakata, M. Takata, *Science* **2002**, *298*, 2358–2361.
[3] a) S. S. Y. Chui, S. M. F. Lo, J. P. H. Charmant, A. G. Orpen, I. D. Williams, *Science* **1999**, *283*, 1148–1150; b) L. Pan, K. M. Adams, H. E. Hernandez, X. Wang, C. Zheng, Y. Hattori, K. Kaneko, *J. Am. Chem. Soc.* **2003**, *125*, 3062–3067.
[4] a) B. Kesanli, W. Lin, *Coord. Chem. Rev.* **2003**, *246*, 305–326; b) J. S. Seo, D. Whang, H. Lee, S. I. Jun, J. Oh, Y. J. Jeon, K. Kim, *Nature* **2000**, *404*, 982–986.
[5] R.-G. Xiong, X.-Z. You, B. F. Abrahams, Z. Xue, C.-M. Che, *Angew. Chem. Int. Ed.* **2001**, *40*, 4422–4425.
[6] O. R. Evans, H. L. Ngo, W. Lin, *J. Am. Chem. Soc.* **2001**, *123*, 10395–10396.
[7] Y. Cui, S. J. Li, W. Lin, *J. Am. Chem. Soc.* **2003**, *125*, 6014–6015.
[8] X. Shi, G.-S. Zhu, S.-L. Qiu, K.-L. Huang, J.-H. Yu, R.-R. Xu, *Angew. Chem. Int. Ed.* **2004**, *43*, 6482–6485.
[9] M. A. Alam, M. Nethaji, M. Ray, *Inorg. Chem.* **2005**, *44*, 1302–1308.
[10] J. D. Ranford, J. J. Vittal, D. Wu, X. Yang, *Angew. Chem. Int. Ed.* **1999**, *38*, 3498–3501.
[11] a) N. Ohata, H. Masuda, O. Yamauchi, *Angew. Chem. Int. Ed. Engl.* **1996**, *35*, 531–532; b) N. Ohata, H. Masuda, O. Yamauchi, *Inorg. Chim. Acta* **2000**, *300*, 749–761; c) N. Ohata, H. Masuda, O. Yamauchi, *Inorg. Chim. Acta* **1999**, *286*, 37–45.
[12] T. Moriuchi, M. Nishiyama, K. Yoshida, T. Ishikawa, T. Hirao, *Org. Lett.* **2001**, *3*, 1459–1461.
[13] M. A. Alam, M. Nethaji, M. Ray, *Angew. Chem. Int. Ed.* **2003**, *42*, 1940–1942.
[14] S. Cukierman, *Biophys. J.* **2000**, *78*, 1825–1834.
[15] K. M. Jude, S. K. Wright, C. Tu, D. N. Silverman, R. E. Viola, D. W. Christianson, *Biochemistry* **2002**, *41*, 2485–2491.
[16] H. Kandori, *Biochim. Biophys. Acta* **2000**, *1460*, 177–191.
[17] R. Ludwig, *Angew. Chem. Int. Ed.* **2003**, *42*, 258–260.
[18] S. Pal, N. B. Sankaran, A. Samanta, *Angew. Chem. Int. Ed.* **2003**, *42*, 1741–1743.
[19] L. E. Cheruzel, M. S. Pometun, M. R. Cecil, M. S. Mashuta, R. J. Wittebort, R. M. Buchanan, *Angew. Chem. Int. Ed.* **2003**, *42*, 5452–5455.
[20] A. Mukherjee, M. K. Saha, M. Nethaji, A. R. Chakravarty, *Chem. Commun.* **2004**, 716–717.
[21] B. Sreenivasulu, J. J. Vittal, *Angew. Chem. Int. Ed.* **2004**, *43*, 5769–5772.
[22] a) L. Infantes, J. Chisholm, S. Motherwell, *CrystEngComm* **2003**, *5*, 480–486; b) L. Infantes, S. Motherwell, *CrystEngComm* **2002**, *4*, 454–461.
[23] G. M. Sheldrick, Bruker *SHELSTL-PC*, University of Göttingen, Germany, **1997**.
[24] H. D. Flack, *Acta Crystallogr.* **1983**, *A39*, 876–881.

Received April 19, 2005
Published Online: July 6, 2005

 © 2005 Wiley-VCH Verlag GmbH & Co. KGaA, Weinheim

Reaction of 1,3,5-Triazacyclohexanes with $TiCl_4$: Formation of Cationic Complexes

Randolf D. Köhn,*[a] Philip Kampe,[a,b] and Gabriele Kociok-Köhn[a]

Dedicated to Professor Herbert Schumann on the occasion of his 70th birthday

Keywords: N ligands / Tridentate ligands / Titanium

N-substituted 1,3,5-triazacyclohexanes [R_3TAC; R = cyclohexyl, *p*-fluorobenzyl or Ph$(CH_2)_n$ (*n* = 1, 2, 3)] react with excess $TiCl_4$ to give the corresponding cationic κ^3 complexes $[(R_3TAC)TiCl_3][Ti_2Cl_9]$. Attempts to prepare complexes with titanium-free anions at lower Ti:R_3TAC ratio or with added Me_3SiOTf lead to the same cations with $[Ti_2Cl_{10}]^{2-}$ and $[Ti_2Cl_8(OTf)]^-$ anions. Five complexes as well as (*p*-fluorobenzyl)$_3$TAC have been characterised by X-ray crystallography. The ring C–H bonds engage in hydrogen bonding interactions in the crystals and strongly solvent and anion dependent ^{1}H NMR signals are detected in solution.

(© Wiley-VCH Verlag GmbH & Co. KGaA, 69451 Weinheim, Germany, 2005)

Introduction

Many complexes containing triazacyclononane and larger macrocyclic amines are known.[1,2] They are used, for example, as bioinorganic model systems, reagents with high metal ion selectivity or as olefin polymerisation catalysts. The smaller *N*-substituted 1,3,5-triazacyclohexanes (R_3TAC) are much easier to prepare by the reaction of formaldehyde with primary amines allowing for a large variety of alkyl substituents. However, their coordination chemistry has mostly been explored only in the past ten years. A wide range of complexes with transition metals (like titanium complex **A**[3] in Scheme 1) and main group elements are well established. MAO activated chromium(III) complexes[4] (e.g. **B** in Scheme 1) are highly active homogeneous catalysts for the polymerisation and selective trimerisation of olefins.[5] Recently alternative catalysts for the selective trimerisation of ethylene based on aryl-substituted $CpTiCl_3$, **C**, have been discovered.[6] Since many features of the metal complexes containing R_3TAC, such as the ring centroid-metal distance, donor orbital orientation or positions of the ring substituents resemble those of analogous Cp rather than triazacyclononane complexes, we were interested in the preparation of analogous $[(R_3TAC)TiCl_3]^+$ complexes. The only previously described types of triazacyclohexane complexes of titanium are the neutral imido complexes **A** shown in Scheme 1.[3,7,8] In this paper we describe the synthesis of cationic 1,3,5-triazacyclohexane complexes by the reaction of the ligand with $TiCl_4$ (Scheme 2).

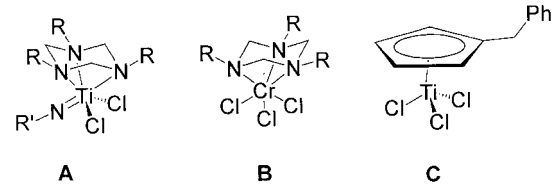

Scheme 1.

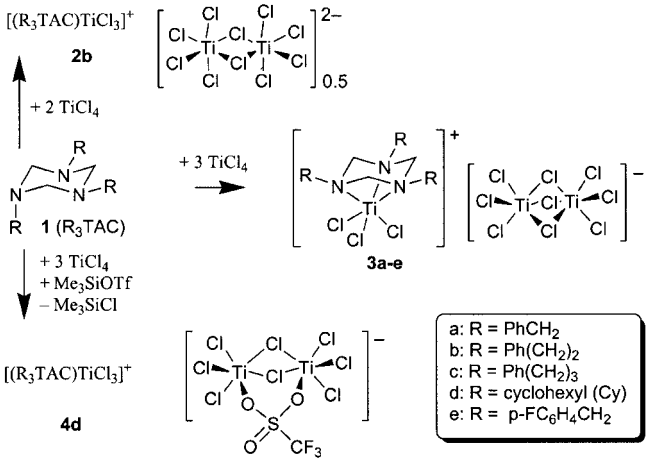

Scheme 2.

[a] Department of Chemistry, University of Bath, Bath, BA2 7AY, UK
E-mail: r.d.kohn@bath.ac.uk
[b] Current address: TU Darmstadt, 64287 Darmstadt, Germany
E-mail: Kampe@ct.chemie.tu-darmstadt.de
Supporting information for this article is available on the WWW under http://www.eurjic.org or from the author.

Results and Discussion

Treatment of $TiCl_4$ with one equivalent of *N*-substituted triazacyclohexanes **1** gave complex mixtures of products. However, a few yellow crystals of **2b** grew from this mixture as in the case of R = $Ph(CH_2)_2$ (**1b**). X-ray crystallography revealed a cationic complex $[(R_3TAC)TiCl_3]^+$ with $[Ti_2Cl_{10}]^{2-}$ anions. Apparently, excess $TiCl_4$ can abstract chloride ions to produce cationic R_3TAC complexes. Indeed, reaction of excess $TiCl_4$ with **1** gave high yields of often crystalline orange compounds. The optimal ratio of $TiCl_4$ to R_3TAC for a clean reaction was found to be 3:1. The crystal structures of **3a**, **3b** and **3d** contain the same cations as in **2b** but with the relatively more titanium rich anions $[Ti_2Cl_9]^-$. Similar ionisation of $TiCl_4$ has previously been observed in the reaction of hexaalkylbenzene with three equivalents of $TiCl_4$ giving $[(arene)TiCl_3][Ti_2Cl_9]$[9] Contrary to these arene complexes, the formation of **3** is irreversible on dilution. Thus, triazacyclohexanes are much stronger ligands than the arenes. The similarity of this reaction and the structures of the products show that the coordination chemistry of triazacyclohexanes share many characteristics with cyclic π ligands in the orientation of the donor orbitals, the position of the substituents near the plane of the donor atoms as well as the steric requirements.

The well-defined complexes **3** show only limited solubility in most inert organic solvents. The isolated crystalline solids are poorly soluble even in chlorinated solvents. The concentrations of saturated solutions of **3a** and **3d** in CH_2Cl_2 were found to be 2×10^{-4} and 2×10^{-3} mol cm^{-3}, respectively, by ^{1}H NMR spectroscopy. We generally find low solubility of triazacyclohexane complexes, probably due to hydrogen bonding interactions between ring–CH and Cl of the anion (or the complex itself) found in many solid-state structures. Thus, long-chain *N*-substituents or strong donor solvents are usually required for sufficient solubility. The concentration of **3e** was high enough to obtain ^{1}H and ^{19}F NMR spectra in pure $CDCl_3$ (about 4×10^{-3} mol cm^{-3} by NMR spectroscopy). All complexes **3** dissolved well in a mixture of $CDCl_3$ and $SOCl_2$ without apparent decomposition. Solutions in this mixture remained stable for many days even when exposed to air. Comparison of the NMR spectra of **3e** in neat $CDCl_3$ and those in 1:1 $CDCl_3/SOCl_2$ showed little differences except for the chemical shift of the two doublets for the ring CH_2 signals (4.89 and 4.74 ppm in $CDCl_3$ vs. 4.98 and 4.48 ppm in $CDCl_3/SOCl_2$). The observation of these two doublets for the equatorial and axial hydrogen atoms in the ring is also the best evidence for κ^3-R_3TAC coordination to a metal as observed previously.[10] The chemical shift and shift difference appears to be highly dependent on the environment (solvent, anion), probably due to C–H···X hydrogen bonding interactions. The shift difference varies from 0.1–0.9 ppm and is significantly smaller than the difference found in the neutral imido complexes of type **A** (1–2 ppm).[3,7,8]

In an attempt to obtain analogous cationic titanium complexes with titanium free anions we added Me_3SiOTf to the reaction mixture. Me_3SiCl was formed, however, a crystal structure of the product, **4d**, revealed the same cation not with an isolated triflate anion but with the titanium containing anion $[Ti_2Cl_6(\mu\text{-}Cl)_2(\mu\text{-}OTf)]^-$. Elemental analysis of the bulk product indicates that a mixture of **4d** and **3d** was obtained.

Addition of one equivalent of $LiB(C_6F_5)_4$ to a $CDCl_3/SOCl_2$ solution of **3d** leads to a significant change in the chemical shift of the pair of ring CH_2 signals of the ^{1}H NMR spectrum without changing the rest of the spectrum (4.96 and 4.62 ppm vs. 4.97 and 4.77 ppm in **3d**) indicating an anion exchange. Preparative scale metathesis of **3** or $TiCl_4$/**1** with $LiB(C_6F_5)_4$ allows the isolation of analogous salts **5** with largely $B(C_6F_5)_4$ anions, although no pure samples could be obtained due to anion contamination. **5d** had an NMR spectrum identical to the NMR tube experiment mentioned above and the spectra for **5b** (4.91 and 4.30 ppm vs. 5.03 and 4.81 ppm in **3b**) and for **5c** (3.60 and 3.45 ppm vs. coinciding peaks at 4.83 for **3c**) showed an increasing effect of the anion exchange (up-field shift and larger separation) for decreasing bulk of the *N*-substituents. A mixture of **5b** and **3b** leads to NMR signals at average positions indicating fast anion exchange on the NMR time-scale.

The strong dependence of the ring CH_2 ^{1}H NMR signals on the anion and the solvent indicates significant interactions of these C–H bonds with the environment.

X-ray Crystal Structures

All structures contain the $[(R_3TAC)TiCl_3]^+$ cation with titanium containing anions. Except for one feature, structural differences between cations with different anions (**2b**, **3b** and **3d**, **4d**) as well as anions with different cations (**3a**, **3b**, **3d**) are small and allow a separate discussion of the anions and cations.

Structural parameters of the coordination environment around titanium in the cations $[(R_3TAC)TiCl_3]^+$ shown in Figure 1 are summarised in Table 1. The structures are very similar to the neutral $[(R_3TAC)CrCl_3]$ where the analogous structure for R = $PhCH_2CH_2$ is known.[5] However, the Ti–N bond (2.23 Å) is much longer than in the chromium complex (2.10 Å) whereas the Ti–Cl bonds (2.20 Å) are shorter than in the chromium complex (2.28 Å), despite nearly identical ionic radii for Cr^{III} and Ti^{IV}.[11] Thus the higher charge on titanium favours the chloride bonding over the amine bonding. As in other triazacyclohexane complexes the nitrogen lone pair cannot be directed towards the metal and results in a bent-bonding situation. However, the Ti–N bonding is improved by bending the N-substituent towards the N_3 plane and therefore the lone pair towards the metal as shown in Scheme 3.

This bending can be expressed by the Ti–N–C angle or better the distance Δ of the α-C of the N-substituent above (or below) the N_3 plane. This can also be compared to the free ligand; the published structure[12] of **1a** has severe temperature dependent disorder between axial and equatorial benzyl groups making it difficult to obtain reliable Δ values. We crystallised the known ligand **1e** (R = *p*-fluorobenzyl)

 © 2005 Wiley-VCH Verlag GmbH & Co. KGaA, Weinheim

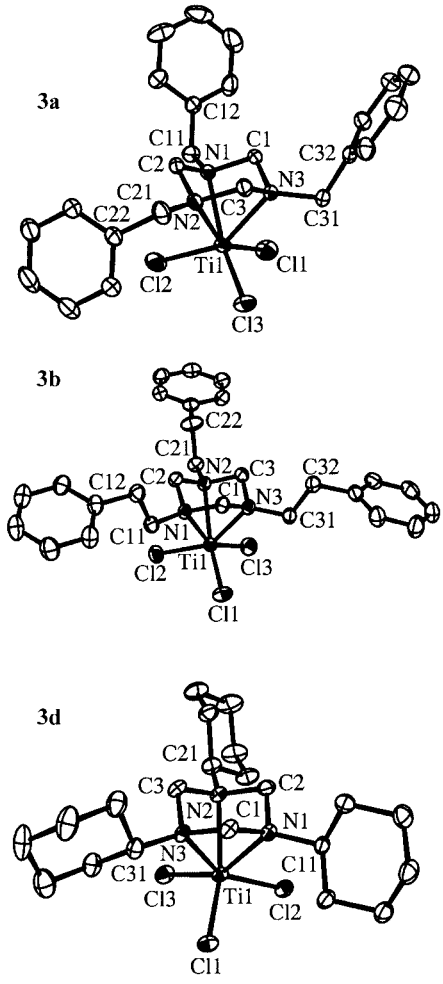

Figure 1. Structure of the cations in **3a**, **3b** and **3d**. The cations in **2b** and **4d** look nearly identical.

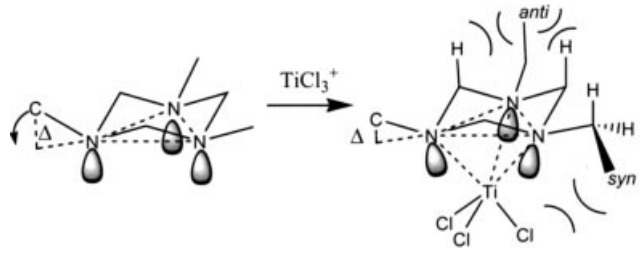

Scheme 3. Bent-bonding situation in triazacyclohexane complexes, definition of Δ, and the *syn* and *anti* conformation of the N-substituent.

and obtained a crystal structure without such disorder.[13] The structure of **1e** shows the most common conformation for free triazacyclohexanes with one axial and two equatorial N-substituents as shown in Figure 2. Δ for the two equatorial carbon atoms is +0.47 and +0.55 Å and close to the value of +0.49 Å expected for a ring with perfect tetrahedral angles and equal C–N bond lengths of 1.46 Å (average found in **1e**). The observed Δ values for the titanium complexes fall into three groups: +0.12 and +0.16 Å

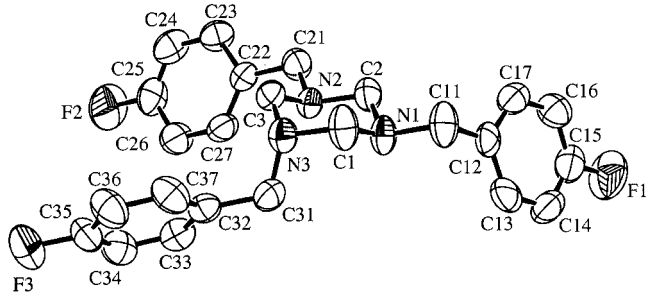

Figure 2. Structure of the complex **1e**.

Table 1. Selected averaged distances [Å] and angles [°] in $[(R_3TAC)TiCl_3]^+$ of **2**, **3** and **4**.

	R = $PhCH_2$ **3a**	R = $PhCH_2CH_2$ **2b** [**3b**]	R = cyclohexyl **3d** [**4d**]
Ti1–N1	2.221(1)[b]	2.205(2)[b] [2.236(2)[b]]	2.240(3) [2.236(2)]
Ti1–N2	2.254(1)[a]	2.218(2)[b] [2.230(2)[b]]	2.232(3) [2.239(2)]
Ti1–N3	2.228(1)[b]	2.227(2)[a] [2.223(2)[b]]	2.235(3) [2.227(2)]
av. Ti–N_{syn}	2.25	2.23 [–]	2.24 [2.23]
av. Ti–N_{anti}	2.22	2.21 [2.23]	
Ti1–Cl1	2.201(1)	2.208(1) [2.206(1)]	2.197(1) [2.204(1)]
Ti1–Cl2	2.191(1)	2.206(1) [2.196(1)]	2.213(1) [2.203(1)]
Ti1–Cl3	2.205(1)	2.199(1) [2.189(1)]	2.201(1) [2.212(1)]
av. Ti–Cl	2.20	2.20 [2.20]	2.20 [2.21]
Δ(C11)[c]	+0.02[b]	–0.01[b] [–0.02[b]]	+0.04 [+0.04]
Ti1–N1–C11	126.5(1)	125.7(2) [125.7(2)]	128.7(2) [128.2(1)]
Δ(C21)[c]	+0.16[a]	–0.01[b] [+0.03[b]]	+0.06 [+0.03]
Ti1–N2–C21	133.2(1)	126.1(2) [127.7(2)]	128.4(2) [127.8(1)]
Δ(C31)[c]	–0.02[b]	+0.12[a] [–0.07[b]]	+0.08 [+0.05]
Ti1–N3–C31	125.2(1)	131.5(2) [123.4(2)]	129.3(2) [128.2(1)]
av. Δ/Ti–*N*–C_{syn}	0.16/133	0.12/132 [–]	0.06/129 [0.04/128]
av. Δ/Ti–*N*–C_{anti}	0.00/126	–0.01/126 [–0.02/126]	
av. N–Ti–N	61.7	62.2 [61.9]	61.9 [62.1]
av. Cl–Ti–Cl	106	106 [106]	104 [104]
av. Ti–*N*–C–C_{syn}	54	75 [–]	55 [57]
av. Ti–*N*–C–C_{anti}	173	177 [177]	177 [176]

[a] *syn* conformation of R. [b] *anti* conformation of R. [c] Distance Δ above the N_3 plane (negative number on metal side).

 © 2005 Wiley-VCH Verlag GmbH & Co. KGaA, Weinheim

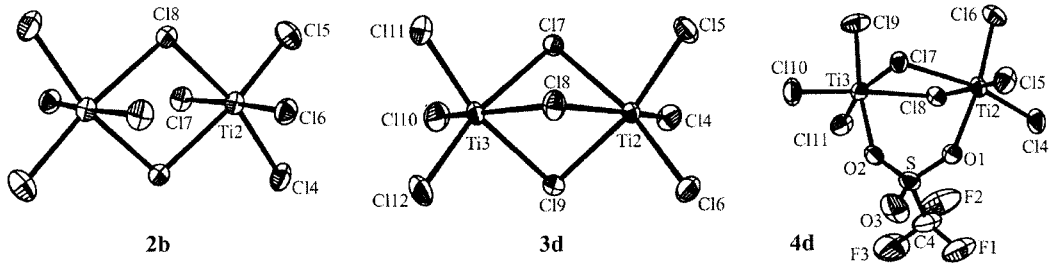

Figure 3. Structure of the anions in **2b**, **3d** and **4d**. The anions in **3a** and **3b** look nearly identical to that in **3d**.

for N-substituents in the *syn* conformation, –0.07 to +0.03 (av. –0.01) Å for the *anti* conformation and +0.03 to +0.08 (av. +0.05) Å for the cyclohexyl substituent (β-C in both *syn* and *anti* position). All values indicate a substantial bending of the N-substituent position towards the N_3 plane upon complexation in order to obtain better N-metal overlap. However, steric repulsion leads to less bending in the *syn* conformation (β-C···Cl) and increased bending in the *anti* conformation (β-C···axial ring C–H) with an intermediate case for cyclohexyl with repulsion at both β-C positions. The intermediate values for the cyclohexyl substituent show that both steric repulsions are important.

It is informative to compare the bonding parameters in these cationic $[(R_3TAC)TiCl_3]^+$ complexes with the neutral imido complexes **A**. The Ti–N bond lengths *trans* to Ti–Cl are nearly the same (2.23 Å) unless R is the bulky *t*Bu group (>2.30 Å) whereas the Ti–Cl bonds are substantially shorter in the cationic complexes (2.20 vs. 2.33–2.36 Å in **A**) but similar to those in the cationic arene complexes $[(arene)TiCl_3]^+$ (2.19 Å).[9] However, the Δ values for N-substituents *trans* to Cl in the imido complexes are much larger (+0.15 to 0.24 Å) than those found in the cationic complexes (–0.07 to +0.16 Å). Thus the tighter bonding of R_3TAC in cationic complexes is expressed as an improved nitrogen lone pair orientation (smaller Δ) rather than shorter Ti–N bonds.

All anions (Figure 3) contain two octahedrally coordinated titanium atoms. The two metals share one edge (two chloride bridges) in **2** or one face (three chloride bridges) in **3**. The anion in **4** contains a triflate bridge in addition to two chloride bridges and results in structural features intermediate between **2** and **3** as shown in Table 2. The anions in **2** and **3** have been observed before while the anion in **4** is new.[14]

The structures also allow us to look at the C–H···X interactions in the crystal and the effect of varying the N-substituents and anions. A CSD review of C–H···Cl interactions revealed H···Cl distances of 2.8–2.9 Å and C–H···Cl angles of 140–180° as the best parameters for this hydrogen bonding interaction when Cl is part of an anion.[15] The structures of all complexes in this work contain C–H···Cl contacts of this length or shorter and involve at least one ring C–H bond. Each anion has several contacts to neighbouring cations leading to an extended 3D network rationalising the poor solubility. However, there are noteworthy differences between the structures. The shortest contacts in **3** with the anion increase from **3b** (2.68 Å, R = $PhCH_2CH_2$) to **3a** (2.76 Å, R = $PhCH_2$) and **3d** (2.85 Å, R = cyclohexyl) as expected for increasing steric bulk exhibited by the substituent. In the latter case as well as in the similar **4d** (shortest C–H···Cl 2.78 Å + C–H···O(Tf) 2.51 Å) additional contacts of similar lengths with C–H groups of the substituents exist. The single short C–H···Cl contact in **3b** is replaced by two slightly longer contacts of 2.73 Å (ring CH) and 2.72 Å (α-CH_2 of R) reflecting the probably tighter binding of the Ti_2Cl_{10} dianion.

Table 2. Selected averaged distances [Å] and angles for the anions of **2**, **3** and **4**.

	$[Ti_2Cl_{10}]^{2-}$ **2b**	$[Ti_2Cl_9]^-$ **3a** [**3b**] {**3d**}	$[Ti_2Cl_8(OTf)]^-$ **4d**
Ti–(μ-Cl)	2.50	2.49 [2.49] {2.49}	2.48
Ti–Cl	2.27	2.22 [2.21] {2.21}	2.21
Ti–O			2.10
Ti···Ti	3.84	3.40 [3.43] {3.39}	3.75
Ti–(μ-Cl)–Ti	101°	86° [87°] {86°}	98°
(μ-Cl)–Ti–(μ-Cl)	79°	78° [78°] {79°}	80°
Cl–Ti–Cl	*cis*: 94°	98° [99°] {99°}	99°

The above study demonstrates that cationic triazacyclohexane complexes of titanium can be obtained by the reaction of the ligand with excess $TiCl_4$. The N-substituents are more bent towards the metal than in neutral complexes with improved metal–N bonding. The ring C–H bonds of the triazacyclohexanes interact with the environment through significant hydrogen-bonding interactions leading to surprisingly poor solubility of these 3D networks in chlorinated solvents.

Experimental Section

General Details: All manipulations of air- and moisture-sensitive compounds were carried out under nitrogen or argon using standard Schlenk-line or glove box techniques. Solvents were dried according to standard methods and collected by distillation. R_3TAC except for **1c** are known and have been prepared analogous to the method described for **1c**. **1a**,**b**,**d**,**e** were crystallised from petroleum ether. ^1H and ^{13}C NMR spectra were recorded with a Varian Mercury-400 or Bruker Avance-300 or 400 at 20 °C and assignments were confirmed by COSY spectra. Mr Alan Carver (University of

 © 2005 Wiley-VCH Verlag GmbH & Co. KGaA, Weinheim

Bath) carried out the elemental analyses with an Exeter Analytical Instruments CE-440 Elemental Analyser.

Phenylpropyl$_3$TAC (1c): Phenylpropylamine (11.37 g, 84.22 mmol) and paraformaldehyde (2.53 g, 84.22 mmol) were dissolved in toluene (50 mL). The solution was heated to distil off the produced water as an azeotropic mixture with toluene. After 30 min the remaining solvent was removed by distillation under reduced pressure. The remaining pale yellow oil was dissolved in methanol (250 mL) and stored at 0 °C. The separated oil was washed with ethanol and dried under reduced pressure to give a colourless oil. ^{1}H NMR (300 MHz, $CDCl_3$): δ = 7.31–7.28 (6 H, C_6H_5–), 7.23 (9 H, C_6H_5–), 3.36 (br. s, 6 H, ring–CH_2), 2.69 (m, 6 H, –CH_2–Ph), 2.51 (m, 6 H, N–CH_2–), 1.83 (m, 6 H, Bz–CH_2–CH$_2$–N). ^{13}C{^{1}H} NMR (75 MHz, $CDCl_3$): δ = 142.1 (1-C_6H_5), 128.4 (3-C_6H_5), 128.2 (2-C_6H_5), 125.7 (4-C_6H_5), 74.5 (N–CH$_2$–N), 52.0 (PhEt–CH$_2$–N), 33.5 (Ph–CH$_2$–), 29.2 (Bz–CH$_2$–).

[(Benzyl$_3$TAC)TiCl$_3$]$^+$[Ti$_2$Cl$_9$]$^-$ (3a): I A solution of (PhCH$_2$)$_3$TAC (0.415 g, 1.16 mmol) in dichloromethane (25 mL) was added to a stirred solution of $TiCl_4$ (0.865 g, 4.56 mmol) in dichloromethane (25 mL) at room temperature under a stream of dinitrogen. After 5 h pale yellow platelets deposited. Washing with dichloromethane (10 mL) and drying in vacuo yielded clear yellow crystals. Yield: 0.56 g (52%). **II** A solution of (PhCH$_2$)$_3$TAC (1.24 g, 3.47 mmol) in toluene (25 mL) was added to a stirred solution of $TiCl_4$ (1.73 g, 9.12 mmol) in toluene (25 mL) at room temperature under a stream of dinitrogen. Dichloromethane (50 mL) was slowly added by condensation under reduced pressure. After 1 h of stirring, further $TiCl_4$ (1.73 g, 9.12 mmol) was added to give a dark orange solution. After another hour little orange crystals started to precipitate. These were dried under reduced pressure. Yield: 1.89 g (59%). ^{1}H NMR (300 MHz, $CDCl_3$/$SOCl_2$): δ = 7.48 m (9 H, C_6H_5–), 7.30 m (6 H, C_6H_5–), 5.06 and 4.14 (d, J = 9 Hz, 3 H, N–CH_2–N), 4.31 (s, 6 H, N–CH_2–Ph) ppm. ^{1}H NMR (400 MHz, saturated in CH_2Cl_2, 0.2 mM): δ = 7.5 (9 H, C_6H_5–), 7.3 (6 H, C_6H_5–), 4.75 and 4.25 (3 H, N–CH_2–N), 4.34 (s, 6 H, N–CH_2–Ph). ^{1}H NMR (400 MHz, saturated in CH_2Cl_2/$SOCl_2$, 1.0 mM): δ = 7.45 (9 H, C_6H_5–), 7.33 (6 H, C_6H_5–), 5.01 and 4.32 (d, 3 H, N–CH_2–N), 4.29 (s, 6 H, N–CH_2–Ph) ppm. ^{13}C{^{1}H} NMR (75 MHz, $CDCl_3$/$SOCl_2$): δ = 130.7 (1-C_6H_5), 130.6 (3-C_6H_5), 129.9 (2-C_6H_5), 127.6 (4-C_6H_5), 76.5 (N–CH$_2$–N), 60.9 (Ph–CH$_2$–N). $C_{24}H_{27}N_3Ti_3Cl_{12}$ (926.58): calcd. C 31.11, H 2.94, N 4.54; found C 30.9, H 2.99, N 4.52 ppm.

[(Phenylethyl$_3$TAC)TiCl$_3$]$^+$[Ti$_2$Cl$_9$]$^-$ (3b): A solution of (PhC$_2$H$_4$)$_3$-TAC (1 g, 2.5 mmol) in dichloromethane (25 mL) was added slowly to a solution of $TiCl_4$ (1.330 g, 7.01 mmol) in dichloromethane (25 mL) at room temperature under a stream of dinitrogen to give a clear brown solution. The product was cautiously precipitated by slow addition of hexane (20 mL). After 48 h a brownish yellow precipitate was separated and dried under reduced pressure to give a brownish yellow powder. Yield: 2.17 g (96%). ^{1}H NMR (300 MHz, $CDCl_3$/$SOCl_2$): δ = 7.41–7.34 (9 H, C_6H_5–), 7.26–7.23 (6 H, C_6H_5–), 5.03 and 4.81 (d, J = 9.2 Hz, 3 H, N–CH_2–N), 3.55 (t, 6 H, Ph–CH_2–), 2.98 (t, 6 H, Bz–CH_2–N) ppm. ^{13}C{^{1}H} NMR (75 MHz, $CDCl_3$/$SOCl_2$): δ = 135.3 (1-C_6H_5), 129.3 (3-C_6H_5), 128.5 (2-C_6H_5), 127.7 (4-C_6H_5), 77.9 (N–CH$_2$–N), 58.1 (Bz–CH$_2$–N), 30.5 (Ph–CH$_2$–) ppm. $C_{27}H_{33}N_3Ti_3Cl_{12}$ (968.66): calcd. C 33.48, H 3.43, N 4.34; found C 33.4, H 3.52, N 4.34.

[(Phenylpropyl$_3$TAC)TiCl$_3$]$^+$[Ti$_2$Cl$_9$]$^-$ (3c): A solution of (PhC$_3$H$_6$)$_3$-TAC (1 g, 2.26 mmol) in dichloromethane (25 mL) was added slowly to a solution of $TiCl_4$ (1.29 g, 6.80 mmol) in dichloromethane (25 mL) at room temperature under a stream of dinitrogen to give a clear dark brown solution. The product was cautiously precipitated by slow addition of hexane (20 mL). After 24 h a dark orange-brown precipitate was separated and dried under reduced pressure to give a brownish yellow crystal-like powder. Yield: 1.81 g (79%). ^{1}H NMR (300 MHz, $CDCl_3$/$SOCl_2$): δ = 7.34–7.27 (9 H, C_6H_5–), 7.24–7.18 (6 H, C_6H_5–), 4.85 and 4.81 (d, J = 9.6 Hz, 3 H, N–CH_2–N), 3.21 (m, 6 H, PhEt–CH_2–N) 2.68 (m, 6 H, Ph–CH_2), 1.98 (m, 6 H, PhCH$_2$–CH_2–) ppm. ^{13}C{^{1}H} NMR (75 MHz, $CDCl_3$/$SOCl_2$): δ = 139.1 (1-C_6H_5), 128.7 (3-C_6H_5), 128.3 (2-C_6H_5), 126.6 (4-C_6H_5), 77.5 (N–CH$_2$–N), 56.2 (PhEt–CH$_2$–N), 32.4 (Ph–CH$_2$–), 25.1 (PhCH$_2$–CH$_2$) ppm. $C_{30}H_{39}N_3Ti_3Cl_{12}$ (1010.74): calcd. C 35.65, H 3.89, N 4.16; found C 36.0, H 3.76, N 4.24.

[(Cyclohexyl$_3$TAC)TiCl$_3$]$^+$[Ti$_2$Cl$_9$]$^-$ (3d): A solution of Cy$_3$TAC (1 g, 3.00 mmol) in dichloromethane (25 mL) was added slowly to a solution of $TiCl_4$ (1.71 g, 9.01 mmol) in dichloromethane (25 mL) at room temperature under a stream of dinitrogen to give a clear brown solution. A bright yellow solid began to precipitate from the dark solution. After 48 h in the refrigerator the precipitate was isolated, washed with dichloromethane (20 mL) and dried under reduced pressure to give bright yellow crystals. Yield: 2.03 g (75%). ^{1}H NMR (300 MHz, $CDCl_3$/$SOCl_2$): δ = 4.97 and 4.77 (d, J = 8.8, 3 H, N–CH_2–N), 3.22 [3 H, CH–N], 2.20 [6 H, eq. –CH_2–CHN)], 2.00 [6 H, eq. –CH_2–CH$_2$CHN], 1.72 (3 H, eq. –CH_2–CH$_2$CH$_2$CHN), 1.38 [12 H, ax. –CH_2–CH_2–CHN] 1.2 (3 H, ax. –CH_2–CH$_2$CH$_2$CHN) ppm. ^{1}H NMR (400 MHz, saturated in CH_2Cl_2, 2.3 mM): δ = 4.927 and 4.85 (d, J = 8.5, 3 H, N–CH_2–N), 3.2 [3 H, CH–N], 2.18 [6 H, eq. –CH_2–CHN)], 1.94 [6 H, eq. –CH_2–CH$_2$CHN], 1.70 (3 H, eq. –CH_2–CH$_2$CH$_2$CHN), 1.34 [12 H, ax. –CH_2–CH_2–CHN] 1.12 (3 H, ax. –CH_2–CH$_2$CH$_2$CHN) ppm. ^{1}H NMR (400 MHz, saturated in CH_2Cl_2/$SOCl_2$ (3:1), 2.8 mM): δ = 4.93 and 4.88 (3 H, N–CH_2–N), 3.2 [3 H, CH–N], 2.2 [6 H, eq. –CH_2–CHN)], 1.94 [6 H, eq. –CH_2–CH$_2$CHN], 1.70 (3 H, eq. –CH_2–CH$_2$CH$_2$CHN), 1.34 [12 H, ax. –CH_2–CH_2–CHN] 1.12 (3 H, ax. –CH_2–CH$_2$CH$_2$CHN) ppm. ^{13}C{^{1}H} NMR (75 MHz, $CDCl_3$/$SOCl_2$): δ = 74.6 (N–CH$_2$–N), 66.6 (CH–N), 27.5 (CH$_2$–CHN), 25.2 (CH$_2$–CH$_2$CHN), 24.7 (CH$_2$–CH$_2$CH$_2$CHN) ppm. $C_{21}H_{39}N_3Ti_3Cl_{12}$ (902.64): calcd. C 27.94, H 4.36, N 4.66; found C 27.9, H 4.35, N 4.65.

[(Cyclohexyl$_3$TAC)TiCl$_3$]$^+$[[Ti$_2$Cl$_8$(OTf)]$^-$ (4d): Trimethylsilyl trifluoromethanesulfonate (0.67 mL, 3.7 mmol) was added to 5 mL of a 0.6 M solution of $TiCl_4$ in toluene (3 mmol) at 0 °C. The resulting deep red-brown solution was stirred for 30 min and then Cy$_3$TAC (1.0 g, 3.0 mmol) was added at 0 °C. After warming to ambient temperature and stirring for 1 h, hexane (30 mL) was added to give an orange precipitate. The solution was decanted and the residue dried under vacuum, washed with 50 mL of hexane and dried again under vacuum to give an orange-brown solid (2.6 g, 85%). Elemental analysis (CHN) of this product fits that of a mixture of complexes containing the cation with a 2:1 mixture of [Ti$_2$Cl$_8$(OTf)]$^-$ and [Ti$_2$Cl$_{10}$]$^{2-}$ anions. Crystals of **4d** were grown from a solution in $SOCl_2$/chloroform. ^{1}H NMR (300 MHz, $CDCl_3$/$SOCl_2$): δ = 4.92 and 4.87 (d, J = 9.4, 3 H, N–CH_2–N), 3.20 [3 H, CH–N], 2.19 [6 H, eq. –CH_2–CHN)], 1.98 [6 H, eq. –CH_2–CH$_2$CHN], 1.71 (3 H, eq. –CH_2–CH$_2$CH$_2$CHN), 1.4 [12 H, ax. –CH_2–CH_2–CHN] 1.2 (3 H, ax. –CH_2–CH$_2$CH$_2$CHN) ppm. ^{13}C{^{1}H} NMR (75 MHz, $CDCl_3$/$SOCl_2$): δ = 77.9 (N–CH$_2$–N), 67.0 (CH–N), 27.3 (CH$_2$–CHN), 25.0 (CH$_2$–CH$_2$CHN), 24.6 (CH$_2$–CH$_2$CH$_2$CHN) ppm. $C_{22}H_{39}N_3Ti_3Cl_{11}SO_3F_3$ (1016.26): calcd. C 26.00, H 3.87, N 4.14. Calcd for the mixture $C_{22}H_{39}N_3Ti_{2.5}Cl_{9.5}S_{0.5}O_{1.5}F_{1.5}$: C 30.35, H 4.52, N 4.83; found C 30.1, H 4.65, N 4.48.

[(Fluorobenzyl$_3$TAC)TiCl$_3$]$^+$[Ti$_2$Cl$_9$]$^-$ (3e): A solution of (*p*-F–PhCH$_2$)$_3$TAC (0.163 g, 0.40 mmol) in dichloromethane (10 mL) was added to a stirred solution of $TiCl_4$ (0.16 mL, 0.28 g,

 © 2005 Wiley-VCH Verlag GmbH & Co. KGaA, Weinheim

Table 3. Crystal data, data collection and refinement parameters for **2b, 3a, 3b, 3d and 4d**.

	2b·(toluene)	**3a**	**3b**	**3d**·(CH_2Cl_2)	**4d**
Empirical formula	$C_{41}H_{49}Cl_8N_3Ti_2$	$C_{24}H_{27}Cl_{12}N_3Ti_3$	$C_{27}H_{33}Cl_{12}N_3Ti_3$	$C_{22}H_{41}Cl_{14}N_3Ti_3$	$C_{22}H_{39}Cl_{11}F_3N_3O_3STi_3$
M [g mol^{-1}]	963.23	926.54	968.66	987.58	1016.27
Crystal colour	yellow	yellow	yellow	yellow	yellow
Crystal size [mm]	0.4×0.25×0.2	0.45×0.38×0.38	0.4×0.33×0.2	0.4×0.3×0.2	0.3×0.3×0.08
Crystal system	monoclinic	monoclinic	triclinic	monoclinic	triclinic
Space group	$P2_1/a$ (no.14)	$P2_1/c$ (no.14)	$P\bar{1}$ (no.2)	$P2_1/c$ (no.14)	$P\bar{1}$ (no.2)
a [Å]	11.3330(2)	11.6700(1)	11.5000(4)	13.5980(2)	13.0210(2)
b [Å]	23.7790(4)	15.7590(1)	12.1700(5)	10.4900(2)	13.4030(2)
c [Å]	16.6530(4)	20.5150(2)	15.7990(7)	28.1290(4)	14.6230(2)
α [°]			69.985(2)		65.2640(8)
β [°]	96.9650(7)	103.2280(4)	83.7330(17)	94.8570(5)	68.9630(9)
γ [°]			69.130(2)		64.0170(8)
V [Å^3]	4454.66(15)	3672.76(5)	1941.09(14)	3998.00(11)	2034.78(5)
Z	4	4	2	4	2
D_c [g cm^{-3}]	1.436	1.676	1.657	1.641	1.659
μ(Mo-K_α) [mm^{-1}]	0.871	1.532	1.453	1.542	1.392
F(000)	1984	1848	972	1992	1024
$2\theta_{range}$ [°]	7–55	8–60	8–55	7–55	7–55
Collected data	71226	68831	21139	38570	35951
Unique data $I > 2\sigma(I)$	10005, R(int) = 0.087	10694, R(int) = 0.036	8525, R(int) = 0.049	8970, R(int) = 0.1625	9257, R(int) = 0.041
Refined parameter	487	379	407	379	415
min./max. density [e Å^{-3}]	–0.560/0.903	–0.891/0.778	–0.513/0.533	–1.028/0.758	–0.655/0.532
Extinction coeff.[a]			0.0033(6)		
R_1[b] [$I > 2\sigma(I)$]	0.0472	0.0297	0.0399	0.0626	0.0356
wR_2[c] [$I > 2\sigma(I)$]	0.0998	0.0700	0.0990	0.1454	0.0908
Gof[d]	1.038	1.047	1.059	1.046	1.049

[a] $F_c^* = kF_c[1 + 0.001F_c^2\lambda^3/\sin(2\theta)]^{-1/4}$. [b] $R_1 = \Sigma||F_o| - |F_c|| / \Sigma|F_o|$. [c] $wR_2 = \{\Sigma[w(F_o^2 - F_c^2)^2] / \Sigma[w(F_o^{2)2}]\}^{1/2}$. [d] Gof = $S = \{\Sigma[w(F_o^2 - F_c^2)^2]] / (n - p)\}^{1/2}$.

1.46 mmol) in dichloromethane (20 mL) at room temperature under a stream of dinitrogen. The solution was slowly concentrated to 2 mL and cooled to –20 °C. Yellow crystals grew overnight and were isolated by decanting the remaining solution, washing with two 1 ml portions of CH_2Cl_2 and drying in a stream of nitrogen. This results in about 1.5 or 2.5 remaining CH_2Cl_2 per **3e** according to elemental analysis and NMR spectroscopy, respectively. Yield: 0.29 g (74%). ^{1}H NMR (400 MHz, saturated solution in $CDCl_3$, 4 mM): δ = 7.40 (m, 6 H, C_6H_4F), 7.21 (6 H, C_6H_4F), 4.89 and 4.74 (d, J = 8.7 Hz, 3 H, N–CH_2–N), 4.26 (s, 6 H, N–CH_2–Ph) ppm. ^{1}H NMR (400 MHz, $CDCl_3$/$SOCl_2$): δ = 7.38 (m, 6 H, C_6H_4F), 7.18 (6 H, C_6H_4F), 4.98 and 4.48 (d, J = 8.9 Hz, 3 H, N–CH_2–N), 4.25 (s, 6 H, N–CH_2–Ph) ppm. ^{13}C{^{1}H} NMR (101 MHz, $CDCl_3$/$SOCl_2$): 164.1 (d, 1-C_6H_4F, J = 252 Hz), 133.4 (d, 3-C_6H_4F, J = 8.8 Hz), 117.2 (d, 2-C_6H_4F, J = 21.6 Hz), 124.0 (d, 4-C_6H_4F, J = 3.3 Hz), 76.7 (N–CH$_2$–N), 59.9 (Ph–CH$_2$–N) ppm. ^{19}F NMR (376 MHz, $CDCl_3$): –108.2 ppm. ^{19}F NMR (376 MHz, $CDCl_3$/$SOCl_2$): δ = –108.2 ppm. $C_{24}H_{24}F_3N_3Ti_3Cl_{12}$ (980.55): calcd. C 29.40, H 2.47, N 4.29, and for **3e**$(CH_2Cl_2)_{1.5}$ (1107.95): calcd. C 27.64, H 2.46, N 3.79; found C 27.7, H 2.58, N 3.89.

X-ray Crystallography: Intensity data for **1e**[13] were collected with a STOE STADI4 and for **2b**, **3a**, **3b**, **3d** and **4d** with a Nonius KappaCCD diffractometer. Details of the crystal structure determinations are shown in Table 3. Structure solution, followed by full-matrix least-squares refinement was performed using the WINGX-1.64 suite of programs throughout.[16]

CCDC-257783–257788 contain the crystallographic data for this paper. These data can be obtained free of charge from The Cambridge Crystallographic Data Centre via www.ccdc.cam.ac.uk/data_request/cif.

Supporting Information: Plots of the C–H···Cl contacts and NMR spectra (see also footnote on the first page of this article).

Acknowledgments

We thank Prof. A. C. Filippou (HU Berlin/Germany) for diffractometer time for compound **1e**.

[1] P. Chaudhuri, K. Wieghard, *Prog. Inorg. Chem.* **1987**, *35*, 329.
[2] S. Y. Bylikin, D. A. Robson, N. A. H. Male, L. H. Ress, P. Mountford, M. Schröder, *J. Chem. Soc., Dalton Trans.* **2001**, 170.
[3] P. J. Wilson, A. J. Blake, P. Mountford, M. Schröder, *J. Organomet. Chem.* **2000**, *600*, 71.
[4] R. D. Köhn, M. Haufe, S. Mihan, D. Lilge, *Chem. Commun.* **2000**, 1927.
[5] R. D. Köhn, D. Smith, M. F. Mahon, M. Prinz, S. Mihan, G. Kociok-Köhn, D. Lilge, *J. Organomet. Chem.* **2003**, *683*, 200.
[6] a) B. Hessen, *J. Mol. Catal. A: Chem.* **2004**, *213*, 129; b) P. J. W. Deckers, B. Hessen, J. H. Teuben, *Organometallics* **2002**, *21*, 5122; c) P. J. W. Deckers, B. Hessen, J. H. Teuben, *Angew. Chem. Int. Ed.* **2001**, *40*, 2516.
[7] M. V. Baker, M. C. Palermo, B. W. Skelton, A. H. White, *Austr. J. Chem.* **1999**, *52*, 179.
[8] P. J. Wilson, P. A. Cooke, A. J. Blake, P. Mountford, M. Schröder, *New J. Chem.* **1999**, *23*, 271.
[9] P. Kiprof, J. Li, C. L. Renish, E. K. Kalombo, V. G. Young, Jr., *J. Organomet. Chem.* **2001**, *620*, 113; E. Solari, C. Floriani, A. Chiesi-Villa, C. Guastini, *J. Chem. Soc., Chem. Commun.* **1989**, 1747.
[10] M. Haufe, R. D. Köhn, R. Weimann, G. Seifert, D. Zeigan, *J. Organomet. Chem.* **1996**, *520*, 121.
[11] R. D. Shannon, *Acta Crystallogr., Sect. A* **1976**, *32*, 751.
[12] G. A. Sim, *J. Chem. Soc., Chem. Commun.* **1987**, 1118.
[13] Crystallographic data for **1e**: $C_{24}H_{24}F_3N_3$, M = 411.46, monoclinic, space group $P2_1/n$, a = 9.977(2), b = 14.591(5), c = 15.490(4) Å, β = 107.30(3)°, V = 2152.9(10), Z = 4, D_c = 1.269 Mg m^{-3}, μ(Mo-K_α) = 0.094 mm^{-1}, T = 293 K, 6387 reflec-

tions collected, 3044 unique, (*R*int = 0.0304) final residuals $R_1[I > 2\sigma(I)] = 0.0463$, $wR_2 = 0.1068$.
[14] J. Eicher, P. Klingelhöfer, U. Müller, K. Dehnicke, *Z. Anorg. Allg. Chem.* **1984**, *514*, 79.
[15] C. B. Aakeröy, T. A. Evans, K. R. Seddon, I. Pálinkó, *New J. Chem.* **1999**, 145.
[16] L. J. Farrugia, *J. Appl. Crystallogr.* **1999**, *32*, 837.
Received: February 9, 2005
Published Online: June 17, 2005

 © 2005 Wiley-VCH Verlag GmbH & Co. KGaA, Weinheim

Dinuclear Oxomolybdate(V) Species with Oxalato and Pyridine Ligands Revisited: *cis*/*trans* Isomerization of $[Mo_2O_4(\eta^2\text{-}C_2O_4)_2(R\text{-}Py)_2]^{2-}$ (R-Py = Pyridine, Alkyl-Substituted Pyridine) in Water Evidenced by NMR Spectroscopy

Barbara Modec,*[a] Darko Dolenc,[a] Jurij V. Brenčič,[a] Jože Koller,[a] and Jon Zubieta[b]

Keywords: Isomerization / Molybdenum / N ligands / NMR spectroscopy / Polyoxometalates

The simple oxohalomolybdate(V) ions $[MoOCl_4(H_2O)]^-$ and $[MoOBr_4]^-$ were reacted with oxalic acid in mixtures containing an alcohol and a pyridine (R-Py) to form the dinuclear anions $[Mo_2O_4(\eta^2\text{-}C_2O_4)_2(R\text{-}Py)_2]^{2-}$ based on the $\{Mo_2O_4\}^{2+}$ structural core. The dinuclear anion exists in two isomeric forms – as a *trans* and as a *cis* isomer. A *trans* arrangement of the pyridine ligands relative to the $Mo_2(\mu_2\text{-}O)_2$ bridge was observed for $(PyH)_2[Mo_2O_4(\eta^2\text{-}C_2O_4)_2Py_2]$ (**1**), $(PyH)_2[Mo_2O_4(\eta^2\text{-}C_2O_4)_2(3,5\text{-}Lut)_2]$ (**2**), $[MeNC_5H_3(Me)_2]_2[Mo_2O_4(\eta^2\text{-}C_2O_4)_2(3,5\text{-}Lut)_2]\cdot H_2O$ (**3**), $(4\text{-}MePyH)_2[Mo_2O_4(\eta^2\text{-}C_2O_4)_2(4\text{-}MePy)_2]\cdot 1/2(4\text{-}MePy)$ (**5**), and $[(C_6H_5)_4P]_2[Mo_2O_4(\eta^2\text{-}C_2O_4)_2Py_2]\cdot H_2O$ (**7**) [Py = pyridine; 3,5-Lut = 3,5-lutidine; $MeNC_5H_3(Me)_2^+$ = *N*-methyl-3,5-lutidinium cation and 4-MePy = 4-methylpyridine], while a *cis* arrangement was found in only two compounds, namely $(4\text{-}EtPyH)_2[Mo_2O_4(\eta^2\text{-}C_2O_4)_2(4\text{-}EtPy)_2]$ (**4**) (4-EtPy = 4-ethylpyridine) and $(4\text{-}MePyH)_3[Mo_2O_4(\eta^2\text{-}C_2O_4)_2(4\text{-}MePy)_2]Br$ (**6**). The solution chemistry of the *trans*-$[Mo_2O_4(\eta^2\text{-}C_2O_4)_2Py_2]^{2-}$ anion was monitored by ^1H and ^{13}C variable temperature NMR spectroscopy and showed evidence of two processes: the substitution of a pyridine ligand for water, coupled with *cis*/*trans* isomerization. Both reactions were exploited in the preparation of *trans*-$(PyH)_2[Mo_2O_4(\eta^2\text{-}C_2O_4)_2(H_2O)_2]$ (**8**) from a water/methanol solution of *cis*-$(4\text{-}EtPyH)_2[Mo_2O_4(\eta^2\text{-}C_2O_4)_2(4\text{-}EtPy)_2]$ (**4**). *trans*-$(PyH)_2[Mo_2O_4(\eta^2\text{-}C_2O_4)_2(H_2O)_2]$ (**8**) was seen to react with methanol with the rupture of the molybdenum-to-oxalate bonds resulting in the cyclic octanuclear anion which crystallizes as a pyridinium salt, $(PyH)_2[Mo_8O_{16}(OCH_3)_8(\mu_8\text{-}C_2O_4)]\cdot 2CH_3OH$ (**9**). The compounds were fully characterized by X-ray structural analysis and IR spectroscopy. MO calculations were performed on the isomeric pair of $[Mo_2O_4(\eta^2\text{-}C_2O_4)_2(4\text{-}MePy)_2]^{2-}$ in order to establish their relative energies.

(© Wiley-VCH Verlag GmbH & Co. KGaA, 69451 Weinheim, Germany, 2005)

Introduction

The MoO^{3+} structural unit pervades in the chemistry of molybdenum in the +5 oxidation state.[1] The metal displays a marked tendency to dimerize through one or two oxygen bridges with the formation of the $\{Mo_2O_3\}^{4+}$ and $\{Mo_2O_4\}^{2+}$ dinuclear fragments. In the case of the $\{Mo_2O_4\}^{2+}$ structural core a direct interaction between two molybdenum atoms, conveniently described as a single metal–metal bond, is formed. The X-ray structural analyses of numerous $\{Mo_2O_4\}^{2+}$ compounds have shown that the basic structural properties of the $\{Mo_2O_4\}^{2+}$ core are independent of the ligands which complete the five- or sixfold coordination environments of the metal.[1,2] In the absence of ligands, the metal centers attain coordinative saturation through further assembly of $\{Mo_2O_4\}^{2+}$ units which share their originally μ_2-bridging oxo groups to form discrete oligonuclear clusters.[3] For instance, the association of four $\{Mo_2O_4\}^{2+}$ units through the agency of methoxide ions has been shown to produce two different types of octanuclear metal oxide cores: (i) a ring-like $\{Mo_8O_8(\mu_2\text{-}O)_8(\mu_2\text{-}OCH_3)_8\}$,[4,5] and (ii) a more compact $\{Mo_8O_8(\mu_3\text{-}O)_4(\mu_2\text{-}O)_4(\mu_3\text{-}OCH_3)_2(\mu_2\text{-}OCH_3)_4\}^{2+}$ core.[6] In the presence of suitable ligands, their ligation to the $\{Mo_2O_4\}^{2+}$ core normally precedes the self-assembly of dinuclear subunits. Multidentate oxygen donor ligands, in particular oxalate, with its well-known ability to adopt different coordination modes, can theoretically connect the dinuclear $\{Mo_2O_4\}^{2+}$ units into polymeric materials. True polymeric $\{Mo_2O_4\}^{2+}$ species where multidentate oxygen donor ligands link the dinuclear building blocks into infinite structures are extremely rare. The only examples are $[Mo_2O_4(C_2O_4)Cl_2]_n^{2n-}$ and $[Mo_2O_4(C_2O_4)_2(H_2PO_4)]_n^{3n-}$, with infinite chain structures, and $[Mo_2O_4(PO_4)(HPO_4)]_n^{3n-}$, with an infinite layer structure.[7–9] The bridging ligand in $[Mo_2O_4(C_2O_4)Cl_2]_n^{2n-}$ is oxalate, while in the other two polymers the phosphate

[a] Department of Chemistry and Chemical Technology, University of Ljubljana, Aškerčeva 5, 1000 Ljubljana, Slovenia.
Fax: +386-1-2419-220
E-mail: barbara.modec@guest.arnes.si
[b] Department of Chemistry, Syracuse University, Syracuse, New York 13244, USA
E-mail: jazubiet@syr.edu
Supporting information for this article is available on the WWW under http://www.eurjic.org or from the author.

 © 2005 Wiley-VCH Verlag GmbH & Co. KGaA, Weinheim **DOI: 10.1002/ejic.200500023**

serves to link the dinuclear subunits. The literature also reports on another type of polymeric compound where the repeating structural unit is a tetranuclear, cube-like metal oxide core with the formula $\{Mo_4O_4(\mu_3\text{-}O)_4\}^{4+}$ and the bridging ligands are the phosphates.[10] The cube-like core may be considered as the assembly of two $\{Mo_2O_4\}^{2+}$ units. Apparently, under the reaction conditions employed, the assembly of $\{Mo_2O_4\}^{2+}$ units took place first and was followed by phosphate coordination to the periphery of the $\{Mo_4O_4(\mu_3\text{-}O)_4\}^{4+}$ core.

We have demonstrated in our previous work that a series of complexes with the oxalate bonded in different ways can be obtained by tuning the oxalate-to-molybdenum ratio: $[Mo_8O_{16}(OCH_3)_8(\mu_8\text{-}C_2O_4)]^{2-}$ and $[Mo_2O_4(\mu_2\text{-}C_2O_4)Cl_2]_n^{2n-}$ when the oxalate amounts were small, and *trans*-$[Mo_2O_4(\eta^2\text{-}C_2O_4)Py_2]^{2-}$ and $[\{Mo_2O_4(\eta^2\text{-}C_2O_4)_2\}_2(\mu_4\text{-}C_2O_4)]^{6-}$ when the amounts of the ligand were large.[7,11] Furthermore, with an even larger amount of the oxalate, $\{Mo_2O_4\}^{2+}$ no longer formed, but rather the $\{Mo_2O_3\}^{4+}$ core with four coordination sites per metal center. The species obtained, $[Mo_2O_3(\eta^2\text{-}C_2O_4)_4]^{4-}$, thus contains two oxalato ligands per molybdenum. Although the X-ray structure analyses provided unambiguous characterization of the above-listed complexes, their solubility in water and their diamagnetic nature enabled NMR solution studies. The spectrum of the pyridine-coordinated complex *trans*-$[Mo_2O_4(\eta^2\text{-}C_2O_4)Py_2]^{2-}$ displays broadening of the pyridine resonances, which suggested substitution reactions in water solutions. Further studies were therefore initiated with the aim to provide an adequate explanation of these observations.

Results and Discussion

Structural Studies

Structures of Compounds with trans- and cis-$[Mo_2O_4(\eta^2\text{-}C_2O_4)_2(R\text{-}Py)_2]^{2-}$ Anions

The *trans* and *cis* geometric isomers of the $[Mo_2O_4(\eta^2\text{-}C_2O_4)_2(R\text{-}Py)_2]^{2-}$ ion are depicted in Figures 1 and 2, respectively. A central $\{Mo_2O_4\}^{2+}$ core, with a pyridine ligand and a bidentate oxalate completing the six-coordinate environment of each metal, may be recognized in both isomers. The position of the pair of pyridine ligands or oxalates can be either on the opposite sides of the plane defined by the Mo=O groups (*trans* isomer) or on the same side (*cis* isomer). The *trans* arrangement was observed for R-Py = pyridine (**1** and **7**), 3,5-lutidine (**2** and **3**), and 4-methylpyridine (**5**), while *cis* isomers were found for 4-ethylpyridine (**4**) and 4-methylpyridine (**6**). Both isomers were isolated only in the case of 4-methylpyridine. The two isomeric forms of the dinuclear anion differ in symmetry: neglecting the alkyl substituents on the pyridine rings, the *trans* isomer belongs to the C_2 point group, and the *cis* isomer to the C_s point group. However, the above-stated symmetry of the anions is rarely realized in solid-state structures. The exceptions are the *trans* anions in **1** and **2**, where the center of the $Mo(\mu_2\text{-}O)_2Mo$ group sits on a crystallographic twofold rotation axis and only half of the anion defines the asymmetric unit. The geometric parameters of the $\{Mo_2O_4\}^{2+}$ core in compounds **1**–**7** do not differ significantly and have similar values to those determined previously for many other $\{Mo_2O_4\}^{2+}$ compounds:[1,2] (i) a short Mo–Mo distance in the range 2.5430(3)–2.5559(5) Å for *trans* isomers and 2.5519(2)–2.5520(3) Å for *cis* isomers, signifying a single metal–metal bond, and (ii) a nonplanar $Mo(\mu_2\text{-}O)_2Mo$ moiety with fold angles in the ranges 149.5(2)–154.07(9)° and 152.17(5)–153.88(6)° for *trans* and *cis* isomers, respectively. The *trans* influence of the terminal oxo group is reflected in the nonequivalence of the two molybdenum-to-oxalate oxygen bond lengths. Relevant geometric parameters for the anions in **1**–**7** are summarized in Tables 1 and 2.

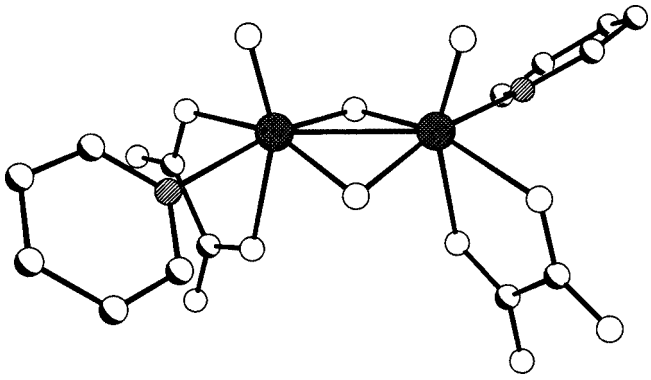

Figure 1. Ball-and-stick representation of the *trans*-$[Mo_2O_4(\eta^2\text{-}C_2O_4)_2(Py)_2]^{2-}$ anion in **1**. Mo sites are cross-hatched, nitrogen atoms are lined bottom left to top right, and oxygen atoms are small, unshaded and carbon atoms small, shaded spheres. The same drawing scheme is used throughout.

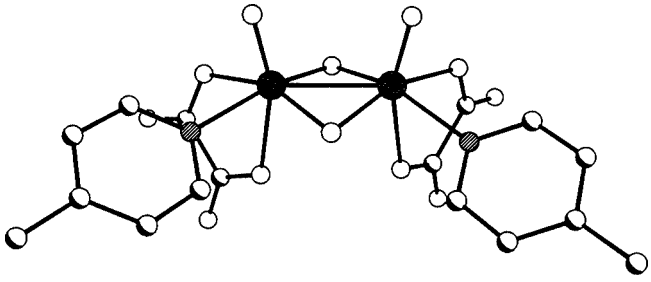

Figure 2. Ball-and-stick representation of the *cis*-$[Mo_2O_4(\eta^2\text{-}C_2O_4)_2(4\text{-}MePy)_2]^{2-}$ anion in **6**.

Interesting patterns of hydrogen bonds are observed for compounds **1**–**7**. The oxalato ligands, which can act as acceptors of hydrogen bonds, are matched with protonated pyridine molecules, and these are seen to form either a hydrogen bonding interaction with one noncoordinated oxygen atom from the oxalate or a bifurcated interaction with both noncoordinated oxygen atoms of the oxalate (Figure 3). The former type is present in **1**, with relatively short N···O distances of 2.642(2) Å, while the latter occurs in **2** and **5**. In the case of bifurcated hydrogen bonds, one is shorter than the other, as illustrated by **2**, where the N···O distances are 2.700(2) and 2.984(2) Å. Another type of hy-

 © 2005 Wiley-VCH Verlag GmbH & Co. KGaA, Weinheim

Table 1. Selected geometric parameters [Å, °] for *trans*-$[Mo_2O_4(\eta^2\text{-}C_2O_4)_2(R\text{-}Py)_2]^{2-}$.

Compound	Mo–O(oxalate)	Mo–Mo	Fold angle[a]	Mo–N
1	2.135(1) vs. 2.189(1)	2.5490(3)	149.56(4)	2.257(2)
2	2.132(1) vs. 2.185(1)	2.5525(3)	151.58(4)	2.266(2)
3	2.129(2) vs. 2.167(1)	2.5488(2)	149.87(4)	2.246(2)
				2.257(2)
	2.127(2) vs. 2.180(2)			
5[b]	2.135(3) vs. 2.195(3)	2.5559(5)	150.2(2)	2.246(3)
				2.260(3)
	2.140(3) vs. 2.198(3)			
	2.130(3) vs. 2.200(3)	2.5492(5)	149.5(2)	2.247(4)
				2.253(4)
	2.142(3) vs. 2.184(3)			
7	2.118(2) vs. 2.176(2)	2.5430(3)	154.07(9)	2.268(2)
				2.310(2)
	2.127(2) vs. 2.155(2)			

[a] Defined as the dihedral angle between two $Mo(\mu_2\text{-}O)_2$ planes. [b] Two sets of parameters are listed, one for each anion in the asymmetric unit.

Table 2. Selected geometric parameters [Å, °] for *cis*-$[Mo_2O_4(\eta^2\text{-}C_2O_4)_2(R\text{-}Py)_2]^{2-}$.

Compound	Mo–O(oxalate)	Mo–Mo	Fold angle	Mo–N
4	2.115(1) vs. 2.212(1)	2.5520(3)	153.88(6)	2.241(2)
				2.260(2)
	2.086(1) vs. 2.185(1)			
6	2.117(1) vs. 2.229(1)	2.5519(2)	152.17(5)	2.233(1)
				2.251(1)
	2.113(1) vs. 2.207(1)			

drogen-bonding interaction is observed for the *cis* isomers: the position of the protonated aromatic ring is such as to form two interactions to two closest coordinated oxygen atoms of two different oxalates (Figure 3). As exemplified by **4**, one of the two N···O distances is shorter than the other [2.728(2) vs. 2.977(2) Å]. In **3** and **7**, with no cations able to participate in hydrogen-bonding interactions, hydrogen bonds occur between the oxalato ligands and the water molecules of crystallization instead. For instance, in **3** each water molecule forms two hydrogen bonds to two noncoordinated oxalate oxygens from two different anions, with O···O distances of 2.904(3) and 2.986(3) Å. Infinite chains of alternating dinuclear anions and water molecules are thus formed (Figure 3). In **3** the chains propagate along the *b* axis.

Structure of trans-(PyH)$_2$[Mo$_2$O$_4$(η^2-C$_2$O$_4$)$_2$(H$_2$O)$_2$] (8)

The structure of **8** consists of dinuclear *trans*-$[Mo_2O_4(\eta^2\text{-}C_2O_4)_2(H_2O)_2]^{2-}$ anions (shown in Figure 4) and protonated pyridine molecules as countercations. The asymmetric unit

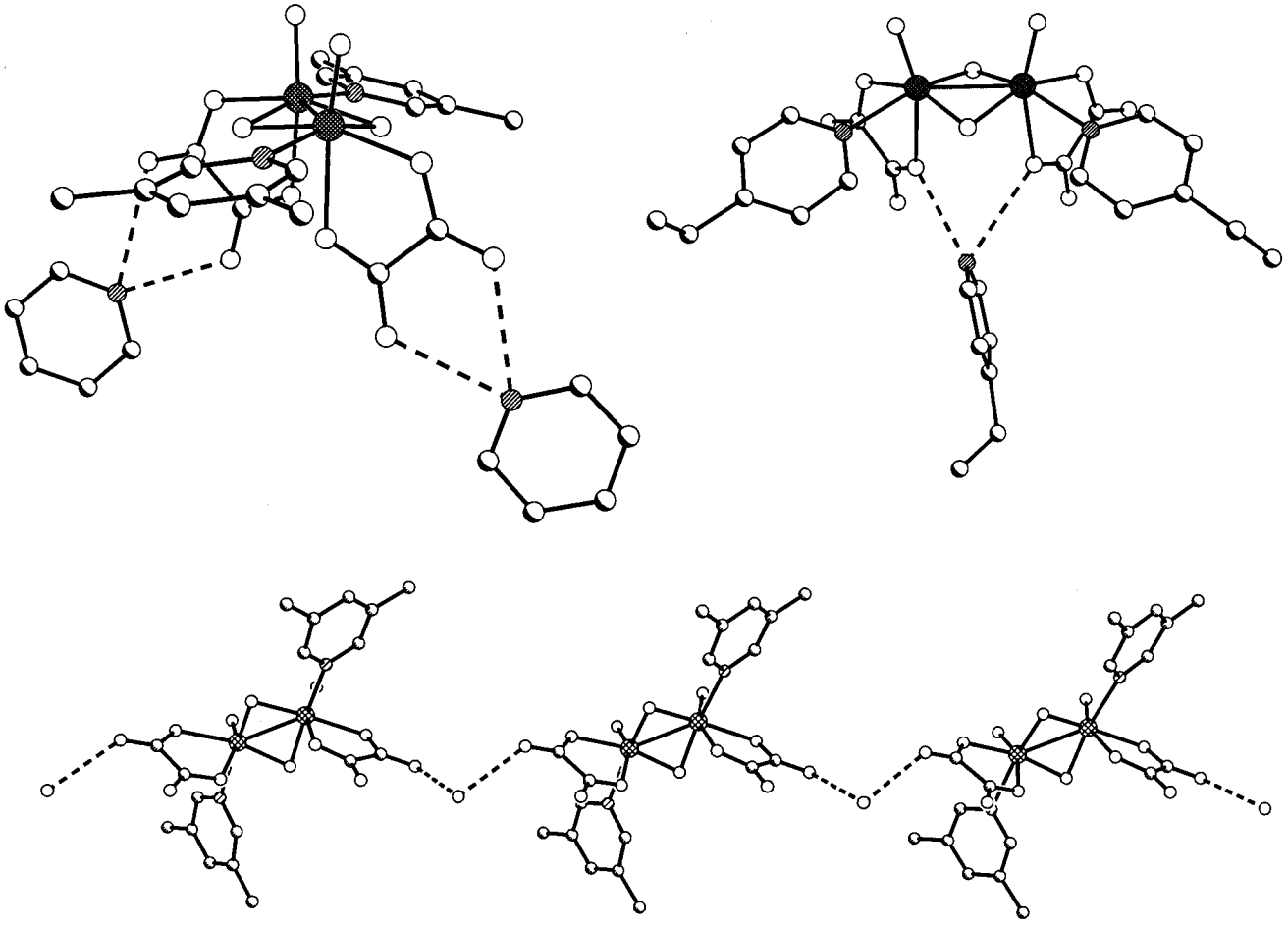

Figure 3. Types of hydrogen bonds in $[Mo_2O_4(\eta^2\text{-}C_2O_4)_2(R\text{-}Py)_2]^{2-}$ compounds.

 © 2005 Wiley-VCH Verlag GmbH & Co. KGaA, Weinheim

contains two dinuclear anions and four pyridinium cations. The bonding pattern within the two crystallographically independent *trans*-$[Mo_2O_4(\eta^2\text{-}C_2O_4)_2(H_2O)_2]^{2-}$ anions is basically the same (see Table 3). Owing to the *trans* influence of the terminal oxo group, one of the two molybdenum-to-oxalate oxygen bond lengths is short and the other is long. The molybdenum-to-water bond lengths are comparable to those observed for $[Mo_4O_8(OH)_2(H_2O)_2(C_4O_4)_2]^{2-}$ [2.148(6) Å],[12] $Ba[Mo_2O_4(\eta^2\text{-}C_2O_4)_2(H_2O)_2]\cdot 3H_2O$ [2.198(4) Å], and $Cs_2[Mo_2O_4(\eta^2\text{-}C_2O_4)_2(H_2O)_2]\cdot H_2O$ [2.12(1) and 2.15(1) Å].[13,14]

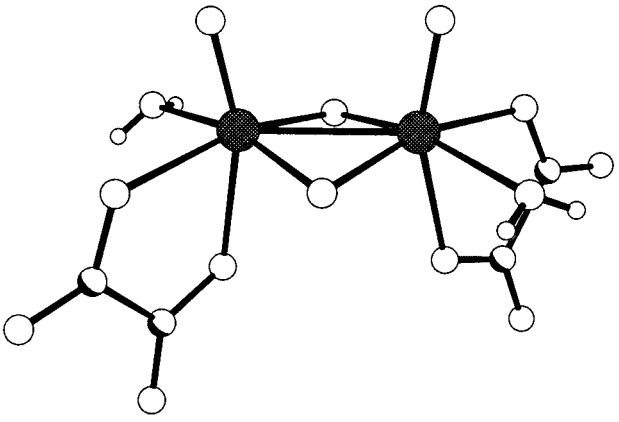

Figure 4. Drawing of the *trans*-$[Mo_2O_4(\eta^2\text{-}C_2O_4)_2(H_2O)_2]^{2-}$ anion in **8**.

Table 3. Selected geometric parameters [Å, °] for the *trans*-$[Mo_2O_4(\eta^2\text{-}C_2O_4)_2(H_2O)_2]^{2-}$ anion in **8**.[a]

Mo–O(oxalate)	Mo–Mo	Fold angle	Mo–O(water)
2.124(2) vs. 2.187(2)	2.5620(4)	153.6(1)	2.159(2)
			2.161(2)
2.143(2) vs. 2.164(2)			
2.115(2) vs. 2.197(2)	2.5626(4)	155.0(1)	2.160(2)
			2.150(2)
2.142(2) vs. 2.184(2)			

[a] Two sets of parameters are listed, one for each anion in the asymmetric unit.

A complicated pattern of hydrogen bonds is formed in **8**. Each water ligand forms two hydrogen bonds, one to the doubly-bridging oxo group of the adjacent anion, with O···O distances in the range 2.675(3)–2.720(3) Å, and one to the noncoordinated oxygen of the oxalate, also from the adjacent anion, with O···O distances in the range 2.643(3)–2.662(3) Å. Each anion forms a total of eight hydrogen bonds to four neighboring anions, two to each neighbor. Infinite layers that are coplanar with the (110) unit-cell plane are thus formed. Pyridinium cations are attached to the oxalate oxygen atoms on both sides of these layers through the agency of hydrogen bonds with lengths in the range 2.744(4)–3.125(5) Å.

The structure of the $[Mo_2O_4(\eta^2\text{-}C_2O_4)_2(H_2O)_2]^{2-}$ anion has been determined previously. It is of interest to note that the X-ray structure determination of *trans*-$Ba[Mo_2O_4(\eta^2\text{-}C_2O_4)_2(H_2O)_2]\cdot 3H_2O$ was also the first on a compound containing the $\{Mo_2O_4\}^{2+}$ unit and, as such, unambiguously confirmed the existence of the previously assumed $\{Mo_2O_4\}^{2+}$ structural core.[13] In contrast to the uniform tendency of Mo=O bonds to weaken bonds *trans* to themselves, no significant *trans* influence was observed. This phenomenon was ascribed to a low *trans* susceptibility of the oxalato ligand.[15] However, later structural determinations on the *trans*-$[Mo_2O_4(\eta^2\text{-}C_2O_4)_2(H_2O)_2]^{2-}$ anion clearly indicated the existence of a *trans* influence.[14] The pyridinium salt of this anion has also been reported, but with a different composition, $H(PyH)_3[Mo_2O_4(\eta^2\text{-}C_2O_4)_2(H_2O)_2]_2\cdot 2H_2O$.[16] In the case of the thio-bridged derivative of the dinuclear aqua-ligated anion, i.e., $[Mo_2O_2(\mu_2\text{-}S)_2(\eta^2\text{-}C_2O_4)_2(H_2O)_2]^{2-}$, the *cis* geometric isomer has been isolated as well. A *cis* arrangement of the ligands was observed in two caesium salts, *cis*-$KCs_3[Mo_2O_2S_2(\eta^2\text{-}C_2O_4)_2(H_2O)_2]_2\cdot 4H_2O$,[14] and *cis*-$NaCs_3[Mo_2O_2S_2(\eta^2\text{-}C_2O_4)_2(H_2O)_2]_2\cdot 6H_2O$.[17] These were the only known *cis* isomers prior to this study.

Structure of $(PyH)_2[Mo_8O_{16}(OCH_3)_8(\mu_8\text{-}C_2O_4)]\cdot 2CH_3OH$ (9)

Compound **9** crystallizes in a triclinic unit cell with one octanuclear anion $[Mo_8O_{16}(OCH_3)_8(\mu_8\text{-}C_2O_4)]^{2-}$, two protonated pyridine molecules as countercations, and two methanol molecules. The asymmetric unit consists of one half of the anion, with the other half generated by the inversion center located at the center of the ring. Each cyclic anion consists of four $\{Mo_2O_4\}^{2+}$ units arranged around the μ_8-oxalate and linked together by pairs of μ_2-bridging methoxides (Figure 5). The bonding pattern in the anion is very similar to that determined previously for $(Bu_4N)_2[Mo_8O_{16}(OCH_3)_8(\mu_8\text{-}C_2O_4)]$[18] and $(MeNC_5H_5)_2[Mo_8O_{16}(OCH_3)_8(\mu_8\text{-}C_2O_4)]$:[11] the Mo–Mo bonds are 2.5767(4)–2.5876(4) Å, the nonbonding Mo···Mo contacts

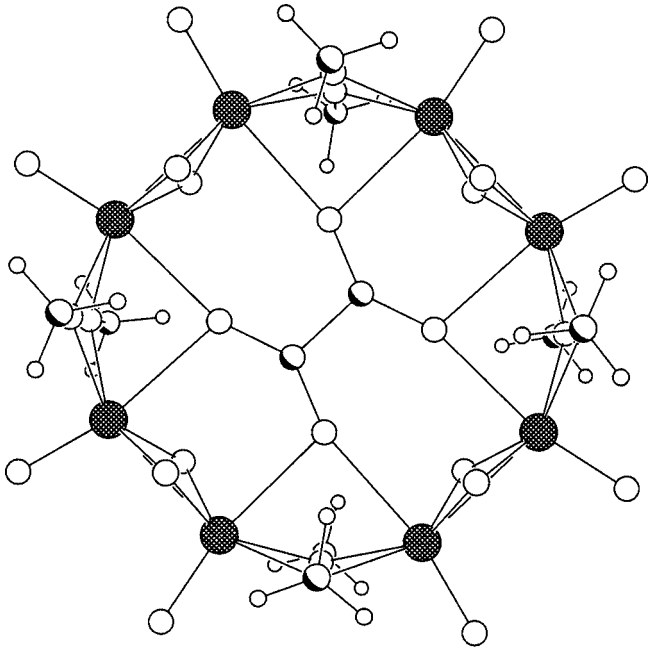

Figure 5. Drawing of the $[Mo_8O_{16}(OCH_3)_8(\mu_8\text{-}C_2O_4)]^{2-}$ anion in **9**.

 © 2005 Wiley-VCH Verlag GmbH & Co. KGaA, Weinheim

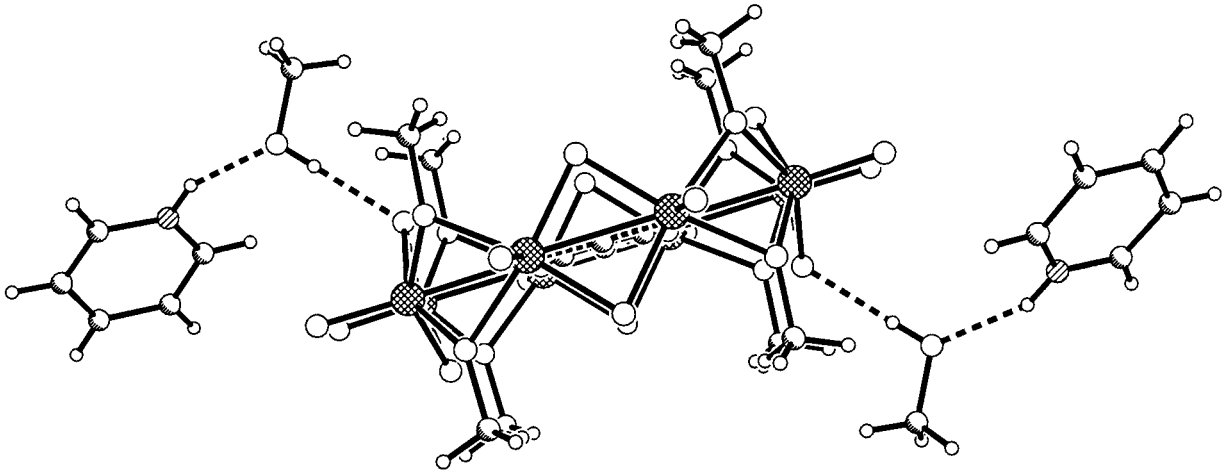

Figure 6. Octanuclear anion in **9** with a pair of hydrogen bonded methanol molecules and pyridinium cations.

spanning the methoxide bridges are 3.2489(4)–3.2548(4) Å, and the molybdenum-to-oxalate bond lengths are 2.357(3)–2.386(3) Å. Each octanuclear anion has a pair of methanol molecules linked by hydrogen bonds to the doubly-bridging oxo groups with lengths of 2.745(4) Å. Methanol participates in another hydrogen-bonding interaction with the protonated pyridine nitrogen, where it acts as the acceptor of the hydrogen bond (Figure 6). The corresponding O···N distance is 2.686(4) Å. Recently, a related octanuclear ring, $[Mo_8S_4O_{12}(OH)_8(C_2O_4)]^{2-}$, was reported. It is built of four $\{Mo_2O_2(\mu_2\text{-}O)(\mu_2\text{-}S)\}^{2+}$ subunits.[19] It supplements a series of octanuclear, cyclic anions built either of $\{Mo_2O_4\}^{2+}$ units or thio-bridged analogs, i.e., $\{Mo_2O_2(\mu_2\text{-}O)(\mu_2\text{-}S)\}^{2+}$ and $\{Mo_2O_2(\mu_2\text{-}S)_2\}^{2+}$.[17] This series confirms the ability of the structurally related, yet chemically markedly different, dinuclear cores to assemble in a similar manner with the formation of clusters with the same architectures. A structural similarity was observed with several other molybdenum(v) oxalato complexes, namely *trans*-$[Mo_2O_4(\eta^2\text{-}C_2O_4)_2(H_2O)_2]^{2-}$ and its thio analog *trans*-$[Mo_2O_2S_2(\eta^2\text{-}C_2O_4)_2(H_2O)_2]^{2-}$,[15,20] and a series of tetranuclear anions, i.e., $[\{Mo_2O_4(\eta^2\text{-}C_2O_4)_2\}_2(\mu_4\text{-}C_2O_4)]^{6-}$,[11] $[\{Mo_2O_3S(\eta^2\text{-}C_2O_4)_2\}_2(\mu_4\text{-}C_2O_4)]^{6-}$,[20,21] and $[\{Mo_2O_2S_2(\eta^2\text{-}C_2O_4)_2\}_2(\mu_4\text{-}C_2O_4)]^{6-}$.[17] It is of interest to note that the recently reported hexanuclear species $[\{Mo_2O_2S_2\}_3(OH)_4(\eta^2\text{-}C_2O_4)_2(\mu_6\text{-}C_2O_4)]^{4-}$ has only been observed for the $\{Mo_2O_2(\mu_2\text{-}S)_2\}^{2+}$ series of compounds.[22]

Synthetic Considerations

The basic reaction system inspected was that with a pyridine, oxalic acid, acetonitrile, an alcohol, and $(PyH)_5[MoOCl_4(H_2O)]_3Cl_2$ or $(PyH)[MoOBr_4]$. Both molybdenum starting materials possess labile sites (aqua and halo ligands), which in the mixtures of pyridine and methanol undergo a facile substitution chemistry with the formation of the $\{Mo_2O_4\}^{2+}$ structural unit or discrete clusters, as demonstrated before.[3] With a sufficient amount of oxalate, i.e. a ligand to metal ratio greater than 1, the formation of *trans*-$[Mo_2O_4(\eta^2\text{-}C_2O_4)_2Py_2]^{2-}$ takes place. The dinuclear anion was isolated in two salts, one with protonated pyridine molecules as countercations and the other as an *N*-methylpyridinium salt.[11] The two salts have different solubilities. While the pyridinium salt of *trans*-$[Mo_2O_4(\eta^2\text{-}C_2O_4)_2Py_2]^{2-}$ is only soluble in water, the *N*-methylpyridinium salt is also soluble in methanol. Contrary to our expectations, the *N*-alkylation of pyridine which occurs in the latter case did not turn out to be a general reaction:[23] it was observed only in the case of methanol. When other alcohols were used, such as ethanol, 2-propanol and *tert*-butanol, the only solid isolated was *trans*-$(PyH)_2[Mo_2O_4(\eta^2\text{-}C_2O_4)_2Py_2]$ (**1**). It is pertinent to note that the reaction mixture in the absence of alcohol also produced **1**. Although not required for the formation of dinuclear anions, the use of alcohols was justified by the fact that most oxalate salts, either with protonated or *N*-methylated pyridines, exhibit good alcohol solubility and the only product which crystallizes from the reaction mixture is that with the $[Mo_2O_4(\eta^2\text{-}C_2O_4)_2(R\text{-}Py)_2]^{2-}$ anion.

By using 4-methylpyridine in place of pyridine we hoped to prepare analogous compounds of *trans*-$[Mo_2O_4(\eta^2\text{-}C_2O_4)_2(4\text{-}MePy)_2]^{2-}$, which, provided they were also methanol soluble, would be a better choice for NMR solution studies as the anion $[Mo_2O_4(\eta^2\text{-}C_2O_4)_2(4\text{-}MePy)_2]^{2-}$ would not only display a simpler pattern of aromatic resonances than pyridine, but also a methyl singlet in a different spectral region which could serve as a probe for monitoring the substitution reactions. However, the reaction mixture described for the preparation of **6** afforded two crystalline phases whose identities were revealed by X-ray structure analyses as *trans*-$(4\text{-}MePyH)_2[Mo_2O_4(\eta^2\text{-}C_2O_4)_2(4\text{-}MePy)_2]\cdot 1/2(4\text{-}MePy)$ (**5**) and *cis*-$(4\text{-}MePyH)_3[Mo_2O_4(\eta^2\text{-}C_2O_4)_2(4\text{-}MePy)_2]Br$ (**6**). The described reaction shows that the formation of both isomeric forms of the $[Mo_2O_4(\eta^2\text{-}C_2O_4)_2(4\text{-}MePy)_2]^{2-}$ anion takes place simultaneously from the same reaction mixture, under the same conditions. MO calculations performed on the isomeric pair of $[Mo_2O_4(\eta^2\text{-}C_2O_4)_2(4\text{-}MePy)_2]^{2-}$ anions revealed insignificant differences in their energy. According to the most reliable approach of the three used, the B3LYP density functional with a 6-31G*

 © 2005 Wiley-VCH Verlag GmbH & Co. KGaA, Weinheim

basis set and pseudopotential, the *trans* isomer of $[Mo_2O_4(\eta^2\text{-}C_2O_4)_2(4\text{-}MePy)_2]^{2-}$ has a lower energy than the corresponding *cis* isomer by only 7.24 kJ mol^{-1}. With so small an energy difference, the formation of either is equally probable unless the pair differs in solubility. The stereochemistry of the product thus depends to a larger extent upon its solubility rather than on the reaction conditions employed.

NMR Solution Studies

The ^{1}H NMR spectrum of an aqueous solution of *trans*-$(PyH)_2[Mo_2O_4(\eta^2\text{-}C_2O_4)_2Py_2]$ (**1**) recorded at room temperature reveals six broad resonances in the aromatic spectral region, indicating that the pyridine ligands are involved in an exchange process. The temperature-dependent nature of these reactions was confirmed by recording the spectra at higher temperatures, at 10 K intervals up to 343 K, where the six resonances coalesce into three [δ = 8.25 (2 H, 3-H), 8.74 (1 H, 4-H), and 9.20 ppm (2 H, 2-H)] and the signals corresponding to pyridine, in coordinated and free form, and pyridinium cation became indistinguishable. The NMR spectra of aqueous solutions of *trans*-$(4\text{-}MePyH)_2[Mo_2O_4(\eta^2\text{-}C_2O_4)_2(4\text{-}MePy)_2]\cdot 1/2(4\text{-}MePy)$ (**5**) and *cis*-$(4\text{-}MePyH)_3[Mo_2O_4(\eta^2\text{-}C_2O_4)_2(4\text{-}MePy)_2]Br$ (**6**) gave evidence for another process. Apart from different values of integrals due to differences in the composition of **5** and **6**, their spectra are the same: a set of broad resonances in the aromatic spectral region and two, also broadened, methyl resonances. The isomerization of the *cis* into the *trans* isomer and vice versa was assumed to take place. The use of methanol-soluble *trans*-$(MeNC_5H_5)_2[Mo_2O_4(\eta^2\text{-}C_2O_4)_2Py_2]$ enabled NMR experiments at temperatures below 273 K and a quantitative evaluation of this process. Since the *N*-methylpyridinium cation does not participate in the exchange process in the way the pyridinium cation does, its resonances (three in the aromatic part of the spectrum and the methyl singlet) are consequently sharp and their integrals remain constant. Upon lowering the temperature, the previously broad pyridine resonances become sharper and at 243 K are resolved into seven signals, shown by COSY to belong to three sets, denoted as A, B and C (Figure 7). The signals C2, C3, and C4 were unambiguously identified by the addition of a small amount of pyridine as belonging to free pyridine.[24] Its presence can be accounted for only if the complex is partially dissociated, but in that case, an additional set of signals belonging to the mono-substituted $[Mo_2O_4(\eta^2\text{-}C_2O_4)_2Py(H_2O)]^{2-}$ is expected. Two isomeric forms are also possible for the mono-substituted complex. Since the environments of pyridine ligands in both are very similar, we assume that the pair is indistinguishable in the ^{1}H NMR spectrum. Accordingly, the mono-substituted complex is considered throughout the text as one species only. The bis(aqua)-ligated $[Mo_2O_4(\eta^2\text{-}C_2O_4)_2(H_2O)_2]^{2-}$ is also present; however this species is invisible in the ^{1}H NMR spectrum. The remaining four signals belong to sets A and B. Only the resonances of 2,6-H protons were clearly separated (A2 doublet centered at δ = 9.30 ppm and B2 doublet centered at δ = 9.16 ppm), while the resonances of the 4-H and 3,5-H protons were superimposed on each other (A4, B4 and A3, B3 signals). It is reasonable to expect that the immediate coordination environment is mostly experienced by the 2,6-H pair and to a significantly smaller extent by the 4-H proton or the 3,5-H pair. Set A was therefore assigned to belong to coordinated pyridine ligands in *cis*-$[Mo_2O_4(\eta^2\text{-}C_2O_4)_2Py_2]^{2-}$ and set B to *trans*-$[Mo_2O_4(\eta^2\text{-}C_2O_4)_2Py_2]^{2-}$ and the mono-substituted $[Mo_2O_4(\eta^2\text{-}C_2O_4)_2Py(H_2O)]^{2-}$ together. This assignment was based on the values of integrals of signals A2, B2, and C2[25] and the fact that the environment of the pyridine ligands in the *trans* isomer differs significantly from that in the *cis* isomer and that the environment of pyridine in the mono-substituted complex resembles that in the *trans* isomer very closely. On the basis of the chemical shifts of sets A and B, one can assume that the protons will resonate at lower field when the two pyridine rings are placed close to each other, as in the case of the *cis* isomer. In order to provide experimental support for the above-described assignment, two additional experiments were performed at 243 K. The solution of *trans*-$(MeNC_5H_5)_2[Mo_2O_4(\eta^2\text{-}C_2O_4)_2Py_2]$ was divided into two aliquots, of which one was repeatedly diluted and the other was titrated with pyridine. An increase in the concentration of free pyridine upon dilution was paralleled with the gradual decrease of the amount of coordinated pyridine, as monitored by the sum of integrals of signals A2 and B2 relative to the integral of the cation (Figure S1). The relative heights of A2 and B2 changed as well: a gradual decrease in the integral of A2 was observed, while B2 remained virtually constant within this concentration range. The signal B2 became slightly deformed, indicating two overlapping resonances. The pyridine titration had the opposite effect: the signal A2 started to gain in intensity, while B2 remained constant (Figure S2). The total amount of coordinated pyridine increased upon pyridine titration. The sum of integrals of signals A2 and B2 gravitated towards the integral of the cation. It was also observed that even with large additions of pyridine, {0.254 mmol of pyridine per 0.0405 mmol of $[Mo_2O_4(\eta^2\text{-}C_2O_4)_2Py_2]^{2-}$; Figure S2, spectrum f} the dissociation of pyridine was not entirely suppressed. Assuming that the extent of dissociation of the second pyridine ligand is very small and the amount of bis(aqua) complex negligible, approximate amounts of the mono-substituted complex and both major species, *cis*-$[Mo_2O_4(\eta^2\text{-}C_2O_4)_2Py_2]^{2-}$ and *trans*-$[Mo_2O_4(\eta^2\text{-}C_2O_4)_2Py_2]^{2-}$, could be calculated. Under these conditions, an excess of pyridine and a temperature of 243 K, around 8% of dinuclear complex exists in the mono-substituted form, while the *cis* isomer of $[Mo_2O_4(\eta^2\text{-}C_2O_4)_2Py_2]^{2-}$ exceeds its *trans* isomer in concentration by a factor of 1.8.

With the expectation that the oxalate carbon resonances would provide extra information about the major species in the solution, the ^{13}C NMR spectra were recorded. Of the three coordination sites of each metal in the $\{Mo_2O_4\}^{2+}$ moiety, the two sites that are in the *cis* position to the Mo=O group may be denoted as the equatorial ones, and

 © 2005 Wiley-VCH Verlag GmbH & Co. KGaA, Weinheim

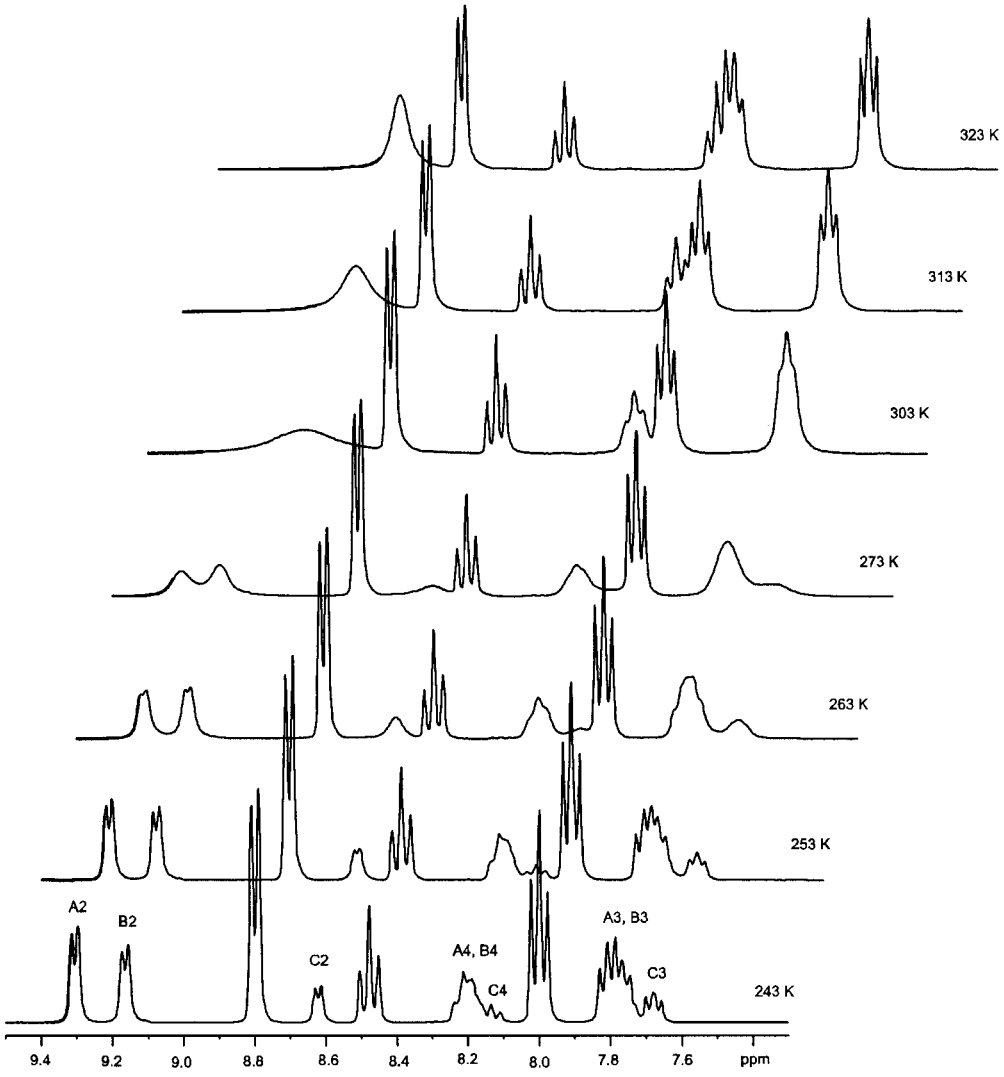

Figure 7. Variable temperature ^{1}H NMR spectra of *trans*-$(MeNC_5H_5)_2[Mo_2O_4(\eta^2\text{-}C_2O_4)_2Py_2]$. Labels A, B, and C refer to different pyridine species, and 2, 3, and 4 to pyridine protons 2,6, 3,5, and 4, respectively.

the remaining site, i.e. the one *trans* to the terminal oxo group, as the apical one. With the oxalate bonded in the bidentate manner as in the title compounds **1**–**8**, where one coordinated oxygen occupies the equatorial position and the other the apical position, the two oxalate carbon atoms are not chemically equivalent. Furthermore, the coordination environment of the oxalato ligand in *cis*-$[Mo_2O_4(\eta^2\text{-}C_2O_4)_2Py_2]^{2-}$ differs from that in *trans*-$[Mo_2O_4(\eta^2\text{-}C_2O_4)_2Py_2]^{2-}$. The room temperature ^{13}C NMR spectrum of *trans*-$(MeNC_5H_5)_2[Mo_2O_4(\eta^2\text{-}C_2O_4)_2Py_2]$ reveals two broad resonances at δ = 165.7 and 166.9 ppm, which resolved upon cooling to 243 K into three major ones at δ = 166.2, 166.5, and 167.7 ppm, and a minor one at δ = 167.5 ppm. However, no signal appeared at around δ = 173 ppm that would suggest the presence of free, noncoordinated oxalate.[26] In order to establish the dependence of the carbon oxalate frequencies upon the oxalate coordination mode, the ^{13}C NMR spectrum of $(MeNC_5H_5)_6[\{Mo_2O_4(\eta^2\text{-}C_2O_4)_2\}_2(\mu_4\text{-}C_2O_4)]$ was recorded. The oxalato ligands in the latter complex are bonded differently than in compounds **1**–**8** (Figure 8). Each of the four bidentate oxalates is bonded with both oxygen atoms in *cis* positions relative to the molybdenyl group, causing the chemical equivalence of the two carbon atoms. The carbon atoms of the tetraunidentate oxalate are equivalent as well. The ^{13}C NMR spectrum of $(MeNC_5H_5)_6[\{Mo_2O_4(\eta^2\text{-}C_2O_4)_2\}_2(\mu_4\text{-}C_2O_4)]$ reveals two resonances that could be associated with the oxalate moiety, an intense one at δ = 166.6 ppm and a weak one at δ = 173.0 ppm. The latter confirms the presence of free oxalate as a consequence of the rupture of the tetranuclear structure in solution. This result is not surprising in view of the results of the X-ray diffraction analysis, which showed that the bonds to μ_4-oxalate are weakened due to the labilizing *trans* influence of the four terminal oxo groups.[11] The cleavage of the tetranuclear anion produces two dinuclear $[Mo_2O_4(C_2O_4)_2]^{2-}$ fragments, each of which possesses two vacant coordination sites. Addition of one equivalent of pyridine per molybdenum results in a solution whose ^{1}H and ^{13}C NMR spectra are identical to the spectra of *trans*-$(MeNC_5H_5)_2[Mo_2O_4(\eta^2\text{-}C_2O_4)_2Py_2]$, differing only in the

 © 2005 Wiley-VCH Verlag GmbH & Co. KGaA, Weinheim

ratios between the *N*-methylpyridinium cation and pyridine. Since the bidentate oxalato ligands in *trans*-$[Mo_2O_4(\eta^2\text{-}C_2O_4)_2Py_2]^{2-}$ and in $[\{Mo_2O_4(\eta^2\text{-}C_2O_4)_2\}_2(\mu_4\text{-}C_2O_4)]^{6-}$ do not occupy the same coordination sites of the $\{Mo_2O_4\}^{2+}$ unit, the equivalence of the NMR spectra indicates rearrangements on the sites occupied by the oxalates as well. The conversion of one isomer into another presumably proceeds via a five-coordinate intermediate state (Scheme 1). The intermediate species in which the bidentate oxalate is coordinated to the two equatorial sites and the free apical position remains to be occupied with a unidentate ligand, i.e. pyridine or water, is also probable. Its relative instability may be explained in terms of the *trans* influence of the terminal oxo group: it is more favorable if the apical position, which is subject to the *trans* influence, is occupied by one terminus of the bidentate ligand rather than by a unidentate ligand. Binding of pyridine to the apical position is therefore weaker and the ligand exchange at this position too fast, even at low temperatures, to be observed in the NMR spectrum. The dissociation of coordinated pyridine as the rate-determining step of the whole process was confirmed by measuring the rates of exchange in the 253–293 K temperature interval in the ^{1}H NMR spectra of $[Mo_2O_4(\eta^2\text{-}C_2O_4)_2Py_2]^{2-}$ prepared in situ. The rate constants were measured on the basis of the line broadening of signal A2, which belongs to the pyridine ligands of *cis*-$[Mo_2O_4(\eta^2\text{-}C_2O_4)_2Py_2]^{2-}$.[27] The shape of signal A2 at each temperature was compared with the corresponding signal in the simulated spectrum. The activation parameters for the dissociation of pyridine from *cis*-$[Mo_2O_4(\eta^2\text{-}C_2O_4)_2Py_2]^{2-}$ were calculated from Eyring plot (Figure 9): $\Delta H^{\ddagger} = 82 \pm 4$ kJ mol^{-1} and $\Delta S^{\ddagger} = 79 \pm 14$ J mol^{-1} K^{-1}. The positive activation entropy is in agreement with the proposed dissociative mechanism. The determined value of the activation enthalpy could serve as a rough estimate of the molybdenum-to-pyridine bond strength.

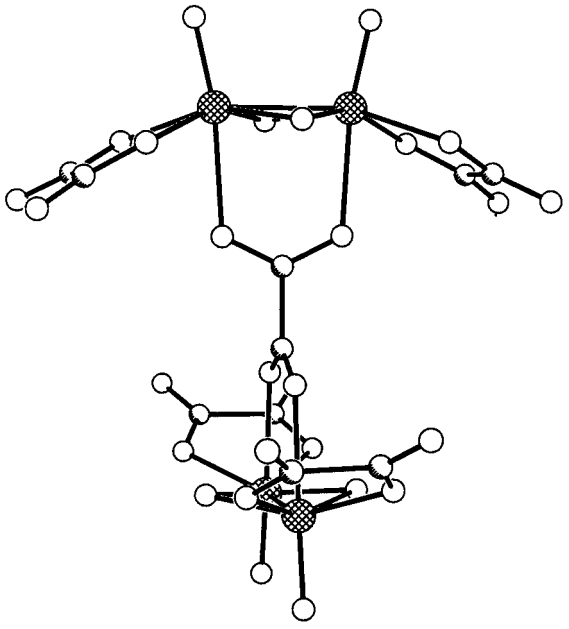

Figure 8. Oxalato ligands in $[\{Mo_2O_4(\eta^2\text{-}C_2O_4)_2\}_2(\mu_4\text{-}C_2O_4)]^{6-}$ adopt two binding modes: (i) the bidentate oxalates occupy the equatorial positions of the $\{Mo_2O_4\}^{2+}$ moiety, and (ii) the μ_4-oxalate occupies the apical positions of two $\{Mo_2O_4\}^{2+}$ moieties.[11]

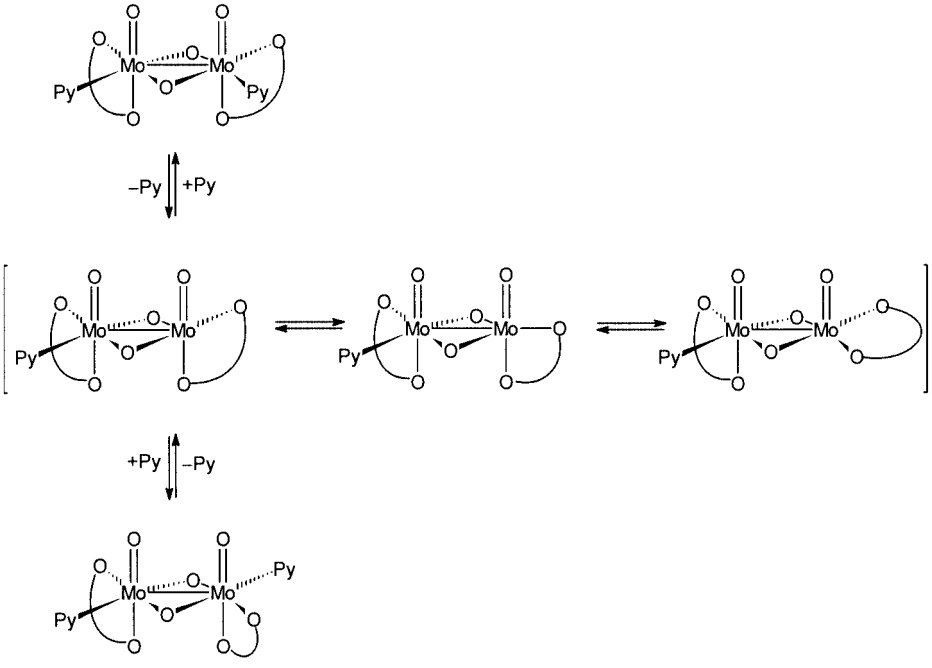

Scheme 1. Proposed *cis*/*trans* isomerization of $[Mo_2O_4(\eta^2\text{-}C_2O_4)_2Py_2]^{2-}$ with intermediate states included in square brackets. For simplicity, only the rearrangements on one metal center of the dinuclear anion are shown.

 © 2005 Wiley-VCH Verlag GmbH & Co. KGaA, Weinheim

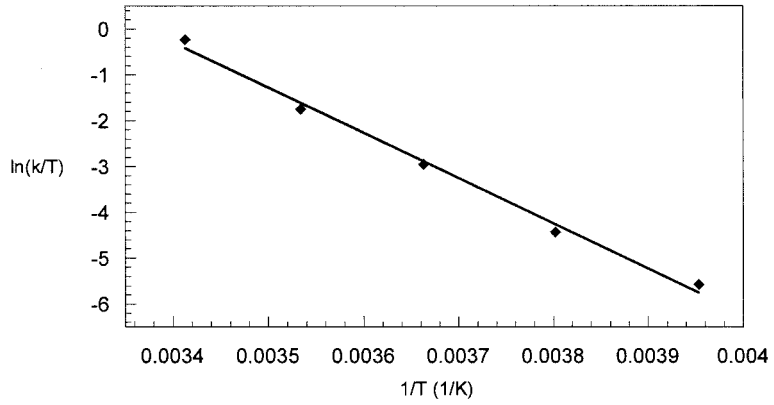

Figure 9. Eyring plot in the 253–293 K interval for the dissociation of pyridine from *cis*-$[Mo_2O_4(\eta^2\text{-}C_2O_4)_2Py_2]^{2-}$ in D_2O/CD_3OD solution. The solid line represents the equation $y = -9876 \cdot x + 33.284$ ($r^2 = 0.9934$) from the linear regression analysis.

Speculations on the Solution Chemistry of *cis*- and *trans*-$[Mo_2O_4(\eta^2\text{-}C_2O_4)_2(R\text{-}Py)_2]^{2-}$

Reports of oxalato complexes of molybdenum(v) date back almost a century, when the preparations of barium, potassium, and pyridinium salts of *trans*-$[Mo_2O_4(\eta^2\text{-}C_2O_4)_2(H_2O)_2]^{2-}$ were reported.[28] In a later study, the substitution chemistry of *trans*-$[Mo_2O_4(\eta^2\text{-}C_2O_4)_2(H_2O)_2]^{2-}$ with several ligands, including pyridine, was explored.[29] It was observed that the addition of pyridine to the sodium salt of *trans*-$[Mo_2O_4(\eta^2\text{-}C_2O_4)_2(H_2O)_2]^{2-}$ did not result in the coordination of pyridine; rather, the coordination sphere remained intact and the product was the pyridinium salt of the same anion. The substitution of water for pyridine in *trans*-$[Mo_2O_4(\eta^2\text{-}C_2O_4)_2(H_2O)_2]^{2-}$ was reported to be slow, with the equilibrium favoring the aqua complex. $(PyH)_2[Mo_2O_4(\eta^2\text{-}C_2O_4)_2Py_2]$ could only be prepared from $(PyH)_2[Mo_2O_4(\eta^2\text{-}C_2O_4)_2(H_2O)_2]$ upon prolonged refluxing in boiling pyridine. In reactions with some other ligands two other processes were suggested: a rupture of the doubly oxo-bridged structure to afford a singly oxo-bridged $\{Mo_2O_2(\mu_2\text{-}O)\}^{4+}$, and a substitution of the bidentate oxalate. Since the stereochemistry of the starting material was not known, no isomerization processes were proposed.

In line with the previous findings, we observed that both geometric isomers of $[Mo_2O_4(\eta^2\text{-}C_2O_4)_2(R\text{-}Py)_2]^{2-}$ react in water with the substitution of coordinated pyridine for water molecules, which are present in huge excess. This substitution is, as evidenced by NMR spectroscopy, accompanied by another process, namely isomerization of the *trans* isomer into the *cis* and vice versa. The crystallization of *trans*-$(PyH)_2[Mo_2O_4(\eta^2\text{-}C_2O_4)_2(H_2O)_2]$ (**8**) from a water/methanol solution of *cis*-$(4\text{-}EtPyH)_2[Mo_2O_4(\eta^2\text{-}C_2O_4)_2(4\text{-}EtPy)_2]$ (**4**) after the addition of pyridinium sulfate adds firm support for both processes. Slow evaporation of a solution of *trans*-$(PyH)_2[Mo_2O_4(\eta^2\text{-}C_2O_4)_2Py_2]$ (**1**) also afforded a dinuclear species with coordinated water – *trans*-$(PyH)_2[Mo_2O_4(\eta^2\text{-}C_2O_4)_2(H_2O)_2]$ (**8**). On the other hand, when the pyridinium cations in the solution of *trans*-$(PyH)_2[Mo_2O_4(\eta^2\text{-}C_2O_4)_2Py_2]$ (**1**) were neutralized with a strong base, followed by the addition of tetraphenylphosphonium bromide, no substitution occurred. The product was a water solvate – *trans*-$[(C_6H_5)_4P]_2[Mo_2O_4(\eta^2\text{-}C_2O_4)_2Py_2]\cdot H_2O$ (**7**) – which retains the original, *trans*, configuration of the ligands. Although water solutions of $[Mo_2O_4(\eta^2\text{-}C_2O_4)_2Py_2]^{2-}$ contain isomeric pairs of $[Mo_2O_4(\eta^2\text{-}C_2O_4)_2Py_2]^{2-}$, partially substituted $[Mo_2O_4(\eta^2\text{-}C_2O_4)Py(H_2O)]^{2-}$ and fully substituted, aqua-ligated $[Mo_2O_4(\eta^2\text{-}C_2O_4)_2(H_2O)_2]^{2-}$, we were not able either to isolate any of the two isomeric forms of $[Mo_2O_4(\eta^2\text{-}C_2O_4)_2Py(H_2O)]^{2-}$ or carry out the transformation of *trans*-$[Mo_2O_4(\eta^2\text{-}C_2O_4)_2Py_2]^{2-}$ into the *cis* isomeric form on a preparative scale.

In the context of the above-discussed reactions of $[Mo_2O_4(\eta^2\text{-}C_2O_4)_2Py_2]^{2-}$ anions in water, the reaction of *trans*-$(PyH)_2[Mo_2O_4(\eta^2\text{-}C_2O_4)_2(H_2O)_2]$ (**8**) with methanol has to be briefly mentioned. Although **8** is sparingly soluble in methanol, it slowly reacts with it. Evaporation of a lightly colored, saturated methanol solution yields orange crystals of $(PyH)_2[Mo_8O_{16}(OCH_3)_8(\mu_8\text{-}C_2O_4)]\cdot 2CH_3OH$ (**9**). The formation of this octanuclear anion supports several other processes. The coordinated oxalate is shown to be labile under certain conditions and can be substituted with other ligands, methoxide being such a ligand. Due to the rupture of the molybdenum-to-oxalate bonds, the oxalate content in the resulting species is greatly reduced. Since the variable temperature NMR studies were carried out in a water/methanol mixture, the formation of **9** shows that the role of methanol is not restricted solely to that of a solvent.

Vibrational Spectroscopy

The most relevant feature of the IR spectra of the title compounds concerns the carbon-oxygen frequencies of the oxalato ligand because they are diagnostic of its coordination mode.[30] Several absorption bands observed for ν_{as}(OCO) in the range 1710–1633 cm^{-1}, two bands for ν_s(OCO) in the range 1418–1249 cm^{-1}, and a single band for δ(OCO) at 789–780 cm^{-1} (see Table 4) are typical for the bidentate coordination mode found in complexes **1**–**8**. The observed frequencies agree very well with the data observed for $Ba[Mo_2O_4(\eta^2\text{-}C_2O_4)_2(H_2O)_2]\cdot 3H_2O$ {1710, 1680, 1653 [ν_{as}(OCO)], 1430, 1289 [ν_s(OCO)], 793 [δ(OCO)]}.[13] For

 © 2005 Wiley-VCH Verlag GmbH & Co. KGaA, Weinheim

the anion in **9** with all oxalate oxygen atoms engaged in coordination and metal–oxygen distances of approximately equal length, bands at 1661, 1650 [ν_{as}(OCO)], 1389, 1283 [ν_s(OCO)], and 814 [δ(OCO)] cm^{-1} were observed. Their frequencies do not differ from those reported for the *N*-methylpyridinium salt of this anion.[11]

Table 4. Characteristic oxalate absorptions [cm^{-1}] in $[Mo_2O_4(\eta^2\text{-}C_2O_4)_2(R\text{-}Py)_2]^{2-}$ compounds and in *trans*-$(PyH)_2[Mo_2O_4(\eta^2\text{-}C_2O_4)_2(H_2O)_2]$ (**8**).

Compound	ν_{as}(OCO)	ν_s(OCO)	δ(OCO)
1	1707, 1681, 1638	1418, 1279	789
2	1707, 1671	1415, 1275	780
3	1710, 1662	1376, 1294	785
4	1708, 1669, 1634	1417, 1272	785
5	1709, 1667	1414, 1275	784
6	1707, 1682, 1633	1417, 1277	789
7	1707, 1687, 1672	1376, 1249	784
8	1650[a]	1392, 1287	788

[a] A single, very broad band is displayed. The water bending mode absorbs in the same spectral region.

The antisymmetric and symmetric O–H stretching modes of the lattice water in **3** appear at 3533 and 3464 cm^{-1}, and in **7** at 3526 and 3396 cm^{-1}. Their frequencies fall in the usually observed region (3550–3200 cm^{-1}).[31] The absorptions assigned to coordinated water in the spectrum of **8** are seen as very broad bands. A broad band centered at about 2900 cm^{-1} may be attributed to both types of O–H stretching vibrations. The typical region for the water bending vibration (1630–1600 cm^{-1})[31] overlaps with the ν_{as}(OCO) vibration of the oxalate.

Conclusions

A series of compounds containing the *trans* or *cis* isomeric form of the $[Mo_2O_4(\eta^2\text{-}C_2O_4)_2(R\text{-}Py)_2]^{2-}$ anion has been prepared. *trans*-$(4\text{-}MePyH)_2[Mo_2O_4(\eta^2\text{-}C_2O_4)_2(4\text{-}MePy)_2]\cdot 1/2(4\text{-}MePy)$ (**5**) and *cis*-$(4\text{-}MePyH)_3[Mo_2O_4(\eta^2\text{-}C_2O_4)_2(4\text{-}MePy)_2]Br$ (**6**) are the only examples where both isomers were isolated. The stepwise substitution of pyridine for water in solutions of $[Mo_2O_4(\eta^2\text{-}C_2O_4)_2Py_2]^{2-}$ produces the mono-substituted $[Mo_2O_4(\eta^2\text{-}C_2O_4)_2Py(H_2O)]^{2-}$, whose presence was detected by NMR spectroscopy, and the bis-(aqua)-ligated $[Mo_2O_4(\eta^2\text{-}C_2O_4)_2(H_2O)_2]^{2-}$. The isolation of *trans*-$(PyH)_2[Mo_2O_4(\eta^2\text{-}C_2O_4)_2(H_2O)_2]$ (**8**) from a solution of *cis*-$(4\text{-}EtPyH)_2[Mo_2O_4(\eta^2\text{-}C_2O_4)_2(4\text{-}EtPy)_2]$ (**4**) adds firm support for simultaneous *cis*/*trans* isomerization accompanying the substitution reactions. The latter result is in accordance with the MO calculations on the *trans* and *cis* isomer of $[Mo_2O_4(\eta^2\text{-}C_2O_4)_2(4\text{-}MePy)_2]^{2-}$, which revealed insignificant differences in their energy.

Experimental Section

General Remarks: Reagents were purchased from Aldrich and used without further purification. $(PyH)_5[MoOCl_4(H_2O)]_3Cl_2$ and $(PyH)[MoOBr_4]$ were prepared by published procedures.[32,33] Pyridinium sulfate was isolated as a white solid by neutralizing sulfuric acid with two equiv. of pyridine and drying in vacuo. The solvothermal reactions were carried out in sealed glass tubes under autogenous pressure. Several synthetic procedures are described for some compounds. The IR and far-IR spectra were measured on solid samples as Nujol or poly(chlorotrifluoroethylene) mulls using Perkin–Elmer 2000 series FT-IR spectrometer. ^1H and ^{13}C spectra were recorded on a Bruker Avance DPX 300 spectrometer referenced to the solvent. Elemental analyses were performed by the Chemistry Department service at the University of Ljubljana. The compounds **1**, **2**, **4**, and **6** were found to decompose on prolonged exposure to the air.

NMR Spectroscopy of *trans*-$(MeNC_5H_5)_2[Mo_2O_4(\eta^2\text{-}C_2O_4)_2Py_2]$: *trans*-$(MeNC_5H_5)_2[Mo_2O_4(\eta^2\text{-}C_2O_4)_2Py_2]$ (63 mg, 0.0809 mmol), prepared following the previously published procedure,[11] was dissolved in 0.6 mL of D_2O/CD_3OD mixture (1:1 volume ratio). The variable temperature ^1H NMR spectra (the aromatic region) are shown in Figure 7. The signals for the *N*-methylpyridinium cation in the spectrum recorded at 243 K are at δ = 4.36 (s, 3 H, $CH_3NC_5H_5$), 8.00 (m, 2 H, 3-H), 8.48 (t, J = 7.8 Hz, 1 H, 4-H), and 8.80 (d, J = 5.9 Hz, 2 H, 2-H) ppm. The assignments of other signals are described in the text.

NMR Spectroscopy of $(MeNC_5H_5)_6[\{Mo_2O_4(\eta^2\text{-}C_2O_4)_2\}_2(\mu_4\text{-}C_2O_4)]$: $(MeNC_5H_5)_6[\{Mo_2O_4(\eta^2\text{-}C_2O_4)_2\}_2(\mu_4\text{-}C_2O_4)]$ was prepared following the previously published procedure.[11] ^1H NMR (D_2O, 300 MHz): δ = 4.35 (s, 3 H, $CH_3NC_5H_5$), 8.00 (m, 2 H, 3-H), 8.48 (t, J = 7.9 Hz, 1 H, 4-H), 8.73 (d, J = 5.9 Hz, 2 H, 2-H) ppm. ^{13}C NMR (D_2O, 75 MHz): δ = 48.5 ($CH_3NC_5H_5$), 128.4 (C-3), 145.4 (C-2), 145.6 (C-4), 166.6 (coordinated oxalate), 173.0 (free oxalate) ppm.

NMR Determination of the Exchange Rates: $(MeNC_5H_5)_6[\{Mo_2O_4(\eta^2\text{-}C_2O_4)_2\}_2(\mu_4\text{-}C_2O_4)]$ (22 mg, 14.5 mmol) was dissolved in D_2O (0.3 mL), followed by the addition of CD_3OD (0.3 mL). An excess of pyridine (15.4 mg, 0.1927 mmol) was added to this solution. The relative amounts of *cis*-$[Mo_2O_4(\eta^2\text{-}C_2O_4)_2Py_2]^{2-}$, *trans*-$[Mo_2O_4(\eta^2\text{-}C_2O_4)_2Py_2]^{2-}$, and $[Mo_2O_4(\eta^2\text{-}C_2O_4)_2Py(H_2O)]^{2-}$ were calculated from the integrals of the corresponding signals. The spectra were measured at 10 K intervals in the temperature range 233–333 K.

***trans*-$(PyH)_2[Mo_2O_4(\eta^2\text{-}C_2O_4)_2Py_2]$ (1):** A glass tube was charged with $(PyH)_5[MoOCl_4(H_2O)]_3Cl_2$ (50 mg, 0.117 mmol of Mo), $H_2C_2O_4\cdot 2H_2O$ (20 mg, 0.159 mmol), acetonitrile (0.5 mL), *tert*-butanol (1 mL), and pyridine (4 mL). The tube was sealed and heated for 90 h in an electric oven maintained at 115 °C. The tube was then allowed to cool slowly to room temperature. Orange, block-shaped crystals of **1** were collected by filtration and washed with dichloromethane. Yield: 73% (32 mg). *Note.* Other alcohols (ethanol, 2-propanol) can be used instead of *tert*-butanol. The yields are comparable (77% for the reaction mixture with ethanol and 80% for the reaction mixture with 2-propanol). IR: $\tilde{\nu}$ = 3130 cm^{-1} (w), 3089 (w), 3053 (w), 2168 (w), 2066 (w), 1707 (vvs), 1681 (vvs), 1638 (vvs), 1542 (vs), 1487 (vvs), 1418 (vvs), 1279 (vvs), 1224 (vs), 1203 (vs), 1171 (w), 1137 (w), 1078 (m), 1046 (m), 1016 (m), 997 (m), 955 (vvs), 935 (vs), 907 (s), 789 (vvs), 773 (vvs), 760 (vs), 742 (vvs), 691 (vvs), 641 (m), 603 (vs), 528 (s), 491 (vs), 477 (s), 441 (m), 400 (m), 361 (s), 341 (w), 318 (s), 291 (w), 279 (w), 269 (m), 247 (m), 228 (w) cm^{-1}. $C_{24}H_{22}Mo_2N_4O_{12}$ (750.3): calcd. C 38.42, H 2.96, N 7.47; found C 38.18, H 2.99, N 7.30.

***trans*-$(PyH)_2[Mo_2O_4(\eta^2\text{-}C_2O_4)_2(3,5\text{-}Lut)_2]$ (2):** $(PyH)_5[MoOCl_4(H_2O)]_3Cl_2$ (200 mg, 0.466 mmol of Mo) and $H_2C_2O_4\cdot 2H_2O$ (200 mg, 1.59 mmol) were added to a mixture of 3,5-lutidine (2 cm^3), methanol (2.5 mL), and acetonitrile (0.5 mL) in an Erlenmeyer flask. The reaction mixture was allowed to stand in the

 © 2005 Wiley-VCH Verlag GmbH & Co. KGaA, Weinheim

closed flask under ambient conditions for ten days. Orange crystals of **2** were collected by filtration and washed with dichloromethane. Yield: 24% (45 mg). IR: $\tilde{\nu}$ = 3061 cm^{-1} (w), 1707 (vvs), 1671 (vvs), 1604 (s), 1595 (s), 1523 (s), 1482 (vs), 1415 (vs), 1325 (w), 1275 (vvs), 1248 (w), 1198 (m), 1169 (w), 1153 (vvs), 1093 (w), 1044 (m), 1022 (m), 1003 (m), 952 (vvs), 938 (vs), 907 (s), 875 (m), 780 (vvs), 768 (vvs), 740 (vvs), 705 (s), 694 (vs), 637 (w), 608 (m), 540 (w), 529 (m), 489 (vs), 480 (s), 430 (w), 397 (m), 363 (s), 345 (m), 317 (s), 256 (s) cm^{-1}. $C_{28}H_{30}Mo_2N_4O_{12}$ (806.4): calcd. C 41.70, H 3.75, N 6.95, found C 41.49, H 3.86, N 6.82.

***trans*-[$MeNC_5H_3(Me)_2]_2[Mo_2O_4(\eta^2\text{-}C_2O_4)_2$(3,5-Lut)$_2]\cdot H_2O$ (3):** A glass tube was charged with (PyH)[$MoOBr_4$] (120 mg, 0.235 mmol), $H_2C_2O_4\cdot 2H_2O$ (100 mg, 0.794 mmol), tetraphenylphosphonium bromide (100 mg, 0.239 mmol), 3,5-lutidine (4 mL), methanol (0.5 mL), and acetonitrile (0.5 mL). The tube was sealed and heated for 90 h in an electric oven maintained at 115 °C. The reaction mixture was then allowed to cool slowly to room temperature. Orange, block-like crystals of **3** were separated manually from unidentified crystalline material of a light yellow color, probably the *N*-methyl-3,5-lutidinium salt of oxalic acid. Yield: 49% (52 mg). IR: $\tilde{\nu}$ = 3533 cm^{-1} (w), 3464 (w), 1710 (vvs), 1662 (vvs), 1376 (s), 1307 (s), 1294 (s), 1254 (vs), 1215(w), 1205(m), 1185 (m), 1153 (s), 1052 (m), 1039 (m), 1028 (m), 943 (vvs), 923 (vs), 899 (vs), 867 (s), 785 (vs), 772 (vs), 739 (vs), 724 (vs), 699 (m), 677 (vs), 612 (w), 588 (w), 525 (m), 474 (vs), 416 (w), 397 (m), 353 (m), 314 (s), 296 (w), 277 (m), 261 (w) cm^{-1}. $C_{34}H_{44}Mo_2N_4O_{13}$ (908.6): calcd. C 44.95, H 4.88, N 6.17, found C 44.87, H 4.69, N 6.03.

***cis*-(4-EtPyH)$_2$[$Mo_2O_4(\eta^2\text{-}C_2O_4)_2$(4-EtPy)$_2$] (4). Procedure a:** A glass tube was charged with $(PyH)_5[MoOCl_4(H_2O)]_3Cl_2$ (50 mg, 0.117 mmol of Mo), $H_2C_2O_4\cdot 2H_2O$ (20 mg, 0.159 mmol), and 4-ethylpyridine (3 mL). The tube was sealed and heated for 90 h in an electric oven maintained at 115 °C. The tube was then allowed to cool slowly to room temperature. Large, orange, plate-like crystals of **4** were collected by filtration and washed with dichloromethane. Yield: 79% (40 mg). **Procedure b:** A glass tube was charged with (PyH)[$MoOBr_4$] (75 mg, 0.147 mmol), $H_2C_2O_4\cdot 2H_2O$ (20 mg, 0.159 mmol), 4-ethylpyridine (3 mL), 2-propanol (0.5 mL), and acetonitrile (0.5 mL). The tube was sealed and heated for 90 h in an electric oven maintained at 115 °C. The tube was then allowed to cool slowly to room temperature. Large, orange, plate-like crystals of **4** were collected by filtration and washed with dichloromethane. Yield: 82% (52 mg). IR: $\tilde{\nu}$ = 3068 cm^{-1} (w), 2922 (m), 2851 (m), 1708 (s), 1669 (vs), 1634 (vs), 1615 (vs), 1495 (m), 1455 (w), 1417 (s), 1314 (w), 1272 (m), 1224 (w), 1201 (m), 1108 (w), 1066 (m), 1028 (m), 946 (vvs), 930 (s), 904 (m), 833 (vs), 785 (vs), 740 (vs), 720 (m), 662 (w), 647 (w), 580 (w), 560 (w), 521 (w), 486 (s), 404 (w), 362 (m), 347 (w), 313 (s), 285 (w), 273 (w), 254 (m) cm^{-1}. $C_{32}H_{38}Mo_2N_4O_{12}$ (862.5): calcd. C 44.56, H 4.44, N 6.50, found C 44.34, H, 4.38, N, 6.41.

***trans*-(4-MePyH)$_2$[$Mo_2O_4(\eta^2\text{-}C_2O_4)_2$(4-MePy)$_2$]·1/2(4-MePy) (5):** A glass tube was charged with $(PyH)_5[MoOCl_4(H_2O)]_3Cl_2$ (50 mg, 0.117 mmol of Mo), $H_2C_2O_4\cdot 2H_2O$ (50 mg, 0.397 mmol), 4-methylpyridine (4 mL), 2-propanol (0.5 mL), and acetonitrile (0.5 mL). The tube was sealed and heated for 90 h in an electric oven maintained at 115 °C. The tube was then allowed to cool slowly to room temperature. Yellow, needle-shaped crystals of **5** were collected by filtration. Yield (based on the dried sample): 32% (15 mg). IR: $\tilde{\nu}$ = 3512 cm^{-1} (w), 3416 (w), 3062 (m), 1709 (vvs), 1667 (vvs), 1501 (vvs), 1462 (vvs), 1414 (vs), 1306 (w), 1275 (s), 1230 (m), 1212 (m), 1200 (m), 1097 (w), 1071 (m), 1032 (s), 1010 (m), 950 (vvs), 904 (m), 830 (m), 813 (vs), 784 (vvs), 742 (vvs), 668 (w), 522 (m), 491 (vs), 402 (w), 363 (m), 346 (w), 315 (s), 251 (m), 238 (w) cm^{-1}. *Note.* No elemental analysis was performed, since the crystals lost the 4-methylpyridine solvent of crystallization when removed from the solution.

***cis*-(4-MePyH)$_3$[$Mo_2O_4(\eta^2\text{-}C_2O_4)_2$(4-MePy)$_2$]Br (6). Procedure a:** A glass tube was charged with (PyH)[$MoOBr_4$] (120 mg, 0.235 mmol), $H_2C_2O_4\cdot 2H_2O$ (200 mg, 1.59 mmol), 4-methylpyridine (4 mL), 2-propanol (0.5 mL), and acetonitrile (0.5 mL). The tube was sealed and heated for 90 h in an electric oven maintained at 115 °C. After cooling to room temperature, the reaction mixture consisted of a clear, orange solution. Over a period of two weeks two types of crystals grew from the solution: yellow, needle-like crystals of **5** and orange, block-like crystals of **6**. The total amount of solid material was 62 mg. **Procedure b:** A glass tube was charged with (PyH)[$MoOBr_4$] (120 mg, 0.235 mmol), $H_2C_2O_4\cdot 2H_2O$ (100 mg, 0.794 mmol), and 4-methylpyridine (4 mL). The tube was sealed and heated for 90 h in an electric oven maintained at 115 °C. The reaction mixture was allowed to cool slowly to room temperature. Orange, block-shaped crystals of **6** were separated manually from the colorless, needle-like crystals of 4-methylpyridinium oxalate. Yield: 71% (82 mg). IR: $\tilde{\nu}$ = 2921 cm^{-1} (m), 2846 (m), 1707 (vvs), 1682 (vvs), 1633 (vvs), 1503 (vs), 1417 (vs), 1307 (s), 1277 (vs), 1232 (m), 1202 (m), 1098 (m), 1059 (m), 1032 (s), 1006 (m), 949 (vvs), 932 (vs), 904 (m), 813 (vs), 789 (vs), 748 (vs), 722 (vs), 666 (w), 651 (w), 553 (m), 519 (s), 503 (vs), 483 (vvs), 476 (vvs), 402 (m), 365 (s), 349 (m), 321 (vs), 294 (m), 273 (w), 247 (m), 218 (w) cm^{-1}. $C_{34}H_{38}BrMo_2N_5O_{12}$ (980.5): calcd. C 41.65, H 3.91, N 7.14, found C 41.58, H 3.64, N 6.98.

***trans*-[$(C_6H_5)_4P]_2[Mo_2O_4(\eta^2\text{-}C_2O_4)_2Py_2]\cdot H_2O$ (7):** Compound **1** (250 mg, 0.333 mmol) was dissolved in water (10 mL). After the addition of potassium hydroxide (42 mg, 0.749 mmol), the clear, orange solution turned cloudy. The solution was then filtered and a solution of tetraphenylphosphonium bromide (315 mg, 0.754 mmol) in acetonitrile (7 mL) was added to the filtrate. The volume of the filtrate was reduced to one half by pumping on the vacuum line. The concentrated solution was kept in a closed flask at ambient conditions. Red crystals of **7** grew after two days and were collected by filtration and washed with dichloromethane. Yield: 41% (178 mg). IR: $\tilde{\nu}$ = 3526 cm^{-1} (w), 3396 (w), 1707 (m), 1687 (s), 1672 (vs), 1642 (s), 1603 (m), 1581 (m), 1481 (m), 1436 (s), 1376 (s), 1314 (w), 1249 (m), 1218 (m), 1160 (w), 1107 (vs), 1069 (w), 1042 (w), 1015 (w), 997 (m), 937 (vs), 919 (m), 898 (m), 845 (w), 784 (s), 755 (s), 743 (s), 721 (vs), 691 (vs), 634 (w), 528 (vs), 471 (m), 317 (m), 264 (w). $C_{62}H_{52}Mo_2N_2O_{13}P_2$ (1286.9): calcd. C 57.87, H 4.07, N 2.18, found C 57.68, H 4.28, N 2.09.

***trans*-(PyH)$_2$[$Mo_2O_4(\eta^2\text{-}C_2O_4)_2(H_2O)_2$] (8):** Compound **1** (250 mg, 0.333 mmol) was dissolved in water (10 mL). Methanol (10 mL) and pyridinium sulfate (256 mg, 1.00 mmol) were then added to the clear, orange solution. The solution was left in an open beaker under ambient conditions. Within a few hours orange crystals of **8** started to deposit from the solution. The crystals were collected by filtration and washed with dichloromethane. Yield: 67% (140 mg). IR: $\tilde{\nu}$ = 2900 cm^{-1} (br), 1650 (vvs), 1483 (s), 1418 (s), 1392 (s), 1287 (s), 1258 (s), 1197 (m), 1166 (m), 1058 (m), 1007 (m), 964 (vvs), 945 (vvs), 910 (vs), 856 (m), 788 (vs), 750 (vs), 722 (vs), 678 (vs), 609 (s), 588 (s), 534 (s), 490 (vvs), 447 (m), 393 (m), 350 (w), 311 (s), 260 (s), 180 (w) cm^{-1}. $C_{14}H_{16}Mo_2N_2O_{14}$ (628.2): calcd. C 26.77, H 2.57, N 4.46, found C 26.71, H 2.49, N 4.49.

Isomerization of *cis*-(4-EtPy)$_2$[$Mo_2O_4(\eta^2\text{-}C_2O_4)_2$(4-EtPy)$_2$] (4): Compound **4** (140 mg, 0.162 mmol) was dissolved in water (7.5 mL) and methanol (7.5 mL) and pyridinium sulfate (130 mg, 0.508 mmol) were added to the solution. The solution was allowed to stand in an open beaker under ambient conditions for three

 © 2005 Wiley-VCH Verlag GmbH & Co. KGaA, Weinheim

days. Orange crystals of **8** were collected by filtration and washed with dichloromethane. Yield: 81% (82 mg).

$(PyH)_2[Mo_8O_{16}(OCH_3)_8(\mu_8\text{-}C_2O_4)]\cdot 2CH_3OH$ (9): Compound **8** (220 mg, 0.350 mmol) was added to methanol (15 mL) in an Erlenmeyer flask, which was stoppered and the reaction mixture stirred under ambient conditions for three days. The unreacted starting material (150 mg) was filtered off and the resulting filtrate was allowed to stand in an open beaker under ambient conditions overnight. Orange, needle-shaped crystals of **9** grew from the solution. Yield (based on the dried product and taking into the account only the reacted starting material): 84% (37 mg). IR: $\tilde{\nu}$ = 2925 cm^{-1} (s), 2851 (m), 2825 (m), 1661 (vs), 1650 (m), 1610 (w), 1528 (m), 1484 (m), 1444 (m), 1389 (s), 1283 (w), 1253 (w), 1200 (w), 1168 (m), 1027 (vs), 969 (vvs), 814 (vs), 750 (vvs), 721 (vvs), 676 (m), 539 (vvs), 462 (vvs), 380 (m), 339 (m), 275 (s), 221 (m) cm^{-1}. *Note.* No elemental analysis was performed since the crystals quickly lost the methanol solvent of crystallization when removed from the solution.

Computational Details: MO calculations on the *trans* and *cis* isomeric forms of $[Mo_2O_4(\eta^2\text{-}C_2O_4)(4\text{-}MePy)_2]^{2-}$ were performed in order to determine their relative stabilities using three different methods: (i) semi-empirical PM3, (ii) ab initio Hartree–Fock with the 3-21G basis set, and (iii) density functional B3LYP with the 6-31G* basis set and a pseudopotential. The SPARTAN′02 program was used.[34] The atomic coordinates of the anions in **5** and **6** were taken from the X-ray diffraction study. No geometric optimization was applied. The calculated energy differences are too small to have any significance. According to the first method, the energy of the *cis* isomer is 0.95 $kJ\,mol^{-1}$ lower than that of the *trans* isomer. The other two methods show the *trans* isomer as the more energetically favored, by 11.59 $kJ\,mol^{-1}$ using the second method and by 7.24 $kJ\,mol^{-1}$ using the third method.

X-ray Crystallographic Study: Crystals were mounted on the tip of a glass fiber with a small amount of silicon grease and transferred to the goniometer head. Data for **4** and **6** were collected on a Bruker P4 diffractometer equipped with a SMART CCD system.

Table 5. Crystallographic data for compounds **1**–**5**.

	1	**2**	**3**	**4**	**5**
Empirical formula	$C_{24}H_{22}Mo_2N_4O_{12}$	$C_{28}H_{30}Mo_2N_4O_{12}$	$C_{34}H_{44}Mo_2N_4O_{13}$	$C_{32}H_{38}Mo_2N_4O_{12}$	$C_{31}H_{33.5}Mo_2N_{4.5}O_{12}$
Formula mass	750.34	806.44	908.61	862.54	852.99
Crystal system	monoclinic	monoclinic	monoclinic	monoclinic	triclinic
Space group	*C*2/*c*	*C*2/*c*	$P2_1/n$	$P2_1$	$P\bar{1}$
T [K]	200(2)	150(2)	150(2)	94(2)	110(2)
a [Å]	22.0725(2)	22.0750(3)	13.3334(1)	10.3678(8)	12.4664(2)
b [Å]	8.7841(1)	8.4565(1)	16.4482(2)	15.399(1)	17.3974(2)
c [Å]	15.1629(2)	17.3676(3)	17.2333(2)	11.0861(9)	18.0972(3)
α [°]	90	90	90	90	93.8446(6)
β [°]	113.3504(4)	97.7975(8)	92.0718(4)	91.902(2)	108.9105(7)
γ [°]	90	90	90	90	92.8035(6)
V [$Å^3$]	2699.11(5)	3212.16(8)	3776.97(7)	1768.9(2)	3694.4(1)
Z	4	4	4	2	4
μ [mm^{-1}]	1.002	0.848	0.733	0.776	0.742
Collected reflections	5947	6908	16799	22565	28754
Unique reflections, R_{int}	3087, 0.0149	3651, 0.0133	8586, 0.0178	11276, 0.0236	16441, 0.0251
Observed reflections	2699	3354	7264	11088	13525
*R*1 [$I > 2\sigma(I)$]	0.0217	0.0221	0.0284	0.0251	0.0503
*wR*2 (all data)	0.0551	0.0565	0.0739	0.0652	0.1414

Table 6. Crystallographic data for compounds **6**–**9**.

	6	**7**	**8**	**9**
Empirical formula	$C_{34}H_{38}BrMo_2N_5O_{12}$	$C_{62}H_{52}Mo_2N_2O_{13}P_2$	$C_{14}H_{16}Mo_2N_2O_{14}$	$C_{22}H_{44}Mo_8N_2O_{30}$
Formula mass	980.48	1286.88	628.17	1584.11
Crystal system	monoclinic	monoclinic	triclinic	triclinic
Space group	$P2_1/n$	$P2_1/n$	$P\bar{1}$	$P\bar{1}$
T [K]	91(2)	293(2)	293(2)	150(2)
a [Å]	10.0050(5)	14.4105(1)	12.5884(2)	8.6323(1)
b [Å]	14.4475(7)	26.0364(2)	13.0228(2)	12.2594(2)
c [Å]	27.838(1)	15.2125(1)	13.5288(2)	12.2558(2)
α [°]	90	90	89.2790(6)	94.4216(6)
β [°]	96.538(1)	98.4308(4)	70.3024(7)	105.3578(7)
γ [°]	90	90	76.6323(6)	110.2995(7)
V [$Å^3$]	3997.7(3)	5646.01(7)	2026.33(5)	1152.34(3)
Z	4	4	4	1
μ [mm^{-1}]	1.691	0.569	1.316	2.195
Collected reflections	50588	23321	16410	9530
Unique reflections, R_{int}	13204, 0.0224	12915, 0.0218	9171, 0.0176	5250, 0.0138
Observed reflections	11878	10290	6834	4843
*R*1 [$I > 2\sigma(I)$]	0.0273	0.0340	0.0314	0.0268
*wR*2 (all data)	0.0736	0.1006	0.0842	0.0821

 © 2005 Wiley-VCH Verlag GmbH & Co. KGaA, Weinheim

Data processing was accomplished with the SAINT program.[35] Absorption corrections were made using SADABS.[36] Data for **1**, **2**, **3**, **5**, **7**, **8**, and **9** were collected on a Nonius Kappa CCD diffractometer. Data reduction and integration were performed with the software package DENZO-SMN.[37] Averaging of the symmetry-equivalent reflections largely compensated for the absorption effects. For all compounds, the coordinates of some or all of the non-hydrogen atoms were found by direct methods using the structure solution program SHELXS.[38] The positions of the remaining non-hydrogen atoms were located by use of a combination of least-squares refinement and difference Fourier maps in the SHELXL-97 program.[38] With the exception of **5** and **9**, all non-hydrogen atoms were refined anisotropically. The asymmetric unit of **5** contains two 4-methylpyridine molecules of crystallization, one of which is badly disordered, in addition to two dinuclear anions and four protonated 4-methylpyridine molecules. The disorder could not be modeled satisfactorily, resulting in relatively large *R* factors and residual density in the final difference Fourier map. The nitrogen and carbon atoms of both solvent molecules were refined isotropically. The oxalate ion in **9** is disordered over two positions. The carbon atoms C(6) and C(7) of the disordered oxalate ion were refined isotropically, each with an occupancy factor of 0.5. The hydrogen atoms were included in the structure factor calculations at idealized positions. Figures depicting the structures were prepared with SHELXTL.[39] Cell parameters and refinement results are summarized in Tables 5 and 6. CCDC-258550 (**1**), -258551 (**2**), -258552 (**3**), -258553 (**4**), -258554 (**5**), -258555 (**6**), -258556 (**7**) -258557 (**8**), and 258558 (**9**) contain the supplementary crystallographic data for this paper. These data can be obtained free of charge from The Cambridge Crystallographic Data Centre via www.ccdc.cam.ac.uk/data_request/cif.

Supporting Information (see also footnote on the first page of this article): Contains Figure S1 {^{1}H NMR spectra of the diluted D_2O/CD_3OD solutions of *trans*-$(MeNC_5H_5)_2[Mo_2O_4(\eta^2\text{-}C_2O_4)_2Py_2]$, recorded at 243 K} and Figure S2 {^{1}H NMR spectra of D_2O/CD_3OD solutions of *trans*-$(MeNC_5H_5)_2[Mo_2O_4(\eta^2\text{-}C_2O_4)_2Py_2]$ titrated with pyridine, recorded at 243 K}.

Acknowledgments

The work was supported by the Slovenian Ministry of Education, Science and Sport (grant P1-0134) and by the National Science Foundation (Grant CHE-0242153). We are grateful to Prof. Alojz Demšar for his help with the simulation of NMR spectra.

[1] E. I. Stiefel, *Prog. Inorg. Chem.* **1977**, *22*, 1–223.
[2] H. K. Chae, W. G. Klemperer, T. A. Marquart, *Coord. Chem. Rev.* **1993**, *128*, 209–224.
[3] B. Modec, J. V. Brenčič, *J. Cluster Sci.* **2002**, *13*, 279–302 and references cited therein.
[4] D. J. Darensbourg, R. L. Gray, T. Delord, *Inorg. Chem. Acta* **1985**, *98*, L39–L42.
[5] B. Modec, J. V. Brenčič, L. Golič, *Polyhedron* **2000**, *19*, 1219–1225.
[6] B. Modec, J. V. Brenčič, R. C. Finn, R. S. Rarig, J. Zubieta, *Inorg. Chim. Acta* **2001**, *322*, 113–119.
[7] B. Modec, J. V. Brenčič, D. Dolenc, J. Zubieta, *J. Chem. Soc., Dalton Trans.* **2002**, 4582–4586.
[8] M.-Y. Lee, S.-L. Wang, *Chem. Mater.* **1999**, *11*, 3588–3594.
[9] L. A. Mundi, R. C. Haushalter, *Inorg. Chem.* **1990**, *29*, 2879–2881.
[10] a) L. A. Mundi, R. C. Haushalter, *J. Am. Chem. Soc.* **1991**, *113*, 6340–6341; b) E. W. Corcoran Jr., *Inorg. Chem.* **1990**, *29*, 157–158; c) R. C. Haushalter, K. G. Strohmaier, F. W. Lai, *Science* **1989**, *246*, 1289–1291.
[11] B. Modec, J. V. Brenčič, J. Koller, *Eur. J. Inorg. Chem.* **2004**, 1611–1620.
[12] L. Lisnard, P. Mialane, A. Dolbecq, J. Marrot, F. Secheresse, *Inorg. Chem. Commun.* **2003**, *6*, 503–505.
[13] F. A. Cotton, S. M. Morehouse, *Inorg. Chem.* **1965**, *4*, 1377–1381.
[14] B. Kamenar, B. Kaitner, N. Strukan, *Croat. Chem. Acta* **1991**, *64*, 329–341.
[15] W. S. McDonald, *Acta Crystallogr., Sect. B* **1978**, *34*, 2850–2853.
[16] R. Yang, X. Yu, *Chin. J. Struct. Chem.* **1985**, *4*, 1–4.
[17] A. Dolbecq, B. Salignac, E. Cadot, F. Secheresse, *Bull. Pol. Acad. Sci.* **1998**, *46*, 237–271.
[18] Q. Chen, S. Liu, J. Zubieta, *Angew. Chem. Int. Ed. Engl.* **1988**, *27*, 1724–1725.
[19] X.-P. Zhan, C.-Z. Lu, W.-B. Yang, H.-W. Ma, C.-D. Wu, Q.-Z. Zhang, *Dalton Trans.* **2003**, 1457–1458.
[20] K. Mennemann, R. Mattes, *J. Chem. Res.* **1979**, *100*, 1343.
[21] T. Shibahara, S. Ooi, H. Kuroya, *Bull. Chem. Soc. Jpn.* **1982**, *55*, 3742–3746.
[22] C. du Peloux, A. Dolbecq, E. Cadot, J. Marrot, F. Secheresse, *J. Mol. Struct.* **2003**, *656*, 37–44.
[23] We observed that pyridine *N*-methylation with methanol took place in the presence of oxalic acid at elevated temperature. The fact that *N*-methylpyridinium salts result from a nucleophilic attack of pyridine on methyl halide formed from methanol and hydrogen halide does not provide a valid explanation. The latter reaction requires strongly acidic conditions, while the reaction medium in our case contains mostly pyridine. Moreover, the halogenation of alcohols is known to proceed more readily with tertiary and secondary alcohols, but not with methanol. The exact nature of this process is currently under investigation.
[24] A downfield shift was observed for the signals of free pyridine [243 K spectrum: δ = 7.67 (C-3), 8.14 (C-4), 8.62 (C-2) ppm], suggesting that pyridine is not entirely free. The corresponding pyridine frequencies in water solution appear at δ = 7.24, 7.66, and 8.32 ppm.
[25] The integral of signal C2, which belongs to free pyridine, is smaller than the integrals of signals A2 and B2. This observation rules out an alternative explanation: an equilibrium between only one isomeric form of $[Mo_2O_4(\eta^2\text{-}C_2O_4)_2Py_2]^{2-}$ (set A), the mono-substituted complex (set B), and the bis(aqua)-ligated complex. In the latter situation the integral of C2 would be larger than the integral of B2 because the amount of free pyridine is twice the amount of the bis(aqua)-ligated complex plus the amount of the mono-substituted complex.
[26] For comparison, the carbonate carbon resonances in water solution of $[(Mo_2O_4)_3(\mu_6\text{-}CO_3)(\mu_2\text{-}CO_3)_3(\mu_2\text{-}OH)_3]^{5-}$ with two distinctly different carbonato ligands appear in the same spectral region: two major signals at δ = 160 and 165 ppm with a 1:3 intensity ratio and three minor ones at δ = 160.5, 164.5, and 165.5 ppm. [M. J. Manos, A. D. Keramidas, J. D. Woollins, A. M. Z. Slawin, T. A. Kabanos, *J. Chem. Soc., Dalton Trans.* **2001**, 3419–3420.] The ^{13}C NMR spectrum of an aqueous solution of ammonium oxalate reveals a resonance at δ = 173.9 ppm.
[27] P. H. M. Budzelaar, *gNMR* Version 5.0.1.0. NMR Simulation Program, IvorySoft, Oxford, **2002**.
[28] a) R. G. James, W. Wardlaw, *J. Chem. Soc.* **1927**, 2145–2156; b) H. M. Spittle, W. Wardlaw, *J. Chem. Soc.* **1928**, 2742.
[29] P. C. H. Mitchell, *J. Chem. Soc. A* **1969**, 146–152.
[30] a) N. F. Curtis, *J. Chem. Soc. A* **1968**, 1584–1587; b) P. Roman, A. Luque, C. Guzman-Miralles, J. I. Beitia, *Polyhedron* **1995**, *14*, 2863–2869.
[31] K. Nakamoto, *Infrared and Raman Spectra of Inorganic and Coordination Compounds. Part B: Applications* in *Coordination, Organometallic and Bioinorganic Chemistry*, 5th ed., Wiley In-

 © 2005 Wiley-VCH Verlag GmbH & Co. KGaA, Weinheim

terscience, New York, Chichester, Weinheim, Brisbane, Singapore, Toronto, **1997**, pp. 53–57.
[32] B. Modec, J. V. Brenčič, *Eur. J. Inorg. Chem.* **2005**, 1698–1709.
[33] G. R. Hanson, A. A. Brunette, A. C. McDonell, K. S. Murray, A. G. Wedd, *J. Am. Chem. Soc.* **1981**, *103*, 1953–1959.
[34] *Spartan'02*, Wavefunction, Inc., Irvine, CA, **2002**.
[35] *SMART* and *SAINT*, Siemens Analytical Instruments Inc., Madison, WI, **1990**.
[36] G. M. Sheldrick, *SADABS, A Program for Absorption Correction with the Siemens SMART Area-Detector system*, Universität Göttingen, **1996**.
[37] Z. Otwinowski, W. Minor, *Methods Enzymol.* **1997**, *276*, 307–326.
[38] G. M. Sheldrick, *SHELXS-97* and *SHELXL-97*, Universität Göttingen, **1997**.
[39] *SHELXTL, Software Package for Crystal Structure Determination*, Version 5.03, Siemens Analytical X-ray Instrument Division, Madison, WI, **1994**.

Received: January 10, 2005
Published Online: July 12, 2005

 © 2005 Wiley-VCH Verlag GmbH & Co. KGaA, Weinheim

Syntheses, Structures, and Optical Properties of β-Ferrocenylacrylate Metal Polymers

Lin Ke Li,[a] Ying Lin Song,[b] Hong Wei Hou,*[a] Yao Ting Fan,[a] and Yu Zhu[a]

Keywords: Cadmium / Lead / Nonlinear optics / Organic–inorganic hybrid composites / Polymers

The zero-dimensional polymer $[Pb_6(\mu_2OOCCH{=}CHFc)_2(\mu_3\text{-}OOCCH{=}CHFc)_2(\mu_2\text{-}\eta^2\text{-}OOCCH{=}CHFc)_2(\eta^2\text{-}OOCCH{=}CHFc)_2(\mu_4\text{-}O)_2]$ (**1**), the one-dimensional chain polymers $[Pb(\eta^1\text{-}\mu_2\text{-}OOCCH{=}CHFc)_2(phen)]_n$ (phen = phenanthroline; (**2**), $\{[Cd(\mu_2\text{-}\eta^2\text{-}OOCCH{=}CHFc)(\eta^2\text{-}OOCCH{=}CHFc)(H_2O)_2](H_2O)_4\}_n$ (**3**), and the two-dimensional hybrid polymer $\{[Cd(\eta^2\text{-}OOCCH{=}CHFc)(bbbm)_{1.5}Cl]\cdot 1.5H_2O\}_n$ [bbbm = 1,1′-(1,4-butanediyl)bis-1*H*-benzimidazole; **4**] have been prepared by the reaction of sodium β-ferrocenylacrylate [FcCH=CHCOONa, Fc = $(\eta^5\text{-}C_5H_5)Fe(\eta^5\text{-}C_5H_4)$] with the appropriate metal salts. Solution-state differential pulse voltammetry for **1**–**4** indicated that the half-wave potentials of the ferrocenyl moieties in these polymers are all shifted to positive potential compared with that of sodium β-ferrocenylacrylate. The four polymers' third-order nonlinear optical (NLO) properties were determined by the Z-scan technique in DMF solutions. The results show that these polymers possess good nonlinear optical refraction effects. Their hyperpolarizability (γ) values are calculated to be 4.80×10^{-30}, 5.19×10^{-30}, 1.57×10^{-29}, and 2.04×10^{-29} esu for **1**–**4**, respectively. The γ values of the Cd^{II} polymers (**3** and **4**) are slightly larger than those of the Pb^{II} polymers (**1** and **2**), which indicates that the metal ions play an important role in the NLO properties of these polymers.

(© Wiley-VCH Verlag GmbH & Co. KGaA, 69451 Weinheim, Germany, 2005)

Introduction

Currently, the rational design and synthesis of metal–organic polymeric complexes containing multifunctional groups have received much attention because of their widespread potential applications in molecular sensor technology, peptide mimetic models, charge-transfer complexes, non-linear optical materials, organic synthesis, homogeneous catalysis, materials chemistry, and so on.[1–5] Due to the fascinating properties of the ferrocene moiety as well as the versatile coordination modes[6] and strong coordinating capability of the carboxylate groups, ferrocenecarboxylate compounds have been extensively used as functional ligands.[7–14] Furthermore, the introduction of ferrocenyl carboxylate groups into metal–organic frameworks provides an effective way to prepare new functional materials with unique features.

Ferrocenecarboxylate and ferrocenedicarboxylate were among the first to be prepared and studied in synthetic strategies, and lots of metal-based polymers containing them have been described.[12,13,15–20] However, relatively few reports have appeared on other ferrocenecarboxylate–metal polymers. In recent years, various groups and ourselves have put effort into the synthesis and property investigations of other ferrocenecarboxylate–metal polymers,[10,11] such as the structures and the redox properties of the polymers $[Pb(o\text{-}OOCC_6H_4COFc)(\eta^2\text{-}o\text{-}OOCC_6H_4COFc)(bpe)]_n$, $\{[Zn(o\text{-}OOCC_6H_4COFc)_2(4,4'\text{-}bpy)(H_2O)_2]\cdot 2MeOH\cdot 2H_2O\}_n$, $\{[Cd(o\text{-}OOCC_6H_4COFc)_2(bpe)(MeOH)_2]\cdot 2H_2O\}_n$, $\{[Pb\{\mu_2\text{-}\eta^2\text{-}OOCCH{=}(CH_3)CFc\}_2]\cdot MeOH\}_m$,[10] and $\{[Cd(\mu_2\text{-}OOCH_4C_6Fc)(\eta^2\text{-}OOCH_4C_6Fc)(bbp)](CH_3OH)\}_n$,[11] and the magnetic properties of $\{[Mn(OOCH_4C_6Fc)_2(\mu_2\text{-}OH_2)(H_2O)_2](H_2O)\}_n$ and $[Mn(\mu_2\text{-}OOCH_4C_6Fc)_2(phen)]_n$,[11] etc., but no reports have touched on the third-order NLO properties of ferrocenecarboxylate–metal polymers.

Following our earlier studies on ferrocenecarboxylate–metal polymers, we report here the syntheses and structures of a series of novel polymers constructed from FcCH=CHCOONa with Pb^{II} or Cd^{II} ions and subsidiary ligands. The third-order NLO studies in DMF solution show that all these polymers display self-focusing behaviors. This result is consistent with the previous conclusion that the NLO properties of coordination polymers are controlled by the valence shell structures of the central metal ions. Their thermal and electrochemical properties were also investigated.

Results and Discussion

Preparation of the Polymers

Polymers **1**–**4** were obtained by treatment of FcCH=CHCOONa with the appropriate metal salts and subsidiary

[a] Department of Chemistry, Zhengzhou University, Henan 450052, P. R. China
Fax: +86-371-7761744
E-mail: houhongw@zzu.edu.cn
[b] Department of Applied Physics, Harbin Institute of Technology, Heilongjiang 150001, P. R. China

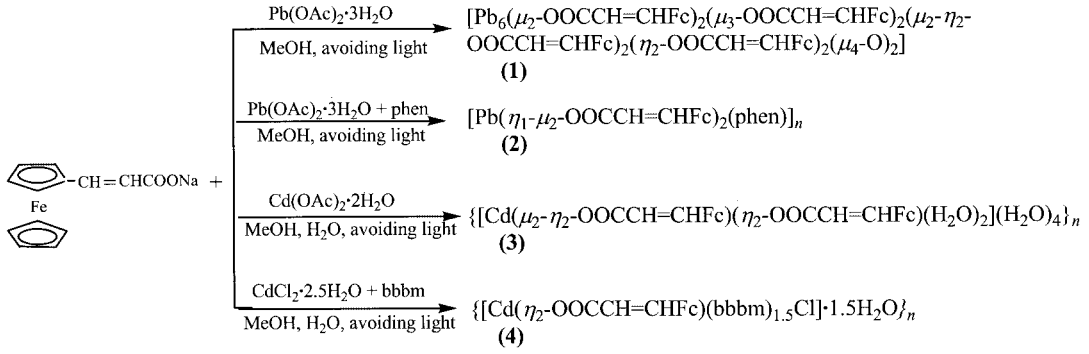

Scheme 1.

ligands in different solvents (Scheme 1). Crystals suitable for X-ray crystallography of polymers **1**–**4** were also obtained by slow evaporation of the solvents in the dark due to the reasons mentioned previously.[21] These crystals are only soluble in highly polar solvents such as DMSO and DMF, etc.

Under similar reaction conditions, the reactions of $Pb(OAc)_2$ with different ferrocenecarboxylates generate different structural geometries. For example, treatment of $Pb(OAc)_2$ with FcCOONa or $FcC(CH_3)$=CHCOONa gives the one-dimensional chain structural polymers $\{[Pb_2(OOCFc)(\eta^2\text{-}OOCFc)(\mu_2\text{-}\eta^2\text{-}OOCFc)(\mu_3\text{-}\eta^2\text{-}OOCFc)(MeOH)]\cdot 1.5MeOH\cdot H_2O\}_n$[6e] or $\{[Pb\{\mu_2\text{-}\eta^2\text{-}OOCCH=(CH_3)CFc\}_2]\cdot MeOH\}_n$,[10] while when FcCH=CHCOONa was treated with $Pb(OAc)_2$ a zero-dimensional polymer (**1**) was obtained whose structure displays significant difference from the former two polymers. The addition of phen to the reaction system of **1** led to the formation of the one-dimensional polymer **2**. Up to now, the synthesis of two-dimensional polymers containing ferrocenecarboxylate was still a great challenge. On the basis of self-assembly of coordination polymers, we successfully prepared a novel, two-dimensional hybrid polymer **4** with the organic bridging ligand bbbm.

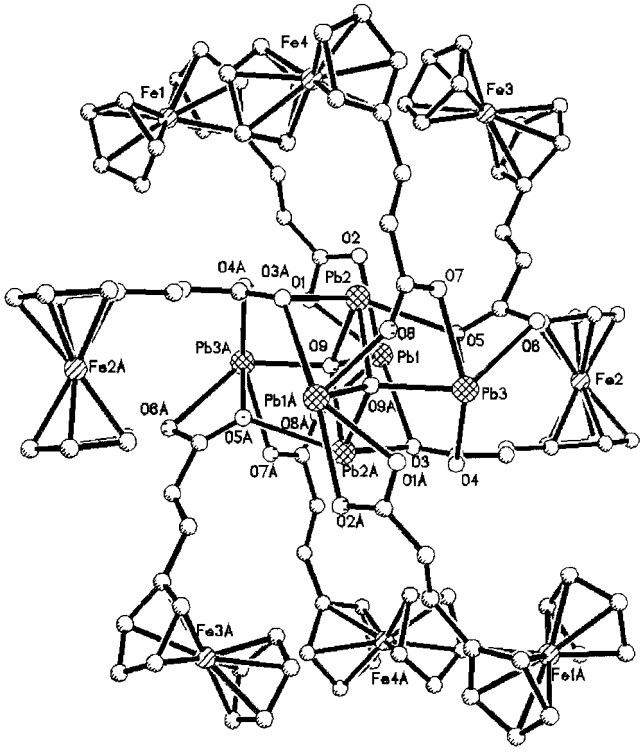

Figure 1. Crystal structure of $[Pb_6(\mu_2\text{-}OOCCH=CHFc)_2(\mu_3\text{-}OOCCH=CHFc)_2(\mu_2\text{-}\eta^2\text{-}OOCCH=CHFc)_2(\eta^2\text{-}OOCCH=CHFc)_2(\mu_4\text{-}O)_2]$ (**1**) with heteroatom labeling scheme.

Crystal Structure of $[Pb_6(\mu_2\text{-}OOCCH=CHFc)_2(\mu_3\text{-}OOCCH=CHFc)_2(\mu_2\text{-}\eta^2\text{-}OOCCH=CHFc)_2(\eta^2\text{-}OOCCH=CHFc)_2(\mu_4\text{-}O)_2]$ (1)

The molecule crystallizes in the space group $P\bar{1}$. X-ray diffraction analysis revealed that **1** is a zero-dimensional Pb^{II} polymer (Figure 1). The structure shows a giant, scroll-wheel-like arrangement of the eight ferrocene units in four kinds of coordination modes with a presumed Pb_6 octahedron core (the six Pb^{II} ions inhabit the six apexes of the presumed octahedron), and the six Pb^{II} ions are bridged by two $\mu_4\text{-}O^{2-}$ anions from the inner of the Pb_6 octahedron core, simultaneously. The molecule sits astride a center of inversion.

The eight $FcCH=CHCOO^-$ units surround the Pb_6 core and bridge the six Pb^{II} ions to form a stable Pb_6 octahedron. It is interesting that the eight $FcCH=CHCOO^-$ units display four kinds of coordination modes: bidentate (η^2-OOCCH=CHFc), bidentate (μ_2-OOCCH=CHFc), tridentate (μ_3-OOCCH=CHFc), and tridentate ($\mu_2\text{-}\eta^2$-OOCCH=CHFc). As for the Pb_6 octahedron, the mean deviation of the plane Pb2–Pb2A–Pb3–Pb3A (**A**), Pb1–Pb1A–Pb2–Pb2A (**B**), or Pb1–Pb1A–Pb3–Pb3A (**C**) is 0.000 Å. The dihedral angle between planes **A** and **B** is 68.8°, that between **A** and **C** is 85.5°, and that between **B** and **C** is 85.8°. The Pb1–Pb1A, Pb2–Pb2A, and Pb3–Pb3A distances are 6.621, 3.725, and 6.546 Å, respectively.

 © 2005 Wiley-VCH Verlag GmbH & Co. KGaA, Weinheim

The six Pb^{II} ions lie in three kinds of coordination environments, considering an arbitrary length of approximately 2.8 Å to define maximum bonding interactions (this being the sum of the two ionic radii[22]). Pb1 and Pb3 are pentacoordinate. Each Pb1 binds to five oxygen atoms, two from a chelating η^2-OOCCH=CHFc$^-$ unit, one from bidentate μ_2-OOCCH=CHFc$^-$, one from tridentate μ_3-OOCCH=CHFc$^-$, and one from the μ_4-O^{2-} anion from the inner core of the Pb_6 octahedron. For Pb3, the five oxygen atoms are two from μ_2-η^2-OOCCH=CHFc$^-$, one from μ_3-OOCCH=CHFc$^-$, one from μ_2-OOCCH=CHFc$^-$, and one from the μ_4-O^{2-} anion. The coordination number of Pb2 is four, with four oxygen atoms from μ_2-η^2-OOCCH=CHFc$^-$, μ_3-OOCCH=CHFc$^-$, and two μ_4-O^{2-} anions. The Pb–O distances are in the range 2.264(8)–2.694 Å. This contrasts with the Pb atoms in the acetate, formate, and pentafluorobenozate complexes, where eightfold coordination is found;[23] coordination numbers of 7,[24] 9,[25] and 10[26] are also known in other Pb^{II} carboxylates.

The eight ferrocene fragments are located around the Pb_6 octahedron. Fe1, Fe4, Fe1A, and Fe4A are co-planar, as are Fe2, Fe3, Fe2A, and Fe3A, and the dihedral angle between the two planes is 89.8°, that is to say they are nearly perpendicular to each other.

It has previously been reported that bridging oxygen atoms are present at the center of a polyhedron formed by transition[27] and main- group[28] metals or hetero-polymetal containing Pb atoms,[29] for example the zero-dimensional Zn^{II} polymers $[(Zn_4O)(O_2CR)_6]$ (R = diethylamino, piperidino, or pyrrolidino),[30] and $[Zn_4(\mu_2\text{-}FcCOO)_6(\mu_4\text{-}O)]$.[6e] Reports on Pb^{II} carboxylate complexes containing an oxide ligand bridging the metal atoms in a homometallic polyhedron of Pb^{II} ions are very scare.[23]

Crystal Structure of $[Pb(\eta^1\text{-}\mu_2\text{-}OOCCH=CHFc)_2(phen)]_n$ (2)

The 1D chain structure of polymer **2** is formed by a double monatomic bridge connecting the adjacent Pb^{II} ions (Figure 2). Each Pb^{II} ion adopts a distorted octahedral PbN_2O_4 coordination environment. The repeated Pb_2O_2 rings construct the basic skeleton structure of the one-dimensional chain: the dimensions of the rhomboid are 2.549×2.734 Å^2, the dihedral angle between the two adjacent Pb_2O_2 rhomboid is 81.8°, and the Pb···Pb intrachain distance is 4.202 Å. The phen rings lie on alternate sides of each chain, parallel to the *c*-axis. The $Pb–N_{(phen)}$ distance [2.612(11) Å] is consistent with those in $\{[Pb(phen)_2(ox)]\cdot 5H_2O\}_n$ (ox = oxalate) [2.721(2) Å],[31] $[Pb(phen)(O_2CCH_3)(O_2NO)]_n$ [2.519(3) and 2.579(3) Å],[32] $[Pb(phen)_2(O_2CCH_3)(ClO_4)]$, and $[Pb(phen)_2(O_2CCH_3)(NCS)]_2$,[32] etc.

The Pb_2O_2 ring in **2** is different from those in dimeric $[Pb(phen)(O_2CCH_3)_2]_2$[33] and $[Pb(phen)(O_2CCH_3)(NCS)]_2$[34] and polymeric $[Pb(phen)(O_2CCH_3)(O_2ClO_2)]_n$[35] and $[Pb(phen)(O_2CCH_3)(O_2NO)]_n$,[36] where the Pb_2O_2 rings share edges with PbOCO quadrilaterals to form the dimer core. The long edge of the Pb_2O_2 ring in **2** (2.734 Å) is similar in length to those in $[Pb(phen)(O_2CCH_3)(O_2NO)]_n$ (2.80 Å) and $[Pb(phen)(O_2CCH_3)(O_2ClO_2)]_n$ (2.74 Å), but considerably shorter than those in $[Pb(phen)(O_2CCH_3)(NCS)]_2$ (3.19 Å) and $[Pb(phen)(O_2CCH_3)_2]_2$

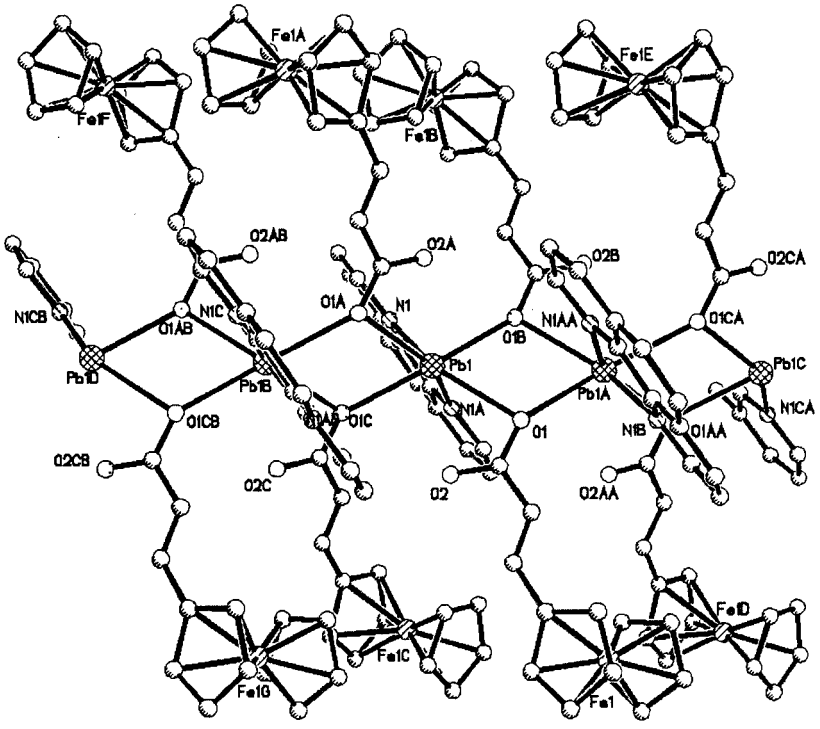

Figure 2. Perspective view of the 1D chain structure of $[Pb(\eta^1\text{-}\mu_2\text{-}OOCCH=CHFc)_2(phen)]_n$ (**2**) with only the heteroatoms labeled.

 © 2005 Wiley-VCH Verlag GmbH & Co. KGaA, Weinheim

(3.37 Å). This indicates the strong coordinating ability of the FcCH=CHCOO$^-$ anion.

Since the distance between adjacent phen rings (8.270 Å) on one side of the 1D chain is out of the range of π–π stacking interactions there are no such interactions in the crystal structure, and it is the intermolecular interaction that is responsible for the packing in the solid-state structure.

Crystal Structure of {[Cd(μ$_2$-η^2-OOCCH=CHFc)-(η^2-OOCCH=CHFc)(H$_2$O)$_2$](H$_2$O)$_4$}$_n$ (3)

The X-ray diffraction analysis revealed that **3** crystallizes in the space group $P2_1/n$. As can be seen from Figure 3, each Cd^{II} ion is seven-coordinate and the adjacent [Cd(η^2-OOCCH=CHFc)(H$_2$O)$_2$] groups are linked by μ$_2$-η^2-OOCCH=CHFc$^-$ units into a one-dimensional chain polymer.

In the structural unit, each Cd^{II} ion binds to atoms O1 and O2 from a chelating η^2-OOCCH=CHFc$^-$, O3, O4, and O4A atoms from two μ$_2$-η^2-OOCCH=CHFc$^-$, groups and the O5 and O6 atoms from two coordinated H$_2$O molecules. The Cd–O$_{(OOCCH=CHFc^-)}$ distances are in the range 2.242(4)–2.580(5) Å. The Cd^{II} ions are not in a straight line: the adjacent Cd···Cd separation is 4.637 Å and the Cd–Cd–Cd angle is 105.5°. The one-dimensional [Cd(μ$_2$-η^2-OOCCH=CHFc)(η^2-OOCCH=CHFc)(H$_2$O)$_2$] chain extends along the *b*-direction. Viewed along the *b*-axis, two kinds of ferrocene fragments are located along both sides of the one-dimensional chain, and they alternate along this chain. The one-dimensional chains are connected by O–H···O hydrogen bonds and intermolecular interactions (Figure 4). The structure is similar to the reported 1-D infinite zigzag chain polymer [Cd{Fc(CO$_2$)$_2$}(DMF)$_2$(H$_2$O)]$_n$,[19] in which the Cd^{II} atoms are connected by the 1,1′-ferrocenedicarboxylate ligand in a 1,3′-disubstituted bridging mode.

Crystal Structure of {[Cd(η^2-OOCCH=CHFc)-(bbbm)$_{1.5}$Cl]·1.5H$_2$O}$_n$ (4)

The crystal structure analysis demonstrates that **4** crystallizes in the space group $P\bar{1}$. As shown in the structural unit (Figure 5), each Cd^{II} ion is six-coordinate in a slightly distorted octahedral environment with two oxygen atoms from a chelating η^2-OOCCH=CHFc$^-$ unit, three nitrogen atoms from three bridging bbbm ligands, and one Cl atom. The O1, O2, N3, Cl1, and Cd1 atoms are nearly co-planar (the mean deviation from the ideal CdCNO$_2$ plane is 0.0322 Å), and define the equatorial plane [Cd1–O1 = 2.273(12), Cd1–O2 = 2.476(12) Å, Cd1–N3 = 2.301(14) Å, and Cd1–Cl1 = 2.506(4) Å]. The N1 and N5 atoms of the other two bbbm units occupy the axial positions [Cd1–N1 = 2.520(13), Cd1–N5 = 2.347(12) Å], and the axial angle N1–Cd1–N5 is 166.3(4)°. All the Cd^{II} ions are bridged by the bbbm with ferrocene units in the side chain leading to an infinite two-dimensional network (Figure 6). The sheet extends along the [010] crystallographic plane.

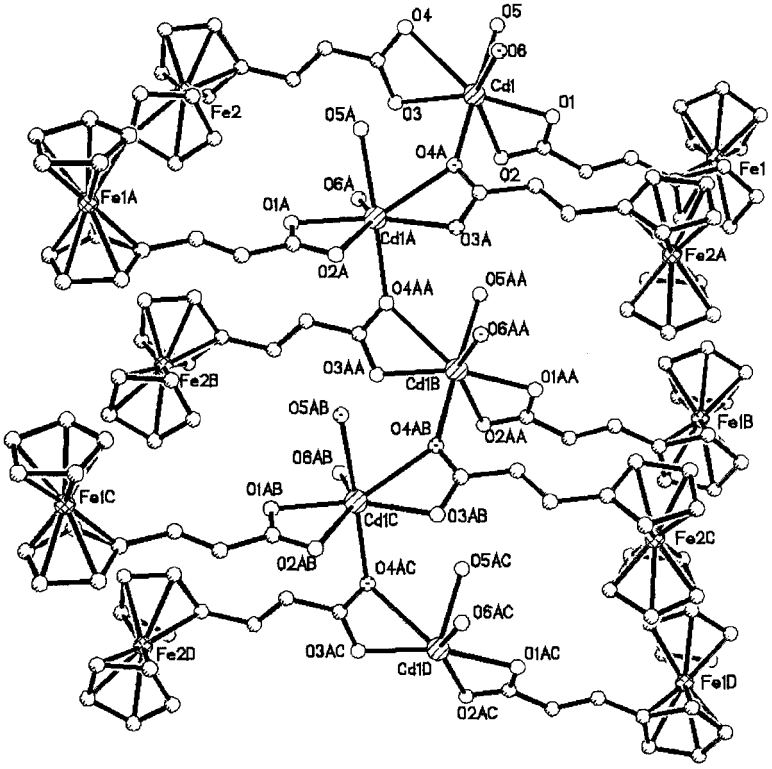

Figure 3. One-dimensional chain structure of {[Cd(μ$_2$-η^2-OOCCH=CHFc)(η^2-OOCCH=CHFc) (H$_2$O)$_2$](H$_2$O)$_4$}$_n$ (**3**) with only heteroatoms labeled.

 © 2005 Wiley-VCH Verlag GmbH & Co. KGaA, Weinheim

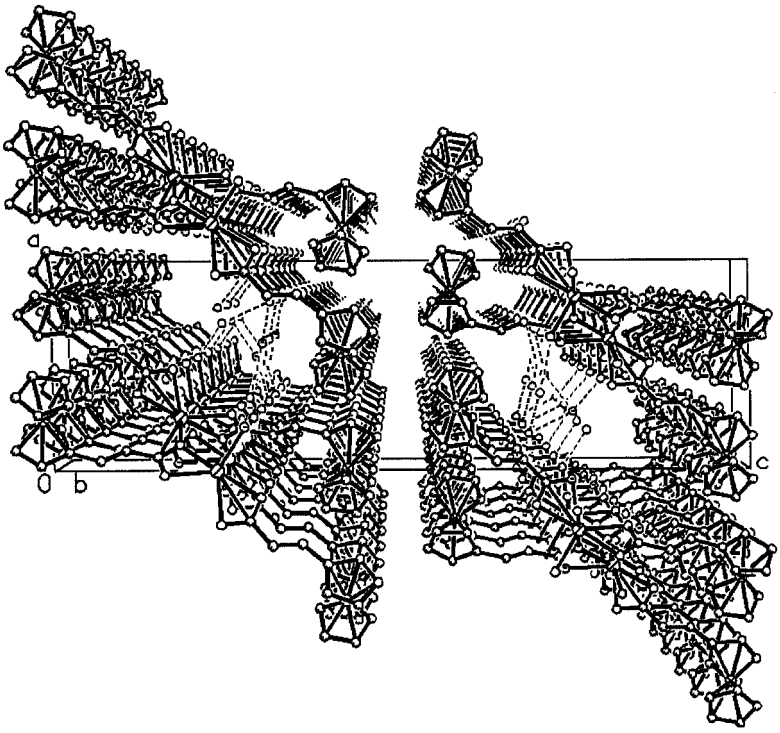

Figure 4. The solid-state structure of $\{[Cd(\mu_2\text{-}\eta^2\text{-}OOCCH{=}CHFc)(\eta^2\text{-}OOCCH{=}CHFc)(H_2O)_2](H_2O)_4\}_n$ (**3**).

Hybrid polymers with ferrocene units in the side chain have been published in our recent papers,[6e,10,11] such as the one-dimensional, ladder-like polymers $\{[Zn(OOCFc)_2(bpt)]\cdot 2.5H_2O\}_n$, $[Zn(OOCFc)(\eta^2\text{-}OOCFc)(bbp)]_n$, and $\{[Cd(\mu_2\text{-}OOCH_4C_6Fc)(\eta^2\text{-}OOCH_4C_6Fc)(bbp)](CH_3OH)\}_n$, the zigzag chain polymer $[Pb(FcCOO)(\mu_2\text{-}FcCOO)(bpe)]_n$, and the linear chain polymer $\{[Zn(o\text{-}OOCC_6H_4COFc)_2(4,4'\text{-}bpy)(H_2O)_2]\cdot 2MeOH\cdot 2H_2O\}_n$. However, two-dimensional ferrocenecarboxylate-containing hybrid polymers have not been reported up to now. Using the organic bridging ligand bbbm, we have successfully prepared the novel two-dimensional hybrid polymer **4** containing a ferrocenearboxylate component.

Thermogravimetric Analysis

The TG-DTA data of **1**–**4** were determined in the range 25–900 °C in air. It can be seen from the TG curve that **1** begins to lose weight at 212 °C, and the process of weight

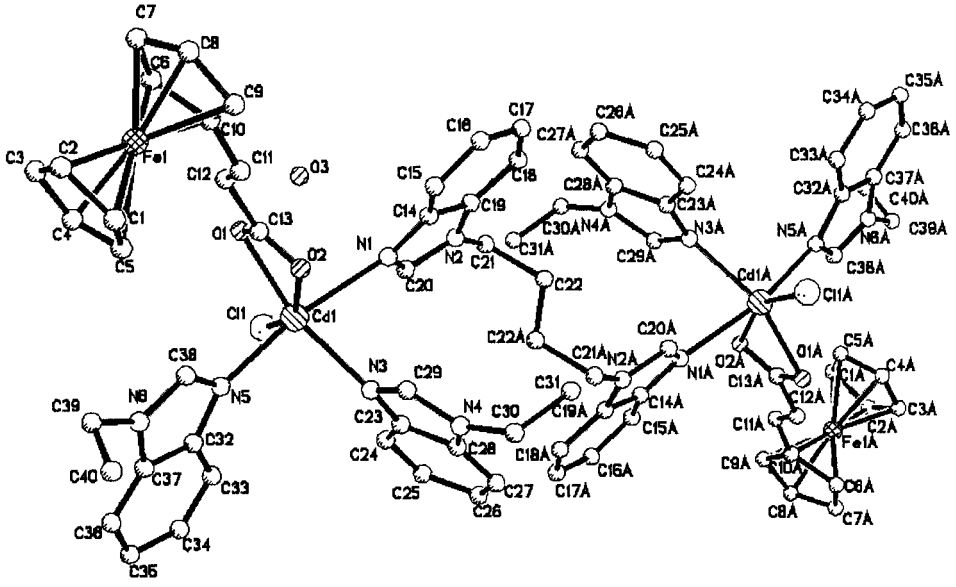

Figure 5. ORTEP diagram showing the structure unit of $\{[Cd(\eta^2\text{-}OOCCH{=}CHFc)(bbbm)_{1.5}Cl]\cdot 1.5H_2O\}_n$ (**4**). H atoms have been omitted for clarity.

 © 2005 Wiley-VCH Verlag GmbH & Co. KGaA, Weinheim

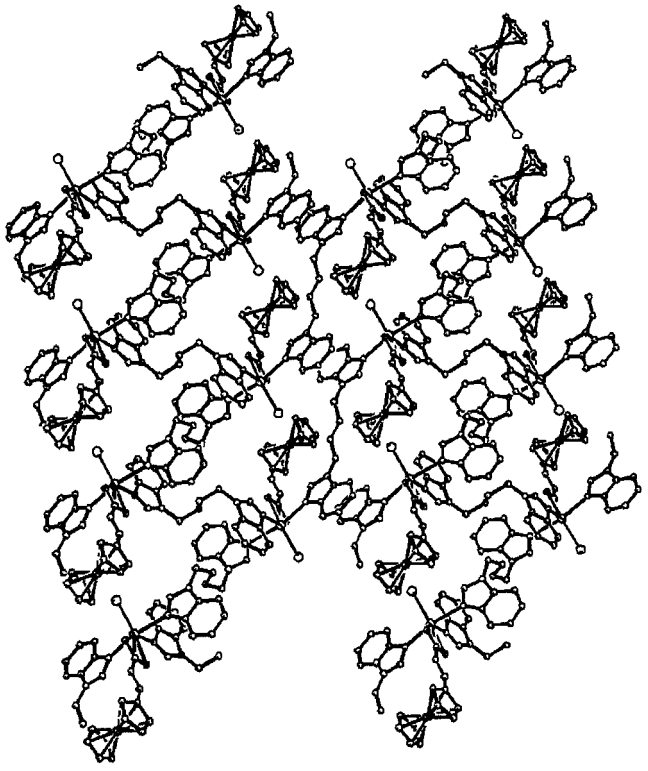

Figure 6. Two-dimensional sheet structure of $\{[Cd(\eta^2\text{-}OOCCH{=}CHFc)(bbbm)_{1.5}Cl]\cdot 1.5H_2O\}_n$ (**4**). H atoms have been omitted for clarity.

loss is sustained up to 381 °C; this corresponds to the decomposition of the FcCH=CHCOO⁻ anions. A plateau region is then observed from 381 to 900 °C. Finally, a brown amorphous residue was left, which can be assigned to 1.5PbO + 2FeO. There are two weak exothermic peaks at 258 and 304 °C, and a very strong exothermic peak at 399 °C on the DTA curve of **1**.

For polymer **2**, the weight-loss process begins at 183 °C and it goes through multiple weight loss steps, which can be assigned to the loss of the phen molecule and the decomposition of FcCH=CHCOO⁻ anions; this process is sustained up to 411 °C. A clear plateau region is then observed from 411 to 900 °C in the TGA plot. Finally, the brown amorphous residue is presumed to be PbO + 2FeO. There is one weak exothermic peak at 249 °C and one very strong exothermic peak at 390 °C on the DTA curve of **2**.

We find from the TG curve that **3** begins to lose weight at 35 °C, and this process is maintained up to 159 °C, corresponding to the loss of uncoordinated H_2O molecules. After a plateau region from 159 to 225 °C in the TG curve, it goes through complicated multiple weight-loss steps from 225 to 555 °C, corresponding to the loss of coordinated H_2O and the decomposition of the FcCH=CHCOO⁻ units. There is then a plateau region from 555 to 900 °C. The brown residue can be assigned to the residual CdO + 2FeO. There is one middle exothermic peak at 280 °C and one very strong exothermic peak at 414 °C on the DTA curve.

In the TG curve of **4**, the weight loss process from 164 to 232 °C can be assigned to the loss of H_2O molecules, then it goes through complicated multiple weight-loss steps in the temperature range of 232 to 600 °C, which can be assigned to the decomposition of bbbm and the FcCH=CHCOO⁻ anions. The final brown residue corresponds to CdO + FeO. The weight remains constant from 600 to 900 °C. In the DTA curve of **4**, there is a weak exothermic peak at 260 °C, a middle exothermic peak at 395 °C, and a very strong exothermic peak at 478 °C.

Redox Properties

The solution-state differential pulse voltammograms of **1**–**4** and FcCH=CHCOONa are shown in Figure 7. It can be seen from this figure that all these polymers show a single peak with a half-wave potential ($E_{1/2}$ vs. SCE) at 0.56 V for **1**, 0.54 V for **2**, 0.53 V for **3**, and 0.52 V for **4**, which can be assigned to the electron-transfer process of the ferrocenyl moiety. Relative to free FcCH=CHCOONa (0.51 V), the half-wave potentials of **1**–**4** are all shifted to slightly higher potential. It is apparent that these shifts can be attributed to the influence of the central metal ions, and this is consistent with the previous results of transition metal–ferrocenyl systems.[9,37] The reason for this is that the conjugated π-electron systems between the two metals allow communication,[38] and the electron-withdrawing nature of the coordinated metal centers makes the ferrocene unit harder to oxidize.[39]

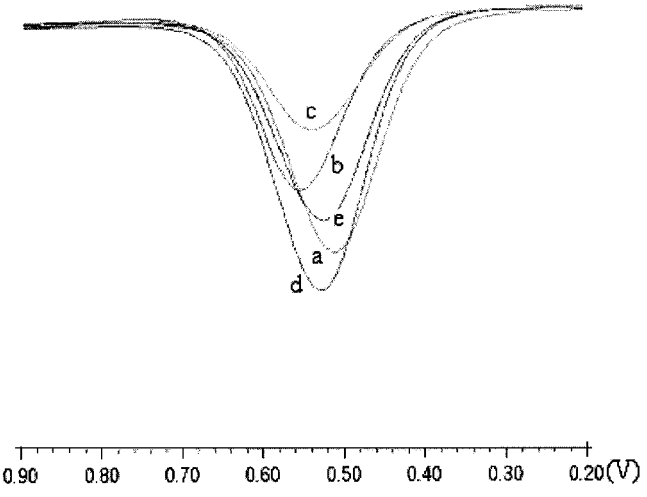

Figure 7. Differential pulse voltammogram of (a) NaOOCCH=CHFc (0.51 V), (b) **1** (0.56 V), (c) **2** (0.54 V), (d) **3** (0.53 V), (e) **4** (0.52 V) all at concentrations of approximately 1.0×10^{-3} M in DMF containing nBu$_4$NClO$_4$ (0.1 M) at a scanning rate of 20 mV s^{-1} (vs. SCE).

Nonlinear Optical Properties

The second-order NLO properties of ferrocenyl derivatives have been extensively studied,[40] but reports on the third-order NLO properties of ferrocenyl derivatives, especially ferrocenecarboxylate polymers, are very limited.

 © 2005 Wiley-VCH Verlag GmbH & Co. KGaA, Weinheim

The UV/Vis spectra of **1**–**4** were determined in DMF solutions. From a previous study,[41,42] we know that ferrocene exhibits two characteristic absorptions in the UV/Vis spectra at 440 nm (assigned to the $^1E_{1g} \leftarrow {}^1A_{1g}$ transition) and 325 nm (assigned to the $^1E_{2g} \leftarrow {}^1A_{1g}$ transition). Similarly, the four polymers also show two characteristic bands at around 315 and 445 nm (Figure 8). All four polymers have a relatively low linear absorption ranging from 500 to 1000 nm, similar to other known organic–metal polymers.[42] This indicates low intensity loss and little temperature change caused by photon absorption when light propagates in the materials.

The NLO properties of **1**–**4** were investigated with a 532-nm laser pulse for 8 ns in a 1.21×10^{-4} M (**1**), 1.12×10^{-4} M (**2**), 1.37×10^{-4} M (**3**), or 1.16×10^{-4} M (**4**) DMF solution.

Figures 9a–d depict the Z-scan data for **1**–**4**, respectively. We find that all these polymers possess good nonlinear optical refraction effects. It is obvious that the theoretical curves (solid curves) reproduce well the general pattern of the observed experimental data (black dot). This fact suggests that the experimentally obtained NLO effects are effectively third-order in nature. The data show that these polymers have the same positive sign for the refractive nonlinearity, which gives rise to self-focusing behavior.

The NLO refractive effects were assessed by dividing the normalized Z-scan data obtained in the closed-aperture configuration by the normalized Z-scan data obtained in the open-aperture configuration.

The third-order NLO refractive index, n_2, can be derived from Equations (1), (2), and (3)[43]

$$T(Z,S)=\frac{\int_{-\infty}^{+\infty}\varepsilon_0 cn_0\pi\int_0^r|E_a(r,t,z)|^2 r\,dr\,dt}{S\int_{-\infty}^{+\infty}\frac{I_0\pi\omega_0^2}{2}e^{-(t/t_0)^2}dt} \quad (1)$$

$$E_a(r,t,z)=\frac{2\pi}{i\lambda(l-z)}e^{[i\pi r^2/\lambda(l-z)]}\int_0^\infty E(r',t,z)J_0\frac{2\pi r'r}{\lambda(l-z)}e^{[i\pi r'^2/\lambda(l-z)]}r'dr \quad (2)$$

$$E(r',t,z)=2\sqrt{\frac{I(r',t,z)}{\varepsilon_0 cn_0}}e^{\{(kn_2/\alpha_2)\ln[1+q(r',t,z)]\}} \quad (3)$$

where Z is the distance of the sample from the focal point, ε_0 and c are the permittivity and speed of light in vacuo, respectively, n_0 and n_2 are the linear and nonlinear refractive indices of the sample, respectively, r is the radial coordinate, t is the time, t_0 is the pulse width, I_0 is the peak irradiation intensity at focus, and $Z_0 = \pi\omega_0^2/\lambda$, with ω_0 being the spot radius of the laser beam at focus and λ being the wavelength of the laser; l is the distance between the aperture and focus, α_2 is the nonlinear absorption coefficient, and $S = 1 - \exp[-2(r_a/\omega_a)^2]$ is the linear aperture transmittance.

Based on Equation (1), the refractive index, n_2, was calculated to be 1.43×10^{-18} m^{2}W^{-1} for **1**, 1.43×10^{-18} m^{2}W^{-1} for **2**, 1.59×10^{-18} m^{2}W^{-1} for **3**, and 1.75×10^{-18} m^{2}W^{-1} for **4**. In accordance with the n_2 values, the effective third-order susceptibility $\chi^{(3)}$ can be calculated by $|\chi^{(3)}| = cn_o^2n_2/80\pi$; the $\chi^{(3)}$ values of **1**–**4** are 1.05×10^{-12}, 1.05×10^{-12}, 3.88×10^{-12}, and 4.27×10^{-12} esu, respectively.

The corresponding modulus of the hyperpolarizability, γ, was obtained from $|\gamma| = \chi^{(3)}/NF^4$, where N is the number density of the compound (concentration), F^4, the local field correction factor, is 3. The γ values (4.80×10^{-30} esu for **1**, 5.19×10^{-30} esu for **2**, 1.57×10^{-29} esu for **3**, and 2.04×10^{-29} esu for **4**) are larger than those observed in other ferrocenyl complexes, whose γ values range from 10^{-35} to 10^{-31} esu.[44] In general, nonlinear optical behavior governed by the nonlinear hyperpolarizability, γ, of the materials: the larger the γ value, the better the materials' NLO properties. On the other hand, from these data we can see that the γ values of the same metal ions are very close, and the γ values of **3** and **4** (Cd^{II} polymers) are a little larger than those of **1** and **2** (Pb^{II} polymers). This may be attributed to the influence of the central metal ions. The influence of these polymers' dimensionality on the third-order NLO properties is not very noticeable. Upon summarizing the limited literature relating to the third-order NLO properties of coordination polymers, we find that the coordina-

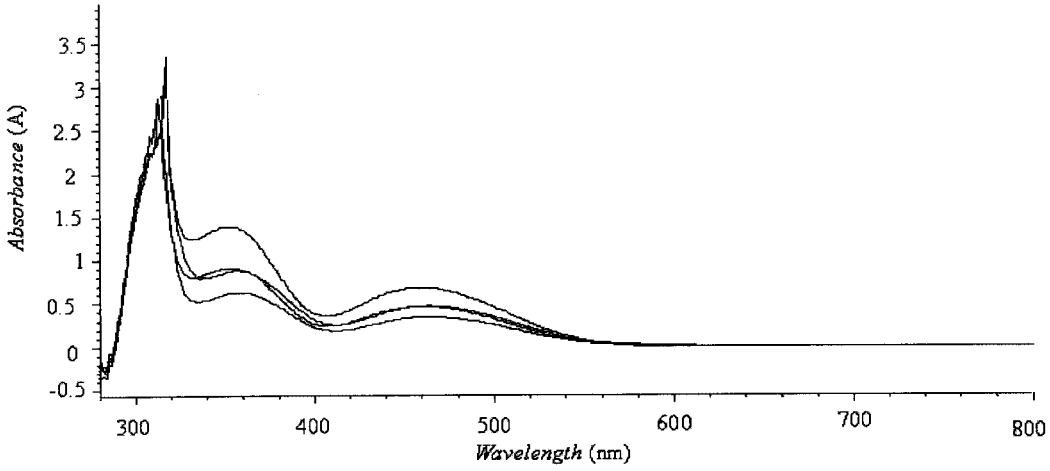

Figure 8. The UV/Vis spectra of polymers **1**–**4** in DMF solution.

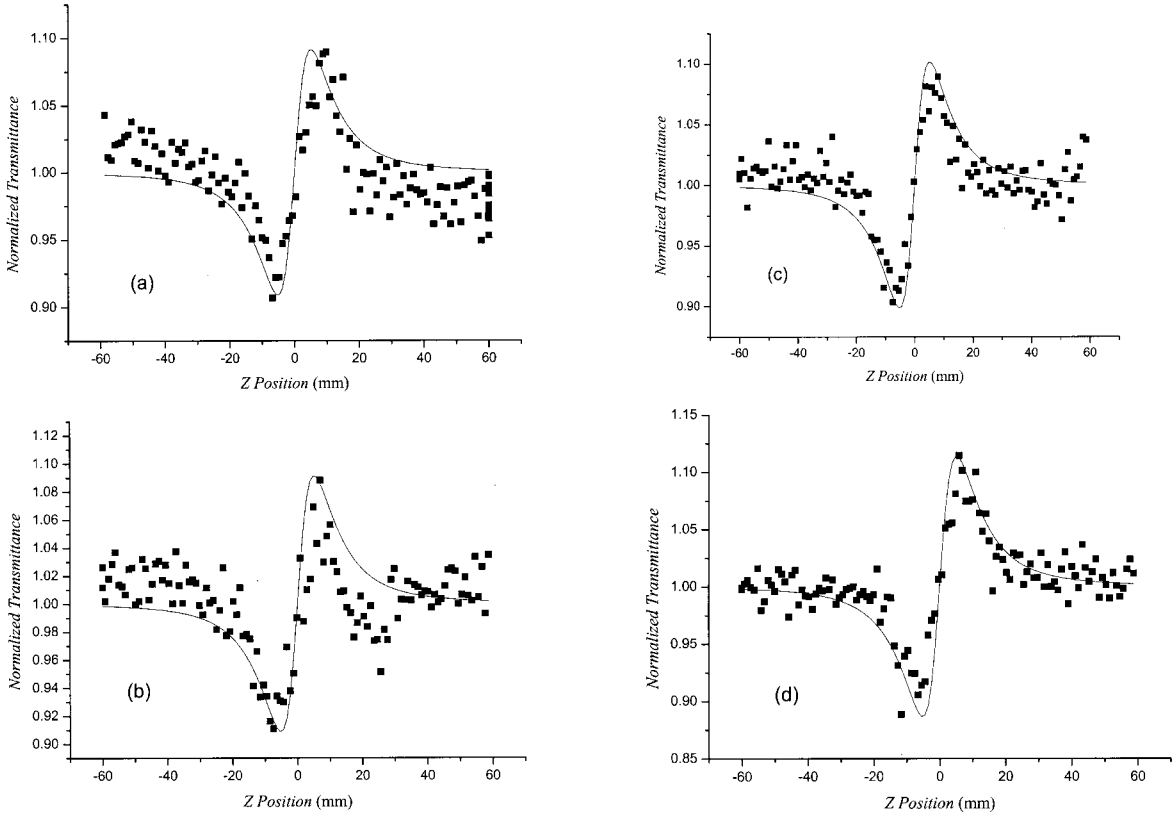

Figure 9. Z-scan data for **1**–**4**. The data were assessed by dividing the normalized Z-scan data obtained in the closed-aperture configuration by the normalized Z-scan data obtained in the open-aperture configuration. The black dots are the experimental data, and the solid curve is the theoretical fit. (a) The self-focusing effects of **1** in 1.21×10^{-4} M DMF solution at 532 nm. (b) The self-focusing effects of **2** in 1.12×10^{-4} M DMF solution at 532 nm. (c) The self-focusing effects of **3** in 1.37×10^{-4} M DMF solution at 532 nm. (d) The self-focusing effects of **4** in 1.16×10^{-4} M DMF solution at 532 nm.

tion polymers' large NLO properties may mainly be ascribed to the effect of metal ions, because the incorporation of transition metal ions into polymers can extend the π-conjugation length of the molecules, and the large π-conjugation system is favorable to increase the NLO susceptibility $\chi^{(3)}$ values.[45,46]

All the four polymers display self-focusing behavior, which is consistent with the previous conclusion[45] that the NLO properties of polymers are further controlled by the valence shell structures of the central metal ions. Nearly all the reported polymers with d^{10} valence shell metal ions give self-focusing behaviors, such as theorganic–metal polymers $[Zn(bbbt)(NCS)_2]_n$, $[Zn(pbbt)(NCS)_2]_n$,[45] $[HgI_2(4,4'\text{-azopyridine})]_n$, $[HgI_2(bpea)]_n$, $[Pb(NCS)_2(bpea)]_n$,[47] $[Cd(en)(NO_3)_2(4,4'\text{-bpy})]_n$,[48] and the ferrocenyl complexes $[Zn(4\text{-PFA})_2(NO_3)_2](H_2O)$, $[Hg_2(OAc)_4(4\text{-BPFA})_2](CH_3OH)$, $[Cd_2(OAc)_4(4\text{-BPFA})_2]$[4] etc. Other than the valence shell structures of the central metal ions, some other factors also have an effect on the intensity of the third-order optical nolinearity, such as the orbital overlap, orbital symmetry, degree of electron delocalization, linear polarizability etc. Further studies on the structure and third-order NLO properties relationship in these polymers are still underway. We believe that the study of third-order NLO properties of this kind of polymer may provide some promising candidates for the design of optical materials.

Conclusion

From the above discussion we can conclude that β-ferrocenylacrylate [FcCH=CHCOONa, Fc = $(\eta^5\text{-}C_5H_5)Fe(\eta^5\text{-}C_5H_4)$] is an excellent candidate to form extended structures whose versatile coordination modes can lead to the various and unpredictable structural geometries of different polymers. These metal–organic polymers possess good nonlinear optical refraction effects, and the metal ions play important roles in their NLO properties, because the incorporation of transition metal ions in polymers can extend the π-conjugation length of molecules, and the large π-conjugation system is favorable to increase the NLO susceptibility $\chi^{(3)}$ values.[45,46]

Experimental Section

General Details: All chemicals were of reagent grade from commercial sources and were used without further purification. β-Ferrocenylacrylic acid (FcCH=CHCOOH) was prepared according to the literature,[49] and its sodium salt was prepared by reaction with sodium methoxide. 1,1′-(1,4-Butanediyl)bis-1*H*-benzimidazole (bbbm) was prepared according to the literature.[50]

Preparation of $[Pb_6(\mu_2\text{-}OOCCH=CHFc)_2(\mu_3\text{-}OOCCH=CHFc)_2(\mu_2\text{-}\eta^2\text{-}OOCCH=CHFc)_2(\eta^2\text{-}OOCCH=CHFc)_2(\mu_4\text{-}O)_2]$ (1): FcCH=CHCOONa (27.8 mg, 0.10 mmol) in methanol (4 mL) was

 © 2005 Wiley-VCH Verlag GmbH & Co. KGaA, Weinheim

added dropwise to a methanol solution (5 mL) of $Pb(OAc)_2 \cdot 3H_2O$ (38.0 mg, 0.1 mmol). The resultant pale-orange solution was allowed to stand at room temperature in the dark. Good quality red crystals were obtained several days later (yield: 6 mg, 58%). $C_{26}H_{22}Fe_2O_{4.5}Pb_{1.5}$ (828.92): calcd. C 37.67, H 2.68; found C 37.62, H 2.72. IR (KBr): $\tilde{\nu}$ = 3440 m, 3111 m, 2361 w, 1627 s, 1483 s, 1389 s, 1247 s, 818 m, 674 m, 489 m cm^{-1}.

Preparation of $[Pb(\eta^1\text{-}\mu_2\text{-}OOCCH{=}CHFc)_2(phen)]_n$ (2): Polymer **2** was prepared in a manner analogous to that used to prepare **1**, except that another kind of subsidiary ligand phen (phen = phenanthroline) (19.8 mg, 0.1 mmol) was added. The resultant red solution was allowed to stand at room temperature in the dark. Good quality red crystals were obtained after two weeks (yield: 28 mg, 62%). $C_{38}H_{30}Fe_2N_2O_4Pb$ (897.53): calcd. C 50.85, H 3.37, N 3.12; found C 50.39, H 3.56, N 3.38. IR (KBr): $\tilde{\nu}$ = 3445 m, 3094 s, 1637 s, 1540 s, 1372 s, 1244 m, 1101 m, 975 m, 846 m, 726 m, 670 m, 489 m cm^{-1}.

Preparation of $\{[Cd(\mu_2\text{-}\eta^2\text{-}OOCCH{=}CHFc)(\eta^2\text{-}OOCCH{=}CHFc)(H_2O)_2](H_2O)_4\}_n$ (3): FcCH=CHCOONa (55.6 mg, 0.2 mmol) in 3 mL of methanol was added dropwise to a 3 mL aqueous solution of $Cd(OAc)_2 \cdot 2H_2O$ (21.1 mg, 0.1 mmol). The resultant red solution was allowed to stand at room temperature in the dark. Good quality red crystals were obtained after a week (yield: 55 mg, 76%). $C_{26}H_{34}CdFe_2O_{10}$ (730.63): calcd. C 42.74, H 4.69; found C 42.68, H 4.73. IR (KBr): 3439 s, 3125 s, 2360 w, 1636 s, 1527 m, 1401 s, 1254 m, 1037 m, 815 m, 682 m, 488 m cm^{-1}.

Preparation of $\{[Cd(\eta^2\text{-}OOCCH{=}CHFc)(bbbm)_{1.5}Cl]\cdot 1.5H_2O\}_n$ (4): A methanol solution (5 mL) of bbbm (29 mg, 0.1 mmol) was added dropwise to an aqueous solution (2 mL) of $CdCl_2 \cdot 2.5H_2O$ (22.8 mg, 0.1 mmol) to give a clear solution. FcCH=CHCOONa (27.8 mg, 0.1 mmol) in 6 mL of methanol was then added dropwise to this mixture. Two weeks later good quality red crystals were obtained from the resultant red solution at room temperature in the dark (yield: 28 mg, 48%). $C_{40}H_{41}CdClFeN_6O_{3.5}$ (865.49): calcd. N 9.72, C 55.54, H 4.72; found C 55.49, H 4.72, N 9.70. IR (KBr): $\tilde{\nu}$ = 3432 s, 3114 s, 1633 s, 1541 s, 1398 s, 1252 m, 819 m, 750 m, 684 m, 491 m cm^{-1}.

X-ray Crystallography: Crystal data and experimental details for **1**–**4** are contained in Table 1. All the data were collected on a Rigaku RAXIS-IV imaging plate area detector diffractometer using graphite monochromated Mo-K_α radiation (λ = 0.71073 Å). Red, prismatic single crystals of **1**–**4** were selected and mounted on a glass fiber. The data were collected at a temperature of 291(2) K and corrected for Lorenz-polarization effects. A correction for secondary extinction was applied. The structures were solved by direct methods and expanded using Fourier techniques. The non-hydrogen atoms were refined anisotropically. Hydrogen atoms were included but not refined. The final cycle of full-matrix least-squares refinement was based on observed reflections and variable parameters. All calculations were performed using the SHELXL-97 program.[51] Selected bond lengths and bond angles are given in Table 2.

CCDC-233289, -261304, -233290, and -233291 for **1**–**4**, respectively, contain the supplementary crystallographic data for this paper. These data can be obtained free of charge from The Cambridge Crystallographic Data Center via www.ccdc.cam.ac.uk/data_request/cif.

Physical Measurements: C, H, and N analyses were carried out on a MOD 1106 analyzer. IR data were recorded on a Bruker Tensor 27 spectrophotometer with KBr pellets in the 400–4000 cm^{-1} region. TGA-DTA measurements were performed by heating the sample from 25 °C to 900 °C at a rate of 10 °C min^{-1} in air in a Perkin–Elmer DTA-7 or TGA-7 differential thermal analyzer.

Differential pulse voltammetry studies were recorded with a CHI650 electrochemical analyzer utilizing the three-electrode configuration of a Pt working electrode, a Pt auxiliary electrode, and a commercially available saturated calomel electrode as the reference electrode with a pure N_2 gas inlet and outlet. The measurements were performed in DMF solution containing tetraethylammonium perchlorate (nBu_4NClO_4) (0.1 M) as supporting electrolyte, with a

Table 1. Crystallographic data for **1**–**4**.

	1	**2**	**3**	**4**
Formula	$C_{26}H_{22}Fe_2O_{4.5}Pb_{1.5}$	$C_{38}H_{30}Fe_2N_2O_4Pb$	$C_{26}H_{34}CdFe_2O_{10}$	$C_{40}H_{41}CdClFeN_6O_{3.5}$
Mol. mass	828.92	897.53	730.63	865.49
Crystal system	triclinic	monoclinic	monoclinic	triclinic
Crystal size [mm]	0.21 × 0.20 × 0.19	0.20 × 0.18 × 0.18	0.22 × 0.20 × 0.19	0.20 × 0.20 × 0.18
Space group	$P\bar{1}$	$C2/c$	$P2_1/n$	$P\bar{1}$
a [Å]	10.315(2)	36.790(7)	10.746(2)	9.7369(19)
b [Å]	15.429(3)	10.477(2)	7.380(15)	10.200(2)
c [Å]	15.790(3)	8.2697(17)	35.632(3)	19.829(4)
α [°]	104.82(3)	90	90	102.76(3)
β [°]	97.59(3)	92.09(3)	91.13(3)	96.48(3)
γ [°]	91.65(3)	90	90	95.22(3)
V [Å^3]	2403.0(8)	3185.4(11)	2825.4(10)	1894.6(6)
D_c [Mg m^{-3}]	2.291	1.872	1.718	1.517
Z	4	4	4	2
μ [mm^{-1}]	11.700	6.216	1.813	1.062
Refl. collected/unique	6745/6745; R(int) = 0.0000	4485/2517; R(int) = 0.0867	6153/3740; R(int) = 0.0558	4320/4320; R(int) = 0.0000
Data/restraints/parameters	6745/6/599	2517/0/214	3740/0/353	4320/2/495
R[a]	0.0553	0.0754	0.0439	0.0974
R_w[b]	0.1230	0.2012	0.0679	0.2258
GOF on F^2	1.011	1.102	0.956	1.045
$\Delta\rho_{min}$ and $\Delta\rho_{max}$ [e Å^{-3}]	–2.311 and 2.006	–3.019 and 2.411	–0.635 and 0.681	–1.529 and 0.975

[a] $R_1 = \Sigma||F_o| - |F_c||/\Sigma|F_o|$. [b] $R_W = \{\Sigma[w(F_o^2 - F_c^2)^2]/\Sigma[w(F_o^2)^2]\}^{1/2}$.

Table 2. Selected bond lengths [Å] and angles [°] for **1**–**4**.[a]

1			
Pb(1)–O(9)	2.264(8)	Pb(2)–O(5)	2.610(11)
Pb(1)–O(1)	2.400(12)	Pb(2)–Pb(3)	3.687(12)
Pb(1)–O(8)#1	2.432(12)	Pb(3)–O(9)#1	2.267(9)
Pb(1)–O(2)	2.644(13)	Pb(3)–O(7)	2.473(11)
Pb(1)–O(3)	2.694(11)	Pb(3)–O(5)	2.536(13)
Pb(2)–O(9)	2.325(9)	Pb(3)–O(6)	2.597(14)
Pb(2)–O(9)#1	2.367(8)	Pb(3)–O(4)	2.607(10)
Pb(2)–O(3)#1	2.489(9)	O(8)–Pb(1)#1	2.432(12)
O(9)–Pb(3)#1	2.267(9)	O(9)–Pb(2)#1	2.367(8)
O(3)–Pb(2)#1	2.489(9)		
O(9)–Pb(1)–O(1)	81.4(4)	O(3)#1–Pb(2)–Pb(3)	99.2(2)
O(9)–Pb(1)–O(8)#1	83.1(4)	O(5)–Pb(2)–Pb(3)	43.4(3)
O(1)–Pb(1)–O(8)#1	75.7(5)	O(9)#1–Pb(3)–O(7)	76.2(3)
O(9)–Pb(1)–O(2)	76.5(3)	O(9)#1–Pb(3)–O(5)	75.2(3)
O(1)–Pb(1)–O(2)	49.7(5)	O(7)–Pb(3)–O(5)	74.7(4)
O(8)#1–Pb(1)–O(2)	123.6(4)	O(9)#1–Pb(3)–O(6)	122.7(4)
O(9)–Pb(1)–O(3)	72.8(3)	O(7)–Pb(3)–O(6)	74.1(4)
O(1)–Pb(1)–O(3)	147.3(4)	O(5)–Pb(3)–O(6)	50.2(4)
O(8)#1–Pb(1)–O(3)	81.5(4)	O(9)#1–Pb(3)–O(4)	79.6(3)
O(2)–Pb(1)–O(3)	137.2(3)	O(7)–Pb(3)–O(4)	145.1(3)
O(9)–Pb(2)–O(9)#1	74.9(3)	O(5)–Pb(3)–O(4)	75.1(4)
O(9)–Pb(2)–O(3)#1	104.5(3)	O(6)–Pb(3)–O(4)	99.2(4)
O(9)#1–Pb(2)–O(3)#1	75.1(3)	O(9)#1–Pb(3)–Pb(2)	38.2(2)
O(9)–Pb(2)–O(5)	84.1(4)	O(7)–Pb(3)–Pb(2)	52.4(2)
O(9)#1–Pb(2)–O(5)	72.2(4)	O(5)–Pb(3)–Pb(2)	45.0(3)
O(3)#1–Pb(2)–O(5)	142.6(4)	O(6)–Pb(3)–Pb(2)	85.5(3)
O(9)–Pb(2)–Pb(3)	94.5(2)	O(4)–Pb(3)–Pb(2)	93.4(2)
O(9)#1–Pb(2)–Pb(3)	36.4(2)	Pb(2)#1–O(3)–Pb(1)	97.1(3)
Pb(1)–O(9)–Pb(2)	107.7(4)	Pb(3)–O(5)–Pb(2)	91.5(4)
Pb(1)–O(9)–Pb(2)#1	114.2(3)	Pb(1)–O(9)–Pb(3)#1	110.8(3)
Pb(2)–O(9)–Pb(2)#1	105.1(3)	Pb(3)#1–O(9)–Pb(2)	113.6(3)
Pb(3)#1–O(9)–Pb(2)#1	105.4(4)		
2			
Pb(1)–O(1)#1	2.549(12)	Pb(1)–O(1)#3	2.734(12)
Pb(1)–O(1)#2	2.549(12)	Pb(1)–O(1)	2.734(12)
Pb(1)–N(1)	2.612(11)	O(1)–Pb(1)#1	2.549(11)
Pb(1)–N(1)#3	2.612(11)		
O(1)#1–Pb(1)–O(1)#2	150.3(6)	N(1)–Pb(1)–O(1)#3	90.8(4)
O(1)#1–Pb(1)–N(1)	81.1(4)	N(1)#3–Pb(1)–O(1)#3	149.1(4)
O(1)#2–Pb(1)–N(1)	73.7(4)	O(1)#1–Pb(1)–O(1)	74.7(4)
O(1)#1–Pb(1)–N(1)#	73.7(4)	O(1)#2–Pb(1)–O(1)	121.8(4)
O(1)#2–Pb(1)–N(1)#3	81.1(4)	N(1)–Pb(1)–O(1)	149.1(4)
N(1)–Pb(1)–N(1)#3	63.8(5)	N(1)#3–Pb(1)–O(1)	90.8(4)
O(1)#1–Pb(1)–O(1)#3	121.8(4)	O(1)#3–Pb(1)–O(1)	118.2(5)
O(1)#2–Pb(1)–O(1)#3	74.7(4)	Pb(1)#1–O(1)–Pb(1)	105.3(4)
3			
Cd(1)–O(1)	2.242(4)	Cd(1)–O(5)	2.395(5)
Cd(1)–O(3)	2.274(4)	Cd(1)–O(4)	2.579(4)
Cd(1)–O(6)	2.313(4)	Cd(1)–O(2)	2.580(5)
Cd(1)–O(4)#1	2.356(5)	O(4)–Cd(1)#2	2.356(5)
O(1)–Cd(1)–O(3)	142.98(17)	O(5)–Cd(1)–O(4)	71.80(15)
O(1)–Cd(1)–O(6)	92.27(16)	O(1)–Cd(1)–O(2)	53.78(15)
O(3)–Cd(1)–O(6)	124.73(15)	O(3)–Cd(1)–O(2)	89.57(15)
O(1)–Cd(1)–O(4)#1	97.51(16)	O(6)–Cd(1)–O(2)	144.52(14)
O(3)–Cd(1)–O(4)#1	84.23(15)	O(4)#1–Cd(1)–O(2)	87.27(16)
O(6)–Cd(1)–O(4)#1	87.57(16)	O(5)–Cd(1)–O(2)	93.28(17)
O(1)–Cd(1)–O(5)	80.75(17)	O(4)–Cd(1)–O(2)	136.12(15)
O(3)–Cd(1)–O(5)	98.37(15)	Cd(1)#2–O(4)–Cd(1)	139.94(19)
O(6)–Cd(1)–O(5)	90.48(17)	O(1)–Cd(1)–O(4)	150.72(17)
O(4)#1–Cd(1)–O(5)	177.34(16)	O(3)–Cd(1)–O(4)	54.13(14)
O(6)–Cd(1)–O(4)	78.25(15)	O(4)#1–Cd(1)–O(4)	109.53(6)
4			
Cd(1)–O(1)	2.273(12)	Cd(1)–O(2)	2.476(12)
Cd(1)–N(3)	2.301(14)	Cd(1)–Cl(1)	2.506(4)
Cd(1)–N(5)	2.347(12)	Cd(1)–N(1)	2.520(13)
O(1)–Cd(1)–N(3)	148.5(5)	N(3)–Cd(1)–N(1)	79.6(4)
O(1)–Cd(1)–N(5)	91.9(4)	N(5)–Cd(1)–N(1)	166.3(4)
N(3)–Cd(1)–N(5)	88.9(4)	O(2)–Cd(1)–N(1)	89.3(4)
O(1)–Cd(1)–O(2)	54.9(4)	Cl(1)–Cd(1)–N(1)	91.4(3)
N(3)–Cd(1)–O(2)	94.0(5)	N(3)–Cd(1)–Cl(1)	108.4(3)
N(5)–Cd(1)–O(2)	84.0(4)	N(5)–Cd(1)–Cl(1)	99.5(3)
O(1)–Cd(1)–Cl(1)	102.5(4)	O(2)–Cd(1)–Cl(1)	157.4(4)
O(1)–Cd(1)–N(1)	94.0(4)		

[a] Symmetry transformations used to generate equivalent atoms: for **1**: #1 $-x + 2$, $-y + 1$, $-z + 1$; for **2**: #1 $-x + 1$, $-y - 2$, $-z - 1$; #2 x, $-y - 2$, $z + 1/2$; #3 $-x + 1$, y, $-z - 1/2$; for **3**: #1 $-x + 5/2$, $y + 1/2$, $-z + 1/2$; #2 $-x + 5/2$, $y - 1/2$, $-z + 1/2$; for **4**: #1 $-x + 4$, $-y - 3$, $-z + 2$; #2 $-x + 3$, $-y - 3$, $-z + 2$; #3 $-x + 2$, $-y - 3$, $-z + 1$.

 © 2005 Wiley-VCH Verlag GmbH & Co. KGaA, Weinheim

50-ms pulse width and a 20-ms sample width. The potential was scanned from +0.2 to +0.9 V at a scan rate of 20 $mV\,s^{-1}$.

A DMF solution of **1**–**4** was placed in the 1-mm quartz cuvette for NLO measurements. The nonlinear refraction was measured with linearly polarized laser light (λ = 532 nm; pulse width: 8 ns) generated from a Q-switched and frequency-doubled Nd-YAG laser. The spatial profiles of the optical pulses were nearly Gaussian. The laser beam was focused with a 25-cm focal-length focusing mirror. The radius of the beam waist was measured to be 35 ± 5 μm (half-width at $1/e^2$ maximum). The interval between the laser pulses was chosen to be about 5 s for operational convenience. The incident and transmitted pulse energies were measured simultaneously by two Laser Precision detectors (RjP-735 energy probes), which were linked to a computer by an IEEE interface. The NLO properties of the samples were manifested by moving the samples along the axis of the incident beam (Z-direction) with respect to the focal point.[43] An aperture 0.5 mm in radius was placed in front of the detector to assist the measurement of the self-focusing effect.

Caution! Although no problems were encountered in this work, perchlorate salts are potentially explosive. They should therefore be prepared in small quantities and handled with care.

Acknowledgments

The authors thank the National Natural Science Foundation of China (numbers 20001006 and 20371042), the Excellent Young Teachers Program in Higher Education Institute, and Henan Province for financial support.

[1] a) A. Togni, T. Hayashi, *Ferrocene, Homogeneous Catalysis*, in *Organic Synthesis and Materials Science*, VCH, Weinheim, **1995**; b) *Metallocenes* (Eds.: A. Togni, R. L. Haltermann), Wiley-VCH, New York, **1998**; c) N. J. Long, *Metallocenes*, Blackwell, Oxford, **1998**.

[2] a) N. J. Long, *Angew. Chem. Int. Ed. Engl.* **1995**, *34*, 21–38; b) M. Kira, T. Matsubara, H. Shinohara, M. Sisido, *Chem. Lett.* **1997**, 89–90; c) A. Nomoto, T. Moriuchi, S. Yamazaki, A. Ogawa, T. Hirao, *Chem. Commun.* **1998**, 1963–1964; d) H. Plenio, C. Aberle, *Organometallics* **1997**, *16*, 5950–5957.

[3] a) T. J. Pechham, A. J. Lough, I. Manners, *Organometallics* **1999**, *18*, 1030–1040; b) H. Fink, N. J. Long, A. J. Martin, G. Opromolla, A. J. P. White, D. J. Williams, P. Zanello, *Organometallics* **1997**, *16*, 2646–2650; c) P. D. Beer, F. Szemes, V. Balzani, C. M. Sala, M. G. B. Drew, S. W. Dent, M. Maestri, *J. Am. Chem. Soc.* **1997**, *119*, 11864–11875.

[4] G. Li, Y. L. Song, H. W. Hou, L. K. Li, Y. T. Fan, Y. Zhu, X. R. Meng, L. W. Mi, *Inorg. Chem.* **2003**, *42*, 913–920.

[5] a) S. S. Sun, D. T. Tran, O. S. Odongo, A. J. Lees, *Inorg. Chem.* **2002**, *41*, 132–135; b) J. A. Mata, S. Uriel, R. Llusar, E. Peris, *Organometallics* **2000**, *19*, 3797–3802; c) J. D. Carr, S. J. Coles, M. B. Hursthouse, M. E. Light, E. L. Munro, J. H. R. Tucker, J. Westwood, *Organometallics* **2000**, *19*, 3312–3315.

[6] a) Y. H. Liu, Y. L. Lu, H. C. Wu, J. C. Wang, K. L. Lu, *Inorg. Chem.* **2002**, *41*, 2592–2597; b) X. Lei, M. Shang, A. Patil, E. E. Wolf, T. P. Fehlner, *Inorg. Chem.* **1996**, *35*, 3217–3222; c) G. Baskar, K. Landfester, M. Antonietti, *Macromolecules* **2000**, *33*, 9228–9232; d) D. N. Hendrickson, S. M. J. Aubin, R. C. Squire, K. Folting, W. E. Streib, G. Christou, *Angew. Chem. Int. Ed. Engl.* **1995**, *34*, 887–889; e) H. W. Hou, L. K. Li, G. Li, Y. T. Fan, Y. Zhu, *Inorg. Chem.* **2003**, *42*, 3501–3508.

[7] C. Ramon, L. Concepción, M. Elies, E. Enric, *Inorg. Chem.* **1998**, *37*, 5686–5689.

[8] D. Guo, B. G. Zhang, C. Y. Duan, X. Cao, Q. J. Meng, *Dalton Trans.* **2003**, 282–284.

[9] G. L. Zheng, J. F. Ma, Z. M. Su, L. K. Yan, J. Yang, Y. Y. Li, J. F. Liu, *Angew. Chem. Int. Ed.* **2004**, *43*, 2409–2411.

[10] G. Li, H. W. Hou, L. K. Li, X. R. Meng, Y. T. Fan, Y. Zhu, *Inorg. Chem.* **2003**, *42*, 4995–5004.

[11] H. W. Hou, L. K. Li, Y. Zhu, Y. T. Fan, Y. Q. Qiao, *Inorg. Chem.* **2004**, *43*, 4767–4774.

[12] V. Chandrasekhar, S. Nagendran, S. Bansal, M. A. Kozee, D. R. Powell, *Angew. Chem. Int. Ed.* **2000**, *39*, 1833–1835.

[13] K. C. Kumara Swamy, S. Nagabrahmanandachari, K. Raghuraman, *J. Organomet. Chem.* **1999**, *587*, 132–135.

[14] X. R. Meng, G. Li, H. W. Hou, H. Y. Han, Y. T. Fan, Y. Zhu, C. X. Du, *J. Organomet. Chem.* **2003**, *679*, 153–161.

[15] a) F. A. Cotton, L. R. Fallvello, A. H. Reid, J. H. Tocher, *J. Organomet. Chem.* **1987**, *319*, 87–97; b) M. R. Churchill, Y. J. Li, D. Nalewajer, P. M. Schaber, P. M. Dorfman, *Inorg. Chem.* **1985**, *24*, 2684–2687.

[16] X. R. Meng, H. W. Hou, G. Li, B. X. Ye, T. Z. Ge, Y. T. Fan, Y. Zhu, H. Sakiyama, *J. Organomet. Chem.* **2004**, *689*, 1218–1229.

[17] R. Graziani, U. Casellato, G. Plazzogna, *J. Organomet. Chem.* **1980**, *187*, 381–690.

[18] N. Prokopuk, D. F. Shriver, *Inorg. Chem.* **1997**, *36*, 5609–5613.

[19] D. Guo, H. G. Mo, C. Y. Duan, F. Lu, Q. J. Meng, *J. Chem. Soc., Dalton Trans.* **2002**, 2593–2594.

[20] D. Guo, B. G. Zhang, C. Y. Duan, X. Cao, Q. J. Meng, *Dalton Trans.* **2003**, 515–516.

[21] H. W. Hou, G. Li, L. K. Li, Y. Zhu, X. R. Meng, Y. T. Fan, *Inorg. Chem.* **2003**, *42*, 428–435.

[22] R. D. Shannon, *Acta Crystallogr., Sect. A* **1976**, *32*, 751–767.

[23] P. R. Harrison, A. T. Steel, *J. Organomet. Chem.* **1982**, *239*, 105–113.

[24] a) D. J. Williams, S. J. Maginn, R. J. Davey, *Polyhedron* **1994**, *13*, 1683–1688; b) M. R. S. J. Foreman, M. J. Plater, J. M. S. Skakle, *J. Chem. Soc., Dalton Trans.* **2001**, 1897–1903.

[25] R. G. Bryant, V. P. Chacko, M. C. Etter, *Inorg. Chem.* **1984**, *23*, 3580–3584.

[26] Y. G. Shin, M. J. Hampden-Smith, T. T. Kodas, E. N. Duesler, *Polyhedron* **1993**, *12*, 1453–1458.

[27] a) C. Caffney, P. G. Harrision, T. J. King, *J. Chem. Soc., Chem. Commun.* **1980**, 1251–1253; b) S. Asirvatham, M. A. Khan, K. M. Nicholas, *Inorg. Chem.* **2000**, *39*, 2006–2007; c) A. M. Atria, A. Vega, M. Contreras, J. Valenzuela, E. Spodine, *Inorg. Chem.* **1999**, *38*, 5681–5685; d) Y. Yang, J. Pinkas, M. Noltemeyer, H. G. Schmidt, H. W. Roeskey, *Angew. Chem. Int. Ed.* **1999**, *38*, 664–666.

[28] a) D. C. Bradley, H. Chudzynska, D. M. Frigo, M. E. Hammond, M. B. Hursthouse, M. A. Mazid, *Polyhedron* **1990**, *9*, 719–726; b) C. S. Weinert, I. A. Guzei, A. L. Rheingold, L. R. Sita, *Organometallics* **1998**, *17*, 498–500; c) M. Cesari, *Gazz. Chim. Ital.* **1980**, *110*, 365; d) J. B. Parise, Y. Ko, *Chem. Mater.* **1994**, *6*, 718–720.

[29] a) A. Pandey, V. D. Gupta, H. Noth, *Eur. J. Inorg. Chem.* **1999**, 1291–1293; b) L. Mam, D. A. Payne, *Chem. Mater.* **1994**, *6*, 875–877; c) L. G. Hubert-Pfalzgraf, S. Daniele, R. Papiernik, M. C. Massiani, B. Septe, J. Vaissermann, J. C. Daran, *J. Mater. Chem.* **1997**, *7*, 753–762; d) J. Caruso, M. J. Hampden-Smith, E. N. Duesler, *J. Chem. Soc., Chem. Commun.* **1995**, 1041–1042.

[30] C. S. McCowan, T. L. Groy, M. T. Caudle, *Inorg. Chem.* **2002**, *41*, 1120–1127.

[31] L. H. Zhu, M. H. Zeng, B. H. Ye, X. M. Chen, *Z. Anorg. Allg. Chem.* **2004**, *630*, 952–955.

[32] A. Morsali, A. R. Mahjoub, S. J. Darzi, M. J. Soltanian, *Z. Anorg. Allg. Chem.* **2003**, *629*, 2596–2599.

[33] J. M. Harrowfield, H. Miyamae, B. W. Skelton, A. A. Soudi, A. H. White, *Aust. J. Chem.* **1996**, *49*, 1165–1170.

[34] A. R. Mahjoub, A. Morsali, *Polyhedron* **2002**, *21*, 197–203.

[35] A. K. Hall, J. M. Engelhard, A. Morsali, A. A. Soudi, A. Yanovsky, *CrystEngComm* **2000**, 13.

[36] A. Morsali, M. Payheghader, M. S. Salehi, *Z. Anorg. Allg. Chem.* **2002**, *628*, 12–14.

 © 2005 Wiley-VCH Verlag GmbH & Co. KGaA, Weinheim

[37] a) R. Horikoshi, T. Mochida, H. Moriyama, *Inorg. Chem.* **2002**, *41*, 3017–3024; b) A. Ion, M. Buda, J. C. Moutet, E. Saint-Aman, G. Royal, I. Gautier-Luneau, M. Bonin, R. Ziessel, *Eur. J. Inorg. Chem.* **2002**, 1357–1366; c) C. Y. Duan, Y. P. Tian, Z. H. Liu, X. Z. You, T. C. W. Mak, *J. Organomet. Chem.* **1998**, *570*, 155–162; d) E. M. Barranco, O. Crespo, M. C. Gimeno, P. G. Jones, A. Laguna, M. D. Villacampa, *J. Organomet. Chem.* **1999**, *592*, 258–264; e) Y. M. Xu, P. Saweczko, H. B. Kraatz, *J. Organomet. Chem.* **2001**, *637*, 335–342.

[38] a) P. D. Beer, C. Blackburn, J. F. McAleer, H. Sikanyika, *Inorg. Chem.* **1990**, *29*, 378; b) J. D. Carr, S. J. Coles, M. B. Hursthouse, M. E. Light, E. L. Munro, J. H. R. Tucker, J. Westwood, *Organometallics* **2000**, *19*, 3312–3315.

[39] E. M. Barranco, O. Crespo, M. C. Gimeno, P. G. Jones, A. Laguna, C. Sarroca, *J. Chem. Soc., Dalton Trans.* **2001**, 2523–2529.

[40] a) J. T. Lin, S. S. Sun, J. J. Wu, Y. C. Liaw, K. J. Lin, *J. Organomet. Chem.* **1996**, *517*, 217–226; b) J. T. Lin, S. S. Sun, J. J. Wu, L. Lee, K. J. Lin, Y. F. Huang, *Inorg. Chem.* **1995**, *34*, 2323–2333; c) L. K. Yeung, J. E. Kim, Y. K. Chung, P. H. Rieger, D. A. Sweigart, *Organometallics* **1996**, *15*, 3891–3897; d) O. Briel, K. Sünkel, I. Krossing, H. Nöth, E. Schmälzlin, K. Meerholz, C. Bräuchle, W. Beck, *Eur. J. Inorg. Chem.* **1999**, 483–490; e) J. Mata, S. Uriel, E. Peris, R. Llusar, S. Houbrechts, A. Persoons, *J. Organomet. Chem.* **1998**, *562*, 197–202; f) I. S. Lee, Y. K. Chung, J. Mun, C. S. Yoon, *Organometallics* **1999**, *18*, 5080–5085; g) I. S. Lee, S. S. Lee, Y. K. Chung, D. Kim, N. W. Song, *Inorg. Chim. Acta* **1998**, *279*, 243–248.

[41] Y. S. Sohn, D. N. Hendrickson, H. B. Gray, *J. Am. Chem. Soc.* **1971**, *93*, 3603–3612.

[42] A. T. Armstrong, A. T. Smith, E. Elder, S. P. McGlynn, *J. Chem. Phys.* **1967**, *46*, 4321–4328.

[43] a) M. Sheik-Bahae, A. A. Said, T. H. Wei, D. J. Hagan, E. W. V. Stryland, *IEEE J. Quantum Electron.* **1990**, *26*, 760–769; b) H. W. Hou, X. Q. Xin, J. Liu, M. Q. Chen, S. Shi, *J. Chem. Soc., Dalton Trans.* **1994**, 3211–3214.

[44] a) Y. P. Tian, Z. L. Lu, X. Z. You, *Acta Chim. Sin. (Chin. Ed.)* **1999**, *57*, 1068–1072; b) S. Ghosal, M. Samoc, P. N. Prasad, J. J. Tufariello, *J. Phys. Chem.* **1990**, *94*, 2847–2851; c) Z. Yuan, G. Stringer, I. R. Jobe, D. Kreller, K. Scott, L. Koch, N. J. Taylor, T. B. Marder, *J. Organomet. Chem.* **1993**, *452*, 115–120.

[45] X. R. Meng, Y. L. Song, H. W. Hou, Y. T. Fan, G. Li, Y. Zhu, *Inorg. Chem.* **2003**, *42*, 1306–1315.

[46] a) H. W. Hou, X. R. Meng, Y. L. Song, Y. T. Fan, Y. Zhu, H. J. Lu, C. X. Du, W. H. Shao, *Inorg. Chem.* **2002**, *41*, 4068–4075; b) H. W. Hou, Y. L. Wei, Y. L. Song, Y. Zhu, L. K. Li, Y. T. Fan, *J. Mater. Chem.* **2002**, *12*, 838–843.

[47] Y. Y. Niu, Y. L. Song, T. N. Chen, Z. L. Xue, X. Q. Xin, *CrystEngComm* **2001**, 36.

[48] L. K. Li, B. Y. Chen, Y. L. Song, G. Li, H. W. Hou, Y. T. Fan, L. W. Mi, *Inorg. Chim. Acta* **2003**, *344*, 95–101.

[49] G. D. Broadhead, J. M. Osgerby, P. L. Pauson, *J. Chem. Soc.* **1958**, 650–654.

[50] X. J. Xie, G. S. Yang, L. Cheng, F. Wang, *Huaxue Shiji (Chin. Ed.)* **2000**, *22*, 222–223.

[51] G. M. Sheldrick, *SHELX-97*, Program for the Solution and Refinement of Crystal Structures, University of Göttingen, Germany, **1997**.

Received: January 22, 2005
Published Online: July 12, 2005

 © 2005 Wiley-VCH Verlag GmbH & Co. KGaA, Weinheim

Formation of C–C Bonds in Diiron Complexes by Addition of Carbanions to Alkynyl(methoxy)carbene Ligands

Luigi Busetto,*[a] Fabio Marchetti,[a] Stefano Zacchini,[a] and Valerio Zanotti[a]

Keywords: Carbanions / Carbene ligands / C–C coupling / Iron

Addition of cyanide ions to the alkynyl(methoxy)carbene complexes $[Fe_2\{\mu\text{-}CN(Me)(R)\}(\mu\text{-}CO)(CO)\{C_\alpha(OMe)C_\beta{\equiv}C_\gamma R'\}(Cp)_2]^+$ (R = Xyl, R′ = Tol, **1a**; R = Xyl, R′ = Ph, **1b**; R = Xyl, R′ = Me_3Si, **1c**; R = Me, R′ = Tol, **1d**; R = Me, R′ = Ph, **1e**) occurs selectively at C_α to afford the 1,1-disubstituted σ-propargyl complexes $[Fe_2\{\mu\text{-}CN(Me)(R)\}(\mu\text{-}CO)(CO)\{C(OMe)(CN)(C{\equiv}CR')\}(Cp)_2]$ (R = Xyl, R′ = Tol, **2a**; R = Xyl, R′ = Ph, **2b**; R = Xyl, R′ = Me_3Si, **2c**; R = Me, R′ = Tol, **2d**; R = Me, R′ = Ph, **2e**). Conversely, the stabilised carbanaions $[CH(R)_2]^-$ (R = CN, CO_2Me) add at the C_γ position with subsequent hydrogen migration to C_β to give the 1-σ-buta-1,3-dienyl complexes $[Fe_2\{\mu\text{-}CN(Me)(Xyl)\}(\mu\text{-}CO)(CO)\{C_\alpha(OMe){=}C_\beta HC_\gamma(Tol){=}C_\delta(R)_2\}(Cp)_2]$ (R = CN, **3a**; CO_2Me, **3b**). No migration is possible in the absence of hydrogen atoms at C_δ, therefore addition of $[C(Me)(CO_2Me)_2]^-$ to **1a** results in the formation of the σ-allenyl complex $[Fe_2\{\mu\text{-}CN(Me)(Xyl)\}(\mu\text{-}CO)(CO)\{C_\alpha(OMe){=}C_\beta{=}C_\gamma(Tol)C_\delta(Me)(CO_2Me)_2\}(Cp)_2]$ (**4**). Protonation of the neutral complexes **3b** and **4** affords the vinyl(methoxy)carbene complexes $[Fe_2\{\mu\text{-}CN(Me)(Xyl)\}(\mu\text{-}CO)(CO)\{C_\alpha(OMe)C_\beta H{=}C_\gamma(Tol)C_\delta(R)(CO_2Me)_2\}]^+$ (R = H, **5**; Me, **6**), which exist in solution as mixtures of (*E*)- and (*Z*)-isomers in dynamic equilibrium, as shown by VT NMR studies. The cationic complex **6** shows electrophilic behaviour. Thus, addition of CN^- results in the σ-allyl complex $[Fe_2\{\mu\text{-}CN(Me)(Xyl)\}(\mu\text{-}CO)(CO)\{C_\alpha(OMe)(CN)[C_\beta H{=}C_\gamma(Tol)C_\delta(Me)(CO_2Me)_2]\}(Cp)_2]$ (**7**), whereas the reaction with Me_2NH affords the vinyl acyl complex $[Fe_2\{\mu\text{-}CN(Me)(Xyl)\}(\mu\text{-}CO)(CO)\{C_\alpha(O)C_\beta H{=}C_\gamma(Tol)C_\delta(Me)(CO_2Me)_2\}(Cp)_2]$ (**8**). The crystal structures of **2b** and **3a·CH_2Cl_2** have been determined.

(© Wiley-VCH Verlag GmbH & Co. KGaA, 69451 Weinheim, Germany, 2005)

Introduction

Alkynyl(alkoxy)carbenes represent a quite important class of organometallic complexes, since they are potentially useful reagents for the synthesis of organic compounds.[1] Most of the studies that have appeared to date concern mononuclear chromium and tungsten compounds of the type $(CO)_5M{=}C(OEt)C{\equiv}CR$. Their reactivity includes addition of protic nucleophiles (amines, imines, alcohols, thiols, phosphanes, carboxylic acids)[2–4] and carbon nucleophiles (alkynes, enamines, enaminones, enol ethers),[5–7] together with a large variety of cyclisation reactions.[8–10] We have recently reported the synthesis and the reactivity towards amines of the diiron alkynyl(methoxy)carbene complexes $[Fe_2\{\mu\text{-}CN(Me)(R)\}(\mu\text{-}CO)(CO)\{C_\alpha(OMe)C_\beta{\equiv}C_\gamma R'\}(Cp)_2]^+$ (R = Xyl, R′ = Tol, **1a**; R = Xyl, R′ = Ph, **1b**; R = Xyl, R′ = Me_3Si, **1c**; R = Me, R′ = Tol, **1d**; R = Me, R′ = Ph, **1e**).[11] The addition of amines to **1** was found to be completely regioselective at C_γ, whereas in the case of the mononuclear species $(CO)_5M{=}C(OEt)C{\equiv}CR$, addition at the carbene carbon C_α has also been observed.[1] The different regiochemistry observed could be due to either steric and/or electronic factors. In order to shed more light on this point, we decided to study the reactivity of **1** with other nucleophiles, and here we report some reactions involving **1** and different carbanions, such as CN^-, $[CH(R)_2]^-$ (R = CN, CO_2Me) and $[CMe(CO_2Me)_2]^-$. These reactions represent a direct way to form new C–C bonds in a diiron complex and, therefore, are potentially interesting in order to build new coordinated organic species.

[a] Dipartimento di Chimica Fisica ed Inorganica, Università di Bologna,
Viale Risorgimento 4, 40136 Bologna, Italy
Fax: +39 0512093690
E-mail: busetto@ms.fci.unibo.it

Results and Discussion

The reaction of the alkynyl(methoxy)carbene complexes $[Fe_2\{\mu\text{-}CN(Me)(R)\}(\mu\text{-}CO)(CO)\{C_\alpha(OMe)C_\beta{\equiv}C_\gamma R'\}(Cp)_2]^+$ (R = Xyl, R′ = Tol, **1a**; R = Xyl, R′ = Ph, **1b**; R = Xyl, R′ = Me_3Si, **1c**; R = Me, R′ = Tol, **1d**; R = Me, R′ = Ph, **1e**) with $(nBu_4N)(CN)$ in CH_2Cl_2 solution (Scheme 1) results in the selective addition of the cyanide ion to the carbene carbon to give the 1,1-disubstituted σ-propargyl complexes $[Fe_2\{\mu\text{-}CN(Me)(R)\}(\mu\text{-}CO)(CO)\{C(OMe)(CN)(C{\equiv}CR')\}(Cp)_2]$ (R = Xyl, R′ = Tol, **2a**; R = Xyl, R′ = Ph, **2b**; R = Xyl, R′ = Me_3Si, **2c**; R = Me, R′ = Tol, **2d**; R = Me, R′ = Ph, **2e**) in good yields (70–80%). The reaction can be completely reversed by addition of CF_3SO_3Me.

The IR spectra of **2** show, as expected,[12] ν(CO) at around 1970 and 1790 cm^{-1} for the terminal and bridging carbonyls, respectively, and a weak ν(CN) absorption (at

 DOI: 10.1002/ejic.200500093

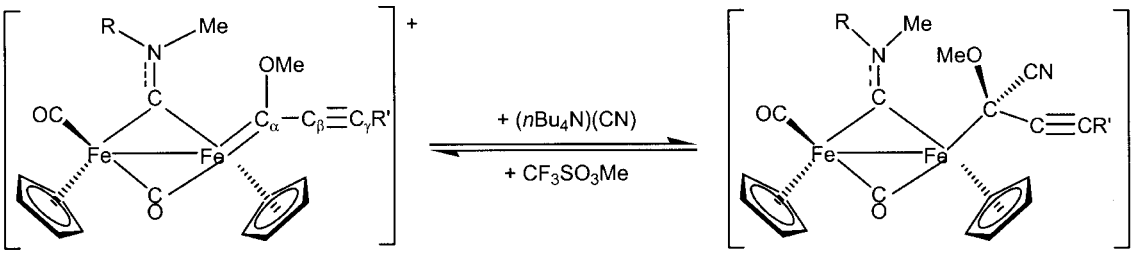

R	R'	
Xyl	Tol	**1a**
Xyl	Ph	**1b**
Xyl	$SiMe_3$	**1c**
Me	Tol	**1d**
Me	Ph	**1e**

R	R'	
Xyl	Tol	**2a**
Xyl	Ph	**2b**
Xyl	$SiMe_3$	**2c**
Me	Tol	**2d**
Me	Ph	**2e**

Scheme 1.

2190 cm^{-1} for **2a**) that is shifted to 2142 cm^{-1} in [Fe_2{μ-CN(Me)(Xyl)}(μ-CO)(CO){C(OMe)(^{13}CN)(C≡CTol)}-$(Cp)_2$] (prepared from the reaction of **1a** with K^{13}CN) because of an isotope effect. The NMR spectra of **2** evidence the presence in solution of one single isomer. This is interesting, since complexes **1** are chiral and the addition of CN^- produces a second chiral centre, thus making possible the presence of diastereomeric species. The fact that only one form is present in solution indicates that the cyanide addition is regio- and stereoselective, occurring at one specific face of the plane containing the alkynyl(methoxy)carbene ligand; therefore, a racemic mixture of one single diastereomer is selectively formed.

Three low-field resonances in the ^{13}C NMR spectra are attributable to the bridging carbyne ($\delta \approx 335$ ppm), and to the bridging and the terminal carbonyls ($\delta \approx 270$ and 215 ppm, respectively). The CN carbon resonates at $\delta \approx 126$ ppm, whereas the C≡C group shows two distinct signals at $\delta = 94$–105 and 89–99 ppm. Finally, the sp^3 propargylic carbon resonates in the high-field region of the spectra, as expected for a metal-bound alkyl ($\delta \approx 50$ ppm).

The molecular structure of complex **2b** has been determined by single-crystal X-ray analysis (Figure 1 and Table 1). The molecule contains a terminal C(OMe)(CN)(C≡CPh) ligand bound to Fe_2{μ-CN(Me)(Xyl)}(μ-CO)(CO)$(Cp)_2$, which shows a *cis* geometry of the Cp ligands with the Xyl group placed in the opposite side of the

Table 1. Selected bond lengths [Å] and angles [°] for complex **2b**.

Fe(1)–Fe(2)	2.5271(10)	C(13)–N(1)	1.317(5)
Fe(2)–C(11)	1.763(6)	C(14)–N(1)	1.468(6)
Fe(1)–C(12)	1.856(5)	C(23)–O(1)	1.430(5)
Fe(2)–C(12)	1.992(5)	C(24)–O(1)	1.426(5)
Fe(1)–C(13)	1.839(4)	C(23)–C(25)	1.463(7)
Fe(2)–C(13)	1.897(4)	C(25)–N(2)	1.144(6)
Fe(1)–C(23)	2.091(5)	C(23)–C(26)	1.470(7)
C(11)–O(11)	1.140(6)	C(26)–C(27)	1.188(6)
C(12)–O(12)	1.172(5)	C(27)–C(28)	1.437(7)
Fe(1)–C(23)–O(1)	110.9(3)	C(23)–C(26)–C(27)	174.8(5)
Fe(1)–C(23)–C(25)	108.0(3)	C(26)–C(27)–C(28)	176.5(5)
Fe(1)–C(23)–C(26)	107.3(3)	O(1)–C(23)–C(25)	108.6(4)
C(23)–C(25)–N(2)	177.5(6)	O(1)–C(23)–C(26)	111.2(4)

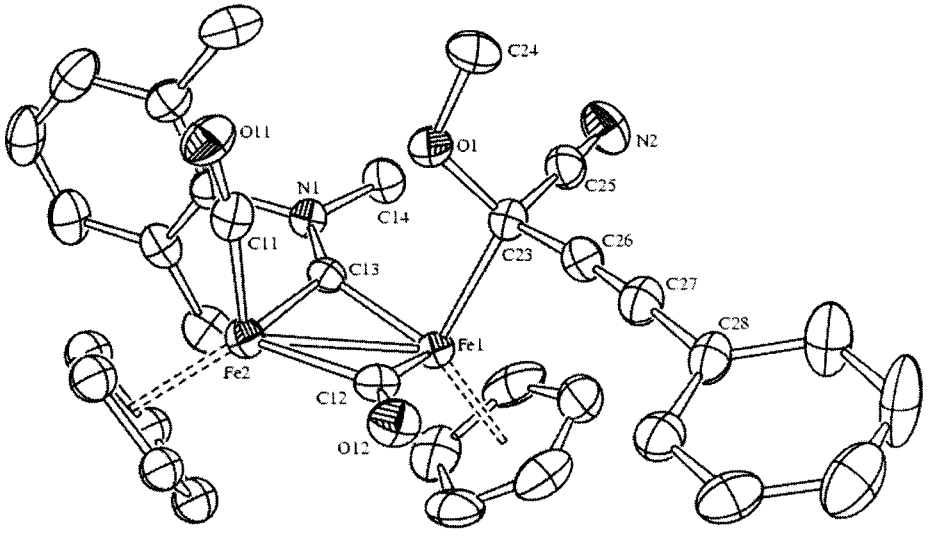

Figure 1. Molecular structure of **2b**, with key atoms labelled (all H atoms have been omitted). Displacement ellipsoids are at 30% probability level. Only the main image of the disordered Cp bound to Fe(2) is drawn.

 © 2005 Wiley-VCH Verlag GmbH & Co. KGaA, Weinheim

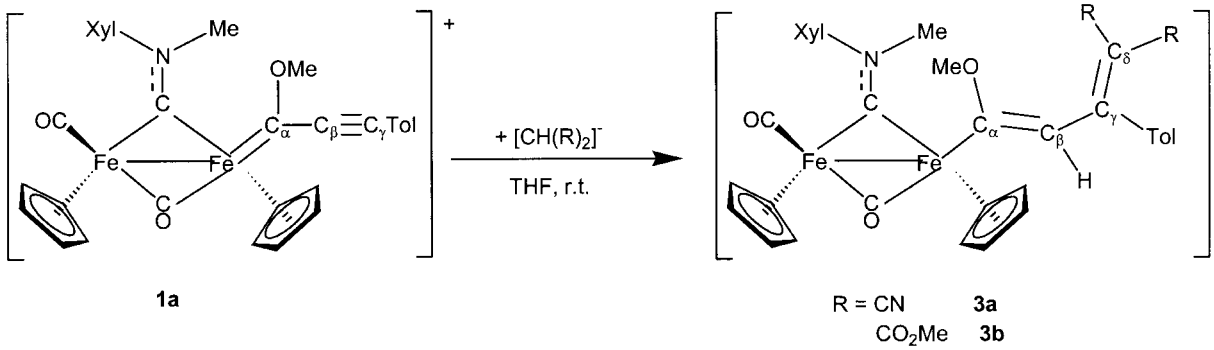

Scheme 2.

σ-propargyl, as previously found in analogous diiron and diruthenium complexes.[13,14] As in **1a**,[11] the C(13)–N(1) interaction [1.317(5) Å] suggests some double-bond character, and thus the aminocarbyne ligand can be alternatively described as a bridging iminium ion.

The bridging CO shows a marked asymmetry [Fe(1)–C(12) = 1.856(5) and Fe(2)–C(12) = 1.992(5) Å] as consequence of the different electronic properties of the terminal ligands [i.e. the σ-propargyl and CO]. Similarly, the bridging aminocarbyne is also asymmetric, although to a lesser extent [Fe(1)–C(13) = 1.839(4) and Fe(2)–C(13) = 1.897(4) Å]; an analogous behaviour has been observed previously in other diiron complexes containing bridging aminocarbyne and bridging carbonyl ligands.[12b,12c,13b,13c,15] The Fe(1)–C(23) distance [2.091(5) Å] is that of a pure Fe–C(sp^3) σ-bond and is similar to that found in the cyanomethyl complex [$Fe_2\{\mu$-$CN(Me)_2\}(\mu$-$CO)(CO)(CH_2CN)(Cp)_2$] [2.068(3) Å].[15] The propargylic nature of the ligand is indicated by the fact that the C(23)–C(26) interaction [1.470(7) Å] is a single bond whereas C(26)–C(27) [1.188(6) Å] is a triple bond; moreover, the C(23)–C(26)–C(27)–C(28) chain is almost linear [C(23)–C(26)–C(27) = 174.8(5)°; C(26)–C(27)–C(28) = 176.5(5)°]. The C(25)–N(2) interaction [1.144(6) Å] is typical for the triple bond in organic nitriles, and C(25) shows sp hybridisation [C(23)–C(25)–N(2) = 177.5(6)°].

Table 2. Selected bond lengths [Å] and angles [°] for complex **3a**.

Fe(1)–Fe(2)	2.5110(9)	C(13)–N(1)	1.318(4)
Fe(2)–C(11)	1.758(4)	C(23)–O(1)	1.348(4)
Fe(1)–C(12)	1.859(3)	C(23)–C(25)	1.413(5)
Fe(2)–C(12)	2.008(3)	C(25)–C(26)	1.406(5)
Fe(1)–C(13)	1.834(3)	C(26)–C(27)	1.411(5)
Fe(2)–C(13)	1.894(3)	C(27)–C(28)	1.421(5)
Fe(1)–C(23)	1.936(3)	C(28)–N(2)	1.158(4)
C(11)–O(11)	1.153(4)	C(27)–C(29)	1.440(7)
C(12)–O(12)	1.178(4)	C(29)–N(3)	1.149(5)
Fe(1)–C(23)–O(1)	116.6(2)	C(26)–C(27)–C(28)	122.5(3)
Fe(1)–C(23)–C(25)	121.9(2)	C(26)–C(27)–C(29)	121.6(3)
O(1)–C(23)–C(25)	121.5(3)	C(28)–C(27)–C(29)	115.9(3)
C(23)–C(25)–C(26)	132.6(3)	C(27)–C(28)–N(2)	179.6(4)
C(25)–C(26)–C(27)	124.5(3)	C(27)–C(29)–N(3)	179.2(4)

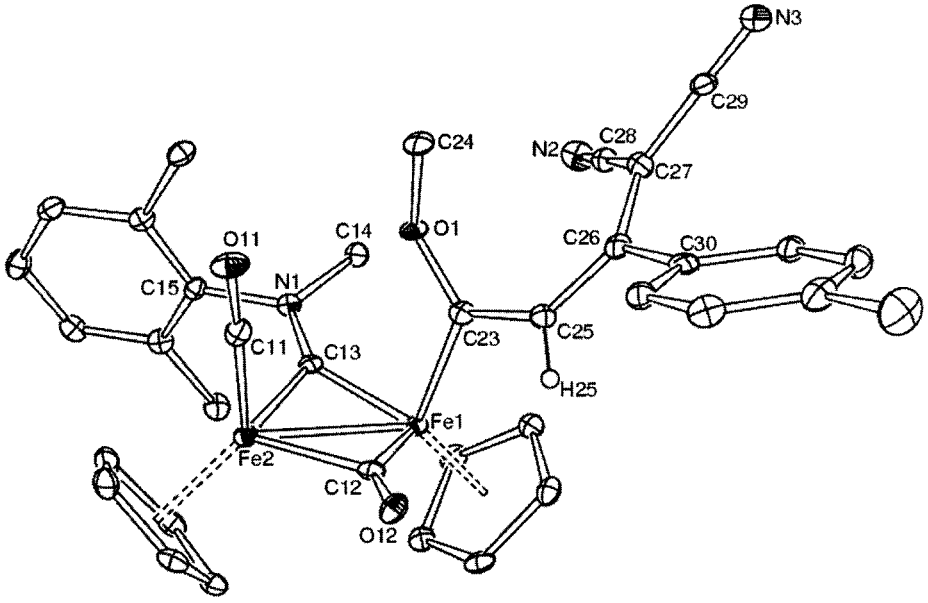

Figure 2. Molecular structure of **3a**, with key atoms labelled [all H atoms, except H(25), have been omitted]. Displacement ellipsoids are at 30% probability level.

 © 2005 Wiley-VCH Verlag GmbH & Co. KGaA, Weinheim

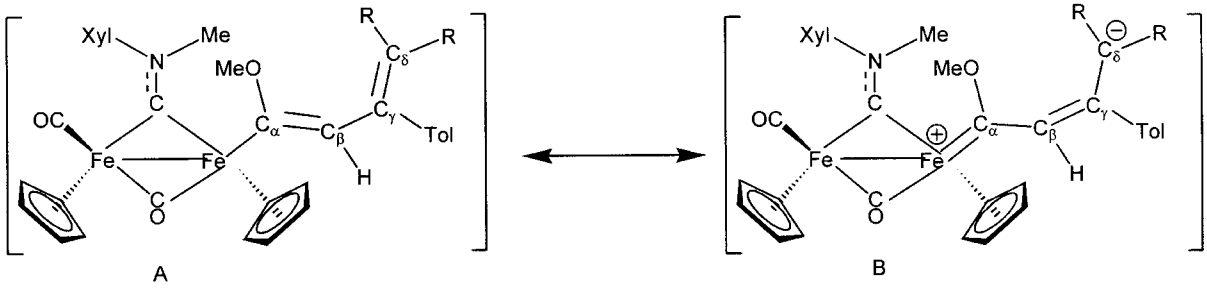

Scheme 3.

The molecular structure of **2b** indicates that cyanide addition has occurred stereoselectively from a single side of the plane containing the alkynyl(methoxy)carbene ligand, thus explaining the observed formation of a single isomer.

The addition of stabilised carbanions of the type $[CH(R)_2]^-$ (R = CN, CO_2Me) to **1a** occurs differently (Scheme 2) and results in the formation of the 1-σ-buta-1,3-dienyl complexes $[Fe_2\{\mu\text{-}CN(Me)(Xyl)\}(\mu\text{-}CO)(CO)\{C_\alpha(OMe)=C_\beta HC_\gamma(Tol)=C_\delta(R)_2\}(Cp)_2]$ (R = CN, **3a**; CO_2Me, **3b**) in good yields (60–70%). Compounds **3** have been fully characterised spectroscopically and, moreover, the crystal structure of **3a** has been determined by X-ray diffraction (Figure 2 and Table 2).

The molecule retains the $Fe_2\{\mu\text{-}CN(Me)(Xyl)\}(\mu\text{-}CO)(CO)(Cp)_2$ core present in the parent compound **1a**, to which the new terminal 1-σ-buta-1,3-dienyl ligand $C_\alpha(OMe)=C_\beta HC_\gamma(Tol)=C_\delta(CN)_2$ is bound. The almost equal C(23)–C(25) [1.413(5) Å], C(25)–C(26) [1.406(5) Å] and C(26)–C(27) [1.411(5) Å] distances indicate a strong delocalisation inside the butadienyl ligand, probably because of the presence of the strongly electron-withdrawing cyano groups. It is noteworthy that σ-butadienyl ligands usually show an alternating trend of the C–C bonds as, for example in $[Fe(Cp)(CO)_2(CH=CHCH=CHBr)]$ [1.341(4), 1.426(4) and 1.320(4) Å].[16] The delocalisation in the ligand causes some π-back-donation from the metal and, in fact, the Fe(1)–C(23) bond length [1.936(3) Å] is shorter than a pure Fe–C(sp^2) σ-interaction; for instance, 1.971(3) Å in $[Fe(Cp)(CO)_2(CH=CHCH=CHBr)]$[16] and 1.956(7) Å in the vinyl complex $[Fe_2\{\mu\text{-}CN(Me)(Xyl)\}(\mu\text{-}CO)(CO)\{C(OMe)=CHC(=NPh)(Tol)\}(Cp)_2]$.[11] For comparison, the Fe=C(carbene) distance in the parent compound **1a** is 1.849(7) Å.[11] These data suggest that the1-σ-buta-1,3-dienyl complex **3a** can be alternatively described as a zwitterionic vinyl carbene (resonance form B in Scheme 3), although the first form prevails.

From a stereochemical point of view, the C(23)=C(25) bond possesses an *E* configuration, whereas the ligand adopts an *s-cis* conformation about C(25)–C(26); the fact that the latter has a partial double-bond character also makes this conformation rigid in solution. This is fully confirmed by NOE experiments, which show a strong enhancement of the Tol protons after irradiation of H(25).

The NMR spectra of **3** show the presence of a single species in solution, therefore the reactions are completely regio- and stereoselective. The main feature of the ^1H NMR spectra is represented by the resonances at δ = 5.98 (**3a**) and 5.43 ppm (**3b**) attributable to C_β-H. The C_β and C_γ carbons of the 1-σ-buta-1,3-dienyl ligand appear at similar chemical shifts in both **3a** and **3b** [δ = 118.9 and 121.4 ppm (C_β) and 134.9 and 133–138 ppm (C_γ)], whereas the resonances of C_α and C_δ differ considerably [δ = 262.8 and 221.8 ppm (C_α) and 59.7 and 114.8 ppm (C_δ)]. The latter is directly influenced by the different substituents at C_δ, and this also has some important effects on the nature of the ligand. In fact, the low-field value of δ_{C_α} for **3a** (δ = 262.8 ppm) suggests the presence of some methoxy carbene character; for example, in the parent alkynyl(methoxy)carbene complex **1a**, we have δ_{C_α} = 281.4 ppm. Conversely, the value of δ_{C_α} for **3b** (δ = 221.8 ppm) is typical for an Fe–C(sp^2) single bond as found in σ-vinyl and σ-butadienyl complexes; for instance, the related complex $[Fe_2\{\mu\text{-}CN(Me)(Xyl)\}(\mu\text{-}CO)(CO)\{C_\alpha(OMe)=C_\beta HC_\gamma(Tol)=NPh\}(Cp)_2]$,[11] which contains a 1-σ-4-azabuta-1,3-dienyl ligand, has δ_{C_α} at δ = 204.0 ppm. This indicates that **3b** can be mainly described by the 1-σ-buta-1,3-dienyl form (A), whereas the zwitterionic form (B) becomes more important in the case of **3a**, as also indicated by its crystal structure.

The formation of **3** very likely proceeds by addition of $[CH(R)_2]^-$ to C_γ of **1a** to give a σ-allenyl intermediate, followed by hydrogen migration from C_δ to C_β (Scheme 4); an example of the latter process has been described for the formation of the zwitterionic η^3-allyl complex $[Pt\{\eta^3\text{-}CH_2C[C(CO_2Me)_2]CHPh\}(PPh_3)_2]$ from $[Pt(\eta^3\text{-}CH_2CCH)(PPh_3)_2]^+$ and $[CH(CO_2Me)_2]^-$.[17]

In order to confirm this, we studied the reaction between **1a** and $[C(Me)(CO_2Me)_2]^-$ (Scheme 5). As expected, no methyl migration is observed and, thus, the σ-allenyl complex $[Fe_2\{\mu\text{-}CN(Me)(Xyl)\}(\mu\text{-}CO)(CO)\{C_\alpha(OMe)=C_\beta=C_\gamma(Tol)C_\delta(Me)(CO_2Me)_2\}(Cp)_2]$ (**4**) can be isolated in good yield (78%).

The IR spectrum of **4** shows ν(CO) at 1963 and 1787 cm^{-1} for the terminal and bridging carbonyls, respectively, and $\nu(CO_2Me)$ at 1734 cm^{-1}. The NMR spectra indicate the presence in solution of two isomers in a 2:1 ratio, with similar but distinct resonances. This suggests that the addition of $[C(Me)(CO_2Me)_2]^-$ to **1a** is not stereoselective, but can occur on both sides of the plane containing the alkynyl(methoxy)carbene ligand (Scheme 6). Therefore, the two isomers differ only in the relative orientation of the Tol and $C_\delta(Me)(CO_2Me)_2$ substituents; in particular, in one isomer (A), the Tol group points towards the μ-

 © 2005 Wiley-VCH Verlag GmbH & Co. KGaA, Weinheim

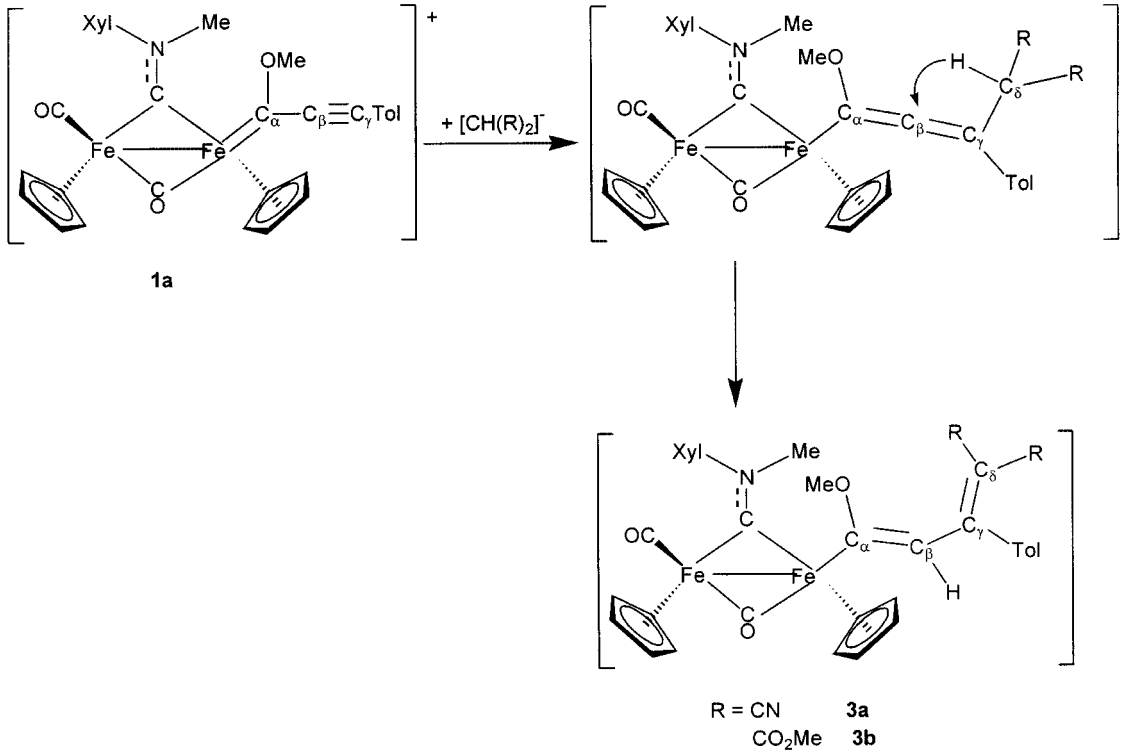

Scheme 4.

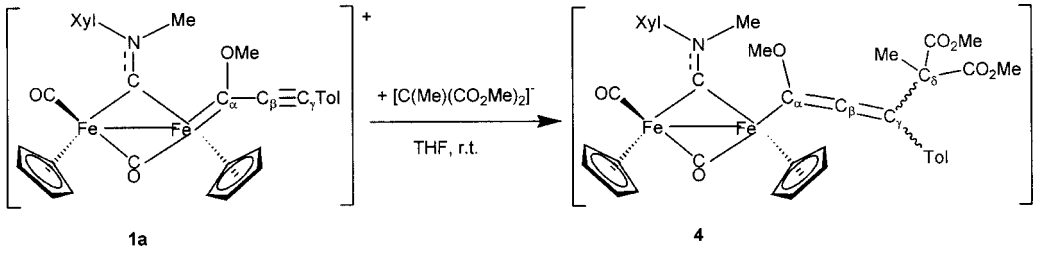

Scheme 5.

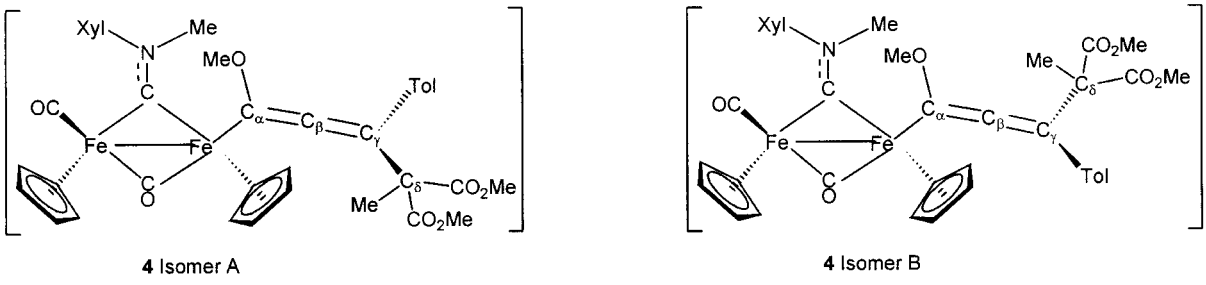

Scheme 6.

CN(Me)(Xyl) ligand, whereas in the other (B) it is directed to the same side as μ-CO.

It is quite interesting to compare this reaction with the addition of CN^- reported in Scheme 1. The latter is completely stereoselective, probably because it involves a site of the alkynyl(methoxy)carbene ligand (C_α) which is very close to the diiron core of the molecule and, thus, is sterically protected by the other ligands. Conversely, C_γ is sterically free and therefore very little control of the stereochemistry of the addition is possible. Some steric control is probably exerted also on the regiochemistry of these nucleophilic additions. In fact, the small CN^- ion can easily access C_α,

 © 2005 Wiley-VCH Verlag GmbH & Co. KGaA, Weinheim

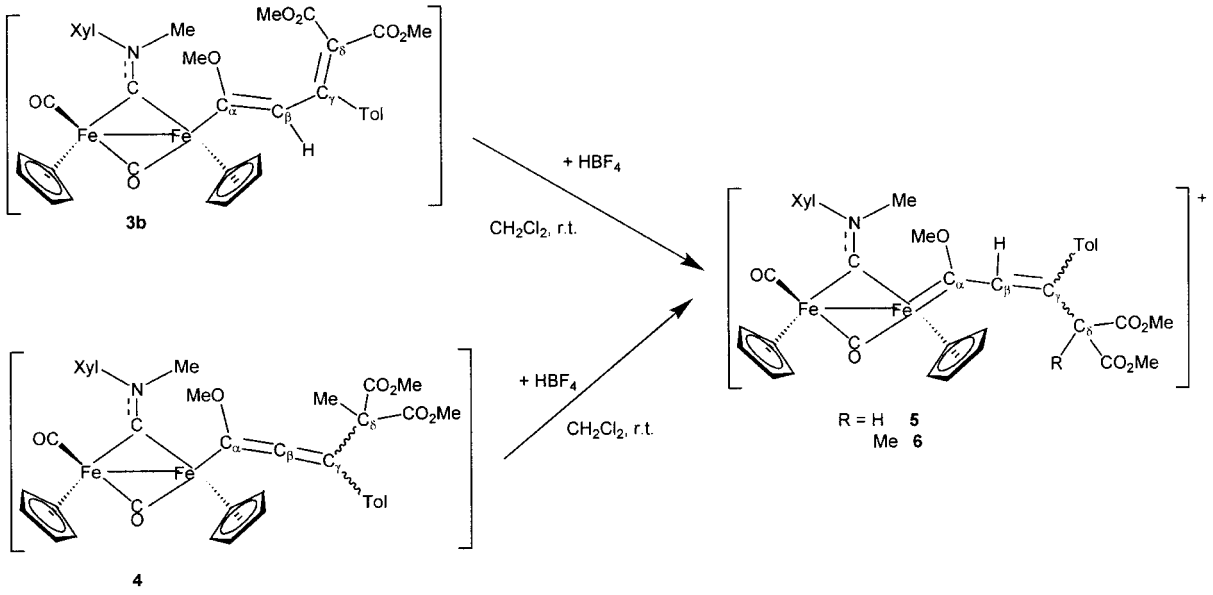

Scheme 7.

whereas the more cumbersome $[CH(R)_2]^-$ and $[C(Me)(CO_2Me)_2]^-$ add to C_γ.

The σ-allenyl ligand in **4** shows characteristic resonances in the ^{13}C NMR spectrum[18] at δ = 144–147, 195 and 104 ppm for C_α, C_β and C_γ, respectively. The aliphatic C_δ atoms resonate at $\delta \approx 59$ ppm, whereas its Me group resonates at $\delta \approx 22$ ppm.

Both complexes **3b** and **4** react quantitatively with strong acids to afford the cationic vinyl(methoxy)carbene complexes $[Fe_2\{\mu\text{-}CN(Me)(Xyl)\}(\mu\text{-}CO)(CO)\{C_\alpha(OMe)C_\beta H{=}C_\gamma(Tol)C_\delta(R)(CO_2Me)_2\}]^+$ (R = H, **5**; Me, **6**; Scheme 7). Conversely, the reaction of **3a** and **2a**–**e** with acids results in a complex mixture of decomposition products.

The regiochemistry of the protonation reactions is quite interesting as complex **3b** adds H^+ selectively at the C_δ carbon of the 1-σ-buta-1,3-dienyl ligand in order to favour the delocalisation of the positive charge along the entire ligand and the diiron frame. The same result is obtained in the case of the reaction of **4** by selective protonation of C_β.

The reactivity of σ-allenyl complexes towards nucleophiles has been widely studied, whereas data on reactions with electrophiles are quite scarce.[18] It is, however, been reported that electrophiles usually react at C_γ and not C_β. For instance, the protonation of $[Re(Cp)(NO)(PPh_3)(\sigma\text{-}CH{=}C{=}CH_2)]$ with HBF_4 results in the formation of $[Re(Cp)(NO)(PPh_3)(\eta^2\text{-}CH{\equiv}CCH_3)]^+$ by addition of H^+ to C_γ.[19] Thus, the reaction reported here represents a rare case of electrophilic attack at C_β of a σ-allenyl complex.

Complexes **5** and **6** were fully characterised spectroscopically. Their IR spectra show ν(CO) shifted by about 30 cm^{-1} towards higher frequencies with respect to the parent complexes **3b** and **4**, as expected for cationic compounds. The NMR spectra at room temperature indicate the presence of an exchange process, which can be frozen-out at 243 K. Under these conditions, two species can clearly be distinguished in solution in ratios of 1.3:1 for **5** and 1.5:1 for **6**. These were fully characterised by gs-HSQC and gs-HMBC experiments[20] at 243 K, and their stereochemistry assigned by NOE measurements conducted at 218 K to avoid saturation-transfer effects.[21] The two species are isomers which differ only in the configuration of the vinyl double bond $C_\beta{=}C_\gamma$ (Scheme 8). In both cases the major isomer is the one in which the C_β-H hydrogen is *cis* to the Tol group; because of the different nature of the substituents on C_δ, this possesses an (*E*)-configuration in **5** and a (*Z*)-configuration in **6**. Therefore, the minor isomers have the configuration (*Z*)-**5** and (*E*)-**6**. The two isomers can be easily distinguished from the ^1H chemical shift of C_β-H, which resonates at lower field in the major isomers [(*E*)-**5**: δ = 6.69 ppm; (*Z*)-**6**: δ = 6.53 ppm), than in the minor isomers [(*Z*)-**5**: δ = 6.49 ppm; (*E*)-**6**: δ = 6.24 ppm)], where it is *trans* to Tol. For example, NOE studies on **6** show that irradiation of the C_β-H resonance in the minor isomer (δ = 6.24 ppm) generates a strong enhancement of the C_δ-*Me* resonance, in agreement with the proposed (*E*)-configuration. The carbene nature of the ligand is supported by the typical ^{13}C chemical shift of C_α ($\delta \approx 315$ ppm); conversely, C_β and C_γ resonate at values characteristic of olefinic protons ($\delta \approx 140$ and 135 ppm, respectively).

The reaction of the vinyl(methoxy)carbene complex **6** with CN^- was then studied (Scheme 9). As in the case of the analogous reaction of **1**, the cyanide ion selectively adds to the carbene carbon to afford the σ-allyl complex $[Fe_2\{\mu\text{-}CN(Me)(Xyl)\}(\mu\text{-}CO)(CO)\{C_\alpha(OMe)(CN)[C_\beta H{=}C_\gamma(Tol)\text{-}C_\delta(Me)(CO_2Me)_2]\}(Cp)_2]$ (**7**) in good yield (68%). This reaction is also completely regio- and stereoselective, resulting in the formation of a single species whose spectroscopic and NOE data suggest a (*Z*)-configuration of the double bond.

Finally, the reactivity of **6** with a neutral nucleophile such as Me_2NH was considered (Scheme 10). This results in the formation of the neutral organometallic species $[Fe_2\{\mu\text{-}CN(Me)(Xyl)\}(\mu\text{-}CO)(CO)\{C_\alpha(O)C_\beta H{=}C_\gamma(Tol)C_\delta(Me)\text{-}$

 © 2005 Wiley-VCH Verlag GmbH & Co. KGaA, Weinheim

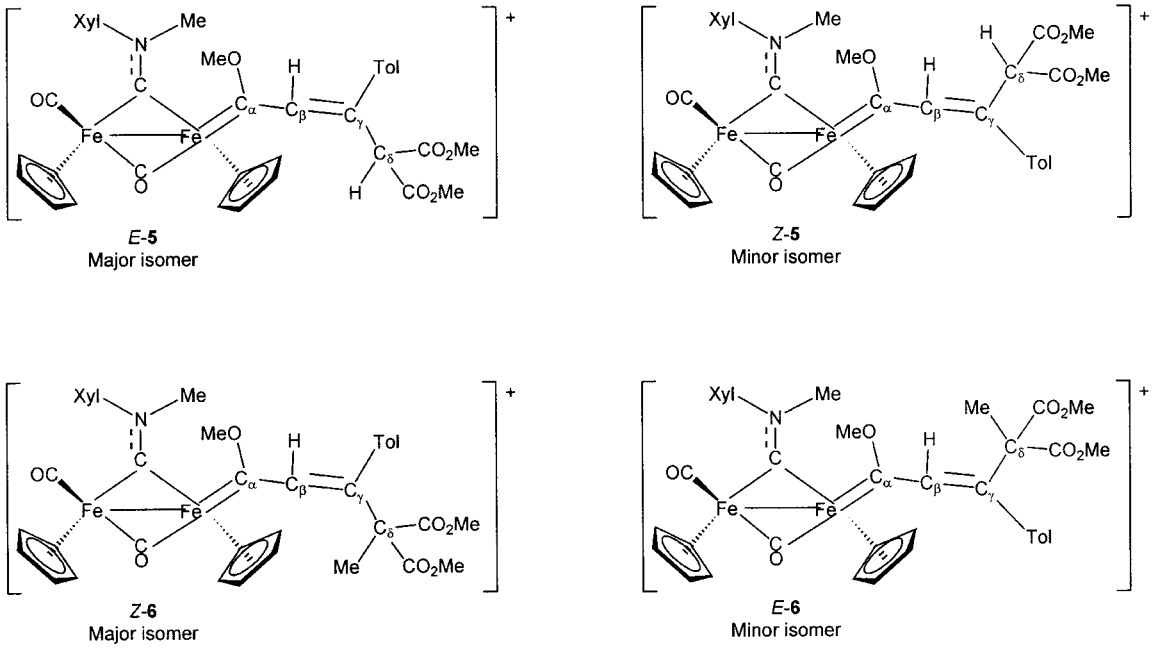

Scheme 8.

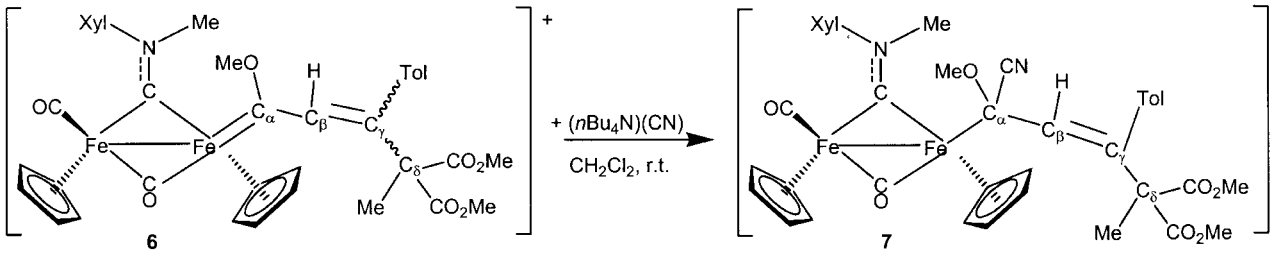

Scheme 9.

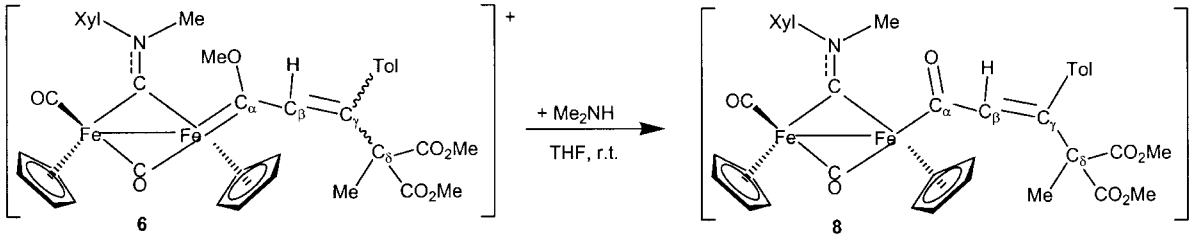

Scheme 10.

$(CO_2Me)_2\}(Cp)_2]$ (**8**), which can be recovered in good yield (76%) after column chromatography. The same species can also be obtained by direct chromatography of **6** through an Al_2O_3 column (previously treated with 4% water) with CH_2Cl_2/THF (1:1) as eluent. In the case of the reaction of **6** with Me_2NH, IR spectroscopy clearly indicates that **8** is already present in solution before chromatography. Complex **8** contains a vinylacyl ligand, as clearly indicated by its NMR spectra. In particular, the acyl carbon resonates at δ = 265.8 ppm, and the vinyl atoms show characteristic resonances (i.e. C_γ: δ = 125.6 ppm; C_β: δ = 143.3 ppm (^{13}C NMR) and C_β-H: δ = 6.45 ppm (^1H NMR). A single species is present in solution, for which, on the basis of its spectroscopic features, we can assume a (*Z*)-configuration for the double bond.

Conclusions

The results reported in this paper indicate that the alkynyl(methoxy)carbene ligand in **1** contains two different sites available for nucleophilic attack, i.e. C_α and C_γ. The regiochemistry of the reactions studied is mainly controlled by steric factors; thus, the small CN^- ion adds at C_α, whereas the bulkier $[CH(R)_2]^-$ and $[C(Me)(CO_2Me)_2]^-$ react selectively at C_γ. In the same way, it can be considered that the

 © 2005 Wiley-VCH Verlag GmbH & Co. KGaA, Weinheim

addition of amines to **1** is also mainly sterically controlled and therefore it occurs at C_γ, as observed previously.[11] Electronic factors must also be considered, and they point to the same conclusions. Thus, the hard CN^- nucleophile attacks in a 1,2 manner, accordingly to the HSAB theory, whereas the softer $[CH(R)_2]^-$ and $[C(Me)(CO_2Me)_2]^-$ anions react in a 1,4 manner.

The addition of carbanions to **1** results in the formation of new C–C bonds and, hence, different types of ligands are formed. In particular, addition at C_α generates 1,1-disubstituted σ-propargyl compounds, whereas σ-allenyl complexes are formed in the case of reaction at C_γ. The latter species can evolve further when a hydrogen is present on C_δ, resulting eventually in the formation of 1-σ-buta-1,3-dienyl complexes. All the ligands formed are terminally coordinated to the diiron frame, even though they are known to be able to act also as bridging ligands in different coordination modes.[18,22]

Finally, we have shown that the neutral complexes **3** and **4** can react with electrophiles and that the resultant cationic products can be further modified by nucleophilic additions. This represents an interesting step-by-step sequence for the building up of highly functionalised ligands in diiron species.

Experimental Section

All reactions were carried out routinely under nitrogen using standard Schlenk techniques. Solvents were distilled immediately before use under nitrogen from appropriate drying agents. Infrared spectra were recorded on a Perkin–Elmer Spectrum 2000 FT-IR spectrophotometer and elemental analyses were performed on a ThermoQuest Flash 1112 Series EA Instrument. All NMR measurements were performed on Varian Gemini 300 and Varian Mercury 400 instruments. The chemical shifts for ^1H and ^{13}C are referenced to internal TMS. The spectra were fully assigned by ^1H,^{13}C correlation measured using gs-HSQC and gs-HMBC experiments.[20] Monodimensional NOE measurements were recorded using the DPFGSE-NOE sequence.[23] All chemicals were used as received from Aldrich Co., except $[Fe_2\{\mu\text{-}CN(Me)(R)\}(\mu\text{-}CO)(CO)\{C_\alpha(OMe)C_\beta{\equiv}C_\gamma R'\}(Cp)_2][SO_3CF_3]$ (R = Xyl, R′ = Tol, **1a**; R = Xyl, R′ = Ph, **1b**; R = Xyl, R′ = Me_3Si, **1c**; R = Me, R′ = Tol, **1d**; R = Me, R′ = Ph, **1e**)[11] which were prepared by published methods. The anions $Na[CH(CN)_2]$, $Na[CH(CO_2Me)_2]$ and $Na[C(Me)(CO_2Me)_2]$ were prepared just before use by the reaction of Na with $CH_2(CN)_2$, $CH_2(CO_2Me)_2$ and $CH(Me)(CO_2Me)_2$, respectively, in THF.

Synthesis of $[Fe_2\{\mu\text{-}CN(Me)(R)\}(\mu\text{-}CO)(CO)\{C(OMe)(CN)(C{\equiv}CR'')\}(Cp)_2]$ (R = Xyl, R′ = Tol, 2a; R = Xyl, R′ = Ph, 2b; R = Xyl, R′ = Me_3Si, 2c; R = Me, R′ = Tol, 2d; R = Me, R′ = Ph, 2e): (n-Bu_4N)(CN) (110.0 mg, 0.417 mmol) was added to a solution of **1** (0.220 mmol) in CH_2Cl_2 (15 mL) and the mixture stirred at room temperature for 20 min; during this time, the solution changed from red to brown. The solvent was then removed under reduced pressure and the residue dissolved in CH_2Cl_2 (5 mL) and chromatographed through Al_2O_3. The final product was obtained as a brown fraction using CH_2Cl_2 as eluent.

2a: $C_{34}H_{32}Fe_2N_2O_3$ (628.32): calcd. C 64.99, H 5.13, N 4.46; found C 65.11, H 5.01, N 4.21. Yield 110.6 mg (80%). ^1H NMR (399.939 MHz, $CDCl_3$, 293 K): δ = 2.34 (s, 3 H, p-C_6H_4Me), 2.13, 2.62 (s, 6 H, $C_6H_3Me_2$), 2.86 (s, 3 H, O*Me*), 4.28, 4.64 (s, 10 H, Cp), 4.71 (s, 3 H, N*Me*), 7.12–7.50 (m, 7 H, arom). $^{13}C\{^1H\}$ NMR (100.575 MHz, $CDCl_3$, 293 K): δ = 17.6, 18.3 ($C_6H_3Me_2$), 21.2 (p-C_6H_4Me), 50.8 (Fe-*C*), 50.9 (N-*Me*), 52.7 (O*Me*), 86.5, 89.4 (Cp), 89.7, 94.5 (*C*≡*C*), 121.2 (C_{ipso} Tol), 126.2 (*C*≡N), 127.9, 128.0, 128.7, 129.8, 131.0, (*C*-H arom), 132.3, 134.0, 137.3 (*C*-Me Xyl + Tol), 149.4 (C_{ipso} Xyl), 215.0 (*C*O), 266.5 (μ-*C*O), 338.3 (μ-*C*) ppm. IR (CH_2Cl_2, 293 K): $\tilde{\nu}$ = 2192(s) (CN), 1970(vs) (CO), 1791(s) cm^{-1} (μ-CO).

2b: $C_{33}H_{30}Fe_2N_2O_3$ (614.29): calcd. C 64.52, H 4.92, N 4.56; found C 64.68, H 5.11, N 4.28. Yield 102.7 mg (76%). ^1H NMR (399.939 MHz, $CDCl_3$, 293 K): δ = 2.15, 2.64 (s, 6 H, $C_6H_3Me_2$), 2.88 (s, 3 H, O*Me*), 4.30, 4.69 (s, 10 H, Cp), 4.72 (s, 3 H, N*Me*), 7.20–7.59 (m, 8 H, arom) ppm. $^{13}C\{^1H\}$ NMR (100.575 MHz, $CDCl_3$, 293 K): δ = 16.6, 18.2 ($C_6H_3Me_2$), 50.4 (Fe-*C*), 50.8 (N-*Me*), 52.7 (O*Me*), 86.5, 89.3 (Cp), 90.4, 94.3 (*C*≡*C*), 124.2 (C_{ipso} Tol), 126.0 (*C*≡N), 127.2, 127.8, 127.9, 129.7, 130.9 (*C*-H arom), 132.2, 133.9 (*C*-Me Xyl), 149.2 (C_{ipso} Xyl), 214.9 (*C*O), 266.5 (μ-*C*O), 338.1 (μ-*C*) ppm. IR (CH_2Cl_2, 293 K): $\tilde{\nu}$ = 2192(s) (CN), 1970(vs) (CO), 1790(s) cm^{-1} (μ-CO).

2c: $C_{33}H_{30}Fe_2N_2O_3Si$ (642.38): calcd. C 61.70, H 4.71, N 4.36; found C 61.43, H 4.95, N 4.29. Yield 92.2 mg (72%). ^1H NMR (399.939 MHz, $CDCl_3$, 293 K): δ = 0.29 (s, 9 H, Me_3Si), 2.13, 2.65 (s, 6 H, $C_6H_3Me_2$), 2.83 (s, 3 H, O*Me*), 4.30, 4.65 (s, 10 H, Cp), 4.72 (s, 3 H, N*Me*), 7.24–7.34 (m, 3 H, arom) ppm. $^{13}C\{^1H\}$ NMR (100.575 MHz, $CDCl_3$, 293 K): δ = 1.1 (Me_3Si), 17.0, 18.7 ($C_6H_3Me_2$), 51.2 (N-*Me*), 52.8 (O*Me*), 86.7, 89.8 (Cp), 99.0, 105.6 (*C*≡*C*), 126.4 (*C*≡N), 128.0, 130.1 (*C*-H arom), 132.3, 138.5 (*C*-Me Xyl), 149.7 (C_{ipso} Xyl), 215.1 (*C*O), 264.8 (μ-*C*O), 338.4 (μ-*C*) ppm. IR (CH_2Cl_2, 293 K): $\tilde{\nu}$: 2193(s) (CN), 1969(vs) (CO), 1793(s) cm^{-1} (μ-CO).

2d: $C_{27}H_{26}Fe_2N_2O_3$ (538.20): calcd. C 60.25, H 4.87, N 5.21; found C 60.07, H 4.93, N 5.05. Yield 82.9 mg (70%). ^1H NMR (399.939 MHz, $CDCl_3$, 293 K): δ = 2.42 (s, 3 H, p-C_6H_4Me), 2.89 (s, 3 H, O*Me*), 4.14, 4.58 (s, 6 H, NMe_2), 4.66, 4.80 (s, 10 H, Cp), 7.20–7.53 (m, 4 H, arom) ppm. $^{13}C\{^1H\}$ NMR (100.575 MHz, $CDCl_3$, 293 K): δ = 21.4 (p-C_6H_4Me), 50.4 (Fe-*C*), 50.1, 53.9, (NMe_2), 53.6 (O*Me*), 86.6, 89.4, (Cp), 94.4 (*C*≡*C*), 121.6 (C_{ipso} Tol), 127.0 (*C*≡N), 128.9 (*C*-Me Tol), 128.7–131.5 (*C*-H arom), 214.6 (*C*O), 276.0 (μ-*C*O), 333.3 (μ-*C*) ppm. IR (CH_2Cl_2, 293 K): $\tilde{\nu}$ = 2192(m) (CN), 1969(vs) (CO), 1790(s) cm^{-1} (μ-CO).

2e: $C_{26}H_{24}Fe_2N_2O_3$ (524.17): calcd. C 59.56, H 4.62, N 5.34; found C 59.23, H 4.59, N 5.52. Yield 88.8 mg (77%). ^1H NMR (399.939 MHz, $CDCl_3$, 293 K): δ = 2.84 (s, 3 H, O*Me*), 4.10, 4.53 (s, 6 H, NMe_2), 4.60, 4.76 (s, 10 H, Cp), 7.30–7.530 (m, 5 H, arom) ppm. $^{13}C\{^1H\}$ NMR (100.575 MHz, $CDCl_3$, 293 K): δ = 49.9 (Fe-*C*), 49.8, 53.3 (O*Me* + NMe_2), 86.6, 89.1 (Cp), 90.6, 94.2 (*C*≡*C*), 124.3 (*C*≡N), 125.6 (C_{ipso} Ph), 127.1–130.8 (*C*-H arom), 214.7 (*C*O), 267.9 (μ-*C*O), 332.3 (μ-*C*) ppm. IR (CH_2Cl_2, 293 K): $\tilde{\nu}$ = 2192(m) (CN), 1969(vs) (CO), 1789(s) cm^{-1} (μ-CO).

Synthesis of $[Fe_2\{\mu\text{-}CN(Me)(Xyl)\}(\mu\text{-}CO)(CO)\{C_\alpha(OMe){=}C_\beta HC_\gamma(Tol){=}C_\delta(R)_2\}(Cp)_2]$ (R = CN, 3a; CO_2Me, 3b): $Na[CH(R)_2]$ (0.500 mmol in 7 mL of THF) was added to a solution of **1a** (200.0 mg, 0.260 mmol) in THF (10 mL) and the mixture stirred at room temperature for 5 min. It was then filtered through an Al_2O_3 pad and the solvent removed from the filtrate under reduced pressure. The residue was dissolved in CH_2Cl_2 (5 mL) and chromatographed through Al_2O_3. The final product was obtained as a brown fraction using THF as eluent.

3a: $C_{36}H_{33}Fe_2N_3O_3$ (667.36): calcd. C 64.79, H 4.98, N 6.30; found C 64.58, H 4.75, N 6.09. Yield 121.4 mg (70%). ^1H NMR

 © 2005 Wiley-VCH Verlag GmbH & Co. KGaA, Weinheim

(399.939 MHz, $CDCl_3$, 293 K): δ = 2.34 (s, 3 H, *p*-C_6H_4*Me*), 2.37, 2.55 (s, 6 H, C_6H_3*Me*$_2$), 3.30 (s, 3 H, O*Me*), 4.47 (s, 3 H, N*Me*), 4.29, 4.79 (s, 10 H, Cp), 5.98 (s, 1 H, =C_β*H*), 7.14–7.34 (m, 7 H, arom) ppm. $^{13}C\{^1H\}$ NMR (100.575 MHz, $CDCl_3$, 293 K): δ = 17.5, 18.5 (C_6H_3*Me*$_2$), 21.4 (*p*-C_6H_4*Me*), 53.1 (N-*Me*), 59.7 (C_δ), 63.6 (O*Me*), 86.9, 90.2 (Cp), 118.0 (C_βH), 118.9 (*C*≡N), 128.4, 128.5, 128.8, 129.6, 130.0 (*C*-H arom), 132.9, 133.6 (*C*-Me Xyl), 134.9 (C_γ), 140.7 (*C*-Me Tol), 148.1 (C_{ipso} Xyl), 158.8 (C_{ipso} Tol), 213.4 (*C*O), 262.8 (Fe-C_α), 266.2 (μ-*C*O), 336.3 (μ-*C*) ppm. IR (CH_2Cl_2, 293 K): $\tilde{\nu}$ = 2199(s) (CN), 1968(vs) (CO), 1791(s) cm^{-1} (μ-CO).

3b: $C_{38}H_{39}Fe_2NO_7$ (733.41): calcd. C 62.23, H 5.36, N 1.91; found C 62.48, H 5.04, N 2.15. Yield 114.4 mg (60%). ^1H NMR (399.939 MHz, $CDCl_3$, 293 K): δ = 2.25, 2.58, 2.89 (s, 9 H, C_6H_3*Me*$_2$ + *p*-C_6H_4*Me*), 3.15 (s, 3 H, O*Me*), 3.52 (s, 6 H, CO_2*Me*), 4.38 (s, 3 H, N*Me*), 4.23, 4.83 (s, 10 H, Cp), 5.54 (s, 1 H, =C_β*H*), 6.92–7.22 (m, 7 H, arom) ppm. $^{13}C\{^1H\}$ NMR (100.575 MHz, $CDCl_3$, 293 K): δ = 17.8, 18.7 (C_6H_3*Me*$_2$), 21.4 (*p*-C_6H_4*Me*), 51.5 (CO_2*Me*), 52.2 (N-*Me*), 61.6 (O*Me*), 86.4, 89.1 (Cp), 114.8 (C_δ), 121.4 (C_βH), 127.9, 128.0, 128.3, 128.6, 129.9 (*C*-H arom), 133.0, 134.1, 137.7, 138.5 (*C*-Me Tol + *C*-Me Xyl + C_γ), 148.2 (C_{ipso} Xyl), 152.6 (C_{ipso} Tol), 168.1 (*C*O$_2$Me), 214.4 (*C*O), 221.8 (Fe-C_α), 265.4 (μ-*C*O), 337.5 (μ-*C*) ppm. IR (CH_2Cl_2, 293 K): $\tilde{\nu}$ = 1960(vs) (CO), 1784(s) (μ-CO), 1736(s) cm^{-1} (CO_2Me).

Synthesis of [Fe_2{μ-CN(Me)(Xyl)}(μ-CO)(CO){C_α(OMe)=C_β=C_γ(Tol)C_δ(Me)(CO_2Me)$_2$}(Cp)$_2$] (4): Na[C(Me)(CO_2Me)$_2$] (0.300 mmol, in 5 mL THF) was added to a solution of **1a** (200.0 mg, 0.260 mmol) in THF (10 mL) and the mixture stirred at room temperature for 5 min. It was then filtered through an Al_2O_3 pad and the solvent removed from the filtrate under reduced pressure. The residue was dissolved in CH_2Cl_2 (5 mL) and chromatographed through Al_2O_3. The final product was obtained as a brown fraction using THF as eluent. $C_{39}H_{41}Fe_2NO_7$ (747.44): calcd. C 62.67, H 5.53, N 1.87; found C 62.98, H 5.38, N 1.95. Yield 151.5 mg (78%). ^1H NMR (399.939 MHz, $CDCl_3$, 293 K). – Isomer A: δ = 1.66 (s, 3 H, C_δ*Me*), 2.24 (s, 3 H, *p*-C_6H_4*Me*), 2.12, 2.55 (s, 6 H, C_6H_3*Me*$_2$), 2.95 (s, 3 H, O*Me*), 3.61, 3.84 (s, 6 H, CO_2*Me*), 4.16 (s, 3 H, N*Me*), 4.19, 4.63 (s, 10 H, Cp), 6.96–7.30 (m, 7 H, arom) ppm. – Isomer B: δ = 1.76 (s, 3 H, C_δ*Me*), 2.28 (s, 3 H, *p*-C_6H_4*Me*), 2.15, 2.59 (s, 6 H, C_6H_3*Me*$_2$), 2.88 (s, 3 H, O*Me*), 3.66, 3.68 (s, 6 H, CO_2*Me*), 4.28 (s, 3 H, N*Me*), 4.22, 4.66 (s, 10 H, Cp), 6.96–7.30 (m, 7 H, arom) ppm. Isomer ratio: A/B = 2. $^{13}C\{^1H\}$ NMR (100.575 MHz, $CDCl_3$, 293 K). – Isomer A: δ = 17.0, 18.4 (C_6H_3*Me*$_2$), 20.9 (*p*-C_6H_4*Me*), 22.8 (C_δ*Me*), 51.7 (N-*Me*), 52.2, 52.5 (CO_2*Me*), 56.3 (O*Me*), 59.5 (C_δ), 85.7, 89.1 (Cp), 104.6 (=C_γ), 127.2–129.8 (*C*-H arom), 133.2–138.8 (C_{ipso} Tol + *C*-Me Tol + *C*-Me Xyl), 144.7 (Fe-C_α=), 148.4 (C_{ipso} Xyl), 172.6, 173.5 (*C*O$_2$Me), 195.3 (=C_β=), 215.4 (*C*O), 265.3 (μ-*C*O), 339.5 (μ-*C*) ppm. – Isomer B: δ = 16.9, 18.5 (C_6H_3*Me*$_2$), 20.9 (*p*-C_6H_4*Me*), 22.3 (C_δ*Me*), 51.7 (N-*Me*), 52.1, 52.3, (CO_2*Me*), 55.8 (O*Me*), 59.7 (C_δ), 85.7, 89.4, (Cp), 104.5 (=C_γ), 127.2–129.8 (*C*-H arom), 133.2–138.8 (C_{ipso} Tol + *C*-Me Tol + *C*-Me Xyl), 147.5 (Fe-C_α=), 148.3 (C_{ipso} Xyl), 173.0, 173.1 (*C*O$_2$Me), 194.5 (=C_β=), 215.8 (*C*O), 265.1 (μ-*C*O), 340.1 (μ-*C*) ppm. IR (CH_2Cl_2, 293 K): $\tilde{\nu}$ = 1963(vs) (CO), 1787(s) (μ-CO), 1734(s) cm^{-1} (CO_2Me).

Synthesis of [Fe_2{μ-CN(Me)(Xyl)}(μ-CO)(CO){C_α(OMe)C_βH=C_γ(Tol)C_δH(CO_2Me)$_2$}(Cp)$_2$][BF_4] (5): HBF_4 (0.100 mL, 54 wt.% in Et_2O, 0.726 mmol) was added to a solution of **3b** (238.3 mg, 0.325 mmol) in CH_2Cl_2 (10 mL) and the mixture stirred at room temperature for 5 min until complete formation of the final product. The solvent was then removed under reduced pressure and the residue washed with Et_2O (2×10 mL) and petroleum ether (2×10 mL). $C_{38}H_{40}BF_4Fe_2NO_7$ (821.22): calcd. C 55.58, H 4.91, N 1.71; found C 55.21, H 5.04, N 1.98. Yield 241.0 mg (90%). ^1H NMR (399.939 MHz, $CDCl_3$, 243 K). – (*E*)-isomer: δ = 2.24 (s, 3 H, *p*-C_6H_4*Me*), 2.36, 2.53 (s, 6 H, C_6H_3*Me*$_2$), 3.50 (s, 3 H, O*Me*), 3.76, 3.82 (s, 6 H, CO_2*Me*), 4.13 (s, 3 H, N*Me*), 4.75 (s, 1 H, C_δ*H*), 4.52, 5.12 (s, 10 H, Cp), 6.69 (s, 1 H, =C_β*H*), 7.01–7.79 (m, 7 H, arom) ppm. – (*Z*)-Isomer: δ = 2.28 (s, 3 H, *p*-C_6H_4*Me*), 2.33, 2.50 (s, 6 H, C_6H_3*Me*$_2$), 3.46 (s, 3 H, O*Me*), 3.73, 3.78 (s, 6 H, CO_2*Me*), 3.90 (s, 3 H, N*Me*), 4.67 (s, 1 H, C_δ*H*), 4.52, 5.06 (s, 10 H, Cp), 6.49 (s, 1 H, =C_β*H*), 7.01–7.79 (m, 7 H, arom) ppm. Isomer ratio *E*/*Z* = 1.3. $^{13}C\{^1H\}$ NMR (100.575 MHz, $CDCl_3$, 243 K). – (*E*)-Isomer: δ = 16.8, 18.4 (C_6H_3*Me*$_2$), 21.4 (*p*-C_6H_4*Me*), 52.9 (N-*Me*), 53.7, 53.8 (CO_2*Me*), 57.2 (C_δ), 63.0 (O*Me*), 88.5, 92.8 (Cp), 126.9–130.1 (*C*-H arom), 132.3–139.7 (C_{ipso} Tol + *C*-Me Xyl + C_γ), 140.7 (*C*-Me Tol), 140.9 (C_βH), 147.2 (C_{ipso} Xyl), 168.0, 168.5 (*C*O$_2$Me), 212.7 (*C*O), 259.5 (μ-*C*O), 313.6 (Fe=C_α), 332.7 (μ-*C*) ppm. – (*Z*)-Isomer: δ = 16.7, 18.4 (C_6H_3*Me*$_2$), 21.3 (*p*-C_6H_4*Me*), 53.7 (N-*Me*), 53.6, 54.2 (CO_2*Me*), 57.0 (C_δ),64.5 (O*Me*), 88.8, 92.8 (Cp), 126.9–130.1 (*C*-H arom), 132.3–139.7 (C_{ipso} Tol + *C*-Me Xyl + C_γ), 138.2 (C_βH), 139.7 (*C*-Me Tol), 146.8 (C_{ipso} Xyl), 167.9, 168.3 (*C*O$_2$Me), 212.1 (*C*O), 261.9 (μ-*C*O), 317.1 (Fe=C_α)331.2 (μ-*C*) ppm. IR (CH_2Cl_2, 293 K): $\tilde{\nu}$ = 1991(vs) (CO), 1816(s) (μ-CO), 1755(ms), 1739(s) cm^{-1} (CO_2Me).

Synthesis of [Fe_2{μ-CN(Me)(Xyl)}(μ-CO)(CO){C_α(OMe)C_βH=C_γ(Tol)C_δ(Me)(CO_2Me)$_2$}(Cp)$_2$][BF_4] (6): HBF_4 (0.100 mL, 54 wt.% in Et_2O, 0.726 mmol) was added to a solution of **4** (300.0 mg, 0.402 mmol) in CH_2Cl_2 (10 mL) and the mixture stirred at room temperature for 5 min until complete formation of the final product. The solvent was then removed under reduced pressure and the residue washed with Et_2O (2×10 mL) and petroleum ether (2×10 mL). $C_{39}H_{42}BF_4Fe_2NO_7$ (835.25): calcd. C 56.08, H 5.07, N 1.68; found C 55.84, H 5.34, N 1.47. Yield 308.9 mg (92%). ^1H NMR (399.939 MHz, $CDCl_3$, 243 K). – (*Z*)-Isomer: δ = 1.58 (s, 3 H, C_δ*Me*), 2.31 (s, 3 H, *p*-C_6H_4*Me*), 2.11, 2.44 (s, 6 H, C_6H_3*Me*$_2$), 3.56 (s, 3 H, O*Me*), 3.73, 3.75 (s, 6 H, CO_2*Me*), 4.07 (s, 3 H, N*Me*), 4.40, 5.11 (s, 10 H, Cp), 6.53 (s, 1 H, =C_β*H*), 6.82–7.28 (m, 7 H, arom) ppm. (*E*)-Isomer: δ = 1.51 (s, 3 H, C_δ*Me*), 2.26 (s, 3 H, *p*-C_6H_4*Me*), 2.14, 2.44 (s, 6 H, C_6H_3*Me*$_2$), 3.50 (s, 3 H, O*Me*), 3.69, 3.87 (s, 6 H, CO_2*Me*), 3.71 (s, 3 H, N*Me*), 4.49, 5.06 (s, 10 H, Cp), 6.24 (s, 1 H, =C_β*H*), 6.82–7.28 (m, 7 H, arom) ppm. Isomer ratio *Z*/*E* = 1.5. $^{13}C\{^1H\}$ NMR (100.575 MHz, $CDCl_3$, 243 K). – (*Z*)-Isomer: δ = 16.8, 18.3 (C_6H_3*Me*$_2$), 21.4 (*p*-C_6H_4*Me*), 22.6 (C_δ*Me*), 53.7, 53.8 (CO_2*Me*), 54.4 (N-*Me*), 60.5 (C_δ), 63.4 (O*Me*), 88.4, 92.6 (Cp), 127.5–129.9 (*C*-H arom), 132.5, 132.9, 133.1, 134.8 (C_{ipso} Tol + *C*-Me Xyl + C_γ),139.9 (*C*-Me Tol), 141.0 (C_βH), 147.1 (C_{ipso} Xyl), 171.6, 172.1 (*C*O$_2$Me), 212.3 (*C*O), 258.3 (μ-*C*O), 314.5 (Fe=C_α),332.6 (μ-*C*) ppm. – (*E*)-Isomer: δ = 16.2, 18.3 (C_6H_3*Me*$_2$), 21.3 (*p*-C_6H_4*Me*), 22.3 (C_δ*Me*), 53.7 (N-*Me*), 53.7, 53.8 (CO_2*Me*), 60.4 (C_δ),64.6 (O*Me*), 88.8, 92.7 (Cp), 127.5–129.9 (*C*-H arom), 132.2, 132.4, 132.6, 133.2 (C_{ipso} Tol + *C*-Me Xyl + C_γ), 138.6 (C_βH), 138.8 (*C*-Me Tol), 146.8 (C_{ipso} Xyl), 171.6, 171.9 (*C*O$_2$Me), 212.2 (*C*O), 262.1 (μ-*C*O), 316.9 (Fe=C_α), 331.2 (μ-*C*) ppm. IR (CH_2Cl_2, 293 K): $\tilde{\nu}$ = 1992(vs) (CO), 1817(s) (μ-CO), 1730(s) cm^{-1} (CO_2Me).

Synthesis of [Fe_2{μ-CN(Me)(Xyl)}(μ-CO)(CO){C_α(OMe)(CN)[C_βH=C_γ(Tol)C_δ(Me)(CO_2Me)$_2$]}(Cp)$_2$] (7): (nBu$_4$N)(CN) (110.0 mg, 0.417 mmol) was added to a solution of **6** (200.0 mg, 0.268 mmol) in CH_2Cl_2 (10 mL) and the mixture stirred at room temperature for 1 h. The solvent was then removed under reduced pressure and the residue dissolved in CH_2Cl_2 (5 mL) and chromatographed through Al_2O_3. The final product was obtained as an orange-brown fraction using THF as eluent. $C_{40}H_{42}Fe_2N_2O_7$ (774.46): calcd. C 62.03, H 5.47, N 3.62; found C 62.35, H 5.17, N 3.95. Yield

 © 2005 Wiley-VCH Verlag GmbH & Co. KGaA, Weinheim

Table 3. Crystal data and experimental details for **2b** and **3a**·CH_2Cl_2.

Complex	**2b**	**3a**·CH_2Cl_2
Formula	$C_{33}H_{30}Fe_2N_2O_3$	$C_{37}H_{35}Cl_2Fe_2N_3O_3$
Mol. mass	614.29	752.28
T [K]	293(2)	100(2)
λ [Å]	0.71073	0.71073
Crystal system	monoclinic	monoclinic
Space group	$P2_1/n$	$P2_1/c$
a [Å]	9.5892(19)	13.561(3)
b [Å]	18.320(4)	28.916(6)
c [Å]	16.215(3)	8.9896(18)
β [°]	96.26(3)	105.73(3)
V [Å^3]	2831.7(10)	3393.2(12)
Z	4	4
D_c [g cm^{-3}]	1.441	1.473
μ [mm^{-1}]	1.062	1.054
F(000)	1272	1552
Crystal size [mm]	0.25 × 0.21 × 0.16	0.23 × 0.18 × 0.12
θ limits [°]	1.65–25.02	1.41–25.55
Reflections collected	24789	31265
Independent reflections	5019 (R_{int} = 0.0992)	6350 (R_{int} = 0.0872)
Data/restraints/parameters	5019/ 38/361	6350/0/429
Goodness on fit on F^2	0.948	1.053
R_1 [$I > 2\sigma(I)$]	0.0528	0.0507
wR_2 (all data)	0.1440	0.1254
Largest diff. peak and hole [e Å^{-3}]	0.439/–0.476	0.594/–1.010

125.9 mg (68%). ^{1}H NMR (399.939 MHz, $CDCl_3$, 293 K): δ = 1.44 (s, 3 H, $C_\delta Me$), 2.26 (s, 3 H, p-C_6H_4Me), 2.00, 2.53 (s, 6 H, $C_6H_3Me_2$), 2.67 (s, 3 H, O*Me*), 3.76 (s, 6 H, CO_2Me), 4.54 (s, 3 H, N*Me*), 4.19, 4.60 (s, 10 H, Cp), 6.07 (s, 1 H, =$C_\beta H$), 6.91–7.27 (m, 7 H, arom) ppm. ^{13}C{^{1}H} NMR (100.575 MHz, $CDCl_3$, 293 K): δ = 17.2, 18.7 ($C_6H_3Me_2$), 21.5 (p-C_6H_4Me), 22.4 ($C_\delta Me$), 51.4 (N-*Me*), 52.7 (O*Me*), 52.8 (CO_2Me), 57.6 (Fe-C_α),62.5 (C_δ), 87.1, 89.4 (Cp), 123.5 (*C*N), 127.0 (C_{ipso} Tol), 128.1–130.1 (*C*-H arom), 132.2 (C_γ), 133.2, 134.6 (*C*-Me Xyl), 136.3 (C_βH), 137.3 (*C*-Me Tol), 149.9 (C_{ipso} Xyl), 172.4 (*C*O_2Me), 216.1 (*C*O), 271.8 (μ-*C*O), 337.0 (μ-*C*) ppm. IR (CH_2Cl_2, 293 K): $\tilde{\nu}$ = 2191(m) (CN), 1967(vs) (CO), 1774(s) (μ-CO), 1729(s) cm^{-1} (CO_2Me).

Synthesis of [Fe_2{μ-CN(Me)(Xyl)}(μ-CO)(CO){C_α(O)C_βH=C_γ(Tol)–C_δ(Me)(CO_2Me)$_2$}(Cp)$_2$] (8): Me_2NH (3.0 mL, 2.0 M in THF, 6.0 mmol) was added to a solution of **6** (200.0 mg, 0.268 mmol) in THF (15 mL), and the mixture stirred at room temperature for 30 min. The solvent was then removed in vacuo and the residue dissolved in CH_2Cl_2 and chromatographed through Al_2O_3. The final product was obtained as a green fraction using CH_2Cl_2/THF (1:1) as eluent. $C_{38}H_{39}Fe_2NO_7$ (733.41): calcd. C 62.23, H 5.36, N 1.91; found C 62.51,; H 5.12, N 1.77. Yield: 149.4 mg (76%). ^{1}H NMR (399.939 MHz, $CDCl_3$, 293 K): δ = 1.42 (s, 3 H, $C_\delta Me$), 2.24 (s, 3 H, p-C_6H_4Me), 2.43, 2.45 (s, 6 H, $C_6H_3Me_2$), 3.38 (s, 3 H, N*Me*), 3.71, 3.83 (s, 6 H, CO_2Me), 4.22, 4.82, (s, 10 H, Cp), 6.45 (s, 1 H, =$C_\beta H$), 6.99–7.24 (m, 7 H, arom) ppm. ^{13}C{^{1}H} NMR (100.575 MHz, $CDCl_3$, 293 K): δ = 17.5, 18.5 ($C_6H_3Me_2$), 21.3 (p-C_6H_4Me), 22.2 ($C_\delta Me$), 51.0 (N-*Me*), 52.7, 52.9 (CO_2Me), 60.6 (C_δ), 86.1, 89.5 (Cp), 125.6 (C_γ), 127.7–131.0 (*C*-H arom + C_γ), 133.4, 134.4, 135.4, 136.6 (*C*-Me Tol + *C*-Me Xyl + C_{ipso} Tol), 143.3 (C_βH), 148.1 (C_{ipso} Xyl), 172.3, 172.5 (*C*O_2Me), 215.4 (*C*O), 265.8 (Fe-C_α), 267.2 (μ-*C*O), 337.5 (μ-*C*) ppm. IR (CH_2Cl_2, 293 K): $\tilde{\nu}$ = 1965(vs) (CO), 1774(s) (μ-CO), 1733(s) cm^{-1} (CO_2Me).

X-ray Crystallographic Study: Compounds **2b** and **3a**·CH_2Cl_2 were crystallised from CH_2Cl_2/pentane. Crystal data and collection details are reported in Table 3. The diffraction experiments were carried out on a Bruker SMART 2000 diffractometer equipped with a CCD detector using Mo-K_α radiation. Data were corrected for Lorentz polarisation and absorption effects (empirical absorption correction SADABS).[24] Structures were solved by direct methods and refined by full-matrix least-squares based on all data using F^2.[25] Hydrogen atoms were fixed at calculated positions and refined by a riding model. All non-hydrogen atoms were refined with anisotropic displacement parameters, unless otherwise stated. One Cp ligand in **2b** is disordered. Disordered atomic positions were split and refined isotropically using similar distance and similar U restraints and one occupancy parameter per disordered group. CCDC-261569 (for **2b**) and CCDC-261570 (for **3a**·CH_2Cl_2) contain the supplementary crystallographic data for this paper. These data can be obtained free of charge from The Cambridge Crystallographic Data Centre via www.ccdc.cam.ac.uk/data_request/cif.

Acknowledgments

We thank the Ministero dell'Università e della Ricerca Scientifica e Tecnologica (MIUR) (project: "New strategies for the control of reactions: interactions of molecular fragments with metallic sites in unconventional species") and the University of Bologna ("Funds for Selected Research Topics") for financial support. We also thank one of the referees for useful suggestions.

[1] a) A. de Meijere, H. Schirmer, M. Duetsch, *Angew. Chem. Int. Ed.* **2000**, *39*, 3964–4002; b) A. de Meijere, *Pure Appl. Chem.* **1996**, *68*, 61–72; c) R. Aumann, H. Nienaber, *Adv. Organomet. Chem.* **1997**, *41*, 163–242.

[2] a) E. O. Fisher, F. R. Kreissl, *J. Organomet. Chem.* **1972**, *35*, C47–C51; b) R. Aumann, B. Jasper, R. Fröhlich, *Organometallics* **1995**, *14*, 3173–3177; c) A. Rahm, W. D. Wulff, A. L. R. Rheingold, *Organometallics* **1993**, *12*, 597–599; d) M. Duetsch, F. Stein, R. Lackmann, E. Pohl, R. Herbst-Irmer, A. de Meijere, *Chem. Ber.* **1992**, *125*, 2051–2065; e) F. Stein, M. Duetsch, E. Pohl, R. Herbst-Irmer, A. de Meijere, *Organometallics* **1993**, *12*, 2556–2564.

 © 2005 Wiley-VCH Verlag GmbH & Co. KGaA, Weinheim

[3] a) F. Stein, M. Duetsch, R. Lackmann, M. Noltemeyer, A. de Meijere, *Angew. Chem. Int. Ed. Engl.* **1991**, *30*, 1658–1660; b) R. Aumann, R. Fröhlich, S. Kotila, *Organometallics* **1996**, *15*, 4842–4851; c) F. Camps, A. Llebaria, J. M. Moretó, S. Ricart, J. M. Viñas, J. Ros, R. Yáñea, *J. Organomet. Chem.* **1991**, *401*, C17–C19.
[4] a) R. Aumann, K. B. Roths, M. Kößmeier, R. Fröhlich, *J. Organomet. Chem.* **1998**, *556*, 119–127; b) R. Aumann, P. Hinterding, *Chem. Ber.* **1993**, *126*, 421–427.
[5] a) A. G. Meyer, R. Aumann, *Synlett* **1995**, 1011–1013; b) R. Aumann, A. G. Meyer, R. Fröhlich, *Organometallics* **1996**, *15*, 5018–5027; c) R. Aumann, M. Kößmeier, C. Mück-Lichtenfeld, F. Zippel, *Eur. J. Org. Chem.* **2000**, 37–49.
[6] a) R. Aumann, K. Roths, R. Fröhlich, *Organometallics* **1997**, *16*, 5893–5899; b) R. Aumann, K. Roths, R. Fröhlich, *J. Organomet. Chem.* **2001**, *617–618*, 322–328.
[7] a) R. Aumann, M. Kößmeier, K. Roths, R. Fröhlich, *Tetrahedron* **2000**, *56*, 4935–4949; b) R. Aumann, K. Roths, M. Grehl, *Synlett* **1993**, 669–671; c) R. Aumann, M. Kößmeier, K. Roths, R. Fröhlich, *Synlett* **1994**, 1041–1044; d) K. L. Faron, W. D. Wulff, *J. Am. Chem. Soc.* **1988**, *110*, 8727–8729.
[8] a) K. S. Chan, W. D. Wulff, *J. Am. Chem. Soc.* **1986**, *108*, 5229–5236; b) K. S. Chan, *J. Chem. Soc., Perkin Trans. 1* **1991**, 2602–2603; c) K. S. Chan, M. L. Yeung, W.-K. Chan, R.-J. Wang, T. C. Mak, *J. Org. Chem.* **1995**, *60*, 1741–1747.
[9] a) W. D. Wulff, D. C. Yang, *J. Am. Chem. Soc.* **1984**, *106*, 7565–7567; b) J. Barluenga, F. Aznar, S. Barluenga, A. Martín, S. García-Granda, E. Martín, *Synlett* **1998**, 473–474; c) A. de Meijere, L. Wessjohann, *Synlett* **1990**, 20–32; d) K. L. Faron, W. D. Wulff, *J. Am. Chem. Soc.* **1990**, *112*, 6419–6420; e) F. Camps, J. M. Moretó, S. Ricart, J. M. Viñas, *Angew. Chem. Int. Ed. Engl.* **1991**, *30*, 1470–1472.
[10] a) W. D. Wulff, D. C. Yang, *J. Am. Chem. Soc.* **1983**, *105*, 6726–6727; b) K. H. Dötz, W. Kuhn, G. Müller, B. Huber, H. G. Alt, *Angew. Chem. Int. Ed. Engl.* **1986**, *25*, 826–827; c) K. H. Dötz, R. Noack, K. Harms, G. Müller, *Tetrahedron* **1990**, *46*, 1235–1252; d) B. A. Anderson, W. D. Wulff, T. S. Powers, S. Tribbitt, A. L. Rheingold, *J. Am. Chem. Soc.* **1992**, *114*, 10784–10792; e) H. Adam, T. Albrecht, J. Sauer, *Tetrahedron Lett.* **1994**, *35*, 557–560.
[11] L. Busetto, F. Marchetti, S. Zacchini, V. Zanotti, *Inorg. Chim. Acta* **2005**, *358*, 1469–1484.
[12] a) V. Zanotti, S. Bordoni, L. Busetto, L. Carlucci, A. Palazzi, R. Serra, V. G. Albano, M. Monari, F. Prestopino, F. Laschi, P. Zanello, *Organometallics* **1995**, *14*, 5332–5341; b) V. G. Albano, S. Bordoni, L. Busetto, F. Marchetti, M. Monari, V. Zanotti, *J. Organomet. Chem.* **2003**, *684*, 37–43; c) V. G. Albano, L. Busetto, M. Monari, V. Zanotti, *J. Organomet. Chem.* **2000**, *606*, 163–168; d) V. G. Albano, L. Busetto, F. Marchetti, M. Monari, S. Zacchini, V. Zanotti, *Organometallics* **2004**, *23*, 3348–3354; e) V. G. Albano, L. Busetto, F. Marchetti, M. Monari, S. Zacchini, V. Zanotti, *Organometallics* **2003**, *22*, 1326–1331; f) V. G. Albano, L. Busetto, F. Marchetti, M. Monari, S. Zacchini, V. Zanotti, *J. Organomet. Chem.* **2004**, *689*, 528–538.
[13] a) L. Busetto, F. Marchetti, S. Zacchini, V. Zanotti, *Eur. J. Inorg. Chem.* **2004**, 1494–1504; b) V. G. Albano, L. Busetto, C. Camiletti, C. Castellari, M. Monari, V. Zanotti, *J. Chem. Soc., Dalton Trans.* **1997**, 4671–4676; c) V. G. Albano, S. Bordoni, L. Busetto, C. Camiletti, M. Monari, A. Palazzi, F. Prestopino, V. Zanotti, *J. Chem. Soc., Dalton Trans.* **1997**, 4665–4670; d) L. Busetto, F. Marchetti, S. Zacchini, V. Zanotti, E. Zoli, *J. Organomet. Chem.* **2005**, *690*, 348–357.
[14] a) K. Boss, C. Dowling, A. R. Manning, *J. Organomet. Chem.* **1996**, *509*, 197–207; b) K. Boss, M. G. Cox, C. Dowling, A. R. Manning, *J. Organomet. Chem.* **2000**, *612*, 18–35.
[15] V. G. Albano, L. Busetto, F. Marchetti, M. Monari, V. Zanotti, *J. Organomet. Chem.* **2002**, *649*, 64–69.
[16] R. Ferede, M. Noble, A. W. Cordes, N. T. Allison, J. Lay, *J. Organomet. Chem.* **1988**, *339*, 1–6.
[17] P. W. Blosser, D. G. Schimpff, J. C. Gallucci, A. Wojcicki, *Organometallics* **1993**, *12*, 1993–1995.
[18] S. Doherty, J. F. Corrigan, A. J. Carty, E. Sappa, *Adv. Organomet. Chem.* **1995**, *37*, 39–130.
[19] J. Pu, T. S. Peng, A. M. Arif, J. A. Gladysz, *Organometallics* **1992**, *11*, 3232–3241.
[20] W. Wilker, D. Leibfritz, R. Kerssebaum, W. Beimel, *Magn. Reson. Chem.* **1993**, *31*, 287–292.
[21] a) S. Forsén, R. A. Hoffman, *J. Chem. Phys.* **1963**, *39*, 2892–2901; b) G. A. Morris, R. Freeman, *J. Magn. Reson.* **1978**, *29*, 433–462.
[22] a) A. Wojcicki, *Inorg. Chem. Commun.* **2002**, *5*, 82–97; b) B. J. Brisdon, R. A. Walton, *Polyhedron* **1995**, *14*, 1259–1276.
[23] K. Stott, J. Stonehouse, J. Keeler, T. L. Hwang, A. J. Shaka, *J. Am. Chem. Soc.* **1995**, *117*, 4199–4200.
[24] G. M. Sheldrick, *SADABS*, Program for empirical absorption correction, University of Göttingen, Germany, **1996**.
[25] G. M. Sheldrick, *SHELX97*, Program for crystal structure determination, University of Göttingen, Germany, **1997**.

Received: January 25, 2005
Published Online: July 14, 2005

 © 2005 Wiley-VCH Verlag GmbH & Co. KGaA, Weinheim

Towards Molecular Conductors with a Spin-Crossover Phenomenon: Crystal Structures, Magnetic Properties and Mössbauer Spectra of [Fe(salten)Mepepy][M(dmit)$_2$] Complexes

Christophe Faulmann,*[a] Stéphane Dorbes,[a] Bénédicte Garreau de Bonneval,[a] Gábor Molnár,[a] Azzedine Bousseksou,[a] Carlos J. Gomez-Garcia,[b] Eugenio Coronado,[b] and Lydie Valade[a]

Keywords: Conducting materials / Magnetic properties / Moessbauer spectroscopy / Spin crossover / X-ray diffraction

Three new iron(III) compounds of formula [Fe(salten)-Mepepy][M(dmit)$_2$]·CH_3CN (M = Ni, Pd, Pt; H_2salten = 4-aza-heptamethylene-1,7-bis(salicylideneiminate); Mepepy = 1-(pyridin-4-yl)-2-(*N*-methylpyrrol-2-yl) ethane; dmit^{2-} = 1,3-dithiole-2-thione-4,5-dithiolato) have been synthesised and the crystal structure of each compound has been solved at different temperatures. The structures consist of alternating layers of [M(dmit)$_2$]$^-$ units and [Fe(salten)Mepepy] cations. In the Ni compound photo-isomerisation of the Mepepy ligand can be observed in dichloromethane solution. The temperature dependence of the magnetic susceptibility of the compounds reveals a gradual $S = 5/2 \rightleftharpoons S = 1/2$ spin crossover of the Fe^{III} ions. This phenomenon is confirmed by Mössbauer spectroscopy for the Ni compound, which also reveals a magnetic component at 4.5 K with a hyperfine magnetic field, H_i, of 442(3) Oe. Theoretical analysis of the thermal variation of the high-spin proportion allows us to calculate the thermodynamical parameters of the spin-crossover behaviour in this compound: energy-gap (Δ) = 1536 cm^{-1}, entropy change (ΔS) = 33 J K^{-1} mol^{-1} and a cooperative interaction, J, of 0 cm^{-1} (non-cooperative spin crossover). The fractional oxidation state complex [Fe(salten)Mepepy][Ni(dmit)$_2$]$_3$ has been obtained after electrooxidation of [Fe(salten)Mepepy]-[Ni(dmit)$_2$] in acetonitrile. It exhibits a gradual spin conversion coupled with antiferromagnetic interactions. Its room temperature electrical conductivity is 0.1 S cm^{-1}.
(© Wiley-VCH Verlag GmbH & Co. KGaA, 69451 Weinheim, Germany, 2005)

Introduction

Since the discovery of the organic metal TTF–TCNQ (TTF = tetrathiafulvalene; TCNQ = tetracyanoethylene) much work has been devoted to the research of new conducting systems involving either donor–acceptor complexes or fractional oxidation-state compounds. These studies resulted in the discovery of several superconductors [derived, for example, from the BEDT-TTF molecule[1] (BEDT-TTF = bis(ethylenedithio)tetrathiafulvalene) or from the M(dmit)$_2$ complex[2] (dmit^{2-} = 1,3-dithiole-2-thione-4,5-dithiolato)]. In addition, these compounds are also now being used in a new area of research by a few groups, which consists in designing hybrid materials with a combination of different physical properties such as conductivity and magnetism,[3] conductivity and optical activity,[4] or magnetism and non-linear optics.[5] The possibilities offered by this hybrid approach in the field of the molecular conductors have been highlighted very recently.[6] In this kind of materials one might either just observe coexistence between these two properties, or an interplay due to a mutual interaction between the two effects. A good example of the coexistence of properties is found in the salt β′′-(BEDT-TTF)$_4$-[Fe(ox)$_3$](H_3O)·C_6H_5CN (ox = oxalate), reported by Day and co-workers,[7] which is the first example of a paramagnetic superconductor. An interplay between conductivity and magnetism has been observed, for example, in BETS-derived complexes [BETS = bis(ethylenedithio)tetraselenafulvalene].[8] Thus, λ-[(BETS)$_2$FeCl$_4$] undergoes a metal–insulator transition at 8 K and becomes metallic again below this temperature when a magnetic field of 10 T is applied.[9] Recently, Coronado et al.[10,11] succeeded in obtaining (BEDT-TTF)$_3$[MnCr(ox)$_3$](CH_2Cl_2) and (BETS)$_3$[MnCr(ox)$_3$]-(CH_2Cl_2), which exhibit the coexistence of conductivity and ferromagnetism.

In the above-discussed complexes, each property is carried by a distinct network: the organic part is at the origin of the conductivity, due to a charge transfer or a partial oxidation state of the organic donor, whereas the inorganic part is involved in the magnetic properties. In such compounds, observation of an interplay between the properties will depend on eventual interactions between the two networks. These electronic interactions can be favoured by short contacts and/or hydrogen bonding between the ade-

[a] Laboratoire de Chimie de Coordination,
205 Route de Narbonne, 31077 Toulouse Cedex, France
E-mail: faulmann@lcc-toulouse.fr
[b] Instituto Ciencia Molecular, Universidad de Valencia
Dr. Moliner 50, 46100 Burjassot, Spain
Supporting information for this article is available on the WWW under http://www.eurjic.org or from the author.

quate molecules, although the occurrence of the desired interplay is still not controllable. An attractive way of increasing the π–d interactions between the two networks consists of connecting them by covalent linkages. This has been attempted by Ouahab and co-workers in $[Cu(hfac)_2(TTF\text{-}py)_2](PF_6)\cdot 2CH_2Cl_2$[12] [hfac = hexafluoroacetylacetonate and TTF-py = 4-(2-tetrathiafulvalenylethenyl)pyridine], by connecting TTF to the Cu^{II} complex by unsaturated bonds and rings. So far, however, this approach has led to molecular compounds with very poor conducting properties and lack of magnetic properties of interest.

Some of us have also been interested in combining conductivity and magnetism by using metallocenium and $M(dmit)_2$ complexes.[13] Despite the interesting magnetic properties observed in $(Cp^*_2Mn)[Ni(dmit)_2]$, no fractional oxidation-state compound has been obtained with metallocenium and, consequently, the compound is an insulator. Another way of introducing a magnetic component into $M(dmit)_2$ complexes is to use spin-crossover cations. Spin crossover (abbreviated as SCO) in certain transition metal complexes has been known for a long time and has been well described and studied by several authors.[14] From the perspective of the present work, it should be noted that a slight modification in the ligand or in the nature of the solvent might result in a change of the value of the transition temperature, or even in the vanishing of the SCO phenomenon.

The ultimate goal of this work is to obtain a molecular conductor, and consequently a complex in a fractional oxidation state, that exhibits a spin crossover in such a way that the bistability of this magnetic switch may affect the conducting properties of the material. The choice of the starting SCO complex is crucial in the sense that it must not lose its magnetic properties when combined with the $M(dmit)_2$ complex. It must also not decompose or undergo any transformation during the oxidation process necessary to obtain the fractional oxidation state of the complex. In this context, Fe^{III} complexes seem promising as their oxidation state should not change during the synthesis of the fractional oxidation-state complex.

Several Fe^{III} complexes displaying SCO have already been described (see ref.[15] for a comprehensive review). In six-coordinate Fe^{III} systems an $S = 1/2 \leftrightharpoons S = 5/2$ conversion was observed in most cases. In these Fe^{III} SCO complexes, similar to the "benchmark" Fe^{II} complexes, the LS to HS spin-state change is accompanied by an increase of the metal–ligand distances ($\Delta r \approx 8$–15%). However, the average bond length change is significantly smaller in the case of Fe^{III} ions ($\Delta r \approx 5\%$) than for Fe^{II}. Due to this fact, the rate of interconversion of spin states is, in general, faster in Fe^{III} systems to such an extent that in many instances the ^{57}Fe Mössbauer spectra do not show separate HS and LS contributions. It is mainly for this reason that, in contrast to Fe^{II} compounds, a light-induced spin-state trapping (LIESST) effect is rarely observed in Fe^{III} complexes.[16–18] Furthermore, the majority of Fe^{III} SCO complexes display a gradual spin-state change as a function of temperature, while abrupt transitions with thermal hysteresis have been reported in only a few cases.[19–25] Although in a less straightforward way, this tendency may also be related to the smaller bond length changes in Fe^{III} complexes, given that the lattice expansion is a major ingredient for the cooperative interactions (elastic interactions) determining the gradual/abrupt nature of the spin-transition curves.[26]

For another attempt to obtain SCO properties in a molecular conductor (see ref.[19] for the first attempt), we chose the SCO complex [Fe(salten)Mepepy](BPh_4), previously reported by Sour et al.[27] [H_2salten = 4-azaheptamethylene-1,7-bis(salicylideneiminate); Mepepy = 1-(pyridin-4-yl)-2-(*N*-methylpyrrol-2-yl) ethane]. This Fe^{III} complex exhibits a gradual, thermally induced SCO.[27] Moreover, it also undergoes a partial photoinduced spin-state change in solution due to the photoisomerizable ligand Mepepy. Such a physical property might also play a role in the electrical properties of the final compound.

In this paper, we report the synthesis and X-ray characterisation of three new iron(III) compounds of formula [Fe(salten)Mepepy][$Ni(dmit)_2$] and [Fe(salten)Mepepy]-[$M(dmit)_2$]·CH_3CN (M = Pd, Pt), together with magnetic, spectroscopic and Mössbauer studies of the Ni derivative.

Results and Discussion

Description of the Structures

To the best of our knowledge this is the first time that the structure of complexes containing the Fe(salten)-(Mepepy) unit has been reported. The triclinic unit cell of each compound contains one $M(dmit)_2$ unit and one Fe(salten)(Mepepy) unit, with one acetonitrile molecule for the Pd and Pt complexes only (Figure 1).[28] Selected crystallographic data for every compound are reported in the Experimental Section (general crystallographic data can be found in the Supporting Information, Table S1).

Considering the cell parameters, the cell volume decreases upon lowering the temperature for every compound (see Table 1). For the Pd and Pt complexes, this decrease is accompanied by a decrease of the value for all parameters except the angles β and γ, whose values increase slightly. The Ni complex exhibits other features: only the β value increases when lowering the temperature, although the b and a values first decrease (from 295 to 240 K), and then increase again down to 100 K.

The intramolecular distances and angles within the $M(dmit)_2$ units are similar to those observed in other monoanionic $M(dmit)_2$ complexes.[29] In every complex, the Fe atom is in an octahedral environment, with the two oxygen atoms in a *trans* configuration. The two largest bond lengths around Fe are Fe–N21 and Fe–N32; the two shortest are Fe–O11 and Fe–O12. Thus, the [FeO_2N_4] octahedron can be regarded as axially elongated along the N32–Fe–N21 direction or axially compressed along the O11–Fe–O12 direction. The Mepepy fragment is not planar due to a slight distortion around the central C=C ethene bond:

 © 2005 Wiley-VCH Verlag GmbH & Co. KGaA, Weinheim

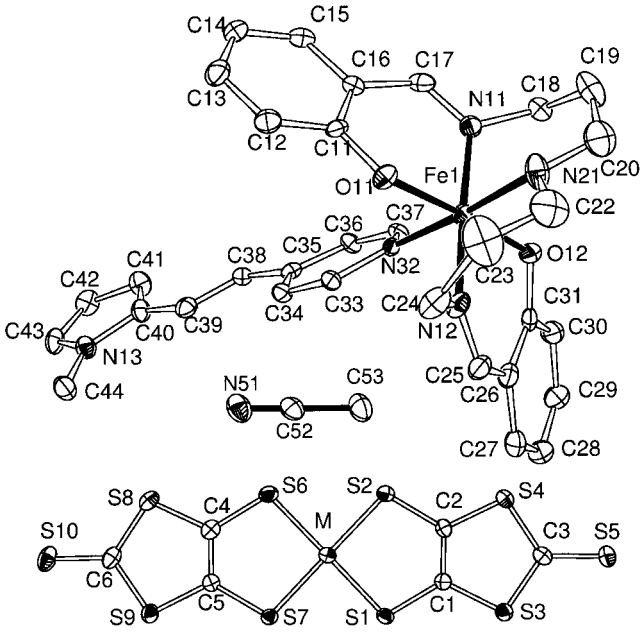

Figure 1. Asymmetric unit showing the atomic labelling of [Fe(salten)Mepepy][M(dmit)$_2$] (M = Ni, Pd, Pt) with acetonitrile present for M = Pd and Pt.

Table 1. Variations of the cell parameters (%, vs. parameters at 295 K) for **1**, **2** and **3** at 240, 160 and 100 K.

	T	Δ*a*/*a*	Δ*b*/*b*	Δ*c*/*c*	Δ*a*/*a*	Δ*β*/*β*	Δ*γ*/*γ*	Δ*V*/*V*
	240	–0.4	–0.2	–1.2	–0.2	0.2	–0.4	–1.7
Ni	160	–0.9	–0.1	–1.8	–0.2	0.2	–0.4	–2.8
	100	–1.1	–0.1	–1.9	–0.1	0.4	–0.4	–3.3
	240	–0.3	0.0	–0.5	–0.1	0.1	0.1	–0.9
Pd	160	–0.7	–0.3	–1.0	–0.2	0.2	0.1	–2.3
	100	–0.9	–0.4	–1.3	–0.3	0.3	0.2	–3.0
	240	–0.6	–0.2	–0.8	–0.2	0.1	0.0	–1.7
Pt	160	–1.0	–0.5	–1.3	–0.2	0.2	0.1	–2.9
	100	–1.2	–0.6	–1.7	–0.4	0.3	0.2	–3.7

the dihedral angle of C35–C38–C39–C40 ranges between 173.62(45)° (Ni, 100 K) and –179.90(41)° (Pd, 160 K; see Figure 2 and Table 2).

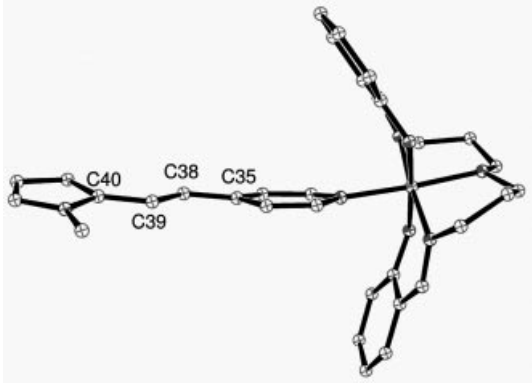

Figure 2. View of the [Fe(salten)Mepepy]$^+$ cation showing the non-planarity of the Mepepy part.

Table 2. Dihedral angle around C35–C38–C39–C40 and angle between the pyridine ring and the methylpyrrole ring in **1**, **2** and **3** at various temperatures.

		295 K	240 K	160 K	100 K
Dihedral angle around	Ni	176.0(8)	176.1(6)	175.9(6)	173.6(5)
C35–C38–C39–C40	Pd	179.6(5)	179.7(4)	–179.9(4)	–179.4(4)
	Pt	178.8(6)	178.6(8)	179.1(6)	179.6(53)
Angle between the pyridine ring	Ni	10.7(7)	11.0(5)	12.0(5)	11.4(4)
and the methylpyrrole ring	Pd	14.0(4)	14.3(4)	14.3(4)	14.5(3)
	Pt	12.7(5)	12.9(6)	13.0(5)	13.4(4)

Three different temperature effects are observed for each complex: for the Ni complex, lowering the temperature induces a decrease of this torsion angle [from 176.0(8)° to 173.6(5)°], whereas it increases in the Pt complex [from 178.8(6)° to 179.6(5)°]. For the Pd complex, a rocking motion is observed from 179.6(5)° to –179.4(4)°. These variations in the dihedral angle around the central C=C bond also induce a non-planarity between the two rings of the Mepepy fragment. The angle between the pyridine ring and the methylpyrrole ring ranges between 10.7(7)° (Ni, 295 K) and 14.5(3)° (Pd, 100 K; see Table 2). Whatever the complex, this angle always increases when the temperature is lowered. In regard to the latter two parameters (dihedral angle and inter-planar angle), the largest deviations are observed for the Ni complex.

The bond lengths around Fe also decrease when lowering the temperature (see Table 3). The bonds Fe–N32 and Fe–N11 are the most sensitive to the temperature: they exhibit variations up to around –3.2% between 295 K and 100 K (for the Pt complex, bond Fe–N32). For every complex, a decrease of the temperature tends to reduce the gap between the different bond lengths: indeed, since the longest bond lengths are subject to the largest decrease, this induces a more regular distribution of the bond lengths around the Fe atom.

Depending on the temperature, the twelve angles subtended at the Fe atom do not vary similarly as some decrease whereas others increase. A noticeable point is the following: whatever the complex, the O11–Fe–N12 and N12–Fe–N32 angles decrease down to around –2.5% and the O11–Fe–N11 angle increases by up to about 2.0% when compared to their value at room temperature. The Pd complex is the one for which there are the smallest variations in the values of distances and angles around the Fe atom.

Deformations of the octahedron around Fe can be estimated from the angles between the three equatorial planes defined by the six Fe-coordinating atoms, together with the deviation of the central Fe atom from these planes. These planes are almost orthogonal to each other, as reflected by the values all larger than 88° (Table S2 in the Supporting Information), and the Fe atom always lies very close to these planes (max. deviation of 0.024 Å). The angles between the eight opposite faces of the octahedron around Fe also define its deformation: at room temperature, these values lie between 3.99° and 6.31°, thus indicating that the faces are not parallel (Table S2 in the Supporting Infor-

 © 2005 Wiley-VCH Verlag GmbH & Co. KGaA, Weinheim

Table 3. Bond lengths around the Fe atom with their variations [%] relative to the room temperature values for **1**, **2** and **3** at various temperatures.

		Ni		Pd		Pt	
		Bond length	Δ%	Bond length	Δ%	Bond length	Δ%
Fe(1)–O(11)	295	1.926(5)	0.0	1.884(4)	0.00	1.892(5)	0.00
	240	1.890(4)	–1.8	1.877(3)	–0.37	1.900(5)	0.42
	160	1.885(4)	–2.1	1.872(3)	–0.64	1.887(4)	–0.32
	100	1.891(3)	–1.8	1.872(3)	–0.64	1.880(4)	–0.63
Fe(1)–O(12)	295	1.884(6)	0.0	1.899(4)	0.00	1.901(5)	0.00
	240	1.868(4)	–0.8	1.889(3)	–0.53	1.906(5)	0.26
	160	1.871(4)	–0.7	1.887(3)	–0.63	1.874(5)	–1.42
	100	1.873(3)	–0.6	1.884(3)	–0.79	1.877(4)	–1.26
Fe(1)–N(11)	295	1.979(9)	0.0	1.965(4)	0.00	1.971(5)	0.00
	240	1.949(5)	–1.5	1.953(3)	–0.61	1.959(7)	–0.61
	160	1.916(6)	–3.2	1.946(3)	–0.97	1.947(5)	–1.27
	100	1.930(4)	–2.5	1.947(3)	–0.92	1.930(5)	–2.08
Fe(1)–N(12)	295	1.979(8)	0.0	1.972(4)	0.00	1.987(6)	0.00
	240	1.925(5)	–2.7	1.961(4)	–0.56	1.990(7)	0.15
	160	1.937(5)	–2.1	1.958(3)	–0.71	1.971(5)	–0.86
	100	1.935(4)	–2.2	1.959(3)	–0.66	1.957(5)	–1.51
Fe(1)–N(21)	295	2.057(10)	0.0	2.033(5)	0.00	2.044(7)	0.00
	240	2.033(5)	–1.2	2.016(4)	–0.84	2.003(8)	–2.01
	160	1.994(6)	–3.1	2.018(4)	–0.74	1.999(6)	–2.05
	100	2.013(4)	–2.1	2.019(4)	–0.69	2.009(5)	–1.71
Fe(1)–N(32)	295	2.049(7)	0.0	2.036(4)	0.00	2.052(5)	0.00
	240	2.023(4)	–1.3	2.006(3)	–1.47	2.019(6)	–1.61
	160	1.983(6)	–3.2	1.994(3)	–2.06	2.001(5)	–2.53
	100	1.993(4)	–2.7	1.994(3)	–2.06	1.986(5)	–3.22

mation). In most cases a decrease of the temperature tends to reduce these angles (up to –3.23° for the Ni complex). These features, together with those discussed above, clearly show that the distorted octahedral environment around Fe tends to become more and more regular as well as more compact upon decreasing the temperature.

The structure can also be viewed as layers of iron complexes together with acetonitrile, separated from each other by layers of $M(dmit)_2$ units (Figure 3).

Each layer spreads out almost in the $(01\bar{1})$ plane. There are several short intermolecular contacts (around the sum of the van der Waals radii) within each layer. Within the $M(dmit)_2$ layers, short intermolecular contacts below 3.7 Å involve parallel $M(dmit)_2$ units connected through S–S interactions (Figure 3). Depending on M and the temperature, the units are connected through 1, 3, 5 or 7 contacts (≤3.7 Å) between S atoms. For a given M, the lower the temperature the larger the number of contacts (see Supporting Information, Table S3).

In addition, there are also some short intermolecular contacts (interatomic distances ≤ sum of the van der Waals radii[30]) between the sheets of $M(dmit)_2$ units and the layer of iron complexes and solvent (see Supporting Information, Table S4).

There is no contact between the acetonitrile and $M(dmit)_2$ units, whatever M is. Acetonitrile, if present, is connected through short contacts (see Supporting Information, Table S5) to the Fe units only.

The iron complexes are also connected to each other through several short contacts (see Supporting Information, Table S6), but no real hydrogen bonds exist. As for the interactions between the $M(dmit)_2$ units, the lower the temperature the larger the number of contacts between the various components of these compounds.

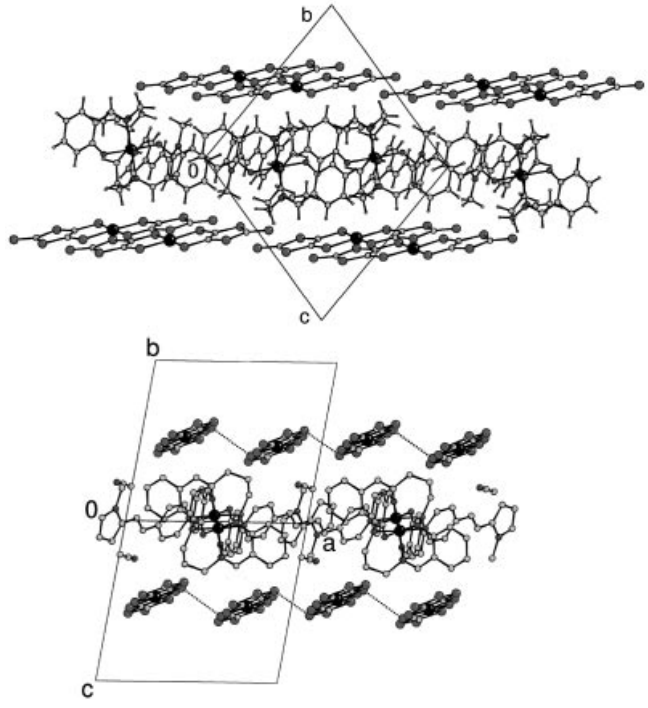

Figure 3. View of the structural arrangement in **1**, **2** and **3** along the *a* direction (left) and along the *bc* direction (right).

 © 2005 Wiley-VCH Verlag GmbH & Co. KGaA, Weinheim

UV/Vis Spectroscopy and Light Irradiation Effects

The UV/Vis absorption spectrum of [Fe(salten)Mepepy](BPh$_4$) in CH_2Cl_2 is shown in Figure 4. It shows two strong and broad absorption bands (λ = 370 nm, ε = 17757 $M^{-1}cm^{-1}$; λ = 401 nm, ε = 16656 $M^{-1}cm^{-1}$) and a very weak band (λ = 486 nm, ε = 4803 $M^{-1}cm^{-1}$). This latter is due to a ligand-to-metal charge transfer (LMCT).[27] Whereas only one band (λ = 375 nm) is observed in CH_3CN,[27] the splitting and broadening of this transition in CH_2Cl_2 is probably due to solvent effects (smaller polarity of CH_2Cl_2 compared with CH_3CN), which change the energy of the electronic transitions and induce bathochromic and hypsochromic shifts. Nevertheless, the transitions at 370 and 401 nm can be assigned to a ligand-centred $\pi\rightarrow\pi^*$ transition similar to that observed in CH_3CN.[27] Upon irradiation, these transitions are slightly blue-shifted (from 371 to 364 nm, and from 401 to 397 nm), and their intensities are significantly decreased (from 17757 to 11667 $M^{-1}cm^{-1}$, and from 16656 to 11109 $M^{-1}cm^{-1}$). As in CH_3CN, the LMCT transition at 486 nm is not affected by light.[27] From this study on the starting [Fe(salten)Mepepy](BPh$_4$) salt, it can be concluded that this complex also undergoes a *trans* to *cis* isomerisation of the Mepepy ligand in CH_2Cl_2.

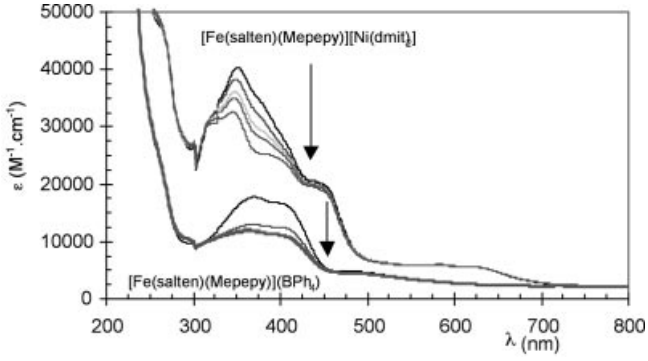

Figure 4. UV/Vis spectra and evolution upon irradiation of [Fe(salten)Mepepy](BPh$_4$) (lower curves) and [Fe(salten)Mepepy][Ni(dmit)$_2$ (upper curves) in CH_2Cl_2. Arrows indicate decrease of the intensity of the transitions upon irradiation.

The effect of light was then studied for the [Fe(salten)Mepepy][Ni(dmit)$_2$] complex in solution. The UV/Vis spectrum of this complex exhibits several absorption peaks. The main absorption band lies around 351 nm (ε = 40288 $M^{-1}cm^{-1}$) and contains several shoulders at shorter and longer wavelengths. This broad peak is the superposition of several transitions within the $[Ni(dmit)_2]^-$ unit ($\pi\rightarrow\pi^*$ and MLCT transitions[31]) and includes the transitions previously observed in the starting salt [Fe(salten)Mepepy](BPh$_4$). A satellite band is observed at 443 nm ($\pi\rightarrow\pi^*$, $\varepsilon \approx$ 20412 $M^{-1}cm^{-1}$) and two weaker bands at 582 nm ($n_S\rightarrow\pi^*$[31]) and 620 nm (with $\varepsilon \approx$ 6000 and 5600 $M^{-1}cm^{-1}$, respectively), attributed to MLCT transitions.[32] Irradiation results in a blue shift of the most important absorption (from 351 to 345 nm), accompanied by a decrease of ε = 32407 $M^{-1}cm^{-1}$. The shoulders also become more pronounced, and one is clearly visible at 385 nm (ε = 24992 $M^{-1}cm^{-1}$). The bands at 443, 582 and 620 nm are unaffected by irradiation. The absorption at 385 nm can be attributed to the ligand-centred $\pi\rightarrow\pi^*$ transition {initially at 370 nm in the starting salt [Fe(salten)Mepepy](BPh$_4$)}. Upon irradiation, this transition exhibits a decrease of around 25% of its intensity. The parallel evolution of the starting salt [Fe(salten)Mepepy](BPh$_4$) and [Fe(salten)Mepepy][Ni(dmit)$_2$] suggests that the $[Fe(salten)Mepepy]^+$ unit also undergoes an isomerisation in solution when associated with the $[Ni(dmit)_2]^-$ unit.

Raman Studies of the [Fe(salten)Mepepy]-Based Complexes

It is possible to evaluate the charge transfer in complexes containing $[Ni(dmit)_2]^{n-}$ units (in an entire or fractional oxidation state) by Raman spectroscopy.[33] The Raman spectrum of [Fe(salten)Mepepy][Ni(dmit)$_2$] is shown in Figure 5a. The lines at 599, 1435 and 1598 cm^{-1} were assigned to the Fe(salten) fragment in comparison with the spectra of [Fe(salten)]Cl (see Figure S2, Supporting Information). The lines at 134, 338, 357, 508, 1051 and 1395 cm^{-1} were assigned to the $[Ni(dmit)_2]^-$ unit by comparison with literature data,[33] and confirm that the charge transfer, ρ, is equal

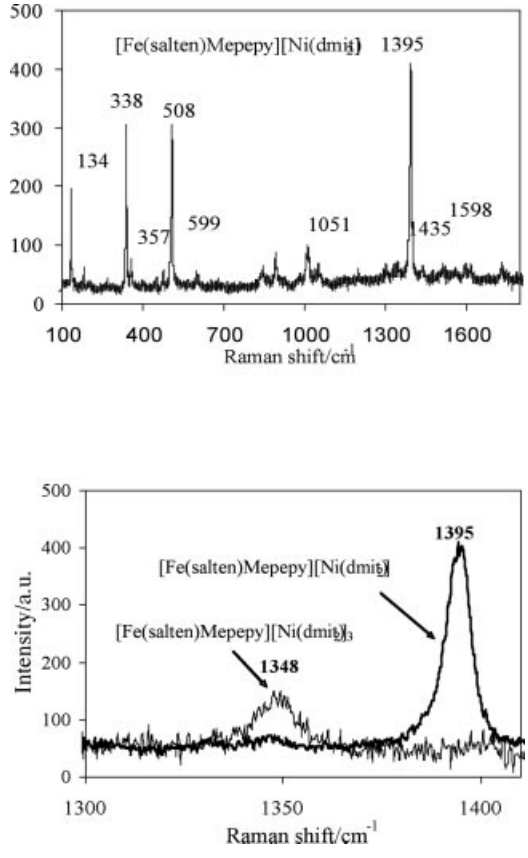

Figure 5. Raman spectra of a single crystal of [Fe(salten)Mepepy][Ni(dmit)$_2$] (top) and [Fe(salten)Mepepy][Ni(dmit)$_2$]$_3$ (bottom).

 © 2005 Wiley-VCH Verlag GmbH & Co. KGaA, Weinheim

to 1. In [Fe(salten)Mepepy][Ni(dmit)$_2$] the band at 1395 cm^{-1} is due to the C=C bond stretching mode. In [Fe(salten)Mepepy][Ni(dmit)$_2$]$_x$, this line (Figure 5b) is found at 1348 cm^{-1}. This band, whose position is very sensitive to the amount of charge transfer, allows us to determine a ρ value of around 0.3. The others lines of this spectrum are due to the Ni(dmit)$_2$ fragment and are in agreement with this ratio (Table S7, Supporting Information).

Magnetic Properties of Non-Fractional Oxidation State Complexes

For the Ni and Pt complexes (Figure 6), the temperature dependence of the $\chi_M T$ product shows a rapid but gradual decrease down to about 235 K, followed by a slightly descending plateau down to 2 K, with a slope about 10 times smaller than in the previous region and with a $\chi_M T$ product close to 0.9 cm^3 K mol^{-1} (χ_M = molar magnetic susceptibility).

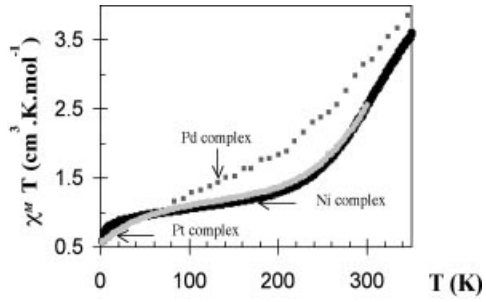

Figure 6. Variations of $\chi_M T$ as a function of the temperature for **1**, **2** and **3**.

For the Ni complex the magnetic properties are the same with or without acetonitrile in the complex (see Supporting Information, Figure S1). The Pd complex, which has been measured only between 80 and 350 K, exhibits almost similar behaviour, but with a smaller change in the slope at around 210 K. No plateau is observed down to 80 K. The behaviours of the Ni and Pt complexes are very close and similar to that observed for the starting iron salt [Fe(salten)-Mepepy](BPh$_4$).[27] For a given complex, the magnetic behaviour in the warming and cooling modes does not show any detectable thermal hysteresis loop. The 1:1 stoichiometry of the complexes [Fe(salten)Mepepy][M(dmit)$_2$] (M = Ni, Pd, Pt)} shows they are built on the association of an Fe^{III} complex with a formally M^{III} complex with S = 1/2.

Neglecting any magnetic interaction between Fe^{III} and M^{III}, as well as the orbital contributions, the expected "spin-only" value of $\chi_M T$ is equal to 4.38 cm^3 K mol^{-1} for Fe^{III} ions in the high-spin (HS) state (S = 5/2) and 0.37 cm^3 K mol^{-1} for both the M^{III} ions and the Fe^{III} ions in the low-spin (LS) state (S = 1/2). At the highest temperatures of the measurements, the experimental values are about 3.5 cm^3 K mol^{-1}, which are clearly below the expected values (ca. 4.8 cm^3 K mol^{-1}). In the low-temperature regime the experimental plateau is above the expected value (ca. 1.0 cm^3 K mol^{-1} compared to 0.74 cm^3 K mol^{-1}). These observations indicate that the spin transition is incomplete both at low and at high temperatures, i.e. at 350 K a fraction of Fe^{III} ions is still in the LS form, while there is a residual HS fraction even at the lowest temperatures, as confirmed by the Mössbauer data (see below).

Fitting the temperature dependence of the HS fraction (curve not shown) with the well-known Ising-like model[34–36] leads to the thermodynamic parameters of the spin crossover in this compound: an energy gap between the HS and LS levels, Δ, of 1536 cm^{-1} and a reasonable entropy change upon the spin crossover of ΔS = 33 J K^{-1} mol^{-1}. The fitting also leads to a very weak cooperative interaction ($J \approx 0$ cm^{-1}), in accordance with a non-cooperative system.

In summary, these results clearly show that the spin conversion is maintained in the Fe complex, even after the substitution of the BPh$_4^-$ anion by the [M(dmit)$_2$]$^-$ anion. This latter seems, therefore, to have a "neutral" effect on the magnetic properties of the [Fe(salten)Mepepy]$^+$ complex, whereas it has a "positive" effect when combined with [Fe(sal$_2$trien)]$^+$ (appearance of a strong cooperativity and a hysteresis loop, never observed before in this family of SCO complexes).[19]

Magnetic Properties of the Fractional Oxidation State Complex

A plot of the $\chi_M T$ product vs. temperature is shown in Figure S3 (Supporting Information). $\chi_M T$ is equal to 1.47 cm^3 K mol^{-1} at room temperature, and decreases almost linearly down to a value of 0.04 cm^3 K mol^{-1} at 2 K. Such a behaviour can be explained by a gradual spin conversion of the [Fe(salten)Mepepy]$^+$ unit from the HS state to the LS state, coupled to an antiferromagnetic interaction between the two components, which leads at low temperature to a non-magnetic ground spin state. This explanation is in agreement with a lack of magnetisation at 2 K (see Figure S4 in the Supporting Information).

Mössbauer studies were not possible in the present case because of the small amount of sample available (0.8 mg). For the same reason, room temperature electrical conductivity was only measured on the powder by the two-probes method. A value as large as 0.1 S cm^{-1} was obtained, which is indicative of the presence of a significant electron delocalisation in this compound.

Mössbauer Spectroscopy

The ^{57}Fe Mössbauer spectra of [Fe(salten)Mepepy]-[Ni(dmit)$_2$] were recorded between 4.5 K and 330 K. Figure 7 show selected spectra obtained in the cooling mode. The fitted Mössbauer parameters at each temperature are given in Table 4.

 © 2005 Wiley-VCH Verlag GmbH & Co. KGaA, Weinheim

Table 4. Least-squares-fitted Mössbauer data for [Fe(salten)Mepepy][Ni(dmit)$_2$].

	Low spin[a,b]			High spin			
T [K]	δ [mm s^{-1}]	ΔE_Q [mm s^{-1}]	$\Gamma/2$ [mm s^{-1}]	δ [mm s^{-1}]	ΔE_Q [mm s^{-1}]	$\Gamma/2$ [mm s^{-1}]	A_{HS}/A_{tot}
4.5	0.23(1)	1.74(1)	0.31(1)	0.41(5)	–0.6(1)	0.51(8)	19(2)
80	0.254(2)	1.649(4)	0.277(3)	0.466(8)	0.68(1)	0.277(3)	24(1)
150	0.242(3)	1.528(6)	0.266(5)	0.446(5)	0.64(2)	0.266(5)	31(1)
185	0.227(3)	1.451(8)	0.233(6)	0.426(6)	0.65(1)	0.233(6)	34(1)
220	0.225(3)	1.392(7)	0.223(6)	0.413(5)	0.646(9)	0.223(6)	39(1)
260	0.22(2)	1.14(3)	0.24(1)	0.39(2)	0.67(3)	0.24(1)	50(3)
300	0.14(3)	1.05(8)	0.24(5)	0.34(1)	0.658(2)	0.24(1)	80(4)
330	0.2(1)	0.8(2)	0.27(1)	0.349(5)	0.62(1)	0.27(1)	78(5)

[a] δ = isomer shift; ΔE_Q = quadrupole splitting; $\Gamma/2$ = half-height width of the line; A_{HS}/A_{tot} = area ratio. [b] Error bars are given in parentheses; isomer-shift values refer to metallic iron at room temperature. Between 80 and 330 K both components were fitted with the same linewidth.

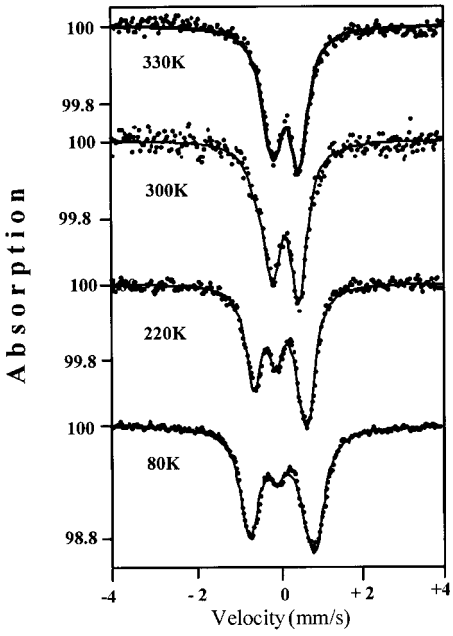

Figure 7. Selected Mössbauer spectra of [Fe(salten)Mepepy][Ni(dmit)$_2$] obtained in the cooling mode between 330 and 80 K. The solid lines represent fitted curves.

At 330 K, the spectrum for [Fe(salten)Mepepy][Ni(dmit)$_2$] consists chiefly (80%) of one component with isomer-shift and quadrupole-splitting values characteristic of HS Fe^{III}. The ratio of the LS component increases gradually with decreasing temperature. This component is characterised by somewhat larger isomer-shift and quadrupole-splitting values. It is important to note that, in contrast to the first doublet, this second spectrum exhibits almost no temperature dependence of the quadrupole splitting. Taking into account that in the ^{6}S configuration of Fe^{III} no low-lying excited levels are expected and its $^2T_{2g}$ configuration shows an appreciable thermal population of close-lying excited levels when slightly distorted, the low-temperature main doublet (76%) can be assigned unambiguously to a low-spin Fe^{III} species and the high-temperature main doublet (78%) corresponds to a high-spin Fe^{III} species. The distinct spectra obtained for the two spin-states indicate that the spin interconversion rates are slow compared to the hyperfine frequencies of Mössbauer spectroscopy (ca. 10^{-7}–10^{-8} s^{-1}]). The area ratio A_{HS}/A_{tot}, which is in a first approximation proportional to the HS fraction, decreases gradually from 330 K (≈78%) to 80 K (≈24%). It must be emphasised that the Mössbauer data were collected for the same sample that was studied with magnetic susceptibility. In spite of this, the HS fraction that can be deduced from the Mössbauer spectra (Table 4) and magnetic susceptibility data (Figures 6 and 7) are slightly different, especially in the high-temperature region (300 and 330 K). Among the reasons for this discrepancy one should note that the magnetic data are difficult to convert into HS fractions since the susceptibilities of the pure HS and LS species are not known. Furthermore, the high-temperature Mössbauer spectra are not sufficiently resolved (due to the close isomer-shift and quadrupole-splitting values of Fe^{III} in both states) and therefore there is a large uncertainty in the fits. On the whole, however, the Mössbauer data clearly confirm the gradual and incomplete $S = 1/2 \leftrightharpoons S = 5/2$ spin crossover of Fe^{III} species in [Fe(salten)Mepepy][Ni(dmit)$_2$].

Upon further cooling to 4.5 K a magnetic hyperfine splitting appears. The spectrum (Figure 8) shows that only the quadrupolar doublet corresponding to the residual HS fraction is converted into a magnetic hyperfine Mössbauer splitting.

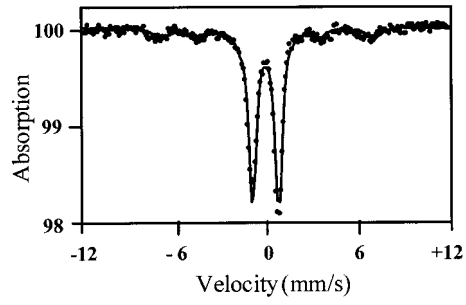

Figure 8. Mössbauer spectrum of [Fe(salten)Mepepy][Ni(dmit)$_2$] at 4.5 K. The solid line represents the fitted curve with both quadrupolar and magnetic components.

The spectrum was fitted by an axial hyperfine magnetic field parallel to the principal axis of the electric field gradient (EFG). The fit shows unambiguously that the principal EFG component is negative. In addition, the corresponding

 © 2005 Wiley-VCH Verlag GmbH & Co. KGaA, Weinheim

hyperfine magnetic field, H_i, was evaluated to be 430 kOe. This value falls in the range expected for HS Fe^{III}.[37] The magnetic component of the spectrum was fitted with quite a large line-width [$\Gamma/2 = 0.51(8)$ mm s^{-1}], thus indicating the presence of some magnetic relaxation in the system. It should be noted, however, that the H_i value obtained here (430 kOe) is somewhat smaller than what can be expected from the $220<S_z>$ rule, which leads to a theoretical value of $H_i = 550$ kOe. This is due to the fact that the magnetic ordering at 4.5 K is not totally achieved and needs a lower temperature to be complete, in good agreement with the observation of the broadening of the linewidth at this temperature. One can attribute this magnetic splitting at 5 K either to a slow paramagnetic relaxation or to a long-range cooperative order. Considering the first possibility (slow paramagnetic relaxation), the dilute nature of the complex is evidenced by a shortest inter-complex Fe^{III}–Fe^{III} distance of about 6.9 Å, a magnitude which is large enough to result in long spin-spin relaxation times for high-spin iron(III). Considering the possibility of a long-range order, on the basis of the magnetic data we cannot exclude the possibility of the existence of magnetic couplings, even though it seems more reasonable to describe the low-temperature variation of magnetic properties in terms of zero-field splitting effects. We note that these limiting behaviours can be distinguished by Mössbauer spectroscopy by analysis of the temperature dependence of the spectra using the Mössbauer magnetic relaxation theory established by Blume and Tijon.[38] It can be also achieved experimentally using a weak external applied magnetic field, which may freeze the magnetic fluctuations.[39] These laborious approaches, however, are beyond the scope of this paper.

Conclusions

In attempt to combine conductivity and spin-crossover properties in the same material, we have synthesised three new compounds with the general formula [Fe(salten)Mepepy][M(dmit)$_2$]·CH_3CN (M = Ni, Pd, Pt). We have shown by magnetic susceptibility and Mössbauer measurements that the Fe^{III} ions preserve their spin-crossover properties in the new crystal lattice, although the spin crossover of the Ni complex is not complete at low temperature (80 K). Mössbauer spectroscopy has shown that the remaining high-spin state is magnetically ordered at 4.5 K, leading to a promising way to combine magnetic properties and bistability in inorganic molecular compounds. Preliminary attempts to synthesise fractional oxidation-state complexes have resulted in the synthesis of a conductive powder that exhibits a spin conversion with antiferromagnetic interactions. Although not structurally characterised, this compound is one of the first complexes to combine spin conversion and electrical properties. Work is currently in progress to combine such SCO compounds with metal-bisdithiolene complexes.[19]

Experimental Section

Synthesis: All reactions were performed under an inert atmosphere of argon, using Schlenk technique, and sheltered from daylight. Solvents were dried and distilled under argon prior to use.

[Fe(salten)Mepepy](BPh$_4$) and (NBu$_4$)[M(dmit)$_2$] (M = Ni, Pd, Pt) were synthesised following literature methods.[27,40]

Synthesis of [Fe(salten)Mepepy][M(dmit)$_2$]·CH_3CN (M = Ni, Pd, Pt): (NBu$_4$)[M(dmit)$_2$] (M = Ni, Pd, Pt; 0.24 mmol) was dissolved in a mixture of acetonitrile and acetone (30 and 20 mL, respectively) and a solution of [Fe(salten)Mepepy](BPh$_4$) (214 mg, 0.24 mmol) in acetonitrile (10 mL) was added dropwise. The resulting solution was stirred for 5 min and stored at 4 °C overnight. The precipitate obtained was filtered, washed with 5 × 5 mL of acetonitrile, 2 × 3 mL of diethyl ether, and dried under vacuum. Every compound was obtained as shiny, crystalline blocks, which were used for subsequent characterisations. Initially, the Ni complex was obtained with acetonitrile (its structure was solved at 160 K, see below). The same crystal, when analysed again a few weeks later on the diffractometer, did not contain acetonitrile.

1: [Fe(salten)Mepepy][Ni(dmit)$_2$]. $C_{38}H_{35}FeN_5NiO_2S_{10}$ (1028.9): calcd. C 44.36, H 3.43, N 6.81; found C 44.95, H 3.53, N 6.89.

2: [Fe(salten)Mepepy][Pd(dmit)$_2$]·CH_3CN. $C_{40}H_{38}FeN_6O_2PdS_{10}$ (1117.6): calcd. C 42.98, H 3.43, N 7.52; found C 42.95, H 3.58, N 7.10.

3: [Fe(salten)Mepepy][Pt(dmit)$_2$]·CH_3CN. $C_{40}H_{38}FeN_6O_2PtS_{10}$ (1206.3): calcd. C 39.82, H 3.18, N 6.97; found C 40.50, H 3.04, N 6.46.

Synthesis of [Fe(salten)Mepepy][Ni(dmit)$_2$]$_3$: This complex was obtained either by galvanostatic or potentiostatic oxidation of [Fe(salten)Mepepy][Ni(dmit)$_2$] in acetonitrile, using Pt electrodes.

UV/Vis Spectroscopy/Irradiation: Measurements were performed with [Fe(salten)Mepepy](BPh$_4$) and [Fe(salten)Mepepy][Ni(dmit)$_2$] at room temperature in CH_2Cl_2 solution with a Perkin–Elmer Lambda 5 equipment. Irradiation was performed with a 200 W (Hg) Oriel lamp (filter 400 nm).

X-ray Structure Analysis: X-ray data for each compound, were collected at 295, 240, 160 and 100 K on an IPDS diffractometer (Stoe) or on an Xcalibur (Oxford Diffraction) diffractometer, with monochromatic Mo-K_α radiation ($\lambda = 0.71073$ Å). Crystallographic data are given in Table 5. X-ray structure analysis was performed using the WinGX package.[41] H atoms were included at their calculated positions as riding on their adjacent atom. SIR97[42] or Shelxs97[43] were used for the structure solutions, Shelxl97[44] for the refinements, Platon[45] for structure analysis, and Ortep3[46] or Cameron[47] for the production of the crystallographic illustrations. CCDC-262730 to -262742 contain the supplementary crystallographic data for this paper. These data can be obtained free of charge from The Cambridge Crystallographic Data Centre via www.ccdc.cam.ac.uk/data_request/cif.

Magnetic Measurements: Magnetic measurements were performed on powders (Pd and Pt complexes containing acetonitrile; Ni complex without acetonitrile) using either an MPMS SQUID magnetometer (Quantum Design) operating at 1 T or a Faraday-type magnetometer equipped with a DRUSH electromagnet (operating in the range 0.4–1.4 T), a Sartorius balance and a continuous-flow Oxford Instruments cryostat. The magnetic susceptibility values were calibrated against Hg[Co(SCN)$_4$]. Data were corrected for magnetisation of the sample holder and for diamagnetic contributions, which were estimated from Pascal's constants.

 © 2005 Wiley-VCH Verlag GmbH & Co. KGaA, Weinheim

Table 5. Crystallographic data for the complexes [Fe(salten)Mepepy][M(dmit)$_2$] at various temperatures.

	[Fe(salten)Mepepy][Ni(dmit)$_2$] (**1**)				[Fe(salten)Mepepy][Pd(dmit)$_2$]·CH$_3$CN (**2**)				[Fe(salten)Mepepy][Pt(dmit)$_2$]·CH$_3$CN (**3**)			
Empirical formula	$C_{38}H_{35}FeN_5NiO_2S_{10}$				$C_{40}H_{38}FeN_6O_2PdS_{10}$				$C_{40}H_{38}FeN_6O_2PtS_{10}$			
M	1028.87				1117.61				1206.30			
Temperature [K]	293	240	160	100	280	240	160	100	293	240	160	100
Crystal system	triclinic				triclinic				triclinic			
Space group	$P\bar{1}$				$P\bar{1}$				$P\bar{1}$			
Z	2				2				2			
a [Å]	13.384(2)	13.335(3)	13.262(3)	13.239(1)	13.433(2)	13.394(1)	13.333(5)	13.306(1)	13.464(2)	13.384(1)	13.332(2)	13.303(3)
b [Å]	12.995(2)	12.971(3)	12.983(3)	12.987(1)	13.541(2)	13.536(2)	13.503(5)	13.483(2)	13.556(1)	13.522(2)	13.485(2)	13.469(3)
c [Å]	14.972(2)	14.785(3)	14.699(3)	14.684(1)	14.811(2)	14.740(2)	14.658(5)	14.613(2)	14.832(2)	14.712(1)	14.635(2)	14.587(3)
α [°]	99.69(2)	99.51(2)	99.54(2)	99.555(6)	98.55(2)	98.46(1)	98.338(5)	98.27(1)	98.91(1)	98.746(8)	98.71(1)	98.54(2)
β [°]	114.98(2)	115.20(2)	115.24(2)	115.478(7)	115.68(2)	115.79(1)	115.953(5)	116.04(1)	115.41(1)	115.521(8)	115.61(1)	115.75(2)
γ [°]	98.38(2)	97.98(2)	97.99(2)	97.982(6)	99.58(1)	99.63(1)	99.690(5)	99.74(1)	99.50(1)	99.526(8)	99.56(1)	99.68(2)
V [Å^3]	2257.3(6)	2218.5(8)	2194.4(7)	2183.9(3)	2319.2(5)	2298.8(4)	2266.7(14)	2250.0(4)	2332.9(4)	2293.6(4)	2264.9(6)	2247.4(8)
$D_{calcd.}$ [g cm^{-3}]	1.514	1.540	1.557	1.565	1.600	1.615	1.638	1.650	1.717	1.747	1.769	1.783
μ (Mo-K_α) [mm^{-1}]	1.241	1.262	1.276	1.282	1.193	1.204	1.221	1.230	3.796	3.861	3.910	3.940
No. of collected refls.	22405	23958	23690	94870	23066	21904	27590	27229	23144	24197	68385	96901
No. of unique refls.	8278	14122	13968	16671	8548	8445	10195	10064	8570	14580	16363	17135
R(int)	0.1227	0.0921	0.1011	0.1405	0.0796	0.0610	0.0754	0.0645	0.0678	0.0973	0.1161	0.1535
R_1	0.0472	0.0499	0.0503	0.0520	0.0442	0.0419	0.0444	0.0419	0.0397	0.0551	0.0525	0.0512
wR_2	0.0911	0.0617	0.0620	0.0794	0.0759	0.0794	0.0867	0.0851	0.0653	0.0755	0.0841	0.0562
No. of parameters	515	515	515	515	543	543	543	543	543	543	543	543

Raman Spectroscopy: Raman measurements were performed with a Dilor XY micro-Raman (source: 632.8 nm line of a He-Ne laser; laser power density: ≈10^5 W cm^{-2}). The spectra were recorded at VV polarisation.

Mössbauer Spectroscopy: The variable-temperature Mössbauer measurements were obtained on a constant-acceleration spectrometer with a 50 mCi source of ^{57}Co (Rh matrix). The isomer shift values (δ) are given with respect to metallic iron at room temperature. The absorber was a sample of microcrystalline powder enclosed in a 2-cm-diameter cylindrical plastic sample holder, the size of which was determined to optimise the absorption. The variable-temperature spectra were obtained in the range 4.5–330 K using a He bath cryostat (Air Liquid DTA). Fitting parameters for all spectra were obtained by using a least-squares computer program.[48] The standard deviations of statistical origin are given in parentheses.

Supporting Information (see footnote on the first page of this article) contains four figures {magnetic behaviour of **1** with or without solvent, magnetic behaviour and magnetisation of [Fe(salten)-Mepepy][Ni(dmit)$_2$]$_3$, and Raman spectra of [Fe(salten)]Cl, [Fe(salten)Mepepy](BPh$_4$) and [Fe(salten)Mepepy][Ni(dmit)$_2$]} and seven tables (crystallographic data, geometrical data, short intermolecular distances and assignments of the Raman spectra).

Acknowledgments

The support and sponsorship of COST Action D14/0003/98 are acknowledged. S. D. thanks COST D14 for funding a Short Term Scientific Mission in Valencia.

[1] J. M. Williams, J. R. Ferraro, R. J. Thorn, K. D. Carlson, U. Geiser, H. H. Wang, A. M. Kini, M.-H. Whangbo, *Organic Superconductors (Including Fullerene): Synthesis Structure, Properties and Theory*, Prentice Hall, Englewood Cliff, NJ, **1992**.

[2] C. Faulmann, P. Cassoux, *Solid State Properties (Electronic, Magnetic, Optical) of Dithiolene Complex-based Compounds*, in *Progress in Inorganic Chemistry (Dithiolene Chemistry: Synthesis Properties, and Applications)* (Ed.: E. I Stiefel), John Wiley & Sons, Inc., **2004**, vol. 52, pp. 399–489.

[3] E. Coronado, P. Day, *Chem. Rev.* **2004**, *104*, 5419–5448.

[4] E. Coronado, J. R. Galán-Mascarós, *Inorg. Chem.* **2004**, *43*, 8072–8077.

[5] O. Margeat, P. G. Lacroix, J. P. Costes, B. Donnadieu, C. Lepetit, K. Nakatani, *Inorg. Chem.* **2004**, *43*, 4743–4750.

[6] E. Coronado, J. R. Galán-Mascarós, *J. Mater. Chem.* **2005**, *15*, 66–74.

[7] M. Kurmoo, A. W. Graham, P. Day, S. J. Coles, M. B. Hursthouse, J. L. Caufield, J. Singleton, F. L. Pratt, W. Hayes, L. Ducasse, P. Guionneau, *J. Am. Chem. Soc.* **1995**, *117*, 12209–12217.

[8] H. Kobayashi, A. Kobayashi, P. Cassoux, *Chem. Soc. Rev.* **2000**, *29*, 325–333.

[9] M. Tokumoto, T. Naito, H. Kobayashi, A. Kobayashi, V. N. Laukhin, L. Brossard, P. Cassoux, *Synth. Met.* **1997**, *86*, 2161–2162.

[10] A. Alberola, E. Coronado, J. R. Galan-Mascaros, C. Gimenez-Saiz, C. J. Gomez-Garcia, *J. Am. Chem. Soc.* **2003**, *125*, 10774–10775.

[11] A. Alberola, E. Coronado, J. R. Galan-Mascaros, C. Gimenez-Saiz, C. J. Gomez-Garcia, E. Martinez-Ferrero, A. Murcia-Martinez, *Synth. Met.* **2003**, *135–136*, 687–689.

[12] F. Setifi, L. Ouahab, S. Golhen, Y. Yoshida, G. Saito, *Inorg. Chem.* **2003**, *42*, 1791–1793.

[13] C. Faulmann, E. Riviere, S. Dorbes, F. Senocq, E. Coronado, P. Cassoux, *Eur. J. Inorg. Chem.* **2003**, 2880–2888.

[14] P. Gütlich, H. A. Goodwin, *Spin Crossover in Transition Metal Compounds I–III*, in *Topics in Current Chemistry*, **2004**; Vol. 233–235.

[15] P. J. van Koningsbruggen, Y. Maeda, H. Oshio, *Top. Curr. Chem.* **2004**, *233*, 259–324.

[16] S. Hayami, K. Inoue, S. Osaki, Y. Maeda, *Chem. Lett.* **1998**, 987–988.

[17] G. Juhasz, S. Hayami, O. Sato, Y. Maeda, *Chem. Phys. Lett.* **2002**, *364*, 164–170.

[18] S. Hayami, Z.-Z. Gu, M. Shiro, Y. Einaga, A. Fujishima, O. Sato, *J. Am. Chem. Soc.* **2000**, *122*, 11569.

[19] S. Dorbes, L. Valade, J. A. Real, C. Faulmann, *Chem. Commun.* **2005**, 69–71.

[20] S. Floquet, M.-L. Boillot, E. Riviere, F. Varret, K. Boukheddaden, D. Morineau, P. Negrier, *New J. Chem.* **2003**, *27*, 341–348.

[21] M. D. Timken, S. R. Wilson, D. N. Hendrickson, *Inorg. Chem.* **1985**, *24*, 3450.

 © 2005 Wiley-VCH Verlag GmbH & Co. KGaA, Weinheim

[22] N. S. Gupta, M. Mohan, N. K. Jha, W. E. Antholine, *Inorg. Chim. Acta* **1991**, *184*, 13–21.
[23] M. S. Haddad, M. W. Lynch, W. D. Federer, D. N. Hendrickson, *Inorg. Chem.* **1981**, *20*, 123–131.
[24] F. V. Wells, S. W. McCann, H. H. Wickman, S. L. Kessel, D. N. Hendrickson, R. D. Feltham, *Inorg. Chem.* **1982**, *21*, 2306.
[25] A. Earnshaw, E. A. King, L. F. Larkworthy, *J. Chem. Soc. A* **1969**, 2459.
[26] H. Spiering, *Top. Curr. Chem.* **2004**, *235*, 171–195 and references cited therein.
[27] A. Sour, M.-L. Boillot, E. Riviere, P. Lesot, *Eur. J. Inorg. Chem.* **1999**, 2117–2119.
[28] An acetonitrile molecule was also found in the complex of Ni and its structure was solved at 160 K; it is similar to that of the Pd and Pt complexes (see Supporting Information for the X-ray data and CCDC-262733). Its magnetic properties are also similar to the properties of the Ni complex without solvent (see Supporting Information, Figure S1).
[29] A. E. Pullen, R. M. Olk, *Coord. Chem. Rev.* **1999**, *188*, 211–262.
[30] A. Bondi, *J. Phys. Chem.* **1964**, *68*, 441–451.
[31] G. N. Schrauzer, V. P. Mayweg, *J. Am. Chem. Soc.* **1965**, *87*, 3585–3592.
[32] R. M. Olk, R. Kirmse, E. Hoyer, C. Faulmann, P. Cassoux, *Z. Anorg. Allg. Chem.* **1994**, *620*, 90–100.
[33] K. I. Pokhodnya, C. Faulmann, I. Malfant, R. A. Solano, P. Cassoux, A. Mlayah, D. Smirnov, J. Leotin, *Synth. Met.* **1999**, *103*, 2016–2019.
[34] R. Boca, *Theoretical Foundations of Molecular Magnetism*, in *Current Methods in Inorganic Chemistry*, Elsevier, Amsterdam, **1999**; Vol. 1.
[35] A. Bousseksou, G. Molnár, G. G. Matouzenko, *Eur. J. Inorg. Chem.* **2004**, 4353–4369.
[36] A. Bousseksou, G. Molnar, *C. R. Chimie* **2003**, *6*, 1175–1183.
[37] N. N. Greenwood, T. C. Gibbs, *Mössbauer Spectroscopy,* Chapman Hall, New York, **1971**.
[38] M. Blume, *Phys. Rev.* **1968**, *174*, 351–358.
[39] J.-M. Vincent, S. Menage, J.-M. Latour, A. Bousseksou, J.-P. Tuchagues, A. Decian, M. Fontecave, *Angew. Chem. Int. Ed. Engl.* **1995**, *34*, 205–207.
[40] G. Steimecke, H. J. Sieler, R. Kirmse, E. Hoyer, *Phosphorus Sulfur* **1979**, *7*, 49–55.
[41] L. J. Farrugia, *J. Appl. Crystallogr.* **1999**, *32*, 837–838.
[42] A. Altomare, M. C. Burla, M. Camalli, G. L. Cascarano, C. Giacovazzo, A. Guagliardi, A. G. G. Moliterni, G. Polidori, R. Spagna, *J. Appl. Crystallogr.* **1999**, *32*, 115–119.
[43] G. M. Sheldrick *SHELXS97 – A Program for Automatic Solution of Crystal Structure (Release 97-2)*, University of Göttingen, Germany, **1997**.
[44] G. M. Sheldrick *SHELXL97 – Programs for Crystal Structure Analysis (Release 97-2)*, University of Göttingen, Germany, **1998**.
[45] A. L. Spek *PLATON, A Multipurpose Crystallographic Tool*, Utrecht University, Utrecht, The Netherlands, **1998**.
[46] *ORTEP3 for Windows*: L. J. Farrugia, *J. Appl. Crystallogr.* **1997**, *30*, 565.
[47] D. M. Watkin, L. Pearce, C. K. Prout *CAMERON – A Molecular Graphics Package*, Chemical Crystallography Laboratory, University of Oxford, **1993**.
[48] F. Varret, Indian National Science Academy, New Delhi, Jaipur, India, **1981**.

Received: February 10, 2005
Published Online: July 12, 2005

 © 2005 Wiley-VCH Verlag GmbH & Co. KGaA, Weinheim

Supramolecular Cations of (*S*)-, (*R*)-, and (*RS*)-Indan-1-aminium(dibenzo[18]crown-6) in Magnetic $[Ni(dmit)_2]^-$ Salts

Tomoyuki Akutagawa,*[a–c] Kazumasa Matsuura,[b] Sadafumi Nishihara,[b] Shin-ichiro Noro,[a,b] and Takayoshi Nakamura*[a–c]

Keywords: Crown compounds / Magnetic properties / Supramolecular chemistry / Chirality / S ligands

Magnetic crystals were formed using supramolecular cation structures that consist of (*S*)-AIH^+(dibenzo[18]crown-6), (*R*)-AIH^+(dibenzo[18]crown-6), or (*RS*)-AIH^+(dibenzo[18]crown-6) (AIH^+ = indan-1-aminium) as the counter cation to $[Ni(dmit)_2]^-$ ions ($dmit^{2-}$ = 2-thioxo-1,3-dithiole-4,5-dithiolate), which bear one S = 1/2 spin. The resulting salts, (*S*)-AIH^+(dibenzo[18]crown-6)$[Ni(dmit)_2]$ (**1**), (*R*)-AIH^+(dibenzo[18]crown-6)$[Ni(dmit)_2]$ (**2**), and (*RS*)-AIH^+(dibenzo[18]crown-6)$[Ni(dmit)_2]$ (**3**), feature supramolecular cations that are formed through the inclusion of the ammonium moiety of AIH^+ into the cavity of dibenzo[18]crown-6 through N–H···O hydrogen bonds. Salts **1**, **2**, and **3** possess space groups of $P2_1$, $P2_1$, and $P2/m$, respectively, and possess similar molecular packings. Chiral cations (*S*)-AIH^+ (salt **1**) and (*R*)-AIH^+ (salt **2**) yielded chiral crystals, whereas racemic (*RS*)-AIH^+ (salt **3**) afforded a racemic crystal with a mirror plane. Within the crystals, alternating layers of $[Ni(dmit)_2]^-$ ions and (AIH^+)(dibenzo[18]crown-6) cations formed a layered structure along the *b* axis. Since the 2_1 axis of salts **1** and **2** were observed along the *b* axis, effective chiral magnetic interactions between the $[Ni(dmit)_2]^-$ ions were not observed. In the *ac* plane, weak interactions among the $[Ni(dmit)_2]^-$ ions formed a two-dimensional layer. Temperature-dependent magnetic susceptibilities of salts **1**, **2**, and **3** exhibited a Curie–Weiss-type behavior, which shows weak antiferromagnetic interactions between the $[Ni(dmit)_2]^-$ ions, with Weiss temperatures of –2.9, –2.9, and –4.2 K, respectively.

(© Wiley-VCH Verlag GmbH & Co. KGaA, 69451 Weinheim, Germany, 2005)

Introduction

Structures of organic ammonium RNH_3^+(crown ether) assemblies in the solid state depend on both the structure of the cation and on the size of the crown ether ring.[1] Various types of RNH_3^+ structures (R = H, CH_3, $C_6H_5CH_2$, NH_2, etc.) have been shown to form stable ammonium(crown ether) complexes in the solid state.[1] In these structures, the N–H^+···O hydrogen bonds and electrostatic interactions play important roles in binding the ammonium moiety into the cavity of the crown ethers.[2] Because it has been shown that the ionic radius of NH_4^+ matches the cavity size of [18]crown-6, it is reasonable to assume that N–H^+···O hydrogen bonds help form stable RNH_3^+([18]crown-6) complexes in the solid state. Although the cation-binding ability of dibenzo[18]crown-6 (1,4,7,10,13,16-hexaoxa-2,3:11,12-dibenzocyclooctadeca-2,11-diene) is similar to that of [18]crown-6,[3] the two benzene rings that are fused onto [18]crown-6 greatly affect the cationic structure of the RNH_3^+(dibenzo[18]crown-6) complexes and the molecular packing within the crystals. Comparatively, the O_6 plane of NH_4^+([18]crown-6) is nearly planar,[4] while the molecular structure of NH_4^+(dibenzo[18]crown-6) can be defined as a V-shaped conformation with the two benzene rings forming a bent structure in relation to the O_6 plane of the [18]crown-6 moiety.[5] The solid-state supramolecular cation structures of RNH_3^+ and dibenzo[18]crown-6, therefore, have the potential to yield a completely different type of cation assembly, as compared to those with [18]crown-6.

We have been involved in preparing supramolecular cationic structures and forming salts with $[Ni(dmit)_2]$ ($dmit^{2-}$ = 2-thioxo-1,3-dithiole-4,5-dithiolate).[6] Such an approach has allowed us to modify the assembled structures of the $[Ni(dmit)_2]^-$ ions, each bearing one S = 1/2 spin, and thus adjust the magnetic properties of the $[Ni(dmit)_2]^-$ salts. Among the salts, assembled structures between RNH_3^+ and [18]crown-6, such as anilinium([18]crown-6),[7] *p*-phenylenediammonium([18]crown-6)$_2$,[7] and *p*-xylylenediammonium([18]crown-6)$_2$ supramolecules,[8] yielded a variety of $[Ni(dmit)_2]^-$ ion assemblies that possess magnetic properties such as isolated spins, linear one-dimensional Heisenberg

[a] Research Institute for Electronic Science, Hokkaido University, N12W6 kita-ku, Sapporo 060-0812, Japan
Fax: +81-11-706-4972
E-mail: takuta@imd.es.hokudai.ac.jp
tnaka@imd.es.hokudai.ac.jp
[b] Graduate School of Environmental Earth Science, Hokkaido University, Sapporo 060-0810, Japan
[c] CREST, Japan Science and Technology Agency (JST), Kawaguchi 332-0012, Japan
Supporting information for this article is available on the WWW under http://www.eurjic.org or from the author.

 DOI: 10.1002/ejic.200500131 © 2005 Wiley-VCH Verlag GmbH & Co. KGaA, Weinheim

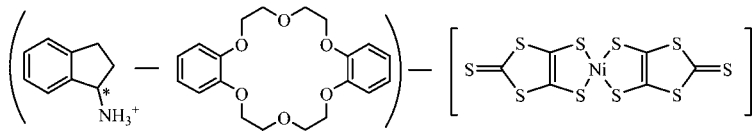

Scheme 1. Chemical structures of (*S*)-, (*R*)-, and (*RS*)-indan-1-aminium(dibenzo[18]crown-6)[Ni(dmit)$_2$] salts.

chains, and spin-ladders, according to the shape of the cationic structures. Introduction of chirality into the RNH_3^+ cations can potentially enhance the $[Ni(dmit)_2]^-$ ion assemblies within the crystals. A slight chemical modification of the cationic structures, specifically from anilinium([18]-crown-6) to *p*-phenylenediammonium([18]crown-6)$_2$, was found to modulate the $[Ni(dmit)_2]^-$ ion assemblies,[7a] and to drastically change the magnetic properties, from that of spin-ladder to that of singlet dimers.[7b] In the present study, we examined the effects of relatively small structural perturbations of the hydrogen-bonded supramolecular cations of RNH_3^+(dibenzo[18]crown-6) structures by modifying the chirality of the RNH_3^+ units in the $[Ni(dmit)_2]^-$ salts. For this purpose, chiral cations (*S*)- and (*R*)-indan-1-aminium [(*R*)-AIH$^+$ and (*S*)-AIH$^+$, respectively] and racemic (*RS*)-indan-1-aminium [(*RS*)-AIH$^+$] were utilized to form the hydrogen-bonded (AIH$^+$)(dibenzo[18]crown-6) structures in the magnetic $[Ni(dmit)_2]$ salts (Scheme 1). Because the NH_3^+ moiety of AIH$^+$ has the capacity to hydrogen-bond to the six oxygen atoms of the dibenzo[18]crown-6 molecule, it can be suggested that the asymmetric carbon center of (*S*)- and (*R*)-AIH$^+$ may affect the chirality of the crystals.

Results and Discussion

Crystal Structures

As expected, salts of (*S*)-AIH$^+$(dibenzo[18]crown-6)-[Ni(dmit)$_2$] (**1**), (*R*)-AIH$^+$(dibenzo[18]crown-6)[Ni(dmit)$_2$] (**2**), and (*RS*)-AIH$^+$(dibenzo[18]crown-6)[Ni(dmit)$_2$] (**3**) have the same stoichiometry. The data for the X-ray structural analyses for salts **1**, **2**, and **3** were obtained at 297 K (Table 1). The crystal symmetry of salts **1** and **2** were chiral $P2_1$ due to the existence of an asymmetric center within the chiral (*S*)- and (*R*)-AIH$^+$ ions, while that of salt **3** was achiral $P2_1/m$ due to the racemic (*RS*)-AIH$^+$ ion. For all the salts, the ammonium moiety of AIH$^+$ lies above the cavity of dibenzo[18]crown-6, thus forming the AIH$^+$(dibenzo-[18]crown-6) cationic structure. Furthermore, the molecular arrangements of the $[Ni(dmit)_2]^-$ ions and the AIH$^+$(dibenzo[18]crown-6) cations are similar to each other. Because the LUMO of the $[Ni(dmit)_2]^-$ ion is occupied by a single electron, which bears one $S = 1/2$ spin, the salts can be described as magnetic crystals.

The structures of the supramolecular cations of salts **1**–**3** are shown in Figure 1. As shown in Figure 1a, the ammonium moiety of (*S*)-AIH$^+$ lies above the cavity of dibenzo[18]crown-6, which possesses a V-shaped conformation. As a note, X-ray structural analyses confirmed that the absolute chirality of (*S*)-AIH$^+$ (salt **1**) and (*R*)-AIH$^+$ (salt **2**) corresponded to that of the starting (*S*)- and (*R*)-AIH$^+$ ions (Figures 1b and 1c), respectively. For salt **3**, on the other hand, the N1 and C9–C16 atoms define a mirror plane, which allows the isomers (*S*)- and (*R*)-AIH$^+$ ions equal probability (50%) of occupation, thus reflecting the racemic nature of the cation (Figure 1d).

The structural parameters of the cationic structures for salts **1**–**3** are summarized in Table 2. In each case, effective N–H···O hydrogen bonding between the NH_3^+ group of AIH$^+$ and the six oxygen atoms of dibenzo[18]crown-6 was observed. The N–O hydrogen bonding distances range from 2.917(6) to 3.132(6) Å, in which the average N–O distance

Table 1. Crystal data, data collection, and reduction parameters of salts **1**–**3**.

	1	**2**	**3**
Empirical formula	$C_{35}H_{36}O_6NNiS_{10}$	$C_{35}H_{36}O_6NNiS_{10}$	$C_{35}H_{36}O_6NNiS_{10}$
Formula mass	945.97	945.97	945.97
Space group	$P2_1$ (#4)	$P2_1$ (#4)	$P2_1/m$ (#11)
a [Å]	8.55(2)	8.57(3)	8.62(2)
b [Å]	20.53(3)	20.57(5)	20.32(4)
c [Å]	11.79(3)	11.81(3)	11.79(2)
β [°]	101.67(7)	101.7(1)	101.35(8)
V [Å^3]	2027(6)	2037(9)	2026(7)
Z	2	2	2
$D_{calcd.}$ [g cm^{-1}]	1.550	1.541	1.550
T [K]	297	297	297
μ [cm^{-1}]	10.4	10.33	10.39
Reflections measured	34337	30802	33339
Independent reflections	8785	8797	4767
Reflections used	5169	5269	3270
R[a]	0.034	0.036	0.034
$R_w(F^2)$[a]	0.074	0.090	0.083
GOF	0.983	0.950	1.128

[a] $R = \Sigma||F_o| - |F_c||/\Sigma|F_o|$ and $R_w = (\Sigma\omega(|F_o| - |F_c|)^2/\Sigma\omega F_o^2)^{1/2}$.

 © 2005 Wiley-VCH Verlag GmbH & Co. KGaA, Weinheim

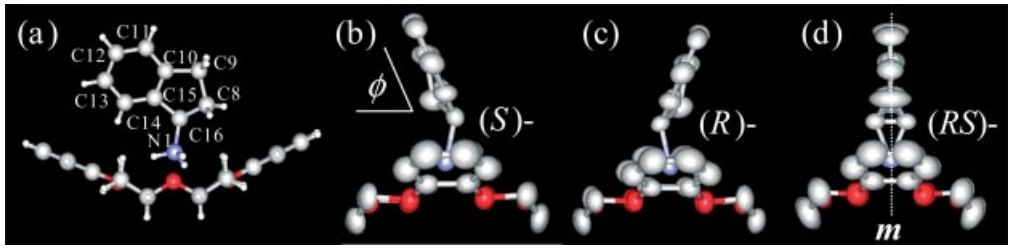

Figure 1. AIH^+(dibenzo[18]crown-6) structures of salts **1**–**3**. (a) Cation unit of salt **1** viewed parallel to the O_6 plane of dibenzo[18]crown-6. Configurations of (b) (*S*)-AIH^+, (c) (*R*)-AIH^+, and (d) (*RS*)-AIH^+ units viewed along the π plane of AIH^+. Hydrogen atoms are omitted for clarity.

for salts **1**, **2**, and **3** are 3.00, 3.02, and 3.02 Å, respectively. The greater average N–O distances, in comparison to the standard distance for the N–O hydrogen bond (2.87 Å),[9] indicate that the AIH^+(dibenzo[18]crown-6) structures involve six weak $NH_3^+\cdots O$ hydrogen-bond interactions. For salts **1** and **2**, the distance between N1 and the O_6 plane of dibenzo[18]crown-6 ($d_{N-O_{plane}}$) is 1.23 Å, while that of racemic salt **3** is slightly longer (1.27 Å). The dihedral angle (φ) between the O_6 plane of dibenzo[18]crown-6 and the C_6 plane of the AIH^+ benzene moiety for salts **1** and **2** is 66.04 and 66.24°, respectively. In contrast, the racemic nature of the (*RS*)-AIH^+ ion of salt **3** exhibits an average structure of 50% probability of each configuration. In this case, the static disorder of the (*R*)-AIH^+ and (*S*)-AIH^+ configuration yields a mirror plane as defined by the N1 and C9–C16 atoms resulting in φ = 90°. These structural differences in the cations, however, do not affect the $[Ni(dmit)_2]^-$ arrangements within the crystals.

Table 2. Structural parameters of the cations for salts **1**–**3**.[a]

	1	**2**	**3**
N1–O1, N1–O4	3.119(6), 3.002(5)	3.131(6), 2.952(5)	2.996(4)
N1–O2, N1–O5	2.963(6), 2.900(6)	2.918(6), 2.958(6)	2.937(3)
N1–O3, N1–O6	2.955(5), 3.110(6)	3.010(5), 3.122(6)	3.119(5)
$N1–O_{AV}$	3.00	3.02	3.02
$d_{N-O_{plane}}$	1.23	1.23	1.27
φ	66.04	66.24	90

[a] The parameters $d_{N-O_{plane}}$ and φ are defined in the text.

The unit cell of salt **1** viewed along the *a* axis is shown in Figure 2. Although the space group of salt **3** is different from those of salts **1** and **2**, the overall molecular packing in crystal **3** is comparable to those of salts **1** and **2**. The AIH^+(dibenzo[18]crown-6) cations and $[Ni(dmit)_2]^-$ ions are independently arranged within the *ac* plane, whereas the cation and anion layers are alternately arranged along the *b* axis. Moreover, the cation layer disrupts the intermolecular interactions between the $[Ni(dmit)_2]^-$ layers along the *b* axis. Since the spiral 2_1 axis is parallel to the *b* axis, effective chiral intermolecular interactions between the $[Ni(dmit)_2]^-$ anions were not expected within the crystals.

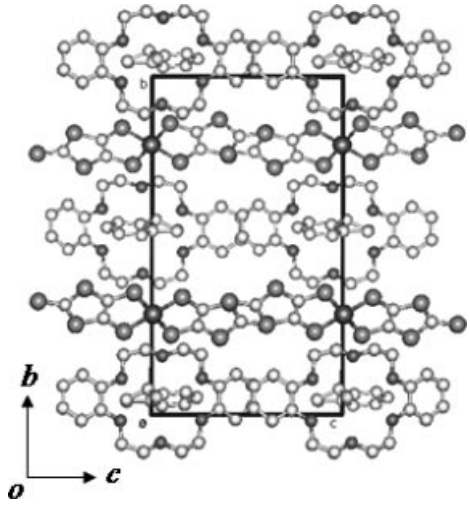

Figure 2. Unit cell of salt **1** viewed along the *a* axis. Hydrogen atoms are omitted.

The arrangements of the cations and anions within the *ac* plane are shown in Figure 3. The AIH^+(dibenzo[18]crown-6) units are stacked along the *a* axis, in which the V-shaped dibenzo[18]crown-6 units in the *ac* plane are arranged in the same direction along the *a* axis. Although a large dipole moment was expected in the *ac* plane, each cationic layer is arranged in a 2_1 symmetry, thus cancelling the dipole moment of the overall crystal. The $[Ni(dmit)_2]^-$ ions within the *ac* plane interact through weak lateral interatomic S···S contacts along the *c* and *a*+*c* axis. Despite the lack of significant π–π overlap between the $[Ni(dmit)_2]^-$ ions, a layered structure is formed by two-dimensional lateral S···S contacts in the *ac* plane. The magnitude of intermolecular interactions between the $[Ni(dmit)_2]^-$ ions was estimated from the calculated values of the transfer integrals (*t*) of LUMO based on extended Hückel molecular orbital calculations (Table 3). The transfer integrals of salts **1**, **2**, and **3** along the *a*+*c* axis (t_1) are 21.8, 21.5, and 26.9 meV, respectively, which are larger than those along the *c* axis (t_2 = 4.04, 4.15, and 4.98 meV for salts **1**, **2**, and **3**, respectively). Since the t_1 interactions are two- or threefold larger than the t_2 interactions, intermolecular interactions between $[Ni(dmit)_2]^-$ ions are dominated by those in the one-dimensional linear chain along the *a*+*c* axis. Each chain is ar-

 © 2005 Wiley-VCH Verlag GmbH & Co. KGaA, Weinheim

ranged through weak interchain interactions (t_2) along the *c* axis. Because the magnitude of the intrachain interactions (t_1) for salt **3** is roughly 20% greater than those of salts **1** and **2**, slightly larger magnetic interactions should be present for salt **3** than for salts **1** and **2**.

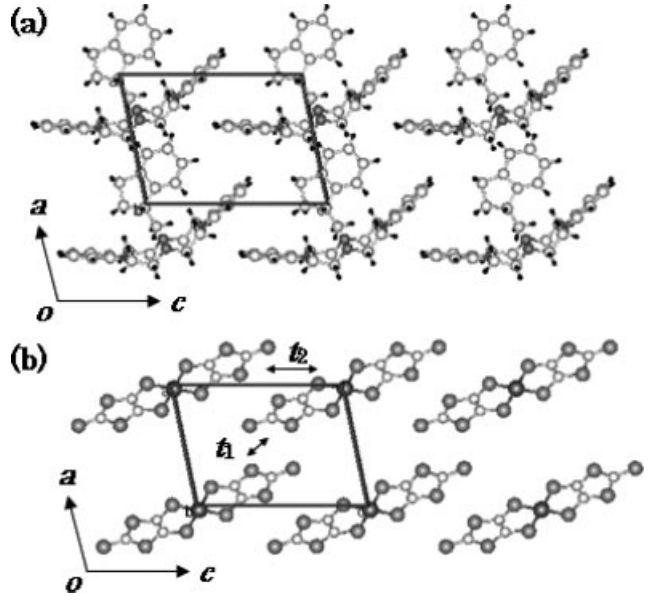

Figure 3. Crystal structures of salt **1**. (a) AIH^+(dibenzo[18]crown-6) cation and (b) $[Ni(dmit)_2]^-$ ion arrangements within the *ac* plane {intermolecular transfer integrals, t_1 and t_2, between the $[Ni(dmit)_2]^-$ ions are shown}.

Table 3. Transfer integral ($t \times 10^{-3}$ eV)[a] and magnetic parameters of salts **1**–**3**.

	1	**2**	**3**
t_1	21.8	21.5	26.9
t_2	4.04	4.15	4.98
C [emu K mol^{-1}]	0.367	0.374	0.372
θ [K]	-2.9	-2.9	-4.2

[a] The transfer integrals (t) were obtained by the LUMO of $[Ni(dmit)_2]^-$ based on the extended Hückel calculation ($t = -10S$ eV); S is the overlap integral.

Circular dichroism (CD) spectra of salts **1**–**3** with KBr pellets were measured to confirm the chiral intermolecular interactions between $[Ni(dmit)_2]^-$ ions. The intermolecular charge-transfer absorption between $[Ni(dmit)_2]^-$ ions has been observed at an energy around 8×10^3 cm^{-1}, while the intramolecular localized excitation bands of the $[Ni(dmit)_2]^-$ ion appear in the visible energy region with the absorption maxima around 12, 13, and 18×10^3 cm^{-1}.[10] Weak responses of CD spectra of salts **1** and **2** were observed at ca. 15 and ca. 20×10^3 cm^{-1} as a positive and negative rotation angle, respectively, while there was no meaningful response in the CD spectrum of racemic salt **3**. Therefore, the chiral arrangements of AIH^+ ions induced the circular dichroism in the intramolecular localized excitations of $[Ni(dmit)_2]^-$ ion along the *b* axis through intermolecular interactions between the $[Ni(dmit)_2]^-$ and AIH^+ ions.

Magnetic Properties

The magnetism of the crystals were determined by estimating the magnetic exchange energy (J), which is proportional to the square of t, i.e. magnitude of the intermolecular interaction.[11] Each $[Ni(dmit)_2]^-$ ion possesses one S = 1/2 spin, and therefore the molecular assemblies are directly related to the magnetism. Temperature-dependent magnetic susceptibilities (χ_{mol} vs. T) are similar among salts **1**–**3** (Figure 4 and Table 3); such similarity is also indicated by the comparable $[Ni(dmit)_2]^-$ arrangements among the crystals. The χ_{mol} vs. T of salts **1** and **2** exhibit Curie–Weiss behavior, in which the magnetic parameters C and θ are 0.367 emu K mol^{-1} and –2.9 K, respectively. Although salt **3** also exhibits Curie–Weiss behavior, the greater intrachain interactions (t_1 = 26.9 meV) of salt **3**, than those of salts **1** and **2**, provides a slightly larger Weiss constant of θ = –4.2 K (Figure 4b). In salt **3**, the magnitude of intermolecular t_1 and t_2 interactions between $[Ni(dmit)_2]^-$ anions are slightly larger than those of salts **1** and **2**, which increases the $|J|$ and $|\theta|$ values. The disordered arrangements of racemic AIH^+ ions in salt **3** affects the crystal lattice, which slightly changes the anionic arrangements to increase the intermolecular interactions between the $[Ni(dmit)_2]^-$ ions.

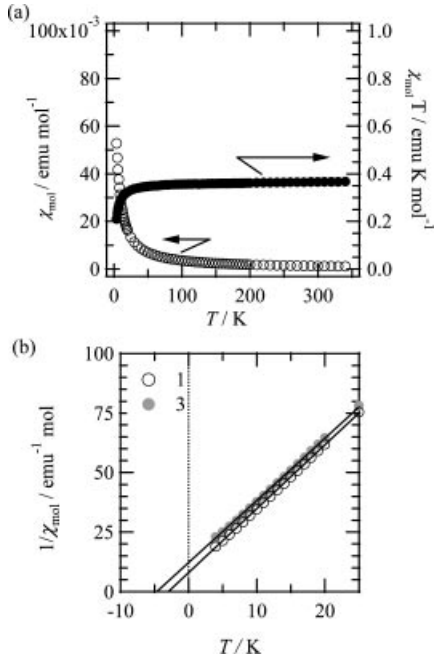

Figure 4. Temperature-dependent molar magnetic susceptibility (χ_{mol}) per one $[Ni(dmit)_2]^-$ ion for salts **1**–**3**. (a) χ_{mol} vs. T (left scale) and $\chi_{mol}T$ vs. T (right scale) plots for salt **1**. (b) χ_{mol}^{-1} vs. T plots for salts **1** and **3**.

Summary

Supramolecular cationic structures of (*S*)-AIH^+(dibenzo[18]crown-6), (*R*)-AIH^+(dibenzo[18]crown-6), and (*RS*)-AIH^+(dibenzo[18]crown-6) (AIH^+ = indan-1-aminium) were incorporated into $[Ni(dmit)_2]^-$ salts. Supra-

 © 2005 Wiley-VCH Verlag GmbH & Co. KGaA, Weinheim

molecular assemblies were formed through hydrogen-bond interactions between the NH_3^+ moieties of the AIH^+ ion and the oxygen atoms in the dibenzo[18]crown-6 molecule. Chiral (*S*)-AIH^+ and (*R*)-AIH^+ and racemic (*RS*)-AIH^+ yielded isomorphous crystals with a stoichiometry of AIH^+(dibenzo[18]crown-6)$[Ni(dmit)_2]$. The chiral salts possess a chiral space group of $P2_1$, while the latter salt possesses an achiral $P2_1/m$ space group. However, the molecular packing and temperature-dependent magnetic susceptibilities of the three salts are comparable to each other. The AIH^+(dibenzo[18]crown-6) cations are packed within the *ac* plane, whereas the $[Ni(dmit)_2]^-$ ions form a two-dimensional layer separated by a layer of cations. The transfer integrals in the $[Ni(dmit)_2]$ layer exhibit weak one-dimensional intermolecular interactions between the $[Ni(dmit)_2]$ molecules, which yield weak antiferromagnetic interactions between the $[Ni(dmit)_2]^-$ ions. Chiral cations (*S*)- and (*R*)-AIH^+ were successfully introduced into the supramolecular cationic structures in $[Ni(dmit)_2]$-based molecular magnets. Introduction of chirality into the crown ethers are currently underway in an attempt to achieve chiral intermolecular interaction between the $[Ni(dmit)_2]$ molecules.

Experimental Section

Preparation of $[Ni(dmit)_2]$ Salts: The precursor monovalent salt $n(Bu_4N)[Ni(dmit)_2]$ was prepared according to the literature.[12] The ammonium salts of (*S*)-, (*R*)-, and (*RS*)-$AIH^+BF_4^-$ were prepared by neutralization of commercially available chiral (*S*)-, (*R*)-, and racemic (*RS*)-AIH^+ using 42% aqueous HBF_4. Single crystals of salts **1**–**3** were grown by slow diffusion of $n(Bu_4N^+)[Ni(dmit)_2]^-$ and $AIH^+BF_4^-$ in vials charged with CH_3CN (ca. 20 mL). The compositions of crystals **1**–**3** were determined by X-ray structural analysis and by elemental analysis. Salt **1**: $C_{35}H_{36}NNiO_6S_{10}$ (946.01): calcd. C 44.44, H 3.84, N 1.48; found C 44.11, H 3.69, N 1.24. Salt **2**: $C_{35}H_{36}NNiO_6S_{10}$ (946.01): calcd. C 44.44, H 3.84, N 1.48; found C 44.64, H 3.91, N 1.67. Salt **3**: $C_{35}H_{36}NNiO_6S_{10}$ (946.01): calcd. C 44.44, H 3.84, N 1.48; found C 44.29, H 3.54, N 1.62.

Crystal Structure Determination: Crystallographic data (Table 1) were collected with a Rigaku Raxis-Rapid diffractometer with Mo-K_α (λ = 0.71073 Å) radiation from a graphite monochromator. Structure refinements were performed using the full-matrix least-squares method on F^2. Calculations were carried out using Crystal Structure software packages.[13] Parameters were refined using anisotropic temperature factors with the exception of those for the hydrogen atoms. CCDC-263460 (**1**), -263461 (**2**), and -263462 (**3**) contain the supplementary crystallographic data for this paper. These data can be obtained free of charge from The Cambridge Crystallographic Data Centre via www.ccdc.cam.ac.uk/data_request/cif.

Magnetic Susceptibility: Temperature-dependent magnetic susceptibilities were measured with a Quantum Design Model MPMS-XL SQUID magnetometer for polycrystalline samples. The applied magnetic field was 1 T for all measurements.

Calculation of Transfer Integrals: Transfer integrals (t) were calculated within the tight-binding approximation using the extended Hückel molecular orbital method. The LUMO of the $[Ni(dmit)_2]^-$ ion was used as the basis function.[14] Semi-empirical parameters for Slater-type atomic orbitals were obtained from the literature.[14] The t values between each pair of molecules were assumed to be proportional to the overlap integral (S) using the equation, $t = -10S$ eV.

Supporting Information (see also footnote on the first page of this article): Preparations of $HAI^+BF_4^-$ and salts **1**–**3**, the atomic numbering scheme, and CD spectra of salts **1**–**3**.

Acknowledgments

This work was partly supported by a Grant-in-Aid for Science Research from the Ministries of Education, Culture, Sports, Science, and Technology of Japan. The authors thank Dr. K. Ichimura and Prof. K. Nomura for the use of their SQUID magnetometer and Miss W. Kaneko, Prof. M. Ohba, and Prof. S. Kitagawa for the use of their CD spectrometer.

[1] a) E. Weber, J. L. Toner, I. Goldberg, F. Vögtle, D. A. Laidler, J. F. Stoddart, R. A. Bartsch, C. L. Liotta, in *Crown ethers and analogs* (Eds.: S. Patai, Z. Rappoport), John Wiley & Sons, New York, **1989**; b) G. W. Gokel, in *Crown Ethers & Cryptands* (Ed.: J. F. Stoddart), RSC, Cambridge, **1994**.

[2] Y. L. Ha, A. K. Chakraborty, *J. Phys. Chem.* **1992**, *96*, 6410–6417.

[3] a) R. M. Izatt, J. S. Bradshaw, S. A. Nielsen, J. D. Lamb, J. J. Christensen, D. Sen, *Chem. Rev.* **1985**, *85*, 271–339; b) R. M. Izatt, K. Pawlak, J. S. Bradshaw, R. L. Bruening, *Chem. Rev.* **1991**, *91*, 1721–2085.

[4] O. Nagao, A. Kobayashi, Y. Sasaki, *Bull. Chem. Soc. Jpn.* **1978**, *51*, 790–792.

[5] a) S. T. Malinovskii, Yu. A. Simonov, T. I. Malinovskii, V. E. Zubareva, D. G. Batir, I. M. Reibel, *Kristallografiya* **1984**, *29*, 466–470; b) J. A. A. de Bore, D. N. Reinhouldt, J. W. H. M. Uiterwijk, S. Harkema, *J. Chem. Soc., Chem. Commun.* **1982**, 194–196.

[6] a) T. Akutagawa, T. Nakamura, T. Inabe, A. E. Underhill, *J. Mater. Chem.* **1997**, *7*, 183–184; b) T. Akutagawa, T. Nakamura, T. Inabe, A. E. Underhill, *Thin Solid Films* **1998**, *331*, 264–271; c) T. Akutagawa, T. Nakamura, *Coord. Chem. Rev.* **2000**, *198*, 297–311; d) T. Akutagawa, Y. Nezu, T. Hasegawa, T. Nakamura, K. Sugiura, Y. Sakata, T. Inabe, A. E. Underhill, *Chem. Commun.* **1998**, 2599–2600; e) N. Robertson, T. Akutagawa, T. Nakamura, S. Roehrs, A. E. Underhill, *J. Mater. Chem.* **1999**, *9*, 1233–1236; f) T. Akutagawa, T. Hasegawa, T. Nakamura, T. Inabe, K. Sugiura, Y. Sakata, A. E. Underhill, *Synth. Met.* **1999**, *102*, 1747–1748; g) T. Akutagawa, T. Hasegawa, T. Nakamura, S. Takeda, T. Inabe, K. Sugiura, Y. Sakata, A. E. Underhill, *Inorg. Chem.* **2000**, *39*, 2645–2651; h) T. Nakamura, T. Akutagawa, K. Honda, A. E. Underhill, A. T. Coomber, R. H. Friend, *Nature* **1998**, *394*, 159–160; i) T. Akutagawa, T. Hasegawa, T. Nakamura, S. Takeda, T. Inabe, K. Sugiura, Y. Sakata, A. E. Underhill, *Chem. Eur. J.* **2001**, *7*, 4902–4912; j) T. Akutagawa, T. Hasegawa, T. Nakamura, T. Inabe, *J. Am. Chem. Soc.* **2002**, *124*, 8903–8911; k) T. Akutagawa, K. Shitagami, S. Nishihara, S. Takeda, T. Hasegawa, T. Nakamura, Y. Hosokoshi, K. Inoue, S. Ikeuchi, Y. Miyazaki, K. Saito, *J. Am. Chem. Soc.* **2005**, *127*, 4397–4402.

[7] a) S. Nishihara, T. Akutagawa, T. Hasegawa, T. Nakamura, *Chem. Commun.* **2002**, 408–409; b) S. Nishihara, T. Akutagawa, T. Hasegawa, S. Fujiyama, T. Nakamura, T. Nakamura, *J. Solid State Chem.* **2002**, *168*, 661–667.

[8] a) T. Akutagawa, A. Hashimoto, S. Nishihara, T. Hasegawa, T. Nakamura, *J. Phys. Chem. B.* **2003**, *107*, 66–74; b) T. Akutagawa, A. Hashimoto, S. Nishihara, T. Hasegawa, T. Nakamura, *J. Supramol. Chem.* **2002**, *2*, 175–186.

[9] a) G. A. Jeffrey, in *An Introduction to Hydrogen Bonding* (Ed.: D. G. Truhlar), Oxford University Press, New York, **1997**; b) G. C. Pimentel, A. L. McClellan, in *The Hydrogen Bond*, Free-

 © 2005 Wiley-VCH Verlag GmbH & Co. KGaA, Weinheim

mann, San Francisco, **1960**; c) W. C. Hamilton, J. A. Ibers, in A. *Hydrogen Bonding in Solids* (Ed.: R. Breslow, M. Karplus), Benjamin Inc, NY, **1968**.H.B.
[10] H. L. Liu, D. B. Tanner, A. E. Pullen, K. A. Abboud, J. R. Reynolds, *Phys. Rev. B.* **1996**, *53*, 10557–10568.
[11] a) J. S. Scott, in *Semiconductor and Semimetals. High Conducting Quasi-One-Dimensional Organic Crystals* (Ed.: E. Conwell), Academic Press, New York, **1988**, p. 385; b) R. L. Carlin, in *Magnetochemistry*, Springer-Verlag, Heidelberg, **1986**; c) O. Kahn, in *Molecular Magnetism*, VCH, New York, **1993**..
[12] G. Steinmecke, H. J. Sieler, R. Krimes, E. Hoyer, *Phosphorus Sulfur* **1979**, *7*, 49–55.
[13] Crystal Structure: *Single crystal structure analysis software*, version 3.6, Rigaku Corporation and Molecular Structure Corporation, **2004**.
[14] T. Mori, A. Kobayashi, Y. Sasaki, H. Kobayashi, G. Saito, H. Inokuchi, *Bull. Chem. Soc. Jpn.* **1984**, *57*, 627–633.
Received: February 15, 2005
Published Online: July 14, 2005

 © 2005 Wiley-VCH Verlag GmbH & Co. KGaA, Weinheim

Extended Networks of Co^{2+} and Mn^{2+} Bridged by NCS^-/N_3^- Anions and Flexible Long Spacers: Syntheses, Structures, and Magnetic Properties

Xin-Yi Wang,[a] Bao-Long Li,*[b] Xia Zhu,[b] and Song Gao*[a]

Keywords: Thiocyanate / Azide / Cobalt / Manganese / 1,2-Bis(imidazol-1-yl)ethane / 1,2-Bis(1,2,4-triazol-1-yl)ethane / Magnetic properties

Four new metal-organic polymers with SCN^-/N_3^- anion bridges and flexible long spacers L {L = bim [1,2-bis(imidazol-1-yl)ethane] and bte [1,2-bis(1,2,4-triazol-1-yl)ethane]}, $[Co(SCN)_2(bim)]$ (**1-Co**), $[Co(SCN)_2(bte)]$ (**2-Co**), $[Mn(N_3)_2(bte)]$ (**3-Mn**), and $[Mn(N_3)_2(bim)]$ (**4-Mn**), were synthesized and characterized by single-crystal X-ray diffraction studies and their magnetic properties were investigated. Complex **1-Co** is a triple-bridging chain complex with double end-to-end SCN^- anions and single *gauche*-bim spacers as bridges. Complexes **2-Co** and **3-Mn** both contain 1D chains bridged by double end-to-end SCN^- or N_3^- anions and these chains are further extended to 2D (4,4) layers by the *anti*-bte spacers. Complex **4-Mn** has a topological 3D diamond structure constructed through 1D double end-on azide-bridged Mn^{II} chains and extended through the *anti*-bim spacers. Magnetic measurements reveal that **1-Co** and **3-Mn** remain paramagnetic; the dominant magnetic coupling between Co^{II} is weak ferromagnetic and that between Mn^{II} is strong antiferromagnetic. As for **2-Co** and **4-Mn**, they show metamagnetic behavior below T_N = 2.9 and 3.0 K, respectively. Our results show that a combination of the short anion bridges (SCN^-/N_3^-) and flexible bidentate long spacers can be used to construct coordination polymers with novel topologies and interesting magnetic properties.
(© Wiley-VCH Verlag GmbH & Co. KGaA, 69451 Weinheim, Germany, 2005)

Introduction

In the attractive field of supermolecular chemistry and crystal engineering, long bidentate spacers provide a useful approach to new functional materials with a variety of multi-dimensional arrays and networks.[1] Because of the large separation and the inefficiency to transmit magnetic interactions, these long spacers were seldomly used to construct molecule-based magnetic materials with high magnetic-ordering temperatures. However, their abilities to form new architectures with novel topologies and interesting magnetic properties still attracts intensive attention, such as compounds constructed by rigid *N*,*N*′-bidentate spacers like 4,4′-bipyridine (4,4′-bpy), (*E*)-1,2-bis(4-pyridinyl)ethene, pyrazine, and other related ligands.[2–4] Very recently, we reported a series of compounds $M(CHOO)_2(4,4'\text{-bpy})\cdot nH_2O$ (M = Mn, Co, n = 0; M = Co, Ni, n = 5) with all 3D structures and magnetically long-range ordering.[2d] As with its azide analog $M(N_3)_2(4,4'\text{-bpy})$ (M = Mn, Fe),[2a–2c] the bidentate long spacer 4,4′-bpy efficiently tuned the topologies of these compounds and led to weak ferromagnetism.

The design of coordination polymers is highly influenced by several factors such as the coordination geometry of the central atom, the structural characteristics of the ligand molecule, the solvent system and the counterion. When rigid bifunctional ligands are used as spacers to connect metal centers, the topology of the network is usually determined by the coordination geometry of the central metal preference. Contrary to rigid ligands, the flexible ligands with conformational flexibility induce a variety of structures and may lead to the formation of the supramolecular isomers.[3i,3j] Some coordination polymers with flexible ligands have been investigated.[3,4] For example two remarkable polyrotaxane-like polymers based on 1,4-bis(imidazol-1-ylmethyl)benzene (bix) were synthesized by Robson and coworkers.[3k,3l] The flexible ligands 1,2-bis(imidazol-1-yl)ethane (bim) and 1,2-bis(1,2,4-triazol-1-yl)ethane (bte) can adopt either *gauche* (angular) or *anti* (linear) conformations (Scheme 1).[4a] We previously reported several coordination polymers in which the ligands also exhibit either *gauche* or *anti* conformations.[4] Complex $[Mn(\textit{gauche}\text{-bte})_2(NCS)_2]_n\cdot[Mn(\textit{anti}\text{-bte})(H_2O)_2(NCS)_2]_n$ contains both a double-stranded chain and a single chain in the same crystal and both *gauche* and *anti* conformations of the bte spacer.[4c]

[a] State Key Laboratory of Rare Earth Materials Chemistry and Applications & PKU-HKU Joint Laboratory on Rare Earth Materials and Bioinorganic Chemistry, College of Chemistry and Molecular Engineering, Peking University,
Beijing 100871, P. R.China
Fax: 86-10-62751708
E-mail: gaosong@pku.edu.cn
[b] College of Chemistry and Chemical Engineering, The Key Laboratory of Organic Synthesis of Jiangsu Province, Suzhou University,
Street Shizi No. 1, Suzhou 215006, P. R.China
Fax: 86-512-65224783
E-mail: blli1965@pub.sz.jsinfo.net
Supporting information for this article is available on the WWW under http://www.eurjic.org or from the author.

 DOI: 10.1002/ejic.200500151 © 2005 Wiley-VCH Verlag GmbH & Co. KGaA, Weinheim

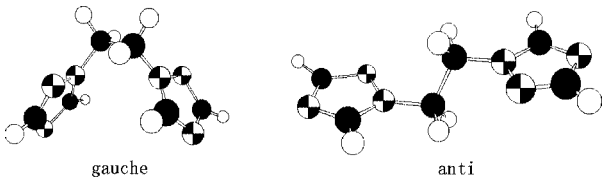

Scheme 1. The *gauche* and *anti* conformations of the bte and bim spacers (bte as example).

Of course, the main approach to constructing molecule-based magnetic materials is to employ short bridging ligands, which are efficient to mediate the magnetic coupling, to connect paramagnetic transition metal ions. Among the widely used anion ligands, the pseudohalide azide has been demonstrated to be the all-important one, if not the most, due to the versatility and the ability to mediate strong magnetic coupling, either ferro- or antiferromagnetic. Most commonly, the azide ion can adopt two possible bridging modes: end-to-end (*EE*) associated with antiferromagnetic (AF) coupling, and end-on (*EO*) related with ferromagnetic exchange.[5] In our previous reports,[2d,6] we explored another three-atom bridging ligand, the formate anion, which is a natural analog of azide, to construct new formate compounds with structures and magnetic properties similar to or different from those of azide. Furthermore, we investigated another pseudohalide anion: the thiocyanato ion (SCN^-). Like azide and formate, SCN^- can also mediate magnetic coupling between the metal ions, with the sign and the magnitude depending on the bridging modes and the localized structural details.[7–14] Owing to the two different donor groups (N and S) within it, the thiocyanate ion has less versatility and is less efficient as a magnetic coupler than the azide ligand. In contrast with the large number of azide-bridged compounds studied from a magnetic and structural point of view, there are fewer reports on the divalent first-row transition metal complexes bridged by SCN^-. Fully studied complexes are mainly compounds of Ni^{II}[8,9] and Cu^{II},[10–12] such as dimers,[8,10] 1D chains,[9,11] and 2D layers.[12] For Mn^{II} and Co^{II} compounds, the existing results are quite rare.[13,14] The 2D compounds $M(SCN)_2(ROH)_2$ (M = Mn, Co; R = CH_3, C_2H_5, C_3H_7)[13b,14] and the proposed 1D chain compounds $M(SCN)_2$(2,2-bipyridine) (M = Mn, Co) are rare examples that have been investigated thoroughly.[13a] New thiocyanate-bridged compounds, especially of Co^{II}, are needed to be explored further.

Taking into account the above-mentioned aspects, we report here the syntheses, structures and the magnetic properties of four new coordination polymers: $Co(L)(SCN)_2$ [L = bim (**1-Co**) and bte (**2-Co**)] and $Mn(L)(N_3)_2$ [L = bte (**3-Mn**) and bim (**4-Mn**)]. All four of these polymers assemble through both the flexible-bidentate long spacers (bim/bte) and the short anion ligands (SCN^-/N_3^-) as bridges. Among them, **1-Co** is a triple-bridging 1D compound bridged by double *EE*-SCN^- ligands and single *gauche*-bim spacers. **2-Co** is a 2D metamagnet with double *EE*-SCN^- ligands and *anti*-bte spacers as bridges. **3-Mn** has a very similar structure to that of **2-Co** and behaves as a magnetic AF chain. As for **4-Mn**, the double *EO*-azides and the *anti*-bim spacers lead to a metamagnet with a distorted 3D diamondoid structure.

Results and Discussion

Crystal Structures

Single-crystal X-ray diffraction of **1-Co** reveals that it crystallizes in the orthorhombic space group $Pna2_1$ and the structure is presented in Figure 1. In **1-Co**, each Co^{II} center is octahedrally coordinated by two nitrogen atoms from two bridging bim ligands in *trans* positions, two nitrogen and two sulfur atoms from four bridging *EE*-SCN^- groups. Lengthened along the S1–Co1–S2 axis, the octahedron is of an approximate D_{4h} point group. The bond lengths are as follows: Co1–N1 2.083(2), Co1–N3 2.076(2), Co1–N5 2.127(2), Co1–N6 2.122(2), Co1–S1 2.660(2), and Co1–S2 2.635(1) Å. The bond angles of D–Co1–D (D represents N or S atoms) are in the range of 88–92°. The angles of Co1–S2–C10 and Co1A–S1A–C9 are ca. 98°, which are close to a right angle, and the angles of Co1–N5–C9 and Co1A–N6A–C10 are 160° or so. So the geometry of the $Co_2(SCN)_2$ ring is close to that of a rectangle although with poor coplanarity. The geometrical feature of $Co_2(SCN)_2$ has already been observed in other thiocyanato-containing metal complexes and it is believed to have a very important influence on the magnetic coupling between the transition metal ions, especially Ni^{II}.[7a–7c,9c] It is well demonstrated that, because of the orthogonality of the orbitals, the more rectangular the geometry, the greater the possibility of ferromagnetic coupling will be.[7a–7c]

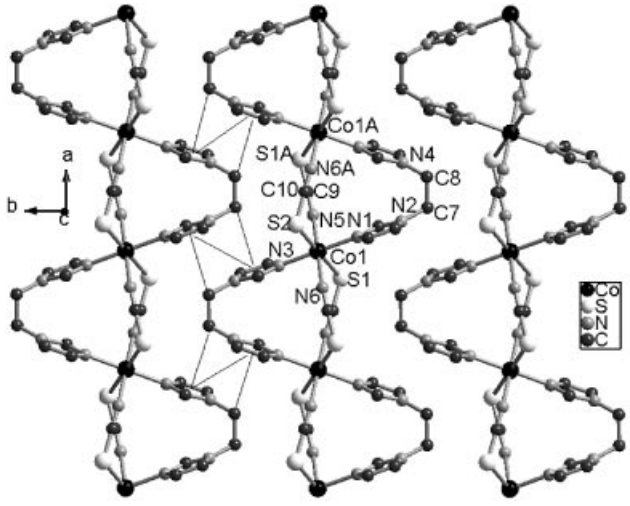

Figure 1. Toothed chain structures and the 2D layer of **1-Co**. Hydrogen atoms are omitted for clarity. The thin lines represent the π–π and C–H···π interactions between adjacent chains.

The SCN^- anion is almost linear [S1A–C9–N5 and S2–C10–N6A are 179.2(2) and 178.8(2)°, respectively] and the bim ligand is of the *gauche* conformation [torsion angle of N2–C7–C8–N4 is 59.2(3)°]. Both of these ligands act as bridges to connect adjacent Co^{II} ions to form a triple-bridg-

ing 1D toothed chain along the [100] crystallographic direction. Parallel chains stack in the [010] direction such that the convex bim bow of one chain extends into the concave section of the neighboring chain. There are obvious C–H···π interactions between the hydrogen atoms of alkanes and imidazole rings of adjacent chains (C–H···π angles 110.1 and 109.5°, and C···π distances 3.294 and 3.294 Å). Also, there are π–π interactions between the imidazole rings of the adjacent chains (perpendicular distance between centroids of the imidazole rings: 4.054 Å, dihedral angle: 0.6°). Thus, the 2D layer parallel with the *ab* plane is stabilized by these C–H···π and π–π interactions (Figure 1 and Table S1). The shortest intra- and interchain distances between Co^{II} ions are 5.625(2) and 9.095(2) Å, respectively. The layers stack together along the *c* direction in the sequence ···A–B–A–B··· with a slide of 4.55 Å (*b*/2) and the shortest Co–Co interlayer distance is about 8.170(2) Å.

Although **2-Co** has a similar composition to **1-Co** by replacing bim with bte, its structure and properties are different from **1-Co** (Figure 2). **2-Co** crystallizes in the triclinic space group $P\bar{1}$ and the Co^{II} atom is located in the symmetrical center. The cobalt atom in **2-Co** is also in the same elongated octahedron of an approximate D_{4h} point group formed by two *trans*-N atoms from bte, two *trans*-N and S atoms from four symmetry-related SCN^- anions of an *EE* mode. The bond lengths and the angles of D–Co–D are close to those of **1-Co** and the details can be found in the CIF file. Unlike **1-Co**, the ring of $Co_2(SCN)_2$ is almost coplanar and results in an approximate rectangle where the angles of Co–S–C and Co–N–C are ca. 165° and 100°, respectively, slightly larger than those in **1-Co**. Bridged by SCN^- only, **2-Co** forms 1D $[Co(SCN)_2]_n$ chains along the *a* axis; and the adjacent octahedra align parallel to one another. Different from the *gauche*-bim spacer in **1-Co**, the bte ligand in **2-Co** is of the *anti* conformation with the torsion angle N1–C3–C3A–N1A of 180.0 (2)°. Through this linear conformation, bte links adjacent cobalt chains to form a 2D neutral (4,4) network, which is very similar to that in $[Cd(NCS)_2(bte)]_n$.[4b] The 2D network in **2-Co** is completely different from the 1D toothed chain in **1-Co** only because bim in **1-Co** is replaced by bte in **2-Co**. This difference shows the subtle modulations of the bidentate spacers to construct novel topologies. The nearest Co–Co intrachain distance is 5.691(3) Å and that of the interchain is 12.014(56) Å. In the 2D network, there are no obvious π–π interactions between the adjacent triazole rings (shortest perpendicular distance between centroids of the triazole rings: 5.691 Å, dihedral angle: 0°). But, obvious π–π interactions between the 2D networks can be found (perpendicular distance between centroids of the triazole rings: 3.886 Å, dihedral angle: 0°), and there are C–H···π interactions between the hydrogen atoms of alkane and triazole rings of adjacent 2D networks (C3–H···π angles 124.5°, C···π distances 3.811 Å) (Table S2). All these weak interactions stack the 2D layers along the [011] direction in the sequence ···A–B–C–A–B–C··· to form the whole architecture (Figure S1).

The structure of **3-Mn** is very similar to that of **2-Co** (Figure 3), except that the bridging ligand is the *EE*-N_3^- anion instead of SCN^-. Also, this structure is very similar to that of $[Mn(N_3)_2(bpa)]_n$,[3m] except that the flexible bte spacer is present instead of the flexible bpa spacer. The 1D $[Mn(N_3)_2]_n$ chain is linked by bte to form a two-dimensional (4,4) layer and the layers stack along the [011] direction also in the ···A–B–C··· mode (Figure S2). There are no π–π interactions between the adjacent triazole rings in the 2D networks (shortest perpendicular distance between centroids of the triazole rings: 5.236 Å). Different from **2-Co**, the π–π interactions between adjacent 2D layers are negligibly weak (perpendicular distance between centroids of the triazole rings: 4.334 Å, dihedral angle: 0°). The coordination octahedron of Mn^{II} is more regular than that of **2-Co**; the bond lengths of Mn–N are in the range of 2.21–2.27 Å and the bond angles are from 87.0 to 93.0°. The metal–metal distance of 5.236(5) Å within the chain is shorter than that of 5.691(3) Å in **2-Co**, originating from the short length of the N_3^- ion as compared to SCN^- [2.348(8) and 2.799(10) Å for N_3^- and SCN^-, respectively]. The interchain M–M distance [11.948(56) Å] is similar to that of **2-Co** due to the same bridging ligand *anti*-bte.

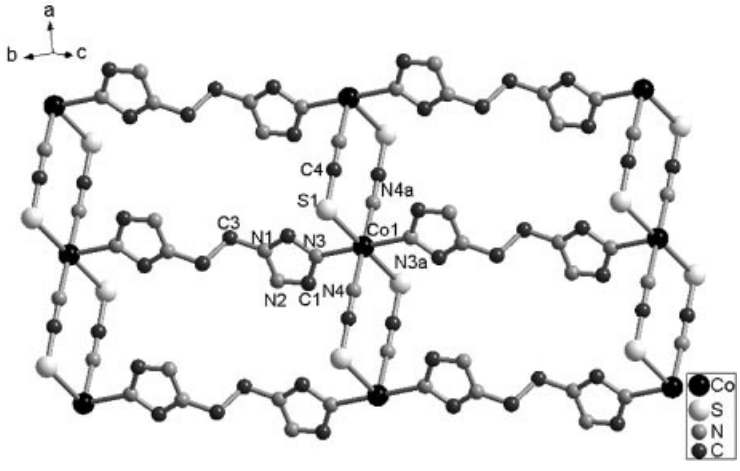

Figure 2. Two-dimensional (4,4) layer bridged by double end-to-end SCN^- and *anti*-bte ligands of **2-Co**.

 © 2005 Wiley-VCH Verlag GmbH & Co. KGaA, Weinheim

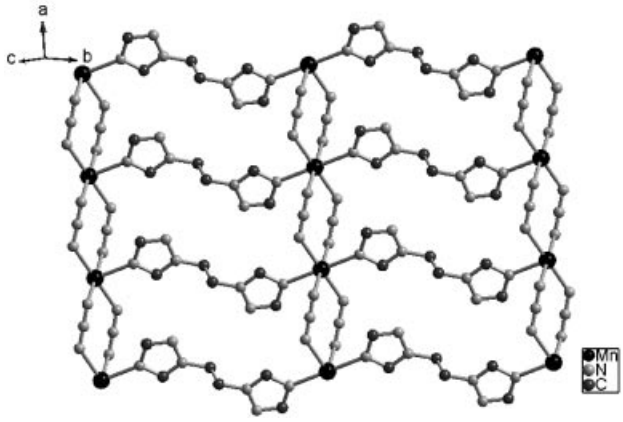

Figure 3. Two-dimensional (4,4) layer bridged by double end-to-end N_3^- and *anti*-bte ligands of **3-Mn**.

The crystal structure of **4-Mn** has some interesting characteristics. The change from the bte ligand in **3-Mn** to bim in **4-Mn** leads to very different crystal structures, which shows the importance that ancillary ligands play in tuning the crystal structure. As can be seen from Figure 4a, every Mn^{II} atom in **4-Mn** is also coordinated by six nitrogen atoms, two from the *cis*-imidazole rings of the bim ligand and the others from four *EO*-azide anions. The octahedron is largely distorted with the Mn–N bond lengths from 2.223(5) to 2.299(3) Å and N–Mn–N bond angles from 74.03(11) to 100.17(11)°. The Mn–N bond lengths do not vary much but the N–Mn–N angles deviate much from 90°, especially those of the N_{azide}–Mn–N_{azide} angles [e.g., N5–Mn1–N5a = 74.03(11)°, N8–Mn1–N8a = 77.44(11)°, and N5–Mn1–N8 = 100.17(11)°]. The detailed bond lengths and bond angles can be found in the CIF file. **4-Mn** is different from **3-Mn** in that there are two symmetrically independent azide anions (N5–N6–N7 and N8–N9–N10) and they both act as *EO* bridges, linking Mn^{II} ions to form a 1D zigzag $[Mn(N_3)_2]_n$ chain along the *a* direction (Figure 4b). The bond angles of Mn–N5–Mn and Mn–N8–Mn are 105.97(13) and 102.56(12)°, respectively, giving rise to two metal–metal intrachain distances, 3.614(5) and 3.535(5) Å, respectively. These kinds of double *EO*-azide-bridged Mn^{II} ions form a ferromagnetic chain in **4-Mn** as in two reported compounds.[2e,15]

The bim ligands in the *anti* conformation all act as bridges to expand the $[Mn(N_3)_2]_n$ chains into a 3D architecture. No obvious weak interactions can be found in **4-Mn** as the bim ligands are sufficiently separated from each other. Along the chain, the bim ligands of the Mn^{II} ions point in four different directions alternatively (Figure 4c), leading to an interesting shape of a "molecular windmill", with bim

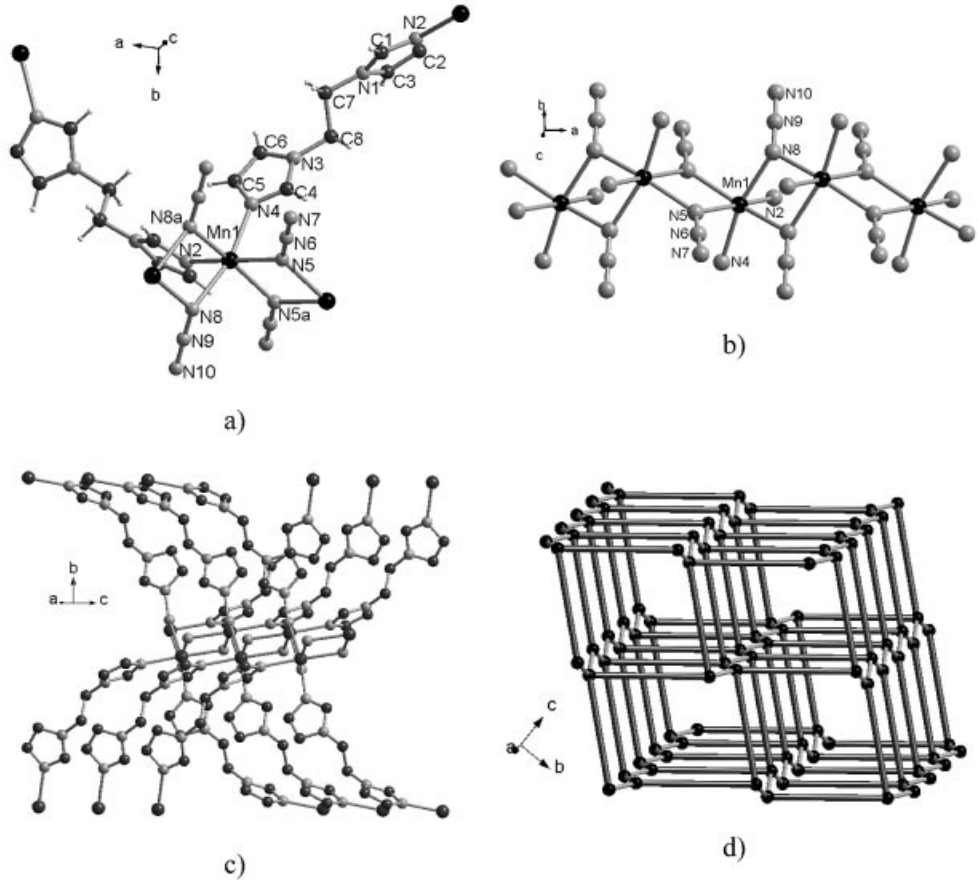

Figure 4. a) Coordination environment of Mn1 in **4-Mn**. b) Chain structure bridged by *EO*-azide anions along the *a* direction. c) Connections between adjacent chains. d) 3D distorted diamondoid topology of **4-Mn**. The long sticks represent the *anti*-bim ligands and the short ones *EO*-azide anions.

 © 2005 Wiley-VCH Verlag GmbH & Co. KGaA, Weinheim

ligands in four directions as four arms. As a result of this connection mode, every Mn^{II} atom is a four-connected node, and thus the topology of **4-Mn** is a distorted 3D diamond, as can be seen in Figure 4d. If a dimer Mn^{II} bridged by azide is considered as one node, the structure can also be viewed as a simple cubic topology. The distance between the Mn^{II} ions bridged by bim is 11.460(14) Å, and such a long distance leads to porous channels along the *a* direction.

Magnetic Properties

1-Co

The plots of $\chi_M T$ versus T and χ_M^{-1} versus T measured from 2 to 300 K in 1 kOe are displayed in Figure 5. At 300 K, the $\chi_M T$ value is 3.10 $cm^3 K mol^{-1}$ and decreases to a minimum of 1.71 $cm^3 K mol^{-1}$ at 8 K, then it increases abruptly to 5.78 $cm^3 K mol^{-1}$ at 2 K. Fitting the data above 30 K using the Curie–Weiss law, $\chi_M = C/(T - \theta)$, gives a Curie constant C = 3.31 $cm^3 K mol^{-1}$, significantly larger than the spin-only value of 1.875 $cm^3 K mol^{-1}$ for Co^{2+}, and a negative Weiss constant θ of –18.8 K. Commonly, this kind of behavior of $\chi_M T$ and the negative θ value may indicate the occurrence of a dominant antiferromagnetic coupling between the spin carriers. However, because the spin-orbit coupling itself can lead to a negative θ value and a decrease of $\chi_M T$ at high temperatures, caution must be paid concerning those spins with large spin-orbit coupling, such as the Co^{2+} ion in an octahedral ligand field. Actually, the increase of $\chi_M T$ below 8 K indicates the possibility of ferromagnetic coupling. Although difficult, some efforts have been made to calculate the spin-orbit coupling parameter λ (λ = –170 cm^{-1} for the free ion), the axial splitting parameter Δ (and then the axial zero-field splitting parameter D), and/or the exchange coupling parameter J for some mono- and dinuclear Co^{II} ions in the octahedral field.[16–18] In the case of **1-Co**, we fitted the susceptibility data by considering a mononuclear Co^{2+} ion with spin-orbit coupling parameter λ ($H = -\lambda LS$) in a molecular-field approximation. The χ_{mono} for a mononuclear Co^{2+} in an octahedral environment can be calculated from Equation (1)[16] with $x = \lambda/k_B T$.

The parameter A gives a measure of the crystal field strength relative to the interelectronic repulsions and is equal to 1.5 for a weak crystal field, 1.32 for a free ion, and 1.0 for a strong field. Considering the molecular-field theory with zJ as the total exchange parameter, we can fit our experimental data above 30 K with Equation (2).[19]

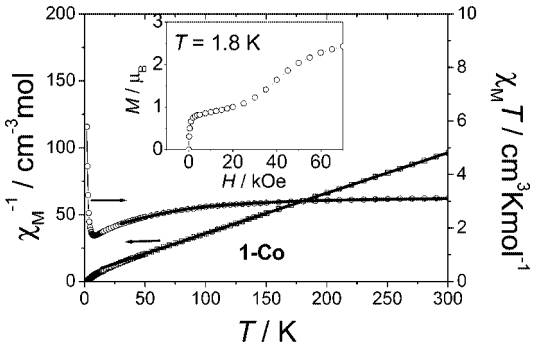

Figure 5. Plots of $\chi_M T$ versus T and χ_M^{-1} versus T from 2 to 300 K of **1-Co**. The line across χ_M^{-1} is the fit using the Curie–Weiss law and that along $\chi_M T$ represents the best fit using the model mentioned in the text. Inset: the field-dependent isothermal magnetization $M(T,H)$ for **1-Co** at 1.8 K.

$$\chi = \frac{\chi_{mono}}{1 - (2zJ/Ng^2\beta^2)\chi_{mono}} \quad (2)$$

In Equations (1) and (2), N, g, β, k_B, and T have their usual meanings. The best fit (Figure 5) gives λ = –117 cm^{-1} = –168 K, A = 1.24, and zJ = 0.42 cm^{-1} = 0.61 K with $R = 1.3 \times 10^{-5}$ [$R = \Sigma(\chi_{obsd.} - \chi_{calcd.})^2/\Sigma(\chi_{obsd.})^2$].

Although our results are semi-quantitative due to the impreciseness of the molecular-field theory, the evaluated positive zJ shows the possibility of the ferromagnetic interaction between Co^{II} neighbors. It is also evidenced by the isothermal magnetization measurement at 1.8 K (inset of Figure 5). The magnetization increases very fast from zero to about 0.7 μ_B at 2 kOe, which indicates the occurrence of ferromagnetic coupling and might suggest the occurrence of a phase transition. After a slow increase to about 1.0 μ_B at 20 kOe, the magnetization increases faster again to 2.43 μ_B at 70 kOe. To clarify the occurrence of a phase transition, the temperature dependence of the zero-field-cooled and field-cooled magnetization (ZFCM and FCM) at 20 Oe from 1.8 to 8 K, and the *ac* susceptibility under H_{dc} = 0 Oe and H_{ac} = 3 Oe from 1.8 to 4 K were measured, and the results are presented in Figure S3. All these results show no sign of long-range ordering at the lowest temperature limit of 1.8 K of our SQUID system.

2-Co

The temperature dependence of the susceptibility χ_M of **2-Co** was measured in a magnetic field of 5 kOe from 2 to 300 K and the result is plotted as $\chi_M T$ versus T and χ_M^{-1} versus T in Figure 6. After decreasing slowly upon cooling to a minimum of 3.49 $cm^3 K mol^{-1}$ at 40 K (inset of Figure 6), $\chi_M T$ increases abruptly to a peak at 4.5 K, and then

$$\chi_{mono} = \frac{1}{T} \times \frac{\frac{7(3-A)^2 x}{5} + \frac{12(2+A)^2}{25A} + \left\{\frac{2(11-2A)^2 x}{45} + \frac{176(2+A)^2}{675A}\right\} \times \exp\left(\frac{-5Ax}{2}\right) + \left\{\frac{(5+A)^2 x}{9} - \frac{20(2+A)^2}{27A}\right\} \exp(-4Ax)}{\frac{8x}{3}\left\{3 + 2\exp\left(\frac{-5Ax}{2}\right) + \exp(-4Ax)\right\}} \quad (1)$$

 © 2005 Wiley-VCH Verlag GmbH & Co. KGaA, Weinheim

drops again until 2 K. The data in the range of 30–300 K obeys the Curie–Weiss law with $C = 3.79\ cm^3\,K\,mol^{-1}$ and a negative θ value of –3.50 K. As is discussed for **1-Co**, the small negative θ value does not necessarily come from the AF coupling through the *EE*-SCN^- ion but from the spin-orbit coupling. Similar to that of **1-Co**, the $\chi_M T$ data above 30 K can also be fitted by Equations (1) and (2) with a small temperature-independent paramagnetic constant $\chi_{TIP} = 0.0003\ cm^3\,mol^{-1}$. The best fit (Figure 6) gives $\lambda = -85.6\ cm^{-1} = -124$ K, $A = 1.45$ and $zJ = 2.43\ cm^{-1} = 3.51$ K with $R = 5\times10^{-6}$ [$R = \Sigma(\chi_{obsd.} - \chi_{calcd.})^2/\Sigma(\chi_{obsd.})^2$]. The A value shows the weak ligand field and the positive zJ clearly indicates the existence of the dominant ferromagnetic coupling between the adjacent Co^{II} ions, consistent with the result of **1-Co**.

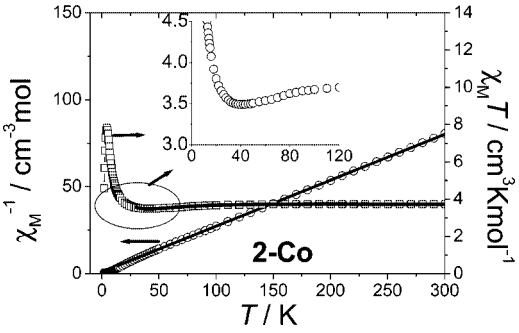

Figure 6. Plots of $\chi_M T$ versus T and χ_M^{-1} versus T from 2 to 300 K of **2-Co**.The line across χ_M^{-1} is the fit using the Curie–Weiss law and that along $\chi_M T$ represents the best fit using the model mentioned in the text. Inset: the expansion of the minimum of $\chi_M T$.

To prove the long-range ordering of **2-Co**, suggested by the peak of $\chi_M T$ at 4.5 K, we performed other measurements at low temperatures. The isothermal magnetization at 1.80 K with the field up to 50 kOe shows a pronounced sigmoid behavior of a metamagnet. The magnetization first increases slowly with increasing field strength, then shows a sharp transition to a ferromagnetic state (or a paramagnetic one) (Figure 7). At 50 kOe, the magnetization value is 2.80 μ_B, close to the expected saturated value of high-spin Co^{II}. The critical field is ca. 0.65 kOe at 1.8 K, estimated from the sharp peak of dM/dH, which is the field strength of the steepest point of the $M(H,T)$ curve. We also measured the *ac* isothermal magnetization at $H_{ac} = 3$ Oe with a dc field from –6 to + 6 kOe and a frequency of 666 Hz (Figure S4) and the FCM from 2 to 6 K at different fields (200, 400, 500, 600 and 800 Oe) (inset of Figure 7). The sharp peak of χ_M' is consistent with that of dM/dH; and the peak of χ_M in the FCM shifts to low temperatures with increasing external fields and finally disappears when the field is larger than the critical field. Also, the temperature-dependent ac susceptibility under $H_{dc} = 0$ Oe and $H_{ac} = 3$ Oe with frequencies of 277, 666, 1633, and 4111 Hz was measured from 2 to 6 K (Figure 8). The in-phase signal shows a sharp peak at ca. 2.9 K, and no detectable out-of-phase signal or frequency dependence was observed.

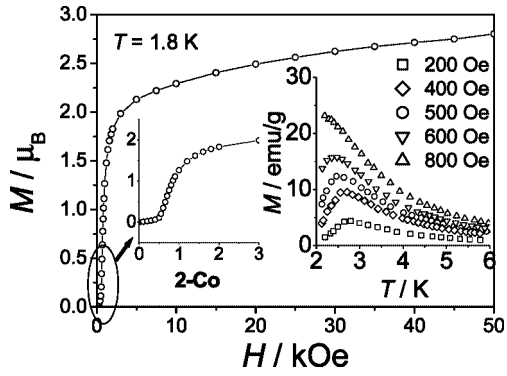

Figure 7. Field-dependent isothermal magnetization $M(T,H)$ for **2-Co** at 1.8 K. The low-field region is expanded for clarity. Inset: field-cooled magnetization from 2 to 6 K at different fields.

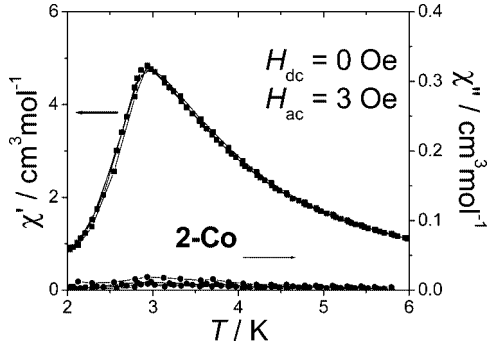

Figure 8. Ac susceptibilities from 2 to 6 K in zero applied dc field and an ac field of 3 Oe at different frequencies (277, 666, 1633, 4111 Hz) for **2-Co**.

All of the measured data indicates that **2-Co** is a metamagnet below the critical temperature 2.9 K, and the critical field for the metamagnetic transition is ca. 650 Oe at 1.8 K. Considering the structure, the metamagnetism of **2-Co** can be rationalized as a result of the competition between the weak antiferromagnetic coupling among the ferromagnetic $[Co(SCN)_2]_n$ chains and the external field. External fields larger than 650 Oe overcome the antiferromagnetic stacking of the chains and turn the AF ground state into a paramagnetic one.

3-Mn

The magnetic susceptibility χ_M of **3-Mn** measured at 10 kOe from 2 to 300 K shows a broad peak at about 50 K (Figure S5), which is typical for an AF-coupled system. As can be seen from Figure 9, the $\chi_M T$ value at 300 K is $3.61\ cm^3\,K\,mol^{-1}$, which is significantly lower than the spin-only value of $4.375\ cm^3\,K\,mol^{-1}$, and decreases continuously to $0.0387\ cm^3K\,mol^{-1}$ at 2 K. Fitting of the data above 130 K with the Curie–Weiss law gives $C = 4.94\ cm^3\,K\,mol^{-1}$ and $\theta = -108$ K, indicating a strong antiferromagnetic coupling between the Mn^{II} ions bridged by the *EE*-N_3^- anion. At 1.8 K, the isothermal magnetization $M(T,H)$ increases almost linearly from 0 to 50 kOe and reaches 0.2 μ_B per Mn^{II} atom at 50 kOe, far from the saturation value $M_S = 5\ \mu_B$ for a spin-only Mn^{II} ion, confirming the antiferromagnetic coupling between the Mn^{II} ions. Considering the

 © 2005 Wiley-VCH Verlag GmbH & Co. KGaA, Weinheim

low-dimensional structure of **3-Mn**, we can fit the susceptibility data χT above 30 K using Equation (3) based on the molecular-field theory;[19] χ_{chain} is the susceptibility of the Fisher model of a 1D equally spaced Hensenberg chain for a classical spin (S = 5/2) with the Hamiltonian $H = -2J\Sigma_{<i,j>}S_i \cdot S_j$ [Equation (4)][19a] with u represented by Equation (5).

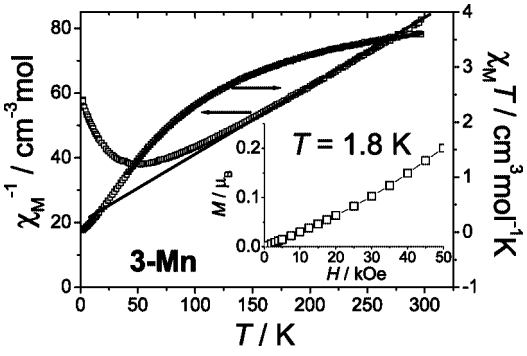

Figure 9. Plots of $\chi_M T$ versus T and χ_M^{-1} versus T from 2 to 300 K of **3-Mn**. The line across χ_M^{-1} is the fit using the Curie–Weiss law and that along $\chi_M T$ represents the best fit using the chain model mentioned in the text. Inset: field-dependent isothermal magnetization $M(T,H)$ for **3-Mn** at 1.8 K.

$$\chi = \frac{\chi_{chain}}{1 - (2zJ/Ng^2\beta^2)\chi_{chain}} \quad (3)$$

$$\chi_{chain} = \frac{Ng^2\beta^2S(S+1)}{3kT}\frac{1+u}{1-u} \quad (4)$$

$$u = \coth[\frac{JS(S+1)}{kT}] - [\frac{kT}{JS(S+1)}] \quad (5)$$

In Equations (3)–(5), S = 5/2; J and zJ represent the magnetic coupling constants of the intra- and interchains. The best fit (Figure 9) gives $J = -8.08(3)\ cm^{-1} = -11.7$ K, $zJ = -0.9(1)\ cm^{-1} = -1.3$ K, and $g = 2.057$ with $R = 4.7 \times 10^{-5}$ [$R = \Sigma(\chi_{obsd.}T - \chi_{calcd.}T)^2/\Sigma(\chi_{obsd.}T)^2$]. The negative J and zJ values show that an AF interaction exists both within and between the chains.

4-Mn

As can be seen from the plots of $\chi_M T$ versus T and χ_M^{-1} versus T measured from 2 to 300 K in 10 kOe displayed in Figure S6, the value of $\chi_M T$ increases gradually with decreasing temperature and shows a peak at 10 K. This behavior suggests intrachain ferromagnetic coupling; the decrease of $\chi_M T$ below 10 K may be due to interchain antiferromagnetic coupling or saturation effect of the field. Fitting of the data above 100 K with the Curie–Weiss law gives C = 4.16 $cm^3\,K\,mol^{-1}$ and a positive θ value of +23.5 K, also indicating the dominant ferromagnetic coupling between Mn^{II} ions transmitted by the *EO*-azide anion.

To further clarify the nature of the low-temperature phase, we have measured the FCM in different fields (200, 500, 1500 Oe) (inset of Figure 10) and the ac susceptibility under H_{dc} = 0 Oe and H_{ac} = 2 Oe from 2 to 15 K (Figure 10). The FCM at low fields of 200 and 500 Oe shows peaks at about 3.0 K but the peak disappears in the high-field region (1.5 kOe). This behavior is quite similar to that of **2-Co** and indicates a phase transition from an antiferromagnetic state to a ferromagnetic one above some critical field. Actually, the ac susceptibility under zero dc field is typical for an antiferromagnet; the in-phase signal shows a sharp peak at 3.0 K, and no detectable out-of-phase signal nor frequency dependence was observed. In order to investigate the phase transition with increasing field, the isothermal magnetization $M(T,H)$ with fields up to 70 kOe at 1.8 K (Figure 11) was measured. As a whole, the magnetization increases fast at low fields and almost reaches saturation at about 10 kOe. At the highest field of 70 kOe, the saturation value is 5.1 μ_B, very close to the saturated value of 5 μ_B for S = 5/2. Careful examination of the low-field range between 0 and 3 kOe reveals two obvious abrupt steps, with H_{c1} = 0.23 kOe and H_{c2} = 0.82 kOe, defined as the H values with the steepest slopes of the $M(H,T)$ curve (inset of Figure 11). The plateau region at 1.8 K is presumably associated with the familiar spin-flop state at the intermediate field values $H_{c1} < H < H_{c2}$. The ac isothermal magnetization under a field of H_{ac} = 2 Oe with H_{dc} from 0 to 3 kOe and a frequency of 666 Hz at 1.8 K (Figure S7) supports these two transitions. Two obvious peaks, χ'_M and χ''_M, are consistent with the peaks of dM/dH.

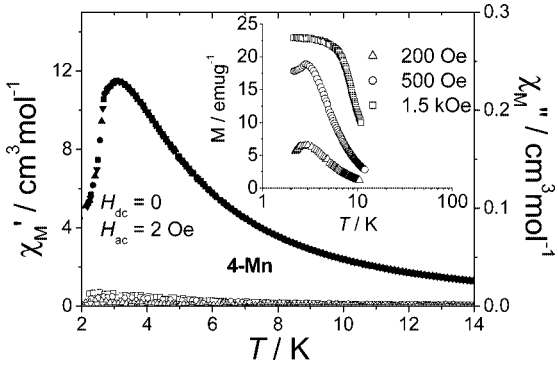

Figure 10. Ac susceptibilities from 2 to 6 K in the zero applied dc field and an ac field of 2 Oe at different frequencies (277, 666, 1633, 4111 Hz) for **4-Mn**. Inset: field-cooled magnetization at different fields.

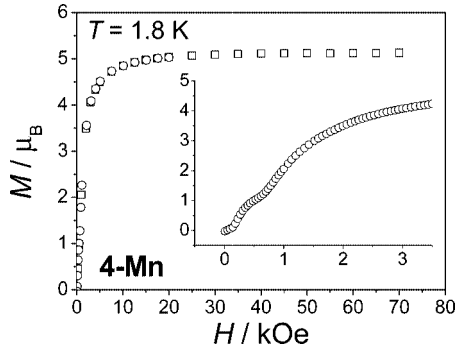

Figure 11. Field-dependent isothermal magnetization $M(T,H)$ for **4-Mn** at 1.8 K. Inset: expansion of the low-field region.

Based on the structure of **4-Mn** and the magnetic data, we rationalize that this phenomenon is a metamagnetic

 © 2005 Wiley-VCH Verlag GmbH & Co. KGaA, Weinheim

transition coexisting with a spin-flop transition. The metamagnetic transition originates from competition between the external field and the AF coupling among ferro- or ferrimagnetic chains or layers. And the spin-flop transition is quite common for many antiferromagnets with weak anisotropy (for Mn^{II}, the ^6S ground state makes it one of the weakest anisotropic ions). The moment orientation switches from the easy axis to an orientation perpendicular to the applied field only when the fields are larger than a critical field H_{c1}.[19c] From the magnetic point of view, **4-Mn** can be considered as a 1D ferromagnetic chain because of the very large interchain Mn–Mn distances [11.460(14) Å] as compared to the short intrachain distances of 3.614(5) and 3.535(5) Å. The intrachain coupling transferred by the *EO*-N_3^- anion is ferromagnetic since the angles of Mn–N_{azide}–Mn are about 103° and 106°, and there are numerous reports concluding that this kind of bridging azide favors the ferromagnetic coupling between Mn^{II} ions.[2e,5a,15] With the weak AF coupling between the chains, these ferromagnetic chains are aligned in an *anti*-parallel fashion to each other at low external fields. As the field increases to a spin-flop field H_{c1} = 0.23 kOe, **4-Mn** transfers from the AF state to a spin-flop one and the antiparallel magnetizations of the two sub-lattices flop from the direction of the easy axis to that perpendicular to it. Further increase of the external field to a critical field H_{c2} = 0.82 kOe can totally overwhelm the interchain AF coupling and the state turns into a ferromagnetic one. Similar behavior was also observed in a compound where Mn^{II} and Ni^{II} ions were ferromagnetically bridged by NO_2^- anions to form a ferromagnetic chain.[20]

Conclusions

By using two flexible long ligands [1,2-bis(1,2,4-triazol-1-yl)ethane (bte) and 1,2-bis(imidazol-1-yl)ethane (bim)], and two short anion bridges SCN^- and N_3^-, we successfully synthesized four new coordination polymers formulated as $[Co(SCN)_2(bim)]$ (**1-Co**), $[Co(SCN)_2(bte)]$ (**2-Co**), $[Mn(N_3)_2(bte)]$ (**3-Mn**), and $[Mn(N_3)_2(bim)]$ **(4-Mn)**. **1-Co** crystallizes as a triple-bridging chain compound with double *EE*-SCN^- and single *gauche*-bim ligands as bridges. **2-Co** and **3-Mn** have very similar 2D (4,4) layer structures with an *anti*-bte ligand connecting $[Co(SCN)_2]_n$ or $[Mn(N_3)_2]_n$ chains bridged by double *EE*-SCN^-/N_3^- anions. **4-Mn** forms a distorted diamondoid structure through double *EO*-N_3^- and *anti*-bim bridging ligands. Magnetic measurement reveals that the dominant magnetic coupling between the Co^{II} ions in **1-Co** and **2-Co** is ferromagnetic. **1-Co** remains paramagnetic up to 1.8 K and **2-Co** is a metamagnet below T_N = 2.9 K with a critical field H_C = 650 Oe at 1.8 K. For **3-Mn**, the strong AF coupling leads to an AF chain compound without long-range ordering above 1.8 K. For **4-Mn**, the AF ground state exists below T_N = 3.0 K and a metamagnetic transition coexisting with a field-induced spin-flop transition was observed with the H_{c1} = 0.23 kOe and H_{c2} = 0.82 kOe. Our results show that a combination of short anion bridges (SCN^-/N_3^-) and flexible-bidentate long spacers can be used to construct coordination polymers with novel topologies and interesting magnetic properties.

Experimental Section

General Remarks: All starting materials were commercially available, reagent grade, and used as purchased without further purification. The ligands bim and bte were prepared according to a literature method.[21] Elemental analyses of C, H, N were carried out with a Perkin–Elmer 240C analyzer. FTIR spectra were obtained for KBr pellets with a Nicolet 170SX FTIR spectrophotometer in the 4000–400 cm^{-1} region. Variable-temperature magnetic susceptibility, zero-field ac magnetic susceptibility measurements, and field dependence of magnetization were performed with an Oxford Maglab 2000 System or a Quantum Design MPMS XL-5 SQUID system. The experimental susceptibilities were corrected for the diamagnetism of the constituent atoms (Pascal's tables).

Synthesis

$[Co(SCN)_2(bim)]$ (1-Co): $Co(NO_3)_2{\cdot}6H_2O$ (0.146 g, 0.5 mmol), KSCN (0.097 g, 1.0 mmol) and bim (0.081 g, 0.5 mmol) in 14 mL of water were heated in a Teflon-lined autoclave (20 mL) at 180 °C for 4 d. After slow cooling to room temperature, purple prism-shaped crystals suitable for single-crystal X-ray crystallographic analysis were obtained. The crystals were filtered from the mother liquor and washed with ethanol. Yield: 0.110 g (65%). $C_{10}H_{10}CoN_6S_2$ (337.29): calcd. C 35.61, H 2.99, N, 24.92; found C 35.54, H 2.96, N 24.86. IR: $\tilde{\nu}$ = 3129 (w), 2099 (vs), 1605 (w), 1520 (s), 1439 (w), 1373(w), 1285 (w), 1246 (w), 1107 (m), 1103 (m), 941 (w), 837 (w), 752 (m), 656 (m), 629 (m) and 471 (w) cm^{-1}.

$[Co(SCN)_2(bte)]$ (2-Co): $Co(NO_3)_2{\cdot}6H_2O$ (0.146 g, 0.5 mmol) and KSCN (0.097 g, 1.0 mmol) in a 20 mL solution of H_2O/EtOH (1:1, v/v) was added to one side of an H-shaped tube, and 20 mL of an H_2O/EtOH solution (1:1, v/v) of bte (0.082 g, 0.5 mmol) was added to the other side of the H-shaped tube. After approximately 3 months, purple crystals suitable for X-ray analysis were obtained. Yield: 0.090 g (53%). $C_8H_8CoN_8S_2$ (339.3): calcd. C 28.32, H 2.38, N 33.04; found C 28.24, H 2.29, N 32.86. IR: $\tilde{\nu}$ = 3121 (w), 2114 (vs), 1524 (m), 1451 (w), 1385 (m), 1319 (w), 1285 (m), 1208 (w), 1127(s), 1012 (m), 992 (m), 874 (w), 698 (w), 679 (m), 648 (m) and 463 (w) cm^{-1}.

$[Mn(N_3)_2(bte)]$ (3-Mn): A methanolic solution (20 mL) of bte (0.082 g, 0.5 mmol) was slowly added to an aqueous solution (20 mL) of $MnSO_4{\cdot}H_2O$ (0.085 g, 0.5 mmol) and excess NaN_3 (0.163 g, 2.5 mmol) while stirring. The mixtures were stirred at room temperature and the resultant solution was filtered. After the filtrate was allowed to stand in the air for 1 week, well-shaped pale yellow crystals were obtained. Yield: 0.126 g (83%). $C_6H_8MnN_{12}$ (303.1): calcd. C 23.77, H 2.66, N 55.45; found C 23.72, H 2.58, N 55.35. IR: $\tilde{\nu}$ = 3124 (w), 2076 (vs), 1780 (w), 1523 (s), 1461 (w), 1367 (w), 1281 (m), 1207 (m), 1154 (w), 1123 (m), 1010 (m), 985 (m), 893 (w), 700 (w), 679 (w), 654 (w) and 419 (w) cm^{-1}.

$[Mn(N_3)_2(bim)]$ (4-Mn): For this synthesis, $MnSO_4{\cdot}H_2O$ and bim were used in a 1:0.5 molar ratio with excess NaN_3 because the reaction of $MnSO_4{\cdot}H_2O$ and bim in a 1:1 molar ratio with excess NaN_3 will produce the complex $[Mn(N_3)_2(bim)_2]_n$.[4d] An aqueous solution (10 mL) of excess NaN_3 (0.163 g, 2.5 mmol) was mixed with 10 mL of an aqueous solution of $MnSO_4{\cdot}H_2O$ (0.170 g, 1.0 mmol) and stirred for 20 min. An ethanol solution (10 mL) of bim (0.081 g, 0.5 mmol) was then slowly added to the above solu-

 © 2005 Wiley-VCH Verlag GmbH & Co. KGaA, Weinheim

Table 1. Crystallographic data for compounds **1**–**4**.

	1-Co	**2-Co**	**3-Mn**	**4-Mn**
Empirical formula	$C_{10}H_{10}CoN_6S_2$	$C_8H_8CoN_8S_2$	$C_6H_8MnN_{12}$	$C_8H_{10}MnN_{10}$
M_r [gmol^{-1}]	337.29	339.27	303.18	301.20
Crystal system	orthorhombic	triclinic	triclinic	monoclinic
Space group	$Pna2_1$	$P\bar{1}$	$P\bar{1}$	$P2_1/c$
a [Å]	11.249(3)	5.691(3)	5.236(5)	6.214(2)
b [Å]	9.095(2)	6.432(4)	6.419(6)	18.984(5)
c [Å]	12.585(3)	8.840(5)	8.760(8)	10.382(3)
α [°]	90	102.608(12)	102.752(12)	90
β [°]	90	100.220(9)	90.290(10)	89.624(5)
γ [°]	90	94.753(10)	94.551(13)	90
V [Å^3]	1287.6(6)	308.3(3)	286.2(4)	1224.6(5)
Z	4	1	1	4
$\rho_{calcd.}$ [g cm^{-3}]	1.740	1.827	1.759	1.634
Crystal size [mm^{-1}]	0.12×0.16×0.4	0.11×0.20×0.20	0.3×0.3×0.4	0.1×0.2×0.2
μ(Mo-K_α) [mm^{-1}]	1.650	1.728	1.163	1.083
Measured reflections	13604	3464	2120	11816
Independent reflections	2935	1391	1212	2166
Observed reflections[a]	2819	1264	1196	2056
No. of parameters	173	88	88	172
F(000)	684	171	153	612
GOF	1.077	1.070	0.989	1.242
Max/min [e Å^{-3}]	0.293/–0.354	0.286/–0.336	0.330/–0.237	0.227/–0.366
T_{max}/T_{min}	0.827/0.731	0.829/0.714	0.705/0.661	0.901/0.802
R_1[b]	0.0277	0.0306	0.0231	0.0535
wR_2[c]	0.0586	0.0696	0.0605	0.1169

[a] Observation criterion: $I > 2\sigma(I)$. [b] $R_1 = \Sigma||F_o| - |F_c||/\Sigma|F_o|$. $I > 2\sigma(I)$. [c] $wR_2 = \{\Sigma[w(F_o^2 - F_c^2)^2]/\Sigma[w(F_o^2)^2]\}^{1/2}$, for all data.

tion. The mixture was stirred at room temperature for 30 min and the resultant solution was filtered. After the filtrate was allowed to stand in the air for 2 weeks, well-shaped yellow crystals were obtained. Yield: 0.117 g (78%). $C_8H_{10}MnN_{10}$ (301.2): calcd. C 31.90, H 3.35, N 46.51; found C 31.79, H 3.32, N 46.38. IR: $\tilde{\nu}$ = 3125 (w), 2072 (vs), 2033 (s), 1609 (w), 1512 (m), 1466 (w), 1385 (w), 1335 (m), 1292 (w), 1261 (w), 1231 (m), 1111 (w), 1084 (s), 1022 (w), 934 (m), 830 (m), 752 (m), 664 (m) and 413 (w) cm^{-1}.

Single-Crystal X-ray Crystallography: All data collections were performed at a temperature of 193.15 K except for the crystal data collection of **2-Co** which was performed at 298(2) K with a Rigaku Mercury CCD diffractometer with ω-scan technique. The structures were solved by direct methods and refined with full-matrix least-squares techniques based on F^2 using the SHELXS-97 and SHELXL-97 programs. Anisotropic thermal parameters were assigned to all non-hydrogen atoms. The hydrogen atoms of the bte and bim ligands were generated geometrically. Details of the crystallographic data are listed in Table 1. CCDC-221765 and -260333 to -260335 contain the supplementary crystallographic data for this paper. These data can be obtained free of charge at www.ccdc.cam.ac.uk/conts/retrieving.html [or from the Cambridge Crystallographic Data Centre, 12, Union Road, Cambridge CB2 1EZ, UK; Fax: +44-1223/336-033; E-mail, deposit@ccdc.cam.ac.uk]. Also, CIF files of these four compounds can be found in the Supporting Information.

Supporting Information Available: Tables of the details of the π–π and C–H···π interactions of **1-Co** and **2-Co**, the stack of the layers of **2-Co** and **3-Mn**, ac susceptibility and ZFCM/FCM of **1-Co**, ac isothermal magnetization of **2-Co** and **4-Mn**, $\chi_M T$ versus T of **3-Mn**, $\chi_M T$ versus T, χ_M^{-1} versus T, and dM/dH of **4-Mn**.

Acknowledgments

We acknowledge support from the National Science Fund for Distinguished Young Scholars (20125104), NSFC Nos. 20221101, 20490210, and the Natural Science Foundation of the University of Jiangsu Province (No. 03KJB150118), and the Funds of The Key Laboratory of Organic Synthesis of Jiangsu Province, P. R. China. We also acknowledge Mr. Zhang Yong for the single-crystal structural determination.

[1] For examples, see: a) A. J. Blake, N. R. Champness, S. S. M. Chung, W.-Sh. Li, M. Schröder, *Chem. Commun.* **1997**, 1005–1006; b) K. N. Power, T. L. Hennigar, M. J. Zawarotko, *Chem. Commun.* **1998**, 595–596; c) C. V. K. Sharma, R. D. Rogers, *Chem. Commun.* **1999**, 83–84; d) Q.-M. Wang, G.-C. Guo, T. C. W. Mak, *Chem. Commun.* **1999**, 1849–1850; e) C. M. Grunert, J. Schweifer, P. Weinberger, W. Linert, K. Mereiter, G. Hilscher, M. Muller, G. Wiesinger, P. J. van Koningsbruggen, *Inorg. Chem.* **2004**, *43*, 155–165; f) K. Uemura, S. Kitagawa, K. Fukui, K. Saito, *J. Am. Chem. Soc.* **2004**, *126*, 3817–3828.

[2] a) S. Han, J. L. Manson, J. Kim, J. S. Miller, *Inorg. Chem.* **2000**, *39*, 4182–4185; b) S. Martín, M. G. Barandika, L. Lezama, J. L. Pizarro, Z. E. Serna, J. I. R. De Larramendi, M. I. Arriortua, T. Rojo, R. Cortés, *Inorg. Chem.* **2001**, *40*, 4109–4115; c) A.-H. Fu, X.-Y. Huang, J. Li, T. Yuen, Ch.-L. Lin, *Chem. Eur. J.* **2002**, *8*, 2239–2247; d) X.-Y. Wang, H.-Y. Wei, Z.-M. Wang, S. Gao, Zh.-D. Chen, *Inorg. Chem.* **2005**, *44*, 572–583; e) J. L. Manson, A. M. Arif, J. S. Miller, *Chem. Commun.* **1999**, 1479–1480; f) X. Hao, Y.-G. Wei, Sh.-W. Zh, *Chem. Commun.* **2000**, 2271–2272.

[3] For examples see: a) M. L. Hernández, M. G. Barandika, M. K. Urtiaga, R. Cortés, L. Lezama, M. I. Arriortua, T. Rojo, *J. Chem. Soc., Dalton Trans.* **1999**, 1401–1406; b) P. J. van Kon-

 © 2005 Wiley-VCH Verlag GmbH & Co. KGaA, Weinheim

ingsbruggen, Y. Garcia, H. Kooijman, A. L. Spek, J. G. Haasnoot, O. Kahn, J. Linares, E. Codjovi, F. Varret, *J. Chem. Soc., Dalton Trans.* **2001**, 466–471; c) Y. Carcia, P. J. van Koningsbruggen, H. Kooijman, A. L. Spek, J. G. Haasnoot, O. Kahn, *Eur. J. Inorg. Chem.* **2000**, 307–314; d) S. Konar, E. Zangrando, M. G. B. Drew, T. Mallah, J. Ribas, N. R. Chaudhuri, *Inorg. Chem.* **2003**, *42*, 5966–5973; e) R. Bronisz, *Inorg. Chim. Acta* **2004**, *357*, 396–404; f) Q.-H. Zhao, H.-F. Li, X.-F. Wang, Zh.-D. Chen, *New J. Chem.* **2002**, *26*, 1709–1710; g) F. M. Tabellion, S. R. Seidel, A. M. Arif, P. J. Stang, *J. Am. Chem. Soc.* **2001**, *123*, 11982–11990; h) A. K. Ghosh, D. Ghoshal, T.-H. Lu, G. Mostafa, N. R. Chaudhuri, *Cryst. Growth Des.* **2004**, *4*, 851–857; i) T. L. Hennigar, D. C. Macquarrie, P. Losier, R. D. Rogers, M. J. Zaworotko, *Angew. Chem. Int. Ed. Engl.* **1997**, *36*, 972–973; j) B. Moulton, M. J. Zaworotko, *Chem. Rev.* **2001**, *101*, 1629–1658; k) B. F. Hoskins, R. Robson, D. A. Slizys, *J. Am. Chem. Soc.* **1997**, *119*, 2952–2953; l) B. F. Hoskins, R. Robson, D. A. Slizys, *Angew. Chem. Int. Ed. Engl.* **1997**, *36*, 2336–2338; m) M. L. Hernandez, M. G. Barandika, K. K. Urtiaga, R. Cortes, L. Lezama, M. I. Arriortua, *J. Chem. Soc., Dalton Trans.* **2000**, 79–84.

[4] a) B.-Z. Li, X. Zhu, B.-L. Li, Y. Zhang, *J. Mol. Struct.* **2004**, *691*, 159–163; b) B.-L. Li, X. Zhu, J.-H. Zhou, Y.-F. Peng, Y. Zhang, *Polyhedron* **2004**, *23*, 3133–3141; c) J.-H. Zhou, X. Zhu, Y.-N. Zhang, Y. Zhang, B.-L. Li, *Inorg. Chem. Commun.* **2004**, *7*, 949–952; d) B.-L. Li, X. Zhu, J.-H. Zhou, Y. Zhang, *Acta Crystallogr., Sect. C* **2004**, *60*, m373–m374; e) X. Zhu, B.-L. Li, J.-H. Zhou, B.-L. Li, Y. Zhang, *Acta Crystallogr., Sect. C* **2004**, *60*, m191–m193; f) L. P. Wu, Y. Yamagiwa, T. Kuroda-Sowa, T. Kamikawa, M. Munakata, *Inorg. Chim. Acta* **1997**, *256*, 155–159.

[5] For examples, see: a) J. Ribas, A. Escuer, M. Monfort, R. Vicente, R. Cortés, L. Lezama, T. Rojo, *Coord. Chem. Rev.* **1999**, *193–195*, 1027–1068; b) E.-Q. Gao, Y.-F. Yue, S.-Q. Bai, Z. He, C.-H. Yan, *J. Am. Chem. Soc.* **2004**, *126*, 1419–1429; c) T.-F. Liu, D. Fu, S. Gao, Y.-Z. Zhang, H.-L. Sun, G. Su, Y.-J. Liu, *J. Am. Chem. Soc.* **2003**, *125*, 13976–13977.

[6] X.-Y. Wang, L. Gan, S.-W. Zhang, S. Gao, *Inorg. Chem.* **2004**, *43*, 4615–4625.

[7] a) M. Kabešová, R. Boca, M. Melnícк, D. Valigura, M. Dunaj-Jurco, *Coord. Chem. Rev.* **1995**, *140*, 115–135; b) K. K. Narang, J. P. Pandey, *Synth. React. Inorg. Met.-Org. Chem.* **1994**, *24*, 73–93; c) A. H. Norbury, *Adv. Inorg. Chem. Radiochem.* **1975**, *17*, 231–386; d) R. A. Bailey, S. L. Kozak, T. W. Michelsen, W. N. Mills, *Coord. Chem. Rev.* **1971**, *6*, 407–445.

[8] a) D. M. Duggan, D. N. Hendrickson, *Inorg. Chem.* **1974**, *13*, 2929–2940; b) A. P. Ginsberg, R. L. Martin, R. W. Brookes, R. C. Sherwood, *Inorg. Chem.* **1972**, *11*, 2884–2889; c) M. Monfort, J. Ribas, X. Solans, *Inorg. Chem.* **1994**, *33*, 4271–4276; d) A. P. Ginsberg, R. C. Sherwood, R. W. Brookes, R. L. Martin, *J. Am. Chem. Soc.* **1971**, *93*, 5927–5928; e) M. Taniguchi, A. Ouchi, *Bull. Chem. Soc. Jpn.* **1986**, *59*, 3277–3278; f) J. C. Trofimenko, J. K. Calabrese, S. Wolowiec, F. B. Hulsbergen, J. Reedijk, *Inorg. Chem.* **1992**, *31*, 3943–3950; g) T. Rojo, R. Cortés, L. Lezama, M. I. Arriortus, K. Urtiga, G. Vilenueve, *J. Chem. Soc., Dalton Trans.* **1991**, 1779–1783.

[9] a) A. Escuer, S. B. Kumar, F. Mautner, R. Vicente, *Inorg. Chim. Acta* **1998**, *269*, 313–316; b) R. Vicente, A. Escuer, J. Ribas, X. Solans, *J. Chem. Soc., Dalton Trans.* **1994**, 259–262; c) B. W. Dockum, W. M. Reiff, *Inorg. Chem.* **1982**, *21*, 2613–2619.

[10] a) R. Vicente, A. Escuer, E. Peñalba, X. Solan, M. Font-Bardía, *Inorg. Chim. Acta* **1997**, *255*, 7–12; b) M. B. Cingi, A. M. Manotti Lanfredi, A. Tiripicchio, J. G. Haasnot, J. Reedijk, *Inorg. Chim. Acta* **1983**, *72*, 81–88; c) J. G. Haasnot, W. L. Driessen, J. Reedijk, *Inorg. Chem.* **1984**, *23*, 2803–2807; d) V. Kettmann, J. Krätsmár-Smogrovic, O. Svajlenová, M. Zemlicka, *Z. Naturforsch., Teil B.* **1992**, *47*, 1565–1570; e) P. C. Christidis, C. A. Bolos, G. Brauer, G. Will, N. S. Trendafilova, G. St. Nikolov, *Inorg. Chim. Acta* **1995**, *228*, 173–185.

[11] a) P. Domiano, A. Musatti, M. Nardelli, C. Peizzi, G. Predieri, *J. Chem. Soc., Dalton Trans.* **1975**, 2357–2360; b) M. Kabešová, M. Dunaj-Jurco, J. Sodánova, *Inorg. Chim. Acta* **1987**, *130*, 105–111; c) H. Yamaguchi, Y. Inomata, T. Takeuchi, *Inorg. Chim. Acta* **1990**, *172*, 105–112; d) C. A. White, G. P. A. Yap, N. P. Raju, J. E. Greedan, R. J. Crutchley, *Inorg. Chem.* **1999**, *38*, 2548–2549; e) M. Julve, M. Verdaguer, G. De Munno, J. A. Real, G. Bruno, *Inorg. Chem.* **1993**, *32*, 795–802; f) J. Ribas, C. Diaz, X. Solans, M. Font-Bardía, *J. Chem. Soc., Dalton Trans.* **1996**, 35–38; g) J. Ribas, C. Diaz, X. Solans, M. Font-Bardía, *Inorg. Chim. Acta* **1995**, *231*, 229–232; h) R. Cortés, M. K. Urtiaga, L. Lezama, J. I. R. Larramendi, M. I. Arriortua, T. Rojo, *J. Chem. Soc., Dalton Trans.* **1993**, 3685–3694; i) J. A. R. Navarro, M. A. Romero, J. M. Salas, M. Quirós, E. R. T. Tiekink, *Inorg. Chem.* **1997**, *36*, 4988–4991.

[12] S. Ferlay, G. Francese, H. W. Schmalle, S. Decurtins, *Inorg. Chim. Acta* **1999**, *286*, 108–113.

[13] a) B. W. Dockum, G. A. Eisman, E. H. Witten, W. M. Reiff, *Inorg. Chem.* **1983**, *22*, 150–156; b) G. C. Defotis, C. K. Barlowe, W. R. Shangraw, *J. Magn. Magn. Mater.* **1986**, *54–57*, 1493–1494; c) H.-J. Chen, X.-M. Chen, *Inorg. Chim. Acta* **2002**, *329*, 13–21.

[14] a) G. C. DeFotis, E. D. Remy, C. W. Scherrer, *Phys. Rev. B* **1990**, *41*, 9074–9086; b) J. N. McElearney, L. L. Balagot, *Phys. Rev. B* **1979**, *19*, 306–317; c) G. C. DeFotis, E. M. McGhee, K. R. Echols, R. S. Wiese, *J. Appl. Phys.* **1988**, *63*, 3569–3571; d) A. K. Gregson, N. T. Moxon, *Inorg. Chem.* **1982**, *21*, 586–590; e) G. C. DeFotis, B. T. Wimberly, E. M. McGhee, *J. Phys. (Paris), Colloq.* **1988**, *49*, 855–856.

[15] M. A. M. Abu-Youssef, A. Escuer, D. Gatteschi, M. A. S. Goher, F. A. Mautner, R. Vicente, *Inorg. Chem.* **1999**, *38*, 5716–5723.

[16] F. E. Mabbs, D. J. Machin, *Magnetism and Transition Metal Complexes*; Chapman and Hall, London, **1973**.

[17] B. N. Figgis, M. Gerloch, J. Lewis, F. E. Mabbs, G. A. Webb, *J. Chem. Soc. A* **1968**, 2086–2093. And references therein.

[18] H. Sakiyama, *J. Chem. Software* **2001**, *7*, 171–178. And references therein.

[19] a) O. Kahn, *Molecular Magnetism*, VCH, New York, **1993**; b) R. L. Carlin, A. J. Van-Duyneveldt, *Magnetic Properties of Transition Metal Compounds*; Springer-Verlag, New York, **1977**; c) R. L. Carlin, *Magnetochemistry*; Springer-Verlag, Berlin, Heidelberg, **1986**.

[20] R. Feyerherm, C. Mathonière, O. Kahn, *J. Phys. Condens. Matter* **2001**, *13*, 2639–2650.

[21] J. Torres, J. L. Lavandera, P. Cabildo, R. M. Claramunt, J. Elguero, *J. Heterocycl. Chem.* **1988**, *25*, 771–787.

Received: February 21, 2005
Published Online: July 14, 2005

 © 2005 Wiley-VCH Verlag GmbH & Co. KGaA, Weinheim

Variability in the Structures of Luminescent [2-(Aminomethyl)pyridine]silver(I) Complexes: Effect of Ligand Ratio, Anion, Hydrogen Bonding, and π-Stacking

Rodney P. Feazell,[a] Cody E. Carson,[a] and Kevin K. Klausmeyer*[a]

Keywords: Silver / N ligands / X-ray diffraction / Coordination modes

The reaction of 2-(aminomethyl)pyridine (2-amp) with silver(I) salts of triflate (OTf^-), trifluoroacetate (tfa^-), and tetrafluoroborate (BF_4^-) produce monomeric, dimeric, bridged, and polymeric structural motifs. The structural characteristics are dependent upon the ratio of ligand/metal in the structure as well as the ability of the anion to coordinate to the metal centers and form hydrogen bonds to the bound ligands. The silver coordination environment takes on several geometries including near linear (**6**), trigonal (**4**), tetrahedral (**1**), and both trigonal-bipyramidal and square-based pyramidal in a single structure (**2**). Structures **2**, **3**, and **5** also display short Ag–Ag contacts ranging from 2.8958(3) to 3.0305(4) Å. The species with metal–metal interactions, which are connectively very similar to their metal-isolated counterparts of **1**, **4**, and **6**, are held together only by weak π-stacking interactions or hydrogen bonds to their respective anions. Low-temperature luminescence spectra were collected for all compounds and are compared.
(© Wiley-VCH Verlag GmbH & Co. KGaA, 69451 Weinheim, Germany, 2005)

Introduction

Progress in the field of crystal engineering has been greatly complemented by coordination studies of the coinage metals.[1–8] Studies of silver in particular have had much to offer. This is because of the flexibility in its coordination sphere and the ease with which it varies the coordination number.[9–13] Many silver coordination architectures are readily obtainable through slight variations in ligand and/or anion and include discrete, small molecules, supramolecular arrays, and 1-, 2-, and 3-dimensional coordination networks.[13–17] Several systematic studies of the structural dependence on anions have been nicely demonstrative of the diversity possible with small changes in counterion properties such as coordinating or hydrogen-bonding ability.[18–23] A related area of this research that has proved lacking, however, is that concerned with the ligand/metal ratio dependence of these structures.[24] To the best of our knowledge, no thorough report has been given that shows the effects of changing the ratio of ligand/metal in bidentate silver(I) systems of various anions. This led us to investigate the changes in the solid-state structures of [2-(aminomethyl)-pyridine]silver(I) complexes that are caused by altering the ratio of ligand/metal in the reaction mixtures. One resulting feature that is of particular interest in these and other silver complexes is the closed-shell metal–metal interaction that is very well known to occur in the monovalent group 11 elements.[25–31] While not as broadly represented or studied as the aurophilic attraction that holds the gold–gold interaction intact, a small surge of recent work has been dedicated to examining the properties of this argentophilic contact.[32–37] Included in this group are a handful of theoretical studies that put the strength of the interaction along the same intensity as that of a hydrogen bond with an idealized internuclear separation of 3.137–3.208 Å.[38–41]

Herein we demonstrate that not only can the molecular architecture of silver(I) coordination complexes be altered by changes in the counterion, but they can also be largely affected by the ratio of ligand/metal. The 2-(aminomethyl)-pyridine ligand, whose small bite angle imposes a predisposition for chelation, is seen to construct a range of coordination motifs, shown in Figure 1, from simple monomers to coordination polymers with various silver(I) salts simply by changing its ratio in solution. The resulting complexes contain a number of interesting structural features and physical properties including several short, sterically unfavored Ag–Ag interactions, bridging 2-amp ligands and a pronounced luminescence.

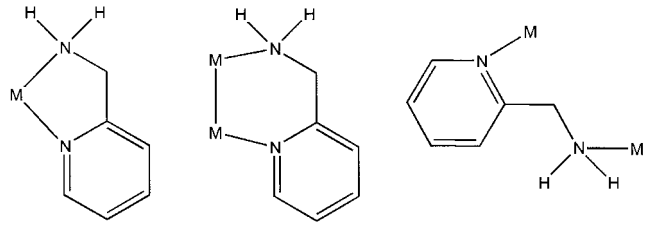

Figure 1. Binding modes that are seen with the 2-(aminomethyl)-pyridine ligand in the silver(I) structures described herein.

[a] Department of Chemistry and Biochemistry, Baylor University, Waco, TX 76798-7348, USA
Fax: +1-254-710-4272
E-mail: kevin_klausmeyer@baylor.edu
Supporting information for this article is available on the WWW under http://www.eurjic.org or from the author.

Results and Discussion

Preparation and NMR Spectroscopy

The 2-(aminomethyl)pyridine complexes **1**–**7** (Schemes 1, 2, and 3) were all prepared by the direct reaction of the ligand with silver(I) salts in varying ratios. The 1:1 $AgBF_4$ structure has already been discussed in a previous study.[23] The many intriguing structural features of the complexes presented here are seen to stem directly from the ratio of ligand/metal, with the ratio itself often being influenced by the properties of the anion present. An example of this is the silver triflate complex which we have been unable to force beyond a 3:2 ratio of ligand/metal, while that of the trifluoroacetate has not been isolable at 3:2 but proceeds directly to 2:1. Hydrogen bonding between the amine protons and the anions are a major determining factor in the structure, orientation, and 3-dimensional growth of the complexes.

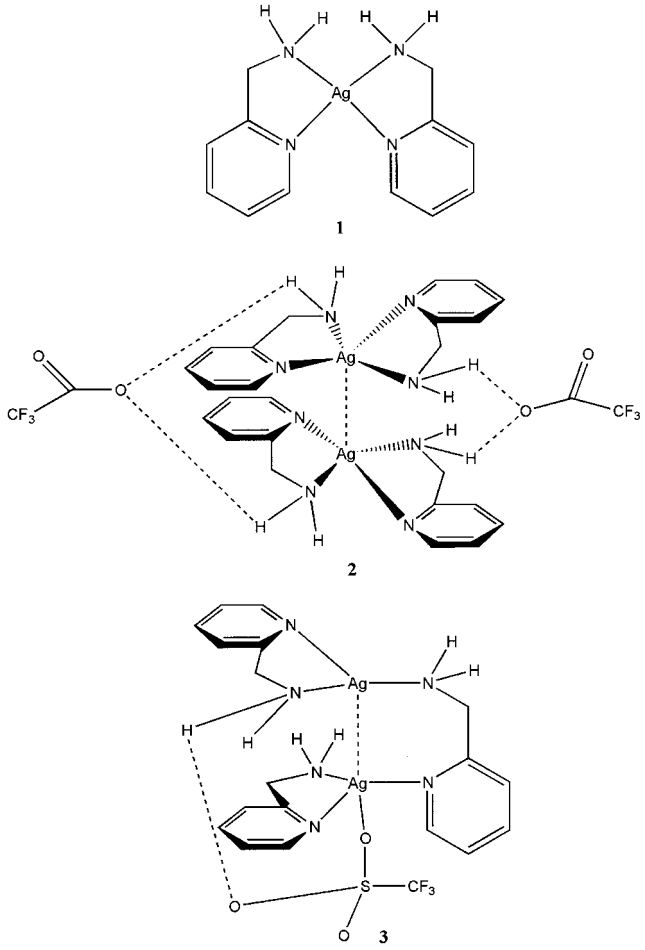

Scheme 1.

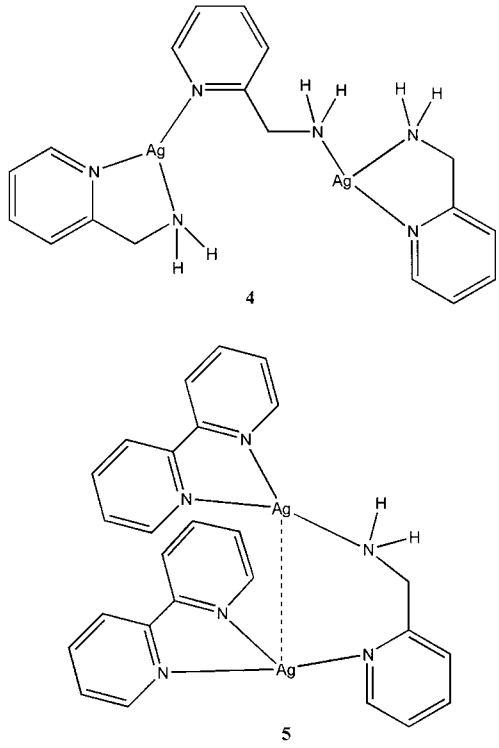

Scheme 2.

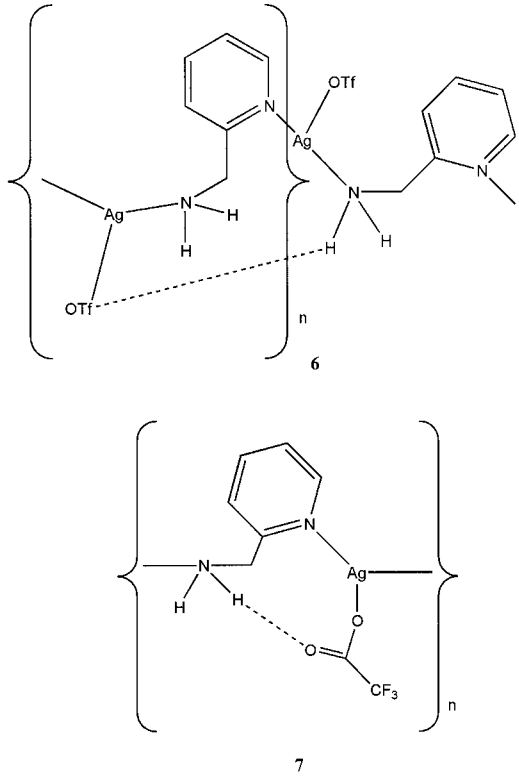

Scheme 3.

The ^1H NMR spectra of all the compounds are, as expected, generally similar. Signal shifts of the amine protons as well as of the *ortho*-*N*-hydrogen atoms on the pyridine rings are demonstrative of the differences in coordinated silver environments caused by the different anions present. The greatest shifts are seen examining the $–NH_2–$ protons in the presence of silver, ranging from 1.3 to 2.0 ppm downfield of the δ = 1.67 ppm chemical shift of the free 2-amp ligand in solution (NMR spectroscopic data for the free

 © 2005 Wiley-VCH Verlag GmbH & Co. KGaA, Weinheim

ligand is available in the Supporting information; for Supporting information see also the footnote on the first page of this article). These shifts are implicative of solution-state complexation.

X-ray Crystallography

Structural confirmation of all the complexes mentioned herein was provided by X-ray diffraction studies. Single crystals of all compounds were analyzed and structural diagrams are displayed in Figures 2–10. A summary of the X-ray data is presented in Tables 1 and 2. Collections of selected bond lengths, angles, interatomic distances and hydrogen bonds are given in Tables 3, 4, and 5.

Description of the Crystal Structures

The ratio of 2-amp ligand/Ag in the structures of both compounds **1** and **2** is 2:1. A significant change in both the metal geometries and the ligand–metal bond lengths are seen when going from **1** to **2**, and are the result of differences in interaction of the BF_4^- and tfa^- anions. The structure of **2** contains a rather short Ag–Ag interaction[38] that is obtained at the expense of the relaxed tetrahedral environment of the metal-separated structure of **1**.

The expansion of the silver coordination environment from linear in a two-coordinate polymeric setting[23] to near tetrahedral upon the addition of 2 equiv. of the chelating 2-(aminomethyl)pyridine ligand to produce compound **1** was as expected. In the former structure, the only way to achieve the two-coordinate environment necessary to accommodate a 1:1 ratio of 2-amp/$AgBF_4$ is with an outward twisting of the ligand. In this way the amino and pyridine donors of separate 2-amp ligands are utilized, linking the linearly coordinated silver ions into a one-dimensional coordination polymer. In the latter, the increased coordination number allows for the formation of a chelated complex which is easily achieved by the 2-amp ligand creating the distorted tetrahedron that is shown in Figure 2. The deformation of the tetrahedral bond angles in this compound is caused by the small bite angle of the coordinated 2-amp ligands which averages 73°. The interligand angles are thus made more obtuse, ranging from 125.9(2)° to 133.9(2)°. BF_4^- ions are held in place in the lattice by H-bonding with the amine protons. The crystal structure of compound **1** contains two independent molecules of $(2\text{-amp})_2AgBF_4$ caused by slight differences in conformation. Amine–Ag and pyridine–Ag bonds cannot be distinguished from one another in this structure by bond lengths alone. Considerable overlap is seen with the amine–Ag distances ranging from 2.293(6) to 2.371(5) Å and the pyridine–Ag distances ranging from 2.262(6) to 2.368(4) Å.

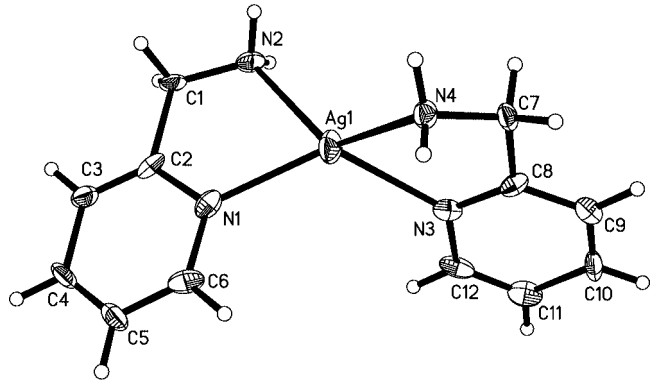

Figure 2. Molecular structure of one of the unique cationic monomers of **1**. Ellipsoids are drawn at the 50% probability level.

Table 1. Crystallographic data for compounds **1**–**4**.

	1	**2**	**3**	**4**
Empirical formula	$C_{24}H_{32}Ag_2B_2F_8N_8$	$C_{56}H_{64}Ag_4F_{12}N_{16}O_8$	$C_{20}H_{24}Ag_2F_6O_6S_2$	$C_{18}H_{24}Ag_2B_2F_8N_6$
Formula mass	821.94	1748.71	838.31	713.79
a [Å]	7.8817(5)	7.4205(6)	8.1167(9)	7.112(1)
b [Å]	14.0058(8)	13.284(1)	22.930(4)	8.335(2)
c [Å]	7.2894(4)	18.049(2)	15.625(2)	21.471(4)
α [°]	106.208(2)	69.342(4)		97.23(3)
β [°]	93.211(2)	89.255(4)	97.430(5)	98.51(3)
γ [°]	100.710(3)	80.621(4)		99.10(3)
V [Å^3]	754.25(8)	1640.8(2)	2883.7(7)	1228.4(4)
Z	1	1	4	2
Space group	$P\bar{1}$	$P\bar{1}$	$P2_{1/n}$	$P\bar{1}$
T [K]	110(2)	110(2)	110(2)	110(2)
$D_{calcd.}$ [g cm^{-3}]	1.810	1.770	1.931	1.930
μ [mm^{-1}]	1.379	1.275	1.588	1.675
$2\theta_{max.}$ [°]	28.31	26.43	28.30	28.39
Reflections measured	15414	54807	66994	14615
Reflections used (R_{int})	5828(0.0267)	12763(0.0401)	7095(0.0308)	5935(0.0226)
Restraints/parameters	7/391	3/865	0/397	10/341
R_1 [$I > 2\sigma(I)$]	0.0174	0.0274	0.0177	0.0274
wR_2 [$I > 2\sigma(I)$]	0.0465	0.0635	0.0432	0.0678
$R(F_o^2)$ (all data)	0.0184	0.0364	0.0226	0.0317
$R_w(F_o^2)$ (all data)	0.0472	0.0675	0.0443	0.0705
GOF on F^2	1.028	1.016	1.063	1.034

 © 2005 Wiley-VCH Verlag GmbH & Co. KGaA, Weinheim

Table 2. Crystallographic data for compounds **5**–**7**.

	5	**6**	**7**
Empirical formula	$C_{26}H_{24}Ag_2B_2F_8N_6$	$C_7H_8AgF_3N_2O_3S$	$C_8H_8AgF_3N_2O_2$
Formula mass	809.87	365.08	329.03
a [Å]	10.5634(6)	12.982(6)	4.7270(8)
b [Å]	13.6804(9)	11.458(4)	9.898(2)
c [Å]	19.709(1)	7.709(5)	22.111(4)
α [°]			
β [°]		101.40(3)	
γ [°]			
V [Å^3]	2848.3(3)	1124(1)	1034.6(3)
Z	4	4	4
Space group	$P2_12_12_1$	$P2_{1/c}$	$P2_12_12_1$
T [K]	110(2)	110(2)	110(2)
$D_{calcd.}$ [g cm^{-3}]	1.889	2.157	2.112
μ [mm^{-1}]	1.457	2.017	1.978
$2\theta_{max}$ [°]	28.29	28.37	26.45
Reflections measured	33450	39350	13577
Reflections used (R_{int})	7004(0.0291)	2751(0.0310)	2121(0.0626)
Restraints/parameters	0/397	0/154	0/145
R_1 [$I > 2\sigma(I)$]	0.0174	0.0194	0.0200
wR_2 [$I > 2\sigma(I)$]	0.0408	0.0491	0.0443
$R(F_o^2)$ (all data)	0.0194	0.0232	0.0229
$Rw(F_o^2)$ (all data)	0.0412	0.0502	0.0450
GOF on F^2	1.067	1.067	1.067

Table 3. Selected bond lengths [Å], angles [°], and distances for the compounds $(2\text{-amp})_2AgBF_4$ (**1**) and $(2\text{-amp})_2Ag(tfa)$ (**2**).

1			
Ag1–N1	2.262(6)	Ag1–N3	2.319(5)
Ag1–N4	2.336(6)	Ag1–N2	2.371(5)
Ag2–N6	2.293(6)	Ag2–N7	2.310(5)
Ag2–N8	2.322(5)	Ag2–N5	2.368(4)
N1–Ag1–N3	125.6(2)	N1–Ag–1N4	131.9(2)
N3–Ag1–N4	72.5(2)	N1–Ag1–N2	74.61(2)
N3–Ag1–N2	133.9(2)	N4–Ag1–N2	128.3(2)
N6–Ag2–N7	133.4(2)	N6–Ag2–N8	126.5(2)
N7–Ag2–N8	74.4(2)	N6–Ag2–N5	73.3(2)
N7–Ag2–N5	125.9(2)	N8–Ag2–N5	133.3(2)
N2–H···F2[1]	3.123(7)	N6–H···F7[4]	3.146(6)
N2–H···F3[2]	3.068(6)	N6–H···F8[5]	3.031(6)
N4–H···F1[1]	3.049(6)	N8–H···F6[6]	3.070(7)
N4–H···F4[3]	3.101(6)	N8–H···F5[5]	3.090(7)
Symmetry transformations used to generate atoms: #1: $x-1, y, z+1$; #2: $x-1, y, z$; #3: $x, y, z+1$; #4: $x, y, z-1$; #5: $x+1, y, z-1$; #6: $x+1, y, z$.			
2			
Ag1–N2	2.309(3)	Ag1–N4	2.326(3)
Ag1–N3	2.402(3)	Ag1–N1	2.418(3)
Ag2–N–8	2.265(3)	Ag2–N6	2.273(3)
Ag2–N5	2.499(3)	Ag2–N7	2.558(3)
Ag3–N10	2.298(3)	Ag3–N12	2.339(3)
Ag3–N11	2.390(3)	Ag3–N9	2.425(3)
Ag4–N16	2.277(3)	Ag4–N14	2.292(3)
Ag4–N13	2.459(3)	Ag4–N15	2.516(3)
Ag1–Ag2	3.0077(4)	Ag3–Ag4	3.0305(4)
N2–Ag1–N4	146.3(1)	N2–Ag1–N3	119.4(1)
N4–Ag1–N3	71.5(1)	N2–Ag1–N1	72.6(1)
N4–Ag1–N1	113.8(1)	N3–Ag1–N1	151.7(1)
N2–Ag1–Ag2	105.64(8)	N4–Ag1–Ag2	107.98(7)
N3–Ag1–Ag2	76.79(7)	N1–Ag1–Ag2	75.17(7)
N8–Ag2–N6	174.6(1)	N8–Ag2–N5	112.8(1)
N6–Ag2–N5	72.5(1)	N8–Ag2–N7	71.7(1)
N6–Ag2–N7	106.1(1)	N5–Ag2–N7	124.9(1)
N8–Ag2–Ag1	91.69(8)	N6–Ag2–Ag1	84.96(8)
N5–Ag2–Ag1	116.92(7)	N7–Ag2–Ag1	117.73(7)
N10–Ag3–N12	147.3(1)	N10–Ag3–N11	118.9(1)
N12–Ag3–N11	71.2(1)	N10–Ag3–N9	73.5(1)
N12–Ag3–N9	113.5(1)	N11–Ag3–N9	151.3(1)
N10–Ag3–Ag4	108.08(8)	N12–Ag3–Ag4	104.59(7)
N11–Ag3–Ag4	73.78(7)	N9–Ag3–Ag4	77.76(7)
N16–Ag4–N14	176.1(1)	N16–Ag4–N13	110.8(1)
N14–Ag4–N13	72.7(1)	N16–Ag4–N15	72.7(1)
N14–Ag4–N15	107.0(1)	N13–Ag4–N15	124.3(1)
N16–Ag4–Ag3	90.13(8)	N14–Ag4–Ag3	86.76(8)
N13–Ag4–Ag3	113.12(7)	N15–Ag4–Ag3	122.55(7)
N2–H···O8[1]	2.993(4)	N10–H···O1	2.905(4)
N2–H···O5[2]	2.945(4)	N10–H···O3	2.988(4)
N4–H···N7[3]	3.380(4)	N12–H···O6	2.949(4)
N4–H···O2	3.087(4)	N12–H···N13[3]	3.144(4)
N6–H···O4[4]	2.965(4)	N14–H···O6	3.076(4)
N6–H···O2	3.060(4)	N14–H···O7[6]	2.974(4)
N8–H···O8[5]	2.965(4)	N16–H···O1	3.049(4)
N8–H···O5[2]	3.060(4)	N16–H···O3[4]	2.960(4)
Symmetry transformations used to generate atoms: #1: $x, y, z-1$; #2: $x, y+1, z-1$; #3: $x-1, y, z$; #4: $x+1, y, z$; #: 5 $x+1, y, z-1$; #6: $x+1, y-1, z$.			

The crystal structure of complex **2** is shown in Figure 3 and is demonstrative of the strong effects that hydrogen bonding and the exchange of anion can have upon the structural characteristics of these compounds. Stoichiometrically identical to **1**, the use of the strong H-bond-accepting trifluoroacetate results in an unexpected sandwiching of two of the cationic units that are present in **1**. The increased propensity of the trifluoroacetate ion to hydrogen bonds enables it to act as a bridge pulling two amine groups of what would be separate units into close proximity of one another. This bridging activity is seen to occur on both sides of a now dimetallic cluster utilizing all four amine groups. The result is that the metal centers are pulled into such proximity to one another as to form a significant metal–metal interaction at 3.0077(4) Å. Similar distances are

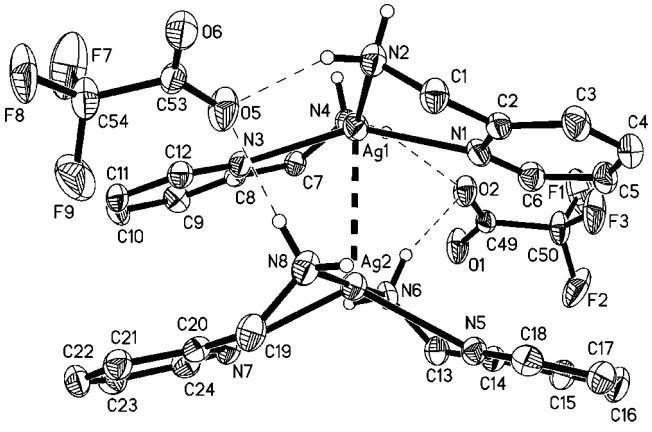

Figure 3. Molecular structure of one of the unique metal dimers of **2** showing how H-bonding to the anions hold the "sandwich" together. Ellipsoids are drawn at the 50% probability level. All hydrogen atoms except for those on the amine nitrogen atoms have been removed for clarity.

 © 2005 Wiley-VCH Verlag GmbH & Co. KGaA, Weinheim

Table 4. Selected bond lengths [Å], angles [°], and distances for the compounds (2-amp)$_3$Ag$_2$(OTf)$_2$ (**3**), (2-amp)$_3$Ag$_2$(BF$_4$)$_2$ (**4**), and 2,2′-bpy$_2$(2-amp)Ag$_2$(BF$_4$)$_2$ (**5**).

3			
Ag1–N3	2.211(1)	Ag1–N2	2.277(1)
Ag1–N1	2.396(1)	Ag1–O1	2.591(1)
Ag2–N4	2.199(1)	Ag2–N6	2.236(1)
Ag2–N5	2.403(1)	Ag1–Ag2	2.9137(3)
N3–Ag1–N2	159.77(4)	N3–Ag1–N1	122.35(4)
N2–Ag1–N1	73.09(4)	N3–Ag1–O1	88.42(4)
N2–Ag1–O1	96.65(4)	N1–Ag1–O1	114.76(4)
N3–Ag1–Ag2	74.26(3)	N2–Ag1–Ag2	85.69(3)
N1–Ag1–Ag2	130.76(3)	O1–Ag1–Ag2	111.41(2)
N4–Ag2–N6	165.33(5)	N4–Ag2–N5	119.63(4)
N6–Ag2–N5	74.73(4)	N4–Ag2–Ag1	80.05(4)
N6–Ag2–Ag1	91.03(3)	N5–Ag2–Ag1	115.98(3)
N2–H···O2^1	3.1438(17)	N4–H···O4	2.9911(17)
N2–H···O6^2	3.1422(17)	N6–H···O2	3.0426(18)
N4–H···O5^2	2.9799(17)	N6–H···O3^1	3.0810(18)

Symmetry transformations used to generate atoms: #1: $-x + 1, -y, -z$; #2: $-x + 1, -y, -z + 1$.

4			
Ag1–N3	2.185(2)	Ag1–N2	2.267(2)
Ag1–N1	2.355(2)	Ag2–N4	2.186(2)
Ag2–N6	2.287(2)	Ag2–N5	2.313(2)
Ag1–Ag2	5.794(2)		
N3–Ag1–N2	154.73(8)	N3–Ag1–N1	130.16(7)
N2–Ag1–N1	74.86(8)	N4–Ag2–N6	146.26(8)
N4–Ag2–N5	135.55(7)	N6–Ag2–N5	74.97(7)
N2–H···F8A^1	3.055(16)	N4–H···F4	3.112(3)
N2–H···F5^1	3.094(3)	N4–H···F1^1	2.982(3)
N2–H···F8^1	3.330(4)	N6–H···F4^2	3.133(3)
N2–H···F7A	2.97(3)	N6–H···F1^2	3.384(3)
N2–H···F7	3.211(5)	N6–H···F2	3.000(3)

Symmetry transformations used to generate atoms: #1: $x + 1, y, z$; #2: $-x + 2, -y, -z + 1$.

5			
Ag1–N1	2.150(2)	Ag1–N3	2.270(1)
Ag1–N4	2.284(2)	Ag2–N2	2.178(2)
Ag2–N6	2.287(2)	Ag2–N5	2.329(2)
Ag1–Ag2	2.8958(3)		
N1–Ag1–N3	136.91(6)	N1–Ag1–N4	148.32(6)
N3–Ag1–N4	73.34(5)	N1–Ag1–Ag2	82.92(4)
N3–Ag1–Ag2	100.56(4)	N4–Ag1–Ag2	81.52(4)
N2–Ag2–N6	142.97(6)	N2–Ag2–N5	145.38(6)
N6–Ag2–N5	71.65(5)	N2–Ag2–Ag1	86.46(4)
N6–Ag2–Ag1	85.99(4)	N5–Ag2–Ag1	99.82(4)
N2–H···F5^1	2.977(2)	N2–H···F2^1	3.1257(19)
N2–H···F3^1	3.099(2)		

Symmetry transformations used to generate atoms: #1: $x, y + 1, z$.

Table 5. Selected bond lengths [Å], angles [°], and distances for the compounds (2-amp)AgOTf (**6**) and (2-amp)Ag(tfa) (**7**).

6			
Ag1–N2^1	2.144(2)	Ag1–N1	2.145(2)
Ag1–O2	2.644(2)	Ag1–Ag1^2	5.977(2)
N2^1–Ag1–N1	171.93(6)		
N2–H···O1^3	2.913(2)	N2–H···O1^5	2.993(3)
N2–H···O3^4	2.967(3)		

Symmetry transformations used to generate atoms: #1: $-x + 2, y + 1/2, -z + 1/2$; #2: $-x + 2, y - 1/2, -z + 1/2$; #3: $-x + 1, y - 1/2, -z + 1/2$; #4: $-x + 1, -y + 1, -z$; #5: $-x + 1, -y + 1, -z + 1$.

7			
Ag1–N2^1	2.186(2)	Ag1–N1	2.188(2)
Ag1–O1	2.498(2)	Ag1–Ag1^2	5.437(1)
N2^1–Ag1–N1	152.96(9)	N2^1–Ag1–O1	94.27(8)
N1–Ag1–O1	110.63(8)		
N2–H···O2	2.922(3)	N2–H···O1^3	2.904(3)

Symmetry transformations used to generate atoms: #1: $-x + 1, y + 1/2, -z + 1/2$; #2: $-x + 1, y - 1/2, -z + 1/2$; #3: $-x + 2, y - 1/2, -z + 1/2$.

normally found only in complexes where the interacting silver ions are being bridged directly by another donor or anion.[27] This is a noteworthy interaction seeing as how the tetrahedral environments of the individual metal centers have to undergo considerable distortions in order to achieve a geometry that allows for the contact to occur. The resulting metal–metal interaction hence seems not only to be lightly supported, but even unfavored. The reasoning behind the fact that the complex does not snap apart to become isostructural with **1** lies in the fact that the silver(I) ion is extremely flexible in its coordination sphere. In order to accommodate the silver–silver interaction the two metal centers must contort into two quite different conformations. The top silver ion adopts a distorted square-based pyramidal arrangement. For this to occur the N–Ag bond lengths are stretched to suit the new setting with the pyridine–silver bonds being stretched more, making it now possible to distinguish between the two types of donors on the basis of bond lengths. Amine–silver lengths range from 2.298(3) to 2.339(3) Å whereas the pyridine–silver lengths are stretched slightly longer to between 2.390(3) and 2.425(3) Å. The bottom silver ion suffers a similar contortion that leaves it in a trigonal-bipyramidal setting with both amine groups occupying the axial positions. Pyridine donors and the metal–metal interaction hold the equatorial spaces. This distinct difference in coordination sites assists in broadening the division between the lengths of the amine– and pyridine–silver separations; the axial amine–silver distances range from 2.265(3) to 2.292(3) Å while the equatorial pyridine–silver distances range from 2.459(3) to 2.558(3) Å. Looking outward from the initial interdimeric H-bonded bridge it is noticed that each oxygen atom of the trifluoroacetate ion is used to hold a separate set of these stacked complexes on top of each other such that the anion acts in an η^2,μ_4-fashion. This effectively constructs a linear chain of dimetallic clusters held together by hydrogen bonds.

The molecular structures of compounds **3** and **4** offer another example of the marked effect that changes in the H-bond-accepting ability of the anion has upon the conformation of the molecule. Ratios of ligand/metal in both complexes are 3:2 such that the structural differences again are being caused solely by the anion. The addition of a more strongly interacting anion has the effect of closing the 3:2 structure onto itself.

In **3**, the ratio of ligand/metal is controlled, or at least limited, by the anion. It is seen that even a fivefold excess of 2-amp does not force a ratio higher than 3:2 in the crystal structure shown in Figure 4. This is accredited to a bifunctional role of the triflate ion in the complex: its first function is to act as a coordinating anion to one of the

 © 2005 Wiley-VCH Verlag GmbH & Co. KGaA, Weinheim

metal ions, and its second is to concomitantly engage in an intramolecular H-bond through a separate oxygen atom. The addition of more than 1 equiv. of 2-amp disrupts the linear coordination environment that the silver ion has when the ligand is present in only 1 equiv. (as in compound **6**). The first 0.5 equiv. of ligand that is added past an initial 1:1 ratio forms a bridge joining two 2-amp-chelated silver(I) units. After this point, a triflate ion that binds to one of the metal centers through a single oxygen atom halts the addition of a full second equivalent of 2-amp ligand to the silver ions. In this orientation the triflate ion is then able to H-bond through a second oxygen atom to the amine protons of the ligand chelating the opposite silver ion. The effect is similar to that seen in compound **2**; H-bonding with the anion holds the silver ion bound only to nitrogen atoms sufficiently close to the anion-bound silver ion to create a strong metal–metal interaction. However, the geometry of the SO_3 portion of the triflate allows it to be involved in both coordination and H-bonding, thus forcing the structural difference with **2**. The bridging 2-amp ligand acts as a hinge as the H-bonded anion squeezes the silver ions to within 2.9137(3) Å of one another. In this structure there is a notable difference in bond lengths between the two types of ligands present. This should be expected as the stress of the five-membered ring is relieved in going from a chelating to a more relaxed bridging six-membered system. The chelated amine–silver distances are 2.277(1) and 2.236(1) Å and the chelated pyridine–silver distances are 2.396(1) and 2.403(1) Å. The same distances measured for the bridging ligand are noticeably shorter at 2.199(1) and 2.211(1) Å, respectively. The coordinating O1 atom has a bond length to Ag1 of 2.590(1) Å. In this structure, as in the last two, intermolecular H-bonding again plays a role in determining the packing of the complex with another 1-D "polymer" being constructed of the dimetallic units held together by H-bonds to the anions. H-bonds to O2 and O3 fashion a sort of dimer, while those to the non-coordinating anions assemble these dimers into a chain.

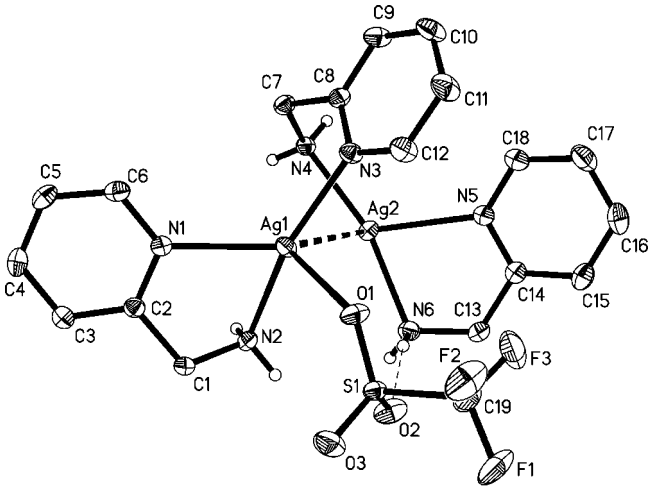

Figure 4. Molecular structure of the monopositive cation in **3**. Ellipsoids are drawn at the 50% probability level. All hydrogen atoms except for those on the amine nitrogen atoms have been removed for clarity.

In the absence of an anion capable of strongly receiving an H-bond the cationic closed structure of compound **3** opens to form the flat 3:2 complex **4**. The structure, as shown in Figure 5, is an intermediate one that bridges the gap between the polymer formed by 2-amp and $AgBF_4$ in the 1:1 ratio and the discrete structure of compound **1** with its 2:1 ratio, making $AgBF_4$ the only silver salt studied with which all three of these ratios were able to be achieved. Without the H-bonding of the anion to hold them together, the metal centers situate themselves widely separated by 5.794(2) Å on opposite sides of the bridging ligand. Each silver ion is then chelated by another 2-amp ligand creating a nearly planar dimetallic complex. Although twists and rotations about the center bridging ligand are likely to be occurring in solution, stacking of the molecules into sheets, as well as π–π interactions help keep them flat in the solid state. The distance between the planes of the aromatic rings averages around 3.2 Å from one layer to the next in the crystal structure. The BF_4^- anions can be seen to fit nicely into holes formed by this stacking of molecules and are held in place by weak H-bonds to the amine nitrogen atoms. The chelating amine–silver distances in **4** are 2.267(2) and 2.287(2) Å and the pyridine–silver distances are 2.313(2) and 2.355(2) Å. The bridging amine–silver and pyridine–silver distances are again seen to be quite shorter at 2.186(2) and 2.185(2) Å. Angles around the silver ions are distorted from the ideal 120° trigonal geometry due to the small bite angle of the chelating 2-amp ligand and have values ranging from 74.97(7) to 154.73(8)°. However, deviations of the silver ions from their respective three-nitrogen planes are small at 0.054(1) Å for Ag1 and 0.170(1) Å for Ag2, showing that they are still very much in a planar environment.

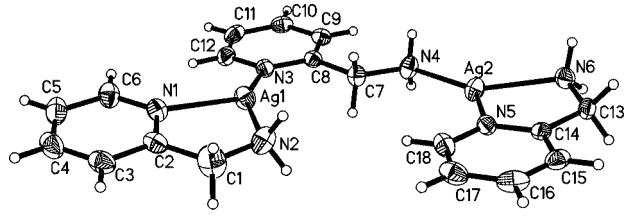

Figure 5. View of the cationic complex of **4**. Ellipsoids are drawn at the 50% probability level.

Compound **5** was prepared in an attempt to mimic the structural characteristics of **4** using 2,2′-bipyridine as the chelating ligand that caps the ends of the dimetallic structure. The addition of 2 equiv. of 2,2′-bipyridine to a solution that is 1:2 in 2-amp/$AgBF_4$ does indeed produce a compound that is stoichiometrically identical to **4** (when the bipyridine is substituted for the chelating 2-amp ligands). However, what resulted was the unexpected hybrid shown in Figure 6 that contains features of both **3** and **4**. The 2-amp ligand acts as expected in the presence of an excess of $AgBF_4$, bridging two separate metal centers. The addition of 2,2′-bipyridine results in two 2,2′-bipyridine-chelated silver ions separated by the bridging 2-amp ligand.

 © 2005 Wiley-VCH Verlag GmbH & Co. KGaA, Weinheim

The connectivity of the structure formed is analogous to that seen in **4**. Otherwise, the similarities between this and **4** are few. Instead of opening up to make a flat structure, the amine-bound silver ion twists back around to form an interaction with the pyridine-bound silver ion. The resulting hairpin structure bears closer resemblance to the triflate salt in **3**. A major difference here is that there are no good H-bond donors on the bipyridine ligands and no strongly H-bond-accepting anion to link the chelating ligands, as in **2** and **3**. This leaves only the weaker π-stacking forces of the two bipyridine ligands to account for the conformation of this compound. The angle of the bipyridine planes from one another is a rather obtuse 28.4° and the ring centers are separated by an average of 4.546 Å. This lends itself to the observation that the argentophilic interaction in these compounds is a highly favored one and the 2-amp ligand bridging two interacting silver ions appears to be only slightly higher in energy than the conformation in which the silver ions are completely separated. There is also fairly prominent intermolecular π-stacking of the bipyridine rings both above and below each molecule with the parallel ring planes averaging only 3.316 Å from one another. The N–Ag distances here are quite short, second only to those seen in the polymer complex **6**. The Ag1–pyridine bond length is 2.150(2) Å and the Ag2–amine distance is 2.178(2) Å. The bipyridine-N–Ag distances are more along the lines of the lengths that have been displayed so far and range from 2.271(1) to 2.330(2) Å.

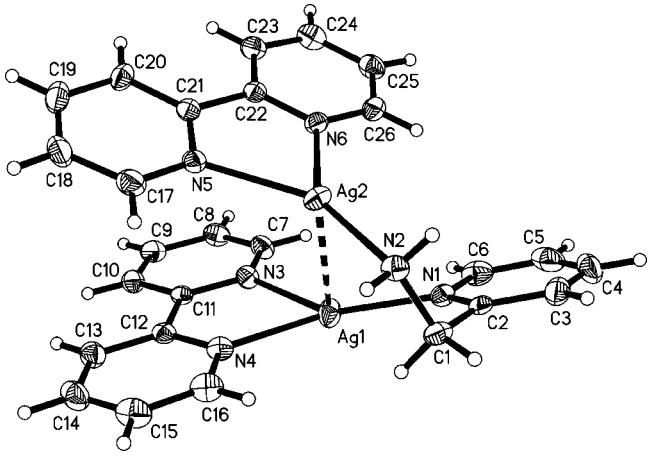

Figure 6. View of the cationic complex of **5**. Ellipsoids are drawn at the 50% probability level.

Compounds **6** and **7** show the result of the addition of the 2-amp ligand to silver triflate and trifluoroacetate salts in a 1:1 ratio. In the absence of a sufficient amount of strong donor sites to construct at least a three-coordinate environment around the metal center (in this case N-donors), each silver ion attempts to adopt its desired linear coordination environment. Since a maximum bite angle of around only 75° is obtainable with the chelating 2-amp ligand, donors from two separate ligands must be used in order to achieve this arrangement. The results are linear zigzag coordination polymers similar to those seen previously with noncoordinating anions.[23] In the case of **6** and **7**, the anions display an increasing coordination ability resulting in varying degrees of perturbation of the metal centers from their ideal linear geometry. They also allow for H-bonding within the polymer and to adjacent polymers, adding to the dimensionality of the structure.

2-(Aminomethyl)pyridine together with 1 equiv. of silver triflate assembles into a zigzagging 1-dimensional coordination polymer containing silver ions with a T-shape geometry, compound **6**. The unique portion of the polymer, shown in Figure 7, contains one silver ion bound in near-linear coordination by an amine nitrogen atom and its symmetry-equivalent pyridine nitrogen atom. The triflate anion is coordinated as well through a stretched bond to O1. When perpetuated, the 2-(aminomethyl)pyridine backbone of the polymer, shown in Figure 8, is seen to be nearly planar both perpendicular to and in the direction of its growth. This is similar to the conformation displayed in compound **4** and is likely the result of a combination of ring stacking and hydrogen bonding. The linear chains are stacked one on top of another with each row slightly offset from the previous as to accommodate the anions protruding into the next layer. The layers are held together throughout the length of the polymers by the interpolymeric hydrogen bonding of each triflate ion to an amine group both above and below the plane in which it is in. The triflate ions are held in the plane of the polymer by intrapolymeric H-bonding to an amine in the next unit. This also likely assists in keeping the planarity of the polymer. The triflate-O–Ag bond is a weak one at 2.644 Å, which is apparent from the only slight bending of the amine–Ag–pyridyl angle of

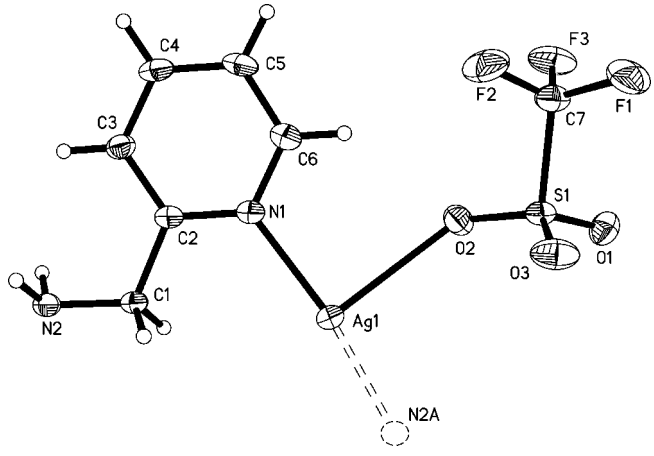

Figure 7. View of the unique portion of the polymer of **6** with the coordination environment about the silver ion shown complete. Ellipsoids are drawn at the 50% probability level.

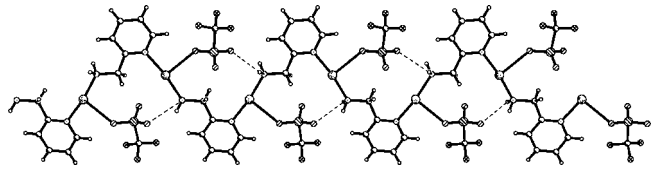

Figure 8. View of the 1-D polymer of **6** showing the intrapolymeric H-bonding.

 © 2005 Wiley-VCH Verlag GmbH & Co. KGaA, Weinheim

171.93(6)°. The N–Ag distances of this polymer are the shortest displayed herein at 2.145(2) Å for the pyridine–Ag length and 2.144(2) Å for the amine–silver distance.

The unique portion of compound **7**, shown in Figure 9, again contains a single silver ion, 2-amp ligand, and anion. It is made apparent here that trifluoroacetate acts as a stronger coordinating anion than triflate when there are insufficient N-donors to saturate the coordination sites of the silver ion. The 1-dimensional coordination polymer backbone of **7** that is seen in Figure 10 is connectively very similar to that of **6**. The more strongly interacting anion, while generally occupying the same spaces in the polymer as those held by triflate in the previous structure, imparts structural features not formerly seen. O1 coordinates strongly to Ag with a bond length of 2.498(2) Å, distorting the pyridine–Ag–amine angle to 152.96(9)°. This distortion causes the amino nitrogen atom to be pushed out of its planar position to give the linear polymer an overall helical appearance seen looking down the length of the polymer. With its remaining oxygen atom, the trifluoroacetate ion extends a bridge both above and, by symmetry equivalence, below the original polymer to link to silver ions of adjacent polymers. This stretched interaction at 2.715(2) Å crosslinks the helical polymers into a pseudo-2-dimensional pleated sheet structure. The intrapolymeric H-bonding here serves to help hold the 1-dimensional polymer into its spiraling conformation. The N–Ag bond lengths are quite short in this polymer as they were in compound **6**, though the presence of the more strongly donating anion causes them to lengthen slightly. The pyridine–Ag distance is 2.188(2) Å and the amine–Ag distance is 2.186(2) Å.

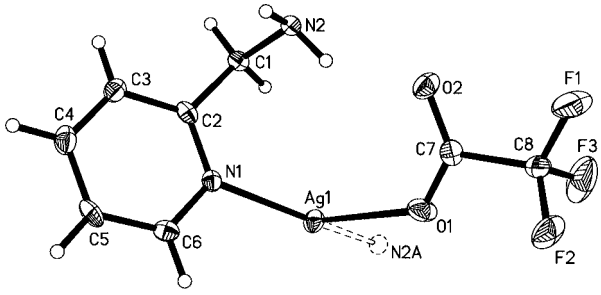

Figure 9. Molecular diagram of the unique portion of **7** with the coordination environment about the silver ion shown complete. Ellipsoids are drawn at the 50% probability level.

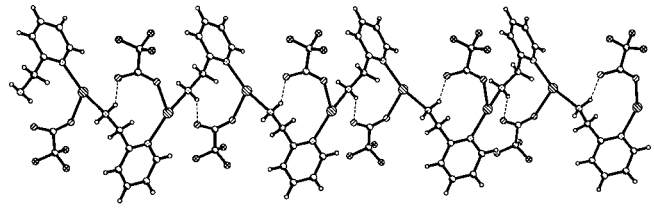

Figure 10. View of the helical 1-D polymer formed by compound **7** showing the intrapolymeric H-bonding.

Luminescence Properties

Interest in hybrid inorganic–organic polymers for application as potential new "organic" light-emitting devices (OLEDs) has been on a steady rise over the past decade. Their versatility comes from the ability to tune their absorption and emission spectra by (typically) facile modifications to the metal environment. Such tuning is not an easy option for the strictly organic LEDs, which often require drastic synthesis and modifications to alter their photoluminescent properties.[42] All excitation and emission spectra were recorded at concentrations of 1×10^{-4} M in acetonitrile glasses at 77 K. The low-temperature solution luminescence was collected to give a general representation of what the solid-state excitation and emission would be, given that in the 77 K glasses there is substantial complex character (polymeric character in the case of compounds **6** and **7**).[18,43,44] Luminescence spectra of representative compounds are displayed in Figure 11. A more complete collection of spectra are available in the supporting information.

Discussion of Luminescence

The resemblance of the excitation spectra of compounds **1**–**7** with that of the free 2-(aminomethyl)pyridine ligand suggests that the luminescent behavior of these complexes is initiated by a ligand-based absorption, which then decays by means of ligand-to-metal charge transfer. Excitation maxima of all compounds are presented in

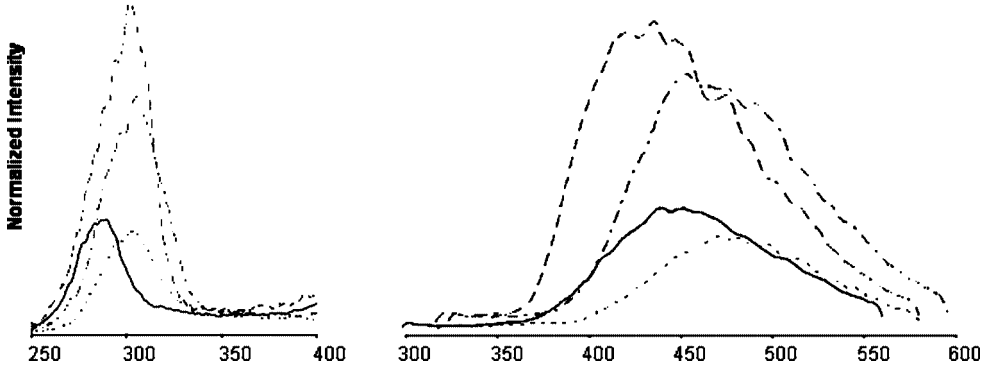

Figure 11. Normalized excitation and emission spectra of compounds **1**, **3**, **6**, and **7** taken in acetonitrile glasses at 1×10^{-4} M concentration at 77 K. —— = (2-amp)AgOTf, – – – = (2-amp)Ag(tfa), ····· = $(2\text{-amp})_2AgBF_4$, –·–·– = $Ag_2(2\text{-amp})_3(OTf)_2$.

 © 2005 Wiley-VCH Verlag GmbH & Co. KGaA, Weinheim

Table 6 along with the local emission maxima. The emission spectra of the various compounds cover a modest range of the spectrum with local maxima spanning approximately 100 nm. The strongest emissions are seen to be produced by the compounds that have the most interacting anions, OTf and tfa, and of these the coordination polymer **7**, likely accredited to the extended networks of electronic interaction, shows a stronger emission. It is seen that the most intense luminescence, that of the 1:1 (2-amp)Ag(tfa) polymer, also occurs at the most energetic wavelengths with three strong transitions at 422, 436, and 448 nm. As a general trend, as the intensity of the luminescence drops off, so does the energy of the transitions. The next most intense emission comes from the 3:2 (2-amp)AgOTf cluster **3** with its strongest maxima at 453 nm, followed by the silver "sandwich" complex **2** at 460 nm. The triflate polymer **6** and the tetrafluoroborate monomers of **1** show similar intensity with maxima at 441 and 473 nm, respectively.

Table 6. Luminescent spectral data for compounds **1**–**7** at 77 K and 1×10^{-4} M in CH_3CN.

Compound	Excitation λ_{max} [nm]	Emission local λ_{min} [nm]
2-amp	318	378
1	303	472, 483, 500, 516
2	303	460, 470, 495
3	307	454, 468, 477, 492
4	300	446, 454, 462, 475
5	369	392, 435
6	290	440, 452, 462
7	302	422, 437, 449, 476

Conclusions

We have demonstrated here that a variety of silver(I) complexes can be formed with the bidentate nitrogen ligand 2-(aminomethyl)pyridine. The complexes, their structures and luminescent characteristics are seen to be highly dependent not only on the hydrogen-bonding and coordinating ability of the anion but also on the ratio of ligand/metal. The simplicity of the 2-amp ligand made it a desirable prospect for this concentration/counterion study that produced molecular structures ranging from simple monomers to folded dimetallic metal–metal interacting species to elaborate multidimensional polymers. This same type of behavior is currently being investigated in the 3- and 4-(aminomethyl)pyridines which have demonstrated great potential for the formation of coordination polymers and macromolecules by removing the ability to chelate that has been so prevalent in the 2-amp structures. Results of these studies will form the basis of further publications.

Experimental Section

General Remarks: All experiments were carried out under argon using a Schlenk line and standard Schlenk techniques. Glassware was dried at 120 °C for several hours prior to use. All reagents except 2,2′-bipyridine, which was stored in a bench top dessicator, were stored in a glovebox with an inert gas. Acetonitrile and diethyl ether were distilled from calcium hydride and sodium/benzophenone ketyl, respectively, immediately before use. 2-(Aminomethyl)-pyridine and 2,2′-bipyridine were purchased from Aldrich and used as received. Silver(I) trifluoroacetate, silver(I) trifluoromethanesulfonate, and silver(I) tetrafluoroborate were purchased from Strem Chemicals Inc. and used as received. ^{1}H NMR spectra were recorded at 300.13 MHz with a Bruker Spectrospin 300 MHz spectrometer. Elemental analyses were performed by Atlantic Microlabs Inc. in Norcross, Georgia. Excitation and emission spectra were recorded with an Instruments S. A. Inc. Fluoromax-2 model spectrometer using band pathways of 5 nm for both excitation and emission and are presented uncorrected.

General Synthesis: General procedures for the synthesis of compounds **1**–**4**, **6**, and **7** involved the addition of an acetonitrile solution (5 mL) of 2-(aminomethyl)pyridine to a stirred solution of the appropriate silver salt in acetonitrile (5 mL). The mixtures were stirred for 10 min then dried in vacuo to leave white to off-white powders. All flasks were shielded from light with aluminum foil to prevent the photodecomposition of the silver compounds. Crystals of compound **2** were grown by slow diffusion of hexanes into a dichloromethane solution at 5 °C. Crystals of compound **5** were grown by slow diffusion of diethyl ether into a dichloromethane solution at 5 °C. Crystals of all other compounds were obtained by slow diffusion of diethyl ether into acetonitrile solutions at 5 °C. The amount of reagents used, yields, and analytical data are presented in the following paragraphs as well as any modifications to the general synthetic procedure. Yields are based on the amount of silver salt used.

Synthesis of $Ag(2\text{-amp})_2BF_4$ (1): This reaction used 2 equiv. of 2-(aminomethyl)pyridine (0.111 g, 1.03 mmol) added to $AgBF_4$ (0.100 g, 0.51 mmol) to leave a white flaky solid in 92% (0.19 g, 0.47 mmol) yield upon solvent evaporation. Colorless block-shaped crystals were formed. ^{1}H NMR (298 K, CD_3CN): δ = 2.93 (br. s, 4 H, NH_2), 4.14 (s, 4 H, CH_2), 7.28 (m, 2 H), 7.739 (td, J_{H-Ho} = 7.5, J_{H-Hm} = 1.5 Hz, 4 H), 8.49 (d, J_{H-Ho} = 6.0 Hz, 2 H) ppm. $AgC_{12}H_{16}N_4BF_4$ (410.95): calcd. C 35.07, H 3.92, N 13.63; found C 35.03, H 3.78, N 13.33.

Synthesis of $Ag(2\text{-amp})_2(tfa)$ (2): This reaction used 2 equiv. of 2-(aminomethyl)pyridine (0.098 g, 0.91 mmol) added to Ag(tfa) (0.100 g, 0.45 mmol) to leave a light-brown fluffy solid in 82% (0.16 g, 0.37 mmol) yield upon evaporation of the solvent. Colorless block-shaped crystals were formed. ^{1}H NMR (298 K, CD_3CN): δ = 3.47 (br. s, 4 H, NH_2), 3.83 (s, 4 H, CH_2), 7.29 (m, 2 H), 7.77 (d, J_{H-Ho} = 6.0 Hz, 4 H), 8.48 (s, 2 H) ppm. $AgC_{14}H_{16}N_4O_2F_3$ (437.17): calcd. C 38.46, H 3.69, N 12.82; found C 38.24, H 3.57, N 12.54.

Synthesis of $Ag_2(2\text{-amp})_3(OTf)_2$ (3): This reaction used 3 equiv. of 2-(aminomethyl)pyridine (0.063 g, 0.58 mmol) added to 2 equiv. of AgOTf (0.100 g, 0.39 mmol). An oily yellow solid was left upon evaporation of the solvent in vacuo. This was then redissolved in a small amount of CH_3CN and precipitated with ether to leave a fluffy white solid in 76% (0.12 g, 0.15 mmol) yield upon drying. Colorless block-shaped crystals were formed. ^{1}H NMR (298 K, CD_3CN): δ = 3.32 (br. s, 6 H, NH_2), 4.11 (s, 6 H, CH_2), 7.28 (m, 3 H), 7.74 (td, J_{H-Ho} = 7.5, J_{H-Hm} = 1.5 Hz, 6 H), 8.49 (d, J_{H-Ho} = 6.0 Hz, 3 H) ppm. $Ag_2C_{20}H_{24}N_6O_6F_6S_2$ (838.31): calcd. C 28.86, H 2.89, N 10.02; found C 29.29, H 2.92, N 10.00.

Synthesis of $Ag_2(2\text{-amp})_3(BF_4)_2$ (4): This reaction used 3 equiv. of 2-(aminomethyl)pyridine (0.150 g, 1.39 mmol) added to 2 equiv. of $AgBF_4$ (0.180 g, 0.92 mmol). A white powder was left in 84% yield (0.278 g, 0.39 mmol) upon evaporation of the solvent in vacuo.

 © 2005 Wiley-VCH Verlag GmbH & Co. KGaA, Weinheim

Colorless block-shaped crystals were formed. ^{1}H NMR (298 K, CD_3CN): δ = 3.12 (br. s, 6 H, NH_2), 4.15 (s, 6 H, CH_2), 7.29 (m, 3 H), 7.75 (td, $J_{H–Ho}$ = 7.4, $J_{H–Hm}$ = 1.5 Hz, 6 H), 8.50 (s, 3 H) ppm.

Synthesis of $Ag_2$2,2′-bpy$_2$(2-amp)$(BF_4)_2$ (5): This reaction used 2-(aminomethyl)pyridine (0.050 g, 0.46 mmol) added to 2 equiv. of $AgBF_4$ (0.180 g, 0.93 mmol). This solution was stirred for 10 min, then 2 equiv. of 2,2′-bipyridine (0.144 g, 0.92 mmol) in 5 mL of CH_3CN was added. This was stirred an additional 5 min, then dried in vacuo to leave an off-white powder in 90% (0.126 g, 0.22 mmol) yield. Colorless block-shaped crystals were formed. ^{1}H NMR (298 K, CD_3CN): δ = 3.19 (br. s, 2 H, NH_2), 4.05 (s, 2 H, CH_2), 7.43 (m, 8 H), 7.89 (m, 9 H), 7.98 (d, $J_{H–Ho}$ = 8.1 Hz, 2 H), 8.36 (d, $J_{H–Ho}$ = 4.8 Hz, 1 H) ppm.

Synthesis of Ag(2-amp)OTf (6): This reaction used 2-(aminomethyl)-pyridine (0.042 g, 0.39 mmol) added to AgOTf (0.100 g, 0.39 mmol) to leave an oily brown solid upon evaporation of the solvent. This solid was then redissolved in a small amount of CH_3CN and precipitated with diethyl ether to leave a brown solid in 85% (0.120 g, 0.33 mmol) yield. Colorless block-shaped crystals were formed. ^{1}H NMR (298 K, CD_3CN): δ = 3.42 (br. s, 2 H, NH_2), 4.16 (s, 2 H, CH_2), 7.25 (m, 1 H), 7.77 (td, $J_{H–Ho}$ = 6.9, $J_{H–Hm}$ = 1.0 Hz, 2 H), 8.52 (d, $J_{H–Ho}$ = 3.6 Hz, 1 H) ppm. $AgC_7H_8N_2O_3SF_3$ (365.08): calcd. C 25.80, H 2.47, N 8.56; found C 26.27, H 2.33, N 8.77.

Synthesis of Ag(2-amp)(tfa) (7): This reaction used 2-(aminomethyl)-pyridine (0.049 g, 0.45 mmol) added to Ag(tfa) (0.100 g, 0.45 mmol) to leave an off-white powder in 75% (0.11 g, 0.34 mmol) yield upon evaporation of the solvent. Colorless plates were formed. ^{1}H NMR (298 K, CD_3CN): δ = 3.68 (s, 2 H, NH_2), 4.11 (s, 2 H, CH_2), 7.28 (m, 1 H); 7.75 (td, $J_{H–Ho}$ = 7.5, $J_{H–Hm}$ = 1.5 Hz, 2 H), 8.53 (d, $J_{H–Ho}$ = 6.0 Hz, 1 H) ppm. $AgC_8H_8N_2O_2F_3$ (329.03): calcd. C 29.20, H 2.45, N 8.51; found C 29.38, H 2.39, N 8.40.

X-ray Crystallographic Study: Crystallographic data were collected on crystals with dimensions 0.181 × 0.150 × 0.100 mm for **1**, 0.210 × 0.150 × 0.090 mm for **2**, 0.279 × 0.216 × 0.202 mm for **3**, 0.310 × 0.270 × 0.250 mm for **4**, 0.245 × 0.231 × 0.199 mm for **5**, 0.167 × 0.143 × 0.094 mm for **6**, and 0.240 × 0.150 × 0.080 mm for **7**. Crystals of all compounds were immobilized on a cryoloop by encasing them in Paratone-N oil then cooling them in a nitrogen cold stream. Data were collected at 110 K with a Bruker X8 Apex. Graphite-monochromated Mo-K_α radiation (λ = 0.71073 Å) was used throughout. All structures were solved by direct methods after processing with SAINT-Plus and correction of the data using SADABS.[45] All of the data were processed with the Bruker AXS SHELXTL software, version 6.10.[43] All non-hydrogen atoms were refined anisotropically and hydrogen atoms were placed in calculated positions except for the amine hydrogen atoms of compound **3**, whose positions were allowed to refine. The crystal structures of compounds **1** and **2** each contain 2 unique monomers of their respective compounds. The structure of compound **4** contains a BF_4^- anion disordered over 2 positions. The anisotropic displacement parameters for the two orientations of the disorder are constrained to be equal and the site occupancies were refined as 0.825(3)/0.173(3) [for B(1/1a), F(1/1a), F(2/2a), F(3/3a), F(4/4a)]. CCDC-260748 (**1**), -260750 (**2**), -260753 (**3**), -262119 (**4**), -260752 (**5**), -260751 (**6**), and -260749 (**7**) contain the supplementary crystallographic data for this paper. These data can be obtained free of charge from The Cambridge Crystallographic Data Centre via www.ccdc.cam.ac.uk/data_request/cif.

Supporting Information (see footnote on the first page of this article): Additional figures showing extended H-bonding networks, stacking, and 3-D growth of compounds **2**, **6**, and **7** are available as well as full excitation and emission spectra for all compounds reported.

Acknowledgments

This research was supported by funds provided by grant from the Robert A. Welch Foundation (AA-1508). The Bruker X8 APEX diffractometer was purchased with funds received from the National Science Foundation Major Research Instrumentation Program Grant CHE-0321214.

[1] J. Y. Lu, *Coord. Chem. Rev.* **2003**, *246*, 327–347.
[2] C. Janiak, *J. Chem. Soc., Dalton Trans.* **2003**, 2781–2804.
[3] Y.-B. Xie, J.-R. Li, X.-H. Bu, *Polyhedron* **2005**, *24*, 413–418.
[4] J. T. Sampanthar, J. J. Vittal, *Cryst. Eng.* **2000**, *3*, 117–133.
[5] Z.-L. You, H.-L. Zhu, W.-S. Liu, *Acta Crystallogr., Sect. C* **2004**, *60*, m620–m622.
[6] R. P. Feazell, C. E. Carson, K. K. Klausmeyer, *Acta Crystallogr., Sect. C* **2004**, *60*, m598–m600.
[7] M. A. S. Goher, A. K. Hafez, M. A. M. Abu-Youssef, A. M. A. Badr, C. Gspan, F. A. Mautner, *Polyhedron* **2004**, *23*, 2349–2356.
[8] Y.-B. Dong, X. Zhao, R.-Q. Huang, M. D. Smith, H.-C. z. Loye, *Inorg. Chem.* **2004**, *43*, 5603–5612.
[9] D. J. Eisler, R. J. Puddephatt, *Cryst. Growth Des.* **2005**, *5*, 57–59.
[10] A. L. Pickering, D.-L. Long, L. Cronin, *Inorg. Chem.* **2004**, *43*, 4953–4961.
[11] M. Vetrichelvan, Y.-H. Lai, K. F. Mok, *Eur. J. Inorg. Chem.* **2004**, 2086–2095.
[12] A. N. Khlobystov, A. J. Blake, N. R. Champness, D. A. Lemenovskii, A. G. Majouga, N. V. Zyk, M. Schröder, *Coord. Chem. Rev.* **2001**, *222*, 155–192.
[13] S.-L. Zheng, M.-L. Tong, X.-M. Chen, *Coord. Chem. Rev.* **2003**, *246*, 185–202.
[14] S. Sailaja, M. V. Rajasekharan, *Inorg. Chem.* **2000**, *39*, 4586–4590.
[15] Y. J. K. Ok-Sang Jung, Y.-A. Lee, H. K. Chae, H. G. Jang, J. Hong, *Inorg. Chem.* **2001**, *40*, 2105–2110.
[16] M. Hong, W. Su, R. Cao, M. Fujita, J. Lu, *Chem. Eur. J.* **2000**, *6*, 427–431.
[17] S.-L. Zheng, M.-L. Tong, R.-W. Fu, X.-M. Chen, S.-W. Ng, *Inorg. Chem.* **2001**, *40*, 3562–3569.
[18] R. P. Feazell, C. E. Carson, K. K. Klausmeyer, *Inorg. Chem.* **2005**, *44*, 996–1005.
[19] K. K. Klausmeyer, R. P. Feazell, J. H. Reibenspies, *Inorg. Chem.* **2004**, *43*, 1130–1136.
[20] C. Seward, J. Chan, D. Song, S. Wang, *Inorg. Chem.* **2003**, *42*, 1112–1120.
[21] Y. Kang, S. S. Lee, K.-M. Park, S. H. Lee, S. O. Kang, J. Ko, *Inorg. Chem.* **2001**, *40*, 7027–7031.
[22] D. L. Reger, R. F. Semeniuc, M. D. Smith, *Inorg. Chem.* **2001**, *40*, 6545–6546.
[23] S. Sailaja, M. V. Rajasekharan, *Inorg. Chem.* **2003**, *42*, 5675–5684.
[24] P. L. Caradoc-Davies, L. R. Hanton, W. Henderson, *J. Chem. Soc., Dalton Trans.* **2001**, 2749–2755.
[25] V. J. Catalano, S. J. Horner, *Inorg. Chem.* **2003**, *42*, 8430–8438.
[26] R. J. Puddephatt, *Coord. Chem. Rev.* **2001**, *216–217*, 313–332.
[27] P. Pyykkö, *Chem. Rev.* **1997**, *97*, 597–636.
[28] A. Codina, E. J. Fernández, P. G. Jones, A. Laguna, J. M. López-de-Luzuriaga, M. Monge, M. E. Olmos, J. Pérez, M. A. Rodríguez, *J. Am. Chem. Soc.* **2002**, *124*, 6781–6786.

 © 2005 Wiley-VCH Verlag GmbH & Co. KGaA, Weinheim

[29] E. J. Fernández, J. M. López-de-Luzuriaga, M. Monge, M. E. Olmos, J. Pérez, A. Laguna, A. A. Mohamed, J. John, P. Fackler, *J. Am. Chem. Soc.* **2003**, *125*, 2022–2023.
[30] R. E. Bachman, M. S. Fioritto, S. K. Fetics, T. M. Cocker, *J. Am. Chem. Soc.* **2001**, *123*, 5376–5377.
[31] D. E. Harwell, M. D. M. B. Knobler, F. A. L. Anet, M. F. Hawthorne, *J. Am. Chem. Soc.* **1996**, *118*, 2679–2685.
[32] V. J. Catalano, M. A. Malwitz, *Inorg. Chem.* **2003**, *42*, 5483–5485.
[33] A. A. Mohamed, L. M. Pérez, J. John, P. Fackler, *Inorg. Chim. Acta* **2005**, *358*, 1657–1662.
[34] C.-M. Che, M.-C. Tse, M. C. W. Chan, K.-K. Cheung, D. L. Phillips, K.-H. Leung, *J. Am. Chem. Soc.* **2000**, *122*, 2464–2468.
[35] Q.-M. Wang, T. C. W. Mak, *J. Am. Chem. Soc.* **2001**, *123*, 7594–7600.
[36] M. A. Omary, T. R. Webb, Z. Assefa, G. E. Shankle, H. H. Patterson, *Inorg. Chem.* **1998**, *37*, 1380–1386.
[37] H. Abbas, A. L. Pickering, D.-L. Long, P. Kögerler, L. Cronin, *Chem. Eur. J.* **2005**, *11*, 1071–1078.
[38] P. Pyykko, N. Runeberg, F. Mendizabal, *Chem. Eur. J.* **1997**, *3*, 1451–1457.
[39] P. Pyykko, N. Runeberg, F. Mendizabal, *Chem. Eur. J.* **1997**, *3*, 1458–1465.
[40] H. L. Hermann, G. Boche, P. Schwerdtfeger, *Chem. Eur. J.* **2001**, *7*, 5333–5342.
[41] E. J. Fernández, J. M. López-de-Luzuriaga, M. Monge, M. A. Rodríguez, M. Olga Crespo, C. Gimeno, A. Laguna, P. G. Jones, *Inorg. Chem.* **1998**, *37*, 6002–6006.
[42] A. Bacher, C. H. Erdelen, W. Paulus, H. Ringsdorf, H.-W. Schmidt, P. Schuhmacher, *Macromolecules* **1999**, *32*, 4551–4557.
[43] J. A. Jiménez, R. M. Claramunt, O. Mó, M. Yáñez, F. Wehrmann, G. Buntkowsky, H.-H. Limbach, R. Goddard, J. Elguero, *Phys. Chem. Chem. Phys.* **1999**, *1*, 5113–5120.
[44] Y. Ba, D. Chagolla, *J. Phys. Chem. B* **2002**, *106*, 5250–5257.
[45] G. M. Sheldrick, *SADABS*, University of Göttingen, Göttingen, Germany, **1997**.

Received: March 11, 2005
Published Online: July 6, 2005

 © 2005 Wiley-VCH Verlag GmbH & Co. KGaA, Weinheim

Synthesis and Crystal Structure of a Cocrystalline Compound of a Rare Earth Metalloporphyrin with Fullerene $\{[TPPYb(\mu\text{-}OH)_2Yb(THF)TPP]\cdot C_{60}\}_n$

Jie Zhang,*[a] Ruifang Cai,[a] Minqing Chen,[b] Linhong Weng,[a] and Xigeng Zhou*[a]

Keywords: Metalloporphyrin / Fullerenes / Cocrystal / Ytterbium

The reaction of $YbI_2(THF)_2$ with $TPPLi_2$ (TPP = 5,10,15,20-tetraphenylporphyrin) in THF, and then with 0.5 equiv. of C_{60}, which was solvated in toluene beforehand, gave the title compound $\{[TPPYb(\mu\text{-}OH)_2Yb(THF)TPP]\cdot C_{60}\}_n$, which is the first example of a rare earth metallofullerene cocrystal compound. X-ray structural analyses indicate that this compound displays a complicated supramolecular structure, which contains some unique noncovalent interactionsbetween C_{60} and the rare earth metalloporphyrin units.

(© Wiley-VCH Verlag GmbH & Co. KGaA, 69451 Weinheim, Germany, 2005)

Introduction

The fullerene (C_{60}) molecule has attracted much current attention due to its chemical properties, and uniform, spherical, and nanoscale physical structure, and its potential application in optical and electronic materials, superconductors, and sensors.[1] The organometallic chemistry of fullerene is becoming a flourishing subdiscipline of fullerene research.[2,3] However, research efforts are primarily focused on organotransition metal fullerene complexes in which the fullerene essentially behaves as a weak electron-deficient alkene ligand.[4] In the field of lanthanofullerene chemistry, only the chemistry of endohedral complexes with encapsulated metal atoms, $Ln@C_{2n}$ has been investigated.[5] These species are prepared by the arc vaporization of a mixture of graphite and lanthanoid oxide or carbide under helium.[6] Owing to the high electron-deficient character of lanthanide metal centers, the synthesis of exohedral lanthanide fullerene complexes poses a fundamental problem. The chemistry of exohedral lanthanide fullerene complexes has remained relatively unexplored.[2,7]

On the other hand, the weak noncovalent interactions of curved/flat or curved/curved molecular surfaces have recently attracted much attention in supramolecular chemistry and crystal engineering.[8] The curved π surface of C_{60} shows a tendency to interact with other molecules, making it an interesting candidate for engineering supramolecular arrays. It has been confirmed that the ball-shaped C_{60} molecule can cocrystallize with planar molecules such as porphyrins or metalloporphyrins through the interaction of the curved π surface of the fullerene with the planar π surface of the porphyrin, without the need to match convex surfaces with concave surfaces.[8] Many molecular complexes of fullerenes with transition metalloporphyrins have been obtained and structurally characterized.[9–11] However, no examples of cocrystals consisting of rare earth metalloporphyrins with fullerenes have been reported. In this contribution, we report the synthesis and structural characterization of a novel rare earth metalloporphyrin compound cocrystallized with C_{60} molecules, $\{[TPPYb(\mu\text{-}OH)_2Yb(THF)TPP]\cdot C_{60}\}_n$ (**1**). The X-ray structural analysis of **1** provides some insight into the supramolecular assembly between the fullerenes and metalloporphyrins, which incorporates some unique supramolecular interactions.

Results and Discussion

Bochkarev et al. synthesized the first fulleride complexes of low valence lanthanocene derivatives and confirmed the valence flexibility of Ln^{II} ions in these charge-transfer compounds by temperature-dependent ESR spectroscopy.[7] When considering the noncovalent interactions between the porphyrin rings and the fullerene molecules, we anticipate that strong interactions will be observed between the low valence ytterbium porphyrins and the C_{60} molecules. However, the reaction of $TPPYb^{II}$ with C_{60} leads only to an oxidation product. The reactions of $TPPLi_2$ with $YbI_2(THF)_2$ in THF, and the subsequent reaction with 0.5 equiv. of C_{60} which was solvated in toluene beforehand gave the ytterbium(III) porphyrinate complex cocrystallized with fullerene (**1**) [Equation (1)]. The oxidation of the Yb^{II} units may be caused by trace amounts of oxygen gas and moisture in the inert atmosphere, as similarly observed for another rare earth metalloporphyrin.[12] To obtain a crystal of complex **1** suitable for X-ray diffraction analysis, the selection of an appropriate solvent may be important. Owing to

[a] Department of Chemistry, Fudan University, Shanghai 200433, People's Republic of China
Fax: +86-21-6564-1740
E-mail: zhangjie@fudan.edu.cn
[b] Centre for Analyses and Measurement, Fudan University, Shanghai 200433, People's Republic of China

 DOI: 10.1002/ejic.200500229

C_{60} being almost insoluble in THF, and the ytterbium complex of tetraphenylporphyrin being hardly soluble in toluene, we chose for our experiments a solvent mixture of THF and toluene (THF/toluene, 11:1.5). In fact, the final product **1** is also poorly soluble in THF and toluene. It should be noted that we could not obtain the analogous Samarofullerene compound under the same conditions.

$$H_2TPP \xrightarrow[2)\ YbI_2(THF)_2\ \ 3)\ C_{60}/\ toluene]{1)\ nBuLi} \underset{\mathbf{1}}{[TPPYb(OH)_2Yb(THF)TPP]\cdot C_{60}}$$

TPP = 5,10,15,20-tetraphenylporphyrin

(1)

Unambiguous structure determination of complex **1** was completed by X-ray crystallographic analysis of a single crystal, which had been obtained by the slow diffusion of *n*-hexane into the THF and toluene solution of **1**. The molecular structure of **1** is shown in Figure 1. Selected bond lengths and short contact distances are given in Table 1 and Table 2, respectively. The asymmetric unit of **1** consists of one C_{60} molecule and one dinuclear ytterbium porphyrinate, in which the two ytterbium atoms are connected by two hydroxy-bridges. Compound **1** crystallizes in such a way that two dinuclear ytterboporphyrin units surround each fullerene. Within this unit the fullerene is positioned asymmetrically between the two [TPPYb(μ-OH)$_2$Yb(THF)-TPP] units. X-ray single crystal structure analysis reveals that supramolecular interactions between the curved/flat molecule interfaces exist. The most obvious noncovalent interaction is found between the planes of porphyrin rings and the curved surface of the fullerenes. The C_{60} molecule is centered over the porphyrins giving two different short contact modes. In the first mode, one porphyrin plane interacts with the 5:6 ring-junction C–C bonds of C_{60}, and in the other mode, the porphyrin plane interacts with the 5:6 and 6:6 ring-junction C–C bonds of another C_{60} molecule, as shown in Figure 2. This is significantly different form the results observed for most porphyrins or metalloporphyrins, which prefer to interact with the electron-rich 6:6 ring junction.[9,10] The mechanism of interaction of porphyrin with the 6:6 or 5:6 ring junctions of fullerene is unclear.[9g,10a] The N···C(C_{60}) distances in **1** are in the range of 3.08–3.09 Å and lie at the lower end of the range of van der Waals contacts, and well below the "standard" contact distance (3.2–3.3 Å), and are similar to the corresponding distances in metal-free porphyrin fullerene complexes.[13] However, these distances are significantly longer than the corresponding distances in transition metalloporphyrin fullerene cocrystals.[9–11] This may be attributed to the electron-deficient character of rare earth metal ions, and the electron-acceptor nature of fullerene, resulting in weaker interactions between the metalated porphyrin units and the fullerenes.

Table 1. Selected bond lengths [Å] for the ytterbium porphyrin unit in **1**.

Yb(1)–O(1)	2.1819(9)	Yb(2)–O(1)	2.2451(9)
Yb(1)–O(2)	2.1893(9)	Yb(2)–O(2)	2.2497(9)
Yb(1)–N(8)	2.2935(10)	Yb(2)–N(2)	2.3313(10)
Yb(1)–N(7)	2.3090(9)	Yb(2)–N(1)	2.3449(9)
Yb(1)–N(5)	2.3166(9)	Yb(2)–N(4)	2.3515(10)
Yb(1)–N(6)	2.3323(11)	Yb(2)–N(3)	2.3567(12)
Yb(1)–Yb(2)	3.6237(2)	Yb(2)–O(3)	2.3821(10)

Table 2. Selected short contact distances [Å] in **1**.

N(8)···C(128)^{1}	3.0861	C(86)···C(132)$^{1\#}$	3.3524
C(54)···C(149)^{1}	3.3941	H(91A)···C(123)^{2}	2.8569
C(55)···C(149)^{1}	3.3875	Yb(1)···C(128)^{1}	4.0835
C(58)···C(127)^{1}	3.3390	Yb(1)···C(129)^{1}	3.8940
N(1)···C(113)$^{2\#}$	3.0920	Yb(2)$^{2\#}$···C(112)	4.0517
N(3)···C(112)$^{2\#}$	3.0881	Yb(2)$^{2\#}$···C(113)	3.9158
C(6)···C(154)$^{2\#}$	3.3733		

Symmetry transformations used to generate equivalent atoms: 1: *x*, *y*, *z*; 1#: –*x*, –*y*, –*z*; 2: 1/2 – *x*, 1/2 + *y*,1/2 – *z*; 2#: 1/2 + *x*, 1/2 – *y*, 1/2 + *z*.

As shown in Figure 3, the THF molecules may play a unique role in the crystal structure of **1**. This contrasts with other fullerene cocrystals of metalloporphyrins and metal-free porphyrins, in which the solvent molecules only exist in the crystal lattice.[9–11] Only one THF molecule in **1** is

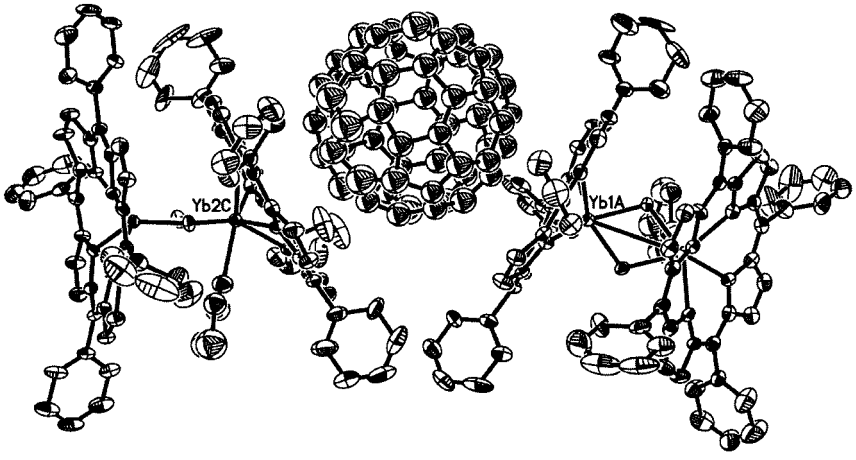

Figure 1. ORTEP diagram of the [TPPYb(μ-OH)$_2$Yb(THF)TPP]·C_{60} unit with the thermal ellipsoids drawn at the 30% probability level. Hydrogen atoms have been omitted for clarity.

 © 2005 Wiley-VCH Verlag GmbH & Co. KGaA, Weinheim

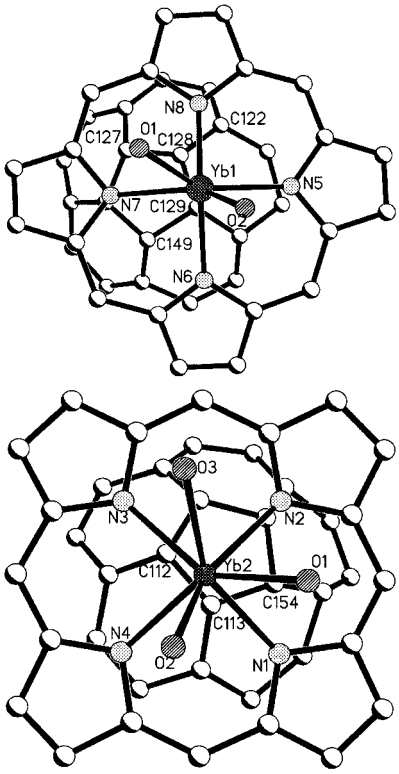

Figure 2. Orientation of C_{60} with respect to the ytterboporphyrin plane, as seen in **1**.

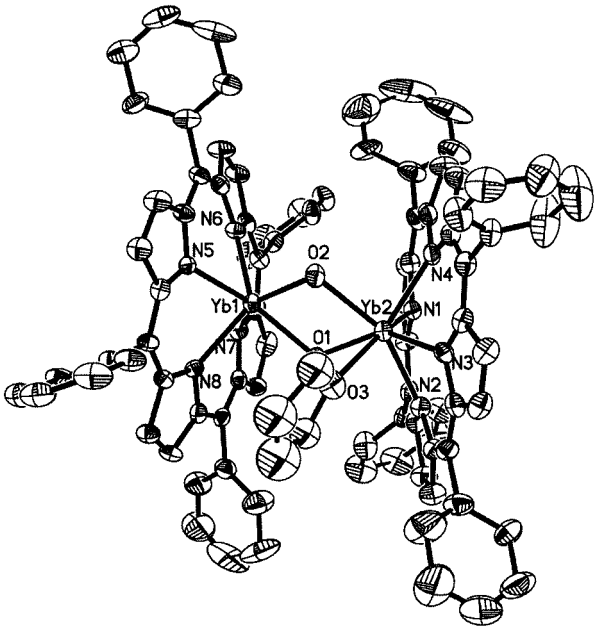

Figure 3. ORTEP diagram of the [TPPYb(μ-OH)$_2$Yb(THF)TPP] unit in **1** with the thermal ellipsoids drawn at the 30% probability level. Hydrogen atoms have been omitted for clarity.

coordinated to one Yb^{3+} ion, and this results in different coordination environments around the metal centers, in that one Yb^{3+} ion is seven-coordinate, while the other Yb^{3+} ion is six-coordinate. This causes the two porphyrin rings in the dinuclear ytterbium porphyrin units to lie unparallel, the dihedral angle between them is 31.91(1)°. This angle is comparable to the corresponding values found in the unique example of [{Yb^{III}(TTP)}$_2$(μ-OH)(μ-$OCH_2CH_2OCH_3$)] where the dihedral angle between the two porphyrin ring planes is 30.5°.[12] The difference in the metal coordination environments also means that the average distance of Yb(1) to the nitrogen atoms of one porphyrin ring [3.313(1) Å] is significantly shorter than the average distance of Yb(2) to the nitrogen atoms of another porphyrin ring [3.346(1) Å]. Also, the Yb(1)–O(1) and Yb(1)–O(2) distances [2.1819(9) Å, 2.1893(9) Å] are significantly shorter than the Yb(2)–O(1) and Yb(2)–O(2) distances [2.2451(9) Å, 2.2497(9) Å]. It should be noted that dinuclear rare earth metalloporphyrin complexes containing such an unsymmetrical coordination mode are rarely reported,[12] and the unparallel arrangement of the porphyrin planes in the metalloporphyrin units may cause the differences in the short contacts between the two porphyrin rings and the C_{60} molecule.

In **1**, the fullerene is too far from the ytterbium atoms for any covalent bond to form between them. The ytterbium atoms are displaced significantly out of the N4 planes of the porphyrins, in the direction opposite to that of the porphyrin-fullerene contacts, and as a result of this there is no possibility of a direct exohedral interaction forming between the ytterbium atoms and the fullerene molecules. This is significantly different from the results observed for the late transition metalloporphyrin fullerene cocrystals, in which strong noncovalent interactions exists between the metal centers and the fullerene molecules because of the electron-rich characters of these metal ions.[9,10] Interestingly, the fullerene is positioned so that the closest contact with the ytterbium atom involves 5:6 ring junctions, and it is significantly shorter than the van der Waals radii of the atoms involved. This may be attributed to the strong covalent interactions of the ytterbium atoms with the porphyrin rings through the hydroxyl bridges.

Within the cocrystal structures of metalloporphyrin with fullerene, there are two kinds of noncovalent interactions in the supramolecular assembly: one is the interaction of the planes of the porphyrin rings with the curved surfaces of the fullerenes, and the other is the porphyrin/porphyrin face-to-face contacts, which pair the porphyrin units. In the aryl-substituted metalloporphyrin fullerene cocrystalline complexes, the porphyrin/porphyrin contact is very weak due to the repulsive interactions of the terminal aryl substituents. Usually, in aryl-substituted porphyrin complexes only one metalloporphyrin unit interacts with two C_{60} molecules.[10c] In complex **1**, in addition to the fullerene/porphyrin interactions, there are covalent interactions between the Yb^{3+} ions and the two hydroxyl bridges between the two tetraphenyl-metalloporphyrins. This combination of covalent and noncovalent interactions produces helical ribbons that wind their way through the crystal (Figure 4).

Another feature of the structure of complex **1** is that there is a noncovalent interaction between the phenyl substituents of the porphyrin rings and the fullerene molecules. Although plenty of cocrystal complexes of fullerenes with

 © 2005 Wiley-VCH Verlag GmbH & Co. KGaA, Weinheim

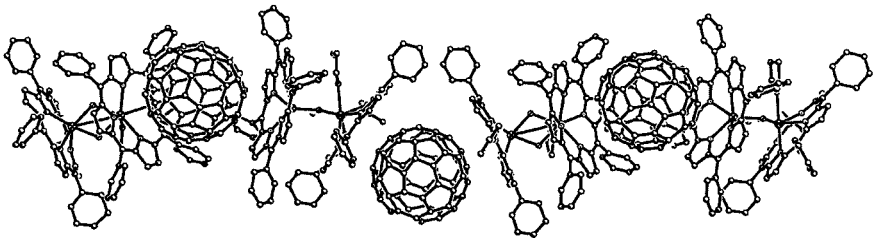

Figure 4. View of the helical chain in **1**.

transition metalloporphyrins have been obtained and structurally characterized, aryl-substituted metalloporphyrin fullerene cocrystalline complexes are very rare. Some researchers regard the modification of the structure of the terminal phenyl groups as very important in order to make the curved C_{60} surface match the planar surface of the porphyrin to enable cocrystal growth.[10b] In complex **1**, one of the phenyl substituents of the dinuclear ytterboporphyrin units forms a contact with a third C_{60} molecule, with the shortest C···C distance of 3.35 Å. To the best our knowledge, only one example of the phenyl substituents participating in noncovalent interactions has been reported, this previous example was of a metal-free porphyrin cocrystallized with C_{60} molecules.[10c] In **1**, this interaction may be attributed to the unparallel arrangement of the porphyrin plane which allows the phenyl substituent to move closer to the C_{60} molecules.

Conclusions

In summary, in this paper we have reported the successful synthesis of the first crystallographically confirmed cocrystalline compound of a rare earth metalloporphyrin with fullerene. This compound displays a complicated supramolecular structure containing unique noncovalent interactions between the fullerene molecules and the dinuclear rare earth metalloporphyrin units.

Experimental Section

General Procedure: All operations involving air- and moisture-sensitive compounds were carried out under purified argon or nitrogen using standard Schlenk techniques. The solvents THF, toluene, and *n*-hexane were refluxed and distilled over sodium benzophenone ketyl under nitrogen immediately prior to use. Tetraphenylporphyrin and *n*BuLi (2.0 M in cylcohexane) were purchased from Aldrich, and were used without further purification. Infrared spectra were obtained with a NICOLET FT-IR 360 spectrometer, with samples prepared as KBr pellets.

Synthesis of 1: *n*-Butyllithium (1.96 M, 120 μL in cyclohexane) was added dropwise to a solution of H_2TPP (76 mg, 0.118 mmol) in THF (20 mL) at ambient temperature. After stirring for 12 h a THF solution of $YbI_2(THF)_2$ (68 mg, 0.118 mmol, 15 mL) was slowly added to the reaction mixture, which was then stirred for a further 12 h. Then a toluene solution of C_{60} (42.6 mg, 0.59 mmol, 30 mL) was injected into the reaction solution. Towards the end of addition, brown solid precipitated from the dark purple solution. The reaction solution was stirred for 24 h at ambient temperature, and the precipitate was then filtered off. Crystallization by the slow diffusion of *n*-hexane into the pellucid dark purple solution yielded dark purple crystals of **1** after several months. IR (KBr): $\tilde{\nu}$ = 3436 (m), 1596 (m), 1477 (m), 1439 (s), 1330 (m), 1220 (m), 1182 (m), 1069 (s), 1006 (s), 990 (s), 798 (s), 751 (m), 722 (m), 700 (s), 656 (m), 632 (w), 577 (m), 527 (s) cm^{-1}.

Crystallographic Data for 1: Suitable single crystals of complex **1** for X-ray structural analysis were sealed under argon in Lindemann glass capillaries. Diffraction data were collected on a Bruker SMART Apex CCD diffractometer using graphite-monochromated Mo-K_α (λ = 0.71073 Å) radiation. During the collection of the intensity data, no significant decay was observed. Frames were integrated to the maximum 2θ angle of 50.02° with the Siemens SAINT program to yield a total 44738 reflections, of which 18883 were independent (R_{int} = 0.0795). The Laue symmetry indicated a monoclinic crystal system, and the final unit cell parameters were determined from the full-matrix least-squares refinement on F^2 employing the 18883 unique reflections. The intensities were corrected

Table 3. Crystal and data collection parameters for **1**.

	1
Formula	$C_{152}H_{66}N_8O_3Yb_2$
Molecular weight	2398.21
Crystal color	purple
Crystal dimensions [mm]	0.20×0.15×0.10
Crystal system	monoclinic
Space group	*P*21/*n*
a [Å]	17.0274(14)
b [Å]	29.097(2)
c [Å]	22.6793(18)
β [°]	107.150(1)
V [Å^3]	10736.6(15)
Z	4
$D_{calcd.}$ [g cm^{-3}]	1.484
μ [mm^{-1}]	1.797
F (000)	4792
Radiation (λ = 0.710730 Å)	Mo-K_α
Temperature [K]	298(2)
Scan type	$\omega - 2\theta$
θ range [°]	1.17 to 25.01
h,*k*,*l* range	$-15 \le h \le 20$, $-34 \le k \le 29$, $-26 \le l \le 26$
No. of reflections measured	44738
No. of unique reflections	18883 (R_{int} = 0.0795)
Completeness to θ	99.8% (θ = 25.01)
Max. and min. transmission	0.8407 and 0.7151
Refinement method	Full-matrix least-squares on F^2
Data/restraints/parameters	18883/148/1166
Goodness-of-fit on F^2	0.942
Final *R* indices [$I > 2\sigma(I)$]	R_1 = 0.0732, wR_2 = 0.1900
R indices (all data)	R_1 = 0.1454, wR_2 = 0.2173
Largest diff. peak and hole [e Å^{-3}]	1.831 and –0.989

 © 2005 Wiley-VCH Verlag GmbH & Co. KGaA, Weinheim

for Lorentz-polarization effects and empirical absorption with the SADABS program.[14] The structure was solved by direct methods using the SHELXL-97 program.[15] All non-hydrogen atoms were found from the difference Fourier syntheses. The H atoms were included at calculated positions, with their isotropic thermal parameters related to those of the supporting carbon atoms, and were not included in the refinement. Further refinement led to the final R indices [$I > 2\sigma(I)$] $R_1 = 0.0732$. All calculations were performed using the SHELXL-97 program. A summary of the crystallographic data is given in Table 3. CCDC-250532 (**1**) contains the supplementary crystallographic data for this paper. These data can be obtained free of charge from The Cambridge Crystallographic Data Centre via www.ccdc.cam.ac.uk/data_request/cif.

Acknowledgments

We thank the National Natural Science Foundation of China (No. G20271013) and Fudan University Young Teacher Science Foundation for financial support.

[1] a) J. L. Segura, N. Martín, D. M. Guldi, *Chem. Soc. Rev.* **2005**, *34*, 31–47; b) M. Bendikov, F. Wudl, D. F. Perepichka, *Chem. Rev.* **2004**, *104*, 4891–4945; c) J. F. Nierengarten, *New J. Chem.* **2004**, *28*, 1177–1191.

[2] A. L. Balch, M. M. Olmstead, *Chem. Rev.* **1998**, *98*, 2123–2166.

[3] a) M. Toganoh, Y. Matsuo, E. Nakamura, *Angew. Chem. Int. Ed.* **2003**, *42*, 3530–3532; b) M. Toganoh, Y. Matsuo, E. Nakamura, *J. Am. Chem. Soc.* **2003**, *125*, 13974–13975; c) H. Song, C. H. Lee, K. Lee, J. T. Park, *Organometallics* **2002**, *21*, 2514–2520.

[4] a) G. Lee, Y. J. Cho, B. K. Park, K. Lee, J. T. Park, *J. Am. Chem. Soc.* **2003**, *125*, 13920–13921; b) D. M. Thompson, M. Bengough, M. C. Baird, *Organometallics* **2002**, *21*, 4762–4770.

[5] a) M. M. Olmstead, A. de Bettencourt-Dias, J. C. Dauchamp, S. Stevenson, D. Marciu, H. C. Dorn, A. L. Balch, *Angew. Chem. Int. Ed.* **2001**, *40*, 1223–1225; b) C. R. Wang, T. Kai, T. Tomiyama, T. Yoshida, Y. Kobayshi, E. Nishibori, M. Takata, M. Sakata, H. Shinohara, *Angew. Chem. Int. Ed.* **2001**, *40*, 397–399; c) M. M. Olmstead, A. de Bettencourt-Dias, J. C. Dauchamp, S. Stevenson, H. C. Dorn, A. L. Balch, *J. Am. Chem. Soc.* **2000**, *122*, 12220–12226; d) M. M. Olmstead, H. M. Lee, J. C. Duchamp, S. Stevenson, D. Marciu, H. C. Dorn, A. L. Balch, *Angew. Chem. Int. Ed.* **2003**, *42*, 900–903.

[6] a) S. Stevenson, G. Rice, T. Glass, K. Harich, F. Cromer, M. R. Jordan, J. Craft, E. Hadju, R. Bible, M. M. Olmstead, K. Maitra, A. J. Fisher, A. L. Balch, H. C. Dorn, *Nature* **1999**, *401*, 55–57; b) F. T. Edelmann, *Angew. Chem. Int. Ed. Engl.* **1995**, *34*, 981–985.

[7] M. N. Bochkarev, I. L. Fedushkin, V. I. Nevodchikov, A. V. Protchenko, H. Schumann, F. Girgsdies, *Inorg. Chim. Acta* **1998**, *280*, 138–142.

[8] a) D. V. Konarev, S. S. Khasanov, A. Otsuka, Y. Yoshida, G. Saito, *J. Am. Chem. Soc.* **2002**, *124*, 7648–7649; b) Y. Wang, Z. Lin, *J. Am. Chem. Soc.* **2003**, *125*, 6072–6073; c) T. Kawase, K. Tanaka, N. Fujiwara, H. R. Darabi, M. Oda, *Angew. Chem. Int. Ed.* **2003**, *42*, 1624–1628; d) M. Wang, X. Zhang, Q. Zheng, *Angew. Chem. Int. Ed.* **2004**, *43*, 838–842; e) D. Gust, T. A. Moore, A. L. Moore, *Acc. Chem. Res.* **2001**, *34*, 40–48; f) H. Imahori, *J. Phys. Chem. B.* **2004**, *108*, 6130–6143; g) D. M. Guldi, *Chem. Soc. Rev.* **2002**, *31*, 22–36; h) H. Imahori, *Org. Biomol. Chem.* **2004**, *2*, 1425–1433.

[9] a) M. M. Olmstead, D. A. Costa, K. Maitra, B. C. Noll, S. L. Phillips, P. M. Van Calcar, A. L. Balch, *J. Am. Chem. Soc.* **1999**, *121*, 7090–7097; b) D. H. Hochmuth, S. L. J. Michel, A. J. P. White, D. J. Williams, A. G. M. Barrett, B. M. Hoffman, *Eur. J. Inorg. Chem.* **2000**, 593–596; c) J. Zheng, K. Tashiro, Y. Hirabayashi, K. Kinbara, K. Saigo, T. Aida, S. Sakamoto, K. Yamaguchi, *Angew. Chem. Int. Ed.* **2001**, *40*, 1857–1861; d) F. D. Souza, N. P. Rath, G. R. Deviprasad, M. E. Zandler, *Chem. Commun.* **2001**, 267–268; e) M. M. Olmstead, A. de Bettencourt-Dias, H. M. Lee, D. Pham, A. L. Balch, *Dalton* **2003**, 3227–3232; f) D. I. Schuster, P. Cheng, P. D. Jarowski, D. M. Guldi, C. Luo, L. Echegoyen, S. Pyo, A. R. Holzwarth, S. E. Braslavsky, R. M. Williams, G. Klihm, *J. Am. Chem. Soc.* **2004**, *126*, 7257–7270; g) D. Sun, F. S. Tham, C. S. Reed, L. Chaker, P. D. W. Boyd, *J. Am. Chem. Soc.* **2002**, *124*, 6604–6612.

[10] a) P. D. W. Boyd, M. C. Hodgson, C. E. F. Rickard, A. G. Oliver, L. Chaker, P. J. Brothers, R. D. Bolskar, F. S. Tham, C. A. Reed, *J. Am. Chem. Soc.* **1999**, *121*, 10487–10495; b) T. Ishii, R. Kanehama, N. Aizawa, M. Yamashita, H. Matsuzaka, K. Sugiura, H. Miyasaka, T. Kodama, K. Kikuchi, I. Ikemoto, H. Tanaka, K. Marumoto, S. Kuroda, *J. Chem. Soc. Dalton Trans.* **2001**, 2975–2980; c) D. V. Konarev, I. S. Neretin, Y. L. Slovokhotov, E. I. Yudanova, N. V. Drichko, Y. M. Shul′ga, B. P. Tarasov, L. L. Gumanov, A. S. Batsanov, J. A. K. Howard, R. N. Lyubovskaya, *Chem. Eur. J.* **2001**, *7*, 2605–2616; d) D. V. Konarev, A. Y. Kovalevsky, X. Li, I. S. Neretin, A. L. Litvinov, N. V. Drichko, Y. L. Slovokhotov, P. Coppens, R. N. Lyubovskaya, *Inorg. Chem.* **2002**, *41*, 3638–3646; e) D. V. Konarev, S. S. Khasanov, G. Saito, R. N. Lyubovskaya, Y. Yoshida, A. Otsuka, *Chem. Eur. J.* **2003**, *9*, 3837–3848; f) A. L. Litvinov, D. V. Konarev, A. Y. Kovalevsky, A. N. Lapshin, E. I. Yudanova, N. V. Drichko, P. Coppens, R. N. Lyubovskaya, *Eur. J. Inorg. Chem.* **2003**, 3914–3917.

[11] a) T. Ishii, N. Aizawa, M. Yamashita, H. Matsuzaka, T. Kodama, K. Kikuchi, I. Ikemoto, Y. Iwasa, *J. Chem. Soc. Dalton Trans.* **2000**, 4407–4412; b) T. Ishii, N. Aizawa, R. Kanehama, M. Yamashita, H. Matsuzaka, T. Kodama, K. Kikuchi, I. Ikemoto, *Inorg. Chim. Acta* **2001**, *317*, 81–90.

[12] W. Wong, L. Zhang, F. Xue, T. C. W. Mak, *J. Chem. Soc. Dalton Trans.* **1999**, 3053–3062.

[13] D. V. Konarev, A. Yu. Kovalevsky, A. L. Litvinov, N. V. Drichko, B. P. Tarasov, P. Coppens, R. N. Lyubovskaya, *J. Solid State Chem.* **2002**, *168*, 474–485.

[14] G. M. Sheldrick, *SADABS, A Program for Empirical Absorption Correction*, Göttingen, Germany, **1998**.

[15] G. M. Sheldrick, *SHELXL-97, Program for the refinement of crystal structures*, University of Göttingen, Germany, **1997**.

Received: March 17, 2005
Published Online: July 14, 2005

 © 2005 Wiley-VCH Verlag GmbH & Co. KGaA, Weinheim

Lanthanide(III)-Induced Conversion of 12-Metallacrown-4 to 5-Metallacrown-5 Complexes in Solution

Antoine Pacco,[a] Tatjana N. Parac-Vogt,[a] Els van Besien,[a] Kristine Pierloot,[a] Christiane Görller-Walrand,[a] and Koen Binnemans*[a]

Keywords: Lanthanides / Hydroxamic acids / Metallacrowns / N,O ligands / Rare earths

The conversion of 12-metallacrown-4 complexes with copper(II) in the central cavity to 15-metallacrown-5 complexes with lanthanide(III) ions in the central cavity upon addition of trivalent lanthanide ions was analysed in solution by electrospray ionisation mass spectrometry (ESI-MS), absorption spectrophotometry, circular dichroism and proton NMR spectroscopy. In all cases, copper(II) ions were the ring metals. The lanthanide-induced shifts of the proton resonances in the NMR spectra of different lanthanide(III)-containing 15-metallacrown-5 complexes with tyrosinehydroximate ligands were studied. The dynamics of ligand exchange of α-aminohydroximate-based lanthanide(III)-containing 15-metallacrown-5 complexes were studied in methanol solutions. The ring structure of the 12-metallacrown-4 complex that acts as starting compound for the formation of the 15-metallacrown-5 complexes was optimized by DFT methods using alaninehydroximate as a model ligand.

(© Wiley-VCH Verlag GmbH & Co. KGaA, 69451 Weinheim, Germany, 2005)

Introduction

Metallacrowns, a class of macrocyclic compounds discovered by Pecoraro and coworkers in 1989, are inorganic analogues of crown ethers where heteroatoms and metals substitute for the ring carbons.[1,2] Several types of metallacrown complexes with different metals, ligands and ring sizes have been developed.[3] The stoichiometry of the metallacrown complexes depends on the type of ligand used. Aminohydroximate ligands, which are derivatives of hydroxamic acids with an additional amino group as a potential coordinating group, are suitable ligands for metallacrown formation because they can act as bridging ditopic ligands. These ligands form a metallamacrocycle ring with a metal-nitrogen-oxygen backbone in the presence of copper(II) ions. β-Aminohydroximate ligands can form connected six- and five-membered chelate rings giving rise to 12-metallacrown-4 complexes (12-MC-4) with four copper(II) ions in the macrocyclic ring. A fifth copper(II) ion is encapsulated by the four oxygen atoms of the ring leading to a pentanuclear copper(II) complex Cu^{II}[12-MC-4] whose crystal structure has been determined.[4]

On the other hand, α-aminohydroximate ligands form 15-metallacrown-5 (15-MC-5) compounds because these ligands chelate the metals by connected five-membered rings giving rise to a planar metallamacrocycle ring with five copper atoms in the ring. The cavity size of this ring is larger than the cavity size of the 12-metallacrown-4 complexes and affords the incorporation of lanthanide(III)[5–11] or uranyl ions.[11–13] 15-Metallacrown-5 complexes of lanthanide(III) ions with either chiral or nonchiral α-aminohydroximate ligands have been structurally characterized.[5–10] Careri and coworkers showed that α-aminohydroximate ligands form the 12-metallacrown-4 structural motif in aqueous solution in the absence of lanthanide(III) ions.[14] However, those Cu^{II}[12-MC-4] metallacrowns are less stable than those containing β-alaninehydroxamic acid as the ligand. No single crystal structure of 12-metallacrown-4 complexes containing α-aminohydroximate ligands has been determined yet, but solution studies have shown that Cu^{II}[12-MC-4] complexes are converted into (UO_2)[15-MC-5] complexes in aqueous solution upon addition of a uranyl salt.[13]

Although the lanthanide(III)-containing 15-metallacrown-5 complexes with α-aminohydroximate ligands have been thoroughly characterised in the solid state, their formation and self-assembly in solution still remain elusive. The formation of 12-metallacrown-4 complexes with salicylhydroximate ligands has been investigated in solution and data pointed out that some dimeric nickel(II) salicylhydroximate intermediates reorganize in basic solvents to form a 12-metallacrown macrocycle. It was also found that 12-metallacrown-4 copper(II) complexes with salicylhydroximate ligands maintain their structure in solution in the presence of excess ligand or metal ions.[3] In this study, we demonstrate that in the self-assembly of copper(II)-containing 15-metallacrown-5 complexes derived from α-aminohydroximate ligands, the final 15-metallacrown-5 is formed through the lanthanide(III)-templated reassembly of the 12-

[a] Katholieke Universiteit Leuven, Department of Chemistry, Celestijnenlaan 200F, 3001 Leuven, Belgium
Fax: +32-16-327992
E-mail: Koen.Binnemans@chem.kuleuven.be

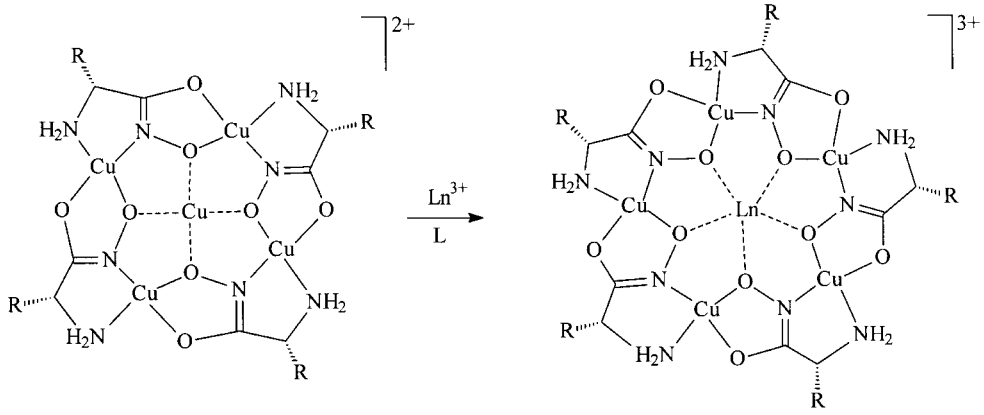

Scheme 1. Schematic representation of lanthanide-induced conversion of 12-metallacrown-4 (left) to 15-metallacrown-5 (right).

metallacrown-4 complex (Scheme 1). Since the structure of the 12-metallacrown-4 complex has not been determined yet, its ring structure with alaninehydroximate as a model ligand was optimized by DFT methods. The solution properties and ligand exchange of 15-metallacrown-5 complexes with α-aminohydroximate ligands and copper(II) ions were studied by a combination of several experimental techniques such as electron spray mass spectrometry (ESI-MS), paramagnetic nuclear magnetic resonance techniques, circular dichroism and UV/Vis spectrophotometry. The evaluation of the properties of metallacrown compounds in solution is important if one envisages solution-based applications of metallacrowns, for example, as sequestering agents for selective recognition of actinide or lanthanide ions and as contrast agents for magnetic resonance imaging applications.

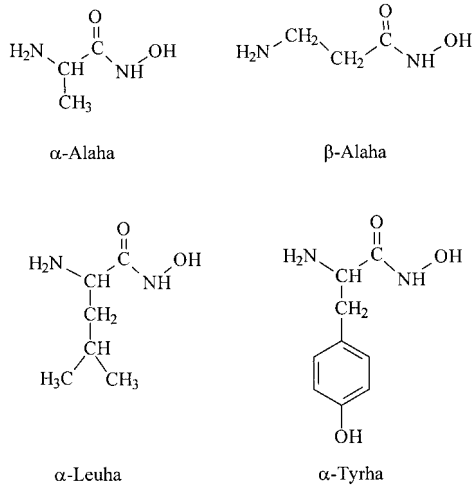

Scheme 2. Schematic representation of α-alaninehydroxamic acid (α-Alaha), β-alaninehydroxamic acid (β-Alaha), α-leucinehydroxamic acid (α-Leuha) and α-tyrosinehydroxamic acid (α-Tyrha).

Results and Discussion

Structure Optimization of Cu^{II}[12-MC-4] by DFT Methods

The structures of the ligands used in this study are presented in Scheme 2. The crystal structures of copper(II)-containing 12-metallacrown-4 complexes, Cu^{II}[12-MC-4], with β-aminohydroximate ligands were determined in the past,[4,8] but to the best of our knowledge no crystal structures of Cu^{II}[12-MC-4] with α-aminohydroximate ligands have been determined. The crystal structure of Cu^{II}[12-MC-4] with β-aminohydroximate ligands shows that the ligands form five- and six-membered chelate rings with the metal ions arranged in an almost planar ring. Dallavalle and coworkers have commented on the structure of Cu^{II}[12-MC-4] with the α-aminohydroximate ligands derived from phenylalanine-, tryptophan- and alaninehydroxamic acid. Because those ligands can form only five-membered chelate rings, this would give rise to a strained structure if planar, so they propose an arrangement of the rings in a cup-conformation with four sp^3-hybridised oxygen atoms bridging the peripheral and central copper(II) ions.[14–15]

In order to gain more insight into the structure of Cu^{II}[12-MC-4] with α-aminohydroximate ligands, we performed density functional theory (DFT) calculations (Figure 1). For comparison, we have also calculated the structure of Cu^{II}[12-MC-4] with β-aminohydroximate ligands by the same method. In both types of complexes (with α-alaninehydroxamic or β-alaninehydroxamic acid as the ligand), the four peripheral copper(II) ions form an almost planar structure. The central copper(II) ion is situated above this quasi-plane. For the complex formed with the α-aminohydroximate ligands, the deviation from planarity is larger than for the complex with β-aminohydroximate ligands. This can clearly be seen by comparing the dihedral angles between the four copper(II) ions: 1.4° in the β-form and 3.0° in the α-form. There is also a difference in the position of the central copper(II) ion above the quasi-plane: in the complex with α-aminohydroximate ligands the distance between the central copper(II) ion and a virtual line connecting two opposite copper(II) ions is 0.98 Å, whereas in the β-form it is only 0.50 Å. Another difference is the coordination of the

 © 2005 Wiley-VCH Verlag GmbH & Co. KGaA, Weinheim

copper(II) ions in the ring. In the complex with β-aminohydroximate ligands the copper(II) ions have a nearly planar coordination, whereas the deviation from planarity is more pronounced in the complex with α-aminohydroximate ligands. This can be related to the stability of these two structures in solution: the calculated complex-formation constant for Cu^{II}[12-MC-4] with α-Alaha ($\log\beta = 40$) is lower than that with β-Alaha ($\log\beta = 49$).[14] The difficulties of growing crystals of the α-form could lie in the subtle differences in the proposed structures.

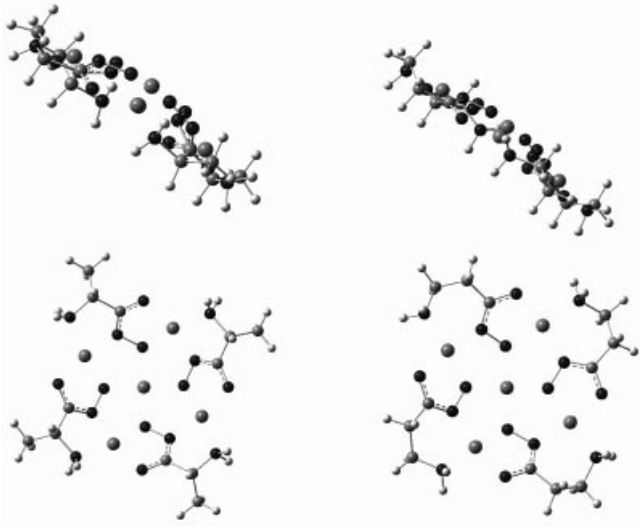

Figure 1. Structure of Cu^{II}[12-MC-4] with α-alaninehydroxamic acid (left) and β-alaninehydroxamic acid (right) resulting from the DFT calculation.

Titration of $[Cu_5L_4]^{2+}$ with Lanthanide(III) Ions Monitored by Optical Spectroscopy

Complex formation between α-aminohydroxamic acid and copper(II) ions can lead to several species depending on the pH of the solution. When copper(II) ions and α-Alaha are mixed in a 1:3 ratio, the distribution diagram shows that, in the pH range 4.5–5.5, the pentanuclear $[Cu_5(\alpha\text{-Alaha})_4]^{2+}$ complex is the most abundant species in solution.[14] When copper(II) ions and α-Leuha are mixed in a 1:1 ratio and the pH of the final solution is around 4.5, the only detectable complex in solution is also a pentanuclear $[Cu_5(\alpha\text{-Leuha})_4]^{2+}$ complex.[13] In the present study, the starting solutions for the titrations were also prepared by mixing the ligand and copper(II) acetate in a 1:1 ratio, so we can assume that under these conditions the pentanuclear complex is the most abundant species in solution. This was confirmed by ESI-MS results and will be discussed later.

The UV/Vis absorption spectrum of $[Cu_5(\alpha\text{-Leuha})_4]^{2+}$ at pH 4.5 is characterised by two prominent absorption bands with maxima at 650 nm and 343 nm. Similarly, the maximum absorbance for $[Cu_5(\alpha\text{-Tyrha})_4]^{2+}$ has been observed at 660 and 346 nm. The λ_{max} values in the visible region are in agreement with those calculated for $[Cu_5(\alpha\text{-Pheha})_4]^{2+}$ and $[Cu_5(\alpha\text{-Trpha})_4]^{2+}$ metallacrowns.[15] Bands at 352 and 336 nm have also been observed in these complexes and could be assigned to $N^-\text{–}O^-_{(nitrogen)} \rightarrow Cu^{II}$ and $N^-\text{–}O^-_{(oxygen)} \rightarrow Cu^{II}$ charge-transfer transitions.

Since the α-aminohydroxamic acids used in this study are chiral, their copper(II) complexes are expected to be optically active as well. The CD spectrum of $[Cu_5(\text{D-}\alpha\text{-Leuha})_4]^{2+}$ shows a positive Cotton effect at 350 nm and two negative peaks at 558 and 646 nm. The two latter peaks

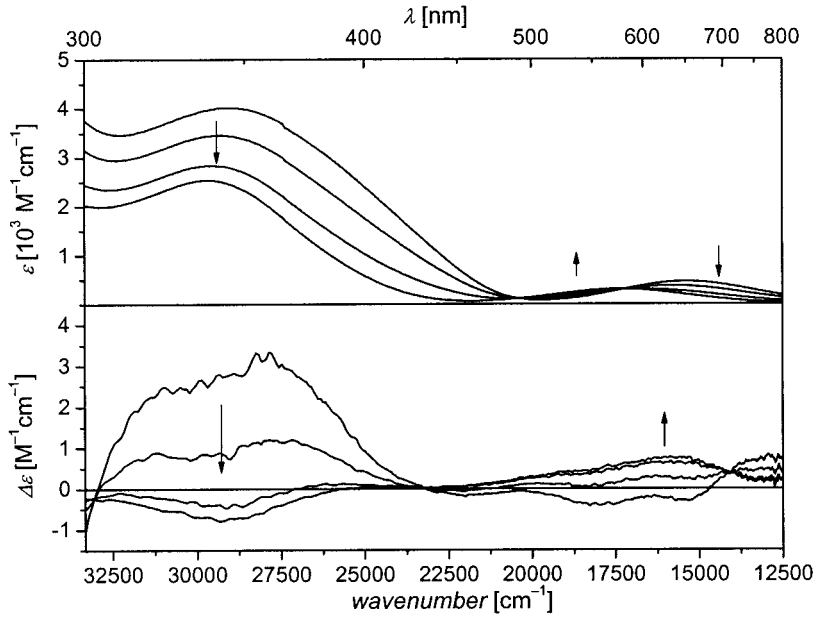

Figure 2. Changes in UV/Vis and CD absorption spectra of Cu^{2+}/D-α-Leuha solutions in water upon addition of Gd^{3+}. The Gd^{3+} ion was added in 0.33-equivalent increments relative to the 12-metallacrown-4 concentration.

 © 2005 Wiley-VCH Verlag GmbH & Co. KGaA, Weinheim

are either due to d-d transitions of the copper(II) ion or due to the presence of nonequivalent chromophores in the metallacrown. If L-α-Leuha was used as the ligand, the CD spectrum of the resulting $[Cu_5(L\text{-}\alpha\text{-Leuha})_4]^{2+}$ looked as a mirror image of the $[Cu_5(D\text{-}\alpha\text{-Leuha})_4]^{2+}$ spectrum, with two bands at 558 and 646 nm having positive Cotton effects and a band at a 350 nm having a negative Cotton effect. The CD spectrum of $[Cu_5(L\text{-}\alpha\text{-Tyrha})_4]^{2+}$ showed a weak positive Cotton effect at 350 nm and a weak negative Cotton effect at 672 nm. The stepwise addition of Gd^{3+} to the aqueous solution of $[Cu_5(D\text{-}\alpha\text{-Leuha})_4]^{2+}$ and $[Cu_5(L\text{-}\alpha\text{-Tyrha})_4]^{2+}$ caused significant changes both in the UV/Vis and in the CD spectra. As seen in Figure 2, the UV/Vis and CD spectra are characterised by isosbestic points, suggesting the presence of only two interconverting species in the solutions. At the end point of the titration of $[Cu_5(L\text{-}\alpha\text{-Tyrha})_4]^{2+}$ with Gd^{3+}, one band having a negative Cotton effect is observed at 557 nm. The ligand field analysis of lanthanide(III)-containing 15-metallacrown-5 copper(II) species was in accordance with this finding and suggested that three d-d transitions should be expected in the ligand field region, and the transition around ca. 556 nm should be the most intense.[5] After titration of $[Cu_5(L\text{-}\alpha\text{-Tyrha})_4]^{2+}$ with Gd^{3+}, the UV/Vis spectra are characterised by two prominent absorption bands with maxima at 581 nm and 340 nm. Similar absorption spectra have also been observed for the other lanthanide(III)-containing 15-metallacrown-5 complexes with L-α-Tyrha as ligand (Ln^{3+} = Y^{3+}, La^{3+}, Nd^{3+}, Sm^{3+}, Eu^{3+}, Tb^{3+}, Dy^{3+}, Ho^{3+}, Er^{3+}, Tm^{3+}). The absorption spectra of the different lanthanide-containing metallacrown complexes are virtually independent of the lanthanide(III) ions. The peak maxima in the spectra differ less than 2 nm from those of the gadolinium(III)-containing metallacrowns.

$[Cu_5L_4]^{2+}$ Titration with Lanthanide(III) Monitored by ESI-MS

Electrospray ionisation mass spectrometry (ESI-MS) is an effective method for studying the speciation of metal complexes in solution and was applied in studies of different metallacrown systems.[16] The method has been proven to be very useful in providing solution molecular weights of the formally neutral metallacrown complexes after the loss of bound anions. ESI-MS results indicate that solutions containing a copper(II) salt and α-Leuha in a 1:1 ratio form exclusively 12-MC-4 species in the solution, with peaks at 447 and 930 *m/e*, which could be assigned to the pentanuclear species $[Cu_5(\alpha\text{-Leuha})_5]^{2+}$ (447.2 calcd.) and $[Cu_5(\alpha\text{-Leuha})_5](Cl)^+$ (929.8 calcd.), respectively.

As seen in Figure 3, the addition of gadolinium(III) to the $[Cu_5(\alpha\text{-Leuha})_4]^{2+}$ solution caused disappearance of the peaks which were assigned to the 12-MC-4 species and the appearance of new peaks at 627 and 1319 *m/e*, which could be assigned to the 15-MC-5 species $[Gd(NO_3)Cu_5(\alpha\text{-Leuha})_5]^{2+}$ (628.9 calcd.) and $[Gd(NO_3)_2Cu_5(\alpha\text{-Leuha})_5]^+$ (1319.8 calcd.), respectively.

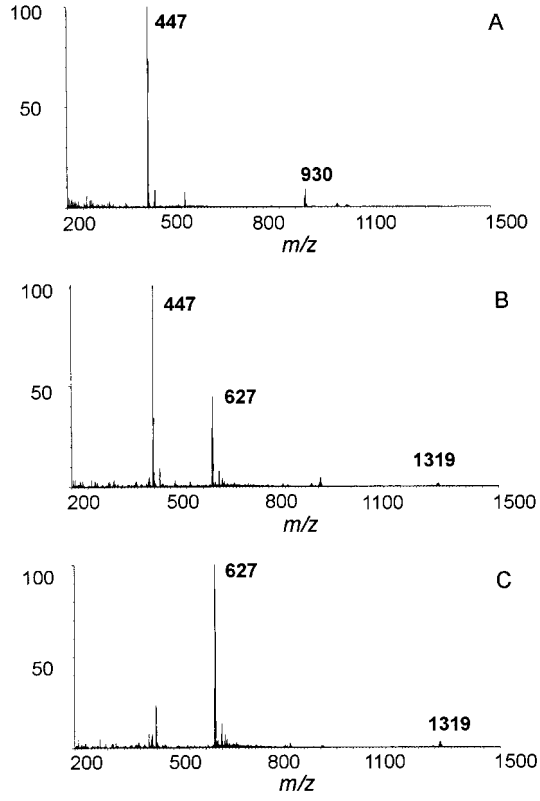

Figure 3. Positive-ion mode ESI-MS spectra of Cu^{2+}/Leuha solutions containing different amounts of Gd^{3+} relative to the 12-metallacrown-4 concentration: (a) 0.0 equiv., (b) 0.5 equiv., (c) 1.0 equiv.

A similar trend was observed upon addition of Gd^{3+} to the solution of $[Cu_5(\alpha\text{-Tyrha})_4]^{2+}$: the peaks corresponding to $[Cu_5(\alpha\text{-Tyrha})_4]^{2+}$ disappeared, and new positive-mode ESI-MS peaks appeared at *m/e* = 753 and 1570 corresponding to $[(Gd)Cu_5(\alpha\text{-Tyrha})_5](NO_3)^{2+}$ (753.9 calcd.) and $[(Gd)Cu_5(\alpha\text{-Tyrha})_5](NO_3)_2^+$ (1569.9 calcd.), respectively. In the ESI-MS spectra taken in the negative mode, only one peak at 1693 *m/e* appeared corresponding to $[(Gd)Cu_5(\alpha\text{-Tyrha})_5](NO_3)_4^-$ (1692.8 calcd.). These results indicate that after addition of 1 equiv. gadolinium relative to the 12-metallacrown-4, complete conversion of 12-metallacrown-4 to 15-metallacrown-5 occurs, and that the gadolinium(III)-containing 15-metallacrown-5 is the only species formed in solution.

$[Cu_5L_4]^{2+}$ Titration with Lanthanide(III) Monitored by NMR

In paramagnetic molecules, the NMR signals of protons close to the paramagnetic centres are broadened. Metallacrowns containing paramagnetic copper(II) ions and a paramagnetic lanthanide(III) ion in the cavity are therefore expected to give very broad signals with bad resolution. The extent of paramagnetic-induced line broadening depends on the electronic relaxation time of the paramagnetic metal centres. Broad lines are expected for complexes with copper(II) ions because of the relatively long electronic relax-

 © 2005 Wiley-VCH Verlag GmbH & Co. KGaA, Weinheim

ation time of this ion (τ_s = 1–5 × 10^{-9} s).[17] However, a shortening of the electronic relaxation times of the metal ions involved can occur as a consequence of magnetic coupling.[18] The copper(II) ions in the 15-MC-5 ring are antiferromagnetically coupled so that the τ_s value is lower than it would be in the absence of magnetic coupling.[6,16] As a consequence, one could in principle observe signals in high resolution NMR experiments.

We studied the conversion of a 12-metallacrown-4 to a 15-metallacrown-5 in [D_4]MeOH by solution proton NMR spectroscopy. Spectra of solutions containing equimolar amounts of the copper(II)/aminohydroximate ligand (L-Leuha) and different amounts of lanthanide(III) ions were recorded after one day (Figure 4). The four different samples prepared contained 0.00, 0.33, 0.66 and 1.00 equiv. $Nd(NO_3)_3$ (relative to the amount of 12-metallacrown-4). The first spectrum, without any neodymium(III), shows only one broad peak at ca. 1 ppm. In the sample with 0.33 equiv. of neodymium(III), the signal at 1 ppm disappears and two new signals appear at approximately. 31 ppm and 16 ppm in addition to four other signals that appear between δ = 0 and 4 ppm (Figure 4). 2D-COSY experiments revealed that the peaks experiencing the largest paramagnetic shift, at 31 ppm and 16 ppm, belong to the α and γ protons of L-Leuha, respectively. The peaks of the methyl groups appear at δ = 0.5 and 1.5 ppm, indicating that these two groups are magnetically nonequivalent. The other two weak signals that appear between δ = 0 and 4 ppm are from the magnetically nonequivalent β-protons of the ligand. Addition of more neodymium(III) ions increased the intensity of all peaks, and only a slight shift to lower field was observed. We attempted a similar NMR titration experiment for the metallacrown system with L-Tyrha ligands. Unfortunately, solutions containing equimolar amounts of copper(II) and L-Tyrha *without* lanthanide(III) were turbid at those high concentrations and no NMR spectra of the starting solutions could be obtained. On the other hand, copper(II)/L-Tyrha solutions *with* lanthanide(III) ions were clear, and their NMR spectra are discussed later.

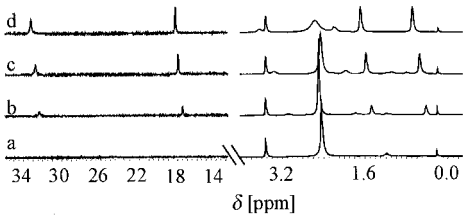

Figure 4. Proton NMR spectra of Cu^{2+}/Leuha solutions in [D_4]MeOH containing different amounts of Nd^{3+} relative to the 12-metallacrown-4 concentration: (a) 0.00 equiv., (b) 0.33 equiv., (c) 0.66 equiv., (d) 1.00 equiv.

It is interesting to note that in the case of 12-metallacrown-4, which is formed in the absence of any lanthanide(III) in solution, most of the NMR signals could not be detected. However, in the case of 15-metallacrown-5 complexes, which are formed upon addition of neodymium(III), the NMR signals of the ligand become observable. This difference points to the different electronic relaxation of the copper(II) ions in the 12-metallacrown-4 and 15-metallacrown-5. This difference is not surprising if one considers that the coordination around copper(II) ions is nearly square planar in 15-metallacrown-5,[12] but square pyramidal in 12-metallacrown-4, as shown by our DFT calculations.

NMR Analysis of $Ln(NO_3)_3$[15-$MC_{Cu^{II}N(L–Tyrha)}$-5]

Paramagnetic shift reagents, which are used to induce large NMR shifts in organic molecules to which they are coordinated, are available for most classes of compounds. One factor that has led to the widespread application of lanthanide-containing shift reagents (LSR) is that the shifts observed in the NMR spectrum are highly predictable.[19–22] This is a result of the magnetic properties of the lanthanide ions. In this study we do not focus on the effect that paramagnetic metallacrown compounds have on nuclei of a substrate molecule, but on the lanthanide induced shift (LIS) of the ligand protons of the metallacrown compounds. ^{1}H NMR spectra of $Ln(NO_3)_3$[15-$MC_{Cu^{II}N(L–Tyrha)}$-5] containing different lanthanide(III) ions in the central cavity were recorded in [D_4]MeOH solutions to examine the influence of lanthanide(III) ions on the chemical shift. The values of ^{1}H NMR resonances of the metallacrowns formed with Ln^{3+} (Ln = La, Ce, Pr, Nd, Sm, Eu, Tb, Dy, Ho, Er, Tm) and Y^{3+} are shown in Figure 5.

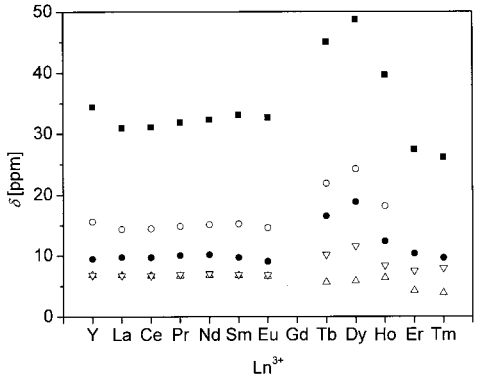

Figure 5. Proton NMR resonances for $Ln(NO_3)_3$[15-$MC_{Cu^{II}N(L–Tyrha)}$-5] with different Ln^{3+} ions and Y^{3+} [α-protons (squares), β-protons (empty and filled circles), aromatic protons (triangles pointing upwards and downwards)].

The assignment of the peaks was made with the help of 2D-COSY experiments with $Nd(NO_3)_3$[15-$MC_{Cu^{II}N(L–Tyrha)}$-5] (see below). The magnitude of the shift for the aromatic protons is less than that for the signals of the two β-protons and the α-proton. This is consistent with the fact that the proton in closest proximity to a paramagnetic centre is shifted farthest. $La(NO_3)_3$[15-$MC_{Cu^{II}N(L–Tyrha)}$-5] has four distinct proton resonances [at ≈ 31 ppm (1H), ≈ 14 ppm (1H), ≈ 10 ppm (1H) and at 6.7 ppm (4H)] that are paramagnetically shifted due to the copper(II) ions in the me-

 © 2005 Wiley-VCH Verlag GmbH & Co. KGaA, Weinheim

tallacrown ring. The spectra of the 15-metallacrown-5 complexes with $Y^{3+}$and Ce^{3+} are similar to the spectrum of the complex with La^{3+}. For the $Ln(NO_3)_3$[15-$MC_{Cu^{II}N(L\text{–}Tyrha)}$-5] complexes with Ln^{3+} = Pr^{3+}, Nd^{3+}, Sm^{3+} and Eu^{3+} the signals of the aromatic protons appear as two separate resonances. 2D-COSY experiments with $Nd(NO_3)_3$[15-$MC_{Cu^{II}N(L\text{–}Tyrha)}$-5] showed a coupling between the resonances at ca. 15 ppm and ca. 10 ppm belonging to the two β-protons of the CH_2 group of the ligand. Interestingly, only one of these signals (the one at ca. 10 ppm) couples with the signal belonging to the α-proton (at ca. 32 ppm). From this, we infer that the β-protons of the CH_2 group are magnetically nonequivalent. The spectrum of $Gd(NO_3)_3$[15-$MC_{Cu^{II}N(L\text{–}Tyrha)}$-5] exhibits excessive line broadening of the signals due to the paramagnetic gadolinium(III) ion and is not discussed here. For the $Ln(NO_3)_3$[15-$MC_{Cu^{II}N(L\text{–}Tyrha)}$-5] complexes with Ln^{3+} = Tb^{3+}, Dy^{3+} and Ho^{3+} the paramagnetic shift is even larger. The signals belonging to the α- and the β-protons of the complex with Dy^{3+} experience the largest upfield shifts of the lanthanide series. One resonance signal of the aromatic protons of those three metallacrowns has shifted upfield, the other has shifted slightly downfield. 2D-COSY experiments with $Dy(NO_3)_3$[15-$MC_{Cu^{II}N(L\text{–}Tyrha)}$-5] showed only one coupling signal between the resonances belonging to the aromatic protons. The integration values of the peak belonging to the α-proton (1H), the two peaks belonging to the β-protons (1H each) and the two signals belonging to the aromatic protons (2H each) are consistent with this assignment. However if we consider the spectra of the $Ln(NO_3)_3$[15-$MC_{Cu^{II}N(L\text{–}Tyrha)}$-5] complexes with Ln = Er^{3+} and Tm^{3+} one proton resonance is missing. Again, 2D-COSY experiments with $Er(NO_3)_3$[15-$MC_{Cu^{II}N(L\text{–}Tyrha)}$-5] showed only one coupling signal between the resonances belonging to the aromatic protons. Presumably, the missing resonance must belong to one β-proton.

Lanthanide-induced shifts (LIS) for nuclei of a ligand upon coordination arise by two possible mechanisms. These two mechanisms are the pseudocontact and contact shift.[23] The contact shift of a nucleus directly bound to a lanthanide(III) ion is usually very large, but decreases rapidly as the number of bonds between the lanthanide(III) ion and the nucleus under study increases. Because there are at least four bonds between the central lanthanide(III) ion of the metallacrown and the ligand protons, the contribution of the contact shift is negligible, and the pseudocontact shift contribution can be considered as the most important one. In addition, shifts resulting from the pseudocontact mechanism are highly predictable.[19] If we look at the shifts belonging to the α-proton of the different $Ln(NO_3)_3$[15-$MC_{Cu^{II}N(L\text{–}Tyrha)}$-5] complexes, it can be seen that complexes with Ln = Pr, Nd, Sm, Eu, Tb, Dy and Ho have a similar effect as upfield shift reagents with a relative ordering of the shifts Dy > Tb > Ho > Sm > Eu > Nd > Pr, whereas complexes with erbium(III) and thulium(III) have a similar effect as downfield shift reagents. It is not surprising that the direction of the shifts and the relative ordering is nearly the same as the shifts of a substrate recorded in the presence of the shift reagent [Ln(dpm)$_3$], where the shifts also result mainly from the pseudocontact mechanism.[24]

Ligand Exchange in Ln^{III}[15-MC-5] Complexes

Previous ligand exchange studies for the copper(II) based metallacrowns Cu[12-$MC_{Cu^{II}N(shi)}$-4] and Cu[12-$MC_{Cu^{II}N(anha)}$-4] showed the kinetic inertness towards ligand exchange in methanol.[16] On the other hand, vanadyl-containing metallacrown complexes [9-$MC_{(VO)N(shi)}$-3] and [9-$MC_{(VO)N(nha)}$-3], unable to sequester metal ions in their cavities, were found to be kinetically labile in methanol.[25]

We tested the dynamics of ligand exchange of α-aminohydroximate-based 15-metallacrown-5 complexes with central lanthanide(III) cavity ions in methanol. ^{1}H NMR was used to monitor the ligand exchange for 15-metallacrown-5 complexes containing L-Tyrha and L-Pheha aminohydroximate ligands. The equimolar solutions of Nd[15-$MC_{Cu^{II}N(L\text{–}Tyrha)}$-5] (**1**) and Nd[15-$MC_{Cu^{II}N(L\text{–}Pheha)}$-5] (**2**) were mixed and after 1 h the ^{1}H NMR spectrum of the mixture shows two sets of peaks appearing at the same ppm values as for the separate solutions of **1** and **2** (Figure 6). After 1 d at room temperature, new peaks appeared in the spectra. When this mixture was kept for 2 d at 37 °C, some of those new peaks were resolved into multiplets. A similar spectrum was obtained in an experiment where the ligands L-Tyrha and L-Pheha were mixed in the presence of copper(II) and neodymium(III). We were wondering whether some metallacrowns containing both L-Tyrha and L-Pheha ligands (mixed-ligand metallacrowns) were forming in solution after a long period of time or initially at the time of their synthesis with both L-Tyrha and L-Pheha in the reaction mixture. If this takes place, the environment of the protons of one ligand will depend on the adjacent ligand in the metallacrown ring and they will not be magnetically equivalent anymore. This can be an explanation why the peaks are resolved into multiplets.

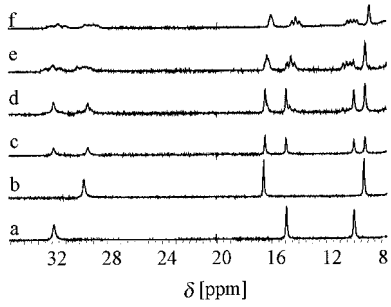

Figure 6. Proton NMR spectra of (a) Nd[15-$MC_{Cu^{II}N(L\text{–}Tyrha)}$-5] (**1**), (b) Nd[15-$MC_{Cu^{II}N(L\text{–}Pheha)}$-5] (**2**), (c) a 1:1 mixture of **1** and **2** after 1 h, (d) 1 d, (e) 2 d at 37 °C, (f) control experiment in which the metallacrown is synthesised from a [D_4]MeOH solution containing both L-Tyrha and L-Pheha, copper(II) and neodymium(III) in the reaction mixture.

In order to further understand the exchange process we used ESI-MS to probe the mass distribution of the complexes in solution. When initially both L-Tyrha and L-Pheha ligands (1:1) were allowed to react with the copper(II) and

 © 2005 Wiley-VCH Verlag GmbH & Co. KGaA, Weinheim

lanthanide(III) ions, a uniform distribution of ESI-MS peaks with values corresponding to different Ln^{III}[15-$MC_{Cu^{II}N(L–Pheha)_x(L–Tyrha)_y}$-5] complexes with the *x*/*y* ratios 5:0, 4:1, 3:2, 2:3, 1:4 and 0:5 was observed. This distribution points to the formation of mixed-ligand metallacrowns and means that there is no preference for one of the two ligands.

The copper(II) and lanthanide(III) metal ions can be viewed as templates around which the macrocyclic ring in 15-metallacrown-5 complexes is formed. However the reactants, the α-aminohydroximate ligands, are forming a ring only through coordination with the copper(II) ions and not through inter- or intramolecular reaction of the ligands between themselves. This could allow easy rearrangement and mixing of the different ligands since they are only coupled together through coordination bonds to the copper(II) ions. This is not surprising, as it is known that copper(II) complexes are among the most labile complexes of the d-block metal(II) ions.[26]

Conclusions

The easy conversion of Cu^{II}[12-MC-4] to a Ln^{III}[15-MC-5] is accomplished by addition of Ln^{III} ions in solution. Evidence for the presence of only two metallacrown species in the conversion process was obtained by UV/Vis and CD spectrophotometry. Complete disappearance of Cu^{II}[12-MC-4] and formation of Ln^{III}[15-MC-5] was proved by ESI-MS spectrometry and NMR spectroscopy. Due to the labile copper(II)–ligand bond, easy mixing of the different α-aminohydroxamate ligands can take place in solution, leading to a mixture of different metallacrown complexes.

Experimental Section

Reagents: L-Leucine methyl ester hydrochloride, D-leucine methyl ester hydrochloride, L-tyrosine methyl ester hydrochoride and L-phenylalanine methyl ester hydrochoride were obtained as pure products from Acros Organics. All other chemicals and solvents were reagent grade. L-Leucine hydroxamic acid, D-leucine hydroxamic acid, L-tyrosine hydroxamic acid and L-phenylalanine hydroxamic acid were prepared via their respective methyl esters as reported in ref.[27].

Equipment and Techniques: Positive- and negative-mode electrospray mass spectra (ESI-MS) were obtained with a Q-tof 2 (Micromass, Manchester UK) instrument. The samples were injected into the apparatus after dissolution in acetonitrile or in methanol.

UV/Vis absorption spectra were recorded with a Shimadzu UV-1601PC spectrophotometer using quartz cells of 1 cm path length. Circular dichroism spectra were measured with a JASCO J-810 spectropolarimeter using quartz cells of 2 cm path length. The spectra were collected in the 200–900 nm range. The solutions for the measurements were always freshly prepared before measurement. The concentration of the copper(II) and α-aminohydroxamic acid solutions was 2 mM. The pH of the solution was determined before and after each measurement.

^1H NMR spectra were recorded in deuterated water (D_2O) or methanol ([D_4]MeOH) solutions with a Bruker Avance 300 spectrometer operating at 300 MHz. In the titration experiment, to four 500-μL solutions in [D_4]MeOH containing equimolar amounts of $Cu(OAc)_2$ and L-leucine hydroxamic acid (0.1 M) were added 0.00, 0.33, 0.66 and 1.00 equiv. $Nd(NO_3)_3$. This was achieved by adding respectively 0, 20, 40 and 60 μL of a neodymium(III) nitrate solution in [D_4]MeOH (0.166 M) and adjusting the total volume of the NMR samples to 600 μL. Solutions of $Ln(NO_3)_3$[15-$MC_{Cu^{II}N(L–Tyrha)}$-5] complexes with different lanthanide(III) ions and yttrium(III) were prepared by dissolving some crystals in [D_4]-MeOH. In the ligand-exchange experiments, two solutions containing metallacrown complexes (0.02 M in [D_4]MeOH) with different α-aminohydroxamic acids were mixed together. This NMR sample was also heated for 2 d at 37 °C in a water bath. In the control experiment, metallacrown was formed by adding neodymium(III) nitrate solution (240 μL, 0.166 M) in [D_4]MeOH to a solution of $Cu(OAc)_2$ (0.2 mmol) and both α-aminohydroxamic acids (0.1 mmol of each). Chemical shifts were referenced to sodium 2,2-dimethyl-2-silapentane-5-sulfonate (DSS) or to the solvent peak. Two-dimensional proton–proton correlation spectroscopy (2D COSY) was performed by applying the standard Bruker pulse sequence, and confirmed the assignment of the proton resonances.

Computational Details: The optimisation of the geometrical structures was accomplished by density-functional theory (DFT) as implemented in the Amsterdam Density Functional program package[28,29] ADF2002.03.[30] A triple zeta (TZP) basis set of Slater type orbitals was used. The frozen core approximation was employed, including all orbitals up to 2p for the copper atoms and 1s for the carbon, nitrogen and oxygen atoms. The local density functional of Vosko, Wilk and Nusair[31] was used, with the exchange and correlation corrections from Becke[32] and Perdew[33], respectively (BP86). The complexes were fully optimized without symmetry constraints.

Acknowledgments

T.N.P.V. and K.B. acknowledge the F. W. O.-Flanders (Belgium) for Postdoctoral Fellowships and the K. U. Leuven for financial support (VIS/01/006.01/20002–06/2004 and GOA 03/03). Financial support by the IWT-Vlaanderen to A.P. is gratefully acknowledged. The authors thank Prof. Thierry Verbiest for access to his CD spectrometer.

[1] M. S. Lah, V. L. Pecoraro, *J. Am. Chem. Soc.* **1989**, *111*, 7258–7259.
[2] M. S. Lah, M. L. Kirk, W. Hatfield, V. L. Pecoraro, *J. Chem. Soc., Chem. Commun.* **1989**, 1606–1608.
[3] V. L. Pecoraro, A. J. Stemmler, B. R. Gibney, J. J. Bodwin, H. Wang, J. W. Kampf, A. Barwinski, *Prog. Inorg. Chem.* **1997**, *45*, 83–177.
[4] B. Kurzak, E. Farkas, T. Glowiak, H. Kozlowski, *J. Chem. Soc., Dalton Trans.* **1991**, *2*, 163–167.
[5] A. J. Stemmler, A. Barwinski, M. J. Baldwin, V. Young, V. L. Pecoraro, *J. Am. Chem. Soc.* **1996**, *118*, 11962–11963.
[6] A. J. Stemmler, J. W. Kampf, M. L. Kirk, B. H. Atasi, V. L. Pecoraro, *Inorg. Chem.* **1999**, *38*, 2807–2817.
[7] A. D. Cutland, R. G. Malkani, J. W. Kampf, V. L. Pecoraro, *Angew. Chem. Int. Ed.* **2000**, *39*, 2689–2691.
[8] J. J. Bodwin, A. D. Cutland, R. G. Malkani, *Coord. Chem. Rev.* **2001**, *216*, 489–512.
[9] A. D. Cutland, J. A. Halfen, J. W. Kampf, V. L. Pecoraro, *J. Am. Chem. Soc.* **2001**, *123*, 6211–6212.
[10] A. D. Cutland, J. W. Kampf, V. L. Pecoraro, *Angew. Chem. Int. Ed.* **2002**, *41*, 4667–4670.
[11] A. J. Stemmler, V. L. Pecoraro, *Inorg. Synth.* **2002**, *33*, 67–70.
[12] A. J. Stemmler, J. W. Kampf, V. L. Pecoraro, *Angew. Chem. Int. Ed. Eng.* **1996**, *35*, 2841–2843.

 © 2005 Wiley-VCH Verlag GmbH & Co. KGaA, Weinheim

[13] T. N. Parac-Vogt, A. Pacco, C. Görller-Walrand, K. Binnemans, *J. Inorg. Biochem.* **2005**, *99*, 497–504.
[14] M. Careri, F. Dallavalle, M. Tegoni, I. Zagnoni, *J. Inorg. Biochem.* **2003**, *93*, 174–180.
[15] F. Dallavalle, M. Tegoni, *Polyhedron* **2001**, *20*, 2697–2704.
[16] B. R. Gibney, D. P. Kessissoglou, J. W. Kampf, V. L. Pecoraro, *Inorg. Chem.* **1994**, *33*, 4840–4849.
[17] I. Bertini, C. Luchinat, S. Aime, *Coord. Chem. Rev.* **1996**, *150*, 77–110.
[18] I. Bertini, C. Luchinat, S. Aime, *Coord. Chem. Rev.* **1996**, *150*, 131–161.
[19] T. J. Wenzel, *NMR shift reagents*, CRC Press, Boca Raton, **1987**.
[20] C. Piguet, C. F. G.C Geraldes, Paramagnetic NMR Lanthanide Induced Shifts for Extracting Solution Structures, in: *Handbook on the Physics and Chemistry of Rare Earths*, K. A. Gschneidner Jr., J.-C. G. Bünzli, V. Pecharsky, Eds., Vol. 33, Ch. 215, pp 353–463, Elsevier, Amsterdam, **2003**.
[21] S. Rigault, C. Piguet, *J. Am. Chem. Soc.* **2000**, *122*, 9304–9305.
[22] S. Rigault, C. Piguet, G. Bernardinelli, G. Hopfgartner, *J. Chem. Soc., Dalton Trans.* **2000**, 4587–4600.
[23] J. A. Peters, J. Huskens, D. J. Raber, *Prog. NMR Spectrosc.* **1996**, *28*, 283–350.
[24] W. D. Horrocks, J. P. Sipe, *Science* **1972**, *177*, 994.
[25] B. R. Gibney, A. J. Stemmler, S. Pilotek, J. W. Kampf, V. L. Pecoraro, *Inorg. Chem.* **1993**, *32*, 6008–6015.
[26] D. F. Shriver, P. W. Atkins, *Inorganic Chemistry*, Oxford University Press **1999**.
[27] C. R. Hauser, W. B. Renfrow, Jr., *Org. Synth.* **1945**, *2*, 67–68.
[28] G. te Velde, F. M. Bickelhaupt, S. J. A. van Gisbergen, C. Fonseca Guerra, E. J. Baerends, J. G. Snijders, *J. Comput. Chem.* **2001**, *22*, 931–967.
[29] C. Fonseca Guerra, J. G. Snijders, G. te Velde, E. J. Baerends, *Theor. Chem. Acc.* **1998**, *99*, 391.
[30] ADF2002.03, SCM, Theoretical Chemistry, Vrije Universiteit, Amsterdam, The Netherlands, http://www.scm.com.
[31] S. H. Vosko, L. Wilk, M. Nusair, *Can. J. Phys.* **1980**, *58*, 1200.
[32] A. D. Becke, *Phys. Rev. A* **1988**, *38*, 3098.
[33] J. P. Perdew, *Phys. Rev. B* **1986**, *33*, 8822.

Received: March 20, 2005
Published Online: July 14, 2005

 © 2005 Wiley-VCH Verlag GmbH & Co. KGaA, Weinheim

Imino- and Oxazolino-Functionalised Pyrrolylphosphanes and Pyrrolylphosphinites: An Unexploited Class of Chiral *P,N*-Bidentate Ligands with Unusual Electronic Properties

Konstantin N. Gavrilov,[a] Vasily N. Tsarev,*[b] Stanislav I. Konkin,[a] Sergey E. Lyubimov,[b] Alexander A. Korlyukov,[b] Mikhail Yu. Antipin,[b] and Vadim A. Davankov[b]

Keywords: Allylic substitution / Asymmetric catalysis / Palladium / *P,N*-bidentate ligands / Rhodium

Enantiopure *P,N*-bidentate pyrrolylphosphanes and pyrrolylphosphinites have been prepared based upon chiral imino- and oxazolino-containing compounds. Complexation of the new ligands with $[Rh(CO)_2Cl]_2$ and $[Pd(allyl)Cl]_2$ has been found to give the chelate complexes $[Rh(CO)Cl(\eta^2\text{-}P,N)]$ and $[Pd(allyl)(\eta^2\text{-}P,N)]^+BF_4^-$, respectively. Imino- and oxazolino-functionalised pyrrolylphosphanes and pyrrolylphosphinites have been shown to be a novel class of *P,N*-bidentate ligands possessing exceptional π-acceptor and original σ-donor properties. With these ligands, up to 77 % *ee* has been achieved in the asymmetric Pd-catalyzed sulfonylation of 1,3-diphenyl-2-propenyl acetate with sodium *p*-toluenesulfinate. In the enantioselective alkylation of 1,3-diphenyl-2-propenyl acetate with dimethyl malonate, up to 93 % enantioselectivity has been achieved by using $[Pd(allyl)(\eta^2\text{-}P,N)]^+BF_4^-$ complexes as chiral catalysts.
(© Wiley-VCH Verlag GmbH & Co. KGaA, 69451 Weinheim, Germany, 2005)

Introduction

In the last decade, (1-pyrrolyl)phosphanes ($PPh_x(NC_4H_4)_{3-x}$, x = 0–2), phosphinites and phosphonites ($P(OPh)_x(NC_4H_4)_{3-x}$, x = 1–2) have been successfully applied in the synthesis of rhodium[1–7] and cobalt[8] complexes, as well as in Rh-catalyzed hydroformylation.[9,10] A set of spectroscopic, structural, and thermochemical measurements[1–7,10] showed that these substances are exceptional π-acceptor ligands. The rationale for this π-acceptor character is best demonstrated by the resonance forms **A**–**D**, Figure 1.

Aromatic delocalisation of the nitrogen lone pair into the five-membered ring places a partial positive charge adjacent to the phosphorus atom. This contribution in **B** and **C** would be expected to render the pyrrolyl substituent an effective electron-withdrawing group. Relative to phenyl, resonance form **D** would also be expected to contribute in an electron-withdrawing fashion, since a more electronegative nitrogen atom replaces carbon.[3] As a result, the substituent parameter χ_i for the 1-pyrrolyl functionality is approximately 12, and the π-acceptor character of these ligands is thus found to exceed that of arylphosphites (–OPh, χ_i = 9.7) and fluorinated aromatic phosphanes (–C_6F_5 χ_i = 11.2).[3]

The higher frequencies of the metal carbonyl stretch for rhodium complexes with pyrrolylphosphanes and pyrrolylphosphonites compared with rhodium complexes with phosphites (Table 1) are consistent with pyrrolyl-based ligands being a better π-acceptor than phosphites, as anticipated from the greater number of 1-pyrrolyl substituents, which reduces the back-donation to the metal carbonyl.

As for σ basicity, the $^1J_{P,Se}$ coupling constants in the ^{31}P NMR spectra of corresponding selenide derivatives indicate

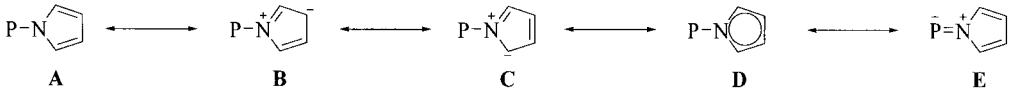

Figure 1. Resonance forms of pyrrolylphosphanes.

[a] Department of Chemistry, Ryazan State Pedagogic University, 46 Svoboda str., Ryazan, 390000, Russia
Fax: +7-0912-775-498
E-mail: chem@ttc.ryazan.ru
[b] Institute of Organoelement Compounds, Russian Academy of Sciences,
28 Vavilova str., Moscow, 119991, Russia
Fax: +7-095-135-6471
E-mail: tsarev@ineos.ac.ru

that $P(NC_4H_4)_3$ ($^1J_{P,Se}$ for $Se{=}P(NC_4H_4)_3$ = 970 Hz) is more basic than $P(OPh)_3$ and constrained phosphites ($^1J_{P,Se}$ for Se=L = 1099–1011 Hz) and less basic than $P(NR_2)_3$ ($^1J_{P,Se}$ for Se=L = 854–784 Hz).[6] For estimating the σ basicity of pyrrolylphosphanes, we suggest a well-known criterion that the values of $^1J_{P,Rh}$ coupling constants in the ^{31}P NMR spectra of corresponding chlorocarbonyl complexes

 DOI: 10.1002/ejic.200500075 © 2005 Wiley-VCH Verlag GmbH & Co. KGaA, Weinheim

Table 1. Spectroscopic data for the complexes [Rh(acac)(CO)L] and *trans*-[RhCl(CO)L_2].

Complex	ν(CO) [cm^{-1}] (CH_2Cl_2)	$^1J_{P,Rh}$, [Hz] ($CDCl_3$)
[Rh(acac)(CO){P(NC_4H_4)$_3$}][5]	2012	251
[Rh(acac)(CO){P(OPh)$_3$}][4,5]	2006	293
[Rh(acac)(CO){P(OEt)$_3$}][11]	1990	267
[Rh(CO){P(NC_4H_4)$_3$}$_2$Cl][1,2]	2024	180
[Rh(CO){P(NC_4H_4)$_2$(OPh)}$_2$Cl][10]	2018	190
[Rh(CO){P(OPh)$_3$}$_2$Cl][2]	2016	210

of rhodium(I) strongly correlate with the s character of the phosphorus lone pair.[11,12] According to this criterion, pyrrolylphosphanes are strong σ bases comparable not only with P(OPh)$_3$ and constrained phosphites, but also with alkyl phosphites (Table 1). A possible reason is a significant contribution of the resonance form with partial negative charge at the phosphorus atom, and easy polarization of the aromatic group.[13] Values of $^1J_{P,Se}$ and $^1J_{P,Rh}$ seem to be more correct criteria for σ basicity than the bond lengths Rh–P used by some authors.[14] On the basis of the X-ray data for the isostructural complexes [Rh(acac)(CO){P(OPh)$_3$}] (Rh–P 2.170 Å) and [Rh(acac)(CO){P(NC_4H_4)$_3$}] (Rh–P 2.166 Å), they made a conclusion about stronger σ-donor properties of P(OPh)$_3$ in comparison to P(NC_4H_4)$_3$. However, bond lengths M–P are dependent not only on σ basicity, but also on π acidity of the ligand.[6] Thus, in another pair of isostructural compounds [Rh(acac){P(OPh)$_3$}$_2$] (Rh–P 2.147, 2.156 Å) and [Rh(acac){P(NC_4H_4)$_3$}$_2$] (Rh–P 2.161, 2.176 Å), bonds Rh–P are longer in the complex with P(NC_4H_4)$_3$,[4] while $^1J_{P,Rh}$ is 291 and 261 Hz, respectively (compare also with the data in Table 1).

Therefore, pyrrolylphosphanes and pyrrolylphosphinites are characterised by rather paradoxical electronic properties, and are both more potent π acids and σ bases than phosphites, representing a novel and efficient group of optically active ligands.[15–17] It should be noted that the –P(NC_4H_4)$_2$ building block and the common chiral ligand –PPh$_2$ fragment are practically the same size, according to their Tolman's cone angle values.[1,4] One could expect that such unusual electronic and steric properties of ligands with –P(NC_4H_4)$_2$ fragments make these compounds promising for asymmetric catalysis, but to the best of our knowledge no examples of their catalytic application are known. In the present communication we report previously unknown chiral pyrrolylphosphanes and pyrrolylphosphinites and pioneering results of their application in the coordination chemistry of palladium and in asymmetric Pd-catalysed allylation.

Results and Discussion

The new *P,N*-bidentate pyrrolylphosphinites **2a**–**c** and pyrrolylphosphanes **2d**,**e** were obtained from chlorobis(1-pyrrolyl)phosphane in one step (Scheme 1).

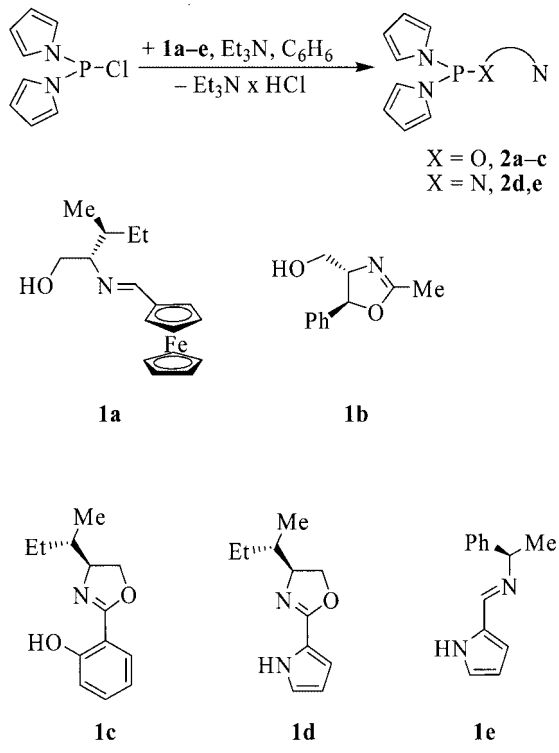

Scheme 1.

Compounds **2a**–**e** are soluble in common nonprotic solvents and stable under dry conditions. Unlike P(NC_4H_4)$_3$, ligands **2d** and **2e** are moisture sensitive. A possible reason for this, as in the case of the keto-functionalised ligand P(NC_4H_4)$_2$(NC_4H_3C(O)Me-2),[7] is that a functionalised pyrrole ring represents a better leaving group than the unfunctionalised pyrrolyl groups and, additionally, is able to form hydrogen bonds with incoming protic nucleophiles.

Using the compounds **2a**–**e**, neutral and cationic *cis*-chelate metal complexes were obtained (Scheme 2).

Some important spectroscopic data of the complexes are summarised in Table 2.

The $^1J_{P,Rh}$ and ν(CO) data for complexes **3a**–**e** are in good agreement with the suggested structures.[18] IR and ^{13}C NMR spectroscopic characteristics of the carbonyl ligands in complexes **3a**–**e** (δ_C = 186.2 ppm, $^1J_{C,Rh}$ = 72 Hz, ^2J(C,P) = 16 Hz for **3a** and δ_C = 184.9 ppm, $^1J_{C,Rh}$ = 68 Hz, $^2J_{C,P}$ = 17 Hz for **3e**) indicate that **2a**–**e** represent a novel group of highly π-accepting *P,N*-bidentate ligands.[4,7,19] Notably, the ν(CO) values of **3d**,**e** prove that

 © 2005 Wiley-VCH Verlag GmbH & Co. KGaA, Weinheim

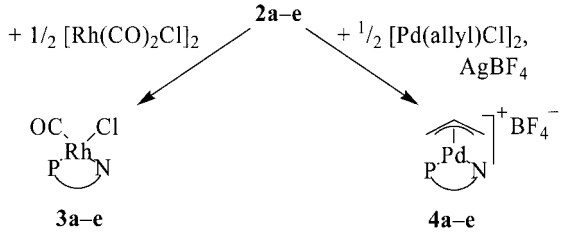

Scheme 2.

Table 2. Selected spectroscopic data for compounds **3a**–**e** and **4a**–**e** (in $CHCl_3$).

Compound	^{31}P NMR Spectroscopy δ_P	^1J(P,Rh) [Hz]	IR Spectroscopy ν(CO) [cm^{-1}]
3a	116.7	242	2032
3b	116.3	242	2034
3c	126.2	256	2036
3d	93.4	245	2039
3e	94.9	249	2040
4a	113.1, 112.6	–	–
4b	115.6, 115.1	–	–
4c	125.5, 124.7	–	–
4d	89.3, 88.8	–	–
4e	92.5	–	–

ligands **2d**,**e** bearing three pyrrole rings, are the most π acidic in the group. A comparison of the $^1J_{P,Rh}$ and ν(CO) data for compounds **3a**–**c** (Table 2) and isostructural rhodium complexes previously described by us[18,20,21] (Table 3)

Table 3. Selected spectral parameters for [Rh(CO)Cl(η^2-*P,N*)] complexes with *P,N*-bidentate arylphosphite ligands.

Ligand	ν(CO), cm^{-1} ($CHCl_3$)	$^1J_{P,Rh}$, Hz ($CHCl_3$)
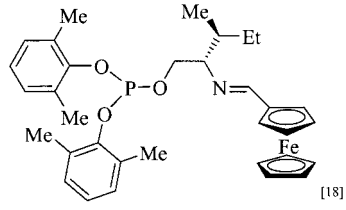 [18]	2025	279
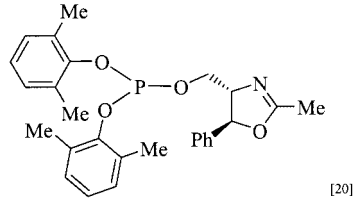 [20]	2030	277
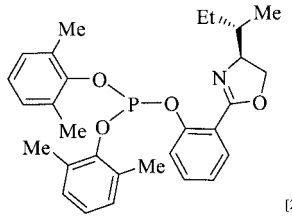 [21]	2024	287

supports a general conclusion about higher σ-donor and π-acceptor properties of pyrrolylphosphanes and pyrrolylphosphinites with respect to phosphites.

It is rather difficult to determine the best σ donor among the ligands **2a**–**e**, since the $^1J_{P,Rh}$ values in chloro carbonyl rhodium chelate complexes depend largely on the nature of a nitrogen-containing fragment (see ref.[18] and references cited therein). But in the case of **3c** and **3d**, the ^{31}P NMR spectroscopic data (Table 2) indicate that pyrrolylphosphane **2d** is a stronger σ donor than pyrrolylphosphinite **2c**.

Complexes **3a**, **3c** and **3d** were characterised by X-ray diffraction. Their molecular structures are shown in Figure 2, Figure 3 and Figure 4, and selected bond lengths and angles are given in Table 4.

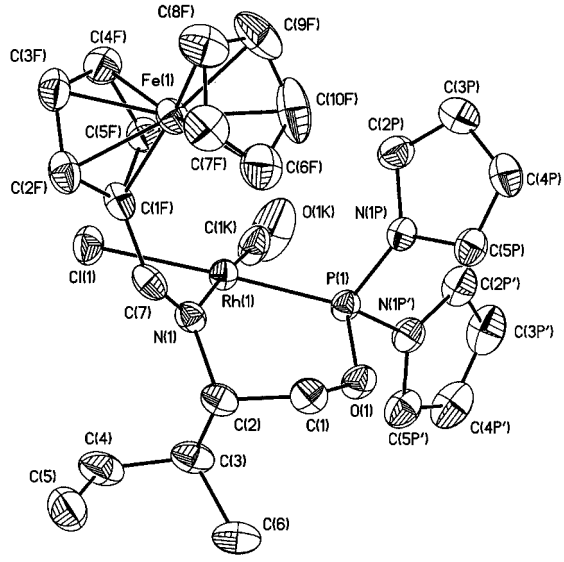

Figure 2. Molecular structure of complex **3a**. Atoms are given by thermal ellipsoids at 50% probability. Principal bonds and angles (Å and °): Rh(1)–C(1K) 1.837(3), Rh(1)–N(1) 2.141(2), Rh(1)–P(1) 2.1576(8), Rh(1)–Cl(1) 2.3742(9), P(1)–O(1) 1.598(2), P(1)–N(1P) 1.691(2), P(1)–N(1P′) 1.703(2), O(1)–C(1) 1.444(3), O(1K)–C(1K) 1.134(4); O(1)–P(1)–N(1P) 103.34(12), O(1)–P(1)–N(1P′) 96.27(12), N(1P)–P(1)–N(1P′) 100.49(11), O(1)–P(1)–Rh(1) 116.68(8), N(1P)–P(1)–Rh(1) 116.72(8), N(1P′)–P(1)–Rh(1) 119.95(9).

From X-ray studies it was found that in the crystal the molecules of **3a**,**c**,**d** are characteried by *S* configurations of C(2) and C(3) for **3a**, C(4) and C(5) for **3c**, and C(4) and C(5) for the **3d** asymmetric atoms, respectively.

The distorted sofa conformation (the deviation of the P(1) atom from the basal plane is 0.81 Å) of the six-membered metallacycle is observed in compound **3d**. In compound **3a,** where the fused five-membered cyclic fragments are absent, the six-membered metallacycle adopts the distorted chair conformation with deviations of the P(1) and C(2) atoms by 0.57 and 0.79 Å, respectively. The chair conformation of the six-membered metallacycle is also observed in previously studied complexes with the 1,3-diaza-2-phosphabicyclo[3.3.0]octane ligand.[22] So, it can be concluded that the distorted sofa conformation in **3d** is caused by the presence of five-membered cycles fused with the metallacycle.

 © 2005 Wiley-VCH Verlag GmbH & Co. KGaA, Weinheim

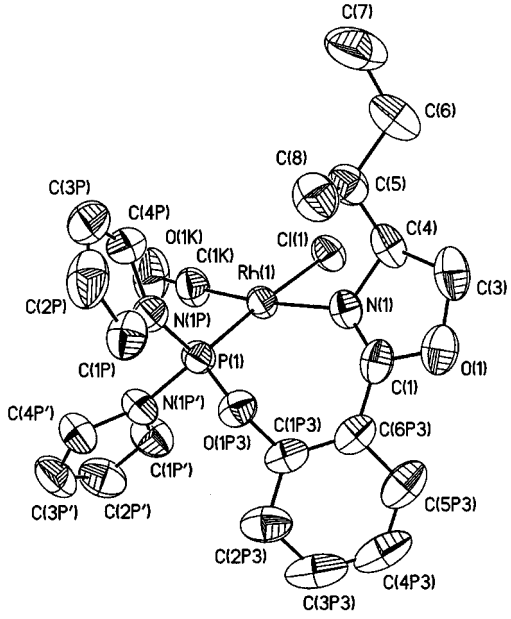

Figure 3. Molecular structure of complex **3c**. Atoms are given by thermal ellipsoids at 50% probability. Principal bonds and angles (Å and °): Rh(1)–C(1K) 1.828(3), Rh(1)–N(1) 2.1020(19), Rh(1)–P(1) 2.1553(9), Rh(1)–Cl(1) 2.3810(9), P(1)–O(1P3) 1.6166(17), P(1)–N(1P) 1.691(2), P(1)–N(1P′) 1.696(2), O(1K)–C(1K) 1.134(3); O(1P3)–P(1)–N(1P) 94.72(10), O(1P3)–P(1)–N(1P′) 103.95(10), N(1P)–P(1)–N(1P′) 102.73(10), O(1P3)–P(1)–Rh(1) 116.33(6), N(1P)–P(1)–Rh(1) 119.85(8), N(1P′)–P(1)–Rh(1) 116.05(8).

The seven-membered metallacycle in **3c** is fused with phenyl and oxazoline moieties and its conformation may be described as a distorted boat. Atoms C(1P3), C(6P3) and Rh(1) deviate from the plane P(1)O(1P3)N(1)C(1) by 0.93, 0.98 and 0.68 Å, respectively.

Table 4. Selected bond lengths [Å] and angles [°] for complexes **3a**, **3c** and **3d**.

	3a	**3c**	**3d**
Rh(1)–C(1K)	1.837(3)	1.828(3)	1.838(3)
Rh(1)–N(1)	2.141(2)	2.1019(19)	2.111(2)
Rh(1)–P(1)	2.158(1)	2.155(1)	2.145(1)
Rh(1)–Cl(1)	2.374(1)	2.381(1)	2.363(1)
O(1K)–C(1K)	1.134(4)	1.134(3)	1.129(4)
N(1)–Rh(1)–P(1)	88.36(7)	90.20(6)	86.54(6)
C(1K)–Rh(1)–P(1)	89.81(9)	91.13(9)	93.67(10)
C(1K)–Rh(1)–Cl(1)	89.00(9)	89.48(9)	89.35(10)
N(1)–Rh(1)–Cl(1)	92.67(7)	89.64(6)	90.64(6)
P(1)–Rh(1)–Cl(1)	177.35(3)	176.05(2)	174.45(3)
O(1K)–C(1K)–Rh(1)	178.0(3)	176.9(3)	178.1(3)

The oxazoline cycles in **3c** and **3d** have different conformations. In the former case this cycle is planar, while in the latter it adopts the envelope conformation with deviation of the C(4) atom by 0.15 Å. The ferrocenyl substituent in **3a** occupies a pseudoequatorial position.

The *endo*-cyclic rhodium atom has an almost ideal square-planar geometry, its deviation from the basal plane does not exceed 0.02 Å. On the other hand in **4** the deviation of the Rh^{I} atom from the basal plane is more pronounced (0.06 Å), which may be explained by steric overcrowding of the six-membered metallacycle. The P(1)–Rh(1) bonds in **3a**,**c**,**d** are somewhat shorter than those in the previously investigated 1,3-diaza-2-phosphabicyclo[3,3,0]octane ligand complex[22]. On the other hand, the shortening of the P(1)–Rh(1) bond did not lead to respective elongation of the Rh(1)–Cl(1) bond in comparison to the analogous bond in the previously described complex.[22] So, the *trans*-effect of a $P(C_4H_4N)_3$ moiety is almost the same as

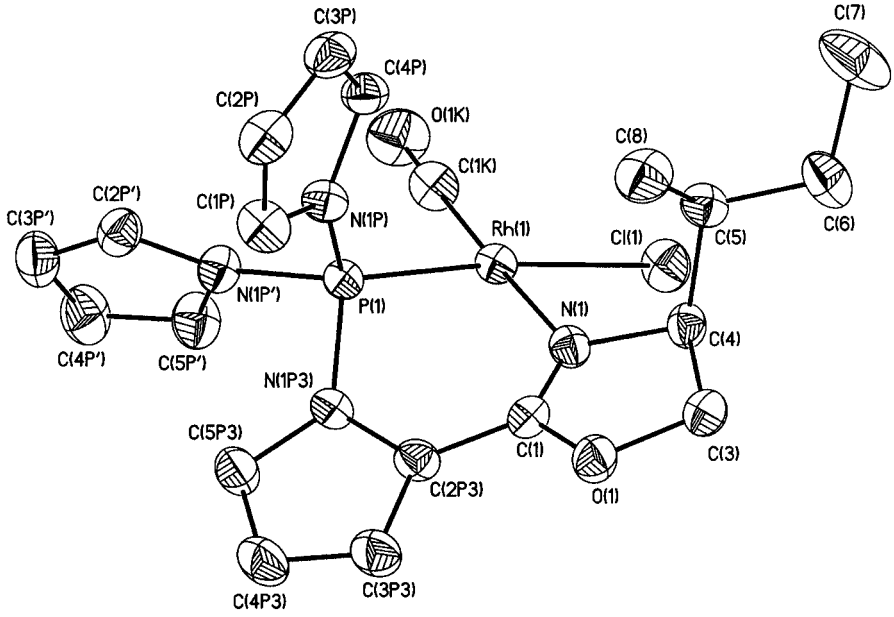

Figure 4. Molecular structure of complex **3d**. Atoms are given by thermal ellipsoids at 50% probability. Principal bonds and angles (Å and °): Rh(1)–C(1K) 1.838(3), Rh(1)–N(1) 2.111(2), Rh(1)–P(1) 2.1448(8), Rh(1)–Cl(1) 2.3631(9), P(1)–N(1P) 1.681(2), P(1)–N(1P′) 1.698(2), P(1)–N(1P3) 1.717(2), C(1K)–O(1K) 1.129(4); N(1P)–P(1)–N(1P′) 102.52(12), N(1P)–P(1)–N(1P3) 99.87(12), N(1P′)–P(1)–N(1P3) 100.44(11), N(1P)–P(1)–Rh(1) 118.26(8), N(1P′)–P(1)–Rh(1) 121.83(9), N(1P3)–P(1)–Rh(1) 110.46(8).

 © 2005 Wiley-VCH Verlag GmbH & Co. KGaA, Weinheim

in the case of the 1,3-diaza-2-phosphabicyclo[3.3.0]octane fragment.

The geometry of the P(1) atom in **3a** and **3c** is distorted tetrahedral, the bond angles at this atom vary in the range of 94–119°. It should be noted that endocyclic P–O bonds in **3a**,**c**,**d** have almost the same lengths as in previously studied compound.[22]

There is no correlation between $^1J_{P,Rh}$ values and Rh–P bond lengths, because, as mentioned above, the Rh–P bond length depends not only on σ basicity but also on the π acidity of the P ligand. Thus, the shortest Rh–P bonds were found in the complexes with the most π-acceptor pyrrolylphosphanes [Rh(CO)($P(NC_4H_4)_2(NC_4H_3C(O)Me$-2))Cl] [2.147 Å, $^1J_{P,Rh}$ = 237 Hz, $\tilde{\nu}$(CO) = 2017 cm^{-1} (KBr)],[7] [Rh(CO)($P(NC_4H_4)_2$(7-aza-1-indolyl))Cl] and **3d** (Table 5); **3d** has the shortest Rh–P bond among these complexes and related compounds like [Rh(acac)(CO){$P(NC_4H_4)_3$}]. The data in Table 5 clearly demonstrate that *ν*(CO) in the IR spectra of [Rh(CO)(L)Cl] complexes is strongly affected by changings in the π acidity of *P,N*-bidentate ligands. In particular, pyrrolylphosphane $P(NC_4H_4)_2$(7-aza-1-indolyl) is a much stronger π acceptor than $P(Ph)_2$(7-aza-1-indolyl), but weaker than **2d**,**e**. It is notable that whereas *ν*(CO) for the rhodium complexes varies significantly from 1986 to 2040 cm^{-1} ($\Delta\tilde{\nu}$(CO) = 54 cm^{-1}), $\Delta^1J_{C,Rh}$ does not exceed a mere 6 Hz (Table 5). Moreover, the $\tilde{\nu}$(CO) magnitudes of [Rh(CO)($P(Ph)_2$(7-aza-*N*-indolyl))Cl] and [Rh(CO)-($P(NC_4H_4)_2$(7-aza-*N*-indolyl)Cl] differ by 22 cm^{-1}, while their $^1J_{C,Rh}$ values are equal. These facts are in good agreement with a conclusion made earlier by us that $^1J_{C,Rh}$ for *cis-P,N*-chelate chlorocarbonyl complexes [Rh(CO)(L)Cl] lie within a narrow interval of 68–75 Hz and are practically indifferent to electronic characteristics of a phosphorus atom environment.[20] Duplication of peaks in the ^{31}P NMR spectra of compounds **4a**–**d** (Table 2) indicates the presence of their *exo*- and *endo*-isomers.[18,21] Sharp singlets in the ^{31}P NMR spectrum of **4e** can be rationalised either by fast interconversion of the isomers or by an absence of one of them.

Pyrrolylphosphanes and pyrrolylphosphinites **2a**–**e** and complexes **4c**,**d** were tested in asymmetric Pd-catalysed allylic substitution reactions (Scheme 3).

The results of allylic sulfonylation are summarised in Table 6. Good optical (up to 77% *ee*) and moderate chemi-

Table 5. Some spectral and structural parameters of *cis-P,N*-chelate chlorocarbonyl complexes [Rh(CO)(L)Cl].

Ligand	ν(CO), cm^{-1} ($CHCl_3$)	$^1J_{P,Rh}$ ($^2J_{C,P}$), Hz ($CDCl_3$)	$^1J_{P,Rh}$, Hz ($CHCl_3$)	Rh–P, Å
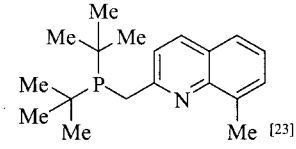 [23]	1986	74 (21)	167	–
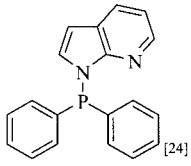 [24]	2005	70 (23)	180	2.198
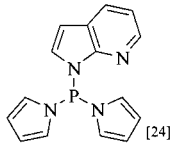 [24]	2027	70 (23)	242	2.165
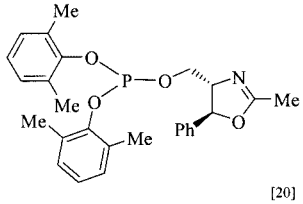 [20]	2030	72 (19)	277	2.173
2a	2032	72 (16)	242	2.158
2c	2036	–	256	2.155
2d	2039	–	245	2.145
2e	2040	68 (17)	249	–

 © 2005 Wiley-VCH Verlag GmbH & Co. KGaA, Weinheim

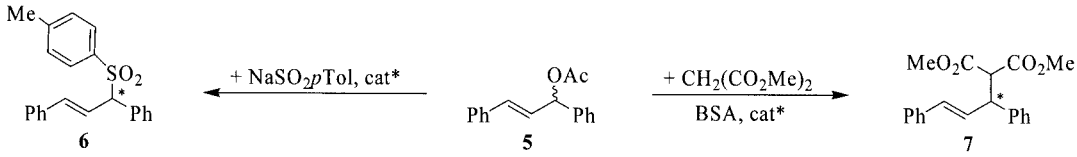

Scheme 3.

cal (up to 60%) yields of product **6** were achieved. **2b** (entry 5) was found to be the most stereoselective ligand, while **2a**, **2c** and **2e** showed basically the same enantioselectivity (54–64%), and no conversion was observed with **2d** (entries 10–12). An increased L*/Pd molar ratio in the processes catalysed by $[Pd(allyl)Cl]_2$ resulted in higher optical and chemical yields (entries 1,2; 4,5). Worth noting is that the most successful catalyst precursor for **2c** happened to be $[Pd_2(dba)_3]\times CHCl_3$ (entries 7–9).

Table 6. Enantioselective allylic sulfonylation of **5** with $NaSO_2pTol$ (in THF).

Entry	Catalyst precursor	Ligand	L*/Pd	Isolated yield [%]	*ee* [%][a]
1	$[Pd(allyl)Cl]_2$	**2a**	1:1	17	32 (*R*)
2	$[Pd(allyl)Cl]_2$	**2a**	2:1	60	64 (*R*)
3	$[Pd_2(dba)_3]\times CHCl_3$	**2a**	1:1	16	33 (*R*)
4	$[Pd(allyl)Cl]_2$	**2b**	1:1	0	–
5	$[Pd(allyl)Cl]_2$	**2b**	2:1	26	77 (*R*)
6	$[Pd_2(dba)_3]\times CHCl_3$	**2b**	1:1	15	15 (*S*)
7	$[Pd(allyl)Cl]_2$	**2c**	1:1	37	7 (*S*)
8	$[Pd(allyl)Cl]_2$	**2c**	2:1	30	7 (*S*)
9	$[Pd_2(dba)_3]\times CHCl_3$	**2c**	1:1	25	54 (*S*)
10	$[Pd(allyl)Cl]_2$	**2d**	1:1	0	–
11	$[Pd(allyl)Cl]_2$	**2d**	2:1	0	–
12	$[Pd_2(dba)_3]\times CHCl_3$	**2d**	1:1	0	–
13	$[Pd(allyl)Cl]_2$	**2e**	1:1	22	57 (*R*)
14	$[Pd(allyl)Cl]_2$	**2e**	2:1	31	58 (*R*)

[a] *ee* measured by HPLC [(*R*,*R*)-Whelk-01, hexane/*i*PrOH = 4:1, 1 mL/min, 254 nm].

For the asymmetric allylic alkylation (Scheme 3, Table 7), ligands **2a** and **2c** provided the best results (entries 1,2,5). Thus, cationic complex **4c** afforded the product in 93% *ee* (93% conversion, entry 7).

Table 7. Enantioselective allylic alkylation of **5** with dimethyl malonate (in THF, L*/Pd = 1:1).

Entry	Catalyst	Conv. [%][a]	*ee* [%][b]
1	$[Pd(allyl)Cl]_2$/**2a**	99	83 (*R*)
2	$[Pd_2(dba)_3]\times CHCl_3$/**2a**	91	81 (*R*)
3	$[Pd(allyl)Cl]_2$/**2b**	99	44 (*R*)
4	$[Pd_2(dba)_3]\times CHCl_3$/**2b**	99	38 (*R*)
5	$[Pd(allyl)Cl]_2$/**2c**	46	88 (*S*)
6	$[Pd_2(dba)_3]\times CHCl_3$/**2c**	12	61 (*S*)
7	**4c**	93	93 (*S*)
8	$[Pd(allyl)Cl]_2$/**2d**	19	64 (*S*)
9	$[Pd_2(dba)_3]\times CHCl_3$/**2d**	8	36 (*R*)
10	**4d**	0	–
11	$[Pd(allyl)Cl]_2$/**2e**	11	80 (*S*)
12	$[Pd_2(dba)_3]\times CHCl_3$/**2e**	10	67 (*S*)

[a] Measured by HPLC. [b] Determined by HPLC (Daicel Chiralcel OD-H, hexane/*i*PrOH = 99:1; 0.5 mL/min, 254 nm).

Stereoinduction of pyrrolylphosphane **2e** is close to **2a** and **2c** (entry 11), but conversion is low. Ligands **2b** and **2d** demonstrated moderate enantioselectivity (up to 64% *ee*) with substantially low conversion in the case of **2d**. In contrast to allylic sulfonylation, $[Pd(allyl)Cl]_2$ was a superior catalyst precursor for all ligands.

Conclusions

Several chiral imino- and oxazolino-functionalised pyrrolylphosphanes and pyrrolylphosphinites were obtained for the first time by a simple one-step synthesis. These compounds have been shown to be a novel class of *P,N*-bidentate ligands possessing exceptional π-acceptor and original σ-donor properties. The new ligands were used in asymmetric Pd-catalyzed allylic substitution where up to 93% *ee* was achieved in the benchmark test with 1,3-diphenyl-2-propenyl acetate and dimethyl malonate. It should be pointed out, however, that the present work describes only five substances in this general class. A tremendous variety of similar substituents such as substituted pyrroles, indoles, imidazoles, pyrazoles, etc., are commercially available or obtainable by synthetic means.[1] The simple synthesis of pyrrolylphosphanes and pyrrolylphosphinites, their outstanding electronic properties, together with the wide variety of accessible pyrrolelike precursors make it an attractive area of research with great promise.

Experimental Section

General Remarks: All reactions were performed under argon in dehydrated solvents. IR spectra were recorded with a Specord M80 instrument. ^{31}P and ^{13}C NMR spectra were recorded with a Bruker AMX 400 instrument (162.0 MHz for ^{31}P, 100.6 MHz for ^{13}C). The assignments of the signals in the ^{13}C NMR spectra were made with the use of the DEPT technique and, for pyrrolyl substituents, using literature data.[10] Chemical shifts (ppm) are given relative to Me_4Si (^{13}C NMR) and 85% H_3PO_4 (^{31}P NMR). Mass spectra were recorded with a Kratos MS890 spectrometer (EI), an MSVKh TOF spectrometer with ionization by Cf-252 fission fragments (plasma desorption technique, PD) and AMD 402 spectrometer (FAB). Optical rotations were measured on a Perkin–Elmer 141 polarimeter. Elemental analyses were performed at the Laboratory of Microanalysis (Institute of Organoelement Compounds, Moscow).

$[Rh(CO)_2Cl]_2$,[25] $[Pd(allyl)Cl]_2$,[26] $[Pd_2(dba)_3]\times CHCl_3$,[27] chlorobis(1-pyrrolyl)phosphane,[10] compounds **1a**,[18] **1c**,[28] **1d**[29] and **1e**[30] were synthesised using literature procedures. 4-Hydroxymethyl-2-methyl-5-phenyl-2-oxazoline (**1b**) was purchased from Fluka. The syntheses of rhodium(I) complexes **3a**–**e** and palladium(II) complexes **4a**–**e** were performed by techniques similar to that reported.[18,31]

$NaSO_2pTol$, $CH_2(CO_2Me)_2$ and *N*,*O*-bis(trimethylsilyl)acetamide (BSA) were purchased from Acros Organics. Compound **5** was syn-

 © 2005 Wiley-VCH Verlag GmbH & Co. KGaA, Weinheim

thesised as published.[26] The catalytic experiments were carried out according to published procedures.[22]

Preparation of Ligands. General Technique: A solution of chlorobis(1-pyrrolyl)phosphane (4.2×10^{-3} mol) in benzene (15 mL) was added dropwise to a stirred solution of the appropriate compound **1a**–**e** (4.2×10^{-3} mol) and Et_3N (0.6 mL, 4.2×10^{-3} mol) in the same solvent (15 mL) at 0 °C. The reaction mixture was then heated to boiling point, allowed to cool down, stirred for 0.5 h at 50 °C, allowed to cool to room temperature and filtered. The solvent was removed in vacuo (40 Torr), and the residue was concentrated and dried in vacuo (1 Torr, 2 h).

{(2*S*)-2-(Ferrocenylmethylideneamino)-2-[(1*S*)-1-methylpropyl]-ethoxy}bis(1-pyrrolyl)phosphinite (2a): Yield: 1.85 g, 93%; dark red oil. $[a]_D^{21}$ = +151.4 (*c* = 0.5, $CHCl_3$). ^{13}C NMR ($CDCl_3$): δ_C = 161.7 (CH=N), 121.1 (d, ^2J = 14.9 H, CHNP), 120.9 (d, ^2J = 14.7 Hz, CHNP), 111.7 (d, ^3J = 6.5 Hz, *C*HCHNP), 111.6 (d, ^3J = 6.1 Hz, *C*HCHNP), 80.4 [$C_{Fc(ipso)}$], 76.3 (d, ^3J = 5.3 Hz, CHN), 70.1, 69.9, 69.1, 67.5 (all C_{Fc}), 69.2 (d, ^2J = 16.3 Hz, CH_2OP), 68.7 (C_{Cp}), 36.1 (*C*HCH$_3$), 25.2 (*C*H$_2$CH$_3$), 15.7 (CH*C*H$_3$), 10.8 (CH$_2$*C*H$_3$) ppm. ^{31}P NMR ($CDCl_3$): δ_P = 113.6 ppm. MS (70 eV, EI): *m*/*z* (%): 475 (6) $[M]^+$, 409 (64) [M – pyrrolyl]$^+$, 264 (95), 121 (100). MS (PD): *m*/*z* (%): 475 (80) $[M]^+$, 409 (100) [M – pyrrolyl]$^+$. MS (FAB): *m*/*z* (%): 475 (16) $[M]^+$, 409 (85) [M – pyrrolyl]$^+$, 264 (100). Elemental analysis for $C_{25}H_{30}FeN_3OP$ (475.2): calcd. C 63.17, H 6.36, N 8.84; found C 63.31, H 6.29, N 8.71.

[(4*S*,5*S*)-(2-Methyl-5-phenyl-2-oxazolin-4-yl)methoxy]bis(1-pyrrolyl)phosphinite (2b): Yield 1.33 g, 90%; light yellow oil. $[a]_D^{21}$ = –158.3 (*c* = 1, $CHCl_3$). ^{13}C NMR ($CDCl_3$): δ_C = 166.0 (C=N), 139.8, 128.5, 128.1, 125.1 (all C_{Ph}), 121.0 (d, ^2J = 10.3 Hz, CHNP), 120.9 (d, ^2J = 10.1 Hz, CHNP), 111.9 (d, ^3J = 5.3 Hz, *C*HCHNP), 111.8 (d, ^3J = 5.0 Hz, *C*HCHNP), 82.6 (CHO), 74.6 (d, ^3J = 6.5 Hz, CHN), 68.3 (d, ^2J = 18.3 Hz, CH_2OP), 13.5 (CH_3) ppm. ^{31}P NMR ($CDCl_3$): δ_P = 114.5 ppm. MS (PD): *m*/*z* (%): 353 (7) $[M]^+$, 313 (55), 101 (100). MS (FAB): *m*/*z* (%): 353 (2) $[M]^+$, 287 (100) [M – pyrrolyl]$^+$, 182 (83). Elemental analysis for $C_{19}H_{20}N_3O_2P$ (353.1): calcd. C 64.58, H 5.70, N 11.89; found C 64.39, H 5.77, N 12.01.

{2-[(4*S*)-4-*sec*-Butyl-2-oxazolin-2-yl]phenoxy}bis(1-pyrrolyl)phosphinite (2c): Yield 1.46 g, 92%; light yellow oil. $[a]_D^{21}$ = –17.5 (*c* = 1, $CHCl_3$). ^{13}C NMR ($CDCl_3$): δ_C = 160.6 (C=N), 151.4 (d, ^2J = 10.3 Hz), 132.0, 130.9, 124.4, 120.6, 116.4 (all C_{Ar}), 121.6 (d, ^2J = 15.9 Hz, CHNP), 121.5 (d, ^2J = 16.4 Hz, CHNP), 111.9 (d, ^3J = 5.0 Hz, *C*HCHNP), 111.8 (d, ^3J = 4.6 Hz, *C*HCHNP), 71.3 (CHN), 69.1 (CH_2O), 38.8 (*C*HCH$_3$), 25.7 (*C*H$_2$CH$_3$), 14.2 (CH*C*H$_3$), 11.2 (CH$_2$*C*H$_3$) ppm. ^{31}P NMR ($CDCl_3$): δ_P = 107.6 ppm. MS (PD): *m*/*z* (%): 381 (7) $[M]^+$, 315 (49) [M – pyrrolyl]$^+$, 217 (100). Elemental analysis for $C_{21}H_{24}N_3O_2P$ (381.2): calcd. C 66.13, H 6.34, N 11.02; found C 66.38, H 6.29, N 11.11.

{2-[(4*S*)-4-*sec*-Butyl-2-oxazolin-2-yl]-(1-pyrrolyl)}bis(1-pyrrolyl)-phosphane (2d): Yield 1.32 g, 89%; light orange oil. $[a]_D^{21}$ = –36.1 (*c* = 1, $CHCl_3$). ^{13}C NMR ($CDCl_3$): δ_C = 156.7 (C=N), 126.4 (d, ^2J = 3.8 Hz), 124.7 (d, ^2J = 8.7 Hz), 117.3, 111.7 (all C_{Pyr}), 122.6 (d, ^2J = 15.2 Hz, CHNP), 122.2 (d, ^2J = 14.4 Hz, CHNP), 112.4 (d, ^3J = 4.2 Hz, *C*HCHNP), 112.2 (d, ^3J = 4.2 Hz, *C*HCHNP), 71.3 (CHN), 69.9 (CH_2O), 39.1 (*C*HCH$_3$), 25.4 (*C*H$_2$CH$_3$), 14.3 (CH*C*H$_3$), 11.2 (CH$_2$*C*H$_3$) ppm. ^{31}P NMR ($CDCl_3$): δ_P = 71.9 ppm. MS (PD): *m*/*z* (%): 354 (12) $[M]^+$, 288 (36) [M – pyrrolyl]$^+$, 193 (100). Elemental analysis for $C_{19}H_{23}N_4OP$(354.2): calcd. C 64.39, H 6.54, N 15.81; found C 64.12, H 6.63, N 15.96.

{2-[(1*R*)-1-Phenylethyliminomethyl]-(1-pyrrolyl)}bis(1-pyrrolyl)phosphane (2e): Yield 1.31 g, 87%; red oil. $[a]_D^{21}$ = +68.0 (*c* = 0.8, $CHCl_3$). ^{13}C NMR ($CDCl_3$): δ_C = 148.8 (CH=N), 144.8, 128.2, 126.5, 126.3 (all C_{Ph}), 134.7 (d, ^2J = 2.7 Hz), 126.6 (d, ^2J = 4.2 Hz), 118.5, 112.1 (all C_{Pyr}), 122.5 (d, ^2J = 14.4 Hz, CHNP), 122.2 (d, ^2J = 14.0 Hz CHNP), 112.0 (d, ^3J = 3.8 Hz, *C*HCHNP), 111.8 (d, ^3J = 3.8 Hz, *C*HCHNP), 68.6 (CHN), 24.7 (CH_3) ppm. ^{31}P NMR ($CDCl_3$): δ_P = 68.7 ppm. MS (FAB): *m*/*z* (%): 360 (8) $[M]^+$, 294 (44) [M – pyrrolyl]$^+$, 105 (100). Elemental analysis for $C_{21}H_{21}N_4P$ (360.2): calcd. C 69.99, H 5.87, N 15.55; found C 70.23, H 5.78, N 15.63.

Rhodium Complexes

[Rh(CO)(2a)Cl] (3a): Yield 0.22 g, 94%; red powder; m.p. 215–216 °C (dec.). ^{13}C NMR ($CDCl_3$): δ_C = 171.8 (CH=N), 121.9 (CHNP), 113.1 (*C*HCHNP), 81.0 [$C_{Fc(ipso)}$], 76.1 (CHN), 73.3, 73.1, 72.8, 72.1 (all C_{Fc}), 70.9 (CH_2OP), 69.7 (C_{Cp}), 36.9 (*C*HCH$_3$), 25.2 (*C*H$_2$CH$_3$), 14.3 (CH*C*H$_3$), 10.3 (CH$_2$*C*H$_3$) ppm. IR (KBr): $\tilde{\nu}$(CO) = 2019 cm^{-1}. Elemental analysis for $C_{26}H_{30}ClFeN_3O_2PRh$ (641.0): calcd. C 48.66, H 4.71, N 6.55; found C 48.83, H 4.62, N 6.68.

[Rh(CO)(2b)Cl] (3b): Yield 0.17 g, 90%; light-brown powder; m.p. 208–210 °C (dec.). IR (KBr): $\tilde{\nu}$(CO) = 2016 cm^{-1}. Elemental analysis for $C_{20}H_{20}ClN_3O_3PRh$ (519.0): calcd. C 46.22, H 3.88, N 8.09; found C 46.41, H 3.72, N 7.90.

[Rh(CO)(2c)Cl] (3c): Yield 0.18 g, 89%; orange powder; m.p. 199–200 °C (dec.). IR (KBr): $\tilde{\nu}$(CO) = 2022 cm^{-1}. Elemental analysis for $C_{22}H_{24}ClN_3O_3PRh$ (547.0): calcd. C 48.24, H 4.42, N 7.67; found C 48.45, H 4.51, N 7.53.

[Rh(CO)(2d)Cl] (3d): Yield 0.17 g, 92%; light-brown powder; m.p. 207–208 °C (dec.). IR (KBr): $\tilde{\nu}$(CO) = 2025 cm^{-1}. Elemental analysis for $C_{20}H_{23}ClN_4O_2PRh$ (520.0): calcd. C 46.13, H 4.45, N 10.76; found C 46.29, H 4.33, N 10.61.

[Rh(CO)(2e)Cl] (3e): Yield 0.17 g, 90%; brown powder; m.p. 186–188 °C (dec.). ^{13}C NMR ($CDCl_3$): δ_C = 152.9 (CH=N), 140.9, 128.8, 127.8, 127.5 (all C_{Ph}), 131.5 (d, ^2J = 16.0 Hz), 126.4 (d, ^2J = 4.4 Hz), 114.4, 110.5 (d, $^3J_{C,P}$ = 9.2 Hz) (all C_{Pyr}), 123.1 (d, ^2J = 10.4 Hz, CHNP), 122.9 (d, ^2J = 10.4 Hz, CHNP), 114.0 (d, ^3J = 5.6; *C*HCHNP), 113.9 (d, ^3J = 6.4 Hz, CH*C*HNP), 63.9 (CHN), 21.1 (CH_3). IR (KBr): $\tilde{\nu}$(CO) = 2010 cm^{-1}. Elemental analysis for $C_{22}H_{21}ClN_4OPRh$ (526.0): calcd. C 50.16, H 4.02, N 10.64; found C 50.32, H 3.93, N 10.51.

Palladium Complexes

[Pd(2a)(allyl)]$^+$BF$_4^-$ (4a): Yield 0.25 g, 90%; red powder; m.p. 170–172 °C (dec.). MS (FAB): *m*/*z* (%): 622 (100) [M – BF_4]$^+$, 581 (8) [M – BF_4 – allyl]$^+$, 409 (22). Elemental analysis calcd. (%) for $C_{28}H_{35}BF_4FeN_3OPPd$ (709.1): C, 47.39; H, 4.97; N, 5.92; found: C, 47.57; H, 6.08; N, 6.11.

[Pd(2b)(allyl)]$^+$BF$_4^-$ (4b): Yield 0.21 g, 88%; light-brown powder; m.p. 162–164 °C (dec.). MS (FAB): *m*/*z* (%): 500 (100) [M – BF_4]$^+$, 459 (17) [M – BF_4 – allyl]$^+$, 287 (47). Elemental analysis for $C_{22}H_{25}BF_4N_3O_2PPd$ (587.1): calcd. C 44.96, H 4.29, N 7.15; found C 45.21, H 4.41, N 7.29.

[Pd(2c)(allyl)]$^+$BF$_4^-$ (4c): Yield 0.22 g, 91%; deep-orange powder; m.p. 169–171 °C (dec.). MS (FAB): *m*/*z* (%): 528 (100) [M – BF_4]$^+$, 487 (9) [M – BF_4 – allyl]$^+$, 315 (95). Elemental analysis for $C_{24}H_{29}BF_4N_3O_2PPd$ (615.1): calcd. C 46.82, H 4.75, N 6.82; found C 47.05, H 4.62, N 6.69.

[Pd(2d)(allyl)]$^+$BF$_4^-$ (4d): Light-brown powder; 0.21 g, 90% yield; m.p. 168–170 °C (dec.). MS (FAB): *m*/*z* (%): 501 (100) [M – BF_4]$^+$, 460 (19) [M – BF_4 – allyl]$^+$, 193 (95). Elemental analysis for $C_{22}H_{28}BF_4N_4OPPd$ (588.1): calcd. C 44.89, H 4.79, N 9.52; found C 45.18, H 4.86, N 9.65.

 © 2005 Wiley-VCH Verlag GmbH & Co. KGaA, Weinheim

[Pd(2e)(allyl)]$^+$BF$_4^-$ (4e): Yield 0.21 g, 89%; deep-brown powder; m.p. 173–175 °C (dec.). MS (FAB): *m*/*z* (%): 507 (100) [M – BF_4]$^+$, 466 (24) [M – BF_4 – allyl]$^+$, 199 (97). Elemental analysis for $C_{24}H_{26}BF_4N_4PPd$ (594.1): calcd. C 48.47, H 4.41, N 9.42; found C 48.61, H 4.52, N 9.55.

Catalytic Experiments

Palladium-Catalysed Allylic Sulfonylation of 1,3-Diphenylallyl Acetate with Sodium *p*-Toluenesulfinate: A solution of [Pd(allyl)Cl]$_2$ (0.0037 g, 0.01 mmol) or [$Pd_2(dba)_3$]×$CHCl_3$ (0.0103 g, 0.01 mmol) and the appropriate ligand (0.02–0.04 mmol) in THF (5 mL) was stirred for 40 min. 1,3-Diphenylallyl acetate **5** (0.1 mL, 0.5 mmol) was added to the solution and the reaction mixture was stirred for 15 min. Sodium *p*-toluenesulfinate (0.178 g, 1.00 mmol) was then added and the reaction mixture was stirred for 48 h, quenched with brine (10 mL) and extracted with THF (3×7 mL). The organic layer was washed with brine (2×7 mL) and dried over $MgSO_4$. The solvent was evaporated at reduced pressure (40 Torr). Crystallization of the residue from EtOH followed by desiccation in vacuo (10 Torr, 12 h) gave the product **6** as white crystals. All spectroscopic data of compound **6** were in good agreement with the literature.[32]

Palladium-Catalysed Allylic Alkylation of 1,3-Diphenylallyl Acetate with Dimethyl Malonate: A solution of [Pd(allyl)Cl]$_2$ (0.0037 g, 0.01 mmol) or [$Pd_2(dba)_3$]×$CHCl_3$ (0.0103 g, 0.01 mmol) and the appropriate ligand (0.02 mmol) in THF (5 mL) was stirred for 40 min [alternatively, the appropriate presynthesised complex (0.02 mmol) was dissolved in THF (5 mL)]. 1,3-Diphenylallyl acetate **5** (0.1 mL, 0.50 mmol) was added to the solution and the reaction mixture was stirred for 15 min. Dimethyl malonate (0.10 mL, 0.87 mmol), BSA (0.22 mL, 0.87 mmol), and sodium acetate (0.002 g) were also added. The reaction mixture was stirred for 48 h, diluted with THF (5 mL) and filtered through Celite. The filtrate was evaporated at reduced pressure (40 Torr) giving, after in vacuo desiccation (10 Torr, 12 h), product **7** as a colourless oil solidifying upon standing. All spectroscopic data of compound **7** were in good agreement with the literature.[33]

X-ray Crystallographic Study: Crystallographic data for **3a**, **3c** and **3d** are presented in Table 8. All X-ray diffraction measurements were carried out with a SMART 1000 CCD diffractometer at 100 K. The frames were corrected for absorption by the SADABS program.[34]

The principal experimental and crystallographic parameters are presented in Table 8. The structures of **3a**,**c**,**d** were solved by direct methods and refined by full-matrix techniques against F^2 in anisotropic approximations using the SHELXTL 5.1 program package.[35] The positions of hydrogen atoms were calculated geometrically and included in refinement in the rigid body approximation. The absolute configuration of **3a**,**c**,**d** was determined by using the Flack parameter. CCDC-261125 (for **3a**), -261126 (for **3c**) and -261124 (for **3d**) contain supplementary crystallographic data for this paper. These data can be obtained free of charge at www.ccdc.acm.ac.uk/retrieving.html or from the Cambridge Crystallographic Data Centre 12, Union Road, Cambridge CB2 1EZ, UK [Fax: +44-1223-336033].

Acknowledgments

The authors thank Dr. P.V. Petrovskii (Institute of Organoelement Compounds, Moscow) for assistance in characterising the products and Dr. A.V. Korostylev (Leibniz-Institut für Organische Katalyse an der Universitat Rostock, Germany) for assistance in preparation of the manuscript. The authors gratefully acknowledge receiving the chiral HPLC columns (*R*,*R*) WHELK-01 from Regis Technologies (USA) and Chiralcel OD-H from Daicel Chemical Industries,

Table 8. The principal experimental and crystallographic parameters of structures **3a**, **3c** and **3d**.

	3a	**3c**	**3d**
Molecular formula	$C_{26}H_{30}ClFeN_3O_2PRh$	$C_{22}H_{24}ClN_3O_3PRh$	$C_{20}H_{23}ClN_4O_2PRh$
Formula mass	641.71	547.77	520.75
Colour	red	red	yellow
Dimension [mm]	0.40×0.10×0.10	0.50×0.05×0.05	0.20×0.10×0.10
Crystal system	orthorhombic	orthorhombic	orthorhombic
Space group	$P2_12_12_1$	$P2_12_12_1$	$P2_12_12_1$
a [Å]	8.448(3)	9.734(3)	8.704(2)
b [Å]	13.009(5)	10.459(3)	10.883(3)
c [Å]	24.601(9)	23.548(7)	23.190(6)
V [Å^3]	2703.7(17)	2397.3(13)	2196.8(10)
Z	4	4	4
$\rho_{calcd.}$ [g/cm^3]	1.576	1.518	1.575
Temperature [K]	120	293	120
Min./max. 2Θ [°]	1.77/30.00	1.73/29.96	2.07/30.02
Scan type	ω	ω	ω
Radiation, λ(Mo-K_α) [Å]	0.71073	0.71073	0.71073
Linear absorption (μ) [cm^{-1}]	13.33	9.18	9.95
$T_{min.}/T_{max.}$	0.8782/0.6177	0.9555/0.6568	0.9070/0.8258
F(000)	1304	1112	1056
Total refl. (R_{int})	21171 (0.0219)	28694 (0.0369)	17056 (0.0309)
Number of independent reflections	7594	6928	6391
Number of independent refl. with $I > 2\sigma(I)$	6928	5792	6008
Parameters	318	280	264
wR_2	0.0785	0.0479	0.0892
R_1 [for reflections with $I > 2\sigma(I)$]	0.0306	0.0271	0.0329
GOF	0.996	0.990	1.025
Flack parameter	–0.032(16)	–0.031(18)	–0.04(2)
$\rho_{max.}/\rho_{min.}$, [e/Å^3]	1.676/–0.407	0.530/–0.241	1.925/–1.120

 © 2005 Wiley-VCH Verlag GmbH & Co. KGaA, Weinheim

Ltd. (Japan). This work was partially supported by the Russian Foundation for Basic Research (Grant No. 03-03-32181) and Grant of the President of RF for young scientists – doctors of sciences (No. MD -21.2003.03).

[1] K. G. Moloy, J. L. Petersen, *J. Am. Chem. Soc.* **1995**, *117*, 7696–7710.
[2] S. Serron, S. P. Nolan, K. G. Moloy, *Organometallics* **1996**, *15*, 4301–4306.
[3] A. Huang, J. E. Marcone, K. L. Mason, W. J. Marshall, K. G. Moloy, S. Serron, S. P. Nolan, *Organometallics* **1997**, *16*, 3377–3380.
[4] A. M. Trzeciak, T. Glowiak, R. Grzybek, J. J. Ziolkowski, *J. Chem. Soc., Dalton Trans.* **1997**, 1831–1838.
[5] S. Serron, J. Huang, S. P. Nolan, *Organometallics* **1998**, *17*, 534–539.
[6] T. S. Barnard, M. R. Mason, *Organometallics* **2001**, *20*, 206–214.
[7] A. D. Burrows, R. W. Harrington, M. F. Mahon, M. T. Palmer, F. Senia, M. Varrone, *J. Chem. Soc., Dalton Trans.* **2003**, 3717–3726.
[8] J. Castro, A. Moyano, M. A. Pericas, A. Riera, M. A. Maestro, J. Mahia, *Organometallics* **2000**, *19*, 1704–1712.
[9] R. Jackstell, H. Klein, M. Beller, K.-D. Wiese, D. Rottger, *Eur. J. Org. Chem.* **2001**, 3871–3877.
[10] S. C. van der Slot, J. Duran, J. Luten, P. C. J. Kamer, P. W. N. M. van Leeuwen, *Organometallics* **2002**, *21*, 3873–3883.
[11] E. E. Nifantyev, A. V. Shishin, A. T. Teleshev, A. R. Bekker, N. N. Nevskii, N. N. Baturin, *Russ. J. Gen. Chem.* **1991**, *61*, 2481–2493.
[12] P. S. Pregosin, R. W. Kunz, in: *^{31}P NMR and ^{13}C NMR of Transition Metal Phosphine Complexes* (in series NMR Basic Principles and Progress), Springer Verlag: New York, **1979**, p. 16.
[13] C. Reichardt, in: *Solvents and Solvent Effects in Organic Chemistry*; VCH Verlagsgesellschaft: Weinheim, **1988**, p. 141.
[14] W. Simanko, K. Mereiter, R. Schmid, K. Kirchner, A. M. Trzeciak, J. J. Ziolkowski, *J. Organomet. Chem.* **2000**, *602*, 59–64.
[15] J. Ansell, M. Wills, *Chem. Soc. Rev.* **2002**, *31*, 259–268.
[16] O. Molt, T. Schrader, *Synthesis* **2002**, 2633–2670.
[17] K. N. Gavrilov, O. G. Bondarev, A. I. Polosukhin, *Russ. Chem. Rev.* **2004**, *73*, 671–700.
[18] K. N. Gavrilov, O. G. Bondarev, R. V. Lebedev, A. A. Shiryaev, S. E. Lyubimov, A. I. Polosukhin, G. V. Grintselev–Knyazev, K. A. Lyssenko, S. K. Moiseev, N. S. Ikonnikov, V. N. Kalinin, V. A. Davankov, A. V. Korostylev, H.-J. Gais, *Eur. J. Inorg. Chem.* **2002**, 1367–1376.
[19] K. N. Gavrilov, *Russ. J. Inorg. Chem.* **1997**, *42*, 368–384.
[20] A. I. Polosukhin, O. G. Bondarev, S. E. Lyubimov, A. V. Korostylev, K. A. Lyssenko, V. A. Davankov, K. N. Gavrilov, *Tetrahedron: Asymmetry* **2001**, *12*, 2197–2204.
[21] O. G. Bondarev, S. E. Lyubimov, A. A. Shiryaev, N. E. Kadilnikov, V. A. Davankov, K. N. Gavrilov, *Tetrahedron: Asymmetry* **2002**, *13*, 1587–1588.
[22] K. N. Gavrilov, V. N. Tsarev, A. A. Shiryaev, O. G. Bondarev, S. E. Lyubimov, E. B. Benetsky, A. A. Korlykov, M. Yu. Antipin, V. A. Davankov, H.-J. Gais, *Eur. J. Inorg. Chem.* **2004**, 629–634.
[23] A. J. Deeming, I. P. Rothwell, M. B. Hursthouse, K. M. Abdul Malik, *J. Chem. Soc., Dalton Trans.* **1980**, 1974–1982.
[24] A. D. Burrows, M. F. Mahon, M. Varrone, *J. Chem. Soc., Dalton Trans.* **2003**, 4718–4730.
[25] J. A. McCleverty, G. Wilkinson, *Inorg. Synth.* **1966**, *8*, 211–214.
[26] P. R. Auburn, P. B. McKenzie, B. Bosnich, *J. Am. Chem. Soc.* **1985**, *107*, 2033–2046.
[27] K. Moseley, P. M. Maitlis, *J. Chem. Soc., Dalton Trans.* **1974**, 169–175.
[28] H. Yang, M. A. Khan, K. M. Nicholas, *Organometallics* **1993**, *12*, 3485–3494.
[29] H. Brunner, B. Habler, *Z. Naturforsch., Teil B* **1998**, *53*, 476–480.
[30] H. Brunner, B. Reiter, G. Riepl, *Chem. Ber.* **1984**, *117*, 1330–1354.
[31] K. N. Gavrilov, O. G. Bondarev, R. V. Lebedev, A. I. Polosukhin, A. A. Shiryaev, S. E. Lyubimov, P. V. Petrovskii, S. K. Moiseev, V. N. Kalinin, N. S. Ikonnikov, V. A. Davankov, A. V. Korostylev, *J. Organomet. Chem.* **2002**, *655*, 204–217.
[32] D. Seebach, E. Devaquet, A. Ernst, M. Hayakawa, F. N. M. Kuhlne, W. B. Schweizer, B. Weber, *Helv. Chim. Acta* **1995**, *78*, 1636–1645.
[33] S. Breeden, M. Wills, *J. Org. Chem.* **1999**, *64*, 9735–9738.
[34] G. M. Sheldrick, *SADABS*, v.2.01, Bruker/Siemens Area Detector Absorption Correction Program, Bruker AXS, Madison, Wisconsin, USA.
[35] G. M. Sheldrick, *SHELXTL-97*, V5.1, Bruker AXS Inc., Madison, WI 53719, USA, **1997**.

Received: January 24, 2005
Published Online: July 6, 2005

 © 2005 Wiley-VCH Verlag GmbH & Co. KGaA, Weinheim

Tetranuclear Polypyridyl Complexes of Ru^{II} and Fe^{II}: Synthesis, Electrochemical, Photophysical and Photochemical Behaviour

Jean Lombard,[a] Sophie Romain,[a] Stéphane Dumas,[a] Jérôme Chauvin,[a] Marie-Noëlle Collomb,[a] Denis Daveloose,[b] Alain Deronzier,*[a] and Jean-Claude Leprêtre*[a]

Keywords: Bridging ligands / Electrochemistry / Iron / Photochemistry / Ruthenium

Three heterotetranuclear complexes $[\{Ru^{II}(bpy)_2(LL_n)\}_3Fe^{II}]^{8+}$ {bpy = 2,2′-bipyridine, n = 2, 4, 6; denoted $[\{Ru(LL_n)\}_3Fe]^{8+}$}, in which one iron centre is complexed by three Ru^{II}-tris-bipyridine-like moieties containing covalently bridging bis-bipyridine LL_n ligands, have been synthesised and characterised. The stability and the electrochemical, photophysical and photochemical properties of these complexes have been investigated in CH_3CN. The cyclic voltammograms of all complexes exhibit two successive reversible oxidation processes in the positive region, corresponding to the Fe^{II}/Fe^{III} and Ru^{II}/Ru^{III} redox couples. These systems are clearly separated ($\Delta E_{1/2}$ about 300 mV), which indicates the absence of an electronic connection between the two subunits. In the negative region, three successive reversible four-electron systems are observed, corresponding to the ligand-based reduction processes. The two oxidized forms of the complexes $[\{Ru^{II}(LL_n)\}_3Fe^{III}]^{9+}$ and $[\{Ru^{III}(LL_n)\}_3Fe^{III}]^{12+}$, which are obtained by two successive exhaustive electrolyses, are very stable. The $[\{Ru(LL_n)\}_3Fe]^{8+}$ complexes are luminescent, which shows that the covalent linkage between the Ru^{II}-tris-bipyridine and Fe^{II}-tris-bipyridine subunits leads to an only partial quenching of the Ru^{II*} excited states by energy transfer to the Fe^{II} centre. The luminescence lifetime and quantum yield are found to be independent of the complexes′ concentration, thus indicating that the energy-transfer process is only due to an intramolecular electron-exchange mechanism. Quantitative photoinduced oxidation of the tetranuclear complexes has been performed by continuous photolysis experiments in the presence of a large excess of a diazonium salt, which plays the role of a sacrificial oxidant. Two successive oxidation processes ($Fe^{II} \rightarrow Fe^{III}$ and $Ru^{II} \rightarrow Ru^{III}$) are observed.
(© Wiley-VCH Verlag GmbH & Co. KGaA, 69451 Weinheim, Germany, 2005)

Introduction

In recent years, important synthetic efforts have been made to mimic the function of the donor site of the photosystem II (PSII) by the development of superstructured heterometallic complexes.[1–3] The main strategy to elaborate models of PSII involves the covalent coupling of a photoactive $[Ru^{II}(bpy)_3]^{2+}$ (bpy = 2,2′-bipyridine) moiety, which plays the role of the P_{680} chlorophyll photosensitizer, to some monomanganese(II), binuclear (II,III) or (III,III) and trinuclear (II,II,II) complexes that model the catalytic centre that oxidizes water into oxygen.[4–7] It has been reported for the mononuclear manganese(II) complexes that an intramolecular electron transfer can occur from the Mn^{II} site to the photogenerated Ru^{III} species in the presence of an external electron acceptor like viologen in acetonitrile.[8] However, the rate constant for this process is fairly slow and the efficiency of the process depends on the distance between the two metallic centres. In addition, the system is complicated, since the Mn^{II}/Mn^{III} redox couple is only poorly reversible as the Mn^{III} species reacts with residual water to form binuclear Mn^{III}/Mn^{IV} oxo complexes.[9–11] Moreover, in most cases the Mn^{II} sites quench the excited state of the ruthenium(II) complex, presumably by an energy-transfer process.[8,12,13] With a view to studying this kind of intramolecular electron transfer, we have recently reported the photoredox behaviour of a series of heterobinuclear metallic complexes of Ru^{II} and Fe^{II}, namely $[Ru^{II}(bpy)_2(LL_n)\text{-}Fe^{II}(bpy)_2]^{4+}$ (denoted $[Ru(LL_n)Fe]^{4+}$), based on the use of bridging bis-bipyridine ligands LL_n (Scheme 1).[14] This system is simpler than the Ru^{II}/Mn^{II} one, since Fe^{II}/Fe^{III} is a perfectly reversible redox couple, with the oxidation of the $[Fe^{II}(bpy)_3]^{2+}$-like complex occurring at a potential close to that of $[Mn^{II}(bpy)_3]^{2+}$. In this previous study, we demonstrated that the ^{3}MLCT excited state of the Ru^{II}-tris-bipyridine centre is strongly quenched by the Fe^{II}-tris-bipyridine

[a] Laboratoire d′Electrochimie Organique et de Photochimie Rédox, Université Joseph Fourier,
UMR CNRS 5630, Institut de Chimie Moléculaire de Grenoble, FR CNRS 2607
B. P. 53, 38041 Grenoble Cedex 9, France
Fax: +33-4-7651-4267
E-mail: jean-claude.lepretre@ujf-grenoble.fr
alain.deronzier@ujf-grenoble.fr
[b] Centre de Recherches du Service de Santé des Armées "Emile Pardé", Laboratoire de Biospectrométrie,
24 Avenue des Maquis du Grésivaudan, BP 87, 38702 La Tronche, Cedex, France

 © 2005 Wiley-VCH Verlag GmbH & Co. KGaA, Weinheim **DOI: 10.1002/ejic.200500106**

unit through an energy-transfer process that is mainly intermolecular. Nevertheless, this strong energy transfer can be easily short-circuited in the presence of an external irreversible electron acceptor like an aryldiazonium salt (ArN_2^+) by an electron transfer that leads finally to the photoinduced formation of $[Ru^{II}(LL_n)Fe^{III}]^{5+}$ species with high efficiency. It has been shown that the electron transfer between the ground state of the Ru^{III} and Fe^{II} species essentially occurs by an intermolecular process. In order to gain more information about these photoprocesses, we have synthesised a series of new heterobimetallic complexes of Ru^{II} and Fe^{II}: $[\{Ru^{II}(bpy)_2(LL_n)\}_3Fe^{II}]^{8+}$ {n = 2, 4, 6; denoted $[\{Ru(LL_n)\}_3Fe]^{8+}$} in which one iron centre is complexed by three Ru^{II}-tris-bipyridine moieties (Scheme 1). A previous publication reported some photophysical data of this kind of complex, but these compounds were only prepared in situ.[15] Under these conditions, the presence of some uncomplexed $[Ru^{II}(bpy)_2(LL_n)]^{2+}$ {denoted $[Ru^{II}(LL_n)]^{2+}$} species in the medium prevented the drawing of clear conclusions about the photophysical properties of the $[\{Ru(LL_n)\}_3Fe]^{8+}$ complexes. In the present study, we report the synthesis and characterisation of the three heterotetranuclear complexes $[\{Ru(LL_n)\}_3Fe]^{8+}$, their main redox and photophysical properties and the comparison of the latter properties with those of the heterobinuclear complexes $[Ru(LL_n)Fe]^{4+}$. Moreover, we have investigated the possibility to photoinduce the oxidation of the tetranuclear complexes in the presence of ArN_2^+. The expected multi-step oxidation process is summarised in Scheme 2.

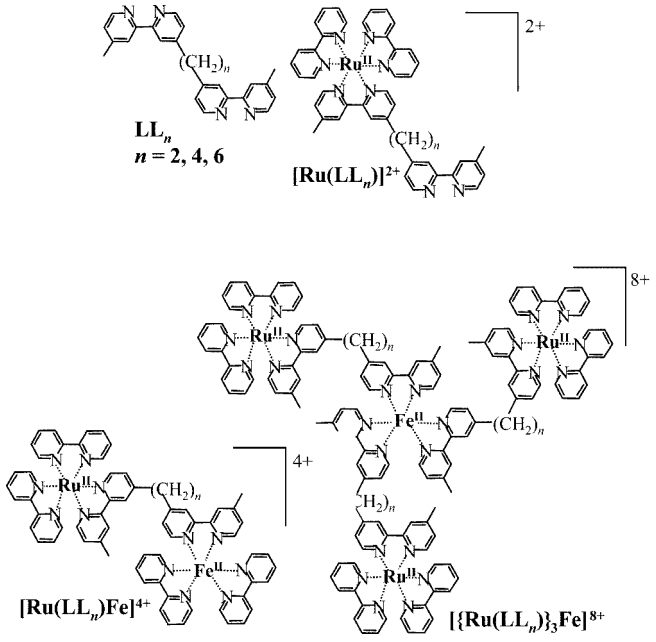

Scheme 1. Chemical structure of the ligands LL_n and of the complexes $[Ru(LL_n)]^{2+}$, $[Ru(LL_n)Fe]^{4+}$ and $[\{Ru(LL_n)\}_3Fe]^{8+}$.

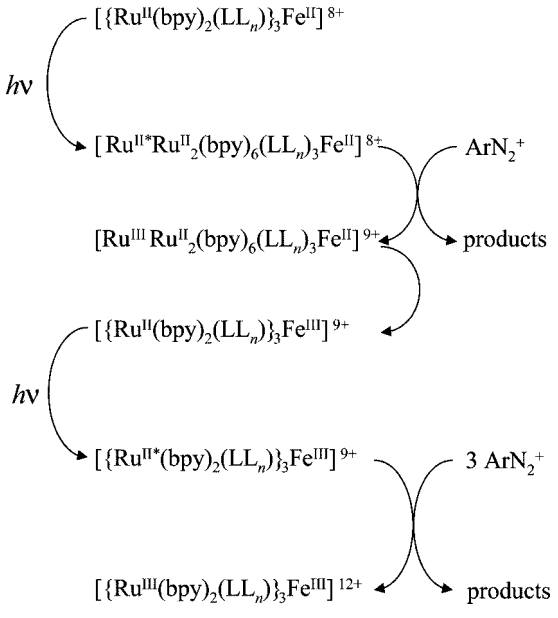

Scheme 2. Schematic presentation of the photooxidation mechanism of $[\{Ru(LL_n)\}_3Fe]^{8+}$ in the presence of an external electron acceptor (ArN_2^+).

Results and Discussion

Synthesis and Stability of the Complexes

Eliott and co-workers[15] have reported that the complexation of some $[Ru^{II}(bpy)_2(L\text{-}L)]^{2+}$ complexes (L-L = covalently linked bipyridines) with Fe^{2+} in situ in methanol/water (1:1) forms the tetranuclear complexes $[\{Ru^{II}(bpy)_2(L\text{-}L)\}_3Fe^{II}]^{8+}$. However, in this medium, it has been shown that such compounds undergo some dissociation (association constants between 10^{13} and 10^{15}). As a result, the presence of uncomplexed $[Ru^{II}(bpy)_2(L\text{-}L)]^{2+}$ species leads to the observance of a double exponential for the emission decay. The fast component of the decay corresponds to emission from ruthenium "ligands" complexed to iron, and the long one to the uncomplexed $[Ru^{II}(bpy)_2(L\text{-}L)]^{2+}$ centres. Moreover, isolation of tetranuclear complexes in a pure form by this group was unsuccessful. In this work, we have synthesised, isolated and purified three heterotetranuclear complexes $[\{Ru(LL_n)\}_3Fe]^{8+}$ (n = 2, 4 and 6) by the treatment of 0.4 equivalents of Fe^{2+}, as its perchlorate salt, with one equivalent of the corresponding $[Ru(bpy)_2(LL_n)]^{2+}$ complexes in ethanol/water (12:1). This synthetic method allows us to obtain the expected compounds with fairly good yields; their purity was checked by TLC and elemental analysis. In order to determine their photophysical properties in CH_3CN solution properly, we also verified their stability in this solvent by UV/Vis spectroscopy. The visible absorption spectra of $[\{Ru(LL_n)\}_3Fe]^{8+}$ in the concentration range 10^{-4}–10^{-7} M exhibit the expected regular bands at 356, 396 (shoulder), 430 (shoulder), 454 and 530 nm (shoulder) corresponding to the superimposition of the absorbance of the Ru^{II}- and Fe^{II}-tris-bipyridine subunits (Table 1).[15] For the three complexes $[\{Ru(LL_n)\}_3Fe]^{8+}$, there is no significant variation of the ratio of the absorbance values at 356, 454 and 530 nm with concentration (in the range 10^{-4} and 10^{-7} M), showing that no dissociation of the complexes occurs. The linearity of the absorbance vs.

 © 2005 Wiley-VCH Verlag GmbH & Co. KGaA, Weinheim

Table 1. UV/Vis data for $[Ru^{II}(LL_n)]^{2+}$ and $[\{Ru^{II}(LL_n)\}_3Fe^{II}]^{8+}$ in deoxygenated CH_3CN + 0.1 M Bu_4NClO_4 at 25 °C.

Complexes	λ_{abs} (ε)	Ref.
$[Fe^{II}(dmbpy)_3]^{2+}$	356 nm (7100 $M^{-1}cm^{-1}$), 395[a] (4000) 494[a] (7400), 528 (8000)	this work
$[Fe^{III}(dmbpy)_3]^{3+}$	417 (2200)	this work
$[Ru^{II}(LL_2)]^{2+}$	354[a] (5500), 396[a] (5100) 430[a] (10300), 454 (12000)	[14]
$[Ru^{II}(LL_4)]^{2+}$	354[a] (5500), 396[a] (5200) 430[a] (10700), 454 (12300)	[14]
$[Ru^{II}(LL_6)]^{2+}$	354[a] (5700), 396[a] (5400) 430[a] (11000), 454 (12700), 356[a] (25000)	[14]
$[\{Ru^{II}(LL_2)\}_3Fe^{II}]^{8+}$	396[a] (20500), 430[a] (35000) 455 (40900), 530[a] (9300)	this work
$[\{Ru^{II}(LL_4)\}_3Fe^{II}]^{8+}$	356[a] (26000), 396[a] (21400), 430[a] (36600) 454 (42500), 530[a] (11800)	this work
$[\{Ru^{II}(LL_6)\}_3Fe^{II}]^{8+}$	356[a] (27300), 396[a] (22200), 430[a] (36600) 454 (42300), 530[a] (12700)	this work

[a] Shoulder.

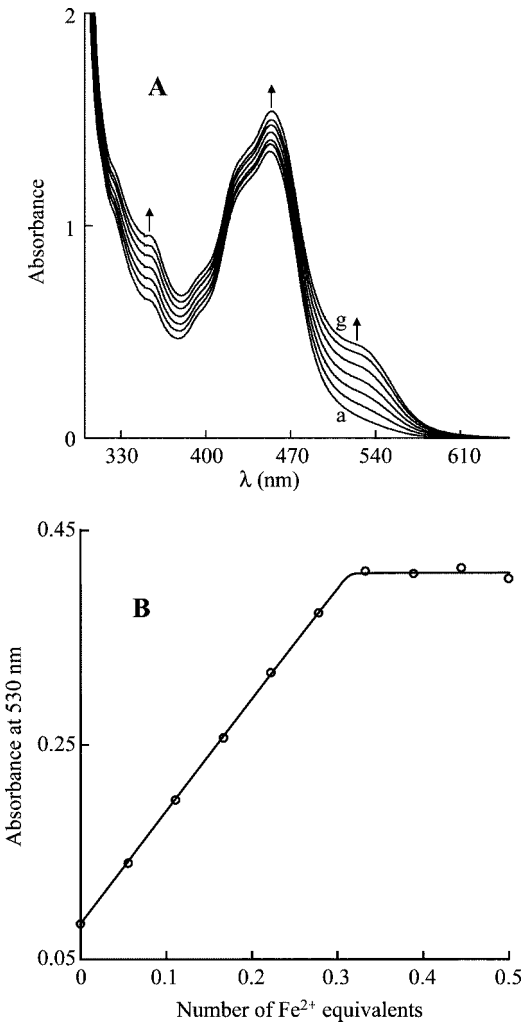

Figure 1. A) Evolution of the visible spectrum of a solution of $[Ru(LL_4)]^{2+}$ (0.105 mM) in CH_3CN + 0.1 M Bu_4NClO_4 during the addition of $Fe(ClO_4)_2 \cdot 8H_2O$: a) initial solution, b) after addition of 0.055 equiv. of Fe^{2+}, (c) 0.11, (d) 0.167, (e) 0.22, (f) 0.28, (g) 0.33 and 0.5. B) Evolution of the absorbance at 530 nm (l = 1 cm).

addition of Fe^{2+} allows the determination of the association constant as being greater than 10^{22}. This constant value is higher than those estimated in a methanol/water mixture (10^{13}–10^{15}),[15] presumably due to the more dissociative properties of this medium compared to the acetonitrile one. This high stability was also confirmed by following the absorbance at 530 nm of a $[Ru(LL_n)]^{2+}$ acetonitrile solution after progressive addition of $Fe(ClO_4)_2 \cdot 8H_2O$ (Figure 1). The absorbances at 356 and 530 nm increase linearly during the addition of Fe^{2+} until a maximum is reached for the expected ratio of one iron for every three $[Ru(LL_n)]^{2+}$ units. Addition of an excess of Fe^{2+} does not lead to any spectroscopic changes. The absence of free $[Ru(LL_n)]^{2+}$ is also confirmed by luminescence measurements in CH_3CN, since, for all synthesised complexes, the emission decay curves are clean single exponentials (see below).

Electrochemistry

In CH_3CN containing 0.1 M Bu_4NClO_4 the electrochemical behaviour of the three $[\{Ru(LL_n)\}_3Fe]^{8+}$ complexes is similar (see Table 2). The length of the aliphatic bridges has only a slight effect on the $E_{1/2}$ values of the oxidative and reductive processes. In the negative region, although the successive one-electron reductions of the bipyridine ligands in the $[Fe(dmbpy)_3]^{2+}$ (dmbpy = 4,4′-dimethyl-2,2′-bipyridine) and $[Ru(LL_n)]^{2+}$ complexes are clearly separated (by 115–140 mV, see Table 2), the reduction pattern of the $[\{Ru(LL_n)\}_3Fe]^{8+}$ complexes shows only three successive reduction waves {see Figure 2 for $[\{Ru(LL_4)\}_3Fe]^{8+}$}, as observed previously for the binuclear $[Ru(LL_n)Fe]^{4+}$ complexes.[14] Moreover, only the first reduction wave is clearly seen. A strong adsorption phenomenon coupled to the second reduction process leads to an important distortion of the third one. It should be mentioned that each reversible redox system corresponds to the overall exchange of four electrons corresponding to the one-electron reduction of one bipyridine unit per metallic centre. The exchange of

 © 2005 Wiley-VCH Verlag GmbH & Co. KGaA, Weinheim

Table 2. Electrochemical data for $[Ru^{II}(bpy)_2(LL_n)]^{2+}$ and $[\{Ru^{II}(LL_n)\}_3Fe^{II}]^{8+}$ in deoxygenated CH_3CN + 0.1 M Bu_4NClO_4 using a platinum electrode at a scan rate of 100 mV s^{-1}.[a]

Complexes	Fe^{II}/Fe^{III}	Ru^{II}/Ru^{III}	Reduction processes 1	2	3	Ref.
$[Fe^{II}(dmbpy)_3]^{2+}$	0.585 (60)	–	–1.775 (60)	–1.970 (70)	–2.195 (70)	this work
$[Ru^{II}(LL_2)]^{2+}$	–	0.912 (60)	–1.665 (50)	–1.855 (50)	–2.105 (50)	[14]
$[Ru^{II}(LL_4)]^{2+}$	–	0.905 (60)	–1.665 (50)	–1,862 (50)	–2.115 (50)	[14]
$[Ru^{II}(LL_6)]^{2+}$	–	0.905 (60)	–1.665 (50)	–1.865 (50)	–2.125 (50)	[14]
$[\{Ru^{II}(LL_2)\}_3Fe^{II}]^{8+}$	0.607 (60)	0.907 (60)	–1.687 (60)	–1.827 (80)	[b]	this work
$[\{Ru^{II}(LL_4)\}_3Fe^{II}]^{8+}$	0.588 (60)	0.905 (60)	–1.647 (70)	–1.806 (50)	[b]	this work
$[\{Ru^{II}(LL_6)\}_3Fe^{II}]^{8+}$	0.588 (60)	0.902 (60)	–1.658 (60)	–1.818 (70)	[b]	this work

[a] $E_{1/2}$ (V) (ΔEp in mV) vs. Ag/Ag^+ (0.01 M $AgNO_3$ in CH_3CN + 0.1 M Bu_4NClO_4). [b] This value cannot be accurately measured since the waves are strongly distorted by adsorption phenomena (see text).

four electrons is confirmed by the fact that the height of the first reduction wave at a rotating disk electrode is equal to the sum of the heights of the two oxidation waves (see below and Figure 2).

In the positive region, the cyclic voltammograms of the three $[\{Ru(LL_n)\}_3Fe]^{8+}$ complexes exhibit two well-separated reversible redox systems (Figure 2). The potentials of these systems are closed to those of the mononuclear complexes $[Fe(dmbpy)_3]^{2+}$ and $[Ru(LL_n)]^{2+}$, thus allowing us to assign the first oxidative process to the Fe^{II}/Fe^{III} redox couple and the more anodic one to that of the Ru^{II}/Ru^{III} system (Table 2). Moreover, rotating disk electrode experiments confirmed that the complexes are obtained in pure form and that no dissociation occurs in CH_3CN, since the height of the Ru^{II}/Ru^{III} wave is three times that of Fe^{II}/Fe^{III}, in accordance with the 3:1 Ru/Fe stoichiometry in the tetranuclear complexes [Equations (1) and (2)].

$$[\{Ru^{II}(bpy)_2(LL_n)\}_3Fe^{II}]^{8+} \rightarrow [\{Ru^{II}(bpy)_2(LL_n)\}_3Fe^{III}]^{9+} + e^- \quad (1)$$

$$[\{Ru^{II}(bpy)_2(LL_n)\}_3Fe^{III}]^{9+} \rightarrow [\{Ru^{III}(bpy)_2(LL_n)\}_3Fe^{III}]^{12+} + 3e^- \quad (2)$$

As previously observed for the $[Ru(LL_n)Fe]^{4+}$ complexes,[14] the $E_{1/2}$ values of the Fe^{II}/Fe^{III} and Ru^{II}/Ru^{III} redox systems decrease slightly upon increasing the number of methylenes in the aliphatic bridge (Table 2). This $E_{1/2}$ variation is due to a slightly higher electron-donor effect of the LL_6 ligand compared to LL_4, and of the latter to LL_2.

Otherwise, the Ru^{II}/Ru^{III} redox system involves the simultaneous exchange of three electrons. In order to estimate the magnitude of the electronic connexion between the three ruthenium centres, computational fitting of the cyclic voltammetry curves of $[\{Ru(LL_n)\}_3Fe]^{8+}$ was performed, which led to the determination of the formal potentials E_f^1, E_f^2 and E_f^3 for the three ruthenium oxidation steps (Table 3) (see Figure 3 for $[\{Ru(LL_4)\}_3Fe]^{8+}$ and Experimental Section).[16,17] Since the difference between the extreme E_f values ($\Delta E_f^{3-1} = E_f^3 - E_f^1$) is close to the theoretical value (57 mV) for the three tetranuclear complexes,[16] the absence of an electronic connexion within the studied compounds is confirmed. One can see, as observed for the Fe^{II}/Fe^{III} system, that these E_f values are in accordance with the electron-donor character of the bridging ligand; the $E_{1/2}$ value of the Ru^{II}/Ru^{III} couple decreases slightly

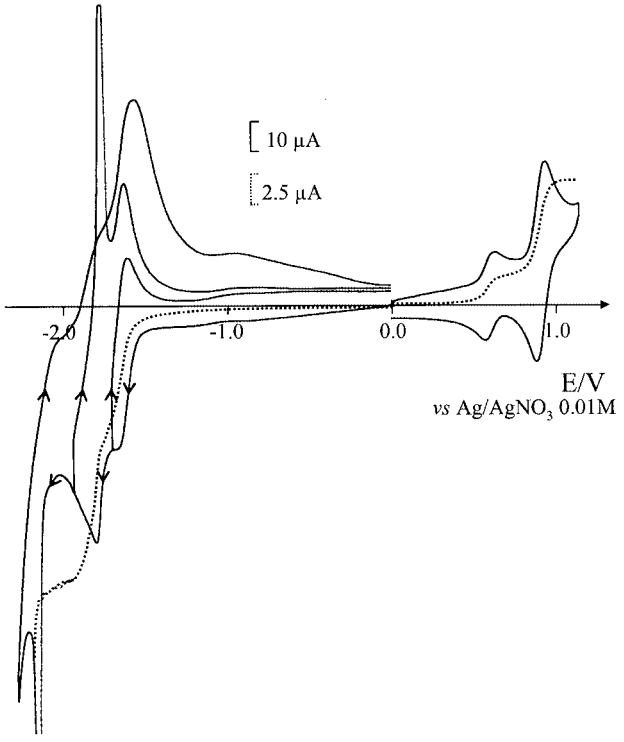

Figure 2. (–) Cyclic voltammograms of a 0.32 mM solution of $[\{Ru(LL_4)\}_3Fe]^{8+}$ in CH_3CN + 0.1 M Bu_4NClO_4 at a platinum electrode; scan rate: 100 mV s^{-1}. (---) Voltammograms at a platinum rotating disk electrode at ω = 600 r min^{-1}; scan rate: 10 mV s^{-1}.

(10 mV) in the order $LL_2 > LL_4 > LL_6$. Since the two oxidized forms of the complexes, $[\{Ru^{II}(LL_n)\}_3Fe^{III}]^{9+}$ and $[\{Ru^{III}(LL_n)\}_3Fe^{III}]^{12+}$ are expected to be produced during the photoinduced electron-transfer processes (Scheme 2), the stabilities of these species were evaluated by exhaustive electrolyses. Taking into account the large potential difference between the Fe^{II}/Fe^{III} and Ru^{II}/Ru^{III} redox systems ($\Delta E_{1/2}$ = 296 mV for LL_2, 315 for LL_4 and 317 for LL_6), the mixed-valent $[\{Ru^{II}(LL_n)\}_3Fe^{III}]^{9+}$ species are perfectly stable. Indeed, two successive exhaustive electrolyses carried out at 0.80 and 1.10 V consumed one and three electrons, respectively, per $[\{Ru(LL_n)\}_3Fe]^{8+}$, and allowed the bulk build-up of $[\{Ru^{II}(LL_n)\}_3Fe^{III}]^{9+}$ and $[\{Ru^{III}(LL_n)\}_3Fe^{III}]^{12+}$. This is illustrated by the evolution of the absorption spectra of the solutions after these sequential electrolyses

 © 2005 Wiley-VCH Verlag GmbH & Co. KGaA, Weinheim

Table 3. Oxidation potentials of $[\{Ru(LL_n)\}_3Fe]^{8+}$ determined by fitting of the experimental cyclic voltammograms.

	$E_{1/2}$ [mV] vs. Ag/Ag^+ 10 mM				
Complexes	Fe^{II}/Fe^{III} $E_{1/2}$	Ru^{II}/Ru^{III} E_f^1	Ru^{II}/Ru^{III} E_f^2	Ru^{II}/Ru^{III} E_f^3	Ru^{II}/Ru^{III} $E_{1/2}^{moy}$ (ΔE_f^{3-1})
$[\{Ru^{II}(LL_2)\}_3Fe^{II}]^{8+}$	614	882 ± 1	915 ± 2	934 ± 3	910 (58)
$[\{Ru^{II}(LL_4)\}_3Fe^{II}]^{8+}$	584	860 ± 2	906 ± 2	931 ± 2	899 (71)
$[\{Ru^{II}(LL_6)\}_3Fe^{II}]^{8+}$	572	852 ± 1	897 ± 4	818 ± 10	889 (66)

(see Figure 4 for LL_4). The typical initial bands of the Fe^{II}-tris-bipyridine unit (λ = 356 and 530 nm) disappear after one electron per complex has been passed (Table 1). After exchange of three other electrons, the bands of the Ru^{II}-tris-bipyridine units (λ = 356 and 454 nm) disappear and are replaced by those of the Ru^{III} ones (428 and 644 nm). Both oxidized forms are stable for several hours. Finally, we found that exhaustive reduction of all these oxidized species leads to the nearly quantitative recovery of the starting material, thus demonstrating the high reversibility of the process.

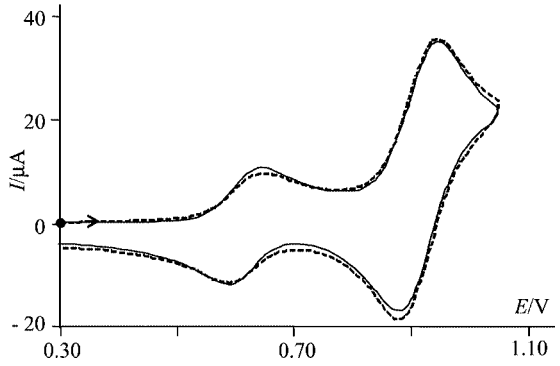

Figure 3. Cyclic voltammograms of a 0.14 mM solution of $[\{Ru(LL_4)\}_3Fe]^{8+}$ in CH_3CN + 0.1 M Bu_4NClO_4 at a platinum electrode; scan rate 200 mV s^{-1}: (---) experimental curve, (−) fitted curve.

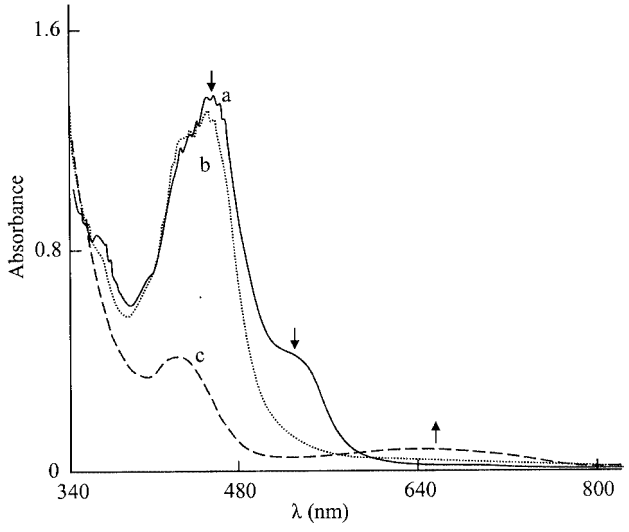

Figure 4. Absorption spectra of a 0.32 mM solution of $[\{Ru(LL_4)\}_3Fe]^{8+}$ in CH_3CN + 0.1 M Bu_4NClO_4: (a) initial solution, (b) after exhaustive electrolysis at 0.80 V, (c) after exhaustive electrolysis at 1.10 V (l = 1 mm).

Energy Transfer

The emission wavelength (λ_{emis}), luminescence lifetime (τ), and luminescence quantum yield (φ_L) of the $[\{Ru(LL_n)\}_3Fe]^{8+}$ complexes are reported in Table 4, along with those obtained for the corresponding $[Ru(LL_n)]^{2+}$ and $[Ru(LL_n)Fe]^{4+}$ parent complexes. On the nanosecond timescale, the luminescence decay of all $[\{Ru(LL_n)\}_3Fe]^{8+}$ complexes appears as a single exponential with a luminescence lifetime slightly lower than those of the monometallic $[Ru(LL_n)]^{2+}$ complexes. Further experiments were performed on a subnanosecond timescale using a picosecond Ti:Sapphire laser and single photon counting detection. No additive short component in the decay was observed. Nevertheless, if the luminescence is detected, it is largely quenched. Indeed, compared to the $[Ru(LL_n)]^{2+}$ complexes, the luminescence quantum yield is lowered from a factor of 6 for $[\{Ru(LL_6)\}_3Fe]^{8+}$ to almost 10 for $[\{Ru(LL_4)\}_3Fe]^{8+}$ (Table 4). These data indicate that, as observed for $[Ru(LL_n)Fe]^{4+}$, the Fe^{II}-tris-bipyridine unit quenches the ^3MLCT excited state in the $[\{Ru(LL_n)\}_3Fe]^{8+}$ complexes.

The luminescence lifetime and quantum yield of the $[\{Ru(LL_n)\}_3Fe]^{8+}$ complexes were found to be independent of the concentration of the samples (concentration range used from 10^{-6} to 2×10^{-5} M), which means that, in contrast to what we demonstrated for the binuclear $[Ru(LL_n)Fe]^{4+}$ complexes, the intermolecular quenching is not efficient in such tetranuclear systems. As a result, the partial inhibition of the luminescence of the Ru^{II} centre is only due to an intramolecular interaction with the central Fe^{II}-tris-bipyridine unit.

Electron transfer (ET) between Ru^{II}* and Fe^{II} centres has to be ruled out for this quenching pathway. Indeed, considering the potential values of the $Ru^{II}*/Ru^{I}$ [in the range 0.34–0.38 V for $[\{Ru(LL_n)\}_3Fe]^{8+}$ vs. Ag/Ag^+ in CH_3CN with 0.1 M Bu_4NClO_4][18] and Fe^{II}/Fe^{III} (in the range 0.58–0.60 V) redox couples, the electron-transfer quenching process is strongly endergonic (≥0.2 V). Likewise, the potential value of the $Ru^{II}*/Ru^{III}$ redox couple (between –1.12 and –1.14 V) compared to that of the first reduction potential of the iron unit (between –1.647 and –1.687) leads to a strongly endergonic process (≥0.52 V). Thus, a pure electronic energy transfer (EET) can be considered as the main quenching process.[14,19]

The quenching rate constant (k_q) was determined from Equation (3), where φ_L^{Ref} and φ_L^{S} are the luminescence quantum yields of the $[Ru(LL_n)]^{2+}$ and $[\{Ru(LL_n)\}_3Fe]^{8+}$ complexes, respectively, and τ^{Ref} the luminescence lifetime of $[Ru(LL_n)]^{2+}$.

 © 2005 Wiley-VCH Verlag GmbH & Co. KGaA, Weinheim

Table 4. Photophysical data determined for deoxygenated solutions of the ruthenium complexes in CH_3CN + 0.1 M Bu_4NClO_4 at 25 °C.

Complexes	λ_{emis} [nm]	τ [μs]	φ_L	k_q[a]	Ref.
$[Ru^{II}(bpy)_3]^{3+}$	603	1.06	0.062	9.0×10^9 $M^{-1}s^{-1}$[b]	[14,29]
$[Ru^{II}(LL_2)]^{2+}$	611	1.11	0.060	1.4×10^{10} $M^{-1}s^{-1}$[b]	[14]
$[Ru^{II}(LL_4)]^{2+}$	612	1.12	0.054	1.8×10^{10} $M^{-1}s^{-1}$[b]	[14]
$[Ru^{II}(LL_6)]^{2+}$	612	1.13	0.059	1.8×10^{10} $M^{-1}s^{-1}$[b]	[14]
$[Ru^{II}(LL_2)Fe^{II}]^{4+}$	612	1.10[c]	0.022[c]	3.5×10^8 $M^{-1}s^{-1}$	[14]
$[Ru^{II}(LL_4)Fe^{II}]^{4+}$	612	1.03[c]	0.019[c]	2.2×10^9 $M^{-1}s^{-1}$	[14]
$[Ru^{II}(LL_6)Fe^{II}]^{4+}$	612	1.00[c]	0.023[c]	3.3×10^9 $M^{-1}s^{-1}$	[14]
$[\{Ru^{II}(LL_2)\}_3Fe^{II}]^{8+}$	612	1.07	0.008	5.9×10^6 s^{-1}	this work
$[\{Ru^{II}(LL_4)\}_3Fe^{II}]^{8+}$	612	1.03	0.005	8.8×10^6 s^{-1}	this work
$[\{Ru^{II}(LL_6)\}_3Fe^{II}]^{8+}$	612	1.04	0.009	4.9×10^6 s^{-1}	this work
$[\{Ru^{II}(LL_2)]_3Zn^{II}\}^{8+}$	–	1.07	0.06	–	this work

[a] Quenching rate constant of the electronic energy transfer (EET) between Ru^{II}* and Fe^{II}. [b] Values determined in the presence of $[Fe(bpy)_3]^{2+}$. [c] Values determined for a 0.04 mM solution of binuclear complexes.

$$k_q = \left(\frac{\phi_L^{Ref}}{\phi_L^{S}} - 1\right) \times \frac{1}{\tau^{Ref}} \quad (3)$$

The same order of magnitude of k_q ($5\times10^6 \leq k_q \leq 9\times10^6$ s^{-1}; Table 4) was obtained for all three compounds, which shows that the EET process is moderately efficient and clearly not connected to the length to the aliphatic chain of the bridging ligand. Eliott and co-workers[15] have obtained a similar magnitude of k_q ($8\times10^6 \leq k_q \leq 197\times10^6$ s^{-1}) in aqueous methanolic solution, but, in contrast to our results, these authors found a dependence of the k_q value with the distance beween Ru^{II} and Fe^{II}: the more important the Ru^{II}–Fe^{II} distance, the weaker the k_q value. One can suggest that the nature of the solvent might have an influence on the deactivation process. This influence of solvation conditions is confirmed by the lower τ values obtained in aqueous methanolic medium for the precursor ruthenium complexes {τ = 356 ns for $[Ru(LL_2)]^{2+}$}.[15]

EET processes occur according to two mechanisms − Dexter (or electron exchange interaction)[20] and Förster (or coulombic interaction)[21] − both of which involve the spectral overlap of the luminescence of the donor with the absorption spectra of the acceptor. The Dexter mechanism requires contact between the donor and the acceptor, whereas the Förster one proceeds over a larger distance. For the Förster process, a critical transfer distance, R_0, can be calculated according to Equation (4)

$$R_0 = 1.25\times10^{17} \frac{\phi_D}{n^4} \int_0^\infty F_D(\bar{\nu})\varepsilon_A(\bar{\nu})\frac{d(\bar{\nu})}{\bar{\nu}^4} \quad (4)$$

where φ_D is the donor emission quantum yield {i.e. $[Ru(LL_n)]^{2+}$}, n the solvent refractive index and the integral term represents the spectral overlap of the normalised donor emission with the acceptor absorption. For the three $[\{Ru(LL_n)\}_3Fe]^{8+}$ complexes, an R_0 value of 20 ± 1 Å has been calculated, whereas the distance between the ruthenium and iron centres in theses structures is in the range from 10 to 12 Å according to space-filling molecular models.[15] When the estimated distance between both metallic centres is less than R_0, energy transfer is faster than radiative and non-radiative relaxation of the donor. Nevertheless, the fact that τ does not exhibit a systematic dependence on the Ru–Fe distance in the $[\{Ru(LL_n)\}_3Fe]^{8+}$ series suggests that the Förster mechanism should be considered as minor. Thus, the deactivation mainly proceeds by the Dexter mechanism. Therefore, since it involves the contact between the acceptor and the donor, the folding up of the molecule is required. Taking into account that the length of the alkyl chain does not lead to an important variation in τ, and that the deactivation process is mainly intramolecular, the experimental luminescence data can be understood if one considers that the tetranuclear complexes coexist in at least two forms in a thermodynamic equilibrium after irradiation in the MLCT band of the $[Ru(LL_n)]^{2+}$ subunit (Scheme 3). At the ground state level, the more stable geometry of the complexes is presumably the one which presents the four cationic metallic centres sufficiently distant to minimize the electrostatic repulsion. Quickly after the laser pulse irradiation, at the excited state level, the complexes undergo a sub-nanosecond (less than 30 ps) rearrangement, which cannot be detected by our setup, into two forms A and B (Scheme 3). In the A form, the relatively important Ru^{II}/Fe^{II} distance does not allow an efficient energy transfer (via a Dexter mechanism) and the luminescence of the ruthenium centre is detected with almost no perturbation due to the presence of the iron centre. It is well-known that, after irradiation in the MLCT band of the $[Ru(LL_n)]^{2+}$ moieties, an electron from the HOMO, which is localised around the metallic centre, is injected into the LUMO, which is delocalised over the bipyridine ligand, to form the transient $bpy^{\cdot-}$ radical anion.[22,23] In the B form, the two linked cationic metallic centres fold up in a way that confines the $bpy^{\cdot-}$ radical. Because two metallic centres are close, an efficient intramolecular EET is now feasible and contributes to the extinction of the luminescence of the complexes. From the luminescence quantum yield measurements, it appears that the B form is the more stable one at room temperature since φ_L decreases drastically from a factor of between 6 and 10 compared to that of $[Ru(LL_n)]^{2+}$ (Table 4). Moreover, if the A form and the B form are in rapid equilibrium, the excited state lifetime of the tetranuclear samples would be shorter than the corresponding

 © 2005 Wiley-VCH Verlag GmbH & Co. KGaA, Weinheim

$[Ru(LL_n)]^{2+}$ as the relaxation channel for the B form is much faster than for the A form.[24] This effect is weak for $[\{Ru(LL_2)\}_3Fe]^{8+}$ {τ = 1.07 μs compared to 1.11 μs for $[Ru(LL_2)]^{2+}$} and larger for complexes having a longer aliphatic bridge such as n = 4 and n = 6 (Table 4).

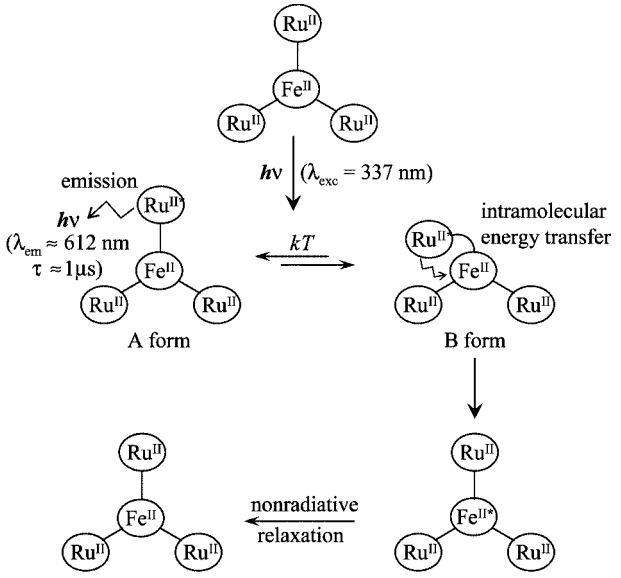

Scheme 3. Illustration of the photophysical behaviour of $[\{Ru(LL_n)\}_3Fe]^{8+}$ in CH_3CN + 0.1 M Bu_4NClO_4 after irradiation at 337 nm.

Although this phenomenon involves the proximity of cationic species, and therefore electrostatic repulsion, such an EET mechanism has already been suspected for other systems containing a $[Ru(bpy)_3]^{2+}$*-like donor with cationic iron[14,15] or manganese[12,25] complexes as acceptor. Nevertheless, the luminescence quantum yield of the $[\{Ru(LL_n)\}_3Fe]^{8+}$ complexes is much lower than that of $[Ru(LL_n)Fe]^{4+}$. To understand the reason for this difference, and to investigate the possibility of a self-quenching phenomenon of the Ru^{II}-tris-bipyridine units in the tetranuclear structure, we synthesised a similar tetranuclear complex in which Fe^{2+} is replaced by Zn^{2+}, namely $[\{Ru^{II}(bpy)_2(LL_2)\}_3Zn^{II}]^{8+}$ {denoted $[\{Ru(LL_2)\}_3Zn]^{8+}$}. The Zn^{II}-tris-bipyridine centre has no absorption in the visible region and, as expected, the absorption spectrum of the $[\{Ru(LL_2)\}_3Zn]^{8+}$ complex is close to that of $[Ru(LL_2)]^{2+}$. That excludes any possibility of an energy transfer between the Ru^{II}-tris-bipyridine units and the Zn^{II}-tris-bipyridine one after light irradiation. Moreover, since the Zn^{2+} site is not able to be oxidized, a quenching of the Ru^{II}* luminescence by an electron transfer is thermodynamically prohibited. The quantum yield and luminescence lifetime of $[\{Ru(LL_2)\}_3Zn]^{8+}$ were determined to be φ_L = 0.06 and τ = 1.07 μs, respectively. These values are similar to those obtained for $[Ru(LL_2)]^{2+}$ (φ_L = 0.06, τ = 1.11 μs), only the lifetime is weakly decreased as for $[\{Ru(LL_2)\}_3Fe]^{8+}$, indicating that the possible self-quenching of the similar $[Ru(LL_2)]^{2+}$ centre has to be considered as a minor process. Thus, the drastically lowered φ_L value for the $[\{Ru(LL_n)\}_3Fe]^{8+}$ complexes compared to $[Ru(LL_n)Fe]^{4+}$ can only be due to a higher probability of a dynamic quenching between Fe and Ru by folding up of the molecule in the tetranuclear structures than in the binuclear ones.

Photoinduced Electron Transfer

It has been established previously[14,26,27] that addition of an irreversible electron acceptor like 4-bromophenyldiazonium tetrafluoroborate ($ArN_2^+BF_4^-$) to a solution of the $[Ru^{II}(bpy)_3]^{2+}$ complex in CH_3CN + 0.1 M Bu_4NClO_4 allows the efficient production of $[Ru^{III}(bpy)_3]^{3+}$ under continuous irradiation (quantum yield 0.34). This permanent build up of $[Ru^{III}(bpy)_3]^{3+}$ arises because of the following electron transfer quenching reaction [Equations (5) and (6)]; the back-electron transfer reaction between $[Ru^{III}(bpy)_3]^{3+}$ and $ArN_2^{\cdot}$ radical is avoided by the rapid evolution of $ArN_2^{\cdot}$ into ArH and N_2.[25,26]

$$[Ru^{II}(bpy)_3]^{2+}* + ArN_2^+ \rightarrow [Ru^{III}(bpy)_3]^{3+} + ArN_2^{\cdot} \quad (5)$$

$$ArN_2^{\cdot} \xrightarrow{CH_3CN} ArH + N_2 \quad (6)$$

In the binuclear $[Ru(LL_n)Fe]^{4+}$ complexes, it has been demonstrated that ArN_2^+ can also react preferentially with the excited state of the $[Ru(LL_n)]^{2+}$ subunit to advantageously short-circuit the energy transfer.[14] For tetranuclear complexes, a similarly efficient photogeneration of the corresponding Ru^{III} species, i.e. $[Ru^{III}Ru^{II}_2(bpy)_6(LL_n)_3Fe^{II}]^{9+}$ is expected (Scheme 2). Indeed, the quenching of the Ru^{II}* centre in the $[\{Ru(LL_n)\}_3Fe]^{8+}$ complexes by EET is incomplete and the luminescence lifetime of the Ru^{II}* excited state is sufficiently long-lived (1 μs) to allow a bimolecular reaction using an external electron acceptor. In addition, the lifetime of the excited state of the Fe^{II} moiety is too short (<1 ns) to undergo an efficient bimolecular electron transfer with ArN_2^+.[19]

In order to photoinduce the oxidation of the $[\{Ru(LL_n)\}_3Fe]^{8+}$ complexes, ArN_2^+ was added to a solution of the complexes in deoxygenated CH_3CN + 0.1 M Bu_4NClO_4. Since the photogenerated Ru^{III} subunit plays the role of oxidant towards Fe^{II} (see electrochemical part), irradiation should lead, in a first step, to $[\{Ru^{II}(LL_n)\}_3Fe^{III}]^{9+}$ (Scheme 2). In a second step, the formation of the final $[\{Ru^{III}(LL_n)\}_3Fe^{III}]^{12+}$ species is expected as ArN_2^+ is added in excess. The rate constant of oxidant quenching (k_{ET}) of the excited state of the tetranuclear complexes by ArN_2^+ was determined from the Stern–Volmer plot, see Equation (7)

$$\tau/\tau_{Ar} = 1 + k_{ET}\cdot\tau\cdot[ArN_2^+] \quad (7)$$

where τ and τ_{Ar} are the luminescence lifetime of the complexes without and with a variable concentration of ArN_2^+, respectively, and k_{ET} is the rate constant of the electron transfer reaction according to Equation (8).

 © 2005 Wiley-VCH Verlag GmbH & Co. KGaA, Weinheim

$$[Ru^{II}*Ru^{II}_2(bpy)_6(LL_n)_3Fe^{II}]^{8+} + ArN_2^+ \xrightarrow{k_{ET}} [Ru^{III}Ru^{II}_2(bpy)_6(LL_n)_3Fe^{II}]^{9+} + ArN_2^{\cdot} \quad (8)$$

The Stern–Volmer plots are linear for the three complexes (Figure 5). This indicates that the electron transfer is a simple bimolecular reaction, i.e. only one Ru^{II} centre reacts each time with ArN_2^+. The k_{ET} values obtained for the tetranuclear $[\{Ru(LL_n)\}_3Fe]^{8+}$ compounds ($>10^9$ $M^{-1}s^{-1}$) depend only slightly on the Ru–Fe distance in the complexes, and are around 10 times greater than the k_{ET} values determined for the binuclear $[Ru(LL_n)Fe]^{4+}$ complexes (Table 5). The markedly faster electronic quenching process in the case of tetranuclear complexes is presumably due to the lower efficiency of the competitive energy transfer by the Fe^{2+} centre (Table 4). Nevertheless, it is difficult to compare the energy-transfer constants of these two kinds of complexes since, for the tetranuclear complexes, the energy transfer occurs via an intramolecular process while for the binuclear ones it is intermolecular.

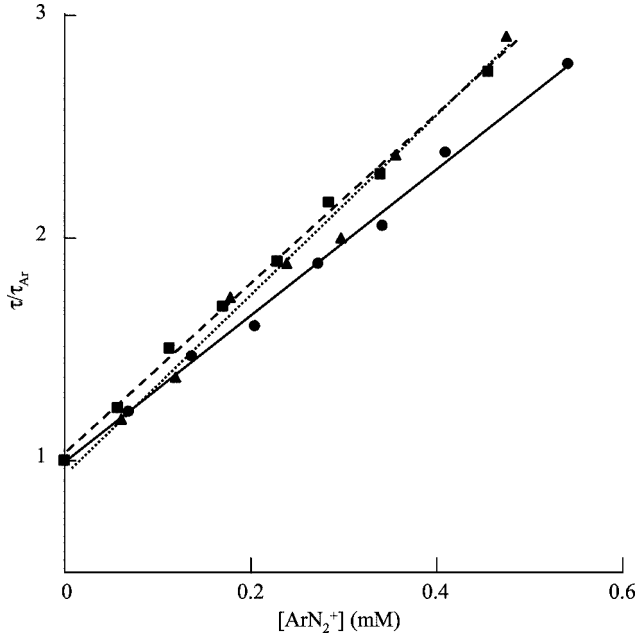

Figure 5. Stern–Volmer plots for the $[\{Ru(LL_n)\}_3Fe]^{8+}$ complexes in deoxygenated CH_3CN (0.01 mM) with ArN_2^+ (between 0 and 0.6 mM): $[\{Ru(LL_2)\}_3Fe]^{8+}$ (■), $[\{Ru(LL_4)\}_3Fe]^{8+}$ (●) and $[\{Ru(LL_6)\}_3Fe]^{8+}$ (▲).

Table 5. Electron transfer rate constant, k_{ET}, for $[Ru(LL_n)Fe]^{4+}$ and $[\{Ru(LL_n)\}_3Fe]^{8+}$ in the presence of a variable concentration of ArN_2^+ at room temperature in CH_3CN + 0.1 M Bu_4NClO_4.

Complexes	k_{ET} [$M^{-1}s^{-1}$]
$[Ru^{II}(LL_2)Fe^{II}]^{4+}$	3.7×10^8
$[Ru^{II}(LL_4)Fe^{II}]^{4+}$	5.3×10^8
$[Ru^{II}(LL_6)Fe^{II}]^{4+}$	6.4×10^8
$[\{Ru^{II}(LL_2)\}_3Fe^{II}]^{8+}$	3.6×10^9
$[\{Ru^{II}(LL_4)\}_3Fe^{II}]^{8+}$	3.2×10^9
$[\{Ru^{II}(LL_6)\}_3Fe^{II}]^{8+}$	4.0×10^9

Photooxidation by Continuous Irradiation

Successive photogeneration of the oxidized $[\{Ru^{II}(LL_n)\}_3Fe^{III}]^{9+}$ and $[\{Ru^{III}(LL_n)\}_3Fe^{III}]^{12+}$ species (Scheme 2) was followed by UV/Vis absorption spectroscopy. Solutions containing $[\{Ru(LL_n)\}_3Fe]^{8+}$ (0.03–0.04 mM) in the presence of an excess of ArN_2^+ (15 mM) in CH_3CN + 0.1 M Bu_4NClO_4 were irradiated with a mercury lamp (250 W). Two successive changes of the absorption spectrum were observed during the irradiation. In the first step, the band of the Fe^{II} unit at 530 nm decreases regularly until it disappears totally, in accordance with the formation of $[\{Ru^{II}(LL_n)\}_3Fe^{III}]^{9+}$ via the transient photogenerated Ru^{III} species (Figure 6). In a second step, irradiation induces the quantitative formation of $[\{Ru^{III}(LL_n)\}_3Fe^{III}]^{12+}$, as illustrated by the decrease of the MLCT band of the Ru^{II} unit at around 455 nm and the appearance of two new ones at 428 and 644 nm typical of the Ru^{III} species.

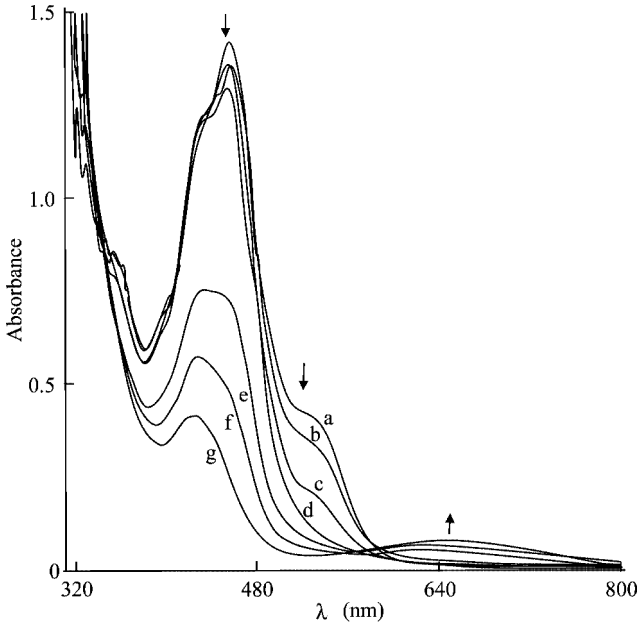

Figure 6. Spectral change of a mixture of $[\{Ru(LL_6)\}_3Fe]^{8+}$ (0.032 mM) and ArN_2^+ (15 mM), under visible irradiation: (a) initial solution, (b) 3 s, (c) 12 s, (d) 24 s, (e) 120 s, (f) 220 s, (g) 700 s, (l = 1 cm).

From a kinetic point of view, one can consider that, during the first step, there is a steady-state concentration of the Ru^{II} and Ru^{III} species since the sacrificial oxidant is present in large excess. Thus, the overall kinetic law for the oxidation of the Fe^{II}-tris-bipyridine unit can, as we previously proposed,[14] be approximated to a pseudo-first-order equation [Equation (9)], where $[Ru^{II}]$ and $[Fe^{II}]$ represent the concentration of the two subunits of the $[\{Ru(LL_n)\}_3Fe]^{8+}$ complexes in solution.

$$v = k[Ru^{II}][Fe^{II}][ArN_2^+] = K_{Fe}[Fe^{II}] = -d[Fe^{II}]/dt \quad (9)$$

In a similar fashion, during the second step involving the formation of $[\{Ru^{III}(LL_n)\}_3Fe^{III}]^{12+}$, a pseudo-first-order equation is also obtained, see Equation (10).

 © 2005 Wiley-VCH Verlag GmbH & Co. KGaA, Weinheim

Table 6. Apparent oxidation rate constants for $[\{Ru(LL_n)\}_3Fe]^{8+}$ during irradiation in the presence of a large excess of ArN_2^+.

Complexes	K_{Fe} [s^{-1}]	K_{Ru} [s^{-1}]
$[\{Ru^{II}(LL_2)\}_3Fe^{II}]^{8+}$	$5.4\times10^{-2}\pm0.8\times10^{-2}$	$4.99\times10^{-3}\pm4\times10^{-5}$
$[\{Ru^{II}(LL_4)\}_3Fe^{II}]^{8+}$	$8.4\times10^{-2}\pm0.6\times10^{-2}$	$6.63\times10^{-3}\pm6\times10^{-5}$
$[\{Ru^{II}(LL_6)\}_3Fe^{II}]^{8+}$	$11.7\times10^{-2}\pm1\times10^{-2}$	$12.24\times10^{-3}\pm3\times10^{-5}$

$$v = k'[Ru^{II}][Fe^{III}][ArN_2^+] = K_{Ru}[Ru^{II}] = -d[Ru^{II}]/dt \quad (10)$$

These two oxidation steps were followed by the evolution of the absorbance at 530 and 454 nm, respectively, with the irradiation time. In all cases the absorbance variation was fitted by a monoexponential curve, as illustrated in Figure 7, in accordance with Equations (9) and (10), thus allowing the determination of K_{Fe} and K_{Ru} for the three heterotetranuclear complexes. These values are given in Table 6. It appears that both the Fe^{II} and Ru^{II} oxidation rate depend on the nature of the bridging ligand, and that the efficiency of the photoassisted process increases when the length of the alkyl chain increases, oxidation of $[\{Ru(LL_6)\}_3Fe]^{8+}$ being twice as fast as oxidation of $[\{Ru(LL_2)\}_3Fe]^{8+}$.

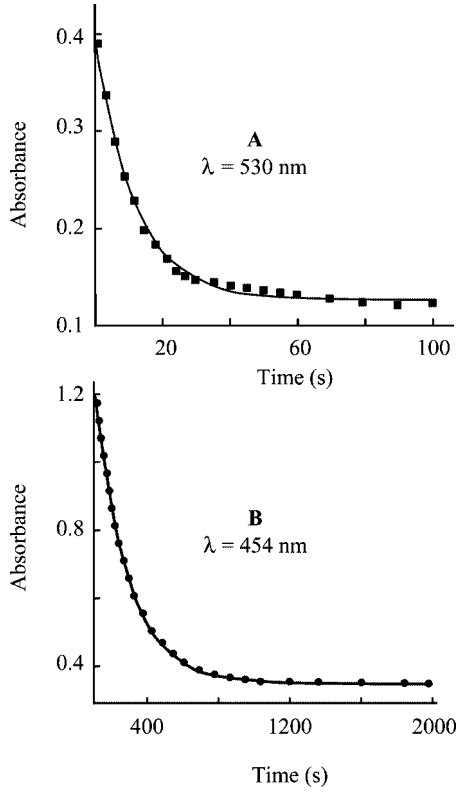

Figure 7. Evolution of the absorption intensity at 530 nm (A) and 454 nm (B) with irradiation time for the $[\{Ru(LL_6)\}_3Fe]^{8+}$ complexes (0.032 mM) in CH_3CN + 0.1 M Bu_4NClO_4, in the presence of ArN_2^+ (15 mM) (l = 1 cm). Bold lines correspond to the fit using a monoexponetial function. The fit parameters K_{Fe} and K_{Ru} are given in Table 6.

Two processes can control the overall efficiency of the oxidation steps and explain the influence of the aliphatic chain length on the photooxidation rate. The first one is the photogeneration of the Ru^{III} moieties. This process requires contact between two cationic species {i.e. ArN_2^+ and $[\{Ru(LL_n)\}_3Fe]^{8+}$} and involves an electrostatic repulsion phenomenon which should be important for the complex exhibiting the smaller Ru–Fe distance − $[\{Ru(LL_2)\}_3Fe]^{8+}$ − whereas it is less pronounced for $[\{Ru(LL_6)\}_3Fe]^{8+}$. The second process involves the oxidation of Fe^{II} into Fe^{III}. Since the electron transfer operates according to an intramolecular process, it requires the folding-up of the complex in order to allow the formation of Fe^{III} through the photogenerated Ru^{III} moieties. Taking into account that the flexibility of the aliphatic bridging ligand increases with the number of methylene units, the contact between Ru^{III} and Fe^{II} should be favoured in the case of $[\{Ru(LL_6)\}_3Fe]^{8+}$, whereas for $[\{Ru(LL_2)\}_3Fe]^{8+}$ the folding-up is more difficult and therefore the photooxidation rate is lowered.

Finally, the quantum yield of formation of $[\{Ru^{II}(LL_n)\}_3Fe^{III}]^{9+}$ (φ_F) was determined in CH_3CN (see Experimental Section) and was found to be equal to 0.22 for the most efficient system, i.e. $[\{Ru(LL_6)\}_3Fe]^{8+}$.

Conclusions

In this study we have demonstrated that for the tetranuclear $[\{Ru^{II}(LL_n)\}_3Fe^{II}]^{8+}$ complexes a partial energy transfer from the ^{3}MLCT excited state of the Ru^{II}-tris-bipyridine centres to the Fe^{II}-tris-bipyridine unit occurs by a pure intramolecular process, in contrast to what was observed for the corresponding binuclear complexes. This is a consequence of the structure of the tetranuclear complexes, in which the presence of the three Ru^{II} subunits prevents the close contact of the Fe^{II} centre with the Ru^{II} subunits of another tetranuclear complex and therefore an intermolecular energy transfer. The rate constant of the process is not clearly connected to the length of the aliphatic chain of the bridging ligand. This energy-transfer process can be easily short-circuited in the presence of an external irreversible electron acceptor by an electron-transfer process, leading, with a high quantum yield, to the photoinduced oxidation of the iron(II) subunit of the tetranuclear complexes (φ_F = 0.22) followed by that of the ruthenium(II) subunits.

An extension of this work is currently underway with similar tetranuclear polypyridyl complexes of Ru^{II} and Mn^{II}. An efficient photoinduced oxidation phenomenon is also expected for this kind of complex since the energy transfer between the two different metallic subunits is known to be less efficient than for the parent Fe^{II} compounds.

 © 2005 Wiley-VCH Verlag GmbH & Co. KGaA, Weinheim

Experimental Section

General: Acetonitrile (Rathburn, HPLC grade) was used as received and stored under argon in a glovebox. Tetra-*n*-butylammonium perchlorate (Bu_4NClO_4, Fluka) was used as received. ^1H NMR spectra were recorded on a Bruker AC 250 spectrometer. The electrospray ionisation mass spectrometry (ESI-MS) experiments were performed on a triple quadrupole mass spectrometer Quattro II (micromass, Altrincham, UK). The ESI source was heated to 80 °C. The sampling cone voltage was set within the range 6–17 V according to the complex studied. Complexes in solution (1 mg mL^{-1} in CH_3CN) were injected using a syringe pump at a flow rate of 10 μL min^{-1}. The electrospray probe (capillary) voltage was optimised in the range 2–5 kV for positive ion electrospray. Elemental analyses were performed by the Service Central d'Analyse du CNRS at Vernaison (France). UV/Vis spectra were obtained using a Cary 1 and a Cary 100 absorption spectrophotometers on 1-mm path-length quartz cells for electrochemical experiments and 1-cm cells for irradiation experiments.

Electrochemistry: All electrochemical measurements were performed under argon in a glovebox at room temperature. Cyclic voltammetry and controlled potential electrolysis experiments were performed using an EG&G PAR model 173 potentiostat/galvanostat equipped with a PAR model universal programmer and a PAR model 179 digital coulometer. A CHI440 Electrochemical Analyzer (CH Instruments, Texas, USA) was used for the determination of formal potentials. A standard three-electrode electrochemical cell was used. Potentials were referenced to an Ag/10 mM $AgNO_3$ reference electrode in CH_3CN + 0.1 M Bu_4NClO_4. Potentials referred to that system can be converted into the ferrocene/ferrocenium couple by subtracting 87 mV and to SCE or NHE by adding 298 mV or 548 mV, respectively.[28] The working electrode was a platinum disk polished with 2-μm diamond paste (Mecaprex Presi) with a diameter of 5 mm for cyclic voltammetry [E_{pa}: anodic peak potential; E_{pc}: cathodic peak potential; $E_{1/2} = (E_{pa} + E_{pc})/2$; $\Delta E_p = E_{pa} - E_{pc}$] and 2 mm for rotating disk electrode experiments (RDE). Exhaustive electrolyses were carried out with a platinum plate. The auxiliary electrode was a Pt wire in CH_3CN + 0.1 M Bu_4NClO_4. For electrochemical experiments, electronic absorption spectra were recorded on a Hewlett–Packard 8452 A diode array spectrophotometer. Initial and electrolyzed solutions were transferred to a conventional 1-mm quartz cell in the glovebox.

Luminescence: The steady-state emission spectra were recorded on a Photon Technology International (PTI) SE-900M spectrofluorimeter. All the samples for luminescence and photooxidation experiments were prepared in a glovebox in deoxygenated CH_3CN + 0.1 M Bu_4NClO_4 and contained in a 1-cm quartz cell. The samples were maintained under aerobic conditions with a Teflon cap. The luminescence lifetime of the complexes was recorded after irradiation at λ = 337 nm with a 4-ns pulsed laser (spectra physics 337-201) and recorded at λ = 600 nm using a monochromator and a photomultiplicator tube (Hammamatsu R928) coupled with an ultra-fast oscilloscope (Tektronix TDS 520A). For subnanosecond decay experiments, sample excitation was performed at 400 nm, which was obtained by the second harmonic of a Titanium: Sapphire laser (picosecond Tsunami laser at an 80-MHz repetition rate). For decay acquisition, a GaAs microchannel plate photomultiplier (Hamamatsu model R 3809 U-51) followed by a homemade single-photon correlator were used. The ultimate time resolution of the entire chain was close to 30 ps. The emission quantum yield, φ_L, was determined at 25 °C in deoxygenated acetonitrile solutions with a CH_3CN solution of $[Ru^{II}(bpy)_3](PF_6)_2$ ($\varphi_L^{ref} = 0.062$)[29] according to Equation (11)

$$\phi_L^S = \frac{I_L^S}{I_L^{Ref}} \frac{(1-10^{-OD^{Ref}})}{(1-10^{-OD^S})} \phi_L^{Ref} \quad (11)$$

where the emission intensity, I_L, was calculated from the spectrum area $\int I(\lambda)d\lambda$, and OD represents the optical density at the excitation wavelength (450 nm). The superscripts "S" and "Ref" refer to the sample and to the standard, respectively.

Continuous Irradiation: The irradiation experiments were performed using a mercury lamp (Oriel 66901, 250 W) whose UV and IR radiations were filtered with a large band-pass filter centred around λ = 560 nm (irradiation range between 410 and 710 nm). The solutions contained a mixture of $[\{Ru(LL_n)\}_3Fe]^{8+}$ complex (0.03–0.04 mM) and ArN_2^+ (15 mM) in order to obtain an absorbance below 1.5 at 454 nm in CH_3CN + 0.1 M Bu_4NClO_4. Under these conditions the concentration of ArN_2^+ can be considered as constant during the experiments.

The quantum yields of formation of $[\{Ru^{II}(LL_n)\}_3Fe^{III}]^{9+}$, φ_F, measured after continuous irradiation at 436 nm, were performed with a 250-W Hg Lamp (Oriel 66901). The desired mercury emission line was isolated using a band-pass filter. The quantum yields were determined by actinometry at the wavelength of the maximum absorption of $[Fe(bpy)_3]^{2+}$ (526 nm) by comparing the absorption of the sample before and after irradiation and using the quantum yield formation of $[Ru(bpy)_3]^{3+}$ in the system $[Ru(bpy)_3]^{2+}/ArN_2^+$ as reference ($\varphi_F^{Ref} = 0.34$).[26] Samples were prepared with the same absorbance (Abs = 2) at 454 nm and the variation of absorbance during irradiation was checked to be less than 0.1. The quantum yield of formation, φ_F^S, of the sample was deduced from Equation (12).

$$\phi_F^S = \left[\frac{(\Delta OD)^S_{526\,nm}}{(\Delta OD)^{Ref}_{454\,nm}}\right]_{t,\lambda^{irr}=436\,nm} \times \phi_F^{Ref} \quad (12)$$

Synthesis of the Diazonium Salt: 4-bromophenyl diazonium tetrafluoroborate *p*-$BrC_6H_4N_2^+ \cdot BF_4^-$ ($ArN_2^+ \cdot BF_4^-$) was synthesised as described previously.[26]

Synthesis of Ligands LL_n and of $[Ru^{II}(bpy)_2(LL_n)](PF_6)_2$: The ligands 1,2-bis[4-(4′-methyl-2,2′-bipyridinyl)]ethane (LL_2), 1,2-bis[4-(4′-methyl-2,2′-bipyridinyl)]butane (LL_4), 1,2-bis[4-(4′-methyl-2,2′-bipyridinyl)]hexane (LL_6) and the $[Ru^{II}(bpy)_2(LL_2)](PF_6)_2$, $[Ru^{II}(bpy)_2(LL_4)](PF_6)_2$, $[Ru^{II}(bpy)_2(LL_6)](PF_6)_2$ complexes were synthesised as described previously.[14]

Synthesis of $[\{Ru^{II}(bpy)_2(LL_n)\}_3Fe^{II}](PF_6)_8$: An aqueous solution of 0.4 molar equivalents of $Fe(ClO_4)_2 \cdot 8H_2O$ was added to an orange solution of $[Ru^{II}(bpy)_2(LL_n)](PF_6)_2$ (100 mg) in ethanol (10 mL) at 60 °C, leading to the formation of the red-orange complex $[\{Ru^{II}(bpy)_2(LL_n)\}_3Fe^{II}]^{8+}$. After stirring the solution for one hour at 60 °C, the ethanol was removed under reduced pressure and the heterotetranuclear complex was extracted with CH_2Cl_2. The resulting solution was washed three times with an aqueous KPF_6 solution (0.1 M) in order to exchange the ClO_4^- anion with PF_6^-, and then twice with water. After drying over Na_2SO_4, CH_2Cl_2 was removed under reduced pressure. The red-orange product obtained corresponding to $[\{Ru^{II}(bpy)_2(LL_n)\}_3Fe^{II}](PF_6)_8$ was reprecipitated in CH_3CN/diethyl ether, washed with diethyl ether, and dried under vacuum. The purity of each complex was confirmed by elemental analysis, ^1H NMR spectroscopy and by the observation of a single spot by TLC [eluent H_2O/CH_3CN (10:90) containing KPF_6 (10 mM)].

 © 2005 Wiley-VCH Verlag GmbH & Co. KGaA, Weinheim

$[\{Ru^{II}(bpy)_2(LL_2)\}_3Fe^{II}](PF_6)_8$ ($[\{Ru(LL_2)\}_3Fe]^{8+}$): 51 mg (45%). $C_{132}H_{114}F_{48}Fe_1N_{24}P_8Ru_3{\cdot}6H_2O$ (3663.3): calcd. C 43.28, H 3.46, N 9.18; found C 43.42, H 3.33, N 9.36. ESI-MS: *m/z* (%) = 3410.28 $[M - PF_6]^+$, 1632.70 (2) $[M - 2PF_6]^{2+}$, 1040.15 (6) $[M - 3PF_6]^{3+}$, 743.87 (10) $[M - 4PF_6]^{4+}$, 566.10 (42) $[M - 5PF_6]^{5+}$.

$[\{Ru^{II}(bpy)_2(LL_4)\}_3Fe^{II}](PF_6)_8$ ($[\{Ru(LL_4)\}_3Fe]^{8+}$): Yield: 46 mg (41%). $C_{138}H_{126}F_{48}Fe_1N_{24}P_8Ru_3{\cdot}6H_2O$ (3747.5): calcd. C 44.34, H 3.71, N 9.04; found C 44.82, H 3.72, N 9.03. ESI-MS: *m/z* (%): 3494.44 $[M - PF_6]^+$, 1674.75 (1) $[M - 2PF_6]^{2+}$, 1068.18 (8) $[M - 3PF_6]^{3+}$, 764.90 (17) $[M - 4PF_6]^{4+}$, 582.92 (53) $[M - 5PF_6]^{5+}$.

$[\{Ru^{II}(bpy)_2(LL_6)\}_3Fe^{II}](PF_6)_8$ ($[\{Ru(LL_6)\}_3Fe]^{8+}$): Yield: 24 mg (22%). $C_{144}H_{138}F_{48}Fe_1N_{24}P_8{\cdot}Ru_36H_2O$ (3831.65): calcd. C 45.14, H 3.94, N 8.78; found C 45.63, H 3.91, N 8.96. ESI-MS: *m/z* (%): 3578.60 $[M - PF_6]^+$, 1726.80 (1) $[M - 2PF_6]^{2+}$, 1096.22 (8) $[M - 3PF_6]^{3+}$, 785.92 (22) $[M - 4PF_6]^{4+}$, 599.74 (59) $[M - 5PF_6]^{5+}$.

Synthesis of $Zn(CF_3SO_3)_2$: Pure CF_3SO_3H (1 mL, 11.2 mmol) was added to a solution of CH_3CN (10 mL) containing Zn powder (7.13 g, 112 mmol). After stirring for one day, the excess of Zn was removed by filtration. Addition of diethyl ether to the filtrate yielded the formation of a white precipitate of $Zn(CF_3SO_3)_2$, which was filtered off, washed with diethyl ether and dried under vacuum (yield: 1.02 g, 50%).

Synthesis of $[\{Ru^{II}(bpy)_2(LL_2)\}_3Zn^{II}](PF_6)_8$: Solid $Zn(CF_3SO_3)_2$ (2.36 mg, 6.48 μmol) was added to a solution of $[Ru^{II}(bpy)_2(LL_2)](PF_6)_2$ (20.8 mg, 19.4 μmol) in ethanol (80 mL), leading to the formation of the $[\{Ru^{II}(bpy)_2(LL_2)\}_3Zn^{II}\}^{8+}$ complex. This solution was stirred for one hour at reflux. After cooling to room temperature, an aqueous solution (20 mL) of KPF_6 (15 mg, 64.8 μmol) was added and then the ethanol was removed under reduced pressure. The heterotetranuclear complex was extracted from the aqueous phase with CH_2Cl_2. The resulting CH_2Cl_2 solution was washed three times with an aqueous KPF_6 solution (0.1 M), and then twice with water. After drying over Na_2SO_4, CH_2Cl_2 was removed under reduced pressure. The orange product obtained corresponding to $[\{Ru^{II}(bpy)_2(LL_2)\}_3Zn^{II}](PF_6)_8$ was reprecipitated from CH_3CN/diethyl ether, washed with diethyl ether, and dried under vacuum (yield: 18.5 mg, 80%). $C_{132}H_{114}F_{48}N_{24}Ru_3P_8Zn_1$ (3564.8): calcd. C 44.47, H 3.22, N 9.43; found C 44.49, H 3.29, N 9.60.

Acknowledgments

We thank Dr. Jean-Claude Vial from the Laboratoire de Spectrométrie Physique (CNRS UMR 5588, Université Joseph Fourier, Grenoble I) for allowing us to use his picosecond emission decay setup. We also thank one referee for pointing out that the kinetics of two excited states in rapid equilibrium were worked out thoroughly by J. N. Demas.

[1] M. R. Wasielewski, *Chem. Rev.* **1992**, *92*, 435.
[2] V. Balzani, A. Juris, M. Venturi, *Chem. Rev.* **1996**, *96*, 759.
[3] C. A. Bignozzi, J. R. Schoonover, F. Scandola, *Prog. Inorg. Chem.* **1997**, *44*, 1, special volume on molecular level artificial photosynthetic materials (Eds.: G. J. Meyer, K. D. Karlin), John Wiley & Sons, New York.
[4] L. Sun, L. Hammarström, B. Akermark, S. Styring, *Chem. Soc. Rev.* **2001**, *30*, 36.
[5] L. Hammarström, *Curr. Opin. Chem. Biol.* **2003**, *7*, 666.
[6] D. Burdinski, K. Wieghardt, S. Steenken, *J. Am. Chem. Soc.* **1999**, *30*, 10781.
[7] D. Burdinski, B. Eberhardt, K. Wieghardt, *Inorg. Chem.* **2000**, *39*, 105.
[8] K. E. Berg, A. Tran, M. K. Raymond, M. Abrahamsson, J. Wolny, S. Redon, M. Andersson, L. Sun, L. Hammarström, H. Toftlund, B. Akermark, *Eur. J. Inorg. Chem.* **2001**, 1019.
[9] M. M. Morrisson, D. T. Sawyer, *Inorg. Chem.* **1978**, *17*, 333.
[10] M. N. Collomb Dunand-Sautier, A. Deronzier, *J. Electroanal. Chem.* **1997**, *428*, 65.
[11] M. N. Collomb Dunand-Sautier, A. Deronzier, I. Romero, *J. Electroanal. Chem.* **1997**, *436*, 219.
[12] H. Berglund-Baudin, L. Sun, R. Davidov, M. Sundahl, S. Styring, B. Akermark, M. Almgren, L. Hammarström, *J. Phys. Chem. A* **1998**, *102*, 2512.
[13] M. Abrahamsson, H. Baudin, A. Tran, C. Philouze, K. E. Berg, M. K. Raymond-Johansson, L. Sun, B. Akermark, S. Styring, L. Hammarström, *Inorg. Chem.* **2002**, *41*, 1534.
[14] F. Lafolet, J. Chauvin, M.-N. Collomb, A. Deronzier, H. Laguitton-Pasquier, J.-C. Leprêtre, J.-C. Vial, B. Brasme, *Phys. Chem. Chem. Phys.* **2003**, *5*, 2520.
[15] R. H. Schmehl, R. A. Auerbach, W. F. Wacholtz, C. M. Elliott, R. A. Freitag, J. W. Merkert, *Inorg. Chem.* **1986**, *25*, 2440.
[16] A. E. Kaifer, M. Gomez-Kaifer, *Supramolecular Electrochemistry*, Chap. 8 "Electrochemical Considerations for Supramolecular Systems", Wiley-VCH Weinheim, Germany ,**1999**, p. 89.
[17] J. B. Flanagan, S. Margel, A. J. Bard, F. C. Anson, *J. Am. Chem. Soc.* **1977**, *100*, 4248.
[18] The potentials of the Ru^{II*}/Ru^{I} and Ru^{II*}/Ru^{III} redox couples were estimated by subtracting 2.03 eV (λ_{emis} = 612 nm) from the potential of Ru^{II}/Ru^{I} and Ru^{II}/Ru^{III} of the $[\{Ru(LL_n)\}_3Fe]^{8+}$ complexes.
[19] C. Creutz, M. Chou, T. Netzel, M. Okumura, N. Sutin, *J. Am. Chem. Soc.* **1980**, *102*, 1309.
[20] L. D. Dexter, *J. Chem. Phys.* **1953**, *21*, 838.
[21] T. H. Förster, *Discuss. Faraday Soc.* **1959**, *27*, 7.
[22] A. Juris, V. Balzani, F. Barrigelletti, S. Campagna, P. Belser, A. von Zelewsky, *Coord. Chem. Rev.* **1988**, *84*, 85–277.
[23] G. F. Strousse, J. R. Schoonover, R. Duesing, S. Boyde, W. E. Jones, T. J. Meyer, *Inorg. Chem.* **1995**, *34*, 473.
[24] J. N. Demas, *Excited State Lifetime Measurements*, Academic Press, New York, **1983**.
[25] C. Baffert, S. Dumas, J. Chauvin, J.-C. Leprêtre, M.-N. Collomb, A. Deronzier, *Phys. Chem. Chem. Phys.* **2005**, *7*, 202.
[26] H. Cano-Yelo, A. Deronzier, *J. Chem. Soc., Faraday Trans. 1* **1984**, *80*, 3011.
[27] H. Laguitton-Pasquier, A. Martre, A. Deronzier, *J. Phys. Chem. B* **2001**, *105*, 4801.
[28] V. V. Pavlishchuk, A. W. Addison, *Inorg. Chim. Acta* **2000**, *298*, 97.
[29] J. V. Caspar, T. J. Meyer, *J. Am. Chem. Soc.* **1983**, *105*, 5583.

Received: February 2, 2005
Published Online: July 7, 2005

 © 2005 Wiley-VCH Verlag GmbH & Co. KGaA, Weinheim

Ab initio Study of Some Intramolecularly Donor-Stabilized Silenes

Dirk Wandschneider,[a] Manfred Michalik,[b] Hartmut Oehme,[c] and Andreas Heintz*[a]

Keywords: Silenes / Ab initio calculations / Donor-acceptor systems

Ab initio calculations were performed to predict geometric structures, stabilizing energies and rotational barriers of some intramolecularly donor-stabilized silenes. Calculations were performed using the HF, MP2, and B3LYP method with the 6-31G(d) and 6-31++G(d,p) basis set. Results were compared to experimentally available X-ray structures and energy barriers known from temperature dependent ^{1}H NMR measurements. Various approaches were applied to get an insight into the remarkable stability of these thermodynamically stabilized Si=C compounds. The results indicate a strong stabilizing effect of the intramolecular Si–N donor-acceptor bond.
(© Wiley-VCH Verlag GmbH & Co. KGaA, 69451 Weinheim, Germany, 2005)

1. Introduction

Silenes, silicon derivatives with an Si=C double bond, are extremely labile compounds. In absence of scavenger reagents they undergo rapid dimerizations or oligomerizations, if they are not stabilized. A kinetic stabilization can be achieved by means of bulky substituents attached to the Si=C group. Some highly congested silenes could be isolated and structurally characterized.[1,2] Coordination of donor molecules like amines, THF or fluoride anions to the electrophilic silene silicon atom leads to an effective thermodynamic stabilization of the compounds.[3–6] A particularly effective stabilization is expected, when substituents with donor groups are introduced to the silenes and intramolecular donor–acceptor interaction between this donor group and the electrophilic silicon center is possible. Such intramolecular N→Si coordination was concluded from theoretical calculations of Gusel′nikov et al.[7] for a 1-methylene-5-methyl-2,8-dioxa-5-aza-1-silacyclooctane, and a stable dibenzosilafulvene with an 8-dimethylaminomethyl-1-naphthyl group at the silicon atom was isolated by Chernyshev et al.[8,9] However, no X-ray crystal structure analysis of the compound could be performed to validate their results.

Recently we were able to obtain the following silenes (Figure 1):[10–12]

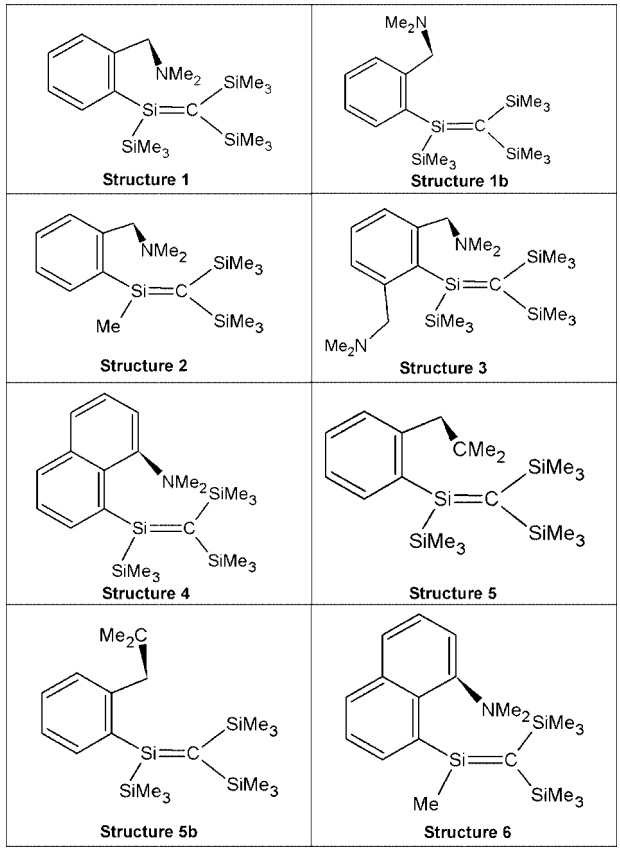

Figure 1. Selected structures of studied substances (schematically).

1-[2-(dimethylaminomethyl)phenyl]-1,2,2-tris(trimethylsilyl)silene (**1**),

1-[2-(dimethylaminomethyl)phenyl]-1-methyl-2,2-bis(trimethylsilyl)silene (**2**),

1-[2,6-bis(dimethylaminomethyl)phenyl]-1,2,2-tris(trimethylsilyl)silene (**3**), and

[a] Institute of Chemistry, University of Rostock, Department of Physical Chemistry,
18055 Rostock
Fax: +49-3814986502
E-mail: andreas.heintz@chemie.uni-rostock.de
[b] Leibniz-Institute for Organic Catalysis,
Rostock
[c] Institute of Chemistry, University of Rostock, Department of Inorganic Chemistry,
18055 Rostock
Supporting information for this article is available on the WWW under http://www.eurjic.com or from the authors.

1-(8-dimethylamino-1-naphthyl)-1,2,2-tris(trimethylsilyl)-silene (**4**).

They were clearly characterized by X-ray structural analyses as intramolecularly donor-stabilized silenes. They proved to be thermally stable up to 140 °C and have a dramatically reduced reactivity compared with uncomplexed silenes.

In this paper we report some ab initio calculations of the geometric structures and energies of **1**, as well as some related compounds. The aim of these calculations was to estimate the impact of the intramolecular Si–N donor bond on the Si=C double bond. Additionally, the temperature dependent ^{1}H NMR spectra of **1**, **2** and **3** were interpreted in form of a hindered rotation about the Si=C bond and evaluated quantitatively by comparison of experimental data for the Gibbs activation energy $\Delta G^{\neq}$ with values calculated by ab initio methods.

2. Results and Discussions

The experimentally available X-ray structures of **1**, **2** and **3**[10–12] can be compared to the quantum mechanically fully optimized geometric structures of the isolated species. Obviously, some deviations between the isolated species and the species in the solid phase are to be expected, since packaging effects in the solid phase could not be accounted for in the ab initio calculations. Nevertheless, the geometric structure obtained by using the HF/6-31++G(d,p) method agrees favorably with the X-ray structure, as the results in Table 1 show for **1**. Worth mentioning is the short interatomic Si···N distance of about 2.0 Å, which is much shorter than the sum of the van der Waals radii (3.5 Å) and longer than a covalent Si–N bond (about 1.8 Å), supporting the idea of an Si···N donor–acceptor stabilized interaction. Therefore a distinct pyramidalization at the silene silicon center (sum of angles < 350°) is observed, whereas the configuration at the silene carbon atom is trignonal planar (sum of angles > 359°). The Si=C bond length is about 1.76 Å. This is distinctly longer than in the similarly substituted stable silene $Me_2Si=C(SiMe_3)(SiMe{t}Bu_2)_2$ (1.702 Å),[4] where no donor stabilization takes place. The Si=C distance is in good agreement with the corresponding distance in the intermolecular adduct of the silene $Me_2Si=C(SiMe_2Ph)_2$ with ethyldimethylamine (1.761 Å).[5] This supports the idea that the interaction of silenes with donor groups leads to an elongation of the Si=C bond[3–6] caused by a weakening of the Si–C π interaction. The Si=C distances of the kinetically stabilized silenes $(Me_3Si)_2Si=C(OSiMe_3)Ad$ (1.764 Å, Ad = 1-adamantyl)[13] and $(Me_3Si)({t}BuMe_2Si)=Ad'$ (1.741 Å, Ad′ = 2-adamantylidene)[14] are almost the same as those of the thermodynamically stabilized silenes, but these elongations were accounted for by the electronic effects of the substituents.[14,15]

For compound **3** the situation is quite comparable to compound **1**, as the results in Table 2 show. Only one of the two dimethylamino groups interacts with the tetra-coordinated silene silicon atom. This leads again to a pyramidalization at the silene silicon atom and one short interatomic Si···N distance. The configuration at the silene carbon atom is perfectly trigonal planar and the Si=C bond length is only slightly longer than in compound **1**.

There are several possibilities to calculate the stabilizing effect of the Si–N donor-acceptor interaction on the stability of the silenes and in particular of the Si=C double bond. For intermolecularly donor-stabilized silenes this energy can easily be calculated from the difference between the total energy of the complex and of the isolated molecules, using the so-called supermolecule approximation.

Table 1. Selected structural parameters of compound **1**.

	HF/6-31++G(d,p)	B3LYP/6-31++G(d,p)	X-ray results
Distance (Si=C) [Å]	1.755	1.761	1.748
Distance (Si···N) [Å]	2.096	2.175	2.004
Distance (C–$SiMe_3$) [Å]	1.854	1.858	1.824
Distance (C–$SiMe_3$) [Å]	1.865	1.869	1.832
Distance (Si–Ph) [Å]	1.907	1.910	1.890
Distance (Si–$SiMe_3$) [Å]	2.431	2.422	2.381
Angle (Ph–Si=C–$SiMe_3$) [°]	0.671	–0.071	–3.405
Sum of angles (silene Si) [°]	346.94	348.44	343.60
Sum of angles (silene C) [°]	359.83	359.81	359.35

Table 2. Selected structural parameters of compound **3**.

	HF/6-31++G(d,p)	B3LYP/6-31++G(d,p)	X-ray results
Distance (Si=C) [Å]	1.760	1.765	1.758
Distance (Si···N) [Å]	2.119	2.199	2.035
Distance (Si···N) [Å]	3.812	3.818	3.441
Distance (C–$SiMe_3$) [Å]	1.862	1.865	1.837
Distance (C–$SiMe_3$) [Å]	1.867	1.870	1.839
Distance (Si–Ph) [Å]	1.919	1.919	1.892
Distance (Si–$SiMe_3$) [Å]	2.444	2.422	2.402
Angle (Ph–Si=C–$SiMe_3$) [°]	19.40	18.13	20.66
Sum of angles (silene Si) [°]	350.00	350.71	348.48
Sum of angles (silene C) [°]	359.99	359.97	360.00

 © 2005 Wiley-VCH Verlag GmbH & Co. KGaA, Weinheim

Unfortunately, since donor and acceptor are subunits in the same molecule in **1**, **2** and **3**, this strategy does not work. There is no direct way to calculate this stabilizing contribution since it is superimposed by other effects like steric repulsion. Nevertheless, several approaches were undertaken and will be described in the following sections.

2.1. Calculations with the NBO Model

The stabilizing influence of the N→Si donor–acceptor interaction and the resulting elongation of the Si=C double bond in the intramolecularly donor-stabilized silenes can easily be rationalized by a mesomeric interpretation which predicts an ylide-like nature of the donor stabilized silenes (see Figure 2).

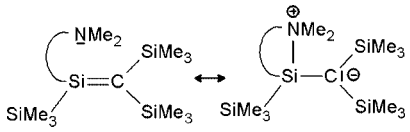

Figure 2. Mesomeric structures of compounds **1**, **3**, and **4**.

A similar conclusion is reached by using the Natural Bond Orbital (NBO) analysis.[16–18] This method transforms the delocalized Hartree–Fock orbitals into localized electron orbitals ("natural bond orbitals") that are closely tied to chemical bonding concepts and resembles the well known Lewis structure. Deviations from "normal" Lewis structures are represented as antibonding orbitals. The orbitals can interact very strongly. The energetic importance of the possible interaction between "filled" (donor) and "empty" (acceptor) NBO's can be estimated by using the NBODel keyword. In this method, the interactions between user defined orbitals are switched off to calculate their influence on the molecular stability. For compound **1** as well as for the conformer **1b**, where the CH_2–NMe_2 group is turned away from the electrophilic silicon atom, calculations were performed using the HF/6-31G(d) method. For compound **1**, the energy attributed to hyperconjugation between the lone pair at N and the empty orbital at the silene silicon atom is calculated as 277 kJ/mol and the Si–C π interaction is calculated as 87 kJ/mol. For compound **1b**, no N–Si interaction is possible, and the hyperconjugative Si–C π interaction is calculated as 168 kJ/mol. When the Si–N donor acceptor interaction takes place, the Si–C π interaction is strongly diminished and a reduction of the rotational barrier about the Si=C double bond in comparison to uncomplexed silenes in the order of 80 kJ/mol is conceivable. Since the occupation of the antibonding Si–C orbital is increased, an elongation of the Si=C bond has to be expected in comparison to silenes without a donor stabilization.

The very high value for the N–Si hyperconjugation interaction as predicted in the framework of the NBO model does not represent the net stabilization energy of the Si–N donor acceptor interaction. Other effects like Pauli exchange repulsion and to a lesser extent electrostatic interactions drastically diminish the stabilizing effect of the hyperconjugation, as was pointed out in the discussions concerning the internal rotational barrier of ethane.[19–22] This net stabilization energy has to be computed by other methods.

2.2. Influence of the Si–N Distance

If the CH_2–NMe_2 group is pointed towards the Si atom in the Si=C bond as in compound **1**, a Si–N donor-acceptor interaction is possible [d(Si–N) ≈ 2.0–2.1 Å]. If the direction of the CH_2–NMe_2 group is changed to point away from the Si atom as in conformer **1b**, no such interaction is possible [d(N–Si) ≈ 4.5 Å]. Both geometric structures were optimized using the HF/6-31++G(d,p) method. The structures show some distinctive deviations. In the conformer with the long Si–N distance, the Si=C double bond is shortened to 1.722 Å in comparison to 1.755 Å in the conformer with short Si–N distance. In the same way, the conformer **1b** shows no longer a pyramidalization at the silene silicon atom (sum of angles at the silene Si atom = 359.16°). Both results agree with our interpretation of the influence of the Si–N interaction on the Si=C double bond as a donor-acceptor interaction between the lone pair at N and the π* orbital of the silene double bond. This picture is also qualitatively supported by the contour plots of the HOMO and LUMO of conformer **1**, which are shown in Figures 3 and 4. A recognizable overlap between the n(N)- and the π(Si=C)-orbital is observed for the conformer with the short Si–N distance, whereas the HOMO and LUMO of the other conformer do not indicate any interaction between the N and Si atom.

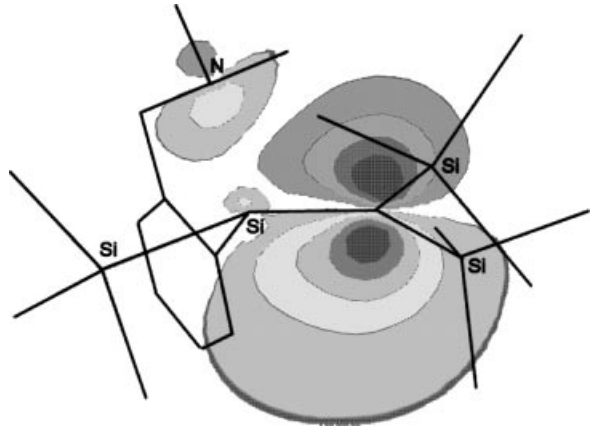

Figure 3. Contour plot of the HOMO orbital of compound **1**. The Figure shows the HOMO in the plane containing the N atom and the Si=C double bond.

Energy calculations of the conformers **1** and **1b** were performed using the MP2/6-31++G(d,p) method. These calculations showed that the structure with the short Si–N distance is energetically favored by 77 (37) kJ/mol at the MP2 (HF) level. This energy consists of the Si–N donor-acceptor stabilization energy and the steric repulsion effects in both conformers and is in reasonable accordance with the value of 82 (92) kJ/mol found by Gusel′nikov et al.[7] for the intramolecularly N-donor-stabilized 1-methylene-5-methyl-2,8-

 © 2005 Wiley-VCH Verlag GmbH & Co. KGaA, Weinheim

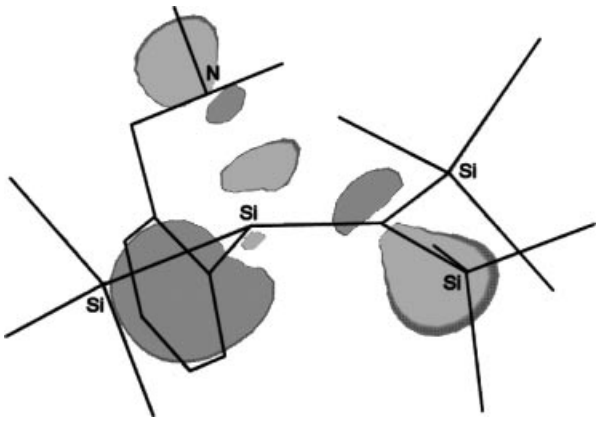

Figure 4. Contour plot of the LUMO orbital of compound **1**. The Figure shows the LUMO in the plane containing the N atom and the Si=C double bond.

dioxa-5-aza-1-silacyclooctane (MADS), calculated by the same method but using the smaller 6-31G(d) basis set. In contrast to the calculations of Gusel′nikov, a strong deviation between the results obtained with the MP2 and the HF method was observed for compound **1**, showing that electron correlation can not be neglected in this case.

The hypothetical intermolecular stabilization of dimethylsilene with NH_3 was calculated by Gusel′nikov et al.[7] as 31 kJ/mol using the MP2/6-31G(d) method in the supermolecular approximation. This value is smaller than the value obtained for silene **1**, showing that the electronic and steric effect of the different substituents can not be neglected.

To understand the influence of the steric repulsion on our results, some calculations were performed with model compound **5** (see Figure 1). In this compound, the dimethylamino group of **1** is replaced with the sterically similar isopropyl group. Again, configurations with a short (2.4 Å) and a long (4.7 Å) distance between this group and the silene silicon atom were calculated, representing the structures **5** and **5b**, respectively. In contrast to the NMe_2 group, no donor–acceptor interaction with the electrophilic silicon atom is expected for the isopropyl group. The energy difference between both conformers of **5** should thus be determined solely by steric repulsions. This leads to a strong stabilization of the configuration with the long isopropyl-silene silicon atom distance of 75 (122) kJ/mol calculated at the MP2/6-31++G(d,p) [HF/6-31++G(d,p)] level.

Under the assumptions made above, the Si···N interaction energy without steric repulsion effects can now be calculated as the difference between the two stabilization energies of the different conformers of compounds **1** and **5**. As a result, the Si···N interaction energy without the influence of steric repulsion is calculated as 152 (159) kJ/mol using the MP2/6-31++G(d,p) [HF/6-31++G(d,p)] method. This energy shows only a small dependence on electron correlation, since the errors in the HF calculations, which are mainly due to incorrect interorbital pair correlations, cancel out each other favorably.

2.3. Comparison of Stabilization Effect of NMe_2 Group on Silenes and Silanes

The results obtained above indicate a strong donor–acceptor interaction of the free electron pair of the N atom with the Si=C bond. Without the Si–C antibonding orbital of the Si=C bond, no strong donor-acceptor interaction should be possible. If the dimethylamino group is exchanged for an isopropyl group, again no strong donor–acceptor interaction is possible, regardless whether there exists a Si=C double bond or not. In the hydrogenation reactions of **1** and **5b** with H_2 leading to the saturated compounds **1c** and **5c** these effects determine the difference in the following two standard reaction energies:

1 + H_2 → **1c**; $\Delta E_{H(1)}$

5b + H_2 → **5c**; $\Delta E_{H(5)}$

The stabilizing effect of the NMe_2 group on the Si=C bond can be calculated from the difference between the hydrogenation reactions:

$\Delta E_{stab} = \Delta E_{H(1)} - \Delta E_{H(5)}$

As a result, a stabilizing effect ΔE_{stab} of 74 kJ/mol (41 kJ/mol) was obtained at the MP2/6-31++G(d,p) [HF/6-31++G(d,p)] level. These stabilization energies agree nearly quantitatively with the energies obtained from the investigation in section 2.2. A strong influence of electron correlation is also observed in these results.

Again it has to be assumed that other factors like higher steric repulsions in compound **1** in comparison to compound **5b** have a major impact on these stabilization energies. Using the results from the study of model compounds **5** and **5b** in section 2.2., a stabilization energy without the influence of steric repulsion of 149 (163) kJ/mol can be attributed to the Si···N interaction using the MP2/6-31++G(d,p) [HF/6-31++G(d,p)] method.

2.4. Rotational Barrier About the Si=C Double Bond

For compound **1**, **3** and the structurally quite similar compound **6**, temperature-dependent ^1H NMR studies were performed.[23] As expected, at room temperature two separate signals were found for the two nonequivalent trimethylsilyl groups at the carbon atom of the above-mentioned compounds. For compound **1** and **6** the dynamic ^1H NMR studies revealed that at elevated temperatures a coalescence of the signals of the $CSiMe_3$ groups occurred. For compound **3**, at temperatures of up to 80 °C no coalescence of these two signals could be observed. The data were used to determine the rotational barrier $\Delta G^{\neq}$ about the Si=C bond. The following approximate equation derived from the Eyring equation was used:[24]

$$\Delta G^{\neq} = T_c \cdot 19.13 \cdot (9.97 + \lg\frac{T_c}{\Delta \nu_c})$$

$\Delta G^{\neq}$ is the free energy barrier, T_c the coalescence temperature and $\Delta \nu_c$ is the signal separation of the $CSiMe_3$ groups extrapolated to the coalescence temperature.

These results can be compared to some data obtained from ab initio calculations. The rotational barrier of the Si=C bond was determined by performing a relaxed poten-

 © 2005 Wiley-VCH Verlag GmbH & Co. KGaA, Weinheim

tial energy surface scan involving the dihedral angle Ph–Si=C–$SiMe_3$ of compounds **1**, **2**, and **3** using the HF/6-31G(d) method. The resulting energy vs. dihedral angle diagram is show in Figure 5. The geometries belonging to the maximal values of these curves were then recalculated using the higher 6-31++G(d,p) basis set at the HF and the MP2 level. The difference between these absolute energies corresponds approximately to the rotational barrier of the Si=C double bond. Since the rotational barrier is strictly speaking a difference of Gibbs energies, the following corrections were applied to the calculated energies $\Delta E^{\neq}_{elec}$ using the HF/6-31G(d) method:

$$\Delta G^{\neq} = \Delta E^{\neq}_{elec} + \Delta ZPE^{\neq} + \Delta E^{\neq}_{vib} + \Delta E^{\neq}_{rot} - T\Delta S^{\neq}$$

$\Delta ZPE^{\neq}$ is the correction due to zero point energy, $\Delta E^{\neq}_{vib}$ + $\Delta E^{\neq}_{rot}$ are the contributions due to vibration and rotation and $\Delta S^{\neq}$ is the entropy difference.

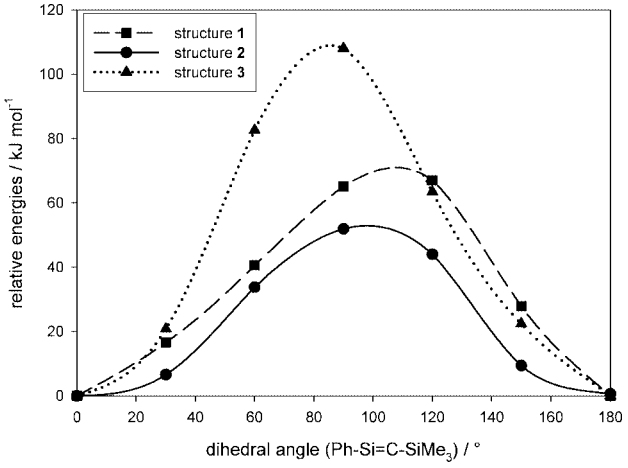

Figure 5. Rotational barrier of the Si=C double bond calculated at the HF/6-31G(d) level.

The resulting free energies as well as the energies obtained at the HF/6-31++G(d,p), the MP2/6-31++G(d,p) level and the experimental ^{1}H NMR results are shown in Table 3. Our best estimates for the rotational barrier in Table 3 (column 6) are obtained by using the results from the MP2 single point energy calculation (column 5) and applying the corrections according to the equation above by using the HF/6-31G(d) method (difference between column 3 and column 2). The rotational barriers determined by this quantum mechanical approach agree surprisingly well with the spectroscopically determined rotational barriers, supporting our interpretation of the experimental data.

These values are also very close to values found for intermolecular silene adducts

THF·Me_2Si=C($SiMe_3$)SiMe*t*Bu_2 and NMe_3·Me_2Si=C-($SiMe_3$)SiMe*t*Bu_2, where values of 50 kJ/mol and 65 kJ/mol, respectively, were reported.[25]

The calculated rotational barriers of isomer interconversion are smaller than in uncomplexed silenes, which were found to be about 160 kJ/mol.[1] This shows that the interaction of donor groups with the Si=C bond leads to a weakening of the Si–C π interaction in the order of 60–100 kJ/mol, in qualitative agreement with our results from the NBO calculation. The value for the cis/trans isomerization in alkenes, which amounts to approximately 250 kJ/mol,[26] is considerably higher than the value for the silenes, as expected.

3. Conclusions

The ab initio calculations on the silene compounds **1**, **2**, and **3** in the gas phase are in good agreement with data from X-ray structural analysis. Both methods show an Si–N distance that is shorter than in saturated counterparts. A strong interaction between the free N orbital and the antibonding orbital at the electrophilic silicon atom was observed. This is accompanied by a weakening of the Si=C double bond, which results in the elongation of the Si=C bond and the reduction of the rotational barrier about the Si=C bond. The stabilization energy gained of the donor-stabilized silenes in comparison to unstabilized silenes by coordination with the dimethylamino group is in the order of about 75 kJ/mol. This energy consists of a stabilizing donor-acceptor interaction (app. 150 kJ/mol) and a weakening steric repulsion effect (app. 75 kJ/mol).

The spectroscopically determined rotational barriers about the Si=C double bond of compounds **1**, **3** and **6** could be quantitatively reproduced by our ab initio calculations.

4. Computational Details

All calculations were performed for isolated species using the GAUSSIAN98 and GAUSSIAN03 program package.[27] At first, a full geometry optimization was performed using the 6-31G(d) basis set on the RHF level. All calculated structures represent minima on the potential energy surface; this means no negative frequencies were observed. The calculated frequencies were used to obtain the zero point energies and other thermodynamic properties of those structures. Some further geometry optimizations using the 6-

Table 3. Rotational barriers from ab initio calculation (kJ/mol).

Structure	$\Delta E^{\neq}$ (HF/6-31G(d))	$\Delta G^{\neq}$ (HF/6-31G(d))	$\Delta E^{\neq}$ (HF/6-31++G(d,p))	$\Delta E^{\neq}$ (MP2/6-31++G(d,p))	$\Delta G^{\neq}$ (best estimate)	Experiment[20] (^{1}H NMR)
1	70.9	73.4	64.5	64.3	66.8	71.5
2	52.6	52.7	57.4	56.2	56.3	63.3[a]
3	108.0	114.9	107.6	93.8	100.7	> 100[b]

[a] Similar compound **6**. [b] Up to 80 °C no coalescence could be observed.

 © 2005 Wiley-VCH Verlag GmbH & Co. KGaA, Weinheim

31++G(d,p) basis set on the HF and the B3LYP level were performed for the most important structures. All main structural elements from the X-ray structures could be reproduced qualitatively with both of the applied ab initio methods. The results from the B3LYP/6-31++G(d,p) geometry optimization show larger deviations from the X-ray structure (see Tables 1 and 2). This may be due to problems of B3LYP in describing steric interactions correctly. Therefore, we decided to use the geometric structures obtained from the HF calculations as the foundation for any further calculations like frequency calculations or single point energy calculations using the more sophisticated but also very time consuming MP2 method. Due to the high computational cost of the MP2 method for these large molecules, only single point energy calculations were performed using the MP2/6-31++G(d,p) method on the geometric structures obtained at the HF level. No geometry optimization was attempted at the MP2 theoretical level.

All NBO calculations were performed with NBO version 3.1[28] as incorporated in Gaussian03.

The calculation of the rotational barrier about the Si=C double bond was accomplished at the HF/6-31G(d) level by using the Opt = ModRedundant keyword of GAUSSIAN03. We changed the dihedral angle Ph–Si=C–$SiMe_3$ in 5 steps of 30°, starting with the value of approximately 0° corresponding to the fully optimized geometry.

Supporting Information: The supporting information (see also the footnote on the first page of this article) includes the coordinates and total energies of the above mentioned structures as well as the thermodynamic corrections.

[1] A. G. Brook, M. A. Brook, *Adv. Organomet. Chem.* **1996**, *39*, 71–258.
[2] T. Müller, W. Ziche, N. Auner, in: *The Chemistry of organic silicon compounds* (Eds.: Z. Rappoport, Y. Apeloig), Wiley, New York, **1998**, vol. 2, p. 857–1062.
[3] N. Wiberg, H. Köpf, *J. Organomet. Chem.* **1986**, *315*, 9–18.
[4] N. Wiberg, G. Wagner, G. Reber, J. Riede, G. Müller, *Organometallics* **1987**, *6*, 35–41.
[5] N. Wiberg, K.-S. Joo, K. Polborn, *Chem. Ber.* **1993**, *126*, 67–69.
[6] N. Wiberg, G. Wagner, G. Müller, J. Riede, *J. Organomet. Chem.* **1984**, *271*, 381–386.
[7] V. G. Avakyan, L. E. Gusel′nikov, V. A. Pestunovich, A. A. Bagaturyants, N. Auner, *Organometallics* **1999**, *18*, 4692–4699.
[8] N. N. Zemljanskii, I. V. Borisova, A. K. Shestakova, Y. A. Ustynyuk, E. A. Chernyshev, *Izv. Akad. Nauk Ser. Khim.* **1998**, *47*, 486–491.
[9] N. N. Zemljanskii, I. V. Borisova, A. K. Shestakova, Y. A. Ustynyuk, E. A. Chernyshev, *Russ. Chem. Bull.* **1998**, *47*, 469–474.
[10] M. Mickoleit, K. Schmohl, R. Kempe, H. Oehme, *Angew. Chem.* **2000**, *112*, 1679–1681; *Angew. Chem. Int. Ed.* **2000**, *39*, 1610–1612.
[11] M. Mickoleit, R. Kempe, H. Oehme, *Chem. Eur. J.* **2001**, *7*, 987–992.
[12] M. Pötter, U. Bäumer, M. Mickoleit, R. Kempe, H. Oehme, *J. Organomet. Chem.* **2001**, *621*, 261–266.
[13] A. G. Brook, S. C. Nyburg, F. Abdesaken, B. Gutekunst, G. Gutekunst, R. K. M. R. Kallury, Y. C. Poon, Y.-M. Chang, W. Wong-Ng, *J. Am. Chem. Soc.* **1982**, *104*, 5667–5672.
[14] Y. Apeloig, M. Bendikov, M. Yuzefovich, M. Nakash, D. Bravo-Zhivotovskii, D. Bläser, R. Boese, *J. Am. Chem. Soc.* **1996**, *118*, 12228–12229.
[15] Y. Apeloig, M. Karni, *J. Am. Chem. Soc.* **1984**, *106*, 6676–6682.
[16] J. P. Foster, F. Weinhold, *J. Am. Chem. Soc.* **1980**, *102*, 7211–7218.
[17] A. E. Reed, F. Weinhold, *J. Chem. Phys.* **1983**, *78*, 4066–4073.
[18] A. E. Reed, L. A. Curtiss, F. Weinhold, *Chem. Rev.* **1988**, *88*, 899–926.
[19] L. Goodman, H. Gu, V. Pophristic, *J. Chem. Phys.* **1999**, *110*, 4268–4275.
[20] L. Goodman, V. Pophristic, F. Weinhold, *Acc. Chem. Res.* **1999**, *32*, 983–993.
[21] F. M. Bickelhaupt, E. J. Baerends, *Angew. Chem.* **2003**, *115*, 4315–4320.
[22] F. Weinhold, *Angew. Chem.* **2003**, *115*, 4315–4320.
[23] M. Mickoleit, K. Schmohl, M. Michalik, H. Oehme, *Eur. J. Inorg. Chem.* **2004**, *7*, 1538–1544.
[24] H. Kessler, *Angew. Chem.* **1970**, *82*, 237–253; *Angew. Chem. Int. Ed. Engl.* **1970**, *9*, 219–235.
[25] N. Wiberg, H.-S. Hwang-Park, H.-W. Lerner, S. Dick, *Chem. Ber.* **1996**, *129*, 471–478.
[26] H. Beyer, W. Walter, *Lehrbuch der Organischen Chemie*, Hirzel, Leipzig, **1998**.
[27] M. J. Frisch, G. W. Trucks, H. B. Schlegel, G. E. Scuseria, M. A. Robb, J. R. Cheeseman, J. A. Montgomery, Jr., T. Vreven, K. N. Kudin, J. C. Burant, J. M. Millam, S. S. Iyengar, J. Tomasi, V. Barone, B. Mennucci, M. Cossi, G. Scalmani, N. Rega, G. A. Petersson, H. Nakatsuji, M. Hada, M. Ehara, K. Toyota, R. Fukuda, J. Hasegawa, M. Ishida, T. Nakajima, Y. Honda, O. Kitao, H. Nakai, M. Klene, X. Li, J. E. Knox, H. P. Hratchian, J. B. Cross, C. Adamo, J. Jaramillo, R. Gomperts, R. E. Stratmann, O. Yazyev, A. J. Austin, R. Cammi, C. Pomelli, J. W. Ochterski, P. Y. Ayala, K. Morokuma, G. A. Voth, P. Salvador, J. J. Dannenberg, V. G. Zakrzewski, S. Dapprich, A. D. Daniels, M. C. Strain, O. Farkas, D. K. Malick, A. D. Rabuck, K. Raghavachari, J. B. Foresman, J. V. Ortiz, Q. Cui, A. G. Baboul, S. Clifford, J. Cioslowski, B. B. Stefanov, G. Liu, A. Liashenko, P. Piskorz, I. Komaromi, R. L. Martin, D. J. Fox, T. Keith, M. A. Al-Laham, C. Y. Peng, A. Nanayakkara, M. Challacombe, P. M. W. Gill, B. Johnson, W. Chen, M. W. Wong, C. Gonzalez, J. A. Pople, *Gaussian 03 Revision B.04*, Gaussian, Inc., Pittsburgh PA, **2003**.
[28] E. D. Glendening, A. E. Reed, J. E. Carpenter, F. Weinhold, *NBO Version 3.1*.

Received: February 11, 2005
Published Online: July 6, 2005

 © 2005 Wiley-VCH Verlag GmbH & Co. KGaA, Weinheim

Copper, Cobalt and Platinum Complexes with Dithiothiophene-Based Ligands

Dulce Belo,[a] Mauro J. Figueira,[a] Joana Mendonça,[a] Isabel C. Santos,[a] Manuel Almeida,*[a] Rui T. Henriques,[b] Maria Teresa Duarte,[c] Concepció Rovira,[d] and Jaume Veciana[d]

Keywords: S ligands / Coordination chemistry / Copper / Cobalt / Platinum

The preparation and characterisation of new thiophenedithiolate complexes of Cu, Co and Pt with the ligands α-tpdt and tpdt (α-tpdt = 2,3-thiophenedithiolate, tpdt = 3,4-thiophenedithiolate) is reported. The Co and Pt complexes present regular square-planar coordination geometry and low oxidation potentials when compared with complexes with simpler ligands, but their monoanionic state is found to be rather unstable. The $Co(tpdt)_2$ complex can be isolated both in the monoanionic and dianionic states as a stable compound but the $Co(\alpha\text{-tpdt})_2$ and the Pt complexes can be obtained only in the dianionic state, while their monoanionic state is unstable. The Co and Pt complexes can, however, be easily oxidised to the neutral state, giving a fine-powdered microcrystalline material without high electrical conductivity. With Cu only a less frequent geometry based on a tetrametallic Cu^I cluster and three ligands is observed as $[Cu_4(\alpha\text{-tpdt})_3]^{2-}$ and $[Cu_4(tpdt)_3]^{2-}$.

(© Wiley-VCH Verlag GmbH & Co. KGaA, 69451 Weinheim, Germany, 2005)

Introduction

Transition metal dithiolene complexes, $M(S_2X)_2$, because of a rich variety of coordination geometry and a vivid redox behaviour, have attracted continuing interest during the last 30 years.[1] Depending on the metal, M, coordination geometry and oxidation state, these complexes can be diamagnetic or carry different magnetic moments and therefore have been choice building blocks for the design of functional molecular materials.[2] Square-planar coordination geometries are favoured, with metals of Ni and Cu group in the anionic form $[M(S_2X)_2]^-$, and such complexes have been widely used as counterions in charge transfer solids with a variety of donors, often giving rise to new molecular materials displaying unconventional electrical and magnetic properties, including ferromagnetism,[3] metallic[4] and even superconducting properties.[5]

[a] Instituto Tecnológico e Nuclear / CFMC,
Estrada nacional 10, 2686-953 Sacavém, Portugal
Fax: +351-219-941455
E-mail: malmeida@itn1.itn.pt
[b] Instituto de Telecomunicações, Pólo de Lisboa, IST,
Av Rovisco Pais, 1049-001 Lisboa, Portugal
Fax: +351-21-8417862
E-mail: rth@ist.utl.pt
[c] Centro de Quimica Estrutural, Instituto Superior Técnico,
Av Rovisco Pais, 1049-001 Lisboa, Portugal
Fax: +351-21-8417862
E-mail: Teresa.duarte@ist.utl.pt
[d] Institut de Ciència de Materials de Barcelona (CSIC),
Campus Universitari de Bellaterra,
08193 Cerdanyola, Spain
Fax: +344-93-5805729
E-mail: cun@icmab.es

Another common coordination geometry in bisdithiolene complexes is the square pyramidal, 4+1, in dimerised arrangements, $[M(S_2X)_2]_2^{2-}$, favoured for M = Fe, Co and to a smaller extent occurring also for Ni.[6,7] Other geometries are known in metal bisdithiolene complexes and, for example, for Co, trimerised, $[Co(S_2X)_2]_3^{2-}$,[8] and even polymeric, $[Co(S_2X)_2]_n^{n-}$,[9] arrangements of square planar units also have been described.

The accessibility to different oxidation states in these complexes is greatly dependent on the type of ligand because their contribution to the HOMO and LUMO is often dominant. Extended π ligands favour both a lower oxidation potential and larger solid state interactions between neighbouring units in stacked structures of square-planar complexes. Sulfur-rich ligands with additional sulfur atoms in the periphery of the complex are expected to provide intermolecular S···S contacts that may enhance the magnitude and the dimensionality of the solid state intermolecular interactions.

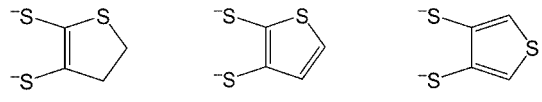

In this context we recently focused our efforts on exploring complexes based on thiophenedithiolate ligands (α-tpdt = 2,3-thiophenedithiolate, dtpdt = 2,3-dihydro-5,6-thiophenedithiolate and tpdt = 3,4-thiophenedithiolate, Scheme 1). Previously we described the properties of the first Au[10] and Ni[11] complexes with thiophenedithiolate

ligands, which are generally characterised by rather low oxidation potentials. Many of these complexes can be obtained as a neutral species such as Au(α-tpdt)$_2$, one of the rare electrically conducting compounds based on a neutral molecule, and the first one showing metallic transport properties in spite of being characterised only as a polycrystalline sample.[10] The paramagnetic Ni^{III} complex was the key component of an interesting charge transfer salt displaying a metamagnetic transition.[11] More recently, other neutral Ni complexes based on more extended bisdithiolene ligands have been obtained as single crystals and were characterised as unimolecular metallic systems.[12]

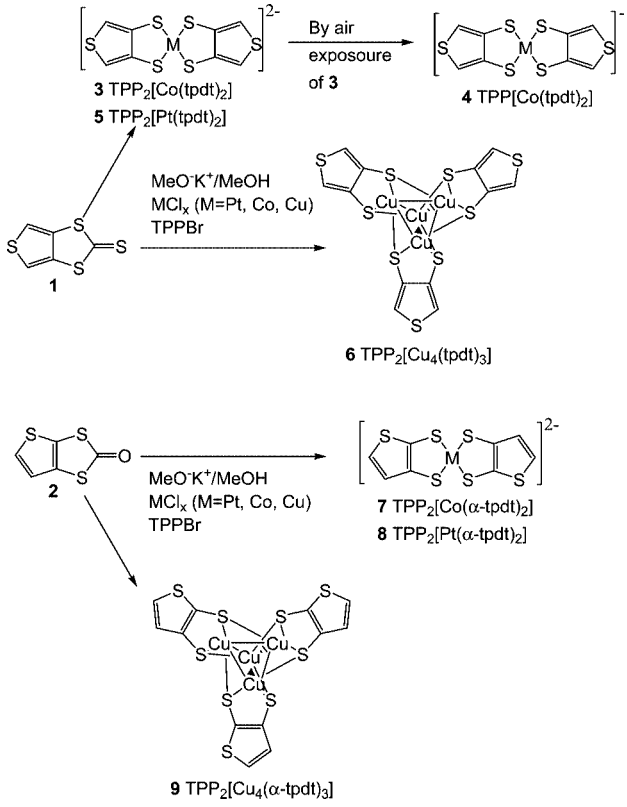

Scheme 1. Preparation of the transition metal complexes **4**–**9**.

These results led us to prepare similar bisthiophenedithiolate complexes with different transition metals and to explore their possible use as building blocks for the preparation of magnetic or electrically conducting materials. In this paper we report on the preparation and properties of new thiophenedithiolate complexes of Cu, Co and Pt with the ligands α-tpdt and tpdt having diverse oxidation states and geometries.

Results and Discussion

The synthesis of TPP$_y$M(xtpdt)$_z$ followed a procedure (Scheme 1) similar to the one previously described for other transition metal complexes with dithiolatethiophene ligands, with minor modifications. The previous preparation of Au[10] and Ni[11] complexes with thiophenedithiolate ligands was made as tetrabutylammonium (TBA) salts. However, difficulties in crystallising the salts of these complexes with such cations led us to work with larger cations such as tetraphenylphosphonium (TPP), which favours the crystallisation process. The ligands were obtained in methanol solution from 5,6-thieno[2,3-*d*]-1,3-dithiol-2-one (**1**) for [M(α-tpdt)$_2$]$^{x-}$ salts, and from thieno[3,4-*d*]-1,3-dithiol-2-thione (**2**) in the case of [M(tpdt)$_2$]$^{x-}$ complexes, by cleavage with potassium methoxide. These ligands, without intermediate isolation, were immediately treated with the appropriate metal chloride to give the Co^{II}, Pt^{II} and Cu^{I} complexes, which precipitated as red (**5**), green (**3**), orange (**8**), dark brown (**7**) and golden brown (**6**, **9**) TPP salt, by treatment with TPPBr. These reactions were carried out in strictly anaerobic conditions inside a glovebox. The TPP[Co(tpdt)$_2$] complex (**4**) was obtained as a dark blue precipitate, just by stirring an acetonitrile solution of **3** under air. After recrystallisation, all compounds give air-stable crystals with yields ranging from 50 to 80%. The Pt complex **8** in acetonitrile solution, when exposed to air, changes colour to green, indicating that an oxidation process takes place, in agreement with the low oxidation potential observed in the cyclic voltammetry data (see below). However, possibly because of decomposition and instability of the Pt^{III} complexes, it was not possible to isolate the monoanionic species. Although with only a slightly larger oxidation potential the Pt(tpdt)$_2^{2-}$ complex **5** does not undergo any oxidation upon air exposure.

With the exception of the copper salts **6** and **9**, the abovementioned synthetic procedure leads to the dianionic species M^{II} with M = Co and Pt in a square-planar coordination geometry. Cu complexes are always obtained with a different stoichiometry, of four metals to three ligands. This stoichiometry, although unexpected, is not entirely new as it has been previously reported for a few [Cu$_4$(S$_2$X)$_3$]$^{2-}$ complexes.[13] However in most of these previous examples the stoichiometry of the complexes obtained is controlled by the metal–ligand proportion, the ligand excess favouring the formation of the square-planar Cu^{II} complex. In the present case we were not able to obtain the square-planar Cu coordination, even with a large excess of the ligands.

The crystal structures of complexes **4**–**9** were solved by single-crystal X-ray diffraction and their crystal and structure refining data are listed in Table 1 and Table 2. The Co and Pt complexes present identical, essentially planar, geometry (Figure 1 and Figure 2), with small nonplanar deviations observed only in the thiophenic sulfur atoms of complex **5**, which are displaced towards opposite directions giving rise to a very small chair-type distortion.

By contrast, this usual square-planar coordination geometry, found also in the previously described Au and Ni complexes with these ligands,[10,11] was not observed in the Cu complexes **6** and **9**, which present a different stoichiometry and structure: [Cu$_4$(xtpdt)$_3$]$^{2-}$. In these complexes the dianion is composed by four Cu^{I} atoms, each one coordinated to the other three Cu atoms. The Cu2, Cu3 and Cu4 atoms are chelated to two sulfurs from one dithiothiophene ligand and to another sulfur atom from a neighbouring ligand. Although Cu1 is also coordinated to three sulfur atoms,

 © 2005 Wiley-VCH Verlag GmbH & Co. KGaA, Weinheim

Table 1. Crystal data and structure refinement of compounds **4**, **5**, **7** and **8**.

	$TPP_2[Co(\alpha\text{-}tpdt)_2]$ (**7**)	$TPP[Co(tpdt)_2]$ (**4**)	$TPP_2[Pt(tpdt)_2]$ (**5**)	$TPP_2[Pt(\alpha\text{-}tpdt)_2]$ (**8**)
Empirical formula	$C_{56}H_{44}CoP_2S_6$	$C_{32}H_{24}CoPS_6$	$C_{56}H_{44}P_2PtS_6$	$C_{56}H_{44}P_2PtS_6$
Formula mass	1030.14	690.77	1166.30	1166.30
Temperature [K]	293(2)	293(2)	120(2)	293(2)
Crystal system, space group	monoclinic, $P2_1/n$	triclinic, $P\bar{1}$	monoclinic, $P2_1/n$	monoclinic, $P2_1/n$
a [Å]	11.4352(18)	9.6591(11)	11.5361(2)	11.396(2)
b [Å]	14.649(3)	10.0699(9)	14.4982(2)	14.6302(18)
c [Å]	14.5746(15)	16.6435(15)	14.4816(3)	14.632(2)
α [°]	90.0	93.428(7)	90.0	90.0
β [°]	94.209(5)	106.465(8)	93.3204(5)	93.856(9)
γ [°]	90.0	92.886(8)	90.0	90.0
Volume [Å^3]	2434.9(6)	1545.9(3)	2418.02(7)	2433.9(7)
Z, D_{calcd} [Mg/m^3]	2, 1.405	2, 1.484	2, 1.602	2, 1.591
μ [mm^{-1}]	0.714	1.034	3.266	3.244
$F(000)$	1066	708	1168	1168
Crystal size [mm]	0.6 × 0.4 × 0.2	0.5 × 0.3 × 0.12	0.36 × 0.108 × 0.02	0.5 × 0.3 × 0.2
θ range [°]	1.97–26.01	2.03–26.04	2.91–27.48	1.97–25.98
Index range (h,k,l)	–0/14, 0/18, –17/+17	0/11,–12/12, –20/19	–14/14, –18/16, –18/18	0/14, –17/0, –18/17
Reflections collected/unique	4974/4733 [R_{int} = 0.0187]	6369/5992 [R_{int} = 0.0236]	25490/5440 [R_{int} = 0.0520]	4969/4728 [R_{int} = 0.037]
Absorption correction	Psi-scan	Psi-scan	SORTAV	Psi-scan
T_{max} and T_{min}	0.9994 and 0.9262	0.9995 and 0.8675	0.39761 and 0.36873	0.9991 and 0.7707
Data/parameters	4733/323	5992/364	5440/295	4728/323
Goodness-of-fit on F^2	1.106	1.044	1.021	0.938
Final R indices [$I > 2\sigma(I)$]	R_1 = 0.0421, wR_2 = 0.0851	R_1 = 0.0508, wR_2 = 0.0862	R_1 = 0.0264, wR_2 = 0.0599	R_1 = 0.0456, wR_2 = 0.0688
$\Delta\rho_{max./min.}$ [e/A^3]	0.341/–0.276	0.348/–0.343	0.911/–1.206	0.904/–0.515

Table 2. Crystal data and structure refinement of compounds **6** and **9**.

	$TPP_2[Cu_4(\alpha\text{-}tpdt)_3]$ (**9**)	$TPP_2[Cu_4(tpdt)_3]$ (**6**)
Empirical formula	$C_{60}H_{46}Cu_4P_2S_9$	$C_{60}H_{46}Cu_4P_2S_9$
Formula mass	1371.61	1371.61
Temperature [K]	293(2)	293(2)
Wavelength [Å]	0.71073	0.71069
Crystal system, space group	monoclinic, $P2_1/c$	hexagonal, $P61$
a []	12.1360(19)	13.5743(14)
b [Å]	21.0210(17)	13.5743(14)
c [Å]	23.3280(19)	53.931(8)
α [°]	90.000(5)	90.000(5)
β [°]	100.808(9)	90.000(5)
γ [°]	90.000(5)	120.000(5)
Volume [Å^3]	5845.7(11)	8606.1(18)
Z, $D_{calcd.}$ [Mg/m^3]	4, 1.558	6, 1.588
μ [mm^{-1}]	1.851	1.886
$F(000)$	2784	4176
Crystal size [mm]	0.5 × 0.2 × 0.1	
θ range [°]	1.71–25.98	1.73–25.03
Index range (h,k,l)	0/14, 0/25, –28/28	–16/13, 0/16, –64/0
Reflections collected/unique	11986/11428 [R_{int} = 0.1083]	15903/5090 [R_{int} = 0.2518]
Absorption correction	Psi-scan	
T_{max} and T_{min}	0.9998 and 0.9702	
Refinement method	full-matrix least-squares on F^2	full-matrix least-squares on F^2
Data/restraints/parameters	11428/78/676	5090/1/676
Goodness-of-fit on F^2	0.881	1.012
Final R indices [$I > 2\sigma(I)$]	R_1 = 0.1023, wR_2 = 0.1739	R_1 = 0.0835, wR_2 = 0.0833
$\Delta\rho_{max./min.}$ [e/A^3]	0.809 and –0.489	0.488 and –0.434

 © 2005 Wiley-VCH Verlag GmbH & Co. KGaA, Weinheim

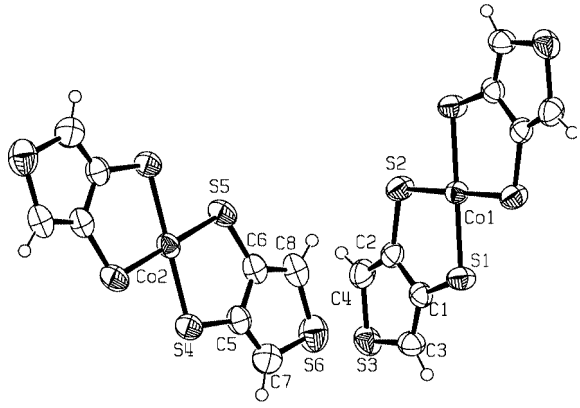

Figure 1. ORTEP views and atomic numbering scheme of $[Co(tpdt)_2]^{-}$ with thermal ellipsoids at 40% probability level. The atomic numbering scheme is the same in the case of $[Pt(tpdt)]^{2-}$.

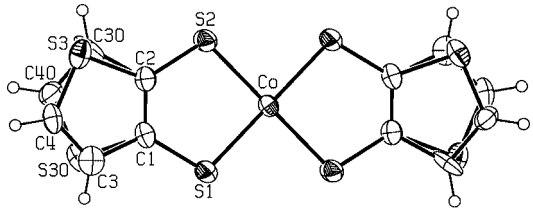

Figure 2. ORTEP views and atomic numbering scheme of $[Co(\alpha\text{-}tpdt)_2]^{2-}$ with thermal ellipsoids at 40% probability level. The atomic numbering scheme is the same in the case of $[Pt(\alpha\text{-}tpdt)_2]^{2-}$.

each one belongs to different dithiothiophene ligands (Figure 3 and Figure 4). The Cu–Cu distances range from 2.740 to 2.640 Å and 2.729 to 2.655 Å, for complexes **6** and **9**, respectively, values which are comparable to the few similar complexes with other dithiolate ligands.[13] The Cu–S distances can be divided into two different ranges: one, Cu–S_L, involving sulfur atoms in the same ligand that range from 2.264 to 2.320 Å in salt **6** and 2.252 to 2.336 Å in salt **9**, and the other with slightly shorter bond lengths between

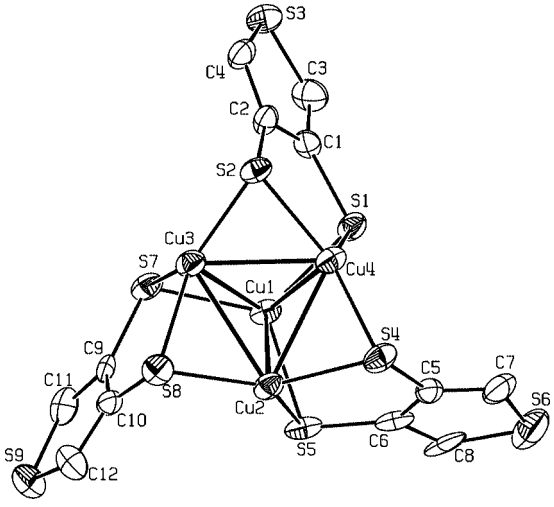

Figure 3. ORTEP views and atomic numbering scheme of $[Cu_4(tpdt)_3]^{2-}$ with thermal ellipsoids at 40% probability level.

the sulfur atom in the neighbouring ligand, Cu–S_N, that range from 2.216 to 2.231 and 2.212 to 2.240 for complexes **6** and **9**, respectively.

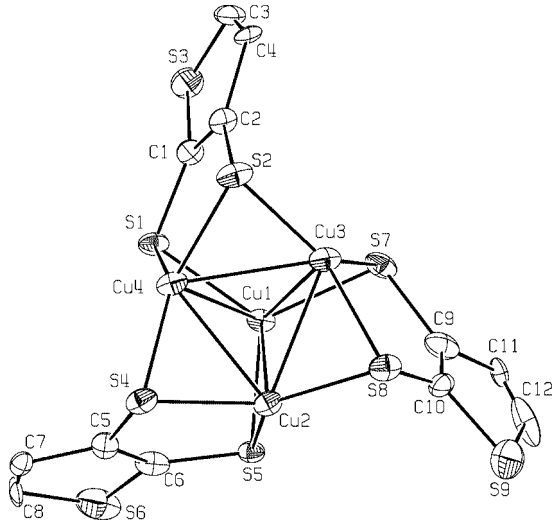

Figure 4. ORTEP views and atomic numbering scheme of $[Cu_4(\alpha\text{-}tpdt)_3]^{2-}$ with thermal ellipsoids at 40% probability level.

The angles between the average planes of each ligand are close to 70° (Figure 3 and Figure 4). In all cases, within the ligand, the bond lengths in the thiophenic ring are very close to those found in the corresponding Ni and Au analogues (Table 3 and Table 4).[10,11] The α-tpdt complexes of Co (**7**) and Pt (**8**) present a disorder in the orientation of the thiophenic sulfur of the ligands (Figure 2), making it impossible to distinguish between a *cis* or *trans* conformation of the complex, as both configurations with orientation disorder in the crystal could give the observed results. As the $Ni(\alpha\text{-}tpdt)_2$[11] and $Au(dtpdt)_2$[10] complexes previously studied were found to crystallise in the *trans* configuration, the observed disorder is most likely the result of orientational disorder of the complex in the *trans* configuration. In this respect it should be mentioned that in those cases one specific orientation of the complexes is favoured by several hydrogen bonds and strong S···S contacts involving the thiophenic ring, and therefore preventing possible orientational disorder of the complex in those structures. This is at variance with the structure of **7** and **8** where there are no strong thiophenic S···S contacts and the existing hydrogen bonds do not present any specific orientation.

Two different types of crystal packing were found on the studied salts. The first one consists of isolated anions, surrounded by the TPP cations and this type of crystal packing is shared for complexes **5**, **6**, **7**, **8** and **9** (Figure 5 and Figure 6). Although they are not isostructural, they present the same crystal packing pattern. The interactions between the anions and the cations are established through several hydrogen bonds. The interactions found are of the C–H···S type, involving both the thiophenic and the coordination sulfur atoms (Table 5). The effect on the crystal structure

 © 2005 Wiley-VCH Verlag GmbH & Co. KGaA, Weinheim

Table 3. Selected bond lengths [Å] for $[M(L)_2]^{x-}$ in complexes **4**, **5**, **7** and **8**.

	$[Co(\alpha\text{-tpdt})]^{2-}$	$[Co(tpdt)]^{-}$	$[Pt(tpdt)]^{2-}$	$[Pt(\alpha\text{-tpdt})]^{2-}$
M–S1	2.2139(7)	2.177(1)	2.3109(6)	2.306(2)
M–S2	2.2215(8)	2.182(1)	2.3113(6)	2.314(2)
M–S4	–	2.178(1)	–	–
M–S5	–	2.167(1)	–	–
S1–C1	1.743(3)	1.749(4)	1.759(3)	1.740(8)
S2–C2	1.736(3)	1.760(4)	1.754(3)	1.731(7)
S4–C5	–	1.753(4)	–	–
S5–C6	–	1.746(4)	–	–
S3–C2	1.713(4)	--	–	1.736(16)
S3–C4	1.689(10)	1.709(4)	1.715(3)	1.690(40)
S3–C3	–	1.710(4)	1.721(3)	–
S30–C1	1.717(14)	–	–	1.718(13)
S30–C40	1.72(2)	–	–	1.710(30)
S6–C7	–	1.702(4)	–	–
S6–C8	–	1.708(5)	–	–
C1–C2	1.355(4)	1.420(5)	1.437(3)	1.351(10)
C5–C6	–	1.417(5)	–	–
C1–C3	1.47(2)	1.359(5)	1.362(4)	1.530(40)
C3–C4	1.39(2)	–	–	1.470(60)
C2–C4	–	1.345(5)	1.370(3)	–
C2–C30	1.55(3)	–	–	1.410(50)
C5–C7	–	1.361(5)	–	–
C6–C8	–	1.368(5)	–	–
C30–C40	1.45(3)	–	–	1.420(80)

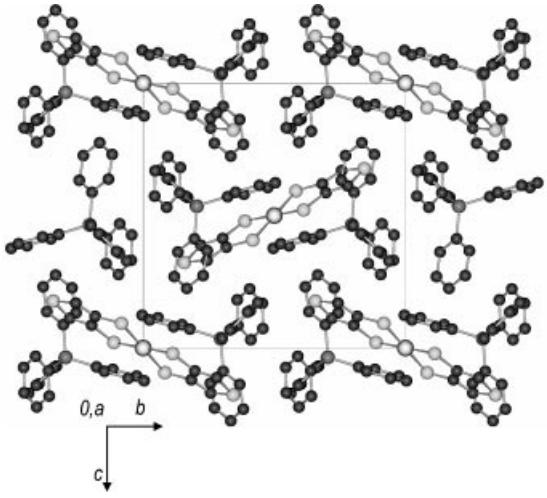

Figure 5. View of the crystal structure of **7** along *a*. The crystal packing for complexes **5** and **8** is very similar.

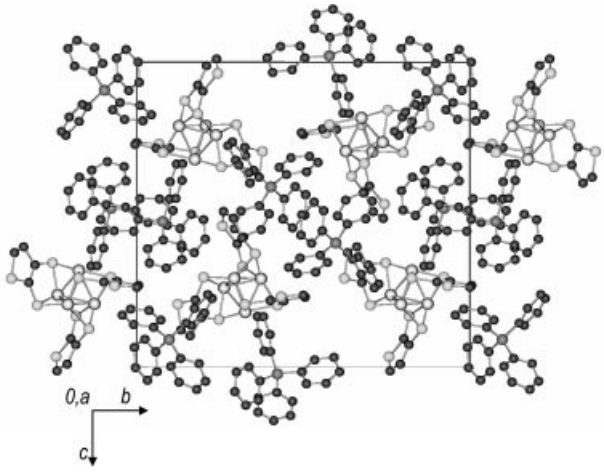

Figure 6. View of the crystal structure of **9** along *a*.

of the sulfur atom position in the thiophenic ring (tpdt or α-tpdt) is negligible.

The crystal structure of **4** is composed by layers of dithiolate anions parallel to the *bc* plane, with TPP cations sitting in holes in these layers. The anionic layers are due to a network of short contacts. Anions of one type are connected between the terminal sulfur atoms by short S(3)···S(3)* [3.492(2) Å] contacts making regular chains along *b*. These chains are interconnected by another dithiolate anion, placed almost perpendicularly to the first ones, through short S6···C1 contacts [3.436(2) Å] (Figure 7). This last contact may denote a weak interaction between this S atom and the carbon π system. The TPP cations are sitting over the spaces left in this anionic layer.

Cyclic voltammetry of all $TPP_yM(xtpdt)_z$ was performed in acetonitrile versus Ag/AgCl and the redox potential values of the different processes observed are listed in Table 6. As in the case of the Au and Ni compounds previously described, these new transition metal complexes with dithiolatethiophene ligands present lower oxidation potentials than complexes with more simple bisdithiolene ligands such as maleonitrile dithiolate (mnt) or even benzodithiolate (bdt). With the exception of the copper complexes, which present a different stoichiometry and coordination environment, when going from tpdt to α-tpdt ligands the redox potentials decrease, showing an increasing facility of these complexes to be oxidised. The complexes with M = Co, Pt present at negative values a reversible process ascribed to

 © 2005 Wiley-VCH Verlag GmbH & Co. KGaA, Weinheim

Table 4. Selected bond lengths [Å] for $[Cu_4(L)_3]^{2-}$ in complexes **6** and **9**.

	tpdt	α-tpdt
Cu1–Cu2	2.696(2)	2.727(2)
Cu1–Cu3	2.675(2)	2.688(2)
Cu1–Cu4	2.690(2)	2.690(2)
Cu2–Cu3	2.740(2)	2.670(2)
Cu2–Cu4	2.641(2)	2.652(2)
Cu3–Cu4	2.640(2)	2.681(3)
Cu1–S1	2.284(4)	2.280(4)
Cu1–S5	2.286(4)	2.290(3)
Cu1–S7	2.303(4)	2.294(3)
Cu2–S8	2.216(4)	2.233(4)
Cu2–S4	2.276(4)	2.256(5)
Cu2–S5	2.314(5)	2.308(4)
Cu3–S2	2.231(4)	2.211(4)
Cu3–S8	2.280(4)	2.288(4)
Cu3–S7	2.320(4)	2.312(5)
Cu4–S4	2.220(4)	2.235(4)
Cu4–S2	2.264(4)	2.274(4)
Cu4–S1	2.316(4)	2.333(4)
S1–C1	1.765(15)	1.703(13)
S2–C2	1.757(14)	1.768(12)
S3–C3	1.723(16)	1.733(16)
S3–C4	1.732(15)	–
S3–C1	–	1.706(12)
S4–C5	1.803(16)	1.734(16)
S5–C6	1.733(17)	1.714(15)
S6–C8	1.701(18)	1.860(20)
S6–C7	1.710(19)	–
S6–C6	–	1.711(12)
S7–C9	1.758(13)	1.675(15)
S8–C10	1.755(15)	1.788(19)
S9–C11	1.692(15)	–
S9–C12	1.706(14)	1.742(12)
S9–C10	–	1.733(14)
C2–C1	1.466(17)	1.397(15)
C5–C6	1.424(19)	1.412(17)
C9–C10	1.457(18)	1.330(20)
C1–C3	1.354(17)	–
C2–C4	1.331(16)	1.567(16)
C3–C4	–	1.250(20)
C5–C7	1.319(18)	1.505(15)
C6–C8	1.349(19)	–
C7–C8	–	1.130(30)
C9–C11	1.349(17)	1.620(19)
C10–C12	1.326(15)	–
C11–C12	–	1.130(12)

Table 5. Selected hydrogen bonds and short contacts in the crystal structure of complexes **4**–**9**.

4	*d* [Å]	Angle [°]
S3···S3[a]	3.492(2)	–
S6···C1	3.436(2)	–
C14–H14···S5	2.815(1)	137
C33–H33···S5	2.980(1)	158
5	*d* [Å]	Angle [°]
C24–H24···S1	2.895(1)	170
C33–H33···S2	2.821(1)	152
C44–H44···S3	2.897(1)	139
6	*d* [Å]	Angle [°]
C22–H24···S5	2.855(3)	141
C64–H64···S6	2.919(6)	148
C36–H36···S8	2.909(4)	137
7	*d* [Å]	Angle [°]
C43–H43···S1	2.851(1)	144
C24–H24···S2	2.940(1)	171
C12–H12···S3	2.942(4)	129
C12–H12···S30	2.798(13)	177
8	*d* [Å]	Angle [°]
C43–H43···S1	2.832(2)	145
C24–H24···S2	2.944(2)	173
C12–H12···S3	2.941(17)	129
C12–H12···S30	2.759(13)	176
9	*d* [Å]	Angle [°]
C22–H22···S2	2.934(5)	135
C94–H94···S5	2.966(4)	124
C53–H53···S6	2.833(6)	160
C75–H75···S7	2.860(4)	147
C86–H86···S9	2.951(10)	120

[a] $-x + 1, -y + 2, -z + 1$.

the $M(xtpdt)_2^{2-}/M(xtpdt)_2^{-}$ couple. These low values are in agreement with the fact that the $Co(tpdt)_2^{-}$ complex was obtained from the dianionic species upon air oxidation and with the previously mentioned fact that $Pt(\alpha\text{-}tpdt)_2^{2-}$ changes colour upon air exposure, indicative of oxidation. In spite of not so different oxidation potentials, $Co(\alpha\text{-}tpdt)_2^{2-}$ and $Pt(tpdt)_2^{2-}$ do not denote any air oxidation and the monoanionic species could not be isolated, probably because of instability associated with dismutation in the neutral and dianionic species. The Co and Pt complexes also show an irreversible process at more positive potentials, possibly associated with the formation of the insoluble neutral complexes, which could be obtained by chemical oxidation (see below). The Cu complexes also undergo two redox processes, a reversible wave for $Cu_4(tpdt)_3$ at –0.330 V, quasireversible for $Cu_4(\alpha\text{-}tpdt)_3$ at about –0.392 V (–0.506, –0.278) and an irreversible oxidation at higher potentials of about 0.18 V.

As suggested by the cyclic voltammetry data, in the case of Pt and Co complexes, the corresponding neutral metal(IV) complexes were easily obtained by chemical oxidation as fine and very insoluble precipitates. The same products, as judged by elemental analysis and IR, were also obtained by electrochemical oxidation from acetonitrile solutions containing the $TPP_y[M(xtpdt)_2]$ salts. Using standard electrocrystallisation galvanostatic conditions with a current density of 1 $\mu A/cm^2$ for about 7–12 days, in a two-compartment cell with platinum electrodes, only an equally fine and insoluble microcrystalline dark powder was obtained. The elemental analysis of these products is consistent with the neutral complex. Further characterisation of these products was hampered by the difficulty in the preparation of single crystals because of the large insolubility of these neutral complexes in most solvents. However, the measurements of the electrical conductivity by the four-probe method in compressed powder pellets indicated conductivity lower than 10^{-6} S/cm.

 © 2005 Wiley-VCH Verlag GmbH & Co. KGaA, Weinheim

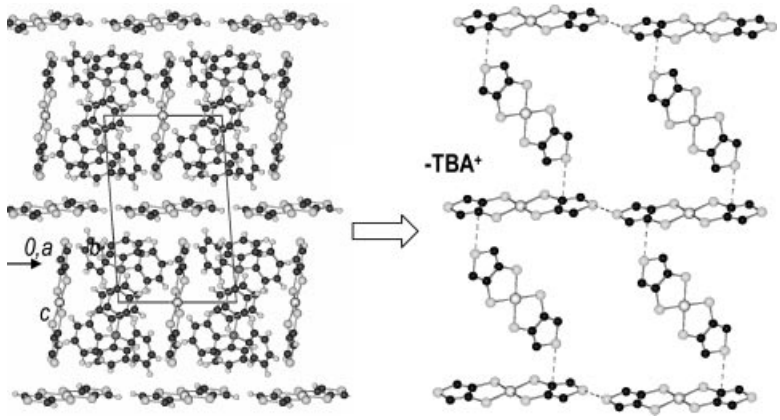

Figure 7. View of the crystal structure of **4** along *a*. On the right side the anionic layer in **4** is shown in detail, emphasising the short S3···S3* and S6···C1 contacts, responsible for the two-dimensional dithiolate network.

Table 6. Cyclic voltammetry of $[M(L)_2]^{x-}$ complexes.

Compound	$E_{1/2}(M^{I}\rightarrow M^{II})$ [mV]	$E_{1/2}(M^{II}\rightarrow M^{III})$ [mV]	$E_{1/2}(M^{III}\rightarrow M^{IV})$ [mV]	Ref.
TPP[Co(tpdt)$_2$]		–618	+497	this work
TPP$_2$[Co(α-tpdt)$_2$]		–591	–257/–175/–8	this work
TPP$_2$[Pt(tpdt)$_2$]		–253	+416	this work
TPP$_2$[Pt(α-tpdt)$_2$]		–519	+69/+152/+278	this work
TBA[Au(α-tpdt)$_2$]		–1162	+456	[10]
TBA[Au(tpdt)$_2$]		–900	+754[a]/+1319	[10]
TBA[Ni(α-tpdt)$_2$]		–562	+253	[11]
TBA$_2$[Co(mnt)$_2$]		–384[a]		[1a]
TBA$_2$[Pt(mnt)$_2$]		–231[a] (–160)	+853 (+720)	[1a] [b], ([19] [c])
TPP$_2$[Cu$_4$(tpdt)$_3$]	–330	+148/+293		this work
TPP$_2$[Cu$_4$(α-tpdt)$_3$]	–506/–278	+182/+430		this work

[a] $M^{III} \rightarrow M^{III/IV}$. [b] In DMF, vs. Ag/AgCl. [c] In acetonitrile vs. Ag/Ag^+.

Summary

New thiophenedithiolate complexes of Cu, Co and Pt with the ligands α-tpdt and tpdt were prepared. The Cu complexes obtained, independently of the metal to ligand ratio, present a tetrametallic Cu^I cluster and three ligands: $[Cu_4(\alpha\text{-tpdt})_3]^{2-}$ and $[Cu_4(tpdt)_3]^{2-}$. The Co and Pt complexes, with square-planar coordination geometry, are obtained in the dianionic state. In spite of their low oxidation potential, only for Co(tpdt)$_2$ was it possible to isolate the monoanionic complex and in other cases this oxidation state is rather unstable. Further oxidation of these complexes to the neutral state gives an electrically insulating powder material.

Experimental Section

General Remarks: All manipulations were carried out with exclusion of air under dry nitrogen or argon unless otherwise stated. All solvents were purified following standard procedures. Thieno[3,4-*d*]-1,3-dithiol-2-thione (**1**) and 5,6-thieno[2,3-*d*]-1,3-dithiol-2-one (**2**) were synthesised as described previously. Other chemicals were commercially obtained and used without any further purification. Column chromatography was carried out using silica gel (0.063–0.2 mm) from S.D.S. UV/Vis spectra were recorded with a Cary 5G spectrophotometer (Varian). IR spectra were obtained with a Perkin–Elmer 577 spectrophotometer. MALDI mass spectra were obtained in time-of-flight negative linear mode with an apparatus Kratus Kompact Maldi 2 K probe (KRATOS Analytical) operated with pulsed extraction of the ions. Cyclic voltammetry data were obtained by using a BAS C3 Cell Stand. The measurements were performed at room temperature in acetonitrile solutions containing nBu$_4$PF$_6$ as supporting electrolyte, with a scan rate of 100 mV/s, platinum wire working and counter electrodes and using a Ag/AgCl as a reference electrode.

Tetraphenylphosphonium Salt of Cobalt(III) Bis(3,4-thiophenedithiolate), TPPCo(tpdt)$_2$ (4): Whilst stirring, thieno[3,4-*d*]-1,3-dithiol-2-thione (**1**) (100 mg, 5.25×10^{-4} mol) was added to a solution of potassium methoxide in methanol (10 mL, 2 M). The formed yellow solution was filtered and added to a solution (2 mL) of $CoCl_2\cdot6H_2O$ (63 mg, 2.6×10^{-4} mol) in methanol, turning to a green mixture. The inorganic precipitate was removed and the liquor added to 1 mL of a solution of tetraphenylphosphonium bromide (222 mg, 5.25×10^{-4} mol) in methanol giving a green precipitate, **3**. The green solid obtained was dissolved in acetonitrile and stirred under air. Just a few minutes later the solution turned from green to dark blue. After an hour this solution was filtered and evaporated, giving **4** as a blue precipitate. The stirring was maintained, in all steps, only until no visible modifications were observed. The best crystals of **4**, suitable for X-ray measurements, were obtained from crystallisation in acetonitrile/ethyl ether. Total

 © 2005 Wiley-VCH Verlag GmbH & Co. KGaA, Weinheim

yield: 79%, 142 mg; $C_{56}H_{44}CoP_2S_6$ (**3**) (1030.20): calcd. C 65.29, H 4.30, S 18.67; found C 64.61, H 3.85, S 17.63; $C_{32}H_{24}PS_6Co$ (**4**) (690.81): calcd. C 55.64, H 3.50, S 27.84; found C 56.23, H 3.68, S 26.95. FTIR (KBr) $\tilde{\nu}$ = 3060 (m) (arom. C–H), 1580 (s) (C=C str.), 1480 (s) (C–H, ring C=C str.), 1460 (s) (=C–H, ring C=C), 1310 (s), 1125 (s), 990 (s), 840 (s), 760 (s), 725 (s) (C–S), 690 (s) (C–S), 630 (m) (C–S), 530 (s) cm^{-1}. UV/Vis (CH_3CN) λ_{max} = 1915 nm; m.p. 67 °C dec. MS: *m*/*z* (%) = 352 (100) [M^-].

Bis(tetraphenylphosphonium) Salt of Platinum(II) Bis(3,4-thiophenedithiolate), $TPP_2Pt(tpdt)_2$ (5): The compound was prepared using the same method as for **4**, using $NaPtCl_4{\cdot}3H_2O$ instead of $CoCl_2{\cdot}6H_2O$. The product was obtained as dark red plate crystals, directly by synthesis, allowing the final solution to rest overnight. Yield: 50%, 152 mg; $C_{56}H_{44}P_2PtS_6$ (1166.36): calcd. C 57.67, H 3.80, S 16.49; found C 56.79, H 3.94, S 16.89; FTIR (KBr) $\tilde{\nu}$ = 3520 (m), 3440 (m) (C–H arom.), 1440 (s) (P-φ), 1300 (s), 1105 (s), 720 (s) (C–S), 690 (m) (C–S), 530 (s) cm^{-1}. UV/Vis (CH_3CN): λ_{max} = 871, 1915 nm; m.p. gradual decomposition 300 °C. MS: *m*/*z* (%) = 487.5 (100) [M^-].

Bis(tetraphenylphosphonium) Salt of Copper(I) Tris(3,4-thiophenedithiolate), $TPP_2Cu_4(tpdt)_3$ (6): The compound was prepared using the same method as for **4**, using $CuCl_2{\cdot}2H_2O$ instead of $CoCl_2{\cdot}6H_2O$. The product was obtained as a brown precipitate. The best crystals, suitable for X-ray measurements, were obtained by recrystallisation in acetonitrile/ethyl ether. Yield: 62%, 55 mg; $C_{60}H_{46}Cu_4P_2S_9$ (1371.69): calcd. C 52.54, H 3.38, S 21.03; found C 53.88, H 3.52, S 20.66; FTIR (KBr) $\tilde{\nu}$ = 1584 (m), 1482 (m), 1439 (m) (C-φ), 1277 (m), 1109 (s), 997 (m), 839 (m), 755 (s), 726 (s), 689 (s) (C–S), 531 (s) cm^{-1}. UV/Vis (CH_3CN): λ_{max} = 1912 nm; m.p. 120 °C dec. MS: *m*/*z* (%) = 325 (100) [$C_8H_4S_5Cu$], 209.7 [$C_4H_2S_3Cu$], 693.5 [M^-].

Tetraphenylphosphonium Salt of Cobalt(III) Bis(2,3-thiophenedithiolate), $TPP_2Co(\alpha\text{-}tpdt)_2$ (7): The compound was prepared using the same method as for **4**. The initial reactive was 5,6-thieno[2,3-*d*]-1,3-dithiol-2-one (**2**). The product was obtained as dark brown crystals after recrystallisation in acetonitrile/ethyl ether. Total yield: 80%, 214 mg; $C_{56}H_{44}CoP_2S_6$ (1030.20): calcd. C 65.29, H 4.30, S 18.67; found C 64.90, H 3.95, S 18.75; $\tilde{\nu}$ = 3440 (m), 3050 (m) (C–H arom.), 1650 (m), 1640 (m), 1590 (s), 1490 (s), 1445 (s) (P-φ), 1310 (m), 1240 (m), 1160 (m), 1110 (s), 1020 (m), 1000 (m), 755 (m), 730 (s), 700 (s), 630 (m), 54 (s) cm^{-1}. UV/Vis (CH_3CN): λ_{max} = 581, 795, 1912 nm; m.p. 117.8–119.5 °C. MS: *m*/*z* (%) = 144.7 (100) [S_3C_4] [M^-].

Bis(tetraphenylphosphonium) Salt of Platinum(II) Bis(2,3-thiophenedithiolate), $TPP_2Pt(\alpha\text{-}tpdt)_2$ (8): The compound was prepared from 5,6-thieno[2,3-*d*]-1,3-dithiol-2-one (II) following the same method as in **5**. After recrystallisation the compound was obtained as orange plate-shaped crystals. Yield: 53%, 161 mg; $C_{56}H_{44}P_2PtS_6$ (1166.36): calcd. C 57.67, H 3.80, S 16.49; found C 56.93, H 3.69, S 16.25; $\tilde{\nu}$ = 3054 (m) (C–H arom.), 1578 (m), 1429 (m) (P-φ), 1377 (s), 716 (s) (C–S), 682 (s) (C–S) cm^{-1}. UV/Vis (CH_3CN): λ_{max} = 990, 1912 nm. MS: *m*/*z* (%) = 487.5 (100) [M^-].

Bis(tetraphenylphosphonium) Salt of Copper(I) Tris(2,3-thiophenedithiolate), $TPP_2Cu_4(\alpha\text{-}tpdt)_3$ (9): Using as starting material **2** and following the same procedure used for **6**, the product was obtained as golden brown crystals. Yield: 59%, 53 mg; $C_{60}H_{46}Cu_4P_2S_9$ (1371.69): calcd. C 52.54, H 3.38, S 21.03; found C 53.27, H 3.47, S 20.35; $\tilde{\nu}$ = 1482 (m), 1439 (m) (P-φ), 1110 (m), 998 (m), 864 (m), 757 (m), 726 (s) (C–S), 692 (s) (C–S), 601 (m), 514 (s) cm^{-1}. UV/Vis (CH_3CN): λ_{max} = 432, 1418, 1908 nm; m.p. 213.3–214.4 °C dec. MS: *m*/*z* (%) = 144.9 [$C_4H_2S_3$], 324.8 [$C_8H_4S_5Cu$], 353 [$C_8H_4S_6Cu$].

Cobalt(IV) Bis(3,4-thiophenedithiolate), $Co(tpdt)_2$ (10): A solution of iodine in acetone was added to a solution of **4** in acetone (10 mL, 1.5×10^{-2} M), dropwise in stoichiometric amounts. The fine dark precipitate obtained was isolated by centrifugation, washed by Soxhlet extraction with acetone and dried in vacuo. Yield 32%, 17 mg; $C_8H_4CoS_6$ (351.41: calcd. C 27.34, H 1.15, S 54.74; found C 27.11, H 1.07, S 53.15.

Platinum(IV) Bis(3,4-thiophenedithiolate), $Pt(tpdt)_2$ (11): Using as starting material **5** and following the same procedure used for **10**, the neutral species was obtained as a fine-powdered dark solid. Yield 28%, 20 mg; $C_8H_4PtS_6$ (487.57): calcd. C 19.71, H 0.83, S 39.45; found C 19.03, H 0.95, S 37.14.

Cobalt(IV), Bis(2,3-thiophenedithiolate), $Co(\alpha\text{-}tpdt)_2$ (12): Using as starting material **7** and following the same procedure used for **10**, the neutral species was obtained as a fine-powdered dark solid. Yield 45%, 24 mg; $C_8H_4CoS_6$ (351.41): calcd. C 27.34, H 1.15, S 54.74; found C 26.94, H 1.14, S 53.04.

Platinum(IV), Bis(2,3-thiophenedithiolate), $Pt(\alpha\text{-}tpdt)_2$ (13): Using as starting material **8** and following the same procedure used for **10**, the neutral species was obtained as a fine-powdered dark solid. Yield 37%, 27 mg, $C_8H_4PtS_6$ (487.57): calcd. C 19.71, H 0.83, N 0.00, S 39.45; found C 19.94, H 1.14, N 0.00, S 35.83.

X-ray Crystallographic Study: The data collection was performed at room temperature for all compounds on an Enraf–Nonius CAD4 diffractometer equipped with a graphite monochromatised Mo-K_α radiation (λ = 0.71069 Å) in the ω-2θ-scan mode, except in the case of compound **5**, where data were collected at 120 K with a Nonius KAPPA CCD using a Mo rotating anode using φ- and ω-scans. Data collection and refinement details are presented in Table 1.

The structures were solved by direct methods using SIR97[14] and refined by full-matrix least-squares methods using the program SHELXL97[15] and the winGX software package.[16] All non-hydrogen atoms were refined anisotropically. Hydrogen atoms were placed in idealised positions and allowed to refine riding on the parent C atom. Molecular graphics were prepared using ORTEP 3[17] and SCHAKAL-97.[18] Crystal data and structure refinement are summarised in Tables 5 and 6. Experimental details, atomic coordinates, and bond lengths and angles have been deposited in the Cambridge Crystallographic Data Centre (CCDC). CCDC-263500–263505 for compounds **4**–**9** contain the supplementary crystallographic data for this paper. These data can be obtained free of charge from the CCDC via www.ccdc.cam.ac.uk/data_request/cif.

Acknowledgments

This work was partially supported by Fundação para a Ciência e Tecnologia (Portugal) under contracts POCTI/35342/QUI/2000 and POCTI/QUI/4508/2002 and by DGI project BQU2003–00760, and by DGR Catalonia, project 2001SGR00362 (Spain). The collaboration between the team members of Sacavém and Barcelona was supported under the CSIC-ICCTI bilateral agreement. This work also benefited from COST action D14.

[1] a) J. A. McCleverty, *Prog. Inorg. Chem.* **1968**, *10*, 29; b) D. Coucouvanis, *Prog. Inorg. Chem.* **1970**, *11*, 233; c) R. Eisenberg, *Prog. Inorg. Chem.* **1971**, *12*, 295; d) L. Alcácer, H. Novais in *Extended Linear Chain Compounds* (Ed.: J. S. Miller), Plenum Press, New York, **1983**, vol. 3, ch. 6, p. 319; e) S. Alvarez, V. Ramon, R. Hoffman, *J. Am. Chem. Soc.* **1985**, *107*, 6253; f) *Progress in Inorganic Chemistry*, vol. 52, *Dithiolene Chemistry:*

Synthesis Properties, and Applications (Eds.: K. D. Karlin, E. I. Tiefel), John Wiley & Sons, New York, **2004**.
[2] N. Robertson, L. Cronin, *Coord. Chem. Rev.* **2002**, *227*, 93.
[3] A. T. Coomber, D. Beljonne, R. H. Friend, J. L. Bredas, A. Charlton, N. Robertson, A. E. Underhill, M. Kurmoo, P. Day, *Nature* **1996**, *380*, 144.
[4] a) M. Ahmad, A. E. Underhill, *J. Chem. Soc., Chem. Commun.* **1981**, 67; b) M. M. Ahmad, D. J. Turner, A. E. Underhill, C. S. Jacobsen, K. Mortensen, K. Carneiro, *Phys. Rev. B* **1984**, *29*, 4796.
[5] a) P. Cassoux, L. Valade in *Inorganic Materials*, 2nd ed. (Eds.: D. W. Bruce, D. O'Hare), John Wiley & Sons, Chichester, **1996**, pp. 1–64; b) P. Cassoux, J. S. Miller in *Chemistry of Advanced Materials* (Eds.: L. V. Interrante, M. J. Hampden-Smith), Wiley-VCH, New York, **1998**, pp. 19–72.
[6] D. Simão, H. Alves, D. Belo, S. Rabaça, E. B. Lopes, V. Gama, M. T. Duarte, R. T. Henriques, H. Novais, M. Almeida, *Eur. J. Inorg. Chem.* **2001**, 3119–3126.
[7] H. Alves, D. Simão, I. C. Santos, V. Gama, R. T. Henriques, H. Novais, M. Almeida, *Eur. J. Inorg. Chem.* **2004**, *6*, 1318–1329.
[8] V. Gama, R. T. Henriques, M. Almeida, L. Veiros, M. J. Calhorda, A. Meetsma, J. L. de Boer, *Inorg. Chem.* **1993**, *32*, 3705–3711.
[9] V. Gama, R. T. Henriques, G. Bonfait, M. Almeida, A. Meetsma, S. Van Smaalen, J. L. de Boer, *J. Am. Chem. Soc.* **1992**, *114*, 1986–1989.
[10] D. Belo, H. Alves, E. B. Lopes, M. T. Duarte, V. Gama, R. T. Henriques, M. Almeida, A. Pérez-Benítez, C. Rovira, J. Veciana, *Chem. Eur. J.* **2001**, *7*, 511–519.
[11] D. Belo, H. Alves, S. Rabaça, L. C. Pereira, M. T. Duarte, V. Gama, R. T. Henriques, M. Almeida, E. Ribera, C. Rovira, J. Veciana, *Eur. J. Inorg. Chem.* **2001**, 3127–3132.
[12] H. Tanaka, Y. Okano, H. Kobayashi, W. Susuki, A. Kobayashi, *Science* **2001**, *291*, 285.
[13] a) G.-E. Matsubayashy, A. Yokozawa, *Chem. Commun.* **1991**, 68; b) J. Dai, M. Munakata, Y. Ohno, G. Q. Bian, Y. Suenaga, *Inorg. Chim. Acta* **1999**, *285*, 332; c) J. R. Nicholson, I. L. Abrahams, C. D. Garner, *Inorg. Chem.* **1985**, *24*, 1092.
[14] A. Altomare, M. C. Burla, M. Camalli, G. Cascarano, G. Giacovazzo, A. Guagliardi, A. G. G. Moliterni, G. Polidori, R. Spagna, *J. Appl. Cryst.* **1999**, *32*, 115–119.
[15] G. M. Sheldrick, *SHELXL97*, A Program for Crystal Structure Refinement, University of Göttingen, Germany, **1997**.
[16] L. J. Farrugia, *J. Appl. Cryst.* **1999**, *32*, 837–838.
[17] ORTEP3 for Windows: L. J. Farrugia, *J. Appl. Crystallogr.* **1997**, *30*, 565.
[18] E. Keller, SCHAKAL-97, A Computer Program for the Representation of Molecular and Crystallographic Models, Kristallographisches Institut der Universität Freiburg, Germany, **1997**.
[19] L. Persaud, C. H. Langford, *Inorg. Chem.* **1985**, *24*, 3562.

Received: February 16, 2005
Published Online: July 4, 2005

 © 2005 Wiley-VCH Verlag GmbH & Co. KGaA, Weinheim

Self-Assembly by Ligand-Exchange Reactions

Dillip Kumar Chand,*[a] Ramalingam Manivannan,[a] Himansu S. Sahoo,[a] and Kandasamy Jeyakumar[a]

Dedicated to Prof. Makoto Fujita on his 47th birthday

Keywords: Cage compounds / NMR spectroscopy / Metallacycles / Palladium / Ligand exchange

An interesting phenomenon of ligand exchange is observed in the DMSO solution of certain self-assembled molecules generated from *cis*-protected Pd^{II} and organic ligands. Upon heating, assemblies such as $[\{Pd(en)\}_x(ligand)_y](NO_3)_{2x}$ change to $[Pd_m(ligand)_n](NO_3)_{2m}$ and $[Pd(en)_2](NO_3)_2$. The change is also possible at room temperature when 0.5 equiv. $Pd(en)(NO_3)_2$ is added in excess to the system. The transformation is incomplete when the ligand moiety is monodentate in nature, for example in the case of 4-phenylpyridine. However, multinuclear assemblies containing nonchelating, polydentate ligands used in this study entirely favor the transformation. This process is not possible with some related Pt^{II} compounds.

(© Wiley-VCH Verlag GmbH & Co. KGaA, 69451 Weinheim, Germany, 2005)

Introduction

Creation of discrete and definite molecular architectures using organic ligands and selected metal ions through self-assembly has received much attention in organic synthesis because of the inherent simplicity of the method.[1,2] Self-assembled structures that would result from the complexation of a metal ion with a designed ligand may be assumed to be fixed a priori.[2] However, the mode of arrangement of the participating components depends on the steric requirements, thermodynamic stability, and entropy cost of the final assembly, as well as on the guest molecule, if any, and on the solvent.[3] In the solution state, two or more isomers or structures may coexist in dynamic equilibrium depending upon the directionality/flexibility of the ligand, in particular when the metal–ligand bond of the system is labile in nature.[4] It has also been shown that it is possible in certain cases to shift such equilibria to favor one of the compounds as a single/major product by suitably controlling parameters like solvent, guest molecule, temperature, time etc.[5]

The construction of self-assembled structures under the influence of stereochemical details of the complex and the choice of pyridine-appended ligands have been studied well by Fujita[2e] and Stang[2c] in the coordination chemistry of palladium(II). Polynuclear complexes $(M_xL_y)^{n+}$ of different geometries and conformations have also been realized by the use of polydentate nonchelating ligands. Usually *cis*-protected Pd^{II}, e.g., $Pd(en)^{2+}$, has been employed,[2c,2e] and the area has been a subject of extensive study and review. Such systems require control over only two coordination sites of each metal center involved, because the other two positions are already protected. In contrast, there exist very few examples[6] of assemblies achieved from Pd^{II} where all four sites are available for coordination during the assembly process. The use of particular ligands for both *cis*-protected Pd^{II} and unprotected Pd^{II} is published as a comparative study.[6e]

[a] Department of Chemistry, Indian Institute of Technology Madras,
Chennai 600036, India
Fax: +91-044-2257-8241-4202
E-mail: dillip@iitm.ac.in

Results and Discussion

We are interested in the dynamic nature of the Pd^{II}-driven self-assembly processes. The ligand **1** (Figure 1) and *cis*-protected $Pd(en)(NO_3)_2$ at a ratio of 1:1 form a binuclear M_2L_2 macrocycle, $[\{Pd(en)\}_2(\mathbf{1})_2](NO_3)_4$ (**5**), as a major product along with a tetranuclear macrocyclic compound, $[\{Pd(en)\}_4(\mathbf{1})_4](NO_3)_8$ (**6**) (Scheme 1), as reported earlier.[6e] The assembly process was performed in DMSO by stirring at 60 °C for 10 min. While taking another look at the dynamic equilibrium of the two self-assembled structures (**5** and **6**) resulting from ligand **1** and *cis*-protected Pd^{II}, we observed an interesting phenomenon. Our effort was to shift the equilibrium in favor of one of these two structures. When temperature was chosen as a parameter to vary, instead of the possible shift in equilibrium, we observed scrambling of the assemblies, giving rise to yet other

 © 2005 Wiley-VCH Verlag GmbH & Co. KGaA, Weinheim **DOI: 10.1002/ejic.200500192**

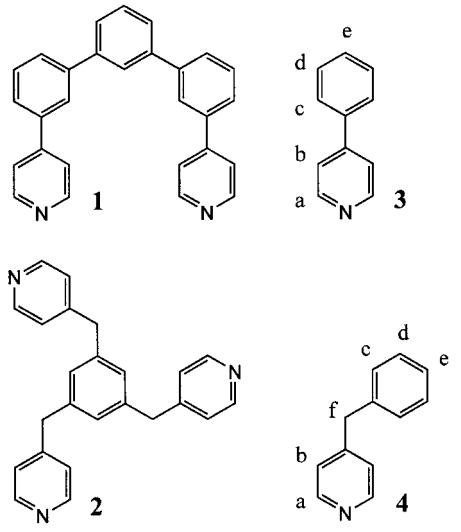

Figure 1. Structures of the ligands **1**, **2**, **3**, and **4**.

assemblies (Scheme 1). Scrambling is also observed in some other related systems and is discussed in this report.

It is observed here that for the complexation of **1** with *cis*-protected $Pd(en)(NO_3)_2$, heating or stirring is not required, and the system in DMSO gives rise to assemblies spontaneously at room temperature as a result of the simple combination of the components. The two compounds **5** and **6** are of course in dynamic equilibrium (Scheme 1), as is evident from the concentration-dependent nature of the equilibrium. Upon increasing the concentration, the bigger molecule **6** is favored, and with decreasing concentration, the smaller molecule **5** is favored. However, it was not possible to push the equilibrium of **5** and **6** exclusively in favor of one compound by varying the concentration.

In order to shift the equilibrium in favor of one of the assemblies we decided to vary other possible parameters. What is more interesting is the effect of heat on the dynamic equilibrium behavior. Experiments were performed at different temperatures; around 90 °C was found to be a good temperature for studying this process.[7] At a particular con-

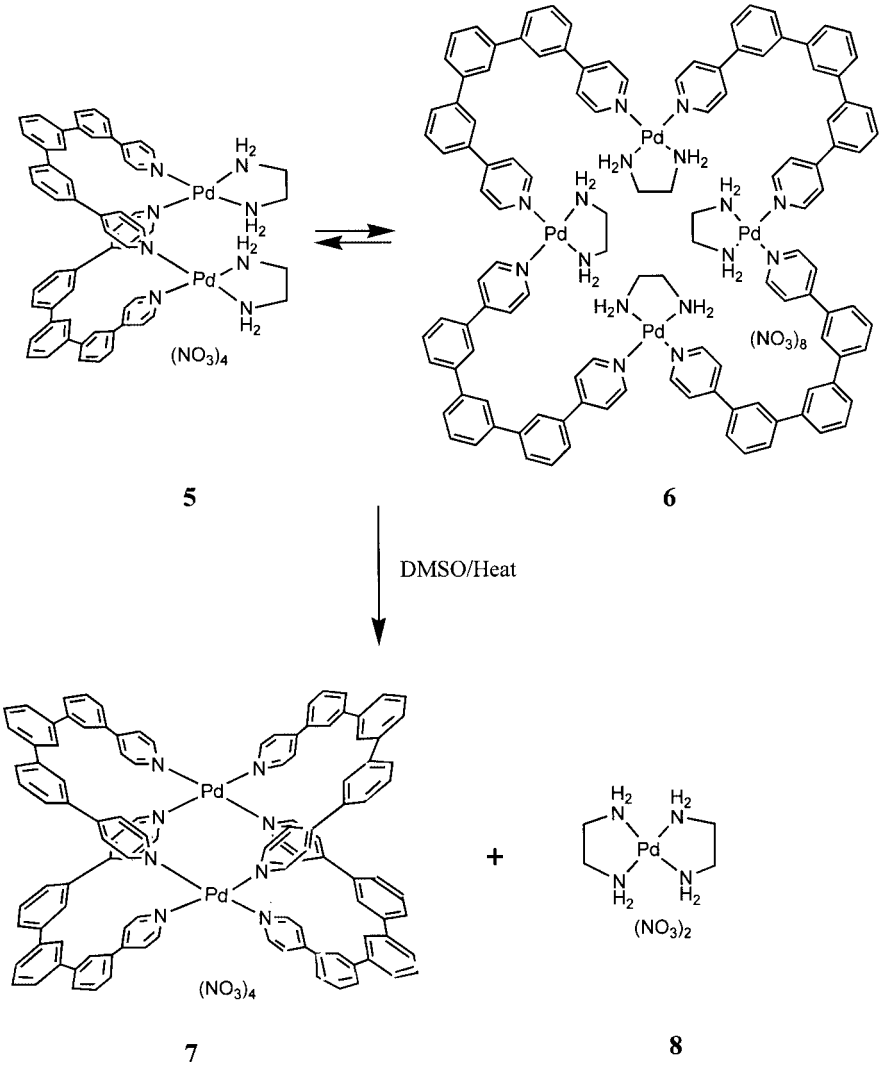

Scheme 1. Transformation of a dynamic equilibrium of **5** and **6** to a mixture of **7** and **8** occurred by ligand exchange (see ref.[6b,6e] for the synthesis of **5**, **6**, and **7**).

 © 2005 Wiley-VCH Verlag GmbH & Co. KGaA, Weinheim

centration, with the increase in temperature (heating) we could not observe a shift of equilibrium in [D_6]DMSO. Rather, new peaks were observed in the proton NMR at the expense of **5** and **6**. The assemblies were identified in due course as the M_2L_4 assembly $[(Pd)_2(\mathbf{2})_4](NO_3)_4$ (**7**)[6b] and $[Pd(en)_2](NO_3)_2$ (**8**).[8] The proportion of the complexes at any given time is calculated from the integration ratio of the corresponding py_α protons as observed in their ^1H NMR spectra (e.g., Figure 2). It is worthwhile to mention here that compound **7** can be prepared by combining the ligand **1** and $Pd(NO_3)_2$ at a ratio of 2:1 in DMSO and stirring at 90 °C for 10 min. Thus, a mixture of **5** and **6** changes, upon heating, to a mixture of **7** and **8**. At an intermediate stage all four compounds **5**, **6**, **7**, and **8** coexist, and finally only **7** and **8** are detected (Figure 2). We attribute such an observation to a ligand exchange around the metal centers promoted by the increase in temperature and the solvent.

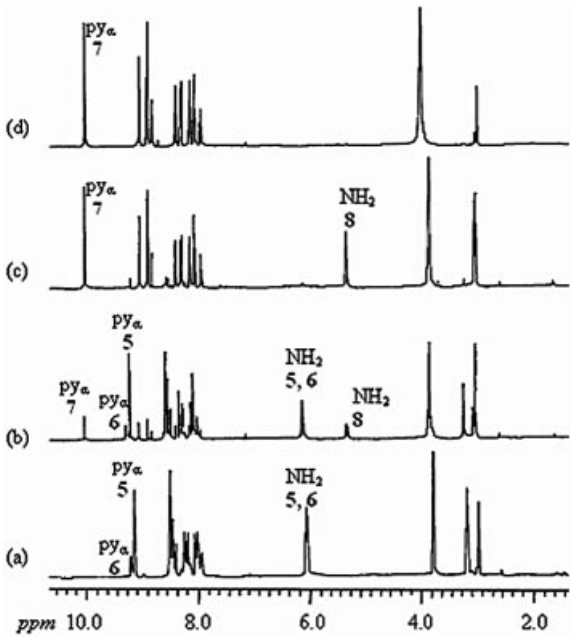

Figure 2. ^1H NMR spectra of a dynamic equilibrium mixture of $[\{Pd(en)\}_2(\mathbf{1})_2](NO_3)_4$ (**5**) and $[\{Pd(en)\}_4(\mathbf{2})_4](NO_3)_8$ (**6**), and the evolution, after this mixture was heated at 90 °C in [D_6]DMSO, of a mixture of $[(Pd)_2(\mathbf{2})_4](NO_3)_4$ (**7**) and $[Pd(en)_2](NO_3)_2$ (**8**) due to ligand exchange. NMR peaks are due to (a) **5** and **6** at t = 0 h (ref. [6e]); (b) **5**, **6**, **7**, and **8** at t = 6 h, an intermediate stage; (c) **7** and **8** at t = 48 h, completed scrambling; and (d) pure **7** (ref. [6e]) for comparison.

Another system considered was the assembly from ligand **2**. Ligand **2** and $Pd(en)(NO_3)_2$, at a ratio of 2:3, provide an M_3L_2 compositional assembly $[\{Pd(en)\}_3(\mathbf{2})_2](NO_3)_6$ (**9**) along with a mixture of other oligomeric compounds[9] in aqueous[5b] or DMSO solution.[6e] The assembly of ligand **2** with $Pd(NO_3)_2$ at a ratio of 8:6 gives a designed M_6L_8 molecular sphere, $[(Pd)_6(\mathbf{2})_8](NO_3)_{12}$ (**10**).[6d] As the scrambling of the ligand described (vide supra) for the ligand system **1** seemed interesting, the ligand system **2** was subjected to a similar set of experiments. A mixture of **9** and its oligomers, existing in dynamic equilibrium, was heated in [D_6]-DMSO, with the expectation of forming **10** and **8**. Once again, ligand exchange was observed around the Pd^{II} centers, and the dynamic equilibrium was transformed completely to a mixture of **10** and **8** (Scheme 2).

In the ligand-exchange process observed in this work, multinuclear assemblies containing *cis*-protected Pd^{II} centers, i.e. $[\{Pd(en)\}_x(ligand)_y](NO_3)_{2x}$, change to multinuclear assemblies containing simple Pd^{II} centers, i.e. $[Pd_m(ligand)_n](NO_3)_{2m}$, along with $[Pd(en)_2](NO_3)_2$. When the total number of Pd^{II} ions per molecule in the resulting assembly is "m" then it is associated with "m" numbers of $[Pd(en)_2](NO_3)_2$ molecules.

So far, we have discussed the findings with the polydentate nonchelating ligands **1** and **2**. An immediate comparison is necessary with a monodentate ligand reminiscent of these ligands. Thus 4-phenylpyridine (**3**) and 4-benzylpyridine (**4**) (Figure 1) were used for a similar study. The ligands **3** and **4** being monodentate, their complexes with *cis*-protected Pd^{II} and unprotected Pd^{II} are only mononuclear, and the synthesis of these new complexes (**11**–**14**) is described in this work. The complex $[Pd(en)(\mathbf{3})_2](NO_3)_2$ (**11**) was expected to give $[(Pd)(\mathbf{3})_4](NO_3)_2$ (**12**) and $[Pd(en)_2](NO_3)_2$ (**8**) as before upon heating (Scheme 3). This time the expected transformation proceeded, but not to completion (Figure 3, Figure 4). Structure **11** remained in a dynamic equilibrium with a mixture of **12** and **8**. A similar result was obtained with the ligand system **4**. Here $[Pd(en)(\mathbf{4})_2](NO_3)_2$ (**13**) remained in a dynamic equilibrium with a mixture of $[(Pd)(\mathbf{4})_4](NO_3)_2$ (**14**) and **8**.

Comparison of the scrambling process observed with the different ligand systems presented in this work reveals the following points. When $[\{Pd(en)\}_x(ligand)_y](NO_3)_{2x}$, having a Pd concentration of 10 mM is heated, the speed at which the scrambling proceeds to give the resulting assemblies depends upon the ligand of choice. Probably the process is also controlled by the composition and thermodynamic stability of the concerned self-assemblies. The ligand system **2** leads to the final stage of the process very quickly in 12 h, while **1** requires more than 2 days (Figure 4). The ligands **3** and **4** also form the expected new assemblies initially; however, after a certain amount is formed (about 18–20% of the ligand in the new assembly), a dynamic equilibrium is established, and the process is incomplete.

Some experiments were performed in [D_6]DMSO to understand the stability vs. lability of the complexes through proton NMR studies. When the required amount of ethylene diamine was added to any of the Pd^{II} complexes **5**–**7** or **9**–**14**, in each case the Pd^{II} ion was sequestered as $[Pd(en)_2](NO_3)_2$ (**8**) immediately, and the corresponding ligands were released. However, addition of any of the ligands **1**–**4** to **8** caused no changes. This indicates that the above-mentioned acyclic or nonchelated cyclic complexes are kinetically labile. However, the chelated complex **8** behaved in a kinetically nonlabile manner under the conditions employed. To throw some light on stability, the following experiments were performed. Complex **8** was added to a solution of assembly **7**. Compound **7** remained un-

 © 2005 Wiley-VCH Verlag GmbH & Co. KGaA, Weinheim

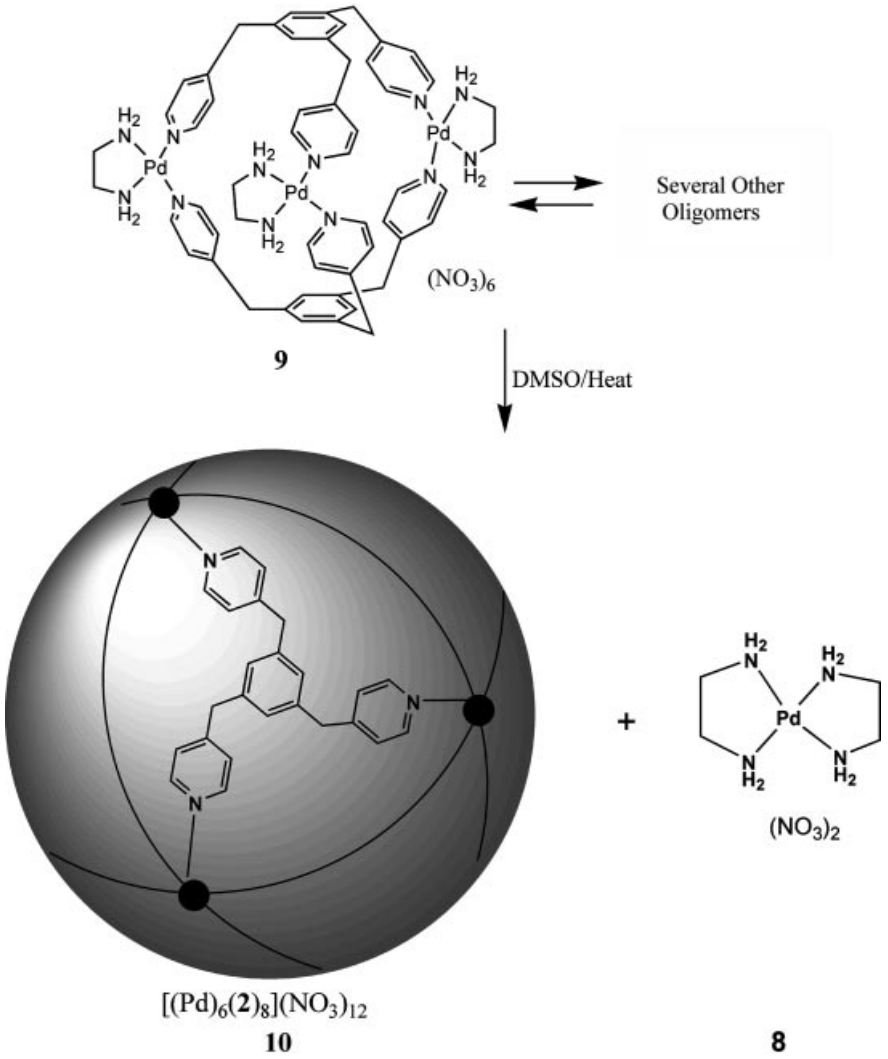

Scheme 2. Transformation of a dynamic equilibrium of **9** and its oligomers to a mixture of **10** and **8** occurred due to ligand exchange (see ref. [5b] for the synthesis of **9** and ref. [6d] and [6e] for that of **10**).

changed as observed from the proton NMR of the mixture. A similar experiment was performed by the addition of **8** to **10**; the result was that **10** also remained unchanged. However, when **8** was combined with a solution of **12**, a considerable amount of **11** was generated immediately at room temperature, and once again, an equilibrium mixture of **11**, **12**, and **8** was observed. In line with the behavior of **12**, the complex **14**, upon being combined with **8**, also generated **13**. Thus, it is possible to suggest that **7** and **10** are, although kinetically labile, still comparatively stable enough to drive the ligand-exchange reaction for the ligand systems **1** and **2** and completely in favor of **7** and **10**, respectively. As for **12** and **14**, these two complexes are labile; however thermodynamically not stable enough to drive the equilibrium completely in the forward direction. In addition, the presence of **12** or **14** with **8** allows ligand exchange around the Pd^{II} center of relatively inert **8**. Hence, there exists a final equilibrium as a result of the interplay of all participating molecules.

Another control experiment was performed to find out whether the dissociation of $Pd(en)^{2+}$ and ligands from $[\{Pd(en)\}_x(ligand)_y](NO_3)_{2x}$ occurred and whether the dissociated $Pd(en)^{2+}$ was involved in promoting the ligand-exchange process observed. Thus we added a 0.5-equiv. excess of $Pd(en)(NO_3)_2$ to each one of the systems and found that the speed of scrambling was increased in the case of the ligand systems **1** and **2**. Interestingly, the ligand exchange could be observed in this situation even at room temperature. However, no detectable increase in speed was observed in the cases of **3** or **4** when 0.5 equiv. excess of $Pd(en)(NO_3)_2$ was added.

As the *trans*-effect is important in the chemistry of Pt^{II}, we checked the possibility of similar scrambling phenomena in Pt^{II}-driven self-assemblies. When $[\{Pt(en)\}_x(\mathbf{2})_y](NO_3)_{2x}$ assemblies were heated in $[D_6]$DMSO, we could not observe the formation of any trace of $[(Pt)_6(\mathbf{2})_8](NO_3)_{12}$; rather the system decomposed to unidentified products upon prolonged heating.[10] The kinetic inertness of the Pt–N bond compared to the lability of the Pd–N bond[11] suggests that self-correction is inefficient in the Pt^{II} system at the given reaction conditions in this work to give discrete products through a ligand-exchange pathway.

 © 2005 Wiley-VCH Verlag GmbH & Co. KGaA, Weinheim

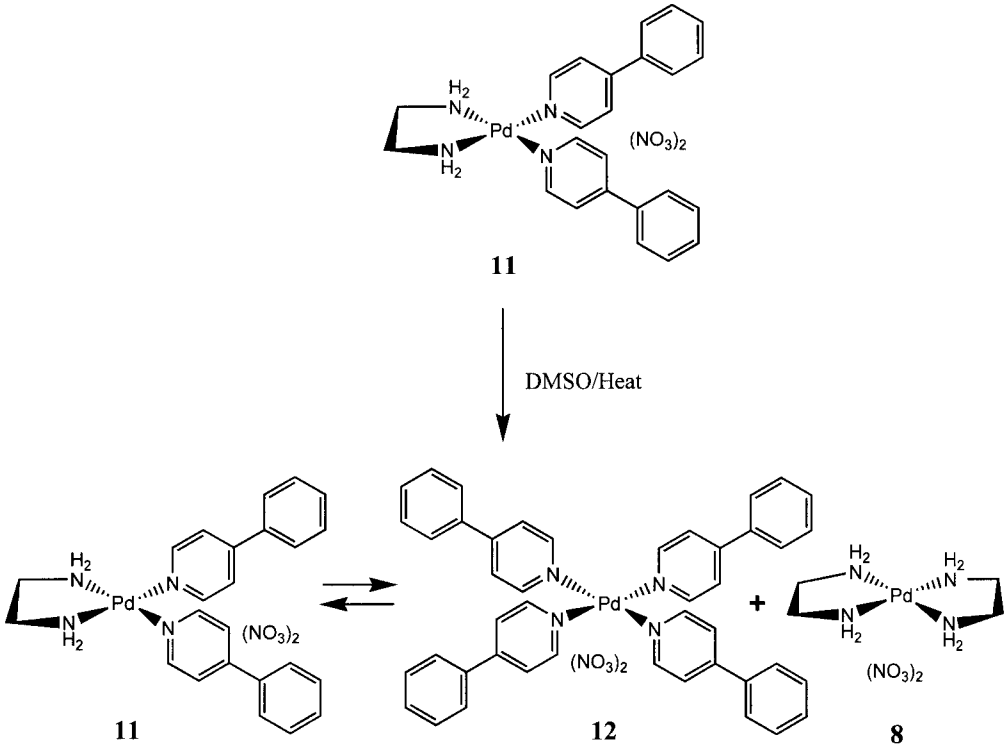

Scheme 3. Dynamic equilibrium of **11** and a mixture of **12** and **8** resulting from ligand exchange (approximately 18% of the ligand is present in **12** and 82% in **11**).

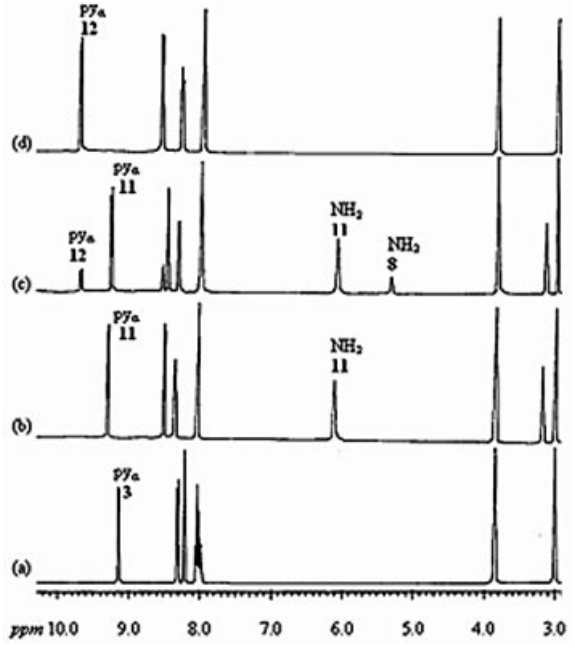

Figure 3. ^{1}H NMR spectra in [D$_6$]DMSO for (a) ligand **3**; (b) [Pd(en)(**3**)$_2$](NO$_3$)$_2$ (**11**); (c) the final equilibrium mixture of [Pd(en)(**3**)$_2$](NO$_3$)$_2$ (**11**), [Pd(**3**)$_4$](NO$_3$)$_2$ (**12**), and [Pd(en)$_2$](NO$_3$)$_2$ (**8**) obtained by heating a solution of **11** at 90 °C for 10 h; and (d) pure **12**.

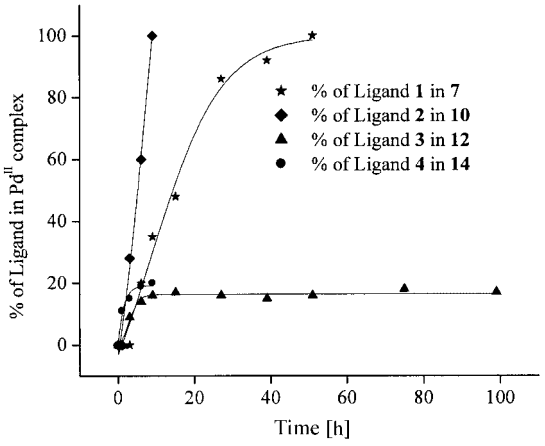

Figure 4. Percentage of ligand in the Pd^{II} complex, generated as a function of time, when [{Pd(en)}$_x$(ligand)$_y$](NO$_3$)$_{2x}$ is heated at 90 °C.

In conclusion, the result opens up a concern in Pd^{II} chemistry for further study to give more generalization on the ligand-exchange process. Consideration of other parameters like the solvent, the substituent on the ligand as well as that on the protecting group is certainly required to enrich the chemistry and explain the observations.

Experimental Section

The ligands **1** and **2** and complexes **5**–**10** have been synthesized by the methods reported earlier,[6e,8] while **3** and **4** are obtained from Lancaster. The complexes **11**–**14** are new and reported here. The downfield shift of the pyridine protons in **11**–**14** are attributed to complexation with Pd^{II}; the nature of the shift is in line with other related complexes. Deuterated solvent ([D$_6$]DMSO) was acquired from Aldrich and used as such for the complexation reactions for

 © 2005 Wiley-VCH Verlag GmbH & Co. KGaA, Weinheim

NMR study. ^{1}H NMR spectroscopic data were obtained with a Bruker 400 MHz NMR spectrometer using external TMS in $CDCl_3$ as the reference. The assemblies of general formula $[\{Pd(en)\}_x(ligand)_y](NO_3)_{2x}$ prepared in [D$_6$]DMSO were heated at 90 °C in NMR tubes. The desired temperature was achieved by immersing the tubes in a constant-temperature bath. The sample tubes were taken out of the bath at chosen intervals of time, and ^{1}H NMR spectra are recorded at room temperature. Formation of $[Pd_m(ligand)_n](NO_3)_{2m}$ and $[Pd(en)_2](NO_3)_2$ in the reaction mixture was confirmed by comparing with the data of the corresponding pure samples. The proportion of the assemblies of interest was calculated from the integration ratio of the Py_α protons in question. Proton NMR spectroscopic data of the ligands **3** and **4** and of the complex $[Pd(en)_2](NO_3)_2$ (**8**) in [D$_6$]DMSO was required for this work and is reported here ^{1}H NMR (400 MHz, [D$_6$]DMSO, TMS): For **3**: δ = 9.136 (d, 2 H, a), 8.306 (d, 2 H, b), 8.212 (dd, 2 H, c), 8.049–7.960 (m, 3 H, d and e) ppm; for **4**: δ = 8.961 (broad, 2 H, a), 7.79–7.71(broad m, 7 H, b,c,d, and e), 4.440 (s, 2 H, f) ppm; for **8:** δ = 5.360 (s, 8 H, CH_2), 3.00 (s, 8 H, NH_2, merged with the residual solvent peaks) ppm.

Synthesis of 11–14

$[Pd(en)(3)_2](NO_3)_2$ (11): To a solution of $Pd(en)(NO_3)_2$, (14.5 mg, 0.05 mmol) in MeCN (5 mL) was added the ligand **3** (15.5 mg, 0.1 mmol). The mixture was stirred to get a clear solution. Subsequent addition of diethyl ether precipitated the complex **11** as a white solid (24 mg, 80%). ^{1}H NMR (400 MHz, [D$_6$]DMSO, TMS): δ = 9.333 (d, 4 H, a), 8.540 (d, 4 H, b), 8.388 (m, 4 H, c), 8.062 (m, 6 H, d and e), 6.130 (s, 4 H, NH_2), 3.189 (s, 4 H, CH_2) ppm. $C_{24}H_{26}N_6O_6Pd$: calcd. C 47.97, H 4.36, N 13.99; found C 48.08, H 4.46, N 13.78.

$[Pd(en)(4)_2](NO_3)_2$ (12): Following the synthesis of **11**, to a solution of $Pd(en)(NO_3)_2$, (14.5 mg, 0.05 mmol) in MeCN (5 mL) was added the ligand **4** (16.9 mg, 0.1 mmol). Subsequent addition of diethyl ether precipitated a white solid, the complex **12** (26 mg, 83%). ^{1}H NMR (400 MHz, [D$_6$]DMSO, TMS): δ = 9.097 (d, 4 H, a), 8.010 (d, 4 H, b), 7.810–7.744 (m, 10 H, c, d and e), 5.980 (s, 4 H, NH_2), 4.527 (s, 4 H, f), 3.103 (s, 4 H, CH_2) ppm. $C_{26}H_{30}N_6O_6Pd$: calcd. C 49.65, H 4.81, N 13.36; found C 49.74, H 4.99, N 13.58.

$[Pd(3)_4](NO_3)_2$ (13): To a solution of $Pd(NO_3)_2$, (11.7 mg, 0.05 mmol) in MeCN (5 mL) was added the ligand **3** (31.0 mg, 0.2 mmol), whereupon a white solid was precipitated out. The mixture was heated for a further period of 10 min at 90 °C, and the solid was separated (36 mg, 85%). ^{1}H NMR (400 MHz, [D$_6$] DMSO, TMS): δ = 9.758 (d, 8 H, a), 8.608 (d, 4 H, b), 8.345–8.322 (m, 8 H, c), 8.063–8.021 (m, 12 H, d and e) ppm. $C_{44}H_{36}N_6O_6Pd$: calcd. C 62.08, H 4.26, N 9.87; found C 62.26, H 4.30, N 9.71.

$[Pd(4)_4](NO_3)_2$ (14): To a solution of $Pd(NO_3)_2$, (11.7 mg, 0.05 mmol) in MeCN (5 mL) was added the ligand **4** (33.8 mg, 0.2 mmol), whereupon a white solid precipitated out. The mixture was heated for a further period of 10 min at 90 °C, and the solid was separated (35 mg, 78%). ^{1}H NMR (400 MHz, [D$_6$]DMSO, TMS): δ = 9.461 (d, 8 H, a), 7.956 (d, 8 H, b), 7.791–7.664 (m, 20 H, c, d and e), 4.462 (s, 8 H, f) ppm. $C_{48}H_{44}N_6O_6Pd$: calcd. C 63.54, H 4.89, N 9.26; found C 63.39, H 5.02, N 9.11.

Acknowledgments

This study was supported by a grant in aid for scientific research from the Department of Science and Technology (DST), New Delhi, India (No.SR/S1/IC-18/2003). We highly appreciate the NMR instrumentation facility provided by the DST under the FIST program to the Department of Chemistry, IIT Madras. Authors also acknowledge the help of Mr. Mohan in recording the ^{1}H NMR spectra.

[1] *Templating, Self-Assembly and Self-Organization* (Eds.: J. P. Sauvage, M. W. Hosseini) in *Comprehensive Supramolecular Chemistry*, *Vol. 9* (Ed.: J.-M. Lehn), Pergamon, Oxford, **1995**.

[2] a) P. J. Stang, B. Olenyuk, *Acc. Chem. Res.* **1997**, *30*, 502–518; b) D. L. Caulder, K. N. Raymond, *Acc. Chem. Res.* **1999**, *32*, 975–982; c) S. Leininger, B. Olenyuk, P. J. Stang, *Chem. Rev.* **2000**, *100*, 853–907; d) R. W. Saalfrank, E. Uller, B. Demleitner, I. Bernt, *Struct. Bonding (Berlin)* **2000**, *96*, 149–175; e) M. Fujita, K. Umemoto, M. Yoshizawa, N. Fujita, T. Kusukawa, K. Biradha, *Chem. Commun.* **2001**, 509–518; f) B. J. Holliday, C. A. Mirkin, *Angew. Chem. Int. Ed.* **2001**, *40*, 2022–2043; g) G. F. Swiegers, T. J. Malefeste, *Chem. Eur. J.* **2001**, *7*, 3636–3643; h) F. A. Cotton, C. Lin, C. A. Murillo, *Acc. Chem. Res.* **2001**, *34*, 759–771.

[3] a) A. Hori, K. Kumazawa, T. Kusukawa, D. K. Chand, M. Fujita, S. Sakamoto, K. Yamaguchi, *Chem. Eur. J.* **2001**, *7*, 4142–4149; b) R. W. Saalfrank, H. Glaser, B. Demleitner, F. Hamplel, M. M. Chowdhry, V. Schünemann, A. X. Trautwein, G. B. M. Vaughan, R. Yeh, A. V. Davis, K. N. Raymond, *Chem. Eur. J.* **2002**, *8*, 493–497; c) Y. Kubota, S. Sakamoto, K. Yamaguchi, M. Fujita, *Proc. Natl. Acad. Sci. USA* **2002**, *99*, 4854.

[4] a) M. Fujita, O. Sasaki, T. Mitsuhashi, T. Fujita, J. Yazaki, K. Yamaguchi, K. Ogura, *Chem. Commun.* **1996**, 1535; b) T. Beissel, R. E. Powers, T. N. Parac, K. N. Raymond, *J. Am. Chem. Soc.* **1999**, *121*, 4200; c) M. Albrecht, M. Napp, M. Schneider, P. Weis, R. Frohlich, *Chem. Commun.* **2001**, 409; d) A. Sautter, D. G. Schmid, G. Jung, F. Wuerthner, *J. Am. Chem. Soc.* **2001**, *123*, 5424; e) R. W. Saalfrank, B. Demleitner, H. Glaser, H. Maid, D. Bathelt, F. Hamplel, W. Bauer, M. Teichert, *Chem. Eur. J.* **2002**, *8*, 2679–2683; f) T. Yamamoto, A. M. Arif, P. J. Stang, *J. Am. Chem. Soc.* **2003**, *125*, 12309–12317.

[5] a) S. Anderson, H. L. Anderson, J. K. M. Sanders, *Acc. Chem. Res.* **1993**, *26*, 469–475; b) M. Fujita, S. Nagao, K. Ogura, *J. Am. Chem. Soc.* **1995**, *117*, 1649–1650; c) A. Bilyk, M. M. Harding, *J. Chem. Soc., Chem. Commun.* **1995**, 1697–1698; d) B. Hasenknopf, J.-M. Lehn, N. Boumediene, A. Dupont-Gervais, A. van Dorsselaer, B. O. Kneisel, D. Fenske, *J. Am. Chem. Soc.* **1997**, *119*, 10956–10962; e) K. Umemoto, K. Yamaguchi, M. Fujita, *J. Am. Chem. Soc.* **2000**, *122*, 7150–7151; f) Y. Yamanoi, Y. Sakamoto, T. Kusukawa, M. Fujita, S. Sakamoto, K. Yamaguchi, *J. Am. Chem. Soc.* **2001**, *123*, 980–981.

[6] a) D. A. McMorran, P. J. Steel, *Angew. Chem. Int. Ed.* **1998**, *37*, 3295–3297; b) D. K. Chand, K. Biradha, M. Fujita, *Chem. Commun.* **2001**, 1652–1653; c) H. Liu, X. Tong, *Chem. Commun.* **2002**, 1316–1317; d) D. K. Chand, K. Biradha, M. Fujita, S. Sakamoto, K. Yamaguchi, *Chem. Commun.* **2002**, 2486–2487; e) D. K. Chand, M. Fujita, K. Biradha, S. Sakamoto, K. Yamaguchi, *Dalton Trans.* **2003**, 2750–2756; f) M. Tominaga, K. Suzuki, M. Kawano, T. Kusukawa, T. Ozeki, S. Sakamoto, K. Yamaguchi, M. Fujita, *Angew. Chem. Int. Ed.* **2004**, *43*, 5621–5625; g) N. L. S. Yue, D. J. Eisler, M. C. Jennings, R. J. Puddephatt, *Inorg. Chem.* **2004**, *43*, 7671–7678; h) M. Tominaga, T. Kusukawa, S. Sakamoto, K. Yamaguchi, M. Fujita, *Chem. Lett.* **2004**, *33*, 794–795; i) A. Hori, K. Yamashita, T. Kusukawa, A. Akasaka, K. Biradha, M. Fujita, *Chem. Commun.* **2004**, 1798–1799.

[7] At higher temperatures, e.g., 120 °C, the process is faster and sometimes causes decomposition on prolonged heating. At lower temperatures, e.g., 60 °C, the process is slow, and hence more time is required for the study.

[8] L. V. Popov, N. N. Zheligovskaya, A. M. Grevtsev, E. A. Kharina, V. I. Spitsyn, *Izv. Akad. Nauk. SSSR Ser. Khim.* **1977**, 1677–1679.

[9] However, the M_3L_2 compositional assembly $[\{Pd(en)\}_3(\mathbf{2})_2](NO_3)_6$ (**9**) could be obtained exclusively in aqueous solution

 © 2005 Wiley-VCH Verlag GmbH & Co. KGaA, Weinheim

by using a suitable template, e.g., 4-methoxyphenyl acetate, as described in ref.[5b].

[10] When ligand **2** was treated with $Pt(NO_3)_2$ and heated at 90 °C for 10 min, it gave a complicated mixture, unlike the complexation of **2** with $Pd(NO_3)_2$. The suitable conditions for achieving $[(Pt)_6(\mathbf{2})_8](NO_3)_{12}$ from **2** and $Pt(NO_3)_2$ were found to be heating at 120 °C for 24 h.

[11] Substitution on Pd^{II} center shows 10^5-fold greater reactivity compared to Pt^{II}. See *Comprehensive Coordination Chemistry: The Synthesis, Reactions, Properties and Applications of Coordination Compounds*, *Volume 1* (Eds.: G. Wilkinson, R. D. Gillard, J. A. McCleverty), Pergamon, Oxford, **1987**, p. 311.

Received: March 2, 2005
Published Online: July 6, 2005

 © 2005 Wiley-VCH Verlag GmbH & Co. KGaA, Weinheim

Atom Transfer Radical Additions with the Cationic Half-Sandwich Complex $[Cp^*Ru(PPh_3)_2(CH_3CN)]OTf$

Laurent Quebatte,[a] Rosario Scopelliti,[a][‡] and Kay Severin*[a]

Keywords: ATRA reaction / Homogeneous catalysis / Radical reaction / Ruthenium

The cationic ruthenium half-sandwich complex $[Cp^*Ru(PPh_3)_2(CH_3CN)][OTf]$ (**2**) ($Cp^* = \eta^5$-C_5Me_5, OTf = SO_3CF_3) was synthesized by reduction of $[Cp^*RuCl_2]_2$ with zinc in the presence of NaOTf and subsequent reaction with PPh_3. When NaOTf was omitted, the corresponding tetrachlorozincate salts were obtained. Complex **2**, as well as the salts $[Cp^*Ru(CH_3CN)_3]_2[ZnCl_4]$ (**3**) and $[Cp^*Ru(PPh_3)_2(CH_3CN)]_2[ZnCl_4]$ (**4**), were characterized by single-crystal X-ray analysis. Complex **2** proved to be a potent catalyst for the atom transfer radical addition of CCl_4 and $CHCl_3$ to terminal olefins, displaying a performance superior to that of the previously described neutral catalyst $[Cp^*RuCl(PPh_3)_2]$. For the addition of $CHCl_3$ to styrene, a total turnover number of 890 was achieved.
(© Wiley-VCH Verlag GmbH & Co. KGaA, 69451 Weinheim, Germany, 2005)

Introduction

The atom transfer radical addition (ATRA) of polyhalogenated compounds to olefins ("Kharasch reaction")[1] is a versatile method for C–C bond formation and has found several applications in organic synthesis.[2] In 1973, it was reported that the complex $[RuCl_2(PPh_3)_3]$ is able to efficiently catalyze this type of reaction and it was subsequently used as the catalyst of choice for more than 20 years.[3] Over the last 6 years, however, several new ruthenium-based catalysts with superior performance have been reported.[4] Among these, the complex $[Cp^*RuCl(PPh_3)_2]$ (**1**) is of special interest since it is one of the few catalysts, which allows to carry out the addition of CCl_4 and $CHCl_3$ to olefins at ambient temperatures.[5,6] Despite its high activity, complex **1** suffers from poor long term stability, a characteristic shared by many other highly active catalysts for the Kharasch reaction.[4]

Nagashima et al. have reported that the ATRA activity of the dinuclear complex $[Cp^*Ru\{\mu_2$-*i*PrN=C(Me)-N*i*Pr$\}RuClCp^*]$ could be increased by transforming it into a cationic species using $NaPF_6$ or $NaBPh_4$.[7] Similarly, the activity of ruthenium chloro catalysts for the closely related atom transfer radical polymerization (ATRP)[8] could be enhanced by chloride abstraction with silver salts.[9] For Ru vinylidene catalysts, on the other hand, it was reported that the abstraction of a chloro ligand lead to a decrease in ATRA activity.[10] In the following we show that the cationic complex $[Cp^*Ru(PPh_3)_2(CH_3CN)][OTf]$ (**2**) is a very potent catalyst for ATRA reactions. Its stability is significantly higher than that of the neutral counterpart **1**. Consequently, good turnover numbers (TONs) were observed, even for "difficult" reactions such as the addition of $CHCl_3$ to styrene.

Results and Discussion

Cationic complexes of the general formula $[Cp^*Ru(PR_3)_2(CH_3CN)]X$ (X^- = weakly coordinating anion) have been obtained by reaction of complex **1** with MX in acetonitrile ($M^+ = Ag^+$, NH_4^+)[11] or by reaction of $[Cp^*Ru(CH_3CN)_3]X$ with PR_3 in CH_2Cl_2 (Scheme 1).[12] For the synthesis of the complex $[Cp^*Ru(PPh_3)_2(CH_3CN)][OTf]$ (**2**), we decided to use the latter pathway since the trisacetonitrile complex $[Cp^*Ru(CH_3CN)_3]X$ is easily accessible by reduction of $[Cp^*RhCl_2]_n$ with zinc in acetonitrile in the presence of MX salts.[12]

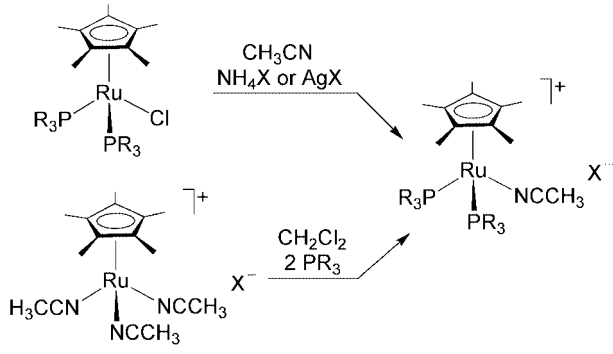

Scheme 1. Synthesis of cationic complexes of the general formula $[Cp^*Ru(PR_3)_2(CH_3CN)]X$ (X^- = weakly coordinating anion).

Following this synthetic route it was possible to prepare the cationic complex **2** in 95% yield by reaction of

[a] Institut de Sciences et Ingénierie Chimiques, École Polytechnique Fédérale de Lausanne (EPFL)
1015 Lausanne, Switzerland
Fax: +41-21-693-9305
E-mail: kay.severin@epfl.ch
[‡] X-ray structural analysis.

 DOI: 10.1002/ejic.200500321 © 2005 Wiley-VCH Verlag GmbH & Co. KGaA, Weinheim

$[Cp^*RuCl_2]_2$ with zinc in acetonitrile in the presence of NaOTf and direct conversion of the product with two equivalents of PPh_3 (Scheme 2). Complex **2** displays a good solubility in polar organic solvents such as THF, dichloromethane and chloroform, and a moderate solubility in toluene. The identity of **2** was confirmed by NMR spectroscopy, elemental analysis and single-crystal X-ray analysis (Figure 1).

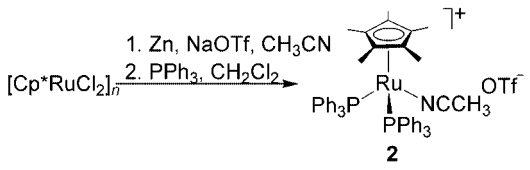

Scheme 2. Synthesis of complex **2**.

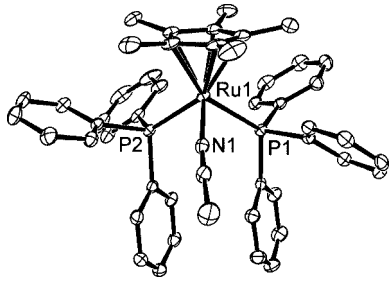

Figure 1. ORTEP[22] drawing of the molecular structure of **2** in the crystal. The OTf^- anion and the hydrogen atoms are omitted for clarity. Selected bond lengths [Å] and angles [°]: Ru1–N1 2.056(2), Ru1–P1 2.3709(6), Ru1–P2 2.3462(7); P2–Ru1–P1 99.41(2), N1–Ru1–P1 87.97(5), N1–Ru1–P2 87.95(6).

The cation of complex **2** displays the expected pianostool geometry. As a consequence of the steric demand of the triphenylphosphane ligands, the P–Ru–P angle [99.41(2)°] is larger than the N–Ru–P angles [N1–Ru1–P1 87.97(5)°; N1–Ru1–P2 87.95(6)°]. The Ru–P bond lengths [Ru1–P1 2.3709(6) Å, Ru1–P2 2.3462(7) Å] are similar to what has been found for the neutral complex **1**.[13]

In order to investigate the influence of the NaOTf salt during the synthesis of complex **2**, we have performed the reduction of $[Cp^*RuCl_2]_2$ with zinc in acetonitrile in the absence of this salt. The formation of a trisacetonitrile complex $[Cp^*Ru(CH_3CN)_3]^+$ (**3**) was observed but as the counterion, the tetrachlorozincate anion was formed as revealed by single-crystal X-ray analysis (Scheme 3, Figure 2). Complex **3** proved to be not suited for a clean synthesis of a bis(triphenylphosphane) adduct: when two equivalents of PPh_3 were added to a solution of **3** in CD_2Cl_2, the desired cationic bisadduct **4** was formed but along with the neutral complex **1**, the monoadduct **5**,[14,15] and free PPh_3 as evidenced by ^1H and ^{31}P NMR spectroscopy. From this mixture, it was possible to obtain single crystals of complex **4** by addition of pentane. A graphic representation of the structure of **4** is depicted in Figure 3.

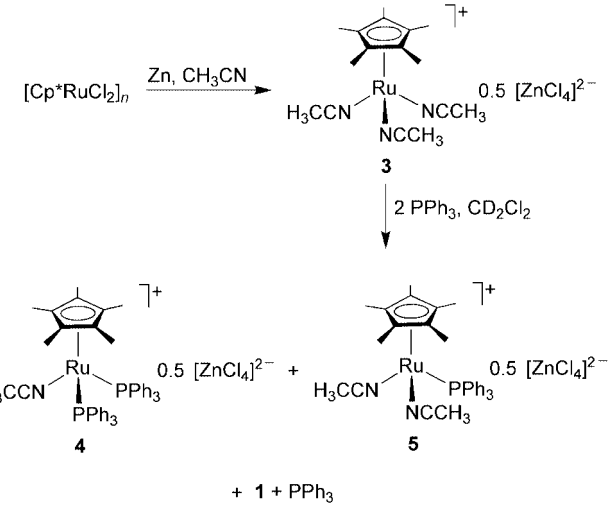

Scheme 3. Synthesis of the tetrachlorozincate complex **3** and its reaction with PPh_3.

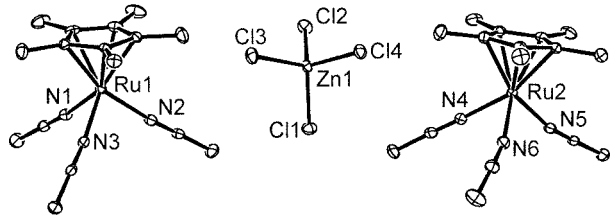

Figure 2. ORTEP[13] drawing of the molecular structure of **3** in the crystal. The hydrogen atoms are omitted for clarity. Selected bond lengths [Å] and angles [°]: Ru1–N1 2.095(2), Ru1–N2 2.108(2), Ru1–N3 2.103(2), Ru2–N4 2.110(2), Ru2–N5 2.102(2), Ru2–N6 2.109(2); N1–Ru1–N2 88.19(8), N1–Ru1–N3 84.67(8), N3–Ru1–N2 90.60(7), N5–Ru2–N4 90.84(8), N5–Ru2–N6 91.66(8), N–Ru2–N4 81.76(8).

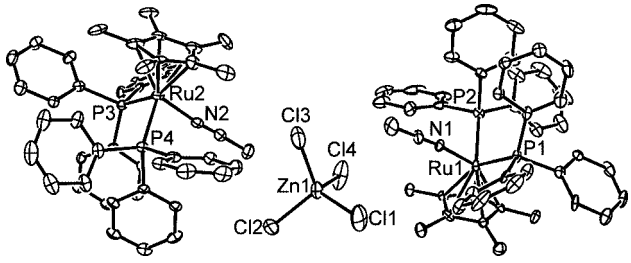

Figure 3. ORTEP[13] drawing of the molecular structure of **4** in the crystal. The hydrogen atoms and the solvent molecules ($3\times CH_2Cl_2$) are omitted for clarity. Selected bond lengths [Å] and angles [°]:Ru1–N1 2.037(6), Ru1–P1 2.3568(19), Ru1–P2 2.343(2), Ru2–N2 2.061(7), Ru2–P3 2.3556(19), Ru2–P4 2.346(2); N1–Ru1–P1 87.44(16), N1–Ru1–P2 88.12(18), P2–Ru1–P1 99.00(7), N2–Ru2–P4 89.28(18), N2–Ru2–P3 90.17(17), P4–Ru2–P3 97.19(7).

The bond lengths and angles found for the two crytallographically independent cations of complex **3** are very similar to those observed for other $[Cp^*Ru(CH_3CN)_3]^+$ complexes.[16] The N–Ru–N angles are close to 90°. The geometry of the cations can thus be described as pseudo-octahe-

 © 2005 Wiley-VCH Verlag GmbH & Co. KGaA, Weinheim

dral with the Cp* ligand occupying three facial coordination sites. As it was observed for complex **2**, the P–Ru–P angles of **4** [99.00(7) and 97.19(7)°] are larger than the P–Ru–N angles [P–Ru–N 87.44(16)–90.17(17)°].

To evaluate the ability of the cationic complex **2** to catalyze ATRA reactions, we first investigated the addition of CCl_4 to styrene at 60 °C using a molar ratio of **2**/styrene/CCl_4 = 1:300:432. The complete conversion of the olefin was observed within 2 h. For the neutral complex **1**, a conversion of 97% was reported after 5 h.[5] In order to obtain more information about differences in activity and stability of the catalysts **1** and **2**, we have investigated the time course of the reaction between styrene and CCl_4 at room temperature in chloroform with a molar ratio of Ru/styrene/CCl_4 = 1:300:600 (Figure 4). For reactions with the cationic catalyst **2**, a quantitative reaction was observed after ca. 4 h. For reactions catalyzed by the neutral complex **1**, on the other hand, a very fast product formation was found for the first 20 min, but then the rates dropped dramatically and the conversion reached a plateau at around 40%. When the solvent was changed to toluene and the CCl_4 concentration was reduced, an increased lifetime of the catalyst was observed but still the final conversion (60%) was lower than what was found for **2**. This data suggested that the neutral catalyst **1** shows a higher intrinsic activity than the cationic complex **2** but a significantly lower stability. This is in agreement with the observation of Simal et al. that complex **1** rapidly decomposed in presence of CCl_4: when 10 equivalents of CCl_4 were added to a solution of **1** in toluene at 20 °C, the complete conversion into a paramagnetic Ru^{III} compound occurred within 2 h.[5] When a similar experiment was performed with the cationic complex **2**, only 40% decomposition was observed after 2 h. For complex **1** it was suggested that PPh_3 dissociation is required to activate the catalyst.[5] This step is likely to be faster for the neutral complex **1** as compared to the cationic complex **2**, which may explain the higher initial activity of the former. The higher stability of the cationic complex **2**, on the other hand, may be due to a different activity of the Ru^{III} species formed by atom transfer but further investigations are needed to clarify this point.

The good performance of the cationic catalyst **2** was confirmed in other ATRA reactions (Table 1). As mentioned above, the reaction between styrene and CCl_4 could be completed within 5 h using 0.33 mol% of complex **2** at room temperature (entry 1). Using only 0.02 mol% catalyst, a total TON of 3050 was measured after 5 weeks.[17] A remarkably fast and clean reaction was observed with methyl methacrylate (MMA) and CCl_4 as the substrates (entry 2). After 2 h at room temperature, a yield of 93% was obtained. For the neutral catalyst **1**, for comparison, a yield of only 36% was found after 24 h.[5] The olefins *n*-butyl acrylate (entry 3) and 1-decene (entry 4) gave lower yields of 67 and 77%, respectively. For the former substrate, this was due to competing oligomerization reactions.

In order to perform ATRA reactions with the significantly less active substrate $CHCl_3$, the reaction temperature was increased to 40 °C and a catalyst concentration of 1 mol% was employed (entries 5–9). Under these conditions, catalyst **2** provided the chloroform adducts of the aromatic olefins styrene, *p*-chlorostyrene, and *p*-methoxystyrene with good yields (entries 5–7). A TON of 890 was obtained for the addition of $CHCl_3$ to styrene using 0.1 mol% of complex **2**. This is – to the best of our knowledge – the highest value ever reported for a ruthenium-based catalyst. For acrylate substrates, almost complete conversions were determined after 24 h. The yields of the desired addition products, however, were very modest due to competing polymerization reactions (entries 8 and 9).

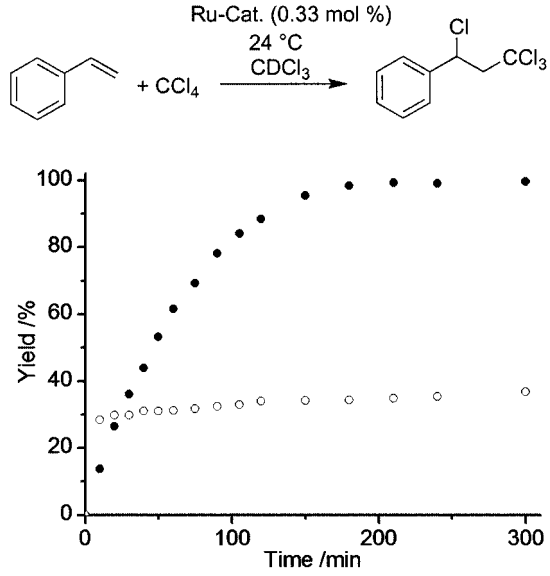

Figure 4. Time course of the reaction between styrene and CCl_4 catalyzed by complexes **1** (○) or **2** (●). Reaction conditions: Ru/styrene/CCl_4 = 1:300:600; solvent = $CDCl_3$; [Ru] = 4.6 mM; 24 °C. The yield is based on the formation of the product as determined by ^1H NMR spectroscopy.

Table 1. ATRA reactions catalyzed by complex **2**.[a]

Entry	Olefin	$CXCl_3$	*T* [°C]	*t* [h]	Conv. [%]	Yield [%]
1	styrene	CCl_4	24	5	100	97
2	methyl methacrylate	CCl_4	24	2	100	93
3	*n*-butyl acrylate	CCl_4	24	10	98	67
4	1-decene	CCl_4	40	24	80	77
5	styrene	$CHCl_3$	40	24	96	88
6	*p*-chlorostyrene	$CHCl_3$	40	48	95	92
7	*p*-methoxystyrene	$CHCl_3$	40	48	96	90
8	methyl methacrylate	$CHCl_3$	40	24	96	33
9	*n*-butyl acrylate	$CHCl_3$	40	24	99	15

[a] Reaction conditions: **2**/olefin/CCl_4 = 1:300:600, [**2**] = 4.6 mM, solvent: $CHCl_3$ or **2**/olefin/$CHCl_3$ = 1:100, [**2**] = 13.8 mM, solvent = $CHCl_3$. The conversion is based on the consumption of the olefin and the yield is based on the formation of the product as determined by GC or ^1H NMR spectroscopy after the time given.

Conclusions

Over the last few years, several highly active ruthenium-based catalysts for ATRA reactions have been described.[4]

 © 2005 Wiley-VCH Verlag GmbH & Co. KGaA, Weinheim

These catalysts allow to perform Kharasch reactions under very mild conditions with few side products. But still, there are some important challenges that need to be addressed by future research in this area. First of all, the mechanistic understanding of ruthenium-catalyzed ATRA reactions is rudimentary which hampers a more rational approach towards catalyst discovery (e.g. stereoselective catalysts) and optimization. Furthermore, catalyst stability is a problem for several of the newly developed complexes and apart from optimizing the reaction conditions (temperature, concentrations etc.), solutions to this dilemma are not evident. The results described above demonstrate that a simple modification such as the conversion of a chloro complex into a cationic acetonitrile complex may result in a significantly increased catalyst stability. Although it remains to be seen whether similar effects can be observed for other catalysts, it seems worthwhile to consider modifications of this type in future investigations.

Experimental Section

General: All reactions were performed under a dry dinitrogen atmosphere. The solvents and substrates were distilled from appropriate drying agents and stored under dinitrogen. Zn dust (< 10 micron; 98+%) was obtained from Aldrich, NaOTf (97+%) and PPh_3 (98.5+%) were obtained from Fluka. The complexes $[Cp^*RuCl_2]_2$[18] and $[Cp^*RuCl(PPh_3)_2]$[19] were prepared according to literature procedures. The ^1H, ^{13}C, and ^{31}P NMR spectra were recorded on a Bruker Advance DPX 400 spectrometer with the solvents as internal standards (^1H, ^{13}C) or a solution of H_3PO_4 in D_2O as external standard (^{31}P). All spectra were recorded at room temperature. GC-MS analyses were performed with a WCOT Fused Silica column (30 m) coupled to a Varian Saturn 2200 mass spectrometer.

Synthesis of Complex 2: Zn (0.2 g, 3.1 mmol) and NaOTf (84 mg, 488 μmol) were added to a solution of $[Cp^*RuCl_2]_2$ (100 mg, 162 μmol) in CH_3CN (5 mL) and the mixture was stirred for 2 h at room temperature. The yellow solution was filtered and the remaining Zn was washed with additional solvent (2 × 3 mL). After evaporation of the solvent, the resulting powder was dissolved in CH_2Cl_2 (5 mL), filtered, and the filtrate was washed with additional CH_2Cl_2 (2 × 3 mL). PPh_3 (256 mg, 976 μmol) was added to the combined solutions whilst stirring. After for 20 min, the mixture was concentrated to 2 mL and poured into a flask containing hexane (15 mL) to precipitate the product as a yellow powder, which was isolated by filtration, washed with hexane (2 × 3 mL), and dried under vacuum. Yield: 294 mg (95%). Single crystals were obtained by diffusion of pentane into a solution of **2** in CH_2Cl_2. ^1H NMR (400 MHz, CD_2Cl_2): δ = 1.13 (t, $^4J_{H,P}$ = 1.6 Hz, 15 H, Cp*), 2.65 (t, $^5J_{H,P}$ = 0.6 Hz, 3 H, CH_3CN), 7.13–7.46 (m, 30 H, Ph) ppm. ^{13}C NMR (101 MHz, CD_2Cl_2): δ = 5.9 (CH_3CN), 9.7 (CH_3, Cp*), 93.1 (C, Cp*), 128.2–134.2 (Ph), 129.3 (CH_3CN) ppm. ^{31}P NMR (162 MHz, CD_2Cl_2): δ = 42.20 ppm. Elemental analysis: calcd. (%) for $C_{49}H_{48}F_3NO_3P_2RuS \times H_2O$ (969.0): C 60.73, H 5.20, N 1.45; found C 60.84, H 5.17, N 1.56.

Synthesis of Complex 3: A solution of $[Cp^*RuCl_2]_2$ (736 mg, 1196 μmol) in CH_3CN (35 mL) was added Zn (5.0 g, 76.5 mmol) and stirred for 5 h at room temperature. The initial dark brown color changed to bright yellow. The solution was filtered and the remaining Zn was washed with additional solvent (15 mL). After evaporation of the solvent under vacuum, the resulting powder was suspended in Et_2O (15 mL), isolated by filtration, washed with additional Et_2O (15 mL) and dried under vacuum. Yield: 1030 mg (93%). Single crystals were obtained by slow diffusion of Et_2O into a solution of **3** in CH_3CN. ^1H NMR (400 MHz, CD_3CN): δ = 1.59 (s, 15 H, Cp*) ppm. ^{13}C NMR (101 MHz, CD_3CN): δ = 9.7 (CH_3, Cp*), 80.6 (C, Cp*) ppm. Elemental analysis: calcd. (%) for $C_{32}H_{48}Cl_4N_6Ru_2Zn \times 3/4\ CH_3CN$ (956.9): C 42.05, H 5.29, N 9.88; found: C 42.36, H 5.36, N 9.47.

Reaction of Complex 3 with PPh_3: PPh_3 (5.7 mg, 21.7 μmol) was added to a solution of complex **3** (5.0 mg, 5.4 μmol) in CD_2Cl_2 (500 μL). The resulting bright orange solution was analyzed by ^1H and ^{31}P NMR spectroscopy. Single crystals of **4** were obtained by slow diffusion of pentane into the reaction mixture. NMR [400 (^1H), 162 (^{31}P) MHz, aromatic protons, free CH_3CN and PPh_3 are omitted]: **4:** ^1H: δ = 1.13 (t, $^4J_{H,P}$ = 1.6 Hz, 15 H, Cp*), 2.87 (t, $^5J_{H,P}$ = 1.4 Hz, 3 H, CH_3CN) ppm. ^{31}P: δ = 43.0 ppm. **1:** ^1H: δ = 1.01 (t, $^4J_{H,P}$ = 1.4 Hz, 15 H, Cp*) ppm. ^{31}P: δ = 41.0 ppm. **5:** ^1H: δ = 1.42 (d, $^4J_{H,P}$ = 1.6 Hz, 15 H, Cp*), 2.22 (d, $^5J_{H,P}$ = 1.2 Hz, 6 H, CH_3CN) ppm. ^{31}P: δ = 48.9 ppm.

General Procedure for the ATRA of CCl_4 to Olefins: 1000 μL of a $CDCl_3$ stock solution of the olefin, CCl_4, and the internal standard mesitylene were added to a 1.5 mL vial containing the solid catalyst **2** (final conc.: [**2**] = 4.6 mM, [olefin] = 1.38 M, [CCl_4] = 2.76 M, [mesitylene] = 0.36 M). For 1-decene, the resulting solution was placed in an oil bath tempered at 40 °C. After the given time, a sample (20 μL) was removed from the reaction mixture, diluted with $CDCl_3$ (550 μL) and analyzed by ^1H NMR spectroscopy or gas chromatography. The kinetic experiments were performed in an analogous fashion by removing several samples at regular time intervals.

General Procedure for the ATRA of $CHCl_3$ to Olefins: 500 μL of a $CDCl_3$ stock solution of the olefin and the internal standard mesitylene were added to a 1.5 mL vial containing the solid catalyst **2** (final conc.: [**2**] = 13.8 mM, [olefin] = 1.38 M, [mesitylene] = 0.36 M). The resulting solution was placed in an oil bath tempered at 40 °C. After the given time, a sample (20 μL) was removed from the reaction mixture, diluted with $CDCl_3$ (550 μL) and analyzed by ^1H NMR spectroscopy or gas chromatography.

Decomposition Experiment: Complex **2** (2.8 mg, 2.9 μmol) and CCl_4 (2.9 μL, 30.1 μmol) were dissolved in CD_2Cl_2 (500 μL). The reaction followed by ^1H and ^{31}P NMR (400 and 162 MHz, respectively) for 10 h at 21 °C.

X-ray Crystallography: Details about the crystals and their structure refinement are listed in Table 2 and Table 3 whereas some relevant geometrical parameters are included into the picture captions. Data collection were performed at 140(2) K on a 4-circle goniometer having kappa geometry and equipped with an Oxford Diffraction KM4 Sapphire CCD. Data reduction was carried out with CrysAlis RED, release 1.7.0.[20] Absorption correction has been applied to all data sets. Structure solution and refinement were performed with the SHELXTL software package, release 5.1.[21] The structures were refined using the full-matrix least-squares on F^2 with all non-H atoms anisotropically defined. H atoms were placed in calculated positions using the "riding model". CCDC-268907–268909 contain the supplementary crystallographic data for this paper. These data can be obtained free of charge from The Cambridge Crystallographic Data Centre via www.ccdc.cam.ac.uk/data_request/cif.

 © 2005 Wiley-VCH Verlag GmbH & Co. KGaA, Weinheim

Table 2. Crystallographic data for the complexes **2** and **3**.

	2	**3**
Empirical formula	$C_{49}H_{48}F_3NO_3P_2RuS$	$C_{32}H_{48}Cl_4N_6Ru_2Zn$
Molecular weight [g mol^{-1}]	950.95	926.07
Crystal size	0.16 × 0.13 × 0.11	0.18 × 0.13 × 0.09
Crystal system	triclinic	triclinic
Space group	$P\bar{1}$	$P\bar{1}$
a [Å]	10.5409(4)	9.3648(4)
b [Å]	13.3793(7)	12.9800(8)
c [Å]	16.2230(9)	18.3753(10)
α [°]	88.977(4)	72.891(5)
β [°]	86.567(4)	88.514(4)
γ [°]	75.659(4)	72.566(5)
Volume [Å^3]	2212.64(18)	2031.94(18)
Z	2	2
Density [g cm^{-3}]	1.427	1.514
Temperature [K]	140(2)	140(2)
Absorption coefficient [mm^{-1}]	0.529	1.611
Θ range [°]	3.12 to 25.03	3.15 to 25.03
Index ranges	–10 → 10, –15 → 15, –19 → 19	–10 → 11, –15 → 15, –21 → 20
Reflections collected	13077	12149
Independent reflections	6823 (R_{int} = 0.0200)	6273 (R_{int} = 0.0225)
Absorption correction	semi-empirical	empirical
Max. and min. transmission	0.9638 and 0.8015	0.887 and 0.620
Data/restraints/parameters	6823/0/541	6273/0/406
Goodness-of-fit on F^2	1.044	0.985
Final R indices [$I > 2\sigma(I)$]	R_1 = 0.0307, wR_2 = 0.0799	R_1 = 0.0219, wR_2 = 0.0567
R indices (all data)	R_1 = 0.0340, wR_2 = 0.0822	R_1 = 0.0265, wR_2 = 0.0581
Largest diff. peak/hole [e·Å^{-3}]	0.653 and –0.810	0.466 and –0.675

Table 3. Crystallographic data for the complex **4**.

	4 × 3CH_2Cl_2
Empirical formula	$C_{99}H_{102}Cl_{10}N_2P_4Ru_2Zn$
Molecular weight [g mol^{-1}]	2065.72
Crystal size	0.22 × 0.20 × 0.11
Crystal system	monoclinic
Space group	$P2_1$
a [Å]	10.6258(4)
b [Å]	21.7283(11)
c [Å]	20.4384(11)
α [°]	90
β [°]	90.815(4)
γ [°]	90
Volume [Å^3]	4718.3(4)
Z	2
Density [g cm^{-3}]	1.454
Temperature [K]	140(2)
Absorption coefficient [mm^{-1}]	0.966
Θ range [°]	2.99 to 25.03
Index ranges	–11 → 10, –25 → 25, –24 → 24
Reflections collected	27665
Independent reflections	15206 (R_{int} = 0.0498)
Absorption correction	empirical
Max. and min. transmission	0.823 and 0.458
Data/restraints/parameters	15206/1/1063
Goodness-of-fit on F^2	0.923
Final R indices [$I > 2\sigma(I)$]	R_1 = 0.0517, wR_2 = 0.1063
R indices (all data)	R_1 = 0.0715, wR_2 = 0.1135
Largest diff. peak/hole [e·Å^{-3}]	1.158 and –0.707

Acknowledgments

We gratefully acknowledge support by the Swiss National Science Foundation and by the EPFL.

[1] M. S. Kharasch, E. V. Jensen, W. H. Urry, *Science* **1945**, *102*, 128.
[2] a) F. Minisci, *Acc. Chem. Res.* **1975**, *8*, 165; b) J. Iqbal, B. Bhatia, N. K. Nayyar, *Chem. Rev.* **1994**, *94*, 519.
[3] H. Matsumoto, T. Nakano, Y. Nagai, *Tetrahedron Lett.* **1973**, *14*, 5147.
[4] For reviews see: a) L. Delaude, A. Demonceau, A. F. Noels, *Top. Organomet. Chem.* **2004**, *7*, 155; b) K. Severin, *Curr. Org. Chem.*, in press.
[5] a) F. Simal, L. Wlodarczak, A. Demonceau, A. F. Noels, *Tetrahedron Lett.* **2000**, *41*, 6071; b) F. Simal, L. Wlodarczak, A. Demonceau, A. F. Noels, *Eur. J. Org. Chem.* **2001**, *14*, 2689.
[6] For other complexes, which catalyze ATRA reactions under mild conditions see a) L. Quebatte, E. Solaris, R. Scopelliti, K. Severin, *Organometallics* **2005**, *24*, 1404; b) L. Quebatte, M. Haas, E. Solari, R. Scopelliti, Q. T. Nguyen, K. Severin, *Angew. Chem. Int. Ed.* **2005**, *44*, 1084; c) L. Quebatte, R. Scopelliti, K. Severin, *Angew. Chem. Int. Ed.* **2004**, *43*, 1520; d) O. Tutusaus, S. Delfosse, A. Demonceau, A. F. Noels, C. Vinas, F. Teixidor, *Tetrahedron Lett.* **2003**, *44*, 8421; e) O. Tutusaus, C. Vinas, R. Nunez, F. Teixidor, A. Demonceau, S. Delfosse, A. F. Noels, I. Mata, E. Molins, *J. Am. Chem. Soc.* **2003**, *125*, 11830.
[7] Y. Motoyama, M. Gondo, S. Masuda, Y. Iwashita, H. Nagashima, *Chem. Lett.* **2004**, *33*, 442.
[8] M. Kamigaito, T. Ando, M. Sawamoto, *Chem. Rev.* **2001**, *101*, 3689.
[9] a) T. Opstal, F. Verpoort, *New J. Chem.* **2003**, *27*, 257; b) T. Opstal, F. Verpoort, *Angew. Chem. Int. Ed.* **2003**, *42*, 2876; c) B. de Clercq, F. Verpoort, *Macromolecules* **2002**, *35*, 8943.
[10] T. Opstal, F. Verpoort, *Tetrahedron Lett.* **2002**, *43*, 9259.
[11] a) K. S. Singh, P. J. Carroll, M. R. Kollipara, *Polyhedron* **2005**, *24*, 391; b) K. M. Rao, E. K. Rymmai, *Polyhedron* **2003**, *22*, 307; c) R. Torres-Lubián, M. J. Rosales-Hoz, A. M. Arif, R. D. Ernst, M. A. Paz-Sandoval, *J. Organomet. Chem.* **1999**, *585*, 68.
[12] B. Steinmetz, W. A. Schenk, *Organometallics* **1999**, *18*, 943.

 © 2005 Wiley-VCH Verlag GmbH & Co. KGaA, Weinheim

[13] I. A. Guzei, M. A. Paz-Sandoval, R. Torres-Lubian, P. Juarez-Saavedra, *Acta Crystallogr., Sect. C* **1999**, *55*, 1090.
[14] A. A. Zlota, M. Tilset, K. G. Caulton, *Inorg. Chem.* **1993**, *32*, 3816.
[15] When complex **2** is dissolved in CD_3CN, the formation of the monotriphenylphosphane adduct can be observed by NMR spectroscopy.
[16] a) M. J. Burk, A. J. Arduengo III, J. C. Calabresem, R. L. Harlow, *J. Am. Chem. Soc.* **1989**, *111*, 8938; b) C. Gemel, A. LaPensee, K. Mauthner, K. Mereiter, R. Schmid, K. Kirchner, *Monatsh. Chem.* **1997**, *128*, 1189.
[17] Reaction conditions: **2**/styrene/CCl_4 = 1:5000:7500; solvent: [D_8]toluene. [**2**] = 0.28 mM; 24 °C.
[18] U. Koelle, J. Kossakowski, D. Grumbine, T. D. Tilley, *Inorg. Synth.* **1992**, *29*, 225.
[19] M. S. Chinn, D. M. Heinekey, *J. Am. Chem. Soc.* **1990**, *112*, 5166.
[20] Oxford Diffraction Ltd., Abingdon, Oxfordshire, UK, **2003**.
[21] G. M. Sheldrick, University of Göttingen, Germany, **1997**; Bruker AXS, Inc., Madison, Wisconsin, 53719, USA, **1997**.
[22] ORTEP 3 for Windows version 1.076. L. J. Farrugia, *J. Appl. Crystallogr.* **1997**, *30*, 565.

Received: April 18, 2005
Published Online: July 7, 2005

 © 2005 Wiley-VCH Verlag GmbH & Co. KGaA, Weinheim

Synthesis, Crystal Structure, and Magnetic Properties of a Three-Dimensional Hydroxide Sulfate: $Mn_5(OH)_8SO_4$

Yong Fan,[a] Guang Hua Li,[a] Lei Yang,[a] Zhi Ming Zhang,[a] Yan Chen,[a] Tian You Song,*[a] and Shou Hua Feng*[a]

Keywords: Hydroxy sulfate / Hydrothermal synthesis / Magnetic properties / Thermodiffractometry / Structure elucidation

A 3D hydroxysulfate, $Mn_5(OH)_8SO_4$, formed from a mild hydrothermal reaction has been reported. The compound crystallizes in the triclinic system $P\bar{1}$ with cell parameters a = 7.5501(5) Å, b = 8.5558(6) Å, c = 8.6059(5) Å, α = 98.122(4)°, β = 102.370(4)°, γ = 99.646(4)°, V = 526.19(6) Å^3 and Z = 2. The crystal structure consists of a 3D framework with channels along the c-axis. In this structure, the manganese atoms in the distorted pentahedra and octahedra are interconnected by OH groups to form layers along the bc plane. These layers are further connected with MnO_5 distorted pentahedra, MnO_6 octahedra and $[SO4]^{2-}$ tetrahedra, resulting in a complicated network. The temperature dependence of the magnetic susceptibility shows a weak antiferromagnetic interaction in the compound.
(© Wiley-VCH Verlag GmbH & Co. KGaA, 69451 Weinheim, Germany, 2005)

Introduction

Recently, there has been growing interest in the study of structurally and chemically diverse microporous materials, especially those containing transition elements, because they have potential applications as ion exchangers, catalysts, and advanced materials with novel magnetic and electronic properties.[1–8] The discovery of structures with novel topologies and properties is dependent upon creative synthesis from combinations of tetrahedral anions and polyhedrally coordinated transition metal cations.[9–13] In these materials, anions such as phosphates, germanates, and arsenates are often involved as $[TO_4]$ units (T = tetrahedrally coordinated elements) of inorganic frameworks. Frameworks containing sulfate anions have been considerably less investigated, which is surprising since sulfates are known to promote a wide range of structural arrangements in inorganic solids.[14] From the synthetic chemistry point of view, transition-metal sulfates are very difficult to obtain as single crystals by hydrothermal techniques.

Since the pioneering works of Rao et al. some hybrid porous sulfates and inorganic sulfates containing transition elements have been reported. Wang et al. reported a double-chain copper sulfate.[15] Paul et al. recently reported several Kagomé lattices and other types of layered iron and cobalt sulfates.[16–20] S. Vilminot et al. reported a layered cobalt sulfate.[21] M. J. Rosseinsky et al. have also reported several layered cobalt sulfates.[22,23] M. I. Khan et al. reported a layered vanadium sulfate.[24] In most of the previous compounds prepared by hydrothermal techniques, the layers were like modified brucite, having some of the $[MO_6]$ (M = octahedrally coordinated metal element) octahedra replaced by $[TO_4]$ tetrahedra above and below the vacancies, whereas now a truly brucite-type magnetic layered compound has been reported by S. Vilminot et al.[25] There are much fewer 3D compounds reported. Wright et al. reported a 3D scandium sulfate.[26] C. N. R. Rao et al. have reported a 3D nickel sulfate.[27] S Vilminot et al. reported another nickel sulfate.[28] O. Hare et al. have synthesized several uranium sulfates, one of which has a 3D structure.[29–31] Metal sulfates without entrained organic cations also exhibit interesting catalytic, ion-exchange, and magnetic properties, and they have higher thermal stability relative to metal sulfate hybrids.

There is only one manganese sulfate compound, reported by S. Vilminot et al[32], which has a layered structure. Here we report the synthesis and structure of a 3D manganese sulfate, $Mn_5(OH)_8SO_4$, which has the highest metal/sulfur ratio yet reported. It is another member of the well-known basic transition-metal sulfate family.[33–37] The magnetic properties of this compound are also reported. A thermodiffractometric study reveals that the compound has a high thermal stability.

Results and Discussion

Characterization

The ICP analysis of the product shows the wt.-% of Mn and S to be 54.11 and 6.18, respectively, indicating a Mn/S

[a] State Key Laboratory of Inorganic Synthesis and Preparative Chemistry, College of Chemistry, Jilin University, Changchun 130012, P. R. China
Fax: +86-431-5168624
E-mail: shfeng@mail.jlu.edu.cn
Supporting information for this article is available on the WWW under http://www.eurjic.org or from the author.

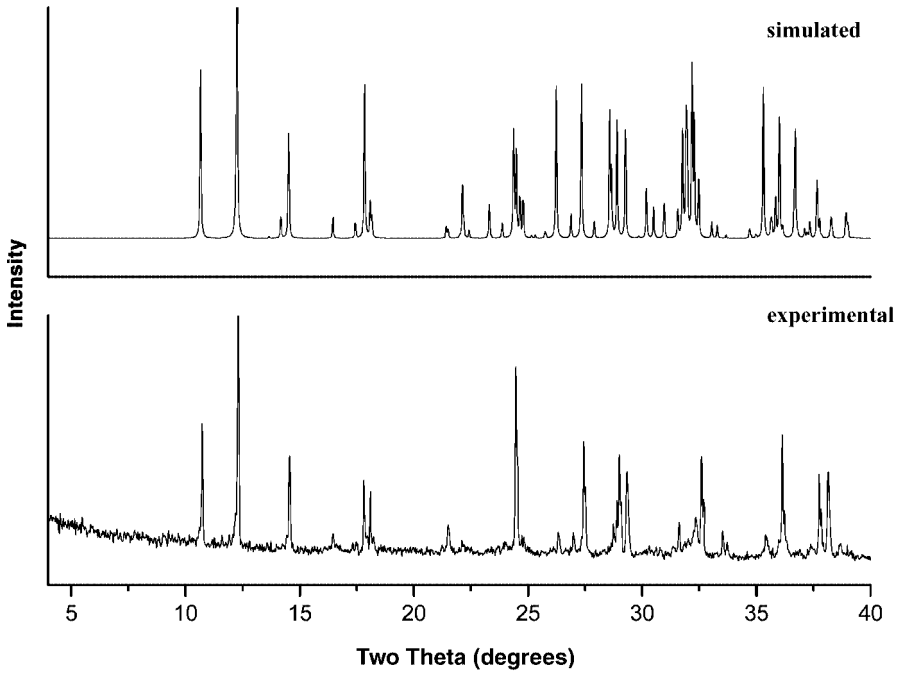

Figure 1. Experimental and simulated powder X-ray diffraction patterns for **1**.

ratio of 5:1, which is in agreement with the experimental wt.-% values of 54.26 and 6.36 based on the ideal formula given by single-crystal X-ray diffraction analysis.

The powder X-ray diffraction pattern was consistent with the simulated one as shown in Figure 1. The positions of the diffraction peaks in both patterns correspond well, which indicates the phase purity of the as-synthesized sample. The difference in reflection intensities between the simulated and experimental patterns was due to the variation in the crystal orientation of the powder sample.

An IR spectrum was recorded between 4000 and 400 cm^{-1} (Figure S2, Supporting Information; for Supporting Information see also the footnote on the first page of this article). The series of sharp bands in the 3635–3430-cm^{-1} and the 850–650-cm^{-1} regions are attributed to O–H. The typical vibrational bands of SO_4^{2-} are observed in the 1150–590-cm^{-1} range. The ν_3 and ν_4 vibrational bands of the sulfate group appear at 1150–1045 cm^{-1} and 650–590 cm^{-1}, respectively. The bands centered at 916 cm^{-1} are attributed to ν_1 vibrational bands of the sulfate group. The bands centered at 470 cm^{-1} and 425 cm^{-1} are attributed to O–Mn vibrations.

The combined thermogravimetric analysis-differential thermal analysis (TGA-DTA) of $Mn_5(OH)_8SO_4$ was carried out in air from room temperature to 900 °C by using a heating rate of 10 °C·min^{-1} and is shown in Figure 2. The results show three mass losses, two sharp and one broad. The first mass loss of about 10.9%, occurring in the region 198–362 °C, with a strong endotherm centered at 299 °C, corresponds to the loss of three H_2O groups (calcd. 10.7%) from six OH groups. The second mass loss of 3.9%, in the region 362–571 °C, corresponds to the loss of one H_2O from two OH groups (calcd. 3.6%). Two weak exotherms, centered at 336 °C and 381 °C, indicate structural changes. After that there is a slight weight gain starting at 571 °C, three weak exotherms centered at 542 °C, 597 °C, and 647 °C, indicating that some of the Mn^{II} ions have been oxidized. However, it is difficult to determine this weight gain accurately, as this process overlaps slightly with the weight loss due to the decomposition of the SO_4^{2-} fraction. Decomposition of

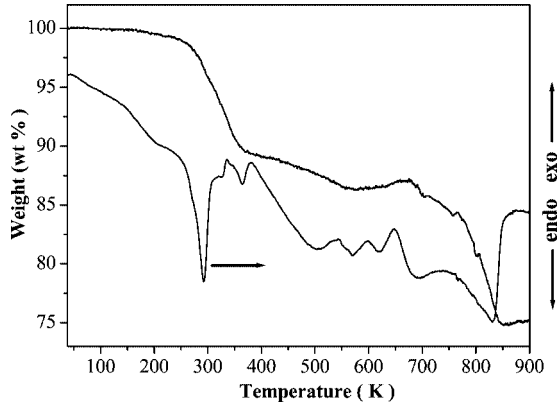

Figure 2. TGA-DTA curves for **1**.

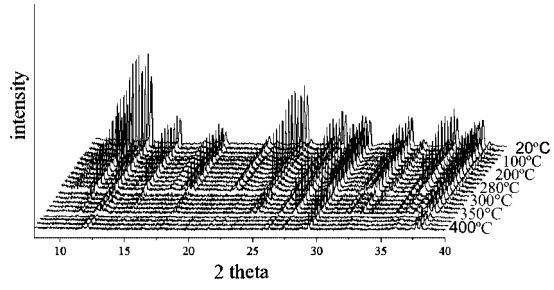

Figure 3. X-ray thermodiffractometric pattern for **1**.

 © 2005 Wiley-VCH Verlag GmbH & Co. KGaA, Weinheim

the SO_4^{2-} fraction starts to take place at 830 °C as a strong exothermic effect. The TG curve shows a continuous weight loss in this region. The final thermal decomposition product is Mn_2O_3 with its standard powder diffraction pattern (PDF database No: 41–1442).

A thermodiffractometric study of **1** (Figure 3) was undertaken to characterize the water loss. Compound **1** is only stable up to 280 °C; above this temperature water is lost.

Description of Structure

The asymmetric unit of **1** contains 29 non-hydrogen atoms (5 Mn, 1 S, and 23 O atoms) as shown in Figure 4. The Mn atoms adopt three different types of coordination: pentahedral, distorted pentahedral, and distorted octahedral, which is more complex than other basic sulfates.[33–37] In other metal sulfates, the metal atoms adopt only one octahedral or tetrahedral coordination, only $Zn(OH)_2$·$ZnSO_4$ adopts octahedral and tetrahedral coordination. Mn(1) is coordinated to five oxygen atoms [O(1), O(2), O(2A), O(3), and O(4)] from five different OH groups and shows as a slightly distorted pentahedron. O(2), O(2A), O(3), and O(4) form a plane with O(1) occupying the axial position. The Mn atom is slightly above or below the plane of the pyramid. The Mn(1)–O bond lengths range from 2.151(3) to 2.168(3) Å. Mn(2), Mn(3), and Mn(5) all adopt octahedral coordination: Mn(2) and Mn(3) are coordinated to six oxygen atoms from five different OH groups and a sulfate group, Mn(5) is coordinated to six oxygen atoms from four different OH groups and two different sulfate groups, with typical geometrical parameters {d_{av}[Mn(2)–O] = 2.211(3) Å, d_{av}[Mn(3)–O] = 2.217(3) Å, and d_{av}[Mn(5)–O] = 2.239(3) Å}. Mn(4) is coordinated by five oxygen atoms from five different OH groups; O(6A), O(8), and O(9A) form a distorted plane, whereas O(1) and O(9) occupy the axial positions, forming a distorted pentahedron. It is worth noting that the bond lengths of Mn(1)–Mn(3), Mn(1)–Mn(2), and Mn(2)–Mn(2)$^{\#2}$ are 3.1639(10) Å, 3.1729(9) Å, and 3.0933(14) Å, respectively.

The sulfate group in each asymmetric unit is tetrahedrally coordinated through its two oxygen atoms, O(10) and O(11A), and bonded to two different Mn atoms, Mn(2) and Mn(3), through the μ_3-O(7) bridge. O(12), the shortest of the S–O bonds, is a terminal oxygen with d_{av}(S–O) = 1.469(4) Å.

Formation of the 3D structure (Figure 5) can be explained by the linking of layers (Figure 6) through columns (Figure 7), which form empty channels. Each layer is obtained by linking chains of Mn atoms, bridged by O atoms. There is no similarity to the well-known structures of most basic hydroxide sulfates of divalent metals in which there are 1D chains or 2D layers linked by hydrogen bonding to form more complex networks. Mn(1)O(5), Mn(2)O(6), and Mn(3)O(6) form a chain (Chain 1), and Mn(1A)O(5), Mn(2A)O(6), and Mn(3A)O(6) form a neighboring chain (Chain 2). In Chain 1, Mn(1) is bridged to Mn(2) through 2 O atoms [O(1) and O(2)] on one side and to Mn(3) through 2 O atoms [O(3) and O(4)] on the other side. The fifth O atam [O(2A)] bridges Mn(2) to Mn(1A) and Mn(2A) of Chain 2. Mn(2) is further bridged to Mn(3) through two O atoms [O(6) and O(7)]. O(2) bridges Chain 1 to the Mn(1A) of Chain 2. O(5) and O(5A) bridge Mn(2) to Mn(2A) of Chain 2′, which faces the opposite direction to that of Chain 2. O(1) bridges Mn(1), Mn(2), and Mn(4)

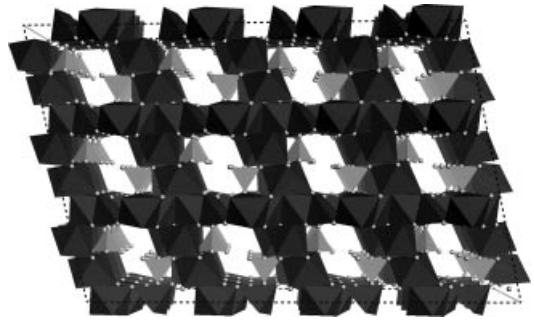

Figure 5. View of the crystal structure of the complex along the *c*-axis. SO_4^{2-} tetrahedra are gray and MnO_x polyhedra are black.

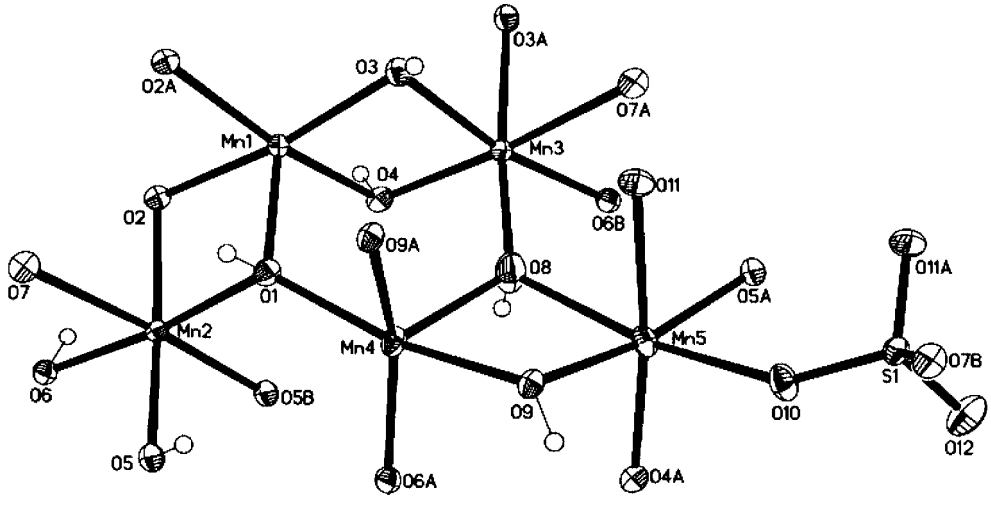

Figure 4. ORTEP drawing of the asymmetric unit of **1** showing the atom-labeling scheme (50% thermal ellipsoids).

 © 2005 Wiley-VCH Verlag GmbH & Co. KGaA, Weinheim

of the column which lie perpendicular to the layer of the chains. Mn(3) is bridged to Mn(1) and Mn(2) in the same type of chain as explained earlier for Mn(1) and Mn(2) using four of its coordination sites. Its fifth coordinating oxygen, O(8), bridges it to Mn(4) and Mn(5) of the column, which runs out of the layer, and the sixth oxygen, O(3), bridges it to Mn(1A) and Mn(3A) of Chain 2. Thus the two neighboring chains run parallel but in opposite directions to each other. They are linked together through bridging O atoms to form a complex layer (Figure 6).

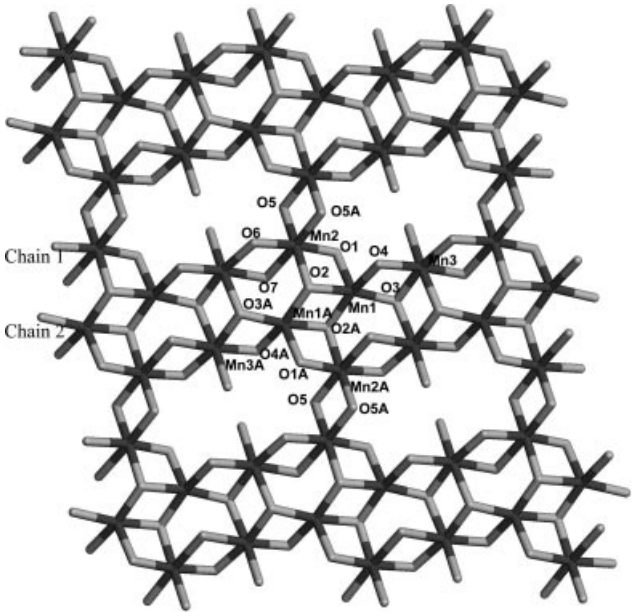

Figure 6. View of the structure perpendicular to the plane of the Mn/O/H layer orientated in the [100] plane.

Between the layers are complex columns formed by $Mn(5)O_6$ octahedra, $Mn(4)O_5$ distorted pentahedra and sulfate tetrahedra. In each column, two $Mn(5)O_6$ octahedra, two $Mn(4)O_5$ distorted pentahedra, and two sulfates are tetrahedrally linked together through edge or corner sharing to form a unit. These units are linked to form the infinite column (Figure 7).

The 3D structure is obtained by linking the layers in a unique pattern. The consecutive layers are linked to each other through complex columns which are perpendicular to them and thus form empty channels that can be viewed along the *c*-axis (Figure 5).

Magnetic Susceptibility

The temperature dependence of magnetic susceptibility at 5000 Oe was measured for **1** in the range 4–300 K (Figure 8). The experimental data were fitted by using the Curie–Weiss equation $\chi_m = C_m/(T - \Theta)$. The Curie constant is 21.72 emu·K·mol^{-1}. The Weiss constant, Θ, was determined to be –134.35 K in the temperature range of 25 K to 300 K, which suggests rather strong antiferromagnetic interactions between neighboring Mn atoms. This behavior is fully confirmed by the onset of a net maximum in the χ_m vs. T curve at 8.3 K; this maximum can be ascribed to the Neel temperature. The effective magnetic moment at 300 K, calculated from $\mu_{eff} = (8\chi_m T/5)^{1/2}$, is 5.64 μ_B per Mn, which is slightly lower than the theoretically expected value of 5.92 μ_B for Mn^{2+} in a high-spin d^5 system. This may be caused by the interaction of Mn atoms.

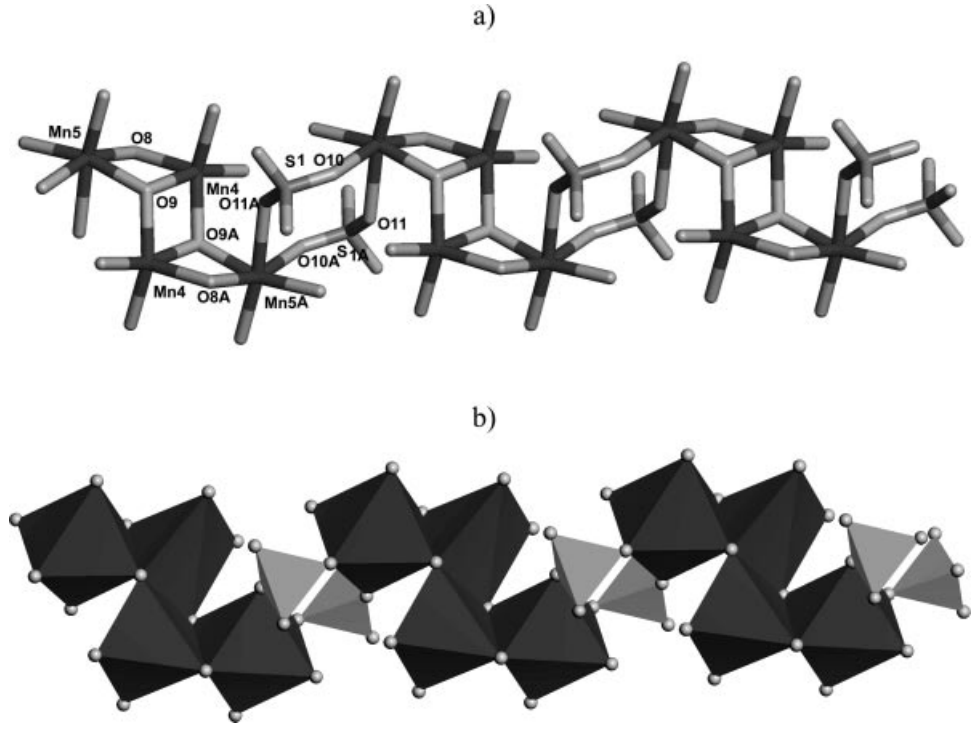

Figure 7. Complex column formed by $Mn(5)O_6$ octahedra, $Mn(4)O_5$ distorted pentahedra and sulfate tetrahedra.

 © 2005 Wiley-VCH Verlag GmbH & Co. KGaA, Weinheim

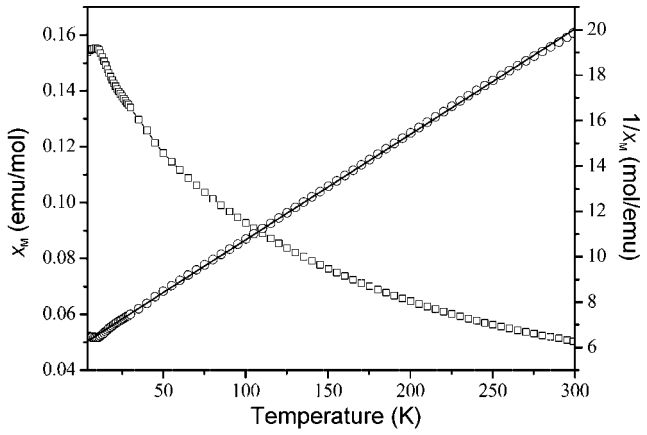

Figure 8. Thermal evolution of χ_m (□), linear curve (-) and $1/\chi_m$ (O) curves of **1**.

Conclusions

A 3D compound, $Mn_5(OH)_8SO_4$, has been synthesized hydrothermally from Mn^{II} ions and H_2SO_4. It has been structurally characterized by single-crystal X-ray diffraction analysis. The phase purity of the product has been confirmed by powder X-ray diffraction. The structure consists of alternately connected $\{MnO_x\}$ and $\{SO_4\}$ units which form a complex network. This compound is stable below 280 °C. The temperature dependence of the magnetic susceptibility shows a rather strong antiferromagnetic interaction in the compound.

Experimental Section

Characterization: The product was prepared by a hydrothermal method. In a typical synthesis, $MnCl_2{\cdot}4H_2O$ (0.199 g) was dissolved in water (10 mL) with stirring, and H_2SO_4 (0.1 mL) was added to form a solution. Cyclohexyl amine (2.4 mL) was added to this solution with continuous stirring until a homogeneous reaction mixture was formed. The final mixture with a molar ratio of $MnCl_2{\cdot}4H_2O/H_2SO_4$/cyclohexyl amine of 1:5:20 was crystallized in a 23-mL PTFE-lined acid digestion bomb at 170 °C for 5 d. The resultant product of pink sticks was filtered and washed thoroughly with distilled water. The yield was 25% based on Mn. Inductively coupled plasma (ICP) analysis was performed with a Perkin–Elmer Optima 3300DV ICP instrument. X-ray powder diffraction (XRD) data were collected with a Siemens D5005 diffractometer with Cu-K_α radiation (λ = 1.5418 Å). The step size was 0.02°, and the count time was 4 s. The infrared (IR) spectrum was recorded within the 400–4000 cm^{-1} region on a Nicolet Impact 410 FTIR spectrometer using KBr pellets. A Perkin–Elmer DTA 1700 was used to obtain the differential thermal analysis (DTA) and a Perkin–Elmer TGA 7 to obtain thermogravimetric analysis (TGA) curves in an air with a heating rate of 10 °C·min^{-1}. X-ray thermodiffractometry was performed in the furnace of a Siemens D-5000 diffractometer in the θ-θ mode in air. Magnetic susceptibility data were collected on the basis of a 0.0227 g sample over the temperature range of 4–300 K at a magnetic field of 5 kG with a Quantum Design MPMS-7 SQUID magnetometer.

X-ray Crystallographic Study: A suitable pink single crystal with dimensions $0.35\times0.32\times0.30$ mm^3 was glued to a thin glass fiber and mounted on a Siemens Smart CCD diffractometer equipped with a normal-focus, 2.4-kW sealed-tube X-ray source (graphite-monochromatic Mo-K_α radiation (λ = 0.71073 Å). Intensity data were collected at a temperature of 293 ± 2 K. Data processing was accomplished with the SAINT processing program.[38] The total number of measured reflections and observed unique reflections were 2885 and 1822, respectively. Intensity data of 1822 independent reflections ($-7 \le h \le 8$, $-10 \le k \le 7$, $-10 \le l \le 10$) were collected in the ω scan mode. An empirical absorption correction was applied using the SADABS program with T_{max} = 0.4000 and T_{min} = 0.3001). The structure was solved in the space group $P\bar{1}$ by direct methods and refined on F^2 by full-matrix least-squares using SHELXTL97.[39] The sulfur and manganese atoms were located first. Oxygen was then found in the difference Fourier map. The hydrogen atoms were placed geometrically. All non-hydrogen atoms were refined with anisotropic thermal parameters. The compound crystallizes in the triclinic system $P\bar{1}$ with cell parameters a = 7.5501(5) Å, b = 8.5558(6) Å, c = 8.6059(5) Å, α = 98.122(4)°, β = 102.370(4)°, γ = 99.646(4)°, V = 526.19(6) $Å^3$ and Z = 2. A summary of the crystallographic data is presented in Table 1. Further details of the crystal-structure investigation(s) may be obtained from the Fachinformationszentrum Karlsruhe, 76344 Eggenstein-Leopoldshafen, Germany, on quoting the depository number CSD-391307 (Crysdata@FIZ-Karlsruhe.de).

Table 1. Crystal data for title compound **1**.[a]

Empirical formula	$H_8Mn_5O_{12}S$
Formula weight	506.82
Temperature	293(2) K
Wavelength	0.71073 Å
Crystal system	Triclinic
Space group	$P\bar{1}$
Unit cell dimensions	a = 7.5501(5) Å
	b = 8.5558(6) Å
	c = 8.6059(5) Å
	α = 98.122(4)°
	β = 102.370(4)°
	γ = 99.646(4)°
Volume	526.19(6) $Å^3$
Z	2
Calculated density	3.199 m^3
Absorption coefficient	6.092
F(000)	490
Crystal size	$0.35\times0.32\times0.30$ mm
Reflections collected/unique	2885/1822 [R_{int} = 0.0365]
Data/restraints/parameter	1822/4/193
Goodness-of-fit on F^2	1.071
Final R indices [$I > 2\sigma(I)$]*	R_1 = 0.0366, wR_2 = 0.0868

[a] $R_1 = \Sigma||F_o|-|F_c||/\Sigma|F_o|$; $wR_2 = \{\Sigma[w(F_o^2-F_c^2)^2]/\Sigma[w(F_o^2)]^2\}^{1/2}$.

Acknowledgments

We thank the National Natural Science Foundation of China (Grant No. 20071013 and 20301007) and the State Basic Research Project of China (Grant G2000077507).

[1] T. Pinnavaia, *Science* **1983**, *220*, 365–371.
[2] T. Shichi, K. Takagi, Y. Sawaki, *Chem. Commun.* **1996**, 2027–2028.
[3] J. M. Thomas, *Angew. Chem.* **1994**, *106*, 963–989.
[4] M. E. Davis, *Chem. Eur. J.* **1997**, *3*, 1745–1750.
[5] T. Bein, *Chem. Mater.* **1996**, *8*, 1636–1653.
[6] D. W. Lewis, D. J. Willock, C. R. A. Catlow, J. M. Thomas, G. J. Hutchings, *Nature* **1996**, *382*, 604–606.
[7] S. P. Newman, W. Jones, *New J. Chem.* **1998**, *22*, 105–115.

 © 2005 Wiley-VCH Verlag GmbH & Co. KGaA, Weinheim

[8] K. Cheetham, G. Férey, T. Loiseau, *Angew. Chem. Int. Ed.* **1999**, *38*, 3269–3292.
[9] I. Bull, P. S. Wheatley, P. Lightfoot, R. E. Morris, E. Sastre, A. Wright, *Chem. Commun.* **2002**, 1180–1181.
[10] J. Rocha, M. W. Anderson, *Eur. J. Inorg. Chem.* **2000**, *5*, 801–818.
[11] J. Rocha, P. Ferreira, Z. Lin, P. Brandao, A. Ferreira, J. D. P. de Jesus, *J. Phys. Chem. B* **1998**, *102*, 4739–4744.
[12] J. Rocha, P. Ferreira, L. D. Carlos, A. Ferreira, *Angew. Chem. Int. Ed.* **2000**, *39*, 3276–3279.
[13] D. Ananias, A. Ferreira, J. Rocha, P. Ferreira, J. P. Rainho, C. Morais, L. D. Carlos, *J. Am. Chem. Soc.* **2001**, *123*, 5735–5742.
[14] M. S. Wickleder, *Chem. Rev.* **2002**, *102*, 2011–2087.
[15] L. Xu, E. B. Wang, J. Peng, R. D. Huang, *Inorg. Chem. Commun.* **2003**, *6*, 740–743.
[16] C. N. R. Rao, E. V. Sampathkumaran, R. Nagarajan, G. Paul, J. N. Behera, A. Choudhury, *Chem. Mater.* **2004**, *16*, 1441–1446.
[17] G. Paul, A. Choudhury, E. V. Sampathkumaran, C. N. R. Rao, *Angew. Chem. Int. Ed.* **2002**, *41*, 4297–4300.
[18] G. Paul, A. Choudhury, C. N. R. Rao, *Chem. Commun.* **2002**, 1904–1905.
[19] G. Paul, A. Choudhury, C. N. R. Rao, *Chem. Mater.* **2003**, *15*, 1174–1180.
[20] J. N. Behera, G. Paul, A. Choudhury, C. N. R. Rao, *Chem. Commun.* **2004**, 456–457.
[21] M. B. Salah, S. Vilminot, M. R. Plouet, G. Andre, T. Mhirid, M. Kurmoo, *Chem. Commun.* **2004**, 2548–2549.
[22] A. Rujiwatra, C. J. Kepert, M. J. Rosseinsky, *Chem. Commun.* **1999**, 2307–2308.
[23] A. Rujiwatra, C. J. Kepert, J. B. Claridge, M. J. Rosseinsky, H. Kumagai, M. Kurmoo, *J. Am. Chem. Soc.* **2001**, *123*, 10584–10594.
[24] M. I. Khan, S. Cevik, R. J. Doedens, *Inorg. Chim. Acta* **1999**, *292*, 112–116.
[25] M. B. Salah, S. Vilminot, M. Richard-Plouet, G. Andre, T. Mhiri, M. Kurmoo, *Chem. Commun.* **2004**, 2548–2549.
[26] I. Bull, P. S. Wheatley, P. L. Russe, E. Morris, E. Sastre, P. A. Wright, *Chem. Commun.* **2002**, 1180–1181.
[27] N. Behera, K. V. Gopalkrishnan, C. N. R. Rao, *Inorg. Chem.* **2004**, *43*, 2636–2642.
[28] S. Vilminot, M. R. Plouet, G. Andre, D. Swierczynski, F. B. Vigneron, M. Kurmoo, *Inorganic Chemistry* **2003**, *42*, 6859–6967.
[29] M. Doran, A. J. Norquist, D. O'Hare, *Chem. Commun.* **2002**, 2946–2947.
[30] J. Norquist, P. M. Thomas, M. Doran, D. O'Hare, *Chem. Mater.* **2002**, *14*, 5179–5184.
[31] P. M. Thomas, A. J. Norquist, M. B. Doran, D. O'Hare, *J. Mater. Chem.* **2003**, *13*, 88–92.
[32] M. B. Salah, S. Vilminot, T. Mhiri, M. Kurmoo, *Eur. J. Inorg. Chem.* **2004**, 2272–2276.
[33] V. Y. Ittaka, H. R. Oswald, S. Locchi, *Acta Crystallogr.* **1962**, *15*, 559.
[34] V. K. Mereiter, *Acta Crystallogr. Sect. B* **1979**, *35*, 579–585.
[35] M. Gentsch, K. Weber, *Acta Crystallogr. Sect. C* **1984**, *40*, 1309–1311.
[36] I. J. Bear, I. E. Grey, I. C. Madsen, I. E. Newnham, L. J. Rogers, *Acta Crystallogr. Sect. B* **1986**, *42*, 32–39.
[37] E. Dubler, H. R. Oswald, *Die Kristallstruktur von Trikobalt(II)-dihydrodisulfat-dihydrat, $Co_3(OH)_2(SO_4)_2{\cdot}2H_2O$*, Teil der Dissertation von E. Dubler, University of Zürich, **1970**.
[38] Software Packages SMART and SAINT, Siemens AnalyticalX-ray Instruments, Inc., Madison, WI, **1996**.
[39] SHELXTL, version 5.1; Siemens Industrial Automation, Inc, Madison, WI, **1997**.

Received: February 3, 2005
Published Online: July 7, 2005

 © 2005 Wiley-VCH Verlag GmbH & Co. KGaA, Weinheim

Periodates of Tetravalent Titanium, Zirconium, Hafnium and Thorium: Synthesis, Characterisation and EXAFS Study

Andrew L. Hector*[a] and William Levason[a]

Keywords: Periodates / Polyoxometalates / EXAFS spectroscopy / Group 4 elements / Thorium

Reaction of $TiO(SO_4)\cdot xH_2O$ with periodic acid in aqueous solution at pH = 2 yields a precipitate of $Ti_2O_2HIO_6\cdot 5H_2O$, while reaction of zirconyl, hafnyl or thorium nitrate with periodic acid in hot aqueous nitric acid solutions yields $MHIO_6\cdot xH_2O$ (M = Zr, Hf, Th; x = 4 or 5). The thorium periodate is soluble in aqueous KOH and $KThIO_6\cdot 4H_2O$ can be precipitated from these solutions. The zirconium, hafnium and both thorium periodates are shown by EXAFS to consist of edge-sharing chains of MO_8 and IO_6 units, IR and Raman studies indicate protonation of periodate in the $MHIO_6$ modifications. The titanium periodate contains vertex-sharing IO_6 groups.
(© Wiley-VCH Verlag GmbH & Co. KGaA, 69451 Weinheim, Germany, 2005)

Introduction

Polyoxometalates of electropositive metals have a number of interesting properties. For example, zirconium phosphates can be produced with microporous or mesoporous structures and have potential uses in ion exchange, intercalation, ion conductivity, catalysis and molecular sorption.[1–3] Polymeric structures are found for many oxo anion compounds of Ti, Zr, Hf and Th. Periodate anions $[H_{5-n}IO_6]^{n-}$ function as strong O-donor ligands towards many metal ions of the p and later d blocks, often stabilising unusually high oxidation states, for example Pd^{IV}, Ni^{IV}, Ru^{VI}, Pb^{IV}, Tl^{III} or Cu^{III}.[4–8] In contrast, their compounds with early d-block metals are relatively little investigated.[4] In the case of the oxophilic M^{IV} ions of the group 4 metals (Ti, Zr, Hf) the brief mentions of periodate species in the literature are over 50 years old and contain only compositions derived from classical "wet" analyses, leading to rather unlikely formulations $7TiO_2\cdot I_2O_7$, and $(ZrO_2)_n\cdot I_2O_7\cdot xH_2O$ (x = 3, 4 or 6).[9,10] In the f-block tetravalent thorium is also reported to form periodate complexes.[9,11] The orange cerium(IV) compounds $CeHIO_6\cdot 4H_2O$ and $M'CeIO_6\cdot xH_2O$ (M′ = K, Rb or Cs) were described in the older literature[4,9] and have more recently[12] been characterised by IR and UV/Vis spectroscopy and possible structures proposed based upon extended X-ray absorption fine structure (EXAFS) data from these amorphous and insoluble solids. There are also reports of the stabilization of Tb^{IV} in periodate media.[14,15] Recently, open-framework uranyl periodate compounds have been described,[13] showing the potential to produce useful porous materials with electropositive metals. We report here an investigation of the periodate complexes of these early d-block metals in the oxidation state IV and some experiments on the f-block systems.

[a] School of Chemistry, University of Southampton, Southampton SO17 1BJ, UK
Fax: +44-23-8059-6805
E-mail: A.L.Hector@soton.ac.uk

Results and Discussion

The products we obtained from the reaction of periodic acid or alkali metal periodates with various group 4 metal reagents proved to be insoluble in water except at very low and sometimes at high pH, amorphous by powder X-ray diffraction (PXD) and often of variable composition. In large part, this is a result of the complex and only partially understood solution chemistry of the group 4 M^{IV} ions in which oxo- or hydroxo-bridge oligomeric hydrolysis products are common features.[16,17] Often this results in rather intractable chemistry. Our general approach was to carry out a variety of exploratory syntheses, examine the products formed by energy dispersive X-ray analysis (EDX) to establish the elements present and their ratios, and use IR spectroscopy to examine the form ($[IO_4]^-$ or $[H_{5-n}IO_6]^{n-}$) of any periodate present.[4] Preparations which yielded species of reproducible composition and which were homogeneous by EDX (spectra collected on a series of points) were selected for detailed study.

Titanium

The addition of $TiCl_4$ to aqueous solutions of H_5IO_6, boiling freshly precipitated titanium dioxide with aqueous H_5IO_6, or reaction of $TiCl_4$ dissolved in glacial acetic acid with H_5IO_6 and KNO_3 in water (the last gave $KM''IO_6$ for M″ = Ge or Sn[7]), formed white precipitates which contained only small amounts of iodine (EDX evidence) and

 DOI: 10.1002/ejic.200500169 © 2005 Wiley-VCH Verlag GmbH & Co. KGaA, Weinheim

were mainly the hydrated dioxide. Similarly, heating freshly precipitated TiO_2 with H_5IO_6 or H_5IO_6/KIO_4 in water in hydrothermal bombs at ca. 150 °C for 3–4 d gave products containing very little iodine (the temperatures are limited by the stability of H_5IO_6 which decomposes above ca. 175 °C[18]). The addition of concentrated aqueous H_5IO_6 solution to one of $TiOSO_4{\cdot}xH_2O$ in hot aqueous H_2SO_4 or to a solution of freshly precipitated TiO_2 in hot aqueous nitric acid was more successful, producing white precipitates of constant composition. If carried out as described in the Exp. Sect. at pH = 2, after washing with water and prolonged drying in vacuo, the products have a reproducible heavy atom ratio of Ti/I = 2:1 and conventional analysis data are consistent with a composition $Ti_2O_2HIO_6{\cdot}5H_2O$. The thermogravimetric analysis (TGA) trace (Figure 1) is very simple, the first weight loss (< 200 °C) corresponding to $-5H_2O$, and the second to –"HIO_4", which is complete at ca. 700 °C leaving TiO_2 (identity confirmed by PXD).

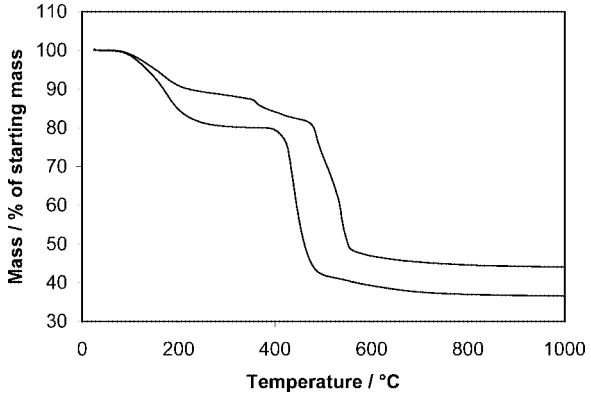

Figure 1. TGA traces of $ThHIO_6{\cdot}5H_2O$ (top) and $Ti_2O_2HIO_6{\cdot}5H_2O$ (bottom) recorded in oxygen.

If the reactions are carried out at higher pH, for example by adding KOH/KIO_4 solution to the acid solution of titanium, the white precipitates have variable composition and presumably are mixtures containing titanium dioxide. In the reactions carried out in the presence of KIO_4, or if the isolated product is treated with 2 M KOH solution no potassium is incorporated. The white powder $Ti_2O_2HIO_6{\cdot}5H_2O$ is insoluble and unaffected by water, dissolves in concentrated aqueous nitric or perchloric acids, and is decomposed by 10 M KOH on heating with precipitation of titanium dioxide.

The IR spectrum of this material shows vibrations due to H_2O, "IO_6" groups and a weak feature at 1135 cm^{-1} assigned to δ(IOH)[4] consistent with the protonation of the periodate required by charge balance. The spectral profile is similar to those found in other complexes containing HIO_6^{4-} species.[4,5] The low-frequency region is dominated by the strong broad absorptions of the coordinated periodate group and these probably obscure features due to Ti–O–Ti units. The compound fluoresces in the Raman spectrometer and this limits the spectral quality, but in addition to strong features at 791 (sh), 654 and 476 cm^{-1} associated with the periodate groups, there is a medium-intensity feature at 936 cm^{-1} which may be due to a Ti–O–Ti unit. The diffuse reflectance spectrum shows a broad feature in the near UV at ca. 36000 cm^{-1} which is tentatively assigned as overlapping internal absorptions of the coordinated periodate ligand and $O\rightarrow Ti^{IV}$ charge transfer (CT). The $Ti_2O_2HIO_6{\cdot}5H_2O$ is amorphous but some structural data were obtained by iodine-*K* edge EXAFS studies (see EXAFS section).

Zirconium and Hafnium

Reactions similar to those described for titanium, including attempted reactions of the freshly precipitated dioxides with H_5IO_6 in hydrothermal bombs or with refluxing aqueous H_5IO_6 failed to give periodato compounds. However, the addition of a concentrated aqueous periodic acid solution to a solution of zirconyl nitrate, $ZrO(NO_3)_2{\cdot}xH_2O$, in hot aqueous nitric acid, produced a white precipitate with a Zr/I = 1:1 composition. The hafnium analogue was obtained similarly using $HfO(NO_3)_2{\cdot}xH_2O$.[19] Provided the precipitation occurs at pH ≈ 2 and the products are washed thoroughly with hot water and dried in vacuo at room temperature to constant weight, they had a reproducible composition of $MHIO_6{\cdot}xH_2O$. These materials were found to be amorphous by PXD but homogeneous by EDX over a series of points. Both the conventional analyses and the TGA weight loss suggest that the thoroughly dried compounds have $x = 4$ for Zr and 5 for Hf. The differences between the two formulations are small but greater than the experimental uncertainty and are reproducible, although we cannot rule out that the water content may be slightly variable. As observed with titanium, working at a higher pH seems to lead to products containing appreciable amounts of the dioxides, and if preparations are carried out in the presence of KIO_4, or the freshly isolated $MHIO_6{\cdot}xH_2O$ is treated with 2 M KOH, no significant amount of potassium is incorporated. In contrast to the titanium periodate described above, the compounds $MHIO_6{\cdot}xH_2O$ dissolve in 10 M aqueous KOH to give a clear solution, but the white products precipitated from these solutions by addition of ethanol had a highly variable K/I/M ratio and have not been purified or identified. The compounds $MHIO_6{\cdot}xH_2O$ are amorphous, insoluble in water, but dissolve in concentrated HNO_3 or $HClO_4$. Their IR spectra show water, "IO_6" groups and a weak broad feature at 1150–1165 cm^{-1} assigned as δ(IOH). If the samples are treated with D_2O for 48 h, the IR spectra of the products show this band has diminished in intensity and a new feature at ca. 820 cm^{-1} is present assigned as δ(IOD). The Raman spectra of the two compounds (Figure 2) are very similar showing only small variations in relative band intensities and frequencies suggesting similar structural units present. The TGA data show decomposition to MO_2 at ca. 650 °C.

For many later transition metal ions, the periodate complexes have related tellurate analogues (containing $H_{6-n}TeO_6]^{n-}$ ligands[4]), but addition of telluric acid to solutions of Zr^{IV} or Hf^{IV} in nitric acid under the conditions

 © 2005 Wiley-VCH Verlag GmbH & Co. KGaA, Weinheim

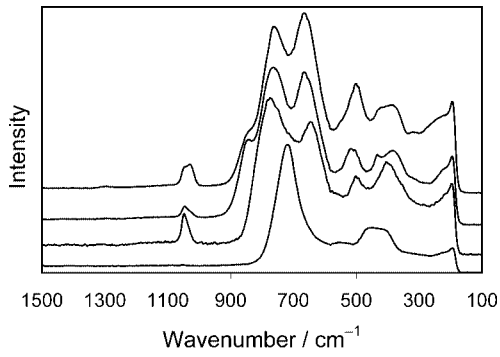

Figure 2. Raman spectra of (top to bottom) $ZrHIO_6{\cdot}4H_2O$, $HfHIO_6{\cdot}5H_2O$, $ThHIO_6{\cdot}5H_2O$ and $KThIO_6{\cdot}4H_2O$.

used to prepare the periodates gave no precipitation. It seems probable that the weaker telluric acid is fully protonated at these pH values and does not coordinate to the group 4 metal.

Thorium

Thorium(IV) is much less prone to hydrolysis and oligomerisation in aqueous solution than the group 4 metal ions, and treatment of aqueous thorium nitrate solution with an aqueous H_5IO_6 solution in the pH range 2–4 produces a white precipitate of composition $ThHIO_6{\cdot}5H_2O$. The IR and Raman spectra of this compound are very similar to those of the Zr and Hf compounds suggesting related structural units. The compound dissolves in concentrated mineral acids and in strong aqueous alkali solution. The TGA plot showing thermal decomposition to ThO_2 (Figure 1) is simple, showing water loss in two steps and then loss of "HIO_4" with no other intermediates formed.

When $ThHIO_6{\cdot}5H_2O$ is stirred with 5 M KOH solution, it slowly dissolves to give a colourless solution, from which slow addition of ethanol precipitates a white powder identified by analysis as $KThIO_6{\cdot}4H_2O$. The IR and Raman spectra of this product (Figure 2 and Exp. Sect.) are clearly different to that of $ThHIO_6{\cdot}5H_2O$, in particular the "IO_6" region is simpler and the weak features attributed in the latter to δ(IOH) modes are absent. The compound is amorphous and insoluble in water, except at very low pH. The behaviour of $ThHIO_6{\cdot}5H_2O$ in alkali is reminiscent of that of $CeHIO_6{\cdot}4H_2O$,[12] and contrasts with that of the Zr and Hf systems.

Cerium, Praseodymium and Terbium

Reaction of $[NH_4]_2Ce(NO_3)_6$ in aqueous HNO_3 with periodic acid precipitates deep yellow $CeHIO_6{\cdot}4H_2O$;[12] this can also be prepared from cerium(III) ions and periodic acid oxidised with ozonised oxygen[12] and (impure) from cerium(III) nitrate and aqueous periodic acid.[20] Since stable and soluble Pr^{IV} or Tb^{IV} precursors are unavailable, ozonisation of aqueous Pr^{III} and Tb^{III} nitrate solutions containing H_5IO_6 at pH = 2 was explored, but even after several hours there was no evidence for oxidation of the lanthanide (in situ UV/Vis spectra). There are several reports[14,15,21–24] that in alkaline solution at least partial conversion to the M^{IV} state is possible, either electrochemically or by using strong chemical oxidants such as peroxodisulfate or ozone. If $Pr(NO_3)_3$ solution is added dropwise to a 5 M KOH solution containing KIO_4, through which ozonised oxygen is passing, a brown colour appears and after several hours a deep yellow solution with a yellow-brown precipitate is formed. The UV/Vis spectra of the yellow solution is dominated by a strong broad band at ca. 34000 cm^{-1}, similar in energy to features reported for other Pr^{IV} species and assigned as $O \rightarrow Pr^{IV}$ CT.[21] The yellow solution decomposes slowly producing a white precipitate and a green solution of Pr^{III}. Filtration and addition of saturated KNO_3 solution to the filtrate produced a fawn-yellow precipitate which became darker on drying. EDX data on this precipitate showed it contained K, I and Pr but was inhomogeneous. The IR spectrum is similar to that of $KCeIO_6{\cdot}xH_2O$.[12] Once isolated, the material is insoluble in water or aqueous alkali and decomposes to green Pr^{III} instantly by acids. The solid decomposes to green Pr^{III} over a few hours/days. Similar ozonisation of a solution of $Tb(NO_3)_3$, KOH and KIO_4 produced a deep red brown solution and a brown precipitate. Filtration and addition of saturated aqueous KNO_3 to the filtrate gave a red-brown solid. EDX data on this solid showed K, Tb and I, although again the ratios differed from sample to sample. The IR spectrum showed water and "IO_6" and the UV spectrum, both of the original red-brown solution and the isolated solid, contained a strong broad feature at ca. 25500 cm^{-1} assigned as $O \rightarrow Tb^{IV}$ CT. Formation of Tb^{IV} in periodate media has been reported several times before[15,22] and Ying and Rudong[15] claimed the isolation and characterisation of $MTbIO_6{\cdot}xH_2O$ (M = Li, x = 14; M = Na, x = 7; M = K, x = 8) complexes by this route. Our spectroscopic data are in good agreement with those reported, but despite very many attempts we have been unable to obtain species which have a constant composition or are homogeneous.

We conclude that substances which probably contain $KMIO_6{\cdot}xH_2O$ (M = Pr or Tb) analogous to the cerium complex do form, but it is very doubtful if they can be obtained even approximately pure, and this precludes work to establish the structural units present.

EXAFS Studies

All the tetravalent periodate materials discussed herein are amorphous; all attempts to produce crystalline materials by varying the synthesis conditions and hydrothermal growth failed. The EXAFS study was undertaken with the aim of discovering some information about their local structures. EXAFS data were recorded at both the metal (Zr-K, Hf-L_{III}, Th-L_{III}) and iodine (K) edges for $MHIO_6{\cdot}xH_2O$ (M = Zr, Hf, Th) and $KThIO_6{\cdot}4H_2O$. For $Ti_2O_2HIO_6{\cdot}5H_2O$, only iodine-K edge data were recorded since the titanium-K edge lies in the iodine-L region.

The iodine edge spectra of $ZrHIO_6{\cdot}4H_2O$ were fitted readily with a first shell of 6 oxygen atoms at a distance

 © 2005 Wiley-VCH Verlag GmbH & Co. KGaA, Weinheim

of 1.88 Å. A second shell was clearly visible in the Fourier transform at 3.27 Å and this could be fitted, with very similar statistics, with one or two zirconium atoms. A larger number of zirconium atoms resulted in deterioration of the fit statistics. The zirconium EXAFS contained a strong first shell at 2.18 Å. This shell gave a poor fit with six oxygen atoms which improved markedly with eight-coordination. The fit with seven-coordinate Zr was indistinguishable from the eight-coordinate model. A second shell at 3.26 Å was modelled with two iodine atoms, similarly to the iodine data, a single iodine atom gave a reasonable fit but a larger number did not. The background-subtracted spectra and Fourier transforms are shown in Figure 3 and structural data are presented in Table 1.

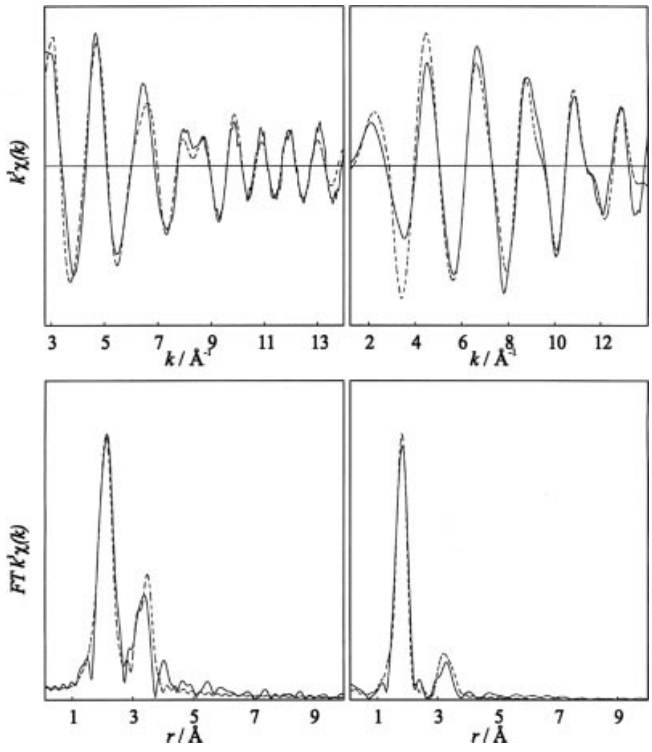

Figure 3. Fitted zirconium- (left) and iodine-*K* (right) edge EXAFS (top) and Fourier transformed EXAFS (bottom) spectra of $ZrHIO_6{\cdot}4H_2O$. Experimental data is shown as solid lines and calculated spectra as broken lines.

The Zr···I distances observed in both the Zr and I edge data are consistent with edge-sharing polyhedra, with a Zr–O–I bond angle of 108°. Based on this and the observed coordination numbers, two structural models for $ZrHIO_6{\cdot}4H_2O$ are plausible based on this EXAFS data. The first is that chains are formed with alternating IO_6 and ZrO_8 groups; this is the case if the second shell in both data sets is modelled with two atoms. The second model arises from the possibility of a single atom in the second shell and would give rise to dimeric species containing a periodate ion and one zirconium atom. This second model does not fit with the insolubility of the material, but more importantly is not plausible due to the composition. In the chain model the edge-sharing periodate ions fill four coordination sites on Zr, the remaining four can be occupied by water molecules (probably hydrogen-bonded to neighbouring chains). With dimers, six water molecules would be needed for ZrO_8. Seven-coordinate Zr is also consistent with the EXAFS data, but this would still require five water molecules. Thus, edge-sharing chains with alternating ZrO_8 and IO_6 groups (Figure 4) is considered the most likely structure of this material.

Table 1. EXAFS data for $MHIO_6{\cdot}xH_2O$ (M = Zr, Hf, Th) and $KThIO_6{\cdot}4H_2O$ (the calculated standard deviations are from the EXAFS fitting software and a 1% error in the distances should be considered more reasonable).

Metal edge EXAFS (Zr-*K*, Hf-L_{III}, Th-L_{III})[a]						
M	M–O [Å]	σ^2	M···I [Å]	σ^2	E_F	*R* (%)
Zr	2.177(6)	0.023(1)	3.261(5)	0.012(1)	–1.4	26.0
Hf	2.15(2)	0.035(3)	3.22(2)	0.017(6)	–8.9	32.4
Th	2.46(1)	0.029(2)	3.501(8)	0.012(1)	–6.7	33.9
KTh	2.46(2)	0.014(3)	3.54(1)	0.010(2)	–6.8	47.2
I-*K* edge EXAFS[b]						
M	I–O [Å]	σ^2	I···M [Å]	σ^2	E_F	R (%)
Zr	1.875(4)	0.007(1)	3.267(5)	0.011(2)	–14.3	28.2
Hf	1.863(4)	0.009(1)	3.25(3)	0.015(3)	–11.4	26.2
Th	1.844(7)	0.011(2)	3.41(2)	0.010(3)	–8.9	34.8
KTh	1.868(9)	0.007(2)	3.5(3)	0.05(12)	–10.7	27.0

[a] Coordination numbers: M–O = 8; M···I = 2. [b] Coordination numbers: I–O = 6; I···M = 2.

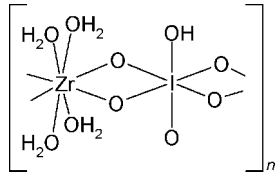

Figure 4. Proposed structural motif in $ZrHIO_6{\cdot}4H_2O$.

The EXAFS data quality for $HfHIO_6{\cdot}5H_2O$, $ThHIO_6{\cdot}5H_2O$ and $KThIO_6{\cdot}4H_2O$ was poorer than for the Zr system discussed above. The Hf-L_{III} edge data was noisy and had to be truncated; only 1.5–9 $Å^{-1}$ were used, but it was possible to obtain meaningful information from these data, albeit with slightly high *R* factors. The Th-L_{III} edge data suffered with two major monochromator glitches and the relevant data points were deleted. Similarly, a major glitch in the iodine edge EXAFS data, which was not observed in the other samples, became apparent in both Th samples and a section had to be cut from the data. This has resulted in high *R* factors for the Th data at both edges and unreliable second-shell information in the I-*K* edge fits.

Examination of the data in Table 1 shows that $HfHIO_6{\cdot}5H_2O$ is very similar to $ZrHIO_6{\cdot}4H_2O$ and the same structure appears to be adopted. The small reduction in the M–O distance is consistent with ionic radii[25] and the agreement between the Hf···I and I···Hf distances, though poorer than with Zr, is still within error. The M–O bond lengths for the Zr and Hf compounds are in excellent agreement with those in the $[M_4(OH)_8(H_2O)_{16}]^{8+}$ ions.[17] Interestingly, even accepting their lower reliability, the fits to the

 © 2005 Wiley-VCH Verlag GmbH & Co. KGaA, Weinheim

data collected on the protonated and potassium-exchanged thorium periodates are also compellingly similar to $ZrHIO_6{\cdot}4H_2O$. The first-shell distance increase for Th compared with Zr is slightly larger than the 0.21 Å suggested by ionic radii and this could be taken to imply nona-coordinate Th in $ThHIO_6{\cdot}5H_2O$, though the distance is the same in $KThIO_6{\cdot}4H_2O$ where the number of water molecules is insufficient for nona-coordinate Th. The EXAFS data of $ZrHIO_6{\cdot}4H_2O$ is also markedly similar to that of $CeHIO_6{\cdot}4H_2O$.[12] The chain structure which we consider likely here was also proposed in this earlier work, though it was only possible to fit one shell to the Ce EXAFS data and the chain structure was based on the iodine edge data only. Thus, we suggest that the same core structure is adopted throughout the series of tetravalent periodates with these electropositive metals containing $ZrHIO_6{\cdot}4H_2O$, $HfHIO_6{\cdot}5H_2O$, $CeHIO_6{\cdot}4H_2O$, $ThHIO_6{\cdot}5H_2O$ and $KThHIO_6{\cdot}4H_2O$. The fifth water molecule observed in some of these compounds is likely to be loosely associated. The potassium ion in $KThIO_6{\cdot}4H_2O$ does not appear to change the EXAFS data at either edge, but in all the metal edge spectra there are features in the Fourier transform beyond the second shell which have not been modelled. Vertex-sharing potassium would be in this region. The Raman spectra of the thorium compounds (Figure 2) show the change in the symmetry of the periodate ion on exchange of the proton in $ThHIO_6{\cdot}5H_2O$ with potassium to yield $KThIO_6{\cdot}4H_2O$ and are consistent with an increased symmetry on deprotonation but an otherwise similar environment.

The iodine-*K* edge data for $Ti_2O_2IO_6{\cdot}5H_2O$ were fitted (R = 20.92) with six oxygen atoms at 1.861(3) Å and two titanium atoms at 3.51(2) Å; Debye–Waller factors were 0.006(1) and 0.014(5) $Å^2$, respectively. Whilst the information which can be derived from one edge is clearly less, it is possible to see that this material is structurally different from those described above. Assuming a typical octahedral Ti^{IV}–O distance of 1.97 Å, the Ti–O–I bond angle would be around 133°; thus, it is likely that the structure of this material is based around vertex-sharing polyhedra. A second shell with more than two titanium atoms does not give a good fit, ruling out higher symmetry structures, and there are not enough oxide/hydroxide/water groups for a discrete molecular structure. Hence, a structure based on chains or sheets is likely.

Experimental Section

General: Physical measurements were made as described previously.[5] For analysis known weights of the compounds were boiled with 2 M H_2SO_4 and excess aqueous SO_2 which achieved dissolution and reduction to iodide. Iodine was determined gravimetrically as AgI and potassium gravimetrically as $KBPh_4$, and the group IV metals and Th as the dioxides by pyrolysis to constant weight in flowing O_2/N_2. Water contents were estimated from the TGA traces. All samples were examined by PXD and found to be fully amorphous. X-ray absorption data were collected at ambient temperature in transmission mode from powdered samples diluted with BN on station 9.3 of the SRS with an Si 220 monochromator. Background subtraction was performed with PAXAS[26] and EXAFS data were fitted using EXCURVE.[27] $ZrO(NO_3)_2{\cdot}xH_2O$, $TiO(SO_4){\cdot}xH_2O$, $Pr(NO_3)_3{\cdot}xH_2O$ and $Tb(NO_3)_3{\cdot}xH_2O$ (Aldrich), and $Th(NO_3)_4{\cdot}5H_2O$ (BDH), were used as received. $HfO(NO_3)_2{\cdot}xH_2O$ was prepared as described elsewhere.[19]

$Zr[HIO_6]{\cdot}4H_2O$: $ZrO(NO_3)_2{\cdot}xH_2O$ (0.26 g, ca. 1.0 mmol) was dissolved in hot aqueous nitric acid (5:1 v/v, H_2O/HNO_3, 200 mL) and the solution stirred vigorously, whilst a solution of H_5IO_6 (0.34 g, 1.5 mmol) in water (20 mL) was added dropwise. Immediately, a white precipitate formed, and after stirring for 30 min the hot solution was filtered, the solid washed with hot water (3 × 50 mL) and dried in vacuo for 24 h (0.35 g, 90%). $H_9IO_{10}Zr$ (387.19): calcd. I 32.8, Zr 23.6; found I 33.3, Zr 23.8. IR (Nujol): $\tilde{\nu}$ = 3380 (st, br), 1624 (m), 1153 (w), 780 (sh), 720 (vs), 494 (s), 379 (m) cm^{-1}. Raman: $\tilde{\nu}$ = 3300 (w, br) 1580 (w), 1038 (m), 825 (sh), 761 (vs), 662 (vs), 502 (m), 381 (m), 192 (m) cm^{-1}. UV/Vis (neat diffuse reflectance): $\tilde{\nu}$ = 45450, 35700, ca. 33000 (sh) cm^{-1}.

$Hf[HIO_6]{\cdot}5H_2O$: This compound was prepared similarly using $HfO(NO_3)_2{\cdot}xH_2O$. Yield 86%. $H_{11}HfIO_{11}$ (492.48): calcd. Hf 36.2, I 25.8; found Hf 35.8, I 24.9. IR (Nujol): $\tilde{\nu}$ = 3380 (st, br), 1615 (m), 1161 (w), 760 (sh), 720 (vs), 502 (s), 379 (m) cm^{-1}. Raman: $\tilde{\nu}$ = 3300 (w, br), 1580 (w), 1036 (m), 844 (sh), 765 (vs), 666 (vs), 514 (m), 434 (m), 381 (m), 194 (m) cm^{-1}. UV/Vis (neat diffuse reflectance): $\tilde{\nu}$ = 45450, 35700, ca. 34000 (sh) cm^{-1}.

$Th[HIO_6]{\cdot}5H_2O$: Thorium nitrate hydrate (0.24 g, 0.48 mmol) was dissolved in water (20 mL), concd. HNO_3 (1 mL) added and the mixture heated to ca. 80 °C. A solution of H_5IO_6 (0.15 g, 0.65 mmol) in water (10 mL) was added and the mixture stirred for 30 min. The white precipitate was filtered off, rinsed with hot water (3 × 20 mL) and dried in vacuo (0.22 g, 85%). $H_{11}IO_{11}Th$ (546.02): calcd. I 23.2, Th 42.5; found I 23.8, Th 42.4. IR (Nujol): $\tilde{\nu}$ = 3380 (st, br), 1620 (m), 1161 (w), 760 (sh), 725 (vs), 447 (s), 370 (m) cm^{-1}. Raman: $\tilde{\nu}$ = 3300 (w, br), 1580 (w), 1040 (m), 772 (vs), 640 (vs), 498 (m), 396 (m), 200 (m) cm^{-1}. UV/Vis (neat diffuse reflectance): $\tilde{\nu}$ = 44800, 36000 cm^{-1}.

$Ti_2O_2[HIO_6]{\cdot}5H_2O$: Powdered $TiO(SO_4){\cdot}xH_2O$ (1.6 g, 10 mmol) was suspended in hot water (300 mL) and the mixture vigorously stirred whilst aqueous ammonia (25% w/v, 10 mL) was added, producing a flocculent white precipitate. The mixture was boiled for 10 min, then filtered hot and the white solid washed with copious amounts of hot water to remove residual ammonia. The wet solid was added to a hot mixture of water and concd. nitric acid (4:1 v/v, 100 mL), where it dissolved slowly on stirring to give a clear solution. Periodic acid (2.3 g,10 mmol) in water (10 mL) was added to this solution resulting in a white precipitate. After 10 min, the precipitate was filtered off, washed with hot water (3 × 20 mL) and dried in vacuo. (1.8 g, 82%). $H_{11}IO_{13}Ti_2$ (441.72): calcd. I 28.7, Ti 21.7; found I 28.5, Ti 21.9. IR (Nujol): $\tilde{\nu}$ = 3300 (st, vbr), 1625 (m), 1135 (m), 890 (sh), 730 (s, br), 473 (s), 370 (m) cm^{-1}. Raman: $\tilde{\nu}$ = 936 (m, sh), 791 (s, sh), 654 (vs), 476 (s), 294 (s) cm^{-1}. UV/Vis (neat diffuse reflectance): $\tilde{\nu}$ = 44000, 35800 cm^{-1}.

$KThIO_6{\cdot}5H_2O$: $Th[HIO_6]{\cdot}5H_2O$ (0.2 g, 0.37 mmol) was suspended in 5 M KOH (10 mL) and stirred for 1 h, where it dissolved to give a clear solution. Ethanol (20 mL) was added dropwise to the rapidly stirred solution producing a white precipitate. This was filtered off, washed with ethanol/water (1:1 v/v, 20 mL) and dried in vacuo (0.18 g, 86%). $H_{10}IKO_{11}Th$ (584.11): calcd. I 22.3, K 6.7; found I 22.4, K 6.8. IR (Nujol): $\tilde{\nu}$ = 3350 (st, br), 1640 (m), 698 (vbr, s), 668 (sh), 440 (br, m) cm^{-1}. Raman: $\tilde{\nu}$ = 3300 (w, br), 1580 (w), 720 (vs), 540 (m), 466 (br, m), 200 (m) cm^{-1}.

 © 2005 Wiley-VCH Verlag GmbH & Co. KGaA, Weinheim

Acknowledgments

A. L. H. is supported through a Royal Society University Research Fellowship. Beamtime at the SRS for EXAFS studies was provided by CCLRC through award number 43033. Thanks to Dr. R. D. Oldroyd for preliminary studies on the lanthanide systems, Miss H. L. Turner for measuring the Raman spectra and Mrs. R. P. Bell for advice on handling and transport of the thorium samples.

[1] A. Clearfield, *Comments Inorg. Chem.* **1990**, *10*, 89.
[2] G. Alberti, M. Casciola, U. Constantino, R. Vivandi, *Adv. Mater.* **1996**, *8*, 291.
[3] S. Shen, B. Tian, C. Yu, S. Xie, Z. Zhang, B. Tu, D. Zhao, *Chem. Mater.* **2003**, *15*, 4046.
[4] W. Levason, *Coord. Chem. Rev.* **1997**, *161*, 33.
[5] A. L. Hector, W. Levason, M. Webster, *Inorg. Chim. Acta* **2003**, *343*, 90.
[6] D. B. Currie, W. Levason, R. D. Oldroyd, M. T. Weller, *J. Chem. Soc., Dalton Trans.* **1994**, 1483.
[7] D. B. Currie, W. Levason, R. D. Oldroyd, M. T. Weller, *J. Mater. Chem.* **1993**, *3*, 447.
[8] N. Binsted, A. L. Hector, W. Levason, *Inorg. Chim. Acta* **2000**, *298*, 116.
[9] R. C. Raychoudhury, *J. Ind. Chem. Soc.* **1941**, *18*, 335.
[10] R. K. Bahl, S. Singh, N. K. Bali, *J. Ind. Chem. Soc.* **1943**, *20*, 141.
[11] Y. Ying, S. Yongwen, Y. Rudong, *Radiochim. Acta* **1998**, *80*, 147.
[12] W. Levason, R. D. Oldroyd, *Polyhedron* **1996**, *15*, 409.
[13] T. A. Sullens, R. A. Jensen, T. Y. Shvareva, T. E. Albrecht-Schmitt, *J. Am. Chem. Soc.* **2004**, *126*, 2676.
[14] Y. Yang, Y. Rudong, *Polyhedron* **1992**, *11*, 963.
[15] Yu. M. Kiselev, A. S. Baranov, *Zh. Neorg. Khim.* **2002**, *47*, 779.
[16] E. Hollink, D. W. Stephan, in *Comprehensive Coordination Chemistry II* (Eds.: J. A. McCleverty, T. J. Meyer), Elsevier, Oxford, **2004**, vol. 4, p. 105.
[17] C. Hagfeldt, V. Kessler, I. Persson, *Dalton Trans.* **2004**, 2142.
[18] A. L. Hector, S. J. Henderson, W. Levason, M. Webster, *Z. Anorg. Allg. Chem.* **2002**, *628*, 198.
[19] C. Favotto, M. Mansori, L. Tortet, K. Jardet, P. Satre, *Ann. Chim. Sci. Mater.* **2001**, *26*, 71.
[20] A. H. Lokio, *Acta Chem. Scand.* **1973**, *27*, 147.
[21] D. E. Hobart, K. Samhoun, J. P. Young, V. E. Norvell, G. Mamantov, J. R. Peterson, *Inorg. Nucl. Chem. Letts.* **1980**, *16*, 321.
[22] a) W. Dong, Y. Rudong, *Huaxue Xuebao* **1986**, *44*, 563; b) *Chem. Abstr.* **1986**, *105*, 85819.
[23] G. Varlashkin, G. M. Begum, J. R. Peterson, *J. Less Common Met.* **1985**, *109*, 123.
[24] A. S. Saprykin, V. P. Shilov, V. I. Spit*syn*, N. N. Krot, *Dok. Akad. Nauk. SSSR* **1976**, *226*, 853.
[25] R. D. Shannon, *Acta Crystallogr. Sect. A* **1976**, *32*, 751.
[26] N. Binsted, *PAXAS*, University of Southampton, **1994**.
[27] a) N. Binsted, *EXCURVE 9.2.7.1*, University of Southampton, **2004** (*K* edges); b) S. Tomic, B. G. Searle, A. Wander, N. M. Harrison, A. J. Dent, J. F. W. Mosselmans, J. E. Inglesfield, *DL_EXCURV 1.0*, CCLRC Tech. Rep. DL-TR-2005-001, ISSN 1362-0207, **2005** (L_{III} edges).

Received: February 24, 2005
Published Online: July 12, 2005

 © 2005 Wiley-VCH Verlag GmbH & Co. KGaA, Weinheim

Lithium *tert*-Butyl[phenyl(2,2,6,6-tetramethylpiperidino)boryl]amide: A Versatile Reagent

Ulrike Braun,[a] Tassilo Habereder,[a] and Heinrich Nöth*[a]

Keywords: Lithium *tert*-butyl[phenyl(2,2,6,6-tetramethylpiperidino)boryl]amide / *N*−Metalborylamides

Figure 1 on page 3632 of the original article[1] is actually a copy of Figure 2; the correct Figure 1 is shown below.

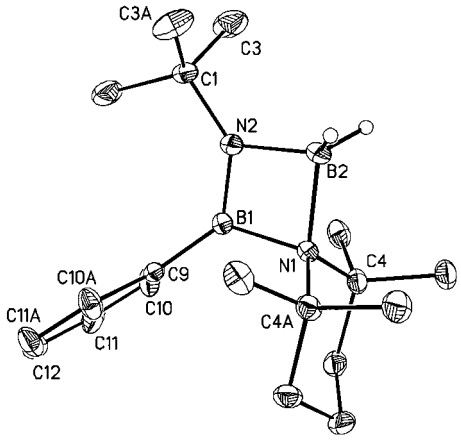

[1] U. Braun, T. Habereder, H. Nöth, *Eur. J. Inorg. Chem.* **2004**, 3629−3643.

Received: June 27, 2005
The Editors

[a] Department of Chemistry, University of Munich, Butenandtstr. 5−13, 81377 München, Germany
E-mail: H.Noeth@lrz.uni-muenchen.de

 DOI: 10.1002/ejic.200500564 © 2005 Wiley-VCH Verlag GmbH & Co. KGaA, Weinheim

μ-η¹:η¹-*N*,*N*′-Imidazolidine-Bridged Dicopper(II/II) Complexes of a New Dinucleating μ-Bis(tetradentate) Schiff Base Ligand: Synthesis, Structural Characterization, ^{1}H NMR Spectroscopy, and Magnetic Coupling

Manindranath Bera,[a] Wing Tak Wong,[b] Guillem Aromí,[c] and Debashis Ray*[a]

Keywords: N,O ligand / Imidazolidine / Copper complexes / Magnetic properties

The dicopper oxidation state in the title of the original article[1] is erroneously given as (II/III); however, it should be (II/II) as shown in the correct title above.

[1] M. Bera, W. T. Wong, G. Aromí, D. Ray, *Eur. J. Inorg. Chem.* **2005**, 2526−2535.

Received: June 27, 2005
The Editors

[a] Department of Chemistry, Indian Institute of Technology, Kharagpur 721 302, India,
E-mail: dray@chem.iitkgp.ernet.in
[b] Department of Chemistry, University of Hong Kong, Pokfulam Road, Pokfulam, Hong Kong SAR, P.R. China
[c] Departament de Química Inorgànica, Universitat de Barcelona, Diagonal, 647, 08028 Barcelona, Spain

 © 2005 Wiley-VCH Verlag GmbH & Co. KGaA, Weinheim **DOI: 10.1002/ejic.200500565**

EurJIC
European Journal of Inorganic Chemistry

Issue 17/2005

Pages 3377–3544

Papers available ahead of print in Early View at www.interscience.wiley.com

Earliest available Table of Contents:
Automatically, free of charge by e-mail through
www.interscience.wiley.com/alerts

COVER PICTURE

The cover picture shows the X-ray structures of some new half-sandwich (or piano-stool) Ru^{II}-[9]aneS_3 complexes ([9]aneS_3 = 1,3,7-trithiacyclononane) against a background of cells in culture. The complexes of the type $[RuCl_2(L)([9]aneS_3)]$, $[RuCl(L)_2([9]aneS_3)][CF_3SO_3]$, and $[Ru(dmsoS)(L)_2([9]aneS_3)][CF_3SO_3]_2$ (L = 1,3,5-triaza-7-phosphaadamantane, PTA; $(L)_2$ = 2 PTA or chelating N-ligand) were prepared from Ru-[9]aneS_3-dmso precursors and structurally characterized, both in solution and in the solid state. Some of them are analogues of known cytotoxic half-sandwich $Ru^{II}(\eta^6$-arene) organometallic compounds of the type $[RuCl(en)(\eta^6$-arene)$][PF_6]$ and $[RuCl_2(PTA)(\eta^6$-arene)], in which the aromatic fragment is replaced by the sulfur macrocycle [9]aneS_3 while the rest of the coordination sphere is left unchanged. Preliminary in vitro tests performed on some complexes against the mouse adenocarcinoma cancer cell line (TS/A) and the human mammary normal cell line (HBL-100) showed that, in general, the Ru-[9]aneS_3 compounds have a cytotoxicity comparable to that of the corresponding organometallic analogues. These results suggest that the aromatic fragment of the piano-stool Ru^{II} compounds is not an essential feature for the in vitro anticancer activity, and it might be effectively replaced by another face-capping ligand with a low steric demand, such as [9]aneS_3. Details are discussed in the article by E. Alessio et al. on p. 3423 ff. This work was performed within the framework of COST Action D20, a collaboration between WG 0001 and WG 0005.

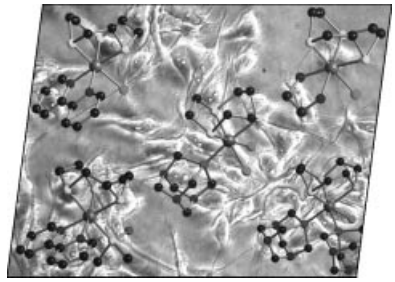

MICROREVIEW

Contents

3393 **M. Trueba,* S. P. Trasatti**

γ-Alumina as a Support for Catalysts: A Review of Fundamental Aspects

Keywords: Alumina / Materials science / Micro- and macrostructures / Supported catalysts

 © 2005 Wiley-VCH Verlag GmbH & Co. KGaA, Weinheim

SHORT COMMUNICATIONS

3405 **C. P. Pradeep, P. S. Zacharias,* S. K. Das***

A Chiral Copper Complex Forms Supramolecular Homochiral Helices via O−H···Cl−Cu Interactions

Keywords: Copper / Helical structures / Hydrogen bonds / Schiff bases / Self-assembly / Supramolecular chemistry

3409 **P. Gómez-Saiz, R. Gil-García, M. A. Maestro, J. L. Pizarro, M. I. Arriortua, L. Lezama, T. Rojo, J. García-Tojal***

Unexpected Behaviour of Pyridine-2-carbaldehyde Thiosemicarbazonatocopper(II) Entities in Aqueous Basic Medium − Partial Transformation of Thioamide into Nitrile

Keywords: Copper complexes / Desulfurization / Structure elucidation / Thiosemicarbazone complexes

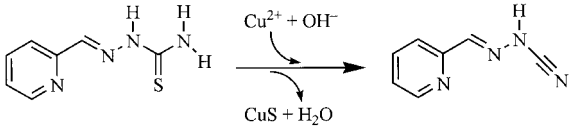

3414 **J. Lewiński,* W. Bury, T. Kopeć, E. Tratkiewicz, I. Justyniak, J. Lipkowski**

Unprecedented Coordination Mode Variation of Group 13 Metal−Alkyl Compounds Derived from Methyl Thiosalicylate

Keywords: Aluminum / Indium / Noncovalent interactions / Thiolates

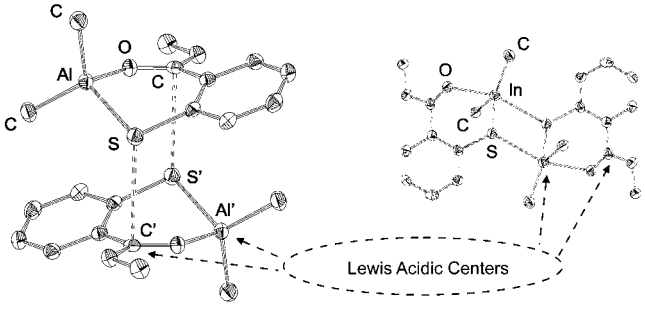

3418 **X.-L. Wang, C. Qin, E.-B. Wang,* L. Xu**

An Unusual 3D Interdigitated Architecture Self-Assembled from Sidearm-Containing 2D Bilayer Motifs with a Cuboidal Framework

Keywords: Bilayers / Interdigitation / Luminescence / Supramolecular chemistry / Zinc

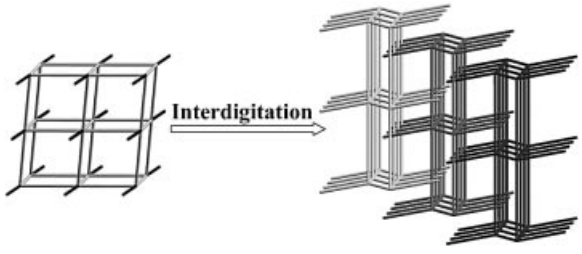

FULL PAPERS

3423 **B. Serli, E. Zangrando, T. Gianferrara, C. Scolaro, P. J. Dyson, A. Bergamo, E. Alessio***

Is the Aromatic Fragment of Piano-Stool Ruthenium Compounds an Essential Feature for Anticancer Activity? The Development of New Ru^{II}-[9]aneS_3 Analogues

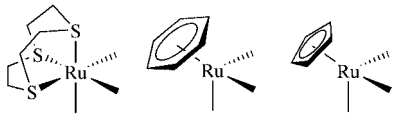

Keywords: Antitumor agents / Facial coordination / Half-sandwich complexes / Ruthenium / S ligands

3435 **E. Fujiwara, H. Fujiwara, B. Z. Narymbetov, H. Kobayashi, M. Nakata, H. Torii, A. Kobayashi,* K. Takimiya, T. Otsubo, F. Ogura**

Molecular Conductors Based on *peri*-Ditellurium-Bridged Donors, 2,3-DMTTeA and TMTTeN

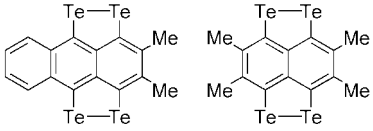

2,3-DMTTeA TMTTeN

Keywords: Tellurium / Conducting materials / Magnetic properties / Band structure

3450 **K. Heinze,* M. Beckmann**

Conformational Analysis of Chiral Ferrocene–Peptides

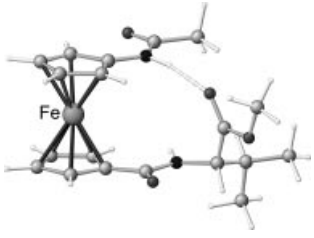

Keywords: Conformational analysis / Hydrogen bonds / Metallocenes / Modelling / Peptides

3458 **Q.-Y. Liu, L. Xu***

Novel Structure Evolution of Lanthanide–SIP Coordination Polymers (NaH_2SIP = 5-Sulfoisophthalic Acid Monosodium Salt) from a 1D Chain to a 3D Network as a Consequence of the Lanthanide Contraction Effect

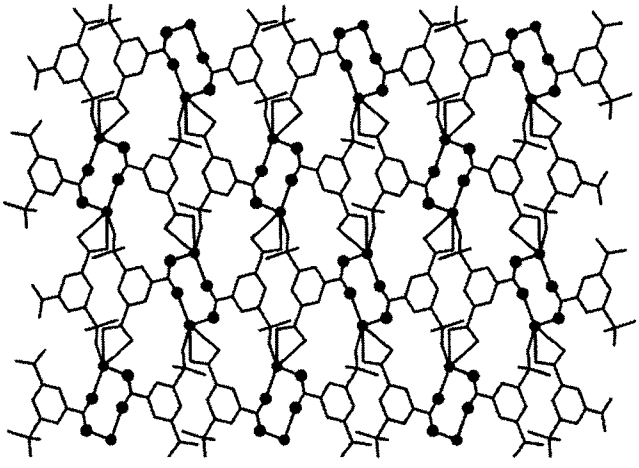

Keywords: Crystal structures / Hydrothermal synthesis / Lanthanides / Lanthanide contraction

 © 2005 Wiley-VCH Verlag GmbH & Co. KGaA, Weinheim

3467 **D. A. Garnovskii, N. A. Bokach, A. J. L. Pombeiro,* M. Haukka, J. J. R. Fraústo da Silva, V. Yu. Kukushkin***

Microwave-Assisted and Pd^{II}-Mediated Nitrile−Oxime Coupling

Keywords: Microwave synthesis / Metal-mediated synthesis / Nitriles / Oximes / Nitrile−oxime coupling / Palladium complexes

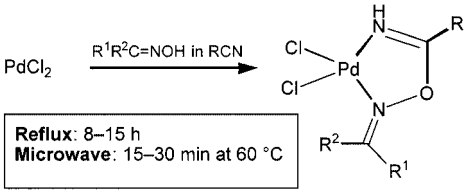

3472 **G. Paolucci,* M. Vignola, S. Formenti, W. Massa**

4f-*ansa*-Metallocenes−Dinuclear Complexes where the *ansa*-Dicyclopentadienyl Ligands Simultaneously Act in a Chelating and Bridging Mode − Crystal Structure of $(LY)_2(\mu\text{-}L)$ [L = 2,6-Pyridinediylbis(methylcyclopentadienyl)]

Keywords: Yttrium / Praseodymium / Dinuclear *ansa*-lanthanocenes / Metallocenes

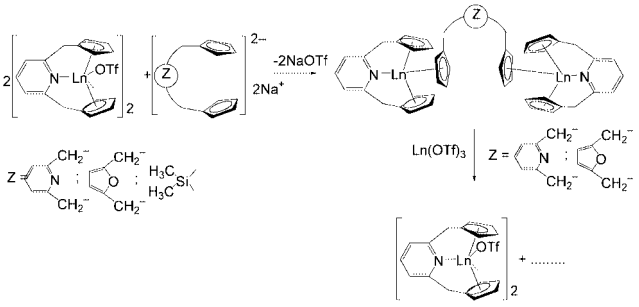

3479 **M. Vázquez, M. R. Bermejo,* M. Licchelli, A. M. González-Noya, R. M. Pedrido, C. Sangregorio, L. Sorace, A. M. García-Deibe, J. Sanmartín**

Non-Covalent Aggregation of Discrete Metallo-Supramolecular Helicates into Higher Assemblies by Aromatic Pathways: Structural and Chemical Studies of New Aniline-Based Neutral Metal(II) Dihelicates

Keywords: Fluorescence / Helical structures / Pi interactions / Self-assembly / Supramolecular chemistry

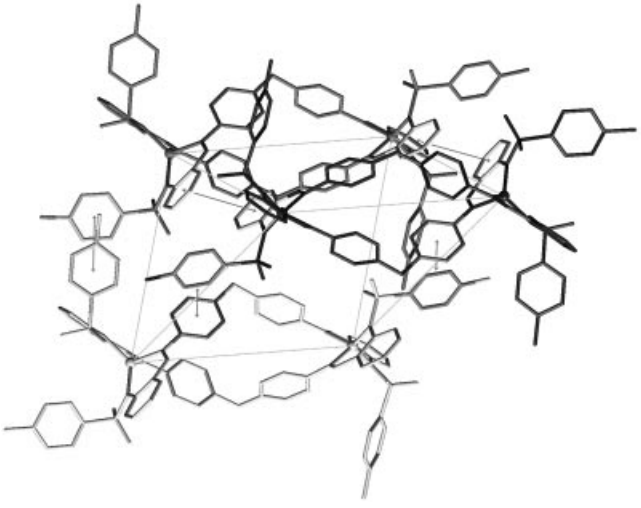

3491 **A. T. Chaviara, A. C. Tsipis,* P. J. Cox, C. A. Bolos***

Synthesis, Structural Characterization, and Density Functional Study of Homo- and Heteropolyhalide Complexes of Cu^{II} with Dien and Dpta Ligands: Crystal Structure of [Bis(3-aminopropyl)amine](bromo)(diiodobromo)copper(II)

Keywords: Copper / Density functional calculations / Halides / N ligands

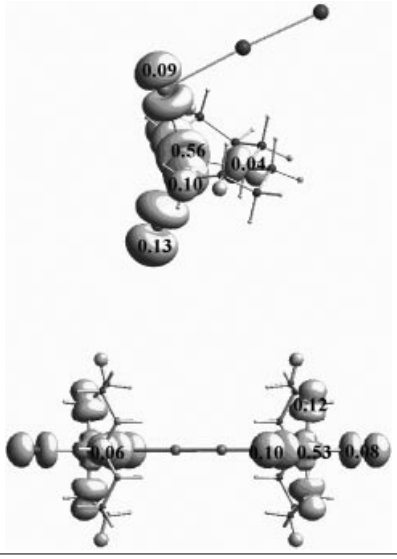

 © 2005 Wiley-VCH Verlag GmbH & Co. KGaA, Weinheim

3503 **S. Kaizaki,* D. Shirotani, Y. Tsukahara, H. Nakata**

First Observation of NIR 4f−4f Luminescence through the Energy Transfer from the SOMO π* Doublet in Nitronyl Nitroxide Radical Lanthanide(III) Complexes

Keywords: Near infrared 4f−4f luminescence / Lanthanide(III) complexes / Nitronyl nitroxide radical / Energy transfer / Antenna effect

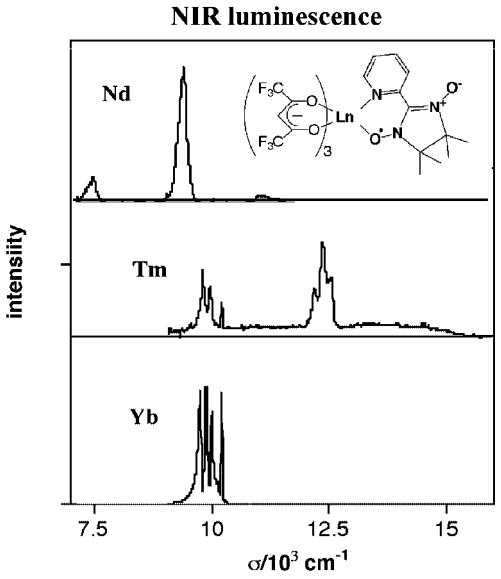

3506 **C. Zimmermann, F. W. Heinemann, A. Grohmann***

A Tetraphosphane Imine Ligand Which Enforces Square-Pyramidal Coordination

Keywords: Tetrapodal pentadentate ligand / Phosphane ligands / Chelates / Cobalt / Nickel

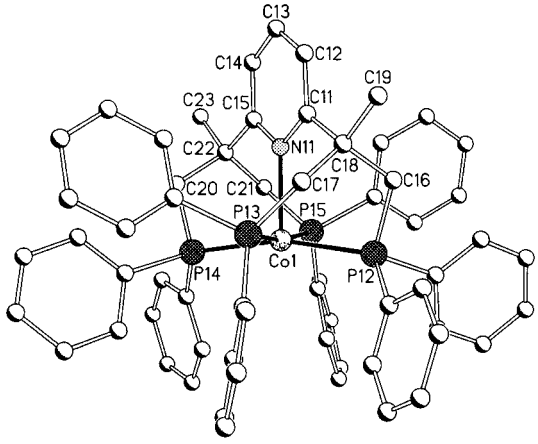

3513 **S. Durot, C. Policar,* F. Cisnetti, F. Lambert, J.-P. Renault, G. Pelosi, G. Blain, H. Korri-Youssoufi, J.-P. Mahy**

Series of Mn Complexes Based on *N*-Centered Ligands and Superoxide − Reactivity in an Anhydrous Medium and SOD-Like Activity in an Aqueous Medium Correlated to Mn^{II}/Mn^{III} Redox Potentials

Keywords: N,O ligands / Manganese / Superoxide / SOD mimics / Imidazole / Phenolate

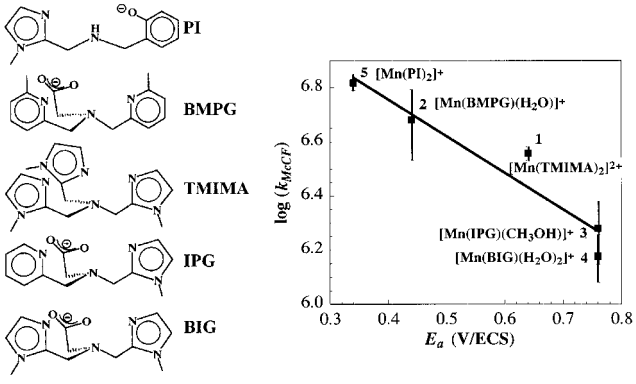

 © 2005 Wiley-VCH Verlag GmbH & Co. KGaA, Weinheim

3524 **H. Nöth,* A. Troll**

The *N*-Lithiation of 2,4,6-Triphenylborazine

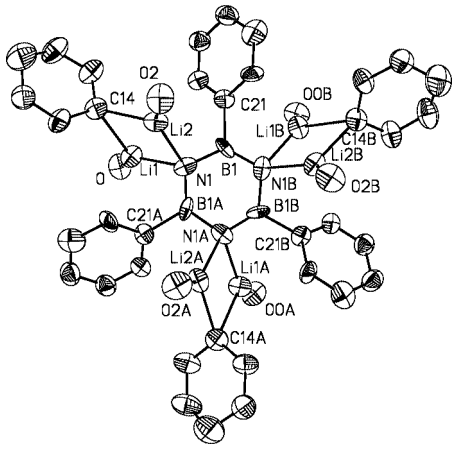

Keywords: Lithium / Boron / Deprotonation reactions / Tetraphenylborazinates

3536 **C. Knapp, R. Mews***

Complexes of the Bicyclic Multifunctional Sulfur-Nitrogen Ligand $F_3CCN_5S_3$ with Co^{2+}, Zn^{2+}, Cu^{2+}, and Cd^{2+}

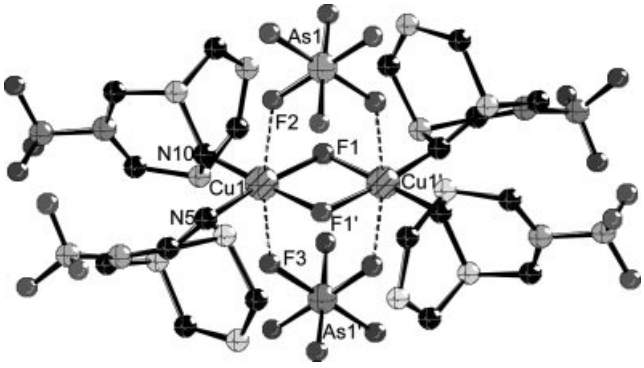

Keywords: Bridging ligands / Heterocycles / N ligands / S ligands / Transition metals

γ-Alumina as a Support for Catalysts: A Review of Fundamental Aspects

Monica Trueba*[a] and Stefano P. Trasatti[a]

Keywords: Alumina / Materials science / Micro- and macrostructures / Supported catalysts

The present review discusses the most important aspects to take into consideration to improve the properties of γ-Al_2O_3 as a support for catalytic applications. We show that the synthetic route to γ-Al_2O_3 is the starting point that determines the micro- and macrostructure of the oxide and, consequently, allows control of the support characteristics. The relevance of the adequate structural characterization of the oxide as well as of its surface sorption behavior through the proton-affinity distributions, are considered. The usefulness of the latter during supported catalyst preparation, for catalytic active sites characterization, and for stability evaluation after calcination are discussed for the Co/γ-Al_2O_3 system in particular.

(© Wiley-VCH Verlag GmbH & Co. KGaA, 69451 Weinheim, Germany, 2005)

0. Introduction

Among the different transition aluminas known, γ-alumina (γ-Al_2O_3) is perhaps the most important with direct application as a catalyst and catalyst support in the automotive and petroleum industries.[1,2] The usefulness of this oxide can be traced to a favorable combination of its textural properties, such as surface area, pore volume, and pore-size distribution and its acid/base characteristics, which are mainly related to surface chemical composition, local microstructure, and phase composition. Nevertheless, the chemical and hydrothermal stability of γ-Al_2O_3 are still a critical point for catalytic applications.

For example, the use of γ-Al_2O_3 as a support for Co-based catalysts in the Fischer–Tropsch (FT) process for the production of clean fuels[3,4] is not lacking in practical problems. The most common undesirable situations are: 1) alumina dissolution during supported catalyst preparation (usually in aqueous media), which affects the nature of the resulting Co species, 2) γ-Al_2O_3 rehydration during catalyst implementation because of the H_2O produced in the FT process, and 3) thermal degradation (sintering and phase transformation) in the catalyst regeneration step (hot-

[a] Department of Physical Chemistry and Electrochemistry, University of Milan,
Via C. Golgi 19, 20133, Milan, Italy
Fax: +39-02-5031-4300
E-mail: monica.trueba@unimi.it

Monica Trueba is a Ph.D. student in the Department of Physical Chemistry and Electrochemistry at the University of Milan (Italy). She is working on alumina supports for catalytic applications.

Stefano P. Trasatti is presently a researcher in the Physical Chemistry and Electrochemistry Department of the University of Milan. He received a PhD in Industrial Chemistry in 1995. In the same year he was awarded the Oronzio De Nora prize for the best work in the field of electrochemistry. He worked in a private company from 1996 to 2002 where he was responsible for surface treatments and material testing. He is the author of more than 20 papers and two patents in the field of metallic corrosion. His research interests include corrosion in refinery, corrosion monitoring and control, as well as the use of artificial intelligence systems in the study of corrosion.

MICROREVIEWS: This feature introduces the readers to the authors' research through a concise overview of the selected topic. Reference to important work from others in the field is included.

spots). It is clear that these side-reactions, which affect catalyst stability, activity, and selectivity, are principally related to support stability.

In the present work, the main aspects to be taken into account when trying to improve the properties of γ-Al_2O_3 as a support for catalysts are reviewed. First, the micro- and macroscopic nature of the support are described because without an adequate knowledge of them any applications will always be less than optimal. Next, the significance of the synthesis route is discussed, followed by the γ-Al_2O_3/H_2O interface and acid/base properties due to the effect of H_2O on support stability during both catalyst preparation and implementation. The importance of studying the oxide surface sorption behavior through the proton-affinity distributions is also considered. Finally, some practical implications for the Co/γ-Al_2O_3 system are presented.

1. γ-Alumina Structure

1.1. Microstructure

The principal features of the γ-Al_2O_3 microstructure are usually reported for the oxide obtained by the thermal dehydration (calcination) of aluminum hydroxides and oxyhydroxides. The transformation sequence during this process has been studied for many years, and it also gives other metastable phases of α-Al_2O_3 depending on the calcination temperature [Equation (1)].[2,5–10]

$$\text{Boehmite/amorphous } Al_2O_3 \rightarrow \gamma\text{-}Al_2O_3 \rightarrow \delta\text{-}Al_2O_3 \rightarrow \theta\text{-}Al_2O_3 \rightarrow \alpha\text{-}Al_2O_3 \quad (1)$$

γ-Al_2O_3 is reported to appear at temperatures between 350 and 1000 °C when it is formed from crystalline[11] or amorphous[12] precursors, and is stable at temperatures as high as 1200 °C when the latter is used as the starting material.

The structural characterization of γ-Al_2O_3 is commonly performed by techniques such as IR spectroscopy,[6,13–16] NMR spectroscopy,[10,14,15,17] X-ray diffraction (XRD),[10,14,17,18] transmission electron microscopy (TEM),[16,19] and BET adsorption.[16,17] Additional information from the use of relatively new methods such as neutron vibrational spectroscopy (NVS), prompt-gamma activation analysis (PGAA), and small-angle X-ray scattering (SAXS), is also available.[10,16] Nevertheless, despite the variety of experimental and computational[9,20,21] studies, there is still a considerable debate about the structure of γ-Al_2O_3 as well as many of the transitional Al_2O_3 phases.

The structure of γ-Al_2O_3 is traditionally considered as a cubic defect spinel type, whose experimental unit cell is illustrated in Figure 1<yigr1>. The defective nature derives from the presence of only trivalent Al cations in the spinel-like structure, i.e., the magnesium atoms in the ideal spinel $MgAl_2O_4$ are replaced by aluminum atoms. The oxygen lattice is built up by a cubic close-packed stacking of oxygen layers, with Al atoms occupying the octahedral and tetrahedral sites. To satisfy the γ-Al_2O_3 stoichiometry some of the

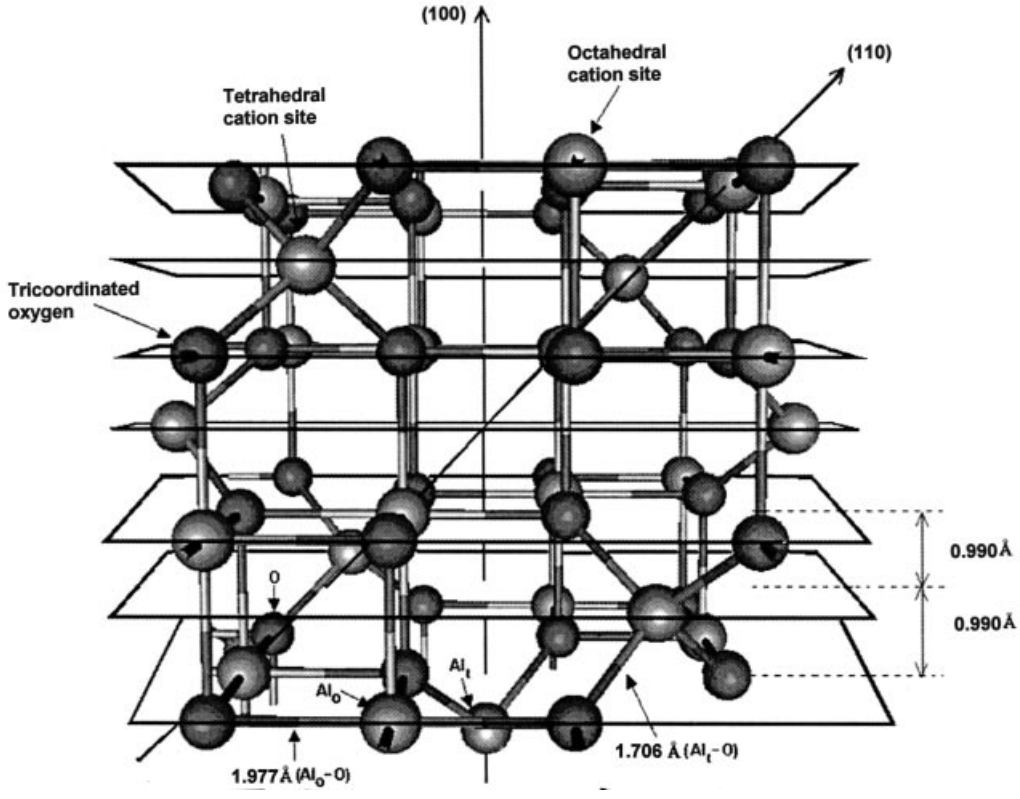

Figure 1. Experimental cubic γ-Al_2O_3 spinel-type unit cell.[21]

 © 2005 Wiley-VCH Verlag GmbH & Co. KGaA, Weinheim

lattice positions remain empty (vacancies), although their precise location is still controversial.

When γ-Al_2O_3 is derived from amorphous aluminas it has always been reported to possess a cubic lattice.[12,22–25] Both a cubic lattice[26–28] and tetragonal distortion[29,30] are found for boehmite [AlO(OH)]- or gibbsite [$Al(OH)_3$]-derived γ-Al_2O_3. Other studies, however, have proposed the existence of only a tetragonal structure.[10,16,31] Recently, tetragonal γ-Al_2O_3 obtained from highly crystalline boehmite was reported to be present between 450–750 °C.[10] A reduction of the tetragonal distortion can be produced by increasing the temperature, but at no stage is cubic γ-Al_2O_3 obtained. A new phase has been identified with more obvious cation ordering above 750 °C, designated as γ′-Al_2O_3, which approaches the structure of δ-Al_2O_3 above 900 °C.

It should be pointed out that some discrepancies exist with respect to the δ-phase, which is usually an intermediate phase between γ- and θ-Al_2O_3 [Equation (1)]. Some studies have reported that there is no distinct difference between δ- and γ-Al_2O_3.[30,32] The main difference is considered to be in the arrangement of the Al atoms: the vacancies are distributed between octahedral and tetrahedral sites in γ-Al_2O_3, while they are only in octahedral sites in δ-Al_2O_3; the oxygen lattice is the same for both phases. Other works, however, report no occurrence of the δ-phase at all.[7,11]

Many studies of γ-Al_2O_3 by means of XRD, NMR spectroscopy, and TEM have demonstrated the preference for vacancies in octahedral sites with the Al cation in tetrahedral positions,[7,26,28] whereas other authors support the opposite conclusion, i.e., the vacancies tend to reside in tetrahedral positions.[15,29] On the other hand, it has also been suggested that the cationic vacancies should be more realistically imagined as being distributed randomly between tetrahedral and octahedral cavities.[30] Further, it has also been reported that γ-Al_2O_3 contains significant portions of cations occupying "non-spinel" sites, i.e., sites that are vacant in the ideal spinel structure.[27]

The role of hydrogen has also been stressed. Some works claim that a considerable amount of hydrogen is present in the bulk structure of γ-Al_2O_3,[7,13,33,34] although the possibility of the hydrogen spinel (HAl_5O_8) as a structural candidate instead of the OH species has been ruled out.[14,27,34] Computational studies show that this spinel structure is thermodynamically unstable.[9] A relatively well-ordered bulk crystalline γ-Al_2O_3 that contains no interstitial hydrogen has been reported in recent studies[16] where the H-containing species are localized at the surface and within amorphous regions.

The removal of OH groups during high temperature treatment creates coordinatively unsaturated surface (*cus*) cations where tetrahedral (Al^{IV}) and octahedral (Al^{VI}) aluminum coordinations are the most widely accepted.[10,14,35] However, variable amounts of pentahedrally coordinated aluminum (Al^{V}), concentrated principally at the surface, have also been found.[13,15,36,37] It has been reported that the Al^{V} content is strictly related to the pore-size distribution, crystallinity, and surface area such that a high Al^{V} amount implies low crystallinity and a high surface area.[13] Three-coordinate Al on the surface is unlikely, despite the fact that its presence would be expected based on the bulk structure.[14] The partly uncoordinated metal cations and oxide anions that lie at the surface of γ-Al_2O_3 can act as acids and bases, respectively, according to the Lewis definition.[35] The strongest acid sites are considered to be the Al^{IV} *cus* ions, which are mainly located in crystallographically defective configurations and are responsible for the high catalytic activity of highly dehydrated aluminas. Nevertheless, the defective configurations, which yield the reactive surface sites, tend to be annihilated during high-temperature dehydration. The tendency of the Al coordination number to be lowered on H_2O desorption produces a new kind of OH group. The last OH groups to be removed are not related to those which were present on the initial hydroxylated surface and whose structure determines the properties of the *cus* surface cations.

The most important surface features of γ-Al_2O_3 have been determined by means of IR[6,35,38] and NMR spectroscopy,[38–40] although the precise nature of the surface acid sites is still unknown. Up to now, the most accepted and frequently used empirical model to describe γ-Al_2O_3 surfaces was that developed by Knözinger and Ratnasamy:[6]

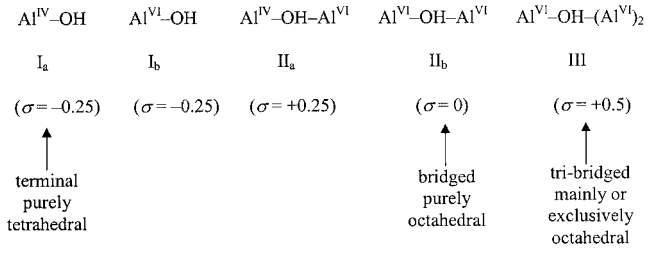

Accordingly, five different types of OH groups are present on the surface that exhibit a distinct "net electric charge" (σ), depending on the number of Al neighbors and on Al coordination. This model, however, has serious limitations due to its crude description of ideal γ-alumina surfaces that neglects surface hydroxylation/dehydroxylation process induced by temperature effects. Recently, using density functional (DFT) calculations, realistic models of the γ-Al_2O_3 surface have been proposed that account for the above process.[41] These models show that the behavior of various types of surface hydroxy groups depends strongly on the local chemical environment, morphology (exposed surfaces), and composition of the oxide, which are greatly influenced by the alumina precursors (starting materials) and synthetic methods used.

1.2. Macrostructure

Conventional γ-alumina is typically prepared by thermal dehydration of coarse particles of well-defined boehmite at a temperature above 400–450 °C.[2] The oxide obtained usually presents a surface area and pore volume below

 © 2005 Wiley-VCH Verlag GmbH & Co. KGaA, Weinheim

Table 1. Point of zero charge (*pzc*) of γ-Al_2O_3.

Preparation procedure	Experimental method	*pzc*
Thermal treatment and aging of the hydrolysis product of Al ethoxide	Microelectrophoresis[69]	6.7–9.2
Commercial (Degussa Corp.)	Direct potentiometric titration[73]	8.6
	back titration[73]	7.5
Commercial (American Cyanamid)	Mass titration[79]	8.3
Commercial (American Cyanamid)	Direct potentiometric titration[77]	
	γ-Al_2O_3	7.0
	modified with F^-	3.4
	at different temperatures[80]	6.3–8.0
Commercial (unspecified)	Potentiometric titration and electrophoresis[81]	8.0
Commercial (Alfa Aesar)	Discontinuous titration[74]	6.7
Commercial (Condea)	Direct potentiometric titration[49]	
	γ-Al_2O_3 (5–10% δ-phase)	8.25
	γ-Al_2O_3 (56% δ-phase)	not *cip*
	γ-Al_2O_3 + 5% silica	5.7
	γ-Al_2O_3 + 5% zirconium	6.9
	γ-Al_2O_3 + 5% lanthanum	7.5

250 $m^2 g^{-1}$ and 0.50 $cm^3 g^{-1}$, respectively. Also, its stability is greatly affected by steam, which accelerates the transformation of γ-Al_2O_3 into α-Al_2O_3, with a consequent marked drop of surface area as a result of sintering.

Besides thermal decomposition, several methods for γ-Al_2O_3 synthesis that use traditional techniques of preparative chemistry, such as precipitation and hydrolysis, have been developed to improve the oxide's textural properties and hydrothermal stability.[17,19,33,42–47] Moreover, the addition of thermal stabilizing modifiers (Zr^{4+}, Ca^{2+}, Th^{4+}, and La^{3+}) is quite popular. The latter inhibit the transformation of transition aluminas into the α-phase, opposite to the effect obtained with In^{3+}, Ga^{3+}, and Mg^{2+}. However, the acid-base behavior of the modified oxide can be very different with respect to the γ-Al_2O_3 itself (Table 1).[48,49] The Al_2O_3-SiO_2 system has also been widely studied.[50–53]

Since the transition of metastable phases into α-Al_2O_3 occurs predominantly at the contact between primary particles, the key for suppressing the rate of sintering (without additives) is to prepare active aluminas in a morphological state in which the area of contact between primary particles is minimized, such as those with a fibrillar crystalline structure.[33] It is well known that microcrystalline solids show slower decomposition kinetics (e.g. dissolution).[54] Furthermore, it is preferable to avoid high-temperature treatments during calcination/decomposition of hydroxide and/or oxide mixtures because the solid-state reactions could be affected.

The past few years have witnessed marked progress in the synthesis of γ-aluminas. Due to the recent advancements in mesostructured silicas and other oxides,[55,56] efforts have been devoted to the synthesis of mesostructured aluminas with a well-ordered arrangement of pores that is essentially preserved after calcination. Many attempts have been made to synthesize ordered mesoporous alumina by supramolecular templating methods, where nonionic, anionic or cationic surfactants, or nonsurfactant molecules have been used as structural directing agents for the synthesis.[17,57–61] However, most of the aluminas obtained in this way present mainly amorphous framework walls that limit their hydrothermal stability, which greatly compromises their usefulness in catalytic applications.

A novel three-step assembly pathway for the formation of a mesostructured alumina with framework pore-walls made of crystalline, lathlike γ-Al_2O_3 nanoparticles has been reported recently.[62–64] The textural properties, like surface area and pore volume (300–350 $m^2 g^{-1}$ and 0.45–0.75 $cm^3 g^{-1}$, respectively), are improved with respect to the conventional γ-alumina. Moreover, the morphological characteristics obtained, i.e., crystallinity and fibrillar-like structure, greatly improve the oxide's thermal and hydrolytic stability. These new mesostructures can be readily impregnated with transition metal precursors from aqueous solutions without loss of porosity, surface area, or pore volume, thus making them promising for applications in catalysis.

Sol-gel is the preferred method for the synthesis of aluminosilicates since it provides a low-temperature synthesis with excellent control over mixing.[50] In particular, slow simultaneous hydrolysis of the two alkoxides (precursors) is preferred to pre-hydrolysis since a higher yield of heterolinkages can be obtained. It has been shown that the nature of the precursor and the manner in which precursor hydrolysis is performed determine the properties of the resulting Al_2O_3-SiO_2 mixed oxide.[52,53] A decrease of the surface area (larger than the single oxides) with an increase of silica amount is obtained when aluminosilicates are prepared by slow simultaneous hydrolysis of Al and Si precursors.[53] A different tendency is reported for alumina-silica xerogels obtained by pre-hydrolysis.[52]

The wide experimental evidence indicates that the preparation history has an important effect on the type of γ-Al_2O_3 structure that is produced (phase composition, bulk and surface chemical composition, and local microstructure of the oxide) as well as on oxide stability and textural properties. The reaction sequence and kinetics depend on the properties of the precursor and this applies not only to its different forms, for example gelatinous or highly crystalline

 © 2005 Wiley-VCH Verlag GmbH & Co. KGaA, Weinheim

types, but also to the conditions under which the precursor is prepared.

2. γ-Al_2O_3/H_2O Interface

The existence of Lewis acid sites (*cus* cations) and basic sites (oxide anions) at the γ-Al_2O_3 surface allows its rehydroxylation (or rehydration) by interaction with H_2O, so that *cus* cations and anions can, in part, be converted into surface hydroxy groups.[6,13,21,35,37] This interaction has been represented as a two-step process for γ-Al_2O_3 under atmospheric conditions[21,37] that involves nondissociative adsorption of H_2O on Lewis sites (*cus* Al), which essentially consists in a transfer of electron density to a Lewis acid site

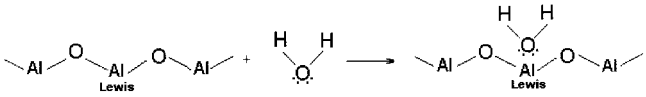

followed by dissociative chemisorption of H_2O and modification of surface Al coordination with the hydroxy group bonded to the Al atom, i.e., the two-coordinate oxygen atom adjacent to the Al site is protonated.

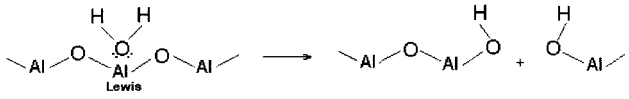

The rehydration of γ-alumina corresponds to the loss of tetrahedrally coordinated Al surface species and an increase of hydroxylated octahedral Al that can also involve some Al^{V}.[13] The reactivity towards water depends on the layers exposed at each surface.

When the oxide particles are dispersed in water, the surface oxo and hydroxo groups at the solid/solution interface can associate with protons to form positively charged surface complexes.[33,54,65] The term "surface complex" does not imply a particular bonding structure but is used simply to indicate that chemical and/or noncoulombic physical interactions between the ionized surface sites and the associating ion lead to a kind of surface complex. The proton binding by oxo or hydroxy groups produces –OH and $–OH_2$ species at the surface that will react according to their own proton affinity constant [Equations (2) and (3)]:[33]

$$[(M^{\nu})_n\text{-O}]^{\Sigma\nu-2} + H^+ \rightleftharpoons [(M^{\nu})_n\text{-OH}]^{\Sigma\nu-1},\ K_i^{\Sigma\nu-2} \quad (2)$$

$$[(M^{\nu})_n\text{-OH}]^{\Sigma\nu-1} + H^+ \rightleftharpoons [(M^{\nu})_n\text{-OH}_2]^{\Sigma\nu},\ K_i^{\Sigma\nu-1} \quad (3)$$

where $K_i^{\Sigma\nu-2}$ and $K_i^{\Sigma\nu-1}$ represent the intrinsic affinity constants that depend, for various types of surface groups, on the local configuration of the surface, especially the number (n) of surrounding metal (M) cations and their effective bond valence (ν). It follows that the oxide/solution interface may be very complex and consist of different surface species that can reside at the same time on the oxide surface.

As a result of γ-Al_2O_3 surface/H_2O interactions, the dissolution of the alumina oxide may be induced by adsorption of H^+ ions.[54,65] Earlier, the extent of dissolution was assumed to be controlled by thermodynamics. Presently, there is general agreement that this process is often controlled by slow chemical reactions occurring at the oxide/H_2O interface.[66–68] A dissolution reaction, more akin to etching, takes place preferentially along crystal defects induced by dislocations that may considerably accelerate kinetic processes while exerting only slight effects on the thermodynamic properties. The OH groups of the alumina surface determine not only its chemical and electrochemical properties but also the activity in the etching process. Thus, release of Al ions can be affected by any process that modifies the hydroxy group coverage of the oxide, such as temperature of calcination and cooling conditions, adsorption on surfaces, irreversible exchange of OH groups, etc.

Studies dedicated to clarifying the dissolution mechanism of anodic polycrystalline alumina membranes[67] have shown that the ratio of Al ion release into the solution depends on the alumina preparation, electrolyte conditions, such as ionic strength, and surface rehydroxylation. The authors considered that the different types of Al ions present on the surface are more active during the first treatment, since a decrease of the concentration of Al ions in solution is obtained upon repeated treatment with acid or base. They suggested that continuation of the etching is preceded by the rehydroxylation or hydrolysis of Al–O–Al bonds [Equation (4)]:

$$\text{Al–O–Al} + H_2O \rightarrow 2\,\text{AlO(OH)} \quad (4)$$

It is worth mentioning that the adsorption of small amounts of alumina on the surface of amorphous silica reduces the rate of silica dissolution in water even when much less than a monolayer of aluminum ions is present.[51] It has been postulated that negative aluminosilicate ion sites on the surface prevent hydroxy ions, which are required to catalyze the dissolution of silica, from approaching the interface.

3. Acid/Base Properties of γ-Al_2O_3

3.1. General Considerations

Most solid oxides develop pH-dependent surface charges when immersed in aqueous solution, according to the general equilibria given in Equations (5) and (6)]:[33,65,68,70]

$$\equiv\text{S–OH}_2^+ \rightleftharpoons \equiv\text{S}_{\text{basic}}\text{–OH} + H^+ \quad (5)$$

$$\equiv\text{S}_{\text{acid}}\text{–OH} + OH^- \rightleftharpoons \equiv\text{S–O}^- + H_2O \quad (6)$$

where $\equiv S_{basic}–OH$ and $\equiv S_{acid}–OH$ represent hydrated sites at the oxide surface with basic and acidic character and may have different local configurations. Depending on the concentration of either one or another type of sites, the oxides may show a dominant tendency to adsorb cations (SiO_2, SiO_2-Al_2O_3, zeolites), anions (MgO, La_2O_3, ZnO), or

 © 2005 Wiley-VCH Verlag GmbH & Co. KGaA, Weinheim

both cations in basic solution and anions in acidic solution (Al_2O_3, TiO_2, Cr_2O_3).

Acid and basic sites behave exactly as acid and basic substances in solution. Therefore, they respond reversibly to a change in solution pH with the concomitant variation of the total surface charge, with the H^+ and OH^- ions usually being regarded as potential determining ions (absence of specific adsorption).

If Γ_{OH^-} is the surface concentration of negatively charged groups and Γ_{H^+} is the surface concentration of positively charged groups, the net surface charge of the oxide (σ_{ox}) is defined according to Equation (7),[71,72] where Γ is measured in mol cm^{-2} and σ_{ox} in C cm^{-2}.

$$\sigma_{ox} = F(\Gamma_{H^+} - \Gamma_{OH^-}) \quad (7)$$

The pH at which $\sigma_{ox} = 0$, that is where $\Gamma_{H^+} = \Gamma_{OH^-}$, is called the point of zero charge (*pzc*). This does not correspond to the situation of undissociated OH groups but more realistically to the condition of positive surface groups being at the same concentration as negative surface groups. Generally, the surface charge of solid oxide is positive at low pH and negative at high pH.

It should be pointed out that the terminology employed in the literature for "zero point" is plenty, and terms like isoelectric point of the solid (*ieps*),[69,70] point of zero salt effect (*pzse*),[73] point of zero net charge (*pznc*),[74] point of zero net proton charge (*pznpc*),[74–76] and pristine point of zero charge (*ppzc*)[77,78] can be found.

Besides *pzc*, another important quantity that characterizes oxide/solution interfaces is the isoelectric point (*iep*), which corresponds to the pH at which the so-called zeta (ζ) potential is zero.[70–72] This potential is related only to the presence of the free charges in the diffuse layer in solution and can be determined by means of electrokinetic experiments like electrophoresis.

According to the *pzc* and *iep* concepts, the difference between these characteristics is a substantial one. The *pzc* measures the condition of neutrality of the oxide surface while the *iep* is a measure of the condition of zero diffuse charge on the solution side. In the absence of specific adsorption the condition of neutrality corresponds to $\sigma_{ox} = 0$ on the solution side, hence *pzc* = *iep*. If specific adsorption is present, the net charge in the liquid phase of the interface may be different from zero, i.e., $\zeta \neq 0$ and *pzc* ≠ *iep*. Conversely, at the *iep*, the fact that the total charge is zero does not necessarily mean that $\Gamma_{H^+} = \Gamma_{OH^-}$ due to the possible presence of extra charge associated with specifically adsorbed non-potential-determining ions.

The *pzc* is commonly determined by potentiometric titration[52,53,73,76,77,79–81] as these results can be directly converted into proton-adsorption isotherms. The relative surface concentration of protons is frequently obtained by mass balance between the proton (or hydroxide) ions added to solution and the measured proton concentration in solution at equilibrium.[53,73,77–80] The titration procedure is usually performed for different concentrations of the inert electrolyte, i.e., at different solution ionic strengths. If the potential-determining ions are H^+ and OH^- for acid and base titration, respectively (absence of specific adsorption), the titration (charging) curves as well as adsorption isotherms should pass through a common intersection point (*cip*), identified as *pzc*. It should be pointed out that potentiometric titration is reliable only if the amount of protons exchanged by the oxide sample is larger than that involved in the autoprotolysis of water, which is pH dependent.[82] Accordingly, the pH window whereby useful information is obtained is from pH = 3 to 11 (outside this region the buffering effect of H_2O prevails).

3.2. Point of Zero Charge of γ-Al_2O_3

The surface sorption behavior of γ-Al_2O_3 has been widely studied, although the *pzc* for this oxide is not reported as a unique value or in a narrow range of pH values but between 6 and 9.[49,65,69,73,74,76,77,80–83] This is related mainly to the differences in material preparation that influence the micro- and macrostructure of the oxide, and to the experimental method used for *pzc* determination. General trends have been proposed, like the variation of the *pzc* with degree of sample hydration, impurities, structure defects, etc. Some of the available data are summarized in Table 1.

Recently, a discontinuous titration procedure that allows simultaneous measurement of protons and background electrolyte has shown that whereas proton adsorption/desorption gives rise to a positive/negative surface charge, Al dissolution does not.[74] This result supports previous studies which concluded that Al dissolution consumes H^+ ions without affecting the surface charge.[73,84,85] For example, increasing the amounts of soluble Al or CO_2 in solution lowers the phenolphthalein end-point (8.3) to 7.9 and 7–7.3, respectively.[85]

Two mechanisms of acid-base consumption have been proposed,[74] namely significant proton consumption at low values of pH as a result of either proton adsorption [Equation (8)] or Al dissolution [Equation (9)], and base consumption that reflects proton dissociation at higher pH (>6) [Equation (10)] and/or mineral dissolution [Equation (11)].

$$\equiv AlOH + H^+ \rightleftharpoons \equiv AlOH_2^+ \quad (8)$$

$$0.5\,Al_2O_{3(s)} + 3\,H^+ \rightleftharpoons Al^{3+} + 1.5\,H_2O \quad (9)$$

$$\equiv AlOH + OH^- \rightleftharpoons \equiv AlO^- + H_2O \quad (10)$$

$$0.5\,Al_2O_{3(s)} + 1.5\,H_2O + OH^- \rightleftharpoons Al(OH)_4^- \quad (11)$$

These two mechanisms cannot be distinguished on the basis of titration data alone, and independent measurement of the background ion adsorption and Al dissolution are required, as was stressed in other research papers.[76]

Traditional titration methods do not properly consider the solubility of γ-Al_2O_3, which is pH dependent, since various concentrations of Al in solution exert different effects on the shape of the colloidal titration curve. For a correct estimation of the adsorbed proton concentration only,

 © 2005 Wiley-VCH Verlag GmbH & Co. KGaA, Weinheim

Schulthess and Parks[73] have developed a back-titration technique that allows the consideration of all sources that consume hydrogen ions and properly adjusts the titration curve for the changes in solubility as the pH changes. This method more accurately reveals the adsorption behavior of H^+ on the surface of γ-Al_2O_3. In fact, the obtained *pzc* values differ by more than one pH unit as forwards (8.60) and back (7.50) titration is performed.

Several studies have demonstrated that polyvalent cations in electrolyte solution compete successfully with protons for adsorption on the active sites of the alumina surface by means of a cation–proton exchange reaction.[54,69,74,75,79,86,87] It has been shown that this process constitutes an alternative method for the estimation of dissolution active sites, since it inhibits oxide dissolution (blocking effect).[53]

For γ-Al_2O_3, specific cationic adsorption is proposed because the *cip* is localized in the alkaline pH region and the H^+ adsorption is different from zero.[49,73,79,86] The common intersection point (*cip*), however, cannot be considered as the *pzc*, according to the previous definition. The competitive adsorption has been interpreted as follows.[73] If electrolyte cations/anions are specifically adsorbed over H^+/OH^- ions, an increase in apparent proton desorption/adsorption is produced. Each H^+/OH^- ion removed from the surface by cation/anion exchange would neutralize a OH^-/H^+ species in solution and this would not be readily distinguished from H^+ ion removal by adsorption. At the *cip*, the amounts of H^+ and OH^- displaced from the surface site are equal and no apparent change in pH is detected with changes in salt concentration (ionic strength). The fact that the *cip* is not coincident with the *pzc* indicates that the surface charge is not equivalent to the proton isotherms, and at high ionic strengths only apparent proton isotherms are obtained due to electrolyte cation/anion competition. The asymmetry (*cip* shift) of the charging curves also depends on the nature of the electrolyte ions and/or on the presence of differently reacting crystal planes.

The effect of the amount of γ-Al_2O_3 in solution on its surface behavior has also been investigated. It has been reported that the *pzc* decreases with concentration from about 9.5 at 1.0 wt.-% to 8.6 at 10 wt.-%,[76] thus indicating that the proton surface data obtained for dilute suspensions do not directly reflect the surface charge characteristics of concentrated suspensions. In a previous work it was found that the amount of oxide present in suspension does not influence the amount of protons consumed/released upon dissolution of γ-Al_2O_3; however, the concentration of the solid in solution was considerably lower (1–3 wt.-%).[77]

The acid-base properties of aluminosilicates have also been studied[33,50–53,88,89] due to the usefulness of these materials in catalytic applications. It has been reported that the surface charge and *pzc* of the mixed oxide increase with Al content,[53] although Lewis acid sites of similar strength are present on the surface independently of the Al/Si atomic ratio. Brønsted acidity also exists, especially in the samples with a higher percentage of silica, which arises from silanol groups (terminal silanol and bridging OH groups). The *pzc* of γ-Al_2O_3-SiO_2 also depends on the way γ-Al_2O_3 silanization is performed as well as on the silanization agent. For example, the use of ethyltriethoxysilane instead of dimethyldimethoxysilane lowers the *pzc* value from 7.1 to 6.25.[49]

3.3. γ-Al_2O_3 Surface Heterogeneity

Heterogeneity effects in the adsorption of oxide/electrolyte solutions were first considered by Leckie et al. in 1978.[90] Since then, many models[65,78,81,87,91,92] as well as a great variety of materials such as inorganic metal oxides,[82,86,87,93] mixed oxides,[94] clays,[95–97] carbons,[98,99] and humic substances[100,101] have been used to describe proton-binding behavior at oxide/solution interfaces. Most site-binding models are a combination of surface reactions and an electrostatic approach, and these models can often describe proton adsorption data quite satisfactorily, although their physical chemistry picture is very different. As a result, an objective picture of the intrinsic properties of the oxide/solution interface is difficult to obtain due to the dependence of the calculated parameters on the specific model applied.

An important result derived from γ-Al_2O_3 surface heterogeneity experimental studies[33,77,80] is the resolution of three or four categories of surface sites, making use of proton-binding isotherms from potentiometric titration and proton-affinity distributions. These sites contribute to proton binding and surface-charge development between pH = 3 and 11 and will react specifically with solution protons, depending on their log K_i and solution pH, as follows:

$$[Al^{VI}\text{–}O\text{–}Al^{IV}]^{-0.75} + H^+ \rightleftharpoons [Al^{VI}\text{–}OH\text{–}Al^{IV}]^{+0.25} \qquad \log K_{IIa} \approx 4.1$$

$$[Al^{IV}\text{–}OH]^{-0.25} + H^+ \rightleftharpoons [Al^{IV}\text{–}OH_2]^{+0.75} \qquad \log K_{Ia} \approx 6.8$$

$$[Al^{VI}\text{–}OH]^{-0.5} + H^+ \rightleftharpoons [Al^{VI}\text{–}OH_2]^{+0.5} \qquad \log K_{Ib} \approx 9.8$$

$$[(Al^{VI})_3\text{–}O]^{-0.5} + H^+ \rightleftharpoons [(Al^{VI})_3\text{–}OH]^{+0.5} \qquad \log K_{III} \approx 2.5$$

Nonactive surface sites over the mentioned pH range have also been proposed:

$$[Al^{VI}\text{–}OH\text{–}Al^{VI}]^0 + H^+ \rightleftharpoons [Al^{VI}\text{–}OH_2\text{–}Al^{VI}]^{+1} \qquad \log K_{IIb1} \approx -2$$

$$[Al^{VI}\text{–}O\text{–}Al^{VI}]^{-1} + H^+ \rightleftharpoons [Al^{VI}\text{–}OH\text{–}Al^{VI}]^0 \qquad \log K_{IIb2} \approx 12.5$$

Protonation of hydroxy groups is more difficult because of the proton–proton repulsion in the $–OH_2$ species. Only surface hydroxy groups with negative uncompensated charge (types I_a and I_b, according to Knözinger and Ratnasamy[6]) can be protonated in the pH interval used.

A direct consequence of this is that at any pH the oxide surface exhibits sites which carry positive charges (log $K_i >$ pH) and sites with negative charges (log $K_i <$ pH), which are disposed in regular arrays on different crystal planes at the surface. Another consequence is that, even at the pH

 © 2005 Wiley-VCH Verlag GmbH & Co. KGaA, Weinheim

corresponding to *pzc*, some of the above sites can still be charged.

A knowledge of the proton distribution and proton-binding properties for various surface sites (strength and number), synonymous of surface heterogeneity, is needed to predict the pH dependence of the surface charge. It has been shown that the occurrence of the *cip* in charging curves depends on the actual distribution of the surface sites.[49,73,77,93,102] This applies not only to γ-Al_2O_3 modified with anionic and/or cationic species but also when its phase composition changes. As illustrated in Table 1, no definite *cip* is obtained for γ-Al_2O_3 samples containing 56% of the δ-phase[49] as a result of the increase of surface and bulk heterogeneity. Success in obtaining a meaningful and accurate proton adsorption distribution generally depends on the method of its evaluation, the quality of the experimental data, and the appropriate choice of adsorption model.[103] Among the variety of methods for the quantitative estimation of the surface heterogeneity of metal oxides,[103–106] a new method based on the determination of proton-affinity distribution by plotting titration data as derivatives of the proton/hydroxy ion adsorption as a function of pH has been proposed.[107] This approach is considered more realistic from a physical point of view.

Additional necessary information is the temperature dependence of the equilibrium constant and the influence of the temperature on the proton-affinity distribution at the oxide/electrolyte interface, both of which are also vital for any attempt at understanding proton-induced surface dissolution. Studies of the effect of temperature on the proton-affinity distribution at the γ-Al_2O_3/electrolyte interface have shown that temperature variations can affect proton binding in a different way on various groups of surface sites, depending on their enthalpy and entropy changes for specific proton adsorption.[80] The effect of temperature and electrolyte is twofold: proton-affinity constants depend on temperature like all free-energy functions, but the development of the surface charge is also perturbed by electrostatic repulsion in the double layer, which is dependent on the electrolyte concentration.

It is worth mentioning that the use of proton-affinity distributions allows us to obtain reliable quantitative information on the Brønsted acidity of mixed oxide systems such as aluminosilicates.[33,52] Methods like IR[50] or titration with Hammett color indicators[108] often meet with the difficulty of separating the contributions of Brønsted and Lewis acidity.

The adsorption properties of oxides as a function of solution pH may be predicted, at least in principle, by the knowledge of their *pzc*. However, the heterogeneity of acid/base sites on their surface raises some questions about the significance of a global *pzc*. For every heterogeneous surface the concept of *pzc* must be more carefully considered, although, in reality, *pzc* is an overall surface property rather than a thermodynamically meaningful constant. The proton-binding properties for various surface sites allow us to predict the γ-Al_2O_3 adsorption capacity as a function of pH more accurately.

4. γ-AL_2O_3 as a Support

4.1. General Aspects

Transition aluminas are frequently used as pre-shaped supports for preparing multiphase catalysts that consist of an active phase dispersed on a carrier or support.[33] The properties of the active phase depend mainly on the manner in which the active component of the catalyst (precursor) is introduced onto the support and the nature and strength of precursor–support interactions.

The major route for supported catalyst preparation makes use of aqueous media by simple impregnation (wet impregnation or incipient wetness) or by homogeneous deposition-precipitation, ion exchange, and specific adsorption. The choice of one or the other route is usually made by considering the nature and strength of the support–precursor interactions. Common subsequent steps are washing and drying, accompanied by irreversible transformation of the catalyst (its activation).

Different kinds of precursor–support interactions have been considered. Surface interactions for small ions are generally accepted to be predominantly electrostatic, which is supported by experimental results where the extent of adsorption of positive/negative ions increases with a pH rise/decrease. Nevertheless, some experimental evidence reflects exceptions from the simple rule of electrostatic adsorption with the existence of "specific" or "chemical" surface–adsorbate interactions that may compete with coulombic repulsion, as in the adsorption of cations such as Ni^{2+}, Co^{2+}, and Pb^{2+} onto a positively charged alumina surface.[109,110] These results support the existence of specific sites on the hydroxylated surface that act in adsorption of the catalyst precursor and are related to the intrinsic acid/base properties of the surface. Moreover, the adsorption by ligand substitution, i.e., surface hydroxyls "become members" of the coordination sphere of the adsorbate, has been suggested for halide complexes of Pt, Pd, Rh, Ir, Au, and Ru on alumina[111] and for amine complexes of Co^{2+}, Ni^{2+}, and Cu^{2+} on titania.[112]

The surface density of adsorption sites is usually low, which gives a high metal dispersion but insufficient loading. Regulation of the adsorption capacity of amphoteric supports like γ-Al_2O_3 can be done by doping solid oxides with electropositive (Na^+, Li^+) or electronegative (F^-, Cl^-) ions, which results in an increase/decrease of the apparent *pzc* values of supports. However, the introduction of basic or acidic modifiers may also change important properties of the catalysts (Table 1). Another possibility for increasing metal concentration is variation of the temperature of the impregnation solution.

In spite of the advantages of precursor impregnation from an aqueous phase, such as easy scale up at relatively low cost, the use of the metal is inefficient because of its incomplete loading and reduction and uncontrolled sintering during high-temperature salt decomposition. This has motivated researchers to study other ways to prepare supported catalysts, directed mainly at avoiding the use of H_2O

 © 2005 Wiley-VCH Verlag GmbH & Co. KGaA, Weinheim

as the impregnation phase.[33] Organic media, vapour, and solid phases have been investigated. The most straightforward way for preparing dispersed metal catalysts consists in mounting metallic atoms or small clusters of metal atoms in their zero-valent state onto an appropriate support, which eliminates the need for any subsequent activation and the catalyst can be obtained in a single preparation step. For example, metallic Pt particles mounted on TiO_2 by means of a microemulsion method have been reported recently.[47] Metal–support interactions are not observed and the Pt/TiO_2 catalysts show higher catalytic activity than the same material prepared by the impregnation technique.

4.2. Co/γ-Al_2O_3 Catalysts

It is well known that supported catalysts containing metallic cobalt or as an oxide or sulfide are very important in heterogeneous catalysis. The actual interest is focused on the Co deposition mechanism and its dependence on the support surface features. It is not easy to explain why the maximum rate of deposition is obtained in the first stages of impregnation where a negligible amount of Al^{3+} ions have been released, especially considering that γ-Al_2O_3 surface dissolution is a slow process. A systematic kinetic study of Co^{2+} deposition together with γ-Al_2O_3 surface dissolution is thought to be the best way to clarify this mechanistic aspect.

Another important challenge is the elucidation of the local structure of the deposited Co^{2+} species. The first direct evidence for the formation of inner sphere Co^{2+} complexes on a γ-Al_2O_3 surface was obtained in the 1990s by means of extended X-ray absorption fine-structure (EXAFS). At present, it is not clear why an Al-Co precipitate with a hydrotalcite structure predominates in the cases where the deposition of Co^{2+} on γ-Al_2O_3 takes place through the $Co(H_2O)_6^{2+}$ species.

Studies to elucidate the mechanism of Co^{2+} adsorption on γ-Al_2O_3 have been developed since the early 1970s and were reviewed recently.[114] Most of the work reported uses Co^{II} aqua complexes as precursors. In general, Co^{2+} adsorption on γ-Al_2O_3 increases considerably with solution pH in the range from 5 to 8, although the process becomes increasingly masked by precipitation of $Co(OH)_2$ at higher pH values. Restoring the initial pH value by addition of acid or base has been proposed since the decrease of impregnation solution pH during Co^{2+} adsorption on γ-Al_2O_3 decreases the extent of the deposition process markedly. In this way, Co^{2+} precipitation inside the pores is avoided and Co/γ-Al_2O_3 catalysts with very highly active surfaces can be obtained. The extent of adsorption can also be increased by increasing the temperature during impregnation, thus influencing the resulting structure of the adsorbate. For example, $Co(OH)_2$ predominates under ambient conditions while $CoAl_2O_4$ becomes important at higher temperatures. Co^{2+} adsorption has also been studied on γ-Al_2O_3 modified with F^- ions − the adsorption increases with higher F^- content.

Studies of adsorption of Co^{2+} and Ni^{2+} amino complexes on γ-Al_2O_3 have demonstrated that alumina should not be considered inert during impregnation, even under mild conditions such as at ambient temperature, with a pH close to the *pzc* of the support, and with reasonable contact times.[83,115] Alumina dissolution is promoted not only by protons or hydroxy ions but also by the presence of Co and Ni ions in solution. The authors suggest that the following phenomena take place at the same time at the γ-Al_2O_3/solution interface during impregnation:
– adsorption of ions which, in certain cases, may even accelerate the rate of support dissolution;
– dissolution of alumina, which depends on the characteristics of the alumina surface;
– precipitation of cations released from the support with metal ions in solution;
– alumina rehydration.

The use of proton-affinity distributions for characterization of the active sites of γ-Al_2O_3/Co and γ-Al_2O_3/Co-Mo catalysts has been reported.[113] Potentiometric titration in combination with proton-affinity distributions has been proposed as a powerful method for the characterization of a supported catalyst surface.

The picture that emerges from the recent literature emphasizes the importance of the intrinsic heterogeneity of adsorption sites on the support for catalyst preparation. The proton-binding properties of various surface sites, i.e. the pH-dependent surface development, are also needed when the precursor salt is present in solution. Another important issue is the stability of the Co^{2+} complexes on γ-Al_2O_3 and the evolution of the system during subsequent preparation steps such as drying and calcination for the evaluation of the properties of the supported catalyst (activity and selectivity).

5. Conclusions

There is no doubt that the preparation history of γ-Al_2O_3 strongly determines its properties. Consequently, the phase composition, bulk and surface chemical composition, local microstructure, as well as stability and textural properties of the oxide can be controlled by varying the synthetic route for the application of γ-Al_2O_3 as a catalyst support. The frequent use of aqueous media for supported catalyst preparation implies that rigorous γ-Al_2O_3 characterization is important not only from a structural point of view. The oxide acid/base properties and adsorption capacity as a function of solution pH (and temperature) should be taken into consideration for both γ-Al_2O_3/electrolyte and γ-Al_2O_3/Co^{2+} salt solution systems as only the *pzc* value is not enough. Information from surface heterogeneity can help to understand and to regulate the adsorption mechanism as well as the occurrence of secondary reactions such as γ-Al_2O_3 dissolution. Further, the nature of the active sites of the supported catalyst and its stability should be evaluated prior to testing catalyst activity and selectivity.

 © 2005 Wiley-VCH Verlag GmbH & Co. KGaA, Weinheim

[1] K. Oberlander, *Applied Industrial Catalysis* (Ed.: B. E. Leach), Academic Press, New York, **1984**, p. 63.
[2] K. Wefers, *Alumina Chemicals: Science and Technology Handbook* (Ed.: L. D. Hart), The American Ceramic Society, Westerville, Ohio, **1990**, p. 13.
[3] M. E. Dry, *Appl. Catal. A: General* **1996**, *138*, 319–344.
[4] C. L. Bianchi, *Catal. Lett.* **2001**, *76*, 155–159.
[5] S. J. Wilson, M. H. Stacey, *J. Colloid Interface Sci.* **1981**, *82*, 507–517.
[6] C. Morterra, G. Magnacca, *Catal. Today* **1996**, *27*, 497–532.
[7] J. A. Wang, X. Bokhimi, A. Morales, O. Novaro, T. López, R. Gómez, *J. Phys. Chem. B* **1999**, *103*, 299–303.
[8] K. Shimizu, Y. Kato, H. Yoshida, A. Satsuma, T. Hattori, T. Yoshida, *Chem. Commun.* **1999**, *17*, 1681–1682.
[9] C. Wolverton, K. C. Hass, *Phys. Rev. B* **2000**, *63*, 1–16 024102-1–024102-16.
[10] G. Paglia, C. E. Buckley, A. L. Rohl, R. D. Hart, K. Winter, A. J. Studer, B. A. Hunter, J. V. Hanna, *Chem. Mater.* **2004**, *16*, 220–236.
[11] B. A. Latella, B. H. O'Connor, *J. Am. Ceram. Soc.* **1997**, *80*, 2941–2944.
[12] T. C. Chou, D. Adamson, J. Mardinly, T. G. Nieh, *Thin Solid Films* **1991**, *205*, 131–139.
[13] A. A. Tsyganenko, P. P. Mardilovich, *J. Chem. Soc., Faraday Trans.* **1996**, *92*, 4843–4852.
[14] K. Sohlberg, S. J. Pennycook, S. T. Pantelides, *J. Am. Chem. Soc.* **1999**, *121*, 10999–11001.
[15] C. Pecharroman, I. Sobrados, J. E. Iglesias, T. González-Carreño, J. Sanz, *J. Phys. Chem. B* **1999**, *103*, 6160–6170.
[16] G. Paglia, C. E. Buckley, T. J. Udovic, A. L. Rohl, F. Jones, C. F. Maitland, J. Connolly, *Chem. Mater.* **2004**, *16*, 1914–1923.
[17] V. González-Peña, I. Díaz, C. Márquez-Alvarez, E. Sastre, J. Pérez-Pariente, *Microporous Mesoporous Mater.* **2001**, *44–45*, 203–210.
[18] A. K. Bhattacharya, D. R. Pyke, G. S. Walker, C. R. Werrett, *Appl. Surf. Sci.* **1997**, *108*, 465–470.
[19] T. Ren, Z. Yuan, B. Su, *Langmuir* **2004**, *20*, 1531–1534.
[20] X. Krokidis, P. Raybaud, A. Gobichon, B. Rebours, P. Euzen, H. Toulhoat, *J. Phys. Chem. B* **2001**, *105*, 5121–5130.
[21] A. Ionescu, A. Allouche, J. P. Aycard, M. Rajzmann, F. Hutschka, *J. Phys. Chem. B* **2002**, *106*, 9359–9366.
[22] I. Levin, L. A. Bendersky, D. G. Brandon, M. Ruhle, *Acta Mater.* **1997**, *45*, 3659–3669.
[23] M. Plummer, *J. Appl. Chem.* **1958**, *8*, 35–44.
[24] R. McPherson, *J. Mater. Sci.* **1973**, *8*, 851–858.
[25] R. McPherson, *J. Mater. Sci.* **1980**, *15*, 3141–3149.
[26] K. P. Sinha, A. P. B. Sinha, *J. Phys. Chem.* **1957**, *61*, 758–761.
[27] R. S. Zhou, R. L. Snyder, *Acta Crystallogr., Sect. B* **1991**, *47*, 617–630.
[28] Y. G. Wang, P. M. Bronsveld, J. Th. M. Dehosson, B. Djuricic, D. McGarry, S. Pickering, *J. Am. Ceram. Soc.* **1998**, *81*, 1655–1660.
[29] S. J. Wilson, *J. Solid State Chem.* **1979**, *30*, 247–255.
[30] S. J. Wilson, J. D. C. McConnell, *J. Solid State Chem.* **1980**, *34*, 315–322.
[31] T. Tsuchida, R. Furuichi, T. Ishii, *Thermochim. Acta* **1980**, *39*, 103–115.
[32] R. H. French, H. Mullejans, D. J. Jones, *J. Am. Ceram. Soc.* **1998**, *81*, 2549–2557.
[33] J. A. Schwarz, C. Contescu, A. Contescu, *Chem. Rev.* **1995**, *95*, 477–510.
[34] K. Sohlberg, S. J. Pennycook, S. T. Pantelides, *J. Am. Chem. Soc.* **1999**, *121*, 7493–7499.
[35] G. Busca, *Catal. Today* **1998**, *41*, 191–206.
[36] D. Coster, J. J. Fripiat, *Chem. Mater.* **1993**, *5*, 1204–1210.
[37] D. Coster, J. J. Fripiat, M. Muscas, A. Auroux, *Langmuir* **1995**, *11*, 2615–2620.
[38] K. Sohlberg, S. J. Pennycook, S. T. Pantelides, *Chem. Eng. Commun.* **2000**, *181*, 107–135.
[39] C. S. John, N. C. M. Alma, G. R. Hays, *Appl. Catal.* **1983**, *6*, 341–346.
[40] D. Coster, A. L. Blumenfeld, J. J. Fripiat, *J. Phys. Chem.* **1994**, *98*, 6201–6211.
[41] M. Digne, P. Sautet, P. Raybaud, P. Euzen, H. Toulhoat, *J. Catal.* **2002**, *211*, 1–5.
[42] S. F. Tikhov, V. B. Fenelonov, V. I. Zaikovskii, Yu. V. Potapova, V. A. Sadykov, *Microporous Mesoporous Mater.* **1999**, *33*, 137–142.
[43] W. Deng, P. Bodart, M. Pruski, B. H. Shanks, *Microporous Mesoporous Mater.* **2002**, *52*, 169–177.
[44] Nanotechnology in mesostructured materials: Y. Kim, Ch. Kim, J. W. Choi, P. Kim, J. Yi, *Stud. Surf. Sci. Catal.* **2003**, *146*, 209–212.
[45] Ch. Kim, Y. Kim, P. Kim, J. Yi, *Korean J. Chem. Eng.* **2003**, *20*, 1142–1144.
[46] M. I. F. Macedo, C. C. Osawa, C. A. Bertran, *J. Sol-Gel Sci. Technol.* **2004**, *30*, 135–140.
[47] X. Zhang, F. Zhang, K. Chan, *Mater. Lett.* **2004**, *58*, 2872–2877.
[48] Acidity and Basicity of Solids: A. Lycourghiotis, *ASI Series, Series C: Mathem. Phys. Sci.* **1994**, *444*, 415–444.
[49] S. P. Trasatti, B. Sacchi, *Study of the Degradation Process of Catalyst Supports by Means of Electrochemical Techniques*, University of Milan, **2004**, Report 3/2004, p. 1–35.
[50] J. B. Miller, E. I. Ko, *Catal. Today* **1997**, *35*, 269–292.
[51] R. K. Iler, *J. Colloid Interface Sci.* **1973**, *43*, 399–408.
[52] T. J. Bandosz, C. Lin, J. A. Ritter, *J. Colloid Interface Sci.* **1998**, *198*, 347–353.
[53] V. La Parola, G. Deganello, S. Scirè, A. M. Venezia, *J. Solid State Chem.* **2003**, *174*, 482–488.
[54] B. Wehrli, E. Wieland, G. Furrer, *Aquat. Sci.* **1990**, *52*, 1–31.
[55] P. Yang, D. Zhao, D. I. Margolese, B. F. Chmelka, G. D. Stucky, *Nature* **1998**, *396*, 152–155.
[56] A. Sayari, S. Hamoudi, Y. Yang, I. L. Moudrakovski, J. R. Ripmeester, *Chem. Mater.* **2000**, *12*, 3857–3863.
[57] S. Cabrera, J. El Haskouri, J. Alamo, A. Beltran, D. Beltran, S. Mendioroz, M. D. Marcos, P. Amoros, *Adv. Mater.* **1999**, *11*, 379–381.
[58] S. Valange, J. Guth, F. Kolenda, S. Lacombe, Z. Gabelica, *Microporous Mesoporous Mater.* **2000**, *35–36*, 597–607.
[59] X. Liu, Y. Wei, D. Jin, W. Shih, *Mater. Lett.* **2000**, *42*, 143–149.
[60] F. Schüth, *Chem. Mater.* **2001**, *13*, 3184–3195.
[61] Z. Zhang, R. W. Hicks, T. R. Pauly, T. J. Pinnavaia, *J. Am. Chem. Soc.* **2002**, *124*, 1592–1593.
[62] Z. Zhang, T. J. Pinnavaia, *J. Am. Chem. Soc.* **2002**, *124*, 12294–12301.
[63] R. W. Hicks, T. J. Pinnavaia, *Chem. Mater.* **2003**, *15*, 78–82.
[64] R. W. Hicks, Z. Zhang, T. J. Pinnavaia, Patent WO03011759 **2003**, 1–12.
[65] *Aquatic Surface Chemistry* (Ed.: P. W. Schindler, W. Stumm), Wiley-InterScience, New York, **1987**, p. 83.
[66] V. E. Henrich, P. A. Cox, *The Surface Science of Metal Oxides*, Cambridge Univ. Press, Cambridge, UK, **1994**.
[67] P. P. Mardilovich, A. N. Govyadinov, N. I. Mazurenko, R. Paterson, *J. Membr. Sci.* **1995**, *98*, 143–155.
[68] G. E. Brown, Jr., V. E. Henrich, W. H. Casey, D. L. Clark, C. Eggleston, A. Felmy, D. W. Goodman, M. Grätzel, G. Maciel, M. I. McCarthy, K. H. Nealson, D. A. Sverjensky, M. F. Toney, J. M. Zachara, *Chem. Rev.* **1999**, *99*, 77–174.
[69] G. A. Parks, *Chem. Rev.* **1965**, *65*, 177–198.
[70] J. P. Brunelle, *Pure Appl. Chem.* **1978**, *50*, 1211–1229.
[71] A. Daghetti, G. Lodi, S. Trasatti, *Mater. Chem. Phys.* **1983**, *8*, 1–90.
[72] J. Lyklema, *Fundamentals of Interface and Colloid Science*, Academic Press Inc., San Diego, **1991**.
[73] C. P. Schulthess, D. L. Sparks, *Soil. Sci. Soc. Am. J.* **1986**, *50*, 1406–1411.

 © 2005 Wiley-VCH Verlag GmbH & Co. KGaA, Weinheim

[74] K. W. Goyne, A. R. Zimmerman, B. L. Newalkar, S. Komarneni, S. L. Brantley, J. Chorover, *J. Porous Mater.* **2002**, *9*, 243–256.
[75] J. Ganor, J. Cama, V. Metz, *J. Colloid Interface Sci.* **2003**, *264*, 67–75.
[76] C. R. Evanko, R. F. Delisio, D. A. Dzombak, J. W. Novak, Jr.., *Colloids Surf. A: Physicochem. Eng. Aspects* **1997**, *125*, 95–107.
[77] C. Contescu, J. Jagiello, J. A. Schwarz, *Langmuir* **1993**, *9*, 1754–1765.
[78] K. Nagashima, F. D. Blum, *J. Colloid Interface Sci.* **1999**, *217*, 28–36.
[79] S. Subramanian, J. S. Noh, J. A. Schwarz, *J. Catal.* **1988**, *114*, 433–439.
[80] C. Contescu, A. Contescu, J. A. Schwarz, *J. Phys. Chem.* **1994**, *98*, 4327–4335.
[81] T. Hiemstra, H. Yong, W. H. Van Riemsdijk, *Langmuir* **1999**, *15*, 5942–5955.
[82] C. Contescu, V. T. Popa, J. A. Schwarz, *J. Colloid Interface Sci.* **1996**, *180*, 149–161.
[83] J. L. Paulhiac, O. Clause, *J. Am. Chem. Soc.* **1993**, *115*, 11602–11603.
[84] J. C. Parker, L. W. Zelazny, S. Sampath, W. G. Harris, *Soil Sci. Soc. Am. J.* **1979**, *43*, 668–674.
[85] W. Stumm, J. J. Morgan, *Aquatic Chemistry. An Introduction Emphasizing Chemical Equilibria*, in *Natural Waters*, 2nd ed., John Wiley & Sons, Inc., New York, **1981**.
[86] L. J. Criscenti, D. A. Sverjensky, *Am. J. Sci.* **1999**, *299*, 828–899.
[87] K. Bourikas, T. Hiemstra, W. H. Van Riemsdijk, *Langmuir* **2001**, *17*, 749–756.
[88] K. Shibata, T. Kiyoura, J. Kitagawa, T. Sumiyoshi, K. Tanabe, *Bull. Chem. Soc. Jpn.* **1973**, *46*, 2985–2988.
[89] C. Contescu, V. T. Popa, J. B. Miller, E. I. Ko, J. A. Schwarz, *Chem. Eng. J.* **1996**, *64*, 265–272.
[90] J. A. Davis, J. O. Leckie, *J. Colloid Interface Sci.* **1978**, *67*, 90–107.
[91] L. K. Koopal, W. H. Van Riemsdijk, M. G. Roffey, *J. Colloid Interface Sci.* **1987**, *118*, 117–135.
[92] W. Piasecki, *Phys. Chem. Chem. Phys.* **2003**, *5*, 713–719.
[93] C. Contescu, J. A. Schwarz, *Appl. Catal. A: General* **1994**, *118*, L5–L10.
[94] C. Contescu, V. T. Popa, J. B. Miller, E. I. Ko, J. A. Schwarz, *J. Catal.* **1995**, *157*, 244–258.
[95] J. Jagiello, T. J. Bandosz, K. Putyera, J. A. Schwarz, *J. Colloid Interface Sci.* **1995**, *172*, 341–346.
[96] T. J. Bandosz, J. Jagiello, J. A. Schwarz, *J. Phys. Chem.* **1995**, *99*, 13522–13527.
[97] T. J. Bandosz, J. Jagiello, J. A. Schwarz, *J. Phys. Chem.* **1996**, *100*, 15569–15574.
[98] T. J. Bandosz, J. Jagiello, C. Contescu, J. A. Schwarz, *Carbon* **1993**, *31*, 1193–1202.
[99] A. M. Puziy, O. I. Poddubnaya, J. A. Ritter, A. D. Ebner, Ch. E. Holland, *Carbon* **2001**, *39*, 2313–2324.
[100] J. C. M. de Wit, W. H. Van Riemsdijk, L. K. Koopal, *Environ. Sci. Technol.* **1993**, *27*, 2015–2022.
[101] M. N. Nederlof, J. C. M. de Wit, W. H. Van Riemsdijk, L. K. Koopal, *Environ. Sci. Technol.* **1993**, *27*, 846–856.
[102] G. H. Bolt, W. H. Van Riemsdijk, *Aquatic Surface Chemistry* (Ed.: W. Stumm), Wiley, New York, **1987**, p. 127–164.
[103] J. Jagiello, *Langmuir* **1994**, *10*, 2778–2785.
[104] F. Villiéras, J. L. Michot, F. Bardot, J. M. Cases, M. François, W. Rudziński, *Langmuir* **1997**, *13*, 1104–1117.
[105] M. Černik, M. Borkovec, J. C. Westall, *Environ. Sci. Technol.* **1995**, *29*, 413–425.
[106] J. Bersillon, F. Villiéras, F. Bardot, T. Gorner, J. Cases, *J. Colloid Interface Sci.* **2001**, *240*, 400–411.
[107] B. Prélot, R. Charmas, P. Zarzycki, F. Thomas, F. Villiéras, W. Piasecki, W. Rudziński, *J. Phys. Chem. B* **2002**, *106*, 13280–13286.
[108] J. Kijenski, A. Baiker, *Catal. Today* **1989**, *5*, 1–120.
[109] P. Chu, E. E. Petersen, C. J. Radke, *J. Catal.* **1989**, *117*, 52–70.
[110] L. Vordonis, N. Spanos, P. G. Koutsoukos, A. Lycourghiotis, *Langmuir* **1992**, *8*, 1736–1743.
[111] J. C. Summers, S. A. Ausen, *J. Catal.* **1978**, *52*, 445–452.
[112] K. Hadjiivanov, D. Klissurski, M. Kantcheva, A. Davydov, *J. Chem. Soc., Faraday Trans.* **1991**, *87*, 907–911.
[113] M. Adachi, C. Contescu, J. A. Schwarz, *J. Catal.* **1996**, *158*, 411–419.
[114] K. Bourikas, Ch. Kordulis, J. Vakros, A. Lycourghiotis, *Adv. Colloid Interface Sci.* **2004**, *110*, 97–120.
[115] J. B. d'Espinose de la Caillerie, M. Kermarec, O. Clause, *J. Am. Chem. Soc.* **1995**, *117*, 11471–11481.

Received: April 22, 2005
Published Online: August 2, 2005

 © 2005 Wiley-VCH Verlag GmbH & Co. KGaA, Weinheim

A Chiral Copper Complex Forms Supramolecular Homochiral Helices via O–H···Cl–Cu Interactions

Chullikkattil P. Pradeep,[a] Panthapally S. Zacharias,*[a] and Samar K. Das*[a]

Keywords: Copper / Helical structures / Hydrogen bonds / Schiff bases / Self-assembly / Supramolecular chemistry

An enantiopure ligand H_2L [Schiff base prepared from (*S*)-(+)-2-phenylglycinol and 2-hydroxy-5-nitrobenzaldehyde] reacts with $CuCl_2{\cdot}2H_2O$ to yield a chiral copper complex [Cu(HL)Cl] (**1**) that forms right-handed supramolecular helices via O–H···Cl–Cu hydrogen bonds.

(© Wiley-VCH Verlag GmbH & Co. KGaA, 69451 Weinheim, Germany, 2005)

The influence of metal centers on hydrogen bonding has become a topic of intense research recently since metal-directed hydrogen bonding has far-reaching importance in inorganic supramolecular chemistry, materials chemistry, and bioinorganic chemistry. Metal-directed hydrogen bonding can show considerable strength and directionality and thereby is able to control the self-assembly of the building blocks, thus resulting in a variety of interesting supramolecular architectures.[1] Among these, hydrogen-bonded systems involving metal halides (M–X) have been well studied in materials chemistry and organometallic chemistry.[2] Halogens act as strong hydrogen-bond acceptors when bound to transition metals, in contrast to their limited ability to serve as weak hydrogen-bond acceptors when bound to carbon. The directional properties of metal halides in the formation of hydrogen bonds have been shown independently by the groups of Brammer and Orpen.[3]

Among the various metallo-supramolecular architectures, helical structures are of considerable interest because of their intrinsic chirality and their potential for yielding materials with novel chemical, electronic, biological, and optical properties.[4] Of particular interest are chiral helices prepared by the self-assembly of chiral building blocks.[5] We have recently reported a supramolecular homochiral helical architecture assembled by C–H···Cl–M hydrogen-bonding interactions.[6] However, to the best of our knowledge, there is no report on homochiral helices based on O–H···Cl–M interactions. In the present communication we wish to report a chiral, mononuclear, square-planar copper complex that self-assembles through O–H···Cl–Cu interactions to form homochiral helices in the crystal packing.

The reaction of a 1:1 mixture of (*S*)-(+)-2-phenylglycinol and 2-hydroxy-5-nitrobenzaldehyde in methanol yielded the tridentate chiral ligand H_2L in moderate yield. Reaction of H_2L with $CuCl_2{\cdot}2H_2O$ in methanol at room temperature gave a green solid of [Cu(HL)Cl] (**1**), which on recrystallization from methanol gave X-ray quality crystals. The molecular structure of the complex is shown in Figure 1. The structure consists of a neutral, mononuclear, four-coordinate copper(II) complex with the chiral tridentate Schiff-base ligand providing the ONO donor atom set. The fourth position is occupied by a chloride ion. The overall coordination geometry of the compound is distorted square-planar, with the copper ion lying approximately at the center of the plane consisting of the ligand donor atoms Cl(1), O(1), N(1), and O(2).

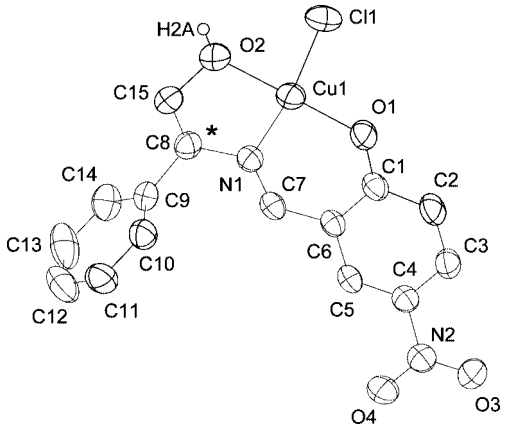

Figure 1. Thermal ellipsoidal plot (50%) of **1**. Hydrogen atoms are omitted for clarity. The asterisk mark indicates the chiral center. Selected bond lengths [Å] and angles [°]: Cu(1)–O(1) 1.880(2), Cu(1)–O(2) 1.968(2), Cu(1)–N(1) 1.954(2), Cu(1)–Cl(1) 2.2482(8), O(1)–C(1) 1.289(3), N(1)–C(7) 1.265(4); O(1)–Cu(1)–N(1) 94.04(9), O(1)–Cu(1)–O(2) 172.12(11), N(1)–Cu(1)–O(2) 81.37(10), O(1)–Cu(1)–Cl(1) 94.99(6), N(1)–Cu(1)–Cl(1) 170.74(7), O(2)–Cu(1)–Cl(1) 89.88(8).

[a] School of Chemistry, University of Hyderabad, Hyderabad, 500046, India
Fax: +91-40-2301-2460
E-mail: skdsc@uohyd.ernet.in

Supporting information for this article is available on the WWW under http://www.eurjic.org or from the author.

 DOI: 10.1002/ejic.200500261 © 2005 Wiley-VCH Verlag GmbH & Co. KGaA, Weinheim

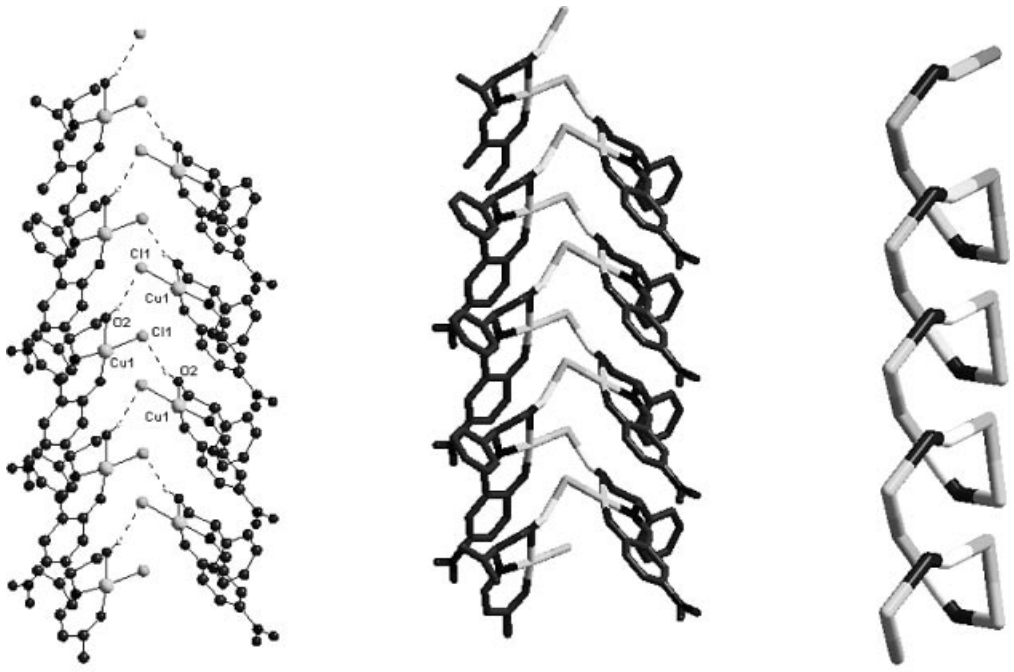

Figure 2. Intermolecular O–H···Cl–Cu hydrogen-bonding interactions between adjacent molecules that lead to the formation of homochiral helices. Ball-and-stick (left) and wire-frame (center) representations; helical backbone (right) (wire-frame representation).

The molecular packing in the crystal structure of **1** reveals strong O–H···Cl–Cu intermolecular hydrogen-bonding interactions involving the hydrogen atom on O(2) and the Cl(1) anion coordinated to the copper center (Figures 1 and 2). This results in the formation of supramolecular hydrogen-bonded helices that extend indefinitely throughout the crystal lattice (Figure 2) [selected hydrogen bonding parameters: H–O = 0.80(4) Å, H···Cl = 2.26(4) Å, O···Cl = 3.024(3) Å, and O–H···Cl = 159(4)°].

The O–H···Cl distance observed in this study [2.26(4) Å] is appreciably shorter than the sum of the van der Waals radii for the H and the neutral Cl atoms (2.95 Å). This can be classified as a strong interaction (those less than 2.52 Å are termed strong).[7a] Similar strong M–X···H–O bonds are known in the literature but they do not result in helical structures. Representative examples include a Cu–Cl···H–O hydrogen bond (H–O = 0.84 Å, H···Cl = 2.25 Å, O···Cl = 3.08 Å, and O–H···Cl = 173.3°) in the crystal structure of $[CuCl(C_{19}H_{19}N_3O)]$[7b] and a Cu–Cl···H–O hydrogen bond (H–O = 0.98 Å, H···Cl = 2.26 Å, O···Cl = 3.228 Å, and O–H···Cl = 171°) in the compound $[CuCl(C_5H_9N_3)(C_{12}H_8N_2)]Cl{\cdot}H_2O$.[7c] The strength of the interaction can be attributed to the strong hydrogen-bond donor ability of the O–H group due to its greater acidity and to the strong H-bonding acceptor property of the metal-bound chloride.

The path of the helix can easily be traced by following the hydrogen bonds clockwise around the twofold screw axis of the helix. Three copper complex fragments form one helix turn in **1** with a pitch of 5.831 Å (Figure 2). We believe that the turn required to generate a perfect periodic self-assembly of [Cu(HL)Cl] (**1**) in a helical fashion is induced by the chirality of the building block coupled with the strong O–H···Cl–Cu hydrogen-bonding interactions. The rigidity of the Schiff-base ligand, which occupies three binding sites of the Cu atom, may also have some role in dictating such a helical arrangement in this self-assembly process. The absolute configuration of complex **1** was successfully determined by refining the Flack parameter [0.029(13)].[8]

Since we have described (above) a supramolecular helical feature of the copper complex [Cu(HL)Cl] (**1**) in the solid state, we decided to perform spectral studies in the solid state. The solid-state circular dichroism (CD) and electronic reflectance spectra of [Cu(HL)Cl] (**1**) are presented in Figure 3. The CD spectrum shows both positive and negative bands. The overall feature of the solid-state reflectance electronic spectrum is not identical to its solution spectrum (see Supporting Information). This can be correlated to the intermolecular interactions in the solid state of complex **1**, as shown in Figure 2. The bands observed in the electronic and CD spectra of complex **1** at around 700 nm are assigned to d–d transitions. The EPR spectrum (Figure 4) of a powdered sample of complex **1** at liquid nitrogen temperature exhibits a typical axial feature with $g_{\|} = 2.22$ and $g_{\perp} = 2.08$ for a Cu^{II} (d^9) system. The feature remains the same even at room temperature. The solution EPR spectrum (see Supporting Information) of complex **1** in frozen methanol shows an axial feature too, but with copper hyperfine coupling for a typical monomeric tetragonal Cu^{II} complex with a $d_{x^2-y^2}$ ground-state doublet.

To summarize, we have synthesized and characterized a chiral, mononuclear, square-planar Cu^{II} complex [Cu(HL)Cl] (**1**), which self-assembles through strong O–H···Cl–Cu intermolecular hydrogen-bonding interactions to form a homochiral helical arrangement. The advantages of this

 © 2005 Wiley-VCH Verlag GmbH & Co. KGaA, Weinheim

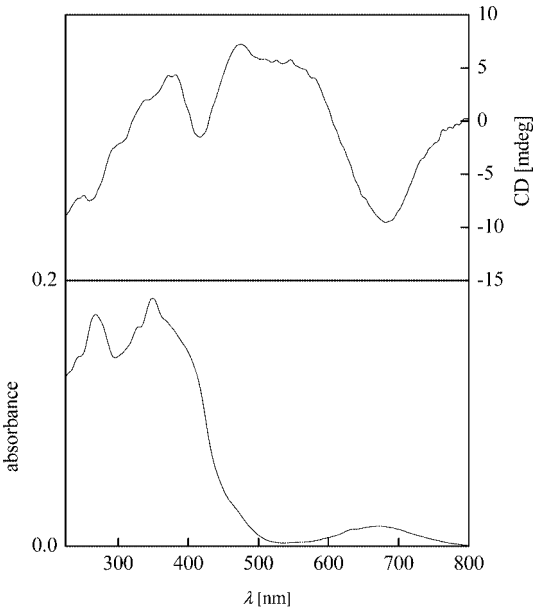

Figure 3. Circular dichroism and diffuse electronic reflectance spectra of **1** in the solid state (compound **1** was mixed with KBr to prepare a pellet).

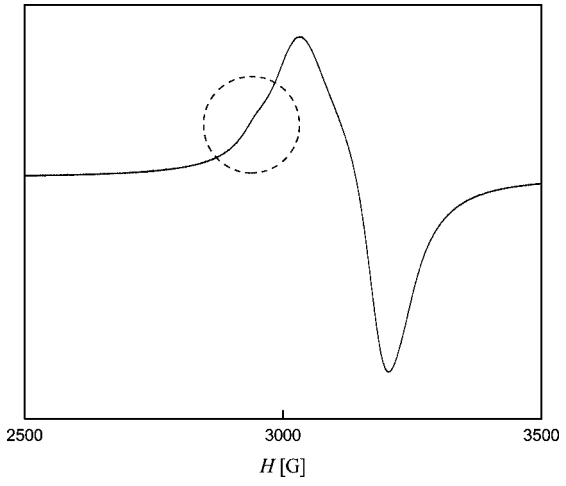

Figure 4. EPR spectrum of a powdered sample of **1** at liquid nitrogen temperature (the circle highlights the $g_{\|}$ feature).

system are that it is simple, easy to prepare, and provides potential for further explorations. The CD and electronic reflectance spectral studies (solid state vs. solution) of **1** support the intermolecular interactions in the solid state, which is consistent with the formation of supramolecular homochiral helices in the crystal. These intermolecular interactions may be lost in solution phase, as evidenced by EPR spectral studies.

Experimental Section

General: Microanalytical (C, H, N) data were obtained with a Flash EA 1112 Series CHNS Analyzer. A Shimadzu 3101 PC UV/Vis/NIR spectrophotometer was used to record the electronic spectra. Infrared spectra were recorded on KBr pellets with a JASCO-5300 FT-IR spectrophotometer. ^{1}H NMR spectra of the ligand in $CDCl_3$ solution were recorded with a Bruker 400 MHz spectrometer using $Si(CH_3)_4$ as an internal standard. The CD spectra were measured with a JASCO J-810 spectropolarimeter. The EPR spectrum was recorded with a JEOL JES-FA200 spectrometer.

Synthesis of Enantiopure Ligand H_2L: (*S*)-(+)-2-Phenylglycinol (0.137 g, 1 mmol) and 2-hydroxy-5-nitrobenzaldehyde (0.167 g, 1 mmol) were stirred together in methanol (15 mL) at room temperature for 3 h. The resulting yellow solution was filtered and the filtrate was allowed to slowly concentrate. The resulting yellow solid was collected by filtration, washed with hexane, and dried at room temperature (0.25 g, 87%). $C_{15}H_{14}N_2O_4$ (286.28): calcd. C 62.93, H 4.93, N 9.79; found C 63.11, H 4.76, N 9.87. ^{1}H NMR ($CDCl_3$): δ = 4.00 (d, J = 7.2 Hz, 2 H, CH_2), 4.61 (t, J = 6.4 Hz, 1 H, CH), 7.00–7.45 (m, 6 H, Ar), 8.20–8.27 (m, 2 H, Ar), 8.52 (s, 1 H, H–C=N). IR (KBr): $\tilde{\nu}$ = 3272, 1649, 1615, 1545, 1350, 1225, 1070, 901, 835, 696 cm^{-1}. UV/Vis (CH_3OH): λ_{max} (ε) = 390 nm (6141 M^{-1}cm^{-1}), 324 (9655), 259 (18238), 240 (16123).

Synthesis of the Chiral Copper Complex [Cu(HL)Cl] (1): $CuCl_2{\cdot}2H_2O$ (0.17 g, 1 mmol) was added to a methanolic solution of the ligand H_2L (0.286 g, 1 mmol). The mixture was stirred at room temperature in air overnight. The resultant green solution gave a green, needle-shaped crystalline product on slow concentration, which was collected by filtration and recrystallized from methanol (0.265 g, 69%). $C_{15}H_{13}ClCuN_2O_4$ (384.27): calcd. C 46.88, H 3.41, N, 7.29; found C 47.02, H 3.49, N 7.18. IR (KBr): $\tilde{\nu}$ = 1634, 1600, 1549, 1468, 1387, 1308, 1094 cm^{-1}. Diffuse electronic reflectance (KBr pellet): λ_{max} = 270, 375, 700 nm. UV/Vis (CH_3CN): λ_{max} (ε) = 252 nm (20271 M^{-1}cm^{-1}), 235 (20105), 355 (18137), 690 (104).

X-ray Crystallographic Study: $C_{15}H_{13}ClCuN_2O_4$, M = 384.26 g mol^{-1}, monoclinic, space group $P2_1$, a = 11.3232(8), b = 5.8314(4), c = 12.3108(9) Å, β = 112.3110(10)°, V = 752.03(9) Å^3, Z = 2, $D_{calcd.}$ = 1.697 g cm^{-3}, μ = 1.651 mm^{-1}, F(000) = 390, crystal size 0.31 × 0.08 × 0.08 mm. A total of 8757 reflections were collected of which 3368 unique reflections (R_{int} = 0.0262) were used. R = 0.0338 for 3056 reflections with $I > 2\sigma(I)$. Data were collected at 298(2) K with a Bruker SMART APEX CCD area detector system

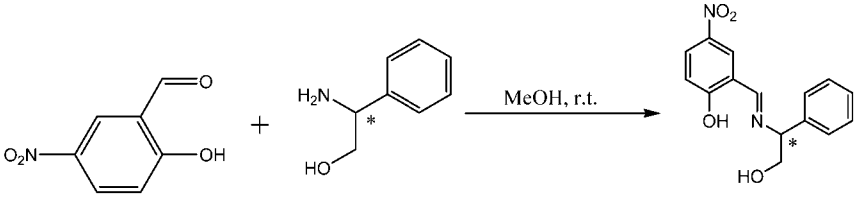

H_2L

 © 2005 Wiley-VCH Verlag GmbH & Co. KGaA, Weinheim

[λ(Mo-K_α) = 0.71073 Å] fitted with a graphite monochromator; 2400 frames were recorded with an ω-scan width of 0.3°, each for 15 s; crystal–detector distance: 60 mm; collimator: 0.5 mm. Data reduction with SAINTPLUS,[9] structure solution with SHELXS-97,[10] and refined with SHELXL-97.[11] All non-hydrogen atoms were refined anisotropically. Hydrogen atoms were introduced in calculated positions and included in the refinement as riding on their respective parent atoms. The final Fourier difference synthesis showed minimum and maximum peaks of 0.566 and –0.223 e Å^{-3}. CCDC-265514 contains the supplementary crystallographic data for this paper. These data can be obtained free of charge from The Cambridge Crystallographic Data Centre via www.ccdc.cam.ac.uk/data_request/cif.

Acknowledgments

We thank the Department of Science and Technology, Government of India, for financial support. The National X-ray Diffractometer facility at the University of Hyderabad by the Department of Science and Technology, Government of India, is also gratefully acknowledged. We are grateful to UGC, New Delhi, for providing infrastructure facilities at the University of Hyderabad under UPE grant. C. P. P. thanks UGC, New Delhi, for a fellowship.

[1] a) L. Brammer, *Chem. Soc. Rev.* **2004**, *33*, 476–489; b) L. Brammer, *Dalton Trans.* **2003**, 3145–3157; c) L. M. Epstein, E. S. Shubina, *Coord. Chem. Rev.* **2002**, *231*, 165–181; d) D. Braga, F. Grepioni, *Acc. Chem. Res.* **2000**, *33*, 601–608; e) R. H. Crabtree, P. E. M. Siegbahn, O. Eisenstein, A. L. Rheingold, T. F. Koetzle, *Acc. Chem. Res.* **1996**, *29*, 348–354; f) A. D. Burrows, C.-W. Chan, M. M. Chowdhry, J. E. McGrady, D. M. P. Mingos, *Chem. Soc. Rev.* **1995**, *24*, 329–339.

[2] U. Bentrup, M. Feist, E. Kemnitz, *Prog. Solid State Chem.* **1999**, *27*, 75–129; L. Brammer, E. A. Bruton, P. Sherwood, *Cryst. Growth Des.* **2001**, *1*, 277–290; R. Kuhlman, *Coord. Chem. Rev.* **1997**, *167*, 205–232; M. J. Riley, D. Neill, P. V. Bernhardt, K. A. Byriel, C. H. L. Kennard, *Inorg. Chem.* **1998**, *37*, 3635–3639; D. V. Yandulov, K. G. Caulton, N. V. Belkova, E. S. Shubina, L. M. Epstein, D. V. Khoroshum, D. G. Musaev, K. Morokuma, *J. Am. Chem. Soc.* **1998**, *120*, 12553–12563; D.-H. Lee, H. J. Kwon, B. P. Patel, L. M. Liable-Sands, A. L. Rheingold, R. H. Crabtree, *Organometallics* **1999**, *18*, 1615–1621; Z. Mazej, K. L. Borrmann, B. Zemva, *Inorg. Chem.* **1998**, *37*, 5912–5914.

[3] J. C. Mareque Rivas, L. Brammer, *Inorg. Chem.* **1998**, *37*, 4756–4757; G. R. Lewis, A. G. Orpen, *Chem. Commun.* **1998**, 1873–1874; A. L. Gillon, A. G. Orpen, J. Starbuck, X.-M. Wang, Y. Rodríguez-Martín, C. Ruiz-Pérez, *Chem. Commun.* **1999**, 2287–2288; A. L. Gillon, G. R. Lewis, A. G. Orpen, S. Rotter, J. Starbuck, X.-M. Wang, Y. Rodríguez-Martín, C. Ruiz-Pérez, *J. Chem. Soc., Dalton Trans.* **2000**, 3897–3905; A. Angeloni, A. G. Orpen, *Chem. Commun.* **2001**, 343–344.

[4] J.-M. Lehn, *Supramolecular Chemistry − Concepts and Perspectives*, VCH, Weinheim, **1995**; E. C. Constable, in *Comprehensive Supramolecular Chemistry* (Eds.: J. P. Sauvage, M. W. Hosseini), Pergamon Press, Oxford, **1996**, vol. 9, p. 213–252; E. C. Constable, C. E. Housecroft, M. Neuburger, D. Phillips, P. R. Raithby, E. Schofield, E. Sparr, D. A. Tocher, M. Zehnder, Y. Zimmermann, *J. Chem. Soc., Dalton Trans.* **2000**, 2219–2228; C. Piguet, J.-C. G. Bünzli, *Chem. Soc. Rev.* **1999**, *28*, 347–358; M. Albrecht, *Chem. Rev.* **2001**, *101*, 3457–3497; M. J. Hannon, V. Moreno, M. J. Prieto, E. Moldrheim, E. Sletten, I. Meistermann, C. J. Isaac, K. J. Sanders, A. Rodger, *Angew. Chem. Int. Ed.* **2001**, *40*, 879–884.

[5] U. Knof, A. von Zelewsky, *Angew. Chem. Int. Ed.* **1999**, *38*, 302–322; C. Piguet, G. Bernardinelli, G. Hopfgartner, *Chem. Rev.* **1997**, *97*, 2005–2062; G. Baum, E. C. Constable, D. Fenske, C. E. Housecroft, T. Kulke, *Chem. Eur. J.* **1999**, *5*, 1862–1873 and references cited therein.

[6] M. Prabhakar, P. S. Zacharias, S. K. Das, *Inorg. Chem.* **2005**, *44*, 2585–2587.

[7] a) G. Aullón, D. Bellamy, L. Brammer, E. A. Bruton, A. G. Orpen, *Chem. Commun.* **1998**, 653–654; b) M. M. Olmstead, T. E. Patten, C. Troeltzsch, *Inorg. Chim. Acta* **2004**, *357*, 619–624; c) E. Y. Bivián-Castro, S. Bernès, J. Escalante, G. Mendoza-Díaz, *Acta Crystallogr., Sect. C* **2004**, *60*, m205–m207.

[8] H. D. Flack, *Acta Crystallogr., Sect. A* **1983**, *39*, 876–881.

[9] Software for the CCD Detector System, Bruker Analytical X-ray Systems Inc., Madison, WI, **1998**.

[10] G. M. Sheldrick, *Program for structure solution*, University of Göttingen, Germany, **1997**.

[11] G. M. Sheldrick, *Program for crystal structure analysis*, University of Göttingen, Germany, **1997**.

Received: March 25, 2005
Published Online: August 1, 2005

Unexpected Behaviour of Pyridine-2-carbaldehyde Thiosemicarbazonatocopper(II) Entities in Aqueous Basic Medium – Partial Transformation of Thioamide into Nitrile

Patricia Gómez-Saiz,[a] Rubén Gil-García,[a] Miguel A. Maestro,[b] José Luis Pizarro,[c] María Isabel Arriortua,[c] Luis Lezama,[d] Teófilo Rojo,[d] and Javier García-Tojal*[a]

Keywords: Copper complexes / Desulfurization / Structure elucidation / Thiosemicarbazone complexes

Unusual species are obtained from the HL/Cu^{II}/NO_3^- system (HL = pyridine-2-carbaldehyde thiosemicarbazone) in basic aqueous solutions. A partial desulfurization process occurs for 1:1 Cu/HL molar ratio which gives rise to the precipitation of the mixed ligand [Cu(L)(L^{CN})] (**1**) complex [HL^{CN} = $C_7H_6N_4$, (pyridin-2-ylmethylene)hydrazinecarbonitrile]. This compound contains Cu^{II} ions in a square-pyramidal environment. On the other hand, distorted octahedral [$Cu(L)_2$] (**2**) entities are isolated in excess of the thiosemicarbazone ligand. Desulfurization of the thiosemicarbazone is detected even at physiological pH values. However, this reaction does not take place in absence of Cu^{II} ions, and HL·2.25H_2O (**3**) or HL·H_2O are obtained in these conditions.

(© Wiley-VCH Verlag GmbH & Co. KGaA, 69451 Weinheim, Germany, 2005)

Introduction

The copper(II) derivatives of pyridine-2-carbaldehyde thiosemicarbazone (HL = $C_7H_8N_4S$) exhibit relevant biological properties, in particular related to the cytotoxic effects against tumoral cells.[1] Spectroscopic studies in aqueous solution led to propose the existence of the $[Cu(HL)]^{2+}$, $[Cu(L)]^+$ and [Cu(L)(OH)] species, corresponding to two acid–base equilibria with proton dissociation constants pK_{a1} = 2.40 (deprotonation of the $N_{hydrazinic}$ atom in the ligand) and pK_{a2} = 8.30, respectively.[2] In fact, the high stability of the metal–ligand system has allowed the attainment and structural characterization of several compounds containing $[Cu(HL)]^{2+}$ and $[Cu(L)]^+$ entities.[3] They show a 1:1 metal–thiosemicarbazone stoichiometry, with the thiosemicarbazone acting as an NNS terdentate ligand. However, as far as we are aware, attempts to isolate either the basic [Cu(L)(OH)] species or its derivatives have not been carried out.

The present work deals with the structural studies developed on solids obtained from the pyridine-2-carbaldehyde thiosemicarbazone–nitrate–copper(II) system in aqueous solutions at high pH values. In this way, unexpected [Cu(L)(L^{CN})] (**1**) and [$Cu(L)_2$] (**2**) compounds have been obtained [HL^{CN} = $C_7H_6N_4$, (pyridin-2-ylmethylene)hydrazinecarbonitrile] together with the thiosemicarbazone ligand in a new structural arrangement, HL·2.25H_2O (**3**). Surprisingly, we have not found any evidence of the existence of [Cu(L)(OH)] derivatives in the solids isolated.

Results and Discussion

The addition of sodium hydroxide to an aqueous solution of the Cu(L)(NO_3) complex at pH = 9–11 yields complex **1** as a major component of a dark brown powdery solid. Unfortunately, attempts to purify this compound have been unsuccessful. In spite of this, it has been possible to obtain some small crystals and to solve the molecular structure[4,5] of the monomeric species, which is shown in Figure 1. As can be seen, one of the thiosemicarbazone ligands in compound **1** is converted into a new carbonitrile derivative which acts as a bidentate ligand. The geometry around the Cu^{II} ions is square-pyramidal (τ = 0.25).[6] Distances in the NCN terminal moiety are 1.312(8) and 1.129(9) Å for C14–N7 and C14–N8, respectively. The latter is closer to a C≡N link, but the first one exhibits some double bond character. Therefore, cyanamide (N–C≡N) and carbodiimide (N=C=N) contributions must be considered. Furthermore, it must be taken into account the conjugation along all the system. On the other hand, this car-

[a] Departamento de Química, Universidad de Burgos, Plaza Misael Bañuelos s/n, 09001 Burgos, Spain
Fax: +34-47-258831
E-mail: qipgatoj@ubu.es
[b] Servicios Generales de Apoyo a la Investigación, Universidade da Coruña, Edificio Anexo a Facultade de Ciencias, Campus da Zapateira s/n, 15071 A Coruña, Spain
[c] Departamento de Mineralogía y Petrología, Universidad del País Vasco, Aptdo. 644, 48080 Bilbao, Spain
[d] Departamento de Química Inorgánica, Universidad del País Vasco, Aptdo. 644, 48080 Bilbao, Spain
Supporting information for this article is available on the WWW under http://www.eurjic.org or from the author.

bonitrile ligand is unusual from a structural point of view, being the closest related C=N–N–C≡N structure found that corresponding to the C-biphenylene–N(1)-(4-iodophenyl)–N(2)-cyano–azomethinimine compound.[7]

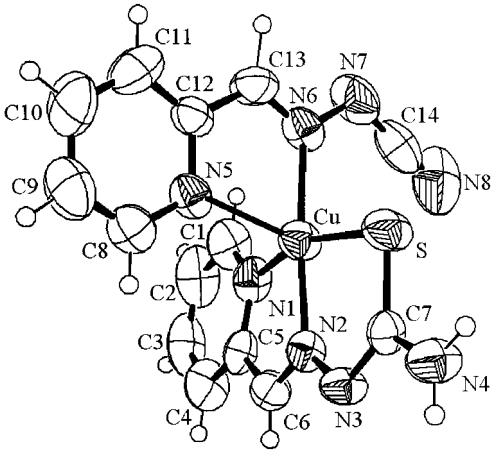

Figure 1. Crystal structure of compound **1**. Selected bond lengths [Å] and angles [°]: Cu–N1 2.025(4), Cu–N2 1.961(4), Cu–S 2.263(2), Cu–N5 2.222(5), Cu–N6 2.039(5), N2–C6 1.288(6), N2–N3 1.351(5), N3–C7 1.330(5), S–C7 1.720(6), N4–C7 1.334(5), N6–C13 1.279(6), N6–N7 1.360(6), N7–C14 1.312(8), N8–C14 1.129(9), N1–Cu–S 159.5(1), N1–Cu–N2 80.7(2), N1–Cu–N6 99.7(2), N5–Cu–N6 78.1(2), N1–Cu–N5 96.0(2), N2–Cu–N6 174.8(2), closest intermolecular Cu···Cu distance 6.528(2)[ii] ([ii] = $-x + 1, -y, -z + 1$).

The structure of compound **1** resembles that of complex **2** (see Figure 2) which was prepared with high purity following a 1:2 metal-to-ligand molar ratio in a basic medium.[8] The crystal building of **2** contains isolated distorted octahedral entities where each Cu^{II} ion is bonded to two NNS terdentate thiosemicarbazone ligands. The N1 atom can be considered as pseudocoordinated to the metal centre due to the long Cu–N1 bond length being the topology better described as a [5+1] coordination. Because of the Jahn–Teller effect in the Cu^{II} ion, there are few bis-chelate copper(II) complexes containing terdentate thiosemicarbazone ligands (to the best of our knowledge, less than 5% of the structures reported in the literature).[9]

The desulfurization of the thiosemicarbazone ligand to give the compound **1** is a complex process very sensitive to temperature, pH, time of reaction and stoichiometry. Variations in the experimental conditions at pH values above 7.0 give rise to differences in the composition of the solids. Most of the products obtained in our experiments exhibit very low crystallinity and dark colours. Because of this, it is very difficult to identify the components of the powders. Besides this, the amorphous precipitates show very low solubility in water and other solvents. This fact prevents purification of the samples without inducing important changes in the experimental conditions. All these problems make it necessary to find characteristic parameters to follow the process. In this sense, the strong infrared band at 2108 cm^{-1} corresponding to ν(CN) in compound **1** has allowed us to check the presence of desulfurized species in solid powdered samples obtained at different pH values. EPR measurements have also been used to identify the presence of **1** and

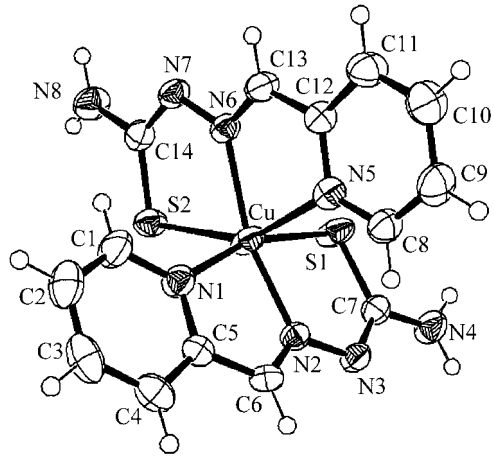

Figure 2. Crystal structure of compound **2**. Selected bond lengths [Å] and angles [°]: Cu–N1 2.515(3), Cu–N2 2.144(3), Cu–S1 2.505(1), Cu–N5 2.059(3), Cu–N6 2.002(3), Cu–S2 2.309(1), N2–C6 1.283(4), N2–N3 1.377(4), N3–C7 1.319(4), S1–C7 1.729(3), N4–C7 1.359(4), N6–C13 1.290(4), N6–N7 1.356(4), N7–C14 1.333(4), S2–C14 1.729(3), N8–C14 1.340(4), N1–Cu–S1 149.61(9), N1–Cu–N2 71.5(1), N1–Cu–N6 84.3(1), N5–Cu–S2 161.83(8), N5–Cu–N6 79.5(1), N1–Cu–N5 85.8(1), N2–Cu–N6 155.7(1), S1–Cu–S2 97.37(4), closest intermolecular Cu···Cu distance 5.9909(7)[i] ([i] = $-x + 1, -y + 2, -z + 1$).

2 in the precipitates. Thus, a degree of desulfurization process has been detected even at physiological pH = 7.4 values in aqueous solutions of $Cu(L)(NO_3)$ at 40 °C. On the other hand, organic fragments are absent in the black solids collected when the reactions are maintained for more than 1 h at pH = 13 and temperatures higher than 40 °C (IR bands in the 4000–400 cm^{-1} region practically disappear if the products are washed with water after filtering off).

A three-step mechanism can be proposed for this reaction (Scheme 1). The resulting HL^{CN} ligand would link to a $[Cu(L)]^+$ entity and deprotonate in basic media. Note that CuS is only a nominal formula to refer the unidentified inorganic species present in the mixture. Nevertheless, qualitative evidences of the presence of sulfide and sulfate have been achieved for some of the samples analysed.[10]

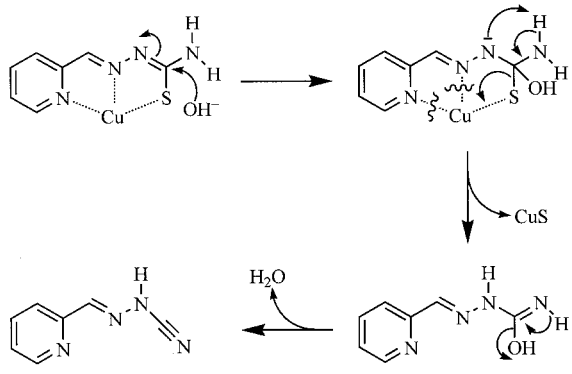

Scheme 1.

Assays using KOH, NEt_3, or 0.5 M $Na_2CO_3/NaHCO_3$ buffer instead of NaOH lead to similar results. The nitrile derivative is also obtained when $Cu(L)(NO_3)$ is replaced by $[\{Cu(L)Cl\}_2]$[3b,3c,3i] as starting material.

 © 2005 Wiley-VCH Verlag GmbH & Co. KGaA, Weinheim

No evidence of nitrile formation has been found in the absence of Cu^{II} ions, even not when the aqueous solutions were evaporated to dryness. Instead, the yellow $HL{\cdot}2.25H_2O$ (**3**) compound was obtained at pH ≈ 13. The molecular structure of **3**[11] (Figure 3) shows bond lengths and angles very similar to those reported in the literature for $HL{\cdot}H_2O$[12] but, surprinsingly, the *syn* conformation of the N(1) and N(2) atoms with respect to the C(5)–C(6) bond resembles the crystal features of the pyridinium H_2L^+ derivatives obtained at very low pH values.[13] On the other hand, evaporation of aqueous solutions of the free ligand at pH ≈ 11 to dryness yields red crystals with the same structure reported by Byushkin et al. for $HL{\cdot}H_2O$ (see Supporting Information).

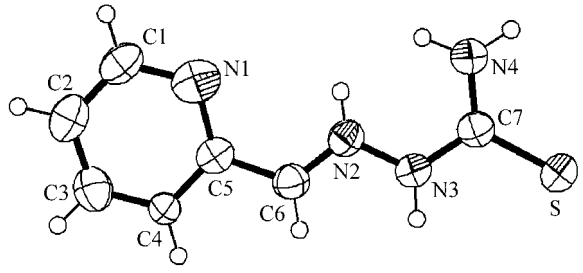

Figure 3. Crystal structure of compound **3**. Selected bond lengths [Å]: N2–C6 1.277(4), N2–N3 1.363(3), N3–C7 1.351(4), S–C7 1.695(3), N4–C7 1.314(4).

Taking into account the extensive literature dealing with the conversion of thioamides and thioureas into carbonitriles, cyanamides and carbodiimides,[14] one could expect that the reaction reported here is also quite common for thiosemicarbazone compounds. However, as far as we are aware, transformation of thiosemicarbazones into carbonitrile derivatives induced by basic media is an unprecedent process. In fact, we have tried the attainment of HL^{CN} by reaction of HL with HgO, but the $[Hg(L)_2]$ compound was obtained.[15] In the same way, previous attempts of desulfurization of HL using $HgCl_2$ + Na in methanol and $Pb(CH_3COO)_2{\cdot}3H_2O$ + KOH in water were unsuccessful.[1j] These results are probably due to the stability that the conjugation induces in this thiosemicarbazone system.

Recently, desulfurization of dithiocarbamatocadmium(II) complexes in the presence of amines has been reported.[16] In addition, there are indirect evidences of desulfurization of an analogous thiosemicarbazonecopper(II) system in aqueous basic medium.[17] However, the reactions described in these papers do not yield carbonitrile derivatives.

The presence of such a process in physiological conditions could lead to a re-interpretation of the biological properties of some thiosemicarbazone systems, mainly those aspects related to the possible therapeutic uses. Furthermore, this reaction opens an inexpensive way to achieve the synthesis of new ligands. In a more general scope, the transformation of thioamides into carbonitriles in the presence of Cu^{II} ions suggests possible pathways for the syntheses of biomolecules in sulfur-rich environments, e.g. prebiotic conditions.[18]

Supporting Information Available: IR and EPR spectra, powder diffractograms of samples at different pH values and a summary of the cif output for the $HL{\cdot}H_2O$ compound.

Acknowledgments

We thank Drs. J. J. Delgado and V. Diez-Gómez (SCAI, Universidad de Burgos, Spain), and Jon P. Chapman (Servicio General de Rayos X, Universidad del País Vasco, Spain) for the elemental analyses and some of the X-ray measurements. This work has been carried out with the financial support of the Dirección General de Investigación del Ministerio de Ciencia y Tecnología. BQU2002–00435 and the Junta de Castilla y León BU15/03. P. G.-S. thanks to the Universidad de Burgos for her Doctoral Fellowship.

[1] For instance: a) W. E. Antholine, J. M. Knight, D. H. Petering, *J. Med. Chem.* **1976**, *19*, 339–341; b) W. E. Antholine, J. M. Knight, H. Whelan, D. H. Petering, *Mol. Pharmacol.* **1977**, *13*, 89–98; c) L. A. Saryan, E. Ankel, C. Krishnamurti, D. H. Petering, *J. Med. Chem.* **1979**, *22*, 1218–1221; d) L. A. Saryan, K. Mailer, C. Krishnamurti, W. Antholine, D. H. Petering, *Biochem. Pharmacol.* **1981**, *30*, 1595–1604; e) W. E. Antholine, F. Taketa, *J. Inorg. Biochem.* **1982**, *16*, 145–154; f) W. E. Antholine, F. Taketa, *J. Inorg. Biochem.* **1984**, *20*, 69–78; g) S. B. Padhye, G. B. Kauffman, *Coord. Chem. Rev.* **1985**, *63*, 127–160; h) D. X. West, S. B. Padhye, P. B. Sonawane, *Struct. Bonding* **1991**, *76*, 1–50; i) D. X. West, A. E. Liberta, S. B. Padhye, R. C. Chikate, P. B. Sonawane, A. S. Kumbhar, R. G. Yerande, *Coord. Chem. Rev.* **1993**, *123*, 49–71; j) E. W. Ainscough, A. M. Brodie, W. A. Denny, G. J. Finlay, J. D. Ranford, *J. Inorg. Biochem.* **1998**, *70*, 175–185; k) J. García-Tojal, A. García-Orad, A. Alvarez Díaz, J. L. Serra, M. K. Urtiaga, M. I. Arriortua, T. Rojo, *J. Inorg. Biochem.* **2001**, *84*, 271–278.

[2] a) W. E. Antholine, D. H. Petering, *Proc. Am. Assoc. Cancer Res.* **1974**, *15*, 16; b) D. J. Legget, W. A. E. McBryde, *Talanta* **1974**, *21*, 1005–1011; c) W. E. Antholine, J. M. Knight, D. H. Petering, *Inorg. Chem.* **1977**, *16*, 569–574; d) H. Beraldo, L. Tosi, *Inorg. Chim. Acta* **1986**, *125*, 173–182.

[3] a) C. F. Bell, C. R. Theocharis, *Acta Crystallogr., Sect. C* **1987**, *43*, 26–29; b) A. G. Bingham, H. Bögge, A. Müller, E. W. Ainscough, A. M. Brodie, *J. Chem. Soc., Dalton Trans.* **1987**, 493–499; c) C. F. Bell, K. A. K. Lott, N. Hearn, *Polyhedron* **1987**, *6*, 39–44; d) H. K. Parwana, G. Singh, *Indian. J. Chem.* **1987**, *26A*, 581–583; e) E. W. Ainscough, E. N. Baker, A. M. Brodie, R. J. Cresswell, J. D. Ranford, J. M. Waters, *Inorg. Chim. Acta* **1990**, *172*, 185–190; f) E. W. Ainscough, A. M. Brodie, J. D. Ranford, J. M. Waters, *J. Chem. Soc., Dalton Trans.* **1991**, 1737–1742; g) E. W. Ainscough, A. M. Brodie, J. D. Ranford, J. M. Waters, *J. Chem. Soc., Dalton Trans.* **1991**, 2125–2131; h) E. W. Ainscough, A. M. Brodie, J. D. Ranford, J. M. Waters, K. S. Murray, *Inorg. Chim. Acta* **1992**, *197*, 107–115; i) J. García-Tojal, M. K. Urtiaga, R. Cortés, L. Lezama, T. Rojo, M. I. Arriortua, *J. Chem. Soc., Dalton Trans.* **1994**, 2233–2238; j) J. García-Tojal, J. García-Jaca, R. Cortés, T. Rojo, M. K. Urtiaga, M. I. Arriortua, *Inorg. Chim. Acta* **1996**, *249*, 25–32; k) E. W. Ainscough, A. M. Brodie, J. D. Ranford, J. M. Waters, *J. Chem. Soc., Dalton Trans.* **1997**, 1251–1255; l) J. García-Tojal, L. Lezama, J. L. Pizarro, M. Insausti, M. I. Arriortua, T. Rojo, *Polyhedron* **1999**, *18*, 3703–3711; m) P. Gómez-Saiz, J. García-Tojal, A. Mendia, B. Donnadieu, L. Lezama, J. L. Pizarro, M. I. Arriortua, T. Rojo, *Eur. J. Inorg. Chem.* **2003**, 518–527; n) P. Gómez-Saiz, J. García-Tojal, M. A. Maestro, J. Mahía, L. Lezama, T. Rojo, *Eur. J. Inorg. Chem.* **2003**, 2123–2132; o) P. Gómez-Saiz, J. García-Tojal, M. A. Maestro, J.

 © 2005 Wiley-VCH Verlag GmbH & Co. KGaA, Weinheim

Mahía, F. J. Arnáiz, L. Lezama, T. Rojo, *Eur. J. Inorg. Chem.* **2003**, 2639–2650.

[4] Synthesis of **1**: published methods with small modifications were used to synthesize HL[5] and Cu(L)(NO_3).[3b] The best way that we have found to obtain **1** with a less amount of impurities consists on the dropwise addition of a solution of HL (0.180 g, 1.0 mmol) in water (30 mL) previously basified with 5 M NaOH just to solution of the ligand (pH ≈ 11), to another aqueous solution of $Cu(NO_3)_2{\cdot}3H_2O$ (0.100 g, 0.5 mmol) with heating (70 °C). Once the addition was completed, the heating was stopped and the reaction was maintained for 1.5 h. The brown precipitate was filtered off, washed with water at pH ≈ 11 (2 × 20 mL) and dried over vacuum. Good results were also obtained starting from Cu(L)(NO_3) (0.152 g, 0.5 mmol) in water (30 mL) at 80 °C by addition of NaOH 0.1 M to reach pH = 9.0 and further reaction for 1 h maintaining the temperature and pH. Other trials were carried out at different pH values (7.4, 9.0, 11.0, and 13.0), temperatures (40, 50, and 80 °C) and reaction times (1 and 5 h) yielding compounds with varied compositions. **1** is present in some of these solids, except for those obtained in extreme conditions (e. g. reactions for 5 h at 80 °C and any pH value yielded black unidentified amorphous inorganic solids). Brown crystals of **1** suitable for X-ray analysis were separated from the mother liquours of the reaction of $Cu(NO_3)_2{\cdot}3H_2O$ and HL (stoichimetries 2:3) by slow evaporation at room temperature. $C_{14}H_{12}CuN_8S$ (387.92): calcd. C 43.3, H 3.1, N 28.9, S 8.3; found C 40.6, H 3.0, N 26.9, S 7.5. Selected IR bands (cm^{-1}, KBr): 3426 w, br., 3290 m, br., 3070 m, br., 3018 w, 2966 w, 2194 vw, 2108 vs, 1646 m, 1596 s, 1526 s, 1483 w, 1468 m, 1446 s, 1427 vs, sh, 1383 s, 1346 m, 1320 m, 1296 w, 1226 s, 1166 vs, 1155 vs, 1016 vw, 897 vw, 880 vw, 766 w, 738 w, 627 w. EPR (X-band, solid sample): room temp. to 120 K, g_1 = 2.168, g_2 = 2.057, g_3 = 2.029. Crystal data: $C_{14}H_{12}CuN_8S$, M_W = 387.92, triclinic, space group $P\bar{1}$, a = 8.119(1), b = 8.678(1), c = 13.761(2) Å, α = 72.97(1), β = 85.98(1), γ = 62.83(1)°, U = 822.4(2) Å^3, Z = 2, μ(Mo-K_α) = 1.468 mm^{-1}, T = 293(2) K, 4987 reflections collected, 2496 were unique (R_{int} = 0.0552). Final R values, $R1$ [$I > 2\sigma(I)$] = 0.0527, $wR2$ [$I > 2\sigma(I)$] = 0.0574, $R1$ (all data) = 0.1436, $wR2$ (all data) = 0.0718. CCDC-252369, -252370, and -252371 contain the supplementary crystallographic data for this paper. These data can be obtained free of charge from The Cambridge Crystallographic Data Centre via www.ccdc.cam.ac.uk/data_request/cif.

[5] F. E. Anderson, C. J. Duca, J. V. Scudi, *J. Am. Chem. Soc.* **1951**, *73*, 4967–4968.

[6] A. W. Addison, T. N. Rao, J. Reedijk, J. van Rijn, G. C. Verschoor, *J. Chem. Soc., Dalton Trans.* **1984**, 1349–1356.

[7] F. Brandl, W. Hoppe, *Z. Kristallogr. Kristallogeom. Kristallchem.* **1967**, *125*, 80.

[8] Synthesis of **2**: A solution containing Cu(L)(NO_3) (0.152 g, 0.5 mmol) in water (30 mL) was added dropwise with constant stirring to another solution of HL (0.090 g, 0.5 mmol) in water (30 mL) previously basified with NaOH 1 M to pH = 11.0. The reaction mixture was stirred for 2 h at 40 °C. The brown precipitate was filtered off and washed with hot water (2 × 20 mL) and acetone (2 × 20 mL) and dried over vacuum (0.178 g, 84%). Single crystals were obtained from aqueous solutions of HL (in basic medium) and $Cu(NO_3)_2{\cdot}3H_2O$ slowly mixed by means of a diffusion device. $C_{14}H_{14}CuN_8S_2$ (421.99): calcd. C 39.8, H 3.3, N 26.6, S 15.2; found C 39.4, H 3.0, N 26.2, S 15.0. Selected IR bands (cm^{-1}, KBr): 3474 m, 3364 w, 3273 m, 3084 m, br., 1627 m, 1614 m, 1600 m, 1590 m, 1548 m, 1477 w, 1406 vs, 1316 m, 1297 m, 1230 m, 1149 s, sh, 1051 w, 883 w, 768 w, 763 w, 732 m, 636 w, 618 w, 516 w, 449 w. EPR (X-band, solid sample): room temp. to 120 K, g_1 = 2.186, g_2 = 2.046, g_3 = 2.038. Crystal data: $C_{14}H_{14}CuN_8S_2$, M_W = 421.99, triclinic, space group $P\bar{1}$, a = 7.810(1), b = 8.695(1), c = 12.993(2) Å, α = 100.508(2), β = 92.539(2), γ = 102.674(2)°, U = 843.0(2) Å^3, Z = 2, μ(Mo-K_α) = 1.559 mm^{-1}, T = 298(2) K, 4834 reflections collected, 3345 were unique (R_{int} = 0.0224). Final R values, $R1$ [$I > 2\sigma(I)$] = 0.0435, $wR2$ [$I > 2\sigma(I)$] = 0.1170, $R1$ (all data) = 0.0569, $wR2$ (all data) = 0.1264.

[9] a) P. Souza, A. I. Matesanz, V. Fernández, *J. Chem. Soc., Dalton Trans.* **1996**, 3011–3013; b) M. A. Ali, R. J. Butcher, J. C. Bryan, *Inorg. Chim. Acta* **1999**, *287*, 8–13; c) M. A. Ali, A. H. Mirza, A. M. S. Hossain, M. Nazimuddin, *Polyhedron* **2001**, *20*, 1045–1052.

[10] Qualitative tests used to detect the presence of (a) sulfide and (b) sulfate: (a) HCl(c) (0.5 mL) was added to 0.030 g of each sample in a test tube, being the top of the tube covered with a paper wet with a solution of $Pb(NO_3)_2$ 0.5 M. H_2S evolution leads to the PbS formation; (b) addition of HCl(c) (1.0 mL) to 0.030 g of the solid, filtration, and addition of $Ba(NO_3)_2$ 0.04 M (0.5 mL) to the acid solution. White $BaSO_4$ precipitates if sulfate ions are present.

[11] Synthesis of **3**: several drops of 5 M NaOH were added to a suspension of HL (0.180 g, 1 mmol) in water (20 mL) to reach a pH ≈ 13 with heating. Some minutes later, the solid disappeared leading to a pale yellow solution. The reaction mixture was allowed to react 1 h after which a white crystalline compound was filtered off, washed with water at basic pH (2 × 20 mL) and dried (0.132 g, 60%). Pale yellow crystals suitable for X-ray studies were separated from a solution of HL in water at pH ≈ 13. $C_7H_{12.5}N_4O_{2.25}S$ (220.77): calcd. C 38.1, H 5.9, N 25.4, S 14.5; found C 38.3, H 5.4, N 25.2, S 14.7. Selected IR bands (cm^{-1}, KBr): 3457 m, br., 3350 s, sh, 3189 m, sh, 3045 w, 2956 w, br., 2804 w, br., 1616 s, 1603 m, 1590 s, 1566 m, 1540 vs, br., 1488 w, 1467 vs, 1433 s, 1360 s, 1285 vs, 1249 s, sh, 1152 m, 1113 s, 1090 m, 1066 m, 1051 m, 998 m, 940 m, 900 w, 880 m, 812 m, 775 m, 745 m, 546 m, br., 623 m, 555 w, 518 w, 452 w, 419 w. ^1H NMR (400 MHz; [D_6]acetone, 25 °C), δ = 10.72 (s, 1 H, NH), 8.58 (d, $^3J_{H,H}$ = 5 Hz, 1H, 1-H), 8.21 (s, 1 H, 6-H), 8.17 (d, $^3J_{H,H}$ = 8 Hz 1 H, 4-H), 8.04 (s, 1 H, $NH_{terminal}$), 7.8 (m, 1H, 3-H), 7.62 (s, 1 H, $NH_{terminal}$), 7.36 (m, 1 H, 2-H). Crystal data: $C_7H_{12.5}N_4O_{2.25}S$, M_W = 220.77, tetragonal, space group $I4_1/a$, a = b = 13.6755(8), c = 22.122(2) Å, α = β = γ = 90°, U = 4137.3(5) Å^3, Z = 16, μ(Mo-K_α) = 0.298 mm^{-1}, T = 293(2) K, 11986 reflections collected, 2124 were unique (R_{int} = 0.0404). Final R values, $R1$ [$I > 2\sigma(I)$] = 0.0593, $wR2$ [$I > 2\sigma(I)$] = 0.1827, $R1$ (all data) = 0.0788, $wR2$ (all data) = 0.2018.

[12] V. N. Byushkin, Y. M. Chumakov, N. M. Samus, I. O. Baka, *Zh. Strukt. Khim.* **1987**, *28*, 140–142.

[13] a) M. K. Urtiaga, M. I. Arriortua, J. García-Tojal, T. Rojo, *Acta Crystallogr., Sect. C* **1995**, *51*, 2172–2174; b) A. Morsali, A. Ramazani, F. Jamali, F. Gouranlou, *Z. Kristallogr. New Cryst. Struct.* **2001**, *216*, 607–608.

[14] For instance: a) W. Weith, *Ber. Dtsch. Chem. Ges.* **1873**, *6*, 1389; b) F. Kurzer, *J. Chem. Soc.* **1949**, 3033–3038; c) F. Kurzer, K. Douraghi-Zadeh, *Chem. Rev.* **1967**, *67*, 107–145; d) H. Ulrich, A. A. R. Sayigh, *Angew. Chem. Int. Ed. Engl.* **1966**, *5*, 704–712; e) K. Friedich, K. Wallenfels, *Isonitrile Chemistry*, I. Ugi Academic, New York, **1971**; f) X. Shen, X. Shi, B. Kang, Y. Tong, Y. Liu, L. Gu, Q. Liu, Y. Huang, *Polyhedron* **1999**, *18*, 33–37; g) L. Kovacs, E. Ösz, Z. Györgydeák, *Carbohydr. Res.* **2002**, *337*, 1171–1178; h) O. López, I. Maya, V. Ulgar, I. Robina, J. Fuentes, J. G. Fernández-Bolaños, *Tetrahedron Lett.* **2002**, *43*, 4313–4316; i) J. C. Manimala, E. V. Anslyn, *Eur. J. Org. Chem.* **2002**, 3909–3922; j) Y.-M. Zhang, L. Xian, T.-B. Wei, K.-B. Yu, *J. Chem. Research (S)* **2003**, *798*–799; k) E. V. Kudrik, A. Theodoridis, R. van Eldik, S. V. Makarov, *Dalton Trans.* **2005**, 1117–1122, and references therein.

[15] Drops of 5 M NaOH were added over a solution of $HgCl_2$ (0.070 g, 2.5 mmol) in water (30 mL) just to complete precipitation of yellow HgO, which was filtered off and washed with water (2 × 20 mL) and acetone (20 mL). The freshly prepared oxide was put into a flask with a small amount of acetone and HL (0.180 g, 1 mmol) was added dropwise. The reaction was kept with reflux for 5 h. A yellow solid was collected and

washed with acetone (20 mL). This compound is a mixture of $[Hg(L)_2]$ + HgO. For a complete characterization of $[Hg(L)_2]$, see ref.[1j]

[16] L. H. Van Poppel, T. L. Groy, T. Caudle, *Inorg. Chem.* **2004**, *43*, 3180–3188.

[17] P. Gómez-Saiz, J. García-Tojal, V. Díez-Gómez, R. Gil-García, J. L. Pizarro, M. I. Arriortua, T. Rojo, *Inorg. Chem. Commun.* **2005**, *8*, 259–262.

[18] F. Duvernay, T. Chiavassa, F. Borget, J.-P. Aycard, *J. Am. Chem. Soc.* **2004**, *126*, 7772–7773.

Received: April 19, 2005
Published Online: July 20, 2005

 © 2005 Wiley-VCH Verlag GmbH & Co. KGaA, Weinheim

Unprecedented Coordination Mode Variation of Group 13 Metal–Alkyl Compounds Derived from Methyl Thiosalicylate

Janusz Lewiński,*[a] Wojciech Bury,[a] Tomasz Kopeć,[a] Ewa Tratkiewicz,[a] Iwona Justyniak,[b] and Janusz Lipkowski[b]

Keywords: Aluminum / Indium / Noncovalent interactions / Thiolates

The X-ray structure analysis of the alkylaluminum and -indium compounds derived from methyl thiosalicylate, $Me_2Al(SC_6H_4\text{-}2\text{-}CO_2Me)$ and $[Me_2In(\mu\text{-}SC_6H_4\text{-}2\text{-}CO_2Me)]_2$, revealed that the intermolecular S···C(π) interaction between the Al–S thiolate units and the ester π-surface can effectively compete with the hypercoordinate sulfur–metal dative bond. The former compound exists as the noncovalently bonded dimer involving the thiolate sulfur atom and the electrophilic carbon atom of the ester functionality, whereas the indium complex is a five-coordinate dimer with the $In_2(\mu\text{-}S)_2$ central core.

(© Wiley-VCH Verlag GmbH & Co. KGaA, 69451 Weinheim, Germany, 2005)

Introduction

The chemistry of five-coordinate aluminum complexes has an extensive literature[1] and the significance of the fifth coordinate site for aluminum-based reagent/catalyst function and/or selectivity is gradually emerging.[2] In spite of many contributions in this area, less direct information has been gleaned about the nature of bonding, stability, and reactivity of this class of compounds, and the identity of both active centers and transition-state structures remains elusive.[3] Therefore, detailed structural information concerning the extent of coordination and association in alkylaluminum complexes as well as the magnitude of the donor–aluminum interaction in five-coordinate species are crucial in understanding their physical behavior and chemical reactivity. In this regard, investigations based on the dialkylaluminum chelate complexes derived from donor-functionalized alcohols or unsaturated bifunctional O,X-H proligands, i.e., $[R_2Al(O,X)]_n$-type complexes, have appeared particularly fruitful.[4] Recently, our group has reported the results concerning the relationship between intra- and intermolecular forces resulting from donor–acceptor and hydrogen-bonding interactions using group 13 chelate complexes.[5] For instance, we have demonstrated that in the solid state dialkylaluminum chelate complexes have a tendency to form $[R_2Al(\mu\text{-}O,O')]_2$-type adducts with five-coordinate metal centers (Scheme 1, structure **I**) with the intermolecular Al–O distance varying from ca. 2.05 Å to the van der Waals surface (i.e., over 3.5 Å).[4f] Conversely, the structure investigations of the group 13 chelate complexes with salicylideneiminate anion (saldR′) revealed that the crystal structure of $R_2M(saldR')$ (M = Al or Ga) complexes is determined by distinct intermolecular hydrogen-bond motifs (structure **II**), while the indium analogue formed a five-coordinate dimer with $In_2(\mu\text{-}O)_2$ bridges in the solid state.[5a,5b] As an extension of this work, we report herein on structure investigations of alkylaluminum and -indium compounds derived from methyl thiosalicylate, which revealed that the intermolecular S···C(π) interaction between the Al–S thiolate units and the π-surface of the ester functionality (structure **IV**) can compete with the putative sulfur–aluminum hypercoordinate bond (structure **III**).

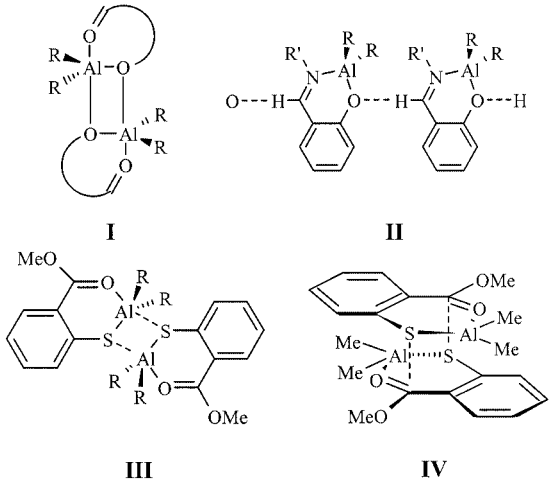

I **II** **III** **IV**

Scheme 1.

[a] Department of Chemistry, Warsaw University of Technology, Noakowskiego 3, 00-664 Warsaw, Poland
E-mail: lewin@ch.pw.edu.pl
[b] Institute of Physical Chemistry, Polish Academy of Sciences, Kasprzaka 44, 01-224 Warsaw, Poland

Supporting information for this article is available on the WWW under http://www.eurjic.org or from the author.

 © 2005 Wiley-VCH Verlag GmbH & Co. KGaA, Weinheim **DOI: 10.1002/ejic.200500418**

Results and Discussion

The reaction of Me_3Al with methyl thiosalicylate in an equimolar ratio results in the quantitative formation of $Me_2Al(SC_6H_4\text{-}2\text{-}CO_2Me)$ (**1**). The resulting complex has been characterized in solution by NMR spectroscopy and molecular weight measurements (see Exp. Sect.), and in the solid state its structure has been determined by X-ray crystallography. Compound **1** exists as a monomer in solution and crystallizes as a noncovalently bonded dimer (Figure 1). The monomeric units of **1** consist of the tetrahedral aluminum center. The salient structural feature of **1** is the conformation of the chelate-ring system S(1)–C(3)–C(8)–C(9)–O(1)–Al(1), which highly deviates from planarity with a puckering amplitude Q = 0.579(2) Å.[6] This deformation is realized by the bending on the sulfur atom, while the metal–ester linkage remains essentially planar; the torsion angles Al(1)–S(1)–C(3)–C(8) and Al(1)–O(1)–C(9)–C(8) are equal to 30.3(3)° and 1.2(4)°, respectively. The ester group is rotated relative to the phenyl ring with an O(1)–C(9)–C(8)–C(3) torsion angle of 23.9(4)°. Most strikingly, the analysis of the crystal-packing patterns of **1** shows notably short intermolecular S···C(π) [3.379(3) Å] distances between a pair of adjacent molecules that represents a type of weak attractive interaction of the sulfur atom to the π-system of the ester group. The observed S···C(π) distance remains significantly below the sum of the van der Waals radii,[7,8] and should be considered as denoting a bonding interaction. This assumption is further supported by the relative orientation of the thiolate and ester groups: the S···C=O angle is 88.7°, and both the Al–S···C(π) and the C–S···C(π) angles are close to the tetrahedral values indicating that the sulfur sp^3 lone pair is oriented approximately perpendicular to the ester group.

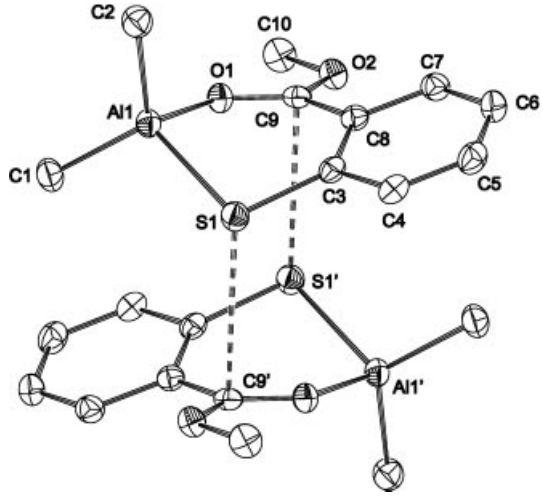

Figure 1. Molecular structure of **1** with thermal ellipsoids drawn at the 40% probability; hydrogen atoms are omitted for clarity.

The structural motif for **1** is surprising as both the participation of thiolate ligands in the formation of the $R_2Al(\mu\text{-}SR')_2AlR_2$ bridges and the Lewis acid properties of the metal center in tetrahedral dialkylaluminum chelate complexes are well recognized.[1] We have previously determined the following order for the Lewis acidity of the group 13 metal centers in the four-coordinate $R_2M(O,O')$ complexes: In ≥ Al > Ga,[4c] and it was of interest to see which type of coordination mode would be adopted by the alkylindium derivative of methyl thiosalicylate. The reaction of Me_3In with the pro-ligand results in the formation of $[Me_2In(\mu\text{-}SC_6H_4\text{-}2\text{-}CO_2Me)]_2$ (**2**) which is found to exist as a monomer/dimer equilibrium based on solution molecular weight studies (calcd. for dimeric **2** 623.72, found 530). A similar equilibrium was observed for dimethylindium acetylacetonate complex,[9] while the related dimethylindium complexes supported by methyl salicylate[4c] or *N*-phenylsalicylideneimine[5a] occurred exclusively in the dimeric form in benzene solution.

The X-ray crystallographic analysis revealed that in contrast to the aluminum complex **1**, the indium derivative **2** adopts the five-coordinate motif with the $In_2(\mu\text{-}S)_2$ central core (see Figure 2). The conformation of the chelate-ring system S(1)–C(3)–C(8)–C(9)–O(1)–In(1) is even more pleated than the related heterocyclic ring in **1** [with a puckering amplitude Q = 0.922(3) Å]. The In–S distances are dissimilar [2.561(5) and 2.853(2) Å], with that in the equatorial position being 0.292 Å shorter. The In(1)–O(1) distance of 2.452(4) Å is longer than the corresponding linkage in the related five-coordinate dimer derived from methyl salicylate, $[Me_2In(\mu\text{-}OC_6H_4\text{-}2\text{-}CO_2Me)]_2$ [2.165(4) Å].[4c] Thus, the five-coordinate dimeric motif observed for **2** demonstrates that group 13 metal–alkyl compounds supported by the monoanionic methyl thiosalicylate ligand are capable of aggregating through dative bridging bonds between the metal center and the thiolate group.

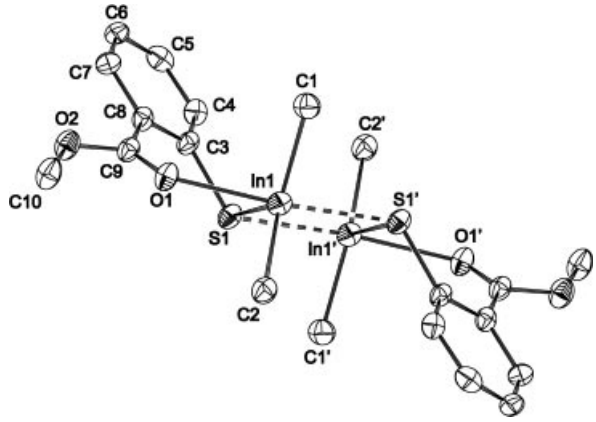

Figure 2. Molecular structure of **2** with thermal ellipsoids drawn at the 40% probability; hydrogen atoms are omitted for clarity.

Conclusions

In conclusion, the reported results clearly indicate that for the methylaluminum complex supported by the methyl thiosalicylate ligand the structure of type **IV** is preferred over the adduct of type **III** with the dative bond between the thiolate sulfur atom and the aluminum five-coordinate site. To the best of our knowledge, this is the first report

 © 2005 Wiley-VCH Verlag GmbH & Co. KGaA, Weinheim

on the competition of the intermolecular n→π* interaction, involving the thiolate sulfur atom and the electrophilic carbon atom of the ester functionality, with the hypercoordinate bond in metal complexes and opens up an interesting area for further studies. Studies of both the relationship between the hypercoordinate bonds in the group 13 metal–alkyl complexes and noncovalent interactions, and the significance of the intermolecular S···C(π) interaction between M–S thiolate units and the π-surface of the carbonyl functionality in various systems are in progress.

Experimental Section

General Remarks: All reactions were carried out under dry nitrogen using standard Schlenk techniques. Solvents were dried and distilled prior to use. NMR spectra were recorded with a Varian Mercury 400 spectrometer.

$Me_2Al(SC_6H_4$-2-$CO_2Me)$ (1): $AlMe_3$ (0.312 g, 4.32 mmol) was added to a solution of methyl thiosalicylate (0.727 g, 4.32 mmol) in hexane (7 mL) at –78 °C. After the addition was completed, the reaction mixture was allowed to warm to room temperature and a pale yellow solid precipitated. The product was dissolved under heating to 40 °C and yellow block-shaped crystals were obtained at 0 °C. Yield: 0.934 g (96%). $C_{10}H_{13}AlO_2S$ (224.24): calcd. C 53.32, H 6.26, S 14.23; found C 53.07, H 6.32, S 14.11; molecular weight studies: calcd. 224.24, found 238. ^{1}H NMR (200 MHz, C_6D_6): δ = –0.17 (s, 6 H, $AlCH_3$), 2.88 (s, 3 H, OCH_3), 6.51–7.68 (m, 4 H, Ar) ppm. ^{13}C NMR (50 MHz, C_6D_6): δ = –8.3, 55.0, 123.2, 123.8, 132.7, 134.8, 137.3, 152.1, 175.9 (C=O) ppm. ^{27}Al NMR (104 MHz, C_6D_6): δ = 158 ppm.

$Me_2In(\mu$-SC_6H_4-2-$CO_2Me)$ (2): The reaction was carried out according to the same procedure as described for **1**, using $InMe_3$ (0.141 g, 0.89 mmol) and methyl thiosalicylate (0.152 g, 0.89 mmol) in toluene (7 mL). Colorless block-shaped crystals were obtained from a toluene/hexane solution at –20 °C after 24 h. Yield 0.27 g (98%). $C_{20}H_{26}In_2O_4S_2$ (624.19): calcd. C 38.49, H 4.20, S 10.27; found C 38.12, H 4.11, S 9.98. ^{1}H NMR (200 MHz, C_6D_6): δ = 0.42 (s, 6 H, $InCH_3$), 3.17 (s, 3 H, OCH_3), 6.67–7.64 (m, 4 H, Ar) ppm. ^{13}C NMR (50 MHz, C_6D_6): δ = –2.9, 52.5, 124.4, 129.6, 131.8, 132.2, 136.7, 143.7, 172.0 (C=O) ppm.

X-ray Crystallographic Study: A single crystal of **1** and **2** suitable for X-ray diffraction studies was placed in a thin-walled capillary tube (Lindemann glass 0.5 mm) under an inert gas. The tube was plugged with grease, then flame-sealed and mounted on a goniometer head. **1:** Triclinic, space group $P\bar{1}$ (no. 2), a = 8.4030(4), b = 8.6340(6), c = 9.9590(5) Å, α = 88.776(4), β = 66.253(3), γ = 62.170(3)°, V = 572.34(6) Å^3, Z = 2, F(000) = 236, $D_{calcd.}$ = 1.301 g m^3, T = 150(2) K. **2:** Monoclinic, space group $P2_1/c$ (no. 14), a = 8.1080(17), b = 13.151(3), c = 11.423(2) Å, β = 108.0.94(15)°, V = 1157.8(4) Å^3, Z = 4, F(000) = 759, $D_{calcd.}$ = 2.198 g m^3, T = 150(2) K. Nonius Kappa-CCD diffractometer, μ(Mo-K_a) = 4.19 mm^{-1}. The structures of **1** and **2** were solved by direct methods using the SHELXS-97[10] program and were refined by full-matrix least squares on F^2 using the program SHELXL-97.[11] Refinement converged at R_1 = 0.0514, wR_2 = 0.1185 for all data and 130 parameters [R_1 = 0.0443, wR_2 = 0.1145 for 1600 reflections with $I_o > 2\sigma(I_o)$], GOF = 1.07 for **1**; R_1 = 0.0514, wR_2 = 0.1185 for all data and 130 parameters [R_1 = 0.0443, wR_2 = 0.1145 for 1600 reflections with $I_o > 2\sigma(I_o)$], GOF = 1.053 for **2**. CCDC-240417 (**1**) and -240418 (**2**) contain the supplementary crystallographic data for this paper. These data can be obtained free of charge from The Cambridge Crystallographic Data Centre via www.ccdc.cam.ac.uk/data_request/cif.

Supporting Information: Selected bond lengths and angles in **1** and **2** (see footnote on the first page of this article).

Acknowledgments

The work was supported by the Polish State Committee for Scientific Research (Grant No. 3 T08E 053 27).

[1] For reviews see: a) G. H. Robinson (Ed.), *Coordination Chemistry of Aluminum*, VCH Publishers, Inc., New York, **1993**; b) D. A. Atwood, *Struct. Bonding* **2003**, *105*, 167; c) D. J. Linton, A. E. H. Wheatley, *Struct. Bonding* **2003**, *105*, 67.

[2] See for example: a) M. Shibasaki, M. Kanai, K. Funabashi, *Chem. Commun.* **2002**, 1989; b) B. J. O'Keefe, M. A. Hillmyer, W. B. Tolman, *J. Chem. Soc., Dalton Trans.* **2001**, 2215; c) J. Lewiński, J. Zachara, P. Goś, E. Grabska, T. Kopeć, I. Madura, W. Marciniak, I. Prowotorow, *Chem. Eur. J.* **2000**, *6*, 3215; d) J. Lewiński, P. Horeglad, M. Dranka, I. Justyniak, *Inorg. Chem.* **2004**, *43*, 5789; e) J. Lewiński, P. Horeglad, E. Tratkiewicz, J. Lipkowski, E. Kołodziejczyk, *Macromol. Rapid Commun.* **2004**, *25*, 1939.

[3] For example, this concerns: a) Maruoka's concepts involving the hypervalent R_3Al complexes as intermediates in several chelation-controlled nucleophilic and electrophilic reactions of various substrates, K. Maruoka, T. Ooi, *Chem. Eur. J.* **1999**, *5*, 829; b) the incorporation of the dsp^3 Al hybridization in the catalytically active aluminum complexes, S. G. Nelson, B. K. Kim, T. Peelen, *J. Am. Chem. Soc.* **2000**, *122*, 9318.

[4] For selected examples see: a) D. G. Hendershot, M. Barber, R. Kumar, J. P. Oliver, *Organometallics* **1991**, *10*, 3302; b) J. Lewiński, J. Zachara, I. Justyniak, *Organometallics* **1997**, *16*, 3859; c) J. Lewiński, J. Zachara, K. B. Starowieyski, *J. Chem. Soc., Dalton Trans.* **1997**, 4217; d) J. A. Francis, C. N. McMahon, S. G. Bott, A. R. Barron, *Organometallics* **1999**, *18*, 4403; e) J. A. N. Francis, S. G. Bott, A. R. Barron, *Polyhedron* **1999**, *18*, 2211; f) J. Lewiński, J. Zachara, I. Justyniak, *Chem. Commun.* **2002**, 1586; g) H. Schumann, F. Girgsdies, S. Dechert, J. Gottfriedsen, M. Hummert, S. Schutte, J. Pickardt, *Z. Anorg. Allg. Chem.* **2002**, *628*, 2625.

[5] a) J. Lewiński, J. Zachara, K. B. Starowieyski, Z. Ochal, I. Justyniak, T. Kopeć, P. Stolarzewicz, M. Dranka, *Organometallics* **2003**, *22*, 3773; b) J. Lewiński, J. Zachara, P. Stolarzewicz, M. Dranka, E. Kołodziejczyk, I. Justyniak, J. Lipkowski, *New J. Chem.* **2004**, *28*, 1320; c) J. Lewiński, J. Zachara, T. Kopeć, K. B. Starowieyski, J. Lipkowski, I. Justyniak, E. Kołodziejczyk, *Eur. J. Inorg. Chem.* **2001**, 1123; d) C. S. Branch, J. Lewiński, I. Justyniak, S. G. Bott, J. Lipkowski, A. R. Barron, *J. Chem. Soc., Dalton Trans.* **2001**, 1253; e) J. Lewiński, I. Justyniak, J. Lipkowski, J. Zachara, *Inorg. Chem. Commun.* **2000**, *3*, 700.

[6] We have recently demonstrated that for π-conjugated bidentate ligands the strength of the interaction between donor sites and the metal center, and hence the Lewis acidity of the metal center, is significantly controlled by the conformation of the chelate ring, J. Lewiński, P. Goś, T. Kopeć, J. Lipkowski, R. Luboradzki, *Inorg. Chem. Commun.* **1999**, *2*, 374.

[7] a) The corresponding sum of the van der Waals radii was assumed to fall in the range of 3.50–3.80 Å; A. Bondi, *J. Phys. Chem.* **1964**, *68*, 441; b) S. C. Nyburg, C. H. Faerman, *Acta Crystallogr., Sect. B* **1985**, *41*, 274; c) however, according to Morgan et al., the distance minimum for S···C(sp^2) van der Waals contacts is ca. 5 Å, R. S. Morgan, C. E. Tatsch, R. H. Goushard, J. M. McAdon, P. K. Warne, *Int. J. Peptide Protein Res.* **1978**, *11*, 209.

 © 2005 Wiley-VCH Verlag GmbH & Co. KGaA, Weinheim

[8] For discussions concerning the borderline distances of noncovalent attractive forces see for example ref.[4f] and I. Dance, *New J. Chem.* **2003**, *27*, 22.
[9] O. T. Beachley, Jr., D. J. MacRae, M. R. Churchill, A. Yu. Kovalevsky, E. S. Robirds, *Organometallics* **2003**, *22*, 3991.
[10] G. M. Sheldrick, *SHELXS-97, Program for Structure Solution*, Universität Göttingen, **1997**.
[11] G. M. Sheldrick, *SHELXL-97, Program for Structure Refinement*, Universität Göttingen, **1997**.

Received: May 09, 2005
Published Online: August 1, 2005

 © 2005 Wiley-VCH Verlag GmbH & Co. KGaA, Weinheim

An Unusual 3D Interdigitated Architecture Self-Assembled from Sidearm-Containing 2D Bilayer Motifs with a Cuboidal Framework

Xin-Long Wang,[a] Chao Qin,[a] En-Bo Wang,*[a] and Lin Xu[a]

Keywords: Bilayers / Interdigitation / Luminescence / Supramolecular chemistry / Zinc

The new complex [Zn(H_2bptc)(bpy)]·0.5bpdo (**1**) [H_4bptc = 3,3′,4,4′-biphenyltetracarboxylic acid, bpy = 4,4′-bipyridine, and bpdo = 4,4′-bipyridine *N*,*N*′-dioxide] has been synthesized and characterized. It exhibits a novel (2D→3D) interdigitated architecture that is obtained for the first time from the self-assembly of sidearm-containing bilayer motifs with a cuboidal framework, in which each cuboidal box of one bilayer is interdigitated by two arms that belong to two adjacent bilayers. The luminescent properties of **1** are discussed.

(© Wiley-VCH Verlag GmbH & Co. KGaA, 69451 Weinheim, Germany, 2005)

Introduction

The interest in entangled systems is rapidly increasing not only for their potential applications as functional materials[1] but also their aesthetic and often complicated architectures and topologies.[2] Interpenetrating networks are the most popular among the entangled polymeric systems, and many appealing interpenetrated frameworks have been constructed, aided by the rapid growth of network-based crystal engineering, and have been well discussed in two comprehensive reviews by Robson and Batten.[3] More recently, a complete analysis of all 3D interpenetrated metal-organic framework structures contained in the CSD database has been proposed with a rationalization and classification of the topology of interpenetration.[4] A characteristic feature of interpenetration is that it is necessary to break internal connections in order to separate the individual nets. In contrast, other types of polymeric supramolecular architectures can, in principle, be disentangled without the need for breaking links (hereafter referred to as "extricable entanglement"), and their resulting overall architectures are more flexible than the usual networks entirely based on coordination bonds − a functional property that has potential applications ranging from drug-delivery vehicles to sensor devices.[5] Unfortunately, these species are much less known, as evidenced by a recent review by Ciani and co-workers.[6] At present, limited examples include infinite multiple helices,[7] cloth-like warp-and-weft sheet structures,[8] interdigitation,[9] and polypseudo-rotaxane structures.[10] Up to now, of the previously reported interdigitated examples, almost all are related to highly undulating *single* layers containing small and cramped windows,[9a,9b] including two exceptional cases in which interdigitation occurs between two different structural motifs (a 1D chain and a 2D puckered layer).[9c,9d] A molecular bilayer as a new structural motif was not reported until recently,[11] although since then several types of bilayer architectures have been fabricated by the assembly of T-shaped,[12] non-T-shaped,[13] or rectangular segments.[14] To the best of our knowledge, the only known interdigitated species containing *double* layer motifs is [Ag(bpe)($L_{0.5}$)]·H_2O [bpe = 1,2-bis(4-pyridyl)ethane; L = 4,4′-biphenyldicarboxylate,[9e] which is comprised of two sets of polycatenated T-shaped bilayers and where, quite surprisingly, the closest bilayers belonging to the different sets are interdigitated in pairs in a tongue-and-groove fashion.[15] An interesting question that arises from this is whether interdigitated structures can also be generated by the aggregation of other types of bilayers, and, if so, what would they be like.

Fortunately, by trial and error we have isolated such a complex, namely [Zn(H_2bptc)(bpy)]·0.5bpdo (**1**) [H_4bptc = 3,3′,4,4′-biphenyltetracarboxylic acid, bpy = 4,4′-bipyridine, and bpdo = 4,4′-bipyridine *N*,*N*′-dioxide], which, for the first time, defines a 3D interdigitated architecture assembled by sidearm-containing bilayer motifs with a cuboidal framework.

Results and Discussion

Single-crystal X-ray diffraction reveals that **1** (see Exp. Sect. for synthesis) is an extended 3D interdigitated network involving 2D bilayers with dangling arms. Each Zn^{II} atom is coordinated by three carboxylate oxygen atoms from three different bptc ligands and two nitrogen atoms from two bpy ligands to give a distorted trigonal-bipyrami-

[a] Institute of Polyoxometalate Chemistry, Department of Chemistry, Northeast Normal University,
Changchun, 130024, China
Fax: +86-431-509-8787
E-mail: wangenbo@public.cc.jl.cn

Supporting information for this article is available on the WWW under http://www.eurjic.org or from the author.

 © 2005 Wiley-VCH Verlag GmbH & Co. KGaA, Weinheim **DOI: 10.1002/ejic.200500440**

dal geometry (Figure 1). Two crystallographically equivalent zinc atoms are bridged by a pair of bptc carboxylate ends into a dinuclear zinc unit with a Zn···Zn distance of 3.82(7) Å. The dizinc carboxylate moieties are linked by four *exo*-tridentate bptc ligands (two of the four carboxylate groups do not take part in coordination but are pendent) to two adjacent dinuclear zinc units, thus generating a 1D $[Zn_2(Hbptc)_2]_n$ double chain (Figure S1). The zinc ions have an affinity for a five-coordinate environment, as discussed above, three of which have been used in the construction of the double chain, therefore the remaining two provide additional binding sites, i.e. two bpy ligands coordinate *trans* to each metal center in an axial position, thereby further connecting adjacent double chains into a unique 2D bilayer containing cuboidal boxes of approximate dimensions 11.4×13.0×3.8 Å, as illustrated in Figure 2. The 2D bilayer framework can also be considered as being constructed by two (4,4) grid sheets of composition $[Zn(H_2bptc)(bpy)]$ linked by μ_2-carboxylato groups of bptc.

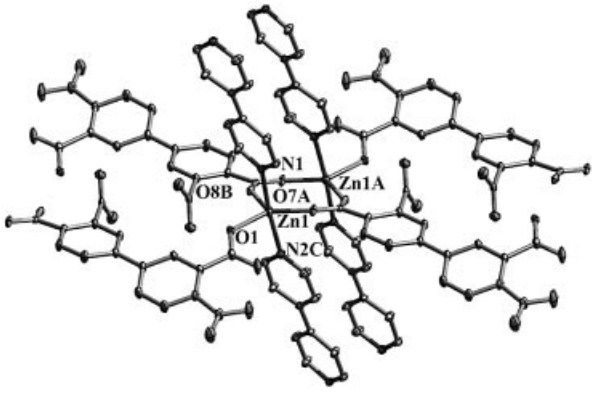

Figure 1. ORTEP view of the Zn^{II} coordination environments. Selected bond lengths [Å]: Zn(1)–O(1) 1.9935(15), Zn(1)–O(7A) 2.0007(14), Zn(1)–O(8B) 2.0189(14), Zn(1)–N(1) 2.1642(16), Zn(1)–N(2C) 2.1665(17). Symmetry codes: A: *x*, *y*, *z* + 1; B: –*x* + 1, –*y* + 1, –*z* + 1; C: *x*, *y* – 1, *z*.

It should be noted that, different from the previously reported bilayers assembled from rectangular building blocks, the unusual bilayer structure reported here has lateral arms pointing out from both sides of the bilayer (Figure 2, bottom). This remarkable feature is a necessary condition for the formation of interdigitation. To sum up, three factors can be envisaged to play roles in the generation of mutual interdigitation in **1**: (i) the presence within the 2D bilayer motifs of very large cuboidal boxes (with dimensions 11.4×13.0×3.8 Å) built up by four pairs of dizinc units, four bptc, and four bipy ligands, (ii) the existence of dangling bptc groups that are disposed in a mutual *anti* orientation with respect to the bilayer plane, and (iii) the fact that all the bilayers are stacked parallel at a distance of about 5.72 Å, while the effective length of each dangling arm is around 8.64 Å (from the baricenter of the dizinc unit to the uncoordinated carboxyl oxygen atom end), thus providing, obviously, the possibility for the ultimate realization of mutual interdigitation. Under these premises, the lateral arms of each bilayer point into the cuboidal voids of the adjacent

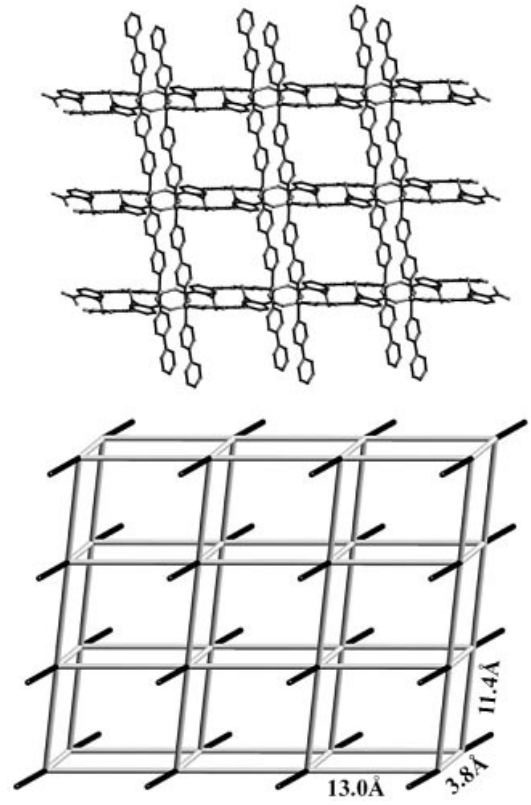

Figure 2. View of the 2D bilayer (top) and a schematic representation of the sidearm-containing 2D bilayer with large cuboidal boxes (bottom).

bilayers, in a mutual relationship. Each cuboidal box is therefore interdigitated by two arms that belong to two different bilayers, one entering from one side and the other from the opposite one, as shown in Figure 3. Finally, this unique fashion originated by the entanglement of three adjacent polymeric motifs at a time gives the novel (2D→3D) interdigitated array of compound **1** (see Figure 4). The aromatic rings of bptc pointing into the cuboidal box are parallel to those of edges bridged by bptc ligands, thus generating the π–π stacking interactions with a face-to-face separation of 3.61 Å that stabilize the whole entanglement. The schematic representation of the "mutual interdigitation" in this species shows that two adjacent bilayers are displaced by about one third of the polymer period along the direction of extension. The sequence of the bilayers in the 3D network is therefore of the ABCABC type (Figure 4).

A potential driving force for interdigitation is the need to fill the void space of a single network. However, in spite of this feature, the resulting 3D network still contains one-dimensional channels running along the *a*-axis and the effective free volume is 20.2%, as calculated by PLATON (Figure S2). Guest bpdo molecules reside in the channels and are hydrogen-bonded to the uncoordinated carbonyl oxygen atom of the bptc [O(6)···O(9) 2.577(3) Å]. Moreover, they form significant π–π stacking interactions with the arm moieties [interplanar distance of 3.55(6) Å], thereby stabilizing the whole 3D host-guest network.

 © 2005 Wiley-VCH Verlag GmbH & Co. KGaA, Weinheim

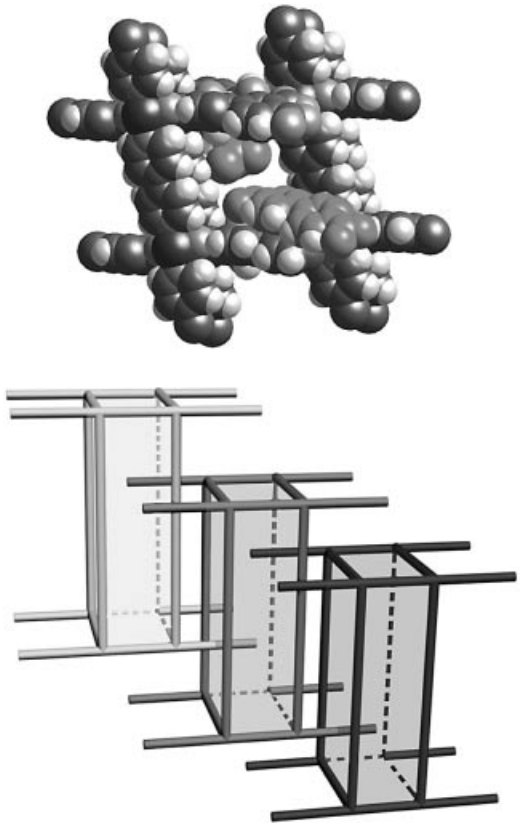

Figure 3. A space-filling model of a cuboidal box of the bilayer showing the two interdigitated arms (top), and a schematic illustration of the mutual interdigitation of three cuboidal boxes from three polymeric bilayers (bottom).

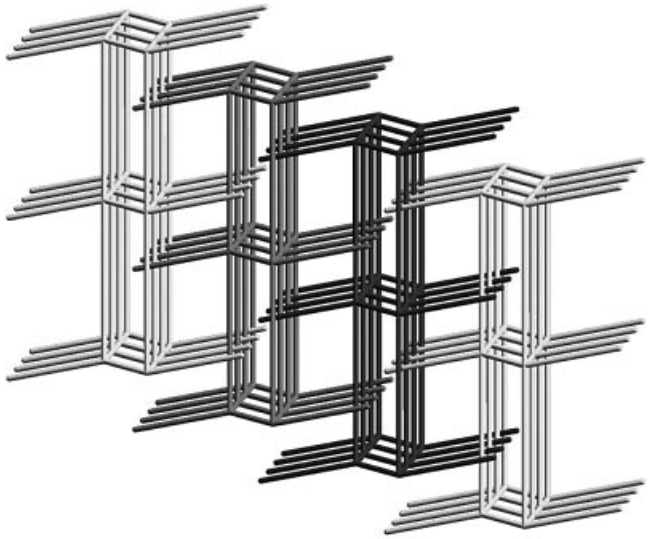

Figure 4. Schematic view of the (2D→3D) interdigitated array showing the relative displacement of the adjacent bilayers.

Compound **1** shows a strong photoluminescence in the solid state at room temperature, with a maximum emission band at 456 nm upon excitation at 338 nm (Figure 5). As there are no obvious emissions observed for the organic components under the same experimental conditions, the intense luminescence in compound **1** may be attributable to ligand-to-metal charge transfer.[16]

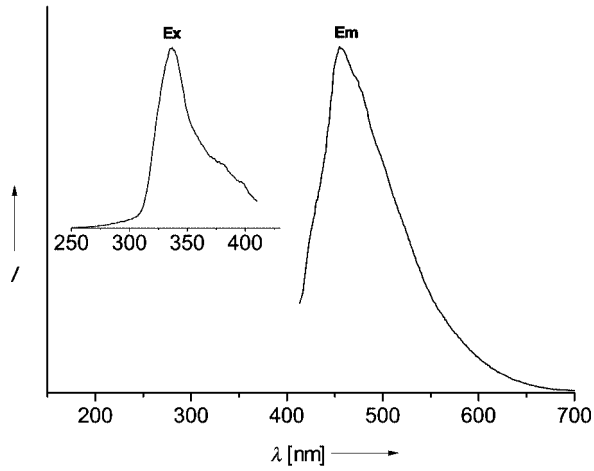

Figure 5. Photoluminescent spectra of **1** in the solid state at room temperature. Ex = excitation, Em = emission.

Conclusions

In summary, this work has, for the first time, demonstrated that an interdigitated structure can be produced by the assembly of bilayer motifs with a cuboidal framework. Compound **1**, besides adding a new member to the class of extricable entanglement, provides a remarkable new structural motif for the entangled system. Based on this new motif, one can envisage using it to construct another unknown entangled type − polythreading of bilayers − when the lateral arms are long enough to ensure complete threading through the cuboidal box. Further development and study of this interesting molecular module are in progress in our laboratories.

Experimental Section

Synthesis of 1: A mixture of $Zn(NO_3)_2 \cdot 6H_2O$ (149 mg, 0.5 mmol), H_4bptc (165 mg, 0.5 mmol), bpy (78 mg, 0.5 mmol), bpdo (47 mg, 0.25 mmol), triethylamine (0.05 mL, 0.35 mmol), and water (10 mL) in a 23-mL Teflon-lined reactor were heated at 160 °C under autogenous pressure for 5 d and then cooled to room temperature at a rate of 10 °C h^{-1} to give colorless crystals of **1** (yield: 135 mg, 42% based on Zn). $C_{31}H_{20}N_3O_9Zn$ (643.87): calcd. C 58.72, H 3.13, N 6.53; found C 58.35, H 3.47, N, 6.46. FT-IR (KBr): $\tilde{\nu}$ = 1715 (s), 1604 (vs), 1519 (s), 1491 (s), 1410 (s), 1380 (vs), 1210 (m), 1170 (m), 1150 (m), 805 (m), 782 (m) cm^{-1}.

X-ray Crystallographic Study: The data were collected with a Rigaku R-AXIS RAPID IP diffractometer with Mo-K_α monochromated radiation (λ = 0.71073 Å) at 173(2) K. An empirical absorption correction was applied. The structures were solved by direct methods and refined by the full-matrix least-squares method on F^2 using the SHELXTL crystallographic software package.[17] Anisotropic thermal parameters were used to refine all non-hydrogen atoms. The hydrogen atoms were included at idealized positions. Crystal data for **1**: $C_{31}H_{20}N_3O_9Zn$, M = 643.87, triclinic, space group $P\bar{1}$, a = 9.6477(19), b = 11.410(2), c = 12.980(3) Å, α =

 © 2005 Wiley-VCH Verlag GmbH & Co. KGaA, Weinheim

98.34(3)°, β = 96.44(3)°, γ = 111.36(3)°, V = 1295.4(4) Å^3, Z = 2, μ = 1.016 mm^{-1}, 12679 reflections measured, 5776 unique (R_{int} = 0.0202), final R [$I > 2\sigma(I)$] R_1 = 0.0311, wR_2 = 0.0892. CCDC-271719 contains the supplementary crystallographic data for this paper. These data can be obtained free of charge from the Cambridge Crystallographic Data Centre via www.ccdc.cam.ac.uk/data_request/cif.

Supporting Information Available (see footnote on the first page of this article): Additional figures (Figures S1 and S2) for **1**.

Acknowledgments

We are indebted to Dr. L. Carlucci for helpful analysis of the structure. This work was financially supported by the National Natural Science Foundation of China (no. 20371011).

[1] a) D. M. Proserpio, R. Hoffman, P. Preuss, *J. Am. Chem. Soc.* **1994**, *116*, 9634–9637; b) J. S. Miller, *Adv. Mater.* **2001**, *13*, 525–527; c) O. Ermer, *Adv. Matter.* **1991**, *3*, 608–611; d) J. P. Sauvage, *Acc. Chem. Res.* **1998**, *31*, 611–619; e) R. Kitaura, K. Seki, G. Akiyama, S. Kitagawa, *Angew. Chem. Int. Ed.* **2003**, *42*, 428–431.

[2] a) L. Carlucci, G. Ciani, M. Moret, D. M. Proserpio, S. Rizzato, *Angew. Chem. Int. Ed.* **2000**, *39*, 1506–1510; b) S. A. Bourne, J. Lu, B. Moulton, M. J. Zaworotko, *Chem. Commun.* **2001**, 861–862; c) Y. H. Li, C. Y. Su, A. M. Goforth, K. D. Shimizu, K. D. Gray, M. D. Smith, H. C. zur Loye, *Chem. Commun.* **2003**, 1630–1631.

[3] a) S. R. Batten, R. Robson, *Angew. Chem. Int. Ed.* **1998**, *37*, 1460–1494; b) S. R. Batten, *CrystEngCommun.* **2001**, *3*, 67–73.

[4] V. A. Blatov, L. Carlucci, G. Ciani, D. M. Proserpio, *CrystEngCommun.* **2004**, *6*, 377–395.

[5] a) J. P. Sauvage, *Acc. Chem. Res.* **1998**, *31*, 611–619; b) K. Kim, *Chem. Soc. Rev.* **2002**, *31*, 96–107.

[6] L. Carlucci, G. Ciani, D. M. Proserpio, *Coord. Chem. Rev.* **2003**, *246*, 247–289.

[7] a) L. Carlucci, G. Ciani, D. W. V. Gudenberg, D. M. Proserpio, *Inorg. Chem.* **1997**, *36*, 3812–3813; b) S. Sailaja, M. V. Rajasekharan, *Inorg. Chem.* **2000**, *39*, 4586–4590; c) Y. Cui, S. J. Lee, W. Lin, *J. Am. Chem. Soc.* **2003**, *125*, 6014–6015; d) X. C. Huang, J. P. Zhang, Y. Y. Lin, X. M. Chen, *Chem. Commun.* **2005**, 1–4.

[8] a) P. M. Van Calcar, M. M. Olmstead, A. L. Balch, *J. Chem. Soc., Chem. Commun.* **1995**, 1773–1774; b) L. Carlucci, G. Ciani, A. Gramaccioli, D. M. Proserpio, S. Rizzato, *CrystEngCommun.* **2000**, *2*, 154–163; c) Y. H. Li, C. Y. Su, A. M. Goforth, K. D. Shimizu, K. D. Gray, M. D. Smith, H. C. zur Loye, *Chem. Commun.* **2003**, 1630–1631.

[9] a) L. Carlucci, G. Ciani, P. Macchi, D. M. Proserpio, S. Rizzato, *Chem. Eur. J.* **1999**, *5*, 237–243; b) S. R. Batten, B. F. Hoskins, R. Robson, *Chem. Eur. J.* **2000**, *6*, 156–161; c) P. Ayyappa, O. R. Evans, W. Lin, *Inorg. Chem.* **2002**, *41*, 3328–3330; d) X. L. Wang, C. Qin, E. B. Wang, L. Xu, Z. M. Su, C. W. Hu, *Angew. Chem. Int. Ed.* **2004**, *43*, 5036–5040; e) Z. Y. Fu, X. T. Wu, J. C. Dai, S. M. Hu, W. X. Du, *New J. Chem.* **2002**, *26*, 978–980.

[10] a) C. V. K. Sharma, R. D. Rogers, *Chem. Commun.* **1999**, 83–84; b) M. B. Zaman, M. D. Smith, H. C. zur Loye, *Chem. Commun.* **2002**, 2256–2257; c) K. Biradha, M. Fujita, *Chem. Commun.* **2002**, 1866–1867; d) G. F. Liu, B. H. Ye, Y. H. Ling, X. M. Chen, *Chem. Commun.* **2002**, 1442–1443; e) L. Carlucci, G. Ciani, D. M. Proserpio, *Chem. Commun.* **1999**, 449–450; f) M. L. Tong, H. J. Chen, X. M. Chen, *Inorg. Chem.* **2000**, *39*, 2235–2238; g) C. Qin, X. L. Wang, L. Carlucci, M. L. Tong, E. B. Wang, C. W. Hu, L. Xu, *Chem. Commun.* **2004**, 1876–1877.

[11] a) M. Kondo, T. Yoshitomi, K. Seki, H. Matsuzaka, S. Kitagawa, *Angew. Chem. Int. Ed. Engl.* **1997**, *36*, 1725–1727; b) T. L. Hennigar, D. C. MacQuarrie, P. Losier, R. D. Rogers, M. J. Zaworotko, *Angew. Chem. Int. Ed. Engl.* **1997**, *36*, 972–973.

[12] a) K. N. Power, T. L. Hennigar, M. J. Zaworotko, *New J. Chem.* **1998**, *22*, 177–181; b) J. C. Dai, X. T. Wu, Z. Y. Fu, C. P. Cui, S. M. Hu, W. X. Du, L. M. Wu, H. H. Zhang, R. Q. Sun, *Inorg. Chem.* **2002**, *41*, 1391–1396; c) C. J. Kepert, M. J. Rosseinsky, *Chem. Commun.* **1999**, 375–376; d) A. Rujiwatra, C. J. Kepert, M. J. Rosseinsky, *Chem. Commun.* **1999**, 2307–2308; e) S. Kitagawa, M. Kondo, *Bull. Chem. Soc. Jpn.* **1998**, *71*, 1739; f) M. J. Zaworotko, *Chem. Commun.* **2001**, 1–2; g) J. Zhang, Z. J. Li, J. K. Cheng, Y. Kang, Y. Y. Qin, Y. G. Yao, *New J. Chem.* **2005**, *29*, 421–423.

[13] J. C. Dai, S. M. Hu, X. T. Wu, Z. Y. Fu, W. X. Du, H. H. Zhang, R. Q. Sun, *New J. Chem.* **2003**, *27*, 914–918.

[14] a) S. M. F. Lo, S. S. Y. Chui, L. Y. Shek, Z. Y. Lin, X. X. Zhan, G. H. Wen, I. D. Williams, *J. Am. Chem. Soc.* **2000**, *122*, 6293–6294; b) Z. Y. Fu, X. T. Wu, J. C. Dai, L. M. Wu, C. P. Cui, S. M. Hu, *Chem. Commun.* **2001**, 1856–1857; c) J. H. Luo, M. C. Hong, R. H. Wanf, R. Cao, L. Han, D. Q. Yuan, Z. Z. Lin, Y. F. Zhou, *Inorg. Chem.* **2003**, *42*, 4486–4488; d) X. L. Wang, C. Qin, E. B. Wang, Y. G. Li, C. W. Hu, L. Xu, *Chem. Commun.* **2004**, 378–379; e) R. J. Hill, D. L. Long, M. S. Turvey, A. J. Blake, N. R. Champness, P. Hubberstey, C. Wilson, M. Schröder, *Chem. Commun.* **2004**, 1792–1793.

[15] L. Carlucci, G. Ciani, D. M. Proserpio, *CrystEngCommun.* **2003**, *5*, 269–279.

[16] a) A. Meijerink, G. Blasse, M. Glasbeek, *J. Phys.: Condens. Matter* **1990**, *2*, 6303–6313; b) R. Bertoncello, M. Bettinelli, M. Cassrin, A. Gulino, E. Tondello, A. Vittadini, *Inorg. Chem.* **1992**, *31*, 1558–1565; c) J. Tao, J. X. Shi, M. L. Tong, X. X. Zhang, X. M. Chen, *Inorg. Chem.* **2001**, *40*, 6328–6330.

[17] a) G. M. Sheldrick, *SHELXS-97, A Program for the Solution of Crystal Structures from X-ray Data*, University of Göttingen, Germany, **1997**; b) G. M. Sheldrick, *SHELXL-97, A Program for the Refinement of Crystal Structures from X-ray Data*, University of Göttingen, Germany, **1997**.

Received: May 16, 2005
Published Online: August 1, 2005

 © 2005 Wiley-VCH Verlag GmbH & Co. KGaA, Weinheim

Is the Aromatic Fragment of Piano-Stool Ruthenium Compounds an Essential Feature for Anticancer Activity? The Development of New Ru^{II}-[9]aneS_3 Analogues

Barbara Serli,[a] Ennio Zangrando,[a] Teresa Gianferrara,[b] Claudine Scolaro,[c] Paul J. Dyson,[c] Alberta Bergamo,[d] and Enzo Alessio*[a]

Keywords: Antitumor agents / Facial coordination / Half-sandwich complexes / Ruthenium / S ligands

New half-sandwich Ru^{II}-[9]aneS_3 complexes ([9]aneS_3 = 1,4,7-trithiacyclononane), namely [$RuCl_2$(PTA)([9]aneS_3)] (**4**), [RuCl(PTA)$_2$([9]aneS_3)][OTf] (**5**), [RuCl(en)([9]aneS_3)][OTf] (**6**), [RuCl(enac)([9]aneS_3)][OTf] (**7**), [RuCl(bipy)([9]aneS_3)][OTf] (**8**), and [Ru(dmso-S)(bipy)([9]aneS_3)][OTf]$_2$ (**9**) [PTA = 1,3,5-triaza-7-phosphaadamantane; enac = 1,2-bis-(isopropyleneimino)ethane; OTf = $CF_3SO_3^-$] were prepared from Ru-[9]aneS_3–dmso precursors and structurally characterized, both in solution and in the solid state by X-ray crystallography. Some of them are analogs of known cytotoxic organometallic Ru^{II}-(η^6-arene) and Ru^{II}-(η^5-cyclopentadienyl) compounds, in which the aromatic fragment is replaced by the sulfur macrocycle 1,4,7-trithiacyclononane, while the rest of the coordination sphere is left unchanged. Similarly to the aromatic analogs for which data are available, in aqueous solution the Ru-[9]aneS_3 complexes (with the exception of **5**) hydrolyze a chloride (or a dmso in the case of **9**) to give the corresponding aquo species. This process is rapidly reversed in the presence of free chloride, and coordination of phosphate is likely to occur to the aquo species in phosphate buffered solutions at physiological pH. Preliminary in vitro tests performed on complexes **4**–**6** against the mouse adenocarcinoma cancer cell line (TS/A) and the human mammary normal cell line (HBL-100) showed that, in general, the Ru-[9]aneS_3 compounds have a cytotoxicity comparable to that of the corresponding organometallic analogs. These results suggest that the aromatic fragment of the piano-stool Ru^{II} compounds is not an essential feature for the in vitro anticancer activity, and it might be effectively replaced by another face-capping ligand with a low steric demand, such as [9]aneS_3.

(© Wiley-VCH Verlag GmbH & Co. KGaA, 69451 Weinheim, Germany, 2005)

Introduction

The field of anticancer ruthenium drugs is attracting growing interest because some compounds have proved to have very encouraging pharmacological profiles;[1] in particular, they show in vivo activity against tumors that are resistant to cisplatin and carboplatin and a generally lower toxicity (and hence side-effects) than platinum drugs. The most advanced representatives of this new class of anticancer agents are the two Ru^{III} coordination compounds KP1019 {[indH][*trans*-$RuCl_4$(ind)$_2$]; ind = indazole}, developed in the Eighties by Keppler and co-workers,[2] and NAMI-A {[imH][*trans*-$RuCl_4$(dmso-S)(im)]; im = imidazole}, developed in the Nineties by some of us.[3] NAMI-A is selectively active against metastases of solid tumors,[4] while KP1019 is active against colorectal tumors.[5] Both compounds were recently tested on humans because of their promising activities against platinum-resistant malignancies; NAMI-A has completed a phase-I trial and is scheduled to begin phase-II trials soon,[6] while KP1019 is currently in phase-I trials.[7] Contrary to platinum anticancer compounds, the activity of NAMI-A seems to be unrelated to direct cytotoxicity.

More recently, an entirely different class of Ru^{II} compounds developed by Sadler and co-workers has shown very promising anticancer activity both in vitro and in vivo.[8] This class comprises organometallic half-sandwich Ru^{II}–arene complexes of the type [RuCl(en)(η^6-arene)][PF_6] (arene = benzene, *p*-cymene, tetrahydroanthracene, dihydroanthracene, biphenyl), also called "piano-stool" complexes because of their geometry (Figure 1). Such complexes exhibit IC_{50} values (IC_{50} = concentration of compound that kills 50% of cell population) in vitro in the range 6–200 μM against a human ovarian cancer cell line, compared with values of 0.5 μM for cisplatin and 6 μM for carboplatin.[8] The initial in vitro and in vivo studies sug-

[a] Dipartimento di Scienze Chimiche, University of Trieste, Via L. Giorgieri 1, 34127 Trieste, Italy
E-mail: alessi@univ.trieste.it
[b] Dipartimento di Scienze Farmaceutiche, University of Trieste, Piazzale Europa 1, 34127 Trieste, Italy
[c] Institut des Sciences et Ingénierie Chimiques, Ecole Polytechnique Fédérale de Lausanne (EPFL), 1015 Lausanne, Switzerland
[d] Callerio Foundation Onlus, Via A. Fleming 22–31, 34127 Trieste, Italy
Supporting information for this article is available on the WWW under http://www.eurjic.org or from the author.

gested that the most active complexes contain the most hydrophobic η^6-arene ligands. For example, [RuCl(en)(η^6-biphenyl)][PF_6] is active in the A2780 human ovarian cancer xenograft and is not cross-resistant in the A2780cis xenograft.[9] The target for these Ru^{II}–arene complexes might be DNA.[10] Investigations with natural DNA in a cell-free medium indicated that they bind preferentially to guanine residues; binding involves mono-functional coordination to G N7 (after chloride release) and noncovalent, hydrophobic interactions between the arene ligand and DNA, which may include arene intercalation and minor groove binding.[11]

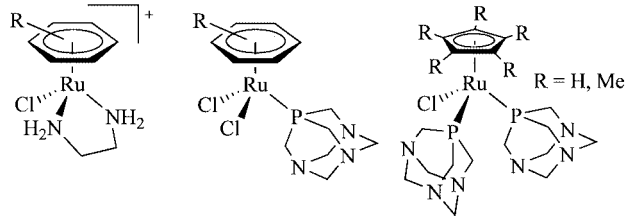

Figure 1. Schematic drawings of the cytotoxic organometallic piano-stool compounds. [RuCl(en)(η^6-arene)]$^+$, [$RuCl_2$(PTA)(η^6-arene)], and [RuCl(PTA)$_2$(η^5-C_5R_5)].

The biological activities of other piano-stool organometallic Ru^{II} complexes have been investigated at different levels. The 1,3,5-triaza-7-phosphaadamantane (PTA) complex [$RuCl_2$(PTA)(η^6-*p*-cymene)] (Figure 1) has proved to have in vitro pH-dependent DNA binding properties and to induce apoptosis in neuroblastoma cells at nanomolar concentrations.[12] It was observed that for the Ru^{II}–arene PTA complexes loss of the arene can occur on binding to an oligonucleotide.[13] In vivo, [$RuCl_2$(PTA)(η^6-*p*-cymene)] has been found to be capable of inhibiting lung metastases in CBA mice bearing the MCa mammary carcinoma, reducing both their number and weight.[14] Related compounds have also been shown to exhibit antimicrobial properties.[15] In vitro anticancer properties have been demonstrated for the compounds [RuCl(BESE)(η^6-*p*-cymene)]$^+$ [BESE = $EtS(O)(CH_2)_2S(O)Et$][16] and [RuCl(PTA)$_2$(η^5-C_5Me_5)] (interestingly, the corresponding η^5-C_5H_5 complex is not cytotoxic, perhaps due to its lower lipophilicity).[17] In addition, [$RuCl_2$(Y)(η^6-C_6H_6)] compounds (Y = dmso, 3-aminopyridine, aminoguanidine, *p*-aminobenzoic acid) have been shown to have topoisomerase II poisoning and in vitro anticancer activity (at 100–300 μM concentrations); interaction of these compounds with DNA in vitro and formation of ternary cleavage complexes of topo II-drug-DNA has been demonstrated.[18] Coordination of the known anticancer agent 1-β-hydroxyethyl-2-methyl-5-nitroimidazole (metronidazole) to the Ru^{II}–benzene fragment affords [$RuCl_2$(metronidazole)(η^6-C_6H_6)], which has superior selective cytotoxicity to metronidazole itself and topoisomerase II activity.[19] Sheldrick and co-workers have published some ruthenium(II)–arene compounds with alanine- and guanine-derived co-ligands,[20] and while their anticancer activity was not included in the report, they were found to be cytotoxic towards P388 leukaemia cells.[21]

All these organometallic compounds are characterized by the presence of a face-capping aromatic ligand, either neutral (η^6-arene) or negatively charged (η^5-cyclopentadienyl), firmly bound to ruthenium. We were interested to establish whether the aromatic fragment is an essential feature for the biological activity of these piano-stool Ru^{II} complexes or if another face-capping ligand with a low steric demand would play the same role. For this reason we synthesized a new series of half-sandwich Ru^{II} complexes similar to the organometallic compounds described above, in which the aromatic fragment is replaced by the sulfur macrocycle 1,4,7-trithiacyclononane ([9]aneS_3), while the rest of the coordination sphere is left unchanged. The capability of [9]aneS_3 to coordinate to transition metal centers (and to ruthenium in particular) as a robust, face-capping, six-electron donor ligand, in analogy to the η^6-arene and η^5-cyclopentadienyl fragments (Figure 2), is well known.[22–27]

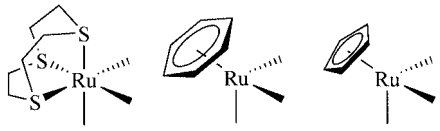

Figure 2. Schematic structural comparison of three half-sandwich Ru^{II} fragments with different face-capping ligands.

We report here the synthesis and structural characterization, both in solution and in the solid state, of the following complexes: [$RuCl_2$(PTA)([9]aneS_3)] (**4**), [RuCl(PTA)$_2$([9]aneS_3)][OTf] (OTf = triflate, $CF_3SO_3^-$) (**5**), and [RuCl(en)([9]aneS_3)][OTf] (**6**), which are analogs of some of the organometallic compounds described above; in addition, we have also prepared and characterized [RuCl(enac)([9]aneS_3)][OTf] [enac = 1,2-bis(isopropyleneimino)ethane] (**7**), [RuCl(bipy)([9]aneS_3)][OTf] (**8**), and [Ru(dmso-S)(bipy)([9]aneS_3)][OTf]$_2$ (**9**). The chemical behavior of these complexes in aqueous solution and at physiological pH have been investigated, and the in vitro tumor cell growth inhibition effects of **4**–**6** assessed.

Results and Discussion

The Precursors

Precursors for the new piano-stool compounds described below were the Ru-[9]aneS_3-dmso complexes [$RuCl_2$(dmso-S)([9]aneS_3)] (**1**), [RuCl(dmso-S)$_2$([9]aneS_3)][OTf] (**2**), and [Ru(dmso)$_3$([9]anoS_3)][OTf]$_2$ (**3**; Figure 3), in which the sulfoxides are quite easily replaced by stronger ligands. Compound **1** was first described by Landgrafe and Sheldrick in 1994,[24a] while **2** and **3** were more recently prepared by us by treatment of **1** with one or two equivalents of AgOTf, respectively.[28] Complex **3** crystallizes as [Ru(dmso-O)(dmso-S)$_2$([9]anoS_3)][OTf]$_2$ but in noncoordinating solvents it rapidly equilibrates with its linkage isomer [Ru(dmso-O)$_2$(dmso-S)([9]aneS_3)][OTf]$_2$, which is slightly more stable. Incidentally, complex **2** closely resembles the disulfoxide complex [RuCl(BESE)(η^6-*p*-cymene)][PF_6], for which James and co-workers had reported in vitro anti-cancer activity,[16] with [9]aneS_3 in place of *p*-cymene and two

 © 2005 Wiley-VCH Verlag GmbH & Co. KGaA, Weinheim

S-bonded dmso's in place of the doubly S-bonded disulfoxide $EtS(O)(CH_2)_2S(O)Et$ (BESE).

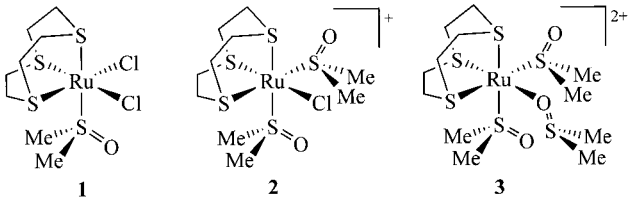

Figure 3. Schematic drawings of the precursors **1**–**3**.

All the products described below were characterized by elemental analysis, spectroscopic techniques in solution (NMR and UV/Vis spectroscopy), and in the solid state by IR spectroscopy and by X-ray diffraction analysis.

PTA Compounds

The reaction of **1** with one equivalent of 1,3,5-triaza-7-phosphaadamantane (PTA) in refluxing nitromethane led, upon selective replacement of dmso, to the isolation of the neutral compound $[RuCl_2(PTA)([9]aneS_3)]$ (**4**) in high yield (Scheme 1).

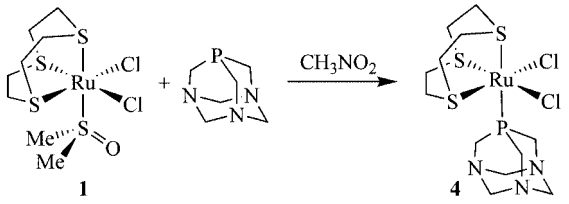

Scheme 1.

The ^1H NMR spectrum of **4** in D_2O (the only solvent in which the complex is highly soluble), recorded immediately after dissolution, shows a manifold of partially overlapping multiplets (δ = 2.6–3.0 ppm) attributed to the CH_2 protons of the [9]aneS_3 ligand,[29] and two equally intense signals (narrow unresolved multiplets) for the PTA ligand (δ = 4.22 and 4.55 ppm). By comparison with the spectrum of $[RuCl_2(PTA)(\eta^6\text{-}p\text{-cymene})]$,[12a] the downfield singlet was assigned to the CH_2 protons in the nitrogen heterocycle of PTA and the other to the CH_2 protons in the phosphorus-nitrogen heterocycle of PTA. The ^{31}P NMR spectrum shows a singlet at δ = –33.41 ppm {cf. δ = –36.63 ppm for $[RuCl_2(PTA)(\eta^6\text{-}p\text{-cymene})]$ in $CDCl_3$}.

In the solid state, the metal exhibits the expected distorted octahedral geometry (Figure 4). The Ru–ligand bond lengths are slightly different in the two independent molecules (A and B) identified in the asymmetric unit. The Ru–P bond lengths [2.290(3) Å and 2.279(2) Å] are similar to those observed in $[RuCl_2(PTA)(\eta^6\text{-}p\text{-cymene})]$.[12a] The Ru–Cl distances fall in a range from 2.429(3) to 2.459(3) Å and are similar to those in the precursor **1**.[24a] The three Ru–S bond lengths are remarkably different: those *trans* to Cl are significantly shorter [2.233(3)–2.275(3) Å, similar to those in precursors **1**] than that *trans* to the PTA phosphorus donor [2.365(3) and 2.349(3) Å in A and B, respectively]. The latter are comparable to the Ru–S bond length *trans* to phosphorus found in $[RuCl_2(PPh_3)([9]aneS_3)]$ [2.356(2) Å].[30] Water molecules (two for each complex unit) occupy voids in the crystal lattice and interact through H-bonds with the chloride ligands and with the PTA nitrogens.

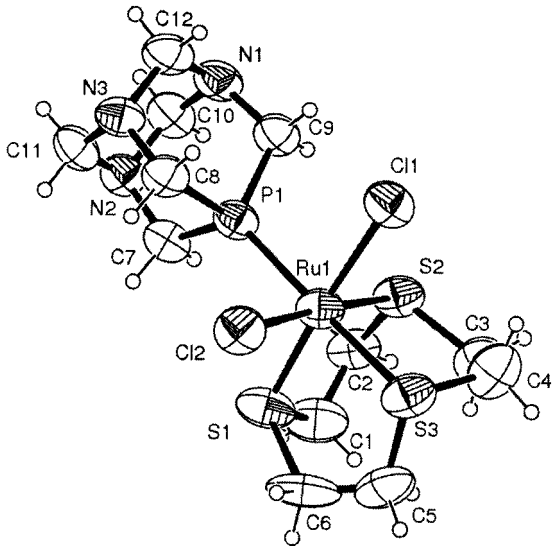

Figure 4. X-ray molecular structure of one of the two independent complexes of $[RuCl_2(PTA)([9]aneS_3)]\cdot 2(H_2O)$ (**4**). Selected bond lengths [Å] and angles [°], with data in parentheses referring to the second unit: Ru(1)–S(1) 2.248(3) [2.233(3)], Ru(1)–S(2) 2.275(3) [2.261(3)], Ru(1)–S(3) 2.365(3) [2.349(3)], Ru(1)–Cl(1) 2.429(3) [2.445(3)], Ru(1)–Cl(2) 2.429(3) [2.459(3)], Ru(1)–P(1) 2.290(3) [2.279(2)]; P(1)–Ru(1)–S(3) 175.2(1) [175.4(1)], S(1)–Ru(1)–Cl(1) 175.7(1) [174.5(1)], S(2)–Ru(1)–Cl(2) 175.5(1) [177.1(1)].

Treatment of $[RuCl(dmso)_2([9]aneS_3)][OTf]$ (**2**) with two equivalents of PTA in refluxing methanol yielded the cationic compound $[RuCl(PTA)_2([9]aneS_3)][OTf]$ (**5**) (Scheme 2).

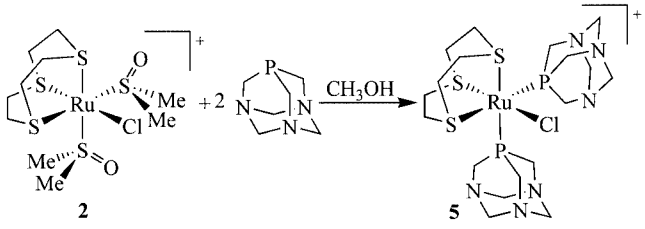

Scheme 2.

The ^1H NMR spectrum of **5** in D_2O is similar to that of **4**: the two equivalent PTA ligands give two resonances, integrating for 12 protons each, at δ = 4.25 and 4.59 ppm. The ^{31}P NMR spectrum shows a single resonance at δ = –33.45 ppm for the two equivalent phosphorus atoms. In the solid state (Figure 5), the two Ru–P bond lengths [2.317(2) and 2.315(2) Å] and the Ru–Cl distance [2.442(2) Å] present a trend similar to that found in the crystal of **4**, with values comparable to those found in

 © 2005 Wiley-VCH Verlag GmbH & Co. KGaA, Weinheim

$[RuCl(PTA)_2(\eta^5\text{-}C_5Me_5)]$.[17] As previously observed (complex **4**), the Ru–S bond length *trans* to Cl [2.295(2) Å] is shorter than those *trans* to the PTA ligands [2.395(2) and 2.372(2) Å].

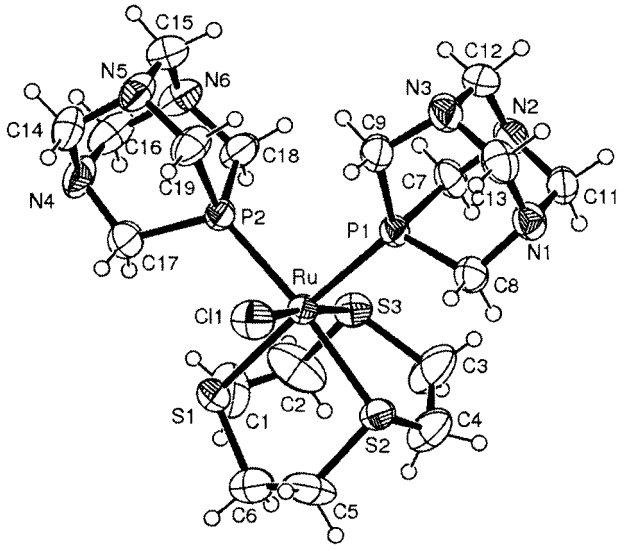

Figure 5. X-ray molecular structure of the complex cation of $[RuCl(PTA)_2([9]aneS_3)][OTf]\cdot(CH_3OH)$ (**5**). Selected bond lengths [Å] and angles [°]: Ru–S(1) 2.395(2), Ru–S(2) 2.372(2), Ru–S(3) 2.295(2), Ru–Cl(1) 2.442(2), Ru–P(1) 2.317(2), Ru–P(2) 2.315(2); P(1)–Ru–S(1) 176.66(7), P(2)–Ru–S(2) 174.17(7), S(3)–Ru–Cl(1) 174.68(7).

Ethylenediamine Compounds

The reaction of $[RuCl(dmso\text{-}S)_2([9]aneS_3)][OTf]$ (**2**) with one equivalent of ethylenediamine in refluxing nitromethane yielded, upon replacement of the two dmso ligands, the cationic compound $[RuCl(en)([9]aneS_3)][OTf]$ (**6**) (Scheme 3).

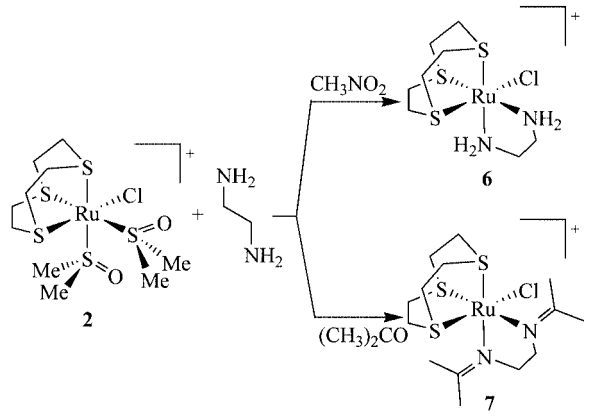

Scheme 3.

According to the X-ray structural analysis (Figure 6), the Ru–N and Ru–Cl bond lengths, as well as the chelating N–Ru–N angle, are comparable with the values found by Sadler and co-workers for the $[RuCl(en)(\eta^6\text{-arene})][PF_6]$ compounds.[10] The Ru–S distance *trans* to Cl [2.256(1) Å] is similar to the shortest one in **4**, and those *trans* to the N atoms agree with values documented for [9]aneS$_3$ *trans* to nitrogen ligands.[24a,25,28]

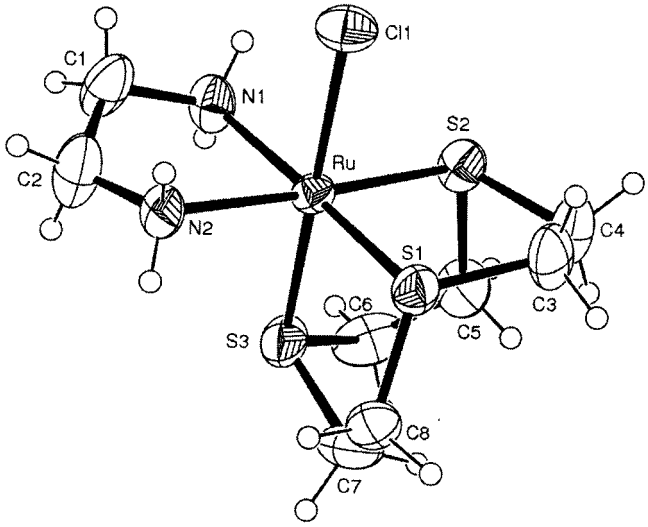

Figure 6. X-ray molecular structure of the complex cation of $[RuCl(en)([9]aneS_3)][OTf]$ (**6**). Selected bond lengths [Å] and angles [°]: Ru–S(1) 2.268(3), Ru–S(2) 2.290(3), Ru–S(3) 2.256(1), Ru–Cl(1) 2.443(1), Ru–N(1) 2.119(9), Ru–N(2) 2.180(7); N(1)–Ru–N(2) 80.7(1), N(1)–Ru–S(1) 175.4(2), N(2)–Ru–S(2) 176.3(3), S(3)–Ru–Cl(1) 179.7(1).

The $^{13}C\{^1H\}$ NMR spectrum of **6** in CD_3NO_2 (three resonances for the six CH_2 groups of [9]aneS$_3$ and a single resonance for the two CH_2 groups of the en ring) shows that the symmetry of the complex in solution (C_s) is higher than that observed in the solid state. Owing to rapid conformational equilibration of the [9]aneS$_3$ and en ligands, the complex has a plane of symmetry in solution that contains the S–Ru–Cl axis and bisects the [9]aneS$_3$ and the opposite en ligand. The ^1H NMR spectrum of **6** in CD_3NO_2 shows, besides the multiplets for [9]aneS$_3$, four equally intense, well-resolved signals for the coordinated ethylenediamine (Supporting Information). In accordance with the C_s symmetry {and by comparison with the assignements of $[RuCl(en)(\eta^6\text{-arene})]^+$ compounds}, the relatively broad resonances at δ = 3.35 and 3.91 ppm (coupled in the H-H COSY spectrum) were assigned to the two pairs of diastereotopic protons on the equivalent NH_2 groups, while the multiplets at δ = 2.83 and 2.94 ppm (coupled in the H-H COSY spectrum) were assigned to the two pairs of diastereotopic protons on the CH_2 groups. These latter resonances are coupled to the CH_2 signal of en at δ = 45.9 ppm in the H-C COSY spectrum. The ^1H NMR spectrum in D_2O is similar, but the two CH_2 resonances overlap with the multiplets of [9]aneS$_3$ (see below).

When the reaction between **2** and ethylenediamine was performed in refluxing acetone, condensation between the ligand and the solvent occurred to give 1,2-bis(isopropyleneimino)ethane (enac), which binds to ruthenium as a chelate. The cationic species $[RuCl(enac)([9]aneS_3)][OTf]$ (**7**) was thus obtained in good yield as a yellow solid and the structure was confirmed by X-ray analysis (Figure 7).

 © 2005 Wiley-VCH Verlag GmbH & Co. KGaA, Weinheim

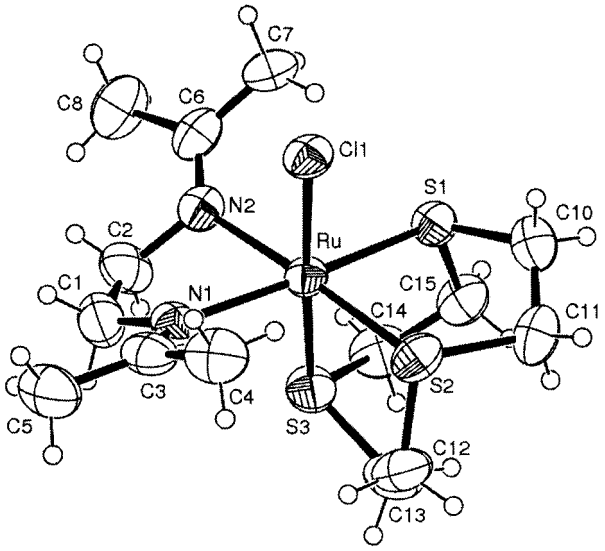

Figure 7. X-ray molecular structure of the complex cation of [RuCl(enac)([9]aneS_3)][OTf]·0.75H_2O (**7**). Selected bond lengths [Å] and angles [°]: Ru–S(1) 2.378(2), Ru–S(2) 2.414(2), Ru–S(3) 2.132(2), Ru–Cl(1) 2.296(2), Ru–N(1) 2.220(6), Ru–N(2) 2.239(5); N(1)–Ru–N(2) 74.3(2), N(1)–Ru–S(1) 173.4(1), N(2)–Ru–S(2) 177.4(1), S(3)–Ru–Cl(1) 176.26(7).

Complex **7** exhibits geometrical features that are remarkably different to the other structures reported and to those expected for similar Ru species. In fact, the Ru–N bond lengths are significantly longer than those found in compound **6** with the en ligand [2.220(6) and 2.239(5) Å vs. 2.119(9) and 2.180(7) Å]. In addition, the two Ru–S bond lengths *trans* to N [2.3776(18), 2.4139(18) Å] are extremely long if compared with those in **6**. Conversely, the Ru–Cl and the *trans* Ru–S bonds are exceptionally short: 2.296(2) and 2.132(2) Å, respectively [the Ru–Cl distance has to be compared with the value of 2.443(1) Å found in **6**]. These features can be ascribed to the steric requirements of the chelating N ligand that presents a bowed arrangement with coplanar N=C$(Me)_2$ groups that make an angle of 43.8(3)°. Methyls C(4) and C(7) point towards the chloride at a distance of around 3.54 Å.

The ^{1}H NMR spectrum of **7** in CD_3NO_2 shows, besides the [9]aneS_3 resonances, an unresolved multiplet at δ = 3.90 ppm for the four CH_2 protons and two singlets (6 H each) at δ = 2.23 and 2.57 ppm for the two pairs of diastereotopic methyl groups of the 1,2-bis(isopropyleneimino)-ethane ligand.

2,2′-Bipyridine Compounds

The reaction between [RuCl(dmso-S)$_2$([9]aneS_3)][OTf] and one equivalent of 2,2′-bipyridine (bipy) in refluxing methanol led again to the selective replacement of the two sulfoxides and formation of the cationic compound [RuCl(bipy)([9]aneS_3)][OTf] (**8**) (Scheme 4). The analogous complex [RuCl(bipy)([9]aneS_3)]Cl, as the chloride salt, has been prepared (and structurally characterized) by Goodfellow and co-workers upon reaction of **1** with a slight excess of bipy in refluxing ethanol.[26a]

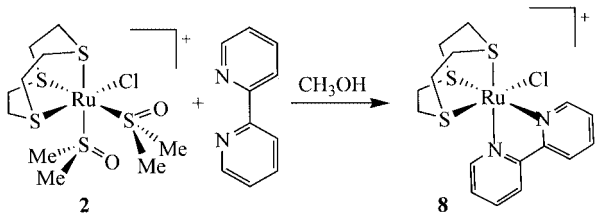

Scheme 4.

The geometry of the product was confirmed by X-ray crystallography (Figure 8). The Ru–N [2.094(4) and 2.102(4) Å], Ru–Cl [2.426(1) Å], and Ru–S [2.280(1) Å *trans* to Cl; 2.298(1) (Å) *trans* to N] bond lengths are consistent with those previously reported for the chloride derivative.[26a]

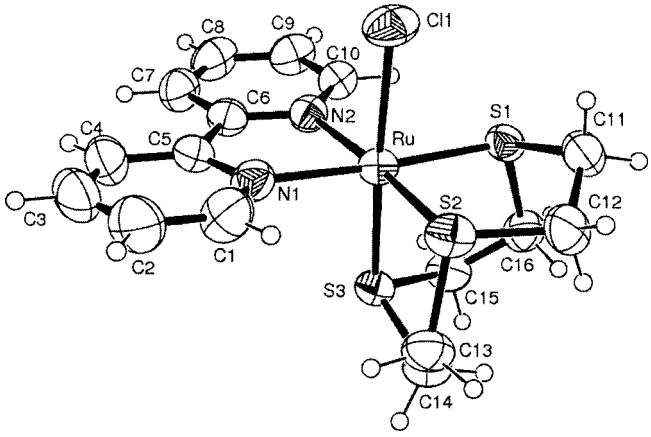

Figure 8. X-ray molecular structure of the complex cation of [RuCl(bipy)([9]aneS_3)][OTf] (**8**). Selected bond lengths [Å] and angles [°]: Ru–S(1) 2.298(1), Ru–S(2) 2.299(1), Ru–S(3) 2.280(1), Ru–Cl(1) 2.426(1), Ru–N(1) 2.102(4), Ru–N(2) 2.094(4); N(2)–Ru–N(1) 77.9(2), N(1)–Ru–S(1) 175.6(1), N(2)–Ru–S(2) 174.5(1), S(3)–Ru–Cl(1) 176.12(5).

The ^{1}H NMR spectrum of **8** in CD_3NO_2 shows four equally intense signals in the aromatic region for the coordinated bipy, indicating that the two halves of the chelate are equivalent.

Similarly, [Ru(dmso-S)(bipy)([9]aneS_3)][OTf]$_2$ (**9**), in which the chloride of **8** is formally replaced by a dmso-S ligand, was obtained by treatment of the dicationic precursor [Ru(dmso)$_3$([9]aneS_3)][OTf]$_2$ (**3**) with one equivalent of 2,2′-bipyridine in refluxing methanol (Scheme 5). The X-ray structure of **9** is shown in Figure 9. The coordination bond lengths and angles are in agreement with the parameters found in **8**, but the Ru–S(3) bond length *trans* to dmso is slightly longer than the corresponding value *trans* to Cl in **8** [2.339(3) vs. 2.280(1) Å], thus indicating a different *trans* influence for dmso and chlorine, as previously observed.[24a] The Ru–S(dmso) bond length of 2.285(3) Å is very similar to that in the precursor **1** [2.287(2) Å]. The plane of bipy forms a dihedral angle of about 12° with the N(1), N(2), S(1), and S(2) donors, away from the axial dmso ligand.

 © 2005 Wiley-VCH Verlag GmbH & Co. KGaA, Weinheim

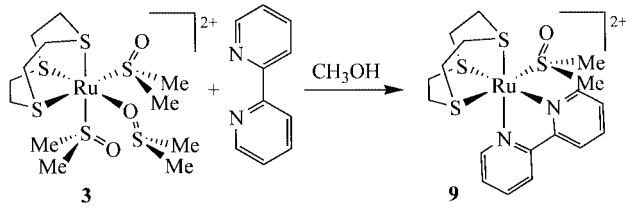

Scheme 5.

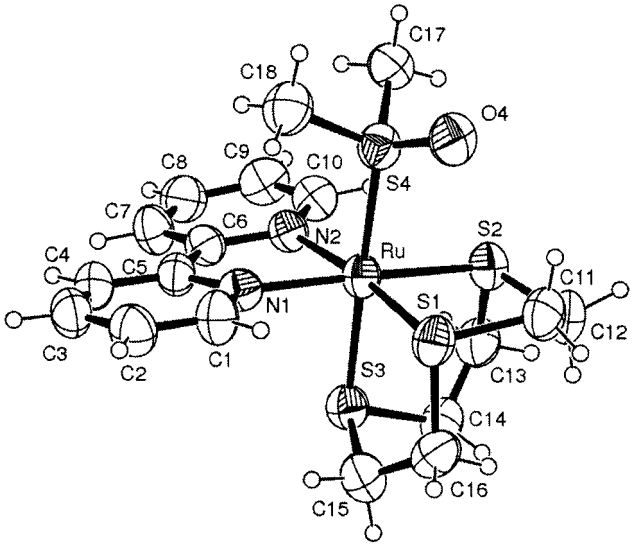

Figure 9. X-ray molecular structure of the complex cation of $[Ru(dmso\text{-}S)(bipy)([9]aneS_3)][OTf]_2{\cdot}2(H_2O)$ (**9**). Selected bond lengths [Å] and angles [°]: Ru–S(1) 2.322(3), Ru–S(2) 2.311(2), Ru–S(3) 2.339(3), Ru–S(4) 2.285(3), Ru–N(1) 2.071(7), Ru–N(2) 2.100(7); N(1)–Ru–N(2) 77.8(3), N(1)–Ru–S(2) 174.0(2), N(2)–Ru–S(1) 173.1(2), S(4)–Ru–S(3) 178.48(9).

The ^{1}H NMR spectrum of **9** in D_2O is similar to that of **8**, with an additional singlet at δ = 2.83 for the equivalent methyl groups of the dmso-S ligand. This resonance is remarkably upfield-shifted for a dmso coordinated through S, and actually falls in the region typical for dmso-O, because of the shielding cone of the adjacent bipy, as becomes apparent from the X-ray structure (Figure 9). The S=O stretching vibration in the solid state falls at an unusually high energy (1160 cm^{-1}), suggesting that in this dicationic complex dmso-S acts mainly as a σ-donor.

Llobet et al. have stated that $[9]aneS_3$ exerts a strong steric interaction on the *cis* ligands on the basis that in $[Ru(H_2O)(phen)([9]aneS_3)][ClO_4]_2$ the *cis* X–Ru–S angles are larger than 90°.[27b] However, in all structures reported the S–Ru–S angles involving the $[9]aneS_3$ are in a range from 82.68(7) to 89.6(1)°, and these values are likely to be dependent on the nature of the macrocycle. A careful inspection of the *cis* X–Ru–S bond angles reveals that these are larger than 90° in **4** and **5** (X = P), due to the bulk of the PTA ligand, and in **6**–**9** (X = N) because of the small bite angle of the chelating nitrogen ligand. Thus, these slight deformations are not ascribable to the bulk of the $[9]aneS_3$ ligand but, rather, to the geometrical requirements of the other ligands, as confirmed by the fact that the *cis* Cl–Ru–S bond angles are close to, or slightly less than, 90°.

As a conclusion it is worthwhile to note that X-ray diffraction studies indicate close geometrical similarities between the present complexes and the piano-stool Ru^{II} compounds bearing an η^6-arene ligand instead of the $[9]aneS_3$ tripodal group.

Chemical Behavior in Aqueous Solution

These new piano-stool ruthenium complexes were prepared with the aim of comparing their biological activities with those of the corresponding organometallic compounds bearing an aromatic fragment in place of the $[9]aneS_3$ ligand. Thus, as a first step, the chemical behavior of compounds **4**–**9** was investigated in water, in the presence of 100 mM NaCl (that mimics the extracellular chloride concentration), and in PBS buffer solution at physiological pH (0.01 M phosphate buffer, pH 7.4, 0.9% NaCl) by ^{1}H NMR and UV/Vis spectroscopy.

Both the ^{1}H NMR and UV/Vis spectra of the neutral PTA complex $[RuCl_2(PTA)([9]aneS_3)]$ (**4**) changed quite rapidly during the first 30 min after dissolution in water due to dissociation of one chloride to give $[RuCl(H_2O)(PTA)([9]aneS_3)]^+$ (**4a**). The evolution of the absorption spectrum is characterized by two isosbestic points at 330 and 408 nm (Supporting Information). In the ^{1}H NMR spectrum the two PTA resonances of **4** (δ = 4.22, 4.55 ppm) are gradually replaced by those of **4a** (δ = 4.23, 4.57 ppm), which are only slightly shifted downfield; no signals for the free ligands were observed.[31] The spectra remained unchanged afterwards, even after prolonged periods (weeks), indicating that **4a** is stable. Addition of 100 mM NaCl to a D_2O solution of **4a** reversed the hydrolytic process completely, and the original NMR spectrum of **4** was immediately re-obtained (Supporting Information). A pK_a value of 3.3 for coordinated PTA in **4a** was obtained from a ^{31}P NMR pH titration curve in D_2O (Supporting Information). For comparison, a pK_a value of 3.13 has been estimated from a ^{31}P NMR titration for coordinated PTA in the $[RuCl_2(PTA)(\eta^6\text{-}p\text{-cymene})]$ complex,[14] while a pK_a value of 10.1 was similarly obtained for the coordinated water molecule in $[Ru(H_2O)(phen)([9]aneS_3)]^{2+}$.[27b] Conversely, the p$K_a$ values of the coordinated water in $[Ru(H_2O)(en)(\eta^6\text{-arene})]^{2+}$ adducts, as determined by ^{1}H NMR spectroscopy, are in the range 7.71–8.25.[32]

In phosphate buffered saline (pH 7.4) the hydrolysis of **4** to **4a** occurs as in water, but is followed by a further slow reaction leading to a new species **4b**. In the ^{1}H NMR spectrum this process is accompanied by the gradual decrease of the two PTA resonances of **4a** and simultaneous growth of two new signals (δ = 4.28 and 4.60 ppm) for **4b**. After 15 days at ambient temperature **4a** and **4b** are present in solution in approximately equal amounts. This slow process is perhaps due to partial dissociation of the chloride of **4a** to yield $[Ru(H_2O)_2(PTA)([9]aneS_3)]^{2+}$ (**4b**); however, coordination of phosphate, as observed in the $[Ru(H_2O)(en)(\eta^6\text{-ar-}$

 © 2005 Wiley-VCH Verlag GmbH & Co. KGaA, Weinheim

ene)]$^{2+}$ and [Ru(H_2O)Cl(PTA)(η^6-arene)]$^+$ species,[14,32] cannot be excluded (see below).

The cationic PTA complex [RuCl(PTA)$_2$([9]$aneS_3$)][OTf] (**5**) was found to be remarkably inert both in water and at physiological pH. No significant spectral changes were observed over a period of two weeks. Addition of 100 mM Cl induced no spectral changes (Supporting Information). A pK_a value of 2.4 for coordinated PTA in **5** was obtained from a ^{31}P NMR pH titration curve in D_2O (Supporting Information).

Investigation of the behavior of [RuCl(en)([9]$aneS_3$)][OTf] (**6**) in aqueous solution by ^{1}H NMR spectroscopy is difficult due to overlap of the signals of the CH_2 protons of en and [9]$aneS_3$. In the ^{1}H NMR spectrum of **6** in D_2O immediately after dissolution two sets of NH_2 signals, belonging to two species in an approximate 3:1 ratio, are observed (Supporting Information). The spectrum remained basically unchanged for days. Addition of 100 mM NaCl reversed the initial ratio between the two sets of NH_2 resonances immediately, suggesting the presence of an equilibrium between the two species (Supporting Information). Thus, the resonances of the most intense set (δ = 3.87, 4.70 ppm) were assigned to the aquated species [Ru(H_2O)(en)([9]$aneS_3$)]$^{2+}$ (**6a**), while those of the minor set (δ = 3.65, 4.54 ppm) were attributed to the parent compound **6**, which becomes predominant in the presence of excess chloride. The ^{1}H NMR spectrum in buffer solution, besides the NH_2 signals of **6** and **6a**, shows two other less-intense broad resonances at δ = 4.35 and 4.45 ppm, assigned to the NH_2 of coordinated en in a new species **6b**. The signals of **6** decrease slowly with time while those of **6a** and **6b** correspondingly increase, and after one week **6b** was the main species in solution. Tentatively, **6b** might form from **6a** upon phosphate coordination (no signals for free ethylendiamine or [9]$aneS_3$ were observed to grow with time).

The ^{1}H NMR spectrum of [RuCl(enac)([9]$aneS_3$)][OTf] (**7**) in D_2O recorded immediately after dissolution is similar to that in CD_3NO_2 (see above) and remains unchanged with time. However, upon addition of NaCl the resonances of a new species, of almost equal intensity, appear immediately beside those of the original species (Supporting Information). Thus, the resonances of the original set were assigned to the aquated species [Ru(H_2O)(enac)([9]$aneS_3$)]$^{2+}$ (**7a**; for example, the singlets of the methyl groups appear at δ = 2.23 and 2.57 ppm), while those of the new set (methyl groups at δ = 2.22 and 2.61 ppm) were attributed to the parent compound **7**, which is in equilibrium with **7a**. In the absence of free chloride, this equilibrium is completely shifted towards **7a** at NMR concentrations. The ^{1}H NMR spectrum in phosphate-buffered saline solution shows, besides the signals of **7** and **7a**, the resonances of yet another species with coordinated enac, **7b**, which were found to grow slowly with time (days). No signals for the free ligands were observed during these processes. Most likely, also in this case **7b** is derived from **7a** upon coordination of phosphate.

[RuCl(bipy)([9]$aneS_3$)][OTf] (**8**) is relatively labile in aqueous solution. The ^{1}H NMR spectrum recorded immediately after dissolution of the complex in D_2O shows two sets of signals for the coordinated bipy in an approximate 3:2 ratio (Supporting Information). The most abundant set was assigned to **8** and the other, which grows with time, to the dicationic aquated species [Ru(H_2O)(bipy)([9]$aneS_3$)]$^{2+}$ (**8a**).[33] After 30 min the ratio between **8** and **8a** was about 1:2 (Supporting Information), and the equilibrium could be reversed by the addition of chloride. During the hydrolytic process, no signals for free bipy or [9]$aneS_3$ were observed. The same aquo species **8a** was obtained, but much more slowly (days), from [Ru(dmso-S)(bipy)([9]$aneS_3$)][OTf]$_2$ (**9**) upon dissociation of the dmso ligand (Scheme 6). In this case the process could also be followed by monitoring the growth of the resonance of free dmso at δ = 2.72 ppm.

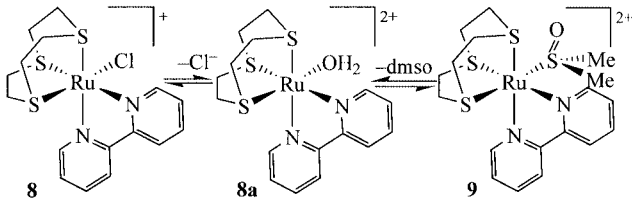

Scheme 6.

The behavior of **8** and **9** at pH 7.4 is similar to that found in water and is mainly influenced by the presence of free chloride in the buffer. Thus, for both complexes the equilibrium amount of **8a** is lower than in pure water and compound **9** slowly equilibrates also with **8** (Scheme 6). In addition, for both complexes the signals of a new species with coordinated bipy, presumably with phosphate bound in the place of water, were observed to grow slowly with time.

Cell Growth Inhibition Effects on TS/A Adenocarcinoma Cells and on HBL-100 Mammary Cells

The MTT test, which measures mitochondrial dehydrogenase activity as an indication of cell viability, was carried out with the water-soluble compounds [$RuCl_2$(PTA)([9]$aneS_3$)] (**4**), [RuCl(PTA)$_2$([9]$aneS_3$)][OTf] (**5**), and [RuCl(en)([9]$aneS_3$)][OTf] (**6**) using two different cell lines − tumour mouse TS/A cells and normal human HBL-100 cells. The effects of compounds **4**–**6** on the cell growth were evaluated after treatment for 24, 48, and 72 h. The cell viability after these times was determined by the MTT assay and the results from these studies are summarized in Figure 10. The experiments were performed in quadruplicate and repeated twice for all three compounds; the IC_{50} values resulting from an average over the two experiments are listed in Table 1.

Compounds **4**–**6** show different in vitro behaviors against the mouse adenocarcinoma cancer cell line (TS/A) and against the human mammary nontumor cell line (HBL-100). Complex **4** is scarcely cytotoxic and shows IC_{50} values that are high and very similar in both cell lines. It is worth comparing these data with the aromatic [$RuCl_2$(PTA)(η^6-arene)] analogs of complex **4**, values for which are also given in Table 1.

 © 2005 Wiley-VCH Verlag GmbH & Co. KGaA, Weinheim

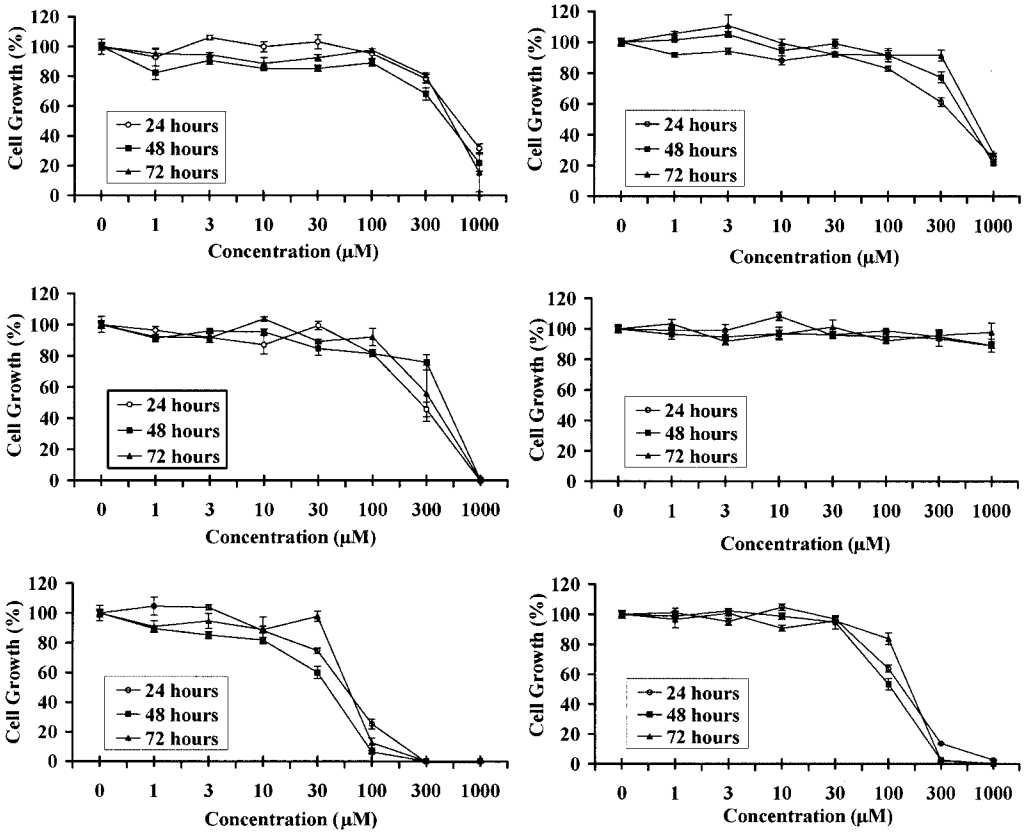

Figure 10. Effects of [$RuCl_2$(PTA)([9]$aneS_3$)] (**4**) (top), [RuCl(PTA)$_2$([9]$aneS_3$)][OTf] (**5**) (middle), and [RuCl(en)([9]$aneS_3$)][OTf] (**6**) (bottom) on TS/A (left) and HBL-100 (right) cell proliferation. The cells were sown on day 0 and treated on day 1 with a range of concentrations between 1–1000 μM of compounds **4**–**6** for 24, 48, and 72 hours. Cell growth was evaluated using the MTT test at the end of the treatment.

Table 1. IC_{50} values of [$RuCl_2$(PTA)([9]$aneS_3$)] (**4**), [RuCl(PTA)$_2$([9]$aneS_3$)][OTf], (**5**) and [RuCl(en)([9]$aneS_3$)][OTf], (**6**) on the TS/A and HBL-100 cell lines after incubation for 72 h.

Compound	IC_{50} (TS/A) [μM]	IC_{50} (HBL-100) [μM]
[$RuCl_2$(PTA)([9]$aneS_3$)] (**4**)	650	738
[RuCl(PTA)$_2$([9]$aneS_3$)][OTf] (**5**)	388	>1000
[RuCl(en)([9]$aneS_3$)][OTf] (**6**)	65	175
[$RuCl_2$(PTA)(η^6-*p*-cymene)][a]	507	>1000
[$RuCl_2$(PTA)(η^6-benzene)][a]	231	>1000

[a] IC_{50} values taken from ref. 14.

A larger difference in cytotoxicity between the two cell lines is observed for complex **5**, which is mildly active against the TS/A adenocarcinoma cells with an IC_{50} value of 388 μM after 72 h of incubation, but is essentially nontoxic to the HBL-100 normal cells under analogous conditions, even at very high concentrations (IC_{50} > 1000 μM). It thus appears that the presence of two PTA ligands is important to have a selectivity of the compounds towards the cancer cells.

Complex **6** is the most cytotoxic among those tested and it is also somewhat selective towards cancer cells (Table 1). The aromatic analogs of complex **6**, developed by Sadler and co-workers,[8,9] also show greater cytotoxicity than Ru^{II}–arene PTA complexes (aromatic analogs of complex **4**).[14] A direct comparison between **6** and the corresponding [RuCl(en)(η^6-arene)][PF_6] complexes is difficult as cytotoxicity tests were performed against different cell lines; for example, [RuCl(en)(η^6-*p*-cymene)][PF_6] has an IC_{50} value of 10 μM against A2780 cells. Nevertheless, from these data it appears that the aromatic fragment is not essential for cytotoxicity and that the [9]$aneS_3$ ligand can be used in its place.

Conclusions

In summary, some new half-sandwich Ru^{II}-[9]$aneS_3$ complexes, namely [$RuCl_2$(PTA)([9]$aneS_3$)] (**4**), [RuCl(PTA)$_2$([9]$aneS_3$)][OTf] (**5**), [RuCl(en)([9]$aneS_3$)][OTf] (**6**), [RuCl(enac)([9]$aneS_3$)][OTf] (**7**), [RuCl(bipy)([9]$aneS_3$)][OTf] (**8**), and [Ru(dmso-S)(bipy)([9]$aneS_3$)][OTf]$_2$ (**9**) have been prepared from Ru-[9]$aneS_3$-dmso precursors and structurally characterized. Some of them are analogs of known cytotoxic organometallic Ru^{II}-(η^6-arene) and Ru^{II}-(η^5-cyclopentadienyl) compounds, in which the aromatic fragment is replaced by the sulfur macrocycle 1,4,7-trithiacyclononane while the rest of the coordination sphere is left unchanged.

For all new complexes, the results from the X-ray studies are consistent with the NMR spectroscopic data, thus indi-

 © 2005 Wiley-VCH Verlag GmbH & Co. KGaA, Weinheim

cating that the structures observed in the solid state are maintained in solution. Owing to rapid conformational equilibration of the [9]aneS_3 (and en ligand in **6**), the symmetry of each complex in solution (C_s) is higher than in the solid state. In solution they have a plane of symmetry that contains the S–Ru–X axis (X = P in **4**; X = Cl in **5**–**8**; X = S in **9**) and bisects the [9]aneS_3 and the opposite ligands (either two equal monodentate ligands as in **4** and **5**, or a chelate as in **6**–**9**). Similarly to the aromatic analogs for which data are available, in aqueous solution the Ru-[9]-aneS_3 complexes (with the exception of **5**) hydrolyze a chloride (or a dmso in the case of **9**) to give the corresponding aquo species. This process is rapidly reversed in the presence of free chloride, and coordination of phosphate to the aquo species is likely to occur in phosphate-buffered solutions at physiological pH. No dissociation of [9]aneS_3 or of the other ligands was observed.

Preliminary in vitro tests were performed on three complexes (**4**–**6**) against the mouse adenocarcinoma cancer cell line (TS/A) and the human mammary normal cell line (HBL-100). In general, the Ru-[9]aneS_3 compounds have a cytotoxicity comparable to that of the corresponding organometallic analogs. The most cytotoxic complex among those tested was [RuCl(en)([9]aneS_3)][OTf] (**6**), with IC_{50} values of 65 μM (TS/A) and 175 μM (HBL-100). Most interestingly, compounds **5** and **6** are more cytotoxic against the cancer cell line (TS/A) than against the human mammary normal cell line (HBL-100); thus, they might lead to anticancer activity with low general toxicity and hence low side-effects.

In conclusion, the results of the in vitro studies suggest that the aromatic fragment of the piano-stool Ru^{II} compounds is not an essential feature for the in vitro anticancer activity, and it might be effectively replaced by another face-capping ligand with a low steric demand such as [9]-aneS_3. As Sadler and co-workers have shown that there is a direct correlation between cytotoxicity and the size (and therefore the lipophilicity) of the arene, it is possible that in the future the cytotoxicity of the Ru-[9]aneS_3 complexes might similarly be increased by using more lipophilic ligands.

Experimental Section

UV/Vis spectra were obtained on a Jasco V-550 spectrometer in quartz cells. ^1H and ^{13}C NMR spectra were recorded at room temperature at 400 and 100.5 MHz, respectively, on a JEOL Eclipse 400 FT instrument. All spectra were recorded at room temperature. Proton peak positions were referenced to 2,2-dimethyl-2,2-silapentane-5-sulfonate (DSS, set at δ = 0.00 ppm) in D_2O, or to the peak of residual non-deuterated solvent set at δ = 4.33 ppm in CD_3NO_2. Carbon peak positions were referenced to DSS (set at δ = 0.0 ppm) in D_2O, or to the central peak of the solvent set at δ = 62.8 ppm in CD_3NO_2. ^{31}P NMR spectra were recorded on a Bruker Avance DPX 400 MHz spectrometer at 161.9 MHz. Infrared spectra (KBr) were recorded on a Perkin–Elmer 983G spectrometer or on a Perkin–Elmer 2000 NIR FT-Raman spectrometer. ESI mass spectra of the complexes were obtained on a Thermofinigan LCQ Deca XP Plus quadrupole ion trap instrument set in positive mode (solvent: methanol; flow rate: 5 μL min^{-1}; spray voltage: 5 kV; capillary temperature: 100 °C; capillary voltage: 20 V), as described previously.[34] Elemental analysis (C, H, N) was performed at the Dipartimento di Scienze Chimiche, Università di Trieste. [$RuCl_2$(dmso-S)([9]aneS_3)] (**1**),[24] [RuCl(dmso-S)$_2$([9]aneS_3)][OTf] (**2**),[28] [Ru(dmso)$_3$([9]anoS_3)][OTf]$_2$ (**3**),[28] and PTA[35] were prepared according to literature procedures. Trithiacyclononane was purchased from Aldrich.

The pH titration curves, reporting the chemical shift of the ^{31}P NMR spectra vs. the pD values, were fitted to the Henderson–Hasselbalch equation using the program Micromath® Scientist® with the assumption that the observed chemical shifts are weighted averages according to the populations of the protonated and deprotonated species. The resonance frequencies change smoothly with pH between the chemical shifts of the charged form HA^+, and those of the neutral, deprotonated form A, which is present at high pH. At any pH, the observed chemical shift is a weighted average of the two extreme values $\delta(HA^+)$ and $\delta(A)$:

$$\delta_{av} = \frac{\delta(HA^+)[HA^+]+\delta(A)[A]}{[HA^+]+[A]}$$

The midpoint of the titration curve occurs when the concentrations of the acid and its conjugate base are equal: $[HA^+] = [A]$, i.e. when the pH equals the pK_a of the compound.

[$RuCl_2$(PTA)([9]aneS_3)] (4): PTA (37 mg, 0.16 mmol) was added to [$RuCl_2$(dmso-S)([9]aneS_3)] (**1**; 100 mg, 0.16 mmol) partially dissolved in nitromethane (15 mL). The mixture was then heated to reflux to yield a yellow solution after 2–3 min, and a yellow-orange solid after about 10 min. After 2 h reflux, the precipitate was removed by filtration, washed with cold nitromethane and diethyl ether, and vacuum dried. Yield: 51 mg (62%). $C_{12}H_{24}Cl_2N_3PRuS_3$ (509.47): calcd. C 28.3, H 4.75, N 8.25; found C 28.2, H 5.11, N 8.13. ^1H NMR (400 MHz, D_2O, 25 °C): δ = 3.00–2.60 (m, 12 H, [9]aneS_3), 4.23 (s, 6 H, PTA), 4.55 (s, 6 H, PTA) ppm. $^{31}P\{^1H\}$ NMR (161.9 MHz, D_2O, 25 °C): δ = –33.41 (s) ppm. UV/Vis (H_2O, 25 °C): λ_{max} (ε) = 317 nm (632 $M^{-1}cm^{-1}$), 362 (542), 423 (390). ES-MS (MeOH): *m*/*z* = 512 (calcd. 511) [$RuCl_2$(PTA)([9]aneS_3) + $H]^+$, 492 (calcd. 492) [RuCl(H_2O)(PTA)([9]aneS_3)]$^+$, 474 (calcd. 474) [RuCl(PTA)([9]aneS_3)]$^+$.

[$RuCl(PTA)_2$([9]aneS_3)][OTf] (5): PTA (45 mg, 0.29 mmol) was added to [RuCl(dmso-S)$_2$([9]aneS_3)][OTf] (**2**; 90 mg, 0.144 mmol) partially dissolved in methanol (15 mL) and the mixture was refluxed for 2 h. The yellow solution was then concentrated in vacuo to ca. 3 mL, and a few drops of diethyl ether were added. A yellow solid formed upon standing, which was removed by filtration, washed with cold methanol and diethyl ether, and vacuum dried. Yield: 75 mg (60%). $C_{19}H_{36}ClF_3N_6O_3P_2RuS_4$ (780.24): calcd. C 29.2, H 4.65, N 10.77; found C 29.1, H 4.29, N 10.50. ^1H NMR (400 MHz, D_2O, 25 °C): δ = 2.62 (m, 2 H, [9]aneS_3), 2.92 (m, 10 H, [9]aneS_3), 4.25 (s, 12 H, PTA), 4.59 (s, 12 H, PTA) ppm. ^1H NMR (400 MHz, CD_3CN, 25 °C): δ = 2.38 (m, 2 H, [9]aneS_3), 2.78 (m, 8 H, [9]aneS_3), 2.99 (m, 2 H, [9]aneS_3), 4.20 (s, 12 H, PTA), 4.50 (s, 12 H, PTA) ppm. $^{13}C\{^1H\}$ NMR (100.5 MHz, CD_3CN, 25 °C): δ = 32.1, 34.2, 41.2 (CH_2, [9]aneS_3), 54.2, 73.2 (CH_2, PTA), 123.7, 125.5 (CF_3, OTf) ppm. $^{31}P\{^1H\}$ NMR (161.9 MHz, D_2O, 25 °C): δ = –33.45 (s) ppm. UV/Vis (H_2O, 25 °C): λ_{max} (ε) = 357 nm (480 $M^{-1}cm^{-1}$), 296 (1000). ES-MS (MeOH): *m*/*z* = 631 (calcd. 631) [$RuCl(PTA)_2$([9]aneS_3)]$^+$.

[RuCl(en)([9]aneS_3)][OTf] (6): Ethylenediamine (10.7 μL, 0.16 mmol) was added to [RuCl(dmso-S)$_2$([9]aneS_3)][OTf] (**2**; 150 mg, 0.16 mmol) dissolved in nitromethane (10 mL) and the mixture was refluxed for 2 h. The yellow solution was concentrated

 © 2005 Wiley-VCH Verlag GmbH & Co. KGaA, Weinheim

in vacuo to ca. 5 mL, filtered through paper, and a few drops of diethyl ether were added. A yellow-brown microcrystalline solid formed upon standing, which was removed by filtration, washed with cold nitromethane and diethyl ether, and vacuum dried. Yield: 110 mg (87%). $C_9H_{20}ClF_3N_2O_3RuS_4$ (526.03): calcd. C 20.5, H 3.83, N 5.32; found C 20.4, H 3.52, N 4.95. ^{1}H NMR (400 MHz, CD_3NO_2, 25 °C): δ = 2.8–2.3 (m, 12 H, [9]aneS$_3$), 2.83 (br., 2 H, en), 2.94 (br., 2 H, en), 3.35 (br., 2 H, NH), 3.91 (br., 2 H, NH) ppm. ^{13}C{^{1}H} NMR (100.5 MHz, CD_3NO_2, 25 °C): δ = 32.7, 33.1, 35.9 (CH_2, [9]aneS$_3$), 45.9 (CH_2, en), 120.8, 124.0 (CF_3, OTf) ppm. UV/Vis (H_2O, 25 °C): λ_{max} (ε) = 370 nm (490 M^{-1}cm^{-1}). Selected IR (KBr): $\tilde{\nu}$ = 3295 cm^{-1} (w, νNH$_2$), 3250 (w, νNH$_2$), 1577 (m, δNH$_2$), 1257, 1140, 1026 cm^{-1} (s, νOTf). ES-MS (MeOH): *m*/*z* = 377 (calcd. 377) [RuCl(en)([9]aneS$_3$)]$^+$.

[RuCl(enac)([9]aneS$_3$)][OTf] (7): Ethylenediamine (15 μL, 0.225 mmol) was added to [RuCl(dmso-S)$_2$([9]aneS$_3$)][OTf] (**2**; 140 mg, 0.1125 mmol) dissolved in acetone (20 mL) and the mixture was refluxed for 2 h. The yellow solution was concentrated in vacuo to ca. 5 mL and a few drops of diethyl ether were added. A yellow microcrystalline solid formed on standing, which was removed by filtration, washed with cold acetone and diethyl ether, and vacuum dried. Yield: 40 mg (59%). $C_{15}H_{28}ClF_3N_2O_3RuS_4$ (606.15): calcd. C 29.7, H 4.65, N 4.62; found C 30.4, H 4.34, N 4.47. ^{1}H NMR (400 MHz, D_2O, 25 °C): δ = 2.23 (s, 6 H, CH_3), 2.8–2.4 (m, 12 H, [9]aneS$_3$), 2.57 (s, 6 H, CH_3), 3.93 (m, 4 H, CH_2 enac) ppm. ^{1}H NMR (400 MHz, CD_3NO_2, 25 °C): δ = 2.24 (s, 6 H, CH_3), 2.8–2.4 (m, 12 H, [9]aneS$_3$), 2.69 (s, 6 H, CH_3), 3.90 (m, 4 H, CH_2 enac) ppm. UV/Vis (H_2O, 25 °C): λ_{max} (ε) = 275 nm (4300 M^{-1}cm^{-1}), 376 (580). Selected IR (KBr): $\tilde{\nu}$ = 1625 cm^{-1} (m, νC=N), 1267, 1148, 1031 (s, νOTf) cm^{-1}.

[RuCl(bipy)([9]aneS$_3$)][OTf] (8): 2,2′-Bipyridine (25 mg, 0.16 mmol) was added to [RuCl(dmso-S)$_2$([9]aneS$_3$)][OTf] (**2**; 100 mg, 0.16 mmol) partially dissolved in methanol (10 mL) and the mixture was refluxed for 1 h. After about 10 min the solution turned orange. Upon concentration in vacuo to ca. 3 mL an orange solid formed, which was removed by filtration, washed with cold methanol and diethyl ether, and vacuum dried. Yield: 65 mg (65%). $C_{17}H_{20}ClF_3N_2O_3RuS_4$ (622.11): calcd. C 32.8, H 3.24, N 4.50; found C 32.1, H 3.34, N 4.30. ^{1}H NMR (400 MHz, CD_3NO_2, 25 °C): δ = 3.1–2.5 (m, 12 H, [9]aneS$_3$), 7.63 (t, 2 H, H5,5′), 8.14 (t, 2 H, H4,4′), 8.48 (d, 2 H, H3,3′), 9.08 (d, 2 H, H6,6′) ppm. UV/Vis (H_2O, 25 °C): λ_{max} (ε) = 286 nm (13800 M^{-1}cm^{-1}), 420 (2350).

[Ru(dmso-S)(bipy)([9]aneS$_3$)][OTf]$_2$ (9): 2,2′-Bipyridine (11.4 mg, 0.073 mmol) was added to [Ru(dmso)$_3$([9]aneS$_3$)][OTf]$_2$ (**3**; 60 mg, 0.073 mmol) dissolved in methanol (15 mL) and the mixture was refluxed for 1 h. Upon concentration in vacuo to ca. 3 mL a yellow solid formed, which was removed by filtration, washed with cold methanol and diethyl ether, and vacuum dried. Yield: 50 mg (84%). $C_{20}H_{26}N_2F_6O_7S_4Ru$ (813.85): calcd. C 29.5, H 3.22, N 3.44; found C 29.2, H 3.14, N 3.30. ^{1}H NMR (400 MHz, D_2O, 25 °C): δ = 3.3–2.7 (m, 12 H, [9]aneS$_3$), 2.83 (s, 6 H dmso-S), 7.81 (t, 2 H, H5,5′), 8.31 (t, 2 H, H4,4′), 8.60 (d, 2 H, H3,3′), 9.05 (d, 2 H, H6,6′) ppm. Selected IR (KBr): $\tilde{\nu}$ = 163 cm^{-1} (s, νSO, dmso-S), 517 (m, νRuS, dmso-S), 1267, 1258, 1150, 1030 (s, νOTf) cm^{-1}. UV/Vis (H_2O, 25 °C): λ_{max} (ε) = 268 nm (16000 M^{-1}cm^{-1}), 306 (9800), 316 (13000), 344 (3220).

X-ray Crystallography: Diffraction data for all compounds were collected at room temperature on a Nonius DIP-1030H system with graphite-monochromated Mo-K_α radiation, with the exception of the data set of compound **4**, which was collected at 220(2) K with a Bruker–Nonius FR591 rotating anode (Cu-K_α) equipped with a KappaCCD detector. Cell refinement, indexing, and scaling of the data sets were performed with the programs Denzo and Scalepack.[36] The structures were solved by Patterson and Fourier analyses and refined by the full-matrix least-squares method based on F^2 with all observed reflections.[37] A Flack parameter of 0.55(7) for space group $P2_1$ in **6** indicates racemic twinning of the crystal. The ΔF maps revealed water molecules in **4** and **9** (two molecules per complex unit) and in **7** (residuals accounting for 0.75 water oxygen), and methanol (one molecule) in **5**. The hydrogen atoms were located at geometrically calculated positions except those of disordered water. The structural figures were drawn with ORTEP3 for Windows (ellipsoids at 40% probability level),[38] and all the calculations performed with the WinGX System, Ver 1.64.05.[39] Crystal data and details of structure refinements for compounds **4**–**9** are reported in Tables 2 and 3.

CCDC-265997–266002 (for **4**–**9**) contain the supplementary crystallographic data for this paper. These data can be obtained free

Table 2. Crystal data and details of structure refinement for compounds **4**–**6**.

	4·2H$_2$O	**5**·CH$_3$OH	**6**
Formula	$C_{12}H_{28}Cl_2N_3O_2PRuS_3$	$C_{20}H_{40}ClF_3N_6O_4P_2RuS_4$	$C_9H_{20}ClF_3N_2O_3RuS_4$
Formula mass	545.49	812.28	526.03
Crystal system	monoclinic	triclinic	monoclinic
Space group	$P2_1/n$	$P\bar{1}$	$P2_1$
a [Å]	19.271(4)	7.896(3)	7.975(3)
b [Å]	7.523(3)	14.354(4)	9.223(3)
c [Å]	28.721(4)	14.303(4)	12.235(4)
α [°]		103.33(2)	
β [°]	94.58(2)	99.63(2)	96.04(2)
γ [°]		91.83(3)	
V [Å^3]	4151(2)	1551.0(8)	894.9(5)
Z	8	2	2
$D_{calcd.}$ [g cm^{-3}]	1.746	1.739	1.952
μ [mm^{-1}]	12.142[a]	1.022	1.532
Reflections collected	47588	16888	11536
Reflections unique (R_{int})	6128 (0.0488)	5919 (0.0524)	4979 (0.0351)
Reflections $I > 2\sigma(I)$	3674	3476	3820
R_1	0.0644	0.0551	0.0382
wR_2 [$I > 2\sigma(I)$][b]	0.1846	0.1381	0.0953
Residuals [e Å^{-3}]	0.912, –0.524	0.934, –0.848	0.576, –0.529

[a] Copper radiation. [b] $R_1 = \Sigma||F_o| - |F_c||/\Sigma|F_o|$, $wR_2 = [\Sigma w(F_o^2 - F_c^2)^2/\Sigma w(F_o^2)^2]^{1/2}$.

 © 2005 Wiley-VCH Verlag GmbH & Co. KGaA, Weinheim

Table 3. Crystal data and details of structure refinement for compounds **7**–**9**.

	7·H_2O	**8**	**9**·2(H_2O)
Formula	$C_{15}H_{29.50}ClF_3N_2O_{3.75}RuS_4$	$C_{17}H_{20}ClF_3N_2O_3RuS_4$	$C_{20}H_{30}F_6N_2O_9RuS_6$
Formula mass	619.67	622.11	849.89
Crystal system	monoclinic	monoclinic	triclinic
Space group	$P2_1/n$	$C2/c$	$P\bar{1}$
a [Å]	7.769(3)	24.811(4)	10.087(4)
b [Å]	10.722(3)	11.803(3)	12.625(3)
c [Å]	31.968(5)	16.384(3)	14.134(4)
α [°]			88.02(2)
β [°]	94.02(3)	100.39(3)	75.50(3)
γ [°]			68.76(2)
V [Å^3]	2656.3(13)	4719.3(17)	1621.1(9)
Z	4	8	2
$D_{calcd.}$ [g cm^{-3}]	1.549	1.751	1.741
μ [mm^{-1}]	1.047	1.177	0.953
Reflections collected	20925	19338	17550
Reflections unique (R_{int})	4900 (0.0359)	4518 (0.0679)	7909 (0.0675)
Reflections $I > 2\sigma(I)$	3058	2633	3414
R_1	0.0590	0.0394	0.0594
wR_2 [$I > 2\sigma(I)$][a]	0.1742	0.0893	0.1335
Residuals [e Å^{-3}]	0.825, –0.518	0.377, –0.476	0.623, –0.576

[a] $R_1 = \Sigma||F_o| - |F_c||/\Sigma|F_o|$, $wR_2 = [\Sigma w(F_o^2 - F_c^2)^2/\Sigma w(F_o^2)^2]^{1/2}$.

of charge from The Cambridge Crystallographic Data Centre via www.ccdc.cam.ac.uk/data_request/cif.

In vitro Tests: TS/A murine adenocarcinoma cell line, initially obtained from Dr. G. Forni (CNR, Centro di Immunogenetica ed Oncologia Sperimentale, Torino, Italy) belongs to the tumor cell panel of the Callerio Foundation (Trieste) and is stored in liquid nitrogen. Cells were cultured according to a standard procedure,[40] and maintained in RPMI-1640 medium (EuroClone, Wetherby, U.K.) supplemented with 10% Fetal Bovine Serum (FBS, Invitrogen, Milano, Italy), 2 mM L-glutamine (EuroClone) and 50 μg mL^{-1} gentamycin sulfate solution (EuroClone). The cell line was kept in a CO_2 incubator with 5% CO_2 and 100% relative humidity at 37 °C. Cells from a confluent monolayer were removed from flasks by a trypsin-EDTA solution (EuroClone). HBL-100 nontumorigenic epithelial cells were maintained in McCoy's 5A medium (SIGMA, St. Louis, MO, USA) supplemented with 10% FBS, 2 mM L-glutamine, 100 UI mL^{-1} penicillin, and 100 μg mL^{-1} streptomycin (EuroClone) in a humidified atmosphere with 5% CO_2 at 37 °C.

Cell viability was determined by the trypan blue dye exclusion test. For experimental purposes, the cells were sown in multi-well cell culture plastic plates (Corning Costar Italia, Milano, Italy). Cell growth was determined by the MTT viability test.[41] Cells were sown on 96-well plates and 24 h after showing were incubated with the appropriate compound at concentrations of 1–1000 μM, prepared by dissolving in a medium containing 5% of serum for 24, 48, and 72 h. Analysis was performed at the end of the incubation time. Briefly, MTT [3-(4,5-dimethylthiazol-2-yl)-2,5-diphenyltetrazolium bromide] dissolved in PBS (5 mg mL^{-1}) was added to all wells (10 μL per 100 μL of medium) and the plates were then incubated at 37 °C with 5% CO_2 and 100% relative humidity for 4 h. After this time, the medium was discarded and 100 μL of dmso (SIGMA) was added to each well according to the method of Alley and co-workers.[42] The optical density was measured at 570 nm on a SpectraCount Packard (Meriden, CT) instrument.

Supporting Information: ^{31}P NMR pH titration curves in D_2O for [RuCl(H_2O)(PTA)([9]aneS_3)]$^+$ (**4a**) and [RuCl(PTA)$_2$([9]aneS_3)][OTf] (**5**). UV/Vis spectral variations of [RuCl$_2$(PTA)[9]aneS_3] (**4**) in aqueous solution within 30 min after dissolution. ^1H NMR spectrum of [RuCl(en)([9]aneS_3)][OTf] (**6**) in CD_3NO_2. ^1H NMR spectra of [RuCl$_2$(PTA)([9]aneS_3)] (**4**), [RuCl(PTA)$_2$([9]aneS_3)][OTf] (**5**), [RuCl(en)([9]aneS_3)][OTf] (**6**), [RuCl(enac)([9]aneS_3)][OTf] (**7**), and [RuCl(bipy)([9]aneS_3)][OTf] (**8**) in D_2O, immediately after dissolution and after addition of 100 mM NaCl.

Acknowledgments

This work was performed within the framework of COST Action D20 (WG 0001 and WG 0005) and contributed by LINFA-MADE CRTrieste. We wish to thank Engelhard Italiana S.p.A. for a generous loan of hydrated $RuCl_3$.

[1] M. J. Clarke, *Coord. Chem. Rev.* **2003**, *236*, 209–233.
[2] a) B. K. Keppler, W. Rupp, U. M. Juhl, H. Enders, R. Niebl, W. Balzer, *Inorg. Chem.* **1987**, *26*, 4366–4370; b) B. K. Keppler, M. R. Berger, M. H. Henn, *Cancer Treat. Rev.* **1990**, *17*, 261–277.
[3] G. Sava, E. Alessio, A. Bergamo, G. Mestroni, in *Topics in Biological Inorganic Chemistry*, Vol. 1 "*Metallo-pharmaceutical*" (Eds.: M. J. Clarke, P. J. Sadler), Springer, Berlin, **1999**, pp. 143–169.
[4] a) E. Alessio, G. Mestroni, A. Bergamo, G. Sava, in *Metal Ions and Their Complexes in Medication and in Cancer Diagnosis and Therapy*, Vol. 42 of *Met. Ions Biol. Syst.* (Eds.: A. Sigel, H. Sigel), M. Dekker, New York, **2004**, pp. 323–351; b) E. Alessio, G. Mestroni, A. Bergamo, G. Sava, *Curr. Top. Med. Chem.* **2004**, *4*, 1525–1535.
[5] M. Galanski, V. B. Arion, M. A. Jakupec, B. K. Keppler, *Curr. Pharm. Des.* **2003**, *9*, 2078–2089.
[6] J. M. Rademaker-Lakhai, D. van den Bongard, D. Pluim, J. H. Beijnen, J. H. M. Schellens, *Clin. Canc. Res.* **2004**, *10*, 3717–3727.
[7] E. Reisner, V. B. Arion, M. F. C. Guedes da Silva, R. Lichtenecker, A. Eichinger, B. K. Keppler, V. Yu. Kukushkin, A. J. L. Pombeiro, *Inorg. Chem.* **2004**, *43*, 7083–7093.
[8] R. E. Morris, R. E. Aird, P. del Socorro Murdoch, H. Chen, J. Cummings, N. D. Hughes, S. Parsons, A. Parkin, G. Boyd, D. I. Jodrell, P. J. Sadler, *J. Med. Chem.* **2001**, *44*, 3616–3621.

 © 2005 Wiley-VCH Verlag GmbH & Co. KGaA, Weinheim

[9] R. E. Aird, J. Cummings, A. A. Ritchie, M. Muir, R. E. Morris, H. Chen, P. J. Sadler, D. J. Jodrell, *Br. J. Cancer* **2002**, *86*, 1652–1657.
[10] a) H. Chen, J. A. Parkinson, S. Parsons, R. A. Coxall, R. O. Gould, P. J. Sadler, *J. Am. Chem. Soc.* **2002**, *124*, 3064–3082; b) H. Chen, J. A. Parkinson, R. E. Morris, P. J. Sadler, *J. Am. Chem. Soc.* **2003**, *125*, 173–186.
[11] O. Novakova, H. Chen, O. Vrana, A. Rodger, P. J. Sadler, V. Brabec, *Biochemistry* **2003**, *42*, 11544–11554.
[12] a) C. S. Allardyce, P. J. Dyson, D. J. Ellis, S. L. Heath, *Chem. Commun.* **2001**, 1396–1397; b) C. S. Allardyce, P. J. Dyson, *Platinum Met. Rev.* **2001**, *45*, 62–69.
[13] A. Dorcier, P. J. Dyson, C. Gossens, U. Rothlisberger, R. Scopelliti, I. Tavernelli, *Organometallics* in press.
[14] C. Scolaro, A. Bergamo, L. Brescacin, R. Delfino, M. Cocchietto, G. Laurenczy, T. J. Geldbach, G. Sava, P. J. Dyson, *J. Med. Chem.* in press.
[15] C. S. Allardyce, P. J. Dyson, D. J. Ellis, P. A. Salter, R. Scopelliti, *J. Organomet. Chem.* **2003**, *668*, 35–42.
[16] L. A. Huxham, E. L. S. Cheu, B. O. Patrick, B. R. James, *Inorg. Chim. Acta* **2003**, *352*, 238–246.
[17] D. N. Akbayeva, L. Gonsalvi, W. Oberhauser, M. Peruzzini, F. Vizza, P. Brüggeller, A. Romerosa, G. Sava, A. Bergamo, *Chem. Commun.* **2003**, 264–265.
[18] a) Y. N. Vashisht Gopal, D. Jayaraju, A. K. Kondapi, *Biochemistry* **1999**, *38*, 4382–4388; b) Y. N. Vashisht Gopal, N. Konuru, A. K. Kondapi, *Arch. Biochem. Biophys.* **2002**, *401*, 53–62.
[19] L. Dale, J. H. Tocher, T. M. Dyson, D. I. Edwards, D. A. Tocher, *Anti-Cancer Drug Des.* **1992**, *7*, 3–14.
[20] S. Korn, W. S. Sheldrick, *J. Chem. Soc., Dalton Trans.* **1997**, 2191–2199.
[21] S. Heeb, PhD dissertation, Ruhr-Universität Bochum, **1990**.
[22] a) S. R. Cooper, *Acc. Chem. Res.* **1988**, *21*, 141–146.
[23] a) M. Schröder, *Pure Appl. Chem.* **1988**, *60*, 517–524; b) A. J. Blake, M. Schröder, *Adv. Inorg. Chem.* **1990**, *35*, 1–80.
[24] a) C. Landgrafe, W. S. Sheldrick, *J. Chem. Soc., Dalton Trans.* **1994**, 1885–1893; b) K. Brandt, W. S. Sheldrick, *J. Chem. Soc., Dalton Trans.* **1996**, 1237–1243.
[25] a) S. Roche, C. Haslam, H. Adams, S. L. Heath, J. A. Thomas, *Chem. Commun.* **1998**, 1681–1682; b) S. Roche, H. Adams, S. E. Spey, J. A. Thomas, *Inorg. Chem.* **2000**, *39*, 2385–2390; c) S. Roche, S. E. Spey, H. Adams, J. A. Thomas, *Inorg. Chim. Acta* **2001**, *323*, 157–162; d) C. S. Araujo, M. G. B. Drew, V. Félix, L. Jack, J. Madureira, M. Newell, S. Roche, T. M. Santos, J. A. Thomas, L. Yellowlees, *Inorg. Chem.* **2002**, *41*, 2250–2259.
[26] a) B. J. Goodfellow, V. Félix, S. M. D. Pacheco, J. Pedrosa de Jesus, M. G. B. Drew, *Polyhedron* **1997**, *16*, 393–401; b) J. Madureira, T. M. Santos, B. J. Goodfellow, M. Lucena, J. Pedrosa de Jesus, M. G. Santana-Marques, M. G. B. Drew, V. Félix, *J. Chem. Soc., Dalton Trans.* **2000**, 4422–4431.
[27] a) X. Sala, I. Romero, M. Rodriguez, A. Llobet, G. González, M. Martinez, J. Benet-Buchholz, *Inorg. Chem.* **2004**, *43*, 5403–5409; b) X. Sala, A. Poater, I. Romero, M. Rodriguez, A. Llobet, X. Solans, T. Parella, T. M. Santos, *Eur. J. Inorg. Chem.* **2004**, 612–618.
[28] E. Iengo, E. Zangrando, E. Baiutti, F. Munini, E. Alessio, *Eur. J. Inorg. Chem.* **2005**, 1019–1031.
[29] This NMR feature is shared by all the following complexes (see Experimental Section) and will not be repeated in the text.
[30] N. W. Alcock, J. C. Cannadine, G. R. Clark, A. F. Hill, *J. Chem. Soc., Dalton Trans.* **1993**, 1131–1135.
[31] In general, for each complex, the manifold of multiplets of [9]aneS_3 also changes during hydrolysis but, owing to the diffused overlap of peaks, these resonances are difficult to use for monitoring the process.
[32] a) F. Wang, H. Chen, S. Parson, I. D. H. Oswald, J. E. Davidson, P. J. Sadler, *Chem. Eur. J.* **2003**, *9*, 5810–5820; b) R. Fernandez, M. Melchart, A. Habtemariam, S. Parsons, P. J. Sadler, *Chem. Eur. J.* **2004**, *10*, 5173–5179.
[33] The presence of two sets of resonances in the D_2O NMR spectrum of [RuCl(bipy)([9]aneS_3)]$^+$ (and of the analogous phen complex) was erroneously attributed by Goodfellow and coworkers to two different conformations of the thioether ring in slow equilibrium on the NMR timescale.[26a]
[34] P. J. Dyson, J. S. McIndoe, *Inorg. Chim. Acta* **2003**, *354*, 68–74.
[35] D. J. Daigle, A. B. Pepperman Jr., S. L. Vail, *J. Heterocycl. Chem.* **1974**, *11*, 407–408. .
[36] Z. Otwinowski, W. Minor, *Processing of X-ray Diffraction Data Collected in Oscillation Mode*, in *Methods in Enzymology, Volume 276: Macromolecular Crystallography, part A* (Eds.: C. W. Carter, Jr., & R. M. Sweet), Academic Press, **1997**, p.307–326.
[37] *SHELX97 Programs for Crystal Structure Analysis* (Release 97-2). G. M. Sheldrick, University of Göttingen, Germany, **1998**.
[38] *ORTEP3 for Windows*; L. J. Farrugia, *J. Appl. Crystallogr.* **1997**, *30*, 565.
[39] L. J. Farrugia, *J. Appl. Crystallogr.* **1999**, *32*, 837–838.
[40] P. Nanni, C. De Giovanni, P. L. Lollini, G. Nicoletti, G. Prodi, *Clin. Exp. Metastasis* **1983**, *1*, 373–385.
[41] T. Mosmann, *J. Immunol. Methods* **1983**, *65*, 55–63.
[42] M. C. Alley, D. A. Scudiero, A. Monks, M. L. Hursey, M. J. Czerwinski, D. L. Fine, B. J. Abbott, J. G. Mayo, R. H. Shoemaker, M. R. Boyd, *Cancer Res.* **1988**, *48*, 598–601.

Received: March 9, 2005
Published Online: June 21, 2005

 © 2005 Wiley-VCH Verlag GmbH & Co. KGaA, Weinheim

Molecular Conductors Based on *peri*-Ditellurium-Bridged Donors, 2,3-DMTTeA and TMTTeN

Emiko Fujiwara,[a] Hideki Fujiwara,[b] Bakhyt Zh. Narymbetov,[b] Hayao Kobayashi,[b] Masahiro Nakata,[a] Hajime Torii,[c] Akiko Kobayashi,*[a] Kazuo Takimiya,[d] Tetsuo Otsubo,[d] and Fumio Ogura[e]

Keywords: Tellurium / Conducting materials / Magnetic properties / Band structure

Molecular conductors based on *peri*-ditellurium-bridged polyacene donor molecules 3,4-dimethylanthra[1,9-*cd*:4,10-*c′d′*]bis[1,2]ditellurole (2,3-DMTTeA) and 2,3,6,7-tetramethylnaphtho[1,8-*cd*:4,5-*c′d′*]bis[1,2]ditellurole (TMTTeN) were prepared. The crystal structure analyses of neutral 2,3-DMTTeA molecule and its cation radical salts revealed that these crystals involve an orientational disorder of the asymmetrical molecule, 2,3-DMTTeA, and that the intermolecular network through tellurium atoms is very strong and dominant in terms of the construction of the crystal frameworks. In the crystal of $(TMTTeN)_2M(CN)_2$ (M = Ag and Au), the crystal structure analyses and the extended Hückel tight-binding band calculations indicated that these salts are quasi three-dimensional conductors. These salts are highly conductive (720–760 $S\,cm^{-1}$) and maintain metallic states down to about 50 K. Furthermore, the $Ag(CN)_2^-$ salt exhibited a Pauli paramagnetic behavior down to 2 K [χ(para) ≈ 2.0–2.5×10^{-4} $emu\,mol^{-1}$]. In the crystal of $(TMTTeN)(SCN)_{0.88}$, the donor molecules are stacked to form one-dimensional columns and construct a three-dimensional network between the columns through the intermolecular Te···Te contacts. The SCN^- salt is also highly conductive (590 $S\,cm^{-1}$) and maintains a metallic behavior down to 4.2 K. Almost temperature-independent paramagnetic susceptibility of $(TMTTeN)(SCN)_{0.88}$ indicates Pauli paramagnetism of this salt [χ(para) ≈ $1.6–1.9 \times 10^{-4}$ $emu\,mol^{-1}$]. A tight-binding band structure calculation indicates that the Fermi surface of the SCN^- salt is open along the b^* and c^* directions, but the intermolecular interactions between the donor columns are not so weak because of the three-dimensional network mediated by the protruded tellurium atoms.

(© Wiley-VCH Verlag GmbH & Co. KGaA, 69451 Weinheim, Germany, 2005)

Introduction

Over the past few decades, a considerable number of studies have been performed on the chemistry and physics of organic conductors.[1] The main principle of the molecular design of conductors with stable metallic states has been considered to be an achievement of the two-dimensional electronic state of molecular crystals that is realized by an introduction of sulfur and selenium atoms into π electron systems. These heavy chalcogen atoms included in π donor molecules are expected to increase the intermolecular interactions in the solid state and to yield wide conduction bands. In this sense, tellurium-containing molecular conductors are of special interest. However, very few attempts have been made on the tellurium-containing donor molecules,[2] such as tetratellurafulvalene (TTeF)[3] and hexamethylene-TTeF (HMTTeF),[4] because of difficulties of synthesis and poor solubilities to common organic solvents. Among them, crystal structures of $(HMTTeF)_4(PF_6)_2$ and $(HMTTeF)_2[Pt(dmit)_2]$,[5] where dmit is dimercaptoisotrithione, have been reported and revealed their unique donor arrangements. In addition, several years ago $(HMTTeF)(Et_2TCNQ)(THF)_x$ was reported to be metallic around room temperature, where Et_2TCNQ is 2,5-diethyl-7,7,8,8-tetracyano-*p*-quinodimethane.[6] However, no HMTTeF salt has been known to show a metallic behavior down to low temperatures. Therefore, no systematic research has been carried out thoroughly in terms of both the electrical conductivities and structure analyses of the HMTTeF salts. On the other hand, the TCNQ complex of TTeF showed a metallic behavior down to 2 K with a very high room temperature conductivity of 2200 $S\,cm^{-1}$ in comparison with those of its sulfur and selenium analogs.[7] This result indicates

[a] Research Centre for Spectrochemistry, School of Science, The University of Tokyo,
Hongo, Bunkyo-ku, Tokyo 113-0033, Japan
Fax: +81-3-5841-4417
E-mail: akiko@chem.s.u-tokyo.ac.jp
[b] Institute for Molecular Science,
Myodaiji, Okazaki 444-8585, Japan
[c] Department of Chemistry, School of Science, The University of Tokyo,
Hongo, Bunkyo-ku, Tokyo 113-0033, Japan
[d] Department of Applied Chemistry, Faculty of Engineering, Hiroshima University,
Kagamiyama, Higashi-Hiroshima 739-8527, Japan
[e] Department of Industrial Chemistry, Faculty of Engineering, Kinki University,
Umenobe-1, Takaya, Higashi-Hiroshima 739-2116, Japan

that organic metals possessing high conductivities and wide bandwidths can be realized by the substitution for tellurium atoms.

From the viewpoint of the crystal structures, furthermore, conducting salts based on tellurium-containing donors are interesting because the formation of a tellurium network seems to be dominant in terms of the construction of crystal structures. Polyacene donor molecules containing *peri*-ditellurium bridges are considered to utilize the atomic character of their protruded tellurium atoms more directly than the TTeF donors such as TTeF and HMTTeF. Needless to say, the tellurium crystal that has a three-dimensional Te···Te network shows a semimetallic behavior under ambient pressure and brings a superconducting transition at 3.3 K under pressure of 4.5 GPa,[8] which is extremely lower than the pressures required for a sulfur crystal (10.1 K under 93 GPa and 14 K under 157 GPa)[9] and a selenium crystal (6.8 K under 13 GPa).[10,11] Therefore, the tellurium-containing molecular conductors deserve much attention if such a nature of the tellurium crystal is reflected in their physical properties.

Tetratellurotetracene (TTeT)[12,13] is a well-known donor molecule containing *peri*-ditellurium bridges. However, few cation radical salts and charge transfer complexes of TTeT have been reported owing to its extremely poor solubility and their crystal structures have not been made clear so far.[14] Therefore, we focused on the other donors containing *peri*-ditellurium bridges such as 3,4-dimethylanthra-[1,9-*cd*:4,10-*c′d′*]bis[1,2]ditellurole (2,3-DMTTeA)[15] and 2,3,6,7-tetramethylnaphtho[1,8-*cd*:4,5-*c′d′*]bis[1,2]ditellurole (TMTTeN),[16] because their solubilities to organic solvents are considerably improved in comparison to other reported tellurium-containing donors because of the existence of methyl groups. We report here the structures of the neutral 2,3-DMTTeA and TMTTeN molecules, and the structures and physical properties of their cation radical salts.[17–19]

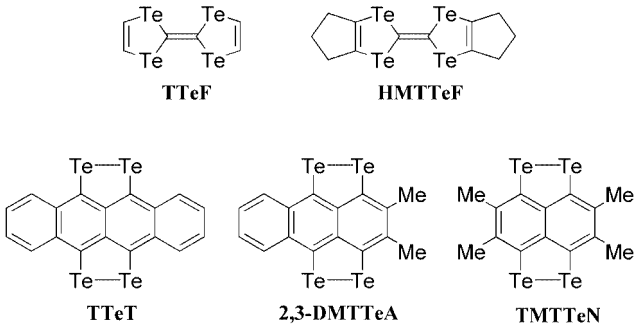

Results and Discussion

Molecular Structures and the Highest Occupied Molecular Orbital (HOMO)

In the early 1980s, we proposed to estimate the "dimensionality" of molecular conductors from their Fermi surfaces calculated by an extended Hückel tight-binding band approximation.[20] By virtue of the successful studies on low-temperature magnetotransport experiments of two-dimensional conductors around 1990,[21] the extended Hückel tight-binding band calculation was accepted as a conventional method to evaluate the dimensionality of electronic structures of organic conductors. Although sufficiently reliable empirical parameters of atomic orbitals that are used in the extended Hückel band calculations are hardly obtained even for selenium atoms, the accumulated information on the band structures of the organic conductors composed of selenium-containing tetrathiafulvalene (TTF)-like donors, such as tetramethyltetraselenafulvalene (TMTSF) and bis(ethylenedithio)tetraselenafulvalene (BETS), permits us fairly good band structure calculations. However, it is still not so clear whether a similar calculation could be applied to the tellurium-containing systems, especially to the conductors composed of non-TTF-type donors.

An ab initio molecular orbital (MO) calculation has been made on the TMTTeN molecule. The calculated HOMO has a π character as shown in Figure 1. Because the HOMO has an *anti*-bonding character at the Te–Te bond, the Te–Te bond length is expected to be shortened in its cationic state. As described later, the X-ray crystal structure analyses of TMTTeN systems with various formal charges of the molecules (δ) have been made. In Table 1, the formal charge (δ) dependence of the average bond lengths of $TMTTeN^{+\delta}$ molecules {δ = 0 (neutral crystal), 0.5 [the $Ag(CN)_2^-$ and $Au(CN)_2^-$ salts], 0.7 (the AsF_6^- salt) and 0.9 (the ClO_4^- and SCN^- salts)} is summarized (see also Figure 2).

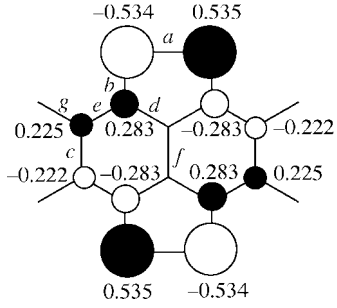

Figure 1. Schematic drawing of the HOMO of TMTTeN. Atomic orbital coefficients are also shown.

As shown in Figure 2, there seems to be a good correlation between δ and bond lengths in terms of the bonds *a* and *c* (see Figure 1, a). The shortening of the Te–Te (*a*) and C–C (*c*) bonds in the cationic state indicates the antibonding nature of the HOMO at these bonds, which is consistent with the result of the MO calculation. Thus, the HOMO will have an a_u symmetry with a node at the Te–Te bond. It is easily imagined that the node at the Te–Te bond is not favorable for the construction of molecular conductors with two- (or three-) dimensional electronic bands, despite the introduction of tellurium atoms. In contrast to the conductors based on TTF-like donors, whose HOMO has the same sign at every chalcogen atom, the transverse intermolecular interaction between TMTTeN molecules may be cancelled

 © 2005 Wiley-VCH Verlag GmbH & Co. KGaA, Weinheim

Table 1. Bond lengths [Å] of TMTTeN. The bond lengths are averaged by assuming D_{2h} symmetry.[a]

	Neutral D[b]		$(D)_2Ag(CN)_2$	$(D)2Au(CN)^2$	$D(AsF_6)_{0.7}$	$D(SCN)_{0.88}$	$D(ClO_4)_{0.88}$
Formal charge (δ)	0		0.5	0.5	0.7	0.88	0.88
	Molecule A	Molecule B					
Te–Te (a)	2.7011(7)	2.6983(6)	2.664(1)	2.664(1)	2.666(2)	2.662(1)	2.666(3)
Te–C (b)	2.126(4)	2.218(4)	2.160(7)	2.113(8)	2.17(2)	2.113(8)	2.15(2)
C–C (c)	1.446(8)	1.427(8)	1.39(1)	1.41(2)	1.35(4)	1.39(1)	1.38(3)
C–C (d)	1.422(6)	1.429(5)	1.371(9)	1.42(1)	1.39(2)	1.410(7)	1.37(2)
C–C (e)	1.371(6)	1.387(6)	1.374(10)	1.38(1)	1.39(2)	1.400(7)	1.35(2)
C–C (f)	1.45(1)	1.42(1)	1.36(2)	1.42(2)	1.40(4)	1.46(2)	1.36(4)
C–C (g)	1.505(6)	1.500(6)	1.52(1)	1.50(1)	1.55(3)	1.510(7)	1.52(2)

[a] D indicates the TMTTeN molecule. [b] Molecule A and molecule B represent two crystallographically independent molecules.

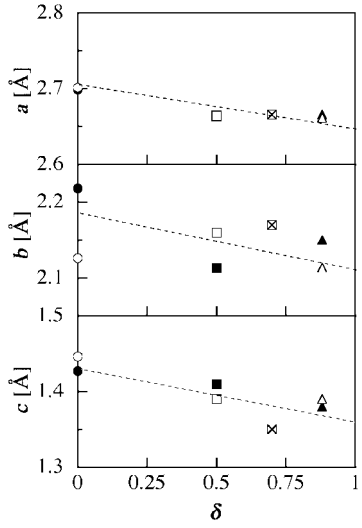

Figure 2. Formal charge (δ) dependences of three bond lengths of $TMTTeN^{+\delta}$ (*a*, *b* and *c*) that show large δ-dependence: neutral TMTTeN molecule A (open circles) and molecule B (black circles), $Ag(CN)_2^-$ salt (open squares), $Au(CN)_2^-$ salt (black squares), SCN^- salt (open triangles), ClO_4^- salt (black triangles), and AsF_6^- salt (x in box).

out as a result of the sum of the positive and negative Te···Te overlap integrals.

Crystal Structure Analyses

Neutral 2,3-DMTTeA Molecule

Figure 3 shows the crystal structure of the neutral 2,3-DMTTeA molecule recrystallized from carbon disulfide. There is one crystallographically independent donor molecule in the crystal. The 2,3-DMTTeA molecule has a planar structure. The molecular structure of 2,3-DMTTeA is subject to an orientational disorder that is caused by the unsymmetry of the molecule, which makes 2,3-DMTTeA appear as if it has a tetracene framework instead of the actual anthracene framework. Such an orientational disorder was not observed in the sulfur and selenium analogs of 2,3-DMTTeA.[15b] These facts indicate that the network formed by the tellurium atoms is very strong and dominant in terms of the construction of the crystal structures in comparison to the interaction between the anthracene moieties. As Figure 3 (parts a and b) indicate, the donor molecules form columns with a short interplanar distance of 3.78 Å along the *b*-axis, whereas a slip distance (5.41 Å) is very large along the donor short axis. Consequently, there is no intermolecular Te···Te contact that is less than the sum of the van der Waals radii (4.2 Å) in the donor columns. On the other hand, there are several short intercolumnar contacts, as shown in part b of Figure 3. To put it briefly, the molecules form side-by-side arrays along the *c*-axis through the short Te···Te contacts.

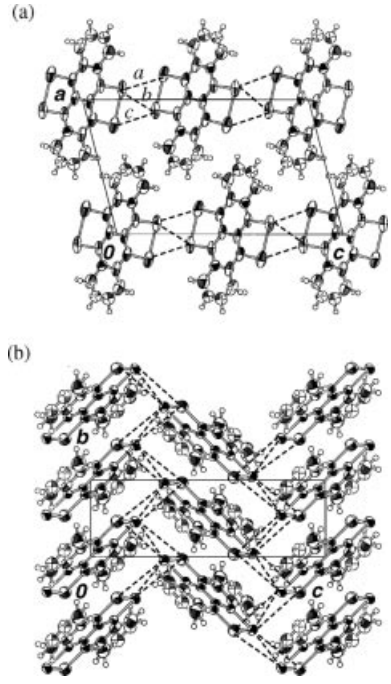

Figure 3. Crystal structures of the neutral 2,3-DMTTeA molecule projected on (a) the *ac*-plane and (b) the *bc*-plane. Owing to the orientational disorder, the occupation probability of two terminal CH_2 groups is 50%, and 2,3-DMTTeA molecule is drawn as if it has a tetracene framework. Intermolecular contacts [Å]: Te(1)···Te(2), a = 4.052(1); Te(1)···Te(2), b = 3.838(1); and Te(1)···Te(1), c = 4.100(1).

Neutral TMTTeN Molecule

An X-ray crystal structure analysis was performed on the neutral crystal of TMTTeN recrystallized from carbon disulfide. As shown in Figure 4 (part a and b), the crystal

 © 2005 Wiley-VCH Verlag GmbH & Co. KGaA, Weinheim

includes carbon disulfide as an interstitial solvent. TMTTeN has no orientational disorder as in the molecular structure of 2,3-DMTTeA, because of the symmetrical shape of TMTTeN. Two kinds of crystallographically independent donor molecules (A and B) exist in the crystal (see Figure 4 (part a and b). Among them, molecule B is located on the inversion center. As Figure 4 (b) indicates, each of the donor molecules A and B form independent stacking columns along the *c*-axis. However, there is no intermolecular short Te···Te contact in both the donor columns of molecules A and B. On the other hand, there are several short intercolumnar intermolecular Te···Te contacts between the donor columns of molecules A and B, and the three-dimensional network formed by the protruded tellurium atoms of the donor molecules is developed in the crystal.

Cation Radical Salts of 2,3-DMTTeA

X-ray crystal structure analyses were performed on the cation radical salts of 2,3-DMTTeA with BF_4^-, ClO_4^-, ReO_4^-, PF_6^-, AsF_6^-, and Br^- anions. The BF_4^- and ReO_4^- salts are isostructural to the ClO_4^- salt and the PF_6^- salt is isostructural to the AsF_6^- salt. For this reason, only the crystal structures of the ClO_4^- and AsF_6^- salts are discussed among the tetrahedral and octahedral anion salts, respectively.

Crystal Structure of (2,3-DMTTeA)$_3$(ClO$_4$)$_2$

Overlap mode and crystal structure of the ClO_4^- salt of 2,3-DMTTeA are shown in Figure 5. The compositions of

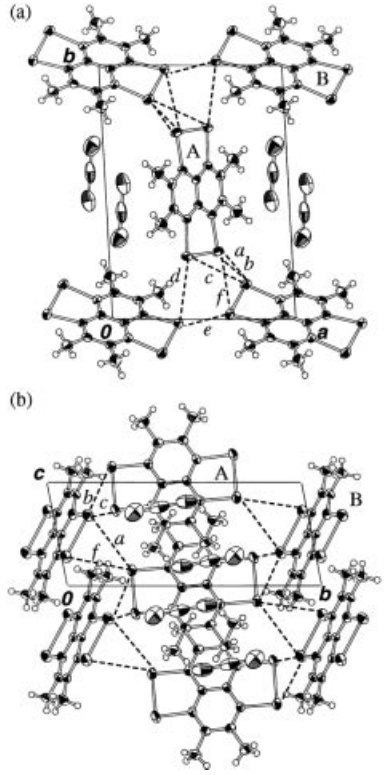

Figure 4. Crystal structures of the neutral TMTTeN molecule projected on (a) the *ab*-plane and (b) the *bc*-plane. Intermolecular contacts [Å]: Te(2)···Te(3), a = 4.0860(7); Te(2)···Te(3), b = 3.9032(8); Te(1)···Te(3), c = 3.820(1); Te(1)···Te(4), d = 3.9133(6); Te(4)···Te(4), e = 3.908(1); and Te(2)···Te(4), f = 3.8651(6).

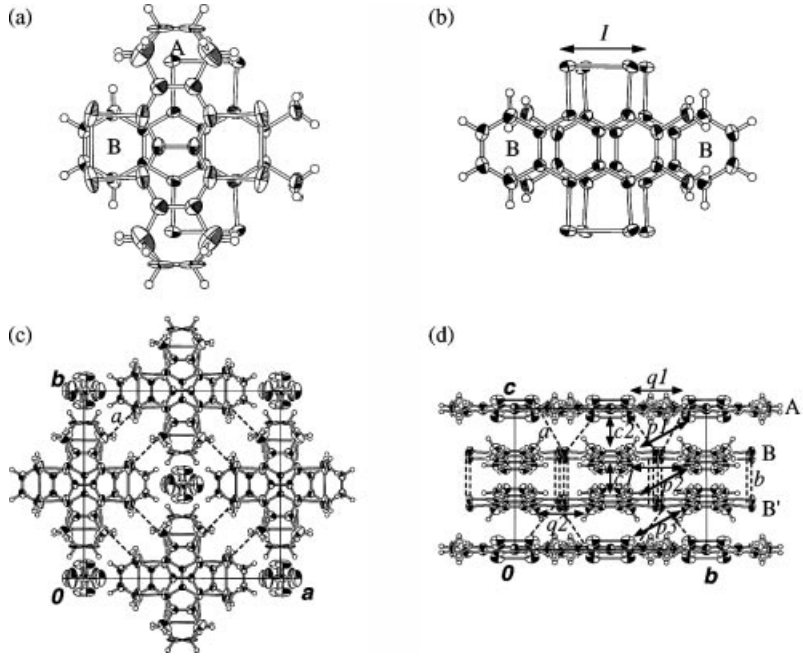

Figure 5. Overlap modes of the donor molecules in (2,3-DMTTeA)$_3$(ClO$_4$)$_2$ projected on the molecular planes (a) between molecules A and B, (b) between molecules B and B′. The occupation probability of two terminal CH_2 groups of molecule A is 50%. Interplanar distances [Å]: between molecules A and B, 3.81; and between molecules B and B′, 3.83. Slip distance [Å]: between molecules B and B′, I = 0.54. (c) Crystal structure of (2,3-DMTTeA)$_3$(ClO$_4$)$_2$ projected on the *ab*-plane. (d) Donor arrangement in (2,3-DMTTeA)$_3$(ClO$_4$)$_2$ viewed along the *a*-axis. Intermolecular contacts [Å]: Te(2)···Te(3), a = 4.1695(6); and Te(1)···Te(2), b = 3.9381(6). Overlap integrals ($\times 10^{-3}$): $c1$ = –24.75, $c2$ = 0.85, $p1$ = –0.96, $p2$ = 0.97, $p3$ = 0.53, $q1$ = 0.14, and $q2$ = 0.06.

 © 2005 Wiley-VCH Verlag GmbH & Co. KGaA, Weinheim

the BF_4^-, ClO_4^-, and ReO_4^- salts were determined to be $(2,3\text{-DMTTeA})_3(\text{anion})_2$. There are two crystallographically independent fragments of the donor [a quarter (A) and a half (B) of the donor molecule] and a half of the ClO_4^- anion, resulting in an average oxidation state of the donor molecule of +2/3. The anion molecules are located in the channel surrounded by 2,3-DMTTeA molecules (see Figure 5, c). As shown in Figure 5 (a and b), molecule A has an orientational disorder of the anthracene moiety that is similar to the case of the neutral 2,3-DMTTeA molecule, whereas molecule B has no orientational disorder. Molecules A and B form A–B–B′-type stacking columns along the *c*-axis in which their long axes are rotated by 90° at the A–B overlap (see Figures 5, a and d). On the other hand, the overlap mode of molecules B and B′ is so-called "head-to-tail overlap" as shown in part b of Figure 5. As Figure 5 indicates (c and d), a three-dimensional Te···Te network is formed through several intermolecular short Te···Te contacts. The interplanar distance between molecules A and B (3.81 Å) is almost the same as that between molecules B and B′ (3.83 Å). On the contrary, the intracolumnar overlap integral between molecules A and B ($c2 = 0.85\times10^{-3}$) is much smaller than that between molecules B and B′ ($c1 = -24.75\times10^{-3}$) and is rather similar to those along the side-by-side directions ($p1 = -0.96\times10^{-3}$, $p2 = 0.97\times10^{-3}$, $p3 = 0.53\times10^{-3}$, $q1 = 0.14\times10^{-3}$, and $q2 = 0.06\times10^{-3}$), because the overlap mode between molecules A and B is not preferable and there is no short Te···Te contact between molecules A and B, where these intermolecular overlap integrals were calculated using the extended Hückel approximation. From the viewpoint of the intermolecular interaction, these results suggest the isolation of the dimers (molecules B and B′) in the donor column, giving rise to very low electrical conductivities of the tetrahedral anion salts ($\sigma_{rt} \approx 10^{-2}$ to 10^{-3} S cm^{-1}) as discussed later.

Crystal Structure of (2,3-DMTTeA)(AsF$_6$)$_{0.2}$

Figure 6 shows the overlap mode and crystal structure of the AsF_6^- salt of 2,3-DMTTeA. The orientational disorder of the 2,3-DMTTeA molecule is also observed in this salt. The compositions of the PF_6^- and AsF_6^- salts could not be determined by population refinement because of a heavy positional disorder of the anion molecules. Consequently, the compositions of $2,3\text{-DMTTeA}(\text{anion})_{0.2}$ were determined by electron probe microanalyses (EPMA). The anion molecules are located in the channels surrounded by the donor molecules, which is similar to the case of the tetrahedral anion salts. The anions are disordered along the donor stacking axis, and there are two kinds of possible positions of the AsF_6^- anion in a channel. Diffuse X-ray diffraction patterns are observed by an oscillation photograph and revealed that the AsF_6^- salt has a fivefold structure along the *a*-axis, suggesting that one AsF_6^- anion molecule exists per five unit cells. This result is consistent with the composition of the salt (5:1) determined by EPMA. As shown in Figure 6 (a and c), the donor molecules form uniform stacks along the *a*-axis. The dihedral angle of two donor molecules is 32.34° between the adjacent columns along the *b*-axis. An intermolecular interplanar distance is 3.81 Å and slip distances are 1.13 Å (*I*) and 1.21 Å (*II*) along the molecular long and short axes, respectively, indicating the relatively good overlap mode of the donors in the stack. As Figure 6 (b and c) indicates, there are several interstack Te···Te contacts [Te(1)···Te(1); a = 3.828(3) Å and Te(2)···Te(2); b = 3.882(3) Å] that are shorter than the intrastack one [Te(1)···Te(2); c = 4.155(2) Å]. The intermolecular interaction along the donor stacking direction shows a large overlap integral ($a1 = -20.96\times10^{-3}$) in comparison with the other ones ($c1 = -0.19\times10^{-3}$, $p1 = -2.22\times10^{-3}$, and $q1 = -0.46\times10^{-3}$). Hence, the intracolumnar conduction path of the AsF_6^- and PF_6^- salts is considered to be much better than those of the above-mentioned tetrahedral anion salts of 2,3-DMTTeA, but this salt showed a semiconducting behavior probably because of the strong one-dimensionality of the intermolecular interaction along the *a*-axis.

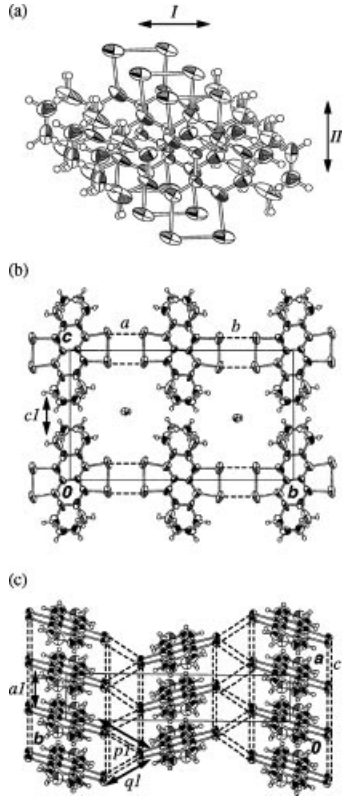

Figure 6. (a) Overlap mode of the donor molecules in $(2,3\text{-DMTTeA})(AsF_6)_{0.2}$ projected on the molecular planes. Interplanar distance [Å]: 3.81. Slip distances [Å]: I = 1.13 and II = 1.21. (b) Crystal structure of $(2,3\text{-DMTTeA})(AsF_6)_{0.2}$ projected on the *bc*-plane. (c) Donor arrangement in $(2,3\text{-DMTTeA})(AsF_6)_{0.2}$ viewed along the *c*-axis. Intermolecular contacts [Å]: Te(1)···Te(1), a = 3.828(3); Te(2)···Te(2), b = 3.882(3); and Te(1)···Te(1), c = 4.155(2). Overlap integrals ($\times10^{-3}$): $a1$ = –20.96, $c1$ = –0.19, $p1$ = –2.22, and $q1$ = –0.46. Dihedral angle between the adjacent donor molecules along the *b*-axis [°]: 32.34.

Crystal Structure of (2,3-DMTTeA)$_2$Br

The overlap mode and crystal structure of the Br^- salt of 2,3-DMTTeA are shown in Figure 7. In spite of use of the tetra-*n*-butylammonium salt of the $GaBr_4^-$ anion as a sup-

 © 2005 Wiley-VCH Verlag GmbH & Co. KGaA, Weinheim

porting electrolyte, an EPMA measurement revealed that the gallium atom is not contained in the obtained crystal. The orientational disorder of the donor molecule is also observed in this salt. The composition was determined to be $(2,3\text{-DMTTeA})_2Br$ by EPMA. The anion molecules are disordered along the *c*-axis and occupy only one of two kinds of channels, which is surrounded by tellurium atoms of the donor molecule as if the anion avoids the steric hindrance of the outer benzene-ring of 2,3-DMTTeA molecules. As Figure 7 indicates, the donor arrangement of the Br^- salt is isostructural to that of a quasi one-dimensional metal $(TSeT)_2Cl$ with a tetragonal lattice, where TSeT is tetraselenotetracene, reported by Shibaeva et al. in 1978.[22,23] The donor molecules form uniform columns along the *c*-axis with a very short interplanar distance of 3.31 Å and a large slip distance along the molecular long axis (4.31 Å) (see Figure 7, a and c). The donor molecules are inclined with a dihedral angle of 53.99° between the adjacent donor columns. As shown in Figure 7 (b and c), no intermolecular Te···Te contact appears between the donor columns, whereas short contacts [Te(1)···Te(1); *a* = 3.699(4) Å] are developed in the column, suggesting a tight one-dimensional nature along the *c*-axis. The overlap integral between the donor molecules along the *c*-axis (*c1* = 53.81×10^{-3}) is very much larger than those of interstack ones (*p1* = -2.62×10^{-3}, *p2* = -1.22×10^{-3}, *q1* = -0.13×10^{-3}, and *q2* = -1.22×10^{-3}). These results also suggest its strong one-dimensional character along the stacking direction, which results in a quite high conductivity ($\sigma_{rt} \approx 1500\ S\,cm^{-1}$) and a semiconducting behavior.

Cation Radical Salts of TMTTeN

X-ray crystallographic analyses were performed on the cation radical salts of TMTTeN with $Ag(CN)_2^-$, $Au(CN)_2^-$, SCN^-, ClO_4^-, and AsF_6^- anions. Because the crystal structures of the $Ag(CN)_2^-$ and $Au(CN)_2^-$ salts are similar to each other, only the crystal structure of the $Ag(CN)_2^-$ salt is discussed here in respect of these two salts.

Crystal Structure of $(TMTTeN)_2Ag(CN)_2$

Figure 8 shows the overlap mode and crystal structure of the $Ag(CN)_2^-$ salt. The composition of the $Ag(CN)_2^-$ and $Au(CN)_2^-$ salts was determined to be $(TMTTeN)_2$(anion)

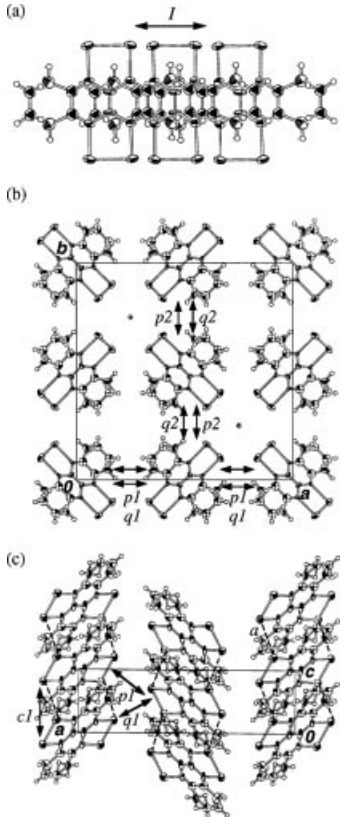

Figure 7. (a) Overlap mode of the donor molecules in $(2,3\text{-DMTTeA})_2Br$ projected on the molecular planes. Interplanar distance [Å]: 3.31. Slip distances [Å]: *I* = 4.31. (b) Tetragonal lattice of $(2,3\text{-DMTTeA})_2Br$ projected on the *ab*-plane. (c) Donor arrangement of $(2,3\text{-DMTTeA})_2Br$ viewed along the *b*-axis. Intermolecular contact [Å]: Te(1)···Te(1), *a* = 3.699(4). Overlap integrals ($\times10^{-3}$): *c1* = 53.81, *p1* = –2.62, *p2* = –1.22, *q1* = –0.13, and *q2* = –1.22. Dihedral angles between the adjacent donor molecules [°]: 53.99.

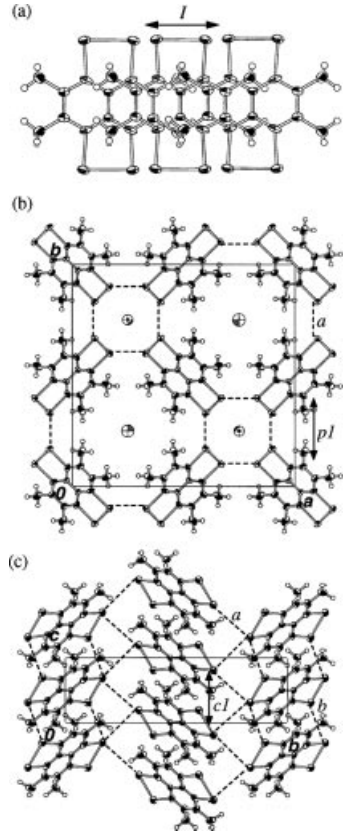

Figure 8. (a) Overlap mode of the donor molecules in $(TMTTeN)_2$-$Ag(CN)_2$. Interplanar distance [Å]: 3.41. Slip distance [Å]: *I* = 4.13. (b) Crystal structure of $(TMTTeN)_2Ag(CN)_2$ projected on the *ab*-plane. (c) Donor stacking columns of $(TMTTeN)_2Ag(CN)_2$ viewed along the *a*-axis. Intermolecular contacts [Å]: Te(1)···Te(1), *a* = 4.0199(8); and Te(1)···Te(1), *b* = 3.709(1). Overlap integrals ($\times10^{-3}$): *c1* = 90.96 and *p1* = –6.99. Dihedral angle between the adjacent donor molecules [°]: 71.4.

 © 2005 Wiley-VCH Verlag GmbH & Co. KGaA, Weinheim

by a population refinement. The projections of the crystal structure of the $Ag(CN)_2^-$ salt on the *ab*- and *bc*-planes are shown in Figure 8 (b and c, respectively). The donor molecules are stacked along the *c*-axis and take the same orientation with a short interplanar distance of 3.41 Å and a large slip distance of 4.13 Å. The dihedral angle of the donor molecules is 71.4° between the adjacent donor columns. The $Ag(CN)_2^-$ anions are located on the 4_2-axes and are heavily disordered along the *c*-axis. However, the structure was refined to an R-factor of 3%. The crystal structure of this salt is quite similar to those of $(2,3\text{-DMTTeA})_2Br$ and $(TSeT)_2Cl$[23] with tetragonal lattices, but the positions of the anion molecules are different from the other salts. That is, the $Ag(CN)_2^-$ anions occupy all four channels in the unit cell that is surrounded by the donor molecule, because the methyl groups of TMTTeN are considerably smaller than the disordered large benzene ring of 2,3-DMTTeA and, as a result, there is enough space for the anions compared to $(2,3\text{-DMTTeA})_2Br$ (see Figure 8, b). As shown in Figure 8 (b and c), there are several intermolecular Te···Te contacts, and a three-dimensional network through tellurium atoms is developed between the intracolumns and intercolumns in contrast to the one-dimensional character of $(2,3\text{-DMTTeA})_2Br$. The one-dimensionality of the intermolecular interaction is weaker than that of $(2,3\text{-DMTTeA})_2Br$: $c1/p1 \approx 13$ in $(TMTTeN)_2Ag(CN)_2$, where $c1$ (90.96×10^{-3}) and $p1$ (-6.99×10^{-3}) are the overlap integrals parallel and perpendicular to the *c*-axis (the donor stacking axis), respectively, while $c1/p1 \approx 20$ in $(2,3\text{-DMTTeA})_2Br$, resulting in a stable metallic behavior of $(TMTTeN)_2Ag(CN)_2$ as discussed later.

Crystal Structure of (TMTTeN)(SCN)$_{0.88}$

The overlap mode and crystal structure of the SCN^- salt are shown in Figure 9. In spite of preparation from the solution containing both the SCN^- and ClO_4^- anions, the composition of the obtained salt was determined to be $(TMTTeN)(SCN)_{0.88}$ by a population refinement and no ClO_4^- anion was discovered, which is consistent with the result of the EPMA measurement that shows no trace of chlorine atom. Although the crystals of the SCN^- salt with the same shape were also prepared from the solution that contains only the SCN^- anion by an electrocrystallization, the obtained crystals were very small. The projections of the crystal structure of the SCN^- salt on the *bc*-, *ab*- and *ac*-planes are shown in parts b–d in Figure 9. The donor molecules are stacked to form columns along the *a*-axis with a short intermolecular interplanar distance of 3.62 Å and a large slip distance of 4.03 Å. The anions are located in the channels that are formed by TMTTeN molecules. The donor molecules are inclined with a dihedral angle of 72.2° between the two adjacent donor columns along the *b*-axis. The donor arrangement of $(TMTTeN)(SCN)_{0.88}$ is almost

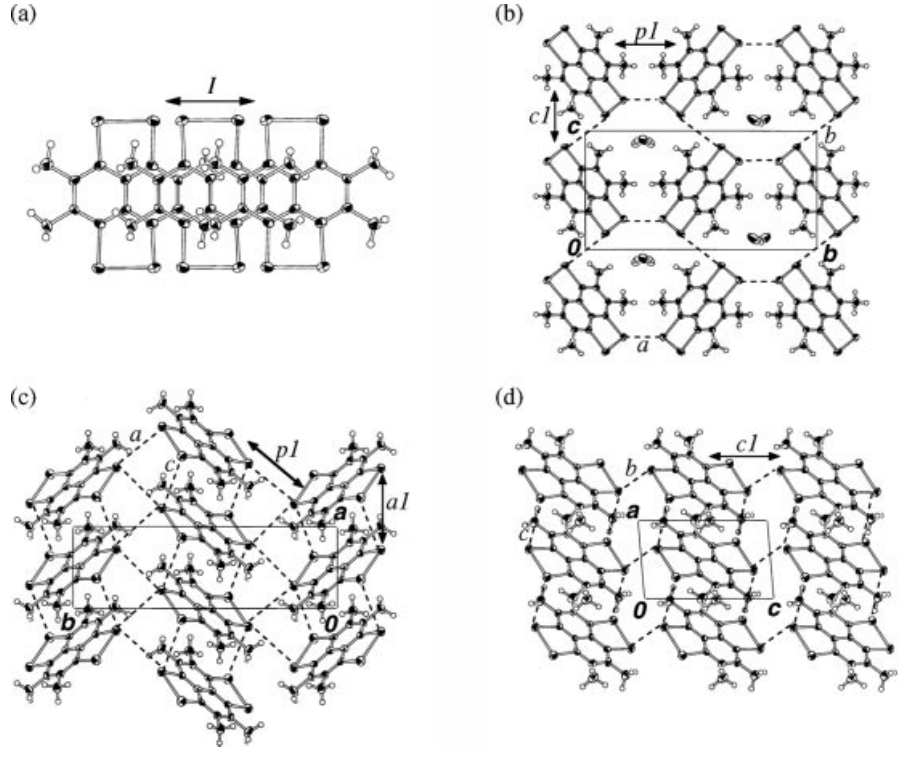

Figure 9. (a) Overlap mode of donor molecules in $(TMTTeN)(SCN)_{0.88}$. Interplanar distance [Å]: 3.62. Slip distance [Å]: I = 4.03. (b) Crystal structure of $(TMTTeN)(SCN)_{0.88}$ projected on the *bc*-plane. Donor stacking columns of $(TMTTeN)(SCN)_{0.88}$ viewed (c) along the *c*-axis and (d) along the *b*-axis. Intermolecular contacts [Å]: Te(1)···Te(1), a = 4.048(1); Te(2)···Te(2), b = 4.123(1); and Te(1)···Te(2), c = 3.788(2). Overlap integrals ($\times10^{-3}$): $a1$ = 82.83, $c1$ = –24.36, and $p1$ = –7.23. Dihedral angle between the adjacent donor molecules along the *b*-axis [°]: 72.2.

 © 2005 Wiley-VCH Verlag GmbH & Co. KGaA, Weinheim

the same as that of previously reported $(TSeT)_2SCN$.[23,24] This crystal structure belongs to a monoclinic lattice and is not isostructural to those of the $Ag(CN)_2^-$ and $Au(CN)_2^-$ salts with tetragonal lattices. That is, the penetration of the SCN^- anion into the TMTTeN lattice results in a modification of the packing pattern of TMTTeN molecules along the *c*-axis of the crystals, but the arrangements of TMTTeN molecules along the other two axes are almost the same as those of the $Ag(CN)_2^-$ and $Au(CN)_2^-$ salts. On the other hand, the atomic positions of the SCN^- anions are disordered along the donor stacking axis. As shown in Figure 9 (b–d), there are many intermolecular Te···Te contacts and a three-dimensional network is developed through tellurium atoms in the crystal. The overlap integral along the stack is fairly large ($a1 = 82.83 \times 10^{-3}$) compared to the others ($c1 = -24.36 \times 10^{-3}$ and $p1 = -7.23 \times 10^{-3}$) because of the tight stacking structure of TMTTeN molecules. On the other hand, the interstack overlap integral *c1* is about three times larger than *p1* because of a parallel arrangement of two TMTTeN molecules in the interaction *c1* in contrast to an almost orthogonal arrangement in the interaction *p1*. The large interaction *c1* also originates from the structural situation where two intermolecular Te···Te overlaps between each tellurium pair with longer Te···Te distance and shorter Te···Te distance cannot cancel each other out in spite of the nodal plane at the Te–Te bond. Thus, the overlap integral along the stacking axis (*a1*) is only three times larger than that of the side-by-side direction (*c1*), suggesting relatively strong quasi two-dimensionality in the *ac*-plane, which results in a stable metallic behavior down to 4.2 K.

Crystal Structure of (TMTTeN)$(ClO_4)_{0.88}$

The overlap mode and crystal structure of the ClO_4^- salt are shown in Figure 10. The composition of the ClO_4^- salt was determined to be $(TMTTeN)(ClO_4)_{0.88}$ by a population refinement. The donor arrangement of the ClO_4^- salt is a little different from those of the $Ag(CN)_2^-$ and $Au(CN)_2^-$ salts. Namely, the donor molecules form the columns with uniform stackings along the *c*-axis and the anion molecules are disordered along the donor stacking axis on the special position of the 4_2-axes in a similar manner to the $Ag(CN)_2^-$ and $Au(CN)_2^-$ salts. However, the gradient between the donor molecules is very gentle, with a dihedral angle of 26.9° between the two adjacent donor columns, compared to that of the $Ag(CN)_2^-$ salt (71.4°). As it turned out, the lattice constants of the *a*- and *b*-axes of the ClO_4^- salts are longer by about 2.4 Å, and the *c*-axis of the ClO_4^- salt is shorter by about 1.3 Å than those of the $Ag(CN)_2^-$ and $Au(CN)_2^-$ salts. Furthermore, the donor molecule has a small slip distance (1.08 Å), but the interplanar distance (3.87 Å) is larger than that of the $Ag(CN)_2^-$ salt (3.41 Å) (see parts a in Figure 8 and Figure 10). This large interplanar distance might be related to a larger positive charge on the TMTTeN molecule (+0.88) than the case of the $Ag(CN)_2^-$ salt (+0.5). As shown in Figure 10 (b and c), a three-dimensional network mediated by tellurium atoms that is similar to the other TMTTeN salts is developed in the crystal. Consequently, not only a strong intermolecular interaction is observed in the donor stacking direction (*c1* $= -80.61 \times 10^{-3}$), but a comparatively strong interaction also exists between stacking columns ($p1 = -5.45 \times 10^{-3}$). However, this salt showed a semiconducting behavior with a relatively low conductivity of $\sigma_{rt} \approx 0.8\ S\,cm^{-1}$, probably because of the difference of the stacking mode of the donors.

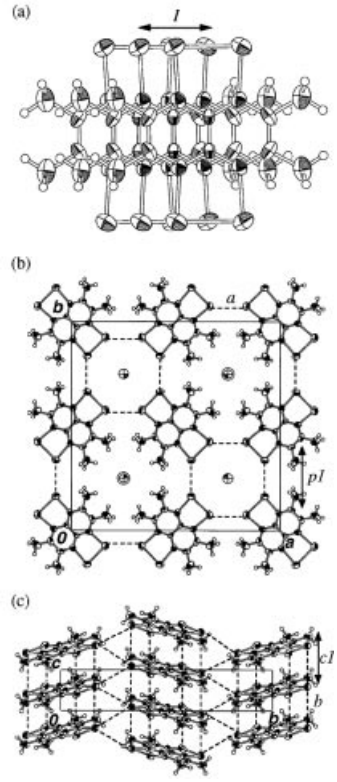

Figure 10. (a) Overlap mode of the donor molecules in (TMTTeN)$(ClO_4)_{0.88}$. Interplanar distance [Å]: 3.87. Slip distance [Å]: $I = 1.08$. (b) Crystal structure of $(TMTTeN)(ClO_4)_{0.88}$ projected on the *ab*-plane. (c) Donor stacking columns of $(TMTTeN)(ClO_4)_{0.88}$ viewed along the *a*-axis. Intermolecular contacts [Å]: Te(1)···Te(1), $a = 4.112(2)$; and Te(1)···Te(1), $b = 4.020(2)$. Overlap integrals ($\times 10^{-3}$): $c1 = -80.61$ and $p1 = -5.45$. Dihedral angle between the adjacent donor molecules [°]: 26.9.

Crystal Structure of (TMTTeN)$(AsF_6)_{0.7}$

Figure 11 shows the overlap mode and crystal structure of the AsF_6^- salt. The space group of this salt ($P42_1m$) is different from the other tetragonal salts ($P4_2/ncm$), and a half of the donor molecule is a crystallographically independent unit. The composition of the AsF_6^- salts is determined to be $(TMTTeN)(AsF_6)_{0.7}$ by a population refinement. The donor arrangement, interplanar distance of 3.44 Å and slip distance of 4.06 Å in the AsF_6^- salt is almost the same as those of the $Ag(CN)_2^-$ salt, suggesting that the donor molecules of these salts possess almost the same degree of positive charge. Although the anion molecules are located on all four channels that are formed by the donor molecules, only the anions in the two channels that are surrounded by tellurium atoms of the donor molecules are disordered along the *c*-axis. As shown in Figure 11 (b and c), a three-dimensional network through tellurium atoms is also devel-

 © 2005 Wiley-VCH Verlag GmbH & Co. KGaA, Weinheim

oped and is similar to the linear anion salts like the $Ag(CN)_2^-$ and $Au(CN)_2^-$ salts. Intermolecular overlap integrals are comparatively large ($c1 = 89.01\times10^{-3}$, $p1 = -8.60\times10^{-3}$, $p2 = -8.63\times10^{-3}$, $q1 = -7.08\times10^{-3}$, and $q2 = -6.80\times10^{-3}$).

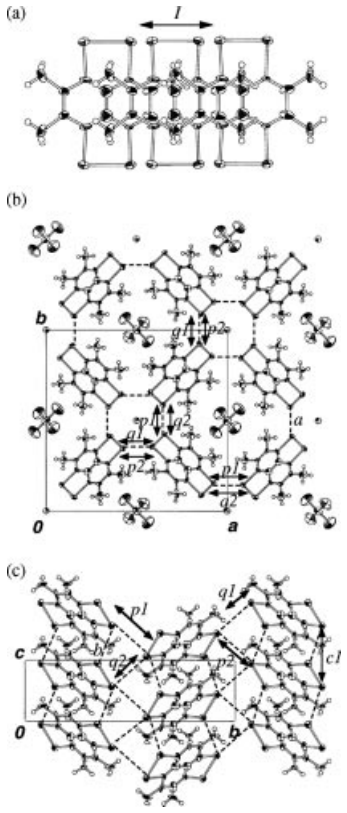

Figure 11. (a) Overlap mode of the donor molecules in $(TMTTeN)(AsF_6)_{0.7}$. Interplanar distance [Å]: 3.44. Slip distance [Å]: $I = 4.06$. (b) The crystal structure of $(TMTTeN)(AsF_6)_{0.7}$ projected on the *ab*-plane. (c) Donor stacking columns of $(TMTTeN)(AsF_6)_{0.7}$ along the *a*-axis. Intermolecular contacts [Å]: Te(1)···Te(2), $a = 4.054(3)$; and Te(1)···Te(2), $b = 3.716(2)$. Overlap integrals ($\times10^{-3}$): $c1 = 89.01$, $p1 = -8.60$, $p2 = -8.63$, $q1 = -7.08$ and $q2 = -6.80$. Dihedral angle between the adjacent donor molecules [°]: 65.24.

Physical Properties

Conducting Properties of the 2,3-DMTTeA Salts

Room temperature conductivities and activation energies of the obtained 2,3-DMTTeA salts are summarized in Table 2. The resistivities of the BF_4^-, ClO_4^-, ReO_4^-, PF_6^-, AsF_6^-, and SbF_6^- salts were measured down to about 80 K along the donor stacking axes. The BF_4^-, ClO_4^-, and ReO_4^- salts showed semiconducting behaviors with low conductivities of $\sigma_{rt} \approx 10^{-2}$ to 10^{-3} S cm^{-1} owing to their inadequate conduction paths along the donor stacking axes that originate from the crossed overlap mode of molecules A and B (Figure 5) and the strong dimerization of molecules B and B′. The temperature dependence of electrical resistivities of the PF_6^-, AsF_6^-, and SbF_6^- salts are also semiconducting with relatively high room temperature conductivities of 1.0–20 S cm^{-1} and low activation energies of 0.02–0.09 eV because of their quasi one-dimensional structures that indicate a strong one-dimensional nature along the donor stacking axis. On the other hand, the Br^- and SCN^- salts showed quite high conductivities of σ_{rt} = 1300 and 890 S cm^{-1} and semiconducting behaviors with very low activation energies of 0.01 and 0.004 eV, respectively, owing to the tight one-dimensional character along the donor stacking direction and the disorders of the donor and anion molecules. The CuI_2^- salt showed a semiconducting behavior with a low room temperature conductivity of 10^{-3} S cm^{-1} and a large activation energy of 0.17 eV. The NO_3^- salt indicates a semiconducting behavior with a relatively large room temperature conductivity of 4.7 S cm^{-1} and a large activation energy of 0.031 eV. As a result, no metallic salt has been discovered in the 2,3-DMTTeA salts, probably because of the strong one-dimensionality of their electronic structures and the disorder effect of 2,3-DMTTeA molecules in the crystal.

Conducting Properties of the TMTTeN Salts

Room temperature conductivities and activation energies of the TMTTeN salts are listed in Table 3. All the salts except for the $Ag(CN)_2^-$, $Au(CN)_2^-$, and SCN^- salts are semiconductors or insulators. Among them, the $Cu(SCN)_2^-$ and

Table 2. Electrical properties of the 2,3-DMTTeA salts.[a]

Anions[b]	Solvents[c]	Current [μA]	Electrical properties	$\sigma_{293\,K}$ [S cm^{-1}]	E_a [eV]
BF4$^-$	THF	0.05–0.3	semiconducting	9.7×10^{-3}	0.17
ClO4$^-$	THF or PhCl	0.05–0.2	semiconducting	7.1×10^{-3}	0.16
ReO_4^-	THF	0.1–0.7	semiconducting	5.5×10^{-3}	0.16
PF_6^-	THF	0.1–0.3	semiconducting	1.0	0.090
AsF_6^-	THF	0.1–0.5	semiconducting	17	0.019
SbF_6^-	THF	0.1–0.5	semiconducting	10	0.048
Br^-[d]	THF	0.1–0.7	semiconducting	1300	0.010
SCN^-	TCE	0.1–0.4	semiconducting	890	0.004
CuI_2^-	THF	0.1–0.3	semiconducting	3.0×10^{-3}	0.17
NO_3^-	THF	0.05–0.3	semiconducting	4.7	0.031

[a] All preparations were carried out at room temperature under nitrogen. [b] All the supporting electrolytes were tetra-*n*-butylammonium salts except for the $GaBr_4^-$ anion. Tetraethylammonium salt was used in the $GaBr_4^-$ salt. [c] THF = tetrahydrofuran, PhCl = chlorobenzene and TCE = 1,1,2-trichloroethane. [d] This salt was prepared with tetra-*n*-butylammonium salt of $GaBr_4^-$ as a supporting electrolyte.

 © 2005 Wiley-VCH Verlag GmbH & Co. KGaA, Weinheim

Table 3. Electrical properties of the TMTTeN salts.[a]

Anions[b]	Solvents[c]	Current [μA]	Electrical properties	$\sigma_{293\,K}$ [S cm^{-1}]	E_a [eV]
$Ag(CN)_2^-$	10% EtOH/TCE	0.1–0.2	metallic down to ca. 50 K	760	
$Au(CN)_2^-$	10% EtOH/TCE	0.1–0.2	metallic down to ca. 50 K	720	
SCN^-[d]	10% EtOH/TCE	0.1–0.2	metallic down to 4.2 K	590	
$Cu(SCN)_2^-$	THF	0.1	semiconducting	840	0.055
$N(CN)_2^-$	PhCN	0.1	insulating	$<10^{-6}$	
BF_4^-	10% EtOH/PhCl	0.1	semiconducting	9.9	0.11
ClO_4^-	PhCl	0.1	semiconducting	7.6×10^{-1}	0.072
$GaBr_4^-$	10% EtOH/PhCl	0.1	semiconducting	360	0.028
PF_6^-	10% EtOH/PhCl	0.1	semiconducting	7.7×10^{-1}	0.054
AsF_6^-	10% EtOH/PhCl	0.1	semiconducting	13	0.015
SbF_6^-	THF or PhCl	0.1	semiconducting	3.0×10^{-1}	0.10
Br^-	10% EtOH/PhCl	0.1	semiconducting	6.0×10^{-2}	0.12
$Mo_6O_{19}^{2-}$	10% EtOH/PhCl	0.1	semiconducting	2.4	0.038

[a] All preparations were carried out at 40 °C under nitrogen. [b] All the supporting electrolytes were tetra-*n*-butylammonium salts except for the $Cu(SCN)_2^-$, $N(CN)_2^-$, BF_4^-, and SbF_6^- salts. Tetraethylammonium salt was used in the BF_4^- salt and tetraphenylphosphonium salt was used in the $N(CN)_2^-$ salt. In the $Cu(SCN)_2^-$ and SbF_6^- salts, bis(triphenylphosphoranylidene)ammonium salts were used. [c] EtOH = ethanol, TCE = 1,1,2-trichloroethane, THF = tetrahydrofuran, PhCN = benzonitrile and PhCl = chlorobenzene. [d] This salt was prepared under existence of two kinds of anion complexes, tetra-*n*-butylammonium salts of SCN^- and ClO_4^- anions.

$GaBr_4^-$ salts showed very high room temperature conductivities of 840 and 360 S cm^{-1} with low activation energies of 0.02–0.04 eV, respectively. On the other hand, the ClO_4^- salt showed a low room temperature conductivity of 10^{-1} S cm^{-1}. The linear $Ag(CN)_2^-$, $Au(CN)_2^-$, and SCN^- anion salts showed very high room temperature conductivities (590–760 S cm^{-1}). As shown in Figure 12, the temperature dependences of the resistivities of the $Ag(CN)_2^-$ and $Ag(CN)_2^-$ salts are metallic down to about 50 K, below which the resistivities increase very slowly down to 4.2 K with decreasing temperature. On the other hand, Figure 12 also shows that the temperature dependence of electrical resistivities of the SCN^- salt is metallic down to 4.2 K without any increase of resistivities, in contrast to the $Ag(CN)_2^-$ and $Ag(CN)_2^-$ salts. Although the temperature dependence of its resistivity is very small, like those of the $Ag(CN)_2^-$ and $Au(CN)_2^-$ salts, this SCN^- salt displays no increase in resistivity. Therefore, the SCN^- salt is revealed to be a genuine stable metal down to low temperatures. As mentioned before, this system has a strong transverse intermolecular interaction (see *c1* in Figure 9), which is the origin of its stable metallic state. On the other hand, the AsF_6^- salt also has a relatively high conductivity of 13 S cm^{-1}, but showed a semiconducting behavior at room temperature. Considering it has almost the same donor arrangement as the metallic $Ag(CN)_2^-$ and $Au(CN)_2^-$ salts, this semiconducting behavior may suggest that the large disorder effect of the octahedral AsF_6^- anion prevents a metallic conducting behavior.

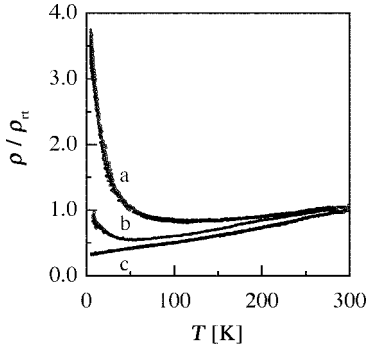

Figure 12. Temperature dependence of the electrical resistivities of the metallic TMTTeN salts. a, $(TMTTeN)_2Au(CN)_2$; b, $(TMTTeN)_2Ag(CN)_2$; and c, $(TMTTeN)(SCN)_{0.88}$.

Magnetic Properties of the TMTTeN Salts

The magnetic susceptibilities of $(TMTTeN)_2Ag(CN)_2$ and $(TMTTeN)(SCN)_{0.88}$ were measured using SQUID magnetometer down to 2 K at 30 kOe. The susceptibility of the neutral TMTTeN crystal was also measured in order to estimate the diamagnetic contribution of the TMTTeN molecule, which was performed by subtracting that of carbon disulfide included in the crystal of the neutral TMTTeN molecule. Figure 13 shows the temperature dependence of paramagnetic susceptibilities of $(TMTTeN)_2Ag(CN)_2$ and $(TMTTeN)(SCN)_{0.88}$. The paramagnetic susceptibility of $(TMTTeN)_2Ag(CN)_2$, which is corrected by subtracting a diamagnetic contribution and a small low-temperature Curie component due to paramagnetic impurities and/or lattice defects, was almost constant throughout the temperature range, indicating a Pauli paramagnetism based on metal electrons ($2.0–2.5\times10^{-4}$ emu mol^{-1}). No anomaly that corresponds to the gradual resistivity increase around 50 K was observed, suggesting the stable metallic nature of this salt. On the other hand, the paramagnetic susceptibilities of $(TMTTeN)(SCN)_{0.88}$ are also almost constant throughout the temperature range, indicating the Pauli paramagnetism of the system ($1.6–1.9\times10^{-4}$ emu mol^{-1}). Therefore, as revealed by the low-temperature resistivity behaviors, these salts are the first systems that possess metallic ground state among the *peri*-ditellurium-bridged donors. Because these TMTTeN conductors have an approximately one-dimensional cosine band along the molecular stacking direction, the smaller susceptibility of $(TMTTeN)(SCN)_{0.88}$ and larger susceptibility of $(TMTTeN)_2Ag(CN)_2$ seem to be related to the difference in not only their bandwidths but also their band-

 © 2005 Wiley-VCH Verlag GmbH & Co. KGaA, Weinheim

fillings; namely, the ratio $\sin(\pi \times 0.5/2)/\sin(\pi \times 0.88/2) \approx 0.72$, is nearly equal to the ratio of the susceptibilities of these salts. In addition, the magnitude of these susceptibilities is about half that of the well-known κ-type BEDT-TTF superconductors ($\approx 5 \times 10^{-4}$ emu mol^{-1}),[25] where BEDT-TTF is bis(ethylenedithio)-TTF. Their small susceptibilities suggest large bandwidths of $(TMTTeN)_2Ag(CN)_2$ and $(TMTTeN)(SCN)_{0.88}$, which are brought about by the strong intermolecular interaction, and are consistent with the organic metals based on tellurium-containing donors such as (TTeF)(TCNQ).[26]

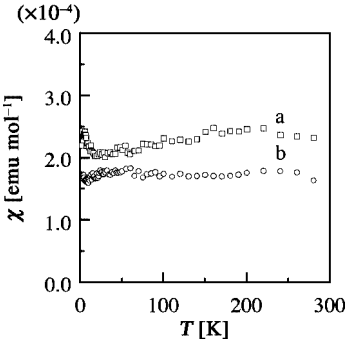

Figure 13. Temperature dependence of the paramagnetic susceptibilities of the TMTTeN salts. a, $(TMTTeN)_2Ag(CN)_2$; and b, $(TMTTeN)(SCN)_{0.88}$.

Band Structure Calculations

We have previously reported the results of the extended Hückel tight-binding band calculation on $(TMTTeN)_2Ag(CN)_2$.[18] However, the extended Hückel tight-binding band is calculated anew, because the empirical parameters used here are redetermined on the basis of the results of the ab initio MO calculations. As the first step of the band structure calculation, an extended Hückel MO was obtained as approximately the same as the ab initio MO. The calculated intermolecular overlap integrals of the individual salts have already been presented, together with their crystal structures. Generally speaking, the transverse interactions became much smaller than the interaction along the direction of the molecular stacking, because of the nodal plane at the Te–Te bond. The energy dispersion curves of conduction bands and the Fermi surfaces of $(TMTTeN)_2Ag(CN)_2$ and $(TMTTeN)(SCN)_{0.88}$ are shown in Figures 14 and 15, respectively.

Energy Dispersion Curves and Fermi Surface of $(TMTTeN)_2Ag(CN)_2$

Owing to the tetragonal lattice symmetry, the obtained band dispersions are doubly degenerated on the XM line (see Figure 14), which makes the Fermi surfaces that are composed of two corrugated one-dimensional Fermi surfaces quasi three-dimensional. A large bandwidth (≈4.0 eV) is consistent with the observed small Pauli susceptibility. The Fermi surfaces are closed in the a^*c^*- and b^*c^*-planes and also in the plane perpendicular to the c^*-axis [an example of the cross section of the Fermi surface at the plane (Γ′X′Y′) perpendicular to the c^*-axis is presented], as shown in Figure 14. As mentioned before, the analogous selenium-donor system $(TSeT)_2Cl$ showed a metal–semi-

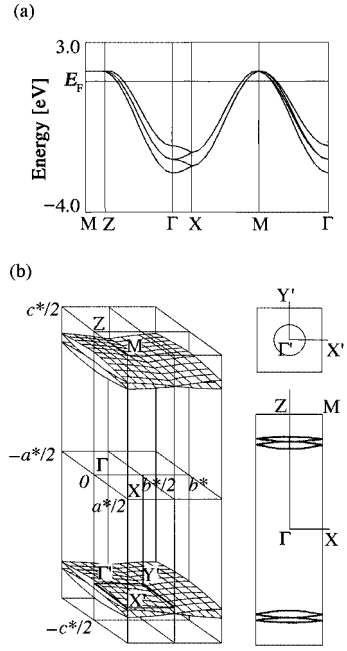

Figure 14. Energy band structures and three-dimensional Fermi surfaces of $(TMTTeN)_2Ag(CN)_2$ obtained by the extended Hückel tight-binding band calculation and their cross sections at the plane through ΓXZ and Γ′X′Z′, where Γ = (0, 0, 0), X = (a^*/2, 0, 0), Z = (0, 0, c^*/2), Γ′ = (0, 0, –0.35c^*), X′ = (a^*/2, 0, –0.35c^*), and Y′ = (0, b^*/2, –0.35c^*).

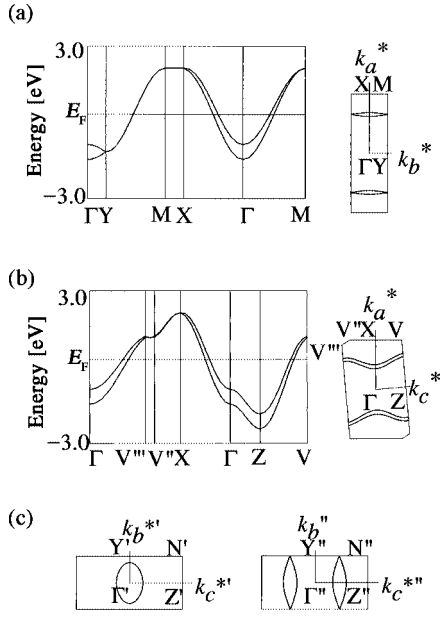

Figure 15. Energy band structures and cross sections of Fermi surfaces of $(TMTTeN)(SCN)_{0.88}$ obtained by the extended Hückel tight-binding band calculation. Γ = (0, 0, 0), X = (a^*/2, 0, 0), Y = (0, b^*/2, 0), Z = (0, 0, c^*/2), Γ′ = (0.23a^*, 0, 0), Y′ = (0.23a^*, b^*/2, 0), Z′ = (0.23a^*, 0, c^*/2), Γ″ = (0.28a^*, 0, 0), Y″ = (0.28a^*, b^*/2, 0), and Z″ = (0.28a^*, 0, c^*/2).

 © 2005 Wiley-VCH Verlag GmbH & Co. KGaA, Weinheim

metal transition around 20 K, where a susceptibility drop that indicates a partial disappearance of the Fermi surfaces was observed. The stable metallic state of $(TMTTeN)_2Ag(CN)_2$ is attributable to the stronger three-dimensionality of the band structure. Therefore, $(TMTTeN)_2Ag(CN)_2$ is the first organic conductor that has a stable metallic state and "quasi three-dimensional Fermi surfaces" at ambient pressure on the basis of the tellurium-containing π donors.

Energy Dispersion Curves and Fermi Surface of (TMTTeN)(SCN)$_{0.88}$

As Figure 15a indicates, the band dispersions are doubly degenerated on the YM line. A large bandwidth (≈4.5 eV) is consistent with the observed small Pauli susceptibility. The Fermi surface of the SCN^- salt is open along the *b**- and *c**-directions, but the intermolecular interactions between the donor columns are fairly strong, as mentioned before. As shown in part c of Figure 15, cross sections of the Fermi surface perpendicular to the *a**-axis indicate a two- or quasi two-dimensional metallic state. Consequently, the Fermi surfaces are considered to be stable against the nesting of the Fermi surfaces. This may be an origin of the stable metallic state of the SCN^- salt.

Conclusions

Crystal structures and physical properties of various cation radical salts based on the *peri*-ditellurium-bridged polyacene donor molecules 2,3-DMTTeA and TMTTeN were examined. We have obtained the stable metallic cation radical salts of the TMTTeN molecule. Compared with usual organic conductors, the molecular conductors based on these tellurium-containing π donors show a very strong tendency to form a three-dimensional network mediated by tellurium atoms. Owing to the strong Te···Te network, the anions have very small contributions to the architecture of the crystal structures and are located fairly randomly in the channels that are formed by the donor molecules in most cases. New conducting systems with ordered crystal structures will be obtained by suitable selection of counteranions, which will afford a new class of three-dimensional organic metals with bandwidths much wider than the hitherto-obtained organic metals.

Experimental Section

General Remarks: 2,3-DMTTeA and TMTTeN were synthesized according to the reported methods.[15,16] Tetrahydrofuran (THF) was freshly distilled from sodium and benzophenone under nitrogen prior to use. Chlorobenzene (PhCl) was washed three times with concd. sulfuric acid, then with aqueous sodium hydrogen carbonate solution and water, followed by drying with calcium chloride and distilled from diphosphorus pentaoxide. Ethanol (EtOH) was distilled from magnesium ethoxide under nitrogen. Benzonitrile (PhCN) was dried with calcium chloride and distilled from diphosphorus pentaoxide under reduced pressure. 1,1,2-Trichloroethane (TCE) was washed three times with concd. sulfuric acid, then with aqueous sodium hydrogen carbonate solution and water, followed by drying with calcium chloride and was distilled under nitrogen. All the supporting electrolytes were recrystallized several times with organic solvents.

Electrocrystallization: The crystals of cation radical salts were grown by an electrochemical oxidation in the solvent shown in Table 2 for the 2,3-DMTTeA salts and Table 3 for the TMTTeN salts in the presence of the donor and the tetraalkylammonium, tetraphenylphosphonium, or bis(triphenylphosphoranylidene)ammonium salts of the corresponding anions under a constant current of 0.05–0.7 μA at room temperature in the case of the 2,3-DMTTeA salts and at 40 °C in the case of the TMTTeN salts.

Crystal Structure Determination: X-ray crystal structure analyses were performed on the neutral 2,3-DMTTeA and TMTTeN molecules recrystallized from carbon disulfide and their cation radical salts. Intensity data were measured with Rigaku AFC5R or AFC7R automated four-circle diffractometers or R-AXIS IV imaging plate area detector [only for $TMTTeN(AsF_6)_{0.7}$] by using graphite-monochromated Mo-K_α radiation at room temperature. Experimental details and crystal data are listed in Table 4, Table 5, and Table 6. Anisotropic temperature factors were applied for the non-hydrogen atoms. The calculated positions of hydrogen atoms were not refined but included in the final calculation. All calculations were performed using the teXsan[27] crystallographic software package of the Molecular Structure Corporation. CCDC-118377–118378, 121877–121880, 142670, and 264456–264461 contain the supplementary crystallographic data for this paper. These data can be obtained free of charge from The Cambridge Crystallographic Data Centre via www.ccdc.cam.ac.uk/data_request/cif.

Table 4. Crystallographic data of the neutral 2,3-DMTTeA and TMTTeN.

	2,3-DMTTeA	TMTTeN·CS_2
Formula	$C_8H_5Te_2$	$C_{15}H_{12}S_2Te_4$
Formula mass	356.33	766.78
Crystal color, habit	black, needle	black, rod
Crystal system	monoclinic	triclinic
a [Å]	9.976(5)	10.812(5)
b [Å]	5.137(1)	14.588(6)
c [Å]	16.186(1)	6.295(3)
α [°]		100.49(4)
β [°]	104.28(2)	106.75(4)
γ [°]		89.90(4)
V [Å^3]	803.8(3)	933.5(7)
Space group	$P2_1/c$ (#14)	$P\bar{1}$ (#2)
Z	4	2
$D_{calcd.}$ [g cm^{-3}]	2.944	2.728
μ(Mo-K_α) [cm^{-1}]	71.75	64.04
Diffractometer	Rigaku AFC7R	Rigaku AFC5R
Radiation	Mo-K_α (λ = 0.71069 Å)	Mo-K_α (λ = 0.71069 Å)
Temperature [K]	294	296
Measured reflections	total: 2722, unique: 2588	total: 5714, unique: 5445
Structure solution	Direct methods (SHELXS86)	Direct methods (SHELXS86)
Refinement	Full-matrix least-squares	Full-matrix least-squares
No. observations	1200 [$I>3.00\sigma(I)$]	3883 [$I>3.00\sigma(I)$]
No. variables	90	190
Residuals: R;[a] R_w[b]	0.054; 0.040	0.034; 0.033

[a] $R = \Sigma||F_o| - |F_c||/\Sigma|F_c|$. [b] $R_w = [\Sigma\omega(|F_o| - |F_c|)^2/\Sigma\omega F_o^2]^{1/2}$.

Electron Probe Microanalysis (EPMA): Several single crystals were attached on a carbon tape, and several points on each crystal were examined by Scanning Electron Microscope, S-450 (Hitachi, Co.

 © 2005 Wiley-VCH Verlag GmbH & Co. KGaA, Weinheim

Table 5. Crystallographic data of the 2,3-DMTTeA salts.

	(2,3-DMTTeA)$_3$(BF$_4$)$_2$	(2,3-DMTTeA)$_3$(ClO$_4$)$_2$
Formula	$C_{12}H_{7.50}B_{0.50}F_2Te_3$	$C_{12}H_{7.50}Cl_{0.50}O_2Te_3$
Formula mass	577.89	584.22
Crystal color, habit	black, prismatic	black, prismatic
Crystal system	monoclinic	monoclinic
a [Å]	16.437(5)	16.538(3)
b [Å]	14.585(4)	14.681(2)
c [Å]	11.623(4)	11.612(4)
β [°]	111.19(2)	111.48(2)
V [Å^3]	2597(1)	2623(1)
Space group	$C2/m$ (#12)	$C2/m$ (#12)
Z	8	8
$D_{calcd.}$ [g cm^{-3}]	2.955	2.958
μ(Mo-K_α) [cm^{-1}]	66.92	67.17
Diffractometer	Rigaku AFC7R	Rigaku AFC7R
Radiation	Mo-K_α (λ = 0.71069 Å)	Mo-K_α (λ = 0.71069 Å)
Temperature [K]	295	295
Measured reflections	total: 4067, unique: 3941	total: 4146, unique: 3974
Structure solution	Direct methods (SHELX86)	Direct methods (SIR92)
Refinement	full-matrix least-squares	full-matrix least-squares
No. observations	2614 [I>3.00$\sigma(I)$]	2568 [I>3.00$\sigma(I)$]
No. variables	164	169
Residuals: R;[a] R_w[b]	0.052; 0.049	0.034; 0.023
	(2,3-DMTTeA)$_3$(ReO$_4$)$_2$	(2,3-DMTTeA)$_5$PF$_6$
Formula	$C_{12}H_{7.50}O_2Re_{0.50}Te_3$	$C_8H_5F_{0.60}P_{0.10}Te_2$
Formula mass	659.59	370.82
Crystal color, habit	black, prismatic	black, prismatic
Crystal system	monoclinic	monoclinic
a [Å]	16.617(2)	4.155(2)
b [Å]	14.990(2)	19.854(8)
c [Å]	11.569(2)	11.519(4)
β [°]	111.015(9)	94.66(4)
V [Å^3]	2690.0(6)	947.0(6)
Space group	$C2/m$ (#12)	$P2_1/a$ (#14)
Z	8	4
$D_{calcd.}$ [g cm^{-3}]	3.257	2.601
μ(Mo-K_α) [cm^{-1}]	109.29	61.20
Diffractometer	Rigaku AFC5R	Rigaku AFC7R
Radiation	Mo-K_α (λ = 0.71069 Å)	Mo-K_α (λ = 0.71069 Å)
Temperature [K]	296	296
Measured reflections	total: 4196, unique: 4069	total: 2548, unique: 2256
Structure solution	Direct methods (SIR92)	Direct methods (SIR92)
Refinement	Full-matrix least-squares	Full-matrix least-squares
No. observations	2281 [I>3.00$\sigma(I)$]	1182 [I>3.00$\sigma(I)$]
No. variables	172	109
Residuals: R;[a] R_w[b]	0.051; 0.037	0.085; 0.108
	(2,3-DMTTeA)$_5$AsF$_6$	(2,3-DMTTeA)$_2$Br
Formula	$C_8H_5As_{0.10}F_{0.60}Te_2$	$C_4H_{2.50}Br_{0.12}Te$
Formula mass	375.22	188.15
Crystal color, habit	black, needle	black, needle
Crystal system	monoclinic	tetragonal
a [Å]	4.155(2)	18.655(2)
b [Å]	19.898(3)	
c [Å]	11.572(7)	5.438(3)
β [°]	94.85(9)	
V [Å^3]	953.3(6)	1892(1)
Space group	$P2_1/a$ (#14)	$P4_2/ncm$ (#138)
Z	4	16
D_{calcd} [g cm^{-3}]	2.614	2.641
μ(Mo-K_α) [cm^{-1}]	64.07	71.54
Diffractometer	Rigaku AFC5R	Rigaku AFC5R
Radiation	Mo-K_α (λ = 0.71069 Å)	Mo-K_α (λ = 0.71069 Å)
Temperature [K]	296	296
Measured reflections	total: 3201, unique: 2853	total: 1313
Structure solution	Direct methods (SIR92)	Direct methods (SIR92)
Refinement	Full-matrix least-squares	Full-matrix least-squares
No. observations	1400 [I>3.00$\sigma(I)$]	578 [I>3.00$\sigma(I)$]
No. variables	109	56
Residuals: R;[a] R_w[b]	0.067; 0.082	0.095; 0.119

[a] $R = \Sigma||F_o| - |F_c||/\Sigma|F_c|$. [b] $R_w = [\Sigma\omega(|F_o| - |F_c|)^2/\Sigma\omega F_o^2]^{1/2}$.

Table 6. Crystallographic data of the TMTTeN salts.

	(TMTTeN)$_2$Ag(CN)$_2$	(TMTTeN)$_2$Au(CN)$_2$
Formula	$C_{3.5}H_3Ag_{0.12}Te$	$C_{3.5}H_3Au_{0.12}Te$
Formula mass	185.61	196.30
Crystal color, habit	black, needle	black, needle
Crystal system	tetragonal	tetragonal
a [Å]	18.2911(9)	18.322(1)
c [Å]	5.352(1)	5.350(3)
V [Å^3]	1790.5(4)	1795.9(9)
Space group	$P4_2/ncm$ (#138)	$P4_2/ncm$ (#138)
Z	16	16
D_{calcd} [g cm^{-3}]	2.754	2.904
μ(Mo-K_α) [cm^{-1}]	69.46	103.33
Diffractometer	Rigaku AFC7R	Rigaku AFC7R
Radiation	Mo-K_α (λ = 0.71069 Å)	Mo-K_α (λ = 0.71069 Å)
Temperature [K]	296	296
Measured reflections	total: 1582	total: 1586
Structure solution	Direct methods (SHELXS86)	Direct methods (SHELXS86)
Refinement	Full-matrix least-squares	Full-matrix least-squares
No. observations	927 [I>3.00$\sigma(I)$]	947 [I>3.00$\sigma(I)$]
No. variables	55	48
Residuals: R;[a] R_w[b]	0.035; 0.034	0.042; 0.044
	TMTTeN(SCN)$_{0.88}$	TMTTeN(ClO$_4$)$_{0.88}$
Formula	$C_{7.44}H_6NO_{0.44}S_{0.44}Te_2$	$C_{3.50}H_3Cl_{0.22}Te$
Formula mass	370.88	180.46
Crystal color, habit	black, prismatic	black, needle
Crystal system	monoclinic	tetragonal
a [Å]	5.419(3)	20.660(2)
b [Å]	17.493(2)	
c [Å]	8.941(2)	4.019(2)
β [°]	94.77(3)	
V [Å^3]	844.7(5)	1715(1)
Space group	$P2_1/a$ (#14)	$P4_2/ncm$ (#138)
Z	4	16
$D_{calcd.}$ [g cm^{-3}]	2.916	2.795
μ(Mo-K_α) [cm^{-1}]	69.40	68.58
Diffractometer	Rigaku AFC5R	Rigaku AFC7R
Radiation	Mo-K_α (λ = 0.71069 Å)	Mo-K_α (λ = 0.71069 Å)
Temperature [K]	296	296
Measured reflections	total: 2215, unique: 2013	total: 1534
Structure solution	Patterson methods (DIRDIF92 PATTY)	Direct methods (SHELXS86)
Refinement	Full-matrix least-squares	Full-matrix least-squares
No. observations	1223 [I>3.00$\sigma(I)$]	641 [I>3.00$\sigma(I)$]
No. variables	101	48
Residuals: R;[a] R_w[b]	0.035; 0.034	0.055; 0.068
	TMTTeN(AsF$_6$)$_{0.7}$	
Formula	$C_7H_6As_{0.35}F_{1.50}Te_2$	
Formula mass	400.04	
Crystal color, habit	black, needle	
Crystal system	tetragonal	
a [Å]	18.373(2)	
c [Å]	5.3236(9)	
V [Å^3]	1797.15	
Space group	P-42$_1m$ (#14)	
Z	8	
$D_{calcd.}$ [g cm^{-3}]	2.957	
μ(Mo-K_α) [cm^{-1}]	77.29	
Diffractometer	R-AXIS IV	
Radiation	Mo-K_α (λ = 0.71070 Å)	
Temperature [K]	296	
Measured reflections	total: 974	
Structure solution	Direct methods (SHELXS86)	
Refinement	Full-matrix least-squares	
No. observations	845 [I>3.00$\sigma(I)$]	
No. variables	111	
Residuals: R;[a] R_w[b]	0.072; 0.073	

[a] $R = \Sigma||F_o| - |F_c||/\Sigma|F_c|$. [b] $R_w = [\Sigma\omega(|F_o| - |F_c|)^2/\Sigma\omega F_o^2]^{1/2}$.

 © 2005 Wiley-VCH Verlag GmbH & Co. KGaA, Weinheim

Ltd.). Data were accumulated for 100 s with time constants of 12 μs. Data collections and analyses were controlled by the Delta Class Analyzer (Kevex).

Magnetic Susceptibility Measurement: The magnetic susceptibilities were measured at a field of 30 kOe in the temperature range from 300 to 2 K using a Quantum Design MPMS-7 SQUID magnetometer. The samples were wrapped with clean aluminum foil whose magnetic susceptibility was separately measured and subtracted. The data were corrected for the diamagnetic contribution estimated from Pascal's constants, and the actual measurement of the neutral TMTTeN molecule [$\chi^{dia} = 7.47 \times 10^{-4}$ emu mol^{-1} for the $Ag(CN)_2^-$ salt and $\chi^{dia} = 3.63 \times 10^{-4}$ emu mol^{-1} for the SCN^- salt] and Curie impurities [0.05 mol-% for the $Ag(CN)_2^-$ salt and no subtraction of Curie impurities for the SCN^- salt].

Electrical Resistivity Measurement: The electrical resistivities were measured by a four-probe method along the donor stacking axis of the single crystals using Huso Electro Chemical System HECS 944C1 and/or HECS 944C Multi-channel 4-terminal conductometer. Electrical contacts were achieved with gold wires (Ø 0.015 mm) and gold paste.

Molecular Orbital (MO) and Band Structure Calculations: In order to use the simple extended Hückel type tight-binding band calculation for the molecular conductors based on *peri*-ditellurium-bridged polyacene donor molecules, reliable determination of the highest occupied molecular orbital (HOMO), from which a conduction band is formed, had to be made beforehand. The ab initio MO calculations of TMTTeN were performed by replacing the methyl groups with hydrogen atoms using Gaussian 94[28] on a Hewlett–Packard workstation (Apollo 9000 series model 735) at the Research Centre for Spectrochemistry of the University of Tokyo. The Huzinaga-Dunning double zeta basis set was used.[29] The Los Alamos effective core potential plus double zeta basis set (LanL2DZ) was used for tellurium atoms.[30]

The overlap integrals, band structures, and Fermi surfaces were calculated by a tight-binding method based on the extend Hückel approximation. Slater-type atomic orbitals were used for the calculation of MOs. The parameters for tellurium atoms were determined on the basis of the ab initio MO calculations and crystallographic analyses discussed before in this paper. The exponent ζ and the ionization potential (eV) were: Te 5s, 2.33, –17.41; Te 5p, 2.01, –8.98; Te 5d, 1.64, –4.76; C 2s, 1.625, –21.4; C 2p, 1.625, –11.4; H 1s, 1.0, –13.6. In the case of 2,3-DMTTeA salts, overlap integrals were calculated by using the coordinates of only one side of two conformations of the disordered molecule.

Acknowledgments

This work was supported by a Grand-in-Aid for Scientific Research on Priority Areas (No. 10149103 "Physical Properties of Solid-state Metal-assembled Complexes") from the Ministry of Education, Science, Sport and Culture, Japan.

[1] a) J. M. Williams, J. R. Ferraro, R. J. Thorn, K. D. Carlson, U. Geiser, H. H. Wang, A. M. Kini, M.-H. Whangbo, *Organic Superconductors (Including Fullerenes)*, Prentice Hall, New Jersey, **1992**; b) T. Ishiguro, K. Yamaji, G. Saito, *Organic Superconductors*, 2nd ed., Springer-Verlag, Berlin, Heidelberg, **1998**.

[2] a) A. Kobayashi, Y. Sasaki, R. Kato, H. Kobayashi, *Chem. Lett.* **1986**, 387–390; b) D. O. Cowan, A. Kini in *The Chemistry of Organic Selenium and Tellurium Compounds* (Ed.: S. Patai), John Wiley & Sons, London, **1987**, vol. 2, pp. 463–494; c) D. O. Cowan, R. McCullough, A. Bailey, K. A. Lerstrup, D. Talham, D. Herr, M. Mays, *Phosphorus Sulfur Silicon Relat. Elem.* **1992**, *67*, 277–294.

[3] R. D. McCullough, G. B. Kok, K. A. Lerstrup, D. O. Cowan, *J. Am. Chem. Soc.* **1987**, *109*, 4115–4116.

[4] E. Aharon-Shalom, J. Y. Becker, J. Bernstein, S. Bittner, S. Shaik, *Tetrahedron Lett.* **1985**, *26*, 2783–2786.

[5] a) K. Kikuchi, K. Yakushi, H. Kuroda, I. Ikemoto, K. Kobayashi, M. Honda, C. Katayama, J. Tanaka, *Chem. Lett.* **1985**, 419–422; b) Z. S. Li, S. Matsuzaki, R. Kato, H. Kobayashi, A. Kobayashi, M. Sano, *Chem. Lett.* **1986**, 1105–1108.

[6] G. Saito, S.-S. Pac, O. O. Drozdova, *Synth. Met.* **2001**, *120*, 667–670.

[7] D. O. Cowan, M. D. Mays, T. J. Kistenmacher, T. O. Poehler, M. A. Beno, A. M. Kini, J. M. Williams, Y. K. Kwok, K. D. Carlson, L. Xiao, J. J. Novoa, M.-H. Whangbo, *Mol. Cryst. Liq. Cryst.* **1990**, *181*, 43–58.

[8] a) M. A. Il'ina, E. S. Itskevich, *JETP Lett.* **1971**, *13*, 15–18; b) I. V. Berman, Z. I. Bynzarov, Y. P. Kurkin, *Sov. Phys. Solid State* **1973**, *14*, 2192–2194; c) M. A. Il'ina, E. S. Itskevich, *Sov. Phys. Solid State* **1976**, *17*, 2266–2267.

[9] a) E. N. Yakovlev, G. N. Stepanov, Y. A. Timofeev, B. V. Vinogradov, *JETP Lett.* **1978**, *28*, 340–342; b) V. V. Struzhkin, R. J. Hamley, H.-K. Mao, Y. A. Timofeev, *Nature* **1997**, *390*, 382–384.

[10] a) J. Witting, *Phys. Rev. Lett.* **1965**, *15*, 159–159; b) A. R. Moodenbaugh, C. T. Wu, R. Viswanathan, *Solid State Commun.* **1973**, *13*, 1413–1416.

[11] a) F. P. Bundy, K. J. Dunn, *Phys. Rev. B* **1980**, *22*, 3157–3164; b) Y. Akahama, M. Kobayashi, H. Kawamura, *Solid State Commun.* **1992**, *84*, 803–806.

[12] D. J. Sandman, J. C. Stark, B. M. Foxman, *Organometallics* **1982**, *1*, 739–742.

[13] D. J. Sandman, J. C. Stark, G. P. Hamill, W. A. Burke, B. M. Foxman, *Mol. Cryst. Liq. Cryst.* **1982**, *86*, 1819–1825.

[14] a) D. J. Sandman, J. C. Stark, M. Rubner, R. A. Acampora, L. A. Samuelson, B. M. Foxman, *Mol. Cryst. Liq. Cryst.* **1983**, *93*, 293–305; b) R. Kato, H. Kobayashi, A. Kobayashi, *Physica B+C* **1986**, *143*, 304–306.

[15] a) K. Takimiya, Y. Aso, T. Otsubo, F. Ogura, *Bull. Chem. Soc. Jpn.* **1991**, *64*, 2091–2102; b) For the sulfur and the selenium isologues of 2,3-DMTTeA, see: K. Takimiya, A. Ohnishi, Y. Aso, T. Otsubo, F. Ogura, K. Kawabata, K. Tanaka, M. Mizutani, *Bull. Chem. Soc. Jpn.* **1994**, *67*, 766–772.

[16] T. Otsubo, N. Sukenobe, Y. Aso, F. Ogura, *Synth. Met.* **1988**, *27*, B509–B514. Refs.[17–19] are preliminary communications.

[17] M. Nakata, A. Kobayashi, T. Saito, H. Kobayashi, K. Takimiya, T. Otsubo, F. Ogura, *J. Chem. Soc. Chem. Commun.* **1997**, 593–594.

[18] a) E. Arai, H. Fujiwara, H. Kobayashi, A. Kobayashi, K. Takimiya, T. Otsubo, F. Ogura, *Inorg. Chem.* **1998**, *37*, 2850–2851; b) A. Kobayashi, M. Nakata, E. Arai, H. Fujiwara, H. Kobayashi, K. Takimiya, T. Otsubo, F. Ogura, *Synth. Met.* **1999**, *103*, 1865–1868.

[19] E. Ojima, B. Z. Narymbetov, H. Fujiwara, H. Kobayashi, A. Kobayashi, K. Takimiya, T. Otsubo, F. Ogura, *Chem. Lett.* **1999**, 845–846.

[20] For example, a) T. Mori, A. Kobayashi, Y. Sasaki, H. Kobayashi, *Chem. Lett.* **1982**, 1923–1926; b) H. Kobayashi, R. Kato, A. Kobayashi, *Synth. Met.* **1997**, *19*, 623–628; c) A. Kobayashi, H. Kim, Y. Sasaki, H. Kobayashi, *Solid State Commun.* **1987**, *62*, 57–64.

[21] For example, a) K. Oshima, T. Mori, H. Inokuchi, H. Urayama, H. Yamochi, G. Saito, *Phys. Rev. B* **1988**, *38*, 938–941; b) W. Kang, G. Montambaux, J. R. Cooper, D. Jérome, P. Batail, C. Lenoir, *Phys. Rev. Lett.* **1989**, *62*, 2559–2562; c) K. Kajita, Y. Nishio, T. Takahashi, R. Kato, H. Kobayashi, W. Sasaki, A. Kobayashi, Y. Iye, *Solid State Commun.* **1989**, *70*, 1189–1193.

[22] R. P. Shibaeva, V. F. Kaminskii, *Sov. Phys. Crystallogr. Engl. Transl.* **1978**, *23*, 669–672.

 © 2005 Wiley-VCH Verlag GmbH & Co. KGaA, Weinheim

[23] a) I. F. Shchegolev, E. B. Yagubskii in *Extended Linear Chain Compounds* (Ed.: J. S. Miller), Plenum Press, New York, **1982**, vol. 2, pp. 385–434; b) R. P. Shibaeva in *Extended Linear Chain Compounds* (Ed.: J. S. Miller), Plenum Press, New York, **1982**, vol. 2, pp. 435–467.
[24] R. P. Shibaeva, V. F. Kaminskii, A. I. Kotov, E. B. Yagubskii, M. L. Khidekel, *Kristallografiya* **1979**, *24*, 271–275.
[25] a) N. Toyota, T. Sasaki, Y. Watanabe, *Physica C* **1991**, *178*, 339–344; b) A. Kawamoto, K. Miyagawa, Y. Nakazawa, K. Kanoda, *Phys. Rev. Lett.* **1995**, *74*, 3455–3458.
[26] The width of the donor band of (TXF)(TCNQ) (X = S, Se, and Te) has been reported to be 0.85 eV (X = S), 1.52 (X = Se), and 2.49 (X = Te). E. D. Herr, M. D. Mays, R. D. McCullough, A. B. Bailey, D. O. Cowan, *J. Org. Chem.* **1996**, *61*, 7006–7011.
[27] *teXsan*, Crystal Structure Analysis Package, Molecular Structure Cooperation, **1985** and **1992**.
[28] M. J. Furisch, G. W. Trucks, H. B. Schlegel, P. M. W. Gill, B. G. Johnson, M. A. Robb, J. R. Cheeseman, T. Keith, G. A. Petersson, J. A. Montgomery, K. Raghavachari, M. A. Al-Laham, V. G. Zakrzewski, J. V. Ortiz, J. B. Foresman, J. Cioslowski, B. B. Stefanov, A. Nanayakkara, M. Challacombe, C. Y. Peng, P. Y. Ayala, W. Chen, M. W. Wong, J. L. Andres, E. S. Replogle, R. Gomperts, R. L. Martin, D. J. Fox, J. S. Binkley, D. J. Defrees, J. Baker, J. J. P. Stewart, M. Head-Gordon, C. Gonzalez, J. A. Pople, *Gaussian 94*, Gaussian, Inc., Pittsburgh, PA, **1995**.
[29] T. H. Dunning Jr., P. J. Hay in *Modern Theoretical Chemistry* (Ed.: H. F. Schaefer), Plenum, New York, **1976**, vol. III, pp. 1–28.
[30] W. R. Wadt, P. J. Hay, *J. Chem. Phys.* **1985**, *82*, 284–298.

Received: February 24, 2005
Published Online: July 20, 2005

 © 2005 Wiley-VCH Verlag GmbH & Co. KGaA, Weinheim

Conformational Analysis of Chiral Ferrocene–Peptides

Katja Heinze,*[a] and Manuela Beckmann[a]

Dedicated to Professor Gottfried Huttner on the occasion of his 68th birthday

Keywords: Conformational analysis / Hydrogen bonds / Metallocenes / Modelling / Peptides

Ferrocene-containing dipeptides Ac-Fca-AA-OMe (AA = L-Val, L-Ile) with the artificial amino acid 1′-aminoferrocene-1-carboxylic acid (Fca) and chiral α-amino acid building blocks display hydrogen-bonded structures that result in organised helical ferrocene units in solution, as evidenced by spectroscopic and theoretical investigations.
(© Wiley-VCH Verlag GmbH & Co. KGaA, 69451 Weinheim, Germany, 2005)

Introduction

Short peptides usually exist as an ensemble of rapidly interconverting conformers in solution. However, intramolecular forces (hydrogen bonds, salt bridges, π-interactions) may stabilise a few preferred conformations even in small molecules.[1] In recent years, bioorganometallic chemistry has developed as a rapidly growing field, and this holds especially true for ferrocene as the organometallic ingredient.[2] The favourable electrochemical properties of ferrocenes have been exploited for use as redox probes in ferrocene-containing biomolecules. The almost unhindered rotational freedom of the ferrocene cyclopentadienyl rings might give rise to new structural and dynamic aspects in 1,1′-disubstituted ferrocene bioconjugates.[3]

We recently investigated the solid-state and solution structure of the *N*-protected active ester of 1′-aminoferrocene-1-carboxylic acid (Fca), benzotriazol-1-yl 1′-(acetylamino)ferrocene-1-carboxylate (Ac-Fca-OBt; Ac = acetyl, Bt = benzotriazol-1-yl) and found an intramolecular hydrogen bond both in the solid state and in solution with an activation barrier for the interconversion between enantiomeric conformations of 43 kJ mol^{-1}.[3] Kraatz et al. have reported the Boc-protected analogue and proposed a similar solution structure.[4]

Recently, Rapić and Metzler-Nolte reported the solid-state structure of the tetrapeptide Boc-Ala-Fca-Ala-Ala-OMe, which possesses two intramolecular hydrogen bonds that result in a (*P*)-helical arrangement of the Cp rings.[5] Similar observations on disubstituted ferrocene–peptide conjugates of ferrocenedicarboxylic acid have been reported by Hirao,[6,7] Kraatz[8] and Metzler-Nolte,[9] while the monosubstituted ferrocene–peptide conjugates of ferrocenecarboxylic acid frequently employed for labelling purposes do not exhibit a preferred helical arrangement at the ferrocene moiety.[6,7,9]

Simple chiral dipeptides of Fca, such as Ac-Fca-AA-OMe (AA = α-amino acid), possess just one chiral carbon atom in the vicinity of the ferrocene unit but should be able to display an intramolecular hydrogen bond which could result in a preferred conformation of the dipeptides in solution. Here we describe our results of a conformational analysis of Ac-Fca-AA-OMe (AA = L-Val, L-Ile) dipeptides in solution using spectroscopic and theoretical methods.

Results and Discussion

The dipeptides **1** and **2** were synthesised starting from the activated ester Ac-Fca-OBt[3] and H-Val-OMe·HCl and H-Ile-OMe·HCl, respectively (Scheme 1). The conjugates were fully characterised by mass spectrometry, showing the expected [M$^+$] peaks at m/z = 400 and 414, respectively, elemental analyses, IR spectroscopy (see Exp. Sect.) and cyclic voltammetry (oxidation waves at 535 and 565 mV vs. SCE, respectively).

In order to investigate the possible conformations of **1** and **2** in CH_2Cl_2 solution we performed NMR, IR and CD spectroscopic experiments with **1** and **2** in solution together with a theoretical analysis. The following discussion will at first focus on the conformations of **1** and subsequently a generalised conclusion will be attempted.

The ^{1}H NMR spectra of analytically pure samples of **1** in CD_2Cl_2 (Figure 1, Table 1) show two distinct species groups in the amide proton region and for the methyl group CH_3(A) in an approximate ratio of 10:1, which do not interconvert on the NMR timescale at 303 K {major con-

[a] Anorganisch-Chemisches Institut der Universität Heidelberg, Im Neuenheimer Feld 270, 69120 Heidelberg, Germany
Fax: +49-6221-545-707
E-mail: katja.heinze@urz.uni-heidelberg.de
Supporting information for this article is available on the WWW under http://www.eurjic.org or from the author.

 © 2005 Wiley-VCH Verlag GmbH & Co. KGaA, Weinheim DOI: 10.1002/ejic.200500268

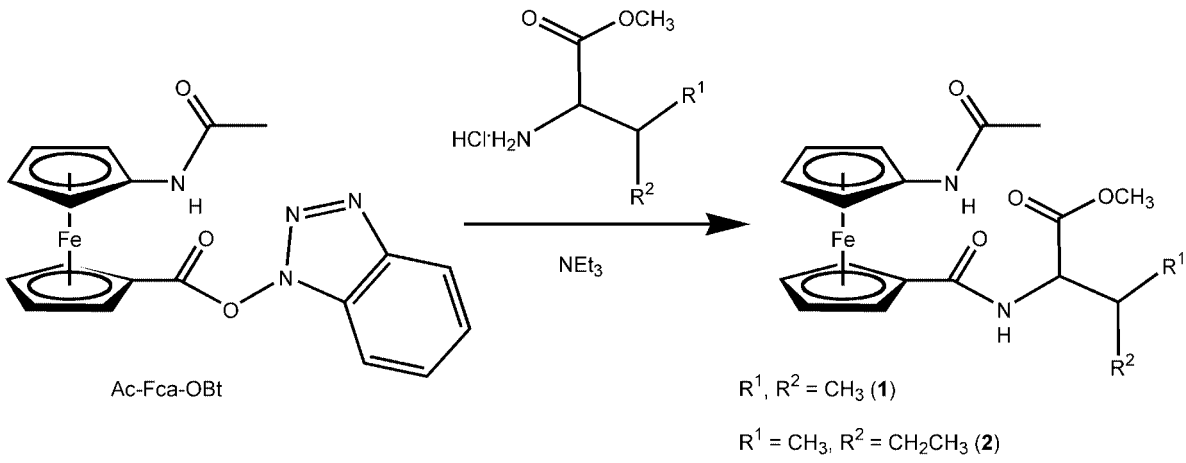

Scheme 1.

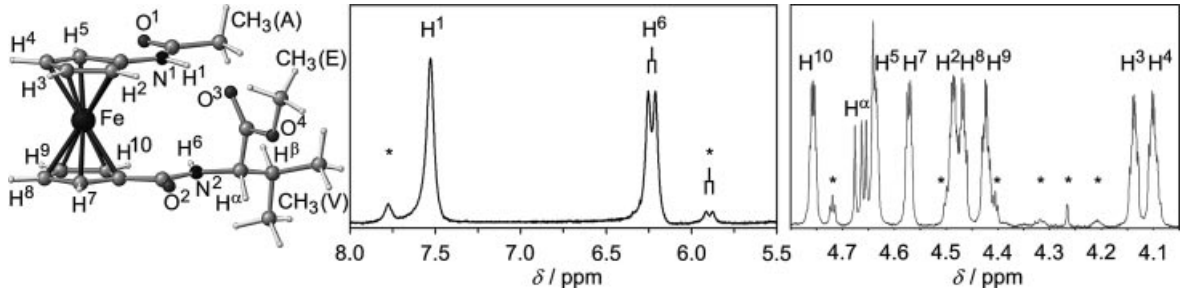

Figure 1. Left: atom numbering of **1**. ^{1}H NMR spectra of **1** in CD_2Cl_2 (10 mM); centre: amide region; right: Cp-H region (peaks labelled with an asterisk belong to minor conformations).

Table 1. ^{1}H NMR spectroscopic data of **1** and **2** (atom numbering according to Figure 1).

	1 (major)	**1** (minor)	**2** (major)	**2** (minor)
H^1	7.57 (m)	7.78 (s)	7.59 (m)	7.80 (s)
H^2/H^5	4.42 (m)/4.57 (m)		4.47 (m)/4.56 (m)	
H^3/H^4	4.04 (m)/4.07 (m)		4.03 (m)/4.07 (m)	
H^6	6.30 (d, 8.2 Hz)	5.84 (d, 8.0 Hz)	6.33 (d, 8.5 Hz)	5.7 (br)
H^7/H^{10}	4.51 (m)/4.69 (m)		4.50 (m)/4.69 (m)	
H^8/H^9	4.36 (m)/4.40 (m)		4.36 (m)/4.40 (m)	
H^α	4.59 (dvd, 8.8 Hz, 5.3 Hz)		4.63 (dvd, 8.5 Hz, 5.3 Hz)	
H^β	2.25 (dvqvq, 5.2 Hz, 7.0 Hz, 7.0 Hz)		1.97 (m)	
CH_3(A)	1.99 (s)	2.02 (s)	1.99 (s)	[a]
CH_3(E)	3.78 (s)		3.77 (s)	
CH_3(V)	0.97 (d, 7.2 Hz)		0.95 (pt, 7.4 Hz)	
CH_3(V)	0.99 (d, 7.2 Hz)		0.96 (d, 6.8 Hz)	
CH_2	–	–	1.26 (m), 1.50 (m)	

[a] Not observed due to overlap with H^β signal.

formers: $\delta(H^1)$ = 7.57 ppm, $\delta(H^6)$ = 6.30 ppm, $\delta[CH_3(A)]$ = 1.99 ppm; minor conformers: $\delta(H^1)$ = 7.78 ppm, $\delta(H^6)$ = 5.84 ppm, $\delta[CH_3(A)]$ = 2.02 ppm at 303 K}.

The cyclopentadienyl proton signals of the major conformers were assigned by 2D NMR experiments and a literature comparison[3,5,10] (Figure 1, Table 1). The expected NOE cross-peaks (intra-Cp, amide-Cp and within the L-valine unit) are observed in the NOESY spectra, while no cross-peaks are observed between the substituents. For the major species in CD_2Cl_2 solution all Cp protons are magnetically non-equivalent as the chiral carbon centre C^α of the L-amino acid part generates diastereotopic sides of the ferrocene both in the "lower" Cp ring (H^7/H^{10}: δ = 4.51/4.69 ppm; H^8/H^9: δ = 4.36/4.40 ppm) *and* in the "upper" Cp ring (H^2/H^5: δ = 4.42/4.57 ppm; H^3/H^4: δ = 4.04/4.07 ppm) which demonstrates that the chiral information is effectively transferred from the α-amino ester to the "lower" Cp *and* to the "upper" Cp ring. An analogous stereodiscrimination is found for the cyclopentadienyl carbon atoms (C^7/C^{10}: δ = 69.1/69.3 ppm; C^8/C^9: δ = 71.0/71.3 ppm; C^2/C^5: δ = 63.7/64.3 ppm; C^3/C^4: δ = 65.8/65.9 ppm).

Variable-temperature ^{1}H NMR spectra between 193 and 303 K allowed us to investigate the hydrogen-bonding situation of both conformer groups of **1** by monitoring the tem-

 © 2005 Wiley-VCH Verlag GmbH & Co. KGaA, Weinheim

perature dependence of all amide proton signals. For the major conformers $\Delta\delta(H^1)$ = –6.8 ppb K^{-1} and $\Delta\delta(H^6)$ = –3.3 ppb K^{-1} (determined by a regression analysis between 243 and 303 K), thus showing that only H^1 is involved in a dynamic hydrogen bond, whereas for the minor conformers $\Delta\delta(H^1)$ = –5.9 ppb K^{-1} and $\Delta\delta(H^6)$ = –11.1 ppb K^{-1}, which suggests that *both* H^1 and H^6 are dynamically hydrogen-bonded [cf. non-hydrogen bonded Fc-NH-C(=O)-CH_3: $\Delta\delta(H^1)$ = –2.9 ppb K^{-1} and hydrogen-bonded Fc-NH-C(=O)-Fc-NH-C(=O)CH_3: $\Delta\delta(H^1)$ = –6.6 ppb K^{-1} and $\Delta\delta(H^6)$ = –11.0 ppb K^{-1}[3]].

The solution IR spectra of **1** (Figure 2) display signals due to hydrogen-bonded NH groups (3357 and 3325 cm^{-1}) together with free NH groups (3433 cm^{-1}), as well as absorption bands corresponding to hydrogen-bonded ester carbonyl groups (1728 cm^{-1}) and free ester groups (1739 cm^{-1}) in addition to several amide I (1664–1653 cm^{-1}) and amide II bands (1546–1512 cm^{-1}).

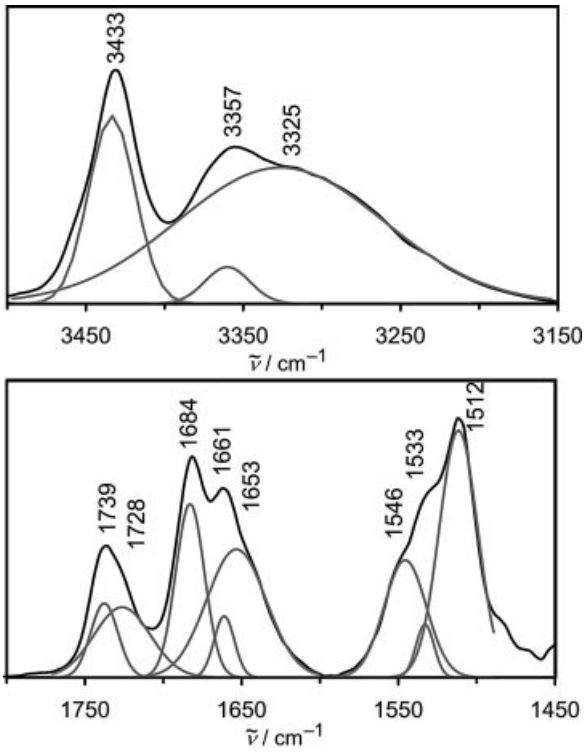

Figure 2. IR spectra of **1** in CH_2Cl_2 (left: amide A region; right: amide I+II region).

In the UV/Vis spectra the typical ferrocene absorption is observed at around 440 nm (see Exp. Sect.). The CD spectra of **1** and **2** in CH_2Cl_2 (Figure 3) display a positive Cotton effect at the ferrocene absorption (M_θ = 7440 and 6490 mdeg M^{-1} cm^{-1} at 450 nm for **1** and **2**, respectively) which is usually interpreted as a (*P*)-helical conformation of the ferrocene.[5,6,9] The CD signal intensity is diminished (M_θ = 3570 and 3210 mdeg M^{-1} cm^{-1} for **1** and **2**, respectively) by the addition of 20% (v/v) methanol, which might compete for hydrogen-bonding sites and result in a reduction of the helicity at the ferrocene. The negative CD at 500 nm might arise from minor conformations of **1** and **2** with (*M*)-helical ferrocene units or freely rotating Cp rings.[11]

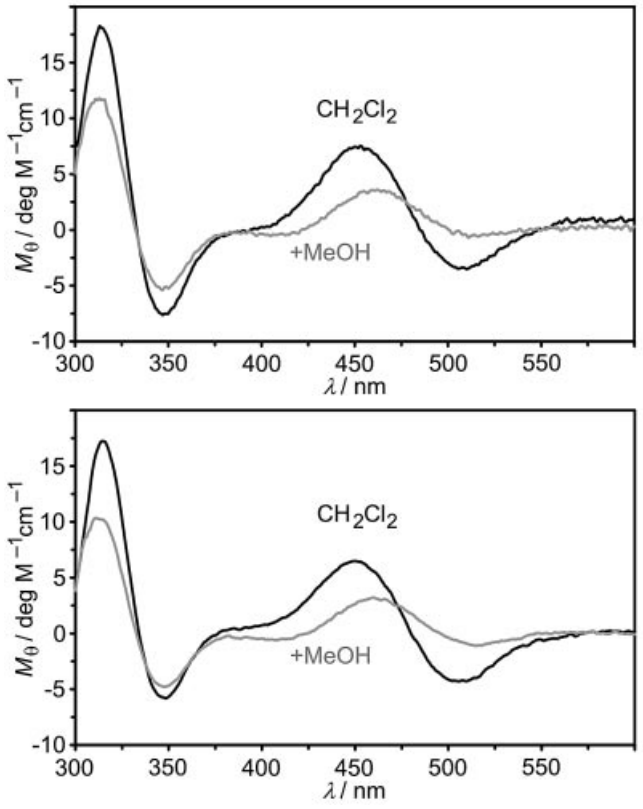

Figure 3. CD spectra of **1** (left) and **2** (right) (1 mM) in CH_2Cl_2 (dark line) and CH_2Cl_2/MeOH 20% (v/v) (light line).

Thus, ferrocene conjugates **1** and **2** appear to have similar helical conformations in CH_2Cl_2 solution that are destroyed in coordinating solvents. Additionally, NMR spectra in CD_2Cl_2/D_2O and CD_2Cl_2/DMSO/D_2O solvent mixtures reveal a different pattern in the Cp-H region between δ = 3.9 and 4.8 ppm, thus indicating different conformations in these solvent mixtures. In addition to the different pattern in the Cp-H region, the amide protons are exchanged against deuterium, with amide proton H^6 having a larger half-life than H^1, probably due the higher steric shielding of H^6 by the ester and alkyl groups of the α-amino acid part than for H^1.

A modelling study was performed in order to obtain more insight into the possible conformational space of the ferrocene–dipeptides. As force fields used in molecular mechanics calculations and dynamics simulations are currently not available for ferrocene derivatives, we employed the DFT method. DFT calculations (B3LYP, LanL2DZ) on **1** in the gas phase with varying starting geometries resulted in an ensemble of ten stable hydrogen-bonded conformations (Figure 4, Table 2), which fall into four categories (**RL**, **LR**, **LL** and **RR**) that differ in the relative orientation of the NH vectors (R and L denote a clockwise and anticlockwise rotation, respectively, of the N^1H^1 and N^2H^6 vectors when looking along the [centroid C^1–C^5]–[centroid C^6–C^{10}] axis). Different types of intramolecular hydrogen bonds (**a**:

 © 2005 Wiley-VCH Verlag GmbH & Co. KGaA, Weinheim

$H^1\cdots O^3$; **b**: $H^1\cdots O^2$; **c**: $H^6\cdots O^1$) are observed within these groups. No minimum structure could be found for conformers **RL-c** and **LR-c** with the NH vectors directed towards each other and with a hydrogen bond between H^6 and O^1 as the geometry optimisations always converge to structures **RL-b** and **LR-b**, respectively. In fact, **RL-c** rather corresponds to the transition state of the isomerisation **RL-a** → **LL-c** (Table 2). Likewise, the non-hydrogen-bonded geometries **RL-d**, **LL-d** and **RR-d** represent transition states with one imaginary frequency for the Cp ring rotation rather than minimum structures, while **LR-d** again represents a local minimum (Figure 5, Table 2).

The relative energies of the different conformations fall into a narrow region of 0–30 kJ mol^{-1} as expected for a small peptide (Table 2). In spite of these small energy differences, an attempt to explain the experimental data on the basis of the calculated geometries and energies was undertaken. From the conformer population data it is reasonable to include only conformers **RL-a**, **RL-b**, **LR-b**, **LL-a**, **LL-b** and **LL-c** in the following interpretation of the experimental data (Figure 4, highlighted structures; see also Table 2 and Scheme 2).

The observation of hydrogen-bonded ester carbonyl groups (type **a** hydrogen bond: **RL-a** and **LL-a**) together

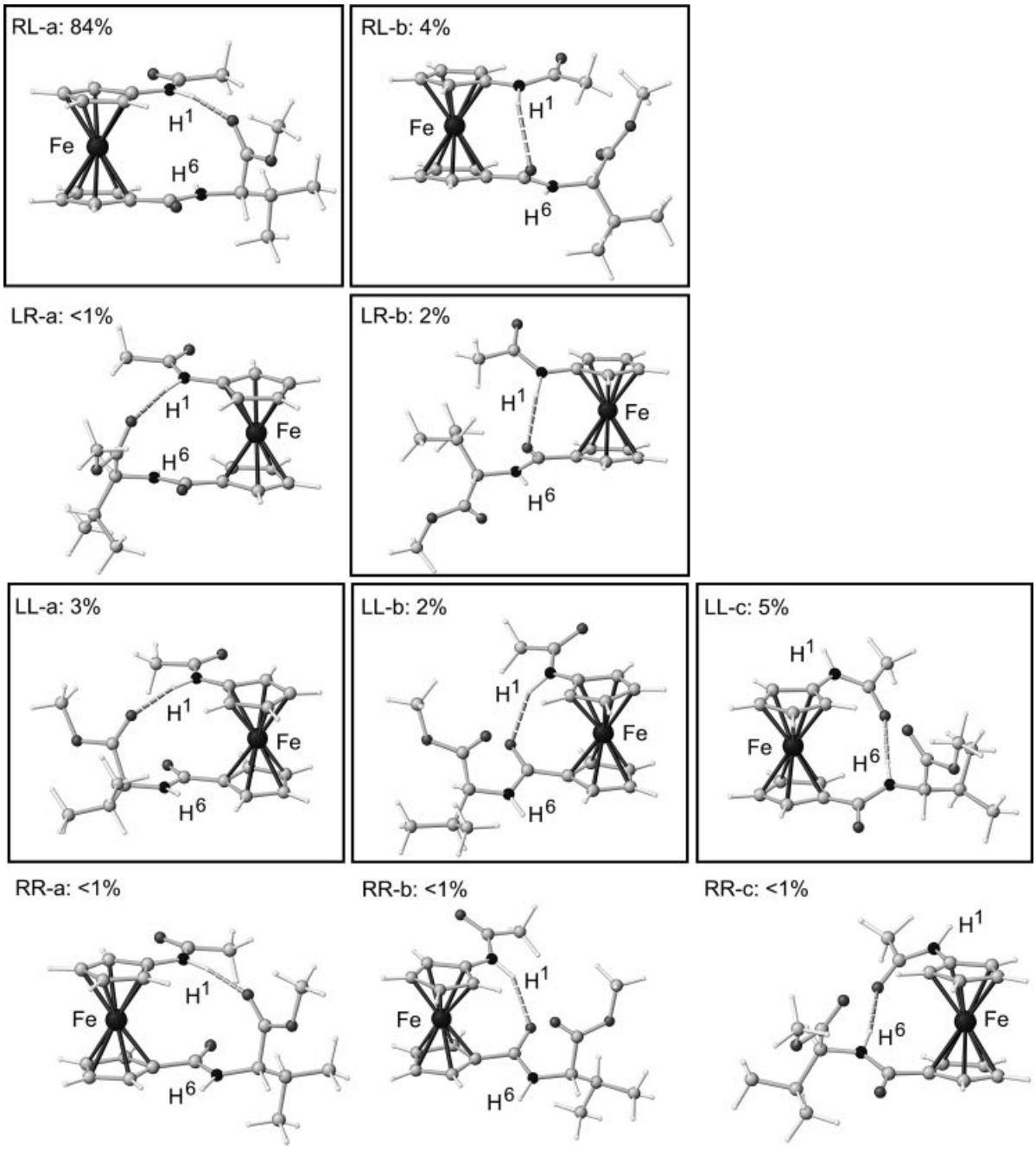

Figure 4. Ensemble of DFT-calculated hydrogen-bonded minimum structures of **1** with the major conformations highlighted.

 © 2005 Wiley-VCH Verlag GmbH & Co. KGaA, Weinheim

Table 2. Energetic and geometric parameters calculated for the conformers of **1** by DFT methods (B3LYP, LanL2DZ).

Conformer	Relative energy [kJ mol^{-1}]	Conformer population [%][a]	α [°][b]	Hydrogen bond [Å]
RL-a	0	83.9	+46.4	$H^1\cdots O^3$ = 1.92
RL-b	7.5	4.1	–7.2	$H^1\cdots O^2$ = 2.44
LR-a	19.6	<1	–38.9	$H^1\cdots O^3$ = 1.92
LR-b	9.1	2.1	+4.7	$H^1\cdots O^2$ = 2.04
LL-a	8.3	2.9	–32.0	$H^1\cdots O^3$ = 1.94
LL-b	9.3	2.0	–48.4	$H^1\cdots O^2$ = 2.01
LL-c	7.0	5.0	+84.2	$H^6\cdots O^1$ = 1.91
RR-a	20.9	<1	+27.2	$H^1\cdots O^3$ = 1.95
RR-b	26.7	<1	+48.3	$H^1\cdots O^2$ = 2.02
RR-c	21.9	<1	–82.1	$H^6\cdots O^1$ = 1.83
RL-d	24.9[c]	–	–177.8	–
LR-d	12.1[d]	<1	+149.9	–
LL-d	21.8[e]	–	+166.4	–
RR-d	23.4[f]	–	–179.3	–
RL-a → LL-c	24.6[g]	–	+38.5	$H^6\cdots O^1$ = 2.25 ($H^1\cdots O^3$ = 3.43)
LL-a → LL-b	16.2[h] (7.9[i])	–	–42.1	($H^1\cdots O^3$ = 3.04) $H^1\cdots O^2$ = 2.39

[a] Conformer populations were calculated by using a Boltzmann distribution at 298 K. [b] The torsion angle, α, is defined as C^1–[centroid C^1–C^5]–[centroid C^6–C^{10}]–C^6. [c] This geometry corresponds to a transition state with N_{imag} = 1 (16.7i cm^{-1}; Cp ring rotation). [d] This geometry corresponds to a minimum (N_{imag} = 0). [e] This geometry corresponds to a transition state with N_{imag} = 1 (5.5i cm^{-1}; Cp ring rotation). [f] This geometry corresponds to a transition state with N_{imag} = 1 (11.0i cm^{-1}; Cp ring rotation). [g] This geometry corresponds to a transition state with N_{imag} = 1 (45.7i cm^{-1}; combined Cp ring rotation, *N*-acetyl rotation and hydrogen-bond breaking). [h] This geometry corresponds to a transition state with N_{imag} = 1 (32.6i cm^{-1}; combined Cp ring rotation and hydrogen-bond breaking). [i] Energy relative to **LL-a**.

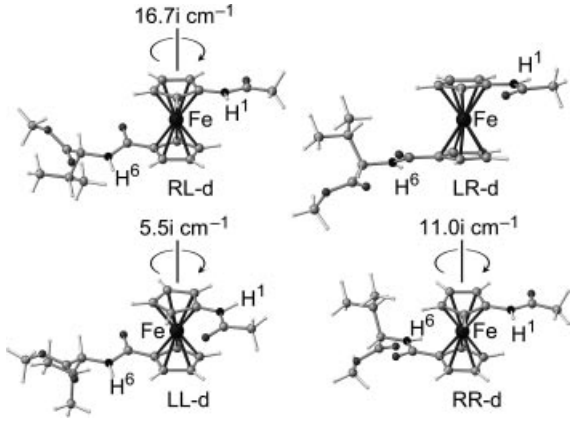

Figure 5. Non-hydrogen bonded structures of **1**.

with free ester carbonyl groups, as well as hydrogen-bonded amide carbonyl groups (type **b** and **c** hydrogen bonds: **RL-b**, **LR-b**, **LL-b**, **LL-c**) together with free amide carbonyl groups, in the calculated conformers is in agreement with the experimental IR spectroscopic data (Figures 2 and 4).

On the basis of their relative abundance, the two signal sets with relative intensity of 91% and 9% observed in the ^{1}H NMR spectra are assigned to groups **RL** (calculated conformer population 88%) and **LL** (calculated conformer population 10%), respectively, while populations of group **LR** and group **RR** fall below the detection limit of NMR spectroscopy.

Interconversion within the NMR-observable conformer groups **RL** and **LL** is fast on the NMR timescale as only time-averaged NMR signals are observed for each group (Scheme 2). Thus, the activation barrier for the involved processes hydrogen-bond breaking and Cp-ring rotation should be rather small. The activation barriers for these elementary steps can be estimated to be 8 kJ mol^{-1} for hydrogen-bond breaking and 5–10 kJ mol^{-1} for Cp-ring rotation[12] (13–18 kJ mol^{-1} for both steps; cf. energies of non-hydrogen-bonded species **d** in Table 2). In fact, a transition state for the conformational rearrangement **LL-a** → **LL-b** could be located only 7.9 kJ mol^{-1} above **LL-a**.

However, for the transformation **RL** → **LL**, in addition to hydrogen-bond breaking and Cp-ring rotation, the *N*-acetyl group has to flip relative to the Cp plane, which results in an additional activation barrier of 17–25 kJ mol^{-1} [rotational barrier estimated for the model compound (acetylamino)ferrocene Ac–NH–Fc; Figure 6[13]]. Thus, in total the energy required for this stepwise pathway **RL-a** → **RL-d** → *N*-acetyl rotation → **LL-d** → **LL-a**/**LL-b**/**LL-c** can be estimated to lie in the range 30–43 kJ mol^{-1}. For **RL-a** → **LL-c** a direct low-energy hydrogen-bond-assisted pathway combining *N*-acetyl rotation and Cp-ring rotation could be found with a transition state 24.6 kJ mol^{-1} higher in energy than **RL-a** (Figure 7, Scheme 2). Even the energy for this direct pathway is substantially higher than that estimated for the easy transformation between **a**, **b** and **c** conformers. Thus, the DFT calculations provide a qualitative rationale for the observation of two slowly interconverting species groups (Scheme 2).

The assignment of the major conformers to group **RL** and the minor conformers to group **LL** was further supported by the variable-temperature ^{1}H NMR spectra as the major conformers only possess $H^1\cdots$O hydrogen bonds (**RL-a**, **RL-b**) while the minor conformers have $H^1\cdots$O *and* $H^6\cdots$O hydrogen bonds (**LL-a**, **LL-b** and **LL-c**, Figure 4, Scheme 2) in agreement with the observed large temperature dependence of the signal for proton H^6 in the minor species group.

 © 2005 Wiley-VCH Verlag GmbH & Co. KGaA, Weinheim

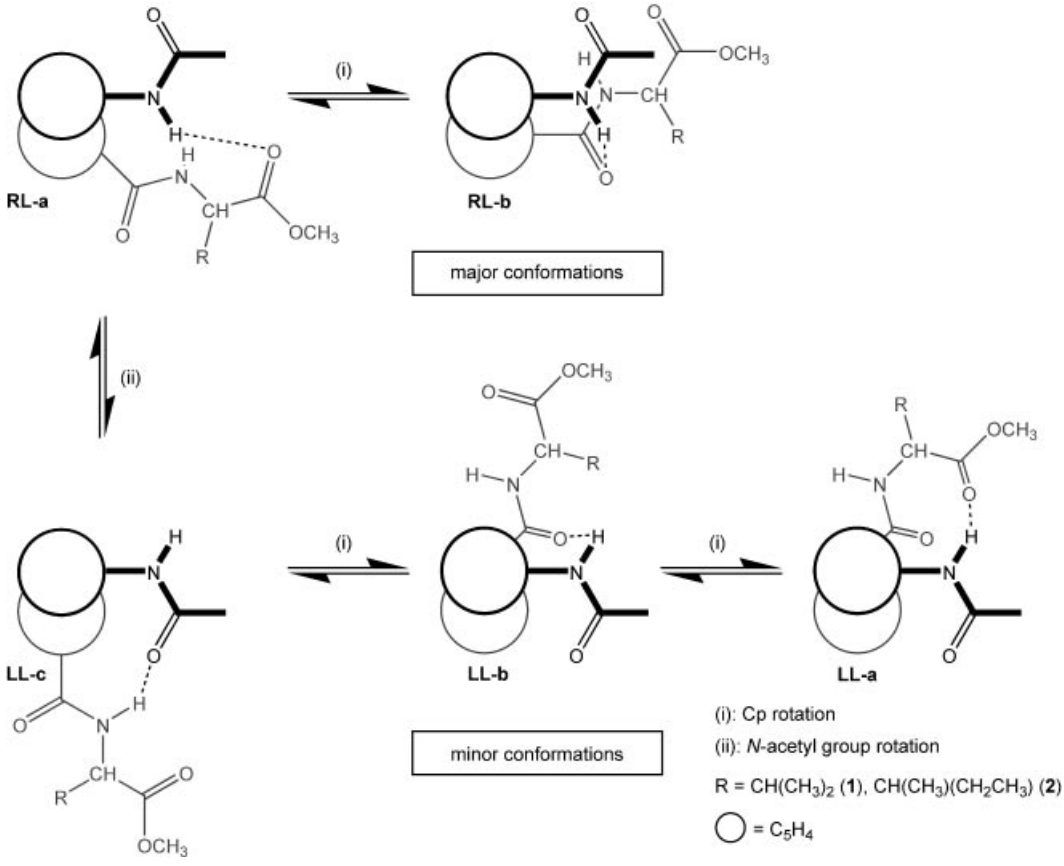

Scheme 2.

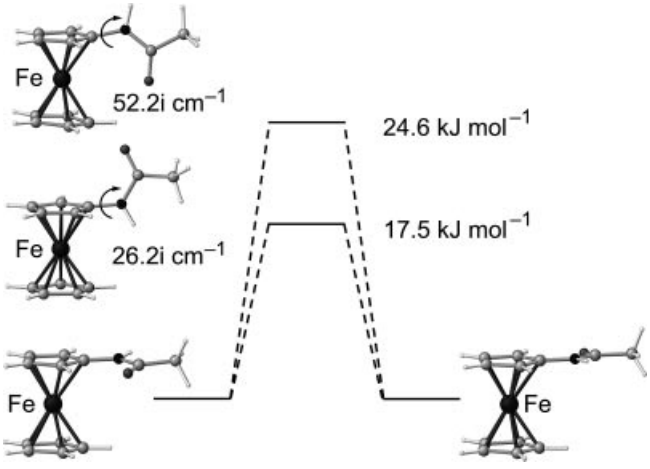

Figure 6. Energy profile for the *N*-acetyl group rotation in the model complex Ac-NH-Fc.

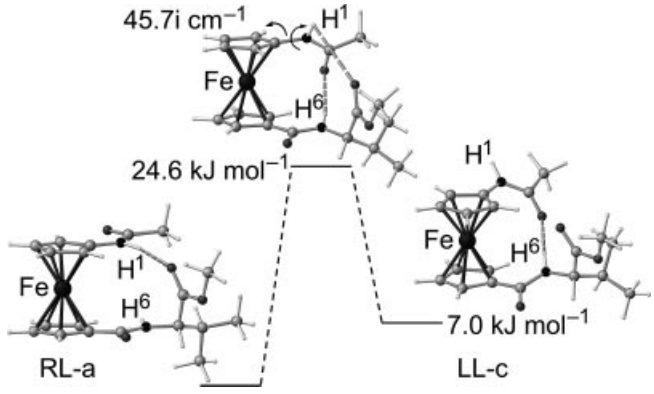

Figure 7. Energy profile for the hydrogen-bond-assisted direct conversion **RL-a** → **LL-c**.

Due to the restrained relative orientation of the ferrocene chromophore and the chiral centre due to the hydrogen bonding the ferrocene itself gains helical chirality, which results in fairly large Cotton effects compared to those of monosubstituted ferrocenes with a chiral centre in the substituent.[11] The dominant (*P*)-helical conformation of the ferrocene unit suggested by the CD spectra (Figure 3) can be explained by conformers **RL-a**, **LR-b** and **LL-c** with positive torsion angles *a*, which together amount to 91% of the species according to the calculations (Table 2). Thus, the DFT modelling of the conformational space of **1**, albeit not in a strictly quantitative sense, can explain all the experimental findings (IR, NMR and CD data).

For the isoleucine derivative **2** the experimental data are almost identical to those of **1** (see Exp. Sect. and Supporting Information), thereby suggesting a similar conformation of **2** in solution. Figure 8 depicts the calculated minimum structure of **2** (analogous to **RL-a** with a population of 62%; see Supporting Information), which has a Cp torsion angle, *a*, of +47.3°. This observation points to the fact

 © 2005 Wiley-VCH Verlag GmbH & Co. KGaA, Weinheim

that a second chiral carbon centre (C^{β}) in the side-chain of the isoleucine moiety has only a marginal influence on the ferrocene conformation and that the preferred ferrocene helicity in these dipeptides is determined by the configuration of the C^{α} atom of the α-amino acid.

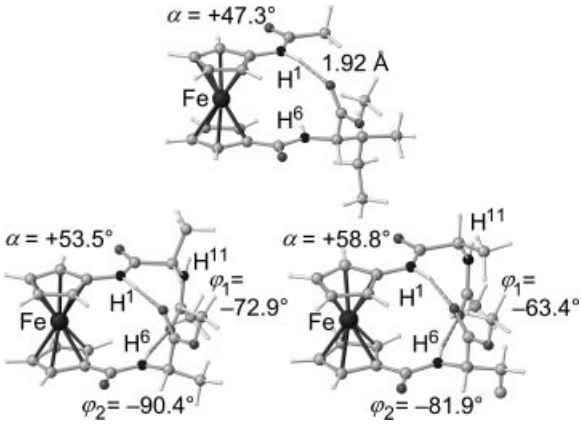

Figure 8. DFT calculated minimum structure of **2** (top), Ac-Ala-Fca-Ala-OMe (bottom left) and Ac-D-Ala-Fca-Ala-OMe (bottom right) [φ_1 and φ_2 are the C(=O)–C^{α}–N–C(=O) torsion angles].

To further corroborate the above interpretations the tripeptides Ac-Ala-Fca-Ala-OMe and Ac-D-Ala-Fca-Ala-OMe, which possess two intramolecular hydrogen bonds, were modelled (Figure 8) and the ferrocene helicity and amide backbone torsion angles φ [C(=O)-N–C^{α}-C(=O)] compared to those of the structurally characterised tetrapeptide Boc-Ala-Fca-Ala-Ala-OMe.[5] For the tetrapeptide, values of $\alpha = +60.7°$, $\varphi_1 = -81.3°$ and $\varphi_2 = -90.1°$ have been determined in the solid state, and these compare well with the calculated values for the tripeptide Ac-Ala-Fca-Ala-OMe ($\alpha = +53.5°$, $\varphi_1 = -72.9°$ and $\varphi_2 = -90.4°$), further supporting the above interpretations. This finding suggests that the ferrocene helicity is determined by the configuration of the first C-terminal amino acid rather than the configuration of the N-terminal amino acid. In fact, replacing the N-terminal L-Ala by D-Ala results in a very similar conformation (Ac-D-Ala-Fca-Ala-OMe: $\alpha = +58.8°$, $\varphi_1 = -63.4°$ and $\varphi_2 = -81.9°$; Figure 8).

Conclusions

One chiral carbon atom within the C-terminal substituent at the organometallic amino acid Fca is sufficient to induce helical chirality at the ferrocene provided that an efficient hydrogen-bonding pathway exists between the two cyclopentadienyl rings. The conformer **RL-a**, which accounts for the major conformation of **1** and **2** in solution, possesses a (*P*)-helical ferrocene unit. The helicity is induced by a single intramolecular amide-to-ester hydrogen bond as the chirality-transfer pathway. The organised chiral secondary structures of small Fca-containing peptides open up an opportunity to design selective receptors[14–17] and homodisperse oligomers[13a,18] with well-defined secondary structures containing neutral or cationic ferrocene units in the backbone. Further work in these directions is currently in progress.

Experimental Section

General: Unless noted otherwise, all manipulations were carried out under argon by means of standard Schlenk techniques. All solvents were dried by standard methods and distilled under argon prior to use. All other reagents were used as received from commercial sources. NMR: Bruker Avance DPX 200 at 200.15 MHz and Varian Unity Plus 400 at 399.89 MHz (^{1}H); chemical shifts (δ) in ppm with respect to residual solvent peaks as internal standard: CD_2Cl_2 (^{1}H: δ = 5.32 ppm). IR spectra were recorded with a BioRad Excalibur FTS 3000 spectrometer using CaF_2 cells in CH_2Cl_2. Cyclic voltammetry was performed using an EG&G model 273 potentiostat, a glassy carbon electrode, a platinum electrode and an SCE electrode, 10^{-3} M in 0.1 M nBu$_4$NBF$_4$/CH_2Cl_2; potentials are given relative to that of SCE; $E_{1/2}$ of the Fc/Fc$^+$ couple under the experimental conditions is 420(10) mV vs. SCE. Circular dichroism spectra were recorded with a JASCO J-810 spectropolarimeter in 1-cm Suprasil cells thermostatted at 20 °C under argon. Mass spectra were recorded with a Finnigan MAT 8400 spectrometer with 4-nitrobenzyl alcohol as the matrix (FAB). Elemental analyses were performed by the microanalytical laboratory of the Organic Chemistry Department, University of Heidelberg. Melting points were determined with a Gallenkamp capillary melting point apparatus MFB 595 010 and are uncorrected.

Computational Methods: Density functional calculations were carried out with the Gaussian03/DFT[19] series of programs. The B3LYP formulation of density functional theory was used with the LanL2DZ basis set.[19] Geometry optimisations were performed using the Berny algorithm as implemented in Gaussian03. Convergence criteria were as follows: maximum force 0.00045; root-mean-square of forces 0.0003; maximum displacement 0.0018; root-mean-square displacements 0.0012. All points were characterised as minima ($N_{imag} = 0$) or first-order saddle points ($N_{imag} = 1$) by frequency analysis.

Synthesis of 1 and 2: A solution of the activated ester Ac-Fca-OBt in THF was treated with 1 equiv. of H-Val-OMe·HCl (for **1**) or H-Ile-OMe·HCl (for **2**) and 1 equiv. of NEt_3 and stirred at ambient temperature for 3 h. The solvent was then removed under reduced pressure and the residue was dissolved in dichloromethane. The solution was washed with water, aqueous $NaHCO_3$, saturated NaCl and 2% citric acid. The organic layer was dried with $MgSO_4$ and the solvent was removed under reduced pressure to give an orange powder. **1:** Yield: 160 mg, 0.40 mmol (82%). $C_{19}H_{24}FeN_2O_4$ (400.26): calcd. C 57.02, H 6.04, N 7.00; found C 57.20, H 6.09, N 7.18. UV/Vis (CH_2Cl_2): λ = 441 nm (270 M^{-1}cm^{-1}). ^{13}C{^{1}H} NMR (CD_2Cl_2): δ = 173.1 (C=O$_{ester}$), 169.8 (C=O$_{acetyl}$), 168.7 (C=O$_{amide}$), 94.6 (Cp-C_q), 76.5 (Cp-C_q), 71.3, 71.0 (C^8, C^9), 69.3, 69.1 (C^7, C^{10}), 65.9, 65.8 (C^3, C^4), 64.3 (C^2), 63.7 (C^5), 57.2 (C^{α}), 52.1 [CH_3(E)], 31.2 (C^{β}), 23.9 [CH_3(A)], 19.4, 18.3 [CH_3(V)] ppm. MS (FAB): *m/z* (%) = 400 (95) [M$^+$]. IR (CsI): $\tilde{\nu}$ = 3290 (NH), 3094, 2966, 2935 2874, 2857 (CH), 1745 (CO$_{ester}$), 1668, 1636 (amide I), 1560, 1539 (amide II) cm^{-1}. M.p. 66 °C. **2:** Yield: 194 mg, 0.46 mmol (78%). $C_{20}H_{26}FeN_2O_4$ (414.28): calcd. C 57.98, H 6.33, N 6.76; found C 57.96, H 6.32, N 7.40. UV/Vis (CH_2Cl_2): λ = 438 nm (300 M^{-1}cm^{-1}) ppm. ^{13}C{^{1}H} NMR (CD_2Cl_2): δ = 173.1 (C=O$_{ester}$), 169.8 (C=O$_{acetyl}$), 168.8 (C=O$_{amide}$), 94.7 (Cp-C_q), 76.5 (Cp-C_q), 71.3, 71.0 (C^8, C^9), 69.3, 69.2 (C^7, C^{10}), 65.9, 65.8 (C^3, C^4), 64.3 (C^2), 63.7 (C^5), 56.5 (C^{α}), 52.1 [CH_3(E)], 37.1 (C^{β}), 25.1 (CH_2), 23.2 [CH_3(A)], 15.3 [CH_3(V)], 11.0 (CH_2CH_3) ppm. MS (EI): *m/z* (%)

 © 2005 Wiley-VCH Verlag GmbH & Co. KGaA, Weinheim

= 414 (100) [M^+]. IR (CsI): $\tilde{\nu}$ = 3298 (NH), 3091, 2965, 2934 2878, 2856 (CH), 1746 (CO_{ester}), 1670, 1636 (amide I), 1562, 1542 (amide II) cm^{-1}. IR (CH_2Cl_2): $\tilde{\nu}$ = 3431, 3355, 3325 (sh) (NH), 1735 (CO_{ester}), 1682, 1660, 1654 (sh) (amide I), 1550 (s), 1533 (sh), 1512 (amide II) cm^{-1}. M.p. 68 °C.

Supporting Information (see footnote on the first page of this article): Coordinates of all minimum structures and transition states, a table of energetic and geometric parameters calculated for the conformers of **2** by DFT methods (B3LYP, LanL2DZ) and IR spectra of **1** and **2** in CH_2Cl_2.

Acknowledgments

This work was supported by the Deutsche Forschungsgemeinschaft, the Fonds der Chemischen Industrie and the Dr. Otto Röhm Gedächtnisstiftung. The generous support of Prof. Dr. G. Huttner is gratefully acknowledged. We thank Prof. Dr. N. Metzler-Nolte for valuable discussions and for giving us access to the CD spectropolarimeter.

[1] N. Sewald, H.-D. Jakubke, *Peptides: Chemistry and Biology*, Wiley-VCH **2002**.
[2] D. N. van Staveren, N. Metzler-Nolte, *Chem. Rev.* **2004**, *104*, 5931–5985.
[3] K. Heinze, M. Schlenker, *Eur. J. Inorg. Chem.* **2004**, 2974–2988.
[4] K. A. Mahmoud, Y.-T. Long, G. Schatte, H.-B. Kraatz, *Eur. J. Inorg. Chem.* **2005**, 173–180.
[5] L. Barišić, M. Dropucic, V. Rapić, H. Pritzkow, S. I. Kirin, N. Metzler-Nolte, *Chem. Commun.* **2004**, 2004–2005.
[6] T. Moriuchi, A. Nomoto, K. Yoshida, T. Hirao, *Organometallics* **2001**, *20*, 1008–1013.
[7] T. Moriuchi, A. Nomoto, K. Yoshida, A. Ogawa, T. Hirao, *J. Am. Chem. Soc.* **2001**, *123*, 68–75.
[8] F. E. Appoh, T. C. Sutherland, H.-B. Kraatz, *J. Organomet. Chem.* **2004**, *689*, 4669–4677.
[9] X. de Hatten, T. Weyhermüller, N. Metzler-Nolte, *J. Organomet. Chem.* **2004**, *689*, 4856–4867.
[10] H.-B. Kraatz, J. Lusztyk, G. D. Enright, *Inorg. Chem.* **1997**, *36*, 2400–2405.
[11] Amino acid conjugates of ferrocenecarboxylic acid Fc-CO-NH-CHR-COOEt show weak, positive Cotton effects at 450 nm and stronger, negative Cotton effects at 500 nm. For R = $CH_2CH(CH_3)_2$: M_θ = 50 mdeg M^{-1} cm^{-1} (450 nm) and M_θ = –100 mdeg M^{-1} cm^{-1} (500 nm): H. Falk, C. Krasa, K. Schlögl, *Monatsh. Chem.* **1969**, *100*, 1552–1563. For R = $CH_2CH_2SCH_3$: M_θ = 402 mdeg M^{-1} cm^{-1} (460 nm) and M_θ = –1610 mdeg M^{-1} cm^{-1} (500 nm): Ref.[9]
[12] The experimental rotational barrier of unsubstituted ferrocene has been determined to be 1–5 kJ mol^{-1}: a) L. N. Mulay, A. Atalla, *J. Am. Chem. Soc.* **1963**, *85*, 702–706; b) A. Haaland, J. E. Nilsson, *J. Chem. Soc., Chem. Commun.* **1968**, *2*, 88–89; c) S. Sorriso, G. Cardaci, S. M. Murgia, *J. Organomet. Chem.* **1972**, *44*, 181–184; d) A. B. Gardner, J. Howard, T. C. Waddington, R. M. Richardson, J. Tomkinson, *Chem. Phys.* **1981**, *57*, 453–460. The rotational barrier calculated for ferrocene by DFT is 6.0 kJ mol^{-1} (44.6i cm^{-1}), which is in good agreement with the experiment. The barrier calculated for Ac-NH-Fc by DFT is 7.1 kJ mol^{-1} (16.9i cm^{-1}). See Supporting Information.
[13] The barrier for the N-ring rotation in acetanilide has been recently calculated as 18 kJ mol^{-1}, which is in very good agreement with the low-energy barrier calculated for Ac-NH-Fc: a) R. J. Doerksen, B. Chen, D. Liu, G. N. Twe, W. F. DeGrado, M. L. Klein, *Chem. Eur. J.* **2004**, *10*, 5008–5016; b) W. Caminati, A. Maris, A. Millemaggi, *New J. Chem.* **2000**, *24*, 821–824. The amide-plane rotation barrier calculated for Fc-CO-NH_2 is higher (estimated 35–40 kJ mol^{-1}) due to the onset of double-bond localisation: L. Lin, A. Berces, H.-B. Kraatz, *J. Organomet. Chem.* **1998**, *556*, 11–20.
[14] K. Heinze, M. Schlenker, *Eur. J. Inorg. Chem.* **2005**, 66–71.
[15] P. D. Beer, *Acc. Chem. Res.* **1998**, *31*, 71–80.
[16] P. D. Beer, P. A. Gale, *Angew. Chem.* **2001**, *113*, 502–532; *Angew. Chem. Int. Ed.* **2001**, *40*, 486–516.
[17] T. Schrader, A. D. Hamilton, *Functional Synthetic Receptors*, Wiley-VCH **2005**.
[18] a) J. S. Nowick, M. Pairish, I. Q. Lee, D. L. Holmes, J. W. Ziller, *J. Am. Chem. Soc.* **1997**, *119*, 5413–5424; b) H. Q. Zeng, R. S. Miller, R. A. Flowers, B. Gong, *J. Am. Chem. Soc.* **2000**, *122*, 2635–2644; c) J. T. Ernst, J. Becceril, H. S. Park, H. Yin, A. D. Hamilton, *Angew. Chem.* **2003**, *115*, 553–557; *Angew. Chem. Int. Ed.* **2003**, *42*, 535–539; d) D. Liu, S. Choi, B. Chen, R. J. Doerksen, D. J. Clements, J. D. Winkler, M. L. Klein, W. F. DeGrado, *Angew. Chem.* **2004**, *116*, 1178–1182; *Angew. Chem. Int. Ed.* **2004**, *43*, 1158–1162.
[19] M. J. Frisch, G. W. Trucks, H. B. Schlegel, G. E. Scuseria, M. A. Robb, J. R. Cheeseman, J. A. Montgomery, Jr., T. Vreven, K. N. Kudin, J. C. Burant, J. M. Millam, S. S. Iyengar, J. Tomasi, V. Barone, B. Mennucci, M. Cossi, G. Scalmani, N. Rega, G. A. Petersson, H. Nakatsuji, M. Hada, M. Ehara, K. Toyota, R. Fukuda, J. Hasegawa, M. Ishida, T. Nakajima, Y. Honda, O. Kitao, H. Nakai, M. Klene, X. Li, J. E. Knox, H. P. Hratchian, J. B. Cross, C. Adamo, J. Jaramillo, R. Gomperts, R. E. Stratmann, O. Yazyev, A. J. Austin, R. Cammi, C. Pomelli, J. W. Ochterski, P. Y. Ayala, K. Morokuma, G. A. Voth, P. Salvador, J. J. Dannenberg, V. G. Zakrzewski, S. Dapprich, A. D. Daniels, M. C. Strain, O. Farkas, D. K. Malick, A. D. Rabuck, K. Raghavachari, J. B. Foresman, J. V. Ortiz, Q. Cui, A. G. Baboul, S. Clifford, J. Cioslowski, B. B. Stefanov, G. Liu, A. Liashenko, P. Piskorz, I. Komaromi, R. L. Martin, D. J. Fox, T. Keith, M. A. Al-Laham, C. Y. Peng, A. Nanayakkara, M. Challacombe, P. M. W. Gill, B. Johnson, W. Chen, M. W. Wong, C. Gonzalez, J. A. Pople, *Gaussian 03*, revision B.03, Gaussian, Inc., Pittsburgh, PA, USA, **2003**.

Received: March 29, 2005
Published Online: August 1, 2005

 © 2005 Wiley-VCH Verlag GmbH & Co. KGaA, Weinheim

Novel Structure Evolution of Lanthanide–SIP Coordination Polymers (NaH_2SIP = 5-Sulfoisophthalic Acid Monosodium Salt) from a 1D Chain to a 3D Network as a Consequence of the Lanthanide Contraction Effect

Qing-Yan Liu[a,b] and Li Xu*[a]

Keywords: Crystal structures / Hydrothermal synthesis / Lanthanides / Lanthanide contraction

The new series of lanthanide–SIP coordination polymers $[\{Ln(SIP)(H_2O)_5\}(H_2O)_3]_n$ (Ln = Lu (**1**), Yb (**2**), Tm (**3**), and Er (**4**)], $[\{Ln(SIP)(H_2O)_4\}]_n$ (Ln = Ho (**5**), Dy (**6**), Tb (**7**), Sm (**8**), Pr (**9**), and Nd (**10**)], and $[\{La(SIP)(H_2O)_3\}(H_2O)]_n$ (**11**), have been synthesized by hydrothermal reactions of Ln_2O_3 and 5-sulfoisophthalic acid monosodium salt (NaH_2SIP) at 160 °C and characterized by single-crystal X-ray diffraction. The unprecedented three structure types ongoing from Lu^{III} to La^{III} have been established: type I for the small ions, Lu, Yb, Tm, and Er; type II for the medium ions including Ho, Dy, Tb, Sm, Pr, and Nd; and type III for the largest La ion. Type I adopts a one-dimensional zigzag chain-like structure, type II exhibits a two-dimensional undulate layer structure, and type III features a two-dimensional double-layer pillared by sulfonate groups to form a three-dimensional open framework. The progressive structural changes from type I to type II and to type III with increasing atomic number were rationalized by the effect of the lanthanide contraction. Their spectroscopic properties and thermal stability were also investigated.
(© Wiley-VCH Verlag GmbH & Co. KGaA, 69451 Weinheim, Germany, 2005)

Introduction

The design and construction of coordination polymers is one of the most active areas of materials research. The intense interest in these materials is driven by both their interesting network topologies and their potential applications in catalysis, molecular magnets, sensors, ion exchange, adsorption, and phase separation.[1–6] Numerous coordination polymers with varied dimensions and topologies have been obtained through a judicious choice of organic linkers and metal ions.[7–14] Many of the efforts have so far been devoted to the study of transition-metal-based coordination polymers.[15–19] The chemistry of lanthanide coordination polymers has been less-well investigated despite their useful luminescent, catalytic, and magnetic properties.[20–25] For example, our knowledge about how the lanthanide contraction works in crystal-structure formation is limited because of few systematic investigations across the lanthanide series with a single ligand.[26–28] This contribution deals with the self-assembly of the lanthanide series with the single SIP ligand. SIP was selected for several reasons: (1) it contains a soft sulfonate group that may serve as a more sensitive probe in the exploration of the effect of the lanthanide contraction; (2) it has three functional groups that allow the formation of structures of higher dimensions; (3) π–π stacking interactions between the aromatic rings may facilitate ordered, noninterpenetrated open frameworks; (4) it has an asymmetric geometry that may lead to acentric crystal structures that are needed for the development of non-linear optical materials. This new series of lanthanide–SIP coordination polymers prepared by hydrothermal reactions displays three types of polymeric structures, ranging from one-dimensional chains to a three-dimensional framework on going from Lu to La.

[a] State Key Laboratory of Structural Chemistry, Fujian Institute of Research on the Structure of Matter, Chinese Academy of Sciences,
Fuzhou, Fujian, 350002, P. R. China
Fax: +86-591-8370-5045
E-mail: xli@fjirsm.ac.cn
[b] Graduate School of the Chinese Academy of Sciences,
Beijing 100039, P. R. China
Fax: +86-591-8370-5045
E-mail: qyliu@fjirsm.ac.cn
Supporting information for this article is available on the WWW under http://www.eurjic.org or from the author.

Results and Discussion

Preparation of the Complexes

We prepared the series of Ln^{III}–SIP compounds **1**–**11** with the structures $[\{Ln(SIP)(H_2O)_5\}(H_2O)_3]_n$ [Ln = Lu (**1**), Yb (**2**), Tm (**3**), and Er (**4**)], $[\{Ln(SIP)(H_2O)_4\}]_n$ [Ln = Ho (**5**), Dy (**6**), Tb (**7**), Sm (**8**), Pr (**9**), and Nd (**10**)], and $[\{La(SIP)(H_2O)_3\}(H_2O)]_n$ (**11**) (excluding the rare and radioactive Pm as well as Eu^{III} and Gd^{III} reported previously[29]) by a hydrothermal reaction of Ln_2O_3 and NaH_2-SIP in aqueous solution. The preparative reactions were carried out at different temperatures (140 °C, 160 °C, and 180 °C) to investigate the temperature dependence of their solid structures. X-ray diffraction analyses of the products

 © 2005 Wiley-VCH Verlag GmbH & Co. KGaA, Weinheim DOI: 10.1002/ejic.200500271

indicated that the same results were obtained at these reaction temperatures although the purity and yields were slightly different, indicative of the thermodynamic nature of the hydrothermal reactions. Attempts to get single crystals of the Ce–SIP compound by reacting CeO_2 with NaH_2SIP were unsuccessful. This compound has been reported previously but the crystal structure was not determined. The crystalline compounds **1**–**11** could not be isolated from the conventional reaction of Ln_2O_3 with NaH_2SIP in aqueous solution at room temperature, indicating the kinetic nature of the reactions. The different results between the conventional solutions and hydrothermal reactions may be caused by a different reaction mechanism: the hydrothermal reaction mechanism is shifted from the kinetic to the thermodynamic domain when compared to a conventional solution reaction.[30–32]

Table 1. Selected bond lengths [Å] for compounds **1**–**4**.[a]

	Lu (**1**)	Yb (**2**)	Tm (**3**)	Er (**4**)
Ln–O1	2.392(11)	2.401(15)	2.415(5)	2.415(3)
Ln–O2	2.443(11)	2.438(16)	2.463(6)	2.447(3)
Ln–O3A	2.392(12)	2.406(16)	2.410(5)	2.463(3)
Ln–O4A	2.443(13)	2.456(16)	2.437(5)	2.423(3)
Ln–O8	2.285(13)	2.291(17)	2.306(6)	2.310(3)
Ln–O9	2.297(12)	2.306(16)	2.315(6)	2.326(3)
Ln–O10	2.300(13)	2.314(16)	2.321(6)	2.333(3)
Ln–O11	2.360(13)	2.370(19)	2.385(7)	2.393(3)
Ln–O12	2.455(13)	2.468(16)	2.471(6)	2.460(3)
Ln–O (av.)	2.374	2.383	2.391	2.397
O···O (av.)	2.857	2.864	2.856	2.686
π–π interacting distances (face-to-face)	3.715	3.705	3.715	3.687
Dihedral angle of benzene rings in the chain [°]	51.0	51.4	51.7	48.4

[a] Symmetry transformation for equivalent atoms: A: $x - 1/2, -y + 1/2, z - 1/2$.

Crystal Structures

The X-ray diffraction analyses of compounds **1**–**11** revealed three types of solid structures on going from Lu to La: a 1D chain (**1**–**4**, Lu–Er), a 2D sheet (**5**–**10**, Ho–Pr), and a 3D network (**11**, La). These structure types result from the different coordination modes of SIP, as illustrated in Scheme 1, presumably as a consequence of the lanthanide contraction, as will be detailed below.

Type I: Structure of $[\{Ln(SIP)(H_2O)_5\}(H_2O)_3]_n$ [Ln = Lu (1), Yb (2), Tm (3), and Er (4)]

The type I structure features a one-dimensional ribbon, as exemplified in Figure 1 for **4** (Ln = Er). Each Er^{III} ion is coordinated to nine oxygen atoms, four from the carboxylate groups and five from water molecules (Figure 1a). SIP uses the two carboxylate arms to chelate to the Er^{III} ions, as illustrated in Scheme 1(a), to form an infinite zigzag chain (Figure 1b). The Er–O distances given in Table 1 range from 2.310(3) to 2.463(3) Å (average value 2.397 Å). The phenyl rings in the chain are not parallel but are twisted relative to each other with a dihedral angle of around 48.4°. The uncoordinated sulfonate group forms hydrogen bonds with coordinated and lattice water molecules.

The extensive interchain hydrogen bonds link the zigzag chains into a three-dimensional supramolecular layer structure, as illustrated in Figure 2. Two types of hydrogen bonds are observed between the chains: hydrogen bonds between the coordinated water molecules and carboxylate oxygen atoms (O···O = 2.723–2.900 Å), and hydrogen bonds between the coordinated water molecules and sulfonate oxygen atoms (O···O = 2.675, 2.814, and 2.929 Å). The supramolecular layer structures are further stabilized by π–π interactions between the parallel aromatic rings in an off-set fashion, with a face-to-face distance of about 3.687 Å. Similar hydrogen bonds and π–π interactions between aromatic rings have also been reported in the cadmium complexes recently reported.[33,34] The lattice water molecules located in the cavities of the supramolecular open framework are hydrogen bonded to each other and the chain, with O···O distances ranging from 2.703 to 3.081 Å.

The Lu (**1**), Yb (**2**), and Tm (**3**) complexes possess a similar structure. Selected bond lengths, hydrogen bonds, and π–π stacking distances between aromatic rings are listed in Table 1. The results indicate that the Ln–O bond lengths increase from Lu (**1**) to Er (**4**), as expected for the lanthanide contraction.

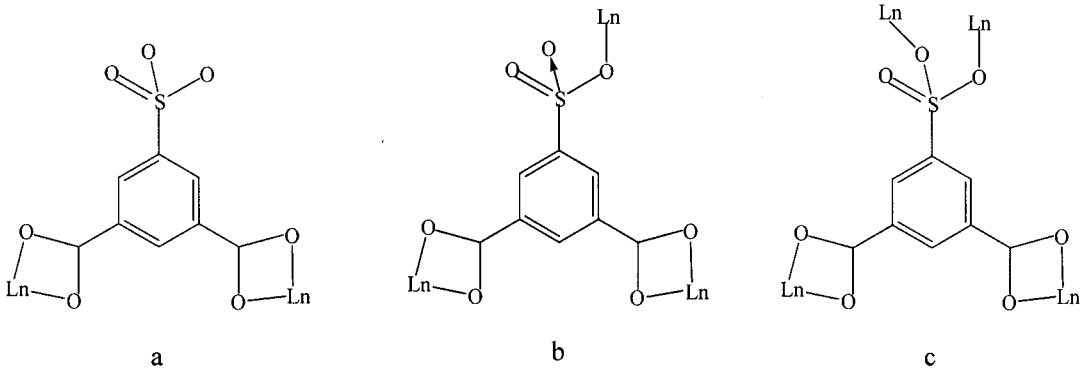

Scheme 1. The three different coordination modes of the SIP ligand observed in complexes **1**–**11**.

 © 2005 Wiley-VCH Verlag GmbH & Co. KGaA, Weinheim

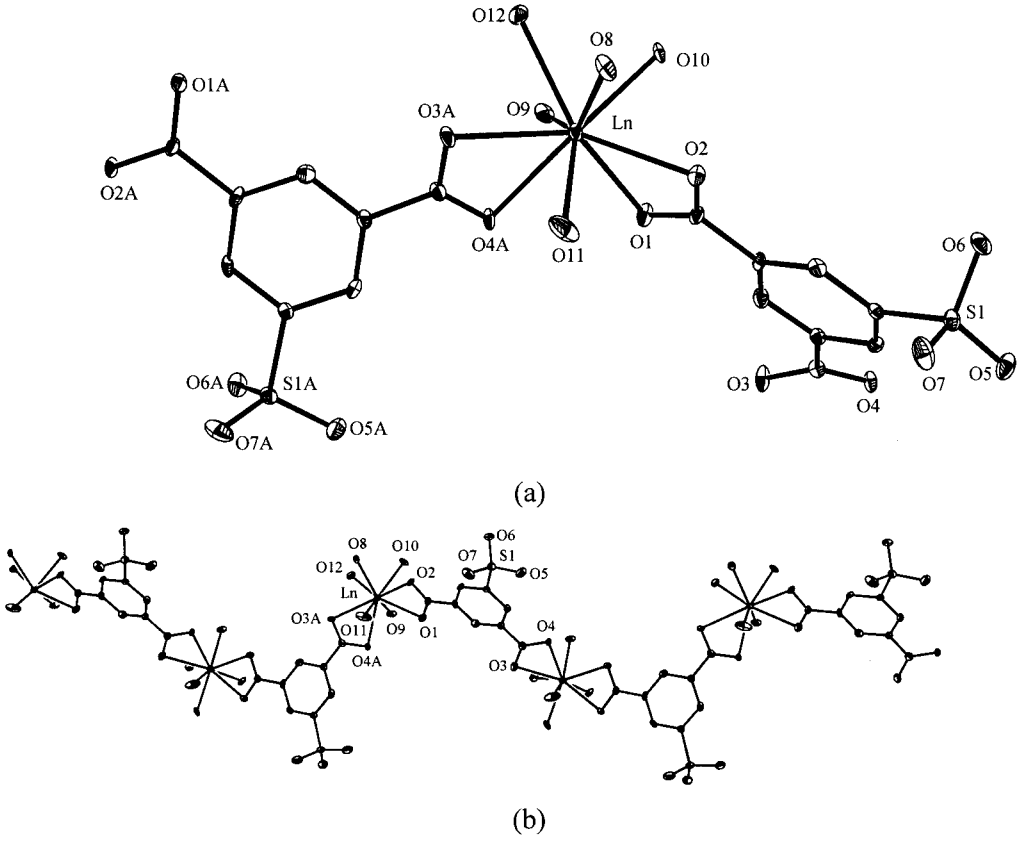

Figure 1. a) Local coordination environment of the lanthanide ions [Ln = Lu (**1**), Yb (**2**), Tm (**3**), and Er (**4**)]. b) Infinite zigzag chain of complexes **1**–**4**.

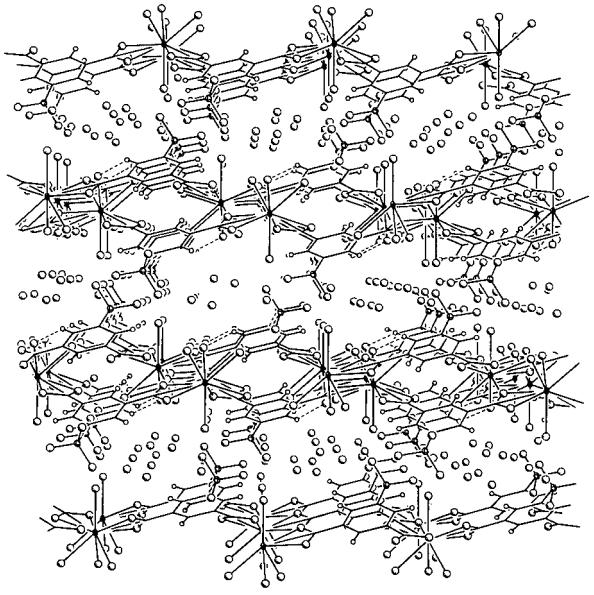

Figure 2. Three-dimensional supramolecular framework of **1**–**4**. The lattice water molecules occupy the interlayer space. The interlamellar interactions between the neighboring layers are hydrogen bonds (not shown).

Type II: Structure of [{Ln(SIP)(H$_2$O)$_4$}]$_n$ [Ln = Ho (5), Dy (6), Tb (7), Sm (8), Pr (9), and Nd (10)]

The lanthanide ions Ho (**5**), Dy (**6**), Tb (**7**), Sm (**8**), Pr (**9**), and Nd (**10**) form type II structures with the acentric crystal system, space group $Pna2_1$. They have similar crystal structures, as displayed in Figure 3a for Ln = Pr. Their selected bond lengths, hydrogen bonds, and π–π stacking distances are listed in Table 2. The type II structure can be described as an undulating, two-dimensional, sheet-like structure constructed from fused $[Pr(SIP)_3(H_2O)_4]$ pseudo-hexagonal grids (Figure 3b). The tridentate SIP ligand links the three surrounding Pr^{III} atoms through two chelating carboxylate groups and one sulfonate oxygen atom, as illustrated in Scheme 1(b). The presence of intermolecular hydrogen bonds and π–π interactions finally results in a three-dimensional supramolecular structure, as depicted in Figure 4. Compounds **5**–**10** are isomorphous with the previously reported Eu^{III} and Gd^{III} complexes.[29] A structural comparison with type I compounds may give an insight into the formation of type II species. Both types of compounds have nine-coordinate lanthanide ions in a similar coordination geometry. The type II structure may best be understood as resulting from interchain replacement of one of the coordinated waters by one sulfonate oxygen atom in a type I structure. The resultant Ln–O_3S bonding links the

 © 2005 Wiley-VCH Verlag GmbH & Co. KGaA, Weinheim

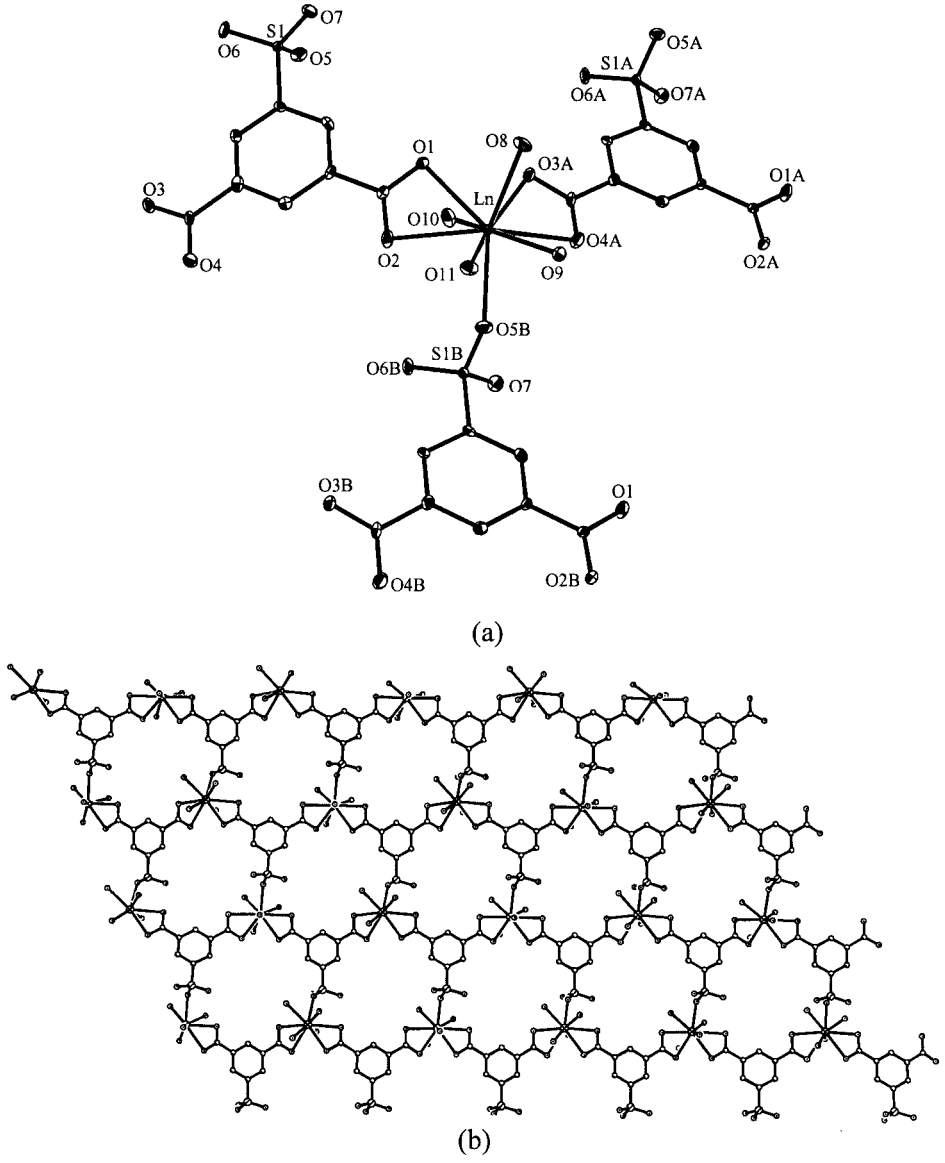

Figure 3. a) Local coordination environment of the lanthanide ions [Ln = Ho (**5**), Dy (**6**), Tb (**7**), Sm (**8**), Pr (**9**), and Nd (**10**)]. b) Two-dimensional network structure of complexes **5–10**.

Table 2. Selected bond lengths [Å] for compounds **5–9**.[a]

	Ho (**5**)	Dy (**6**)	Tb (**7**)	Sm (**8**)	Pr (**9**)
Ln–O1	2.415(8)	2.466(12)	2.442(5)	2.502(18)	2.519(4)
Ln–O2	2.494(7)	2.539(14)	2.504(5)	2.540(16)	2.560(3)
Ln–O3A	2.436(7)	2.472(10)	2.462(4)	2.476(16)	2.536(3)
Ln–O4A	2.491(6)	2.550(11)	2.520(4)	2.541(15)	2.579(3)
Ln–O5B	2.384(7)	2.447(12)	2.409(5)	2.460(18)	2.476(4)
Ln–O8	2.363(9)	2.434(15)	2.392(7)	2.409(19)	2.472(4)
Ln–O9	2.375(8)	2.451(11)	2.400(4)	2.439(15)	2.482(3)
Ln–O10	2.376(6)	2.469(14)	2.403(6)	2.469(18)	2.517(3)
Ln–O11	2.420(5)	2.496(10)	2.434(4)	2.491(14)	2.541(3)
Ln–O (av.)	2.417	2.480	2.441	2.481	2.520
O···O (av.)	2.863	2.866	2.845	2.884	2.847
π–π distance	3.652	3.686	3.588	3.681	3.636
Dihedral angle [°]	8.0	6.9	8.1	8.6	7.2

[a] Symmetry transformation for equivalent atoms: A: $-x + 1/2$, $y + 1/2$, $z - 1/2$; B: $-x + 1/2$, $y + 1/2$, $z + 1/2$.

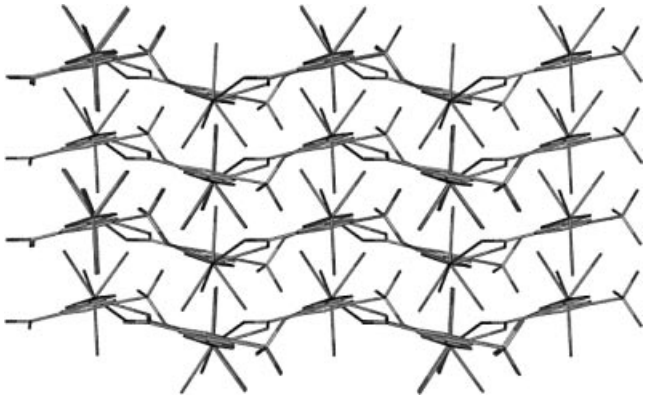

Figure 4. View of complexes **5–10** along the *b* axis. The interlayer interactions between the neighboring layers are hydrogen bonds (not shown).

 © 2005 Wiley-VCH Verlag GmbH & Co. KGaA, Weinheim

zigzag chains into a 2D sheet. Such structure evolution suggests a stronger trend for the type II lanthanide ions to bind to anionic sulfonate groups, as will be detailed later.

Type III: 3D Open Framework Structure of [{La(SIP)-$(H_2O)_3$}(H_2O)]$_n$ (11)

Only lanthanum, which has the largest ionic radius in the lanthanide series, was found to form a 3D coordination polymer, namely [{La(SIP)$(H_2O)_3$}(H_2O)]$_n$ (**11**). As shown in Figure 5a, each La^{III} ion is coordinated by nine oxygen atoms, six from five SIP ligands and three from water molecules. The five SIP ligands are coordinated to the La^{III} center in three distinct modes, two by one carboxylate oxygen, two through one sulfonate oxygen, and one by a chelating carboxylate group. The La–O distances (Table 3) range from 2.451(5) to 2.596(5) Å (av. 2.544 Å), with the longest La–O distance associated with the sulfonate oxygen atoms. The S–O bond lengths are normal[35] [1.439(5), 1.443(5) and 1.446(5) Å] and similar to each other, as expected for the strong conjugation of sulfonate. As shown in Scheme 1 (c), SIP functions as an unprecedented hexadentate ligand with only one sulfonate oxygen atom uncoordinated. Of the three functional groups of SIP, one chelating carboxylate group and one unidentate oxygen atom of sulfonate group, together with the similar ones from a neighboring SIP, connect the two neighboring La^{III} ions to form the sixteen-

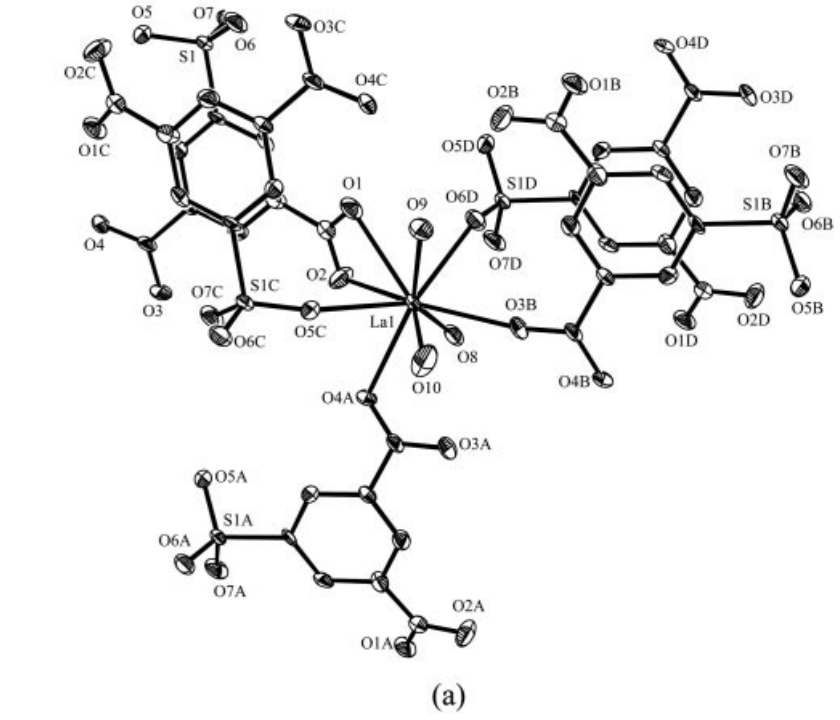

(a)

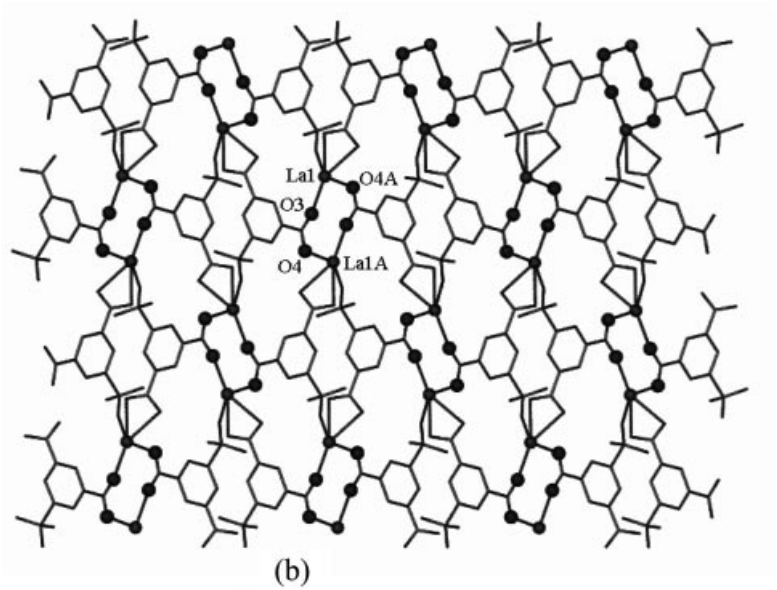

(b)

Figure 5. a) Local coordination environment of compound **11**. b) Two-dimensional sheet-like structure viewed along the *a* axis.

 © 2005 Wiley-VCH Verlag GmbH & Co. KGaA, Weinheim

membered ring depicted in Figure 5b. Of interest is the other carboxylate group, which, together with the similar one from neighboring SIP, bridges a pair of La^{III} ions to form an $[La_2O_4C_2]$ eight-membered ring with an La···La separation of 4.982 Å, as shown in Figure 5a. Two types of rings connected by SIP propagate along the crystallographic *bc* plane to yield a two-dimensional sheet-like structure (Figure 5a). As described above, SIP uses five of its six donor atoms to form a 2D sheet. The sixth donor atom from the sulfonate group functions as a linker between the layers to form a 3D open framework, as depicted in Figure 6, with an approximate interlamellar separation of 3.884 Å. The free oxygen atom of the sulfonate group is involved in hydrogen bonding with the coordinated water molecules at a distance of 2.687–2.968 Å. The lattice water molecules are located in the cavities of the structure, forming a number of hydrogen bonds with carboxylate oxygen atoms, sulfonate oxygen atoms, and coordinated water molecules (O···O = 2.596–2.991 Å). The coordination polymer is further stabilized by π–π stacking interactions between the parallel aromatic rings in an off-set fashion, with a face-to-face distance of about 3.517 and 3.642 Å.

Table 3. Selected bond lengths [Å] for compound **11**.[a]

Bond	Distance [Å]	Bond	Distance [Å]
Ln–O1	2.583(5)	Ln–O2	2.586(5)
Ln–O3A	2.468(5)	Ln–O4B	2.507(4)
Ln–O5C	2.565(5)	Ln–O6D	2.596(5)
Ln–O8	2.451(5)	Ln–O9	2.565(5)
Ln–O10	2.574(5)	Ln–O (av.)	2.544

[a] Symmetry transformation for equivalent atoms: A: $x - 1/2, -y + 1/2, z - 1/2$; B: $-x + 1/2, y + 1/2, -z + 5/2$; C: $-x, -y, -z + 2$; D: $-x + 1/2, y + 1/2, -z + 3/2$.

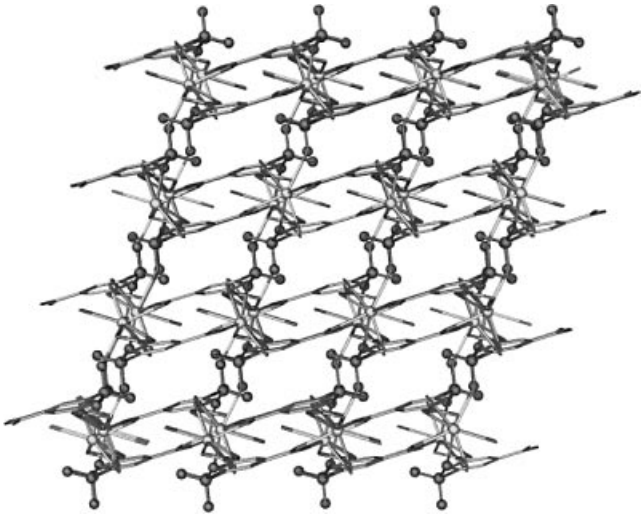

Figure 6. Three-dimensional pillared structure of complex **11** viewed along the *b* axis (the sulfonate groups and lanthanum atoms are represented as spheres).

Discussion of Structure Evolution

The self-assembly of the lanthanide series with a single ligand was found to form three unprecedented types of structures, ranging from a 1D chain to a 2D sheet and a 3D framework, wherein all lanthanide ions are nine-coordinate and trivalent. This intriguing structure evolution across the lanthanide series may be attributable to the effect of the lanthanide contraction. The structure evolution (from Lu to La) results from the extent to which the coordinated water molecules are replaced by the sulfonate oxygen atoms of the SIP ligand. Thus, the effect of the lanthanide contraction should be responsible for the water substitution with the sulfonate anions during the structure evolution. The preference to bond to anionic ligands can be measured as follows:

$$\Phi = Z/r$$

where Φ is the basicity, Z is the oxidation state, and r is the ionic radius.[36]

La^{III} has the largest ionic radius and thus the smallest basicity in the lanthanide(III) series. In other words, La^{III} has the greatest tendency to form La^{III}–O_3S bonds, thus accounting for the replacement of water by one sulfonate oxygen during the 2D → 3D structure evolution. Moreover, the large ionic radius allows the presence of five surrounding SIP ligands. The lighter lanthanide ions from Ho^{III} to Pr^{III} adopt a 2D sheet-like structure as a consequence of both their slightly higher basicity and smaller ionic radii. The lightest four lanthanide ions (Lu^{III}–Er^{III}) show no substantial interactions with the sulfonate oxygen donor atoms in their chain-like structures, consistent with their larger basicity and smallest radii. In summary, the sulfonate group of SIP is a comparatively soft oxygen donor ligand and is thus able to serve as a more sensitive probe for investigating the effect of the lanthanide contraction in crystal-structure formation of the lanthanide series, thereby accounting for the unprecedented three structure types observed in this lanthanide–SIP system.

FT-IR Spectra and Thermogravimetric Analyses

The FT-IR spectra of these complexes exhibit broad absorption bands in the range 3500–3200 cm^{-1} due to the presence of water molecules in the structures. The strong bands at 1360–1670 cm^{-1} for all complexes are characteristic of the carboxylate group. The absorptions in the region 1000–1230 cm^{-1} for all complexes are typical of the sulfonate group.[37] Interestingly, the characteristic bands of the carboxylate group show some changes from type I to type II, even though the coordination mode of the carboxylate groups in the two structure types is identical. In the type I structure these peaks are observed in the range 1668–1397 cm^{-1}, while in the type II structure these absorptions are in the range 1605–1381 cm^{-1} with two weak shoulders in the range 1665–1630 cm^{-1}. The IR spectrum of the La–SIP compound (type III) is nearly identical to that of the type II structure. However, the characteristic bands of the sulfonate group do not show any obvious change from type I to type III.

To assess the thermal stability of these compounds and their structural variation as a function of the temperature,

 © 2005 Wiley-VCH Verlag GmbH & Co. KGaA, Weinheim

thermogravimetric analyses (TGA) were performed on single-phase polycrystalline samples of these materials (Figure S1). Since compounds of the same structure type show similar thermal behavior, the results of only three representative compounds − Yb (**2**) of type I, Tb (**7**) of type II, and La (**11**) of type III − are discussed. The TGA measurements for Yb (**2**) exhibit three distinct weight-loss steps. The first weight loss occurs between 60 and 110 °C due to the release of three lattice water molecules (weight loss: measured 9.55%; calculated 9.64%). The second weight loss in the temperature range 110–240 °C corresponds to the removal of the coordinated water molecules (observed 14.65%; calculated 16.07%). A further increase of the temperature leads to the decomposition of the compound at 540 °C. The thermogravimetric analysis of Tb (**7**) shows that the initial weight loss occurs in the temperature range 120–200 °C, attributable to the release of all coordinated water molecules (observed 14.67%; calculated 15.19%). The thermogravimetric analysis of La (**11**) indicates that the loss of the water (14.95%) takes place between 100 °C and 160 °C, corresponding to the release of all water molecules (calculated: 15.85%).

Conclusions

In conclusion, the self-assembly of the lanthanide series with a single (SIP) ligand with soft sulfonate probes leads to the formation of the unprecedented three structural types I (1D), II (2D), and III (3D). The compounds of the heaviest lanthanides (Lu, Yb, Tm, and Er) adopt a type I structure without Ln–sulfonate bonds, the Ho, Dy, Tb, Sm, Pr, and Nd compounds belong to type II, with one Ln–sulfonate bond, and the largest, La, forms a type III structure with two La–sulfonate bonds. The progressive structural changes resulting from the distinct preference for the lanthanide series to bind to anionic sulfonate groups are believed to due to their different basicity as a consequence of the effects of the lanthanide contraction. In addition, the SIP ligand displays diverse coordination modes, which together with the versatile coordination ability of the bridging ligand makes it adaptable to lanthanide ions of different sizes and leads to the various topologies of the coordination networks.

Experimental Section

General Remarks: All chemicals were purchased commercially and used without further purication, including 5-sulfoisophthalic acid monosodium salt (Alfa). Elemental analyses were carried out with an Elementar Vario EL III analyzer and IR spectra (KBr pellets) were recorded with a Perkin–Elmer Spectrum One. The thermogravimetric measurements were performed with a Netzsch STA449C apparatus under nitrogen with a heating rate of 10 °C min^{-1} from 25 to 800 °C. All complexes were synthesized by a hydrothermal method under autogenous pressure.

$[\{Lu(SIP)(H_2O)_5\}(H_2O)_3]_n$ (1): In a typical synthesis, solid Lu_2O_3 (0.04 g, 0.1 mmol) was dispersed in an aqueous solution (15 mL) of 5-sulfoisophthalic acid monosodium salt (0.03 g, 0.12 mmol) with a pH value of ca. 3–4. The mixture was placed in a Teflon-lined stainless-steel autoclave (30 mL), and the autoclave was sealed, heated to 160 °C under autogenous pressure for 5 d, and then cooled to room temperature at a rate of 6 °C h^{-1}. The resulting colorless, crystalline product was filtered, washed with distilled water, and dried at ambient temperature (0.035 g, yield 62% based on Lu). $C_8H_{19}LuO_{15}S$ (562.26): calcd. C 17.08, H 3.38; found C 17.01, H 3.33. IR (KBr pellet): $\tilde{\nu}$ = 3388(vs), 1664(s), 1612(vs), 1542(vs), 1460(s), 1396(vs), 1211(s), 1175(s), 1119(m), 1043(vs), 746(m), 628(s) cm^{-1}.

$[\{Yb(SIP)(H_2O)_5\}(H_2O)_3]_n$ (2): The synthetic procedure for **2** was similar to that for **1** but replacing Lu_2O_3 with Yb_2O_3. A colorless, crystalline product was obtained (0.042 g, yield 75% based on Yb). $C_8H_{19}O_{15}SYb$ (560.33): calcd. C 17.14, H 3.39; found C 17.00, H 3.36. IR (KBr pellet): $\tilde{\nu}$ = 3391(vs), 1667(s), 1614(vs), 1538(vs), 1462(s), 1397(vs), 1208(s), 1175(s), 1120(m), 1042(vs), 746(m), 628(s) cm^{-1}.

$[\{Tm(SIP)(H_2O)_5\}(H_2O)_3]_n$ (3): The synthetic procedure for **3** was similar to that for **1** but replacing Lu_2O_3 with Tm_2O_3. A pale-orange, crystalline product was obtained (0.037 g, yield 66% based on Tm). $C_8H_{19}O_{15}STm$ (556.22): calcd. C17.27, H 3.42; found C 17.19, H 3.41. IR (KBr pellet): $\tilde{\nu}$ = 3389(vs), 1667(s), 1614(vs), 1540(vs), 1460(s), 1395(vs), 1210(s), 1176(s), 1119(m), 1042(vs), 745(m), 628(s) cm^{-1}.

$[\{Er(SIP)(H_2O)_5\}(H_2O)_3]_n$ (4): The synthetic procedure for **4** was similar to that for **1** but replacing Lu_2O_3 with Er_2O_3. A pale-red, crystalline product was obtained (0.043 g, yield 78% based on Er). $C_8H_{19}ErO_{15}S$ (554.55): calcd. C17.31, H 3.43; found C 17.30, H 3.41. IR (KBr pellet): $\tilde{\nu}$ = 3391(vs), 1668(s), 1614(vs), 1538(vs), 1460(s), 1396(vs), 1210(s), 1176(s), 1120(m), 1042(vs), 745(m), 630(s) cm^{-1}.

$[\{Ho(SIP)(H_2O)_4\}]_n$ (5): The synthetic procedure for **5** was similar to that for **1** but replacing Lu_2O_3 with Ho_2O_3. A colorless, crystalline product was obtained (0.028 g, yield 59% based on Ho). $C_8H_{11}HoO_{11}S$ (480.16): calcd. C 20.04, H 2.29; found C 19.86, H 2.21. IR (KBr pellet): $\tilde{\nu}$ = 3390(vs), 3232(vs), 1658(w), 1642(w), 1605(vs), 1559(vs), 1458 vs), 1391(vs), 1208(m), 1180(s), 1115(w), 1042(s), 744(w), 628(m) cm^{-1}.

$[\{Dy(SIP)(H_2O)_4\}]_n$ (6): The synthetic procedure for **6** was similar to that for **1** but replacing Lu_2O_3 with Dy_2O_3. A colorless, crystalline product was obtained (0.030 g, yield 63% based on Dy). $C_8H_{11}DyO_{11}S$ (477.73): calcd. C 20.15, H 2.31; found C 20.14, H 2.25. IR (KBr pellet): $\tilde{\nu}$ = 3405(vs), 3232(vs), 1658(w), 1641(w), 1601(vs), 1538(vs), 1451(vs), 1382(s), 1223(m), 1206(m), 1180(s), 1116(w), 1043(s), 738(w), 620(m) cm^{-1}.

$[\{Tb(SIP)(H_2O)_4\}]_n$ (7): The synthetic procedure for **7** was similar to that for **1** but replacing Lu_2O_3 with Tb_4O_7. A colorless, crystalline product was obtained (0.031 g, yield 66% based on Tb). $C_8H_{11}O_{11}STb$ (474.15): calcd. C 20.25, H 2.32; found C 20.22, H 2.28. IR (KBr pellet): $\tilde{\nu}$ = 3391(vs), 3210(vs), 1664(w), 1639(w), 1602(vs), 1536(vs), 1458(vs), 1392(vs), 1208(m), 1177(m), 1116(m), 1042(s), 777(m), 742(m), 625(m) cm^{-1}.

$[\{Sm(SIP)(H_2O)_4\}]_n$ (8): The synthetic procedure for **8** was similar to that for **1** but replacing Lu_2O_3 with Sm_2O_3. A colorless, crystalline product was obtained (0.028 g, yield 61% based on Sm). $C_8H_{11}O_{11}SSm$ (465.58): calcd. C 20.65, H 2.36; found C 20.60, H 2.32. IR (KBr pellet): $\tilde{\nu}$ = 3408(vs), 3201(vs), 1653(w), 1634(w),

 © 2005 Wiley-VCH Verlag GmbH & Co. KGaA, Weinheim

1602(vs), 1537(vs), 1448(vs), 1383(vs), 1222(vs), 1203(m), 1166(m), 1109(m), 1046(s), 773(m), 738(m), 630(m), 583(m) cm^{-1}.

$[\{Pr(SIP)(H_2O)_4\}]_n$ (9): The synthetic procedure for **9** was similar to that for **1** but replacing Lu_2O_3 with Pr_6O_{11}. A colorless, crystalline product was obtained (0.015 g, yield 34% based on Pr). $C_8H_{11}O_{11}PrS$ (456.14): calcd. C 21.05, H 2.41; found C 20.94, H 2.33. IR (KBr pellet): $\tilde{\nu}$ = 3410(vs), 3249(vs), 1650(w), 1633(w), 1601(vs), 1531(vs), 1447(vs), 1381(vs), 1223(vs), 1203(m), 1164(m), 1109(m), 1045(s), 773(m), 736(m), 627(m), 585(m) cm^{-1}.

$[\{Nd(SIP)(H_2O)_4\}]_n$ (10): The synthetic procedure for **10** was similar to that for **1** but replacing Lu_2O_3 with Nd_2O_3. A pink, crystalline product was obtained (0.024 g, yield 51% based on Nd).

Table 4. Crystallographic data for **1**–**5**.

	Lu (**1**)	Yb (**2**)	Tm (**3**)	Er (**4**)	Ho (**5**)
Empirical formula	$C_8H_{19}LuO_{15}S$	$C_8H_{19}O_{15}SYb$	$C_8H_{19}O_{15}STm$	$C_8H_{19}ErO_{15}S$	$C_8H_{11}HoO_{11}S$
Formula mass	562.26	560.33	556.22	554.55	480.16
Temperature [K]	273(2)	293(2)	293(2)	293(2)	293(2)
Crystal size [mm]	0.20×0.18×0.04	0.45×0.20×0.05	0.33×0.24×0.06	0.45×0.35×0.04	0.25×0.23×0.22
Space group	$P2_1/n$	$P2_1/n$	$P2_1/n$	$P2_1/n$	$Pna2_1$
Z	4	4	4	4	4
a [Å]	9.44700(10)	9.4630(5)	9.4681(17)	9.422(4)	7.2351(10)
b [Å]	10.4895(4)	10.5142(5)	10.5316(18)	10.526(4)	16.456(2)
c [Å]	17.1948(4)	17.2285(10)	17.252(3)	17.102(7)	10.3183(14)
β [°]	101.8210(10)	101.779(2)	101.8150(10)	101.312(4)	90
V [Å^3]	1667.77(8)	1678.07(15)	1683.8(5)	1663.2(11)	1228.5(3)
$D_{calcd.}$ [g cm^{-3}]	2.239	2.218	2.194	2.215	2.596
μ [mm^{-1}]	6.122	5.774	5.469	5.248	6.671
Measured reflections	5171	10289	12721	12505	8952
Independent reflections	2899	2953	3842	3816	2704
Observed reflections [$I > 2\sigma(I)$]	2276	2553	3593	3243	2603
Parameters	250	265	271	274	211
Completeness [%]	97.8	99.7	99.6	99.8	99.6
θ range [°]	2.94–25.08	2.99–25.03	2.28–27.48	2.28–27.48	2.33–27.48
hkl ranges	–10/11	–11/11	–12/11	–12/12	–9/8
	–6/12	–8/12	–13/13	–13/9	–21/16
	–20/20	–20/20	–22/12	–22/22	–12/13
R_1 (obsd. refl.)	0.0730	0.0348	0.0253	0.0306	0.0145
wR_2 (all refl.)	0.1739	0.0828	0.0611	0.0764	0.0337
Largest diff. peak/hole [e Å^{-3}]	1.761/–1.893	1.362/–2.349	1.551/–1.487	2.306/–1.162	0.615/–0.800

Table 5. Crystallographic data for **6**–**9** and **11**.

	Dy (**6**)	Tb (**7**)	Sm (**8**)	Pr (**9**)	La (**11**)
Empirical formula	$C_8H_{11}ODy_{11}S$	$C_8H_{11}O_{11}STb$	$C_8H_{11}O_{11}SSm$	$C_8H_{11}O_{11}PrS$	$C_8H_{11}LaO_{11}S$
Formula mass	477.73	474.15	465.58	456.14	454.14
Temperature [K]	273(2)	293(2)	273(2)	293(2)	273(2)
Crystal size [mm]	0.32×0.14×0.14	0.18×0.16×0.12	0.10×0.10×0.08	0.18×0.15×0.10	0.52×0.50×0.10
Space group	$Pna2_1$	$Pna2_1$	$Pna2_1$	$Pna2_1$	$P2_1/n$
Z	4	4	4	4	4
a [Å]	7.3006(7)	7.260(2)	7.2839(6)	7.1969(17)	7.9076(2)
b [Å]	16.6036(15)	16.508(5)	16.5781(14)	16.695(4)	15.2955(4)
c [Å]	10.4270(10)	10.353(3)	10.3919(8)	10.489(3)	10.4404(3)
β [°]	90	90	90	90	92.686(2)
V [Å^3]	1263.9(2)	1240.7(7)	1254.86(18)	1260.3(5)	1261.39(6)
$D_{calcd.}$ [g cm^{-3}]	2.511	2.538	2.464	2.404	2.391
μ [mm^{-1}]	6.136	5.928	4.905	4.091	3.611
Measured reflections	5968	9150	3814	9206	3907
Independent reflections	2190	2847	1602	2627	2274
Observed reflections [$I > 2\sigma(I)$]	1834	2634	1301	2490	2140
Parameters	147	214	142	214	208
Completeness[%]	99.7	99.8	99.9	99.8	98.4
2θ range[°]	2.31–25.06	2.47–27.48	2.31–25.09	3.08–27.48	2.36–25.35
hkl ranges	–8/7	–9/9	–8/8	–9/9	–9/8
	–17/9	–16/21	–19/14	–21/21	–15/18
	–12/12	–13/13	–6/12	–13/10	–8/12
R_1 (obsd. refl.)	0.0507	0.0267	0.0602	0.0225	0.0403
wR_2 (all refl.)	0.1276	0.0586	0.1354	0.0560	0.1013
Largest diff. peak/hole [e Å^{-3}]	1.945/–0.840	1.120/–0.701	1.113/–1.179	0.758/–0.556	1.298/–2.841

 © 2005 Wiley-VCH Verlag GmbH & Co. KGaA, Weinheim

$C_8H_{11}NdO_{11}S$ (459.47): calcd. C 20.92, H 2.40; found C 20.88, H 2.36. IR (KBr pellet): $\tilde{\nu}$ = 3410(vs), 3251(vs), 1650(w), 1636(w), 1601(vs), 1534(vs), 1448(vs), 1382(vs), 1223(vs), 1204(m), 1167(m), 1109(m), 1049(s), 773(m), 737(m), 626(m), 583(m) cm^{-1}.

$[\{La(SIP)(H_2O)_3\}(H_2O)]_n$ (11): The synthetic procedure for **11** was similar to that for **1** but replacing Lu_2O_3 with La_2O_3. A colorless, crystalline product was obtained (0.035 g, yield 76% based on La). $C_8H_{11}LaO_{11}S$ (454.14): calcd. C 20.25, H 2.32; found C 20.24, H 2.30. IR (KBr pellet): $\tilde{\nu}$ = 3446(vs), 3218(vs), 1644(m), 1599(s), 1564(s), 1538(vs), 1451(s), 1436(s), 1378(vs), 1217(s), 1179(m), 1112(m), 1051(s), 775(m), 726(m), 619(m) cm^{-1}.

X-ray Crystallographic Study: X-ray diffraction data for complexes **2–5**, **7**, **9**, and **10** were collected with a Rigaku Mercury CCD diffractometer equipped with graphite-monochromated Mo-K_α radiation (λ = 0.71073 Å). The CrystalClear software package was used for data reduction and empirical absorption correction.[38] Data collection for complexes **1**, **6**, **8**, and **11** was performed with a Siemens Smart CCD diffractometer with graphite-monochromated Mo-K_α radiation (λ = 0.71073 Å). Empirical absorption corrections were applied using the SADABS program.[39] All structures were solved by direct methods and successive Fourier difference syntheses, and refined by the full-matrix least-squares method on F^2 (SHELXTL Version 5.1[40]). All non-hydrogen atoms were refined with anisotropic thermal parameters for all structures except **1**, **6**, and **8**. In the structures of **1**, **6**, and **8** all non-hydrogen atoms were refined anisotropically except several carbon and oxygen atoms, which were refined isotropically in order to prevent some of them being "non-positive-definite". Aromatic hydrogen atoms were assigned to calculated positions with isotropic thermal parameters fixed at 1.2-times that of the attached carbon atom. Some water hydrogen atoms were placed in calculated positions with isotropic thermal parameters fixed at 1.5-times that of the attached oxygen atom. Other water hydrogen atoms were located from difference maps and refined with O–H distances restrained to 0.95 Å, and isotropic thermal parameters fixed at 1.5-times that of the respective oxygen atom. The R_1 values are defined as $R_1 = \Sigma||F_o| - |F_c||/\Sigma|F_o|$ and $wR_2 = \{\Sigma[w(F_o^2 - F_c^2)^2]/\Sigma[w(F_o^2)^2]\}^{1/2}$. The crystallographic data for **1–11** (except **10**) are listed in Tables 4 and 5. Selected bond lengths together with some nonbonding interactions for **1–4**, **5–9**, and **11** are listed in Tables 1, 2, and 3, respectively. CCDC-267294 to -267303 (for **1–9** and **11**) contain the supplementary crystallographic data for this paper. These data can be obtained free of charge from The Cambridge Crystallographic Data Centre via www.ccdc.cam.ac.uk/data_request/cif.

Acknowledgments

We gratefully acknowledgment the financial support of the "One Hundred Talents Program" of the Chinese Academy of Sciences and National Science Foundation of China (grant no. 20473092).

[1] B. Moulton, M. J. Zaworotko, *Chem. Rev.* **2001**, *101*, 1629–1658.
[2] O. R. Evans, R. Xiong, Z. Wang, G. K. Wong, W. Lin, *Angew. Chem.* **1999**, *111*, 557–559; *Angew. Chem. Int. Ed.* **1999**, *38*, 536–538.
[3] D. L. Reger, T. D. Wright, R. F. Semeniuc, T. C. Grattan, M. D. Smith, *Inorg. Chem.* **2001**, *40*, 6212–6219.
[4] T. Bein, *Supramolecular Architecture*, American Chemical Society, Washington, DC, **1992**.
[5] O. Sato, T. Iyoda, A. Fujishima, K. Hashimoto, *Science* **1996**, *271*, 49–51.
[6] M. Fujita, Y. J. Kwon, S. Washizu, K. Ogura, *J. Am. Chem. Soc.* **1994**, *116*, 1151–1152.
[7] M. Munakata, L. P. Wu, T. Kuroda-Sowa, M. Maekawa, Y. Suenaga, K. Furuichi, *J. Am. Chem. Soc.* **1996**, *118*, 3305–3306.
[8] Y. C. Liang, M. C. Hong, R. Cao, J. B. Weng, W. P. Su, *Inorg. Chem.* **2001**, *40*, 4574–4582.
[9] J. H. Yang, S. L. Zheng, X. L. Yu, X. M. Chen, *Cryst. Growth Des.* **2004**, *4*, 831–834.
[10] X. M. Zhang, H. S. Wu, X. M. Chen, *Eur. J. Inorg. Chem.* **2003**, 2959–2964.
[11] S. H. Feng, R. R. Xu, *Acc. Chem. Res.* **2001**, *34*, 239–247.
[12] C. Ruiz-Pérez, P. A. Lorenzo-Luis, M. Hernández-Molina, M. M. Laz, F. S. Delgado, P. Gili, M. Julve, *Eur. J. Inorg. Chem.* **2004**, 3873–3879.
[13] S. K. Ghosh, G. Savitha, P. K. Bharadwaj, *Inorg. Chem.* **2004**, *43*, 5495–5497.
[14] S. K. Ghosh, R. Joan, P. K. Bharadwaj, *Cryst. Growth Des.* **2005**, *5*, 623–629.
[15] D. F. Sun, R. Cao, Y. Q. Sun, W. H. Bi, D. Q. Yuan, Q. Shi, X. Li, *Chem. Commun.* **2003**, 1528–1529.
[16] D. F. Sun, R. Cao, Y. Q. Sun, X. Li, W. H. Bi, M. C. Hong, Y. J. Zhao, *Eur. J. Inorg. Chem.* **2003**, 94–98.
[17] J. Tao, X. Yin, Z. B. Wei, R. B. Huang, L. S. Zheng, *Eur. J. Inorg. Chem.* **2004**, 125–133.
[18] Z. M. Sun, J. G. Mao, Y. Q. Sun, H. Y. Zeng, A. Clearfield, *Inorg. Chem.* **2004**, *43*, 336–341.
[19] D. S. Kim, P. M. Forster, R. L. Toquin, A. K. Cheetham, *Chem. Commun.* **2004**, 2148–2149.
[20] S. K. Ghosh, P. K. Bharadwaj, *Inorg. Chem.* **2004**, *43*, 2293–2298.
[21] D. M. L. Goodgame, S. P. W. Hill, D. J. Williams, *Inorg. Chim. Acta* **1998**, *272*, 131–140.
[22] C. V. K. Sharma, R. D. Rogers, *Chem. Commun.* **1999**, 83–84.
[23] X. J. Zheng, Z. M. Wang, S. Gao, F. H. Liao, C. H. Yan, L. P. Jin, *Eur. J. Inorg. Chem.* **2004**, 2938–2973.
[24] L. Tei, A. J. Blake, C. Wilson, M. Schröder, *Dalton Trans.* **2004**, 1945–1952.
[25] P. C. R. Soares-Santos, T. Trindade, A. C. Tomé, J. Rocha, R. A. Sá Ferreira, L. D. Carlos, F. A. A. Paz, J. Klinowski, H. I. S. Nogueira, *New J. Chem.* **2004**, *28*, 1352–1358.
[26] L. Pan, X. Y. Huang, J. Li, Y. G. Wu, N. W. Zheng, *Angew. Chem. Int. Ed.* **2000**, *39*, 527–530.
[27] X. Li, Q. Shi, D. F. Sun, W. H. Bi, R. Cao, *Eur. J. Inorg. Chem.* **2004**, *4*, 2747–2753.
[28] Z. He, E. Q. Gao, Z. M. Wang, C. H. Yan, M. Kurmoo, *Inorg. Chem.* **2005**, *44*, 862–874.
[29] Z. Wang, M. Strobele, K. L. Zhang, H. J. Meyer, X. Z. You, Z. Yu, *Inorg. Chem. Commun.* **2002**, *5*, 230–234.
[30] R. M. Barrer, *Hydrothermal Chemistry of Zeolite*, Academic Press, London, **1982**.
[31] G. Bemazeau, *J. Mater. Chem.* **1999**, *9*, 15–18.
[32] S. H. Feng, R. R. Xu, *Acc. Chem. Res.* **2001**, *34*, 239–247.
[33] Q. Y. Liu, L. Xu, *Inorg. Chem. Commun.* **2005**, *8*, 401–405.
[34] Q. Y. Liu, L. Xu, *CrystEngComm* **2005**, *7*, 87–89.
[35] A. Onoda, Y. Yamada, M. Doi, T. Okamura, N. Ueyama, *Inorg. Chem.* **2001**, *40*, 516–521.
[36] T. Moeller, *The Chemistry of the Lanthanides*, Pergamon Press, New York, **1975**.
[37] G. Socrates, *Infrared Characteristic Group Frequencies*, John Wiley & Sons, Stonebridge Press, Bristol, **1980**.
[38] *CrystalClear version 1.3*, Rigaku Corp., **2000**.
[39] G. M. Sheldrick, *A program for the Siemens Area Detector ABSorption correction*, University of Göttingen, **1997**.
[40] G. M. Sheldrick, *SHELXS 97*, *Program for Crystal Structure Solution*, University of Göttingen, **1997**.

Received: March 30, 2005
Published Online: August 1, 2005

 © 2005 Wiley-VCH Verlag GmbH & Co. KGaA, Weinheim

Microwave-Assisted and Pd^{II}-Mediated Nitrile–Oxime Coupling

Dmitrii A. Garnovskii,[a] Nadezhda A. Bokach,[b] Armando J. L. Pombeiro,*[a] Matti Haukka,[c] João J. R. Fraústo da Silva,[a] and Vadim Yu. Kukushkin*[b]

Keywords: Microwave synthesis / Metal-mediated synthesis / Nitriles / Oximes / Nitrile–oxime coupling / Palladium complexes

Refluxing $PdCl_2$ with the ketoximes $R^1R^2C{=}NOH$ (R^1R^2 = MeMe, MeEt, C_5H_{10}) in RCN (R = Me, Et, *n*Pr, Ph) for 2–3 h results in precipitation of the oxime complexes $[PdCl_2(R^1R^2C{=}NOH)_2]$, whereas further reflux of the reaction mixture for an additional 6–12 h leads to formation of the chelated species $[PdCl_2\{NH{=}C(R)ON{=}CR^1R^2\text{-}\kappa^2N\}]$ (R/R^1R^2 = Me/MeMe **1**; Et/MeMe **2**; *n*Pr/MeMe **3**; Me/MeEt **4**; Me/C_5H_{10} **5**; Ph/MeMe **6**) by a Pd^{II}-mediated coupling between the oximes and the nitriles; complexes **1**–**6** were isolated in the solid state in 60–75 % yields. The reaction time could be drastically reduced, to 15–30 min, when the system was additionally irradiated with microwaves (100 W, about 60 °C). Compounds **1**–**6** can also be obtained without isolation of the intermediate oxime complexes either by refluxing for 8–15 h or by microwave irradiation (100 W, about 60 °C) for 15–30 min. The formulation of **1**–**6** is based upon satisfactory C, H, and N elemental analyses, FAB mass spectrometry, and IR, ^1H and $^{13}C\{^1H\}$ NMR spectroscopy, while the structures of **1**·(Me_2CO), **1**·($CHCl_3$), **2**·(H_2O), and **6**·½(H_2O) were determined by X-ray single-crystal diffraction.
(© Wiley-VCH Verlag GmbH & Co. KGaA, 69451 Weinheim, Germany, 2005)

Introduction

In the past five years, microwave irradiation (MWI) has become an increasingly useful tool in synthetic chemistry.[1–12] The major advantages of microwave-assisted syntheses are associated with a substantial decrease of reaction times, an increase of the selectivities of the processes, and, consequently, better purity of the products formed.[2,4,6–8,10–12] In the overwhelming majority of cases, MWI has been applied in organic synthesis. However, some reports on the application of MWI in the synthesis of coordination compounds are also present in the literature.[13–25] In particular, microwave syntheses have been used for the preparation of nanophases and nanocrystalline materials starting from metal complexes,[16,19,20] for preparations by substitution,[17,18,21] and for phthalocyanine syntheses.[13–15,22,23] Recently, some of us have demonstrated that MWI also efficiently promotes reactions of coordinated ligands, such as in the [2+3]-cycloaddition[24] and the addition of hydroxamic acids to metal-bound nitriles.[25]

In the current work, we have extended our previous results on microwave-assisted reactions of ligated nitriles to another system by applying MWI for the nitrile–oxime coupling to form the imino species $HN{=}C(R)ON{=}CR'R''$. In a series of previous papers,[26] we have found that these processes are especially efficient when metal centers are in high oxidation states, for example Pt^{IV},[27] Re^{IV},[28] or Rh^{III},[29] whereas low-oxidation-state metal centers, such as Pt^{II},[30] are insufficiently strong activators to provide the coupling under conventional conditions. Hence, we believed that MWI could provide an additional activation for the addition of oximes to nitriles complexed by low-oxidation-state metal centers and to expand, in this way, the number of this type of compounds with their potential application in organic[31] and phthalocyanine syntheses.[32]

Results and Discussion

In organic chemistry, oximes are known as ambidentate nucleophiles and their reactions with electrophilic reagents, such as acylation, have been extensively studied and reviewed.[33] Metal-mediated oxime–nitrile coupling (or, in other words, iminoacylation by complexed nitriles), is a little-explored area and only recently have publications on this subject started to appear in the literature. The largest fraction of these reports is devoted to the coupling induced by high-oxidation-state metal centers, while reactions at low-oxidation-state metal centers, such as Pd^{II}, are scarce. It is important to note that the first data on metal-mediated iminoacylation, reported at a conference,[34] deal with the reaction between 3,3-dimethyl-2-butanone oxime and $[PdCl_2(PhCN)_2]$ to yield, among other products, the imino

[a] Centro de Química Estrutural, Complexo I, Instituto Superior Técnico, Av. Rovisco Pais,
1049-001 Lisboa, Portugal
E-mail: pombeiro@ist.utl.pt
[b] Department of Chemistry, St. Petersburg State University,
198904 Stary Petergof, Russian Federation
E-mail: kukushkin@VK2100.spb.edu
[c] Department of Chemistry, University of Joensuu,
P. O. Box 111, 80101 Joensuu, Finland
E-mail: matti.haukka@joensuu.fi

complex $[PdCl_2\{NH=C(Ph)ON=CMetBu\}_2]$. The latter observation, which was not developed further, prompted us to investigate the coupling at a Pd^{II} center under both microwave and conventional thermal conditions. For this work we used $PdCl_2$ in neat RCN (R = Me, Et, *n*Pr, Ph) and the ketoximes $R^1R^2C=NOH$ (R^1R^2 = MeMe, MeEt, C_5H_{10}).

Refluxing $PdCl_2$ with the ketoximes $R^1R^2C=NOH$ in RCN for 2–3 h results in precipitation of the known[35] oxime complexes $[PdCl_2(R^1R^2C=NOH)_2]$ (Scheme 1, route **A**). However, further reflux of the reaction mixture for an additional 6–12 h leads to formation of the chelated species $[PdCl_2\{NH=C(R)ON=CR^1R^2\text{-}\kappa^2N\}]$ (**1**–**6**) (route **C**); these complexes were isolated in the solid state in 60–75% yields.

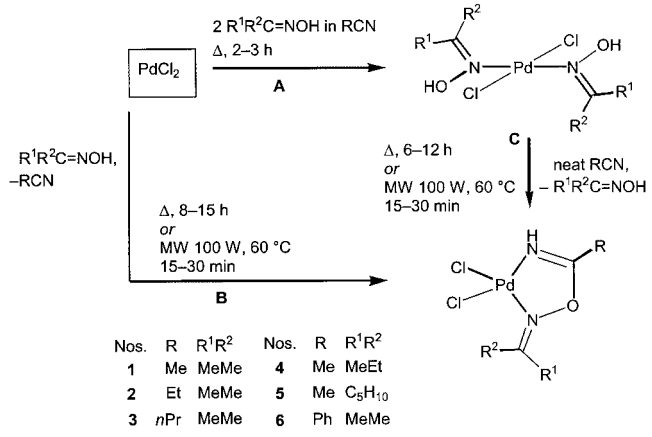

Scheme 1.

The reaction time could be drastically reduced, to 15–30 min, when the system was additionally irradiated with microwaves (100 W, about 60 °C). The yields of the complexes for both conventional and microwave methods were almost identical. Compounds **1**–**6** can also be obtained by route **B** without isolation of the intermediate oxime complexes.

We believe that a plausible mechanism for the oxime–nitrile coupling at the Pd^{II} center involves the formation of the bis(oxime) complexes $[PdCl_2(R^1R^2C=NOH)_2]$, which, in neat RCN, can form an equilibrium concentration of $[PdCl_2(R^1R^2C=NOH)(RCN)]$ by displacement of one oxime ligand. In the latter intermediate, the ligated nitrile is subject to intramolecular attack by the adjacent oxime (or oximato ligand formed upon deprotonation). In general, the coupling between electrophilically activated species and nucleophiles is highly probable when the two species are bound to a common metal center,[36] and, moreover, the chelate effect also drives the reaction.

All isolated compounds (**1**–**6**) gave satisfactory C, H, and N elemental analyses and the expected molecular ion and fragmentation patterns in the FAB^+ mass spectra. The IR spectrum of each product displays two strong ν(C=N) bands in the range between 1672 and 1613 cm^{-1} and a strong band in the high frequency region between 3265 and 3217 cm^{-1} that can be attributed to the ν(N–H) stretching vibration. The ^1H NMR spectra of **1**–**6** in $[D_6]$acetone show a broad peak for the =N*H* group at δ = 9.01–9.44 ppm. This range is specific for imino hydrogens involved in hydrogen bonding.[27] The latter was unambiguously determined in the solid state for the solvates **1**·(Me_2CO), **2**·(H_2O), and **6**·½(H_2O) (see below). We anticipate that complexes **1**–**6** should also exhibit a similar type of H-bond with either $[D_6]$acetone or with traces of water in the commercially available solvent. In the ^1H NMR spectrum, complex **4** displays two set of signals for the alkyl groups (two Me's and Et) of the chelated ligand [the latter derived from the coupling with a mixture of *syn*/*anti*-MeC(=NOH)Et] due to *syn*/*anti*-isomers of the ligand.

The structures of **1**·(Me_2CO), **1**·($CHCl_3$), **2**·(H_2O), and **6**·½(H_2O) were determined by single-crystal X-ray diffraction; the molecular structure of **1**·(Me_2CO) is depicted in Figure 1. The atoms in the other similar structures are numbered correspondingly and bond lengths and angles are given in Table 1.

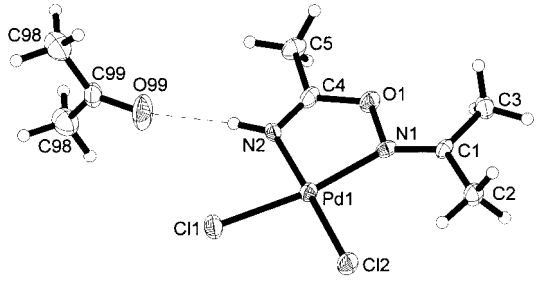

Figure 1. Thermal ellipsoid view of $[PdCl_2\{NH=C(Me)ON=CMe_2\text{-}\kappa^2N\}]$·($Me_2CO$) (**1**·$Me_2CO$) with the atomic numbering scheme. Thermal ellipsoids are drawn with 50% probability. N(2)···O(99) = 2.954(6) Å.

Table 1. Selected bond lengths [Å] and angles [°] **1**·(Me_2CO), **1**·($CHCl_3$), **2**·(H_2O), and **6**·½(H_2O).

	1·(Me_2CO)	**1**·($CHCl_3$)	**2**·(H_2O)	**6**·½(H_2O)
Pd(1)–Cl(1)	2.2769(14)	2.2883(4)	2.2846(13)	2.2810(10)
Pd(1)–Cl(2)	2.3058(13)	2.3022(4)	2.3054(14)	2.3119(11)
Pd(1)–N(1)	2.068(4)	2.0622(15)	2.052(4)	2.069(3)
Pd(1)–N(2)	1.968(4)	1.974(2)	1.965(4)	1.980(4)
N(1)–O(1)	1.463(5)	1.4615(19)	1.454(5)	1.454(4)
N(2)–C(4)	1.271(7)	1.267(2)	1.262(6)	1.260(5)
C(4)–O(1)	1.342(6)	1.339(2)	1.333(5)	1.352(5)
Cl(1)–Pd(1)–Cl(2)	88.93(5)	88.87(2)	87.38(5)	88.48(4)
N(1)–Pd(1)–N(2)	79.2(2)	79.20(6)	78.80(15)	79.12(13)
Pd(1)–N(1)–O(1)	110.0(3)	109.66(10)	110.3(2)	109.5(2)
Pd(1)–N(2)–C(4)	117.0(4)	117.05(13)	117.6(3)	117.6(3)
C(4)–O(1)–N(2)	113.0(4)	113.57(13)	113.3(3)	114.4(3)

Inspection of Table 1 shows that the relevant bond lengths and angles of the four complexes agree with each other within 3σ and they are also well-coherent with the normal bond lengths and angles.[37]

In conclusion, one should note that (*i*) the observed oxime coupling is metal-mediated (as we have shown previously,[1] the addition of oximes to nonactivated organonitriles RCN, i.e. those with a donor group R, does not proceed in the absence of any metal complex even under rather harsh reaction conditions) and (*ii*) the reaction is dramatically accelerated by microwave irradiation, thus al-

 © 2005 Wiley-VCH Verlag GmbH & Co. KGaA, Weinheim

lowing the formation of (imino)Pd^{II} complexes in a short time.

Experimental Section

Materials and Instrumentation: All reagents and solvents were obtained from commercial sources and used as received. C, H, and N elemental analyses were carried out by the Microanalytical Service of the Instituto Superior Técnico. Melting points were determined on a Kofler Table. For TLC, Merck UV 254 SiO_2 plates were used. Positive-ion FAB mass spectra were obtained on a Trio 2000 instrument by bombarding 3-nitrobenzyl alcohol (NBA) matrices of the samples with 8 keV (ca. 1.28×10^{15} J) Xe atoms. Mass calibration for the data system acquisition was achieved with CsI. IR spectra (4000–400 cm^{-1}) were recorded on a JASCO FT/IR-430 instrument in KBr pellets. ^1H NMR spectra were measured on a Varian UNITY 300 spectrometer at ambient temperature. The microwave irradiation experiments were undertaken in a focused microwave CEM Discover®LabMate™ reactor (100 W, 2.45 Hz) fitted with a rotational system and an IR temperature detector; reactions were performed in 10-mL pressure-rated reaction tubes, volumes of reaction mixtures were about 3 mL. Detailed information on the reactor is given at http://www.combichemlab.com/website/files/Combichem/Microwave/cem.htm.

[$PdCl_2${NH=C(R)ON=CMe_2-κ²*N*}] (R = Me 1, Et 2, *n*Pr 3, Ph 6): $PdCl_2$ (20.0 mg, 0.11 mmol) and 2-propanone oxime (17.0 mg, 0.23 mmol) were suspended in the corresponding RCN (1 mL) and the reaction mixture was heated under reflux conditions for 2–3 h until the yellow solid complex [$PdCl_2$(HON=CMe_2-κ*N*)$_2$] had formed. However, if the reaction mixture was refluxed for an additional 6 (**1**), 8 (**2**), or 9 h (**3**), it leads to (*i*) R = Me: the release of orange complex **1**, which was filtered off, washed three times with a small amount of acetonitrile and dried in vacuo. Yield: 25 mg (76%). The latter reaction was also performed under MW irradiation (100 W, about 60 °C) and was complete in 15 min (yield: 24 mg, 73%). (*ii*) R = Et and *n*Pr: formation of an orange solution. The solvent was removed under a gentle stream of nitrogen and the orange solid was washed with diethyl ether and dried in vacuo. Yields: 23 mg (67%; **2**) and 25 mg (69%; **3**). The latter reaction was also performed under MW irradiation (100 W, about 60 °C) and was complete in 30 min. Yields: 22 mg (64%; **2**) and 27 mg (74%; **3**). (*iii*) After refluxing for more than 10 h (R = Ph), the dissolution of the oxime complex was complete and the solution turned orange. The solvent was removed under a gentle stream of nitrogen and the orange crystalline residue was washed three times with diethyl ether and dried in vacuo. Yield: 23.5 mg (59%; **6**). The use of MW irradiation (100 W, about 60 °C) allowed the completion of this reaction in 30 min.

1: $C_5H_{10}Cl_2N_2OPd$ (291.5): calcd. C 20.60, H 3.46, N 9.61; found C 20.80, H 3.42, N 9.31. FAB$^+$-MS: *m*/*z* = 313 [M – H + Na]$^+$, 289 [M – 2H]$^+$, 255 [M – HCl]$^+$. M.p. 187–188 °C. IR (KBr): $\tilde{\nu}$ = 3239 s cm^{-1} ν(N–H), 1672 s and 1625 s ν(C=N). ^1H NMR ([D_6]-acetone): δ = 2.36 (s, 3 H, Me), 2.44 (s, 3 H, Me), 2.68 (s, 3 H, Me), 9.01 (br. s, 1 H, NH) ppm.

2: $C_6H_{12}Cl_2N_2OPd$ (305.5): calcd. C 23.60, H 3.93, N 9.18; found C 23.82, H 3.69, N 9.19. FAB$^+$-MS: *m*/*z* = 306 [M + H]$^+$, 271 [M + H – Cl]$^+$, 235 [M + H – 2Cl]$^+$. M.p. 194–195 °C. IR (KBr): $\tilde{\nu}$ = 3217 s cm^{-1} ν(N–H), 1665 s and 1621 s ν(C=N). ^1H NMR ([D_6]-acetone): δ = 1.27 (t, $^3J_{H,H}$ = 6.8 Hz, 3 H, Me from Et), 2.38 (s, 3 H, Me), 2.69 (s, 3 H, Me), 2.95 (q, $^3J_{H,H}$ = 6.8 Hz, 2 H, CH_2 from Et), 9.13 (br. s, 1 H, NH) ppm.

3: $C_7H_{14}Cl_2N_2OPd$ (319.5): calcd. C 26.33, H 4.38, N 8.77; found C 25.98, H 4.06, N 8.81. FAB$^+$-MS: *m*/*z* = 320 [M + H]$^+$, 285 [M + H – Cl]$^+$. M.p. 174–175 °C. IR (KBr): $\tilde{\nu}$ = 3222 s cm^{-1} ν(N–H), 1667 s and 1620 s ν(C=N). ^1H NMR ([D_6]acetone): δ = 0.98 (t, $^3J_{H,H}$ = 6.6 Hz, 3 H, CH_3), 1.76 (q, $^3J_{H,H}$ = 6.6 Hz, 2 H, CH_2), 2.37 (s, 3 H, Me), 2.69 (s, 3 H, Me), 2.77 (t, $^3J_{H,H}$ = 6.6 Hz, 2 H, CH_2), 9.11 (br. s, 1 H, NH) ppm.

6: $C_{10}H_{12}Cl_2N_2OPd$ (353.5): calcd. C 34.09, H 3.44, N 7.96; found C 34.17, H 3.23, N 8.25. FAB$^+$-MS: *m*/*z* = 319 [M – Cl + 3H]$^+$, 317 [M – Cl + H]$^+$, 316 [M – Cl]$^+$. M.p. 169–170 °C. IR (KBr): $\tilde{\nu}$ = 3218 s cm^{-1} ν(N–H), 1649 s and 1617 s ν(C=N), 1579 s ν(C=C). ^1H NMR ([D_6]acetone): δ = 2.55 (s, 3 H, CH_3), 2.76 (s, 3 H, CH_3), 7.61–8.13 (m, 5 H, Ph), 9.44 (br. s, 1 H, NH) ppm.

[$PdCl_2${NH=C(Me)ON=CMeEt-κ²*N*}] (4): $PdCl_2$ (20.0 mg, 0.11 mmol) and 2-butanone oxime (20.0 mg, 0.23 mmol; a mixture of *syn* and *anti* isomers) were suspended in acetonitrile (1 mL). The reaction mixture was refluxed for 9 h until the complete dissolution of $PdCl_2$ to give an orange solution, whereupon acetonitrile was evaporated with a flow of nitrogen and the yellow oily residue was crystallized under a layer of diethyl ether to give an orange yellow solid that was filtered off and dried in air at room temperature. Yield: 23 mg (67%). The latter reaction was also performed under MW irradiation (100 W, about 60 °C) and was complete in 15 min. Yield: 22 mg (63%). $C_6H_{12}Cl_2N_2OPd$ (305.5): calcd. C 23.60, H 3.93, N 9.18; found C 22.97, H 3.91, N 9.13. FAB$^+$-MS: *m*/*z* = 305 [M]$^+$, 269 [M – HCl]$^+$. IR (KBr): $\tilde{\nu}$ = 3237 s cm^{-1} ν(N–H), 1670 s and 1617 s ν(C=N). ^1H NMR ([D_6]acetone): two *syn*-*anti* isomers in ca. 3:2 ratio. Major isomer: δ = 1.16 (t, $^3J_{H,H}$ = 7.2 Hz, 3 H) and 3.16 (q, $^3J_{H,H}$ = 7.2 Hz, 2 H) (C_2H_5), 2.37 (s, 3 H, CH_3), 2.44 (s, 3 H, CH_3 from oxime), 9.05 (br. s, 1 H, NH); minor isomer: δ = 1.22 (t, $^3J_{H,H}$ = 7.2 Hz, 3 H) and 2.75 (q, $^3J_{H,H}$ = 7.2 Hz, 2 H) (C_2H_5), 2.68 (s, 3 H, CH_3 from oxime), 2.45 (s, 3 H, CH_3), 9.05 (br. s, 1 H, NH) ppm.

[$PdCl_2${NH=C(Me)ON=C(C_5H_{10})-κ²*N*}] (5): $PdCl_2$ (20.0 mg, 0.11 mmol) and cyclohexanone oxime (26.0 mg, 0.23 mmol) were suspended in acetonitrile (1 mL) and refluxed for 4 h, whereupon a yellow, crystalline precipitate of [Pd{HON=C(C_5H_{10})}$_2$] formed. If this suspension was refluxed for an additional 11 h, the oxime complex gradually dissolved to give an orange solution. The solvent was removed under a stream of nitrogen and the orange solid was washed with diethyl ether and dried in vacuo. Yield: 26 mg (69%). The latter reaction was also performed under MW irradiation (100 W, 60 °C) for 30 min. Yield: 25 mg (68%). $C_8H_{14}Cl_2N_2OPd$ (331.5): calcd. C 29.00, H 4.22, N 8.45; found C 28.72, H 3.71, N 8.69. FAB$^+$-MS: *m*/*z* = 331 [M]$^+$, 330 [M – H]$^+$, 260 [M – 2Cl]$^+$. M.p. 191–193 °C. IR (KBr): $\tilde{\nu}$ = 3265 s cm^{-1} ν(N–H), 1658 s and 1613 s ν(C=N). ^1H NMR ([D_6]acetone): δ = 1.65 (m, 2 H, C_5H_{10}), 1.85 (m, 4 H, C_5H_{10}), 2.46 (s, 3 H, CH_3), 2.50 (m, 2 H, C_5H_{10}), 2.60 (m, 2 H, C_5H_{10}), 9.20 (br. s, 1 H, NH) ppm.

X-ray Structure Determinations. Crystals were immersed in cryo-oil, mounted in a Nylon loop, and measured at a temperature of 100 K or 110 K. The X-ray diffraction data were collected with a Nonius KappaCCD diffractometer using Mo-K_α radiation (λ = 0.71073 Å). The Denzo-Scalepack[38] or EvalCCD[39] program packages were used for cell refinements and data reduction. The structures were solved by direct methods using SIR2000[40] or by the Patterson method with DIRDIF-99.[41] A multiscan absorption correction based on equivalent reflections (XPREP in SHELXTL v. 6.14)[42] was applied to all of the data (the T_{min}/T_{max} values were 0.7411/0.8986, 0.5614/0.8510, 0.5097/0.8461, and 0.4884/0.8636 for **1**·(Me_2CO), **1**·($CHCl_3$), **2**·(H_2O), and **6**·½(H_2O), respectively). Structural refinements were carried out with SHELXL-97 with the WinGX graphical user interface.[43,44] NH and H_2O were located from the difference Fourier map but not refined in **6**·½(H_2O) [N(2)

 © 2005 Wiley-VCH Verlag GmbH & Co. KGaA, Weinheim

Table 2. Crystallographic data for **1**·(Me_2CO), **1**·($CHCl_3$), **2**·(H_2O), and **6**·½(H_2O).

	1·(Me_2CO)	**1**·($CHCl_3$)	**2**·(H_2O)	**6**·½(H_2O)
Empirical formula	$C_8H_{16}Cl_2N_2O_2Pd$	$C_6H_{11}Cl_5N_2OPd$	$C_6H_{14}Cl_2N_2O_2Pd$	$C_{10}H_{13}Cl_2N_2O_{1.5}Pd$
Formula mass	349.53	410.82	323.49	362.52
Temperature [K]	100(2)	100(2)	110(2)	100(2)
λ [Å]	0.71073	0.71073	0.71073	0.71073
Crystal system	monoclinic	triclinic	monoclinic	triclinic
Space group	*C*2/*m*	$P\bar{1}$	$P2_1/n$	$P\bar{1}$
a [Å]	20.8502(12)	7.7792(2)	7.112(2)	7.1582(6)
b [Å]	6.8143(3)	8.9921(3)	11.014(3)	8.1661(7)
c [Å]	9.2995(5)	10.4116(3)	14.391(3)	11.5194(11)
α [°]	90	105.127(2)	90	110.343(5)
β [°]	100.117(3)	96.913(2)	101.245(17)	90.897(5)
γ [°]	90	105.504(2)	90	95.358(6)
V [Å^3]	1300.72(12)	663.19(3)	1105.6(5)	627.77(10)
Z	4	2	4	2
$\rho_{calcd.}$ [Mg m^{-3}]	1.785	2.057	1.944	1.918
μ(Mo-K_α) [mm^{-1}]	1.821	2.382	2.134	1.888
R_1[a] [$I \geq 2\sigma(I)$]	0.0277	0.0181	0.0375	0.0388
wR_2[b] [$I \geq 2\sigma(I)$]	0.0705	0.0425	0.0666	0.0993

[a] $R_1 = \Sigma||F_o| - |F_c||/\Sigma|F_o|$. [b] $wR_2 = [\Sigma\{w(F_o^2 - F_c^2)^2\}/\Sigma\{w(F_o^2)^2\}]^{1/2}$.

and O(99)] but refined as riding atoms with a fixed distance of 0.85 Å. Other hydrogens were placed in idealized position and constrained to ride on their parent atom. The crystal water in **6**·½(H_2O) is disordered over two sites with equal occupancy of 0.5. The crystallographic data are summarized in Table 2, with selected bond lengths and angles given in Table 1. CCDC-267621 to -267624 [for **1**·(Me_2CO), **1**·($CHCl_3$), **2**·(H_2O), and **6**·½(H_2O), respectively] contain the supplementary crystallographic data for this paper. These data can be obtained free of charge from The Cambridge Crystallographic Data Centre via ww.ccdc.cam.ac.uk/data_request/cif.

Acknowledgments

This work was supported by the Fundação para a Ciência e a Tecnologia (FCT), Portugal, and its POCTI program (POCTI/QUI/43415/2001 project, which is FEDER funded). D. A. G. expresses gratitude to the FCT and the POCTI program for a fellowship (grant SFRH/BPD/11685/2002). M. H. and V. Yu. K. would like to thank the Academy of Finland for financial support. V. Yu. K. thanks FCT for a grant for Cientista Convidado/Professor at the Instituto Superior Técnico. D. A. G., N. A. B., and V. Yu. K. are very much obliged to the Russian Fund for Basic Research for grants 03-03-32363 and 05-03-32140. The authors also thank NATO for the Collaborative Linkage Grant PST.CLG.979289.

[1] F. Mavandadi, P. Lidstrom, *Curr. Top. Med. Chem.* **2004**, *4*, 773.
[2] A. Corsaro, U. Chiacchio, V. Pistara, G. Romeo, *Curr. Org. Chem.* **2004**, *8*, 511.
[3] M. Nuchter, B. Ondruschka, W. Bonrath, A. Gum, *Green Chem.* **2004**, *6*, 128.
[4] H. Will, P. Scholz, B. Ondruschka, *Chem. Eng. Technol.* **2004**, *27*, 113.
[5] M. Nüchter, U. Müller, B. Ondruschka, A. Tied, W. Lautenschläger, *Chem. Eng. Technol.* **2003**, *26*, 1207.
[6] K. M. K. Swamy, W. B. Yeh, M. J. Lin, C. M. Sun, *Curr. Med. Chem.* **2003**, *10*, 2403.
[7] N. Kuhnert, *Angew. Chem. Int. Ed.* **2002**, *41*, 1863.
[8] M. Larhed, C. Moberg, A. Hallberg, *Acc. Chem. Res.* **2002**, *35*, 717.
[9] V. Santagada, E. Perissutti, G. Caliendo, *Curr. Med. Chem.* **2002**, *9*, 1251.
[10] P. Lidström, J. Tierney, B. Wathey, J. Westman, *Tetrahedron* **2001**, *57*, 9225.
[11] M. Larhed, A. Hallberg, *Drug Discovery Today* **2001**, *6*, 406.
[12] C. R. Strauss, R. W. Trainor, *Austr. J. Chem.* **1995**, *48*, 1665.
[13] M. O. Liu, A. T. Hu, *J. Organomet. Chem.* **2004**, *689*, 2450.
[14] M. O. Liu, Ch.-H. Tai, W.-Y. Wang, J.-R. Chen, A. T. Hu, T.-H. Wei, *J. Organomet. Chem.* **2004**, *689*, 1078.
[15] H. I. Beltran, R. Esquivel, A. Sosa-Sanchez, J. L. Sosa-Sanchez, H. Hopfl, V. Barba, N. Farfan, M. G. Garcia, O. Olivares-Xometl, L. S. Zamudio-Rivera, *Inorg. Chem.* **2004**, *43*, 3555.
[16] S. Komarneni, *Curr. Sci.* **2003**, *85*, 1730.
[17] M. Ardon, P. D. Hayes, G. Hogarth, *J. Chem. Educ.* **2002**, *79*, 1249.
[18] X. M. Xiao, J. Sakamoto, M. Tanabe, S. Yamazaki, S. Yamabe, T. Matsumura-Inoue, *J. Electroanal. Chem.* **2002**, *527*, 33.
[19] A. V. Murugan, R. S. Sonawane, B. B. Kale, S. K. Apte, A. V. Kulkarni, *Mater. Chem. Phys.* **2001**, *71*, 98.
[20] O. Palchik, R. Kerner, Z. Zhu, A. Gedanken, *J. Solid State Chem.* **2000**, *154*, 530.
[21] N. Yoshikawa, Y. Masuda, T. Matsumura-Inoue, *Chem. Lett.* **2000**, *10*, 1207.
[22] C. Ungurenasu, *Synthesis* **1999**, *10*, 1729.
[23] D. R. Baghurst, S. R. Cooper, D. L. Greene, D. M. P. Mingos, S. M. Reynolds, *Polyhedron* **1990**, *9*, 893.
[24] M. A. J. Charmier, V. Yu. Kukushkin, A. J. L. Pombeiro, *J. Chem. Soc., Dalton Trans.* **2003**, 2540.
[25] K. V. Luzyanin, V. Yu. Kukushkin, M. L. Kuznetsov, D. A. Garnovskii, M. Haukka, A. J. L. Pombeiro, *Inorg. Chem.* **2002**, *41*, 2981.
[26] For reviews see: a) V. Yu. Kukushkin, A. J. L. Pombeiro, *Chem. Rev.* **2002**, *102*, 1771; b) A. J. L. Pombeiro, V. Yu. Kukushkin, *Reactions of Coordinated Nitriles*, in *Comprehensive Coordination Chemistry*, 2nd ed., Elsevier, Amsterdam, **2004**, vol. 1, chapter 1.34, pp. 639–660; c) N. A. Bokach, V. Yu. Kukushkin, *Uspekhi Khimii* **2005**, *74*, 164; *Russ. Chem. Rev.* **2005**, *74*, 153.
[27] a) V. Yu. Kukushkin, T. B. Pakhomova, Yu. N. Kukushkin, R. Herrmann, G. Wagner, A. J. L. Pombeiro, *Inorg. Chem.* **1998**, *37*, 6511; b) V. Yu. Kukushkin, T. B. Pakhomova, N. A. Bokach, G. Wagner, M. L. Kuznetsov, M. Galanski, A. J. L. Pombeiro, *Inorg. Chem.* **2000**, *39*, 216; c) G. Wagner, T. B. Pakhomova, N. A. Bokach, J. J. R. Fraústo da Silva, J. Vicente, A. J. L. Pombeiro, V. Yu. Kukushkin, *Inorg. Chem.* **2001**, *40*, 1683; d) M. L. Kuznetsov, N. A. Bokach, V. Yu. Kukushkin, T.

 © 2005 Wiley-VCH Verlag GmbH & Co. KGaA, Weinheim

Pakkanen, G. Wagner, A. J. L. Pombeiro, *J. Chem. Soc., Dalton Trans.* **2000**, 4683; e) A. V. Makarycheva-Mikhailova, M. Haukka, N. A. Bokach, D. A. Garnovskii, M. Galanski, B. K. Keppler, A. J. L. Pombeiro, V. Yu. Kukushkin, *New J. Chem.* **2002**, *26*, 1085; f) D. A. Garnovskii, A. J. L. Pombeiro, M. Haukka, P. Sobota, V. Yu. Kukushkin, *Dalton Trans.* **2004**, 1097.

[28] G. Wagner, A. J. L. Pombeiro, N. A. Bokach, V. Yu. Kukushkin, *J. Chem. Soc., Dalton Trans.* **1999**, 4083.

[29] a) V. Yu. Kukushkin, I. V. Ilichev, G. Wagner, J. J. R. Fraústo da Silva, A. J. L. Pombeiro, *J. Chem. Soc., Dalton Trans.* **1999**, 3047; b) V. Yu. Kukushkin, I. V. Ilichev, M. A. Zhdanova, G. Wagner, A. J. L. Pombeiro, *J. Chem. Soc., Dalton Trans.* **2000**, 1567.

[30] C. M. P. Ferreira, M. F. C. Guedes da Silva, J. J. R. Fraústo da Silva, A. J. L. Pombeiro, V. Yu. Kukushkin, R. A. Michelin, *Inorg. Chem.* **2001**, *40*, 1134.

[31] a) M. N. Kopylovich, V. Yu. Kukushkin, M. F. C. Guedes da Silva, M. Haukka, J. J. R. Fraústo da Silva, A. J. L. Pombeiro, *J. Chem. Soc., Perkin Trans. 1* **2001**, 1569; b) M. N. Kopylovich, A. J. L. Pombeiro, A. Fischer, L. Kloo, V. Yu. Kukushkin, *Inorg. Chem.* **2003**, *42*, 7239; c) M. N. Kopylovich, V. Yu. Kukushkin, M. Haukka, J. J. R. Fraústo da Silva, A. J. L. Pombeiro, *Inorg. Chem.* **2002**, *41*, 4798; d) A. J. L. Pombeiro, V. Yu. Kukushkin, M. N. Kopylovich, J. J. R. Fraústo da Silva, Patent PT 102 618 P (priority date May 30, **2001**).

[32] M. N. Kopylovich, V. Yu. Kukushkin, M. Haukka, K. V. Luzyanin, A. J. L. Pombeiro, *J. Am. Chem. Soc.* **2004**, *126*, 15040.

[33] a) E. Abele, E. Lukevics, *Org. Prep. Proced. Int.* **2000**, *32*, 235; b) E. Abele, E. Lukevics, *Heterocycles* **2000**, *53*, 2285; c) J. P. Adams, *J. Chem. Soc., Perkin Trans. 1* **2000**, 125; d) J. P. Adams, *Contemp. Org. Synth.* **1997**, *4*, 517; e) S. Kurbanov, A. Sirit, N. Sen, *Org. Prep. Proced. Int.* **1999**, *31*, 681; f) E. Guler, N. Sen, A. Sirit, S. Kurbanov, R. Mirzaoglu, *Org. Prep. Proced. Int.* **1998**, *30*, 195; g) S.-C. Tsay, H. V. Patel, J. R. Hwu, *Synlett* **1998**, 939.

[34] L. Caglioti, B. Galli, F. Gasparrini, G. Natile, in *Congresso Interdivisionale della Societa Chimica Italiana*, San Benedetto del Tronto, Atti, **1990**, p. 521.

[35] a) A. G. Constable, W. S. McDonald, L. C. Sawkins, B. L. Shaw, *J. Chem. Soc., Dalton Trans.* **1980**, 1992; b) P. J. Dunn, W. J. Holland, *Mikrochim. Acta* **1977**, *2*, 373; c) P. J. Dunn, W. J. Holland, R. J. Walker, *Mikrochim. Acta* **1975**, *2*, 129; d) Y. Kitano, K. Kobori, M. Tanimura, Y. Kinoshita, *Bull. Chem. Soc. Jpn.* **1974**, *47*, 2969; e) W. J. Holland, R. A. Dimenna, R. J. Walker, *Mikrochim. Acta* **1972**, 183.

[36] a) V. Yu. Kukushkin, A. J. L. Pombeiro, *Inorg. Chim. Acta* **2005**, *358*, 1; b) T. A. Steitz, J. A. Steitz, *Procl. Natl. Acad. Sci.* **1993**, *90*, 6498.

[37] a) F. H. Allen, O. Kennard, D. G. Watson, L. Brammer, A. G. Orpen, R. Taylor, *J. Chem. Soc., Perkin Trans. 2* **1987**, S1; b) A. G. Orpen, L. Brammer, F. H. Allen, O. Kennard, D. G. Watson, R. Taylor, *J. Chem. Soc., Dalton Trans.* **1989**, S1.

[38] Z. Otwinowski, W. Minor, "Processing of X-ray Diffraction Data Collected in Oscillation Mode", in *Methods in Enzymology*, vol. 276 (Macromolecular Crystallography, Part A) (Eds.: C. W. Carter, Jr., R. M. Sweet), Academic Press, New York, **1997**, pp. 307–326.

[39] A. J. M. Duisenberg, L. M. J. Kroon-Batenburg, A. M. M. Schreurs, *J. Appl. Crystallogr.* **2003**, *36*, 220.

[40] M. C. Burla, M. Camalli, B. Carrozzini, G. L. Cascarano, C. Giacovazzo, G. Polidori, R. J. Spagna, *J. Appl. Crystallogr.* **2003**, *36*, 1103.

[41] P. T. Beurskens, G. Beurskens, R. de Gelder, S. Garcia-Granda, R. O. Gould, R. Israel, J. M. M. Smits, *The DIRDIF-99 program system*, Crystallography Laboratory, University of Nijmegen, Nijmegen, The Netherlands, **1999**.

[42] G. M. Sheldrick, *SHELXTL*, Version 6.14, Bruker Analytical X-ray Systems, Bruker AXS, Inc., Madison, Wisconsin, USA, **2003**.

[43] G. M. Sheldrick, *SHELXL-97, Program for Crystal Structure Refinement*, University of Göttingen, **1997**.

[44] L. J. Farrugia, *J. Appl. Crystallogr.* **1999**, *32*, 837.

Received: April 5, 2005
Published Online: July 20, 2005

 © 2005 Wiley-VCH Verlag GmbH & Co. KGaA, Weinheim

4f-*ansa*-Metallocenes−Dinuclear Complexes where the *ansa*-Dicyclopentadienyl Ligands Simultaneously Act in a Chelating and Bridging Mode − Crystal Structure of $(LY)_2(\mu\text{-}L)$ [L = 2,6-Pyridinediylbis(methylcyclopentadienyl)]

G. Paolucci,*[a] M. Vignola,[a] S. Formenti,[a] and W. Massa[b]

Keywords: Yttrium / Praseodymium / Dinuclear *ansa*-lanthanocenes / Metallocenes

The reaction between $[L^NYX]_2$ [X = Cl, OTf; L^N = 2,6-pyridinediylbis(methylcyclopentadienyl] and $L'Na_2$ [L′ = L^N = 2,6-pyridinediylbis(methylcyclopentadienyl; L^{Si} = dimethylsilanediylbis(cylopentadienyl); L^O = 2,5-furanediylbis(methylcyclopentadienyl)] in a 2:1 molar ratio affords dinuclear complexes of formula $(LY)_2(\mu\text{-}L')$, in which the *ansa*-bis(cyclopentadienyl) ligands simultaneously act both in a chelating and bridging mode. The X-ray crystal structure of $(L^NY)_2(\mu\text{-}L^N)$, determined at 193 K shows an arrangement close to trigonal planar of the centroids C_g of the three Cp ligands around the Y atoms. The reactivity of the $(L^NLn)_2(\mu\text{-}L')$ species containing different bridging *ansa*-bis(cyclopentadienyl) groups with an additional free donor atom was tested to verify the possibility of coordination of a third lanthanide ion. The rearrangement reactions that occur, finally leading to the formation of the only $[L^NLnX]_2$ species, are likely to depend on the presence of the further coordinating atom in the ligand bridging the two metal ions.
(© Wiley-VCH Verlag GmbH & Co. KGaA, 69451 Weinheim, Germany, 2005)

Introduction

ansa-Bis(cyclopentadienyl) ligands usually bind to early d-transition,[1] lanthanoid,[2] and actinide[3] metal ions exclusively as metal-chelating ligands (isomeric species **I**). However, the *ansa*-bis(cyclopentadienyl) ligands in dimeric *ansa*-lanthanocene complexes can, in principle, behave both in a chelating and bridging mode with formation of the isomeric species **I** and **II**, respectively. Some examples of dimeric complexes in which each *ansa*-bis(cyclopentadienyl) ligand bridges the two metal ions (**II**) are known both in complexes of d-[4,5] and f-elements.[6–10] To date, no example of completely characterized dinuclear complexes containing the *ansa*-bis(cyclopentadienyl) ligands simultaneously acting in the two binding modes have been reported.

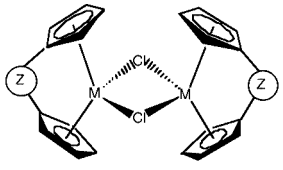

Isomer I

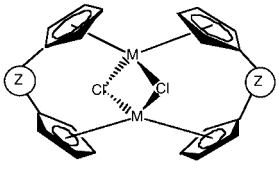

Isomer II

Recently, we have observed that the disodium salt of 2,6-bis(cyclopentadienylmethyl)pyridine (L^NNa_2) affords Pr^{III} or U^{IV} complexes of the type $[(L^NPr)_2(\mu\text{-}L^N)]$[11] and $[(L^NUCl)_2(\mu\text{-}L^N)]$,[12] respectively, where the ligand simultaneously acts both in a chelating and bridging mode. The $[(L^NPr)_2(\mu\text{-}L^N)]$ complex firstly obtained[11] as a by-product in the synthesis of the complex $[L^NPrCl]_2$ was successively prepared in moderate yield (60–70%) by reaction of L^NNa_2 and $PrCl_3$ in a 3:2 molar ratio. Here we report an improved synthesis of $[(L^NPr)_2(\mu\text{-}L^N)]$ together with the synthesis and characterization of some $(L^NY)_2(\mu\text{-}L^N)$, $(L^NY)_2(\mu\text{-}L^{Si})$, and $(L^NY)_2(\mu\text{-}L^O)$ dinuclear complexes [L^N = 2,6-$(C_5H_4CH_2)_2$-C_5H_3N; L^{Si} = $Me_2Si(C_5H_4)_2$; L^O = 2,5-$(C_5H_4CH_2)_2$-C_4H_2O]. The presence of the additional free donor atom in the bridging ligand in the complexes $(L^NY)_2(\mu\text{-}L^N)$ and $(L^NY)_2(\mu\text{-}L^O)$, prompted us to investigate the possibility of coordinating a third metal ion, thus obtaining homo- and heterotrinuclear species.

Results and Discussion

Synthesis and Characterization of $[(L^NLn)_2(\mu\text{-}L^N)]$ (Ln = Y, Pr) and $[(L^NY)_2(\mu\text{-}L')]$ (L′ = L^{Si}, L^O)

In a previous work dealing with the synthesis of the complex $[L^NPrCl]_2$, we observed[11] the presence of an impurity which, on the basis of analytical and ^1H NMR spectroscopic data, was defined as $[L^NPr]_2[\mu\text{-}L^N]$. As a confirmation, the same compound was obtained by reaction of L^NNa_2 and $PrCl_3$ in a 3:2 molar ratio. This complex was also prepared by reaction of $[L^NPrCl]_2$ and L^NNa_2 in a 2:1 molar ratio. However, the workup of the reaction mixture was difficult and any attempt to purify the complex to obtain crystals suitable for X-ray analysis was unsuccessful, mainly due to the very similar solubilities of the reagents

[a] Dipartimento di Chimica, Università Ca' Foscari di Venezia, Dorsoduro 2137, 30123 Venezia, Italy
[b] Fachbereich Chemie, Philipps Universität Marburg, Hans-Merweein-Strasse, Marburg, Germany

 © 2005 Wiley-VCH Verlag GmbH & Co. KGaA, Weinheim **DOI: 10.1002/ejic.200500280**

and the product. By using as starting materials the *ansa*-lanthanocene triflates, $[L^NLnOSO_2CF_3]_2$ (Ln = Y, Pr), more soluble and reactive species than the analogous chlorides $[L^NLnCl]_2$, the yields of the resulting $[L^NLn]_2[\mu\text{-}L^N]$ complexes are very high, thus making the workup and purification of the reaction products easier (Scheme 1).

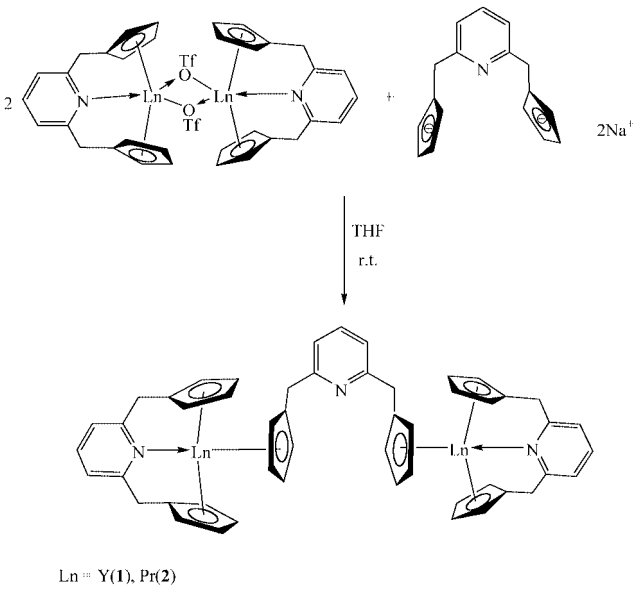

Scheme 1.

The NMR (^1H and ^{13}C) characterization of the diamagnetic complex $[L^NY]_2[\mu\text{-}L^N]$ (**1**) was simple and clearly indicative of its structure in solution (Figure 1).

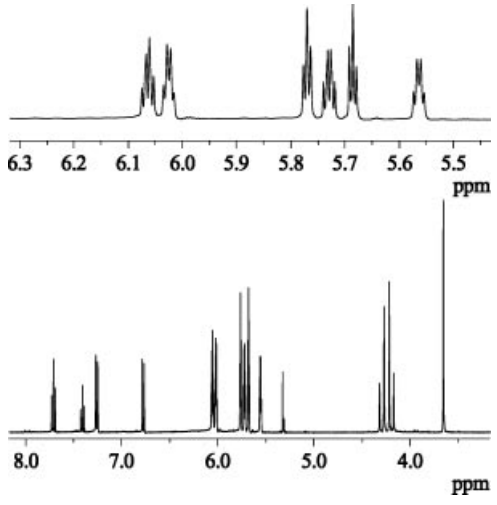

Figure 1. ^1H NMR of $[L^NY]_2[\mu\text{-}L^N]$ (**1**) ([D$_2$]dichloromethane, 400 MHz) (bottom) and its expanded part in the range δ = 6.3–5.5 ppm (top).

As reported in Figure 1, the ^1H NMR spectrum of **1** shows, in addition to a signal pattern similar to that observed in the ^1H NMR spectrum of the complex $[L^NYOSO_2CF_3]_2$ where the ligands act exclusively in a chelating mode,[2c] an additional rather simple pattern of signals readily assignable to the ligand acting in the bridging mode, with an intensity halved with respect to the signals of the two chelating ligands. In fact, the AB systems at δ = 6.06, 6.03, 5.73, 5.56 ppm correspond to the C_5H_4 protons of the chelating ligands, as the rigidity due to the additional coordination of the pyridine nitrogen atoms typical of these chelate systems makes the four C_5H_4 protons non-equivalent. On the contrary, in the case of the ligand bridging the two yttrium ions, the absence of evidence of substantial N→Y coordination makes the two pyridine-bonded C_5H_4 units virtually equivalent so that the two α-C_5H_4 and the two β-C_5H_4 protons give rise to two pseudo-triplets at δ = 5.77 and 5.69 ppm (A_2B_2 system), respectively. More diagnostic of the different rigidity of the two types of ligand L^N of **1** (i.e. in the chelating and bridging modes) are the resonances of the relative methylene groups. In fact in the case of the chelating ligands the two methylene protons are diastereotopic and give rise to an AB system centered at δ = 4.25 ppm, while in the ligand bridging the two yttrium ions free rotation makes all the methylene protons equivalent (singlet at δ = 3.66 ppm).

In the case of the paramagnetic complex $[L^NPr]_2[\mu\text{-}L^N]$ (Ln = Pr: **2**) the previously proposed structure[11] similar to that of the yttrium complex **1** could again be deduced from its ^1H NMR spectrum.

Crystal Structure of 1·CH_2Cl_2

The results of a single-crystal X-ray analysis of **1** (Figure 2) confirms the presence of discrete $[Y_2L^N{}_3]$ molecules, involving two chelating and one bridging ligand L^N. Somewhat surprisingly, the μ-L^N ligand displays a conformation with *anti*-oriented C_5H_4 rings rendering the two (*chel*-L^N)Y fragments non-equivalent. Interestingly, the N2–Y2–N3 angle is not far from 180°, suggesting some weak N2→Y2 interaction, in spite of a rather long N2–Y2 distance of 3.39 Å. Another reason for the unsymmetrical conformation of μ-L^N could be the formation of more favorable crystal packing. Within both (*chel*- L^N)Y fragments N–Y distances of 2.528(3) Å (N1–Y1) and 2.571(3) Å (N3–Y2), respectively, were found, which are in excellent agreement with data reported for $[YL^N(\mu\text{-OTf})]_2$ [2.506(4) Å[2i]], $[YL^N(\mu\text{-OH})]_2$ [2.621(3) Å[2j]], and $[YL^{ind}N(SiHMe_2)_2]$ [2.511(2) Å; L^{ind} carries two indenyl units instead of two C_5H_4 rings[20]]. Thus, substantial N→Y interaction must be assumed to take place within each (*chel*-L^N)Y fragment of **1**, as confirmed by the NMR spectrum of dissolved **1** (vide supra).

Each Y ion formally adopts a coordination number of 10, owing to three η^5-C_5H_4 rings and one N atom. The arrangement of the centers C_g of the three C_5H_4 ligands around the Y atoms is close to trigonal-planar symmetry (Table 1). There is no significant difference in the distances Y–C_g between the chelating and the bridging C_5H_4 ligands. The N-atoms are on the top of the pyramids with the $Y(C_5H_4)_3$ base plane. A packing diagram is shown in Figure 3. The dichloromethane molecules are positioned in gaps between five complex molecules. According to the criteria of Takahashi et al.,[22] a CH–π interaction can be dis-

 © 2005 Wiley-VCH Verlag GmbH & Co. KGaA, Weinheim

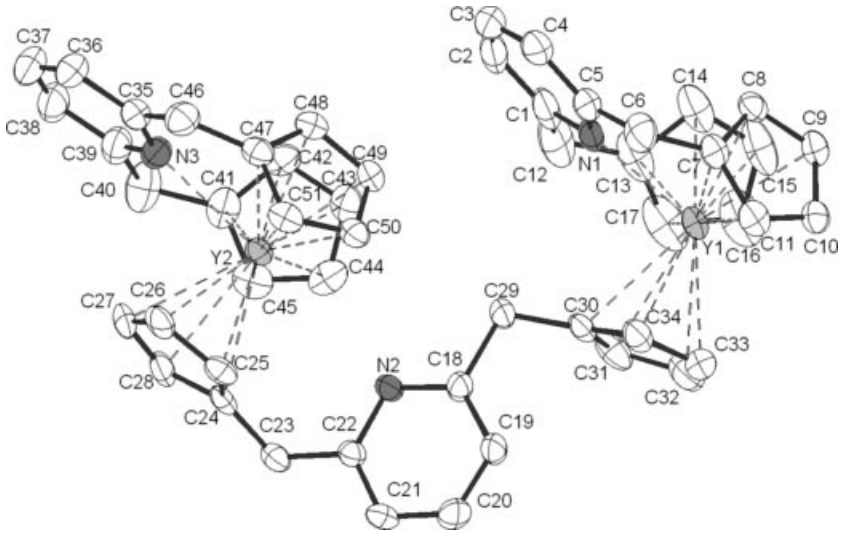

Figure 2. Perspective drawing of the molecular structure of $(L^NY)_2(\mu\text{-}L^N)$ (**1**). Displacement ellipsoids at the 50% probability level.[21]

cussed in relation to one of these neighbors. The distance of H60A (from CH_2Cl_2) to the best plane of ring 6 (C47–C51) is only 2.39 Å, with shortest contacts of 2.44 Å and 2.60 Å to C49 and C48, respectively (Figure 3), and angles C60–H60A–C49 of 142° and C60–H60A–C48 of 139°.

Table 1. Selected bond lengths [Å] and angles [°] including ring centroids (C_g) of **1**·CH_2Cl_2.

Bond lengths	
Y1–C_g2	2.428(2)
Y1–C_g3	2.465(2)
Y2–C_g4	2.454(2)
Y2–C_g5	2.442(2)
Y2–C_g6	2.430(2)
Y1–N1	2.528(3)
Y2–N3	2.571(3)
Bond angles	
C_g1–Y1–C_g2	119.25(8)
C_g1–Y1–C_g3	118.37(7)
C_g2–Y1–C_g3	119.98(8)
N1–Y1–C_g1	90.65(8)
N1–Y1–C_g2	90.50(1)
N1–Y1–C_g3	104.30(1)
C_g5–Y2–C_g6	121.41(7)
C_g4–Y2–C_g6	117.56(6)
C_g4–Y2–C_g5	120.91(6)
N3–Y2–C_g4	95.16(8)
N3–Y2–C_g5	88.78(9)
N3–Y2–C_g6	89.63(8)
Center definitions:	
C_g1: C7–C11	C_g2: C13–C17
C_g3: C30–C34	C_g4: C24–C28
C_g5: C41–C44	C_g6: C47–C51

To verify if there is a possibility that one additional *ansa*-bis(cyclopentadienyl) unit bridging two chelated $[L^NLnOSO_2CF_3]_2$ units could be extended to other *ansa*-bis(cyclopentadienyl) ligands, containing an, in principle additional, coordinating atom in the side chain, the two new yttrium species $[L^NY]_2[\mu\text{-}L^{Si}]$ (**3**) and $[L^NY]_2[\mu\text{-}L^O]$ (**4**) were prepared [L^{Si} = dimethylsilanediylbis(cyclopentadienyl), L^O =

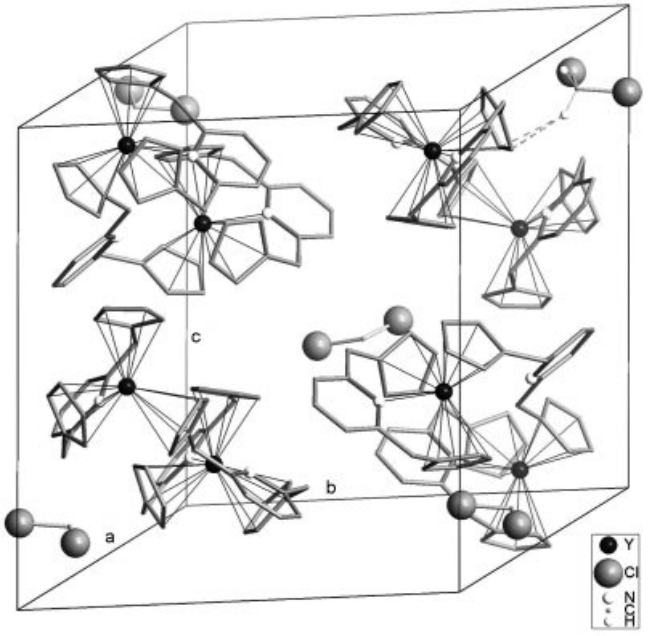

Figure 3. Packing diagram of **1**·CH_2Cl_2. Hydrogen atoms omitted. Possible CH–π interaction marked with dashed lines (H60A···C48, C49) for the upper right CH_2Cl_2 molecule only.

2,5-furanediylbis(methylcyclopentadienyl)] by reaction of $[L^NYOSO_2CF_3]_2$ with $L^{Si}Li_2$ and L^ONa_2 in a 1:1 molar ratio (Scheme 2).

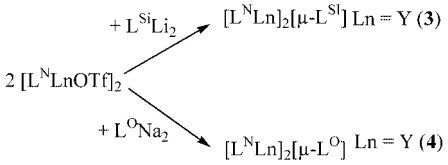

Scheme 2.

The ^{1}H NMR spectrum of **3** suggests a greater flexibility of the two L^NY systems derived from the presence of a

 © 2005 Wiley-VCH Verlag GmbH & Co. KGaA, Weinheim

broad singlet at δ = 4.23 ppm instead of the AB system (due to the diastereotopic methylene protons) observed in the case of **1**. The cyclopentadienyl protons of the L^N unities are still non-equivalent giving rise to four pseudoquadruplets centered at δ = 6.23, 6.18, 6.07, and 5.83 ppm, while the signals of the α- and β-cyclopentadienyl protons of the bridging ligand L^{Si} appear at δ = 6.17 and 6.05 ppm, respectively.

The ^{1}H NMR spectrum of species **4** suggests either a higher or lower rigidity with respect to species **3** and **1**, as shown by the AB pattern at δ = 4.26 ppm for the diastereotopic methylene protons of the two L^N units, while the methylene protons of the L^O unit give rise to a singlet at δ = 3.40 ppm. The cyclopentadienyl protons of the chelated L^N units originate four pseudoquadruplets at δ = 6.00–5.85 (m), 5.67 (q), 5.64–5.58 (m), and 5.43 (q) ppm, partially superimposed with the triplets of the α- and β-cyclopentadienyl protons of the bridging L^O unity.

Reactivity Tests of $[LY]_2[M\text{-}L]$ Complexes

By considering the presence of an uncoordinated pyridine nitrogen atom in the bridging ligand of **1**, and with the aim to verify the possibility of access to homo- and heterotrinuclear complexes by coordination of a third metal ion into the bridging unity, the dinuclear yttrium complex **1** was treated with an equimolar amount of $Y(OTf)_3$. Not quite unexpectedly, the only isolated product was the complex $[L^NYOTf]_2$.

$$[L^NY]_2[\mu\text{-}L^N] + Y(OTf)_3 \rightarrow 3/2\ [L^NYOTf]_2$$

The same behavior was observed by treating the complex $[L^NPr]_2[\mu\text{-}L^N]$ with $Pr(OTf)_3$ in a 1:1 molar ratio and under the same experimental conditions. Also in this case, the ^{1}H NMR spectrum of the final product is consistent with the formulation of $[L^NPrOTf]_2$.

One possible explanation could imply a preliminary coordination of the third lanthanide ion by the free pyridine nitrogen atom, followed by a rapid intramolecular rearrangement through redistribution of the ligands as shown in Scheme 3.

On the basis of the proposed reaction pathway, the driving force could be the presence of the coordinating pyridine nitrogen atom of the bridging ligand unity. As a consequence, this type of intramolecular rearrangement must be absent in complexes of the type $[L^NLn]_2[\mu\text{-}L']$ where the bridging unit does not contain further coordinating atoms.

Accordingly, by treating $[L^NY]_2[\mu\text{-}L^{Si}]$ (**3**) with $Y(OTf)_3$ under the same experimental conditions as for complex **1**, no change of the initial ^{1}H NMR spectrum was observed even after 36 h of reaction at room temperature.

To confirm that the coordination step of the third metal ion by the coordinating atom of the bridging ligand into the molecule plays a fundamental role in allowing the intramolecular rearrangement, the same reaction was carried out with the complex $[L^NY]_2[\mu\text{-}L^O]$ (**4**) and, as expected, the rearrangement took place and dinuclear $[L^NYOTf]_2$ was isolated (Figure 4). From the mother liquor a mixture of other hardly separable complexes, probably containing the species $[L^OYOTf]_2$ and $[L^NY(\mu\text{-}OTf)(\mu\text{-}OTf)YL^O]$ was recovered.

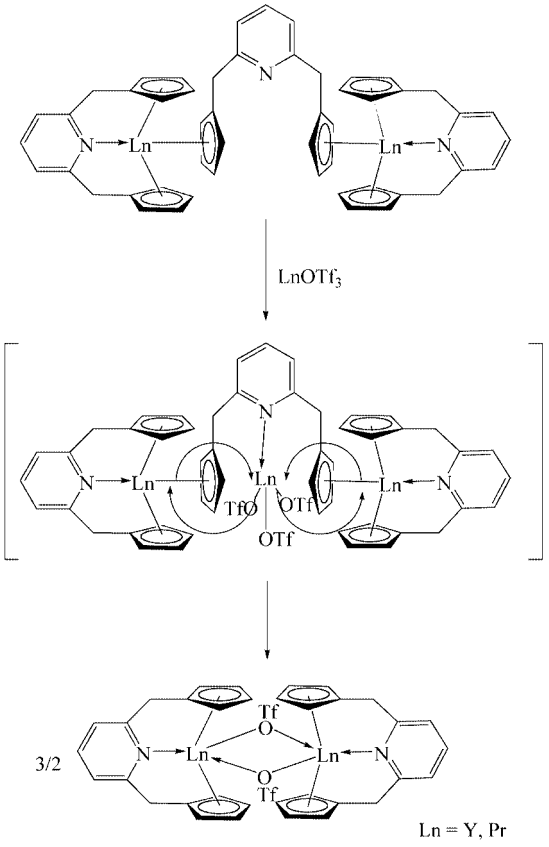

Scheme 3.

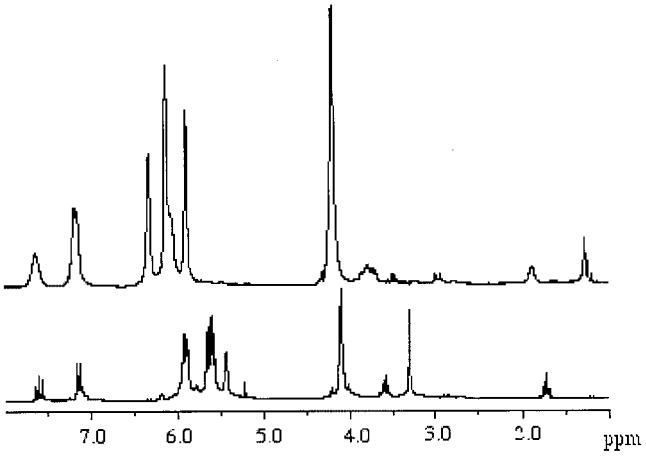

Figure 4. ^{1}H NMR spectra of $[L^NY]_2[\mu\text{-}L^O]$ (bottom) and of the reaction mixture $[L^NY]_2[\mu\text{-}L^O]$ + $Y(OTf)_3$ (top).

Conclusions

ansa-Lanthanocene complexes of the type L^NLnX (X = OTf, Cl) react in a 2:1 molar ratio with *ansa*-bis(cyclopentadienyl) ligands with, or devoid of, an additional coordinat-

 © 2005 Wiley-VCH Verlag GmbH & Co. KGaA, Weinheim

ing atom in the chain bridging the two cyclopentadienyl rings to give dinuclear species containing the *ansa*-bis(cyclopentadienyl) ligands simultaneously acting in a chelating and bridging mode. In the case of the species $[L^NLn]_2[\mu\text{-}L']$ (Ln = Y, Pr), where the bridging ligand L′ contains an additional coordinating atom, any attempt to introduce a third Ln^{III} ion to form homo- or heterotrinuclear complexes failed due to an intramolecular ligand redistribution reaction affording L^NLnX species.

Experimental Section

General Procedures: All manipulations were carried out under purified nitrogen in a glove-box apparatus (MBraun G200). The commercially available solvents, tetrahydrofuran, toluene, *n*-hexane, and diethyl ether, were firstly distilled from $LiAlH_4$ and then from sodium benzophenone ketyl under nitrogen. Dichloromethane was distilled from CaH_2. Deuterated [D_8]toluene was dried with Na/K alloy and collected by thaw cycles. CD_2Cl_2 and $CDCl_3$ were dried with CaD_2 and collected by taw cycles. Yttrium and praseodymium trifluoromethanesulfonates were prepared according to literature methods.[13] *n*BuLi (Aldrich) in THF and pentane or *n*-hexane solutions were titrated before use. The disodium salt of the ligands (L^NNa_2,[14] $L^{Si}Na_2$,[15] L^ONa_2[16]) and the complexes $[L^NLnOTf]_2$[17] were prepared as reported in the literature. NMR spectra were recorded with a Bruker AC 200 or a Varian Unity 400 spectrometer. Chemical shifts (ppm) for ^1H and ^{13}C spectra were internally referenced to the residual undeuterated solvent resonances and related to tetramethylsilane (δ = 0 ppm).

$[(L^NY)_2(\mu\text{-}L^N)]$ (1): To a solution of $[L^NYOTf]_2$ (0.942 g, 1.0 mmol) in THF (20 mL) a solution of L^NNa_2 (0.139 g, 0.5 mmol) in THF (20 mL) was slowly added at room temperature under magnetic stirring, and the mixture reacted at room temperature overnight. After removal of the solvent and volatiles under vacuum, the solid residue was added to dichloromethane (50 mL) and the insoluble sodium triflate filtered off. The volume of the resulting yellow solution was then reduced to 20 mL under vacuum and the solution left to crystallize at –20 °C to give pale yellow crystals (0.799 g, 91.1% yield). $C_{51}H_{45}N_3Y_2$ (877.75): calcd. C 69.79, H 5.17, N 4.79; found C 69.65, H 5.25, N 4.65. ^1H NMR (400 MHz, CD_2Cl_2, 25 °C): δ = 7.72 (t, $^3J_{H,H}$ = 7.7 Hz, 2 H, Py^a-4), 7.41(t, $^3J_{H,H}$ = 7.6 Hz, 1 H, Py^b-4), 7.26 (d, $^3J_{H,H}$ = 7.7 Hz, 4 H, Py^a-3,5), 6.70 (d, $^3J_{H,H}$ = 7.6 Hz, 2 H, Py^b-3,5), 6.06 (AB system, δ_A = 6.07, δ_B = 6.06, J_{AB} = 3.0 Hz, 4 H, Cp^a), 6.03 (AB system, δ_A = 6.03, δ_B = 6.02, J_{AB} = 2.4 Hz, 4 H, Cp^a), 5.77 (A_2B_2 system, J_{AB} = 2.6 Hz, 4 H, Cp^b), 5.73 (AB system, δ_A = 5.74, δ_B = 5.72, J_{AB} = 3.0 Hz, 4 H, Cp^a), 5.69 (A_2B_2 system, J_{AB} = 2.6 Hz, 4 H, Cp^b), 5.56 (AB system, δ_A = 5.57, δ_B = 5.56, J_{AB} = 2.4 Hz, 4 H, Cp^a), 4.25 (AB system, δ_A = 4.29, δ_B = 4.21, J_{AB} = 18.5 Hz, 8 H, CH_2^a), 3.66 (s, 4 H, CH_2^b) ppm. ^{13}C NMR (100 MHz, CD_2Cl_2, 25 °C): δ = 166.33, 162.12, 136.66 (C9), 136.99 (C26), 123.29, 122.35 (C8), 121.40, 120.10 (C25), 119.34 (C4), 114.11 (C2), 112.63 (C18), 109.23 (C19), 108.03 (C1), 103.27 (C3), 38.90 (C23), 37.65 (C6) ppm.

$[(L^NPr)_2(\mu\text{-}L^N)]$ (2): The compound was prepared in a manner analogous to that for **1** from $[L^NPrOTf]_2$ (1.047 g, 2 mmol) and L^NNa_2 (0.279, 1 mmol) in a 2:1 molar ratio. Dark green crystals of **2** were obtained (0.863 g, 88% yield). $C_{51}H_{45}N_3Pr_2$ (981.76): calcd. C 62.39, H 4.62, N 4.28; found C 62.50, H 4.55, N 4.50.

$[(L^NY)_2(\mu\text{-}L^{Si})]$ (3): To a solution of $[L^NYOTf]_2$ (0.942 g, 1.0 mmol) in THF (20 mL) a solution of $L^{Si}Li_2$ (0.100 g, 0.5 mmol) in THF (20 mL) was slowly added at room temperature under magnetic stirring, and the mixture reacted at room temperature overnight. After removal of the solvent and volatiles under vacuum, the solid residue was added to dichloromethane (50 mL) and the insoluble lithium triflate filtered off. The volume of the resulting yellow solution was reduced to 20 mL under vacuum and the solution left to crystallize at –20 °C to give pale yellow crystals (0.706 g, 85% yield). $C_{46}H_{44}N_2SiY_2$ (830.77): calcd. C 66.50, H 5.34, N 3.37; found C 66.60, H 5.40, N 3.50. ^1H NMR (200 MHz, $CDCl_3$, 25 °C): δ = 7.69 (t, $^3J_{H,H}$ = 7.7 Hz, 2 H, Py-4), 7.21 (d, $^3J_{H,H}$ = 7.7 Hz, 4 H, Py-3,5), 6.23 (AB system, J_{AB} = 3.0 Hz, 4 H, Cp^a), 6.18 (m, 8 H, Cp^a + Cp^b), 6.07 (AB system, J_{AB} = 3.0 Hz, 4 H, Cp), 6.05 (A_2B_2 system, J_{AB} = 2.6 Hz, 4 H, Cp^b), 5.83 (AB system, J_{AB} = 3.0 Hz, 4 H, Cp^a), 4.23 (br. s, 4 H, CH_2^a), –0.18 (s, 6 H, CH_3) ppm.

$[(L^NY)_2(\mu\text{-}L^O)]$ (4): To a solution of $[L^NYOTf]_2$ (0.942 g, 1.0 mmol) in THF (20 mL) a solution of L^ONa_2 (0.134 g, 0.5 mmol) in THF (20 mL) was slowly added at room temperature under magnetic stirring, and the mixture reacted at room temperature overnight. After removal of the solvent and volatiles under vacuum, the solid residue was added to dichloromethane (30 mL) and the sodium triflate filtered off. The volume was reduced to 20 mL under vacuum and the yellow solution left to crystallize at –20 °C giving yellow-orange crystals (0.719 g, 83% yield). $C_{50}H_{44}N_2OY_2$ (866.72): calcd. C 69.29, H 5.12, N 3.23; found C 69.35, H 5.20, N 3.30. ^1H NMR (200 MHz, $CDCl_3$, 25 °C): δ = 7.68 (t, $^3J_{H,H}$ = 7.6 Hz, 2 H, Py-4), 7.24 (d, $^3J_{H,H}$ = 7.6 Hz, 4 H, Py-3,5), 6.12–5.92(m, 8 H, Cp^b), 5.75 (AB system, J_{AB} = 2.6 Hz, 4 H, Cp^a), 5.72–5.69 (m, 8 H, Cp^a + Fur), 5.68 (AB system, J_{AB} = 3.0 Hz, 4 H, Cp^a), 5.55 (AB system, J_{AB} = 2.6 Hz, 4 H, Cp^a), 4.21 (A_2B_2, J_{AB} = 18.5 Hz, 8 H, CH_2^a), 3.40 (s, CH_2^b) ppm.

X-ray Crystal Structure Determination: A single crystal was mounted under inert oil in a glass capillary and investigated at 193 K with an IPDS image plate system. The data were corrected for Lorentz and polarization effects, and a numerical absorption correction based on indexed faces was applied. The structure was solved by direct methods (SHELXS-97)[18] and difference Fourier syntheses in space group $P2_1/c$ and refined against all F^2 data using the SHELXL-97 program.[19] All hydrogen atoms were kept riding on calculated positions (C–H 0.95 Å) with isotropic displacement factors taken as 1.2 times the U_{eq} value of the corresponding C atom. All heavier atoms were refined with anisotropic displacement parameters. No disorder was observed for the CH_2Cl_2 solvent molecule. Details of the experimental and crystal data are summarized in Table 2. CCDC-261469 contains the supplementary crystallographic data for this paper. These data can be obtained free of charge from The Cambridge Crystallographic Data Centre via www.ccdc.cam.ac.uk/data_request/cif.

Reactivity Test of $[(L^NY)_2(\mu\text{-}L^N)]$ (1) with $Y(OTf)_3$: To a solution of $[(L^NY)_2(\mu\text{-}L^N)]$ (**1**) (0.439 g, 0.5 mmol) in THF (20 mL) a solution of $Y(OTf)_3$ (0.268 g, 0.5 mmol) in the same solvent (15 mL) was added at room temperature under vigorous magnetic stirring, and the mixture reacted overnight at room temperature. After solvent removal under vacuum, the solid residue was completely dissolved in dichloromethane (20 mL). By slow evaporation of the solvent, pale yellow microcrystals of $[L^NYOTf]_2$ were obtained (0.629 g, 89% yield) as confirmed by elemental analysis, NMR spectroscopic data, and comparison with an authentic sample.

Reactivity Test of $[(L^NPr)_2(\mu\text{-}L^N)]$ (2) with $Pr(OTf)_3$: To a deep green solution of $[(L^NPr)_2(\mu\text{-}L^N)]$ (**2**) (0.491 g, 0.5 mmol) in THF (20 mL) a solution of $Pr(OTf)_3$ (0.294 g, 0.5 mmol) in the same solvent (15 mL) was added at room temperature under vigorous magnetic stirring, and the resulting green reaction mixture reacted

 © 2005 Wiley-VCH Verlag GmbH & Co. KGaA, Weinheim

Table 2. Crystal and data collection parameters for $Y_2L_3{\cdot}CH_2Cl_2$ (**1**·CH_2Cl_2).

Empirical formula	$C_{52}H_{47}Cl_2N_3Y_2$
Formula mass [g/mol]	962.65
Color, habit	yellow-brown, column
Column crystal size [mm]	0.60 × 0.23 × 0.14
Crystal system	monoclinic
Space group	*P*21/*c* (no. 14)
a [Å]	16.949(1)
b [Å]	15.997(1)
c [Å]	16.442(1)
β [°]	108.121(5)
Volume [Å^3]	4236.8(3)
Z	4
Calcd. density [Mg/m^3]	1.509
Temperature [K]	193(2)
λ (Mo-K_α) [Å]	0.71073
Absorption coefficient [mm^{-1}]	2.893
F(000)	1968
2θ range [°]	5.54–60.72
Reflections: total, unique, >4σ(*F*)	44912, 11702, 6145
No. of parameters	532
Final *R* index [$F > 4\sigma(F)$]	0.0474
wR_2 (all reflections)	0.1100
Goodness-of-fit on F^2	0.824
Residual electrondensity [e/Å^3]	0.67, –0.86

overnight at room temperature. The solvent was removed under vacuum and the solid residue completely dissolved in dichloromethane (20 mL). By slow evaporation of the solvent, green microcrystals of $[L^NPrOTf]_2$ were separated (0.465 g, 89% yield) as confirmed by elemental analysis, NMR spectroscopic data, and comparison with an authentic sample.

Reactivity Test of $[(L^NY)_2(\mu\text{-}L^{Si})]$ (3) with $Y(OTf)_3$: To a solution of $[(L^NY)_2(\mu\text{-}L^{Si})]$ (**3**) (0.415 g, 0.5 mmol) in THF (20 mL) a solution of $Y(OTf)_3$ (0.268 g, 0.5 mmol) in the same solvent (15 mL) was added at room temperature under magnetic stirring, and the mixture reacted overnight at room temperature. The solvent was removed under vacuum and the solid residue was added to dichloromethane (20 mL) where it was partially soluble. The solid residue was filtered off and characterized by elemental analysis as unreacted $Y(OTf)_3$. By addition of *n*-hexane to the solution, pale yellow microcrystals of $[(L^NY)_2(\mu\text{-}L^{Si})]$ separated.

Reactivity Test of $[(L^NLn)_2(\mu\text{-}L^O)]$ (4) with $Ln(OTf)_3$: To a solution of $[(L^NY)_2(\mu\text{-}L^O)]$ (**4**) (0.433 g, 0.5 mmol) in THF (20 mL) a solution of $Y(OTf)_3$ (0.268 g, 0.5 mmol) in the same solvent (15 mL) was added at room temperature under vigorous magnetic stirring, and the mixture reacted overnight at room temperature. The solvent was removed under vacuum and the solid residue was dissolved in dichloromethane (20 mL). The solvent was then removed under vacuum at room temperature to give, as the main product, pale yellow microcrystals of $[L^NYOTf]_2$ (0.193 g, 41% yield), as confirmed by elemental analysis and NMR spectroscopic data. From the mother liquor a mixture of compounds hardly separable was recovered.

Acknowledgments

The work was supported by a grant from the Italian Ministry of the University and of Scientific and Technologic Research (MURST, PRIN-2004). G. P. is grateful to Dr. Luca Coletto and Dr. Jacopo Zanon for their contribution to the syntheses of the complexes and for useful discussions.

[1] a) A. Togni, R. L. Halterman (Eds.), *Metallocenes*, Wiley-VCH, Weinheim, **1998**, vols. 1 and 2; b) C. S. Bajgur, W. R. Tikkenen, J. L. Petersen, *Inorg. Chem.* **1985**, *24*, 2539; c) W. Abriel, J. Heck, *J. Organomet. Chem.* **1986**, *302*, 363; d) W. Kaminsky, K. Kulper, H. H. Brintzinger, F. R. W. P. Wild, *Angew. Chem. Int. Ed. Engl.* **1985**, *24*, 507; e) W. Spalek, F. Kuber, A. Winter, J. Rohrmann, B. Bachmann, M. Antberg, V. Dolle, E. F. Paulus, *Organometallics* **1994**, *13*, 954; f) H. H. Britzinger, D. Fischer, R. Mulhaupt, B. Rieger, R. M. Waymouth, *Angew. Chem. Int. Ed. Engl.* **1995**, *34*, 1143; g) H. Deng, H. Winkelbach, K. Taeji, W. Kaminski, K. Soga, *Macromolecules* **1996**, *29*, 6371; h) A. Antinolo, M. Fajardo, S. Gomez-Ruiz, I. Lopez-Solera, A. Otero, S. Prashar, A. Rodriguez, *J. Organomet. Chem.* **2003**, *683*, 11.

[2] a) G. Jeske, L. E. Schock, P. N. Swepston, H. Schumann, T. J. Marks, *J. Am. Chem. Soc.* **1985**, *107*, 8103; b) K. Kiao, E. B. Coughlin, J. E. Bercaw, *J. Am. Chem. Soc.* **1992**, *114*, 7606; c) J. Gräper, R. D. Fischer, G. Paolucci, *J. Organomet. Chem.* **1994**, *471*, 87; d) J. P. Mitchell, S. Hajela, S. K. Brookhart, K. L. Hardcastle, L. M. Henling, J. E. Bercow, *J. Am. Chem. Soc.* **1996**, *118*, 1045; e) C. M. Haar, C. L. Stern, T. J. Marks, *Organometallics* **1996**, *15*, 1765; f) W. A. Hermann, J. Eppinger, M. Spiegler, O. Runte, R. Anwander, *Organometallics* **1997**, *16*, 1813; g) C. Qian, G. Zou, J. Sun, *J. Chem. Soc., Dalton Trans.* **1998**, 1607; h) I. L. Fedushkin, S. Dechert, H. Schumann, *Angew. Chem. Int. Ed.* **2001**, *40*, 561; i) G. Paolucci, J. Zanon, V. Lucchini, W.-E. Damrau, E. Siebel, R. D. Fischer, *Organometallics* **2002**, *21*, 1088; j) W. E. Damrau, G. Paolucci, J. Zanon, E. Siebel, R. D. Fischer, *Inorg. Chem. Commun.* **1998**, *1*, 424.

[3] a) C. M. Fendrick, E. A. Mintz, L. D. Schertz, T. J. Marks, V. W. Day, *Organometallics* **1984**, *3*, 819; b) G. Paolucci, R. D. Fischer, F. Benetollo, R. Seraglia, G. Bombieri, *J. Organomet. Chem.* **1991**, *412*, 327; c) A. K. Dash, Y. Gurevitz, J. Q. Wang, J. Wang, M. Kapon, M. S. Eisen, *Organometallics* **2001**, *20*, 5084; d) A. K. Dash, Y. Gurevitz, J. Q. Wang, J. Wang, M. Kapon, M. S. Eisen, *J. Alloys Compd.* **2002**, *344*, 65.

[4] a) J. Weaver, P. Woodward, *J. Chem. Soc., Dalton Trans.* **1973**, 1439; b) P. A. Wegner, V. A. Uski, R. P. Kiester, S. Dabestani, V. W. Day, *J. Am. Chem. Soc.* **1977**, *99*, 4876.

[5] M. E. Wright, T. M. Mezza, G. O. Nelson, N. R. Armstrong, *Organometallics* **1983**, *2*, 1711.

[6] N. Höck, W. Oroschin, G. Paolucci, R. D. Fischer, *Angew. Chem. Int. Ed. Engl.* **1986**, *25*, 738.

[7] T. Aknoukh, J. Müller, K. Qiao, X. F. Li, R. D. Fischer, *J. Organomet. Chem.* **1991**, *408*, 47.

[8] K. Qiao, R. D. Fischer, G. Paolucci, *J. Organomet. Chem.* **1993**, *456*, 185.

[9] a) C. Qian, W. Nie, J. Sun, *Organometallics* **2000**, *19*, 4134; b) W. Nie, C. Qian, Y. Chen, S. Jie, *J. Organomet. Chem.* **2002**, *647*, 114.

[10] M. G. Klimpel, P. Sirsch, W. Scherer, R. Anwander, *Angew. Chem. Int. Ed.* **2003**, *42*, 574.

[11] G. Paolucci, R. D'Ippolito, C. Ye, C. Qian, J. Gräper, R. D. Fischer, *J. Organomet. Chem.* **1994**, *471*, 97.

[12] G. Paolucci et al., unpublished results.

[13] F. T. Edelmann (Ed.), *Synthetic Methods of Organometallic and Inorganic Chemistry*, Georg Thieme Verlag, Stuttgart, New York, **1997**, vol. 6, p. 36.

[14] G. Paolucci, R. D. Fischer, F. Benetollo, R. Seraglia, R. G. Bombieri, *J. Organomet. Chem.* **1991**, *412*, 342.

[15] $L^{Si}Na_2$ was prepared by adding a THF solution of Me_2SiCl_2 (15.65 mmol) to a THF solution of NaCp (62.60 mmol) at –30 °C. Once the addition was complete, the reaction mixture was left at room temperature overnight. The solvent and volatiles were removed under vacuum. The resulting oily product was treated with toluene to give a pale yellow solid.

[16] C. Qian, D. Zhu, *J. Chem. Soc., Dalton Trans.* **1994**, 1599.

[17] G. Paolucci, J. Zanon, V. Lucchini, W.-E. Damrau, E. Siebel, R. D. Fischer, *Organometallics* **2002**, *21*, 1088–1094.

 © 2005 Wiley-VCH Verlag GmbH & Co. KGaA, Weinheim

[18] G. M. Sheldrick, *SHELXS-97, Program for the solution of crystal structures*, University of Göttingen, **1997**.
[19] G. M. Sheldrick, *SHELXL-97, Program for the refinement of crystal structures*, University of Göttingen, **1997**.
[20] J. Eppinger, Doctoral Dissertation, Technische Universität München, **1999**, 166.
[21] K. Brandenburg, *DIAMOND* 3.0a, Crystal Impact GbR, Bonn, **2004**.
[22] O. Takahashi, Y. Kohno, S. Iwasaki, K. Saito, M. Iwaoka, S. Tomoda, Y. Uezawa, S. Tsuboyama, M. Nisho, *Bull. Chem. Soc. Jpn.* **2001**, *47*, 2421.

Received: March 31, 2005
Published Online: August 1, 2005

 © 2005 Wiley-VCH Verlag GmbH & Co. KGaA, Weinheim

Non-Covalent Aggregation of Discrete Metallo-Supramolecular Helicates into Higher Assemblies by Aromatic Pathways: Structural and Chemical Studies of New Aniline-Based Neutral Metal(II) Dihelicates

Miguel Vázquez,[a][‡] Manuel R. Bermejo,*[b] Maurizio Licchelli,[a] Ana M. González-Noya,[b] Rosa M. Pedrido,[b] Claudio Sangregorio,[c] Lorenzo Sorace,[c] Ana M. García-Deibe,[b] and J. Sanmartín[b]

Keywords: Fluorescence / Helical structures / Pi interactions / Self-assembly / Supramolecular chemistry

Neutral manganese(II), iron(II), cobalt(II), nickel(II), zinc(II) and cadmium(II) complexes with an *N*-tosyl-substituted N_4-donor Schiff base containing a 4,4′-methylenedianiline residue as spacer [H_2L^a: *N*,*N*′-bis(2-tosylaminobenzylidene)-4,4′-methylenedianiline], and the zinc(II) complex with an analogous ligand [H_2L^b: *N*,*N*′-bis(2-tosylaminobenzylidene)-4,4′-oxodianiline] have been prepared by an electrochemical procedure. FAB and ESI mass spectra of the complexes show peaks due to species corresponding to a general formula $[M_2(L^{a,b})_2 + H]^+$, thereby suggesting their dinuclear nature. A detailed study of the crystal packing in the unit cell of the zinc(II) complex with H_2L^a shows that the helicates aggregate to form discrete prismatic moieties containing three molecules held together by π–π and σ–π interactions. Moreover, the Zn^{II} neutral dihelicate with H_2L^b forms a 3D network in the solid state due to intermolecular π-stacking interactions. ^1H NMR studies of the diamagnetic compounds reported herein have been performed. Finally, the ligand H_2L^a and its Zn^{II} and Cd^{II} complexes have been studied by spectrophotometric and spectrofluorimetric techniques in order to get a better understanding of the formation mechanisms of the complexes and of the nature of their fluorescence emission. Emission studies show that the Zn^{II} and Cd^{II} dihelicates with H_2L^a display a green fluorescence in acetonitrile solution (λ = 473 nm, Φ = 0.03 and λ = 476 nm, Φ = 0.01, respectively).

(© Wiley-VCH Verlag GmbH & Co. KGaA, 69451 Weinheim, Germany, 2005)

Introduction

Metallo-helicates are a dynamic research field in supramolecular chemistry.[1–3] However, predicting the result of a self-assembly process is still not easy as it depends on numerous factors, such as the coordination and stereochemical preferences of the metal centres, the structure of the ligand strands or the existence of weak inter- or intramolecular non-covalent connections, such as hydrogen bonds[4] or interactions between aromatic groups.[5]

Aromatic interactions are a very important class of non-covalent intermolecular forces in biology, chemistry and materials science.[6] It has been demonstrated that, in the absence of strong hydrogen-bond donors and acceptors, aromatic groups tend to aggregate via π–π interactions, σ–π (C–H···π) connections, or both, and this trend is magnified when the aromatic groups are electron-poor ring systems.[7] These weak non-covalent bonds can sustain supramolecular architectures,[8] such as the vertical base–base interaction in DNA,[9] the tertiary and quaternary structures of peptides and proteins,[11] the packing of aromatic molecules in crystals,[10] or supramolecular host–guest bonding.[12] Furthermore, Hannon et al. have recently illustrated how metal–ligand and π–π interactions can be used in concert to force the aggregation of helicates into larger nanoscale arrays, such as chiral balls[13] or metallo-supramolecular cylinders.[14] The synthetic method employed to build these assemblies, the so-called "second supramolecular event approach", consists of using an initial supramolecular event to construct small supramolecular units, which are then used as building blocks in a second supramolecular event to give a higher order aggregate.

We have recently embarked upon a program to exploit the helical structural motif as a means of producing larger supramolecular architectures through non-covalent aggregation. In a first approach, we have reported how the introduction of an OH group into an alkyl spacer can provoke the aggregation of neighbouring fluorescent helicates through hydrogen bonding.[15] After that, we decided to ex-

[‡] Present adress: Departamento de Química Inorgánica, Facultade de Química, Universidade de Vigo, 36310 Vigo, Spain
E-mail: miguel.vazquez@uvigo.es
[a] Laboratorio di Chimica Supramolecolare, Dipartimento di Chimica Generale, Università di Pavia, 27100 Pavia, Italy
[b] Departamento de Química Inorgánica, Facultade de Química, Universidade de Santiago de Compostela, 15782 Santiago de Compostela, Spain
E-mail: qimb45@usc.es
[c] UdR INSTM and Dipartimento di Chimica, Università di Firenze, 50019 Sesto Fiorentino (Fi), Italy

plore new routes to employ other non-covalent interactions in the aggregation processes. For this reason we have designed the Schiff-base ligand H_2L^a (Scheme 1), which contains four aniline groups that are potentially electron-deficient ring moieties when coordinating to a metal centre, with the hope that they should induce the aggregation of neighbouring helicate units through aromatic interactions.[16] H_2L^a is also equipped with a long and flexible spacer unit that effectively drives the self-assembly of dihelicates.[17] We have succeeded in synthesising the dinuclear complex of Cu^{II} of this ligand,[18] and herein we describe the synthesis, structural characterisation and absorption, emission and magnetic properties of the manganese(II), iron(II), cobalt(II), nickel(II), zinc(II) and cadmium(II) derivatives of this ligand. Moreover, in order to shed more light on the impact that a change in the flexibility of the spacer could have on the aggregation properties of these complexes, the zinc(II) derivative with an analogous ligand H_2L^b (Scheme 1) has been synthesised and structurally characterised.

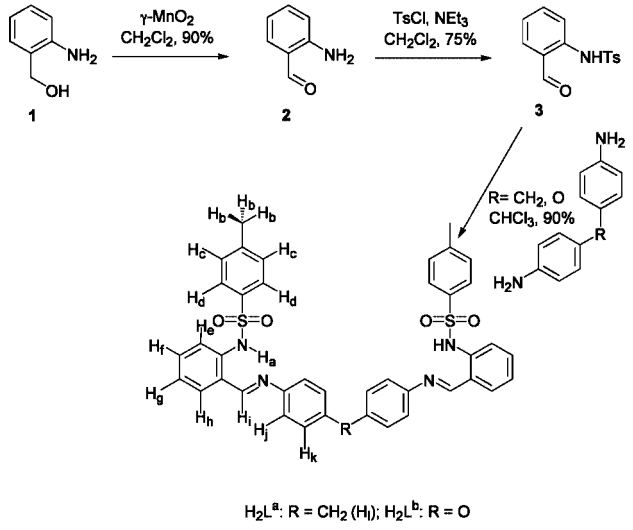

Scheme 1. Synthesis of the ligands H_2L^a and H_2L^b.

Results and Discussion

Synthesis of *N*,*N*′-Bis(2-tosylaminobenzylidene)-4,4′-methylenedianiline (H_2L^a) and *N*,*N*′-Bis(2-tosylaminobenzylidene)-4,4′-oxodianiline (H_2L^b)

Ligands H_2L^a and H_2L^b were synthesised with an overall yield of 60% according to a three-step procedure (Scheme 1).[19] The first step involves the oxidation of 2-aminobenzyl alcohol (**1**) with γ-MnO_2 in dry dichloromethane for 24 h at room temperature, under argon to give 2-aminobenzaldehyde (**2**).[20] Subsequently, the *N*-tosylation of **2** with tosyl chloride and triethylamine to give 2-tosylaminobenzaldehyde (**3**) was performed. Compound **3** has also been prepared and structurally characterised by us by another method.[21] Finally, Schiff-base condensation of **3** and 4,4′-methylenedianiline or 4,4′-oxodianiline in chloroform at reflux temperature afforded ligands H_2L^a and H_2L^b, respectively. These ligands were satisfactorily characterised (see Exp. Sect.).

Electrochemical Synthesis of the Complexes

A series of metal neutral complexes was obtained by electrochemical oxidation[22] of the corresponding metal anode in an acetonitrile solution of the corresponding ligand in the presence of a small quantity of tetraethylammonium perchlorate as supporting electrolyte. The electrochemical efficiencies of the cells were close to 0.5 mol F^{-1}, which are compatible with the following reaction scheme:

Cathode: $2\ H_2L^{a,b} + 4e^- \rightarrow 2\ H_2\ (g) + 2\ (L^{a,b})^{2-}$

Anode: $2\ (L^{a,b})^{2-} + 2M \rightarrow [M(L^{a,b})]_2 + 4\ e^-$

This synthetic procedure allowed us to obtain neutral metal complexes of the type $[M(L^{a,b})]_2{\cdot}(CH_3CN)_n$ (n = 0–2) with high purity and in very good yield. The empirical formulae found, namely $[M(L^a)]{\cdot}(CH_3CN)_n$ (M = Mn, Fe, Co, Ni, Zn, Cd; n = 0–2) and $[Zn(L^b)]{\cdot}(H_2O)_4$, suggest that the metals react with the ligands in a 1:1 molar ratio. All of them seem to be stable in the solid state and, with the exception of the manganese(II) and iron(II) complexes with H_2L^a, also in solution. They are fairly soluble in the most common polar aprotic organic solvents, but totally insoluble in both apolar or protic media.

The complexes with H_2L^a show a shift of the ν(C=N) absorption to lower wavenumbers (7–25 cm^{-1}; cf. 1621 cm^{-1} in the free ligand). In addition, a shift of the ν(C–N) absorption to lower wavenumbers is also observed (34–48 cm^{-1}; cf. 1337 cm^{-1} in the free ligand). Moreover, the zinc(II) complex with H_2L^b shows a slight shift of 7 cm^{-1} for ν(C=N) (1617 cm^{-1} in the free ligand) and a shift of 40 cm^{-1} for ν(C–N) (1340 cm^{-1} in the free ligand), both to lower wavenumbers. These IR data suggest that both imine and amide nitrogen atoms are involved in coordination to the metal centres in all the complexes.

The FAB mass spectra of the complexes show peaks due to fragments $[M_2(L^{a,b})_2 + H]^+$. Such results imply a successful coordination of the ligands to the metals and suggest the dinuclear nature of the complexes. Fragments containing solvent molecules were not observed, which points to the solvate nature rather than to a coordination behaviour of the solvent molecules. Higher molecular weight peaks, which could suggest the presence of supramolecular aggregates, were not observed in any spectra. In order to assess the identity of the complex species formed in solution by the ligands H_2L^a and H_2L^b more clearly, further investigations were performed by electrospray ionisation mass spectroscopy (ESI-MS). All the spectra exhibit base peaks (ca. 100%) corresponding to $[M_2(L^{a,b})_2 + H]^+$ fragments. These data suggest that the [2+2] complexes are the main species in solution.

 © 2005 Wiley-VCH Verlag GmbH & Co. KGaA, Weinheim

Crystal Structure of $[Zn(L^a)]_2 \cdot CH_3CN$ (5)

Recrystallisation of **5** from acetonitrile by slow concentration afforded yellow crystals for which we determined the molecular structure by X-ray crystallography.[23]

The asymmetric unit of the zinc(II) dihelicate **5** (Figure 1) contains two Zn atoms, two ligands and one acetonitrile molecule. The Zn–Zn distance is 11.83 Å and the ligands wrap around the two zinc centres to form a double helix with helical twists of 140.0° ([Zn1–N3–N2–Zn2) and 143.5° (Zn1–N7–N6–Zn2). The distortion from an ideal tetrahedral geometry is shown by the angles between the nitrogen and zinc atoms, which range from 93.0° to 126.8° for Zn1, and from 93.6° to 126.9° for Zn2.

Each ligand forms two six-membered chelate rings, which are nearly planar, one around each zinc atom. The angle between these chelate rings at both metal centres are 96.03(1)° for Zn1 and 103.94(1)° for Zn2. Two oxygen atoms from the tosyl groups interact weakly with each metal centre (Zn–O distances range from 2.65 to 2.87 Å). All other bond lengths are similar to those found in other tetrahedral zinc(II) complexes with related Schiff-base ligands.[15,19,24] The phenyl rings of the diarylmethane spacer are face-to-face π-stacked with those on the adjacent ligand strand [centroid–centroid distances: rings C22 to C27 and C63 to C68 = 4.19 Å; rings C15 to C20 and C55 to C60 = 4.01 Å; angles between ring planes: rings C22 to C27 and C63 to C68 = 27.11(2)°, rings C15 to C20 and C55 to C60 = 18.02(2)°]. All these distances and angles reveal the non-equivalence of the environment of the two zinc atoms and of both ligand units, which gives rise to a certain degree of asymmetry.[5a,19] This coordinative asymmetry leads to the formation of two grooves of different size in the main body of the metallo-organic double helix, reminiscent of the structure of DNA.[25] A good approximation to the wrapping angle of the helicate could be the torsion angle formed by the two metal ions, that define the helical axis of the helicate, and the outer donor atoms of the same ligand strand that coordinate these two metal centres. In our case these torsion angles are 279.5° for N8–Zn1–Z2–N5 and 280.4° for N4–Zn1–Zn2–N1.

A great number of intermolecular face-to-face and edge-to-face aromatic interactions between neighbouring helicates are present in the crystal cell. A detailed study of the

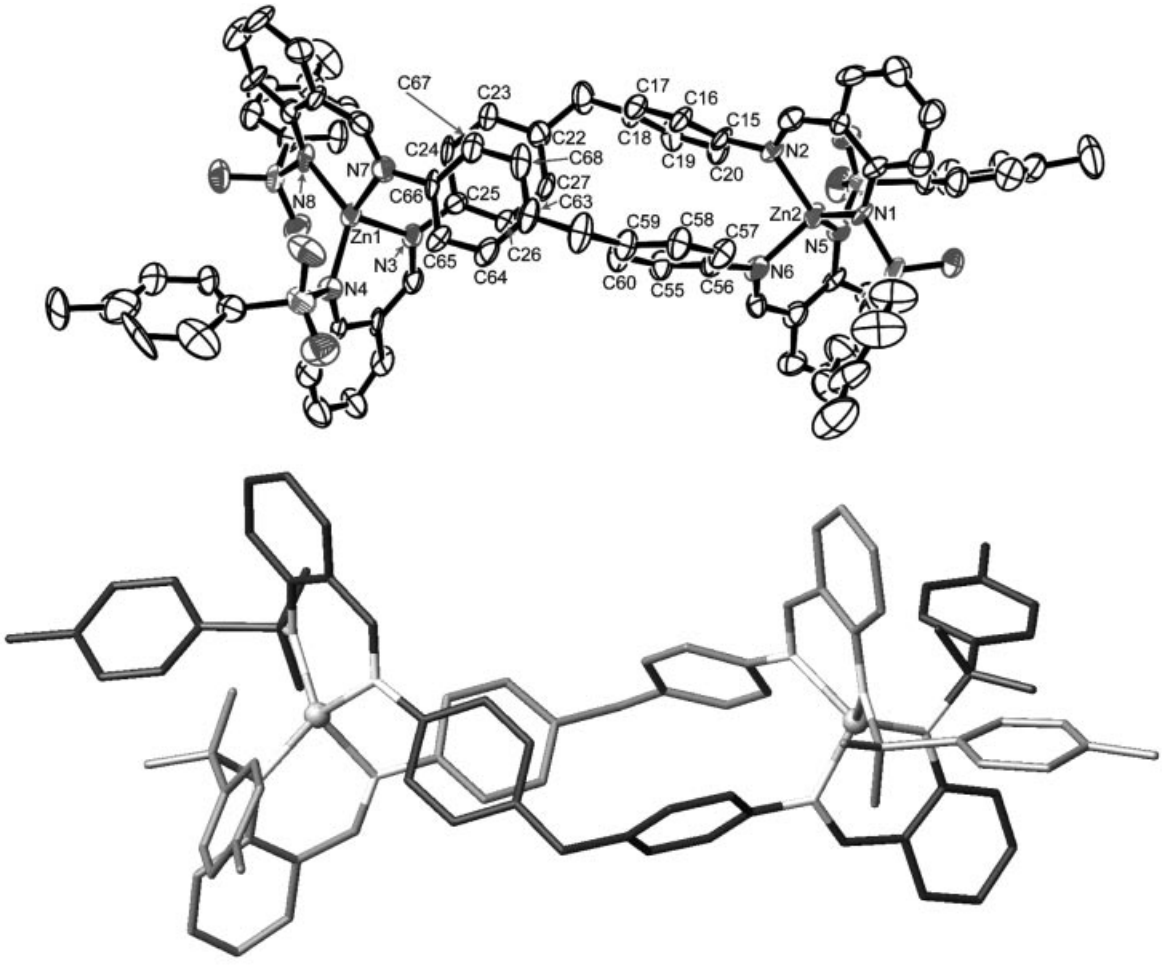

Figure 1. Top: ORTEP representation of the molecular structure of $[Zn(L^a)]_2 \cdot CH_3CN$ (**5**). Thermal ellipsoids are shown at the 40% probability level. Bottom: Stick representation of the X-ray crystal structure of **5**. Hydrogen atoms and the solvent molecule have been omitted for clarity.

 © 2005 Wiley-VCH Verlag GmbH & Co. KGaA, Weinheim

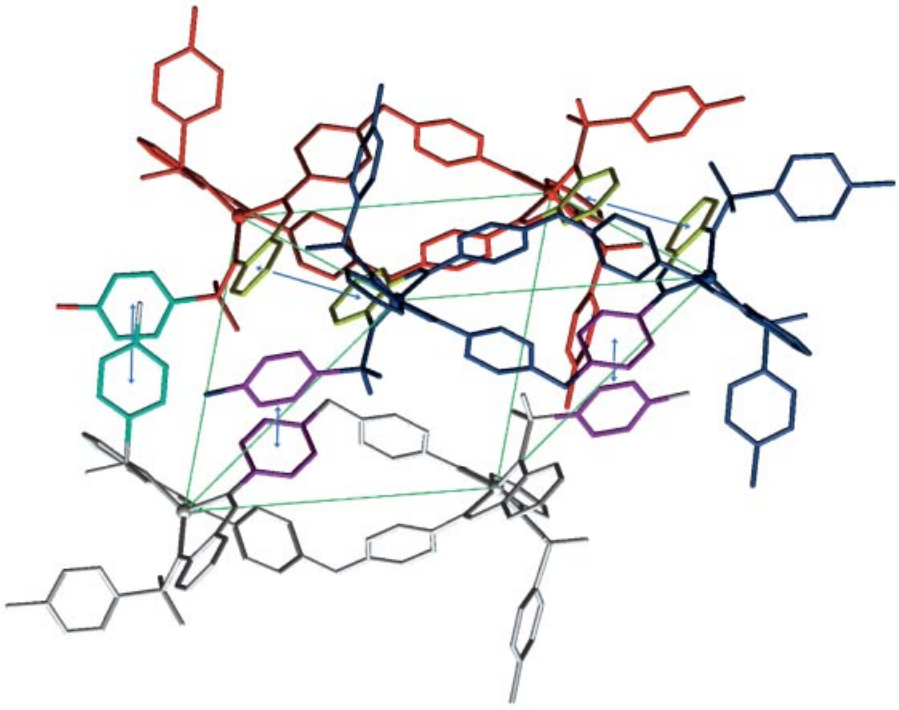

Figure 2. Part of the unit cell of **5** exhibiting the three different types of intermolecular aromatic interactions (cyan, yellow and pink) between three adjacent dihelicates (blue, grey and red). The dinuclear helicates aggregate to form discrete supramolecular prismatic assemblies of three molecules.

crystal packing reveals that the Zn^{II} dihelicates aggregate to form discrete prismatic moieties of three metallo-supramolecular members held together by π–π and σ–π connections.

There are three aromatic supramolecular interactions of different nature in each "triangular prism"; they are coloured cyan, yellow and pink in Figure 2. Both the yellow and cyan interactions are offset π–π interactions, while the pink ones are σ–π. The red dihelicate is connected to the blue one through two identical offset π–π interactions (yellow) between the aromatic rings of their benzylidene binding moieties ($centroid_{red}$–$centroid_{blue}$ distance = 3.89 Å). Moreover, the red dihelicate is connected to the grey one through a unique offset π–π interaction (cyan) between the aromatic rings of their terminal tosyl groups ($centroid_{red}$–$centroid_{white}$ distance = 4.07 Å). Finally, the white dihelicate is connected to the blue one through two identical edge-to-face interactions (pink) using one aromatic ring from the spacer and another from the terminal tosyl group, in a double contact (H_{blue}–$centroid_{white}$ distance = 3.18 Å). These distances are similar to those reported in the literature by us[18] and others[26] for analogous helicates, but shorter than that found for $[Zn(L^b)]_2$ (see below).

Figure 3 shows two different views of two adjacent triangular prisms, painted red and green. There are no π–π or σ–π aromatic interactions between neighbouring prismatic aggregates − they are discrete moieties. Each prism contains both types of helical enantiomer (left-handed and right-handed). The red prism (Figure 3b, left) contains one left-handed and two right-handed helicates, while the green prism (Figure 3b, right) contains one right-handed and two left-handed helicates. The unit cell encloses both isomers in 50% yield.

In summary, the discrete dinuclear dihelicates aggregate in the solid state into groups of three molecules that form an unprecedented assembly of six Zn^{II} ions and six ligands. The volume of the triangular prism defined by the six Zn^{II} ions is 598 $Å^3$ (Figure 4).

Crystal Structure of $[Zn(L^b)]_2 \cdot CH_3CN$

Yellow crystals of $[Zn(L^b)]_2 \cdot CH_3CN$ suitable for X-ray studies[27] were obtained by slow concentration of a saturated acetonitrile solution of $[Zn(L^b)]_2 \cdot (H_2O)_4$ (**7**). The structure of this complex (Figure 5) reveals the formation of a binuclear zinc(II) complex, with the ligands spanning both metal centres and intertwined to give a perfectly symmetrical double helix (symmetry space group of the unit cell = *Fddd*). A racemic mixture of both enantiomers (left- and right-handed) is observed in the crystal cell.

Each zinc(II) centre occupies a four-coordinate distorted tetrahedral environment, being bound by two aminobenzylidenimine units, one from each ligand. Thus, both ligands act as bisbidentate N_4 donors. The distortion from an ideal tetrahedral geometry is shown by the angles between the nitrogen and zinc atoms, which range from 92.2° to 128.0°. Each ligand forms two six-membered chelate rings, which are nearly planar, one around each metal atom. The angle between the chelate rings in both metal centres is 112.9°. Two oxygen atoms from the tosyl groups interact

 © 2005 Wiley-VCH Verlag GmbH & Co. KGaA, Weinheim

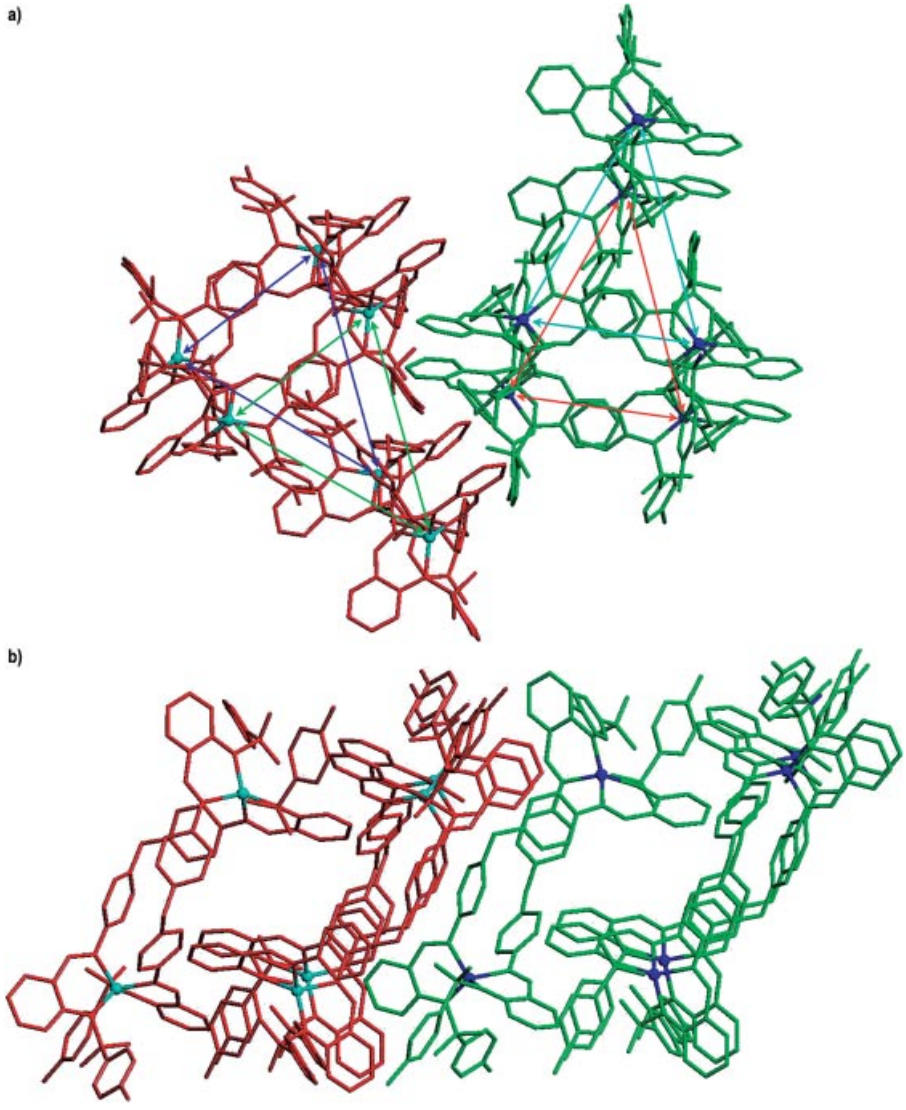

Figure 3. Two different views of two neighbouring prisms (red and green) in the unit cell of **5**. There are no aromatic interactions (π–π or σ–π) between adjacent prismatic aggregates.

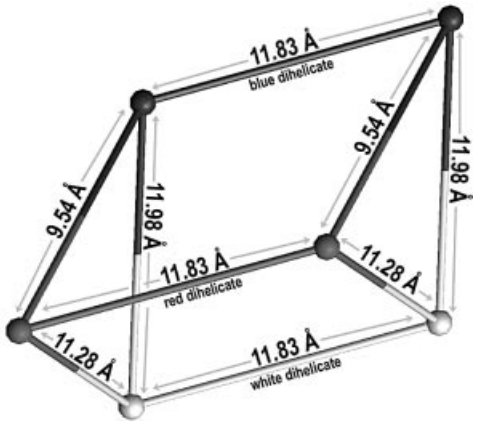

Figure 4. Schematic representation of the supramolecular triangular prism of zinc(II) dihelicates in **5** showing the inter- and intramolecular Zn–Zn distances. The spheres represent the zinc(II) ions, and their colour indicates their original dihelicate, as shown in Figure 2. The volume of the geometrical solid defined by the six Zn^{II} ions is 598 $Å^3$.

weakly with each metal centre (Zn–O distance = 2.69 Å). All the other bond lengths are similar to those found in other tetrahedral zinc(II) complexes with similar N_4 Schiff bases.[15,19,24]

The phenyl rings of the oxodianiline spacer are face-to-face π-stacked with those on the adjacent ligand strand (centroid–centroid distance = 3.99 Å; angle between ring planes = 12.9°). To achieve this, the two ligand units are pulled symmetrically along the helical axis. The helical twist of the ligand strands around the helical axis, defined by the N(1)–Zn(1)–Zn(1_3)–N(1_4) dihedral angle, is 268.8°.

The intermolecular π-stacking interactions present in this crystal structure, which are responsible for the aggregation of the discrete zinc(II) helicate units into a polymeric 3D network of helicates, are very similar to those described in our previous communication.[18] Each Zn^{II} dihelicate uses two aromatic rings to connect to another helical unit, one from the oxodianiline spacer and the other from the benzylidene binding moiety, in a double interaction. Overall, each

 © 2005 Wiley-VCH Verlag GmbH & Co. KGaA, Weinheim

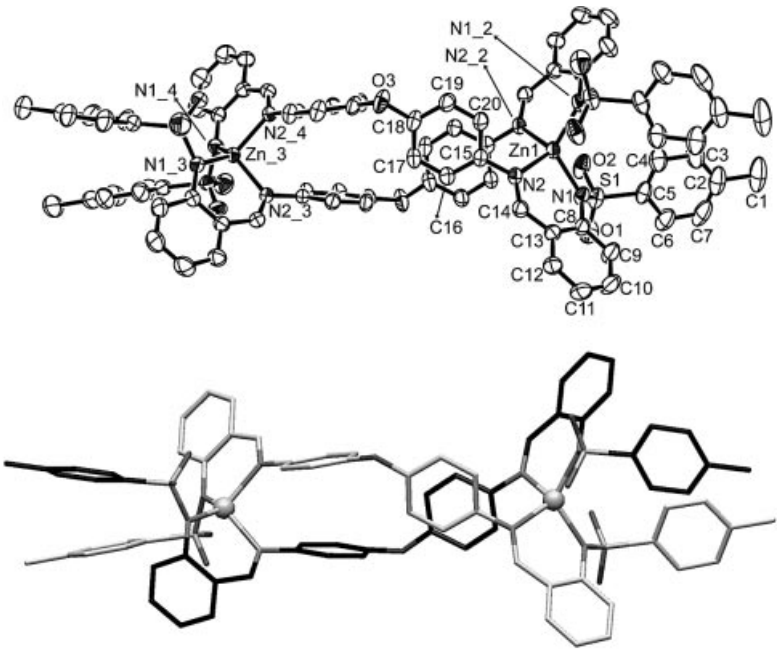

Figure 5. Top: ORTEP representation of the molecular structure of $[Zn(L^b)]_2{\cdot}CH_3CN$ Thermal ellipsoids are shown at the 50% probability level. Bottom: Stick representation of the X-ray crystal structure of $[Zn(L^b)]_2{\cdot}CH_3CN$. Hydrogen atoms and the solvent molecule have been omitted for clarity.

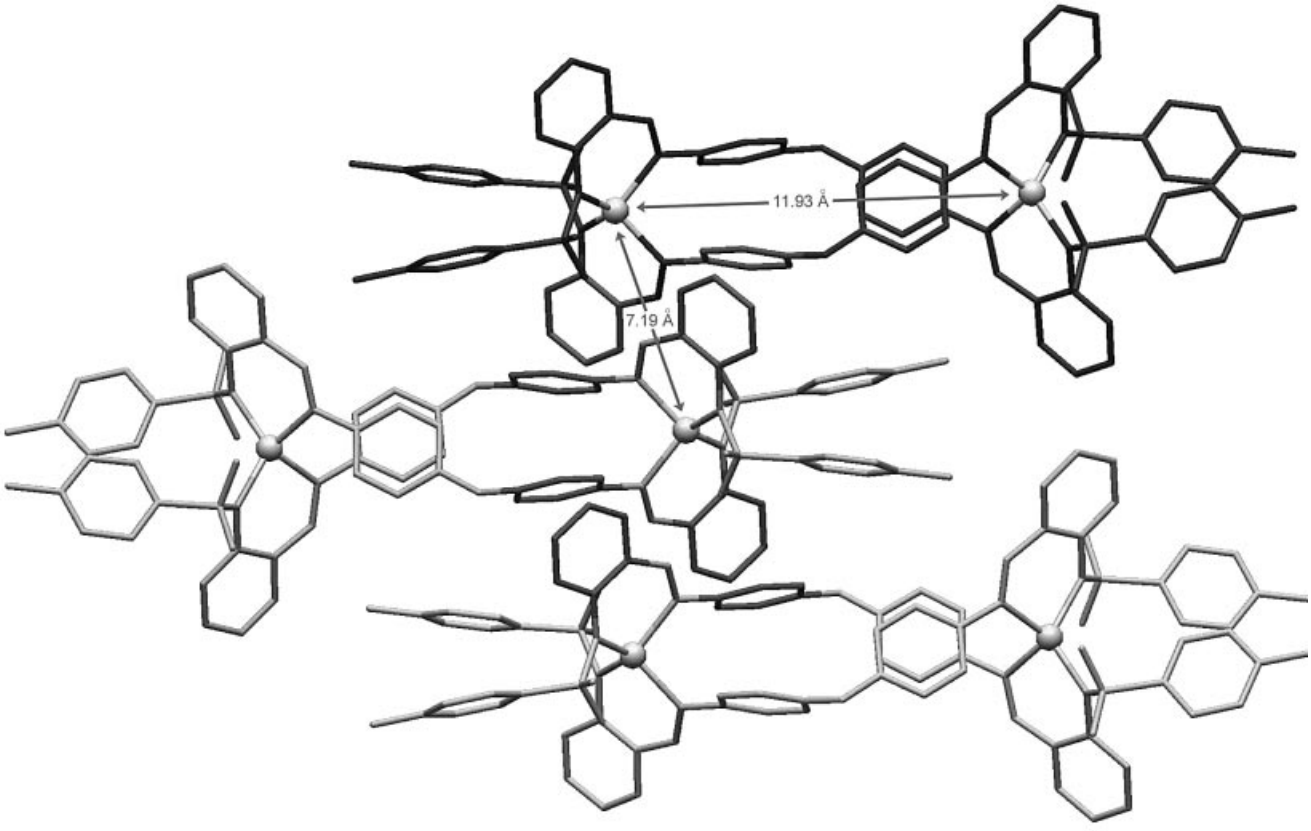

Figure 6. A representation of part of the unit cell of $[Zn(L^b)]_2{\cdot}CH_3CN$, showing the double π-stacking connections established between adjacent dihelicates. This is a 2D view of the crystal cell; π–π connections on the left side of the central dihelicate that grow normal to the plane of the paper must be considered equivalent. Interestingly, the intermolecular Zn–Zn distance (7.19 Å) is shorter than the intramolecular one (11.93 Å).

 © 2005 Wiley-VCH Verlag GmbH & Co. KGaA, Weinheim

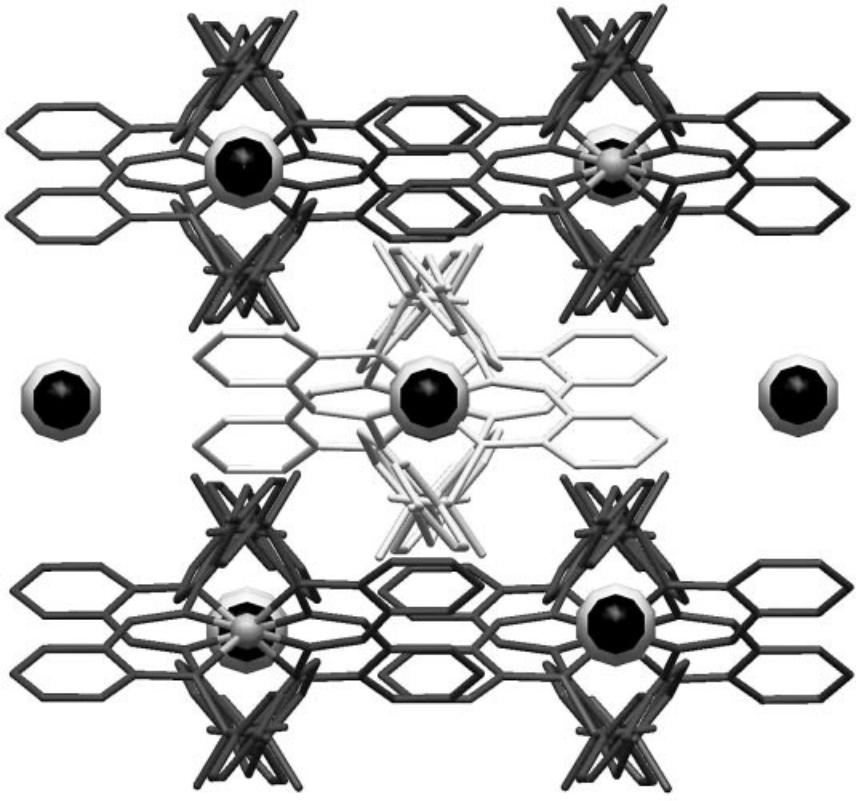

Figure 7. A perspective of the unit cell of $[Zn(L^b)]_2 \cdot CH_3CN$. It can be considered as a 3D supramolecular solid into which acetonitrile guest molecules (white-black spheres) are absorbed.

helicate is connected to another four molecules, through eight identical offset π–π interactions, forming a 3D network of helicates (Figure 6). The distance between the centroids of the intermolecular stacked aromatic rings is 4.80 Å. The "displacement angle" between these stacked rings, defined as the angle between the centroids vector and the normal to the benzylidene ring plane, is 21.7°. Moreover, the distance between the two closest zinc(II) centres of connected dihelicates is shorter (7.19 Å) than the intramolecular Zn–Zn distance (11.93 Å).

Another interesting structural feature of this complex is the presence of two, totally unbound acetonitrile molecules per formula unit that fill the 3D body of the network (Figure 7). This fact shows the capability of the array to include a large number of small, neutral guest molecules.[28] It must be noted that while a number of open frameworks have been assembled by the reactions of metal ions with a large variety of organic molecules, such as di-, tri-, and polytopic N-bound organic linkers or carboxylate linkers (i.e. 4,4-bipyridine[29] and benzene-1,3,5-tricarboxylate[30]), those sustained by π–π interactions are still rare or lacking.[31] Moreover, the use of helical metal-organic architectures as building blocks for the formation of 3D networks has been explored only recently.[26]

This supramolecular situation is quite different to that described above for the other Zn^{II} helicate **5**, where the π–π and σ–π interactions between the aromatic rings of different complexes allow the formation of discrete prismatic aggregates of three helicates. However, it is very similar to that found for the recently reported Cu^{II} derivative with H_2L^a,[18] the difference being that the metal centres in the copper(II) dihelicate occupy very distorted (near square-planar) tetrahedral environments.

The ligand H_2L^b is more rigid than H_2L^a due to the substitution of the CH_2 group in the spacer by an oxygen atom. In addition, the Zn^{II} ion is coordinatively more flexible than Cu^{II}. Taking all this into account, we reasoned that the introduction of more rigidity into any of the building blocks that form a helicate (the ligands or the metal centres) leads to the formation of more-symmetric dihelicates. Moreover, this high symmetry seems to support the self-aggregation of the helicates into polymeric arrays rather than discrete assemblies. Therefore, we suggest that more-rigid building blocks facilitate the self-aggregation of the dihelicates into 3D frameworks.

Magnetic Studies

The occurrence of a coupling between metal centres reported for the Cu^{II} derivative of the ligand H_2L^a[18] could not be confirmed by measurements on the other paramagnetic complexes. The magnetic moments of all the paramagnetic complexes reported herein were recorded in the solid state between 2 and 300 K. The values of the magnetic moments, obtained by the Curie–Weiss fit of susceptibility

 © 2005 Wiley-VCH Verlag GmbH & Co. KGaA, Weinheim

data, are in the range expected for magnetically diluted tetrahedral metal(II) ions.[32] The temperature dependence of the magnetic susceptibilities for all the complexes shows deviation from Curie behaviour at low temperature ($T < 30$ K).

The occurrence of a coupling between metal centres could not be confirmed by measurements of the magnetic susceptibilities on these paramagnetic complexes. Indeed, even if present, the coupling is so weak that its presence would be masked in all the other complexes by zero-field splitting effects, whose energies are comparable to, or even larger in magnitude than, those involved in exchange-coupling. In particular, it should be noted that the electronic ground state in tetrahedral coordination for Ni^{II} ($^3T_1$) and Fe^{II} ($^5T_2$) is orbitally degenerate (although this degeneracy can be removed by low-symmetry effects) and that the magnetic behaviour of tetrahedral Co^{II} is largely affected by spin-orbit coupling of the low-lying excited $^4T_2$ state and the ground $^4A_1$ one. In this framework the observed deviation from Curie–Weiss behaviour observed at low temperature for these systems should be more likely attributed to single-ion effects than to exchange interactions.[33]

NMR Studies

All the NMR experiments carried out with the ligand H_2L^a and the Zn^{II} and Cd^{II} complexes **5** and **6** were recorded with $CDCl_3$ as solvent. The NMR studies with the ligand H_2L^b and the Zn^{II} complex **7** were recorded in [D_6]-DMSO. Assignment of the signals was based on previous results[15,19,24] and on the available literature.[17,34] A comparison between the spectra of the free ligand and those of their respective complexes highlights some interesting features. The NH protons (H_a in Scheme 1) present in the free ligands disappear in the spectra of the complexes, in agreement with the deprotonation of the sulfonamide groups, and the imine hydrogen atoms (H_i) show a shift to higher field for the three complexes (ca. 0.15 ppm), thus demonstrating the coordination of the imine groups to the metal centre. Moreover, the imine protons of the cadmium complex **6** are flanked by satellites arising from spin-spin coupling to $^{111/113}Cd$, suggesting that the complex is kinetically inert on the NMR timescale. The FAB and ESI mass spectra of **5** and **6** suggest the existence of dinuclear $[M(L^a) + H]_2$ species in solution. In addition, their room temperature ^1H NMR spectra in chloroform reveal single sharp sets of proton resonances, indicating the existence of just one species in solution for both complexes. The non-diastereotopic CH_2 protons of the spacer (H_l) of the ligand H_2L^a permitted us to identify their nature. In a dihelical structure, these two protons will be equivalent and a singlet must therefore be observed: in both spectra, a single set of resonance signals are detected, and there is no evidence of the pair of doublets which is characteristic of the CH_2 group in the non-helical box architecture. Thus, the NMR spectroscopic data lead us to conclude that these solution species must also be neutral dimeric helicates of $[M(L^a)]_2$ stoichiometry. The substitution of the non-diastereotopic CH_2 protons by an oxygen in H_2L^b makes it impossible to prove whether the dihelical nature of the [2+2] species of **7** is present in solution.

UV/Vis Absorption and Fluorescence Emission Studies

Absorption and fluorescence data recorded for the ligand and its metal complexes are reported in Table 1. The UV/Vis absorption spectrum of H_2L^a, in acetonitrile solution, exhibits three strong bands (244, 328 and 342 nm). Coordination to M^{II} ions leads to a substantial variation of the absorption spectra. In particular, a new band appears with a maximum in the 370–390 nm range. Unfortunately, all attempts to record the UV/Vis absorption spectra of the manganese(II) and iron(II) derivatives with H_2L^a were unsuccessful because of their poor stability in solution.

Table 1. Absorption and fluorescence data recorded in CH_3CN.

Compound	λ [nm]	ε [$M^{-1}\,cm^{-1}$]	λ_{em} [nm]	Φ
H_2L[a]	244 328 342	49200 26400 26100	475	$<10^{-3}$
3	244 302 384	84800 47300 28700	–	–
4	246 292 388	154900 63500 41400	–	–
5	246 316 379	110000 52100 40700	473	0.03
6	243 318 371	74700 32500 27600	476	0.01

[a] UV/Vis spectra recorded in DMSO.

Fluorescence emission studies in acetonitrile solution show that H_2L^a has a residual luminescence at about 475 nm ($\Phi < 0.001$). The chelation of metal ions to $(L^a)^{2-}$ induces an enhancement of the fluorescence emission (CHEF effect), which is significantly more pronounced for zinc(II), as indicated by the quantum yields values determined for both complexes in acetonitrile ($\Phi = 0.03$ and 0.01 for Zn^{II} and Cd^{II}, respectively). Complex **5** displays a single exponential fluorescence decay at 473 nm, with a lifetime of $\tau = 1.75 \pm 0.03$ ns. The fluorescence lifetime of **6** could not be measured because it is shorter than the response time of our equipment ($\tau < 1$ ns). Moreover, the excitation spectrum of **5** ($\lambda_{em} = 473$ nm) is coincident with the absorption spectrum. Finally, it must be noted that complex **5** does not exhibit triplet emission at low temperature.

Although the origin of the luminescence[15,19] displayed by these compounds remains unknown we have recently proposed that the fluorescence active unit of similar tosylimine derivatives is located on the 2-tosylaminobenzaldehyde residue, since this exhibits an intense luminescence at

 © 2005 Wiley-VCH Verlag GmbH & Co. KGaA, Weinheim

about 498 nm in CH_3CN solution. These new data confirm the important role that the spacer group of this family of tosylimine ligands plays on their fluorescence properties: 4,4′-methylenedianiline, (1*R*,2*R*)-diaminocyclohexane and 1,3-diamino-2-propanol spacers quench the luminescence of the 2-tosylaminobenzaldehyde residue effectively, whereas other spacers such as 1,2-diaminoethane or 1,3-diaminopropane do not prevent the fluorescence emission of their corresponding free ligands.

The relative stability of **5** and **6** was studied by spectrophotometric and spectrofluorimetric experiments. Trifluoroacetic acid (TFA) was added to an acetonitrile solution of these complexes in order to test their behaviour in acidic media. No aqueous solvents were used due to the low solubility of **5** and **6** in these media. For both complexes, the addition of an excess of TFA makes the absorption spectra to become superimposable on that of the free ligand. Such evidence suggests that a demetallation reaction takes place with a protonation of the $(L^a)^{2-}$ species. The titration profiles indicate that the demetallation is complete after addition of about 5 equiv. of TFA for the Zn^{II} complex and about 1 equiv. for the Cd^{II} complex. Therefore, the zinc complex appears to show a higher stability towards acidis. In addition, the formation of only one isosbestic point in the UV/Vis spectra of **5** and **6** during the addition of TFA suggests the existence of only two species in solution: the corresponding complex and the free ligand. Figure 8 shows the variation of the UV/Vis absorption spectra of **5** upon the addition of a standard acetonitrile solution of TFA.

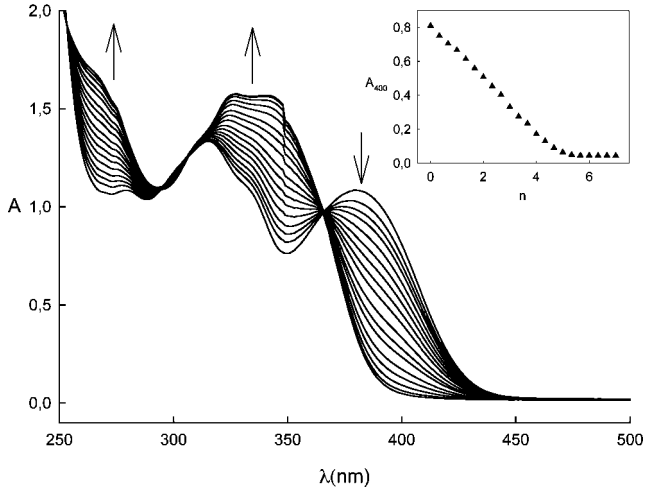

Figure 8. Spectrophotometric titration of an acetonitrile solution of **5** (3×10^{-5} M) with a standard solution of TFA. Inset: absorption intensity at 400 nm (A_{400}) vs. equiv. of TFA (n).

Similar results were obtained by fluorescence measurements. Figure 9 shows the variation of the emission spectra of **5** upon the addition of a standard acetonitrile solution of TFA. The successive addition of acid leads to a progressive decrease of the fluorescence intensity at 473 nm, which, at the end of the titration (after approx. 5 equiv. of TFA), results in a residual emission ($\Phi < 10^{-3}$) characteristic of the free ligand. In the case of the cadmium(II) complex the fluorescence at 476 nm ($\Phi = 0.01$) is completely quenched after the addition of about 1 equiv. of TFA. These data are consistent with the demetallation reaction mentioned above.

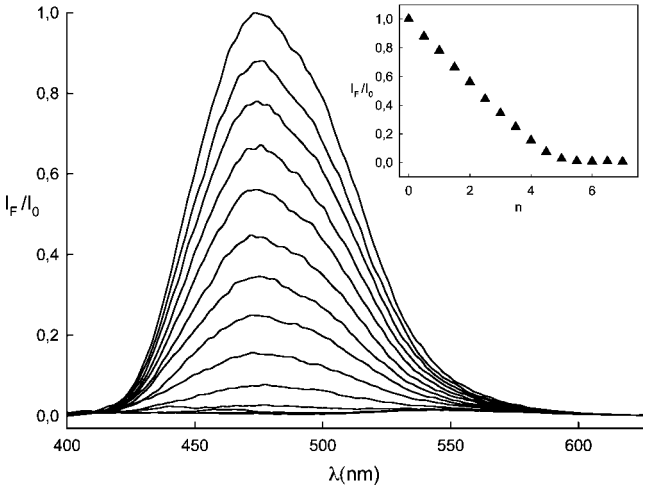

Figure 9. Spectrofluorimetric titration (λ_{exc} = 366 nm) of an acetonitrile solution of **5** (3×10^{-5} M) with a standard solution of TFA. On acid addition, the emission band at 473 nm decreases and the green fluorescence is quenched. Inset: fluorescence intensity at 473 nm (I_F/I_0) vs. equiv. of TFA (n).

Conclusions

In this work we have confirmed the capability of the N_4 Schiff-base ligands *N*,*N*′-bis(2-tosylaminobenzylidene)-4,4′-methylenedianiline (H_2L^a) and *N*,*N*′-bis(2-tosylaminobenzylidene)-4,4′-oxodianiline (H_2L^b) to support the aggregation of discrete helicates into higher supramolecular assemblies through intermolecular non-covalent aromatic interactions. The ligand H_2L^b is more rigid than H_2L^a due to the substitution of the CH_2 group in the spacer by an oxygen atom. The molecular structure of the zinc(II) dihelicate with H_2L^a shows that the discrete complexes aggregate to form discrete prismatic moieties of three molecules held together by π–π and σ–π interactions. The resulting nanoscale structure is a supramolecular assembly of six Zn^{II} ions and six ligands. The volume of the nanoscale triangular prism defined by the six Zn^{II} ions is 598 Å^3. The Zn^{II} complex with H_2L^b forms a polymeric 3D framework in the solid state due to π-stacking interactions between the aniline moieties of discrete dihelicates. Taking into consideration these two structures and those of the previously reported Cu^{II} dihelicate with the ligand H_2L^a,[18] we suggest that an increment of the "rigidity" in any of the building blocks that form this class of neutral dihelicates (aniline ligands and metal centres) definitively favours the self-aggregation of the complexes into 3D polymeric frameworks rather than discrete assemblies.

In addition, the ligand H_2L^a and its diamagnetic Zn^{II} and Cd^{II} complexes have been studied by NMR, spectrophotometric and spectrofluorimetric techniques, leading to

 © 2005 Wiley-VCH Verlag GmbH & Co. KGaA, Weinheim

an understanding of their formation mechanism as well as their structure in solution. Fluorescence studies also confirmed the emissive properties of the tosylaminobenzylidene moiety and the important role that the spacer group of this family of tosylimine ligands plays in this sense. The 4,4′-methylenedianiline spacer avoids luminescence of the 2-tosylaminobenzylidene residue, and only the chelation of Zn^{II} to $(L^a)^{2-}$ involves a significant enhancement of the fluorescence emission (λ_{em} = 473 nm, Φ = 0.03). On the other hand, the Cd^{II} dihelicate displays a low green fluorescence in acetonitrile solution (λ = 476 nm, Φ = 0.01). Finally, it must be noted that the Zn^{II} dihelicate displays a single exponential fluorescence decay at 473 nm, with a lifetime, τ, of 1.75 ± 0.03 ns.

We are currently exploring how to integrate further supramolecular interactions to design more-sophisticated assembly pathways based on multiple recognition events.

Experimental Section

Materials: All the starting materials were purchased from Aldrich and used without further purification. All metals were used as plates, except manganese metal, which was used as pellets. All of them were washed with a dilute solution of hydrochloric acid prior to the electrolysis.

Physical Measurements: Elemental analyses were performed with a Carlo Erba EA 1108 analyzer. The infrared spectra were recorded as KBr pellets with a Bio-Rad FTS 175 spectrophotometer in the range 4000–600 cm^{-1}. Fast atom bombardment (FAB) mass spectra were recorded with a Kratos MS-50 mass spectrometer, employing Xe atoms at 70 keV with *m*-nitrobenzyl alcohol as the matrix. ESI spectra were obtained with an LCQDECA ion-trap mass spectrometer equipped with an electrospray ionisation ion source and controlled by Xcalibur software 1.1 (Thermo-Finnigan). Magnetic susceptibilities of paramagnetic complexes were measured between 2 and 300 K with applied magnetic fields of 0.1 and 1 Tesla using a Cryogenic S600 SQUID magnetometer. Given the expected large anisotropy of Fe^{II}, Co^{II} and Ni^{II} derivatives, they were pressed into pellets to avoid the orientation of polycrystalline powders. Data were corrected for the magnetism of the sample holder, which was determined separately in the same temperature range and field, and the underlying diamagnetism of each sample was estimated from Pascal's constants.[35] The NMR spectra were recorded with a Bruker DPX-250 spectrometer, with $CDCl_3$ and $[D_6]$DMSO as solvents. UV/Vis spectra were recorded with a Varian Cary 100 spectrophotometer; emission and excitation spectra were recorded with a Perkin–Elmer LS-50B luminescence spectrometer. Spectrophotometric and spectrofluorimetric titrations were performed on 10-mL samples of solutions of the complexes (3×10^{-5} M) in CH_3CN, by microaddition of CH_3CN stock solutions of TFA. In each experiment, the overall addition was limited to about 200 μL, so that the volume increment was not significant. The fluorescence decay curves were recorded with an Edinburgh Instruments Model FL 900 time-correlated single-proton counting spectrometer, at the Centro Grandi Strumenti (Università di Pavia). The instrument was operated with a flash lamp filled with H_2 at a pressure of 0.4 atm, with a frequency of 40 kHz and a pulse width of 1.0 ns. The relative fluorescence quantum yields were obtained by the optically diluted method,[36] with dansyl amide (Φ = 0.37 in CH_3CN) as reference.[37]

2-Aminobenzaldehyde (2): 2-Aminobenzyl alcohol (1 g, 8.0 mmol) was dissolved in dry dichloromethane (50 mL) and γ-MnO_2 (0.70 g, 8.0 mmol) was added under argon. The reaction mixture was stirred at room temperature for 24 h. After this, the resulting mixture was filtered through a silica gel bed. The filtrate was concentrated under reduced pressure to leave an oily residue. The residue was then passed through a short silica gel column (silica gel, hexane/ethyl acetate, 5:1) to afford the pure aldehyde **2**.[20] Yield: 0.861 g (90%). FAB MS: *m*/*z* = 122.1 [M^+ + H]. C_7H_7NO: calcd. C 69.4, H 5.8, N 11.6; found C 69.3, H 5.9, N 11.6.

2-Tosylaminobenzaldehyde (3): Aldehyde **2** (0.86 g, 7.10 mmol) was dissolved in dry dichloromethane (50 mL) and tosyl chloride (1.36 g, 7.10 mmol) and triethylamine (5.0 mL, 35.5 mmol) were added under argon. The reaction mixture was heated at reflux temperature for 8 h. After this, the resulting mixture was filtered through a thin Celite bed. The solution was then treated with acid water (pH = 4–5, 3 × 100 mL) and the organic solution dried with Na_2SO_4. The solvent and the excess of triethylamine were removed in vacuo and the residue was recrystallised from chloroform.[19,21] Yield: 1.487 g (75%). FAB MS: *m*/*z* = 276.1 [M^+ + H]. $C_{14}H_{13}NO_3S$: calcd. C 61.1, H 4.7, N 5.1, S 11.6; found C 69.3, H 4.6, N 5.1, S 11.7.

***N*,*N*′-Bis(2-tosylaminobenzylidene)-4,4′-methylenedianiline (H_2L^a):** 4,4′-Methylenedianiline (0.50 g, 2.54 mmol) was added to a chloroform solution (150 mL) of **3** (1.40 g, 5.08 mmol). This mixture was heated (70 °C) and the volume of the solution was reduced to about 30 mL over period of 3 h in a Dean–Stark trap. The resulting solution was filtered and then concentrated. The orange powdery solid was collected by filtration, washed with diethyl ether (25 mL), and dried in vacuo. Yield: 1.501 g (80%). FAB MS: *m*/*z* = 713.1 [M^+ + H]. $C_{41}H_{36}N_4O_4S_2$: calcd. C 69.1, H 5.1, N 7.8, S 9.0; found C 69.1, H 5.2, N 7.9, S 8.9. IR (KBr): $\tilde{\nu}$ = 1621 $\nu_{C=N}$, 1337 ν_{C-N}, 1287 ν_{asSO_2}, 1156 ν_{sSO_2} cm^{-1}. ^1H NMR (250 MHz, $CDCl_3$, 25 °C): δ = 12.98 (s, 2 H, H_a), 8.48 (s, 2 H, H_i), 7.73 (d, ^3J = 8.1 Hz, 4 H, H_d), 7.66 (d, ^3J = 7.8 Hz, 2 H, H_e), 7.37–7.15 (m, 16 H, $H_{c,f,h,j,k}$), 7.05 (t, ^3J = 7.8 Hz, 2 H, H_g), 4.04 (s, 2 H, H_l), 2.32 (s, 6 H, H_b) ppm. UV/Vis (CH_3CN): λ_{max} (ε) = 244 (49200 $M^{-1}cm^{-1}$), 328 (26400), 342 (26100) nm. Fluorescence (CH_3CN): λ = 475 ($\Phi < 10^{-3}$) nm.

***N*,*N*′-Bis(2-tosylaminobenzylidene)-4,4′-oxodianiline (H_2L^b):** 4,4′-Oxodianiline (0.30 g, 1.50 mmol) was added to a chloroform solution (150 mL) of **3** (0.82 g, 3.00 mmol). This mixture was heated (70 °C) and the volume of the solution was reduced to about 30 mL over period of 6 h in a Dean–Stark trap. The resulting solution was filtered and then concentrated. The obtained powdery solid was collected by filtration, washed with diethyl ether (30 mL), and dried in vacuo. Yield: 1.02 g (95%). FAB MS: *m*/*z* = 715.1 [M^+ + H]. $C_{40}H_{34}N_4O_5S_2$: calcd. C 67.14, H 4.76, N 7.83, S 8.95; found C 66.37, H 4.80, N 7.92, S 8.63. IR (KBr): $\tilde{\nu}$ = 3439 ν_{N-H}, 1617 $\nu_{C=N}$, 1340 ν_{C-N}, 1289 ν_{asSO_2}, 1157 ν_{sSO_2} cm^{-1}. ^1H NMR (250 MHz, $[D_6]$-DMSO, 25 °C): δ = 12.62 (s, 2 H, H_a), 8.80 (s, 2 H, H_i), 7.76 (d, ^3J = 8.2 Hz, 2 H, H_e), 7.70 (d, ^3J = 8.2 Hz, 4 H, H_d), 7.44 (m, 8 H, $H_{h,f,k}$), 7.33 (d, ^3J = 8.2 Hz, 4 H, H_c), 7.20 (m, 6 H, $H_{f,j}$), 2.31(s, 6 H, H_b) ppm.

Metal Complexes: The neutral metal complexes $[Mn(L^a)]_2 \cdot CH_3CN$ (**1**), $[Fe(L^a)]_2 \cdot (CH_3CN)_2$ (**2**), $[Co(L^a)]_2 \cdot CH_3CN$ (**3**), $[Ni(L^a)]_2$ (**4**), $[Zn(L^a)]_2 \cdot CH_3CN$ (**5**), $[Cd(L^a)]_2$ (**6**) and $[Zn(L^b)]_2 \cdot (H_2O)_4$ (**7**) were obtained using an electrochemical procedure.[19] An acetonitrile solution of the corresponding ligand (H_2L^a or H_2L^b) containing tetraethylammonium perchlorate as supporting electrolyte was electrolyzed using a platinum wire as the cathode and a metal plate as the anode. The cell can be summarised as Pt(–)$|H_2L^{a,b}$ + MeCN|M(+), where M stands for the metal. The synthesis method is similar for all the metals except in the cases of manganese(II) and

 © 2005 Wiley-VCH Verlag GmbH & Co. KGaA, Weinheim

iron(II) complexes. These two compounds were prepared in a closed cell under argon. The synthesis is typified by the preparation of **5**: A suspension (0.1 g, 0.14 mmol) of H_2L^a in acetonitrile (80 mL), containing 10 mg of tetraethylammonium perchlorate, was electrolysed for 1.5 h, using a zinc plate as anode, with a current of 10 mA. (***Caution:*** Although no problem was encountered in this work, all perchlorate salts are potentially explosive and should therefore be handled with the appropriate care!) Concentration of the resulting yellow solution to a third of its initial volume yielded a yellow solid that was washed with diethyl ether and dried under vacuum. All metal complexes were obtained with high purity and yield. Crystallisation from acetonitrile produced crystals of **5**. Unfortunately, all attempts to crystallise the other complexes were unsuccessful.

$[Mn(L^a)]_2\cdot CH_3CN$ (1): Yield: 0.081 g (84%). MS FAB: *m*/*z* = 1532.4 $[Mn_2(L^a)_2 + H]^+$. ESI MS: *m*/*z* = 1531.6 $[Mn_2(L^a)_2 + H]^+$. $C_{84}H_{71}Mn_2N_9O_8S_4$: calcd. C 64.1, H 4.5, N 8.0, S 8.1; found C 64.0, H 4.4, N 8.0, S 8.3. IR (KBr): $\tilde{\nu}$ = 1614 $\nu_{C=N}$, 1294 (C–N), 1260 ν_{asSO_2}, 1128 ν_{sSO_2} cm^{-1}.

$[Fe(L^a)]_2\cdot(CH_3CN)_2$ (2): Yield: 0.084 g (74%). MS FAB: *m*/*z* = 1534.1 $[Fe_2(L^a)_2 + H]^+$. ESI MS: *m*/*z* = 1533.4 $[Fe_2(L^a)_2 + H]^+$]. $C_{86}H_{74}Fe_2N_{10}O_8S_4$: calcd. C 63.9, H 4.6, N 8.7, S 7.9; found C 64.0, H 4.4, N 8.8, S 8.0. IR (KBr): $\tilde{\nu}$ = 1613 $\nu_{C=N}$, 1290 ν_{C-N}, 1261 ν_{asSO_2}, 1131 ν_{sSO_2} cm^{-1}.

$[Co(L^a)]_2\cdot CH_3CN$ (3): Yield: 0.095 g (86%). MS FAB: *m*/*z* = 1540.1 $[Co_2(L^a)_2 + H]^+$. ESI MS: *m*/*z* = 1539.2 $[Co_2(L^a)_2 + H]^+$. $C_{84}Co_2H_{71}N_9O_8S_4$: calcd. C 63.8, H 4.5, N 8.0, S 8.1; found C 64.0, H 4.4, N 8.1, S 8.1. IR (KBr): $\tilde{\nu}$ = 1596 $\nu_{C=N}$, 1294 ν_{C-N}, 1257 ν_{asSO_2}, 1138 ν_{sSO_2} cm^{-1}. UV/Vis (MeCN): λ_{max} (ε) = 244 (84800 $M^{-1}cm^{-1}$), 302 (47300), 384 (28700) nm.

$[Ni(L^a)]_2$ (4): Yield: 0.081 g (75%). MS FAB: *m*/*z* = 1539.8 $[Ni_2(L^a)_2 + H]^+$. ESI MS: *m*/*z* = 1539.2 $[Ni_2(L^a)_2 + H]^+$. $C_{82}H_{68}N_8Ni_2O_8S_4$: calcd. C 63.9, H 4.4, N 7.3, S 8.3; found C 64.1, H 4.4, N 7.4, S 8.1. IR (KBr): $\tilde{\nu}$ = 1601 $\nu_{C=N}$, 1303 ν_{C-N}, 1264 ν_{asSO_2}, 1131 ν_{sSO_2} cm^{-1}. UV/Vis (MeCN): λ_{max} (ε) = 246 (154900 $M^{-1}cm^{-1}$), 292 (63500), 388 (41400) nm.

$[Zn(L^a)]_2\cdot CH_3CN$ (5): Yield: 0.094 g (84%). MS FAB: *m*/*z* = 1553.5 $[Zn_2(L^a)_2 + H]^+$. ESI MS: *m*/*z* = 1552.9 $[Zn_2(L^a)_2 + H]^+$. $C_{84}H_{71}N_9O_8S_4Zn_2$: calcd. C 64.9, H 4.6, N 8.1, S 8.2; found C 64.8, H 4.5, N 8.1, S 8.3. IR (KBr): $\tilde{\nu}$ = 1614 $\nu_{C=N}$, 1299 ν_{C-N}, 1260 ν_{asSO_2}, 1141 ν_{sSO_2} cm^{-1}. ^1H NMR (250 MHz, $CDCl_3$, 25 °C): δ = 8.33 (s, 4 H, H_i), 7.91 (d, ^3J = 8.5 Hz, 8 H, H_d), 7.46–6.85 (m, 40 H, $H_{c,e-h,j,k}$), 3.89 (s, 4 H, H_l), 2.34 (s, 12 H, H_b) ppm. UV/Vis (MeCN): λ_{max} (ε) = 246 (110000 $M^{-1}cm^{-1}$), 316 (52100), 379 (40700) nm. Fluorescence (MeCN): λ = 473 (Φ = 0.03) nm.

$[Cd(L^a)]_2$ (6): Yield: 0.084 g (73%). MS FAB: *m*/*z* = 1647.7 $[Cd_2(L^a)_2 + H]^+$. ESI MS: *m*/*z* = 1646.8 $[Cd_2(L^a)_2 + H]^+$. $C_{82}H_{68}Cd_2N_8O_8S_4$: calcd. C 59.7, H 4.1, N 6.8, S 7.8; found C 59.8, H 4.0, N 6.9, S 7.9. IR (KBr): $\tilde{\nu}$ = 1603 $\nu_{C=N}$, 1289 ν_{C-N}, 1262 ν_{asSO_2}, 1127 ν_{sSO_2} cm^{-1}. ^1H NMR (250 MHz, $CDCl_3$, 25 °C): δ = 8.33 (s, 4 H, H_i), 7.93 (d, ^3J = 8.5 Hz, 8 H, H_d), 7.75 (d, ^3J = 8.5 Hz, 8 H, H_c), 7.68 (d, ^3J = 8.3 Hz, 4 H, H_e), 7.39–6.83 (m, 28 H, $H_{f-h,j,k}$), 3.95 (s, 4 H, H_l), 2.34 (s, 12 H, H_b) ppm. UV/Vis (MeCN): λ_{max} (ε) = 243 (74700 $M^{-1}cm^{-1}$), 318 (32500), 371 (27600) nm. Fluorescence (MeCN): λ = 476 (Φ = 0.01) nm.

$[Zn(L^b)]_2\cdot(H_2O)_4$ (7): Yield: 0.091 (80%). MS FAB: *m*/*z* = 1557.7 $[Zn_2(L^b)_2 + H]^+$. ESI MS: *m*/*z* = 1557.0 $[Zn_2(L^b)_2 + H]^+$. $C_{80}H_{72}N_8O_{14}S_4Zn_2$: calcd. C 58.95, H 4.42, N 6.88, S 7.86; found C 60.11, H 4.04, N 7.08, S 7.74. IR (KBr): $\tilde{\nu}$ = 1610 $\nu_{C=N}$, 1300 ν_{C-N}, 1243 ν_{asSO_2}, 1140 ν_{sSO_2} cm^{-1}. ^1H NMR (250 MHz, [D_6]-DMSO, 25 °C): δ = 8.66 (s, 4 H, H_i), 7.87 (d, ^3J = 8.2 Hz, 8 H, H_d), 7.73 (d, ^3J = 8.2 Hz, 4 H, H_e), 7.40 (m, 8 H, $H_{f,h}$), 7.29 (d, ^3J = 8.2 Hz, 8 H, H_c), 7.16 (d, ^3J = 8.2 Hz, 8 H, H_k), 6.99 (dd, ^3J = 8.2, ^3J = 6.4 Hz, 4 H, H_g), 6.87 (d, ^3J = 8.2 Hz, 8 H, H_j), 2.34 (s, 12 H, H_b) ppm.

Crystallographic Measurements: The structure determinations of **5** and $[Zn(L^b)]_2\cdot CH_3CN$ were performed at room temperature with a Siemens CCD diffractometer, using graphite-monochromated Mo-K_α radiation from a fine focus sealed tube source. Intensities were corrected for absorption (SADABS). The structures were successfully solved by direct methods (SIR97),[38b] which gave the positions of most of the non-hydrogen atoms. Remaining atoms were identified by successive Fourier difference syntheses. Refinements were carried out on F^2 by full-matrix least-square techniques using SHELXL-97.[38a] Hydrogen atoms were added in calculated positions assuming idealised bond geometries.

Acknowledgments

M. V. and M. L. thank the EU network "Molecular Level Devices and Machines" for financial support. L. S. and C. S. thank the EU network Molnanomag, MIUR and CNR for financial support. M. R. B. thanks Xunta de Galicia (PGIDIT03PXIB20901PR and PGIDIT04PXIC20902PN) and Ministerio de Educación y Ciencia of Spain (BQU2003-00167) for financial support.

[1] a) J.-M. Lehn, *Supramolecular Chemistry – Concepts and Perspectives*, VCH, Weinheim, **1995**; b) E. C. Constable, in *Comprehensive Supramolecular Chemistry* (Eds.: J. L. Atwood, J. E. D. Davies, J.-M. Lehn, D. D. MacNicol, F. Vögtle), Pergamon, Oxford **1996**, vol. 9, p. 213; c) C. Piguet, G. Bernardinelli, G. Hopfgartner, *Chem. Rev.* **1997**, *97*, 2005; d) M. Albrecht, *Chem. Rev.* **2001**, *101*, 3457; e) R. M. Yeh, A. V. Davis, K. N. Raymond, in *Comprehensive Coordination Chemistry II* (Eds.: J. A. McCleverty, T. J. Meyer), Elsevier Ltd., Oxford, **2004**, vol. 7, p. 327; f) M. J. Hannon, L. J. Childs, *Supramol. Chem.* **2004**, *16*, 7.

[2] a) M. Elhabiri, R. Scopelliti, J.-C. Buenzli, C. Piguet, *J. Am. Chem. Soc.* **1999**, *121*, 10747; b) M. J. Hannon, V. Moreno, M. J. Prieto, E. Moldrheim, E. Sletten, I. Meistermann, C. J. Isaac, K. J. Sanders, A. Rodger, *Angew. Chem. Int. Ed.* **2001**, *40*, 880; c) D. Kalny, M. Elhabiri, T. Moav, A. Vaskevich, I. Rubinstein, A. Shanzer, A.-M. Albrecht-Gary, *Chem. Commun.* **2002**, 1426; d) V. Amendola, L. Fabbrizzi, P. Pallavicini, E. Sartirana, A. Taglietti, *Inorg. Chem.* **2003**, *42*, 1632; e) C. J. Matthews, S. T. Onions, G. Morata, L. J. Davis, S. L. Heath, D. J. Price, *Angew. Chem. Int. Ed.* **2003**, *42*, 3166.

[3] a) G. Ercolani, *J. Am. Chem. Soc.* **2003**, *125*, 1609; b) M. R. Bermejo, R. Pedrido, A. M. González-Noya, M. J. Romero, M. Vázquez, L. Sorace, *New J. Chem.* **2003**, *27*, 1753; c) B. Conerney, P. Jensen, P. E. Kruger, C. MacGloinn, *Chem. Commun.* **2003**, 1274; d) S. Mizukami, H. Houjou, M. Kanesato, K. Hiratani, *Chem. Eur. J.* **2003**, *9*, 1521; e) S. D. Reid, A. J. Blake, W. Köckenberger, C. Wilson, J. B. Love, *Dalton Trans.* **2003**, 4387; f) V. Amendola, Y. Díaz Fernández, C. Mangano, M. Montalti, P. Pallavicini, L. Prodi, N. Zaccheroni, M. Zema, *Dalton Trans.* **2003**, 4340; g) R. Prabaharan, N. C. Fletcher, *Dalton Trans.* **2003**, 2558; h) K. Zeckert, J. Hamacek, J.-P. Rivera, S. Floquet, A. Pinto, M. Borkovec, C. Piguet, *J. Am. Chem. Soc.* **2004**, *126*, 11589; i) M. Elhabiri, J. Hamacek, J.-C. G. Bünzli, A.-M. Albrecht-Gary, *Eur. J. Inorg. Chem.* **2004**, 51; V. Maurizot, G. Linti, I. Huc, *Chem. Commun.* **2004**, 924; j) L. P. Harding, J. C. Jeffery, T. Riis-Johannessen, C. R. Rice, Z. Zeng, *Chem. Commun.* **2004**, 654; k) B. Quinodoz, G. Labat, H. Stoeckli-Evans, A. von Zelewsky, *Inorg. Chem.* **2004**, *43*, 7994; l) F. Tuna, M. R. Lees, G. J. Clarkson, M. J. Hannon, *Chem. Eur. J.* **2004**, *10*, 5737; m) H. Houjou, N. Schneider, Y. Nagawa, M. Kanesato, R. Ruppert, K. Hiratani, *Eur. J. Inorg.*

 © 2005 Wiley-VCH Verlag GmbH & Co. KGaA, Weinheim

Chem. **2004**, 4216; n) R. Pedrido, M. R. Bermejo, M. J. Romero, M. Vázquez, A. M. González-Noya, M. Maneiro, M. J. Rodríguez, M. I. Fernández, *Dalton Trans.* **2005**, 572; o) M. Albrecht, I. Janser, R. Fröhlich, *Chem. Commun.* **2005**, 157; p) N. W. Alcock, G. Clarkson, P. B. Glover, G. A. Lawrance, P. Moore, M. Napitupulu, *Dalton Trans.* **2005**, 518.

[4] a) V. Berl, I. Huc, R. G. Khoury, J.-M. Lehn, *Chem. Eur. J.* **2001**, *7*, 2810; b) A. Lavalette, F. Tuna, G. Clarkson, N. W. Alcock, M. J. Hannon, *Chem. Commun.* **2003**, 2666; c) S. G. Telfer, R. Kurod, *Chem. Eur. J.* **2005**, *11*, 57.

[5] a) M. J. Hannon, C. L. Painting, N. W. Alcock, *Chem. Commun.* **1999**, 2023; b) S. Mizukami, H. Houjou, K. Sugaya, E. Koyama, H. Tokuhisa, T. Sasaki, M. Kanesato, *Chem. Mater.* **2005**, *17*, 50.

[6] a) C. A. Hunter, J. K. M. Sanders, *J. Am. Chem. Soc.* **1990**, *112*, 5525; b) G. R. Desiraju, T. Steiner, *The Weak Hydrogen Bond in Structural Chemistry and Biology*, Oxford University Press, Oxford, UK, **1999**; c) W. B. Jennings, B. M. Farrell, J. F. Malone, *Acc. Chem. Res.* **2001**, *34*, 885; d) R. G. Hicks, M. T. Lemaire, L. Öhrström, J. F. Richardson, L. K. Thompson, Z. Xu, *J. Am. Chem. Soc.* **2001**, *123*, 7154.

[7] a) G. R. Desiraju, A. Gavezzotti, *J. Chem. Soc., Chem. Commun.* **1989**, 621; b) W. L. Jorgensen, D. L. Severance, *J. Am. Chem. Soc.* **1990**, *112*, 4768; c) P. M. Zorky, O. N. Zrukya, *Adv. Mol. Struct. Res.* **1993**, *3*, 147; d) K. Biradha, M. J. Zaworotko, *J. Am. Chem. Soc.* **1998**, *120*, 6431.

[8] a) D. B. Amabilino, J. F. Stoddart, *Chem. Rev.* **1995**, *95*, 2725; b) K. Biradha, C. Seward, M. J. Zaworotko, *Angew. Chem. Int. Ed.* **1999**, *38*, 492; c) M. Munakata, L. P. Wu, T. Kuroda-Sowa, *Adv. Inorg. Chem.* **1999**, *46*, 173; d) M. J. Zaworotko, *Chem. Commun.* **2001**, 1.

[9] a) W. Saengew, *Principles of Nucleic Acid Structures*, Springer-Verlag, New York, **1984**, pp 132–140; b) M. R. Arkin, E. D. A. Stemp, R. E. Holmlin, J. K. Barton, A. Hormann, E. J. C. Olson, P. A. Barbara, *Science* **1996**, *273*, 475; c) S. O. Kelley, R. E. Holmlin, E. D. A. Stemp, J. K. Barton, *J. Am. Chem. Soc.* **1997**, *119*, 9861.

[10] a) P. Hobza, H. L. Selzle, E. W. Schlag, *Chem. Rev.* **1994**, *94*, 1767; b) H.-C. Weiss, D. Bläser, R. Boese, B. M. Doughan, M. M. Haley, *Chem. Commun.* **1997**, 1703; c) X.-M. Chen, G.-F. Liu, *Chem. Eur. J.* **2002**, *8*, 4811.

[11] a) S. K. Burley, G. A. Petsko, *Science* **1985**, *229*, 23; b) S. K. Burley, G. A. Petsko, *Adv. Protein Chem.* **1988**, *39*, 125.

[12] a) C. A. Hunter, *Chem. Soc. Rev.* **1994**, 101; b) M. C. T. Fyfe, J. F. Stoddart, *Acc. Chem. Res.* **1997**, *30*, 393.

[13] L. J. Childs, N. W. Alcock, M. J. Hannon, *Angew. Chem. Int. Ed.* **2002**, *41*, 4244.

[14] L. J. Childs, N. W. Alcock, M. J. Hannon, *Angew. Chem. Int. Ed.* **2001**, *40*, 1079.

[15] M. R. Bermejo, M. Vázquez, J. Sanmartín, A. García-Deibe, M. Fondo, C. Lodeiro, *New J. Chem.* **2002**, 1365.

[16] C. Janiak, *J. Chem. Soc., Dalton Trans.* **2000**, 3885.

[17] a) M. J. Hannon, C. L. Painting, N. W. Alcock, *Chem. Commun.* **1999**, 2023; b) N. Yoshida, K. Ichikawa, M. Shiro, *J. Chem. Soc., Perkin Trans. 2* **2000**, 17; c) P. E. Kruger, N. Martin, M. Nieuwenhuyzen, *J. Chem. Soc., Dalton Trans.* **2001**, 1966.

[18] M. Vázquez, A. Taglietti, D. Gatteschi, L. Sorace, C. Sangregorio, A. M. González, M. Maneiro, R. Pedrido, M. R. Bermejo, *Chem. Commun.* **2003**, 1840.

[19] M. Vázquez, M. R. Bermejo, J. Sanmartín, A. M. García-Deibe, C. Lodeiro, J. Mahía, *J. Chem. Soc., Dalton Trans.* **2002**, 870.

[20] W. K. Anderson, D. K. Dalvie, *J. Heterocycl. Chem.* **1993**, *30*, 1533.

[21] J. Mahía, M. Maestro, M. Vázquez, M. R. Bermejo, A. M. González, M. Maneiro, *Acta Crystallogr., Sect. C* **1999**, *55*, 2158.

[22] M. Vázquez, M. R. Bermejo, M. Fondo, A. M. González, J. Mahía, L. Sorace, D. Gatteschi, *Eur. J. Inorg. Chem.* **2001**, 1863, and references cited therein.

[23] Crystal structure analysis of **5**. X-ray diffraction data were collected from a yellow plate crystal (ca. $0.99 \times 0.25 \times 0.03$ mm) by means of a Smart CCD-1000 Bruker diffractometer using graphite-monochromated Mo-K_α radiation (λ = 0.71073 Å). Crystal data for $C_{84}H_{71}N_9O_8S_4Zn_2$: M = 1593.48, T = 293(2) K, monoclinic *I*2*a*, a = 34.066(9), b = 11.283(3), c = 40.426(10) Å, β = 94.673(5)°, V = 15486(7) Å^3, Z = 8, $\rho_{calcd.}$ = 1.367 g cm^{-3}, μ = 0.790 mm^{-1}, 9259 measured reflections, 9259 independent reflections with $I_0 > 2\sigma(I_0)$, 949 parameters refined, *GOF* = 0.973, R_1 = 0.0776 [$I_0 > 2\sigma(I_0)$], 0.2176 (for all data), wR_2 = 0.1979 [$I_0 > 2\sigma(I_0)$] and 0.2840 (for all data), largest difference peak and hole 1.394 and –0.782 e Å^{-3}. CCDC-231784 contains the supplementary crystallographic data for this paper. These data can be obtained free of charge from The Cambridge Crystallographic Data Centre via www.ccdc.cam.ac.uk/data_request/cif.

[24] M. Vázquez, M. R. Bermejo, M. Fondo, A. M. García-Deibe, A. M. González, R. Pedrido, *Eur. J. Inorg. Chem.* **2002**, 465.

[25] J. D. Watson, F. C. H. Crick, *Nature* **1953**, *171*, 737.

[26] a) M. Hong, G. Dong, D. Chun-Ying, L. Yu-Ting, M. Qing-Jin, *J. Chem. Soc., Dalton Trans.* **2002**, 3422; b) M. Hong, F. Chen-Jie, D. Chun-Ying, L. Yu-Ting, M. Qing-Jin, *Dalton Trans.* **2003**, 1229.

[27] Crystal structure analysis of $[Zn(L^b)]_2 \cdot CH_3CN$. X-ray diffraction data were collected from a yellow prismatic crystal (ca. $0.38 \times 0.37 \times 0.32$ mm) by means of a Smart CCD-1000 Bruker diffractometer using graphite-monochromated Mo-K_α radiation (λ = 0.71073 Å). Crystal data for $C_{82}H_{67}N_9O_{10}S_4Zn_2$: M = 1597.43, T = 293(2) K, orthorhombic *Fddd*, a = 17.102(2), b = 22.031(3), c = 40.644(6) Å, V = 15314(4) Å^3, Z = 8, $\rho_{calcd.}$ = 1.386 g cm^{-3}, μ = 0.801 mm^{-1}, 23525 measured reflections, 3791 independent reflections with $I_0 > 2\sigma(I_0)$, 242 parameters refined, *GOF* = 1.070, R_1 = 0.0441 [$I_0 > 2\sigma(I_0)$] and 0.0646 (for all data), wR_2 = 0.1287 [$I_0 > 2\sigma(I_0)$] and 0.1493 (for all data), largest difference peak and hole 0.948 and –0.275 e Å^{-3}. CCDC-261940 contains the supplementary crystallographic data for this paper. These data can be obtained free of charge from The Cambridge Crystallographic Data Centre via www.ccdc.cam.ac.uk/data_request/cif.

[28] O. M. Yaghi, H. Li, C. Davis, D. Richardson, T. L. Groy, *Acc. Chem. Res.* **1998**, *31*, 474.

[29] K. Biradha, H. Hongo, M. Fujita, *Angew. Chem. Int. Ed.* **2000**, *39*, 3843.

[30] J. Kim, B. Chen, T. M. Reineke, H. Li, M. Eddaoudi, D. B. Moler, M. O'Keeffe, O. M. Yaghi, *J. Am. Chem. Soc.* **2001**, *123*, 8239.

[31] S. Lai, C. Cheng, K. Lin, *Chem. Commun.* **2001**, 1082.

[32] E. A. Boudreax, L. N. Mulay, *Theory and Application of Molecular Paramagnetism*, Wiley, New York, **1976**.

[33] a) R. Krämer, I. O. Fritsky, H. Pritzkow, L. A. Kovbasyuk, *J. Chem. Soc., Dalton Trans.* **2002**, 1307; b) C. J. Matthews, S. T. Onions, G. Morata, L. J. Davis, S. L. Heath, D. J. Price, *Angew. Chem. Int. Ed.* **2003**, *42*, 3166 and references cited therein.

[34] E. Gottlieb, V. Kotlyar, A. Nudelman, *J. Org. Chem.* **1997**, *62*, 7512.

[35] C. J. O'Connor, *Prog. Inorg. Chem.* **1982**, *29*, 203.

[36] J. N. Demas, G. A. Crosby, *J. Phys. Chem.* **1971**, *75*, 991.

[37] Y.-H. Li, L.-M. Chan, L. Tyler, R. T. Moody, C. M. Himel, D. M. Hercules, *J. Am. Chem. Soc.* **1975**, *97*, 3118.

[38] a) G. M. Sheldrick, *SHELX-97 (SHELXS-97 and SHELXL-97), Programs for Crystal Structure Analyses*, University of Göttingen, Germany, **1998**; b) A. Altomare, M. C. Burla, M. Camalli, G. L. Cascarano, C. Giacovazzo, A. Guagliardi, A. G. G. Moliterni, G. Polidori, R. Spagna, *J. Appl. Crystallogr.* **1999**, *32*, 115.

Received: February 17, 2005
Published Online: August 2, 2005

 © 2005 Wiley-VCH Verlag GmbH & Co. KGaA, Weinheim

Synthesis, Structural Characterization, and Density Functional Study of Homo- and Heteropolyhalide Complexes of Cu^{II} with Dien and Dpta Ligands: Crystal Structure of [Bis(3-aminopropyl)amine](bromo)(diiodobromo)copper(II)

Aikaterini T. Chaviara,[a] Athanasios C. Tsipis,*[b] Philip J. Cox,[c] and Christos A. Bolos*[a]

Keywords: Copper / Density functional calculations / Halides / N ligands

Polyhalide mononuclear $[CuX(L)(XY_2)]$ and dinuclear $[\{CuX(L)\}_2(\mu\text{-}XY_2X)]$ Cu^{II} complexes [L = diethylenetriamine (dien) or dipropylenetriamine (dpta); X = Cl, Br and Y = Br, I] have been obtained by treating the precursor $[CuX_2(L)]$ complexes with Br_2 or I_2 in 1:1 and 2:1 molar ratios. The new homo- and heteropolyhalide Cu^{II} complexes, either mononuclear or dinuclear, were predicted to be five-coordinate Cu^{II} complexes exhibiting a distorted square-pyramidal configuration. DFT calculations at the B3LYP level of theory provided a satisfactory description of the structures of all complexes, while the distorted square-pyramidal structure of a representative complex, namely $[CuBr(dpta)(BrI_2)]$, was further substantiated by a single-crystal X-ray diffraction study. In the square-pyramidal structure of $[CuBr(dpta)(BrI_2)]$, the basal plane of the pyramid involves three Cu–N contacts [1.990(7), 2.065(7), and 1.989(7) Å] from dpta and the Br(1) atom, while Br(2), which participates in the formation of the terminal $[BrI_2]^-$ ligand, occupies the apical position. The Cu–Br(1) and Cu–Br(2) bond lengths were found to be 2.5797(14) Å (terminal) and 2.735(14) Å (bridging), respectively, while the Br1–Cu–Br2 bond angle is 98.83(5)°. The terminal $[BrI_2]^-$ ligand is almost linear [Br–I–I bond angle of 174.48(3)°]. DFT calculations, spectroscopic measurements, including far-IR and EPR studies, and magnetic measurements of the dinuclear complexes predict that the bridging tetrahalide XY_2X moiety adopts a linear configuration as well. The bonding, electronic, and related properties of the complexes are also discussed in the framework of density functional theory.

(© Wiley-VCH Verlag GmbH & Co. KGaA, 69451 Weinheim, Germany, 2005)

Introduction

Polyhalides are an interesting class of complex materials, which have drawn the attention of synthetic, theoretical, and applied scientists for many years. The tendency of the heavier halogens, particularly iodine, to form stable polyhalide anions $[X_mY_nZ_p]^-$, (X, Y and Z are identical or different halogen atoms; $m + n + p$ is an odd number that can be 3, 5, 7 or 9) or $[X_4]^{2-}$ dianions of variable stoichiometry has been studied thoroughly.[1–3] The formation of a particular polyhalide species depends not only on the specific halogen (X = I, Br, Cl) but also on the bulkiness and polarizability of the cation, the relative concentrations of the components, and, in some cases, on the synthetic route used.[4] The homo- and heterotrihalide anions $[X_3]^-$ and $[X_2Y]^-$ may be considered as donor–acceptor adducts resulting from the addition of a halide anion (Lewis base) to a halogen or interhalogen molecule (Lewis acids).[5] The bonding in the $[X_3]^-$ species can be described by delocalized three-center four-electron (3c-4e) interactions or, alternatively, by a σ-dative $X \rightarrow X_2$ donor–acceptor interaction.[6] The polyhalide species have found a wealth of applications as useful optical materials,[7] superconducting polymers,[8] electric and magnetic materials,[9] oxidizing[10] or halogenating reagents,[11] recyclable oxidizing reagents,[12] or recyclable reagents for the selective iodination of amines and phenols.[13] The halide ions can be used for the halogenation of organic substrates, thus giving products that are important as potent antitumor, antifungal, antibacterial, antineoplastic, anti-inflammatory, and antiviral agents.[14] Polyhalides are generally prepared[5] by the reaction of an ionic halide with the appropriate halogen under conditions specified by the relevant reactivity of the reactants and products through an ion–dipole interaction. The two reacting species can be combined by direct exposure of the halide to the gaseous halogen, by mixing in an appropriate solvent, by in situ reaction following the production of the interhalogen compound, and finally by the exchange reaction of halogens of different atomic number. The product's stability is governed by the size and the polarizability of the specific halogen atoms.

Although a vast number of polyiodide compounds of univalent cations (Cs^+, K^+, Na^+, NR_4^+) have been pre-

[a] Laboratory of Inorganic Chemistry, Department of General and Inorganic Chemistry, Faculty of Chemistry, Aristotle University of Thessaloniki,
54124 Thessaloniki, Greece
[b] Laboratory of Inorganic Chemistry, Department of Chemistry, University of Ioannina,
451 10 Ioannina, Greece
[c] School of Pharmacy, The Robert Gordon University, Schoolhill,
Aberdeen AB10 1FR, Scotland

pared, the synthetic attempts to synthesize polyhalide coordination compounds of transition metals are limited. In this work we report on the synthesis, structural characterization, electronic structure, and bonding of novel Cu^{II} polyhalide complexes obtained by the reaction of the $[Cu(dien)X_2]$ and $[Cu(dpta)X_2]$ complexes with iodine and bromine. The study of the new halometalate derivatives provides further structural information about different linking motifs of halogen-rich compounds.

Results and Discussion

Synthesis

Mononuclear copper(II) trihalide complexes of the general formula $[CuX(L)(XY_2)]$ and the tetrahalide-bridged dicopper(II) loose associations formulated as $[\{CuX(L)\}_2(\mu\text{-}XY_2X)]$ (L = dien, dpta; X = Cl, Br; Y = Br, I) were prepared by treating the precursor $[CuX_2(L)]$ (L = dien, dpta; X = Cl, Br) complexes with Br_2 or I_2 in 1:1 or 2:1 molar ratios, respectively. The precursor $[CuX_2(L)]$ (X = Br, L = dien, **1**;X = Cl, L = dien, **2**; X = Br, L = dpta, **3**; X = Cl, L = dpta, **4**) complexes undergo ligand dissociation in methanol solution to afford the cation $[CuX(L)]^+$ (L = dien, dpta) and X^- anions. The halide anions formed serve as the nucleophilic active center, thus fulfilling one of the highly desirable criteria of such specific addition reactions. The Cu^{II} polyhalide complexes isolated are deeply colored brown or green, crystalline or amorphous powders that are stable at low temperatures.

Structural Characterization

The new compounds were characterized by elemental analysis (C, H, N, Cu) and spectroscopic (IR, UV/Vis), magnetic, and molar conductivity measurements. Moreover, equilibrium structures of all the complexes studied were determined by electronic structure calculation methods at the B3LYP/LANL2DZ level of theory. Furthermore, the crystal structure of the representative mononuclear complex $[CuBr(dpta)(BrI_2)]$ (**5**) was determined by X-ray crystallography.

Vibrational Spectra

The infrared and far-infrared spectra of the compounds, recorded in the ranges 4000–250 cm^{-1} and 400–100 cm^{-1}, respectively, show all the expected strong bands of the coordinated dien and dpta ligands, which confirms the tridentate[15,16] bonding mode of their coordination to the Cu^{II} centers. The peaks at 255–311 cm^{-1} and 223–311 cm^{-1} are typical of copper halides and are attributed to the ν(Cu–Cl) and ν(Cu–Br) stretching vibrations, respectively, of the terminal halide ligands.[17] The computed unscaled harmonic vibrational frequencies of $[CuX(L)(XY_2)]$ (X = Br, Y = I, L = dien, **5**; X = Cl, Y = Br, L = dpta, **6**; X = Br, Y = Br, L = dien, **7**) and $[\{CuX(L)\}_2(\mu\text{-}XY_2X)]$ (X = Cl, Y = Br, L = dien, **8**; X = Cl, I; L = dpta; **9**, X = Br Y = Br, L = dpta, **10**; X = Br, Y = I, L = dien, **11**), due to ν(Cu–Cl) and ν(Cu–Br) stretching vibrations are found in the regions 220–245 and 170–190 cm^{-1}, respectively. The normal vibrational modes of the polyhalide moieties in **5**–**11** appear in the far-IR region of the spectra as two strong bands located at around 158 and 188 cm^{-1} for the mononuclear complexes and as a weak and very broad band at 123–182 cm^{-1} for the dinuclear ones. The weak, broad band due to the bridging $[X–Y–Y–X]^{2-}$ polyhalide unit, which corresponds to an IR-inactive normal mode, is indicative of the linearity of the tetrahalide bridge; this was further corroborated by the DFT calculations of the equilibrium geometries of the respective compounds. The computed far-infrared harmonic vibrational frequencies due to the stretching and bending vibrational normal modes of the polyhalide moieties, along with their assignments, are compiled in Table 1. Notice that the computed bending modes of the polyhalide moieties in **5**–**11** occur in the same region as $\delta(IBr_2)$ and $\delta(I_3Br)$ of the $[I_3Br_4]^-$ anion in the $[PPh_4][I_3Br_4]$ molecule (72–97 cm^{-1}).[18]

Table 1. Far-infrared harmonic vibrational frequencies [cm^{-1}] due to the vibrational normal modes of the polyhalide moieties of complexes **5–11** computed at the B3LYP/LANL2DZ level.

Complex	Frequency[a]		Assignment
	Calcd.	Exp.	
5	54 (1)		$\delta(BrI_2)$
	116 (8)		ν_s(BrCuBr)
	153 (82)	158 (m)–173 (m)	$\nu_{as}(BrCuBrI_2)$
	163 (5)		$\nu_s(BrCuBrI_2)$
6	77 (1)		$\delta(ClBr_2)$
	174 (35)	170 (m)–188 (m)	$\nu_s(ClBr_2)$
	228 (125)		$\nu_{as}(ClCuClBr_2)$
7	68 (0)		$\delta(Br_3)$
	91 (4)		$\delta(Br_3)$
	119 (15)		$\nu_s(CuBrBr_2)$
	131 (12)	143 (m)–178 (m)	$\nu_s(Br_3)$
	220 (60)		$\nu_{as}(Br_3)$
8	82 (1)		$\delta(ClBr_2)$
	134 (3)	128–181 (w, br)	ν_s(Cl–Br–Br–Cl)
	168 (50)		$\nu_s(ClCuClBr_2)$
	217 (15)		$\nu_{as}(ClCuClBr_2)$
9	58 (1)		$\delta(ClI_2)$
	110 (1)	123 (w, br)	ν_s(Cl–I–I–Cl)
	157 (3)		ν_{as}(Cl–I–I–Cl)
10	23 (0)		δ(Br–Br–Br–Br)
	123 (0)		ν_s(Br–Br–Br–Br)
	140 (2)		ν_s(–Br–Br–)
	188 (5)	160–180 (w, br)	ν_{as}(BrCuBr)
11	61 (6)		$\delta(BrI_2)$
	105 (0)		ν_s(–I–I–)
	122 (97)		ν_{as}(Br–I–I–Br)
	185 (25)	170–180 (w, br)	ν_{as}(BrCuBr)

[a] Figures in parentheses are the intensities of the absorption bands (km mol^{-1}).

Electronic Spectra

The electronic absorption spectra of the complexes in DMF solution and in the solid state (Nujol mulls) exhibit

 © 2005 Wiley-VCH Verlag GmbH & Co. KGaA, Weinheim

two or three absorption bands in the ultraviolet and in the visible region of the spectra. To help assignment of the bands and evaluate the properties of the excited states of the Cu^{II} polyhalide complexes, TD-DFT calculations were employed for the precursor complexes **1**–**4** and the mononuclear complexes **5**–**7** in their doublet ground states. Because of the large size of the dinuclear complexes in their triplet ground states, all attempts to compute their principal singlet–singlet electronic transitions were unsuccessful with the computational resources available. The TD-DFT principal singlet–singlet electronic transitions, excitation energies, and oscillator strengths of the mononuclear polyhalide complexes and their precursors are compiled in Table 2.

The computed electronic transitions of the polyhalide Cu^{II} complexes are in excellent agreement with the experimental ones. Thus, all polyhalide complexes exhibit an intense band in the UV region of the spectra at about 360 nm and a broad band in the visible region at 588–645 nm. According to the TD-DFT calculations the high mixing of excited configurations due to the low symmetry of the complexes does not allow us to classify the calculated transitions into the well-known intraligand (LL) or interligand (LL′), ligand-to-metal (LMCT) or metal-to-ligand (MLCT), and ligand field (LF) transitions. The absorption bands arise from electronic transitions between highly delocalized MOs resulting from the mixing of excited configurations having large coefficients in the CI wavefunctions. To intuitively understand the absorption processes, representative density diagrams of the participating MOs for the mononuclear complex **5** are depicted in Figure 1.

For the mononuclear precursor dihalide complexes **1**–**4** the absorption bands in the region of 200–300 nm could be classified as LMCT bands resulting from a combination of dipole-allowed X→Cu and L→Cu (X = Cl, Br; L = dien, dpta) excitations. On the other hand, the absorption bands in the region 300–600 nm correspond to a combination of ligand-field *d*→*d* and X→Cu LMCT transitions. The interligand nature of the LLCT transitions occurring between different ligands of the complexes is worthy of note (Figure 1).

Table 2. Principal electronic transitions, wavelengths (λ), and oscillator strengths (f) for the mononuclear [Cu(L)(X_2)] and [CuX(L)(XY_2)] (L = dien, dpta; X = Cl, Br and Y = Br, I) complexes computed at the B3LYP/LANL2DZ level of theory.

Compound	λ [nm]	f[a]	Assignment
[Cu(dien)Br_2] (**1**)	533	0.0510	LMCT (Br → Cu) + *d* → *d*
	420	0.0768	*d* → *d*
	285	0.0753	LMCT (dien → Cu)
	214	0.0279	LMCT (Br → Cu)
	209	0.0439	LMCT(Br → Cu)
[Cu(dien)Cl_2] (**2**)	565	0.0015	*d* → *d* + LMCT (Cl → Cu)
	448	0.0295	LMCT (Cl → Cu) + *d* → *d*
	369	0.0845	*d* → *d* + LMCT (Cl → Cu)
	278	0.0881	LMCT (dien → Cu)
	202	0.0169	LMCT(Cl → Cu)
[Cu(dpta)Br_2] (**3**)	488	0.0165	LMCT (Br → Cu) + *d* → *d*
	408	0.1184	*d* → *d* + LMCT (Br → Cu)
	334	0.0202	*d* → *d* + LMCT (dpta → Cu)
	276	0.0688	LMCT (dpta → Cu)
	238	0.0305	LMCT (Br → Cu)
	230	0.1092	LMCT (Br → Cu)
	217	0.0429	LMCT (Br → Cu)
[Cu(dpta)Cl_2] (**4**)	457	0.0173	LMCT (Cl → Cu) + *d* → *d*
	373	0.0917	*d* → *d* + LMCT (Cl → Cu)
	320	0.0203	*d* → *d* + LMCT (dpta → Cu
	283	0.1160	LMCT (dpta → Cu)
	196	0.0449	LMCT (dpta → Cu)
[CuBr(dpta)(BrI_2)] (**5**)	754	0.0192	*d* → *d* + LMCT (Br → Cu)
	459	0.0214	LMCT (I_2Br → Cu) + LLCT (I_2Br→ I_2Br)
	404	0.1926	*d* → *d* + LMCT (I_2Br→ Cu)
	324	0.1025	LMCT (I_2Br → Cu) + *d* → *d*
[CuCl(dpta)($ClBr_2$)] (**6**)	737	0.0080	LMCT (Cl → Cu) + *d* → *d*
	352	0.0431	LMCT (Br_2Cl → Cu)
	343	0.0662	LMCT (Cl, Br_2Cl → Cu)
	311	0.0590	*d* → *d* + LMCT (Br_2Cl → Cu)
	278	0.0357	LLCT(dpta→ Br_2Cl)
[CuBr(dien)(Br_3)] (**7**)	757	0.0178	LMCT (Br → Cu) + *d* → *d*
	462	0.0150	LLCT(Br→ Br_3)
	416	0.0174	LMCT (Br_3 → Cu)
	387	0.0197	LLCT(dpta→ Br_3)
	376	0.1215	*d* → *d* + LMCT (Br, Br_3 → Cu)
	330	0.0175	*d* → *d* + LMCT (Br → Cu)
	291	0.1092	MLCT (Cu → Br_3)
	287	0.2934	LMCT (Br → Cu

[a] Only transitions with oscillator strengths larger than 0.015 are considered.

 © 2005 Wiley-VCH Verlag GmbH & Co. KGaA, Weinheim

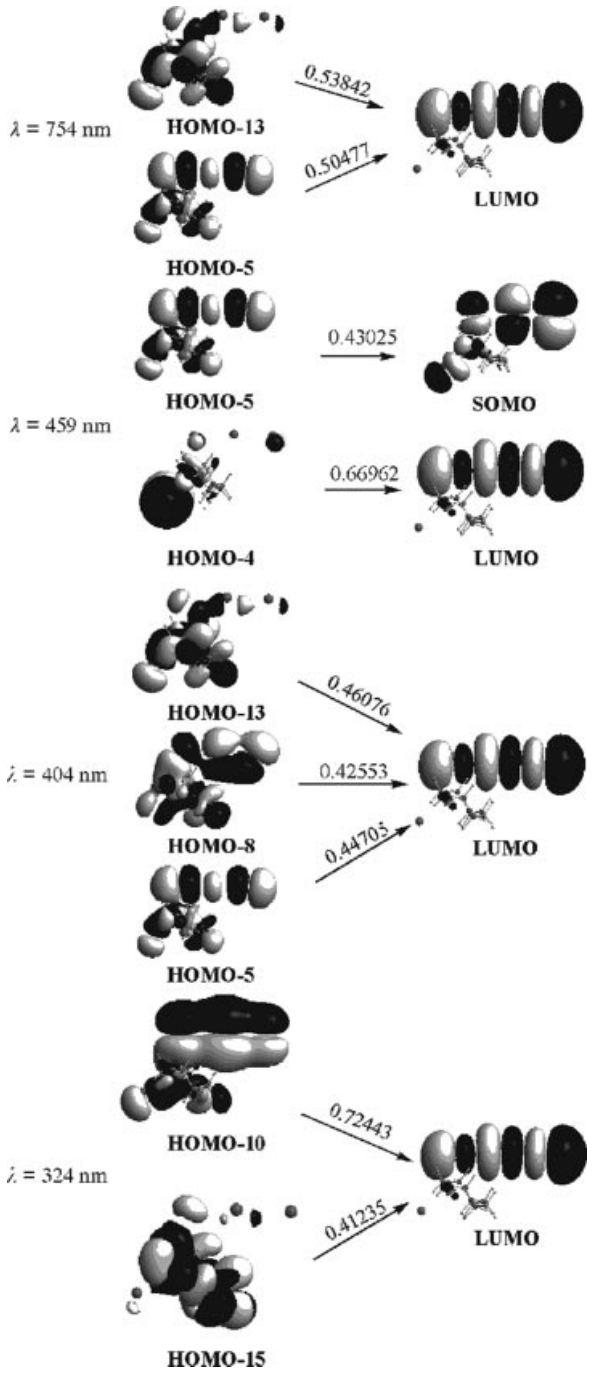

Figure 1. Single-electron transitions with the CI coefficients in the TD-DFT calculations for the more intense bands of [CuBr(dpta)-(BrI_2)] (**5**).

Magnetic Moments, Spin Densities, and Conductivity Measurements

The mononuclear and dinuclear structures of the polyhalide complexes exhibit normal μ_{eff} values per Cu^{II} in the range 1.65–2.19 BM. The room temperature μ_{eff} values of the dinuclear complexes are indicative of a triplet ground state, which was further corroborated by the DFT calculations, as will be discussed later on. In effect, the μ_{eff} values of the complexes are consistent with the computed spin-density distribution. The total spin-density surfaces (SDS) of the polyhalide complexes, along with the numerical values of the spin density at each atom, are displayed in Scheme 1.

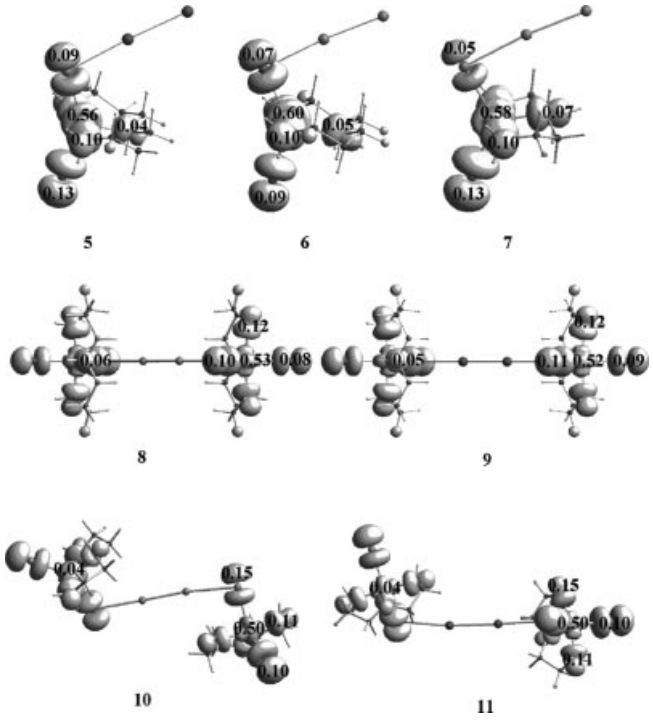

Scheme 1.

It can be seen that the spin density is mainly localized on the central Cu^{II} atoms and the N donor atoms of the dien or dpta ligands. In the dinuclear complexes the spin density distribution follows a similar pattern, but with the spin density localized on the Cu^{II} central atoms being slightly lower, in line with the lower μ_{eff} values of the dinuclear complexes. It is important to note that no spin density is delocalized onto the incoming halogen to form the terminal trihalide or the bridging tetrahalide ligands. Moreover, the computed $<S^2>$ values of 0.754 and 2.005 for the mononuclear and dinuclear complexes, respectively, indicate minimal artificial spin contamination in the calculations.

The molar conductivity measurements of the mononuclear complexes in DMF solution illustrate their essentially 1:1 electrolytic character.[19] As far as the dinuclear complexes are concerned, their $\Lambda\mu$ values are generally slightly higher than those of the mononuclear species, but within the 1:1 range, the only exception being complex **10**, the $\Lambda\mu$ value of which (147 $\mu S\,cm^{-1}$) indicates 2:1 dissociation. The easy dissociation of the dinuclear complexes to mononuclear [$CuX(L)(XY_2)$] ones and the [$CuX_2(L)$] precursors did not allow us, despite many attempts, to isolate crystals suitable for an X-ray diffraction study of their molecular structures. In light of this, the dinuclear complexes can be considered as loose associations between the mononuclear

 © 2005 Wiley-VCH Verlag GmbH & Co. KGaA, Weinheim

$[CuX(L)(XY_2)]$ complexes and their $[CuX_2(L)]$ precursors, in line with the DFT results (see below).

Crystal Structure of $[CuBr(dpta)(BrI_2)]$ (5)

A perspective drawing exhibiting the atom numbering is shown in Figure 2.

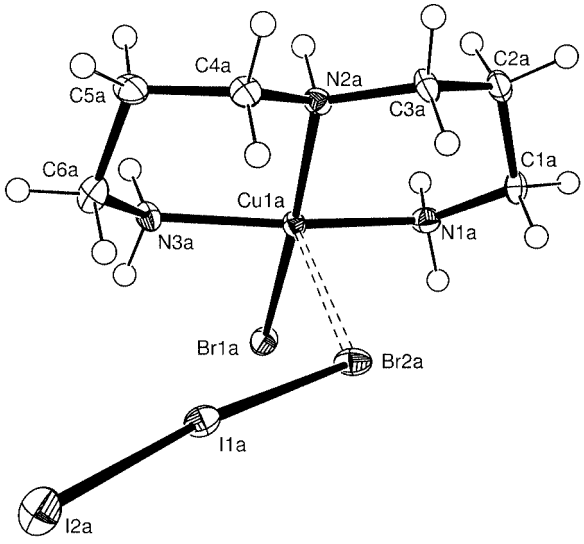

Figure 2. ORTEP plot showing the molecular structure of the $[CuBr(dpta)(BrI_2)]$ with the atom numbering scheme. Thermal ellipsoids are presented at the 50% probability level.

There are 16 formula units per cell and two molecules (**5a** and **5b**) in the asymmetric unit of the structure, with their structural differences being only marginal. Selected bond lengths and angles for **5a** and **5b** are given in Tables 3 and 4, respectively.

Table 3. Selected bond lengths [Å] and angles [°] for **5a**.

I(1A)–I(2A)	2.7619(8)	I(1A)–Br(2A)	2.9484(10)
Br(1A)–Cu(1A)	2.5797(14)	Br(2A)–Cu(1A)	2.7351(14)
Cu(1A)–N(1A)	1.990(7)	Cu(1A)–N(3A)	1.989(7)
Cu(1A)–N(2A)	2.065(7)		
I(2A)–I(1A)–Br(2A)	174.48(3)	Cu(1A)–Br(2A)–I(1A)	119.85(4)
N(1A)–Cu(1A)–N(3A)	162.9(3)	N(3A)–Cu(1A)–N(2A)	92.5(3)
N(1A)–Cu(1A)–N(2A)	94.3(3)	N(3A)–Cu(1A)–Br(1A)	86.6(2)
N(1A)–Cu(1A)–Br(1A)	84.2(2)	N(1A)–Cu(1A)–Br(2A)	92.2(2)
N(2A)–Cu(1A)–Br(1A)	170.4(2)	N(2A)–Cu(1A)–Br(2A)	90.7(2)
N(3A)–Cu(1A)–Br(2A)	103.4(2)	Br(1A)–Cu(1A)-Br(2A)	98.83(5)

The gross geometry of complex **5** appears to be that of a distorted square pyramid and is characterized by *trans*-N–Cu–N (162.9°) and N–Cu–Br (170.4°) bond angles that deviate slightly from the ideal value of 180°. In this distorted CuN_3Br_2 square-pyramidal environment, three nitrogen atoms [N(1A), N(2A) and N(3A)] of the dien or dpta ligands and one bromine atom [Br(1A)] lie in the equatorial plane, whereas the axial position is occupied by the bromine atom [Br(2A)] of the trihalide $[BrI_2]^-$ ligand. The copper atoms Cu(1A) and Cu(1B) are displaced by 0.226(4) and 0.210(4) Å from the plane towards the apical Br(2A) and Br(2B), respectively. The N3–Cu–N2, N2–Cu–N1, N3–Cu–Br1, and Br1–Cu–N1 bond angles in the equatorial plane have values of 92.5(3)°, 94.3(3)°, 86.6(2)°, and 84.2(2)°, respectively, which deviate from the ideal value of 90° for a perfect square plane. The three Cu–N bond lengths span the range of 1.989(7) to 2.065(7) Å, and are consistent with those found in square-pyramidal Cu^{II} complexes with nitrogen donor ligands. The Cu–Br(1) bond length [2.5797(14) Å] in the basal plane is, as expected, shorter than that of the axial Cu–Br(2) bond length [2.7351(14) Å]. Note that the axially coordinated Br(2) atom involved in the formation of the trihalide $[BrI_2]^-$ ligand is not perpendicular to the equatorial plane, the relevant N3–Cu–Br2 and Br1–Cu–Br2 bond angles being 103.4° and 98.83°, respectively. The chair conformation adopted by the six-membered chelate ring formed upon coordination of the dpta ligand to the copper(II) central atom is noteworthy. The trihalide $[BrI_2]^-$ ligand coordinated through the bromine donor atom is almost linear; the Br–I–I bond angle (174.48°) compares well with the respective bond angles of the isostructural CsI_3 (176.3°) and CsI_2Br (178.0°) species. The Br–I bond length of 2.9484 Å is slightly longer than the I–I bond length of 2.7619 Å. These data are in line with the relevant structural features of the $[BrI_2]^-$ moiety in CsI_2Br,[20] which exhibits Br–I and I–I bond lengths of 2.906 and 2.777 Å, respectively.

Table 4. Selected bond lengths [Å] and angles [°] for **5b**.

I(1B)–I(2B)	2.7856(8)	I(1B)–Br(2B)	2.8549(10)
Br(1B)–Cu(1B)	2.5451(13)	Br(2B)–Cu(1B)	2.8118(14)
Cu(1B)–N(1B)	1.991(7)	Cu(1B)–N(3B)	1.984(7)
Cu(1B)–N(2B)	2.060(7)		
I(2B)–I(1B)–Br(2B)	177.50(3)	Cu(1B)–Br(2B)–I(1B)	102.72(4)
N(3B)–Cu(1B)–N(1B)	165.9(3)	N(1B)–Cu(1B)–N(2B)	94.4(3)
N(3B)–Cu(1B)–N(2B)	92.9(3)	N(1B)–Cu(1B)–Br(1B)	83.9(2)
N(3B)–Cu(1B)–Br(1B)	86.6(2)	N(2B)–Cu(1B)–Br(1B)	168.6(2)
N(1B)–Cu(1B)–Br(2B)	95.7(2)	N(3B)–Cu(1B)–Br(2B)	96.2(2)
N(2B)–Cu(1B)–Br(2B)	91.9(2)	Br(1B)–Cu(1B)-Br(2B)	99.50(4)

The equilibrium structures of the whole series of mononuclear and dinuclear polyhalide complexes of Cu^{II} were also determined using computational techniques at the DFT level of theory.

EPR Spectra

The EPR spectrum for powdered $[\{CuBr(dien)\}_2(\mu\text{-}Br_4)]$ and $[\{CuBr(dien)\}_2(\mu\text{-}Br_2I_2)]$ samples (Figure 3) are dominated by a broad derivative centered at $g \approx 2$ plus a weaker feature at $g \approx 4$. Linewidth limitations did not allow us to resolve the hyperfine couplings. The feature at $g \approx 4$ is a semi-forbidden $|\Delta m_s| = 2$ transition[21] that is indicative of pairs of interacting Cu^{II} paramagnetic centers. Similar spec-

 © 2005 Wiley-VCH Verlag GmbH & Co. KGaA, Weinheim

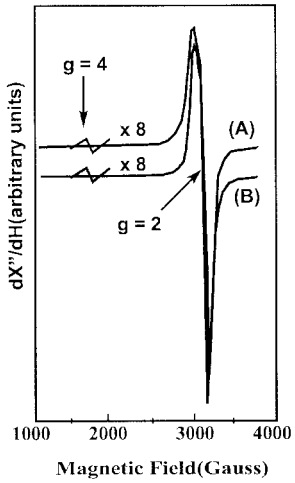

Figure 3. Powder EPR spectrum of powderered [{CuBr(dien)}$_2$(μ-Br_4)] (A) and [{CuBr(dien)}$_2$(μ-Br_2I_2)] (B). Experimental conditions: Temperature: 10.1 K; microwave frequency: 9.42 GHz; modulation amplitude: 10 G peak to peak; microwave power: 32 mW; modulation frequency: 100 kHz. The inset g = 4 signals were recorded using an eightfold larger gain and at 64 mW.

tra have been previously reported for other dinuclear Cu^{II} complexes.[22–24] Accordingly, the present EPR data show that both [{CuBr(dien)}$_2$(μ-Br_4)] and [{CuBr(dien)}$_2$(μ-Br_2I_2)] consist of dinuclear Cu^{II} centers. The details of the lineshape of coupled spin systems depend critically on the relative size of the dipolar and exchange interaction terms, i.e. D and J.[21]

Computational Studies by DFT – Equilibrium Geometry, Electronic Structure, and Bonding Mechanism in Mononuclear Cu^{II} Polyhalide Complexes

The next goal of this work was to determine the details of the electronic structure and, in particular, the nature of the bonding of the polyhalide $[XY_2]^-$ ligand in a series of mononuclear [CuX(L)(XY_2)] (L = dien or dpta; X = Cl, Br and Y = Br, I) compounds and explore the effect of the nature of the halogens on the formation and stability of the polyhalide ligands. Selected geometric, energetic, and electronic parameters for the mononuclear complexes com-

Table 5. Selected structural, energetic, and electronic properties of the mononuclear [CuX(L)(XY_2)] complexes computed at the B3LYP/LANL2DZ level of theory.

	[CuCl(dien)($ClBr_2$)]	[CuCl(dien)(ClI_2)]	[CuBr(dien)($BrBr_2$)]	([CuBr(dpta)($BrBr_2$)])
E [hartrees]	–576.788386	–576.788386	–573.231294	–569.683534
	(–655.351999)	(–655.351999)	(–651.790088)	(–648.246996)
ΔE_1[a] [kcal mol^{-1}]	12.5	12.5	15.8	10.6
	(12.9)	(12.9)	(13.4)	(11.1)
ΔE_2[b] [kcal mol^{-1}]	88.7	88.7	86.2	80.6
	(87.7)	(87.7)	(83.1)	(80.5)
R_e(Cu–X) [Å]	2.339	2.339	2.566	2.531
	(2.480)	(2.480)	(2.669)	(2.658)
R_e(Cu–XY_2) [Å]	2.603	2.603	2.693	2.709
	(2.514)	(2.514)	(2.740)	(2.691)
R_e(X–Y) [Å]	2.760	2.760	2.898	3.129
	(2.775)	(2.775)	(2.901)	(3.120)
R_e(Y–Y) [Å]	2.630	2.630	2.658	2.976
	(2.624)	(2.624)	(2.648)	(2.976)
X–Cu–X [°]	131.2	131.2	131.5	133.6
	(137.7)	(137.7)	(135.2)	(143.8)
Cu–X–Y [°]	103.0	103.0	90.5	107.2
	(90.8)	(90.8)	(84.4)	(100.0)
X–Y–Y [°]	175.1	175.1	174.1	176.4
	(174.8)	(174.8)	(173.8)	(176.8)
μ_e [D]	10.3	10.3	6.5	7.8
	(5.1)	(5.1)	(4.9)	(5.6)
η [eV]	1.62	1.62	1.46	1.41
	(1.50)	(1.50)	(1.42)	(1.41)
Q(Cu)	0.28	0.28	0.23	0.22
	(0.25)	(0.25)	(0.23)	(0.22)
Q(XY_2)	–0.38	–0.38	–0.27	–0.35
	(–0.34)	(–0.34)	(–0.45)	(–0.34)
Q(Y_{int})	–0.05	–0.05	–0.09	–0.06
	(–0.05)	(–0.05)	(–0.08)	(–0.06)
Q(Y_{term})	–0.22	–0.22	–0.24	–0.20
	(–0.22)	(–0.22)	(–0.23)	(–0.21)
bop(X–Y_{int})	0.013	0.013	0.016	0.008
	(0.010)	(0.010)	(0.010)	(0.005)

[a] $\Delta E_1 = \{[E_{[CuX_2(L)]} + E_{(Y_2)}] - E_{[CuX(L)(XY_2)]}\}$. [b] $\Delta E_2 = \{[E_{[CuX(L)]^+} + E_{(XY_2)^-}] - E_{[CuX(L)(XY_2)]}\}$.

 © 2005 Wiley-VCH Verlag GmbH & Co. KGaA, Weinheim

puted at the B3LYP/LANL2DZ level of theory are compiled in Table 5.

It can be seen that the B3LYP/LANL2DZ calculations reproduce well the molecular structure of complex **5** determined by X-ray crystallography. In all mononuclear complexes the trihalide $[XY_2]^-$ ligand adopts an almost linear configuration with the X–Y–Y bond angle ranging from 173.8° up to 176.8°. The $[XY_2]^-$ ligand occupying the axial position in the distorted square pyramidal geometry of the complexes is coordinated to the Cu^{II} central atom in a bent fashion. The computed Cu–X–Y bond angles found in the range of 84.4–107.2° depend on the nature of the halides involved in the formation of the $[XY_2]^-$ ligands. In general terms, the Cu–X–Y bond angles are smaller in the dpta than in the dien complexes.

The association of the incoming Y_2 molecule with the halide X^- ligand to afford the coordinated trihalide $[XY_2]^-$ ligand corresponds to a relatively weak interaction. The association energies, ΔE_1, computed at the B3LYP/LANL2DZ level of theory amount to only 10.6–15.8 kcal mol^{-1} and are comparable to those of hydrogen bonds. However, the trihalide $[XY_2]^-$ ligands interact strongly with the Cu^{II} central atom, the computed Cu–XY_2 bond-dissociation energy, ΔE_2, being 80.5–88.7 kcal mol^{-1}.

Generally, the trihalide $[XY_2]^-$ ligands form slightly stronger coordination bonds in the dien than in the dpta complexes. In both series of complexes the ΔE_2 values follow the trend $[ClBr_2]^- > [ClI_2]^- > [Br_3]^- > [BrI_2]^-$.

Upon association of the Y_2 molecule with the halide X^- ligand there is a charge transfer from the X^- ligand towards the Y_2 molecule, with the transferred electron density mainly localized on the terminal Y atom, which acquires a negative net atomic charge of about –0.20 to –0.24 charge units. The internal Y atom acquires only –0.02 to –0.09 charge units. Moreover, the X atom of the coordinated $[XY_2]^-$ ligands acquires a negative net atomic charge amounting to about –0.27 to –0.45 charge units. Obviously, repulsive electrostatic interactions of the negatively charged X and Y_{int} atoms in the $[XY_2]^-$ ligands do exist, therefore the weak X···Y_{int} interactions could be attributed to covalent interactions. In effect, the X···Y_{int} bonding mechanism could be described as donor–acceptor interactions with the incoming Y–Y molecule acting as acceptor through its σ* LUMO, and the coordinated halide ligand X of the $[CuX(L)(XY_2)]$ mononuclear complex acting as the donor through the HOMO, which is mainly localized on that ligand (Scheme 2). These donor–acceptor interactions give rise to both charge transfer from the donor to the acceptor and weakening of the bonding within the acceptor through partial accumulation of electron density on the antibonding σ* LUMO of the acceptor, which is reflected in the elongation of the Y–Y bond length by 0.099 to 0.148 Å. A thorough search of the molecular orbitals of the trihalide complexes reveals that there are bonding MOs describing the X···Y_{int} interactions. Such MOs, along with the doubly degenerate singly occupied (SOMO) and the lowest unoccupied (LUMO) MOs for a representative complex **5** and its precursor complex **1** are also displayed in Scheme 2.

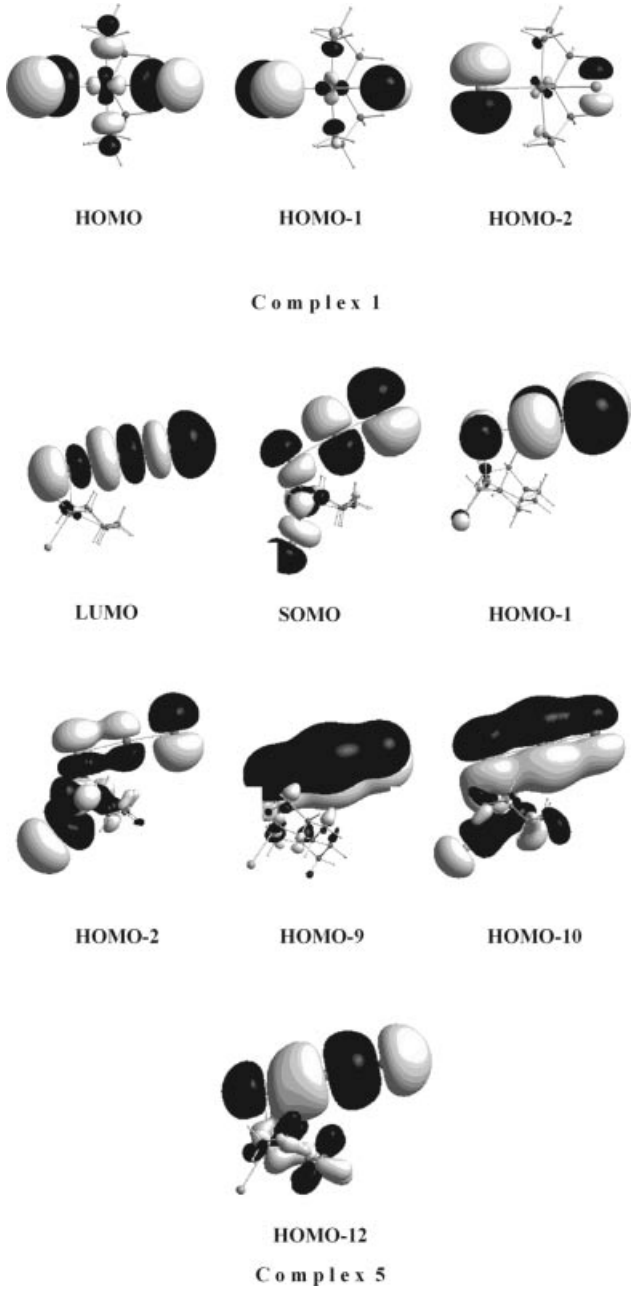

Scheme 2.

The multicenter bonding interactions in HOMO-9 and HOMO-10 and the antibonding ones in SOMO and HOMO-1 should be noted. The HOMO-9 and HOMO-10 correspond to π MOs constructed from the p_π orbitals of the halogen atoms of the X–Y–Y moiety, while the HOMO-12 is a σ-type MO constructed from the p_σ orbitals of the halogen atoms of the X–Y–Y moiety. The SOMO and HOMO-1 correspond to the antibonding π* counterparts of the π_{XYY} MOs. On the other hand, the LUMO corresponds to a σ* MO resulting from the antibonding interaction of p_σ orbitals of the halogen atoms of the X–Y–Y moiety. The computed bond overlap population (bop) values of the X···Y_{int} bonds (Table 5) illustrate the weak nature of the X···Y_{int} interactions. In general terms, these interactions

 © 2005 Wiley-VCH Verlag GmbH & Co. KGaA, Weinheim

follow the trend $Br\cdots Br_{int} > Cl\cdots Br_{int} > Br\cdots I_{int} > Cl\cdots I_{int}$, thus suggesting that the strength of the $X\cdots Y_{int}$ interactions increases as the difference of electronegativity of the constituent halogen atoms decreases. Finally, the hardness, η, given by $(\varepsilon_{LUMO} - \varepsilon_{HOMO})/2$, was found to be in the range of 1.41–1.62 eV; it reflects the relative stability of the complexes (Table 5).

Equilibrium Geometry, Electronic Structure, and Bonding Mechanism in Dinuclear Cu^{II} Polyhalide-Bridged Complexes

The dinuclear [{CuX(L)}$_2$(μ-XY$_2$X)] (L = dien, dpta; X = Cl, Br and Y = Br, I) complexes adopt the triplet ground state. The singlet states correspond to local minima in the PES and are 33–37 kcal mol^{-1} higher in energy than the triplet ground states. Selected geometric, energetic, and electronic parameters for the dinuclear complexes computed at the B3LYP/LANL2DZ level of theory are compiled in Table 6.

The two metal centers in the dinuclear complexes exhibit the same stereochemistry, being five coordinate with a distorted square-pyramidal geometry resembling that of the respective precursor [CuX$_2$(L)] complexes. This is indicative of the loose association of the Y$_2$ molecule with the two [CuX$_2$(L)] moieties. The computed dissociation energy of the Y$_2$ molecule from the dinuclear complexes amounts to 15.1–18.3 kcal mol^{-1} at the B3LYP/LANL2DZ level. On the other hand, the dissociation energy of the dinuclear complexes to the [CuX$_2$(L)] and [CuX(L)(XY$_2$)] species was predicted to be only 2.5–4.6 kcal mol^{-1}, thus illustrating that the dinuclear complexes are easily dissociated into the more stable mononuclear [CuX(L)(XY$_2$)] species. The weak X···Y interaction is mirrored by the relatively long X···Y distances (Table 6).

The trihalide [XY$_2$] moiety in all dinuclear complexes is almost linear, with the X–Y–Y bond angle ranging from 174.3° up to 176.8°. However, the Cl–Br–Br–Cl (complex **8**) and Cl–I–I–Cl (complex **9**) bridging units are almost linear, with the torsion angles being about 177°, while the Br–Br–Br–Br (complex **10**) and Br–I–I–Br (complex **11**) bridging units form dihedral angles of 144.9 and –86.5°, respectively. These configuration preferences of the X–Y–Y–X bridging units could be due to electronegativity effects.

The bonding mechanism of the Y$_2$ molecule from each side with the halide X$^-$ ligands of the two mononuclear [CuX$_2$(L)] species corresponds to donor–acceptor interactions giving rise to both a charge transfer from the X$^-$ donor ligands to Y acceptor atoms while the orbital interactions result in the weakening of the Y–Y bond. Both Y atoms acquire a negative net atomic charge of about –0.15 charge units. On the other hand, the elongation of the Y–Y bond length by 0.123 to 0.165 Å is, as expected, higher in the dinuclear than in the mononuclear complexes. A search of the molecular orbitals of the dinuclear complexes reveals that the presence of bonding MOs that describe the X···Y···Y···X interactions. The relevant MOs, along with the doubly degenerate SOMOs and the LUMO for a representative complex (**9**), are displayed in Scheme 3.

Conclusions

In this paper we have reported the synthesis, structural characterization, and DFT study of novel mono- and dinuclear polyhalide Cu^{II} complexes with general formulae [CuX(L)(XY$_2$)] and [{CuX(L)}$_2$(μ-XY$_2$X)] (L = dien or dpta; X = Cl, Br and Y = Br, I). The vibrational spectra confirm the tridentate bonding mode of the dien or dpta ligands to the central Cu^{II} atom and show the characteristic bands related to polyhalide moieties, thus indicating the lin-

Table 6. Selected structural, energetic, and electronic properties of the dinuclear [{CuX$_2$(L)}$_2$(μ-XY$_2$X)}] (L = dien, dpta; X = Cl, Br and Y = Br, I) complexes computed at the B3LYP/LANL2DZ level of theory.

Property	**8**	**9**	**10**	**11**
E_T [hartrees]	–1284.382307	–1280.839568	–1120.133222	–1116.588499
E_S [hartrees]	–1284.324165	–1280.780849	–1120.076554	–1116.535873
ΔE_{T-S}[a] [kcal mol^{-1}]	–36.5	–36.8	–35.4	–33.0
ΔE_1[b] [kcal mol^{-1}]	4.6	4.2	2.5	4.5
ΔE_2[c] [kcal mol^{-1}]	17.5	15.4	18.3	15.1
R_e(Cu–X) [Å]	2.538	2.525	2.545	2.539
R_e(Cu–XY$_2$) [Å]	2.463	2.447	2.673	2.675
R_e(X–Y) [Å]	2.974	3.165	3.135	3.307
R_e(Y–Y) [Å]	2.654	2.986	2.675	3.002
X–Cu–X [°]	135.6	139.6	141.6	138.2
Cu–X–Y [°]	85.0	95.0	100.8	110.4
X–Y–Y [°]	175.6	176.6	174.3	176.8
X–Y–Y–X [°]	176.7	–177.4	144.9	–86.5
μ_e [D]	0.11	0.26	5.8	7.1
η [eV]	1.39	1.50	1.36	1.41
Q(Cu)	0.23	0.23	0.20	0.20
Q(X)	–0.50	–0.49	–0.41	–0.40
Q(**X**Y$_2$)	–0.37	–0.39	–0.37	–0.39
Q(Y)	–0.15	–0.14	–0.18	–0.15

[a] $\Delta E_{T-S} = E_T - E_S$. [b] $\Delta E = [E_{[CuX_2(L)]} + E_{[CuX(L)(XY_2)]} - E_{[\{CuX(L)\}_2(\mu\text{-}XY_2X)\}]}$. [c] $\Delta E = [2E_{[CuX(L)]^+} + E_{Y_2}] - E_{[\{CuX_2(L)\}_2(\mu\text{-}XY_2X)\}]}$.

 © 2005 Wiley-VCH Verlag GmbH & Co. KGaA, Weinheim

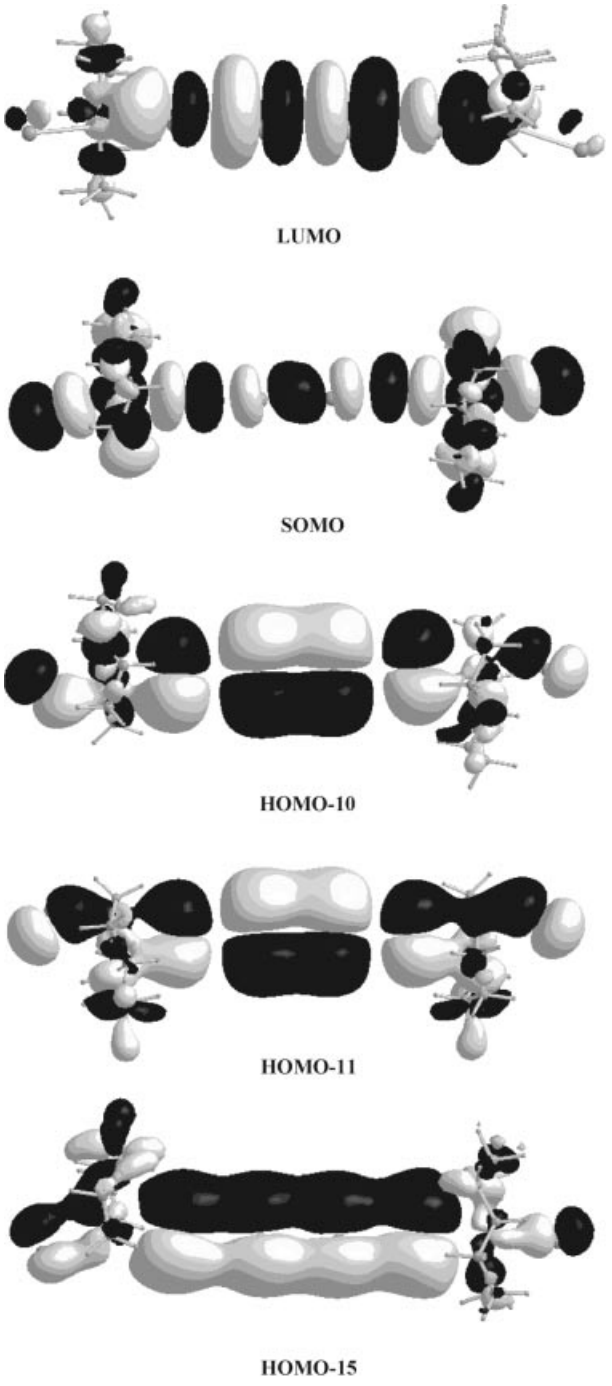

Scheme 3.

earity of the $[X–Y–Y–X]^{2–}$ tetrahalide bridges. According to X-ray data the mononuclear $[CuBr(dpta)(BrI_2)]$ complex adopts a distorted square-pyramidal structure with the apical position occupied by a Br atom that participates in the linear terminal $[BrI_2]^–$ ligand. On the other hand, DFT calculations support a distorted square-pyramidal structure for the $[CuX(L)(XY_2)]$ complexes, in agreement with the experimental findings. The Y_2 molecule in these complexes is weakly bound to the $X^–$ anion, with association energies estimated to be 10.6–15.8 kcal mol$^{–1}$ at the B3LYP/LANL2DZ level. In contrast, the Cu–XY_2 bond-dissociation energies are much larger (80.5–88.7 kcal mol$^{–1}$). The Cu–XY_2 BDEs, which are higher in the dpta than the dien complexes, follow the trend $[ClBr_2]^– > [ClI_2]^– > [Br_3]^– > [BrI_2]^–$.

Both X and Y_{int} atoms in the $[XY_2]^–$ ligand acquire negative charges that give rise to a weak electrostatic interaction. The quite long X···Y_{int} separation distance could be ascribed as a donor–acceptor interaction, with the incoming Y_2 molecule acting as the acceptor through its σ* LUMO and the coordinated $X^–$ ligand being the donor through the HOMO of the $[CuX(L)(XY_2)]$ complex, which is mainly localized on the halide ligands.

The dinuclear $[\{CuX(L)\}_2(\mu\text{-}XY_2X)]$ complexes adopt a triplet ground state while the singlet state corresponds to a local minimum that is about 33–37 kcal mol$^{–1}$ higher in energy. This is corroborated by the μ_{eff} values of the dinuclear complexes, which point to a triplet ground state without any appreciable magnetic interaction. The two metal centers exhibit a distorted square-pyramidal geometry resembling that of the mononuclear $[CuX(L)(XY_2)]$ complexes. The dinuclear $[\{CuX(L)\}_2(\mu\text{-}XY_2X)]$ complexes can easily dissociate into $[CuX(L)(XY_2)]$ and $[CuX_2(L)]$ species due to the very weak X–Y_2 interactions (BDEs are only 2.5–4.6 kcal mol$^{–1}$). The $[XY_2]$ moiety in all dinuclear complexes is almost linear. Finally, the bonding mechanism in the dinuclear $[\{CuX(L)\}_2(\mu\text{-}XY_2X)]$ complexes is described by donor–acceptor interactions which give rise to both charge transfer from the coordinated $X^–$ ligands to the Y_2 moiety at each side and orbital interactions resulting in the elongation of the Y–Y bond, which is greater in the dinuclear than in mononuclear complexes.

Experimental Section

Materials and Instruments: All chemicals were purchased from Aldrich, EDH Chemicals, or Merck and were reagent grade. Carbon, hydrogen, and nitrogen were determined by microanalysis using a Perkin–Elmer 2400 elemental analyser. Copper was determined with a Perkin–Elmer model 403 Atomic Absorption Spectrometer equipped with the appropriate hollow cathode lamps. Molar conductivities were measured with a WTW conductivity bridge employing a calibrated dip-type cell and $10^{–3}$ M solutions in DMF. Magnetic susceptibility measurements on powder samples were performed at room temperature (25 °C) employing the Faraday method with a home-built balance calibrated against $Hg[Co(NCS)_4]$. Diamagnetic corrections were estimated from Pascal's constants. Infrared spectra were obtained by the KBr disc technique and were recorded with a Perkin–Elmer FT-IR Spectrum One spectrometer. Far-infrared spectra (400–100 cm$^{–1}$) were recorded for polyethylene disks with a Bruker 113V Spectrum spectrometer. A 6.25-μm thickness Mylar beam splitter was used for these studies. Electronic spectra in DMF solutions (range 200–1100 nm) and in solid state (Nujol mull, range 400–1100 nm) were measured with a Shimadzu 160A instrument in the range 200–1100 nm. Continuous-wave EPR spectra were recorded at liquid helium temperatures with a Bruker ER 200D X-band spectrometer equipped with an Oxford Instruments cryostat. The microwave frequency and the magnetic field were measured with a microwave frequency counter HP 5350B and a Bruker ER035 M NMR-gaussmeter, respectively.

 © 2005 Wiley-VCH Verlag GmbH & Co. KGaA, Weinheim

Computational Details: The structural, electronic, and energetic properties of all compounds were computed with the Becke three-parameter hybrid functional[25,26] combined with the Lee–Yang–Parr correlation functional,[27] abbreviated as B3LYP, using the LANL2DZ basis set[28] that includes Dunning–Huzinaga full double-ζ on the first row and Los Alamos ECPs plus DZ on the copper and halogen atoms. This hybrid B3LYP functional was used since it gives acceptable results for molecular energies and geometries, as well as proton donation, and weak and strong H-bonds.[29–35] No constraints were imposed on the geometry in any of the computations. Full geometry optimization was performed for each structure using Schlegel's analytical gradient method,[36] and the attainment of the energy minimum was verified by calculating the vibrational energy that results in the absence of imaginary eigenvalues. All the stationary points were identified for minimum (number of imaginary frequencies NIMAG = 0) or transition states (NIMAG = 1). Time-dependent density functional theory (TD-DFT)[37–39] calculations were performed on the equilibrium ground state geometries employing the same density functionals and basis sets as used in the geometry optimization. The Davidson algorithm was used, in which the error tolerance in the square of the excitation energies and trial-vector orthonormality criterion were set to 10^{-8} and 10^{-10}, respectively. The success of the TD-DFT method in calculating excitation energies of transition metal complexes has been demonstrated in several recent studies.[40–42] All calculations were performed using the GAUSSIAN03 series of programs.[43] The qualitative concepts and the graphs derived from the Chem3D program suite[44] highlight the basic interactions resulting from the DFT calculations.

Synthesis of the Complexes: The precursors [$CuBr_2$(dien)] (**1**) and [$CuCl_2$(dien)] (**2**) were prepared by literature methods,[45] while the analogous complexes [$CuBr_2$(dpta)] (**3**) and [$CuCl_2$(dpta)] (**4**) were prepared as described below.

[$CuBr_2$(dpta)] (3): dpta (1.41 mL) was added dropwise to a methanolic suspension (ca. 30 mL) containing 2.23 g (10^{-2} mol) of $CuBr_2$. After vigorous stirring for 20 min, a blue precipitate was formed, which was then separated by filtration, washed several times with diethyl ether, and dried in vacuo. Yield: 2.16 g (61%).

[$CuCl_2$(dpta)] (4): The [$CuCl_2$(dpta)] complex, due to its high solubility in methanol, cannot be isolated, therefore the trihalide [CuCl(dpta)($ClBr_2$)] and the tetrahalide [{Cu(dpta)Cl}$_2$(μ-Cl_2I_2)] complexes were prepared in situ.

[CuBr(dpta)(BrI_2)] (5): A methanolic solution (20 mL) of I_2 (1.27 g, 5 mmol) was added dropwise to a methanolic suspension (30 mL) of [$CuBr_2$(dpta)] (1.775 g, 5 mmol). Diethyl ether (10 mL) was added to the resulting dark-green solution, which was further left at low temperature (4 °C) for 24 h, after which the formation of high-quality, dark-green crystals suitable for X-ray diffraction analysis was observed. The crystals formed were isolated by filtration and dried in air. Yield: 1.61 g (53%). $C_6H_{17}Br_2CuI_2N_3$ (608.38): calcd. C 11.84, H 2.82, Cu 10.44, N 6.91; found C 12.00, H 2.83, Cu 10.25, N 6.96. IR: ṽ = 3277 s, 3203 ws, 3126 vs, 504 m, 252 w, 223 cm^{-1} w. Λ_μ (DMF) = 68 μS cm^{-1}. UV/Vis (DMF): λ_{max} (log ε) = 680 nm (2.42); (Nujol): λ_{max} = 740, 451, 410 nm. μ_{eff} = 1.85 μ_B.

[CuCl(dpta)($ClBr_2$)] (6): A methanolic solution containing 1.41 mL of dpta was added to a solution of $CuCl_2 \cdot 2H_2O$ (1.71 g, 10 mmol) in the same solvent. Br_2 (0.55 mL in 10 mL of methanol) was added to the resulting blue solution. After 1 h, the solution was filtered to remove any impurities, ethanol (10 mL) was added to the filtrate, and the brown precipitate was isolated by filtration, washed several times with ethanol and diethyl ether, and dried in vacuo to give red brown microcrystals of **6** (1.19 g, 28%). $C_6H_{17}Br_2Cl_2CuN_3$ (425.38): calcd. C 16.94, H 4.03, Cu 14.93, N 9.88; found C 17.10, H 4.11, Cu 14.80, N 9.85. IR: ṽ = 3260 vs, 3205 vs, 3113 vs, 511 w, 383 w, 326 cm^{-1} w. Λ_μ (DMF) = 75 μS cm^{-1}. UV/Vis (DMF): λ_{max} (log ε) = 720 (1.97), 921 sh, 434 nm sh; (Nujol): λ_{max} = 792, 530 sh, 461 nm sh. μ_{eff} = 1.65 μ_B.

[CuBr(dien)(Br_3)] (7): A methanolic solution (ca. 5 mL) of 0.1 mL of Br_2 was added to another methanolic solution (ca. 20 mL) of [$CuBr_2$(dien)] (0.650 g, 2 mmol). Upon addition, the blue solid turned green. After stirring for 30 min, the solid formed was separated by filtration, washed several times with diethyl ether, and dried in vacuo to give green microcrystals of **7** (0.272 g, 28%). $C_4H_{13}Br_4CuN_3$ (486.33): calcd. C 9.88, H 2.68, Cu 13.06, N 8.64; found C 9.78, H 2.56, Cu 13.20, N 8.57. IR: ṽ = 3290 vs, 3230 vs, 3157 vs, 523 w, 336 w, 315 cm^{-1} w. Λ_μ (DMF) = 82 μS cm^{-1}. UV/Vis (DMF): λ_{max} (log ε) = 618 nm (2.21); (Nujol): λ_{max} = 651, 444, 403 nm sh. μ_{eff} = 2.19 μ_B.

[{CuCl(dien)}$_2$(μ-Cl_2Br_2)] (8): [$CuCl_2$(dien)] (4.75 g, 20 mmol) was dissolved in ca. 30 mL of methanol. After 30 min of vigorous stirring, 0.55 mL of Br_2 in 10 mL of methanol was added and the color of the solution turned from blue to green. The green solid formed was then separated by filtration, washed several times with diethyl ether, and dried in vacuo to give green microcrystals of **8** (4.51 g, 71%). $C_8H_{26}Br_2Cl_4Cu_2N_6$ (635.04): calcd. C 15.13, H 4.13, Cu 20.01, N 13.23; found C 15.23, H 4.20, Cu 19.85, N 13.36. IR: ṽ = 3300 vs, 3244 vs, 3169 vs, 516 w, 383 w, 311 cm^{-1} w. Λ_μ (DMF) = 106 μS cm^{-1}. UV/Vis (DMF): λ_{max} (log ε) = 683 (2.01), 902 nm (1.92); (Nujol): λ_{max} = 684, 449, 404 nm sh. μ_{eff} = 1.89 μ_B.

[{CuCl(dpta)}$_2$(μ-Cl_2I_2)] (9): A methanolic solution of 1.41 mL of dpta was added to a solution of $CuCl_2 \cdot 2H_2O$ (1.71 g, 10 mmol) in 20 mL of methanol. A solution of iodine (1.27 g, 5 mmol) in 20 mL of methanol was added to the resulting blue solution. After 1 h of stirring, the green solution was left to stand and then 10 mL of diethyl ether was added. After 1 h, a microcrystalline dark-green product had formed, which was isolated by filtration, washed twice with 5 mL of diethyl ether and dried in vacuo to give green microcrystals of **9** (2.24 g, 57%). $C_{12}H_{34}Cl_4Cu_2I_2N_6$ (785.15): calcd. C 18.36, H 4.36, Cu 16.19, N 10.70; found C 18.69, H 4.40, Cu 16.01, N 10.56. IR: ṽ = 3250 vs, 3207 vs, 3130 vs, 506 m, 338 w, 255 cm^{-1} w. Λ_μ (DMF) = 88 μS cm^{-1}. UV/Vis (DMF): λ_{max} (log ε) = 647 nm sh; (Nujol): λ_{max} = 783, 460 nm sh. μ_{eff} = 1.76 μ_B.

[{CuBr(dien)}$_2$(μ-Br_4)] (10): A methanolic solution (ca. 5 mL) of 0.15 mL of Br_2 was added to another methanolic solution (ca. 20 mL) of [$CuBr_2$(dien)] (1.63 g, 5 mmol). Upon addition, the blue solid turned dark blue. After stirring for 30 min, the solid formed was separated by filtration, washed several times with diethyl ether, and dried in vacuo to give dark-green microcrystals of **10** (1.04 g, 51%). $C_8H_{26}Br_6Cu_2N_6$ (812.85): calcd. C 11.82, H 3.22, Cu 15.63, N 10.34; found C 11.76, H 3.32, Cu 15.49, N 10.29. IR: ṽ = 3300 vs, 3235 vs, 3125 vs, 518 w, 253 w, 246 cm^{-1} w. Λ_μ (DMF) = 142 μS cm^{-1}. UV/Vis (DMF): λ_{max} (log ε) = 598 (2.55), 941 nm (2.12); (Nujol): λ_{max} = 633 sh, 526, 425 nm sh. μ_{eff} = 2.16 μ_B.

[{CuBr(dien)}$_2$(μ-Br_2I_2)] (11): A methanolic solution (ca. 20 mL) of I_2 (0.254 g, 1 mmol) was added to another methanolic solution (20 mL) of [$CuBr_2$(dien)] (0.65 g, 2 mmol). Upon addition, the blue solid turned brown. After stirring for 30 min, the solid formed was separated by filtration, washed several times with diethyl ether, and dried in vacuo to give black microcrystals of **11** (0.79 g, 88%). $C_8H_{26}Br_4Cu_2I_2N_6$ (906.85): calcd. C 10.60, H 2.89, Cu 14.01, N 9.27; found C 10.686, H 2.97, Cu 14.10, N 9.33. IR: ṽ = 3286 s, 3233 vs, 3161 vs, 516 w, 238 cm^{-1} w. Λ_μ (DMF) = 110 μS cm^{-1}. UV/

 © 2005 Wiley-VCH Verlag GmbH & Co. KGaA, Weinheim

Vis (DMF): λ_{max} (log ε) = 617 nm (2.46); (Nujol): λ_{max} = 742, 572, 463, 399 nm. μ_{eff} = 1.99 μ_B.

X-ray Crystallographic Study: X-ray diffraction data were collected with an Enraf–Nonius Kappa CCD area-detector diffractometer. The programs DENZO[46] and COLLECT[47] were used in data collection and cell refinement. Details of data collection and structure refinement are given in Table 7. All crystals produced were twinned such that the data set obtained for a single crystal contained overlapping reflections. After removal of the affected reflections, 51.9% of the data set remained. The structure was solved with the program SIR97[48] and refined with SHELX-97.[49] Molecular plots were obtained with the program ORTEP-3.[50] CCDC-260389 contains the supplementary crystallographic data for this paper. These data can be obtained free of charge from The Cambridge Crystallographic Data Centre via www.ccdc.cam.ac.uk/data_request/cif.

Table 7. Crystal data and structure refinements for [CuBr(dpta)-(BrI_2)] (**5**).

Empirical formula	$C_6H_{17}Br_2CuI_2N_3$
Formula mass	608.39
Temperature	120(2) K
Wavelength	0.71073 Å
Crystal system	monoclinic
Space group	*C*2/*c*
Unit cell dimensions	a = 26.7159(13) Å, α = 90°
	b = 9.01969(10) Å, β = 96.097(3)°
	c = 25.4078(7) Å, γ = 90°
Volume	6087.9(3) $Å^3$
Z	16
Density (calculated)	2.655 $Mg\,m^{-3}$
Absorption coefficient	10.717 mm^{-1}
F(000)	4464
Crystal size	0.32 × 0.18 × 0.08 mm
θ range for data collection	5.04–27.50°
Index ranges	$-34 \le h \le 34$
	$-11 \le k \le 11$
	$-31 \le l \le 31$
Reflections collected	15827
Independent reflections	3633 [R(int) = 0.0403]
Refinement method	Full-matrix least squares on F^2
Data/restraints/parameters	3633/0/254
Goodness-of-fit on F^2	1.082
Final R indices [$I > 2\sigma(I)$]	R_1 = 0.0350, wR_2 = 0.0802
R indices (all data)	R_1 = 0.0521, wR_2 = 0.0846
Largest difference peak/hole	0.838/–0.955 e $Å^{-3}$

Acknowledgments

The financial support of this work by the Greek General Secretariat for Research and Technology and the European Commission within the framework of the PENED01 projects is gratefully acknowledged (grant no. 01EΔ367). We would like to thank Assistant Professor J. Deligiannakis for providing the EPR data and also the EPSRC X-ray crystallography service at the University of Southampton for collecting the X-ray data.

[1] E. Dubler, L. Linowsky, *Helv. Chim. Acta* **1975**, *58*, 2604.
[2] A. Rabenau, H. Schulz, W. Stoeger, *Naturwissenschaften* **1976**, *63*, 245.
[3] M. F. Belicchi, G. G. Fava, C. Pelizzi, *Acta Crystallogr., Sect. B* **1981**, *37*, 924.
[4] E. M. Nour, L. H. Chen, J. Laane, *J. Phys. Chem.* **1986**, *90*, 2841.
[5] J. C. Bailar, H. J. Emeleus, R. Nyholm, A. F. Trotman-Dickenson, *Comprehensive Inorganic Chemistry*, Pergamon Press, Oxford, **1973**, vol. 2.
[6] P. Deplano, J. R. Ferraro, M. L. Mercuri, E. F. Trogu, *Coord. Chem. Rev.* **1999**, *188*, 71.
[7] A. Tracz, J. K. Jeszka, J. Ulanski, T. Pakula, J. P. Rabe, *Synth. Met.* **1998**, *94*, 17.
[8] J. Ulanski, A. Tracz, J. K. Jeszka, E. Laukhina, T. Pakula, *Synth. Met.* **1997**, *85*, 1591.
[9] H. Mittag, P. Cikmacs, H. Fullbier, A. Lusis, G. Petrovskis, L. Schmidt, H. Stegemann, *Soviet Electrochem.* **1989**, *25*, 717.
[10] T. Okamoto, T. Utsunomiya, T. Uesugi, T. Kakinami, S. Kajigaeshi, *Bull. Chem. Soc. Jpn.* **1989**, *62*, 3748.
[11] T. Kakinami, H. Suenaga, T. Yamaguchi, T. Okamoto, S. Kajigaeshi, *Bull. Chem. Soc. Jpn.* **1989**, *62*, 3373.
[12] S. S. Mitra, K. Sreekumar, *Eur. Polym. J.* **1998**, *34*, 561.
[13] S. S. Mitra, K. Sreekumar, *React. Funct. Polym.* **1997**, *32*, 281.
[14] A. Butler, J. V. Walker, *Chem. Rev.* **1993**, *93*, 1937.
[15] K. Nakamoto, *Infrared and Raman Spectra of Inorganic and Coordination Compounds*, Wiley, New York, **1986**.
[16] N. Trendafilova, G. S. Nikolov, G. Bauer, R. Kellner, *Inorg. Chim. Acta* **1993**, *210*, 77.
[17] L. Chen, L. K. Thompson, J. N. Bridson, *Inorg. Chem.* **1993**, *32*, 2938.
[18] R. Minkwitz, M. Berkei, R. Ludwig, *Inorg. Chem.* **2001**, *40*, 25.
[19] W. J. Geary, *Coord. Chem. Rev.* **1971**, *7*, 21.
[20] G. B. Carpenter, *Acta Crystallogr.* **1966**, *20*, 334.
[21] A. Bencini, D. Gatteschi, *EPR of Exchange Coupled Systems*, Springer-Verlag, Berlin, **1990**.
[22] C. F. Martens, A. P. H. J. Schenning, M. C. Feiters, J. Heck, P. T. Beurskens, E. Steinwender, R. J. M. Nolte, *Inorg. Chem.* **1993**, *32*, 3029.
[23] R. J. M. Klein Gebbink, C. F. Martens, P. J. A. Kenis, R. J. Jansen, H.-F. Nolting, V. A. Solé, M. C. Feiters, K. D. Karlin, R. J. M. Nolte, *Inorg. Chem.* **1999**, *38*, 5755.
[24] M. Louloudi, K. Mitopoulou, E. Evaggelou, Y. Deligiannakis, N. Hadjiliadis, *J. Mol. Catal. A: Chem.* **2003**, *198*, 231.
[25] A. D. Becke, *J. Chem. Phys.* **1992**, *96*, 2155.
[26] A. D. Becke, *J. Chem. Phys.* **1993**, *98*, 5648.
[27] C. Lee, W. Yang, R. G. Parr, *Phys. Rev. B* **1988**, *37*, 785.
[28] W. R. Wadt, P. J. Hay, *J. Chem. Phys.* **1985**, *82*, 5284.
[29] J. B. Nicholas, *Top. Catal.* **1997**, *4*, 157.
[30] W. R. Koch, H. Hertwing, *Chem. Phys. Lett.* **1997**, *268*, 345.
[31] L. A. Curtis, K. Raghavachari, P. C. Redfern, J. A. Pople, *Chem. Phys. Lett.* **1997**, *270*, 419.
[32] D. M. Smith, B. T. Golding, L. Radom, *J. Am. Chem. Soc.* **1999**, *121*, 9388.
[33] A. K. Ghandra, M. T. Nguyen, *Chem. Phys.* **1998**, *232*, 299.
[34] J. B. Nicholas, *Top. Catal.* **1999**, *9*, 181.
[35] R. Arnaud, C. Adamo, M. Cossi, A. Millet, Y. Valle, V. Barone, *J. Am. Chem. Soc.* **2000**, *122*, 324.
[36] H. B. Schlegel, *J. Comput. Chem.* **1982**, *3*, 214.
[37] R. Bauernschmitt, R. Ahlrichs, *Chem. Phys. Lett.* **1996**, *256*, 454.
[38] C. Jamorski, M. E. Casida, D. R. Salahud, *J. Chem. Phys.* **1996**, *104*, 5134.
[39] S. J. A. van Gisbergen, F. Kootstra, P. R. T. Schipper, O. V. Gritsenko, J. G. Snijders, E. Baerends, *J. Phys. Rev. A* **1998**, *57*, 1556.
[40] A. Rosa, E. J. Baerends, S. J. A. van Gisbergen, E. van Lenthe, J. A. Groeneveld, J. G. Snijders, *J. Am. Chem. Soc.* **1999**, *121*, 10356.
[41] S. J. A. van Gisbergen, J. A. Groeneveld, A. Rosa, J. G. Snijders, E. J. Baerends, *J. Phys. Chem. A* **1999**, *103*, 6835.
[42] P. Boulet, H. Chermette, C. Daul, F. Gilardoni, F. Rogemond, J. Weber, G. Zuber, *J. Phys. Chem. A* **2001**, *105*, 885.
[43] M. J. Frisch, G. W. Trucks, H. B. Schlegel, G. E. Scusseria, M. A. Robb, J. R. Cheeseman, V. G. Zakrzewski, J. A. Montgomery, R. E. Stratmann, J. C. Burant, S. Dapprich, J. M. Mil-

 © 2005 Wiley-VCH Verlag GmbH & Co. KGaA, Weinheim

lan, A. D. Daniels, K. N. Kudin, M. C. Strain, O. Farkas, J. Tomasi, V. Barone, M. Cossi, R. Cammi, B. Mennucci, C. Pomelli, C. Adamo, S. Clifford, J. Orchterski, G. A. Petersson, P. Y. Ayala, Q. Cui, K. Morokuma, D. K. Malick, A. D. Rabuck, K. Raghavachari, J. B. Foresman, J. Cioslowski, J. V. Ortiz, B. B. Stefanov, G. Liu, A. Liashenko, P. Piskorz, I. Komaroni, R. Gomperts, R. L. Martin, D. J. Fox, T. Keith, M. A. Al-Laham, C. Y. Peng, A. Nanayakkara, C. Gonzalez, M. Challacombe, P. M. Gill, P. Johnson, W. Chen, M. W. Wong, J. L. Andres, M. Head-Gordon, E. S. Replogle, J. A. Pople, *Gaussian03*, revision A.7, Gaussian Inc., Pittsburgh, PA, **1998**.

[44] Cambridge Scientific Computing Inc., 875 Massachusetts Ave., Suite 41, Cambridge, MA 02139.

[45] N. F. Curtis, H. K. J. Powell, *J. Chem. Soc. A* **1968**, 3069.

[46] Z. Otwinowski, W. Minor, in *Macromolecular Crystallography*, vol. 276 (Eds.: C. W. Carter, Jr., R. M. Sweet), Academic Press, New York, **1997**, p. 307.

[47] R. Hooft, N. B. V., Delft, The Netherlands, **1998**.

[48] A. Altomare, M. C. Burla, M. Camalli, G. L. Cascarano, C. Giacovazzo, A. G. G. Moliterni, G. Polidori, R. Spagna, *J. Appl. Crystallogr.* **1994**, *27*, 435.

[49] G. M. Sheldrick, University of Göttingen, Göttingen, Germany, **1997**.

[50] L. J. Farrugia, *J. Appl. Crystallogr.* **1997**, *30*, 565.

Received: February 18, 2005
Published Online: August 2, 2005

 © 2005 Wiley-VCH Verlag GmbH & Co. KGaA, Weinheim

First Observation of NIR 4f–4f Luminescence through the Energy Transfer from the SOMO π* Doublet in Nitronyl Nitroxide Radical Lanthanide(III) Complexes

Sumio Kaizaki,*[a] Dai Shirotani,[a] Yasunori Tsukahara,[a] and Hiroyasu Nakata[b]

Keywords: Near infrared 4f–4f luminescence / Lanthanide(III) complexes / Nitronyl nitroxide radical / Energy transfer / Antenna effect

This study demonstrates the first observation of energy transfer from the doublet state of the nitronyl nitroxide radical ligand in Ln^{III} complexes, exerting the light-harvesting antenna effect on the NIR luminescence for the first time.

(© Wiley-VCH Verlag GmbH & Co. KGaA, 69451 Weinheim, Germany, 2005)

Introduction

With the aim of obtaining low-cost near-infrared (NIR) light sources for communications or sensing and biological applications, there have been a number of investigations concerning lanthanide(III) complexes with aromatic imines or organic dyes where the triplet states and/or ligand-to-metal charge transfer (LMCT) play crucial roles in the energy transfer as photosensitizers exerting antenna effects.[1–3] Lanthanide complexes having nitroxide radical(s) could have intriguing emitting properties with regards to the differences in the spin multiplicity of ligand excited states on going from triplet (organic compounds) to doublet (radicals) states. From magnetic studies on nitroxide radical complexes,[4] Luneau and Reber et al. reported the luminescence spectra of uncoordinated[5] and coordinated nitroxides,[6] where attempts were made to understand the electronic states[5] or to seek qualitative trends between the luminescence and the magnetic interaction.[6] During our endeavor to reveal the magneto-optical properties of metal complexes with nitronyl or imino nitroxide radicals such as NIT2py [4,4,5,5-tetramethyl-2-(2′-pyridyl)-4,5-dihydro-1*H*-imidazol-1-oxyl 3-oxide] or IM2py [4,4,5,5-tetramethyl-2-(2′-pyridyl)-4,5-dihydro-1*H*-imidazol-1-oxyl][7–9] as well as of the Ln^{III}–Cr^{III} dinuclear complexes,[10–11] the emission spectra afforded information on the energy transfer from the nitroxide SOMO π* or the Cr^{III} ^2E state to the 4f state. Therefore, the SOMO π* of the nitroxide radical in lanthanide complexes could be expected to become a potential light harvesting antenna. However, there has been no report on Ln^{III} complexes exhibiting NIR 4f–4f luminescence associated with the SOMO π* of the NIT2py radical ligand to 4f energy transfer.

In this article the NIR luminescence is examined for the $[Ln^{III}(hfac)_3(NIT2py)]$ complex in the solid state (Scheme 1) with regards to energy transfer or the antenna effect.

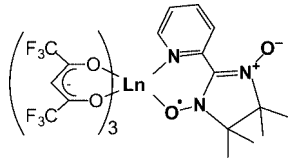

Scheme 1. Schematic molecular structure of $[Ln(hfac)_3(NIT2py)]$.

Results and Discussion

The employed lanthanide(III) complexes are classified into three groups: (i) non-emissive (Lu^{III}: **1**), (ii) Vis-emissive (Eu^{III}: **2**; Sm^{III}: **3**), (iii) NIR-emissive (Nd^{III}: **4**; Tm^{III}: **5**; Yb^{III}: **6**).

The lanthanide complexes **1–6** show similar UV/Vis band patterns with peaks or shoulders near 550 nm and molar absorption coefficients of $\varepsilon_{max} \approx 350–380$ $mol^{-1}\,dm^3$ and $\varepsilon_{514} \approx 250$ $mol^{-1}\,dm^3$, which are assigned to the intraligand n–π* transition of the NIT2py ligand. Therefore, the photoexcitation conditions are not very different from one another at 541 nm.

The absorption and luminescence spectra of the non-emissive 4f–4f complex (**1**) exhibits a vibronic structure (Figure 1). Since the band contours of the two spectra show a mirror image relationship, the luminescence at 9–15×10^3 cm^{-1} is the intraligand doublet-doublet (D-D) luminescence from only one SOMO π* excited state, in con-

[a] Department of Chemistry, Graduate School of Science, Osaka University,
Toyonaka, Osaka, 560-0043, Japan
E-mail: kaizaki@chem.sci.osaka-u.ac.jp
[b] Osaka Kyoiku University,
Kashihara, Osaka, 582-8582, Japan

trast to the (NITBzIm)Ln^{III} complexes which were claimed to have two SOMO π* states from the emission spectra.[8]

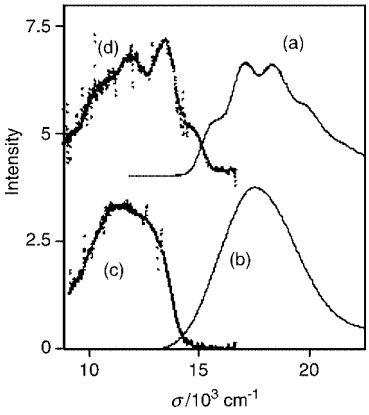

Figure 1. UV/Vis spectra (dotted lines) in CH_2Cl_2 at 180 K and luminescence spectra (solid lines) in the solid state at 180 K of **1** (a) and (d) and NIT2py ligand (b) and (c), respectively.

The Vis-emissive complexes **2** and **3** only demonstrated the intraligand D-D luminescence at 15 K. This results from the energy transfer from the 4f levels to the SOMO π* level, as compared with the cases of [Eu^{III}(hfac)$_3$(IM2py)][7a] and [Eu^{III}(hfac)$_3$(NITBzim or IMBzim)] [hfac = hexafluoroacetylacetonate; NITBzim = 2-(2-benzimidazolyl)-4,4,5,5-tetramethylimidazolin-1-oxyl 3-oxide; IMBzim = 2-(2-benzimidazolyl)-4,4,5,5-tetramethylimidazoline 1-oxide].[6] For [Eu^{III}(hfac)$_3$(IM2py)], the visible 4f–4f luminescence was observed by excitation at 222 nm corresponding to the intraligand hfac transition, but not by excitation at 465 nm corresponding to the intraligand IM2py transition at room temperature; exhibiting the energy transfer from the triplet state of the ancillary hfac ligand.[8a] However, at 5 K the 4f–4f luminescence of the (IM2py)Eu complex was observed by Ar^+ laser excitation.[6b–6d] The present (NIT2py)Eu^{III} complex only gives the intraligand (NIT2py) luminescence, probably due to the lower lying SOMO π* in NIT2py compared with the SOMO π* in IM2py[8a], as shown in Figure 2. On the other hand, the luminescence behavior of [Eu(NITBzim)$_2$(NO$_3$)$_3$] is similar to that of the present NIT2py complex, whereas [Eu(hfac)$_3$(NITBzim or IMBzim)] demonstrates both the intraligand and visible 4f–4f luminescence.[6b–6d] This difference results from the relative location between the SOMO π* band envelope of nitroxide radicals and the emissive 4f energy levels as can be seen in Figure 2.

As shown in Figure 3, the NIR 4f–4f emissive complexes gave typical 4f–4f luminescence at 7490 cm^{-1} ($^4F_{3/2}\rightarrow{}^4I_{13/2}$), 9400 cm^{-1} ($^4F_{3/2}\rightarrow{}^4I_{11/2}$), 11100 cm^{-1} ($^2F_{3/2}\rightarrow{}^4I_{9/2}$) for **4** and 10000 cm^{-1} ($^3H_4\rightarrow{}^3H_6$), 12500 cm^{-1} ($^3F_3\rightarrow{}^3H_6$) for **5** and ca. 10000 cm^{-1} ($^2F_{5/2}\rightarrow{}^2F_{7/2}$) for **6**. These facts indicate that the energy transfers occur from the SOMO π* to the 4f excited levels. The 4f–4f transitions of these complexes are located below the NIT2py SOMO π* state. This behavior is analogous to the case of the energy transfer from the $^2E(Cr^{III})$ to the 4f levels for the Cr–Nd and Cr–Yb dinuclear complexes, [(acac)$_2$Cr(bpypz)Ln(hfac)$_3$],[10d,11] but

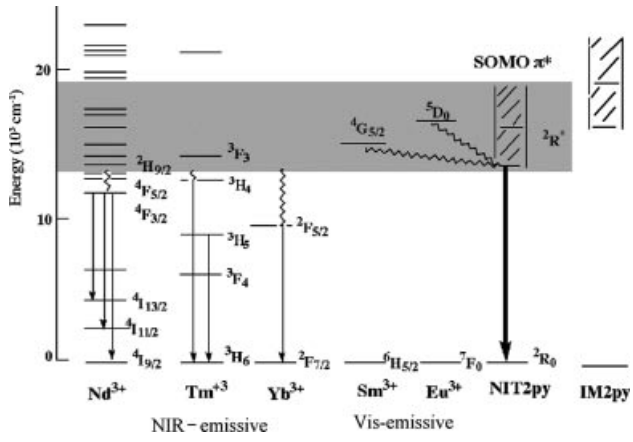

Figure 2. Energy levels for the Ln complexes and nitroxide radicals.

different from that for the corresponding complexes, [(acac)$_2$Cr(ox)Ln(HBpz$_3$)$_2$], which exhibit the simultaneous 3d–3d and 4f–4f luminescence at low temperature.[11] In our recent luminescence study of (NIT2py)- and (IM2py)Cr^{III} complexes, it is found that the NIT2py and IM2py radicals exert the antenna effect, showing a fast energy transfer from the SOMO π* to the $^2E/^2T_1(Cr^{III})$ state.[9] These findings suggest that the SOMO π* doublet state of the nitroxide radical could be of potential for visible-light sensitization of NIR luminescence as a light-harvesting antenna. This could be required for possible candidates of NIR light sources or multiplex assays to simultaneously detect a mixture of lanthanide ions with narrow luminescence peaks by visible-light excitation. This is because of the lower lying NIT2py SOMO π* band range existing within the emissive 4f levels compared with that of IM2py and NITBzim or IMBzim.

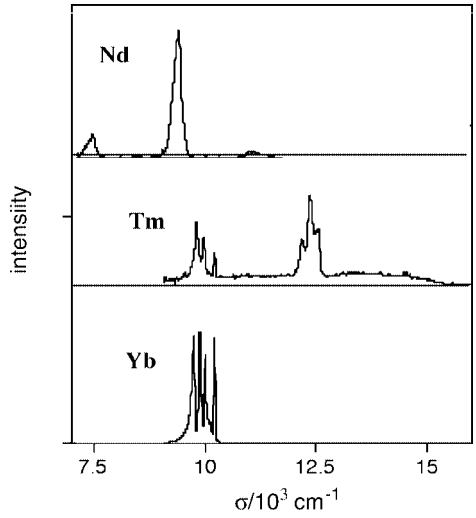

Figure 3. Luminescence spectra in the solid state at 15 K of [Ln(hfac)$_3$(NIT2py)] (top to bottom: **4**, **5**, **6**).

Conclusion

In summary, we observed the 4f–4f NIR luminescence of the (NIT2py)Ln^{III} complexes at 15 K through the direct

 © 2005 Wiley-VCH Verlag GmbH & Co. KGaA, Weinheim

energy transfer from the SOMO π* doublet state to the 4f levels for the first time. Since there was no observation of the simultaneous luminescence for the NIR-emissive Ln^{III} complexes, it appears that the NIT2py radical exerts an antenna effect as a light-harvesting ligand. It is invaluable to clarify the difference between the doublet (SOMO π*)-to-4f direct energy transfer in nitroxide complexes and the triplet-to-4f indirect energy transfer through intersystem crossing from the singlet to triplet state in nonradical organic ligands,[2,3] e.g., in relation with the LMCT for Eu^{III}[12] or Yb^{III} complexes.[13]

Further photophysical and photochemical studies will be needed for the development of new photosensitizers for NIR light sources. This would be made feasible by tuning the emissive states with a variation of the substitution of NIT radicals such as benzimidazole in the nitroxide radical Ln^{III} complexes.

Experimental Section

Measurements: The NIR absorption spectra were recored with a Perkin–Elmer Lambda 19 spectrophotometer at room temperature in chloroform solution. The luminescence spectra were measured with a SPEX 1269 spectrometer with excitation by an Ar^+ laser (514.5 nm). The focus distances for the excitation and emission were 25 cm and 1.3 m, respectively. The excitation and emission slit widths were 4 mm and 2 mm, respectively. The dispersed signal was detected by a Ge-pin photodiode (North Coast EO-817L) cooled by liquid nitrogen.

Preparation of Complexes: The (NIT2py)Ln^{III} complexes were prepared by a modified literature method.[2a] NIT2py (1 mmol) was added to a solution of $[Ln(hfac)_3(H_2O)_2]$ (1 mmol) in $CHCl_3$/EtOH (1:1) (20 mL). The resulting violet solution was stirred at room temperature. After 1 d, violet elongated crystals with no crystallization solvent were obtained. The Eu^{III}, Lu^{III} and Yb^{III} complexes were stable at –5 °C, while the other Ln^{III} complexes were stable at room temperature. $C_{27}H_{19}F_{18}LuN_3O_8$ (1030.40): calcd. C 31.47, H 1.86, N 4.08; found C 31.92, H 1.92, N 4.15. $C_{27}H_{19}F_{18}N_3O_8Yb$ (1028.47): calcd. C 31.53, H 1.86, N 4.09; found C 32.04, H 1.93, N 4.09. $C_{27}H_{19}F_{18}N_3NdO_8$ (999.67): calcd. C 32.44, H 1.92, N 4.20; found C 34.19, H 2.38, N 4.21. $C_{27}H_{19}F_{18}N_3O_8Tm$ (1024.37): calcd. C 31.66, H 1.87, N 4.10; found C 31.43, H 1.80, N 4.11.

[1] a) N. Sabbatini, M. Guardigi, J.-M. Lehn, *Coord. Chem. Rev.* **1993**, *123*, 201; b) H. Maas, A. Currao, G. Calzaferri, *Angew. Chem. Int. Ed.* **2002**, *41*, 2485; c) Y. Hasegawa, T. Ohkubo, K. Sogabe, Y. Kawamura, Y. Wada, N. Nakashima, S. Yanagida, *Angew. Chem. Int. Ed.* **2000**, *39*, 357; d) G. Mancino, A. J. Ferguson, A. Beeby, N. J. Long, T. S. Jones, *J. Am. Chem. Soc.* **2005**, *127*, 524.

[2] a) S. I. Klink, L. Grave, L. D. N. Reinhoudt, F. C. J. M. van Veggel, M. H. V. Werts, F. A. J. Geurts, J. W. Hofstraat, *J. Phys. Chem. A* **2000**, *104*, 5457; b) G. A. Hebbink, L. Grave, L. A. Woldering, D. N. Reinhoudt, F. C. J. M. van Veggel, *J. Phys. Chem. A* **2003**, *107*, 2483; c) N. M. Shavaleev, S. J. A. Pope, Z. R. Bell, S. Faulkner, M. D. Ward, *Dalton Trans.* **2003**, 808.

[3] a) F. Gutierrez, C. Tedeschi, L. Maron, J.-P. Daudey, R. Poteau, J. Azema, P. Tisnés, C. Picard, *Dalton Trans.* **2004**, 1334; b) J. Zhang, P. D. Badger, S. J. Geib, S. Petound, *Angew. Chem. Int. Ed.* **2005**, *44*, 2508.

[4] a) C. Benelli, D. Gatteschi, *Chem. Rev.* **2002**, *102*, 2369; b) M. L. Kahn, J.-P. Sutter, S. Golhen, P. Guionneau, L. Ouahab, O. Kahn, D. Chasseau, *J. Am. Chem. Soc.* **2000**, *122*, 3413; c) C. Lescop, E. Belorizky, D. Luneau, P. Rey, *Inorg. Chem.* **2003**, *42*, 3375; d) M. L. Kahn, R. Ballou, P. Porcher, O. Kahn, J.-P. Sutter, *Chem. Eur. J.* **2002**, *8*, 525.

[5] a) R. Beaulac, G. Bussière, C. Reber, C. Lescop, D. Luneau, *New J. Chem.* **2003**, *27*, 1200; b) C. Hirel, D. Luneau, J. Pécaut, L. Öhrström, G. Bussière, C. Reber, *Chem. Eur. J.* **2002**, *8*, 3157.

[6] a) C. Lescop, D. Luneau, G. Bussière, M. Triest, C. Reber, *Inorg. Chem.* **2000**, *39*, 3740; b) C. Lescop, D. Luneau, P. Rey, G. Bussière, C. Reber, *Inorg. Chem.* **2002**, *41*, 5566; c) G. Bussière, R. Beaulac, H. Bélisle, C. Lescop, D. Luneau, P. Rey, *Top. Curr. Chem.* **2004**, *24*, 97; d) C. Lescop, G. Bussière, R. Beaulac, H. Bélisle, E. Beloeizky, P. Rey, C. Reber, D. Luneau, *J. Chem. Phys. Solid.* **2004**, *65*, 773.

[7] a) S. Kaizaki, *Bull. Chem. Soc. Jpn.* **2003**, *76*, 673; b) T. Yoshida, K. Kanamori, S. Takamizawa, W. Mori, S. Kaizaki, *Chem. Lett.* **1997**, 603; c) T. Yoshida, T. Suzuki, K. Kanamori, S. Kaizaki, *Inorg. Chem.* **1999**, *38*, 1059; d) Y. Tsukahara, A. Iino, T. Yoshida, T. Suzuki, S. Kaizaki, *J. Chem. Soc., Dalton Trans.* **2002**, 181; e) T. Tsukahara, T. Kamatani, T. Suzuki, S. Kaizaki, *Inorg. Chem.* **2002**, *41*, 4363; f) A. Iino, T. Suzuki, S. Kaizaki, *Dalton Trans.* **2003**, 4604**.**

[8] a) T. Tsukuda, T. Suzuki, S. Kaizaki, *J. Chem. Soc., Dalton Trans.* **2002**, 1721; b) T. Tsukuda, T. Suzuki, S. Kaizaki, *Mol. Cryst. Liq. Cryst.* **2002**, *379*, 159; c) T. Tsukuda, M. Ogita, T. Suzuki, S. Kaizaki, *Eur. J. Inorg. Chem.* **2004**, 4463; d) T. Tsukuda, T. Suzuki, S. Kaizaki, *Inorg. Chim. Acta* **2005**, *358*, 1253.

[9] Y. Tsukahara, H. Nakata, S. Kaizaki, *Inorg. Chem.* **2004**, *43*, 4383.

[10] a) T. Sanada, T. Suzuki, S. Kaizaki, *Inorg. Chem.* **1998**, *37*, 4712; b) M. A. Subhan, T. Suzuki, S. Kaizaki, *J. Chem. Soc., Dalton Trans.* **2001**, 492; c) M. A. Subhan, T. Suzuki, S. Kaizaki, *J. Chem. Soc., Dalton Trans.* **2002**, 1416; d) M. A. Subhan, T. Sanada, T. Suzuki, S. Kaizaki, *Inorg. Chim. Acta* **2003**, *353*, 263; e) R. Kawahata, T. Tsukuda, T. Yagi, M. A. Subhan, H. Nakata, A. Fuyuhiro, S. Kaizaki, *Chem. Lett.* **2003**, 1084.

[11] a) M. D. Subhan, T. Suzuki, S. Kaizaki, *Mol. Cryst. Liq. Cryst.* **2002**, *379*, 395; b) M. D. Subhan, T. Suzuki, J. H. Choi, H. Nakata, S. Kaizaki, *J. Lumin.* **2003**, *101*, 307; c) M. D. Subhan, R. Kawahata, H. Nakata, A. Fuyuhiro, T. Tsukuda, S. Kaizaki, *Inorg. Chim. Acta* **2004**, *357*, 3139.

[12] a) S. Petoud, J.-C. G. Bündzli, T. Glanzman, C. Piguet, Q. Xiang, R. P. Thummel, *J. Lumin.* **1999**, *82*, 69; b) P. Dorenbos, *J. Lumin.* **2005**, *111*, 89.

[13] W. D. Horrocks, Jr., J. P. Bolender, W. D. Smith, R. M. Supkowski, *J. Am. Chem. Soc.* **1997**, *119*, 5972.

Received: January 20, 2005
Published Online: August 2, 2005

 © 2005 Wiley-VCH Verlag GmbH & Co. KGaA, Weinheim

A Tetraphosphane Imine Ligand Which Enforces Square-Pyramidal Coordination

Christopher Zimmermann,[a] Frank W. Heinemann,[b] and Andreas Grohmann*[a]

Dedicated to Professor Herbert Schumann on the occasion of his 70th birthday

Keywords: Tetrapodal pentadentate ligand / Phosphane ligands / Chelates / Cobalt / Nickel

The tetrapodal pentadentate NP_4 ligand 2,6-$C_5H_3N[CMe(CH_2PPh_2)_2]_2$, which is readily prepared from the reaction of the corresponding tetrabromide with $KPPh_2$, forms mononuclear complexes with nickel(II) and cobalt(II). In the case of nickel(II), the coordination mode adopted by the ligand is sensitive to the nature of the counterion: Use of $NiCl_2$ gives a chloro complex as one of the products, which, as determined by X-ray crystallography, has a central ion coordinated by three phosphane and one chloro substituent in a distorted square planar fashion; by contrast, the reaction with $Ni(BF_4)_2$ gives a complex of approximate square-pyramidal geometry as the only product, in which all five atoms of the NP_4 set are coordinated to the nickel ion, despite the steric bulk of the eight phenyl substituents. The same type of complex is obtained with $Co(BF_4)_2$ and $Co(ClO_4)_2$. Attempts to increase the coordination number of either complex beyond 5 have been unsuccessful. In particular, the cobalt(II) complex (17 valence electrons) is practically inert to reagents such as O_2, NO, NO^+, I_2, Cl_2 or H_2. Full spectroscopic details for the complexes, as well as X-ray structure analyses, are reported.

(© Wiley-VCH Verlag GmbH & Co. KGaA, 69451 Weinheim, Germany, 2005)

Introduction

Chelating phosphane ligands are widely employed in catalysis and organic synthesis.[1,2] The vast majority of applications in homogeneous catalysis requires bidentate ligands (e.g., in asymmetric hydrogenation).[3] Owing to the necessity for "labile" donors and/or vacant coordination sites in molecular catalysts, ligands of higher denticity such as tridentate $H_3CC(CH_2PPh_2)_3$, "triphos", or tetradentate $P(CH_2CH_2PPh_2)_3$, "pp3", are less prone to give catalytically active species, although specialised applications in the "heterogenisation" of homogeneous catalysts do make use of the increased thermal and kinetic complex stability that such ligands impart.[4] Complexes of polypodal phosphane ligands show a rich coordination and reaction chemistry in their own right, however. This is because of the increasing electron-richness of the metal centre, which is a direct consequence of the increasing number of aryl-, or, better still, alkylphosphane donors. It is in this context that we have begun to extend our study of tetrapodal pentadentate ligands[5] to include tetraphosphane imine ligands. We recently described the C_{2v}-symmetrical NP_4 ligand 2,6-bis{2-(diphenylphosphanyl)-1-[(diphenylphosphanyl)methyl]-1-methylethyl}pyridine ("py{PPh_2}$_4$", **1**).[6] The present contribution summarises coordination chemistry aspects of this ligand with respect to nickel(II) and cobalt(II).

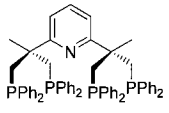

1

Results and Discussion

Coordination Behaviour of py{PPh_2}$_4$ Towards Nickel(II)

A red-brown solid was obtained from the reaction of equimolar amounts of py{PPh_2}$_4$ and $NiCl_2 \cdot 6H_2O$ in refluxing acetonitrile (cf. Experimental Section). Recrystallisation from methanol in the presence of $NaPF_6$ produced a microcrystalline purple material. Structural analysis using a single crystal from this batch revealed a chiral (*) 16 valence electron chloro complex (**2**) with a tetracoordinate nickel(II) centre. The tetraphosphane acts as a tridentate chelator, one diphenylphosphanyl unit and the pyridine nitrogen atom remaining uncoordinated [Equation (1)]. The

[a] Technische Universität Berlin, Institut für Chemie, Sekretariat C2,
Straße des 17. Juni 135, 10623 Berlin
[b] Universität Erlangen-Nürnberg, Institut für Anorganische Chemie,
Egerlandstraße 1, 91058 Erlangen
Fax: +49-30-31422935
E-mail: andreas.grohmann@chem.tu-berlin.de

 DOI: 10.1002/ejic.200500281

complex is also detected in the mass spectrum of the purple material, where it gives rise to a peak at *m*/*z* = 1022 ({[(py{PPh_2}$_4$)NiCl]}$^+$, 20%).

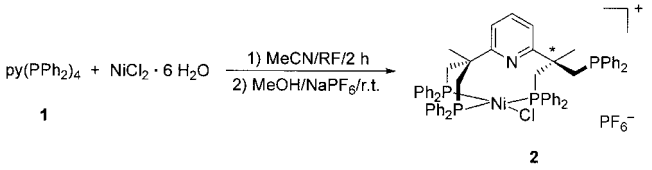

(1)

It should be noted, however, that the percentage of carbon in the solid analyses is consistently too low to be acceptable for pure compound **2**, $C_{61}H_{57}ClF_6NNiP_5$ (1167.14), which requires C 62.78, H 4.92, N 1.20%; a typical analysis is C 56.12, H 4.72, N 1.31%. This indicates that a mixture of products (of different solubilities) is formed, and that the major part of the material may in fact be the bis(hexafluorophosphate) salt, which requires C 57.39, H 4.50, N 1.10%. The ^{1}H, ^{13}C, and ^{31}P NMR spectroscopic data do suggest a highly symmetrical species and are virtually identical to the spectra obtained for the bis(tetrafluoroborate) salt **3** (below).

Apparently, the coordination mode adopted by the ligand is determined by the reaction conditions (solvent, coordinating ability of the counterion); this is evident from the outcome of an overall similar reaction, between stoichiometric amounts of py{PPh_2}$_4$ and $Ni(BF_4)_2 \cdot 6H_2O$ in a methanol/dichloromethane mixed solvent (1:1). In this case, there is only one product, which contains the tetraphosphane as a pentadentate capping ligand. The 18 valence electron complex [(py{PPh_2}$_4$)Ni]$(BF_4)_2$ (**3**), which forms as purple-brown microcrystals in 50% yield [Equation (2)], has the nickel(II) ion in a distorted square-pyramidal coordination environment. In the mass spectrum, the cation appears at *m*/*z* = 987 ({[(py{PPh_2}4)Ni]}$^+$, 75%).

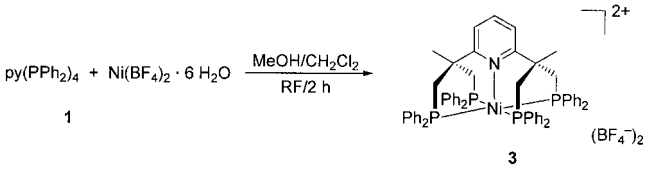

(2)

Compound **3** is readily soluble in acetonitrile and chloroform, and sparingly soluble in methanol. In the IR spectrum (KBr), the band at 1435 cm^{-1} attributed to the P–Ph stretching vibration is second in intensity only to the band diagnostic of BF_4^- (1060 cm^{-1}). Compared to the IR spectroscopic data for uncoordinated py{PPh_2}$_4$, ν_{P-Ph} (str) does not shift upon coordination.[6] Complex **3** is diamagnetic and gives well-resolved NMR spectra at room temperature. The ^{19}F spectrum has a singlet at δ = –149.5 ppm (in CD_2Cl_2), which is due to tetrafluoroborate. In the ^{31}P spectrum, there are two triplets for the diphenylphosphanyl groups at δ = 18.7 ppm and –10.9 ppm (A_2B_2 system). This spin system indicates similar geometries of the cation both in solution and in the solid state, with distortion of diametrically opposed Ni–P bonds from a square-planar towards a tetrahedral arrangement (cf. discussion of the X-ray structure, below). High symmetry in solution is also evident from the ^{1}H and ^{13}C NMR spectra. The pyridine protons give rise to a triplet (δ = 8.74 ppm) and a doublet (δ = 8.39 ppm) in a 1:2 intensity ratio (AB_2 system). Several multiplets between 7.6 ppm and 4.8 ppm are assigned to the diphenylphosphanyl protons. The methylene groups appear as three doublets between 3.3 ppm and 2.3 ppm (equivalent to 2, 2, and 4 protons, respectively), and a singlet at ca. 2.3 ppm accounts for the six methyl protons. In the ^{13}C spectra, there are 12 signals between 169.0 and 123.0 ppm for the aromatic C atoms. One signal each arises from the quaternary (δ = 42.3 ppm) and methyl carbon atoms (δ = 29.2 ppm), whereas the methylene carbon atoms produce two signals at δ = 38.9 ppm and 34.5 ppm, in accordance with the anisochrony observed for the phosphorus atoms.

Molecular Structures of [(py{PPh_2}$_4$)Ni(Cl)](PF$_6$) and [(py{PPh_2}$_4$)Ni](BF$_4$)$_2$

Single crystals suitable for X-ray structure determination had the compositions [(py{PPh_2}$_4$)Ni(Cl)](PF_6)·MeOH (**2**·MeOH) and [(py{PPh_2}$_4$)Ni]$(BF_4)_2$·CH_2Cl_2 (**3**·CH_2Cl_2). Compound **2** is a chiral chloro complex with tridentate coordination of the phosphane ligand (Figure 1); it crystallises as the racemate in the space group $P\bar{1}$. One phosphorus donor and the pyridine nitrogen atom remain uncoordinated [*d*(Ni1···N11) = 301.6(2) pm]. Selected bond lengths and angles are given in Table 1. The chloro ligand is displaced by 122.1(2) pm from the best plane defined by the nickel ion and the three coordinated P atoms, resulting in a coordination geometry around Ni^{II} which is intermediate between square planar and tetrahedral. The Ni–P and Ni–Cl bond lengths are within the range found for other chloro nickel(II) complexes with polyphosphane ligands.[7]

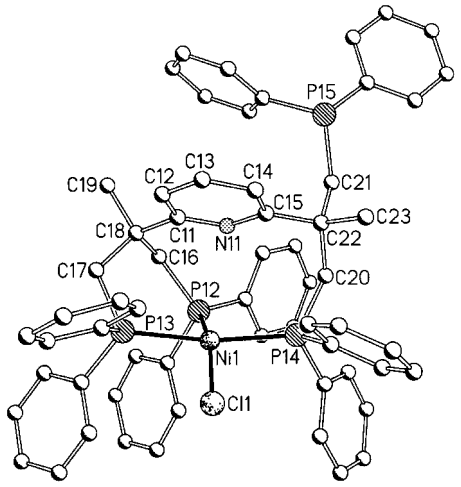

Figure 1. Molecular structure of the cation in the chloro nickel(II) complex **2** (H atoms not shown).

 © 2005 Wiley-VCH Verlag GmbH & Co. KGaA, Weinheim

Table 1. Selected bond lengths [pm] and angles [°] in **2**·MeOH (standard deviations in parentheses).

Ni1–P12	220.0(1)
Ni1–P13	226.2(2)
Ni1–P14	223.6(1)
Ni1–Cl1	218.3(1)
P12–Ni1–P13	88.86(4)
P12–Ni1–P14	97.90(4)
P13–Ni1–Cl1	89.33(4)
P14–Ni1–Cl1	89.85(4)
P12–Ni1–Cl1	155.29(4)
P13–Ni1–P14	165.30(4)

Compound **3** crystallises in the space group *Pccn* and contains distorted square-pyramidal coordinated nickel(II). The structure of the complex cation is shown in Figure 2.

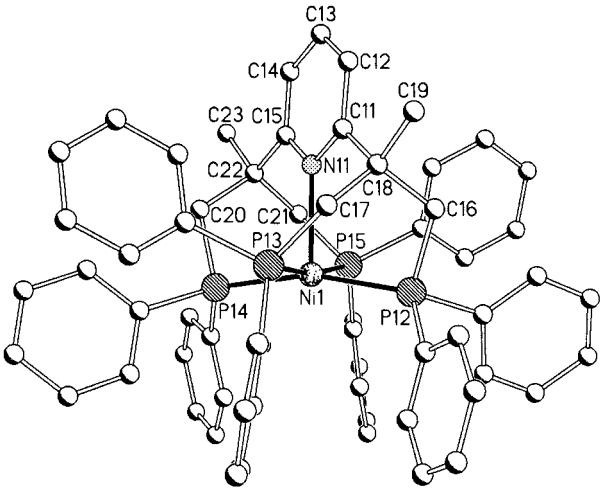

Figure 2. Molecular structure of the cation in the nickel(II) complex **3** (H atoms not shown).

The distortion consists in the pairwise displacement of diametrically opposite phosphane donors below (P12–Ni1–P14) and above (P13–Ni1–P15) the best plane defined by the NiP_4 unit. All phenyl substituents on P12 and P14 are below this plane, whereas donor atoms P13 and P15 have one phenyl ring above and one below. As a consequence, there are two types of Ni–P bond environments in the solid state, which persist in solution and give rise to an A_2B_2 spin system in the ^{31}P NMR spectra of **3**. Selected bond lengths and angles of **3** are listed in Table 3. There are no significant differences between the Ni^{II}–P distances in **3** and **2**.

Coordination Behaviour of py{PPh_2}$_4$ Towards Cobalt(II)

In view of the results obtained for nickel(II), only cobalt(II) salts with weakly coordinating anions were used. Equimolar amounts of py{PPh_2}$_4$ und $Co(ClO_4)_2$·$6H_2O$ in a methanol/dichloromethane solvent mixture (1:1) produce a red-brown solution from which, upon N_2-induced evaporation, [(py{PPh_2}$_4$)Co]$(ClO_4)_2$ (**4**) may be obtained as red-brown microcrystals in moderate yield [25%, Equation (3)]. When $Co(BF_4)_2$·$6H_2O$ is used, the corresponding tetrafluoroborate salt **5** is formed (52%).

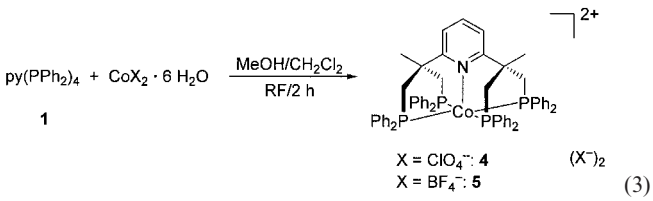

(3)

Both compounds are soluble in CH_2Cl_2 and sparingly soluble in methanol and THF. They are paramagnetic 17-valence-electron complexes of square-pyramidal coordinated cobalt(II), with the parent ion as the base peak in the mass spectra (m/z = 986, [(py{PPh_2}$_4$)Co]$^+$, 100%). The IR (KBr) spectra of **5** and the corresponding nickel(II) complex **3** are virtually identical, as expected. The magnetic moment determined for **4** (μ_{eff} = 1.60(3) BM; Gouy balance) corresponds to one unpaired electron, suggesting a low-spin configuration. (This configuration is assumed for the following discussion; given the possibility of experimental error with this technique, however, a reliable assignment of the spin state will require an ESR spectroscopic investigation). The properties of a number of low-spin cobalt(II) complexes of the type $[CoL_2X]Y$ (L = bidentate neutral ligand with variable donor set, X = coordinating anion; Y = noncoordinating anion) have been published.[8–10] Meek and coworkers reported the series of complexes $[(dppe)_2Co^{II}X](SnX_3)$ [X = Cl, Br, I; dppe = 1,2-bis(diphenylphosphanyl)ethane] and also investigated their magnetic behaviour.[11] Depending on the conditions employed (solvent, temperature, mode of crystallisation), the products have either square-pyramidal or trigonal-bipyramidal coordination geometry, but all complexes are low-spin. Magnetic moments vary slightly and are greater under square-pyramidal coordination geometry (μ_{eff} = 2.03–2.14 BM) than under trigonal-bipyramidal geometry (μ_{eff} = 1.89–1.97 BM). For the series of structurally uncharacterised complexes $[Co(P_4)X](BPh_4)$ (P_4 = hexaphenyl-1,4,7,10-tetraphosphadecane, X = Cl, Br, I, NCS), Sacconi and coworkers reported magnetic moments of μ_{eff} = 1.98–2.13 BM.[12] In spite of their different symmetries, both series of complexes have magnetic moments

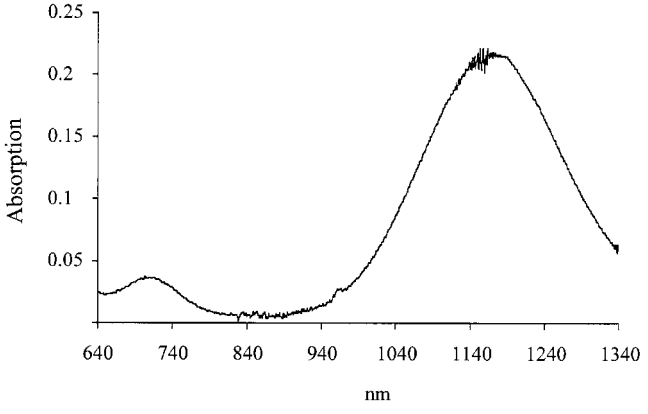

Figure 3. Vis/NIR part of the electronic spectrum of [(py{PPh_2}$_4$)Co]$(ClO_4)_2$ in CH_2Cl_2 (10^{-3} M) at room temperature.

 © 2005 Wiley-VCH Verlag GmbH & Co. KGaA, Weinheim

comparable to a low-spin cobalt(II) complex in an octahedral ligand field ($\mu_{eff} \geq \mu^{s.o.} = 1.73$ BM).[13] By way of comparison, the magnetic moment determined for **4** is smaller by 0.3 to 0.5 BM. The UV/Vis/NIR spectrum of **4** shows two *d-d* transitions at 703 nm (14225 cm^{-1}) and 1166 nm (8576 cm^{-1})(Figure 3).

The ligand field splitting varies with the ligand's position in the spectrochemical series. More weakly coordinating ligands should produce a red shift in the corresponding absorption bands, as has been verified for Sacconi's series, $[Co(P_4)X](BPh_4)$ (P_4 = hexaphenyl-1,4,7,10-tetraphosphadecane, X = Cl, Br, I): Upon going from Cl to I, the two lowest-energy bands shift to lower wavenumbers as shown in Table 2.[12] Assuming square-pyramidal geometry for these complexes in solution, the data obtained for square-pyramidal **4** (Table 2) fit in well, as pyridine is above the halide ions in the spectrochemical series: py > … > Cl > … > Br > I.[13,14]

Table 2. Comparison of the absorption maxima of the two lowest-energy transitions in the solution UV/Vis/NIR spectra of cobalt(II) polyphosphane complexes (see text).

Ionic species	Absorption maximum [cm^{-1}]	Absorption maximum [cm^{-1}]
$[(py\{PPh_2\}_4)Co]^{2+}$[a]	8576	14225
$[Co(P_4)Cl]^{+}$[b]	8270	10520
$[Co(P_4)Br]^{+}$[b]	8000	10000
$[Co(P_4)I]^{+}$[b]	7940	9700

[a] In CH_2Cl_2. [b] In 1,2-dichloroethane.

Preliminary cyclovoltammetric measurements of **4** in CH_2Cl_2 solution at room temperature (internal standard: ferrocene) show one irreversible wave in the cathodic and one in the anodic region. The cathodic wave (–507 mV) may be assigned to the formation of an 18 valence electron cobalt(I) complex ($[(py\{PPh_2\}_4)Co]^+$); the anodic wave, after normalisation on ferrocene, falls outside the voltage range acceptable for CH_2Cl_2 as a CV solvent (–1800 mV to +1500 mV) and thus has no diagnostic value. Renewed measurements, employing both the perchlorate and the tetrafluoroborate salts, in a range of solvents and at different temperatures are expected to clarify whether a cobalt(III) complex is in fact accessible.

Molecular Structure of $[(py\{PPh_2\}_4)Co](ClO_4)_2$

The single crystals used for structure determination had the composition $[(py\{PPh_2\}_4)Co](ClO_4)_2 \cdot 0.75CH_2Cl_2$ (**4**·$0.75CH_2Cl_2$). For $[(py\{PPh_2\}_4)Co](BF_4)_2 \cdot MeOH$, preliminary data confirm the identical structure of the molecular cation. Compound **4** crystallises in the space group $P2_1/c$; the structure of its cation is shown in Figure 4. The metal–nitrogen bond in **4** is ca. 8 pm shorter than in the nickel(II) complex **3**, whereas the metal–phosphorus bonds in **4** are 2–5 pm longer than in **3**. Otherwise, there are no significant structural differences between the cations in both complexes. Table 3 lists a comparison of parameters.

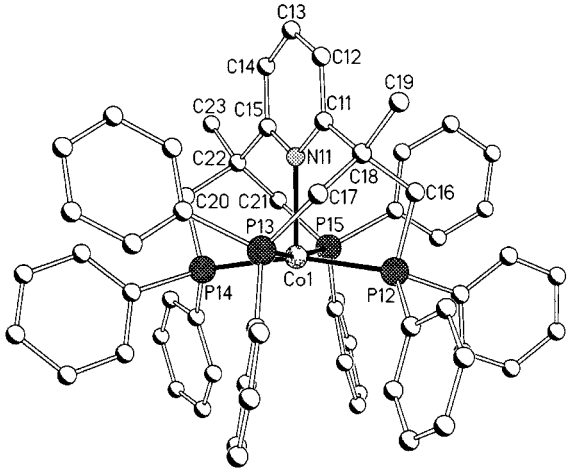

Figure 4. Molecular structure of the cation in the cobalt(II) complex **4** (H atoms not shown).

Table 3. Selected bond lengths [pm] and angles [°] in **3**·CH_2Cl_2 and **4**·$0.75CH_2Cl_2$ (standard deviations in parentheses).

Distance or angle[a]	**3**·CH_2Cl_2	**4**·$0.75CH_2Cl_2$
M–N11	227.8(4)	219.4(3)
M–P12	227.6(2)	232.5(1)
M–P13	223.3(2)	225.1(1)
M–P14	227.4(2)	231.7(1)
M–P15	223.6(2)	225.9(1)
N11–M–P12	98.4(2)	97.65(8)
N11–M–P13	85.2(2)	85.73(8)
N11–M–P14	97.7(2)	97.08(8)
N11–M–P15	85.1(2)	85.40(8)
P12–M–P13	88.21(5)	87.06(3)
P13–M–P14	92.83(6)	93.62(4)
P14–M–P15	88.23(5)	88.46(4)
P15–M–P12	93.42(6)	93.14(4)
P12–M–P14	163.92(5)	165.26(4)
P13–M–P15	170.32(6)	171.07(4)

[a] **3**: M = Ni1; **4**: M = Co1.

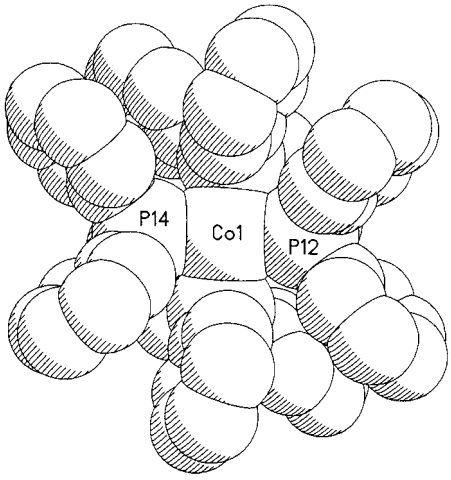

Figure 5. Space-filling model of the cobalt(II) complex **4**, viewed along the Co–N axis.

 © 2005 Wiley-VCH Verlag GmbH & Co. KGaA, Weinheim

The Co–P bond lengths in **4** are within the range observed for other low-spin cobalt(II) complexes with polyphosphane ligands.[11] For example, the average Co–P bond length in $[(dppe)_2CoCl]SnCl_3$ is, under square-pyramidal coordination geometry, 227.6(2) pm, and 225.8(5) pm in the case of trigonal-bipyramidal coordination. The space-filling representation in Figure 5 shows a vacant potential coordination site, which is surrounded by six phenyl rings of the tetraphosphane ligand in a fencelike manner.

The Cobalt(II) Complexes [(py{PPh$_2$}$_4$)Co](X)$_2$ [X = ClO$_4$, BF$_4$] and Their Reactivity Towards CO, NO, NO$^+$, I$_2$, Cl$_2$ and H$_2$

The square-pyramidal cobalt(II) complexes of the new tetraphosphane ligand are remarkably stable towards oxidation, and can be kept in air for extended periods of time without noticeable decomposition. Attempts to increase the coordination number of the cobalt ion beyond 5 in a directed manner, either by simple coordination or by oxidative addition of a small monodentate ligand, have so far met with no success. In keeping with the electrochemical results, a square-pyramidal coordinated, 16-valence-electron cobalt(III) species does not seem accessible. Treatment with I_2 (0.5 equiv., room temperature, 48 h, in THF) reproduces the starting material, whereas the reaction with Cl_2 (0.5 equiv., –50 °C, 2 h, CH_2Cl_2) gives a mixture of products, consisting for the main part of the starting material. Mass spectral features consistent with the formation of the desired chloro complex have a marginal character at best. Whereas the expected steric demand of an iodide or a chloride ligand may preclude its coordination, there is also no indication for the formation of a hydride complex, by oxidative addition of H_2 (**4** in CH_2Cl_2 solution, 40 bar H_2 pressure; mixture monitored by ^{1}H NMR after 1, 4 and 10 d; cf. the synthesis of hydridopentacyanocobaltate(III) from pentacyanocobaltate(II) and H_2[15,16]). Likewise, treatment of solutions of **4** with CO (1 bar, CH_2Cl_2, room temperature, 2 h or MeOH, 50 °C, 1 h) or of **5** with $NOBF_4$ (CH_2Cl_2, room temperature, 48 h) produced no reaction. Only in those cases where solutions of **4** or **5** in CH_2Cl_2 were treated with equimolar amounts of gaseous NO, IR monitoring of solution samples indicated a significant reaction: two bands, one of intermediate intensity at 1856 cm^{-1} and one strong band at 1802 cm^{-1} appear within 1 h; there are no further spectral changes after extended reaction times (16 h). Whether or not this observation indicates the formation of two distinct NO complexes, or a dinitrosyl complex, is as yet unclear. The formation of N_2O [ν_{NN} (str) = 2222 cm^{-1}] with concomitant oxidation of potentially decoordinated phosphane functionalities (a reaction reported to proceed smoothly and quantitatively for free py{PPh$_2$}$_4$ under suitable conditions[6]) is not observed. Both bands (at 1853 and 1797 cm^{-1}) persist with comparable intensity in IR spectra (KBr disc) obtained from the brown solid which remains after evaporation of the solvent. While attempts to obtain single crystals from this material, which would allow structural characterisation, have been unsuccessful, mass spectroscopic data do not rule out the formation of a singly substituted NO complex: the complex ion, $[(py\{PPh_2\}_4)Co]\}^+$, is recorded at m/z = 986 (100%), with a relatively prominent signal at m/z = 1017 (19%); $\Delta(m/z)$ = 31 (fast atom bombardment, matrix: *p*-nitrobenzyl alcohol). Treatment of **4** with NO at 0 °C, however, produced no reaction.

The preparation of ruthenium(II) complexes of the new tetraphosphane ligand will be reported elsewhere. Whereas the phenyl-substituted tetraphosphane ligand **1** may be too sterically encumbered to give complexes with iron(II), such complexes are in fact accessible with the methyl analogue, py(PMe$_2$)$_4$, which we have recently prepared. A study of its coordination behaviour and reactivity is under way.

Conclusions

The new highly symmetrical NP_4 ligand 2,6-$C_5H_3N[CMe(CH_2PPh_2)_2]_2$ forms mononuclear complexes with nickel(II) and cobalt(II), despite the steric bulk of eight phenyl rings on its four phosphorus-substituted "tentacles". The adopted mode of coordination depends on the nature of the counterion: In the case of strongly coordinating chloride, the ligand may in effect be tridentate (P_3) whereas, for weakly coordinating anions (BF_4^-, ClO_4^-), all five donor atoms coordinate to the central ion, to give complexes of approximate square-pyramidal geometry. The cobalt complex is virtually inert with respect to coordination of a sixth monodentate ligand (including dioxygen), owing to a "fence" of phenyl groups shielding the sixth coordination site. The reactivity of these complexes is expected to increase considerably upon the introduction of sterically less demanding and more basic P donors, such as the dimethylphospanyl residue.

Experimental Section

Unless noted otherwise, all reactions were carried out at room temperature in dried solvents under dry dinitrogen, using standard Schlenk techniques. The tetraphosphane ligand py{PPh$_2$}$_4$ was prepared by literature methods;[6] $NiCl_2{\cdot}6H_2O$, $Ni(BF_4)_2{\cdot}6H_2O$, $Co(ClO_4)_2{\cdot}6H_2O$ and $Co(BF_4)_2{\cdot}6H_2O$ were purchased from Fluka or Aldrich and used without further purification. IR spectra of solids were measured using KBr disks; solution IR spectra were recorded in CaF_2 cuvets, with compensation of solvent absorptions. IR spectra were assigned on the basis of literature data.[17] Magnetic moments of polycrystalline samples were determined on a Gouy balance (Johnson-Matthey) at room temperature, with diamagnetic corrections calculated from Pascal's constants.[18] Spectroscopic data were obtained using the following instruments: IR spectroscopy: Perkin–Elmer 1600 FT IR and 16PC FT IR; mass spectrometry: Varian MAT 212 and Jeol JMS 700; NMR spectroscopy: Jeol FT-NMR JNM-EX 270, Lambda LA 400 und ALPHA 500. Signs of coupling constants in the ^{1}H, ^{13}C, and ^{31}P NMR spectra were not determined. Elemental analyses were carried out with Carlo Erba EA 1106 and 1108 analysers. Cyclic voltammograms were recorded with a PAR 264A potentiostat and a three-electrode cell with a glassy carbon ROTEL working electrode and Pt reference and counter electrode (nBu$_4$NPF$_6$, 10^{-1} mol L^{-1}; internal standard $(Cp)_2Fe/(Cp)_2Fe^+$; $E_{1/2}$ = +0.4 V vs. NHE[19]).

 © 2005 Wiley-VCH Verlag GmbH & Co. KGaA, Weinheim

[(py{PPh_2}$_4$)NiCl]PF_6 (2): To a solution of py{PPh_2}$_4$ (375 mg, 0.400 mmol) in acetonitrile (20 mL) was added solid $NiCl_2 \cdot 6H_2O$ (10 mg, 0.40 mmol) in one portion. The resulting reddish-brown suspension was heated to reflux for 30 min, to give a clear solution of the same colour. Stripping of the solvent and drying in vacuo left a red-brown solid, which was dissolved in methanol. Addition of $NaPF_6$ (70 mg, 0.40 mmol) to the warm deep purple solution produced a purple microcrystalline precipitate after 12 h (182 mg). Elemental analysis (CHN) data are consistently too low in carbon. This observation, as well as the fact that the chloroform-soluble fraction gives ^{1}H, {^{1}H}^{13}C, and {^{1}H}^{31}P NMR spectra virtually identical to those of **3**, indicate that a mixture of complexes (with and without coordinated chloride) may have formed (see text). MS (FAB, *p*-NBA): *m*/*z* (%) = 1022 [(py{PPh_2}$_4$)NiCl]$^+$ (20).

[(py{PPh_2}$_4$)Ni]$(BF_4)_2$ (3): The addition of a solution of $Ni(BF_4)_2 \cdot 6H_2O$ (267 mg, 0.780 mmol) in methanol (20 mL) in one portion to a solution of py{PPh_2}$_4$ (724 mg, 0.780 mmol) in dichloromethane (20 mL) instantaneously produced a brown solution, which was heated to reflux for 30 min and subsequently taken to dryness. The obtained purple-brown powder was triturated with n-hexane, separated by filtration, and dried in vacuo. Yield: 465 mg **3**·MeOH (50%). **3**·MeOH: $C_{62}H_{61}B_2F_8NNiOP_4$ (1192.37): calcd. C 62.45, H 5.16, N 1.17; found C 62.09, H 5.21, N 0.83. IR (KBr): $\tilde{\nu}$ = 3048, 1586, 1480, 1435 (str), 1084, 1060, 742, 696, 517 cm^{-1}. MS (FD$^+$, CH_2Cl_2): *m*/*z* (%) = 987 (75) [(py{PPh_2}$_4$)Ni]$^+$, 1073 (15) {[(py{PPh_2}$_4$)Ni]BF_4}$^+$. ^{1}H NMR (400 MHz, CD_2Cl_2, room temp.): δ = 8.74 (t, $^2J_{H,H}$ = 8.0 Hz, 1 H, py-H^4), 8.39 (d, $^2J_{H,H}$ = 8.0 Hz, 2 H, py-H^{3,5}), 7.6–4.8 (m, 40 H, overlaid from low to high field: py-H^{3,5}; C_{ortho}-H, C_{ortho}′-H, C_{meta}-H, C_{meta}′-H, C_{para}-H, C_{para}′-H), 3.24 (d, $^2J_{H,H}$ = 7.8 Hz, 2 H, -C*H*$_2$-), 3.05 (d, $^2J_{H,H}$ = 7.8 Hz, 2 H, -C*H*$_2$-), 2.42 (d, $^2J_{H,H}$ = 7.4 Hz, 4 H, -C*H*$_2$-), 2.29 (s, 6 H, -C*H*$_3$) ppm. {^{1}H}^{13}C NMR (400 MHz, CD_2Cl_2, room temp.): δ = 168.3–123.8 (12 signals, 53 C, py-C^4, py-C^{2,6}, py-C^{3,5}, C_{ipso}, C_{ipso}′, C_{ortho}, C_{ortho}′, C_{meta}, C_{meta}′, C_{para}, C_{para}′), 42.3 (2 C, >C<), 38.8 (2 C, -*C*H$_2$-), 34.5 (2 C, -*C*H$_2$-), 29.3 (2 C, -*C*H$_3$) ppm. {^{1}H}^{19}F NMR (400 MHz, CD_2Cl_2, room temp.): δ = –149.5 (s, 4 F, B*F*$_4$) ppm. {^{1}H}^{31}P NMR (400 MHz, $CDCl_3$, room temp.): δ = 18.7 (t, $^2J_{P,P}$ = 151 Hz, 2 P, -*P*Ph$_2$), –10.9 (t, $^2J_{P,P}$ = 149.5 Hz, 2 P, -*P*Ph$_2$) ppm.

[(py{PPh_2}$_4$)Co]$(ClO_4)_2$ (4): A solution of py{PPh_2}$_4$ (1.10 g, 1.18 mmol) in dichloromethane (20 mL) was slowly added to a stirred solution of $Co(ClO_4)_2 \cdot 6H_2O$ (430 mg, 1.18 mmol) in methanol (30 mL). In the course of the addition, the colour of the resultant solution changed from pink to brown. After heating to reflux for 30 min, the solution was allowed to cool to room temperature, and its volume reduced in a slow stream of dinitrogen. After 72 h, a red-brown microcrystalline precipitate had formed, which was separated by filtration (G4 frit), washed with Et_2O (2 × 10 mL), and dried in a stream of dinitrogen. Yield: 369 mg **4**·2 MeOH (25%). More product was obtained from the mother liquor after evaporation of the solvent mixture in air. **4**·2MeOH: $C_{63}H_{65}Cl_2CoNO_{10}P_4$ (1249.95): calcd. C 60.54, H 5.24, N 1.12; found C 60.31, H 5.37, N 0.94. IR (KBr): $\tilde{\nu}$ = 3427 (br), 3054 (H–C_{aryl}), 2962 (-CH_3), 1573, 1483, 1454, 1435 (str, P–Ph), 1262, 1096 (str, br, ClO_4^-), 803, 742, 694, 623 (ClO_4^-), 516 cm^{-1}. MS (FAB, *p*-NBA): *m*/*z* (%) = 986 (100) [{py{PPh_2}$_4$}Co]$^+$, 1085 (60) {[py{PPh_2}$_4$Co]ClO_4}$^+$. μ_{eff} (spin only) = 1.60(3) BM. UV/Vis (10^{-3} mol L^{-1} in CH_2Cl_2, room temp.): λ (ε) = 1166 nm (218 dm^3 mol^{-1} cm^{-1}), 703 nm (37 dm^3 mol^{-1} cm^{-1}).

[(py{PPh_2}$_4$Co]$(BF_4)_2$ (5): A mixture of solid $Co(BF_4)_2 \cdot 6H_2O$ (347 mg, 1.02 mmol) and solid py{PPh_2}$_4$ (950 mg, 1.02 mmol) was taken up in a methanol/dichloromethane mixture (1:1; 40 mL). The initial pink colour of the solution changed to brown after ca. 5 min. The solution was heated to reflux overnight, allowed to cool to room temperature during several h, taken to dryness in an oil pump vacuum, and the remaining solid triturated with n-hexane, to produce a reddish-tan precipitate, which was filtered (G4 frit), and dried in vacuo. Yield: 751 mg **5** (52%). **5**·4 MeOH: $C_{65}H_{73}B_2CoF_8NO_{12}P_4$ (1416.73): calcd. C 60.58, H 5.71, N 1.09; found C 60.40, H 5.19, N 0.99. IR (KBr): $\tilde{\nu}$ = 3446 (br), 1482, 1458, 1436 (str, P–

Table 4. Selected crystallographic data for **2**·MeOH, **3**·CH_2Cl_2, and **4**·0.75CH_2Cl_2.

Compound	**2**·MeOH	**3**·CH_2Cl_2	**4**·0.75CH_2Cl_2
Molecular formula	$C_{62}H_{61}ClF_6NNiOP_5$	$C_{62}H_{59}B_2Cl_2F_8NNiP_4$	$C_{61.75}H_{58.5}Cl_{3.5}CoNO_8P_4$
M_r [g mol^{-1}]	1199.13	1245.21	1249.48
Crystal size [mm^3]	0.60 × 0.50 × 0.40	0.60 × 0.50 × 0.25	0.60 × 0.55 × 0.45
F (000)	1244	5136	2586
Crystal system	triclinic	orthorhombic	monoclinic
Space group	$P\bar{1}$ (No. 2)	*Pccn* (No. 56)	$P2_1/c$ (No. 14)
a [pm]	1245.2(2)	4211.3(6)	1260.3(2)
b [pm]	1353.9(2)	1530.7(2)	1982.1(2)
c [pm]	1698.9(3)	1808.0(3)	2390.3(2)
α [°]	92.59(1)	90	90
β [°]	93.10(1)	90	94.30(1)
γ [°]	94.46(1)	90	90
V [nm^3]	2.8478(8)	11.655(3)	5.954(2)
Z	2	8	4
ρ_{calc} [g cm^{-3}]	1.398	1.419	1.394
μ [mm^{-1}]	0.591	0.601	0.608
Temperature [K]	200(2)	210(2)	294(2)
2 Θ range [°]	4.6–54.0	5.8–50.1	6.1–52.8
Measured reflections	14180	12180	14664
Unique reflections	12434	10283	12160
Observed reflections [$I > 2\sigma(I)$]	8327	6180	8750
Refined parameters	719	724	728
wR_2 (all data)	0.1462	0.2004	0.1720
R_1 [$I > 2\sigma(I)$]	0.0572	0.0688	0.0577

 © 2005 Wiley-VCH Verlag GmbH & Co. KGaA, Weinheim

Ph), 1060 (BF_4), 742, 694 cm^{-1}. MS (FD^+, CH_2Cl_2): *m*/*z* (%) = 986 (100) $[(py\{PPh_2\}_4)Co]^+$.

X-ray Crystallography of Compounds 2, 3, and 4: Purple single crystals of $[(py\{PPh_2\}_4)Ni(Cl)]PF_6 \cdot MeOH$ (**2**·MeOH) were obtained within 3 d by isothermal diffusion of Et_2O into a saturated solution of the reaction product in methanol. Dark red crystalline blocks of $[(py\{PPh_2\}_4)Ni](BF_4)_2 \cdot CH_2Cl_2$ (**3**·CH_2Cl_2) were similarly obtained from CH_2Cl_2/Et_2O within 2 d. Red crystals of $[(py\{PPh_2\}_4)Co](ClO_4)_2 \cdot 0.75\ CH_2Cl_2$ (**4**·0.75 CH_2Cl_2) formed within 2 d from a dichloromethane solution whose volume was reduced in a slow stream of dry dinitrogen. Suitable crystals were mounted in glass capillaries. Data sets were obtained on a Siemens P4 diffractometer, using Mo-K_α radiation (λ = 71.073 pm) and the ω-scan technique. The structures of all complexes were solved by direct methods and refined using full-matrix least-squares procedures on F^2 (SHELXTL NT 6.12).[20] All non-hydrogen atoms of all complexes were anisotropically refined. Compound **2** crystallises with one molecule of MeOH per formula unit, which is disordered. Two preferential orientations for the C–O unit were refined, with an occupancy of 0.53(2) (O1, C1) and 0.47(2) (O2, C2), respectively. Compound **3** crystallises with one molecule of CH_2Cl_2 and compound **4** with ca. 0.75 CH_2Cl_2 per formula unit. The dichloromethane molecule in **4** is disordered; two preferential positions were determined for one of the chloride atoms, with occupancies refined to 0.53(2) for Cl12 and 0.22(2) for Cl13. Cl13 was only isotropically refined. Treatment of hydrogen atoms: All hydrogen atoms were geometrically positioned and allowed to ride on their carrier atoms during the refinement; their isotropic displacement parameters were tied to those of the adjacent C and O atoms by a factor of 1.2 or 1.5. Crystallographic data are listed in Table 4. CCDC-266966 (**2**·MeOH), CCDC-266967 (**3**·CH_2Cl_2), and CCDC-266968 (**4**·0.75CH_2Cl_2) contain the supplementary crystallographic data for this paper. These data can be obtained free of charge from The Cambridge Crystallographic Data Centre via www.ccdc.cam.ac.uk/data_request/cif.

Acknowledgments

Financial support of this work by the Deutsche Forschungsgemeinschaft is gratefully acknowledged. We appreciate the diligence and helpful suggestions of two referees concerning the products of the complexation reactions with nickel.

[1] J.-C. Hierso, R. Amardeil, E. Bentabet, R. Broussier, B. Gautheron, P. Meunier, P. Kalck, *Coord. Chem. Rev.* **2003**, *236*, 143.
[2] H. A. Mayer, W. C. Kaska, *Chem. Rev.* **1994**, *94*, 1239.
[3] L. Dahlenburg, *Eur. J. Inorg. Chem.* **2003**, 2733.
[4] R. A. Findeis, L. H. Gade, *Eur. J. Inorg. Chem.* **2003**, 99.
[5] A. Grohmann, *Adv. Inorg. Chem.* **2004**, *56*, 179.
[6] C. Zimmermann, W. Bauer, F. W. Heinemann, A. Grohmann, *Z. Naturforsch.* **2002**, *57b*, 1256.
[7] M. Di Vaira, L. Sacconi, *J. Chem. Soc. Dalton Trans.* **1975**, 493.
[8] G. Dyer, D. W. Meek, *J. Am. Chem. Soc.* **1967**, *89*, 3983.
[9] A. Sacco, F. Gorieri, *Gazz. Chim. Ital.* **1963**, *93*, 687.
[10] J. Chatt, F. A. Hart, D. T. Rosevear, *J. Chem. Soc.* **1961**, 5504.
[11] J. K. Stalick, P. W. R. Corfield, D. W. Meek, *Inorg. Chem.* **1973**, *12*, 1668.
[12] M. Bacci, S. Midollini, P. Stoppioni, L. Sacconi, *Inorg. Chem.* **1973**, *12*, 1801.
[13] H. Lueken, *Magnetochemie*, Teubner Verlag, Wiesbaden, **1999**.
[14] U. Müller, *Anorganische Strukturchemie*, 2nd ed., Teubner Verlag, Wiesbaden, **1992**.
[15] J. Halpern, L. Y. Won, *J. Am. Chem. Soc.* **1968**, *90*, 6665.
[16] J. Halpern, M. Pribanić, *Inorg. Chem.* **1970**, *9*, 2616.
[17] G. Socrates, *Infrared Characteristic Group Frequencies*, 2nd ed., Wiley, New York, **1994**.
[18] O. Kahn, *Molecular Magnetism*, Wiley-VCH, New York, **1993**.
[19] H. M. Koepp, H. Wendt, H. Strehlow, *Z. Elektrochem.* **1960**, *64*, 483.
[20] *SHELXTL NT 6.12*, Bruker AXS, Inc., Madison, WI, USA, **2002**.

Received: March 31, 2005
Published Online: August 2, 2005

 © 2005 Wiley-VCH Verlag GmbH & Co. KGaA, Weinheim

Series of Mn Complexes Based on *N*-Centered Ligands and Superoxide – Reactivity in an Anhydrous Medium and SOD-Like Activity in an Aqueous Medium Correlated to Mn^{II}/Mn^{III} Redox Potentials[‡][‡‡]

Stéphanie Durot,[a][‡‡‡] Clotilde Policar,*[a][‡‡‡] Federico Cisnetti,[a] François Lambert,[a] Jean-Philippe Renault,[c] Giorgio Pelosi,[b] Guillaume Blain,[d] Hafsa Korri-Youssoufi,[a] and Jean-Pierre Mahy[a]

Keywords: N,O ligands / Manganese / Superoxide / SOD mimics / Imidazole / Phenolate

Two crystal structures are described in this article: (a) the structure of a monomeric Mn^{II} complex with the tridentate *N*-centered N_3 ligand tris[(1-methyl-2-imidazolyl)methyl]amine (TMIMA) ($[Mn^{II}(TMIMA)_2]^{2+}$); and (b) the structure of a monomeric Mn^{III} complex with the tridentate *N*-centered N_2O ligand 2-{[(1-methyl-2-imidazolyl)methyl]amino}phenolate (PI^-)[2] ($[Mn^{III}(PI)_2]^+$) (**5**). The latter was isolated both in the Mn^{II} and in the Mn^{III} state, although only Mn^{III} crystals were successfully grown. They are part of a series of Mn complexes prepared as SOD mimics, namely $[Mn(BMPG)(H_2O)]^+$ (**2**) {BMPG = *N*,*N*-bis[(6-methyl-2-pyridyl)methyl]glycinate}, $[Mn(IPG)(MeOH)]^+$ (**3**) {IPG = *N*-[(1-methyl-2-imidazolyl)methyl]-*N*-(2-pyridylmethyl)glycinate}, $[Mn(BIG)(H_2O)_2]^+$ (**4**) {BIG = *N*,*N*-bis[(1-methyl-2-imidazolyl)methyl]glycinate}. The reactivity of Mn^{II} complexes **1** and **2** in an anhydrous medium is described and compared to that of complexes **3** and **4**, the data for which was previously published. The cyclic voltammograms of the whole complex series were recorded in an aqueous medium (collidine buffer). Their SOD-like activities were estimated by the McCord–Fridovich test (*IC*50 with 22 μM cytc Fe^{III}: 1.6 ± 0.1 μmol L^{-1} for **1**, 1.2 ± 0.5 μmol L^{-1} for **2**, 3.0 ± 0.2 μmol L^{-1} for **3**, 3.7 ± 0.6 μmol L^{-1} for **4**, 0.8 ± 0.1 μmol L^{-1} for **5**). *IC*50 values were converted into the corresponding kinetic constant k_{McCF} values. A linear correlation between E_a and $\log(k_{McCF})$ was obtained, indicating that in this series the conversion to Mn^{III} is probably the rate-limiting step. This is of substantial importance for further Mn–SOD mimic design in this series.
(© Wiley-VCH Verlag GmbH & Co. KGaA, 69451 Weinheim, Germany, 2005)

Introduction

Superoxide ($O_2^{\cdot-}$), as the first species in the dioxygen reduction cascade, is a toxic species involved in oxidative stress.[3–5] Its concentration is controlled in vivo by superoxide dismutases, metalloenzymes that catalyze its dismutation. Superoxide is considered to be responsible for several pathological situations. There is a pharmaceutical requirement for molecules that could scavenge or, even better, catalytically dismutate superoxide.[6–8] The design of low molecular weight complex SOD mimics requires greater understanding of the effect of the metal environment on the SOD-like activity. In the field of superoxide dismutase mimics, copper, iron, manganese and cobalt complexes have been described.[7–12] Mn is the least toxic of these metal ions.[8] In our laboratory, we design Mn complexes and test them as SOD mimics. In this article, the crystal structure of a monomeric Mn^{II} complex (**1**) derived from $\mathbf{L^1}$ {tris[(1-methyl-2-imidazolyl)methyl]amine or TMIMA} is presented $\{[Mn^{II}(TMIMA)_2](PF_6)_2\}$. The crystal structure of a monomeric Mn^{III} complex derived from $\mathbf{L^2}$ (2-{[(1-methyl-2-imidazolyl)methyl]amino}phenolate or PI^-) is also described $\{[Mn^{III}(PI)_2](PF_6)\}$. In the latter case, both Mn^{II} (**5′**) and Mn^{III} states (**5**) could be isolated, although only Mn^{III} crystals were successfully obtained. Complexes **1** and **5** are part of a series of Mn complexes prepared as SOD mimics, previously published, namely $[Mn(BMPG)(H_2O)]^+$ (**2**) {BMPG = *N*,*N*-bis[(6-methyl-2-pyridyl)methyl]-glycinate},[13] $[Mn(IPG)(MeOH)]^+$ (**3**) {IPG = *N*-[(1-methyl-2-imidazolyl)methyl]-*N*-(2-pyridylmethyl)glycinate}, $[Mn(BIG)(H_2O)_2]^+$ (**4**) {BIG = *N*,*N*-bis[(1-methyl-2-imidazolyl)methyl]glycinate}.[1] A general approach to reaction with superoxide has already been published.[1] Firstly, this

[‡] Part 2 of a series. Part 1: Ref.[1]
[‡‡] Abbreviations: Ref.[2]
[a] Laboratoire de Chimie Bio-organique et Bio-inorganique, UMR8124, Bâtiment 420, Université Paris XI, 91405 Orsay Cedex, France
Fax: +33-1-69157231
E-mail: cpolicar@icmo.u-psud.fr
[b] Dipartimento di Chimica Generale ed Inorganica, Chimica Analitica, Chimica Fisica, Università di Parma, Parco Area delle Scienze 17A, 43100 Parma, Italy
[c] Laboratoire de Radiolyse CEA Saclay (DSM/DRECAM/SCM-URA331), 91405 Orsay Cedex, France
[d] Laboratoire de Chimie Inorganique, UMR8613, Bâtiment 420, Université Paris XI, 91405 Orsay Cedex, France
[‡‡‡] These two authors contributed equally to this work.
Supporting information for this article is available on the WWW under http://www.eurjic.org or from the author.

article consists of a study of the reactivity of Mn^{II} complexes with superoxide in an anhydrous medium (DMSO). Secondly, the reactivity in an aqueous solution is evaluated with the conventional McCord–Fridovich assay and/or pulse radiolysis. Presented is a brief study of the Mn^{II} complexes (**1** and **2**) in the anhydrous medium and an evaluation of the SOD activity of complexes **1**, **2**, and **5** with the McCord–Fridovich assay. These activities are presented here in terms of a recalculated kinetic constant, k_{McCF}. For two of the complexes, namely, **3** and **4**, k_{McCF} values are compared with the kinetic constants measured by pulse radiolysis. For the whole series the relationship between redox potential and k_{McCF} has been investigated.

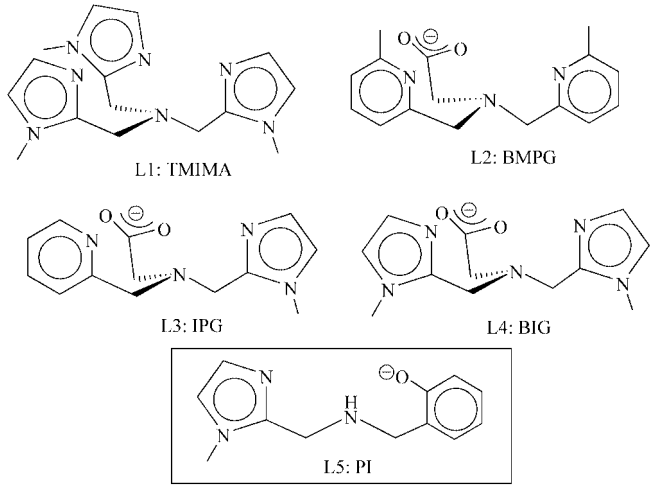

Figure 1. Structure of the ligands.

Results

Syntheses

Ligand Synthesis

The synthesis of the $\mathbf{L^1}$ ligand is already known.[14,15] A new synthetic pathway is presented in the Exp. Sect., involving an amine tertiarization by reductive amination instead of a nucleophilic substitution. The new method displayed a higher yield (90% vs. 62% from bis[2-(1-methyl-2-imidazolyl)methyl]amine.

Ligand $\mathbf{L^5}$ was synthesized as shown in Scheme 1 by a two-step synthesis. The yield was moderate but the procedure was very easy. 2-(Methylamino)phenol was obtained by catalytic hydrogenation (Ni) of 2-cyanophenol. It was reductively coupled to *N*-methyl-2-imidazolcarboxaldehyde obtained according to a published procedure.[16]

Preparation of the Complexes

Mn^{II} complex **1** was obtained from $\mathbf{L^1}$ (see Figure 1) with PF_6^- as the counter-anion in MeOH/H_2O (1:1). X-ray suitable crystals were successfully grown providing the monomeric $[Mn^{II}(TMIMA)_2](PF_6)_2$ compound **1**. Experimental details are described in the Exp. Sect.

Mn^{II} complex **5′** was obtained from $\mathbf{L^5}$ (see Figure 1) under strictly controlled anaerobic conditions. A white precipitate was obtained, but no crystal has been successfully grown so far. The powder could be recrystallized from CH_3CN by diffusion of *t*BuOMe as $[Mn^{III}(PI)_2](PF_6)(CH_3CN)$. When the synthesis was carried out in the presence of dioxygen, a dark violet precipitate of an Mn^{III} complex (**5**) was directly obtained.

Description of the Structure of $[Mn(TMIMA)_2](PF_6)_2$ (1)

An X-ray diffraction study was carried out on the $[Mn(TMIMA)_2](PF_6)_2$ complex **1** and the experimental details are reported in Table 6 (Exp. Sect.). The asymmetric unit consists of a cationic moiety, formed by two neutral tridentate ligands coordinated to a central Mn^{II} ion, lying on a center of symmetry, and two hexafluorophosphate anions (see Figure 2). Selected distances and angles are reported in Table 1.

The hexafluorophosphate anions are found in two positions with an occupancy of 0.5. The manganese(II) ion is coordinated to six imidazole nitrogen atoms with distances of 2.364(2), 2.366(3), and 2.307(2) Å (by symmetry, the other Mn–N distances are identical). These distances are larger than the average value found using the Cambridge Crystallographic Database (CCDC)[17] for manganese complexes with ligands containing the imidazole ring [av. 2.226(12) Å on the basis of 42 fragments; see the list in the Supporting information].

The $Mn–N_{tripod}$ distance is 2.916(2) Å, which is longer than the sum of their van der Waals radii (2.82 Å). This is due both to the complete metal coordination sphere and to

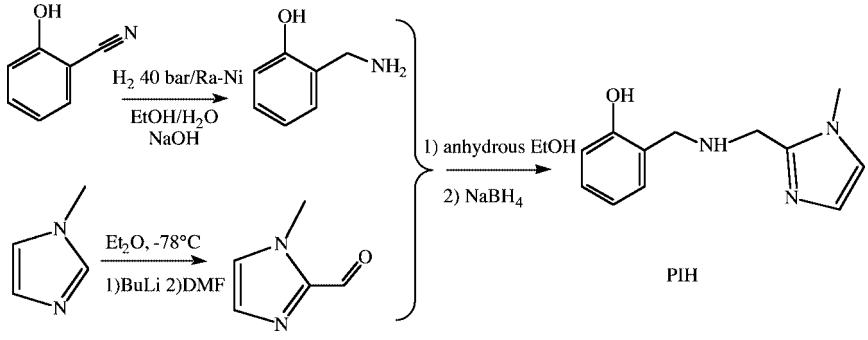

Scheme 1. Synthetic pathway to PIH.

 © 2005 Wiley-VCH Verlag GmbH & Co. KGaA, Weinheim

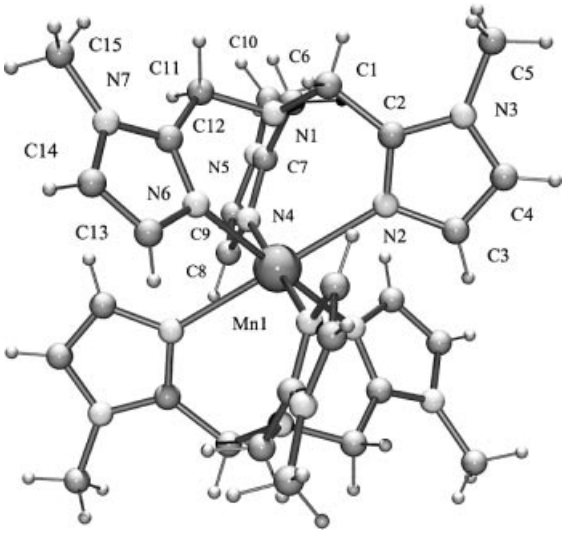

Figure 2. Representation of cationic complex **1**.

Table 1. Selected bonds and angles (symmetry operator A: $1 - x$, $-y$, $1 - z$).

Bonds	[Å]	Angles	[°]
Mn1–N2	2.364(2)	N2–Mn1–N4	98.73(7)
Mn1–N4	2.307(2)	N2–Mn1–N6	99.91(8)
Mn1–N6	2.366(3)	N4–Mn1–N6	100.48(7)
Mn1–N2A	2.364(2)	N2–Mn1–N4A	81.28(7)
Mn1–N4A	2.307(2)	N2–Mn1–N6A	80.09(7)
Mn1–N6A	2.366(3)	N4–Mn1–N6A	79.52(7)

the steric constraints imposed by the presence of two bulky ligands. In comparable structures, with a single tripodal ligand and a monodentate donor that completes the octahedron, the tripodal nitrogen atom is much closer to the central ion and forms a coordination bond: the average distance in these cases is 2.53(4) Å (on the basis of the same 42 fragments listed in the Supporting information). Deviation from the octahedral structure is also noticeable in the angle values (see Table 1).

Sheets of complex molecules, interacting through van der Waals contacts, pile up running parallel to the *xz* plane and are held together by a complex system of hydrogen bonds formed by the fluorine atoms of the hexafluorophosphate anions with the methyl and methylene groups of the ligand. The shortest distance between manganese ions is Mn···Mn (x, $-y - 1/2$, $+z - 1/2$) and is 9.413(1) Å. The magnetic properties of complex **1** are that of a Curie-law Mn^{II} ion, with a $\chi_{mol}T$ value of 4.4 $cm^3 mol^{-1} K$ from ambient temperature down to 2 K (results not shown), with no efficient Mn^{II}–Mn^{II} intermolecular through-space interaction at such distances.[13]

Description of the Structure of $[Mn(PI)_2](PF_6)(CH_3CN)$ (5)

An X-ray diffraction study has been carried out on the complex $[Mn(PI)_2](PF_6)(CH_3CN)$ (**5**). An ORTEP view of the manganese complex is shown in Figure 3 and the experimental details regarding data collection are reported in Table 6 (Exp. Sect.). The structure consists of two cationic moieties made up of manganese atoms lying on centers of symmetry surrounded by two tridentate monoanionic ligands. Manganese(III) ions present a slightly distorted octahedral coordination geometry as can be seen from the coordination distances and angles (Table 2), with a compression along the $O_{phenolato}$–Mn–$O_{phenolato}$.

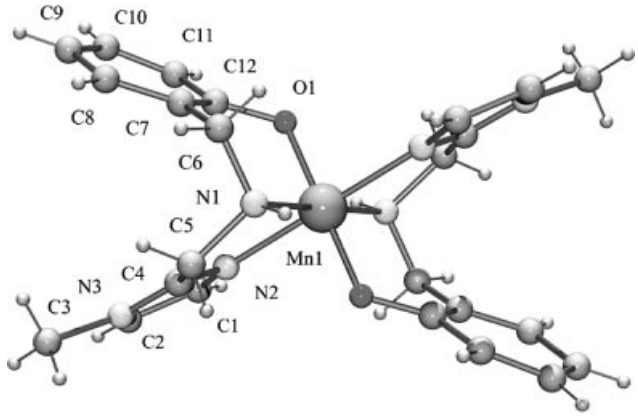

Figure 3. Representation of cationic complex **5**.

Table 2. Selected distances and angles for **5**.

Distances	[Å]	Angles	[°]
Mn1–O1	1.82(1)	O1–Mn1–N1	91.6(7)
Mn1–N1	2.20(2)	O1–Mn1–N2	92.3(7)
Mn1–N2	2.17(2)	N1–Mn1–N2	78.9(8)
Mn2–O2	1.85(1)	O2–Mn2–N4	91.7(6)
Mn2–N4	2.19(2)	O2–Mn2–N5	93.3(6)
Mn2–N5	2.18(2)	N4–Mn2–N5	79.0(7)

It is noteworthy that a hydrogen bond exists in the two independent molecules between the amino NH group and the phenol oxygen atom of the centrosymmetrically related ligand molecule [N1···O1 2.81(2) Å and N4···O2 2.83(2) Å]. A hexafluorophosphate anion compensates the charge of the cationic complex. Hydrogen bonds between fluorine atoms of PF_6^- and N1 and N4 are responsible for the overall packing. The structure also contains an acetonitrile crystallization molecule that occupies the remaining interstices.

Reactivity of the Mn^{II} Complexes with Superoxide in an Anhydrous Medium

In the series **1**, **2**, **3**, and **4**, Mn^{II} ions bear 0, 1 or 2 H_2O molecules, and show different bulkiness around Mn. The reactivity of both $[Mn^{II}(BMPG)(H_2O)]^+$ (**2**) and $[Mn^{II}(TMIMA)_2]^{2+}$ (**1**) was studied as described previously in the case of both **3** and **4**.[1]

Successive amounts of superoxide were added to a 10^{-3} mol L^{-1} solution of the complex in anhydrous DMSO. EPR spectra were recorded at 10 K. For **2**, the initial Mn^{II} signal[18] decreased from 0 to 1.5 equiv. superoxide. From 1.5 to 3 equiv., the solution was EPR-silent; and above

 © 2005 Wiley-VCH Verlag GmbH & Co. KGaA, Weinheim

Table 3. Reactivity of superoxide in anhydrous DMSO with Mn^{II} complexes from the N-tripodal series: amount of superoxide consumed deduced from the EPR spectrum.

	$Mn^{II}(TMIMA)_2^{2+}$	$Mn^{II}(IPG)(MeOH)^+$	$Mn^{II}(BMPG)(H_2O)^+$	$Mn^{II}(BIG)(H_2O)_2^+$
Number of water bound to Mn	0	0	1	2
$O_2^{\cdot-}$ consumed (equiv./Mn^{II})	1 equiv.	1 equiv.	3 equiv.	>5 equiv.

4 equiv., a signal from superoxide was finally obtained and quantified (data not shown, see Exp. Sect. and Table 3). For **1**, the 6-line hyperfine signal from Mn^{II} decreased upon superoxide addition; and at 2 equiv., the superoxide EPR signal was recovered and quantified (see Exp. Sect., Table 3 and Figure 4).

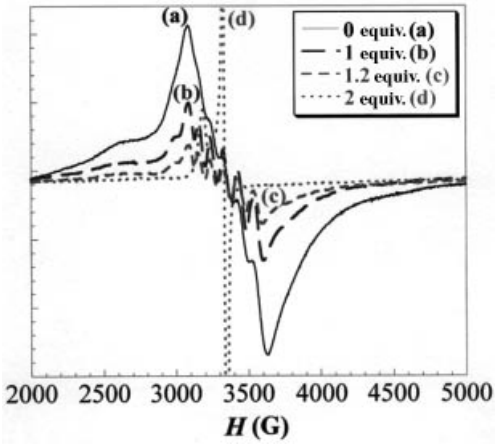

Figure 4. Reactivity of $[Mn(TMIMA)_2]^{2+}$ (**1**) with superoxide in anhydrous DMSO. $[Mn(TMIMA)_2](PF_6)_2$ (10^{-3} mol L^{-1}), 100 K, ν = 9.38 GHz, att. 20 dB, mod. amp. 5 G, t_c = 41 ms.

These results show that both **1** and **2** react with superoxide. No multiline signal was observed, showing that the formation of $Mn^{III}Mn^{IV}$ di-μ-oxo dimers, previously observed with **3** and **4**,[1,19] was not obtained in the case of **1** and **2**. This can be tentatively assigned to the steric crowding due the methyl groups in **2** and to the complete coordination sphere in **1**.

The superoxide signal was recovered at a different $O_2^{\cdot-}$/Mn stoichiometry for these complexes and quantified. The amount of $O_2^{\cdot-}$ consumed was determined (see Table 3). It appears that the more water molecules are coordinated to the Mn^{II}, the more equivalents of superoxide are consumed. The presence of the Mn ion is necessary since water alone, at the same concentration and under the same experimental conditions, did not switch off the superoxide signal.

Tuning Redox Potentials to Tune the SOD-Like Activity

Redox Potential and SOD Activity

The catalysis of the superoxide dismutation is a redox process, involving both Mn^{II} and Mn^{III} oxidation states. To make this redox catalysis efficient, the redox potential of the Mn^{III}/Mn^{II} couple should be, as encountered in SODs,[20] between the potential of the two couples $O_2/O_2^{\cdot-}$ and $O_2^{\cdot-}/H_2O_2$−that is, at pH = 7, –0.40 V and +0.65 V/SCE, respectively (see Figure 5).[9,21–24] Theoretically, the closer the potential of the two couples, the faster the reaction between them. Hitherto, the value optimizing the kinetics of both oxidation and reduction is the midway potential, i.e. 0.12 V/SCE.[9,20]

The Mn^{III}/Mn^{II} redox potential is controlled by the coordination sphere around the metal center, either through the nature of the Lewis bases coordinated to the Mn center, by electronic effect on the Lewis bases,[25] or by the geometry around the Mn center. Increasing the number of the O^- donor will lower the potential by increasing the electron density onto the metal center. Mn^{III}, as a d^4 ion, will prefer a geometric distortion from the octahedric structure. The redox potential of the Mn^{III}/Mn^{II} couple can be lowered by

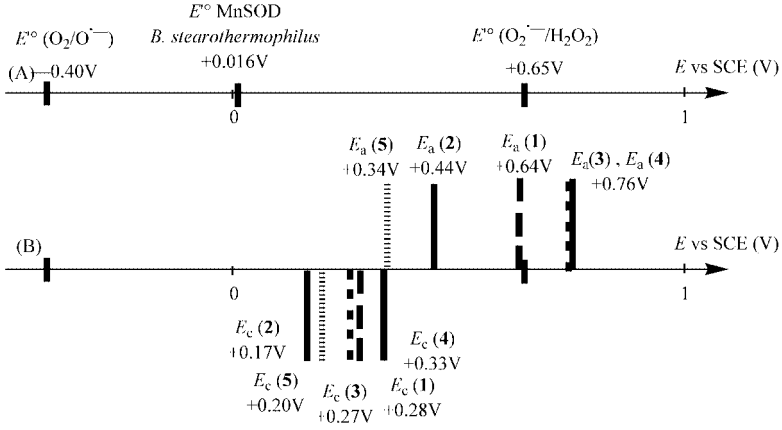

Figure 5. (A) Apparent standard redox potential for superoxide couples at pH = 7. (B) Anodic and cathodic half-wave potentials for the complexes in collidine pH 7.5 buffer.

 © 2005 Wiley-VCH Verlag GmbH & Co. KGaA, Weinheim

controlling the geometry around the metal center, that is by imposing some deformation with regards to the octahedral environment.[26]

No electrochemical wave was observed for the Mn^{II} complexes of this series in dimethyl sulfoxide, acetonitrile or phosphate buffer. This is not uncommon for Mn^{II} complexes.[27–29] In collidine buffer (pH = 7.5)[30] however, irreversible waves were recorded (see Figure 6 in the case of **4**). Anodic and cathodic potentials (Table 4 and Figure 5) are within (**2**, **5**, and **1**) or at the limit (**3** and **4**) of the required region for effective superoxide dismutation. Potentials for **3** and **4** are close, which is consistent with the similar environment around the metal cations. They are close to the potential previously reported for a Mn^{II} coordinated with *N*,*N*-bis(2-pyridylmethyl)-(*S*)-histidine, which shows a similar coordination sphere (2 imidazoles, 1 pyridine, 1 carboxylate).[30] For **1** and **2**, the anodic wave potentials are less positive. The conversion of Mn^{II} into Mn^{III} is thus easier. This can be assigned to the steric crowding encountered in **1** and **2**, which may favor a distorted environment around the metal center. In **5**, the N_4O_2 environment favors the Mn^{III} by comparison with the nitrogen-richer environment for the other complexes.

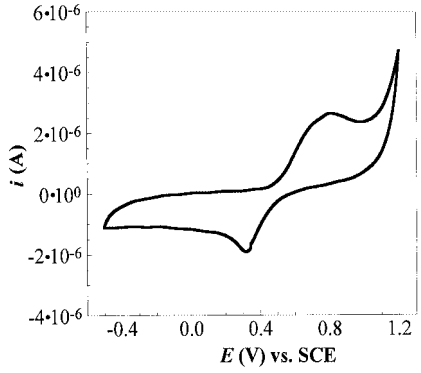

Figure 6. Voltammogram of **4** [2×10^{-3} mol L^{-1} (on the basis of Mn content)], collidine buffer (50 mM), pH = 7.5, 100 mV s^{-1}. Working electrode: vitrous carbon disk.

Table 4. Redox potential for the anodic and cathodic waves for complexes **1**–**5**.

Complex	E_a[a]	E_c[a]
1	0.64	0.28
2	0.44	0.17
3	0.76	0.27
4	0.76	0.33
5	0.34	0.20

[a] V vs. SCE.

Evaluation of the SOD-Like Activity: McCord–Fridovich Assay

Reactivity towards the superoxide was investigated in an aqueous phosphate buffer (pH = 7.8) with the McCord–Fridovich assay, using the xanthine-xanthine oxidase system to produce the superoxide. The test is based on a kinetic competition for superoxide reduction between the putative superoxide scavenger and ferricytochrome c.[31] The reduction of ferricytochrome c was monitored spectrophotometrically at 550 nm. This test requires several preliminary checks in order to ensure its reliability (see Exp. Sect.).[1,8,32,33]

Complexes **1**–**5** inhibited the reduction of ferricytochrome c. The inhibition percentage was measured for several complex concentrations and the *IC*50 value was then deduced by two graphical methods (see Figure 7 and Exp. Sect. for details).[1,31,32,34,35] They are reported in Table 5.

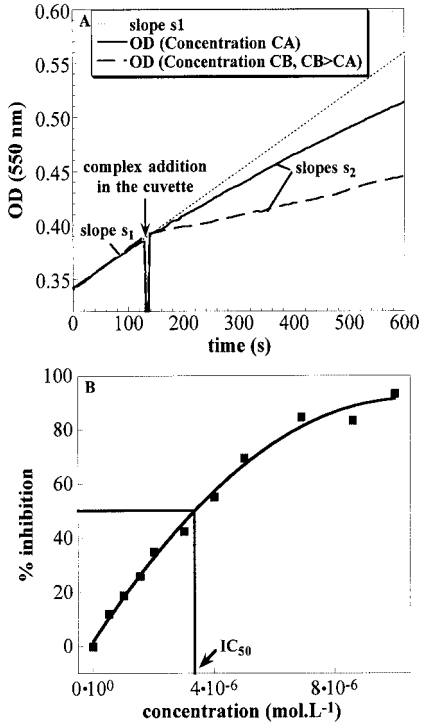

Figure 7. A. Kinetics of the reduction of ferricytochrome c (550 nm) without and with the putative SOD mimic **4**. B. Inhibition percentage as a function of **4**: *IC*50 determination.

It should be noted that reported *IC*50 values are dependent both on the detector used [usually cytochrome c Fe^{III} or nitroblue tetrazolium (NBT)] and on its concentration. For a given putative SOD mimic, the smaller the detector concentration, the smaller the *IC*50 value. Therefore, *IC*50 values are not appropriate for comparisons with the literature. From the measured *IC*50 values, it is possible to calculate a kinetic constant value (k_{McCF}), which is independent of both detector concentration and nature. At the *IC*50 concentration, superoxide reacts at the same speed with the detector and the putative SOD mimic. Then, $k_{McCF} = k_{detector}\cdot[detector]/IC50$.[36] In the case of cytochrome c Fe^{III} as the detector, $k_{Cyt\ c}$ (pH = 7.8; 21 °C) = 2.6×10^5 mol^{-1} Ls^{-1}.[37] In the case of NBT, k_{NBT} (pH = 7.8) = 5.94×10^4 mol^{-1} Ls^{-1}.[38]

Table 5 reports some values from the literature. The tested compounds **1**–**4** are within the range of the activities

 © 2005 Wiley-VCH Verlag GmbH & Co. KGaA, Weinheim

Table 5. *IC*50 values and kinetic catalytic constants: comparison with the literature.

Complex	*IC*50[a]	k_{cat} [$mol^{-1}Ls^{-1}$] [c]	Ref.
$[Fe^{III}(IPG)Cl_2]$	$IC50_{22\ \mu m\ Cyt\ c} = 2.7\times10^{-4}\ mol\ L^{-1}$	2.1×10^{4} IT	[39]
$[Mn^{II}(ClO_4)_2]$ + EDTA	$IC50_{22\ \mu m\ Cyt\ c} = 1.67\pm3\times10^{-4}\ mol\ L^{-1}$	$3.4\pm0.1\times10^{4}$ IT	[1]
$[Fe^{III}(BIG)Cl_2]$	$IC50_{22\ \mu m\ Cyt\ c} = 1.4\times10^{-4}\ mol\ L^{-1}$	4.1×10^{4} IT	[39,40]
$[Mn^{III}(DFB)]$	$IC50_{6.7\ \mu m\ Cyt\ c} = 1.04\times10^{-5}\ mol\ L^{-1}$	1.0×10^{6} IT	[32]
$[Mn^{III}(TBAP)]^{+}$	$IC50_{10\ \mu m\ Cyt\ c} = 9.2\times10^{-6}\ mol\ L^{-1}$	2.8×10^{5} IT	[41]
$[Mn^{II}(PA)_2(PAH)(H_2O)]$	$IC50_{50\ \mu m\ NBT} = 6.5\times10^{-6}\ mol\ L^{-1}$	4.6×10^{5} IT	[42,43]
$[Mn^{III}(TPAC)]$	$IC50_{XTT} = (0.33\pm0.014)\times10^{-5}\ mol\ L^{-1}$ [b]	$(9.3\pm0.4)\times10^{5}$ IT	[44]
$[Mn^{II}(TPAA)](PF_6)_2$	$IC50_{22\ \mu m\ cyt\ c} = 4.3\times10^{-6}\ mol\ L^{-1}$	1.3×10^{6} IT; 1.05×10^{7} PR	[28]
$[Mn^{II}(ClO_4)_2]$	$IC50_{22\ \mu m\ cyt\ c} = 4.5\pm0.5\times10^{-6}\ mol\ L^{-1}$	$1.3\pm0.2\times10^{6}$ IT	[1]
4	$IC50_{22\ \mu m\ cyt\ c} = 3.7\pm0.6\times10^{-6}\ mol\ L^{-1}$	$1.5\pm0.3\times10^{6}$ IT; $1.4\pm0.1\times10^{6}$ PR	[1]; this work
3	$IC50_{22\ \mu m\ cyt\ c} = 3.0\pm0.6\times10^{-6}\ mol\ L^{-1}$	$1.9\pm0.5\times10^{6}$ IT; $3.8\pm0.2\times10^{6}$ PR	[1]; this work
1	$IC50_{22\ \mu m\ cyt\ c} = 1.6\pm0.1\times10^{-6}\ mol\ L^{-1}$	$3.6\pm0.2\times10^{6}$ IT	this work
$[Mn^{II}(NTB)(salicylate)]ClO_4$	$IC50_{46\ \mu m\ NBT} = 0.7\times10^{-6}\ mol\ L^{-1}$	3.9×10^{6} IT	[45]
$Mn^{II}(Obz)(3,5\text{-}iPr_2pzH)(HB(3,5\text{-}iPr_2pz)_3)$	$IC50_{50\ \mu m\ NBT} = 0.75\times10^{-6}\ mol\ L^{-1}$	4.0×10^{6} IT	[42]
$[Mn^{II}(NTB)(terephthalate)]$	$IC50_{46\ \mu m\ NBT} = 0.64\times10^{-6}\ mol\ L^{-1}$	4.3×10^{6} IT	[46]
2	$IC50_{22\ \mu m\ cyt\ c} = 1.2\pm0.5\times10^{-6}\ mol\ L^{-1}$	$4.8\pm1.4\times10^{6}$ IT	this work
5	$IC50_{22\ \mu m\ cyt\ c} = 8.7\pm0.6\times10^{-7}\ mol\ L^{-1}$	$6.6\pm0.5\times10^{6}$ IT	this work
$[Mn^{II}\{N,N\text{-bis(2-pyridylmethyl)-(}S\text{)-histidinate}\}(H_2O)]_2(ClO_4)_2$	$IC50_{10\ \mu m\ Cyt\ c} = 2.9\times10^{-7}\ mol\ L^{-1}$	9.0×10^{6} IT	[30]
$[Mn^{II}(EDTB)(Ac)]Ac\cdot EtOH$	–	1.0×10^{7} IT	[38]
M40403	–	1.6×10^{7} SF	[47]
$[Mn^{III}(BVDME)]_2$	$IC50_{10\ \mu m\ Cyt\ c} = 5.0\times10^{-8}\ mol\ L^{-1}$	5.0×10^{7} IT	[48]
$[Mn^{III}TE\text{-}2\text{-}PyP(OH_2)]^{5+}$	$IC50_{10\ \mu m\ Cyt\ c} = 4.5\times10^{-8}\ mol\ L^{-1}$	5.8×10^{7} IT	[23]
$[Mn^{III}Cl_4\ TE\text{-}2\text{-}PyP]^{5+}$	$IC50_{10\ \mu m\ Cyt\ c} = 6.5\times10^{-9}\ mol\ L^{-1}$	4.0×10^{8} IT	[49]
S,*S*-Dimethyl-M40403	–	1.6×10^{9} SF	[50]

[a] 50% inhibition concentration. Indices specify the UV/Vis probe (cytc Fe^{III} or NBT) concentration used for the test. k_{cat} is the catalytic constant directly measured by pulsed radiolysis or stopped-flow techniques and k_{McCF} are recalculated kinetic constants from the *IC*50 value. [b] Measured with XTT as UV/Vis probe. [51] k_{cat} was directly provided in the article, by comparison with SOD.[52] [c] IT: indirect test; SF: stopped flow; PR: pulsed radiolysis. DFB: desferrioxamine B; TBAP: 5,10,15,20-tetrakis(4-benzoic acid)porphyrin; PA: picolinate; TPAC: *cis*,*cis*-1,3,5-tri{(5-trimethylammonium)-2-hydroxypicolyl)amino}cyclohexane; salen: *N*,*N*′-bis(salicylideneamino)ethane; TPAA: tris{2-[*N*-(2-pyridylmethyl)amino]ethyl}amine; NTB: tris(2-benzimidazolylmethyl)amine; XTT: 3′-{1-[(phenylamino)carbonyl]-3,4-tetrazolium}bis(4-methoxy-6-nitrobenzenesulfonic acid) hydrate; Obz: benzoate; $HB(3,5\text{-}iPr_2pz)_3$: hydrotris(3,5-diisopropyl-1-pyrazolyl)borate; EDTB: *N*,*N*,*N*′,*N*′-tetrakis(2′-benzimidazolylmethyl)-1,2-ethanediamine; M40403 and *S*,*S*-dimethyl-M40403: Mn^{II} complexes from modified 1,4,7,10,13-pentaazacyclopentadecane ligands; BVDME: biliverdine IX dimethyl ester; TE-2-PyP: 5,10,15,20-tetrakis(*N*-ethylpyridinium-2-yl)porphyrin.

reported for Mn^{II} complexes. Compound **5** is the best within this series. *IC*50 values for Mn^{II} complexes **3** and **4** are far better than those reported for the corresponding Fe^{III} complexes. Mn seems to be a most suitable ion for SOD mimics, as it is the least toxic of the Fe, Co, Ni, Cu, Mn series. Moreover, the best SOD mimic reported so far is a Mn^{II} complex (see Table 5).

Pulse Radiolysis (for 3 and 4)

This McCord–Fridovich assay, as a determination of catalytic SOD-like activity is controversial. It has been shown, using stopped-flow techniques,[8,33] or pulse radiolysis,[28] that such an indirect test can be positive in the case of both a catalytic and a stoichiometric superoxide scavenger. As a matter of fact, in the McCord–Fridovich assay, superoxide is produced in low amounts. For compounds displaying high *IC*50 values (over 1 μmol L^{-1}), the conditions required to probe a catalytic behavior may not be fulfilled if $n_{complex} >> n_{superoxide}$ in the experiment. However, this test remains relevant as the X/XO system provides a stationary state of superoxide of low concentration, which is closer to what is usually encountered in vivo.[11,24] Moreover, in the case of a small *IC*50 value indicative of a catalytic activity, the k_{McCF} value derived from the *IC*50 value (see above) corresponds to the k_{cat}.

To test the catalytic behavior within the series, we studied the reactivity of **3** and **4** by pulse radiolysis. They were chosen because they have the highest *IC*50 values of the series, i.e. they were the slowest of the series.

Pulse radiolysis was used to produce the superoxide radical by irradiation of oxygenated aqueous solutions with high energy ionizing radiation.[53] Primary radicals ($H^{\cdot}$, e^{-}_{aq}, $HO^{\cdot}$) are rapidly and quantitatively converted into either superoxide $O_2^{\cdot-}$ or its protonated form hydroperoxyl $HO_2^{\cdot}$, in the presence of either formate or alcohols.[54,55] Propan-2-ol was chosen as formate might coordinate to Mn. The aqueous solution, driven at a constant rate through the UV/Vis microcell, was irradiated for a short time period with an irradiation frequency (1 Hz) chosen so that between two pulses the solution was totally renewed. Absorbances were averaged over 100 pulses. This setup provides an improvement of the signal to noise ratio, by comparison with generally used single-pulse experiments.[56–59]

Superoxide decay was directly monitored at 270 nm, in aqueous phosphate buffer solutions (5 mmol L^{-1}, pH = 7.8). Spontaneous decay of $O_2^{\cdot-}$ followed a second order rate law, as expected for autodismutation of superoxide. The ob-

served rate constant had a value of $1.3\times10^5\,mol^{-1}\,L\,s^{-1}$, consistent with that reported in the literature[54] at pH = 7.8 ($1.0\times10^5\,mol^{-1}\,L\,s^{-1}$). The effect of either **3** or **4** on the superoxide decay was tested for different concentrations of complex (2×10^{-7}, $10^{-5}\,mol\,L^{-1}$ for **3** and 2.14×10^{-7}, 2.14×10^{-6}, and $2.14\times10^{-5}\,mol\,L^{-1}$ for **4**, with an initial superoxide concentration $[O_2^{\cdot-}]_0 = 7.3\times10^{-5}\,mol\,L^{-1}$). From the absorbance decay at 270 nm, kinetic constants were deduced (see Exp. Sect.). The catalytic rate constants k_{cat} were obtained (see Exp. Sect.). They are reported in Table 5.

The apparent first-order kinetics observed for the superoxide decay in the presence of either complex, under conditions where $n_{complex} < n_{superoxide}$, showed that both **3** and **4** act as true catalysts for superoxide dismutation. The derived catalytic rate constant for **3** is of the same order of magnitude than that calculated from the *IC*50 values obtained by the McCord–Fridovich assay. For **4**, rate constants obtained from both methods are in good agreement.[60]

This pulse radiolysis experiment is strong evidence for the catalytic behavior of **3** and **4**. This conclusion concerning **3** is reinforced by further pulse radiolysis experiments that is described elsewhere.[61]

Correlation between SOD Activity and Potentials

As shown above, all redox potentials of the complexes of this series are in the expected range for the catalysis of superoxide dismutation. A linear correlation can be found between anodic half-wave potentials for the Mn^{III}/Mn^{II} couple and $\log(k_{McCF})$ with a negative slope, as shown in Figure 8. Within this series, the activity can be improved by a stabilization of the +III oxidation state: the rate-limiting step is the oxidation into Mn^{III}. Similar correlations have been described previously: (a) in the case of different series of Mn^{III}–porphyrins,[9,23,49] with a positive slope, indicating that the reduction to Mn^{II} was the rate-limiting step and; (b) in the case of Fe^{II} complexes with a negative slope, indicating that the oxidation to iron(III) was the rate-limiting step.[62]

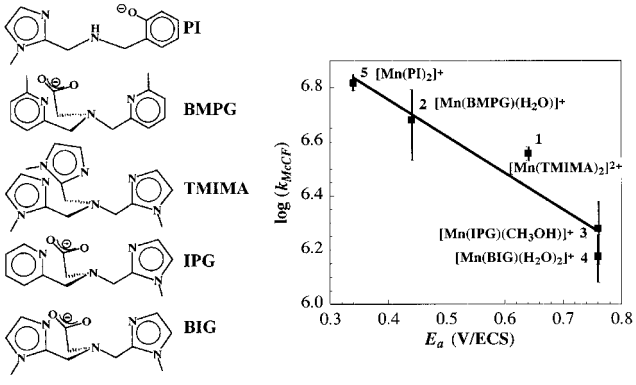

Figure 8. Correlation between E_a and $\log(k_{McCF})$.

Conclusions

The new Mn complexes **1** and **5**, whose structures are presented here, are part of a series of Mn complexes that were studied as SOD mimics. Reactivity in an anhydrous medium was described for **1** and **2** and compared with that of **3** and **4**, previously published.[1] The SOD activity was evaluated through the McCord–Fridovich assay and pulse radiolysis. *IC*50 values directly obtained from the McCord–Fridovich assay, are dependent on the experimental conditions used−that is on the concentration of the detector and its concentration. The results are thus provided and discussed here as derived values, k_{McCF}. We suggest that k_{McCF} should be more commonly used, as *IC*50 values are not comparable from one experiment to the other if different detectors or different concentrations of the same detector were used. The SOD activity in this series is found to be within the reported range for Mn^{II} compounds (see Table 5). The redox properties of the complexes from this series were studied by cyclic voltammetry in a collidine buffer. The potentials of the complexes of the series were tuned both by inducing steric constraints and by increasing the Lewis donor character of the ligands. The present article shows a linear trend between the anodic half-wave potential and $\log(k_{McCF})$ with a negative slope, indicating that the SOD activity in such a series can be improved by lowering the redox potential. Some new compounds are now under investigation to improve SOD activity.

Experimental Section

General: IR spectra (KBr) were recorded with a Bruker IFS 66 FT-IR spectrometer. ^1H NMR spectra were recorded with a Bruker AM 250 spectrometer (^1H, 250 MHz) or a Bruker AC 360 (^1H, 360 MHz). Cyclic voltammetry experiments were performed with an AUTOLAB potentiostat. Electronic absorption spectra were recorded with a Safas 190 DES double-mode spectrophotometer. Chemical reagents were purchased either from Aldrich or Acros and used without further purification. Xanthine oxidase and ferricytochrome c were purchased from Sigma.

Syntheses and Characterization

***N*,*N*,*N*-Tris[(1-methyl-2-imidazolyl)methyl]amine (TMIMA):** A solution of *N*,*N*-bis[(1-methyl-2-imidazolyl)methyl]amine[40] (see also refs.[14,63,64]) (4.1 g, 0.02 mol) with 1-methyl-2-imidazolcarbaldehyde (2.5 g, 0.02 mol)[16] in non-anhydrous MeOH (150 mL) was hydrogenated in the presence of Pd/C (10%) for 3 d. Pd/C was removed by filtration and the supernatant was concentrated to dryness. The white solid was purified by precipitation in CH_3Cl/Et_2O. Yield: 90%. M.p. 200 °C. ^1H NMR (250 MHz, CD_3OD): δ = 3.0 (s, 9 H, CH_3N), 3.8 (s, 6 H, 3 im-CH_2N), 6.7 (d, J = 2.3 Hz, 3 H, H_{im}), 6.9 (d, J = 2.3 Hz, 3 H, H_{im}) ppm. ^{13}C NMR (62 MHz, CD_3OD): δ = 31.7 (CH_3N), 48.7 (NCH_2-im), 121.3 (C_{4im}), 127.3 (C_{5im}), 145.4 (C_{2im}) ppm. IR (KBr; strong bands only): $\tilde{\nu}$ = 1495.8 (ν_{im}), 749.3 (δ_{im}) cm^{-1}. ESI-MS: *m*/*z* (%) = 300.2 (30) [M + H], 322.2,(10) [M + Na].

[2-(Methylamino)phenol]: This protocol was inspired from a published aliphatic nitrile reduction procedure.[65] 2-Cyanophenol (4 g, 33.6 mmol) was dissolved in EtOH (120 mL). An aqueous solution (20 mL) of NaOH (5 g, 125 mmol) and Raney nickel (about 3 g) were then added. The resulting suspension was stirred under H_2 (40 bars) for 4 h. After decantation of the nickel, the solution was filtered and EtOH was evaporated. CH_2Cl_2 (30 mL) was added and the pH of the aqueous phase was brought to 9.3 by addition of 2 N

 © 2005 Wiley-VCH Verlag GmbH & Co. KGaA, Weinheim

HCl. The organic phase was decanted and the aqueous phase was further extracted 3 times with small portions of CH_2Cl_2. The organic phase was dried (Na_2SO_4) and the solvents were evaporated. 2-(Methylamino)phenol (2.42 g, yield 59%) was obtained as a white solid. The nonquantitative yield is probably due to the formation of the Ni^{II} complex which gives a blue-green coloration to the aqueous phase. ^1H NMR (250 MHz, $CDCl_3$): δ = 1.25 (br. s, NH_2), 4.14 (s, 2 H, CH_2), 6.81 (m, 2 H, Ar), 6.98 (d, J = 5 Hz, 1 H, Ar), 7.18 (t, J = 7.5 Hz, 1 H, Ar) ppm.

2-({[(1-Methyl-2-imidazolyl)methyl]amino}methyl)phenol (PIH): 2-(Methylamino)phenol (1 g, 8.1 mmol) and 1-methyl-2-imidazolecarbaldehyde (0.89 g, 8.1 mmol), synthesized according to a published procedure[16] were dissolved in anhydrous EtOH (80 mL). This solution was heated to reflux over 3 h and thencooled to ambient temperature. $NaBH_4$ (0.384 g, 10.2 mmol) was then added in small portions over 15 min and the resulting solution was refluxed for 5 min. 2 N aqueous HCl was then added until the end of gaseous release. EtOH was evaporated and CH_2Cl_2 (30 mL) was added. The pH of the aqueous phase was brought to 9.5 by addition of a 2 N aqueous NaOH solution. The organic phase was decanted and the aqueous phase was further extracted 3 times with small portions of CH_2Cl_2. The joint organic phases were dried (Na_2SO_4) and the solvents evaporated. PIH (1.2 g, yield 68%) was obtained as an orange oil. ^1H NMR (360 MHz, $CDCl_3$): δ = 3.45 (s, 3 H, NCH_3), 3.72 (s, 2 H, CH_2), 3.87 (s, 2 H, CH_2), 7.01 (t, J = 8 Hz, 1 H, Ar), 6.94 (d, J = 7.3 Hz, 1 H, Ar), 6.87 (br s, 1 H, Ar), 6.74 (br. m, 3 H, Ar) ppm. ^{13}C NMR (90 MHz, $CDCl_3$): δ = 32.3 ($N_{im}CH_3$), 43.3 and 51.0 ($N_{im}CH_2$ and $N_{Ar}CH_2$), 116.0, 118.9, 121.1, 122.8, 126.7, 128.5, 128.9, 145.2 (phenol and imidazole), 157.5 ($C_{phenol}OH$) ppm. IR (KBr; strong bands only): $\tilde{\nu}$ = 1456 and 1489 (ν_{im}), 1255 (ν_{phenol}), 756 (δ_{im}) cm^{-1}. ESI-MS: m/z (%) = 218.1 (100) [M + H].

$Mn(TMIMA)_2(PF_6)_2$ (1): An $MnBr_2$ solution in distilled water (125 mg in 7 mL) was added after deoxygenation (argon) to a hot (40 °C) deoxygenated methanolic solution of TMIMA (150 mg in 7 mL). After 1.5 h at 40 °C, it was allowed to cool to room temp. A deoxygenated solution of ammonium hexafluorophosphate (288 mg) in MeOH/H_2O (5 mL, 1:1) was then added. Crystals suitable for X-ray diffraction were grown by slow concentration over 24 h. Yield: 50%. $C_{30}H_{42}F_{12}MnN_{14}P_2$ (943.6): calcd. C 38.19, H 4.49, F 24.16, Mn 5.82, N 20.78, P 6.56; found C 38.00, H 4.39, F 24.60, Mn 5.83, N 20.70, P 6.48. IR (KBr): $\tilde{\nu}$ = 1503 (ν_{im}), 839 (PF_6^-), 741 (δ_{im}), 556 (PF_6^-) cm^{-1}. Crystals of $[Mn(TMIMA)_2](PF_6)_2$ (**1**) were obtained from a water/methanol solution as prismatic crystals. One of these, the size of which was 0.3 × 0.6 × 0.6 mm, was mounted on a SMART 1000 Bruker AXS diffractometer with Mo-K_α radiation (λ = 0.7107 Å). Atomic scattering factors were taken from ref.[66] The structure was solved by direct methods using SIR97[67] and refined using SHELXL-97[68] on F^2 by full-matrix least squares with anisotropic displacement parameters for all non-hydrogen atoms. All hydrogen atoms were calculated in ideal geometrical positions. Final refinement gave R_1 = 0.0348 and wR_2 = 0.0984. Experimental details for the X-ray data collection are reported in Table 6. The refinement procedure was carried out using the WinGX package[69] with the program PARST[70] for the geometrical description of the structures and ORTEP[71] and PLUTO[72] for the structure drawings.

$[Mn(PI)_2](CH_3CN)(PF_6)$ (5): A deoxygenated aqueous solution (8 mL) of $MnBr_2$ (124 mg, 0.58 mmol) was added to a deoxygenated methanolic solution (8 mL) of PIH (0.70 mmol). Et_3N (0.025 g, 0.25 mmol) was added. The resulting solution was allowed to stand for 1.5 h at ambient temperature under positive argon pressure. A deoxygenated solution (2.5 mL H_2O/2.5 mL MeOH) of NH_4PF_6 (0.25 g, 1.53 mmol, 2.6 equiv.) was then added. A white powder was then precipitated. The solid was filtered off and redissolved in CH_3CN. The solution turned violet and crystals of $[Mn(PI)_2](PF_6)\cdot CH_3CN$ suitable for X ray diffraction were obtained in low yield (50% from the powder) from acetonitrile by diffusion of tBuOMe as tiny dark crystals (see below). When the preparation was carried out at a higher temperature (50 °C) and under dioxygen, a purple black solution was obtained and a purple black powder was precipitated upon NH_4PF_6 addition. $C_{24}H_{28}F_6N_6O_2MnP(CH_3CN)_{0.5}(H_2O)_{1.5}$ (679.66): calcd. C 44.14, H 4.82, Mn 8.08, N 13.39, P 4.56; found C 44.30, H 4.51, Mn 7.99, N 13.37, P 4.66. IR (KBr; strong bands only): $\tilde{\nu}$ = 3438 and 3339 (ν_{NH}), 1595, 1507, 1477, 1268 ($\nu_{COphenol}$), 841 (PF_6), 779, 767 (δ_{im}), 557 (PF_6) cm^{-1}. Among the crystals obtained a few specimens were chosen and tested for diffraction. All of them were very small and badly twinned. The best crystal found (0.1 × 0.1 × 0.3 mm) was mounted on a Philips diffractometer with Mo-K_α radiation (λ = 0.7107 Å). Tabulated atomic scattering factors were taken from ref.[66] The structure was solved by direct methods using SIR97[67] and refined using SHELXL-97[68] on F^2 by full-matrix least squares with anisotropic displacement parameters for all atoms but the acetonitrile molecule and the hydrogen atoms. All hydrogen atoms were calculated in ideal geometrical positions. Because of its very small size the crystal used for structure characterization gave extremely weak diffraction. The final refinement suffers therefore from a very low ratio between the parameters to refine and the number of observed reflections. Final refinement gave R_1 = 0.117 and wR_2 = 0.36. Experimental details for the X-ray data collection are reported in Table 6. The refinement procedure was carried out using the WinGX package[69] with the program PARST[70] for the geometrical description of the structures and ORTEP[71] and PLUTO[72] for the structure drawings.

CCDC-245983 contains the supplementary crystallographic data for this paper. These data can be obtained free of charge from The Cambridge Crystallographic Data Centre via www.ccdc.cam.ac.uk/data_request/cif.

Reactivity in Anhydrous DMSO with Superoxide: The protocol for studying the reactivity with Mn^{II} complexes was the same as that previously published (preparation of superoxide solutions, spectrophotometric titration).[1] Several aliquots were prepared with a final volume of 1 mL, containing the complex and n equiv. of superoxide. After the superoxide was added, the aliquot was manually stirred. 100 μL was introduced in an EPR tube which was immediately frozen in an EtOH/N_2(liq) bath and then kept in N_2(liq). EPR spectra were then recorded. For each experiment, the superoxide was quantified by EPR from the intensity of the g_{xy} = 2.00 peak and a linear correlation with concentration was found (see Supporting information). This was used to quantify the remaining superoxide within each EPR tube.

Cyclic Voltammetry Experiments: Cyclic voltammetry experiments were performed at room temperature with an argon stream in a collidine buffer (pH = 7.5; 50 mmol L^{-1}). The working electrode was a vitreous carbon disk. The reference electrode was an SCE, saturated with KCl. Concentrations of the complexes were 2×10^{-3} mol L^{-1} and 6×10^{-4} mol L^{-1} on the basis of Mn^{II} content.

McCord–Fridovich Assay or Xanthine-Xanthine Oxidase-Cytochrome c Assay: The superoxide anion was supplied to the system from the xanthine-xanthine oxidase reaction.

Reliability of the McCord–Fridovich Assay: To check that the tested compounds do not inhibit the production of superoxide by xanthine oxidase, the rate of conversion of xanthine to urate (see be-

Table 6. Crystal data for complexes $[Mn(TMIMA)_2](PF_6)_2$ (**1**) and $[Mn(PI)_2](PF_6)(CH_3CN)$ (**5**).

	1	**5**
Empirical formula	$C_{30}H_{42}F_{12}MnN_{14}P_2$	$C_{26}H_{31}MF_6n_1N_7O_2P$
Formula mass	943.622	673.5
Crystal system	monoclinic	triclinic
Space group	$P2_1/c$	$P\bar{1}$
a [Å]	12.295(2)	11.815(11)
b [Å]	13.879(3)	13.318(13)
c [Å]	12.720(2)	10.770(9)
α [°]	90	94.91(5)
β [°]	109.43(2)	112.79(7)
γ [°]	90	80.84(7)
V [Å^3]	2129.4(8)	1542(3)
Z	2	2
F(000)	966	692
$D_{calcd.}$ [mg m^{-3}]	1.531	1.45
μ(Mo-K_α) [mm^{-1}]	0.4987	0.71069
Crystal size [mm]	0.4 × 0.6 × 0.6	0.1 × 0.1 × 0.3
T [K]	293	293
No. of reflections measured	18649	5409
θ range [°]	2.00 < 2θ < 50.00	3.00 < 2θ < 60.00
hkl ranges	–13, 13; –15, 15; –14, 14	–14,12; –15, 15; 0, 12
No. of unique reflections	2950	5409
No. of reflections observed [$I > 2\sigma(I)$]	2381	887
No. of parameters	323	372
R_1[a]	0.0348	0.117
Weight (A, B)[b]	0.0523, 0.54	0.1122, 0.00
wR_2[c]	0.0984	0.368
Max. Fourier difference [e/Å^3]	0.28, –0.16	0.56, –0.64

[a] $R_1 = \Sigma||F_o| - |F_c||/\Sigma|F_o|$. [b] $1/\sigma^2(F_o^2) + (A\cdot P)^2 + B\cdot P]$ where $P = [\mathrm{Max}(F_o^2,0) + 2\cdot F_c^2]/3$. [c] $wR_2 = \{\Sigma[w(F_o^2 - F_c^2)^2/\Sigma[w(F_o^2)^2]\}^{1/2}$.

low) was determined by measuring the increase in absorbance at 290 nm over a 2-min period with and without the tested compounds. At concentrations higher than the *IC*50 value, no inhibition of this conversion was recorded. We also checked that ferricytochrome c was stable in the presence of the putative SOD mimics.

Xanthine to Urate Assay: To measure the rate of conversion of xanthine to urate, xanthine oxidase (30 μL of 0.77 U mL^{-1} XO) was added to a solution of potassium phosphate buffer (pH = 7.8; 50 mmol L^{-1}) containing xanthine (150 μmol L^{-1}) at a final volume of 1.0 mL at 25 °C. Urate production was monitored at 290 nm. No difference in the slope was recorded with or without the putative SOD mimics.

Reduction of Ferricytochrome c: Activities were measured using ferricytochrome c reduction.[1,31,33,73] The assay was performed at 25 °C in 3 mL of reaction buffer (50 mmol L^{-1} potassium phosphate buffer, pH = 7.8) containing ferricytochrome c (22 μmol L^{-1}), xanthine (200 μM), and an amount of xanthine oxidase such as to give a rate of ΔOD_{550nm} = 0.025 min^{-1} (about 0.01 U mL^{-1}) in the absence of a putative SOD mimic. A reduction of ferricytochrome c was monitored at 550 nm. After 2 min, different amounts of the putative SOD mimic were added. Rates were linear for at least 8 min. Both rates in the absence and in the presence of the complex were determined for each concentration of complex added. The *IC*50 value represents the concentration of putative-SOD mimic that induces a 50% inhibition of the reduction of cytochrome c. If *s1* is the slope before addition of the putative SOD mimic and *s2* is the slope after addition of the putative SOD mimic, the inhibition percentage is given by I (%) = (*s1* – *s2*)/*s1*×100. For an *IC*50 value determination, I is measured for several concentrations in the range of the *IC*50. *IC*50 is obtained for I = 50%; (*s1* – *s2*)/*s2* was also plotted against the complex concentration, providing a linear correlation. *IC*50 is then obtained for (*s1* – *s2*)/*s2* = 1.[34]

Pulse Radiolysis Experiments: The pulse radiolysis experiment was carried out using a 10 MeV Titan β linear accelerator at the Laboratory of Radiolysis, CEA Saclay. Pulses can last between 5 ns and 1 μs, and the frequency between two pulses is adjustable. A 10 ns pulse corresponds to a 20 Gray dose. Solutions saturated with oxygen are driven in a quartz circulating microcell (spectral path length 1 cm, volume 400 μL) at a constant flux (1 mL min^{-1}). The spectroscopic and temporal analysis is mediated by an optical fiber, linked to a monochromator, then to a photomultiplier and lastly to a Tektronix numerical oscilloscope allowing the observation of the temporal evolution of absorbance. Absorbance was averaged over 100 pulses. It provides an improvement of the signal/noise ratio, by comparison with generally used single-pulse experiments. The amount of superoxide generated during pulse radiolysis was established by the absorbance value at 260 nm, assuming that ε_{260} = 1940 mol L^{-1} cm^{-1}[54] All measurements were carried out in propan-2-ol (100 mmol L^{-1}) in phosphate buffer (5 mmol L^{-1}) at pH = 7.8 and 25 °C. Various amounts of complexes MnIPG or MnBIG were dissolved in that buffer. Solutions were oxygen-saturated by bubbling O_2 for at least 60 min. The electron pulse lasted 1 μs, generating a 7.3×10^{-5} mol L^{-1} superoxide solution. The irradiation frequency was 1 Hz, so that the cell content was totally renewed between two pulses. The disappearance of superoxide was monitored at 270 nm (ε_{270} = 1479 mol L^{-1} cm^{-1} at pH = 7.8 and 23 °C[53]). Rates were derived assuming, either second-order kinetics corresponding to the auto-dismutation of superoxide [$OD = OD_0/(1 + k_{obs}\ OD_0 t)$], or a pseudo-first order kinetics in the presence of complexes {$OD = OD_0[\exp(-k_{obs}t)] + B$, $k_{obs} = k_{cat}$[complex] + A}. Simulations of kinetic traces are performed using Gepasi3 (auto-dismutation) or Kaleidagraph (complex catalyzed dismutation).

Supporting Information: See also the footnote on the first page of this article. A. Reference for statistical analysis of the Mn–N dis-

 © 2005 Wiley-VCH Verlag GmbH & Co. KGaA, Weinheim

tances; B. additional crystallographic data for **1**; C. EPR quantification of the superoxide content.

Acknowledgments

We would like to acknowledge the European Community for financial support (TMR contract FMRX-CT980174).

[1] C. Policar, S. Durot, F. Lambert, M. Cesario, F. Ramiandrasoa, I. Morgenstern-Badarau, *Eur. J. Inorg. Chem.* **2001**, 1807–1818.
[2] Abbreviations: IPG = *N*-[(1-methyl-2-imidazolyl)methyl]-*N*-(2-pyridylmethyl)glycinate; BIG = *N*,*N*-bis[(1-methyl-2-imidazolyl)methyl]glycinate; TMIMA = tris[(1-methyl-2-imidazolyl)methyl]amine; BMPG = *N*,*N*-bis[(6-methyl-2-pyridyl)-methyl]glycinate; PI = 2-{[(1-methyl-2-imidazolyl)methyl]-amino}phenolate; EPR = electron paramagnetic resonance; *IC*50 = concentration that induces a diminution of 50% in the kinetic of reduction of ferricytochrome c in the McCord–Fridovich assay; SOD = superoxide dismutase; SCE: saturated calomel electrode; cyt c = Cytochrome c Fe^{III}; NBT: nitro-blue tetrazolium; X/XO = xanthine/xanthine oxidase. See also Table 5.
[3] I. Fridovich, *Arch. Biochem. Biophys.* **1986**, *247*, 1–11.
[4] I. Fridovich, *Ann. Rev. Biochem.* **1995**, *64*, 97–112.
[5] I. Fridovich, *J. Biol. Chem.* **1997**, *272*, 18515–18517.
[6] C. X. Zhang, S. J. Lippard, *Curr. Opin. Chem. Biol.* **2003**, *7*, 481–489.
[7] D. Salvemini, C. Muscoli, D. P. Riley, S. Cuzzocrea, *Pulm. Pharmacol. Ther.* **2002**, *15*, 439–447.
[8] D. P. Riley, *Chem. Rev.* **1999**, *99*, 2573–2587.
[9] I. Batinic-Haberle, I. Spasojevic, R. D. Stevens, P. Hambright, P. Neta, A. Okado-Matsumoto, I. Fridovich, *J. Chem. Soc., Dalton Trans.* **2004**, 1696–1702.
[10] J. R. Anacona, M. Azocar, O. Nusetti, C. Rodriguez-Barbarin, *Transition Met. Chem.* **2003**, *28*, 24–28.
[11] J.-L. Pierre, P. Chautemps, S. Refaif, C. Beguin, A. El Marzuki, G. Serratrice, E. Saint-Aman, P. Rey, *J. Am. Chem. Soc.* **1995**, *117*, 1965–1973.
[12] M. A. Bailey, M. J. Ingram, D. P. Naughton, *Biochem. Biophys. Res. Commun.* **2004**, *317*, 1155–1158.
[13] S. Durot, C. Policar, F. Bisceglie, G. Pelosi, T. Mallah, J.-P. Mahy, *Inorg. Chem.* **2003**, *42*, 8072–8080.
[14] K. J. Oberhausen, R. J. O'Brien, J. F. Richardson, R. M. Buchanan, R. Costa, J.-M. Latour, H.-L. Tsai, D. N. Hendrickson, *Inorg. Chim. Acta* **1990**, *173*, 145.
[15] K. J. Oberhausen, R. J. O'Brien, J. F. Richardson, R. M. Buchanan, R. Costa, J.-M. Latour, H.-L. Tsai, D. N. Hendrickson, *Inorg. Chem.* **1993**, *32*, 4561–4565.
[16] P. E. Iberson, H. Lund, *Acta Chem. Scand.* **1966**, *20*, 2649.
[17] F. H. Allen, *Acta Crystallogr., Sect. B* **2002**, *58*, 380–388.
[18] The six hyperfine lines are broadened because of intermolecular interactions.
[19] In the case of **3**, the formation of a di-μ-oxo–$Mn^{III}Mn^{IV}$ species was observed after addition 0.5 equiv. of superoxide. The di-μ-oxo–$Mn^{III}Mn^{IV}$ species has been shown to be further reduced to a di-μ-oxo–$Mn^{III}Mn^{III}$ species (1 equiv. of superoxide). In the case of **4**, a similar behaviour was recorded upon addition of superoxide, but with a different stoichiometry. The $Mn^{III}Mn^{IV}$–di-μ-oxo complex was obtained after addition of 1.5 equiv. of superoxide and the EPR-silent $Mn^{III}Mn^{III}$–di-μ-oxo species was obtained after addition of 2 equiv. of superoxide. A mechanism involving the oxidation of the starting Mn^{II} complex to an $Mn^{III}Mn^{IV}$–di-μ-oxo and then a reduction to the $Mn^{III}Mn^{III}$–di-μ-oxo species has been proposed.
[20] W. C. J. Barrette, D. T. Sawyer, J. A. Fee, K. Asada, *Biochemistry* **1983**, *22*, 624–627.
[21] W. H. Koppenol, F. Levine, T. L. Hatmaker, J. Epp, J. D. Rush, *Arch. Biochem. Biophys.* **1986**, *251*, 594–599.
[22] J. Stein, J. P. Fackler, G. J. Mcclune, J. A. Fee, L. T. Chan, *Inorg. Chem.* **1979**, *18*, 3511–3518.
[23] I. Batinic-Haberle, I. Spasojevic, P. Hambright, L. Benov, A. L. Crumbliss, I. Fridovich, *Inorg. Chem.* **1999**, *38*, 4011–4022.
[24] J.-L. Pierre, *Regard sur la Biochimie* **2000**, 17–20.
[25] E. A. Lewis, J. R. Lindsay-Smith, P. H. Walton, S. J. Archibald, S. P. Foxo, G. M. P. Giblin, *J. Chem. Soc., Dalton Trans.* **2001**, 1159_1161.
[26] M. G. B. Drew, C. J. Harding, V. Mckee, G. G. Morgan, J. Nelson, *J. Chem. Soc. Chem. Commun.* **1995**, 1035–1038.
[27] F. C. Frederick, W. M. Coleman, L. T. Taylor, *Inorg. Chem.* **1983**, *22*, 792–795.
[28] A. Deroche, I. Morgenstern-Badarau, M. Cesario, J. Guilhem, B. Keita, L. Nadjo, C. Houée-Levin, *J. Am. Chem. Soc.* **1996**, *118*, 4567–4573.
[29] Y. Nishida, N. Tanaka, A. Yamazaki, T. Tokii, N. Hashimoto, K. Ide, K. Iwasawa, *Inorg. Chem.* **1995**, *34*, 3616–3620.
[30] K. Yamato, I. Miyahara, A. Ichimura, K. Hirotsu, Y. Kojima, H. Sakurai, D. Shiomi, K. Sato, T. Takui, *Chem. Lett.* **1999**, 295–296.
[31] J. M. McCord, I. Fridovich, *J. Biol. Chem.* **1969**, *244*, 6049–6055.
[32] K. M. Faulkner, R. D. Stevens, I. Fridovich, *Arch. Biochem. Biophys.* **1994**, *310*, 341–346.
[33] R. H. Weiss, A. G. Flickinger, W. J. Rivers, M. M. Hardy, K. W. Aston, U. S. Ryan, D. P. Riley, *J. Biol. Chem.* **1993**, *268*, 23049–23054.
[34] Y. Sawada, I. Yamazaki, *Biochim. Biophys. Acta* **1973**, *327*, 257–265.
[35] M. Baudry, S. Etienne, A. Bruce, M. Palucki, E. Jacobsen, B. Malfroy, *Biochem. Biophys. Res. Commun.* **1993**, *192*, 964–968.
[36] R. F. Pasternack, B. Halliwell, *J. Am. Chem. Soc.* **1979**, *101*, 1026–1031.
[37] J. Butler, W. H. Koppenol, E. Margoliash, *J. Biol. Chem.* **1982**, *257*, 10747–10750.
[38] Z.-R. Liao, X.-F. Zheng, B.-S. Luo, L.-R. Shen, D.-F. Li, H.-L. Liu, W. Zhao, *Polyhedron* **2001**, *20*, 2813–2821.
[39] M. C. Rodriguez, Thesis, Université Paris-Sud, **1996**, p. 249.
[40] M. C. Rodriguez, I. Morgenstern-Badarau, M. Cesario, J. Guilhem, B. Keita, L. Nadjo, *Inorg. Chem.* **1996**, *35*, 7804–7810.
[41] P. J. Gauuan, M. P. Trova, L. Gregor-Boros, S. B. Bocckino, J. D. Crapo, B. J. Day, *Bioorg. Med. Chem.* **2002**, *10*, 3013–3021.
[42] N. Kitajima, M. Osawa, N. Tamura, Y. Moro-Oka, T. Hirano, M. Hirobe, T. Nagano, *Inorg. Chem.* **1993**, *32*, 1879–1880.
[43] K. S. Yamaguchi, L. Spencer, D. T. Sawyer, *FEBS Lett.* **1986**, *197*, 249–252.
[44] E. A. Lewis, H. H. Khodr, R. C. Hider, J. R. Lindsay-Smith, P. H. Walton, *J. Chem. Soc., Dalton Trans.* **2004**, 187–188.
[45] D. F. Xiang, C. Y. Duan, X. S. Tan, Q. W. Hang, W. X. Tang, *J. Chem. Soc., Dalton Trans.* **1998**, 1201–1204.
[46] D. F. Xiang, X. S. Tan, Q. W. Hang, W. X. Tang, B.-M. Wu, T. C. W. Mak, *Inorg. Chim. Acta* **1998**, *277*, 21–25.
[47] D. Salvemini, Z.-Q. Wang, J. L. Zweier, A. Samouilov, H. Macarthur, T. P. Misko, M. G. Currie, S. Cuzzocrea, J. A. Sikorski, D. P. Riley, *Science* **1999**, *286*, 304–305.
[48] I. Spasojevic, I. Batinic-Haberle, R. D. Stevens, P. Hambright, A. N. Thorpe, J. Grodkowski, P. Neta, I. Fridovich, *Inorg. Chem.* **2001**, *40*, 726–739.
[49] R. Kachadourian, I. Batinic-Haberle, I. Fridovich, *Inorg. Chem.* **1999**, *38*, 391–396.
[50] K. W. Aston, N. Rath, A. Naik, U. Slomczynska, O. F. Schall, D. P. Riley, *Inorg. Chem.* **2001**, *40*, 1779–1789.
[51] H. Ukeda, S. Maeda, T. Ishii, M. Sawamura, *Anal. Biochem.* **1997**, *251*, 206–209.
[52] P. H. Walton, Department of Chemistry, University of York, personal communication.
[53] B. H. J. Bielski, *Photochem. Photobiol.* **1978**, *28*, 645–649.
[54] B. H. J. Bielski, D. E. Cabelli, R. L. Arudi, A. B. Ross, *J. Phys. Chem. Ref. Data* **1985**, *14*, 1041–1100.

 © 2005 Wiley-VCH Verlag GmbH & Co. KGaA, Weinheim

[55] B. H. J. Bielski, R. L. Arudi, *Anal. Biochem.* **1983**, *133*, 170–178.
[56] D. E. Cabelli, B. H. J. Bielski, *J. Phys. Chem.* **1984**, *88*, 3111–3115.
[57] D. E. Cabelli, B. H. J. Bielski, *J. Phys. Chem.* **1984**, *88*, 6291–6294.
[58] A. Deroche, I. Morgenstern-Badarau, M. Cesario, J. Guilhem, B. Keita, L. Nadjo, C. Houée-Levin, *J. Am. Chem. Soc.* **1996**, *118*, 4567–4573.
[59] S. Goldstein, G. Czapski, D. Meyerstein, *J. Am. Chem. Soc.* **1990**, *112*, 6489–6492.
[60] In ref. 1[1], two *IC*50 values are reported for each complex. One value corresponds to that reported here. The other one, labeled specific *IC*50 or $IC50_{spe}$, was measured in the presence of an excess of ligand. This was done to estimate the effect of decoordination which could occur at a low concentration. For **3**, $IC50_{spe} = 2.0 \pm 0.2\ \mu mol\,L^{-1}$ ($k_{catspe} = 2.9 \pm 0.5\ 10^6\,mol^{-1}\,Ls^{-1}$) and for **4**, $IC50_{spe} = 1.7 \pm 0.2\ \mu mol\,L^{-1}$ ($k_{catspe} = 3.4 \pm 0.4\ 10^6\,mol^{-1}\,Ls^{-1}$). These values are closer to the pulse radiolysis values.
[61] S. Durot, F. Lambert, J.-P. Renault, C. Policar, *Eur. J. Inorg. Chem.* **2005**, 2789–2793.
[62] M. Tamura, Y. Urano, K. Kikuchi, T. Higuchi, M. Hirobe, T. Nagano, *Chem. Pharm. Bull.* **2000**, *48*, 1514–1518.
[63] S. Chen, J. F. Richardson, R. M. Buchanan, *Inorg. Chem.* **1994**, *33*, 2376–2382.
[64] K. J. Oberhausen, J. F. Richardson, R. M. Buchanan, W. Pierce, *Polyhedron* **1989**, *8*, 659–668.
[65] H. Geneste, M. Hesse, *Tetrahedron* **1996**, *15*, 15199.
[66] *International Tables for X-ray Crystallography*, Kluwer Academic Publishers, Dordrecht/Boston/London, **1995**.
[67] A. Altomare, M. C. Burla, M. Camalli, G. L. Cascarano, C. Giacovazzo, A. Guagliardi, A. G. G. Moliterni, G. Polidori, R. Spagna, *J. Appl. Crystallogr.* **1999**, *32*, 115–119.
[68] G. M. Sheldrick, *SHELXL-97*, University of Göttingen, **1997**.
[69] L. J. Farrugia, *J. Appl. Crystallogr.* **1999**, *32*, 837–838.
[70] M. Nardelli, *J. Appl. Crystallogr.* **1995**, *28*, 659.
[71] C. K. Johnson, M. N. Burnett, *Report ORNL-6895*, Oak Ridge National Laboratory, Oak Ridge, Tennessee, USA, **1996**.
[72] A. L. Spek, *PLATON, A Multipurpose Crystallographic Tool*, University of Utrecht, **1999**.
[73] K. M. Faulkner, S. I. Liochev, I. Fridovich, *J. Biol. Chem.* **1994**, *269*, 23471–23476.

Received: October 6, 2004
Published Online: August 2, 2005

 © 2005 Wiley-VCH Verlag GmbH & Co. KGaA, Weinheim

The *N*-Lithiation of 2,4,6-Triphenylborazine[‡]

Heinrich Nöth,*[a] and Alexander Troll[a]

Dedicated to Prof. Dr. Dr. h. c. mult. Rolf Huisgen on the occasion of his 85th birthday

Keywords: Lithium / Boron / Deprotonation reactions / Tetraphenylborazinates

The reaction of the borazine $Ph_3B_3N_3H_3$, **1**, with a diethyl ether solution of LiMe/LiI/TMEDA yields [$(Ph_4B_3N_3H_3)$Li(tmeda)LiI(tmeda)], **2**. However, when halide free LiMe is used in the presence of TMTA, then $(Ph_4B_3N_3H_3)$Li(tmta), **3**, is formed which shows that a Me/Ph exchange occurs with the formation of LiPh which adds to **1** to form the borazinate **3**. A Bu/Ph exchange is also observed in the reaction of **1** with Li*t*Bu/tmta. The product isolated from THF is compound [$(Ph_4B_3N_3H_2Li$–Li$(thf)_3$], **6c**, which results from deprotonation of and LiPh addition to **1**. A straightforward 1:1 LiPh addition reaction is observed on treatment of the borazine $Ph_3B_3N_3Me_3$, **4**, with LiPh in diethyl ether solution to give the borazinate $(Ph_4B_3N_3Me_3)$Li(OEt_2), **5**. Reaction of **1** with LiPh (ratio 1:1) in diethylether produces $(Ph_4B_3N_3H_2Li)$-[$Ph_3B_3N_3H_2$Li$(OEt_2)_2$], **7**, while an excess of LiPh leads to triple deprotonation and LiPh addition to the N atoms of compound $(Ph_3B_3N_3Li_3)$ to give the adduct [$Ph_3B_3N_3Li_3(OEt_2)_3$]-[LiPh(OEt_2)], **8**. All new compounds have been characterized by spectroscopic methods and X-ray structure determinations.
(© Wiley-VCH Verlag GmbH & Co. KGaA, 69451 Weinheim, Germany, 2005)

Introduction

Borazines of type $R_3B_3N_3H_3$ can be deprotonated at the NH groups by organyllithium compounds. The resulting *N*-lithioborazine derivatives have been used to synthesize new organylborazines by treating them with organyl halides.[2,3] So far, only *N*-monolithio-borazines, $R_3B_3N_3H_2Li$ (R = Me, *t*Bu, NMe_2) have been characterized structurally as complexes with ligands such as diethyl ether (OEt_2), tetrahydrofuran (THF), tetramethyl diethylene diamine (TMEDA) or 1,3,5-trimethyl-1,3,5-hexahydrotriazine (TMTA).[1] Deprotonation proceeds by an addition-elimination process as demonstrated for the reaction of $tBu_3B_3N_3H_3$ with *t*BuLi.[1] Solvates of *N*-lithioborazines $R_3B_3N_3H_2Li$ (R = Me, *t*Bu, Me_2N) are usually present in the solid state in the form of dimers. Monomers are obtained with bulky ligands such as TMTA and/or large substituents (*t*Bu) located at the boron atoms.[1]

In 2,4,6-triphenylborazine, **1**, the phenyl groups are twisted against the borazine plane by about 29°[4] leaving a cleft between the phenyl groups. Due to this geometry, it was expected that **1** might behave differently towards LiR compounds compared with 2,4,6-trimethylborazine. And this is indeed the case as we will show here.

Reaction of $Ph_3B_3N_3H_3$, 1, with MeLi and LiBu

Because of the fact that **1**[5] is much more soluble in diethyl ether or tetrahydrofuran than in hydrocarbons its behaviour towards organyllithium compounds was studied mostly in ether solvents. Scheme 1 gives an overview of the results.

LiMe was first used as a solution in diethyl ether which contained an equivalent amount of LiI. The 1:1 reaction in the presence of TMEDA led to the monodeprotonated triphenylborazine $Ph_3B_3N_3H_2$Li(tmeda) cocrystallizing with LiI(tmeda) to give the product **2** (see Scheme 1). On the other hand, when halide free LiMe, prepared from Li metal and MeCl in diethyl ether, was activated by TMTA then the isolated compound **3** proved to be the Li complex of the 2,4,4,6-tetraphenylborazinate anion. This demonstrates that a LiMe/LiPh exchange has taken place, and that the generated LiPh has added to **1**. Compound **3** was isolated in 78% yield which fits well with Equations (1) and (2).

An organyl group exchange was also observed when **1** was treated with a solution of LiBu and TMTA in diethyl ether. The tmta complex **6b** could not be characterized, but crystallization of the reaction product from THF gave crystals of **6c** which proved to be a lithium (*N*-lithio-tetraphenylborazinate) isolated as its THF solvate [$(Ph_4B_3N_3H_2Li)$-Li$(thf)_3$]. Its formation is shown in Equations (3) and (4). A different solvate of this lithium *N*-lithio-tetraphenylborazinate could be isolated from a 1:1 reaction of LiPh in

[‡] Contributions to the Chemistry of Boron, 257. Part 256: Ref.[1]
[a] Department of Chemistry, University of Munich, Butenandtstr. 5–13, 81 377 München, Germany

 DOI: 10.1002/ejic.200500135

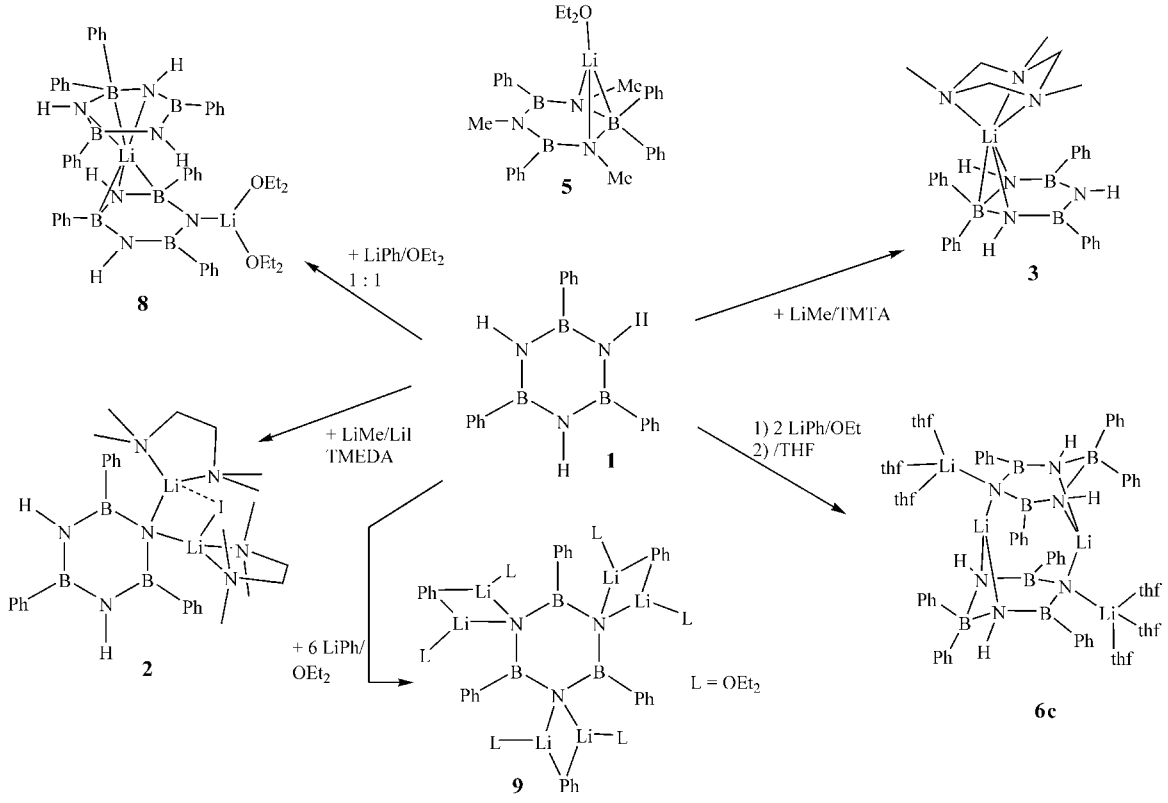

Scheme 1. Reactions of **1** with LiMe/LiI, LiMe and LiPh.

$$Ph_3B_3N_3H_3 + 3\ LiMe + 3\ TMTA \rightarrow Me_3B_3N_3H_3 + 3\ LiPh(tmta) \quad (1)$$

$$\underset{\mathbf{1}}{3\ Ph_3B_3N_3H_3} + 3\ LiPh(tmta) \rightarrow \underset{\mathbf{3}}{3\ (Ph_4B_3N_3H_3)Li(tmta)} \quad (2)$$

diethyl ether with **1**. It was isolated as its bis(diethyl ether) adduct $[Ph_4B_3N_3H_2Li]Li(OEt_2)_2$, **6a**, which on treatment with THF converted to **6c**. These results suggest that **1** adds LiPh preferentially to give a stable tetraphenylborazinate. In order to test this assumption LiPh was allowed to react with $Ph_3B_3N_3Me_3$, **4**, where no deprotonation at the N atoms is expected. Indeed, LiPh adds readily to **4** producing a lithiumborazinate as shown in Equation (5) which was isolated as its mono diethyl ether adduct **5**.

$$5\ Ph_3B_3N_3H_3 + 6\ LiBu(tmta) \rightarrow$$
$$2\ Bu_3B_3N_3H_3 + 3\ Ph_4B_3N_3H_2Li_2(tmta)_n + 3\ PhH + 6 - n\ TMTA$$
$$\mathbf{6b} \quad (3)$$

$$Ph_4B_3N_3H_2Li_2(tmta)_n + 3\ THF \rightarrow \underset{\mathbf{6c}}{Ph_4B_3N_3H_2Li_2(thf)_3} + n\ TMTA \quad (4)$$

$$\underset{\mathbf{4}}{Ph_3B_3N_3Me_3} + LiPh + OEt_2 \rightarrow \underset{\mathbf{5}}{Ph_4B_3N_3Me_3Li(OEt_2)} \quad (5)$$

It was, therefore, of interest to test how LiPh in diethyl ether solution would react with **1**. As depicted in Scheme 1 and Equations (6) and (7), reactions indeed occur but are always accompanied by the deprotonation of **1**. In the case of the 1:1 reaction [Equation (6)] the isolated crystals proved to be composed of the components $Ph_3B_3N_3H_2Li$ and $Ph_4B_3N_3H_3Li(OEt_2)_2$, **7**, which are linked by Li–N and Li–B bonds as shown by its molecular structure determined by X-ray crystallography (see Figure 2a).

$$2\ Ph_3B_3N_3H_3 + 2\ LiPh + 2\ OEt_2 \rightarrow$$
$$\underset{\mathbf{7}}{[(Ph_4B_3N_3H_3Li(OEt_2)_2][Ph_3B_3N_3H_2Li]} + 2\ PhH \quad (6)$$

$$Ph_3B_3N_3H_3 + 2\ LiPh + 2\ OEt_2 \rightarrow \underset{\mathbf{6a}}{Ph_4B_3N_3H_2Li_2(OEt_2)_2} + PhH \quad (7)$$

When **1** was allowed to react with LiPh in a 1:2 ratio in diethyl ether, both addition and deprotonation of **1** occurred within a single molecule of **1** to give $[Ph_4B_3N_3H_2Li]$-Li. The compound was isolated as its bis(diethyl ether) solvate, $Ph_4B_3N_3H_2Li_2(OEt_2)_2$, **6a**, which readily looses most of its diethyl ether in vacuo. This compound can be transferred like **6b** into its tris(THF) complex **6c**, but single crystals of good quality were obtained only by its preparation according to Equations (3) and (4). This compound is also formed when the ratio of **1**/LiPh was increased up to 1:4 (as shown by ^1H and ^{11}B NMR spectroscopy). However, when this ratio was increased to 1:6 then a new compound **8** (see Scheme 1) could be isolated. This compound proved

 © 2005 Wiley-VCH Verlag GmbH & Co. KGaA, Weinheim

to be the triply deprotonated borazine **1**, $Ph_3B_3N_3(Li{\cdot}OEt_2)_3$, stabilized by 3 equiv. of $LiPh(OEt_2)$ [Equation (8)].

$$Ph_3B_3N_3H_3 + 6\ LiPh + 6\ OEt_2 \rightarrow \underset{\mathbf{8}}{Ph_3B_3N_3Li_3(OEt_2)_3{\cdot}(LiPh{\cdot}OEt_2)_3} \quad (8)$$

The conclusion that we can draw is that a detailed study of the behaviour of borazines $R_3B_3N_3H_3$ with active organylmetal compounds offers an interesting new area of research akin to metal aryls.

Molecular Structures

Although single crystals were obtained of the new compounds [with the exception of **6a** and **6b** most of them showed only weak diffracting power even at low temperature (–80 °C)]. The molecular structures of compounds **2** to **8** are depicted in Figures 1–6, and relevant bonding parameters of B_3N_3 rings are presented in Tables 1 and 2. Two types of B_3N_3 rings can be compared: (a) *N*-lithioborazines in compounds **2** and **7**, with **6c** as a special case; and (b) lithioborazinates containing a tetracoordinated boron atom as found in compounds **3**, **5**, **6c** and **7**. For all cases the numbering in the figures starts with N1 (or the analogous atom N4 in combined borazines/borazinates or if two independent molecules are present in the unit cell) carrying one or two Li atoms. Atoms B2 (and/or B5) stand in *para* position to N1 (N4). In the case of the borazinates, B2 (and/or B5) are tetracoordinate B atoms. For centrosymmetric dimers only the asymmetric unit will be discussed in addition to the bonds from the Li atom that bridges the two rings. However, when there are two independent molecules in the unit cell, then the data of only one of them will be described provided that there are no strong deviations in the bonding parameters. This is, for instance, the case for **6c**. A selection of additional parameters is listed in the captions to the figures. While most of the observed Li–N distances were found in the range of 2.0 to 2.3 Å there are also short Li–B distances (2.2–2.4 Å) that we take as Li–B bonds. Li–B distances that are larger than 2.5 Å were considered to be nonbonded distances.

Compound **2** (see Figure 1) is a molecular complex of LiI with the *N*-lithioborazine $Ph_3B_3N_3H_2Li$. Each of the Li atoms is coordinated to one molecule of TMEDA, respectively. The LiN_2 planes of the tmeda ligands at Li1 and Li2 stand almost perpendicular to one another. The four N–Li–N bond angles at atom Li2 range from 84.2(2) to 116.3(2) indicating a distorted tetrahedral array. The Li2–I1 distance is 2.769(5) Å, similar to that found for $LiI(thf)_3$ [2.741(7) Å] [6] or LiI(pmdta) [2.75(3), 2.67(3) Å][7] while compound $[(tmeda)_2Li]I$ has an ionic structure.[8] Atom Li1 of **2** is

Table 1. Bond lengths [Å] and bond angles [°] of compounds **2** and **7** containing a $Ph_3B_3N_3H_2Li$ unit. Values for **7a/7b** refer to the two independent molecules in the unit cell. Numbering scheme for **7b** refers to the equivalent atoms in **7a**.

	N1–B1	B1–N2	N2–B2	B2–N3	N3–B3	B3–N1	N1–Li1
2	1.421(3)	1.449(5)	1.419(4)	1.423(4)	1.445(3)	1.425(3)	1.999(5)
7a*	1.423(5)	1.440(5)	1.419(5)	1.415(5)	1.443(5)	1.435(5)	1.991(7)
7b*	1.432(6)	1.431(5)	1.423(6)	1.419(5)	1.434(5)	1.442(6)	2.000(7)
	B1–N1–B3	N1–B1–N2	B1–N2–B2	N2–B2–N3	B2–N3–B3	N3–B3–N1	Li1–N1–Li2
2	117.4(2)	120.4(2)	122.9(2)	115.4(2)	122.9(9)	120.3(2)	104.9(2)
7a*	117.3 (3)	120.7(3)	122.6(3)	115.4(3)	122.8(3)	120.7(3)	130.2(3)
7b*	117.0(4)	121.5(3)	122.4(4)	115.3(4)	123.6(3)	119.8(4)	126.3(3)

Table 2. Bond lengths [Å] and bond angles [°] of compounds containing a lithium tetraphenylborazinate unit. Values for **5a/5b** and **7a/7b** refer to the independent molecules in the unit cell.

	N1–B1	B1–N2	N2–B2	B2–N3	N3–B3	B3–N1
3	1.444(5)	1.407(5)	1.559(5)	1.574(5)	1.421(5)	1.439(5)
5a*	1.458(3)	1.407(3)	1.566(3)	1.587(4)	1.419(3)	1.442(3)
6c	1.442(4)	1.425(4)	1.555(4)	1.549(4)	1.430(4)	1.434(4)
	N4–B4	B4–N5	N5–B5	B5–N6	N6–B6	B6–N4
5b*	1.455(3)	1.411(3)	1.602(3)	1.599(4)	1.396(3)	1.459(3)
7a**	1.423(5)	1.414(5)	1.560(5)	1.564(5)	1.425(5)	1.433(5)
7b**	1.429(6)	1.410(6)	1.569(5)	1.563(5)	1.411(5)	1.442(5)
	B1–N1–B3	N1–B1–N2	B1–N2–B2	N2–B2–N3	B2–N3–B3	N3–B3–N1
3	121.4(3)	117.1(4)	125.3(3)	104.0(3)	122.5(3)	118.4 (3)
5a*	119.0(2)	118.4(2)	125.9(2)	106.6(2)	125.9(2)	118.1(2)
6c	115.9(2)	121.4(3)	123.8(2)	102.3(2)	124.3(2)	121.8(3)
	B4–N4–B6	N4–B4–N5	B4–N5–B5	N5–B5–N6	B5–N6–B6	N6–B6–N4
5b*	120.2(2)	117.1(2)	124.5(2)	106.9(2)	127.2(2)	118.2(2)
7a**	122.8(4)	116.6(4)	123.6(3)	102.2(3)	124.4(3)	116.8(3)
7b**	122.6(3)	116.9(′3)	124.4(4)	102.2(3)	123.7(3)	116.7(3)

 © 2005 Wiley-VCH Verlag GmbH & Co. KGaA, Weinheim

tricoordinate and is located in a planar environment of three N atoms (sum of bond angles = 359.8°). Quite unusual is the very open N1–Li1–N4 bond angle of 166.5(3)°. This arrangement seems to be due to a weak dipolar interaction of Li1 with I1. The Li1···I1 distance is 3.78 Å. A comparatively sharp bond angle is observed for Li1–N1–Li2 with 104.9(2)°.

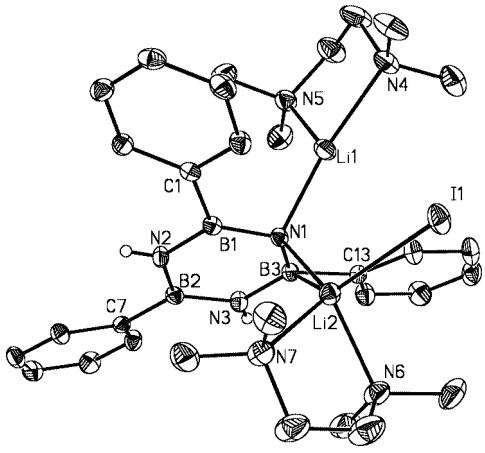

Figure 1. ORTEP plot of the molecular structure of **2**. Thermal ellipsoids are represented at a 25% probability scale. Selected bond lengths [Å] and angles [°]: B1–C1 1.595(4), B3–C13 1.598(4), B2–C7 1.582 (4), Li1–N1 1.999(5), Li1–N4 2.148(5), Li1–N5 2.140(6), Li2–N1 2.094(5), Li2–N6 2.152 (5), Li2–N7 2.223(5), Li2–I1 2.769(5), Li1···Li2 3.245(7). Li1–N1–Li2 104.9(2), B1–N1–Li1 107.3(2), B3–N1–Li1 111.6(2), B1–N1–Li2 109.5(2), B3–N1–Li2 105.3(2), N5–Li1–N4 85.3(2), N1–Li1–N5 108.2(2), N1–Li1–N4 166.5(3), N1–Li2–N6 126.2(2), N1–Li2–N7 116.3(2), N6–Li2–N7 84.2(2), B1–C1–C2 120.9(2), B2–C7–C8 121.7(2), C8–C7–C12 116.4(2), B3–C13–C14 122.6(2), C18–C13–C14 115.9(2). Torsion angles [°]: B2–N2–B1–C1 173.4, B2–N3–B3–C13 171.2, C8–C7–B2–N2 –20.7.

The geometry of the $Ph_3B_3N_3H_2Li$ unit is close to that found for $Me_3B_3N_3H_2Li$.[1] The borazine ring is not planar as shown by an interplanar angle of 7.4° for B1N1B3/B1N2N3B3. Angles B1–N1–B3 and N2–B2–N3 are smaller than 120° with 117.4(2)° and 115.4(2)° while all other endocyclic bond angles are 120° or a few degrees larger (see Table 1). Thus, the borazine unit is elongated along the N1···B2 vector. Typical are the B1–N2 and N3–B3 bonds which are elongated with respect to all the other B–N bonds. The phenyl groups are arranged in a propeller-like fashion and form torsion angles with the borazine ring of 14.7, 18.3, and 19.3° at atoms B3, B1 and B2 respectively, i.e. they are less twisted than in the parent compound **1**.

An *N*-lithioborazine unit is also present in compound **7** which is a borazine borazinate (see Figure 2a). Its two B_3N_3 rings are joined by atom Li2 coordinated to three N and two B atoms of the two rings while the second lithium atom (Li1) is coordinated to the N1 atom and two diethyl ether molecules.[9] The *N*-lithioborazine part (N1 to B3, N1A to B3A) is planar and stands almost parallel to the N4B4N5N6 plane of the borazinate unit (interplanar angle = 5.2°). Quite open are the Li1–N1–Li2 and N1–Li2–N6 bond angles with 126.2(3)° and 136.4(3)°, respectively. As shown in Table 1, the molecular parameters of the borazine ring are similar to those of compound **2**. The bonding, however, is drastically different in the borazinate unit due to the presence of the tetracoordinate B5 atom. This has the consequence that the B_3N_3 ring deviates strongly from planarity and adopts a tub shape with the B5 and N4 atoms pushed outside of the ring plane B4N5N6B6. Interplanar angles are N6B5N5/N6B6N5B4 = 31.3° and B6N4B4/B6N6B4N5 = 6.1°. This distortion of the borazine ring into a tub shape is obviously not only the consequence of the presence of the tetracoordinate B5 atom but also a consequence of the fact that the Li2 atom coordinates to N5 and N6 of the borazinate ring and to N1 of the borazine unit with Li2–N5, Li2–N6 and Li2–N1 distances of 2.157(7), 2.187(7) and 2.250 (6) Å, respectively. The sum of the bond angles at atom Li1 is 353.6° while it is 334.7° for atom Li2 (to atoms N1, N5, and N6) which joins the two B_3N_3 rings. There are two independent molecules in the unit cell. Figure 2b) depicts the core structures of the two independent molecules of **7** which are rather similar. There are no Li–Li bonding interactions.

Compound **3** crystallizes in two isomeric forms as a lithium tetraphenylborazinate (see Figure 3a,b). Its essential bonding parameters are listed in Table 2. As found for the borazinate part in compound **7** the Li atom coordinates with N atoms of the ring adjacent to the tetracoordinate B atom. In this case the atom Li1 is pentacoordinate by five N atoms, e.g. there are three Li–N bonds to the tmta molecule which range from 2.170 to 2.202(6) Å, while those to the borazinate atoms N2 and N3 are 2.222(6) and 2.184(7) Å, respectively. In addition Li1 coordinates also to atom C7. Figure 3b shows the core structure of compound **3** demonstrating that its Li atom is in an interesting coordinative situation as four N atoms and the Li atom form a plane while atoms N5 and C7 lie outside of this plane. This results in a strongly distorted octahedral coordination of the Li1 atom [bond angles: B2–Li1–C13 178.3(4), N3–Li1–N6 174.9(3), C7–Li1–N5 169.8(3), N2–Li1–N4 172.5(3), C7–Li1–N4 107.3(3), C7–Li1–N6 106.6(3)].

The sum of bond angles at atoms B1 and B3 is 360°. Nevertheless, the B_3N_3 ring in **3** is no longer planar and adopts like the corresponding ring in **5** a tub conformation with interplanar angles B2B3N3/N2B2B1N3 of 27.1°, and B1N1N2/N2B2B1N3 of 11.9°. All endocyclic bond angles at the B atoms are smaller than 120° while those at the N atoms are larger. B–N and B–C bonds to the tetracoordinate atom B2 are longer than those to the tricoordinate atoms. A new feature is that the B–N bonds next to the B2–N bonds are shorter than those to atom N1. This distinguishes the borazinates from the *N*-lithioborazines, and this has also been observed for the borazinates **3**, **5**, and **6c**, although the latter is a special case.

The borazinate **5** shows almost the same features as compound **3**. Once again there are two independent molecules in the unit cell which differ by the coordination of the Li atoms. These two molecules are shown in Figure 4a,b. In molecule **5a** the Li1 atom coordinates to the O atom of

 © 2005 Wiley-VCH Verlag GmbH & Co. KGaA, Weinheim

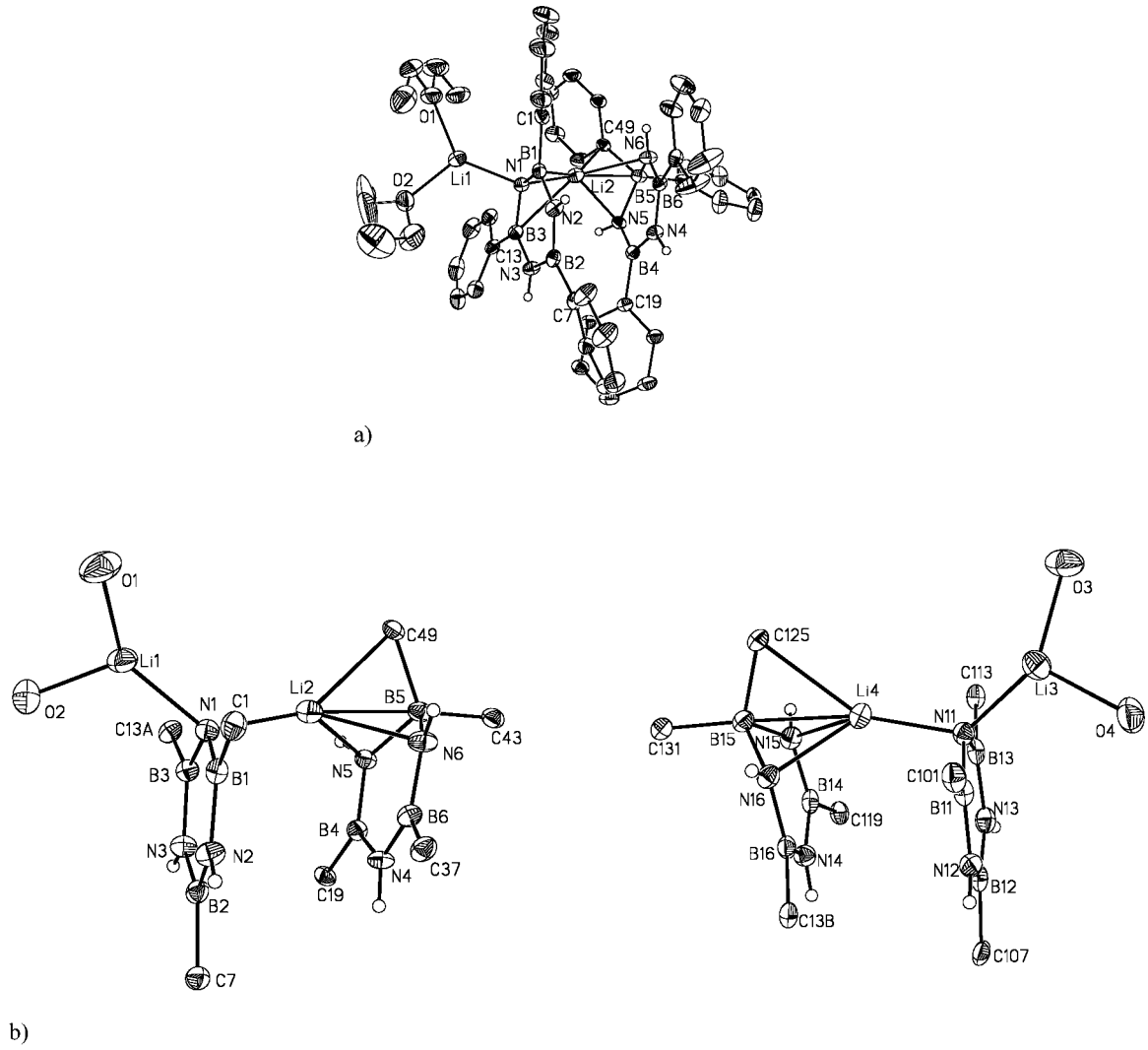

Figure 2. (a) Molecular structure of compound **7**. Thermal ellipsoids are represented at a 25% probability scale. Selected bond lengths [Å] and angles [°]: O1–Li1 1.961(7), O2–Li1 1.968(9), N1–Li1 1.991(8), N1–Li2 2.025(8), N5–Li2 2.178(7), N6–Li2 2.213(8), B5–Li2 2.298(8), C49–Li2 2.416(7), O3–Li3 1.941(9), O4–Li3 1.950(9), N11–Li3 2.000(8), N11–Li4 2.012(7), N15–Li4 2.180(7), Li–N16 2.158(7), B1–C1 1.653(6), B1–C7 1.636(5), B2–C13 1.576(6), B3–C19 1.595(5), B4–C25 1.584(6), B5–C31 1.602(5), B6–C37 1.581(6), B7–C43 1.644(6), B7–C49 1.648(5), B8–C55 1.589(5), B9–C61 1.573(5), B10–C67 1.598(5), B11–C73 1.574(5), B12–C79 1.583(5), B1–C1 1.602(5), B2–C7 1.584(6), B3–C13 1.581(6), N4–C19 1.576(6), B5–C25 1.653(6), B5–C37 1.595(5), B5–C31 1.636(5), B6–C37 1.5895(5). O1–Li1–O2 104.6(4), O1–Li1–N1 111.9(4), O2–Li1–N1 137.1(4), N1–Li2–N5 131.3(4), N5–Li2–N6 67.3(2), N1–Li2–N6 136.1(3), Li1–N1–Li2 126(3), B1–N1–Li1 100.3(3), B1–N1–Li2 95.4(3), B3–N1–Li1 116.5(3), B1–N1–B3 117.0(3). Interplanar angles [°]: B1N2B3N3/B1N1B3 4.5, B1N2B3N3/N2B2N3 5.2, B1N2B3N3/C18C13C14 19.3, B1N2B3N3/C7C8C12 19.9, B1N2B3N3/C C16C 26.3; B4N5N6B6/B4N4B6 33.2, B4N5N6B6/N5B5N6 26,7, B4N5N6B6/C20C19C24 69.5, B4N5N6B6/ C38C37C42 16.7, N5B5N6/C44C43C48 90.5, N5B5N6/ C50C49C54 52.5. Second molecule: B11N12N13B13/B1111B13 2.7, B11N12N13B13/N12B23N13 4.7, B11N12N13B13/C102C101C106 150.2, B11N12N13B13/C108C107C112 14.8, B11N12N13B13/C114C113C118 6.9. (b) The core structure of the two independent molecules of **7**.

the diethyl ether molecule and to two N atoms next to the tetracoordinate B atom of the borazinate ring. In addition there is a weak Li–C interaction. While the Li2 atom of the second isomer shows less symmetry because the Li–N bonds involve not only one N atom next to the tetracoordinate atom B5 but also one to atom N4.

Compound **6c** (see Figure 5) is a special case because it combines both a borazinate and a deprotonated N atom within a single borazine ring. It crystallizes from THF as $Ph_4B_3N_3H_2Li_2(thf)_3$. This molecule is present in the solid state as a dimer where the Li atom of the two borazinate units binds the two rings together each forming three Li–N bonds. Therefore, all ring nitrogen atoms are involved in bonding. Both independent Li atoms (Li1 and Li2) show tetracoordination. The Li atom of the *N*-lithioborazine part is coordinated to the N1 atom of its ring and three O atoms of the THF molecules. Figure 5a shows the dimeric molecule (for clarity two phenyl groups are depicted only by their *ipso*-C atoms) while Figure 5b depicts the disorder of two of the three THF molecules.

In all compounds with a borazinate unit there are Li···B interactions. In **5** the shortest Li–B contact is Li1–B2 with

 © 2005 Wiley-VCH Verlag GmbH & Co. KGaA, Weinheim

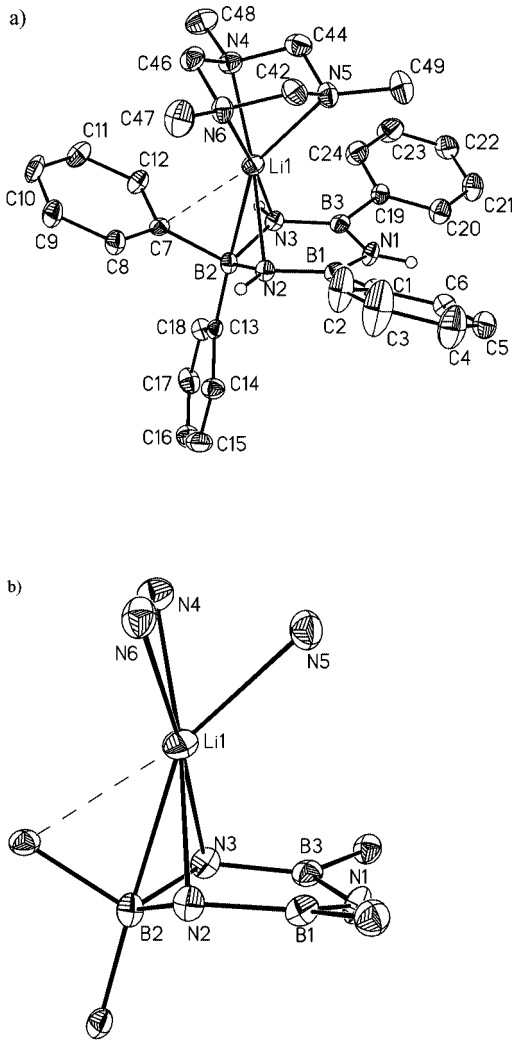

Figure 3. (a) ORTEP plot of the molecular structure of **3**. Thermal ellipsoids are represented at a 25% probability scale. Selected bond lengths [Å] and angles [°]: Li1–N2 2.186(7), Li1–N3 2.235(7), Li1–N4 2.165(7), Li1–N5 2.188(7), Li1–N6 2.196(7), Li1–C7 2.453(7), B1–C1 1.580(5), B2–C7 1.650(5), B2–C13 1.630(6), B3–C19 1.585(6). N2–Li1–N4 172.5(3), N2–Li1–N5 118.3(3), N2–Li1–N6 109.5(3), N3–Li1–N4 117.1(3), N3–Li1–N4 117.0(3), N3–Li1–N5 120.6(3), N3–Li1–N6 174.9(4), N4–Li1–N5 65.1(2), N4–Li1–N6 65.1(2), N5–Li1–N6 64.5(2), N1–B1–C13 119.8(3), N2–B1–C1 122.9(3), N2–B2–C7 109.6(3), N2–B2–C13 112.0(3), C7–B2–C13 107.2(3), N3–B3–C19 121.8(3), B1–N2–Li1 98.1(3), B2–N3–Li1 72.5(2), B2–N2–Li1 74.2(3), B3–N3–Li1 99.6(3). Torsion angles [°]: N1–B1–N2–B2 11.2, B1–N2–B2–N3 –32.4, N2–B2–N3–B3 35.2, B2–N3–B3–N1 –17.7, N3–B3–N1–B1 –10.6, B3–N1–B1–N2 13.8. Interplanar angles [°]: B1N2B3N3/B1N1B3 10.9, B1N2B3N3/N2B2N3 27.4, B1N2B3N3/C6C1C2 22.1, B1N2B3N3/C8C7C12 68.8, B1N2B3N3/C14C13C18 77.1, B1N2B3N3/C20C19C24 23.6. (b) Core structure of compound **3** showing the geometry around the Li1 atom.

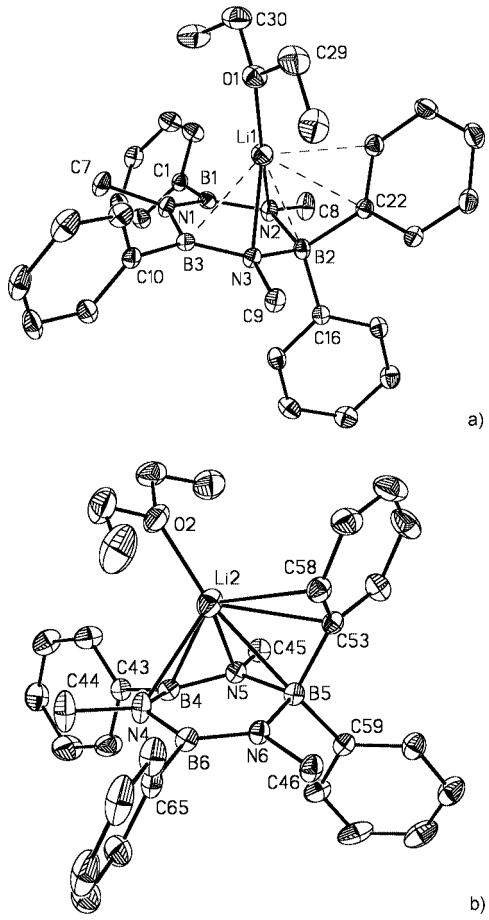

Figure 4. (a) ORTEP plot of one of the two isomeric molecules of compound **5a**. Thermal ellipsoids are represented at a 25% probability scale. Selected bond lengths [Å] and angles [°]: Li1–O1 1.928(4), Li1–N1 2.167(5), Li1–N2 2.349(4), Li1–N3 2.518(5), Li1–B2 2.652(5), Li1–B3 2.420(5), Li1–C4 2.454(5), Li1–O1 1.928(5), B1–C1 1.587(4), B2–C16 1.632(4), B2–C22 1.665(3), B3–C10 1.584(3). O1–Li1–N1 120.5(2), O1–Li1–N2 157.4(3), O1–Li1–N3 134.2(3), N1–Li1–N2 60.6(1), N1–Li1–N3 62.8(1), N2–Li1–N3 67.9(1). Interplanar angles [°]: B1N2N3B3/B1N1B3 14.0, B1N2N3B3/N2B2N3 10.8. B1N23N3B3/C1C2C6 120.0, B1N2N3B3/C10C11C15 107.4, B1N23N3B3/C16C17C21 91.5, B1N2N3B3/C22C23C27 117.4. (b) The structure of the second isomer of compound **5b**. Selected bond lengths [Å] and angles [°]: Li2–N4 2.143(6), Li2–N5 2.426(3), Li2–B4 2.485(6), Li2–B5 2.400(5), Li2–C53 2.414(6), Li2–C58 2.399(6), B4–C43 1.587(4), B5–C53 1.662(4), B5–C59 1.628(4), B6–C65 1.569(4). O2–Li2–N4 114.6(2), O2–Li2–N5 136.5(3), N4–Li2–N5 64.4(2), N4–B4–Li2 73.4(2), N5–B4–Li2 62.2(2), B4–N4–Li2 71.5(2), B4–N5–Li2 82.2(2). Interplanar angles [°]: B4N4N6B6/B4N4B6 10.7, B4N5N6B6/N5B5N6 2.8.

2.314(8) Å, in **6c** the Li–B distances are 2.342(8) Å for Li1–B2, 2.213(3) for Li1–B3, 2.400(5) for Li2–B4, and 2.485(6) Å for Li2–B5, while the distance Li2–B3a is 2.701(6) Å. Moreover, in compound **3** the shortest Li–B distances are Li2–B5 with 2.298(8) and Li4–B15 2.277(8) Å; all other Li–B distances are larger ranging from 2.583 to 2.694(4) Å. Taking these distances into account there are obviously η-(BN)Li interactions in these compounds similar to the Li–C interactions of aryllithium compounds.[10] However, in contrast to $(Et_3B_3N_3Me_3)Cr(CO)_6$[11] with its puckered borazine ring, the B_3N_3 rings deviate either only slightly from planarity or adopt a tub or a twist conformation for borazinates. Thus, the *N*-lithioborazines and borazinates are structurally quite different compared to aryllithium compounds.

 © 2005 Wiley-VCH Verlag GmbH & Co. KGaA, Weinheim

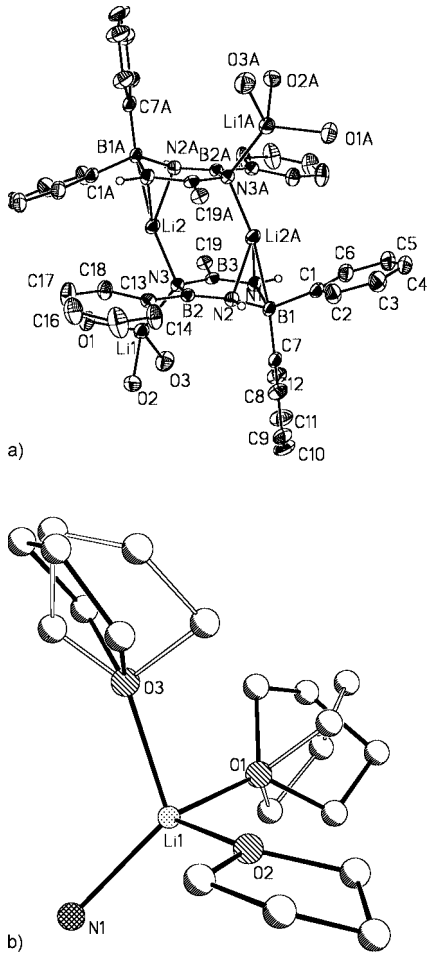

Figure 5. (a) Molecular structure of compound **6c**. Thermal ellipsoids are depicted on a 25% probability scale. Only the *ipso*-C atoms of the phenyl groups are shown for clarity. Selected bond lengths [Å] and angles [°]: Li1–O1 1.977(6), Li1–O2 2.024(6), Li1–O3 2.084(6), Li1–N1 2.073(6), Li2–N1 2.003(6), Li2–N2A 2.137(6), Li2–N3A 2.169(6), Li2···Li2A 3.29(1), Li2A–B1 2.641(6), Li2–B1A 2.311(6), B1–C1 1.601(4), B2–C7 1.635(5), B2–C13 1.652(5), B3–C19 1.603(4). O1–Li1–O2 103.9(3), O1–Li1–O3 95.9(2), O2–Li1–O3 95.3(3), N1–Li1–O1 124.1(3), N1–Li1–O2 113.1(3), N1–Li1–O3 119.7(3), N1–Li2–N2A 132.5(3), N1–Li2–N3A 135.0(3), N2A–Li2–N3A 68.3(2), Li1–N1–Li2 118.3(2), B1–N1–Li1 111.2(2), B3–N 1–Li1 107.0(2), B1–N1–Li2 101.5(2), B3–N1–Li2 103.0(2). Interplanar angles [°]: B1N1N3B3/B1N1B3 2.6, B1N1N3B3/N2B2N3 27.8, B1N1N3B3/C19C20C24 12.9, B1N1N3B3/C2C1C6 7.6, N2B2N3/C14C13C18 50.5, N2B2N3/C8C7C12 125, C13C14C18/C8C7C12 75.5. (b) Plot of the disordered THF molecules in compound **6c**.

Finally, Figure 6 represents the molecular structure of compound **8**. Several crystals were subjected to data collection, but all of them diffracted very weakly even when fairly large crystals were used. Therefore, we will not discuss any bonding parameters, but use the result of the "best" crystal structure solution (R_1 = 16.2%) to show its rather unusual structure which can be looked at as a triply *N*-lithiated 2,4,6-triphenylborazine stabilized by three molecules of phenyllithium. Each Li atom binds to one diethyl ether molecule.

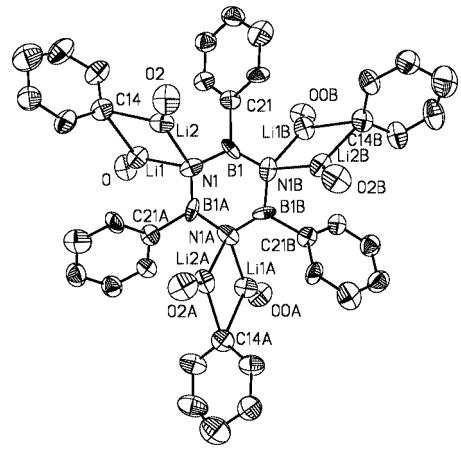

Figure 6. ORTEP plot of the molecular structure of compound **8**. Thermal ellipsoids represent a 25% probability. Selected bond lengths [Å] and angles [°]: Li1–O1 1.96(2), Li1–N1 2.03(2), Li1–C14 2.15(2), Li1···Li2 2.35(2), Li2–O2 1.92(2), Li2–N1 2.02(9), Li2–C14 2.22(2), Li2···B1 2.71(2), B1–N1 1.43(1), B1–N1B 1.46(1), B1–C14 1.63(2), B1···Li1B 2.60(2), N1–B1A 1.46(1). O1–Li1–N1 132(1), O1–Li1–C14 110.8(9), N1–Li1–C14 113.4(9), O2–Li2–N1 127.4(9), O2–Li2–C14 117(1), N1–Li2–C14 110.7(8), N1–B1–N1B 126(1), N1B–B1–C21 117.(1), B1–N1–B1A 114(1), B1–N1–Li2 103(1), B1–N1–Li1 137.0(8), Li1–N1–Li2 71.0(7), B1A–N1–Li2 136.5(9), B1A–N1–Li1 95.2(9), Li1–C14–Li2 64.9(7). Interplanar angles [°]: B_3N_3/C1C2C6 39.9, B3N3/N1Li1Li2 53.8, N1Li1Li2/C14C15C19 90.0, C7Li1Li2/C14C15C19 90.0.

NMR and IR Spectra

^{11}B NMR spectroscopic data allow a clear distinction between *N*-lithioborazines and lithium borazinates (see Tables 3 and 4). For the former, the ^{11}B resonance is practically the same as for **1** with somewhat broader line widths. For **2** a slightly better shielded ^{11}B nucleus is observed although two kinds of tricoordinate B atoms might have been detected. This suggests that either this molecule is fluxional in solution or that the shift difference between the boron atoms B1 and B3 that are adjacent to the deprotonated nitrogen atom N1 and to the boron atom B2 is marginal. We prefer this latter alternative as two kinds of phenyl groups are observed both in the ^{13}C and ^{1}H NMR spectra. The borazinates, however, show two ^{11}B NMR signals in a 1:2 ratio for the tetracoordinate B2 atoms and the tricoordinate B1 and B3 atoms. The latter are in general slightly better shielded – by about 1 ppm – than those of the parent compound **1**. As expected, the ^{11}B NMR signal of the tetracoordinate B2 atoms are observed at lower frequencies with δ^{11}B at about –5 ppm. They also show much sharper signals compared to the tricoordinate B atoms (Table 3 and Table 4).

The ^{7}Li resonances indicate that the structures found for the solid state are retained in solution as compounds **2**, **6**, and **7** show two different ^{7}Li NMR signals. We assign the signals in the higher field (in the range of 0.9 to –0.39 ppm) to the "terminal" Li atoms while those in the range from 1.58 to 2.4 ppm are assigned to those of the borazinates where the Li atom binds to the borazinate nitrogen atoms.

There are two sets of signals for the C atoms of the phenyl groups bound to B1/B3 and B2 atoms in compounds

 © 2005 Wiley-VCH Verlag GmbH & Co. KGaA, Weinheim

Table 3. Chemical shifts for ^1H, ^7Li, and ^{11}B NMR of compounds **1**–**7** (in C_6D_6; ppm) and line widths in brackets [Hz].

	δ^1H(NH)	B–Ph			δ^{11}B	δ^7Li
		ortho	*meta*	*para*		
1	5.89	7.53	7.28	7.29	34.8	
2	5.70	7.74 (B-2)	7.26 (B-2)	7.34 (B-2)	34.1	2.4 [50]
		7.91 (B-1,3)	7.31 (B-1,3)	7.38 (B-1,3)	350	
3	4.77 (N-2,3-H)	7.95 (B-2)	6.80 (B-2)	7.58 (B-2′)	–5.2 [150]	2.1 [40]
	5.81 (N-1-H)	8.03 (B-2)	6.95 (B-2′)	7.65 (B-2)	33.1 [400]	
		8.11 (B-1,3)	7.15 (B-1,3)	7.86 (B-1,3)		
4	2.72 (NMe)		7.2–7.9			
5	2.49 (N-2,3-Me)	7.35 (B-1,3)	7.13 (B-1,3′)	7,25 (B-2′)	1.9 [130]	2.1 [40]
	2.71 (N-1-Me)	7.59 (B-2,2)	7.17 (B-2)	7.26 (B-2)		
			7.19 (B-2)	7.30 (B-1,3)		
7	4.64 (2′,3′-H)		6.94–7.58		–4.6 [170]	0.9 [80]
	5.57 (N-2,3-H)				33.5 [360]	2.4 [120]
	5.74 (N-1′-H)					
6a	5.78 (br.)	7.51 (B-2)	6.93 (B-2)	7.21 (B-2)	–5.9 [130]	–0.39 [150]
		7.71 (B-2′)	6.99 (B-2′)	7.27 (B-2′)	36.8 [800]	3.0 [150]
		8.02 (B-1,3)	7.10 (B-1,3)	7.42 (B-1,3)		
6c	5.78 (br.)	7.55 (B-2)	6.95 (B-2)	7.29 (B-2)	–3.5 [170]	–0.39 [40])
		7.71 (B-2′)	7.19 (B-2′)	7.33 (B-2′)	34.2 [400]	1.58 [10]
		7.73 (B-1,3)	7.25 (B-2,4)	7.49 (B-1,3)		
8	–	7.70 (B)	6.87 (PhB)	7.35 (BPh)	39.6 [800]	2.9 [190]
		8.01 (PhLi)	7.15 (PhLi)	7.21 (PhLi)		
PhLi		8.01	6.96	7.01		

Table 4. ^{13}C chemical shifts of the phenyl groups attached to the boron atoms of compounds **2**–**7** (in C_6D_6); B^{13}C carbon signals have not been observed.

	δ^{13}C(PhB)	
1	128.4, 130.1, 132.4	
2	B-2	B-1,3
	127.9, 128.5, 132.3	128.0, 128.8, 132.6
3	B-2	B-1,3
	127.6,127.8,129.0	128.1 130.0, 132.1
	129.8, 131.7, 131.9	
4	B-2	B-1,3
	127.6, 127.9, 128.4	128.3, 128.6, 133.4
	128.5, 131.0, 131.4	
5	B-2,5	B-1,3,4,6
	127.3, 127.4, 129.2,	128.1, 128.3, 129.0,
	128.2, 128.5, 129.3,	130.2, 131.8, 132.1
	131.6, 132.4, 132.5	
6a	B-2	B-1,3
	127.4, 127.5, 128.9,	128.5, 129.9, 132.5
	129.0, 131.9, 132.0	
6c	B-2	B-1,3
	127.3, 127.6, 129.0,	128.4, 129.8, 132.4
	129.1, 131.8, 132.2	
7a,**b**	B-5	B-2
	127.3, 127.4, 129.2	128.2, 128.5, 132.5
	129.3, 131.6, 132.4	B-1,3
	B-4,6	128.3, 129.0, 132.1s
	128.1, 130.2, 131.8	
8	B-Ph	Li-Ph
	127.4, 128.5, 129.0	121.8, 133.5, 143.6, 145.4
PhLi	121.7, 126.7, 127.7	
	143.8	

having an *N*-lithioborazine skeleton while for the borazinates the two phenyl groups at the tetracoordinate boron atom B2 are chemically and magnetically different (see data in Table 3). ^{13}C NMR signals for the boron bonded *ipso*-C atoms could not be observed. This is a well-known phenomenon. The ^{1}H NMR signals of the phenyl groups show the expected ^3J(H,H) coupling with a value of 7 Hz. All NH proton signals are slightly deshielded compared with those of **1**. In the case of the borazinates two broad signals are observed in contrast to a single resonance for the *N*-lithioborazines.

B–N stretching bands of the BN ring modes are found in a range from 1475 to 1370 cm^{-1}. In most cases the band at 1472 cm^{-1} of **1** is shifted to smaller wave numbers indicating a weakening of the B–N bonding.

Discussion and Conclusion

The question of bonding in borazines in comparison to benzene is still not definitely settled[12] and whether borazines are supposed to be antiaromatic or aromatic depends on whether one discusses magnetic properties or bond energies. However, there is consent that borazines are much more reactive than benzene and its derivatives due to the B–N bond polarity. This not only relates to the ready addition of electrophiles to its N atoms but also of nucleophiles to the B atoms, and borazinate formation is a typical example of the latter. In addition, borazines of type $R_3B_3N_3H_3$ are also weak protic acids as was first shown by Wagner and Bradford[2,3] and delineated also in this and the previous study.[1] In the resulting *N*-lithioborazines and lithium borazinates the Li atoms coordinate in most cases to two N atoms of a B_3N_3 ring, but also all three atoms may be used for this purpose (**6c**). The resulting lithium tetraphenylborazinates add LiI or $Ph_3B_3N_3H_2Li$ in a 1:1 ratio (compounds **2** and **7**) or the borazinates may even dimerize (compounds **6** and **7**). Quite unusual is the 1:1 deprotonation and borazinate formation at a single borazine

 © 2005 Wiley-VCH Verlag GmbH & Co. KGaA, Weinheim

ring as found for the 1:2 reaction of LiPh with **1** to give compound **7**. And in the case of the 1:6 ratio of **1** with LiPh even a triple deprotonation was observed, the compound $Ph_3B_3N_3Li_3$, being stabilized by the addition of three molecules of LiPh, **8**. These are reactions unprecedented compared with the behaviour of benzene derivatives.

The ring planarity of the B_3N_3 ring is lost by the formation of the borazinate anion which adopts a tub shape conformation or contains twisted B_3N_3 rings. In these cases, the Li cation coordinates to two or even three ring N atoms. In the latter case, one observes dimerization via two Li bridges between two B_3N_3 rings (**6c** and **7**). Borazinate formation is accompanied with a strengthening of the two B–N bonds adjacent to the tetracoordinate boron atoms, while these bonds are weaker (longer) in the *N*-lithioborazines. This indicates that the electron distribution in these two ring systems is different. Although the monolithioborazines may be looked at as isoelectronic counterparts to aryllithium compounds[9,10] this statement may be far too shortfetched. Observed Li–N and Li–B interactions are not necessarily an indication of η-(NB)Li bonding. In the case of $(Et_3B_3N_3Et_3)Cr(CO)_3$, this type of interaction has been disputed because the borazine ring is puckered and the CO bonds are close to linearity with the Cr–C bonds.[13] However, a more recent theoretical treatment of the bonding in borazine tricarbonylchromium compounds is in favour of π-bonding.[14] One argument given is that the puckering of the ring is only weak and not comparable with a hexahydrotriazine.

The *N*-lithioborazines are also structurally not close to the $Cr(CO)_3$ complexes of borazines.[11] None of the compounds contain a Li atom that sits symmetrically above the B_3N_3 ring plane. An approximation is, however, found in one of the two isomers of **5** but two of its three Li–B distances are >2.5 Å. Thus, the structural chemistry of *N*-lithioborazine and lithium borazinates is unique which is, of course, due to the B–N bond polarity of the borazine ring system. One may try, however, to find similarities between the structures of *N*-lithioborazines and lithium carboranates.[15,16] In the latter class of compounds the solvated Li cation may be coordinated to a B–B, B–C or a C–C bond or to an open face of the carborane as found for *closo-exo*-5,6-[μ-H_2Li(thf)$_2$][1-Li(thf)$_2$-2-(Me_3Si)-3-(R)-2,4-(Me_3Si)-2,4-$C_2B_4H_4$] (R = $SiMe_3$, Me).[17] In this complex, one Li cation sits on top of an open C_2B_3 face while the second is bonded sidewise to a B–B bond. This lithium carboranate on reaction with YCl_3 produces the complex [Li(thf)$_4$]{(1-Cl-1-H_6)-2,2′,3,3′(Me_3Si)$_4$-4,4′,5,5′-Li(thf)[1,1′-*commo*-Y(2,3-$C_2B_4H_4$)$_2$]}[18] where the Li cation of the yttriate coordinates to four B atoms (2 each per carborane unit) with Li–B distances of 2.31(4), 2.27(4), and 2.49(4) Å. In the starting material the Li–B distances are Li1–B3 2.291(9), Li1–B4 2.371(9), and Li1–B5 2.237(10) Å.[17] A totally different situation results for the lithium salt of the triboracyclobutane dianion {[Me_3Si(CH_2SiMe_3)B][B(duryl)]$_2$}$^{2-}$ where both THF-solvated Li cations coordinate to two boron atoms of the BBB triangle with Li–B distances of 2.309(5), 2.325(5) for the Li(thf) group and 2.323(5) and 2.529(5) Å for the Li(thf)$_2$ unit. The Li atom lies almost in the B_3 plane.[19] Reduction of the six-membered [MeB(CHMe)]$_3$ by Li metal in diethyl ether or THF occurs in several steps leading finally to an *arachno*-borane structure for [MeBCH(Me)-Li]$_3$.[20] In this molecule the Li atoms bridge to basal adjacent C atoms but binds also to B atoms with distances ranging from 2.239(6) and 3.251(6) Å. Li–C bond lengths are somewhat longer at 2.247–2.456(6) Å.

Obviously, there are no close similarities between *N*-lithioborazines and lithium carboranates, the closest ones are those in which a Li atom coordinates to two borazine rings or to two open faces of two carborane anions. η^6-Coordination of an *N*-lithioborazine results in one of the isomers of compound **5**, but only when relatively long Li–N and Li–B distances are included. Carborane anions usually offer a pentagonal face as the most basic site for Li coordination while in *N*-lithioborazines Li–N coordination prevails. This situation may change for the following five-membered rings (Scheme 2) which on deprotonation may behave more like the carboranes.

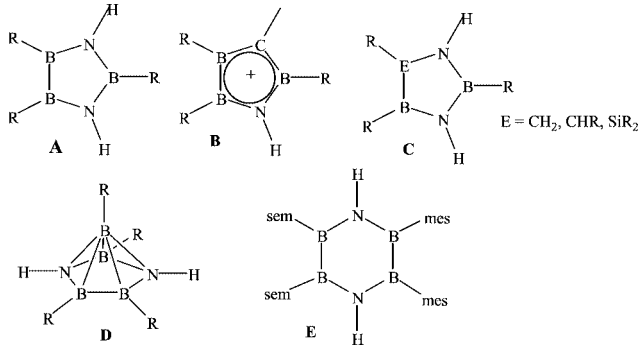

Scheme 2.

Moreover, the deprotonation of the *arachno*-diazahexaborane and/or its classical isomer, 1,4-diazatetraborinane should provide interesting examples for studying the relationships between carboranes offering a B_3C_2 open face and its isoelectronic BN analogue.

Experimental Section

General Remarks: All experiments were carried out using standard Schlenk techniques under argon. Organyllithium compounds were obtained as diethyl ether or hexane solutions from Chemetall AG. Solvents were dried and distilled under nitrogen. NMR spectra were recorded with a Jeol EX00 for ^{1}H, ^{7}Li, ^{11}B, ^{13}C NMR (399.782, 157.48, 128.262, 100.531 MHz, respectively) spectra using $SiMe_4$ and C_6D_6 as internal standards with a 1 M aqueous LiCl solution, or BF_3·OEt_2 as the external standard. A Siemens P4 diffractometer equipped with the low-temperature device LT2 was used for intensity data collection with Mo-K_α radiation and a CCD area detector. Data were recorded at –80 °C.

2,4,6-Triphenylborazine (1):[4,13] Freshly distilled ($Me_3Si)_2NH$ (93.8 mL, 72.6 g, 450 mmol) was dissolved in dichloromethane (250 mL) and the solution cooled to –78 °C. Then $PhBCl_2$ (75.0 g, 472 mmol) was added with stirring. The mixture was then kept at 55 °C for 10 d. Within this period the ^{11}B NMR signal for the

 © 2005 Wiley-VCH Verlag GmbH & Co. KGaA, Weinheim

PhB(Cl)NHSiMee$_3$ (δ^{11} B = 37.6 ppm) vanished and only the signal for **1** was observed (δ^{11}B = 34.8 ppm). All volatiles (CH_2Cl_2, Me_3SiCl) were then removed in vacuo and the residue crystallized from diethyl ether. Yield: 45.4 g, 98%. M.p. 180–185 °C. ^{13}C NMR (C_6D_6): δ = 128.4, 130.1, 132.4 ppm. ^{11}B NMR: δ = 34.8 ppm.

(Tetramethylethylenediamine)lithium–2,4,6-triphenylborazine–(tetramethylethylenediamine)lithium Iodide (2): 1 (1.03 g, 3.34 mmol) was dissolved in diethyl ether (60 mL) at 0 °C. With stirring, a solution of commercial LiMe (containing LiI) in diethyl ether (2.20 mL, 3.52 mmol) and TMEDA (1.0 mL) was added drop wise to the borazine solution. After warming to ambient temperature, the clear solution was stirred for 2 d and then reduced in volume to about 20 mL. At –5 °C colorless prisms separated from the slightly brown solution. Yield: 2.10 g, 92%. M.p. 173–175 °C. ^{1}H NMR (C_6D_6): δ = 2.00 (s, 24 H, NCH_3), 2.14 (s, 8 H, NCH_2) ppm. ^{13}C NMR: δ = 46.0, 58.2 ppm. ^{11}B NMR: δ = 34.1 ($h_{1/2}$ = 350 Hz) ppm. $C_{30}H_{49}B_3IN_7Li_2$ (680.98): calcd. C 52.91, H 7.25, I 18.63, N 14.40; found C 52.86, H 7.13, I 18.51, N 14.22.

(1,3,5-Trimethylhexahydrotriazine)lithium 2,4,4,6-Tetraphenylborazinate (3): 1 (1.17 g, 3.79 mmol) was placed into a flask containing diethyl ether (60 mL). The suspension was cooled to 0 °C. To a solution of LiMe (prepared from Li grains and MeCl in diethyl ether, 4.0 mmol, 2 5 mL, 1.6 M) diluted with diethyl ether (10 mL) was added trimethylhexahydrotriazine (1.1 mL, 7.8 mmol). This LiMe reagent was slowly added dropwise into the diethyl ether solution of **1** at 0 °C. A clear solution resulted which was stirred for 2 d and then reduced in volume in vacuo. On keeping the solution at –5 °C, colorless prisms of **3** separated (1.90 g, 3.63 mmol, 95%). M.p. 91–95 °C. ^{1}H NMR (C_6D_6): δ = 1.95 (s, 9 H, NCH_3), 3.01 (s, 6 H, NCH_2) ppm. ^{13}C NMR: δ = 38.4, 76.6 ppm (azin). ^{11}B NMR: δ = –5.2 ($h_{1/2}$ = 150 Hz), 33.1 ($h_{1/2}$ = 400 Hz) ppm (ratio 1:2). ^{7}Li NMR: δ = 2.1 ($h_{1/2}$ = 40 Hz) ppm. IR (Nujol/Hostaflon; only medium to strong signals): $\tilde{\nu}$ = 3411 m, 3077 m, 3053 m, 3030 m, 3013 m, 2992 m, 2050 m, 2870 m, 2795 m, 2734 m, 2720 m, 2711 m, 1600 m, 1502 st, 1474 st, 1441 vst, 1422 vst, 1408 vst, 1347 m, 1314 m, 1272 st, 1502 st, 1474 st, 1441 vst, 1408 vst, 1347 m, 1314 m, 1272 st, 1195 m, 1157 m, 1118 vst, 1029 m, 1016 st, 939 st, 930 m, 866 m, 762 m, 756 m, 732 st, 704 vst, 671 st, 6521 m, 581 m, 557 m cm^{-1}. $C_{30}H_{38}B_3LiN_6$ (522.06): calcd. C 69.02, H 7.34, N 16.10; found C 68.08, H 7.42, N 15.71.

(Diethyl ether)lithium 1,3,5-Trimethyl-2,4,6,6-tetraphenylborazinate (5): To a stirred solution of $(PhBNMe)_3$, **4**,[13] in diethyl ether (0.304 g, 0.86 mmol, 40 mL) was added at 0 °C a solution of LiPh (0.45 mL, 0.9 mmol) in diethyl ether/cyclohexane (1:1). The resulting clear yellow solution was stirred for 2 d at ambient temperature and then reduced to a volume of ca. 20 mL in vacuo. On storing the solution at –5 °C crystals separated within a few days. Yield: 0.42 g of **5**, 95%. M.p. 165 °C (dec.). ^{1}H NMR (C_6D_6): δ = 0.68 (t, 6 H, CH_2CH_3), 2.49 (s, 6 H, 1,5-NCH_3), 2.71 (s, 3 H, 3-NCH_3), 2.90 (q, 4 H, OCH_2), 7.13 (t, 4 H, *m*-PhB-2,6, $^3J_{H,H}$ = 7.0 Hz), 7.17 (t, 2 H, *m*-PhB-4, $^3J_{H,H}$ = 7.0 Hz), 7.19 (t, 2 H, *m*-PhB, $^3J_{H,H}$ = 7.0 Hz), 7.25 (t, 1 H, *p*-PhB-4, $^3J_{H,H}$ = 7.0 Hz), 7.26 (t, 1 H, *p*-PhB-4′, $^3J_{H,H}$ = 7.0 Hz), 7.30 (t, 2 H, *m*-PhB-2,6, $^3J_{H,H}$ = 7.0 Hz), 7.35 (dd, 4 H, *o*-PhB-2,6, $^3J_{H,H}$ = 7.0, $^4J_{H,H}$ = 1.0 Hz), 7.59 (d, 4 H, *o*-PhB-2,2′, $^3J_{H,H}$ 7.0 Hz) ppm. ^{13}C NMR (C_6D_6): δ = 14.9 (CH_2CH_3), 36.6 (NCH_3), 37.2 (NCH_3), 64.6 (OCH_2) ppm. ^{11}B NMR: δ = 1.9 ($h_{1/2}$ = 130 Hz), 37.2 ($h_{1/2}$ = 400 Hz) ppm. ^{7}Li NMR: δ = 2.1 ($h_{1/2}$ = 40 Hz) ppm. IR (Nujol/Hostaflon; only medium to very strong signals): $\tilde{\nu}$ = 3067 st, 3044 st, 3006 st, 2997 st, 2982 st, 2945 st, 2894 st, 2852 m, 2819 m, 1595 st, 1567 m, 1497 st, 1481 st, 1466 st, 1431 st, 1397 vst, 1368 st, 1355 vst, 1298 vst, 1265 st, 1258 st, 1194 m, 1160 m, 1146 st, 1111 m, 1064 st, 1044 m, 1019 st, 999 m, 912 m, 900 m, 854 m, 845 m, 756 wt, 721 st, 716 st, 704 vst, 621 m, 617 m, 486 m cm^{-1}. $C_{31}H_{39}B_3LiN_3O$ (509.05): calcd. C 73.15, H 7.72, N 8.25; found C 71.88, H 7.73, N 8.16.

Bis(diethyl ether)lithium 2,4,6,6-Tetraphenylborazinate–lithium–2,4,6-triphenylborazine (7): To a stirred solution of **1** (0.858 g, 2.7 mmol) in diethyl ether (50 mL) was slowly added a 2 M solution of LiPh (1.39 mL, 2.78 mmol) in diethyl ether/cyclohexane. The brownish solution was then stirred for 5 d at ambient temperature followed by reduction of its volume to 20 mL in vacuo. The solution was kept at –5 °C. Colorless crystals separated from the slightly brown solution. Yield: 1.05 g of **7**, 91%. M.p. 130–132 °C (dec.). ^{1}H NMR (C_6D_6): δ = 1.07 (t, 12 H, CH_2CH_3, $^3J_{H,H}$ = 7 Hz), 3.20 (q, 8 H, OCH_2, $^3J_{H,H}$ = 7 Hz), 4.64 (br. s, 2 H, N-1′,5′-H), 5.57 (br. s, 2 H, N-3,5-H) 6.94–7.58 (m, 35 H, PhB) ppm. ^{13}C NMR: δ = 15.2 (CH_2CH_3), 65.8 (OCH_2) ppm. ^{11}B NMR: δ = –4.6 ($h_{1/2}$ = 170 Hz), 33.5 ($h_{1/2}$ = 360 Hz) ppm. ^{7}Li NMR: δ = 0.9 ($h_{1/2}$ = 80 Hz), 2.4 ($h_{1/2}$ = 120 Hz) ppm. IR (Nujol, Hostaflon; only medium to very strong bands quoted): $\tilde{\nu}$ = 3446 m, 3430 m, 3074 m, 3049 st, 3009 st, 2997 st, 2977 st, 2931 st, 2898 m, 2862 m, 1599 vst, 1571 m, 1501 vst, 1479 st, 1424 vst, 1399 vst, 1359 m, 1339 m, 1312 st, 1300 m, 1264 m, 874 m, 752 st, 743 m, 705 vst, 663 m, 652 m, 682 m, 515 m cm^{-1}. $C_{50}H_{60}B_6Li_2N_6O_2$ (855.82): calcd. C 70.17, H 7.07, N 9.82; found C 70.95, H 7.89, N 9.43.

Bis(diethyl ether)lithium *N*-Lithio-tetraphenylborazinate (6a): To a stirred solution of **1** (0.640 g, 2.07 mmol) in diethyl ether (60 mL) a solution of LiPh in diethyl ether/cyclohexane (2 M, 2.15 mL, 4.3 mmol) was added dropwise at 0 °C. The mixture was stirred 4 d at ambient temperature. Then its volume was reduced to about 20 mL in vacuo. The brown solution was stored at –5 °C. After a few days, colorless crystals were isolated. Yield: 0.962 g of **6a**, 85%. The same compound was also obtained by treating **1** with 3 or 4 equiv. of LiPh (only tested by ^{11}B NMR). When compound **6a** was kept in vacuo, 1.5 equiv. of diethyl ether was lost. M.p. 140–142 °C. ^{1}H NMR: δ = 1.07 (t, CH_2CH_3, $^3J_{H,H}$ = 7 Hz), 3.20 (q, $^3J_{H,H}$ = 7 Hz, 8 H, OCH_2), 5.78 (br. s, 4 H, HN-1,1′,5,5′) ppm. ^{13}C NMR: δ = 15.3 (CH_2CH_3), 65.7 (OCH_2) ppm. ^{11}B NMR: δ = –5.9 ($h_{1/2}$ = 130 Hz), 36.8 ($h_{1/2}$ = 800 Hz) ppm. ^{7}Li NMR: δ = –0.39 ($h_{1/2}$ = 150 Hz), 3.0 ($h_{1/2}$ = 150 Hz) ppm. IR (Nujol, Hostaflon; only medium to very strong bands quoted): $\tilde{\nu}$ = 3096 m, 3047 m, 2926 m, 1596 m, 1499 m. 1483 m, 1434 st, 1343 vst, br, 1278 st, 1245 m, 1188 m, 1070 m, 1027 m, 851 st, 805 m, 755 m, 737 st, 703 vst, 683 st, 585 m, 491 m cm^{-1}. $C_{52}H_{54}B_6Li_4N_6O$ (891.67) [dimeric mono(diethyl ether) adduct]: calcd. C 71.65, H 6.24, N 9.64; found C 71.39, H 6.27, N 9.03.

Tris(tetrahydrofuran)lithium *N*-Lithio-2,2,4,6-tetraphenylborazinate (6c): *N*,*N*′,*N*′′-trimethylhexahydrotriazine (1.83 g, 14.2 mol) was added to a hexane solution of *n*BuLi (5.0 mL. 1.6 M, 8.0 mmol). This slightly yellow solution was then added to a stirred solution of **1** (2.34 g, 7.76 mmol) in hexane (40 mL). Gas evolution was noted after a few drops had been added. After addition, the mixture was kept at reflux for 14 h. The solid (1.65 g, most likely **6b**) was isolated by filtration and was then dissolved in THF (25 mL). After removal of the solvent, a brown oil remained. Most of the oil solidified on storing for several days. The resulting colorless crystals were isolated and washed with a small amount of pentane. Yield: 1.62 g of **6c**, 56%. M.p. 148–151 °C. Several of the crystals had single-crystal quality. By dissolving **6a** in THF the same compound separated from a concentrated solution kept at –25 °C. ^{1}H NMR: δ = 1.37 (t, $^3J_{H,H}$ = 7 Hz, 24 H, OCH_2CH), 3.54 (q, $^3J_{H,H}$ = 7 Hz, 24 H, OCH_2), 5.78 (br. s, 4 H, N-1,1′,5,5′) ppm. ^{13}C NMR: δ = 26.2 (OCH_2CH_2), 68.3 (OCH_2) ppm. ^{11}B NMR: δ = –3.5, 34.2 ppm. ^{7}Li NMR: δ = –0.39 ($h_{1/2}$ = 40 Hz), 1.58 ($h_{1/2}$ = 10 Hz) ppm.

 © 2005 Wiley-VCH Verlag GmbH & Co. KGaA, Weinheim

IR (Nujol, Hostaflon; only medium to very strong bands quoted): $\tilde{\nu}$ = 3011 m, 2982 m, 1950 m, 2799 m, 1599 m, 1502 st, 1449 st, 1425 st, 1399 st, 1339 cm^{-1}. $C_{36}H_{46}B_3Li_2N_3O_3$ (615.13): calcd. C 70.30, H 7.54, N 6.83; found C 69.41, H 7.34, N 6.67.

1,3,5-Tris[(diethyl ether)lithio]-2,4,6-triphenylborazine–Tris(phenyllithium–diethyl ether) (8): To a stirred solution of **1** (450 mg, 1.47 mmol) in diethyl ether (40 mL), a solution of PhLi in diethyl ether/cyclohexane (1:1, 4.5 mL, 9.0 mmol) was slowly added at 0 °C. The brown solution was stirred for 3 d. Then its volume was reduced to ca. 20 mL. Moisture-sensitive crystals separated from the solution within a few days at –5 °C. Some of them had single-crystal quality but showed low diffracting power. Yield: 1.37 g of **8**, 1.34 mmol, 92%. M.p. 166–168 °C. ^{1}H NMR (C_6D_6): δ = 0.75 (t, $^3J_{H,H}$ = 6 Hz, 36 H, CH_2CH_3), 2.90 (q, $^3J_{H,H}$ = 6 Hz, 24 H, OCH_2), 6.87 (t, $^3J_{H,H}$ = 7 Hz, 6 H, *m*-PhB), 7.15 (t, $^3J_{H,H}$ = 7 Hz, 6 H, *m*-PhLi), 7.21 (t, $^3J_{H,H}$ = 7 Hz, 3 H, *p*-PhLi), 7.35 (t, $^3J_{H,H}$ = 7 Hz, 3 H, *p*-PhB), 7.70 (d, $^3J_{H,H}$ = 7 Hz, 6 H, *o*-PhB), 8.01 (d, $^3J_{H,H}$ = 7 Hz, 6 H, *o*-PhLi) ppm. ^{13}C NMR: δ = 14.6 (CH_2CH_3), 65.1 (OCH_2), 121.8 (*i*-PhLi), 127.4 (*p*-PhLi), 128.5 (*m*-PhLi), 129.0 (*p*-PhB), 133.5 (*m*-PhB), 143.6 (*o*-PhB), 145.4 (*o*-PhB) ppm. ^{11}B NMR: δ = 39.6 ($h_{1/2}$ = 800 Hz). ^{7}Li NMR: δ = 2.9 ($h_{1/2}$ = 190 Hz). IR (Nujol, Hostaflon; only medium to very strong bands quoted): $\tilde{\nu}$ = 3063 m,3048 m, 2979 m, 2936 m, 2889 m, 1594 m, 1483 m, 1467 m, 1457 m, 1447 m, 1430 st, 1408 m, 1387 m, 1330 vst, 1316 vst, 1261 st, 1210 m, 1189 st, 1153 m, 1095 m, 1064 st, 1044 m, 1023 m, 1005 m, 978 m, 836 m, 789 m, 764 m, 740 st, 726 st, 675 m, 622 m, 616 st, 593 m, 445 m, 434 st cm^{-1}. $C_{60}H_{90}B_3Li_6N_3O_6$ (1023.47): calcd. C 70.41, H 8.86, N 4.11; found C 68.78, H 8.49, N 4.79.

X-ray Crystal Structure Analyses: Crystals were placed under a blanket of a cold stream of N_2 in perfluoroether oil (stock point –40 °C). The selected single crystal was mounted on the tip of a glass fiber and placed on a supporting copper rod which was transferred onto the goniometer head cooled to –80 °C with a Bruker LT2 device. After centering the crystal, data on 5 different sets of 15 frames each were recorded using a Siemens P4 diffractometer equipped with a CCD detector. These data were used to determine the unit cell with the program SMART.[21] Data collection was performed using the hemisphere mode of the program SMART. Data on 1200 frames were collected which were reduced with the program SAINT.[22] The normalized data set was then used to obtain a model structure.[23] As most data sets showed only weak reflection beyond $2\theta > 30°$, several cycles of isotropic refinements of found non-hydrogen positions were necessary to complete the non-hydrogen framework. After refinement with anisotropic thermal parameters, most hydrogen positions were observed after several cycles. Only the found positions for NH hydrogen atoms were isotropically refined. The CH hydrogen atoms were placed in calculated positions and refined with a riding model in the final cycles of refinement (not so for compound **5** where several hydrogen positions at the phenyl groups were freely refined but in the final cycles with fixed U_i values). The U_{ij} values of the carbon atoms of the diethyl ether molecule showed too long C–O bonds and too short C–C distances, suggesting site disorder. However, a split-model calculation did not significantly improve the *R* value. Therefore, the data of the unsplit situation is quoted. On the other hand, two of the three THF molecules of **6c** were site-disordered. The refinement showed about equal occupancy of the two positions. Therefore, in the final cycles SOF was fixed to 0.5. In case of compound **8** data

Table 5. Crystallographic data for compounds **2**–**8**.

	2	**3**	**4**	**5**	**6c**	**8**
Empirical formula	$C_{30}H_{49}B_3ILi_2N_7$	$C_{30}H_{37}B_3LiN_6$	$C_{31}H_{39}B_3LiN_3O$	$C_{100}H_{121}B_{12}Li_4N_{12}O_4$	$C_{72}H_{92}B_6Li_4N_6O_6$	$C_{60}H_{84}B_3Li_6N_3O_6$
Formula mass	680.97	521.03	509.02	1712.57	1230.14	1017.37
Crystal size [mm]	0.40×0.40×0.60	0.2×0.27×0.5	0.20×0.30×0.30	0.20×0.20×0.30	0.2×0.2×0.3	0.4×0.49×0.55
Crystal system	monoclinic	orthorhombic	triclinic	monoclinic	monoclinic	hexagonal
Space group	*P*21/*c*	*Pbca*	*P*1	*P*21/*c*	*P*21/*n*	*R*3
a [Å]	13.6330(4)	15.2568(2)	11.5296(8)	23.4276(3)	12.9042(8)	22.005(3)
b [Å]	14.6656(5)	16.7596(3)	16.147(1)	20.7481(3)	20.106(1)	22.005(3)
c [Å]	18.9577(7)	23.8982(1)	17.208(1)	23.5936(1)	14.2005(8)	23.604(5)
α [°]	90.00	90.00	103.238(1)	90.00	90.00	90.00
β [°]	106.025(1)	90.00	103.286(1)	119.16 (1)	105.574(1)	90.00
γ [°]	90.00	90.00	92.420(2)	90.00	90.00	120.00
V [Å^3]	3643.0(2)	6110.7(1)	3005.5(4)	10014.9(2)	3549.1(4)	9898(3)
Z	4	8	4	4	2	6
ρ(calcd.) [Mg/m^3]	1.242	1.133	1.125	1.136	1.151	1.024
μ [mm^{-1}]	0.908	0.066	0.066	0.067	0.070	0.062
F(000)	1408	2216	1088	3636	1312	3276
Index range	$-17 \le h \le 17$	$-16 \le h \le 16$	$-12 \le h \le 12$	$-30 \le h \le 29$	$-15 \le h \le 13$	$-22 \le h \le 22$
	$-17 \le k \le 17$	$-18 \le k \le 18$	$-16 \le k \le 716$	$-25 \le k \le 25$	$-23 \le k \le 23$	$-21 \le k \le 21$
	$-23 \le l \le 3$	$-26 \le l \le 26$	$-19 \le l \le 9$	$-30 \le l \le 29$	$-16 \le l \le 16$	$-23 \le l \le 23$
2θ [°]	57.98	46.52	46.52	51.5	49.42	41.62
T [K]	193(2)	193	193	183	193	193
Reflections collected	20309	25177	13520	54348	17491	11121
Reflections unique	7184	4372	7007	16329	5692	2297
Reflections observed (4σ)	5948	2627	5469	12140	3479	1359
R(int.)	0.0183	0.1064	0.0174	0.0359	0.0404	0.1279
No. of variables	404	361	712	1298	498	235
Weighting scheme[a] *x*/*y*	0.0452/3.5395	0.0422/5.6631	0.0683/1.4601	0.0553/17.9596	0.0810/2.5368	0.1321/105.16
GOOF	1.053	1.105	1.021	1.153	1.024	1.101
Final *R* (4σ)	0.0356	0.0751	0.0471	0.0900	0.0697	0.1607
Final wR_2	0.0904	0.1320	0.1289	0.1960	0.1660	0.3715
Largest residual peak [e/Å^3]	0.899	0.438	0.381	0.811	0.369	0.283

[a] $w^{-1} = \sigma^2F_o^2 + (xP)^2 + yP$; $P = (F_o^2 + 2F_c^2)/3$.

 © 2005 Wiley-VCH Verlag GmbH & Co. KGaA, Weinheim

for several crystals were measured. But even the "best" set of data gave no R_2 value better than 37%. Selected crystallographic data are found in Table 5. Additional data related to the X-ray structures are deposited with the Cambridge Crystallographic Data Centre. CCDC-260218 to -260223 contain the supplementary crystallographic data for this paper. These data can be obtained free of charge from The Cambridge Crystallographic Data Centre via www.ccdc.cam.ac.uk/data_request/cif.

Acknowledgments

We would like to thank Chemetall GmbH, Frankfurt, for generous support, as well as Fonds der Chemischen Industrie. Mrs. D. Ewald, Mr. P. Mayer, and Mrs. E. Kiesewetter were very helpful in recording NMR, MS, and IR data. We also acknowledge the help of Mr. F. Stahl in some of the experiments, Mr. P. Schulz for elemental analyses, and Drs. T. Habereder, J. Knizek, and W. Ponikwar for their help in crystal structure analyses.

[1] H. Nöth, S. Rojas-Lima, A. Troll, *Eur. J. Inorg. Chem.* **2005**, 1895–1906.
[2] R. I. Wagner, J. L. Bradford, *Inorg. Chem.* **1962**, *1*, 93–98.
[3] R. I. Wagner, J. L. Bradford, *Inorg. Chem.* **1962**, *1*, 99–106.
[4] H. Schwenk, Ph. D. Thesis, Univ. of Munich, **1998**.
[5] J. Bielawsky, M. K. Das, E. Hanecker, K. Niedenzu, H. Nöth, *Inorg. Chem.* **1986**, *25*, 4623–4628. The procedure described here for the preparation of **1** is a modification. Monitoring the reaction by ^{11}B NMR, we found that 10 d are required to convert the starting materials quantitatively into **1**.
[6] H. Nöth, R. Waldhör, *Z. Naturforsch.* **1998**, *53b*, 1525–1530.
[7] C. L. Raston, B. W. Skelton, C. R. F. Whitaker, A. H. White, *J. Chem. Soc., Dalton Trans.* **1988**, 987–990.
[8] A. Troll, Ph. D. Thesis, Univ. of Munich, **1999**.
[9] W. N. Setzer, P. v. R. Schleyer, *Adv. Organomet. Chem.* **1985**, 354–441.
[10] P. v. R. Schleyer, *Methoden der Organischen Chemie* (*Houben-Weyl*), Georg Thieme Verlag, Stuttgart, New York, **1993**, vol. E19d, p. 1–99.
[11] H. Werner, R. Prinz, E. Deckelmann, *Chem. Ber.* **1969**, *102*, 95–103.
[12] B. Kiran, A. K. Phukan, E. D. Jemmis, *Inorg. Chem.* **2001**, *40*, 3615–3618.
[13] H. Nöth, *Z. Naturforsch.* **1961**, *16b*, 618–620.
[14] R. N. Grimes (Ed.), *Metal Interactions with Boron Clusters*, Plenum Press, New York, London, **1982**.
[15] One of the referees suggested a comparison of the structures of the *N*-lithioborazines and borazinates with lithium carbaborates.
[16] R. N. Hosmane, "Carboranes and Metallacarboranes; Chemistry in New Directions", in *Contemporary Boron Chemistry* (Eds.: M. Davidson, A. K. Hughes, T. B. Marder, K. Wade), Royal Society of Chemistry, Special Publication 253, **2000**, p. 299–307.
[17] N. S. Hosmane, A. K. Saxena, R. F. D. Barreto, H. Zhang, J. A. Maguire, L. Jia, Y. Wang, A. R. Oki, K. V. Grover, S. J. W. Shitten, K. Dawson, M. A. Tolle, U. Siriwardane, T. Demissie, J. S. Fagner, *Organometallics* **1993**, *12*, 3001–3014.
[18] N. S. Hosmane, D. Zhu, H. Zhang, A. D. F. R. Oki, J. A. Maguire, *Organometallics* 1**998**, *17*, 3196–3203.
[19] P. Ameris, W. Mesbak, C. Präsung, M. Hofmann, G. Geisel, W. Mauer, A. Berndt, *Organometallics* **2003**, *22*, 1594–1596.
[20] W. Lößlein, H. Pritzkow, P. v. R. Schleyer, L. R. Schmitz, W. Siebert, *Angew. Chem.* **2000**, *112*, 1333–1335; *Angew. Chem. Int. Ed.* **2003**, *35*, 1276–1278.
[21] Bruker, *SMART*, Version 5.1, Bruker Analytical Instruments, Madison.
[22] Bruker, *SAINT*, Version 5.1, Bruker Analytical Instruments, Madison.
[23] G. W. Sheldrick, *SHELXTL*, Version 5.1, Bruker Analytical Instruments, Madison, **1997**; G. W. Sheldrick, *SHELX-93*, University of Göttingen, **1993**.

Received: February 16, 2005
Published Online: August 2, 2005

 © 2005 Wiley-VCH Verlag GmbH & Co. KGaA, Weinheim

Complexes of the Bicyclic Multifunctional Sulfur-Nitrogen Ligand $F_3CCN_5S_3$ with Co^{2+}, Zn^{2+}, Cu^{2+}, and Cd[‡]

Carsten Knapp[a] and Rüdiger Mews*[a]

Keywords: Bridging ligands / Heterocycles / N ligands / S ligands / Transition metals

The ability of the sulfur-nitrogen-carbon bicycle $F_3CCN_5S_3$ to act as a donor towards transition metal cations has been investigated. $F_3CCN_5S_3$ forms complexes with $[M(SO_2)_2](AsF_6)_2$ [M = Co, Cu, Zn, Cd] in the ratio 2:1 of the composition $[M(F_3CCN_5S_3)_2(OSO)_2(FAsF_5)_2]$ [M = Co (**1**), Zn (**3**)], $[Cu(F_3CCN_5S_3)_2(\mu\text{-}F)(\mu\text{-}F_2AsF_4)]_2$ (**4**), and $[Cd(F_3CCN_5S_3)(\mu\text{-}F_3CCN_5S_3)(\eta^2\text{-}F_2AsF_4)_2]_2$ (**5**) in liquid sulfur dioxide. In the octahedral Co and Zn complexes $F_3CCN_5S_3$ coordinates as a monodentate ligand through the bridging nitrogen atom N5, which carries the highest negative charge according to theoretical calculations. With Cu^{2+} a dinuclear structure with a central planar, four-membered Cu_2F_2 ring is formed, which has the shortest Cu···Cu distance of all structurally characterized Cu_2F_2 units. Similar to the Co and Zn complexes, $F_3CCN_5S_3$ acts as a terminal monodentate ligand in the Cu compound. The reaction with the larger and softer Cd^{2+} cation results in a dinuclear complex that contains terminal and bridging $F_3CCN_5S_3$ ligands. The bridging ligands coordinate through N5 and a nitrogen atom neighboring the carbon atom. In addition, a third weak bonding interaction between one fluorine atom of the trifluoromethyl substituent and the Cd^{2+} center is observed. The formation of the different structures and the versatile coordination modes of the $F_3CCN_5S_3$ ligand are discussed.
(© Wiley-VCH Verlag GmbH & Co. KGaA, 69451 Weinheim, Germany, 2005)

Introduction

Recently, we reported the syntheses, crystal structures, and solid-state packing of $1\lambda^4,3\lambda^4,5\lambda^4$-trithia-2,4,6,8,9-pentaazabicyclo[3.3.1]nona-1(9),2,3,5,7-pentaenes (RCN_5S_3) with different alkyl and aryl substituents.[1] Based on quantum chemical calculations,[1a,2] these bicyclic sulfur-nitrogen heterocycles were proposed to act as versatile multifunctional ligands in coordination chemistry. The presence of several lone pairs and energetically low-lying orbitals of different symmetries should allow different coordination modes and a versatile chemistry. The calculations showed that the nitrogen atoms carry a high negative partial charge and the sulfur atoms a high positive one. The highest negative charge was found to be at the bridging nitrogen atom N5, independent of the substituent R.[1a] Thus, RCN_5S_3 might act as either a donor or an acceptor. Electrophiles exclusively attack the heterobicycle at the sulfur atom of the sulfurdiimide bridge, as was shown in reactions with EPh_3 (E = P, As)[3,4a] and in the structure determination of $[(Me_2N)_3S]^+[F_3CCN_5S_3NC(NH_2)CF_3]^-$.[4a] Reactions with Lewis acids, however, are more versatile. The Lewis acid AsF_5 attacks, as expected, at the bridging nitrogen atom N5 of $F_3CCN_5S_3$, while the proton, the simplest Lewis acid, interacts with a nitrogen atom neighboring the ring carbon atom.[4]

In this report we will focus on reactions of $F_3CCN_5S_3$ with $[M(SO_2)_x](AsF_6)_2$. The trifluoromethyl-substituted derivative $F_3CCN_5S_3$ is a representative example of this class of compounds. In addition, the sulfur-nitrogen heterocycle is stabilized by the F_3C group.[1a,5] Transition metal sulfur dioxide hexafluoroarsenates in liquid sulfur dioxide are an excellent system to introduce even very weak donor ligands into coordination chemistry.[6,7] Due to the weakly coordinating SO_2 ligands and AsF_6^- counteranions, the metal centers are almost "naked". Thus, even very weak donors can be attached to the metal centers. Until now only two metal complexes of $F_3CCN_5S_3$ were known,[2] namely $[Ni(F_3CCN_5S_3)_2(SO_2)_2(AsF_6)_2]$, formed from $[Ni(SO_2)_6](AsF_6)_2$, where, similar to the AsF_5 adduct, the $F_3CCN_5S_3$ acts as an N-ligand and coordinates through the bridging nitrogen atom N5 to the metal center, and the silver complex $[Ag(F_3CCN_5S_3)(\mu\text{-}F_3CCN_5S_3)]_2(AsF_6)_2$, which contains two differently coordinating $F_3CCN_5S_3$ molecules as terminal and bridging ligands, respectively. These two examples show that the coordination modes of the ligand depend on the metal center. Therefore it seemed worthwhile to extend our investigations to other metals.

In this paper reactions of the metal sulfur dioxide hexafluoroarsenates $[M(SO_2)_2](AsF_6)_2$ (M = Co, Cu, Zn, Cd) with $F_3CCN_5S_3$ are reported. The X-ray structures of the

[‡] Part of this work was presented at the 10th International Symposium on Inorganic Ring Systems (Burlington, VT, USA, August 2003) and at the 14th European Symposium on Fluorine Chemistry (Poznan, Poland, July 2004).

[a] Institut für Anorganische und Physikalische Chemie, Universität Bremen
Postfach 330440, 28344 Bremen, Germany
Fax: +49-421-218-4267
E-mail: mews@chemie.uni-bremen.de

 © 2005 Wiley-VCH Verlag GmbH & Co. KGaA, Weinheim **DOI: 10.1002/ejic.200500396**

resulting complexes and the different coordination modes of the ligand $F_3CCN_5S_3$ are discussed.

Results and Discussion

The reaction of $F_3CCN_5S_3$ with the transition metal cations $Co^{2+}$and Zn^{2+} in liquid sulfur dioxide yielded orange crystals of $[M(F_3CCN_5S_3)_2(OSO)_2(FAsF_5)_2]$ [M = Co (**1**), Zn (**3**)], which are isostructural with the known Ni^{2+} complex **2**.[2] The presence of O-coordinated SO_2 in these complexes can be concluded from the S–O stretching mode in the IR spectra; O-coordination is preferred by hard metal centers.[6,8] The As–F stretching vibrations for the AsF_6^- counteranions are split and partly shifted to higher wavenumbers, in agreement with a distorted coordinated AsF_6^- (Scheme 1).

A different result is expected for the reaction with Cu^{2+}, because Cu^{2+} compounds (d^9) are strongly affected by the Jahn–Teller distortion. Very air-sensitive blue crystals were obtained from the reaction of $F_3CCN_5S_3$ with $[Cu(SO_2)_x](AsF_6)_2$ in liquid sulfur dioxide. The IR spectrum shows no absorptions in the region of S–O stretching vibrations, in agreement with the results of the X-ray structure determination (see below). The isolated dinuclear complex of the formula $[Cu(F_3CCN_5S_3)_2(\mu\text{-}F)(\mu\text{-}F_2AsF_4)]_2$ (**4**) contains a central four-membered Cu_2F_2 ring with two Cu^{2+} cations bridged by two fluoride and two AsF_6^- anions. In addition, each Cu^{2+} ion coordinates two $F_3CCN_5S_3$ ligands. The bridging fluoride ions result from the decomposition of AsF_6^- anions. It has been known for a long time that $[Cu(AsF_6)_2]$ readily loses AsF_5 with formation of $[CuF_n(AsF_6)_{2-n}]$ of ill-defined composition.[9] Recently, $[CuF(AsF_6)]$[10] has been structurally characterized[11] and might allow the straightforward preparation of **4** in the future (Scheme 2).

Cd^{2+} is a "softer" metal cation, due to its larger ionic radius than the cations of the first row transition metals discussed above, therefore a different behavior is observed: the reaction of $[Cd(SO_2)_x](AsF_6)_2$ with $F_3CCN_5S_3$ in liquid sulfur dioxide yields the dinuclear complex $[Cd(F_3CCN_5S_3)(\mu\text{-}F_3CCN_5S_3)(\eta^2\text{-}F_2AsF_4)_2]_2$ (**5**), similar to the silver complex we described earlier (Scheme 3).[2]

Structural Investigations

Structures of $[M(F_3CCN_5S_3)_2(OSO)_2(FAsF_5)_2]$ [M = Co (1), Zn (3)]

Single crystals of all compounds suitable for X-ray diffraction were obtained by slow evaporation of the solvent (liquid sulfur dioxide) at room temperature. Complexes **1** and **3** are isostructural and crystallize in the monoclinic space group $P2_1/n$ (Figure 1). The metal cation lies on an inversion center and is surrounded by two $F_3CCN_5S_3$ ligands. In addition, the two AsF_6^- counteranions are linked to the cation by bridging fluoride ions, with the remaining two free coordination sites being filled by sulfur dioxide solvent molecules to complete the octahedral coordination sphere (Figure 1). For comparison, selected average bond lengths are included in Table 1 together with the data for $F_3CCN_5S_3$ and $F_3CCN_5S_3{\cdot}AsF_5$.

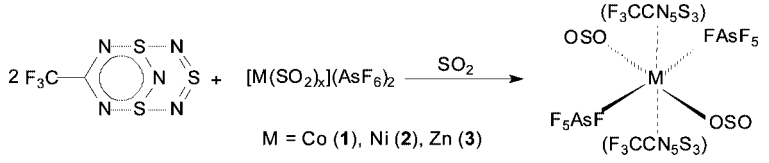

Scheme 1.

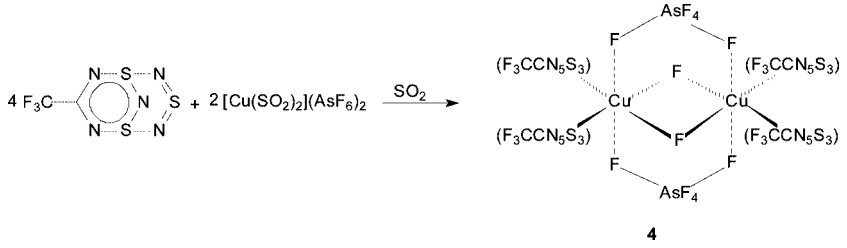

Scheme 2.

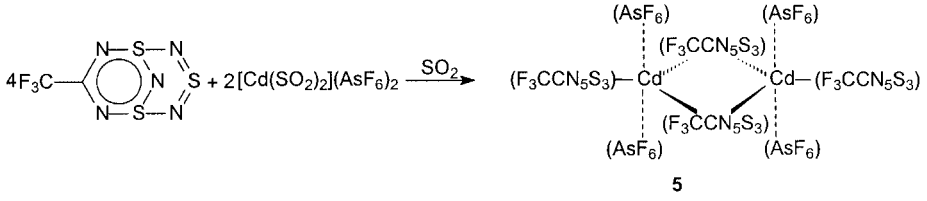

Scheme 3.

 © 2005 Wiley-VCH Verlag GmbH & Co. KGaA, Weinheim

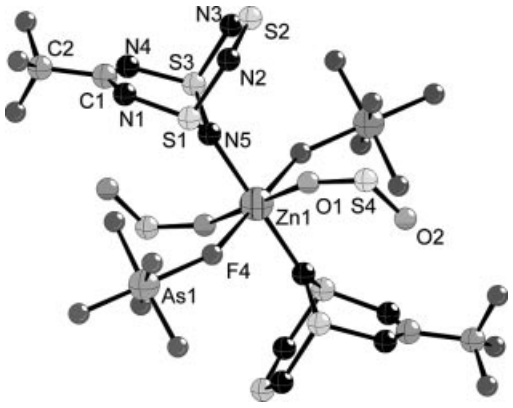

Figure 1. Structure of $[Co(F_3CCN_5S_3)_2(SO_2)_2(FAsF_5)_2]$ (**1**), which is isostructural to $[Zn(F_3CCN_5S_3)_2(SO_2)_2(FAsF_5)_2]$ (**3**). Selected bond lengths [pm] for **1**: Co(1)–N(5) 205.8(2), Co(1)–F(4) 209.53(16), Co(1)–O(1) 214.0(2), C(1)–N(1) 131.3(4), C(1)–N(4) 132.0(4), C(1)–C(2) 153.7(4), N(1)–S(1) 162.7(2), S(1)–N(5) 164.7(2), S(1)–N(2) 170.9(3), N(2)–S(2) 154.4(3), S(2)–N(3) 154.8(3), N(3)–S(3) 171.4(3), S(3)–N(4) 162.6(3), S(3)–N(5) 165.1(2), O(1)–S(4) 144.4(2), S(4)–O(2) 141.1(3), As(1)–F(4) 179.13(17), average As–F 169.9. Selected bond lengths [pm] for **3**: Zn(1)–N(5) 203.42(19), Zn(1)–F(4) 210.44(15), Zn(1)–O(1) 218.14(18), C(1)–N(1) 131.5(3), C(1)–N(4) 132.1(3), C(1)–C(2) 153.0(3), N(1)–S(1) 162.3(2), S(1)–N(5) 164.9(2), S(1)–N(2) 170.9(2), N(2)–S(2) 154.4(3), S(2)–N(3) 155.1(3), N(3)–S(3) 171.1(3), S(3)–N(4) 162.4(2), S(3)–N(5) 165.1(2), O(1)–S(5) 144.08(19), S(5)–O(2) 141.2(2), As(1)–F(4) 178.65(15), average As–F 169.8.

The $F_3CCN_5S_3$ ligand coordinates to the metal center through the bridging nitrogen atom N5, which carries the highest negative charge according to theoretical calculations.[4a] The M–N distance of about 205 pm in **1**, **2**, and **3** [203.42(19) pm in **1** and 206.3(4) in **2**] is in agreement with the similar ionic radii of the cations. The changes of the bond length within the sulfur-nitrogen heterocycle on coordination to a transition metal cation and on adduct formation with AsF_5 compared with the free ligand follow the same pattern as discussed previously.[4a]

The M···O distance increases from M = Zn to M = Ni by about 8 pm and is approximately 7 pm longer than in complexes containing only SO_2, such as $[Ni(OSO)_6](AsF_6)_2$ [203.3(3)–204.3(3) pm][13] and $[Co(OSO)_4(FAsF_5)_2]$ [205.9(4)–207.5(4) pm].[7]

In agreement with accepted bonding models,[14] the end-on coordination of the SO_2 ligand to the cation results in two different S–O bond lengths. Compared to the free SO_2 molecule (143 pm),[15] the M···O–S bond is slightly stretched (144 pm), whereas the terminal S–O bond is slightly shortened (140–141 pm). This distortion is a function of the Lewis acidity of the acceptor and decreases with the weakening of the M···O interaction from M = Zn to M = Ni.[2]

Similar to the M···O distances, the M···F distances [209.53(16) pm in **1**] are longer than in the complexes containing only SO_2 as additional ligands {e.g. $[Co(OSO)_4(FAsF_5)_2]$: 201.8(3)–202.6(3) pm}.[7] The counteranion acts as a monodentate ligand resulting in a distortion of the AsF_6^- octahedron. The As–F bond of the bridging fluoride F4 in **3** is about 10 pm longer than the average of the other As–F bond lengths.

Structure of $[Cu(F_3CCN_5S_3)_2(\mu\text{-}F)(\mu\text{-}F_2AsF_4)]_2$ (4)

Blue crystals suitable for X-ray diffraction were also obtained by slow evaporation of the liquid sulfur dioxide. Structure solution and refinement were realized in the triclinic space group $P\bar{1}$. The dinuclear complex contains a central planar, four-membered Cu_2F_2 ring (Figure 2). Two $F_3CCN_5S_3$ ligands coordinate through the bridging nitrogen atom N5 to each copper, completing a square-planar environment around the Cu^{2+} ion. In addition, the two metal centers are bridged by the AsF_6^- counteranions above and below the Cu_2F_2 unit. The contacts within the plane are much stronger than the Cu–F contacts perpendicular to the plane due to the Jahn–Teller effect. This view is supported by applying Brown's bond valence approach,[16] which assigns 0.28 v.u. (valency units) for the Cu–N contacts and 0.42 v.u. for the Cu–F bonds within the Cu_2F_2 ring, but only 0.13 v.u. for the Cu–F contacts to the bridging hexafluoroarsenate ions. Only a few compounds containing a Cu_2F_2 ring have been structurally characterized, and the Cu···Cu distance is normally in the range of 290–340 pm.[17] The title compound contains the shortest Cu···Cu distance of all Cu_2F_2 four-membered rings [287.5(2) pm], which might be a result of the AsF_6^- bridges. Since the Cu···F–AsF_4–F···Cu interactions are weak, the hexafluoroarsenate ions are less distorted than in the com-

Table 1. Selected average bond lengths [pm] for $[M(F_3CCN_5S_3)_2(OSO)_2(FAsF_5)_2]$ [M = Co (**1**), Ni (**2**), Zn (**3**)], $F_3CCN_5S_3{\cdot}AsF_5$, and $F_3CCN_5S_3$. The values in square brackets are valency units [v.u.] according to Brown's bond valence approach.[16]

	$F_3CCN_5S_3$[12]	**1**	**2**[2]	**3**	$F_3CCN_5S_3{\cdot}AsF_5$[4a]
M–N5		205.8(2) [0.33]	206.3(4) [0.33]	203.42(19) [0.43]	
M–O1		214.0(2) [0.29]	210.0(4) [0.30]	218.14(18) [0.28]	
M–F4		209.53(16) [0.29]	204.5(3) [0.31]	210.44(15) [0.27]	
F4–As1		179.13(17)	179.5(3)	178.65(15)	
average As–F		169.9	169.1	169.7	
C1–C2	152.4(4)	153.7(4)	153.9(8)	153.0(3)	153.2(8)
C1–N1	132.1	131.6	131.0	131.8	131.6
N1–S1	163.1	162.6	162.6	162.3	161.9
S1–N5	163.0	164.9	164.0	165.0	166.1
S1–N2	172.5	170.1	171.4	170.0	171.0
N2–S2	154.5	154.6	153.7	154.7	155.1

 © 2005 Wiley-VCH Verlag GmbH & Co. KGaA, Weinheim

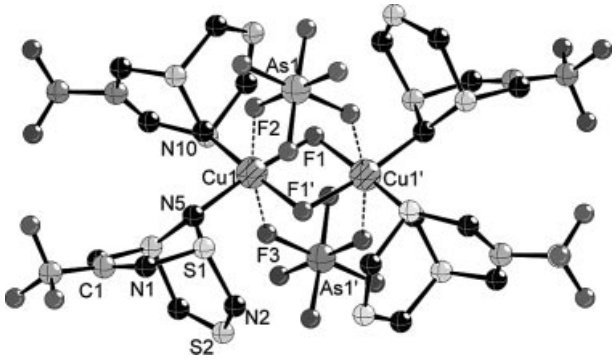

Figure 2. Structure of $[Cu(\mu\text{-}F)(\mu\text{-}F_3CCN_5S_3)(\mu\text{-}F_2AsF_4)]_2$ (**4**). Selected bond lengths [pm] and angles [°]: Cu(1)–F(1) 191.3(5), Cu(1)–F(1′) 191.9(5), Cu(1)–N(5) 197.4(7), Cu(1)–N(10) 199.4(8), Cu(1)–F(3) 235.3(5), Cu(1)–F(2′) 236.5(6), Cu(1)–Cu(1′) 287.5(2), C(1)–N(1) 131.0(12), C(1)–N(4) 133.5(12), C(1)–C(2) 151.9(13), N(1)–S(1) 163.2(7), S(1)–N(5) 165.4(7), S(1)–N(2) 170.8(8), N(2)–S(2) 154.3(8), S(2)–N(3) 154.4(8), N(3)–S(3) 171.1(8), S(3)–N(4) 162.5(8), S(3)–N(5) 165.1(7), C(3)–N(6) 131.2(12), C(3)–N(9) 132.4(12), C(3)–C(4) 154.5(13), N(6)–S(4) 160.3(8), S(4)–N(10) 165.7(8), S(4)–N(7) 172.5(9), N(7)–S(5) 153.6(9), S(5)–N(8) 154.8(9), N(8)–S(6) 171.1(9), S(6)–N(9) 161.6(9), S(6)–N(10) 163.4(8); F(1)–Cu(1)–F(1′) 82.8(2), F(1)–Cu(1)–N(5) 90.0(3), F(1′)–Cu(1)–N(5) 172.8(3), F(1)–Cu(1)–N(10) 175.2(3), F(1′)–Cu(1)–N(10) 93.0(3), N(5)–Cu(1)–N(10) 94.2(3). Symmetry transformation to generate primed atoms: $-x$, $-y + 2$, $-z + 1$.

plexes discussed above. The influence of the metal center on the average bond lengths of the $F_3CCN_5S_3$ ligands is small: the changes within the heterocycle are in the expected range for $F_3CCN_5S_3$ coordinated to an acceptor.[4a]

Magnetic measurements on **4** were not carried out but might be interesting as structural[17] and theoretical investigations[18] on Cu_2F_2 rings of similar geometry have shown antiferromagnetic coupling between the Cu^{2+} centers.

Structure of $[Cd(F_3CCN_5S_3)(\mu\text{-}F_3CCN_5S_3)(\eta^2\text{-}F_2AsF_4)_2]$ (5)

Orange crystals suitable for X-ray diffraction were also obtained by slow evaporation of the liquid sulfur dioxide solvent. The structure solution and refinement were realized in the monoclinic space group $P2_1/n$. The complex has a structure similar to that of the corresponding silver compound $[Ag(F_3CCN_5S_3)(\mu\text{-}F_3CCN_5S_3)]_2(AsF_6)_2$.[2] The dinuclear structure contains two different kinds of $F_3CCN_5S_3$ ligands − bridging and terminal (Figure 3). As usual, the terminal $F_3CCN_5S_3$ coordinates through the bridging nitrogen atom N5. The second $F_3CCN_5S_3$ acts as a bidentate ligand through the bridging nitrogen atom (here N10) and the nitrogen atom (N6) next to the trifluoromethyl substituent, and bridges the two metal cations to form an eight-membered $Cd_2N_4S_2$ metallacycle. The Cd–N6 distance [232.25(18) pm (M = Cd), 249.7(4) pm (M = Ag)] is much shorter, and the Cd–N10 distance [240.54(19) pm (M = Cd), 228.1(4) pm (M = Ag)] much longer, than in the corresponding silver compound, while the Cd–N5 distance to the terminal ligand is not influenced by the metal [225.79(19) pm (M = Cd), 222.3(5) pm (M = Ag)]. This is the result of an additional weak bonding interaction between one fluorine atom of the trifluoromethyl substituent and the cadmium center. Bidentate hexafluoroarsenate ions complete the coordination sphere around the metal center, to give a coordination number of eight. Bidentate hexafluoroarsenate ions are less common, but have been observed before in Ag^+ and Cd^{2+} complexes.[19] By applying the bond valence approach,[16] the relative strengths of the different contacts become obvious (Figure 4). The Cd–N contacts are the dominating interactions (0.30–0–45 v.u.), while the Cd–F contacts to the bidentate hexafluoroarsenate ions are weaker (0.13–0.20 v.u.). The additional bonding between

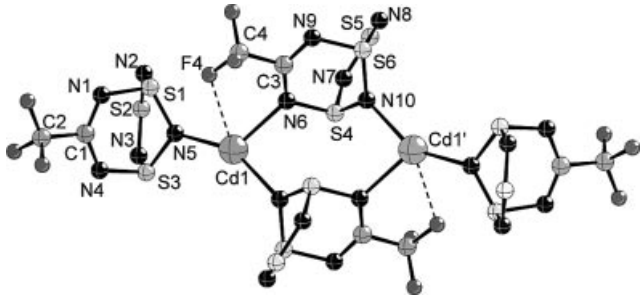

Figure 3. Structure of $[Cd(F_3CCN_5S_3)(\mu\text{-}F_3CCN_5S_3)]_2^{4+}$. Anions have been omitted for clarity. Selected bond lengths [pm] and angles [°]: Cd(1)–N(5) 225.79(19), Cd(1)–N(6) 232.25(18), Cd(1)–F(7) 240.07(13), Cd(1)–N(10′) 240.54(19), Cd(1)–F(14) 244.36(15), Cd(1)–F(13) 247.51(15), Cd(1)–F(8) 256.61(14), C(1)–N(1) 131.6(3), C(1)–N(4) 133.1(3), C(1)–C(2) 153.0(3), N(1)–S(1) 163.62(19), S(1)–N(5) 164.87(19), S(1)–N(2) 171.9(2), N(2)–S(2) 154.9(2), S(2)–N(3) 154.5(2), N(3)–S(3) 172.2(2), S(3)–N(4) 161.4(2), S(3)–N(5) 167.13(18), C(2)–F(3) 131.5(3), C(2)–F(1) 132.5(3), C(2)–F(2) 132.6(3), C(3)–N(9) 130.8(3), C(3)–N(6) 134.8(3), C(3)–C(4) 153.4(3), N(6)–S(4) 166.98(18), S(4)–N(10) 164.06(19), S(4)–N(7) 168.8(2), N(7)–S(5) 156.4(2), S(5)–N(8) 154.3(2), N(8)–S(6) 171.1(2), S(6)–N(9) 164.35(19), S(6)–N(10) 164.61(18), C(4)–F(6) 131.8(3), C(4)–F(5) 132.6(3), C(4)–F(4) 134.9(3); N(5)–Cd(1)–N(6) 122.82(6), N(5)–Cd(1)–N(10′) 152.02(6), N(6)–Cd(1)–N(10′) 84.68(6). Symmetry transformation to generate primed atoms: $-x$, $-y$, $-z$.

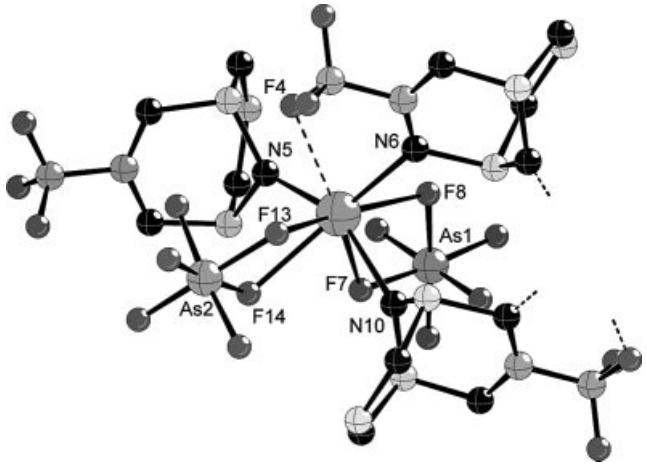

Figure 4. Part of the structure of $[Cd(F_3CCN_5S_3)(\mu\text{-}F_3CCN_5S_3)(\eta^2\text{-}F_2AsF_4)_2]_2$ showing the environment around the Cd^{2+} ion. For selected bond lengths and angles see caption to Figure 3. Selected valency units: Cd–N5 0.45, Cd–N6 0.38, Cd–N10 0.30, Cd–F4 0.10, F4–C4 0.92, average F–C4 1.00, Cd–F7 0.20, Cd–F8 0.13, Cd–F13 0.17, Cd–F14 0.18.

 © 2005 Wiley-VCH Verlag GmbH & Co. KGaA, Weinheim

the trifluoromethyl group and the metal center is much weaker (0.10 v.u.), but strongly influences the structure.

Conclusions

The large number of different lone pairs and low-lying orbitals enables the versatile chemistry of $F_3CCN_5S_3$. It can act as a donor to Lewis acids in many different ways. Coordination through the bridging nitrogen atom N5, which, according to theoretical calculations, carries the highest negative charge, is preferred by hard transition metal cations. $F_3CCN_5S_3$ can coordinate as a terminal ligand, but is also able to bridge Lewis acid centers through the bridging nitrogen atom and a nitrogen atom next to the ring carbon. This allows the formation of eight-membered metallacycles. Surprisingly, even the fluorine atoms of the trifluoromethyl group are able to form an additional bond, which makes $F_3CCN_5S_3$ a tridentate ligand. A comparison of the different complexes shows that $F_3CCN_5S_3$ is a very flexible ligand, which can be seen as well in the possible angle between the S–N5–S plane and the N5–metal contact, which varies in a wide range between –13.1° (M = Cd) and +27.5° (M = Cu). The resulting structures depend on the ionic radii and the hardness of the metal cations. Scheme 4 shows the four possible coordination modes known so far. Together with the known reactions with Lewis bases, the chemistry of $F_3CCN_5S_3$ is very versatile and makes the bicycles of the type RCN_5S_3 an interesting class of compounds to investigate and understand the chemistry of sulfur-nitrogen compounds. Reactions with ligands containing other organic substituents and with other transition metals have been performed as well. They resulted in decomposition of the sulfur-nitrogen heterocycle, but in some cases, when decomposition products can be isolated, an interesting chemistry can be anticipated. These investigations, for example the formation of the eight-membered planar heterocycle $[RCN_4S_3]^+[AsF_6]^-$ from the reaction of RCN_5S_3 with $[Hg(SO_2)_x](AsF_6)_2$, will form part of a separate publication.[20]

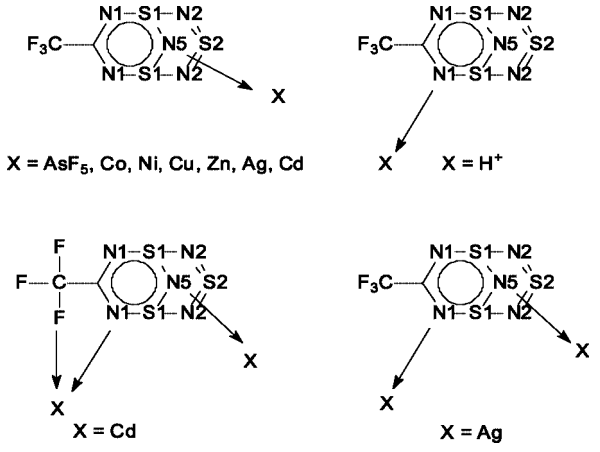

Scheme 4. Observed coordination modes of $F_3CCN_5S_3$.

Experimental Section

General: All manipulations of the solid, air-sensitive materials were performed with the exclusion of oxygen and moisture under dry nitrogen. The reactions were carried out in lambda-type glass vessels with Teflon valves using liquid sulfur dioxide as solvent, which was transferred via a vacuum line. Sulfur dioxide was dried over P_4O_{10} and distilled prior to use. The starting materials $F_3CCN_5S_3$[1a] and $[M(SO_2)_x](AsF_6)_2$ (M = Co, Zn, Cu, Cd)[7] were prepared according to published procedures. IR spectra were obtained with a Perkin–Elmer Paragon 500 FT-IR spectrometer as Nujol or Kel-F mulls. ^{19}F NMR spectra were recorded with a Bruker DPX 200 spectrometer in CD_3CN (chemical shifts are given with respect to $CFCl_3$), and melting points with a Gallenkamp melting point apparatus in sealed melting point capillaries.

$[Co(F_3CCN_5S_3)_2(OSO)_2(FAsF_5)_2]$ (1): A 10 mL portion of SO_2 was condensed onto a mixture of $F_3CCN_5S_3$ (0.25 g, 1.0 mmol) and $[Co(SO_2)_4](AsF_6)_2$ (0.35 g, 0.5 mmol) at –196 °C via a vacuum line. The reaction mixture was allowed to warm slowly to room temperature, and a brown-black solution was formed. After slow removal of the solvent, a brown-black solid remained. Careful washing of the reaction mixture with cold (–40 °C) liquid sulfur dioxide yielded orange crystals of the title compound (0.35 g, 0.3 mmol, 60%), m.p. 100–110 °C (dec.). ^{19}F NMR (200 MHz, CD_3CN, 20 °C): δ = –67.1 (q, $^1J_{F,As}$ = 930 Hz, 12 F, AsF_6^-), –75.9 (s, 12 F, CF_3) ppm. IR: $\tilde{\nu}$ = 1335 w, 1313 m, 1290 sh, 2112 m, 1295 sh, 1181 m, 1133 m, 1030 m, 1018 m, 968 w, 895 w, 816 w, 796 w, 777 m, 750 sh, 719 s, 704 m, 670 m, 661 m, 586 m, 529 m, 518 m, 506 m, 491 w cm^{-1}.

$[Zn(F_3CCN_5S_3)_2(OSO)_2(FAsF_5)_2]$ (3): Similar to the preparation of **1**, an orange solution was formed from $F_3CCN_5S_3$ (0.20 g, 0.8 mmol) and $[Zn(SO_2)_2](AsF_6)_2$ (0.23 g, 0.4 mmol). After slow removal of the solvent, a red-black oil remained. Careful washing of the reaction mixture with cold (–40 °C) liquid sulfur dioxide yielded yellow crystals of the title compound (0.27 g, 0.25 mmol, 63%), m.p. 90 °C (dec.). ^{19}F NMR (200 MHz, CD_3CN, 20 °C): δ = –67.3 (q, $^1J_{F,As}$ = 930 Hz, 12 F, AsF_6^-), –75.9 (s, 12 F, CF_3) ppm. IR: $\tilde{\nu}$ = 1509 w, 1482 m, 1455 sh, 1145 m, 1396 m, 1362 m, 1313 s, 1213 s, 1182 s, 1139 s, 1023 m, 1019 m, 968 w, 891 w, 806 w, 788 m, 760 sh, 724 s, 704 m, 661 m, 586 m, 528 m, 517 m, 519 sh, 490 w cm^{-1}.

$[Cu(\mu\text{-}F)(F_3CCN_5S_3)_2(\mu\text{-}F_2AsF_4)]_2$ (4): $F_3CCN_5S_3$ (0.20 g, 0.8 mmol) and $[Cu(SO_2)_2](AsF_6)_2$ (0.23 g, 0.4 mmol) formed a brown-black solution. After slow removal of the solvent, a yellow-brown solid remained. Careful washing of the reaction mixture with cold (–40 °C) liquid sulfur dioxide yielded blue crystals of the title compound (0.20 g, 0.13 mmol, 65%), m.p. 110 °C (dec.). ^{19}F NMR (200 MHz, CD_3CN, 20 °C): δ = –67.1 (q, $^1J_{F,As}$ = 930 Hz, 12 F, AsF_6^-), –75.9 (s, 12 F, CF_3) ppm. IR: $\tilde{\nu}$ = 1344 w, 1300 w, 1246 m, 1218 m, 1199 m, 1178 m, 1146 m, 1023 sh, 1005 m, 979 sh, 957 sh, 894 w, 850 w, 818 w, 805 w, 783 m, 773 m, 754 m, 721 s, 698 m, 663 m, 588 m, 566 w, 552 w, 528 sh, 516 w, 504 w, 489 w, 454 w cm^{-1}.

$[Cd(F_3CCN_5S_3)(\mu\text{-}F_3CCN_5S_3)(\eta^2\text{-}F_2AsF_4)_2]_2$ (5): $F_3CCN_5S_3$ (0.20 g, 0.8 mmol) and $[Cd(SO_2)_2](AsF_6)_2$ (0.25 g, 0.4 mmol) formed an orange solution. After slow removal of the solvent, orange crystals of the title compound (0.39 g, 0.2 mmol, 100%) remained, m.p. 159 °C (dec.). ^{19}F NMR (200 MHz, CD_3CN, 20 °C): δ = –67.0 (q, $^1J_{F,As}$ = 932 Hz, 12 F, AsF_6^-), –75.9 (s, 12 F, CF_3) ppm. IR: $\tilde{\nu}$ = 1498 vs, 1474 s, 1446 s, 1391 w, 1368 s, 1343 m, 1299 w, 1228 m, 1197 m, 1168 m, 1106 sh, 1028 m, 1005 m, 956 w, 814 m, 790 m, 770 s, 750 sh, 725 vs, 710 vs, 666 s, 606 m, 585 m, 571 sh, 550 w, 542 w, 518 sh, 510 m, 490 w cm^{-1}.

 © 2005 Wiley-VCH Verlag GmbH & Co. KGaA, Weinheim

Table 2. Crystal data and structure refinement for **1**, **3**, **4**, and **5**.

	1	**3**	**4**	**5**
Empirical formula	$C_4As_2CoF_{18}N_{10}O_4S_8$	$C_4As_2F_{18}N_{10}O_4S_8Zn$	$C_8As_2Cu_2F_{26}N_{20}S_{12}$	$C_8As_4Cd_2F_{36}N_{20}S_{12}$
Formula mass	1059.39	1065.83	1531.92	1969.48
Crystal system	monoclinic	monoclinic	triclinic	monoclinic
Space group	$P2_1/n$	$P2_1/n$	$P\bar{1}$	$P2_1/n$
a [pm]	944.9(2)	943.50(10)	947.7(3)	1464.2(3)
b [pm]	1361.7(2)	1361.7(2)	1043.7(3)	1016.6(2)
c [pm]	1073.3(2)	1078.10(10)	1206.7(3)	1667.6(3)
α [°]	90	90	66.28(2)	90
β [°]	97.680(10)	97.420(10)	68.70(3)	109.69(3)
γ [°]	90	90	84.27(2)	90
V [nm^3]	1.3686(4)	1.3735(3)	1.0144(5)	2.3371(8)
Z	2	2	1	2
$D_{calcd.}$ [Mg m^{-3}]	2.571	2.577	2.508	2.799
Crystal size [mm]	0.70 × 0.60 × 0.50	0.40 × 0.40 × 0.30	0.30 × 0.20 × 0.20	0.50 × 0.40 × 0.15
θ range	2.64–27.51	2.64–27.51	2.79–22.50	2.27–25.92
Reflections collected	4053	7340	3152	3195
Independent reflections	3132 [R(int) = 0.0181]	3154 [R(int) = 0.0254]	2544 [R(int) = 0.0389]	4496 [R(int) = 0.0465]
Goodnes-of-fit on F^2	1.089	1.028	0.990	1.018
Final R indices R_1, wR_2	0.0289, 0.0705	0.0255, 0.0602	0.0498, 0.1032	0.0182, 0.0446
R indices (all data)	0.0366, 0.0737	0.0329, 0.0632	0.0916, 0.1150	0.0214, 0.0456

Crystallographic Analysis: The single-crystal X-ray structure determinations were carried out with a Siemens P4 diffractometer or a Stoe IPDS using Mo-K_α (λ = 0.71073 Å) radiation with a graphite monochromator. The crystals were mounted onto a thin glass fiber using Kel-F oil. Details of the data collection and refinement are given in Table 2. The structures were solved by direct methods (SHELXS).[21] Subsequent least-squares refinement on F^2 (SHELXL 97-2) located the positions of the remaining atoms in the electron density maps.[21] All atoms were refined anisotropically. Hydrogen atoms were placed in calculated positions using a riding model and refined isotropically in blocks. The data were corrected for absorption (DIFABS).[22] Graphical representations of the structures were prepared with the program DIAMOND.[23] CCDC-265908 (**1**), -265907 (**3**), -265909 (**4**), and -265910 (**5**) contain the supplementary crystallographic data for this paper. These data can be obtained free of charge from The Cambridge Crystallographic Data Centre via www.ccdc.cam.ac.uk/data_request/cif.

Acknowledgments

We are grateful to the BFK NaWi, Universität Bremen, for financial support and Mr. Peter Brackmann for collecting the X-ray data.

[1] a) C. Knapp, E. Lork, T. Borrmann, W.-D. Stohrer, R. Mews, *Eur. J. Inorg. Chem.* **2003**, 3211–3220; b) C. Knapp, E. Lork, R. Mews, A. V. Zibarev, *Eur. J. Inorg. Chem.* **2004**, 2446–2451.

[2] R. Maggiulli, R. Mews, W.-D. Stohrer, M. Noltemeyer, *Chem. Ber.* **1990**, *123*, 29–34.

[3] a) R. T. Boeré, G. Ferguson, R. T. Oakley, *Acta Crystallogr., Sect. C* **1986**, *42*, 900–902; b) R. T. Boeré, A. W. Cordes, S. L. Craig, J. B. Graham, R. T. Oakley, J. A. J. Privett, *J. Chem. Soc., Chem. Commun.* **1986**, 807–808; c) R. T. Boeré, A. W. Cordes, R. T. Oakley, *J. Am. Chem. Soc.* **1987**, *109*, 7781–7785.

[4] a) C. Knapp, E. Lork, R. Maggiulli, P. G. Watson, R. Mews, T. Borrmann, W.-D. Stohrer, U. Behrens, *Z. Anorg. Allg. Chem.* **2004**, *630*, 1235–1244; b) C. Knapp, T. Borrmann, E. Lork, P. G. Watson, W.-D. Stohrer, R. Mews, *Phosphorus Sulfur Silicon Relat. Elem.* **2004**, *179*, 887–890.

[5] R. T. Boeré, J. Fait, K. Larsen, J. Yip, *Inorg. Chem.* **1992**, *31*, 1417–1423.

[6] R. Mews, E. Lork, P. G. Watson, B. Görtler, *Coord. Chem. Rev.* **2000**, *197*, 277–320 and references cited therein.

[7] E. Lork, R. Mews, J. Petersen, M. Schröter, B. Žemva, *J. Fluorine Chem.* **2001**, *110*, 109–116 and references cited therein.

[8] W. A. Schenk, *Angew. Chem.* **1987**, *99*, 101–112; *Angew. Chem. Int. Ed. Engl.* **1987**, *26*, 98–109.

[9] C. D. Desjardins, J. Passmore, *J. Fluorine Chem.* **1975**, *6*, 379–388.

[10] B. Frelec, D. Gantar, J. H. Holloway, *J. Fluorine Chem.* **1982**, *20*, 385–396.

[11] Z. Mazej, I. Arčon, P. Benkič, A. Kodre, A. Tressaud, *Chem. Eur. J.* **2004**, *10*, 5052–5058.

[12] R. Maggiulli, R. Mews, W.-D. Stohrer, M. Noltemeyer, G. M. Sheldrick, *Chem. Ber.* **1988**, *121*, 1881–1889.

[13] E. Lork, J. Petersen, R. Mews, *Angew. Chem.* **1994**, *106*, 1724–1725; *Angew. Chem. Int. Ed. Engl.* **1994**, *33*, 1663–1665.

[14] a) J. W. Moore, H. W. Baird, H. B. Miller, *J. Am. Chem. Soc.* **1968**, *90*, 1358–1359; b) R. J. Gillespie, F. G. Riddell, D. R. Slim, *J. Am. Chem. Soc.* **1976**, *98*, 8069–8072.

[15] B. Post, R. S. Schwartz, I. Fankuchen, *Acta Crystallogr.* **1952**, *8*, 372–374.

[16] The contacts s [in valance units (v.u.)] have been defined as $s = \exp[(R_0 - R)/B]$, where R is the observed distance, R_0 is the value of the bond length with the unit bond valence, and B = 0.37 is a constant. Used constants: Cu···F R_0 = 1.6, Cu···N R_0 = 1.520; Co···F R_0 = 1.64, Co···N R_0 = 1.66, Co···O R_0 = 1.685; Ni···F R_0 = 1.596, Ni···N R_0 = 1.647, Ni···O R_0 = 1.670; Zn···F R_0 = 1.62, Zn···N R_0 = 1.72, Zn···O R_0 = 1.704; Cd···F R_0 = 1.811, Cd···N R_0 = 1.96, C···F R_0 = 1.32; The constants are available from: a) http://ccp14.sims.nrc.ca/ccp/web-mirrors/i_d_brown/bond_valence_param/; b) I. D. Brown, *The Chemical Bond in Inorganic Chemistry – The Bond Valence Model*, Oxford University Press, Oxford, **2002**.

[17] a) R. W. M. ten Hoedt, J. Reedijk, G. C. Verschnoor, *Recl. Trav. Chim. Pays-Bas* **1981**, *100*, 400–405; b) W. C. Velthuizen, J. G. Haasnoot, A. J. Kinneging, F. J. Rietmeijer, J. Reedijk, *J. Chem. Soc., Chem. Commun.* **1983**, 1366–1368; c) F. J. Rietmeijer, R. A. G. de Graaff, J. Reedijk, *Inorg. Chem.* **1984**, *23*, 151–156; d) E. van der Voort, P. van der Sluis, A. L. Spek, *Acta Crystallogr., Sect. C* **1987**, *43*, 887–890; e) F. S. Keij, R. A. G. de Graaff, J. G. Haasnoot, A. J. Oosterling, E. Pedersen, J. Reedijk, *J. Chem. Soc., Chem. Commun.* **1988**, 423–425; f) A. J. Oosterling, R. A. G. Graaff, J. G. Haasnoot, F. G. Keij, J. Reedijk, E. Pedersen, *Inorg. Chim. Acta* **1989**, *163*, 53–58; g) R. R. Jacobs, Z. Tyeklár, K. D. Karlin, J. Zubieta, *Inorg. Chem.* **1991**,

 © 2005 Wiley-VCH Verlag GmbH & Co. KGaA, Weinheim

30, 2035–2040; h) S. C. Lee, R. H. Holm, *Inorg. Chem.* **1993**, *32*, 4745–4753; i) D. A. Handley, P. B. Hitchcock, T. H. Lee, G. J. Leigh, *Inorg. Chim. Acta* **2001**, *316*, 59–64; j) I. Blain, M. Pierrot, M. Giorgi, M. Réglier, *C. R. Acad. Sci. Ser. IIc* **2001**, *4*, 1–10; k) X. Liu, A. C. McLaughlin, M. P. de Miranda, E. J. L. McInnes, C. A. Kilner, M. A. Halcrow, *Chem. Commun.* **2002**, 2978–2979.

[18] A. Rodríguez-Fortea, P. Alemany, S. Alvarez, E. Ruiz, *Inorg. Chem.* **2002**, *41*, 3769–3778.

[19] a) H. W. Roesky, J. Schimkowiak, M. Noltemeyer, G. M. Sheldrick, *Z. Naturforsch., Teil B* **1988**, *43*, 949–951; b) H. W. Roesky, T. Gries, P. G. Jones, K.-L. Weber, G. M. Sheldrick, *J. Chem. Soc., Dalton Trans.* **1984**, 1781–1784.

[20] C. Knapp, P. G. Watson, E. Lork, R. Mews, T. Borrmann, W.-D. Stohrer, A. Decken, to be published.

[21] G. M. Sheldrick, *SHELX-97, Programs for Crystal Structure Analysis*, release 97-2, Institut für Anorganische Chemie der Universität Göttingen, **1997**.

[22] N. Walker, D. Stuart, *Acta Crystallogr., Sect. A* **1983**, *39*, 158–166.

[23] *Diamond-Visual Crystal Structure Information System*, Crystal Impact, Bonn.

Received: May 3, 2005
Published Online: August 2, 2005

 © 2005 Wiley-VCH Verlag GmbH & Co. KGaA, Weinheim

New Avenues in Inorganic Chemistry

Among the chemical disciplines, inorganic chemistry has traditionally been open to new directions into materials. Visions of future technologies challenge the inorganic chemist to produce materials with new and, in particular, designer properties, sometimes with surprising results. For instance, the demand for miniaturization led to the discovery that a decrease in size does not give a continuous trend in properties.

Inorganic chemistry has a role in materials science

Nanoscience, and in consequence nanotechnology, both deal with the special properties and the pattern of behaviour of any kind of material on the nanometer scale. At these dimensions the classical differences between physics, chemistry, and biology become meaningless. This can be considered as a scientifically new, holistic concept. Nanoscience and -technology, therefore, are not to be considered as novel scientific disciplines in a classical sense. Rather they unify apparently different fields on the nanoscale. Classical physical laws can no longer be applied to describe the propeties of a particle of any chemical composition if its dimension falls below a critical dimension. The investigation of individual nanoparticles, especially with respect to their electronic, optical or magnetic properties, has therefore been in the focus of interest for many research groups around the world over the last few decades. Consequently, our knowledge on the properties of, for instance, semiconductor and metal nanoparticles, is quite advanced. We indeed now understand the dramatic change of properties on the way from the bulk state to the nano state: quantum size effects begin to dominate and corresponding theories replace those of classical physics.

Nanoscience blurs the borders between disciplines

There is, however, still a dramatic gap in our knowledge on the behaviour of three-, two- and one-dimensional arrangements of those nanoparticles. How do they communicate? What is the role of the matter in between? Which kind of forces hold organized particles together? How do nanoparticles interact with biomolecules? Numerous other questions can be formulated for these arrangements. Last but not least, it is important to think about applications of communicating nanoparticles in future electronic devices, sensors, storage systems etc.

In many countries, funding bodies have initiated projects with the goal of bringing together physicists and chemists in order to find answers to the numerous questions arising in connection with the organinization of nanoparticles. Some of the relevant results of a research program supported by the Deutsche Forschungsgemeinschaft (SPP 1072), entitled "Semiconductor and Metal Nanoparticles as Building Blocks for Organized Structures" are now published as peer reviewed papers in this issue of the *European Journal of Inorganic Chemistry*. Besides producing a series of important results, a second effect has been reached by the program: several groups started successful collaborations, especially fruitful between physical and chemical research partners, since, as mentioned before, these disciplines meet each other on the nanoscale. From the publishing point of view another consequence was evident: since the peer review was necessarily international, cross-border stimulation of ideas was a interesting side-effect, illuminating new aspects of the study. Some authors specifically mentioned that the comments were particularly valuable.

International and interdisciplinary contacts stimulate innovative research

As a large part of the acquired results has already been published elsewhere in the course of the last past years, this issue contains an unusual number of microreviews. We hope that this collection of results from cooperative research will stimulate still more groups to initiate interdisciplinary and international collaborations in the field of nanoscience and nanotechnology.

Günter Schmid
(Editorial Board, EurJIC)

Karen Hindson
(Editor, EurJIC)

 © 2005 Wiley-VCH Verlag GmbH & Co. KGaA, Weinheim

EurJIC
European Journal of Inorganic Chemistry

Issue 18/2005

Pages 3545–3772

Papers available ahead of print in Early View at www.interscience.wiley.com

Earliest available Table of Contents:
Automatically, free of charge by e-mail through
www.interscience.wiley.com/alerts

COVER PICTURE

The cover picture shows one-, two- and three-dimensional arrays of nanoparticles (represented by the cluster in the centre). The bottom right corner illustrates the self-assembly of a monolayer of nanoparticles from a drop of solution. Also displayed is the AFM imaging of nanoparticles (top right), the interaction of a nanoparticle array with an electrical field (top left), and the immobilisation of nanoparticles on DNA (bottom left). All these interactive aspects of research on nanoparricles that are used as buiding blocks for organized systems are covered in a series of papers in this issue. The artwork was performed by Michael Noyong, RWTH Aachen.

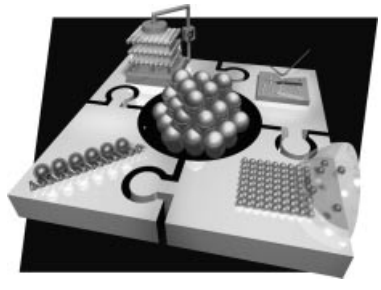

MICROREVIEWS

Contents

3561 **A. Müller,* S. Roy**

Linking Giant Molybdenum Oxide Based Nano-Objects Based on Well-Defined Surfaces in Different Phases

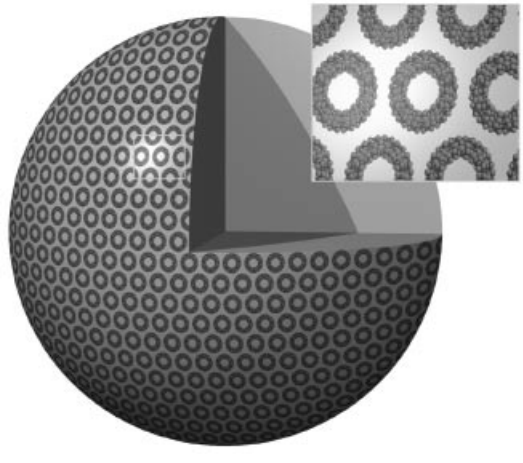

Keywords: Hydrophilic surfaces / Monolayers / Nanochemistry / Polyoxomolybdates / Surfactant-encapsulated clusters / Surface structures / Vesicles

 © 2005 Wiley-VCH Verlag GmbH & Co. KGaA, Weinheim

3571 **M. Giersig,* M. Hilgendorff***

Magnetic Nanoparticle Superstructures

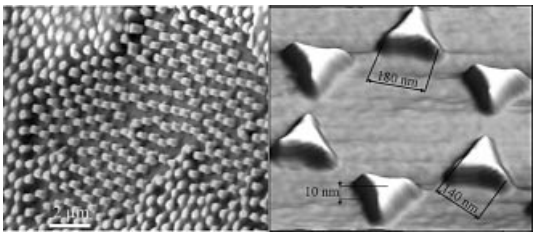

Keywords: Nanoparticles / Ferrofluids / Nanosphere lithography / Nanoshadows

3585 **J. Frenzel, J.-O. Joswig, P. Sarkar, G. Seifert, M. Springborg***

The Effects of Organisation, Embedding and Surfactants on the Properties of Cadmium Chalcogenide (CdS, CdSe and CdS/CdSe) Semiconductor Nanoparticles

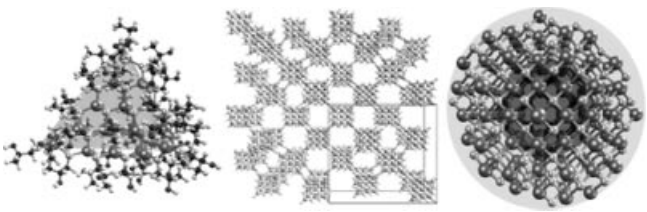

Keywords: Cadmium sulfide / Cluster compounds / Density-functional calculations / Nanostructures / Semiconductors

3597 **F. J. Brieler, P. Grundmann, M. Fröba,* L. Chen, P. J. Klar,* W. Heimbrodt, H.-A. Krug von Nidda, T. Kurz, A. Loidl**

Comparison of the Magnetic and Optical Properties of Wide-Gap (II,Mn)VI Nanostructures Confined in Mesoporous Silica

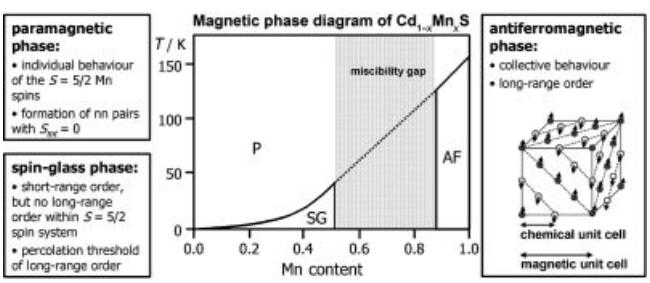

Keywords: Mesoporous materials / Diluted magnetic semiconductors / Host−guest systems / Nanostructures / $Cd_{1-x}Mn_xS$ / $Cd_{1-x}Mn_x$-Se / $Zn_{1-x}Mn_xS$

3613 **A. Shavel, N. Gaponik, A. Eychmüller***

The Assembling of Semiconductor Nanocrystals

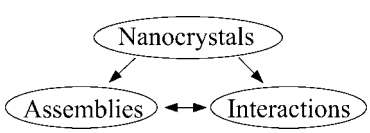

Keywords: Nanostructures / Colloids / Layer-by-layer assembly / Interactions

 © 2005 Wiley-VCH Verlag GmbH & Co. KGaA, Weinheim

3625 **F. Wen, N. Waldöfner, W. Schmidt, K. Angermund, H. Bönnemann,* S. Modrow, S. Zinoveva, H. Modrow, J. Hormes, L. Beuermann, S. Rudenkiy, W. Maus-Friedrichs, V. Kempter, T. Vad, H.-G. Haubold**

Formation and Characterization of Pt Nanoparticle Networks

Keywords: Colloids / Cross-linking / Nanostructures / Platinum / Self-assembly

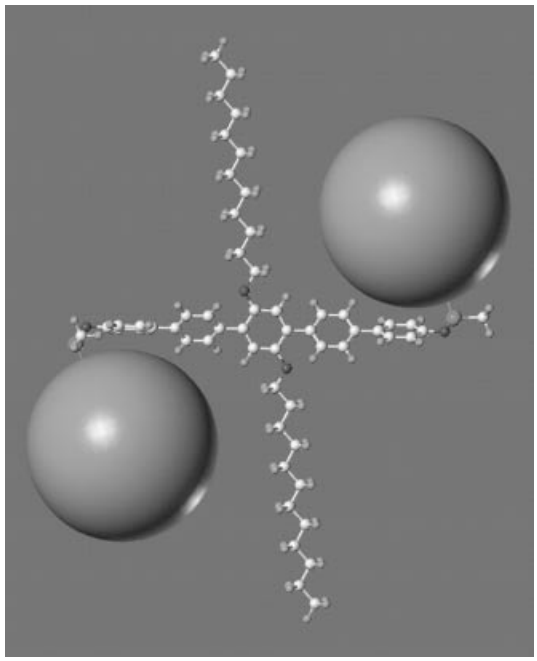

3641 **C. M. Niemeyer,* U. Simon***

DNA-Based Assembly of Metal Nanoparticles

Keywords: DNA / Materials science / Nanoparticles / Self-Assembly / Supramolecular Chemistry

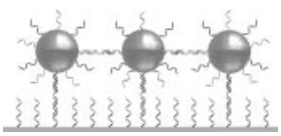

SHORT COMMUNICATION

3657 **R. Köppe,* G. Schmid, S. Schneider, H. Schnöckel***

Template-Fabricated Gold Nanowires from Gas-Phase Transport Reactions

Keywords: Chemical vapour transport / Gold / Iodine / Nanostructures / Template synthesis

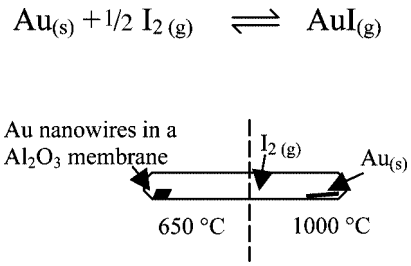

FULL PAPERS

3663 **L. Yong, S. D. Hoffmann, T. F. Fässler***

Crystal Structures of $[K(2.2.2\text{-crypt})]_4[Pb_9Mo(CO)_3]$ − Isolation of the Novel Isomers $[(\eta^5\text{-}Pb_9)Mo(CO)_3]^{4-}$ beside $[(\eta^4\text{-}Pb_9)Mo(CO)_3]^{4-}$

Keywords: Cluster compounds / Cryptands / Isomers / Packing / Zintl anions

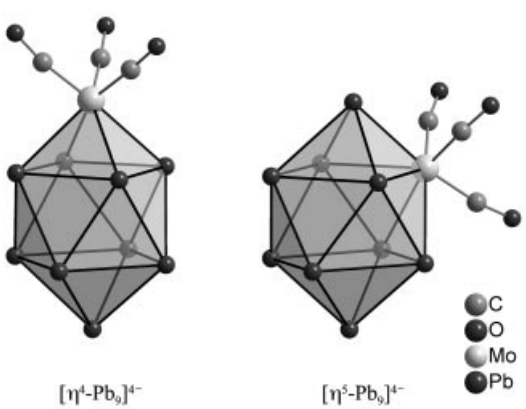

 © 2005 Wiley-VCH Verlag GmbH & Co. KGaA, Weinheim

3670 **T. Reuter, S. Neumeier, G. Schmid,***
E. Koplin, U. Simon

Generation and Characterization of Multilayer Systems Consisting of $Au_{55}(PPh_3)_{12}Cl_6$ Double Layers and SiO_2 Barrier Films

Keywords: Gold / Multilayers / Impedance spectroscopy / Bénard–Marangoni effect / Crystallisation

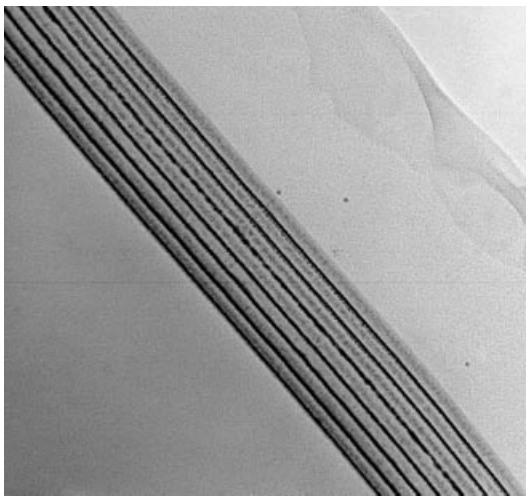

3679 **S. Neumeier, T. Reuter, G. Schmid***

The Electronic Interaction Between $Au_{55}(PPh_3)_{12}Cl_6$ Monolayers Through SiO_2 Films

Keywords: Monolayers / Gold / Multilayers / Electronic tunnelling / Current-voltage characteristics

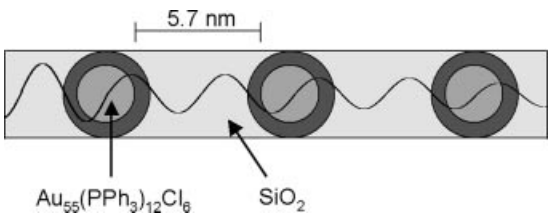

3683 **V. Jacobsen, T. Zhu, W. Knoll, M. Kreiter***

Current-Voltage Characterisation of Monolayer-Supported Au-Nanoclusters by Scanning Tunnelling Microscopy under Ambient Conditions

Keywords: Scanning probe microscopy / Surface plasmon resonance / Colloids / Monolayers / Nanostructures / Self-assembly

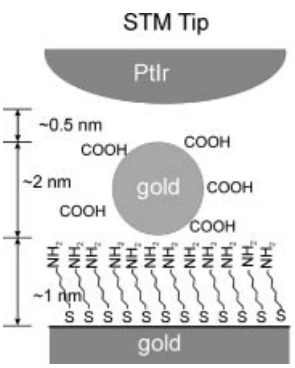

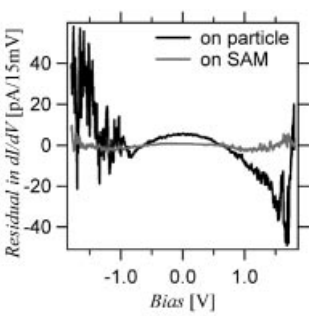

3691 **G. Kästle, A. Schröder, H.-G. Boyen,**
A. Plettl, P. Ziemann, O. Mayer, J. Spatz,*
M. Möller, M. Büttner, P. Oelhafen

Electrical Resistivity of Epitaxial Au Films Surface-Modulated by Arrays of Pt Nanoparticles

Keywords: Thin films / Gold / Conductivity / Platinum nanoparticles

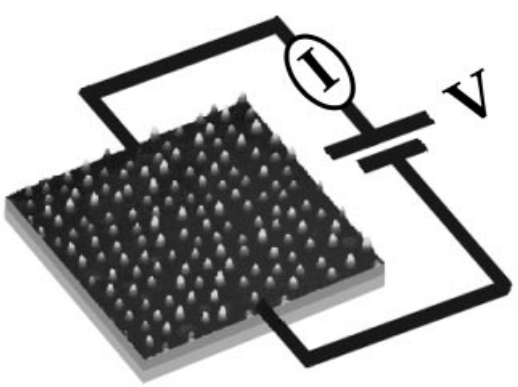

 © 2005 Wiley-VCH Verlag GmbH & Co. KGaA, Weinheim

3699 **M. Veith,* J. Frères, P. König, O. Schütt, V. Huch, J. Blin**

Nanoscaled Sn and Pb Particles Aligned in Al_2O_3 Tubes Obtained from Molecular Precursors

Keywords: Tin and lead clusters / Nanoparticles / Al_2O_3 tubes / Alignment of metal clusters / Alkoxy- and siloxyaluminium amides

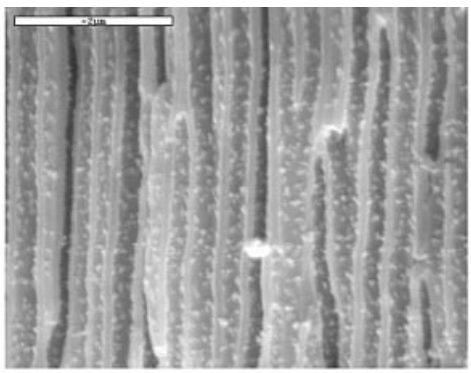

3711 **C. M. Intelmann, H. Dietz, W. Plieth***

Preparation of Gold Nanoparticles on Ultrathin Films of Polythiophene and Polythiophene Derivatives

Keywords: Gold / Nanoparticles / Ultrathin films / Polythiophene / Polymer modification

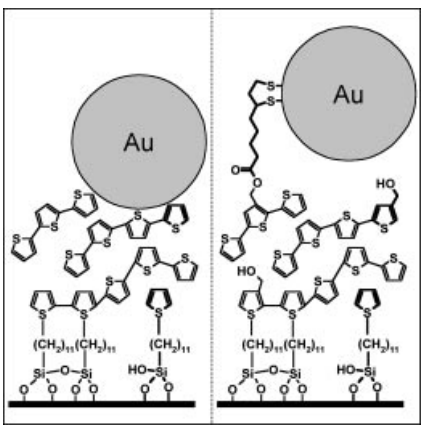

3717 **A. M. Bittner,* X. C. Wu, S. Balci, M. Knez, A. Kadri, K. Kern**

Bottom-Up Synthesis and Top-Down Organisation of Semiconductor and Metal Clusters on Surfaces

Keywords: Cadmium sulfide / Nanocrystals / Metal clusters / Microcontact printing / Nanostructures / Template synthesis

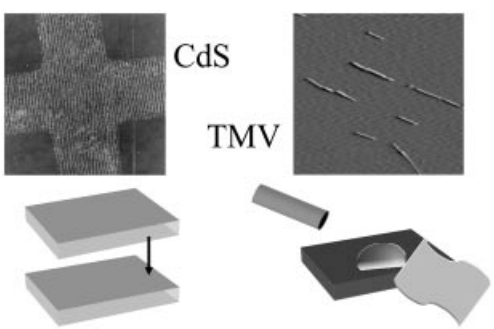

3729 **X. C. Wu, L. F. Chi,* H. Fuchs**

Patterning of Semiconductor Nanoparticles via Microcontact Printing

Keywords: Microcontact printing / Interaction / Interfaces / Nanocluster / Patterning / Semiconductors

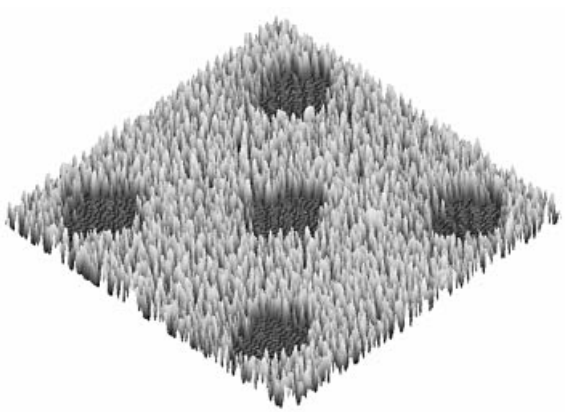

 © 2005 Wiley-VCH Verlag GmbH & Co. KGaA, Weinheim

3734 **Y.-P. Tong, S.-L. Zheng,* X.-M. Chen***

Structures, Photoluminescence and Theoretical Studies of Two Zn^{II} Complexes with Substituted 2-(2-Hydroxyphenyl)benzimidazoles

Keywords: Density functional calculations / N,O ligands / Photoluminescence / Pi interactions / Zinc

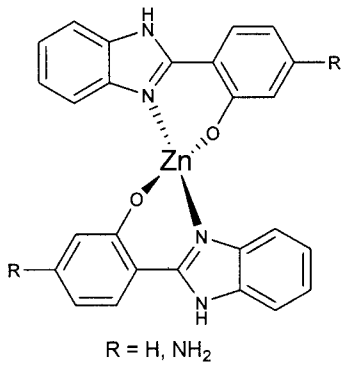

3742 **R. Andrés,* E. De Jesús,* F. Javier de la Mata, J. C. Flores, R. Gómez**

Carbosilane Dendrons Functionalized at Their Focal Point

Keywords: Dendrimers / Metallocenes / Silanes / Titanium / Zirconium

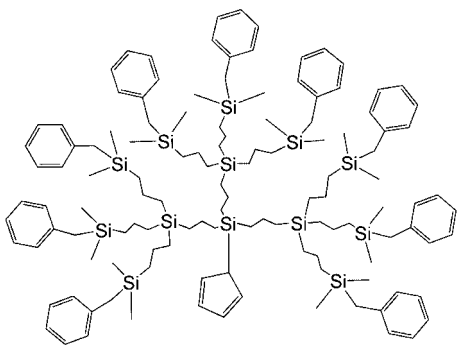

3750 **M. Saito,* R. Haga, M. Yoshioka**

Synthesis and Structures of Bi(1,1-stannole)s

Keywords: Metallacycles / Tin / UV/Vis spectroscopy

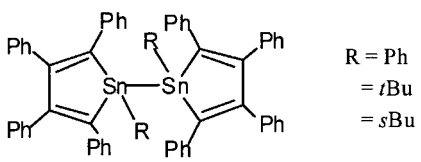

3756 **V. G. Vaidyanathan, B. U. Nair***

A Platinium(II)-Based Molecular Light Switch for Proteins

Keywords: Fluorescent probes / Platinum / Proteins / Tridentate ligands

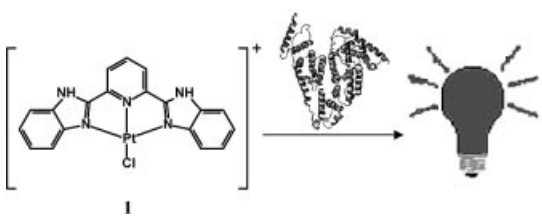

3760 **C.-M. Jin, C. Ye, C. Piekarski, B. Twamley, J. M. Shreeve***

Mono and Bridged Azolium Picrates as Energetic Salts

Keywords: Azides / Heats of formation / Ionic liquids / Materials science / Nitrogen heterocycles

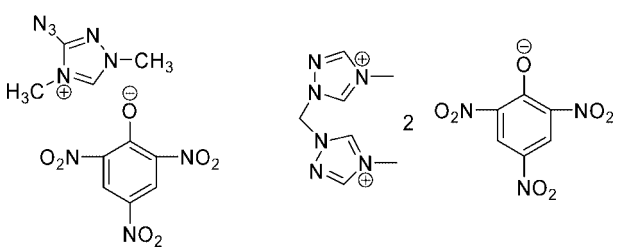

Linking Giant Molybdenum Oxide Based Nano-Objects Based on Well-Defined Surfaces in Different Phases

Achim Müller*[a] and Soumyajit Roy[a]

Keywords: Films / Hydrophilic surfaces / Monolayers / Nanochemistry / Polyoxomolybdates / Surfactant-encapsulated clusters / Surface structures / Vesicles

The linking of nanosized clusters is especially interesting if the following conditions are fulfilled: The nano-objects, as in the present case, have interesting properties like *well-defined* functionalized external and internal surfaces, linking processes follow *well-defined* rules and occur with respect to formation of discrete as well as extended structures under mild conditions in different phases, i.e. in the gas, solution and solid phase. In the present microreview it is shown that the wheel- and sphere-shaped nanosized molybdenum-oxide based clusters fulfil these conditions while extensive linking is observed even under one-pot conditions, which means that the clusters primarily formed by self-assembly can become further linked in the same phase.

(© Wiley-VCH Verlag GmbH & Co. KGaA, 69451 Weinheim, Germany, 2005)

The chemistry of varying connectivity is a fascinating subject. Nature has long made use of this phenomenon as a means to induce structural diversity. From dazzling diamonds to charry coals, from liquid aniline to its conducting plastic polymer,[1] the varying fluidity of the membranes,[2a] from a basic building unit to a variety of supramolecular structures,[2b–2f] from crystalline quartz to ornate shells of diatoms and related bio- (or bio-mimetic) architectures,[2g–2k] are but only a few illustrations of varying connectivity. The underlying principle in all cases is nearly the same, varied but iterative linking of basic building blocks. The tale becomes especially interesting from a chemist's point of view if the above principle can be deliberately realized in a reaction system which has the intrinsic potential to show connectivity variability under different conditions,

[a] Lehrstuhl für Anorganische Chemie I, Fakultät für Chemie der Universität,
Postfach 100131, 33501 Bielefeld, Germany
Fax: +49-521-106-6003
E-mail: a.mueller@uni-bielefeld.de

Achim Müller (left) studied chemistry and physics at the University of Göttingen and received his Ph.D. (1965) and his Habilitation (1967) there. In 1971, he became professor at the University of Dortmund (Germany), and in 1977 accepted the chair of Inorganic Chemistry at the University of Bielefeld, where he is still Professor of the Faculty of Chemistry. His research involves the chemistry of transition metals, particularly inorganic supramolecular chemistry and bioinorganic chemistry in synthesis, spectroscopy, and theory. He has published, besides numerous original papers, more than 35 reviews and is coeditor of several books, including "The Chemistry of Nanomaterials" with C. N. R. Rao and A. K. Cheetham in 2004 (Wiley-VCH). The latest of his very many national and international awards in 2005 are an honorary doctorate of the University Pierre et Marie Curie (Paris) and an award, the Premio Elhuyar Goldschmidt, of the Real Sociedad Española de Química (RSEQ, Spanish Chemical Society). He also delivered this year's annual Lewis Lecture at the University of Cambridge.

S. Roy (right) obtained his M. Sc from the Indian Institute of Technology, Delhi, India, and has just completed his doctoral dissertation under the supervision of Prof. A. Müller at the University of Bielefeld.

MICROREVIEWS: This feature introduces the readers to the authors' research through a concise overview of the selected topic. Reference to important work from others in the field is included.

e.g. in the gas phase, in solution or under solid-state conditions. The solutions of oxoanions of the early transition metals, in particular the polyoxomolybdates under reducing conditions considered here, provide spectacular possibilities to explore the enormous connectivity variety that can be achieved by linking together metal-oxide based building blocks or even the resulting nanosized clusters.[3] Examples include spherical nanocapsules with unique receptor properties like those of the $\{Mo_{132}\}$ Keplerate type,[4] the giant wheel-type cluster anions like $\{Mo_{154}\}$,[5] and the "blue lemon" $\{Mo_{368}\}$-type species[6] (all formed from metal-oxide fragments as building blocks) as well as the formation of chains or layers from these clusters which themselves act as building blocks. In this microreview an account of such covalent structuring in the solid state leading to periodicity is depicted as a concluding section and is preceded by different types of "super-structuring" in the gas phase, in solution and on surfaces. The unprecedented linking versatility to be illustrated shortly is a consequence not only of the uniformly nanoscaled structured surfaces but especially of the characteristic/unique functionalizations [with the option for an interesting type of "scale chemistry, in which the size of the "secondary building blocks" (SBUs) in a structure is increased while maintaining the same connectivity between them [...]" (see ref.[7])]. With respect to the structural variety of nanosized discrete species, the other polyoxometalates like the polyoxotungstates behave completely different from the polyoxomolybdates, i.e. they do not show the versatility of nanosized structures.

1. Structuring in the Gas Phase

"Uncharged" molybdenum-oxide giant spheres with a molecular mass of about 16 kDa can be "kicked out" like soccer balls into the gas phase using matrix-assisted laser desorption and ionization (MALDI) and be detected by time of flight (TOF) mass spectrometry.[8] These findings confirmed the existence of such giant clusters in the gas phase and opened a wide range of nontrivial experiments, i.e. single-molecule spectroscopy of nano-objects or the epitaxial growth of functionalized supramolecular layers or cluster collectives suitable for electronic devices (quantum-dot cellular automata). The practically neutral spherical clusters studied here, for the aforementioned related investigations, cocrystallized in a matrix of DCTB (2-[(2*E*)-3-(4-*tert*-butylphenyl)-2-methylprop-2-enylidene]malononitrile).

MALDI spectra for two spherical species of the type $[\{(Mo)Mo_5\}_{12}\{M_{30}\}]$ in the DCTB matrix were obtained. As main products, single spheres of the types $[\{Mo\}_{72}\{Fe\}_{30}(Mo)_6]$ (molecular mass 15.93 kDa with nearly all decorations, but without the crystal water), $[\{Mo_{72}\}\{Mo_{30}\}]$ (15.94 kDa) singly and doubly charged, and remarkably, also oligomers with 2, 3, 4 and 5 spheres, again singly and doubly charged, were found. Taking into account the molecular mass of DCTB (250 Da), the mass distribution over the peaks covers the complete range from the fully ligand decorated (together with only a few matrix molecules) to the completely undecorated giant spheres (Figure 1).

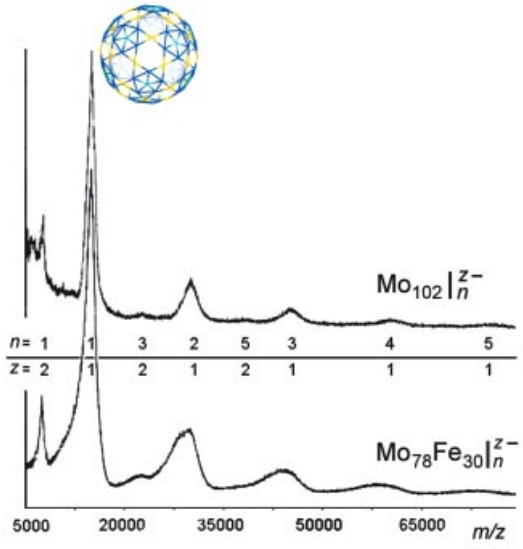

Figure 1. MALDI TOF mass spectra of the $[\{(Mo)Mo_5\}\{M\}_{30}]$-type species (M = Fe, Mo) and their oligomers (for details see ref.[8]).

2. Super Structuring in Solution

An interesting cluster connectivity was accomplished with super-structuring, and highlighted also as "rounding up"[9] of a huge number of $\{Mo_{154}\}$-type nanowheels in aqueous solution to vesicular nanoassemblies, i.e. to an inorganic skinned drop of water (for details on the topic not mentioned here, see ref.[10]).

The $\{Mo_{154}\}$ based vesicles, almost monodisperse, were characterized by light-scattering data (DLS and SLS) as well as transmission and scanning electron microscopy, which revealed spherical hollow structures with an average, hydrodynamic radius of about 45 nm and comprising approximately 12×10^2 $\{Mo_{154}\}$ wheel-shaped clusters (Figure 2). The clusters appear to lie flat and homogeneously distributed on the vesicle surface. A question may arise as to whether those entities are really hollow and not solid. It can be shown that they are, apart from the solvent inside.[11]

The unique/unprecedented phenomenon of self-assembling $\{Mo_{154}\}$-type nano-objects into a spherical vesicle is still not completely understood. However, it is expected that here the counter cations Na^+, H^+ and especially the different types of confined structured water play, besides attracting van der Waals forces, a crucial role in the story of vesicular stabilization. (The aqueous solution of the clusters is a medium strong acid, even "dissolving" metals like Zn.) Assuming that all the nanowheels are distributed on the surface in almost hexagonal closest packing, the center-to-center distance between two adjacent nanowheels would be around 4.9 nm, whereas the diameter of an individual nanowheel is according to X-ray crystallography 3.6 nm. This infers that the nanowheels are not touching each other on the vesicle surface.

As mentioned above, water assemblies and counter cations are expected to play an important role in filling gaps and holding the overall assemblies together, while the struc-

 © 2005 Wiley-VCH Verlag GmbH & Co. KGaA, Weinheim

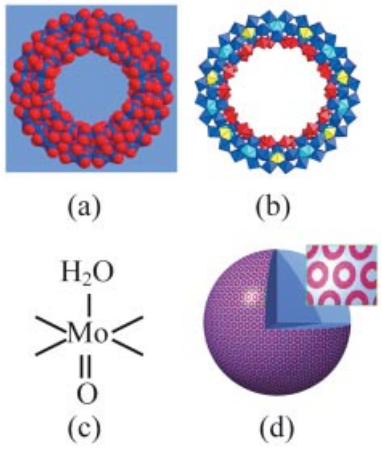

Figure 2. Structure of the 3.6 nm size $\{Mo_{154}\}$-type nanowheel with a hydrophilic surface and nanosized central cavity as well as the related vesicle. (a) Space-filling representation (Mo atoms blue and light blue; O atoms red). (b) Polyhedral representation, demonstrating the abundance of pentagonal $\{(Mo)Mo_5\}$ units (in blue) probably influencing the water structure ($\{Mo_2\}$ units red; $\{Mo_1\}$ units yellow). (c) The typical smallest fragment with a metal atom and its coordination sphere, i.e., with one of the 70 H_2O ligands causing the extreme hydrophilic nature that is responsible for the interaction with solvents such as water. (d) Schematic plot of the vesicle structure ($\approx$ 45 nm radius) formed from ca. 12×10^2 nanowheels in aqueous solution; the inset shows enlarged nanowheels.

tured water would in a way especially explain the stability of the vesicles! Indeed, the integration of a large number of nano-objects on an ordered spherical surface seems to be highly *anti*-entropic and hence a highly unlikely event (Figure 2). But the release of some of the "local" strongly hydrogen bonded water molecules from the vicinity of the clusters to the "bulk" water pays the high price for the mentioned entropy decrease.

These results are also interesting as the molecular $\{Mo_{154}\}$-type wheels show, because of the abundance of 70 coordinated H_2O ligands, an extremely hydrophilic surface causing a well-defined hydration shell. This again causes extreme solubility, which for more than 200 years prevented chemists from the time of Scheele and Berzelius who performed the first related experiments, from isolating them in a crystalline state.[12a] Now it can be shown by dielectric relaxation studies[12b] that there are different kinds of confined water in and on these systems; for instance the water inside the wheel-type cavity is more strongly fixed (thus less mobile) than the water at the surface, while both are probably involved in the stabilization of the vesicles. This correlates with the above-mentioned hydrophilicity and especially the strong cluster surface water interaction.

3. Encapsulation by Surfactants and Surface Structuring: Films and Monolayers

The motivation to examine "Surfactant Encapsulated Clusters" (SECs) rather than only "naked" ones had the following base: the surfactant shell improves the *stability* of the encapsulated cluster against *fragmentation*, enhances the *solubility* in nonpolar, aprotic organic solvents, neutralizes their *charge*, thus leading to discrete, *electrostatically neutral* assemblies, while altering the *surface chemical properties* (e.g. self-aggregation, surface adhesion, wetting behavior) in a predictable manner. Some related investigations[13,14] are reviewed here, also deliberately with respect to some details.

The discrete hybrid $(DODA)_{40}(NH_4)_2[(H_2O)_n \subset Mo_{132}O_{372}(CH_3COO)_{30}(H_2O)_{72}]$ ($n \approx 50$) for example is formed by spontaneous self-assembly (see Figure 3). It consists of a hollow giant spherical isopolyoxomolybdate core covered by a hydrophobic shell of dimethyldioctadecylammonium

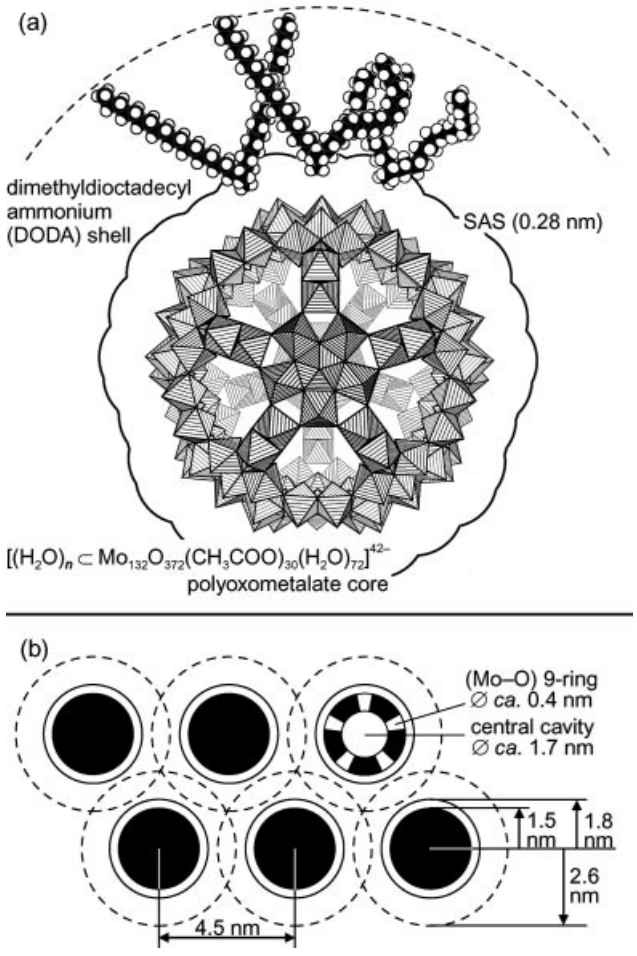

Figure 3. (a) Schematic representation of the surfactant-encapsulated cluster (SEC). The Mo–O framework of the $\{Mo_{132}\}$-type cluster is shown in polyhedral representation. The DODA amphiphiles, only a fraction of which are represented in the Scheme, form a hydrophobic shell around the cluster. Molecular dynamics simulations of a single SEC placed within a periodic solvent-filled ($CHCl_3$) box indicate that in solution the relative density of the appending C_{18} chains decreases as the radial distance from the cluster increases. Due to the conformational flexibility of the C_{18} chains, the external boundary of the SEC (represented by the broken line) is not sharply defined. (b) Schematic representation of a single SEC layer according to TEM data and molecular models. The SECs arrange on a 2D lattice to form a closest packing. Surfactant shells of neighboring SECs locally interpenetrate one another. One of the SECs is displayed cross-sectioned to further highlight the supramolecular architecture.

 © 2005 Wiley-VCH Verlag GmbH & Co. KGaA, Weinheim

(DODA) cations, which was the basis for the generation of well-defined films and monolayers.[13] The structural characterization of the nanoporous core-shell particles was based on small-angle X-ray scattering (SAXS) data (on solutions of the encapsulated clusters), transmission electron microscopy (TEM) investigations, FT-IR and UV/Vis spectroscopy, as well as the determination of the molecular area of the encapsulated cluster by Langmuir–Blodgett (LB) film investigations.[13] Computer modeling of the solvent-accessible surface of the encapsulated cluster yielded a central cavity with a volume of 1.5(±0.3) nm^3. The cavity is occupied by approximately 50(±15) H_2O molecules, which are, in the case of the present acetate system with a hydrophobic shell interior, not densely packed. The covered surface area of 84 $Å^2$/DODA indicates a rather tight packing of the amphiphiles at the cluster/capsule surface.

The discrete cluster hybrids have been directly imaged by transmission electron microscopy.[13] Figure 4a shows a thin film originally cast onto a water surface. The inorganic cores of $(DODA)_{40}(NH_4)_2[(H_2O)_n \subset Mo_{132}O_{372}(CH_3COO)_{30}(H_2O)_{72}]$ ($n \approx 50$) appear as dark spots embedded in a bright matrix of surfactant molecules. Both the diameter of the dark objects (ca. 3 nm), as well as the average distance between them (ca. 4.5 nm), match the film structure depicted in Figure 4b. The image shows monolayer regions, regions consisting of a bilayer (darker) and the uncovered substrate (brighter), while small domains exhibit hexagonal arrays of SECs corresponding to a two-dimensional dense packing of spherical particles (arrows). The order improves in thicker films and becomes three-dimensional. An ordered region is shown in Figure 4b; the related electron diffraction pattern (insert) clearly reveals long-range order (spots rather than rings) and a threefold symmetry for the pattern of reflections corresponding to a spacing of 4.2 nm. In accordance with the presence of local fourfold symmetry projections it can be assumed that the SECs are arranged on a fcc lattice with the most dense (111) planes preferentially oriented parallel to the substrate, as is the case of latex films. It may therefore be concluded that the diffraction pattern reflects the structure from the triangular array of particles in a (111) plane at normal orientation to the beam, and that the packing of the SECs is best described within a fcc lattice with a cubic unit-cell axis of approximately 6 nm.

A characteristic feature of the present type of SEC is that it spreads at the air-water interface. This property was used to measure its molecular area. From the compression isotherm of a monolayer of the cluster (Figure 5), a molecular area of 15 nm^2 at the collapse point could be determined, which corresponds to the densest possible packing. Based on the assumption of a void-free monolayer in which the inorganic cluster cores are packed in a hexagonal array (Figure 3b), a core-to-core distance of 4.2 nm was obtained, a result that is in excellent agreement with the TEM data. The molecular area for noninteracting SECs determined at the onset of the isotherm ($\pi = 0$) is 32 nm^2, which corresponds to a diameter (of the spherical projection) of 6.4 nm.

Due to the unique supramolecular architecture of the surfactant encapsulated cluster (SEC) as well as its high solubility in common organic solvents, this aggregate shows promising perspectives for future applications in host-guest chemistry and homogeneous size-selective catalysis.

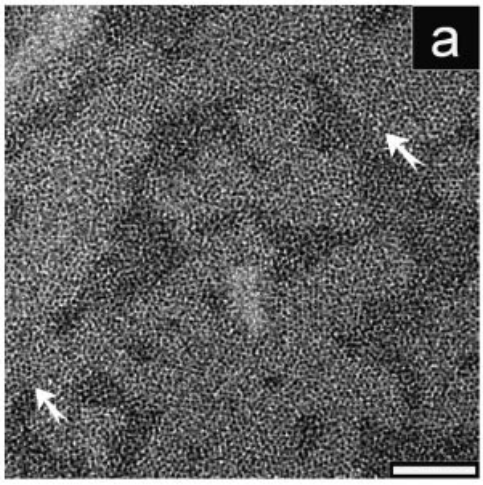

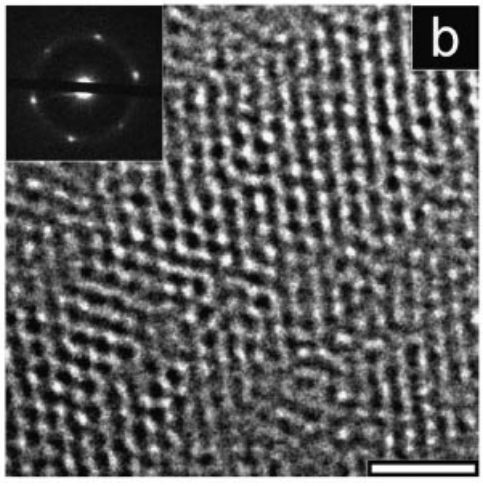

Figure 4. Shown is (a) a TEM micrograph of a thin film of SECs (scale bar 50 nm). Extended monolayers, interspersed with holes and doublelayer regions, are clearly visible (two arrows mark some regions of apparent hexagonal order). (b) TEM micrograph of an ordered region of a thicker film at high magnification (scale bar 20 nm). The insert shows a low-angle electron diffraction pattern (elastically filtered) recorded from a larger area (5 μm^2) containing the region shown.

4. Extended Structuring in the Solid State

Controlled assembly of building blocks by *specific linking* in a self-assembly process following an "Aufbau" principle leading to the metal-oxide based nanoscaled clusters as mentioned above, inevitably comes up with an imminent question. Is it possible to use those self-assembled structures as "secondary building blocks" to generate even "*extended*" complex topologies by "*extended" linking*? In our

 © 2005 Wiley-VCH Verlag GmbH & Co. KGaA, Weinheim

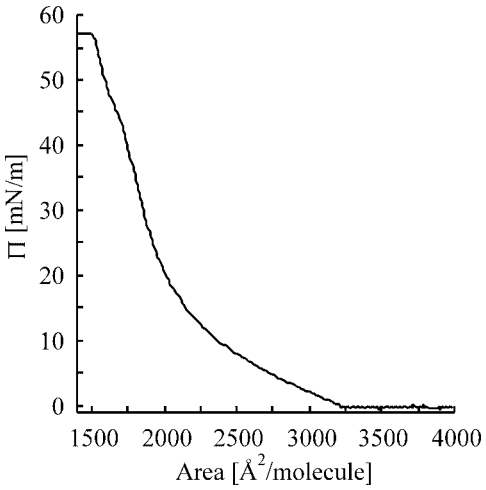

Figure 5. Surface pressure-area ($\pi - A$) isotherm of the SEC at the air-water interface.

case the question was whether it is possible to "trigger" a special aggregation-type process to extensively link [(pentagon)$_{12}$(linker)$_{30}$]-type species and/or the circular {Mo$_{154}$}-type nano-objects, as "secondary building blocks". In fact it was possible to find an easy solution to the problem. A simple condensation-type reaction with the loss of water molecules solves the problem by triggering a self-organization type process even under solid-state conditions at room temperature, thereby getting the primarily formed parent-type nano-objects linked in the same phase. In the following Section we will discuss five prototypal cases of such processes, which elegantly demonstrate the basic principles of "scale chemistry"[7a] in the context of connectivity.

4.1 Cross-Linking the [{(Mo)Mo$_5$}$_{12}${Fe}$_{30}$]-Type Capsules According to Their Acidic Properties to 2D Layers: A Remarkable Room-Temperature Solid-State Reaction

A well-known reaction in inorganic chemistry is a condensation process in aqueous solution between acidic [M^{III}(H$_2$O)$_6$]$^{3+}$-type complexes with the resulting loss of protons and water that leads to the formation of iron polycations via M–O–M linkages.[15] Such a reaction has a very low activation energy and hence could in principle proceed in the present [{(Mo)Mo$_5$}$_{12}${Fe}$_{30}$]-type capsule situation because of the abundance of 30 [Fe(H$_2$O)$_2$]$^{3+}$groups as linkers.[16a]

Correspondingly, it was in fact observed that even in a room-temperature solid-state reaction the [{(Mo)Mo$_5$}$_{12}$-{Fe}$_{30}$]-type nano-objects become cross-linked.[16b,16c] The rapid loss of loosely bound crystal water molecules leads to a situation where the discrete spherical clusters are abundant in the compound [{(Mo)Mo$_5$}$_{12}$Fe$_{30}$O$_{252}$(CH$_3$COO)$_{12}${Mo$_2$O$_7$(H$_2$O)}$_2${H$_2$Mo$_2$O$_8$ (H$_2$O)}(H$_2$O)$_{91}$]·ca. 150 H$_2$O, i.e. the corresponding freshly filtered monoclinic crystals can come into contact, which is a condition for the interaction. This finally leads to the formation of [H$_4$Mo$_{72}$Fe$_{30}$O$_{254}$(CH$_3$COO)$_{10}${Mo$_2$O$_7$(H$_2$O)}{H$_2$Mo$_2$O$_8$(H$_2$O)}$_3$(H$_2$O)$_{87}$]·ca. 80 H$_2$O, with a layered structure forming platelike crystals (see Schemes 1 and 2 and Figure 6). It is assumed that the finally released H$^+$ ions protonate the spherical cluster units. (Note: [{(Mo)-Mo$_5$}$_{12}${Fe}$_{30}$]-type clusters can also be obtained as discrete entities in rhombohedral crystals, where the reaction does not proceed, probably because of a different type of packing.) The (nearly) electrical neutrality of the cluster units facilitates the easy loss of water and hence cross-linking. The reaction steps (see Scheme 1 and Scheme 2) involved in cross-linking clearly show as expected a decrease in the volume of the unit cell.

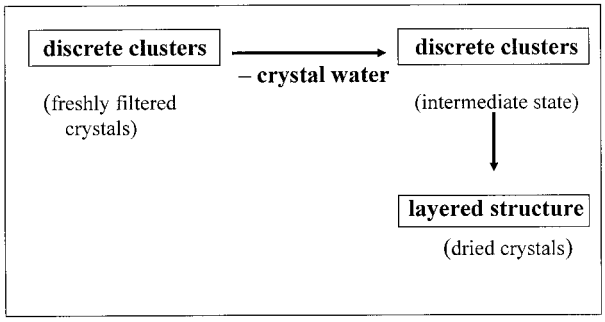

Scheme 1.

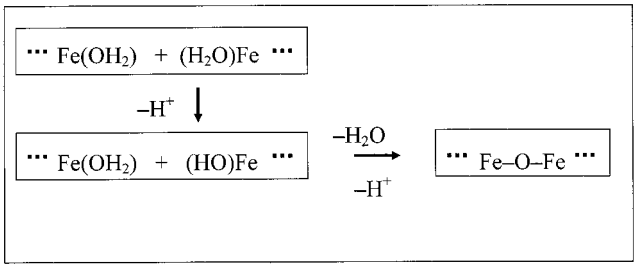

Scheme 2.

4.2 "Necklace"-Type Linking of Spherical Capsules

From two-dimensional layers to a one-dimensional chain or necklace, a transition, which might initially seem problematic but, which in fact, follows the same thread of chemical logic. The formation of one-dimensional chains of related similar nano-objects involves, in principle, a reaction of the same type, which is based on a compound containing (nearly neutral) discrete [{(Mo^{VI})Mo$^{VI}_5$}$_{12}${Mo$^{V}_6$Fe$^{III}_{24}$}-(CH$_3$COO)$_{20}$O$_{258}$(H$_2$O)$_{84}$]$^{2-}$ clusters. When the black crystals containing the mentioned clusters are dried, the latter becomes linked to form one-dimensional chains with the stoichiometry [{(Mo^{VI})Mo$^{VI}_5$}$_{12}$ {Mo$^{V}_6$Fe$^{III}_{24}$} (CH$_3$COO)$_{20}$-O$_{258}$(H$_2$O)$_{82}$]$^{2-}$. The reaction is triggered by the rapid loss of crystal water molecules (Figure 7 and Figure 8),[17] which causes the obligatory decrease of inter-sphere distances and leads to the situation where an Mo=O group of one discrete sphere can formally act as a ligand while replacing H$_2$O groups attached to Fe^{III} centers of an adjacent sphere in an

 © 2005 Wiley-VCH Verlag GmbH & Co. KGaA, Weinheim

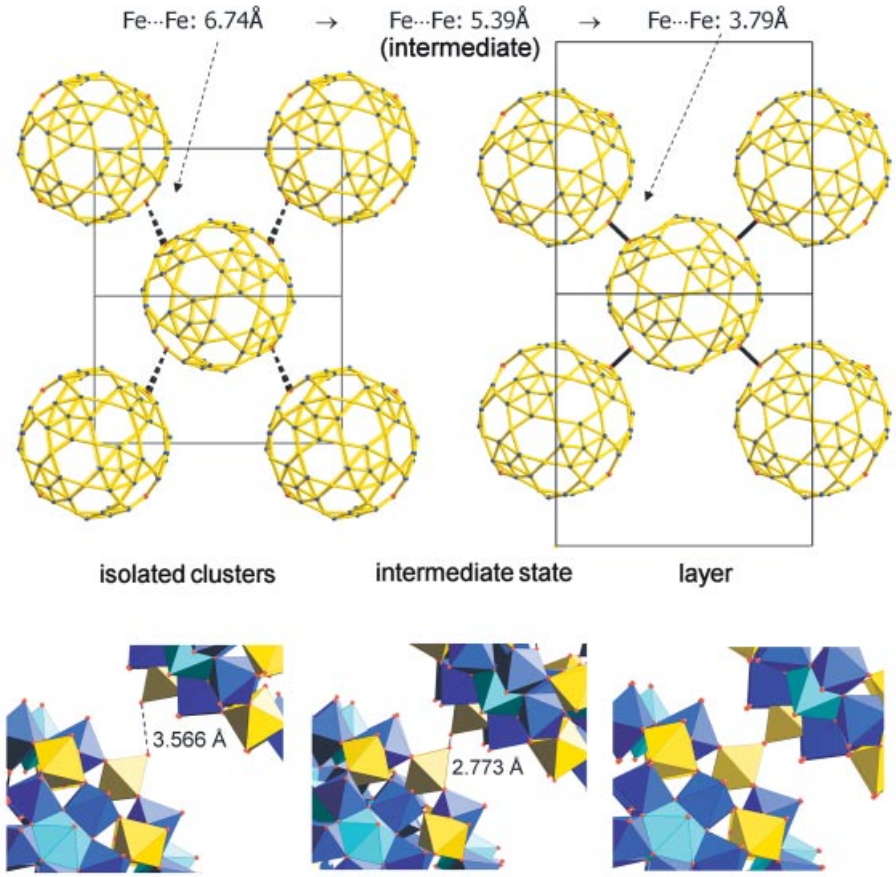

Figure 6. Wireframe representation (in yellow/blue) of the metal skeleton of the $\{Mo_{72}Fe_{30}\}$-type cluster units indicating their covalent cross-linking to a layer structure (top right). The solid-state room-temperature conversion process leading to its formation takes place according to Scheme 1 and Scheme 2 given in the text. The reaction proceeds from discrete cluster units (top left) present in the wet monoclinic crystals, freshly filtered from the mother liquor, via an intermediate state (top middle) with discrete units positioned at the minimum possible distances without covalent bond formation to the final (rhombic) crystalline product. (Note: the same does not occur for rhombohedral crystals with discrete units.[16a]) The related segment demonstrating the linking is given in polyhedral representation (FeO_6 yellow; Mo polyhedra blue).

S_N-type reaction. It is important to note that this mechanism is much more complicated than that in the above-mentioned cross-linking case. It should further be noted that the present clusters due to their lower symmetry do not allow an easy further higher-symmetrical cross-linking, i.e. with two-dimensional periodicity.

In the present case and in that of the previous Section (4.1), it should in principle also be possible to form oligomers when the existing boundary conditions prevent extended linking.

4.3 Cross-Linking of the Spherical Clusters Exhibiting Encapsulated "Guests", i.e. Composites with Nucleus-Shell Topology

The chemistry of connectivity could become even more exciting if it is possible to "cross-link" not only empty spherical capsules like those described above, but also "host-guest"-type composites – especially those with unusual host-guest interactions – to a network. The above-mentioned experiments have shown that it is possible to connect $[\{(Mo)Mo_5\}_{12}\{Fe\}_{30}]$-type moieties, but the question arises, can such moieties, which are reacting to become linked, contain guests?

Interestingly, the cavities inside the (practically uncharged) $[\{(Mo)Mo_5\}_{12}\{Fe\}_{30}]$-type clusters are large enough to host Keggin-type anions with a diameter of ca. 14 Å. The latter can be incorporated into the cavity of the former by merely adding them to a solution ambient to the generation of the host cluster shells.[18] The resulting molybdenum-oxide based "host-guest" composite with an encapsulated Keggin ion presents an unprecedented noncovalent, i.e. supramolecular host-guest interaction (Figure 9).[19] Here the Keggin ion (guest) can, in principle, also act as a "kind of template" for the generation of the host as it accelerates its formation.

It finally turned out that these "host-guest" supramolecular nanocomposites can be linked in a way that is identical to that of the empty spherical capsules to form layers (see Section 4.1). In other words, these host-guest nanocomposites also undergo a cross-linking type of solid-state condensation reaction at room temperature to form a layered net-

 © 2005 Wiley-VCH Verlag GmbH & Co. KGaA, Weinheim

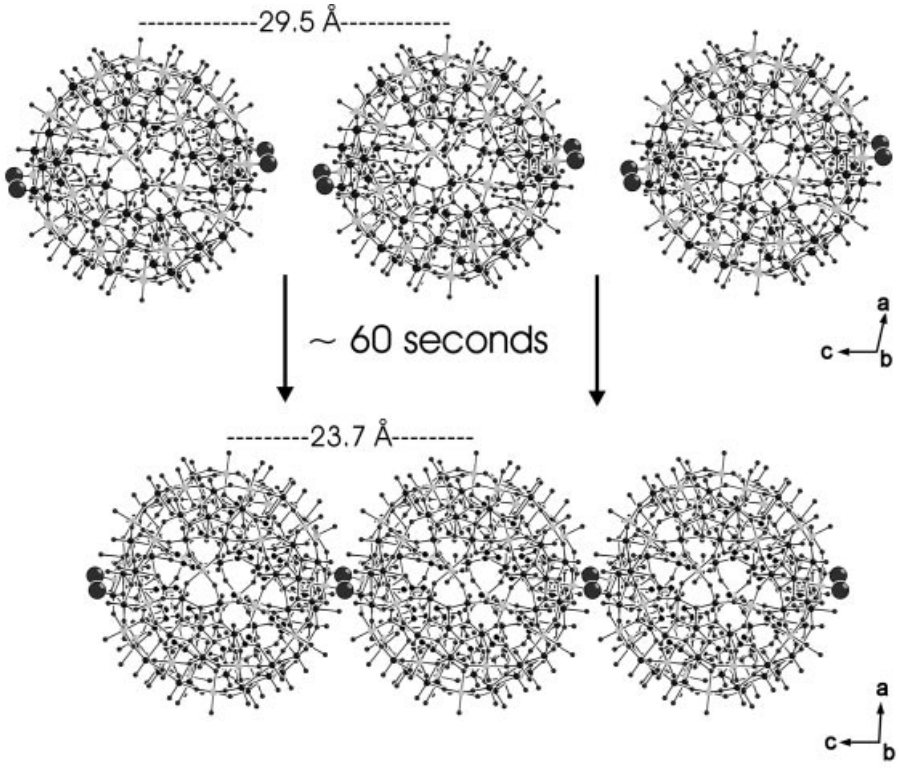

Figure 7. Schematic representation of the room-temperature solid-state reaction (see also Figure 8) leading to the formation of the chain (bottom) present in the compound $Na_2[\{(Mo^{VI})Mo^{VI}_5\}_{12}\{Mo^{V}_6Fe^{III}_{24}\}(CH_3COO)_{20}O_{258}(H_2O)_{82}]$·ca. 80 H_2O caused by linking the discrete spheres $[\{(Mo^{VI})Mo^{VI}_5\}_{12}\{Mo^{V}_6Fe^{III}_{24}\}(CH_3COO)_{20}O_{258}(H_2O)_{84}]^{2-}$ (top).[17] Note the (small) error limit in the number of Mo^{V} centers and the corresponding (possible) cluster charge.

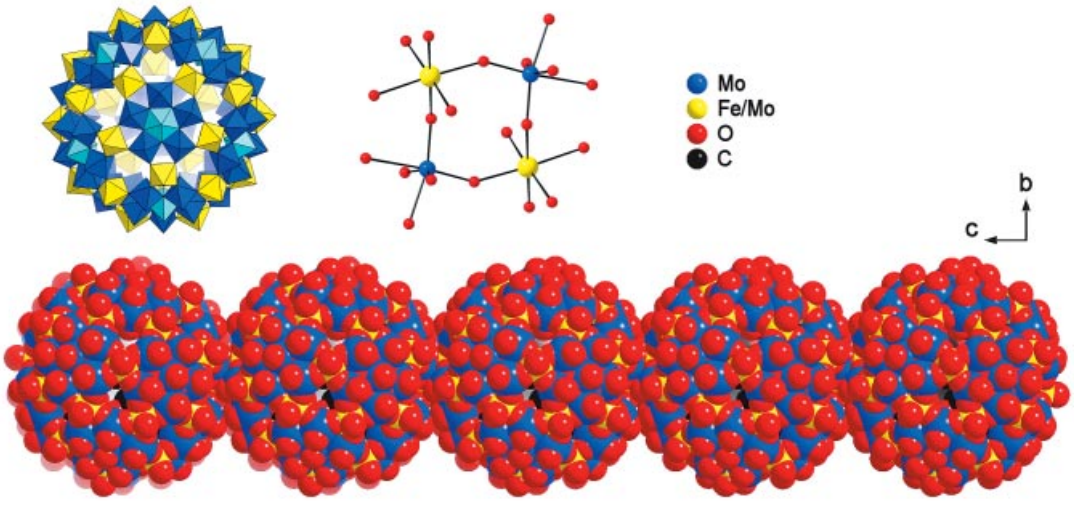

Figure 8. More detailed representation of the structures depicted in Figure 7 showing 1) the discrete anion (polyhedral representation, top left) in crystals of $Na_2[\{(Mo^{VI})Mo^{VI}_5\}_{12}\{Mo^{V}_6Fe^{III}_{24}\}(CH_3COO)_{20}O_{258}(H_2O)_{84}]$·ca. 150 H_2O, and 2) the anionic chain (Figure 7) in these crystals (bottom, space-filling representation). The linking area is separately given in ball-and-stick representation (top right); bond lengths [Å] and angles [°] in the M_4O_4 (M = Mo/Fe) ring: Mo–O: 1.72/1.78; Fe–O: 1.96/1.98; Mo–O–Fe: 147.0/149.9; O–Mo–O: 101.5; O–Fe–O: 93.2.[17]

 © 2005 Wiley-VCH Verlag GmbH & Co. KGaA, Weinheim

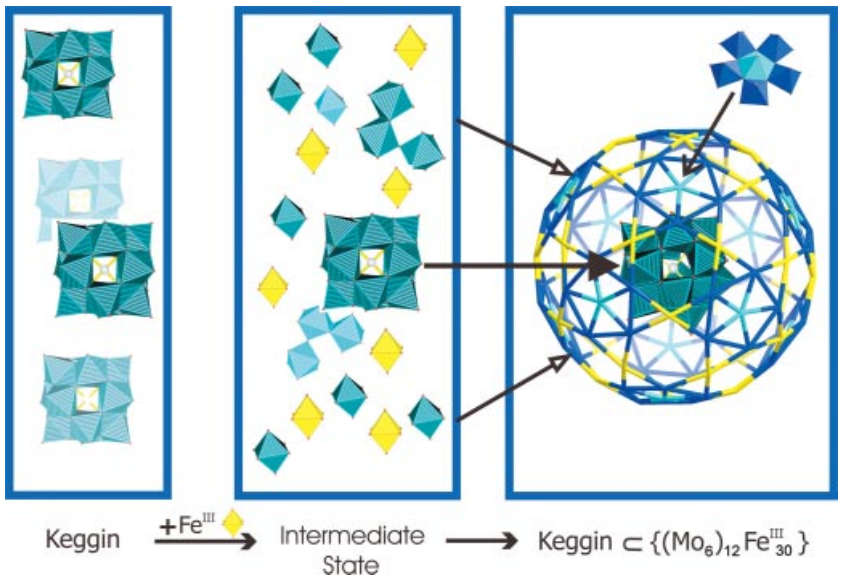

Figure 9. Reaction Scheme showing the decomposition of part of the Keggin anions $\{PMo_{12}O_{40}\}^{3-}$ (left, polyhedral representation) in the presence of Fe^{3+} in aqueous solution, leading finally to the formation of the spherical $\{(Mo)Mo_5\}_{12}\{Fe\}_{30}$-type cage [with wireframe representation of the capsule's Mo atoms (in cyan and dark blue) and Fe atoms (in yellow)] which has one of the remaining nondecomposed Keggin anions encapsulated (polyhedral representation) thus forming the unusual supramolecular species with core-shell topology: guest ⊂ [(pentagon)$_{12}$(linker)$_{30}$] (FeO_6 octahedra yellow).

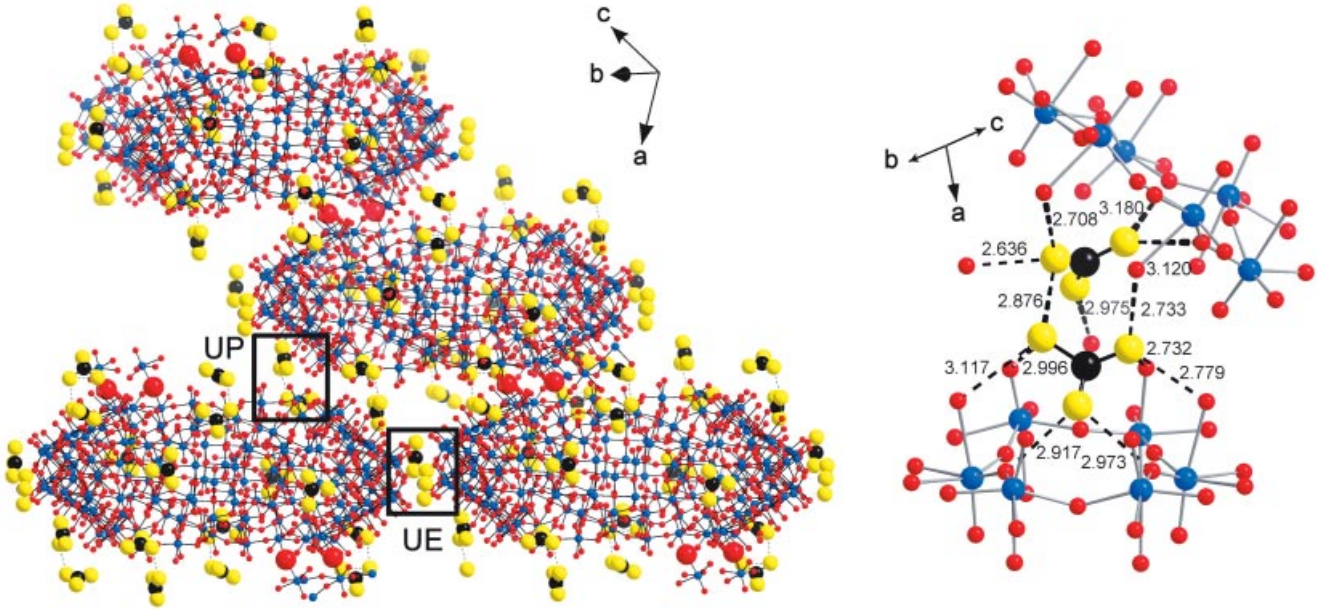

Figure 10. Left: ball-and-stick representation of four $\{Mo_{154}\}$-type rings of the compound $^{1}_{\infty}\{(NH_3CONH_2)_{14}[Mo^{VI}_{126}Mo^{V}_{28}O_{462}H_{14}(H_2O)_{68}]\}\cdot$ca. 350 H_2O "glued" with two types of protonated urea molecules [viz., equatorial (UE) as well as polar (UP)]. The atoms of the urea (type) units and the oxygen atoms which covalently connect adjacent rings have been enlarged for clarity (molybdenum blue; oxygen red; carbon black; nitrogen and oxygen atoms of urea units which could not be clearly distinguished using single-crystal X-ray structure analysis, yellow). Right: interaction between polar UP-type units among themselves as well as with oxygen atoms of two hexagonal $\{Mo_6O_6\}$ ring sites showing the (weak) potential receptor property of the cluster. The difficulty of distinguishing exactly between O and N atoms of UP is mainly caused by a O=Mo–H_2O disorder at the cluster surface (for details see ref.[20]).

 © 2005 Wiley-VCH Verlag GmbH & Co. KGaA, Weinheim

work, where each individual nanocomposite acts as a "secondary building block".

4.4 Linking the {Mo_{154}}-Type Circular Clusters to Chains

Like the [(pentagon)$_{12}$(linker)$_{30}$]-type nano-objects above, the {Mo_{154}}-type wheels can also be linked to form a one-dimensional chain of the type $^{1}_{\infty}${Mo_{154}}. For instance, using protonated urea as a "gluing" agent it is possible to achieve such linking. The protonated urea reduces the repulsion of approaching negatively charged rings, thereby facilitating condensation between them and ultimately leading to a covalent Mo–O–Mo connectivity (see Figure 10 and ref.[20]). These findings can lead to new gateways in host-guest chemistry as the protonated urea molecules are "attached" to the nucleophilic {Mo_6O_6}-type "receptors" on the cluster surface [note also a new (A. Müller et al., unpublished) synthetic method for the formation of $^{1}_{\infty}${Mo_{154}}-type chains with "guest free" {Mo_6O_6} rings as well as with other cationic substrates like guanidinium].

4.5 Linking the {Mo_{154}}-Type Circular Clusters to Layers

The {Mo_{154}}-type units are not only one-dimensionally connected to form chains but also into $^{2}_{\infty}${Mo_{154}}-type layers. The basic principle involves the assembly of {Mo_{154}}-type rings as synthons by inducing a synergetically activated functional complementarity on their surface sites. The title of the corresponding paper was "*Assembling nanosized ring-shaped synthons to an anionic layer structure based on the synergetically induced functional complementarity of their surface sites*: $Na_{21}[Mo_{126}^{VI}Mo_{28}^{V}O_{462}H_{14}(H_2O)_{54}(H_2PO_2)_7]\cdot xH_2O$ ($x \approx 300$)".[21] Because of the increased electron density (or nucleophilicity) of the considered Mo=O group (pointing outside of the ring), caused by the coordinated $H_2PO_2^-$ ligand, the related ring formally acts as a ligand resulting in the substitution of the H_2O ligand at a corresponding Mo=O group of another adjacent ring which has no coordinated $H_2PO_2^-$ ligand. (Four such covalent connectivities are formed per ring.) The layered structure also leads, topologically speaking, to the formation of a system of "tubular"-type nanochannels (Figure 11). They present a possibility for the construction of a new class of materials with well-defined channel cavities (3.4 nm diameter) once the channels are freed of water and cations! Such layered networks with specific channel dimensions might be useful for size- and shape-selective reactions especially under catalytical conditions. These systems are especially attractive as they are electron rich (note: the delocalized electrons cause the blue color). It should further be mentioned that not only linking to extended structures with periodicity could be achieved but also the formation of a dimeric species.[22]

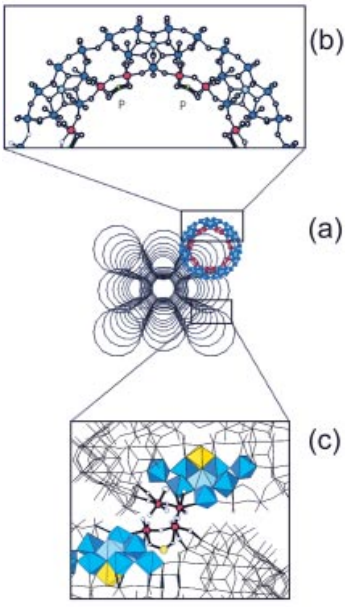

Figure 11. (a) Perspective view of the cluster framework of $Na_{21}[Mo^{VI}_{126}Mo^{V}_{28}O_{462}H_{14}(H_2O)_{54}(H_2PO_2)_7]\cdot$ca. 300 H_2O along the crystallographic *c* axis, showing the abundance of nanotubes. For clarity, only one complete ring (without the $H_2PO_2^-$ ligands) is shown in polyhedral representation. With respect to the other rings, only the centers of the {Mo_1} units are given and connected. (b) Ball-and-stick representation of the upper half of a ring segment showing the principal positions of the $H_2PO_2^-$ ligands. (c) Detailed view [perpendicular to (a) and (b)] of the bridging region between two cluster rings emphasizing one {Mo_8}, one {Mo_1} unit (in polyhedral representation) as well as one {Mo_2} unit and one $H_2PO_2^-$ ligand (without hydrogen atoms; ball-and-stick representation). The bridging (disordered) oxygen center is depicted as a large hatched circle. Colour code: {Mo_2} red; {Mo_8} blue (central MoO_7 pentagonal-bipyramid, light blue); {Mo_1} yellow; P green.[21]

5. Concluding Remarks

Our investigations touched upon here are especially interesting because of the unprecedented discrete nano-objects' properties. The spherical nanoclusters for example can be considered as "artificial cells" while they also have a strong intrinsic tendency of "responsive reactivity".[23,24] This feature, together with the well-known catalytic properties of polyoxomolybdate clusters, could in principle lead to the emergence of a novel type of molecular catalyst and host-guest system from which functional nanodevices may evolve. One important point in this regard is the fact that several of the nano-objects (the porous capsules are, especially under O_2 free conditions, stable in solution) allow easy and different types of manipulations, for instance the specific affinity of the spherical capsules to cations can be "tuned" due to the modification variability of both the internal cavity shell as well as the overall charge.[3f]

Although in this short voyage, various facets of covalent and noncovalent connectivity related to different states of matter have been highlighted, from "vesicular structuring" in solution via oligomeric assemblies in the gas phase to covalent connectivity in the solid state, it seems that a lot of discoveries in this context are still possible! The reason for the enormous versatility is really a consequence of the nanoscaled and especially appropriately functionalized surfaces, which resulted for instance in an interesting study to observe nucleation intermediates (title of the paper: "Kinetic Precipitation of Solution-Phase Polyoxomolybdate [...]:

 © 2005 Wiley-VCH Verlag GmbH & Co. KGaA, Weinheim

A Window to Solution-Phase Nanostructure").[25] An especially interesting challenge for the future will also be to place (discrete) oligomers observed in the gas phase[8] on surfaces in order to study their electronic properties.

Acknowledgments

The authors thank Priv. Doz. Dr. D. G. Kurth and Dr. H. Bögge for their cooperation. Furthermore, financial support by the Deutsche Forschungsgemeinschaft and the Fonds der Chemischen Industrie is gratefully acknowledged. SR thanks the "Graduiertenkolleg Strukturbildungsprozesse", Universität Bielefeld, for a fellowship.

[1] A. J. Heeger, *Angew. Chem. Int. Ed.* **2001**, *40*, 2591–2611.
[2] a) D. Voet, J. G. Voet, *Biochemistry* 2nd ed.; Wiley: New York, **1995**; b) J.-M. Lehn, *Supramolecular Chemistry: Concepts and Perspectives*, VCH: Weinheim, **1995**; c) J. W. Steed, J. L. Atwood, *Supramolecular Chemistry*, Wiley: Chichester, **2000**; d) F. Vögtle, *Supramolecular Chemistry*, Wiley: Chichester, **1991**; e) J.-P. Behr (Ed.), *Perspectives in Supramolecular Chemistry, vol. 1: The Lock and Key Principle (The State of the Art – 100 Years On)*, Wiley: Chichester, **1994**; f) A. D. Hamilton (Ed.), *Perspectives in Supramolecular Chemistry*, *vol. 3*: *Supramolecular Control of Structure and Reactivity*, Wiley: Chichester, **1996**; g) S. Mann, *Biomineralization: Principles and Concepts in Bioinorganic Materials Chemistry*, Oxford University Press: Oxford, **2001**; h) R. Wetherbee, *Science* **2002**, *298*, 547; i) N. Kröger, S. Lorenz, E. Brunner, M. Sumper, *Science* **2002**, *298*, 584–586; j) S. Mann, *Angew. Chem. Int. Ed.* **2000**, *39*, 3392–3406; k) S. Mann, G. A. Ozin, *Nature* **1996**, *382*, 313–318.
[3] a) A. Müller, P. Kögerler, C. Kuhlmann, *Chem. Commun.* **1999**, 1347–1358; b) A. Müller, P. Kögerler, H. Bögge, *Structure and Bonding (Berlin)* **2000**, *96*, 203–236; c) A. Müller, F. Peters, M. T. Pope, D. Gatteschi, *Chem. Rev.* **1998**, *98*, 239–271; d) A. Müller, S. Roy, *Coord. Chem. Rev.* **2003**, *245*, 153–166; e) L. Cronin, in: (Eds.: J. A. McCleverty, T. J. Meyer), *Comprehensive Coordination Chemistry II*, Elsevier: Amsterdam, **2004**, *Vol. 7*, 1–56; f) A. Müller, S. Roy, in: (Eds.: C. N. R. Rao, A. Müller, A. K. Cheetham), *The Chemistry of Nanomaterials: Synthesis Properties and Applications*, Wiley-VCH: Weinheim, **2004**, pp. 452–475.
[4] a) A. Müller, E. Krickemeyer, H. Bögge, M. Schmidtmann, S. Roy, A. Berkle, *Angew. Chem. Int. Ed.* **2002**, *41*, 3604–3609, and literature cited therein; b) A. Müller, S. K. Das, S. Talismanov, S. Roy, E. Beckmann, H. Bögge, M. Schmidtmann, A. Merca, A. Berkle, L. Allouche, Y. Zhou, L. Zhang, *Angew. Chem. Int. Ed.* **2003**, *42*, 5039–5044.
[5] A. Müller, S. K. Das, E. Krickemeyer, C. Kuhlmann, *Inorg. Synth.* **2004**, *34*, 191–200.
[6] A. Müller, E. Beckmann, H. Bögge, M. Schmidtmann, A. Dress, *Angew. Chem. Int. Ed.* **2002**, *41*, 1162–1167.
[7] a) G. Férey, *Science* **2001**, *291*, 994–995; see also: *J. Solid State Chem.* **2000**, *152*, 37–48; b) A. K. Cheetham, G. Férey, T. Loiseau, *Angew. Chem. Int. Ed.* **1999**, *38*, 3268–3292.
[8] A. Müller, E. Diemann, S. Q. N. Shah, C. Kuhlmann, M. C. Letzel, *Chem. Commun.* **2002**, 440–441.
[9] "Rounding up Nanoclusters: Nanotechnology", *Materials today* (Research News) **2004**, *January Issue*, 10.
[10] T. Liu, E. Diemann, H. Li, A. W. M. Dress, A. Müller, *Nature* **2003**, *426*, 59–62.
[11] The answer also came from a combination of DLS and SLS studies on the solutions containing those vesicles. The results of a DLS measurement performed on the aqueous $\{Mo_{154}\}$ solution showed that the aggregates were almost monodisperse, with an average hydrodynamic radius R_h of 45 nm. SLS data, analyzed through the Zimm plot, indicated that the average radius of gyration R_g was almost equal to the hydrodynamic radius R_h as observed from DLS studies. It is known that for a *solid* spherical particle, the relationship between the two radii is $R_g = 0.77R_h$. If the aggregates were solid spheres with R_h around 45 nm, an R_g value of 34 nm would be expected, which was clearly not the case. As an increasing fraction of the total mass of a spherical object is distributed closer to the sphere's surface, the ratio R_g/R_h increases; the ratio approaches a value of 1 as the corresponding spherical object has all of its mass on its surface. The scattering data thus indicated that the aggregates in solution were not "solid clusters", but vesicle-like hollow spheres. (Solvents inside the spheres do not contribute to the light scattering.) Moreover the mass of the aggregates (M_w) determined from the Zimm plot (which excludes any contained solvent) corresponded approximately to 1,165 individual nanowheels. Because a solid $\{Mo_{154}\}/\{Mo_{152}\}$-type nanocrystal with a 45 nm radius would contain more than 14,000 individual molecules, the estimated M_w value also suggested that those aggregates must have a hollow interior with 1,165 nanowheels homogeneously distributed on the surface of the vesicle.
[12] a) A. Müller, C. Serain, *Acc. Chem. Res.* **2000**, *33*, 2–10; b) A. Oleinikova, H. Weingärtner, E. Diemann, M. Chaplin, A. Müller, (unpublished observation).
[13] D. Volkmer, A. Du Chesne, D. G. Kurth, H. Schnablegger, P. Lehmann, M. J. Koop, A. Müller, *J. Am. Chem. Soc.* **2000**, *122*, 1995–1998.
[14] D. G. Kurth, P. Lehmann, D. Volkmer, A. Müller, D. Schwahn, *J. Chem. Soc. Dalton Trans.* **2000**, 3989–3998.
[15] F. A. Cotton, G. Wilkinson, C. A. Murillo, M. Bochmann, *Advanced Inorganic Chemistry,* 6th ed.; Wiley: New York, **1999**.
[16] a) A. Müller, S. Sarkar, S. Q. N. Shah, H. Bögge, M. Schmidtmann, S. Sarkar, P. Kögerler, B. Hauptfleisch, A. X. Trautwein, V. Schünemann, *Angew. Chem. Int. Ed.* **1999**, *38*, 3238–3241; b) A. Müller, E. Krickemeyer, S. K. Das, P. Kögerler, S. Sarkar, H. Bögge, M. Schmidtmann, S. Sarkar, *Angew. Chem. Int. Ed.* **2000**, *39*, 1612–1614; c) A. Müller, S. K. Das, E. Krickemeyer, P. Kögerler, H. Bögge, M. Schmidtmann, *Solid State Sciences* **2000**, *2*, 847–854.
[17] A. Müller, S. K. Das, M. O. Talismanova, H. Bögge, P. Kögerler, M. Schmidtmann, S. S. Talismanov, M. Luban, E. Krickemeyer, *Angew. Chem. Int. Ed.* **2002**, *41*, 579–582.
[18] A. Müller, S. K. Das, P. Kögerler, H. Bögge, M. Schmidtmann, A. X. Trautwein, V. Schünemann, E. Krickemeyer, W. Preetz, *Angew. Chem. Int. Ed.* **2000**, *39*, 3413–3417.
[19] A. Müller, S. K. Das, H. Bögge, M. Schmidtmann, A. Botar, A. Patrut, *Chem. Commun.* **2001**, 657–658.
[20] A. Müller, S. Roy, M. Schmidtmann, H. Bögge, *Chem. Commun.* **2002**, 2000–2002.
[21] A. Müller, S. K. Das, H. Bögge, C. Beugholt, M. Schmidtmann, *Chem. Commun.* **1999**, 1035–1036.
[22] L. Cronin, C. Beugholt, E. Krickemeyer, M. Schmidtmann, H. Bögge, P. Kögerler, T. K. K. Luong, A. Müller, *Angew. Chem. Int. Ed.* **2002**, *41*, 2805–2808.
[23] A. Müller, D. Rehder, E. T. K. Haupt, A. Merca, H. Bögge, M. Schmidtmann, G. Heinze-Brückner, *Angew. Chem. Int. Ed.* **2004**, *43*, 4466–4470.
[24] A. Müller, E. Krickemeyer, H. Bögge, M. Schmidtmann, S. Roy, A. Berkle, *Angew. Chem. Int. Ed.* **2002**, *41*, 3604–3609.
[25] Y. Zhu, A. Cammers-Goodwin, B. Zhao, A. Dozier, E. C. Dickey, *Chem. Eur. J.* **2004**, *10*, 2421–2427.

Received: May 24, 2005
Published Online: August 22, 2005

 © 2005 Wiley-VCH Verlag GmbH & Co. KGaA, Weinheim

Magnetic Nanoparticle Superstructures

Michael Giersig*[a] and Michael Hilgendorff*[a]

Keywords: Nanoparticles / Ferrofluids / Nanosphere lithography / Nanoshadows

The aim of this microreview is to present recent advances in the preparation of magnetic nanoparticle superstructures from ferrofluids and by nanosphere lithography. Different successes of methods presented in this article to create magnetic nanoparticles will be discussed in view of different requirements of available assembling techniques. Theoretical aspects of nanoparticle assemblies and their assembled layer magnetic properties are not reviewed here.
(© Wiley-VCH Verlag GmbH & Co. KGaA, 69451 Weinheim, Germany, 2005)

1. Introduction

For the design of novel nanostructured devices one needs a technique for preparing highly symmetric periodic particle arrays (PPA) within the range of several microns, on an industrial scale. Different routes have been investigated in the past to obtain small particles, which can be assembled in large areas of high symmetry. These approaches typically apply "scale down" techniques, e.g. ball milling of bulk materials, and "bottom up" techniques, e.g. cluster or nanoparticle growth from precursors in gaseous or liquid phases. The latter, i.e. the wet chemical synthesis of inorganic colloidal particle fluids, is most elegant from a chemist's point of view.[1]

Inorganic colloidal fluids are stable dispersions of nanoscale clusters or fine particles – which can be crystalline or amorphous – in a solvent.[2] If the dispersed material is known to exhibit ferromagnetic behavior in the bulk material, colloidal suspensions thereof are called ferrofluids or magnetic fluids.[3] One can develop PPA with ferrofluids having a standard particle size distribution $< 10\%$ by simply drying a drop of solution on suitable substrates. This self-assembly technique has been improved through use of

[a] caesar Research Center (Center of European Studies and Research),
Ludwig-Erhard-Allee 2, 53175 Bonn, Germany
Fax: +49-228-9656-187
E-mail: giersig@caesar.de; E-mail: hilgendorff@caesar.de

Michael Giersig studied at the A. Mickiewicz University of Poland. He carried out his diploma research work at the Fritz-Haber-Institute of the Max-Planck-Gesellschaft in Berlin and received his diploma in physics at the Freie Universität Berlin in 1984. He continued to work at the Fritz-Haber-Institute. He received his PhD in chemistry at the Freie Universität Berlin in 1988. Subsequently he continued with his postdoctoral work at the Institute for Molecular Genetics of the Max-Planck-Institut in Berlin. At the end of 1989 he took up a post at the Hahn-Meitner-Institute in Berlin, Department of Physical Chemistry, where he was awarded twice with a research prize. In 1995 he received an international accolade in the form of a 2-year stay at the University of Melbourne, Department of Physical Chemistry. After his return he habilitated at the University of Potsdam, Faculty of Physical Chemistry in 1999. In 2000 Michael Giersig was appointed professor at the Technological University, department of physics in Poznan, Poland. He is the author/co-author of over 140 scientific journal and conference articles and book chapters. He joined the research center caesar in April 2003 to establish the group "nanoparticle technology". The work of the group focuses on the creation of 2-D and 3-D nanostructures, based on single nanoparticles as well as the fabrication of nanostructured surfaces with a size of a number of square centimeters. A further focal point is the optical, structural as well as magnetic characterization of nanostructures.

Michael Hilgendorff received his diploma in chemistry in 1993 (University of Hannover), where he investigated the photocatalytic degradation of carbon tetrachloride on platinized titanium dioxide particles. He then worked on ZnO colloids and transparent electrical conductive electrodes at the University of Würzburg, where he received his PhD in 1999. In February 1999 he joined the group of Michael Giersig at the Hahn-Meitner-Institute in Berlin to work within the priority program of the Deutsche Forschungsgemeinschaft (DFG) on "Semiconductors and metal clusters as building blocks for nanostructured materials". He joined the group "nanoparticle technology" at caesar in April 2003, where he is responsible for the development of new and the optimization of existing inorganic colloid syntheses.

MICROREVIEWS: This feature introduces the readers to the authors' research through a concise overview of the selected topic. Reference to important work from others in the field is included.

different coating techniques (e.g. spin coating, dip coating, or spraying) in combination with applied external forces. The origin of these external forces is either mechanical, and is used for the preparation of Langmuir–Blodgett (LB) films,[4] or electrostatic, which is then used for layer-by-layer (LbL) assembly applying polyelectrolytes.[5] The use of external electric and magnetic fields to improve the self-assembly of charged and magnetic nanoparticles, respectively, has also been reported.[6,7]

Despite all those successes, there are some applications that cannot be solved by the use of ferrofluids. One reason is the limitation of perfectly ordered nanostructures to about one micron squared. A second result from the question: "How can we arrange highly ordered magnetic nanoparticles on substrates having a distance larger than 100 nm?". To overcome these problems, a lithographical technique applying organic colloids – Nanosphere Lithography (NSL) – has been further optimized.[8]

The formation of monolayers of self-assembled colloidal particles (mainly polystyrene and silica submicron-sized, monodisperse spheres) is well established and has been widely used in various fields of research.[9] Well-ordered latex particle films were used, among others, as masks that allow the production of regularly arranged triangular-shaped structures on almost arbitrary substrates. Through the evaporation of different materials through the mask, it was possible to prepare nano-sized particles with diverse optical[9,10] or magnetic properties.[10] There are many different monolayer fabrication methods based on electrophoresis,[6] electrostatic deposition,[11] the Langmuir–Blodgett technique, spin-coating,[12] the controlled evaporation of solvents from a solution containing latex particles on a hydrophilic substrate,[13] or non-photolithographic methods.[14] Many authors used the method of Micheletto et al.,[13a] or other drying-based methods and pointed out that a hydrophilic surface is crucial for monolayer depositions.[15] To deposit PS latex particles onto hydrophobic substrates it is necessary to use an alternative method that involves assembly onto a liquid–gas or a liquid–liquid interface.[8]

In this microreview we will provide an overview of assemblies of ferrofluids, as well as some improvements of NSL by changing the shadows below – and the interstices between – hexagonal-ordered monolayers of submicron spheres. For an overview of theoretical aspects of nanoparticle assemblies see.[16] Detailed information on magnetic properties are available by Leslie-Pelecky and Rieke,[17] Binns,[18] and Spasova and Farle.[19] A short summary is given in ref.[20].

2. Superstructures from Ferrofluids

Syntheses: The most important prerequisite for the preparation of magnetic nanoparticle superstructures from ferrofluids is the control over particle size and size distribution during syntheses. Many wet chemical routes have been developed in recent years. Syntheses of monometallic magnetic particles such as Fe,[21] Co,[7b,21a,21b,22] or Ni,[21a,21b,23] have been successfully done by electrochemical reduction,[22i,23d] chemical reduction by Li,[23c] hydroborides,[21b,22j–22l] or polyols[24] of metal salts, thermal decomposition (initiated by conventional methods[7b,21e,22a,22b,22e–22h,22m,23a,23b] or by ultrasound[21d]) of zero-valent metal-organic compounds in organic solvents in the presence of bulky stabilizers such as: *i*) fatty acids (in combination with organic amines or phosphanes); *ii*) polymers, or; *iii*) surfactants. In the case of *i*), the fatty acids act as stabilizing compounds, i.e. to overcome oxidation, Van der Waals, and dipole–dipole interactions, while the amines or phosphanes control the particle growth. Surfactants can be used as stabilizers for inorganic nanomaterials dispersed in organic solvents or as compounds forming stable micelles in heterogeneous oil-in-water systems, e.g. sodium dodecyl sulfate (SDS). Other surfactants, e.g. alkylammonium bromides (DDAB, CTAB) or Aerosol OT (AOT), form a stable emulsion of water droplets in hydrophobic solvents (reverse micelles). Figure 1 shows a typical result of Co-particles prepared by thermal decomposition of octacarbonyldicobalt in dichlorobenzene.

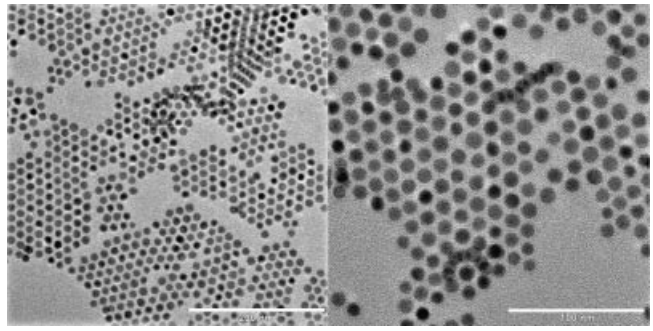

Figure 1. TEM images at different magnifications of monodisperse 10 nm Co particles self-assembled on a carbon-coated Cu grid.

The development of bimetallic ferrofluid syntheses has been based on existing synthetic procedures of monometallic ferrofluids. In general, they have been produced by thermal decomposition of bimetallic zero-valent metal-organic compounds[25] or in-situ or successive thermal decomposition of zero-valent monometallic metal-organic compounds,[26] as well as by in-situ or successive reduction of metal salts,[27,28] or combinations thereof.[29] In summary, bimetallic particles form alloys, core-shell particles, or cluster in cluster particles,[24] are all dependent largely, but not exclusively, on reaction kinetics. Applied methods and properties of these fluids have been summarized in ref.[20].

The most common preparation of magnetite (Fe_3O_4) ferrofluids was developed by Massart about 20 years ago and described in detail in 1987.[30] The synthesis was based on the co-precipitation of Fe^{II} and Fe^{III} salts in aqueous solutions stabilized by repulsive electrostatic forces. TEM investigations show typically aggregated particles, consisting usually of a mixture of ferrimagnetic magnetite, and maghemite (γ-Fe_2O_3), and paramagnetic hematite (αFe_2O_3). The ratio of the different iron oxide phases is directly compared to the expense associated with performing the synthe-

 © 2005 Wiley-VCH Verlag GmbH & Co. KGaA, Weinheim

sis under oxygen free conditions, because γFe_2O_3 and α-Fe_2O_3 are oxidation products of Fe_3O_4. Figure 2 provides typical images of magnetite particles prepared in aqueous medium (a) and after their transfer to toluene (b).

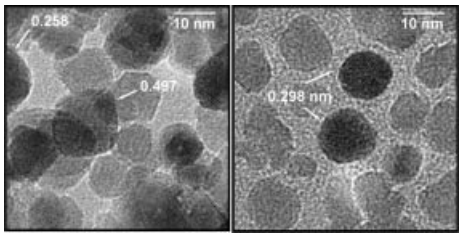

Figure 2. Typical TEM images of iron oxide particles; a) prepared in aqueous solution by Massart method and b) the same particles dried from a toluene solution after adsorbing oleic acid on their surface. The distances shown in the images are the result of fast Fourier analysis, indicating typical lattice planes of magnetite (redrawn with permission from ref.[16a]).

Since these reports, several optimizations have been discovered to produce ferrofluids useful for new applications. One of them was concerned with the possibility of changing the magnetic properties of the inverse Fe_3O_4 spinell by replacing Fe^{II} with Co^{II}, Ni^{II}, Mn^{II}, or Zn^{II} ions.[31]

Additionally, many reports dealt with solving the classic problem of nanoparticle aggregation in aqueous solutions (Figure 2, a). To overcome such aggregation, new preparations have involved micellar solutions,[32] as well as the transfer of iron oxide particles from aqueous to nonpolar solvents by hydrophobizing the surface by adsorbing bulky stabilizers such as fatty acids (Figure 2, b).[33]

Different methods have been applied to decrease particle size distribution. One method that has been successfully applied involves synthesis of iron oxides in reverse micelles. A second method dealt with a size selective precipitation after transfer of iron oxide particles to nonpolar organic solvents. Most recently, Sun et al.[34] have developed a very successful method to achieve monodisperse Fe_3O_4 nanoparticles without a size selection procedure. This method is based on the reduction of iron(III) acetylacetonate by 1,2-hexadecanediol and further thermal decomposition at high temperatures (solvent: diphenyl ether, b.p. 265°C) in the presence of oleic acid and oleylamine as stabilizers. As a result, small Fe_3O_4 nanoparticles (diameter ca. 4 nm) having a particle size distribution of ca. 5% are formed and can be further grown by seed-mediated growth.[35] A further method to obtain monodisperse maghemite (γ-Fe_2O_3) particles based on the preparation of Fe particles by the thermal decomposition of carbonyliron and their further oxidation to the oxide has been published by Hyeon et al.[36] A detailed investigation of the structural, magnetic, and electronic properties of iron oxide nanoparticles prepared by decomposition of iron(II) and iron(0) precursors in the presence of different organic solvents and surfactants has been published in ref.[37].

Table 1 provides an overview of successful syntheses and surface properties, determining the applicability of different assembling methods, of various magnetic colloids.

General observations for wet chemical ferrofluid preparations are increasing particle sizes with decreasing precursor concentrations and decreasing chain length of the stabilizers, and increasing size distributions with increasing final particle sizes. As one challenge of syntheses is to achieve a narrow size distribution, the reverse micelle technique and the so-called "hot injection" technique have been successfully applied, especially for the preparation of larger particles (diameters $>$ 5 nm – 15 nm). Using the latter method, standard size deviations $<$ 10% have been experimentally demonstrated (standard size deviations of ca. 5% have been predicted theoretically by choosing a proper combination of solvent and stabilizers[38]). Moreover, the hot-injection technique has been employed to facilitate a further growth of primary prepared particles (seed particles) by reactive precipitation of precursors on the surface of seed particles.

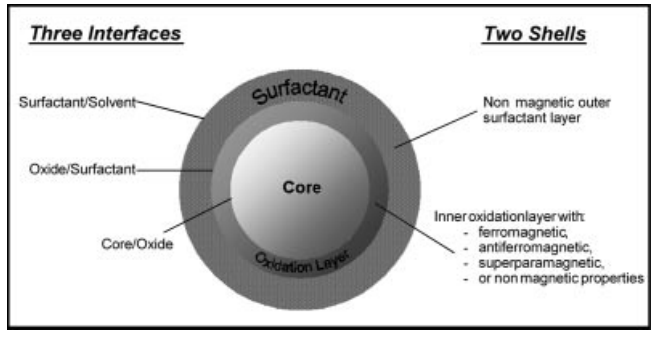

Figure 3. Sketch of a magnetic nanoparticle representing the usual result of colloid chemical synthesis. The desired core material is covered with an inner oxidation layer of the core material and an outer surfactant layer that is necessary to overcome attractive forces. As a result, three interfaces are present, which determine the nanoparticles properties (adapted with permission from ref.[16a]).

Table 1. Overview of successful syntheses and surface properties of various magnetic colloids.

Synthesis		Materials	Surface properties
D	Decomposition	metals, their alloys, and oxides prepared by post oxidation	uncharged, hydrophobic
E	Electrolysis	metals and their alloys	charged, hydrophobic
R	Reverse micelles	metals, their alloys, and oxides	charged, hydrophobic
M	Micelles	magnetic latex spheres formed by emulsion polymerization	charged, hydrophilic
O	Organohydroborate reduction.	metals and their alloys	charged, hydrophobic
P	Polyol reduction	metals and their alloys	various
C	Combination	metal alloys	uncharged, hydrophobic
H	Hydrolysis and condensation	iron oxides	charged, hydrophilic

 © 2005 Wiley-VCH Verlag GmbH & Co. KGaA, Weinheim

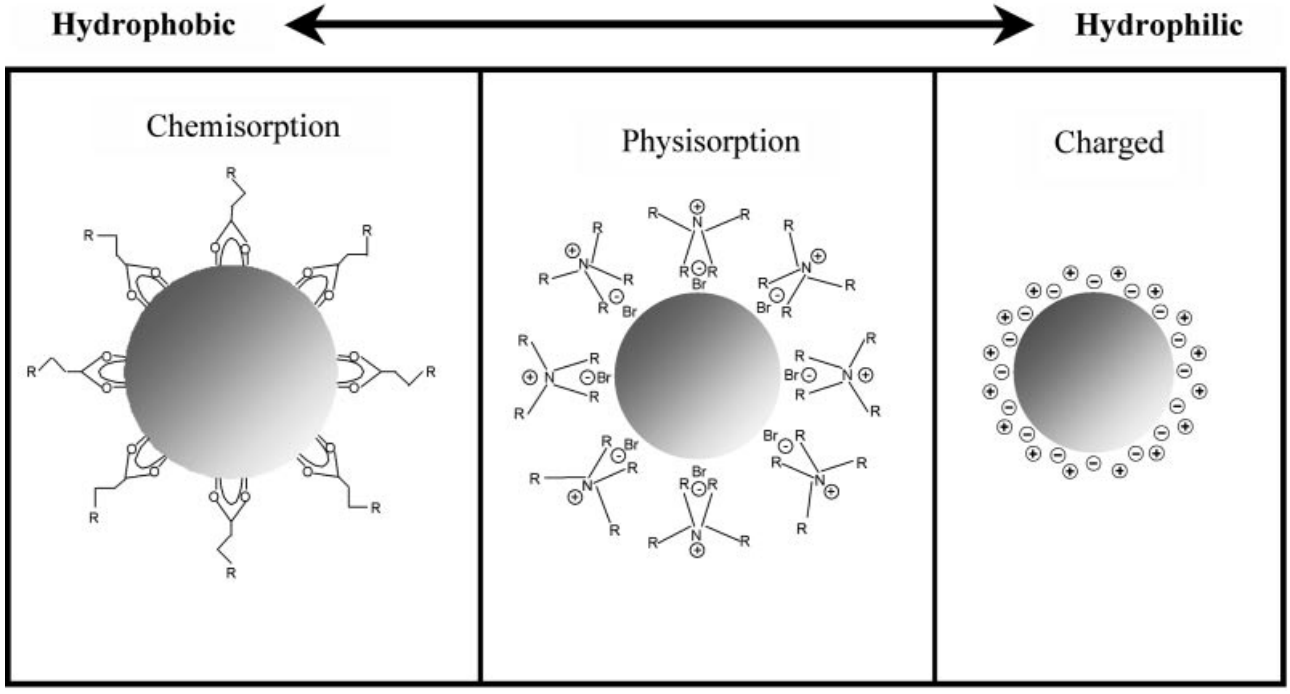

Figure 4. Sketches of models describing the particle surface under different conditions. The chemisorption, i.e. the dissociative adsorption of stabilizers, is most often used in hydrophobic solvents (e.g. toluene). The physisorption has been successfully used to stabilize colloids by tetraalkyl ammonium salts in polar organic solvents (e.g. THF). Simply charged surfaces are in principle limited to aqueous suspensions.

The main result of wet chemical preparations of nanoparticles is the fact that one produces composite particles consisting of a core of the desired material, a protecting outer surface layer, and an intermediate inner surface layer of – most often – unknown composition. Figure 3 and Figure 4 give a schematic overview of the "composite" nanoparticle and its different surface properties (with respect to different preparation routes) that are mainly determined by the outer protecting surface layer.

Assembly: Concerned with the control of particle evolution during syntheses by kinetic rather than thermodynamic control of particle size and particle size distribution, is the phenomenon of self-assembly, which was first investigated using submicron spheres of PS latex or SiO_2 dispersed in water. This work concluded that self-assembly is conditional on the narrow size distribution of the particles (standard deviation ca. 5%), i.e. a narrow distribution of the sum of repulsive and attractive forces between particles in a colloidal solution. Thus, this conclusion is not limited to well-separated single particles. It holds also for aggregates of particles often found in aqueous systems, assuming that equal forces interact between aggregates of similar size.

Various methods have been applied for assembling magnetic colloids in recent years. The different methods and their requirements – mainly concerned to the surface properties of the nanoparticles, which are different for different preparation conditions – are summarized in Table 2 (in view of Table 1).

2.1 Self-Assembly

The most simple particle layer preparation method, which allows the application of external forces, is drying a drop of solution on a flat substrate – solid or liquid. This procedure results in a particle monolayer if the inorganic material concentration of the fluid is in the order of about 10^{-4} M. The monolayer typically consists of particle *sheets* of high symmetry interrupted by *empty* areas containing excess stabilizer (Figure 5).

The particle sheets can self-assemble into hexagonal-ordered arrays as shown in Figure 1, or into cubic-ordered arrays,[39,37] depending on the stabilizers nature and/or the particles shape, respectively. Increasing the ferrofluid concentration can increase the particle area density and the number of layers formed by self-assembly on a substrate. Increasing the concentration results in multilayers forming three-dimensional crystals of various symmetry, e.g. hcp, fcc, bcc, or tetragonal, but with multiple defects. Figure 6 shows a three-dimensional crystal prepared by drying a drop of a monodisperse Co-colloid shown in Figure 1.

One major requirement for technological applications of ferrofluids is their assembly into ordered structures of several mm^2 in size. Self-assembling of colloids on aqueous surfaces allows for the preparation of continuous layers of several mm^2 in size typically consisting of well-ordered *cores* interrupted by grain boundaries between cores of different orientation. There is no principle difference between nano-sized inorganic and micron-sized organic colloids.

 © 2005 Wiley-VCH Verlag GmbH & Co. KGaA, Weinheim

Table 2. Overview of successful assembling methods, their requirements, and their applicability for colloids prepared by methods summarized in Table 1.

Assembling Method		Requirements	Applicable for
SA	**S**elf-**A**ssembly: self organization of colloidal particles into symmetric arrays during their deposition on flat substrates, i.e. flat solid- or liquid surfaces, or their precipitation into large particulate crystals from over-saturated liquids	narrow distribution of interacting forces between the colloidal particles	D, M (latex), R, and C
IA	External field **I**mproved **A**ssembly:		
	LB: mechanical force-improved assembly on aqueous surfaces	hydrophobic properties	D, E, R, O, P, and C
	MDT: magnetic force-improved assembly on flat surfaces	ferro- or superparamagnetic properties	D, R, M, C, and H[a]
	EDT: electric force-improved assembly on flat surfaces	charged colloids	R, M, and H[a] [b]
LbL	**L**ayer-**b**y-**L**ayer assembly: alternative deposition of polymers and colloids on solid surfaces of various geometry	charged colloids and aqueous solvents by use of polyelectrolytes	all[c]

[a] Particles available by the methods E, O, and P are typically too small to be influenced by external electric and magnetic fields during deposition at room temperature. [b] EDT approach has not yet been demonstrated for magnetic colloids to the authors' knowledge. [c] Applicability is dependent on the solubility of polymers in different solvents.

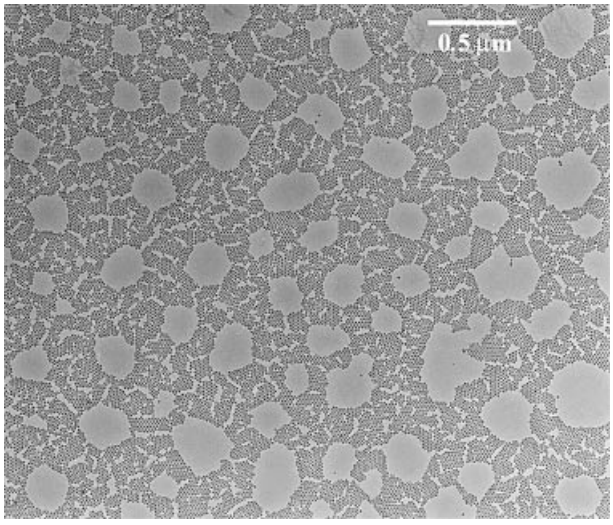

Figure 5. Typical TEM image of a sheet-like self-assembled film obtained by drying a drop of ferrofluid on a carbon-coated Cu grid (adapted with permission from ref.[16b]).

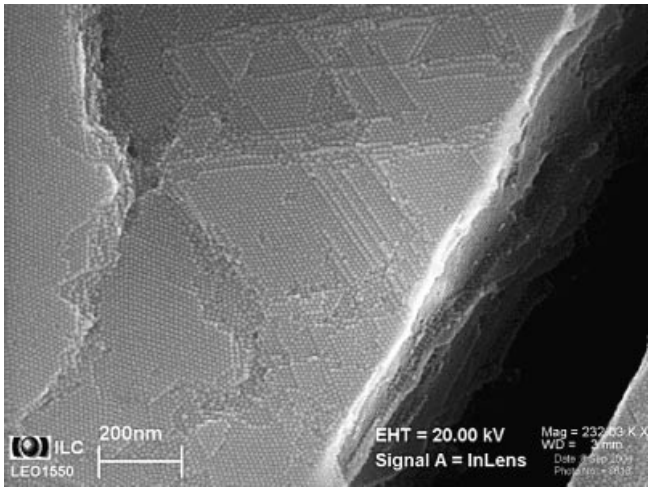

Figure 6. SEM image of a colloidal crystal prepared from a concentrated solution of highly monodispere Co nanoparticles (courtesy of E. Majkova).

The core size can be improved by adding special surfactants (or simply soap) to the aqueous phase that will change its surface tension and/or the interaction of the particulate depletion layer. The latter refers to theoretical descriptions developed by Debye, Hückel, and Onsager (see common textbooks of physical chemistry).

Figure 7 presents a typical result of particle assembly on a water surface. The visible structure results from isolated second layer islands. A perfect monolayer would not be visible at this magnification, demonstrating the problem of TEM investigations to show both, symmetry as well as large-area substrate coverage in case of nanoscale materials. It is obvious from Figure 8 that the symmetry of the assembled layer is decreased compared to the layer shown in Figure 1. Nevertheless, assembling on water surfaces allows (and is limited) to prepare monolayers of, for example, narrow symmetry distribution, but over several mm^2. Furthermore, this technique allows applying external magnetic fields during monolayer formation; static, as well as rotating magnetic fields. The latter may have some advantages in preparing assembled layers of circular geometry.

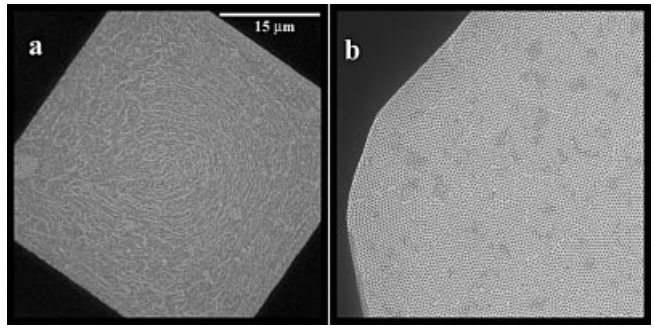

Figure 7. a) One mesh of a complete covered Cu grid. The structure results from islands of a double layer as can be seen in b. b) Higher magnified image showing the degree of ordering (adapted with permission from ref.[16b]).

Further optimizations have been available by applying the LB technique, dealing with mechanical force to increase the core size of self-assembled particle layers on water surfaces.[4] The preparation of large-scale three-dimensional

 © 2005 Wiley-VCH Verlag GmbH & Co. KGaA, Weinheim

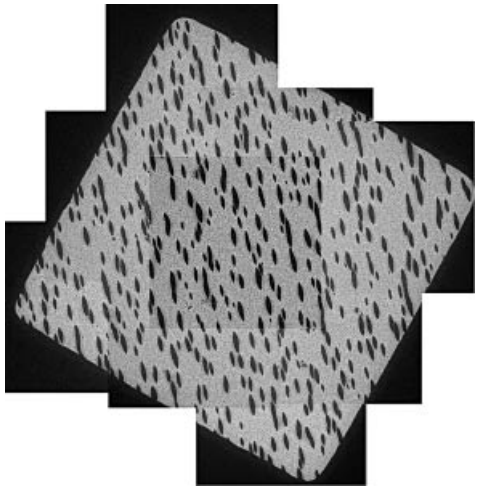

Figure 8. TEM image constructed from 11 micrographs. The mesh is 45 μm × 45 μm. The insert demonstrates that the structure is the same on at least four meshes (adapted with permission from ref.[16b]).

colloidal crystals grown from over-saturated fluids, has also been reported.[29j,29k]

2.2 Magnetophoretic Deposition Technique (MDT)

Ordering phenomenon in ferrofluids placed in external magnetic fields have been observed and theoretically calculated in literature. More recently, the formation of ordered stripes and hexagonal sheets has been experimentally observed while drying a thin liquid film of a ferrofluid on a substrate in an applied external magnetic field.[7b,16] Theoretical calculations of Lacoste and Lubensky showed that the shape of ordered structures, which are obtainable by drying a thin layer of ferrofluid under the influence of an external magnetic field applied in an identical plane to the liquid layer, can be completely different. Stripes as well as hexagonal sheets are available and can be made to coexist simply by changing the strength of the applied magnetic field and/or the concentration of the particles.[40] We found experimentally that the direction of the applied magnetic field is a further important parameter.[7b,16]

Figure 8 is shown for two reasons. Firstly, it demonstrates the coexistence of stripes (triple layers in this case) and sheets (monolayers, not really visible at this magnification) and confirms theoretical calculations. Secondly, it has been constructed from eleven single images to demonstrate large-area ordering within several μm^2, which is one major problem of TEM investigations of nanoscale materials. (One mesh of a carbon-coated copper grid, typically used in TEM investigations of colloids, 45 μm by 45 μm in size, is shown.).

Detailed investigations of MDT showed that the size of stripes (Figure 9) as well as sheets (as in Figure 5) of high symmetry, interrupted by isotropic regions of low (or no) symmetry and *empty* regions,[7b,16] can be increased by increasing the strength of the applied magnetic field. Figure 10 shows TEM images of the creation of multidimensionally ordered diluted Co colloids of the same concentration using MDT with external applied magnetic fields of 0.8 T (monolayer, upper left), 1.5 T (double layer, upper right), and 6 T (triple layer, lower left). The lower right image shows a triple layer prepared in the absence of a magnetic field for comparison.

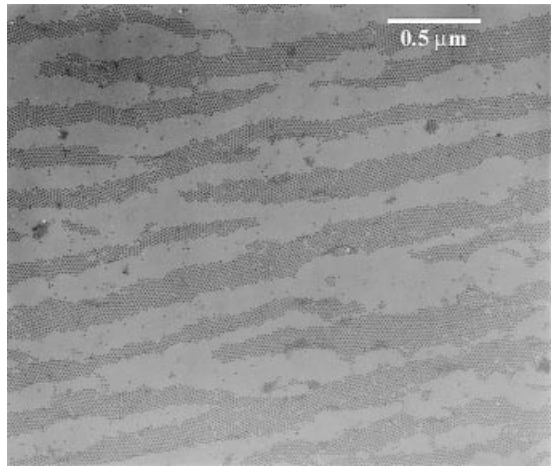

Figure 9. TEM image at low magnification showing a large-area of chains deposited at 0.8 T in perpendicular arrangement (adapted with permission from ref.[7b]).

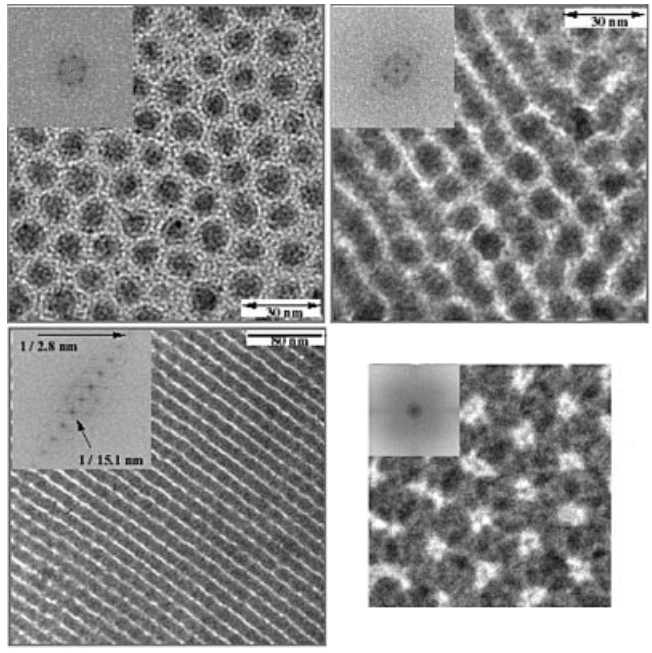

Figure 10. TEM images of the creation of multidimensionally ordered Co colloids of the same concentration using MDT with external applied magnetic fields of 0.8 T, mono layer (upper left), 1.5 T, double layer (upper right), and 6 T, triple layer (lower left). The lower right image shows a triple layer prepared in the absence of a magnetic field for comparison (redrawn with permission from ref.[7b]).

By increasing the concentration of colloids one can obtain micron-sized rod-shaped colloidal crystals by MDT grown perpendicular (magnetic field applied perpendicular to a substrate) or parallel (magnetic field applied parallel to

 © 2005 Wiley-VCH Verlag GmbH & Co. KGaA, Weinheim

a substrate) on a substrate as can be seen in Figure 11 and Figure 12.[41]

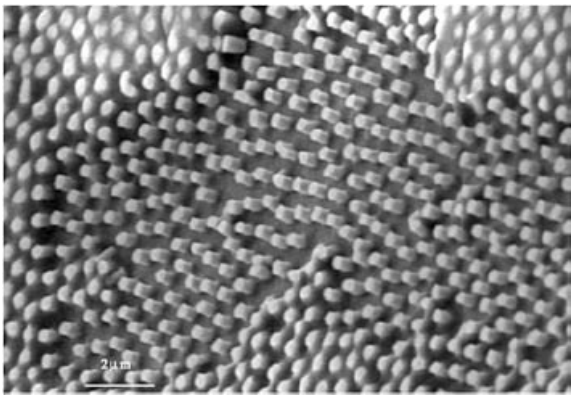

Figure 11. SEM picture of randomly distributed rods prepared by drying in air on substrate in a magnetic field of 0.8 T perpendicular to a Si/Si_3N_4 substrate (adapted with permission from ref.[41]).

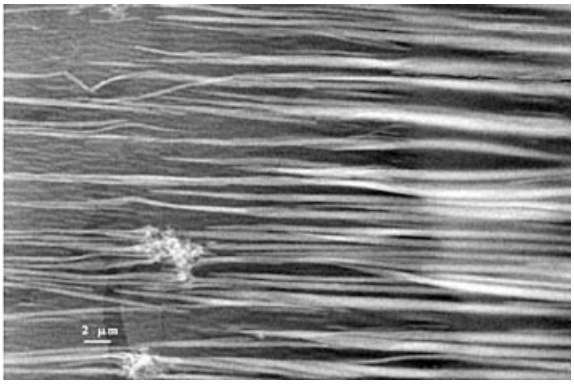

Figure 12. SEM picture of rods prepared like in Figure 11, however, with the magnetic field of 0.8 T parallel to the substrate (adapted with permission from ref.[41]).

Most recently, the perpendicular magnetic field-directed growth of such rods has been discussed in detail by the Pileni group.[42] Meanwhile, the magnetic field-directed growth of rods from bimetallic $CoPt_3$ colloids also has been published.[43]

Despite all those successes, the maximum size of defect-free inner superstructures available by applying MDT is limited to the lower μm range.[7b,16]

2.3 Layer-by-Layer Deposition (LbL)

Different to other assembling methods is the LbL technique, The LbL technique based on polymer-mediated self-assembly by alternatively adsorbing oppositely charged polymers (polyelectrolytes) or polymer and nanoparticles on solid substrates.[5,44] The LbL approach is, in principle, applicable for ferrofluids prepared by all methods presented in Table 1 with one restriction. Dealing with polyelectrolyte (the most common technique) requires typically aqueous solutions and charged colloids; therefore it is generally limited to ferrofluids containing iron oxide. The advantages of this technique are the availability of assembled layers (mainly layers of aggregates in case of aqueous iron oxide colloids) on curved substrates, i.e. latex spheres, and free-standing films including hollow spheres. As a result, nanoparticle layers of different thicknesses alternatively divided by layers of polymer have been published to be available.

A certain number of articles concerning the preparation of photonic crystals from magnetized latex spheres are available.[5d–5f,45] Two different routes were used to prepare magnetic organic/inorganic hybrid spheres. One dealt with the synthesis of magnetite incorporated in polymeric microspheres produced by emulsion polymerization.[46] The second method applied the LbL approach to prepare latex particles covered with magnetite[5c–5f]

These microspheres have then been used for the preparation of three-dimensional crystals. The photonic band gap of these crystals could be varied by varying the distance between the microspheres within a colloidal crystal by applying MDT. Increasing the applied magnetic field resulted in decreasing particle distances and blue shift of the Bragg diffraction wavelength. Unidirectional shifts have been observed with increasing NaCl concentration in aqueous solutions and decreasing dielectric constants of non-aqueous solutions.

The Farle group has used the LbL approach to prepare magnetite-covered latex particles.[5d–5f] Figure 13 shows TEM micrographs of uncoated PS particles (a) and polyelectrolyte-modified PS particles with (b) one, (c) two, (d) three Fe_3O_4 nanoparticles/polyelectrolyte layers. The average diameters of the composite particles are 650, 770, and 960 nm, respectively. The insert pictures in (b) clearly show Fe_3O_4 particles on the PS particles, many of them existing as aggregates.

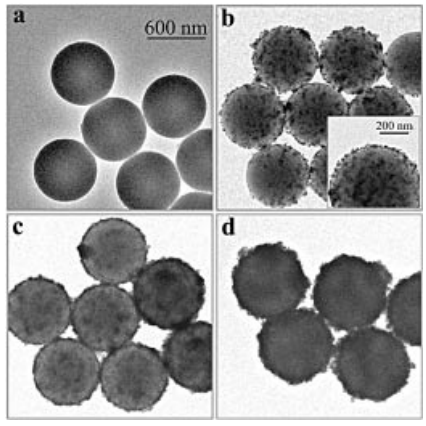

Figure 13. TEM micrographs of uncoated PS particles (a), and polyelectrolyte-modified PS particles with (b) one, (c) two, (d) three Fe_3O_4 nanoparticles/polyelectrolyte layers. The average diameters of the composite particles are 650, 770, and 960 nm, respectively. The insert pictures in (b) show clearly Fe_3O_4 particles on the PS particles; many of them existing as aggregates (adapted with permission from ref.[5g]).

These particles were then coated with SiO_2-covered Au particles.[5e,5f] The use of SiO_2-covered Au particles became necessary because the requirement of a negatively charged surface of Au colloids (as prepared Au particles by the applied method are positively charged). This approach in-

 © 2005 Wiley-VCH Verlag GmbH & Co. KGaA, Weinheim

volves coating of microspheres with a high refractive material prior to the colloid crystal formation. Figure 14 demonstrates the successful preparation of latex@magnetite@gold core-shell nanostructured microspheres. Properties of photonic band gap behavior of colloidal crystals prepared from these particles are under investigation.

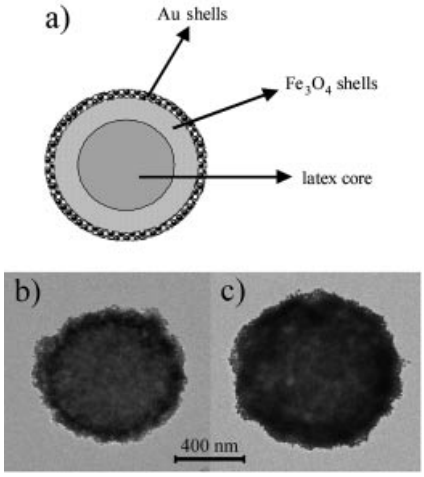

Figure 14. a) Schematic of a core (latex)-shell (Fe_3O_4 and Au nanoparticles) magnetic microsphere. b,c) TEM images of 640 nm PS microspheres: b) covered with two layers of magnetic Fe_3O_4 nanoparticles (d = 750 ± 20 nm) and c) after additional coverage with three layers of Au nanoparticles (d = 860 ± 20 nm) (redrawn with permission from ref.[5e]).

3. Superstructures by Nanosphere Lithography (NSL)

The main prerequisite to obtain highly symmetric nanostructured surfaces of large areas by use of NSL is the successful preparation of ordered monolayers of submicron spheres that are free of grain boundaries. To achieve this, we have developed a modified preparation technique based on the deposition of latex particles similar to a LB film on water. This method, involving surfactant-improved self-assembly on a liquid–gas interface (instead of a mechanical force-improved LB-assembly), allowed us to obtain large monolayers (a few cm^2) that could be applied directly onto various surfaces. Using this simple fabrication technique, it was possible to prepare monolayers as large as a few cm^2 with grain sizes of 1 mm^2 and above (using latex particles with diameters between 1000 nm and 500 nm), and areas of even 50 μm^2 without other structural defects (like point defects). Figure 15 shows one typical result of our modified method (right) in comparison to typical results of other methods (left).[8]

Figure 16 shows AFM images of nanostructured surfaces after evaporation of Ni through different masks and further removal of the latex particles by dissolution in THF. The hexagonal symmetry of triangular-shaped Ni islands is clearly visible.[8]

Those nanostructured substrates have been successfully used for the growth of hexagonal-ordered carbon nanotubes, grown perpendicular on a 1 cm^2 substrate, and having interstices > 100 nm (Figure 17). It has been found that the distance of perpendicular-aligned CNT's on substrates is a critical parameter in the preparation of field emission devices from CNT's.[47]

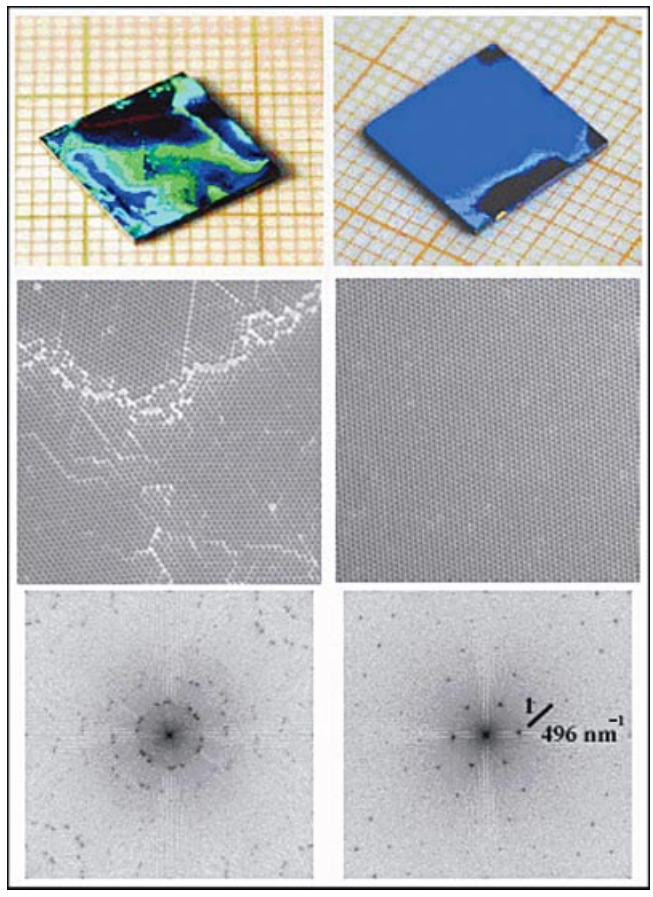

Figure 15. 1 × 1 cm^2 silicon wafers covered with 496 nm PS latex particles deposited as a monolayer. In contrast to the sample on the left side, most of the surface of the right one does not contain any grain boundaries, which are represented as a monochrome light interference (blue) color of the surface (right). In the second row, atomic force microscopy images are shown as representative examples for both samples. Additionally, quantitative information about the structures was obtained from a power spectrum of the pictures. Typical reflections for a polycrystalline structure are shown, in contrast to the right one which shows a power spectrum of perfectly ordered PS latex particles (adapted with permission from ref.[16a]).

3.1 The Shadow Approach

The structures obtained by NSL can become much more complex by varying the shadows below the microspheres of masks during evaporation. We have first developed computer simulations that predicted the structures resulting from the variation of the angle between the evaporation beam and the sample by tilting and/or rotating the sample under process. Figure 18 shows the principle experimental setup of the shadow approach.[48]

Meanwhile, a variety of predicted complex morphologies, ranging from cup-like structures to rods and wires, have

 © 2005 Wiley-VCH Verlag GmbH & Co. KGaA, Weinheim

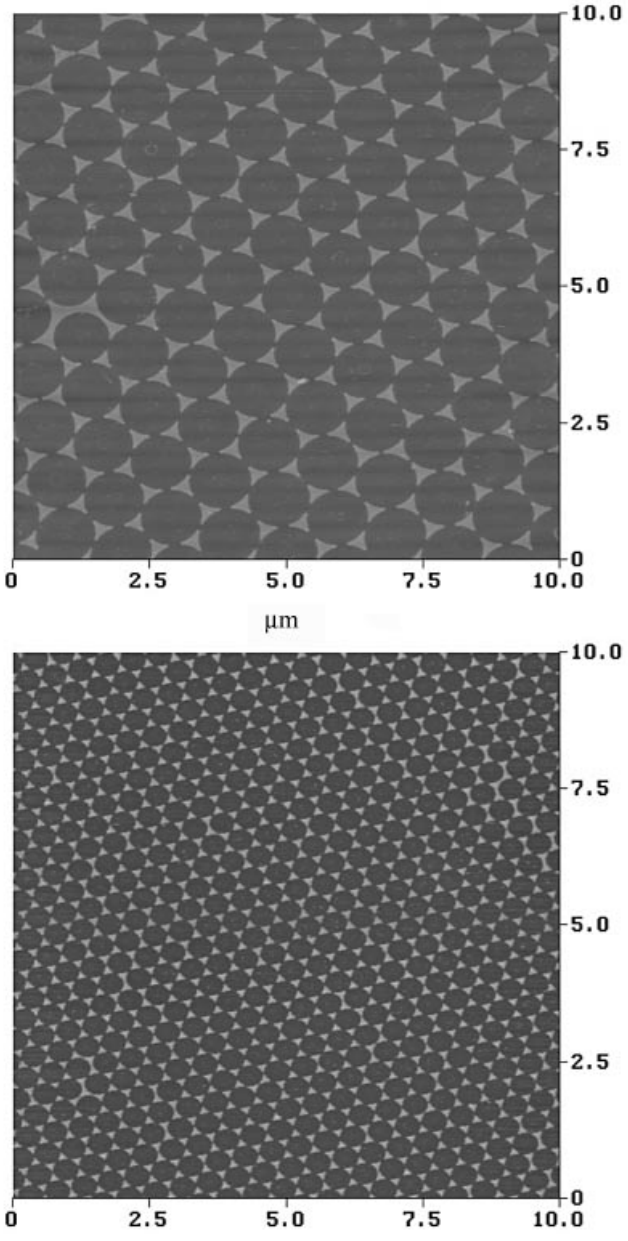

Figure 16. AFM image gallery showing 2-D magnetic Ni nanostructures created by deposition through different PS latex masks.

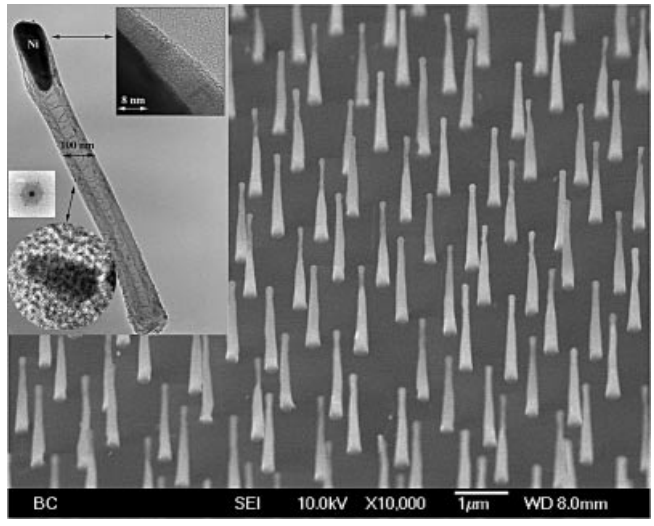

Figure 17. SEM image showing well-aligned carbon nanotubes grown perpendicular on a substrate that was pre-patterned with triangular Ni islands (courtesy of Z. F. Ren).

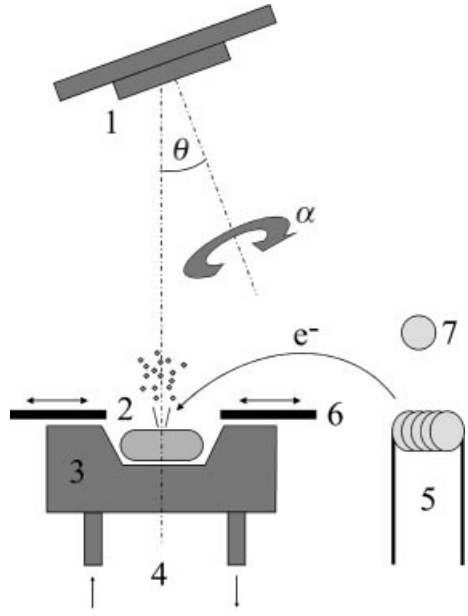

Figure 18. Schematic of the modified evaporation system. (1) Sample holder, (2) evaporation source, (3) crucible, (4) water cooling system, (5) electron beam source, (6) shutter, (7) magnetic field. The evaporation angle is q, and R the rotation angle of the sample (adapted with permission from ref.[48]).

been successfully prepared using this technique. Figure 19 and Figure 20 give examples of simulation and realization for one experimental setup, respectively.[48]

3.2 Fine Tuning of Interstices

The shadow approach could be further improved by changing the mask morphology, i. e. by decreasing the size and by changing the form of the interstices between the spheres through temperature processing. Figure 21 demonstrates the changes of size and form of interstices and the change of the interferometric color of a 540-nm PS latex mask annealed in 25 mL water/ethanol/acetone mixture by (A) 1, (B) 2, (C) 4, (D) 6, (E) 7, and (F) 10 microwave pulses.[49]

Applying temperature-treated masks in the shadow approach allowed for the preparation of particles with morphologies such as rings and rods. The combination of both processes allows an outstanding control of size and morphology of particles deposited on substrates. This efficient way is shown to scale down the size of metallic nanoparticles from 200 nm to 30 nm, while preserving the original nanosphere spacing and order. Nano-sized Fe rings produced by this method, having a diameter of 150 nm, show

 © 2005 Wiley-VCH Verlag GmbH & Co. KGaA, Weinheim

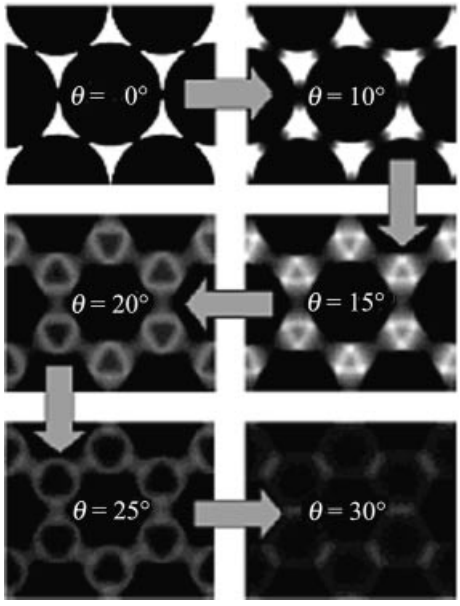

Figure 19. Simulation results for the evaporation through an hcp mask of ordered spheres, with evaporation angles q varying from 0° (perpendicular evaporation) to 30° (adapted with permission from ref.[48]).

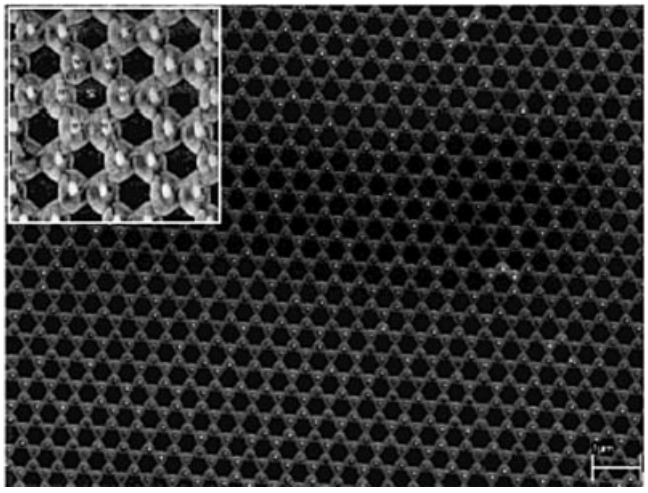

Figure 20. SEM image of a bimetallic structure, obtained by a two-step evaporation process. First step, evaporation of 150 nm Cr (with sample rotation at q = 25°), followed by a normal evaporation (q = 0°) of 15 nm Ni. The inset presents the scan in the AFM tapping phase mode of the same sample, which shows well-separated Ni spots inside the cup-like Cr structures. The diameter of the mask spheres was 540 nm (adapted with permission from ref.[48]).

ferromagnetic behavior, which has been predicted by mathematical modeling. Figure 22 shows a SEM picture of ordered Fe nanorings evaporated over an annealed 540-nm PS latex mask. The outer diameter of single rings is 150 nm and the width of the rings is 20–30 nm.[49]

Computer simulations that showed the possibility of creating periodic arrays of any other geometrical shapes confirmed all experimental results. Some examples are given in Figure 23.[49]

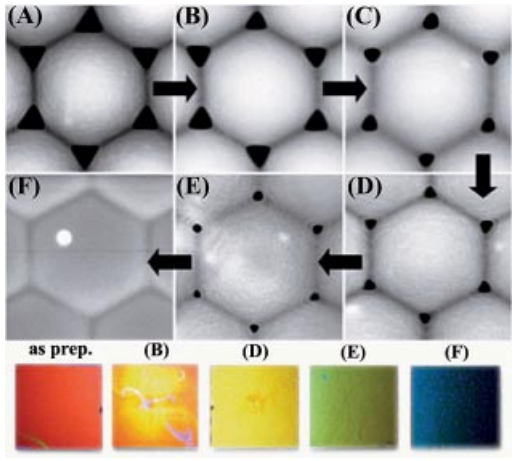

Figure 21. Change of interstices and interferometric color of a 540-nm PS latex mask annealed in 25 mL water/ethanol/ acetone mixture by (A) 1, (B) 2, (C) 4, (D) 6, (E) 7, and (F) 10 microwave pulses (redrawn with permission from ref.[49]).

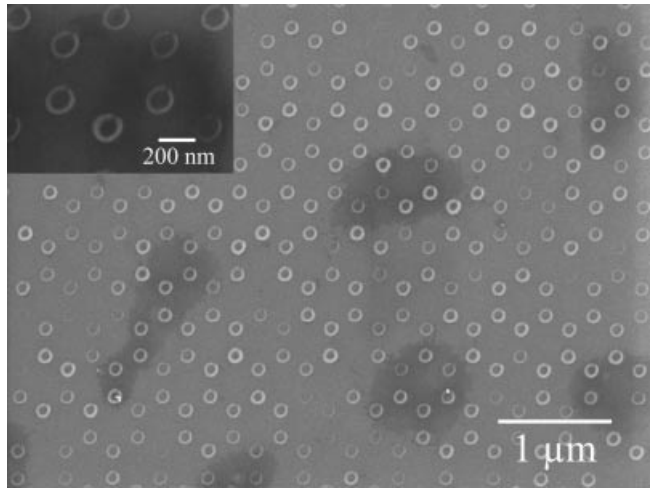

Figure 22. SEM picture of ordered Fe nanorings evaporated over an annealed 540-nm PS latex mask. The outer diameter of the single ring is 150 nm and the width of the ring is 20–30 nm (adapted with permission from ref.[49]).

Concluding Remarks

We have presented some principles of syntheses of inorganic colloidal magnetic particles, their properties, and recent advances in preparing assembled layers thereof on different substrates. The results are, of course, not necessarily limited to magnetic particles. The only restriction for non-magnetic materials is the applicability of MDT. Furthermore, we have shown, that organic colloids, used as lithographic masks, are interesting tools for the development of mm^2-sized nanostructured devices. As reduced size means increased reactivity, colloid chemistry is not able to provide solutions in all fields of device development.

Moreover, the applicability of inorganic colloidal magnetic particles is limited by their composite nature, the NSL is limited to two-dimensional structures and the quality of perfect NSL masks prepared from organic colloids is still a

 © 2005 Wiley-VCH Verlag GmbH & Co. KGaA, Weinheim

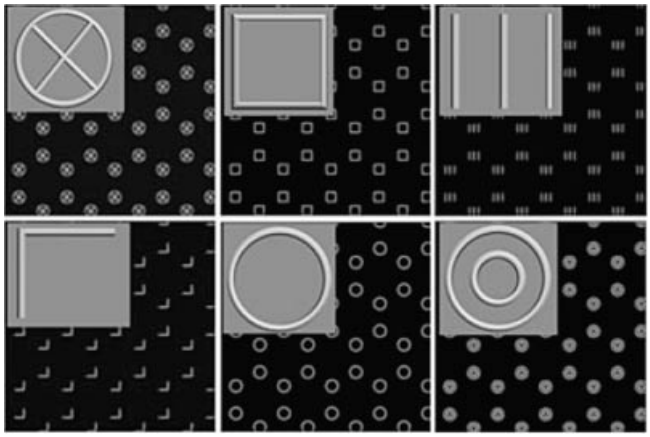

Figure 23. Computer simulation of some structures that should be available theoretically by evaporation through annealed PS masks (adapted with permission from ref.[49]).

challenge when PS latex particles 1000 nm $> d >$ 400 nm are used.

Nevertheless, from the point of view of the ease of sample handling all the methods presented here have great promise in aiding the development of devices relevant to electronic, pharmaceutical, and bioscience technologies.

Acknowledgments

The authors gratefully acknowledge the German Research Community (DFG, Priority Program SPP 1072) for financial support. We also acknowledge a huge number of collaborators whose names are available from the reference section.

[1] a) C. J. Brinker, G. W. Scherer, *Sol-Gel Science*, Academic Press, San Diego, **1990**; b) H.-D. Dörfler, *Grenzflächen- und Kolloidchemie,* Wiley-VCH, Weinheim, **1994** (written in German); c) G. Schmid (Ed.), *Clusters and Colloids: From Theory to Applications*, Wiley-VCH, Weinheim, **1994**; d) J.-H. Fendler (Ed.), *Nanoparticles and Nanostructured Films*, Wiley-VCH, Weinheim, **1998**; e) H. S. Nalwa (Ed.), *Handbook of Surfaces and Interfaces of Materials*, Academic Press, San Diego, **2001**; f) P. Moriarty, *Rep. Prog. Phys.* **2001**, *64*, 297–381; g) L. M. Liz-Marzan, D. Norris (Guest Eds.) New Aspects of Nanocrystal Research, *Mater. Res. Soc. Bull.* **2001**, *26*; h) G. Schmid (Ed.), *Nanoparticles: From Theory to Applications*, Wiley-VCH, Weinheim, **2004**.

[2] W. Ostwald, *Die Welt der vernachlässigten Dimensionen*, Steinkopf, Dresden, **1915** (written in German).

[3] a) R. E. Rosensweig, *Sci. Am.* **1982**, *247*, 124–132; b) R. E. Rosensweig, *Ferrohydrodynamics*, Dover Publishing, New York, **1998**.

[4] a) S. A. Iakovenko, A. S. Trifonov, M. Giersig, A. Mamedov, D. K. Nagesha, V. V. Hanin, E. C. Soldatov, N. A. Kotov, *Adv. Mater.* **1999**, *11*, 388–392; b) T. Fried, G. Shemer, G. Markovich, *Adv. Mater.* **2001**, *13*, 1158–1161.

[5] a) M. A. Correa-Duarte, M. Giersig, N. A. Kotov, L. M. Liz-Marzán, *Langmuir* **1998**, *14*, 6430–6435; b) F. G. Aliev, M. A. Correa-Duarte, A. Mamedov, J. W. Ostrander, M. Giersig, L. M. Liz-Marzán, N. A. Kotov, *Adv. Mater.* **1999**, *11*, 1006–1010; c) F. Caruso, M. Spasova, A. Susha, M. Giersig, R. A. Caruso, *Chem. Mater.* **2001**, *13*, 109–116; d) E. L. Bizdoaca, M. Spasova, M. Farle, M. Hilgendorff, F. Caruso, *J. Magn. Magn. Mater.* **2002**, *240*, 44–46; e) E. L. Bizdoaca, M. Spasova, M. Farle, M. Hilgendorff, L. M. Liz-Marzan, F. Caruso, *J. Vac. Sci. Technol. A* **2003**, *21*, 1515–1518; f) M. Spasova, V. Salgueiriño-Maceira, A. Schlachter, M. Hilgendorff, M. Giersig, L. M. Liz-Márzan, M. Farle, *J. Mater. Chem.* **2005**, *15*, 2095–2098; g) F. Caruso, A. S. Susha, M. Giersig, H. Möhwald, *Adv. Mater.* **1999**, *11*, 950–953.

[6] M. Giersig, P. Mulvaney, *J. Phys. Chem.* **1993**, *97*, 6334–6336.

[7] a) M. Giersig, M. Hilgendorff, *J. Phys. D: Appl. Phys.* **1999**, *32*, L111–L113; b) M. Hilgendorff, B. Tesche, M. Giersig, *Aust. J. Chem.* **2001**, *54*, 497–501.

[8] J. Rybczynski, M. Hilgendorff, M. Giersig, in: *NATO Science Series II*, vol. 91, *Low-Dimensional Systems: Theory, Preparation, and some Applications* (Eds.: L. M. Liz-Marzán, M. Giersig), Kluwer Academic Publishers, Dordrecht, **2003**, pp. 163–172.

[9] S. H. Park, B. Gates, Y. Xia, *Adv. Mater.* **1999**, *11*, 462–466.

[10] B. Gates, Y. Xia, *Adv. Mater.* **2001**, *13*, 1605–1608.

[11] a) H. W. Deckman, J. H. Dunsmuir, *Appl. Phys. Lett.* **1982**, *41*, 377–379; b) A. Rogach, A. Susha, F. Caruso, G. Sukhorukov, A. Kornowski, S. Kershaw, H. Möhwald, A. Eychmüller, H. Weller, *Adv. Mater.* **2000**, *12*, 333–337.

[12] a) J. C. Hulteen, P. R. Van Duyne, *J. Vac. Sci. Techn. A* **1995**, *13*, 1553–1558; b) J. C. Hulteen, D. A. Treichel, M. T. Smith, M. L. Duval, T. R. Jensen, R. P. Van Duyne, *J. Phys. Chem. B* **1999**, *103*, 3854–3863; c) M. Winzer, M. Kleiber, N. Dix, R. Wiesendanger, *Appl. Phys. A* **1996**, *63*, 617–619.

[13] a) R. Micheletto, H. Fukuda, M. Ohtsu, *Langmuir* **1995**, *11*, 3333–3336; b) J. Boneberg, F. Burmeister, C. Schäfle, P. Leiderer, *Langmuir* **1997**, *13*, 7080–7084; c) F. Burmeister, W. Badowsky, T. Braun, S. Wieprich, J. Boneberg, P. Leiderer, *App. Surf. Sci.* **1999**, *144–145*, 461–466; d) F. Burmeister, C. Schäfle, B. Keilhofer, K. M. Bechinger, J. Boneberg, P. Leiderer, *Adv. Mater.* **1998**, *10*, 495–497; e) N. D. Denkov, O. D. Velev, P. A. Kralchevsky, I. B. Ivanov, H. Yoshimura, K. Nagayama, *Langmuir* **1992**, *8*, 3183–3190; f) S. Rakers, L. F. Chi, H. Fuchs, *Langmuir* **1997**, *13*, 7121–7124; g) E. Adachi, A. S. Dimitrov, K. Nagayama, *Langmuir* **1995**, *11*, 1057–1060.

[14] a) Y. Lu, Y. Yin, B. Gates, Y. Xia, *Langmuir* **2001**, *17*, 6344–6350; b) S. H. Park, Y. Xia, *Langmuir* **1999**, *15*, 266–273.

[15] F. Burmeister, C. Schäfle, T. Matthes, M. Böhmisch, J. Boneberg, P. Leiderer, *Langmuir* **1997**, *13*, 2983–2987.

[16] a) M. Giersig, M. Hilgendorff, in: *Nanoscale Materials* (Eds.: P. Kamat, L. M. Liz-Marzán), Kluwer Academic Publishers, Boston, **2003**, pp. 335–370; b) M. Hilgendorff, M. Giersig, in: *Nanoparticle Assemblies and Superstructures* (Ed.: N. Kotov), CRC Press LLC, Boca Raton, **2005**, pp. 385–409.

[17] D. L. Leslie-Pelecky, R. D. Rieke, *Chem. Mater.* **1996**, *8*, 1770–1783.

[18] C Binns, in: *Handbook of Surfaces and Interfaces of Materials,* vol. 2 (Ed.: H. S. Nalwa), Academic Press, San Diego, **2001**, pp. 357–392.

[19] M. Spasova, M. Farle, in: *NATO Science Series II*, vol. 91, *Low-Dimensional Systems: Theory, Preparation, and Some Applications* (Eds.: L. M. Liz-Marzán, M. Giersig), Kluwer Academic Publishers, Dordrecht, **2003**, pp. 173–192.

[20] M. Hilgendorff, in: *Encyclopedia of Nanoscience and Nanotechnology*, vol. 1 (Ed.: H. S. Nalwa), American Scientific Publishers, Stevenson Ranch, **2004**, pp. 213–233.

[21] a) C. B. Murray, S. Sun, H. Doyle, T. Betley, *Mater. Res. Soc. Bull.* **2001**, *26*, 985–991; b) H. Bönnemann, W. Brijoux, R. Brinkmann, E. Dinjus, T. Joussen, B. Korall, *Angew. Chem. Int. Ed. Engl.* **1991**, *30*, 1312–1314; c) J. Rivas, M. A. López-Quintela, M. G. Bonome, R. J. Duro, J. M. Greneche, *J. Magn. Magn. Mater.* **1993**, *122*, 1–5; d) K. S. Suslick, M. Fang, T. Hyeon, *J. Am. Chem. Soc.* **1996**, *118*, 11960–11961; e) T. W. Smith, D. Wychick, *J. Phys. Chem.* **1980**, *84*, 1621–1629.

[22] a) N. Buske, H. Sonntag, T. Götze, *Colloids Surfaces* **1984**, *12*, 195–202; b) M. Respaud, J. M. Broto, H. Rakoto, A. R. Fert, L. Thomas, B. Barbara, M. Verelst, E. Snoeck, P. Lecante, A. Mosset, J. Osuna, T. Ould Ely, C. Amiens, B. Chaudret, *Phys.*

 © 2005 Wiley-VCH Verlag GmbH & Co. KGaA, Weinheim

Rev. B **1998**, *57*, 2925–2935; c) D. P. Dinega, M. G. Bawendi, *Angew. Chem. Int. Ed.* **1999**, *38*, 1788–1791; d) V. F. Puntes, K. M. Krishnan, P. Alivisatos, *Appl. Phys. Lett.* **2001**, *78*, 2187–2189; e) P. H. Hess, P. H. Parker Jr., *J. Appl. Polym. Sci.* **1966**, *10*, 1915–1927; f) E. Papirer, P. Horny, H. Balard, R. Anthore, C. Petipas, A. Martinet, *J. Colloid Interface Sci.* **1983**, *94*, 207–228; g) J. Osuna, D. de Caro, C. Amiens, B. Chaudret, E. Snoeck, M. Respaud, J.-M. Broto, A. Fert, *J. Phys. Chem.* **1996**, *100*, 14571–14574; h) C. Pathmamanoharan, A. P. Philipse, *J. Colloid Interface Sci.* **1998**, *205*, 340–353; i) J. A. Becker, R. Schäfer, R. Festag, W. Ruland, J. H. Wendorff, J. Pebler, S. A. Quaiser, W. Helbig, M. T. Reetz, *J. Chem. Phys.* **1995**, *103*, 2520–2527; j) G. N. Glavee, K. J. Klabunde, C. M. Sørensen, G. C. Hadjipanayis, *Inorg. Chem.* **1993**, *32*, 474–477; k) S. Sun, C. B. Murray, *J. Appl. Phys.* **1999**, *85*, 4325–4330; l) C. Petit, A. Taleb, M. P. Pileni, *J. Phys. Chem. B* **1999**, *103*, 1805–1810; m) J. P. Stevenson, M. Rutnakornpituk, M. Vadala, A. R. Esker, S. W. Charles, S. Wells, J. P. Dailey, J. S. Riffle, *J. Magn. Magn. Mater.* **2001**, *225*, 47–58.

[23] a) A. S. R. Hoon, M. Kilner, G. J. Russell, B. K. Tanner, *J. Magn. Magn. Mater.* **1983**, *39*, 107–110; b) N. Cordente, M. Respaud, F. Senocq, M.-J. Casanove, C. Amiens, B. Chaudret, *Nano Lett.* **2001**, *1*, 565–568; c) D. L. Leslie-Pelecky, S.-H. Kim, M. Bonder, X. Q. Zhang, R. D. Rieke, *Chem. Mater.* **1998**, *10*, 164–171; d) M. T. Reetz, M. Winter, R. Breinbauer, T. Thurn-Albrecht, W. Vogel, *Chem. Eur. J.* **2001**, *7*, 1084–1094.

[24] N. Toshima, T. Yonezawa, *New J. Chem.* **1998**, *22*, 1179–1201.

[25] a) D. B. Lambrick, N. Mason, N. J. Harris, G. J. Russell, S. R. Hoon, M. Kilner, *IEEE Trans. Magn.* **1985**, *21*, 1891–1893; b) D. B. Lambrick, N. Mason, S. R. Hoon, M. Kilner, *J. Magn. Magn. Mater.* **1987**, *65*, 257–260; c) D. B. Lambrick, N. Mason, S. R. Hoon, M. Kilner, J. N. Chapman, *IEEE Trans. Magn.* **1988**, *24*, 1644–1646; d) T. Ould Ely, C. Pan, C. Amiens, B. Chaudret, F. Dassenoy, M.-J. Casanove, A. Mosset, M. Respaud, J.-M. Broto, *J. Phys. Chem. B* **2000**, *104*, 695–702; e) M. C. Fromen, A. Serres, D. Zitoun, M. Respaud, C. Amiens, B. Chaudret, P. Lecante, M. J. Casanove, *J. Magn. Magn. Mater.* **2001**, *242–245*, 610–612; f) D. Zitoun, M. Respaud, M. C. Fromen, M. J. Casanove, P. Lecante, C. Amiens, B. Chaudret, *Phys. Rev. Lett.* **2002**, *89*, 037203(4).

[26] Y. Li, J. Liu, Y. Wang, Z. L. Wang, *Chem. Mater.* **2001**, *13*, 1008–1014.

[27] H. Ago, S. Ohshima, K. Uchida, M. Yumura, *J. Phys. Chem. B* **2001**, *105*, 10453–10456.

[28] a) M. T. Reetz, W. Helbig, S. A. Quaiser, *Chem. Mater.* **1995**, *7*, 2227–2228; b) P. M. Paulus, H. Bönnemann, A. M. van der Kraan, F. Luis, J. Sinzig, L. J. de Jongh, *Eur. Phys. J. D* **1999**, *9*, 501–504; c) H. Bönnemann, W. Brijoux, R. Brinkmann, M. Wagener, *World Patent*, Studiengesellschaft Kohle mbH. **1999**, WO 99/41758; d) H. Bönnemann, in: *Handbook of Surfaces and Interfaces of Materials*, vol. 3 (Ed.: H. S. Nalwa), Academic Press, San Diego, **2001**, pp. 41–64; e) W. Yu, Y. Wang, H. Liu, W. Zheng, *J. Mol. Catal. A* **1996**, *112*, 105–113; f) N. Nunomura, T. Teranishi, M. Miyake, A. Oki, S. Yamada, N. Toshima, H. Hori, *J. Magn. Magn. Mater.* **1998**, *177–181*, 947–948; g) N. Nunomura, H. Hori, T. Teranishi, M. Miyake, S. Yamada, *Phys. Lett. A* **1998**, *249*, 524–530; h) T. Teranishi, M. Miyake, *Chem. Mater.* **1999**, *11*, 3414–3416; i) P. Lu, T. Teranishi, K. Asakura, M. Miyake, N. Toshima, *J. Phys. Chem. B* **1999**, *103*, 9673–9682; j) J. Rivas, R. D. Sánchez, A. Fondado, C. Izco, A. J. García-Bastida, J. García-Otero, J. Mira, D. Baldomir, A. Gonzáles, I. Lado, M. A. López-Quintela, S. B. Oseroff, *J. Appl. Phys.* **1994**, *76*, 6564–6566; k) A. J. García-Bastida, R. D. Sánchez, J. García-Otero, J. Rivas, A. González-Penedo, J. Solla, M. A. López-Quintela, *Mater. Sci. Forum* **1998**, *269–272*, 919–924; l) R. D. Sánchez, M. A. López-Quintela, J. Rivas, A. González-Penedo, A. J. García-Bastida, C. A. Ramos, R. D. Zysler, S. Ribeiro-Guevara, *J. Phys.: Condens. Matter* **1999**, *11*, 5643–5654; m) N. Duxin, N. Brun, P. Bonville, C. Colliex, M. P. Pileni, *J. Phys. Chem. B* **1997**, *101*, 8907–8913; n) N. Duxin, N. Brun, C. Colliex, M. P. Pileni, *Langmuir* **1998**, *14*, 1984–1989; o) E. E. Carpenter, C. T. Seip, C. J. O'Connor, *J. Appl. Phys.* **1999**, *85*, 5184–5186; p) C. J. O'Conner, V. Kolesnichenko, E. E. Carpenter, C. Sangregorio, W. Zhou, A. Kumbhar, J. Sims, F. Agnoli, *Synth. Met.* **2001**, *122*, 547–557; q) B. Ravel, E. E. Carpenter, V. G. Harris, *J. Appl. Phys.* **2002**, *91*, 8195–8197.

[29] a) B. Warne, O. I. Kasyutich, E. L. Mayes, J. A. L. Wiggins, K. K. W. Wong, *IEE Trans. Magn.* **2000**, *36*, 3009–3011; b) S. Sun, C. B. Murray, D. Weller, L. Folks, A. Moser, *Science* **2000**, *287*, 1989–1992; c) S. Yamamuro, D. Farrell, K. D. Humfeld, S. A. Majetich, *Mater. Res. Soc. Symp. Proc.* **2001**, *636*, D.10.8.1(6); d) D. Farrell, S. Yamamuro, S. A. Majetich, *Mater. Res. Soc. Symp. Proc.* **2001**, *674*, U.4.4.1(6); e) K. D. Humfeld, A. K. Giri, E. L. Venturini, S. A. Majetich, *IEEE Trans. Magn.* **2001**, *37*, 2194–2196; f) R. V. Chamberlin, K. D. Humfeld, D. Farrell, S. Yamamuro, Y. Ijiri, S. A. Majetich, *J. Appl. Phys.* **2002**, *91*, 6961–6963; g) S. Yamamuro, D. Farrell, S. A. Majetich, *Phys. Rev. B* **2002**, *65*, 224431(9); h) M. Chen, D. E. Nikles, *Nano Lett.* **2002**, *2*, 211–214; i) M. Chen, D. E. Nikles, *J. Appl. Phys.* **2002**, *91*, 8477–8479; j) K. Ono, Y. Kakefuda, R. Okuda, Y. Ishii, S. Kamimura, A. Kitamura, M. Oshima, *J. Appl. Phys.* **2002**, *91*, 8480–8482; k) E. V. Shevchenko, D. V. Talapin, A. Kornowski, F. Wiekhorst, J. Kötzler, M. Haase, A. L. Rogach, H. Weller, *Adv. Mater.* **2002**, *14*, 287–290; l) E. V. Shevchenko, D. V. Talapin, A. L. Rogach, A. Kornowski, H. Weller, *J. Am. Chem. Soc.* **2002**, *124*, 11480–11485; m) J.-I. Park, J. Cheon, *J. Am. Chem. Soc.* **2001**, *123*, 5743–5746; n) N. S. Sobal, M. Hilgendorff, H. Möhwald, M. Giersig, M. Spasova, T. Radetic, M. Farle, *Nano Lett.* **2002**, *2*, 621–624; o) M. Spasova, T. Radetic, N. Sobal, M. Hilgendorff, U. Wiedwald, M. Farle, M. Giersig, U. Dahmen, *Mater. Res. Soc. Symp. Proc.* **2002**, *721*, 195–200; p) N. S. Sobal, U. Ebels, H. Möhwald, M. Giersig, *J. Phys. Chem. B* **2003**, *107*, 7351–7354; q) N. S. Sobal, M. Giersig, *Aust. J. Chem.* **2005**, *58*, 307–310.

[30] R. Massart, V. Cabuil, *J. Chim. Phys.* **1987**, *84*, 967–973, (in french).

[31] a) R. V. Upadhyay, K. J. Davies, S. Wells, S. W. Charles, *J. Magn. Magn. Mater.* **1995**, *139*, 249–254; b) K. J. Davies, S. Wells, R. V. Upadhyay, S. W. Charles, K. O'Grady, M. El Hilo, T. Meaz, S. Mørup, *J. Magn. Magn. Mater.* **1995**, *149*, 14–18; c) P. C. Fannin, S. W. Charles, J. L. Dormann, *J. Magn. Magn. Mater.* **1999**, *201*, 98–101.

[32] a) M.-P. Pileni, *Adv. Funct. Mater.* **2001**, *11*, 323–336; b) L. Liz, M. A. López Quintela, J. Mira, J. Rivas, *J. Mater. Sci.* **1994**, *29*, 3797–3801; c) J. A. López Pérez, M. A. López Quintela, J. Mira, J. Rivas, S. W. Charles, *J. Phys. Chem. B* **1997**, *101*, 8045–8047.

[33] a) K. J. Davies, S. Wells, S. W. Charles, *J. Magn. Magn. Mater.* **1993**, *122*, 24–28; b) I. Mălăescu, L. Gabor, F. Claici, N. Ştefu, *J. Magn. Magn. Mater.* **2000**, *222*, 8–12; c) T. Fried, G. Shemer, G. Markovich, *Adv. Mater.* **2001**, *13*, 1158–1161.

[34] S. Sun, H. Zeng, *J. Am. Chem. Soc.* **2002**, *124*, 8204–8205.

[35] a) K. R. Brown, M. J. Natan, *Langmuir* **1998**, *14*, 726–728; b) N. R. Jana, L. Gearheart, C. J. Murphy, *Chem. Mater.* **2001**, *13*, 2313–2322; c) H. Yu, P. C. Gibbons, K. F. Kelton, W. E. Buhro, *J. Am. Chem. Soc.* **2001**, *123*, 9198–9199.

[36] a) T. Hyeon, S. S. Lee, J. Park, Y. Chung, H. B. Na, *J. Am. Chem. Soc.* **2001**, *123*, 12798–12801; b) J. Park, K. An, Y. Hwang, J.-G. Park, H.-J. Noh, J.-Y. Kim, J.-H. Park, N.-M. Hwang, T. Hyeon, *Nat. Mater.* **2004**, *3*, 891–895.

[37] F. X. Redl, C. T. Black, G. C. Papaefthymiou, R. L. Sandstrom, M. Yin, H. Zeng, C. B. Murray, S. P. O'Brian, *J. Am. Chem. Soc.* **2004**, *126*, 14583–14599.

[38] D. V. Talapin, A. L. Rogach, M. Haase, H. Weller, *J. Phys. Chem. B* **2001**, *105*, 12278–12285.

[39] C. B. Murray, S. Sun, W. Gaschler, H. Doyle, T. A. Betley, C. R. Kagan, *IBM J. Res. Dev.* **2001**, *45*, 47–56.

[40] D. Lacoste, T. C. Lubensky, *Phys. Rev. E* **2001**, *64*, 41506(8).

 © 2005 Wiley-VCH Verlag GmbH & Co. KGaA, Weinheim

[41] Y. Chushkin, L. Chitu, S. Luby, E. Majkova, A. Satka, V. Holy, J. Ivan, M. Giersig, M. Hilgendorff, T. Metzger, O. Konovalov, *Mater. Res. Soc. Symp. Prog.* **2005**, *877*, accepted.
[42] a) V. Germain, J. Richardi, D. Ingert, M. P. Pileni, *J. Phys. Chem. B* **2005**, *109*, 5541–5547; V. Germain, M. P. Pileni, *J. Phys. Chem. B* **2005**, *109*, 5548–5553.
[43] P. Beecher, E. V. Shevchenko, H. Weller, A. J. Quinn, G. Redmond, *Adv. Mater.* **2005**, *17*, 1080–1083.
[44] a) J. H. Fendler, *Chem. Mater.* **1996**, *8*, 1616–1624; b) G. Decher, *Science* **1997**, *277*, 123–127; c) T. Cassagneau, T. E. Mallouk, J. H. Fendler, *J. Am. Chem. Soc.* **1998**, *120*, 7848–7859; d) G. B. Sukhorukov, E. Donath, H. Lichtenfeld, E. Knippel, M. Knippel, A. Budde, H. Mohwald, *Colloid. Surf. A* **1998**, *137*, 253–266; e) G. B. Sukhorukov, E. Donath, S. Davis, H. Lichtenfeld, F. Caruso, V. I. Popov, H. Möhwald, *Polym. Adv. Technol.* **1998**, *9*, 759–767; f) F. Caruso, R. A. Caruso, H. Möhwald, *Science* **1998**, *282*, 111–1114; g) J. Schmitt, P. Mächtle, D. Eck, H. Möhwald, C. A. Helm, *Langmuir* **1999**, *15*, 3256–3266; h) B. H. Sohn, B. H. Seo, *Chem. Mater.* **2001**, *13*, 1752–1757.
[45] X. Xu, G. Friedman, K. D. Humfeld, S. A. Majetich, S. A. Asher, *Adv. Mater.* **2001**, *13*, 1681–1684.
[46] a) K. Wormuth, *J. Colloid Interface Sci.* **2001**, *241*, 366–377; b) Y. Deng, L. Wang, W. Yang, S. Fu, A. Elaïssari, *J. Magn. Magn. Mater.* **2002**, *257*, 69–78.
[47] a) Z. P. Huang, D. L. Carnahan, J. Rybczynski, M. Giersig, M. Sennett, D. Z. Wang, J. G. Wen, K. Kempa, Z. F. Ren, *Appl. Phys. Lett.* **2003**, *82*, 460–462; b) J. Rybczynski, M. Giersig, *Nano Lett.* **2003**, *3*, 13–18.
[48] A. Kosiorek, W. Kandulski, P. Chudzinski, K. Kempa, M. Giersig, *Nano Lett.* **2004**, *4*, 1359–1363.
[49] A. Kosiorek, W. Kandulski, H. Glaczynska, M. Giersig, *Small* **2005**, *1*, 439–444.

Received: June 2, 2005
Published Online: August 26, 2005

 © 2005 Wiley-VCH Verlag GmbH & Co. KGaA, Weinheim

The Effects of Organisation, Embedding and Surfactants on the Properties of Cadmium Chalcogenide (CdS, CdSe and CdS/CdSe) Semiconductor Nanoparticles

Johannes Frenzel,[a] Jan-Ole Joswig,[b,c] Pranab Sarkar,[b,d] Gotthard Seifert,[a] and Michael Springborg*[b]

Keywords: Cadmium sulfide / Cluster compounds / Density-functional calculations / Nanostructures / Semiconductors

An overview of recent density-functional-based studies on the structure, surface structure and electronic and optical properties of CdS, CdSe and CdS/CdSe semiconductor nanoparticles is given. In particular, the effects of organisation, embedding and surfactants on the properties of these particles are discussed and illustrated by our own results and literature examples. The surface stabilisation by ligands, core/shell embedding or superstructure organisation combined with electronic structure stabilisation of these nanoparticles directly influences their properties: for stabilised nanoparticles a size-dependent decay of the lowest optical excitation energy towards the value of the bulk is found, as observed experimentally.

(© Wiley-VCH Verlag GmbH & Co. KGaA, 69451 Weinheim, Germany, 2005)

1. Introduction

The optical and electronic properties of semiconductor nanoclusters are of great interest for a large variety of potential applications such as displays,[1] quantum dot lasers,[2] solar cells[3] and biological labels.[4,5] Examples of such systems are quantum dots embedded in solid-state structures, colloidal particles on surfaces or clusters in the gas phase. Much progress has been achieved in the controlled synthesis of such particles with a narrow size distribution.[6] Although this allows detailed investigations of the properties of such particles, especially as a function of their size,[7–10] a complete understanding of the basic physical and chemical processes that determine the properties of nanoclusters as a function of size, as well as of the influence of organisation, embedding and surfactants on their properties, is lacking.

The II–VI materials form an important class of semiconductor compounds, with CdS, CdSe, ZnS and ZnSe as their most prominent systems. These materials are often used in a colloidal form in which they form a kind of quantum dot. In the bulk phase, these compounds crystallise preferentially in the zincblende (sphalerite) or the wurtzite structure, although the energetic difference between these two structures is small. Therefore, the existence of both forms in colloidal solutions is not surprising although the basic processes of the structure formation are not yet known in detail. For core/shell nanoparticles, which are formed from a specific II–VI compound, embedded into another II–VI compound, it is known that the stress due to the lattice mismatch may lead to material instabilities and diffusion processes between the two compounds. These instabilities may limit the applicability of such quantum dot structures considerably.

As already mentioned, nanoparticles and colloids of semiconductors are of particular interest due to their electronic and optical properties. Important parameters that characterise these properties are the energies of the orbitals around the Fermi energy and their spatial distribution (e.g.

[a] Institute for Physical Chemistry and Electrochemistry, Technical University of Dresden,
01062 Dresden, Germany
E-mail: johannes.frenzel@chemie.tu-dresden.de
gotthard.seifert@chemie.tu-dresden.de
[b] Institute for Physical and Theoretical Chemistry, University of Saarland,
66123 Saarbrücken, Germany
E-mail: m.springborg@mx.uni-saarland.de
[c] Present address: Laboratory of Physics, Helsinki University of Technology,
P.O. Box 1100, 02015 HUT, Finland
E-mail: joj@fyslab.hut.fi
[d] On leave from: Department of Chemistry, Visva-Bharati University,
Santiniketan, India
E-mail: p.sarkar@mx.uni-saarland.de

MICROREVIEWS: This feature introduces the readers to the authors' research through a concise overview of the selected topic. Reference to important work from others in the field is included.

spatial localisation to the inner part of the particle, or near the surface of the particle, or delocalisation over the whole particle etc.). These properties may be strongly influenced by structural relaxations, the structure of the surface, adsorbed or bonded molecules at the surface (surfactants) and structural changes due to diffusion processes within the particle.

The nanoparticles that are experimentally investigated may contain between a few hundred and some 100000 atoms. Their properties are strongly influenced by the large number of atoms at the surface and their specific bonding properties. The lack of periodicity on the one hand and the relatively large number of atoms on the other hand make theoretical studies of their properties rather difficult. Despite studies of very small systems (see, for example ref.[11]), only a small number of investigations exist that focus on the electronic properties of such particles.[12–15] Very often the structural elements in such investigations are taken from the bulk system. Only in a few cases were the structures of the nanoparticles optimised when considering systems with just a few dozen atoms. Moreover, the precise role of surfactants, embedding, organisation and the surrounding media have been studied only marginally.

In this paper we will review our investigations on the effects of organisation, embedding and surfactants on the properties of CdS, CdSe and CdS/CdSe semiconductor

Johannes Frenzel graduated from the chemistry department of the Technical University of Dresden in 2003 and is now a PhD student in the group of Prof. G. Seifert. His studies are focussed on surface and organisation effects of nanoparticles with respect to their properties.

Jan-Ole Joswig studied chemistry at the Universities of Hamburg, Konstanz and Edinburgh and received his diploma in 1999. He continued working with Michael Springborg at the Universities of Konstanz and Saarland (Saarbrücken) to obtain his PhD in 2003. Currently, he is working as a post-doc at Helsinki University of Technology. His main research interests are the structural, electronic and optical properties of semiconductor and metal clusters and their size dependence.

Pranab Sarkar obtained his MSc in 1991 from the University of Burdwan (India) and his PhD in 1997 from the Indian Association for the Cultivation of Science, Jadavpur. After a post-doc stay at the University of Montreal (Canada) in the years 1997 and 1998, he became a reader in chemistry at the Visva-Bharati University, Santiniketan (India). During the years 2001–03 he undertook extended visits at the University of Saarland, Saarbrücken (Germany). His research interests include theoretical studies on semiconductor nanocrystals and quantum dynamics of real and model systems.

Gotthard Seifert studied Chemistry at the TU Dresden, where he received his diploma in 1975 and graduated with a Dr. rer. nat. (PhD) in 1979. From 1979–1992 he worked as a research assistant at the Institute of Theoretical Physics at the TU Dresden. In 1988 he got his habilitation in theoretical physics. In 1989 and 1990 he worked as a visiting scientist and visiting professor at the International School for Advanced Studies (SISSA) in Trieste and at the EPFL. In 1991 he was a visiting scientist at the Forschungszentrum in Jülich. From 1992–1998 he was again at the Institute of Theoretical Physics at the TU Dresden as a lecturer/professor. In 1998 he moved to the Universität Paderborn (Theoretical Physics) and in 2001 he became a professor of Physical Chemistry at the TU Dresden. His research interests are in the areas of quantum chemistry, cluster physics and chemistry and computational materials research.

Michael Springborg received his diploma in 1980 from the Technical University of Denmark where he also obtained his PhD in 1982. After post-doc stays at the Max Planck Institute for Solid-State Physics in Stuttgart (Germany) and Nordita, Copenhagen (Denmark), he became a scientific staff member in Physical Chemistry at the University of Konstanz in 1989. Since 2000 he is a full professor of Physical and Theoretical Chemistry at the University of Saarland, Saarbrücken (Germany). His research field is the development of theoretical methods and accompanying computer codes for the calculation of electronic and structural properties of materials, in particular of polymers and chain compounds as well as clusters and colloids, as well as fundamental aspects of the electronic density-functional theory. He has published around 150 scientific papers and one monograph on "Methods of Electronic-Structure Calculations" and has edited a book on "Applications of Density-Functional Methods."

 © 2005 Wiley-VCH Verlag GmbH & Co. KGaA, Weinheim

nanoparticles over a wide size range, from clusters containing just a few atoms to nanoparticles with up to about 1000 atoms. The quantum mechanical calculations were done using density-functional theory (DFT) within a tight-binding approximation (DFTB).[16–19] First, the structure and stability of isolated CdS and CdSe clusters, both without and with surfactants, will be discussed as a function of cluster size, followed by a discussion of their electronic structure and optical properties. Subsequently, the so-called core/shell structures will be considered and, finally, the properties of periodically organised clusters will be studied.

2. Structure and Stability

Cadmium chalcogenide nanoparticles are observed with different shapes, e.g. the smaller ones are found to be more tetrahedral[20,21] and the larger particles tend to have a more spherical shape.[22,23] Their geometric structure resembles the structure of the infinite crystal, which in a first approximation can be explained by the existence of directional bonds and, in most cases, tetrahedral coordination as in the bulk.

When considering only naked clusters (i.e. neglecting any surfactants), this tetrahedral coordination is missing for the surface atoms, which leads to the existence of dangling bonds or surface states.[14,24–26] In fact, the influence of the surface becomes very important for particles with a diameter of just a few nanometres or less. For cadmium chalcogenides and other semiconductor particles there is only a small amount of experimental information available for such small clusters. These compounds are mostly dispersed in solutions in Lewis base-type organic solvents, leading to cadmium chalcogenide nanoparticles saturated with tributylphosphane/trioctylphosphane oxide (TOP/TOPO),[23,24] polyphosphate[27] or thiol groups,[20,21,28–31] such that the surface atoms are saturated and the surface states vanish.

In order to obtain some insight into the properties of these systems, naked CdS and CdSe clusters have also been studied theoretically, for example using empirical tight-binding models.[32,33] In these studies the atomic positions are usually fixed, and only a few studies have considered structural relaxations. With an empirical tight-binding scheme these were studied by Whaley et al.,[12–14] whereas a parameter-free density-functional method was used for small CdSe clusters by Eichkorn and Ahlrichs,[11] Troparevsky and Chelikowsky,[34] and Galli et al.[35] We have studied the properties of stoichiometric and nonstoichiometric CdS and CdSe clusters (with up to approximately 1000 atoms)[15,36,37] using a density-functional-based tight-binding method.[16–19] Structural relaxations of these clusters were also considered starting with structures that were cut out from the infinite periodic crystal, (i.e. with either a zincblende or wurtzite structure). However, other structures may also be relevant, for example the boron nitride cage-like structures suggested by Kasuya et al. recently.[38]

In our investigations we optimised all atomic positions of naked CdS and CdSe clusters. We found major structural changes in the outer parts of the clusters, while the inner parts largely kept the initial structure of the bulk material. The size of the surface region turned out to be independent of the particle size and consists of the outermost two layers of atoms (corresponding to a thickness of about 2–3 Å). Outward displacement of the sulfur atoms and inward displacement of the cadmium atoms can be recognised by analysing the radial distribution of the atoms (see Figure 1). Cadmium, as a typical metal atom, prefers high coordination numbers, whereas in many systems sulfur atoms are found with a low coordination number of two. For clusters with a large number of singly bonded surface atoms, Cd–Cd, but no S–S, nearest-neighbour bonds are formed in the structural relaxation (see Figure 2), independent of the initial structure. Other theoretical studies of CdS and CdSe gave similar results to ours,[13,15,36,37,39–41] and Galli et al.[35] found a self healing of the surface similar to previous reports.[34,42]

For clusters, stability is often discussed in relation to the energy gap between occupied and unoccupied states, i.e., in terms of molecular orbital theory, the gap between the highest occupied and lowest unoccupied molecular orbitals (the HOMO–LUMO gap[43,44]). The existence of magic numbers (i.e. of particularly stable clusters) is associated with the existence of a gap between the occupied and unoc-

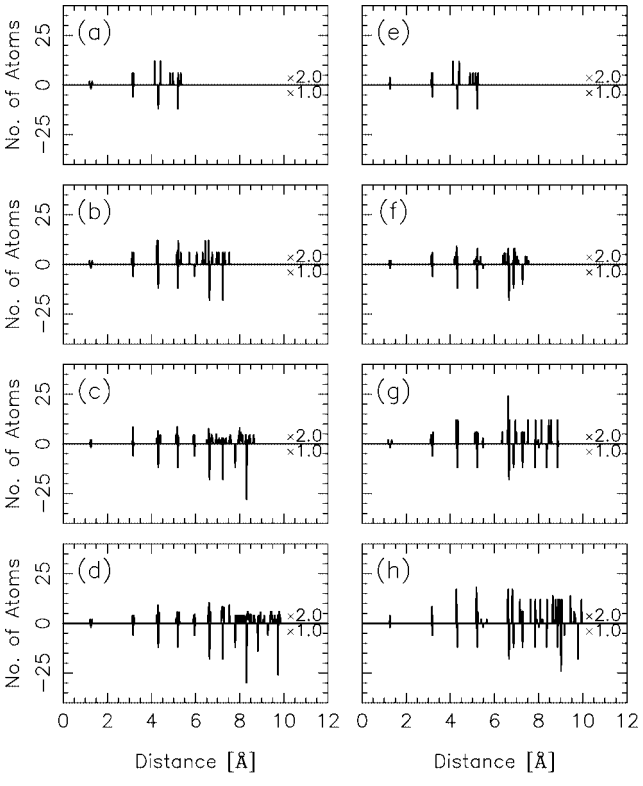

Figure 1. Radial distribution of cadmium and sulfur atoms for zincblende (left column) and wurtzite (right column) clusters of different sizes: (a) and (e) $Cd_{16}S_{16}$; (b) and (f) $Cd_{37}S_{37}$; (c) and (g) $Cd_{57}S_{57}$; (d) and (h) $Cd_{81}S_{81}$. The results for the optimised clusters are shown as curves pointing upward, whereas the curves pointing downward show those for the unrelaxed clusters. Reprinted with permission from ref.[15] Copyright (2000) American Chemical Society.

 © 2005 Wiley-VCH Verlag GmbH & Co. KGaA, Weinheim

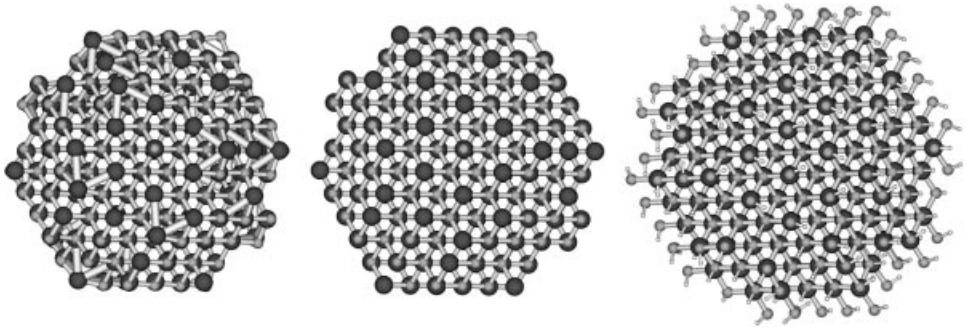

Figure 2. A $(CdS)_{192}$ cluster as a spherical part of the zincblende bulk structure (middle). During structural relaxation Cd–Cd nearest-neighbour bonds are formed (left), while explicit surfactants $[Cd_{192}S_{118}(SH)_{164}]^{16-}$ maintain the initial structure of cluster (right).

cupied orbitals. When discussing the stability of II–VI semiconductor particles, one finds an interplay between structural and electronic effects. When considering the electronic structure in bulk of, for example, CdS, a large bandgap (2.58 eV)[45] arises due to the complete filling of the S 3p-like states (shell closing). The two 5s electrons per Cd atom first fill up this S 3p-like state (two unoccupied orbitals per atom) to form directed bonds that finally result in the tetrahedral coordination.

For singly unsaturated clusters (with underlying bulk structure) this combined atomic structure–electronic structure balance of the bulk is not fulfilled as the structure at the surface causes surface states, as mentioned before. However, it becomes valid for clusters that are modified at the surface, such that the fourfold coordination from the bulk is reconstructed for all cadmium atoms at the surface by sulfur-containing surfactants, e.g. –SR (R = organic residue). Within this approach, the S atoms carrying the surfactants are already saturated in a twofold coordination. Consequently, the resulting final clusters are described as $[Cd_mS_n(SH)_i]^{2(m-n)-i}$, with $2(m - n) - i$ being the charge of the cluster ensuring a non-zero HOMO–LUMO gap. This charge can easily be compensated in solution by the counterions.

In a recent investigation we examined passivated CdS clusters.[36] The results showed only a marginal structural distortion relative to the initial bulk structure without any diffusion of atoms or formation of homonuclear nearest-neighbour bonds at the cluster surface and, moreover, independent of whether the underlying structure was derived from the zincblende or wurtzite crystal structures. These findings are in agreement with experimental results for structurally characterised particles.[20,21,29–31,46–48]

Explicit surfactants have already been considered in the studies by Eichkorn and Ahlrichs,[11] who used density-functional methods for small CdSe clusters, as well as by Gurin[49] for CdS systems using ab initio (Hartree–Fock) methods. Galli et al.[35] did not find any differences in the structures of surfactant-capped and naked CdSe clusters.[50] Furthermore, we should add that surfactant molecules have been treated in other theoretical studies, for example within a tight binding,[13,14] semi-empirical[51] or classical force-field approach.[52]

3. Electronic Structure

One main reason for studying nanoparticles is that their electronic properties are strongly size-dependent and, hence, the possibility exists to tune these by varying the particle size. In the most simple approximation, this quantum-size effect (QSE) or quantum-confinement effect[7,8,53–56] can be understood by using the simple model of a particle in a box. In such a treatment, as well as in effective-mass models,[57–59] the specific structure of the particle is not considered. This means that the significant influence of the structure on the electronic properties, especially for small particles (i.e. those with less than 1000 atoms), is not taken

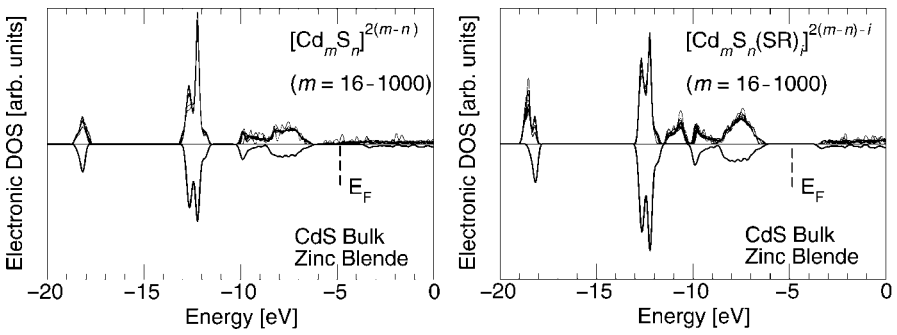

Figure 3. Electronic DOS (calculated with DFTB) of zincblende-derived CdS clusters (left panel, curves pointing upward) and of saturated, zincblende-derived CdS clusters with R = H (right panel curves pointing upward) vs. the bulk CdS electronic DOS (curves pointing downward).

into account. The cases in which the electronic properties were studied with consideration of the underlying structures (of which only a few also included the effects due to structural relaxation) were mentioned above.[11–14,16,17,32,33,57–59]

As for the bulk crystalline structures, the density of states (DOS) profiles of the zincblende- and the wurtzite-based clusters are very similar and they are also rather similar to the DOS of the corresponding bulk structures,[39–41,60–62] even for the smallest clusters (see Figure 3).[12,15,24,49]

The analysis of the radial charge-distribution (see Figure 4) in the clusters clearly indicates a surface region with a thickness of about 2.5 Å for CdS clusters, i.e. the region where significant structural relaxations occur (cf. Section 2). The charge transfer between Cd and S atoms in this region is much stronger than in the inner part of the clusters. No significant differences of this behaviour are observed between zincblende- and wurtzite-based structures. On the other hand, the effect is slightly more pronounced for the unrelaxed structures. This result is very similar to the situation for surfaces of crystalline CdS and CdSe.[39–41]

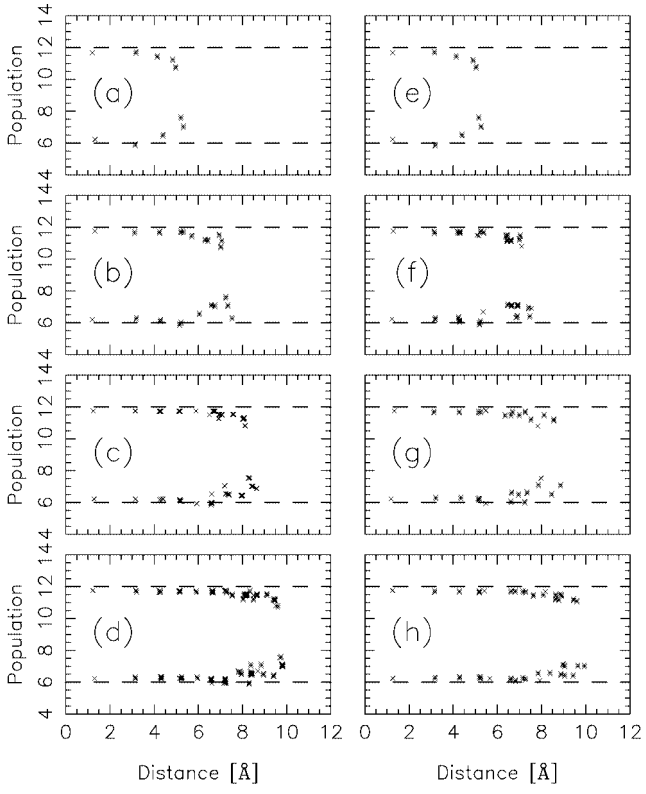

Figure 4. Radial distribution of Mulliken populations for zincblende (left column) and wurtzite (right column) clusters of different sizes: (a) and (e) $Cd_{16}S_{16}$; (b) and (f) $Cd_{37}S_{37}$; (c) and (g) $Cd_{57}S_{57}$; (d) and (h) $Cd_{81}S_{81}$. The horizontal dashed lines mark the number of valence electrons of the neutral atoms (12 for cadmium and 6 for sulfur atoms). Reprinted with permission from ref.[15] Copyright (2000) American Chemical Society.

The frontier orbitals, i.e. the HOMO and LUMO, are important for the reactivity (e.g. the binding of surfactants) as well as for the optical properties. The radial dependence of the HOMO and LUMO is shown for a series of clusters in Figure 5. With N_{ij} being the Mulliken gross population for the *j*th atom and *i*th orbital we define the density as:

$$\rho(\vec{r}) = \sum_j N_{ij} \left(\tfrac{2\alpha}{\pi}\right)^{2/3} \exp\left[-\alpha(\vec{r} - \vec{R}_j)^2\right]$$

with α being chosen "reasonably", i.e. so that illustrative figures result. Subsequently, we calculate the spherical average of this density. As one can see, the HOMO gets increasingly delocalised over the whole cluster with increasing cluster size, whereas, simultaneously, the extent of localisation of the LUMO to surface atoms increases. Therefore, the LUMO depends sensitively on variations of the cluster surface, such as structural relaxations or the presence of surfactants.[36,63]

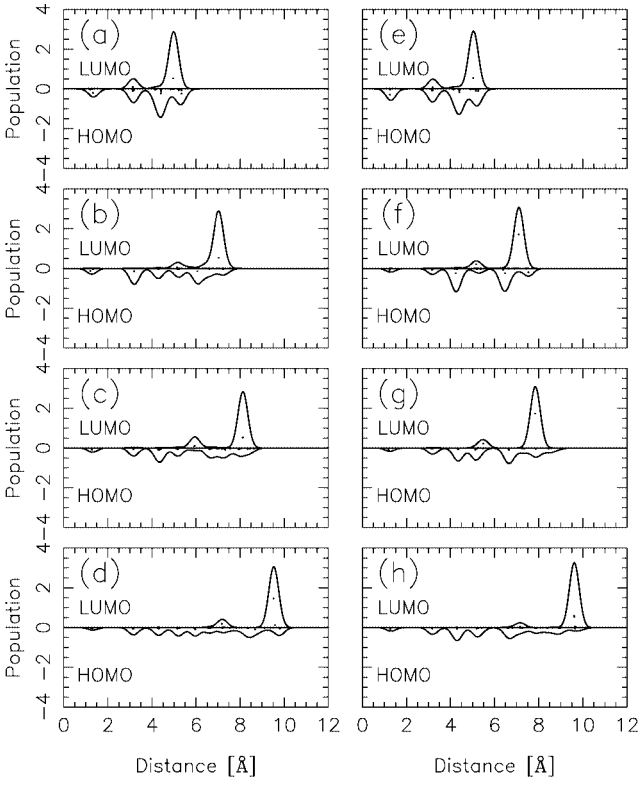

Figure 5. Spherical average of the atomic contributions to HOMO (curves pointing downward) and LUMO (curves pointing upward) broadened with Gaussian functions for zincblende (left column) and wurtzite (right column) clusters of different sizes: (a) and (e) $Cd_{16}S_{16}$; (b) and (f) $Cd_{37}S_{37}$; (c) and (g) $Cd_{57}S_{57}$; (d) and (h) $Cd_{81}S_{81}$. This function is defined in Section 3. Reprinted with permission from ref.[15] Copyright (2000) American Chemical Society.

The HOMO–LUMO energy gaps of both zincblende- and wurtzite-derived clusters are displayed in Figure 6 as a function of cluster size.[63] It can be seen that the relaxation does not have a significant influence on the trends in the size of the energy gaps themselves. However, for clusters with relatively large gaps the gap size is increased, on average by about 0.8 eV, after optimisation of the structures. As a function of cluster size the gap size is oscillating, but

 © 2005 Wiley-VCH Verlag GmbH & Co. KGaA, Weinheim

does show a weak overall decrease with increasing cluster size. The oscillations are mainly due to the varying number of singly bonded surface atoms. The fact that the gap shows an overall decrease with increasing cluster size has also been found by other groups.[23,32,33,64,65]

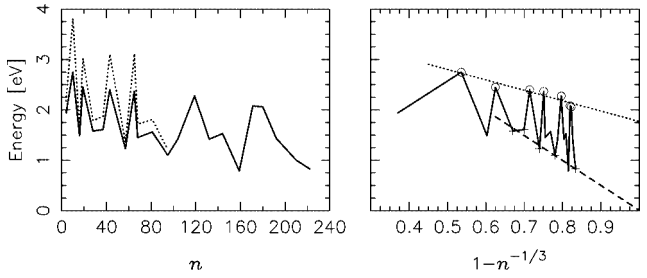

Figure 6. Left panel: HOMO–LUMO gap as a function of cluster size for zincblende-derived clusters. The gap is taken from unrelaxed spherical cut-outs of the zincblende crystal structures (solid curve) and for optimised structures of these clusters (dotted curve). Right panel: HOMO–LUMO gap as function of $1 - n^{-1/3}$, with n being the number of CdS pairs. The gap corresponds to the unrelaxed structures in the left panel. Trend lines are drawn through the gap maxima (dotted, open circles) and minima (dashed, plus signs, excluding the two smallest clusters) to accentuate the size dependence of the HOMO–LUMO gap. Reprinted with permission from ref.[63] Copyright (2003) American Chemical Society.

The gap size is drawn as a function of $1 - n^{-1/2}$ (n being the number of CdS pairs) for unrelaxed clusters in Figure 6. This plot accentuates the size dependence of the gap. Considering only the clusters with relatively large gaps, one can see that an overall decrease is expected for a particle in a box, as observed for CdSe nanoparticles.[66] The extrapolation leads to a bulk limit ($1 - n^{-1/2} \rightarrow 1$) of 1.75 eV. Considering an upward shift of 0.8 eV due to structural relaxation (as mentioned above), this extrapolated gap size is in agreement with the experimental value of the bulk bandgap for CdS (2.58 eV).

In contrast to this result, the gap for the clusters with the smallest gaps approaches a zero gap asymptotically, i.e. metallic behaviour. This result supports the above-mentioned character of the surface states in clusters with unsaturated cadmium surface atoms. In the case of very large particles, this would lead to a metallic-like surface if the metal atoms are not saturated with organic ligands.

With surface saturation in the case of cadmium sulfide clusters leading to $[Cd_mS_n(SH)_i]^{2(m-n)-i}$ (cf. Section 2), the irregularly oscillating behaviour of the HOMO–LUMO gaps and LUMO energies observed in the naked clusters vanishes.[36] Then, both the HOMO (mainly due to S 3p states) and the LUMO (due to Cd 5s states) energies show the same spatial delocalisation as well as a smooth dependence on the particle size, and for all structures the gap decreases toward the bulk value for larger structures (see Figure 7).

This model is rather sensitive to details of the surface structure, as a single missing ligand at one Cd atom already results in a dangling bond which, in turn, leads to a mid-gap state. The same happens if an S or Se atom has two or more dangling bonds.[14,24–26] However, these dangling

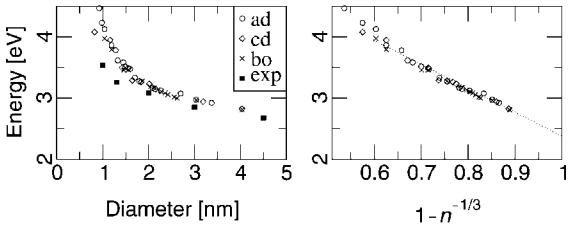

Figure 7. HOMO–LUMO gap of surface-saturated CdS clusters (R = H). The underlying cluster structures are spherical parts of the zincblende bulk structure centred either at a Cd–S nearest-neighbour bond (bo), a cadmium atom (cd) or an adamantane-like cavity (ad) and were fully optimised for the clusters up to 3 nm in diameter. Experimental values from ref.[80] of thiophenol-capped CdS clusters are also given.

bonds are reactive centres, which can easily find a reaction partner for stabilisation in an ionic solution.

To summarise, the surface atoms have a very strong influence on the optical and electronic properties of cadmium sulfide clusters, although this may be less pronounced for nanoparticles with diameters of some tens to hundreds of nanometres.

4. Optical Properties

In the preceding sections we have shown that the electronic structure of II–VI semiconductor nanoparticles is sensitive to the underlying atomic structure and, especially, that the surface has a basic influence on the orbitals closest to the Fermi level. For a more accurate description of optical properties, selection rules and collective effects in the excitation process have to be taken into account. This has been done in previous studies of cadmium sulfide, selenide, and telluride clusters by applying the effective-mass method for the calculation of the energetically lowest optical transitions;[57–59,67,68] in this model the underlying structure of the cluster is not considered. However, the structure has been included in the tight-binding calculations that have also been performed for these systems.[13,14,32,33,64,69–77] Nevertheless, except for a very few studies, structural relaxations as well as collective effects have not been taken into account, with the exceptions being, for example, the work of Whaley and co-workers[13] as well as the density-functional studies of Ahlrichs et al.[11,42] and Galli et al.[35] Chelikowsky et al.[34] have performed calculations of very small Cd_nSe_n clusters ($n \leq 8$) by employing the time-dependent local-density approximation (TDLDA).[78] In an earlier study we presented a systematic study of the optical properties of larger clusters[63] employing time-dependent density-functional response theory (TD-DFRT) as incorporated in the DFTB method (referred to as TD-DFRT-TB).[79] In that work, the optical spectra of naked stoichiometric CdS clusters were investigated. We did not find the onset peaks to be shifted with respect to the joint DOS, which is in agreement with the work of Ahlrichs.[42] Instead, depending on structural changes, the spectra show fluctuations of the lowest excitation energy with increasing cluster

size. Corresponding to the above-mentioned correlation of singly bonded surface atoms and the HOMO–LUMO gap energy oscillations (see Section 3), the smallest excitation energies of such clusters lie below the experimental bulk absorption value of 2.58 eV[45] and the values for the corresponding nanoparticles.[80] When subtracting the local density of states of all singly bonded surface atoms, a spectrum with a gap of about 3 eV is obtained, since the additional states at lower energies arise predominantly from cadmium 5s levels. The intense low-lying excitations in the spectra of clusters with a large number of unsaturated cadmium atoms indicate a collective character, as observed experimentally in metal clusters as surface plasmon excitations.[81]

Alternatively, the experimental results of Lifshitz et al.[82,83] on the excitation relaxation processes for CdSe systems suggest the presence of a sub-bandgap state with a clear dependence on the cluster structure. The authors argue that the recombination takes place at a low-symmetry site, such as one near the surface, and, furthermore, that the hole is delocalised, whereas the electron is localised at the surface, which is similar to our findings for the naked clusters. Using optical measurements Bawendi et al.[24] have observed that one or both charge carriers are surface-trapped. On the other hand, theoretical studies of CdS and CdSe[40,41] have found surface states just above the valence band (both in contrast to our results). In their study of CdSe clusters, Hill and Whaley[12] found surface states similar to ours in some cases, while other groups[14,73] have found surface states appearing close to the bottom of the conduction band.

In a recent study,[36] we explicitly and systematically included surfactants in calculations of the optical spectra of CdS nanoparticles (see Figure 8). For all clusters, the smallest excitation energies are found above 2.58 eV and, when extrapolating the particle size toward infinity (Figure 9), the experimentally observed asymptotic decay toward the bulk value of the absorption is recovered with increasing cluster size. Moreover, for larger particle sizes the HOMO–LUMO energy gap gives a good approximation of the lowest-energy transitions (TD-DFRT-TB spectra) for (CdS) clusters with more than 150 atoms.

Besides the discussed general size-dependence, single or a few unsaturated surface atoms (cf. Section 3) can cause surface-trapped states, which are observable in the optical spectra and may thus affect the luminescence process.

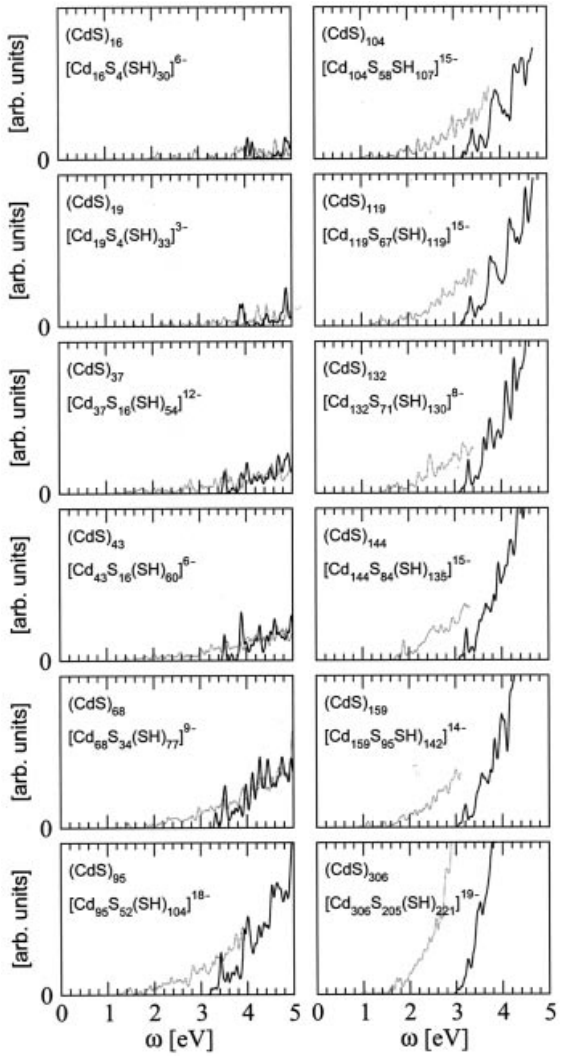

Figure 8. TD-DFRT-TB singlet excitation spectra of naked clusters (grey curves) and saturated clusters (black curves). The underlying structures were optimised, except for $(CdS)_{306}$ and $[Cd_{306}S_{205}(SH)_{221}]^{19-}$.

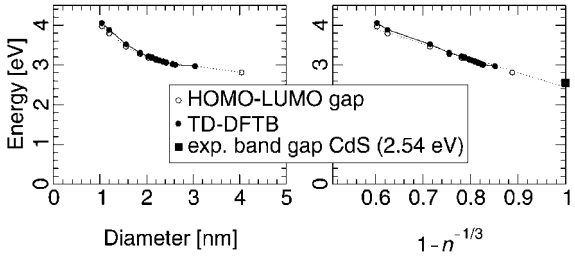

Figure 9. The calculated lowest energy transition (TD-DFRT-TB spectra) vs. HOMO–LUMO gap energy of surface-saturated CdS clusters (R = H, underlying structure: zincblende, bond centred). The results differ for small clusters (max. 2%) while they coincide for larger ones. The underlying structure was relaxed for clusters up to 3 nm in diameter.

5. Embedded Structures (Core/Shell Systems)

As we have seen in the preceding sections, the atoms closest to the surface are chemically active. This means, in turn, that this cluster can be stabilised by passivating the dangling bonds at the surface, with surfactants for example, as we have seen above, or by embedding the cluster in a host, in which case quantum dots may result.

Core/shell nanoparticles are intermediates between these two extremes as they consist of one material embedded into another with the thickness of the shell being finite. A large variety of material properties can be obtained by varying the two materials as well as the sizes of the two parts. Therefore, during the last decade much experimental work has been reported directed toward the synthesis of such

 © 2005 Wiley-VCH Verlag GmbH & Co. KGaA, Weinheim

core/shell nanoparticles with tailored properties.[84–86] Core/shell systems that have been studied include CdSe/ZnS, ZnS/CdS, CdS/HgS, HgS/CdS, CdS/PbS, CdSe/ZnSe, CdSe/CdS, CdS/CdSe etc.[87]

In a recent study,[88] we presented theoretical results for the structural and electronic properties of CdSe/CdS and CdS/CdSe core/shell nanoparticles that have also been the focus of significant experimental interest,[89–92] although theoretical studies of these, or related, systems are extremely scarce.[76,93,94] In particular, only one of these studies[94] included any estimate of the energetics and structural properties of these materials and, to the best of our knowledge, no studies have addressed stability and diffusion processes. These processes, which are of importance for degradation, were also addressed briefly in our work.

The similarity between the CdS and CdSe lattice constants was our main motivation for choosing this semiconductor pair for our investigation. For naked CdS and CdSe clusters, we found[15,37,95] that zincblende- and wurtzite-derived clusters are energetically very close. Therefore, we decided to consider spherical parts of only the zincblende crystal structure with one semiconductor compound outside the other one and, subsequently, let the structures relax to their closest total-energy minima.

In Figure 10 we show the atomic Mulliken gross populations (related to the atomic charges) for the different clusters of our study as a function of the radial distance (i.e. of the distance to the geometric average of all nuclear coordinates). Similar to our previous results,[15,37,95] we observed a larger electron transfer from Cd to S than from Cd to Se in the general case, although the difference is marginal. Moreover, as for the pure, stoichiometric, naked CdS and CdSe clusters, we found an increased electron transfer in the outermost parts of the clusters although, in contrast to our results for the pure clusters, the width of this region depends on the cluster. As for the pure cluster, the absolutely outermost atoms are mainly Se and S atoms, whereas the metal atoms (in particular near the surface) tend to experience a structural relaxation so that they obtain a higher coordination. The pair of core/shell systems $Cd_{21}S_{21}$/$Cd_{16}Se_{16}$ and $Cd_{16}Se_{16}$/$Cd_{21}S_{21}$ is particularly interesting, because it is the only case for which the two systems have exactly the same numbers of Cd, S and Se atoms but where the complete core and shell have been interchanged. For this pair we found that the overall distribution of the Mulliken populations is very similar for the two systems, independent of which of them is the core and which is the shell (cf. the two uppermost panels in Figure 10). Moreover, we found that $Cd_{21}S_{21}$/$Cd_{16}Se_{16}$ is more stable than $Cd_{16}Se_{16}$/$Cd_{21}S_{21}$ by 32.2 eV. For the infinite systems, the gap of CdSe is smaller than that of CdS.[96,97] Therefore, we found that the most stable system is that of the large-gap core embedded into a small-gap shell.

The optical properties are determined by the properties of excitons that, to a first approximation, are mainly derived from the HOMO and LUMO. Therefore, we shall study the latter in some detail. Figure 11 shows a schematic representation of the radial dependence of these orbitals as

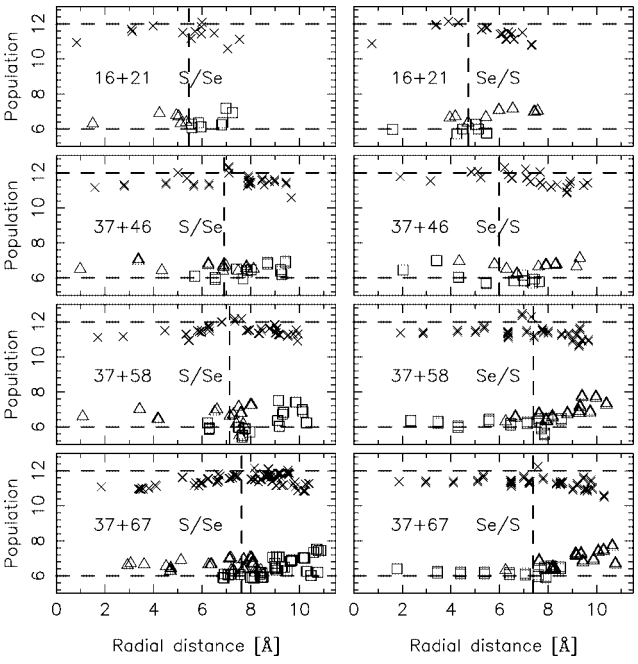

Figure 10. The radial distribution of Mulliken gross populations for different core/shell systems. Crosses, triangles and squares mark the populations of Cd, S and Se atoms, respectively. The horizontal dashed lines mark the number of valence electrons in the neutral atoms (12 for Cd and 6 for S and Se). The labels "N+M" and "A/B" on the panels denote a Cd_NA_N/Cd_MB_M core/shell system with A and B referring to S and Se. The vertical dashed lines show a crude separation of the system into a core and a shell part by being placed at the average of the radial distances of the outermost A atom and innermost B atom.

defined in Section 3. As indicated in the figure, the HOMO is localised to the shell region whereas the LUMO is localised to the core region in only one case ($Cd_{37}S_{37}$/$Cd_{58}Se_{58}$). This means that a charge transfer may take place upon excitation and, accordingly, that the excitons may be very long-lived. We stress that neither the HOMO nor the LUMO is confined to the complete core or shell, but each of the two orbitals is localised on a few atoms in either the core or the shell. Therefore, any standard relaxation process by which the exciton can relax may also be relevant here, although due to the obvious spatial separation of the HOMO and LUMO the process may be slow. This also means that the HOMO and LUMO may also be spatially separated for the other systems of our study, leading to long-lived excitons, but only for this single case does the spatial separation include a separation between core and shell.

For macroscopic CdSe/CdS interfaces the HOMO of the CdSe part lies at a higher energy than the HOMO of the CdS part.[96] On the other hand, the HOMO–LUMO energy gap of crystalline CdSe is smaller than that of crystalline CdS,[96,97] suggesting that the LUMO of CdSe and CdS will appear energetically relatively close to each other. This indicates that the HOMO of the core/shell system will be located on the CdSe part whereas the LUMO may be located on either part. Results like those of Figure 11 show that this simple expectation is only partly true. However, when the HOMO and LUMO are localised on different

 © 2005 Wiley-VCH Verlag GmbH & Co. KGaA, Weinheim

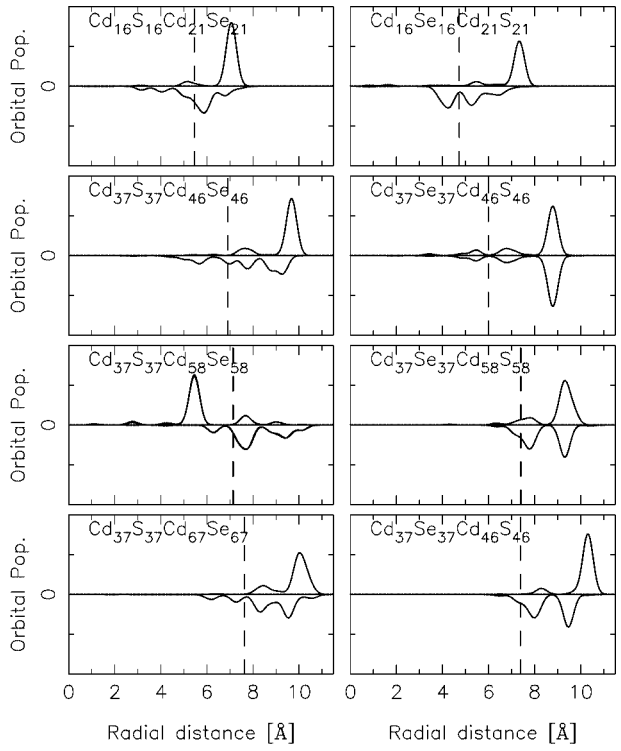

Figure 11. Schematic representation of the radial electron distribution of the HOMO (curves pointing downward) and of the LUMO (upward) for the same systems as in Figure 10. The vertical dashed lines mark the separation into a core and a shell part as in Figure 10. The function is defined in Section 3.

parts of the system, one may have a system that can act as a nanocapacitor whose excitons are particularly long-lived. On the other hand, this simple picture also suggests that the HOMO–LUMO energy gap of the core/shell systems is smaller than that of the individual components. Our calculated energy gaps, at most 1.15 eV, are indeed in agreement with this consensus.

We finally studied the energetics of diffusion of one S (Se) atom from the core to the shell and, simultaneously, one Se (S) atom from the shell to the core in various core/shell systems. This gives some first indications of the stability of these systems towards degradation. First, we simply interchanged two close S and Se atoms and subsequently allowed the structure to relax to the closest total-energy minimum. It turned out that in several cases the total energy (cf. Figure 12) was lowered by some electron volts, whereas it was increased in other cases. Subsequently, we followed the energetics along the reaction path for this interchange of a Se–S pair using the nudged-elastic-band method.[98] The resulting total-energy curves are shown in Figure 12, where it can be seen that the diffusion is connected with a fairly large energy barrier of several electron volts, which makes the diffusion highly unlikely despite the accompanying energy gain. In some of the cases of Figure 12 we observed a change in the HOMO–LUMO gap, but it was not possible to identify a correlation between the energy gain upon the interchange and the change in the gap. Finally, the large energy barrier for the transition suggests that quantum dots, which in principle are core/shell systems with a very thick shell, are also stable against degradation.

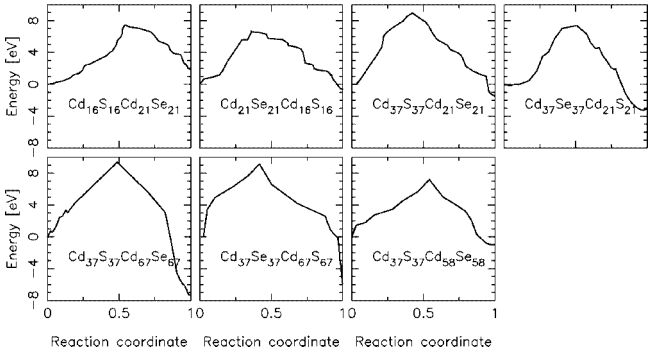

Figure 12. Variation in the total energy accompanying an interchange of a close pair of an S and an Se atom in some selected core/shell systems. The reaction coordinate is defined as being 0 before and 1 after the interchange.

6. Organised Structures

After having discussed the properties of single II–VI semiconductor nanoparticles, we now focus on the effects due to organisation. Because of their potential application as building blocks for electronic and optical devices, solvent-free particles (i.e., a non-liquid phase), either deposited on a substrate or incorporated into a solid phase, are advantageous to obtain adequate material handling. Some effort has been made to organise semiconductor nanoparticles, for example by Samokhvalov et al.[99] and Lahav et al.,[100,101] who have studied the collective electronic properties of self-organised CdS particles in hybrid Langmuir–Blodgett films. Similarly, Hilbron et al.[102] have obtained an arrangement by polymerisation of the surfactants. Recently, Feng et al.[103,104] have fabricated porous CdS frameworks that had been stabilised by metal ions similar to what is found for zeolites.

Weller and co-workers[30,31,105,106] have synthesised tetrahedral Cd_mS_n nanoparticles organised in a tetragonal superstructure. Their building-block structures are similar to those reported previously,[21,29] but have different organic ligands for stabilisation. The stoichiometries within the super network are, thus, $Cd_{17}S_4(SCH_2CH_2OH)_{26}$ and $Cd_{32}S_{14}[SCH_2CH(CH_3)OH]_{36}$ (corresponding to $Cd_{17}S_{32}$ and $Cd_{32}S_{50}$ for the case of naked clusters). These clusters have a tetragonal shape and are connected by shared corner atoms to form a network with a diamond-like superstructure. Both a single tetrahedron and the unit cell of the diamond-like superstructure are shown in Figure 13 for the smaller cluster only.

We have performed calculations using the DFTB method on saturated and unsaturated tetrahedral cadmium sulfide clusters, both in the gas phase and in the tetragonal superstructure. In the singly unsaturated clusters, strong deformations can be observed caused by the structural relaxation. However, less charge transfer within the single cluster

 © 2005 Wiley-VCH Verlag GmbH & Co. KGaA, Weinheim

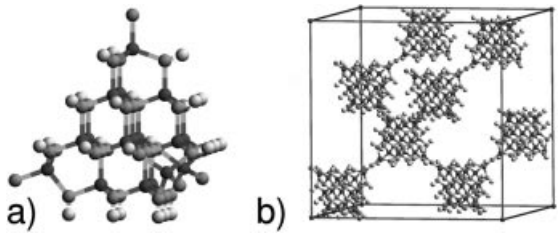

Figure 13. (a) Single tetrahedral $Cd_{17}S_{32}H_{24}$ cluster (unrelaxed) and (b) unit cell of the corresponding superstructure. Cd, S and H atoms are shown as dark grey, light grey and white spheres, respectively.

is observed when saturating the dangling bonds at the surface with hydrogen atoms and, moreover, the structural relaxations are marginal with respect to the initial (experimentally characterised) clusters.

The electronic properties, for example those given by the Mulliken gross populations (Figure 14), show a strong dependence on saturation. An influence of the periodic arrangement on the properties could, however, hardly be observed: the Mulliken populations and the density of states (Figure 15) are very similar for the single clusters and for the periodic structure. Nevertheless, due to their dense packing and covalent linking the surfactants itself are stabilised in the cavity. Likewise, the organisation of such nanoparticles in Langmuir–Blodgett films or their embedding in a polymer matrix strongly influences an ordering/fixation of the ligands. In all cases, the reproducibility of the single nanoparticles' surface structure is increased, thus affecting the cluster's electronic and optical properties (cf. Sections 3 and 4).

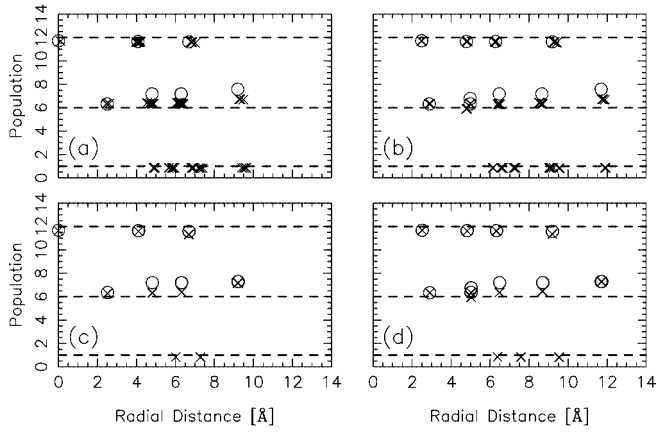

Figure 14. Radial distribution of the Mulliken gross populations in $Cd_{17}S_{32}$ and $Cd_{17}S_{32}H_{26}$ [(a) single tetrahedron, (c) periodic structure], and $Cd_{32}S_{58}$ and $Cd_{32}S_{58}H_{44}$ [(b) single tetrahedron, (d) periodic structure]. Open circles and crosses mark atoms in the unsaturated and the saturated clusters, respectively. The dashed lines mark the number of valence electrons of the single atoms in Cd (12), S (6) and H (1).

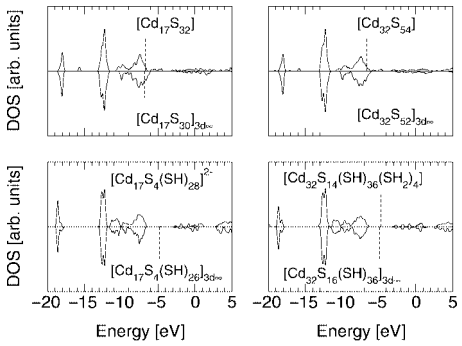

Figure 15. DOS of the tetrahedral clusters $Cd_{17}S_{32}$ (left column) and $Cd_{32}S_{54}$ (right column). The upper panels show the DOS for the clusters without surfactants and the lower panels show the DOS for clusters with surfactants (R = H). In each panel the curve pointing upward refers to the single cluster, whereas the curve pointing downward refers to the periodic superstructure. The dashed lines mark the Fermi levels.

7. Concluding Remarks

In this report we have reviewed results on the structural, electronic and optical properties of CdS and CdSe clusters and the effects of organisation, embedding and surfactants on these properties. In our own studies, we performed calculations for clusters with up to several hundred atoms using the DFTB method. The cluster structures were approximated to be spherical cut-outs of two crystal structures − zincblende and wurtzite − that are of relevance for the macroscopic materials under ambient conditions.

Surfactants attached to the unsaturated atoms of the surface have a strong influence on the structural properties: whereas naked clusters show strong relaxation effects, in particular in the surface layer, the saturation reduces the relaxation significantly such that the surface atoms essentially remain at their initial, unrelaxed positions. We also found that the underlying structure has a large impact on the electronic and, thus, also on the optical properties. The densities of states show, however, no large influence of cluster size on the positions of the evolving bands, but saturation gives additional states in comparison to the bulk DOS. Furthermore, we have shown that in the surface region of naked clusters, i.e. in the region where structural changes take place, the Mulliken gross populations suggest a higher charge transfer than the inner bulk-like part of the clusters. Also, the LUMO is located in this part, whereas the HOMO is delocalised over the entire cluster.

We have also shown that the trends in the size-dependent presentation of the HOMO–LUMO gap are already very well described by naked, unrelaxed clusters. These trends indicate, by extrapolation, that the gap approaches the bulk bandgap value for clusters with only a small number of singly bonded surface atoms and that it approaches a zero gap for clusters with a large number of unsaturated surface atoms. Again, we find a strong dependence of the electronic properties on the nature of the surface and the kind of saturation.

With respect to the optical properties, these findings are affirmed, since in the optical spectra the dependence on the

 © 2005 Wiley-VCH Verlag GmbH & Co. KGaA, Weinheim

number of singly bonded surface atoms was recovered, too. Saturation widens the HOMO–LUMO gap, since it is closed by states of singly bonded cadmium atoms in the gap. Thus, saturated CdS clusters have HOMO–LUMO gaps that are larger than the bulk bandgap, thus supporting using the simple theoretical picture of the particle in a box.

Similar effects could be observed in core/shell systems for which some of the effects could be well described as being due to saturation effects. For example, the Mulliken populations and, in some cases, also the delocalisation of the HOMO do not change at the core/shell interface. However, since the shell is unsaturated itself, it shows the same trends (larger charge transfer) as the one-compound clusters discussed above, although to a lesser extent. Except for one case, the core/shell systems investigated in this study do not show the total spatial separation of HOMO and LUMO that would lead to long-lived excitons. Diffusion between core and shell atoms is found to be rather unlikely, which suggests that embedded systems, and also quantum dots, are stable against degradation.

Finally, we have also investigated the effects of periodic organisation of tetrahedral clusters into superstructures, which have already been synthesised. The effects of saturation discussed above can also be found in these systems despite the different overall structure and the organisation. However, the periodic arrangement does not seem to lead to major changes in the electronic properties. Nevertheless, organisation prevents structural changes at the sites of conjunction, although this may be considered as nothing other than a special type of saturation. This shows again that saturation is a very important effect for properties of clusters, and studying them should be a central subject for any investigation of large, but finite, systems.

Acknowledgments

This work was mainly supported by the Deutsche Forschungsgemeinschaft through the SPP 1072 (project Sp 439/9-1). The authors are also grateful to the Fonds der Chemischen Industrie.

[1] V. L. Colvin, M. C. Schlamp, A. P. Alivisatos, *Nature* **1994**, *370*, 354–357.
[2] V. I. Klimov, A. A. Mikhailovsky, S. Xu, A. Malko, J. A. Hollingsworth, C. A. Leatherdale, H. J. Eisler, M. G. Bawendi, *Science* **2000**, *290*, 314–317.
[3] W. U. Huynh, J. J. Dittmer, A. P. Alivisatos, *Science* **2002**, *295*, 2425–2427.
[4] W. C. W. Chan, S. M. Nie, *Science* **1998**, *281*, 2016–2018.
[5] M. Bruchez, M. Moronne, P. Gin, S. Weiss, A. P. Alivisatos, *Science* **1998**, *281*, 2013–2016.
[6] A. Eychmüller, in *Nanoparticles* (Ed.: G. Schmid), Wiley-VCH, Weinheim, **2004**.
[7] A. D. Yoffe, *Adv. Phys.* **1993**, *42*, 173–266.
[8] A. D. Yoffe, *Adv. Phys.* **2001**, *50*, 1–208.
[9] A. Eychmüller, *J. Phys. Chem. B* **2000**, *104*, 6514–6528.
[10] Y. Wang, N. Herron, *J. Phys. Chem.* **1991**, *95*, 525–532.
[11] K. Eichkorn, R. Ahlrichs, *Chem. Phys. Lett.* **1998**, *288*, 235–242.
[12] N. A. Hill, B. Whaley, *J. Chem. Phys.* **1993**, *99*, 3707–3715.
[13] K. Leung, K. B. Whaley, *J. Chem. Phys.* **1999**, *110*, 11012–11022.
[14] S. Pokrant, K. B. Whaley, *Eur. Phys. J. D* **1999**, *6*, 255–267.
[15] J. O. Joswig, M. Springborg, G. Seifert, *J. Phys. Chem. B* **2000**, *104*, 2617–2622.
[16] D. Porezag, T. Frauenheim, T. Kohler, G. Seifert, R. Kaschner, *Phys. Rev. B* **1995**, *51*, 12947–12957.
[17] G. Seifert, D. Porezag, T. Frauenheim, *Int. J. Quantum Chem.* **1996**, *58*, 185–192.
[18] M. Elstner, D. Porezag, G. Jungnickel, J. Elsner, M. Haugk, T. Frauenheim, S. Suhai, G. Seifert, *Phys. Rev. B* **1998**, *58*, 7260–7268.
[19] T. Frauenheim, G. Seifert, M. Elstner, T. Niehaus, C. Kohler, M. Amkreutz, M. Sternberg, Z. Hajnal, A. Di Carlo, S. Suhai, *J. Phys. Condens. Matter* **2002**, *14*, 3015–3047.
[20] I. G. Dance, *Polyhedron* **1986**, *5*, 1037–1104.
[21] G. S. H. Lee, D. C. Craig, I. Ma, M. L. Scudder, T. D. Bailey, I. G. Dance, *J. Am. Chem. Soc.* **1988**, *110*, 4863–4864.
[22] J. E. B. Katari, V. L. Colvin, A. P. Alivisatos, *J. Phys. Chem.* **1994**, *98*, 4109–4117.
[23] C. B. Murray, D. J. Norris, M. G. Bawendi, *J. Am. Chem. Soc.* **1993**, *115*, 8706–8715.
[24] M. G. Bawendi, W. L. Wilson, L. Rothberg, P. J. Carroll, T. M. Jedju, M. L. Steigerwald, L. E. Brus, *Phys. Rev. Lett.* **1990**, *65*, 1623–1626.
[25] M. A. Hines, P. Guyot-Sionnest, *J. Phys. Chem.* **1996**, *100*, 468–471.
[26] A. C. Carter, C. E. Bouldin, K. M. Kemner, M. I. Bell, J. C. Woicik, S. A. Majetich, *Phys. Rev. B* **1997**, *55*, 13822–13828.
[27] L. Spanhel, M. Haase, H. Weller, A. Henglein, *J. Am. Chem. Soc.* **1987**, *109*, 5649–5655.
[28] T. Vossmeyer, L. Katsikas, M. Giersig, I. G. Popovic, K. Diesner, A. Chemseddine, A. Eychmüller, H. Weller, *J. Phys. Chem.* **1994**, *98*, 7665–7673.
[29] N. Herron, J. C. Calabrese, W. E. Farneth, Y. Wang, *Science* **1993**, *259*, 1426–1428.
[30] T. Vossmeyer, G. Reck, L. Katsikas, E. T. K. Haupt, B. Schulz, H. Weller, *Science* **1995**, *267*, 1476–1479.
[31] T. Vossmeyer, G. Reck, B. Schulz, L. Katsikas, H. Weller, *J. Am. Chem. Soc.* **1995**, *117*, 12881–12882.
[32] L. W. Wang, A. Zunger, *Phys. Rev. B* **1996**, *53*, 9579–9582.
[33] P. E. Lippens, M. Lannoo, *Phys. Rev. B* **1989**, *39*, 10935–10942.
[34] M. C. Troparevsky, J. R. Chelikowsky, *J. Chem. Phys.* **2001**, *114*, 943–949.
[35] A. Puzder, A. J. Williamson, F. Gygi, G. Galli, *Phys. Rev. Lett.* **2004**, *92*, 217401.
[36] J. Frenzel, G. Seifert, manuscript in preparation.
[37] P. Sarkar, M. Springborg, *Phys. Rev. B* **2003**, *68*, 235409.
[38] A. Kasuya, R. Sivamohan, Y. A. Barnakov, I. M. Dmitruk, T. Nirasawa, V. R. Romanyuk, V. Kumar, S. V. Mamykin, K. Tohji, B. Jeyadevan, K. Shinoda, T. Kudo, O. Terasaki, Z. Liu, R. V. Belosludov, V. Sundararajan, Y. Kawazoe, *Nat. Mater.* **2004**, *3*, 99–102.
[39] T. N. Horsky, G. R. Brandes, K. F. Canter, C. B. Duke, A. Paton, D. L. Lessor, A. Kahn, S. F. Horng, K. Stevens, K. Stiles, A. P. Mills, *Phys. Rev. B* **1992**, *46*, 7011–7026.
[40] Y. R. Wang, C. B. Duke, *Phys. Rev. B* **1988**, *37*, 6417–6424.
[41] P. Schroer, P. Kruger, J. Pollmann, *Phys. Rev. B* **1994**, *49*, 17092–17101.
[42] P. Deglmann, R. Ahlrichs, K. Tsereteli, *J. Chem. Phys.* **2002**, *116*, 1585–1597.
[43] M. Brack, *Rev. Mod. Phys.* **1993**, *65*, 677–732.
[44] W. A. de Heer, *Rev. Mod. Phys.* **1993**, *65*, 611–676.
[45] O. Madelung, M. Schulz, *Landholt-Börnstein Numerical Data and Functional Relationships, in Science and Technology, New Series III: Crystal and Solid: Semiconductors*, vol. 22a, Springer, Berlin, **1986**.
[46] I. G. Dance, A. Choy, M. L. Scudder, *J. Am. Chem. Soc.* **1984**, *106*, 6285–6295.
[47] S. Lacelle, W. C. Stevens, D. M. Kurtz, J. W. Richardson, R. A. Jacobson, *Inorg. Chem.* **1984**, *23*, 930–935.
[48] P. Strickle, *J. Chem. Soc. D* **1969**, 655.

 © 2005 Wiley-VCH Verlag GmbH & Co. KGaA, Weinheim

[49] V. S. Gurin, *J. Phys. Chem.* **1996**, *100*, 869–872.
[50] A. Puzder, A. J. Williamson, N. Zaitseva, G. Galli, *Nano Lett.* **2004**, *4*, 2361–2365.
[51] Y. Nosaka, H. Tanaka, *J. Phys. Chem. B* **2002**, *106*, 3389–3393.
[52] E. Rabani, *J. Chem. Phys.* **2001**, *115*, 1493–1497.
[53] A. P. Alivisatos, *J. Phys. Chem.* **1996**, *100*, 13226–13239.
[54] S. Gorer, G. Hodes, in *Semiconductor Nanoclusters − Physical, Chemical, and Catalytic Aspects*, vol. 103 (Eds.: P. V. Kamat, D. Meisel), Elsevier Science Publ. B.V., Amsterdam, **1997**, pp. 297–320.
[55] A. Henglein, *Top. Curr. Chem.* **1988**, *143*, 113–180.
[56] M. Nirmal, D. J. Norris, M. Kuno, M. G. Bawendi, A. L. Efros, M. Rosen, *Phys. Rev. Lett.* **1995**, *75*, 3728–3731.
[57] L. E. Brus, *J. Chem. Phys.* **1983**, *79*, 5566–5571.
[58] H. M. Schmidt, H. Weller, *Chem. Phys. Lett.* **1986**, *129*, 615–618.
[59] G. T. Einevoll, *Phys. Rev. B* **1992**, *45*, 3410–3417.
[60] A. Kobayashi, O. F. Sankey, S. M. Volz, J. D. Dow, *Phys. Rev. B* **1983**, *28*, 935–945.
[61] K. J. Chang, S. Froyen, M. L. Cohen, *Phys. Rev. B* **1983**, *28*, 4736–4743.
[62] D. Vogel, P. Kruger, J. Pollmann, *Phys. Rev. B* **1995**, *52*, 14316–14319.
[63] J. O. Joswig, G. Seifert, T. A. Niehaus, M. Springborg, *J. Phys. Chem. B* **2003**, *107*, 2897–2902.
[64] E. Rabani, B. Hetenyi, B. J. Berne, L. E. Brus, *J. Chem. Phys.* **1999**, *110*, 5355–5369.
[65] L. M. Ramaniah, S. V. Nair, *Phys. Rev. B* **1993**, *47*, 7132–7139.
[66] V. N. Soloviev, A. Eichhofer, D. Fenske, U. Banin, *J. Am. Chem. Soc.* **2000**, *122*, 2673–2674.
[67] L. E. Brus, *J. Chem. Phys.* **1984**, *80*, 4403–4409.
[68] A. I. Ekimov, A. L. Efros, M. G. Ivanov, A. A. Onushchenko, S. K. Shumilov, *Solid State Commun.* **1989**, *69*, 565–568.
[69] N. A. Hill, K. B. Whaley, *J. Chem. Phys.* **1994**, *100*, 2831–2837.
[70] M. V. R. Krishna, R. A. Friesner, *J. Chem. Phys.* **1991**, *95*, 8309–8322.
[71] A. Tomasulo, M. V. Ramakrishna, *J. Chem. Phys.* **1996**, *105*, 3612–3626.
[72] A. Mizel, M. L. Cohen, *Phys. Rev. B* **1997**, *56*, 6737–6741.
[73] S. Y. Ren, S. F. Ren, *J. Phys. Chem. Solids* **1998**, *59*, 1327–1330.
[74] L. W. Wang, A. Zunger, *J. Phys. Chem. B* **1998**, *102*, 6449–6454.
[75] K. Leung, S. Pokrant, K. B. Whaley, *Phys. Rev. B* **1998**, *57*, 12291–12301.
[76] J. Perez-Conde, A. K. Bhattacharjee, *Solid State Commun.* **1999**, *110*, 259–264.
[77] A. Franceschetti, H. Fu, L. W. Wang, A. Zunger, *Phys. Rev. B* **1999**, *60*, 1819–1829.
[78] M. C. Troparevsky, L. Kronik, J. R. Chelikowsky, *Phys. Rev. B* **2002**, *65*, 033311.
[79] T. A. Niehaus, S. Suhai, F. Della Sala, P. Lugli, M. Elstner, G. Seifert, T. Frauenheim, *Phys. Rev. B* **2001**, *63*, 085108.
[80] Y. Wang, N. Herron, *Phys. Rev. B* **1990**, *42*, 7253–7255.
[81] W. A. de Heer, K. Selby, V. Kresin, J. Masui, M. Vollmer, A. Chatelain, W. D. Knight, *Phys. Rev. Lett.* **1987**, *59*, 1805–1808.
[82] E. Lifshitz, I. Dag, I. Litvin, G. Hodes, S. Gorer, R. Reisfeld, M. Zelner, H. Minti, *Chem. Phys. Lett.* **1998**, *288*, 188–196.
[83] E. Lifshitz, I. Dag, I. D. Litvitn, G. Hodes, *J. Phys. Chem. B* **1998**, *102*, 9245–9250.
[84] D. Gerion, F. Pinaud, S. C. Williams, W. J. Parak, D. Zanchet, S. Weiss, A. P. Alivisatos, *J. Phys. Chem. B* **2001**, *105*, 8861–8871.
[85] Y. W. Cao, U. Banin, *J. Am. Chem. Soc.* **2000**, *122*, 9692–9702.
[86] U. Banin, M. Bruchez, A. P. Alivisatos, T. Ha, S. Weiss, D. S. Chemla, *J. Chem. Phys.* **1999**, *110*, 1195–1201.
[87] M. A. Malik, P. O'Brien, N. Revaprasadu, *Chem. Mater.* **2002**, *14*, 2004–2010.
[88] P. Sarkar, M. Springborg, G. Seifert, *Chem. Phys. Lett.* **2005**, *405*, 103.
[89] Y. C. Tian, T. Newton, N. A. Kotov, D. M. Guldi, J. H. Fendler, *J. Phys. Chem.* **1996**, *100*, 8927–8939.
[90] H. Weller, *Adv. Mater.* **1993**, *5*, 88–95.
[91] H. Weller, A. Eychmüller, *Semiconductor Nanoclusters – Physical, Chemical, and Catalytic Aspects* (Eds.: P. V. Kamat, D. Meisel), Elsevier Science B. V., Amsterdam, **1996**.
[92] B. O. Dabbousi, J. Rodriguez-Viejo, F. V. Mikulec, J. R. Heine, H. Mattoussi, R. Ober, K. F. Jensen, M. G. Bawendi, *J. Phys. Chem. B* **1997**, *101*, 9463–9475.
[93] D. Schooss, A. Mews, A. Eychmüller, H. Weller, *Phys. Rev. B* **1994**, *49*, 17072–17078.
[94] N. A. Hill, S. Pokrant, A. J. Hill, *J. Phys. Chem. B* **1999**, *103*, 3156–3161.
[95] J. O. Joswig, S. Roy, P. Sarkar, M. Springborg, *Chem. Phys. Lett.* **2002**, *365*, 75–81.
[96] W. Langbein, M. Hetterich, C. Klingshirn, *Phys. Rev. B* **1995**, *51*, 9922–9929.
[97] O. Zakharov, A. Rubio, X. Blase, M. L. Cohen, S. G. Louie, *Phys. Rev. B* **1994**, *50*, 10780–10787.
[98] H. Jónsson, G. Mills, K. W. Jacobsen, in *Classical and Quantum Dynamics in Condensed Phase Simulations* (Ed.: B. J. e. a. Berne), World Scientific, Singapore, **1998**.
[99] A. Samokhvalov, M. Berfeld, M. Lahav, R. Naaman, E. Rabani, *J. Phys. Chem. B* **2000**, *104*, 8631–8634.
[100] M. Berfeld, A. Samokhvalov, R. Naaman, M. Lahav, *Adv. Mater.* **2001**, *13*, 584.
[101] S. W. Guo, L. Konopny, R. Popovitz-Biro, H. Cohen, H. Porteanu, E. Lifshitz, M. Lahav, *J. Am. Chem. Soc.* **1999**, *121*, 9589–9598.
[102] G. Carrot, S. M. Scholz, C. J. G. Plummer, J. G. Hilborn, J. L. Hedrick, *Chem. Mater.* **1999**, *11*, 3571–3577.
[103] X. H. Bu, N. F. Zheng, P. Y. Feng, *Chem. Eur. J.* **2004**, *10*, 3356–3362.
[104] N. F. Zheng, X. H. Bu, P. Y. Feng, *Nature* **2003**, *426*, 428–432.
[105] H. Döllefeld, H. Weller, A. Eychmüller, *J. Phys. Chem. B* **2002**, *106*, 5604–5608.
[106] H. Döllefeld, H. Weller, A. Eychmüller, *Nano Lett.* **2001**, *1*, 267–269.

Received: May 2, 2005
Published Online: August 1, 2005

 © 2005 Wiley-VCH Verlag GmbH & Co. KGaA, Weinheim

Comparison of the Magnetic and Optical Properties of Wide-Gap (II,Mn)VI Nanostructures Confined in Mesoporous Silica

Felix J. Brieler,[a] Petra Grundmann,[a] Michael Fröba,*[a] Limei Chen,[b] Peter J. Klar,*[b] Wolfram Heimbrodt,[b] Hans-Albrecht Krug von Nidda,[c] Thomas Kurz,[c] and Alois Loidl[c]

Keywords: Mesoporous materials / Diluted magnetic semiconductors / Host–guest systems / Nanostructures / $Cd_{1-x}Mn_xS$ / $Cd_{1-x}Mn_xSe$ / $Zn_{1-x}Mn_xS$

Arrays of highly ordered $Cd_{1-x}Mn_xSe$, $Cd_{1-x}Mn_xS$, and $Zn_{1-x}Mn_xS$ nanoparticles with x ranging from 0.01 to 0.3 and with lateral dimensions of 3, 6, and 9 nm were synthesised within mesoporous SiO_2 host structures of the MCM-41 and SBA-15 type. The hexagonal symmetry of these arrays (space group *p*6*m*) and the high degree of order were confirmed by X-ray diffraction and transmission electron microscope studies. Physisorption measurements show the progressive filling of the pores of the SiO_2 host structures, while photoluminescence excitation (PLE) and electron paramagnetic resonance (EPR) studies confirm the good crystalline quality of the incorporated (II,Mn)VI guest species. The effects of the reduction of the lateral dimensions on the electronic properties of the diluted magnetic semiconductor were studied by PLE spectroscopy. Due to the quantum confinement of the excitons in the nanostructures an increase of the direct band gap with decreasing particle size is observed. The magnitude of the confinement effects increases with increasing excitonic Bohr radius of the (II,Mn)VI, i.e. it is largest for (Cd,Mn)Se and smallest for (Zn,Mn)S. Moreover, an increased band-gap bowing with Mn content is observed for the Cd compounds and can be correlated with the modification of the magnetic properties. Surprisingly, no band-gap bowing with x is observed for the $Zn_{1-x}Mn_xS$ nanostructures. Analysis of the EPR linewidth and EPR intensity show that macroscopic magnetic properties such as the Curie–Weiss temperature are affected by the reduction of the lateral dimensions. The microscopic coupling between the Mn ions (e.g. the exchange constants J_{nn} and J_{nnn}) is not altered to a first approximation.

(© Wiley-VCH Verlag GmbH & Co. KGaA, 69451 Weinheim, Germany, 2005)

1. Introduction

The fabrication of ordered assemblies of particles on the nanometre scale is a challenge in material science, which has become more and more important over the last decades. With the availability of highly ordered arrays of particles well defined in size in the range of a few nanometres only, the understanding of the unusual dependence of electronic, optical and magnetic properties on size and shape of those nanoparticles has increased significantly. Most of the procedures to obtain 2D magnetic semiconductor nanostructures, i.e. quantum wells, require nonequilibrium growth conditions, which can be realised, for example, by molecular beam epitaxy (MBE) under ultra high vacuum or metal-organic vapour-phase epitaxy (MOVPE). In order to fabricate 0D quantum dots or 1D quantum wires, the conventionally used top-down approach (see Figure 1) is to start with two-dimensional quantum wells and to use a lithographic pattern definition followed by a pattern transfer, usually a subsequent etching procedure[1–7] or a controlled local diffusion process due to ion-bombardment.[8,9] Such top-down approaches usually only yield magnetic semiconductor nanostructures of good structural and optical quality for lateral sizes larger than about 50 nm. Below this size, fabrication-induced surface damage deteriorates the quality of the structures and has a strong undesired effect on optical and magnetic properties. This makes it difficult to separate intrinsic and extrinsic properties in a study of the electronic and magnetic properties as a function of lateral size of the nanostructure.

[a] Institute of Inorganic and Analytical Chemistry, Justus Liebig University Gießen,
Heinrich-Buff-Ring 58, 35392 Gießen, Germany
E-Mail: michael.froeba@anorg.chemie.uni-giessen.de
[b] Department of Physics and Material Sciences Center, Philipps University of Marburg,
Renthof 5, 35032 Marburg, Germany
E-Mail: klarp@mailer.uni-marburg.de
[c] Experimental Physics V, Electronic Correlations and Magnetism, Institute of Physics, University of Augsburg,
Universitätsstraße 2, 86135 Augsburg, Germany

MICROREVIEWS: This feature introduces the readers to the authors' research through a concise overview of the selected topic. Reference to important work from others in the field is included.

Felix J. Brieler is a PhD student in the group of Prof. Fröba in Gießen (Germany). He obtained his diploma in Chemistry on nanostructured semiconductors within mesoporous MCM-41 silica phases in the same group in Hamburg (Germany) in 2000. Since then, he has been working on his PhD thesis "nanostructured diluted magnetic semiconductors within mesoporous silica", which he will finish later this year. He stayed in Exeter (Great Britain) from April to May 1998 as an exchange student.

Petra Grundmann was born in 1961 and started her practical training in 1979 in Dresden (Germany). After completion in 1981 she worked in a research laboratory before she came to the Institute of Inorganic and Analytical Chemistry at the Justus Liebig University in Gießen (Germany) in 1993. She has worked in the group of Prof. Fröba since 2001.

Prof. Dr. Michael Fröba was born in Lübeck (Germany) in 1962 and studied chemistry in Würzburg and Hamburg. He obtained his PhD in 1993 in the group of Prof. Wolfgang Metz at the Institute of Physical Chemistry at the University of Hamburg (Germany). After that he stayed at the Lawrence Livermore National Laboratory (California, USA) from 1994 to 1996. He completed his Habilitation in 2000 at the University of Hamburg in Inorganic Chemistry. From 2000 to 2001 he was appointed associate professor (C3) at the University of Erlangen-Nuremberg (Germany). Since 2001 he is a full professor (C4) in Gießen and head of the Institute of Inorganic and Analytical Chemistry. He is author/coauthor of about 100 scientific publications, including several reviews and book articles. His research interests include porous materials with a focus on the template-directed synthesis and characterisation of mesoporous materials with different morphologies as well as the formation of nanostructures within different porous matrices.

Dr. Limei Chen is currently a researcher at the Physics Department of the Philipps-University of Marburg (Germany). She majored in Chemistry at Beijing Normal University (China) and obtained her BSc and MSc degrees in 1988 and 1991, respectively. In 1992 she obtained a scholarship from the British Council and UK Overseas Development Agency and worked at North East Wales Institute (UK) as a trainee where she obtained the Certificate of British Council Technical Training. From 1994 to 1997 she was the recipient of the first Norwich Research Park Studentship and obtained her PhD degree at the University of East Anglia (UK) in Physics. After a short spell as postdoctoral assistant at the University of East Anglia (UK), she started to work as a postdoctoral researcher at the Philipps-University of Marburg in 1998. Limei Chen is author/coauthor of about 25 scientific publications. Her research interests include magnetic and optical properties of novel nanostructures.

Dr. Peter J. Klar is currently a lecturer of Physics at the Philipps-University of Marburg (Germany). He obtained his Diploma in Physics at the University of Hamburg (Germany) in 1993,and his PhD at the University of East Anglia (UK) in 1997. After two short spells as postdoctoral assistant at the University of East Anglia and at the University of Surrey (UK) he moved on to the Philipps-University of Marburg in 1998. There he completed his Habilitation in Experimental Physics in 2004 and was appointed Privatdozent in 2005. He is author/coauthor of about 90 scientific publications, including several reviews and book articles. His research interests include physics of magnetic semiconductors and hybrids for spintronics, of III-N-V semiconductor structures for opto-electronics, of novel nanostructures ranging from nanomagnetism to applications in catalysis, and material and device characterisation in general.

Prof. Dr. Wolfram Heimbrodt was born 1954 in Berlin, Germany. He received his Diploma in Physics in 1980 from the Technical University of Dresden. He carried out his PhD. thesis in the group of Prof. Otfried Goede at the Humboldt-University of Berlin in 1985 working on the optical properties of isovalent impurities in II-VI semiconductors. Since 1986 he has worked as a postdoctoral Research Fellow in the Institute of Optics and Spectroscopy at the HU-Berlin. In 1993 he became the head of Group Spectroscopy of Semiconductor Microstructures in the Institute of Physics at the HU-Berlin and received his Habilitation in 1996, the main research interest being spintronics and magnetic semiconductors. Between 1996 and 1997 he worked as Senior Research Fellow with Prof. J. J. Davies at the University of East Anglia (UK). In 1997 he became a Professor of Experimental Physics at the Philipps-University Marburg (Germany).

Dr. Hans-Albrecht Krug von Nidda is a scientific employee and academic councillor at the University of Augsburg (Germany). He studied Physics at the Technical University in Darmstadt where he obtained his diploma in 1992. He was a PhD student in the group of Prof. Loidl, working on a project within the "Sonderforschungsbereich 252" (electronically highly correlated metallic compounds), and completed his thesis on electron spin resonance in heavy fermion compounds in 1997. Later, he moved with the group of Prof. Loidl to Augsburg where he is working as a postdoc and is supervisor of a sub group on electron spin resonance. Since 2000, he is the head of the subproject on metal-insulator transitions and order of microscopic degrees of freedom within "Sonderforschungsbereich 484" (cooperative phenomena in the solid state). During the winter term of 2001/2002, he stayed at the Kapitza Institute in Moscow within the scope of a Russian-German collaboration about defect states in low dimensional and magnetically frustrated systems. Currently, he is working on his habilitation thesis involving ESR in transition metal oxides.

Thomas Kurz is a PhD student in Augsburg (Germany). He obtained his Diploma in Physics about resistivity and magnetism in manganites in 2001. Since then, he has been working on his PhD thesis "magnetism in nanometer dimensions", which is a cooperation between the Philipps-University of Marburg (Germany) and the University of Augsburg. He is a member of the European Graduate College Marburg/Budapest. He stayed in Budapest (Hungary) as an exchange student in April 2003.

Prof. Dr. Alois Loidl is a full professor at the University of Augsburg. He studied Technical Physics in Vienna (Austria). In 1971, he finished his studies as a graduate engineer (Dipl.-Ing.) in nuclear physics and moved to the University of Frankfurt (Germany) where he performed his PhD in Solid State Physics. In 1981, he completed his Habilitation in Mainz (Germany) and was appointed professor (C2) at the Physical Institute in Mainz in 1983. After offers for a professorship from the University of Missouri-Columbia (Columbia, USA) and the University of Hannover (Germany), both in 1987, he was appointed as a university professor with tenure in Mainz. From 1991 to 1996, he was a full professor (C4) at the Institute of Solid State Physics at the Technical University of Darmstadt (Germany) and while there was also appointed executive director of the Physical Institute (1995). In 1996 he moved to the newly founded Center for Electronic Correlations and Magnetism at the University of Augsburg (Germany). He is an editor of the European Physical Journal B since 2000 and is author or coauthor of more than 400 scientific publications.

 © 2005 Wiley-VCH Verlag GmbH & Co. KGaA, Weinheim

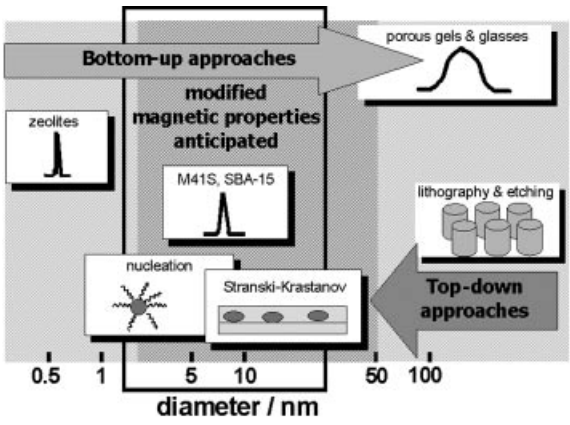

Figure 1. Bottom-up and top-down approaches for fabricating magnetic semiconductor nanostructures.

Alternatively, a large variety of so-called bottom-up approaches can be used to synthesise magnetic semiconductor nanostructures. Some of these approaches are also presented schematically in Figure 1. Examples are methods based on established growth techniques for 2D semiconductor structures (e.g. MBE or MOVPE) such as Stranski-Krastanov growth[10–18] or growth on patterned substrates.[19,20] There are also various fabrication techniques relying on nucleation and precipitation processes either in glass matrices (ranging from RF-sputtering techniques[21–24] to sol-gel methods[25–28]) or in solutions[29,30] (e.g. TOP/TOPO synthesis). All the bottom-up approaches mentioned so far yield good quality nanostructures down to sizes of a few nanometres. However, the ensembles of nanostructures fabricated in this fashion usually exhibit a rather broad Gaussian size distribution, which also manifests itself in measurements of the electronic and magnetic properties. In particular, in conventional magnetic measurements of such ensembles such as measurements of the magnetisation or of magnetic resonance, the results are strongly dominated by the larger magnetic particles, i.e. the "large size" wing of the distribution. The reason is very simple, such measurements are sensitive to the total number of magnetic ions and the amount of magnetic ions per nanostructure scales with its characteristic size e.g. for a spherical nanoparticle with the third power of its diameter. Therefore, it is desirable to define a sharp cut-off of the size distribution of the nanoparticles towards larger sizes.

One way of achieving this is by chemical synthesis of nanoparticle ensembles in a bottom-up approach using size-limiting matrices, which serve as a kind of "mini-reactor". Narrow particle size distributions can be obtained if a high quality of this nanoreactor is realised. As hosts for a size-limited synthesis only a few possibilities are worth considering: firstly, the utilisation of reverse micelles ("water-in-oil" droplets), which are already used widely in the synthesis of nanoparticles,[31–40] and secondly, the use of a porous substance which does not react with the precursors for the actual synthesis. In the large group of different porous substances the mesoporous materials seem to be the most promising approach for nanoparticle syntheses[41] since the size range, in which the pores – and therefore the nanoparticles – can be synthesised, covers a scale of several hundreds of nanometres and in particular sizes below 50 nm where changes of the particle properties due to confinement are anticipated (see also Figure 1).

In the case of reverse micelles the size of the micelle is governed by the volume of the water molecules inside and by the surfactant molecules at the surface of the micelle, i.e. the space inside the micelle where the chemical reaction or coprecipitation takes place can be varied for example by changing the amount of water in the original solution.[42] One of the surfactants often used to form reverse micelles in a nonpolar solvent is sodium di(2-ethylhexyl) sulfosuccinate, mostly denoted as Aerosol OT or Na(AOT). In a typical synthesis (see Figure 2), two micellar solutions, having the same water content (that is to say the same micelle size) and each containing one of the reactants, are mixed. When two of these micelles collide, they exchange their water contents in a micellar exchange process and the desired reaction occurs. After a few microseconds the previously formed "double-micelle" dissociates to form two independent reverse micelles, one containing the product while the other is only filled with water.

Figure 2. Micellar exchange process in a nonpolar solvent. The reaction takes place inside the water micelles (redrawn from ref.[42]).

When using mesoporous materials as hosts for the synthesis of nanoparticles, the narrow size distribution of the guest species is achieved by a narrow pore size distribution of the respective host material. In the last 12 years it has been a major goal in the synthesis of mesoporous substances to obtain materials which exhibit a high degree of long range order on the one hand and a narrow pore size distribution on the other. The quality of mesoporous materials has risen from poorly ordered so-called "disordered mesoporous foams" to high quality materials, which have very sharp pore size distributions. The high degree of long-range order can be demonstrated by TEM investigations or high-quality XRD measurements. A perfect arrangement of the pores over length scales of 300 nm and more is state of the art.[43]

Fine tuning of the pore size can be achieved by varying the nature of the structure directing agent (SDA). At first, long-chain tetraalkylammonium halides were used as SDA's for the synthesis of mesoporous materials of the M41S family. By varying the chain length of the hydrophobic alkyl group (usually containing 12 to 22 carbon atoms) the pore size can be altered very precisely in the range of about 1 nm.[44,45] However, the overall pore size is limited to about 4 nm when using these kinds of surfactants. The utilisation of swelling agents offered the possibility of expanding the

 © 2005 Wiley-VCH Verlag GmbH & Co. KGaA, Weinheim

pore sizes to about 10 nm, but this was always accompanied with an overall loss of structural order, which was achieved in the first instance.

In 1998, new precursors for the synthesis of a new class of mesoporous materials were first introduced. These so-called triblock copolymers offer the possibility of expanding the pore size to about 30 nm.[46] Just by varying the synthesis temperature a fine tuning of the pore diameters was achieved and narrow size distributions with mean diameters in the range of 5 to 10 nm were obtained. However, the distributions do broaden when going to higher mean diameters.

Synthesising mesoporous materials with well defined pore diameters, i.e. narrow pore size distributions, is the first step to preparing reasonable hosts for the synthesis of nanoparticles which are formed inside the pores.

Introducing the precursor compounds into the pores of the respective size-limiting matrices is the next synthetic problem, which has to be addressed. The utilisation of reverse micelles has the advantage of a two-phase system. Using a precursor, which is only soluble in one of the phases (in this case water) prevents desired materials from forming outside of the mini-reactor and results in a very defined synthesis exclusively inside the size-limiting matrix.

In the case of mesopores as the size-limiting matrix, however, the formation of bulk materials outside the pore system can never be fully avoided. Only after the synthesis can one estimate the amount of bulk material formed during the synthesis. Wet impregnation techniques[41] and incorporation of the precursors from supercritical CO_2[47] can be applied to introduce guest molecules into the pores of the host material. Drying the impregnated materials is the crucial step in the synthesis to preventing the formation of bulk material on the outer surface of the host structure. After the introduction of the precursor the other reactants have to be introduced via the gas phase, which is to prevent the extraction of the first precursor from the pores and the consecutive precipitation outside the pores if the second reactant is introduced in a liquid form. Figure 3 gives a schematic representation of a mesopore directed synthesis of nanoparticles.

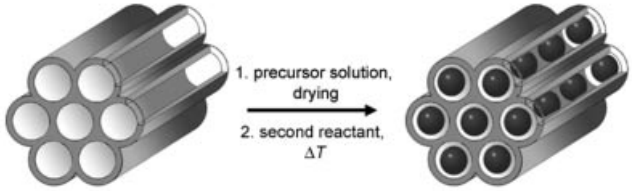

Figure 3. Schematic representation of nanoparticle synthesis inside a mesoporous host.

One of the most investigated semiconductor nanoparticles is cadmium sulphide, CdS.[2,10,31] The occurring quantum confinement, which is mostly reflected by a blue-shift of the band-gap energy, has been discussed extensively.[30,48–54] Other nanoscale semiconductor compounds, such as III-V semiconductors (e.g. GaAs or InP) or other II-VI semiconductors (e.g. CdSe, CdTe, ZnS, ZnSe, ZnTe), have also been studied in great detail (see recent reviews[42,55–58]), but to discuss all of them here would go beyond the scope of this micro-review. Instead, this work focuses on the synthesis and characterisation of Mn doped II-VI semiconductor nanostructures and describes in detail the effects of miniaturisation on the electronic, magnetic and optical properties of these materials.

The synthesis of the so-called "diluted magnetic semiconductor" (DMS) nanostructures is of great interest as semiconducting and magnetic properties are combined in one for the same nanostructure. Therefore, ordered arrays of nanometre-sized magnetic semiconductors are promising components for new devices in magneto- or spin electronics (e.g. magnetic hard disc media, non-volatile computer memory chips).[59] These materials are obtained, when a cation A of a binary semiconductor AB is randomly substituted by a magnetic ion M, leading to a $A_{1-x}M_xB$ formula. Physical properties, for example, band-gap energy or magnetic behaviour, are now not only a function of the particle size but also of the doping level x.

2. Synthesis

The first preparation of manganese doped ZnS nanoparticles with particle sizes ranging between 3.5 and 7.5 nm was reported by Bhargava et al. in 1994.[60] The quantum dots were synthesised by a precipitation approach in which diethylzinc and diethylmanganese in a toluene solution were treated with H_2S. However, in the case of liquid solution precipitation or self-organised growth methods, the particle size distribution is not very well defined. Similar results were also found in other approaches.[61–64] In particular, there is no sharp upper limit for the size, in contrast to the case of nanostructures synthesised inside nanoreactors such as reverse micelles or mesoporous materials. The existence of a sharp upper limit is desired in most investigations of the effects of reduced dimensions on the magnetic properties as the largest particles usually determine the results.

A synthesis of $Cd_{1-x}Mn_xS$ nanoparticles with a very sharp size distribution was reported by Pileni's group, by applying the reverse micelle technique.[65,66] The obtained particle sizes could be varied from an average size of about 1.8 to 3.2 nm and the reported manganese contents were $0 \leq x \leq 0.23$.

DMS nanoparticles were also synthesised inside mesoporous host structures. This approach for a host/guest system was first described in 2002 by our group, when $Cd_{1-x}Mn_xS$ was incorporated inside 3 nm wide pores of MCM-41 silica.[67] First, calcined MCM-41 silica was impregnated with an aqueous solution of cadmium and manganese acetate in the desired molar ratio. Afterwards the precipitate was filtered off, thoroughly dried and treated with H_2S at $T \leq 100$ °C. Powder X-ray diffraction and nitrogen physisorption proved the preservation of the host structure after the intrapore formation of the guest species and showed that the reaction had only taken place inside the pores and

 © 2005 Wiley-VCH Verlag GmbH & Co. KGaA, Weinheim

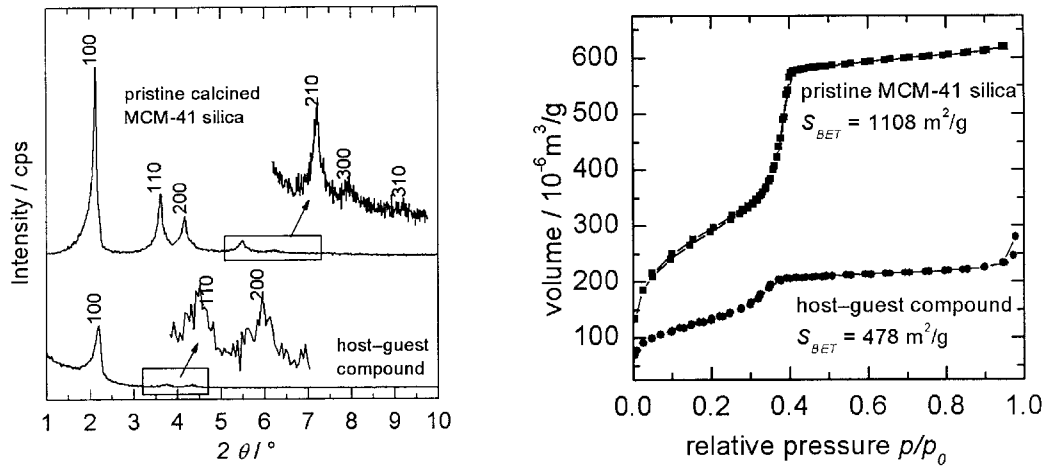

Figure 4. Powder X-ray diffraction patterns (left) and nitrogen physisorption isotherms (right) of MCM-41 silica and MCM-41 silica/$Cd_{1-x}Mn_xS$ host/guest compounds.[67]

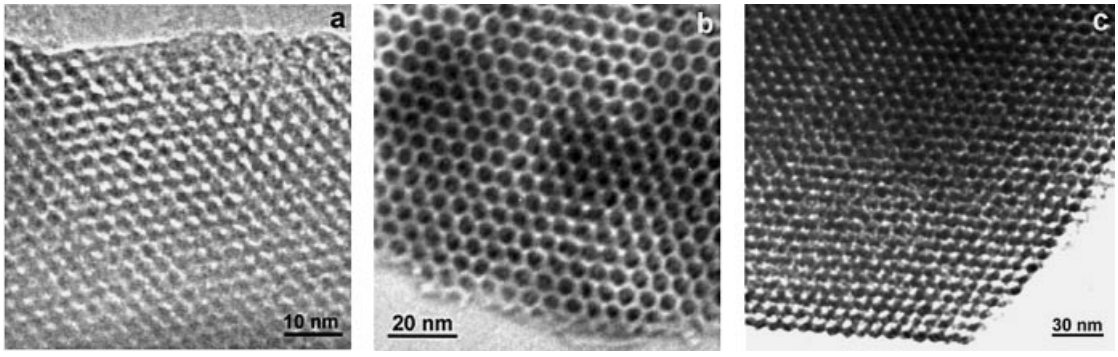

Figure 5. TEM pictures of different mesoporous host structures, a) MCM-41 silica with 3 nm pores, b) SBA-15 silica with 6 nm pores, c) SBA-15 silica with 9 nm pores.[70]

no bulk material was formed (Figure 4). The complete transformation of the acetates to the sulphides was proved by infrared and X-ray absorption spectroscopy. Similar results were obtained for other host/guest system based syntheses of nanoparticles, like $Cd_{1-x}Mn_xSe$ within MCM-41 silica[68] and $Cd_{1-x}Mn_xS$ within mesoporous thin films.[69]

A more detailed discussion on the size dependence of electronic, magnetic and optical properties was given in 2004, when the DMS compound $Zn_{1-x}Mn_xS$ was synthesised inside mesoporous hosts with different pore sizes.[70] For an accurate study three different mesoporous materials, each with cylindrical pores, were used: MCM-41 silica with 3 nm pores and furthermore two SBA-15 silica with 6 and 9 nm pores. The different pore sizes of the host materials were realised using different SDA's and different reaction temperatures (see above). A very high degree of order of the host materials was achieved, which was apparent from X-ray diffraction, sorption analyses and TEM investigations (see Figure 5).

The intrapore formation of the nanoparticles was carried out the same way as described for the $Cd_{1-x}Mn_xY$ (Y = S, Se) nanoparticle preparation, only this time the impregnation/conversion cycle was repeated several times to achieve a higher filling of the pores. Again, no bulk material was formed outside the respective pore system and the mesostructure was still found to be intact after the synthesis.

3. Band Gap and Optical Properties

With photoluminescence-spectroscopic techniques it is possible to measure the dependence of the band-gap variation on particle size and doping level x. This was carried out for various DMS compounds, like $Cd_{1-x}Mn_xS$,[66–68,71,72] $Cd_{1-x}Mn_xSe$[68] and $Zn_{1-x}Mn_xS$,[70,73] synthesised either in reverse micelles or in mesoporous hosts.

Figure 6 shows a schematic diagram of the complex optical processes observable in wide-gap (II,Mn)VI semiconductors. The semiconductor band states with a direct band-gap transition and the 3d shells of the Mn^{2+} ions with their internal transitions form electronic subsystems of the (II,Mn)VI semiconductor which are coupled by energy transfer processes. In addition to semiconductor band-gap related luminescence and absorption, luminescence and absorption bands are observed due to the intra-3d-shell transitions of the Mn^{2+} ions. The states within the 3d shell are strongly affected by the crystal field of the lattice site of the corresponding Mn^{2+} ion. The majority of the Mn^{2+} ions

 © 2005 Wiley-VCH Verlag GmbH & Co. KGaA, Weinheim

are incorporated on cation sites with a tetrahedral crystal field. The lowest state is the $^6A_1$ state originating from the ^6S state of the free ion, and the next highest states are $^4T_1$, $^4T_2$, $^4A_1$ and ^4E originating from the ^4G state of the free ion. Absorption processes can take place between the $^6A_1$ ground state and the excited states. A yellow luminescence between the $^4T_1$ first excited state and the $^6A_1$ ground state is observed for all wide-gap (II,Mn)VI compounds, independent of Mn concentration for Mn incorporated onto the cation site. In addition, there are a few Mn^{2+} ions on other sites. These "defect" sites show a different crystal field splitting between the states of the 3d shell, and this leads to other absorption and luminescence bands. A prominent example is the red Mn^{2+} luminescence. Energy-transfer processes can take place between the band states and the Mn^{2+} 3d shells, as well as between Mn^{2+} 3d shells corresponding to different sites.

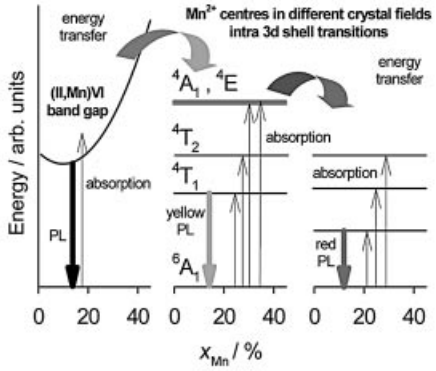

Figure 6. Schematic diagram of the optical processes observable in wide-gap (II,Mn)VI semiconductors. The abscissa values are the same for all three graphs.

In Figure 7 typical optical spectra of $Zn_{0.7}Mn_{0.3}S$ nanoparticles synthesised inside mesoporous hosts with different pore diameters are shown. The PL spectrum is dominated by the strong yellow luminescence originating from the $^4T_1 \rightarrow {}^6A_1$ internal Mn^{2+} 3d shell transition (exemplarily shown for the 6 nm sample, thick line in Figure 7).

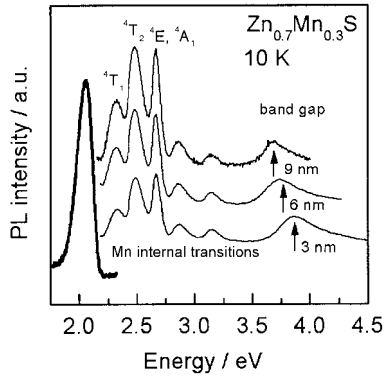

Figure 7. PLE spectra (thin lines) of $Zn_{1-x}Mn_xS$ nanoparticles with diameters of 3, 6 and 9 nm, respectively, detected on the yellow Mn luminescence. The Mn-related yellow PL band (thick line) of the 6 nm sample is shown as a typical example.

The internal Mn transitions arising from the $^4T_1$, $^4T_2$, ^4E and $^4A_1$ states are observable between 2.3 and 2.7 eV (the increase in intensity with increasing particle size simply reflects the increasing total amount of manganese) whereas the peak at the highest energy in each spectrum corresponds to the band gap related absorption. Because of the effective energy transfer from the band states into the Mn subsystem this peak is also detectable on the yellow PL.

The band gap related feature shifts to higher energies with decreasing particle diameter (i.e. shows a quantum confinement effect) whereas the energy positions of the Mn^{2+} internal transitions remain unaffected by the particle size (demonstrating that the energy positions are only determined by the local crystal field of the Mn site). The observed quantum confinement effects prove that during the synthesis $Zn_{1-x}Mn_xS$ is formed inside the SiO_2 pore system only. The energy positions of the Mn^{2+} internal transitions serve as a probe of the crystal field at the Mn site. In Figure 8 the energies of the lowest excited states of a Mn^{2+} $3d^5$ ion in a T_d symmetric ligand field with respect to the $^6A_1$ ground state are depicted for a bulk $Zn_{0.9}Mn_{0.1}S$ sample (full circles) and the $Zn_{0.7}Mn_{0.3}S$ nanostructures of different radii (open symbols). The curves have been calculated in the Tanabe–Sugano model[74] as a function of the crystal field parameter Dq with the Racah parameters B = 50 meV and C = 434 meV. The extracted crystal field parameters using the Tanabe–Sugano method are almost the same for bulk samples and nanostructures indicating the good quality of the nanostructures.

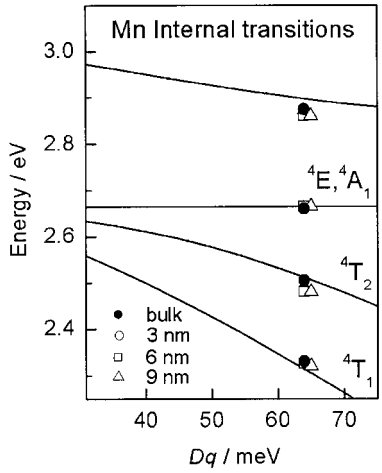

Figure 8. Energies of the internal transitions of Mn^{2+} ions in a T_d symmetric crystal field versus the field parameter Dq using the Racah parameters B = 50 meV and C = 434 meV, calculated in the framework of the Tanabe–Sugano model. Experimental points for $Zn_{0.9}Mn_{0.1}S$ bulk and $Zn_{0.7}Mn_{0.3}S$ nanostructures.

Figure 9 gives a comparison of the energy positions of the band gaps of nanoparticles of three (II,Mn)VI DMS's with different diameters as a function of Mn content x. A bulk reference curve is shown in the case of $Cd_{1-x}Mn_xSe$, but not for $Zn_{1-x}Mn_xS$ and $Cd_{1-x}Mn_xS$. For the sulphides, the band gaps of the 9 nm nanostructures are almost bulk-like. The quantum confinement of the excitons in the nano-

 © 2005 Wiley-VCH Verlag GmbH & Co. KGaA, Weinheim

particles evokes an increase in the direct band gap of about 350 meV for 3 nm $Cd_{1-x}Mn_xSe$ nanoparticles compared with the bulk. For the corresponding $Cd_{1-x}Mn_xS$ nanoparticles the confinement is only about 200 meV. In the case of the 3 nm $Zn_{1-x}Mn_xS$ nanoparticle the confinement energy compared to the bulk is about 180 meV. The decrease of the confinement energy going from (Cd,Mn)Se via (Cd,Mn)S to (Zn,Mn)S has two major reasons: (1) the exciton Bohr radius decreases throughout the series and (2) the corresponding bulk band gap increases, i.e. reduces the height of the confining potential given by the band-gap difference between the SiO_2 barrier and (II,Mn)VI semiconductor. The (Cd,Mn)S as well as the (Zn,Mn)S nanoparticle series clearly show, as expected, that the confinement effects increase with decreasing particle diameter. For both series the energy positions for the 9 nm wires almost correspond with those of the bulk band gaps.

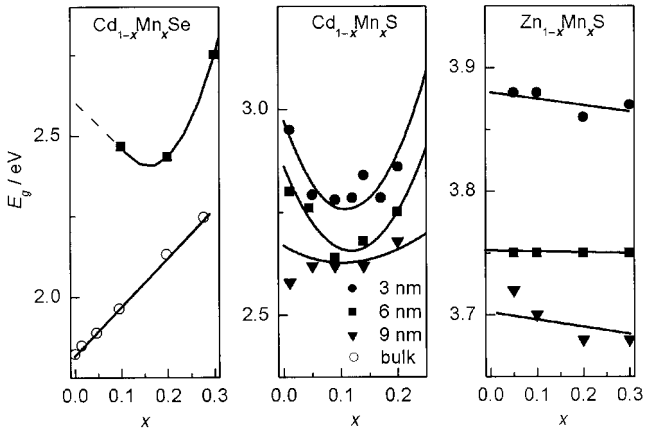

Figure 9. Band gaps of $Cd_{1-x}Mn_xSe$ nanoparticles (left), $Cd_{1-x}Mn_xS$ nanoparticles (middle) and $Zn_{1-x}Mn_xS$ nanoparticles (right) of different diameters as a function of composition x at $T = 10$ K. The solid lines are guides to the eye.

An interesting result is that both Cd-based nanoparticle systems exhibit a larger bowing of the band gap, depending on the Mn concentration, than do the corresponding bulk samples. This agrees with results reported for (Cd,Mn)S quantum dots by Levy et al.,[66] who also showed that the exchange interaction-induced band gap bowing becomes stronger with decreasing diameter for (Cd,Mn)S quantum dots synthesised in reverse micelles. Such a bowing is known for various bulk wide-gap (II,Mn)VI semiconductors.[75–78] Bylsma et al. derived the following expression for the band gap as a function of temperature T and Mn concentration x in DMS nanostructures [Equation (1)]:[79]

$$E_g(x,T) = E_0 + \Delta E x - \frac{AT^2}{T+B} - C\chi T \quad (1)$$

where the first three terms represent the commonly used description of the energy gap of a semiconductor compound comprising a linear shift in composition and a Varshni-like temperature dependence. The last term is specific to DMS and causes the bowing. It describes a contribution due to the magnetic susceptibility χ of the Mn ions. Both, the constant C as well as magnetic susceptibility χ, may be affected by the reduction of the lateral dimensions. The constant C is given by Equation (2).

$$C \sim 3m_c\alpha^2 + (m_{hh} + m_{lh})\beta^2 \quad (2)$$

where m_c, m_{hh}, and m_{lh} are the conduction-band and valence-band masses and α and β are the s–d and p–d coupling parameters. As $\alpha << \beta$ and m_{hh}, $m_{lh} > m_c$ in the (II,Mn)VI compound, the magnitude of C is mainly determined by β for which Larson et al. give the following expression [Equation (3)]:[80]

$$\beta = -32\frac{V_{pd}^2}{N_0}\left[\frac{U_{eff}}{(E_d + U_{eff} - E_{ev})(E_v - E_d)}\right] \quad (3)$$

where V_{pd} and U_{eff} are a hopping parameter depending on the manganese–anion distance and an electron-electron interaction parameter in the Hubbard fashion. The hopping parameter V_{pd} basically represents the hybridisation between the Mn 3d orbitals and the anion p orbitals in the bonding of the ternary (II,Mn)VI semiconductor compound. In the band structure of the (II,Mn)VI compound this is reflected by the energetic overlap of the anion p-orbital derived valence bands and the Mn 3d-orbital derived valence bands in the density of states as shown schematically on the left hand side of Figure 10. The electron-electron interaction parameter U_{eff} represents the on-site Coulomb repulsion energy which is required to add a sixth electron to the half-filled Mn 3d shell as shown schematically on the right of Figure 10. E_v and E_{3d} are representative energies of the p-like valence-band edge states and the Mn 3d related valence-band states, respectively.

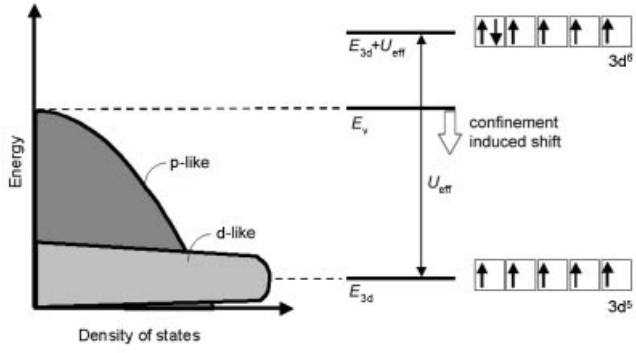

Figure 10. Schematic representation of the parameters contributing to the p–d exchange parameter β in the model by Larson et al.

The p–d coupling parameter β strongly depends on the energy separation between the p- and d-like valence-band states represented by E_v and E_{3d}, respectively [see Equation (3)]. The modified positions (compared to bulk) of the p- and d-related bands in the band structure of the nanoparticle causes an increase of the p–d exchange interaction, resulting in a possible contribution to the enhanced band-gap bowing in the nanostructures. Due to the quantum confinement, the top of the p-like valence band (E_v) of the $Cd_{1-x}Mn_xS$ nanostructures may shift significantly towards the Mn 3d states (E_{3d}), which are positioned about 3 eV below

 © 2005 Wiley-VCH Verlag GmbH & Co. KGaA, Weinheim

the valence-band edge of bulk material (see Figure 10). This enhancement effect is similar to that in bulk $Cd_{1-x}Mn_xY$ with Y = Te, Se, S where an increased p–d hybridization is observed with increasing band gap going from Te to S.[81] Similar results were also reported for the corresponding Zn series where the main Mn 3d photoemission feature was found at 3.5, 3.6 and 3.8 eV below the valence-band maximum of (Zn,Mn)Te, (Zn,Mn)Se and (Zn,Mn)S, respectively.[82]

The susceptibility χ itself is also affected by the reduced dimensionality. In virtual crystal and mean-field approximation, the expression for χ is given by Equation (4):

$$\chi = x_{\text{eff}} \frac{N_A S(S+1) g^2 \mu_B{}^2}{3k_B[T + \Theta(x)]} \quad (4)$$

x_{eff} (which is a magnetically effective Mn concentration accounting for antiferromagnetic pairing) as well as $\Theta(x)$ are modified in a nanostructure due to the increase of the surface-to-volume ratio. The number of nearest neighbours on the cation sublattice is reduced at the surface leading to an increase of the effective x. This also causes a reduction of the Curie–Weiss parameter Θ in a similar fashion (see section 4: "Magnetic properties"). The combination of both effects results in a stronger increase of χ with x in the nanostructures compared to the bulk.

Therefore, both the dependence of the p–d exchange parameter β and that of the susceptibility χ on reduced dimensionality are in accordance with the observed enhancement of the band-gap bowing in $Cd_{1-x}Mn_xS$ and $Cd_{1-x}Mn_xSe$ nanostructures as a function of x. It is worth mentioning here that the former effect is probably of less importance because a good description of the magnetic properties of the paramagnetic phase of the (II,Mn)VI nanostructures is obtained (see section 4), assuming that the exchange coupling between adjacent Mn ions J_{nn} (which is proportional to β^2) is not altered in the nanostructures. Moreover, the dependence of the band gap of bulk $Zn_{1-x}Mn_xS$ and the corresponding nanostructured samples on the Mn concentration x seems to be an exception from a general rule. Although bulk (Zn,Mn)Te[75,83] as well as (Zn,Mn)Se[76,79] exhibit considerable bowing effects, neither the bulk $Zn_{1-x}Mn_xS$[84] nor the nanostructured samples in Figure 9 exhibit significant bowing effects with increasing x.

4. Magnetic Properties

Undoped II-VI compounds (x = 0) are diamagnetic whereas Mn–VI compounds (x = 1) are paramagnetic at high temperatures and exhibit an antiferromagnetic phase at low temperatures. The degree of magnetic coupling between the spins of the Mn ions depends strongly on the average distance between them, i.e. on x. Consequently, a very rich magnetic phase diagram as a function of x and T arises for a typical (II,Mn)VI semiconductor alloy such as (Cd,Mn)S (see Figure 11). Decreasing the concentration x of magnetic ions in diluted magnetic II-VI alloys restricts the spin ordering effects to the lower temperature region. Nevertheless, phases determined by collective magnetic behaviour such as antiferromagnetic (AF) phases as well as a spin-glass phase (SG) are commonly observed in addition to the paramagnetic phase (P) (Figure 12 gives a schematic summary of collective and individual behaviour of magnetic systems). The P phase extends to lower temperatures with decreasing x. For example, for (Cd,Mn)S, a (disordered) AF phase which has a long-range spin ordering occurs below a critical temperature $T_N(x)$ for a sufficiently high Mn concentration $x > 0.8$ (beyond the miscibility gap). The corresponding phase transition is characterised by peaks at T_N in both the magnetic susceptibility and the specific heat. For Mn concentrations below the miscibility gap an SG phase is observed for temperatures below $T_{SG}(x)$. In the case of (Cd,Mn)Te even a transition to the AF phase has been reported for x = 0.7,[85] which means that it is still below the miscibility gap.

The spin-glass phase is characterised by an antiferromagnetic short-range ordering of the spins, as well as by frustration effects. The somewhat diffuse phase transition from the paramagnetic into the spin-glass phase leads to a peak at $T_{SG}(x)$ in the temperature dependence of the magnetic susceptibility, but no anomaly in the specific heat is observable. Neutron-scattering experiments have shown that small antiferromagnetically ordered clusters already appear above T_{SG}, which grow in size with decreasing temperature. Another surprising fact is that a spin-glass phase is observable not only above the percolation limit ($x \approx 0.2$), but also below. In the very low concentration range, a rather long-range interaction is necessary, in addition to the short-range superexchange interaction, to yield a spin-glass phase. The

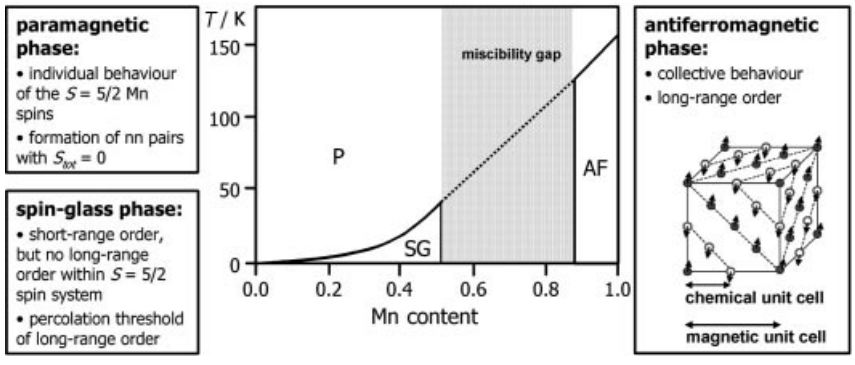

Figure 11. Schematic representation of a typical magnetic phase diagram of a (II,Mn)VI semiconductor.

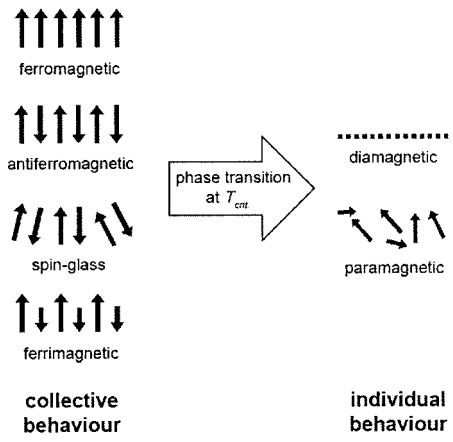

Figure 12. Schematic representation of the collective to the individual behaviour of magnetic systems.

spin freezing temperatures below the percolation concentration are very small, for example, between 0.1 K and 1 K for $x \approx 0.01$. The magnetic dipole-dipole interaction between more distant Mn^{2+} ions is proposed to be the required long-range interaction responsible for this spin-ordering mechanism, despite the fact that the dipole-dipole interaction might be too weak to cause the ordering at finite temperatures.[86]

In bulk (II,Mn)VI materials, the integral EPR signal corresponding to the Mn^{2+} absorption has a Lorentzian lineshape in the paramagnetic regime.[87] The overall intensity I_{tot} as well as linewidth ΔH of the Lorentzian are very sensitive to the spin-spin correlations between the Mn^{2+} ions. Not only changes of the magnetic order with temperature, e.g. transitions from the P phase to the SG phase or from the P phase to the AF phase, are reflected by the temperature dependence of ΔH and I_{tot}, but also by changes of the magnetic interactions within the paramagnetic phase itself due to a reduction of the lateral dimensions.

The EPR spectra for (II,Mn)VI nanoparticles synthesised either in reverse micelles or inside mesoporous hosts are very similar. As a typical example, the EPR spectra of $Zn_{1-x}Mn_xS$ nanoparticles with x varying from 0.01 to 0.3 synthesised inside the 6 nm wide pores of SBA-15 silica are shown in Figure 13.[70] All spectra were taken at 4 K and normalised to the same amplitude. These spectra are typical for exchange coupled Mn^{2+} ions within a II-VI semiconductor compound[88–90] and in nanostructured DMS compounds, for example $Cd_{1-x}Mn_xS$[91] and $Zn_{1-x}Mn_xS$.[70] The spectra can best be explained for low x. They basically consist of a sextet of sharp lines. This sextet, which is centred at a g value of $g = 1.999$, is associated with the allowed ($\Delta m_S = \pm 1$, $\Delta m_I = 0$) magnetic dipolar transitions between the hyperfine-split Zeeman levels of the $^6S_{5/2}$ (or, $^6A_1$) ground state of the Mn^{2+} 3d electrons. The hyperfine structure arises from the interaction between the $S = 5/2$ spin of the unpaired 3d electrons with the $I = 5/2$ spin of the ^{55}Mn nucleus. The hyperfine splitting characteristic for Mn^{2+} in ZnS amounts to about $\delta B_{HFS} = 7.0$ mT between neighbouring allowed transitions in zinc blende as well as in wurtzite structures.[10] The splitting observed in the spectrum of the sample with 1% Mn agrees well with this value.

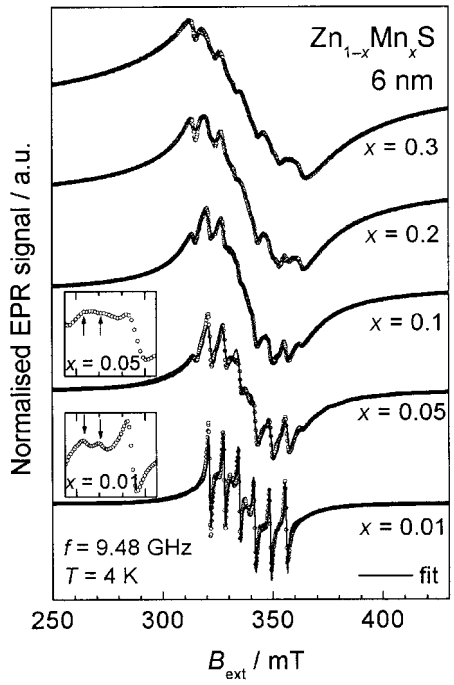

Figure 13. EPR spectra of 6 nm $Zn_{1-x}Mn_xS$ nanoparticles with x varying from 0.01 to 0.3 at $T = 4$ K. Insets: hyperfine transitions on an enlarged field scale for $x = 0.01$ (lower) and $x = 0.05$ (upper), the arrows indicate the positions of the forbidden transitions. Taken from ref.[70].

With increasing Mn content the dipolar interaction and exchange coupling merge the hyperfine structure into one broad resonance line, which is documented best for $x = 0.3$. But this broad line can already be identified for $x = 0.01$. The spectrum for $x = 0.01$ is satisfactorily described by the sum of the broad line and the hyperfine structure of six lines. Both the broad line and the hyperfine lines were assumed to be of Lorentzian shape. In addition it was necessary to take into account a slight linear increase of the hyperfine splitting with the external field due to second-order contributions.

A close inspection reveals that at low Mn concentration each hyperfine line exhibits a pair of satellites at lower external magnetic field associated with the forbidden ($\Delta m_S = \pm 1$, $\Delta m_I = \pm 1$) hyperfine transitions (see lower inset of Figure 13). The forbidden hyperfine transitions in the spectra with the lowest manganese content ($x = 0.01$) are typical for Mn^{2+} ions in the tetrahedral environment of a Zn site in a zinc blende crystal. In the case of a wurtzite crystal these lines are much more prominent and merge with the lines of the allowed hyperfine transitions, as is observed for samples with larger amounts of manganese ($x \geq 0.05$, see upper inset of Figure 13). Thus, it can be concluded that the crystal structure of the incorporated (II,Mn)VI semiconductors is zinc blende only for $x = 0.01$, whereas higher doping levels with Mn^{2+} result in a wurtzite structure. At the same time it has to be noticed that with increasing x an additional hyperfine structure of six lines with a

 © 2005 Wiley-VCH Verlag GmbH & Co. KGaA, Weinheim

larger splitting of about δB_{HFS} = 9.5 mT evolves and persists even at 30% Mn content. This hyperfine structure results from isolated Mn^{2+} ions on the surface of the $Zn_{1-x}Mn_xS$ nanoparticles. From a careful analysis of the intensities of the different signals it can be deduced that the majority of the Mn^{2+} ions are well incorporated into the $Zn_{1-x}Mn_xS$ nanostructures and only a small amount remains weakly bound at their surface.[92] This amount of aggregated Mn ions at the surface of the nanoclusters corresponds to less than 4% of the total amount of Mn in the nanostructure.[70]

The Curie–Weiss parameter Θ of the paramagnetic phase is a measure of the type and strength of the interaction between the manganese ions. It can be obtained experimentally either from plots of the inverse EPR intensity I_{tot}^{-1} versus temperature T or from plots of the inverse susceptibility χ^{-1} versus temperature determined by SQUID measurements. It is found that the experimentally determined Cure–Weiss parameter is usually well described in the high-temperature limit using Equation (5):[93,94]

$$\Theta(x) = -\frac{2}{3k_B}S(S+1)x[J_{nn}z^b_{nn} + J_{nnn}z^b_{nnn}] \quad (5)$$

where J_{nn} and J_{nnn} are the nearest neighbour (nn) and next-nearest neighbour (nnn) exchange coupling constants, respectively, between Mn ions on the cation lattice. The numbers of nn and nnn sites of the cation lattice are denoted by z_{nn} and z_{nnn}, respectively. For both wurtzite and zinc blende crystals z^b_{nn} and z^b_{nnn} are 12 and 6 respectively, in the bulk.

Figure 14 shows plots of the inverse EPR intensity I_{tot}^{-1} of 9 nm $Zn_{1-x}Mn_xS$ nanoparticles with x ranging from 0.01 to 0.3 as a function of the temperature. Similar results were also obtained for a series of $Cd_{1-x}Mn_xS$ nanoparticles with 3 to 9 nm diameters and a series of $Zn_{1-x}Mn_xS$ particles with diameters of 3 and 6 nm, each synthesised within mesoporous hosts. As in the case of bulk (II,Mn)VI, the slope of the $I_{tot}^{-1}(T)$ curve decreases with increasing doping level x and deviates from the Curie–Weiss behaviour at low temperatures, giving the curves a somewhat negative curvature. At first sight surprisingly, the particles with $x \geq 0.2$ do not show any indication for a phase transition into a spin-glass phase, in contrast to bulk material.[95] This result will be discussed further, when the EPR linewidth is analysed. Fitting the $I_{tot}^{-1}(T)$ plots in the high temperature regime (200 K to 300 K) following the Curie–Weiss dependence [Equation (6)]:

$$I_{tot}^{-1}(T) \sim \chi^{-1}(T) \sim (T + \Theta) \quad (6)$$

yields the Curie–Weiss parameter Θ as a function of x.

The corresponding plots for various particle diameters d (obtained by analysing the corresponding EPR data, as shown exemplarily for x = 0.1 in Figure 14, where a straight line is used for extracting the high-temperature Curie–Weiss parameter Θ) are shown in Figure 15 and show some clear trends. As expected, $|\Theta|$ increases with increasing x in each series. The $|\Theta|$ values obtained for the nanostructures are considerably lower than those found in corresponding bulk

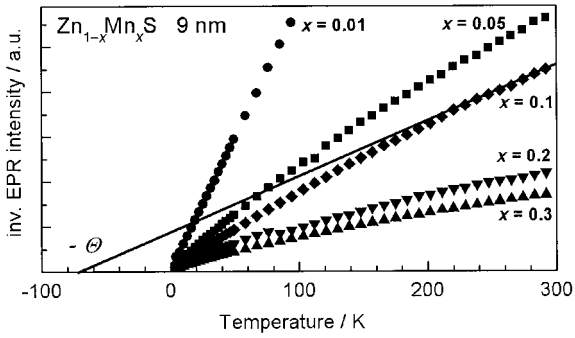

Figure 14. Temperature dependence of the inverse EPR intensity I_{tot}^{-1} of 9 nm $Zn_{1-x}Mn_xS$ nanoparticles.

(II,Mn)VI samples. These are represented by the solid lines in Figure 15 and are calculated using Equation (5). The exchange parameters are taken from the literature:[94,96] J_{nn} = –10.6 K and J_{nnn} = –4.7 K for (Cd,Mn)S and J_{nn} = –16.1 K and J_{nnn} = –0.6 K for (Zn,Mn)S. Moreover, in Figure 15, it appears that the $|\Theta|$ values show a tendency to decrease with decreasing particle diameter d at constant x. Both effects are due to the reduced lateral dimensions of the nanostructures. They occur because Mn ions on the surface of the (II,Mn)VI nanostructures incorporated inside the mesoporous SiO_2 matrices have reduced numbers of nearest neighbours $z^s_{nn} \approx z^b_{nn}/2$ and next-nearest neighbours $z^s_{nnn} \approx z^b_{nnn}/2$ compared to the bulk of the material. This becomes significant as the surface-to-volume ratio is strongly increased in the nanostructures. The effect can be estimated by dividing the volume V of the nanostructure into a volume V^s close to the surface (where the exchange effects differ from bulk) and a remaining bulklike volume $V^b = V - V^s$. The choice of the two volumes will differ for nearest neighbours and next-nearest neighbours because of the length of the scales involved, i.e. the nearest neighbour distance d_{nn} and the next-nearest neighbour distance d_{nnn}, are different. In the following the wurtzite structure is approximated by a zinc blende structure for simplicity. This is a good approximation here as only nearest and next-nearest

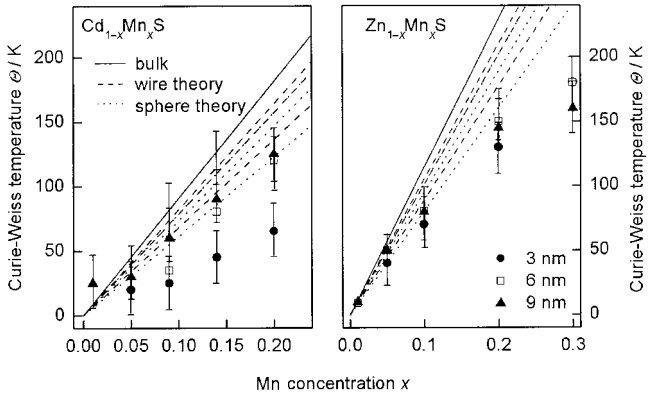

Figure 15. Plots of the Curie–Weiss temperature Θ versus Mn content x in percent obtained by analysing the EPR data of 3, 6, and 9 nm $Cd_{1-x}Mn_xS$ particles (left) and 3, 6, and 9 nm $Zn_{1-x}Mn_xS$ particles (right). The solid line is calculated using Equation (5), the dashed and dotted lines are calculated using Equation (8).

 © 2005 Wiley-VCH Verlag GmbH & Co. KGaA, Weinheim

neighbours are considered. It holds that $d_{nn} = (1/2)^{0.5}a$ and $d_{nnn} = a$ where a is the lattice constant of the zinc blende lattice, $a \approx 0.55$ nm for (Zn,Mn)S and $a \approx 0.58$ nm for (Cd,Mn)S.[97] These values of the lattice constant were used for $Cd_{1-x}Mn_xS$ and $Zn_{1-x}Mn_xS$ independent of x in the following because its dependence on x is not known for the zinc blende modification. Two limiting cases for the shape of the nanostructure shall be considered: (i) an ideal wire structure of infinite length and diameter d and (ii) a spherical nanoparticle with diameter d where d is the pore diameter of the SiO_2 host matrix. One obtains the following definitions [Equation (7)]:

$$V^s_{nn} = V\left(1-\left(\frac{d-2d_{nn}}{d}\right)^{\delta}\right) \qquad V^s_{nnn} = V\left(1-\left(\frac{d-2d_{nnn}}{d}\right)^{\delta}\right) \tag{7}$$

with $\delta = 2$ for infinite wires and $\delta = 3$ for spheres. In both cases it holds that $V^b_{nn} = V - V^s_{nn}$ and $V^b_{nnn} = V - V^s_{nnn}$.

Rewriting Equation (5) including surface effects yields Equation (8).[91]

$$\Theta(x,d) = -\frac{2S(S+1)x}{3Vk_B}\left[J_{nn}\left(V^b_{nn}z^b_{nn} + V^s_{nn}z^s_{nn}\right) + J_{nnn}\left(V^b_{nnn}z^b_{nnn} + V^s_{nnn}z^s_{nnn}\right)\right] \tag{8}$$

Using Equations (5) and (8), the Curie–Weiss parameters have been calculated for $Cd_{1-x}Mn_xS$ and $Zn_{1-x}Mn_xS$ nanostructures assuming a wirelike and a spherical shape. Both the calculations, for the $Cd_{1-x}Mn_xS$ nanostructures as well as for the $Zn_{1-x}Mn_xS$ nanostructures, were carried out for d values of 3, 6, and 9 nm. The results of the calculations are also plotted in Figure 15. In both graphs, the dotted and dashed lines represent the results for a wirelike and a spherical shape, respectively. There are three calculated Θ curves for wire-shaped and three calculated Θ curves for sphere-shaped nanoparticles. For the wire and sphere shapes, the curves are assigned as follows to the corresponding d-values; the steepest curve corresponds to $d = 9$ nm, the intermediate curve to $d = 6$ nm and the least steep curve to $d = 3$ nm. Comparing experimental data and theoretical curves indicates that the theoretically derived reduction of the Curie–Weiss parameters Θ due to surface effects are, as expected, stronger for spherical nanoparticles compared to wire-shaped nanoparticles. The calculated reductions are of the right magnitude for both (Cd,Mn)S and (Zn,Mn)S nanostructures, but still smaller than those found in the experiment. Assuming that spherical particles yields a better agreement, this is in accordance with the TEM analysis of the (II,Mn)VI nanostructures. Figure 16 depicts a TEM image of (Zn,Mn)S nanostructures incorporated into an SBA-15 mesoporous SiO_2 matrix with a pore diameter d of 6 nm in a cross sectional view. The narrow "white" lines represent the SiO_2 walls of the pore systems. The dark regions are the (Zn,Mn)S nanoparticles. This view perpendicular to the pores reveals that the aligned pore channels are filled with the (Zn,Mn)S compound. It can clearly be seen that single "sphere-like" nanoparticles are present, but also that there is a tendency for these nanoparticles to agglomerate to denser "wire-like" structures. There is no evidence for larger particles being formed outside the pore system, i.e. the entire (Zn,Mn)S is confined inside the channels of the mesoporous host.

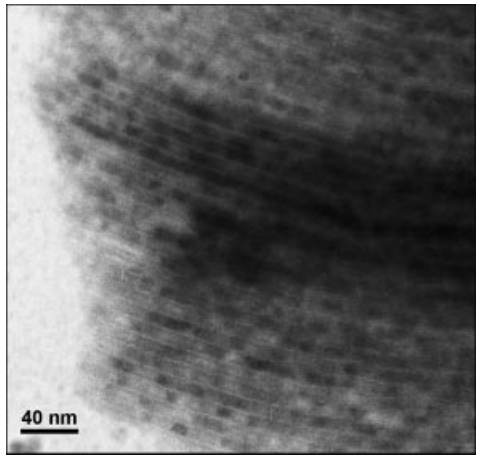

Figure 16. TEM image of (Zn,Mn)S nanostructures incorporated into 6 nm wide pores of SBA-15 silica.

In paramagnetic systems such as the (II,Mn)VI semiconductors, the EPR linewidth behaviour depends intimately on the physics of the inter-manganese spin-spin interactions. The EPR linewidth of bulk (Cd,Mn)- and (Zn,Mn)-chalcogenides has been widely studied.[87,98–101] The experimental results give a consistent picture, which can be summarized as follows: (i) In general, the EPR linewidth is found to increase with increasing Mn content and with decreasing temperature. The EPR line shape is Lorentzian for all samples in the paramagnetic regime. (ii) The EPR linewidth depends very strongly on the anion, i.e. Te, Se and S. For comparable Mn contents x and temperature T, it is found that the EPR line becomes broader as the atomic number of the anion increases from S to Se to Te.[87,98] (iii) There is a much weaker dependence on the type of nonmagnetic cation. The EPR line broadens as the atomic number of the cation decreases, e.g. $Zn_{1-x}Mn_xS$ signals are somewhat weaker and broader than $Cd_{1-x}Mn_xS$ signals for the same x and T.[98]

The EPR linewidth in manganese doped II/VI semiconductors with a high doping level x is found to diverge at low T due to the magnetic phase transition from the paramagnetic phase to the spin-glass phase, in particular for $x > 0.2$, i.e. above the percolation threshold in three dimensions. This additional broadening of the EPR linewidth occurs due to the divergence of the spin-spin correlation length in the vicinity of the paramagnetic to spin-glass phase transition. It is accompanied by a change of the EPR line shape, which becomes asymmetric.

As mentioned earlier $Zn_{1-x}Mn_xS$ and $Cd_{1-x}Mn_xS$ nanoparticles with $x \leq 0.3$ synthesised in mesoporous hosts do not show any signs of a paramagnetic to spin-glass phase transition. This is further substantiated by the correspond-

 © 2005 Wiley-VCH Verlag GmbH & Co. KGaA, Weinheim

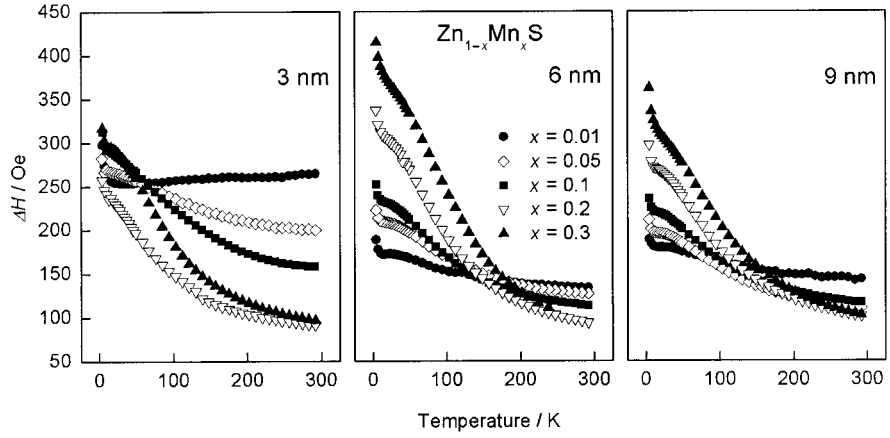

Figure 17. Plots of the EPR linewidth ΔH versus temperature for $Zn_{1-x}Mn_xS$ nanoparticles of different doping levels x and diameters of 3 nm (left), 6 nm (middle) and 9 nm (right).

ing EPR linewidths data in Figure 17 where the linewidth remains finite even at the lowest temperature. The critical Mn concentration x, above which the phase transition occurs, corresponds to the percolation threshold for the Mn ions on the cation sublattice. Obviously, the percolation threshold is increased due to the reduction of the lateral dimensions of the nanostructures and, thus, the magnetic phase transition is suppressed in the nanoparticles. Therefore, the linewidth behaviour is solely determined by the spin-spin interactions within the paramagnetic Mn subsystem.

In the following, the concentration dependence of the linewidth at low temperatures (T = 30 K) and at high temperatures (T = 290 K) will be analysed in more detail. Figure 18a and Figure 18b show plots of the linewidth at these temperatures for $Zn_{1-x}Mn_xS$ nanoparticles with different diameters and $Cd_{1-x}Mn_xS$ nanoparticles with different diameters, respectively. For both material systems, it can be seen from the left graphs that, at T = 30 K, the linewidth depends almost linearly on x. This can be understood as follows. At these temperatures the broadening is determined by a dipolar contribution in addition to an almost constant hyperfine contribution H_{HF}. Exchange narrowing effects due to nearest-neighbour exchange J_{nn} are negligible as basically all Mn ions with manganese nearest neighbours have formed antiferromagnetic pairs. The linewidth at low temperature can be described by Equation (9):

$$\Delta H = H_{HF} + H_{dip} \approx H_{HF} + C_{dip}x \quad (9)$$

where H_{dip} is the dipolar field at the site of a Mn ion in mean-field approximation.[102] The fits in the left graphs of Figure 18 show that the low temperature approximation in Equation (9) describes the observed linewidth behaviour in the nanoparticles very well, in particular for the 6 nm and 9 nm samples of both series. For the (Zn,Mn)S system, the value of H_{HF} of about 150 Oe determined for the 6 nm and 9 nm samples corresponds to half the extension of the six fine structure satellites in Figure 13. The value for the 3 nm samples is slightly larger. The linewidths of the series of $Cd_{1-x}Mn_xS$ nanoparticles show a similar dependence as that of the corresponding Zn-based series, but the linewidth is always smaller. It is worth pointing out that, as in bulk material, this simply reflects the difference in the cation size.

The high temperature behaviour [right graphs of Figure 18a and Figure 18b] can be explained semiquantita-

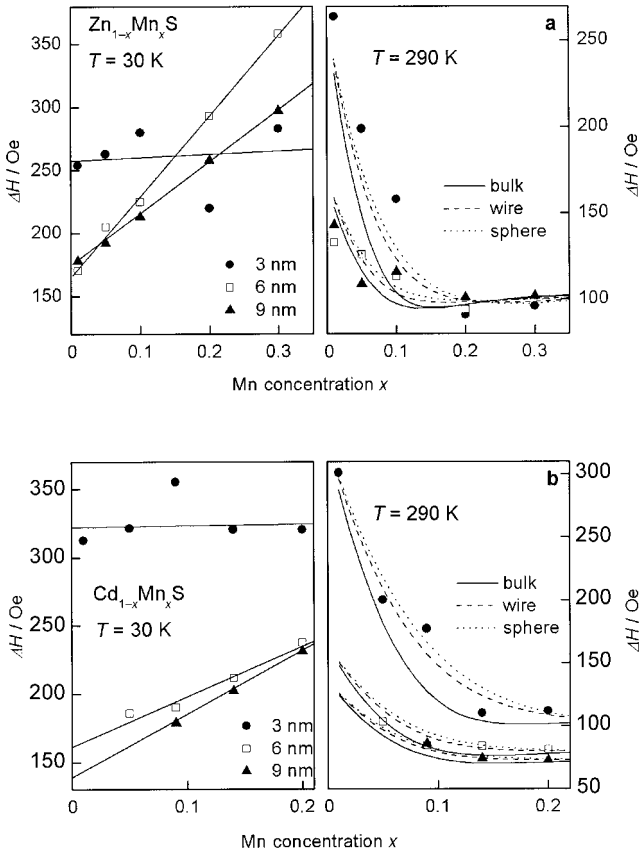

Figure 18. (a) Left: Plots of the EPR linewidth ΔH as a function of the doping level x at T = 30 K for $Zn_{1-x}Mn_xS$ nanoparticles with different diameters. The solid lines are linear fits. Right: Plots of the EPR linewidth ΔH as a function of of the doping level x at T = 290 K for $Zn_{1-x}Mn_xS$ nanoparticles with different diameters. The lines depict the results of model calculations described in the text. (b) corresponding graphs for and $Cd_{1-x}Mn_xS$ nanoparticles with different diameters.

 © 2005 Wiley-VCH Verlag GmbH & Co. KGaA, Weinheim

tively by considering the effect of the nearest-neighbour interaction J_{nn}, which determines the linewidth behaviour at temperatures, where the Mn nearest-neighbour pairs are broken up. For this purpose, the Mn ions in the nanostructure can be divided up into two classes: (i) isolated Mn ions without manganese nearest neighbours and (ii) Mn ions with one or more nearest neighbours. Furthermore, as in the case of the discussion of the Curie–Weiss parameter Θ, the volume of the nanostructure will be divided into a volume close to the surface V^s_{nn} and a bulklike volume V^b_{nn} [see Equation (7)] and the discussion will be based on a zinc blende lattice for simplicity.

The probabilities for the occurrence of two classes of Mn ions as a function of x at the surface and in the bulk of the nanoparticles are given by Equation (10):

$$p^b_{is} = (1 - x)^{z^b_{nn}} \qquad p^b_{nn} = 1 - p^b_{is}$$
$$p^s_{is} = (1 - x)^{z^s_{nn}} \qquad p^s_{nn} = 1 - p^s_{is} \tag{10}$$

The total linewidth as a function of x and diameter d is calculated according to Equation (11):

$$\Delta H(x,d) = \frac{V^b}{V}\sqrt{(\Delta H_{is}p^b_{is})^2 + (\Delta H^b_{nn}p^b_{nn})^2} + \frac{V^s}{V}\sqrt{(\Delta H_{is}p^s_{is})^2 + (\Delta H^s_{nn}p^s_{nn})^2} \tag{11}$$

It is assumed that in both volumes the linewidth contribution ΔH_{is} of the isolated manganese ions is well described by fits of the low temperature linewidth data according to Equation (9).

The linewidth contribution of the Mn ions with nearest neighbours is calculated in a similar fashion as in ref.[103] In both regions Equation (12) holds.

$$\Delta H_{nn} = \frac{H^2_{dip,nn} + H^2_{HF}}{H^i_{ex,nn}} \tag{12}$$

where $H_{dip,nn}$ is the mean dipolar exchange field for a Mn ion with at least one Mn nearest neighbour, which is approximated by Equation (13).

$$\left(H_{dip,nn}\right)^2 \approx \tfrac{3}{4} S(S+1)\mu_B{}^2 g^2 \left[\frac{\gamma}{d^6_{nn}}\right] \tag{13}$$

for the surface as well as the bulk region. γ is basically a scaling factor for the square of the dipolar field due to one nearest neighbour Mn ion.

H_{HF} is the constant value for the hyperfine broadening determined at low T and $H^i_{ex,nn}$ is the isotropic nearest-neighbour exchange field. The latter is calculated according to Anderson and Weiss,[103] Equation (14):

$$H^i_{ex,nn} = 2.83\frac{J_{nn}}{g\mu_0\mu_B}\sqrt{S(S+1)} \tag{14}$$

For both (II,Mn)VI systems, γ is the only free parameter in this calculation and its value is determined by the linewidth limit at high x in the right graphs of Figure 18a and b.

The calculations were carried out for all nanoparticles. In each case, they were performed for bulk as well as for spherical and wirelike shapes. Again $a \approx 0.55$ nm and $a \approx 0.58$ nm were used for (Zn,Mn)S and (Cd,Mn)S, respectively. In the case of the Zn-based nanostructures, the best agreement was obtained for $\gamma = 0.9$ independent of the size of the nanostructure, while, for the Cd-based series, the best agreement was obtained for smaller values of γ, i.e. $\gamma = 0.6$ for the 6 and 9 nm nanostructures and $\gamma = 1$ for the 3 nm nanostructures. Assuming that the Mn–Mn nearest-neighbour distance d_{nn} is MnS-like, $a \approx 0.56$ nm for all Mn pairs, one obtains $\gamma = 1$ for (Zn,Mn)S nanostructures and $\gamma = 0.6$ and 0.5 for (Cd,Mn)S nanostructures. However, considering the crudeness of the model and the uncertainty in the Mn–Mn nearest-neighbour distance, the parameters obtained for γ are reasonable.

The theoretical curves for $Zn_{1-x}Mn_xS$ nanoparticles as well as for $Cd_{1-x}Mn_xS$ nanoparticles are also plotted in the right graphs of Figure 18b. Considering the overall agreement between theory and experiment, it appears better when a spherical shape of the magnetic nanoparticles is assumed. In particular, the linewidth decrease with increasing x is too rapid when a bulklike situation is considered. The corresponding slope is reduced by surface effects as the probability for Mn ions with manganese nearest neighbours is much lower in the surface region V^s_{nn} than in the bulklike volume V^b_{nn} for $0 < x < 0.2$.

In conclusion, changes in the macroscopic observables, e.g. the Curie–Weiss parameter Θ and the EPR linewidth ΔH of the paramagnetic phase of (II,Mn)VI nanoparticles with sizes below 10 nm due to reduced dimensions are observable. It appears that the microscopic coupling between the Mn ions (e. g. the nearest neighbour and next-nearest neighbour exchange constants J_{nn} and J_{nnn}) is not altered to a first approximation. The macroscopic modifications arise mainly due to geometrical restrictions, i.e. the number of neighbours in the various shells around a manganese ion in the surface region are considerably reduced compared to a manganese ion in the bulk of the structure. This effect becomes increasingly important with decreasing lateral dimensions of the nanostructure.

5. Conclusions

We have synthesised and thoroughly characterised (II,Mn)VI nanoparticles with Mn contents ranging from 0 to 0.3 incorporated inside mesoporous SiO_2 matrices with pore sizes of 3, 6, and 9 nm. By careful characterisation of the samples we demonstrate that under these synthesis conditions most of the Mn ions are incorporated on cation

 © 2005 Wiley-VCH Verlag GmbH & Co. KGaA, Weinheim

sites of the II-VI host lattice and that the amount of Mn aggregated at the surface of the nanostructures is negligible. This allows us to thoroughly investigate the effects of reduced dimensionality on the magnetic and electronic properties of the (II,Mn)VI nanoparticles as a function of Mn content x and characteristic diameter d. Both, magnetic as well as electronic properties of the nanoparticles are modified due to the reduced lateral dimensions. We demonstrate by analysis of the EPR linewidth and EPR intensity that macroscopic magnetic properties such as the Curie–Weiss temperature are strongly affected by the reduction of the lateral dimensions whereas the microscopic coupling between the Mn ions (e.g. the exchange constants J_{nn} and J_{nnn}) is not altered to a first approximation. The macroscopic modifications arise mainly due to geometrical restrictions, i.e. the number of neighbours in the cation shells around a Mn ion in the surface region is considerably reduced compared to a Mn ion in the bulk. Due to the quantum confinement of the excitons in the nanostructures an increase of the direct band gap with decreasing particle size is observed. Furthermore, the band-gap bowing as a function of Mn content x is enhanced in the Cd compounds with decreasing nanostructure diameter d. This enhanced band-gap bowing can also be related to the alterations of the macroscopic magnetic properties [i.e. reduction of Curie–Weiss temperature $\Theta(x)$ and increase of effective Mn concentration x_{eff}], which occur due to the increase of the surface-to-volume ratio with decreasing nanostructure size.

Our work demonstrates that incorporating magnetic materials into mesoporous silica host matrices with adjustable, well-defined pore sizes in the range of 2 to 10 nm is an ideal approach for studying nanomagnetic phenomena as a function of particle size.

Acknowledgments

The authors would like to thank Günter Koch (Institute of Inorganic and Analytical Chemistry, Justus Liebig University Gießen) for the transmission electron micrographs. Financial support by the Deutsche Forschungsgemeinschaft (Fr, 1372/4-3 and He 2298/4-3) and the Fonds der Chemischen Industrie is gratefully acknowledged. This work was partially supported by the Bundesministerium für Bildung und Forschung (BMBF) under Contract No. 13N6917/0 (EKM) and by the Optodynamics Center of the Philipps-University.

[1] Y. Oka, J. X. Shen, K. Takabayashi, N. Takahashi, H. Mitsu, I. Souma, R. Pittini, *J. Lumin.* **1999**, *83–84*, 83.
[2] K. Takabayashi, N. Takahashi, I. Yagi, K. Yui, I. Souma, J. X. Shen, Y. Oka, *J. Lumin.* **2000**, *87–89*, 347.
[3] N. Takahashi, K. Takabayashi, I. Souma, J. Shen, Y. Oka, *J. Appl. Phys.* **2000**, *87*, 6469.
[4] A. A. Darhuber, H. Straub, S. O. Ferreira, W. Faschinger, H. Sitter, E. Koppensteiner, G. Brunthaler, G. Bauer, *Mater. Sci. Forum* **1995**, *182–184*, 423.
[5] A. Ribayrol, Y. S. Tang, H. P. Zhou, D. Coquillat, C. M. Sotomayor Torres, J. P. Lascaray, B. Lunn, D. E. Ashenford, G. Feuillet, J. Cibert, *J. Cryst. Growth* **1996**, *159*, 434.
[6] P. J. Klar, D. Wolverson, D. E. Ashenford, B. Lunn, T. Henning, *Semicond. Sci. Technol.* **1996**, *11*, 1863.
[7] P. J. Klar, D. Wolverson, J. J. Davies, W. Heimbrodt, M. Happ, T. Henning, *Phys. Rev. B* **1998**, *57*, 7114.
[8] G. Bacher, T. Kümmell, D. Eisert, A. Forchel, B. König, W. Ossau, C. R. Becker, G. Landwehr, *Appl. Phys. Lett.* **1999**, *75*, 956.
[9] G. Bacher, M. K. Welsch, A. McDonald, T. Kümmell, A. Forchel, B. König, C. Becker, W. Ossau, G. Landwehr, *Phys. Status Solidi A* **2000**, *178*, 359.
[10] S. Kuroda, Y. Terai, K. Takita, T. Okuno, Y. Masumoto, *J. Cryst. Growth* **1998**, *184–185*, 971.
[11] S. Kuroda, Y. Terai, K. Takita, T. Okuno, Y. Masumoto, *J. Cryst. Growth* **1998**, *184–185*, 274.
[12] Y. Terai, S. Kuroda, K. Takita, *Appl. Phys. Lett.* **2000**, *76*, 2400.
[13] Y. Terai, S. Kuroda, K. Takita, T. Takamasu, G. Kido, *J. Lumin.* **2000**, *87–89*, 396.
[14] S. Mackowski, S. Lee, J. K. Furdyna, M. Dobrowolska, G. Prechtl, W. Heiss, J. Kossut, G. Karczewski, *Phys. Status Solidi B* **2002**, *229*, 469.
[15] S. H. Xin, P. D. Wang, A. Yin, C. Kim, M. Dobrowolska, J. L. Merz, J. K. Furdyna, *Appl. Phys. Lett.* **1996**, *69*, 3884.
[16] M. Pinczolits, G. Springholz, G. Bauer, *Phys. Rev. B* **1999**, *60*, 11524.
[17] M. Pinczolits, V. Holy, P. Mayer, K. Wiesauer, T. Roch, G. Bauer, *Surf. Sci.* **2000**, *454–456*, 657.
[18] G. Springholz, M. Pinczolits, P. Mayer, V. Holy, G. Bauer, H. H. Kang, L. Salamanca-Riba, *Phys. Rev. Lett.* **2000**, *84*, 4669.
[19] L. Parthier, S. Luther, O. Portugall, M. von Ortenberg, K. Uchida, H. Kunimatsu, N. Miura, *J. Cryst. Growth* **1998**, *184–185*, 339.
[20] Z. H. Chen, M. C. Debnath, K. Shibata, T. Saitou, T. Sato, Y. Oka, *J. Appl. Phys.* **2001**, *89*, 6701.
[21] K. Yanata, Y. Oka, *Superlatt. Microstruct.* **1994**, *15*, 233.
[22] K. Yanata, K. Suzuki, Y. Oka, *J. Appl. Phys.* **1993**, *73*, 4596.
[23] K. Yanata, Y. Oka, *Jpn. J. Appl. Phys.* **1995**, *34*, 164.
[24] Y. Oka, K. Yanata, *J. Lumin.* **1996**, *70*, 35.
[25] Y. Wang, N. Herron, K. Moller, T. Bein, *Solid State Commun.* **1991**, *77*, 33.
[26] M. A. Chamarro, V. Voliotis, R. Grousson, P. Lavallard, T. Gacoin, G. Counio, J. P. Boilot, R. Cases, *J. Cryst. Growth* **1996**, *159*, 853.
[27] M. Morita, D. Rau, H. Fujii, Y. Minami, S. Murakami, M. Baba, M. Yoshita, H. Akiyama, *J. Lumin.* **2000**, *87–89*, 478.
[28] M. V. Artemyev, L. I. Gurinovich, A. P. Stupak, S. V. Gaponenko, *Phys. Status Solidi B* **2001**, *224*, 191.
[29] A. Henglein, *Ber. Bunsenges. Phys. Chem.* **1986**, *86*, 301.
[30] C. B. Murray, D. J. Norris, M. G. Bawendi, *J. Am. Chem. Soc.* **1993**, *115*, 8706.
[31] C. Petit, P. Lixon, M. P. Pileni, *J. Phys. Chem.* **1990**, *94*, 1598.
[32] C. Petit, T. K. Jain, F. Billoudet, M. P. Pileni, *Langmuir* **1994**, *10*, 4446.
[33] L. Motte, C. Petit, L. Boulanger, P. Lixon, M. P. Pileni, *Langmuir* **1992**, *8*, 1049.
[34] H. Sato, T. Hirai, I. Komasawa, *Ind. Eng. Chem. Res.* **1995**, *34*, 2493.
[35] J. Tanori, N. Duxin, C. Petit, P. Veillet, M. P. Pileni, *Colloid Polym. Sci.* **1995**, *273*, 886.
[36] J. Cizeron, M. P. Pileni, *J. Phys. Chem.* **1995**, *99*, 17410.
[37] J. Cizeron, M. P. Pileni, *J. Phys. Chem. B* **1997**, *101*, 8887.
[38] S. K. Haram, A. R. Mahadeshwar, S. G. Dixit, *J. Phys. Chem.* **1996**, *100*, 5868.
[39] M. P. Pileni, *Langmuir* **1997**, *13*, 3266.
[40] M. L. Curri, A. Agostiano, L. Manna, M. D. Monica, M. Catalano, L. Chiavarone, V. Spagnolo, M. Lugara, *J. Phys. Chem. B* **2000**, *104*, 8391.
[41] K. Moller, T. Bein, *Chem. Mater.* **1998**, *10*, 2950.
[42] M. P. Pileni, *Cryst. Res. Technol.* **1998**, *33*, 1155.
[43] R. Köhn, M. Fröba, *Catal. Today* **2001**, *68*, 227.
[44] J. S. Beck, J. C. Vartuli, W. J. Roth, M. E. Leonowicz, C. T. Kresge, K. D. Schmitt, C. T.-W. Chu, D. H. Olson, E. W. Shep-

 © 2005 Wiley-VCH Verlag GmbH & Co. KGaA, Weinheim

pard, S. B. McCullen, J. B. Higgins, J. L. Schlenker, *J. Am. Chem. Soc.* **1992**, *114*, 10834.
[45] M. Thommes, R. Köhn, M. Fröba, *J. Phys. Chem. B* **2000**, *104*, 7932.
[46] D. Zhao, J. Feng, Q. Huo, N. Melosh, G. H. Fredrickson, B. F. Chmelka, G. D. Stucky, *Science* **1998**, *279*, 548.
[47] J. D. Holmes, D. M. Lyons, K. J. Ziegler, *Chem. Eur. J.* **2003**, *9*, 2144.
[48] L. E. Brus, *J. Chem. Phys.* **1984**, *80*, 4403.
[49] L. E. Nair, S. Sinha, K. C. Rustagi, *Phys. Rev. B* **1987**, *35*, 4098.
[50] A. Henglein, *Chem. Rev.* **1989**, *89*, 1861.
[51] P. E. Lippens, M. Lannoo, *Phys. Rev. B* **1989**, *39*, 10935.
[52] Y. Wang, N. Herron, *Phys. Rev. B* **1990**, *42*, 7253.
[53] T. Vossmeyer, L. Katsikas, M. Giersig, I. G. Popovic, K. Diesner, A. Chemseddine, A. Eychmüller, H. Weller, *J. Phys. Chem.* **1994**, *98*, 7665.
[54] A. P. Alivisatos, *J. Phys. Chem.* **1996**, *100*, 13226.
[55] A. C. Gossard, S. Fafard, *Solid State Commun.* **1994**, *92*, 63.
[56] G. W. Bryant, *J. Lumin.* **1996**, *70*, 108.
[57] R. Nötzel, *Semicond. Sci. Technol.* **1996**, *11*, 1365.
[58] A. Ekimov, *J. Lumin.* **1996**, *70*, 1.
[59] G. A. Prinz, *Science* **1998**, *282*, 1660.
[60] R. N. Bhargava, D. Gallagher, X. Hong, A. V. Nurmikko, *Phys. Rev. Lett.* **1994**, *72*, 416.
[61] A. A. Bol, A. Meijerink, *Phys. Rev. B* **1998**, *58*, R15997.
[62] A. A. Bol, A. Meijerink, *J. Lumin.* **2000**, *87–89*, 315.
[63] D. J. Norris, N. Yao, F. T. Charnock, T. A. Kennedy, *Nanoletters* **2001**, *1*, 3.
[64] M. A. Hines, P. Guyot-Sionnest, *J. Phys. Chem. B* **1998**, *102*, 3655.
[65] L. Levy, J. F. Hochepied, M. P. Pileni, *J. Phys. Chem.* **1996**, *100*, 18322.
[66] L. Levy, N. Feltin, D. Ingert, M. P. Pileni, *J. Phys. Chem. B* **1997**, *101*, 9153.
[67] F. J. Brieler, M. Fröba, L. Chen, P. J. Klar, W. Heimbrodt, H.-A. Krug von Nidda, A. Loidl, *Chem. Eur. J.* **2002**, *8*, 185.
[68] L. Chen, H. Falk, P. J. Klar, W. Heimbrodt, F. Brieler, M. Fröba, H.-A. Krug von Nidda, A. Loidl, Z. Chen, Y. Oka, *Phys. Status Solidi B* **2002**, *229*, 31.
[69] A. V. Kouzema, M. Fröba, L. Chen, P. J. Klar, W. Heimbrodt, *Adv. Funct. Mater.* **2005**, *15*, 168.
[70] F. J. Brieler, P. Grundmann, M. Fröba, L. Chen, P. J. Klar, W. Heimbrodt, H.-A. Krug von Nidda, T. Kurz, A. Loidl, *J. Am. Chem. Soc.* **2004**, *126*, 797.
[71] N. Feltin, L. Levy, D. Ingert, M. P. Pileni, *Adv. Mater.* **1999**, *11*, 398.
[72] M. P. Pileni, *Catal. Today* **2000**, *58*, 151.
[73] L. Chen, P. J. Klar, W. Heimbrodt, F. Brieler, M. Fröba, H.-A. Krug von Nidda, T. Kurz, A. Loidl, *J. Appl. Phys.* **2003**, *93*, 1326.
[74] Y. Tanabe, S. Sugano, *J. Phys. Soc. Jpn.* **1954**, *9*, 753.
[75] A. Twardowski, P. Swiderski, M. von Ortenberg, R. Pauthenet, *Solid State Commun.* **1984**, *50*, 509.
[76] A. Twardowski, T. Dietl, M. Demianiuk, *Solid State Commun.* **1983**, *48*, 845.
[77] C. T. Tsai, S. H. Chen, D. S. Chuu, W. C. Chou, *Phys. Rev. B* **1996**, *33*, 8207.
[78] M. Ikeda, K. Itoh, H. Sato, *J. Phys. Soc. Jpn.* **1968**, *25*, 455.
[79] R. B. Bylsma, W. M. Becker, J. Kossut, U. Debska, *Phys. Rev. B* **1986**, *33*, 8207.
[80] B. E. Larson, K. C. Hass, H. Ehrenreich, A. E. Carlson, *Phys. Rev. B* **1988**, *37*, 4137.
[81] M. Taniguchi, M. Fujimori, M. Fujisawa, T. Mori, I. Souma, Y. Oka, *Solid State Commun.* **1987**, *62*, 431.
[82] R. Weidemann, H.-E. Gumlich, M. Kupsch, H.-U. Middelmann, U. Becker, *Phys. Rev. B* **1992**, *45*, 1172.
[83] Y.R. Lee, A. K. Ramdas, R. L. Aggarwal *Proc. 18th Int. Conf. on Physics of Semiconductors* **1986**, World Scientific.
[84] D. Theis, *Phys. Lett. A* **1976**, *59*, 154.
[85] R. R. Galazka, S. Nagata, P. H. Keesom, *Phys. Rev. B* **1980**, *22*, 3344.
[86] M. A. Novak, O. G. Symko, D. J. Zheng, S. Oseroff, *Phys. Rev. B* **1986**, *33*, 6391.
[87] N. Samarth, J. K. Furdyna, *Phys. Rev. B* **1988**, *37*, 9227.
[88] J. Schneider, S. R. Sircar, A. Z. Räuber, *Z. Naturforsch. A* **1963**, *18*, 980.
[89] J. Lambe, C. Kikuchi, *Phys. Rev. B* **1960**, *119*, 1256.
[90] Y. J. Ishikawa, *J. Phys. Soc. Jpn.* **1966**, *21*, 1473.
[91] F. J. Brieler, P. Grundmann, M. Fröba, L. Chen, P. J. Klar, W. Heimbrodt, H.-A. Krug von Nidda, T. Kurz, A. Loidl, *Chem. Mater.* **2005**, *17*, 795.
[92] P. H. Borse, D. Srinivas, R. F. Shinde, S. K. Date, W. Vogel, S. K. Kulkarni, *Phys. Rev. B* **1999**, *60*, 8659.
[93] J. K. Furdyna, N. Samarth, R. B. Frankel, J. Spalek, *Phys. Rev. B* **1988**, *37*, 3707.
[94] C. Chen, M. Qu, W. Hu, X. Zhang, F. Lin, H. Hu, K. Ma, W. Giriat, *J. Appl. Phys.* **1991**, *69*, 6114.
[95] Y. Q. Yang, P. H. Keesom, J. K. Furdyna, W. Giriat, *J. Sold State Chem.* **1983**, *49*, 20.
[96] Y. Shapira, S. Foner, D. Heiman, P. A. Wolff, C. R. McIntyre, *Solid State Commun.* **1989**, *71*, 355.
[97] Landolt-Börnstein, Numerical Data and Functional Relationships in Science and Technology, Vol. 17b, Springer, Berlin **1982**.
[98] R. E. Kremer, J. K. Furdyna, *Phys. Rev. B* **1985**, *31*, 1.
[99] S. B. Oseroff, *Phys. Rev. B* **1982**, *25*, 6584.
[100] H. A. Sayad, S. M. Bhagat, *Phys. Rev. B* **1985**, *31*, 591.
[101] S. B. Oseroff, R. Calvo, Z. Fisk, F. Acker, *Phys. Lett. A* **1980**, *80*, 311.
[102] J. H. van Vleck, *Phys. Rev.* **1948**, *74*, 1168.
[103] P. W. Anderson, P. R. Weiss, *Rev. Mod. Phys.* **1953**, *25*, 269.

Received: April 26, 2005
Published Online: August 17, 2005

 © 2005 Wiley-VCH Verlag GmbH & Co. KGaA, Weinheim

The Assembling of Semiconductor Nanocrystals

Alexey Shavel,[a] Nikolai Gaponik,[a,b] and Alexander Eychmüller*[a,b]

Keywords: Nanostructures / Colloids / Layer-by-layer assembly / Interactions

Recent accomplishments in arranging semiconductor nanoparticles in a desired manner are reviewed. Coupling mechanisms utilized for this purpose include electrostatic and covalent interactions, methods like layer-by-layer assembly, solvent-controlled precipitation and surface amination for covalent attachment of nanoparticles are employed. Dipole–dipole interactions are operative in nanocrystal solids and fast Förster energy transfer is observed.
(© Wiley-VCH Verlag GmbH & Co. KGaA, 69451 Weinheim, Germany, 2005)

Introduction

Ordered assemblies of nanocrystalline materials have received increasing interest in recent years. Nanoparticles (often referred to as artificial atoms) are used to build up artificial molecules and solids.[1] These arrays and superlattices offer new perspectives for the application of nanoparticles for example in optoelectronic devices. Various approaches toward assembling nanocrystals are known. Three-dimensional superlattices of semiconductor nanoparticles have been built up via self organization[2] and crystallization.[3–5] Another main route towards ordered structures of nanocrystals is covalent binding with and without special linker molecules.[6] These efforts have a direct correlation with the investigations in the fields of covalent coupling of nanoparticles to biomolecules and surface

[a] Institute of Physical Chemistry, University of Hamburg, Grindelallee 117, 20146 Hamburg, Germany
Fax: +49-351-46337164
E-mail: alexander.eychmueller@chemie.tu-dresden.de
[b] Institute of Physical Chemistry and Electrochemistry, Technical University of Dresden, Bergstraße 66b, 01062 Dresden, Germany

Alexander Eychmüller studied physics at the University of Göttingen. In 1987 he obtained his Ph. D., working on proton transfer reactions under the supervision of Dr. K.-H. Grellmann and Prof. A. Weller at the Max Planck Institute for Biophysical Chemistry. After a postdoctoral year at UCLA working with Prof. M. A. El-Sayed on gas phase metal clusters he joined the group of Prof. A. Henglein at the Hahn-Meitner-Institute in Berlin where he became involved in the research on semiconductor quantum dots. In 1994 he moved with Prof. H. Weller to the University of Hamburg focusing his scientific interests on the photophysical and structural properties of semiconductor nanocrystals. The habilitation in 1999 and the venia legendi in 2000 were followed by an offer of a chair in Physical Chemistry and Electrochemistry at the Technical University of Dresden in 2005.

Alexey Shavel was born in 1974 in Vitebsk, Belarus. He studied chemistry at the Belarusian State University from 1991 until 1996. From 1996 to 2002 he worked in the National Academy of Science of Belarus as a junior research scientist. In 2002 he started to work on his Ph. D. under the guidance of Dr. Alexander Eychmüller on the preparation of the nanoparticle superstructures.

Nikolai Gaponik studied chemistry and obtained his Ph. D. (2000) at the Belarusian State University working under the supervision of Prof. D. V. Sviridov on the electrochemical and photoelectrochemical properties of the composite materials based on conducting polymers and semiconductor nanocrystals. He worked as a visiting scientist at the LMU Munich with Dr. M. Gao and Prof. J. Feldmann in 2000. In October 2000 he joined the group of Prof. H. Weller and Dr. A. Eychmüller at the University of Hamburg first as a DAAD-fellow and finally as a research scientist. His current research interest focuses on the synthesis, characterization and applications of semiconductor nanocrystals.

MICROREVIEWS: This feature introduces the readers to the authors' research through a concise overview of the selected topic. Reference to important work from others in the field is included.

functionalization of nanocrystals.[7] Here we report on recent advances made in our Hamburg group in the preparation and the characterization of various assemblies of II-VI semiconductor nanocrystals (SC NCs). We will outline our efforts in the layer-by-layer assembling of SC NCs with and without interfacial polyelectrolytes. This method has been used to coat flat and porous solids as well as spherical microbeads. The latter may also be plated by solvent controlled precipitation of SC NCs onto them as will be shown in the subsequent paragraph. This will be followed by a survey of our experimental work devoted to the covalent coupling of nanoparticles amongst them as well as to flat and curved surfaces. The article will be finalized with a summary of our current theoretical understanding about the interparticle interactions and a kinetic study of Förster energy transfer in SC NC solids.

Layer-by-layer Assembly of Semiconductor Nanocrystals

LbL Assembly on Flat and/or Porous Surfaces

Uniform and multicomponent thin films consisting of functional molecules and/or nanocrystals may be formed by applying the so-called layer-by-layer (LbL) assembly technique. Figure 1 shows, schematically, the LbL procedure which was originally introduced for the assembly of polymer electrolytes[8] and, which was recently adapted to the deposition of charged nanocrystals both on flat[9,10] and on curved surfaces.[11,12] As is seen from Figure 1 the formation of monolayers of deposited material is based on the electrostatic interaction between the nanocrystals and the surface. Alternation of the sign of the charges of the species to be deposited allows the multilayers to grow quite thick, while the introduction of new components in one of the layers yields the opportunity of virtually nonlimited but controllable variations of LbL-multistructure compositions.[13,14] The application of the method described to the modification of artificial opals yielded intrinsically light emitting photonic crystals, which were successfully used for investigations on photonic confinement phenomena.[15,16]

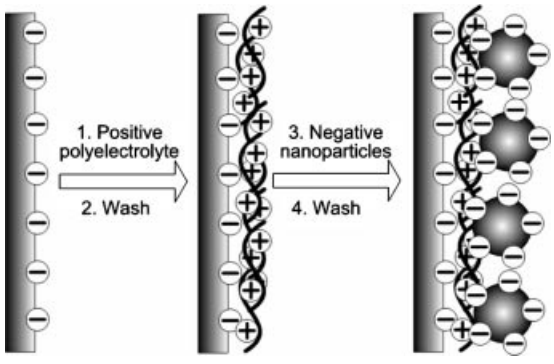

Figure 1. Schematic representation of the LbL assembly involving polyelectrolyte molecules and oppositely charged nanoparticles. The procedures 1–4 can be repeated to assemble more PE/nanoparticles bilayers.

The following standard cyclic procedure is normally used for the preparation of layered structures of negatively charged nanocrystals: (i) dipping of the substrate into a solution of polyelectrolyte (PE) (e.g. 5 mg ml^{-1} in 0.5 M NaCl) for 10 min [poly(ethyleneimine), PEI, was used for the first layer and poly(diallyldimethylammonium chloride), PDDA, for the second and further layers]; (ii) rinsing with water for 1 min; (iii) dipping into aqueous dispersions of the nanocrystals for 20 min; (iv) rinsing with water again for 1 min (cf. Figure 1). On each of the exposed surfaces, this procedure results in a 'bilayer' consisting of a polymer/NC composite. The cycle can be repeated as many times as necessary to obtain a multilayer film of desired thickness. The thickness of the LbL film depends linearly on the number of 'bilayers'. Moreover, a linear dependence of the absorption in the region of the first absorption maximum on the number of bilayers was observed.[17,18]

It is mentioned that in some cases the LbL assembly appeared to be nonefficient. When using freshly prepared colloidal solutions of nanocrystals we occasionally observed incomplete layer formation. Low-molecular weight byproducts of the synthesis as well as the smallest nanocrystal precursors could be responsible for this because they may be attracted by the polyelectrolyte sub-layers with higher efficiency than the nanocrystals themselves. We assume that aging of nanocrystal colloidal solutions leads to the reduction of the activity of those poisoning species due to their association with particle shells, aggregation and precipitation, etc. To avoid this problem, i.e. to make nanocrystal colloidal solutions useful for LbL assembly without aging them, we developed an electrophoretic activation of the colloidal solutions of thiol-capped nanocrystals. The nanocrystal solution that is to be activated is placed in a two-electrode electrochemical cell and a 1.5–2 V potential is applied to the cell. The commonly used electrodes are flat stainless steel or ITO-glass plates with a 1 cm^2 working surface and 5 mm gap in between. The current density drops from ca. 100–120 μA cm^{-2} in the very beginning down to 5–10 μA cm^{-2} after 1 h of this treatment. The above-mentioned byproducts, and possibly other charged species, are electrophoretically assembled or reacted at the electrodes and the thus cleaned activated solutions can be used for the LbL deposition as usual after removal from the cell.

Electrostatic Assembly of NCs

However, in these LbL systems the distance between donors and acceptors can not be shorter than the thickness of the polyelectrolyte monolayer. In order to avoid this limitation, which may be unfavorable for efficient interparticle interactions (see below), a new kind of a LbL structure has been generated.[19] The building blocks of the system were water soluble CdTe NCs with opposite surface charges (the charge of the CdTe NCs depends on the kind of stabilizer[20]), which were LbL assembled without polyelectrolytes between the particle layers. However, we encountered intrinsic limitations such as an easy removal of the already

 © 2005 Wiley-VCH Verlag GmbH & Co. KGaA, Weinheim

deposited layers and the unbeneficial balance of charges during the film growth.[21] These limitations might have less influence in the case of the assembly of only one NC bilayer, while at the same time the inter-layer distance in this case would be further reduced leading to more efficient interactions. Bilayers of oppositely charged NCs can indeed be formed by a direct assembly of water-soluble CdTe NCs capped with amino- and carboxyl-group terminated short chain thiols. The preparation of this layered structure was performed in two steps. In the first step a polyelectrolyte sub-layer was formed followed by this standard procedure: (i) dipping of the substrate into PEI solution for 20 min; (ii) rinsing with water for 1 min; and (iii) dipping into poly-(sodium 4-styrene sulfonate) (PSS) solution (iv) and final rinsing in water. The first PEI layer was used to improve the quality of the layered structure in terms of uniform surface coverage.[10] In the second step, close-packed nanoparticle structures on the surface of the polyelectrolyte's bilayer were assembled as follows. The substrate with the PE bilayer was (i) dipped into aqueous dispersions of the 2-mercaptoethylamine (MA)-capped nanocrystals for 20 min, (ii) rinsed with water for 1 min and finally (iii) dipped into an aqueous dispersion of the mercaptopropionic acid (MPA)- or thioglycolic acid (TGA)-capped nanocrystals, again for 20 min. Such a procedure results in a layered structure consisting of a support/polymer/NCs-NCs composite. Typical absorption and photoluminescence spectra of the system are shown in Figure 2. The composite of the nanoparticles exhibits absorption only from the bottom layer of NCs (the absorption from the top NC layer is below the limit of the sensitivity of our spectrophotometer). At the same time emission associated mainly with the top layer is observed, which is taken as a first hint to efficient energy transfer (see below).

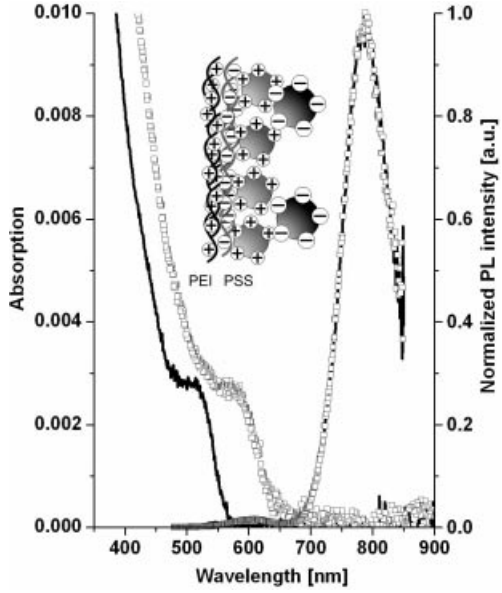

Figure 2. Examples of two close-packed structures utilizing MA-capped CdTe NCs (positively charged) of ca. 2 nm (black solid lines) and 4 nm (open squares) as the bottom layer. MPA-capped nanocrystals (negatively charged) of 6–8 nm in diameter were used as the top layer in both structures shown. While the absorption spectra of the structures show only the features corresponding to the bottom layer, the photoluminescence of the top layer (centered at ca. 780 nm) dominates in both structures.

LbL Assembly on Microbeads

The LbL assembly of NCs on the surface of the polymer [polystyrene, PMMA, melamineformaldehyde (MF) etc.] or silica beads opens up an opportunity to create submicro-sized objects exhibiting the properties of nanosized components.[22,23] In this case the LbL assembly can be done by suspension of the beads in solutions of the corresponding layer component. The contents of the solutions are generally the same as for the procedures described above. Repetitive centrifugations from pure water suspensions are used for washing of the beads and removal of excessive or nonspecifically adsorbed reactants. Figure 3 shows typical TEM images of the LbL modified beads. The modified beads retain the luminescence properties of the NCs used with a slight red shift of the luminescence maximum due to energy transfer from the smallest to the largest NCs in the assembled surface film.[11,24] The comparatively large size of the beads enables them to be manipulated by optical tweezers or to be used as a tip mounted at the end of an optical fiber. Thus, the beads can be used as subwavelength-sized light sources for photonic applications[25] or for the selective amplification of a signal in scanning near-field optical microscopy (SNOM).[26] The LbL modified beads of larger sizes (>2 μm) show an efficient coupling of the light emitted by the NCs with the whispering gallery modes of the spherical microresonators.[27–29] The use of beads made from materials that can be dissolved after LbL deposition of the polyelectrolytes (like e.g. MF, $MnCO_3$, etc.) allows the formation of hollow polyelectrolyte/NCs shells.[30–32] The shells are promising as microcapsules for drug delivery systems where the luminescence of inserted nanocrystals can be used for the monitoring of the delivery process.[33]

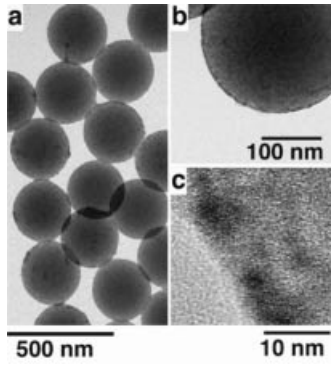

Figure 3. TEM and high-resolution TEM images of CdTe nanocrystals on polystyrene beads with increasing resolution from a) to c). The efficient coverage of the beads with nanocrystals is clearly seen in c) where the crystal structure of individual nanocrystals is resolved. Reproduced from ref.[26] with permission, copyright 2004 American Chemical Society.

 © 2005 Wiley-VCH Verlag GmbH & Co. KGaA, Weinheim

Solvent-Controlled Precipitation

Another method of coating microspheres has been established through the controlled precipitation of nanocrystals by means of their aggregation in solution onto latex spheres.[34] The approach is a variation of heteroaggregation phenomena in a colloidal environment. The aggregation of NCs onto colloidal beads was induced by the solvent-nonsolvent pair precipitation technique which is normally successfully used to separate semiconductor nanocrystals by size. Colloidal cores statistically harvest aggregated nanocrystals, which consequently leads to the formation of a shell. Moreover, the thickness of the shell can efficiently be controlled through the proper choice of the concentration ratio of the colloidal particles serving as the cores and the precipitated species. Luminescent CdTe NCs were stabilized with TGA and thus exhibit a negatively charged surface, which was used to coat negatively charged sulfate stabilized polystyrene spheres, 468 nm in diameter. The latex spheres were precovered by an electrostatically adsorbed monolayer of positively charged polyallylamine hydrochloride (PAH). This modification was done in order to obtain a positively charged surface for better adhesion of the negatively charged NCs. Upon the addition of the NCs into the latex solution a monolayer of the NCs on the surface of the PS latex is formed due to the electrostatic interaction between the carboxylic groups of the NCs' stabilizer and the surface amino groups of the PAH-modified PS latex. The dropwise addition of ethanol (well known as "nonsolvent" for thiol-stabilized NCs[20]) to the latex NCs mixture initiates the aggregation of the NCs and allows for the creation of thicker shells on the beads. In the water/ethanol mixture (80% ethanol) the precipitation of the CdTe NCs on the latex spheres takes only minutes.

Alternatively, CdTe nanocrystals stabilized with MA, and thus being positively charged, were used for the solvent controlled precipitation by governing the pH of the solution. Earlier it has been demonstrated that these nanocrystals are stable and soluble in water in a pH region of 5.5–7 and tend to aggregate at higher pH values. Both, polystyrene and melamine formaldehyde spheres were used for the pH-controlled precipitation. The PS spheres were originally negatively charged and were used as is while the MF spheres were premodified with a monolayer of negatively charged PSS. A pH of 9 was found to be optimal for the complete precipitation of all CdTe NCs present in the solution. Confocal microscopy images of the CdTe-modified PS and MF spheres (Figure 4) demonstrate the efficient coverage and the luminescence properties of the core-shell composites formed.

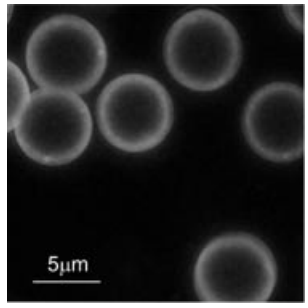

Figure 4. Confocal microscopy image of the luminescent CdTe nanocrystal shells assembled by the solvent controlled precipitation on 5 μm diameter melamine formaldehyde (MF) spheres. Reproduced from ref.[34]

Covalent Coupling of SC NCs

Interparticle Linking

Besides electrostatic coupling of NCs the generation of covalent bonds between selected nanocrystalline entities constitutes a very attractive and vast field. As an example of bridging two different sorts of NCs, we investigated the linkage of CdTe nanocrystals stabilized by TGA and MA.[35] The coupling has been carried out directly at the ligands without using an additional bridging molecule but with the aid of a carbodiimide acting as a mediator for the reaction. The reaction is described in Scheme 1. All solutions used were Ar saturated. The aqueous colloidal solution of TGA-stabilized nanocrystals (ca. 10^{-3} M according to the Cd^{2+} concentration) has been buffered to pH 5.75 by phosphate buffer and mixed with a freshly prepared solution of *N*-cyclohexyl-*N*′-[2-(*N*-methylmorpholino)ethyl]carbodiimide-4 in phosphate buffer (pH 5). After 5 min of stirring the solution was centrifuged and the precipitate redissolved in borate buffer (pH 8.65) using an ultrasonic bath. An aqueous colloidal solution of MA-stabilized nanocrystals (ca. 10^{-3} M according to the Cd^{2+} concentration) has been added and stirred for a further 90 min. While stirring the solution becomes turbid and the assembled CdTe nanocrystals precipitate. A mixture of the CdTe nanocrystal solutions without the addition of carbodiimide, and with the same buffer solutions, was used as a control experiment. In both cases the molar ratio between the different nanocrystals was approximately 1:1. The mixed nanoparticles stabilized with TGA and MA also precipitate because of electrostatic interactions.

The absorption and emission spectra of the linked and mixed nanocrystals were almost identical indicating that no obvious electronic interaction between the different nanocrystal cores seems to occur. Investigations using IR spectroscopy have been carried out in order to prove the assumption of the formation of an amide bond between the MA- and TGA-stabilized nanoparticles. The most pronounced IR absorption bands of the pure CdTe nanocrystals occur at 3500–3000 cm^{-1}, ν(OH, H_2O); 2950 cm^{-1}, $\nu(CH_2)$; 1590 cm^{-1}, $\nu_{as}(COO^-)$; 1450 cm^{-1}, $\nu_s(COO^-)$; and 1400 cm^{-1}, (δ OH) for the TGA-stabilized nanoparticles and at 3460 cm^{-1}, $\nu_{as}(NH_2)$; 3250 cm^{-1}, $\nu_s(NH_2)$; 2800 cm^{-1}, $\nu(CH_2)$; 1600 cm^{-1} (δ NH_3^+); 1490 cm^{-1}, (δ NH_3^+); and 1110 cm^{-1}, ν(CN) for the MA-stabilized nanoparticles. The IR spectra of the MA-stabilized nanocrystals show IR absorption bands that belong to both amine and protonated amine groups, indicating their coexistence on the nanocrystal surface. In the IR spectra of both nanocrystals the S–H

 © 2005 Wiley-VCH Verlag GmbH & Co. KGaA, Weinheim

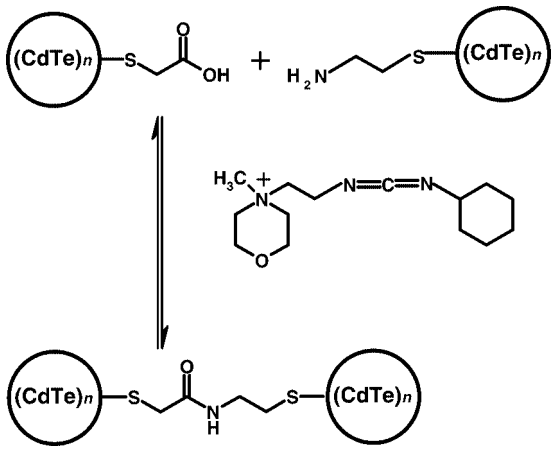

Scheme 1. Principal reaction scheme of the formation of amide bonds between differently stabilized CdTe nanocrystals. Reproduced from ref.[35] with permission of the PCCP Owner Societies.

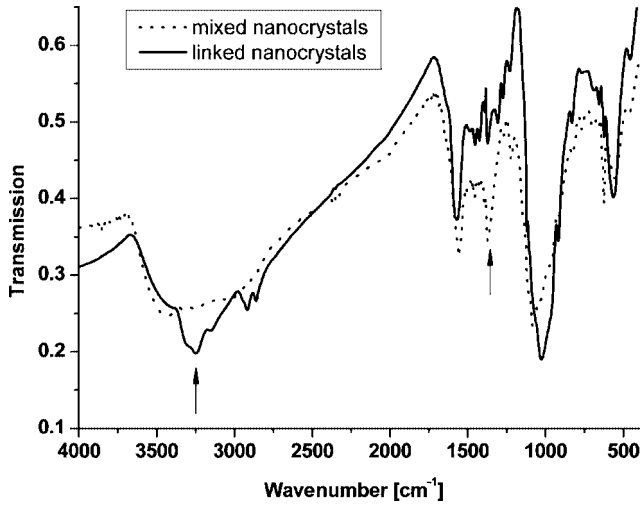

Figure 5. Infrared transmission spectra of mixed and linked CdTe nanocrystals. Reproduced from ref.[35] with permission of the PCCP Owner Societies.

vibrations (ca. 2580 cm^{-1}) are undetectable as is assumed for covalently bound thiols to the nanocrystal surface.

Figure 5 shows the IR spectra of the linked (solid line) and mixed (dotted line) nanocrystals. The main differences between the spectra in Figure 5 are marked with arrows. The IR absorption bands belonging to the valence vibrations of the carboxyl group [1550 cm^{-1}, $\nu_{as}(COO^-)$; 1370 cm^{-1}, $\nu_s(COO^-)$] are red shifted relative to the pure TGA-stabilized nanocrystals because the counterion has been changed. Whereas the spectra of the mixed nanocrystals show a broad band around 3200 cm^{-1} [ν(OH), $\nu(H_2O)$ and $\nu(NH_3^+)$] the band at 3250 cm^{-1} {ν[NH (CONH)]} in the spectra of the linked nanocrystals indicates the existence of an amide bond. Shoulders at this band indicate that some ligands remain unreacted; this is assumed to be because of steric hindrances. In the spectra of the linked nanocrystals the intensity ratio between the two bands belonging to the stretching modes of the carboxyl group has changed when compared to the spectra of the mixed nanocrystals. This is to be expected if a part of the TGA ligands have reacted with the MA. Characteristic amide group vibrations in the fingerprint region cannot be detected because of superimposition with other normal modes. The amide I band (ca. 1650 cm^{-1}), especially, is only indicated as a shoulder in the strong carboxyl group stretching band. The strong absorption bands at 1100 cm^{-1} in both spectra mainly belong to adsorbed phosphate groups originating from the buffer solutions.

Covalent Linking of CdTe NCs to Flat Surfaces

While the covalent coupling of SC NCs is still in infant status the acting chemistry as described in the preceding paragraph may well be applied to the coupling of NCs to pretreated surfaces. Accordingly, we used appropriate fractions of CdTe NCs for the conjugation with various substrates like glass, silica or silicon with different shapes of the surfaces.[36] A general illustration of the binding of the acid-stabilized NCs to aminated surfaces with the aid of carbodiimide as a mediator in the formation of the amide bond is shown in Figure 6 (inset).

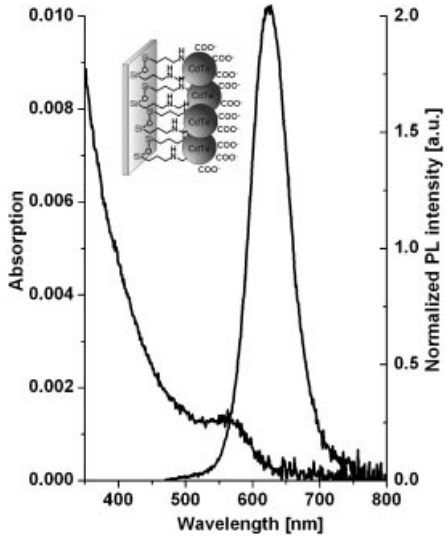

Figure 6. Absorption and luminescence spectra of CdTe NCs conjugated with a flat glass substrate. Excitation wavelength 450 nm. The inset shows a schematic representation of the structure.

The silicon wafers, quartz and glass slides were pretreated before conjugation in the following manner: the glass and quartz slides as well as the silicon wafers (with a 400 nm SiO_2 layer) were cleaned by sonication, first in 0.1 M NaOH solution, then in methanol, and finally in pure water for 15 min each. To form an amino-terminated layer on their surface, the substrates were immersed in a 6 vol.-% solution of 3-(aminopropyl)triethoxysilane in 95% methanol (named below as "3APTES solution") under sonication for 15 min followed by thorough rinsing with methanol. Drying was performed by a thermal treatment at 120 °C for half an hour in an oven.

The details of the linking of the CdTe NCs to flat substrates are as follows. An appropriate amount (0.1–0.5 mL)

 © 2005 Wiley-VCH Verlag GmbH & Co. KGaA, Weinheim

of an aqueous solution of CdTe NCs was mixed with 0.5 mL of MES buffer [2-(*N*-morpholino)ethanesulfonic acid 0,1 mM] and 8 mL of Milli-Q water. The preliminarily cleaned aminated substrate was dipped into this solution. Subsequently, 0.5 mL of a solution of 1-Ethyl-3-[3-(dimethylamino)propyl]carbodiimide hydrochloride 0.025 M and *N*-hydroxysuccinimide 0.025 M (named below as "EDC/NHS solution") was added under vigorous stirring which was continued for another 10 min. After conjugation, the slides were washed three times in Milli-Q water and rinsed thoroughly in acetone and toluene and dried under vacuum conditions. Figure 6 shows optical spectra of the modified slides. The PL properties of the films prepared were found to be at least one order of magnitude more stable in time as compared to analogously LbL-assembled monolayer films. Although the surface coverage estimated from the optical densities of the modified glass slides is roughly 100% (i.e. one monolayer), the formation of islandlike multilayers could not be excluded.[9]

Covalent Linking of CdTe NCs to Spherical Surfaces

The method described is not limited to flat substrates but is of more generality, as seen by our successful attempts to coat glass spheres of micron size by CdTe NCs.[36] A dispersion (5 wt.-% in 10% solution of ethanol in water) of borosilicate glass microspheres (2 ± 0.5 μm, Duke Sci. Co., USA) was treated with 0.1 M NaOH for 15 min under sonication and washed three times in methanol by centrifugation. The treated microspheres were immersed in the 3APTES solution under sonication for 15 min and washed thoroughly with methanol by centrifugation. The final methanol dispersion was heated to boiling point for 1 h. After that, the microspheres were separated from the methanol, redispersed in 0.5 mL of MES buffer and subsequently 0.1 mL of an aqueous solution of CdTe NCs and 0.5 mL of the EDC/NHS solution was added to the dispersion under vigorous shaking which was continued for another 10 min. The conjugation was terminated by the addition of an excess amount of 0.1 M glycine solution. The spheres were washed three times with Milli-Q water and stored in an appropriate solvent, like water or DMF. In Figure 7 we display a fluorescence microscopy image of the glass spheres conjugated with the CdTe NCs. The persistency of the luminescence of the NCs is nicely seen. This luminescence is not altered for at least 3 months. The inset shows a SEM image of one particle of the same sample providing an impression of the coverage of the spheres with nanoparticles.

Figure 8 shows some optical properties of conjugates of CdTe NCs with silica beads. For the generation of these conjugates we used CdTe NCs of two different sizes, namely 3–4 nm in diameter and 6–8 nm in diameter, respectively. The absorption spectra of the conjugates possess well-pronounced first electronic transitions and strong emissions. The position of the absorption and luminescence maxima relate well to the sizes of the NCs in agreement with the size quantization effect operative in semiconductor nanoparticles of such sizes. It is seen that the emission of the larger particles reaches into the near-IR spectral region and that absorption spectra of monolayers of NCs have been gained in this study.

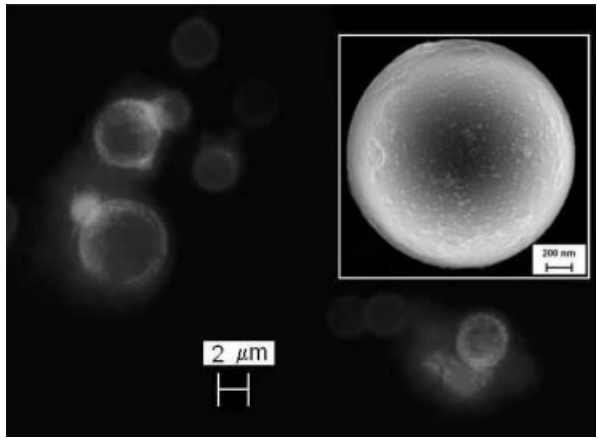

Figure 7. Fluorescence microscopy image of glass spheres conjugated with CdTe NCs. The inset shows a SEM image of one of those particles. Reproduced from ref.[36]

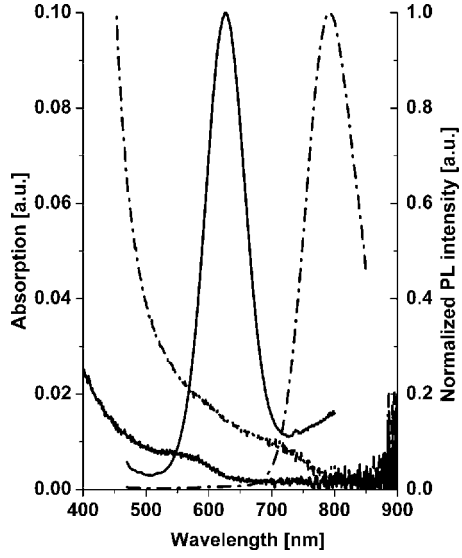

Figure 8. Absorption and luminescence spectra of silica particles conjugated with CdTe NCs of two different sizes. Reproduced from ref.[36]

For the preparation of the silica beads we used a well-known literature method.[37] Tetraethyl orthosilicate (1.5 ml) was added to a solution of ammonium hydroxide (2 mL) in ethanol (50 mL) in order to prepare particles at around 100 nm. The reaction mixture was stirred for 24 h to yield silica nanoparticles. The amino functionalization of the particles' surface was accomplished by the addition of 25 μL of 3APTES to the reaction mixture and continuing stirring for an additional 24 h. After this, the mixture was heated to boiling point for 1 h. The cooled mixture was washed three times with ethanol by centrifugation to give a stable dispersion of amino-functionalized silica spheres. Before conjugation, the silica particles were transferred into

 © 2005 Wiley-VCH Verlag GmbH & Co. KGaA, Weinheim

DMF by consecutive centrifugation with the addition of fresh portions of DMF.

Conjugates of CdTe NCs with aminated silica beads have been prepared as follows. 0.05 mL of aqueous solutions of the CdTe NCs and 0.25 mL of the dispersion of the aminated silica particles in DMF were added to 0.70 mL of DMF. Then, 0.5 mL of the EDC/NHS solution (in DMF) was added with vigorous shaking. The shaking was continued for another 5–20 min. The conjugation was stopped by centrifugation of the silica particles. The conjugated silica particles were washed three times with pure DMF and stored as dispersions in the dark.

Dipole–Dipole Interactions in Layers of Nanocrystals

As described above, various methods of assembling, arranging and coupling of SC NCs have been explored but still only little is known about the properties of the solids evolving from these procedures. Some work has been published by Heath et al. on collective properties of interacting metal nanoparticles.[38,39] Depending on the interparticle distance, those solids reflect dipole–dipole interactions followed by pure electronic coupling when the particles come into closest contact. Later, Remacle and Levine performed theoretical studies on electron-transfer processes with arrays of quantum dots.[40] A shift of the first electronic absorption of small cadmium sulfide clusters to lower energies compared to their solutions was first published by Voßmeyer et al.[41] for closely packed layers of cadmium sulfide nanocrystals. The layers were built up from solutions of the clusters by a spin-coating technique and were examined by absorption spectroscopy. Besides some further studies on Förster energy transfer in semiconductor quantum solids consisting of particles of different sizes[24,42] little is known about the interaction between identical semiconductor nanoparticles. For this purpose cluster crystals are ideal candidates.

For our first studies we chose the cluster crystal compound $Cd_{17}S_4(SCH_2CH_2OH)_{26}$, which had been prepared according to the literature.[3] The structure of this thiol-stabilized molecular-like cadmium sulfide nanocrystal is known from single-crystal X-ray diffraction studies. In Figure 9 the internal structure of the cluster is shown.[3,43] It represents a tetrahedral cut out from the bulk cubic structure consisting of four adamantane-like cages capped with barrelane-like cages at the four tips of the tetrahedron. This tetrahedron has an edge length of 1.4 nm. It is also seen from Figure 9 that neighboring clusters are bound covalently via a bridging sulfur atom from the ligand at each tip of the tetrahedra. A 3D network is formed in this manner in a cubic diamondlike superstructure. Single crystals with sizes in the millimeter range are obtained via this preparation route. Because of absorption coefficients of the clusters as high as 84 000 $L\,mol^{-1}\,cm^{-1}$ it is not possible to perform absorption spectroscopy on these kinds of solids. Consequently, absorption spectra of compact layers created by spin coating of concentrated solutions of the dissolved cluster material were recorded. Figure 10 shows these spectra in comparison with a spectrum of the corresponding cluster solution of $Cd_{17}S_4(SCH_2CH_2OH)_{26}$ nanocrystals.[44] The spectrum of the compact layer recorded in transmission geometry (dashed line) was found to be shifted to lower energies in comparison to the spectrum of the cluster solution (solid line) without showing any significant broadening of the first electronic transition. Surprisingly, the absolute value of the red shift varied with the thickness of the compact layer. The maximum of the red shift in comparison to the spectra of the clusters in solution was about 70 meV at an optical density of about 0.1 at the absorption maximum. Although the compact layers appear totally transparent in the visible region a scattering background is seen in the spectra of compact layers (cf. e.g. Figure 10, dashed line). In order to avoid any measuring artifacts in the experiment an integrating sphere was used. The absorption measurement of the same layer in this different set-up resulted in significantly different signals, i.e. in the removal of the scat-

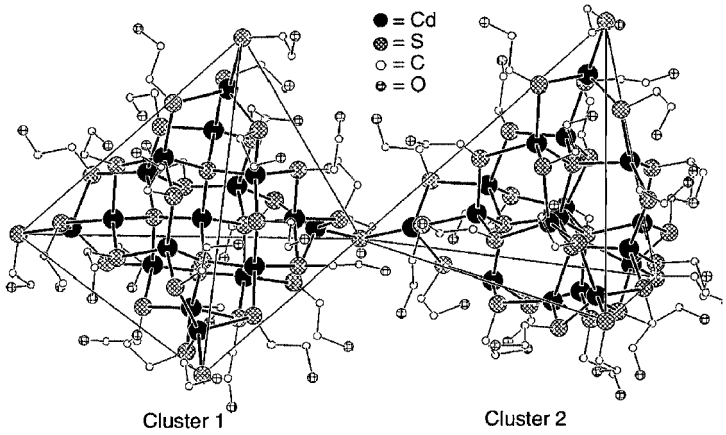

Figure 9. Crystal structure of a superstructure of $Cd_{17}S_4(SCH_2CH_2OH)_{26}$ nanocrystals. Two particles are shown that are bound covalently at the tip of each tetrahedron via a bridging sulfur atom from the ligands. For a better representation of the cores the hydrogen atoms are not shown in this Figure. Reproduced from ref.[3] with permission, copyright 1995 AAAS.

 © 2005 Wiley-VCH Verlag GmbH & Co. KGaA, Weinheim

tering background (dotted line in Figure 10). Furthermore, the spectrum remains red shifted in comparison to the solution spectrum but by a smaller number than deduced before. Additionally, the measurement in the integrating sphere no longer showed a dependence on the thickness of the layers. Thus, regarding the discussion of the energetic position of an absorption band it is extremely important to suppress artifacts caused by scattering. Keeping this in mind a red shift of the first electronic transition in the compact layer of about 29 meV in comparison to the isolated cluster in solution was observed. This energy difference is taken as an indication of cluster–cluster interaction in a closely-packed layer of NCs.

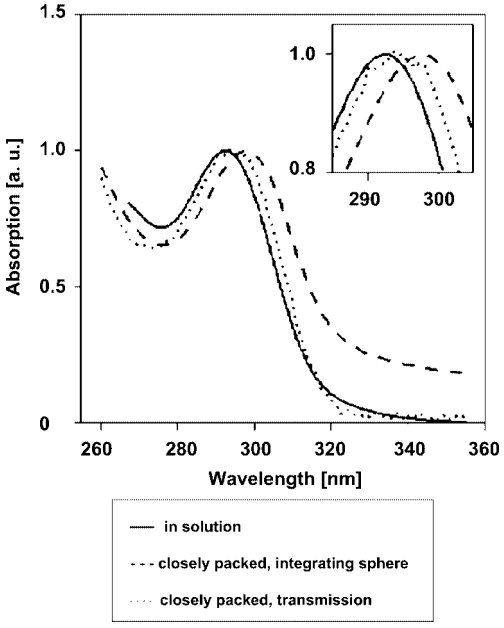

Figure 10. Absorption spectra of a compact layer of $Cd_{17}S_4(SCH_2CH_2OH)_{26}$ nanoparticles in comparison to the spectrum of the same particles in solution (solid line). Significant scattering is observed when the layer is measured in transmission geometry (dashed line) instead of measuring in the integrating sphere (dotted line). The inset provides a closer look on the resulting changes in the position of the maximum of the transition band depending on the experimental setup. (solution: cell thickness: 1 cm, OD = 1.15, calculated concentration: 0.7 μmol/L, integrating sphere: OD = 0.14, calculated film thickness: 30 nm, in transmission: OD = 0.26, calculation of film thickness is difficult because of scattering background, estimated to be 25 nm). Reproduced from ref.[44] with permission, copyright 2002 American Chemical Society.

In Figure 11 the interaction between the transition dipole moment of the absorbing particle and the induced dipole moments in the neighboring particles is sketched schematically. Analogous to the additional coulomb term for the determination of the transition energy by the Brus formula,[45] this interaction lowers the original transition energy of the absorbing particle.

Using text book equations for the values of the oscillator strength, the respective transition dipole moment and the polarizability volume, a potential energy of –51.2 meV for the interaction between the dipole of the absorbing cluster

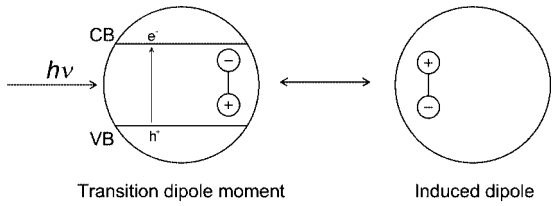

Figure 11. Schematic view of the interaction of the transition dipole moment of a particle appearing with the absorption process and the induced dipole moment of a neighboring particle. Reproduced from ref.[44] with permission, copyright 2002 American Chemical Society.

and the induced dipoles in adjacent clusters (cf. Table 1) is obtained for a distance between the particles (center to center) of 1.4 nm. It was also taken into account that for tetrahedrally shaped particles the polarizability volume decreases (57.0 Å^3), leading to a reduced shift of –14.2 meV to lower energies. Comparing these results with the value of the experiment (–29 meV), these simple calculations readily explain the red shift of the absorption band of the clusters in the compact layer in comparison to the isolated clusters in solution.

Table 1. Red shift of the first electronic transition of compact layers of CdS nanocrystals in comparison to the corresponding transition of the same clusters in solution. The experimental values for the different cluster sizes as well as the calculated results are shown. The theoretical results for both, spherically or tetrahedrally shaped particles are given. Note that for both particle sizes the experimental value fits between the values of the assumed particle shapes.

	Experimental	Calculated spherical	Calculated tetrahedral
cluster sizes	ΔE [meV]	ΔE [meV]	ΔE [meV]
d = 1.8 nm	12	27.2	6.7
d = 1.4 nm	29	51.2	14.2

Comparable results are found for the larger homologue cluster $Cd_{32}S_{14}[SCH_2CH(CH_3)OH]_{36}$ (cf. Table 1).

In an attempt to study the optical properties of the crystalline material itself, i.e. without dissolving the cluster crystals, reflection spectroscopy has been performed. For this, we milled the crystals down to grain sizes of about 2 μm and measured the diffuse reflection in an integrating sphere. In Figure 12 the UV/Vis absorption spectrum of this compound in solution is shown together with the reflection spectrum of the crystalline material. It is clearly seen that in the spectra of the crystalline material the first electronic transition is shifted to lower energies by about 150 meV, which is considerably more than observed in the films (29 meV, see above). Additionally, the transition is broadened from a full width at half maximum of about 390 meV to about 520 meV, which has not been observed in the spin-coated films consisting of the same particles. For the larger red shift a more densely packed structure of the crystals compared to the films is held responsible while for the broadening we propose a model of quantum mechanical coupling. For calculating the dependence of the electronic interaction on the distance between the coupling systems we used a periodical box potential according to Kronig and

 © 2005 Wiley-VCH Verlag GmbH & Co. KGaA, Weinheim

Penney[46] for simulating both the crystalline arrangement of the particles with very small distances between them and the situation in solution with large distances between the particles. In this model, the boxes representing the particles (size 1.4 nm) are separated by potential walls. The height of these energy barriers was chosen to be 3 eV and the separation of the boxes (i.e. the interparticle distance) was varied between 20 nm, reflecting large distances, and 0.7 nm, modeling the situation with neighboring clusters. The effective masses of the charge carriers were taken from the literature (0.2 and 0.7 for electrons and holes, respectively[47]). The 3D arrangement of the particles was taken into account by multiplying the 1D results by three. According to Brus[45] the transition energy is then calculated by addition of the bulk band gap and the Coulomb interaction. For large distances between the clusters a transition energy of 3.92 eV was obtained, which is in fair agreement with the experimental value (4.24 eV). For the clusters with small distances between the inorganic cores we obtained the formation of a sub-band for the electron states, which spans about 75 meV (for 1D) for a separation of 0.7 nm. Due to the larger effective mass of the holes a narrower sub-band (1.5 meV) is observed for this charge carrier. The centers of the sub-bands remain at exactly the same energetic positions as the discrete levels in the case of the solution. Thus, it turns out that for the electronic interaction of semiconductor particles in close contact a broadening of the transition band is expected without a significant change of the transition energy. The shift of the transition energy in the crystalline material is then only due to dipole–dipole interactions of adjacent particles.

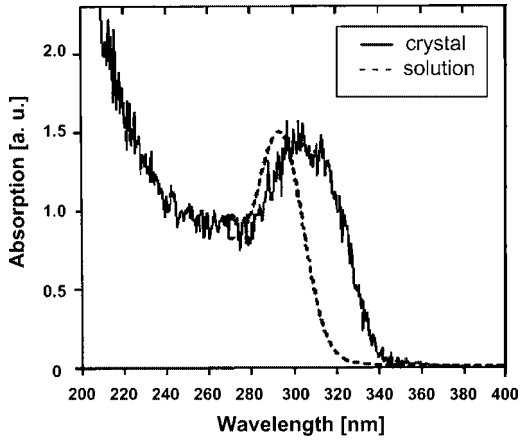

Figure 12. Absorption spectrum of $Cd_{17}S_4(SCH_2CH_2OH)_{26}$ nanocrystals dispersed in solution (dotted line) and reflection spectrum of micron-sized crystals of the same compound (solid line). Reproduced from ref.[43] with permission, copyright 2001 American Chemical Society.

Rapid Förster Energy Transfer

To investigate the Förster energy transfer from smaller (green emitting, PL maximum at approx. 555 nm) to bigger NCs (red emitting, 650 nm) in LbL-layered assemblies, two different structures both consisting of 10 polyelectrolyte/NCs bilayers have been prepared. The first structure consists of five bilayers of the same NCs size followed by five bilayers of the other NCs size on top, while the second structure consists of alternating bilayers of NCs of both sizes, as is schematically shown in Figure 13. The disappearance of the green PL band and the simultaneous relative amplification of the red emission is inherent for both structures and is a consequence of the Förster energy transfer (FRET), i.e. energy transfer takes place between donor and acceptor NCs, when the interparticle distance is smaller than the so-called Förster radius. At the same time the efficiency of the FRET appears to be relatively higher in the case of alternating layers. Indeed, the mean distance between the NCs of different sizes is smaller in the case of the alternating structure. In the other case only the closest red and green NC layers participate in the energy transfer efficiently, while others are too far apart. Furthermore, the applicability of the LbL method to the creation of even more complex structures has been demonstrated. This structure consisted of alternating bilayers of NCs of three different sizes with a gradual decrease of the electronic band gap and it shows PL originating from the biggest NCs only, while the features corresponding to all the NCs' sizes appear in the absorption spectrum (not shown here).

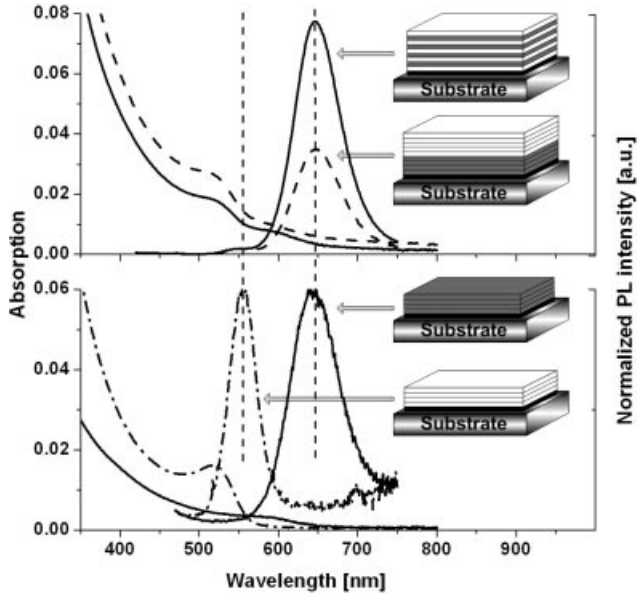

Figure 13. Absorption and PL spectra of the LbL formed assemblies sketched on the right hand side. Green and red layers correspond to the emission color of the particles constituting the assembled PE/NCs bilayers.

The FRET efficiency for thin alternating films of NCs of 2.4 and 3.5 nm in size with PDDA as opposite polyelectrolyte was estimated to be as high as 50% with an average interlayer energy-transfer rate of $(254\ ps)^{-1}$ reaching the value of $(134\ ps)^{-1}$ for certain subspecies in the inhomogeneous distribution of the donor NCs having larger spectral overlap with the acceptor NCs.[48]

 © 2005 Wiley-VCH Verlag GmbH & Co. KGaA, Weinheim

As described above a LbL composite can be prepared with NCs as building blocks only, i.e. without polyelectrolytes in between the NC layers. These structures have been made in order to study Förster energy transfer in nanocrystal solids, assuming that the FRET will be facilitated by a smaller mean interlayer distance. The bilayer structure is supposed to be composed of MA-capped CdTe NCs (donors) in the bottom layer and TGA-capped CdTe NCs (acceptors) in the top layer (Figure 2). For comparison, two monolayer samples comprising only donors (MEA-capped CdTe NCs) or only acceptors (TGA-capped CdTe NCs) are also deposited on the polymer under layer. For both NC sizes the electronic transitions can be distinguished in the absorption spectrum of the bilayer sample, although the contribution of the acceptor NCs is reduced in comparison to the monolayer sample. This is not surprising because the bottom layer of the donor NCs is deposited on a polymer under layer in both cases, favoring the attachment of the NCs, while the top layer of acceptor NCs in the bilayer sample is deposited onto a preformed donor NC layer, which is apparently limited in its ability to attract and accommodate oppositely charged NCs in comparison to a polymer under layer. This is indicated schematically by an incomplete layer of acceptor NCs in the inset of Figure 2. The use of electric-field directed layer-by-layer assembly (EFDLA),[49] which relies on the additional attraction of NCs by applying an electric field to the substrate may allow this problem to be overcome. The absorption spectrum of the bilayer sample can be reproduced by a linear superposition of 1.0× the donor and 0.33× the acceptor absorption spectra. PL spectra show that almost all of the emission from the bilayer sample originates from the acceptor NCs, while the contribution from the donor NCs is strongly diminished. From the quenching of the donor and the enhancement of the acceptor NC PL in the bilayer sample, the efficiency of energy transfer in the bilayer structure is estimated to be ≈80%.

In order to determine the energy-transfer rate, we analyzed streak camera data binned by wavelengths rather than time. Figure 14 compares the PL decay of the donor NCs in the bilayer sample with the PL decay of the donor NCs in the monolayer sample at the same wavelength. To ensure that the donor decay in the bilayer sample is not affected by PL cross-talk from the acceptor NCs we chose a wavelength-binning region of interest from 500 nm to 525 nm. For both samples the PL transients appear as nonexponential decays as is typical for thiol-capped CdTe NCs.[48,50] Nevertheless, one can deduce a *1/e* decay time which decreases from 286 ps for the monolayer sample down to 57 ps for the bilayer sample. A transfer rate of $(71\ \text{ps})^{-1}$ is calculated from these numbers which is 3.5 times higher than the average transfer rate reported before for a CdTe NC bilayer structure with a polymer linker between the layers.[48] If one chooses the wavelength-binning region of interest as being more shifted to the high energy side of the donor spectrum (from 475 to 500 nm), an energy transfer time as low as 50 ps is derived, which is very close to the energy transfer rates of $(38\ \text{ps})^{-1}$ predicted by Klimov et al.[51] We attribute this increase in the energy transfer rate to the reduced average distance between the NC layers by eliminating a polymer linker in between. From the decay times provided above we derive an energy transfer efficiency of 80%, consistent with the efficiency we have calculated from time integrated PL spectra.

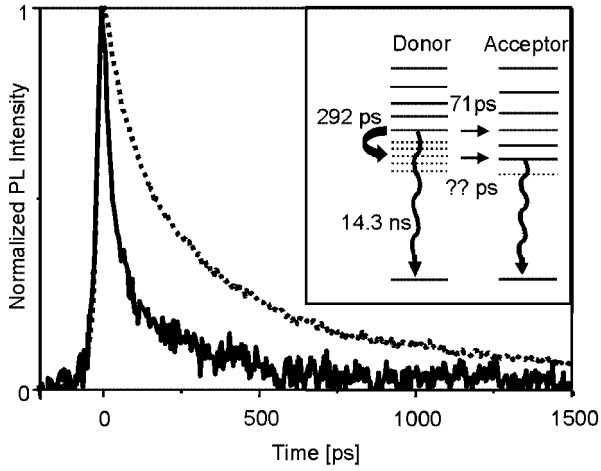

Figure 14. Fluorescence decays of the donor NCs in the monolayer donor sample (dotted line) and the donor NCs in the bilayer sample (solid line). In both samples the PL is integrated from 500 to 525 nm. The *1/e* times are 286 ps and 57 ps, respectively. The inset sketches the different decay channels of an exciton in a NC of the donor layer including the corresponding timescales. Thick solid lines represent the first excitonic transition, thin lines represent vibronic progressions and dashed lines indicate trap states from where the excitons decay nonradiatively. Apart from a resonant energy transfer of excitons in donor NC ground states, a recycling of trapped excitons by resonant transfer to a radiating state in an acceptor NC is also possible on an unknown time-scale. Reproduced from ref.[19]

Acknowledgments

Over the years contributions to this work have been made by Kathrin Hoppe, Joanna Kolny, Herwig Döllefeld, Ekkehard Geidel, Thomas Franzl, Thomas Klar, Dmitri Koktysh, Igor Radtchenko, Gleb Sukhorukov, Andrey Rogach, Jochen Feldmann, and Horst Weller. Their effort is equally appreciated as is the financial support of the DFG and the superior management of the Schwerpunktprogramm by Dr. K.-H. Schmidt and Prof. G. Schmid.

[1] C. P. Collier, T. Vossmeyer, J. R. Heath, *Annu. Rev. Phys. Chem.* **1998**, *49*, 371–404.
[2] C. B. Murray, C. R. Kagan, M. G. Bawendi, *Annu. Rev. Mater. Sci.* **2000**, *30*, 545–610.
[3] T. Vossmeyer, G. Reck, L. Katsikas, E. T. K. Haupt, B. Schulz, H. Weller, *Science* **1995**, *267*, 1476–1479.
[4] D. V. Talapin, E. V. Shevchenko, A. Kornowski, N. Gaponik, M. Haase, A. L. Rogach, H. Weller, *Adv. Mater.* **2001**, *13*, 1868–1871.
[5] A. L. Rogach, D. V. Talapin, E. V. Shevchenko, A. Kornowski, M. Haase, H. Weller, *Adv. Funct. Mater.* **2002**, *12*, 653–664.
[6] A. N. Shipway, E. Katz, I. Willner, *ChemPhysChem* **2000**, *1*, 18–52.
[7] X. Michalet, F. F. Pinaud, L. A. Bentolila, J. M. Tsay, S. Doose, J. J. Li, G. Sundaresan, A. M. Wu, S. S. Gambhir, S. Weiss, *Science* **2005**, *307*, 538–544.

 © 2005 Wiley-VCH Verlag GmbH & Co. KGaA, Weinheim

[8] G. Decher, *Science* **1997**, *277*, 1232–1237.
[9] A. L. Rogach, D. S. Koktysh, M. Harrison, N. A. Kotov, *Chem. Mater.* **2000**, *12*, 1526–1528.
[10] M. Y. Gao, C. Lesser, S. Kirstein, H. Möhwald, A. L. Rogach, H. Weller, *J. Appl. Phys.* **2000**, *87*, 2297–2302.
[11] A. S. Susha, F. Caruso, A. L. Rogach, G. B. Sukhorukov, A. Kornowski, H. Möhwald, M. Giersig, A. Eychmüller, H. Weller, *Colloid Surf. A-Physicochem. Eng. Asp.* **2000**, *163*, 39–44.
[12] M. T. Crisp, N. A. Kotov, *Nano Lett.* **2003**, *3*, 173–177.
[13] T. A. Klar, T. Franzl, A. L. Rogach, J. Feldmann, *Adv. Mater.* **2005**, *17*, 769–773.
[14] A. A. Mamedov, A. Belov, M. Giersig, N. N. Mamedova, N. A. Kotov, *J. Am. Chem. Soc.* **2001**, *123*, 7738–7739.
[15] N. Gaponik, A. Eychmüller, A. L. Rogach, V. G. Solovyev, C. M. Sotomayor Torres, S. G. Romanov, *J. Appl. Phys.* **2004**, *95*, 1029–1035.
[16] S. G. Romanov, D. N. Chigrin, C. M. Sotomayor Torres, N. Gaponik, A. Eychmüller, A. L. Rogach, *Phys. Rev. E* **2004**, *69*, 046606/1–046606/4.
[17] J. W. Ostrander, A. A. Mamedov, N. A. Kotov, *J. Am. Chem. Soc.* **2001**, *123*, 1101–1110.
[18] A. Shavel, N. Gaponik, A. Eychmüller, *J. Phys. Chem. B* **2004**, *108*, 5905–5908.
[19] T. Franzl, A. Shavel, A. L. Rogach, N. Gaponik, T. A. Klar, A. Eychmüller, J. Feldmann, *Small* **2005**, *1*, 392–395.
[20] N. Gaponik, D. V. Talapin, A. L. Rogach, K. Hoppe, E. V. Shevchenko, A. Kornowski, A. Eychmüller, H. Weller, *J. Phys. Chem. B* **2002**, *106*, 7177–7185.
[21] N. A. Kotov, in: *Multilayer Thin Films* (Eds.: G. Decher, J. B. Schlenoff), Wiley-VCH, Weinheim, **2003**, pp. 207–270.
[22] F. Caruso, R. A. Caruso, H. Möhwald, *Science* **1998**, *282*, 1111–1114.
[23] F. Caruso, *Adv. Mater.* **2001**, *13*, 11–22.
[24] C. R. Kagan, C. B. Murray, M. Nirmal, M. G. Bawendi, *Phys. Rev. Lett.* **1996**, *76*, 1517–1520.
[25] P. Olk, B. C. Buchler, V. Sandoghdar, N. Gaponik, A. Eychmüller, A. L. Rogach, *Appl. Phys. Lett.* **2004**, *84*, 4732–4734.
[26] F. Müller, S. Götzinger, N. Gaponik, H. Weller, J. Mlynek, O. Benson, *J. Phys. Chem. B.* **2004**, *108*, 14527–14534.
[27] Y. P. Rakovich, L. Yang, E. M. McCabe, J. F. Donegan, T. Perova, A. Moore, N. Gaponik, A. Rogach, *Sem. Sci. Techn.* **2003**, *18*, 914–918.
[28] Y. P. Rakovich, J. F. Donegan, N. Gaponik, A. L. Rogach, *Appl. Phys. Lett.* **2003**, *83*, 2539–2541.
[29] Y. P. Rakovich, J. F. Donegan, M. Gerlach, A. L. Bradley, T. M. Connolly, J. J. Boland, N. Gaponik, A. Rogach, *Phys. Rev. A* **2004**, *70*, 051801/1–051801/4.
[30] N. Gaponik, I. L. Radtchenko, G. B. Sukhorukov, H. Weller, A. L. Rogach, *Adv. Mater.* **2002**, *14*, 879–882.
[31] N. Gaponik, I. L. Radtchenko, M. R. Gerstenberger, Y. A. Fedutik, G. B. Sukhorukov, A. L. Rogach, *Nano Lett.* **2003**, *3*, 369–372.
[32] N. Gaponik, I. L. Radtchenko, G. B. Sukhorukov, A. L. Rogach, *Langmuir* **2004**, *20*, 1449–1452.
[33] G. B. Sukhorukov, A. L. Rogach, B. Zebli, T. Liedl, A. G. Skirtach, K. Kohler, A. A. Antipov, N. Gaponik, A. S. Susha, M. Winterhalter, W. J. Parak, *Small* **2005**, *1*, 194–200.
[34] I. L. Radtchenko, G. B. Sukhorukov, N. Gaponik, A. Kornowski, A. L. Rogach, H. Möhwald, *Adv. Mater.* **2001**, *13*, 1684–1687.
[35] K. Hoppe, E. Geidel, H. Weller, A. Eychmüller, *Phys. Chem. Chem. Phys.* **2002**, *4*, 1704–1706.
[36] A. Shavel, N. Gaponik, A. Eychmüller, *ChemPhysChem* **2005**, *6*, 449–451.
[37] A. N. Shipway, M. Lahav, R. Gabai, I. Willner, *Langmuir* **2000**, *16*, 8789–8795.
[38] C. P. Collier, R. J. Saykally, J. J. Shiang, S. E. Henrichs, J. R. Heath, *Science* **1997**, *277*, 1978–1981.
[39] G. Markovich, C. P. Collier, S. E. Henrichs, F. Remacle, R. D. Levine, J. R. Heath, *Accounts Chem. Res.* **1999**, *32*, 415–423.
[40] F. Remacle, R. D. Levine, *J. Phys. Chem. B* **2001**, *105*, 2153–2162.
[41] T. Vossmeyer, L. Katsikas, M. Giersig, I. G. Popovic, K. Diesner, A. Chemseddine, A. Eychmüller, H. Weller, *J. Phys. Chem.* **1994**, *98*, 7665–7673.
[42] C. R. Kagan, C. B. Murray, M. G. Bawendi, *Phys. Rev. B* **1996**, *54*, 8633–8643.
[43] H. Döllefeld, H. Weller, A. Eychmüller, *Nano Lett.* **2001**, *1*, 267–269.
[44] H. Döllefeld, H. Weller, A. Eychmüller, *J. Phys. Chem. B* **2002**, *106*, 5604–5608.
[45] L. E. Brus, *J. Chem. Phys.* **1984**, *80*, 4403–4409.
[46] S. Flugge, *Rechenmethoden der Quantentheorie*, 5. verbesserte Auflage, Springer-Verlag, Berlin, Germany, **1993**.
[47] Landolt-Börnstein, "Numerical Data and Functional Relationships", in: *Science and Technology, Vol. 17b, New Series, Group III*, Springer-Verlag, Berlin, **1982**.
[48] T. Franzl, D. S. Koktysh, T. A. Klar, A. L. Rogach, J. Feldmann, N. Gaponik, *Appl. Phys. Lett.* **2004**, *84*, 2904–2906.
[49] M. Gao, J. Sun, E. Dulkeith, N. Gaponik, U. Lemmer, J. Feldmann, *Langmuir* **2002**, *18*, 4098–4102.
[50] A. M. Kapitonov, A. P. Stupak, S. V. Gaponenko, E. P. Petrov, A. L. Rogach, A. Eychmüller, *J. Phys. Chem. B* **1999**, *103*, 10109–10113.
[51] S. A. Crooker, J. A. Hollingsworth, S. Tretiak, V. I. Klimov, *Phys. Rev. Lett.* **2002**, *89*, 186802/1–186802/4.

Received: April 18, 2005
Published Online: August 15, 2005

 © 2005 Wiley-VCH Verlag GmbH & Co. KGaA, Weinheim

Formation and Characterization of Pt Nanoparticle Networks

Fei Wen,[a] Norbert Waldöfner,[a] Wolfgang Schmidt,[a] Klaus Angermund,[a] Helmut Bönnemann,*[a] Stephanie Modrow,[b] Svetlana Zinoveva,[b] Hartwig Modrow,[b] Josef Hormes,[c] Lars Beuermann,[d] Sergiy Rudenkiy,[d] Wolfgang Maus-Friedrichs,[d] Volker Kempter,[d] Thomas Vad,[e] and Heinz-Günter Haubold[e]

Keywords: Colloids / Cross-linking / Nanostructures / Platinum / Self-assembly

Nanoparticle networks can be synthesized by the self-assembly of arrays of metal colloid particles linked by spacer molecules of different sizes. The particles are linked through reactive aluminum sites in a metal–organic shell around the metal particles. Rigid spacer molecules with functional groups at each end are used to bind at these reactive sites. The resulting networks have been characterized by various methods such as transmission electron microscopy (TEM), sorption analysis, X-ray absorption spectroscopy (XAFS), anomalous small angle X-ray scattering (ASAXS), metastable impact electron spectroscopy (MIES), and ultraviolet photoelectron spectroscopy (UPS). These investigations showed that the metal nanoparticles form aggregated networks with average distances between the metal particles that are determined by the sizes of the spacer molecules applied. In this way, porous as well as nonporous networks have been obtained. Whether accessible pores are formed depends on the type of spacer molecule. Furthermore, the properties of the metal particles have proved to be sensitive towards the reaction of the aluminum in the protective shells with the linker molecules.

(© Wiley-VCH Verlag GmbH & Co. KGaA, 69451 Weinheim, Germany, 2005)

Introduction

The assembly of nanosized metal particles into highly ordered arrays has become a new trend in chemistry over the past few years.[1–3] The resulting materials are expected to exhibit novel collective properties that make them very promising with respect to application in microelectronics or optics.[4,5] Superlattices of nanocrystals have already been reported,[6–12] but bottom-up syntheses of three-dimensional structures consisting of nanoparticles still remain a challenge for the synthetic chemist. Over the past couple of years we have developed a synthetic strategy for the preparation of arrays of three-dimensionally connected nanoparticles. The key feature of this synthesis is the formation of a reactive metal–organic colloidal protecting shell around the particles.[13] Reactive alkylaluminum groups in the protective shell allow substitution of the alkyl groups by other organic groups,[14] and the use of bifunctional substituents allows the linking of two metal particles and, consequently, the formation of larger networks of metal particles.[15,16] Using this approach it possible to cross-link different types of metal nanoparticles, such as Pt, Ni, and Co. The synthetic procedures have been adapted to the specific chemistry of the metal species, and the suitability of different alkyl groups in the protective shell has been investigated. The present review gives a survey of these results. In order to provide a consistent thread, however, we will focus here mainly on cross-linked Pt nanoparticles.

[a] Max-Planck-Institut für Kohlenforschung,
Kaiser-Wilhelm-Platz 1, 45470 Mülheim an der Ruhr, Germany
[b] Physikalisches Institut der Universität Bonn,
Nussallee 12, 53115 Bonn, Germany
[c] Center for Advanced Microstructures and Devices,
6980 Jefferson Hwy, Baton Rouge, LA 70806, USA
[d] Institut für Physik und Physikalische Technologien, Technische Universität Clausthal
Leibnizstraße 4, 38678 Clausthal-Zellerfeld
[e] Forschungszentrum Jülich, Institut für Festkörperforschung,
52425 Jülich

Synthesis of Pt Colloids

Different colloid particles, i.e. Pt, Ni, and Co, are considered in this survey, although the general synthetic concept will be demonstrated for Pt particles. In a typical synthesis, the Pt colloids were prepared as follows: $Pt(acac)_2$ (1.97 g, 5 mmol) was dissolved in 200 mL of toluene. Then, $Al(CH_3)_3$ (1.44 g, 20 mmol) was dissolved in 200 mL of tol-

MICROREVIEWS: This feature introduces the readers to the authors' research through a concise overview of the selected topic. Reference to important work from others in the field is included.

uene and carefully added to the first solution over 4 h at 60 °C. After the gas evolution had stopped (24 h), the solution was filtered, and all volatile components were completely evaporated under vacuum to give 2.4 g of colloidal platinum powder in the form of a black, air-sensitive powder. The Pt colloid used for the experiments described here had a composition of 40% Pt, 14% Al, 31% C, and 6% H (by elemental analysis).

H. Bönnemann studied chemistry at the RWTH Aachen, Germany, where he received his PhD and habilitation. After two years of industrial research at Degussa, he became Professor for Industrial Chemistry at the RWTH Aachen, Germany, in 1981. Later on, he worked at the Max-Planck-Institut für Kohlenforschung in Mülheim an der Ruhr, Germany, where he installed a research group with focus on nanoparticles and colloidal metals. In 2004 he became a scientific member of the Forschungszentrum Karlsruhe, Germany, where he has worked as leader of the Nanochemistry Laboratory at the Institute for Industrial Chemistry since January 2005. Fei Wen and Norbert Waldöfner worked as PhD students in his laboratory at the Max-Planck-Institut für Kohlenforschung.

Wolfgang Schmidt studied Chemistry at the University of Mainz, Germany, where he received his PhD in 1994. During his PhD studies, he had a research term at the Boreskov Institute of Catalysis in Novosibirsk, Russia. From 1995 to 1998, he worked as staff scientist at the University of Frankfurt and then became senior scientist in the Department of Heterogeneous Catalysis at the Max-Planck-Institut für Kohlenforschung in Mülheim an der Ruhr. His work is focused on the preparation and characterization of nanoparticles and porous materials.

Klaus Angermund studied chemistry at the Heinrich-Heine University of Düsseldorf, Germany. From 1983 to 1986, he worked as a PhD student in the X-ray department at the Max-Planck-Institut für Kohlenforschung in Mülheim an der Ruhr, Germany. In 1986, he obtained his Ph D in Chemistry from the University of Wuppertal, Germany. In 1987, he was awarded the Otto Hahn scholarship by the Max-Planck Society and worked from 1987 to 1988 as a postdoctoral fellow with Arnold Hagler at Biosym Technologies Inc. in San Diego (USA). Since 1989 he is a scientific co-worker at the Max-Planck-Institut für Kohlenforschung and head of the molecular modeling group. His research focuses on application of molecular modeling techniques to organometallic reactions, force field development and parameterization, and QM/MM methods.

Hartwig Modrow received his PhD in Physics from the University of Bonn, Germany, in 1999. At present, he is Oberassistent at this institute and acting head of the synchrotron radiation group, which specializes in the investigation of electronic and geometric structure of matter and their dynamics. Stephanie Modrow obtained her PhD in that group and is presently working as a patent attorney. Svetlana Zinoveva has been pursuing her PhD Thesis work in the synchrotron radiation group since 2003.

Josef Hormes studied Physics at the University of Bonn, Germany, where he received his PhD in 1975 and habilitation in 1984. After working for the University of Bonn, the Imperial College of London, and Stockholm University (Sweden), he was appointed Professor for Physics at the University of Bonn in 1988. In the period from 1988 to 1999, he was also the Director of the Synchrotron Radiation Laboratory at the University of Bonn. Since 1999, he is Director of the Center for Advanced Microstructures & Devices at the Louisiana State University (LSU) in Baton Rouge, USA, and Professor in the Department of Physics and Astronomy at LSU.

Volker Kempter received his Ph.D. in Physics from the University of Freiburg, Germany, in 1969. He is Prof. of Physics at the Technical University of Clausthal, Germany, where he leads the section for "Molecular Processes on Surfaces". His group specializes on the oxidation and corrosion of films and nanoparticles and on processes on ice surfaces. Lars Beuermann and Sergiy Rudenkiy work as PhD students in his group and Dr. Wolfgang Maus-Friedrichs, as senior scientist, focuses on the investigation of surfaces with relevance for applications in material science.

Heinz-Günter Haubold was leader of the SAXS group at the Institut für Festkörperforschung at the Forschungszentrum Jülich from where he retired in 2003. He designed and built up the user-dedicated ASAXS experiment JUSIFA at the synchrotron facility of HASYLAB at DESY Hamburg, Germany. His coworker Thomas Vad worked on the development of routines and models for the interpretation of ASAXS data.

 © 2005 Wiley-VCH Verlag GmbH & Co. KGaA, Weinheim

Formation of Pt Colloid Networks

As described above, Pt colloid particles were prepared by reducing $[Pt(acac)_2]$ with $Al(CH_3)_3$. These particles have highly reactive methylaluminum groups in the colloidal stabilizer, which allows protonolytic reactions at the protective shell with alcohols or carboxylic acids, while the metallic core remains intact. Several bifunctional organic spacer molecules have been used to cross-link the Pt colloid to form nanoparticle networks. One example using hydroquinone as the spacer is illustrated in Scheme 1.

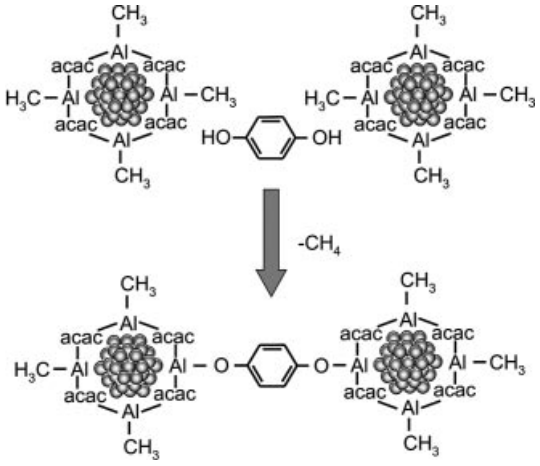

Scheme 1. Principle of the protonolytic cross-linking mechanism.

Further spacer molecules used to cross-link protected colloid particles are shown in Scheme 2. The spacer compounds HBDB, HBP, and HPDB were kindly supplied by Prof. Dr. Joannis Kallitsis[17,18] of the Institute of Chemical Engineering at the University Patras, Greece. For simplicity, the abbreviations given in the scheme will be used when discussing the different molecules.

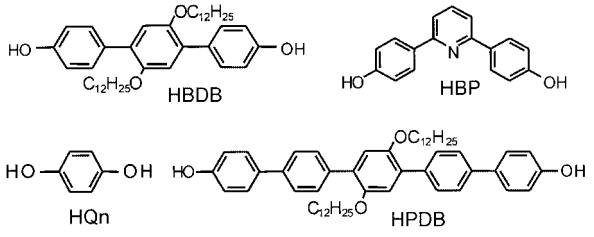

Scheme 2. Structures of the molecular spacers.

All reactions were performed in THF. The ratio of methylaluminum groups in the colloid to hydroxy groups in the molecular spacer was found to be 1:1. The molecular spacers were added dropwise into the Pt colloidal solution over 1 h. The quantity of reactive methylaluminum groups in the colloidal shell can be measured on the basis of the amount of gas (methane) evolved upon adding acetic acid to the Pt colloid. Since the reactive methylaluminum groups are statistically present on the colloidal surfaces, a 3D cross-linked nanoparticle network can be expected. The precipitate formed after the cross-linking reaction between the Pt colloid and the bifunctional molecular spacers can be isolated by simple filtration.

In the present work, several molecular spacers with different rigidity have been used to prepare Pt nanoparticle networks; their structures are depicted in Scheme 2. Here we will focus mainly on the more-rigid molecules hydroquinone (HQn), HBP, HBDB, and HPDB rod-like structures. The spacer lengths depend more or less on their conformational structures.

The introduction of HBDB and HPDB into the Pt colloidal solution caused a precipitate to form in 2 h. Compared with the results using hydroquinone and HBP as the spacers, these precipitates were produced rapidly and were very loosely suspended in the reaction medium. For some samples, the preparation conditions were varied to investigate the effect of this variation on the properties of the resulting materials. For example, the sample Pt/HBP was synthesized at 50 °C, while another sample, Pt/HBP2, was prepared at 25 °C using the same spacer molecule. In a similar manner, Pt/HBDB and Pt/HBDB2 were prepared at 50 and 25 °C, and Pt/HPDB and Pt/HPDB2 at 25 and 50 °C, respectively.

Characterization Methods

Transmission Electron Microscopy (TEM)

TEM measurements were performed using a Hitachi H 7500 instrument operating at an accelerating voltage of 120 kV. Energy-dispersive X-ray spectroscopy (EDX) analyses were performed to obtain a chemical analysis of the particles using an Oxford Instruments INCA EDX spectrometer attached to the microscope. The TEM samples were prepared by placing a drop of the colloidal dispersion onto a copper grid coated with a carbon film. High-resolution TEM measurements were performed on a Hitachi HF 2000 Instrument operating at 200 kV. In order to obtain a chemical analysis of the bimetallic catalysts, point-resolved EDX analyses were performed using a Noran Instruments EDX spectrometer attached to the microscope. The samples were prepared by placing a drop of the colloidal dispersion onto a copper grid coated with a lacey film.

Physisorption Analysis

Nitrogen sorption isotherms were recorded with a Micromeritics ASAP 2010 sorption analyzer at 77 K to evaluate the textural properties of the prepared porous materials. Prior to the measurements, the samples were evacuated at 80 °C for 12 h. The BET (Brunauer–Emmett–Teller) surface area was calculated from the adsorption data in the relative pressure interval from 0.06 to 0.20.

Anomalous Small-Angle X-ray Scattering (ASAXS)

For the characterization of nanostructures with typical metal-particle diameters and interparticle distances in the 1–10 nm regime, small-angle X-ray scattering (SAXS) is amenable for the determination of the structure parameters. Thus, anomalous small-angle X-ray scattering (ASAXS)

 © 2005 Wiley-VCH Verlag GmbH & Co. KGaA, Weinheim

was applied to analyze the inter-particle distances of the as-prepared Pt network products, as the contributions from the organic parts and pore-like voids can be subtracted. Different Pt samples[15] were investigated by ASAXS at the JUSIFA beamline[19] at HASYLAB (DESY Hamburg, Germany). The contrast variation experiments were performed at two X-ray energies, namely E_1 = 11.437 keV and E_2 = 11.535 keV, near the Pt L_3 [$E(L_3)$ = 11.564 keV] absorption edge (for a detailed description, see ref.[16]).

Since ASAXS is not a very common characterization method, the principle of ASAXS measurements will be introduced here.

In the case of a low-concentration ensemble of uniform metal particles in a (negligible) low-molecular matrix, the particle scattering intensity can be written as:

$$\frac{d\Sigma}{d\Omega}(Q) = c_0 n^2 f_0^2 S^2(Q) V^2,$$

where c_0 (= $Nanoparticle_{article}/V_{sample}$) is the number density of the particles, n [= N_{atoms}/V (V = particle volume)] is the number density of the metal atoms within a particle, f_0 is the scattering amplitude, and $S^2(Q)$ is the intraparticle interference factor, i.e., the form factor of a particle.

For a spherical particle of radius R_0, the particle form-factor is defined by

$$S(Q) = 3\frac{\sin(QR_0) - QR_0\cos(QR_0)}{(QR_0)^3},$$

with the magnitude of the scattering vector Q being equal to $4\pi\sin\Theta/\lambda$ (λ is the X-ray wavelength and 2Θ is the scattering angle). In order to obtain more information on the (pure) particle scattering, it is convenient to perform ASAXS experiments. For the two-phase model, the total differential cross-section is given by

$$\frac{d\Sigma}{d\Omega}(Q) = c_0(n_p f_p - n_m f_m)^2 S^2(Q) V^2 + \frac{d\Sigma}{d\Omega_{bg}}(Q),$$

where n_p, f_p, n_m, and f_m are the number densities and atomic form-factors, respectively, of the particles (p) and the surrounding matrix (m). Besides the particle scattering, an additional background scattering term $d\Sigma/d\Omega_{bg}(Q)$ (which is proportional to Q^{-4} in most cases) contributes to the total differential cross-section, which, for the most part, originates from inhomogeneities in the matrix. Therefore, the SAXS intensity almost always contains a (in many cases non-negligible) contribution from the matrix if a SAXS experiment is performed at only one energy. Fortunately, the particle scattering can quite easily be separated from the matrix background if, for example for Pt particles, contrast-variation experiments are carried out at at least two different energies near the Pt L_3 absorption edge [E(Pt L_3) = 11564 eV]. As shown schematically in Figure 1, the atomic form-factors of the Pt particles vary significantly at energies close to the absorption edge, while those of all other elements, i.e. the matrix, remain more or less constant.

Thus, the atomic form-factors

$$f(E) = f_0 + f'(E) + if''(E)$$

of the mainly organic matrix components (C, H, O) remain almost constant in this energy regime. A simple subtraction of two SAXS curves measured at two different energies E_1 and E_2 yields the (almost) pure (Pt) metal-particle scattering

$$\frac{d\Sigma}{d\Omega_p}(Q) = \frac{d\Sigma}{d\Omega}(Q,E_1) - \frac{d\Sigma}{d\Omega}(Q,E_2)$$
$$= c_0 n^2\left[f_{Pt}^2(E_1) - f_{Pt}^2(E_2)\right]S^2(Q)V^2 \times \left\{1 - \frac{2n_m f_m}{n\left[f_{Pt}(E_1) + f_{Pt}(E_2)\right]}\right\}$$

(in the case of negligible f'' correction terms), which reduces to

$$\frac{d\Sigma}{d\Omega_p}(Q) = c_0 n^2\left[f_{Pt}^2(E_1) - f_{Pt}^2(E_2)\right]S^2(Q)V^2$$
$$= c_0\Delta(nf)^2 S^2(Q)V^2$$

$$\text{if } 2n_m f_m / \left\{n\left[f_{Pt}(E_1) + f_{Pt}(E_2)\right]\right\} \ll 1.$$

From the scattering curves thus obtained, the average particle sizes and particle–particle distances are accessible. Figure 2 shows how the thickness of the protective layer and the average distance between particles that are linked by different spacer molecules are accessible from the

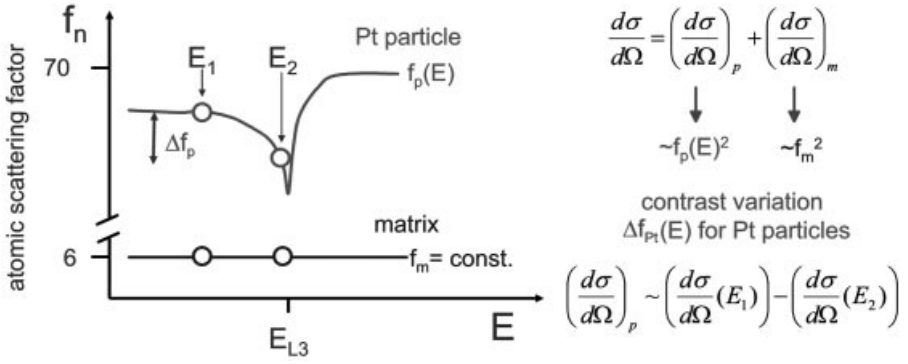

Figure 1. Schematic representation of the dependence of atomic scattering factors from the energies close to the absorption edge of an element (here Pt).

ASAXS data. Knowing the size (R_0) of the pure colloid particle allows calculation of the thickness of the protective shell (t_{ps}) from the particle–particle distance if the protected particles have direct contact, i.e. in solid aggregates of protected particles without spacer molecules. The distance (D_0) between cross-linked particles then allows calculation of the distance (l_{sp}) due to the spacer molecules by considering the thickness of the protective layer according to $l_{sp} = D_0 - (2t_{ps})$.

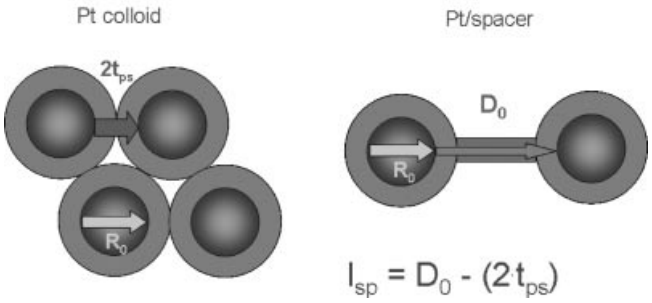

Figure 2. Model to calculate the thickness of the protective layer, t_{ps}, and the distance due to the spacer molecule, I_{sp}, from the particle–particle distance, D_0 (R_0 is the radius of the colloid particle, here Pt colloid).

X-ray Absorption Spectroscopy (XAFS)

The X-ray absorption spectra discussed in this article were measured in transmission mode at two different synchrotron radiation sources: at the ELSA storage ring at University of Bonn, Germany, and at the Center for Advanced Microstructures and Devices (CAMD). Detailed descriptions of the beamlines and instrumentation are found in the literature;[20,21] important parameters of the measurements are summarized in Table 1.

To prepare the samples for measurement at the Al K-edge, a very thin but homogeneous and pinhole-free layer of powder was fixed on an ultra-thin (6 μm) polypropylene film by application of pressure. For all other measurements, the dried colloids were mixed with boron nitride and pressed into pellets. The optimal sample thickness was found by trial and error and was chosen in such a way that the maximum absorption, μd, was not higher than 1.2. The entire process of sample preparation was undertaken in a glove box filled with argon. Sample transfer to the measurement station also took place under an inert gas atmosphere.

XANES data treatment consisted of subtraction of a linear background adapted to the pre-edge and normalization to an edge jump of one at the position given in Table 1. For EXAFS analysis, the UWXAFS package[22] was used.

Metastable Impact Electron Spectroscopy (MIES) and Photoelectron Spectroscopy (UPS)

The characterization of the surface of metal nanoparticles (nanoparticle) is of considerable technological relevance as:

- often a pre-stabilization, i.e. passivation of the particles against air and/or moisture, is required when it is planned to integrate them into nanostructures (or particle networks as in the present application);
- a termination of the nanoparticles by some particular active molecular group, with bifunctional character in the present case, is required in order to be able to interlink the nanoparticles within a customized nanostructure or particle network;
- some applications require a peptization of the nanoparticles, i.e. their embedding into a micelle of specific organic molecules, in order to prevent sintering of the reactive nanoparticles.

Thus, the availability of techniques that are able to concentrate specifically on the chemical properties and the electronic structure of the outermost layer of the nanoparticles is mandatory in order to design, characterize, and manipulate nanoparticles in particle networks or nanostructures in general. Ideally, the depth resolution of the employed surface-analytical technique should be tunable in the sense that, besides the information on the outermost layer, the corresponding information on the sub-surface region of the particles should also be provided for comparison.

MIES metastable He atoms are utilized to eject electrons from surfaces. Metastable He* atoms with thermal energy interact with condensed matter, including nanoparticles, by three different mechanisms depending on the electronic structure of the surface under consideration and its work function.[23,24] In the present work, only Auger neutralization (AN) and Auger deexcitation (AD) are observed. When molecular adsorption onto metals is studied, the situation can become complicated as a change of the mechanism from AN (on clean metals) to AD often takes place as a function of the adsorbate coverage because either an insulating surface is formed or the transfer of the He 2s electron into the metal, which is a prerequisite for the AN process, becomes inhibited because the metal becomes increasingly shielded by adsorbed species from access by the He* probe atoms.

Table 1. Results of Pt L_{III} EXAFS analysis for unconnected and two differently connected nanoparticle systems. Fitting was done in *r*-space between 0.15 and 0.32 nm using a *k*-weight of 3.

Pt L_3 Edge	Backscatterer	R [nm]	N	σ^2 [nm^2]	E_0 [eV]
Unconnected	Al	0.248 ± 0.002	0.8 ± 0.4	$2\times10^{-5}\pm3\times10^{-5}$	0.1 ± 6.3
	Pt	0.270 ± 0.002	4.0 ± 3.3	$11\times10^{-5}\pm6\times10^{-5}$	–0.5 ± 3.6
Connected	O	0.07 ± 0.001	0.7 ± 0.1	$5\times10^{-5}\pm1\times10^{-5}$	8.1 ± 1.6
(sebacic acid)	Al	0.253 ± 0.001	0.4 ± 0.1	$2\times10^{-5}\pm2\times10^{-5}$	2.9 ± 2.8
	Pt	0.267 ± 0.001	4.7 ± 0.6	$9\times10^{-5}\pm1\times10^{-5}$	0.9 ± 0.8
Connected	Al	0.250 ± 0.001	0.8 ± 0.1	$4\times10^{-5}\pm8\times10^{-5}$	11.4 ± 1.6
HBP	Pt	0.279 ± 0.001	6.2 ± 1.4	$2\times10^{-5}\pm1\times10^{-5}$	11.4 ± 1.6

 © 2005 Wiley-VCH Verlag GmbH & Co. KGaA, Weinheim

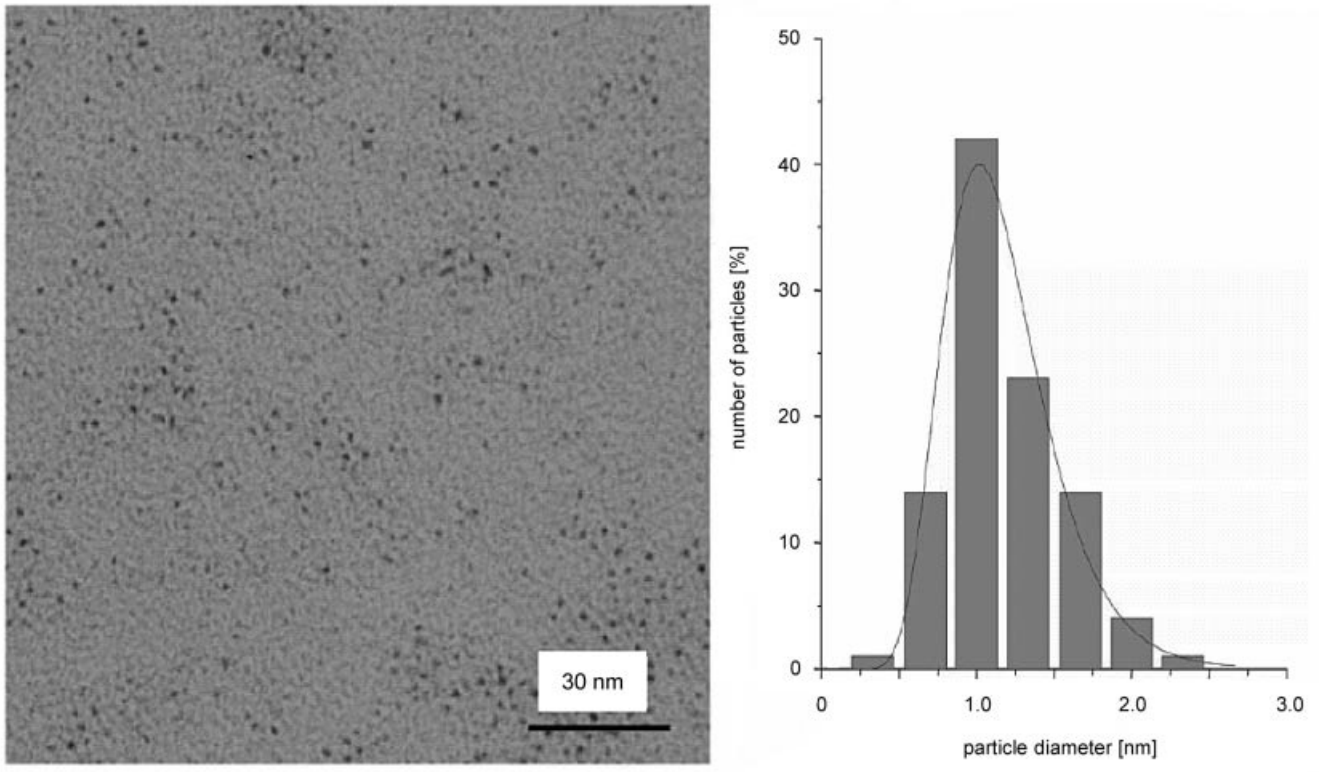

Figure 3. a) TEM image of Pt colloid particles and b) the corresponding particle size distribution (from ref. 16 with permission from IUCr).

While the energy balance of MIES (at least for the AD process) is quite similar to that of UPS (HeI) the depth information of MIES is "zero" because the Auger processes typically take place 4 a.u. in front of the surface and electrons are ejected from species in the outermost layer of the nanoparticles. On the other hand, the depth information of UPS (HeI) is about three monolayers (ML), therefore this technique provides information on the sub-surface region, although averaged over three monolayers. A more detailed introduction to MIES and its various applications in molecular and surface spectroscopy can be found in recent reviews.[23,24] Details of the apparatus employed for the present work can be found elsewhere.[25–27] For the characterization of the chemical composition of the bare surface as well as of films of nanoparticles the apparatus was equipped with a twin anode (Mg/Al) XPS source.

Characterization of Pt Colloids

TEM, ASAXS, and Sorption Analysis

A TEM image of the Pt colloid sample used and the respective particle size distribution is shown in Figure 3. The particles have an average diameter of 1.2 nm.

The particle sizes were confirmed by small-angle X-ray scattering experiments. The particle sizes determined for the Pt colloids by ASAXS were 1.2 ± 0.06 nm. The average distance between neighboring Pt particles in this solid was determined by ASAXS to be 0.36 nm. Assuming a direct contact between the protected particles, the thickness of the protective layer is thus 0.18 nm.

After evaporation of the solvent, nitrogen sorption experiments on the obtained powder resulted in specific surface areas (BET) in the range of only a few square meters per gram. From geometric considerations, spherical 1.2-nm Pt particles should have a specific surface area of about $230\ m^2\,g^{-1}$. This discrepancy can be explained by the extremely small voids that form between densely packed particles of this size − the nitrogen molecules are simply too large to fit into these voids. Thus, only the external surface areas of the Pt particle aggregates contribute to the BET surface area. The majority of the colloid particle surfaces are inside the aggregates and thus not accessible to the nitrogen.

XAFS Characterization of Particles Before Networking

Figure 4 shows the Pt L_3-edge XANES spectra of the Pt nanoparticles that, along with the spacer molecules, form the basic building blocks of the cross-linked systems under investigation in this study. Evidently, clear differences with the reference spectrum of a Pt foil are observed. For example, the characteristic resonances of the reference spectrum are present, but strongly damped. This is to be expected for nanoscaled systems. One reason for this resides in the large number of surface atoms (in this case about 75%) that do not possess complete nearest neighbor shells and for which surface relaxation effects prevent the ideal coherent addition of scattering paths. In addition, nanoscaled particles

 © 2005 Wiley-VCH Verlag GmbH & Co. KGaA, Weinheim

frequently show increased local disorder, which is not described well using the standard Debye–Waller factor approach due to its partially anharmonic nature. A detailed discussion of such effects on nanoparticles[28–30] and a thorough general discussion of the consequences of such inharmonicity[31] can be found in the literature.

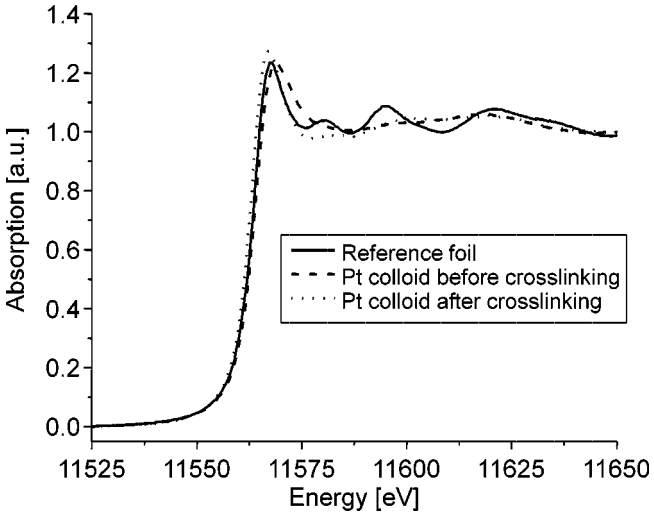

Figure 4. Pt L_3 XANES spectra of (top to bottom): Pt reference foil, Al-organically stabilized Pt colloid after cross-linking with sebacic acid, the same material before cross-linking. Measurements were performed at CAMD.

Intuitively less to be expected are the changes observed in the white-line area, where electronic rather than geometric structure is probed. The maximum intensity of the white-line feature is slightly reduced and shifted to higher excitation energy and features a less-steep slope to the high energy side. Calculations performed in the context of a previous in situ study on the synthesis of such particles[32] suggest that this can indicate an effect of a Pt–Al coordination to surface atoms.

These results are in agreement with the corresponding EXAFS analysis, whose results are summarized in Figure 5 and Table 1: in addition to the expected Pt–Pt coordination at a distance, which is slightly reduced relative to the Pt–Pt distance encountered in bulk Pt, an additional backscatterer located at a distance of about 2.5 Å is needed in order to achieve a fit with reasonably good quality. Clearly, this distance is too high for a second row element such as O or C, but is in good accordance with the distance expected for a coordinated Al atom. A more detailed discussion of the EXAFS analysis of the particles before cross-linking can be found in a previous publication.[33]

MIES and UPS

The concept of the surface characterization of nanoparticles is as follows. Normally, the metal particles need a "shell" that serves two purposes:

· *Passivation*: the long-term stability of the metal particles (the magnetic particles Fe, Ni, and Co in particular) against

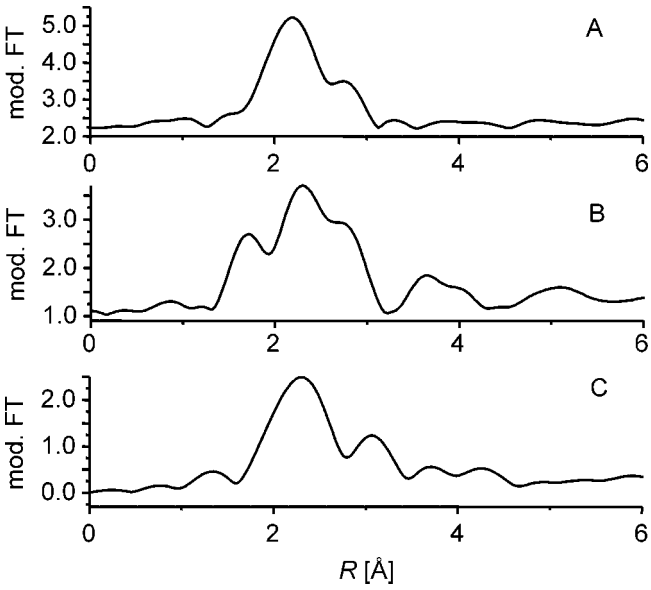

Figure 5. Non-phase-corrected radial distribution functions of (from top to bottom): a) the colloid before cross-linking, b) the colloid network with sebacic acid spacer, c) the colloid networked with HBP.

air and/or moisture has to be guaranteed prior to their integration into a nanoparticle network or, more generally, into a nanostructure;

· *Anchor Function*: the shell must allow for the reliable embedding of the nanoparticles into the custom-designed network, i.e. for the reliable interlinking of the particles in the network by "spacer" molecules.

In general, a two-step procedure must be pursued in order to get information on the composition and the electronic structure of the particles' shell:

· A planar film of the species from which the nanoparticles, Pt in the present case, are composed, has to be studied by MIES and UPS, eventually supported by techniques that give additional information on the chemical composition of the metal film prior to and after being subjected to the shell molecules (XPS), and on the film topology (STM). Then, the interaction of selected atomic and/or molecular species ("shell molecules"; see below) with this film has to be studied in the same way. This step provides "fingerprint spectra" that provide structural information that can be compared with that obtained in the second step on the nanoparticles from the same species as those that constitute the film, and also provide structural information on those molecules that potentially form the shell of the nanoparticles.

· The corresponding analysis is performed on the nanoparticles, which normally possess a shell resulting from wet-chemical procedures. An obvious complication arises from the fact that the composition of the shell produced in this way is, a priori, unknown, i.e. normally cannot be predicted on the basis of the wet-chemical procedures alone. A comparison of the results from the second step with a series of "fingerprint spectra", which have either been gathered in

 © 2005 Wiley-VCH Verlag GmbH & Co. KGaA, Weinheim

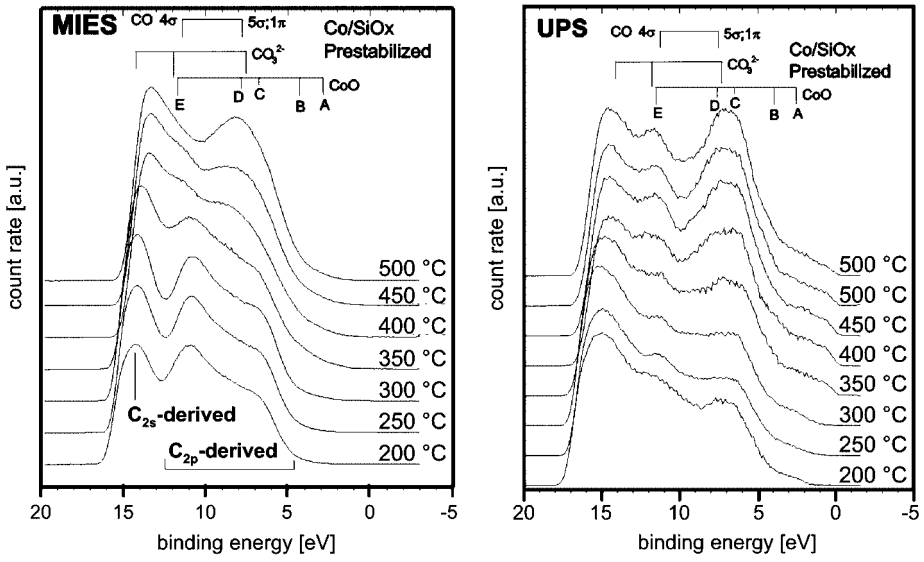

Figure 6. MIES and UPS spectra of Co nanoparticles pre-stabilized by soft oxidation. Deposition on SiO_x. The substrate temperature after deposition was varied between 200 and 500 °C.

the first step or are already available in the literature, is required.

For didactic reasons, the details of the above-mentioned procedure will be illustrated for Co nanoparticles possessing a shell produced by "soft oxidation". First, Co films were produced on SiO_x. These films were then exposed to O_2, CO, and CO_2 with in situ control by MIES/UPS. A detailed presentation of the results and their interpretation can be found elsewhere.[34] Secondly, pre-stabilized Co nanoparticles were deposited on SiO_x substrates from suspensions in toluene.[35] STM indicated that a closed layer of the particles was obtained. Figure 6 displays the MIES (a) and UPS (b) spectra of the surface-deposited, pre-stabilized Co nanoparticles as a function of surface temperature. Also shown are the energetic positions of the main structures resulting from step (1). For completeness, we have also indicated where the spectral features from carbonate (CO_3) groups bound to metallic surfaces[36] should be seen.

Below 250 °C some emission must still be attributed to the ionization of π-type MOs from the aromatic rings of residual toluene solvent molecules on the surface of the particles. From the comparison of the results at higher temperatures with those for gas-exposed planar Co films we estimate that most of the intensity observed in the valence band region (about 70%) is due to (Co–CO_x), with the rest being due to (Co–O) bonds.

For the formation of networks from Pt colloids the existence of an intact Al-organic colloidal protection shell is vital. The reactive methylaluminum groups present in the protecting shell provide the possibility to substitute organic groups at the Al; for the interlinking of the nanoparticles via organic spacer molecules these substituents must be bifunctional. The heating of Al-organic stabilized Pt nanoparticles with in situ control of MIES and UPS (HeI) has provided important information on the thermal properties of the Al-organic stabilization.[37] When heating a colloid network film consisting of Pt nanoparticles cross-linked by hydroquinone spacers, MIES shows the disappearance of the π-emission from the aromatic rings of the spacer molecules at binding energies, E_b, of between 4 and 8 eV. XPS, on the other hand, only indicates a small, unspecific change in the C 1s and O 1s intensities. This suggests the destruction of the spacer molecules (above 200 °C). Moreover, intensity develops at the Fermi level in the MIES spectra. This indicates that the Pt colloids (featuring metallic properties) become accessible to the He* probe atoms utilized for MIES. For temperatures above 200 °C the MIES spectra between E_b = 5 and 10 eV start to resemble more and more those of Al_2O_3 films.[36] This suggests that, as a consequence of the heating procedure, the Pt colloids are surrounded by some sort of (Al–O) network. This implies that most of the emission seen between E_b = 5 and 10 eV after heating would then be due to the ionization of O 2p orbitals from oxygen atoms of the (Al–O) network surrounding the Pt nanoparticles. XPS provides evidence that the Pt nanoparticles are present on the Si substrate employed for deposition up to 600 °C, although they are now stabilized by a Al–O network which has no bifunctional character anymore.

Spacer Molecules

Characterization of the Nanoparticle–Spacer Interaction by MIES and UPS

Some applications require a shell of organic molecules, in particular when the sintering of nanoparticles has to be avoided. Moreover, nanoparticle–organic spacer complexes are natural building blocks for networks of nanoparticles. Both applications impose similar problems for their characterization: the functional group, responsible for the nanoparticle–OM (OM: organic molecule) bond has to be iden-

 © 2005 Wiley-VCH Verlag GmbH & Co. KGaA, Weinheim

tified, and the thermal stability of this bond has to be studied. Essentially the same procedure as described above for the pre-stabilization of the nanoparticles can be pursued, namely a comparison must be made with the fingerprint spectra obtained from the interaction of the same OMs (or at least originating from OMs with the same functional groups) with a planar surface possessing the same termination (the same "shell", see above) as the employed nanoparticles.

Here, we concentrate on the nanoparticle–spacer complexes as the peptization of nanoparticles by long-chain carboxylic acids (possessing a carbonyl group as functional unit) has been dealt with elsewhere.[35]

For illustration, Figure 7 presents MIES and UPS (HeI) spectra for Pt colloids cross-linked by hydroquinone (left) and chlorohydroquinone (right) spacers. For the as-prepared films there is practically no emission for binding energies smaller than 3.5 eV. Together with the fact that the work function of the as-prepared films is 4 eV (as estimated from the low-energy onset of the MIES spectra), we conclude that the studied films possess insulating character, with a bandgap of 7.5 eV. We have not interpreted the MIES/UPS spectra for binding energies above 11.5 eV because this range of binding energies is strongly affected by contributions from secondary and backscattered electrons The coarse structure of the MIES spectra for both networks was identified by comparison with fingerprint spectra available for *p*-CPC films (CPC = *para*-comylphenyl cyanate) on silicon.[38,39] While the MIES/UPS spectra from *p*-CPC show rather well-resolved fine structure due to the ionization of the π-MOs of the aromatic rings in particular, the present spectra show at most indications of a fine structure. From this comparison, we conclude that the emission between 4 and 11 eV is largely due to the ionization of the π- and σ-MOs of the aromatic rings in the spacers. In particular, the emission between 4 and about 8 eV is largely due to the ionization of the π-MOs. Apparently, as the inspection of Figure 7 shows, the main effect of the chlorination of the spacer molecules is a reduction of the emission in the range between 4 and 8 eV, i.e. a reduction in the emission from the ionization of the π-MOs. In addition, we see some fine structure in the MIES spectra in the range E_b = 3 to 7 eV which, as the comparison with the MIES results for 4(2)-CBM (CBM = conduction band minimum) suggests,[40] must be attributed to the ionization of the Cl 3p orbitals.

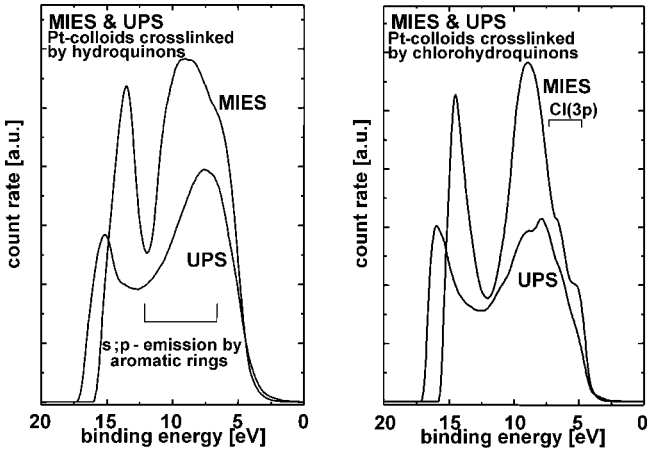

Figure 7. MIES and UPS (HeI) spectra for Al-organic-stabilized Pt colloids cross-linked with hydroquinone (left) and chlorohydroquinone (right) spacers.

Another instructive example for the study of the core–shell interaction is the functionalization of Pd nanoparticles by NR_4Cl molecules (R denotes alkyl groups of different length).[41] The reduction of metal salts with tetraalkylammonium hydrotriorganoborates is a general method for the preparation of metal colloids of elements of groups 6 to 11 in organic solvents. During the colloid formation, the stabilizing tetraalkylammonium salts are formed directly at the reduction center and act as powerful protecting agents for the metal particles. In early publications it was assumed that the protecting groups coordinate to the negatively charged metal cores of the colloid through NR_4 (model 1). The combination of X-ray absorption near edge structure (XANES) measurements with MIES and UPS (HeI) results suggests that the coordination of the stabilizing agent at the particle surface through metal–chlorine bonds is the more appropriate stabilization mode (model 2):[41] if model (1) were applicable, a comparatively well-localized spectral feature from the ionization of the Cl 3p atomic orbital should be seen in the MIES spectra at about E_B = 6 eV because the He* probe atom employed for MIES should interact with the charge cloud of the Cl atom.

Characterization of Pt Colloid Networks

TEM, ASAXS, BET, Modeling

The cross-linked Pt particles form solids which have been investigated by TEM. Comparison of TEM images of the cross-linked samples with those of simply protected Pt colloids show that the particle size of the colloids as well as their monodispersity have not changed after cross-linking (see Figure 8). Furthermore, particles seem to have larger distances between each other if larger spacer molecules are used.

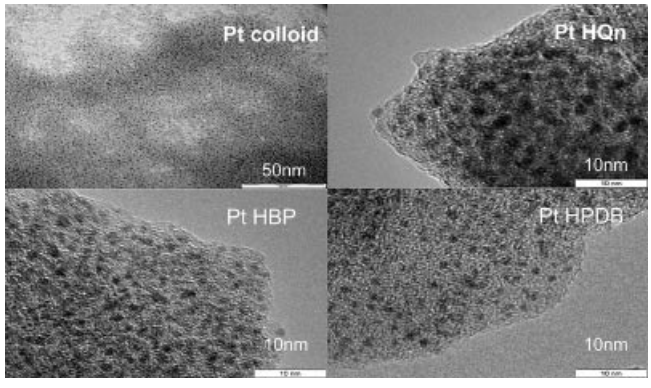

Figure 8. TEM images of protected Pt colloid particles and Pt particles cross-linked with HQn, HBP, and HPDB.

 © 2005 Wiley-VCH Verlag GmbH & Co. KGaA, Weinheim

Because of the large side-chains of Pt/HBDB and Pt/HPDP, one might expect a more linear rather than a three-dimensional network. The TEM images of these samples indeed show areas where one could assume such a chain-like linear arrangement of the particles. The particles are lined up in one direction with more or less identical distances (see part d of Figure 8).

Nitrogen sorption analyses have been used to investigate whether accessible pore systems are obtained after the cross-linking of the Pt particles. The results show that a mesopore system is formed for Pt/HBP (50 °C) with an average pore size of about 31 nm and a pore volume of 0.4680 $cm^3 g^{-1}$. For Pt/HBP2 (25 °C), the pore volume is only 0.0696 $cm^3 g^{-1}$ with an average pore size of only 18 nm. These results show that the temperature applied during the network formation has an influence on the density of the pore system formed. For the networks with the larger molecules HBDP and HPDP, the amount of nitrogen adsorbed in physisorption experiments is extremely low, indicating that no accessible pore system has formed. This can be explained by the large -$OC_{12}H_{25}$ side-chains of the spacer molecules which probably block the pore entrances and the space between the colloid particles.

The small-angle X-ray scattering curves of different cross-linked samples at different energies (ASAXS) are shown in Figure 9.

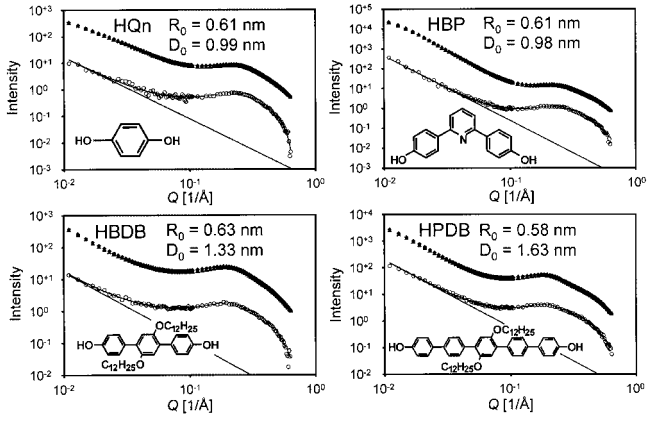

Figure 9. ASAXS curves of Pt particles cross-linked with different spacer molecules. For each plot, the lower curve (circles) is always the difference between the two upper curves (triangles) measured at two different energies (11437 and 11535 eV).

For the modeling of the scattering curves, a modified version of the so-called local monodisperse approximation (Pedersen[42]) is used:

$$\frac{d\sigma}{d\Omega}(Q) = \Delta\rho^2 \int_0^\infty N(D)\left(\int_0^\infty \Phi^2(Q,R)S(Q,R,D,t_{PS})N(R)dR\right)dD$$

where $\Delta\rho^2$ is the scattering contrast, and t_{PS} (= 0.18 nm) is the thickness of the Al-organic protecting shell, which was determined in an earlier study.[16] $\Phi^2(Q,R)$ is the particle form-factor for a sphere of radius R, where

$$\Phi(Q,R) = 3\frac{\sin(QR) - QR\cos(QR)}{(QR)^3}V_0(R),$$

and $V_0(R)$ is the particle volume. $N(R)$ is the log-normal size distribution of the platinum particles

$$N(R) = \frac{1}{\sqrt{2\pi}\sigma R}\exp\left[-\frac{1}{2\sigma^2}\ln^2\left(\frac{R}{R_0}\right)\right],$$

where σ is the half-width at half maximum (HWHM) parameter of the size distribution, and R_0 is the most frequently occurring radius. $N(D)$ is the distribution of the surface-to-surface distances D, which has to be taken into account due to the high flexibility of the spacer molecules. Here, $N(D)$ is modeled by the Gaussian distribution

$$N(D) = \frac{1}{\sqrt{2\pi}\sigma_g}\exp\left[-\frac{1}{2\sigma_g^2}(D - D_0)^2\right],$$

where D_0 denotes the mean distance (spacer–molecule length) between two particles and σ_g is the HWHM of the Gaussian distribution. The structure factor $S(Q, R, D, t_{PS})$ is given by

$$S(Q,R,D,t_{PS}) = (1 + 24\eta G(QL)/(QL))^{-1},$$

(see, for example, Kinning and Thomas[43]), where L is the distance between two particles of radius R,

$$L = 2R + 2t_{PS} + D,$$

η is the volume fraction of a sphere of radius $L/2$, and

$$G(A) = \alpha(\sin(A) - A\cos(A))/A^2 + \beta(2A\sin(A) + (2 - A^2)\cos(A) - 2)/A^3 + \gamma(-A^4\cos(A) + 4[(3A^2 - 6)\cos(A) + (A^3 - 6A)\sin(A) + 6])/A^5$$

with

$$\alpha = (1 + 2\eta)^2/(1 - \eta)^4$$
$$\beta = -6\eta(1 + \eta/2)^2/(1 - \eta)^2$$
$$\gamma = \eta\alpha/2.$$

The scattering behavior at low Q-values is modeled by a Q^{-p} power law, where p is the Porod exponent. This power law provides information on the whole particle system in the sample. The refined structure parameters for the seven samples are given in Table 2.

The Pt particle radii, R_0, as well as the polydispersities, σ, of all samples are in excellent agreement with one another. This can be expected, since the Pt particles used for the preparation of the nanoparticle networks stem from the same synthesis. The scattering contrast parameters, $\Delta\rho^2$, reflect, in general, the different volume fractions of the nanoparticle networks, and show therefore the same trend as the η parameters. The surface-to-surface distances, D_0, show partly significant differences between samples where the same spacer molecule was used for the interconnection of the Pt particles (HPDB, HPDB-2, and HBDB, HBDB-2).

 © 2005 Wiley-VCH Verlag GmbH & Co. KGaA, Weinheim

Table 2. Refined structure parameters for a Pt colloid cross-linked with different spacer molecules according to the Pedersen model.

Sample	R_0 [nm]	σ	D_0 [nm]	σ_g [nm]	$\Delta\rho$ [10^{-4} nm^{-2}]	η	P
HQn	0.50(9)	0.021(8)	0.59(3)	0.10(1)	2.02(2)	0.142(7)	2.07(13)
HBP	0.50(9)	0.021(12)	0.64(3)	0.01(1)	1.82(3)	0.135(12)	3.18(11)
HBP-2	0.51(9)	0.021(9)	0.70(2)	0.01(1)	1.93(2)	0.139(8)	3.22(8)
HBDB	0.52(9)	0.020(8)	0.70(6)	0.01(1)	1.17(3)	0.108(9)	1.90(12)
HBDB-2	0.53(6)	0.019(5)	1.00(5)	0.07(4)	1.39(1)	0.118(6)	2.04(11)
HPDB	0.54(4)	0.020(3)	1.29(9)	0.37(9)	2.05(2)	0.143(7)	2.37(5)
HPDB-2	0.54(5)	0.021(4)	0.96(6)	0.30(1)	1.28(1)	0.113(5)	2.43(16)

The HWHM parameters, σ_g, are also quite different, so that the distance distributions range from almost delta-shaped functions (σ_g = 0.01 nm) to quite broad distributions (σ_g = 0.37 nm). These findings may indicate that these flexible and rather complex spacer molecules are extremely sensitive to small differences in the sample preparation process. The Porod exponents, p, show that the nanoparticle networks of most samples form chain-like structures ($p \approx 2$), and only for the samples HBP and HBP-2 is an exponent of $p \approx 3$ obtained, which indicates the formation of more compact structures (e.g., surface fractals). In order to crosscheck the conclusions drawn from the Porod exponents, the pair-correlation functions $g(r)$ were calculated from the structure factors according to

$$g(r) = 1 + \frac{1}{2\pi^2 c_0}\int_0^\infty (S(Q,R,t_{PS},D) - 1)\frac{\sin(Qr)}{Qr}Q^2 dQ\,.$$

The Pt particle concentration, c_0, is readily obtained from the relation

$$c_0 = \frac{\eta}{V_{HS}}$$

where the hard-sphere volume, V_{HS}, is given by

$$V_{HS} = \frac{\pi}{6}\int_0^\infty N(D)\left(\int_0^\infty N(R)L^3 dR\right)dD$$

$$= \frac{\pi}{6}\int_0^\infty N(D)\left(\int_0^\infty N(R)[2R + 2t_{PS} + D]^3 dR\right)dD\,.$$

Formal coordination numbers $\langle Z\rangle$ are obtained by integration of $g(r)$ over the volume of the first coordination shell:

$$\langle Z\rangle = 4\pi c_0 \int_{r_0-\Delta}^{r_0+\Delta} g(r) r^2 dr$$

where $g(r_0) = max$, and 2Δ is the total width of the coordination peak. Although the coordination numbers will probably not be correct on an absolute scale due to the influence of the polydispersities of the particles and the spacer molecules on the shape of the coordination peak, a qualitative comparison between the different samples is still possible.[16]

The particle concentrations, c_0, hard-sphere volumes, coordination-peak positions, r_0, and the average coordination numbers $\langle Z\rangle$ are given in Table 3.

Table 3. Particle concentrations, c_0, hard-sphere volumes, coordination-peak positions, r_0, and the average coordination numbers, $\langle Z\rangle$, of Pt particles cross-linked with different spacer molecules.

Sample	c_0 [10^{-2} nm^{-3}]	V_{HS} [10^1 nm^3]	r_0 [nm]	$\langle Z\rangle$
HQn	3.38(68)	0.42(8)	2.4(5)	2.4(4)
HBP	3.00(60)	0.45(9)	2.5(5)	2.1(4)
HBP-2	2.83(56)	0.49(9)	2.5(5)	2.2(4)
HBDB	2.10(42)	0.51(10)	2.6(5)	1.6(3)
HBDB-2	1.51(30)	0.79(15)	2.9(6)	1.6(3)
HPDB	1.24(25)	1.16(23)	3.3(6)	2.2(5)
HPDB-2	1.43(28)	0.79(15)	3.0(6)	1.8(4)

The lowest values for the coordination numbers are obtained for those samples with lowest Porod exponents, and higher coordination numbers correspond to larger Porod exponents, i.e. to the networks forming more compact structures. Thus, the results confirm that the scattering contributions at low Q-values are sufficiently well described by the power laws and that the above conclusions are obviously correct.

A further crosscheck of the least-squares results can be obtained from the Fourier transform of the SAXS intensities, the so-called radial distance distribution function[44]

$$\gamma(r) = \frac{r^2}{J_0}\int_0^\infty \frac{d\sigma}{d\Omega}(Q)\frac{\sin(Qr)}{Qr}Q^2 dQ\,,$$

where J_0 is the total scattering power

$$J_0 = \int_0^\infty \frac{d\sigma}{d\Omega}(Q)Q^2 dQ\,.$$

This function contains information on the particle sizes, and interparticle distances. Here, the particle radii are simply given by the corresponding maxima of the first peaks at $\gamma(r = R_1)$. Together with the maxima of the second peaks (at $r = R_2$), the interparticle distances ($d = R_2 - R_1$) and the surface-to-surface distances ($D_0 = d - 2R_1 - 2t_{PS}$) are readily obtained.[16] These values are of course only crude approximations, since the determination of particle radii and/or interparticle distances from the radial distance distribution functions is only reasonable for the case of monodisperse particle systems. Table 4 summarizes the results from the analysis of the distance distribution functions. The parameters are found to be consistent with those obtained from the least-squares analysis, and the significant differences in the D_0 compared to the least-squares results can be attributed to the influence of the particle-size and

 © 2005 Wiley-VCH Verlag GmbH & Co. KGaA, Weinheim

spacer-length distributions, as well as the moderate data quality (the average relative e.s.d.'s for the SAXS intensities are around 15%), which is also reflected by the fairly large e.s.d's of the refined least-squares model parameters (see Table 4).

Table 4. Structure parameters of Pt particles cross-linked with different spacer molecules calculated by the Fourier transform method.

Sample	J_0 [cm^{-1} nm^{-3}]	R_1 [nm]	R_2 [nm]	d [nm]	D_0 [nm]
HQn	20(1)	0.6(1)	3.0(1)	2.4(2)	0.8(3)
HBP	15(1)	0.6(1)	3.0(1)	2.4(2)	0.8(3)
HBP-2	53(1)	0.6(1)	3.1(1)	2.5(2)	0.9(3)
HBDB	45(1)	0.6(1)	3.4(1)	2.8(2)	1.2(3)
HBDB-2	65(1)	0.6(1)	4.0(1)	3.4(2)	1.8(3)
HPDB	135(27)	0.6(1)	4.0(1)	3.4(2)	1.8(3)
HPDB-2	52(1)	0.7(1)	4.1(1)	3.4(2)	1.6(3)

Modeling of the Pt–Spacer Interaction

The interparticle distances analyzed by ASAXS were compared to those calculated from constructed Pt network structures. The spacer lengths were calculated using the MNDO method.[45] The construction of the network structures is based on the assumption of the presence of an Al-organic monolayer on the particle surface, while the corresponding bond lengths were taken from the literature and the Cambridge Structural Database: (1) Al–Pt: 0.232 nm;[46] (2) Al–C: 0.187 nm; (3) Al–O: 0.232 nm. The thus-constructed Pt nanoparticles (1.2 nm) with the cross-linked spacers BDM and HPDB are illustrated in Figures 10 and 11, respectively.

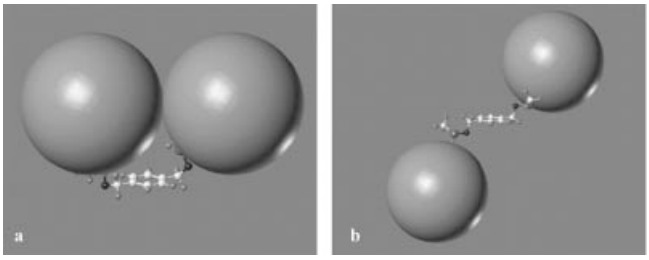

Figure 10. Modeled Pt–spacer–Pt units with BDM as the spacer: a) the minimum interparticle distance; b) the maximum interparticle distance.

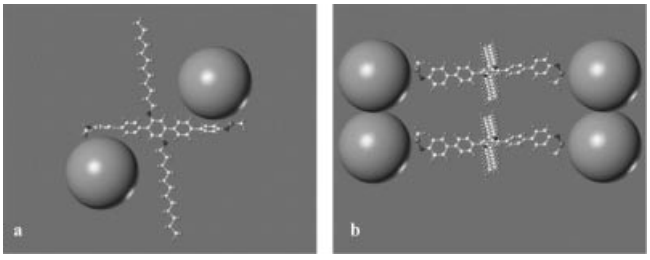

Figure 11. Modeled Pt–spacer–Pt units with HPDB as the spacer: a) the minimum interparticle distance; b) the maximum interparticle distance (another extreme case of minimum particle distance between different interlaced subunits is also shown).

Considering the rotation of Al–O bonds, two extremes are possible, namely the minimum and maximum interparticle distance, although another extreme case of minimum interparticle distance between different interlaced subunits is also shown in Figure 11b. Thus, one has to keep in mind that interparticle distances do not necessarily correspond to the length of the molecular spacers in the obtained network. The more flexible the spacer molecules and the anchoring group, the broader the particle–particle distance distribution is expected to be.

XAFS Characterization of Networked Particles

X-ray absorption spectroscopy can contribute in two ways to the characterization of networked particles, either indirectly, as the (partial) decomposition of the surfactant shell in a networked system should lead to notably reduced rates of agglomeration, and directly, if changes in the electronic structure and the geometry of the metal particles are observed. The indirect characterization is discussed in detail in ref.,[47] therefore here only the main results obtained from XAFS are summarized briefly considering Figures 12 and 13.

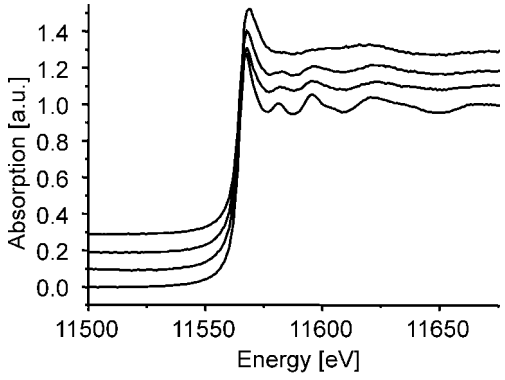

Figure 12. Pt colloid before cross-linking at (from top to bottom) room temperature, 160 °C, and 300 °C in comparison with a Pt foil reference (bottom).

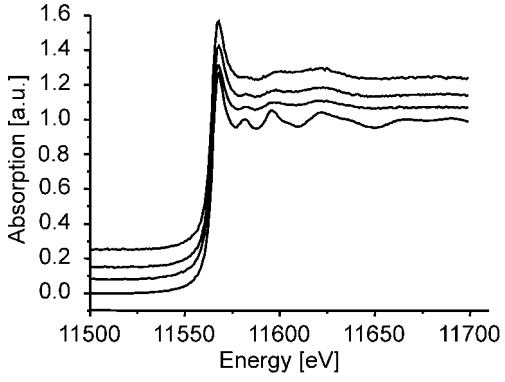

Figure 13. Pt colloid, cross-linked with chlorophenol at (from top to bottom) room temperature, 160 °C, and 300 °C in comparison with a Pt foil reference (bottom).

As the actual intensity of the shape resonances typical for platinum metal allows a rough qualitative estimate of the particle size and degree of ordering present in the sam-

 © 2005 Wiley-VCH Verlag GmbH & Co. KGaA, Weinheim

ple, size-effects and effects of varying spacer molecules at different temperatures can be separated from each other. Only for the unmodified colloid does one observe a significant increase in the intensity of the shape resonances starting at 160 °C, which indicates that the particles undergo significant agglomeration processes at this temperature. In contrast to that, the system with a chlorophenol spacer shows a much smaller trend towards agglomeration even at 300 °C.

At the same time, it is worth noting that the room temperature spectra displayed in Figures 12 and 13 show differences in the white-line region, especially the maximum intensity of the white line and the shape of its high energy slope. The different white-line features change as a function of time in different ways: whereas the agglomerating particles feature a more and more intense white line upon approaching a status more similar to the bulk, the reverse is observed in the cross-linked system. This proves that the observed temperature-dependent changes in the electronic structure shown in Figures 12 and 13 are predominantly due to changes in the decomposing surfactant shell of the colloidal particles, whereas the spacers effectively prevent agglomeration.

With respect to the direct characterization, at first sight it may seem surprising that any changes in the structure of the particles occur at all as a consequence of the networking process even though such changes are clearly visible, as evident from the example presented in Figure 4, where the white-line intensity is increased notably and appears slightly shifted to lower energy, whereas the shape resonance region of the spectra is hardly influenced by the network formation with this type of spacer molecule. TEM studies verify that, in contrast to the situation encountered after the system has been exposed to thermal stress, which was discussed in the above paragraph, the geometry parameters of the individual cores, such as size and shape, remain identical. In addition, the connection of individual metal cores by spacer molecules leads to a preferred interparticular distance although not (necessarily) to a highly ordered long range structure, in which modification of electronic structure can be envisioned due to the necessity to introduce periodic boundary conditions.

Nevertheless, on looking at the Pt L_3-edge XANES spectra displayed in Figure 4 it is evident that the effects of spacer-induced changes in the electronic structure are observed. Therefore, the only explanation for such changes is that the surfactant shell around the particle core is restructured, either geometrically or with respect to the charge distribution, in such a way that considerable influence is exerted on the metal atoms. It is important to stress the implications of this statement, because it means that information on the particle size and shape [as obtained typically from TEM, but also using (A)SAXS] and the nature of the core [as obtained frequently using a diffraction-based technique, such as XRD (X-ray diffraction) or SAED (selected area electron diffraction)] is not sufficient to describe the nature of a nanoparticle, which in turn explains why the macroscopic (e.g. magnetic) properties determined by different researchers on particles of equal size and phase can vary drastically. In fact, a number of theoretical predictions and experimental results based on various experimental techniques,[48–51] including X-ray absorption spectroscopy,[52–57] can be found in the literature to describe such effects. Specifically, a more detailed review on such effects in general is found in ref.,[28] the width of accessible modifications. for example for the case of Co nanoparticles, is discussed in ref.,[56] and a detailed model how these changes influence electronic structure in terms of magnetic properties of Co particles is presented in ref.[57]

Returning to the class of particles discussed in this work, clearly such a modification must be traceable even more directly in the aluminum organic shell. In fact, as shown for selected examples in Figure 14, and discussed in more detail in ref.,[33] the cross-linking with sebacic acid leads to a dramatic change in the electronic structure of Al, increasing the intensity of the white-line drastically and shifting its energy position to a value typical for sixfold (oxygen) coordinated Al. At the same time, the changes induced by cross-linking with a mixture of decanol and sebacic acid spacers lead to a similar trend in the spectra, but to a notably smaller extent. All of these experimental results underline that a spacer-dependent, controlled change in the protection shell is in fact observed, which is especially pronounced when sebacylic acid is used, which leads to a didentate coordination of the spacer to the Al and a sixfold oxygen coordination, but less significant when the connection between the aluminum organic shell and spacer molecule involves just the OH bond.

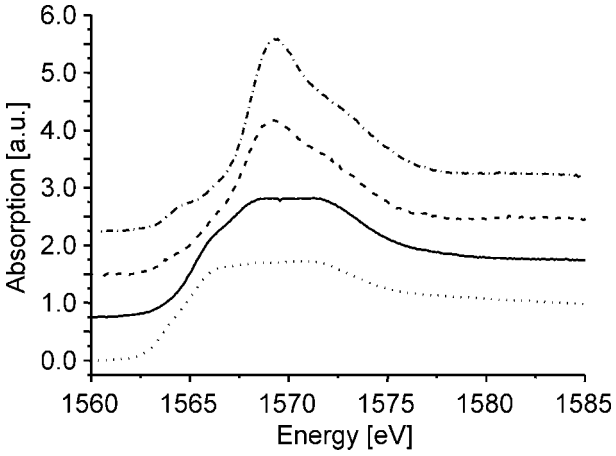

Figure 14. Al K XANES spectra of (from top to bottom) a Pt colloid networked with sebacic acid, the same networked with a mixture of decanol and sebacic acid, the same before networking, and trioctylaluminum.

As discussed in ref.,[33] an almost identical behavior is observed for a related system based on Co nanoparticle precursors, emphasizing once again that one is dealing with a spacer-induced effect on the aluminum organic shell that is dependent on the exact nature of the spacer molecule.

In fact, these differences are also reflected in the Pt L_3 EXAFS evaluation of particles after cross-linking with sebacic acid and HBP, respectively, as shown in Figure 5.

 © 2005 Wiley-VCH Verlag GmbH & Co. KGaA, Weinheim

Table 1 compares the results of this analysis for two such particles, one cross-linked with sebacic acid and the other with HBP. In contrast to the situation encountered for sebacic acid, where it is necessary to use an additional soft backscatterer like oxygen in the fit, this is not the case for HBP. At the same time, the presence of the HBP spacer seems to influence the Pt–Pt distance, which differs beyond the uncertainty of the fitting result and is increased almost to bulk level. As the core of the particles is only 1.2 nm in diameter, such a change can easily be attributed to a variation in core–surfactant interaction as a function of the local charge density on the aluminum atom. Consequently, a controlled tuning of the structure of the Pt core appears possible by choosing the spacer molecules. In fact, the multiplicity of choices becomes evident when looking at the variety of spectral signatures in the white-line region as a function of the spacer molecule, as shown in Figure 15. In combination with a detailed understanding of such effects, this may open a novel approach towards catalysts that are optimized in terms of both activity and accessibility of the catalytic centers.

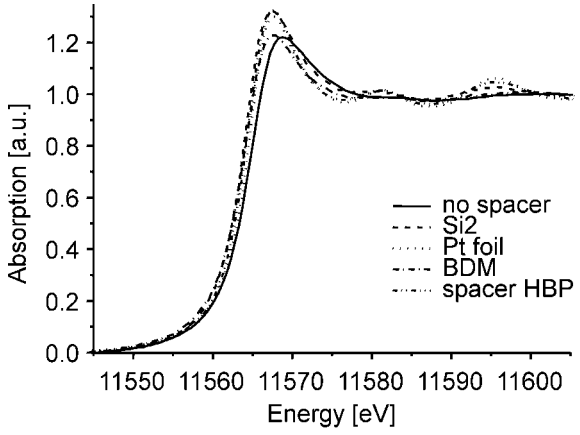

Figure 15. Pt L_3 XANES spectra of colloids with varying spacer molecules and a foil reference.

MIES and UPS Investigations

The obvious problems faced during the characterization of nanoparticle networks produced by a "bottom-up" strategy are threefold:

· Verification of the presence of the spacer molecules in the assembled network;

· Given the presence of the spacers in the nanoparticle–spacer compound, the bonding between the nanoparticles and the spacers needs to be verified;

· The verification of an ordered network composed of nanoparticles and spacers.

As far as the first point is concerned, the main task to be done is to distinguish between the spectral contributions from the organic molecules (OMs) of the particle's shell (Al-organic stabilization in the present case) and those from the spacers. A simple approach is the use of appropriately labeled spacers, i.e. those having a particular ligand atom attached to that produces a clear spectral signature that is well-separated from any of those from the OMs present in the shell. This strategy is similar to that illustrated above for the study of the interaction between and Pt and Pd nanoparticles with their respective protection shells (see above).

The verification of a link between a spacer and adjacent nanoparticles follows the strategy outlined above for obtaining information on the bond formation between nanoparticles and species forming their shell or between nanoparticles and spacer molecules. As a necessary condition, it can be stated that no free, unreacted functional groups (intended for bond formation with the nanoparticles) should be detectable by MIES. However, it is advisable to obtain topological information on the existence of an ordered nanoparticle–spacer structure in addition to the electronic structure information. Our strategy consists in combining MIES/UPS with STM and STS.

STM Investigations

For illustration, we present results for Pt nanoparticles interlinked by HBDB spacers. Figure 16 shows the STM results for Pt nanoparticles (about 1 nm average diameter, as determined by TEM) interlinked by the spacer molecules. The average size of the detected, close-packed aggregates is typically 7 nm. However, the ordered array seen in Figure 16 is apparently not that of single Pt nanoparticles separated by spacers, therefore each aggregate must consist of several interlinked Pt nanoparticles. The simplest structural unit producing aggregates of 7 nm consists of six Pt nanoparticles clustered around a central Pt nanoparticle. Interestingly, we find such compact structures very seldom. This indicates that the nanoparticle networks consist mainly of 1D structures, such as chains, that would escape detection by STM. This agrees with the ASAXS results, which indeed indicate that the nanoparticle networks of most samples consist of chain-like structures (see above).

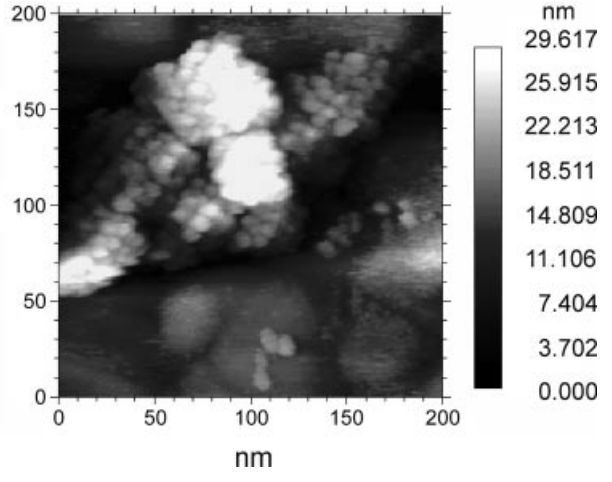

Figure 16. STM image of Pt nanoparticles (average diameter 1 nm) interlinked by HBDB spacers deposited on an Au substrate.

STS measurements, performed as a function of the temperature of the substrate onto which the nanoparticle array is deposited, confirm that the network structure possesses insulating behavior up to 200 °C. More detailed infor-

 © 2005 Wiley-VCH Verlag GmbH & Co. KGaA, Weinheim

mation on the electronic structure of the network is furnished by the MIES/UPS spectra. They confirm the insulating character of the structure, which possesses a bandgap width of about 7 eV and gives spectra (not shown) similar to those of Figure 7.

Summary

Combining different analytical methods, such as TEM, ASAXS, UPS, MIES, XAFS, Sorption analysis, and STM, has allowed us to gain insights into the processes taking place during the network formation of nanoparticles cross-linked with different spacer molecules. Several new spacers with different molecular lengths and rigidity have been used to cross-link Pt colloids via protonolytic reaction to prepare network materials. In general, the materials that form upon cross-linking show no long-range order but rather form network-like structures. When using rigid molecular spacers such as those described above, TEM investigations have revealed that short-length spacers give rise to a densely packed material while long and rigid molecular spacers tend to produce 1D-type structures where the interparticle distance is considerably larger. These results are corroborated by ASAXS investigations. Physical sorption analyses have shown that mesoporous materials are produced for some systems. The shapes of the hysteresis loops of the sorption isotherms strongly depend on the type of molecular spacer used and also on the preparative conditions. Isotherms recorded on products prepared from long-length molecular spacers show that these materials hardly adsorb nitrogen. This is due to the blocking effect from the organic species and poorly defined porous structures. ASAXS measurements have revealed that the interparticle distance only reflects the conformation of the molecular spacers. Varying the preparative conditions with each defined molecular spacer leads to diverse pore structures but identical interparticle distances.

Significant differences between the electronic structures of Pt nanoparticles pre-stabilized with an Al-organic shell and cross-linked particles are observed at room temperature. The properties of the metallic nanoparticles are thus directly influenced by changes of the protective shell. Furthermore, it has proved possible to analyze subtle changes in the protecting shell. Although the Pt colloid modified with 3-chlorohydroquinone differs only in the additional cluster located on the second end of the space molecule, the chlorine can only be detected by MIES in the latter case, thus indicating different equilibrium positions of this molecule. Thermal treatment leads to a disintegration of the spacer molecules, as could be shown by MIES and XANES spectroscopy. A clear trend towards the formation of shape resonances under thermal loads is observed only for the unmodified particles. This indicates that it is driven not by agglomeration but by mere structural reordering within the colloidal metal cores. This agglomeration does not occur as easily for particles that are initially surrounded by spacer molecules, even after destruction of the spacer molecules. It was possible to correlate this observation to a suggested formation of an Al–O protecting shell by MIES.

Acknowledgments

The authors would like to thank Dr. Görigk from the JUSIFA Beamline at the Hasylab, Hamburg, for technical support. Furthermore, we would like to thank Mr. Spliethoff, Mr. Dreier, and Dr. Tesche from the MPI für Kohlenforschung for providing the electron micrographs and Dr. Weidenthaler from the MPI für Kohlenforschung for XPS and XRD investigations. Financial support of the Deutsche Forschungsgemeinschaft, Priority Program SPP 1072 (grant nos. Bo 1135, Ho 887, and Ke 155), and of the Max-Planck-Gesellschaft is gratefully acknowledged.

[1] M. T. Reetz, M. Winter, B. Tesche, *Chem. Commun.* **1997**, 147.
[2] T. Sato, D. Brown, B. F. G. Johnson, *Chem. Commun.* **1997**, 1007.
[3] G. Schmidt, M. Bäumle, N. Beyer, *Angew. Chem. Int. Ed.* **2000**, *39*, 182.
[4] G. Schön, U. Simon, *Colloid Polym. Sci.* **1995**, *273*, 101.
[5] G. Schön, U. Simon, *Colloid Polym. Sci.* **1995**, *273*, 202.
[6] A. Taleb, C. Petit, M. P. Pileni, *Chem. Mater.* **1997**, *9*, 950.
[7] L. Motte, F. Billoudet, E. Lacaze, J. Doulin, M. P. Pileni, *J. Phys. Chem. B* **1997**, *101*, 138.
[8] X. M. Lin, C. M. Sorensen, K. J. Klabunde, *Chem. Mater.* **1999**, *11*, 198.
[9] M. Brust, D. Bethell, D. J. Schiffrin, C. J. Kiely, *Adv. Mater.* **1995**, *7*, 795.
[10] W. Shenton, S. A. Davis, S. Mann, *Adv. Mater.* **1999**, *11*, 449.
[11] S. Connolly, D. Fitzmaurice, *Adv. Mater.* **1999**, *11*, 1202.
[12] B. A. Korgel, S. Fulham, S. Connolly, D. Fitzmaurice, *J. Phys. Chem. B* **1998**, *102*, 8379.
[13] H. Bönnemann, W. Brijoux, R. Brinkmann, U. Endruschat, W. Hofstadt, K. Angermund, *Rev. Roum. Chim.* **1999**, *44*, 1003.
[14] H. Bönnemann, W. Brijoux, R. Brinkmann, German Patent WO 99/59713 (**1999**).
[15] H. Bönnemann, N. Waldöfner, H.-G. Haubold, T. Vad, *Chem. Mater.* **2002**, *14*, 1115.
[16] T. Vad, H.-G. Haubold, N. Waldöfner, H. Bönnemann, *J. Appl. Crystallogr.* **2002**, *35*, 459.
[17] N. Gourdoupi, A. K. Andreopoulou, V. Deimede, J. K. Kallitsis, *Chem. Mater.* **2003**, *15*, 5044.
[18] F. Kakali, J. Kallitsis, T. Pakula, G. Wegner, *Macromolecules* **1998**, *31*, 6190.
[19] H.-G. Haubold, K. Gruenhagen, M. Wagener, H. Jungbluth, H. Heer, A. Pfeil, H. Rongen, G. Brandenberg, R. Moeller, J. Matzerath, P. Hiller, H. Halling, *Rev. Sci. Instr.* **1989**, *60*, 1943.
[20] H. Modrow, S. Bucher, J. Hormes, R. Brinkmann, H. Bönnemann, *J. Phys. Chem. B* **2003**, *107*, 3684.
[21] C. S. S. R. Kumar, M. Aghasyan, H. Modrow, E. Doomes, C. Henke, J. Hormes, R. C. Tittsworth, *J. Nanopart. Res.* **2004**, *6*, 369.
[22] E. A. Stern, M. Newville, B. Ravel, Y. Yacoby, D. Haskel, *Physica B* **1995**, *209*, 117; M. Newville, P. Livins, Y. Yacoby, J. J. Rehr, E. A. Stern, *Phys. Rev. B* **1993**, *47*, 14126; M. Newville, B. Ravel, D. Haskel, E. A. Stern, Y. Yacoby, *Physica B* **1995**, *209*, 145.
[23] Y. Harada, S. Masuda, H. Ozaki, *Chem. Rev.* **1997**, *97*, 1897.
[24] H. Morgner, *Adv. At. Mol. Opt. Phy.* **2000**, *42*, 387.
[25] S. Dieckhoff, V. Schlett, W. Possart, O.-D. Hennemann, J. Günster, V. Kempter, *Appl. Surf. Sci.* **1996**, *103*, 221.
[26] D. Ochs, M. Brause, W. Maus-Friedrichs, V. Kempter, V. Puchin, A. Shluger, L. Kantorovich, *Surf. Sci.* **1996**, *365*, 557.
[27] L. Kantorovich, A. L. Shluger, P. V. Sushko, J. Günster, P. Stracke, D. W. Goodman, V. Kempter, *Faraday Discuss.* **1999**, *114*, 173.

 © 2005 Wiley-VCH Verlag GmbH & Co. KGaA, Weinheim

[28] H. Modrow, *Appl. Spectrosc. Rev.* **2004**, *39*, 183.
[29] A. Di Cicco, M. Berrettoni, S. Stiza, E. Bonetti, G. Cocco, *Phys. Rev. B* **1995**, *50*, 12386.
[30] Y. A. Babanov, L. V. Golovschikova, F. Boscherini, T. Haubold, S. Mobilio, *Nucl. Instrum. Methods. Phys. Res. A* **1995**, *359*, 321.
[31] P. Fornasini, S. A. Beccara, G. Dalba, R. Grisenti, A. Sanson, M. Vaccari, F. Rocca, *Phys. Rev. B* **2004**, *70*, 174301.
[32] K. Angermund, M. Bühl, U. Endruschat, F. T. Mauschick, R. Mörtel, R. Mynott, B. Tesche, N. Waldöfner, H. Bönnemann, G. Köhl, H. Modrow, J. Hormes, E. Dinjus, F. Gassner, H.-G. Haubold, T. Vad, *J. Phys. Chem. B* **2003**, *107*, 7507.
[33] H. Modrow, S. Modrow, J. Hormes, N. Waldöfner, H. Bönnemann, *J. Phys. Chem. B* **2005**, *109*, 900.
[34] M. Frerichs, F. X. Schweiger, M. Maus-Friedrichs, V. Kempter, *Surf. Interface Anal.*, submitted.
[35] S. Rudenkiy, M. Frerichs, F. Voigts, W. Maus-Friedrichs, V. Kempter, R. Brinkmann, N. Matoussevitch, W. Brijoux, H. Bönnemann, N. Palina, H. Modrow, *Appl. Organomet. Chem.* **2004**, *18*, 553.
[36] D. Ochs, M. Brause, W. Maus-Friedrichs, V. Kempter, *J. Electron Spectrosc. Relat. Phenom.* **1998**, *88–91*, 725.
[37] L. Beuermann, W. Maus-Friedrichs, S. Krischok, V. Kempter, S. Bucher, H. Modrow, J. Hormes, N. Waldöfner, H. Bönnemann, *Appl. Organomet. Chem.* **2003**, *17*, 268.
[38] S. Dieckhoff, V. Schlett, W. Possart, O.-D. Hennemann, J. Günster, V. Kempter, *Appl. Surf. Sci.* **1996**, *103*, 221.
[39] S. Dieckhoff, R. Höper, V. Schlett, T. Gesang, W. Possart, O.-D. Hennemann, J. Günster, V. Kempter, *Fresenius J. Anal. Chem.* **1997**, *358*, 258.
[40] J. Stultz, S. Krischok, D. W. Goodman, *Langmuir* **2002**, *18*, 2962.
[41] S. Bucher, J. Hormes, H. Modrow, R. Brinkmann, N. Waldöfner, H. Bönnemann, L. Beuermann, S. Krischok, W. Maus-Friedrichs, V. Kempter, *Surf. Sci.* **2001**, *497*, 321.
[42] J. S. Pedersen, *J. Appl. Crystallogr.* **1994**, *27*, 595.
[43] D. J. Kinning, E. L. Thomas, *Macromolecules* **1984**, *17*, 1712.
[44] L. A. Feigin, D. I. Svergun, *Structure Analysis by Small Angle X-ray and Neutron Scattering*, Plenum Press, New York, **1987**, 38–40.
[45] H. G. Haubold, X. H. Wang, G. Goerigk, W. Schilling, *J. Appl. Crystallogr.* **1997**, *30*, 653.
[46] D. Bakowies, W. Thiel, *J. Comput. Chem.* **1996**, *17*, 87.
[47] L. Beuermann, W. Maus-Friedrichs, S. Krischok, V. Kempter, S. Bucher, H. Modrow, J. Hormes, N. Waldöfner, H. Bönnemann, *Appl. Organomet. Chem.* **2003**, *17*, 268.
[48] C. R. Vestal, Z. J. Zhang, *J. Am. Chem. Soc.* **2003**, *125*, 63.
[49] V. Torma, O. Vidoni, U. Simon, G. Schmid, *Eur. J. Inorg. Chem.* **2003**, 1121.
[50] S. Link, A. Furube, M. B. Mohamed, T. Asahi, H. Masuhara, M. A. El Sayed, *J. Phys. Chem. B* **2002**, *106*, 945.
[51] Y. Diamant, S. G. Chen, O. Melamed, A. Zaban, *J. Phys. Chem. B* **2003**, *107*, 1977.
[52] A. L. Ankudinov, J. J. Rehr, J. Low, S. Bare, *Phys. Rev. Lett.* **2001**, *86*, 1642.
[53] T. Rajh, L. X. Chen, O. Melamed, A. Zaban, *J. Phys. Chem. B* **2002**, *106*, 10543.
[54] P. Zhang, T. K. Sham, *Phys. Rev. Lett.* **2003**, *90*, 245502.
[55] S. Bucher, J. Hormes, H. Modrow, R. Brinkmann, N. Waldöfner, H. Bönnemann, L. Beuermann, S. Krischok, W. Maus-Friedrichs, V. Kempter, *Surf. Sci.* **2002**, *497*, 321.
[56] O. Margeat, C. Amiens, B. Chaudret, P. Lecante, R. E. Benfield, *Chem. Mater.* **2005**, *17*, 107.
[57] J. Hormes, H. Modrow, H. Bönnemann, C. S. S. R. Kumar, *J. Appl. Phys.* in print (**2005**).

Received: May 17, 2005
Published Online: August 24, 2005

 © 2005 Wiley-VCH Verlag GmbH & Co. KGaA, Weinheim

DNA-Based Assembly of Metal Nanoparticles

Christof M. Niemeyer*[a] and Ulrich Simon*[b]

Keywords: DNA / Materials science / Nanoparticles / Self-Assembly / Supramolecular Chemistry

In this microreview we describe the principles of DNA-based assembly of metal nanoparticles in one, two and three dimensions. Different methods of liquid-phase synthesis of metal nanoparticles as well as their functionalisation with DNA are introduced. The concepts developed up to now for the assembly are explained, with selected examples to illustrate the properties of these assemblies as well as emerging applications.
(© Wiley-VCH Verlag GmbH & Co. KGaA, 69451 Weinheim, Germany, 2005)

1. Introduction

Modern chemical synthesis of metal nanoparticles is rooted in the famous experiments of Michael Faraday in the mid-nineteenth century, who showed that the reduction of tetrachloroaurate $[AuCl_4]^-$ with phosphorus as a reducing agent in aqueous solution leads to ruby-red solutions.[1] Today, we know that this reaction leads to the formation of gold nanoparticles in the size range between 3–30 nm,[2] and that the red colour results from the collective oscillation of surface electrons induced by the electric field of the entering light.[3] Since that time many different synthetic routes have been developed in order to obtain metal nanoparticles of different size and shape, all of which, in principle, follow the same strategy, i.e. the reduction of a metal salt in the presence of a stabilizing organic ligand. In the early 1990s these nanoparticles became a new chapter in chemistry. The development of high resolution physical measurements together with the elaboration of theoretical methods applicable to mesoscopic systems brought forth a lot of fascinating ideas about how these nanoparticles can provide new technological breakthroughs, for example in

[a] Universität Dortmund, Fachbereich Chemie, Biologisch-Chemische Mikrostrukturtechnik,
Otto-Hahn Str. 6, 44227 Dortmund
Fax: +49-231-755-7082
E-mail: christof.niemeyer@uni-dortmund.de
[b] Institut für Anorganische Chemie, RWTH Aachen,
Landoltweg 1, 52056 Aachen, Germany
Fax: +49-241-80-99003
E-mail: ulrich.simon@ac.rwth-aachen.de

Ulrich Simon was born in Essen in 1963. He studied chemistry at the University of Essen and obtained his diploma in 1990. In 1992 he obtained his doctorate (Dr. rer. nat.) in Essen and his habilitation in 1999. Since May 2000 he has held the Chair of Inorganic Chemistry and Electrochemistry at the RWTH Aachen University. The main interest of his current research includes the synthesis and electrical properties of metal and semiconductor nanoparticles and of nanoporous materials as well as their application in molecular electronics and chemical sensing.

Christof M. Niemeyer is Professor of Chemistry at the University of Dortmund (Germany) where he holds the chair of Biological and Chemical Microstructuring. He was born in Cloppenburg and studied chemistry at the University of Marburg. His PhD thesis on the development of organometallic receptor molecules at the Max-Planck-Institut für Kohlenforschung in Mülheim/Ruhr under the supervision of Manfred T. Reetz was followed by a postdoctoral fellowship at the Center for Advanced Biotechnology in Boston (USA) with Charles R. Cantor, where he switched research fields to study biomolecular recognition systems. He went back to Germany, where he received his habilitation at the University of Bremen before moving to Dortmund in 2002. He is interested in semisynthetic DNA-protein and nanoparticle-conjugates and their applications in life-sciences, catalysis and molecular nanotechnology.

MICROREVIEWS: This feature introduces the readers to the authors' research through a concise overview of the selected topic. Reference to important work from others in the field is included.

nanoelectronic, diagnostic or sensing devices.[4–10] Basic research has disclosed that nanoparticles exhibit many properties that are somehow between that of a macroscopic solid or bulk material and that of a single atom or molecule.

Nanoparticles with a diameter of between one and several tens of nanometres, which fall in the intermediate size range between molecules and macroscopic solids, exhibit an electronic structure that is somewhere in between the discrete electronic levels of an atom or molecule and the band structure of a bulk material.[11] Although the concept of band structure can still be applied below a certain size these nanoparticles show a size-dependent splitting of the energy levels that replaces the continuum of the energy bands. In this intermediate state matter reveals new physical properties which now depend on the size of the object under consideration. As its origin is in the quantisation of electronic states, this size-dependent change of physical properties is called the *quantum size effect* (QSE) or *size quantisation effect*.

This raises fundamental questions about the design of "artificial molecules" or "artificial solids" built up from nanoscale subunits that finally lead to a new state of matter. This requires the ordered assembly of uniform nanoparticles in one, two or three dimension, leading finally to the formation of an artificial solid or super lattice. Such an array of nanoparticles exhibits delocalised electron states that depend on the strength of the electronic coupling between the adjacent nanoparticles, whereas the electronic coupling depends on the particle size, the nature and the covering density of the stabilizing organic ligands, on the particle spacing, and on the packing symmetry.[11]

Thus it is a great challenge to organize nanoparticles in one to three dimensions in order to study the electronic and optical coupling between the particles, and to even utilize these coupling effects for the set-up of novel nanoelectronic, diagnostic or nanomechanical devices.[9]

Several attempts have been made to assemble metal nanoparticles in one to three dimensions. These range from Langmuir–Blodgett techniques,[12] molecular self-assembly[13] via covalent linkage[14] and electrostatic coupling up to the deposition within or at pre-structured surfaces.[15] However, most of these methods suffer from a lack of recognition and binding specificity.

In contrast, biomolecules, such as proteins and nucleic acids, have almost perfect binding properties and biochemical functionality that have been optimised over billions of years of evolution. Since they are more readily available by synthetic chemical means and are more convenient to handle than proteins, nucleic acids have preferentially been used for the functionalisation of nanoparticles to provide highly specific binding sites.[16,17] Proteins have also been employed to extend the binding capabilities of inorganic nanoparticles, however, instead of simply utilizing their binding properties, a great challenge is the combination of the intrinsic functionality of many proteins, for instance, optic, catalytic, mechanic or switching capabilities, with the distinct properties of nanoparticles.[18] This topic, however, is beyond the scope of this review article, and we will instead focus here on DNA as a construction material in nanosciences.

The enormous specificity of Watson–Crick base-pairing allows the convenient programming of artificial DNA receptor moieties. The power of DNA as a molecular tool is enhanced by our ability to synthesise virtually any DNA sequence by automated methods[19] and to amplify any DNA sequence from microscopic to macroscopic quantities by the polymerase chain reaction (PCR).[20] Another very attractive feature of DNA is the great mechanical rigidity of short double helices, such that they behave effectively like a rigid rod spacer between two tethered functional molecular components on both ends up to approximately 100 nm. Moreover, DNA displays a relatively high physicochemical stability, and Nature provides us with a variety of highly specific enzymes that allow the processing of the DNA material with atomic precision and accuracy on the angstrom level. No other (polymeric) material offers these advantages, which are ideal for molecular construction in the range from about 5 nm up to the micrometer scale. Consequently, DNA has already been used extensively for construction on the nanometre scale,[21] and recent advances indicate its applicability for fabricating nanomechanical devices.[22,23] Hence, DNA holds the promise of allowing the bottom-up self-assembly of complex nanodevices, where, for example, in the course of further miniaturisation, conductive DNA-based structures could reduce time and cost in future nanofabrication.[24]

It is the aim of this microreview to acquaint the reader with the principle of DNA-based assembly of metal nanoparticles. Therefore, the second section introduces the different methods of liquid-phase synthesis of metal nanoparticles and their functionalisation with DNA. The third section will give an overview of the assembly of nanoparticles in one, two and three dimensions. The properties and the emerging applications of these assemblies will be discussed and illustrated with selected examples.

2. Materials Synthesis

2.1. Liquid-Phase Synthesis of Metal Nanoparticles

The synthesis of ligand-stabilized nanoparticles is usually based on the classical routes of colloid or organometallic chemistry. These are suitable for various metals, usually transition metals, as well as for many semiconductors which have technological applications in the bulk state.[7] Besides radiolytic[25] or photochemical[26] techniques and the controlled deposition of metastable organometallic compounds,[27–29] the most common ways of preparation are the chemical reduction of soluble metal salts by suitable reducing agents (e.g., hydrogen, boron hydride, methanol, citric acid, and others), and electrochemical reduction. In order to stabilize the nanoparticles, to control their size and shape and to prevent them from aggregating, organic ligands need to be added. These ligands are typical colloid chemical stabilizers or electron-donor ligands, like amines, phosphanes or thiols, which stabilize the particles electrostatically or ste-

 © 2005 Wiley-VCH Verlag GmbH & Co. KGaA, Weinheim

rically. While the electrostatic stabilisation involves the coulombic repulsion between the particles caused by the charged surface of the nanoparticles and/or by the charge introduced by the respective ligand, steric stabilisation is achieved by ligand molecules that surround the particles as a protective shield. If DNA is used as a ligand, the negative charge of the ribose phosphate backbone introduces negative charge and leads to a predominantly electrostatic stabilisation of the nanoparticles.

The size of the particles is determined by the relative rates of nucleation and particle growth. However, the many control parameters affecting the particle size cannot be analysed separately, so that an established synthesis leading to a well-defined size for one particular metal cannot automatically be transferred to another metal. Nevertheless, many different liquid-phase synthetic routes have been developed which lead to distinct sizes with a narrow particle-size distribution, and which allow the preparation even in multigram scale.

For a detailed description of the synthesis and surface modification of metal nanoparticles the reader might be guided by Daniel and Astruc,[30] Bradley and Schmid,[7] and by Richards and Boennemann.[31] The following chapters will give a brief summary of synthetic routes in the liquid phase, with an emphasis on noble metal nanoparticles, that are typically applied for assembly processes in order to study size and coupling effects.

2.1.1. Chemical Reduction of Metal Salts

The salt reduction route with different types of stabilizing ligands and the wide range of chemical reduction agents has led to a huge variety of metal nanoparticles of different sizes and shapes, with the so-called Schmid cluster $[Au_{55}(PPh_3)_{12}Cl_6]$ being one of the most prominent examples.[32,33] Other examples are $[Pt_{309}phen^*_{36}O_{30}]$[33] or $[Pd_{561}phen_{36}O_{200}]$ (phen* = bathophenanthroline and phen = 1,10-phenanthroline).[34,35] These particles show an extremely narrow particle-size distribution and the idealised formulae of these compounds refer to the so-called geometric magic numbers. According to this model, the metal atoms tend to form a closed geometry of densest sphere packing, where one central atom is surrounded by a closed shell of 12 atoms as next neighbours and a second shell of 42 atoms surrounds this 13-atom arrangement to give a total of 55 atoms, and so on. Larger ligand-stabilized metal nanoparticles are typically not described by their atom number but by their mean diameter, whereas the size distribution typically increases with increasing particle size.

Another approach for the synthesis of nanoparticles involves block copolymers, which are able to form micelles upon addition of a polar or non-polar solvent. These micelles can be regarded as "nanoscopic reactors". After formation of the micelles in a non-polar solvent and addition of a soluble metal salt, the metal ions migrate into the hydrophilic core of the micelles where they are reduced to the metal by addition of a reducing agent. Consequently, the size of the nanoparticles depends on the size of the micelle as well as on the number of metal ions that have been provided to the micelle's core.

As most impressively demonstrated by Möller and coworkers, Au nanoparticles in polystyrene block polyethylene oxide (PS-b-PEO) hexagonally assembled micelles with rather regularly arranged particles 2.5, 4 or 6 nm in diameter can be obtained.[36,37] There, the association of PS-b-PEO for the formation of micelles in a non-polar solvent like toluene was utilized. After adding $LiAuCl_4$ to this solution, the salt was slowly dissolved as the Li^+ ions formed a complex with the polyethylene oxide. Thus, the $AuCl_4$ anions were incorporated as counterions into the micelles, where the nanoparticles were formed by reduction.

2.1.2. Electrochemical Composition of Metal Nanoparticles

An electrochemical route for the synthesis of nanoparticles from Pd or Ni and even from superparamagnetic Co has been developed by Reetz and co-workers.[38] This process, in which the particle size can be controlled in a simple manner by adjustment of the current density, makes use of a simple two-electrode setup in which the sacrificial anode consists of the bulk metal to be transformed into nanoparticles. The supporting electrolyte contains tetraalkylammonium salts, which act as stabilizing ligands in the abovementioned way. Thus, in the overall process the bulk metal is oxidized at the anode, the metal cations migrate to the cathode, and a consecutive reduction takes place with the formation of the ligand-stabilized nanoparticles. Particle sizes in the range of 1.4–4.8 nm and above with a narrow size-distribution can be obtained using this technique. The most striking advantage seems to be the broad variation of the corresponding ligand shell. Since the tetraalkylammonium ions are simply added to the reaction mixture, the thickness of the ligand shell can easily be varied by changing the length of the alkyl chain.

2.2. Synthesis of DNA-Functionalized Nanoparticles

The solid-phase synthesis of DNA oligomers as well as of other native and non-natural nucleic acid derivatives is nowadays routine technology, and DNA sequences up to about 120 nucleotides in length, modified with a large variety of chemical substituents, such as amino and thiol groups attached to the 3′- or 5′-terminus, are readily available by a multitude of commercial suppliers at relatively low costs. These materials are typically used in the synthesis of DNA-modified gold nanoparticles (DNA AuNPs). Most protocols for the synthesis of DNA AuNPs go back to the initial description of these materials by Mirkin and coworkers.[39] Briefly, citrate-stabilized AuNPs are simply mixed with DNA oligomers derivatized with alkylthiol groups at the 3′- or 5′-terminus, incubated for prolonged times of up to several days, and then purified by repeated centrifugation to remove unbound oligomers from the supernatant. The resulting DNA AuNPs are water-soluble and stable for months. Slight variations of the initial protocol have been reported by Mirkin[40] and Niemeyer.[41] The latter, for instance, has reported the synthesis of "oligofunc-

 © 2005 Wiley-VCH Verlag GmbH & Co. KGaA, Weinheim

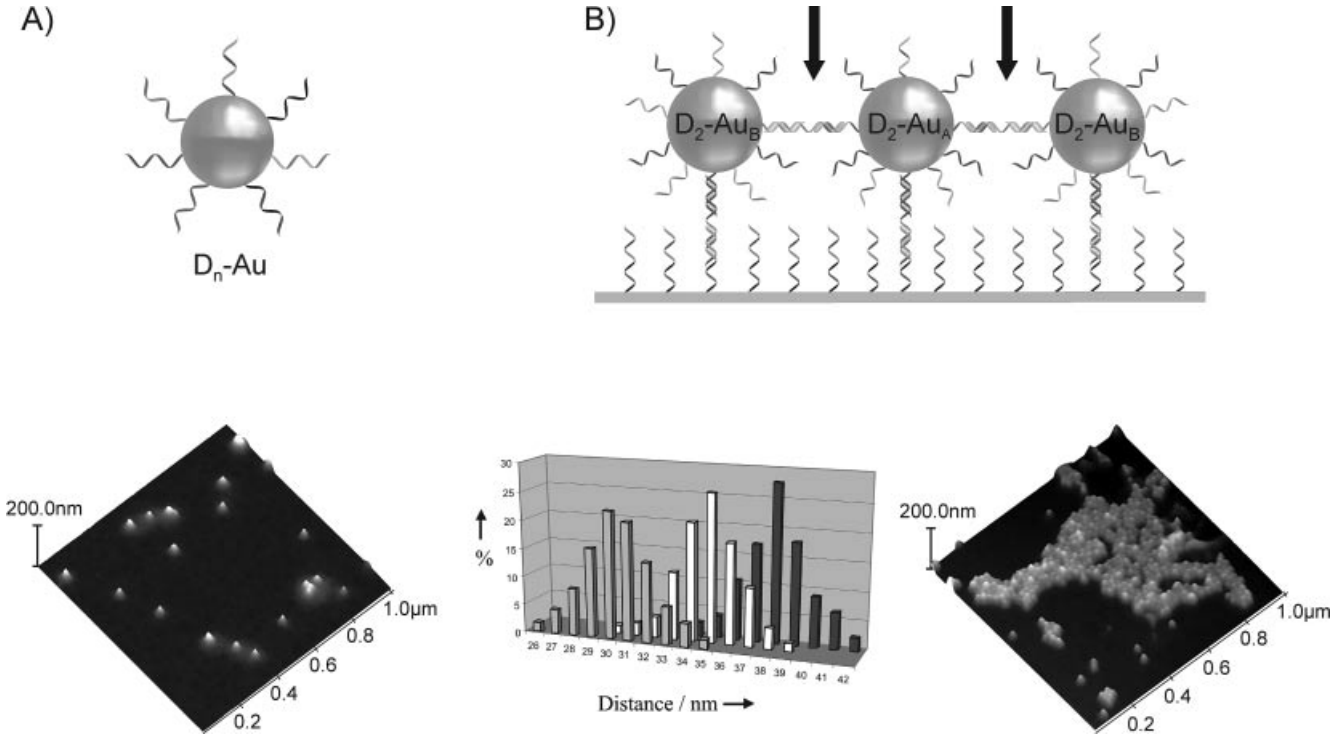

Figure 1. A) Schematic drawing of oligofunctional DNA–gold nanoparticle conjugates (**D_n-Au**) containing various coding oligonucleotides. B) Schematic drawing of DNA-directed immobilisation of cross-linked bifunctional DNA–gold nanoparticles (**D_2-Au**). Two different types of particles (**D_2-Au_A** and **D_2-Au_B**) are immobilized at surface-bound capture oligomers using one of the coding oligonucleotides and are simultaneously cross-linked using the second coding oligonucleotide. Note that both the immobilisation and the interparticle crosslinking is conducted by a trimolecular oligonucleotide linkage. Bottom: AFM images of layer assemblies prepared in the absence (left) or in the presence (right) of crosslinking oligonucleotide.[92] The inset shows the dependency of the particle's centre-to-centre distances on the length of the crosslinking oligomer used.[93]

tional" DNA AuNPs, that contain more than one coding sequence (**D_n-Au** in Figure 1).[42] The index *n* in **D_n-Au** denotes the number of different sequences attached to the nanoparticle, ranging from two (difunctional) up to seven (heptafunctional). The **D_n-Au** nanoparticles reveal almost unaltered hybridisation capabilities as compared to conventional monofunctional conjugates. Due to the extraordinary specificity of Watson–Crick base-pairing, the various oligonucleotide sequences can therefore be individually and selectively addressed as members of an orthogonal coupling system present at the particle's surface.

Applications of such oligofunctional DNA AuNPs are discussed below in Section 3.2.2. It is particularly noteworthy that it is most helpful for many applications to be able to quantify the coverage of the DNA AuNP's surface with DNA oligomers. To achieve this, the fluorescence-based assay of Demers et al.[43] is highly recommended. Moreover, DNA AuNP might, if necessary, be purified by gel electrophoresis, as described by Alivisatos and co-workers.[44,45]

Other approaches have been reported to increase the stability of DNA AuNPs, including the use of polymers[46] and dithiol[47] and trithiol linkers[48] between the DNA moiety and the gold particle. Interestingly, Brust and co-workers have used short peptides with the sequence CALNN to produce very stable AuNPs[49] that can also be further functionalised by attachment of DNA oligomers.

3. Nanoparticle Assemblies & Properties

3.1. Three-Dimensional Assemblies

3.1.1. DNA-Directed Self-Assembly

Following the initial approach of Mirkin's group, DNA hybridisation has been used to generate repetitive, three-dimensionally linked nanoparticle assemblies (Figure 2) where two non-complementary oligonucleotides are coupled in separate reactions with 13-nm gold particles by thiol adsorption.[39] A DNA duplex molecule containing a double-stranded region and two cohesive single-stranded ends, which are complementary to the particle-bound DNA, was used as a linker. Addition of the linker to a mixture of the two oligonucleotide-modified nanoparticles led to the aggregation and slow precipitation of the macroscopic DNA–nanoparticle network. This process is reversible. Since the nanoparticles contain multiple DNA molecules, the oligomerised aggregates are three-dimensionally linked, as can be seen by TEM. Typical images reveal close-packed assemblies of the colloids with uniform particle separations of about 6 nm, corresponding to the length of the DNA linker duplex.

This assembly scheme can also be used for the generation of binary networks comprised of different types of particles. Due to the specificity of Watson–Crick base-pairing, only heterodimeric "A-B" composites of alternating particles are

 © 2005 Wiley-VCH Verlag GmbH & Co. KGaA, Weinheim

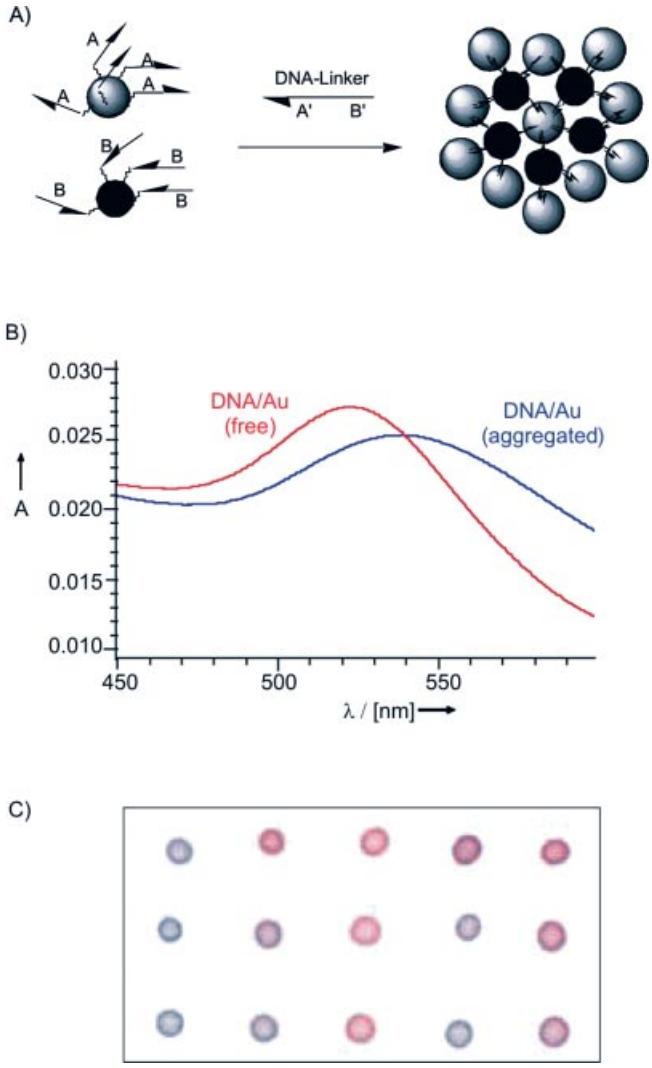

Figure 2. A) Three-dimensional assembly of gold colloids using DNA hybridisation. Two batches of gold particles are derivatized with non-complementary oligonucleotides by either 5′- or 3′-thiol groups. The nanoparticles are oligomerised with a single-stranded nucleic acid linker molecule. Note that only heterodimeric "A–B" linkages are present within the network. B) The network formation leads to a characteristic change in the plasmon absorption. The colour change can be used to macroscopically detect DNA hybridisation using an assay in which DNA/Au conjugates and a sample with potential target DNA is spotted on a hydrophobic membrane. C) Red spots indicate the absence of fully matched DNA, while blue spots are indicative of the presence of complementary target DNA. Data in part C) are reprinted from J.J. Storhoff et al. *Chem. Rev.* **1999**, *99*, 1849–1862. Copyright 1999, American Chemical Society.

formed (Figure 2). For example, two types of gold clusters of either 40 nm or 5 nm diameter have been assembled by DNA hybridisation. In the case of an excess of one particle, satellite-like aggregate structures can be generated and characterised by TEM. Similarly, it has been shown that oligonucleotide-functionalised CdSe/ZnS QDs can be specifically assembled with gold nanoparticles to form binary nanoparticle networks.[50] TEM analysis revealed that the hybrid metal/semiconductor assemblies exhibited the expected A-B structure, and fluorescence and electronic absorption spectroscopy indicated cooperative optical and electronic phenomena within the network materials.

Mirkin et al. have demonstrated that the oligomerisation of DNA-coated gold nanoparticles, depicted in Figure 2, can also be mediated by conjugates comprised of oligonucleotides attached to the streptavidin (STV) protein. Interestingly, the thermodynamically most stable oligomeric networks were only formed upon heating of the kinetically controlled adducts produced initially.[51] Additional topics of fundamental research on DNA/protein nanoparticle interaction concern the investigation of whether and how DNA-functionalised particles can be manipulated by DNA-modifying enzymes.[18] Particles of different morphology, especially rods and sticks, have also been assembled by means of DNA hybridisation.[52,53]

3.1.2. Materials Properties

Studies of DNA-linked gold nanoparticle assemblies concern the influence of the DNA spacer length on the optical,[54] electrical[55] and melting properties[56] of these networks. These experiments provided evidence that the linker length controls the size of the aggregates kinetically, and that the optical properties of the nanoparticle assemblies are governed by aggregate size.[54] In contrast, it has been found that the electrical properties of dry nanoparticle aggregates are not influenced by the linker length.[55] Although SAXS clearly indicates the linker length-dependent distances between particles in solution, the networks collapse upon drying to form bulk materials comprised of nanoparticles covered with an insulating film of DNA. These materials show semiconductor properties that are not influenced by the linker lengths.[55] The strongly cooperative melting effect of the nanoparticle networks[56] results from two key factors: the presence of multiple DNA linkers between each pair of nanoparticles, and a decrease in the melting temperature as DNA strands melt due to a concomitant reduction in local salt concentration. This mechanism, originating from short-range duplex-to-duplex interactions, is independent of DNA base sequences and should be universal for any type of nanostructured probe that is heavily functionalised with oligonucleotides.[56]

3.1.3. Applications

Gold nanoparticles functionalised with proteins have long been used as tools in biosciences.[57] For instance, antibody molecules adsorbed to 10–40-nm colloidal gold are routinely used in histochemistry for the biospecific labelling of certain regions of tissue samples and subsequent TEM analysis. In contrast, applications of DNA-functionalised Au particles were introduced only a few years ago by Mirkin and co-workers.[58] The DNA-directed nanoparticle aggregates depicted in Figure 2 can be used for simple and cheap sensors in biomedical diagnostics, for example for the detection of nucleic acids from pathogenic organisms. Therefore, the major field of applications of AuNP 3D-assemblies concerns the diagnostics of nucleic acid. Many excellent review articles are available[9,16,17,59,60] summarising this field of application. However, most of the analytical

 © 2005 Wiley-VCH Verlag GmbH & Co. KGaA, Weinheim

applications are based on solid-supports (see below), and therefore we will highlight just a few representative examples of 3D assembly in homogeneous solution here.

The sensitive detection of nucleic acids in homogeneous solutions has been achieved by self-assembled oligomerisation[61] or by the use of DNA beacons tethered to nanoparticles.[62] DNA beacons are single-stranded DNA (ssDNA) molecules that form an intramolecular hairpin-loop structure.[63] Both ends are chemically modified with a fluorophore and a quencher dye, the latter of which, due to close spatial proximity, effectively quenches the fluorescence. Upon hybridisation with nucleic acid targets containing a sequence stretch complementary to the loop region of the beacon, the quencher is spatially removed from the fluorophore, which leads to a strong enhancement in fluorescence. A novel class of molecular beacons has been introduced in which the organic quencher dye is replaced by a gold nanoparticle.[62] The quenching efficiency was determined to be about 99.5%, which indicates that the fluorescent signal of the beacon increases about 200-fold upon hybridisation with a complementary target. This type of gold-oligomer-dye hybrid beacon allows the detection of single-base mutations more efficiently than conventional molecular beacons.

Another very interesting observation has been reported by Maeda et al.,[64,65] who discovered that the aggregation of gold nanoparticles even occurs by non-cross-linking DNA hybridisation. This principle might be utilized to design novel assays for the rapid detection of nucleic acid targets.

The DNA-directed assembly of AuNPs has been coupled with functional DNA structures that are capable of carrying out a specific cleavage reaction. With respect to the enzyme-like performance, such a sequence is called a "DNAzyme". The incorporation of a DNAzyme into the particle-interconnecting DNA oligonucleotides allows the rapid and sensitive detection of a range of targets, such as Pb^{2+} ions or adenosine.[66–68]

In addition to the immediate applications of 3D-assembly in diagnostics, the DNA molecules attached to the nanoparticles can also be utilized as actuators for the assembly and switching of (bio)chemical reactions.[22] For instance, gold nanoparticle–DNA molecular beacon conjugates have been exploited for the remote electronic control of DNA hybridisation.[69] Inductive coupling of a radio-frequency magnetic field (RFMF) with a frequency of 1 GHz to the 1.4-nm metal nanoparticle, which functions as an antenna in the DNA constructs, leads to an increase in the local temperature of the bound DNA, thereby inducing denaturation while leaving surrounding molecules relatively unaffected. Since inductive heating has already been applied to the treatment of cancer cells with magnetic-field-induced excitation,[70] the use of gold nanocrystal–DNA conjugates should allow extension of this concept to novel applications. For instance, complex operations, such as gene regulation, biomolecular assembly and enzymatic activity, of distinct portions of nucleic acids or proteins might be controlled, while the rest of the molecule and neighbouring species would remain unaffected. Moreover, because the control is not optical, this technology could even be applicable in highly scattering media.[69]

Another example concerns the reversible switching of gold nanoparticle aggregation by means of "fuelling oligonucleotides" F_a and F_d in Figure 3.[23] The base sequence of F_a is comprised of three stretches, a′ and b′, which are complementary to 23-nm Au-nanoparticle-bound 12-mer oligomers a and b, respectively, as well as stretch c′, which promotes hybridisation of F_a and F_d. The transformation cycle starts with state I, in which the DNA–nanoparticles are dispersed and reveal a characteristic plasmon absorption maximum at 526 nm. Upon addition of oligomer F_a, the particles aggregate (state II in Figure 3), and consequently the plasmon absorption band is damped and shifted towards longer wavelengths at about 625 nm. In the next step, oligomer F_d is added, which is fully complementary to F_a and can hybridize with it, starting at the dangling end stretch c′ of the duplex DNA interconnecting the nanoparticles. This process, schematically shown as an intermediate state III in Figure 3, leads to the formation of a waste duplex and the redispersion of the nanoparticles. Hence, an increase in absorbance at 526 nm occurs again. Because this paper demonstrated for the first time that nanoparticle aggregation can be reversed at room temperature under physiological conditions, applications in the area of switchable (bio)materials for technical purposes and prosthetics might be foreseen.[23]

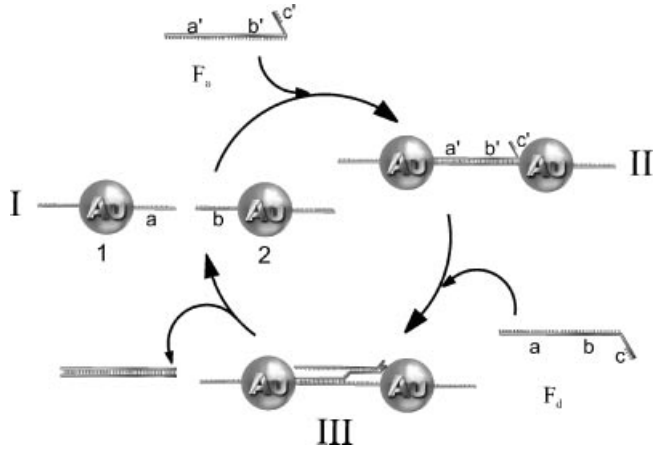

Figure 3. Schematic drawing of the reversible aggregation of DNA-modified gold nanoparticles utilizing fuelling oligonucleotides (F_a and F_d) containing three stretches (a, b and c) that are complementary to the gold-nanoparticle-bound 12-mer oligomers (a and b). Stretch c′ forms a dangling end in the aggregated particles (state II) which promotes the hybridisation of F_a and F_d (intermediate state III). Reprinted with permission, from ref.[23].

3.2. Two-Dimensional Assemblies

3.2.1. Assembly at Interfaces for Diagnostic Applications

In addition to the 3D assembly in homogeneous solution, the use of DNA-functionalised nanoparticles in the heterogeneous nucleic acid hybridisation with capture oligo-

 © 2005 Wiley-VCH Verlag GmbH & Co. KGaA, Weinheim

nucleotides attached to solid supports has recently attracted much attention. Many groups have reported the DNA-directed immobilisation of gold nanoparticles to form supramolecular surface architectures,[71–80] and this approach has also been adopted to the specific sorting of DNA-functionalised quantum dots.[81] The specific nucleic acid-mediated immobilisation of gold nanoparticles can be utilized for the topographic labelling of surface-bound DNA targets. This readily allows the highly sensitive scanometric detection of nucleic acids in DNA-chip analyses by means of the gold-particle-promoted reduction of silver ions (Figure 4), which allows an almost 100-fold increase in sensitivity compared to conventional fluorescent DNA detection.[71] This approach has also been adopted for the array-based electronic detection of nucleic acid analytes.[79] To this end, DNA-functionalised nanoparticles have been immobilized in the gaps of microelectrodes by biospecific interaction. However, the particle density was too low to allow electron conduction between the electrodes. Thus, in a subsequent step, the nanoparticle assembly had to be metallized by reductive deposition of silver, which finally led to a conducting contact between the electrodes. The resulting decrease in ohmic resistance was used as a positive signal for the sensing of the biospecific interaction to be detected.[79]

The use of colloidal gold nanoparticles also allows signal enhancement in DNA hybridisation detection using a quartz crystal microbalance,[72,75] angle-dependent light scattering[82] and surface-plasmon resonance (SPR).[83]

The size-selective light scattering of 50- and 100-nm diameter Au nanoparticles has been used for the two-colour labelling of oligonucleotide arrays.[78] An alternative for the simultaneous determination of multiple DNA targets, the use of Raman-active dye labelled gold nanoparticles, has recently been explored.[84] The gold nanoparticles facilitate the formation of a silver coating that acts as a surface-enhanced Raman scattering promoter for the dye-labelled particles that have been captured by target molecules and an underlying chip in a microarray format. This approach provides the high sensitivity and high selectivity attributes of grey-scale scanometric detection but adds multiplexing and ratioing capabilities because a very large number of probes can be designed based on the concept of using a Raman tag as a narrow-band spectroscopic fingerprint.

DNA-tagged proteins have been immobilized at DNA-functionalised gold nanoparticles by specific nucleic acid hybridisation.[85] This approach has several advantages over the conventional methods to adsorb proteins to colloidal gold. The biofunctionalised nanoparticles not only retain

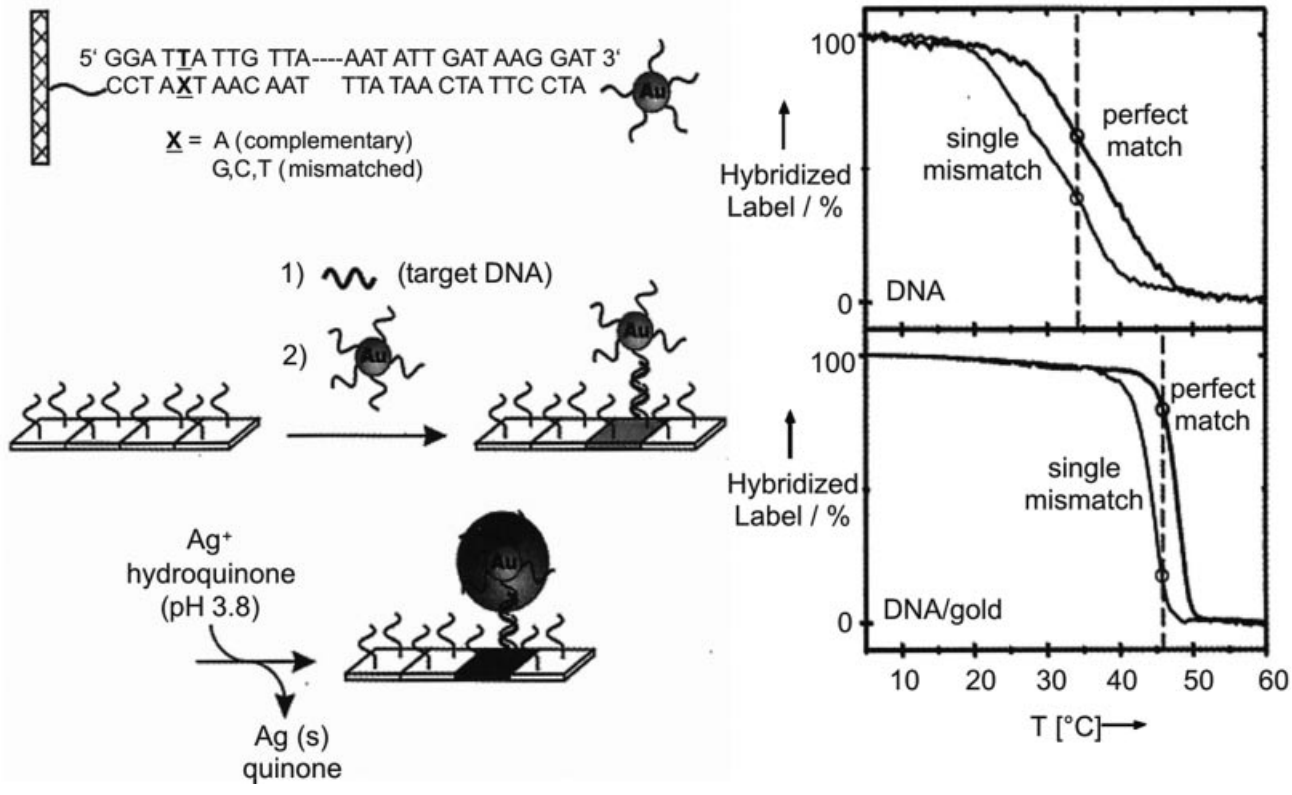

Figure 4. Scanometric detection of nucleic acids in DNA-chip analyses. Capture oligonucleotides immobilized on glass slides are used for specific binding of target nucleic acids. Oligonucleotide-functionalised gold nanoparticles are employed as probes in solid-phase DNA hybridisation detection. Subsequent to a silver enhancement step, the immobilisation of the colloidal gold probe is detected by scanning the glass substrate with a conventional flat-bed scanner. Despite its simplicity, this technique allows for an almost 100-fold increased sensitivity compared to fluorescent DNA detection. Moreover, due to the extraordinarily sharp melting behaviour of the immobilized DNA–nanoparticle networks (see melting curves on the right), this method allows for single-mismatch detection. Reprinted with permission from ref.[71], copyright 2000, American Association for the Advancement of Science.

 © 2005 Wiley-VCH Verlag GmbH & Co. KGaA, Weinheim

the undisturbed recognition properties of the proteins immobilized, but they also reveal an extraordinary stability that even allows for regeneration of the DNA-coated gold particles. These type of bioinorganic hybrid components have been used as reagents in sandwich immunoassays for the detection of proteins using the gold-particle-promoted silver development, allowing for the spatially-addressable detection of femtomolar amounts of chip-immobilized antigens.[85] Recently, this approach was adopted to difunctional DNA AuNPs, thereby significantly enhancing the versatility of nanoparticle probes.[86] Moreover, DNA AuNPs with antibody molecules attached have been used as probes in the sensitive detection of proteins by means of the biobarcode approach.[87–90] These types of metal nanoparticle-based detection systems have been recently reviewed elsewhere.[10,91]

3.2.2. 2D-Assembly for Novel Materials

While monofunctional DNA–nanoparticle conjugates containing just a single recognition site, i.e. an oligonucleotide sequence, were employed in the studies described above, we have recently explored oligofunctional gold nanoparticle conjugates containing different DNA sequences (**D_n-Au** in Figure 1).[42] This type of particle can be considered as a "versatile particle", since, due to the extraordinary specificity of Watson–Crick base-pairing, the various oligonucleotide sequences can be individually and selectively addressed as members of an orthogonal coupling system present at the particle's surface.

As an example, we have shown that difunctional DNA–nanoparticle conjugates (**D_2-Au**) containing two different DNA oligomers self-assemble by DNA hybridisation into surface-bound layers comprised of closely packed, cross-linked nanoparticles (Figure 1).[92] In this approach, the two different DNA sequences of **D_2-Au_A** were utilized such that particle-bound oligomer **1** was used for immobilisation purposes by connecting the particles to surface-bound capture oligomers **4** through the complementary linker **5**. The second type of particle-bound oligomers (**2**) of **D_2-Au_A** was used to establish cross-links to neighbouring particles (**D_2-Au_B** in Figure 1) by means of linker **6**, which is complementary to the sequences **2** and **3** attached to particles **D_2-Au_A** and **D_2-Au_B**, respectively. We reasoned that this approach should lead to densely packed and potentially even ordered monolayers of nanoparticles in which the distance between the individual particles should be adjustable by changing the length of **6**.[92] While the initial study clearly proved the concept of inter-particle DNA cross-linking, no influence of **6** on the interparticle distances was observed by scanning force microscopy (SFM) analysis.[92]

In a recent continuation using in situ SFM studies, we have shown that the self-assembly of difunctional DNA-modified gold nanoparticles at solid substrates does indeed generate particle layers with programmable interparticle spacings.[93] A comparison of these results with earlier work[55,92] indicated that the DNA spacers are highly sensitive to environmental conditions, particularly the degree of hydration of the DNA double helix. Further exploration and refinement of this approach, especially the careful design of the oligomer sequences involved,[94] may eventually pave the way towards nanostructured materials with programmable functionalities for a broad range of applications in materials research and nanobiotechnology.[93]

3.3. One-Dimensional Assemblies

Two fundamentally different approaches have been applied for the formation of one-dimensional assemblies of metal nanoparticles along a DNA backbone. The first approach is to immobilize pre-formed nanoparticles preferably at specific sites along the DNA backbone, while the second approach applies to the direct metallisation of the DNA double strand by reducing the charge-compensation cations (e.g. Ag^+, Pd^{2+}) that were introduced by ion-exchange before. Both procedures have their inherent advantages and disadvantages. While the site-selective immobilisation of pre-formed nanoparticles can take advantage of the precise size control and the defined surface chemistry of the well-elaborated synthetic routes, it is a difficult task to assemble the particles in direct contact to each other over extended domains with an interparticle spacing that is identical and small enough to allow direct dipolar coupling or even electronic transport along the array. The metallisation by metal-ion reduction has successfully led to the formation of highly-conductive nanowires, which could be applied as metallic interconnects. However, the nanoparticles formed during this process suffer from an extraordinarily broad size distribution. Thus, the metal structures along the DNA wires are highly disordered, and none of the size-specific electronic transport properties, which are based on single-electron tunnelling, could be observed or even utilized in nanodevices. In the following section we give an overview of the different methods that have been developed following these two strategies by means of selected examples.

3.3.1. Immobilisation of Nanoparticles on DNA

As previously demonstrated for proteins,[95] Alivisatos and co-workers showed for the first time that a discrete number of water-soluble Au_{55} clusters with one *N*-propylmaleimide ligand per cluster can couple selectively to a sulforyl group incorporated into ssDNA oligomers.[96] Oligonucleotides modified at either the 3′- or 5′-terminus with a free sulforyl group were coupled with an excess of the nanoparticles. After being combined with suitable oligonucleotide templates, parallel (head-to-tail) and antiparallel dimers (head-to-head) were obtained (**7a**–**7c**, respectively, see part B in Figure 5). The linear alignment of the clusters and the centre-to-centre distance, which ranged from 2–6 nm, were illustrated by means of TEM images. These nanoparticle–DNA conjugates have a high flexibility when the DNA backbone is nicked, while an un-nicked double helix significantly lowers the flexibility (for instance, see **7d** in Figure 5). UV/Vis absorbance measurements indicated changes in the spectral properties of the nanoparticles as a consequence of the supramolecular organisation.[97]

 © 2005 Wiley-VCH Verlag GmbH & Co. KGaA, Weinheim

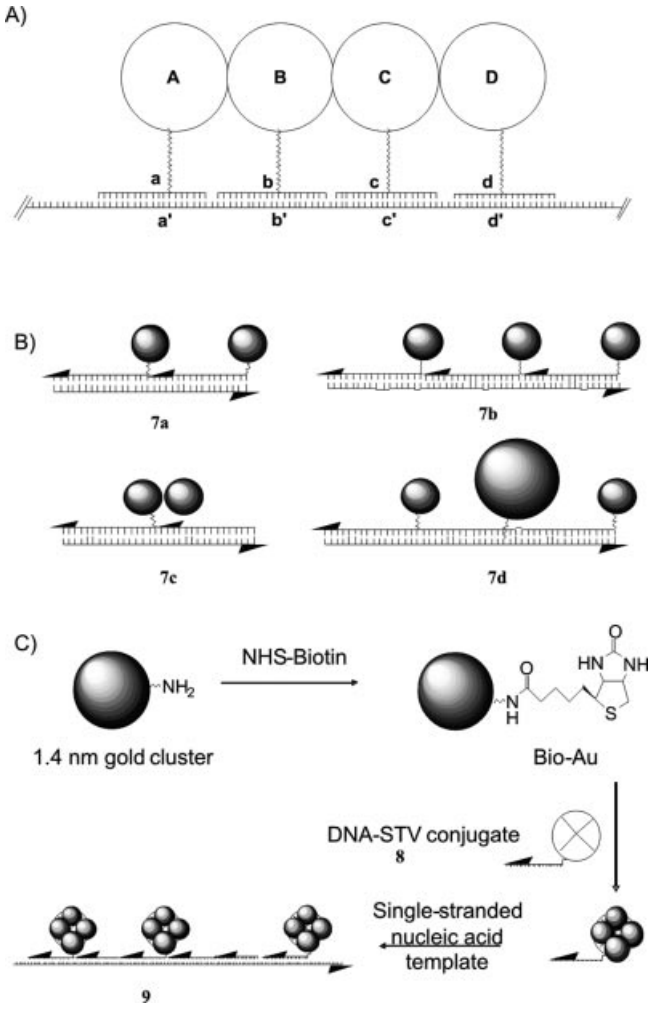

Figure 5. A) Schematic representation of DNA-directed one-dimensional assembly of four different nanoscale building blocks to form a stoichiometrically and spatially defined supramolecular aggregate. B) Assembly of nanocrystal molecules using DNA hybridisation. Conjugates from gold particles (represented as shaded spheres) and 3′- or 5′-thiolated oligonucleotides allow the fabrication of head-to-head (**7a**) or head-to-tail (**7b**) homodimers. A template containing the complementary sequence in triplicate effects the formation of the trimer **7c**. Aggregate **7d** has limited flexibility due to the un-nicked double helical backbone. C) DNA-directed assembly of biotinylated gold nanoclusters using covalent DNA-STV conjugates **8** as molecular adaptors. The nanocluster-loaded STV conjugates self-assemble in the presence of a single-stranded nucleic acid carrier molecule containing complementary sequence stretches to form biometallic aggregates, such as **9**. Reprinted with permission from C. M. Niemeyer, *Angew. Chem. Int. Ed.* **2001**, *40*, 4128–4158.

Noyong et al. have reported the synthesis of string-of-pearl-like alignments of 4-nm Au nanoparticles along DNA strands.[98] In the first step, *cis*-$[PtCl_2(NH_3)_2]$ (cisplatin) is incorporated into DNA-double strands of DNA plasmids. This platinum complex has a high affinity for nitrogen donor sites in nucleotides and therefore binds with high selectivity in neighbouring guanine-guanine nucleobases.[99] This process is well established in medicine, where cisplatin has been used as an anticancer drug for more than 30 years. In its intra-strand position Pt^{2+} is accessible for ligand exchange. Therefore, in a second step, the nanoparticles stabilized by cysteamine can selectively bind to the Pt^{2+} centre by exchange of the NH_3-ligands with H_2N-termini of the ligand shell (Figure 6).

The initial demonstration of the use of DNA as a framework for the precise spatial arrangement of molecular components was carried out with covalent conjugates of single-stranded DNA oligomers and the STV protein.[95] Using the STV-DNA conjugates **8** (Figure 5B) as model systems, a variety of essential basic studies on the DNA-directed assembly of macromolecules were carried out, which have been reviewed earlier.[100] The covalently attached oligonucleotide moiety supplements the STV's four native biotin-binding sites with a specific recognition domain for a complementary nucleic acid sequence. This biospecificity allows the use of DNA-STV conjugates as adapters to assemble basically any biotinylated compound along a nucleic acid template.[100] For example, the strong biotin-STV interaction and the specific nucleic acid hybridisation capabilities of the DNA-STV conjugates **8** have been utilized to organize gold nanoparticles (Figure 5C).[101] To this end, 1.4-nm gold particles containing a single amino substituent have been derivatized with a biotin group and the resulting biotin moiety subsequently used to organize the nanoparticles into a tetrahedral superstructure defined by the biotin-binding sites of the STV. Subsequently, the nanoparticle-loaded proteins self-assemble in the presence of a complementary single-stranded nucleic acid carrier molecule to form nanoparticle assemblies such as **9** (Figure 5C).

The strong biotin–STV interaction together with the specific nucleic acid hybridisation capabilities of DNA have recently been utilized for the controlled assembly of 5-nm Au particles along linear arrays of DNA triple cross-over molecules (TX).[102] As illustrated in Figure 7, the TX molecule consists of seven oligonucleotides, which are hybridized to form three double-stranded helices. These lie in a plane and are linked by strand exchange at four immobile crossover points. The design of the TX molecule is shown in part a of Figure 7. It contains two protruding stem loops, one each from the upper and the lower helices. Thus, a linear array of TX molecules can be obtained by designing three pairs of sticky ends. For illustration, their complementarity is represented by matching colour and geometric shape in part b of Figure 7. In order to template the assembly of 5-nm nanoparticles, streptavidin molecules were selectively bound to biotin groups, which are incorporated into the hairpin loops and are indicated by the small blue dots. In the next step, Au nanoparticles were conjugated to the streptavidin, resulting in a periodic sequence of uniform particles along the linear TX DNA. Figure 7 (parts c and d) shows SEM images of streptavidin/DNA-templated Au nanoparticle arrays. In the first template (c), only one stem loop in each TX molecule is modified with biotin groups, whereas in the second template (d) both stem loops are modified with biotin groups, leading to the formation of single and double rows of nanoparticles, respectively.[102] Kiehl and co-workers have reported similar approaches that use self-assembled DNA nanoarrays comprised of crossover

 © 2005 Wiley-VCH Verlag GmbH & Co. KGaA, Weinheim

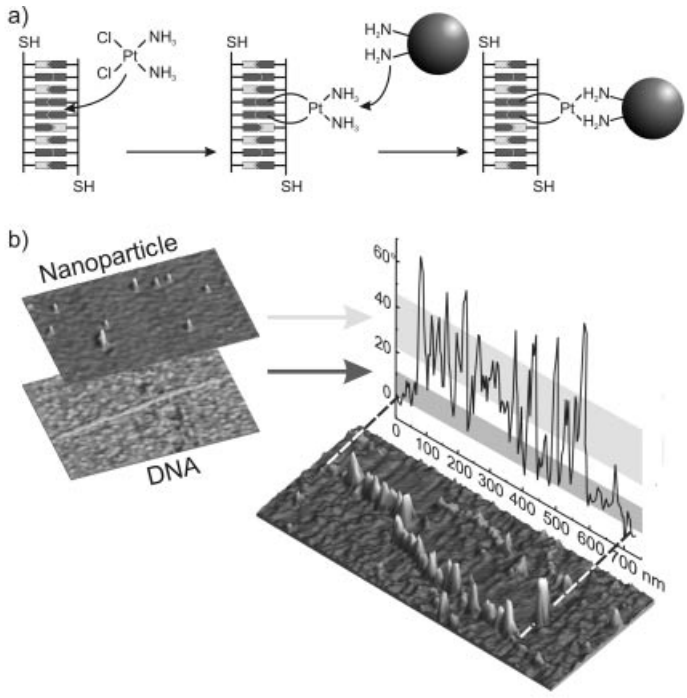

Figure 6. a) Scheme for the organisation of Au nanoparticles along DNA by coupling of NH_2-functionalised (cysteamine) Au nanoparticles at cisplatin-functionalised DNA by simple ligand replacement. b) AFM image (phase contrast) of DNA-aligned Au nanoparticles assembled on a silicon substrate (adapted from ref.[98]).

motifs to produce regular one- and two-dimensional assemblies of gold nanoparticles.[103,104] These reports suggest that programmable DNA arrays will open up novel, powerful routes to the production of precisely assembled nanoparticles.

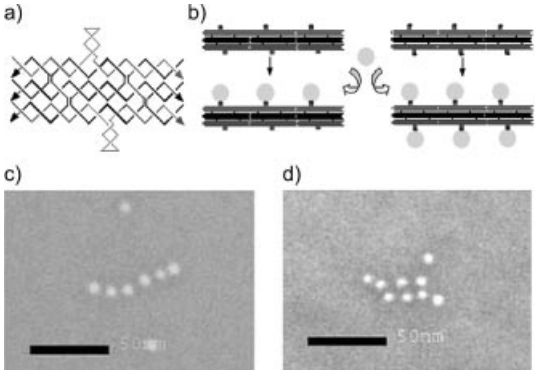

Figure 7. a) Design of the TX molecule and b) schematic drawing of the TX DNA-templated self-assembly of streptavidin linear arrays. c) and d) SEM images of the DNA-templated assembly of 5-nm Au particles (reproduced with permission from ref.[102]).

A first step towards device fabrication has been demonstrated by Kretschmer and Fritsche,[105] who have reported the integration of DNA-templated Au nanoparticles into microelectrode gaps. The microelectrode structures were fabricated by standard photolithography, and the assembly of nanowires consisting of Au nanoparticles in a string-of-pearl-like arrangement spanning the gap was achieved by dielectrophoresis. In a comprehensive study, the different control parameters of formation, the electrical transport properties and the stability of these arrays that lead finally to nanowires consisting of almost uniform nanoparticles that exhibit ohmic behaviour were analysed. The most important results of that work are displayed in Figure 8, which shows SEM images of nanowires bridging an electrode gap of 1 μm. Dielectrophoresis leads to a high number of nanowires, although the magnification shows that the main parts of these wires consist of pearl chains, whereas the diameter of the particles is about 15 nm. The zoom (inset in b) shows the excellent preservation of the individual particles.

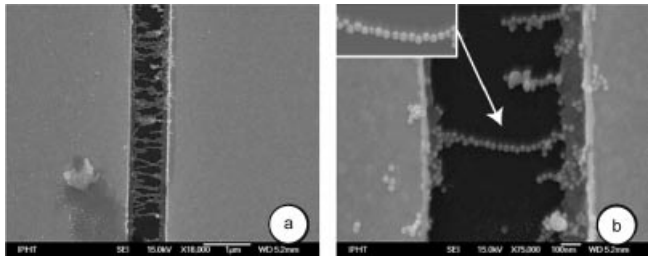

Figure 8. SEM images of microelectrode structure with immobilized DNA-templated nanowires (for explanation see text; reproduced with permission from ref.[105]).

By going to significantly smaller particles of 1.5 nm, which have a much greater potential to serve as building blocks in future nanoelectronic devices due to their enhanced charging energy, Hutchinson and co-workers have elaborated a method to organize the 1.5-nm gold particles

 © 2005 Wiley-VCH Verlag GmbH & Co. KGaA, Weinheim

into linear chains with precisely controlled interparticle spacing over a range of 1.5–2.8 nm.[106,107] These chains are formed in solution by utilizing functional-group-directed self-assembly to organize ligand-stabilized gold nanoparticles onto DNA templates. In this configuration, the spacing between neighbouring nanoparticles is determined by the thickness of the ligand shell stabilizing the nanoparticles and can therefore be tuned at the molecular level by variation of the ligand shell at spacings of 1.5, 2.1 and 2.8 nm with a standard deviation of ≤20%. The ligands that are used for this immobilisation process are (2-mercaptoethyl) trimethylammonium iodide (TMAT, **1**), [2-(2-mercaptoethoxy)ethyl]trimethylammonium toluene-4-sulfonate (MEMA, **6**), and {2-[2-(2-mercaptoethoxy)ethoxy] ethyl}trimethylammonium toluene-4-sulfonate (PEGNME, **11**).

Because the interparticle spacing is enforced by the ligand shell rather than by the scaffold, the spacing is uniform even in nonlinear sections of the chain. This allows the assembly of particles over extended areas up to 1 μm in length and a total coverage of >90%. Figure 9 shows the immobilisation scheme and representative TEM images of linear nanoparticle chains of Au_n-TMAT, Au_n-MEMA and Au_n-PEGNME assembled on λ-DNA. The spacing between neighbouring nanoparticles increases systematically with increasing ligand shell thickness from 1.5 nm ± 0.3 nm in Figure 9A (Au_n-TMAT), through 2.1 ± 0.4 nm in Figure 9B (Au_n-MEMA) to 2.8 nm ± 0.4 nm in Figure 9C (Au_n-PEGNME). The interparticle spacing corresponds to the double thickness of the ligand shell assuming that the stabilizing ligands are in a fully extended conformation, i.e. 1.4 nm for TMAT-functionalised nanoparticles, 2.1 nm for nanoparticles stabilized by MEMA and 2.8 nm for PEGNME-functionalised nanoparticles. The small standard deviations indicate the reproducibility and reliability of this method for generating evenly spaced nanoparticle chains with a high degree of control.

Besides DNA, other chain-like bimolecules have also been used for the one-dimensional assembly. As an example, Bae et al. have recently demonstrated the assembly of one-dimensional arrays of 5-nm Au-nanoparticles using schizophyllan (SPG).[108] SPG is a natural polysaccharide produced by the fungus *Schyzophyllum commune*, which adopts a triple-helical conformation under native conditions. This structure was reversibly dissociated into single chains, which then served as the template for the assembly of the nanoparticles during triple-helix formation.

3.3.2. Metallisation of DNA

Direct metallisation of DNA has been employed by Braun et al. in order to create conductive silver wires.[109] In a multistep process, lithographically fabricated gold elec-

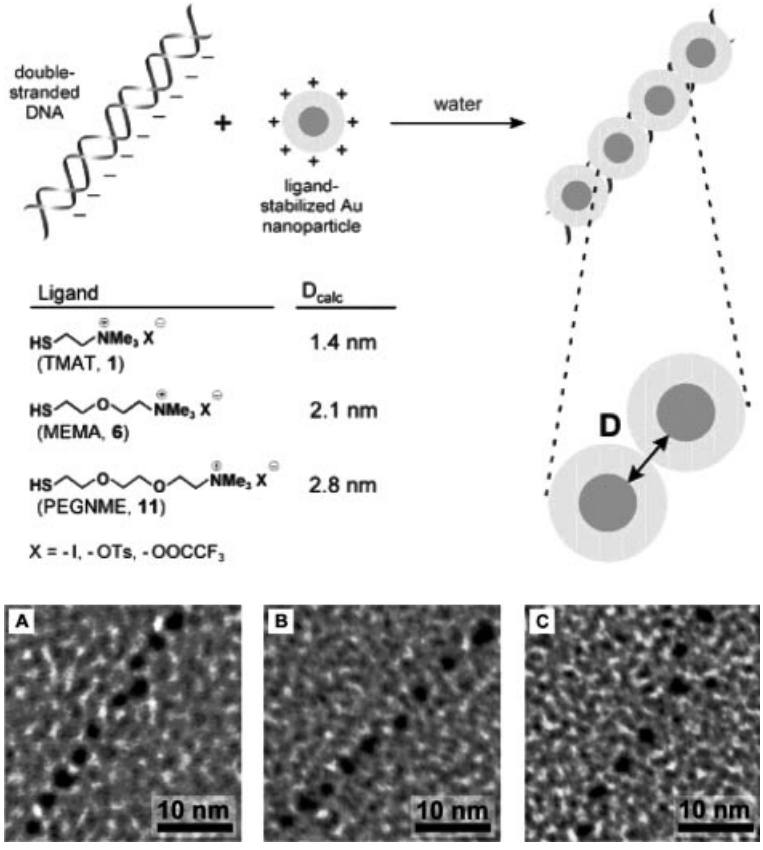

Figure 9. Schematic representation of the solution-phase formation of linear, close-packed DNA–nanoparticle assemblies. The three ligands used are shown in the figure. Below: the TEM images of linear, close-packed nanoparticle–DNA assemblies. The TEM micrographs demonstrate the use of three different ligands to produce linear arrays with different spacing between neighbouring nanoparticles (reproduced with kind permission from ref.[106]).

 © 2005 Wiley-VCH Verlag GmbH & Co. KGaA, Weinheim

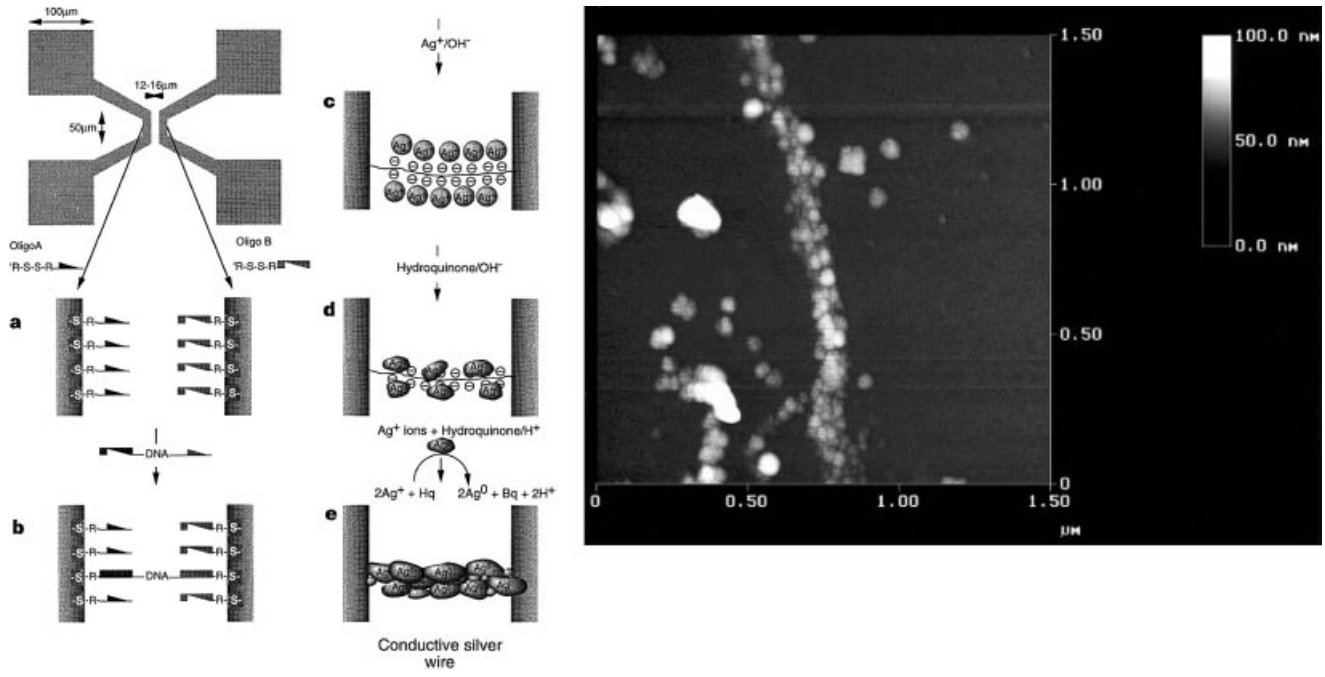

Figure 10. Left: Construction of a nanowire bridging the gap between two gold electrodes. The Ag^+ ions were deposited on the DNA bridge and subsequently reduced to form metallic nanoparticle agglomerates. Right: AFM image of the nanowires illustrating the granular structure (reproduced with permission from ref.[109]).

trodes were functionalised with disulfide-functionalised 12-base oligonucleotides. DNA that contains two 12-base sticky ends, where each of the ends is complementary to one of the two different sequences, was attached to the gold electrodes. Then, an Ag^+ solution was introduced to the surface, which induced an exchange of the charge-compensating Na^+ ions by Ag^+. Reduction with hydroquinone induced the formation of DNA-associated Ag^0 aggregates along the DNA strand. In a following development process, further Ag^+ was reduced to finally provide the metal growths, leading to individual silver nanowires with an average diameter of 100 nm with a pronounced granular structure.

The AFM image in Figure 10 indicates that the wire consists of grains 30–50 nm in diameter deposited along the DNA skeleton. Two-terminal electrical measurements on the silver wire showed that, depending on the silver growth conditions, the differential resistance at voltages beyond the plateau, which is caused presumably by Coulomb charging and/or corrosion effects, varies between 7 and 30 MΩ. Recent continuation of this work has demonstrated original and innovative concepts for tailoring the structural diversity and connectivity of DNA architectures, which is essential for the construction of more complex electronic components and circuits.[110,111]

A similar procedure has also been applied by Harnack et al.[112] and by Richter et al.[113] Harnack et al. have immobilized tris(hydroxymethyl)phosphane-capped gold nanoparticles 1–2 nm in diameter densely on calf thymus DNA. These particles are active catalysts for electroless plating of gold leading to the formation of nanowires with widths of 30–40 nm and electrical conductivities about one-thousandth that of bulk gold. Richter et al. metallized λ-DNA with palladium. The metallisation was accomplished in a two-step chemical deposition of the metal, involving binding of $Pd(CH_3COO)_2$ to the DNA and subsequent reduction with sodium citrate, lactic acid or dimethylborane. This reduction led to the formation of chains of Pd nanoparticles along the DNA (Figure 11). These wires were found to be conducting, exhibiting ohmic behaviour at room temperature. The authors developed this method further by using K_2PtCl_4 and K_2PdCl_4 as a metal source and by slight modification of the reducing conditions.[114] This led to the formation of ordered chains of nanoparticles, thus illustrating a remarkable control over the nucleation and growth processes.

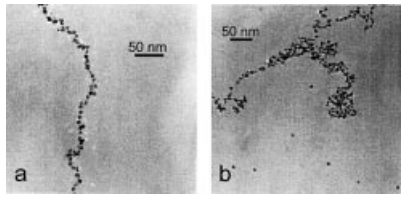

Figure 11. TEM micrographs of chains of a) Pt and b) Pd clusters grown on λ-DNA (reproduced with permission from ref.[114]).

4. Conclusions and Future Directions

This article is intended to provide an overview of the current state-of-the-art of DNA-based assembly of metal nanoparticles in one, two and three dimensions. The examples selected show that interdisciplinary research at the frontier between biomolecular chemistry, inorganic chemis-

 © 2005 Wiley-VCH Verlag GmbH & Co. KGaA, Weinheim

try and materials science leads to new materials with unique properties.

While the assembly process itself is based on the enormous specificity of nucleic acids, which can be tailored by virtue of synthetic organic chemistry, much remains to be done in the development of the basic building blocks, i.e. the DNA AuNPs. As such, there is still a tremendous demand for alternative methods to allow for compensation of typical problems arising in the biofunctionalisation of inorganic nanoparticles. In particular, harsh assembly conditions may lead to ligand-exchange reactions occurring at the colloidal surface. This often prevents the formation of stable bioconjugates and efficient supramolecular assembly. Moreover, the synthesis of nanoparticle–nucleic acid conjugates that are well-defined with respect to their stoichiometric composition is a great challenge, and it is particularly important, from a molecular engineering point of view, to generate sophisticated nanoarchitectures.

Another very important goal concerns the de novo design of nucleic acid sequences that allow efficient two- and three-dimensional self-assembly. Bioinformatic approaches appear to be well suited for solving this task,[94] although much remains to be done in the refinement of such tools. Once developed, one may anticipate a broad scope of applications for designing nucleic acid scaffolds to be used for both the assembly of surface-bound nanoparticle architectures as well as three-dimensional aggregates for bioanalytical and advanced materials research.

When DNA is used as a template for the assembly of nanoparticles, the examples given in this review show impressively that nanowires with metallic conductivity can be obtained. These results have already prompted exciting research on the set-up of functional devices of higher complexity. The works of Williams et al.,[115] who has utilized the recognition of DNA to bind carbon nanotubes to metallic contacts by self-assembly, and by Keren et al.,[110] who has described the self-assembly of segmented nanowires in a multi-step self-assembly process, are emphasised as promising examples. However, it is still a great challenge to develop these processes further in order to realize devices or even device architectures that are robust enough to be applied in nanoelectronic circuitry.

Acknowledgments

Our work is supported by Deutsche Forschungsgemeinschaft (DFG) in Schwerpunktprogramm 1072 through grants Ni399/4-1-3 (CMN), Si609/3-1 and 4-1,2 (US). We thank Bülent Ceyhan and Michael Noyong for help with the figures.

[1] M. Faraday, *Philos. Trans. R. Soc.* **1857**, *147*, 145.
[2] J. M. Thomas, *Pure Appl. Chem.* **1988**, *60*, 1517.
[3] U. Kreibig, M. Vollmer, *Optical Properties of Metal Clusters*, Springer, New York, **1995**.
[4] G. Schoen, U. Simon, *Colloid Polymer Sci.* **1995**, *273*, 101–117.
[5] D. L. Feldheim, C. A. Foss, *Metal Nanoparticles: Synthesis Characterisation, and Applications*, Marcel Dekker, New York, **2002**.
[6] U. Simon, *Adv. Mater.* **1998**, *10*, 1487–1492.
[7] G. Schmid, *Nanoparticles: From Theory to Application*, Wiley-VCH, Weinheim, **2004**.
[8] L. J. De Jongh, *Physics and Chemistry of Metal Cluster Compounds* **1994**.
[9] E. Katz, I. Willner, *Angew. Chem. Int. Ed.* **2004**, *43*, 6042–6108.
[10] N. L. Rosi, C. A. Mirkin, *Chem. Rev.* **2005**, *105*, 1547–1562.
[11] F. Remacle, R. D. Levine, *ChemPhysChem.* **2001**, *2*, 21–36.
[12] G. Markovich, C. P. Collier, J. R. Heath, *Phys. Rev. Lett.* **1998**, *80*, 3807–3810.
[13] G. Schmid, M. Baumle, N. Beyer, *Angew. Chem. Int. Ed.* **2000**, *39*, 181–183; *Angew. Chem.* **2000**, *112*, 187.
[14] G. Schmid, U. Simon, *Chem. Commun.* **2005**, 697–710.
[15] S. Liu, R. Maoz, G. Schmid, J. Sagiv, *Nano Lett.* **2002**, *2*, 1055–1060.
[16] C. A. Mirkin, *Inorg. Chem.* **2000**, *39*, 2258–2272.
[17] C. M. Niemeyer, *Angew. Chem. Int. Ed.* **2001**, *40*, 4128–4158; *Angew. Chem.* **2001**, *113*, 4254–4287.
[18] C. M. Niemeyer, *Angew. Chem. Int. Ed.* **2003**, *42*, 5796–5800; *Angew. Chem.* **2003**, *115*, 5974–5978.
[19] M. H. Caruthers, *Science* **1985**, *230*, 281–285.
[20] K. B. Mullis, *Angew. Chem. Int. Ed. Engl.* **1994**, *33*, 1209–1213; *Angew. Chem.* **1994**, *106*, 1271–1276.
[21] N. C. Seeman, *Nature* **2003**, *421*, 427–431.
[22] C. M. Niemeyer, M. Adler, *Angew. Chem. Int. Ed.* **2002**, *41*, 3779–3783; *Angew. Chem.* **2002**, *114*, 3933–3937.
[23] P. Hazarika, B. Ceyhan, C. M. Niemeyer, *Angew. Chem. Int. Ed.* **2004**, *43*, 6469–6471; *Angew. Chem.* **2004**, *116*, 6631–6633.
[24] R. M. Stoltenberg, A. T. Woolley, *Biomed Microdevices* **2004**, *6*, 105–111.
[25] B. G. Ershov, E. Janata, M. Michaelis, A. Henglein, *J. Phys. Chem.* **1991**, *95*, 8996–8999.
[26] A. Henglein, M. Gutierrez, E. Janata, B. G. Ershov, *J. Phys. Chem.* **1992**, *96*, 4598–4602.
[27] J. R. Thomas, *J. Appl. Phys.* **1966**, *37*, 2914–2915.
[28] W. Yu, W. Tu, H. Liu, *Langmuir* **1999**, *15*, 6–9.
[29] N. A. Dhas, A. Gedanken, *J. Mater. Chem.* **1998**, *8*, 445–450.
[30] M. C. Daniel, D. Astruc, *Chem. Rev.* **2004**, *104*, 293–346.
[31] R. Richards, H. Boennemann, J. Hormes, C. Leuschner, in *Nanofabrication Towards Biomedical Applications* (Eds.: C. S. S. R. Kumar, J. Hormes), Wiley-VCH, Weinheim, **2005**, pp. 3–32.
[32] G. Schmid, R. Boese, R. Pfeil, F. Bandermann, S. Meyer, G. H. M. Calis, J. W. A. van der Velden, *Chem. Ber.* **1981**, *114*, 3634.
[33] G. Schmid, B. Morun, J.-O. Malm, *Angew. Chem. Int. Ed. Engl.* **1989**, *28*, 778–780.
[34] M. N. Vargaftik, V. P. Zagorodnikov, I. P. Stolyarov, I. I. Moiseev, V. A. Likholobov, D. I. Kochubey, A. L. Chuvilin, V. I. Zaikovsky, K. I. Zamaraev, G. I. Timofeeva, *J. Chem. Soc., Chem. Commun.* **1985**, 937–939.
[35] I. I. Moiseev, M. N. Vargaftik, T. V. Chernysheva, T. A. Stromnova, A. E. Gekhman, G. A. Tsirkov, A. M. Makhlina, *J. Mol. Catal. A* **1996**, *108*, 77–85.
[36] J. P. Spatz, A. Roescher, S. Sheiko, G. Krausch, M. Moeller, *Adv. Mater.* **1995**, *7*, 731–735.
[37] J. P. Spatz, A. Roescher, M. Moeller, *Adv. Mater.* **1996**, *8*, 337–340.
[38] M. T. Reetz, W. Helbig, *J. Am. Chem. Soc.* **1994**, *116*, 7401–7402.
[39] C. A. Mirkin, R. L. Letsinger, R. C. Mucic, J. J. Storhoff, *Nature* **1996**, *382*, 607–609.
[40] J. J. Storhoff, R. Elghanian, R. C. Mucic, C. A. Mirkin, R. L. Letsinger, *J. Am. Chem. Soc.* **1998**, *120*, 1959–1964.
[41] P. Hazarika, T. Giorgi, M. Reibner, B. Ceyhan, C. M. Niemeyer, in *Bioconjugation Protocols: Strategies and* Methods (Ed.: C. M. Niemeyer), Humana Press, Totowa, NJ, **2004**, in press.
[42] C. M. Niemeyer, B. Ceyhan, P. Hazarika, *Angew. Chem. Int. Ed.* **2003**, *42*, 5766–5770; *Angew. Chem.* **2003**, *115*, 5944–5948.

 © 2005 Wiley-VCH Verlag GmbH & Co. KGaA, Weinheim

[43] L. M. Demers, C. A. Mirkin, R. C. Mucic, R. A. Reynolds, R. L. Letsinger, R. Elghanian, G. Viswanadham, *Anal. Chem.* **2000**, *72*, 5535–5541.
[44] D. Zanchet, C. M. Micheel, W. J. Parak, D. Gerion, A. P. Alivisatos, *Nano Lett.* **2001**, *1*, 32–35.
[45] W. J. Parak, T. Pellegrino, C. M. Micheel, D. Gerion, S. C. Williams, A. P. Alivisatos, *Nano Lett.* **2003**, *3*, 33–36.
[46] Y. Chen, J. Aveyard, R. Wilson, *Chem. Commun.* **2004**, 2804–2805.
[47] R. L. Letsinger, R. Elghanian, G. Viswanadham, C. A. Mirkin, *Bioconjugate Chem.* **2000**, *11*, 289–291.
[48] Z. Li, R. Jin, C. A. Mirkin, R. L. Letsinger, *Nucleic Acids Res.* **2002**, *30*, 1558–1562.
[49] R. Levy, N. T. Thanh, R. C. Doty, I. Hussain, R. J. Nichols, D. J. Schiffrin, M. Brust, D. G. Fernig, *J. Am. Chem. Soc.* **2004**, *126*, 10076–10084.
[50] G. P. Mitchell, C. A. Mirkin, R. L. Letsinger, *J. Am. Chem. Soc.* **1999**, *121*, 8122–8123.
[51] S.-J. Park, A. A. Lazarides, C. A. Mirkin, R. L. Letsinger, *Angew. Chem. Int. Ed.* **2001**, *40*, 2909–2912; *Angew. Chem.* **2001**, *113*, 2993–2996.
[52] J. K. N. Mbindyo, B. D. Reiss, B. R. Martin, C. D. Keating, M. J. Natan, T. E. Mallouk, *Adv. Mater.* **2001**, *13*, 249–254.
[53] E. Dujardin, L. B. Hsin, C. R. C. Wang, S. Mann, *Chem. Commun.* **2001**, 1264–1265.
[54] J. J. Storhoff, A. A. Lazarides, R. C. Mucic, C. A. Mirkin, R. L. Letsinger, G. C. Schatz, *J. Am. Chem. Soc.* **2000**, *122*, 4640–4650.
[55] S.-J. Park, A. A. Lazarides, C. A. Mirkin, P. W. Brazis, C. R. Kannewurf, R. L. Letsinger, *Angew. Chem. Int. Ed.* **2000**, *39*, 3845–3848; *Angew. Chem.* **2000**, *112*, 4003–4006.
[56] R. Jin, G. Wu, Z. Li, C. A. Mirkin, G. C. Schatz, *J. Am. Chem. Soc.* **2003**, *125*, 1643–1654.
[57] J. Kreuter, in *Microcapsules and Nanoparticles in Medicine and Pharmacy* (Ed.: M. Donbrow), CRC Press, Boca Raton, FL, **1992**, p. 125–148.
[58] J. J. Storhoff, C. A. Mirkin, *Chem. Rev.* **1999**, *99*, 1849–1862.
[59] A. N. Shipway, E. Katz, I. Willner, *ChemPhysChem.* **2000**, *1*, 19–52.
[60] C. M. Niemeyer, C. A. Mirkin (Eds.), *NanoBiotechnology: Concepts, Methods and Applications*, Wiley-VCH, Weinheim, **2004**.
[61] R. Elghanian, J. J. Storhoff, R. C. Mucic, R. L. Letsinger, C. A. Mirkin, *Science* **1997**, *277*, 1078–1081.
[62] B. Dubertret, M. Calame, A. J. Libchaber, *Nat. Biotechnol.* **2001**, *19*, 365–370.
[63] S. Tyagi, F. R. Kramer, *Nat. Biotechnol.* **1996**, *14*, 303–308.
[64] K. Sato, K. Hosokawa, M. Maeda, *J. Am. Chem. Soc.* **2003**, *125*, 8102–8103.
[65] K. Sato, M. Sawayanagi, K. Hosokawa, M. Maeda, *Anal. Sci.* **2004**, *20*, 893–894.
[66] J. Liu, Y. Lu, *J. Am. Chem. Soc.* **2004**, *126*, 12298–12305.
[67] J. Liu, Y. Lu, *Anal. Chem.* **2004**, *76*, 1627–1632.
[68] J. Liu, Y. Lu, *J. Fluoresc.* **2004**, *14*, 343–354.
[69] K. Hamad-Schifferli, J. J. Schwartz, A. T. Santos, S. Zhang, J. M. Jacobson, *Nature* **2002**, *415*, 152–155.
[70] A. Jordan, R. Scholz, P. Wust, H. Fähling, *J. Magn. Magn. Mater.* **1999**, *201*, 413–419.
[71] T. A. Taton, C. A. Mirkin, R. L. Letsinger, *Science* **2000**, *289*, 1757–1760.
[72] L. Lin, H. Zhao, J. Li, J. Tang, M. Duan, L. Jiang, *Biochem. Biophys. Res. Commun.* **2000**, *274*, 817–820.
[73] S. Han, J. Lin, F. Zhou, R. L. Vellanoweth, *Biochem. Biophys. Res. Commun.* **2000**, *279*, 265–269.
[74] R. Möller, A. Csaki, J. M. Köhler, W. Fritzsche, *Nucleic Acids Res.* **2000**, *28*, E91.
[75] F. Patolsky, K. T. Ranjit, A. Lichtenstein, I. Willner, *Chem. Commun.* **2000**, 1025–1026.
[76] T. A. Taton, R. C. Mucic, C. A. Mirkin, R. L. Letsinger, *J. Am. Chem. Soc.* **2000**, *122*, 6305–6306.
[77] C. M. Niemeyer, B. Ceyhan, S. Gao, L. F. Chi, S. Peschel, U. Simon, *Colloid Polym. Sci.* **2001**, *279*, 68–72.
[78] T. A. Taton, G. Lu, C. A. Mirkin, *J. Am. Chem. Soc.* **2001**, *123*, 5164–5165.
[79] S. J. Park, T. A. Taton, C. A. Mirkin, *Science* **2002**, *295*, 1503–1506.
[80] S. Peschel, B. Ceyhan, C. M. Niemeyer, S. Gao, L. F. Chi, U. Simon, *Mater. Sci. Eng., C* **2002**, *19*, 47–50.
[81] D. Gerion, W. J. Parak, S. C. Williamson, D. Zanchet, C. M. Micheel, A. P. Alivisatos, *J. Am. Chem. Soc.* **2002**, *124*, 7070–7074.
[82] G. R. Souza, J. H. Miller, *J. Am. Chem. Soc.* **2001**, *123*, 6734–6735.
[83] L. He, M. D. Musick, S. R. Nicewarner, F. G. Salinas, S. J. Benkovic, M. J. Natan, C. D. Keating, *J. Am. Chem. Soc.* **2000**, *122*, 9071–9077.
[84] Y. C. Cao, R. Jin, C. A. Mirkin, *Science* **2002**, *297*, 1536–1540.
[85] C. M. Niemeyer, B. Ceyhan, *Angew. Chem. Int. Ed.* **2001**, *40*, 3685–3688; *Angew. Chem.* **2001**, *113*, 3798–3801.
[86] P. Hazarika, B. Ceyhan, C. M. Niemeyer, *Small* **2005**, *1*, in press.
[87] J. M. Nam, S. I. Stoeva, C. A. Mirkin, *J. Am. Chem. Soc.* **2004**, *126*, 5932–5933.
[88] J. M. Nam, C. S. Thaxton, C. A. Mirkin, *Science* **2003**, *301*, 1884–1886.
[89] J. M. Nam, S. J. Park, C. A. Mirkin, *J. Am. Chem. Soc.* **2002**, *124*, 3820–3821.
[90] D. G. Georganopoulou, L. Chang, J. M. Nam, C. S. Thaxton, E. J. Mufson, W. L. Klein, C. A. Mirkin, *Proc. Natl. Acad. Sci. USA* **2005**, *102*, 2273–2276.
[91] C. M. Niemeyer, M. Adler, R. Wacker, *Trends Biotechnol.* **2005**, *23*, 208–216.
[92] C. M. Niemeyer, B. Ceyhan, M. Noyong, U. Simon, *Biochem. Biophys. Res. Commun.* **2003**, *311*, 995–999.
[93] B. Zou, B. Ceyhan, U. Simon, C. M. Niemeyer, *Adv. Mater.* **2005**, *17*, 1643–1647.
[94] U. Feldkamp, R. Wacker, W. Banzhaf, C. M. Niemeyer, *ChemPhysChem.* **2004**, *5*, 367–372.
[95] C. M. Niemeyer, T. Sano, C. L. Smith, C. R. Cantor, *Nucl. Acids Res.* **1994**, *22*, 5530–5539.
[96] A. P. Alivisatos, K. P. Johnsson, X. Peng, T. E. Wilson, C. J. Loweth, M. P. Bruchez Jr., P. G. Schultz, *Nature* **1996**, *382*, 609–611.
[97] C. J. Loweth, W. B. Caldwell, X. Peng, A. P. Alivisatos, P. G. Schultz, *Angew. Chem. Int. Ed.* **1999**, *38*, 1808–1812; *Angew. Chem.* **1999**, *111*, 1925–1929.
[98] M. Noyong, K. Gloddek, U. Simon, *Mater. Res. Soc. Symp. Proc.* **2003**, 153–158.
[99] E. R. Jamieson, S. J. Lippard, *Chem. Rev.* **1999**, *99*, 2467–2498.
[100] C. M. Niemeyer, *Chem. Eur. J.* **2001**, *7*, 3188–3195.
[101] C. M. Niemeyer, W. Bürger, J. Peplies, *Angew. Chem. Int. Ed.* **1998**, *37*, 2265–2268; *Angew. Chemie* **1998**, *110*, 2391–2395.
[102] H. Li, S. H. Park, J. H. Reif, T. H. LaBean, H. Yan, *J. Am. Chem. Soc.* **2004**, *126*, 418–419.
[103] S. Xiao, F. Liu, A. E. Rosen, J. F. Hainfeld, N. C. Seeman, K. Musier-Forsyth, R. A. Kiehl, *J. Nanoparticle Res.* **2002**, *4*, 313–317.
[104] J. D. Le, Y. Pinto, N. C. Seeman, K. Musier-Forsyth, T. A. Taton, R. A. Kiehl, *NanoLett.* **2004**, 2343–2347.
[105] R. Kretschmer, W. Fritzsche, *Langmuir* **2004**, *20*, 11797–11801.
[106] G. H. Woehrle, M. G. Warner, J. E. Hutchison, *Langmuir* **2004**, *20*, 5982–5988.
[107] M. G. Warner, J. E. Hutchison, *Nat. Mater.* **2003**, *2*, 272–277.
[108] A.-H. Bae, M. Numata, T. Hasegawa, C. Li, K. Kaneko, K. Sakurai, S. Shinkai, *Angew. Chem. Int. Ed.* **2005**, *44*, 2030–2033; *Angew. Chem.* **2005**, *117*, 2066–2069.
[109] E. Braun, Y. Eichen, U. Sivan, G. Ben-Yoseph, *Nature* **1998**, *391*, 775–778.

 © 2005 Wiley-VCH Verlag GmbH & Co. KGaA, Weinheim

[110] K. Keren, M. Krueger, R. Gilad, G. Ben-Yoseph, U. Sivan, E. Braun, *Science* **2002**, *297*, 72–75.
[111] K. Keren, R. S. Berman, E. Buchstab, U. Sivan, E. Braun, *Science* **2003**, *302*, 1380–1382.
[112] O. Harnack, W. E. Ford, A. Yasuda, J. M. Wessels, *Nano Lett.* **2002**, *2*, 919–923.
[113] J. Richter, M. Mertig, W. Pompe, I. Monch, H. K. Schackert, *Appl. Phys. Lett.* **2001**, *78*, 536–538.
[114] R. Seidel, L. C. Ciacchi, M. Weigel, W. Pompe, M. Mertig, *J. Phys. Chem. B* **2004**, *108*, 10801–10811.
[115] K. A. Williams, P. T. Veenhuizen, B. G. de la Torre, R. Eritja, C. Dekker, *Nature* **2002**, *420*, 761.

Received: May 10, 2005
Published Online: August 26, 2005

 © 2005 Wiley-VCH Verlag GmbH & Co. KGaA, Weinheim

Template-Fabricated Gold Nanowires from Gas-Phase Transport Reactions

Ralf Köppe,*[a] Günter Schmid,[b] Sibylle Schneider,[a] and Hansgeorg Schnöckel*[a]

Keywords: Chemical vapour transport / Gold / Iodine / Nanostructures / Template synthesis

Aluminium oxide membranes are partially filled with solid nanowires of gold by chemical vapour transport (1000 to 650 °C) using iodine as the transport agent. The transport is due to the formation of gas-phase AuI.

(© Wiley-VCH Verlag GmbH & Co. KGaA, 69451 Weinheim, Germany, 2005)

Introduction

The fabrication of solid-state nanostructures has mainly been motivated by their expected quantum-size physical phenomena. In particular, nanowires are interesting entities in which carriers are confined in the radial dimension although transport is possible along their axial dimension. Various fabrication techniques have been developed for the synthesis of the nanowires, including template synthesis[1] and the vapour–liquid–solid growth mechanism.[2]

Porous anodic alumina has frequently been used for the templated synthesis of nanowires since this porous template material consists of a self-assembled honeycomb array of uniformly sized parallel channels. Because of the transparent, thin, sheet-like character of the porous material it is often called "alumina membrane". Thus, arrays of aligned nanowires that are uniform in diameter can be obtained reproducibly by filling the pores of these membranes. Moreover, these membranes are thermally inert up to about 1000 °C.

Two successful strategies to fill these alumina nanotubes have been investigated so far, namely electrochemical deposition processes[3] and chemical processes involving degradation of precursors (inorganic or organometallic[1,4]) after immersing the template material in solution.

In this work we will report on our investigations to fill aluminium oxide membranes by means of chemical transport reactions in the gas phase in a chemical equilibrium. This type of reaction[5] can be characterised in a way where a solid or a liquid substance A reacts with a gas B to form only gaseous products [e.g. C, Equation (1)].

$$i\,A_{s,l} + k\,B_g + \ldots \rightleftharpoons j\,C_g \quad (1)$$

In a temperature gradient, i.e. areas of different temperature in a closed system (e.g. a sealed ampoule), a reversible decomposition of this gaseous product results in the formation of the solid/liquid A and the gas B again. From the outside the situation appears to be a sublimation or distillation of A, although the vapour pressure of the transported species A is negligibly small. In fact, the solid/liquid A is chemically transported.

In order to start with this new technique and to gain experience for the planned incorporation of semiconductor materials (see below), we decided to perform the synthesis of gold colloids inside aluminium oxide nanotubes, which has been thoroughly investigated by several research group before.[4] The chemical transport of gold by means of iodine has only been reported in a qualitative way;[6] the transport effect by chlorine was first described by Biltz.[7,8]

In this work we report on the chemical transport of gold by gaseous iodine in a temperature gradient between 1000 and 650 °C by means of AuI. Gaseous AuI is supposed to be the essential species of the transport mechanism according to Equation (2).

$$(650\,^{\circ}C)\ Au_{(s)} + \tfrac{1}{2}\,I_{2(g)} \rightleftharpoons AuI_{(g)}\ (1000\,^{\circ}C) \quad (2)$$

This mechanism is substantiated by calculations of the partial pressures of the gaseous species. These calculations are based on the thermodynamic data of some halides of gold which were experimentally not accessible until now, but which were recently provided by quantum-chemical investigations.[9,10]

Results

Chemical Vapour Transport

In a typical experiment, both 100 mg of gold and 50 mg of iodine were sealed in an evacuated quartz tube (outer diameter: 10 mm; wall thickness: 1 mm) of about 8 cm^3 vol-

[a] Institut für Anorganische Chemie der Universität Karlsruhe (TH),
Engesserstr. 15, 76128 Karlsruhe
Fax: +49-721-608-4854
E-Mail: schnoeckel@chemie.uni-karlsruhe.de
[b] Institut für Anorganische Chemie der Universität Duisburg-Essen,
Universitätsstr. 5–7, 45117 Essen, Germany

ume. The ampoule was placed in an oven with two independently heated zones at 1000 and 650 °C (at 650 °C the total pressure in the ampoule is estimated to be 2 bar). After two days, irregular shaped crystallites consisting of gold were formed at the low-temperature side of the quartz ampoule. When placing aluminium oxide membranes at the low-temperature side, the colour of the template material changed from colourless before the transport reaction to purplish red after the experiment (Figure 1). This change of colour is an indication of the successful filling of the membrane with gold.[1] Within 48 h about 5 mg of gold are chemically transported. Performing the experiment under identical conditions but without iodine did not lead to any gas-phase transport of gold.

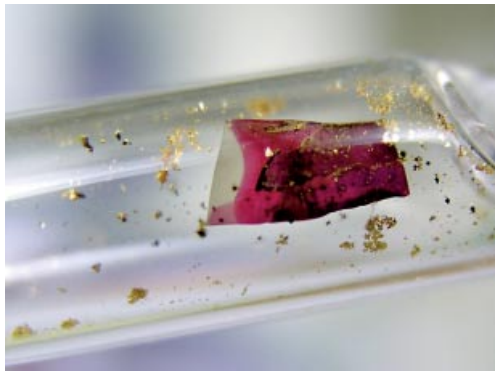

Figure 1. Low-temperature side of a quartz ampoule after chemical transport of gold with iodine.

Transmission Electron Microscopy (TEM)

The membranes were analysed by transmission electron microscopy (TEM). The samples were prepared by milling in a mortar and by suspending the material together with ethanol onto the copper grid by means of an ultrasonic bath. This preparation provides a qualitative view of the dimensions of the membrane and its filling. Figure 2 shows images of the partially filled alumina membrane, including a transverse and a top view of a channel filled with a solid gold nanowire of the exact diameter given by the membrane. As expected from the anodisation voltage of 40 V, channels with a diameter of 50 nm are observed.[1] The aspect ratio of the gold nanorods is about 8. Spherical colloids or flakes, as reported by the groups of Schmid[1] and Martin,[11] are not found.

Further investigations, for example the dissolution of the template material and the analysis of the free gold nanowires by TEM, are underway because, in contrast to the solubility of "as prepared" membranes, the heated template is not soluble in aqueous solutions of acids and bases and therefore this common technique cannot be applied.

Spectroscopic Characterisation

UV/Visible absorption spectra were recorded with an LOT Oriel SPEC II diode array and spectrograph with the

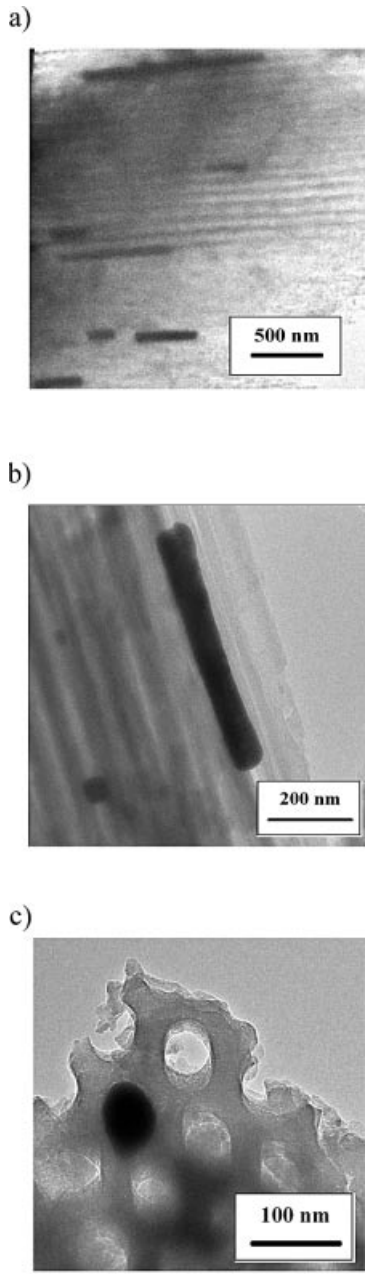

Figure 2. TEM images of the aluminium oxide membrane (channels of 50 nm diameter): a) several solid gold wires, b) transverse view and c) top view of a single wire.

template membranes oriented perpendicular to the incident beam. The absorption spectrum of a filled membrane, with λ_{max} at 550 nm, is shown in Figure 3. This observation is in line with earlier reports on aluminium oxide filled with gold wires and colloids by different methods. Martin et al. have analysed the effects of particle size and aspect ratio on the optical spectra of gold nanowires prepared by electrodeposition.[12] For an aspect ratio of gold nanowires (diameter 60 nm) of between 1.6 and 7.4, an absorbance maximum of 520 nm is reported. Furthermore, Schmid and Sawitowski have reported a bathochromic (red) shift of 20 nm when comparing tempered with untempered alumina (diameter 50 nm) filled with gold colloids. This shift is caused by an

 © 2005 Wiley-VCH Verlag GmbH & Co. KGaA, Weinheim

increase of the dielectric constant after phase transformation leading to crystalline Al_2O_3 upon heating the samples to about 800 °C.[11,13] The extinction maximum (550 nm) found by us is in line with these reports.

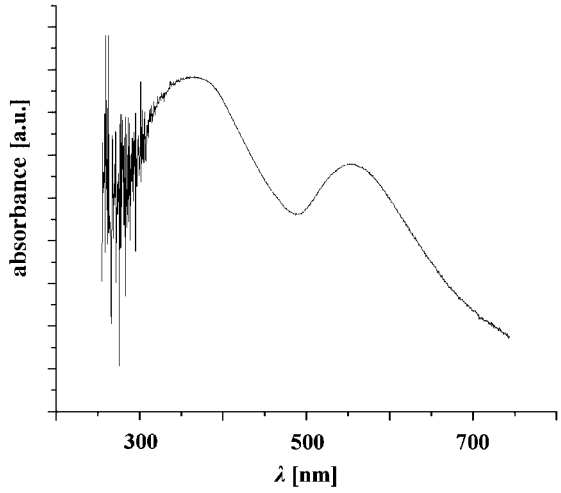

Figure 3. UV/Vis transmission spectrum of an aluminium oxide membrane filled with gold.

Thermodynamic Considerations

In order to obtain information on the gas-phase species responsible for the observed transport of gold, we performed thermodynamic calculations on the partial pressures of the possible gaseous iodides of gold: AuI, AuI_3 and their dimers Au_2I_2 and Au_2I_6.

The reactions inside the quartz ampoule can be described by the following gas phase equilibrium involving Equations (3), (4), (5), (6), (7) and (8):

$$2\,AuI_{(g)} \rightleftharpoons Au_2I_{2(g)} \quad (3)$$

$$2\,AuI_{(g)} + 2\,I_{2(g)} \rightleftharpoons 2\,AuI_{3(g)} \quad (4)$$

$$2\,AuI_{3(g)} \rightleftharpoons Au_2I_{6(g)} \quad (5)$$

$$Au_{(s)} \rightleftharpoons Au_{(g)} \quad (6)$$

$$I_{2(g)} \rightleftharpoons 2\,I_{(g)} \quad (7)$$

$$Au_{(g)} + I_{(g)} \rightleftharpoons AuI_{(g)} \quad (8)$$

The values for the entropy and heat of formation of gaseous I atoms, I_2 and solid and gaseous gold were taken from the collection of thermochemical data of Binnewies.[14] However, experimentally deduced thermodynamic data of the gold iodides are not yet available. Fortunately, these species have been investigated by means of quantum-chemical methods taking into account electron correlation and relativistic effects.[9,10] Thermochemical data on the reactions that may be relevant for the transport experiment in the system gold/iodine are given in Table 1. In addition to the thorough work of Schultz and Hargittai,[10] Schwerdtfeger[9] has reported highly correlated calculations, especially on the AuI molecule. The data obtained − geometric structure, bond dissociation energy and vibrational frequency − are necessary to obtain the heat of formation and entropy of $AuI_{(g)}$, and therefore we mainly use these data for the following discussion. Solid AuI is not relevant for these calculations for the following reason: from thermogravimetric analysis we found that solid AuI is completely decomposed at 140 °C. This observation was confirmed by the calculation of the dissociation pressure by means of the reverse reaction (2′).

$$AuI_{(s)} \rightleftharpoons Au_{(s)} + 1/2\,I_{2\,(g)} \quad (2')$$

According to this calculation the vapour pressure of I_2 over solid AuI at about 200 °C should already be 3 bar, and at 650 °C, as in our experiments, no solid AuI should be present at all because the dissociation pressure should be more than 3 kbar.[14]

In order to describe the complex equilibrium situation in which seven gaseous species are involved (Au, I, I_2, AuI, Au_2I_2, AuI_3, Au_2I_6) quantitatively, one needs the six expressions [Equations (3–8)] of law of mass action given above and, additionally, the equation for the total pressure of iodine describing the mass balance of iodine:

$$p_{total}(I_2) = [p(I) + 2p(I_2) + p(AuI) + 2p(Au_2I_2) + 3p(AuI_3) + 6p(Au_2I_6)]/2$$

where $p_{total}(I_2)$ represents the pressure of I_2 before realisation of the chemical equilibrium. The calculated partial pressures are given in Figure 4 for a typical experiment. The gaseous Au-containing species with the largest partial pressure is monomeric AuI (1300 K: 9×10^{-3} mbar; 1000 K: 1×10^{-5} mbar). All data presented so far are mainly based on the theoretical calculations of Schwerdtfeger[9] (see above). However, the thermodynamic data from the quantum-chemical calculations of Schultz and Hargittai lead to an essentially similar situation.[10] The temperature dependence of $\Delta_R H^0$ and $\Delta_R S^0$ was not taken into account in the calculations due to several other uncertainties (see below).

Discussion

The reaction of gold with iodine in a sealed quartz ampoule in a temperature gradient leads to a chemical transport of gold from the high- to the low-temperature side. From thermochemical calculations we found that, in principle, the reaction given in Equation (2) is responsible for this transport. Gaseous gold is not the transport-relevant species as its vapour pressure in the temperature range under discussion is about three orders of magnitude lower than the partial pressure of AuI.[14] From a rough quantitative estimation of the transport rate based on diffusion processes as the main transport mechanism, only about 0.1 mg of Au should be transported within 24 h. Therefore, the observed higher transportation rate leads to the conclusion that both diffusion and convection contribute to the transport effect. This mechanism seems plausible as the total pressure in the ampoule can reach up to 4 bar in a typical

 © 2005 Wiley-VCH Verlag GmbH & Co. KGaA, Weinheim

Table 1. Thermodynamic data for the formation of gaseous Au_2I_6, AuI_3, Au_2I_2 and AuI from solid Au and gaseous I_2.

Reaction	$\Delta_R H^0$ [kJ mol^{-1}]	$\Delta_R S^0$ [J mol^{-1} K^{-1}]	References
$2\,AuI_{(g)} \rightleftharpoons Au_2I_{2(g)}$	–112.1	–129.6	[9]
$2\,AuI_{(g)} + 2\,I_{2\,(g)} \rightleftharpoons 2\,AuI_{3(g)}$	–117.3	–224.1	[9]
$2\,AuI_{3(g)} \rightleftharpoons Au_2I_{6(g)}$	–135.3	–194.5	[9]
$Au_{(g)} + I_{(g)} \rightleftharpoons AuI_{(g)}$	–200.9	–96.8	$\Delta_f H^0(Au_g)$, $\Delta_f H^0(I_g)$: ref.[14] D_0(AuI): ref.[9] ΔS^0 (AuI) derived from ν(AuI) [9]
$Au_{(s)} \rightleftharpoons Au_{(g)}$	368.4	132.9	[14]
$I_{2(g)} \rightleftharpoons 2\,I_{(g)}$	151.4	101.4	[14]

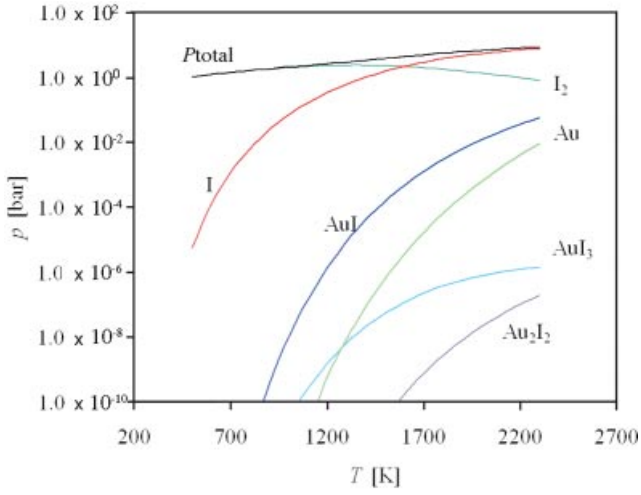

Figure 4. Partial pressures in a typical transport experiment [volume 8 cm^3, $m(I_2)$ = 50 mg].

experiment as the temperature gradient is large. Furthermore, the bond-dissociation energy of AuI is difficult to determine by quantum-chemical means. The calculated value (200.9 kJ mol^{-1}) is lower than the value determined by mass spectrometry [217.7 kJ mol^{-1} > D_0(Au–I) > 267.9 kJ mol^{-1}] [15] and microwave spectroscopy (276.3 kJ mol^{-1}).[16] Consequently, its vapour pressure and the transport rate can only be calculated within this uncertainty. [Estimations of the transport rate using these data lead to values of 0.4 (D_0 = 217.7 kJ mol^{-1}), 42.2 (267.9 kJ mol^{-1}) and 91.7 mg Au/24 h (276.3 kJ mol^{-1}), respectively].

In this work we have presented a novel method to fill aluminium oxide membranes by a gas-phase transport reaction. In order to be useful for this process, these reactions must fulfil the following prerequisites: a) the reaction must transport a bulk material in a temperature gradient and the reaction should work in a temperature range in which the vapour pressure of the relevant gaseous species exhibits significant changes; b) the reaction should take place in a temperature range below 1000 °C where aluminium oxide membranes are known to be thermally stable. Furthermore, the transport gas (here I_2) must be chemically inert with respect to the template material; c) to obtain long solid wires the supersaturation of AuI in the gas phase should be low. A low number of growing crystal seeds inside the template leads to a rather low degree of filling and the aspect ratio of these solid wires is high. In contrast, a high supersaturation, which is a consequence of a high transport rate, leads to a preferential crystallisation of gold outside the channels. Therefore, under these conditions perfect gold crystals are observed on the surface of the membrane.

We believe that this introduction of chemical-transport reactions to nanoscience is only the first step in a strongly developing field. This progress was made possible, and may be expanded in the future, because thermochemical calculations can now be supported by quantum-chemical investigations of unknown thermodynamical data also for hypothetical gaseous species.

Using this method it should be possible to fill almost any metal into alumina membranes, even those with a very low vapour pressure. Furthermore, alloys, mixed crystals with tunable composition[17] and semiconductor materials may be suitable. Therefore, based on the results presented here, we have started experiments for the transport of gold at lower temperatures in order to fill thermally less-stable nanoporous materials (e.g. zeolites). Furthermore, we intend to fill nanoporous aluminium oxide with the semiconductors GaP[18] or GaAs.[19] For this purpose, we first investigated an unexpected chemical-transport reaction [Equation (9)[20]] where only the elements gallium and phosphorus or arsenic are involved such that very pure semiconducting materials can be expected.[18,19]

$$GaX_{(s)} + X_{4(g)} \rightleftharpoons GaX_{5(g)}\ (X = P, As) \quad (9)$$

Experimental Section

Preparation of Aluminium Oxide Membranes: The mesoporous alumina membranes were produced by anodising electropolished, high purity aluminium plates in oxalic acid, using a lead plate cathode. Full details are given elsewhere.[1] The pore diameters are monodisperse and linearly related to the anodising voltage (40 V, 50 nm). The pores are perpendicular to the membrane surface and are packed in an ordered hexagonal array with a wall thickness comparable to the pore diameter. The membrane thickness, ranging up to several hundred microns, can be controlled by the time of the anodising process.

Acknowledgments

This project was supported by the Deutsche Forschungsgemeinshaft (Priority Program: "Semiconductors and Metal Clusters as Components for Organized Structures"). We thank Dr. H.-J. Himmel for recording the UV/Vis spectra. We also acknowledge the electron microscopy laboratory of the University of Karlsruhe.

 © 2005 Wiley-VCH Verlag GmbH & Co. KGaA, Weinheim

[1] M. G. K. Hornyak, R. Pugin, T. Sawitowski, G. Schmid, J.-O. Bovin, G. Karsson, H. Hofmeister, S. Hopfe, *Chem. Eur. J.* **1997**, *3*, 1951.
[2] A. M. Morales, C. M. Lieber, *Science* **1998**, *279*, 208.
[3] G. L. Hornyak, C. J. Patrissi, C. R. Martin, *J. Phys. Chem. B* **1997**, *101*, 1548.
[4] G. Schmid, *J. Mater. Chem.* **2002**, *12*, 1231.
[5] H. Schäfer, *Chemische Transportreaktionen, der Transport organischer Stoffe ueber die Gas-phase und seine Anwendung*, Verlag Chemie, Weinheim, **1962**.
[6] H. Schäfer, M. Trenkel, *Z. Anorg. Allg. Chem.* **1975**, *414*, 137.
[7] W. Biltz, W. Fischer, R. Juza, *Z. Anorg. Allg. Chem.* **1928**, *176*, 121.
[8] W. Fischer, W. Biltz, *Z. Anorg. Allg. Chem.* **1928**, *176*, 81.
[9] T. Söhnel, R. Brown, L. Kloo, P. Schwerdtfeger, *Chem. Eur. J.* **2001**, *7*, 3167.
[10] A. Schulz, M. Hargittai, *Chem. Eur. J.* **2001**, *7*, 3657.
[11] J. C. Hulteen, C. J. Patrissi, D. L. Miner, E. R. Crosthwait, E. B. Oberhauser, C. R. Martin, *J. Phys. Chem. B* **1997**, *101*, 7727.
[12] C. A. Foss, Jr., G. L. Hornyak, J. A. Stockert, C. R. Martin, *J. Phys. Chem.* **1994**, *98*, 2963.
[13] T. Sawitowski, Ph. D. Thesis, University of Essen, **1999**.
[14] M. Binnewies, E. Milke, *Thermochemical Data of Elements and Compounds*, Wiley-VCH, Weinheim, **2002**.
[15] J. R. Brown, P. Schwerdtfeger, D. Schröder, H. Schwarz, *J. Am. Soc. Mass Spectrom.* **2002**, *13*, 485.
[16] C. J. E. L. Reynard, M. C. L. Gerry, *J. Mol. Spectrosc.* **2001**, *205*, 344.
[17] S. Gerighausen, M. Binnewies, *Z. Anorg. Allg. Chem.* **1995**, *621*, 936.
[18] R. Köppe, J. Steiner, H. Schnöckel, *Z. Anorg. Allg. Chem.* **2003**, *629*, 2168.
[19] R. Köppe, H. Schnöckel, *Angew. Chem. Int. Ed.* **2004**, *43*, 2170.
[20] Although the transport of bulk GaP or GaAs takes place in a temperature gradient (1000 to 900 °C) in which the ordered alumina pores are still thermally stable, we were unable to produce nanotubes or nanowires consisting of GaX with a Ga:X ratio of exactly 1:1, probably due to the reaction of X_4 with the membrane material.

Received: April 27, 2005
Published Online: July 20, 2005

 © 2005 Wiley-VCH Verlag GmbH & Co. KGaA, Weinheim

Crystal Structures of $[K(2.2.2\text{-crypt})]_4[Pb_9Mo(CO)_3]$ − Isolation of the Novel Isomers $[(\eta^5\text{-}Pb_9)Mo(CO)_3]^{4-}$ beside $[(\eta^4\text{-}Pb_9)Mo(CO)_3]^{4-}$

Li Yong,[a] Stephan D. Hoffmann,[a] and Thomas F. Fässler*[a]

Dedicated to Prof. Dr. H. H. Karsch on the occasion of his 60th birthday

Keywords: Cluster compounds / Cryptands / Isomers / Packing / Zintl anions

The reaction of $[Mo(CO)_3(MeCN)_3]$ with K_4Pb_9 in the presence of 2.2.2-cryptand (2.2.2-crypt) has been investigated. The transition metal complex $[K(2.2.2\text{-crypt})]_4[(\eta^5\text{-}Pb_9)Mo(CO)_3]$ (**1**), which contains a Pb_9^{4-} Zintl anion coordinated by Mo in an η^5-fashion, is isolated for the first time and characterized by single-crystal X-ray structure analysis. The 10 metal atoms in the $[(\eta^5\text{-}Pb_9)Mo(CO)_3]^{4-}$ anion form a bicapped square antiprism, with the $Mo(CO)_3$ unit occupying a waist vertex position. The IR spectra of single crystals, as well as of the crude product, show clearly that only the $[(\eta^5\text{-}Pb_9)Mo(CO)_3]^{4-}$ ion is formed. In contrast, the reaction of $[Mo(CO)_3(Mes)]$ with K_4Pb_9 under the same reaction conditions gives a mixture of compound **1** and its isomer $[K(2.2.2\text{-crypt})]_4[(\eta^4\text{-}Pb_9)Mo(CO)_3]$ (**2**). Compounds **1** and **2** were isolated without additional solvent molecules. The Pb–Mo, Pb–Pb, and Mo–C bond lengths and Mo–C–O bond angles in the η^4- and η^5-isomers are compared and the packing of compounds **1** and **2** is discussed.
(© Wiley-VCH Verlag GmbH & Co. KGaA, 69451 Weinheim, Germany, 2005)

Introduction

The chemistry of group 14 Zintl ions of the type E_9^{4-} (E = Si, Ge, Sn, Pb) is of growing interest due to the remarkable chemical reactivity of these clusters and their potential application in the preparation of ligand-free nanomaterials.[1] According to Wade's rules, an E_9^{4-} cluster adopts a discrete nine-vertex, 22-electron structure with C_{4v} point symmetry which can be described as a monocapped distorted square antiprism.[2] In the case of the Ge_9^{4-} cluster, progress has been made in the field of oxidative coupling reactions of these Zintl anions. Smaller oligomers such as the dimeric $[Ge_9\text{–}Ge_9]^{6-}$,[3] the trimeric $[Ge_9{=}Ge_9{=}Ge_9]^{6-}$,[4] and the tetrameric $[Ge_9{=}Ge_9{=}Ge_9{=}Ge_9]^{8-}$[5,6] and polymeric representatives[7] have been reported. Recently, a polymeric anion $^1_\infty[HgGe_9]^{2-}$ with Zintl ions as building blocks covalently linked by heteroatoms has been reported by our group.[8] Nucleophilic addition of $BiPh_3$ and $SbPh_3$ has also been realized in order to synthesize functionalized clusters like $[Ph_2Bi\text{–}Ge_9\text{–}BiPh_2]^{2-}$[9] and $[Ph_2Sb\text{–}Ge_9\text{–}SbPh_2]^{2-}$.[10] In the case of the Ge clusters, only one transition metal complex of the composition $[Ge_6\{Cr(CO)_5\}_6]^{2-}$ is known so far.[11]

Oxidative coupling reactions of the heavier homoatomic Sn_9^{4-} cluster have also been studied,[12] although no oligomers and polymers have been reported so far. In the case of the heavier homoatomic Sn_9^{4-} and Pb_9^{4-} Zintl clusters the research interests are mainly focused on their reaction with transition metal complexes. Although a few cases concerning the fragmentation of E_9^{4-} Zintl ions and the formation of clusters of different sizes have been reported recently,[13] in most cases the cluster ions stay intact and act as coordinating ligands to the transition metals. The resulting 10-atom heteroatomic Zintl ions are also called "metalated Zintl ions". The first NMR experiments involving the reaction of E_9^{4-} anions (E = Sn, Pb) with $[Pt(PPh_3)_4]$ in ethylenediamine (en) were described by Rudolph in 1983.[14] However, up to now only a few structurally characterized metalated Zintl ions have been reported, most of which are polystannide complexes, including $[Sn_9M(CO)_3]^{4-}$ (M = Cr, Mo, W),[15–17] $[Sn_9Pt_2(PPh_3)]^{2-}$,[18] and $[Sn_9Ni_2(CO)]^{3-}$.[18] Although the first synthesis of the Pb_9^{4-} Zintl ion by Joannis dates back to 1891,[19] and several important synthetic routes for the preparation of Pb_9^{4-} have been developed since then,[20] the reaction of Pb_9^{4-} with transition metal complexes has remained almost unexplored, and only three metalated complexes of the composition $[Pb_9M(CO)_3]^{4-}$ (M = Cr, Mo, W) have been reported.[16,21] It is worth pointing out that the $[Pb_9Mo(CO)_3]^{4-}$ ion has been characterized in the salt $Mo(CO)_3(en)_2[K(2.2.2\text{-crypt})]_4[Pb_9Mo(CO)_3]\cdot 2.5en$ (**3**), although it could not be obtained without $Mo(CO)_3(en)_2$.[16] In the reported complexes the ML_n fragment usually resides in a capping position, with the *nido*-E_9^{4-} ion

[a] Department Chemie, Technische Universität München, Lichtenbergstraße 4, 85747 Garching, Germany
Fax: +49-89-289-13186
E-mail: thomas.faessler@lrz.tum.de

 DOI: 10.1002/ejic.200500060 © 2005 Wiley-VCH Verlag GmbH & Co. KGaA, Weinheim

bound to the metal atom in an η^4-coordinative fashion (Scheme 1).

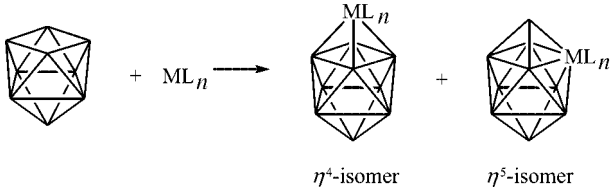

Scheme 1.

Recently, Eichhorn has reported an η^5-coordinated Zintl ion $[Sn_9W(CO)_3]^{4-}$, in which the $W(CO)_3$ unit occupies a waist vertex rather than sitting in a capping position.[17] The obtained product turned out to be a mixture of the η^5- and η^4-isomers in a ratio of 2:1. Metalated Sn_9^{4-} analogs of Ge_9^{4-} and Pb_9^{4-} acting as an η^5-ligand to a transition metal are still unknown. $[M(CO)_3(Mes)]$ (M = Cr, Mo, W) complexes are the most frequently used organometallic complexes for the reaction with E_9^{4-} Zintl ions, whereas their reaction with $[M(CO)_3(MeCN)_3]$ is still unexplored to the best of our knowledge. Herein we report the reaction of K_4Pb_9 with $[Mo(CO)_3(MeCN)_3]$ and the isolation of the first representative of a metalated η^5-Pb_9^{4-} Zintl ion in the solvate-free compound $[K(2.2.2\text{-crypt})]_4[(\eta^5\text{-}Pb_9)Mo(CO)_3]$ (**1**), where 2.2.2-crypt stands for 4,7,13,16,21,24-hexaoxa-1,10-diazabicyclo[8.8.8]hexacosane. According to the results of IR and X-ray analyses, the reaction affords exclusively the η^5-isomer. The reaction of K_4Pb_9 with $[Mo(CO)_3(Mes)]$ was also reinvestigated under the same reaction conditions. In contrast to the previous report,[16] we observed the formation of compound **1** together with its η^4-isomer $[K(2.2.2\text{-crypt})]_4[(\eta^4\text{-}Pb_9)Mo(CO)_3]$ (**2**).

$[K(2.2.2\text{-crypt})]_4[(\eta^5\text{-}Pb_9)Mo(CO)_3]$ (**1**)

$[K(2.2.2\text{-crypt})]_4[(\eta^4\text{-}Pb_9)Mo(CO)_3]$ (**2**)

$Mo(CO)_3(en)_2[K(2.2.2\text{-crypt})]_4[(\eta^4\text{-}Pb_9)Mo(CO)_3]\cdot 2.5en$ (**3**)

$K_2[K(2.2\text{-crypt})]_2[Pb_5\{Mo(CO)_3\}_2](en)_3$ (**4**)

Results and Discussion

Synthesis of Compounds 1 and 2

$[K(2.2.2\text{-crypt})]_4[(\eta^5\text{-}Pb_9)Mo(CO)_3]$ (**1**) was prepared by the slow addition of a toluene solution of $[Mo(CO)_3(MeCN)_3]$[22] to a solution of K_4Pb_9 in ethylenediamine (en) in the presence of 4 equiv. of 2.2.2-crypt. Within 2 h the color of the resulting reaction mixture changed from deep grey to deep reddish-brown. After careful layering with toluene, single crystals of compound **1** started to grow on the walls of the vessel and became visible within a few hours. After one week the solution became colorless, indicating the completeness of the crystallization. Black crystals suitable for single-crystal X-ray diffraction studies were obtained. No additional phases were formed, since the unit cells of several crystals of compound **1** were checked by X-ray diffraction and all of them turned out to be the η^5-complex.

The reaction of K_4Pb_9 with $[Mo(CO)_3(Mes)]$ under the same reaction conditions afforded an isomeric mixture of $[K(2.2.2\text{-crypt})]_4[(\eta^4\text{-}Pb_9)Mo(CO)_3]$ (**2**) and $[K(2.2.2\text{-crypt})]_4[(\eta^5\text{-}Pb_9)Mo(CO)_3]$ (**1**). Surprisingly, compound **2** obtained under these reaction conditions is solvate-free and does not contain an additional $Mo(CO)_3$ fragment as reported for compound **3**.[16] Repetition of the reaction led to variable ratios of the two isomers.

Crystal Structure Analyses of Compounds 1 and 2

Compound 1

The crystal structure analysis of compound **1** shows that the unit cell contains two $[(\eta^5\text{-}Pb_9)Mo(CO)_3]^{4-}$ anions and eight $[K(2.2.2\text{-crypt})]^+$ cations. Four 2.2.2-crypt-coordinated K^+ cations per cluster clearly indicate a charge allocation of –4 for the 10-atom heteroatomic polyanion. Four $[K(2.2.2\text{-crypt})]^+$ units surround the cluster unit at a distance where interionic interactions can be excluded. The shortest Pb–K distance is 7.195 Å. During the refinement, relatively large difference Fourier peaks were located near the Pb atoms, indicating a disorder of the anions which could be resolved by applying a split model (ratio 0.85:0.15). A very similar disorder, even as far as the ratio of occupation is concerned, has been observed for $[(\eta^5\text{-}Sn_9)Mo(CO)_3]^{4-}$.

As emphasized in Figure 1, the $[(\eta^5\text{-}Pb_9)Mo(CO)_3]^{4-}$ ion forms a bicapped square antiprism. The most important feature of this polyhedron is that the $Mo(CO)_3$ unit occupies a waist vertex. This *closo* antiprism is built up by a bottom square plane (Pb2–Pb5), a top square plane (Pb6–Pb8 and Mo), and two capping atoms (Pb1, Pb9). The data of the crystal structure determination of compound **1** are listed in the Exp. Sect., and selected bond lengths and angles for $[(\eta^5\text{-}Pb_9)Mo(CO)_3]^{4-}$ are given in Table 1. The Mo–Pb bond lengths in $[(\eta^5\text{-}Pb_9)Mo(CO)_3]^{4-}$ are different (Table 1), with the contacts of the Mo atom to the apical Pb9 atom and to the Pb2 and Pb5 atoms of the bottom square being remarkably shorter (2.962–3.063 Å) than those to the atoms Pb6 and Pb8 of the top square plane (3.220–3.241 Å). Since these two longer Mo–Pb distances are comparable to the two Pb–Pb contacts within the top square plane (3.278–3.285 Å), the whole cluster can be regarded as regularly shaped, even though the $Mo(CO)_3$ unit is in a waist position. Due to the higher coordination number of the Mo atom in $[(\eta^5\text{-}Pb_9)Mo(CO)_3]^{4-}$, the mean Mo–Pb distance of 3.1074 Å is slightly longer than that in the η^4-isomers (3.028 and 3.032 Å) in compounds **2** and **3**[16] (Table 2). This distance is also significantly longer than the sum of the covalent radii of the metals involved (2.834 Å).[23] The Pb–Pb distances within the top plane are approximately 0.2 Å longer than those in the bottom plane. However, the angles within the bottom plane (90.0 ± 0.9°) lie within a narrower range than those in the top plane (90.0 ± 2.9°). Similar to the different W–C distances in the related η^5- and η^4-$[(Sn_9)W(CO)_3]^{4-}$ complexes, the corresponding Mo–C distances in $[(\eta^5\text{-}Pb_9)Mo(CO)_3]^{4-}$ are

 © 2005 Wiley-VCH Verlag GmbH & Co. KGaA, Weinheim

longer (1.90 Å) than those in the η^4-isomer (1.88 Å). The C–O bonds in $[(\eta^5\text{-}Pb_9)Mo(CO)_3]^{4-}$ are in the range from 1.22 to 1.23 Å and are therefore shorter than those in $[(\eta^4\text{-}Pb_9)Mo(CO)_3]^{4-}$ (1.22–1.27 Å). The Mo–C–O bond angles in $[(\eta^5\text{-}Pb_9)Mo(CO)_3]^{4-}$ deviate strongly from linearity and range from 167 to 171°, which is in contrast to other carbonyl-containing E_9^{4-} moieties like $[(\eta^5\text{-}Sn_9)W(CO)_3]^{4-}$[17] and $[(\eta^4\text{-}Pb_9)Mo(CO)_3]^{4-}$,[16] and also to $[Mo(CO)_3(Mes)]$.[21]

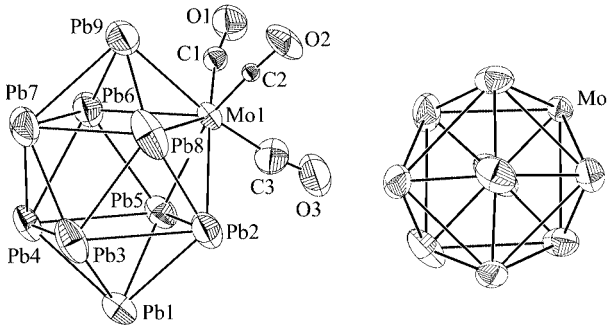

Figure 1. Molecular structure of the *closo*-$[(\eta^5\text{-}Pb_9)Mo(CO)_3]^{4-}$ unit in compound **1** (thermal ellipsoids set at 80% probability).

Table 1. Selected bond lengths [Å] and angles [°] for the $[(\eta^5\text{-}Pb_9)Mo(CO)_3]^{4-}$ unit in compound **1**.

Mo1–Pb2	3.063(1)	Pb4–Pb5	3.390(1)
Mo1–Pb5	3.051(1)	Pb4–Pb6	3.186(1)
Mo1–Pb6	3.220(1)	Pb4–Pb7	3.070(1)
Mo1–Pb8	3.241(1)	Pb5–Pb6	3.011(1)
Mo1–Pb9	2.962(1)	Pb6–Pb7	3.278(1)
Pb1–Pb2	3.069(1)	Pb6–Pb9	3.026(1)
Pb1–Pb3	3.055(1)	Pb7–Pb8	3.285(1)
Pb1–Pb4	3.060(1)	Pb7–Pb9	3.198(1)
Pb1–Pb5	3.070(1)	Pb8–Pb9	3.034(1)
Pb2–Pb3	3.415(1)	Mo1–C1	1.92(1)
Pb2–Pb5	3.272(1)	Mo1–C2	1.89(1)
Pb2–Pb8	3.038(1)	Mo1–C3	1.89(2)
Pb3–Pb4	3.211(1)	C1–O1	1.22(2)
Pb3–Pb7	3.100(1)	C2–O2	1.22(2)
Pb3–Pb8	3.157(1)	C3–O3	1.23(2)
O1–C1–Mo1	167(1)	C1–Mo1–C2	91.9(6)
O2–C2–Mo1	167(1)	C1–Mo1–C3	93.1(6)
O3–C3–Mo1	171(1)	C2–Mo1–C3	95.6(6)
Pb5–Mo1–Pb9	112.38(4)	Pb2–Pb1–Pb4	100.35(2)
Pb2–Mo1–Pb9	112.82(4)	Pb3–Pb1–Pb5	99.96(2)
Pb2–Mo1–Pb6	102.57(3)	Mo1–Pb9–Pb7	99.02(3)
Pb5–Mo1–Pb8	101.72(3)	Pb6–Pb9–Pb8	96.47(2)
Pb6–Mo1–Pb8	88.79(3)	Pb3–Pb2–Pb5	89.07(2)
Mo1–Pb6–Pb7	92.33(3)	Pb2–Pb3–Pb4	90.49(2)
Pb6–Pb7–Pb8	87.05(2)	Pb3–Pb4–Pb5	90.54(2)
Mo1–Pb8–Pb7	91.82(3)	Pb2–Pb5–Pb4	89.90(2)

Table 2. Structural comparison of the anions in compounds **1**, **2**, and **3**.

	1[a]	**2**[a]	**3**[b]
Mean *d*(Pb1 to Pb2, 3, 4, 5) [Å]	3.064	3.074	3.048
Mean *d*(Pb–Pb) in bottom plane [Å][c]	3.322	3.320	3.319
Mean *d*(Pb–Pb/Pb–Mo) in top plane [Å]	3.256	3.202	3.207
Mean *d*(Mo–Pb) [Å]	3.107	3.028	3.032
Mean *d*(Mo–C) [Å]	1.90	1.88	1.93
Mean *d*(C–O) [Å]	1.22	1.23	1.18
Mean Mo–C–O [°]	168	172	178

[a] This work. [b] Ref.[16] [c] The square plane containing the atoms Pb2, Pb3, Pb4, and Pb5 is defined as the bottom plane; the other square plane in the 10-atom polyhedra is defined as the top plane.

Compound 2

The crystal structure analysis of compound **2** shows that the unit cell contains four $[(\eta^4\text{-}Pb_9)Mo(CO)_3]^{4-}$ anions and sixteen $[K(2.2.2\text{-crypt})]^+$ cations. Four 2.2.2-crypt-bound K^+ cations per cluster allow the clear charge allocation of –4 for the 10-atom heteroatomic polyanion. As observed in compound **1**, the four $[K(2.2.2\text{-crypt})]^+$ units in compound **2** are at a large distance from the polyanion and show no coordination to the cluster anion. The distances between the K^+ cations and the polyanions are longer than 7.37 Å. Due to the poor quality of the crystals the reflex intensities were low, and during the refinement relatively large difference Fourier peaks were located near the Pb atoms, indicating a disorder of the anions. Attempts to resolve the disorder were not successful.

As shown in Figure 2, the metal atoms of the $[(\eta^4\text{-}Pb_9)Mo(CO)_3]^{4-}$ ion again form a bicapped square antiprism, but this time with the $Mo(CO)_3$ unit in a capping position. The *closo* antiprism is built up by a bottom square plane (Pb2–Pb5), a top square plane (Pb6–Pb9), and two capping atoms (Pb1, Mo). The data of the crystal structure determination of compound **2** are listed in the Exp. Sect., and selected bond lengths and angles for the $[(\eta^4\text{-}Pb_9)Mo(CO)_3]^{4-}$ anion are given in Table 3. The contacts between the Mo atom and Pb6, Pb7, Pb8, and Pb9 of the top square plane are in the narrow range between 3.014 and 3.048 Å (average 3.028 Å), and are shorter than those observed in compounds **1** (average 3.107 Å) and **3** (average 3.032 Å). The Pb–Pb distances within the top plane range from 3.180 to 3.222 Å and are shorter than those within the bottom plane (3.249–3.428 Å). The Pb–Pb distances between the apical Pb1 and Pb2, Pb3, Pb4, and Pb5 of the bottom plane lie between 3.048 and 3.089 Å (average 3.074 Å) and are longer than those in compounds **1** (average 3.064 Å) and **3** (average 3.048 Å). The two planes have similar dimensions, which gives rise to a more regularly shaped 10-atom cluster than that observed in compounds **1** and **3**. The Pb–Pb distances within the top plane are approximately 0.122 Å shorter than those within the bottom plane. However, the angles within the top plane ($90.0 \pm 0.9°$) lie within a narrower range than those within the bottom plane ($90.0 \pm 1.9°$). In this respect, compound **2** is quite different from compounds **1** and **3**.

Although compounds **2** and **3** contain the same polyhedral core of 10 atoms, the Mo–C–O bond angles in these two compounds are significantly different (Table 2). The mean Mo–C–O bond angle (178°) in compound **3** is almost linear, whereas the corresponding angle in compound **2** deviates strongly from linearity (172°). As shown in Table 2, the Pb–Pb bond lengths within the bottom planes are almost identical (3.322 vs. 3.320 Å) despite the different location of the $Mo(CO)_3$ fragment. The elongation of the mean Mo–Pb distance in the η^5-isomer is a consequence of the higher coordination number. The two elongated bonds

 © 2005 Wiley-VCH Verlag GmbH & Co. KGaA, Weinheim

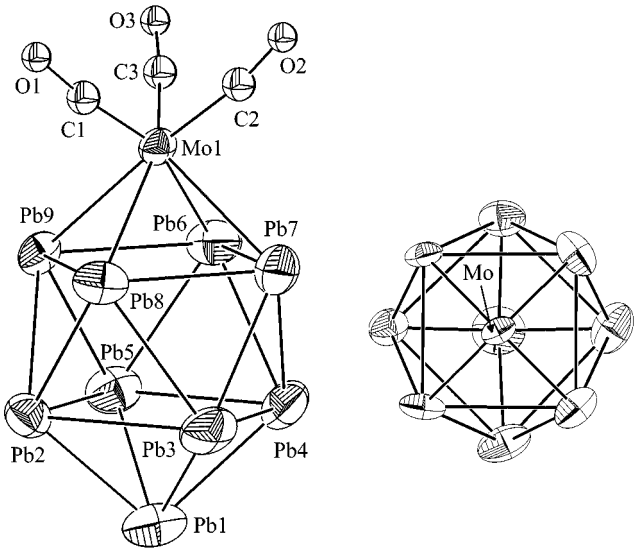

Figure 2. Molecular structure of the *closo*-[(η^4-Pb_9)$Mo(CO)_3$]$^{4-}$ unit in compound **2** (thermal ellipsoids set at 50% probability).

Table 3. Selected bond lengths [Å] and angles [°] for the [(η^4-Pb_9)-$Mo(CO)_3$]$^{4-}$ unit in compound **2**.

Mo1–Pb6	3.030(5)	Pb4–Pb5	3.249(3)
Mo1–Pb7	3.017(4)	Pb4–Pb6	3.137(3)
Mo1–Pb8	3.048(4)	Pb4–Pb7	3.207(3)
Mo1–Pb9	3.014(4)	Pb5–Pb6	3.115(3)
Pb1–Pb2	3.048(3)	Pb5–Pb9	3.138(3)
Pb1–Pb3	3.087(3)	Pb6–Pb7	3.222(3)
Pb1–Pb4	3.089(3)	Pb6–Pb9	3.192(2)
Pb1–Pb5	3.072(3)	Pb7–Pb8	3.215(3)
Pb2–Pb3	3.428(3)	Pb8–Pb9	3.180(2)
Pb2–Pb5	3.293(3)	Mo1–C1	1.83(5)
Pb2–Pb8	3.100(3)	Mo1–C2	1.90(5)
Pb2–Pb9	3.063(3)	Mo1–C3	1.92(5)
Pb3–Pb4	3.309(3)	C1–O1	1.27(5)
Pb3–Pb7	3.100(3)	C2–O2	1.21(5)
Pb3–Pb8	3.149(3)	C3–O3	1.21(5)
O1–C1–Mo1	173(4)	C1–Mo1–C2	92(2)
O2–C2–Mo1	171(4)	C1–Mo1–C3	98(2)
O3–C3–Mo1	172(4)	C2–Mo1–C3	84(2)
Pb7–Mo1–Pb9	97.0(1)	Pb2–Pb1–Pb4	99.53(8)
Pb6–Mo1–Pb8	96.7(1)	Pb3–Pb1–Pb5	99.56(9)
Pb3–Pb2–Pb5	88.79(6)	Pb7–Pb6–Pb9	89.53(6)
Pb2–Pb3–Pb4	88.11(6)	Pb6–Pb7–Pb8	89.71(6)
Pb3–Pb4–Pb5	91.63(7)	Pb7–Pb8–Pb9	89.87(6)
Pb2–Pb5–Pb4	91.47(7)	Pb6–Pb9–Pb8	90.87(6)

(Mo–Pb6, Mo–Pb8) originate from the nonplanarity of the five coordinated Pb atoms.

Very recently, another compound of the composition $K_2[K(2.2\text{-crypt})]_2[Pb_5\{Mo(CO)_3\}_2](en)_3$ (**4**) with Mo–Pb and Pb–Pb bonds has been reported by our group.[24] The structure of the [{$(OC)_3Mo$}Pb_5{$Mo(CO)_3$}]$^{4-}$ anion (Figure 3b) contains a planar five-membered ring of lead atoms. The Pb–Pb bond lengths between 3.014(1) and 3.065(1) Å (average 3.041 Å) in compound **4** are significantly shorter than those in compounds **1** and **2** (d_{Pb-Pb} = 3.011–3.415 Å and 3.048–3.428 Å, respectively). Interestingly, the Mo–Pb distances (3.014–3.048 Å) in compound **2** are very similar to those in compound **4** (3.001–3.093 Å), but differ from those in compound **1** (2.962–3.241 Å). Compound **1** can be regarded as an intermediate in the fragmentation of the Pb_9^{4-} cluster and the formation of the novel Pb_5 cluster fragment in **4** (Figure 3).

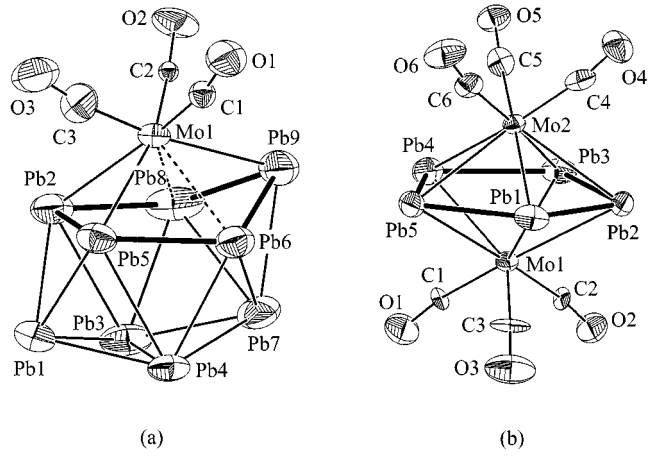

Figure 3. (a) Molecular structure of the *closo*-[(η^5-Pb_9)$Mo(CO)_3$]$^{4-}$ unit in compound **1** (thermal ellipsoids set at 80% probability) (dotted lines represent Mo–Pb distances >3.2 Å). (b) The structure of the *closo*-[η^5-Pb_5{$Mo(CO)_3$}$_2$]$^{4-}$ Zintl anion (thermal ellipsoids set at 80% probability).

Cluster Arrangements

The packing diagrams of compounds **1** and **2** are shown in Figures 4 and 5, respectively. Both compounds form distorted hexagonal layers. The distances between the cluster units within the same layers differ by less than 10% (distance range for **1** from 15.465 to 16.774 Å and for **2** from 15.066 to 16.477 Å). In compound **1** the interlayer distances between the centers of gravity of the clusters are 15.493, 15.853 (2×), and 15.144 Å. The orientation of the $M(CO)_3$ groups with respect to the layers has no significant influence on the distances between the clusters. Irrespective of their orientation the two different layers of clusters (I and II), one of which is shown in Figure 4a, arrange in a cubic-type packing as indicated in Figure 4b by the labels ABCA perpendicular to the *ab* plane (not along *c*).

In compound **2**, the distorted layers are packed pairwise along the *b* direction of the unit cell. Within the AA′ and BB′ layers (Figure 5) the $M(CO)_3$ groups of two layers are oriented towards each other, leading to a larger distance of 14.431 Å between these layers as compared to the A′B and B′A interlayer distance of 12.502 Å. Consequently, different intercluster distances of 16.617 and 14.308 Å occur. The relative orientation of the carbonyl groups of the $Mo(CO)_3$ unit might be the origin of the larger unit cell volume of **2** if compared to **1**.

 © 2005 Wiley-VCH Verlag GmbH & Co. KGaA, Weinheim

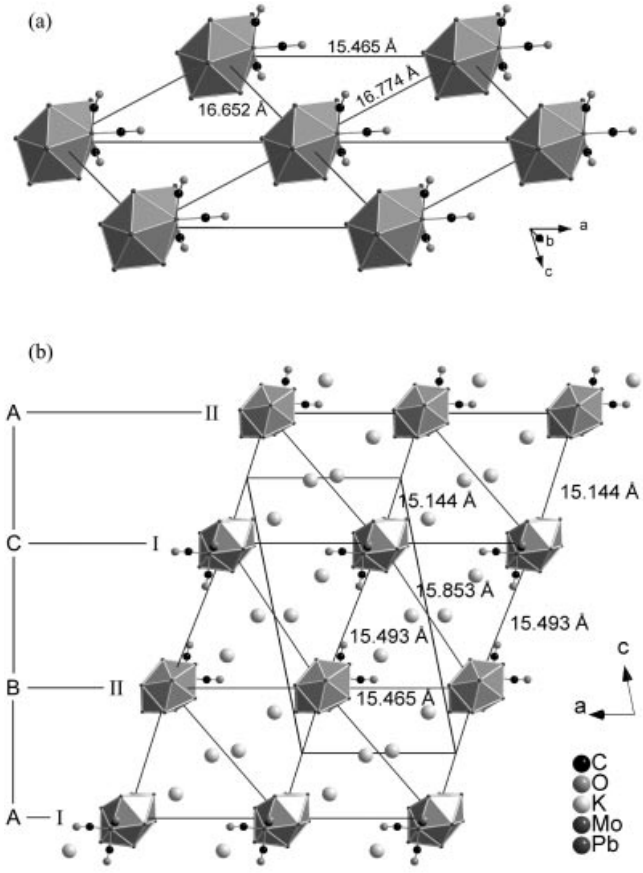

Figure 4. (a) The hexagonal packing in the *ab* plane in the single crystal of compound **1**. (b) The stacking sequence of the layers along the *c* axis in compound **1** (2.2.2-crypt units are not shown).

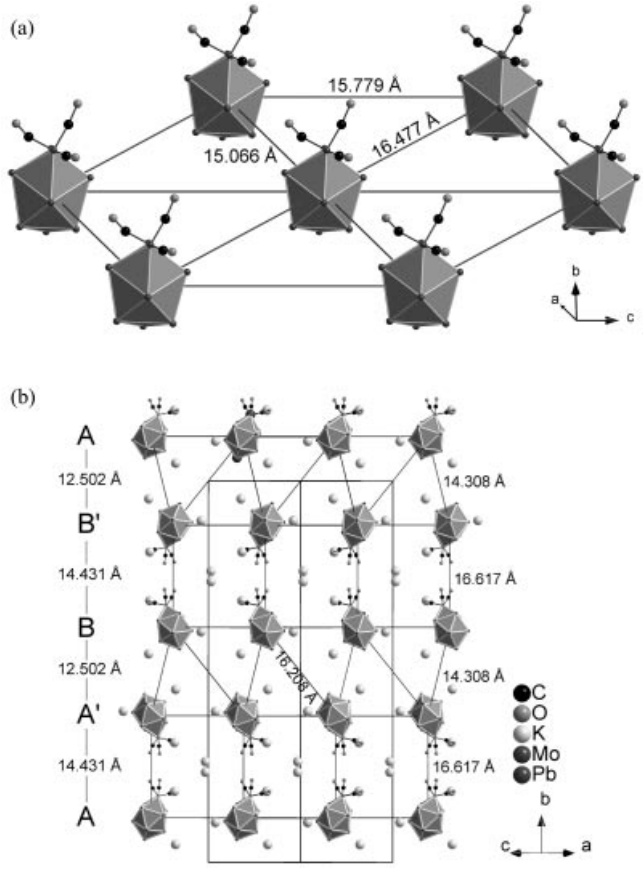

Figure 5. (a) The hexagonal packing in the *ac* plane in the single crystal of compound **2**. (b) The stacking sequence of the layers along the *b* axis in compound **2** (2.2.2-crypt units are not shown).

IR Spectra

Single crystals of **1** and the crude product were carefully checked by solid-state IR analyses. The characteristic CO stretching vibrations of the η^5-isomer are found at 1809 and 1697 cm^{-1}. None of the characteristic peaks of the η^4-isomer ($\tilde{\nu}$ = 1813, 1736, and 1702 cm^{-1})[16] were detected (Table 4). The carbonyl bands of the η^5-isomer are red-shifted relative to those of the η^4-isomer. This red-shift has also been observed for the isomeric compounds $[(\eta^5\text{-}Sn_9)W(CO)_3]^{4-}$ ($\tilde{\nu}$ = 1805, 1701 cm^{-1}) and $[(\eta^4\text{-}Sn_9)W(CO)_3]^{4-}$ ($\tilde{\nu}$ = 1822, 1711, 1701 cm^{-1}; see also Table 4).

As already mentioned above, several crystals of compound **1** were checked by X-ray diffraction and identified as the η^5-isomer. The IR study gave further evidence that the reaction of $[Mo(CO)_3(MeCN)_3]$ with K_4Pb_9 yields exclusively one isomer (**1**). Our attempts to obtain a ^{207}Pb NMR spectrum of compound **1** were unsuccessful due to its poor solubility in the usual solvents (en, DMF, THF, DMSO, and toluene).

Conclusions

The reaction of $[Mo(CO)_3(MeCN)_3]$ with K_4Pb_9 in the presence of 2.2.2-crypt was investigated. A metalated Zintl ion $[K(2.2.2\text{-crypt})]_4[(\eta^5\text{-}Pb_9)Mo(CO)_3]$ (**1**) was isolated and characterized by single-crystal X-ray structure and IR analyses. The carbonyl (CO) stretching vibrations ($\tilde{\nu}$ = 1807, 1697 cm^{-1}) in the IR spectrum of compound **1** clearly show the exclusive formation of the $[(\eta^5\text{-}Pb_9)Mo(CO)_3]^{4-}$ isomer. The $[K(2.2.2\text{-crypt})]_4[(\eta^4\text{-}Pb_9)Mo(CO)_3]$ isomer (**2**), which has been isolated for the first time as a pure product, is formed together with its isomer **1** in the reaction of $[Mo(CO)_3(Mes)]$ with K_4Pb_9 under the same reaction conditions.

Experimental Section

The synthesis of compound **1** was carried out under argon in a glove-box or in a Schlenk line. The IR spectra were recorded from KBr pellets with a JASCO FT/IR-460 spectrometer. The X-ray crystal data were collected with a Nonius Kappa CCD device at the window of a rotating anode X-ray generator and processed with the SHELXS-97 and SHELXL-97 program packages.[25] The crystallographic data for the structures are summarized in Table 5. CCDC-258685 (**1**) and -258686 (**2**) contain the supplementary crystallographic data for this paper. These data can be obtained free of charge from The Cambridge Crystallographic Data Centre via www.ccdc.cam.ac.uk/data_request/cif. The elemental analyses were carried out by the Microanalytical Laboratory at TU Munich. Toluene (Merck) and en (Merck) were dried with K/CaH_2 (Fluka),

 © 2005 Wiley-VCH Verlag GmbH & Co. KGaA, Weinheim

Table 4. The characteristic CO stretching vibrations in E_9 Zintl complexes.

Complexes	ν_{CO} [cm^{-1}]	Ref.
$[K(2.2.2\text{-crypt})]_4[(\eta^4\text{-}Sn_9)Cr(CO)_3]$	1822, 1705	[17]
$[K(2.2.2\text{-crypt})]_4[(\eta^4\text{-}Sn_9)Mo(CO)_3]$	1829, 1708	[17]
$[K(2.2.2\text{-crypt})]_4[(\eta^4\text{-}Sn_9)Mo(CO)_3]$	1830, 1718, 1703	[16]
$[K(2.2.2\text{-crypt})]_4[(\eta^5\text{-}Sn_9)W(CO)_3]$	1805, 1701	[17]
$[K(2.2.2\text{-crypt})]_4[(\eta^4\text{-}Sn_9)W(CO)_3]$	1822, 1711, 1701	[16]
$[K(2.2.2\text{-crypt})]_4[(\eta^4\text{-}Pb_9)Cr(CO)_3]$	1791, 1695, 1681	[21]
$Mo(CO)_3(en)_2[K(2.2.2\text{-crypt})]_4[(\eta^4\text{-}Pb_9)Mo(CO)_3]$	1813, 1736, 1702	[16]
$W(CO)_3(en)_2[K(2.2.2\text{-crypt})]_4[(\eta^4\text{-}Pb_9)W(CO)_3]$	1804, 1697, 1686	[16]
$[K(2.2.2\text{-crypt})]_4[(\eta^5\text{-}Pb_9)Mo(CO)_3]$	1809, 1697	this work
$K_2[K(2.2\text{-crypt})]_2[Pb_5\{Mo(CO)_3\}_2](en)_3$	1889, 1878, 1737	[24]

Table 5. Crystallographic data for compounds **1** and **2**.

	$[K(2.2.2\text{-crypt})]_4[(\eta^5\text{-}Pb_9)Mo(CO)_3]$	$[K(2.2.2\text{-crypt})]_4[(\eta^4\text{-}Pb_9)Mo(CO)_3]$
Empirical formula	$C_{75}H_{144}K_4Mo_1N_8O_{27}Pb_9$	$C_{75}H_{144}K_4MoN_8O_{27}Pb_9$
Formula mass [$g\,mol^{-1}$]	3707.03	3707.03
Temperature [K]	173(2)	120(2)
Wavelength [Å]	0.71073	0.71073
Crystal system	triclinic	monoclinic
Space group	$P\bar{1}$ (no.2)	$P2_1/n$ (no. 14)
a [Å]	15.4651(1)	15.066(1)
b [Å]	16.6519(1)	53.866(1)
c [Å]	25.5701(2)	15.779(1)
α [°]	79.265(1)	90
β [°]	75.144(1)	115.473(1)
γ [°]	62.842(1)	90
Volume [$Å^3$]	5644.9(1)	11560.7(3)
Z	2	4
$\rho_{calcd.}$ [$g\,cm^{-3}$]	2.181	2.130
μ [mm^{-1}]	13.686	13.366
$F(000)$	3444	6888
Crystal size [mm]	$0.40\times0.40\times0.20$	$0.20\times0.10\times0.05$
θ range [°]	1.38 to 25.37	4.09 to 20.85
Index ranges	$0 \le h \le 18$	$-15 \le h \le 13$
	$-17 \le k \le 20$	$0 \le k \le 37$
	$-29 \le l \le 30$	$0 \le l \le 15$
Reflections collected	126980	49478
Independent reflections	20659 (R_{int} = 0.084)	9540 (R_{int} = 0.180)
Goodness-of-fit on F^2	1.067	1.021
Final R indices[$I > 2\sigma(I)$]	R_1 = 0.058, wR_2 = 0.137	R_1 = 0.103, wR_2 = 0.257
R indices (all data)	R_1 = 0.082, wR_2 = 0.148	R_1 = 0.148, wR_2 = 0.287
Largest peak/hole [$e\,Å^{-3}$]	3.107/–2.146	8.597/–3.409

freshly distilled, and degassed. The binary phase of the formal composition "K_4Pb_9" was prepared by a high-temperature reaction (350 °C) from the elements K and Pb in the ratio of 4:9. Tricarbonyl(mesitylene)molybdenum and tris(acetonitrile)tricarbonylmolybdenum were prepared by heating $Mo(CO)_6$ (Alfa Inorganics) in an excess of mesitylene or MeCN under reflux under nitrogen according to the reported methods.[22]

K_4Pb_9 (100 mg, 0.049 mmol) and 2.2.2-crypt (74 mg, 0.2 mmol) were dissolved in en (ca. 1 mL) and stirred for 5 min. A yellow solution of $[Mo(CO)_3(MeCN)_3]$ (16 mg, 0.051 mmol) in toluene (ca. 2 mL) was then added to the green solution of K_4Pb_9. The resulting mixture was stirred at room temperature for another 2 h. After filtration, the filtrate was layered with toluene (2 mL). Within 48 h, dark-brown crystals of $[K(2.2.2\text{-crypt})]_4[Pb_9Mo(CO)_3]$ precipitated (48 mg, ca. 45% with respect to K_4Pb_9). Elemental analysis of the products from this reaction (3707.03): calcd. C 24.30, H 3.92, N 3.02; found C 24.49, H 3.60, N 3.18. The reaction of K_4Pb_9 (100 mg, 0.049 mmol) with $[Mo(CO)_3(Mes)]$ (15 mg, 0.049 mmol) was carried out under the same reaction conditions with the same workup procedure.

Acknowledgments

This work was supported by the Deutsche Forschungsgemeinschaft (SPP 1072). We thank Dr. Klaus Ruhland for his kind assistance with the ^{207}Pb NMR study and Dr. Annette Schier for checking the manuscript.

[1] a) A. Schnepf, *Angew. Chem. Int. Ed.* **2003**, *42*, 2624–2625; b) N. Korber, A. Fleischmann, *J. Chem. Soc., Dalton Trans.* **2001**, 383–385; c) T. F. Fässler, R. Hoffmann, *Angew. Chem. Int. Ed.* **1999**, *38*, 543–546; d) V. Quenéau, E. Todorov, S. C. Sevov, *J. Am. Chem. Soc.* **1998**, *120*, 3263–3264; e) H. G. von Schnering, M. Somer, M. Kaupp, W. Carrillo-Cabrera, M. Baitinger, A. Schmeding, Y. Grin, *Angew. Chem. Int. Ed.* **1998**, *37*, 2359–2361; f) J. R. Heath, *Science* **1995**, *270*, 1315–1316; g) L. Brus,

 © 2005 Wiley-VCH Verlag GmbH & Co. KGaA, Weinheim

Adv. Mater. **1993**, *5*, 286–288; h) M. Ho, A. A. Shvartsbyrg, B. Pan, Z.-Y. Lu, C.-Z. Wang, J. G. Wacker, J. L. Fye, M. F. Jarrold, *Nature* **1998**, *392*, 582–585; i) R. A. Bley, S. M. Kauzlarich, *J. Am. Chem. Soc.* **1996**, *118*, 12461–12462.
[2] Reviews: a) J. D. Corbett, *Chem. Rev.* **1985**, *85*, 383–397; b) T. F. Fässler, *Coord. Chem. Rev.* **2001**, *215*, 347–377; c) T. F. Fässler, *Angew. Chem. Int. Ed.* **2001**, *40*, 4161–4165.
[3] L. Xu, S. C. Sevov, *J. Am. Chem. Soc.* **1999**, *121*, 9245–9246.
[4] a) A. Ugrinov, S. C. Sevov, *J. Am. Chem. Soc.* **2002**, *124*, 10990–10991; b) L. Yong, S. D. Hoffmann, T. F. Fässler, *Z. Anorg. Allg. Chem.* **2005**, in press.
[5] A. Ugrinov, S. C. Sevov, *Inorg. Chem.* **2003**, *42*, 5789–5791.
[6] L. Yong, S. D. Hoffmann, T. F. Fässler, *Z. Anorg. Allg. Chem.* **2004**, *630*, 1977–1981.
[7] a) C. Downie, J.-G. Mao, H. Parmar, A. M. Guloy, *Inorg. Chem.* **2004**, *43*, 1992–1997; b) C. Downie, J.-G. Mao, A. M. Guloy, *Inorg. Chem.* **2001**, *40*, 4721–4725; c) C. Downie, Z. Tang, A. M. Guloy, *Angew. Chem. Int. Ed.* **2000**, *39*, 338–340.
[8] A. Nienhaus, R. Hauptmann, T. F. Fässler, *Angew. Chem. Int. Ed.* **2002**, *41*, 3213–3215.
[9] A. Ugrinov, S. C. Sevov, *J. Am. Chem. Soc.* **2002**, *124*, 2442–2443.
[10] A. Ugrinov, S. C. Sevov, *J. Am. Chem. Soc.* **2003**, *125*, 14059–14064.
[11] a) B. Schiemenz, G. Huttner, *Angew. Chem. Int. Ed. Engl.* **1993**, *32*, 297–298; b) G. Renner, P. Kircher, G. Huttner, P. Rutsch, K. Heinze, *Eur. J. Inorg. Chem.* **2001**, 973–980.
[12] T. F. Fässler, U. Schütz, *J. Organomet. Chem.* **1997**, *541*, 269–276.
[13] a) E. N. Esenturk, J. Fettinger, Y.-F. Lam, B. Eichhorn, *Angew. Chem. Int. Ed.* **2004**, *43*, 2132–2134; b) B. Kesanli, J. Fettinger, B. Eichhorn, *Angew. Chem. Int. Ed.* **2001**, *40*, 2300–2302; c) T. F. Fässler, S. D. Hoffmann, *Angew. Chem. Int. Ed.* **2004**, *43*, 6242–6247.
[14] F. Teixidor, M. L. Leutkens, R. W. Rudolph, *J. Am. Chem. Soc.* **1983**, *105*, 149–150.
[15] a) B. W. Eichhorn, R. C. Haushalter, W. T. Pennington, *J. Am. Chem. Soc.* **1988**, *110*, 8704–8706; b) B. Schiemenz, G. Huttner, *Angew. Chem. Int. Ed. Engl.* **1993**, *32*, 297–298; c) G. Renner, P. Kircher, G. Huttner, P. Rutsch, K. Heinze, *Eur. J. Inorg. Chem.* **2001**, 973–980.
[16] J. Campbell, H. P. A. Mercier, H. Franke, D. P. Santry, D. A. Dixon, G. J. Schrobilgen, *Inorg. Chem.* **2002**, *41*, 86–107.
[17] B. Kesanli, J. Fettinger, B. Eichhorn, *Chem. Eur. J.* **2001**, *7*, 5277–5285.
[18] B. Kesanli, J. Fettinger, D. R. Gardner, B. Eichhorn, *J. Am. Chem. Soc.* **2002**, *124*, 4779–4786.
[19] A. Joannis, *C. R. Hebd. Séances Acad. Sci.* **1891**, *113*, 795–798.
[20] a) T. F. Fässler, R. Hoffmann, *J. Chem. Soc., Dalton Trans.* **1999**, 3339–3340; b) C. J. Warren, R. C. Haushalter, A. B. Bocarsly, *J. Alloys Compd.* **1995**, *229*, 175–205; c) E. Zintl, J. Goubenau, W. Dullenkopf, *Z. Phys. Chem. Abt. A* **1931**, *154*, 1–46; d) C. A. Kraus, *J. Am. Chem. Soc.* **1907**, *29*, 1557–1571.
[21] B. W. Eichhorn, R. C. Haushalter, *J. Chem. Soc., Chem. Commun.* **1990**, 937–938.
[22] a) E. L. Muetterties, J. R. Bleeke, A. C. Sievert, *J. Organomet. Chem.* **1979**, *178*, 197–216; b) C. Li, W. Yeh, S. Peng, G. Lee, *J. Organomet. Chem.* **2001**, *620*, 106–112.
[23] L. Pauling, *The Nature of the Chemical Bond*, 3rd ed., Cornell University Press, Ithaca, NY, **1960**, pp. 116, 256, 261.
[24] L. Yong, S. D. Hoffmann, T. F. Fässler, S. Riedel, M. Kaupp, *Angew. Chem. Int. Ed.* **2005**, *44*, 2092–2096.
[25] G. M. Sheldrick, *SHELXS-97 and SHELXL-97, Programs for the solution and refinement of crystal structures*, University of Göttingen, Germany, **1997**.

Received: January 20, 2005
Published Online: June 21, 2005

 © 2005 Wiley-VCH Verlag GmbH & Co. KGaA, Weinheim

Generation and Characterization of Multilayer Systems Consisting of $Au_{55}(PPh_3)_{12}Cl_6$ Double Layers and SiO_2 Barrier Films

Torsten Reuter,[a] Stefan Neumeier,[a] Günter Schmid,*[a] Eva Koplin,[b] and Ulrich Simon[b]

Keywords: Gold / Multilayers / Impedance spectroscopy / Bénard–Marangoni effect / Crystallisation

Multilayer systems, consisting of $Au_{55}(PPh_3)_{12}Cl_6$ double layers and SiO_2 barrier films of different thickness, have been generated and characterised. The formation of the double layer between the barrier films was carried out by using spin-coating techniques. For the generation of the SiO_2 films, a plasma-assisted physical vapour deposition (PAPVD) procedure has been applied, based on an anodic plasma arc process. Samples of up to nine cluster/SiO_2 combinations have been produced and have been characterised by AFM and SEM. Impedance measurements showed that there is a characteristic thermally activated frequency dependence of the capacitance of the different systems. The cluster layers interact by dipoles formed in the double layers at low frequencies. It has also been shown that multilayer systems with SiO_2 films thicker than 15 nm tend to spontaneously crystallise. Furthermore, wetting problems during the spin-coating processes have been investigated.

(© Wiley-VCH Verlag GmbH & Co. KGaA, 69451 Weinheim, Germany, 2005)

Introduction

Au_{55} clusters, although known for almost 25 years,[1] are still the focus of intensive research, mainly because of their extraordinary electronic properties. The density of states in the valence and in the conduction bands is, compared with that in a bulk piece of metal, dramatically decreased with the result that a metal particle with an extremely small size of 1.4 nm follows quantum mechanical rules instead of the classical laws valid for a bulk metal with an infinitely large number of atoms. Indeed, it has been previously shown that Au_{55} clusters behave as quantum dots that have discrete electronic energy levels.[2,3] Au_{55} clusters act as switches that can be charged and discharged by single electrons, even at room temperature. It is important to mention that individual Au_{55} clusters do not exist in the bare form, and in all cases have to be protected by a shell of appropriate ligand molecules. The nature of such ligand molecules can vary from totally apolar to ionic, with a corresponding change in the solvents in which they are soluble from nonpolar media like alkanes to very polar media like water.[4,5] The existence of a ligand shell is not only necessary for synthetic reasons, but also for prevention of coalescence between bare particles and, last but not least, for profiting from the special electronic properties.

[a] Universität Duisburg Essen,
Universitätsstrasse 5–7, 45117 Essen, Germany
E-mail: guenter.schmid@uni-essen.de
[b] RWTH Aachen,
Landoltweg 1, 52074 Aachen, Germany
E-mail: ulrich.simon@ac.rwth-aachen.de

Our knowledge of the unique electronic properties of Au_{55} clusters prompted us already years ago to look for routes to two-dimensional (2D) organisations, an indispensable condition for the application of these quantum dots in nanoelectronic devices. Perfectly organised monolayers have been generated with limited extension by self-assembly.[6,7] More extended 2D arrangements could be prepared by using chemically modified surfaces[8] or by Langmuir–Blodgett techniques,[9] however, without giving ordered arrays. Artificial structures became available for the first time by using an AFM tip to electrochemically modify pre-prepared surfaces on the nanometre scale.[10] If the order of the clusters is not important, a very simple but effective method can be used. This is the spin coating of dilute solutions of ligand-modified Au_{55} clusters on appropriate surfaces. This technique has been used in the experiments described in this contribution. Spin coating indeed allows to reproducibly generate cluster double layers and, if necessary, monolayers, if the experimental conditions are carefully worked out. Here we report on the generation and on the electric properties of cluster double layers embedded between SiO_2 films of varying thickness. The reason for this research was to find out if thin cluster films, separated from each other by an insulating material, can still communicate with each other, perpendicular to the film plane. From former experiments we know that the horizontal electric conductivity of thin cluster films over extensions of dozens of nanometres is below the detection limit,[11] whereas tunnelling processes between clusters over shorter distances (20 nm) have been observed.[12] Since the layers under investigation are of millimetre dimension, horizontal measurements seem unnecessary. However, the question whether

electron tunnelling between cluster layers that are separated from each other by SiO_2 films of varying thickness will be possible is of general interest.

Results and Discussion

Generation of Cluster/SiO_2 Multilayers

The aim of this work was to generate and electrically characterise multilayer systems as shown schematically in Figure 1 with varying numbers of layers.

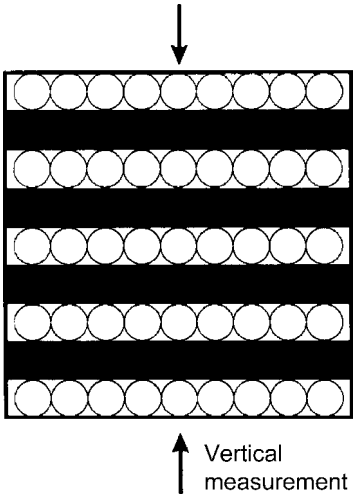

Figure 1. Sketch of a multilayered system consisting of nanoparticles and isolating barrier films.

The construction of the SiO_2 films was performed by plasma-assisted physical vapour deposition (PAPVD). The process is shown in Figure 2.

Figure 2a shows the relevant circuits of the system, and Figure 2b illustrates the process leading to the SiO_2 films. A piece of silicon in a carbon boat, which is linked to the anode, is positioned opposite the cathode, which consists of brass (1). The optimal pressure and the current conditions needed to generate 5 nm SiO_2 films were found to be 2×10^{-2} mbar O_2 and 75 A. After formation of a stable arc (2), the silicon begins to evaporate and moves towards the substrate (3). The jets of the cathode meet the silicon vapour and ionise it resulting in the anodic plasma (4). The anodic plasma expands into the vacuum reaching the substrate with the condensation of the silicon ions (5). Due to the presence of oxygen, SiO_2 is deposited (6). The stoichiometry is not perfect, and there may be a deficit of oxygen to a certain extent, but this should not influence the further steps. The time taken to produce a 5 nm SiO_2 film is only 3 s. As has been shown by the AFM investigations, the roughness of the as-prepared films is only 0.1 nm. Such surfaces are thus best suited for the generation of perfect cluster layers. Figure 3 shows a photograph of the whole apparatus.

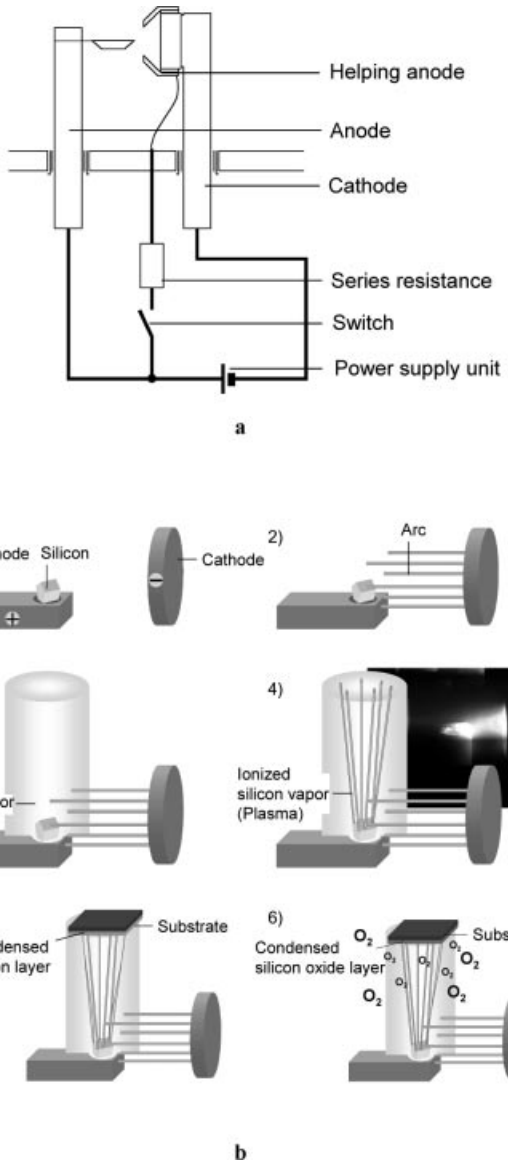

Figure 2. Illustration of the anodic plasma arc process. **a**: circuits for the PAPVD process, **b**: schematic drawing of the coating process using an anodic plasma arc.

To generate cluster double layers, diluted solutions of $Au_{55}(PPh_3)_{12}Cl_6$ clusters in dichloromethane (4.3×10^{-6} M) were used for spin coating. To cover a 1×1 cm^2 area, 50 μL are necessary, which are dropped onto a silicon wafer surface that is rotating at 100 revolutions per minute. After 5 s, the speed is accelerated to 4000 revolutions per minute, resulting in double layers, as can be seen from the AFM image in Figure 4.

The roughness was found to be 0.2 nm. The thickness of the film was determined by generating a cluster-free window by means of the AFM tip. The height profile is also shown in Figure 4. With a value of 5 nm, it agrees perfectly with a cluster double layer.

From the AFM sequences in Figure 5, it can be seen that the coating of the cluster layers with SiO_2 films occurs without destruction by the plasma process.

 © 2005 Wiley-VCH Verlag GmbH & Co. KGaA, Weinheim

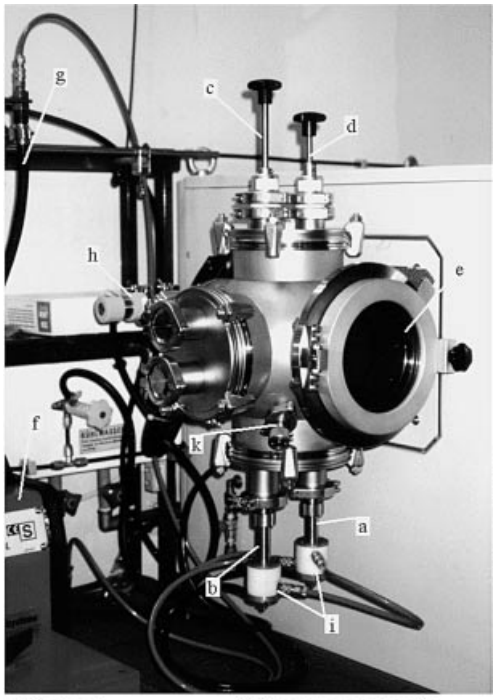

a) Cathode
b) Anode
c) Substrate fastener
d) Shutter
e) Inspection glass
f) Power supply unit
g) Series resistance
h) Needle valve
i) Water supply
k) Valve

Figure 3. Photograph of the whole apparatus for the PAPVD process.

Beginning with a silicon wafer (a), spin coating results in a cluster double layer (b). Coating with a 5-nm SiO_2 film (c) occurs and the surface structure is maintained. As a typical example, Figure 6 shows a transmission electron microscopy image (TEM) of a sectioned piece of a seven-layer system. For better visualisation, a sample with 15-nm SiO_2 layers has been selected. For later electric measurements, only 5 nm films will be considered, since the resistance of the 15 nm films was too high.

As can be seen, the parallel cluster layers consist of individual particles and are without visible defects. The final SiO_2 film still exhibits a low surface roughness of ca. 0.7 nm.

Side Effects

Before discussing the electric properties of multilayers, some side effects will briefly be considered: hydrodynamic instabilities of the cluster layers, and thermodynamic instabilities and optical properties of the multilayers.

The homogeneous coverage of the Si wafers or the SiO_2 films by $Au_{55}(PPh_3)_{12}Cl_6$ clusters from dichloromethane solutions is only possible with solvent that contains moisture (this can be achieved by contact of CH_2Cl_2 with air for a couple of days). The use of absolutely dry solvents results in an insufficient wettability of the wafer surface, actually consisting of a very thin SiO_2 film if handled in air. Absolutely dry solvents cause the Bénard–Marangoni effect.[13–18] This effect deals with the evaporation of thin liquid films

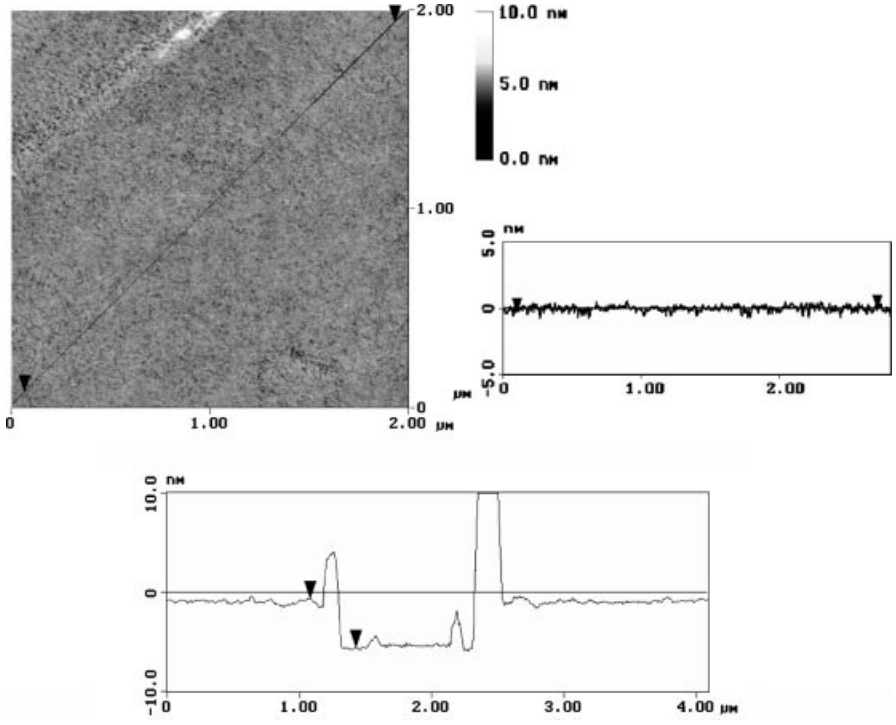

Figure 4. AFM image of a $Au_{55}(PPh_3)_{12}Cl_6$ double layer (left), roughness profile (0.2 nm) (right), and height profile (bottom) of 5 nm, generated by scratching a window into the layer with the AFM tip.

 © 2005 Wiley-VCH Verlag GmbH & Co. KGaA, Weinheim

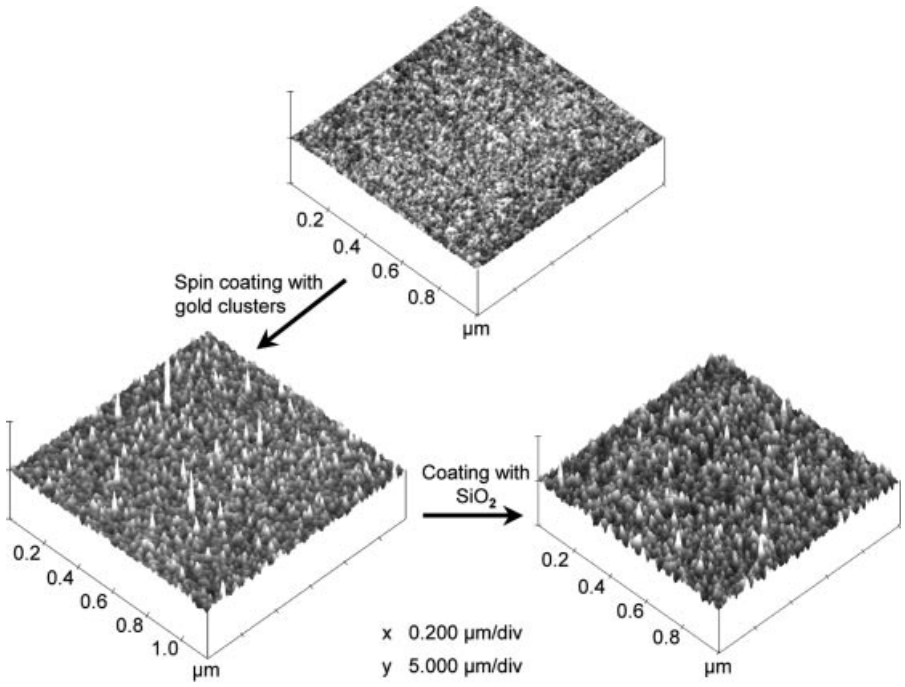

Figure 5. AFM images of a silicon wafer surface (top), a cluster double layer generated by spin coating (left) and a SiO_2 film on top of the cluster film (right), indicating that the SiO_2 does not destroy the cluster layer.

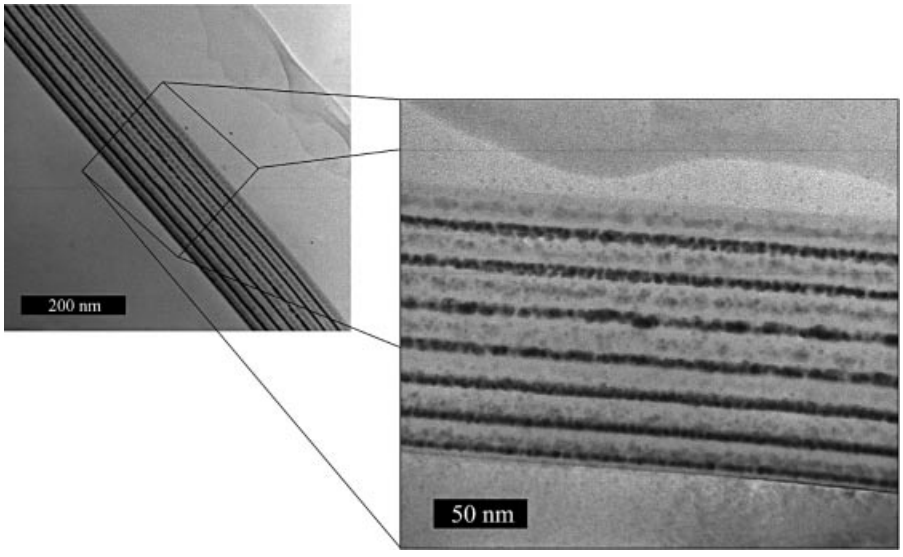

Figure 6. SEM image of a sectioned multilayer system consisting of seven cluster/SiO_2 combinations (black: cluster layers, grey: SiO_2 films).

on substrates. Hydrodynamic instabilities and surface tensions lead to diffusion processes from the warm substrate to the cooler liquid/air interface. A constant flow inside the liquid film is generated, which results in the formation of hexagonally oriented cells. At the borders of these cells, the particles, dissolved in the solvent, are deposited, and finally form hexagonal patterns. Figure 7 illustrates the Bénard–Marangoni effect, and Figure 8 shows light microscopy and scanning electron microscopy (SEM) images of some of the observed hexagonal patterns on glass (top) and on Si wafer (bottom), respectively.

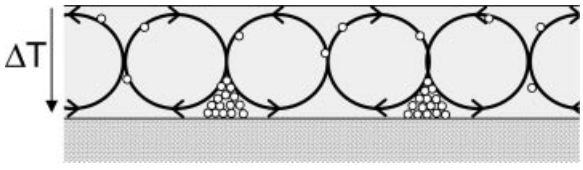

Figure 7. Illustration of the Bénard–Marangoni effect.

It should, however, be mentioned that the formation of such hexagonal structures is not expressed as much when spin-coating techniques are used, relative to simple addition

 © 2005 Wiley-VCH Verlag GmbH & Co. KGaA, Weinheim

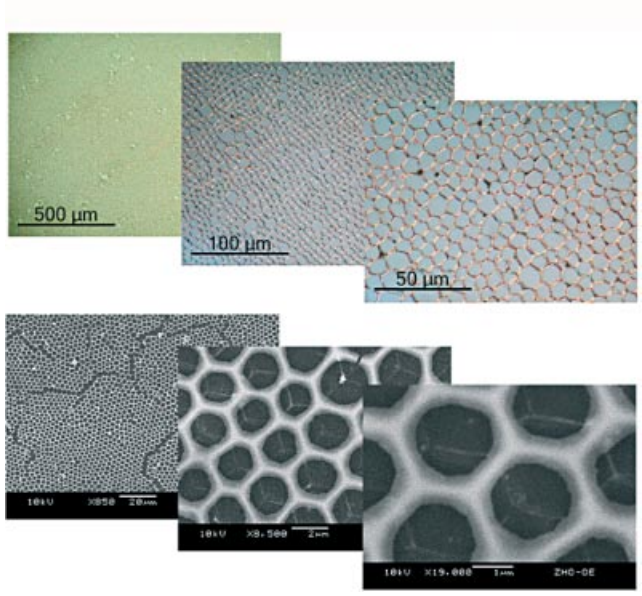

Figure 8. Light microscopy images (top) and SEM images (bottom) of the hexagonal patterns of $Au_{55}(PPh_3)_{12}Cl_6$ clusters on glass substrates (top) and on Si wafers (bottom), respectively. The structures form if the wetting conditions are not appropriate. Bars in the SEM images: 20 µm, 2 µm and 1 µm (from left).

of the cluster solution to the surface of a substrate. The concentrations of the solutions have little influence on the structure formation.

Another effect is observed that indicates the instability of the multilayers in the case of thicker SiO_2 interfaces. The SiO_2 films, generated by the discussed plasma process, are amorphous. In the cases of multilayers with SiO_2 films thicker than 15 nm, there is a tendency of the multilayer to spontaneously crystallise. This tendency is greater as the thickness of the SiO_2 films and the number of layers in-

Figure 9. Photograph of a crystallized multilayer sample.

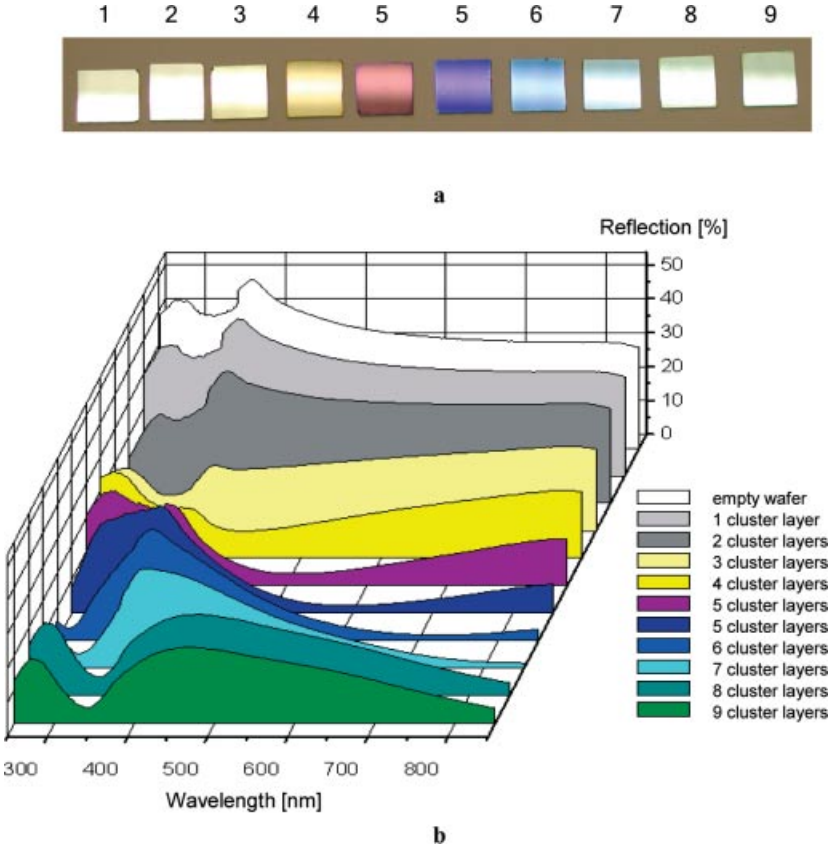

Figure 10. Changes in colour with increasing numbers of layers. **a**: photograph of multilayers consisting of 5-nm cluster layers and 30-nm SiO_2 films. **b**: UV/Vis spectra of the samples shown in **a**, measured in reflection.

 © 2005 Wiley-VCH Verlag GmbH & Co. KGaA, Weinheim

crease. Figure 9 shows an optical image of a crystallised multilayer sample consisting of five cluster/SiO_2 combinations with 40-nm SiO_2 films. Three different types of crystallisation can be seen, macroscopically observable by different colours.

This phenomenon can be compared with the known metal-induced crystallisation of amorphous silicon.[19] Multilayers with SiO_2 intermediates that are <15 nm are stable with respect to crystallisation, whereas pure SiO_2 films that are even more than 15 nm thick are stable in the absence of gold clusters. This clearly indicates cluster-induced crystallisation.

A last phenomenon should be mentioned: the change in colour of the multilayers with increasing numbers of layers. As an example, the colour development and the UV/Vis spectra of a series of layered systems, consisting of cluster double layers and 30-nm SiO_2 films, are shown in Figure 10 (one to nine combinations).

It can be assumed that the reason for this observation is interference between the layers because of reflection and refraction. The fact that various numbers of SiO_2 films do not show any similar effects proves the influence of the gold cluster layers with a different refraction index in between.

Electrical Properties

For vertical measurements, the multilayer systems were contacted from the wafer side with conductive silver paint and from the top SiO_2 film by a gold contact that was made by evaporation of gold through a mask with a central hole with a diameter of 3 mm. As it turned out, reliable and reproducible current–voltage measurements were not possible with as-prepared multilayer systems. One of the reasons was the electrical behaviour of the silicon substrates, which masked the weak additional influence of the multilayers on top. Another reason was assumed to exist in the randomly oriented cluster double layers, which enabled the formation of differing individual conduction paths throughout the samples and therefore prevented reproducibility. In another paper involving this issue, we describe the investigation of multilayer systems with cluster monolayers and gold as a substrate. Thus, in this case perfect current–voltage measurements are possible.

The electric behaviour of the multilayers described in this contribution was investigated by capacitance measurements by means of complex impedance spectroscopy. Impedance spectroscopy (IS) is an experimental method for the analysis of charge carrier dynamics in an electrode/sample system. For this, an alternating electric field with a frequency range of 1–10^7 Hz is applied as an external perturbation of a system that is being tested under equilibrium conditions. By applying an electric field, local as well as translational charge carrier motion may be induced, which leads to the polarization of the sample. Thus, IS is a non-destructive method for the analysis of charge transport as well as of grain boundary and interface polarisation in a solid material. IS has been intensively applied to characterise three-dimensionally organized $Au_{55}(PPh_3)_{12}Cl_6$ clusters.[20–23] The results were very valuable, since for the first time it could be shown that these nanoparticles behave as quantum dots with extremely small capacities between each other allowing single electron transport between individual clusters.

From the impedance investigations of the above-mentioned multilayer systems, we expected information about their electrical capacitance which is dependent on the number of cluster/SiO_2 combinations. For detailed capacitance measurements, multilayers with 5-nm SiO_2 films and 5-nm $Au_{55}(PPh_3)_{12}Cl_6$ double layers have been selected because of the instability of thicker SiO_2 films (see above).

First, we studied the frequency dependence of the capacitance of 5-nm SiO_2 films relative to cluster-containing multilayers. The pure SiO_2 samples show a frequency independent capacitance at frequencies below 10^3 Hz (Figure 11). A dispersion region can be observed at higher fre-

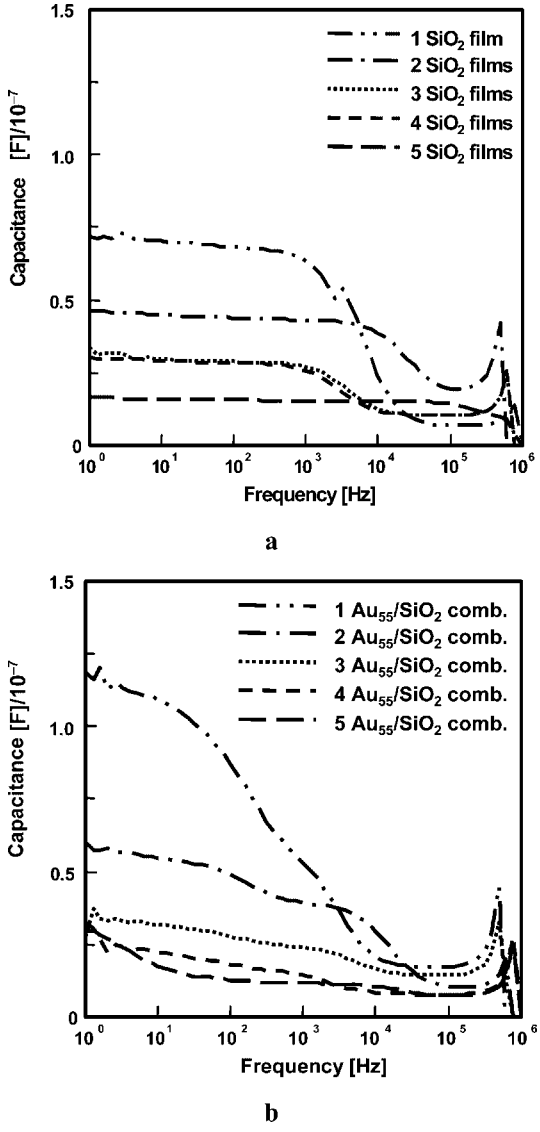

Figure 11. Frequency dependence of the capacitance in multilayered systems consisting of SiO_2 only (**a**) and of cluster/SiO_2 combinations (**b**).

 © 2005 Wiley-VCH Verlag GmbH & Co. KGaA, Weinheim

quencies, where a decrease in the capacitance is observed. Additional peaks at 10^6 Hz are due to measurement artefacts. The cluster-containing samples show a similar behaviour, although higher capacitance values are observed. In samples 1, 2, and 5, an additional dispersion region at low frequencies can be recognised.

The geometry of the sample is an important factor for the experimentally determined capacitance values. In Figure 11, one can see that the capacitance of the samples decreases with increasing thickness of the layers. This is in agreement with the model of a parallel-plate capacitor with the capacitance $C = \varepsilon_r \times \varepsilon_0 \times A/d$, where C = capacitance, ε_r = relative permittivity of the system, ε_0 = permittivity of vacuum, A = square face of the system, and d = total thickness. The geometric effects can be eliminated by calculation of the relative permittivity ε_r of the sample being tested. Physically ε_r describes the transparency of matter in electric fields and, thus, is a measure of the polarisability. Figure 12 shows the relative permittivity of the samples plotted against the layer thickness for two different frequencies.

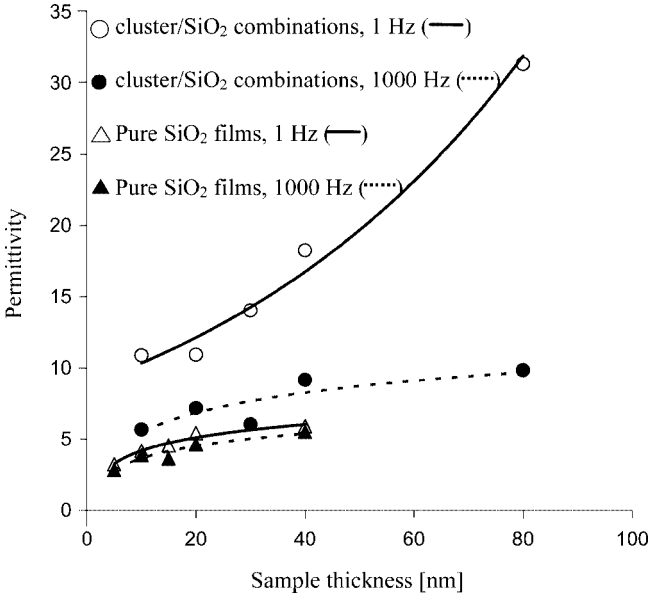

Figure 12. Illustration of the dependence of the relative sample permittivity on the sample thickness for two different measuring frequencies (The lines serve only as a guide for the eye).

It is clearly visible that the pure SiO_2 samples show a significantly smaller permittivity relative to the cluster-containing systems, and the permittivity only slightly increases with increasing layer thickness. The cluster/SiO_2 layer systems show increased permittivity with a pronounced progression as the number of the cluster layers increases. In all measurements, the permittivity at 1 Hz is larger than at 1 kHz, indicating that at low frequencies slow movement of charge carriers leads to an increase in the sample polarisation.

Samples without $Au_{55}(PPh_3)_{12}Cl_6$ clusters do not show significant changes in ε_r with increasing frequencies. Therefore, the increased polarisability of the multilayer systems must result from the presence of the cluster layers. We assign this phenomenon to the formation of dipoles in the cluster double layers and hence the formation of polarisation currents, as is indicated in Figure 13.

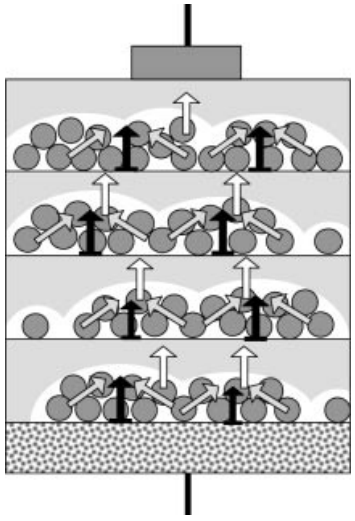

Figure 13. Illustration of the dipole formation in randomly oriented cluster double layers. Black and grey arrows indicate translational motion of charge carriers within the cluster layers parallel (black) to the applied electric field and disoriented (grey) with respect to the applied electric field. White arrows indicate the superposition of the local dipole moments forming a macroscopic dielectric polarisation.

Temperature-dependent capacitance measurements indicate a thermal activation of the polarisation processes in the cluster layers. In Figure 14, experimentally determined permittivity values at 1 Hz are plotted logarithmically versus the inverse temperature in an Arrhenius-like plot.

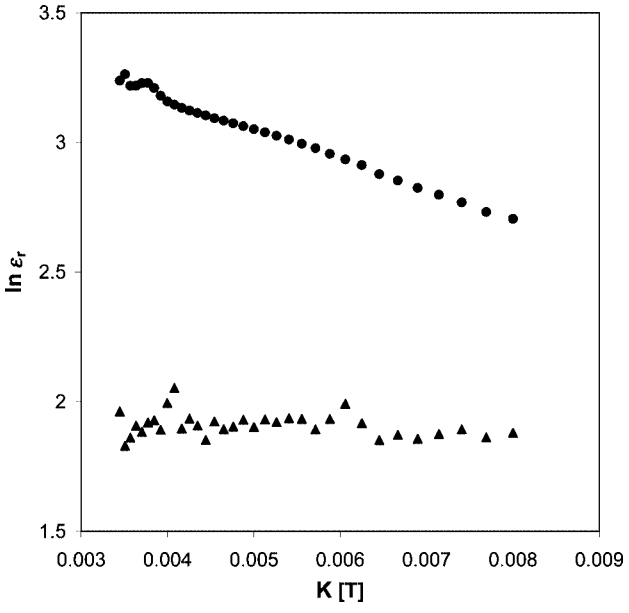

Figure 14. Arrhenius Plot of the temperature dependence of the capacitance for pure SiO_2 systems (triangles) and cluster/SiO_2 systems (dots).

 © 2005 Wiley-VCH Verlag GmbH & Co. KGaA, Weinheim

The permittivity of pure SiO_2 samples is almost temperature independent, whereas cluster/SiO_2 systems show a temperature-dependent behaviour. For the latter structures an increase in the permittivity and therefore the number of polarization processes throughout the sample increases with increasing temperature.

Determination of the activation energy of the polarization processes in the sample by using the Arrhenius-relation gives a remarkably small value of 8.6 meV. However, this value is apparently lower than the activation energies determined for tunnelling processes between Au_{55} clusters, i.e. about 150 meV.[20–23] This might indicate that the polarisation process does not only reflect charge transport between the clusters within the layer, for which the activation energy measured was close to that of previous studies for pure cluster samples. We assume that additional local charge carrier transport occurs via defects in the oxide layer and/or at the interface between the clusters and SiO_2, which may exhibit smaller activation energies.

Conclusions

We have demonstrated the formation of multilayer systems, consisting of $Au_{55}(PPh_3)_{12}Cl_6$ double layers and SiO_2 barrier films of different thickness. The cluster double layer formation between the barrier films was performed by using spin-coating techniques, while the generation of the SiO_2 films resulted from a plasma assisted physical vapour deposition (PAPVD) process. Samples of up to nine cluster/SiO_2 combinations have been produced and have been characterised by AFM and SEM. Impedance measurements showed that there is a characteristic thermally activated frequency dependence of the capacitance of the different systems. The physical interpretation of this behaviour is the formation of dipoles in the non-ordered cluster double layers.

Experimental Section

Reagents and Physical Measurements: $Au_{55}(PPh_3)_{12}Cl_6$ was prepared as described.[24] Silicon wafers were used from SilChem, Freiberg, and consisted of n(As)-doped (111) silicon, 0.003 Ωcm, 375 μm. Silicon for SiO_2 layers: 99.999%, 0.2–1.5 mm, Balzers Materials, Liechtenstein. All solvents were reagent grade and used without further purification. CH_2Cl_2 for spin coating was kept in contact with air for 2–3 d in order to achieve the necessary water content. For optical imaging, a BX41 and a C3030 Zoom from Olympus, Hamburg, were used. AFM measurements were performed with a Nanoscope IIIa, Digital Instruments, Woodbury. SEM investigations were performed with a LEO 1530, LEO Elec-

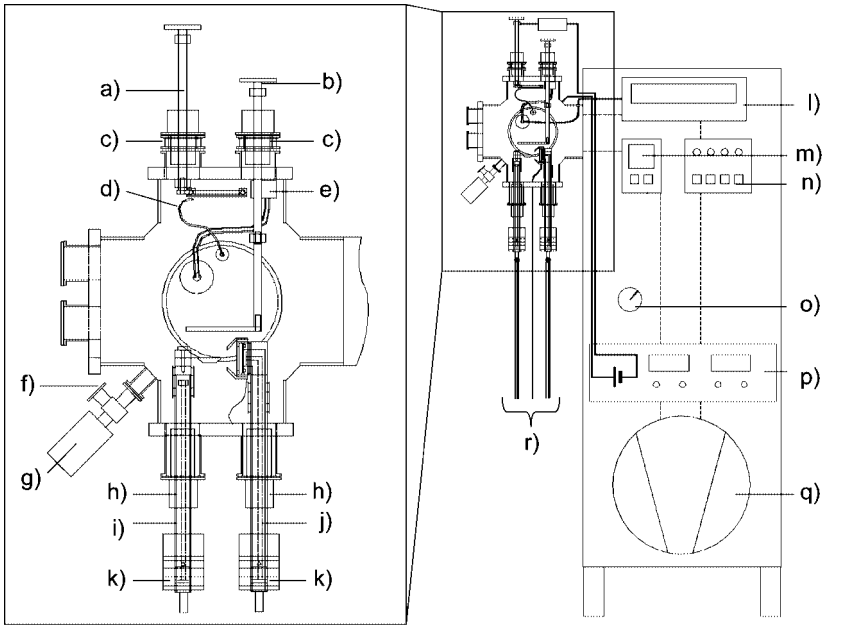

a) Substrate fastener
b) Shutter
c) Isolating lead-trough
d) Pipe for reactive gases
e) Quartz resonator device
f) Gas inlet
g) Needle valve
h) Isolating lead-trough
i) Anode with crucible
j) Cathode with helping anode
k) Water supply
l) Oscillating quartz crystal electronic
m) Pressure measurements
n) Vacuum control unit
o) Main switch
p) High voltage power supply
q) Vacuum pump
r) Electrical connection to power supply and computer-assisted measurements

Figure 15. Technical sketch of the PAPVD system with magnified recipient.

 © 2005 Wiley-VCH Verlag GmbH & Co. KGaA, Weinheim

tron microscopy, Cambridge. For TEM investigations, a CM 200 FEG, Philips, Eindhoven, was used. For a spin coater, Model 6700, Speciality Coating Systems, Indianapolis, was used. The UV/Vis spectra were recorded with a Cary 1Bio, Varian, Palo Alto. The impedance measurements were performed with a Solartron (Farnborough) Impedance Analyzer SI 1260 in combination with a high-impedance input amplifier Solartron (Farnborough) 1296. For the low-temperature measurements, a cryostat of a Physical Property Measuring System by Quantum Design was used.

The device for the anodic plasma arc process was homemade, using commercially available building blocks, if possible. The technical principles behind were taken from patents[25–27] with permission and help from the patent owner Dr. H. Ehrich, Physics Department, University of Duisburg-Essen. A schematic overview over the whole device is shown in Figure 15. Details are also described in ref.[28].

Formation of SiO_2 films: The holder for the silicon was a self-made carbon boat. The silicon wafer was purified with ethanol and dried with a dust-off nozzle before it was fixed by glue 20 cm above the silicon container. The shutter is installed between sample and wafer. The recipient was evacuated to 5×10^{-5} mbar, and oxygen was then allowed to enter up to a pressure of 2×10^{-2} mbar. After reaching a constant pressure, the helping anode was linked with the power circuit. The power between the helping anode and cathode was then increased until a stable discharge between cathode and anode was reached; under the conditions to generate 5-nm SiO_2 films, it was 75 A. After having reached a stable discharge, the supporting anode was separated from the circuit and the shutter was opened. For the measurement of the thickness of the film, a quartz resonator device was used, however, only for films thicker than 10 nm since it is too slow to register thinner films in a few seconds. In those cases a coating parameter had to be determined over the time the sample is in contact with the ion flow. For the 5-nm layers, 3 s are necessary. Usually, the coating rate is 1–3 nm sec^{-1}. It can be adjusted by tuning the power strength and the gas inlet. The temperature in the sample during the coating process was 25–35 °C.

Spin Coating: In a typical spin-coating experiment a 1×1 cm^2 Si wafer was carefully cleaned with ethanol. After drying with a dust-off nozzle, the wafer was fixed on the sample holder of the spin coater by evacuation. Rotation with 100 revolutions per minute was started, and 50 μL of a 4.3×10^{-6} molar cluster solution was dropped on by means of a glass syringe. The whole surface should now be wet. The spin coater was then closed, and the speed was accelerated to 4000 revolutions per minute and kept there for 25 s. Each sample was controlled microscopically before further use. The multilayers were produced by alternative layers of SiO_2 films and the clusters.

Acknowledgments

This work was carried out as a project in the Schwerpunktprogramm 1072 of the Deutsche Forschungsgemeinschaft. We gratefully acknowledge this generous support.

[1] G. Schmid, R. Boese, R. Pfeil, F. Bandermann, S. Meyer, G. H. M. Calis, J. W. A. van der Velden, *Chem. Ber.* **1981**, *114*, 3634.
[2] L. F. Chi, M. Hartig, T. Drechsler, Th. Schwaak, C. Seidel, H. Fuchs, G. Schmid, *Appl. Phys. A* **1998**, *66*, 187.
[3] H. Zhang, G. Schmid, U. Hartmann, *Nanoletters* **2003**, *3*, 305.
[4] G. Schmid, R. Pugin, J.-O. Malm, J.-O. Bovin, *Eur. J. Inorg. Chem.***1998**, 813.
[5] G. Schmid, R. Pugin, W. Meyer-Zaika, U. Simon, *Eur. J. Inorg. Chem.***1999**, 2051.
[6] G. Schmid, M. Bäumle, N. Beyer, *Angew. Chem. Int. Ed.* **2000**, *39*, 181.
[7] G. Schmid, N. Beyer, *Eur. J. Inorg. Chem.* **2000**, 835.
[8] O. Vidoni, St. Neumeier, N. Bardou, J.-L. Pelouard, G. Schmid, *J. Cluster Sci.***2003**, *14*, 325.
[9] A. Vassiliev, H. Rehage, G. Schmid, St. Neumeier, W. Meyer-Zaika, *J. Cluster Sci.* in press.
[10] S. Liu, R. Maoz, G. Schmid, J. Sagiv, *Nanoletters* **2002**, *2*, 1055.
[11] G. Schmid, T. Reuter, St. Neumeier, unpublished results.
[12] Y. Liu, M. Schumann, T. Raschke, C. Radehaus, G. Schmid, *Nanoletters* **2001**, *8*, 405.
[13] P. Y. Su, J. C. Hu, S. l. Cheng, L. J. Chen, J. M. Liang, *Appl. Phys. Lett.* **2004**, *84*, 3480.
[14] V. V. Yaminki, K. Thuresson, B. W. Ninham, *Langmuir* **1999**, *15*, 3683.
[15] A. Oron, S. H. Daivs, S. G. Bankoff, *Rev. Mod. Phys.* **1997**, *69*, 931.
[16] P. C. Ohara, W. M. Gelbart, *Langmuir* **1998**, *14*, 3418.
[17] C. Stowell, B. Korgel, *Nanoletters* **2001**, *1*, 595.
[18] M. Maillard, L. Motte, M. P. Pileni, *Adv. Mater.* **2001**, *13*, 200.
[19] J. H. Kim, J. Y. Lee, *Jpn. J. Appl. Phys.* **1996**, *35*, 2052.
[20] U. Simon, G. Schmid, G. Schön, *Angew. Chem. Int. Ed. Engl.* **1993**, *32*, 250.
[21] G. Schön, U. Simon, *Coll. Polym. Sci.* **1995**, *273*, 101.
[22] U. Simon, *Adv. Mater.* **1998**, *10*, 1487.
[23] V. Torma, G. Schmid, U. Simon, *Chem. Phys. Chem.* **2001**, 5, 321.
[24] G. Schmid, *Inorg. Synth.* **1990**, *7*, 214.
[25] H. Ehrich, *EP 0015897281*, **1993.**
[26] H. Ehrich, *EP 0062086881*, **1995.**
[27] H. Ehrich, B. Hasse, H. P. Hinz, M. Mausbach, *EP* 0056660681, **1995.**
[28] T. Reuter, Ph.D. Dissertation, Universität Duisburg-Essen, **2004**.

Received: April 29, 2005
Published Online: July 20, 2005

 © 2005 Wiley-VCH Verlag GmbH & Co. KGaA, Weinheim

The Electronic Interaction Between $Au_{55}(PPh_3)_{12}Cl_6$ Monolayers Through SiO_2 Films

Stefan Neumeier,[a] Torsten Reuter,[a] and Günter Schmid*[a]

Keywords: Monolayers / Gold / Multilayers / Electronic tunnelling / Current-voltage characteristics

$Au_{55}(PPh_3)_{12}Cl_6$ monolayers embedded between 5-nm SiO_2 barrier films have been successfully generated. The cluster monolayers were obtained by spin coating of very dilute solutions. The SiO_2 films were prepared by means of a special anodic plasma arc technique. Systems of one up to eight cluster/SiO_2 combinations on a gold surface have been generated and investigated. In the voltage region between –5 and +5 mV, all samples exhibited linear current-voltage characteristics. Control samples with only SiO_2 show very different I-U behaviour. We interpret the behaviour observed as a result of electronic tunnelling from the cluster monolayers through the SiO_2 barrier films.
(© Wiley-VCH Verlag GmbH & Co. KGaA, 69451 Weinheim, Germany, 2005)

Introduction

Monolayers of quantum dots are of general interest with respect to the electronic interaction between the dots in only two dimensions (2D). Whereas the electronic situation in individual quantum dots has been investigated by various researchers,[1–3] their interparticle behaviour is rather unknown. $Au_{55}(PPh_3)_{12}Cl_6$ and its derivatives are ideal quantum dots, since this compound is the only metal nanoparticle that shows well-expressed quantum behaviour already at room temperature.[1] Current investigations of the electric conductivity of 2D arrangements of $Au_{55}(PPh_3)_{12}Cl_6$ clusters over about 80 nm indicate that it is below the detection limit,[4] whereas the conductivity of only 20-nm areas shows a typical Coulomb blockade.[5] In this connection, there arose another interesting question, namely the ability of communication of extended monolayers in the vertical direction, separated from each other by insulating barriers. Variations of the insulating barriers (SiO_2) in thickness might provide evidence on the tunnelling limits. Furthermore, we might learn more about the storage capacities of cluster monolayers. Such information is of interest with respect to the development of novel floating gate transistors.[6–10] The corresponding behaviour of cluster double layers or thin films is the subject of another contribution in this issue.[4] There is a principal difference to be expected between thin films and monolayers. Dipolar interactions between cluster layers dominate the behaviour in thin films, whereas electronic tunnelling is observed in the case of monolayers.

In this contribution, we describe the current-voltage behaviour of multilayered systems consisting of $Au_{55}(PPh_3)_{12}Cl_6$ monolayers embedded between 5-nm SiO_2 films.

[a] Universität Duisburg-Essen,
Universitätsstrasse 5–7, 45117 Essen, Germany
E-mail: guenter.schmid@uni-essen.de

Results and Discussion

Generation of Cluster/SiO_2 Multilayers

The generation of the cluster monolayers was performed by means of spin coating and for the formation of the SiO_2 films the same plasma assisted physical vapour deposition (PAPVD) procedure has been applied as is described in detail in the related paper of ref.[4] For the current (I)-voltage (U) investigations we used a novel kind of contacting technique that is shown in Figure 1.

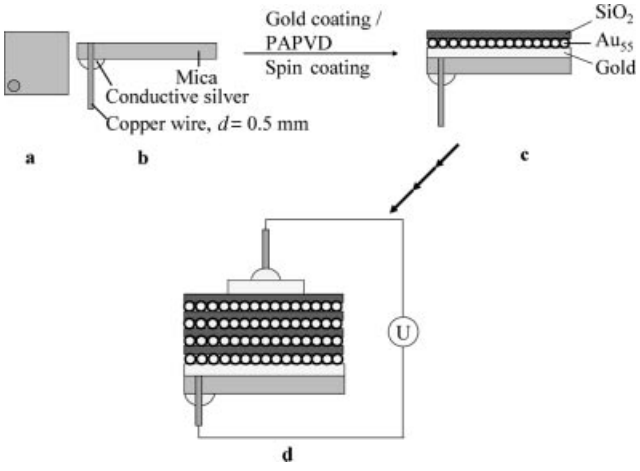

Figure 1. Construction of a $Au_{55}(PPh_3)_{12}Cl_6/SiO_2$ multilayer system.

A 1×1-cm^2 mica platelet was provided with a 0.5-mm borehole at the periphery (a). A 0.5-mm copper wire was plugged in in such a way that it ended exactly at the mica surface and was then fixed by conductive silver on the back side (b). A ca. 400-nm-thick gold film was then generated on the mica by means of PAPVD, followed by a first mono-

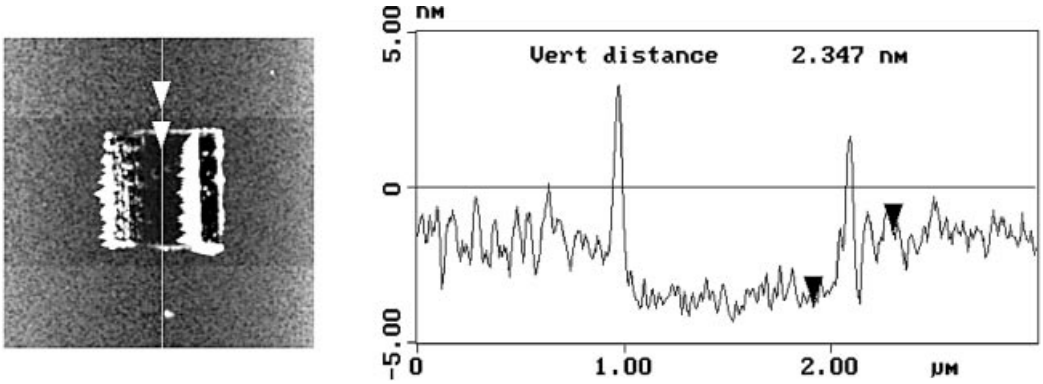

Figure 2. AFM image of a cluster monolayer with a scratched window (left) and the corresponding cross section (right).

layer of $Au_{55}(PPh_3)_{12}Cl_6$ clusters. This was produced by spin coating 50 µL of a 2.8×10^{-7} M cluster solution (c). The spin-coating process is described in detail in ref.[4] The next step consisted of the generation of a first 5-nm SiO_2 film by means of the anodic plasma arc process, also described in detail in ref.[4] Depending on the intended number of layers, the processes were repeated correspondingly. Figure 1d shows a system with four cluster/SiO_2 double layers. The final SiO_2 layer was contacted by a gold electrode 3 mm in diameter that was made by evaporating gold through a corresponding mask. Conductive silver was then used to fix a copper wire on top of the gold electrode. Control of the quality of the cluster monolayers was performed by AFM. Figure 2 views a cluster monolayer with a scratched window from above (left) and a cross section of that sample (right). The height of 2.4 nm agrees perfectly with the existence of a cluster monolayer containing randomly oriented clusters. The quality of the monolayers depends exclusively on the spin-coating conditions and the use of dichloromethane as solvent that has a distinct yield of moisture for improving the wetting conditions.[4]

As an example of the successful generation of cluster/SiO_2 multilayers, a transmission electron microscopic (TEM) image of a four-layered system is shown in Figure 3.

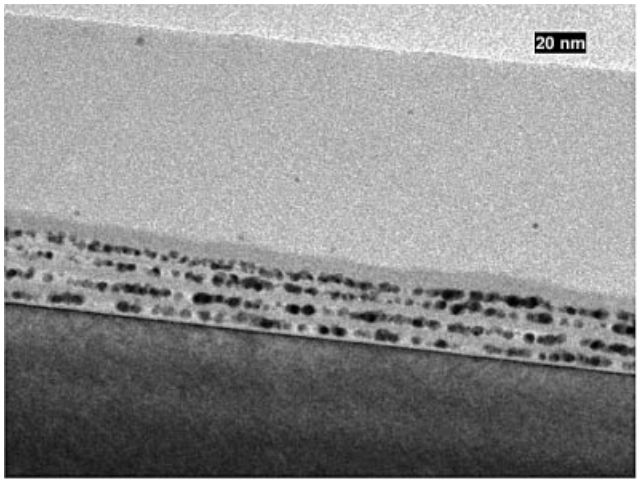

Figure 3. TEM image of a four-layered cluster monolayer/SiO_2 system.

As can be seen, the cluster monolayers are properly separated by the SiO_2 barrier films.

Electrical Measurements

Electrical measurements were performed by current-voltage registrations in the region from –5 to +5 mV. A control experiment with the gold layer alone showed the expected linear I-U characteristic, resulting in a current of 11 mA at 5 mV. Table 1 contains the measured values for four different-layered samples consisting of 1, 2, 4 and 8 cluster/SiO_2 combinations. In addition, two comparative values for 2 and 8 SiO_2 5-nm films are added. As can be seen from the values for the cluster/SiO_2 multilayers, the current values decrease with increasing numbers of layers; however, by far not to the same extent as SiO_2 films alone do.

Table 1. Current values of cluster/SiO_2 and SiO_2-only multilayer systems and of the pure gold surface.

Number of cluster/SiO_2 double layers	Current [mA] Cluster/SiO_2	Current [mA] SiO_2
0 (gold surface)	11	
1	8.8	
2	6.8	3.0
4	4.6	
8	2.9	0.9

Figure 4a shows a typical current-voltage plot for a two-layered cluster/SiO_2 array, resulting in 6.8 mA at 5 mV. The small steps are caused by the measuring technique and so are not system-immanent. In Figure 4b, the dependence of the current on the number of cluster/SiO_2 combinations is plotted and completed by the two SiO_2-only values.

Measurements at higher voltages were not possible because of the critical contact between the macroscopic wire and the nanoscopic part of the device.

These results can be interpreted as follows:

$Au_{55}(PPh_3)_{12}Cl_6$ monolayers, isolated from each other by 5-nm films of SiO_2, are electronically in contact with each other in the voltage region between –5 and +5 mV. This can clearly be followed from the significantly different behaviour of SiO_2 films without cluster monolayers in between. We assume that electronic tunnelling through the barrier

 © 2005 Wiley-VCH Verlag GmbH & Co. KGaA, Weinheim

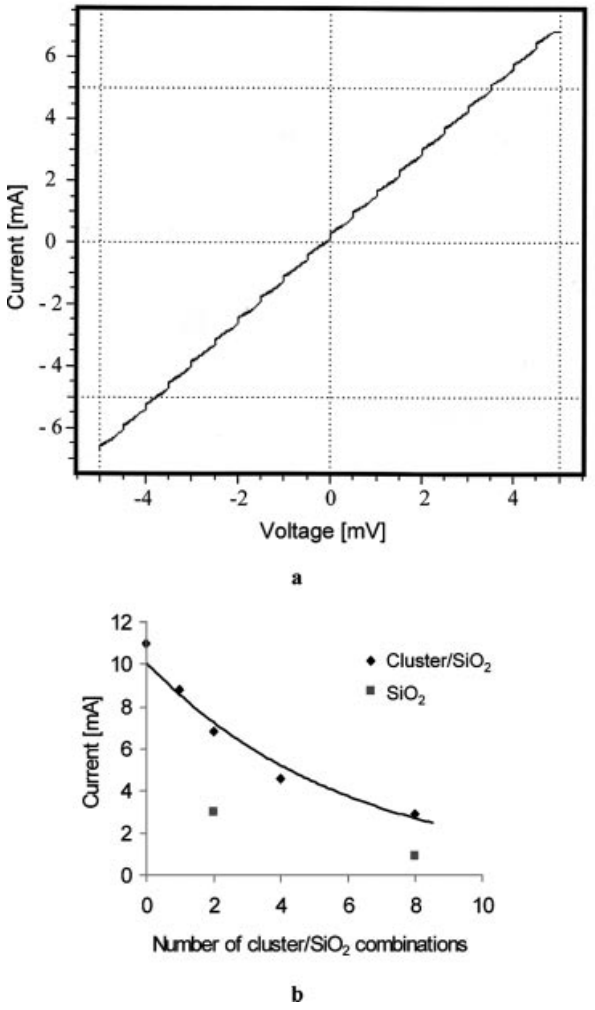

Figure 4. (a) Current-voltage plot of the two-layered $Au_{55}(PPh_3)_{12}Cl_6/SiO_2$ array; (b) dependence of current on the number of cluster/SiO_2 combinations and of SiO_2-only films. (The line serves only as a guide for the eye.).

layers occurs rather than electronic hopping, making the whole multilayer system an electronic unit. With increasing numbers of cluster/SiO_2 combinations, the currents decrease because of increasing tunnelling steps. The linear I-U characteristics, observed for all four investigated samples, indicate that there is no visible tunnelling blockade, which should have been observed in Coulomb blockades, in the layered systems. The tunnelling distance from cluster to cluster is, including the PPh_3 ligand shell, about 5.7 nm (5 nm SiO_2 + 2×0.35 nm for PPh_3). Figure 5 depicts the proposed process formally.

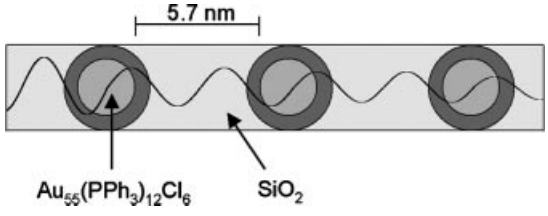

Figure 5. Illustration of the electronic tunnelling through a $Au_{55}(PPh_3)_{12}Cl_6/SiO_2$ multilayer system with decreasing amplitude.

An electronic wave, here arriving from the left, tunnels from cluster to cluster through the ligand shell and the SiO_2 film, however with decreasing amplitude leading to a kind of exponential decrease in current with increasing number of double layers, as can be observed in Figure 4b. The sloping curve approaches asymptotically the value zero for the current at a double-layer number >10. Since arrangements with more than eight layers turned out to be unstable towards crystallisation,[4] they could not be used for reliable measurements.

Conclusions

Multilayer systems consisting of monolayers of $Au_{55}(PPh_3)_{12}Cl_6$ clusters, separated from each other by 5-nm-thick SiO_2 films behave electronically like a tunnelling system, altogether reaching a maximum of over 60 nm in the case of eight cluster/SiO_2 double layers. This is a very valuable result with respect to the question of tunnelling distances. Compared with the behaviour of cluster double layers between SiO_2 barrier films, described in detail in ref.[4], where dipolar interactions between cluster layers dominate, this is obviously not the case with strictly monomolecular cluster layers, where electronic tunnelling happens. These results must be seen in relation to former measurements at three-dimensional assemblies of $Au_{55}(PPh_3)_{12}Cl_6$ clusters.[12–14] Since the gold electrode on top of the multilayer samples has a diameter of 3 mm, the tunnelling process from one electrode to the other is nothing but a kind of 3D system with considerably increased tunnelling distances, namely from 0.7 nm, considering only the PPh_3 ligand shell, up to about 5.7 nm in the samples described here. Since for systems with more than eight cluster/SiO_2 combinations the conductivity approaches that of pure SiO_2, the tunnelling distance reached might somehow be a natural limit. The 5.7 nm tunnelling distance is, compared with distances in former investigations,[15,16] a maximum value.

Experimental Section

Reagents and Physical Measurements: $Au_{55}(PPh_3)_{12}Cl_6$ was prepared as described previously.[11] CH_2Cl_2 for spin coating was kept in contact with air over a couple of days to enrich it with moisture. Mica sheets from PLANO, Wetzlar have been used (0.2 mm). Before use, upper layers were removed by a tape. Current-voltage measurements were performed with an IM 6e from Zahner Meßtechnik GmbH & CoKG, Kronach. Tungsten evaporation boats were from Balzer Materials, Liechtenstein. AFM measurements were performed with a Nanoscope IIIa, Digital Instruments, Woodbury. For spin-coating processes we used Model 6700, Speciality Coating Systems, Indianapolis. The device for PAPVD is described in detail in ref.[4]

Formation of SiO_2/Cluster Double Layers: The generation of the 5-nm SiO_2 barrier layers was performed analogously to the procedure described in ref.[4] For the preparation of the $Au_{55}(PPh_3)_{12}Cl_6$ monolayers, a CH_2Cl_2 solution (50 μL, 2.8×10^{-7} M) was applied for spin coating on the gold surface, generated on 1×1 cm^2 mica

 © 2005 Wiley-VCH Verlag GmbH & Co. KGaA, Weinheim

platelets. For the gold coating, the same PAPVD system was used as the one used for the preparation of the SiO_2 films. Current: 30 A, pressure: 5×10^{-5} mbar. The coating rate was 5 nm/sec. For the evaporation of gold we used tungsten evaporation boats.

Acknowledgments

This work was carried out as a project in the Schwerpunktprogramm 1072 of the Deutsche Forschungsgemeinschaft. We gratefully acknowledge the generous support. We also would like to thank U. Simon for very helpful discussions.

[1] L. F. Chi, M. Hartig, T. Drechsler, Th. Schwaak, C. Seidel, H. Fuchs, G. Schmid, *Appl. Phys. A* **1998**, *66*, 187.
[2] H. Zhang, G. Schmid, U. Hartmann, *Nanoletters* **2003**, *3*, 305.
[3] U. Simon, in *Nanoparticles. From Theory to Application* (Ed.: G. Schmid), Wiley-VCH, Weinheim, **2004.**
[4] T. Reuter, S. Neumeier, G. Schmid, E. Kolpin, U. Simon, *Eur. J. Inorg. Chem.* **2005**.
[5] Y. Liu, M. Schumann, T. Raschke, C. Radehaus, G. Schmid, *Nanoletters* **2001**, *8*, 405.
[6] T. Futatsugi, A. Nakajima, H. Nakao, *Fujitsu Sci. Tech. J.* **1998**, *34*, 142.
[7] D. M. Schaadt, E. T. Yu, S. Sankar, A. E. Berkowitz, *Appl. Phys. Lett.* **1999**, *74*, 472.
[8] B. Dieny, S. Sankar, M. R. McCartney, D. J. Smith, P. Bayle-Guillemaud, A. E. Berkowitz, *J. Magn. Magn. Mater.* **1998**, *185*, 283.
[9] S. W. Kolliopoulou, P. Dimitrakis, P. Normad, H. L. Zhang, N. Cant, S. D. Evans, S. Paul, C. Pearson, A. Molloy, M. C. Petty, D. Tsoukalas, *J. Appl. Phys.* **2003**, *94*, 5234.
[10] S. Paul, C. Pearson, A. Molloy, M. A. Cousins, M. Green, S. Kolliopoulou, P. Dimitrakis, P. Normand, D. Tsoukalas, M. C. Petty, *Nanoletters* **2003**, *3*, 533.
[11] G. Schmid, *Inorg. Synth.* **1990**, *7*, 214.
[12] G. Schön, U. Simon, *Colloid Polym. Sci.* **1995**, *273*, 101.
[13] G. Schön, U. Simon, *Colloid Polym. Sci.* **1995**, *273*, 202.
[14] U. Simon, *Adv. Mater.* **1998**, *10*, 1487.
[15] V. Torma, O. Vidoni, U. Simon, G. Schmid, *Eur. J. Inorg. Chem.* **2003**, 1121.
[16] G. Schmid, U. Simon, *Chem. Commun.* **2005**, 697.

Received: April 29, 2005
Published Online: July 12, 2005

 © 2005 Wiley-VCH Verlag GmbH & Co. KGaA, Weinheim

Current-Voltage Characterisation of Monolayer-Supported Au-Nanoclusters by Scanning Tunnelling Microscopy under Ambient Conditions

Volker Jacobsen,[a,b] Tao Zhu,[a,c] Wolfgang Knoll,[a] and Maximilian Kreiter*[a]

Keywords: Scanning probe microscopy / Surface plasmon resonance / Colloids / Monolayers / Nanostructures / Self-assembly

The current-voltage characteristics of a double-tunnel junction based on a gold crystallite with a diameter of ca. 2 nm, separated from a gold surface by ca. 1 nm was investigated by scanning tunnelling microscopy. The sample architecture was built by attaching gold nanoparticles covered with 2-mercaptosuccinic acid to an atomically flat gold surface which was covered by a self-assembled monolayer (SAM) of 6-amino-1-hexanethiol. Surface plasmon and infrared spectroscopy as well as STM imaging were employed to identify suitable preparation conditions and prove the existence of the desired architecture. No reproducible steps in the current-voltage characteristics are observed on this system under ambient conditions. Nonetheless, a sound signature for tunnelling through the double-tunnel junction is established by a quantitative fit of the averaged experimental data to a theoretical model of a single-tunnel junction. Firstly, the current on the particle is strongly reduced at low absolute external voltage and secondly the current voltage characteristics are asymmetric. Since both deviations from theory are absent in reference experiments on the bare monolayer, they may serve as a robust signature for double-tunnel junctions and open the door to the investigation of single-electron tunnelling under ambient conditions.

(© Wiley-VCH Verlag GmbH & Co. KGaA, 69451 Weinheim, Germany, 2005)

Introduction

The quantization of the electrical current into individual electron charges leads to unique features in the current-voltage characteristics of double-tunnel junctions in which the current flows across an isolated island with a sufficiently small capacitance. In many cases this geometry is realised by the tip of a scanning tunnelling microscope (STM), approaching a metallic nanoparticle, which is isolated from a metallic substrate by a thin isolating layer with a thickness in the nanometer range.[1] This geometry is shown schematically in Figure 1. A complete suppression of current at small applied voltages and a jump to a finite current at a well-defined bias voltage are observed in low temperature experiments, the "Coulomb blockade". If the voltage is further increased, then more current jumps, at a defined voltage spacing, are observed. This feature is termed "Coulomb staircase". Both effects are understood in terms of the charging of the island by single electrons, which leads to a change in its electrostatic potential, resulting in discrete electronic states spaced out in energy. The position of the jumps depends on the geometry of the double-tunnel junction (capacitance of the particle, resistance of the two-tunnel junctions) as well as the offset potential of the island.[2] This potential, although in general due to the charge distribution in the vicinity of the island, is commonly expressed in terms of an equivalent "background charge" which is not quantized and residing on the island itself. It leads to a corresponding shift in electronic potentials and, in turn, to a shift of the applied voltages for which current jumps are

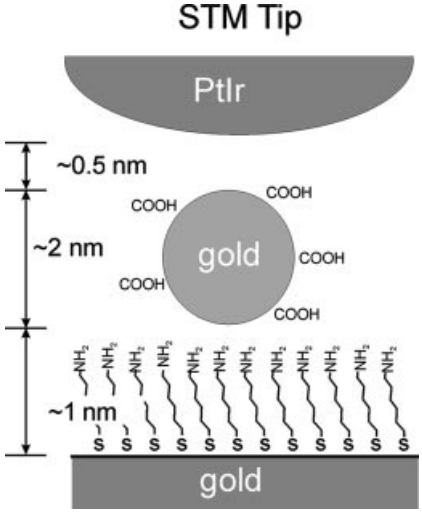

Figure 1. Sketch of a double-tunnel junction with an STM tip, an isolated metal nanoparticle and a monolayer-coated conducting substrate.

[a] Max Planck Institut für Polymerforschung,
Ackermannweg 10, 55128 Mainz, Germany
E-mail: kreiter@mpip-mainz.mpg.de
[b] Current address: Laboratory of Physical Chemistry, Swiss Federal Institute of Technology (ETH),
8093 Zurich, Switzerland
[c] Permanent address: College of Chemistry, Peking University,
Beijing 100871, China

observed. At a finite temperature, the sharp jumps are smeared out in energy on a scale corresponding to the thermal energy. As a consequence, the small steps in energy on systems with a large capacitance (small charging energy) are only observed at low temperature. Room temperature corresponds to a thermal energy of 25 meV. For this reason, only Coulomb blockades on small particles with correspondingly small capacitance can be observed in this temperature regime. An elegant route to small gold particles in a well-defined distance from a conducting substrate is based on the use of self-assembled monolayers as spacer molecules whose thickness can be adjusted to the Angstrom scale and on top of which gold nanoparticles with the appropriate size are deposited.

Several combinations of substrates, particles and organic functionalities of self-assembled monolayers have been used for such studies.

One strategy is based on the deposition of metallic particles coated by an insulating material on bare conducting substrates such as Pt_{309}phenanthroline$_{36}O_{30}$[3] and hexanethiol-capped clusters[4] on clean Au(111) as well as polyvinylpyrrolidone capped Au particles on graphite.[5]

Similarly, bare particles can be deposited on a monolayer-protected surface as was shown for clusters prepared under ultrahigh vacuum (UHV),[6,7] which were deposited on Au(111) protected by a monolayer of *p*-xylene-α-α′-dithiol ($C_8H_{12}S_2$). It must be noted, though, that this approach is restricted to vacuum techniques, since in ambient environments metal clusters need some stabilizing agents, thus preventing the use of bare clusters.

Probably, the best-defined systems are prepared by using a specific organic coating both on the particle and on the substrate, thus avoiding any influence of loosely bound contaminants. Examples for this strategy are heptanethiol-capped clusters on Au(111) coated with a decanethiol self-assembled monolayer,[8] and dodecanethiol-coated particles on Au(111) protected by a monolayer of *p*-xylene-α-α′-dithiol ($C_8H_{12}S_2$).[9] Other experiments on clusters coated with octanethiol/galvinol/mecaptohexylamine on Au coated by hexanethiol[10,11] have been reported.

Most of these experiments were performed under UHV at low temperatures[3,8,12] thus avoiding a smearing out of the steps in the $I(V)$ curve while at the same time avoiding fluctuations of the background charge by immobilizing possible contaminations. Also, at room temperature, Coulomb staircases have been measured under UHV and the results are in agreement with a modified classical theory that takes into account the thermal contribution.[7,12,13]

The high sensitivity of $I(V)$ on the background charge makes the detection of clear $I(V)$ curves under ambient conditions very difficult since all kinds of contaminations will enter and leave the vicinity of the tunnel barrier, leading to a background charge fluctuating quicker in time than the time needed for an $I(V)$ curve. On the other hand, this high sensitivity makes the measurement of single-electron tunnelling events a promising candidate for true transduction of single-molecular switching events if they are accompanied by a change in the associated electrostatic potential.[14] The feasibility of single-electron charging experiments at ambient conditions has been shown by addressing single clusters with an STM tip[10,11,15] and in an electrochemical experiment which was supplemented by STM experiments under UHV.[4] Still, in these cases no quantitative comparison to the classical theory was shown, probably due to the high temporal fluctuations in the overall architecture. It was noted that charged coatings may lead to an increased fluctuation of the background charge,[5] which was corroborated by the remarkable quality of the data from purely aliphatic SAMs.[8] Furthermore, in a polar environment a dielectric response has to be considered that reacts on time scales that are similar or slower than some of the time scales relevant for the experiment. As a consequence, the dynamics of the reorientation of polar species must be considered, leading to additional deviations from the simple picture of a static system with instantaneous dielectric response.[16]

Nonetheless, there are two important reasons to choose charged coatings of the particles and the substrate. Firstly, in order to attach further molecular functionalities some reactivity of the particle coatings is required. Secondly, at ambient conditions the immobilization has to withstand displacement by other molecules and therefore requires some robustness.

In this paper, we are investigating carboxyl-functionalized Au-nanoclusters on an amino-functionalized SAM in air. The goal of this paper is to unravel signatures of tunnelling through a double-tunnel junction in this polar system using STM experiments at ambient conditions. Firstly, the supramolecular geometry consisting of a 6-amino-1-hexanethiol monolayer bound to a gold substrate, decorated by gold nanoparticles coated with mercaptosuccinic acid (MSA) is thoroughly characterized. Scanning tunnelling investigations are shown with an emphasis on the changes of the $I(V)$ characteristics with time. Based on the observation that no reproducible step position of a Coulomb staircase can be identified, an alternative, fully reproducible signature of the $I(V)$ characteristics through a double-tunnel junction is developed which may serve as a signature of single-electron tunnelling even in a strongly fluctuating environment such as ambient air.

Results and Discussion

FTIR and Surface Plasmon Investigations

The deposition of the spacer layer as monitored by surface plasmon spectroscopy is displayed in Figure 2. The evolution of the minimum angle as a function of time (Figure 2b) indicates a quick first adsorption process, which terminates roughly at a thickness corresponding to a self-assembled monolayer of the 6-amino-1-hexanethiol. This process is followed by a second, slower deposition. The reflectivity curves in Figure 2a show that this additional thickness does not decrease upon rinsing with Milli-Q water, indicating a relatively strong affinity. Upon rinsing with 0.1 M HCl, the adlayer thickness is reduced to its value after the first quick deposition. This can be explained by

 © 2005 Wiley-VCH Verlag GmbH & Co. KGaA, Weinheim

some additional 6-amino-1-hexanethiol molecules on top of the first monolayer, which are attached by dimerisation of the head amino groups and are removed after protonation in an acid environment.

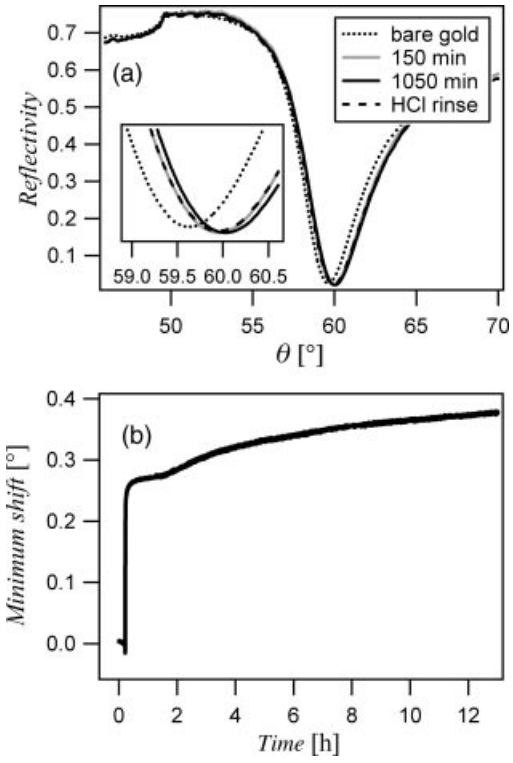

Figure 2. Surface plasmon investigation of the monolayer formation. (a) Reflectivity curves before deposition of 6-amino-1-hexanethiol, after 150 min and 1050 min deposition time and after rinsing with 0.1 M HCl, respectively. (b) Minimum angle shift as a function of time. In this range, the shift in the minimum angle is proportional to the surface coverage.

FTIR spectra of the gold substrates were taken after immersion in the thiol solution and after the rinsing steps. They are displayed in Figure 3.

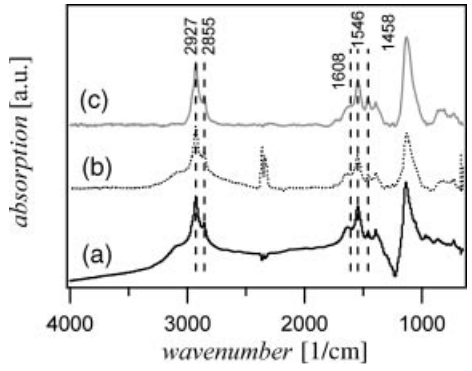

Figure 3. FTIR Spectra of the gold substrate (a) after immersion in the solution containing the 6-amino-1-hexanethiol (b) after rinsing with Milli-Q water (c) after rinsing with 0.1 M HCl.

The characteristic bands for a CH_2 chain are observed: an asymmetric stretching mode at 2927 cm^{-1} and a symmetric stretching mode at 2855 cm^{-1}, as well as a CH_2 scissoring band at 1458 cm^{-1}. The stretching modes are slightly shifted to higher wavenumbers compared to values obtained in solution (2924 cm^{-1} and 2853 cm^{-1}[17]) and in agreement with values found for a disordered monolayer with a density below the one found for the ideal crystalline packing of longer alkanethiols.[18] This finding is reasonable taking into account the influence of the amino head group and the relatively short alkyl chain whose energy in the chain-chain interactions is insufficient to form a 2D crystal. Peaks at 1546 cm^{-1} and at 1608 cm^{-1} are identified as the symmetric and asymmetric NH_3^+ deformation of the amine salt.

It is worth noting that some background signal is obtained before rinsing with HCl. This is attributed to the additional material which is also observed in surface plasmon spectroscopy and is interpreted in terms of additional 6-amino-1-hexanethiol molecules that bind to the self-assembled monolayer by dimerisation of the amino groups and which can be removed in an acid environment. A somewhat ill defined formation of SAMs from amino-terminated thiols is known from the literature. The formation of double layers has been reported,[19] as well as proper single SAMs[20,21] with the formation of carbamate at ambient conditions.[20] There is a possibility of a reverse incorporation of some molecules, i.e. the amino group pointing in the direction of the gold has been reported.[22] In the case discussed here, the clean IR spectrum as well as the thickness, corresponding to a self-assembled monolayer determined by surface-plasmon spectroscopy, point to the existence of a well-defined self-assembled monolayer after rinsing with HCl. From the IR spectra as well as from the observation that no molecular ordering could be resolved with the STM, a disordered monolayer can be deduced.

The deposition of MSA-capped gold particles was monitored in situ by surface plasmon spectroscopy as displayed in Figure 4. After 30 min the deposition speed slows down significantly but does not saturate completely even within 16 h, indicating a slow on-going particle aggregation after saturation of the main binding sites. Rinsing with HCl reduces the amount of Au particles by roughly 30% pointing to the removal of some weakly bound material. Remarkably, in addition to the horizontal shift of the plasmon curve, a slight broadening is observed, which may point towards an increased aggregation of loosely bound particles induced by the rinsing, which is expected to cause significant scattering and therefore an increase in optical absorption.

After deposition of the MSA-capped gold particles, bands at 1719 cm^{-1}, 1578 cm^{-1}, and 1392 cm^{-1} appear in the FTIR spectra (Figure 5), indicating the presence of carboxylic groups on the surface and therefore pointing towards successful deposition of the gold particles.

Imaging of the Particles with the STM

STM images of the substrates with immobilized gold nanoparticles are displayed in Figure 6. Atomically flat

 © 2005 Wiley-VCH Verlag GmbH & Co. KGaA, Weinheim

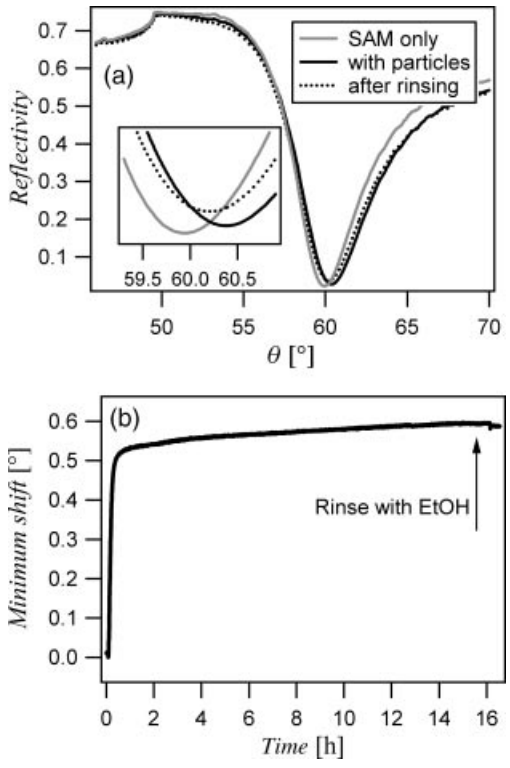

Figure 4. Surface plasmon investigations on particle deposition. (a) Surface plasmon reflectivity curves before and after particle deposition and after rinsing. (b) Kinetics of gold particle deposition.

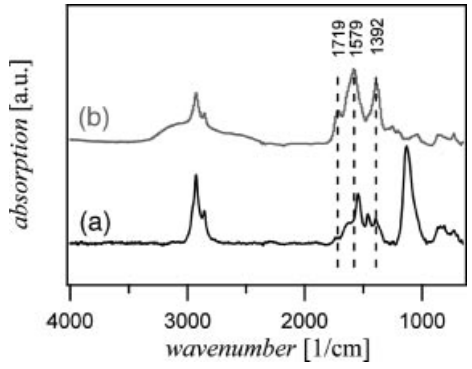

Figure 5. FTIR spectra before (a) and after (b) deposition of Au nanoparticles.

gold terraces with lateral dimensions in the order of 100 nm are clearly seen in Figure 6a. Some particles are only partly visible in the image because they are swept away by the STM tip, these features are indicated by arrows. Figure 6b is obtained at slightly increased bias voltage and a set point current decreased to less than half the value used for the image in (a). Under these conditions stable imaging of the particles is achieved due to the increased distance of the tip to the surface.[23] An image taken on a single particle at reduced image size is shown in Figure 6c with a line profile across the particle displayed in Figure 6d. Firstly it can be seen that the particle has an apparent height of roughly 1.5 nm, which gives an estimate for the real dimension of the particle. Different I(z) characteristics on the particle and on the substrate, may lead to an error of some Angstroms in this height estimate. The apparent lateral size of 6 nm is dominated by the convolution with the geometrical shape of the tip and can therefore only provide an upper limit for the particle size. The surface of the gold terrace appears to be modulated in the range of roughly 1 Å, pointing towards a noncrystalline morphology of the amino-terminated thiol monolayer in agreement with the FTIR investigations. Atomic force microscopy was applied as a complementary method to investigate the surface topography independent from its electric response and an apparent particle height and density was found which was consistent with the results from the STM investigations.

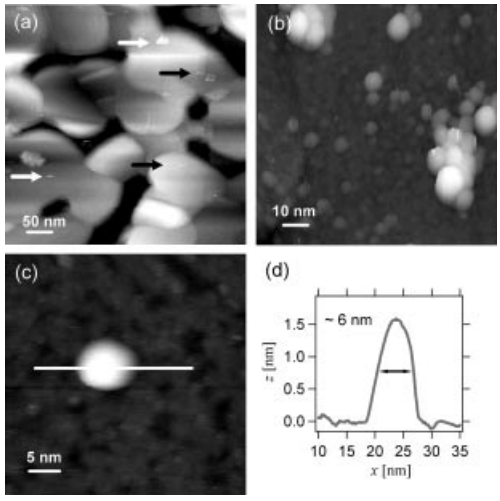

Figure 6. STM images. (a) The arrows indicate particles that are swept away during the imaging (401 mV, 93.4 pA). (b) Decreased tunnel current (500 mV, 38.5 pA). (c) Close-up of (b) (500 mV, 40.7 pA). (d) Line profile through (c).

Spectroscopy was performed by choosing an image frame such that one single particle covers roughly 50% of the image area as shown in Figure 7a, while reference measurements were taken on the same sample for an area without particles. Averaged $I(V)$ curves are displayed in Figure 7b, showing no significant difference between the two experiments, particularly, no pronounced steplike feature as is expected for a Coulomb blockade effect is observed. Single $I(V)$ curves taken on a particle are displayed in Figure 7c and are to be compared with the $I(V)$ curves taken on the pure SAM displayed in Figure 7d. These curves were chosen in a random fashion, i.e. no selection criteria were applied.

Both sets of curves show some differences in the shape of the individual curves, such as a significantly increased current in the uppermost curve in Figure 7d. The saturation at high negative currents is due to the maximum output of the electronics and does not reflect a real physical effect. Typical features of the individual curves taken on the particle are both steplike features as indicated by the vertical lines in the lowest curve and sudden "reverse" jumps which appear as an effective decrease in current at increasing voltage and are marked by arrows in two curves. The individual curves taken on the SAM do not show such behaviour.

 © 2005 Wiley-VCH Verlag GmbH & Co. KGaA, Weinheim

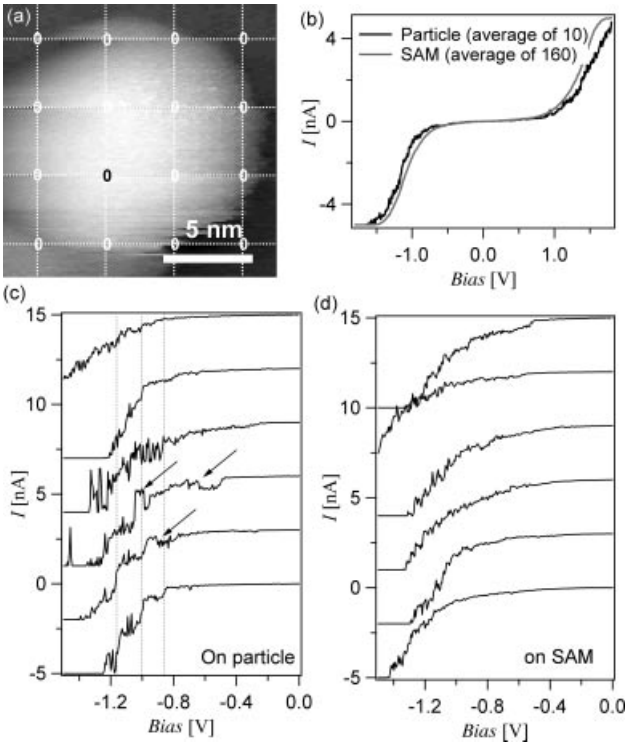

Figure 7. (a) Scanning tunnelling image of a Au nanoparticle (image size 15×15 nm^2). At the indicated 16 points, $I(V)$ spectra were taken during image acquisition (bias = 502 mV, I = 34 pA). (b) Average of 10 $I(V)$ curves obtained, indicated by the position marked in black in (a) compared to the average of all 160 $I(V)$ curves obtained with identical parameters (bias = 502 mV, I = 42.7 pA) on the same sample with no gold particles in the image range. (c) Sequence of individual curves obtained at the position marked by the black "0" in (a). The first six curves that were recorded are displayed, i.e. the data is chosen randomly. The features marked by the arrows and by the vertical dashed lines are explained in the text. (d) Sequence of individual curves randomly chosen from the spectra measured on a sample area without particles and averaged in (b). The curves in (c) and (d) are offset for clarity.

Similar current-voltage steps in single $I(V)$ curves were observed under ambient conditions[10,11,15] and have been assigned to a Coulomb staircase. In the system studied here, a reproducible measurement of the steplike features in the $I(V)$ curve was not possible, thus preventing a clear discrimination as to whether the steps are due to a Coulomb blockade or due to fluctuations of the background charge. The irreproducibility of the $I(V)$ curves as well as the "reverse jumps" may be interpreted as fluctuations of either the background charge or the entire double-tunnel-junction geometry with time, which occurs with high probability in polar systems.[5] On average a smooth $I(V)$ curve is obtained (see Figure 7b) when averaging over a set of experiments and all steplike features are averaged out.

The dI/dV curves acquired simultaneously with the data displayed in Figure 7c and d are shown in Figure 8a and b, respectively. On the SAM, no clear features are seen in the dI/dV representation in agreement with the observations on the $I(V)$ data. The individual curves taken on the particle show some features, which may be interpreted as maxima. They are again highly irreproducible from measurement to measurement. A comparison of the voltage for which apparent steps in the $I(V)$ data occur is made by marking the corresponding voltages in both Figure 7c and Figure 8a. No clear correlation is seen, giving additional evidence that extraction of Coulomb staircase-like behaviour from these experiments is either impossible or would require a very deep and careful statistical analysis.

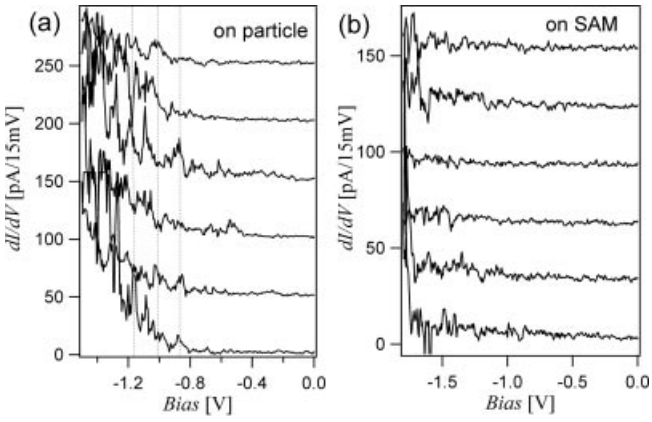

Figure 8. Single scans of the differential conductivity on the particle (a) and on the SAM (b). These data were obtained simultaneously with the curves in Figure 7c and d.

For this reason, an attempt is made with the following to extract information from the only data that can be obtained in a reproducible manner i.e. the averaged curves. Either $I(V)$ or dI/dV may be used for the analysis since they contain redundant information, though the observed effects are better visible with the dI/dV curves, which are therefore discussed below. Such averaged curves taken on a particle and on the SAM are shown in Figure 9a and b and Figure 9c and d, respectively.

A quantitative evaluation of these curves is done by comparing it to a fit based on an approach by Ukraintsev[24] for a single tunnel junction based on the one-dimensional WKB approximation which assumes comparable average density of states at the Fermi level for the tip and sample. This method, originally proposed as the "density of states deconvolution technique" is applied here to quantify the deviation from a normal response of a metal-metal contact. Following Ukraintsev, the measured dI/dV signal can be expressed as

$$\frac{\mathrm{d}I}{\mathrm{d}V}(z,V) = \frac{eA}{2}[T(z,eV/2) + T(z,-eV/2)] \quad (1)$$

with

$$T(z,\xi) = \exp[-2z\frac{8\pi^2 m_e}{\hbar^2}(\bar{\Phi} - \xi)] \quad (2)$$

Where e, m_e, $\hbar$ are the electron charge and mass and Planck's constant respectively, z the tunnelling distance, V the voltage, A a scaling parameter for the absolute value of the tunnel current and $\bar{\Phi}$ the average of the work functions of the tip and substrate material (Φ = 5.31 eV for Au.[25] An identical value is assumed for the Pt/Ir 90:10 alloy that the tip is composed of, based on the literature values of

 © 2005 Wiley-VCH Verlag GmbH & Co. KGaA, Weinheim

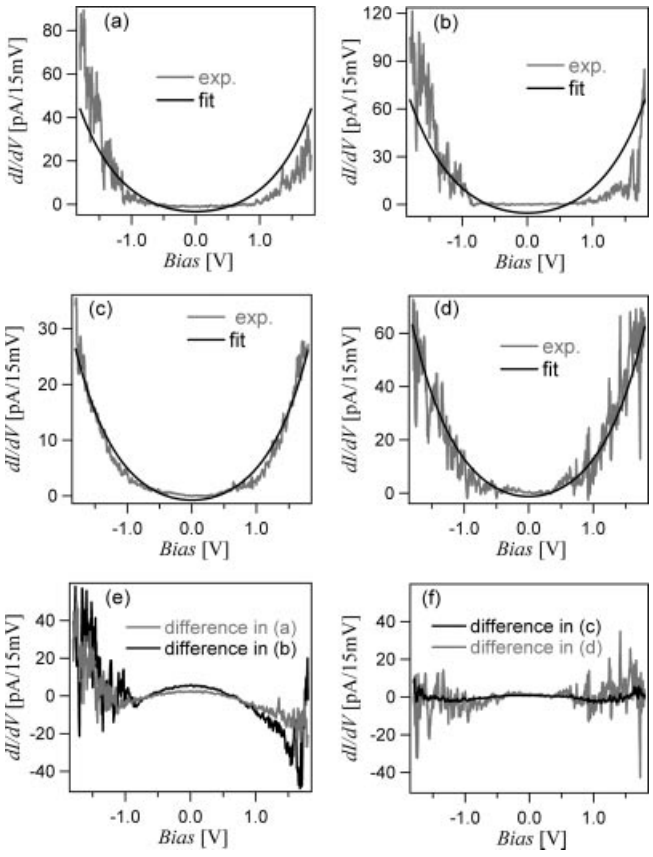

Figure 9. (a) and (b) dI/dV spectra obtained on two different gold nanoparticles The curves are averaged over 10 individual data sets and are representative of 20 particles that were studied. The fit of Equations 1 and 2 to the data using the approach of Ukraintsev is shown as a solid line. The fitting parameters are (d = 1.17 nm, A = 4.29×10^9 V s^{-1}) for (a) and (d = 1.11 nm, A = 1.63×10^9 V s^{-1}) for (b). (c) and (d) were obtained under identical experimental conditions as (a) and (b) on the bare SAM. (c) and (d) are averaged over 150 and 10 individual curves, respectively. The fitting parameters are (d = 1.2 nm, A = 3.92×10^9 V s^{-1}) for (c) and (d = 1.13 nm, A = 2.1×10^9 V s^{-1}) for (d). (e) Residual of the two fits of the gold particle in (a) and (b). (f) Residual of the two fits of the SAM in (c) and (d).

5.65 eV (Pt) and 5.27 eV (Ir)[25]). The remaining free parameters in this fit are the tunnel distance z and the overall scaling parameter A.

A good agreement of the fit with the experimental data was obtained on the pure SAM (Figure 9c and d), justifying the simplifications made by the model a posteriori. The difference spectra (Figure 9f) display only negligible deviations. This good agreement of the Ukraintsev-model, which assumes tunnelling through a vacuum, with our data is remarkable. It shows that a good fit is obtained, although instead of a vacuum, an amino-functionalized thiol is located in the tunnel barrier. The tunnel distance z used for the fit should be regarded as an effective value rather than a true measure of distance. Furthermore, it is noted that the average of 10 traces (Figure 9d) displays more noise that the average of 150 traces (Figure 9c), but the overall response is clearly reproduced in both data sets.

The situation is drastically different for the average spectra taken on the Au particles. The difference between the data and the fit as displayed in Figure 9e exhibits two systematic features, a negative curvature around 0 bias and an asymmetry with respect to the Bias = 0 axis. From the negative curvature a reduced conductivity at a low bias compared to the "normal" case is obvious. When averaging over 10 data sets no systematic steps can be seen as could be anticipated from the strong variations in position of the steps in the individual curves. Though, the steps in the individual curves lead to an increased random noise at higher absolute bias compared to the reference.

There are several possibilities that must be considered as a reason for these features. Single-electron tunnelling effects may play a role, which must be treated in the framework of a slowly reacting polarizable species around the tunnel junction. Furthermore, significant geometrical rearrangements during the scan may occur. Some influence of the chemistry seen at the tip, which consists of amino-terminated molecules on the plane surface. Carboxy groups on the particle may play a role as well. Though, one may argue that if the amino groups present on the plane surface do not lead to a response that differs significantly from the Ukraintsev picture, only small effects are to be expected from a carboxy-terminated surface.

Summary and Outlook

Gold nanoparticles functionalised with mercaptosuccinic acid were immobilized on a gold surface coated with a self-assembled monolayer consisting of 6-amino-1-hexanethiol. The formation of a well-defined geometry was followed by surface plasmon and infrared spectroscopy and proven by STM imaging.

Fluctuations in the $I(V)$ and dI/dV curves obtained with the STM under ambient conditions prevented a reliable observation of a Coulomb staircase in the system studied here. Jumps in the $I(V)$ characteristics are observed which could be interpreted in terms of a Coulomb staircase, but variations in background charge, capacitance or geometry of the double-tunnel junction can equally well account for these observations. These instabilities prevent the reproducible observation of signatures on single-electron tunnelling. A key outcome of this investigation is that we could show that the averaged response of a double-tunnel junction, although not displaying steps, significantly deviates from the response of the metal surface without particles. This was shown by fitting the data to the model proposed by Ukraintsev.[24] While the Ukraintsev model accurately describes the response of the SAM-coated surface on particles a reduced current around zero bias as well as a pronounced asymmetry of the $I(V)$ curves is observed. Although a full understanding of these effects requires further experimental and theoretical efforts, they provide a clear, robust signature for tunnelling through a surface-bound particle that is applicable to ambient conditions. These deviations probably carry a signature of molecular changes in the vicinity of the

 © 2005 Wiley-VCH Verlag GmbH & Co. KGaA, Weinheim

tunnel gap and may therefore be used as nanoscopic reporters for molecular events.

Experimental Section

Substrate Preparation: Microscopy cover slides are cleaned in an Ar/O_2 Plasma (Plasma System, 200G, Technics Plasma, 1 mbar, 90% Ar/10% O_2, 5 min, 300 W) and gold is thermally evaporated on the heated (320°) substrate. A gold film of 50 nm thickness is produced at an evaporation rate of 0.1 nm s^{-1}. This leads to atomically flat Au terraces with typical dimensions of 100 nm which are sufficient for scanning tunnelling experiments.[26] The samples were immersed in a 1 mM solution in ethanol of 6-amino-1-hexanethiol (obtained in the form of its hydrochloride from Dojindo, Japan) for 4 h and subsequently rinsed with ethanol (thrice), Milli-Q water (thrice), 0.1 M HCl (once), Milli-Q water (thrice), and ethanol (once), and dried with a N_2 gun.

Deposition of Au Nanoparticles: Carboxyl-functionalised gold nanoparticles were synthesized as described by Chen et al.,[27] based on the reduction of hydrogen tetrachloroaurate(III) ($HAuCl_4 \cdot 3H_2O$ from Sigma–Aldrich, USA) by sodium borohydride in methanol using 2-mercaptosuccinic acid (MSA, obtained form Acros Organics, Belgium) as the stabilizing thiol ligand. The particle size can be easily controlled by the initial molar ratio of MSA/$HAuCl_4$. In our case, the molar ratio is 1:1. In a 500 mL 3-neck round-bottomed flask, $HAuCl_4 \cdot 3H_2O$ (1.25 mmol) in milli-Q water (5 mL) and MSA (1.25 mmol) in methanol (245 mL) were mixed and vigorously stirred for 30 min at room temperature. A freshly prepared $NaBH_4$ (12.5 mmol) in a water solution (25 mL) was added dropwise at a rate of 60–80 drops per minute, and finished in ca. 5 min. After further stirring for 1 h, the precipitate was collected and washed by a repeated centrifugation-ultrasonic dispersion process in mixed methanol/H_2O, and finally dried in vacuo. The main product was collected as 220 mg powder.

The resulting nanoparticles have diameters of 2 nm with a relatively broad size distribution as confirmed by transmission electron microscopy.

The thiol-modified substrates are immersed in a suspension containing the MSA-capped Au particles ($\approx$ 0.25 mg ml^{-1}, in pH 7.5, 0.1 M Na HEPES Buffer) for between 5 and 60 min depending on the desired particle density on the surface. After deposition, the substrate is subsequently rinsed with Na HEPES Buffer (0.1 M), NaOH solutions (0.1 M), and Milli-Q water and dried with the N_2 gun.

Scanning Tunnelling Microscopy and Spectroscopy: Scanning tunnelling microscopy was performed with a homebuilt scanhead in combination with a commercial controller (RHK SPM 1000). For imaging, the "constant current" mode was used. $I(V)$ spectra that can be unambiguously assigned to topographic features in the image were obtained by interrupting image acquisition and taking the $I(V)$ curves along some preset lines, yielding a complete image with a rectangular grid where $I(V)$ curves were taken. dI/dV spectra were obtained simultaneously by superimposing a sinusoidal modulation on the bias voltage (amplitude 15 mV, frequency 10–40 kHz), which was fed into a lock-in amplifier (Femto, LIA-MVD-200).

Monolayer Analysis: Surface plasmon spectroscopy in the Kretschmann-configuration was performed on a homebuilt set-up, using a HeNe Laser (λ = 633 nm) as light source. This technique, which is described in detail in ref.[28] allows for the monitoring of the thickness of a homogeneous adlayer of known dielectric response from angle-dependent reflectivity measurements. For the deposition of MSA-capped Au particles the coverage as a function of time can be monitored up to an unknown scaling factor, which must be determined by complementary methods. The angle of the reflectivity minimum was monitored as a function of time by measuring three values for each point of the Reflectivity for θ at the last determined minimum position, slightly above and slightly below. The new minimum position was determined as the minimum of a parabola through these three points.

Infrared spectroscopy was performed with a Magna 850 Series II FTIR spectrometer (Nicolet) under grazing incidence.

Acknowledgments

We are grateful to H. Schniepp for supporting us with his scanning probe image viewer and including our file format to it. We acknowledge financial support from the DFG- Schwerpunktprogramm "Hableiter- und Metallcluster als Bausteine für organisierte Strukturen" (DFG-SPP 1072).

[1] A. N. Korotkov, *Coulomb Blockade and Digital Single-Electron Devices*, IUPAC, **1997**.
[2] A. E. Hanna, M. Tinkham, *Phys. Rev. B* **1991**, *44*, 5919.
[3] J. W. Gerritsen, S. E. Shafranjuk, E. J. G. Boon, G. Schmid, H. van Kempen, *Europhys. Lett.* **1996**, *33*, 279.
[4] R. S. Ingram, M. J. Hostetler, R. W. Murray, T. G. Schaaff, J. T. Khoury, R. L. Whetten, T. P. Bigioni, D. K. Guthrie, P. N. First, *J. Am. Chem. Soc.* **1997**, *119*, 9279.
[5] M. Y. Han, L. Zhou, C. H. Quek, S. F. Y. Li, W. Huang, *Chem. Phys. Lett.* **1998**, *287*, 47.
[6] M. Dorogi, J. Gomez, R. Osifchin, R. P. Andres, R. Reifenberger, *Phys. Rev. B* **1995**, *52*, 9071.
[7] R. P. Andres, T. Bein, M. Dorogi, S. Feng, J. I. Henderson, C. P. Kubiak, W. Mahoney, R. G. Osifchin, R. Reifenberger, *Science* **1996**, *272*, 1323.
[8] B. Wang, H. Q. Wang, H. X. Li, C. G. Zeng, J. G. Hou, X. D. Xiao, *Phys. Rev. B* **2001**, 63.
[9] L. E. Harrell, T. P. Bigioni, W. G. Cullen, R. L. Whetten, P. N. First, *J. Vac. Sci. Technol. B* **1999**, *17*, 2411.
[10] L. C. Brousseau, Q. Zhao, D. A. Shultz, D. L. Feldheim, *J. Am. Chem. Soc.* **1998**, *120*, 7645.
[11] W. P. McConnell, L. C. Brousseau, D. L. Feldheim, *Abstracts Of Papers Of The American Chemical Society* **2000**, *219*, U114.
[12] H. Osman, J. Schmidt, K. Svensson, R. E. Palmer, Y. Shigeta, J. P. Wilcoxon, *Chem. Phys. Lett.* **2000**, *330*, 1.
[13] L. F. Chi, M. Hartig, T. Drechsler, T. Schwaack, C. Seidel, H. Fuchs, G. Schmid, *Applied Physics A-Materials Science & Processing* **1998**, *66*, S187.
[14] G. Schmid, G. L. Hornyak, *Current Opinion in Solid State & Materials Science* **1997**, *2*, 204.
[15] W. P. McConnell, J. P. Novak, L. C. Brousseau, R. R. Fuierer, R. C. Tenent, D. L. Feldheim, *J. Phys. Chem. B* **2000**, *104*, 8925.
[16] C. Schoenenberger, H. van Houten, C. W. J. Beenakker, *Physica B* **1993**, *189*, 218.
[17] R. M. Silverstein, C. G. Bassler, T. C. Morill, *Spectrometric Identification of Organic Compounds*, 5 ed., John Wiley and Sons, **1995**.
[18] A. N. Parikh, D. L. Allara, I. B. Azouz, F. Rondelez, *J. Phys. Chem.* **1994**, *98*, 7577.
[19] J. Tien, A. Terfort, G. M. Whitesides, *Langmuir* **1997**, *13*, 5349.
[20] J. M. Brockman, A. G. Frutos, R. M. Corn, *J. Am. Chem. Soc.* **1999**, *121*, 8044.
[21] M. Sprik, E. Delamarche, B. Michel, U. Rothlisberger, M. L. Klein, H. Wolf, H. Ringsdorf, *Langmuir* **1994**, *10*, 4116.
[22] M. L. Wallwork, D. A. Smith, J. Zhang, J. Kirkham, C. Robinson, *Langmuir* **2001**, *17*, 1126.

 © 2005 Wiley-VCH Verlag GmbH & Co. KGaA, Weinheim

[23] H. A. Wierenga, L. Soethout, J. W. Gerritsen, B. E. C. van de Leemput, H. van Kempen, G. Schmid, *Adv. Mater.* **1990**, *2*, 482.
[24] V. A. Ukraintsev, *Phys. Rev. B* **1996**, *53*, 11176.
[25] H. Stöcker, *Taschenbuch der Physik*, 3 ed., Harri Deutsch, Frankfurt a. M., **1998**.
[26] J. Hwang, M. A. Dubson, *J. Appl. Phys.* **1992**, *72*, 1852.
[27] S. H. Chen, K. Kimura, *Langmuir* **1999**, *15*, 1075.
[28] W. Knoll, *Ann. Rev. Phys. Chem.* **1998**, *49*, 569.
Received: March 29, 2005
Published Online: August 1, 2005

 © 2005 Wiley-VCH Verlag GmbH & Co. KGaA, Weinheim

Electrical Resistivity of Epitaxial Au Films Surface-Modulated by Arrays of Pt Nanoparticles

Gerd Kästle,[a] Alexander Schröder,[a] Hans-Gerd Boyen,[a] Alfred Plettl,[a] Paul Ziemann,[a] Oliver Mayer,[b] Joachim Spatz,*[b,c] Martin Möller,[b,d] Michael Büttner,[e] and Peter Oelhafen[e]

Keywords: Thin films / Gold / Conductivity / Platinum nanoparticles

Arrays of Pt nanoparticles with a high degree of hexagonal short-range order are deposited by means of self-assembly of diblock-copolymers on top of high quality epitaxial Au films and their influence on the electrical properties is studied. The temperature-dependent resistivity of the nanomodulated Au films is surprisingly well described by the classical size effect model of Fuchs–Sondheimer, which is based on a mixture of diffuse and specular surface scattering events. Especially, no specific influence of the interparticle distance of the nanoparticle array could be detected even though it was of the same magnitude as the elastic mean free path of the scattering electrons. Rather, the nanomodulation acts as randomly distributed scatterers leading to an overall decreased probability for specular reflections of conduction electrons at the sample surface.

(© Wiley-VCH Verlag GmbH & Co. KGaA, 69451 Weinheim, Germany, 2005)

Introduction

When sample dimensions are reduced as in thin films, surfaces become increasingly important having a strong impact on many of the sample properties like, e.g. electrical conductivity. Although it was speculated already one century ago[1] that the resistivity of thin metal films should deviate from the resistivity of corresponding bulk samples, it was only about 40 years later that Fuchs[2] and Sondheimer,[3] respectively, first developed models to describe the size effect of the electrical resistivity in thin films quantitatively. Along with continuous improvements of the experimental conditions (e.g. purification of starting materials, vacuum technology, analytical tools), sophisticated experiments revealed a large variety of interesting aspects.[4–25]

Common to all of these experiments were either epitaxially grown films with surfaces as flat as possible or polycrystalline films with a finite surface roughness representing a statistical distribution of the film thickness. The influence of a well-defined highly-ordered surface roughness, however, on the electrical resistivity of thin films has not yet been examined. In such a case, it could be speculated that the temperature-dependent resistivity should show deviations from the usually observed behavior whenever the electron mean free path would be a multiple of the characteristic distance between the artificial surface structures.

With the recent developments of powerful methods to produce ensembles of nanostructures on flat surfaces with a high degree of hexagonal short-range order and the individual nanostructures having dimensions approaching the Fermi wavelength of metals (typically some few nanometers), such a study has now become possible. In this work, thin metal films are patterned with a simple bottom-up technique based on molecular self-assembly.[26,27] Arrays of chemically clean Pt nanoparticles are prepared with a diameter of about 3 nm and an interparticle distance of about 30 nm. With these nanoparticles, it is possible to prepare nanomodulated thin metal films with a modulation length comparable to the mean free path of the electrons. The nanomodulated metal films have to fulfill several requirements to be suitable for such transport measurements: First, the metal film itself must be thin enough to ensure the necessary surface sensitivity of the resistivity. Second, it must be epitaxially grown without a magnetic seedlayer to minimize electron scattering within the film as well as additional spin scattering at the film/substrate interface, and third it must be chemically inert because of ex situ steps which are needed for the preparation of the metallic nanoparticles. Finally, the film has to be flat to guarantee that transport properties are governed by the nanomodulation and not by the intrinsic surface roughness of the sample. All these requirements are met by epitaxial Au films grown on sapphire with a Nb seedlayer.[28]

[a] Abteilung Festkörperphysik, Universität Ulm, 89069 Ulm, Germany
[b] Abteilung Organische Chemie III, Universität Ulm, 89069 Ulm, Germany
[c] Present address: Biophysical Chemistry, University of Heidelberg, INF 253, 69120 Heidelberg, Germany
[d] Present address: Deutsches Wollforschungsinstitut, Veltmannplatz 8, 52062 Aachen, Germany
[e] Institut für Physik, Universität Basel, Klingelbergstr. 82, 4056 Basel, Switzerland

Results and Discussion

Size Effect of the Electrical Resistivity

The temperature dependence of the electrical resistivity in bulk metals is described by the Bloch–Grüneisen relation [Equation (1)].

$$\rho_{bulk} = \rho_{0,bulk} + K\left(\frac{T}{\theta_D}\right)^5 \int_0^{\theta_D/T} \frac{x^5 dx}{\left(e^x - 1\right)\left(1 - e^{-x}\right)} \quad (1)$$

Here θ_D is the Debye temperature, K is a material specific factor and $\rho_{0,bulk}$ is the residual resistivity. The electron mean free path due to impurities l_{imp} is related to the residual resistivity by $\rho_{0,bulk} = m \cdot v_{Fermi}/n \cdot e^2 \cdot l_{imp}$. For thin films, however, with a thickness approaching l_{imp}, scattering of the electrons at the surface can no longer be neglected. In the classical size effect model by Fuchs–Sondheimer (FS),[3] surface scattering is included and the resistivity of thin films ρ_{film} can be deduced from the resistivity of the bulk metal [Equation (2)].

$$\frac{\rho_{bulk}}{\rho_{film}} = 1 - \frac{3}{2\kappa} \int_0^1 du \cdot \left(u - u^3\right) \frac{(1-p)\left(1 - e^{-\kappa/u}\right)}{1 - p \cdot e^{-\kappa/u}} \quad (2)$$

Here $\kappa = t/l$ is the ratio between film thickness t and the electron mean free path l in the bulk metal. The so-called specularity parameter p, describes phenomenologically the surface scattering of the electrons. Complete specular scattering corresponds to $p = 1$ whereas complete diffuse scattering corresponds to $p = 0$.

Transport Measurements

Before investigating the influence of a controlled nanomodulation with nanoparticles on the electrical resistivity of the Au films, the resistivity of as-prepared Au films without artificial roughness needs to be addressed, which has been done in a recent study.[23] The high epitaxial quality and the small roughness of the Au films allowed a detailed analysis of the temperature dependence of the resistivity for film thicknesses even down to 2 nm. Surprisingly, the experimental data could be described best within the framework of the classical Fuchs–Sondheimer model[3] while an analysis based on the more physically motivated models of Mayadas–Shatzkes or Soffer[5] gave results that are not physically relevant. Further investigations on medium energy ion irradiated films also confirmed this finding.[24] None of the experiments performed on epitaxially grown Au films gave any hint of a strong influence of the Nb seedlayer on their transport properties. In addition, due to the small thickness of this layer (1 nm), its transition into the superconducting state was found to be suppressed. Furthermore, despite the high quality of the Au films, no influence of quantum effects on the resistivity could be observed and only the original classical size effect model was able to consistently describe the experimental results. Thus, it seems to be justified to analyze the resistivity of the present nanomodulated Au films within the framework of the Fuchs–Sondheimer model.

Nanomodulation of the Film Surface Using Pt Nanoparticles

Arrays of Pt nanoparticles with a high degree of hexagonal short-range order were deposited on top of epitaxially grown Au films (as described in more detail in the experimental section) serving as scattering centers for the conduction electrons. A slight increase in statistical roughness at the Au film surface can be expected due to the plasma treatment[29] necessary to remove organic precursors. However, since all of the preparation procedures have been performed simultaneously on both the nanomodulated as well as the reference film, all sample properties should be identical except for the nanomodulation. Thus, in case of any resistivity changes due to, e.g., the plasma-induced roughening at the surface, this effect will be present in both the nanomodulated as well as the reference Au film.

Figure 1 shows atomic force microscopy (AFM) pictures of an epitaxially grown Au film (thickness t = 25 nm) with one half serving as a reference film (parts a and b in Figure 1) and the other half being nanomodulated with Pt nanoparticles on its surface (parts c and d in Figure 1). Even though the combination of oxygen and hydrogen

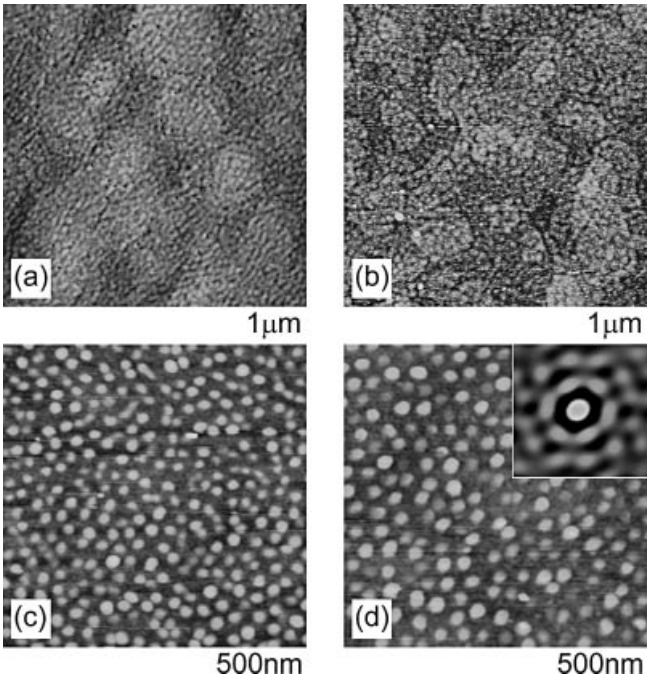

Figure 1. AFM images of the Au reference sample (a, b: z scale 3 nm) and the sample modulated with Pt nanoparticles (c, d: z scale 10 nm). The images were taken after polymer removal by the oxygen plasma (a, c) and after reduction of a thin Au oxide layer (thickness = 4 nm[29]), which is formed in the oxygen plasma by applying an additional hydrogen plasma step (b, d).

 © 2005 Wiley-VCH Verlag GmbH & Co. KGaA, Weinheim

plasmas, which is required for the nanoparticle deposition, leads to a finite film roughness of the reference film of 0.23 nm_{rms} (Figure 1, a) and 0.28 nm_{rms} (Figure 1, b), respectively, the underlying terrace structure of the epitaxial Au film is still visible. After the oxygen plasma treatment, the Pt nanoparticles (Figure l, c) have a spacing of about 32 nm and a height of 3.7 nm, which is reduced to 2.9 nm by the subsequent hydrogen plasma (Figure 1, d). This decrease is due to the reduced nanoparticle volume in the metallic state as compared to the oxidized state, resulting from the exposure to an oxygen plasma. Although not perfectly ordered, the final nanoparticle arrangement exhibits a high degree of hexagonal short-range order as evidenced by the corresponding autocorrelation function shown in the inset of Figure 1 (d). Thus, deviations from the usually observed surface scattering effects induced by a statistical (random) surface roughness[4–25] can indeed be expected.

It has to be emphasized that it is not at all self-evident that stable metallic nanoparticles can be prepared on top of metal films. For Ag clusters, it was found that the clusters dissolve on epitaxial Ag films for temperatures $T > 300$ K whereas they are stable for $T < 225$ K.[30] Although Pt and Au are known to be fully miscible in the bulk, the diffusion constant turns out to be too small for Pt atoms to diffuse from the nanoparticles into the underlying Au film. Assuming a maximum temperature of 80 °C (required for the final conditioning of the nanomodulated sample, see below) which will be kept for a period of 3 days, a diffusion length $L = \sqrt{D \cdot t}$ of well below the interatomic distance can be estimated from published data for the diffusion constant $D = D_0 \cdot e^{-E/k_B T}$ with $D_0 = 9.5 \times 10^{-6}$ $m^2 s^{-1}$ and $E = 2.09$ eV.[31]

This estimate can experimentally be verified by means of X-ray Photoelectron Spectroscopy (XPS). Figure 2 (a) displays the Pt–4f core level spectrum (open symbols) of a nanomodulated sample acquired after annealing to about 80 °C in order to get rid of adsorbed water followed by an additional hydrogen plasma step in order to remove hydrocarbon adsorbates (see below). The Pt–4f spectrum can be well described by fitting[32] a single doublet (solid line) to the data using Doniach–Sunjic type line shapes.[33] As can be recognized in Figure 2 (a), the experimental binding energy position of the Pt–$4f_{7/2}$ core level agrees well with the value measured under identical conditions on a Pt reference sample (vertical solid line), but disagrees with published data[34] for the chemical shift observed in Pt_xAu_{100-x} intermetallic compounds (dashed line: $Pt_{75}Au_{25}$; dotted line: $Pt_{50}Au_{50}$; dash-dotted line: $Pt_{25}Au_{75}$). It is worth mentioning that the size of the final Pt nanoparticles (2.9 nm) matches the information depth of the spectroscopy (twice the photoelectron mean free path corresponding to 3 nm). Thus, significant intermixing between the Pt nanoparticles and the Au substrate can safely be excluded.

In addition to the binding energy position, the analysis of the line shape also provides valuable information about the electronic structure of the nanoparticles, which due to their reduced size of less than 3 nm, could be expected to show molecular/insulating rather than metallic properties. As can be seen in part a of Figure 2, the experimental core level spectrum exhibits a significant asymmetry towards higher binding energies (corresponding to lower kinetic energies of the outgoing photoelectrons) reflecting the creation of electron-hole pairs during photoemission in the vicinity of the Fermi energy E_F. This large asymmetry clearly indicates a high density of states at E_F[35] and, consequently, provides evidence that a particle size of about 3 nm is still large enough to maintain metallic properties of the nanodots allowing a strong coupling to the conduction electrons of the underlying Au film.

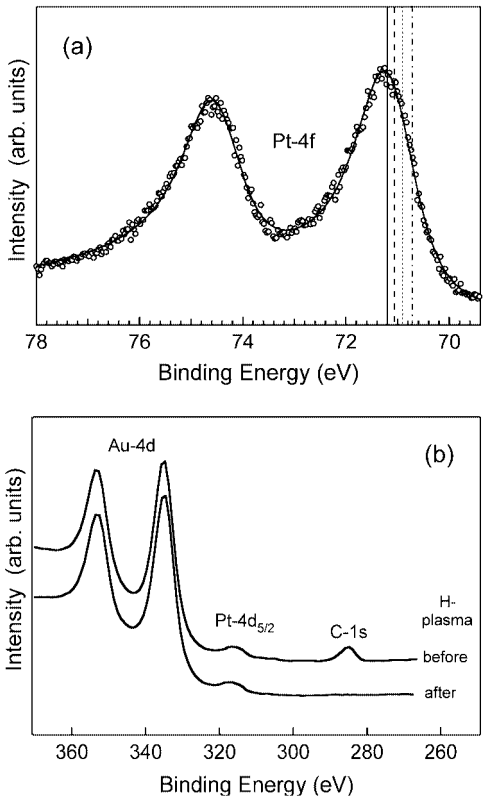

Figure 2. XPS core level spectrum of the Pt–4f doublet acquired after the final H-Plasma step (a) and C-ls binding energy range before and after annealing to about $T = 80$ °C followed by a hydrogen plasma treatment in order to remove adsorbates from the film surface (b). The vertical lines in (a) indicate the position of the Pt–$4f_{7/2}$ core level measured on a Pt reference sample (solid line) as well as the chemical shift observed for Pt_xAu_{100-x} intermetallic compounds[34] (dashed line: $Pt_{75}Au_{25}$, dotted line: $Pt_{50}Au_{50}$, dash-dotted line: $Pt_{25}Au_{75}$).

Surface Sensitivity

Because the resistivity of very thin metallic layers is strongly influenced by surface scattering of the conduction electrons special care has been taken in order to minimize the influence of adsorbates[4,10] like water or hydrocarbons which will accumulate at the surface when exposing the samples to ambient conditions and to various solvents required to perform the lithographic steps. In Figure 3, the resistivity $\rho_{4\,K}$ measured at $T = 4$ K (which corresponds to the residual resistivity ρ_0) and the room temperature resis-

 © 2005 Wiley-VCH Verlag GmbH & Co. KGaA, Weinheim

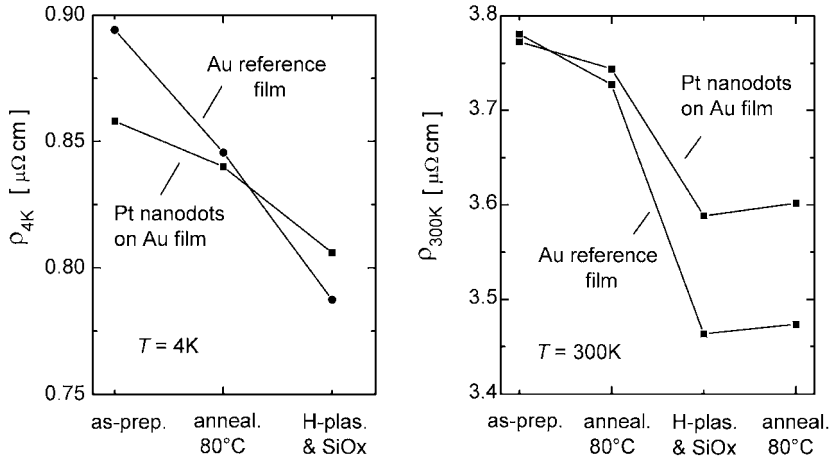

Figure 3. Resistivity at T = 4 K (left) and T = 300 K (right) of the Pt nanomodulated sample as compared to the reference film (thickness of both films: t = 25.4 nm). The resistivity of both samples decreases strongly with increasing surface cleanliness.

tivity $\rho_{300\,K}$ determined at T = 300 K of a nanomodulated Au film is compared with the values acquired from the corresponding Au reference film with both samples being treated simultaneously by the different preparational procedures. In the case of the as-prepared samples and the data taken in the cryostat without any additional treatments, the resistivity of the nanomodulated sample is found to be smaller than the reference film at both temperatures. This is opposite to what is expected for a nanomodulated sample, which should reveal a resistivity enhancement related to a smaller specularity parameter p due to the additional roughness induced by the nanoparticles.

In order to unravel whether adsorbates are responsible for this surprising result, in a first step, all samples were annealed within the cryostat to T = 80 °C for 3 days which is expected to remove the adsorbed water layer from the sample surface. After this procedure both, $\rho_{4\,K}$ and $\rho_{300\,K}$, are found to be reduced with the low temperature value of the reference film still being higher than the corresponding value measured for the nanomodulated film. In a second step, the sample surface was cleaned by removing all hydrocarbon adsorbates in a hydrogen plasma (5 min, 100 W, 0.01 mbar) as evidenced in Figure 2 (b) by means of a vanishing C-ls peak intensity followed by the in situ evaporation of an insulating layer (SiO), in order to protect the metallic film surface from re-adsorption of contaminants during sample transport under ambient conditions to the cryostat. Again, $\rho_{4\,K}$ as well as $\rho_{300\,K}$ are found to be significantly decreased as compared to the previous annealed state of the samples. Additionally and most gratifying, after this cleaning and protecting, the resistivity of the nanomodulated film is observed to be higher than the resistivity of the reference film for both temperatures which is consistent with the expected decrease of the specularity parameter p for the nanomodulated sample.

After carefully characterizing the resistivity as a function of temperature in this state of the samples, a further annealing cycle to T = 80 °C was performed. Since adsorbates/contaminants deposited by the ex situ preparation/transport should be located on top of the SiO protection layer rather than at the interface Au/SiO, in this case, no changes in resistivity are expected due to annealing. Such behavior can most notably be observed in Figure 3 within the experimental uncertainty. Thus, the addition of a protection layer after a hydrogen-plasma induced cleaning step allows for the analysis of the temperature-dependent resistivity $\rho(T)$ dominated by intrinsic surface scattering rather than by surface contaminations. Under these conditions, the influence of modulating a metal film surface by depositing an array of Pt nanoparticles on its electrical transport properties should be detectable.

Temperature Dependence of the Resistivity – Comparison with the FS Model

To determine the characteristic properties of a t = 25.4 nm Au film and to estimate the influence of the nanomodulation on its electrical properties, $\rho(T)$ was measured between 4 K and 300 K using the lock-in technique (Figure 4, open symbols) and the results were compared with the predictions of the classical size effect model of FS (Figure 4, solid lines). This was achieved by means of a numerical fitting procedure (for details see ref.[23,24]). The best fits to the experimental data have been added as solid lines to Figure 4 showing nearly perfect agreement between theory and experiment over the whole temperature range. While such a behavior has already been observed in previous studies on epitaxially grown Au films[23,24] it is rather surprising in the case of the nanomodulated film where deviations from the classical description are expected. On the other hand, after the more qualitative discussion of $\rho_{4\,K}$ and $\rho_{300\,K}$, as shown in Figure 3, the agreement between the experimental and theoretical results within the FS model legitimates extracting all relevant parameters e.g. the specularity parameter p, the electron mean-free path due to impurities l_{imp} and the Debye temperature θ_D. This allows a more detailed analysis of the electrical properties of the

 © 2005 Wiley-VCH Verlag GmbH & Co. KGaA, Weinheim

nanomodulated sample as compared with the corresponding Au reference. The resulting sets of parameters are summarized in Table 1 as obtained for the as-prepared, the annealed, as well as the SiO covered state.

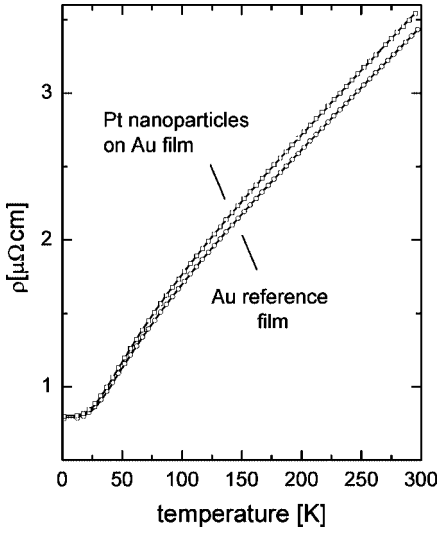

Figure 4. Temperature dependence of the resistivity of a Pt nanomodulated Au thin film sample as compared to the corresponding Au reference film (thickness of both films: t = 25 nm) after exposure to a hydrogen plasma and the in situ deposition of a SiO protection layer (open symbols). The solid lines represent the best fit to the experimental data using the FS model.

Table 1. FS fit parameters derived from the measured $\rho(T)$ curves of the Au reference sample and the nanomodulated sample in the as-prepared, the annealed and the SiO covered state.

	Au reference			Pt nanodots on Au		
	as-prep.	anneal.	SiO	as-prep.	anneal.	SiO
p	0.20	0.21	0.30	0.19	0.19	0.26
l_{imp} [nm]	700	819	697	854	905	805
θ_D [K]	185	190	178	189	191	184

For all measurements, the FS fit gives values for θ_D which are close to the bulk value of 184.6 K as obtained from fitting the temperature dependence of the resisitivity of Au bulk samples[36] with our fitting routine. The latter value itself agrees well with Debye temperatures deduced from resistivity measurements by other groups.[37,38] It is important to note that θ_D values for bulk Au extracted from transport measurements are found to be systematically larger than the corresponding values determined from XRD measurements by analyzing the temperature dependence of the Debye–Waller factor (165–170 K). This might be due to a different weighting of the real phonon density of states by the two different methods.

The similarity of the Debye temperatures extracted for the different states of the reference samples (as-prepared, annealed, SiO covered) confirms that the deposition of Pt nanoparticles on top of the epitaxially grown film using the micellar technique did not change its dynamic properties by, e.g., absorbing a significant amount of hydrogen during the hydrogen plasma treatment. This is also confirmed by analyzing l_{imp}, which determines the residual resistivity of the corresponding bulk material caused by impurities, grain boundaries or other lattice defects. This parameter remains roughly constant for both types of films (reference sample, nanomodulated sample) independent of the condition of the film surface (as-prepared, annealed, covered with SiO). In addition, the order of magnitude observed for l_{imp} in Table 1 also agrees well with the values observed for non-hydrogen plasma treated Au films of similar thickness, studied earlier.[23] Furthermore, the high value of about 800 nm observed for the electron mean free path due to impurities etc. of the corresponding (hypothetical) bulk material also confirms that the concentration of impurities is small and the grain size is large as compared to the sample thickness of t = 25 nm. This adds confidence that the Au films studied here can indeed be used as sensors for surface scattering processes (electron mean free path of the corresponding bulk material is much larger than the film thickness).

It is worth mentioning that by fitting the FS model to the temperature-dependent resistivity of a thin film, reasonable estimates can be extracted for the parameter l_{imp} describing the average distance between impurities or defects within the corresponding bulk material having the same morphology as the thin film. Thus, although the thin film resistivity is enhanced by surface scattering as compared to the bulk resistivity, the above analysis provides insight into the morphology of the thin film by means of impurity/defect concentrations, which is an important issue for the design of metallic interconnects[15,18] in microelectronics.

In Table 1, both parameters θ_D and l_{imp} do not vary significantly when the properties of the sample surface are changed. The appropriate quantity providing information on the condition of the sample surface (cleanliness and nanomodulation) is the specularity parameter p. For the as-prepared Au reference sample, the specularity parameter p = 0.203 is rather small. Only about one fifth of all electrons that contribute to the current are scattered specularly at the film surface or interface. As expected, p is slightly enhanced after moderate annealing of the sample in vacuo and p is increased further to 0.302 after removing all adsorbates by a hydrogen plasma and protecting the sample surface with a SiO layer. The probability of specular surface scattering is obviously significantly reduced by adsorbates on the film surface. Even though the probability of specular reflection is increased by almost 50% for the reference film due to an improved cleanliness at the surface, the absolute value of p is still rather small and only about 1/3 of all electrons are scattered specularly at the film surface or interface.

Once it is known that the specularity coefficient p of the Au reference sample is only 0.302 even in the best case, the effect of the Pt nanomodulation on the transport properties is expected to be comparatively small. To demonstrate the effect of modulating a Au surface by an array of Pt nanoparticles, the specularity coefficients p for the Au reference and the nanomodulated sample as extracted for the different surface conditions are summarized in Figure 5. In every case (as-prepared, annealed, SiO covered), the specularity coefficient p of the nanomodulated sample is

 © 2005 Wiley-VCH Verlag GmbH & Co. KGaA, Weinheim

smaller than that of the Au reference. The reduction of p due to the nanomodulation is most pronounced when the nonmodulated reference Au film exhibits a high degree of specular reflection (SiO covered state). Thus, the main conclusion of the present work is that the decoration or nanomodulation of an otherwise optimized Au surface with arrays of Pt nanoparticles showing a high degree of hexagonal short-range order just reduces the probability of specular reflection, as would be expected for randomly distributed additional scatterers.

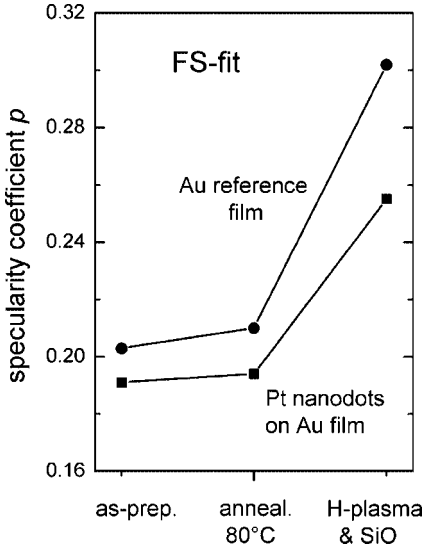

Figure 5. Specularity parameter p for the Au reference and the nanomodulated sample. By improving the surface cleanliness, p is enhanced. The nanomodulation generally leads to an increased probability of diffuse surface scattering as compared to the Au reference.

In order to better understand why diffuse surface/interface scattering dominates in the present experiment, the influence of the Nb seedlayer on electron transport has to be examined in more detail. Comparing the room temperature electrical resistivity of bulk Au (ρ = 2.2 μΩcm) and Nb (ρ = 15 μΩcm) and taking into account the different thickness of both materials (Nb: 1 nm, Au: 25.4 nm) it is obvious that electrical transport through the Nb layer can be neglected. The main impact of the seedlayer on the sample resistivity most likely is a change of the specularity parameter p at the interface between the Au film and the seedlayer as compared to a hypothetical interface between the Au film and the sapphire surface.

Investigations of specular electron scattering in Au films covered with 0.6 nm of Ta were observed to significantly increase the film resistivity by s–d scattering in contrast to Ag or Cu, which did not quench specular reflection.[11] Thus, it is very likely that scattering of the conduction electrons at the Au/Nb interface is not specular but rather diffuse. Unfortunately, this Nb seedlayer cannot be avoided if continuous, flat, epitaxially grown Au films are required as in our study. The only way to achieve Au films of similar quality is to use Fe or Cr seedlayers, which will worsen the conditions when compared with Nb because of the additional strong spin scattering at the interface, an effect which is well known, e.g., from magnetic (GMR) sensors.

Finally, it is worth mentioning, that Pt nanoparticles deposited directly onto the sapphire substrate before growing the Au film in order to avoid surface roughening induced by the plasma treatments did not result in an improved value of the specularity parameter p. Instead, l_{imp} of those films was found to be reduced to about 100 nm (as compared to 800 nm in the case of nanoparticles "on-top") probably due to a distorted epitaxial growth of the Au film on top of the Pt nanoparticles. For this sample configuration, an even further reduced specularity parameter was observed (0–0.1).

Conclusions

The influence of an array of Pt nanoparticles, prepared with a high degree of hexagonal short-range order on top of high quality epitaxial Au films on their electrical properties has been studied. It turned out that the temperature-dependent resistivity of the nanomodulated Au films are well described by the classical size effect model of Fuchs–Sondheimer. No indication could be detected that pointed to a specific effect of the nanoparticle array other than simply increasing the probability of diffuse surface scattering as would be expected for randomly distributed scatterers.

Experimental Section

Micellar Nanoparticles: Pt nanoparticle arrays were prepared using a method based on the self-assembly of suitable diblock-copolymers. A polystyrene(PS)-block-poly(2-vinylpyridine)(P2VP) copolymer was dissolved in an apolar solvent, where the copolymer chains assemble in spherical micellar objects with a hydrophilic P2VP core and a hydrophobic PS shell. The core of the micelle can be loaded with metal salts by adding the appropriate substance to the micellar solution. These metal salt loaded spherical micelles can easily be transferred onto substrates by dip coating, where, again by self-assembly, hexagonal arrays of micelles are formed. With the aid of a combined oxygen and hydrogen plasma process the micellar polymer can be removed, the metal salt can be reduced and spectroscopically clean arrays of metallic particles remain on the substrate. The hexagonal short-range order of the particles was not destroyed by the plasma process. Details on the preparation of micellar solutions and the plasma process can be found elsewhere.[26,27] For the work here, Pt nanoparticles were prepared with a diameter of about 3 nm and a spacing of about 32 nm.

Sample Preparation: The epitaxial Au films were prepared at about 300 °C on c-cut sapphire substrates with a 1 nm Nb seedlayer. The details are described in ref.[28] The samples are structured with standard photo lithography techniques and wet etching in I/KI solution[39] or etched in an RIE-plasma process (Oxford instruments, RIE-PlasmaLab 80Plus). The pattern is shown schematically in Figure 6. Twelve contacts allow four-probe measurements of the resistance on several segments of the sample.

 © 2005 Wiley-VCH Verlag GmbH & Co. KGaA, Weinheim

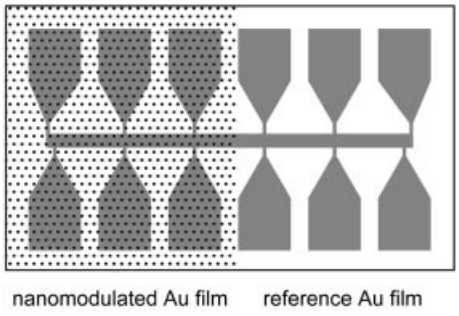

Figure 6. Sketch of a structured nanomodulated Au film sample. One half of the sample is covered with nanoparticles, the other serves as a reference. Four-probe measurements are possible on different segments on both sides.

In the size effect experiments, surface scattering properties of thin films were investigated by the temperature dependence of the resistivity and the specularity parameter p was determined by fitting to FS theory. For experiments on nanomodulated samples, one has to consider the ordinary size effect of thin films and the, probably, small influence of the nanomodulation. For this reason, both a nanomodulated Au film and a Au reference film are prepared in parallel on the same substrate as sketched in Figure 6. In this way, both films can be measured under identical conditions at the same time. All other processes (film growth, plasma exposure, lithography) were performed on the whole sample so that again both films undergo identical treatments and differ only by the nanomodulation. Such a relative measurement should enable the investigation of the influence of nanomodulation on thin film resistivity even if its effect is small.

The thickness of the epitaxial Au films was determined by means of a careful analysis of the Laue oscillations observed in the corresponding X-ray diffraction spectra using the program 'SUPREX'.[40,41] Because of the high quality of the films used in this study, an oscillating intensity could be observed over a wide range of angles covering the small angle as well as the large angle scattering regimes, respectively (for more details, see ref.[23]).

In order to control the chemical state of the Au surface and the Pt nanoparticles after the different preparational steps, the specimens were introduced into the analysis chamber of a commercial electron spectrometer (Fisons ESCALAB-210) and analyzed under ultrahigh vacuum conditions by means of XPS using monochromatized Al-K_α radiation ($h\nu$ = 1486.6 eV, spot size < 1 mm). Data were acquired using an overall energy resolution (electrons and photons) of between 0.5 and 1 eV, full width at half maximum (FWHM). At this point, it is important to note that by combining two separate chambers via a load-lock system, the plasma treatments and the XPS measurements could be performed in situ.

Acknowledgments

Financial support by the Deutsche Forschungsgemeinschaft (DFG) within SPP 1072 as well as SFB 569, the Swiss National Science Foundation (NF), and the NCCR "Nanoscale Science" is gratefully acknowledged.

[1] J. J. Thomson, *Proc. Cambridge Phil. Soc.* **1901**, *11*, 120.
[2] K. Fuchs, *Proc. Cambridge Phil. Soc.* **1938**, *34*, 100–108.
[3] E. H. Sondheimer, *Advan. Phys.* **1952**, *1*, 1–42.
[4] D. Schumacher, in: *Surface Scattering Experiments with Conduction Electrons* (Ed.: G. Holder), Springer Tracts in Modern Physics, Springer, Berlin, **1993**, vol. 128.
[5] S. B. Soffer, *J. Appl. Phys.* **1967**, *38*, 1710–1715.
[6] U. Jacob, J. Vancea, H. Hoffmann, *Phys. Rev. B* **1990**, *41*, 11852–11857.
[7] G. Reiss, E. Hastreiter, H. Brückl, J. Vancea, *Phys. Rev. B* **1991**, *43*, 5176–5179.
[8] G. Reiss, H. Brückl, *Surf. Sci.* **1992**, *270*, 772–776.
[9] J. Ederth, L. B. Kish, E. Olsson, *Phys. Rev. B* **1995**, *51*, 17116–17130.
[10] A. L. Cabrera, W. Garrido-Molina, E. Morales-Leal, J. Espinosa-Gangas, I. K. Schuller, D. Lederman, *Langmuir* **1998**, *14*, 3249–3254.
[11] W. F. Egelhoff, Jr., P. J. Chen, C. J. Powell, D. Parks, G. Serpa, R. D. McMichael, D. Martien, A. E. Berkowitz, *J. Vac. Sci. Technol. B* **1999**, *11*, 1702–1707.
[12] J. Ederth, L. B. Kish, E. Olsson, C. G. Granqvist, *J. Appl. Phys.* **2000**, *88*, 6578–6582.
[13] H. D. Liu, Y. P. Zhao, G. Ramanath, S. P. Murarka, G. C. Wang, *Thin Solid Films* **2001**, *384*, 151–156.
[14] G. Palasantzas, J. T. de Hosson, *Phys. Rev. B* **2001**, *63*, 125404.
[15] R. M. Patrikar, C. Y. Dong, W. J. Zhuang, *Microelectron. J.* **2002**, *33*, 929–934.
[16] O. Pfenningstorf, A. Petkova, Z. Kallassy, M. Henzler, *Eur. Phys. J. B* **2002**, *30*, 111–115.
[17] S. U. Jen, C. C. Yu, C. H. Liu, G. Y. Lee, *Thin Solid Films* **2003**, *434*, 316–322.
[18] C. U. Kim, J. Park, N. Michael, P. Gillespie, R. Augur, *J. Electron. Mater.* **2003**, *32*, 982–987.
[19] I. Vilfan, H. Pfnür, *The European Physical Journal B* **2003**, *36*, 281–287.
[20] S. M. Rossnagel, T. S. Kuan, *J. Vac. Sci. Technol. B* **2004**, *22*, 240–247.
[21] H. Marom, M. Eizenberg, *J. Appl. Phys.* **2004**, *96*, 3319–3323.
[22] R. A. Patrikar, *J. Appl. Surf. Sci.* **2004**, *228*, 213–220.
[23] G. Kästle, H.-G. Boyen, A. Schroder, A. Plettl, P. Ziemann, *Phys. Rev. B* **2004**, *70*, 165414–165419.
[24] G. Kästle, T. Müller, H.-G. Boyen, A. Klimmer, P. Ziemann, *J. Appl. Phys.* **2004**, *96*, 7272–7277.
[25] J. M. Camacho, A. I. Oliva, *Microelectron. J.* **2005**, *36*, 555–558.
[26] J. P. Spatz, S. Mössmer, C. Hartmann, M. Möller, T. Herzog, M. Krieger, H.-G. Boyen, P. Ziemann, B. Kabius, *Langmuir* **2000**, *16*, 407.
[27] G. Kästle, H.-G. Boyen, F. Weigl, G. Lengl, T. Herzog, P. Ziemann, S. Riethmüller, O. Mayer, C. Hartmann, J. P. Spatz, M. Möller, M. Ozawa, F. Banhart, M. G. Garnier, P. Oelhafen, *Adv. Funct. Mater.* **2003**, *13*, 853–861.
[28] G. Kästle, H.-G. Boyen, B. Koslowski, A. Plettl, F. Weigl, P. Ziemann, *Surf. Sci.* **2002**, *498*, 168–174.
[29] B. Koslowski, H.-G. Boyen, C. Wilderotter, G. Kästle, P. Ziemann, R. Wahrenberg, P. Oelhafen, *Surf. Sci.* **2001**, *475*, 1–10.
[30] A. Relitzki, A. Hilger, H. Hovel, U. Kreibig, D. Schumacher, H. Winkes, in: *Science and Technology of atomically engineered materials* (Ed.: P. Jena), World Scientific, **1998**, p. 453.
[31] Landolt-Börnstein, *Group III* ("Condensed Matter"), vol. 26 ("Diffusion in Solid Metals and Alloys"), Springer, Berlin, **1990**.
[32] G. K. Wertheim, P. H. Citrin, *J. Electron Spectrosc. Relat. Phenom.* **1985**, *37*, 57–67.
[33] S. Doniach, M. Sunjic, *J. Phys. C* **1970**, *3*, 285–291.
[34] N. Z. Negm, L. M. Watson, P. R. Norris, A. Szasz, *J. Phys. F: Met. Phys.* **1987**, *17*, 2295–2301.
[35] G. K. Wertheim, P. H. Citrin, *Topics Appl. Phys.* **1978**, *26*, 197–206.
[36] J. Mydosh, P. Ford, M. Kawatra, T. Whall, *Phys. Rev. B* **1974**, *10*, 2845–2856.
[37] J. Jacobs, R. Birtcher, R. Peacock, *J. Vac. Sci. Technol. B* **1969**, *7*, 339.

 © 2005 Wiley-VCH Verlag GmbH & Co. KGaA, Weinheim

[38] N. Karpe, G. Lapogian, J. Bottiger, J. Krog, *Philos. Mag. B* **1995**, *71*, 445.
[39] W. Eidelloth, R. L. Sandstrom, *Appl. Phys. Lett.* **1991**, *59*, 1632–1634.
[40] E. E. Fullerton, J. Guimpel, O. Nakamura, I. K. Schuller, *Phys. Rev. Lett.* **1992**, *69*, 2859–2862.
[41] E. E. Fullerton, I. K. Schuller, H. Vanderstraeten, Y. Bruynseraede, *Phys. Rev. B* **1992**, *45*, 9292–9310.

Received: June 6, 2005
Published Online: August 17, 2005

 © 2005 Wiley-VCH Verlag GmbH & Co. KGaA, Weinheim

Nanoscaled Sn and Pb Particles Aligned in Al_2O_3 Tubes Obtained from Molecular Precursors

Michael Veith,*[a] Jacqueline Frères,[a] Peter König,[a] Oliver Schütt,[a] Volker Huch,[a] and Joel Blin[a]

Keywords: Tin and lead clusters / Nanoparticles / Al_2O_3 tubes / Alignment of metal clusters / Alkoxy- and siloxyaluminum amides

Tin and lead nanoparticles and metal sponges were prepared by reducing $Me_2Si(NtBu)_2Sn$ (**7**) and $Me_2Si(NtBu)_2Pb$ (**9**) with $[H_2AlOtBu]$ (**3**), $[HAl(OtBu)_2]$ (**13**), $[H_2AlOSiMe_2tBu]$ (**8**), and $[(Me_2tBuSiO)_2AlH]$ (**15**). Together with dihydrogen and the metals in their elemental state the monomeric compounds $[Me_2Si(NtBu)_2Al(OSiMe_2tBu)(THF)]$ (**10**) and $[Me_2Si(NtBu)_2Al(OtBu)(THF)]$ (**11**) can be obtained, to mention only two examples. Each monomer is stabilized by a THF molecule coordinated to aluminum, which on sublimation loses its donor molecule and dimerizes through Lewis acid–base interactions to the spiro compounds $[Me_2Si(NtBu)_2AlOSiMe_2tBu]_2$ (**12**) and $[Me_2Si(NtBu)_2AlOtBu]_2$ (**4**), respectively. The molecular structures of **10**, **11**, and **12** were determined by single-crystal X-ray diffraction techniques. The reduction of **7** at –115 °C is gradually indicated by a color change of the reaction mixtures from red to dark brown with increasing temperature and depending on the reducing agent used. The tin powders that were obtained were identified as β-tin using X-ray powder diffraction techniques and their average crystallite size depends on the polarity of the solvent and hydride used. Under certain conditions metal sponges are formed. Pycnometric measurements were carried out on the tin and lead sponges. These showed almost the known densities for the metals when helium was used whereas significantly smaller ones were measured in water. Porous alumina membranes of different pore diameters were filled with tin and lead particles. Metal nanoparticles were prepared within the tubes of the membranes by reduction of the metal amides in the pores. The infiltration process can be repeated up to ten times increasing the amount of particles within the tubes monitored by SEM. The obtained brown or black membranes were characterized by SEM, EDX, and UV/Vis analysis. The filled membranes show sharp impervious ranges in the UV/Vis spectrum between 270 and 525 nm and could therefore be used as wavelength filters.

(© Wiley-VCH Verlag GmbH & Co. KGaA, 69451 Weinheim, Germany, 2005)

Introduction

During the last years metal clusters and colloids have become more and more important as building blocks in the synthesis of organized nanostructured materials. Because of the various applications of metal nanoparticles many articles have emerged, especially in the field of surface-enhanced spectroscopy or photocatalysis. In addition, studies on the size-controlled synthesis and the self-assembly of clusters have appeared.[1,2] Interestingly, the majority of the publications deal with the synthesis and the properties of transition or noble metal nanoparticles,[3] whereas comparatively little is known about colloidal nanoparticles of main group metals.[4]

In this work we describe the preparation of tin and lead colloids and clusters on the nanometer scale using chemical control. The syntheses are based on an organometallic route, which we have already described in former reports.[5,6] In this route, tin and lead amides are reduced by siloxy- or alkoxyalanes in organic solvents leading to tin or lead particles, together with dihydrogen and siloxy or alkoxy compounds. A proposal for the mechanism of the formation of the aluminum compounds is given in this report. By controlling different parameters, e.g. temperature and concentration of the starting materials, it was possible to obtain tin and lead particles either stabilized as colloids or as metal powders and sponges.

We have been able to insert the metal particles into porous alumina membranes of different pore diameters. The membranes were produced for our use by G. Schmid et al., who have already used such membranes for one-dimensional ordering of gold colloids.[7]

Results and Discussion

Syntheses and Reaction Mechanism

Tin and lead particles can be efficiently obtained by reduction of tin or lead amides with siloxy- or alkoxyalanes in organic solvents. Besides dihydrogen, a siloxy- or an alkoxyaluminum amide is formed through ligand exchange.

[a] Institut für anorganische Chemie, Universität des Saarlandes, Postfach 151150, 66041 Saarbrücken, Germany
E-mail: veith@mx.uni-saarland.de

In former publications we reported on the formation of the alkoxy(amino)alane [$(Me_3Si)_2N(H)AlOtBu$] (**1**) in a redox reaction between the lead amide $Pb[N(SiMe_3)_2]_2$ (**2**)[8] and a double equivalent of the *tert*-butoxyalane [$H_2AlOtBu$] (**3**)[9] [Equation (1)].[6] The spirocyclic compounds $[Me_2Si(NtBu)_2AlOtBu]_2$ (**4**) and $[Me_2Si(NtBu)_2AlOSiMe_3]_2$ (**5**) have been obtained by stoichiometric reactions of [$H_2AlOtBu$] (**3**) or [$H_2AlOSiMe_3$] (**6**),[10] respectively, with the cyclic diazastannylene $Me_2Si(NtBu)_2Sn$ (**7**)[11] [Equation (2)].[5]

$$\underset{\mathbf{2}}{Pb[N(SiMe_3)_2]_2} + 2\,\underset{\mathbf{3}}{[tBuOAlH_2]} \longrightarrow \underset{\mathbf{1}}{\{[(Me_3Si)_2N](H)Al(OtBu)\}_2} + H_2 + Pb \quad (1)$$

$$\underset{\mathbf{7}}{Sn(NtBu)_2SiMe_2} + \underset{\mathbf{3,6}}{[(RO)AlH_2]} \longrightarrow \underset{\mathbf{4,5}}{\tfrac{1}{2}\,[Me_2Si(NtBu)_2Al(OR)]_2} + H_2 + Sn \quad (2)$$

R = *t*Bu **3**, **4**; R = $SiMe_3$ **6**, **5**

Using a similar procedure we have recently treated the stannylene $Me_2Si(NtBu)_2Sn$ (**7**) with [$H_2Al(OSiMe_2tBu)$] (**8**) and the plumbylene $Me_2Si(NtBu)_2Pb$ (**9**) with [$H_2AlOtBu$] (**3**) in equimolar ratios [Equations (3)–(5)]. We were able to isolate the monomeric compounds $[Me_2Si(NtBu)_2Al(OSiMe_2tBu)(THF)]$ (**10**) and $[Me_2Si(NtBu)_2Al(OtBu)(THF)]$ (**11**), each monomer being stabilized by a donor solvent molecule [Equation (3)]. If the compounds **10** and **11** are sublimed, they release the solvent donors and dimerize to the spiro compounds $[Me_2Si(NtBu)_2Al(OSiMe_2tBu)]_2$ (**12**) or to **4** [Equation (4)]. Both spirocyclic compounds can also be prepared in solution by heating the reaction mixtures [Equation (4)]. The monomeric compounds **10** and **11** have until now not been observed, and as in our former workup the crude products were directly sublimed [Equation (5)].

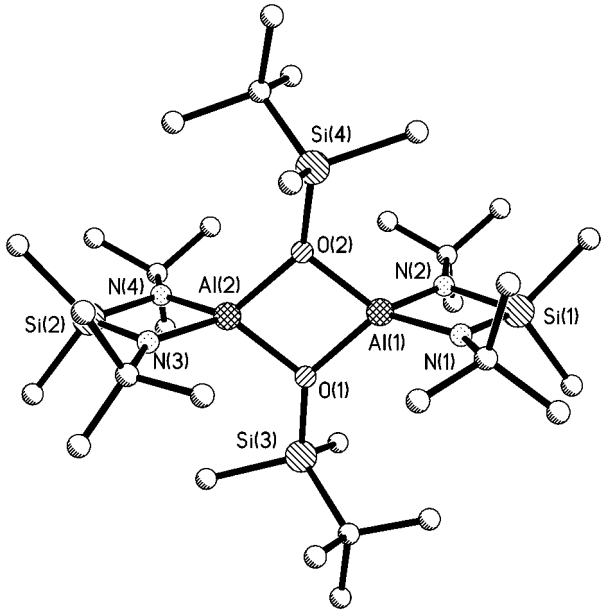

Figure 1. Selected bond lengths [Å] and angles [°] of **12**: Si(1)–N(1)/N(2) 1.746/1.742, Al(1)–N(1)/N(2) 1.838/1.827, Si(2)–N(3)/N(4) 1.746/1.744, Al(2)–N(3)/N(4) 1.832/1.834, Al(1)–O(1) 1.869, Al(1)–O(2) 1.879, Al(2)–O(1) 1.822, Al(2)–O(2) 1.876, O(1)–Si(3) 1.718, O(2)–Si(4) 1.713, N(1)–Si(1)–N(2) 90.89, N(1)–Al(1)–N(2) 85.43, Al(1)–N(1)–Si(1) 91.65, Al(1)–N(2)–Si(1) 92.09, N(3)–Si(2)–N(4) 91.01, N(3)–Al(2)–N(4) 85.59, Al(2)–N(3)–Si(2) 91.65, Al(2)–N(4)–Si(2) 91.65, Al(1)–O(1)–Al(2) 97.54, Al(1)–O(2)–Al(2) 97.42, O(1)–Al(1)-(O2) 82.65, O(1)–Al(2)-(O2) 82.37.

The molecular structure of compound **12** (Figure 1) in the crystal is very similar to those of compounds **4** and **5**.[5] Selected bond lengths and angles are given in the caption of Figure 1 and are found within the expected ranges.

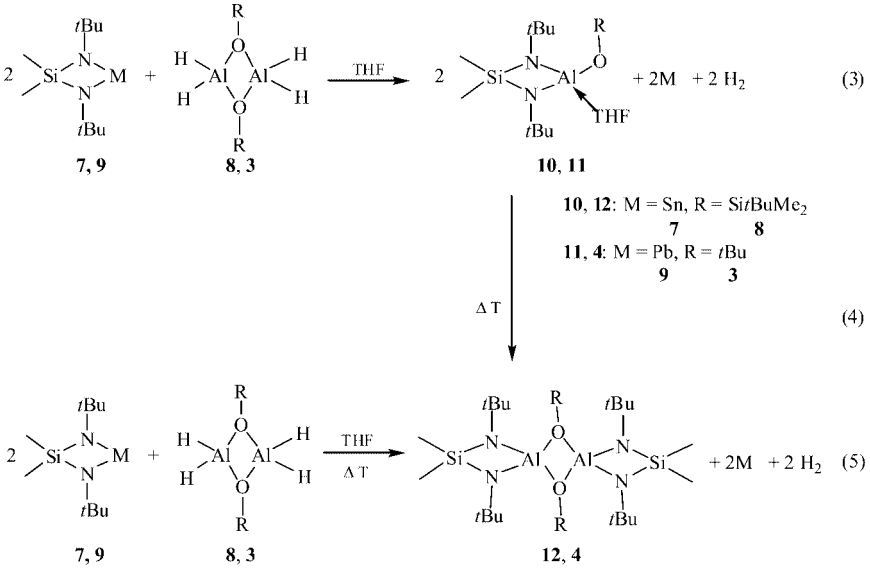

 © 2005 Wiley-VCH Verlag GmbH & Co. KGaA, Weinheim

In Figures 2 and 3 some ball-and-stick representations of the structures of the compounds **10** and **11**, which may be considered as molecular halves of the spirocyclic systems, are shown.

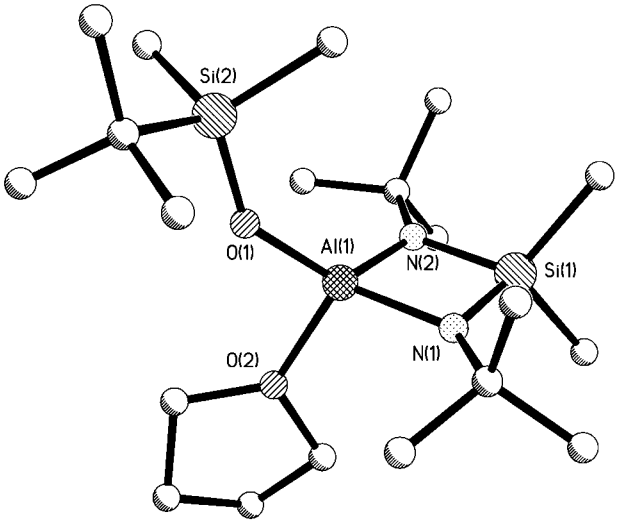

Figure 2. Selected bond lengths [Å] and angles [°] of **10**: Si(1)–N(2) 1.745, Si(1)–N(1) 1.730, Al(1)–N(1) 1.831, Al(1)–N(2) 1.824, Al(1)–O(1) 1.727, Al(1)–O(2) 1.877, O(1)–Si(2) 1,635, N(1)–Si(1)–N(2) 90.83, N(1)–Al(1)–N(2) 85.24, Al(1)–N(1)–Si(1) 92.01, Al(1)–N(2)–Si(1) 91.75, O(2)–Al(1)–O(1) 98.15, C(2)–Si(1)–C(1) 105.68.

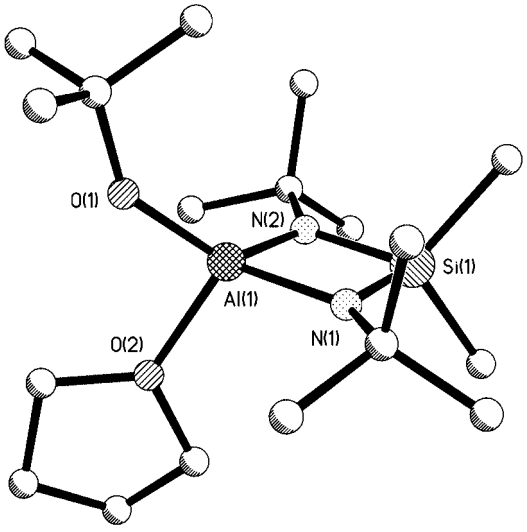

Figure 3. Selected bond lengths [Å] and angles [°] of **11**: Si(1)–N(2) 1.733, Si(1)–N(1) 1.720, Al(1)–N(1) 1.820, Al(1)–N(2) 1.823, Al(1)–O(1) 1.702, Al(1)–O(2) 1.895, N(1)–Si(1)–N(2) 91.15, N(1)–Al(1)–N(2) 85.24, Al(1)–N(1)–Si(1) 92.03, Al(1)–N(2)–Si(1) 91.50, O(2)–Al(1)–O(1) 94.63, C(2)–Si(1)–C(1) 105.5.

Both molecular structures differ from each other only in the oxy ligands at the aluminum atoms. The compounds have a 1,3-diaza-2-sila-4-aluminacyclobutane unit with the aluminum atoms in tetrahedral sites coordinated by two nitrogen and two oxygen atoms. The Al–N–Si–N four-membered rings are almost planar as may be deduced from the sums of the angle of 359.8° for **10** and 359.9° for **11**. The dimensions found in the rings and around the metal atoms are similar to those found in the corresponding spirocyclic molecules.

On treating the plumbylene **9** or the stannylene **7** with a double equivalent of the monohydridoalane [(*t*BuSiO)$_2$AlH] (**13**) in THF, the spiro compound **4** was formed, along with tri-*tert*-butoxyalane (**14**) [Equation (6)]. For this reaction, we assume a mechanism as shown in Figure 4.

$$\underset{\mathbf{7,\,9}}{M(N\mathit{t}Bu)_2SiMe_2} + 2\,\underset{\mathbf{13}}{[(\mathit{t}BuO)_2AlH]} \longrightarrow \tfrac{1}{2}\,\underset{\mathbf{4}}{[Me_2Si(N\mathit{t}Bu)_2Al\mathit{O}t\mathit{B}u]_2} + H_2 + M + \underset{\mathbf{14}}{Al(\mathit{O}t\mathit{B}u)_3} \qquad M = Pb,\ Sn \tag{6}$$

The corresponding reaction between the stannylene **7** and two equivalents of the siloxyalane [(Me$_2$*t*BuSiO)$_2$AlH] (**15**) did not lead to a spiro compound but to the monomeric THF adduct **10** [Equation (7)]. A further product in this reaction is most likely to be the alumosiloxane (Me$_2$*t*BuSiO)$_3$Al (**16**), but we have not been able to isolate or identify this compound yet.

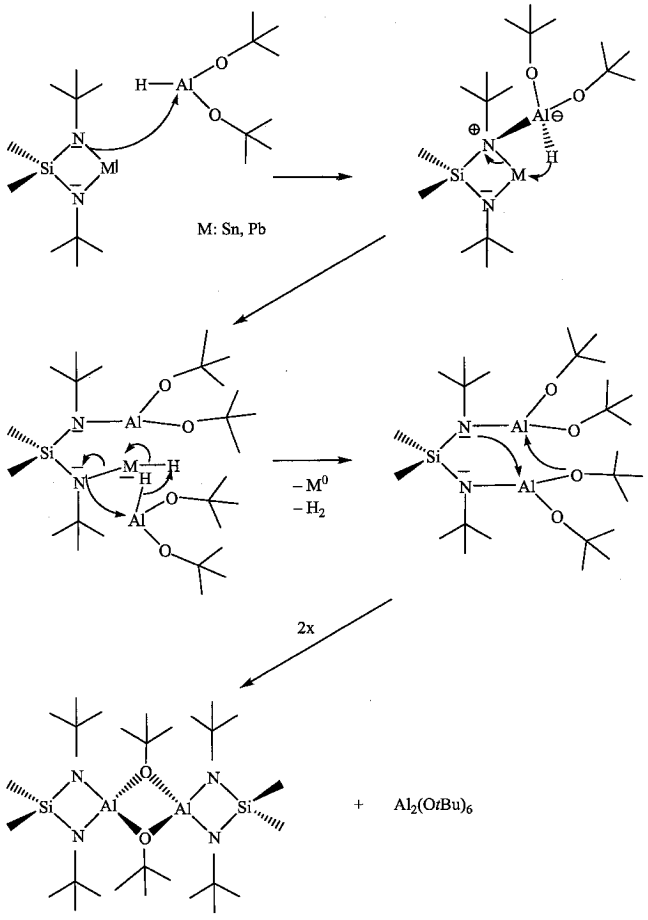

Figure 4. Mechanism for the reaction of Equation (6).

 © 2005 Wiley-VCH Verlag GmbH & Co. KGaA, Weinheim

$$\underset{\mathbf{7}}{Sn(NtBu)_2SiMe_2} + 2\ \underset{\mathbf{15}}{[(Me_2tBuSiO)_2AlH]} \longrightarrow \underset{\mathbf{10}}{[Me_2Si(NtBu)_2Al(O\,SitBuMe_2)(THF)]} + H_2 + Sn + \text{further products}\ \underset{\mathbf{16}}{} \quad (7)$$

Materials Part

By using our reduction procedure of the tin and lead amides it is possible either to stabilize the tin and lead particles as colloids in solution or to obtain them as nanoscaled powders or metal sponges depending on the chosen reaction conditions (temperature or concentration of the starting materials). With regard to the lead formation we have already reported in detail on the different species that may be produced.[6] Here we mainly want to discuss our results from the reduction of the tin compounds.

The polarity of the solvents used has an important influence on the diameters of the tin crystallites that are produced. We studied the reactions of **7** with **3** or **6** [see Equation (2)] in different polar solvents or solvent mixtures, respectively (see Table 1).

Table 1. Average crystallite sizes from analysis of peaks in X-ray powder diffraction data. Reaction of $Me_2Si(NtBu)_2Sn$ (**7**) with $[H_2AlOtBu]$ (**3**) (a), or with $[H_2AlOSiMe_3]$ (**6**) (b).

(a) Medium	Average crystallite size	(b) Medium	Average crystallite size
THF	<20 nm	THF	20–30 nm
THF/thiophene (10%)	60–80 nm	THF/thiophene (10%)	60–80 nm
THF/TMEDA (10%)	160–180 nm	THF/TMEDA (10%)	200–220 nm
Toluene	500–520 nm	Toluene	800–820 nm

When the reaction is started at –115 °C (ethanol/liquid N_2) a clear yellow solution forms. By warming the reaction mixture to room temperature a dramatic color change from red to dark brown takes place. On further heating the mixtures above 40 °C, black suspensions are formed. Obviously, the tin particles are in the first instance formed in a colloidal form (clear intensively colored solutions) and with higher temperatures they grow and agglomerate to finally precipitate. When the siloxyalane **6** is used instead of $[H_2AlOtBu]$ (**3**) in solvents like toluene or THF as reductive agents, the reduction already starts at lower temperatures, since the color change is observed earlier on the temperature scale (Figure 5).

The precipitates that were obtained were isolated at room temperature and characterized by X-ray powder diffraction and revealed to be in all cases β-tin. In the X-ray powder diffraction diagrams of precipitates generated in polar THF, significantly broader diffraction signals appear compared to those of the powders obtained from toluene (Figure 6).

Using a modified Scherrer method it was possible to estimate an average crystallite size from the X-ray diffraction

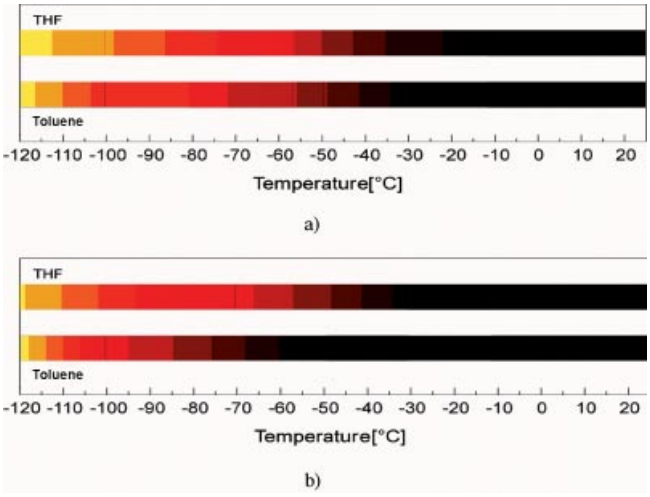

Figure 5. Colors of the reaction mixtures correlated with the temperature. Reaction of $Me_2Si(NtBu)_2Sn$ (**7**) with $[H_2AlOtBu]$ (**3**) (a), or with $[H_2AlOSiMe_3]$ (**6**) (b).

diagrams.[13] The results of this line analysis are shown in Table 1.

The tin particles formed by the reduction of $[Me_2Si(NtBu)_2Sn]$ (**7**) with the more reactive hydride **6** [R = $SiMe_3$, (b) in Table 1] show a larger average crystallite size than those formed when the hydride **3** [R = *t*Bu, (a) in Table 1] is used. This becomes very obvious when toluene is used as a solvent, because then the differences in the sizes are approximately 300 nm. The siloxy groups may have an influence on the most apolar solvent. On the other hand, in the more polar THF, the average crystallite sizes lie in both cases below 30 nm and using hydride **3** the crystallite size may even be below that of 20 nm. Obviously, the donor molecules like THF as well as thiophene and TMEDA in the solvent mixtures are able to stabilize the colloids in such a way that the crystallite growth is hindered. This can also be concluded from experimentally determined carbon/hydrogen contents of the precipitates generated from toluene and THF. They are, for those powders formed in THF, between 7 and 11 times higher than for those generated in toluene (Tables 2 and 3). So it is very likely that solvent molecules are coordinated on the surface of the particles. We have tried to perform HRTEM analyses on the powders, but observed high reactivities with oxygen prior to the measurements, almost excluding a proper experiment. Although we have no data for tin, we assume similar behavior as for lead.[6]

If the metal powders are allowed to interact with one another for longer times, or toluene is used as the solvent, the agglomeration continues and metal sponges are formed. In Figures 7 and 8 fragments of such a tin sponge and the corresponding SEM images are shown. The nanoscopic porosity of the sponges is clearly proved by the SEM images.

Several pycnometric measurements were carried out on the tin sponges. When water was used, an average density of 1.5 g/cm^3 was determined, indicating that some of the holes could not be penetrated by water. With the inert and smaller helium (which is able to fill the pores in a much

 © 2005 Wiley-VCH Verlag GmbH & Co. KGaA, Weinheim

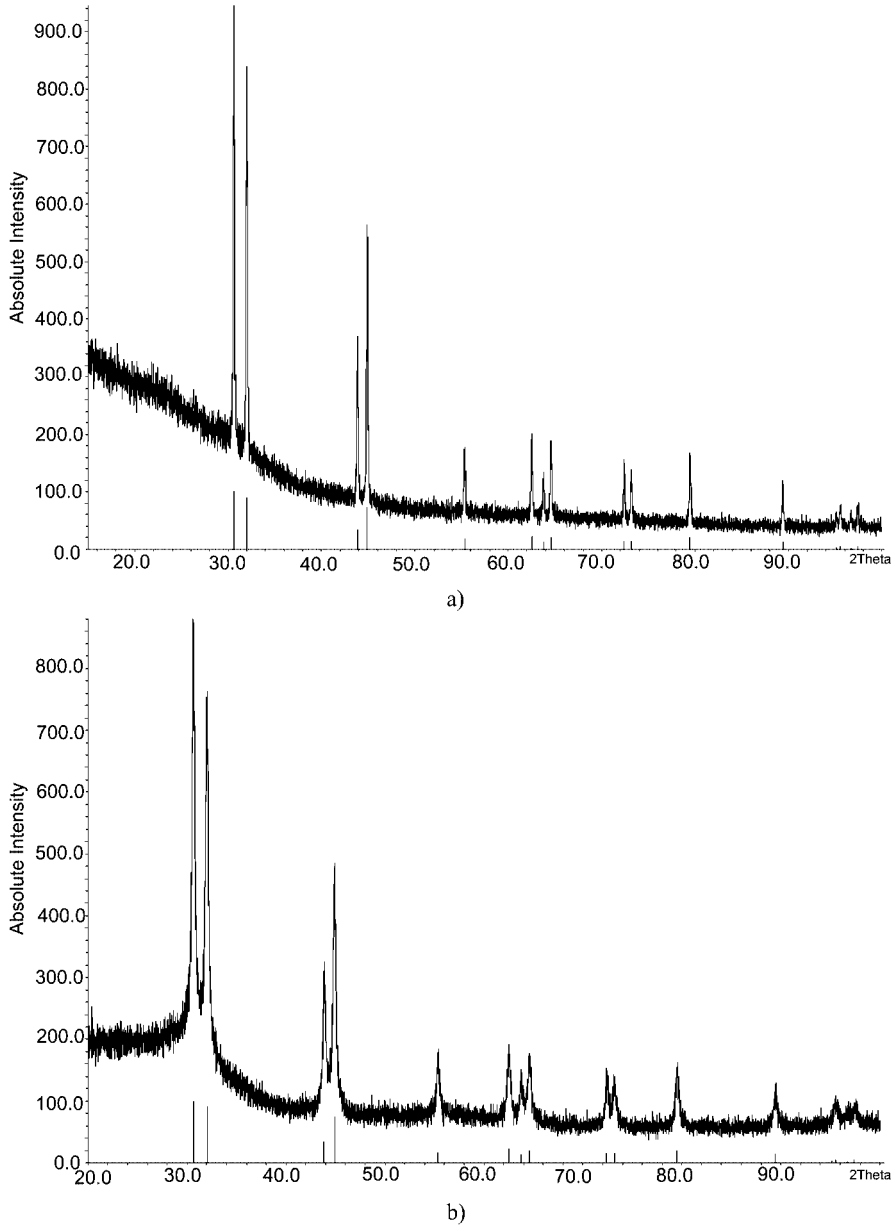

Figure 6. Powder diffraction analysis. Product from the reaction of **7** with **3** a) in toluene and b) in THF with locations of the signals and intensities of β-tin.[12]

Table 2. C and H contents of precipitates generated in toluene.

Reducing agent	C content	H content
$[H_2AlOtBu]_2$ (**2**)	1.47%	0.35%
$[H_2AlOSiMe_3]_n$ (**3**)	0.83%	0.17%

Table 3. C and H contents of precipitates generated in THF.

Reducing agent	C content	H content
$[H_2AlOtBu]_2$ (**2**)	10.86%	2.45%
$[H_2AlOSiMe_3]_n$ (**3**)	7.70%	1.91%

Figure 7. Fragments of a tin sponge. The diameters of the two bigger pieces are around 2 to 3 mm.

better way) we determined an average density of approximately 7 g/cm^3 for the same sponges, which is near the value of 7.3 g/cm^3 for pure tin.[14] For the sake of comparison we also measured the density of the corresponding lead sponges obtained from the reactions between the lead amides and the hydrides (see ref.[6]). With water, a value of almost 8 g/cm^3 was obtained, and with helium the density of approximately 11 g/cm^3 was again close to that of lead

 © 2005 Wiley-VCH Verlag GmbH & Co. KGaA, Weinheim

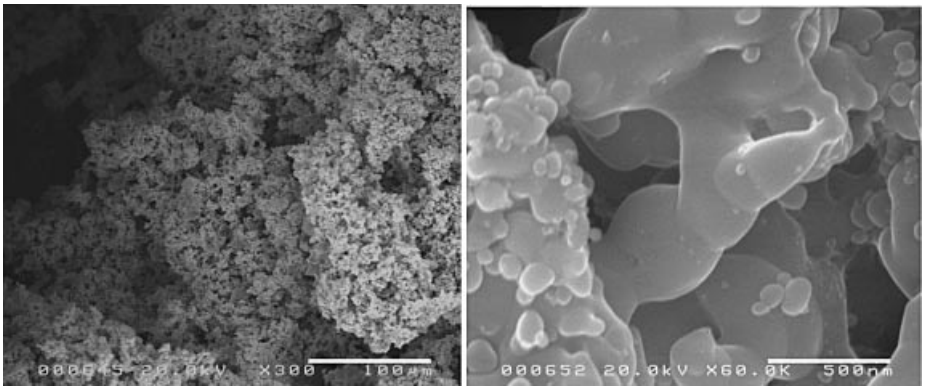

Figure 8. SEM images of a tin sponge to illustrate its high porosity. The two pictures have different scales.

(ref.[14]: 11.3 g/cm^3). The mean values of the pycnometric measurements for the metal sponges in water seem to indicate a higher porosity and smaller diameters of the channels for the precipitates of tin than for those of lead.

To fill porous alumina membranes as templates with lead or tin nanoparticles we used different techniques. We have recently reported on our first attempts to fill the membranes with lead particles.[6] We managed to fill the pores up to a certain extent by treatment of the templates with colloidal solutions of different concentrations, but because of the relatively large diameters of the particles in those colloids (up to 200 nm) they covered mainly the surface of the membranes and did not fill the much smaller pores with diameters of approximately 60 nm.

For new attempts we not only used membranes with various pore diameters of 25, 30, 50, 60, 80, 90, 120 and 300 nm,[7] but also varied the filling techniques. The thickness of the membranes varied between ca. 25 μm and 90 μm and the particle sizes in the membranes are linked to the diameters of the channels as checked by XRD on selected samples after destruction. We finally succeeded in the infiltration of the membranes. Table 4 gives an overview of different possibilities to fill the membranes with tin or lead particles.

Table 4. Possibilities for membrane filling.

(i) membrane + colloidal solution ⟶ diffusion
(ii) membrane + colloidal solution + followed by vacuum induction of the prepared particles
(iii) membrane + lead or tin amide solution ⟶ diffusion of the solution into the pores followed by reactions within the pores by addition of the hydride
(iv) same as in iii but with vacuum induction

For methods (i) and (ii) the membranes were put into already prepared colloidal solutions of the metal and were filled by pure or vacuum-induced diffusion. Methods (i) and (ii) led to dark membranes because of agglomeration of the metal particles on their surfaces. These membranes were not further investigated with regard to their optical properties. For methods (iii) and (iv) the membranes were treated, after careful washing with the solvents and drying, in a first instance with the stannylene or plumbylene solutions. In a second step, they were washed with a small amount of solvent in order to clean the surface. Finally, the metal clusters were synthesized within the membranes by reaction with the added hydrides. The channels of the membranes were filled with the amide solutions using vacuum-assisted diffusion. The routes (iii) and (iv) of Table 4 proved to be the most effective methods to fill the templates. Besides the different filling methods we also varied the concentrations of the reaction solutions, the temperature [<–100 °C for (i) and (ii) and 20 °C for (iii) and (iv)] and the filling time. Finally, we repeated the filling process several times. We cannot completely exclude a side reaction of the metal amides with remaining hydroxy groups on the inner surfaces of the alumina membranes; the concentrations of the stannylene solutions were chosen in such a way that these side reactions may be almost neglected. Furthermore, we could not observe spectroscopically any of the hydrolysis byproducts of the stannylene **7**. Also the molecular byproducts described in the first section of this article have not been isolated and separated for each filling process. In the following, we want to describe in more detail mainly the filling of the membranes with tin. The experiments with lead amides showed similar results, some of which have already been documented.[6] With increasing concentrations and filling time (or repetitions of the filling process) a significant color change of the originally transparent membranes from light brown to dark brown and finally to black is observed. The infiltration can be monitored by EDX analysis. Figure 9 contains spectra of (a) a non-treated 50 nm membrane, (b) a light brown and (c) a dark brown membrane after filling with tin particles.

The signal at 3.5 keV found in the EDX spectra is characteristic for tin and a comparison of these signals with the ones of aluminum at 1.8 keV confirms a higher Sn content for the dark brown membrane. The different intensities in color of the membranes treated with differently concentrated stannylene solutions (up to 210 mmol/L) are reflected in their UV spectra shown in Figure 10. In Figure 10 (a) and (b) the spectra are shown when the hydride **3** was used for reduction, whereas Figures 10 (c) and (d) contain the spectra for when the hydride **6** was used (the self absorption of the membrane is subtracted in the spectra on the right-hand side). With increasing concentrations of stannylene and longer filling times the maxima of the absorptions be-

 © 2005 Wiley-VCH Verlag GmbH & Co. KGaA, Weinheim

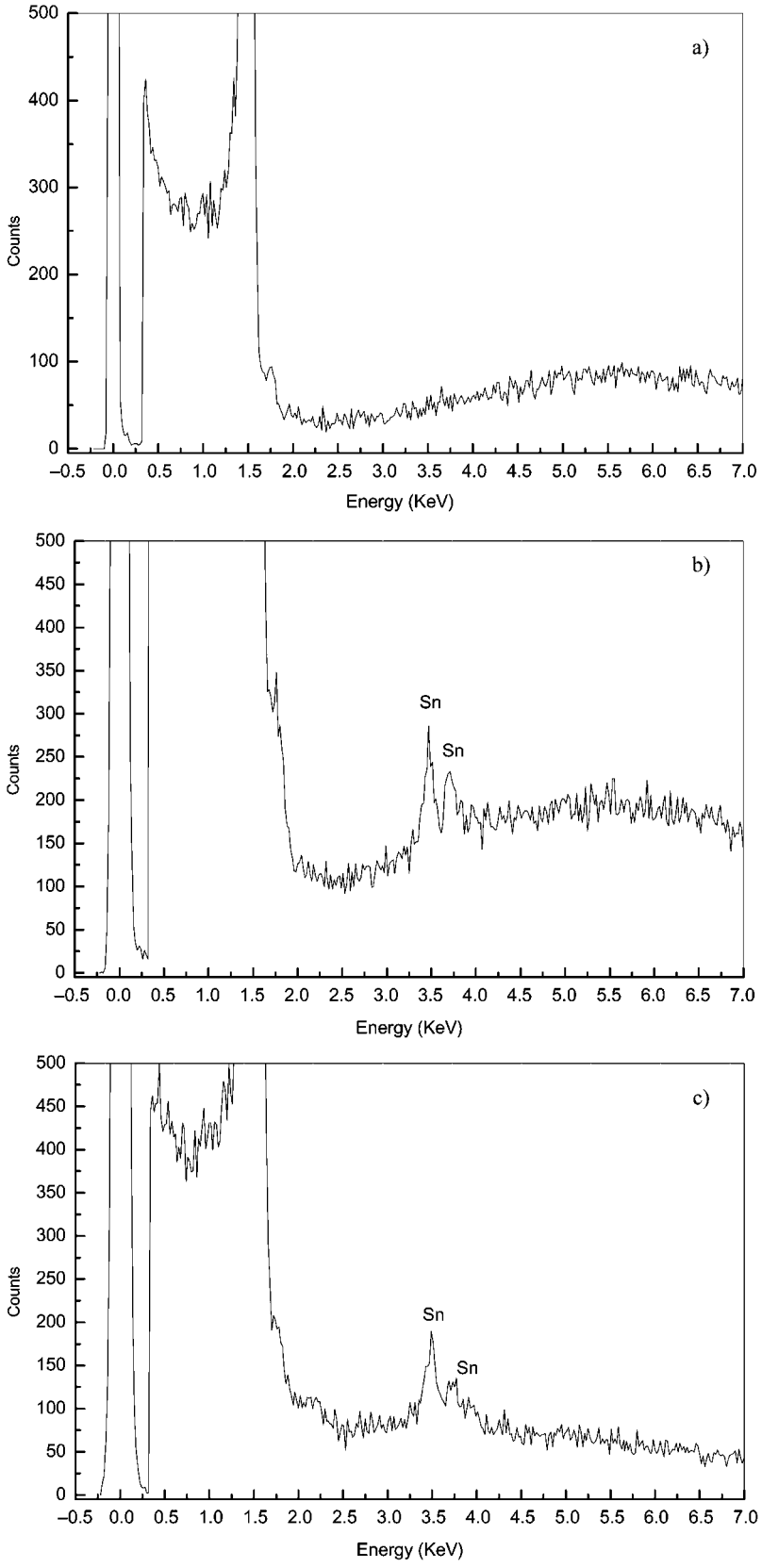

Figure 9. EDX spectra of (a) a nontreated 50 nm membrane, (b) a light brown and (c) a dark brown membrane after filling with tin particles. Experimental conditions: concentration of **7** 137 mmol/L or 411 mmol/L in THF, hydride **3**, method (iv) of Table 4, vacuum induction time 5 min each.

 © 2005 Wiley-VCH Verlag GmbH & Co. KGaA, Weinheim

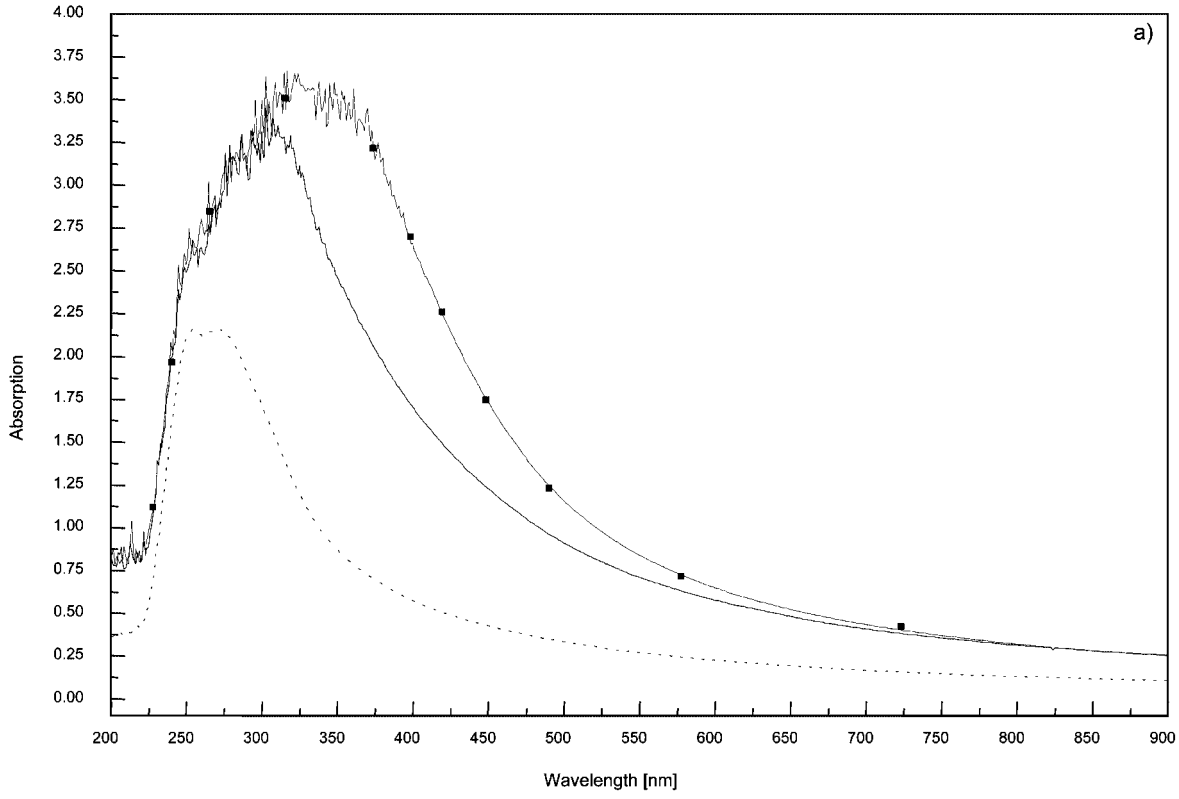
a)
Absorption
Wavelength [nm]
4.00
3.75
3.50
3.25
3.00
2.75
2.50
2.25
2.00
1.75
1.50
1.25
1.00
0.75
0.50
0.25
0.00
200 250 300 350 400 450 500 550 600 650 700 750 800 850 900

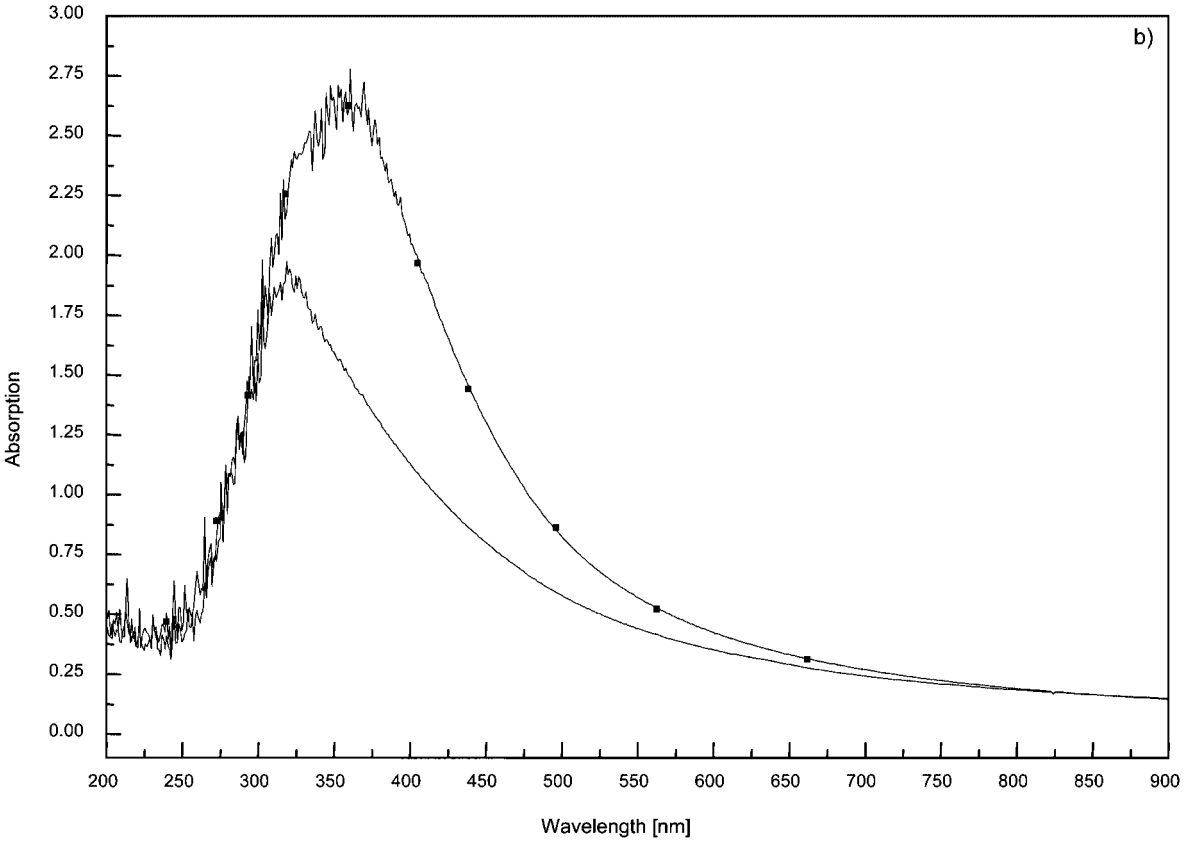
b)
Absorption
Wavelength [nm]
3.00
2.75
2.50
2.25
2.00
1.75
1.50
1.25
1.00
0.75
0.50
0.25
0.00
200 250 300 350 400 450 500 550 600 650 700 750 800 850 900

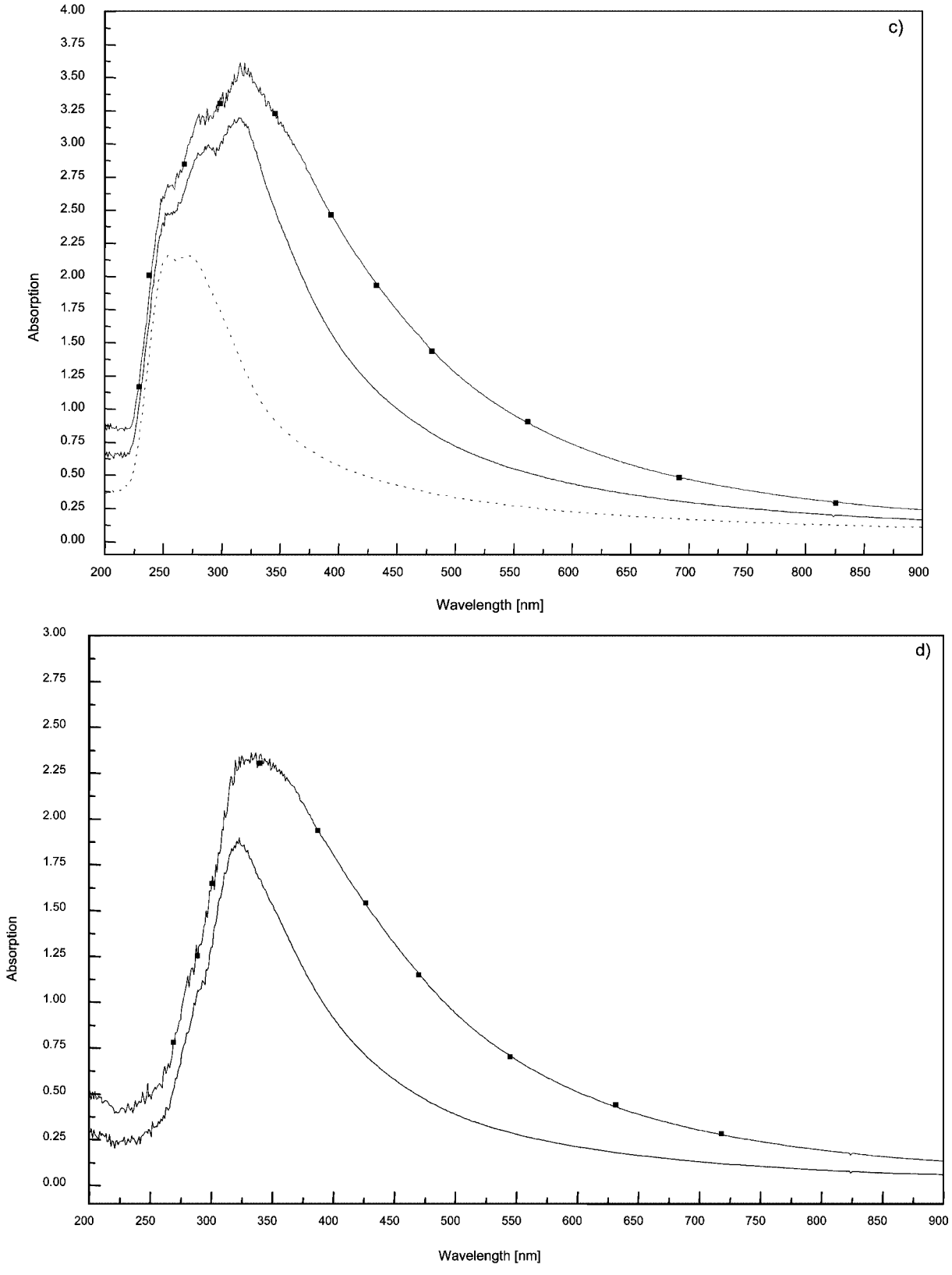

Figure 10. UV spectrum of a 50 nm membrane with respect to the concentration of stannylene **7** and the time of vacuum induction. The reductive agent for (a) and (b) is hydride **3** (– $c_{stannylene}$ = 137 mmol/L, 5 min vacuum induction; –■– $c_{stannylene}$ = 210 mmol/L, 5 min vacuum induction; ··· absorption of the membrane), for (c) and (d), hydride **6** (– $c_{stannylene}$ = 121 mmol/L, 5 min vacuum induction; –■– $c_{stannylene}$ = 200 mmol/L, 10 min vacuum induction; ··· absorption of the membrane). On the right-hand side the absorption of the membrane is subtracted.

 © 2005 Wiley-VCH Verlag GmbH & Co. KGaA, Weinheim

come more intense and the bands are widened due to the bigger sizes and the larger amounts of particles. In addition, the absorption maxima are shifted towards higher wavelengths when the amount of aggregating tin clusters increases leading to an interaction of their plasmon resonances (see also ref.[6] for further discussion).

Already from a visual comparison it becomes evident that the different reactivities of the reductive agents **3** and **6** has only little influence on the color of the treated membranes as shown by their UV spectra. All filled membranes show almost identical absorption curves depending on the concentration of tin clusters.

Dark brown or black membranes result from very high concentrations of stannylene (>350 mmol/L). The absorption spectra show broad signals with very high intensities. Such a spectrum is presented in Figure 11 (concentration of stannylene **7**: 360 mmol/L; reductive agent hydride **3**). It shows an impervious range between 270 and 500 nm. Such a membrane could be used as a wavelength filter, which absorbs the light completely within a well-defined range. The transmission spectrum shown in Figure 12 (concentration of stannylene **7**: 411 mmol/L; reductive agent hydride **6**) underlines this possibility for use. Here one finds an impervious range between 250 and 525 nm.

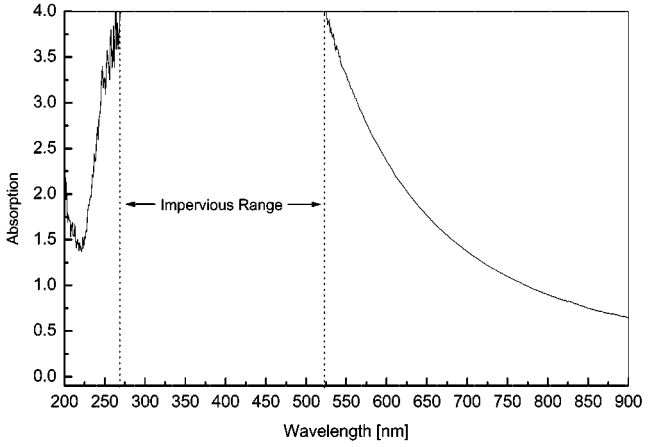

Figure 11. UV/Vis absorption spectrum of a very colored membrane; concentration of stannylene **7**: 360 mmol/L; reductive agent hydride **3**.

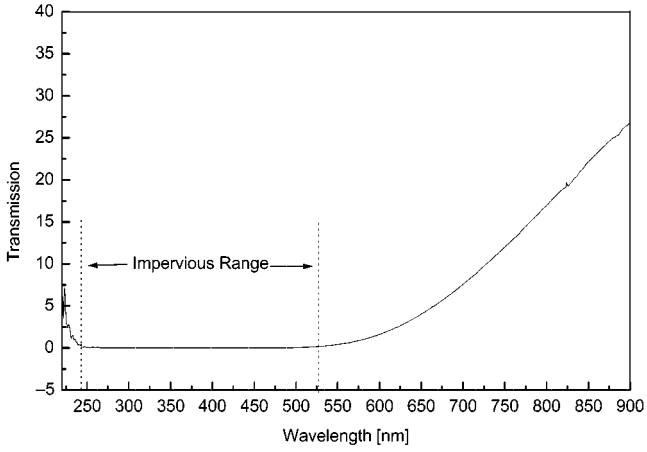

Figure 12. UV/Vis transmission spectrum of a very colored membrane; concentration of stannylene **7**: 411 mmol/L; reductive agent hydride **6**.

As mentioned above, we have used membranes with different pore diameters and the UV spectra of these membranes (filled under similar conditions) show a shift of the absorption maxima towards higher wavelengths (Figure 13). Obviously, the size of the metal clusters plays an important role.[6] As the absorption maxima shift with the pore diameter (with parallel increase of the metal particle diameters) one may use the process to produce wavelength filters of different absorption maxima.

We noticed an improvement in the infiltration of the membranes when we repeated the filling process several times. As expected, the filling of the channels is most effec-

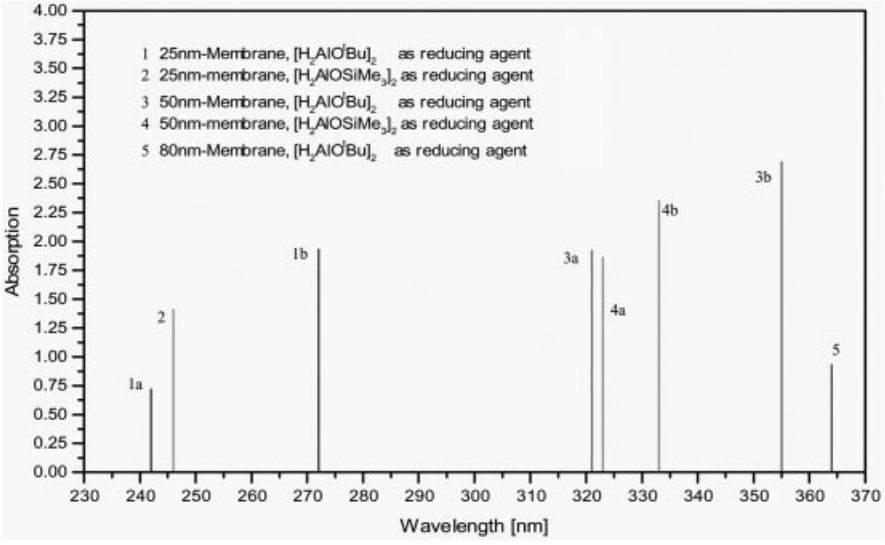

Figure 13. Comparison of the position of the absorption maxima using membranes of different pore diameters filled with tin particles (a and b stand for different probes of the same material).

 © 2005 Wiley-VCH Verlag GmbH & Co. KGaA, Weinheim

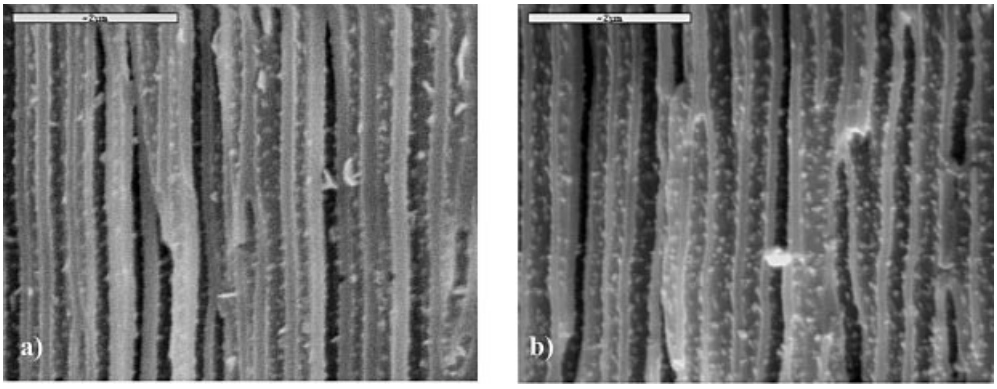

Figure 14. SEM images of (a) 5 and (b) 10 times filled 300 nm Al_2O_3 membranes to show the increase in the amount of lead particles within the pores (ca. 10 kV sputtered with approximately 10 nm Au).

tive for membranes with large pore diameters. The SEM images of a 300 nm Al_2O_3 membrane filled with lead particles after five and ten infiltrations are presented in Figure 14. They show an increase in the amount of lead clusters with repetitive filling. The repetition is nevertheless limited due to a blocking of the pores after ca. 7–8 cycles. The particles in the 300 nm pores have mean diameters of 80–90 nm.

Summary and Conclusion

Tin and lead nanosized particles and metal sponges have been prepared by reduction of molecular tin(II) and lead(II) amides with siloxy- and alkoxyalanes in non-aqueous media. The resulting molecular byproducts have been isolated and (structurally) characterized. Colloidal solutions of tin were obtained when the reaction mixture was slowly warmed from –115 °C to room temperature. With agglomeration of the particles in this solution, tin powders formed and precipitated, and have been identified as β-tin by EDX analysis. Their average particle size diameter can be controlled either by using different donor solvents or different hydrides as reducing agents. The smallest particles were obtained when *tert*-butoxyalane **3** was used as hydride and THF as donor solvent. The metal sponges were characterized by pycnometric measurements with helium and water and show a lower density compared with their value known from literature when water was used because of its surface tension and the high porosity of the metal precipitates. Porous aluminum oxide membranes with different pore diameters were used as templates for ordering tin or lead clusters within the pores. The metal particles were prepared by reduction of the metal amides within the membranes and the amount of particles could be increased by repetition of the filling process, which was an improvement in the infiltration compared to our former attempts. Differently colored membranes resulted from the filling process and were characterized by UV/Vis spectroscopy. Depending on the concentration of the starting materials and the pore diameters of the membranes they showed impervious ranges, which enabled these membranes to be used as wavelength filters.

Experimental Section

Physical Measurements: The elemental analyses of the compounds were carried out using a CHN analyzer from LECO™ Corporation, St. Joseph, MI, U.S.A. The NMR spectra were measured with Bruker 200 MHz spectrometers, model AC 200 F (^{1}H and ^{13}C spectra) and AC 200 P (^{29}Si spectra), using [D_6]benzene as solvent. The single-crystal X-ray analyses were performed either with an Image Plate (IPDS I), or a four-circle diffractometer (STADI 4) (Stoe, Dramstadt). The structure calculations were carried out with SHELXS97[15] and the graphical representation with Diamond 3.[16] The complete crystal structure data are deposited with the Cambridge Crystallographic Data Centre (CCDC), 12 Union Road, Cambridge CB2 1 EZ (UK) [CCDC-270194 (**10**), 270195 (**11**), and 270196 (**12**)]. The powder diffraction measurements of the tin and lead precipitates were performed in a glass capillary with a Stoe diffractometer, model STADIP, using Cu-K_α radiation with a wavelength of 1.540598 Å and a linear PSD detector. The measurements were analyzed with the software WinX^{Pow}. The electron microscopy (SEM) and energy-dispersive X-ray analyses (EDX) were performed with a scanning electron microscope CAMSCAN S4 with Si(Li) semiconductor detectors and with thin windows (Cameca and Noran). To perform the SEM analyses of the filled membranes, the membranes were covered with gold. The UV/Vis spectra were measured with a Perkin–Elmer spectrometer, model Lambda 35.

Synthetic Procedures: All compounds were synthesized under dry nitrogen using standard Schlenk techniques. The solvents were dried by refluxing with appropriate drying agents and distilled before being used.

[Me_2(N*t*Bu)$_2$Al(O*t*Bu)(THF)] (11): $Me_2Si(NtBu)_2Pb$ (**9**) (2.82 g, 6.92 mmol) in THF (25.0 mL) was added dropwise to a stirred solution of $[H_2AlOtBu]_2$ (**3**) (0.71 g, 3.46 mmol) in dry THF (25.0 ml) and allowed to react at room temperature for 24 h. The reaction mixture turned grey, the lead precipitated and gas (hydrogen) evolved. When the reaction was complete, the solution was separated from the lead and concentrated until crystals of [Me_2(N*t*Bu)$_2$Al(O*t*Bu)(THF)] (**11**) formed. After recrystallization of the crude product from THF, **11** (1.48 g, 3.97 mmol) may be obtained, at 4 °C, as colorless crystals (yield: 57%). Molecular mass: 372.60 g/mol. ^{1}H NMR (200 MHz, C_6D_6, 25 °C): δ = 0.45 [s, 3 H, Si(CH_3)$_2$], 0.57 [s, 3 H, Si(CH_3)$_2$], 1.09 (m, 4 H, THF), 1.37 (s, 18 H, N*t*Bu), 1.51 (s, 9 H, O*t*Bu), 3.82 (m, 4 H, THF) ppm. ^{13}C NMR (200 MHz, C_6D_6, 25 °C): δ = 7.09 [s, 1 C, Si(CH_3)$_2$], 7.27 [s, 1 C, Si(CH_3)$_2$], 24.81 (s, 2 C, THF), 34.12 (s, 3 C, O*t*Bu), 36.45 (s, 6 C, N*t*Bu), 49.50 (s, 2 C, quat. C, N*t*Bu), 71.03 (s, 2 C, THF),

 © 2005 Wiley-VCH Verlag GmbH & Co. KGaA, Weinheim

78.16 (s, 1 C, quat. C, O*t*Bu) ppm. ^{29}Si NMR (200 MHz, C_6D_6, 25 °C): δ = –15.55 [s, 1 Si, $Si(CH_3)_2$] ppm. Compound **11** crystallizes in the monoclinic space group *I*2/*a* with Z = 8 [a = 15.724(3), b = 15.529(3), c = 19.917(4) Å, β = 92.97(3)°, V = 4856.8(16) Å^3], 1.84° < θ < 23.92°, 14862 reflections collected, 3738 unique (R_{int} = 0.1329), the structure was solved by direct methods and refined by full-matrix least squares on F^2. Final R_1 = 0.0555 ($I > 2\sigma_I$) and wR_2 = 0.1331 with an electron density left of 0.409/–0.279 e/Å^3.

[Me$_2$Si(N*t*Bu)$_2$Al(OSiMe$_2$*t*Bu)(THF)] (10): Analogous to the synthesis of compound **11** (at room temperature). Yield: 63%. Molecular mass: 430.76 g/mol, calcd. C 55.77, H 11.0, Al 6.26, N 6.5; found C 55.18, H 10.78, Al 6.62, N 6.57. ^{1}H NMR (200 MHz, C_6D_6, 25 °C): δ = 0.28 [s, 6 H, $OSi(CH_3)_2$], 0.44 [s, 3 H, $Si(CH_3)_2$], 0.57 [s, 3 H, $Si(CH_3)_2$], 1.08 (m, 4 H, THF), 1.14 (s, 9 H, Si*t*Bu), 1.34 (s, 18 H, N*t*Bu), 3.8 (m, 4 H, THF) ppm. ^{13}C NMR (200 MHz, C_6D_6, 25 °C): δ = –1.91 [s, 2 C, $OSi(CH_3)_2$], 6.36 [s, 1 C, $Si(CH_3)_2$], 6.7 [s, 1 C, $Si(CH_3)_2$], 18.39 (s, 1 C, quat. C, Si*t*Bu), 24.33 (s, 2 C, THF), 26.26 (s, 3 C, Si*t*Bu), 35.89 (s, 6 C, N*t*Bu), 48.85 (s, 2 C, quat. C, N*t*Bu), 70.74 (s, 2 C, THF) ppm. ^{29}Si NMR (200 MHz, C_6D_6, 25 °C): δ = –14.98 [s, 1 Si, $Si(CH_3)_2$], 4.8 (s, 1 Si, OSi) ppm. Compound **10** crystallizes in the monoclinic space group $P2_1/c$ with Z = 4 [a = 12.095(2), b = 10.637(2), c = 21,629(4) Å, β = 97.67(3)°, V = 2757.8(9) Å^3], 1.90° < θ < 23.99°, 16615 reflections collected, 4214 unique (R_{int} = 0.1215), the structure was solved by direct methods and refined by full-matrix least squares on F^2. Final R_1 = 0.0546 ($I > 2\sigma_I$) and wR_2 = 0.1393 with an electron density left of 0.358/–0.287 e/Å^3.

[Me$_2$Si(N*t*Bu)$_2$Al(OSiMe$_2$*t*Bu)]$_2$ (12): Compound **12** can be synthesized in the same manner as compound **10**, but by heating the reaction mixture under reflux. Yield: 81%. Molecular mass: 789.83 g/mol, calcd. C 48.69, H 9.96, Al 6.84, N 7.1; found C 48.16, H 9.76, Al 6.91, N 6.83. ^{1}H NMR (200 MHz, C_6D_6, 25 °C): δ = 0.51 [s, 18 H, $OSi(CH_3)_2$], 0.61 [s, 12 H, $Si(CH_3)_2$], 1.12 (s, 18 H, Si*t*Bu), 1.38 (s, 36 H, N*t*Bu) ppm. ^{13}C NMR (200 MHz, C_6D_6, 25 °C): δ = –0.41 [s, 4 C, $OSi(CH_3)_2$], 7.27 [s, 4 C, $Si(CH_3)_2$], 19.49 (s, 2 C, quat. C, Si*t*Bu), 27.06 (s, 6 C, Si*t*Bu), 36.27 (s, 12 C, N*t*Bu), 49.62 (s, 4 C, quat. C, N*t*Bu) ppm. ^{29}Si NMR (200 MHz, C_6D_6, 25 °C): δ = –9.39 [s, 2 Si, $Si(CH_3)_2$], 29.46 (s, 2 Si, OSi) ppm. Compound **12** crystallizes in the monoclinic space group $P2_1/n$ with Z = 8 [a = 27.779(6), b = 11.612(2), c = 28.043(6) Å, β = 97.89(3)°, V = 8960(3) Å^3], 1.90° < θ < 24.05°, 55081 reflections collected, 13935 unique (R_{int} = 0.0897), the structure was solved by direct methods and refined by full-matrix least-squares on F^2. Final R_1 = 0.0904 ($I > 2\sigma_I$) and wR_2 = 0.2245 with electron density left: 2.689/–1.741 e/Å^3.

Acknowledgments

Authors thank the "Deutsche Forschungsgemeinschaft (DFG)" for providing financial support in the framework of the research program "Halbleiter und Metallcluster als Bausteine für organisierte Strukturen" (SPP 1072) as well as Prof. Dr. G. Schmid, Essen, for providing the membranes. Dr. M. Ehses, Saarbrücken, is acknowledged for kindly reading the manuscript.

[1] U. Kreibig, M. Vollmer, *Optical Properties of Metal Clusters*, Springer, New York **1995**.
[2] G. Schmid (Ed.), *Clusters and Colloids*, VCH, Weinheim, **1994**.
[3] a) G. Schmid, *Nach. Chem. Tech. Lab.* **1987**, *35*, 249; b) G. Schmid, *Chem. Unserer Zeit* **1988**, *22*, 85; c) G. Schmid, B. Morun, J.-O. Malm, *Angew. Chem.* **1989**, *101*, 772; d) G. Schmid, A. Lehnert, U. Kreibig, Z. Adamczyk, P. Belouschek, *Z. Naturforsch., Teil B* **1990**, *45*, 989–994; e) G. Schmid, R. Küpper, H. Hess, J.-O. Malm, J.-O. Bovin, *Chem. Ber.* **1991**, *124*, 1889–1893; f) G. Schmid, M. Harms, J.-O. Malm, J.-O. Bovin, J. Van Ruitenbeck, H. W. Zandbergen, W. T. Fu, *J. Am. Chem. Soc.* **1993**, *115*, 2046–2048; g) U. Simon, G. Schön, G. Schmid, *Angew. Chem.* **1993**, *105*, 264–267; h) J. G. A. Dubois, J. W. Gerritsen, G. Schmid, H. van Kempen, *Physica B* **1995**, *204*, 51–56; i) S. Peschel, G. Schmid, *Angew. Chem.* **1995**, *107*, 1568–1569; j) J. G. A. Dubois, J. W. Gerritsen, G. Schmid, H. van Kempen, *Physica B* **1996**, *218*, 262; k) A. Bezryadin, C. Dekker, G. Schmid, *Appl. Phys. Lett.* **1997**, *71*, 1273–1275; l) G. Schmid, St. Peschel, T. Sawitowski, *Z. Anorg. Allg. Chem.* **1997**, *623*, 719–723; m) G. Schmid, *J. Chem. Soc., Dalton Trans.* **1998**, 1077–1082; n) G. Schmid, N. Beyer, *Eur. J. Inorg. Chem.* **2000**, 835–837.
[4] a) C. Nayral, T. Ould-Ely, A. Maisonnat, B. Chaudret, P. Fau, L. Lescouzères, A. Peyre-Lavigne, *Adv. Mater.* **1999**, *11*, 61–63; b) C. Nayral, E. Viala, P. Fau, F. Senocq, J. C. Jumas, A. Maisonnat, B. Chaudret, *Chem. Eur. J.* **2000**, *6*, 4082; c) G. Cardenas-Trivino, M. Alvial, K. J. Klabunde, O. Pantoja, H. Soto, *Colloid Polym. Sci.* **1994**, *272*, 310–316; d) P. Cheyssac, M. Geddo, R. Kofman, P. G. Merli, A. Migliori, A. Stella, P. Tognini, *Mater. Sci. Forum* **1995**, *195*, 161; e) B. Ocker, R. Wurster, H. Seiler, *Scanning Microsc.* **1995**, *9*, 63; f) A. Henglein, M. Giersig, *J. Phys. Chem.* **1994**, *98*, 6931–6935; g) G. Sberveglieri, *Sens. Actuators B* **1992**, *6*, 239.
[5] M. Veith, O. Schütt, J. Blin, J. Fréres, S. Becker, V. Huch, *Z. Anorg. Allg. Chem.* **2001**, *628*, 138–146.
[6] M. Veith, S. Mathur, P. König, C. Cavelius, J. Biegler, A. Rammo, V. Huch, H. Shen, G. Schmid, *C. R. Chim.* **2004**, *7*, 509–519.
[7] a) G. Hornyak, M. Kröll, R. Pugin, T. Sawitowski, G. Schmid, J.-O. Bovin, G. Karsson, H. Hofmeister, S. Hopfe, *Chem. Eur. J.* **1997**, *3*, 1951–1956; b) G. Schmid, L. F. Chi, *Adv. Mater.* **1998**, *10*, 515; c) T. Hanaoka, H.-P. Kormann, M. Kröll, T. Sawitowsky, G. Schmid, *Eur. J. Inorg. Chem.* **1998**, 807; d) P. Braunstein, H. P. Kormann, W. Meyer-Zaika, R. Pugin, G. Schmid, *Chem. Eur. J.* **2000**, *6*, 4637–4646.
[8] M. Veith, M. Grosser, *Z. Naturforsch. B. Anorg. Chem.* **1982**, *37*, 1375–1381.
[9] M. Veith, S. Faber, H. Wolfanger, V. Huch, *Chem. Ber.* **1996**, *129*, 381.
[10] J. Blin, Dissertation, Universität des Saarlandes **1999**.
[11] M. Veith, *Angew. Chem.* **1975**, *87*, 278; *Angew. Chem. Int. Ed. Engl.* **1975**, *14*, 263.
[12] JCPDS-Datei, [4-673], from ICDD database.
[13] Steuerungssoftware des STOE-Transmissions-Diffraktometers STADIP: WINXPOW Version 1.03, **1998**, and STOE VISUALXP.
[14] A. F. Holleman, E. Wiberg, N. Wiberg, *Lehrbuch der anorganischen Chemie*, 2nd ed., Walter de Gruyter, Berlin, New York, **1995**.
[15] G. Sheldrick, *Program for Crystal Structure Solution*, version SHELX-97, Göttingen, **1997**.
[16] M. Berndt, K. Brandenburg, H. Putz, *Visual Crystal Structure Information System*, Diamond version 3, Bonn, **1996–2005**.

Received: April 26, 2005
Published Online: August 30, 2005

 © 2005 Wiley-VCH Verlag GmbH & Co. KGaA, Weinheim

Preparation of Gold Nanoparticles on Ultrathin Films of Polythiophene and Polythiophene Derivatives

Carl Matthias Intelmann,[a] Hartmut Dietz,[a] and Waldfried Plieth*[a]

Keywords: Gold / Nanoparticles / Ultrathin films / Polythiophene / Polymer modification

Two different methods were used to immobilise gold nanoparticles on ultrathin films of polythiophene and polythiophene derivatives. The first method utilised ultrathin films of polythiophene to prepare gold nanoparticles by direct reduction of $HAuCl_4$. A uniform coverage of the polythiophene films with randomly distributed gold nanopraticles possesing a polydisperse size distribution was obtained. Size and size distribution of the gold nanoparticles could be controlled by time, concentration of Au^{3+}, and the addition of a cosolvent. With the second method, ultrathin films of polythiophene derivatives were esterified with thioctic acid, using either Steglich or Yamaguchi conditions. The dithiolane moiety of the thioctic acid was utilised to immobilise gold nanoparticles from a monodisperse gold sol. The gold nanoparticles were adhesive on the polymer films and were not removed by scotch tape tests. The samples with the obtained gold nanoparticles of both methods were analysed by scanning electron microscopy (SEM).
(© Wiley-VCH Verlag GmbH & Co. KGaA, 69451 Weinheim, Germany, 2005)

Introduction

Composite materials consisting of conducting polymers and metal nanoparticles are of great interest. Ordered structures as shown in Figure 1 would be the final goal because they are promising for further applications in micro- and optoelectronics.

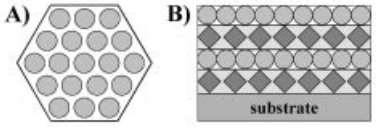

Figure 1. A) lateral hexagonal arrangement, B) sandwich layout.

Some review articles are available on gold nanoparticles, but it would be beyond the scope of this work to give a complete record. For the synthesis the work and reviews of Schmid et al.,[1,2] and for the assembly of gold nanoparticles the review of Daniel et al.[3] should be mentioned.

Holdcroft et al.[4,5] examined the oxidation of poly(3-hexylthiophene) (PHT) with gold trichloride in water-free solvents. The use of thick polymer films (>1 μm) yielded sandwich structures consisting of an oxidised PHT film, covered with a continuous gold layer. However, thinner polymer films (<0.25 μm) yielded only an irregular, nonuniform covering with gold. Holdcroft et al.[5] proposed the following reaction [Equation (1)].

$$3\,[P^0] + 4\,AuCl_3 \rightarrow 3\,[P^+][AuCl_4^-] + Au^0\downarrow \quad (1)$$

P is a sequence of four monomer units (thiophene rings) in the polymer.[5]

To obtain gold nanoparticles rather than nonuniform gold films, the polymer film has to be even thinner than the 0.25 μm that Holdcroft et al. used. For micro- and optoelectronic applications it is necessary to chemically deposit adhesive films especially on insulating substrates. Ultrathin, adhesive, and smooth polythiophene films were described by Fikus et al.[12–14] (Figure 2). These films can be chemically deposited on a variety of substrates, preferentially insulating, with the adhesion promoter 11-(thien-3-yl undecyl) trichlorosilane (TUTS) and are about 100 nm thick.

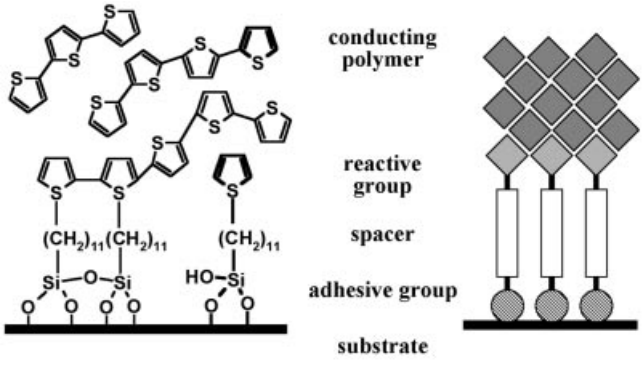

Figure 2. Layout of ultrathin polythiophene films using the adhesion promoter TUTS.

To circumvent complications with the use of water-free solvents it was of interest to determine whether the deposition of gold nanoparticles onto polythiophene films would

[a] Institute of Physical Chemistry and Electrochemistry, Dresden University of Technology,
Mommsenstr. 13, 01062 Dresden, Germany
Fax: +49-351-463-37164
E-mail: waldfried.plieth@chemie.tu-dresden.de

also be possible from aqueous solutions of $HAuCl_4$. Then the following reactions would be possible Equation (2) and Equation (3).

$$3\,[P^0] + HAuCl_4 \rightarrow 3\,[P^+][Cl^-] + Au^0\downarrow + HCl \quad (2)$$

$$3\,[P^0] + 4\,HAuCl_4 \rightarrow 3\,[P^+][AuCl_4^-] + Au^0\downarrow + 4\,HCl \quad (3)$$

Equation (2) was proposed by Freund et al.,[6] while Equation (3) was derived from Equation (1), which was proposed by Holdcroft et al.,[5] assuming that $HAuCl_4$ can be regarded as the hydrochloride of $AuCl_3$. The reduction of $HAuCl_4$ requires the incorporation of a dopant anion into the oxidised polymer to achieve charge neutrality. In the case of an excess of polythiophene, all of the $HAuCl_4$ is reduced and only Cl^- is available as a dopant anion, which is described in Equation (2). On the other hand, in the case of an excess of $HAuCl_4$ all of the polythiophene is oxidised, but not all of the $HAuCl_4$ is reduced. A combination of Equation (2) and Equation (3) is then an appropriate description of the polymer doping, as both anions Cl^- and $AuCl_4^-$ are available in solution and can be incorporated into the oxidised polymer.

The immobilisation of gold nanoparticles can be achieved by different ways,[3] but the most promising approach is the utilisation of the strong interaction between thiols and gold, where a gold–sulfide bond is formed.[10] In this work the dithiolane moiety of thioctic acid (Figure 3) is used to immobilise monodisperse gold nanoparticles. This moiety is a cyclic disulfide, which can be regarded as an equivalent of two thiol moieties and was utilised to form self-assembled monolayers (SAMs)[7,8] or as a stabilising agent for gold nanoparticles.[9] To achieve the immobilisation of the gold nanoparticles out of a gold sol, polymer films containing the thiophene derivative 3-methoxy thiophene (MOT) were prepared. The hydroxyl groups in the polymer (ROH) were then esterified with thioctic acid, as depicted in Figure 3.

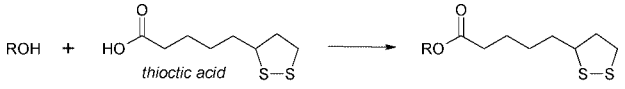

Figure 3. Reaction scheme: esterification with thioctic acid.

Figure 4 shows the layout of the polymer substrates with immobilised gold nanoparticles after the two steps of esterification (1) with thioctic acid and subsequent immobilisation of the gold nanoparticles (2) from a gold sol.

Two different methods were used to immobilise gold nanoparticles on ultrathin films of polythiophene and polythiophene derivatives. With the first method, ultrathin films of polythiophene were utilised to prepare gold nanoparticles by direct reduction of aqueous $HAuCl_4$, to yield polydisperse gold nanoparticles. Size and size distribution of the nanoparticles could be controlled by time, concentration of Au^{3+}, and the addition of a cosolvent. With the second method, ultrathin films of polythiophene derivatives were esterified with thioctic acid, using either Steglich or Yamaguchi conditions. The disulfide moieties of the thioctic acid were utilised to immobilise gold nanoparticles from monodisperse gold sol. The samples with the gold nanoparticles, obtained from both methods, were analysed by scanning electron microscopy (SEM).

Results and Discussion

1) Direct Process

The examined parameters were time, concentration of Au^{3+} and effects of the cosolvent, which are to be discussed. The results are summarised in Figure 5. A continuous gold

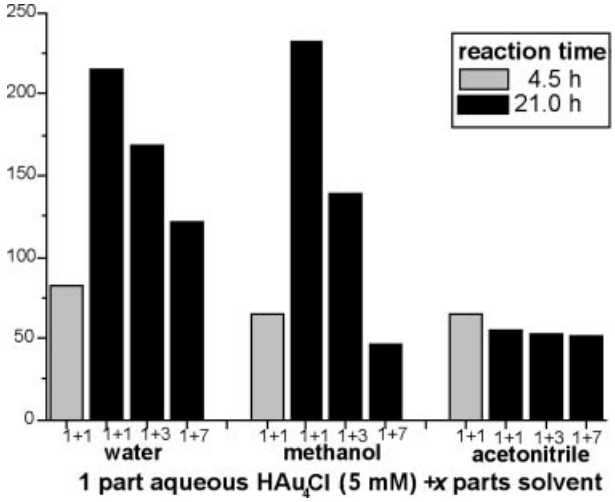

Figure 5. Direct process: mean gold nanoparticle size in relation to concentration, cosolvent, and time.

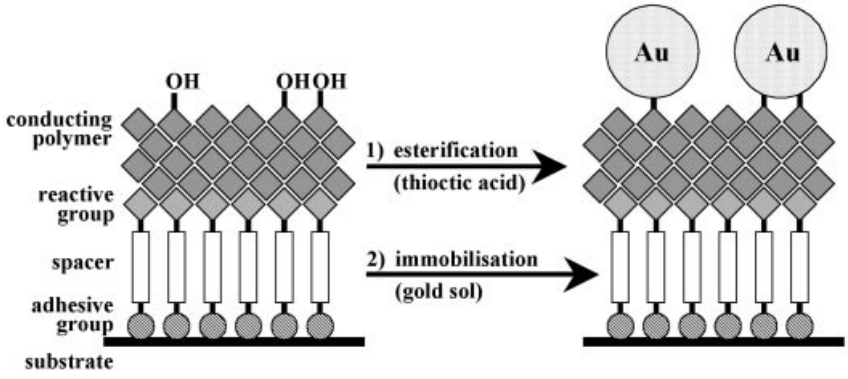

Figure 4. Polymer modification.

 © 2005 Wiley-VCH Verlag GmbH & Co. KGaA, Weinheim

layer on the polythiophene films could not be observed, however, gold nanoparticles were visible on the surface of these films (Figure 6). This outcome was expected from the observations of Holdcroft et al.[4,5] with thin polymer films. The gold particles that were obtained were polydisperse and randomly distributed on the polythiophene films. It could be corroborated that undoped polythiophene was able to reduce aqueous gold salt solutions.

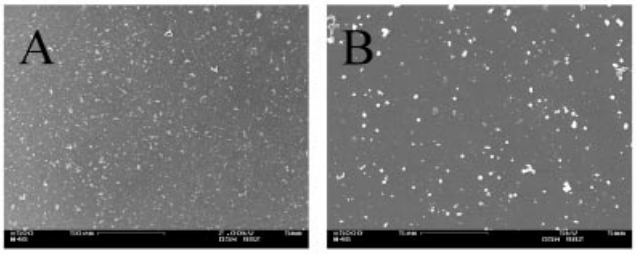

Figure 6. Direct process: typical SEM micrographs: A) 500×. B) 5,000× (5.08 mM of $HAuCl_4$, 4.5 h).

Concentration Dependence

The amount of Au^{3+} in the solutions was the same for all the experiments, because each experiment started with 0.5 mL of an aqueous $HAuCl_4$ solution (5.08 mM) and dilution was achieved by adding, either 0.5 mL, 1.5 mL, or 3.5 mL of solvent into the reaction flask. A decreased concentration of Au^{3+} resulted in smaller particles with a narrower size distribution (parts B and D in Figure 7). This trend could be observed when diluting with water, methanol, and acetonitrile and it was most pronounced with methanol.

Cosolvent Dependence

The presence of a cosolvent (methanol, acetonitrile) resulted in smaller particles with narrower size distributions (parts A and C in Figure 7). The dilution series with methanol yielded results that were little different from the dilution series with water, but were more pronounced, i.e. the decrease in particle size with increasing dilution was larger. The addition of acetonitrile, on the other hand, had a more significant effect on the deposition behaviour of the gold particles. The reduction of Au^{3+} to Au^0 proceeded via Au^+, which is stabilised by acetonitrile. Hence, the deposition of Au was very slow. At a constant number of nucleation centres and nuclei, the size of the nuclei was smaller after a constant time, as the rate of gold deposition was lower, resulting in very small gold particles. The influence of acetonitrile on the deposition was so substantial that there was little change of particle size in the dilution series.

Time Dependence on Particle Size

An increase in reaction time resulted in an increased particle size and a broader size distribution of the particles (parts A and B in Figure 7). Increasing the reaction time from 4.5 h to 21 h and therefore by almost a factor of four, yielded an increase in the particle size of four times.

Summary: Direct Process

The particle size (Figure 5) was increased by the factors, time and concentration. As the particles got larger, the size distribution (Figure 7) also broadened. Adding a second solvent other than water yielded in most cases smaller particles, an effect that could be explained with stabilising effects of the solvent molecules on the different gold species in solution. As a second effect of the solvent addition, the

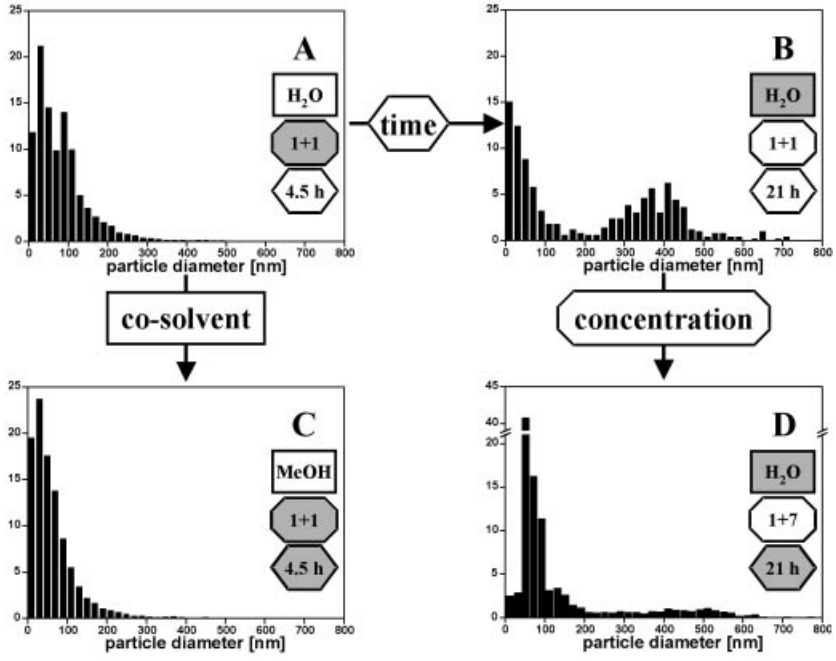

Figure 7. Direct process: particle size distributions.

 © 2005 Wiley-VCH Verlag GmbH & Co. KGaA, Weinheim

size distribution became more homogeneous. To conclude this: Particle size and distribution could be positively influence by the addition of the solvents methanol and acetonitrile.

Polymer Modification

In a second set of experiments the polymer was modified by derivatising it with adhesion groups for the immobilisation of gold nanoparticles out of gold sols. The success of the polymer modifications was checked by adsorption experiments with gold sols. Gold sols of Roche Diagnostics were used. These gold sols were prepared with the citrate reduction method[18] with no further stabilising agent used other than citrate and had a mean particle size of 40 nm. For adsorption of the gold nanoparticles the modified polymer films were immersed into the gold sols. Immobilisation of the gold nanoparticles was achieved by cleavage of the disulfide bond of the thioctic acid and formation of two gold sulfide bonds, which was due to the high affinity of gold to sulfur.[9,10]

Polymer Film Modification through Esterification – Steglich Conditions

In Figure 8, as in all of the SEM micrographs, the gold nanoparticles appear as white to light grey dots, while the substrate with the modified polymer film appears in a dark grey. Figure 8 shows the different affinities of the modified polymer films towards the gold nanoparticles: on the unmodified polythiophene film (Figure 8, A) just a few gold nanoparticles were immobilised. The polythiophene film was used as blank test as it could not be esterified with thioctic acid and had a very low affinity to gold.[11] The modified polymethoxythiophene film (Figure 8, B) on the other hand was densely covered with gold nanoparticles, indicating a successful polymer modification.

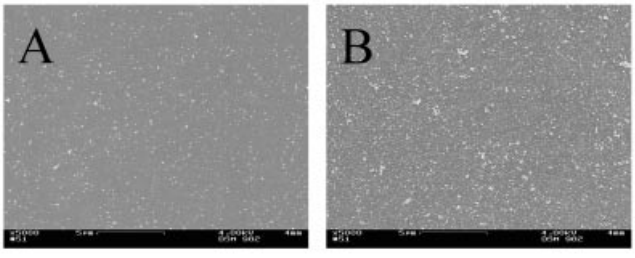

Figure 8. SEM micrographs of immobilised gold nanoparticles on modified polymer films (magnification 5,000): A) polythiophene, B) polymethoxythiophene (modified, Steglich conditions).

The differences in morphology of the copolymer films were examined. The copolymers were prepared from methoxythiophene with thiophene P(T/MOT) and methylthiophene P(MT/MOT), respectively. The films with thiophene (Figure 9, A) had a more homogeneous appearance, than those prepared with methylthiophene (Figure 9, B). This could be explained with a better coupling of the adhesion promoter TUTS with the thiophene, because of a minor steric hindrance of the monomers during polymerisation, due to the absence of the 3-methyl group. Polymer films with regions of different morphology could be observed with the methylthiophene containing copolymers, as shown in part B of Figure 9. These films had a rougher surface, so that more methoxy groups were accessible for esterification with thioctic acid. Thus, locally increased concentrations of dithiolane groups through the thioctic acid ester were available to immobilise more gold nanoparticles on these films. In Figure 9 (see part A) single gold nanoparticles were spread over the unmodified polythiophene film, while in Figure 9 (see part B) inhomogeneities lead to the formation of larger agglomerates of gold nanoparticles. Between the agglomerates regions of homogeneous coverage with single gold nanoparticles were allocated. The regions in the SEM micrograph that had a lighter appearance did not have a higher affinity to the gold nanoparticles compared with the darker regions.

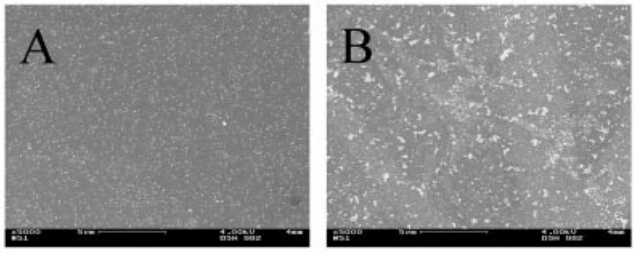

Figure 9. SEM micrographs of immobilised gold nanoparticles on modified polymer films (magnification 5,000): A) P(T/MOT), B) P(MT/MOT) (both modified, Steglich conditions).

The influence of different monomer ratios on the resulting polymers was examined with the copolymers from methoxythiophene with thiophene P(T/MOT). The morphology of the homopolymer films was smooth and homogeneous, as can be seen in Figure 8. With the addition of only small amounts of the other monomer to the polymerisation mixture the copolymer films were still homogeneous, e.g. methoxythiophene in thiophene T/MOT = 90:10 (v/v) (Figure 9, A).

As the monomer ratios were changed further until an equal mixture of the monomers was reached, the morphology of the copolymer films exhibited an increasing roughness. Also, the appearance of regions on the polymer film with different morphologies was observed, which could be indicating that these areas correspond to different segregated copolymers or even homopolymers, respectively.

Adhesion of the gold nanoparticles on the modified polymer films was tested with a scotch tape test. For this, one half of a substrate was covered with scotch tape, which was then quickly removed. SEM was used to examine the samples before and after the test, and no significant loss of gold nanoparticles was detected. Therefore, it can be concluded that the immobilised gold nanoparticles are covalently bound to the modified substrate.

Polymer Film Modification through Esterification – Yamaguchi Conditions

In the experiments examining the Yamaguchi esterification, the quality of the adhesion promoter allowed only the

 © 2005 Wiley-VCH Verlag GmbH & Co. KGaA, Weinheim

deposition of TUTS films with a high coverage of polysiloxane particles originating from the condensation of TUTS molecules. Thus, resulting in inhomogeneously deposited polymer films, as shown in Figure 10. Figure 11 shows that the polymer morphologies could be reproduced, although their surface structure was more coarse than previously described for the Steglich-modified polymer films in Figure 9. The defects in the polymer films (Figures 10 and 11) are due to the film preparation conditions and could not be eliminated. The immediate detection of the gold nanoparticles was impeded by the numerous polymer particles, but with careful examination the gold nanoparticles became apparent.

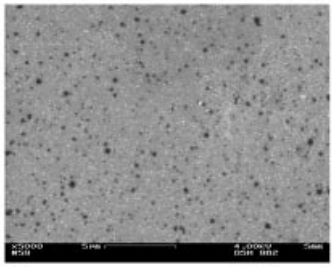

Figure 10. SEM micrograph of immobilised gold nanoparticles on modified polymer film (magnification 5,000): polymethoxythiophene (modified, Yamaguchi conditions).

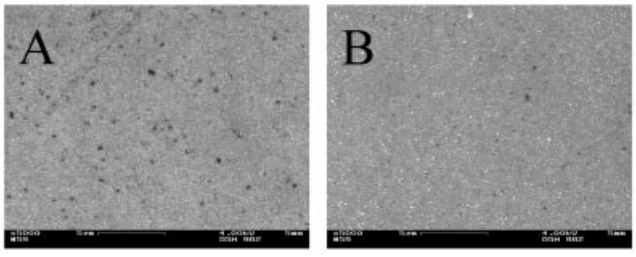

Figure 11. SEM micrographs of immobilised gold nanoparticles on modified polymer films (magnification 5,000): A) P(T/MOT), B) P(MT/MOT) (both modified, Yamaguchi conditions).

When comparing e.g. Figure 8B (Steglich conditions) with Figure 10 (Yamaguchi conditions) in the case of modified polymethoxythiophene, it became obvious that the two pathways for the esterification yielded either agglomerated or separated gold nanoparticles upon subsequent immersion into a gold sol. Also, the coverage of the Yamaguchi-modified polymer films with gold nanoparticles was lower than with the Steglich-modified films. The Yamaguchi-modified polymer films were more porous due to the defects in the pristine polymer films. Therefore, less thioctic acid ester moieties were accessible on the surface by the gold nanoparticles of the gold sol, resulting in a lower coverage of separated gold nanoparticles.

Conclusions

It was shown that gold nanoparticles could be immobilised by two different methods. A direct reduction process, utilising the polymer film of the substrate yielded polydisperse nanoparticles. The particle size of the nanoparticles and their size distribution could be controlled by the factors time, concentration, and the addition of a cosolvent. Monodisperse gold nanoparticles could be immobilised on further modified polymer films. These films were prepared by using thiophene derivatives bearing hydroxyl groups, which were then esterified with thioctic acid using either Steglich or Yamaguchi conditions. The latter method allows the immobilisation of a huge variety of nanoparticles, because those can be prepared ex situ. The only prerequisite for the nanoparticles is that they interact strongly with the dithiolane group of the thioctic acid ester to allow the immobilisation.

Experimental Section

1) Preparation of Ultrathin Films of Polythiophene and Polythiophene Derivatives: The polymer films were chemically deposited on silicon substrates, which were modified with the adhesion promoter 11-(thien-3-yl undecyl) trichlorosilane (TUTS).[12–14]
The pretreatment of the substrates and subsequent modification with TUTS was described in the literature.[12–14] Chemical deposition of the thiophene polymers was carried out in the following manner: the TUTS-modified substrates were placed in a solution of 1.0 g of $FeCl_3$ (anhydrous, Fluka, p.a.) and 25 mL of acetonitrile (<50 ppm water, Fisher Scientific, p.a.), then 100 μL of the respective premixed monomers were added. After 1 h of reaction time, the samples were cleaned in an ultrasonic bath with methanol (Merck, purum). The monomers (Aldrich, p.a.) were thiophene (T), 3-methylthiophene (MT), and 3-methoxythiophene (MOT), the monomer mixtures T/MOT = 90:10 (v/v) and MT/MOT = 90:10 (v/v).

2) Direct Process: Polythiophene substrates were immersed into an aqueous Au^{3+} containing solution: 0.5 mL of $HAuCl_4$ (5.08 mM) + $x \times 0.5$ mL of solvent (x = 0, 1, 3, 7; solvent = dist. water, methanol, acetonitrile). Immersion time was 4.5 h and 21 h, respectively. The examined parameters were time, concentration of Au^{3+} and effects of the cosolvent. After reaction, the substrates were rinsed with copious amounts of distilled water and subsequently dried with argon.

3) Polymer Modification: All the glassware used for the reactions was heated in vacuo and subsequently "aerated" with argon.
Polymer modification reactions were carried out in 100 mL Erlenmeyer flasks, each equipped with a rubber septum. The flasks were moved on a one-dimensional shaker during the reaction. Solvents were freshly dried prior to use, and all other chemicals were used as received.

3a) Polymer Film Modification through Esterification – Steglich Conditions: The esterification was carried out according to Steglich et al.[15] following the working procedure of Echegoyen et al.[16] Each solution was premade and then divided into five parts, which were then added to the different polymer substrates. The thioctic acid (9.4 mmol, 1.94 g) and DMAP (0.65 mmol, 0.08 g) were dissolved in 50 mL of dichloromethane and added to the polymer substrates. After 30 min a DCC solution (11.2 mmol, 2.32 g) in 25 mL of dichloromethane was added. After another 22 h, under gentle movement with the one-dimensional shaker, the modified substrates were cleaned in an ultrasonic bath with distilled water and ethanol for 5 min each and subsequently dried with argon.

3b) Polymer Film Modification through Esterification – Yamaguchi Conditions: The esterification was carried out according to Yamag-

 © 2005 Wiley-VCH Verlag GmbH & Co. KGaA, Weinheim

uchi et al.[17] Each reaction mixture was divided into four parts: three parts for modification of three individual substrates and one part for reaction control with GC-MS. The thioctic acid (1.2 mmol, 245.2 mg) was dissolved in 8 mL of THF, then triethylamine (1.2 mmol, 121.8 mg, 166 μL) was added after which the mixture was stirred for 10 min at 0 °C. 2,4,6-Trichlorobenzoyl chloride (1.2 mmol, 292.8 mg, 457 μL) was then added and stirred for another 10 min at 0 °C, followed by 2 h at room temperature. After removal of triethylamine hydrochloride by filtration through a syringe filter (PTFE, 0.2 μm pore width), the filtrate was evaporated in vacuo and the yellow, viscous residue was dissolved in 8 mL of dichloromethane. A solution of DMAP (2.4 mmol, 293.2 mg) in 8 mL of dichloromethane was then added to this. A polymer substrate was treated with a portion of 4 mL of this resultant solution for 48 h under gentle movement with the one-dimensional shaker. Finally the modified substrates were cleaned in an ultrasonic bath with distilled water and methanol for 5 min each and subsequently dried with argon.

3c) Gold Nanoparticle Adsorption: The modified polymer substrates were immersed in a gold sol for 1 h at 4 °C. The gold sol was prepared by Roche Diagnostics with the citrate reduction method[18] with no further stabilising agent used other than citrate. In the first experiments the substrates were placed face up in the adsorption flask, while later on the substrates were placed slightly tilted upside down in reaction tubes for adsorption. This orientation avoided the deposition of gold nanoparticles, which were destabilised from the gold sol during the progressing experiments. After adsorption the substrates were rinsed with copious amounts of distilled water and subsequently dried with argon.

Acknowledgments

We thank the Deutsche Forschungsgemeinschaft for financial support in the SPP 1072 "Halbleiter und Metallcluster als Bausteine für organisierte Strukturen", Frau Kern for the SEM micrographs, Dr. X. Cai, Dr. E. Jähne, Prof. Dr. H.-J. Adler (Institute for Macromolecular Chemistry, TU Dresden) for synthesis of the adhesion promoter TUTS, and Mr. Th. Kreuzer (Institute for Organic Chemistry, TU Dresden) for help and support during the polymer modifications; Roche Diagnostics for donating the gold sol.

[1] "Clusters and Colloids" (Ed.: G. Schmid), VCH, Weinheim, **1994**.
[2] G. Schmid, B. Corain, *Eur. J. Inorg. Chem.* **2003**, 3081–3098.
[3] M.-C. Daniel, D. Astruc, *Chem. Rev.* **2004**, *104*, 293–346.
[4] M. S. A. Abdou, S. Holdcroft, *Synth. Met.* **1993**, *60*, 93–96.
[5] M. S. A. Abdou, S. Holdcroft, *Chem. Mater.* **1996**, *8*, 26–31.
[6] M. C. Henry, C.-C. Hsueh, B. P. Timko, M. S. Freund, *J. Electrochem. Soc.* **2001**, *148*, D155–D162.
[7] H. Liu, S. Liu, L. Echegoyen, *Chem. Commun.* **1999**, 1493–1494.
[8] K. Bandyopadhyay, H. Liu, S.-G. Liu, L. Echegoyen, *Chem. Commun.* **2000**, 141–142.
[9] L. Maya, K. A. Stevenson, G. Muralidharan, T. G. Thundat, E. A. Kenik, *Langmuir* **2002**, *18*, 2392–2397.
[10] A. Ulman, *J. Chem. Soc., Chem. Rev.* **1996**, *96*, 1533–1554.
[11] F. Elfeninat, C. Fredriksson, E. Sacher, A. Selmani, *J. Chem. Phys.* **1995**, *102*, 6153–6158.
[12] A. Fikus, PhD Thesis, Technische Universität Dresden, **1999**.
[13] D. Appelhans, D. Ferse, H.-J. P. Adler, W. Plieth, A. Fikus, K. Grundke, F.-J. Schmitt, T. Bayer, B. Adolphi, *Colloids Surf. A* **2000**, *161*, 203–212.
[14] A. Fikus, W. Plieth, D. Appelhans, D. Ferse, H.-J. Adler, B. Adolphi, F.-J. Schmitt, *J. Electrochem. Soc.* **1999**, *146*, 4522–4525.
[15] B. Neises, W. Steglich, *Angew. Chem.* **1978**, *90*, 556–557; *Angew. Chem. Int. Ed. Engl.* **1978**, *17*, 522–524.
[16] K. Bandyopadhyay, S.-G. Liu, H. Liu, L. Echegoyen, *Chem. Eur. J.* **2000**, *6*, 4385–4392.
[17] K. Hirata, J. Inanaga, H. Saeki, T. Katsuki, M. Yamaguchi, *Bull. Chem. Soc. Jpn.* **1979**, *52*, 1989–1993.
[18] G. Frens, *Nature - Phys. Sci.* **1973**, *241*, 20–22.

Received: May 3, 2005
Published Online: August 26, 2005

 © 2005 Wiley-VCH Verlag GmbH & Co. KGaA, Weinheim

Bottom-Up Synthesis and Top-Down Organisation of Semiconductor and Metal Clusters on Surfaces

Alexander M. Bittner,*[a] Xiao C. Wu,[a,b] Sinan Balci,[a] Mato Knez,[a,c] Anan Kadri,[d] and Klaus Kern[a]

Keywords: Cadmium sulfide / Nanocrystals / Metal clusters / Microcontact printing / Nanostructures / Template synthesis

Near-spherical dendrimers can be used as templates for bottom-up syntheses of semiconductor clusters. Starting from methanolic solutions of Cd^{2+}, sulfide, and poly(amidoamine) dendrimers, CdS clusters precipitate at the dendrimers. A preparation inside the dendrimers is only possible when the protonation of the latter is carefully controlled. The clusters have diameters above about 2 nm and show blue photoluminescence. The patterning and orientation of CdS/dendrimer clusters on flat surfaces are attained by microcontact printing. Depending on the ripening of the CdS/dendrimer suspension, a sub-micrometer stripe pattern develops inside the micrometer-scaled patterns; it extends over the complete surface. Rod-like plant virions with a different type of lateral organisation can be oriented on a flat substrate by applying mechanical forces during immobilisation from suspensions. These virions can also be employed as templates, in this case for creating metal structures by electroless deposition (chemical metal deposition). The structures are wire-like with diameters of 3–4 nm and are confined inside the central channel of the virions. The early stage of the metallisation process is analysed, and a model that accounts for the selectivity is presented.
(© Wiley-VCH Verlag GmbH & Co. KGaA, 69451 Weinheim, Germany, 2005)

Introduction

The synthesis of well-defined clusters can be carried out by wet chemical means (under mild conditions) when the products are bound to a template. a range of organic templates, for example block copolymers[1] and biotemplates,[2,3] some of which are single molecules, are available for various semiconductor and metal clusters. The template can direct their size and shape, and it can even catalyse the growth. Typical examples are amphiphiles, which may organise into micelles by self-assembly.[1,4] The clusters are more or less strongly bound to the template, which can be removed to liberate pure clusters.[5] However, in many cases (e.g. for optical measurements) this removal is neither required nor an advantage, such as for photoluminescing CdS clusters at dendrimers.[6,7] The physical properties depend mainly on the cluster size and nature. Thus, while metal clusters reach the limit of quantised conductivity only for very small diameters (<2 nm), even relatively large semiconductor clusters (tens of nanometres) show quantised energy levels, which is reflected in their optical properties, especially photoluminescence.[8]

Nanoscale science and nanotechnology rely, in many cases, on the step-by-step assembly of nano-objects on substrate surfaces. An important issue is how to immobilise and orient the objects at defined sites of a given substrate. Considering that the simplest "bottom-up" syntheses for nano-objects employ molecular templates, soft matter manipulation might be important. On the other hand, standard photo- or electron-beam lithography is slow, expensive and often not compatible with soft matter. Hence, new "top-down" methods are called for, and microcontact printing has been developed into one of the most powerful tools in this respect. Recently, very large molecules such as DNA[9] and inorganic nanowires[10] have been shown to be printable.

Dendrimers are branched macromolecules, and the number of branches determines their generation (here eight terminal branches for generation 1, and 16 for generation 2) and hence their size. In contrast to most polymers, dendrimers have an extremely sharp size distribution. They have been used as templates for spherical clusters of metals and semiconductors;[11–17] cluster diameters are usually below 5 nm. Large rod- or tube-like biological molecules and supramolecular aggregates qualify as templates for quasi-one-dimensional nanostructures. They can be well defined in their chemical composition and also in their structure and symmetry. Examples are DNA,[18] plant virions,[19] phages,[20] protein tubes[21,22] and protein fibres,[23,24] all of

[a] Max-Planck-Institut für Festkörperforschung,
Heisenbergstr. 1, 70569 Stuttgart, Germany
Fax: +49-711-689-1079
E-mail: a.bittner@fkf.mpg.de
[b] New address: National Center for Nanoscience and Technology,
Beijing, China
[c] New address: Max-Planck-Institut für Mikrostrukturphysik,
Halle, Germany
[d] Biologisches Institut, Universität Stuttgart,
Pfaffenwaldring 57, 70550 Stuttgart, Germany

 DOI: 10.1002/ejic.200500388 © 2005 Wiley-VCH Verlag GmbH & Co. KGaA, Weinheim

which are increasingly used for nanoscale structuring as functional units or as templates.[18–29] Apart from binding organic molecules, the best-known templating function is binding (or synthesis) of metal clusters and wires, as presented here for the tobacco mosaic virus (TMV).

As mentioned above, possible applications of semiconductor and metal clusters require a transfer to a substrate surface on a selected area in a defined orientation. For templated clusters, it is sufficient to transfer and orient the template as this results automatically in transfer/orientation of the clusters. The transfer method can be by adsorption, although microcontact printing offers selective placement in predefined arrays. Moreover, in certain cases − here aged CdS/dendrimer composites − the printing process results in sub-patterns that develop inside the printed patterns, and hence structuring on two length scales can be achieved in a single step. For many applications, however, the orientation of nonspherical nano-objects, for example in a parallel fashion, is more important than their exact placement. For this, a range of relatively simple methods is available. For example, laterally (parallel to the substrate surface) applied forces that act on a droplet of suspended nano-objects are well known for stretching and orienting DNA;[9,29,30] here they were tested for the orientation of virions.

The theme of this paper is the combination of "top-down" methods for orientation and placement of nano-objects with their "bottom-up" synthesis. Section 1 introduces a new pH-controlled synthesis method for CdS clusters inside poly(amidoamine) (PAMAM) dendrimer templates. The diameter of the clusters is so small that the energy levels are shifted, hence UV-excited photoluminescence is observed in the blue range of the spectrum. CdS/dendrimer composites can be patterned by microcontact printing. This method can, for certain composites, result in "patterned patterns", i.e. in structures with linear substructures. Section 2 is dedicated to linear structures only; it introduces two very simple orientation methods for TMV, namely blow-drying of a droplet, and exerting capillary forces on a droplet by suction with a filter paper. Both methods have been widely applied, but have not been documented in detail for TMV. The virions can be advantageously employed as templates for 3–4-nm-wide metal wires that are confined in the central channel of the virion; the focus is here on the initial stages of the electroless metal deposition process, and on the surprisingly high selectivity for the inner channel of TMV.

Results and Discussions

1. Synthesis and Organisation of Luminescent CdS Clusters in Micrometer and Sub-Micrometer Patterns

The simple and effective one-pot synthesis of CdS clusters from Cd^{2+} and S^{2-} at dendrimers is well documented.[6,7,15–17] When amine-based dendrimers are employed, their protonation has a pronounced effect on the shape, number and location of the formed nanocrystals. Good examples are near-spherical, amine-terminated PAMAM [poly(amidoamine)] dendrimers of generations 4 ($G4NH_2$) and 8 ($G8NH_2$), where the repeat unit is $N–(CH_2CH_2–CONH–CH_2CH_2)_2$ and the terminal groups are primary amines (NH_2). The Cd^{2+} ions appear to bind to the terminal amine groups, thus usually placing the clusters on the surface of the dendrimers rather than inside. However, Section 1.1 shows that a better control of morphology and size can be obtained by careful protonation of some of the amine groups, which has been discussed for poly(propylene imine) (PPI) dendrimers[31] but has not yet been applied for the synthesis of CdS. The use of hydroxy-terminated dendrimers (G4OH) is an interesting and viable alternative since Cd^{2+} binds only weakly to hydroxy groups.

The "bottom-up" synthesis at a template can be complemented by a "top-down" method to organise the dendrimer/CdS composites in a predefined pattern. Microcontact printing is especially attractive due to its speed, simple handling and variability.[7] Pure semiconductor clusters are difficult to print, so a two-step technique is usually employed: first, a thin layer or monolayer of an organic molecule is printed on a flat substrate to achieve a pattern with chemical contrast, for example hydrophilic/hydrophobic. The clusters are thereafter deposited on the structured susbstrate. A much simpler one-step process, in which the complete dendrimer/CdS composite is printed, could therefore be advantageous.[7] In this way, micrometer-sized areas can be selectively and densely covered with CdS clusters. However, the printing density depends on the age of the CdS/dendrimer suspension. Long ageing times (many days) are preferred due to an improvement of the optical quality. Section 1.2 presents and discusses a new organisation phenomenon that operates with composites aged for only two days: the formation of sub-micrometer line patterns inside the patterned areas.

1.1. Synthesis of CdS Clusters at and in Dendrimer Templates

Balogh et al. have defined three different types of metal–dendrimer nanocomposites according to the position of the metal nanoparticles on the dendrimers,[32] namely metal nanoparticles residing inside the dendrimers (internal type), outside the dendrimers (external type) and a mixed type. The formation of the different types is determined by the binding mechanism of the metal ions (which are synthetic precursors for the clusters), by immobilisation reactions, and by metal–dendrimer interactions during the formation of the nanoparticles. The same principle is employed for semiconductor clusters. According to the actual size of the synthesised nanoparticles (D_N), the diameter of the dendrimers (D_D) and the size of the nanoparticles calculated from the number of metal ions bound to each dendrimer (D_C), the constitution of the nanocomposites can be deduced. Thus, when D_N is smaller than both D_D and D_C, several nanoparticles are found per dendrimer. This occurs for large dendrimers (high generation numbers).[33] Here dendrimers can be called "nanoreactors", as nanoparticles are protected by dendrimer "ligands". However, the size of the nanoparticles cannot be simply estimated from the loading

 © 2005 Wiley-VCH Verlag GmbH & Co. KGaA, Weinheim

factor of metal ions to the dendrimer. For example, stable colloidal solutions of CdS/G8NH_2 can be obtained only at NH_2/Cd^{2+} ratios lower than 2 (without control of pH). This indicates that the nucleation sites of the CdS nanoparticles are close to the terminal NH_2 groups. Therefore, CdS clusters are most probably found at the surface regions of the dendrimers, i.e., CdS nanoparticles are (weakly) bound to the terminal NH_2 groups. The diameter (D_N) of the CdS nanoparticles, calculated from the absorption band gap,[34] is about 2 nm,[6] which is smaller than the values of 9.7 and 3.4 nm calculated for D_D and D_C, respectively. Thus, the CdS/G8NH_2 nanocomposites reported by Wu et al.[6,7] belong to the external type, and consist of about two nanoparticles per dendrimer.

When D_N is similar to D_C, one nanoparticle should form per dendrimer. This is the case when the interactions between metal ions and internal functional groups of dendrimers are strong,[35,36] or when the loading of metal ions is confined inside the dendrimers.[15] In this case, the nucleation and also the growth of a nanoparticle is confined within a single dendrimer. The size of nanoparticles can be controlled by the loading factor of metal ions to dendrimers or by the variation of the dendrimer generation. While this is well known for metal/dendrimer composites, semiconductor/dendrimer composites require a more careful control of the protonation.[15] NH_2-Terminated dendrimers undergo various stages of protonation/deprotonation processes at different pH values.[31,37] Therefore, if one can control the protonation of the dendrimers, i.e., only protonate the terminal NH_2 groups and keep the tertiary N groups deprotonated, the CdS clusters should be confined inside the dendrimers. After the synthesis, the NH_3^+ groups can be deprotonated and further chemical modifications can be carried out. Another advantage is that aggregation effects should be reduced due to the repulsive interaction between protonated dendrimers.

1.1.1. pH-Dependent Behaviour of PAMAM Dendrimers

In order to distinguish the protonation processes of tertiary and primary N, various amounts of acid were added to dendrimer (+ Cd^{2+} + S^{2-}) solutions, and conventional pH measurements were carried out. Such measurements are difficult in methanol, but the effects of protonation on the absorption spectra are easily detectable and can be used qualitatively to elucidate the chemical behaviour of the dendrimers. An advantage of the spectroscopic method employed here is that disadvantageous measurement conditions, such as high electrolyte concentration and water as solvent, which are required for accurate pH measurements, can be avoided.

Figure 1 shows the evolution of the absorption spectra of G4OH and G4NH_2 dendrimers in aqueous solution as a function of added amounts of aqueous HCl. G4OH is terminated by OH groups and can therefore not be protonated at its termini, at least in the range of pH values employed. With increasing H^+/NR_3 ratio, the oscillator strength of the C–N bonds (both $\sigma\rightarrow\sigma^*$ and $n\rightarrow\sigma^*$ bonds) in G4OH obviously decreases at first. This can be seen clearly from the variations of absorbance of these two bands with the H^+/NR_3 ratio (see parts a and b in Figure 1) and can be divided into two stages: the rapidly decreasing stage corresponds to the protonation of tertiary N in G4OH, while the flat stage indicates the completion of the protonation process. G4NH_2 (Figure 1, parts c and d) is slightly different to G4OH as it shows a three-stage behaviour. First, the absorption spectra show a small red-shift, and the variation in absorbance is small. After this stage, the changes are similar to those found with G4OH, therefore the first stage should correspond to the protonation of primary N. Note that the changes in the spectra caused by adding HCl can be recovered by adding NaOH. This verifies that the changes are caused by reversible protonation processes.

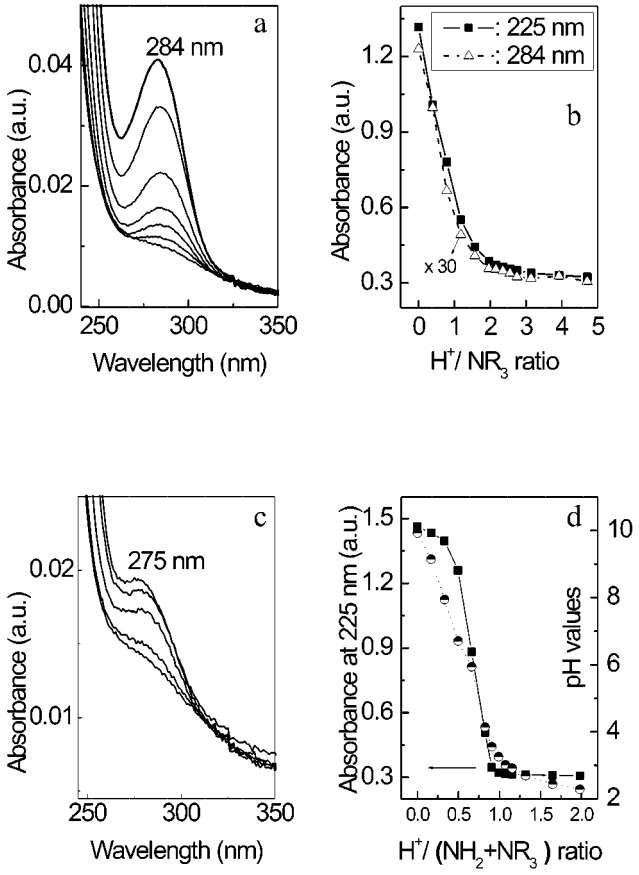

Figure 1. Evolution of absorption spectra of G4OH in aqueous solution, $H^+/(NH_2 + NR_3)$ ratios from top to bottom: 0, 0.39, 0.79, 1.18, 1.57, 2.36, 4.72 (a). Variations of absorbance at 225 and 284 nm vs. H^+/NR_3 ratios; note that the absorption intensity at 284 nm is scaled by a factor of 30 (b). Evolution of absorption spectra of G4NH_2 in aqueous solution, H^+/NR_3 ratio from top to bottom: 0, 0.66, 0.83, 0.91, 0.99 (c). Variations of absorbance (squares) at 225 nm and of pH values (circles) vs. $H^+/(NH_2 + NR_3)$ ratio (d).

In order to check the correlation between the variations in absorption and in protonation, several aliquots from each sample were taken and used for additional pH measurements. They show a good correlation (Figure 1, d). The position of the pH curve at pH 8 corresponds well to the

 © 2005 Wiley-VCH Verlag GmbH & Co. KGaA, Weinheim

turning point of the absorbance at 225 nm [$H^+/(NH_2 + NR_3)$ ratio of 0.3], thus indicating the start of the protonation of the tertiary N. Therefore, the relatively flat part of the curve [H+/(NH_2 + NR_3) ratio 0.3–0.6] can be used to synthesise CdS nanoparticles inside dendrimers: The tertiary amine groups remain deprotonated, thus binding of Cd^{2+} is favoured here.

A good comparison with these results is afforded by the protonation behaviour of poly(propylene imine) (PPI) dendrimers, which has been investigated both experimentally and theoretically.[31] At pH 6–8, PPI dendrimers show the desired protonation behaviour. Compared to PPI dendrimers, NH_2-terminated PAMAM dendrimers possess additional amide groups. Since the protonation of amide groups can be neglected at the pH values discussed here, one can assume that PAMAM dendrimers behave similarly to PPI dendrimers.

These results can be extended to larger dendrimers, namely $G8NH_2$. Figure 2 (a) shows pH values for $G8NH_2$ and $G4NH_2$ plotted against the ratio $H^+/(NH_2 + NR_3)$. The pH values of $G4NH_2$ in 1 M aqueous KCl solution serve as a reference. The pH values for $G8NH_2$ at a low electrolyte concentration with methanol as solvent are similar to those at a high electrolyte concentration with water as solvent. Above pH 5 they overlap well, indicating a similar protonation behaviour. However, methanolic solutions exhibit unstable pH readings and long response times during the experiment, which is well known for non-aqueous systems with low electrolyte concentrations. Figure 2 (b) presents the absorption spectra of CdS/$G8NH_2$ nanocomposites in methanol synthesised at different $H^+/(NH_2 + NR_3)$ ratios. It is known that about two CdS nanoparticles bind per dendrimer at pH 10, which is indicative of at least two final nucleation sites at the surface of the dendrimer. In contrast, at pH 6–7, the CdS particle size increases (compared to the case at pH 10). If Cd^{2+} ions are confined inside the dendrimer, one final nucleation site is preferred. In this case, the CdS cluster size should increase, which was indeed observed. Hence, it is postulated that CdS is encapsulated inside the dendrimer when the synthesis is carried out at pH 6–8. After further decrease of the pH value, precipitates form; for these cases, only the absorption spectrum of the supernatant is shown.

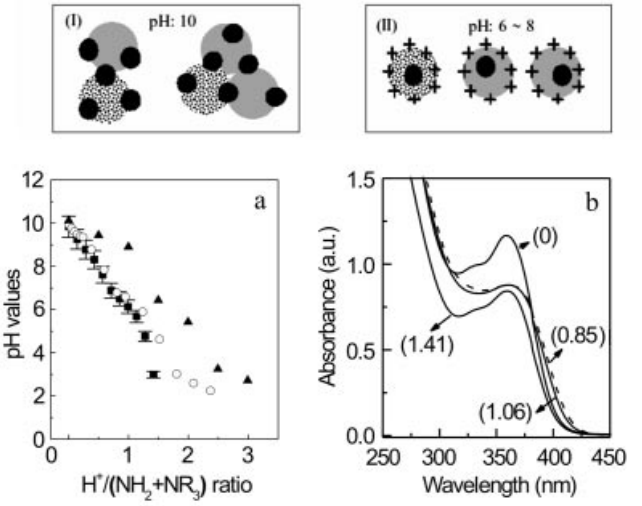

Figure 2. (a) pH values for $G8NH_2$ and $G4NH_2$ at different solvent and electrolyte concentrations vs. ratio $H^+/(NH_2 + NR_3)$. Solid squares: $G8NH_2$ in 0.16 M NaBr in methanol; open squares: $G8NH_2$ in 1 M aqueous NaCl; triangles: $G4NH_2$ in 1 M aqueous NaCl. Upper part (I): Possible morphology of CdS/$G8NH_2$ nanocomposites synthesised at pH 10. (b) Absorption spectra of CdS/$G8NH_2$ nanocomposites in methanol synthesised at selected $H^+/(NH_2 + NR_3)$ ratios; for 1.41 the supernatant was used. Upper part (II): Possible morphology of CdS/$G8NH_2$ nanocomposites synthesised at pH 6–8.

1.1.2. Binding of Cd^{2+} to PAMAM Dendrimers

In the following, syntheses at a pH of around 10 will be discussed for comparison. In these cases, CdS nucleates on

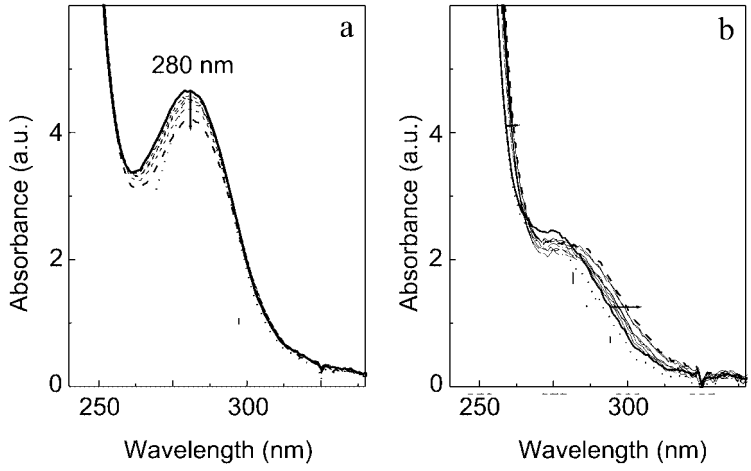

Figure 3. Effects of Cd^{2+} ions on the UV/Vis absorption spectra in methanol: (a) G4OH, ratios Cd^{2+}/NR_3 in direction of arrow (down): 0, 0.2, 0.4, 0.6, 1, 2; bottom spectrum: superposition of absorption spectra of pure G4OH and pure $Cd(CH_3COO)_2$. (b) $G4NH_2$, ratios $Cd^{2+}/(NH_2 + NR_3)$ in direction of arrow (right): 0, 0.08, 0.16, 0.24, 0.32, 0.4, 0.48, 0.64, 0.8; bottom spectrum: superposition of absorption spectra of pure $G4NH_2$ and pure $Cd(CH_3COO)_2$.

 © 2005 Wiley-VCH Verlag GmbH & Co. KGaA, Weinheim

the outer dendrimer surface. The interaction strength of N-containing groups with metal ions normally follows the order $-NH_2 > -NR_3 > -CONHR$ (where R is an alkyl chain).[38,39] The example given in Figure 3 shows the effect of Cd^{2+} ions on the UV/Vis absorption spectra of G4OH and $G4NH_2$. The absorption spectrum of pure dendrimers shows two bands that are related to C–N bonds. The strong one around 220 nm results from the $\sigma\rightarrow\sigma^*$ transition of the C–N bonds, while the weak one around 270 nm corresponds to the $n\rightarrow\sigma^*$ transition of the C–N bonds. In order to show the change of the latter, the strong absorption peak of the former is not shown here. The interaction between Cd^{2+} and N-containing groups can be described as a donor–acceptor interaction (lone pair–cation) and is relatively weak. For the Cd^{2+}/G4OH system, the $\sigma\rightarrow\sigma^*$ and $n\rightarrow\sigma^*$ transitions of the C–N bonds show a small decrease in absorbance intensity and no shift of the band. The superposition of the absorption spectra of pure G4OH and pure $Cd(CH_3COO)_2$ with a Cd^{2+}/NR_3 molar ratio of 2:1 is also shown for comparison. It shows a negligible effect. For the Cd^{2+}-$G4NH_2$ system, the $\sigma\rightarrow\sigma^*$ and $n\rightarrow\sigma^*$ transitions of the C–N bonds show a small red-shift, thereby indicating an increased interference by Cd^{2+} ions compared with the case of G4OH. The superposition of the absorption spectra of pure $G4NH_2$ and pure $Cd(CH_3COO)_2$ with a $Cd^{2+}/(NH_2 + NR_3)$ molar ratio of 0.8 shows a small decrease in absorption due to dilution. Since the difference between G4OH and $G4NH_2$ is that $G4NH_2$ has primary amine groups, the interaction of Cd^{2+} with NH_2 groups must be stronger than its interaction with NR_3 groups, which also follows the usual trend in complex chemistry. Obviously, such an interaction favours binding to the outermost chemical groups, hence external type composites are obtained.

1.2. Microcontact Printing of Dendrimers and CdS\|Dendrimer Composites

The "top-down" patterning of flat substrate surfaces with dendrimers is based on interactions like electrostatic forces or hydrogen binding: the larger the dendrimer, the slower its surface diffusion and hence the simpler its selective transfer by microcontact printing. In this case, patterns do not change during and after printing, which is possible for short- and medium-chain thiols on gold.[40,41] First, a dendrimer solution is contacted with the patterned polymer stamp. In most cases the stamp has to be hydrophilic, which for the standard silicone material [poly(dimethylsiloxane)] (PDMS) is achieved with an O_2 plasma treatment. After drying, the stamp is contacted with the (hydrophilic) substrate. One can apply this process also to dendrimer/nanocluster composites because their transfer properties are imposed by the dendrimers, not by the clusters. In other words, the dendrimer functions as an adhesion promoter for "direct" printing. Thus, the usual two-step process, where a chemically functional (or hydrophobic/hydrophilic) pattern has first to be created before adsorbing the clusters or composites, can be avoided.[42] The transferred composite with CdS retains its luminescence properties, and patterning of various micrometre shapes has been demonstrated.[7] As shown in the following, careful variation of the synthesis and printing parameters allows for a better control and even for new organisation phenomena on the substrate surface.

1.2.1. Adsorption of PAMAM Dendrimers

A prerequisite for surface structuring with molecules (or by composites) is adsorption or immobilisation of the molecules. PAMAM dendrimers terminated by NH_2, COOH and OH groups can adsorb on oxides or OH-terminated surfaces via hydrogen bonds.[6,43] Part a of Figure 4 shows an example of the adsorption of G4OH, $G4NH_2$ and $G8NH_2$ dendrimers from solution onto oxidised Si wafers. The adsorption process is very fast and reaches nominal monolayer thickness (see below) for all three dendrimers within several minutes. Further immersion changes the ellipsometric thickness only slightly. Hence, a nominal monolayer is formed. The heights of the G4 and G8 monolayers

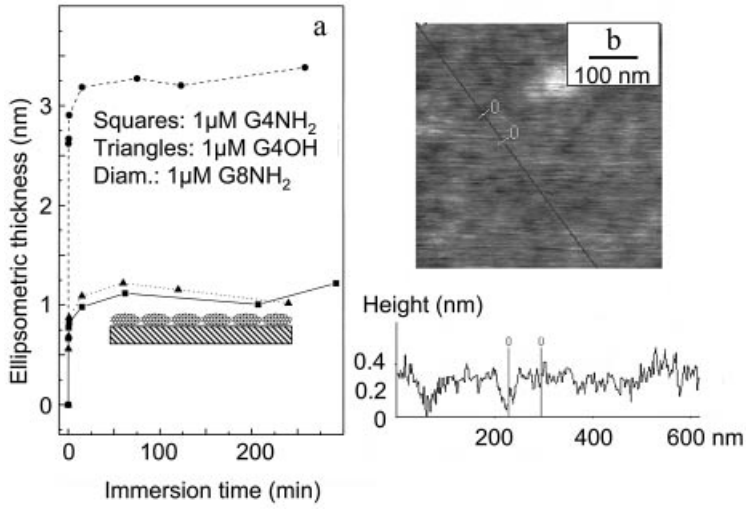

Figure 4. (a) Ellipsometric thickness of G4OH, $G4NH_2$ and $G8NH_2$ on oxidised silicon wafer surfaces measured in air after immersion, rinsing with ethanol and drying with argon. (b) Topographic intermittent contact AFM image of $G4NH_2$ monolayer on an oxidised silicon wafer; bottom part: height profile.

 © 2005 Wiley-VCH Verlag GmbH & Co. KGaA, Weinheim

are around 1.2 and 3.3 nm, respectively, which means large deviations from their ideal spherical diameters of 4.5 and 9.7 nm.[44] The monolayer thicknesses are, however, close to the height of single G4 and G8 dendrimers on hydrophilic surfaces.[45] This indicates that a strong interaction with the hydrophilic surfaces deforms the dendrimers and they show an oblate morphology on these surfaces. A topographic AFM image of a $G4NH_2$ monolayer on a wafer is shown in Figure 4 (b). The white dot in the upper part is a defect, probably due to local multiplayer adsorption. Lateral structures were not observed. The image shows hillocks whose height cannot be determined exactly. The hillocks are ascribed to the $G4NH_2$ monolayer, which is quite flat, as can be seen from the height profile (<1 nm variation). Although the tip geometry plays a role in smoothing out the image, holes in the layer more than 5 nm in diameter should be easily visible. One can deduce that the coverage is smooth and dense. Due to this adsorption behaviour, dendrimers can be printed well on hydrophilic surfaces.[46]

1.2.2. Stripe Patterns of CdS/Dendrimer Composites

In the course of the microcontact printing experiments, an interesting new phenomenon of a "bottom-up" organisation inside "top-down" patterned areas was discovered. For this, only composites that have been aged for a short time (two days at ambient temperature in the synthesis solution) qualify, i.e. particles with a monodisperse size distribution (Figure 5, a).[6] For longer ageing times, Ostwald ripening occurs (for this reason the term "ageing" is preferred over "long term synthesis"). This not only increases the size of the CdS nanoparticles but it also changes the morphology of the whole nanocomposites, which is advantageous for the printing.[6] After two days, the average height (measured by AFM) of the nanocomposites is around 9 nm, and they have a regular shape. In contrast, after 22 days the height of the particles varies from 10 nm to 60 nm, and the distributions of both shape and size broaden considerably (Figure 5, b).

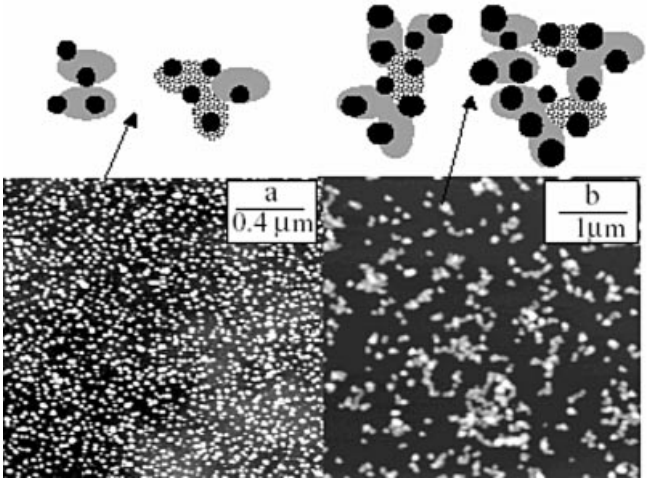

Figure 5. Topographic AFM images of $CdS/G8NH_2$ nanocomposites adsorbed on an oxidised silicon wafer after two days ageing (a) and after 22-days ageing (b). Upper parts: possible morphology for each case.

These relatively large composite aggregates can be organised into predefined micropatterns. First, a PDMS polymer stamp is produced by curing a liquid silicone prepolymer on a patterned silicon master. The patterned stamp is peeled off and treated with an oxygen plasma to create a hydrophilic stamp surface. This surface, in analogy to oxidised silicon wafers (Figure 5), is ideally suited for binding CdS/dendrimer composites aged for 22 d, simply by contacting the solution with the stamp and drying it. Conformal contact with a flat hydrophilic substrate transfers the composites exactly in the predefined pattern.

When the ageing time is reduced to only two days, the distribution of the composites on the substrate does not simply follow the pattern, rather a stripe structure several hundreds of nanometres wide develops inside the pattern, as can be seen in Figure 6. Note that the experiment was carried out in the same way, only the ageing time was shortened. The stripe structure appears to extend over the complete substrate. Hence a sub-micrometer "bottom-up" stripe patterning is obtained by using "top-down" micropatterning (>5 µm width). Height modulations on the stamp surface are not decisive: the same phenomenon occurs with unpatterned (flat) stamps (Figure 7), which are formed on flat, unpatterned silicon wafers. Such flat stamps usually transfer the adsorbed substance uniformly on the substrate.

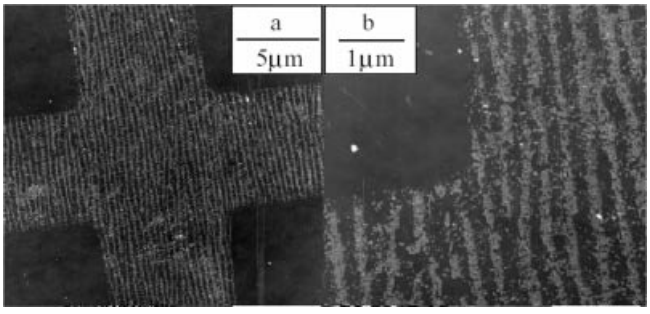

Figure 6. Topographic AFM images of $CdS/G8NH_2$ nanocomposites printed on an oxidised silicon wafer after two days ageing. A sub-micrometre stripe pattern develops inside the imposed cross-shaped pattern during the printing process.

While the structure formation is simple and straightforward, its physical interpretation is still unclear. An interesting question is whether the pattern is already present on the stamps. The inking process is the only chance for a mechanism based on fluid properties, such as dewetting. However, dewetting is excluded since it either results in structures confined to the borders of the printed pattern[47] or it yields foam-like structures in mobile molecular monolayers.[48] For some molecular systems, quite regular, but much larger, pattern widths (tens of micrometers) are found;[49,50] they depend on the orientation of the molecules on the surface, which should not play a role at the low coverages in the system under consideration. Indeed, the stripes presented here do not have uniform widths, but they extend over the complete micropatterned area. Similar, but better ordered,

 © 2005 Wiley-VCH Verlag GmbH & Co. KGaA, Weinheim

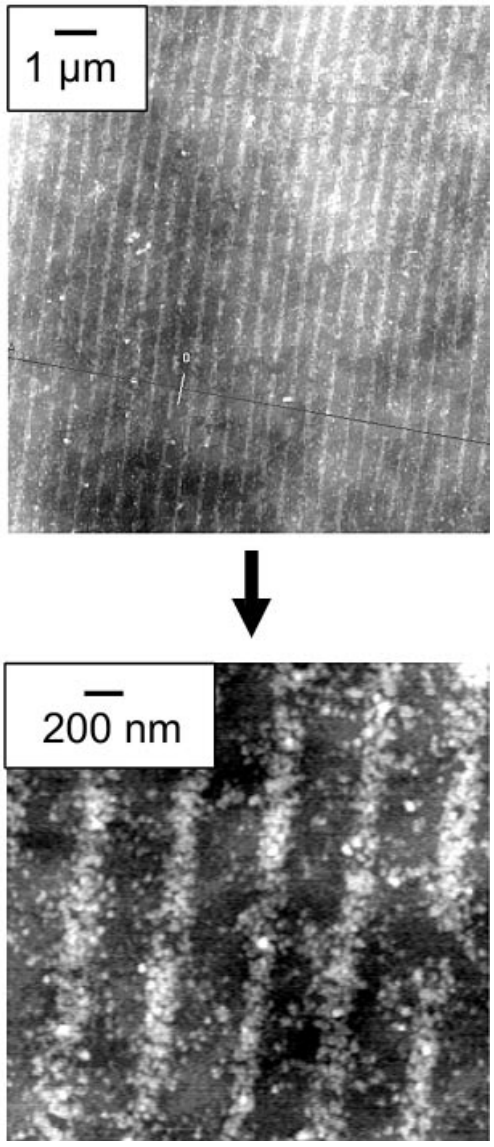

Figure 7. Topographic intermittent contact AFM image of CdS/$G8NH_2$ nanocomposites (aged for two days) printed on an oxidised silicon wafer with a flat stamp.

structures (linear arrays with sub-micrometer widths and a regular spacing) can be formed by dynamic monolayer film instabilities.[51] On the other hand, the composite does not form a complete monolayer, and the large CdS/dendrimer structures are not in all respects comparable with small molecules.

Another interesting point is the huge difference in behaviour between aged and fresh composites. This difference is unlikely to be chemical since both have chemical properties that are similar to pure dendrimers (see above). A clear difference is the (average) mass of the particles, which is relatively low for the fresh composites. However, possible mass-based mechanisms are hard to identify. For example, the stripe formation might suggest buckling, as observed upon heating, oxidation and cooling of PDMS,[52] or a standing wave, although a single acoustic resonance with a micrometre wavelength is unlikely.

2. Orientation of Plant Virions on Surfaces and the Synthesis of Metal Wires in Virions

When one-dimensional nanostructures or linear alignments of clusters are required, several supramolecular biotemplates can be advantageously employed for elegant syntheses (see Introduction). A good template for inorganic nanostructures is the tobacco mosaic virus (TMV). TMV is a tube-like assembly made up from around 2130 identical coat proteins helically organised around a helical single-strand RNA. Its length is about 300 nm and the outer diameter is 18 nm.[53] TMV has an inner channel with a diameter of 4 nm that is clad by the coat proteins. The interior of the channel is thus shielded from the environment; uranyl and most other cations cannot penetrate through the coat, and they have to diffuse in from either end.[26] TMVs are physically and chemically unusually stable − they can be suspended in several polar solvents (e.g. acetone and ethanol) without substantial changes of their structural integrity − and they tend to organise linearly in a head-to-tail fashion; in this way, the channel can be elongated to multiples of 300 nm.[28] Nanostructures can be created on the outer surface or in the interior channel.[28] The first case is analogous to nanostructures on other biomolecules such as DNA, whereas the second case is confinement templating, which has been documented for relatively few cases, for example peptide tubuli,[21] carbon nanotubes[54] and mesoporous silica.[55]

The nature of the coat proteins and the charges (TMV is negatively charged above its pI of 3.5) imply hydrophilicity and hydrogen-bonding capability, hence surfaces such as mica and oxidised silicon wafers are suitable for immobilisation. Due to the adsorption, TMV suffers some compression normal to the substrate surface.[28,56] Note that the adsorption on TEM grids is facile, too, since the standard carbon-coated polymer substrates are at least partially hydrophilic, much different from hydrophobic surfaces such as pure graphite or several polymers. Starting from this point, Section 2.1 investigates how to impose directional order, similar to the CdS/dendrimer stripes presented in Section 1.2.2, to adsorbed or adsorbing virions. Section 2.2 focuses on synthesising clusters and wires on and in a single TMV, so that the clusters are aligned by the linear biotemplate. This is obviously impossible with syntheses in near-spherical templates such as the dendrimers of Section 1.1.

2.1. Organising Tobacco Mosaic Virions in a Parallel Fashion by Lateral Forces

When oriented, but not necessarily patterned, assemblies of biomolecules are required, the simple application of directional mechanical forces during adsorption can be helpful. This method is well known for DNA,[9,29] but less so for much shorter (sub-micrometre) supramolecular units such as TMV. While TMV can organise in liquid-crystalline form at high concentrations, separate single virions form a statistically oriented assembly during adsorption to a substrate. Here it is demonstrated that single TMVs can be

 © 2005 Wiley-VCH Verlag GmbH & Co. KGaA, Weinheim

aligned by applying shear forces during adsorption on a flat substrate surface.

The first approach relies on forces exerted by a directional gas stream (during drying of a droplet) or by a directional flow of solvent (during suction drying of a droplet) (Figure 8). An Mg^{2+}-treated mica surface was covered with a droplet of TMV suspension (0.1 mg/ml), and a stream of argon was directed at it to remove the supernatant. Figure 9 (a) shows the mica surface with aligned adsorbed single virions. Note that the alignment is not perfect (the relative angle between the viral axes is not zero); on the other hand, nearly all virions on a given substrate were found to be oriented. Many virions aggregate linearly, i.e. they organise into objects about 18 nm wide (due to tip convolution effects not detectable by AFM) and hundreds of nanometres long. The pressure of the gas stream has to exceed a certain value ($\approx$ 7 bar); alignment with lower argon pressure was never observed. In a related experiment, a droplet of TMV suspension was placed on a hydrophobic flat PDMS surface and exposed to the argon stream. The aligned virions on the PDMS surface were transferred to an oxidised silicon wafer surface by microcontact printing (Figure 8, b) and visualised by AFM. The results were nearly identical to those shown in Figure 9 (a).

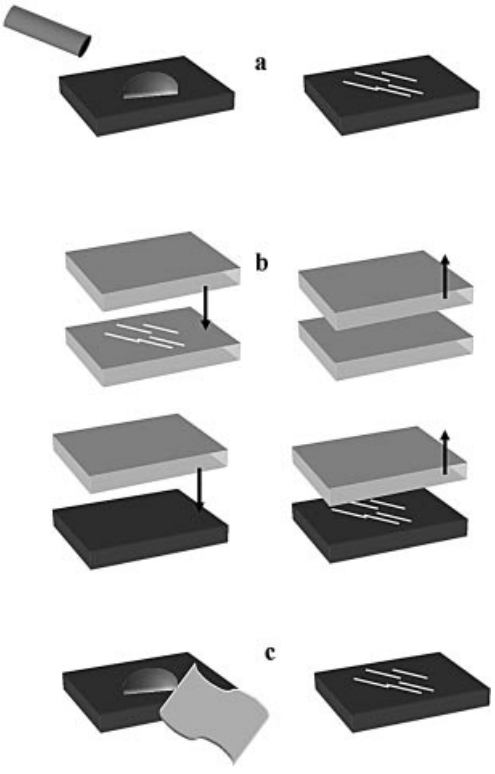

Figure 8. Orientation of nano-objects during their immobilisation by shear forces: (a) drying a droplet with a strong gas stream; (b) transfer of the oriented, adsorbed objects from PDMS to an oxidised wafer by microcontact printing with a flat PDMS stamp (top, arrows); (c) drying a droplet by suction with a filter paper.

An interpretation of this (top-down) process can be based on the initial attachment of only one end of the virion, since this is statistically much more likely than immediate contact of the complete virion. The virion is then free to rotate around the pivotal point for some time before it comes into contact with the substrate over its complete length. At this stage, lateral forces can act to orient the TMVs before they come into complete contact (Figure 8). The orientation is thereafter fixed, since the mobility of adsorbed TMV, especially on hydrophilic substrates, is very low. The alignment should, in both cases, be due to shear forces in the droplet, and it occurs during the diffusion to the surface. It is very unlikely that TMV, which adsorbs strongly on mica or silicon wafers, shows surface diffusion, which was never observed in any AFM experiment on mica or wafers or even graphite. A test verified that once a virion is adsorbed, it cannot reorient: placing a droplet of pure water on a surface coated with randomly adsorbed TMV, and thereafter subjecting it to an argon stream, did not produce aligned virions.

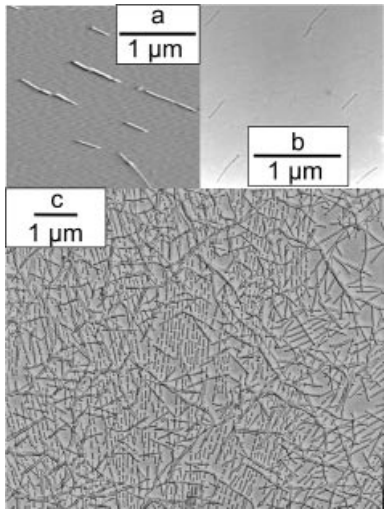

Figure 9. (a) AFM image (error signal) of TMV aligned by drying a droplet with an argon stream during adsorption on Mg^{2+}-treated mica. (b) Transmission electron micrograph (200 kV) of TMVs aligned by lateral forces (suction with filter paper) during adsorption on the carbon-coated polymer surface of a microscopy grid. No uranyl or other stain was applied. (c) as (b), but with higher TMV concentration and with silver shadowing to enhance the contrast (60 kV).

Coverage and orientation are not arbitrary, but in line with expectations: a droplet (max. 0.1 mL) with 0.1 mg mL^{-1} TMV provides sufficient material to deposit about eight monolayers of densely packed TMVs on the employed 1 cm^2 samples. However, coverages of only a tiny fraction of a monolayer were found. The typical diffusion time in the droplet to the surface is in the range of 1 h (for a droplet spread to 1 cm^2), while the droplet contact time was only 1 min, which should result in submonolayer coverage, as observed. In addition, in some cases (e.g. for graphite substrates or for the case of the hydrophobic stamp) a kinetic barrier due to colloid chemical effects can be present.[56] After the droplet contact time, the orienting force was applied; one can assume that the majority of the adsorbed virions are at this time contacting the surface with only one end. The gas stream exerts a force in the nanonew-

 © 2005 Wiley-VCH Verlag GmbH & Co. KGaA, Weinheim

ton range: 7 bar acting on a 300 nm long and 18 nm wide area. This macroscopic force estimate is in line with forces required for (microscopic) AFM manipulation of TMV.[57]

Another promising possibility to align TMVs on a surface is to make use of laterally applied capillary forces, as is also possible for DNA[9] and carbon nanotubes.[58] A TMV suspension (20 μL, 10 mg mL^{-1}) was placed on a transmission electron microscope grid for 1 min, after which the droplet was removed by touching a filter paper to one side of the grid. The shrinking droplet caused a directional flow from the grid to the paper. Again, virions aligned in the direction of the flow, as shown in Figure 9 (see parts b and c). The difference between the figures is based on the much higher concentration of the suspension used for Figure 9 (c). Again, the objects more than 300 nm long are linearly aggregated TMVs. This alignment method, however, is only applicable for surfaces that show relatively weak interaction forces with the virions, such as carbon-coated TEM grids.[56]

In summary, the alignment of TMVs on surfaces can be obtained in several very simple ways based on lateral forces that act on a droplet of TMV suspension, which is, in turn, in contact with a substrate surface.

2.2. Clusters in Virions: Electroless Deposition

Metal clusters can be produced "bottom-up" with electroless deposition on, and also inside, TMV. The advantage of deposition inside the TMV channel is the inherent alignment of the clusters parallel to the viral axis. Here, only the initial and intermediate stages of the process are investigated. The first step is a sensitisation of the suspended virions with sub-2 nm Pd or Pt clusters (sources are Pd and Pt salts in aqueous solution). The clusters are, in fact, so small that identification of single clusters by (conventional) TEM is not possible; rather, the virions appear grey due to the presence of the clusters.[28] After removal of surplus metal ions, the suspension was mixed with a bath that contains the metal ion to be deposited (e.g. Ni^{II}) and a reductant (e.g. hypophosphite or dimethylamine borane, DMAB). The electron transfer from the reductant to the ion is catalysed by the Pd (or Pt) clusters, hence the deposition is limited to the location of the clusters. The deposition is autocatalytic, hence metal is continuously deposited on growing metal clusters. A side reaction is the evolution of hydrogen. The reaction is stopped by adding inhibitors or by drying the suspension, for example for analysis on a TEM grid. An important question is how the growing clusters develop into wires, and this question is obviously linked to the initial phase of the electroless deposition process.

When the original virus suspension contains phosphate, the reaction is limited to the outer viral surface, and relatively large (>30 nm diameter; not shown) coalescing clusters are found. Small clusters (<5 nm diameter) can be obtained by adsorption of noble metal salts, followed by reduction or by "mild" electroless deposition with hypophosphite.[19,26] Whenever the central viral channel can be found (e.g. in a cluster-free region), it is empty, proving the high selectivity of the reaction. The presence of phosphate is thought to result in insoluble deposits of metal phosphates (Co or Ni); these deposits, together with the noble metal clusters, act as very effective nucleation centres for the deposition.

In the absence of phosphate, the selectivity for channel metallisation is high, resulting in the deposition of wires. The selectivity for the channel is not easily explained. Electrostatic and complex chemistry arguments may favour the channel-cladding functional groups;[19,26,28] however, the observation of relatively large (>5 nm) clusters detached from the virions could mean that clusters initially form on the viral coat, but are unable to attach as strongly as in the presence of insoluble metal phosphates (see above). The by-product hydrogen may additionally exert mechanical forces, resulting in this detachment. The production of 3–4-nm-wide wires solely by wet chemical means cannot be achieved by any other process; however, chemical vapour deposition inside carbon nanotubes[54] appears to be an alternative to using TMV, while complete arrays of similar wires can be formed in mesoporous silica.[55] Figure 10 refers to an experiment where TMV was sensitised with Pd and metallised with Ni (in a DMAB-containing bath, see Experimental Section), but the process was interrupted before the time required for wires longer than 200 nm.[28] The lower part of Figure 10 shows the same image with different contrast, and with the positions of the wires marked as black lines. A number of wires already have remarkable lengths (>100 nm). Note that once again the TMVs in Figure 10 are linearly aligned, but that each orifice of the channels is still accessible (white arrows) and thus allows for electrolyte supply inside the TMVs. Hence, all distinct regions (here four) between the orifices appear to be metallised independently from their neighbours, resulting here in four wires.

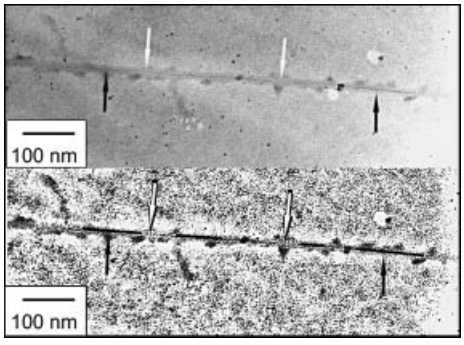

Figure 10. Transmission electron micrograph (200 kV) of Ni wires (<4 nm diameter) inside the TMV channel after electroless deposition in the absence of phosphate. Each gap between two virions is marked by white arrows and the wires by black arrows. The lower image is contrast-enhanced. The wires form upon nucleation and growth of Ni at sub-2 nm Pd clusters.

The mechanism is based on Pd or Pt nuclei that are rapidly covered by the metal (here Ni) that deposits from the electroless bath. Autocatalytic growth can result in depletion of reactive species and thus in size limitation.[59] However, the interior viral channel imposes a natural limit. Another limit is the solution concentration inside the channel: whenever two clusters have formed, a certain amount

 © 2005 Wiley-VCH Verlag GmbH & Co. KGaA, Weinheim

of metal ions is trapped between them. This amount has a maximum of 400 atoms (0.18 M Ni^{II}, 300 nm length, 4 nm diameter), yielding a spherical cluster of less than 3 nm diameter. Hence, more than two clusters inside a single virion can only grow when the first cluster forms deep inside the channel, and the later ones step by step closer to the viral orifice, in line with observations.[19,26] The same argument explains why more than two wires are never found inside a single virion. Wires form when the reductant is DMAB, which is thermodynamically and kinetically superior to hypophosphite (which is used for cluster synthesis). This implies that of the large number of Pd or Pt nuclei, only a very few are highly active. These few clusters start a rapid process of filling the viral channel with the deposit (Figure 11).

Figure 11. Mechanism of electroless cluster and wire deposition inside a channel: (a) tube-like template (e.g. TMV); (b) sensitisation: formation of very small noble metal clusters on the exterior surface and on the interior walls; (c) initial deposition: only a few very active clusters grow fast, the clusters on the exterior surface detach; (d) the clusters inside the channel can grow to, at maximum, two wires per channel when metal ions are supplied from the orifices of the channel.

Conclusions

A simple, wet chemical precipitation process can be used for the "bottom-up" synthesis of semiconductor nanoclusters when dendrimer templates are present. To this end, a synthesis method that produces CdS clusters at the outer surface of poly(amidoamine) dendrimers was modified to yield clusters inside the dendrimers. Control of the pH during synthesis allows for selective protonation of some of the amine groups in the dendrimer; relevant Cd^{2+} binding processes have been identified. The charge of the template is a decisive factor in a successful synthesis and should be considered also in other cluster syntheses. Elegant "top-down" organisation/patterning of the CdS/dendrimer composites on surfaces can be attained with microcontact printing. In addition to simple patterns, sub-micrometre wide stripes, made up from adsorbed composites, develop during printing inside micrometre-sized patterns. Thus, microcontact printing can result in a surprising way (synchronously) in not only "top-down" but also "bottom-up" structuring.

Metal wires 3–4 nm in diameter can be obtained by electroless deposition from solutions containing metal ions and reductants. They grow in the central channels of plant virions; the earlier stages of this process have been analysed, and a mechanism for the selective deposition in the channels presented. Clearly, the method is capable of producing other high aspect structures in narrow tubes. Removal of the coat proteins should be possible by oxidative or enzymatic treatment.[21] Organisation of the virions on flat substrates can be achieved during adsorption by application of external forces to a suspension droplet, resulting in parallel alignment. This method is well known from adsorption studies of other linear biomolecules, but works well even for the relatively short virion length of 300 nm.

Experimental Section

Poly(amidoamine) (PAMAM) dendrimer (generation 8) terminated with amine (Dendritech, Inc., Midland), here referred to as $G8NH_2$, was dissolved in 99.8% ethanol (Roth) with concentrations from 0.5 μM to 50 μM. $G8NH_2$ (200 μL) was diluted with methanol to 10 mL (5.5 μM $G8NH_2$), then 10 mL of 2 mM $Cd(CH_3COO)_2$ and 10 mL of 0.7 mM Na_2S in methanol were added to the dendrimer solution sequentially. After reaction, the nanocomposites were stored in a freezer at –35 °C to reduce the Ostwald ripening growth of nanoparticles, or they were aged at 25 °C for two and 22 days to induce ripening. The final concentration of $G8NH_2$ in the solution was 1.83 μM. The Cd^{2+}/S^{2-} ratio was kept at 3:1 since it was found that at this ratio CdS/$G8NH_2$ nanocomposites could be successfully printed. Before adsorption and printing, nanocomposites were dialysed (Slide-A-Lyzer 10000 MWCO caps, KMF, Lohmar) against methanol. Experiments with generation 4 dendrimers were conducted in a similar manner.

Absorption spectra from solutions were obtained with a Perkin–Elmer UV/Vis spectrometer Lambda 2. Photoluminescence and excitation spectra were taken with a Perkin–Elmer luminescence spectrometer LS 50B. The solutions were placed in quartz cuvettes for both instruments.

Silicon wafers [orientation (100), Crystal, Berlin] were terminated by silicon oxide with hydroxyl groups by the standard RCA procedure: 15 min immersion in a 65–75 °C hot 1:1:5 mixture of 25% NH_4OH (VLSI Selectipur, Merck), 31% H_2O_2 (VLSI Selectipur, Merck) and water (Millipore, 18 MΩcm) followed by 15 min immersion in a 65–75 °C hot 1:1:5 mixture of 37% HCl (Suprapur, Merck), 31% H_2O_2 and water. These samples are termed "oxidised silicon wafers".

Ellipsometric measurements were performed in air with an EL-X-02C ellipsometer (DRE, Ratzeburg) at 70° angle of incidence and 633 nm wavelength. The ellipticity of the HeNe laser beam was minimised with a λ/4 plate. Measurements were made at more than 4 points randomly picked across the sample and averaged. A two-layer transparent film model was used for the thickness calculations of dendrimer layers on oxidised silicon wafers. The refractive index of the dendrimers was fixed at 1.45.

Atomic force microscope (AFM) images of patterns were obtained in intermittent contact mode with a Thermomicroscopes Autoprobe M5, operated in non-contact and intermittent contact mode, with MikroMasch NSC11 tips or NCHR Pointprobe Nanosensors.

Poly(dimethylsiloxane) (PDMS) stamps (Sylgard 184, Dow Corning) were formed on flat polystyrene dishes or on patterned silicon wafer masters [IBM Zürich and Institute for Microelectronics Stuttgart (IMS); before first use the master was rendered hydrophobic with fluoroalkyltrichlorosilane vapour]. The stamps were activated by plasma oxidation in 1 mbar O_2 at 150 mW for 10 s (Technics Plasma 100-E). Hydrophilicity was ensured by contact angle measurements for various exposure times from 0 s to more than 10 s. Freshly activated flat stamps were covered with one drop (≈20 μL) of ink solution for 25 s, and then blown dry with argon. Freshly activated structured stamps were brought into conformal

 © 2005 Wiley-VCH Verlag GmbH & Co. KGaA, Weinheim

contact with the inked flat stamp for 25 s, then peeled off and brought into conformal contact with freshly cleaned silicon wafers for 25 s, and finally peeled off from the substrates.

For the TMV alignment, freshly cleaved mica was treated for 5–15 min with 0.1–1 M aqueous $MgCl_2$. The surface was contacted with a droplet of TMV suspension (0.1 mg mL^{-1}). After 1 min (known to be sufficient for strong adsorption) a strong stream of argon (7–8 bar, 5 mm orifice) was directed at about 65° to the surface normal to remove the supernatant. Alignment by laterally applied capillary forces was achieved as follows: A Formvar/carbon-coated copper grid (300 or 400 mesh, SPI-Supplies) was dipped into ethanol (Roth Rotipuran) and air-dried. TMV suspension (20 μL, 10 mg mL^{-1}) was placed on the grid. After 2–3 min the solution was removed by placing filter paper on one side of the grid. TEM images were obtained with a Philips CM200 at 200 kV and − in this case after silver shadowing − in a Zeiss EM 10 at 60 kV.

TMV was metallised in the following way: First, a TMV suspension (0.1–0.2 mg mL^{-1}) was mixed with an equal volume of a 0.9 mM solution of Na_2PdCl_4 or K_2PtCl_4 (both p.a., Aldrich) in 1 M NaCl (p.a., Fluka), adjusted to pH 5–6 with 0.1 M HCl. After an incubation time of 10 min, the suspension was centrifuged at 14000 rpm for 10 min and the supernatant carefully removed. The pellet was resuspended in water and centrifuged again for 10 min at 14000 rpm in order to remove remaining Pd or Pt. This washing procedure was applied 2–3 times. Ni was deposited from 0.18 M $Ni(CH_3COO)_2{\cdot}4H_2O$ (p.a., Fluka), 0.28 M lactic acid (85% in water, Fluka) and 34 mM DMAB (dimethylamine borane, p.a., Aldrich) in water. The pH was adjusted to 6–7 with 1 M NaOH solution. TEM images were obtained with a Philips CM200 at 200 kV.

[1] M. Möller, J. Spatz, *Curr. Opin. Colloid Interface Sci.* **1997**, *2*, 177–187.
[2] C. M. Niemeyer, *Angew. Chem. Int. Ed.* **2001**, *40*, 4128–4158.
[3] A. M. Bittner, *Naturwissenschaften* **2005**, *92*, 51–64.
[4] M. Pileni, *Cryst. Res. Technol.* **1998**, *33*, 1155–1186.
[5] H.-G. Boyen, K. Fauth, B. Stahl, P. Ziemann, G. Kästle, F. Weigl, F. Banhart, M. Hessler, G. Schütz, N. S. Gajbhiye, J. Ellrich, H. Hahn, M. Büttner, M. G. Garnier, P. Oelhafen, *Adv. Mater.* **2005**, *17*, 574–578.
[6] X. C. Wu, A. M. Bittner, K. Kern, *J. Phys. Chem. B* **2005**, *109*, 230–239.
[7] X. C. Wu, A. M. Bittner, K. Kern, *Adv. Mater.* **2004**, *16*, 413–417.
[8] M. Steigerwald, L. Brus, *Acc. Chem. Res.* **1990**, *23*, 183–188.
[9] H. Nakao, M. Gad, S. Sugiyama, K. Otobe, T. Ohtani, *J. Am. Chem. Soc.* **2003**, *125*, 7162–7163.
[10] Y. Sun, J. A. Rogers, *Nano Lett.* **2004**, *4*, 1953–1959.
[11] E. Strable, J. M. Bulte, B. Moskowitz, K. Vivekanandan, M. Allen, T. Douglas, *Chem. Mater.* **2001**, *13*, 2201–2209.
[12] M. Q. Zhao, R. M. Crooks, *Angew. Chem. Int. Ed.* **1999**, *38*, 364–366.
[13] J. Zheng, M. S. Stevenson, R. S. Hikida, P. V. Van Patten, *J. Phys. Chem. B* **2002**, *106*, 1252–1255.
[14] N. C. B. Tan, L. Balogh, S. F. Trevino, D. A. Tomalia, J. S. Lin, *Polymer* **1999**, *40*, 2537–2545.
[15] B. I. Lemon, R. M. Crooks, *J. Am. Chem. Soc.* **2000**, *122*, 12886–12887.
[16] J. J. J. M. Donners, R. Hoogenboom, A. P. H. J. Schenning, P. A. van Hal, R. J. M. Nolte, E. W. Meijer, N. A. J. Sommerdijk, *Langmuir* **2002**, *18*, 2571–2576.
[17] K. Sooklal, L. H. Hanus, H. J. Ploehn, C. J. Murphy, *Adv. Mater.* **1998**, *10*, 1083–1087.
[18] E. Braun, Y. Eichen, U. Sivan, G. Ben-Yoseph, *Nature* **1998**, *391*, 775–778.
[19] M. Knez, M. Sumser, A. M. Bittner, C. Wege, H. Jeske, T. P. Martin, K. Kern, *Adv. Funct. Mater.* **2004**, *14*, 116–124.
[20] C. E. Flynn, S.-W. Lee, B. R. Peelle, A. M. Belcher, *Acta Mater.* **2003**, *51*, 5867–5880.
[21] M. Reches, E. Gazit, *Science* **2003**, *300*, 625–627.
[22] S. Behrens, K. Rahn, W. Habicht, K.-J. Böhm, H. Rösner, E. Dinjus, E. Unger, *Adv. Mater.* **2002**, *14*, 1621–1625.
[23] M. Mertig, R. Kirsch, W. Pompe, *Appl. Phys. A* **1998**, *66*, S723–S727.
[24] T. Scheibel, R. Parthasarathy, G. Sawicki, X. M. Lin, H. Jaeger, S. L. Lindquist, *Proc. Natl. Acad. Sci. USA* **2003**, *100*, 4527–4532.
[25] J. Richter, M. Mertig, W. Pompe, I. Mönch, H. K. Schackert, *Appl. Phys. Lett.* **2001**, *78*, 536–538.
[26] E. Dujardin, C. Peet, G. Stubbs, J. N. Culver, S. Mann, *Nano Lett.* **2003**, *3*, 413–417.
[27] Q. Wang, T. Lin, L. Tang, J. E. Johnson, M. G. Finn, *Angew. Chem. Int. Ed.* **2002**, *41*, 477–480.
[28] M. Knez, A. M. Bittner, F. Boes, C. Wege, H. Jeske, E. Maiß, K. Kern, *Nano Lett.* **2003**, *3*, 1079–1082.
[29] Z. Deng, C. Mao, *Nano Lett.* **2003**, *3*, 1545–1548.
[30] H. Nakao, H. Shiigi, Y. Yamamoto, S. Tokonami, T. Nagaoka, S. Sugiyama, T. Ohtani, *Nano Lett.* **2003**, *3*, 1391–1394.
[31] R. C. van Duivenbode, M. Borkovec, G. J. M. Koper, *Polymer* **1998**, *39*, 2657–2664.
[32] L. Balogh, R. Valluzzi, K. S. Laverdure, S. P. Gido, G. L. Hagnauer, D. A. Tomalia, *J. Nanopart. Res.* **1999**, *1*, 353–368.
[33] F. Gröhn, B. J. Bauer, Y. A. Akpalu, C. L. Jackson, E. J. Amis, *Macromolecules* **2000**, *33*, 6042–6050.
[34] S. V. Gaponenko, *Optical Properties of Semiconductor Nanocrystals*, Cambridge University Press, **1998**, p. 53.
[35] L. Balogh, D. A. Tomalia, *J. Am. Chem. Soc.* **1998**, *120*, 7355–7356.
[36] M. Q. Zhao, R. M. Crooks, *J. Am. Chem. Soc.* **1998**, *120*, 4877–4878.
[37] G. J. M. Koper, M. H. P. van Genderen, C. Elissen-Roman, M. W. P. L. Baars, E. W. Meijer, M. Borkovec, *J. Am. Chem. Soc.* **1997**, *119*, 6512–6521.
[38] G. G. Guilbault, S. M. Billedeau, *J. Inorg. Nucl. Chem.* **1972**, *34*, 1167.
[39] M. F. Ottaviani, F. Montalti, N. J. Turro, D. A. Tomalia, *J. Phys. Chem. B* **1997**, *101*, 158–166.
[40] E. Delamarche, H. Schmid, A. Bietsch, N. B. Larsen, H. Rothuizen, B. Michel, H. Biebuyck, *J. Phys. Chem. B* **1998**, *102*, 3324–3334.
[41] K. Kuhnke, D. M. P. Hoffmann, X. C. Wu, A. M. Bittner, K. Kern, *Appl. Phys. Lett.* **2003**, *83*, 3830–3832.
[42] N. Lu, X. Chen, D. Molenda, A. Naber, H. Fuchs, D. V. Talapin, H. Weller, J. Müller, J. M. Lupton, J. Feldmann, A. L. Rogach, L. F. Chi, *Nano Lett.* **2004**, *4*, 885–888.
[43] A. M. Bittner, X. C. Wu, K. Kern, *Adv. Funct. Mater.* **2002**, *12*, 432–436.
[44] J. Li, L. T. Piehler, J. R. Baker, D. A. Tomalia, *Langmuir* **2000**, *16*, 5613–5616.
[45] V. V. Tsukruk, F. Rinderspacher, V. N. Bliznyuk, *Langmuir* **1997**, *13*, 2171–2176.
[46] X. C. Wu, A. M. Bittner, K. Kern, *Langmuir* **2002**, *18*, 4984–4988.
[47] Y. Xia, D. Qin, Y. Yin, *Curr. Opin. Colloid Interface Sci.* **2001**, *6*, 54–64.
[48] K. J. Stine, C. M. Knobler, *Phys. Rev. Lett.* **1990**, *65*, 1004–1007.
[49] D. K. Schwartz, J. Ruiz-Garcia, X. Qiu, J. V. Selinger, C. M. Knobler, *Physica A* **1994**, *204*, 606–615.
[50] H. Choi, X. Yang, G. W. Mitchell, C. P. Collier, F. Wudl, J. R. Heath, *J. Phys. Chem. B* **2002**, *106*, 1833–1839.
[51] M. Gleiche, L. F. Chi, H. Fuchs, *Nature* **2000**, *403*, 173–175.
[52] N. Bowden, W. T. S. Huck, K. E. Paul, G. Whitesides, *Appl. Phys. Lett.* **1999**, *75*, 2557–2559.
[53] M. Zaitlin, *AAB Descriptions of Plant Viruses* **2000**, *370*, 8.

 © 2005 Wiley-VCH Verlag GmbH & Co. KGaA, Weinheim

[54] B. K. Pradhan, T. Kyotani, A. Tomita, *Chem. Commun.* **1999**, 1317–1318.
[55] O. Kazakova, D. Erts, T. A. Crowley, J. S. Kulkarni, J. D. Holmes, *J. Magn. Magn. Mater.* **2005**, *286*, 171–176.
[56] M. Knez, M. P. Sumser, A. M. Bittner, C. Wege, H. Jeske, D. M. P. Hoffmann, K. Kuhnke, K. Kern, *Langmuir* **2004**, *20*, 441–447.
[57] M. R. Falvo, S. Washburn, R. Superfine, M. Finch, F. P. Brooks, Jr., V. Chi, R. M. Taylor II, *Biophys. J.* **1997**, *72*, 1396–1403.
[58] Y. Huang, X. Duan, Q. Wei, C. M. Lieber, *Science* **2001**, *291*, 630–633.
[59] H. Kind, A. M. Bittner, O. Cavalleri, K. Kern, T. Greber, *J. Phys. Chem. B* **1998**, *102*, 7582–7589.

Received: April 30, 2005
Published Online: August 17, 2005

 © 2005 Wiley-VCH Verlag GmbH & Co. KGaA, Weinheim

Patterning of Semiconductor Nanoparticles via Microcontact Printing

Xiao Chun Wu,[a] Li Feng Chi,*[a] and Harald Fuchs[a]

Keywords: Microcontact printing / Interaction / Interfaces / Nanocluster / Patterning / Semiconductors

Three general paths for patterning semiconductor nanoparticles stabilized with a short chain stabilizer via microcontact printing (μCP) are presented. The interface between the nanoparticles and surfaces has to be carefully designed to realize a successful direct or indirect printing.

(© Wiley-VCH Verlag GmbH & Co. KGaA, 69451 Weinheim, Germany, 2005)

Introduction

Parallel patterning of functional materials is very important for many photonic and electronic applications, for example multiple color LEDs, color pixels for field-emission displays, and multichannel chemical sensors. Therefore, the parallel schemes of positioning of these functional materials in predetermined areas are of great scientific and technological interest. Apart from the standard patterning techniques such as lithography, recently developed nontraditional patterning methods such as microcontact printing (μCP),[1] nanoimprinting lithography (NIL),[2] scanning probe lithography,[3] and dip-pen nanolithography[4] have attracted a great deal of attention in the field of surface patterning. Among them, μCP and NIL have the advantages of low-cost, simplicity, rapidity, and high throughput (parallel process). μCP is more versatile because many different materials can be used as inks to directly print on flat and curved surfaces.

Generally speaking, the patterning of functional materials can be realized in the following two ways. The first is where the distribution of the functional materials themselves on the surfaces is in a patterned way. Thus, the functionality is naturally patterned.[5–7] For example, Won et al. bound dendrimers on a surface, then let gold ions adsorb to the dendrimers. By UV irradiation with a photomask, patterned Au nanoparticle structures were obtained.[7] The other method is where functional materials are homogeneously distributed on surfaces while another material on top or beneath the functional material is patterned. In this way, through the inhibition or activation of the functionality of functional materials by printed materials, the functionality is realized in a patterned way.[8] For example, Wang et al. first assembled semiconductor nanoparticles on surfaces using a layer-by-layer strategy. Then copper grids were placed on top of the nanoparticle films as an optical mask. Because of the strong enhancement of photoluminescence (PL) from the nanoparticles by irradiation, a strong contrast in PL was observed after removal of the grids.[8]

By means of μCP, there are three possible paths to the patterning of the functional materials: (1) They can be selectively adsorbed to a printed heterogeneous surface, as shown in part a of Scheme 1. (2) They can be bound to a structured stamp and be directly printed on a homogeneous surface, as shown in part b of Scheme 1. (3) They can be brought to a homogeneous layer (e.g. spin coating) on a surface and be patterned by an inactive structure, as shown in Scheme 1 (see part c, the inactive structure can also be beneath the active layers). Although the direct printing of functional materials is desirable, it is not easy to achieve since a compatible stamp-molecule-surface system is needed. Successful printing requires detailed studies of various printing conditions such as ink concentration and time, printing time, and the surface properties of both the stamp and substrate. Therefore, compared to the printing of well-known systems for example self-assembled monolayers (SAMs), the direct printing of functional materials is more complicated.[9–12] Therefore, up to now, the realization of the patterning of functional materials via μCP has been mainly based on the direct printing of SAM layers, rather than the functional materials themselves.[13–17] The advantages of printing SAM layers are that they are relatively simple and the interaction mechanisms among ink, substrate, and stamp are well-studied in these systems,[18–20] but one more step for selective adsorption is needed. Should the first two methods prove difficult to realize, the third method may prove a good choice. For example, Koide et al. first printed alkyltrichlorosilane on an ITO glass substrate, then an organic light-emitting diode was deposited on the patterned substrate by a standard deposition technique.[14] Since the stamped SAM can impede the hole injection into

[a] Physikalisches Institut, Westfälische Wilhelms-Universität Münster and Center for Nanotechnology (CeNTech), 48149 Münster, Germany
E-mail: chi@uni-muenster.de

Supporting information for this article is available on the WWW under http://www.eurjic.org or from the author.

the hole transport layers, this renders the stamped area essentially nonemissive. Although the whole substrate was covered with LED materials, only unpatterned regions show effective emission. In this way, patterned LEDs were obtained.

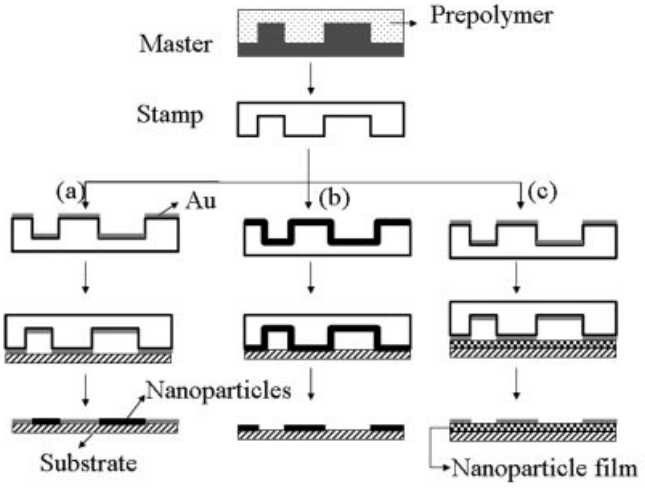

Scheme 1. Patterning of nanoparticles via (a) printing of block layer and adsorption of nanoparticles, (b) direct printing of nanoparticles, and (c) printing of block layer on the top of the nanoparticle layer.

Semiconductor nanoparticles show unique size-dependent optical properties and are of great interest for applications in optoelectronics, photovoltaics, and biological sensing.[21–25] Various chemical synthetic methods have been developed to prepare such nanoparticles. With the progress in the synthesis of nanoparticles using wet chemical syntheses, the synthesis of nanoparticles capped with so-called "stabilizers", which cap the surface of the nanoparticles during their growth, has been greatly improved and produced high-quality nanoparticles. Two different approaches have been developed to synthesize high-quality semiconductor nanoparticles. One is an organometallic synthesis based on the high-temperature thermolysis of precursors, first reported by Murray et al. in 1993,[26] and further improved later.[27–29] An alternative synthesis employs polyphosphates[30] or thiols[31,32] in aqueous media. With the success in obtaining high-quality nanoparticles, assembling them into devices becomes possible. Here we will explore the possibilities provided by the above-mentioned three paths to pattern high-quality CdTe nanoparticles stabilized with a short chain stabilizer (thioglycolic acid, TGA).

Results and Discussion

Selective Adsorption of Nanoparticles on a Patterned Surface

As mentioned in the introduction and shown in Scheme 1a, when nanoparticles show highly selective adsorption or binding onto certain surfaces, the patterning of them can be achieved through producing such surfaces in a patterned way. Recently, Loo et al. reported the direct printing of Au on a –SH terminated surface.[33] Here, we used this procedure to print a Au pattern and used this pattern as marks. Unprinted regions were further modified with different chemical groups in order to study the adsorption behaviors of a CdTe/TGA aqueous solution via hydrogen bonding, ligand exchange, or weak electrostatic forces. Part a of Figure 1 shows a topographic image of a printed Au line on a (3-mercaptoproply)trimethoxysilane (MPTMS) modified Si surface after the removal of MPTMS (O_2 plasma oxidation). A zoom-in image (not shown here) indicated that the unprinted region terminated with –OH groups was quite clean. After 3 h adsorption of a 1 mM CdTe/TGA aqueous solution, images were taken as shown in Figure 1 (b). CdTe nanoparticles showed random and inhomogeneous adsorption both on the hydrophilic –SiOH/Si surface and on the rough Au surface. The density of the nanoparticles was, however, very low. In the case of further modification with MPTMS, the thickness of the Au region increased to over 10 nm, indicating the formation of multilayers of MPTMS on the Au region. After adsorption of nanoparticles for 3 h, in the –SH region, we did not observe obvious adsorption (Supporting Information), indicating that no apparent ligand exchange was taking place between TGA and MPTMS. For (3-aminopropyl)dimethylethoxysilane (APDES) SAMs, the adsorption of nanoparticles on the $–NH_2$ region increased a lot compared to the case of the –SH terminated surface and showed less agglomeration than the –SiOH terminated surface, indicating greater electrostatic forces. However, the density of nanoparticles was still too low. Therefore, Scheme 1 (a) is not an effective path for patterning CdTe/TGA nanoparticles via simple hydrogen bonds, ligand exchange, and weak electrostatic forces.

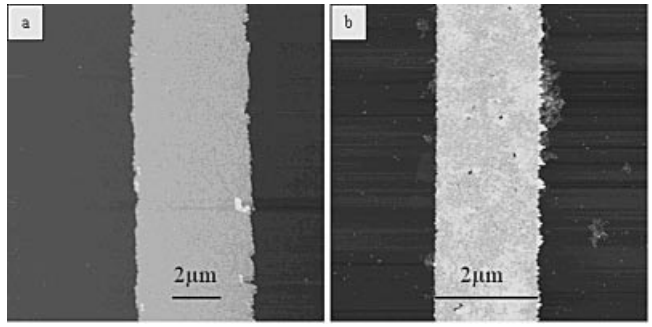

Figure 1. AFM images of Au patterns with –OH groups on unprinted regions before (a) and after (b) adsorption of a CdTe/TGA aqueous solution for 3 h.

Since the surface of the CdTe nanoparticle is capped with a layer of $SHCH_2COOH$ (TGA), the CdTe/TGA can in principle form multiple hydrogen bonds with the SiOH terminated surface. But the low-density inhomogeneous adsorption indicated that the hydrogen bonds between the TGA layer and the surface were weak and ineffective. This provides a hint that the TGA layer cannot be compared to some macromolecules for example poly(amidoamine) dendrimers. Dendrimer-stabilized nanoparticles show effective

 © 2005 Wiley-VCH Verlag GmbH & Co. KGaA, Weinheim

adsorption on surfaces by multiple hydrogen bonds.[34] Here, the roughness of the surface might play a more important role as we could see that more particle aggregates adsorbed on the edges of the Au pattern and on the rough Au pattern. The formation of larger aggregates suggested that the interaction between the nanoparticles was stronger than that between the nanoparticles and the surface. The random adsorption of nanoparticles was also shown by the XPS measurements as signals of Cd, Te, and S from the nanoparticles were obtained (Supporting Information). For the –SH terminated surface, we did not see the obvious ligand exchange between TGA and MPTMS. The main reason for this was that TGA is not a viable ligand. For dodecylamine-stabilized CdSe/CdS core/shell nanoparticles, they showed strong adsorption on an $–NH_2$ or a –SH terminated surface because of strong ligand exchange.[35] This was also verified here by using tri-*n*-octylphosphane (TOPO) stabilized CdSe/CdS nanoparticles as shown in Figure 2. Figure 2 (a) shows an AFM image of printed Au on a –SH terminated surface. Figure 2 (b) presents the AFM image of this surface after adsorption of CdSe/CdS/TOPO in phenyloctane for 3 h. We could see a lot of nanoparticles dispersed on the –SH terminated regions because of strong exchange between TOPO and MPTMS. For the APDES modified surface, the positive charges are determined by the protonation of primary amino groups. The pK_a of the amino groups in solution is 10.6, it is lower in monolayers on solid substrates.[36] The surface pK_a of this layer is 3.9 by force titration and 4.3 by conventional contact angle wetting titration.[37] For a CdTe/TGA aqueous solution, the negative charges are determined by the deprotonation of carboxylate acid groups on the surface of the nanoparticles. The surface pK_a of –COOH terminated surfaces is 5.2 by electrochemical titration and 5.6 by contact angle titration.[38] In our case, the pH of the CdTe/TGA aqueous solution is ca. 7. Therefore the $–NH_2$ groups from the surface are basically uncharged and the –COOH groups from TGA are partially charged. This explains the low density of adsorption.

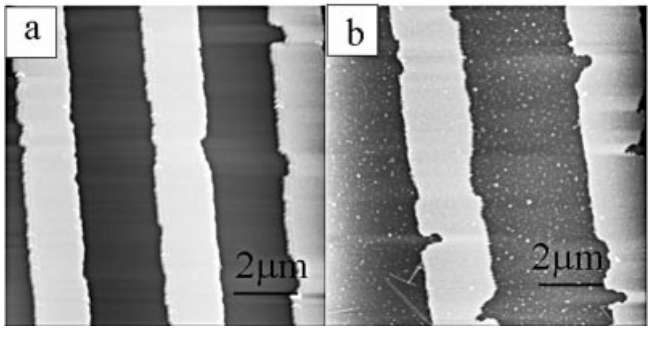

Figure 2. AFM images of Au patterns with –SH groups on unprinted regions before (a) and after (b) adsorption of a CdSe/TOPO solution for 3 h.

Direct Printing of Nanoparticles

We then followed Scheme 1 (b) to explore the possibility of directly printing nanoparticles. Although nanoparticles show no obvious adsorption on a hydrophilic OH terminated Si substrate, enough nanoparticles were left on the stamp by first adding 25 μL of nanoparticle dispersion to a hydrophilic stamp and then blowing it dry with N_2. Figures 3a, b, d, and e show topographic AFM images of printed nanoparticles at two different concentrations. At 1-mM concentration, nanoparticles can be printed homogeneously on the surface. The average height of nanoparticles is ca. 4.6 nm (Figure 3, c), similar to their diameter in solution. For the 2-mM concentration, the density of the nanoparticles on the printed regions was increased as expected. The average height of the nanoparticles is ca. 3.8 nm (Figure 3, e). This suggested that the nanoparticles mainly existed in the single form. Some larger aggregates of nanoparticles also formed at the 2-mM ink concentration as seen in Figure 3 (parts d and e), especially around the pattern edges. This has also been observed in the printing of other materials at higher ink concentrations.[39]

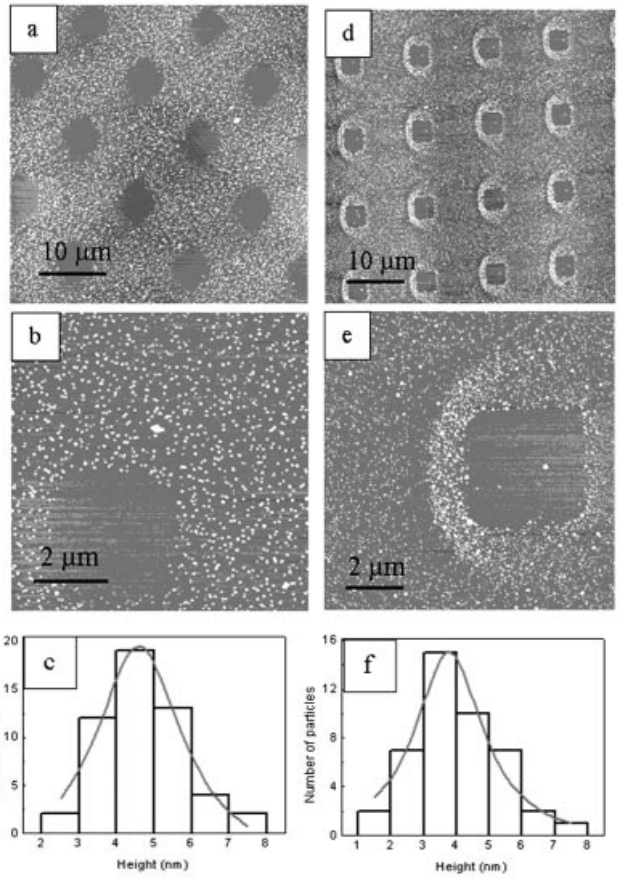

Figure 3. AFM images of printed CdTe/TGA nanoparticles on Si(100) surfaces with ink concentrations of 1 mM for (a) and (b) and of 2 mM for (d) and (e). Size distribution plots for (c) 1 mM and (f) 2 mM ink concentrations.

Printing Metal Structures on a Homogeneous Nanoparticle/Polymer Layer

For many practical applications, the stability of nanoparticles and the easiness of processing play very important

 © 2005 Wiley-VCH Verlag GmbH & Co. KGaA, Weinheim

roles. It is therefore better to disperse the nanoparticles in a matrix, for example a polymer. Recently, Yang's group has succeeded in dispersing high-quality CdTe nanoparticles into polystyrene (PS) and polymethylmethacrylate (PMMA) blocks. The CdTe/PS block can be dissolved in chloroform and then easily spin-coated onto a Si (100) surface.[40] Wang et al. reported that metals deposited on stamps could be transferred to some polymer surfaces by printing above the glass transition temperatures of the polymers under certain pressures.[41] Here we found that metal transference could also be initiated at room temperature under pressure with a slightly longer printing time. Forty-nm Au was thermally evaporated on structured stamps. Through a conformal contact between the Au-coated stamp and the CdTe/PS/Si (100) substrate (1 h in contact with pressure), Au patterns were transferred to the substrate as shown in Figure 4 (a). The fluorescence of CdTe nanopaticles remained as evidenced by the optical bleaching of the fluorescence (Figure 4, b). The bright lines were derived from the gold scattering. The dark lines were from CdTe/PS films. Because of strong scattering from the gold, the photoluminescence from the nanoparticles was shadowed. Therefore, we used PL bleaching to verify the existence of the PL from the nanoparticles. The sample was first placed under a blue light for 10 min and then moved partially out of the irradiation region. A luminescence image was taken immediately after the movement. We could see that the part without the 10 min irradiation showed a strong PL in comparison with that with the 10 min irradiation. The gold part showed no bleaching. A pure CdTe/PS film on a Si substrate underwent a similar bleaching behavior as shown in Figure 4 (c).

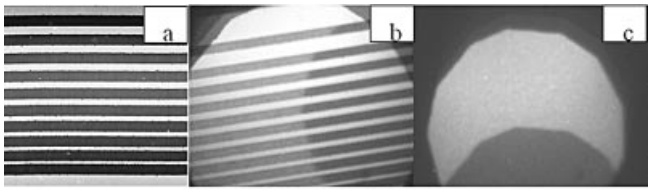

Figure 4. AFM (a) and luminescence (b) images of spin-coated CdTe/PS layer with printed Au patterns on top, and luminescence image (c) of spin-coated CdTe/PS layer.

In conclusion, we have presented several general strategies for the patterning of functional high-quality CdTe/TGA nanoparticles via μCP. Since the synthesis of CdTe/TGA nanoparticles is well-developed, a similar protocol can be adopted for the syntheses of other II-VI nanoparticles[31] or for the post-treatment of nanoparticle surfaces.[42] The patterning methods we have presented here therefore represent a general and easy process for the patterning of functional high-quality CdTe/TGA nanoparticles and also at the same time provide useful guides for patterning similar systems.

Experimental Section

A silicon substrate [WaferNet Co., Type N, 0.5 mm thick, orientation (100), resistivity 2–5 Ω cm] and SiO_2/Si substrate with 300-nm thick thermal SiO_2 were cut and ultrasonicated successively in acetone (p.a.), chloroform (p.a.), 2-propanol (p.a.), and water for 10 min. They were then cleaned with the standard RCA procedure: 15 min immersion into a 70 °C hot 1:1:5 mixture of NH_4OH (25%, Fluka, p.a.), H_2O_2 (31%, Fluka, p.a.) and water (Millipore, 18.2 MΩ cm); followed by a 15 min immersion into a 70 °C hot 1:1:5 mixture of HCl (37%, Aldrich, A.C.S. reagent), H_2O_2 (31%, Fluka, p.a) and water (Millipore, 18.2 MΩ cm). They were finally rinsed with water, and then dried under a stream of nitrogen. MPTMS (3-mercaptopropyltrimethoxysilane, 95%, Aldrich) and APDES [3-aminopropyl(dimethylethoxysilan), 97%, ABCR, Karlsruhe] SAMs were formed on SiO_2 surfaces by vapor deposition in a vacuum chamber for 15 h at room temperature. PDMS stamps (sylgard 184, Dow Corning) were formed on a patterned Si wafer master (IMS Stuttgart, before first use master was rendered hydrophobic with (fluoroalkyl)trichlorosilane vapor).

Printing of Au Structures: Au layers on hydrophobic stamps were deposited by thermal evaporation. A conformal contact between the Au-coated stamp and the MPTMS-modified (or PS-coated) Si substrate was initiated and kept for 1 min for the MPTMS-modified substrate and 1 h under pressure for the PS-coated substrate,[40] then the stamp was peeled off from the substrate. Because of the stronger interaction between Au and the substrate, Au patterns were transferred to the substrate. After 1 min 150-W O_2 plasma treatment, the SH region was oxidized and became an OH region (Templa System 100-E plasma system). This region can be used for further modification via silanization with different chemical groups.

Printing of Nanoparticles: A freshly activated stamp (1 mbar O_2 plasma, 300 W for 20 s) was covered with one drop (25 μL) of CdTe/TGA ink solution for 1 min, and then blown dry with N_2. It was put in a conformal contact with a clean Si (100) substrate for 25 s and then peeled off from the substrate.

Thioglycolic acid-capped CdTe (CdTe/TGA) nanocrystals (ca. 4 nm in size with a band edge photoluminescence maximum at 590 nm, 6% room-temperature quantum efficiency) in aqueous solution were obtained from the Photonics and Optoelectronics Group, Physics Department and CeNS, Ludwig-Maximilians Universität (Munich, Germany). CdTe nanoparticles distributed in a polystyrene (PS) block were obtained from the Key Lab of Supramolecular Structure and Materials, College of Chemistry, Jilin University, Changchun, P. R. China.

AFM measurements were performed with a commercial instrument (Digital Instruments, Nanoscope IIIa, Dimension 3000, Santa Barbara, CA) operated in tapping mode, silicon cantilevers (Nanosensors) of spring constant 250–350 kHz were used. XPS measurements were carried out with a VG ESCALAB 250 imaging XPS spectrometer. The samples were irradiated with monochromatic Al-K_α X-rays (15 kV, 150 W, 500 μm spot size).

Supporting Information Available: AFM images of the Au patterned surface with –SH and $–NH_2$ groups on un-patterned regions before and after adsorption of CdTe/TGA, as well as the XPS spectrum of the Au surface terminated with –OH groups after adsorption of CdTe/TGA.

Acknowledgments

This work was supported by DFG (CH-141). CdTe/TGA nanocrystals were kindly provided by Dr. A. L. Rogach from the Photonics and Optoelectronics Group, Physics Department and CeNS, Ludwig-Maximilians Universität (Munich, Germany) and the CdTe

 © 2005 Wiley-VCH Verlag GmbH & Co. KGaA, Weinheim

nanoparticles distributed in a polystyrene (PS) block were kindly provided by Prof. B. Yang from the Key Lab of Supramolecular Structure and Materials, College of Chemistry, Jilin University, Changchun, P. R. China.

[1] Y. N. Xia, G. M. Whitesides, *Angew. Chem. Int. Ed.* **1998**, *37*, 551–575.
[2] S. Y. Chou, P. R. Krauss, P. J. Renstrom, *Science* **1996**, *272*, 85–87.
[3] R. M. Nyffenegger, R. M. Penner, *Chem. Rev.* **1997**, *97*, 1195–1230.
[4] R. D. Piner, J. Zhu, F. Xu, S. H. Hong, C. A. Mirkin, *Science* **1999**, *283*, 661–663.
[5] V. Erokhin, V. Troitsky, S. Erokhina, G. Mascetti, C. Nicolini, *Langmuir* **2002**, *18*, 3185–3190.
[6] F. Hua, T. H. Cui, Y. Lvov, *Langmuir* **2002**, *18*, 6712–6715.
[7] J. Won, K. J. Ihn, Y. S. Kang, *Langmuir* **2002**, *18*, 8246–8249.
[8] Y. Wang, Z. Y. Tang, M. A. Correa-Duarte, L. M. Liz-Marzan, N. A. Kotov, *J. Am. Chem. Soc.* **2003**, *125*, 2830–2831.
[9] A. Bernard, J. P. Renault, B. Michel, H. R. Bosshard, E. Delamarche, *Adv. Mater.* **2000**, *12*, 1067–1070.
[10] J. Hyun, Y. J. Zhu, A. Liebmann-Vinson, T. P. Beebe, A. Chilkoti, *Langmuir* **2001**, *17*, 6358–6367.
[11] H. Kind, J. M. Bonard, C. Emmenegger, L. O. Nilsson, K. Hernadi, E. Maillard-Schaller, L. Schlapbach, L. Forro, K. Kern, *Adv. Mater.* **1999**, *11*, 1285–1289.
[12] H. Kind, M. Geissler, H. Schmid, B. Michel, K. Kern, E. Delamarche, *Langmuir* **2000**, *16*, 6367–6373.
[13] E. Delamarche, H. Schmid, A. Bietsch, N. B. Larsen, H. Rothuizen, B. Michel, H. Biebuyck, *J. Phys. Chem. B* **1998**, *102*, 3324–3334.
[14] K. Ha, Y. J. Lee, D. Y. Jung, J. H. Lee, K. B. Yoon, *Adv. Mater.* **2000**, *12*, 1614–1617.
[15] Y. Harada, X. L. Li, P. W. Bohn, R. G. Nuzzo, *J. Am. Chem. Soc.* **2001**, *123*, 8709–8717.
[16] Y. Koide, Q. W. Wang, J. Cui, D. D. Benson, T. J. Marks, *J. Am. Chem. Soc.* **2000**, *122*, 11266–11267.
[17] Y. N. Xia, G. M. Whitesides, *J. Am. Chem. Soc.* **1995**, *117*, 3274–3275.
[18] T. Franzl, D. S. Koktysh, T. A. Klar, A. L. Rogach, J. Feldmann, N. Gaponik, *Appl. Phys. Lett.* **2004**, *84*, 2904–2906.
[19] Y. L. Loo, R. L. Willett, K. W. Baldwin, J. A. Rogers, *J. Am. Chem. Soc.* **2002**, *124*, 7654–7655.
[20] Y. N. Xia, M. Mrksich, E. Kim, G. M. Whitesides, *J. Am. Chem. Soc.* **1995**, *117*, 9576–9577.
[21] A. P. Alivisatos, *Science* **1996**, *271*, 933–937.
[22] M. G. Bawendi, M. L. Steigerwald, L. E. Brus, *Annu. Rev. Phys. Chem.* **1990**, *41*, 477–496.
[23] N. Chestnoy, T. D. Harris, R. Hull, L. E. Brus, *J. Phys. Chem.* **1986**, *90*, 3393–3399.
[24] A. Henglein, *Top. Curr. Chem.* **1988**, *143*, 113–180.
[25] M. L. Steigerwald, L. E. Brus, *Acc. Chem. Res.* **1990**, *23*, 183–188.
[26] C. B. Murray, D. J. Norris, M. G. Bawendi, *J. Am. Chem. Soc.* **1993**, *115*, 8706–8715.
[27] X. G. Peng, M. C. Schlamp, A. V. Kadavanich, A. P. Alivisatos, *J. Am. Chem. Soc.* **1997**, *119*, 7019–7029.
[28] Z. A. Peng, X. G. Peng, *J. Am. Chem. Soc.* **2001**, *123*, 183–184.
[29] Z. A. Peng, X. G. Peng, *J. Am. Chem. Soc.* **2002**, *124*, 3343–3353.
[30] L. Spanhel, M. Haase, H. Weller, A. Henglein, *J. Am. Chem. Soc.* **1987**, *109*, 5649–5655.
[31] N. Gaponik, D. V. Talapin, A. L. Rogach, K. Hoppe, E. V. Shevchenko, A. Kornowski, A. Eychmuller, H. Weller, *J. Phys. Chem. B* **2002**, *106*, 7177–7185.
[32] A. Rogach, A. Susha, F. Caruso, G. Sukhorukov, A. Kornowski, S. Kershaw, H. Mohwald, A. Eychmuller, H. Weller, *Adv. Mater.* **2000**, *12*, 333–337.
[33] Y. L. Loo, R. L. Willett, K. W. Baldwin, J. A. Rogers, *Appl. Phys. Lett.* **2002**, *81*, 562–564.
[34] X. C. Wu, A. M. Bittner, K. Kern, *Adv. Mater.* **2004**, *16*, 413–417.
[35] T. Vossmeyer, S. Jia, E. Delonno, M. R. Diehl, S. H. Kim, X. Peng, A. P. Alivisatos, J. R. Heath, *J. Appl. Phys.* **1998**, *84*, 3664–3670.
[36] Z. Y. Tang, Y. Wang, N. A. Kotov, *Langmuir* **2002**, *18*, 7035–7040.
[37] D. V. Vezenov, A. Noy, L. F. Rozsnyai, C. M. Lieber, *J. Am. Chem. Soc.* **1997**, *119*, 2006–2015.
[38] J. W. Zhao, L. Q. Luo, X. R. Yang, E. K. Wang, S. J. Dong, *Electroanalysis* **1999**, *11*, 1108–1111.
[39] T. Pompe, A. Fery, S. Herminghaus, A. Kriele, H. Lorenz, J. P. Kotthaus, *Langmuir* **1999**, *15*, 2398–2401.
[40] H. Zhang, Z. C. Cui, Y. Wang, K. Zhang, X. L. Ji, C. L. Lu, B. Yang, M. Y. Gao, *Adv. Mater.* **2003**, *15*, 777–780.
[41] Z. Wang, J. F. Yuan, J. Zhang, R. B. Xing, D. H. Yan, Y. C. Han, *Adv. Mater.* **2003**, *15*, 1009–1012.
[42] Y. Babayan, J. E. Barton, E. C. Greyson, T. W. Odom, *Adv. Mater.* **2004**, *16*, 1341–1345.

Received: June 10, 2005
Published Online: August 29, 2005

 © 2005 Wiley-VCH Verlag GmbH & Co. KGaA, Weinheim

Structures, Photoluminescence and Theoretical Studies of Two Zn^{II} Complexes with Substituted 2-(2-Hydroxyphenyl)benzimidazoles

Yi-Ping Tong,[a,b] Shao-Liang Zheng,*[a] and Xiao-Ming Chen*[a]

Keywords: Density functional calculations / N,O ligands / Photoluminescence / Pi interactions / Zinc

Two new Zn^{II} complexes of 2-(2-hydroxyphenyl)benzimidazole (Hpbm), and 5-amino-2-(1*H*-benzoimidazol-2-yl)phenol (Hapbm), namely $[Zn(pbm)_2]$ (**1**), and $[Zn(apbm)_2]\cdot C_2H_5OH\cdot H_2O$ (**2**), as well as the ligands themselves, have been prepared and characterized by X-ray crystallography and photoluminescence studies. Both **1** and **2** are neutral, mononuclear molecules that display strong photoluminescence in the blue regionand thus may serve as candidates for blue-light-emitting electroluminescent materials. The electronic transitions in the photoluminescent processes have also been investigated by means of time-dependent density functional theory (TDDFT) energy level and molecular orbitals analyses, which show that their absorption and luminescent properties are ligand-based.
(© Wiley-VCH Verlag GmbH & Co. KGaA, 69451 Weinheim, Germany, 2005)

Introduction

Since the first report of a double-layer green organic electroluminescence (EL) device based on Alq_3 (Hq = quinolin-8-ol) in 1987,[1] metal chelate complexes of Al^{III}, B^{III}, and Zn^{II} have been extensively investigated for their electroluminescent properties.[2,3] Unfortunately, few systematic investigations of the luminescence properties of these complexes have been carried out as extensive structural information is only now becoming available[4,5] and computational techniques have only recently allowed reliable calculations of larger molecules.[5,6] For example, $[Zn(pbt)_2]_2$ [Hpbt = 2-(2′-hydroxyphenyl)benzothiazole] has been studied as an excellent white EL material,[7] even though its molecular structure and electronic characteristics based on the density functional theory (DFT) calculations have only recently been reported.[5]

Although blue-light-luminescent coordination complexes have been an active research field for two decades,[2,8–10] stable and strong blue-emitting metal complexes are still rare, unlike the other basic components of white emission (red and green). It has been shown that some d^{10} metal complexes with N,O-donor ligands may have the high glass transition temperatures required for stable light-emitting diodes and demonstrate nice blue-emitting EL properties.[2,3,5] Among them, Zn^{II} complexes have been proved to be important candidates for EL emitters for their excellent emitting properties[7] and low cost, in comparison with other d^{10} metal (e.g. Au^{I}) complexes.[10] We recently reported a class of blue/green light luminescent d^{10} metal complexes containing the new N,O-donor ligand Hophen (Hophen = 1*H*-[1,10]phenanthrolin-2-one) and the relation between molecular structure and luminescence properties with the help of X-ray single-crystal diffraction analyses and a DFT study of the ground electronic states.[11]

In our continuing efforts to design and synthesize blue-emitting materials, we now extend our focus to benzimidazole derivatives,[12] and report herein the syntheses, crystal structures, and luminescence properties of two neutral, monomeric Zn^{II} complexes, namely $[Zn(pbm)_2]$ (**1**) and $[Zn(apbm)_2]$ (**2**) [Hpbm = 2-(2-hydroxyphenyl)benzimidazole; Hapbm = 5-amino-2-(1*H*-benzoimidazol-2-yl)phenol] (Scheme 1). The electronic transitions in the photoluminescent process have also been studied by means of time-dependent density functional theory (TDDFT) calculations.

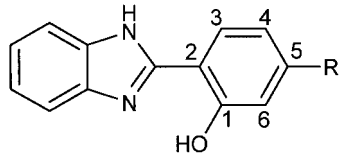

Scheme 1. The structures of Hpbm (R = H) and Hapbm (R = NH_2) with atomic labels.

Results and Discussion

Synthesis and Characterization

For practical applications, neutral coordination compounds are usually required since they may possess impor-

[a] State Key Laboratory of Optoelectronic Materials and Technologies, School of Chemistry and Chemical Engineering, Sun Yat-Sen University,
Guangzhou 510275, China
Fax: +86-20-8411-2245
E-mail: cescxm@zsu.edu.cn
[b] Department of Chemistry, Hanshan Normal College, Chaozhou 521041, China
Supporting information for this article is available on the WWW under http://www.eurjic.org or from the author.

 © 2005 Wiley-VCH Verlag GmbH & Co. KGaA, Weinheim DOI: 10.1002/ejic.200500174

tant characteristics for the performance of their EL properties, such as a relatively high glass transition temperature and thermal stability, easy sublimation, and an ability to form thin films under vacuum.[2,3] Therefore, neutral, mononuclear metal complexes should be expected to be excellent candidates for EL materials. Similar to the other complexes that can easily form thin films under vacuum,[3] both **1** and **2** can be prepared by mixing solutions of zinc acetate and the corresponding ligand in a 1:2 ratio in ethanol. Unfortunately, single crystals for X-ray diffraction were hard to grow, thus different methods, including conventional evaporation, diffusion, and hydrothermal methods were employed. In contrast, many solid EL metal complex materials have, in fact, only been identified by their chemical compositions rather than their structures. Some of their molecular structures may be much more complicated than their empirical formulae, since they may actually be characterized to be dimeric or multinuclear structures in the solid, such as the cases of $[Znq_2]_4$,[13] $[Zn(pbt)_2]_2$,[5] and $[Zn(oz)_2]_2$ [Hoz = 2-(2′-hydroxyphenyl)-2-oxazoline].[9] This fact shows that in the absence of X-ray structures, some conclusions about their luminescence properties may be controversial.[3] Fortunately, both **1** and **2** were found to be neutral, mononuclear molecules by X-ray crystallography, thus systematic investigations of their luminescence properties can be carried out. Our trials also imply that the crystallization conditions are important.

Thermogravimetric analyses (TGA and DTG) of **1** and **2** show their high thermal stability, with decomposition temperatures of 396 and 472 °C, respectively (Figure S1 in the Supporting Information), which are similar to other EL metal-organic materials.[5,12] Preliminary trials also proved that both readily form films under vacuum.

Crystal Structures

Single-crystal X-ray diffraction analyses revealed that both **1** and **2** are neutral, mononuclear molecules with the Zn^{II} ion being tetrahedrally coordinated by two deprotonated pbm or apbm ligands (Figure 1). The dihedral angles between two ligand planes of about 89° and 88°, respectively, indicate a slight distortion from an ideal tetrahedral geometry for **1** and **2**. The N–Zn–N and O–Zn–O angles [122.7(2)° and 110.1(1)° for **1**; 116.2(1)° and 114.0(1)° for **2**] are typical for a tetrahedral geometry. The Zn–O bond lengths of 1.932(1) and 1.931(2) Å in **1** and 1.932(3) and 1.944(3) Å in **2** are slightly shorter than those documented in the literature, whereas the Zn–N bond lengths of 1.951(2) and 1.953(2) Å in **1** and 1.958(3) and 1.975(3) Å in **2** are also slightly shorter than the literature values.[5,13,14] The two crystallographically unique ligands have dihedral angles (ca. 7.2° and 7.3° for **1**; 9.9° and 20.7° for **2**) between the benzimidazole and phenolate moieties which indicate that the ligands are only slightly non-coplanar in **1**, although one ligand is significantly non-coplanar in **2**. Head-to-tail π–π stacking interactions (interligand distance of ca. 3.60 Å) exist between two molecules and give rise to a dimeric supramolecular structure in **1** (Figure 2, a). Such supramolecular dimers are stacked by edge-to-face C–H···π interactions (H···π ca. 2.75 Å) (Figure 2, b) between benzimidazole and phenolate rings of adjacent molecules, giving rise to a three-dimensional supramolecular array, while the π–π stacking interactions are in a nonparallel mode between the ligand planes of adjacent molecules, with face-to-face distances of 3.35–3.60 Å in **2** (Figure 2, c).

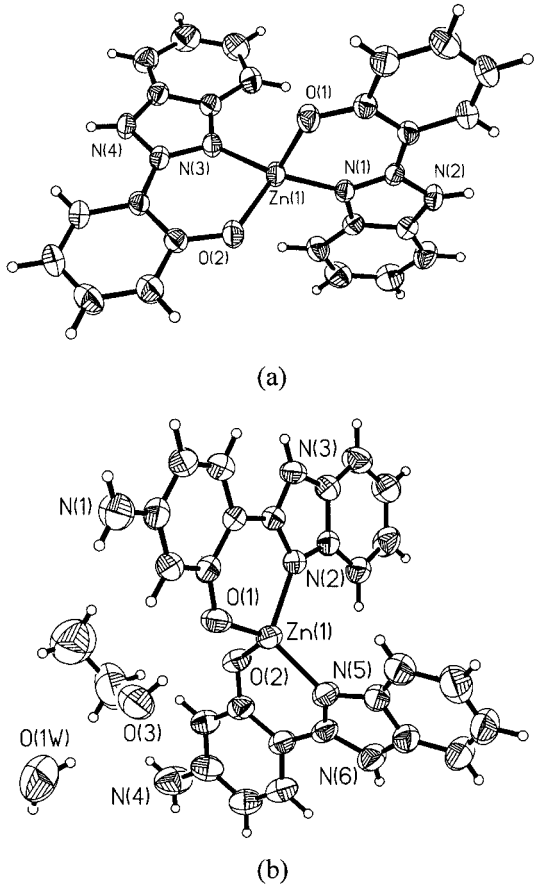

Figure 1. ORTEP views (at the 50% probability level) of **1** (a) and **2** (b).

There are also intermolecular hydrogen-bonding interactions in **1** and **2**. In **1**, the intermolecular hydrogen bonds [N(7)···O(2) = 2.796(2) Å; N(2)···O(3) = 2.822(2) Å] exist between the benzimidazole N–H groups and the deprotonated phenolate oxygen atom, furnishing a supramolecular dimer (Figure 2, a). However, the hydrogen-bonding interactions are more complicated in **2** owing to the existence of lattice water and ethanol molecules. The lattice water molecule forms two hydrogen bonds to two ethanol molecules [O(1w)···O(1) = 2.803(6) Å and O(1w)···O(2) = 2.944(6) Å], and accepts one hydrogen bond from a benzimidazole N–H group [N(1)···O(1w) = 2.855(6) Å] (Figure 3, a). Moreover, the ethanol molecule forms a hydrogen bond to the phenolate oxygen atom [O(1)···O(4) = 2.720(4) Å], and there are also intermolecular hydrogen-bonding interactions between the benzimidazole N–H groups and phenolate oxygen atoms [N(2)···O(6) = 2.791(4) Å; Figure 3, b].

 © 2005 Wiley-VCH Verlag GmbH & Co. KGaA, Weinheim

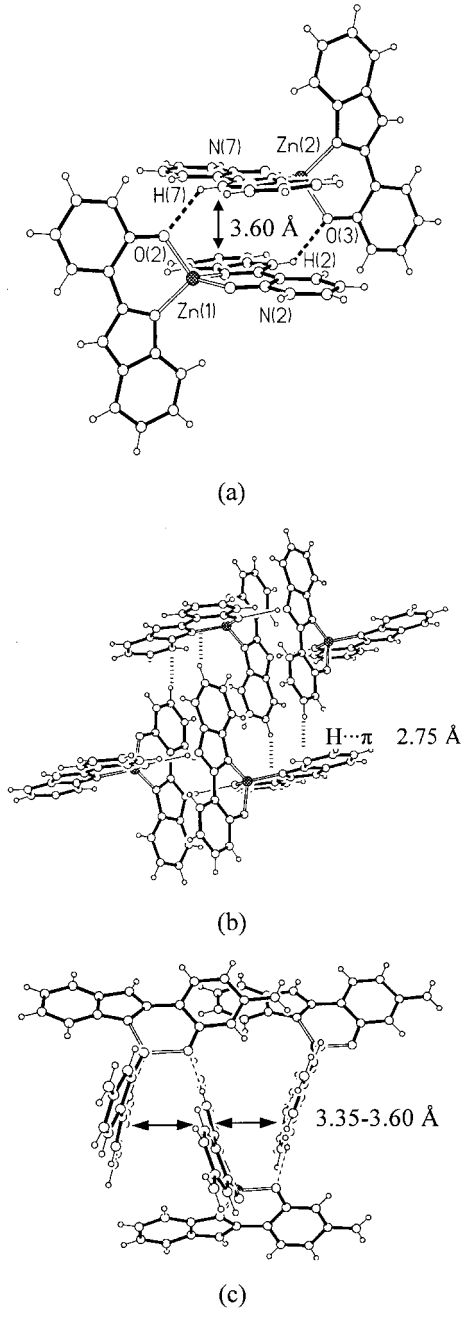

Figure 2. Perspective views of packing patterns in **1** (a, b) and **2** (c).

Neutral Hpbm and Hapbm were also crystallographically characterized. The dihedral angles (ca. 2.2° and 4.2°) between the phenolate and benzimidazole moieties for Hpbm and Hapbm indicate that both are basically coplanar. In the crystal structures of Hpbm and Hapbm, there is an intramolecular hydrogen bond between the phenolic and the imidazole groups [O(1)···N(1) = 2.554(2) Å for Hpbm and 2.563(2) Å for Hapbm] and intermolecular hydrogen bonds between the imidazole N–H groups and phenolic group oxygen atoms [N(2A)···O(1) = 2.821(3) for Hpbm and 2.826(2) Å for Hapbm] (Figure 4). These intermolecular hydrogen bonding and π–π interactions extend adja-

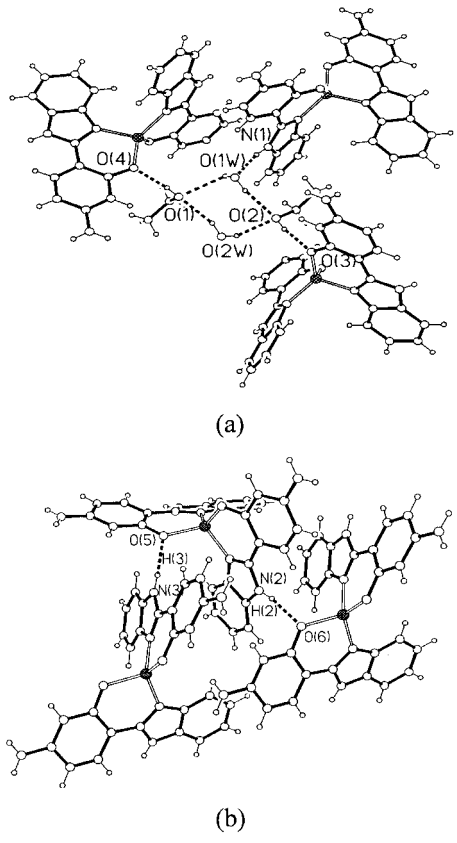

Figure 3. Perspective views of hydrogen-bonding interactions in **2**.

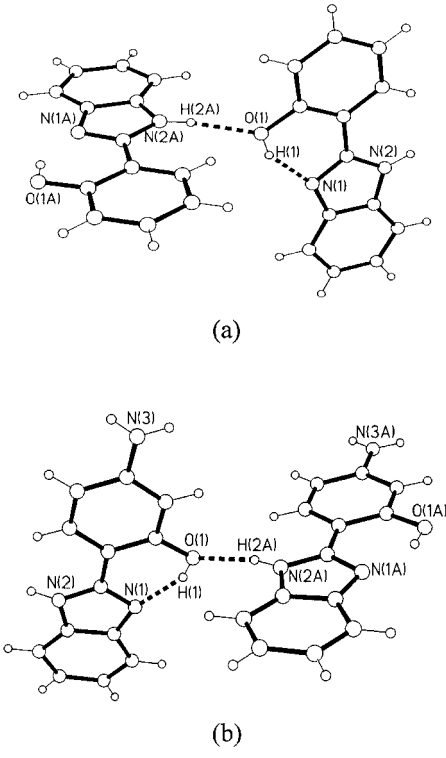

Figure 4. Perspective views of hydrogen-bonding interactions in Hpbm (a) and Hapbm (b).

 © 2005 Wiley-VCH Verlag GmbH & Co. KGaA, Weinheim

cent molecules into helical chains, where each pair of adjacent molecules exhibit offset π–π stacking interactions with face-to-face distances of around 3.43 Å in Hpbm and around 3.41 Å in Hapbm (Figure 5).

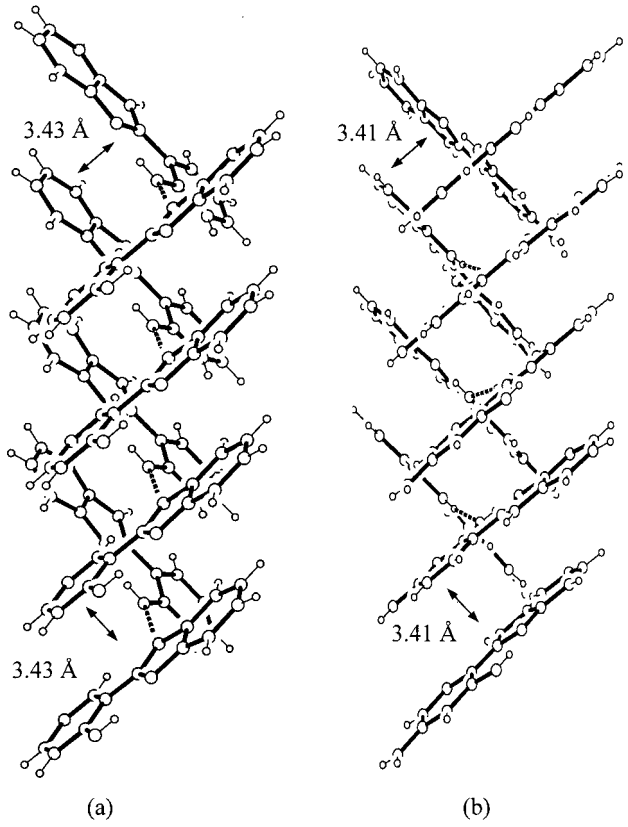

Figure 5. Perspective views of one-dimensional supramolecular arrays packed by hydrogen bonds and π–π stacking interactions in Hpbm (a) and Hapbm (b).

UV/Vis and Luminescent Spectra

The lowest-energy absorption bands of Hpbm and Hapbm in dichloromethane at 298 K occur at 323 and 325 nm, respectively, while those of their Zn^{II} complexes in dichloromethane are red-shifted slightly to 331 nm for **1** and 327 nm for **2,** with discernible shoulders at 343 and 340 nm, respectively (see Figure S2 in the Supporting Information).

The lowest-energy absorption maxima in UV spectra may correspond to S_0–S_n transitions with $n \geq 1$, as the S_0–S_1 transition may have a lower oscillator strength,[15–17] which are fully or partly transition-forbidden and too weak to be observed experimentally. According to our TDDFT calculations (Table 1), the lowest-energy absorption maxima (S_0–S_1 transition) are at 313 and 314 nm, with oscillator strengths of 0.44 and 0.78 for Hpbm and Hapbm, respectively. However, the lowest-energy absorption maximum for **1** should be attributed to the S_0–S_3 transition (wavelength: 364 nm; oscillator strength: 0.24), as the oscillator strength of the S_0–S_1 transition (wavelength: 370 nm) is only 0.04. Similarly, the lowest-energy absorption maximum for **2** can be attributed to the S_0–S_4 transition (wavelength: 344 nm; oscillator strength: 0.34), while its discernible shoulder is the S_0–S_1 transition (wavelength: 354 nm, oscillator strength: 0.16). The excited state–ground state (ES-GS) separations derived from the TDDFT calculations are in agreement with those observed experimentally.

For Hpbm and Hapbm, the S_0–S_1 transitions are mainly associated with transitions from the corresponding HOMOs to the LUMOs, as the coefficients in the configuration interaction wave functions are up to 0.63. As shown in Figure 6, the HOMOs are the π-bonding orbitals, while the LUMOs are the π*-antibonding orbitals, thus S_0–S_1 transitions can be assigned to be π→π* in nature.

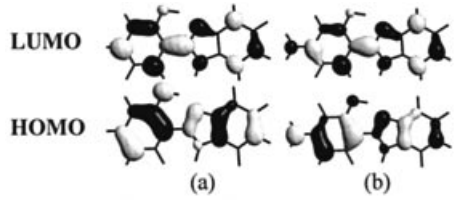

Figure 6. Contour plots of the relevant HOMOs and LUMOs of Hpbm (a) and Hapbm (b).

Similar to the corresponding ligands, the S_0–S_1 transitions of the Zn^{II} complexes are also mainly associated with transitions from the corresponding HOMOs to the LUMOs (Table S1 in the Supporting Information). As shown in Figure 7, the HOMOs are mainly the π-bonding orbitals of one deprotonated ligand, while the LUMOs are the π*-antibonding orbitals of another deprotonated ligand, thus the S_0–S_1 transitions can be assigned to be ligand-centered π→π* in nature (LCCT).

However, the S_0–S_3 transition (lowest-energy absorption maximum) of **1** is in fact mainly associated with the transitions from the corresponding HOMO–1 to LUMO and HOMO to LUMO+1, while the S_0–S_4 transition of **2** is mainly associated with the transitions from the corresponding HOMO–1 to LUMO+1 and HOMO to LUMO+1 (Table S1 in the Supporting Information), although such transitions are also assigned to be π→π* in nature.

Table 1. The calculated and experimental absorption wavelengths [nm] and their transition nature for **1**, **2**, Hpbm, and Hapbm, together with oscillator strengths.

	Transition nature	Wavelength			Oscillator strength
		Calcd.	Exp. in CH_2Cl_2	Exp. in solid	
Hpbm	π→π*	313	323	342	0.44
Hapbm	π→π*	314	325	348	0.78
1	π→π*	364	331	377	0.24
2	π→π*	344	327	368	0.34

 © 2005 Wiley-VCH Verlag GmbH & Co. KGaA, Weinheim

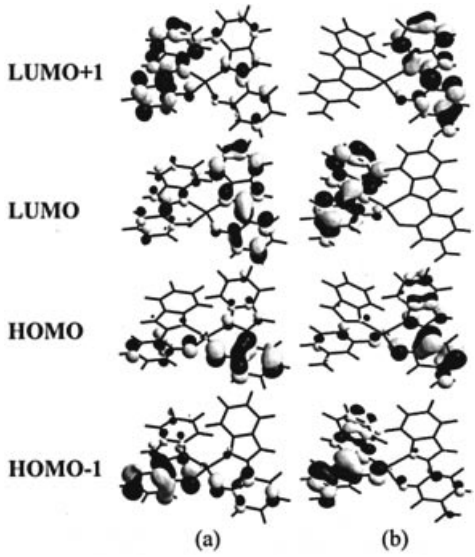

Figure 7. Contour plots of the relevant molecular orbitals (from HOMO–1 to LUMO+1) of **1** (a) and **2** (b).

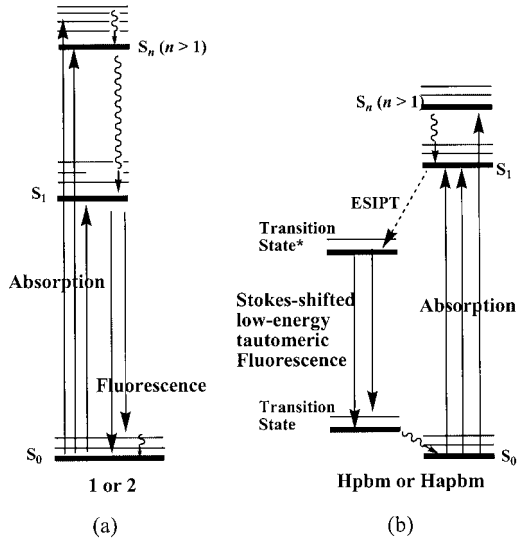

Scheme 2. The electronic transitions in the photoluminescent process of **1** or **2** (a) and Hpbm or Hapbm (b).

As has been noted,[11,18–20] the deprotonation and coordination of organic ligands to d^{10} metal ions can significantly reduce the energy gaps between the HOMOs and LUMOs. The TDDFT energy levels and experimental absorption spectra show that the S_0–S_1 energy separations of both Zn^{II} complexes become smaller than those of the corresponding ligands. According to the energy-gap law for radiationless deactivation,[17,21,22] the luminescence of the Zn^{II} complexes should be red-shifted compared with that of corresponding ligands. However, for the crystalline solid samples, Hpbm and Hapbm emit blue light with a maximum at 444 nm (λ_{ex} = 352 nm) and 426 nm (λ_{ex} = 365 nm) at 298 K, respectively, while **1** and **2** emit at 434 nm (λ_{ex} = 384 nm) and 419 nm (λ_{ex} = 379 nm), respectively (Figure 8). The violation of blue shifts can be ascribed to the excited state intramolecular proton transfer (ESIPT) of such organic compounds, which produces a strongly Stokes-shifted low-energy tautomeric fluorescence (Scheme 2).[12,23–25]

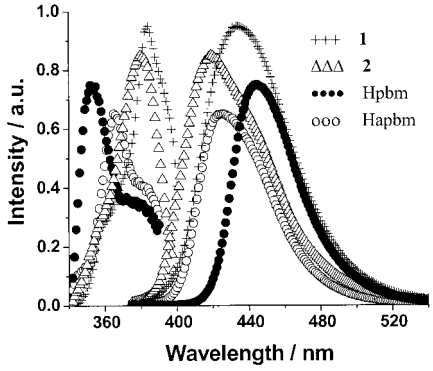

Figure 8. The excitation (left) and emission (right) spectra of **1**, **2**, Hpbm, and Hapbm in the solid state at 298 K. The corresponding excitation wavelengths, λ_{ex}, are 384, 379, 352, and 365 nm, respectively.

Moreover, the weakly electron-donating amino group can increase the electron density of the aromatic group and hence reduce the ES-GS separations slightly, consistent with the S_0–S_1 energy separations found in either the TDDFT energy levels or experimental absorption spectra of the planar Hpbm and Hapbm. On the other hand, in the absence of intramolecular hydrogen-bonding interactions (O–H···N), the 5-amino substitution may further twist the deprotonated ligand plane, as indicated by the experimental dihedral angle variation between the phenolate and benzimidazole rings of **2**, resulting in the reduction of the electron delocalization energy. Such a decrease of the delocalization energy is not favored for a π–π* transition as it may increase the energy separation. Compared with the weak electron-donating effect, the non-coplanar effect may be much stronger in **2**. In the current case, this hypothesis can be verified theoretically, as the higher ES-GS separations of **2** can be found in the TDDFT energy levels. Thus, compared to that of **1**, a significant blue shift (up to 15 nm) is observed in the luminescence of **2**. Similarly, compared to that of Hpbm, the higher emission energy of Hapbm in the non-coplanar ESIPT state is expected, although its S_0–S_1 energy separation is slightly reduced.

To the best of our knowledge, Zn^{II} complexes with aromatic heterocyclic ligands usually exhibit an emission transition that is an intraligand charge-transfer (ILCT). This is in good agreement with the assignment of the π→π* nature of the S_0–S_1 transitions for **1** and **2**. Similar to those of common Zn^{II} complexes,[18,19] the lifetimes of solid **1** and **2** are around 1.90(2) and 1.21(1) ns at room temperature.

Conclusions

Two neutral, mononuclear Zn^{II} complexes and their ligands have been prepared as possible candidates for blue-light-emitting EL materials. Systematic investigations of

 © 2005 Wiley-VCH Verlag GmbH & Co. KGaA, Weinheim

electronic transitions in the photoluminescent process of all compounds have been carried out based on the X-ray structural information, as well as the TDDFT energy level and molecular orbitals analyses, and these show that their absorption and luminescent properties are ligand-based. The photophysical studies further explain the spectral variation along with the effect of complexation with Zn^{II} cations and/or amino substitution.

Experimental Section

General Remarks: All the reagents and solvents employed are commercially available and were used as received without further purification. The C, H, and N microanalyses were carried out with an Elementar Vario El elemental analyzer. ^{1}H NMR spectra were recorded with a Varian INOVA500NB spectrometer. FTIR spectra were recorded with a Bruker Vector22 spectrometer in KBr pellets in the range 4000–400 cm^{-1}. The UV/Vis spectra were recorded with a Varian Cary-100 spectrometer. The steady-state fluorescent and fluorescence lifetimes were determined with an Edinburgh Instrument FLS920 fluorescence spectrophotometer. Thermogravimetric data (TG and DTG) were collected with a Perkin–Elmer TGS-2 analyser in flowing dinitrogen atmosphere at a heating rate of 10 °C min^{-1} by heating the microcrystals.

Synthesis of Hpbm and Hapbm: They were synthesized following methods similar to those reported in the literature.[26] Salicylic acid (0.138 g, 1 mmol) and *o*-phenylenediamine (0.108 g, 1 mmol) were mixed and stirred in syrupy phosphoric acid (3 mL) at a temperature of ca. 520 K for 5 h to give white analytically pure Hpbm after recrystallization of the crude product (ca. 10% yield). X-ray quality crystals were grown by slow evaporation of a solution in $CHCl_3$ for about one week. $C_{13}H_{10}N_2O$ (210.2): calcd. C 74.27, H 4.79, N 13.33; found C 74.02, H 4.81, N 13.49. ^{1}H NMR (500 MHz, [D_6]-DMSO): δ = 13.13 (s, 1 H), 13.12 (s, 1 H), 8.04 (dd, J = 1.50, 8.00 Hz, 1 H), 7.71 (d, J = 8.00 Hz, 1 H), 7.60 (d, J = 7.50 Hz, 1 H), 7.38 (m, 1 H), 7.28 (m, 2 H), 7.03 (m, 2 H) ppm. FTIR (KBr): $\tilde{\nu}$ = 3326 (vs), 1585 (s), 1492 (s), 1417 (s), 1320 (m), 1282 (m), 1262 (s), 1133 (m), 1037 (w), 911 (w), 840 (w), 798 (w), 727 (s), 591 (w), 522 (w), 464 (w) cm^{-1}.

Hapbm was similarly synthesized by reaction of *o*-phenylenediamine (0.108 g, 1 mmol) with 4-aminosalicylic acid (0.153 g, 1 mmol). X-ray quality crystals were grown by very slow evaporation of a solution of DMF over about one month. The yield was ca. 10%. $C_{13}H_{11}N_3O$ (225.2): calcd. C 69.32, H 4.92, N 18.66; found C 69.07, H 4.81, N 18.72. ^{1}H NMR (500 MHz, [D_6]DMSO): δ = 12.96 (s, 1 H), 12.68 (s, 1 H), 7.65 (d, J = 8.10 Hz, 1 H), 7.51 (s, 2 H), 7.17 (dd, J = 3.00, 7.16 Hz, 2 H Hz,), 6.21 (dd, J = 2.10, 8.40 Hz, 1 H), 6.14 (d, J = 1.50 Hz, 1 H), 5.68 (s, 2 H) ppm. FTIR (KBr): $\tilde{\nu}$ = 3471 (m), 3381 (s), 3221 (s), 1631 (s), 1589 (s), 1553 (m), 1424 (s), 1363 (m), 1268 (s), 1198 (m), 1153 (m), 961 (w), 806 (m), 737 (s), 681 (w), 538 (w), 522 (w) cm^{-1}.

Synthesis of [Zn(pbm)$_2$] (1): A mixture of zinc acetate dihydrate (0.110 g, 0.5 mmol), Hpbm (0.210 g, 1.0 mmol), and water (10 mL) was heated in a 23-mL, Teflon-lined stainless-steel container at 110 °C for 4 d. After cooling to room temperature at a rate of 5 K per hour, the colorless crystals of **1** were isolated (yield ca. 0.17 g, 70%). $C_{26}H_{18}N_4O_2Zn$ (483.8): calcd. C 64.54, H 3.75, N 11.58; found C 64.32, H 3.84, N 11.72. ^{1}H NMR (500 MHz, [D_6]DMSO): δ = 13.34 (s, 2 H), 7.98 (d, J = 7.00 Hz, 2 H), 7.58 (d, J = 8.00 Hz, 2 H), 7.25 (d, J = 8.00 Hz, 4 H), 7.05 (q, J = 7.00 Hz, 4 H), 6.80 (d, J = 7.50 Hz, 2 H), 6.68 (t, J = 7.00 Hz, 2 H) ppm. FTIR (KBr): $\tilde{\nu}$ = 3428 (m), 1798 (w), 1567 (s), 1478 (m), 1444 (m), 1407 (m), 1311 (w), 1251 (w), 1140 (w), 876 (w), 738 (w), 654 (w) cm^{-1}.

Table 2. Crystal data and structure refinement for **1**, **2**, Hpbm, and Hapbm.

Complex	**1**	**2**	Hpbm	Hapbm
Empirical formula	$C_{26}H_{18}N_4O_2Zn$	$C_{28}H_{28}N_6O_4Zn$	$C_{13}H_{10}N_2O$	$C_{13}H_{11}N_3O$
Formula mass	483.81	577.93	210.23	225.25
Temperature [K]	293(2)	293(2)	293(2)	293(2)
Crystal system	monoclinic	orthorhombic	orthorhombic	orthorhombic
Space group	$P2_1/n$	*Pbcn*	$Pna2_1$	*Pbca*
a [Å]	10.188(1)	28.900(2)	18.236(16)	12.932(1)
b [Å]	10.010(1)	9.1250(5)	4.8061(17)	8.5641(7)
c [Å]	21.323(1)	20.062(1)	11.990(11)	19.7343(16)
β [°]	94.029(1)	90	90	90
V [Å^3]	2169.2(3)	5290.4(5)	1050.8(14)	2185.5(3)
Z	4	8	4	8
$\rho_{calcd.}$ [mg m^3]	1.481	1.451	1.329	1.369
Abs. coefficient [mm^{-1}]	1.164	0.975	0.087	0.091
F(000)	992	2400	440	944
Crystal size [mm]	0.26 × 0.13 × 0.11	0.46 × 0.24 × 0.08	0.52 × 0.36 × 0.33	0.37 × 0.23 × 0.11
Absorption correction	multi-scan	multi-scan	multi-scan	multi-scan
Index ranges	$-13 \le h \le 10$	$-37 \le h \le 36$	$-23 \le h \le 10$	$-16 \le h \le 15$
	$-12 \le k \le 12$	$-11 \le k \le 11$	$-4 \le k \le 6$	$-9 \le k \le 11$
	$-27 \le l \le 27$	$-26 \le l \le 19$	$-15 \le l \le 14$	$-25 \le l \le 20$
Reflections collected	13051	29997	4138	12220
Unique reflections	4884	6054	2138	2494
Parameters	298	359	146	154
R_{int}	0.0241	0.0599	0.0163	0.0296
Goodness-of-fit	1.050	1.047	1.041	1.072
R_1 [$I > 2\sigma(I)$]	0.0361	0.0612	0.0425	0.0566
wR_2 [$I > 2\sigma(I)$]	0.0914	0.1524	0.1023	0.1247
R_1 (all data)	0.0454	0.1015	0.0484	0.0761
wR_2 (all data)	0.0967	0.1784	0.1057	0.1336
Largest diff. peak and hole [e Å^{-3}]	0.403/–0.321	0.783/–0.425	0.152/–0.190	0.182/–0.157

 © 2005 Wiley-VCH Verlag GmbH & Co. KGaA, Weinheim

Synthesis of $[Zn(apbm)_2]\cdot C_2H_5OH\cdot H_2O$ (2): A filtered solution of Hapbm (0.45 g, 2 mmol) and potassium hydroxide (0.112 g, 2 mmol) in ethanol (80 mL) was added to a solution of zinc acetate dihydrate (0.22 g, 1 mmol) in ethanol (40 mL) at a temperature of 60 °C. The mixture was kept for 4 h at this temperature, and allowed to stand overnight at room temperature. The white precipitate was filtered, washed with ethanol, and dried under reduced atmosphere over silica gel at room temperature for 3 h to give **2** as pale-yellow microcrystals. X-ray quality crystals were obtained by very slow evaporation of a solution in ethanol over about 60 days (ca. 0.29 g, 50% yield based on Zn). $C_{28}H_{28}N_6O_4Zn$ (579.0): calcd. C 58.19, H 4.88, N 14.54; found C 58.33, H 4.58, N 14.42. ^{1}H NMR (500 MHz, [D$_6$]DMSO): δ = 7.62 (d, J = 8.70 Hz, 2 H), 7.42 (d, J = 7.50 Hz, 2 H), 7.11 (t, J = 7.50 Hz, 2 H), 6.96 (t, J = 7.80 Hz, 2 H), 6.86 (d, J = 7.80 Hz, 2 H), 6.01 (dd, J = 2.10, 8.70 Hz, 2 H), 5.91 (d, J = 2.10 Hz, 2 H), 5.39 (s, 4 H). FTIR (KBr): $\tilde{\nu}$ = 3375 (s), 3334 (s), 3211 (m), 1624 (s), 1534 (s), 1478 (s), 1463 (s), 1447 (s), 1396 (w), 1348 (w), 1327 (w), 1296 (w), 1253 (m), 1213 (m), 1157 (m), 980 (w), 848 (w), 811 (w), 751 (m), 602 (w), 539 (w), 508 (w) cm^{-1}.

X-ray Crystallographic Study: Diffraction intensities for **1** and **2**, as well as Hpbm and Hapbm, were collected at 293 K on a Bruker Smart Apex CCD diffractometer (Mo-K_α radiation; λ = 0.71073 Å). Absorption corrections were applied with SADABS.[27] The structures were solved by direct methods and refined with full-matrix least-squares using the SHELXTL program package.[28] The organic hydrogen atoms were generated in ideal positions. Anisotropic thermal parameters were applied to all non-hydrogen atoms. Experimental details of the X-ray analyses are provided in Table 2, with selected bond lengths and angles listed in Table 3.
CCDC-258466 to -258468 (for **1**, **2**, and Hapbm, respectively) and -240084 (Hpbm) contain the supplementary crystallographic data for this paper. These data can be obtained free of charge from The Cambridge Crystallographic Data Centre via www.ccdc.cam.ac.uk/data_request/cif.

Calculation Details: Based on the optimized geometries (selected optimized bond lengths and bond angles are listed in Table S2 in the Supporting Information), time-dependent density functional (TDDFT) calculations were performed at the B3LYP level with a 6-31G** basis set for C, H, N, and O atoms, and effective core potentials basis set LanL2DZ for Zn atoms, employing the Gaussian03 suite of programs.[29] The electron density diagrams of molecular orbitals were obtained with the Gaussview graphics program.

Table 3. Selected bond lengths [Å] and angles [°] for **1**, **2**, Hpbm, and Hapbm.

1			
Zn(1)–O(2)	1.931(2)	Zn(1)–N(1)	1.951(2)
Zn(1)–O(1)	1.932(1)	Zn(1)–N(3)	1.953(2)
O(2)–Zn(1)–O(1)	110.1(1)	O(2)–Zn(1)–N(3)	95.3(1)
O(2)–Zn(1)–N(1)	121.0(1)	O(1)–Zn(1)–N(3)	112.6(1)
O(1)–Zn(1)–N(1)	95.7(1)	N(1)–Zn(1)–N(3)	122.7(1)
2			
Zn(1)–O(1)	1.932(3)	Zn(1)–N(2)	1.958(3)
Zn(1)–O(2)	1.944(3)	Zn(1)–N(5)	1.975(3)
O(1)–Zn(1)–O(2)	114.0(1)	O(1)–Zn(1)–N(5)	126.7(1)
O(1)–Zn(1)–N(2)	94.7(1)	O(2)–Zn(1)–N(5)	95.1(1)
O(2)–Zn(1)–N(2)	110.7(1)	N(2)–Zn(1)–N(5)	116.2(1)
Hpbm			
N(1)–C(7)	1.322(3)	N(2)–C(8)	1.372(3)
N(1)–C(13)	1.389(3)	O(1)–C(1)	1.355(3)
N(2)–C(7)	1.359(3)	C(6)–C(7)	1.457(3)
O(1)–C(1)–C(6)	121.4(2)	N(1)–C(7)–C(6)	123.4(2)
N(2)–C(7)–C(6)	124.9(2)		
Hapbm			
O(1)–C(1)	1.356(2)	N(2)–C(7)	1.354(2)
N(1)–C(7)	1.327(2)	N(2)–C(13)	1.382(2)
N(1)–C(8)	1.389(2)		
O(1)–C(1)–C(6)	121.4(2)	N(2)–C(7)–C(6)	124.7(2)
N(1)–C(7)–C(6)	123.4(2)	N(3)–C(3)–C(4)	121.0(2)

Acknowledgments

This work was supported by the National Natural Science Foundation of China (grant no. 20131020) and the Scientific and Technological Project of Guangdong Province (nos. 2003C103004, 036601, and 04205405).

[1] C. W. Tang, S. A. VanSlyke, *Appl. Phys. Lett.* **1987**, *51*, 913–915.
[2] S.-N. Wang, *Coord. Chem. Rev.* **2001**, *215*, 79–98, and references cited therein.
[3] *Handbook of Luminescence, Display Materials, and Devices* (Eds.: H. S. Nalwa, L. S. Rohwer, A. J. Heeger), American Scientific Publishers, Stevenson Ranch, Calif., **2003**, and references cited therein.
[4] a) M. Brinkmann, G. Gadret, M. Muccini, C. Taliani, N. Masciocchi, A. Sironi, *J. Am. Chem. Soc.* **2000**, *122*, 5147–5157; b) M. Cölle, R. E. Dinnebier, W. Brütting, *Chem. Commun.* **2002**, 2908–2909, and references cited therein.
[5] G. Yu, S. Yin, Y. Liu, Z. Shuai, D. Zhu, *J. Am. Chem. Soc.* **2003**, *125*, 14816–14824.
[6] a) M. D. Halls, H. B. Schlegel, *Chem. Mater.* **2001**, *13*, 2632–2640; b) P. J. Hay, *J. Phys. Chem. A* **2002**, *106*, 1634–1641.
[7] Y. Hamada, T. Sano, H. Fujii, Y. Nishio, H. Takahashi, K. Shibata, *Jpn. J. Appl. Phys.* **1996**, *35*, L1339–L1341.
[8] N. Nakamura, S. Wakabayashi, K. Miyairi, T. Fujii, *Chem. Lett.* **1994**, 1741–1742.
[9] J. Zhang, S. Gao, C.-M. Che, *Eur. J. Inorg. Chem.* **2004**, 956–959.
[10] M. Osawa, M. Hoshino, M. Akita, T. Wada, *Inorg. Chem.* **2005**, *44*, 157–1159.
[11] S.-L. Zheng, J.-P. Zhang, X.-M. Chen, Z.-L. Huang, Z.-Y. Lin, W.-T. Wong, *Chem. Eur. J.* **2003**, *9*, 3888–3896.
[12] Y.-P. Tong, S.-L. Zheng, X.-M. Chen, *Inorg. Chem.* **2005**, DOI: 10.1021/ic0501059.
[13] L. S. Sapochak, F. E. Benincasa, R. S. Schofield, J. L. Baker, K. K. C. Riccio, D. Fogarty, H. Kohlmann, K. F. Ferris, P. E. Burrows, *J. Am. Chem. Soc.* **2002**, *124*, 6119–6125.
[14] Q. Wu, J. A. Lavigne, Y. Tao, M. D'Iorio, S. Wang, *Inorg. Chem.* **2000**, *39*, 5248–5254.
[15] N. J. Turro, K.-C. Liu, M.-F. Show, P. Lee, *Photochem. Photobiol.* **1978**, *27*, 523–529.
[16] a) S.-L. Zheng, P. Coppens, *CrystEngCommun.* **2005**, *7*, 289–293; b) S.-L. Zheng, P. Coppens, *Chem. Eur. J.* **2005**, *11*, 3583–3590.
[17] J. M. Klessinger, J. Michl, *Excited States and Photochemistry of Organic Molecules*, VCH, New York, **1995**.
[18] S.-L. Zheng, J.-H. Yang, X.-L. Yu, X.-M. Chen, W.-T. Wong, *Inorg. Chem.* **2004**, *43*, 830–838.
[19] S.-L. Zheng, X.-M. Chen, *Aust. J. Chem.* **2004**, *57*, 703–712.
[20] V. W.-W. Yam, Y.-L. Pui, K.-K. Cheung, *Inorg. Chem.* **2000**, *39*, 5741–5746.
[21] N. J. Turro, *Modern Molecular Photochemistry*, University Science Books, Sausalito, CA, **1978**.

 © 2005 Wiley-VCH Verlag GmbH & Co. KGaA, Weinheim

[22] D. V. Scaltrito, D. W. Thompson, J. A. O'Callaghan, G. J. Meyer, *Coord. Chem. Rev.* **2000**, *208*, 243–266.
[23] J. Waluk, *Conformational Analysis of Molecules in Excited States*, Wiley-VCH, **2000**, 83–85, and references cited therein.
[24] D. LeGourriérec, V. A. Kharlanov, R. G. Brown, W. Rettig, *J. Photochem. Photobiol. A: Chem.* **2000**, *130*, 101–111.
[25] W. E. Brewer, M. L. Martinez, P.-T. Chou, *J. Phys. Chem.* **1990**, *94*, 1915–1918.
[26] A. W. Addison, P. J. Burke, *J. Heterocycl. Chem.* **1981**, *18*, 803–805.
[27] R. Blessing, *Acta Crystallogr., Sect. A* **1995**, *51*, 33–38.
[28] G. M. Sheldrick, *SHELXTL 6.10*, Bruker Analytical Instrumentation, Madison, Wisconsin, USA, **2000**.
[29] M. J. Frisch, G. W. Trucks, H. B. Schlegel, G. E. Scuseria, M. A. Robb, J. R. Cheeseman, V. G. Zakrzewski, J. A. Montgomery, R. E. Stratmann, J. C. Burant, S. Dapprich, J. M. Millam, A. D. Daniels, K. N. Kudin, M. C. Strain, O. Farkas, J. Tomasi, V. Barone, M. Cossi, R. Cammi, B. Mennuci, C. Pomelli, C. Adamo, S. Clifford, J. Ochterski, G. A. Petersson, P. Y. Ayala, Q. Cui, K. Morokuma, D. K. Malick, A. D. Rabuck, K. Raghavachari, J. B. Foresman, J. Cioslowski, J. V. Oritz, B. B. Stefanov, G. Liu, A. Liashenko, P. Piskorz, I. Komaromi, R. Gomperts, R. L. Martin, D. J. Fox, T. Keith, M. A. Al-Laham, C. Y. Peng, A. Nanayakkara, C. Gonzalez, M. Challacombe, P. M. W. Gill, B. G. Johnson, W. Chen, M. W. Wong, J. L. Andres, M. Head-Gordon, E. S. Replogle, J. A. Pople, *GAUSSIAN03, Revision C.02*; Gaussian, Inc., Pittsburgh, PA, **2003**.

Received: February 27, 2005
Published Online: August 11, 2005

 © 2005 Wiley-VCH Verlag GmbH & Co. KGaA, Weinheim

Carbosilane Dendrons Functionalized at Their Focal Point

Román Andrés,*[a] Ernesto de Jesús,*[a] F. Javier de la Mata,[a] Juan C. Flores,[a] and Rafael Gómez[a]

Keywords: Dendrimers / Metallocenes / Silanes / Titanium / Zirconium

The Si–Ph bond of $PhSi[(CH_2)_3SiMe_2Bz]_3$ (**5**) is cleaved with triflic acid to give $TfOSi[(CH_2)_3SiMe_2Bz]_3$, which, in turn, reacts with triethylammonium chloride or potassium cyclopentadienide to give, respectively, $ClSi[(CH_2)_3SiMe_2Bz]_3$ (**8**) and $(C_5H_5)Si[(CH_2)_3SiMe_2Bz]_3$ (**10**). This strategy can be applied to the post-growth incorporation of nucleophiles to the focal point of carbosilane dendritic wedges. In this way, cyclopentadiene-functionalized dendritic wedges of second and third generation C_5H_5-G*n*-$[(CH_2)_3SiMe_2Bz]_x$ (*n* = 2, *x* = 9, **11**; *n* = 3, *x* = 27, **12**) have been obtained starting from Ph-G*n*-$[(CH_2)_3SiMe_2Bz]_x$ (**6**, **7**). The metallocenes $[\{(BzMe_2SiCH_2CH_2CH_2)_3SiC_5H_4\}_2MCl_2]$ (M = Ti, **14**; Zr, **15**) have also been obtained from **10** and their catalytic behavior in ethylene and propylene polymerization, using MAO as a cocatalyst, has been studied and compared to that of related non-dendritic complexes.

(© Wiley-VCH Verlag GmbH & Co. KGaA, 69451 Weinheim, Germany, 2005)

Introduction

The large number of dendrimers synthesized nowadays from a diversity of cores, repetitive units, and peripheral groups allows the design of macromolecules with tailored properties through the incorporation of suitable functions at the appropriate site of the dendritic molecule (i.e. core, framework, or periphery).[1] Transition metal catalysts are a good example of the relevance of the location of the functional group in the dendritic structure because of the different accessibility of the metal center to the substrate in core- and periphery-functionalized dendrimers.[2,3] In the vast majority of metal-functionalized carbosilane dendrimers the metal complexes reside in the periphery.[4] Some of the exceptions are represented by the metal complexes that van Leeuwen and al. have synthesized from phosphane ligands [triphenylphosphane, bis(diphenylphosphanyl)ferrocene (dppf), bis(diphenylphosphanyl)xanthene (xantphos), or *o*-(diphenylphosphanyl)phenol] located in the core of carbosilane dendrimers.[5] All these phosphanes have been obtained from a family of dendritic wedges whose first generation, **A**, is represented in Scheme 1 and which are grown from *p*-bromostyrene by the usual divergent methodology that alternates hydrosilylation and alkylation steps using $HSiCl_3$ and allylmagnesium bromide, respectively.[6] In the aforementioned dendritic phosphanes, prepared from the lithium derivative of **A**, a styrene spacer separates the phosphorus and the core silicon atoms.

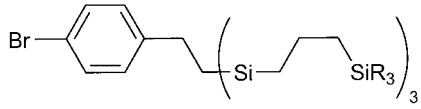

A, R = allyl, Me

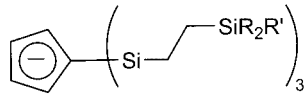

B, R = R' = Et; R = Ph, R' = Me

Scheme 1.

We have previously reported the synthesis of group 4 metallocenes derived from the first-generation dendron **B** that possesses a cyclopentadienide anion (Cp^-) directly linked to its focal point.[7] In contrast to the aryl bromide in **A**, the Cp group is not compatible with the hydrosilylation and alkylation steps and cannot be incorporated before the growth of the dendrimer. Here we describe a strategy for the post-synthetic modification of the focal point of a carbosilane dendritic wedge.

Results and Discussion

Fréchet introduced the term "dendritic wedge" in the description of the convergent strategy for the growth of dendrimers.[8] In this strategy, the dendrimer is assembled from the periphery and each successive generation is synthesized from a single reactive group located at the focal point of a dendritic wedge. The final reaction involves the attachment of the dendritic wedges to a core molecule. For this reason,

[a] Departamento de Química Inorgánica, Universidad de Alcalá, Campus Universitario, 28871 Alcalá de Henares, Madrid, Spain
Fax: +34-91-885-4683
E-mail: ernesto.dejesus@uah.es

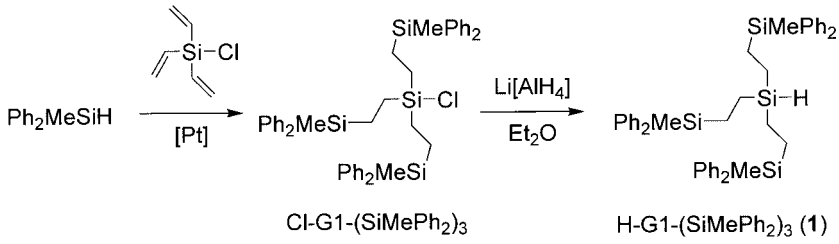

Scheme 2.

the convergent approach has been largely applied to the synthesis of core- or focal-point functionalized dendrimers. Carbosilane dendrimers are, in general, synthesized divergently by a repetitive sequence of hydrosilylation and alkylation steps.[6,9] The sequence of reactions depicted in Scheme 2 illustrates a possible route for the convergent preparation of carbosilane dendrimers in which the Si–Cl bond is reduced to Si–H instead of being alkylated as in a divergent synthesis. Thus, the carbosilane Cl-G1-$[(CH_2)_3SiMePh_2]_3$ was prepared by hydrosilylation of chlorotrivinylsilane with methyldiphenylsilane,[7] and reacted with lithium tetrahydridoaluminate to give H-G1-$[(CH_2)_3SiMePh_2]_3$ (**1**), the first-generation analog of the starting methyldiphenylsilane, quantitatively. The presence of a Si–H bond in **1** was confirmed by the septuplet observed in the ^1H NMR spectrum at $\delta = 3.64$ ppm ($^3J_{H,H} = 2.9$ Hz). Unfortunately, hydrosilylation of chlorotrivinylsilane with **1** always gave mixtures of the second-generation wedge Cl-G2-$[(CH_2)_3SiMePh_2]_3$ with partially hydrosilylated compounds, in spite of the variety of solvents, temperatures, and Pt catalysts (Speier, Karstedt, and Pt/C) tested. This result was not completely unexpected because it is known that both bulky and electron-donating substituents decrease the reactivity of silanes in the platinum-catalyzed hydrosilylation of olefins.[10] Both characteristics are combined in the silane **1** and in its progressively bulkier higher-generation analogs H-G*n*-$[(CH_2)_3SiMePh_2]_3$, which are required for this convergent strategy, in contrast to the divergent growth that uses activated silanes with electron-withdrawing chloro substituents.

The desired focal-point functionalization can also be achieved by an approach in which a protecting group is linked to the core before the dendrimer growth and eliminated at the end of the growing process. In the case of a carbosilane dendrimer, the phenyl group fulfills the main requirements of a silicon-core protector: it is inert towards hydrosilylation and alkylation, but forms bonds with silicon that can undergo protolysis to give a by-product that is easily separable from the dendrimer. Thus, G0, G1, and G2 compounds Ph-G*n*-$(CH_2CHCH_2)_x$ (**2**–**4**, respectively) with 3, 9, and 27 allyl end-groups, respectively, were synthesized from $PhSiCl_3$ by successive allylation and hydrosilylation steps (Scheme 3).[11] The ^1H NMR olefinic resonances at around $\delta = 4.8$ and 5.7 ppm were used to follow the progress of the critical hydrosilylation steps in order to determine their completion and, therefore, the absence of defects in the branches of the final products. The growth was terminated at the desired generation by using benzyldimethylsilane instead of trichlorosilane as the hydrosilylating agent to give Ph-G*n*-$[(CH_2)_3SiMe_2Bz]_x$ (Bz = $CH_2C_6H_5$, **5**–**7**). The reaction of allyl-terminated dendrimers with trichlorosilane in the presence of H_2PtCl_6 as a catalyst occurred smoothly at room temperature, whereas the reaction mixture had to be gently heated for the activation of the trialkylsilane $HSiMe_2Bz$ (^1H NMR monitoring). Dendrimers **5**–**7** were obtained as colorless oils after removal of the volatiles in vacuo and were purified by chromatography on a silica-gel column prior to subsequent use. After isolation, the yields ranged from 93 to 96% for allyl-terminated dendrimers **2**–**4** (for **3** and **4** the values correspond to overall yields from the allyl dendrimer of the previous generation) and 82–83% for **5**–**7**.

Acid-induced cleavage of the Ph–Si bond was attempted with boron trichloride in hexane,[12] HCl and catalytic amounts of aluminum trichloride in diethyl ether,[13] or triflic acid (trifluoromethanesulfonic acid, TfOH) in chloro-

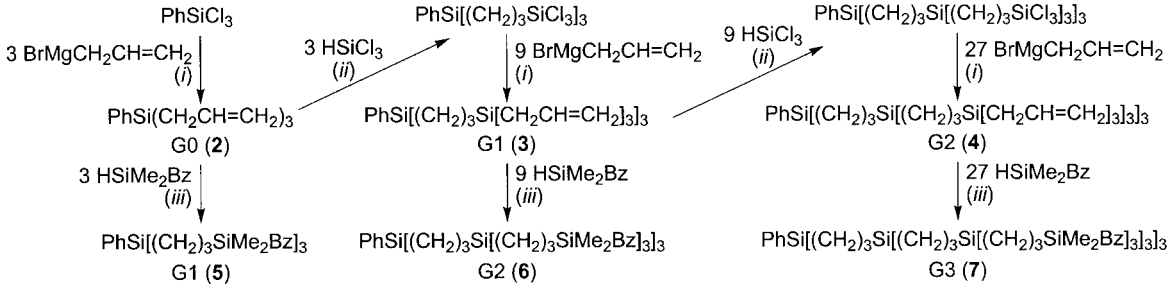

Scheme 3. Synthesis of carbosilane dendritic wedges **2**–**7** with a phenyl group attached to their focal point. Conditions: (*i*) diethyl ether, room temperature, overnight; (*ii*) solvent-free reaction, H_2PtCl_6 in 2-propanol, room temperature, 4 h; (*iii*) solvent-free reaction, H_2PtCl_6 in 2-propanol; see Exp. Sect. for details.

 © 2005 Wiley-VCH Verlag GmbH & Co. KGaA, Weinheim

form.[14] Boron trichloride failed to react with both allyl- and benzyldimethylsilyl-terminated compounds **2** and **5** at room temperature, and protic acids such as HCl or TfOH reacted at the same time with the terminal allyl groups of dendrimers Ph-G*n*-$(CH_2CH{=}CH_2)_x$ (**2**–**4**).[15] Cleavage of the Si–Ph bond with HCl was slow in diethyl ether at room temperature (^{1}H NMR evidence), whereas the Si–Ph bond of dendrimers Ph-G*n*-$[(CH_2)_3SiMe_2Bz]_x$ (**5**–**7**) was cleanly and readily cleaved with triflic acid at 0 °C in chloroform (Scheme 4), with the advantage that the triflate anion TfO^- is a good leaving-group in silyl triflates, undergoing exchange with a wide range of nucleophiles.[16] For the reactions described below, compounds TfO-G*n*-$[(CH_2)_3SiMe_2Bz]_x$ were used without isolation. As shown in Scheme 4, the reaction of $TfOSi[(CH_2)_3SiMe_2Bz]_3$ with triethylammonium chloride in dimethoxyethane (DME) gave $ClSi[(CH_2)_3SiMe_2Bz]_3$ (**8**). Other nucleophiles can be introduced at the focal-point position either from the chlorosilane or directly from the silyl triflate, as exemplified by the preparation of the silanol $HOSi[(CH_2)_3SiMe_2Bz]_3$ (**9**) or the cyclopentadiene $(C_5H_5)Si[(CH_2)_3SiMe_2Bz]_3$ (**10**). The ^{1}H NMR spectrum of **10** shows, at room temperature, broadened temperature-dependent resonances for both types of cyclopentadiene protons, those bonded to sp^2 (δ = 6.4–6.7 ppm) and those bonded to sp^3 carbons (δ = 2.9–3.5 ppm). The related trimethylsilylcyclopentadiene ($C_5H_5SiMe_3$), which is present as a mixture of the three possible isomers, also shows broadened temperature-dependent ^{1}H resonances, which are ascribed to the interconversion of ring protons and isomers by sigmatropic $SiMe_3$ and proton shifts.[17] The ^{1}H NMR behavior of **10** is clearly similar to that of $C_5H_5SiMe_3$, especially in the distribution and temperature dependence of the C(sp^3)–H resonances. Thus, the major isomer of **10** (ca. 70–75%) corresponds to the cyclopentadiene with a C(sp^3)–Si bond (Scheme 5) and gives a broad resonance at δ = 3.4 ppm, whereas the minor isomers show resonances at around δ = 3.0 ppm which are sharper at room temperature. The usefulness of the described methodology for the synthesis of higher-generation dendritic wedges has been demonstrated by the synthesis of the G2 and G3 cyclopentadienes **11** and **12** (Scheme 5). They were obtained as yellow oils in the same conditions described above for **10**, starting from the corresponding triflate TfO-G*n*-$[(CH_2)_3SiMe_2Bz]_x$. The ^{1}H NMR resonances in the cyclopentadiene sp^3 region are similar to those described above for **10**, although they are accompanied by the general broadening of resonances that the restricted mobility of protons causes in higher generations.

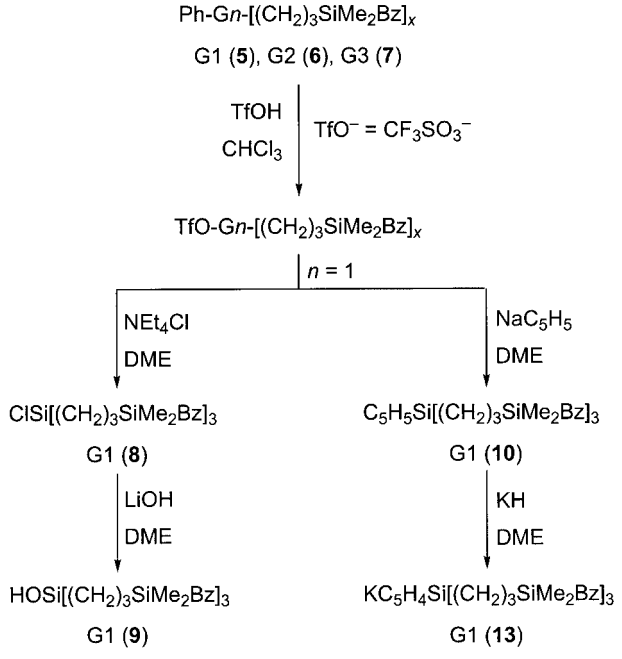

Scheme 4.

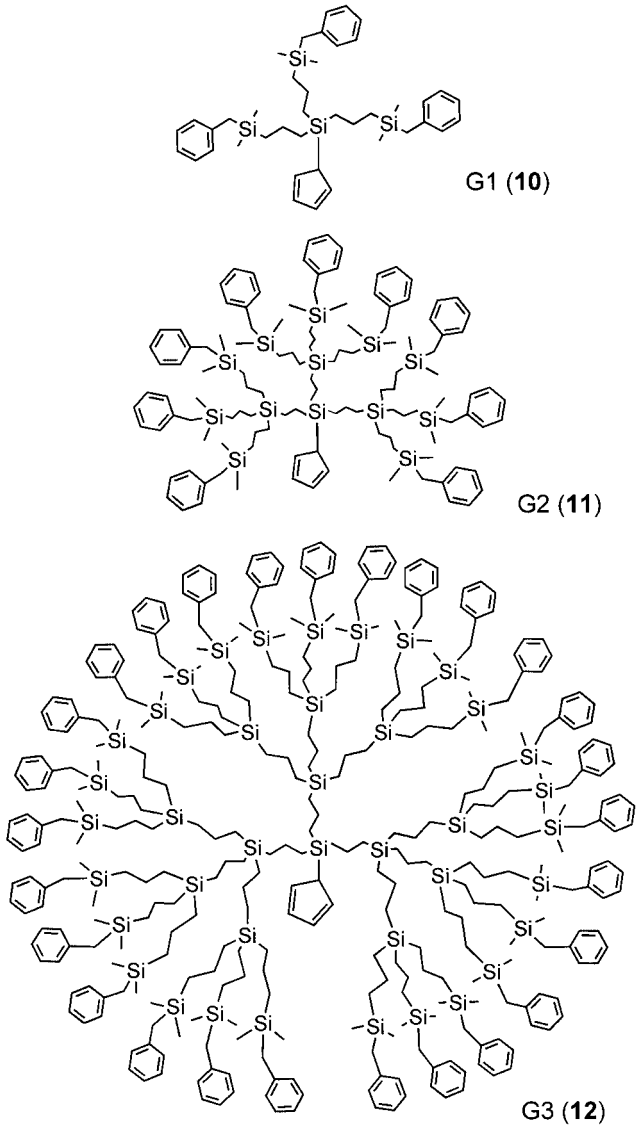

Scheme 5. Cyclopentadienes with carbosilane dendritic wedges of first (**10**), second (**11**), and third generation (**12**). Only the major isomers are represented.

Dendrimers **2**–**12** were characterized by elemental analysis and ^{1}H, ^{13}C{^{1}H}, and ^{29}Si{^{1}H} NMR spectroscopy. Three groups of methylene resonances are observed for the

 © 2005 Wiley-VCH Verlag GmbH & Co. KGaA, Weinheim

$SiCH_2CH_2CH_2Si$ repeating unit in phenyl-protected dendrimers **5**–**7**, at $\delta \approx 0.8$ ppm for the methylene bonded to the core silicon, $\delta = 1.2$–1.3 ppm for the middle CH_2 groups, and $\delta \approx 0.5$ ppm for the rest. Only the core $SiCH_2$ resonance is affected by the modification of the focal-point group, and is progressively shifted to high field when Ph is replaced by Cl, OH, and C_5H_5. In the $^{29}Si\{^1H\}$ NMR spectra, a singlet is observed for every type of silicon atom present in the corresponding molecule. Mass spectra were obtained by ESI or APCI techniques for all the first-generation post-functionalized dendrimers **8**–**10**. Attempts to record MALDI-TOF mass spectra of second- and third-generation cyclopentadiene dendrimers **11** and **12** failed. The purity of phenyl-protected dendrimers **5**–**7**, as well as that of the post-modified cyclopentadienes **10**–**12**, was routinely checked by GPC chromatography in THF. Every chromatogram showed a unique peak with typical polydispersity values of about 1.02–1.03, according to the monodisperse nature of these molecules. As expected, the elution time of the dendrimers increases with the molecular weight. The molecular weights obtained after calibration with a standard of polystyrene were not in good agreement with the theoretical values because of the globular nature of dendrimers. However, a good linear relationship was shown between the logarithm of the theoretical molecular weights and the elution times on GPC traces ($R_2 = 0.984$).[18]

The first-generation cyclopentadienide **13** was synthesized as a potassium salt by reaction of **10** with KH in DME. Dendritic metallocenes **14** (Ti) and **15** (Zr) were subsequently obtained by reaction of two equivalents of cyclopentadienide **13** with $TiCl_4$ or $ZrCl_4$·2THF in toluene (Scheme 6). These products were isolated as red (Ti) or colorless (Zr) oils that were rather stable upon exposure to air. Upon activation with an excess of methylaluminoxane (MAO), complexes **14** and **15** catalyze the polymerization of ethylene. The results are summarized in Table 1 and compared with those of simple metallocenes $[(C_5H_5)_2MCl_2]$ (M = Ti, Zr) obtained under the same conditions. The activity is lowered by one order by the dendritic substituents in the titanocene catalyst, but noticeably there is no such decrease in the zirconocene case. We have previously reported a similar result with vinyl-type carbosilanes $[\{(Ph_2MeSiCH_2CH_2)_3SiC_5H_4\}_2MCl_2]$ (M = Ti, Zr), although in this example a small but significant decrease of 30% was observed for the zirconocene compound.[7] These results can be interpreted in steric terms by taking into account the bigger size of the zirconium atom, and the larger hindrance of vinyl-type carbosilanes when compared with the allyl type reported here. In polymerization of propylene (Table 1), the zirconium complex **15** displays a similar activity to that observed for $[(C_5H_5)_2ZrCl_2]$. Some degree of stereocontrol in the polymerization of α-olefins with metallocenes is, in principle, possible by restricting the rotation of the Cp ligand, for example by means of sterically demanding substituents.[19] The polypropylene obtained with **15**, at both 20 °C and –30 °C, shows the distribution of ^{13}C NMR resonances of a mainly atactic polymer,[20] similar to that obtained with $[(C_5H_5)_2ZrCl_2]$.

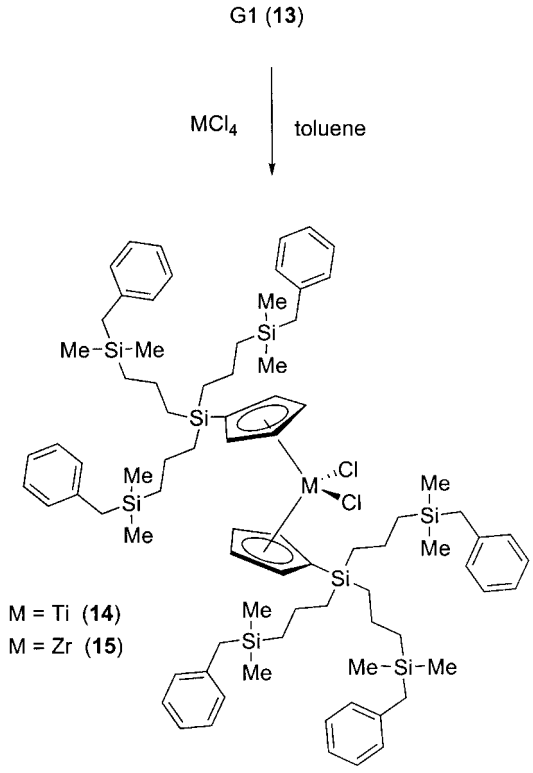

Scheme 6.

In view of these results, we tried the preparation of the second- and third-generation analogs of metallocenes **14** and **15**. Somewhat surprisingly, no reaction was observed between **11** or **12** and KH under the same conditions used for **10**. When *n*-buyllithium was employed instead as a deprotonating agent, the ^1H NMR spectra in C_6D_6 showed the disappearance of the resonances due to the $C(sp^3)$ protons, as expected for the formation of the lithium cyclopentadienides. However, the formation of either mono- or biscyclopentadienyl complexes was never observed when these

Table 1. Ethylene and propylene polymerization results with complexes **14** and **15**.[a]

Precatalyst	Ethylene Yield [g]	Activity [kg_{PE}/mol_M h]	Propylene Yield [g]	Activity [kg_{PP}/mol_M h]
$[Cp_2TiCl_2]$	1.150	5520	–	–
14	0.100	480	–	–
$[Cp_2ZrCl_2]$	2.459	11803	0.446	2141
15	2.549	12235	0.311	1493

[a] Conditions: MAO cocatalyst, Al/M = 1700, 1.25 mmol of catalyst dissolved in 50 mL of toluene, 10 min, 293 K, 1 bar of constant monomer pressure.

 © 2005 Wiley-VCH Verlag GmbH & Co. KGaA, Weinheim

solutions were reacted with $TiCl_4$ or $ZrCl_4$ in the usual solvents (toluene or THF for zirconium), with reaction times of up to two days and temperatures up to 50 °C. The reason for this failure − steric hindrance or inappropriate reaction conditions − is not clear to us at this stage.

Conclusions

The post-synthetic modification of the focal point of a dendrimer is useful for the chemistry of dendrimers and hyperbranched polymers because it permits the incorporation of more-reactive cores.[21] In this paper, we have demonstrated a methodology for such a modification of carbosilane dendrimers that is based on the protolysis of Si–Ph bonds with triflic acid and allows the linking of functional nucleophiles to the focal point of carbosilane wedges. In this way, we have synthesized dendritic cyclopentadienes up to the third generation. We are currently exploring the utility of this strategy for the modification of a variety of ligands.

Experimental Section

Reagents and General Techniques: All operations were performed under argon by using Schlenk or dry-box techniques. Solvents were dried and distilled under argon as described elsewhere.[22] Unless otherwise stated, reagents were obtained from commercial sources and used as received. $Na(C_5H_5)$ was prepared from freshly distilled cyclopentadiene and NaH in THF. $HSiMe_2Bz$ was synthesized from $HSiMe_2Cl$ and BzMgCl in diethyl ether. $ClSi(CH_2CH_2SiMePh_2)_3$ was prepared as previously reported.[7] ^1H, ^{13}C, and ^{29}Si NMR spectra were recorded on Varian Unity 300 or 500 Plus spectrometers. Chemical shifts (δ, ppm) are relative to $SiMe_4$, and were measured by internal referencing to the deuterated solvent (^{13}C and residual ^1H resonances), or by the substitution method (^{29}Si). Coupling constants (J) are given in hertz. The Analytical Services of the Universidad de Alcalá performed the C, and H analyses with a Heraeus CHN–O-Rapid microanalyzer, and the mass spectra with an Automass Multi, ThermoQuest. GPC analyses were carried out with a Varian Inert 9012 and 9065 Polychrom chromatograph, and Polymer Laboratories PL-ELS 1000 Light Scattering detector, using Polymer Laboratories Plgel columns and tetrahydrofuran (THF) as the eluent.

Synthesis of $HSi(CH_2CH_2SiMePh_2)_3$ (1): A solution of $ClSi(CH_2CH_2SiMePh_2)_3$ (1.00 g, 1.35 mmol) in 10 mL of diethyl ether was added to a mixture of lithium aluminum hydride (25 mg, 0.67 mmol) in diethyl ether (25 mL). After stirring the mixture for 6 h at room temperature, the excess of lithium aluminum hydride was hydrolyzed with a 5% solution of HCl in water, and the ethereal and aqueous phases were separated. The aqueous phase was extracted with diethyl ether (2×10 mL) and the ethereal fractions were collected and dried with anhydrous $MgSO_4$. Then, the solvent was removed in vacuo and the residue characterized as $HSi(CH_2CH_2SiMePh_2)_3$ (0.85 g, 89%) as a colorless oil. $C_{45}H_{52}Si_4$ (705.24): calcd. C 76.64, H 7.43; found C 76.31, H 7.39. ^1H NMR ($CDCl_3$): δ = 7.45 (m, 12 H, Ph), 7.32 (m, 18 H, Ph), 3.64 (sept, $^3J_{H,H}$ = 2.9, 1 H, Si*H*), 1.50 (s, 9 H, Me), 0.88 (m, 6 H, $HSiCH_2$), and 0.54 (m, 6 H, $CH_2SiMePh_2$) ppm. $^{13}C\{^1H\}$ NMR ($CDCl_3$): δ = 137.1 (*ipso-Ph*), 134.5 (*meta-Ph*), 129.1 (*para-Ph*), 127.8 (*ortho-Ph*), 7.3 and 2.5 [$Si(CH_2)_2Si$], –5.1 (Me) ppm.

Synthesis of Ph-G*n*-(allyl)$_x$ (2–4): These compounds have been reported previously but complete preparative details were not given.[11] Here, the preparation of Ph-G2-$(allyl)_{27}$ (**4**) is described as representative. Ph-G1-$(allyl)_9$ (**3**; 3.7 g, 5.4 mmol) was added to an excess of trichlorosilane (10 mL, 99 mmol) in the presence of a 2×10^{-3} M solution of H_2PtCl_6 in 2-propanol (0.080 mL, 0.16 μmol) as catalyst. The solution was stirred for 4 h at room temperature and, after verification of the complete hydrosilylation of **3** by ^1H NMR spectroscopy, the excess of silane and other volatiles were removed under vacuum. Subsequently, the crude product was dissolved in diethyl ether (25 mL) and added dropwise (30 min) to an ice-cooled solution of allylmagnesium bromide (180 mmol) in diethyl ether (300 mL). When the addition was finished, the reaction mixture was allowed to warm to room temperature and the stirring was continued overnight. The excess of allylmagnesium bromide was then hydrolyzed with a concentrated aqueous solution of NH_4Cl (100 mL). The organic phase was separated by decantation and the aqueous solution was extracted again with diethyl ether (2×100 mL). The combined organic phase were dried with anhydrous $MgSO_4$, filtered, and the solvents evaporated in vacuo to yield **4** (10.7 g, 96%) as a colorless liquid that was pure by ^1H NMR spectroscopy.

Ph-G0-$(allyl)_3$ (**2**; 13.0 g, 96%) was obtained from $PhSiCl_3$ (9.5 mL, 59 mmol) and allylmagnesium bromide (200 mmol). Ph-G1-$(allyl)_9$ (**3**; 11.4 g, 93%) was obtained from Ph-G0-$(allyl)_3$ (**2**; 4.10 g, 18.0 mmol), trichlorosilane (10 mL, 99 mmol), and allylmagnesium bromide (190 mmol).

Ph-G0-$(allyl)_3$ (2): $C_{15}H_{20}Si$ (228.40): calcd. C 78.88, H 8.83; found C 78.80, H 8.81. ^1H NMR ($CDCl_3$): δ = 7.52 (m, 2 H, Ph), 7.36 (m, 3 H, Ph), 5.80 (m, 3 H, CH_2CH=CH_2), 4.89 (m, 6 H, CH_2CH=CH_2) 1.86 (m, 6 H, CH_2CH=CH_2) ppm. $^{13}C\{^1H\}$ NMR ($CDCl_3$): δ = 135.2 (*ipso*-Ph), 134.2 (CH_2CH=CH_2), 133.8 (*ortho*-Ph), 129.3 (*para*-Ph), 127.7 (*meta*-Ph), 114.3 (CH_2CH=CH_2), 19.5 (CH_2CH=CH_2) ppm. $^{29}Si\{^1H\}$ NMR ($CDCl_3$): δ = –7.90 ppm.

Ph-G1-$(allyl)_9$ (3): $C_{42}H_{68}Si_4$ (685.33): calcd. C 73.61, H 10.00; found C 73.57, H 9.98. ^1H NMR ($CDCl_3$): δ = 7.44 (m, 2 H, Ph), 7.34, (m, 3 H, Ph), 5.74 (m, 9 H, CH_2CH=CH_2), 4.84 (m, 18 H, CH_2CH=CH_2), 1.54 (m, 18 H, CH_2CH=CH_2), 1.37 (m, 6 H, $SiCH_2CH_2CH_2Si$), 0.84 (m, 6 H, $PhSiCH_2CH_2CH_2$), 0.66 (m, 6 H, $PhSiCH_2CH_2CH_2Si$) ppm. $^{13}C\{^1H\}$ NMR ($CDCl_3$): δ = 137.2 (*ipso*-Ph), 134.1 (CH_2CH=CH_2), 133.7 (*ortho*-Ph), 128.6 (*para*-Ph), 127.4 (*meta*-Ph), 113.3 (CH_2CH=CH_2), 19.9 (CH_2CH=CH_2), 18.4, 17.6, and 16.7 [$Si(CH_2)_3Si$] ppm. $^{29}Si\{^1H\}$ NMR ($CDCl_3$): δ = –1.14 (3 Si), –4.01 (1 Si) ppm.

Ph-G2-$(allyl)_{27}$ (4): $C_{123}H_{212}Si_{13}$ (2056.1): calcd. C 71.85, H 10.39; found C 71.81, H 10.36. ^1H NMR ($CDCl_3$): δ = 7.42 (m, 2 H, Ph), 7.30 (m, 3 H, Ph), 5.74 (m, 27 H, CH_2CH=CH_2), 4.85 (m, 54 H, CH_2CH=CH_2), 1.55 (m, 54 H, CH_2CH=CH_2), 1.28 (m, 24 H, $SiCH_2CH_2CH_2Si$), 0.84 (m, 6 H, $PhSiCH_2CH_2CH_2$), 0.54 (m, 42 H, $PhSiCH_2CH_2CH_2Si$ and $SiCH_2CH_2CH_2Si$) ppm. $^{13}C\{^1H\}$ NMR ($CDCl_3$): δ = 137.5 (*ipso*-Ph), 134.3 (CH_2CH=CH_2), 133.9 (*ortho*-Ph), 128.6 (*para*-Ph), 127.6 (*meta*-Ph), 113.4 (CH_2CH=CH_2), 19.8 (CH_2CH=CH_2), 18.6, 18.2, and 16.5 [G1-$Si(CH_2)_3Si$], 18.3, 17.6, and 16.7 [G2-$Si(CH_2)_3Si$] ppm. $^{29}Si\{^1H\}$ NMR ($CDCl_3$): δ = –4.21 (1 Si), 0.42 (3 Si), –1.02 (9 Si) ppm.

Synthesis of Ph-G*n*-[$(CH_2)_3SiMe_2Bz$]$_x$ (5–7): The preparation of Ph-G3-$[(CH_2)_3SiMe_2Bz]_{27}$ (**7**) is given as representative. An excess of benzyldimethylsilane (9.3 mL, 59 mmol) and a 2×10^{-3} M solution of H_2PtCl_6 in 2-propanol (0.080 mL, 0.16 μmol) were added to **4** (4.00 g, 1.95 mmol). The mixture was gently heated until reaction started (the solution became more viscous and turned slightly yellow) and then allowed to recover room temperature. The volatiles

 © 2005 Wiley-VCH Verlag GmbH & Co. KGaA, Weinheim

were evaporated under vacuum at room temperature and the residue was purified by flash chromatography on a silica gel column with hexane as eluent. Dendrimer **7** (9.86 g, 83%) was obtained as a colorless liquid.

Ph-G1-[$(CH_2)_3SiMe_2Bz$]$_3$ (**5**; 4.89 g, 82%) was obtained from benzyldimethylsilane (5.0 mL, 31.6 mmol) and **2** (2.00 g, 8.76 mmol); Ph-G2-[$(CH_2)_3SiMe_2Bz$]$_9$ (**6**; 7.68 g, 83%) was obtained from benzyldimethylsilane (7,0 mL, 44.2 mmol) and **3** (3.10 g, 4.53 mmol).

Ph-G1-[$(CH_2)_3SiMe_2Bz$]$_3$ (5): $C_{42}H_{62}Si_4$ (679.28): calcd. C 74.26, H 9.20; found C 74.21, H 9.19. ^{1}H NMR ($CDCl_3$): δ = 7.44 (m, 2 H, SiPh), 7.35 (m, 3 H, SiPh), 7.18 (m, 6 H, CH_2Ph), 7.05 (m, 3 H, CH_2Ph), 6.95 (m, 6 H, CH_2Ph), 2.04 (s, 6 H, CH_2Ph), 1.33 (m, 6 H, $CH_2CH_2CH_2$), 0.81 (m, 6 H, PhSi$CH_2CH_2CH_2$Si), 0.57 (m, 6 H, PhSi$CH_2CH_2CH_2$Si), –0.07 (s, 18 H, CH_3) ppm. ^{13}C{^{1}H} NMR ($CDCl_3$): δ = 140.4 (*ipso*-CH_2Ph), 137.9 (*ipso*-Ph), 134.0 (*meta*-Ph), 128.7 (*para*-Ph), 128.1 (*ortho*-CH_2Ph), 128.0 (*meta*-CH_2Ph), 127.6 (*ortho*-*Ph*), 123.8 (*para*-CH_2Ph), 27.7 (CH_2Ph), 19.6, 18.3, and 17.3 [Si(CH_2)$_3$Si], –3.51 (Me) ppm. ^{29}Si{^{1}H} NMR ($CDCl_3$): δ = 1.53 (3 Si), –3.99 (1 Si) ppm.

Ph-G2-[$(CH_2)_3SiMe_2Bz$]$_9$ (6): $C_{123}H_{194}Si_{13}$ (2038.0): calcd. C 72.49, H 9.59; found C 72.47, H 9.55. ^{1}H NMR ($CDCl_3$): δ = 7.42 (m, 2 H, Ph), 7.26 (m, 3 H, Ph), 7.17 (m, 18 H, CH_2Ph), 7.03 (m, 9 H, CH_2Ph), 6.95 (m, 18 H, CH_2Ph), 2.04 (s, 18 H, $CH_2C_6H_5$), 1.24 (m, 24 H, Si$CH_2CH_2CH_2$Si), 0.82 (m, 6 H, PhSi$CH_2CH_2CH_2$), 0.50 (m, 42 H, PhSi$CH_2CH_2CH_2$Si and Si$CH_2CH_2CH_2$Si), –0.07 (s, 54 H, Me) ppm. ^{13}C{^{1}H} NMR ($CDCl_3$): δ = 140.4 (*ipso*-CH_2Ph), 137.8 (*ipso*-Ph), 134.0 (*ortho*-Ph), 128.7 (*para*-Ph), 128.1 (*ortho*-CH_2Ph), 128.0 (*meta*-CH_2Ph), 127.6 (*meta*-Ph), 123.8 (*para*-CH_2Ph), 25.8 (CH_2Ph), 19.6, 18.4, and 17.4 [G2-Si(CH_2)$_3$Si], 18.6, 17.8, and 17.7 [G1-Si(CH_2)$_3$Si], –3.5 (Me) ppm. ^{29}Si{^{1}H} NMR ($CDCl_3$): δ = 1.45 (9 Si), 0.47 (3 Si), –4.13 (1 Si) ppm.

Ph-G3-[$(CH_2)_3SiMe_2Bz$]$_{27}$ (7): $C_{366}H_{590}Si_{40}$ (6114.02): calcd. C 71.90, H 9,73; found C 71.60, H 8.75. ^{1}H NMR ($CDCl_3$): δ = 7.42 (m, 2 H, Ph), 7.20 (m, 3 H, Ph), 7.14 (m, 54 H, CH_2Ph), 7.00 (m, 27 H, CH_2Ph), 6.93 (m, 54 H, CH_2Ph), 2.03 (s, 54 H, $CH_2C_6H_5$), 1.24 (m, 78 H, Si$CH_2CH_2CH_2$Si), 0.80 (m, 6 H, PhSi$CH_2CH_2CH_2$), 0.51 (m, 150 H, PhSi$CH_2CH_2CH_2$Si and Si$CH_2CH_2CH_2$Si), –0.07 (s, 162 H, Me) ppm. ^{13}C{^{1}H} NMR ($CDCl_3$): δ = 140.3 (*ipso*-CH_2Ph), 137.8 (*ipso*-Ph), 134.1 (*ortho*-*Ph*), 128.4 (*para*-Ph), 128.1 (*ortho*-CH_2Ph), 128.0 (*meta*-CH_2Ph), 127.6 (*meta*-Ph), 123.9 (*para*-CH_2Ph), 25.8 (CH_2Ph), 18.7, 18.1, and 17.8 [G2-Si(CH_2)$_3$Si], 19.9, 18.5 and 17.5 [G3-Si(CH_2)$_3$Si], –3.4 (Me) ppm; [G1-Si(CH_2)$_3$Si] not found. ^{29}Si{^{1}H} NMR ($CDCl_3$): δ = 1.45 (27 Si), 0.44 (3 Si), 0.40 (9 Si), –4.11 (1 Si) ppm.

Synthesis of Cl-G1-[$(CH_2)_3SiMe_2Bz$]$_3$ (8): Compound **5** (1.00 g, 1.47 mmol) was dissolved in a small volume of chloroform (1 mL). Trifluoromethanesulfonic acid (0.14 mL, 1.6 mmol) was then added dropwise from a syringe to this solution previously cooled to 0 °C. Stirring was continued for 1 h at room temperature, the solvent was removed in vacuo, the residue was dissolved in dimethoxyethane (10 mL), and an excess of solid triethylammonium chloride (0.30 g, 2.2 mmol) was added. After stirring the reaction mixture for 2 h, the volatiles were removed in vacuo and the residue was extracted with hexane (10 mL), the mixture was filtered, and the solvent was evaporated to yield **8** (0.81 g, 86%) as a colorless oil. $C_{36}H_{57}ClSi_4$ (637.63): calcd. C 67.81, H 9.01; found C 67.35, H 9.10. MS (ESI–): *m*/*z* = 653 (calcd. for MOH^-: 653). ^{1}H NMR ($CDCl_3$): δ = 7.19 (m, 6 H, CH_2Ph), 7.04 (m, 3 H, CH_2Ph), 6.98 (m, 6 H, CH_2Ph), 2.06 (s, 6 H, $CH_2C_6H_5$), 1.37 (m, 6 H, Si$CH_2CH_2CH_2$Si), 0.79 (m, 6 H, ClSi$CH_2CH_2CH_2$Si), 0.57 (m, 6 H, ClSi$CH_2CH_2CH_2$), –0.04 (s, 18 H, Me) ppm. ^{13}C{^{1}H} NMR ($CDCl_3$): δ = 140.3 (*ipso*-CH_2Ph), 128.1 (*ortho*-CH_2Ph), 128.0 (*meta*-CH_2Ph), 123.9 (*para*-CH_2Ph), 25.7 ($CH_2C_6H_5$), 20.9, 19.1, and 17.6 [Si(CH_2)$_3$Si], –3.5 (Me) ppm. ^{29}Si{^{1}H} NMR ($CDCl_3$): δ = 30.50 (1 Si), 1.65 (3 Si) ppm.

Synthesis of HO-G1-[$(CH_2)_3SiMe_2Bz$]$_3$ (9): An excess of anhydrous lithium hydroxide (50 mg, 2.1 mmol) was added to a solution of **8** (0.50 g, 0.78 mmol) in dimethoxyethane (10 mL). After stirring the mixture for 3 h at room temperature, the solvent was removed in vacuo, the residue was extracted with hexane (10 mL), the mixture was filtered, and the solvent evaporated to yield **9** (0.41 g, 84%) as a colorless oil. Alternatively, compound **9** can be synthesized by hydrolysis of a solution of **8** in diethyl ether with several drops of water in the presence of an excess of triethylamine. $C_{36}H_{58}OSi_4$ (619.19): calcd. C 69.83, H 9.44; found C 69.43, H 9.43. MS (APCI–): *m*/*z* = 650 (calcd. for $MMeOH^-$: 650). ^{1}H NMR ($CDCl_3$): δ = 7.19 (m, 6 H, CH_2Ph), 7.04 (m, 3 H, CH_2Ph), 6.99 (m, 6 H, CH_2Ph), 2.06 (s, 6 H, $CH_2C_6H_5$), 1.33 (m, 6 H, Si$CH_2CH_2CH_2$Si), 1.20 (s, 1 H, O*H*), 0.61 and 0.54 (m, 12 H, Si$CH_2CH_2CH_2$Si), –0.05 (s, 18 H, Me) ppm. ^{13}C{^{1}H} NMR ($CDCl_3$): δ = 140.3 (*ipso*-CH_2Ph), 128.1 (*ortho*-CH_2Ph), 128.0 (*meta*-CH_2Ph), 123.8 (*para*-CH_2Ph), 25.8 ($CH_2C_6H_5$), 20.0, 19.5, and 17.7 [Si(CH_2)$_3$Si], –3.4 (Me) ppm. ^{29}Si{^{1}H} NMR ($CDCl_3$): δ = 15.49 (1 Si), 1.57 (3 Si) ppm.

Synthesis of C_5H_5-G*n*-[$(CH_2)_3SiMe_2Bz$]$_x$ (10–12): The preparation of C_5H_5-G3-[$(CH_2)_3SiMe_2Bz$]$_{27}$ (**12**) is given as representative. Compound **7** (10.0 g, 1.63 mmol) was dissolved in a small volume of chloroform (4 mL). Trifluoromethanesulfonic acid (0.245 g, 1.63 mmol) was added dropwise from a syringe to this solution previously cooled to 0 °C. Stirring was continued for 1 h at room temperature and then the solvent was removed in vacuo and the residue dissolved in dimethoxyethane (50 mL). Subsequently, solid NaC_5H_5 (0.144 g, 1.63 mmol) was added in a dry box. The reaction mixture was stirred for 3 h, the volatiles removed in vacuo, and the residue extracted with hexane (3 × 20 mL). After evaporation of the solvent, compound **12** (8.5 g, 85%) was obtained as a dark-yellow oil.

C_5H_5-G1-[$(CH_2)_3SiMe_2Bz$]$_3$ (**10**; 8.6 g, 80%) was obtained from **5** (11.0 g, 16.2 mmol), trifluoromethanesulfonic acid (2.43 g, 16.2 mmol), and NaC_5H_5 (1.43 g, 16.2 mmol). C_5H_5-G2-[$(CH_2)_3SiMe_2Bz$]$_9$ (**11**; 2.0 g, 80%) was obtained from **6** (2.50 g, 1.23 mmol), trifluoromethanesulfonic acid (0.184 g, 1.23 mmol), and NaC_5H_5 (0.108 g, 1.23 mmol).

Data for C_5H_5-G1-[$(CH_2)_3SiMe_2Bz$]$_3$ (10): $C_{41}H_{62}Si_4$ (667.27): calcd. C 73.80, H 9.37; found C 73.75, H 9.36. MS (ESI–): *m*/*z* = 666 (calcd. for $M–H^-$: 666). ^{1}H NMR ($CDCl_3$): δ = 7.19 (m, 6 H, CH_2Ph), 7.04 (m, 3 H, CH_2Ph), 6.96 (m, 6 H, CH_2Ph), 6.57, 3.42, and 2.96 (broad resonances, 5 H, C_5H_5), 2.05 (s, 6 H, $CH_2C_6H_5$), 1.27 (m, 6 H, Si$CH_2CH_2CH_2$Si), 0.53 and 0,46 (m, 12 H, Si$CH_2CH_2CH_2$Si), –0.06 (s, 18 H, Me) ppm. ^{13}C{^{1}H} NMR ($CDCl_3$): δ = 140.2 (*ipso*-CH_2Ph), 133.1 (C_5H_5), 129.9 (C_5H_5), 128.0 (*ortho*-CH_2Ph), 127.9 (*meta*-CH_2Ph), 123.8 (*para*-CH_2Ph), 49.7 (C_5H_5), 25.8 ($CH_2C_6H_5$), 19.7, 18.8, and 17.5 [Si(CH_2)$_3$Si], –3.3 (Me) ppm. ^{29}Si{^{1}H} NMR ($CDCl_3$): δ = 2.71 (1 Si), 1.54 (3 Si) ppm.

Data for C_5H_5-G2-[$(CH_2)_3SiMe_2Bz$]$_9$ (11): $C_{122}H_{194}Si_{13}$ (2026.0): calcd. C 72.33, H 9.65; found C 71.86, H 9.27. ^{1}H NMR ($CDCl_3$): δ = 7.16 (m, 18 H, CH_2Ph), 7.02 (m, 9 H, CH_2Ph), 6.95 (m, 18 H, CH_2Ph), 6.54, 3.40, and 2.97 (broad resonances, 5 H, C_5H_5), 2.04 (s, 18 H, $CH_2C_6H_5$), 1.26 (m, 24 H, Si$CH_2CH_2CH_2$Si), 0.51 (m, 48 H, Si$CH_2CH_2CH_2$Si), –0.07 (s, 54 H, Me) ppm. ^{13}C{^{1}H} NMR ($CDCl_3$): δ = 140.4 (*ipso*-CH_2Ph), 132.9 (C_5H_5), 130.1 (C_5H_5), 128.1 (*ortho*-CH_2Ph), 128.0 (*meta*-CH_2Ph), 123.9 (*para*-CH_2Ph),

 © 2005 Wiley-VCH Verlag GmbH & Co. KGaA, Weinheim

49.9 (C_5H_5), 25.8 ($CH_2C_6H_5$), 19.9, 18.5, and 17.5 [G2-Si(CH_2)$_3$Si], 18.9, 18.0 and, 17.9 [G1-Si(CH_2)$_3$Si], –3.4 (Me) ppm. ^{29}Si{^{1}H} NMR ($CDCl_3$): δ = 2.70 (1 Si), 1.58 (9 Si), 0.55 (3 Si) ppm.

Data for C_5H_5-G3-[$(CH_2)_3SiMe_2Bz$]$_{27}$ (12): $C_{365}H_{590}Si_{40}$ (6102.0): calcd. C 71.84, H 9.75; found C 71.15, H 9.44. ^{1}H NMR ($CDCl_3$): δ = 7.14 (m, 54 H, CH_2Ph), 7.02 (m, 27 H, CH_2Ph), 6.92 (m, 54 H, CH_2Ph), 6.50, 3.35, 2.93 (broad resonances, 5 H, C_5H_5), 2.01 (s, 54 H, $CH_2C_6H_5$), 1.25 (m, 78 H, $SiCH_2CH_2CH_2Si$), 0.51 (m, 156 H, $SiCH_2CH_2CH_2Si$), –0.09 (s, 162 H, Me) ppm. ^{13}C{^{1}H} NMR ($CDCl_3$): δ = 140.2 (*ipso*-CH_2Ph), 133.0 (C_5H_5), 130.1 (C_5H_5), 128.1 (*ortho*-CH_2Ph), 127.9 (*meta*-CH_2Ph), 123.8 (*para*-CH_2Ph), 49.5 (C_5H_5), 25.8 ($CH_2C_6H_5$), 19.9, 18.6, and 17.5 [G3-Si(CH_2)$_3$Si], 18.8, 18.3, and 17.9 [G2-Si(CH_2)$_3$Si], –3.3 (Me) ppm; [G1-Si(CH_2)$_3$Si] not found. ^{29}Si{^{1}H} NMR ($CDCl_3$): δ = 2.60 (1 Si), 1.48 (27 Si), 0.43 (9 Si), 0.38 (3 Si) ppm.

Synthesis of KC_5H_4-G1-[$(CH_2)_3SiMe_2Bz$]$_3$ (13): In a dry box, solid potassium hydride (0.60 g, 15 mmol) was added to a solution of **10** (10 g, 15 mmol) in dimethoxyethane (50 mL). The reaction mixture was stirred overnight, filtered, and subsequently the solvent was evaporated in vacuo. Washing the resulting dark-yellow oil, which was insoluble in alkanes, with pentane (3 × 30 mL) yielded 8.7 g (82%) of pure **13**, which is stable enough to be characterized and stored for months in a dry box. MS (ESI+): *m*/*z* = 705 (calcd. for MH^+: 705). ^{1}H NMR (C_6D_6): δ = 7.24 (m, 6 H, CH_2Ph), 7.09 (m, 9 H, CH_2Ph), 6.01 (broad resonance, 4 H, C_5H_4), 2.20 (s, 6 H, $CH_2C_6H_5$), 1.64 (m, 6 H, $CH_2CH_2CH_2$), 0.90 (m, 12 H, $CH_2CH_2CH_2$), 0.17 (s, 18 H, Me) ppm. ^{13}C{^{1}H} NMR (C_6D_6): δ = 140.5 (*ipso*-CH_2Ph), 128.7 (*ortho*-CH_2Ph), 128.5 (*meta*-CH_2Ph), 124.5 (*para*-CH_2Ph), 114.0 (C_5H_5), 109.3 (C_5H_5), 26.6 ($CH_2C_6H_5$), 21.0, 20.8, and 20.3 [Si(CH_2)$_3$Si], –2.5 (Me) ppm; *ipso*-C_5H_4 not found. ^{29}Si{^{1}H} NMR (C_6D_6): δ = –12.03 (1 Si), 1.46 (3 Si) ppm.

Synthesis of [{C_5H_4-G1-[$(CH_2)_3SiMe_2Bz$]$_3$}$_2$TiCl$_2$] (14): A 0.20 M solution of $TiCl_4$ in toluene (3.0 mL, 0.60 mmol) was added from a syringe to a solution of the potassium cyclopentadienide **13** (0.85 g, 1.2 mmol) in toluene (20 mL). The mixture was stirred at room temperature overnight. After filtration, the solution was evaporated in vacuo to dryness. The crude red oil thus obtained was characterized as **14** (0.79 g, 91%). $C_{82}H_{122}Cl_2Si_8Ti$ (1451.3): calcd. C 67.86, H 8.47; found C 67.83, H 8.42. ^{1}H NMR ($CDCl_3$): δ = 7.17 (m, 6 H, CH_2Ph), 7.03 (m, 3 H, CH_2Ph), 6.95 (m, 6 H, CH_2Ph), 6.65 (pseudo t, AA′ part of an AA′BB′ spin system, 2 H, C_5H_4), 6.49 (pseudo t, BB′ part of an AA′BB′ spin system, 2 H, C_5H_4), 2.06 (s, 6 H, $CH_2C_6H_5$), 1.30 (m, 6 H, $SiCH_2CH_2CH_2Si$), 0.81 (m, 6 H, $C_5H_5SiCH_2CH_2CH_2Si$), 0.56 (m, 6 H, $C_5H_5SiCH_2CH_2CH_2Si$), –0.06 (s, 18 H, Me) ppm. ^{13}C{^{1}H} NMR ($CDCl_3$): δ = 140.1 (*ipso*-CH_2Ph), 129.2 (C_5H_4), 127.9 (*ortho*-CH_2Ph), 127.8 (*meta*-CH_2Ph), 123.6 (*para*-CH_2Ph), 119.1 (C_5H_4), 25.9 ($CH_2C_6H_5$), 20.0, 18.8, and 18.3, [Si(CH_2)$_3$Si], –3.1 (Me) ppm; *ipso*-C_5H_4 not found. ^{29}Si{^{1}H} NMR ($CDCl_3$): δ = –5.65 (1 Si), 1.53 (3 Si) ppm.

Synthesis of [{C_5H_4-G1-[$(CH_2)_3SiMe_2Bz$]$_3$}$_2$ZrCl$_2$] (15): Solid $ZrCl_4$·2THF (0.267 g, 0.71 mmol) was added, in a dry box, to a solution of **13** (1.00 g, 1.42 mmol) in toluene. The reaction mixture was stirred overnight, evaporated in vacuo, and extracted with hexane (3 × 10 mL). After filtration, the solvent was evaporated in vacuo to yield **15** (0.89 g, 84%) as a colorless oil. $C_{82}H_{122}Cl_2Si_8Zr$ (1494.66): calcd. C 65.89, H 8.23; found C 65.84, H 8.21. ^{1}H NMR ($CDCl_3$): δ = 7.19 (m, 6 H, CH_2Ph), 7.05 (m, 3 H, CH_2Ph), 6.95 (m, 6 H, CH_2Ph), 6.56 (pseudo t, AA′ part of an AA′BB′ spin system, 2 H, C_5H_4), 6.46 (pseudo t, BB′ part of an AA′BB′ spin system, 2 H, C_5H_4), 2.06 (s, 6 H, $CH_2C_6H_5$), 1.32 (m, 6 H, $SiCH_2CH_2CH_2Si$), 0.85 (m, 6 H, $C_5H_5SiCH_2CH_2CH_2Si$), 0.58 (m, 6 H, $C_5H_5SiCH_2CH_2CH_2Si$), –0.05 (s, 18 H, Me) ppm. ^{13}C{^{1}H} NMR ($CDCl_3$): δ = 140.1 (*ipso*-CH_2Ph), 127.9 (*ortho*-CH_2Ph), 125.5 (C_5H_4), 127.8 (*meta*-CH_2Ph), 123.6 (*para*-CH_2Ph), 115.5 (C_5H_4), 25.9 ($CH_2C_6H_5$), 19.9, 18.8, and 18.3 [Si(CH_2)$_3$Si], –3.1 (Me) ppm; *ipso*-C_5H_4 not found. ^{29}Si{^{1}H} NMR ($CDCl_3$): δ = –6.34 (1 Si), 1.54 (3 Si) ppm.

Ethylene and Propylene Polymerization: A 250-mL flask charged with toluene (50 mL) and equipped with a magnetic stirrer was evacuated and refilled with pre-dried ethylene or propylene gas four times. Whilst keeping the flask pressurized with the corresponding gas (1 bar) and stirring at room temperature, a toluene solution of methylaluminoxane (PMAO-IP 13% Akzo Nobel, 0.50 mL) was syringed through a septum. After 5 min, a toluene solution of the catalyst (0.50 mL, 2.5 mM) was injected into the flask with simultaneous starting of a stopwatch. The polymerization was quenched 10 min later by closing the gas feed, release of the overpressure, and addition of acidified methanol (4% v/v HCl). The mixture was stirred for 6 h and the polymer was filtered, washed with copious amounts of methanol, and dried in an oven to constant weight.

Acknowledgments

We gratefully acknowledge financial support from the DGI-Ministerio de Ciencia y Tecnología (Project BQU2001-1160 and Programa Ramón y Cajal), and the DGI-Comunidad de Madrid (Project GR/MAT/0733/2004).

[1] a) *Dendrimers and Other Dendritic Polymers* (Eds.: J. M. J. Frechet, D. A. Tomalia), Wiley-VCH, Weinheim, **2001**; b) G. R. Newkome, C. N. Moorefield, F. Vögtle, *Dendrimers: Concepts, Syntheses, Applications*, Wiley-VCH, Weinheim, **2001**.

[2] a) G. E. Oosterom, J. N. H. Reek, P. C. J. Kamer, P. W. N. M. van Leeuwen, *Angew. Chem. Int. Ed.* **2001**, *40*, 1828–1849; b) L. J. Twyman, A. S. H. King, I. K. Martin, *Chem. Soc. Rev* **2002**, *31*, 69–82.

[3] a) D. Astruc, F. Chardac, *Chem. Rev.* **2001**, *101*, 2991–3023; b) R. Kreiter, A. W. Kleij, R. J. M. Klein Gebbink, G. van Koten, *Top. Curr. Chem.* **2001**, *217*, 163–199.

[4] O. Rossell, M. Seco, I. Angurell, *C. R. Chimie* **2003**, *6*, 803–817.

[5] a) G. E. Oosterim, R. J. van Haaren, J. N. H. Reek, P. C. J. Kamer, P. W. N. M. van Leeuwen, *Chem. Commun.* **1999**, 1119–1120; b) G. E. Oosterom, S. Steffens, J. N. H. Reek, P. C. J. Kamer, P. W. N. M. van Leeuwen, *Top. Catal.* **2002**, *19*, 61–73; c) J. N. H. Reek, D. de Groot, G. E. Oosterom, P. C. J. Kamer, P. W. N. M. van Leeuwen, *C. R. Chimie* **2003**, *6*, 1061–1077; d) C. Müller, L. J. Ackerman, J. N. H. Reek, P. C. J. Kamer, P. W. N. M. van Leeuwen, *J. Am. Chem. Soc.* **2004**, *126*, 14960–14963.

[6] a) A. W. van der Made, P. W. N. M. van Leeuwen, *J. Chem. Soc., Chem. Commun.* **1992**, 1400–1401; b) A. W. van der Made, P. W. N. M. van Leeuwen, J. C. de Wilde, R. A. C. Brandes, *Adv. Mater.* **1993**, *5*, 466–468; c) L. L. Zhou, J. Rovers, *Macromolecules* **1993**, *26*, 963–968; d) A. M. Muzafarov, O. B. Gorbatsevich, E. A. Rebrov, G. M. Ignat'eva, T. B. Chenskaya, V. D. Myakushev, A. F. Bulkin, V. S. Papkov, *Vysokomol. Soedin.* **1993**, *35*, 1867–1872; *Polym. Sci. Ser A.* **1993**, *35*, 1575–1580; e) B. Alonso, I. Cuadrado, M. Morán, J. Losada, *J. Chem. Soc., Chem. Commun.* **1994**, 2575–2576.

[7] R. Andrés, E. de Jesús, F. J. de la Mata, J. C. Flores, R. Gómez, *Eur. J. Inorg. Chem.* **2002**, 2281–2286.

[8] a) C. Hawker, J. M. J. Fréchet, *J. Chem. Soc., Chem. Commun.* **1990**, 1010–1013; b) C. J. Hawker, J. M. J. Fréchet, *J. Am. Chem. Soc.* **1990**, *112*, 7638–7647.

[9] A convergent synthesis of ferrocene-containing carbosilane denderimers has been reported: I. Cuadrado, C. M. Casado, B.

 © 2005 Wiley-VCH Verlag GmbH & Co. KGaA, Weinheim

Alonso, M. Morán, J. Losada, V. Belsky, *J. Am. Chem. Soc.* **1997**, *119*, 7613–7614.
[10] J. L. Speier, *Adv. Organomet. Chem.* **1979**, *17*, 407–447; L. N. Lewis, *J. Am. Chem. Soc.* **1990**, *112*, 5998–6004.
[11] D. Terumuna, T. Kato, R. Nishio, K. Matsuoka, H. Kuzuhara, Y. Aoki, H. Nohira, *Chem. Lett.* **1998**, 59–60.
[12] See for example: E. Hupe, M. I. Calaza, P. Knochel, *Chem. Commun.* **2002**, 1390–1391.
[13] B. Reiter, K. Hassler, *J. Organomet. Chem.* **1994**, *467*, 21–29.
[14] a) D. Häbich, F. Effenberger, *Synthesis* **1978**, 755–756. b) For a more recent reference see: J. O. Daiss, M. Penka, C. Burschka, R. Tacke, *Organometallics* **2004**, *23*, 4987–4994.
[15] Allyl is a still-better leaving group than phenyl; a) A. R. Bassindale, T. Stout, *J. Organomet. Chem.* **1984**, *271*, C1–C3; K. E. Ruehl, K. Matyjaszewski, *J. Organomet. Chem.* **1991**, *410*, 1–12; b) W. Uhlig, *J. Organomet. Chem.* **1993**, *452*, 29–32.
[16] H. Emde, D. Domsch, H. Feger, U. Frick, A. Götz, H. H. Hergott, K. Hofmann, W. Kober, K. Krägeloh, T. Oesterle, W. Steppan, W. West, G. Simchen, *Synthesis* **1982**, 1–26.
[17] A. J. Ashe, *J. Am. Chem. Soc.* **1970**, *92*, 1233–1235; E. W. Abel, M. O. Dunster, *J. Organomet. Chem.* **1971**, *33*, 161–167.
[18] A. Morikawa, M. Kakimoto, Y. Imai, *Macromolecules* **1992**, *25*, 3247–3253; M. Veith, R. Elsässer, R. P. Krüger, *Organometallics* **1999**, *18*, 656–661.
[19] G. W. Coates, R. M. Waymouth, *Science* **1995**, *267*, 217–219; M. D. Bruce, G. W. Coates, E. Hauptman, R. M. Waymouth, J. W. Ziller, *J. Am. Chem. Soc.* **1997**, *119*, 11174–11182; K. Kimura, K. Takaishi, T. Matsukawa, T. Yoshimura, H. Yamazaki, *Chem. Lett.* **1998**, 571–572.
[20] V. Busico, R. Cipullo, *Prog. Polym. Sci.* **2001**, *26*, 443–533.
[21] P. J. Gittins, L. J. Twyman, *J. Am. Chem. Soc.* **2005**, *127*, 1646–1647.
[22] D. D. Perrin, W. L. F. Armarego, *Purification of Laboratory Chemicals*, 3rd ed., Butterworth–Heinemann Ltd., Oxford, **1988**.

Received: March 1, 2005
Published Online: August 4, 2005

 © 2005 Wiley-VCH Verlag GmbH & Co. KGaA, Weinheim

Synthesis and Structures of Bi(1,1-stannole)s

Masaichi Saito,*[a] Ryuta Haga,[a] and Michikazu Yoshioka[a]

Keywords: Metallacycles / Tin / UV/Vis spectroscopy

The synthesis and structures of bi(1,1-stannole)s are described. Treatment of 1-bromo-4-(dibromophenylstannyl)-1,3-butadiene with *tert*-butyllithium gives the bi(1,1-stannole) having a phenyl group on each tin atom, whereas treatment of 1-bromo-4-(tribromostannyl)-1,3-butadiene with phenyl- or bulky alkyllithiums gives the bi(1,1-stannole) having a phenyl or an alkyl group on each tin atom. The X-ray analysis of the *tert*-butyl-substituted bi(1,1-stannole) is also described. All bi(1,1-stannole)s display two shoulder absorption bands due to π–π^* and σ–π^* transitions.
(© Wiley-VCH Verlag GmbH & Co. KGaA, 69451 Weinheim, Germany, 2005)

Introduction

Group 14 metalloles,[1] or metallacyclopentadienes, have attracted much attention because of interest in them as a possible precursor for the preparation of conjugated polymers having unique electronic structures[2,3] as well as the potential aromaticity of their anions.[4] Since the successful synthesis of some oligo(1,1-silole)s[5,6] and poly(1,1-silole)s, they have been applied to organic electroluminescent (EL) devices.[7,8] Most recently, poly(1,1-germole) has also been reported.[9] In contrast to the silicon and germanium analogs, however, attempts to prepare oligo- and poly(1,1-stannole)s are still unknown. Although the synthesis and some simple reactions of stannoles have been reviewed,[1] even the synthesis of bi(1,1-stannole) has not yet been successful.

In the course of our studies on organotin compounds,[10] we have already reported that bromination of hexaphenylstannole (**1**) gives the ring-opened halogenated product **2** (Scheme 1).[11,12] We have also preliminarily reported that debrominative cyclization of **2** affords the bi(1,1-stannole).[13] We report herein the synthesis, structures, and physical properties of some bi(1,1-stannole)s.

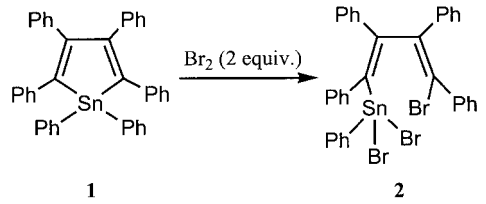

1 **2**

Scheme 1.

[a] Department of Chemistry, Faculty of Science, Saitama University,
Shimo-okubo, Saitama-city, Saitama, 338-8570, Japan
E-mail: masaichi@chem.saitama-u.ac.jp

Results and Discussion

Synthesis of Bi(1,1-stannole) 3

Treatment of **2** with two equivalents of *tert*-butyllithium in THF at –100 °C gave a yellow solution. After usual workup, the mixture was chromatographed to give bi(1,1-stannole) **3** as yellow crystals in 58% yield together with stannole **4** (7%) (Scheme 2). To the best of our knowledge, compound **3** is the first example of bi(1,1-stannole). Two possible mechanisms for the formation of **3** are shown in Scheme 2. The initial step of the reaction is the formation of 1-bromo-1-phenylstannole (**5**), which reacts further with *tert*-butyllithium to give the stannole anion **6** or the stannole radical **7**. The stannole anion **6** then reacts with **5** to give **3**, while the stannole radical **7** couples to itself to also give **3**. Product **4** is formed by nucleophilic substitution at the tin atom of **5** by *tert*-butyllithium. Trapping of the intermediary ionic species **6** by addition of methyl iodide or chlorotrimethylstannane, expecting to obtain a methylated or a stannylated product, failed and the bi(1,1-stannole) **3** was obtained in 71 or 77% yield, respectively. Therefore, a radical mechanism for the formation of **3** is more likely, although the ionic mechanism cannot be ruled out entirely. The yield of **3** was improved (82%) when the reaction was carried out in diethyl ether, although the reason for the solvent-dependent product yield is not clear.

Synthesis of Bi(1,1-Stannole)s Having Various Substituents on the Tin Atom

The synthesis of other bi(1,1-stannole)s having various substituents on the tin atom was achieved by the reaction of 1-bromo-4-(tribromostannyl)-1,3-butadiene (**8**) with lithium reagents.

 © 2005 Wiley-VCH Verlag GmbH & Co. KGaA, Weinheim DOI: 10.1002/ejic.200500274

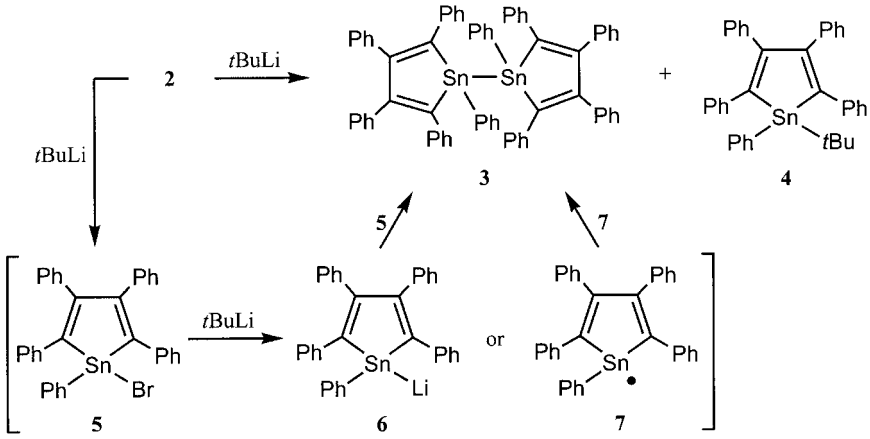

Scheme 2.

Synthesis of 1-Bromo-4-(tribromostannyl)-1,3-butadiene (8)

We attempted to synthesize **8** by the reaction of **1** or **2** with bromine. However, the reaction of **2** with bromine gave a complex mixture. Reaction of hexaphenylstannole (**1**) with excess bromine also gave a complex mixture containing 1,4-dibromo-1,2,3,4-tetraphenylbutadiene.[14]

Since the *p*-methoxyphenyl group on the tin atom is known to be easily removed by halogenation,[15] the reaction of 1,1-di(*p*-methoxyphenyl)stannole (**9**) with bromine was examined. Compound **9** was prepared by the reaction of 1,4-dilithio-1,2,3,4-tetraphenylbutadiene with dichlorodi(*p*-methoxyphenyl)stannane[16] in 58% yield (Scheme 3). Reaction of **9** with bromine (1 equiv.) at –40 °C gave a complex mixture, and treatment of **9** with bromine (2 equiv.) at –20 °C afforded 1,4-dibromo-1,2,3,4-tetraphenylbutadiene (41%).[14] However, the reaction of **9** with excess bromine (10 equiv.) at room temperature gave **8** (96%). The structure of **8** was determined by NMR spectroscopy and elemental analysis (Scheme 3).

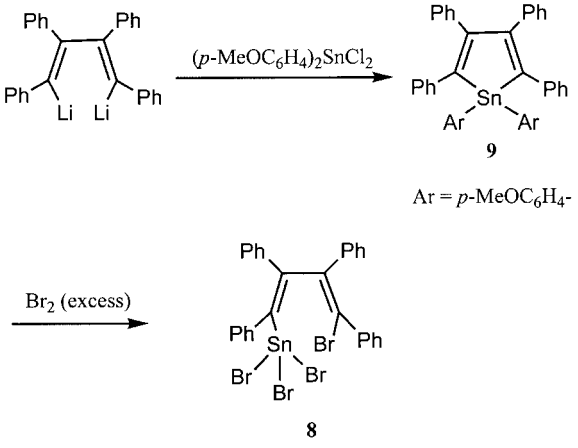

Scheme 3.

Reaction of 8 with Lithium Reagents: Synthesis of Bi(1,1-stannole)s

Treatment of **8** with phenyllithium (2 equiv.) afforded bi(1,1-stannole) **3** (12%) and hexaphenylstannole **1** (33%; Scheme 4). The preferential formation of **1** to **3** may be ascribed to the size of the lithium reagent. In fact, the reaction of **8** with bulkier *tert*-butyllithium (2 equiv.) rather than phenyllithium gave bi(1,1-stannole) **10** having a *tert*-butyl group on each tin atom as the sole product in 55% yield (Scheme 4). Reaction of **7** with *sec*-butyllithium (2 equiv.), a moderately bulky reagent, gave a bi(1,1-stannole) **11** having a *sec*-butyl group on each tin atom as a 1:1 diastereomeric mixture[17] in a relatively good yield (40%; Scheme 4). The diastereomeric ratio was estimated by signal intensities (δ = –60.59 and –60.57 ppm) in the ^{119}Sn NMR spectrum. Contrary to the bulky lithium reagent, the reaction of less bulky methyllithium (1 equiv.) with **8** gave 4-bromo-1,2,3,4-tetraphenyl-1-(trimethylstannyl)-1,3-butadiene (**12**) in 15% yield. Methyllithium would directly attack the tin to afford trimethyl derivative **12** (Scheme 4). Reaction of **8** with methyllithium (3 equiv.) gave **12** (62%) and 1,1-dimethylstannole **13** (27%; Scheme 4).

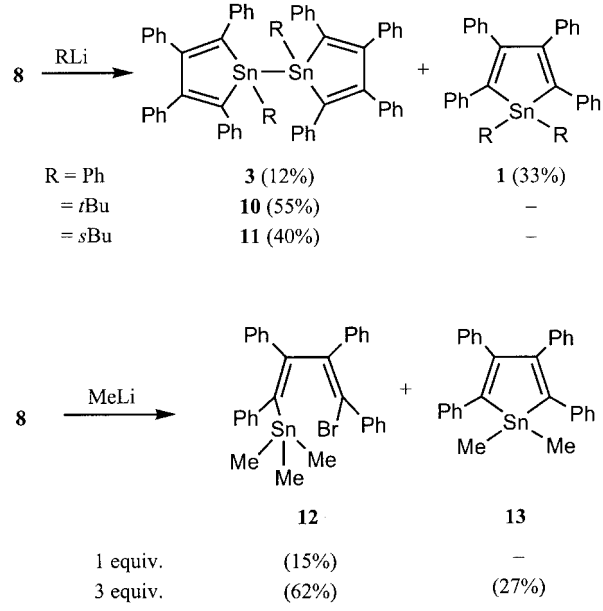

Scheme 4.

 © 2005 Wiley-VCH Verlag GmbH & Co. KGaA, Weinheim

Structures of 3 and 10

Slow evaporation of the solvent from chloroform solutions of **3** and **10** gave X-ray quality crystals. The structure of **3** has been reported previously.[13] Because of the symmetrical structures of **3** and **10** with respect to the Sn–Sn bond, only a half moiety was refined. The ORTEP drawing of **10**, with selected bond lengths and angles, is shown in Figure 1. The length of the Sn–Sn bond is quite normal[18] at 2.7822(7) Å [2.7844(7) Å for **3**].[13] Each stannole ring has a nearly planar structure and is oriented in an *anti* fashion through the Sn–Sn bond probably due to steric reasons. The angle between the stannole plane and the Sn–Sn bond is 67° for **10** (74° for **3**).

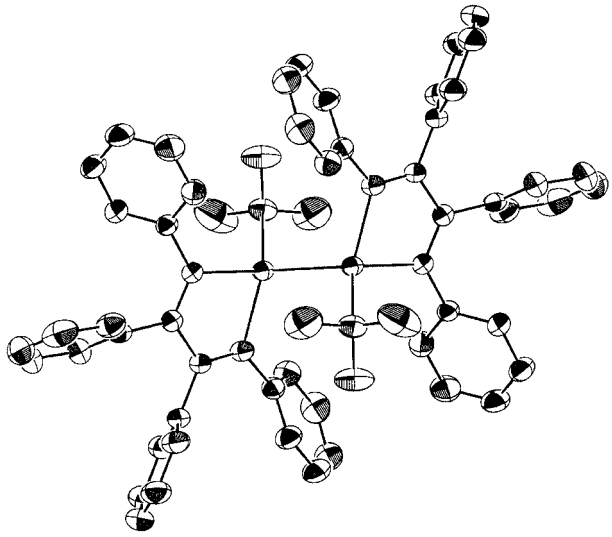

Figure 1. ORTEP drawing of **10** with thermal ellipsoid plots (40% probability for non-hydrogen atoms). Selected bond lengths [Å] and angles [°]: Sn(1)A–Sn(1)B 2.7822(7), Sn(1)A–C(1) 2.143(4), C(1)–C(2) 1.353(5), C(2)–C(3) 1.506(5), C(3)–C(4) 1.352(5), Sn(1)A–C(4) 2.157(4); C(1)–Sn(1)A–C(4) 83.28(14).

Spectroscopic Properties

In the ^{119}Sn NMR spectrum, each central tin atom of the compounds with the stannole skeleton resonates in the range from δ = –100 to –45ppm, in the same region as that of 1,1,2,3,4,5-hexaphenylstannole (δ = –88.7 ppm).[11] The tin atoms of alkyl-substituted bi(1,1-stannole)s **10** and **11** resonate to higher field than that of **3**, as is observed in normal distannanes (δ = –108.7 and –144.7 ppm for $Me_3SnSnMe_3$[19] and $Ph_3SnSnPh_3$,[20] respectively). The $^1J_{^{119}Sn,^{117}Sn}$ coupling constant of 2865 Hz for **3** is a normal value for distannanes (cf. 2748 Hz for $Bu_3SnSnBu_3$).[19] The UV/Vis absorption spectra for **3**, **10**, and **11** are shown in Figure 2. All bi(1,1-stannole)s display two shoulder absorption bands at around 320 and 370 nm. The latter band can be assigned to the π–π* transition of the stannole ring because a similar absorption band is found in 1,1,2,3,4,5-hexaphenylstannole (**1**; λ_{max} = 355 nm).[21] The π–π* transition of group 14 metalloles is observed in the same region, at around 360 nm, because the contributions of the diene moiety to both HOMO and LUMO are predominant rather than that of the metal moiety.[21] The shorter wavelength band can be assigned to the transition from σ(Sn–Sn) to π*(diene) because the corresponding band is absent in **1**. This absorption (320 nm) is red-shifted compared to that of a bi(1,1-silole) (300 nm)[7] because of the higher energy level of a σ(Sn–Sn) bond than that of a σ(Si–Si) bond.

Conclusions

Several bi(1,1-stannole)s combining two stannacyclopentadienyl units through an Sn–Sn bond have been synthe-

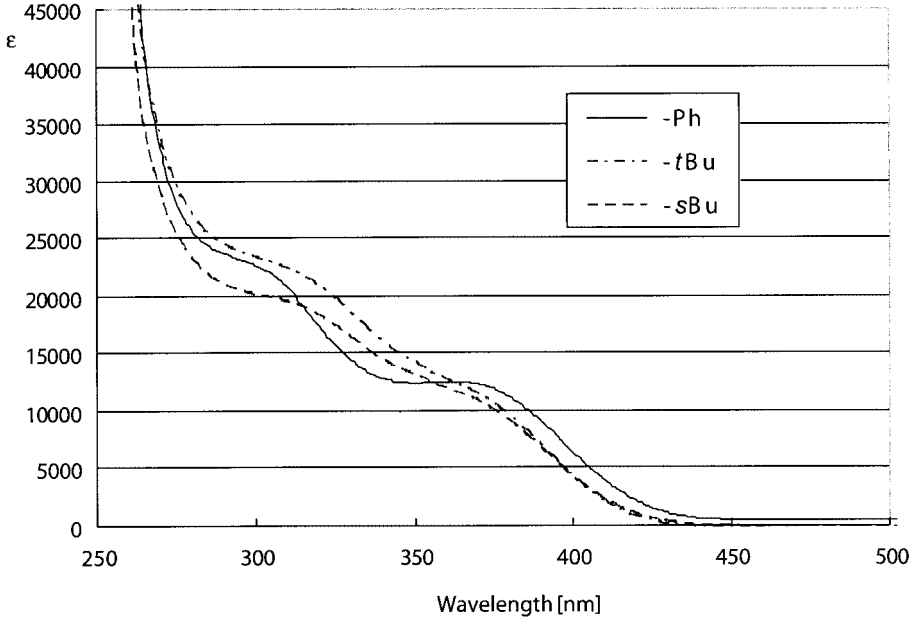

Figure 2. UV/Vis spectra of bi(1,1-stannole)s **3**, **10**, and **11**.

 © 2005 Wiley-VCH Verlag GmbH & Co. KGaA, Weinheim

sized and characterized. The product yield in the formation of bi(1,1-stannole) by the reaction of 1-bromo-4-(tribromophenylstannyl)-1,3-butadiene with lithium reagent is dependent on the size of the lithium reagent used. The X-ray analysis of bi(1,1-stannole) shows a symmetrical structure with respect to the Sn–Sn bond. All bi(1,1-stannole)s display two shoulder absorption bands due to π–π* and σ–π* transitions.

Experimental Section

General Procedures: All reactions were carried out under argon. THF and diethyl ether used in the syntheses were distilled from sodium benzophenone ketyl under argon before use. ^{1}H (400 MHz) and ^{13}C NMR (100 MHz) spectra were recorded on a Bruker AM-400 or an ARX-400 spectrometer in $CDCl_3$ with tetramethylsilane as an internal standard. Although $^nJ_{Sn,^{13}C}$ couplings were observed in the ^{13}C NMR spectra as satellite signals, most of the $^nJ_{^{119}Sn-^{13}C}$ and $^nJ_{^{117}Sn-^{13}C}$ couplings could not be estimated separately because of line broadening. The multiplicities of the signals in the ^{13}C NMR spectra given in parentheses were deduced from DEPT spectra. ^{119}Sn NMR (149 MHz) spectra were recorded on a Bruker ARX-400 spectrometer in $CDCl_3$ with tetramethylstannane as an external standard. Column chromatography was carried out with Merck Kieselgel 60 (SiO_2). All melting points were determined on a Mitamura Riken Kogyo MEL-TEMP apparatus and are uncorrected. Electronic spectra were recorded on a JASCO V-560 UV/Vis spectrometer. Elemental analyses were carried out at the Microanalytical Laboratory of Molecular Analysis and Life Science Center, Saitama University.

Preparation of Bi(1,1-stannole) 3. (a) Method A (in THF): *tert*-Butyllithium (1.60 M in pentane; 3.2 mL, 5.12 mmol) was added at –100 °C to a THF (30 mL) solution of 1-bromo-4-(dibromophenylstannyl)-1,2,3,4-tetraphenyl-1,3-butadiene (**2**; 2030 mg, 2.56 mmol). After warming to room temperature over 4 h, the solvent was evaporated. The residue was subjected to column chromatography (hexane/ethyl acetate = 10:1) to afford bis(1,2,3,4,5-pentaphenylstannacyclopentadienyl) (**3**; 826 mg, 58%) and 1-*tert*-butyl-1,2,3,4,5-pentaphenylstannole (**4**; 103 mg, 7%).
3: M.p. 209 °C (decomp.) (recrystallized from dichloromethane/methanol). ^{1}H NMR: δ = 6.73–6.80 (m, 8 H), 6.84–6.89 (m, 8 H), 6.94–7.00 (m, 24 H), 7.13–7.20 (m, 4 H), 7.24–7.27 (m, 6 H) ppm. ^{13}C NMR: δ = 125.4 (d), 125.9 (d), 127.3 (d), 127.9 (d), 129.0 (d, $J_{Sn,C}$ = 53 Hz), 129.6 (d, $J_{Sn,C}$ = 22 Hz), 130.5 (d), 137.4 (d, $J_{Sn,C}$ = 10, 46 Hz), 138.7 (s), 140.5 (s, $J_{Sn,C}$ = 61 Hz), 142.4 (s, $J_{Sn,C}$ = 47 Hz), 145.9 (s, $J_{Sn,C}$ = 37, 334, 350 Hz), 154.3 (s, $J_{Sn,C}$ = 22, 81 Hz) ppm. ^{119}Sn NMR: δ = –99.3 ppm ($^1J_{^{119}Sn,^{117}Sn}$ = 2865 Hz). $C_{68}H_{50}Sn_2$ (1104.6): calcd. C 73.94, H 4.56; found C 73.30, H 4.31.
4: M.p. 160–161 °C (decomp.) (recrystallized from dichloromethane/methanol). ^{1}H NMR: δ = 1.37 (s, 9 H, $J_{Sn,H}$ = 75, 78 Hz), 6.79–6.80 (m, 4 H), 6.89–6.97(m, 12 H), 7.03–7.06 (m, 4 H), 7.30–7.37 (m, 3 H), 7.48–7.61 (m, 2 H) ppm. ^{13}C NMR: δ = 31.1 (q), 32.7 (s), 125.0 (d), 125.7 (d), 127.2 (d), 127.8 (d), 128.8 (d), 129.0 (d), 129.2 (d), 130.4 (d), 137.2 (d), 139.9 (s), 140.8 (s), 143.4 (s), 144.6 (s), 155.2 (s) ppm. ^{119}Sn NMR: δ = –59.9 ppm. $C_{38}H_{34}Sn$ (609.42): calcd. C 74.90, H 5.62; found C 74.90, H 5.58.

Method B (in Diethyl Ether): *tert*-Butyllithium (1.50 M in pentane; 3.4 mL, 5.10 mmol) was added at –100 °C to a diethyl ether (40 mL) solution of **2** (1999 mg, 2.52 mmol). After warming to room temperature over 4 h, the solvent was evaporated. The residue was subjected to column chromatography (ethyl acetate) followed by recrystallization from hexane and dichloromethane to afford **3** (1141 mg, 82%).

Attempt to Trap Intermediary Ionic Species with Methyl Iodide: *tert*-Butyllithium (1.48 M in pentane; 0.29 mL, 0.43 mmol) was added to a diethyl ether (4 mL) solution of **2** (114 mg, 0.14 mmol) at –100 °C. The color of the solution immediately turned yellow. Methyl iodide (0.05 mL, 0.80 mmol) was added to this solution. After warming to room temperature over 7 h, the solvent was evaporated. Recrystallization from hexane and dichloromethane gave **3** (56 mg, 71%).

Attempt to Trap Intermediary Ionic Species with Chlorotrimethylstannane: *tert*-Butyllithium (1.60 M in pentane; 0.24 mL, 0.38 mmol) was added to a diethyl ether (4 mL) solution of **2** (98 mg, 0.12 mmol) at –100 °C and a diethyl ether (2 mL) solution of chlorotrimethylstannane (30 mg, 0.15 mmol) was then added. After warming to room temperature over 4 h, the solvent was evaporated. Recrystallization from hexane and dichloromethane gave **3** (53 mg, 77%).

Preparation of 1,1-Di(*p*-methoxyphenyl)-2,3,4,5-tetraphenylstannole (9): A suspension of diphenylacetylene (4.40 g, 24.7 mmol) and lithium (171 mg, 24.7 mmol) in diethyl ether (17 mL) was stirred for 4 h at room temperature. A THF (15 mL) solution of di(*p*-methoxyphenyl)dichlorostannane[16] (4.11 g, 10.2 mmol) was added to the resulting suspension and the mixture was refluxed for 3 h. After removal of solvents, any material insoluble in dichloromethane was filtered off. After evaporation, the residue was subjected to column chromatography (hexane/ethyl acetate = 10:1) to give **9** (4.035 g, 58%). M.p. 200 °C (decomp.) (recrystallized from dichloromethane/hexane). ^{1}H NMR: δ = 3.81 (s, 6 H), 6.80–6.86 (m, 4 H), 6.89 (d, J = 8 Hz, 4 H), 6.92–7.05 (m, 16 H), 7.50 (d, J = 8 Hz, 4 H) ppm. ^{13}C NMR: δ = 55.0 (q), 114.9 (d, $J_{Sn,C}$ = 58 Hz), 125.3 (d), 125.8 (d), 127.3 (d), 127.8 (d), 128.3 (s), 129.3 (d, $J_{Sn,C}$ = 22 Hz), 130.3 (d), 138.3 (d, $J_{Sn,C}$ = 46 Hz), 140.7 (s, $J_{Sn,C}$ = 68 Hz), 142.5 (s, $J_{Sn,C}$ = 45 Hz), 143.0 (s), 154.4 (s, $J_{Sn,C}$ = 89 Hz), 160.7 (s) ppm. ^{119}Sn NMR: δ = –79.9 ppm. $C_{40}H_{34}O_2Sn$ (665.44): calcd. C 72.20, H 5.15; found C 72.30, H 4.93.

Reaction of 9 with Bromine (2 equiv.): A carbon tetrachloride (8 mL) solution of bromine (0.02 mL, 0.39 mmol) at –20 °C was added to a carbon tetrachloride (7 mL) solution of **9** (134 mg, 0.19 mmol). After warming to room temperature, the solvent was evaporated. The residue was recrystallized from dichloromethane and methanol to give 1,4-dibromo-1,2,3,4-tetraphenylbutadiene (39 mg, 41%).[14]

Reaction of 9 with Bromine (excess): A carbon tetrachloride (8 mL) solution of bromine (0.89 mL, 17.3 mmol) was added at room temperature to a dichloromethane (15 mL) solution of **9** (1200 mg, 1.74 mmol). The residue was recrystallized from dichloromethane and methanol to give 1-bromo-1,2,3,4-tetraphenyl-4-(tribromostannyl)-1,3-butadiene (**8**; 1328 mg, 96%). M.p. 167–168 °C (decomp.) (recrystallized from dichloromethane/hexane). ^{1}H NMR: δ = 7.06–7.16 (m, 4 H), 7.20–7.39 (m, 14 H), 7.48–7.53 (m, 2 H) ppm. ^{13}C NMR: δ = 128.0 (d), 128.1 (d), 128.2 (d), 128.3 (d), 128.56 (d), 128.58 (d), 128.9 (d), 129.0 (d), 129.8 (d), 129.9 (d), 130.1 (d), 130.8 (d), 136.4 (s), 136.6 (s, $J_{Sn,C}$ = 10 Hz), 136.8 (s), 138.8 (s), 141.0 (s, $J_{Sn,C}$ = 67 Hz), 144.1 (s), 156.69 (s, $J_{Sn,C}$ = 61 Hz) ppm. ^{119}Sn NMR: δ = –285.4 ppm. $C_{28}H_{20}Br_4Sn$ (794.78): calcd. C 42.32, H 2.54; found C 42.65, H 2.50.

Reaction of 8 with Phenyllithium: Phenyllithium (0.88 M in cyclohexane; 0.20 mL, 0.18 mmol) was added at –80 °C to a THF (3 mL) solution of **7** (70 mg, 0.09 mmol). After warming to room temperature over 3.5 h, the volatile substances were removed. After fil-

 © 2005 Wiley-VCH Verlag GmbH & Co. KGaA, Weinheim

tration of material insoluble in dichloromethane, the filtrate was subjected to column chromatography (hexane/ethyl acetate = 10:1) to afford **1** (18 mg, 33%) and **3** (6 mg, 12%).

Reaction of 8 with *tert*-Butyllithium. Formation of Bi(1,1-stannole) 10: *tert*-Butyllithium (1.43 M in pentane; 1.1 mL, 1.57 mmol) was added at –95 °C to a THF (10 mL) solution of **8** (408 mg, 0.51 mmol). After warming to room temperature over 3 h, the volatile substances were removed. After removal of material insoluble in dichloromethane by filtration, the filtrate was recrystallized from dichloromethane and methanol to give bis(1-*tert*-butyl-2,3,4,5-tetraphenylstannacyclopentadienyl) (**10**; 150 mg, 55%). M.p. 270–300 °C (decomp.) (recrystallized from dichloromethane). ^{1}H NMR: δ = 1.10 (s, 18 H, $J_{Sn,H}$ = 85 Hz), 6.80–6.84 (m, 8 H), 6.87–7.04 (m, 32 H) ppm. ^{13}C NMR: δ = 31.6 (q), 35.2 (s), 124.9 (d), 125.6 (d), 127.2 (d), 127.7 (d), 129.6 (d), 130.7 (d), 140.9 (s), 143.5 (s), 148.5 (s), 154.2 (s) ppm. ^{119}Sn NMR: δ = –46.4 ppm. $C_{64}H_{58}Sn_2$ (1064.6): calcd. C 72.21, H 5.49; found C 71.54, H 5.37. The $J_{Sn,Sn}$ and $J_{Sn,C}$ satellites were not observed because of low solubility.

Reaction of 8 with *sec*-Butyllithium: *sec*-Butyllithium (0.96 M in pentane; 0.53 mL, 0.51 mmol) was added at –95 °C to a THF (3 mL) solution of **8** (136 mg, 0.17 mmol). After warming to room temperature over 7 h, the volatile substances were removed. After removal of material insoluble in dichloromethane by filtration, the filtrate was recrystallized from diethyl ether to give a 1:1 diastereomeric mixture of bis(1-*sec*-butyl-2,3,4,5-tetraphenylstannacyclopentadienyl) (**11**; 37 mg, 40%). M.p. 230–233 °C (decomp.) (recrystallized from dichloromethane/methanol). ^{1}H NMR: δ = 0.77 (t, J = 7 Hz, 6 H), 1.03–1.26 (m, 6 H), 1.47–1.58 (m, 4 H), 2.06–2.12 (m, 2 H), 6.76–6.78 (m, 8 H), 6.84–6.87 (m, 8 H), 6.91–6.95 (m, 16 H), 6.98–7.02 (m, 4 H) ppm. ^{13}C NMR: δ = 14.5 (q), 19.7 (q), 19.7 (q), 30.4 (t), 32.1 (d), 124.9 (d), 125.6 (d), 127.2 (d), 127.7 (d), 129.3 (d), 129.3 (d), 130.6 (d), 141.0 (s), 143.5 (s), 148.6 (s), 148.8 (s), 153.7 (s), 153.8 (s) ppm. ^{119}Sn NMR: δ = –60.59, –60.57 ppm. $C_{64}H_{58}Sn_2$ (1064.62): calcd. C 72.21, H 5.49; found C 71.58, H 5.46.

Reaction of 8 with Methyllithium (1 equiv.): Methyllithium (1.02 M in diethyl ether; 0.2 mL, 0.20 mmol) was added at –100 °C to a THF (5 mL) solution of **8** (163 mg, 0.21 mmol). After warming to room temperature, the volatile substances were removed. After removal of material insoluble in dichloromethane by filtration, the filtrate was subjected to column chromatography (hexane/ethyl acetate = 10:1) to give 4-bromo-1,2,3,4-tetraphenyl-1-(trimethylstannyl)-1,3-butadiene (**12**; 19 mg, 15%). M.p. 118 °C (decomp.) (recrystallized from dichloromethane/hexane). ^{1}H NMR: δ = 0.13 (s, 9 H, $J_{Sn,H}$ = 52, 54 Hz), 6.96–7.10 (m, 9 H), 7.13–7.23 (m, 9 H), 7.36–7.40 (m, 2 H) ppm. ^{13}C NMR: δ = –7.0 (q), 124.3 (s), 124.9 (d), 126.4 (d), 127.3 (d), 127.4 (d), 127.7 (d), 127.8 (d), 127.9 (d), 128.0 (d), 128.2 (d), 130.0 (d), 130.1 (d), 130.5 (d), 138.7 (s), 139.7 (s), 140.3 (s), 144.4 (s), 145.3 (s), 148.5 (s), 152.4 (s) ppm. ^{119}Sn NMR: δ = –36.2 ppm. $C_{31}H_{29}BrSn$ (600.20): calcd. C 62.04, H 4.87; found C 62.04, H 4.79.

Reaction of 8 with Methyllithium (3 equiv.): Methyllithium (1.02 M in diethyl ether; 0.4 mL, 0.41 mmol) was added at –90 °C to a THF (4 mL) solution of **8** (101 mg, 0.13 mmol). After warming to room temperature, the volatile substances and material insoluble in dichloromethane were removed. The residue (64 mg) contained 62% of **12** and 27% of 1,1-dimethylstannole **13** by ^{1}H NMR estimation.

Crystal and Experimental Data for 10: Crystals suitable for X-ray diffraction were obtained by slow evaporation of the solvent from a chloroform solution of **10**. Data for the X-ray crystallographic analysis were collected on a Mac Science MXC18K diffractometer with Mo-K_α radiation (λ = 0.71073 Å). The structure was solved by direct methods using SIR[22] and refined by full-matrix least-squares techniques (SHELXL-97)[23] using all independent reflections (5672 reflections) for 298 parameters. The non-hydrogen atoms were refined anisotropically and all the hydrogen atoms were placed at calculated positions [d(C–H) = 0.96 Å]. R_1 = 0.042 [$I > 2\sigma(I)$, 5389 reflections], wR_2 = 0.097 (for all reflections), GOF = 1.094. The crystallographic data and details associated with data collection for **10** are given in Table 1.

Table 1. Crystallographic data for compound **10**.

Formula	$C_{64}H_{58}Sn_2$
Mol. mass	1064.52
Color	yellow
Crystal size [mm]	0.3 × 0.1 × 0.1
Temperature [K]	298
Crystal system	triclinic
Space group	*P*1 (#2)
a [Å]	12.756(2)
b [Å]	11.087(3)
c [Å]	10.685(2)
α [°]	117.650(10)
β [°]	86.180(10)
γ [°]	99.130(10)
V [Å^3]	1321.6(4)
Z	1
$D_{calcd.}$ [g cm^{-3}]	1.34
μ [mm^{-1}]	0.984
Radiation	Mo-K_α
Scan type	ω-2θ
$2\theta_{max}$ [°]	55.0
No. of reflections	5672
No. of parameters	298
R [$I > 2\sigma(I)$]	0.042
wR_2 (all data)	0.097
Goodness of fit	1.094

CCDC-260657 (for **10**) contains supplementary crystallographic data. These data can be obtained free of charge from The Cambridge Crystallographic Data Centre via www.ccdc.cam.ac.uk/data_request/cif.

Acknowledgments

This work was partially supported by Grants-in-Aid for Young Scientists (B), nos. 10740288 (M. S.) and 13740349 (M. S.) from the Ministry of Education, Culture, Sports, Science, and Technology, Japan, and from the Japan Society for the Promotion of Science, respectively. M. Saito acknowledges a Sasakawa Scientific Research Grant from the Japan Science Society and a research grant from the Toray Science Foundation. R. Haga is grateful for Research Fellowships from the Japan Society for the Promotion of Science for Young Scientists.

[1] J. Dubac, A. Laporterie, G. Manuel, *Chem. Rev.* **1990**, *90*, 215–263.
[2] V. N. Khabasheku, V. Balaji, S. E. Boganov, O. M. Nefedov, J. Michl, *J. Am. Chem. Soc.* **1994**, *116*, 320–329.
[3] For examples of reviews, see: a) S. Yamaguchi, K. Tamao, *J. Chem. Soc., Dalton Trans.* **1998**, 3693–3702; b) K. Tamao, S. Yamaguchi, *Pure Appl. Chem.* **1996**, *68*, 139–144.
[4] For examples of reviews, see: a) E. Colomer, R. J. P. Corriu, M. Lheureux, *Chem. Rev.* **1990**, *90*, 265–282; b) J. Dubac, C. Guérin, P. Meunier, in *The Chemistry of Organic Silicon Compounds* (Eds.: Z. Rappoport, Y. Apeloig), John Wiley & Sons, Chiches-

 © 2005 Wiley-VCH Verlag GmbH & Co. KGaA, Weinheim

ter, **1998**, 1961–2036; c) M. Saito, M. Yoshioka, *Coord. Chem. Rev.* **2005**, *249*, 765–780.
[5] S. Yamaguchi, R.-Z. Jin, K. Tamao, *Organometallics* **1997**, *16*, 2486–2488.
[6] K. Kanno, M. Ichinohe, C. Kabuto, M. Kira, *Chem. Lett.* **1998**, 99–100.
[7] H. Sohn, R. R. Huddleston, D. R. Powell, R. West, *J. Am. Chem. Soc.* **1999**, *121*, 2935–2936.
[8] a) S. Yamaguchi, R.-Z. Jin, K. Tamao, *J. Am. Chem. Soc.* **1999**, *121*, 2937–2938; b) K. Tamao, S. Yamaguchi, *J. Organomet. Chem.* **2000**, *611*, 5–11.
[9] H. Sohn, M. J. Sailor, D. Magde, W. C. Trogler, *J. Am. Chem. Soc.* **2003**, *125*, 3821–3830.
[10] a) M. Saito, M. Nitta, M. Yoshioka, *Organometallics* **2001**, *20*, 749–753; b) M. Saito, N. Henzan, M. Nitta, M. Yoshioka, *Eur. J. Inorg. Chem.* **2004**, 743–748.
[11] M. Saito, R. Haga, M. Yoshioka, *Heteroat. Chem.* **2001**, *15*, 349–353.
[12] Zuckerman et al. have reported that the reaction of hexaphenylstannole with bromine gives 1,1-dibromo-2,3,4,5-tetraphenylstannole, see: W. A. Gustavson, L. M. Principe, W.-Z. Min Rhee, J. J. Zuckerman, *J. Am. Chem. Soc.* **1981**, *103*, 4126–4131.
[13] M. Saito, R. Haga, M. Yoshioka, *Chem. Commun.* **2002**, 1002–1003.
[14] H. H. Freedman, *J. Org. Chem.* **1962**, *27*, 2298–2303.
[15] L. R. Sita, *Acc. Chem. Res.* **1994**, *27*, 191–197.
[16] B. N. Biddle, J. S. Gray, A. J. Crowe, *Appl. Organomet. Chem.* **1987**, *1*, 261–265.
[17] Nucleophilic substitution at the silicon by *sec*-butyllithium also gives diastereomeric mixtures, see: J. Ohshita, K. Matsushige, A. Kunai, A. Adachi, K. Sakamaki, K. Okita, *Organometallics* **2000**, *19*, 5582–5588.
[18] K. M. Mackay, in *The Chemistry of Organic Germanium, Tin and Lead Compounds* (Ed.: S. Patai), John Wiley & Sons, Chichester, **1995**, 144–194.
[19] A. G. Davis, *Organotin Chemistry*, VCH, Weinheim, **1997**, and references cited therein.
[20] S. Adams, M. Dräger, B. Mathiasch, *J. Organomet. Chem.* **1987**, *326*, 173–186.
[21] J. Ferman, J. P. Kakareka, W. T. Klooster, J. L. Mullin, J. Quattrucci, J. S. Ricci, H. J. Tracy, W. J. Vining, S. Wallace, *Inorg. Chem.* **1999**, *38*, 2464–2472.
[22] A. Altomare, G. Cascarano, C. Giacovazzo, A. Guagliardi, *J. Appl. Crystallogr.* **1993**, *26*, 343–350.
[23] G. M. Sheldrick, *SHELXL-97*, Program for Crystal Structure Refinement; Göttingen University: Göttingen, Germany, **1997**.
Received: March 30, 2005
Published Online: August 10, 2005

 © 2005 Wiley-VCH Verlag GmbH & Co. KGaA, Weinheim

A Platinium(II)-Based Molecular Light Switch for Proteins

Vaidyanathan G. Vaidyanathan[a] and Balachandran U. Nair*[a]

Keywords: Fluorescent probes / Platinum / Proteins / Tridentate ligands

The platinum(II) complex $[Pt(bzimpy)Cl]^+$ (**1**) [bzimpy = 2,6-bis(benzimidazo-2-yl)pyridine] has been synthesized and characterized by FAB mass spectrometry and UV/Vis, NMR, and emission spectroscopy. Complex **1** emits weakly from its ^{3}MLCT state in aqueous solution but strongly in nonaqueous media. Complex **1** exhibits a molecular light switch effect with a drastic enhancement in its emission intensity and a 72-nm blue shift in the emission maxima in the presence of bovine serum albumin (BSA). Denaturation of BSA in the presence of 6 M urea leads to a decrease in the emission intensity of the complex, which suggests its binding to the hydrophobic pockets of the protein. In the presence of hemoglobin, however, quenching of the emission of the complex is observed due to its binding to Cys104 in subunit C and the resultant fluorescence resonance energy transfer from the platinum(II) complex to the heme.
(© Wiley-VCH Verlag GmbH & Co. KGaA, 69451 Weinheim, Germany, 2005)

In recent years, there has been continuing interest in designing new molecules for the development of novel chemo- and biosensors. However, most of these studies deal with organic molecules as chemo- and biosensors. In recent times, considerable attention has been paid to the synthesis of inorganic chemosensors.[1] Although metal complexes exhibit luminescent behavior like organic molecules, the utility of these metal complexes as biosensors still remain sparse. In the last decade, Barton et al. have demonstrated that $[Ru(dppz)(bpy)_2]^{2+}$ behaves as a molecular light switch for DNA.[2] Despite extensive work on organic fluorophores such as 8-anilino-1-naphthalenesulfonic acid (ANS) as a probe to study the conformational changes of proteins,[3] no metal complex with a similar behavior has yet been reported.

Among the various transition metal ions, platinum plays a vital role in cancer research. While there are a number of reports on the interaction of platinum(II) complexes with DNA, there are relatively few reports on the binding of platinum(II) complexes to proteins.[4,5] Even though most platinum(II) complexes are nonluminescent at room temperature, a few of them have been exploited as chemosensors.[6] Recently, Grove et al. have discussed the vapochromic properties of $[Pt(Me_2bzimpy)Cl]^+$,[7] and Che et al. have recently demonstrated the use of PEG attached $[Pt(CNN)L]^+$ as a molecular light switch for proteins,[8] although studies pertaining to this complex have been limited to albumins. Very recently, the same group has demonstrated the molecular light switch effect specifically to human serum albumin (HSA) exhibited by a platinum(II) complex containing a cyclometalated ligand anchored to amino acids.[9] In this context, we have developed a new platinum-based biosensor with a tridentate ligand, bzimpy, $[Pt(bzimpy)Cl]^+$ (**1**). To the best of our knowledge, this is the first report of a platinum-based transition metal complex that mimics the behavior of an organic molecule such as ANS.

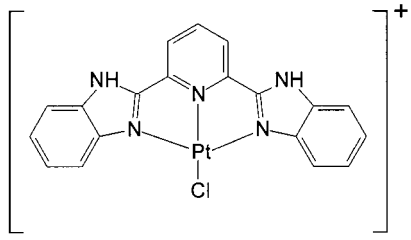

1

Complex **1** was isolated as its PF_6^- salt by refluxing a DMSO solution of bzimpy and K_2PtCl_4 in a 1:1 molar ratio. The absorption spectrum of **1** in DMSO exhibits intense bands at 320 and 380 nm due to an intraligand π–π* transition of the ligand bzimpy. A broad, featureless absorption band at 420 nm has been assigned to a ^{1}MLCT [Pt(5d)–π*(bzimpy)] transition similar to $[Pt(L18)Cl]^+$ [L18 = 2,6-bis(1-octadecylbenzimidazol-2-yl)pyridine].[10] Complex **1** exhibits a very broad and weak ^{3}MLCT emission centered at 625 nm in aqueous solution at room temperature upon excitation at 370 nm. The excited state lifetime of complex **1** is 0.19 μs in Tris buffer solution (pH 7.0) at 298 K. The excited state lifetime of complex **1** is less than that of other platinum(II) complexes such as PtPren and PtPrtmen, whose lifetimes are 4.2 and 3.6 μs, respectively.[11]

[a] Chemical Laboratory, Central Leather Research Institute, Adyar, Chennai 600 020, India
Fax: +91-44-2491-1589
E-mail: bcunchem@rediffmail.com

 © 2005 Wiley-VCH Verlag GmbH & Co. KGaA, Weinheim **DOI: 10.1002/ejic.200500335**

First, the effect of solvents on the emission spectrum of complex **1** was examined. On decreasing the polarity of the solvent, the emission maximum of the complexes shifts towards lower wavelength from 625 to 560 nm, with an increase in the emission intensity (Figure 1). This type of behavior has previously been observed for organic fluorophores such as ANS, where the emission maximum shifts to lower wavelength on decreasing the polarity of the solvent.[2] In order to investigate the molecular light switch effect of complex **1** in the presence of proteins, we investigated the emission properties of complex **1** with bovine serum albumin (BSA), chicken egg albumin, lysozyme, and hemoglobin. These proteins were chosen as they cover a range of hydrophobicity.

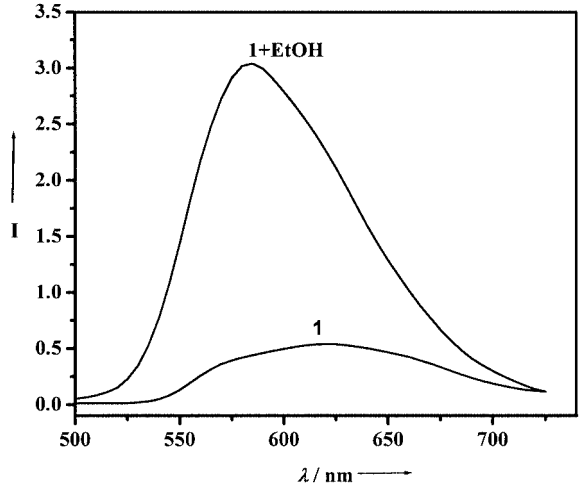

Figure 1. Emission spectra of **1** (50 μM) in the absence and presence of EtOH (λ_{ex} = 370 nm; 298 K; pH 7.0).

Interestingly, on addition of BSA (5 μM), the emission intensity of complex **1** (10 μM) increases 70-fold, with a drastic blue-shift of 72 nm in the emission maximum from 625 nm to 553 nm; the emission band gets sharper on increasing the amount of BSA (Figure 2). A similar behavior of the emission of complex **1** was observed in the presence of chicken egg albumin also. This enhancement in emission intensity has been ascribed to the binding of **1** in the hydrophobic pocket of serum albumin. The binding constants of **1** with BSA and egg albumin were calculated to be $(6.75 \pm 0.1) \times 10^4$ and $(5.4 \pm 0.1) \times 10^4$ M^{-1}, respectively, from the Scatchard plot, and the binding site size number was estimated to be one. Binding of complex **1** to lysozyme, however, resulted in only a marginal increase in its emission intensity. This is not surprising since lysozyme has a less hydrophobic region than the albumins. To understand the effect of albumin on the lifetime of the excited state of complex **1**, emission decay of the complex was monitored in the presence and absence of BSA (Figure 3). From the emission decay profile, the excited-state lifetime of the complex was estimated to be 1.89 μs in the presence of BSA.

Unlike in the case of BSA and lysozyme, the emission intensity of complex **1** decreases on addition of increasing

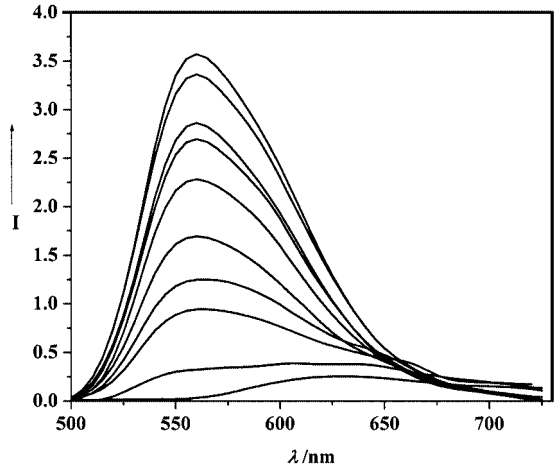

Figure 2. Emission spectra of **1** (10 μM) in the presence of BSA (0–5 μM) (λ_{ex} = 370 nm; pH 7.0).

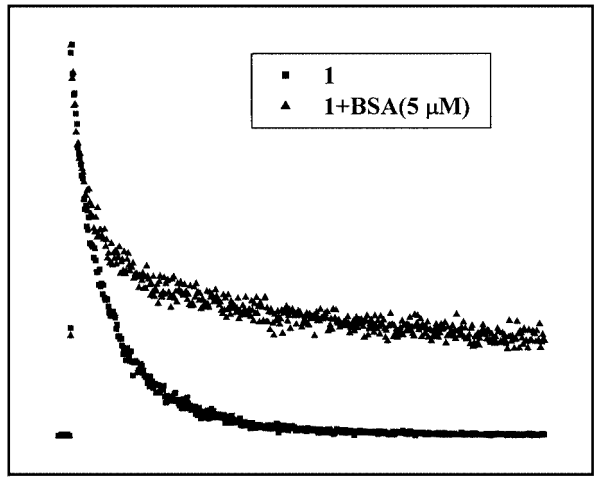

Figure 3. Decay profile of **1** (5 μM) in the absence and presence of BSA (5 μM) (298 K; pH 7.0).

amounts of hemoglobin (Figure 4). In hemoglobin protein, the hydrophobic pocket is occupied by the heme. If complex **1** binds to hemoglobin near the vicinity of heme, one can expect fluorescence resonance energy transfer (FRET) from complex **1** to the heme. This phenomenon of FRET will lead to quenching of the emission of **1** upon binding to hemoglobin. A careful examination of the crystal structure of hemoglobin shows that two sulfur-containing amino acids Met32 and Cys104 in subunit C are at a distance of 0.9 and 1.3 nm from the hydrophobic region where heme is present. Hence, binding of platinum(II) complex to these two sulfur sites will place complex **1** at the appropriate distance from heme for fluorescence energy transfer from **1** to the heme. As platinum(II) has a high affinity for sulfur,[12] complex **1** can be expected to bind to one of these two sulfur-containing amino acids of subunit C, resulting in the observed phenomenon of resonance energy transfer to heme.

In order to support the binding of complex **1** to the sulfur residues, we carried out the absorption titration of com-

 © 2005 Wiley-VCH Verlag GmbH & Co. KGaA, Weinheim

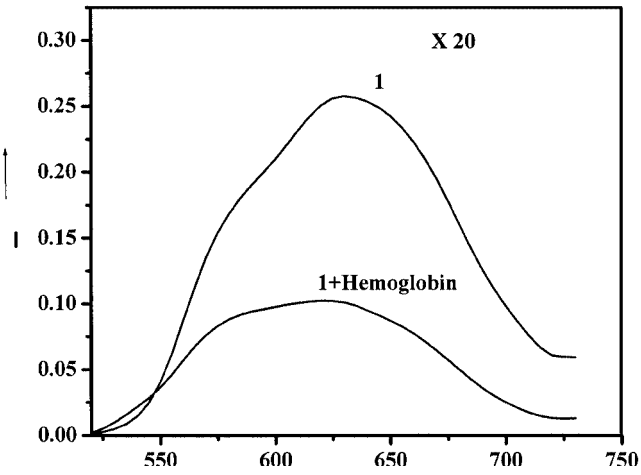

Figure 4. Emission spectra of **1** (50 μM) in the absence and presence of hemoglobin (5 μM) (λ_{ex} = 370 nm; 298 K, pH 7.0).

plex **1** with L-cysteine and L-methionine. Upon addition of increasing amounts of L-cysteine from 0 to 5 μM, the MLCT band of complex **1** shifted towards lower wavelength with the appearance of a new absorption band at 349 nm (Figure 5). The binding constant was determined from the following equation

$$[AA]/(\varepsilon_a - \varepsilon_f) = [AA]/(\varepsilon_b - \varepsilon_f) + 1/K_b(\varepsilon_b - \varepsilon_f)$$

where [AA] is the concentration of amino acid and ε_a, ε_f, and ε_b correspond to A_{obsd}/[Pt], the molar extinction coefficient of the free platinum(II) complex, and the extinction coefficient for the platinum(II) complex in the fully bound form, respectively. A plot of [AA] vs. [AA]/($\varepsilon_a - \varepsilon_f$) gives K_b as the ratio of the slope to the intercept. The binding constant (K_b) was found to be $(3.3 \pm 0.2) \times 10^5$ M^{-1}. However, in the presence of L-methionine, there is no change in the absorption spectrum of complex **1**. The spectral titration

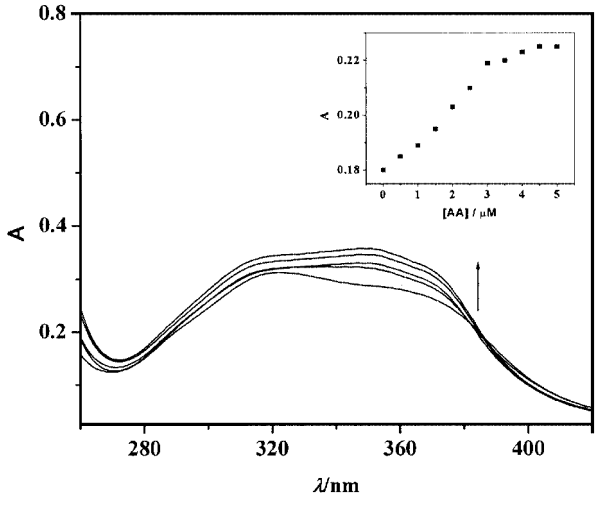

Figure 5. Absorption spectra of complex **1** (5 μM) in the absence and presence of L-cysteine (0–5 μM). Inset: plot of [AA] vs. absorbance at 349 nm.

studies reveal that [Pt(bzimpy)Cl]$^+$ binds more strongly to L-cysteine than to L-methionine. Hence, it can be concluded that complex **1** binds to Cys104 in the subunit C of hemoglobin.

To conclusively establish that complex **1** indeed binds to the hydrophobic regions of the protein, urea-unfolding experiments were carried out. Initially, the emission intensity of **1**-BSA adducts increases significantly with an increase in urea concentration and reaches a maximum at a urea concentration of 4.5 M. No further change in the emission intensity of the **1**-BSA adduct is observed with an increase in urea concentration up to 5 M. At 6 M urea, the emission intensity is the same as that of the native **1**-BSA adduct in the absence of urea. Beyond 6 M urea, however, there is a drastic decrease in the emission intensity of the adduct (Figure 6). Since BSA is a polypeptide with three domains (I, II, and III) extended through helices, the initial increase in emission intensity of the **1**-BSA adduct could be due to tight helical twisting in domain II of the BSA structure. The lack of any decrease in the emission intensity of the adduct in the presence of 4.5–5 M urea is indicative of the retention of the native-like conformation of domain II at this urea concentration. The marked decrease in emission intensity beyond 6 M urea and complete quenching beyond 7 M urea reveals the unfolding of the polypeptide chains followed by separation of domains from each other, which results in loss of hydrophobicity. The results observed here are similar to those observed for bilirubin binding to domain II of the BSA structure.[13] These results confirm that the binding of complex **1** to BSA is through the domain II hydrophobic cavity.

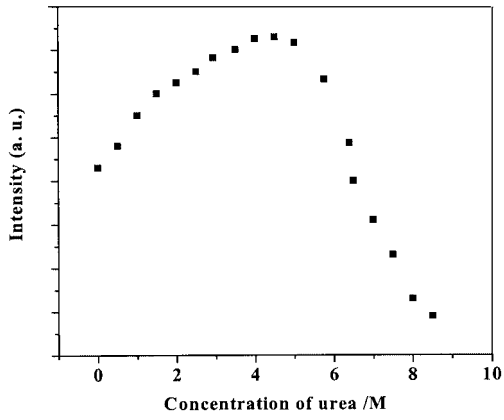

Figure 6. Unfolding of BSA incubated with **1** by urea (measured at 553 nm; λ_{ex} = 370 nm; 298 K).

In summary, we have shown that the present platinum(II) complex can be used as an extrinsic fluorophore for protein-binding studies. We hope that our findings will facilitate a significant development of metal-based sensors for biological applications. Further work is going on to study the uptake of this platinum(II) complex and its distribution in the cell, which can be monitored by fluorescence microscopy without addition of any external fluorophore.

 © 2005 Wiley-VCH Verlag GmbH & Co. KGaA, Weinheim

Experimental Section

Materials: BSA (fraction V powder, lipid free, 66 kDa) and potassium tetrachloroplatinate(II) (K_2PtCl_4) were purchased from Sigma (St. Louis, MO, USA) and used as such without any further purification. 2,6-Pyridinedicarboxylic acid and *o*-phenylenediamine were purchased from Lancaster Chemicals. Tris(hydroxymethyl)aminomethane hydrochloride (Tris-HCl) was purchased from SRL Chemicals. All other reagents were of analytical grade. All the experiments were carried out at pH 7.0 at 25 °C.

Synthesis of [Pt(bzimpy)Cl]PF_6 (1): The ligand bzimpy was prepared as reported in the literature.[14] The platinum(II) complex was prepared by refluxing K_2PtCl_4 (0.48 g, 1 mmol) in DMSO for 2 h followed by the addition of bzimpy (0.311 g, 1 mmol). The resultant yellow precipitate was filtered and dried with diethyl ether. The yellow precipitate was dissolved in acetone and precipitated as its PF_6^- salt by addition of a saturated NH_4PF_6 solution. The yellow precipitate turns red on drying. Yield: 0.6 g (80%). MS: *m*/*z* = 541.5 $[M - Cl]^+$. $C_{19}H_{13}ClF_6N_5PPt$: calcd. C 33.23, H 1.91, N 10.2; found C 32.91, H 1.85, N 10.12. ^1H NMR [(D_6)DMSO]: δ = 8.32 (m, 1 H), 8.05 (d, 2 H), 8.02 (d, 2 H), 7.62 (d, 2 H), 7.33 (t, 2 H), 7.29 (t, 2 H) ppm.

Studies on the Interaction of the Platinum(II) Complex with BSA

Spectroscopic Measurements: All absorption spectra were measured with a Perkin–Elmer Lambda 35 double-beam spectrophotometer. To understand the binding of L-cysteine and L-methionine to complex **1**, the absorption spectra of complex **1** (5 μM) was monitored as a function of concentration of the two amino acids (0–5 μM). The concentration of L-cysteine and L-methionine was varied until there was no appreciable change in the spectrum of the metal complex.

Emission Studies: Steady-state emission studies of the platinum(II) complexes were carried out by varying the concentration of BSA ($0–5 \times 10^{-6}$ M) while keeping the concentration of metal complex constant. The metal complex was excited at 375 nm and emission was monitored between 500 and 850 nm. The binding constant of complex **1** with BSA was determined from the Scatchard plot.[15]

Time-resolved emission for the complex was determined with a picosecond-laser-excited TCSPC spectrometer. The excitation source was a tunable Ti-Sapphire laser (Tsunami Spectrophysics, USA) with a pulse width of less than 2 ps and a repetition rate of 82 MHz. Samples were excited at 370 nm and the emission was monitored with an MCP-PMT (Hamamatsu-C 4878) detector. The decay traces were deconvulated by using a non-linear least-squares analysis with IBH software.

Acknowledgments

V. G. V. thanks the CSIR for a research fellowship. The authors thank the National Center for Ultrafast Processes, Taramani, Chennai, for providing the facilities to carry out time-resolved emission experiments.

[1] a) A. Buryak, K. Severin, *Angew. Chem. Int. Ed.* **2004**, *43*, 4771–4774; b) D. H. Lee, S. Y. Kim, J. Hong, *Angew. Chem. Int. Ed.* **2004**, *43*, 4777–4780; c) S. Charier, O. Ruel, J.-B. Baudin, D. Alcor, J.-F. Allemand, A. Meglio, L. Jullien, *Angew. Chem. Int. Ed.* **2004**, *43*, 4785–4788; d) D. H. Vance, A. W. Czarnik, *J. Am. Chem. Soc.* **1994**, *116*, 9397–9398; e) A. W. Czarnik, *Acc. Chem. Res.* **1994**, *27*, 302–308; f) M. E. Padilla-Tosta, J. M. Lloris, R. Martínez-Máñez, M. D. Marcos, M. A. Miranda, T. Pardo, F. Sancenón, J. Soto, *Eur. J. Inorg. Chem.* **2001**, 1475–1482; g) L. Prodi, F. Bolletta, M. Montalti, N. Zaccheroni, *Eur. J. Inorg. Chem.* **1999**, 455–460; h) S. Furukawa, H. Mihara, A. Ueno, *Macromol. Rapid Commun.* **2003**, *24*, 202–206; i) L. Prodi, M. Montalti, N. Zaccheroni, F. Dallavalle, G. Folesani, M. Lanfranchi, R. Corradini, S. Pagliari, R. Marchelli, *Helv. Chim. Acta* **2001**, *84*, 690–706.

[2] A. E. Friedman, J. C. Chambron, J. P. Sauvage, N. J. Turro, J. K. Barton, *J. Am. Chem. Soc.* **1990**, *112*, 4960–4962.

[3] W. T. Mason, *Fluorescent and Luminescent Probes for Biological Activity*, Academic Press, London, **1999**.

[4] a) B. P. Esposito, R. Najjar, *Coord. Chem. Rev.* **2002**, *232*, 137–149; b) M. D. Hall, T. W. Hambley, *Coord. Chem. Rev.* **2002**, *232*, 49–67.

[5] a) L. T. Lemiesz, H. Kozlowski, B. K. Keppler, *J. Inorg. Biochem.* **1999**, *77*, 141–146; N. Ohta, D. Chen, S. Ito, T. Futo, T. Yotsuyanagi, K. Ikeda, *Int. J. Pharm.* **1995**, *18*, 85–93.

[6] a) H. Q. Liu, S. M. Peng, C.-M. Che, *J. Chem. Soc., Chem. Commun.* **1995**, 509–510; b) C. S. Peyratout, T. K. Aldridge, D. K. Crites, D. R. McMillin, *Inorg. Chem.* **1995**, *34*, 4484–4489.

[7] L. J. Grove, J. M. Rennekamp, H. Jude, W. B. Connick, *J. Am. Chem. Soc.* **2004**, *126*, 1594–1595.

[8] C.-M. Che, J. L. Zhang, L. R. Lin, *Chem. Commun.* **2002**, 2556–2557.

[9] P. K.-M. Siu, D.-L. Ma, C.-M. Che, *Chem. Commun.* **2005**, 1025–1027.

[10] K. Wang, M. Haga, H. Monjushiro, M. Akiba, Y. Sasaki, *Inorg. Chem.* **2000**, *39*, 4022–4028.

[11] H.-F. Xiang, S.-C. Chen, K. K.-Y. Wu, C.-M. Che, P. T. Lai, *Chem. Commun.* **2005**, 1408–1410.

[12] Z. D. Bugarcic, F. W. Heinemann, R. van Eldik, *Dalton Trans.* **2004**, 279–286.

[13] S. Tayyab, N. Sharma, M. M. Khan, *Biochem. Biophys. Res. Commun.* **2000**, *277*, 83–88.

[14] A. W. Addison, P. J. Burke, *J. Heterocycl. Chem.* **1981**, *18*, 803–805.

[15] C. V. Kumar, E. H. Asuncion, *J. Am. Chem. Soc.* **1993**, *115*, 8547–8553.

Received: April 21, 2005
Published Online: August 10, 2005

 © 2005 Wiley-VCH Verlag GmbH & Co. KGaA, Weinheim

Mono and Bridged Azolium Picrates as Energetic Salts

Chuan-Ming Jin,[a] Chengfeng Ye,[a] Crystal Piekarski,[a] Brendan Twamley,[a] and Jean'ne M. Shreeve*[a]

Keywords: Azides / Heats of formation / Ionic liquids / Materials science / Nitrogen heterocycles

The energetic mono and bridged imidazolium, triazolium and tetrazolium picrates **7**–**10**, **14**, and **16**, the dipicrates **23**, **25**, and **26** and the dinitrates **24**, and **27** were synthesized by the quaternization of azolium derivatives (**1**, **2**, **13**, **15**, **19** and **20**) with picric acid and nitric acid or by metathesis of the corresponding quaternary salts (**3**, **6**, **21** and **22**) with silver picrate or silver nitrate. The structures of **14** and **16** were determined by single-crystal X-ray diffraction analysis confirming quaterization on the triazolium and tetrazolium rings. Their physical and thermodynamic properties were determined. In some cases, the salts are thermally stable to ca. 300 °C and they exhibit densities averaging ca. 1.6 g/cm^3. Nearly all have positive heats of formation with the highest calculated value, $\Delta_f H^o_m$ = 611.6 kJ/mol, found for 3-azido-1,4-dimethyl-1,2,4-triazolium picrate (**10**).

(© Wiley-VCH Verlag GmbH & Co. KGaA, 69451 Weinheim, Germany, 2005)

Introduction

Energetic materials are used extensively for both civilian and military applications. There are ongoing research programs worldwide to develop such new materials with higher performance or enhanced insensitivity to thermal or shock insults. In recent years, the synthesis of energetic, heterocyclic compounds have attracted considerable interest. Heterocycles generally have higher heats of formation, density, and oxygen balance than their carbocyclic analogues.[1–3]

Recently, a new class of energetic compounds containing a large number of nitrogen atoms has been studied. These high-nitrogen compounds form a unique class of energetic materials whose energy is derived from their very high positive heats of formation rather than from the combustion of the carbon backbone or the ring/cage strain. The high heat of formation is directly attributable to the large number of inherently energetic N–N and C–N bonds.[4–8]

Most often molecular compounds have been utilized in an energetic role, whereas we and others have recently demonstrated that heterocyclic-based energetic, low-melting salts appear to be of considerable value in this area.[9–13] Energetic materials that are salt-based often possess advantages over non-ionic molecules since these salts tend to exhibit lower vapor pressures and higher densities than their atomically similar non-ionic analogues. Five-membered nitrogen-containing heterocycles are traditional centers for energetic materials, and considerable attention is currently focused on energetic compounds based on azoles.[14,15] *N*-Aminoazolium salts are a family of compounds of increasing interest, since these substituted hetero rings when paired with nitrate or perchlorate anions form new, highly energetic salts.

We have synthesized energetic salts based on *N*-aminoazoles with concomitant determination of structural and thermal properties.[16–18] Increasing the number of nitrogen atoms in heterocycles results in considerable gain in the standard enthalpy of formation in the resulting compounds. The enthalpy criteria of energetic chemical systems are governed by their molecular structure. In moving from imidazole ($\Delta H_f°_{(cryst)}$ = 58.5 kJ/mol)[19] to 1,2,4-triazole ($\Delta H_f°_{(cryst)}$ = 109 kJ/mol) to tetrazole ($\Delta H_f°_{(cryst)}$ = 237.2 kJ/mol),[20] the variation in the trend of the heats of formation is increasingly positive The *N*-amino group behaves as an electron-withdrawing group in high-nitrogen heterocycles.[9]

High-nitrogen compounds containing polyazides possess even more positive heats of formation because their energy content rapidly increases with the number of energetic azido groups in the molecule. However, they tend to be extremely sensitive to spark, friction, and impact as well as to heat.[8] We have reported new energetic salts obtained by the quaternization of azido or nitro derivatives of imidazole, 1,2,4-triazole and substituted derivatives of tetrazole with nitric or perchloric acid or with iodomethane followed by metathesis reaction with silver nitrate or silver perchlorate.[17] While these compounds with azide-containing triazolium cations (nitrate or perchlorate anion) do exhibit marginally high positive heats of formation, recently reported molecular azides of triazine are considerably more energetic with considerably higher heats of formation, e. g., 2,4,6-triazido-1,3,5-triazine (+1053 kJ/mol) and 4,4′,6,6′-tetra(azido)azo-1,3,5-triazine (+2171 kJ/mol).[8]

[a] Department of Chemistry, University of Idaho, Moscow, Idaho, 83844-2343, USA
E-mail: jshreeve@uidaho.edu

 DOI: 10.1002/ejic.200500472

Another area of increasing interest is based on high-energy salts where both the cation and anion are high-nitrogen species.[8,21,22] This is a relatively new area where only a very few such compounds have been studied.[5,10b,22c] One of the more recent and exciting developments in high energy dense materials is salts with high-nitrogen content and with very high positive heats of formation which show remarkable insensitivity to electrostatic discharge, friction, and shock.

We have now extended our studies to salts with energetic mono and bridged azolium cations with picrate as the anion, and have determined their physical and thermodynamic properties. While the typical anions used in these systems are for example, nitrate, perchlorate, and dinitramide, until now their picrate analogues have not been synthesized. In our work, the physical and energetic properties of new picrate salts are compared with those of the salts formed with the former anions. The new salts reported here contain mono or dications and consequently, are either mono or dipicrates. These picrate salts combine an oxygen-rich anion with a high-nitrogen azolium cation thus providing the opportunity for high positive heats of formation. Although anhydrous picric acid tends to be unstable, and its impact and friction sensitivities are higher than that of TNT, many organic and inorganic picrate salts have been created and studied;[23] however, none consists of diazolium cations combined with picrate. The successful syntheses and characterization of these rather stable salts with moderately high positive enthalpies of formation are now reported.

Results and Discussion

Energetic salts, some of which are ionic liquids, have been prepared that contain substituted azolium cations (e. g., imidazolium, triazolium and tetrazolium) in combination with usually small energetic inorganic anions [e. g., NO_3^-, ClO_4^-, and $N(NO_2)_2^-$].[9,10c,16–18,24] Now we have replaced these simple inorganic species by introducing picrate as the energetic anion.

Triazolium or substituted triazolium picrates were prepared either by direct reaction with picric acid in methanol (**7**, **8**) or metathesis with silver picrate after quaternization of the parent triazole with methyl iodide (**9**, **10**) (Scheme 1). The triazolium iodides, **3** and **6**, were prepared based on the literature.[17,25] Although earlier we were able to quaternize azido-substituted triazoles with concentrated nitric or perchloric acid,[17] the analogous reactions of **4** and **5** with picric acid failed under a variety of conditions. This likely arises from the lower acidity of picric acid (pK_a of 0.3) compared to nitric acid (pK_a of –1.44) and with the concomitant decrease in the basicity of the triazolium ring because of the presence of the azide group. However, 3-azido-1,4-dimethyl-1,2,4-triazolium picrate (**10**) can be readily obtained from **6** which was metathesized with silver picrate (Scheme 1).

In their ^1H NMR spectra, all of the compounds **3**, **6**, **7**, and **8**–**10**, with the exception of **12** (shift at δ = 8.3 ppm), have chemical shifts downfield from δ = 9.3 ppm. The latter shifts indicate that these compounds were comprised of quaternized triazolium rings. However, quaternization of 3-amino-1,2,4-triazole (**11**) did not occur at the N-4 position in the triazolium ring, but rather compound **12** resulted from the ready protonation of the 3-amino group (Scheme 1). This same phenomenon was observed when concentrated nitric or perchloric acid was used, that is, a substituted ammonium salt ($RNH_3^+X^-$, X = NO_3^-, ClO_4^-) was formed analogous to **12**.

However, 4-amino-1,2,4-triazole (**13**) was readily quaternized with picric acid in methanol by protonating the ring at N-1 to give the triazolium salt **14** in high yield (Scheme 2). This is supported by signals at δ = 9.5 ppm and δ = 144.1 ppm in the ^1H NMR and ^{13}C NMR spectra, respectively. Additionally, the single-crystal X-ray structure corroborates the quaternization at N-1 (Figure 1).

These results are consistent with the literature where *N*-amino groups in nitrogen-rich heterocycles were quaternized in the ring, not at the *N*-amino group.[9,16,26] This apparently arises because the *N*-amino group acts as an electronegative, electron-withdrawing group in these triazolium systems in contrast to the cases where the triazolium derivatives contain *C*-amino group (s). However, surprisingly, quaternization of 5-amino-tetrazole (*C*-amino group)

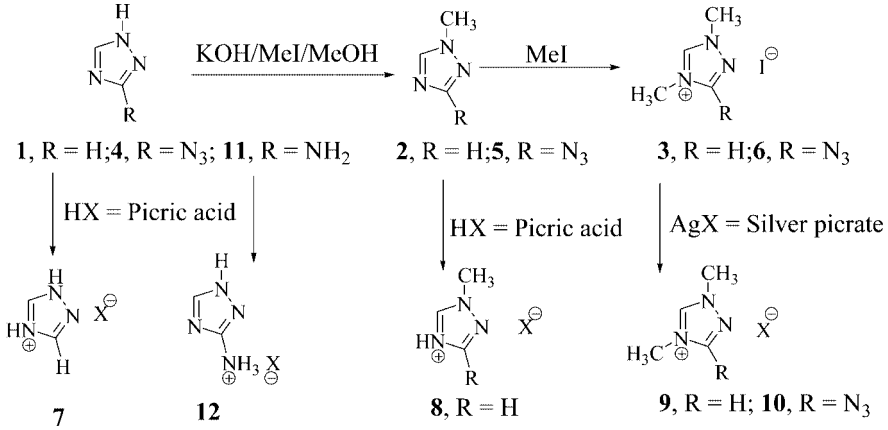

Scheme 1.

 © 2005 Wiley-VCH Verlag GmbH & Co. KGaA, Weinheim

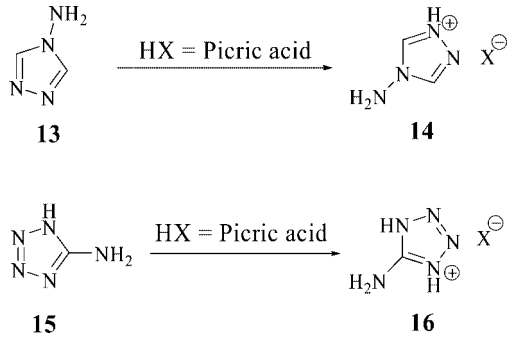

13 14

15 16

Scheme 2.

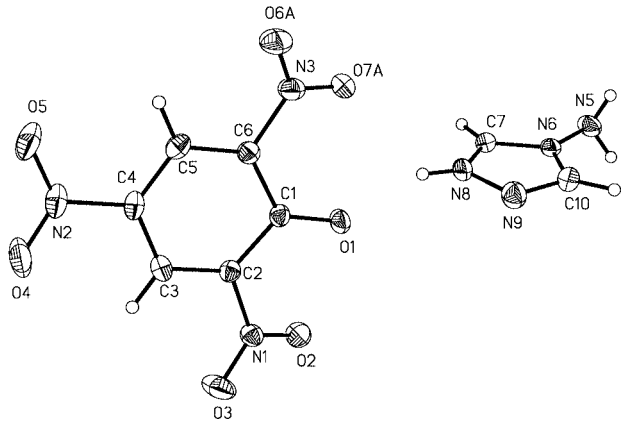

(a)

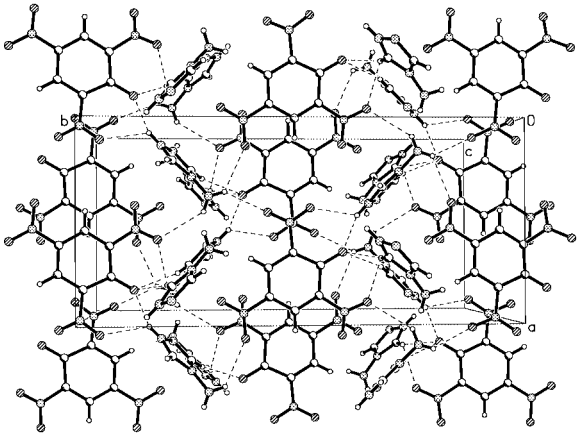

(b)

Figure 1. (a) 30% Probability thermal ellipsoid plot of **14**. Only one conformation for the disordered NO_2 group is shown. Hydrogen atoms are shown but are unlabelled for clarity. (b) A packing diagram of **14**. Dashed lines indicate hydrogen bonding. Zig-zag sheets of triazolium cations tie the rows of picrates into a crosslinked 3D array.

(**15**) (Scheme 2) occurs at the N-4 position in the tetrazolium ring in high yield, and not at the amino group at C-5, to form the salt 5-amino-1,2,4-tetrazolium picrate (**16**). The single-crystal X-ray structure of compound **16** is given in Figure 2.

There is a paucity of energetic salts with bridged cations.[5] In order to examine the physical and thermodynamic properties of mono and diazolium salts containing a common anion, bridged bis(imidazolium) or bis(triazolium) methane compounds were obtained from the reaction of imidazole or triazole with dibromo- or dichloromethane under basic conditions and in the presence of a phase-transfer catalyst (Scheme 3).[27] These bridged azolium species, **19** and **20**, were either: 1) Reacted with picric or nitric acid to form the picrate **23**, or the nitrate **24**; however, compound **20** did not react with picric acid to give the corresponding dipicrate; or 2) quaternized with methyl iodide to give compound **21** and **22**,[27c] which were subsequently metathesized with silver picrate or nitrate forming compound **25**, **26** and **27**. Each of the picrate or nitrate salts was isolated in a yield >88%. Compound **27** is readily soluble in water, but **23**–**26** are not miscible with water. In general, all of these new picrate and nitrate salts are hydrolytically stable.

Physical characteristics and thermochemical properties of the new energetic ionic salts are given in Table 1. The effectiveness of an energetic compound is a function of many properties. Density is crucial since the more grams (mol) of material that can be loaded in a given space, the more efficient the energetic species is. High oxygen balance and a positive, Scheme 3, heat of formation increase the sensitivity of the material as well as performance since the specific impulse is proportional to the square root of heat of formation. For example, the heat of formation is 1075 kJ/mol, the density, 1.60 g/cm^3, and the oxygen balance, –56% are reported for an highly energetic salt, triaminoguanidinium 5,5′-azobis(1*H*-tetrazolate).[8]

Most of the picrates have good thermal stabilities ranging between 176 °C (**10**) and 313 °C (**25**) (TGA), melting points between 91 °C (**8**) and 215 °C (**23**) (DSC), and relatively high densities between 1.48 (**10**) and 1.85 (**16**) g/cm^3 (gas pycnometer). In fact, the latter approaches the density of HMX at 1.91 g/cm^3. However, in general, the bridged azolium picrates are somewhat more stable thermally than their monocationic picrate analogues as shown by their decomposition temperatures, e. g., **26**, T_d = 242 °C, is higher than **8**, T_d = 185 °C. Also, the picrates are more thermally stable than nitrates or perchlorates, e. g., 4-amino-1,2,4-triazolium picrate (**14**) decomposes at 228 °C compared with the nitrate and perchlorate which decompose at 181 °C and 208 °C, respectively.[18]

Similarly, compound **26** (picrate) decomposes at 242 °C, and compound **27** (nitrate) at 162 °C. However, while triazolium picrate (**7**) is thermally unstable at 196 °C, and the nitrate is stable only upto 182 °C, the perchlorate decomposes at 285 °C.[9] Compound **27**, a nitrate salt, exhibits properties of an energetic ionic liquid (T_g –15 °C). In general, the nitrate salt with same azolium cation has a lower

 © 2005 Wiley-VCH Verlag GmbH & Co. KGaA, Weinheim

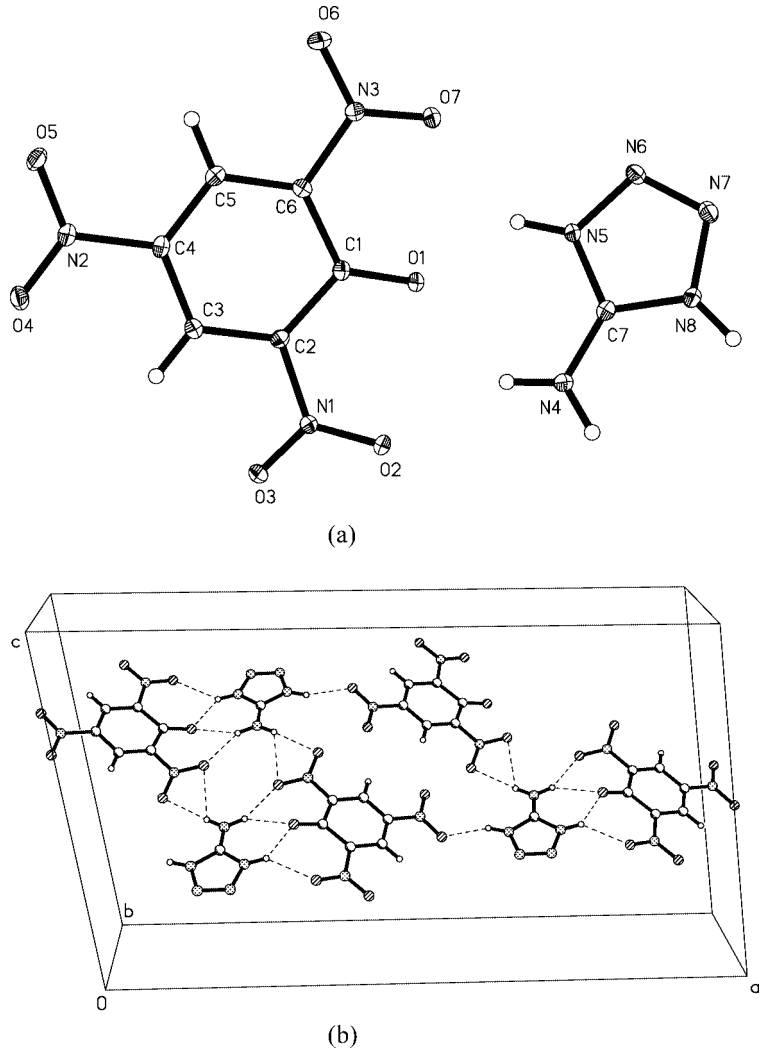

Figure 2. (a) 30% Probability thermal ellipsoid plot of **16**. Hydrogen atoms are shown but are unlabelled for clarity. (b) A packing diagram of **16**. Only one sheet section is shown. Hydrogen bonding is indicated by dashed lines.

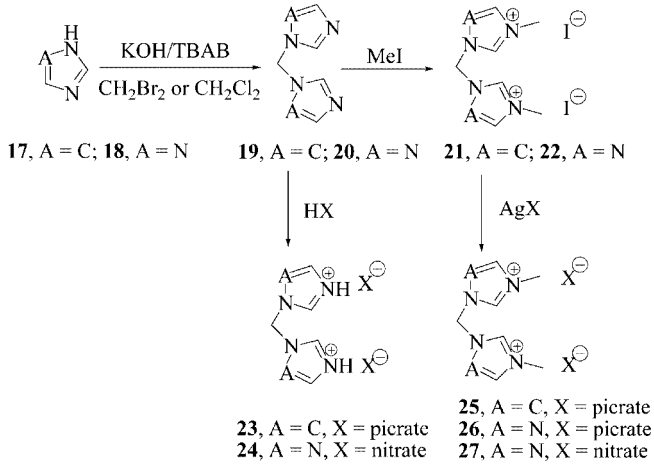

Scheme 3.

melting point than its picrate or perchlorate; e. g. compound **27** is liquid and compound **26** with T_m 216 °C. 4-Amino-1,2,4-triazolium picrate (**14**) with T_m = 197 °C is higher than the nitrate with T_m = 69 °C.[18] Unfortunately, we did not obtain ionic liquids based on picrate; only 1-methyl-1,2,4-triazolium picrate (**8**) with a melting point 91 °C falls into the ionic liquid class. The calculated oxygen balance values range from –36 to –93% which are reasonably close to those for TAG-AT (–73%), TNT (–74%) and picric acid (–43%) (Table 1) and slightly more negative than for HMX (–21%) and RDX (–22%). The molar enthalpy of formation for each sample, e. g., for compound **26**, was derived from the constant volume combustion energy using the following equation:

$\Delta_c H^o_m = \Delta_c U_m + \Delta nRT$ [$\Delta n = \sum n_i$ (products, g) – $\sum n_i$ (reactants, g)]

where $\sum n_i$ is the total molar amount of the gases in products or reactants.

The calculated heat of formation was based on the following reaction:

 © 2005 Wiley-VCH Verlag GmbH & Co. KGaA, Weinheim

$[C_7H_{16}N_{12}O_{14}]^+[C_{12}H_4N_6O_{14}]^-$ (s) + 13/2 O_2 (g) → 19/2 CO_2 (g) + 8 H_2O (l) + 6 N_2 (g)

$\Delta_f H^o_m\{[C_7H_{16}N_{12}O_{14}]^+[C_{12}H_4N_6O_{14}]^-, (s)\} = \{19/2\Delta_f H^o_m[CO_2, (g)] + 8\Delta_f H^o_m[H_2O, (l)]\} - \Delta_c H^o_m\{[C_7H_{16}N_{12}O_{14}]^+[C_{12}H_4N_6O_{14}]^-, (s)\}$

Using the above formula and the literature values for the standard molar enthalpies of formation of CO_2 (g) and H_2O (l) [$\Delta_f H^o_m$ [CO_2, (g)] = –393.5 kJ/mol, $\Delta_f H^o_m$ [H_2O, (l)] = –285.8 kJ/mol],[28] $\Delta_f H^o_m$ for compound **26** was calculated to be 520.4 kJ/mol. All of the quaternary salts have positive heats of formation (ranging from 177.3 kJ/mol to 611.4 kJ/ mol) except for the imidazolium picrate derivatives **23** and **25** with heats of formation at –213.6 kJ/mol and –538.1 kJ/mol, respectively, and 1,1′-methylbis(4-methyltriazolium) dinitrate, and compound **27** with the heat of formation at –195.7 kJ/mol. Not surprisingly, picrate salts have higher heats of formation than the nitrate analogs, for example, $\Delta_f H^o_m$ of compound **26** is 520.4 kJ/mol and that of compound **27** is –195.7 kJ/mol; 4-amino-1,2,4-triazolium

Table 1. Phase transition and decomposition temperatures, densities and thermochemical results of picrates, nitrates and perchlorates.

Compound	Picrate T_m[a]	d[b]	OB[d]	T_d[e]	$\Delta_f H^o_m$[f]	Nitrate T_d[e]	$\Delta_f H^o_m$[f]	Perchlorate T_d[e]	$\Delta_f H^o_m$[f]
7	169	1.77	–67	196	497.7	182	–	285[g]	–
8	91	1.72	–79	185	409.6				
9	141	1.80	–91	271	340.1	160[h]	–	97[h]	–
10	106	1.48	–78	176	611.4	129[h]	–	147[h]	–
12	235	1.60	–66	244	513.2	HMS[i]			
14	197	1.64[c]	–66	228	468.8	181[j]	–109.7	208[j]	298
16	147	1.85[c]	–53	214	198.1				
23	215	1.52	–36	283	–213.6				
24	153	1.54	–46			188	177.3		
25	184	1.63	–93	313	–538.1				
26	216	1.67	–81	242	520.4				
27	–15 (T_g)		–74			162	–195.7		
TAG-AT		1.60	–73		1075[k]				
HMX		1.91	–21		75[k]				
TNT		1.65	–74		–64[k]				
Picric acid		1.77	–43		–213.6				
RDX		–	–22		83.8				

[a] Melting point (T_m) (°C)/phase transition temperature (T_g) (°C). [b] Measured density using pycnometer (g/cm^3). [c] Density from crystal structure for **14** is 1.72 and **16** is 1.84. [d] OB (%) is oxygen balance which was calculated from $OB = 1600[(a + b/2 - d)/FW]$ for a compound with the molecular formula of $C_aH_bN_cO_d$. [e] Thermal degradation temperature (T_d) (°C). [f] Molar enthalpy of formation (kJ/mol). [g] Ref.[9]. [h] Ref.[17]. [i] High melting salt. [j] Ref.[18]. [k] Ref.[8].

Table 2. Crystallographic data for compounds **14** and **16**.

Compound	**14**	**16**
Formula	$C_8H_7N_7O_7$	$C_7H_6N_8O_7$
Mol. mass	313.21	314.20
Crystal system	orthorhombic	monoclinic
Space group	*Pbcn*	*C*2/*c*
a [Å]	9.1757(9)	25.4959(13)
b [Å]	19.8568(18)	6.1793(3)
c [Å]	13.2656(12)	14.5863(8)
β [°]	–	98.069(1)
V [Å^3]	2417.0 (4)	2275.3(2)
Z	8	8
T [K]	297 (2)	86 (2)
λ [Å]	0.71073	0.71073
$\rho_{calcd.}$ [mg/m^3]	1.721	1.834
μ [mm^{-1}]	0.153	0.165
F(000)	1280	1280
Crystal size [mm]	0.62 × 0.61 × 0.29	0.43 × 0.40 × 0.26
θ range [°]	2.05 to 25.25	1.61 to 25.25
Index ranges	$-11 \le h \le 9$, $-23 \le k \le 23$, $-10 \le l \le 15$	$-30 \le h \le 30$, $-7 \le k \le 7$, $-17 \le l \le 17$
No. refl. collected	21722	16834
No. indep. reflections	2184 [R(int) = 0.0222]	2059 [R(int) = 0.0226]
Data/restraints/param.	2184/6/229	2059/0/199
GOF	1.048	1.010
R_1 [$I > 2\sigma(I)$]	0.0419	0.0282
wR_2 [$I > 2\sigma(I)$]	0.1126	0.0787
Largest diff. peak, hole [e·Å^{-3}]	0.230, –0.269	0.239, –0.284

$R_1 = \Sigma|F_o| - |F_c|/\Sigma|F_o|$; w$R_2 = \{\Sigma[w(F_o^2 - F_c^2)^2]/\Sigma[w(F_o^2)^2]\}^{1/2}$

 © 2005 Wiley-VCH Verlag GmbH & Co. KGaA, Weinheim

picrate (**14**) at 468.8 kJ/mol is significantly more positive than the nitrate and the perchlorate salts at –109.7 and 298 kJ/mol, respectively.[17] Not unexpectedly 3-azido-1,4-dimethyl-1,2,4-triazolium picrate (**10**) with $\Delta_f H^o_m$ = 611.6 kJ/mol exhibits the most positive heat of formation in this group of energetic salts.

X-ray Crystallography

Compound **14** crystallizes in an orthorhombic space group, *Pbcn*, and compound **16** in the monoclinic *C*2/*c* space group. Both have eight formula units in the cell and in spite of the different space groups, display similar characteristics. Both consist of discrete crystallographically independent picrate anions and 4-amino-triazolium (**14**) or 5-imino-tetrazolium (**16**) cations. The protonation in compound **14** (part a in Figure 1), has occurred on one of the ring nitrogen atoms, N8, instead of the amino group. This NH^+ is involved in an asymmetric bifurcated hydrogen bond; N8···O1, 2.653(1) and N8···O7a, 2.950(5) Å. The double bonds appear to be localized in the triazolium in spite of the protonation, C7–N8, 1.297(2) Å and N9–C10, 1.296(2) Å. The dihedral angle between the triazolium group and the picrate is 78.4°. The packing diagram (part b in Figure 1) is more complex with rows of picrate anions hydrogen-bonded together by zig-zag sheets of triazolium cations into a cross-linked array. In **16**, the tetrazole double bonds also appear distinct, with N6–N7, 1.269(1) Å and an exocyclic amino C7–N4, 1.310(1) Å, (part a in Figure 2). The picrate and tetrazolium species have a much shallower angle to each other (dihedral angle of 21.9°) compared to **14**. The orientation of the tetrazolium cation to the anion also leads to an asymmetric bifurcated hydrogen bond between N5···O1, 2.624(1) Å, and N5···O7, 2.873(1) Å. Both amino hydrogen atoms are also involved in bifurcated hydrogen bonding, which help extend the system into isolated buckled sheets (part b in Figure 2). Although there are many picrate salts in the literature, there are relatively few associated with triazoles and tetrazoles. Only two of the four examples of each[29–32] display similar asymmetric bifurcated bonding between the tri/tetrazolium and the picrate (N···O, 2.62, 2.64 Å and 2.85, 2.90 Å). Crystallographic data for compounds **14** and **16** were listed in Table 2.

Conclusions

In summary, mono and bridged azolium picrate and nitrate salts were synthesized and their physical and thermochemical properties compared. The thermal stabilities of the salts are dipicrates > picrates > perchlorates > nitrates while the densities are found to average ca. 1.60 g/cm^3. Although it is not possible to quaternize 3-*C*-aminotriazole, the 4-aminotriazole easily reacted at N-1. In contrast, the 5-aminotetrazole (C-5) was readily quaternized at N-4. Their structures were confirmed by single-crystal X-ray analysis. The heats of formation values for picrates are more positive than for analogous nitrates and perchlorates. Oxygen balance values for the mono and bridged azolium picrates and dipicrates fall in the range of many common energetic materials.

Experimental Section

Caution: Although we have not experienced any problems in handling these compounds, their shock and impact sensitivity has not been determined. They should be handled with extreme care.

General Methods: The chemicals were obtained commercially. Silver picrate was prepared based on the literature.[33] A standard Schlenk line system was used for various manipulations. ^{1}H and ^{13}C NMR spectra were recorded on a spectrometer operating at 300 and 75 MHz, respectively, using [D$_6$]DMSO as solvent unless otherwise indicated. Chemical shifts are reported in ppm relative to TMS. DSC data were recorded by heating from 20 °C to 400 °C at 10 °C/min using a differential scanning calorimeter equipped with auto-cool and calibrated using indium. Thermogravimetric analysis (TGA) measurements were made by heating samples at 10 °C/min from 20 °C to 450 °C in a dynamic nitrogen atmosphere. Densities of solid salts were measured at room temperature using a gas pycnometer. The heat of combustion was determined using a semimicro oxygen bomb calorimeter. Elemental analyses were performed commercially. Electrospray mass spectra were recorded using Micromass LCT equipment.

Crystallography: Crystals of compound **14** and **16** were removed from the flasks. A suitable crystal was selected, attached to a glass fiber and placed in the low-temperature nitrogen stream. Data for **14** were collected at 297(2) K and for **16** were collected at 86(2) K using a Bruker/Siemens SMART APEX instrument (Mo-K_α radiation, λ = 0.71073 Å) equipped with a Cryocool NeverIce low temperature device. Data were measured using omega scans of 0.3° per frame for 5 seconds, and a hemisphere of data was collected for compound **14**. A total of 1471 frames were collected with a final resolution of 0.81 Å. The first 50 frames were recollected at the end of data collection to monitor for decay. And a full sphere of data was collected for **16**. A total of 2400 frames were collected with a final resolution of 0.77 Å. The first 50 frames were recollected at the end of data collection to monitor for decay. Cell parameters were retrieved using SMART software[34] and refined using SAINTPlus[35] on all observed reflections. Data reduction and correction for Lp and decay were performed using the SAINTPlus software. Absorption corrections were applied using SADABS.[36] The structure was solved by direct methods and refined by least-squares method on F^2 using the SHELXTL program package.[37] The structure was solved in the space group *Pbcn* (no. 60) for **14** and *C*2/*c* (no. 15) for **16** by analysis of systematic absences. CCDC-271202 (for **14**) and CCDC-271203 (for **16**) contain the supplementary crystallographic data for this paper. These data can be obtained free of charge from The Cambridge Crystallographic Data Centre via www.ccdc.cam.ac.uk/data_request/cif.

1,2,4-Triazolium Picrate (7): In 20 mL methanol were mixed 1,2,4-triazole (0.113 g, 1.6 mmol) and picric acid (0.373 g, 1.6 mmol). The mixture was stirred for 10 hours at 25 °C, and the solvent was removed under reduced pressure. The solid was washed with water (20 mL) and acetone (20 mL) to yield a dark-yellow solid **7** (0.453 g) in 95% yield. M.p. 169 °C. IR (KBr): $\tilde{\nu}$ = 3153, 3068, 2887, 1607, 1571, 1350, 1203, 628 cm^{-1}. ^{1}H NMR: δ = 11.8 (br. s, 2 H), 9.34 (s, 1 H), 9.32 (s, 1 H), 8.60 (s, 2 H) ppm. ^{13}C NMR: δ = 160.8, 143.3, 141.9, 125.3, 124.5 ppm. $C_8H_6N_6O_7$ (298.1): calcd. C 32.23, H 2.03, N 28.19; found C 31.99, H 2.06, N 28.43.

 © 2005 Wiley-VCH Verlag GmbH & Co. KGaA, Weinheim

1-Methyl-1,2,4-triazolium Picrate (8): The procedure was the same as for compound **7** using **2** (0.083 g, 1.0 mmol) and picric acid (0.229 g, 1.0 mmol) at 25 °C for 8 hours. The residue was washed with water (20 mL) and dichloromethane (20 mL) to leave a light-yellow solid **8** (0.291 g) in 93% yield. M.p. 91 °C. IR (KBr): $\tilde{\nu}$ = 3143, 3074, 1608, 1538, 1322, 1274, 664 cm^{-1}. ^1H NMR ([D_6]acetone): δ = 9.42 (s, 1 H), 8.88 (s, 2 H), 8.66 (s, 1 H), 8.18 (br. s, 1 H), 4.21 (s, 3 H) ppm. ^{13}C NMR δ = 158.2, 145.4, 142.1, 140.6, 130.2, 124.9, 3.69 ppm. $C_9H_8N_6O_7$ (312.2): calcd. C 34.62, H 2.58, N 26.92; found C 34.25, H 2.61, N 27.26.

1,4-Dimethyl-1,2,4-triazolium Picrate (9): Silver picrate (0.336 g, 1.0 mmol) was added to **3** (0.225 g, 1.0 mmol) in 20 mL DMF to give a yellow precipitate. The mixture was filtered and solvent was removed from the filtrate under vacuum to leave a yellow solid. The latter was recrystallized from methanol and acetone (1:2) to give a pure yellow solid **9** (0.287 g) in 88% yield. M.p.141 °C. IR (KBr): $\tilde{\nu}$ = 3081, 2953, 1634, 1561, 1337, 1278, 786, 634 cm^{-1}. ^1H NMR δ = 9.97 (s, 1 H), 9.08 (s, 1 H), 8.58 (s, 2 H), 4.06 (s, 3 H), 3.89 (s, 3 H) ppm. ^{13}C NMR δ = 160.9, 145.3, 143.4, 141.8, 125.3, 124.4, 38.6, 34.0 ppm. $C_{10}H_{10}N_6O_7$ (326.2). MS (ESI): (+v e): *m*/*z* = 97.9 [M – Picrate] $^+$; (–v e): *m*/*z* = 227.9 [picrate] $^-$.

3-Azido-1,4-dimethyl-1,2,4-triazolium Picrate (10): The procedure was as used for **9** using **6** (0.18 g, 0.68 mmol) and silver picrate (0.224 g, 0.68 mmol) in 20 mL DMF to form a yellow solid. After removal of solvent, the residue was washed with acetone (30 mL) to leave a dark-yellow solid **10** (0.227 g) in 91% yield. M.p.106 °C. IR (KBr): $\tilde{\nu}$ = 3194, 3095, 2183, 1636, 1550, 1327, 1282, 702, 615 cm^{-1}. ^1H NMR: δ = 9.83 (s, 1 H), 8.59 (s, 2 H), 4.02 (s, 3 H), 3.62 (s, 3 H) ppm. ^{13}C NMR: δ = 161.3, 150.8, 144.1, 142.3, 125.6, 124.7, 39.5, 32.6 ppm. $C_{10}H_9N_9O_7$ (367.2): calcd. C 32.71, H 2.47, N 34.33; found C 32.45, H 2.40, N 33.50.

3-Amino-1,2,4-triazolium Picrate (12): The procedure was as used for **7** from **11** (0.084 g, 1.0 mmol) and picric acid (0.229 g, 1.0 mmol) in 40 mL methanol for 3 h at 45 °C to give a yellow powder **12** (0.298 g) in 95% yield. M.p. 235 °C. IR (KBr): $\tilde{\nu}$ = 3450, 3344, 3098, 1701, 1641, 1551, 1337, 1276, 708, 603 cm^{-1}. ^1H NMR: δ = 8.60 (s, 2 H), 8.32 (s, 1 H), 8.05 (br. s) ppm. ^{13}C NMR: δ = 160.9, 150.8, 141.9, 139.2, 125.3, 124.4 ppm. $C_8H_7N_7O_7$ (313.2): calcd. C 30.68, H 2.25, N 31.31; found C 30.52, H 2.11, N 31.89.

4-Amino-1,2,4-triazolium Picrate (14): Procedure was as used for **12** from **13** (0.094 g, 1.1 mmol) and picric acid (0.26 g, 1.1 mmol) at 45 °C for 6 h to give a yellow solid. Recrystallization from methanol (20 mL) to gave pure **14** (0.317 g) in 92% yield. M.p. 197 °C. IR (KBr): $\tilde{\nu}$ = 3363, 3260, 3122, 2988, 1610, 1543, 1336, 1266, 710, 619 cm^{-1}. ^1H NMR: δ = 9.49 (s, 1 H), 9.48 (s, 1 H), 8.60 (s, 2 H), 6.26 (br. s) ppm. ^{13}C NMR: δ = 160.9, 144.1, 141.9, 125.3, 124.4 ppm. $C_8H_7N_7O_7$ (313.2): calcd. C 30.68, H 2.25, N 31.31; found C 30.64, H 2.09, N 32.36.

5-Aminotetrazolium Picrate (16): Procedure was as used for **8** from **15** (0.124 g, 1.5 mmol) and picric acid (0.345 g, 1.5 mmol) in methanol (20 mL) at 50 °C for 12 h to form a yellow solid. Recrystallization from methanol and dichloromethane (1:2) produced pure **16** (0.424 g) in 90% yield. M.p. 147 °C. IR (KBr): $\tilde{\nu}$ = 3416, 3331, 3209, 2931, 1647, 1587, 1334, 1265, 734, 677 cm^{-1}. ^1H NMR δ = 8.60 (s, 2 H), 7.70 (br. s) ppm. ^{13}C NMR: δ = 160.8, 156.3, 141.9, 125.3, 124.4 ppm. $C_7H_6N_8O_7$ (314.2). MS (ESI): (+v e): *m*/*z* = 84.0 [M – Picrate – 2H] $^+$; (–v e): *m*/*z* = 227.9 [picrate] $^-$.

1,1′-Methylenebis(imidazolium) Dipicrate (23): Procedure was as for **7** from **19** (0.064 g, 0.5 mmol) and picric acid (0.229 g, 1.0 mmol) to give a yellow solid which was washed with acetone (10 mL) and dichloromethane (15 mL) to give a yellow powder **23** (0.288 g) in 95% yield. M.p. 215 °C. IR (KBr): $\tilde{\nu}$ = 3133, 3066, 1611, 1563, 1320, 1272, 709, 621 cm^{-1}. ^1H NMR: δ = 9.34 (s, 2 H), 8.60 (s, 4 H), 7.97 (s, 2 H), 7.74 (s, 2 H), 6.67 (s, 2 H) ppm. ^{13}C NMR: δ = 160.9, 141.9, 137.2, 125.3, 124.5, 121.6, 121.1, 58.0 ppm. $C_{19}H_{14}N_{10}O_{14}$ (606.4): calcd. C 37.63, H 2.33, N 23.10; found C 37.57, H 2.45, N 23.54.

1,1′-Methylenebis(triazolium) Dinitrate (24): Procedure was as for **7** from **20** (0.26 g, 2.0 mmol) and concentrated nitric acid (1.1 g, 70%wt) The solvent was removed in vacuo, the solid was washed with methanol (20 mL) to form a white solid **24** (0.536 g) in 97% yield. M.p. 153 °C. IR (KBr): $\tilde{\nu}$ = 3142, 3029, 1609, 1549, 1309, 1232, 715 cm^{-1}. ^1H NMR: δ = 10.22 (br. s), 9.25 (s, 2 H), 8.32 (s, 2 H), 6.78 (s, 2 H) ppm. ^{13}C NMR: δ = 150.6, 145.4, 60.0 ppm. $C_5H_8N_8O_6$ (276.2): calcd. C 21.75, H 2.92, N 40.37; found C 21.72, H 2.84, N 41.91.

1,1′-Methylenebis(3-methylimidazolium) Dipicrate (25): Procedure was as for **9** from **21** (0.13 g, 0.3 mmol) and silver picrate (0.2 g, 0.6 mmol) in 20 mL DMF to give a yellow solid. Recrystallization from methanol and acetone (1:3) gave pure **25** (0.172 g) in 90% yield. M.p. 184 °C. IR (KBr): $\tilde{\nu}$ = 3104, 3029, 1618, 1567, 1367, 1271, 734, 619 cm^{-1}. ^1H NMR: δ = 9.34 (s, 2 H), 8.60 (s, 4 H), 7.94 (s, 2 H), 7.79 (s, 2 H), 6.64 (s, 2 H), 3.91 (s, 6 H) ppm. ^{13}C NMR: δ = 160.7, 141.7, 137.9, 125.1, 124.4, 124.2, 121.9, 58.2, 36.2 ppm. $C_{21}H_{18}N_{10}O_{14}$ (634.4). MS (ESI): (+v e): *m*/*z* = 178.8 [M – Picrate] $^+$, 89 [M – 2 picrate] $^{2+}$/2; (–v e): *m*/*z* = 227.9 [picrate] $^-$.

1,1′-Methylenebis(4-methyltriazolium) Dipicrate (26): Procedure was as used for **9** from **22** (0.086 g, 0.2 mmol) and silver picrate (0.134 g, 0.4 mmol) to give an orange-yellow solid. Recrystallization from methanol (10 mL) gave pure **23** (0.114 g) in 89% yield. M.p. 216 °C. IR (KBr): $\tilde{\nu}$ = 3060, 1630, 1556, 1313, 1266, 705, 613 cm^{-1}. ^1H NMR: δ = 10.41 (s, 2 H), 9.29 (s, 2 H), 8.60 (s, 4 H), 7.19 (s, 2 H), 3.99 (s, 6 H) ppm. ^{13}C NMR: δ = 160.9, 146.6, 145.7, 141.9, 125.3, 124.3, 62.3, 34.7 ppm. $C_{19}H_{16}N_{12}O_{14}$ (636.4). MS (ESI): (+v e): *m*/*z* = 90.0 [M – 2 picrate] $^{2+}$/2; (–v e): *m*/*z* = 227.9 [picrate] $^-$.

1,1′-Methylenebis(4-methyltriazolium) Dinitrate (27): Compound **22** (0.189 g, 0.44 mmol) was mixed with silver nitrate (0.148 g, 0.88 mmol) in water (20 mL) to form a yellow precipitate. The suspension was filtered. The solvent was removed from the filtrate in vacuo to leave a colorless wax **27** (0.127 g) in 95% yield. M.p. –15.2 °C. IR (KBr): $\tilde{\nu}$ = 3116, 2986, 1637, 1588, 1352, 1233, 760, 617 cm^{-1}. ^1H NMR: δ = 10.46 (s, 2 H), 9.29 (s, 2 H), 7.17 (s, 4 H), 3.97 (s, 6 H) ppm. ^{13}C NMR: δ = 146.6, 145.9, 62.6, 34.6 ppm. $C_7H_{12}N_8O_6$ (304.2). MS (ESI): (+v e): *m*/*z* = 90.0 [M – 2NO_3^-]$^{2+}$/2; (–v e): *m*/*z* = 62.0 [NO_3] $^-$.

Acknowledgments

The authors gratefully acknowledge the support of AFOSR (F49620-03-1-0209), NSF (CHE0315275), and ONR (N00014-02-1-0600). We appreciate the support of Dr. Alex Blumenfeld for NMR analyses. The Bruker (Siemens) SMART APEX diffraction facility was established at the University of Idaho with the assistance of the NSF-EPSCoR program and the M. J. Murdock Charitable Trust, Vancouver, WA, USA.

[1] P. F. Pagoria, G. S. Lee, A. R. Mitchell, R. D. Schmidt, *Thermochim. Acta* **2002**, *384*, 187–204.
[2] A. K. Sikder, N. J. Sikder, *J. Hazardous Materials A* **2004**, *112*, 1–15.
[3] J. P. Agrawal, *Prog. Energy Combust. Sci.* **1998**, *24*, 1–30.

[4] a) A. Hammerl, T. M. Klapötke, H. Nöth, M. Warchhold, G. Holl, M. Kaiser, U. Ticmanis, *Inorg. Chem.* **2001**, *40*, 3570–3575; b) A. Hammerl, T. M. Klapötke, *Inorg. Chem.* **2002**, *41*, 906–912; c) A. Hammerl, G. Holl, M. Kaiser, T. M. Klapötke, H. Piotrowski, *Z. Anorg. Allg. Chem.* **2003**, *629*, 2117–2121.
[5] D. E. Chavez, M. A. Hiskey, R. D. Gilardi, *Org. Lett.* **2004**, *6*, 2889–2891.
[6] M. A. Hiskey, D. E. Chavez, D. L. Naud, S. F. Son, H. L. Berghout, C. A. Bolme, *Proceedings of the International Pyrotechnics Seminar. International Pyrotechnics Seminar* **2000**, *27*, 3–14.
[7] M. A. Hiskey, M. M. Stinecipher, J. E. Brown, *J. Energetic Materials* **1993**, *11*, 157–166.
[8] a) M.-H. V. Huynh, M. A. Hiskey, E. L. Hartline, D. P. Montoya, R. Gilardi, *Angew. Chem. Int. Ed.* **2004**, *43*, 4924–4928, and references cited therein; b) D. E. Chavez, M. A. Hiskey, D. L. Naud, *Propellants Explosives Pyrotechnics* **2004**, *29*, 209–215, and references therein.
[9] a) G. Drake, T. Hawkins, A. Brand, L. Hall, M. Mckay, A. Vij, I. Ismail, *Propellants Explosives Pyrotechnics* **2003**, *28*, 174–180; b) G. W. Drake, US Patent 6,509,473, Jan. 21, **2003**; G. Drake, T. Hawkins, AFOSR Ionic Liquids Workshop, Dulles, VA. October **2002**; G. Drake, AFOSR Ionic Liquids Workshop, Aberdeen, MD. September **2003**.
[10] a) T. M. Klapötke, P. Mayer, A. Schulz, J. J. Weigand, *J. Am. Chem. Soc.* **2005**, *127*, 2032–2033; b) A. Hammerl, G. Holl, M. Kaiser, T. M. Klapötke, P. Mayer, H. Nöth, H. Piotrowski, M. Warchhold, *Eur. J. Inorg. Chem.* **2002**, 834–845; c) J. C. Gálvez-Ruiz, G. Holl, K. Karaghiosoff, T. M. Klapötke, K. Löhnwitz, P. Mayer, H. Nöth, K. Polborn, C. J. Rohbogner, M. Suter, J. J. Weigand, *Inorg. Chem.* **2005**, *44*, 4237–4253.
[11] Y. R. Mirzaei, J. M. Shreeve, *Synthesis* **2003**, 24–26.
[12] Y. R. Mirzaei, H. Xue, J. M. Shreeve, *Inorg. Chem.* **2004**, *43*, 361–367.
[13] a) Y. R. Mirzaei, B. Twamley, J. M. Shreeve, *J. Org. Chem.* **2002**, *67*, 9340–9345; b) H. Xue, B. Twamley, J. M. Shreeve, *J. Org. Chem.* **2004**, *69*, 1397–1400.
[14] Y. Ou, B. Chen, J. Li, H. Jia, *Heterocycles* **1994**, *38*, 1651–1664.
[15] M. S. Pevzner, *Russ. Chem. J.* **1997**, *41*, 73–81.
[16] G. Drake, T. Hawkins, AFRL/PRSP AFOSR Ionic Liquids Workshop. March **2004**, Tampa, FL.
[17] H. Xue, Y. Gao, B. Twamley, J. M. Shreeve, *Chem. Mater.* **2005**, *17*, 191–198.
[18] H. Xue, S. W. Arritt, B. Twamley, J. M. Shreeve, *Inorg. Chem.* **2004**, *43*, 7972–7977.
[19] R. C. Weast, S. M. Selby, *Handbook of Chemistry and Physics*, 48th Edition, **1967**–**1968**, D22–D51.
[20] V. A. Ostrovskii, M. S. Pevzner, T. P. Kofman, I. V. Tselinskii, *Targets in Heterocyclic Systems* **1999**, *3*, 467–526.
[21] W. Ogihara, M. Yoshizawa, H. Ohno, *Chem. Lett.* **2004**, *33*, 1022–1023.
[22] a) A. R. Katritzky, S. Singh, K. Kirichenko, J. D. Holbrey, M. Smiglak, W. M. Reichert, R. D. Rogers, *Chem. Commun.* **2005**, 868–870; b) H. Xue, Y. Gao, B. Twamley, J. M. Shreeve, *Inorg. Chem.* **2005**, *44*, ASAP; c) C. Ye, J.-C. Xiao, B. Twamley, J. M. Shreeve, *Chem. Commun.* **2005**, 2750–2752.
[23] G. Singh, I. P. S. Kapoor, M. Mannan, S. K. Tiwari, *J. Hazardous Materials A* **1999**, *68*, 155–178.
[24] Y. Gao, S. W. Arritt, B. Twamley, J. M. Shreeve, *Inorg. Chem.* **2005**, *44*, 1704–1712.
[25] a) R. J. Granados, *Heterocycl. Chem.* **1976**, *13*, 281–284; b) B. T. Heitke, C. G. McCarty, *J. Org. Chem.* **1974**, *39*, 1522–1526.
[26] R. M. Claramunt, D. Sanz, J. Catalón, F. Fabero, N. A. Garcia, C. Foces-Foces, A. Llamas-Saiz, J. Elguero, *J. Chem. Soc. Perkin Trans. 2* **1993**, 1687–1699.
[27] a) E. Diez-barra, A. De la Hoz, R. I. Rodriguez-Curiel, J. Tejeda, *Tetrahedron* **1997**, *53*, 2253–2260; b) S. Julia, P. Sala, J. Del Mazo, M. Sancho, C. Ochoa, J. Elguero, *J. Heterocyclic Chem.* **1982**, *19*, 1141–1145; c) C. M. Jin, B. Twamley, J. M. Shreeve, *Organometallics* **2005**, *24*, 3020–3023.
[28] a) J. D. Cox, D. D. Wagman and V. A. Medvedev, *CDDATA Key Values for Thermodynamics*; Hemisphere: New York, **1989**; b) J. D. Cox, *J. Chem. Thermodyn.* **1978**, *10*, 903–906.
[29] Q. Wang, Z. Li, H. Yang, F. Li, Z. Ding, F. Tao, *Synthesis* **2003**, 1231–1235.
[30] V. E. Matulis, A. S. Lyakhov, P. N. Gaponik, S. V. Voitekhovich, O. A. Ivashkevich, *J. Mol. Struct.* **2003**, *649*, 309–314.
[31] P. N. Gaponik, S. V. Voitekhovich, O. A. Ivashkevich, A. S. Lyakhov, A. S. Govorova, *Khim. Geterosikl. Soedin.* **1998**, *371*, 6579–665.
[32] S. Sarker, J. H. Cooley, R. D. Willett, A. L. Rheingold, *J. Org. Chem.* **1995**, *60*, 476–478.
[33] R. C. Maurya, P. Sharma, S. Roy, *Synth. React. Inorg. Met.-Org. Chem.* **2003**, *33*, 683–698.
[34] SMART: v.5.626, Bruker Molecular Analysis Research Tool, Bruker AXS, Madison, WI, **2002**.
[35] SAINTPlus: v. 6.36a, Data Reduction and Correction Program, Bruker AXS, Madison, WI, **2001**.
[36] SADABS: v.2.01, an empirical absorption correction program, Bruker AXS Inc., Madison, WI, **2001**.
[37] SHELXTL: v. 6.10, Structure Determination Software Suite, Sheldrick, G. M., Bruker AXS Inc., Madison, WI, **2001**.

Received: May 25, 2005
Published Online: August 9, 2005

 © 2005 Wiley-VCH Verlag GmbH & Co. KGaA, Weinheim

EurJIC
European Journal of Inorganic Chemistry

Issue 19/2005

Pages 3773–3992

Papers available ahead of print in Early View at www.interscience.wiley.com

Earliest available Table of Contents: Automatically, free of charge by e-mail through www.interscience.wiley.com/alerts

COVER PICTURE

The cover picture shows the structures of ferrocene-based phosphanyl-carboxylic acids that have been synthesized, characterized by various physicochemical methods, and further utilized as novel organometallic synthons, ligands in coordination compounds, and components of various catalytic systems over the last ten years that have passed since the discovery of the first representative. Some aspects of the chemistry of these and other related phosphanyl-ferrocenecarboxylic ligands addressed in the Microreview by P. Štěpnička on p. 3787 ff. are indicated in the centre of the cover picture, which is arranged in a chessboard-like manner to emphasize their close, and sometimes causal, relations and complementarity.

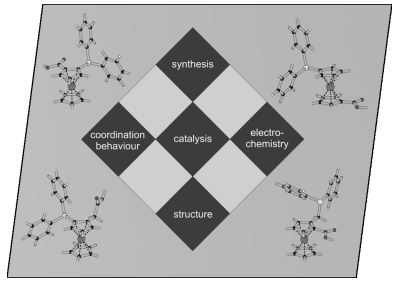

MICROREVIEW

Contents

3787 **P. Štěpnička***

The Chemistry of Phosphanyl-ferrocenecarboxylic Ligands

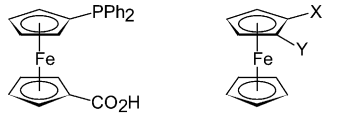

X/Y = PPh_2/CO_2H
CH_2CO_2H/PPh_2
CH_2PPh_2/CO_2H

Keywords: Ferrocene / Phosphanyl-carboxylic ligands / Coordination compounds / Catalysis / Phosphanes / Structure elucidation

 © 2005 Wiley-VCH Verlag GmbH & Co. KGaA, Weinheim

SHORT COMMUNICATION

3805 **K. A. Rufanov,* A. R. Petrov, V. V. Kotov, F. Laquai, J. Sundermeyer***

A Lutetium Cyclopentadienyl-Phosphazene Constrained Geometry Complex (CGC): First Isolobal Analogues of Group 4 Cyclopentadienyl-Silylamido CGC Systems

Keywords: Bridging ligands / Isolobal relationship / Phosphazenes / Constrained geometry complexes / Lutetium

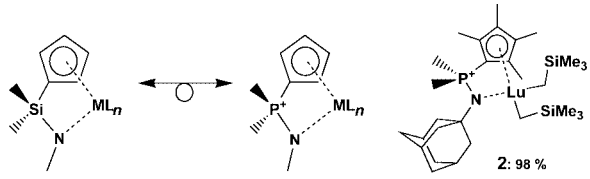

3808 **J. Moussa, K. Boubekeur, H. Amouri***

Self-Assembly of 1-D Coordination Polymers Using Organometallic Linkers and Exhibiting Argentophilic Interactions $Ag^{I}\cdots Ag^{I}$

Keywords: Coordination polymers / Silver / Self-assembly / Quinones / Metal-metal interactions

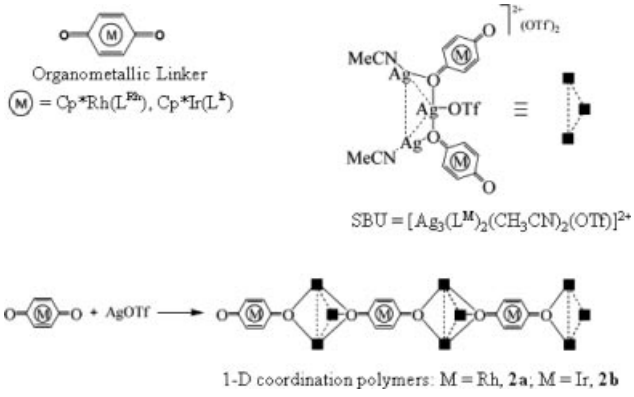

3811 **Z. Shi, X. Gu, J. Peng,* Z. Xin**

An Unprecedented One-Dimensional Chain Constructed from β-Octamolybdate Clusters and Two Kinds of Silver Complex Fragments

Keywords: Chainlike compound / Hydrothermal synthesis / Octamolybdate cluster / Ag complex

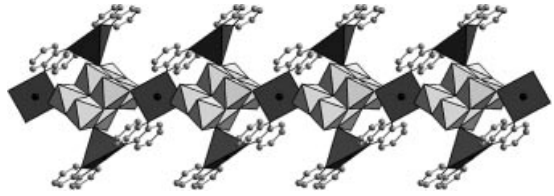

FULL PAPERS

3815 **S. Herres-Pawlis, U. Flörke, G. Henkel***

Tuning of Copper(I)−Dioxygen Reactivity by Bis(guanidine) Ligands

Keywords: Bioinorganic chemistry / Copper / Guanidine ligands / Ligand design / O−O activation

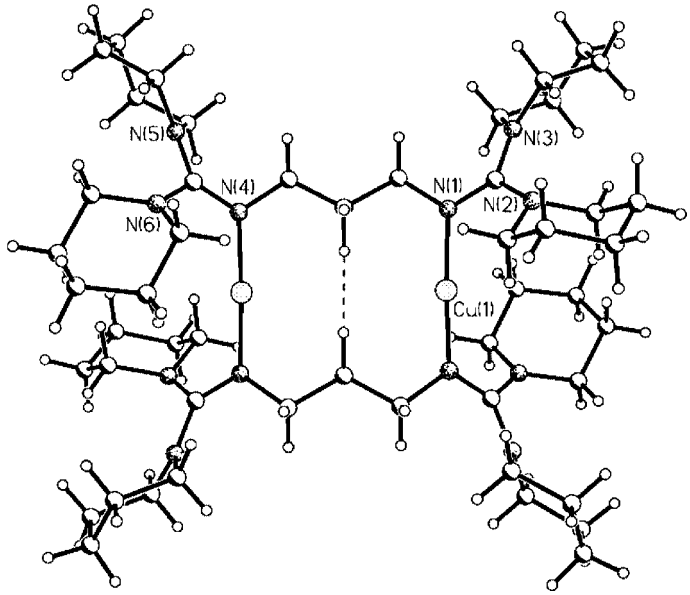

 © 2005 Wiley-VCH Verlag GmbH & Co. KGaA, Weinheim

3825 **J. A. Casares, P. Espinet,***
J. M. Martín-Alvarez,
J. M. Martínez-Ilarduya, G. Salas

Stable Nickel Catalysts for Fast Norbornene Polymerization: Tuning Reactivity

Keywords: Homogeneous catalysis / As ligands / Sb ligands / Nickel / Polymerization / Norbornene / Pentafluorophenyl

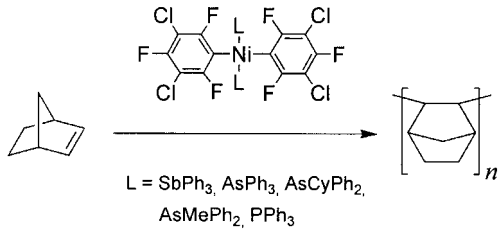

3832 **T. Wada, K. Tanaka***

Reversible Bond Formation and Cleavage of the Oxo Bridge of $[Ru_2(\mu\text{-}O)(dioxolene)_2(btpyxa)]^{3+}$ [btpyxa = 2,7-Di-*tert*-butyl-9,9-dimethyl-4,5-bis(2,2′:6′,2′′-terpyrid-4′-yl)xanthene] Driven by a Three-Electron Redox Reaction

Keywords: Electronic structure / O ligands / Oxidation / Reduction / Ruthenium

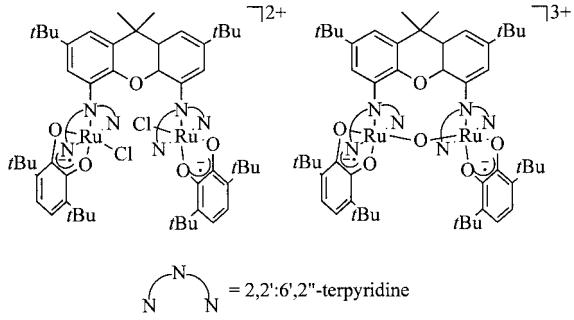

3840 **S. Gençaslan, W. S. Sheldrick***

Bifunctional Bioorganometallic Iridium(III)–Platinum(II) Complexes Incorporating Both Intercalative and Covalent DNA Binding Capabilities

Keywords: Iridium / Platinum / Peptides / DNA binding / Bioinorganic chemistry

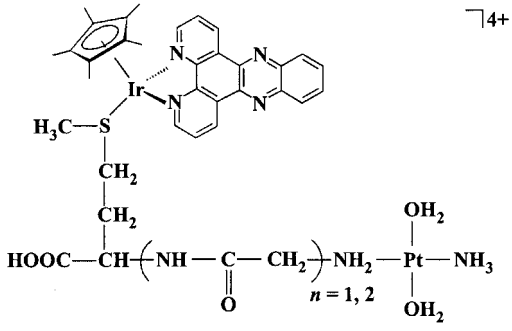

3850 **K. Frąckiewicz, M. Czerwiński, S. Siekierski***

Secondary Periodicity in the Tetrahalogeno Complexes of the Group 13 Elements

Keywords: Quantum calculations / Electronic structure / Group 13 elements / Halogens / Secondary periodicity

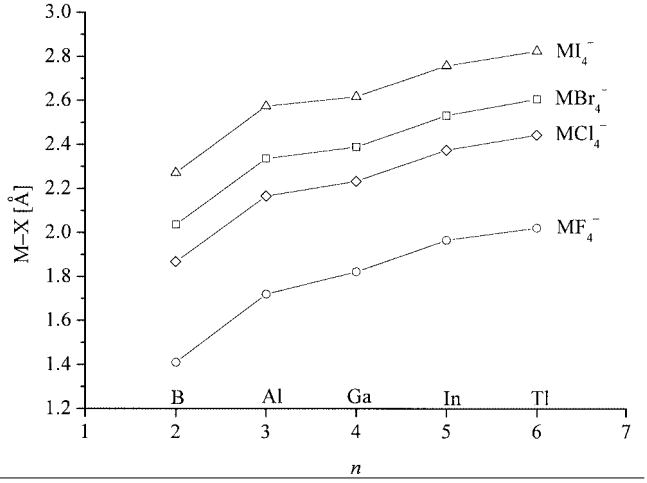

 © 2005 Wiley-VCH Verlag GmbH & Co. KGaA, Weinheim

3857 **E. Annoni, M. Pizzotti,* R. Ugo, S. Quici, T. Morotti, M. Bruschi, P. Mussini**

Synthesis, Electronic Characterisation and Significant Second-Order Non-Linear Optical Responses of *meso*-Tetraphenylporphyrins and Their Zn^{II} Complexes Carrying a Push or Pull Group in the β Pyrrolic Position

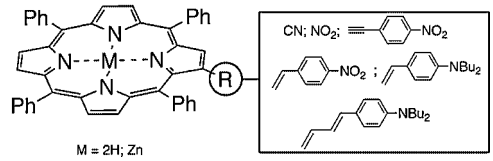

Keywords: Cyclic voltammetry / Nonlinear optics / Porphyrins / UV/Vis spectroscopy / Zinc

3875 **M. Le Hénanf, C. Le Roy, F. Y. Pétillon, P. Schollhammer, J. Talarmin***

Nitrate- and Nitrite-Assisted Conversion of an Acetonitrile Ligand Into an Amidato Bridge at an $\{Mo_2(Cp)_2(\mu\text{-}SMe)_3\}$ Core: Electrochemistry of the Amidato Complex $[Mo_2(Cp)_2(\mu\text{-}SMe)_3\{\mu\text{-}\eta^1,\eta^1\text{-}OC(Me)NH\}]^+$

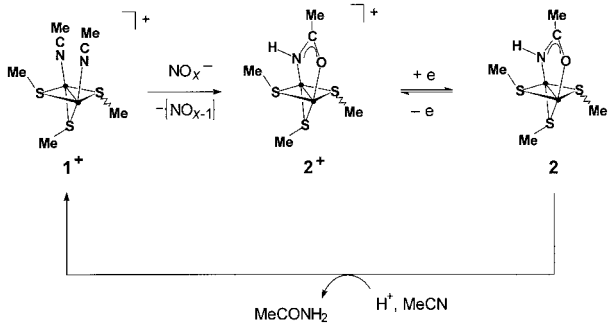

Keywords: Bridging ligands / Cyclic voltammetry / Electrochemistry / Molybdenum / S ligands

3884 **R. Kapoor,* A. Kataria, P. Venugopalan, P. Kapoor, G. Hundal, M. Corbella***

Coordination Chemistry of *N*,*N*,*N*′,*N*′-Tetraethylpyridine-2,6-dithiocarboxamide (*S*-dept) − X-ray Crystal Structures and Magnetic Properties of [Co(*S*-dept)X_2] (X = Br, I, and NCS)

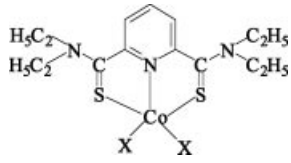

Keywords: *N*,*N*,*N*′,*N*′-Tetraethylpyridine-2,6-dithiocarboxamide / X-ray crystallography / IR / Zero-field splitting / EPR

3894 **I. Ara, N. Chaouche, J. Forniés,* C. Fortuño, A. Kribii, A. Martín**

A Dinuclear Phosphidoplatinum(II) Fragment as a Building Block for Tri-, Tetra-, Hexa-, and Octanuclear Complexes

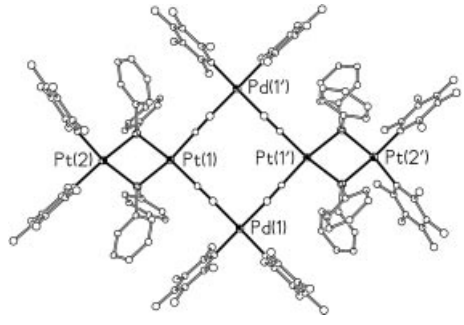

Keywords: Bridging ligands / Cyanides / P ligands / Platinum / Self-assembly

3902 **B.-Q. Ma,* H.-L. Sun, S. Gao***

Vertex-Sharing Water Tape Consisting of Cyclic Hexamers

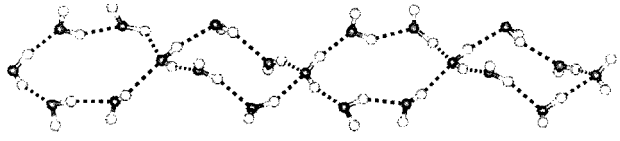

Keywords: Water aggregates / Cyanides / Hydrogen bonds

 © 2005 Wiley-VCH Verlag GmbH & Co. KGaA, Weinheim

3907 **J. D. Crowley, I. M. Steele, B. Bosnich***

Molecular Recognition − Allosterism Generated by Weak Host−Guest Interactions in Molecular Rectangles

Keywords: Host−guest systems / Molecular recognition / Allosterism / Self-assembly / Supramolecular chemistry

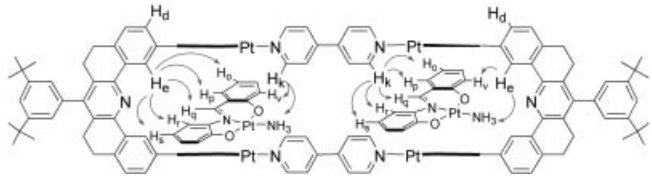

3918 **S. J. Ratnakar, V. Alexander***

Synthesis and Relaxivity Studies of a Gadolinium(III) Complex of ATP-Conjugated DO3A as a Contrast Enhancing Agent for MRI

Keywords: Gadolinium / Imaging agents / Macrocyclic ligands / N ligands

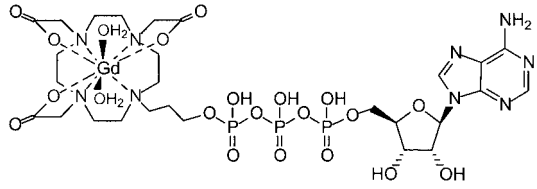

3928 **J. Zhang, S. Morlens, L. G. Hubert-Pfalzgraf,* D. Luneau**

Synthesis, Characterization and Molecular Structures of Yttrium Trifluoroacetate Complexes with O- and N-Donors: Complexation vs. Hydrolysis

Keywords: Carboxylate ligands / Fluorinated ligands / N ligands / Superconductors / Yttrium

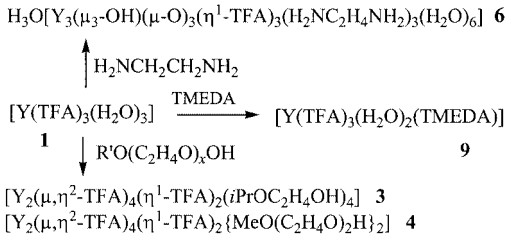

3936 **R. Dreos,* P. Siega, S. Scagliola, L. Randaccio,* G. Nardin, C. Tavagnacco, M. Bevilacqua**

Synthesis, Characterization, and Electrochemical Properties of Dinuclear Complexes Assembled from Asymmetric Co^{III} Bis(dioximates) and Boronic Acids

Keywords: Boronic acid / Cobalt / Dioximes / Enantioselectivity / Electrochemistry

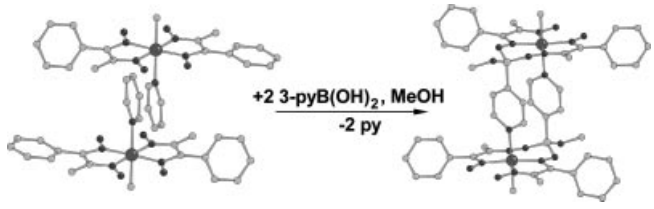

3945 **S. S. Yarovoi, Y. V. Mironov, D. Y. Naumov, Y. V. Gatilov, S. G. Kozlova, S.-J. Kim, V. E. Fedorov***

Octahedral Hexahydroxo Rhenium Cluster Complexes $[Re_6Q_8(OH)_6]^{4-}$ (Q = S, Se): Synthesis, Structure, and Properties

Keywords: Rhenium / Hexahydroxo complexes / Cluster compounds / Electronic structure / Luminescence

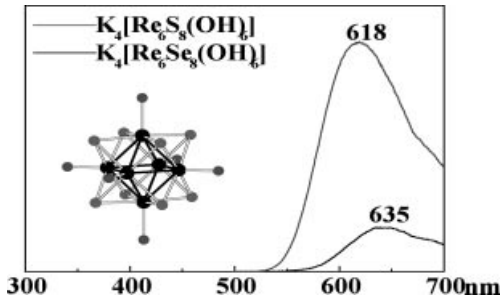

 © 2005 Wiley-VCH Verlag GmbH & Co. KGaA, Weinheim

3950 **W.-K. Lo, W.-K. Wong,* W.-Y. Wong, J. Guo**

Synthesis, Crystal Structures and Photophysical Properties of Novel Tetranuclear Cadmium(II) Schiff-Base Complexes

Keywords: Cadmium / Crystal structures / Phosphorescence / Schiff bases

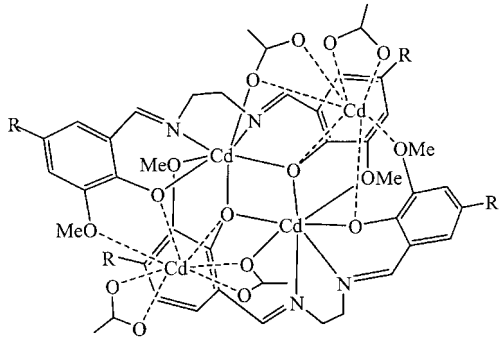

3955 **E. Sebe, I. A. Guzei, M. J. Heeg, L. M. Liable-Sands, A. L. Rheingold, C. H. Winter***

Synthesis Structure, and Properties of Zirconium and Hafnium Complexes Containing η^2-Pyrazolato Ligands

Keywords: Group-4 transition metals / Zirconium / Hafnium / Pyrazolato ligands / N ligands / Intramolecular hydrogen bond

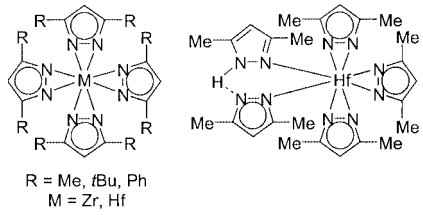

3962 **C. Ramos, P. Royo,* M. Lanfranchi, M. A. Pellinghelli, A. Tiripicchio**

Zirconium and Hafnium Complexes with (Allylsilyl)(η-amidosilyl)-η^5-cyclopentadienyl Ligands: Synthesis, Structure and Reactivity

Keywords: Insertion / Isocyanides / Hafnium / Metallocenes / Zirconium

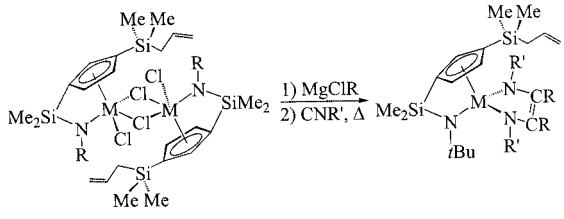

3971 **M. L. Childers, F. Su, A. M. Przyborowska, B. Bishwokarma, G. Park, M. W. Brechbiel, S. V. Torti, F. M. Torti, G. Broker, J. S. Alexander, R. D. Rogers, K. Ruhlandt-Senge, R. P. Planalp***

Pyridine-Ring Alkylation of Cytotoxic *r*-1,*c*-3,*c*-5-Tris[(2-pyridylmethyl)amino]cyclohexane Chelators: Structural and Electronic Properties of the Mn^{II}, Fe^{II}, Ni^{II}, Cu^{II} and Zn^{II} Complexes

Keywords: Antitumor activity / Tripodal ligands / Ligand design / Iron / Zinc / Copper

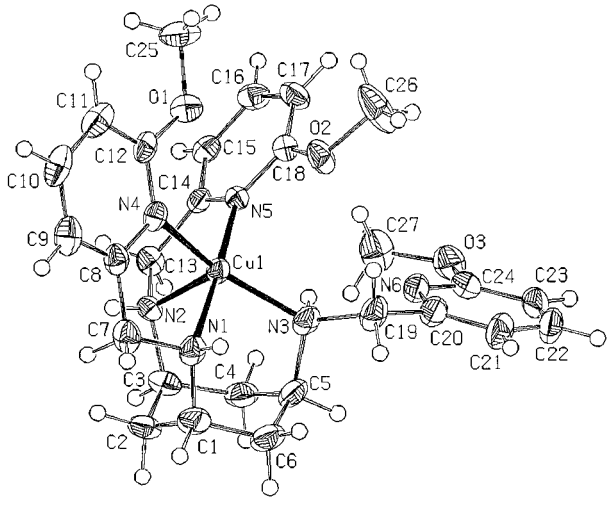

 © 2005 Wiley-VCH Verlag GmbH & Co. KGaA, Weinheim

3983 **Z. Mazej***

Indium(I) Hexafluoropnictates ($InPnF_6$; Pn = P, As, Sb)

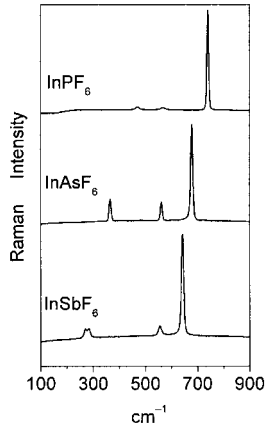

Keywords: Fluorides / Indium / Pnictides / Raman spectroscopy / Structure elucidation

 © 2005 Wiley-VCH Verlag GmbH & Co. KGaA, Weinheim

The Chemistry of Phosphanyl-ferrocenecarboxylic Ligands

Petr Štěpnička*[a]

Keywords: Ferrocene / Phosphanyl-carboxylic ligands / Coordination compounds / Catalysis / Phosphanes / Structure elucidation

The chemistry of ferrocene attracts considerable research interest even more than 50 years after its discovery, being stimulated mainly by applications of ferrocene ligands in catalysis. To the present day, the design of new ferrocene compounds ensued–sometimes by serendipity–the preparation of unprecedented coordination compounds and organometallic materials and, in the case of ferrocene compounds containing appropriate donor sets, led to numerous successful catalytic systems. This review provides a systematic survey of the chemistry of phosphanyl-ferrocenecarboxylic ligands as a specific class of hybrid ferrocene ligands that emerged about ten years ago, illustrating their synthesis, coordination behaviour, and catalytic applications. Attention is also paid to the structural chemistry of these functional ferrocene ligands. (© Wiley-VCH Verlag GmbH & Co. KGaA, 69451 Weinheim, Germany, 2005)

Introduction

It has long been recognised that the introduction of a functional group into a ligand molecule changes its donor properties. Tuning ligand properties by means of the attached substituents proved exceptionally successful in the case of tertiary phosphanes. For instance, the application of carefully "tailored", functionalised phosphane ligands allows for the synthesis of coordination compounds with specific properties and helps in improving the efficacy and selectivity of transition metal mediated reactions.

Among the vast number of modified phosphane ligands reported to date, phosphanyl-carboxylic acids constitute a distinct class of ligands with unique properties.[1] Owing to the chemical properties of both heteroatom donor groups, phosphanyl-carboxylic donors possess great structural variability: the properties of the phosphane part can be varied considerably by changing the substituents at the phosphorus atom whereas the carboxy group can be converted into the corresponding carboxylate (pH-dependent coordination behaviour possible) or to numerous functional derivatives (typically esters and amides). This provides a relatively easy access to the families of related compounds as well as to entirely new types of ligands. Combination of the hard (carboxy) and soft (phosphane) donor groups[2] classify carboxy-phosphanes as typical examples of the so-called hybrid ligands.

The presence of the very different donor sites and chemical variability of the carboxy group enables phosphanyl-carboxylic ligands to coordinate to almost any metal ion and in diverse coordination modes. Soft metals commonly used in catalysis bind phosphanyl-carboxylic ligands predominantly as P-donors; coordination of the O-donor group results in relatively weaker dative bonds and may result in the

[a] Department of Inorganic Chemistry, Faculty of Science, Charles University,
Hlavova 2030, 12840 Prague 2, Czech Republic
E-mail: stepnic@natur.cuni.cz

Petr Štěpnička was born in Liberec, Czech Republic in 1972. He studied inorganic chemistry at the Faculty of Science, Charles University in Prague (1990–1995), where he also received his Ph.D. for the work on phosphanyl-ferrocenecarboxylic acids with Professor Jaroslav Podlaha in 1998. After a postdoctoral fellowship at the Catalysis Research Center, Sapporo University in Japan with Professor Tamotsu Takahashi (1999), he returned to his alma mater and completed his habilitation in 2005, working in the field of phosphanyl-ferrocenecarboxylic ligands. His main research interests include the synthesis and studies on structural, coordination and catalytic properties of ferrocene compounds. He has authored more than 70 papers in reviewed journals.

MICROREVIEWS: This feature introduces the readers to the authors' research through a concise overview of the selected topic. Reference to important work from others in the field is included.

 DOI: 10.1002/ejic.200500485 © 2005 Wiley-VCH Verlag GmbH & Co. KGaA, Weinheim

formation of hemilabile chelates.[1,3] This has a particular impact on the catalytic performance of these ligands since the metal–oxygen dative bonds can be cleaved by the substrate and formed again after the product of the catalytic process is expelled from the coordination sphere of the metal ion. Intermediate chelation makes the catalytic species more robust towards inhibitors and leads to stabilization of reaction intermediates, thus increasing the selectivity and stability of the catalytic system. Furthermore, the presence of carboxy groups increases the solubility of carboxy-phosphanes and their complexes in polar solvents, allowing us to perform some catalysed reactions even in water.[4] Representative examples of successful applications of phosphanyl-carboxylic ligands in catalysis include nickel-catalysed ethene oligomerisation (SHOP process),[5] palladium-catalysed co-dimerisation of ethene with styrene and alternating ethene/CO co-polymerization,[6] and rhodium-catalysed arene hydrogenation.[7] In addition, several chiral phosphanyl-carboxylic acids have been tested in palladium-catalysed enantioselective allylic alkylation.[8]

More recently, progress in organometallic chemistry initiated research on functionalised organometallic derivatives, particularly ferrocene compounds. During the studies involving ferrocene derivatives[9] it had been soon recognised that ferrocene donors differ in many respects from their "organic" counterparts. First, any ferrocene ligand is a coordination compound by itself and its coordination gives rise to multinuclear complexes. Second, the ferrocene molecule represents a conjugated, redox-active system.[9a,10] Monitoring the redox properties of the ferrocene unit within electronically communicating molecules may provide an insight into the nature of chemical interactions between the molecular parts, particularly changes accompanying the coordination of ferrocene donors. Besides, switching the oxidation state of the ferrocene unit may influence reactivity at the coordinated metal centre by changing donor properties of ferrocene ligands. Oxidation of the strongly electron-donating ferrocene moiety creates cationic ferricenium (and vice versa) whose electron-withdrawing character will be reflected by the considerably reduced donor ability of the ligand. Third, the ferrocene skeleton has a well-defined cylindrical shape. It is quite rigid against tilting of the cyclopentadienyl rings, the exception being some 1,1′-bridged derivatives (ferrocenophanes).[11] On the other hand, the energy barrier for the rotation of the rings along the molecular axis is usually very low.[12] This conformational flexibility is particularly important for 1,1′-disubstituted compounds, enabling a favourable arrangement of the donor groups.[13] Finally, ferrocene exhibits an exceptionally high chemical stability among organometallic compounds allowing many synthetic transformations to be performed. The basic synthetic methodology in ferrocene chemistry is well documented including many efficient routes to chiral compounds.[9]

The number of ferrocenylphosphanes bearing further functional groups has grown enormously over the past several decades and investigations into this area has led to the discovery of many useful ligands, some of them having practical importance. However, despite this effort, the field of mixed-donor ferrocene ligands is still strongly dominated by donors of N/P and P/P′ types that are accessible in a stereodefined form through diastereoselective metallation/functionalization of *C*-chiral ferrocene compounds {e.g., [1-(dimethylamino)ethyl]ferrocene, ferrocenyl-dihydrooxazoles, and -dioxanes} and subsequent functional group transformations.[9,14] Even though several potential ferrocene-containing O,P-donors have been reported in the literature, little attention has been paid to their coordination chemistry and catalytic applications.[14e]

Considering the effort devoted separately to the synthesis, coordination, and catalytic chemistry of phosphanyl-carboxylic ligands with purely organic backbones as well as to ferrocene ligands, it is somewhat surprising that ferrocene-containing phosphanyl-carboxylic acids had not been reported until 1996. Since then, a number of phosphanyl-ferrocenecarboxylic derivatives have emerged in the literature—however, as this review focuses exclusively on the synthesis, coordination chemistry, and catalytic and synthetic utility of phosphanyl-carboxylic acids derived from ferrocene, only compounds which have been studied as ligands and catalyst components are included. These comprise mainly—in chronological order—1′-(diphenylphosphanyl)ferrocenecarboxylic acid (Hdpf), its planarly chiral positional isomer, (S_p)-2-(diphenylphosphanyl)ferrocenecarboxylic acid [(S_p)-HL[1]], and homologues of the latter: *rac*-[2-(diphenylphosphanyl)ferrocenyl]acetic acid (*rac*-HL[2]) and *rac*-2-[(diphenylphosphanyl)methyl]ferrocenecarboxylic acid (*rac*-HL[3]; Scheme 1).

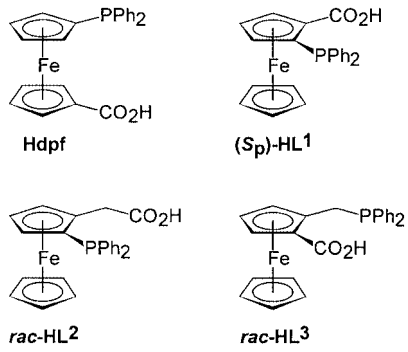

Scheme 1.

Compounds whose coordination and catalytic properties have not been studied systematically (albeit the compounds were often deemed "potentially useful ligands") and those serving just as reaction intermediates do not meet the scope of this review. Examples of such compounds (**1–4**) are shown in Scheme 2.[15] The same applies also for carboxy derivatives of 1,1′-diphosphaferrocene, e.g. to 3,3′,4,4′-tetramethyl-1,1′-diphosphaferrocene-2-carboxylic acid (**5**),[16] representing an alternative but still rather uncommon approach to phosphanyl-ferrocenecarboxylic donors.

 © 2005 Wiley-VCH Verlag GmbH & Co. KGaA, Weinheim

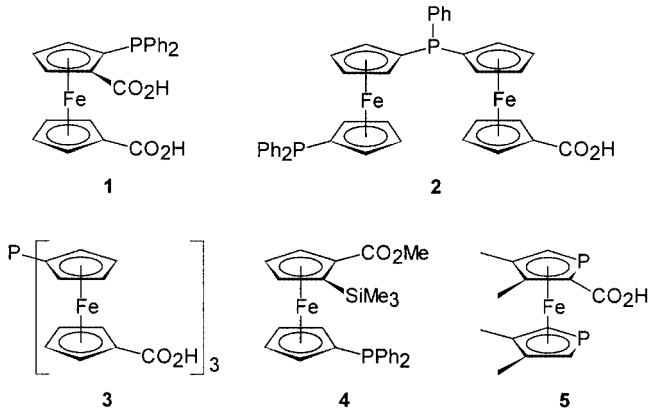

Scheme 2.

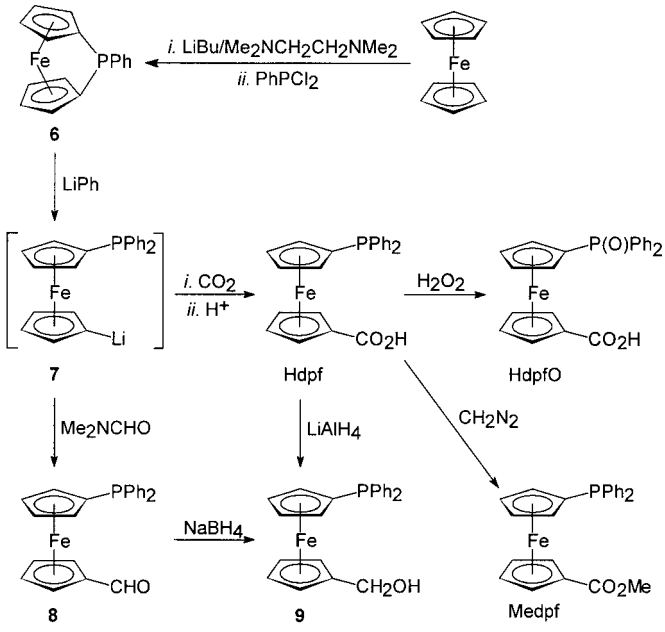

Scheme 3. Synthesis of Hpdf and related compounds.

1′-(Diphenylphosphanyl)ferrocenecarboxylic Acid (Hdpf)

Preparation and Further Synthetic Utilization

In the original synthesis of Hdpf (Scheme 3)[17] we made use of the ring opening in the strained ferrocenophane **6**[18] with phenyllithium to give 1′-(diphenylphosphanyl)lithioferrocene (**7**).[18b,19] In situ carboxylation of **7** with excess solid carbon dioxide and a subsequent acidification of the water-soluble part of the reaction mixture followed by recrystallization of the crude product afforded analytically pure Hdpf as an air-stable, rusty red-brown crystalline solid in typical yields around 80%. A similar methodology has been utilised for the synthesis[20] of 1′-(diphenylphosphanyl) ferrocenecarboxaldehyde (**8**).[21,22]

The acid was further converted into the corresponding phosphane oxide (HdpfO), methyl ester (Medpf), and reduced to alcohol **9** (Scheme 3).[20] A synthesis of Hdpf by stepwise metalation/functionalization of 1,1′-dibromoferrocene has been reported by Butler et al.[22]

In addition to the standard characterization, Hdpf and some related compounds were studied in detail by mass spectrometry[23] and by electrochemical methods.[17] In cyclic voltammograms in acetonitrile, Hdpf shows the expected one-electron oxidation to the corresponding ferricenium at $E^{\circ\prime}$ = +0.32 V vs. ferrocene/ferricenium reference, the shift to higher potential vs. the reference couple being in agreement with the electron-withdrawing nature of both substituents at the ferrocene unit (process **A** in Scheme 4). However, this electrochemical oxidation is followed by chemical complications, resulting in a pseudoreversible behaviour upon back-scan. The product of the following chemical steps was identified as the phosphane oxide HdpfO, an apparent product of the reactions between the electrogenerated ferricenium species and traces of oxygen and/or water. The presence of HdpfO is clearly reflected

 © 2005 Wiley-VCH Verlag GmbH & Co. KGaA, Weinheim

by an additional standard reversible ferrocene/ferricenium wave at more anodic potentials (**C** in Scheme 4). The overall behaviour of Hdpf in the anodic region can be formulated as an ECE process, though with some peculiar features: as the formation of HdpfO definitely involves an attack at the phosphorus atom, one may consider an electron transfer from the phosphorus to the electron-poor iron atom yielding a ferrocenyl-phosphonium cation-radical or its resonance form (see **B** in Scheme 4), which are more reactive at the phosphorus atom than Hdpf.[24] Similar ECE redox behaviour has been observed for 1,1′-bis(diphenylphosphanyl)ferrocene.[25] In contrast, nondissociating complexes with *P*-coordinated Hdpf exhibit normal reversible one-electron oxidations at the ferrocene unit (see below).

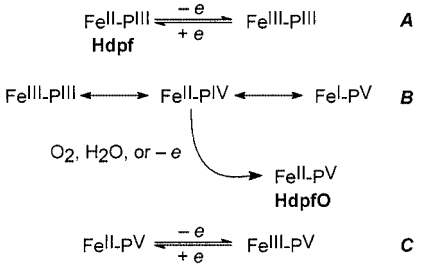

Scheme 4. Schematic depiction of the ECE electrochemical behaviour observed for Hdpf.

In the following work, Hdpf has been used[26] as a precursor for an alternative synthesis of chiral phosphanyloxazoline ligands (Scheme 5).[27] Due to an instability of the phosphanyl group under the reaction conditions, Hdpf was first converted to HdpfO. Then, the carboxy-phosphane oxide was treated with oxalyl chloride yielding the respective acid chloride, which was immediately treated with chiral β-amino alcohols to give amides **10**. Subsequently, the standard oxazoline ring closure reaction with **10** and deprotection of the phosphorus group gave [1′-(diphenylphosphanyl)ferrocenyl]oxazolines **11** (Scheme 5).

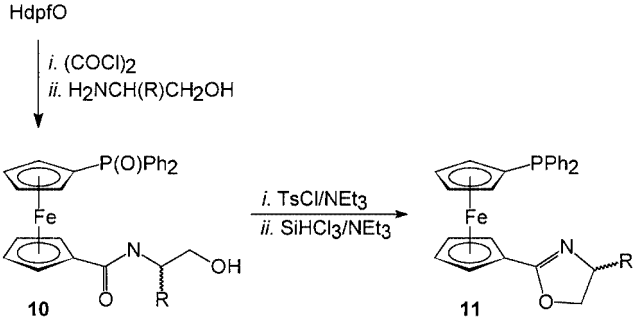

Scheme 5. Synthesis of ferrocenyl-oxazolines [R = (*S*)-*i*Pr, (*R*)-*i*Pr, (*S*)-*t*Bu, (*R*)-Ph].

Oxazolines **11** were tested in palladium-catalysed allylic substitution, giving nearly quantitative yields of the substitution products, though with a lower enantioselectivity than their analogues bearing both functional substituents on one cyclopentadienyl ring. The lowered selectivity can be ascribed to several intermediates with different conformation at the ferrocene unit participating in the catalysed reaction.[14c,27,28] This assumption is supported by spectral evidence and also by the fact, that the conformational equilibrium can be markedly influenced by introducing a stereogenic phosphorus atom.[29]

A different example of the synthetic usefulness of Hdpf represents the preparation of group-6 Fischer-type carbenes bearing the *P*-chelating 1′-(diphenylphosphanyl)ferrocenyl group.[30] In this case, Hdpf was first treated in the presence of peptide-coupling agents {1-hydroxybenztriazole/*N*-[3-(dimethylamino)propyl]-*N*′-ethylcarbodiimide} with secondary amines to give tertiary amides **12**. The reaction of amides **12** with $Na_2[Cr(CO)_5]$ and Me_3SiCl[31] afforded mixtures of the respective *P*-chelated carbenes **13** and phosphane complexes **14** (Scheme 6), which were easily separated by chromatography and fully characterised.

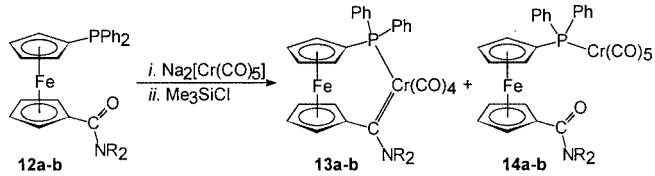

Scheme 6. Preparation of (carbene)chromium(0) compounds [NR_2 = NEt_2 (**a**) and morpholin-4-yl (**b**)].

A similar reaction between **12a** and $Na_2[W(CO)_5]$ under identical conditions (Scheme 7) is more complex, yielding a mixture of nonchelated carbene **15**, trinuclear "W_2Fe" complex **16** and the expected side-product **17**. Removal of **17** by chromatography and heating of the **15/16** mixture in toluene (80 °C, 4 h) afforded another mixture, whose components were separated by column chromatography and characterised as unreacted **16**, the *P*-chelated carbene **18**, and phosphanyl-carbaldehyde complex **19** resulting from decomposition of the carbenes.

The reaction course as observed for tungsten complexes provides strong evidence for a stepwise formation of the *P*-chelated carbenes. Somewhat surprisingly, an analogous reaction with $[Fe(CO)_4]^{2-}$ salts affords—in sharp contrast with the behaviour of organic amides[32]—exclusively the amidophosphane complex [$Fe(CO)_4$(**12a**-κ*P*)] (**20**).

A comparison of the crystal structures for **13a**, **13b**, **18**, and the nonchelated complex **16** (see Figure 1), which is void of possible structural constraints imposed by the chelation, clearly indicates that the $M(CO)_4$ units (M = Cr and W) perfectly fit into the pocket of the chelating ferrocene ligand and that the coordination causes no deformation within either part. An electrochemical study performed with **12a**–**b**, **13a**–**b**, and **14a**–**b** showed that the precursor amides **12** and the phosphane complexes **14a**–**b** behave as standard one ($Fe^{II/III}$) and two localised redox systems ($Fe^{II/III}$ and $Cr^{0/I}$), respectively, whereas the carbene complexes **13a**–**b** represent electronically coupled redox systems, where any redox change involves the entire molecule.

 © 2005 Wiley-VCH Verlag GmbH & Co. KGaA, Weinheim

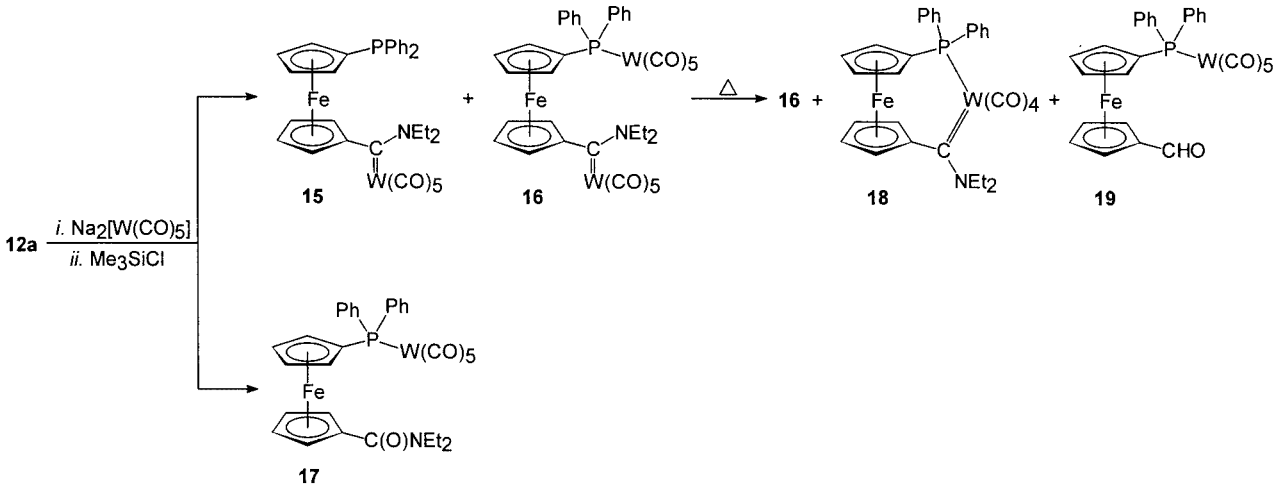

Scheme 7. Carbene-forming reactions with **12a** and pentacarbonyltungstate.

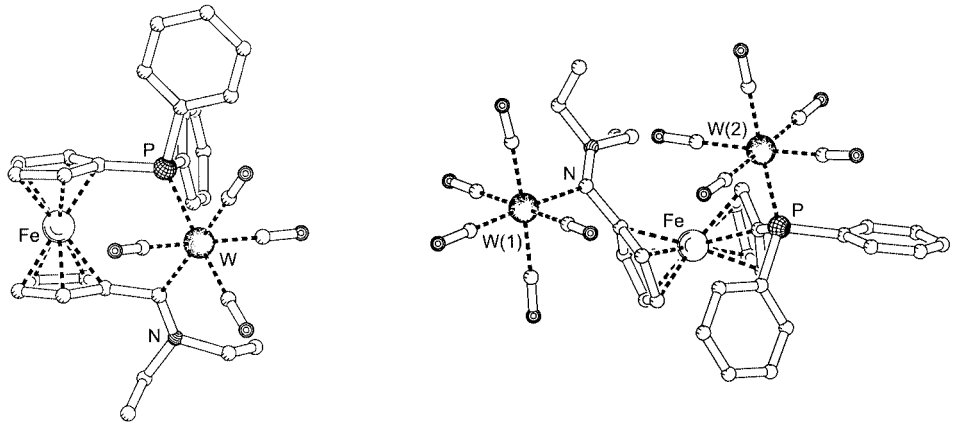

Figure 1. Views of the molecular structures of complexes **18** (left) and **16** (right).

Coordination Chemistry and Catalytic Applications

As Hdpf was the first reported carboxy-ferrocenyl-phosphane, we turned our attention to studying its coordination behaviour towards selected metal ions in order to establish its coordination preferences, which could be expected to differ from the chemistry of either of the related donor-uniform ligands, (diphenylphosphanyl)ferrocene[33] and ferrocenecarboxylic acid.[34]

With soft metals, Hdpf coordinates as a simple tertiary phosphane. For instance, $K_2[PdCl_4]$ and $[Pd(cod)Cl_2]$ (cod = η^2:η^2-cycloocta-1,5-diene) reacted smoothly with 2 equiv. of Hdpf to give the bis(phosphane) complex *trans*-$[PdCl_2(Hdpf\text{-}\kappa P)_2]$ (**21a**). A similar reaction with $[Pd(cod)Br_2]$ gave *trans*-$[PdBr_2(Hdpf\text{-}\kappa P)_2]$ (**21b**). For the case of kinetically inert platinum(II), the isomers *trans*-$[PtCl_2(Hdpf\text{-}\kappa P)_2]$ (**22**) and *cis*-$[PtCl_2(Hdpf\text{-}\kappa P)_2]$ (**23**) were isolated depending on the precursor used.[35] According to the spectroscopic data, all compounds possess the expected square-planar arrangement, which was unambiguously corroborated by the structure determination for **22** and the adducts **21a**·$2CH_3CO_2H$, **22**·$2CH_3CO_2H$, and **23**·$(2+x)CH_2Cl_2$. Solvates **21a**·$2CH_3CO_2H$ and **22**·$2CH_3CO_2H$ obtained by recrystallisation from acetic acid are isostructural, forming molecular crystals built up of molecular triplexes formed by one complex molecule and two molecules of solvating acetic acid, bonded by double hydrogen bonds to the uncoordinated carboxy groups of the ligands (O···O 2.62 Å; Figure 2). The same type of intermolecular interaction is responsible for intermolecular aggregation in **22** and **23**·$(2+x)CH_2Cl_2$ but with a different outcome. The absence of polar solvate molecules in **22** leads to the formation of infinite hydrogen-bonded zig-zag chains (O···O 2.60–2.63 Å) whereas the molecules of **23** assemble by means of double hydrogen bonds into macrocyclic dimers (O···O 2.64 Å; Figure 2), whose conformation is further stabilised by graphite-like π···π stacking of the phenyl groups in *cis*-disposed ligands at a ring-centroid distance of 3.64 Å. The formation of closed supramolecular assembly $[\mathbf{23}]_2$ in the solvate **23**·$(2+x)CH_2Cl_2$ is very likely related to much lower polarity of the crystallization solvent.[35]

In contrast to the very stable palladium(II) and platinum(II) complexes, their nickel(II) analogues are prone to dissociative decomposition in polar solvents. In the series

 © 2005 Wiley-VCH Verlag GmbH & Co. KGaA, Weinheim

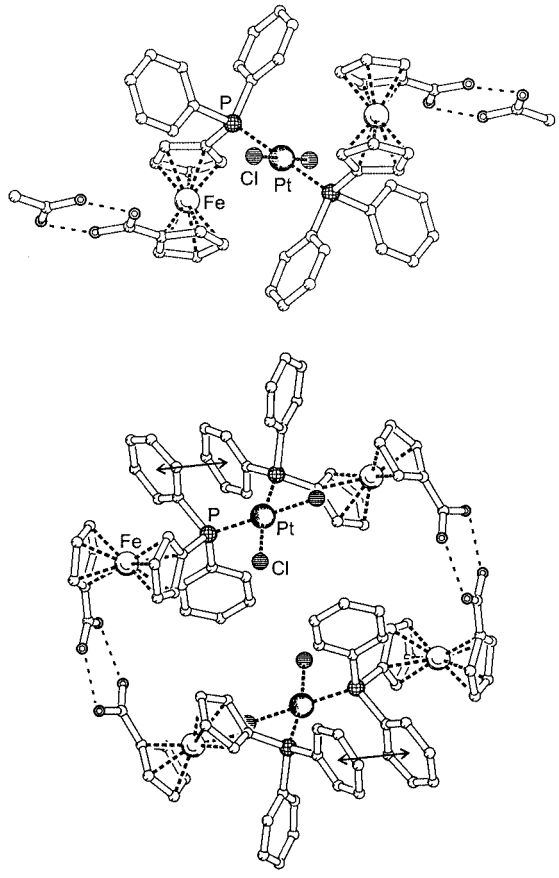

Figure 2. Views of the repeating units in the crystals of **22**·2CH_3CO_2H (top) and **23**·(2+*x*)CH_2Cl_2 (bottom). The O···O hydrogen bonds are shown as thin dashed lines and the π···π stacking interactions of the phenyl rings are indicated by double arrows. Hydrogen atoms and solvating dichloromethane (for the latter compound) are omitted for clarity.

[NiX_2(Hdpf-κ*P*)$_2$] [**24**, X = Cl (**a**), Br (**b**), I (**c**), and SCN-κ*N* (**d**)], the halide complexes **24a**–**c** are paramagnetic and tetrahedral whereas the thiocyanate **24d** is *trans*-square-planar and diamagnetic. Another nickel(II) complex, [Ni(dpf)$_2$] (**25**), was obtained by salt metathesis of nickel(II) sulfate with Nadpf. Compound **25** is an amorphous solid, practically insoluble in organic solvents and water. Hence, its formulation as a coordination polymer involving different nickel(II) sites and multidentate dpf$^-$ anions was based mainly on magnetic measurements and spectroscopic data (IR and photoelectron spectra).[36]

A similar situation has been observed for (Hdpf)mercury(II) complexes. The reaction of Hdpf with mercury(II) halides in acetic acid (bromide and chloride) or dichloromethane (iodide) gave two types of products depending on the stoichiometry of the starting materials: the trinuclear compounds [HgX_2(Hdpf-κ*P*)$_2$] (**26a**–**c**) and the dimeric, tetranuclear complexes [{Hg(μ-X)X(Hdpf-κ*P*)$_2$}$_2$] [**27a**–**c**; X = Cl (**a**), Br (**b**), and I (**c**)]. The complexes are insoluble in common solvents and decompose in strongly donating ones. The solvolytic equilibria are reflected, for example, by extensive broadening of the NMR resonances (spectra recorded for [D_6]DMSO solutions) and by the complexity of the electrochemical behaviour observed for a solution of the complexes in acetonitrile/*N*,*N*-dimethylformamide, explainable as a superposition of the redox response of the dissociated free ligand (see above) and (at least partly) solvolysed mercury complexes.[37]

The crystal structures of the bromide complexes, **26b** and the solvate **27b**·4CH_3CO_2H (Figure 3), revealed a tetrahedral coordination environment around the mercury ion, though with significant deviations from the regular geometry resulting from steric demands of the bulky carboxy-phosphane ligand (note: the overall structures are highly symmetric due to the imposed crystallographic symmetry). In both cases, the ligand carboxy groups do not participate in the coordination but instead take part in hydrogen bonding to either the carboxy group in a neighbouring ligand moiety resulting in infinite twisted chains (**26b**) or to the molecules of solvating acetic acid (**27b**·4CH_3CO_2H). The crystal packing of **27b**·4CH_3CO_2H, unlike the polymeric **26b**, is essentially molecular since two solvate molecules saturate the ligand carboxy groups while the remaining two form hydrogen-bonded dimers $(CH_3CO_2H)_2$ located in structural voids (Figure 3).[37]

Yet another example of carboxy groups of the *P*-coordinated Hdpf associating with solvating acetic acid molecules is the octanuclear heterocubane complex [(μ$_3$-I)$_4${Cu(Hdpf-κ*P*)}$_4$]·2CH_3CO_2H (**28**·2CH_3CO_2H), which is obtained upon refluxing CuI/Hdpf mixtures in glacial acetic acid. Notably, the reaction proceeds with the formation of the well-defined, stable solvate in a relatively broad range of the metal/ligand stoichiometry (Scheme 8).[38]

The structure of **28**·2CH_3CO_2H determined by X-ray crystallography revealed that the {Cu_4I_4} core is quite regular as far as bond lengths and angles are concerned but possesses no higher symmetry. In the crystal, the molecules of solvating acetic acid associate with the uncoordinated carboxy groups of ligands bonded at one face of the heterocubane core (O···O 2.62–2.65 Å). Likewise, the remaining ligand carboxy groups form the usual double hydrogen bridges but with the ligand carboxy groups from the neighbouring molecules (O···O 2.59 and 2.63 Å), thus linking the individual molecules in necklace-like zig-zag chains parallel to the crystallographic *c* axis (Scheme 8).

In further work we turned to mixed-donor carbonyl complexes involving group-6 metals [M(CO)$_5$(Hdpf-κ*P*)], where M = Cr (**29**), Mo (**30**), and W (**31**).[39] Complexes **29** and **31** have been synthesized in good yields by replacement of the weakly coordinated solvent in photogenerated intermediates [M(CO)$_5$(THF)] (THF = tetrahydrofuran), while **30** was obtained from the direct, thermally induced substitution of one carbonyl ligand with Hdpf in [Mo(CO)$_6$]. The compounds are sufficiently stable to be isolated in pure form albeit they slowly decompose in air and under daylight; their decomposition seems to be facilitated by the presence of the acidic carboxy function.

The formulation of compounds **29**–**31** is based mainly on spectroscopic data and further corroborated by the structure determination for **29**. An electrochemical study of the whole series by cyclic voltammetry showed that, upon rais-

 © 2005 Wiley-VCH Verlag GmbH & Co. KGaA, Weinheim

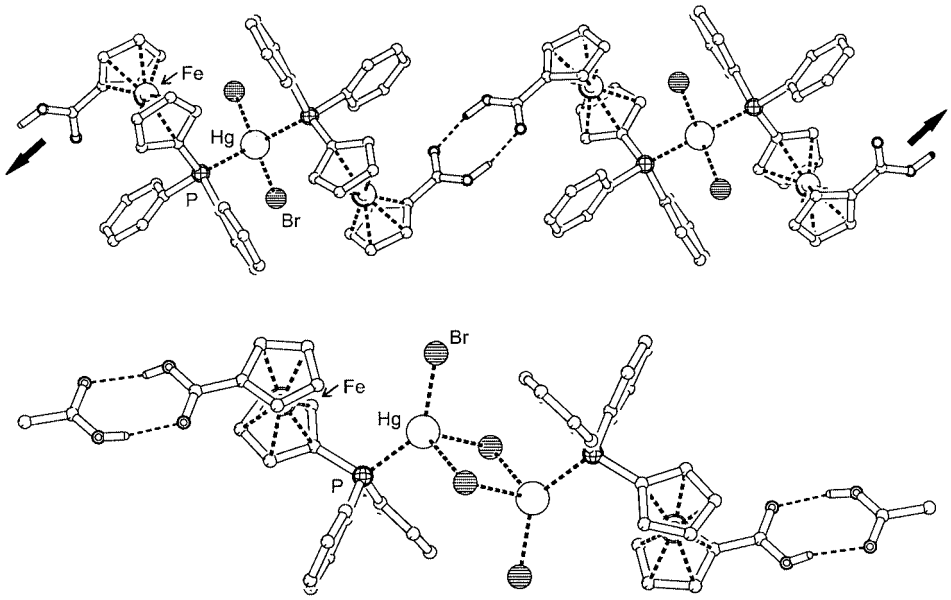

Figure 3. Views of the molecular structures of **26b** (top) and **27b**·$4CH_3CO_2H$ (bottom). The O···O hydrogen bonds are shown as dashed lines and the propagation of the chains in the structure of **26b** is indicated with arrows. The dimers $(CH_3CO_2H)_2$ present in the structure of the solvate are not shown for clarity.

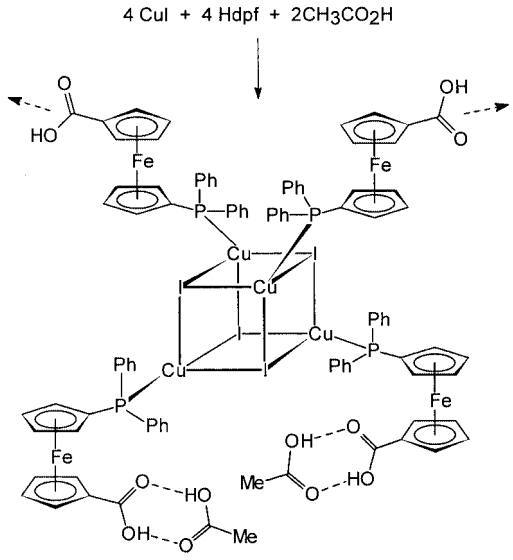

Scheme 8. Preparation and structure of the solvated heterocubane **28**·$2CH_3CO_2H$. Dashed arrows indicate where propagation of the infinite, hydrogen-bonded chains occurs.

ing the external potential, the complexes first undergo a ligand centred, reversible one-electron oxidation (ferrocene/ferricenium) followed by a group-6 metal centred redox process at more positive potentials. The position of the first wave is independent of the group-6 metal and shifted by ca. +180 mV with respect to uncoordinated Hdpf due to electron-density transfer from the ligand to the ligated metal ion. The reversibility of the first redox process indicates that the complexes are stable in both the usual and the oxidised forms under the conditions of measurement (dichloromethane solution, 0.1 $V s^{-1}$ scan rate), which contrasts with the redox behaviour of free Hdpf and solvolytically unstable mercury(II) complexes (see above).

Furthermore, Hdpf together with other phosphanes have been utilised as ligands in the synthesis of an extensive series of (alkoxycarbene)(η^6-hexamethylbenzene)ruthenium(II) compounds (Scheme 9).[40] The starting dichloro(phosphane) complexes **32a**–**d** were prepared by a bridge-splitting reaction from $[\{Ru(\mu\text{-}Cl)Cl(\eta^6\text{-}C_6Me_6)\}_2]$ and then converted into methoxycarbenes **33**. It is assumed that carbene formation starts with a removal of one chloride ligand with $NaPF_6$. The formed cationic, coordinatively unsaturated species coordinates one molecule of terminal alkyne giving an intermediate $[L_nRu(\eta^2\text{-}RC{\equiv}CH)]^+$, which isomerises to a cationic vinylidene complex $[L_nRu{=}C{=}CHR]^+$. Then, the carbene formation is completed by nucleophilic addition of methanol onto the electron-deficient vinylidene C-α atom. For carbenes with R′ = H, (trimethylsilyl)ethyne is used as the alkyne component because the C–Si bond is readily solvolysed under the reaction conditions.[41]

All compounds were characterised by standard spectral methods and the solid-state structure of the solvate **33da**·CH_2Cl_2 was determined by single-crystal X-ray diffraction. Even in this case double hydrogen bonds between carboxy groups of the *P*-coordinated ligand dominate the solid-state assembly, connecting into centrosymmetric dimers the enantiomeric cations (R_{Ru})- and (S_{Ru})-$[(\eta^6\text{-}C_6Me_6)RuCl(Hdpf\text{-}\kappa P)\{{=}C(OMe)CH_2Fc\}]^+$ (Fc = ferrocenyl) which are equally abundant in the racemic crystal (O···O 2.58 Å). In addition, the carboxy OH groups interact with the solvating dichloromethane, thus fixing the solvate in the structure by means of weak O–H···Cl hydrogen bonds, the O···Cl distance being 3.44 Å.

 © 2005 Wiley-VCH Verlag GmbH & Co. KGaA, Weinheim

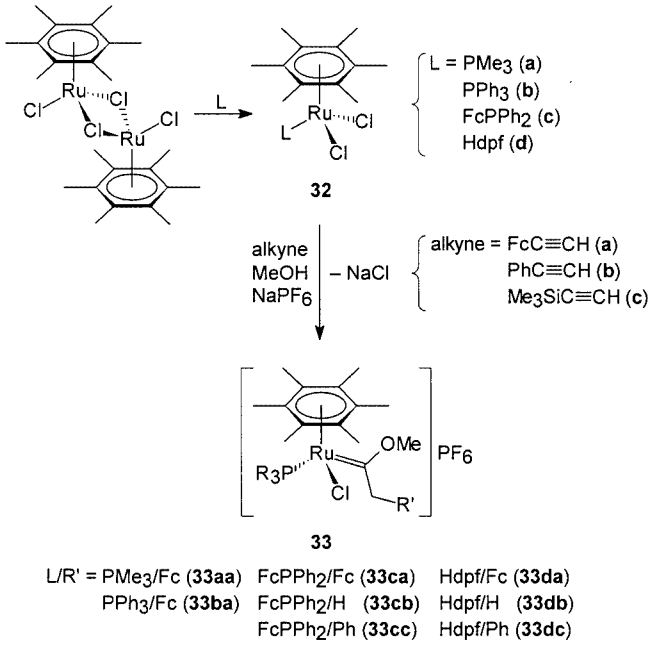

Scheme 9. Synthetic route to cationic (methoxycarbene)ruthenium compounds **33**.

The entire series of phosphane complexes **32** and carbenes **33** was studied by cyclic voltammetry in the anodic region. Analysis of the obtained data allowed for a comparison in both groups as well as across them; the observed trends undoubtedly deserve comment (Figure 4). As for the phosphane complexes, the compounds involving simple phosphanes, **32a** and **32b**, exhibit single redox waves attributable to the reversible oxidation at the central atom ($Ru^{II} \rightarrow Ru^{III}$). The potential of this process varies with the donor properties of the phosphane ligand: PPh_3 as a poorer σ-donor and better π-acceptor makes this oxidation more difficult [$E^{\circ\prime}$ = 0.39 (**32a**), 0.48 V (**32b**); the potentials are given relative to that of the internal ferrocene/ferricenium reference].

The presence of a ferrocenyl-phosphane in **32c** and **32d** is clearly reflected in the voltammograms by an additional one-electron ferrocene/ferricenium wave at lower potentials [$E^{\circ\prime}$ = 0.03 (**32c**), 0.28 V (**32d**)], an anodic shift for the latter compound being in agreement with the presence of an electron-withdrawing carboxy group (Figure 4). However, these redox potentials are slightly lower than those for free ligands, which is in a sharp contrast with the anodic shift typically accompanying coordination of these donors (cf. the data for **29**–**31**[39] and for the related $FcPPh_2$ complexes[42]). Nonetheless, this rather unexpected phenomenon can be explained by an efficient compensation of the ligand-to-metal σ-donation by π-back Ru → P bonding from the electron-rich ruthenium atom. At higher potentials, the ferrocene/ferricenium wave of the ligands is followed by the $Ru^{II} \rightarrow Ru^{III}$ oxidation−however, at much higher potentials than for **32a** and **32b** [$E^{\circ\prime}$ = 0.66 (**32c**), 0.68 V (**32d**)]. The origin of this anodic shift, which does not correspond with the strong electron-donating character of the ferrocene unit, can be accounted for by the preceding

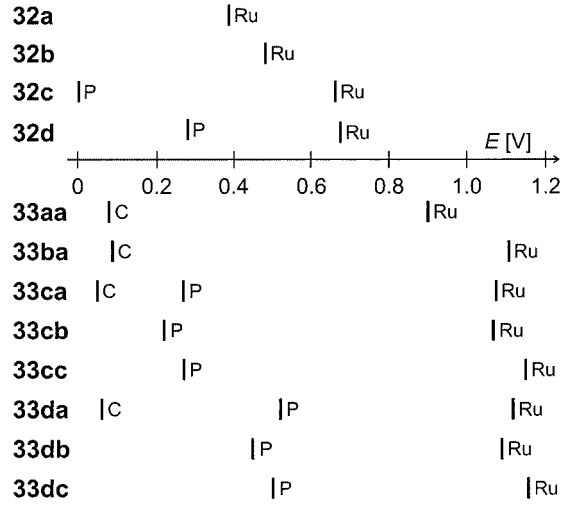

Figure 4. Chart diagram of the anodic redox potentials observed for **32** and **33** in dichloromethane solutions. The redox potentials were determined as an average of the anodic and cathodic peak potentials and given relative to the ferrocene/ferricenium reference. The values are distinguished as follows: the symbol **Ru** indicates a ruthenium-centred oxidation, while **C** and **P** denote the ferrocene/ferricenium potentials for carbene and phosphanyl-ferrocenyl groups, respectively. For compound labels see Scheme 9.

ligand oxidation converting the strongly electron-donating ferrocene into an electron-poor, cationic ferricenium. This change is naturally reflected by the donor properties of the whole phosphanyl-ferrocene ligand and is relayed onto the ruthenium centre (though perhaps in synergism with other factors).

The redox behaviour of the carbenes is similar. However, the redox processes occur at higher potentials due to the cationic nature of these compounds (by ca. 0.5 V for the

 © 2005 Wiley-VCH Verlag GmbH & Co. KGaA, Weinheim

ruthenium-centred oxidations, Figure 4). Another difference can be seen in the position of the ferrocene/ferricenium waves due to the phosphane ligands, which are shifted anodically by 0.24 V as compared to free ligands because the electron density lowering at the ferrocene unit following the coordination cannot be effectively compensated now by back-donation from the electron-poor ruthenium centres.

In summary, the data for compounds bearing the ferrocenyl-phosphanes (**32c**, **32d**, and the respective carbenes) clearly indicate electronic coupling between the ruthenium atom and the ferrocene ligand. On the contrary, the ferrocene unit located in the carbene part (**33aa**, **33ba**, **33ca** and **33da**) remains virtually unaffected by changes occurring in the rest of the molecule, which corresponds with the presence of a nonconjugated linker between the Ru atom and the (carbene)ferrocenyl group. A similar observation has been made also for (arene)ruthenium(II) complexes bearing Ru-coordinated ferrocenyl-phosphanes and ferrocenoyl groups at the terminus of a nonconjugated chain attached to the arene ligand.[43]

Interaction of rhodium(I) compounds with Hdpf leads to two types of complexes differing in coordination of the carboxy-phosphane ligand. The reaction of the dimeric complexes [{Rh(μ-X)(CO)$_2$}$_2$] with 4 equiv. of Hdpf gave the expected square-planar complexes with *P*-monodentate carboxy-phosphane, *trans*-[RhX(CO)(Hdpf-κ*P*)$_2$] [**34**, X = Cl (**a**) and Br (**b**)]. On the other hand, the reactions of Hdpf with rhodium(I) acetylacetonate complexes [Rh(acac)(CO)(L)] [**35**; L = PCy_3 (**a**), PPh_3 (**b**), and $FcPPh_2$ (**c**), acac = pentane-2,4,-dionate(1–)] afforded the corresponding square-planar complexes [Rh(CO)(L)(dpf-κ^2*O,P*)] (**36**) in which the phosphanyl-carboxylate anion dpf$^-$ coordinates as an *O,P*-chelating, bidentate ligand (Scheme 10). The formation of **36** from **35** and Hdpf represents an acid-base reaction with Hdpf acting as the proton donor to the leaving pentane-2,4-dione.[44]

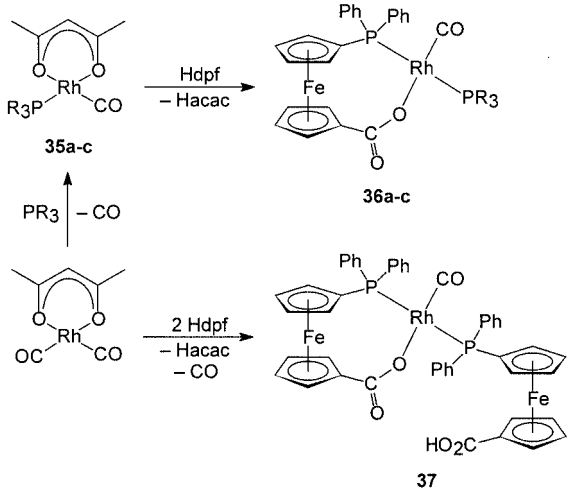

Scheme 10. Preparation of rhodium(I) complexes with *O,P*-chelating phosphanyl-carboxylate dpf$^-$ [PR_3 = PCy_3 (**a**), PPh_3 (**b**), and $FcPPh_2$ (**c**); Cy = cyclohexyl].

Compounds **36a**–**c** are air-stable crystalline solids showing in their IR spectra the characteristic bands due to carboxylate groups ($\nu_{C=O}$ = 1602–1606 cm^{-1}; cf. 1666 cm^{-1} for Hdpf[17]) and the terminal carbonyl ligands ($\nu_{C\equiv O}$ = 1961–1965 cm^{-1}). For all compounds, the NMR spectra indicate *trans*-P–P arrangement around the rhodium atom, as was proven for **36a** by X-ray diffraction analysis (Figure 5).

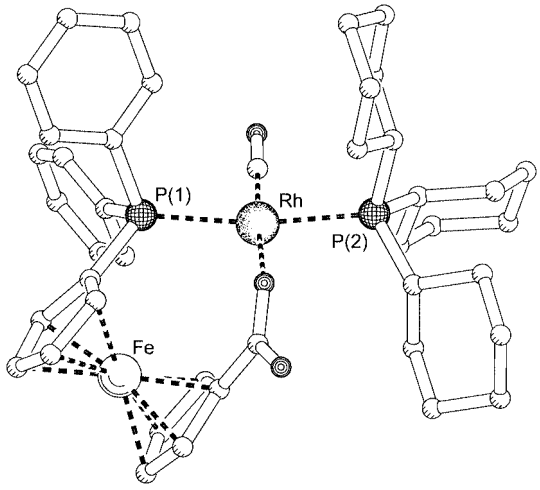

Figure 5. View of the molecular structure of **36a**. Hydrogen atoms are omitted.

Replacing **35** with the dicarbonyl complex [Rh(acac)(CO)$_2$] in the reaction with Hdpf results in an immediate and exclusive formation of complex **37** (Scheme 10). The reaction proceeds with elimination of CO and acetylacetone, requiring 2 equiv. of Hdpf for 1 equiv. of the rhodium complex. For other molar ratios, the reaction stops when one of the starting materials is consumed: for instance, mixing of Hdpf and [Rh(acac)(CO)$_2$] in a 1:1 molar ratio affords an equimolar mixture of **37** and unreacted [Rh(acac)(CO)$_2$]. The IR spectra of **37** display bands assignable to the protonated (1703 cm^{-1}) and deprotonated (1551 cm^{-1}) carboxy group and the band of the terminal carbonyl ligand (1962 cm^{-1}). In contrast, ^{1}H and ^{13}C NMR show only one set of resonances due to "Hdpf" while the ^{31}P NMR spectrum features only one rhodium-coupled signal at δ_P = 20.2 ($^1J_{RhP}$ = 132 Hz) ppm, which is roughly half-way between the values observed for Hdpf in **34a**–**b** (δ_P = 22.2 ppm) and the dpf$^-$ anion in **35a**–**c** (δ_P = 18.4–18.7 ppm). Such a peculiar discrepancy was attributed to hemilabile coordination of the Hdpf/dpf$^-$ ligand pair where the two forms of ligand rapidly exchange the carboxy proton (Scheme 11). The exchange rate is sufficient to cause an averaging on the NMR time scale but definitely not in IR spectra, where both forms of the ligand are clearly observable.

Testing complexes **36a**, **36b** and **37** (pure or with various co-catalysts) and the related metal precursor/ligand mixtures [Rh(acac)(CO)$_2$]/*x*Hdpf, **35a**/Hdpf, **35b**/Hdpf, and

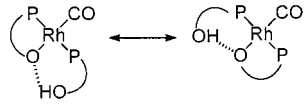

Scheme 11.

 © 2005 Wiley-VCH Verlag GmbH & Co. KGaA, Weinheim

$[RhH(CO)(PPh_3)_3]$/Hdpf in hydroformylation of 1-hexene has shown that most of these pre-catalysts are active, producing aldehyde mixtures in very good yields and with favourable *n*/*iso* ratios; halogen complexes **34a** and **34b** were practically inactive.[45]

Thus, complex **37** as such or generated in situ from $[Rh(acac)(CO)_2]$ and Hdpf represents an efficient hydroformylation catalyst precursor, not requiring any further co-catalyst; additional components may, however, be used to increase the reaction selectivity. For example, at a catalyst/1-hexene ratio of ca. 3.8×10^{-5} under 10 atm of CO/H_2 (1:1 mixture), pre-catalyst **37** gave isomeric heptanals in ca. 80% yield and *n*/*iso* ≈ 2 at 80 °C after 3 h, while the best *n*/*iso* ratio of 4.6 (without diminished yield) was achieved with the **37**/$P(OPh)_3$ system. Besides, complex **37** can be used repeatedly, cf. 84, 89, 83, 69, 48, 13% yields of aldehydes in six consecutive runs when the liquid part of the reaction mixture has been simply decanted from the catalyst residue (*n*/*iso* ratio ranged from 2.1 to 2.7). Spectral data indicate that **37** itself is not the catalytically active species but it is converted under the reaction conditions to the hydride $[RhH(CO)_2(Hdpf\text{-}\kappa P)_2]$.[45]

In our attempts to synthesize compounds featuring a form of Hdpf as an *O*-donor, we pursued the preparation of simple salts. Actually, the reaction of Hdpf with inorganic bases proceeded under the formation of carboxylate salts as evidenced by changes in the carbonyl stretching region of the IR spectra, but the products were ill-defined amorphous materials, tending to retain varying amounts of solvents.[46] Hence, whenever a dpf^- salt is required for synthesis, it is advantageous to generate it only in situ by treating Hdpf with an appropriate base.

The only example of exclusive carboxylate coordination for Hdpf is the paramagnetic titanocene carboxylate $[(\eta^5\text{-}C_5HMe_4)_2Ti(dpf\text{-}\kappa^2O,O')]$ (**38**) obtained by allowing equimolar amounts of "titanocene equivalent" $[(\eta^5\text{-}C_5HMe_4)_2Ti(\eta^2\text{-}Me_3SiC{\equiv}SiMe_3)]$ and Hdpf to react (Figure 6).[47] According to structural data, the dpf^- anion coordinates to the titanium ion as a simple carboxylate without any participation of the phosphane group: the carboxy plane nearly ideally bisects the titanocene fragment, the Ti–O bond lengths being 2.158 and 2.166 Å. Both metallocene units possess the expected geometry and are mutually rotated as exemplified by the dihedral angle subtended by the TiOO′ plane and the plane of the carboxy-substituted ferrocene cyclopentadienyl ring of ca. 25°.

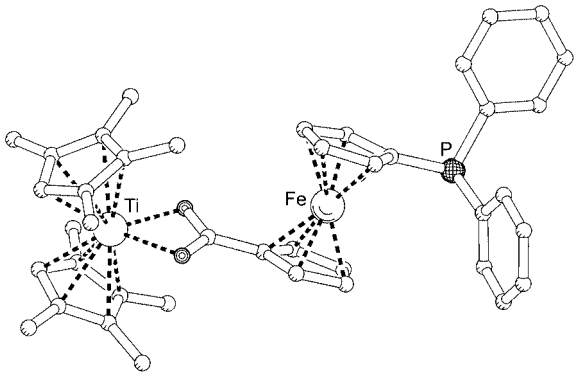

Figure 6. Molecular structure of bis(metallocene) complex **38**.

In order to elucidate the coordination properties of the methyl ester Medpf, we turned to palladium(II) complexes with chelate *C*,*N*-ligands (Scheme 12). The reaction of *ortho*-palladated dimeric complex **39** with Medpf gave the expected bridge-cleavage product **40**. However, the following attempts to synthesize *O*,*P*-chelate complexes failed. Removal of the halide ligand from **40** as well as the direct reaction of bis(acetonitrile) complexes **41** yielded only the phosphane complexes **42** with the acetonitrile molecule completing the coordination sphere around the palladium ion.[48]

Compounds **40**, **42b**, and **21a** as well as some palladium(II) acetate/ligand mixtures (ligand = Hdpf, Medpf, and $FcPPh_2$) were tested as catalyst precursors for Suzuki–Miyaura cross-coupling of 4-bromotoluene and phenylboronic acid.[48] In all cases, the reaction proceeded with excellent isolated yields of 4-methylbiphenyl (≥ 80%). The most active catalysts proved to be the one generated in situ by mixing palladium(II) acetate with 2 equiv. of Hdpf or Medpf, which afforded the product in 96% isolated yield. The least active in the series tested proved to be the $[Pd(cod)Cl_2]$/2Hdpf mixture, a formal analogue to **21a**, which gave only 44% yield.

Recently, Hdpf was tested as an anchoring agent of a transition metal catalyst to a solid support. Treatment of mesoporous molecular sieves MCM-41 with Hdpf and, subsequently, with $[\{Ru(\mu\text{-}Cl)Cl(\eta^6\text{-}p\text{-cymene})\}_2]$ gave an Ru/Hdpf-modified sieve. Because the analytical data for Ru/Hdpf-MCM-41 implied an independent immobilization of the modifiers rather than a surface reaction, a similar material but without Hdpf was prepared from the dimeric ruthenium complex and the sieve. All these materials along with their molecular analogue $[\{RuCl_2(Hdpf\text{-}\kappa P)(\eta^6\text{-}p\text{-cymene})\}_2]$ (**43**) were tested as catalysts in the reaction of benzoic acid with propargyl alcohol to give 2-oxopropyl benzoate. The supported catalysts Ru-MCM-41 and Hdpf/Ru-MCM-41 proved less active than **43**, promoting a side reaction of propargyl alcohol, which further lowered the yield of the ester. In spite of some leaching of the catalytically active species from the solid support, the catalysts could be re-used without any apparent loss of catalytic activity.[49]

(S_p)-2-(Diphenylphosphanyl)ferrocenecarboxylic Acid

(S_p)-2-(Diphenylphosphanyl)ferrocenecarboxylic acid, (S_p)-HL^1, has been reported independently by three groups. The first mention dates back to the year 2000 when this compound was utilised as a chiral synthon for the preparation of chiral diamide ligands,[50] which were further tested in palladium-catalysed alkylation reactions[50a–50d] and the silver(I)-mediated formation of pyrroles.[50c] Notably, the acid itself proved to be a relatively poor ligand for the for-

 © 2005 Wiley-VCH Verlag GmbH & Co. KGaA, Weinheim

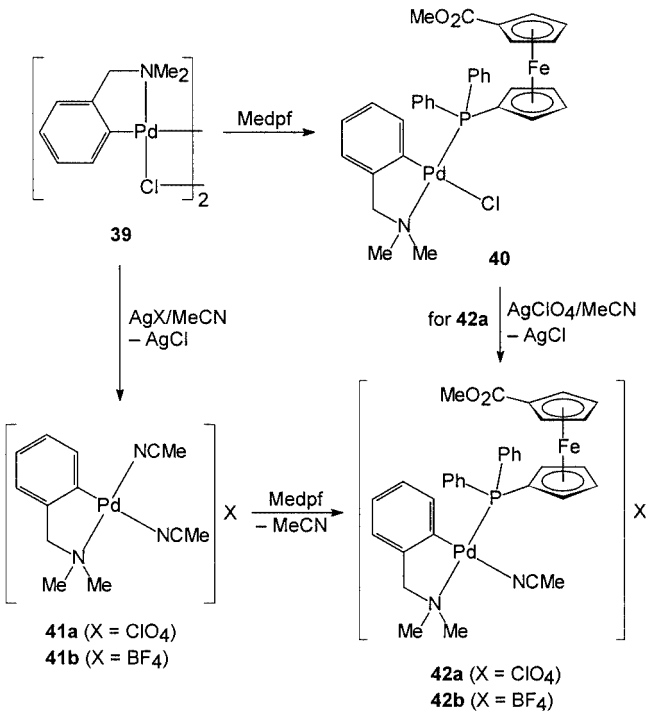

Scheme 12.

mer reaction.[51] More recently, (S_p)-HL^1 has been employed as a chiral auxiliary (catalyst-directing group)[52] and its ester, (S_p)-MeL^1, utilised for the synthesis of ferrocenyl-oxazolines.[53]

The synthetic route leading to (S_p)-HL^1 as reported by all three groups was identical,[50a–50c,54] based the on a chiral protecting/*ortho*-directing group approach (Scheme 13). It starts with chiral ferrocenyl-oxazoline (S,S_p)-**44**, which is accessible in three steps (amidation, oxazoline ring closure, and diastereoselective lithiation/phosphanylation) from ferrocenecarboxylic acid in good yields and stereodefined form. The oxazoline was hydrolysed by the standard protocol: the oxazoline ring was first cleaved by action of aqueous trifluoroacetic acid to give an ammonium salt intermediate, which was directly converted into the more stable amido ester (S,S_p)-**45**. The following saponification of the ester amide with sodium hydroxide, acidification of the reaction mixture and chromatographic purification afforded (S_p)-HL^1 in 60–65% yields vs. (S,S_p)-**44**.

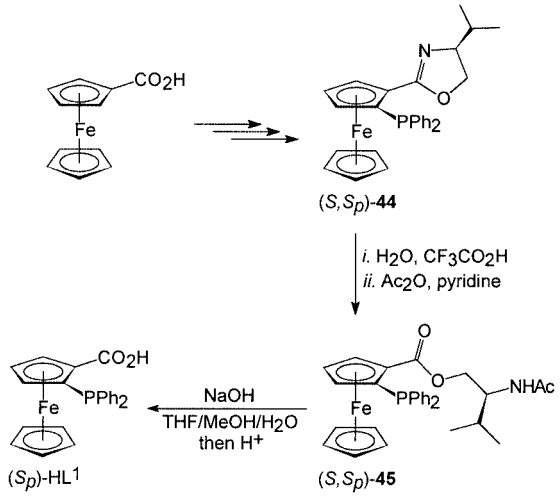

Scheme 13.

It should be noted that a similar methodology with the appropriate oxazolines furnished also 1′-(diphenylphosphanyl)-2-(trimethylsilyl)ferrocenecarboxylic acid,[50c] and esters of C_2-symmetric 2,2′-bis(diphenylphosphanyl)ferrocene-1,1′-dicarboxylic acid.[55] These compounds and amides relating to the later esters[56] were tested as ligands for palladium-catalysed allylic substitution.

Compared to the numerous catalytic applications of (S_p)-HL^1, the coordination chemistry of this carboxy-phosphane remains still unexplored. An exception are (arene)ruthenium(II) complexes with phosphanyl-carboxylate [(S_p)-L^1]$^-$, resulting from the reaction of [{Ru(μ-Cl)Cl(η^6-*p*-cymene)}$_2$] with 2 mol-equiv. of salt K[(S_p)-L^1] generated in situ by neutralization of (S_p)-HL^1 with the equivalent amount of KO*t*Bu. The reaction yields a kinetic 1:1 mixture of diastereoisomeric chelate complexes differing in configuration at the stereogenic ruthenium atom, (R_{Ru},S_p)-**46** and (S_{Ru},S_p)-**46**. However, this mixture undergoes a spontaneous epimerization in favour of the thermodynamically preferred isomer (R_{Ru},S_p)-**46**, which was isolated in 82% yield by crystallization over several days and structurally characterised (Scheme 14, Figure 7).[54]

Apparently, the thermodynamic driving force for this spontaneous equilibration is the destabilization of one of the diastereoisomers, (S_{Ru},S_p)-**46**, due to steric interactions

 © 2005 Wiley-VCH Verlag GmbH & Co. KGaA, Weinheim

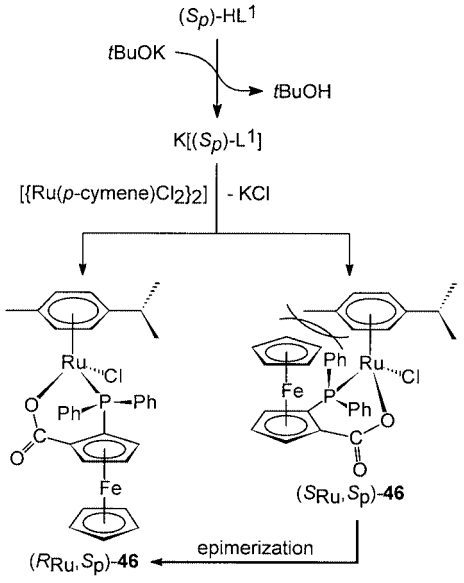

Scheme 14.

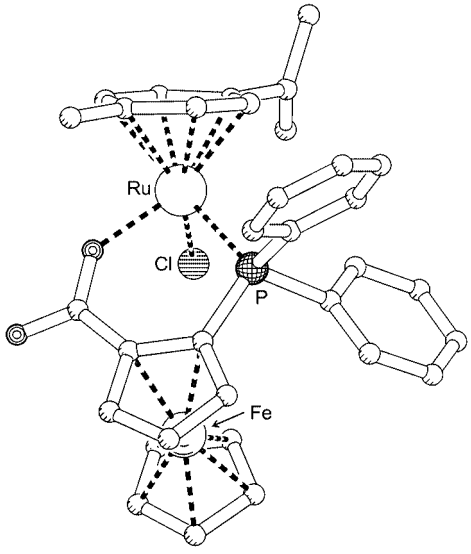

Figure 7. View of the molecular structure of (R_{Ru},S_p)-**46** as obtained for the solvate (R_{Ru},S_p)-**46**·0.7CH_2Cl_2. Molecules of solvating dichloromethane are not shown.

between the rigid ferrocene unit and the bulky η^6-arene ligand. The epimerization occurs most likely via Ru–O bond opening, followed by a rotation along of the ligand moiety into the sterically preferred position and the repetitive closure of the chelate ring. The hemilabile nature of the [(S_p)-L^1]$^-$ ligand evidently facilitates the isomerisation reaction.

rac-[2-(Diphenylphosphanyl)ferrocenyl]acetic Acid

rac-[2-(Diphenylphosphanyl)ferrocenyl]acetic acid, *rac*-HL^2, a formal homologue of (S_p)-HL^1, has been synthesized from the known precursor, *rac*-{[2-(diphenylphosphanyl)ferrocenyl]methyl}dimethylamine (**47**) (Scheme 15). The amine was converted by alkylation with benzyl bromide to ammonium salt **48**, which upon heating with aqueous sodium cyanide gave nitrile **49**. Hydrolysis of the nitrile followed by acidification of the reaction mixture and recrystallisation of the crude acid from aqueous acetic acid yielded *rac*-HL^2 as a yellow, air-stable solid (Scheme 16; ca. 63% yield from **47** over two steps; the salt does not need to be isolated). The acid was further converted into the respective phosphane oxide (**50**), phosphane sulfide (**51**), and methyl ester. The coordination ability of *rac*-HL^2 and *rac*-MeL^2 has been assessed in palladium(II) complexes.[57]

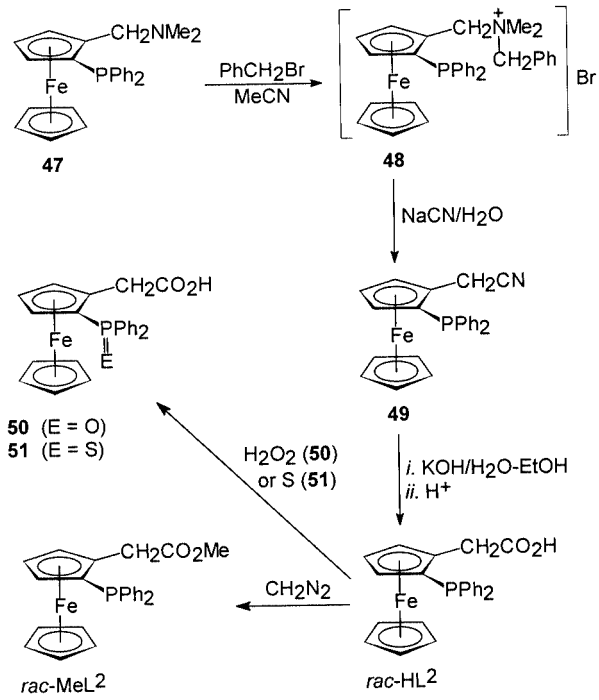

Scheme 15. Preparation of *rac*-HL^2 and its derivatives.

First, we studied palladium(II) complexes containing the 2-[(dimethylamino)methyl]phenyl-κ^2C^1,N spectator ligand (Scheme 16). The reaction of *rac*-MeL^2 with dipalladium precursor **39** gave the expected bridge-cleavage product **52**. Attempts to isolate a similar complex with *rac*-HL^2 failed due to consecutive reactions of the primary product analogous to **52**, most likely an acidolysis of the Pd–C bonds. The removal of the chloride ligand with silver(I) perchlorate from **52** gave cationic chelate complex **53**, which results also from a replacement of acetonitrile ligands in the cationic precursor **42a** (note: the same reaction but with Medpf proceeds with substitution of only one MeCN ligand, see above). The related complex containing the *O*,*P*-chelating [*rac*-L^2]$^-$ anion was obtained by treating dimer **39** with the stoichiometric amount of salt K[*rac*-L^2]$^-$ generated in situ from the acid and KO*t*Bu. The number, types and sequence of atoms within the "L^2-chelate" rings in **53** and **54** are identical and, hence the rings are structurally very similar, which is manifested also by practically identical ligand bite angles O–Pd–C of ca. 98°.[57]

 © 2005 Wiley-VCH Verlag GmbH & Co. KGaA, Weinheim

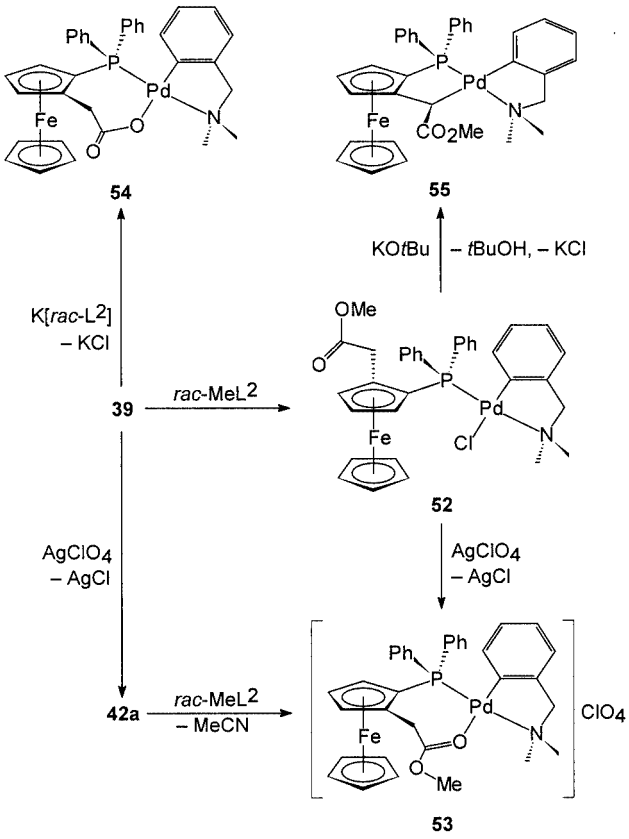

Scheme 16. Synthesis of {[(dimethylamino)methyl]phenyl-κ^2C^1,N}palladium(II) complexes with "L^2 family" ligands.

The reaction of **53** with sodium hydride or potassium *tert*-butoxide in THF provided bis(chelate) complex **55**. A formal dehydrohalogenation **53** → **55** can be rationalised by deprotonation at the activated ligand methylene group and a subsequent intramolecular substitution of the chloride ligand under preservation of the *trans*-P–N donor arrangement around the palladium ion. The reaction diastereoselectively creates a new chiral centre at the deprotonated carbon atom, producing the single diastereoisomer, $(S,R_p)/(R,S_p)$, from the racemic ester.[58] Compared to the related complexes with chelating $[R_2PCHCO_2Et]^-$ anions,[59] compound **55** is chemically very robust, inert to air, CO, SO_2, and some alkynes.

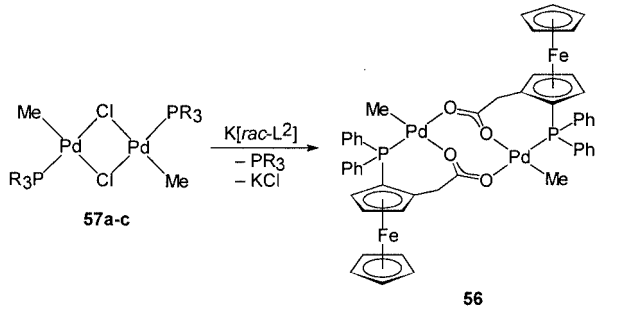

Scheme 17. Formation of dipalladium(II) complex **56** featuring a bridging tridentate $[rac\text{-}L^2]^-$ anion [PR_3 = PMe_3 (**a**), PPh_3 (**b**), and $PFur_3$, where Fur = fur-2-yl (**c**)].

Yet another coordination mode for the $[rac\text{-}L^2]^-$ anion exploiting all (classical) donor atoms has been observed for carboxylate-bridged dipalladium(II) complex **56** resulting from a reaction of dipalladium(II) complex **57** with K[*rac*-L^2] (Scheme 17). The formation of **56** likely involves a substitution of chloride ligands with the carboxylate and chelate-assisted replacement of monodentate phosphanes PR_3 with the phosphanyl group of the carboxylate ligand. Similarly to **55**, complex **56** results in a single diastereoisomer (R_p,S_p)-**56** (i.e., *meso*-form), combining both enantiomers of the racemic ligand in one complex molecule.[60]

rac-[2-(Diphenylphosphanyl) methyl]ferrocenecarboxylic Acid

The ligand *rac*-HL^3 or *rac*-[2-(diphenylphosphanyl) methyl]ferrocenecarboxylic acid is an isomer of the previously discussed compound *rac*-HL^2, differing in the position of the methylene spacer. It has been synthesized from *rac*-[(2-bromoferrocenyl)methyl]dimethylamine (**58**), which was converted to acetate **59** and then to bromo alcohol **60** (Scheme 18). Since the direct phosphanylation[61] commonly operative in ferrocene chemistry failed with compounds **58–60**, we sought for alternative methods. Fortunately, the key phosphanyl bromide **61** was obtained in excellent yield by treating alcohol **60** in acetonitrile with Me_3SiCl/NaI and then with Ph_2PH, as recently reported for some related compounds.[62] Metallation of **61** followed by carboxylation with carbon dioxide and chromatographic purification gave a good yield of *rac*-HL^3. For the sake of comparison with the *rac*-HL^2 family, the acid was further converted into the respective phosphane oxide **62**, phosphane sulfide **62**, and methyl ester *rac*-MeL^3.[63]

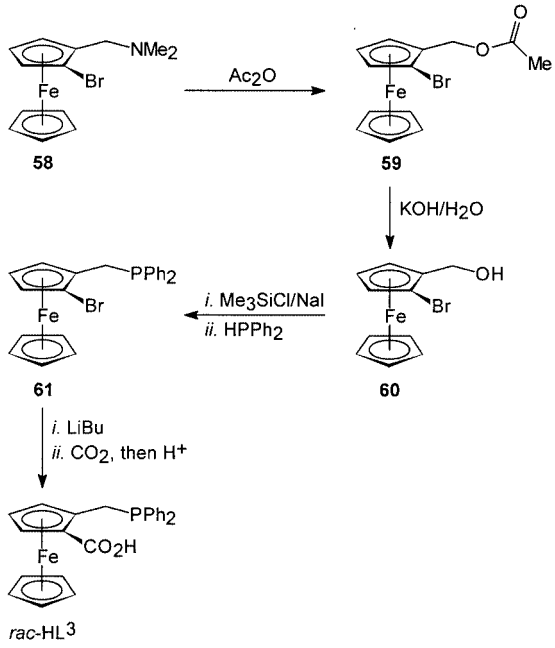

Scheme 18.

The coordination properties of *rac*-HL^3 and the respective ester have been studied up to the present only for rho-

 © 2005 Wiley-VCH Verlag GmbH & Co. KGaA, Weinheim

dium complexes (Scheme 19). (Cyclopentadienyl)rhodium(III) complexes with *P*-monodentate ligands (**64** and **65**) were prepared by bridge cleavage from [{Rh(μ-Cl)Cl(η^5-C_5Me_5)}$_2$] and the respective ligands. Attempts to synthesize *O*,*P*-chelated complexes by treating **64** with bases or from **65** by halide removal failed but, finally, the *O*,*P*-chelating coordination of the [*rac*-L^3]$^-$ anion was attained with a rhodium(I) complex **66** obtained from *rac*-HL^3 and **35a** (see also above).[63]

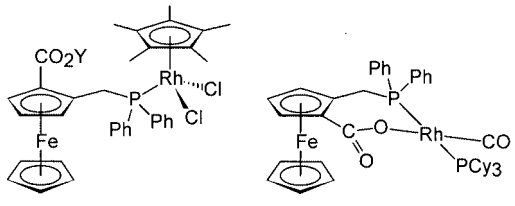

Scheme 19.

Structural Aspects

Hdpf, Medpf, and dpf$^-$ Complexes

The specific steric properties of the ferrocene moiety as mentioned above are obviously reflected in the spatial arrangement of complexes featuring Hdpf and the related forms of this ligand. The number of structurally characterised compounds (Table 1) enables us to draw some general conclusions about the ligand geometry. First, the ferrocene moieties remain quite regular, showing no deformation or tilting of the cyclopentadienyl rings: the maximum dihedral angle of the cyclopentadienyl planes of ca. 7.5° was observed for **29** and **23**·(2+*x*)CH_2Cl_2. Second, the rotation of the carboxy plane from the plane of its parent cyclopentadienyl ring (twist angle θ) does not usually exceed ca. 10°, the exceptions being **36a** (θ = 26°), **38** (θ = 19°) and one of the four ligand moieties in the structure of **28**·2CH_3CO_2H (θ = 16°). Whereas the carboxy rotation in **36a** apparently results from a compromise between the *O*,*P*-chelating coordination of the dpf$^-$ anion and the steric demands of the central atom, twisting of the carboxy group in **38** and **28**·2CH_3CO_2H is probably caused by crystal packing effects. However, in view of DFT calculations for ferrocenecarboxamide,[64] indicating that rotation of the amide moiety from the plane of its bonded cyclopentadienyl ring by as much as 30° reduces orbital interaction of their π-systems by approx. 14%, even such rotations of the carboxy plane do not destabilise the mentioned structures by precluding the carboxy-ferrocene conjugation.

Table 1. Conformation parameter τ for ferrocene units in the structurally characterised Hdpf derivatives and complexes.[a]

Compound	$\lvert\tau\rvert$ [°]
Hdpf and its complexes	
Hdpf[17]	162, 162
HdpfO[17]	146
21a·2CH_3CO_2H[35]	83
22[35]	151, 141, 145
22·2CH_3CO_2H[35]	83
23·(2+*x*)CH_2Cl_2[35]	148, 89
24d·2$CHCl_3$[36]	144
26b[37]	79
27b·4CH_3CO_2H[37]	135
28·2CH_3CO_2H[38]	158, 148, 158, 118
29[39]	68
33da·CH_2Cl_2[40]	148
43·CH_2Cl_2[49]	143, 143
[PdCl{η^3-$CH_2C(CH_3)CH_2$}(Hdpf-κ*P*)][66]	162
dpf$^-$ complexes	
36a[44]	60
38[47]	163
Medpf and its complexes	
Medpf[17]	162
42a[48]	145
42b[48]	146

[a] Parameter τ is defined as the torsion angle (C^P–Cg^P–Cg^C–C^C), where Cg^P and Cg^C denote the centres of gravity of phosphanyl- (P) and carboxy-substituted (C) cyclopentadienyl rings, and C^P and C^C ring carbon atoms bearing the substituents. Absolute values for τ are given to eliminate chirality of the ligand moieties in the solid-state (see ref.[13]). Entries for all crystallographically independent ligand molecules are given where applicable.

The third but most varying parameter is the torsion angle τ (Table 1), which relates to the conformation of the 1,1′-disubstituted ferrocene core (see also ref.[13]). Of the 27 structurally characterised (H)dpf ligand moieties, twenty have τ in the range of 135–160°, i.e. around *anti*-eclipsed conformations [Scheme 20, (a); τ(AB) = 144°]. Such an arrangement apparently minimizes the steric interactions of the substituents at the ferrocene unit by bringing their centres of gravity (not the bonds to the substituents which would lead to *anti*-staggered conformations with τ = 180°) into a mutually opposite position [see side and top views in Scheme 20, (b)]. The minimum τ value of 60° was found for the chelate complex **36a**, where the proximity of both donor groups is enforced by the *O*,*P*-chelating coordination.

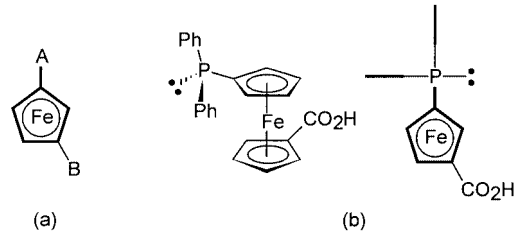

Scheme 20.

Energy changes associated with conformational alterations may be compensated for by an energy gain upon the formation of intermolecular bonds and a favourable crystal assembly.[65] This can be exemplified by six entries with τ = 68–118°, all featuring *P*-monodentate Hdpf, whose carboxy group takes part in the usual double hydrogen bridges to another ligand carboxy group or to solvating acetic acid.

 © 2005 Wiley-VCH Verlag GmbH & Co. KGaA, Weinheim

Intermolecular Interactions

The supramolecular architectures of crystalline organometallic solids are currently gaining increasing attention due to their relation to the rapidly growing research area of organometallic crystal engineering.[67] In this regard, ferrocene chemistry holds great potential for future developments because ferrocene molecules are usually stable, structurally well defined and, most importantly, capable of bearing various polar groups to be used as the structure-assembling tool.

The molecules of ferrocene phosphanyl-carboxylic ligands combine hard polar carboxy moieties with a nonpolar ferrocene skeleton and substituents at the phosphorus atom. Interactions between the polar parts are usually clearly detectable from the structural data and virtually dominate the crystal assembly. However, they operate together with the relatively weaker but important intermolecular forces such as, for example, C–H···X and C–H···π hydrogen bonds (X stands for a heteroatom), and π···π stacking interactions of the aromatic rings.[68]

The summary of the principal intermolecular interactions observed for the discussed ligands and their corresponding phosphane oxides and sulfides is given in Table 2. The phosphane derivatives typically assemble via double hydrogen bridges characteristic for carboxylic acids [Scheme 21, interaction **A**; notation according to graph set theory: $R^2_2(8)$[69]]. A similar assembly is usually encountered also for the respective phosphane sulfides whose thiophosphoryl sulfur atom cannot effectively compete for the hydrogen-bond donor with the carboxy oxygen atoms. On the other hand, the conversion of phosphanes into phosphane oxides is associated with an introduction of a strong hydrogen-bond acceptor, which further increases the structural variability. Among the ferrocene phosphanoyl-carboxylic acids which have been structurally characterised, HdpfO and (S_p)-**67** (see footnotes to Table 2) form one-dimensional zig-zag chains propagating by means of P=O···H–OC(=O) hydrogen bonds (Scheme 21, **B**) whilst **50** forms centrosymmetric cyclic dimers assembled via a pair of the similar P=O···H–OC(O) interactions (Scheme 21, **B**). In contrast, the solvated phosphane oxide **62**·$CHCl_3$ holds the structure of the parent carboxy dimer, forming additional hydrogen bonds to the solvate molecules [P=O···H–CCl_3: O···O 2.986(2) Å; Scheme 21, **D**].

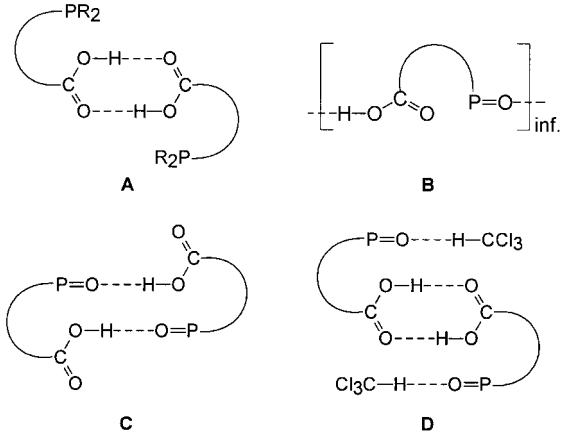

Scheme 21. Hydrogen bonding patterns observed for phosphorus-substituted ferrocenecarboxylic acids.

Table 2. Hydrogen bond lengths for the carboxylic acids.[17,54,57]

Compound	Interaction[a]	*d*(O···O) [Å]
Hdpf	**A**	2.650(6), 2.653(6)[b] [c]
HdpfO	**B**	2.588(4)[b]
(S_p)-**67**[e]	**B**	2.556(4)[d]
rac-HL^2	**A**	2.646(2)[d]
50	**C**	2.596(3)[d]
51	**A**	2.649(2)[d]
rac-HL^3	**A**	2.629(3)[d]
62·$CHCl_3$	**D**	2.646(2)[d]
63·½CH_2Cl_2	**A**	2.663(2)[d]

[a] See text and Scheme 21 for definitions. [b] Determined at room temperature. [c] Entries for two crystallographically independent molecules. [d] Determined at 150 K. [e] (S_p)-2-(diphenylphosphanoyl)ferrocenecarboxylic acid, (S_p)-[HL^1O].

A situation similar to the free ligand has been observed also for a number of complexes with *P*-monodentate Hdpf: the ligand carboxy group typically forms characteristic double hydrogen bonds to an adjacent ligand moiety [**22**, **26b**, **23**·(2+*x*)CH_2Cl_2, **24d**·2$CHCl_3$, **28**·2CH_3CO_2H (see above), **29**, **33da**·CH_2Cl_2, **43**·CH_2Cl_2] or to solvating acetic acid [**21a**·2CH_3CO_2H, **22**·2CH_3CO_2H, **27b**·4CH_3CO_2H, **28**·2CH_3CO_2H (see above)]. In this regard, complex [PdCl{η^3-$CH_2C(CH_3)CH_2$}(Hdpf-κ*P*)] is a notable exception as it forms dimers through Pd–Cl···H–OC(=O) bonds [Cl···O 3.082(2) Å].[66]

Conclusions

The introduction of phosphanyl-ferrocenecarboxylic ligands about ten years ago brought some new aspects into the chemistry of mixed-donor ferrocene ligands. The particular combination of the functional groups and the ferrocene backbone makes these compounds chemically and structurally markedly diverse. Consequently, phosphanyl-ferrocenecarboxylic ligands represent very flexible donors, which typically offer several accessible, sometimes mutually interconvertible, coordination modes, and are capable of hemilabile coordination. From a practical viewpoint, phosphanyl-ferrocenecarboxylic derivatives hold much potential as perspective ligands for catalytic applications and as valuable synthons for the design of supramolecular organometallic materials. The results already obtained are promising and open up new areas for future research, ranging from the development of new ligands and complexes on one side to their applications in catalysis and material science on the other.

Acknowledgments

I am indebted to all my past and present co-workers who have contributed to the research presented here for their enthusiastic

 © 2005 Wiley-VCH Verlag GmbH & Co. KGaA, Weinheim

experimental work and stimulating ideas. Their names appear in the appropriate references. Financial support from the Grant Agency of the Czech Republic and the Grant Agency of Charles University are gratefully acknowledged.

[1] A. Bader, E. Lindner, *Coord. Chem. Rev.* **1991**, *108*, 27–110.
[2] Notation according to the HSAB concept. For a reference, see: R. G. Pearson, *Coord. Chem. Rev.* **1990**, *100*, 403–425.
[3] a) J. C. Jeffrey, T. B. Rauchfuss, *Inorg. Chem.* **1979**, *18*, 2658–2666; b) C. S. Slone, D. A. Weinberger, C. A. Mirkin, *Prog. Inorg. Chem.* **1999**, *48*, 233–350; c) P. Braunstein, F. Naud, *Angew. Chem. Int. Ed.* **2001**, *40*, 680–699.
[4] a) D. C. Mudalige, G. L. Rempel, *J. Mol. Catal. A: Chem.* **1977**, *116*, 309–316 and references cited therein; b) F. Eymery, P. Burattin, F. Mathey, P. Savignac, *Eur. J. Org. Chem.* **2000**, 2425–2431; c) W. A. Herrmann, C. W. Kohlpaintner, *Angew. Chem. Int. Ed. Engl.* **1993**, *32*, 1524–1544 (a review).
[5] For leading references, see: a) S. Mecking, *Angew. Chem. Int. Ed.* **2001**, *40*, 534–540; b) K. Nomura, *Recent Res. Devel. Pure Appl. Chem.* **1989**, *2*, 473–513; c) M. Peuckert, W. Keim, *Organometallics* **1983**, *2*, 594–597; d) W. Keim, *J. Mol. Catal.* **1989**, *52*, 19–25; e) W. Keim, *Angew. Chem. Int. Ed. Engl.* **1990**, *29*, 235–244; f) W. Keim, R. P. Schulz, *J. Mol. Catal.* **1994**, *92*, 21–33.
[6] a) G. J. P. Britovsek, W. Keim, S. Mecking, D. Sainz, T. Wagner, *J. Chem. Soc., Chem. Commun.* **1993**, 1632–1634; b) G. J. P. Britovsek, K. J. Cavell, M. J. Green, F. Gerhards, B. W. Skelton, A. H. White, *J. Organomet. Chem.* **1997**, *533*, 201–212.
[7] M. Onishi, K. Hiraki, M. Yamaguchi, J. Morishita, *Inorg. Chim. Acta* **1992**, *195*, 151–155.
[8] a) G. Knühl, P. Sennhenn, G. Helmchen, *J. Chem. Soc., Chem. Commun.* **1995**, 1845–1846; b) Y. Okada, T. Minami, Y. Umezu, S. Nishikawa, R. Mori, Y. Nakayama, *Tetrahedron: Asymmetry* **1991**, *2*, 667–682; c) T. Minami, Y. Okada, T. Otaguro, S. Tawaraya, T. Furuichi, T. Okauchi, *Tetrahedron: Asymmetry* **1995**, *6*, 2469–2474.
[9] For comprehensive overviews of ferrocene chemistry and catalysis involving ferrocene ligands, see: a) *Ferrocenes: Homogeneous Catalysis, Organic Synthesis and Materials Science* (Eds.: A. Togni, T. Hayashi), VCH, Weinheim, **1995**; b) A. Togni, in *Metallocenes* (Eds.: A. Togni, R. L. Halterman), Wiley-VCH, Weinheim, **1998**, vol. 2, chapter 11, p. 685–721; c) E. G. Perevalova, M. D. Reshetova, K. Y. Grangberg, *Metody elementoorganicheskoy khimii, Ferrocen*, Nauka, Moscow, **1973**; d) A. J. Deeming, in *Comprehensive organometallic chemistry* (Eds.: G. Wilkinson, F. G. A. Stone, E. W. Abel), Pergamon Press, Oxford, **1982**, vol. 4, chapter 31.3.4, p. 475–512.
[10] P. Zanello, *Inorganic electrochemistry*, Royal Society of Chemistry, Cambridge, **2003**.
[11] M. Herbehold, *Angew. Chem. Int. Ed. Engl.* **1995**, *34*, 1837–1839.
[12] The barrier of internal rotation of the cyclopentadiene rings in ferrocene in the gas phase has been established to ca. 4 kJ mol^{-1}, which is lower than the $N_A kT \approx 2.5$ kJ mol^{-1} at 298 K. For the reference, see: A. Haaland, J. E. Nilsson, *Acta Chem. Scand.* **1968**, *22*, 2653–2670.
[13] Fixing the conformations of 1,1′-disubstituted ferrocenes makes their molecules potentially chiral. However, this situation is restricted only to the solid state. In solution, the enantiomeric forms easily interconvert by rotation along the axis connecting the centres of the cyclopentadienyl rings and, hence, cannot be separated.
[14] a) A. Togni, *Angew. Chem. Int. Ed. Engl.* **1996**, *35*, 1475–1477; b) H. B. Kagan, P. Diter, A. Gref, D. Guillaneux, A. Masson-Szymczak, F. Rebiere, O. Riant, O. Samuel, S. Taudien, *Pure Appl. Chem.* **1996**, *68*, 29–36; c) C. J. Richards, A. J. Locke, *Tetrahedron: Asymmetry* **1998**, *9*, 2377–2407; d) T. J. Colacot, *Chem. Rev.* **2003**, *103*, 3101–3118; e) R. C. J. Atkinson, V. C. Gibson, N. J. Long, *Chem. Soc., Rev.* **2004**, *33*, 313–328; f) J. Clayden, *Top. Organomet. Chem.* **2003**, *5*, 251–286; g) H.-U. Blaser, C. Malan, B. Pugin, F. Spindler, H. Steiner, M. Studer, *Adv. Synth. Catal.* **2003**, *345*, 103–151.
[15] a) **1**: I. R. Butler, S. Müssig, M. Plath, *Inorg. Chem. Commun.* **1999**, *2*, 424–427; b) **2**: I. R. Butler, U. Griesbach, P. Zanello, M. Fontani, D. Hibbs, M. B. Hursthouse, K. L. M. A. Malik, *J. Organomet. Chem.* **1998**, *565*, 243–258; c) **3**: I. R. Butler, M. G. B. Drew, A. G. Caballero, P. Gerner, C. H. Greenwell, *J. Organomet. Chem.* **2003**, *679*, 59–64; d) **4**:W.-P. Deng, S.-L. You, X.-L. Hou, L.-X. Dai, Y.-H. Yu, W. Xia, J. Sun, *J. Am. Chem. Soc.* **2001**, *123*, 6508–6519.
[16] a) G. De Lauzon, B. Deschamps, F. Mathey, *New J. Chem.* **1980**, *4*, 683–685; b) A. Kłys, R. B. Nazarski, J. Zakrzewski, *J. Organomet. Chem.* **2001**, *627*, 135–138; c) A. Kłys, J. Zakrzewski, *J. Organomet. Chem.* **2002**, *642*, 143–144; d) L. Sieron, A. Tosik, M. Bukowska-Strzyzewska, *J. Chem. Crystallogr.* **1998**, *28*, 621–628.
[17] J. Podlaha, P. Štěpnička, I. Císařová, J. Ludvík, *Organometallics* **1996**, *15*, 543–550.
[18] a) A. G. Osborne, R. H. Whiteley, R. E. Meads, *J. Organomet. Chem.* **1980**, *193*, 345–357; b) D. Seyferth, H. P. Withers, Jr., *Organometallics* **1982**, *1*, 1275–1282.
[19] D. Seyferth, H. P. Withers, Jr., *J. Organomet. Chem.* **1980**, *185*, C1–C5.
[20] P. Štěpnička, T. Baše, *Inorg. Chem. Commun.* **2001**, *4*, 682–687.
[21] M. D. Wright, *Organometallics* **1990**, *9*, 853–856.
[22] I. R. Butler, R. L. Davies, *Synthesis* **1996**, 1350–1354.
[23] M. Polášek, P. Štěpnička, *J. Mass. Spectrom.* **1998**, *33*, 739–749.
[24] Hdpf is quite stable in solution and is definitely not oxidised spontaneously to HdpfO under the experimental conditions.
[25] a) G. Pilloni, B. Longato, B. Corain, *J. Organomet. Chem.* **1991**, *420*, 57–65; b) P. Zanello, G. Opromolla, G. Giorgi, G. Sasso, A. Togni, *J. Organomet. Chem.* **1996**, *506*, 61–65.
[26] D. Drahoňovský, I. Císařová, P. Štěpnička, H. Dvořáková, P. Maloň, D. Dvořák, *Collect. Czech. Chem. Commun.* **2001**, *66*, 588–604.
[27] W. Zhang, Y. Yoneda, T. Kida, Y. Nakatsuji, I. Ikeda, *Tetrahedron: Asymmetry* **1998**, *9*, 3371–3380.
[28] O. B. Sutcliffe, M. R. Bryce, *Tetrahedron: Asymmetry* **2003**, *14*, 2297–2325.
[29] D. Drahoňovský, P. Štěpnička, D. Dvořák, *Collect. Czech. Chem. Commun.* **2005**, *70*, 361–369.
[30] L. Meca, D. Dvořák, J. Ludvík, I. Císařová, P. Štěpnička, *Organometallics* **2004**, *23*, 2541–2551.
[31] a) R. Imwinkelried, L. S. Hegedus, *Organometallics* **1988**, *7*, 702–706; b) M. A. Schwindt, T. Lejon, L. S. Hegedus, *Organometallics* **1990**, *9*, 2814–2819.
[32] D. Dvořák, *Organometallics* **1995**, *14*, 570–573.
[33] Selected examples: a) A. N. Nesmeyanov, D. N. Kursanov, V. D. Vilchevskaya, N. K. Baranetskaya, A. I. Krylova, V. I. Losilkina, V. N. Setkina, *Dokl. Akad. Nauk SSSR* **1978**, *241*, 111–114; b) P. K. Baker, D. J. T. Sharp, *J. Coord. Chem.* **1988**, *16*, 389–393; c) M. Onishi, K. Hiraki, H. Itoh, H. Eguchi, S. Abe, T. Kawato, *Inorg. Chim. Acta* **1988**, *145*, 105–109; d) T. M. Miller, K. J. Ahmed, M. S. Wrighton, *Inorg. Chem.* **1989**, *28*, 2347–2355; e) S. T. Chacon, W. R. Cullen, M. I. Bruce, O. B. Shawkataly, F. W. B. Einstein, R. H. Jones, A. C. Willis, *Can. J. Chem.* **1990**, *68*, 2001–2010; f) W. R. Cullen, S. J. Rettig, T. C. Zheng, *Can. J. Chem.* **1992**, *70*, 2215–2223; g) F. Estevan, J. Latorre, E. Peris, *Polyhedron* **1993**, *12*, 2153–2156; h) E. Alonso, J. Ruiz, D. Astruc, *J. Cluster Sci.* **1998**, *9*, 271–287; i) S. Otto, *J. Chem. Crystallogr.* **2001**, *31*, 185–190; j) N. J. Long, A. J. P. White, D. J. Williams, M. Younus, *J. Organomet. Chem.* **2002**, *649*, 94–99. See also refs.[40,42–44]
[34] Representative examples: a) A. L. Abuhijleh, C. Woods, *J. Chem. Soc., Dalton Trans.* **1992**, 1249–1252; b) W. Shaozu, L. Benyan, Z. Yulan, *Synth. React. Inorg. Met.-Org. Chem.* **1993**, *23*, 77–83; c) A. L. Abuhijleh, J. Pollitte, C. Woods, *Inorg. Chim. Acta* **1994**, *215*, 131–137; d) M. R. Churchill, Y.-J. Li, D. Nalewajek, P. M. Schaber, J. Dorfman, *Inorg. Chem.* **1985**,

24, 2684–2687; e) F. A. Cotton, L. R. Falvello, A. H. Reid, Jr., J. H. Tocher, *J. Organomet. Chem.* **1987**, *319*, 87–97; f) S.-M. Lee, K.-K. Cheung, W.-T. Wong, *J. Organomet. Chem.* **1996**, *506*, 77–84; g) L. Matas, I. A. Moldes, J. Soler, J. Ros, A. Alvarez-Larena, J. F. Piniella, *Organometallics* **1998**, *17*, 4551–4555; h) R. Costa, C. López, E. Molins, E. Spinosa, *Inorg. Chem.* **1998**, *37*, 5686–5689; i) C. López, R. Costa, F. Illas, E. Molins, E. Spinosa, *Inorg. Chem.* **2000**, *39*, 4560–4565; j) M. W. Cooke, C. A. Murphy, T. S. Cameron, J. C. Swarts, M. A. S. Aquino, *Inorg. Chem. Commun.* **2000**, *3*, 721–725; k) R. Costa, C. López, E. Molins, E. Spinosa, J. Pérez, *J. Chem. Soc., Dalton Trans.* **2001**, 2833–2837; l) H.-W. Hou, L.-K. Li, G. Li, Y.-T. Fan, Y. Zhu, *Inorg. Chem.* **2003**, *42*, 3501–3508; m) I. Wyman, T. J. Burchell, K. N. Robertson, T. S. Cameron, M. A. S. Aquino, *Organometallics* **2004**, *23*, 5353–5364 and references cited therein.

[35] P. Štěpnička, J. Podlaha, R. Gyepes, M. Polášek, *J. Organomet. Chem.* **1998**, *552*, 293–301.

[36] J. Pinkas, Z. Bastl, M. Šlouf, J. Podlaha, P. Štěpnička, *New J. Chem.* **2001**, *25*, 1215–1220.

[37] P. Štěpnička, I. Císařová, J. Podlaha, J. Ludvík, M. Nejezchleba, *J. Organomet. Chem.* **1999**, *582*, 319–327.

[38] P. Štěpnička, R. Gyepes, J. Podlaha, *Collect. Czech. Chem. Commun.* **1998**, *63*, 64–74.

[39] L. Lukešová, J. Ludvík, I. Císařová, P. Štěpnička, *Collect. Czech. Chem. Commuun.* **2000**, *65*, 1897–1910.

[40] P. Štěpnička, R. Gyepes, O. Lavastre, P. H. Dixneuf, *Organometallics* **1997**, *16*, 5089–5095.

[41] H. Le Bozec, P. H. Dixneuf, *Trends Organomet. Chem.* **1994**, *1*, 491–500 and references cited therein.

[42] a) J. C. Kotz, C. L. Nivert, *J. Organomet. Chem.* **1973**, *52*, 387–406; b) J. C. Kotz, C. L. Nivert, J. M. Lieber, R. C. Reed, *J. Organomet. Chem.* **1975**, *91*, 87–95.

[43] B. Therrien, L. Vieille-Petit, J. Jeanneret-Gris, P. Štěpnička, G. Süss-Fink, *J. Organomet. Chem.* **2004**, *689*, 2456–2463.

[44] P. Štěpnička, I. Císařová, *J. Chem. Soc., Dalton Trans.* **1998**, 2807–2811.

[45] A. M. Trzeciak, P. Štěpnička, E. Mieczyńska, J. J. Ziołkowski, *J. Organomet. Chem.* **2005**, *690*, 3260–3267.

[46] a) Ref.[17] (alkali metals); b) P. Štěpnička, J. Podlaha, *Inorg. Chem. Commun.* **1998**, *1*, 332–334 (alkali earth metals).

[47] K. Mach, J. Kubišta, I. Císařová, P. Štěpnička, *Acta Crystallogr., Sect. C: Cryst. Struct. Commun.* **2002**, *58*, m116–m118.

[48] P. Štěpnička, M. Lamač, I. Císařová, *Polyhedron* **2004**, *23*, 921–928.

[49] P. Štěpnička, J. Demel, J. Čejka, *J. Mol. Catal. A: Chem.* **2004**, *224*, 161–169.

[50] a) S.-L. You, X.-L. Hou, L.-X. Dai, B.-X. Cao, J. Sun, *Chem. Commun.* **2000**, 1933–1934; b) J. M. Longmire, B. Wang, X. Zhang, *Tetrahedron Lett.* **2000**, *41*, 5435–5439; c) S.-L. You, X.-L. Hou, L.-X. Dai, *J. Organomet. Chem.* **2001**, *637–639*, 762–766; d) S.-L. You, X.-L. Hou, L.-X. Dai, X.-Z. Zhu, *Org. Lett.* **2001**, *3*, 149–151; e) J. M. Longmire, B. Wang, X. Zhang, *J. Am. Chem. Soc.* **2002**, *124*, 13400–13401.

[51] S.-L. You, Y.-M. Luo, W.-P. Deng, X.-L. Hou, L.-X. Dai, *J. Organomet. Chem.* **2001**, *637–639*, 845–849.

[52] a) B. Breit, D. Breuninger, *J. Am. Chem. Soc.* **2004**, *126*, 10244–10245; b) B. Breit, D. Breuninger, *Synthesis* **2005**, 147–157.

[53] S.-L. You, X.-L. Hou, L.-X. Dai, Y.-H. Yu, W. Xia, *J. Org. Chem.* **2002**, *67*, 4684–7695.

[54] P. Štěpnička, *New J. Chem.* **2002**, *26*, 567–575.

[55] a) W. Zhang, T. Kida, Y. Nakatsuji, I. Ikeda, *Tetrahedron Lett.* **1996**, *37*, 7995–7998; b) W. Zhang, T. Shimanuki, T. Kida, Y. Nakatsuji, I. Ikeda, *J. Org. Chem.* **1999**, *64*, 6247–6251.

[56] W. Zhang, Y. Yoneda, T. Kida, Y. Nakatsuji, I. Ikeda, *J. Organomet. Chem.* **1999**, *574*, 19–23.

[57] P. Štěpnička, I. Císařová, *Organometallics* **2003**, *22*, 1728–1740.

[58] P. Štěpnička, *Inorg. Chem. Commun.* **2004**, *7*, 426–430.

[59] Selected examples: a) P. Braunstein, D. Matt, Y. Dusausoy, J. Fischer, L. Ricard, A. Mitschler, *New J. Chem.* **1980**, *4*, 493–495; b) P. Braunstein, D. Matt, Y. Dusausoy, J. Fischer, A. Mitschler, L. Ricard, *J. Am. Chem. Soc.* **1981**, *103*, 5115–5125; c) P. Braunstein, J. Fischer, D. Matt, M. Pfeffer, *J. Am. Chem. Soc.* **1984**, *106*, 410–421; d) G. Henig, M. Schulz, H. Werner, *Chem. Commun.* **1997**, 2349–2350; e) G. Henig, M. Schulz, B. Windmueller, H. Werner, *J. Chem. Soc., Dalton Trans.* **2003**, 441–448; f) H. Werner, G. Henig, U. Wecker, N. Mahr, K. Peters, H. G. von Schnering, *Chem. Ber.* **1995**, *128*, 1175–1181.

[60] P. Štěpnička, I. Císařová, *Z. Anorg. Allg. Chem.* **2004**, *630*, 1321–1325.

[61] A. Togni, C. Breutel, A. Schnyder, F. Spindler, H. Landert, A. Tijani, *J. Am. Chem. Soc.* **1994**, *116*, 4062–4066. For other examples see refs.[9a,9b,14a,14c,14d]

[62] a) R. Šebesta, Ph. D. Thesis, Comenius University, Bratislava, Slovakia, **2003**. A similar approach has been utilised previously in the synthesis of tertiary (ferrocenylmethyl)amines: b) R. Šebesta, Š. Toma, M. Sališová, *Eur. J. Org. Chem.* **2002**, 692–695.

[63] M. Lamač, I. Císařová, P. Štěpnička, *J. Organomet. Chem.*, accepted for publication.

[64] L. Lin, A. Berces, H.-B. Kraatz, *J. Organomet. Chem.* **1998**, *556*, 11–20.

[65] For instance, the dissociation energy of the formic acid dimer has been established to ca. 60 kJ mol^{-1} by both experimental measurements[65a] and theoretical calculations:[65b] a) A. Winkler, J. B. Mehl, P. Hess, *J. Chem. Phys.* **1994**, *100*, 2717–2727; b) T. Neuheuser, B. A. Hess, C. Reutel, E. Weber, *J. Phys. Chem.* **1994**, *98*, 6459–6467.

[66] P. Štěpnička, I. Císařová, unpublished results.

[67] a) D. Braga, F. Grepioni, G. R. Desiraju, *Chem. Rev.* **1998**, *98*, 1375–1405; b) D. Braga, L. Maini, M. Polito, E. Tagliavini, F. Grepioni, *Coord. Chem. Rev.* **2003**, *246*, 53–71.

[68] A series of ferrocenylmethanol derivatives bearing phosphorus substituents at the ferrocene unit can serve as an example of ferrocene compounds, where the interactions of the bulky nonpolar parts cooperate with the stronger O–H···H hydrogen bonds: P. Štěpnička, I. Císařová, *New J. Chem.* **2002**, *26*, 1389–1396.

[69] M. C. Etter, J. C. MacDonald, *Acta Crystallogr., Sect. B: Struct. Sci.* **1990**, *46*, 256–262.

Received: May 30, 2005
Published Online: August 29, 2005

 © 2005 Wiley-VCH Verlag GmbH & Co. KGaA, Weinheim

A Lutetium Cyclopentadienyl-Phosphazene Constrained Geometry Complex (CGC): First Isolobal Analogues of Group 4 Cyclopentadienyl-Silylamido CGC Systems[‡]

Konstantin A. Rufanov,*[a,b] Alex R. Petrov,[c] Vasili V. Kotov,[c] Frédéric Laquai,[c] and Jörg Sundermeyer*[c]

Dedicated to Prof. Dr. Herbert Schumann on the occasion of his 70th birthday

Keywords: Bridging ligands / Isolobal relationship / Phosphazenes / Constrained geometry complexes / Lutetium

$C_5Me_4HPMe_2$ reacts with 1-adamantyl azide to form the first example of a new family of cyclopentadienylideneaminophosphorane ligands (**1**). Metallation of **1** with $Lu(CH_2SiMe_3)_3(THF)_2$ leads to the first cyclopentadienyl-phosphazene CGC **2**, isolobal to known group 4 cyclopentadienyl-silylamido CGC systems.
(© Wiley-VCH Verlag GmbH & Co. KGaA, 69451 Weinheim, Germany, 2005)

Introduction

Linked cyclopentadienyl-silylamido complexes of early transition metals,[1–4] the so-called "constrained-geometry" catalysts[5] (**A**; Scheme 1), have become one of the best developed classes of specially designed organometallics because of their industrial application as single-site olefin polymerisation catalysts.[4–6] Isolobal analogues of ligands **A** are the chelating cyclopentadienyl-phosphoranylidenes (**B**) and cyclopentadienyl-phosphazenes (**C**).[7]

We found that corresponding ligand systems (**B** and **C**, left) do exist in the thermodynamically more stable tautomeric form of cyclopentadienylidene-*P*-carbo- (**B**, right) and *P*-amino-phosphoranes (**C**, right). In the framework of our current studies on coordination and organometallic chemistry of organophosphorus(v) ligands with different O, S, Se, RN and RCH functionalities, synthesis and molecular structures of the type **B** ligand precursors have been recently developed and reported.[8] In this communication we present synthesis of the first example of type **C** ligands and a new CGC lutetium complex thereof along with their crystal structures.

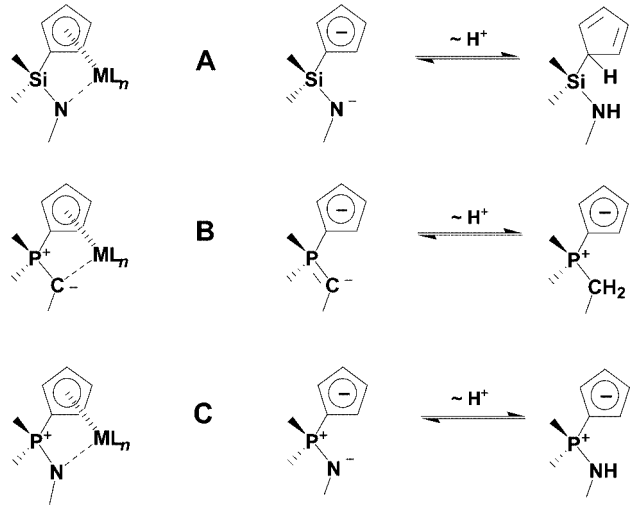

Scheme 1. Isolobally related "constrained-geometry" complexes and corresponding ligand systems.

Results and Discussion

Synthesis of cyclopentadienylidene-phosphorane-C_5Me_4=PMe_2–NHAd (Ad = Adamantyl-1) (**1**) was achieved in 95% yield by the Staudinger reaction of the phosphane $C_5Me_4HPMe_2$, obtained in situ from C_5Me_4HLi and Me_2PCl (Scheme 2), with one equiv. of AdN_3. $^1H/^{13}C$ COSY was used for accurate assignment of all signals. It is

[‡] Part 3 in the series "Organophosphorus(v) Ligands for Coordination and Organometallic Chemistry"; for Part 2 see: K. A. Rufanov, B. Ziemer, M. Meisel, *Dalton Trans.* 2004, 3808–3809.

[a] Institut für Chemie, Humboldt-Universität zu Berlin, Brook-Taylor-Str. 2, 12489 Berlin, Germany
[b] Current address: Leibniz-Institut für Organische Katalyse bei der Universität Rostock, Albert-Einstein-Strasse 29A, 18059 Rostock, Germany
Fax: +49-0381-1281-5000
E-mail: k_rufanov@gmx.de
[c] Fachbereich Chemie der Philipps-Universität Marburg, Hans-Meerwein-Strasse, 35032 Marburg, Germany
Fax: +49-06421-2828917
E-mail: jsu@chemie.uni-marburg.de

Supporting information for this article is available on the WWW under http://www.eurjic.org or from the author.

interesting to note that the N*H* proton appears shifted upfield at δ = 1.38 between the adamantyl-group CH_2 multiplets.[9] The highly pure ligand crystallises from THF/hexane mixtures as colourless plates. Simple metallation of **1** with $Lu(CH_2SiMe_3)_3(THF)_2$ in C_6D_6 at r.t. produced a new "constrained-geometry" lutetium complex [η^5:η^1-$C_5Me_4PMe_2NAd$]$Lu(CH_2SiMe_3)_2$ (**2**) in close to quantitative yield.[10]

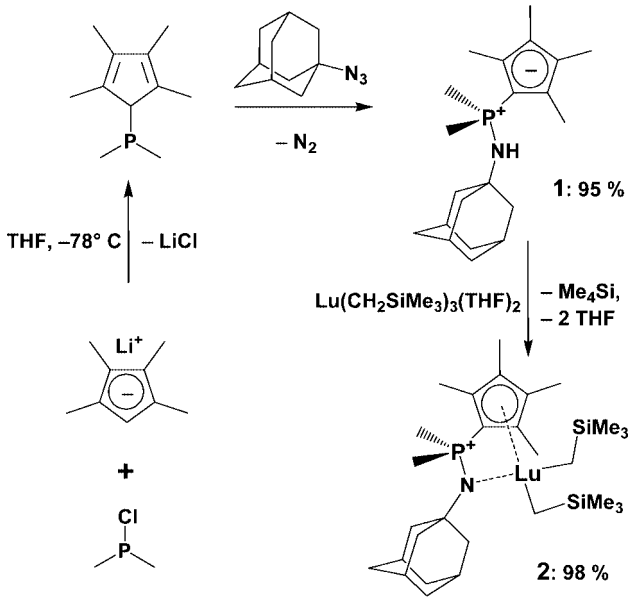

Scheme 2. Synthesis of **1** and **2**.

Metallation of the ligand **1** (δ_P = 17.6) is accompanied by a shift to δ_P = 9.6. Molecules of THF do not coordinate to Lu in THF-containing solutions of **2**, as confirmed by the ^{1}H NMR spectrum: one set of signals of THF protons with distinct coupling is observed. Complex **2** is highly soluble in alkanes and crystallises upon slow evaporation of the reaction mixture at r.t. to give large colourless prisms. Both **1** and **2** are thermally rather stable; their molecular structures are shown in Figure 1.

A comparison of these two structures underlines an increase of the aromatic character of the Cp$^{\#}$ moiety coordinated to the Lu atom: the difference in C–C bond lengths within the Cp$^{\#}$ ring is 0.06 Å for **1** and 0.04 Å for **2**. P–C_{Me} and N–C_{Ad} bonds are only 0.01 Å longer in **2** than in **1**. The P–C_{Cp} bond in **2** is 0.05 Å longer than in **1**, whereas the P–N bond in **2** is almost the same value (0.06 Å) shorter than in **1**. The rather short Lu–N bond (2.28 Å) is much closer to the covalent Lu–N bond lengths (2.21 Å) than to the donor–acceptor ones (2.48 Å) found in the crystal structures of analogous Lu complexes – Cp*Lu(bipy)(NHDip)CH_2SiMe_3 and Cp*Lu(bipy)$(NHDip)_2$.[11] Lu–CH_2 (2.36 Å) and Lu–Cp$^{\#}_{cent}$ (2.33 Å) bond lengths lie in the typical range of Lu σ-alkyl and η^5-Cp* moieties.[11] The 101.2° value of the N–P–C_{Cp} angle is similar to that of N–Si–C_{Cp} in type **A** complexes. In combination with the large radius of Lu, a more open coordination sphere and as a consequence a small but probably nonbonding P···Lu distance (3.08 Å) about 0.7 Å shorter than the sum of the van der Waals radii of these elements (3.80 Å)[12] is observed.

Conclusions

We have introduced the new cyclopentadienyl-phosphazene ligand system **C** and used it for the design of rare earth metal organometallic chelate complexes of the constrained geometry type. A crystal structure analysis of lutetium bisalkyl (**2**) has been presented, confirming that the isolobal relation finds its counterpart in a structural relation to the well-known class of cyclopentadienyl-silylamido complexes of group 4 metals. Systematic synthetic, structural and reactivity aspects of type **B** and **C** ligand systems and a series of new organometallic complexes of *s*-, *p*-, *d*- and *f*-elements will be discussed in a forthcoming full account.[13]

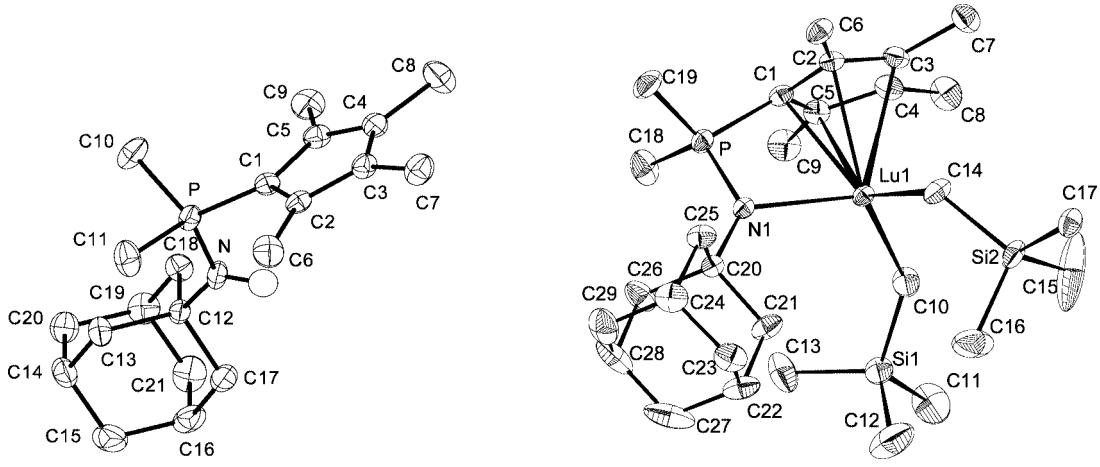

Figure 1. ORTEP illustrations of the ligand **1** (left) and complex **2** (right) showing atom-numbering scheme. Thermal ellipsoids drawn at the 35% probability level. C–*H* hydrogen atoms are omitted for clarity. Selected bond lengths [Å] and bond angles [°] for **1**: C1–C5 1.439(2), C1–C2 1.444(2), C2–C3 1.380(2), P–C1 1.724(2), P–C10 1.803(2), P–N 1.659(1) N1–C12 1.482(2), N–H 0.84(2), P–N1–C12 133.8(1), N–P–C1 108.23(7), N–P–C10 109.63(8). For **2** (right): C1–C5 1.452(6), C1–C2 1.430(6), C2–C3 1.405(6), P–C1 1.774(4), P–C18 1.812(6), P–N1 1.600(3), N1–C20 1.486(5), Lu1–Cp_{cent} 2.343(4), Lu1–N1 2.278(3), Lu1–C10 2.360(4), P–N1–C20 128.2(2), Lu1–N1–C20 128.0(2), P–N1–Lu1 103.7(2), N1–Lu1–C14 109.9(2), N1–Lu1–C10 115.8(2), C14–Lu1–C10 109.9(2).

 © 2005 Wiley-VCH Verlag GmbH & Co. KGaA, Weinheim

Supporting Information: Spectra (see footnote on the first page of this article).

Acknowledgments

K.A.R. and A.R.P. are very grateful to Prof. Manfred Meisel (Institut für Chemie, Humboldt-Universität zu Berlin) for his munificent support during our stay at his research group and in particular to Dr. Brukhard Ziemer for high quality X-ray studies.[14]

[1] a) P. J. Shapiro, E. E. Bunel, W. P. Schaefer, J. E. Bercaw, *Organometallics* **1990**, *9*, 867–871; b) P. J. Shapiro, W. D. Cotter, W. P. Schaefer, J. A. Labinger, J. E. Bercaw, *J. Am. Chem. Soc.* **1994**, *116*, 4623–4640; c) W. E. Piers, P. J. Shapiro, E. E. Bunel, J. E. Bercaw, *Synlett* **1990**, *2*, 74–84.

[2] J. Okuda, *Chem. Ber.* **1990**, *123*, 1649–1651.

[3] J. Okuda, *Dalton Trans.* **2003**, 2367–2378.

[4] a) J. Okuda, T. Eberle in *Metallocenes* (Eds.: R. L. Halterman, A. Togni), Wiley-VCH, Weinheim, **1998**, p. 415; b) W. Kaminsky, *J. Chem. Soc., Dalton Trans.* **1998**, 1413–1418.

[5] a) J. C. Stevens, F. J. Timmers, G. W. Rosen, G. W. Knight, S. Y. Lai (Dow Chemical Co.), *Eur. Pat. Appl.* EP 0 416 815 A2, **1991** (filed August 30, 1990); b) J. A. Canich (Exxon Chemical Co.), *Eur. Pat. Appl.* EP 0 420 436 A1, **1991** (filed September 10, 1990).

[6] a) J. C. Stevens, *Stud. Surf. Sci. Catal.* **1996**, *101*, 11–18; b) A. L. McKnight, R. M. Waymouth, *Chem. Rev.* **1998**, *98*, 2587–2598.

[7] *Note:* if [Si and group 4 metal] of type **A** complexes are replaced by [P and group 3 metal] of type **C** ones, not only isolobal but isoelectronic species result. A theoretical investigation of group 4 constrained geometry complexes featuring phosphazene and phosphinimido arms has been recently published. See: L. Truflandier, C. J. Marsden, C. Freund, B. Martin-Vaca, D. Bourissou, *Eur. J. Inorg. Chem.* **2004**, 1939–1947.

[8] K. A. Rufanov, B. Ziemer, M. Hummert, S. Schutte, *Eur. J. Inorg. Chem.* **2004**, 4759–4763.

[9] Possible explanation of this phenomenon consists in an effective π-shielding of N*H* proton with the C_5Me_4 group, which was partly confirmed by the X-ray structure of **1**, where this proton was located exactly under the phosphorane C_5-aromatic ring.

[10] **Synthesis of 1**: a solution of Me_2PCl (1.5 g, 15.5 mmol) in THF (10 mL) was added to a stirred suspension of C_5Me_4HLi (1.9 g, 14.7 mmol) in a 1:2 THF/hexane mixture (120 mL) for 0.5 h at –78 °C. The reaction mixture was allowed to stir overnight, warming up to r.t. LiCl was filtered off and all volatiles were removed in vacuo giving $C_5Me_4HPMe_2$ as a light yellow oil (2.2 g, 12.1 mmol, about 83% based on C_5Me_4HLi), which was dissolved in THF (10 mL) and treated with a solution of AdN_3 (2.2 g, 12.4 mmol) in THF (10 mL) at r.t. Thus the obtained yellow solution was allowed to stir with a gas-overpressure controller. During gas (N_2) liberation, the reaction solution gradually deepened in colour and after 4 h became dark brown. To complete the reaction it was warmed up to 50 °C for an additional 30 min. THF was removed in vacuo, yielding a light brown residue, which was treated with hexane (50 mL) and thoroughly washed with the same solvent (4 × 50 mL) to give, after drying in vacuo, a white powder of **1**. Yield 3.8 g (95% based on phosphane, 79% based on C_5Me_4HLi). ^{1}H NMR (300 MHz, C_6D_6, +23 °C): δ = 2.44 (s, 6H, C_5Me_4), 2.39 (s, 6H, C_5Me_4), 1.71 (br. s, 3H, CH_{Ad}), 1.40 [br. d, 6H, N–C(CH_2)$_3$], 1.35 (br. s, 1H, N*H*–Ad), 1.30 (br. m, 6H, CH–CH_2–CH), 1.25 [d, J(P,H) = 10 Hz, 6H, Me_2P]. ^{31}P NMR (121.5 MHz, C_6D_6, +23 °C): δ = 17.6 ppm. ^{13}C NMR (75.5 MHz, C_6D_6, +23 °C): δ = 119.7, 117.5 [d, d, J(P,C) = 19, J(P,C) = 18 Hz, *C*(Me)=*C*(Me)], 77.8 [d, J(P,C) = 125 Hz, P-C_{Cp}], 52.4 [d, J(P,C) = 4 Hz, P-NH-C_{ad}], 44.7 [d, J(P,C) = 4 Hz, N-C(CH_2)$_3$], 36.0 (s, CH-CH_2-CH) 29.9 (s, CH_{Ad}), 19.2 [d, J(P,C) = 70 Hz, Me_2P], 14.9 (s, C_5Me_4), 12.1 (s, C_5Me_4). EI-MS: 331, $\mathbf{1}^+$ (36%), 316, $\mathbf{1}^+$ – CH_3 (5%), 286, $\mathbf{1}^+$ – 3 CH_3 (11%), 196, $\mathbf{1}^+$ – Ad (20%). **Synthesis of 2**: a solution of **1** (330 mg, 1 mmol) in C_6D_6 (2 mL) was added to a solution of Lu(CH_2SiMe_3)$_3$(THF)$_2$ (580 mg, 1 mmol) in C_6D_6 (1 mL) at r.t. The pink-coloured solution obtained in this manner (0.6 mL) was transferred into a WILMAD 505-PS 7 NMR tube with a J. Young teflon valve. The rest of the reaction mixture was left in a glovebox for crystallisation at +25 °C giving, after evaporation of benzene, 540 mg of **2** in the form of colourless crystals in – together with the NMR sample – close to quantitative yield. ^{1}H NMR (300 MHz, C_6D_6, +23 °C): δ = 2.11 (s, 6 H, C_5Me_4), 2.04 (s, 6 H, C_5Me_4), 2.01 (br. s, 3 H, CH_{Ad}), 1.73 [br. d, 6 H, N-C(CH_2)$_3$], 1.56 (br. m, 6 H, CH-CH_2-CH), 1.15 [d, J(P,H) = 13 Hz, 6 H, Me_2P], 0.39 (s, 18 H, Me_3Si), –0.90 (q, ^2J = 20, ^4J = 10 Hz, 4 H, Lu-CH_2-Si). ^{31}P NMR (121.5 MHz, C_6D_6, +23 °C): δ = 9.6. ^{13}C NMR (75.5 MHz, C_6D_6, +23 °C): δ = 123.5, 121.5 [d, d, J(P,C) = 14, J(P,C) = 13 Hz, *C*(Me)=*C*(Me)], 83.8 [d, J(P,C) = 115 Hz, P-C_{ipso}], 54.1 [d, J(P,C) = 6 Hz, N-C_{ad}], 47.2 [d, J(P,C) = 8 Hz, N-C-(CH_2)$_3$], 38.3 (s, Lu-CH_2-Si), 36.3 (s, CH-CH_2-CH) 30.2 (s, CH_{Ad}), 21.9 [d, J(P,C) = 54 Hz, Me_2P], 13.9 (s, C_5Me_4), 11.8 (s, C_5Me_4), 4.9 (s, SiMe_3). EI-MS: 679, $\mathbf{2}^+$ (30%), 665.0, $\mathbf{2}^+$ – CH_2 (10%), 591.0, $\mathbf{2}^+$ – Me_4Si (16%). Satisfactory elemental analyses of **1** and **2** were obtained. General experimental details, NMR and EI-MS spectra as well as references on the syntheses of the starting reagents are collected in the Supporting Information; see also the footnote on the first page of this article.

[11] T. M. Cameron, J. C. Gordon, B. L. Scott, *Organometallics* **2004**, *23*, 2995–3002.

[12] A. Bondi, *J. Phys. Chem.* **1964**, *68*, 441–451.

[13] K. A. Rufanov, A. R. Petrov, B. Ziemer, J. Sundermeyer, work in progress.

[14] **Crystal Data for 1:** $C_{21}H_{34}NP$, M = 331.46, orthorhombic, space group $P2_1 2_1 2_1$, a = 10.582(2) Å, b = 13.135(3) Å, c = 13.845(2) Å, V = 1924.5(6) Å^3, Z = 4, $D_{calcd.}$ = 1.144 g cm^{-3}, μ(Mo-K_α) = 0.144 mm^{-1}. Crystal dimensions 0.52 × 0.40 × 0.28 mm. Data were collected with an area detector using ω-scans at 180(2) K on an IPDS STOE diffractometer using graphite-monochromated Mo-K_α radiation (λ = 0.71073 Å). The structure was solved by direct methods and expanded by difference Fourier syntheses using the SHELX-97 software package. G. M. Sheldrick, Program for solution of crystal structures, SHELXS-97; University of Göttingen, **1997**; G. M. Sheldrick, Program for the refinement of crystal structures, SHELXL-97; University of Göttingen, **1997**. 3468 reflections measured, 12951 unique (R_{int} = 0.0332), which were used in all calculations. GoF (on F^2) = 0.995. The final agreement factors were R_1 = 0.0270 [$I > 2.00\sigma(I)$] and wR_2 = 0.0627 (all). For **2**: $C_{29}H_{55}LuNPSi_2$, M = 679.86, monoclinic, space group $P2_1/c$, a = 15.284(2) Å, b = 10.456(1) Å, c = 21.092(2) Å, $\alpha = \gamma$ = 90°, β = 91.97(2)°, V = 3368.7(7) Å^3, Z = 4, D_{calcd} = 1.340 g cm^{-3}, μ(Mo-K_α) = 3.066 mm^{-1}. Crystal dimensions 0.32 × 0.20 × 0.16 mm. Data were collected at 180(2) K as above. The structure was solved as above. The intensities were corrected for Lorentz polarisation and absorption effects using ABSCOR, a modification of DIFABS (T_{min} = 0.4404, T_{max} = 0.6398). N. Walker, D. Stuart, *Acta Crystallogr., Sect. A* **1983**, *39*, 158–166. 6383 reflections measured, 30805 unique (R_{int} = 0.0549), which were used in all calculations. GoF (on F^2) = 1.038. The final agreement factors were R_1 = 0.0398 [$I > 2.00\sigma(I)$] and wR_2 = 0.1034 (all). CCDC-263440 and -263441 contain the supplementary crystallographic data for this paper. These data can be obtained free of charge from The Cambridge Crystallographic Data Centre via www.ccdc.cam.ac.uk/data_request/cif..

Received: June 14, 2005
Published Online: August 19, 2005

 © 2005 Wiley-VCH Verlag GmbH & Co. KGaA, Weinheim

Self-Assembly of 1-D Coordination Polymers Using Organometallic Linkers and Exhibiting Argentophilic Interactions $Ag^{I}\cdots Ag^{I}$

Jamal Moussa,[a] Kamal Boubekeur,[a] and Hani Amouri*[a]

Keywords: Coordination polymers / Silver / Self-assembly / Quinones / Metal-metal interactions

Treatment of the organometallic linkers [Cp*M(η^4-benzoquinone)] [M = Rh, L^{Rh}, (**1a**); M = Ir, L^{Ir} (**1b**)] with excess AgOTf provided the novel 1-D coordination polymers of the formula $\{[Ag_3(L^M)_2(CH_3CN)_2(OTf)][L^M](OTf)_2\}_n$ (**2a**,**b**). Single-crystal X-ray diffraction studies carried out on **2a** and **2b** showed that these polymers exhibit, as an outstanding feature, the presence of $d^{10}\cdots d^{10}$ argentophilic interactions between the silver atoms.
(© Wiley-VCH Verlag GmbH & Co. KGaA, 69451 Weinheim, Germany, 2005)

The design and self-assembly of coordination frameworks exhibiting original architectures[1] and with potential applications as molecular wires,[2] in catalysis,[3] and ion encapsulation[4] offer exciting new prospects for researchers working in the area of material science.[5] Generally, coordination polymers are formed by self-assembly of organic spacers and transition metal ions of different geometrical structures.[6] In this work, we wish to report the 1-D coordination polymers $\{[Ag_3(L^M)_2(CH_3CN)_2(OTf)][L^M](OTf)_2\}_n$ (**2a**,**b**), based on silver coordination chemistry and using [Cp*M(η^4-benzoquinone)] [M = Rh, L^{Rh} (**1a**); M = Ir, L^{Ir} (**1b**)[7]] as organometallic linkers. Interestingly these coordination polymers **2a**,**b** display, as nodes, three silver ions in close proximity with Ag···Ag contacts of 3.3–3.7 Å (Figure 1).

Prior to this work the self-assembly of 1–3-D networks, was reported using the only known organometallic linker [(η^4-benzoquinone)$Mn(CO)_3$][Na].[8] However, none of these polymers contained silver cations. Thus, our 1-D polymers **2a**,**b** are the first coordination polymers with the neutral organometallic linkers [Cp*M(η^4-benzoquinone)] [M = Rh, L^{Rh} (**1a**); M = Ir, L^{Ir} (**1b**)] to be reported.[7] The current compounds differ completely in coordination and properties than those reported previously.

Treatment of [Cp*M(η^4-benzoquinone)] [M = Rh (**1a**); M = Ir (**1b**)] with excess $AgCF_3SO_3$ in CH_2Cl_2 provided a suspension, the solvent was removed under vacuum and the residue was recrystallized from CH_3CN/Et_2O to give golden crystals of **2a** and off-white crystals of **2b** in good yields (see Exp. Sect.). The spectroscopic data of **2a**,**b** are very similar. Thus, the IR spectra of **2a** and **2b** show the presence of two strong bands at 1266 and 1030 cm^{-1} and at 1267 and 1031 cm^{-1}, respectively, which are assigned to the triflate anions; furthermore, two absorptions are visible at 1593 and 1573 cm^{-1} for **2a** and at 1599 and 1580 cm^{-1} for **2b** which are attributed to the C=O groups of the coordinated benzoquinone. The ^1H NMR spectrum of **2a** recorded in [D_6]acetone shows the presence of two singlets at δ = 3.76 ppm assigned to the diene protons and at δ = 2.05 ppm attributed to the methyl protons of the (η^5-Cp*)Rh moiety, while **2b** shows the presence of a singlet at δ = 5.00 ppm for the diene protons and at δ = 2.06 ppm for the (η^5-Cp*)Ir moiety.

To ascertain the identity of these complexes **2a**,**b**, a single-crystal X-ray diffraction study was undertaken (Figure 2).[9] The structures of **2a** and **2b** show the formation of a 1-D coordination polymer. For example, **2b** consists of trimetallic silver nodes of formula $[Ag_3(L^{Ir})_2(CH_3CN)_2(OTf)]^{2+}$ which are linked through linear η^4-benzoquinone ligand L^{Ir} (**1b**). In this linear coordination polymer the trimetallic silver clusters constitute so-called secondary building units (SBUs) (Figure 1).[5] In each SBU, all silver atoms have tetrahedral configurations, the central silver atom Ag2, lies in a plane of symmetry, is coordinated to a triflate anion and to three quinone oxygen atoms while the other two silver atoms, which are symmetrically related, are linked to three quinone oxygen atoms and coordinated to CH_3CN (Figure 1). The Ag2···Ag1 distance between the central silver atom and the peripheral ones is 3.37 Å, indicative of an interatomic contact (sum of van der Waals radii of silver is 3.44 Å[10]), while the peripheral Ag1···Ag1 distance is 3.71 Å suggesting a weak interaction. Interestingly, the organometallic linker L^{Ir} adopts a boat conformation in **2b** with the quinone carbon atoms bent out of the diene plane while acting as a pentadentate ligand, and connecting five silver atoms such that one quinone oxygen atom is biden-

[a] Laboratoire de Chimie Inorganique et Matériaux Moléculaires, UMR CNRS 7071, Université Pierre et Marie Curie,
4 place Jussieu, case 42, 75252 Paris Cedex 05, France
Fax: +33-1-44273841
E-mail: amouri@ccr.jussieu.fr
Supporting information for this article is available on the WWW under http://www.eurjic.org or from the author.

 © 2005 Wiley-VCH Verlag GmbH & Co. KGaA, Weinheim **DOI: 10.1002/ejic.200500605**

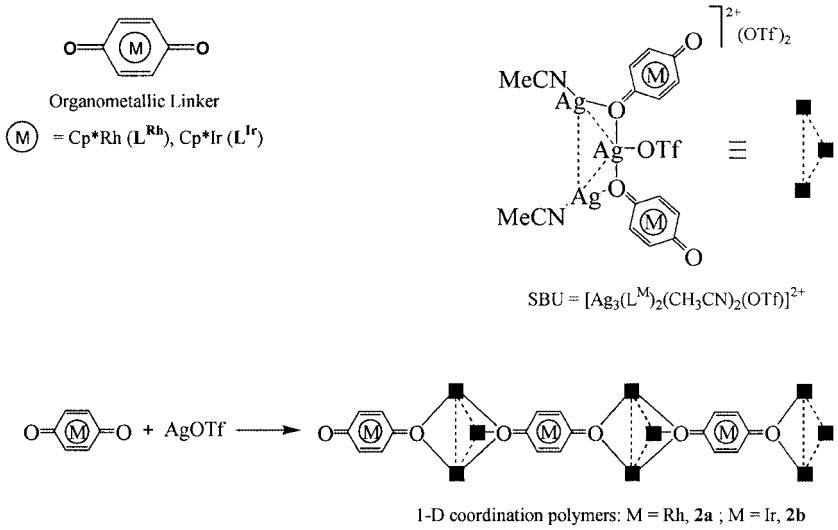

Figure 1. Self-assembly of 1-D polymers **2a**,**b** showing the secondary building units (SBUs) connected by the pentadentate organometallic linkers L^M; M = Rh (**1a**), Ir (**1b**).

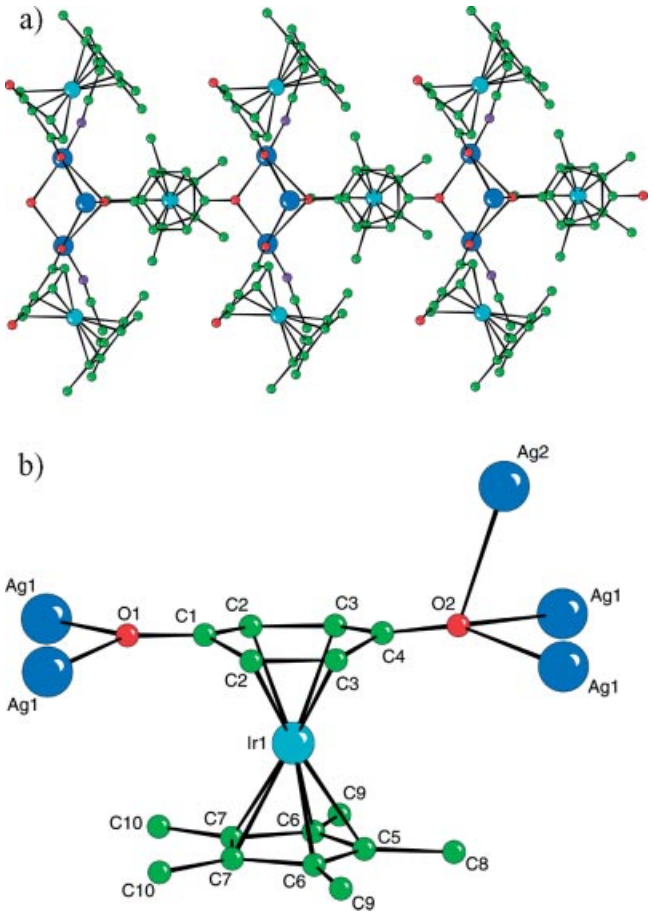

Figure 2. (a) X-ray structure of the 1-D polymer $\{[Ag_3(L^{Ir})_2(CH_3CN)_2(OTf)][L^{Ir}](OTf)_2\}_n$ (**2b**), the triflate anions are omitted for clarity. (b) View of the coordination environment of the pentadentate organometallic linker L^{Ir} in **2b**. Selected bond lengths [Å]: C1–O1 1.293(9), C4–O2 1.281(9), O1–Ag1 2.297(3), O2–Ag1 2.560(4), O2–Ag2 2.508(7), Ir1–C1 2.377(7), Ir1–C2 2.216(5), Ir1–C3 2.220(5), Ir1–C4 2.407(7).

tate (hinge angle θ = 11.85°) and the other one tridentate (hinge angle θ = 11.72°). Such coordination mode has not been reported before (Figure 2b).

Thus, each SBU is connected to the adjacent SBU via a bidentate quinone oxygen atom from one side and through a tridentate quinone oxygen atom from the opposite side, describing a unique architecture for the 1-D coordination polymers $\{[Ag_3(L^M)_2(CH_3CN)_2(OTf)][L^M](OTf)_2\}_n$ (**2a**,**b**).

Discrete trimetallic Ag^I complexes with $d^{10}\cdots d^{10}$ Ag···Ag interactions with luminescent properties continue to generate much interest.[11] The short metal–metal contacts found in these complexes are believed to play a dominant role in excited-state properties.[12] Thus, we intend in the near future to study the photophysical properties of our 1-D polymers **2a**,**b**.

In summary, we have reported a novel class of supramolecular coordination polymers with organometallic linkers exhibiting short argentophilic Ag···Ag interactions. These results illustrate successfully the role of the organometallic ligand linkers L^M (M = Rh, Ir) to produce a novel class of supramolecular species when combined with different metal ions of different geometries. The photoluminescence properties of our coordination polymers will be reported in due course.

Experimental Section

General: All experimental manipulations were carried out under argon using standard Schlenk tube techniques. ^{1}H NMR spectra were recorded with a Bruker AM 300 MHz. IR spectra were recorded as KBr discs with a bio-rad FT-IR spectrometer FTS 165. All solvents were distilled according standard procedures prior to use.

2a: To a suspension of AgOTf (51 mg, 0.2 mmol) in CH_2Cl_2 (15 mL) was added an orange solution of **1a** (35 mg, 0.1 mmol) in CH_2Cl_2 (15 mL). The suspension turned yellow immediately and a solid formed; this mixture was stirred at room temperature for 1 h

 © 2005 Wiley-VCH Verlag GmbH & Co. KGaA, Weinheim

and then the solvent was removed under vacuum, affording a yellow powder which was dried under vacuum and recrystallized by slow diffusion of diethyl ether into a CH_3CN solution to give golden crystals (yield 36 mg, 55%). This compound was identified as $\{[Ag_3(L^{Rh})_2(CH_3CN)_2(OTf)][L^{Rh}](OTf)_2\}_n$. ^1H NMR [300 MHz, $(CD_3)_2CO$]: δ = 2.05 (s, 15 H, Cp*), 3.76 (s, 4 H, benzoquinone) ppm. IR (KBr disc): $\tilde{\nu}$ = 1593, 1572 [ν(C=O)]; 1266 [ν(S–O)]; 1030 [ν(C–F)] cm^{-1}.

2b: To a suspension of AgOTf (80 mg, 0.3 mmol) in CH_2Cl_2 (15 mL) was added a pale yellow solution of **1b** (47 mg, 0.1 mmol). The suspension turned light brown immediately and a solid formed; this mixture was stirred at room temperature for 16 h and then the solvent was removed under vacuum, providing a brown powder which was dried under vacuum and recrystallized by slow diffusion of diethyl ether into a CH_3CN solution to give off-white crystals (yield 45 mg, 60%). This compound was identified as $\{[Ag_3(L^{Ir})_2(CH_3CN)_2(OTf)][L^{Ir}](OTf)_2\}_n$. ^1H NMR (300 MHz, CD_3CN): δ = 2.06 (s, 15 H, Cp*), 5.00 (s, 4 H, benzoquinone) ppm. IR (KBr disc): $\tilde{\nu}$ = 1593, 1572 [ν(C=O)]; 1267 [ν(S–O)]; 1031 [ν(C–F)] cm^{-1}.

Supporting Information: Figures of the coordination polymer **2a**.

Acknowledgments

This work was supported by the CNRS and by the Université Pierre et Marie Curie which we gratefully acknowledge.

[1] a) J.-M. Lehn, *Supramolecular Chemistry, Concept and Perspectives*, VCH, Weinheim, **1995**; b) J. W. Steed, J. L. Atwood, *Supramolecular Chemistry*, Wiley, Chichester, **2000**; c) R. Seidel, P. J. Stang, *Acc. Chem. Res.* **2002**, *35*, 972–983; d) M. Fujita, M. Tominaga, A. Hori, B. Therrien, *Acc. Chem. Res.* **2005**, *38*, 369–378; e) P. D. Custer, J. C. Garrison, C. A. Tessier, W. J. Youngs, *J. Am. Chem. Soc.* **2005**, *127*, 5738–5739.

[2] a) J. A. Ramsden, W. Weng, A. M. Arif, J. A. Gladysz, *J. Am. Chem. Soc.* **1992**, *114*, 5890–5891; b) W. Weng, J. A. Ramsden, A. M. Arif, *J. Am. Chem. Soc.* **1993**, *115*, 3824–3825; c) T. Bartik, W. Weng, J. A. Ramsden, S. Szafert, S. B. Falloon, A. M. Arif, J. A. Gladysz, *J. Am. Chem. Soc.* **1998**, *120*, 11071–11081; d) R. Dembinski, T. Bartik, B. Bartik, M. Jaeger, J. A. Gladysz, *J. Am. Chem. Soc.* **2000**, *122*, 810–822; e) W. Mohr, J. Stahl, F. Hampel, J. A. Gladysz, *Inorg. Chem.* **2001**, *40*, 3263–3264; f) N. Le Narvor, L. Toupet, C. Lapinte, *J. Am. Chem. Soc.* **1995**, *117*, 7129–7138.

[3] a) D. Fiedler, R. G. Bergman, K. N. Raymond, *Angew. Chem.* **2004**, *116*, 6916–6919; *Angew. Chem. Int. Ed.* **2004**, *43*, 6748–6751; b) D. Fiedler, D. H. Leung, R. G. Bergman, K. N. Raymond, *Acc. Chem. Res.* **2005**, *38*, 349–358; M. Fujita, Y. J. Kwon, S. Washizu, K. J. Ogura, *J. Am. Chem. Soc.* **1994**, *116*, 1151–1152.

[4] a) M. Aoyagi, K. Biradha, M. Fujita, *J. Am. Chem. Soc.* **1999**, *121*, 7457–7458; b) A. Tanatani, M. J. Moi, J. S. Moore, *J. Am. Chem. Soc.* **2001**, *123*, 1792–1793; c) K. Biradha, C. Seward, M. J. Zaworotko, *Angew. Chem.* **1999**, *111*, 584–587; *Angew. Chem. Int. Ed.* **1999**, *38*, 492–495.

[5] O. M. Yaghi, M. O'Keeffe, N. W. Ockwig, H. K. Chae, M. Eddaoudi, J. Kim, *Nature* **2003**, *423*, 705–714.

[6] a) L. Raehm, L. Mimassi, C. Guyard-Duhayon, H. Amouri, *Inorg. Chem.* **2003**, *42*, 5654–5659; b) O. Mamula, A. von Zelewsky, T. Bark, G. Bernardinelli, *Angew. Chem.* **1999**, *111*, 3129–3133; *Angew. Chem. Int. Ed.* **1999**, *38*, 2945–2948.

[7] a) J. Le Bras, J. Vaissermann, H. Amouri, *Organometallics* **1998**, *17*, 1116–1121; b) J. Moussa, C. Guyard-Duhayon, P. Herson, H. Amouri, M.-N. Rager, A. Jutand, *Organometallics* **2004**, *23*, 6231–6238.

[8] M. Oh, G. B. Carpenter, D. A. Sweigart, *Acc. Chem. Res.* **2004**, *37*, 1–11 and references cited therein.

[9] Crystal data: **2a**: $C_{48}H_{57}Ag_3O_6Rh_3\cdot(CF_3O_3S)_3\cdot 2(C_2H_3N)$, orthorhombic, $Cmc2_1$, a = 31.820(3), b = 8.5459(8), c = 23.658(2) Å, V = 6433.3(10) $Å^3$, Z = 4, T = 250(2) K, μ = 1.835 mm^{-1}, 18201 reflections measured, 7303 independent (R_{int} = 0.0761), 4555 observed [$I > 2\sigma(I)$], 425 parameters, final R indices R_1 [$I > 2\sigma(I)$] = 0.0649 and wR_2 (all data) = 0.1435, Flack parameter η = –0.03(6), GOF on F^2 = 0.946, max./min. residual electron density = 1.31/–1.57 e·$Å^{-3}$. **2b**: $C_{48}H_{57}Ag_3O_6Ir_3\cdot(CF_3O_3S)_3\cdot 2(C_2H_3N)$, orthorhombic, $Cmc2_1$, a = 31.934(3), b = 8.6198(7), c = 23.842(2) Å, V = 6562.9(10) $Å^3$, Z = 4, T = 250(2) K, μ = 7.121 mm^{-1}, 30911 reflections measured, 9476 independent (R_{int} = 0.0421), 8048 observed [$I > 2\sigma(I)$], 434 parameters, final R indices R_1 [$I > 2\sigma(I)$] = 0.0318 and wR_2 (all data) = 0.0676, Flack parameter η = 0.078(6), GOF on F^2 = 1.007, max./min. residual electron density = 1.09/–1.57 e·$Å^{-3}$. A single crystal of the moisture-sensitive compounds **2a** or **2b** was rapidly selected, mounted onto a glass fiber, and transferred in a cold nitrogen gas stream. Intensity data were collected with a Bruker-Nonius Kappa-CCD with graphite-monochromated Mo-K_α radiation. Unit cell parameters determination, data collection strategy and integration were carried out with the Nonius EVAL-14 suite of programs (A. J. M. Duisenberg, L. M. J. Kroon-Batenburg, A. M. M. Schreurs, *J. Appl. Crystallogr.* **2003**, *36*, 220). The structures were solved by direct methods using the SHELXS-86 program (G. M. Sheldrick, University of Göttingen, **1986**) and refined anisotropically by full-matrix least-squares methods using the SHELXL-97 software package (G. M. Sheldrick, University of Göttingen, Germany, **1997**). CCDC-270623 (**2a**) and -270630 (**2b**) contain the supplementary crystallographic data for this paper. These data can be obtained free of charge from the Cambridge Crystallographic Data Centre via www.ccdc.cam.ac.uk/data_request/cif.

[10] A. Bondi, *J. Phys. Chem.* **1964**, *68*, 441–451.

[11] a) V. J. Catalano, M. A. Malwitz, *Inorg. Chem.* **2003**, *42*, 5483–5485; b) Q.-M. Wang, Y.-A. Lee, O. Crespo, J. Deaton, C. Tang, H. J. Gysling, M. C. Gimeno, C. Larraz, M. D. Villacampa, A. Laguna, R. Eisenberg, *J. Am. Chem. Soc.* **2004**, *126*, 9488–9489.

[12] a) V. W. W. Yam, *Acc. Chem. Res.* **2002**, *35*, 555–563; b) K. M. Lee, H. M. J. Wang, I. J. B. Lin, *J. Chem. Soc., Dalton Trans.* **2002**, 2852–2856; c) C.-M. Che, M.-C. Tse, C. W. Chan, K.-K. Cheung, D. L. Phillips, K.-H. Leung, *J. Am. Chem. Soc.* **2000**, *122*, 2464–2468; d) M. A. Rawashdeh-Omary, M. A. Omary, J. P. Fackler, Jr., *Inorg. Chim. Acta* **2002**, *334*, 376–384; e) M. A. Omary, T. R. Webb, Z. Assefa, G. E. Shankle, H. H. Patterson, *Inorg. Chem.* **1998**, *37*, 1380–1386.

Received: May 18, 2005
Published Online: August 24, 2005

 © 2005 Wiley-VCH Verlag GmbH & Co. KGaA, Weinheim

An Unprecedented One-Dimensional Chain Constructed from β-Octamolybdate Clusters and Two Kinds of Silver Complex Fragments

Zhenyu Shi,[a] Xiaojun Gu,[a] Jun Peng,*[a] and Zhifeng Xin[a]

Keywords: Chainlike compound / Hydrothermal synthesis / Octamolybdate cluster / Ag complex

An unprecedented one-dimensional chainlike compound with green fluorescent emission, $(H_3O)[Ag_3(2,2'\text{-bpy})_2(phnz)_2(\beta\text{-}Mo_8O_{26})]$ (bpy = bipyridine, phnz = phenazine) has been synthesized under hydrothermal conditions. The compound is constructed from β-octamolybdate clusters linked through two kinds of silver-ligand subunits, $[Ag(2,2'\text{-bpy})(phnz)]^+$ and $[Ag(phnz)]^+$.

(© Wiley-VCH Verlag GmbH & Co. KGaA, 69451 Weinheim, Germany, 2005)

Introduction

The significant contemporary interest in the crystal engineering of inorganic-organic hybrid materials not only originates from their diverse structural flexibility, but also from their widely promising potential applications in catalysis, medicine, photochemistry and electromagnetism.[1] Up to now, although a number of inorganic-organic hybrid compounds have been reported,[1f,2] the design and synthesis of novel hybrid materials with highly specific and cooperative functions are still a great challenge. Recently, one synthetic strategy for controlling structure-function relationship has been extensively investigated by choosing suitable building blocks and exploiting the selected or designed organic ligands with the structure-directing properties during the preparation of inorganic-organic hybrid materials, in which the features of the components can be combined to form unique architectures and new properties.[3] An attractive choice of building blocks is polyoxometalate (POM) clusters which, similar to organic ligands, can coordinate to metal centers to construct novel inorganic-organic hybrids.[4] However, among the reported POM-based hybrids, few POM clusters bridged by silver complex fragments have been reported.[5] On the other hand, silver coordination polymers not only are good candidates for potential conducting materials, but also show interesting photophysical and photochemical properties.[6]

As is already known, aromatic chelate ligands such as 2,2′-bipyridine are capable of "passivating" metal sites via the N donors, thus inhibiting expansion of the polymeric frameworks.[7] The polycyclic aromatic bridging ligands such as phenazine with bigger steric hindrance can induce metal ions with flexible coordination spheres to form a complex with a lower coordination number.[1i,8] Therefore, the introduction of two such kinds of organodiamine ligands at a Ag^I site may lead to low-dimensional coordination polymers consisting of π–π stacking interactions and other intermolecular forces which contribute to the physical and chemical behavior of Ag^I complexes.

In this study, we choose 2,2′-bipyridine as a chelate ligand, phenazine as a bridging ligand and Ag^I as the secondary metal, to hydrothermally synthesize a novel one-dimensional chainlike compound with photoluminescence activity, $(H_3O)[Ag_3(2,2'\text{-bpy})_2(phnz)_2(\beta\text{-}Mo_8O_{26})]$ (bpy = bipyridine, phnz = phenazine). The compound represents the first example of octamolybdate clusters bridged by two kinds of organic aromatic amine ligands coordinated to Ag complex fragments.

Results and Discussion

Hydrothermal synthesis has been proved to be a powerful method for the construction of organic-inorganic hybrid materials. Although, in most cases, the reaction mechanisms under hydrothermal conditions are not clear and the control and prediction of crystal structures are difficult, the architecture of the final product directly depends on the interplay of the characteristics of metal ion, ligand, pH values and reaction temperature.[9] In the family of POMs, molybdenum polyoxoanions have received widespread attention owing to their different structures and versatile stoichiometry. It has been documented that the formation of different molybdenum oxoanion subunits can be controlled by the pH values.[3a,10] Generally, mononuclear molybdate $\{MoO_4\}$ exists in basic reaction conditions, while polyoxomolybdate clusters, such as $\{Mo_2O_7\}$, $\{Mo_3O_{10}\}$, $\{Mo_6O_{19}\}$ and $\{Mo_8O_{26}\}$, are most likely isolated under

[a] Institute of Polyoxometalate Chemistry, Department of Chemistry, Northeast Normal University,
Changchun, 130024, P. R. China
E-mail: jpeng@nenu.edu.cn
pjun56@yahoo.com

Supporting information for this article is available on the WWW under http://www.eurjic.org or from the author.

acidic reaction conditions. The β-octamolybdate cluster anion is commonly crystallized from aqueous solutions of molybdate acidified to pH 3–4.

The single-crystal X-ray analysis reveals that the structure of the compound could be described as chains constructed from β-octamolybdates bridged by 2,2′-bipy- and phnz-coordinated Ag^I fragments. As shown in Figure 1, the centrosymmetric octamolybdate $\{Mo_8O_{26}\}$ moiety, which is built up from eight distorted $\{MoO_6\}$ edge-shared octahedrals, is a typical β-octamolybdate. The valence sum calculations show that all molybdenum atoms are in the +6 oxidation state.[11] According to the type of oxygen atoms bonded to the molybdenum atoms, the Mo–O bond lengths are divided into four categories: 1.692(5)–1.706(5) Å for Mo–O(t), 1.754(4)–2.267(4) Å for Mo–O(μ_2), 1.947(4)–2.340(4) Å for Mo–O(μ_3) and 2.135(4)–2.468(4) Å for Mo–O(μ_5) bonds, respectively. All these bond lengths are within the normal ranges and in close agreement with those described in the literature.[4]

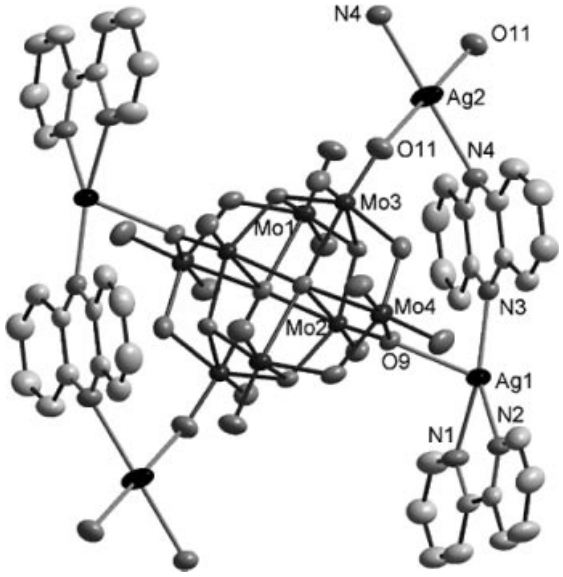

Figure 1. ORTEP drawing of the fundamental building block of the compound with the 50% probability level, showing the coordination environment around Ag and Mo. Only parts of atoms are labeled, and all the hydrogen atoms and water molecules are omitted for clarity.

There are two coordinated dinuclear Ag^I fragments around each β-octamolybdate cluster anion. Two crystallographically independent Ag sites comprise two different distinct environments (see Figure 1). One (Ag1) is coordinated by two nitrogen atoms (N1 and N2) from one 2,2′-bipy ligand, one nitrogen atom (N3) from one phnz ligand, and one bridging oxygen atom (O9) from one β-octamolybdate cluster to complete a trigonal-pyramidal coordination geometry (see Supporting Information, S1a). The atoms N1, N2, N3 and Ag1 nearly lie in the same plane [N3–Ag1–N2 = 144.3(2)°, N2–Ag1–N1 = 71.7(2)°, and N3–Ag1–N1 = 143.2(2)°], while the O9 atom is almost perpendicular to the plane, with the O9–Ag1–N3 angle of 81.5(2)°. The other (Ag2) is coordinated by two nitrogen atoms from two phnz ligands [Ag–N = 2.364(5) Å] and two terminal oxygen atoms from two β-octamolybdate clusters [Ag–O = 2.405(5) Å]. The N4–Ag2–O11 and N4#–Ag2–O11 angles are 82.38(2)° and 97.62(2)°, respectively. The sum of the four N–Ag–O angles is 360.00(4)°, which shows that the Ag(2) site exhibits a distorted square-planar coordination geometry (see Supporting Information, Figure S1b). As is already known, Ag^I generally adopts linear, trigonal, tetrahedral and octahedral coordination geometries, whereas the trigonal-pyramidal and square-planar coordination geometries are less reported. Furthermore, examples of two such kinds of coordination modes existing in the same Ag^I compound have not been documented. The two silver atoms (Ag1 and Ag2) are joined together by one phnz ligand, which acts as a bidentate bridging ligand.

The interesting structural feature of the compound is that β-octamolybdate clusters are linked together by Ag^I fragments through both terminal and bridging oxygen atoms to form a one-dimensional chain (see Figure 2). Interestingly, all the Ag^I ions in the same chain are coplanar. The adjacent one-dimensional chains in the compound are stacked into a two-dimensional supramolecular network (see Figure 3) through offset π–π aromatic stacking interactions with the closest face-to-face distance of ca. 3.40 Å. Protonated water molecules (Ow1) are positioned between the adjacent two-dimensional supramolecular networks and form the hydrogen bonding interactions with the terminal oxygen atoms coming from β-octamolybdate clusters, thus resulting in a three-dimensional supramolecular array (see Supporting Information, Figure S2). The typical hydrogen bonds are as follows: O(6)···Ow(1) 2.892 Å, Ow(1)···O(5) 2.854 Å, Ow(1)···O(8) 2.897 Å, Ow (1)···O(13) 3.001 Å.

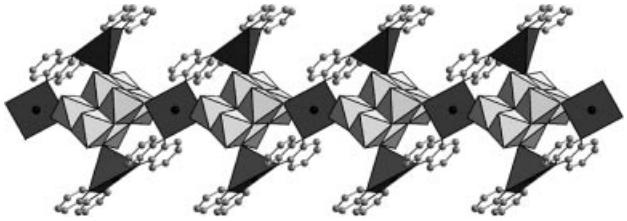

Figure 2. A view of the one-dimensional chain in the compound, all hydrogen atoms and water molecules are omitted for clarity.

Another interesting structural feature is that π–π stacking and Ag^I–π interactions coexist in the compound. To the best of our knowledge, no POM-based Ag^I complexes consisting of π–π stacking and Ag^I–π interactions have been reported. In the compound, the offset face-to-face distance is ca. 3.40 Å. The closest Ag···C contact between adjacent molecules is 3.37(2) Å, which is longer than those found for Ag^I complexes of other polycyclic aromatic compounds (see Figure 4).[6a]

In the infrared spectrum of the compound (as shown in Figure S3), the strong bands at 909, 831, 760, 691, 557 cm^{-1} are attributed to the μ(Mo=O) or μ(Mo–O–Mo) vibrations, while bands in the 1683–1419 cm^{-1} regions can be assigned to characteristic peaks of ligands 2,2′-bipy and phnz.

 © 2005 Wiley-VCH Verlag GmbH & Co. KGaA, Weinheim

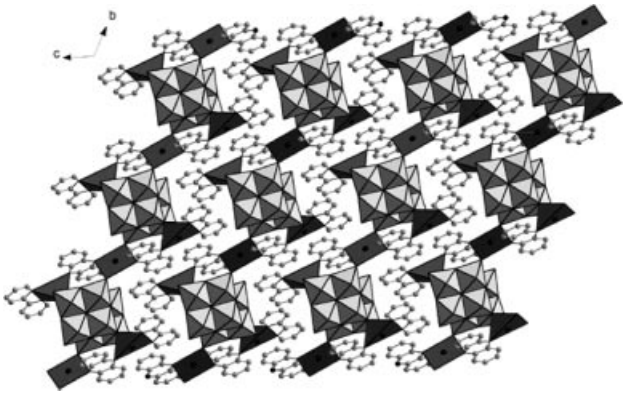

Figure 3. A view of the one-dimensional $\{Ag_3(2,2'\text{-bpy})_2(phnz)_2(\beta\text{-}Mo_8O_{26})\}^-$ chains linked into a two-dimensional layer through supramolecular interactions. All hydrogen atoms are omitted for clarity.

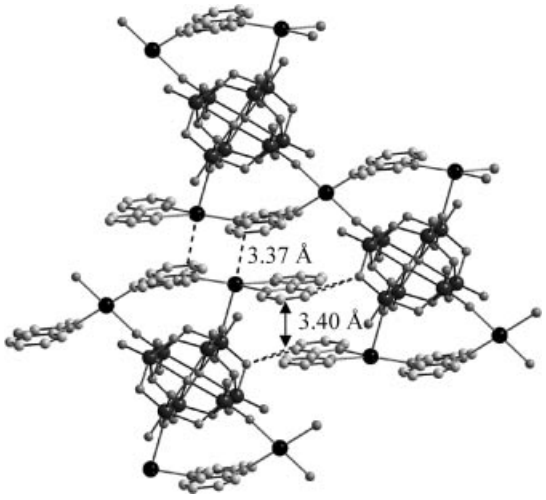

Figure 4. View of the compacted aromatic stacking interactions and significant interactions between the Ag^I ion and aromatic group in the compound.

The thermal gravimetric (TG) curve of the compound exhibits two steps of weight loss in the temperature range 30 to 700 °C (see Figure S4). The first weight loss of 0.63% in the temperature range 40–110 °C corresponds to the release of crystalline water. The second weight loss of 31.08% at 290–430 °C is ascribed to decomposition of organic ligands 2,2′-bipy and phnz. The total weight loss of 31.71% is in good accordance with the calculated value 31.52%.

Generally, Ag^I complexes may emit weak photoluminescence at low temperature.[6b] Whereas, at room temperature the compound in the powdered solid state displays intense photoluminescence with an emission maximum that occurs at 517 nm upon excitation at 420 nm (see Supporting Information, Figure S5). Comparably, the emission bands of the free ligands in the solid state are centered at about 394 nm (λ_{ex} = 330 nm) for 2,2′-bipy and 480, 512 nm (λ_{ex} = 445 nm) for phnz (see Figure S6). It is worth noting that the luminescent properties of the ligands 2,2′-bipy and phnz are very weak, therefore the strong photoluminescence of the compound may originate from the Ag^I–π interactions between Ag^I and the phnz ligand. Since the compound is insoluble in water and common solvents such as ethanol, acetone, acetonitrile and benzene, it may be a good candidate for solvent-resistant green fluorescent material.

In conclusion, a new one-dimensional chainlike compound with green fluorescent emission, constructed from β-octamolybdates linked by two kinds of organic aromatic amine ligands coordinated to Ag^I units, has been successfully synthesized. It represents the first example of POM-based inorganic-organic hybrids in which π–π stacking and Ag^I–π interactions coexist.

Experimental Section

Materials: All reagents and solvents for the syntheses were purchased from commercial and used as received.

Physical Methods: Elemental analyses (C, H, and N) were performed on a PerkinElmer 2400 CHN Elemental Analyzer. Ag and Mo were determined by a Leaman inductively coupled plasma (ICP) spectrometer. IR spectra were obtained on Alpha Centaurt FT/IR spectrometer with KBr pellets in the 400–4000 cm^{-1} region. The TG analyses were performed on a Perkin–Elmer TGA7 instrument in flowing N_2 with a heating rate of 10 °C min^{-1}. Excitation and emission spectra were obtained on a Cary Eclipse.

Synthesis of $(H_3O)[Ag_3(2,2'\text{-bpy})_2(phnz)_2(\beta\text{-}Mo_8O_{26})]$: A mixture of $(NH_4)_6Mo_7O_{24}{\cdot}2H_2O$ (0.4140 g, 0.335 mmol), $AgNO_3$ (0.1138 g, 0.67 mmol), 2,2′-bpy (0.1046 g, 0.67 mmol), phnz (0.0603 g, 0.335 mmol) and H_2O (12 mL) in a mol ratio of 1:2:2:1:2000 was sealed in a Teflon-lined stainless autoclave and heated at 165 °C for 5 days. Yellow crystals of the compound were filtered, washed with water and dried at room temperature. Yield 0.162 g (33% based on silver). Initial pH, 3.8; final pH, 3.3. Elemental analysis for the compound $C_{44}H_{35}Ag_3Mo_8N_8O_{27}$ (2198.91): calcd. C 24.02, H 1.59, N 5.10, Ag 14.73, Mo 34.92; found C 23.96, H 1.46, N 5.18, Ag 14.67, Mo 34.88. IR (KBr): $\tilde{\nu}$ = 3446 (m), 1683 (m), 1558 (m), 1540 (m), 1521 (m), 1490 (m), 1472 (m), 1437 (m), 1419 (m), 909 (m), 831 (w), 760 (w), 691 (m), 557 (w) cm^{-1}.

X-ray Crystallography: Crystal data for the compound was collected on a Rigaku R-AXIS RAPID IP diffractometer, with Mo-K_α-monochromated radiation (λ = 0.71073 Å) at 293 K. An empirical absorption correction was applied.[12] The structure was solved by directed methods and refined by full-matrix least-squares on F^2 using the SHELXTL crystallographic software package.[13] All the non-hydrogen atoms were refined anisotropically. Ow1 was located from difference maps and refined anisotropically, while the hydrogen atoms attached to Ow1 were not located. The positions of hydrogen atoms on carbon atoms were calculated theoretically. Selected bond lengths and angles are listed in Table S1 (see Supporting Information). Crystal data: $C_{44}H_{35}Ag_3Mo_8N_8O_{27}$, triclinic, $P\bar{1}$, M_r = 2198.91 g mol^{-1}, a = 10.132(2) Å, b = 12.106(2) Å, c = 13.283(3) Å, α = 114.43(3)°, β = 107.76(3)°, γ = 90.76(3)°, V = 1394.3(5) $Å^3$, Z = 1, D_c = 2.615 g cm^{-3}, $F(000)$ = 1045, θ range 2.61–27.48°. A total of 9334 reflections were collected and 6204 were independent (R_{int} = 0.0293). The final refinement including hydrogen atoms converged to R = 0.0456, wR = 0.0944, $(\Delta\rho)_{max.}$ = 0.98 e $Å^{-3}$ (0.72 Å from Mo4), $(\Delta\rho)_{min.}$ = –0.98 e $Å^{-3}$ (0.88 Å from Ag2).

CCDC-267510 contains the supplementary crystallographic data for this paper. These data can be obtained free of charge from The Cambridge Crystallographic Data Centre via www.ccdc.cam.ac.uk/data_request/cif.

 © 2005 Wiley-VCH Verlag GmbH & Co. KGaA, Weinheim

Acknowledgments

This research was supported financially by the National Science Foundation of China (20271011).

[1] a) V. Soghomonian, Q. Chen, R. C. Haushalter, J. Zubieta, *Science* **1993**, *259*, 1596–1599; b) O. M. Yaghi, M. O'Keeffe, N. W. Ockwig, H. K. Chae, M. Eddaoudi, J. Kim, *Nature* **2003**, *423*, 705–714; c) P. S. Halasyamani, M. J. Drewitt, D. O'Hare, *Chem. Commun.* **1997**, 867–868; d) Z. Shi, S. H. Feng, S. Gao, L. R. Zhang, G. Y. Yang, J. Hua, *Angew. Chem. Int. Ed.* **2000**, *39*, 2325–2327; e) A. Müller, H. Reuter, S. Dillinger, *Angew. Chem. Int. Ed. Engl.* **1995**, *34*, 2328–2361; f) S. T. Zheng, J. Zhang, G. Y. Yang, *Inorg. Chem.* **2005**, *44*, 2426–2430; g) E. Coronado, C. J. G. Garcia, *Chem. Rev.* **1998**, *98*, 273–296; h) Y. G. Wei, B. B. Xu, C. L. Barnes, Z. H. Peng, *J. Am. Chem. Soc.* **2001**, *123*, 4083–4084; i) A. N. Khlobystov, A. J. Blake, N. R. Champness, D. A. Lemenovskii, A. G. Majouga, N. V. Zyk, M. Schröder, *Coord. Chem. Rev.* **2001**, *222*, 155–192.

[2] a) C. M. Liu, D. Q. Zhang, M. Xiong, D. B. Zhu, *Chem. Commun.* **2002**, 1416–1417; b) J. Y. Niu, D. J. Guo, J. P. Wang, J. W. Zhao, *Cryst. Growth Des.* **2004**, *4*, 241–247; c) L. M. Duan, C. L. Pan, J. Q. Xu, X. B. Cui, F. T. Xie, T. G. Wang, *Eur. J. Inorg. Chem.* **2003**, 2578–2581; d) A. Dolbecq, P. Mialane, L. Lisnard, J. Marrot, F. Sécheresse, *Chem. Eur. J.* **2003**, *9*, 2914–2920.

[3] a) E. Burkholder, V. Golub, C. J. O'Connor, J. Zubieta, *Inorg. Chem.* **2003**, *42*, 6729–6740; b) M. E. Davis, W. B. Lin, *J. Am. Chem. Soc.* **2001**, *123*, 10395–10396.

[4] a) A. Kitamuura, T. Ozeki, A. Yagasaki, *Inorg. Chem.* **1997**, *36*, 4275–4279; b) J. Q. Xu, R. Z. Wang, G. Y. Yang, Y. H. Xing, D. M. Li, W. M. Bu, L. Ye, Y. G. Fan, G. D. Yang, Y. Xing, Y. H. Lin, H. Q. Jia, *Chem. Commun.* **1999**, 983–984; c) D. Hagrman, C. Zubita, D. J. Rose, J. Zubieta, R. C. Haushalter, *Angew. Chem. Int. Ed. Engl.* **1997**, *36*, 873–876; d) C. D. Wu, C. Z. Lu, H. H. Zhuang, J. S. Huang, *Inorg. Chem.* **2002**, *41*, 5636–5637; e) J. Lü, E. H. Shen, Y. G. Li, D. R. Xiao, E. B. Wang, L. Xu, *Cryst. Growth Des.* **2005**, *5*, 65–67; f) D. G. Allis, E. Burkholder, J. Zubieta, *Polyhedron* **2004**, *23*, 1145–1152; g) D. Hagrman, H. D. Hagrman, J. Zubieta, *Inorg. Chim. Acta* **2000**, 212–224.

[5] a) H. Abbas, A. L. Pickering, D. L. Long, P. Kögerler, L. Cronin, *Chem. Eur. J.* **2005**, *11*, 1071–1078; b) S. M. Chen, C. Z. Lu, Y. Q. Yu, Q. Z. Zhang, X. He, *Inorg. Chem. Commun.* **2004**, *7*, 1041–1044; c) E. Burkholder, J. Zubieta, *Solid State Sci.* **2004**, 1421–1428.

[6] a) S. L. Zheng, J. P. Zhang, W. T. Wong, X. M. Chen, *J. Am. Chem. Soc.* **2003**, *125*, 6882–6883; b) M. L. Tong, X. M. Chen, B. H. Ye, L. N. Ji, *Angew. Chem. Int. Ed.* **1999**, *38*, 2237–2240.

[7] Y. G. Li, N. Hao, Y. Lu, E. B. Wang, Z. H. Kang, C. W. Hu, *Inorg. Chem.* **2003**, *42*, 3119–3124.

[8] a) H. Miyasaka, R. Clérac, C. S. Campos-Fernández, K. R. Dunbar, *J. Chem. Soc., Dalton Trans.* **2001**, 858–861; b) A. J. Blake, N. R. Champness, A. N. Khlobystov, D. A. Lemenovskii, W. S. Li, M. Schröder, *Chem. Commun.* **1997**, 1339–1340.

[9] S. O. H. Gutschke, M. Molinier, A. K. Powell, R. E. P. Winpenny, P. T. Wood, *Chem. Commun.* **1996**, 823–824.

[10] C. Z. Lu, C. D. Wu, H. H. Zhuang, J. S. Huang, *Chem. Mater.* **2002**, *14*, 2649–2655.

[11] I. D. Brown, D. Altermatt, *Acta Crystallogr., Sect. B* **1985**, *41*, 244–247.

[12] R. H. Blessing, *Acta Crystallogr., Sect. A* **1995**, *51*, 33–37.

[13] a) G. M. Sheldrick, *SHELXL 97, Program for Crystal Structure Refinement*, University of Göttingen, Germany, **1997**; b) G. M. Sheldrick, *SHELXL 97, Program for Crystal Structure Solution*, University of Göttingen, Germany, **1997**.

Received: April 20, 2005
Published Online: August 29, 2005

 © 2005 Wiley-VCH Verlag GmbH & Co. KGaA, Weinheim

Tuning of Copper(I)–Dioxygen Reactivity by Bis(guanidine) Ligands

Sonja Herres-Pawlis,[a] Ulrich Flörke,[a] and Gerald Henkel*[a]

Dedicated to Professor H. W. Roesky on the occasion of his 70th birthday

Keywords: Bioinorganic chemistry / Copper / Guanidine ligands / Ligand design / O–O activation

A series of bis(guanidine) ligands designed for use in biomimetic coordination chemistry, namely bis(tetramethylguanidino)-, bis(dipiperidinoguanidino)-, and bis(dimethylpropyleno)propane (btmgp, $DPipG_2p$ and $DMPG_2p$, respectively), has been extended to include bis(dimethylethyleneguanidino)propane ($DMEG_2p$), which has both N^{amine} atoms of each guanidine functionality connected by a short ethylene bridge, as a member. From this series, a family of novel bis(guanidine)copper(I) compounds – $[Cu_2(btmgp)_2][PF_6]_2$ (**1**), $[Cu_2(DPipG_2p)_2][PF_6]_2$ (**2**), $[Cu_2(DMPG_2p)_2][PF_6]_2$ (**3**), and $[Cu_2(DMEG_2p)_2][PF_6]_2 \cdot 2MeCN$ (**4**) – has been synthesised. Single-crystal X-ray analysis of **1**–**4** demonstrated that these compounds contain dinuclear complex cations that contain twelve-membered heterocyclic $Cu_2N_4C_6$ rings with the Cu atoms being more than 4 Å apart. Each copper atom is surrounded by a set of two N-donor functions from different ligands, resulting in linear N–Cu–N coordination sites. Depending on their individual substitution patterns, the guanidine moieties deviate from planarity by characteristic propeller-like twists of the amino groups around their $N–C^{imine}$ bonds. The influence of these groups on the reactivity of the corresponding complexes **1**–**4** with dioxygen was investigated at low temperatures by means of UV/Vis spectroscopy. The reaction products can be classified into μ-η^2:η^2-peroxodicopper(II) or bis(μ-oxo)dicopper(III) complex cations that contain the $\{Cu_2O_2\}^{2+}$ core portion as different isomers. The electronic properties of the specific bis(guanidine) ligands are discussed from the viewpoint of their σ-donor and π-acceptor capabilities, and it is shown that μ-η^2:η^2-peroxodicopper(II) complexes are stabilised relative to the bis(μ-oxo)dicopper(III) ones if π conjugation within the guanidine moieties is optimised.
(© Wiley-VCH Verlag GmbH & Co. KGaA, 69451 Weinheim, Germany, 2005)

Introduction

Dioxygen binding in biology is controlled by appropriately designed transition metal active sites. Investigations directed towards an understanding of the mechanisms and a transformation of such processes to technical applications are among the most important research objectives not only in bioinorganic chemistry but also in numerous and diverse arrays of catalytic oxidation reactions.[1–7]

From X-ray structure determinations of the blood dioxygen carrier hemocyanin (for example in arthropods and molluscs)[7,8] it is known that the protein active sites consist of μ-η^2:η^2-peroxodicopper(II) units where each copper ion binds three supporting exogenic N-donor functions originating from histidine imidazole groups. Spectroscopic comparisons suggest that this binding mode occurs also in tyrosinases (phenol → *o*-quinone)[9] and catechol oxidases (*o*-catechol → *o*-quinone).[10,11] $Cu–O_2$ (1:1) adducts are suggested to be involved in the activities of dopamine β-hydroxylase,[12] peptidylglycine α-hydroxylating monooxygenase[1b] and amine oxidases,[12,13] and units containing three copper atoms are found in multicopper oxidases (MCOs) that reduce O_2 to water.[9a]

An understanding of the nature of these reactive intermediates is essential in order to use their principles in coordination chemistry directed towards catalytic applications. Considerable progress towards this aim has been attained through examination of the dioxygen reactivity of synthetic Cu^I complexes, which has resulted in the characterisation of a variety of systems containing μ-η^2:η^2-peroxodicopper(II), bis(μ-oxo)dicopper(III) and bis(μ_3-oxo)tricopper(III,II,II) complex topologies (Figure 1).

A key research objective has been to understand how supporting ligand structural features influence the relative stabilities and interconversions of these species, and especially the effects that control the equilibrium between the P- and O-core that are relevant to proposed metalloprotein active-site intermediates. It has been shown that both units can be supported by neutral, multidentate N-donor ligands and that ligand structural elements (e.g., size of substituents, donor type, bite angle, denticity) play a critical role in determining which units form and how they react.[1,2]

[a] Fakultät für Naturwissenschaften, Department Chemie, Universität Paderborn,
Warburger Strasse 100, 33098 Paderborn, Germany
Fax: +49-5251-603-423
E-mail: biohenkel@uni-paderborn.de
Supporting information for this article is available on the WWW under http://www.eurjic.org or from the author.

 DOI: 10.1002/ejic.200400822 © 2005 Wiley-VCH Verlag GmbH & Co. KGaA, Weinheim

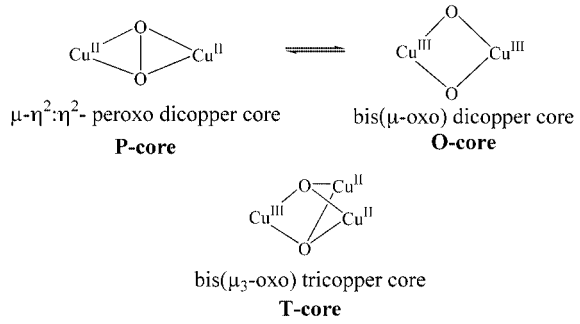

Figure 1. Topologies of Cu/O_2 species where each Cu atom is bonded to both O atoms simultaneously.

The majority of model complexes that imitate the native system make use of tridentate N-donor ligands for copper complexation. These ligands are able to stabilise the Cu_2O_2 core portion by forming square-pyramidal CuO_2N_3 coordination sites with more weakly bonded axial N-donor functions.[3,14,15] However, model complexes that mimic tyrosinase activity are not necessarily dependent on these facial-capping ligands. As has been shown by Stack et al., bidentate N-donor ligands are also capable of forming complexes containing the heterocyclic Cu_2O_2 core portion.[4,16,17] The associated square-planar CuO_2N_2 coordination sites are expected to be more accessible for external substrates that may act as targets for catalytic oxygenation reactions.[18–20] Following this approach, peralkylated diamine ligands have been used to stabilise either the bis(μ-oxo)dicopper(III) (O-core complexes) or the μ-η^2:η^2-peroxodicopper(II) core portion (P-core complexes) depending on the type of substituents.[2a] These systems exhibit tyrosinase-like reactivity as they insert oxygen into C–H bonds. Although the O-core has yet not been detected in enzymatic systems, its relevance for hydroxylation activity seems likely because the equilibria between P- and O-core states proven for model complexes have to be taken into account.[3,16,21–23]

In our search for bifunctional N-donor ligands able to stabilise unusually high metal oxidation states we extended our interest towards guanidine-type systems. Following this approach, bis(tetramethylguanidino)propane (btmgp) was synthesised as the first member of a series of bifunctional peralkylated guanidine ligands designed for use in biomimetic coordination chemistry.[24–26] Attempts to modify the guanidine moieties resulted in the successful preparation of the novel derivatives bis(dimethylpropyleneguanidino)propane ($DMPG_2p$), bis(dipiperidylguanidino)propane ($DPipG_2p$) and bis(dimethylethyleneguanidino)propane ($DMEG_2p$) (Figure 2).[27a,27c]

In this paper we describe a series of dinuclear copper(I) complexes containing these ligands and their reaction behaviour towards molecular oxygen. Depending on the residues attached to the guanidine systems, the resulting Cu_2O_2 species are either bis(μ-oxo)dicopper(III) or μ-η^2:η^2-peroxodicopper(II) complexes.

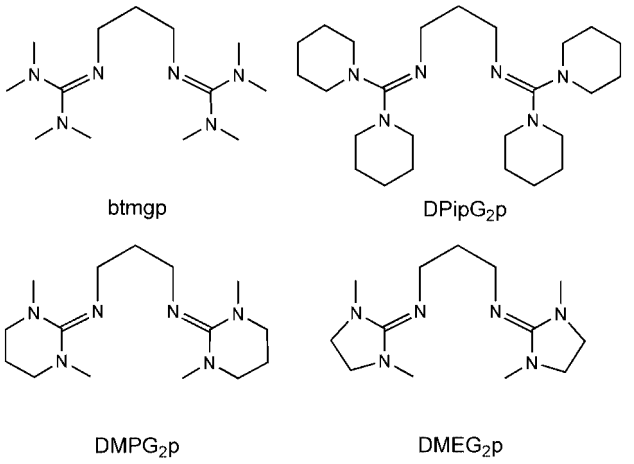

Figure 2. Guanidine-based bifunctional N-donor ligands.

Results and Discussion

Synthesis of the Ligands

The synthesis of the ligands was accomplished according to a general procedure that allows the condensation of almost every urea with an amine to form a guanidine compound via the corresponding Vilsmeier salt.[27b] The Vilsmeier salt is obtained in good yield by reaction of the substituted urea with phosgene in toluene or acetonitrile (Scheme 1).

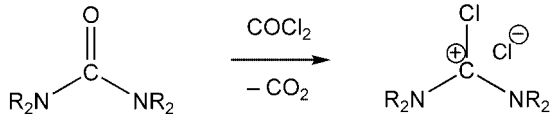

Scheme 1. Generation of the Vilsmeier salts.

The reaction of the Vilsmeier salt with propylene-1,3-diamine, in the presence of triethylamine as an auxiliary base, leads to the corresponding guanidine after deprotonation of the initially formed hydrochloride (Scheme 2). Separation from the by-product Et_3NHCl is accomplished by adding 1 equiv. of NaOH per guanidine functionality and removing the resulting NEt_3 and solvent under reduced pressure. The hydrochloride is not isolated but deprotonated in a two-phase system of MeCN/50% aqueous KOH in order to obtain the pure free base, which needs no further purification.

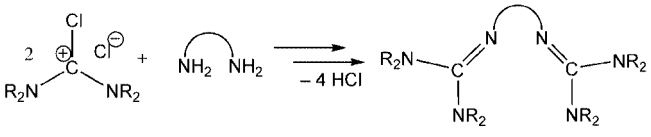

Scheme 2. Reaction between the Vilsmeier salt and the bis(amine).

Synthesis of the Copper Complexes

The complexes were synthesised in good yields by combining $[Cu(MeCN)_4][PF_6]$ with 1.05 equiv. of the bis(guani-

 © 2005 Wiley-VCH Verlag GmbH & Co. KGaA, Weinheim

dine) ligand in dry acetonitrile and stirring for 30 min (Scheme 3). The resulting complex salts **1**–**4** are soluble in polar aprotic media such as MeCN, CH_2Cl_2 and THF, but insoluble in diethyl ether and hydrocarbons.

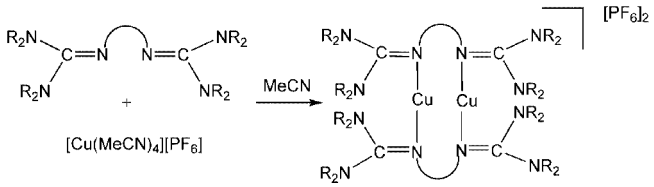

Scheme 3. Complexation of $[Cu(MeCN)_4][PF_6]$ with bis(guanidine) ligands.

All compounds are extremely sensitive to air and moisture due to the high proton affinity of guanidines, which is caused by delocalisation of the positive charge in the guanidine moiety.

Crystal Structures

Single crystals of compounds **1**–**4** suitable for X-ray crystallography were grown by slow diffusion of diisopropyl ether into acetonitrile solutions. The results of the structural analyses are shown in Figures 3, 4, 5, and 6, respectively, while selected bond lengths and angles are collected in Table 1; parameters relating to the data collection and refinement can be found in the Experimental Section.

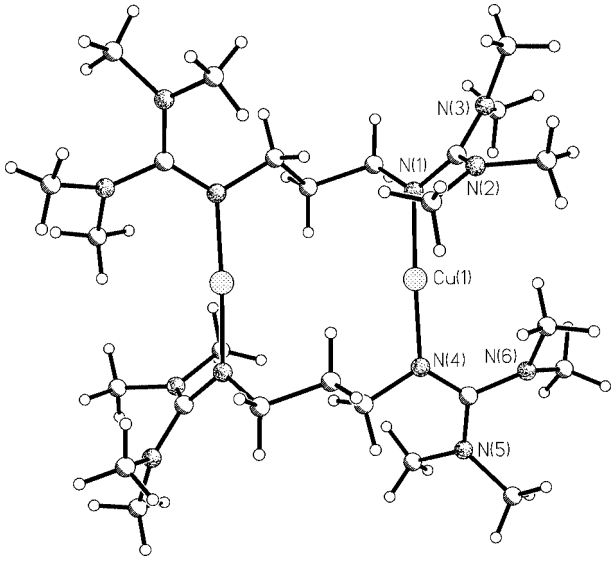

Figure 3. Structure of the $[Cu_2(btmgp)_2]^{2+}$ moiety in crystals of **1**.

The dinuclear complex cations present in all four compounds exhibit molecular ring structures with significant differences in the folding of their propylene chains and in their corresponding interligand H···H separations passing through the centroids of the molecules. The copper centres show almost linear twofold coordination from two N-donor atoms of different ligands with N–Cu–N angles of 176.66(9), 176.77(15), 177.15(6), and 175.29(9)° for **1**–**4**, respectively. The centroids of the molecules lie on crystallographic inversion centres, resulting in perfectly planar

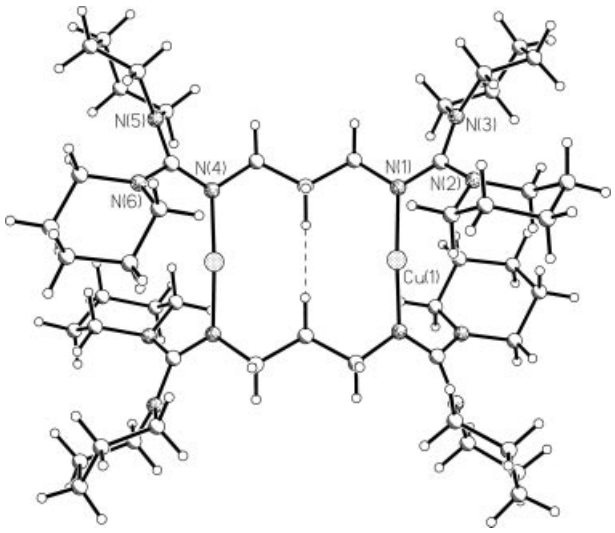

Figure 4. Structure of the $[Cu_2(DPipG_2p)_2]^{2+}$ moiety in crystals of **2**.

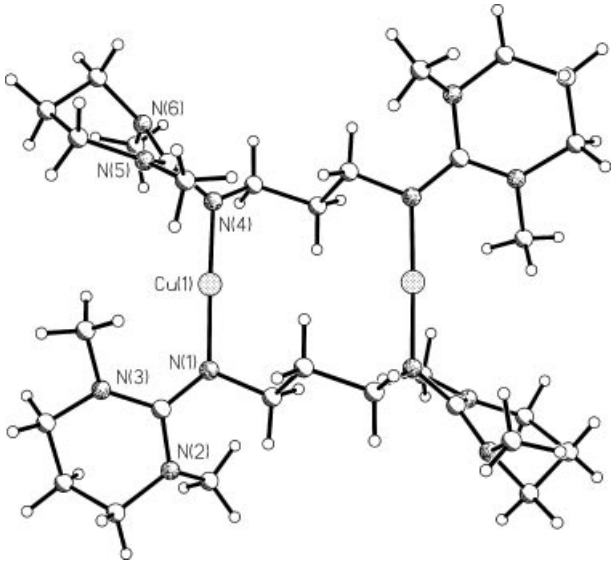

Figure 5. Structure of the $[Cu_2(DMPG_2p)_2]^{2+}$ moiety in crystals of **3**.

Cu_2N_4 moieties. The corresponding Cu–N, N=C, N–C and propyl-bridge C–C distances vary only very slightly from **1** to **4** and are almost identical (averaged values in the order from **1** to **4**): Cu–N: 1.877, 1.866, 1.869, 1.875 Å; N=C: 1.319, 1.309, 1.324, 1.314 Å; C–N(guanidine): 1.358, 1.364, 1.357, 1.359 Å; N–C(propyl): 1.474, 1.471, 1.474, 1.474 Å; C–C(propyl): 1.523, 1.513, 1.523, 1.517 Å. The Cu–N–C and N–C–C ring angles vary slightly in a non-systematic manner, the C–C–C angles are 111.6(2)°, 115.6(3)°, 112.4(1)° and 112.7(2)° for **1**–**4**. These differences may be traced back to variations in the Cu···Cu separations [4.121(1), 4.723(1), 4.358(1), and 4.488(1) Å, respectively]. In **1**, the $N=C(N)_2$ planes of the guanidine moieties are nearly perpendicular to each other with a dihedral angle of 86.3°. For **3**, **2**, and **4** these angles decrease to 80.0°, 71.5° and 68.4°, respectively.

 © 2005 Wiley-VCH Verlag GmbH & Co. KGaA, Weinheim

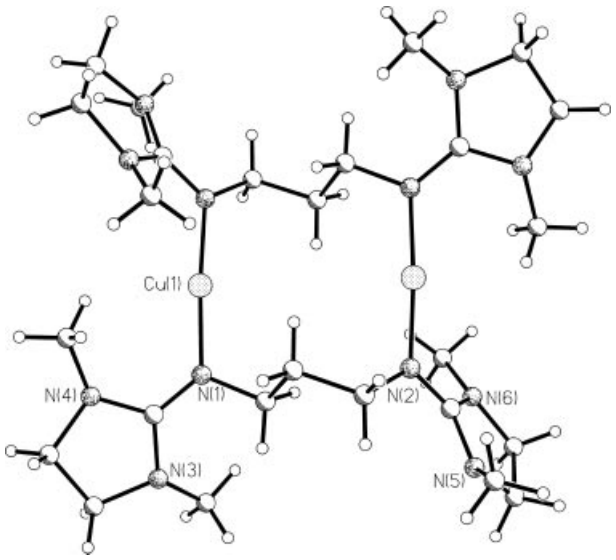

Figure 6. Structure of the $[Cu_2(DMEG_2p)_2]^{2+}$ moiety in crystals of **4**.

Table 1. Selected distances and angles of the complex cations in crystals of **1**–**4**.

Distances [Å]	1	2	3	4
Cu···Cu	4.121(1)	4.723(1)	4.358(1)	4.488(1)
Cu–N^{imine}	1.876(2)	1.876(3)	1.872(1)	1.878(2)
	1.878(2)	1.856(3)	1.867(1)	1.873(2)
N=C	1.323(3)	1.320(5)	1.323(2)	1.310(3)
	1.315(3)	1.297(4)	1.325(2)	1.318(3)
H···H[a]	3.37	2.30	3.26	3.00
Angles [°]				
N^{imine}–Cu–N^{imine}	176.7(1)	176.8(1)	177.2(1)	175.3(1)
N^{amine}–C–N^{amine}	116.0(2)	114.7(4)	117.5(1)	110.0(2)
	116.8(2)	116.0(4)	117.6(1)	110.9(2)

[a] Shortest H···H contact between parallel propylene spacer groups; the H–H vector passes through the centroid of the corresponding complex cation.

Compared with the free ligands $DMPG_2p$ and $DPipG_2p$,[27a] the C=N bonds in **2** and **3** are clearly elongated by about 0.04 Å, whereas the remaining geometric ring parameters show no relevant influence from copper complexation. The $N=C(N)_2$ planes in these ligands show dihedral angles of 23.1 and 31.5°.

Compared with the complexes **1**–**3** (116.4, 115.4, and 117.6°, respectively), the N^{amine}–C–N^{amine} angle in **4** is diminished to 110.5° as the short ethylene linker in the $DMEG_2p$ ligand introduces steric strain.

Table 2 summarises the dihedral angles between the CN_3 guanidine plane and the C^{imine}–N^{amine}–$(C^{alkyl})_2$ planes within the guanidine moieties in the crystalline free bases and in the solid complex salts. It is assumed that the deviation of an individual angle from the mean value mainly reflects packing forces of the crystals. In solution, however, these angles are not subjected to anisotropic interactions with the solvent. For that reason, the following discussion is based on the assumption that the mean angle found in the crystalline state comes close to the situation in solution.

Table 2. Dihedral angles [°] between the CN_3 guanidine plane and the C^{imine}–N^{amine}–$(C^{alkyl})_2$ planes (mean values and ranges of individuals).

Compound	Angle [°]
btmgp	n/a
$DPipG_2p$	40.7 [39.2–42.7]
$DMPG_2p$	25.9 [19.7–31.8]
$DMEG_2p$	n/a
$[Cu_2(btmgp)_2][PF_6]_2$ (**1**)	34.1 [32.3–35.9]
$[Cu_2(DPipG_2p)_2][PF_6]_2$ (**2**)	37.6 [32.2–43.2]
$[Cu_2(DMPG_2p)_2][PF_6]_2$ (**3**)	24.8 [16.7–33.5]
$[Cu_2(DMEG_2p)_2][PF_6]_2$ (**4**)	17.4 [12.7–23.1]

UV/Vis Spectra

Upon reaction of **1** and **2** with O_2, intensive LMCT absorption bands at 300 (ε = 15600) and 390 nm (ε = 17200 $M^{-1}cm^{-1}$) are observed which are characteristic for all O-core complexes known so far (Figure 7).[28a] These species are unstable even at –80 °C in dichloromethane. The initial red solutions change to bluish-green upon warming up to room temperature within 1–2 h.

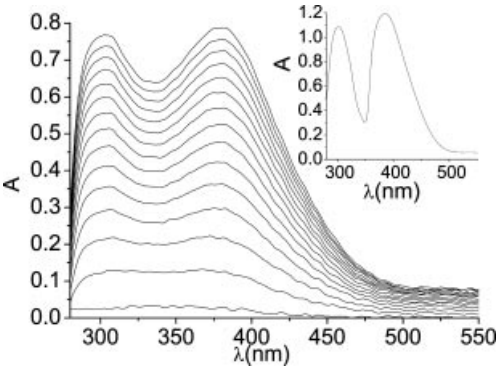

Figure 7. Time-dependent UV/Vis absorption spectra (every 2 min) observed upon introduction of O_2 gas into a CH_2Cl_2 solution of **2** (0.25 mM, –80 °C) during 30 min; inset: spectrum after 2 h (0.33 mM).

Compound **3** reacts with O_2 in dichloromethane with predominant formation of a P-core complex which can be identified by LMCT absorptions at 350 (ε = 21200) and at 550 nm (ε = 900 $M^{-1}cm^{-1}$). The band at about 300 nm (ε = 13500 $M^{-1}cm^{-1}$) originates from O-core components that are formed concomitantly with the P-core (Figure 8). The O-core absorption at 390 nm is not resolved.

In contrast, reaction of **3** with O_2 in acetonitrile at –40 °C results in the immediate formation of an O-core complex, as shown by the UV/Vis absorption bands at 290 (ε = 13000) and 390 nm (ε = 15800 $M^{-1}cm^{-1}$; Figure 9). With MeCN as solvent, the equilibrium between P- and O-core is shifted almost completely to the O-core side. These results show that coordinating solvents are better suited to stabilise the O-core than non-coordinating ones, and thus confirm the reports of other groups.[1a,2,3a]

Treatment of a 0.2 mM solution of **4** in CH_2Cl_2 with dioxygen at –80 °C resulted in a green colour of the solution. At higher concentrations, the solution turns dark brown. The UV/Vis spectrum observed 1 h after introduction of

 © 2005 Wiley-VCH Verlag GmbH & Co. KGaA, Weinheim

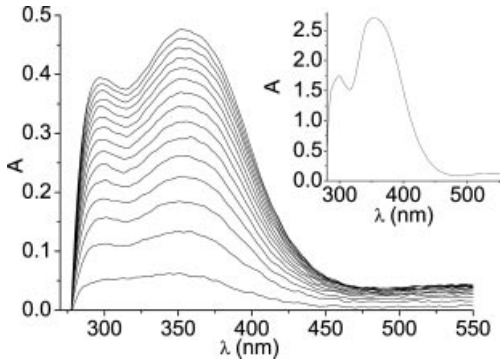

Figure 8. Time-dependent UV/Vis absorption spectra (every 2 min) observed upon introduction of O_2 gas into a CH_2Cl_2 solution of **3** (0.2 mM, –80 °C) during 30 min; inset: spectrum after 2 h (0.5 mM).

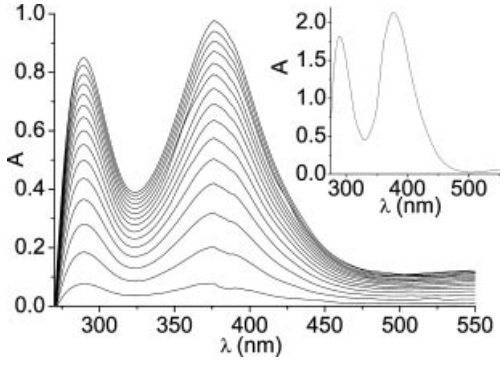

Figure 9. Time-dependent UV/Vis absorption spectra (every 30 s) observed upon introduction of O_2 gas into an MeCN solution of **3** (0.25 mM, –40 °C) during 8 min; inset: spectrum after 1 h (0.5 mM).

molecular oxygen is shown in Figure 10. The spectrum is dominated by a strong absorption band at 355 nm (ε = 17000 $M^{-1}cm^{-1}$) indicative of the predominant formation of the P-core complex. The shoulder at 320 nm (ε = 9500 $M^{-1}cm^{-1}$) is assigned to the formation of O-core contributors.

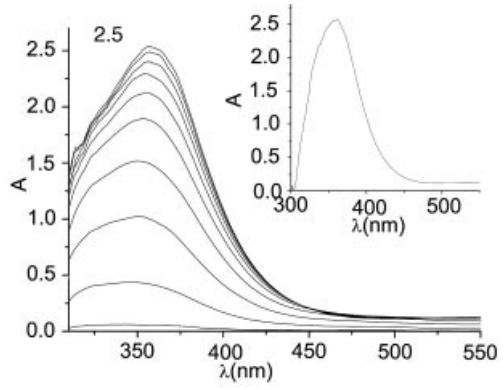

Figure 10. Time-dependent UV/Vis absorption spectrum (every 2 min) observed upon introduction of O_2 gas into a solution of **4** in MeCN/CH_2Cl_2 (1:10) (0.5 mM, –80 °C) during 30 min, inset: spectrum after 1 h (0.25 mM).

Kinetic Aspects

The increase in the absorption bands during the reaction of **1**–**3** with dioxygen in excess obeys first-order kinetics (Figure 11). Moreover, the same first-order rate constants were obtained for reactions starting from different concentrations of **3** in CH_2Cl_2. This observation indicates that the reaction of the copper(I) complexes with oxygen is first-order with respect to the copper complex but of zero-order with respect to O_2 if it is used in excess. The activation parameters ($\Delta H^{\ddagger}$ and $\Delta S^{\ddagger}$) for the formation of the O-core complexes of **1** and **2** and the P-core complex of **3** were determined from the temperature dependence of k (–40 to –80 °C). The first-order rate constants (k) determined at –80 °C and the activation parameters for the formation of the copper–dioxygen species are summarised in Table 3. The kinetic data given below are in accordance with comparable systems reported in the literature, which exhibit small activation enthalpies and very negative activation entropies.[22,23] A small activation enthalpy is indicative of the high driving force for the reaction of a copper(I) complex with dioxygen, whereas a negative activation entropy is the result of a reaction where two molecules are combined to form a new one.

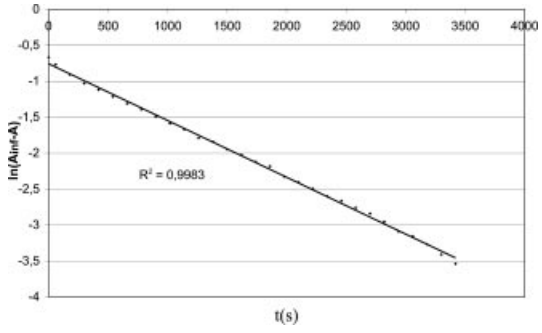

Figure 11. First-order plot based on the absorption change at 350 nm (P-core) for the reaction of **3** at –80 °C with O_2.

Table 3. Kinetic data for the formation of copper–dioxygen species (first-order kinetics).[28b]

Compound	k_1 [s^{-1}]	$\Delta H^{\ddagger}$ [kJ mol^{-1}]	$\Delta S^{\ddagger}$ [J mol^{-1} K^{-1}]
$[Cu_2(btmgp)_2][PF_6]_2$ (**1**)	$1.6(1)\times10^{-1}$	9(1)	–210(5)
$[Cu_2(DPipG_2p)_2][PF_6]_2$ (**2**)	$6.3(3)\times10^{-5}$	42(1)	–104(3)
$[Cu_2(DMPG_2p)_2][PF_6]_2$ (**3**)	$7.9(3)\times10^{-4}$	12(1)	–230(2)

In comparison with **1** and **3**, complex **2** shows a higher activation enthalpy and a smaller negative activation entropy, which can be traced back to the steric demands of the piperidyl units.

Electrochemistry

The copper(I) complexes **1**–**4** were also investigated cyclovoltammetrically to determine their redox activities. In the course of these measurements, irreversible oxidation waves at about –0.2 V attributable to the oxidation of Cu^{I} to Cu^{II} are observed for all the complexes (Table 4). This behaviour is not surprising as the initially linear coordination of Cu^{I} requires subsequent rearrangement processes on changing the oxidation state of copper.

 © 2005 Wiley-VCH Verlag GmbH & Co. KGaA, Weinheim

Table 4. Cyclovoltammetric data (MeCN/TBAP, 2 mm glassy carbon/NHE, v = 100 mV s^{-1}, 25 °C).

Copper complex (+1/+2)	E_{ox} [V]
$[Cu_2(btmgp)_2][PF_6]_2$ (**1**)	–0.18
$[Cu_2(DPipG_2p)_2][PF_6]_2$ (**2**)	–0.29
$[Cu_2(DMPG_2p)_2][PF_6]_2$ (**3**)	–0.21
$[Cu_2(DMEG_2p)_2][PF_6]_2$ (**4**)	–0.23

Interestingly, no correlation between the oxidation potentials of the copper(I) complexes **1**–**4** and their abilities to stabilise P- or O-core complexes could be found.

Mechanism of the Reaction with Oxygen

The observed reaction with molecular oxygen has to be associated with a rearrangement of the bis(guanidine) ligands because the target area of this reaction is affected by significant H···H interactions between protons belonging to adjacent propylene spacers. This interaction is shown by the dashed line in Figure 4 (complex cation **2**). The corresponding ligand conformation represents the maximum stretch of the propylene spacer, which leads to a maximum intraligand N···N separation of 4.821 Å. On going to shorter N···N separations, as realised in the complex cations **1**, **3** and **4**, the propylene chain folds up and allows longer H···H contacts, as can be seen from Table 1 and Figures 3, 5 and 6, respectively. This would principally facilitate potential oxygen insertion, but is in contradiction with the requirements of the resulting $N_2Cu_2O_2N_2$ moiety, which demands intraligand N···N distances of at least 5.5 Å.[27c] Thus, the situation under discussion does not allow any insertion of oxygen into this region without rearrangement of the ligands.

Based on the kinetic data, we propose the following mechanism for the reaction with molecular oxygen (Scheme 4): the Cu^I precursor (complex **a**) reacts in a sequence of first-order reactions with an excess of dioxygen to form the P-core complex. The oxygen uptake within step **A** is rate-determining. In the cases of **1** and **2**, the P-core complexes are less stable than their O-core counterparts, so that the reaction proceeds immediately via step **B**. In the case of **3**, the P-core complex is more stable, and its formation was investigated kinetically.

Reaction step **A** also includes the rearrangement of the bis(guanidine) moieties from nonchelating ligands into chelating ones. The corresponding reaction path is currently under investigation.

σ-Donor and π-Acceptor Capabilities of the Ligands

In order to explain the reaction behaviour of the copper(I) complexes with molecular oxygen, we have to look at the special coordination properties of the guanidine ligands described above. The dihedral angles within the guanidine moieties are decisive for the discussion of these coordination properties (vide supra). Depending on the residues attached to the guanidine systems, the resulting Cu_2O_2 species

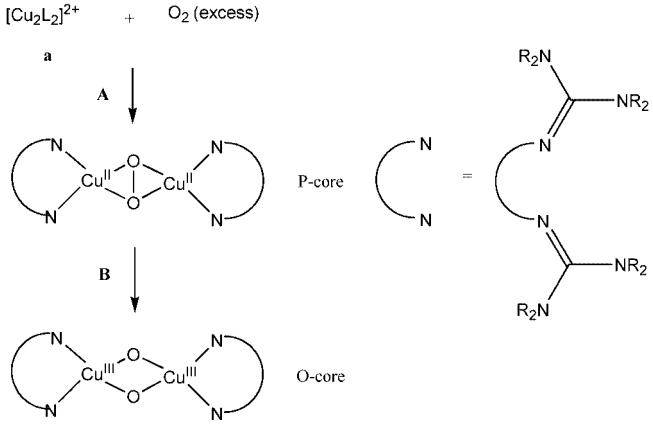

Scheme 4. Proposed mechanism of the reaction of **1**–**4** with dioxygen.

are either bis(μ-oxo)dicopper(III) or μ-η^2:η^2-peroxodicopper(II) complexes, or mixtures of both. The direction in which the equilibrium is driven depends on the degree of planarisation of the guanidine moieties. Within a guanidine residue, the observed structure is predominantly the result of an interplay of two major driving forces, one of them determined by electronic and the other by steric interactions.

Both types of interaction are competing against each other: as the p-orbitals of the peripheral $N^{amine}C_3$ portions search for reasonably good π-interactions with the central CN_3 unit, this prerequisite demands one common plane containing all the involved C and N atoms. On the other hand, the spatial demands of the substituents at the amine nitrogen atoms require propeller-like twists of the NC_3 portions around their N–C^{imine} bonds, which thus prevents a coplanar arrangement with the central CN_3 group. Furthermore, we observed pyramidalisation tendencies of the peripheral $N^{amine}C_3$ portions, which are amplified if both N atoms are part of a heterocyclic ring, as in $DMPG_2p$ and $DMEG_2p$. The degree of pyramidalisation depends on the steric strain in the heterocycle but has no influence on the coordination properties.

It turned out that the result of the interplay between electronic (π-p conjugation) and steric forces (repulsion of the substituents, Figure 12) is decisive for the equilibrium between the bis(μ-oxo)- and the μ-η^2:η^2-peroxodicopper core. Small dihedral angles between adjacent $N^{amine}C_3$ and CN_3 units, indicative of a good conjugation of the π-orbitals in the guanidine moiety, favour the μ-η^2:η^2-peroxodicopper core, whereas moderately larger ones induce a shift of the equilibrium towards the formation of the bis(μ-oxo)dicopper state.

A bonding description of the P-core has been developed by a detailed correlation of spectral features, structural parameters and theoretical calculations by Solomon et al.[9] Furthermore, it is reported that strictly σ-donating ligands should be better suited to stabilise O-core complexes, whereas ligands with π-acceptor properties should favour the formation of their P-core counterparts.[2a,3a]

 © 2005 Wiley-VCH Verlag GmbH & Co. KGaA, Weinheim

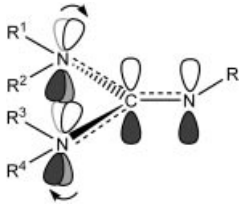

Figure 12. Competition of p-π conjugation and steric repulsion within the guanidine centre; arrows indicate twist from ideal conjugation (pale grey).

The bonding situation comprising a bis(guanidine) ligand attached to the $\{Cu_2O_2\}^{2+}$ core portion is illustrated in Scheme 5. In an attempt to elucidate the principal factors that control the P-core/O-core equilibrium, we correlated the degree of conjugation within the guanidine moiety with the reaction behaviour of the corresponding copper(I) complex towards oxygen. This correlation applies to bis(guanidine) ligands with propylene backbones. In the σ-plane (Scheme 5, left), the interaction of the σ-lobes of the coordinating imine nitrogen atoms with the Cu^{II} $d_{x^2-y^2}$ orbital is denoted. Orthogonally to the σ-plane, the empty π*-orbitals (Scheme 5, right) of the guanidine moieties, representing the LUMO, possess the correct symmetry to accept electron density from the filled d_{xz} and d_{yz} orbitals of Cu^{II}. In the next step, electron density from the peroxide π_v*-orbital can now be transferred into the partially depleted d_{xz} and d_{yz} orbitals of Cu^{II}. At this stage, the degree of p-π conjugation within the guanidine system is of interest. Enhanced p-π overlap lowers the energy of the LUMO of the guanidine residue and makes it more accessible for π-back-donation. In consequence, small modifications of the ligand geometries that change the guanidine conjugation are suited to influence the equilibrium between P- and O-core complex states. In the ligands $DMPG_2p$ and $DMEG_2p$, the alkylene linkers tie the amine nitrogen atoms together and the average guanidine dihedral angles are therefore very small (vide supra). The guanidine conjugation is thus enhanced. However, in btmgp and $DPipG_2p$ the NR_2 moieties are twisted around their N^{amine}–C^{imine} bonds, and the guanidine conjugation is hindered. For that reason, the LUMO is raised in energy, and back-donation is diminished. Now, the σ-donating effect of the imine nitrogen atoms dominates the coordination and the O-core is stabilised.

Conclusions

The novel dipod ligand bis(dimethylethyleneguanidino)-propane ($DMEG_2p$) has been synthesised for use in biomimetic coordination chemistry. $DMEG_2p$ belongs to a new class of bis(guanidine) ligands whose Cu^I complexes are well suited to activate molecular oxygen. Due to their ability to delocalise the positive charge over the guanidine moiety, these ligands are able to stabilise high metal oxidation states, which are established in a variety of copper complexes containing the $\{Cu_2O_2\}^{2+}$ core portion. The analysis of the bonding situation comprising this site attached to a bis(guanidine) residue reveals that the coordination properties of the imine N-donor atoms depend on the substitution pattern within the guanidine moieties. Thus, it is possible to influence the reactivity of the bis(guanidine)copper(I) complexes towards molecular oxygen directly by introducing appropriately designed substituents. Sterically demanding alkyl groups raise the energy of the LUMO, which has the appropriate symmetry to accept electrons from the $\{Cu_2O_2\}^{2+}$ core portion and thus destabilise the P-core state within these complexes. On the other hand, integrating both amine groups of a guanidine residue into a five- or six-membered ring favours the P-core over the O-core state by strengthening the π-conjugation within the ligand and thus lowering the energy of the LUMO. Based on these interrelations between steric features of the ligands and the electron distribution within the $\{Cu_2O_2\}^{2+}$ core portions of dinuclear Cu_2O_2 complexes, new insights into the mechanism of dioxygen activation are provided and strategies towards ligand modification can be developed which are directed towards tailored reaction systems capable of hydroxylating substrates in pre-defined positions.

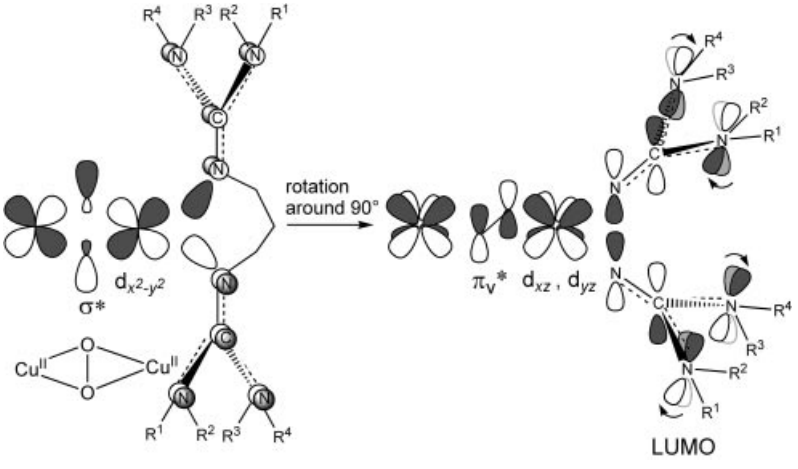

Scheme 5. Bonding situation comprising a bis(guanidine) ligand attached to the $\{Cu_2O_2\}^{2+}$ core portion.

 © 2005 Wiley-VCH Verlag GmbH & Co. KGaA, Weinheim

Experimental Section

General Remarks: All manipulations were performed under pure dinitrogen (99.996%) dried with P_4O_{10} using Schlenk techniques or a glovebox and with absolute solvents. Solvents were purified according to literature procedures and also kept under nitrogen. Triethylamine and 1,3-diaminopropane were used as purchased from Fluka. $[Cu(MeCN)_4][PF_6]$, the Vilsmeier salts and the ligands btmgp, $DMPG_2p$ and $DPipG_2p$ were prepared according to literature procedures.[24,27]

Physical Measurements: Spectra were recorded with the following spectrometers: NMR: Bruker AMX 300 and Avance 500, respectively. IR: Nicolet P510. UV: Perkin–Elmer Lambda 45 in combination with the Hellma UV/Vis low-temperature fibre optic interface (1-cm path length cell), excess O_2, Lauda RL 6 CP cryostat. Copper(I) solutions were transferred into the UV low-temperature cell with a steel capillary under argon pressure. MS (EI, 70 eV): Saturn 2. The elemental analysis for $DMEG_2p$ was performed with a Perkin–Elmer 2400 analysator. Microanalyses for **1**–**4** were performed at the Mikroanalytisches Labor, Ilse Beetz, Kronach, Germany. Cyclic voltammetry (CV) was performed with the electrochemical device Metrohm E 505 equipped with a potentiostat Model VersaStat by EG&G in combination with the PC program Electrochemical Analysis Software 3.0 Model 250 by EG&G. The electrochemical cell was operated under argon, with glassy carbon, glassy carbon and saturated Ag/AgCl serving as working, counter and reference electrodes, respectively. CV curves were obtained at scan rates of 100 mV s^{-1} at 25 °C in MeCN/0.1 M nBu$_4$NPF$_6$. As the complexes are extremely air-sensitive, the copper(I) solutions were transferred into the CV cell with a steel capillary under argon pressure.

Caution! Phosgene is a severe toxic agent that can cause pulmonary embolism and, in the case of prolonged exposure, may be lethal. Use only in a well-ventilated fume hood.

Chloro-*N*,*N*′-bis(1-piperidyl)formamidinium Chloride: According to a literature procedure,[27b] phosgene was passed at 0 °C through a solution of Bis(1-piperidyl) ketone (Aldrich, 12.5 g, 63.8 mmol) in dry MeCN (200 mL) for 30 min. The reaction mixture was stirred at room temperature for 6 h and at 40 °C for another 36 h. After the mixture had cooled down to room temperature, the solvent was evaporated under reduced pressure in order to obtain the product as colourless, slowly crystallising oil. Yield: ca.70% (112 g, 44.7 mmol).

Chloro-*N*,*N*′-ethylene-*N*,*N*′-dimethylformamidinium Chloride: Phosgene was passed at 0 °C through a solution of 1,3-dimethyl-2-imidazolidinone (Fluka, 68.5 g, 600 mmol) in dry toluene (300 mL) for 50 min. The reaction mixture was stirred at room temperature for 2 h and at 40 °C for another 12 h. After the mixture had cooled down to room temperature, the white precipitate formed was collected by filtration, washed three times with dry diethyl ether, and dried in vacuo. Yield: 95% (96 g, 570 mmol).

***N*,*N*′-Bis(1,3-dimethylimidazolidin-2-ylidene)propane-1,3-diamine [Bis(dimethylethyleneguanidino)propane, $DMEG_2p$]:** A solution of chloro-*N*,*N*′-ethylene-*N*,*N*′-dimethylformamidinium chloride (6.76 g, 40 mmol) in dry MeCN (80 mL) was added dropwise, with vigorous stirring, to an ice-cooled solution of 1,3-diaminopropane (1.48 g, 20 mmol) and triethylamine (5.57 mL, 4.04 g, 40 mmol) in dry MeCN (40 mL). After 3 h at reflux, a solution of NaOH (1.6 g, 40 mmol) in water (10 mL) was added. Solvents and Et_3N were then evaporated under vacuum. In order to deprotonate the bis(hydrochloride), 50 wt% KOH (aq., 25 mL) was added and the free base was extracted into the MeCN phase (3 × 25 mL). The organic phase was dried with Na_2SO_4 on charcoal. After filtration through Celite, the solvent was evaporated under reduced pressure. The pure product was obtained as a colourless oil which crystallised after 2 months as needles suitable for X-ray diffraction; yield: 95% (5.05 g, 19 mmol). ^{1}H NMR (500 MHz, $CDCl_3$, 25 °C): δ = 1.57 (m, 2 H, CH_2), 2.60 (s, 12 H, CH_3), 2.95 (br., 8 H, CH_2), 3.26 (t, ^3J = 6.7 Hz, 4 H, CH_2) ppm. ^{13}C NMR (125 MHz, $CDCl_3$, 25 °C): δ = 32.1 (C_a), 36.3 (CH_3), 45.0 (C_b), 49.3 (CH_2), 157.3 (C_{gua}) ppm. IR (film NaCl): $\tilde{\nu}$ = 2931 s, 2831 s, 1660 vs. [ν(C=N)], 1651 vs. [ν(C=N)], 1485 s, 1435 m, 1422 m, 1384 m, 1336 w, 1263 m, 1241 w, 1113 w cm^{-1}. EI-MS: *m*/*z* (%) = 266.2 (39) [M$^+$], 249 (4) [M$^+$ – CH_3], 205 (5), 152 (10), 140 (60) [$CH_2CH_2N{=}CN_2C_4H_{10}^+$], 126 (80) [$CH_2N{=}CN_2C_4H_{10}^+$], 114 (100) [$H_2N{=}CN_2C_4H_{10}^+$], 98 (32), 84 (25), 70 (24). $C_{13}H_{26}N_6$ (266.4): calcd. C 58.61, H 9.84, N 31.55; found C 58.93, H 9.58, N 31.49.

$[Cu_2(btmgp)_2][PF_6]_2$ (1): $[Cu(MeCN)_4][PF_6]$ (372 mg, 1 mmol) was added to a stirred solution of btmgp (284 mg, 1.05 mmol) in MeCN (15 mL). After 30 min of stirring, diethyl ether (20 mL) was added to obtain the colourless product, yield: 90% (430 mg). Crystals suitable for X-ray diffraction were grown by slow diffusion of diethyl ether into an MeCN solution of **1**. ^{1}H NMR (300 MHz, $CDCl_3$, 25 °C): δ = 2.01 (s, MeCN), 2.28 (m, 2 H, H_b), 2.89 (s, 12 H, CH_3), 2.91 (s, 12 H, CH_3), 3.32 (m, 4 H, H_a) ppm. IR (KBr): $\tilde{\nu}$ = 3435 w, 2953 m [ν(CH)], 2931 m [ν(CH)], 2881 m [ν(CH)], 2853 w [ν(CH)], 1564 s [ν(C=N)], 1558 s [ν(C=N)], 1539 s [ν(C=N)], 1477 m [δ(CH)], 1464 m [δ(CH)], 1456 m, 1427 m, 1416 m, 1408 m, 1398 s [ν(C=N)], 1362 m [ν(C=N)], 1337 vw, 1240 w, 1169 m [ν(C=N)], 1161 w, 1123 w, 1070 m [ν(C=N)], 1024 w, 1011 w, 899 w, 876 m, 839 vs, 779 w, 557 m cm^{-1}. UV/Vis (CH_2Cl_2): λ_{max} (ε) = no bands; shoulder at 360 nm (233 M^{-1} cm^{-1}). $C_{26}H_{60}Cu_2F_{12}N_{12}P_2$ (957.9): calcd. C 32.60, H 6.31, N 17.55; found C 32.66, H 6.39, N 17.52.

$[Cu_2(DPipG_2p)_2][PF_6]_2$ (2): $[Cu(MeCN)_4][PF_6]$ (372 mg, 1 mmol) was added to a stirred solution of $DPipG_2p$ (452 mg, 1.05 mmol) in MeCN (15 mL). After 30 min of stirring, diethyl ether (20 mL) was added to obtain the colourless product, yield: 82% (524 mg). Crystals suitable for X-ray diffraction were grown by slow diffusion of diisopropyl ether into an MeCN solution of **2**. ^{1}H NMR (500 MHz, CD_3CN, 25 °C): δ = 1.48–1.58 (m, 24 H, Pip-CH_2), 1.71 (q, ^3J = 7.0 Hz, 2 H, CH_2), 3.05 (t, ^3J = 7.0 Hz, 16 H, Pip-CH_2), 3.55 (t, 4 H, CH_2) ppm. ^{13}C NMR (125 MHz, CD_3CN, 25 °C): δ = 24.0 (Pip), 25.2 (Pip), 25.6 (Pip) 33.8 (C_a), 47.6 (C_b), 49.3 (Pip), 160.2 ($C_{quat.}$) ppm. IR (KBr): $\tilde{\nu}$ = 2934 m, 2852 m, 1626 s [ν(C=N)], 1554 s [ν(C=N)], 1548 s [ν(C=N)], 1491 m [ν(C=N)], 1440 m, 1372 m, 1341 w, 1261 w, 1253 m 1236 w, 1211 w, 1203 w, 1163 m, 1114 w, 1078 m, 1023 m, 1016 w, 985 w, 907 w, 839 vs. [ν(P–F)], 787 m, 705 w, 581 w, 555 m cm^{-1}. $C_{50}H_{92}Cu_2F_{12}N_{12}P_2$ (1278.4): calcd. C 46.98, H 7.25, N 13.15; found C 46.99, H 7.22, N 13.19.

$[Cu_2(DMPG_2p)_2][PF_6]_2$ (3): $[Cu(MeCN)_4][PF_6]$ (372 mg, 1 mmol) was added to a stirred solution of $DMPG_2p$ (308.7 mg, 1.05 mmol) in MeCN (15 mL). After 30 min of stirring, diethyl ether (20 mL) was added to obtain the colourless product, yield: 86% (433 mg). Crystals suitable for X-ray diffraction were grown by slow diffusion of diisopropyl ether into an MeCN solution of **3**. ^{1}H NMR (500 MHz, CD_3CN, 25 °C): δ = 1.62 (m, 2 H, CH_2), 1.71 (m, 4 H, CH_2), 2.95 (s, 12 H, CH_3), 3.15 (m, 8 H, CH_2) ppm. ^{13}C NMR (125 MHz, CD_3CN, 25 °C): δ = 22.3 (CH_2), 34.8 (C_a), 40.1 (CH_3), 46.3 (C_b), 49.7 (CH_2), 160.6 ($C_{quat.}$) ppm. IR (KBr): $\tilde{\nu}$ = 2953 s, 2919 s, 2864 s, 2831 m, 1564 vs. [ν(C=N)], 1552 vs. [ν(C=N)], 1537 vs. [ν(C=N)], 1473 s, 1453 s, 1419 s, 1403 vs. [ν(C=N)], 1376 s, 1354 s, 1325 s, 1313 s, 1272 w, 1236 s, 1206 w, 1162 w, 1113 w, 1084 m, 1050 m, 1014 m, 837 vs. [ν(P–F)], 769 s, 557 s, 511 m cm^{-1}.

 © 2005 Wiley-VCH Verlag GmbH & Co. KGaA, Weinheim

Table 5. Crystal data for compounds **1**–**4**.

	1	**2**	**3**	**4**
Empirical formula	$C_{26}H_{60}Cu_2F_{12}N_{12}P_2$	$C_{50}H_{92}Cu_2F_{12}N_{12}P_2$	$C_{30}H_{60}Cu_2F_{12}N_{12}P_2$	$C_{30}H_{58}Cu_2F_{12}N_{14}P_2$
Formula mass	957.88	1278.38	1005.92	1031.92
Crystal size [mm]	0.25×0.20×0.18	0.22×0.15×0.10	0.40×0.40×0.18	0.20×0.12×0.10
Crystal system	monoclinic	monoclinic	triclinic	triclinic
Space group	$P2_1/n$	$C2/c$	$P\bar{1}$	$P\bar{1}$
a [Å]	8.177(1)	30.457(6)	9.577(1)	7.831(1)
b [Å]	15.574(3)	9.139(2)	10.420(1)	11.650(1)
c [Å]	16.218(3)	21.278(4)	10.703(1)	12.474(1)
α [°]	90	90	103.29(1)	78.02(1)
β [°]	96.47(1)	95.38(1)	96.94(1)	81.70(1)
γ [°]	90	90	90.61(1)	81.18(1)
V [Å^3]	2052.3(6)	5896.6(7)	1031.1(6)	1092.5(6)
Z	2	4	1	1
$D_{calcd.}$ [g cm^{-3}]	1.550	1.440	1.620	1.568
μ(Mo-K_α) [mm^{-1}]	1.205	0.859	1.204	1.140
Temperature [K]	150(2)	120(2)	150(2)	120(2)
Data collection range Θ [°]	1.82 to 28.28	1.34 to 28.52	1.97 to 26.37	1.68 to 28.24
h,k,l	–10/9, –19/20, –21/20	± 40, –11/12, –28/22	±11, ±13, ±13	±10, –14/15, ±16
No. of reflections measured	12491	26613	11105	14028
No. of unique data	4731	7392	4181	5385
Parameters	252	354	266	276
R_1 [$I \geq 2\sigma(I)$]	0.046	0.046	0.026	0.044
wR_2 (all data)	0.115	0.079	0.069	0.095
Min/max ΔF [e Å^{-3}]	–0.42/0.91	–0.45/0.40	–0.18/0.34	–0.57/0.74

$C_{30}H_{60}Cu_2F_{12}N_{12}P_2$ (1005.9): calcd. C 35.82, H 6.01, N 16.71; found C 35.64, H 6.07, N 16.58.

$[Cu_2(DMEG_2p)_2][PF_6]_2$·2MeCN (4): $[Cu(MeCN)_4][PF_6]$ (372 mg, 1 mmol) was added to a stirred solution of $DMEG_2p$ (279 mg, 1.05 mmol) in MeCN (15 mL). After 30 min of stirring, diethyl ether (20 mL) was added to obtain the colourless product, yield: 82% (389 mg). Crystals suitable for X-ray diffraction were grown by slow diffusion of diisopropyl ether into an MeCN solution of **4**. ^{1}H NMR (500 MHz, CD_3CN, 25 °C): δ = 1.82 (m, 2 H, CH_2), 3.00 (s, 12 H, CH_3), 3.46 (br., 8 H, CH_2), 3.65 (t, ^3J = 7.1 Hz, 4 H, CH_2) ppm. ^{13}C NMR (125 MHz, CD_3CN, 25 °C): δ = 35.0 (C_a), 35.6 (CH_3), 45.2 (C_b), 49.2 (CH_2), 162.4 (C_{gua}) ppm. IR (KBr): $\tilde{\nu}$ = 2929 s, 2894 s, 1631 s [ν(C=N)], 1601 vs. [ν(C=N)], 1512 m [ν(C=N)], 1490 m, 1459 m, 1419 m, 1400 m, 1345 w, 1300 s, 1232 w, 1208 w, 1121 w, 1076 w, 1034 w, 970 vw, 839 vs. [ν(P–F)], 723 w, 646 w, 557 vs, 484 w cm^{-1}. $C_{26}H_{52}Cu_2F_{12}N_{12}P_2$ (949.8, after removing the solvent in vacuo): calcd. C 32.88, H 5.52, N 17.70; found C 33.19, H 5.28, N 17.93.

Crystal Structure Analyses: Crystal data for compounds **1**–**4** are presented in Table 5. X-ray diffraction data were collected with a Bruker-AXS SMART APEX CCD diffractometer using Mo-K_α radiation (λ = 0.71073 Å). Data reduction and absorption correction were performed with SAINT and SADABS.[29] The structures were solved by direct and conventional Fourier methods and all non-hydrogen atoms refined anisotropically with full-matrix least-squares procedures based on F^2 (SHELXTL[29]). Hydrogen atoms were derived from difference Fourier maps and placed at idealised positions, riding on their parent C atoms, with isotropic displacement parameters U_{iso}(H) = 1.2U_{eq}(C) and 1.5U_{eq}(C methyl). All methyl groups were allowed to rotate but not to tip. Compound **4** contains two MeCN solvent molecules per unit cell. CCDC-273408 (**1**), -273409 (**2**), -273410 (**3**), and -273411 (**4**) contain the supplementary crystallographic data for this paper. These data can be obtained free of charge from The Cambridge Crystallographic Data Centre via www.ccdc.cam.ac.uk/data_request/cif.

Supporting Information Available (see footnote on the first page of this article): Figures S1, S2 and S3 showing Eyring plots for **1**, **2** and **3**, respectively.

Acknowledgments

We gratefully acknowledge the financial support of the Fonds der Chemischen Industrie (FCI), the Deutsche Forschungsgemeinschaft and the Bundesministerium für Bildung und Forschung. S. H.-P. thanks the FCI for a fellowship.

[1] a) E. A. Lewis, W. B. Tolman, *Chem. Rev.* **2004**, *104*, 1047; b) S. T. Prigge, B. A. Eipper, R. E. Mains, L. M. Amzel, *Science* **2004**, *304*, 864; c) E. I. Tocheva, F. I. Rosell, A. G. Mauk, M. E. P. Murphy, *Science* **2004**, *304*, 867.
[2] a) L. M. Mirica, X. Ottenwaelder, T. D. P. Stack, *Chem. Rev.* **2004**, *104*, 1013; b) H.-C. Liang, M. J. Henson, L. Q. Hatcher, M. A. Vance, C. X. Zhang, D. Lahti, S. Kaderli, R. D. Sommer, A. L. Rheingold, A. D. Zuberbühler, E. I. Solomon, K. D. Karlin, *Inorg. Chem.* **2004**, *43*, 4115.
[3] a) L. Que, Jr., W. B. Tolman, *Angew. Chem.* **2002**, *114*, 1160; *Angew. Chem. Int. Ed.* **2002**, *41*, 1114; b) P. L. Holland, W. B. Tolman, *Coord. Chem. Rev.* **1999**, *190–192*, 855.
[4] T. D. P. Stack, *Dalton Trans.* **2003**, 1881.
[5] a) E. I. Solomon, P. Chen, M. Metz, S.-K. Lee, A. E. Palmer, *Angew. Chem.* **2001**, *113*, 4702; *Angew. Chem. Int. Ed.* **2001**, *40*, 4570; b) R. H. Holm, P. Kennepohl, E. I. Solomon, *Chem. Rev.* **1996**, *96*, 2239; c) J. A. Guckert, M. D. Lowery, E. I. Solomon, *J. Am. Chem. Soc.* **1995**, *117*, 2817.
[6] A. G. Blackman, W. B. Tolman, *Struct. Bonding (Berlin)* **2000**, *97*, 179.
[7] a) K. A. Magnus, H. Ton-That, J. E. Carpenter, *Chem. Rev.* **1994**, *94*, 727; b) K. A. Magnus, B. Hazes, H. Ton-That, C. Bonaventura, J. Bonaventura, W. G. L. Hol, *Proteins: Struct. Funct. Genet.* **1994**, *19*, 302.
[8] M. E. Cuff, K. I. Miller, K. E. Vanholde, W. A. Hendrickson, *J. Mol. Biol.* **1998**, *278*, 855.

 © 2005 Wiley-VCH Verlag GmbH & Co. KGaA, Weinheim

[9] a) E. I. Solomon, U. M. Sundaram, T. E. Machonkin, *Chem. Rev.* **1996**, *96*, 2563; b) M. J. Baldwin, D. E. Root, J. E. Pate, K. Fujisawa, N. Kitajima, E. I. Solomon, *J. Am. Chem. Soc.* **1992**, *114*, 10421.
[10] A. Rompel, H. Fischer, D. Meiwes, K. Buldt-Karentzopoulos, R. Dillinger, F. Tuczek, H. Witzel, B. Krebs, *J. Biol. Inorg. Chem.* **1999**, *4*, 56.
[11] a) C. Gerdemann, C. Eicken, B. Krebs, *Acc. Chem. Res.* **2002**, *35*, 183; b) T. Klabunde, C. Eicken, J. C. Sacchettini, B. Krebs, *Nat. Struct. Biol.* **1998**, *5*, 1084.
[12] J. P. Klinman, *Chem. Rev.* **1996**, *96*, 2541.
[13] C. M. Wilmot, J. Hajdu, M. J. McPherson, P. F. Knowles, S. E. V. Phillips, *Science* **1999**, *286*, 1724.
[14] a) N. Kitajima, Y. Moro-oka, *Chem. Rev.* **1994**, *94*, 737; b) N. Kitajima, K. Fujisawa, C. Fujimoto, Y. Moro-oka, S. Hashimoto, T. Kitagawa, K. Toriumi, K. Tatsumi, A. Nakamura, *J. Am. Chem. Soc.* **1992**, *114*, 1277.
[15] K. Fujisawa, M. Tanaka, Y. Moro-oka, N. Kitajima, *J. Am. Chem. Soc.* **1994**, *116*, 12079.
[16] V. Mahadevan, Z. Hou, A. P. Cole, D. E. Root, T. P. Lal, E. I. Solomon, T. D. P. Stack, *J. Am. Chem. Soc.* **1997**, *119*, 11996.
[17] L. M. Mirica, M. Vance, D. Jackson-Rudd, B. Hedman, K. O. Hodgson, E. I. Solomon, T. D. P. Stack, *J. Am. Chem. Soc.* **2002**, *124*, 9332.
[18] a) A. P. Cole, D. E. Root, P. Mukherjee, E. I. Solomon, T. D. P. Stack, *Science* **1996**, *273*, 1848; b) M. Taki, S. Teramae, S. Nagatomo, Y. Tachi, T. Kitagawa, S. Itoh, S. Fukuzumi, *J. Am. Chem. Soc.* **2002**, *124*, 6367.
[19] P. L. Holland, K. R. Rodgers, W. B. Tolman, *Angew. Chem.* **1999**, *111*, 1210; *Angew. Chem. Int. Ed.* **1999**, *38*, 1139.
[20] V. Mahadevan, J. L. DuBois, B. Hedman, K. O. Hodgson, T. D. P. Stack, *J. Am. Chem. Soc.* **1999**, *121*, 5583.
[21] S. Mahapatra, V. G. Young, Jr., S. Kaderli, A. D. Zuberbühler, W. B. Tolman, *Angew. Chem.* **1997**, *109*, 125–127; *Angew. Chem. Int. Ed. Engl.* **1997**, *36*, 130.
[22] S. Itoh, T. Kondo, M. Komatsu, Y. Oshiro, C. Li, N. Kanehisa, Y. Kai, S. Fukuzumi, *J. Am. Chem. Soc.* **1995**, *117*, 4714.
[23] S. Itoh, H. Nakao, L. M. Berreau, T. Kondo, M. Komatsu, S. Fukuzumi, *J. Am. Chem. Soc.* **1998**, *120*, 2890.
[24] a) S. Pohl, M. Harmjanz, J. Schneider, W. Saak, G. Henkel, *J. Chem. Soc., Dalton Trans.* **2000**, 3473; b) S. Pohl, M. Harmjanz, J. Schneider, W. Saak, G. Henkel, *Inorg. Chim. Acta* **2000**, *311*, 106.
[25] S. Herres, A. J. Heuwing, U. Flörke, J. Schneider, G. Henkel, *Inorg. Chim. Acta* **2005**, *358*, 1089.
[26] a) H. Wittmann, A. Schorm, J. Sundermeyer, *Z. Anorg. Allg. Chem.* **2000**, *626*, 1583; b) V. Raab, J. Kipke, O. Burghaus, J. Sundermeyer, *Inorg. Chem.* **2001**, *40*, 6964; c) H. Wittmann, V. Raab, A. Schorm, J. Plackmeyer, J. Sundermeyer, *Eur. J. Inorg. Chem.* **2001**, 1937.
[27] a) S. Herres, U. Flörke, G. Henkel, *Acta Crystallogr., Sect. C* **2004**, *60*, o358; b) W. Kantlehner, E. Haug, W. W. Mergen, P. Speh, T. Maier, J. J. Kapassakalidis, H.-J. Bräuner, H. Hagen, *Liebigs Ann. Chem.* **1984**, *1*, 108; c) S. Herres, U. Flörke, G. Henkel, *Acta Crystallogr., Sect. C* **2004**, *60*, m659.
[28] a) Resonance-Raman spectra are severely affected by fluorescence emission and thus not suited to contribute to the P-core/O-core question. b) The *k* values for **1**–**3** were determined five times for each temperature step of 5 K between 193 K and 233 K. The average *k* values were calculated and plotted in an Eyring plot (see Supporting Information). The temperature deviation was estimated to be 0.2 K.
[29] SAINT (version 6.02), SHELXTL (version 6.10), SADABS (version 2.03), Bruker AXS, Inc., Madison, Wisconsin, USA, **2002**..

Received: September 30, 2004
Published Online: August 31, 2005

 © 2005 Wiley-VCH Verlag GmbH & Co. KGaA, Weinheim

Stable Nickel Catalysts for Fast Norbornene Polymerization: Tuning Reactivity

Juan A. Casares,[a] Pablo Espinet,*[a] José M. Martín-Alvarez,[a] Jesús M. Martínez-Ilarduya,[a] and Gorka Salas[a]

Keywords: Homogeneous catalysis / As ligands / Sb ligands / Nickel / Polymerization / Norbornene / Pentafluorophenyl

The air-stable complexes *trans*-[Ni($C_6Cl_2F_3$)$_2$L$_2$] (L = $SbPh_3$, **1**; $AsPh_3$, **2**; $AsCyPh_2$, **3**; $AsMePh_2$, **4**; PPh_3, **5**) have been synthesized by arylation of [$NiBr_2$(dme)] (dme = 1,2-dimethoxyethane) in the presence of the corresponding ligand L (for compounds **1**–**4**) or by ligand substitution starting from **1** (for compound **5**). The structures of **1**, **2**, and **5** have been determined by X-ray diffraction and show an almost perfect square-planar geometry in all cases. Their catalytic activity in insertion polymerization of norbornene have been tested showing a strong dependence of the yield and molecular mass of the polymer on the ligand used and the solvent. High yield and high molecular mass values are obtained using complexes with ligands easy to displace from Ni^{II} ($SbPh_3$ is the best) and noncoordinating solvents. Complexes **1**–**3** are suggested as convenient bench-catalysts to have available in the lab.
(© Wiley-VCH Verlag GmbH & Co. KGaA, 69451 Weinheim, Germany, 2005)

Introduction

The increasing interest in the polymerization of cyclic olefins is due to the attractive properties of these polymers, which show high glass transition temperatures, high optical transparency, low dielectric constant and low birefringence. Starting from norbornene (bicyclo[2.2.1]hept-2-ene) and norbornene derivatives, different classes of polymers can be obtained by selecting polymerization conditions that drive the reaction by cationic or radical pathways, by ring-opening metathesis, or by insertion routes (Scheme 1).[1]

Cationic polymerization of norbornene results in the formation of low molecular mass polymers with rearranged norbornanediyl units in the backbone (A). Metal catalyzed ring-opening metathesis polymerization (ROMP) of norbornene derivatives yields polymers containing unsaturations in the backbone (B). Metal-catalyzed insertion polymerization of norbornene, either with early transition metallocene complexes or with late transition organometallics can lead to two different structures, one strictly linear containing norbornanediyl units (C), and another in which norbornanediyl and rearranged norbornanediyl with appended norbornanediyl units alternate (D).[1,2]

A number of nickel complexes are very efficient catalysts for the vinyl polymerization of norbornene, for the copolymerization of functionalized norbornenes, and also for the copolymerization of norbornene with ethene.[1,3–9] Usually the polymerization requires a nickel(II) catalyst and an organometallic co-catalyst [typically methylaluminoxane or

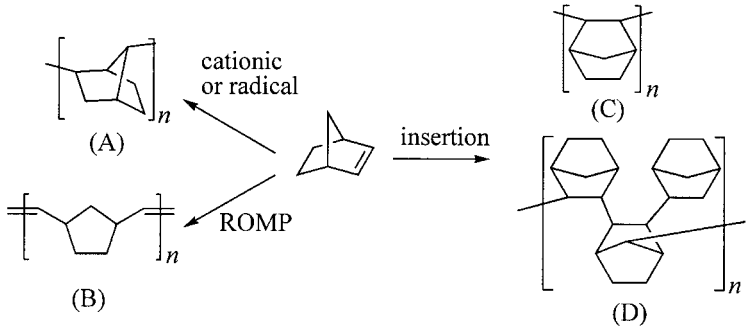

Scheme 1.

$B(C_6F_5)_3$],[1,3,7,8,10] but a few nickel organometallics (cationic allyl complexes such as [Ni(η^3-crotyl)(1,4-COD)]PF_6, some phenyl derivatives, and [Ni(C_6F_5)$_2$(η^6-toluene)]), are very efficient without co-catalyst.[1,8,9] Noteworthy, although the use of monodentate ligands, particularly phos-

[a] Química Inorgánica, Facultad de Ciencias, Universidad de Valladolid,
47005 Valladolid, Spain
E-mail: espinet@qi.uva.es
Supporting information for this article is available on the WWW under http://www.eurjic.org or from the author.

phanes, has been reported in the patent literature,[11] most of the catalysts used are stabilized by multidentate chelating ligands.

In this paper we report the synthesis of complexes *trans*-$[Ni(C_6Cl_2F_3)_2L_2]$ (L = $SbPh_3$, $AsPh_3$, $AsCyPh_2$, $AsMePh_2$, or PPh_3) and their catalytic activity in insertion polymerization of norbornene. In these compounds the monodentate ligands are able to stabilize the complexes allowing their manipulation as solids in the air, but are labile and weak enough to give highly active catalytic systems in solution.

Results and Discussion

Synthesis and Behavior in Solution

The reaction of $[NiBr_2(dme)]$ (dme = 1,2-dimethoxyethane) with $Li(C_6Cl_2F_3)$ and L (molar ratio 1:1:2.2) in diethyl ether affords the yellow air-stable complexes *trans*-$[Ni(C_6Cl_2F_3)_2L_2]$ (L = $SbPh_3$, **1**; $AsPh_3$, **2**; $AsCyPh_2$, **3**; $AsMePh_2$, **4**) (Scheme 2). With PPh_3 this procedure affords *trans*-$[Ni(C_6Cl_2F_3)_2(PPh_3)_2]$ (**5**) along with a number of by-products, not further identified, which lowered the yield. Thus, complex **5** is better prepared by the reaction of **1** with PPh_3 in chloroform (molar ratio 1:2), followed by solvent evaporation, and removal of the displaced ligand $SbPh_3$ with diethyl ether. In fact *trans*-$[Ni(C_6Cl_2F_3)_2(SbPh_3)_2]$ is a fairly general precursor for other $[Ni(C_6Cl_2F_3)_2L_2]$ complexes.

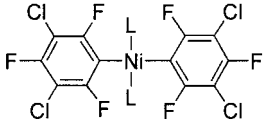

L	Complex
$SbPh_3$	**1**
$AsPh_3$	**2**
$AsCyPh_2$	**3**
$AsMePh_2$	**4**
PPh_3	**5**

Scheme 2.

All the complexes reported in this paper are *trans* isomers. The structures of **1**, **2** and **5** have been determined by X-ray diffraction. They are very similar and only the structure of **5** is shown in Figure 1. Crystallographic data are given in Table 3 (see Experimental Section). Selected interatomic distances and angles are shown in Table 1. The complexes crystallized in the P-1 group with one molecule in the asymmetric unit for compound **5**, and just half a molecule in the asymmetric unit for compounds **1** and **2**. The three compounds are almost perfectly square planar, with angles between adjacent donor atoms very close to 90° and the two haloaryl ligands mutually *trans*. The Ni–C bond lengths are very similar to those found in the two *trans*-bis(pentafluorophenyl)nickel complexes reported to date (1.939 Å in both $[Ni(C_6F_5)_2(PMePh_2)_2]$ and $[Ni(C_6F_5)_2(CNtBu)_2]$).[18,20] The Ni–P distances [2.2467(9) and 2.2544(8) Å] are in the upper limit of the range found in the Cambridge Structural Database for *trans*-bis(triphenylphosphane)nickel complexes (2.220–2.253 Å).[12] The Ni–As and Ni–Sb distances cannot be compared to reference values in the literature because the Ni complexes with $AsPh_3$ or $SbPh_3$ reported (one with each ligand) are not structurally similar.[13,14] The haloaryl rings are almost perpendicular to the coordination plane in the three molecules, with tilting

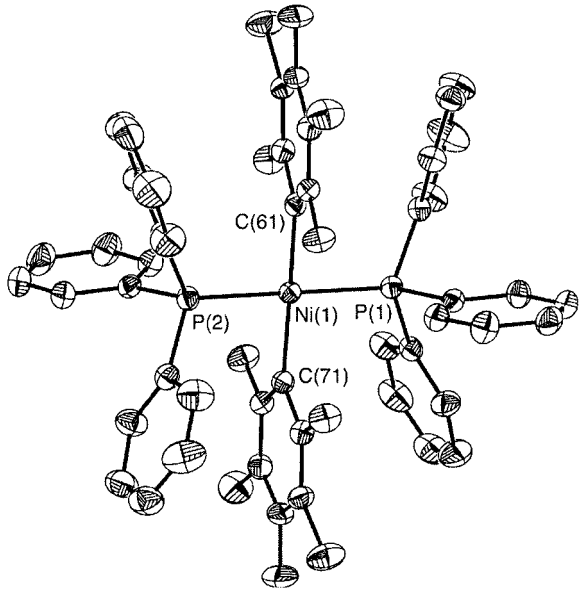

Figure 1. ORTEP diagram of the molecular structure of complex *trans*-$[Ni(C_6Cl_2F_3)_2(PPh_3)_2]$ (**5**). All hydrogen atoms have been omitted for clarity. Atoms are shown as displacement ellipsoids enclosing 30% probability density.

Table 1. Selected bond lengths [Å] and angles [°] for **1**, **2** and **5**.

1		**2**		**5**	
Ni(1)–C(31)	1.926(5)	Ni(1)–C(1)	1.933(3)	Ni(1)–C(61)	1.938(2)
				Ni(1)–C(71)	1.951(2)
Ni(1)–Sb(1)	2.4480(6)	Ni(1)–As(1)	2.3094(7)	Ni(1)–P(2)	2.2467(9)
				Ni(1)–P(1)	2.2544(8)
C(31)–Ni(1)–Sb(1)	88.36(13)	C(1)–Ni(1)–As(1)	90.11(9)	C(61)–Ni(1)–P(1)	91.03(6)
				C(71)–Ni(1)–P(1)	90.45(7)
				C(61)–Ni(1)–P(2)	89.33(7)
				C(71)–Ni(1)–P(2)	89.21(7)

 © 2005 Wiley-VCH Verlag GmbH & Co. KGaA, Weinheim

angles ranging from 83.2(2) to 89.3(2)°. The phosphane ligands are staggered and one phenyl ring on each phosphane is parallel to one haloaryl ring.

The stereochemical preferences of complexes $[Ni(aryl)_2L_2]$ are strongly dependent on the nature of L. Electronically, the *cis* isomers, avoiding *trans* arrangements of substituents with high *trans*-influence, should be preferred, and this is often determinant for Pd and Pt complexes.[15] However, steric factors seem important in the smaller Ni. In fact, structures containing some of the ligands used here have *cis* feature L–Ni–L angles noticeably larger than 90°,[16] indicating steric repulsion between the ligands. This suggests that the preference for the *trans* isomer found here must be largely associated to a minimization of steric repulsions. Related complexes with arylphosphanes also show a preference for *trans* stereochemistry, as found for $[Ni(C_6F_5)_2(PMePh_2)_2]$,[17,18] and $[Ni(4\text{-}C_6BrF_4)_2(PMePh_2)_2]$ in solution ($CDCl_3$ or CD_2Cl_2) and in the solid state.[19] $[Ni(4\text{-}C_6BrF_4)_2(PMePh_2)_2]$ is formed as a mixture of the *cis* and *trans* isomers which slowly converts completely into the most stable *trans* isomer. On the other hand, for complexes involving less sterically demanding ligands, such as $[PPh_3Me][Ni(C_6F_5)_2Br(CO)]$, $[Ni(C_6F_5)_2(CO)_2]$, and $[Ni(C_6F_5)_2(THF)_2]$, only the *cis* isomer is obtained.[20] The NMR spectra of **1**–**5** in $CDCl_3$ show the presence of just one compound in solution. The spectra at room temperature are coincident with those recorded at 213 K on samples dissolved at low temperature, supporting the suggestion that the signals arise from the *trans* isomer present in the solid state.

Complexes **1**–**5** are stable in the solid state and can be stored for long periods, but they decompose slowly in solution in $CDCl_3$ or [D$_6$]acetone at 298 K (in times much larger than the polymerization reactions). The decomposition is faster for **1** than for **2**–**4**, and is very slow for **5**. The major F-containing decomposition product is the coupling compound $C_6Cl_2F_3$–$C_6Cl_2F_3$ (**6**), along with small amounts of $C_6Cl_2F_3H$ (**7**) and other very minor noncharacterized products. A similar decomposition pattern has been reported for related pentafluorophenyl derivatives.[21]

Catalyzed Polymerization of Norbornene

The catalytic reactions were carried out under nitrogen at room temperature. In CH_2Cl_2 the polymerization started in seconds without cocatalysts, producing a white precipitate of polymer. After 30 min the reactions were quenched pouring the reacting mixtures over MeOH. Data concerning the polymers obtained are reported in Table 2. No attempts were made to optimize the yield or M_w of the polymer. Polymerization runs using **1** as a catalyst under air gave the same results.

The ^{13}C NMR spectra of the polynorbornene obtained in these experiments were identical to that reported by Barnes et al. using $[Ni(dpm)_2]/AlEt_3/B(C_6F_5)_3$ (dpm = 2,2,6,6-tetramethyl-3,5-heptanedionate) and (pentafluorophenyl)nickel complexes as catalysts. The absence of resonances in the 20–24 ppm region has been taken as indicative of *exo*-enchained norbornene-based polymers, generated by an insertion mechanism.[9] The ^{19}F NMR spectra in $CDCl_3$ showed mainly three 1:1:1 signals (–112.0, –115.3, –115.5 ppm), together with signals due to the coupling product **6** and smaller signals due to the hydrolysis product **7**, which remain adsorbed to the polymer, and to unidentified products (–105.1, –106.0, –111.9 ppm). Repeated washing with toluene removes the signals of **6** and **7**, but not the other minor signals. The chemical shifts of the 1:1:1 signals are typical of a $C_6Cl_2F_3$ group bonded to a carbon atom and can be assigned to the perhaloaryl group bonded to the polymer. The chemical shift of the $C_6Cl_2F_3$ fluorine nuclei are very sensitive to the group substituents.[22] A similar effect has been observed in the ^{19}F NMR of the pentafluorophenyl group bonded to metal or to carbon atoms.[23] The presence of three signals indicates that the two F_{ortho} atoms are nonequivalent because the rotation of the $C_6Cl_2F_3$ group around the phenyl *ipso*-carbon–norbornene carbon single bond is hindered according to the results reported by Barnes et al.[9] In the case of the $C_6Cl_2F_3$ group the chemical shifts for F_{ortho} and F_{para} do not permit us to assign them unambiguously and an attempt to correlate (hence recognize) the F_{ortho} atoms by spin saturation transfer at 323 K was unsuccessful, revealing that there is no detectable exchange of the two F_{ortho} signals at this temperature. In our compounds we do not see a splitting of any of the F_{ortho} signals, a phenomenon which was reported in the case of C_6F_5 by Barnes et al.[9] This may well be because of the fact that all chemical shift differences are smaller in our system.

Table 2. Norbornene polymerization catalyzed by **1**–**5** (reaction conditions unless otherwise stated: 9.2 mmol of norbornene and 4.6 μmol of catalyst in 3 mL of CH_2Cl_2; reaction time: 30 min).

Entry	Catalyst	Yield [%]	$M_w/10^5$	M_w/M_n
1	**1**	90	12.59	2.4
2	**2**	75	6.06	4.6
3	**3**	72	6.05	4.9
4	**4**	3	2.11	2.1
5	**5**	traces	0.1	
6	**1**[a]	–	–	
7	**1**[b]	17	0.99	
8	**1**[c]	0	–	
9	**1**[d]	18	0.1	

[a] Solvent: acetone. [b] Solvent: acetone; reaction time: 24 h. [c] 5-Norbornene-2-carboxaldehyde instead of norbornene. [d] A 3:1 mixture of norbornene/5-norbornene-2-carboxaldehyde instead of norbornene.

A clear dependence of the yield of the polymer on the ligand in the catalysts is observed: the yield in polymer is high for complexes with $SbPh_3$, $AsPh_3$, and $AsCyPh_2$, but drops dramatically for $AsMePh_2$ and PPh_3. The very high yield and M_W found with complex **1** ($SbPh_3$ as the ligand) are comparable to that found previously for the three component catalyst $[Ni(dpm)_2]/AlEt_3/B(C_6F_5)_3$.[9] The higher stability in the solid state of **1** compared to $[Ni(C_6F_5)_2(\eta^6\text{-toluene})]$, which is air and moisture sensitive, is advantageous. The influence of the ligand on the reaction can be understood assuming that equilibria 1 and 2 govern the

 © 2005 Wiley-VCH Verlag GmbH & Co. KGaA, Weinheim

concentration of the active species in solution. Ligands that are better donors and have less steric requirement shift these equilibria to the left, making the complexes inactive.

$$[Ni(C_6Cl_2F_3)_2L_2] + NB \rightleftharpoons [Ni(C_6Cl_2F_3)_2(NB)L] + L \quad (1)$$

$$[Ni(C_6Cl_2F_3)(P)L_2] + NB \rightleftharpoons [Ni(C_6Cl_2F_3)(P)(NB)L] + L \quad (2)$$

(P = polymer chain)

The effect of the bulkiness of the ligand on the properties of the polymer has been studied by Lipian et al. for cationic allylpalladium(II) complexes with selected phosphanes as the catalyst.[24] For these catalysts the bulkier the phosphane the lower the molecular mass of the polymer, while high conversion is always observed. The opposite trend is observed here comparing complexes **3** (containing $AsCyPh_2$) and **4** (containing $AsMePh_2$). This suggests a different ligand role for both types of catalyst. While no ligand dissociation is required in the palladium complexes employed by Lipian et al. (the bulkier phosphane is simply hindering more norbornene coordination or insertion), in complexes **1**–**5** the displacement of one ligand by the entering norbornene is required to carry out the polymerization process. For similar electronic characteristics displacement of a bulkier ligand $AsCyPh_2$ in equilibria 1 and 2 is favored compared to the displacement of $AsMePh_2$ and this turns out to be the dominant fact. Similarly, the molecular mass of the polymer increases with the same ligands that increase the overall yield of the reaction.

The reaction between **1** and norbornene in CD_2Cl_2 was monitored by ^{19}F NMR (norbornene:**1** = 200:1). No signals of Ni complexes containing $C_6Cl_2F_3$ other than **1** were detected throughout the experiment. This suggests that **1** is a precatalyst, from which the catalyst is formed in a small nonobservable proportion. At low temperature (–60 °C) no reaction takes place at an observable rate. At –10 °C the white polymer starts to precipitate from the solution and very broad $C_6Cl_2F_3$ signals appear corresponding to the ones mentioned earlier. At 0 °C the solution becomes very viscous in a few minutes, giving rise to a broadening of all the signals in the spectrum.

The polymerization of O-functionalyzed norbornenes with Ni catalysts has been reported in the literature, although using a higher catalyst/monomer ratio.[8] Even in these conditions the yield and M_w values are low, and the authors attribute the low reactivity of O-functionalyzed norbornenes in part to the coordinating ability of the oxygen. Examples of the poisoning effect of palladium catalysts due to the coordination of the O-donor groups of functionalyzed norbornenes have been recently reported.[27]

The polymerization of 5-norbornene-2-carboxaldehyde was attempted with **1** as the catalyst, but no reaction was observed after 30 min, in agreement with the observations just discussed. Moreover, 5-norbornene-2-carboxaldehyde inhibits the polymerization in mixtures with norbornene and only a small amount of oligomers is obtained (Table 2, entries 8 and 9). The reaction of 5-norbornene-2-carboxaldehyde with **1** was monitored by ^{19}F NMR spectroscopy. In a 1:1 ratio no reaction takes place. If the ratio of the monomer is increased up to 100:1 no new signals of Ni-bonded $C_6Cl_2F_3$ groups appear, but weak peaks of organic $C_6Cl_2F_3$ arise. Apparently, the aldehyde group is not able to stabilize any Ni intermediate formed after norbornene insertion into the C–Ni bond, nor is the carboxylic group able to displace the $SbPh_3$ ligands coordinated to nickel, at least in a detectable extension. At room temperature the oligomerization of the monomer takes place slowly in the NMR tube, giving very broad signals due to $C_6Cl_2F_3$ bonded to carbon.

Further support of the detrimental effect of the presence of O-donors in norbornene polymerizations, whether intramolecular (O-functionalyzed norbornenes) or external (O-containing solvents) is provided by the results found for polymerization of norbornene in acetone: No polymerization of norbornene was observed after 30 min at 25 °C. Only after 24 h could a small amount of polynorbornene be detected (Table 2, entries 6 and 7). In other words, the catalytic activity is severely reduced, although not completely suppressed, in acetone. The small amount of white polymer precipitated from the acetone solution after 24 h at 25 °C was dissolved in $CDCl_3$ and showed in the ^{19}F NMR spectrum the same signals of $C_6Cl_2F_3$ discussed for the polymers obtained in CH_2Cl_2. However, the M_w of this polymer (Table 2 entry 7) is much lower than the M_w of the polymers obtained in CH_2Cl_2.

^{19}F NMR spectra of solutions of **1** in acetone revealed a complicated equilibrium between four different complexes, arising from partial substitution of $SbPh_3$ by acetone or water, with only 2% remaining as complex **1**.[25] The interpretation of this is that the most active catalyst in solution is complex **1**, which has a lower concentration in an acetone solution than in noncoordinating solvents, hence showing a reduced activity. Moreover, the substitution equilibria 1 and 2, which give rise to the species on which insertion takes place, are now further disfavored by the presence of considerable concentrations of free ligand, displaced from **1** by solvent or water. The rate corresponding to direct catalysis by aquo or acetone complexes is likely to be negligible, given the strong ligation of these O-donor ligands to Ni. This interpretation fits well with the general hypothesis that oxygen donors block the Ni catalyst.[8,24,26,27]

Conclusions

The results show that some *trans* diaryl nickel complexes containing monodentate ligands, stable and easy to store and handle, are very efficient catalysts for norbornene polymerization. There is a strong dependence of the yield and molecular mass of the polymer on the ligand used: yields and M_w's are higher for complexes with $SbPh_3$ (the best), $AsPh_3$, and $AsCyPh_2$, which are ligands easy to displace from Ni^{II}, but ligands more strongly bonded to the metal, such $AsMePh_2$ or PPh_3 (the worst) give less efficient catalysts. The inability of the complexes to polymerize substituted norbornene containing O-donor groups is related to

 © 2005 Wiley-VCH Verlag GmbH & Co. KGaA, Weinheim

the fact that the norbornene olefin bond is not able to displace the O-coordinating ligands even under high concentration conditions. Finally, the use of coordinating O-donor solvents or water is extremely detrimental.

In view of their catalytic activity in norbornene polymerization, their thermal and air stability, and their easy preparation, compounds **1**–**3** are choice reagents to have available.

Experimental Section

General Methods: All reactions were carried out under N_2 except when stated otherwise. Solvents were distilled using standard methods. The starting compound [$NiBr_2$dme],[28] the ligand $AsMePh_2$,[29] and solutions of $LiC_6Cl_2F_3$ were prepared by published methods.[30] Combustion CHN analyses were made with a Perkin–Elmer 2400 CHN microanalyzer. IR spectra were recorded with a Perkin–Elmer FT 1720 X spectrophotometer. Molecular masss of polymer were determined with a Waters SEC system equipped with a refractive index detector, using a three-column bed operating at 40 °C in $CHCl_3$ and calibrated to polystyrene narrow distribution standards. GS-MS data were obtained with a Hewlett–Packard 6890N gas chromatograph mass spectrometer (5973).

NMR spectra: ^{1}H NMR (300.16 MHz), ^{19}F NMR (282.4 MHz), and ^{31}P NMR (121.4 MHz) spectra were recorded with Bruker ARX 300 and AC 300 instruments equipped with a VT-100 variable-temperature probe. Chemical shifts are reported in ppm from $SiMe_4$ (^{1}H), CCl_3F (^{19}F), or H_3PO_4 (85%) (^{31}P) with positive shifts downfield, at ambient probe temperature unless otherwise stated. *J* values are given in Hz. ^{13}C NMR were registered as ^{1}H-^{13}C correlation experiments, which were made with a HMQC sequence with BIRD selection and GARP decoupling during acquisition. Chemical shifts of quaternary carbons are not listed in the experimental data.

Synthesis of $AsBrPh_2$: A solution of $LiAsPh_2$ was prepared from Li (0.557 g, 80.25 mmol), and $AsPh_3$ (9.187 g, 30.00 mmol) in THF (60 mL) as reported in the literature.[31] The solution was filtered with a cannula, cooled to –80 °C and Br_2 (3.1 mL, 60.50 mmol) was added very slowly. The solution was left to warm up to room temperature whilst stirring, whereupon it changed from deep red to orange. Then, solvent was removed and the resulting black residue was treated with CH_2Cl_2 (20 mL) and a saturated solution of NH_4Br in water (40 mL). The organic layer was decanted and the aqueous layer was subsequently extracted with CH_2Cl_2 (2 × 10 mL). Organic layers were dried with anhydrous $MgSO_4$, filtered and the solvent was vacuum evaporated. $AsBrPh_2$ (yellow oil) was obtained from the resulting residue after distillation at 170 °C and 5 mbar. Yield: 4.438 g (48%). $C_{12}H_{10}AsBr$ (309.04): calcd. C 46.64, H 3.26; found C 46.32, H 3.07. ^{1}H NMR ($CDCl_3$, 293 K): δ = 7.67–7.63 (m, 4 H), 7.44–7.40 (m, 6 H) ppm. ^{13}C NMR ($CDCl_3$, 293 K): δ = 134.5, 133.3, 130.8, 129.6 ppm.

Synthesis of $AsCyPh_2$: A solution of MgCyCl in diethyl ether (35 mL) was prepared refluxing Mg (0.509 g, 20.94 mmol) and CyCl (2.0 mL, 16.86 mmol) for 6 h. The mixture was then cooled in an ice bath and a solution of $AsBrPh_2$ (2.321 g, 7.51 mmol) in THF (20 mL) was slowly added dropwise over 15 min. The stirring was maintained for another 30 min. The system was opened to air and acidified water (30 mL) was added. The organic layer was decanted and the aqueous layer was extracted with diethyl ether (3 × 10 mL). The organic solution was dried with anhydrous $MgSO_4$ and filtered and the solvent was vacuum evaporated. $AsCyPh_2$ was obtained as a yellow oil. After one day at –20 °C it became a white crystalline solid. Yield: 1.898 g (81%). $C_{18}H_{21}As$ (312.29): calcd. C 69.23, H 6.78; found C 68.79, H 6.57. ^{1}H NMR ($CDCl_3$, 293 K): δ = 7.50 (m, 4 H, Ph), 7.38–7.31 (m, 6 H, Ph), 2.33 (m, 1 H, C*H*, Cy), 1.77 (m, 5 H, Cy), 1.32 (m, 5 H, Cy) ppm. ^{13}C NMR ($CDCl_3$, 293 K): δ = 139.4, 133.6, 128.4, 128.2 ppm.

Synthesis of *trans*-[$Ni(C_6Cl_2F_3)_2(SbPh_3)_2$] (1): *n*-Butyllithium (8.5 mL of 1.2 M solution in hexane, 10.20 mmol) was added dropwise to a solution of 1,3,5-$C_6Cl_3F_3$ (2.402 g, 10.20 mmol) in dry Et_2O (50 mL), at –78 °C. After the reaction mixture was stirred at this temperature for 1 h, $SbPh_3$ (4.322 g, 12.24 mmol) and [$NiBr_2$(dme)] (1.574 g, 5.10 mmol) were added, and the suspension obtained was stirred overnight and allowed to warm to room temperature. Wet Et_2O (20 mL) was added and the suspension evaporated to dryness. The residue was extracted with $CHCl_3$ (60 mL) and the filtrate was evaporated to 5 mL, treated with ethanol (20 mL), and concentrated to 20 mL. The resulting suspension was filtered and the yellow solid washed with ethanol and air dried. Yield: 2.94 g (50%). $C_{48}H_{30}Cl_4F_6NiSb_2$ (1164.78): calcd. C 49.50, H 2.60; found C 49.14, H 2.76. ^{1}H NMR ($CDCl_3$, 293 K): δ = 7.34–7.25 (m, 30 H, Ph) ppm. ^{19}F NMR ($CDCl_3$, 293 K): δ = –87.47 (s, 4 F, F_{ortho}), –119.46 (s, 2 F, F_{para}) ppm.

Synthesis of *trans*-[$Ni(C_6Cl_2F_3)_2(AsPh_3)_2$] (2): To a solution of $LiC_6Cl_2F_3$ prepared from $C_6Cl_3F_3$ (1.181 g, 5.02 mmol) and BuLi (5.02 mmol) at –78 °C, were added $AsPh_3$ (1.837 g, 6.00 mmol) and [$NiBr_2$(dme)] (0.772 g, 2.50 mmol), the brown suspension obtained was stirred for 12 h and allowed to warm to room temperature. After that time the flask was opened to the air and wet diethyl ether (15 mL) was added in order to hydrolyze the organolithium excess. The solution was filtered and the resulting red solution was concentrated until dryness. The residue was treated with $CHCl_3$ (30 mL), the obtained suspension was filtered, and the resulting orange solution was concentrated until dryness. The crude product was recrystallized from $CHCl_3$/EtOH. Yield: 1.39 g (52%). $C_{48}H_{30}As_2Cl_4F_6Ni$ (1071.10): calcd. C 53.82, H 2.82; found C 53.06, H 2.94. ^{1}H NMR ($CDCl_3$, 293 K): δ = 7.7–7.1 (m, 30 H, Ph) ppm. ^{19}F NMR ($CDCl_3$, 293 K): δ = –89.05 (s, 4 F, F_{ortho}), –120.34 (s, 2 F, F_{para}) ppm.

Synthesis of *trans*-[$Ni(C_6Cl_2F_3)_2(AsCyPh_2)_2$] (3): Prepared as described for **2** but using $AsCyPh_2$ (1.891 g, 6.00 mmol) instead of $AsPh_3$. Yield: 1.323 g (49%). $C_{48}H_{42}As_2Cl_4F_6Ni$ (1083.20): calcd. C 53.22, H 3.91; found C 52.94, H 3.60. ^{1}H NMR ($CDCl_3$, 293 K): δ = 7.4–7.0 (m, 20 H, Ph), 2.11 (m, 2 H, C*H*, Cy), 1.88–0.88 (m, 20 H, Cy) ppm. ^{19}F NMR ($CDCl_3$, 293 K): δ = –88.75 (s, 4 F, F_{ortho}), –120.08 (s, 2 F, F_{para}) ppm.

Synthesis of *trans*-[$Ni(C_6Cl_2F_3)_2(AsMePh_2)_2$] (4): Prepared as described for **2** but using $AsMePh_2$ (1.465 g, 6.00 mmol) instead of $AsPh_3$. Yield: 0.834 g (35%). $C_{38}H_{26}As_2Cl_4F_6Ni$ (946.96): calcd. C 48.20, H 2.77; found C 47.82, H 2.71. ^{1}H NMR ($CDCl_3$, 293 K): δ = 7.31 (m, 20 H, Ph), 1.57 (s, 6 H, Me) ppm. ^{19}F NMR ($CDCl_3$, 293 K): δ = –90.29 (s, 4 F, F_{ortho}), –119.69 (s, 2 F, F_{para}) ppm.

Synthesis of *trans*-[$Ni(C_6Cl_2F_3)_2(PPh_3)_2$] (5): To a solution of PPh_3 (0.0787 g, 0.30 mmol) in $CHCl_3$ (20 mL) solid **1** (0.175 g, 0.15 mmol) was added. After complete dissolution of the nickel compound, the solution was stirred for 30 min, filtered through Celite®, and then the solvent was evaporated to dryness. The solid residue was washed with *n*-hexane (4 × 10 mL) to remove the $SbPh_3$, filtered and vacuum dried. Yield 0.128 g (87%). $C_{48}H_{30}Cl_4F_6NiP_2$ (983.21): calcd. C 58.64, H 3.07; found C 58.31, H 3.00. ^{1}H NMR ($CDCl_3$, 293 K): δ = 7.50 (m, 4 H, Ph), 7.29 (m, 2 H, Ph), 7.19 (m, 4 H, Ph) ppm. ^{19}F NMR ($CDCl_3$, 293 K): δ =

 © 2005 Wiley-VCH Verlag GmbH & Co. KGaA, Weinheim

–89.04 (t, $^4J_{P-F}$ = 2.7 Hz, 4 F, F_{ortho}), –121.21 (t, $^6J_{P-F}$ = 3.4 Hz, 2 F, F_{para}) ppm. $^{31}P\{^1H\}$ NMR ($CDCl_3$, 293 K): δ = 22.4 (m) ppm.

Synthesis of $C_6Cl_2F_3$–$C_6Cl_2F_3$ (6): A solution of **1** (1.400 g, 1.20 mmol) in chloroform (250 mL) was refluxed for 12 h. The resulting brown suspension was evaporated to dryness and the residue was chromatographed (silica gel/hexane). The fraction corresponding to the first eluted compound was evaporated to dryness giving a white solid. Yield: 0.303 g (62%). $C_{12}Cl_4F_6$ (399.93): calcd. C 36.04; found C 36.20. GS-MS: *m*/*z* = 397.8 $[M]^+$. ^{19}F NMR ($CDCl_3$, 293 K): δ = –107.48 (m, 1 F, F_{para}), –110.78 (m, 2 F, F_{ortho}) ppm.

Synthesis of $C_6Cl_2F_3H$ (7): To a solution of $LiC_6Cl_2F_3$ prepared from $C_6Cl_3F_3$ (1.000 g, 4.25 mmol) and BuLi (4.25 mmol) at –78 °C, was added H_2O (0.300 g, 16.65 mmol). The mixture was allowed to warm to room temperature, dried with $MgSO_4$, and the solvents evaporated to dryness, yielding a colorless oil. Yield: 0.717 g (84%). GS-MS: *m*/*z* (%) = 199.9 $[M]^+$. ^1H NMR ($CDCl_3$, 293 K): δ = 6.91 (td, $^3J_{H,F}$ = 8.6 Hz, $^5J_{H,F}$ = 2.4 Hz, 1 H) ppm. ^{19}F NMR ($CDCl_3$, 293 K): δ = –110.64 (m, 1 F, F_{para}), –112.04 (dd, $^3J_{H,F}$ = 8.6 Hz, $^4J_{F-F}$ = 1.8 Hz, 2 F, F_{ortho}) ppm.

Polymerization Experiments: All the polymerization catalysis reactions were carried out under N_2, in Schlenk flasks (25 mL) reacting norbornene with a monomer:catalyst ratio of 2000:1. In a typical experiment norbornene (866.3 mg, 9.2 mmol) was dissolved in deoxygenated CH_2Cl_2 (3 mL). To the stirred solution the solid catalyst (4.9 mg of **2**, 4.6 μmol) was added. The reaction started immediately, giving polynorbornene as a white precipitate (the reaction is better done in a round-bottomed flask, since the heat generated by the reaction makes the solvent boil). The stirring was maintained for 30 min and the reaction mass was poured into MeOH (100 mL). The polymer was filtered, washed several times with MeOH and vacuum dried. Yield: 650 mg (75%). NMR spectroscopic data of the polymers. ^{13}C DEPT NMR spectra ($CDCl_3$) of the polymers were recorded, and in all cases a similar spectra were obtained with broad signals at the following chemical shifts, δ = 54–45 (CH), 45–38 (CH), 38–34 (CH_2), 34–28 (CH_2) ppm.

Experimental Procedure for X-ray Crystallography: Suitable single crystals were mounted in glass fibers, and diffraction measurements were made with a Bruker SMART CCD area-detector diffractometer with Mo-K_α radiation (λ = 0.71073 Å).[32] Intensities were integrated from several series of exposures, each exposure covering 0.3° in ω, the total data set being a hemisphere.[33] Absorption corrections were applied, based on multiple and symmetry-equivalent measurements.[34] The structure was solved by direct methods and refined by least-squares on massed F^2 values for all reflections (see Table 3).[35] All non-hydrogen atoms were assigned anisotropic displacement parameters and refined without positional constraints. Hydrogen atoms were taken into account at calculated positions and their positional parameters were refined. Refinement proceeded smoothly to give R_1 = 0.0423 based on the reflections with $I > 2\sigma(I)$ and wR_2 = 0.0965 for all data. Complex neutral-atom scattering factors were used.[36] Crystallographic data (excluding structure factors) for the structures reported in this paper have been deposited with the Cambridge Crystallographic Data Centre as supplementary publications with the following deposition numbers: CCDC-262216, -262215, and -262214 for complexes **1**, **2**, and **5**, respectively. Copies of the data can be obtained free of charge on application to the CCDC, 12 Union Road, Cambridge CB2 1EZ, UK (Fax: +44-1223-336-033; E-mail: deposit@ccdc.cam.ac.uk).

Supporting Information: Two ORTEP figures for compounds **1** and **2** are provided as Supporting Information (see also the footnote on the first page of this article).

Table 3. Crystal data and structure refinement for **1**, **2** and **5**.

	1	**2**	**5**
Empirical formula	$C_{48}H_{30}Cl_4F_6NiSb_2$	$C_{48}H_{30}As_2Cl_4F_6Ni$	$C_{48}H_{30}Cl_4F_6NiP_2$
Formula mass	1164.73	1071.07	983.17
Temperature	298(2)	298(2) K	293(2) K
Wavelength [Å]	0.71073	0.71073	0.71073
Crystal system	triclinic	triclinic	triclinic
Space group	*P*1	*P*1	*P*1
a [Å]	10.045(3)	10.023(4)	10.062(5)
b [Å]	11.066(3)	11.078(5)	13.769(5)
c [Å]	11.733(3)	11.448(5)	15.780(5)
α [°]	95.747(6)	89.597(8)	86.905(5)
β [°]	112.001(6)	69.929(8)	89.449(5)
γ [°]	103.772(5)	67.957(8)	83.725(5)
V [Å^3]	1148.1(6)	1095.7(8)	2169.9(15)
Z	1	1	2
$D_{calcd.}$ [g cm^{-3}]	1.685	1.623	1.505
Absorption coefficient [mm^{-1}]	1.864	2.245	0.828
F(000)	570	534	996
Crystal size [mm]	0.16 × 0.06 × 0.03	0.24 × 0.12 × 0.08	0.35 × 0.22 × 0.09
Theta range for data collection	1.91 to 23.31°	1.91 to 23.34°	1.49 to 23.27°
Reflections collected	5374	5185	10214
Independent reflections	3286 (R_{int} = 0.0261)	3139 (R_{int} = 0.0215)	6183 (R_{int} = 0.0197)
Absorption correction	SADABS	SADABS	SADABS
Maximum and	1.000000	1.000000	1.000000
minimum transmission factor	0.561030	0.720972	0.823285
Data/restraints/parameters	3286/0/277	3139/0/277	6183/0/551
Goodness-of-fit on F^2	0.946	1.006	1.037
R_1 [$I > 2\sigma(I)$]	0.0347	0.0284	0.0423
wR_2 (all data)	0.0810	0.0779	0.0965

 © 2005 Wiley-VCH Verlag GmbH & Co. KGaA, Weinheim

Acknowledgments

Financial support by the Ministerio de Ciencia y Tecnología (Project CTQ2004–07667) and the Junta de Castilla y León (Project No.VA 060–04) is very gratefully acknowledged.

[1] C. Janiak, P. G. Lassahn, *J. Mol. Catal. A: Chem.* **2001**, *166*, 193–209.
[2] C. Karafilidis, H. Hermann, A. Rufiñska, B. Gabor, R. J. Mynott, G. Breitenbruch, C. Weidenthaler, J. Rust, W. Joppek, M. S. Brookhart, W. Thiel, G. Fink, *Angew. Chem. Int. Ed.* **2004**, *43*, 2444–2446.
[3] B. L. Goodall in *Late Transition Metal Polymerization Catalysis* (Eds.: B. Rieger, L. Saunders Baugh, S. Katcker, S. Striegler), Wiley-VCH, Weinheim, **2003**, chapter 4.
[4] a) M. C. Sacchi, M. Sonzogni, S. Losio, F. Forlini, P. Locatelli, I. Tritto, M. Licchelli, *Macromol. Chem. Phys.* **2001**, *202*, 2052–2058; b) C. Zhao, R. Ribeiro, V. S. Subrahmayam, C. L. Gil, A. P. de Lima, *Polymer* **2001**, *42*, 2455–2462; c) C. Janiak, P.-G. Lasshahn, *Polym. Bull.* **2002**, *47*, 539–546.
[5] S. J. Diamanti, P. Ghosh, F. Shimizu, G. C. Bazan, *Macromolecules* **2003**, *36*, 9731–9735.
[6] B. Y. Lee, Y. H. Kim, H. J. Shin, C. H. Lee, *Organometallics* **2002**, *21*, 3481–3484.
[7] W.-H. Sun, H. Yang, Z. Li, Y. Li, *Organometallics* **2003**, *22*, 3678–3683.
[8] G. M. Benedikt, E. Elce, B. L. Goodall, H. A. Kalamarides, L. H. III McIntosh, L. F. Rhodes, K. T. Selvy, C. Andes, K. Oyler, A. Sen, *Macromolecules* **2002**, *35*, 8978–8988.
[9] D. A. Barnes, G. M. Benedikt, B. L. Goodall, S. S. Huang, H. A. Kalamarides, S. Lenhard, L. H. III McIntosh, K. T. Selvy, R. A. Shick, L. F. Rhodes, *Macromolecules* **2003**, *36*, 2623–2632.
[10] C.-F. Huang, S.-K. Wang, S.-W. Kuo, W.-J. Huang, F.-C. Chang, *J. Appl. Polym. Sci.* **2004**, *92*, 1824–1833.
[11] B. L. Goodall, S. Jayaraman, R. A. Shick, L. F. Rhodes, R. D. Allen, R. A. DiPietro, T. Wallow, *US Patent* **2004**, 6723486.
[12] F. H. Allen, J. E. Davies, J. J. Galloy, D. Johnson, O. Kennard, C. F. Macrae, E. M. Mitcher, G. F. Mitchell, J. M. Smith, D. G. Watson, *J. Chem. Inf. Comput. Sci.* **1991**, *31*, 187–204.
[13] K. Herbst, P. Zanello, M. Corsini, N. D′Amelio, L. Dahlenburg, M. Brorson, *Inorg. Chem.* **2003**, *42*, 974–981.
[14] M. Jimenez-Tenorio, M. C. Puerta, I. Salcedo, P. Valerga, S. I. Costa, P. T. Gomes, K. Mereiter, *Chem. Commun.* **2003**, 1168–1169.
[15] a) J. Vicente, A. Arcas, D. Bautista, *Organometallics* **1997**, *16*, 2127–2138; b) J. Vicente, J. A. Abad, A. D. Frankland, M. C. Ramírez de Arellano, *Chem. Eur. J.* **1999**, *5*, 3066–3075; c) J. Vicente, J. A. Abad, E. Martínez-Viviente, P. G. Jones, *Organometallics* **2002**, *21*, 4454–4467; d) J. Vicente, A. Arcas, D. Bautista, M. C. Ramírez de Arellano, *J. Organomet. Chem.* **2002**, *663*, 164–172.
[16] For L–Ni–L angles larger than 100° with L = PPh_3 in planar complexes see for instance: a) S. D. Ittel, J. A. Ibers, *J. Organomet. Chem.* **1973**, *57*, 389–402; b) K. R. Porschke, Y.-H. Tsay, C. Kruger, *Angew. Chem. Int. Ed. Engl.* **1985**, *24*, 323–324; c) C. Mealli, S. Midollini, S. Moneti, L. Sacconi, J. Silvestre, T. A. Albright, *J. Am. Chem. Soc.* **1982**, *104*, 95–107; d) H. Gorls, B. Schulz, U. Rosenthal, W. Schulz, *Crys. Res. Tecnol.* **1988**, *23*, 25–33; e) R. Countryman, B. R. Penfold, *J. Cryst. Mol. Struct.* **1972**, *2*, 281; f) J. R. Ascenso, A. R. Dias, M. T. Duarte, P. T. Gomes, J. N. Marote, A. F. G. Ribeiro, *J. Organomet. Chem.* **2001**, *632*, 164–174; g) J.-T. Ahlemann, H. W. Roesky, R. Murugavel, E. Parisini, M. Noltemeyer, H.-G. Schmidt, O. Müller, R. Herbst-Irmer, L. N. Markovskii, Y. G. Shermolovich, *Chem. Ber./Recueil* **1997**, *130*, 1113–1121.
[17] a) M. D. Rausch, Y. Tibbetts, *Inorg. Chem.* **1970**, 512–516; b) M. D. Rausch, Y. F. Chang, H. B. Gordon, *Inorg. Chem.* **1969**, 1355–1362.
[18] M. R. Churchill, M. V. Veidis, *J. Chem. Soc. Dalton* **1972**, 670–674.
[19] R. McDonald, K. C. Sturge, A. D. Hunter, L. Shilliday, *Organometallics* **1992**, *11*, 893–900.
[20] J. Forniés, A. Martín, B. Menjón, H. A. Kalamarides, L. F. Rhodes, C. S. Day, V. W. Day, *Chem. Eur. J.* **2002**, *21*, 4925–4934.
[21] T. Yamamoto, M. Abla, Y. Murakami, *Bull. Chem. Soc. Jpn.* **2002**, *75*, 1997–2009.
[22] When bonded to a transition metal atom the F_{ortho} signals appear strongly unshielded, while the F_{para} signal is shielded. The chemical shift difference between F_{ortho} and F_{para} is, in metal complexes, about 30–40 ppm while in organic compounds it is about 2–15 ppm. For chemical shifts of $C_6Cl_2F_3$ bonded to carbon see: A. L. Casado, P. Espinet, *J. Am. Chem. Soc.* **1998**, *120*, 8978–8985. For chemical shifts of metal-bonded $C_6Cl_2F_3$ see for instance; a) M. A. Alonso, J. A. Casares, P. Espinet, J. M. Martínez-Ilarduya, C. Pérez-Briso, *Eur. J. Inorg. Chem.* **1998**, 1745–1753; b) J. A. Casares, P. Espinet, K. Soulantica, I. Pascual, A. Guy Orpen, *Inorg. Chem.* **1997**, *36*, 5251–5256.
[23] See for instance: a) A. C. Albeniz, P. Espinet, Y.-S. Lin, *Organometallics* **1997**, *16*, 4138–4144; b) A. C. Albéniz, P. Espinet, Y.-S. Lin, *Organometallics* **1997**, *16*, 5964–5973.
[24] J. Lipian, R. A. Mimna, J. C. Fondran, D. Yandulov, R. A. Shick, B. L. Goodall, L. F. Rhodes, J. C. Huffman, *Macromolecules* **2002**, *35*, 8969–8977.
[25] Manuscript in preparation.
[26] A. D. Hennis, J. D. Polley, G. S. Long, A. Sen, D. Yandulov, J. Lipian, G. M. Benedikt, L. F. Rhodes, J. Huffman, *Organometallics* **2001**, *20*, 2802–2812.
[27] J. K. Funk, C. E. Andes, A. Sen, *Organometallics* **2004**, *23*, 1680–1683.
[28] R. B. King, *Organometallic Syntheses* (Eds.: J. J. Eisch, R. B. King), Academis Press, New York, **1965**, vol. 1, p. 72.
[29] C. A. Bayse, R. L. Luck, E. J. Schelter, *Inorg. Chem.* **2001**, *40*, 3463–3467.
[30] P. Espinet, J. M. Martínez-Ilarduya, C. Pérez-Briso, A. L. Casado, M. A. Alonso, *J. Organomet. Chem.* **1998**, *551*, 9–20.
[31] W. Levason, C. A. McAuliffe, *Inorganic Syntheses* **1976**, *16*, 188–192.
[32] *SMART*, diffractometer control software, Bruker Analytical X-ray Instruments Inc., Madison, WI, Version 5.051, **1998**.
[33] *SAINT*, integration software, Bruker Analytical X-ray Instruments Inc., Madison, WI, Version 6.02, **1999**.
[34] G. M. Sheldrick, *SADABS*, a program for absorption correction with the Siemens SMART system, University of Göttingen, **1996**.
[35] G. W. Sheldrick, *SHELXTL*, Bruker Analytical Instruments, Madison, Version 5.1, **1998**.
[36] International Tables for Crystallography, Kluwer, Dordrecht, **1992**, vol. C.

Received: February 9, 2005
Published Online: August 31, 2005

 © 2005 Wiley-VCH Verlag GmbH & Co. KGaA, Weinheim

Reversible Bond Formation and Cleavage of the Oxo Bridge of $[Ru_2(\mu\text{-}O)(dioxolene)_2(btpyxa)]^{3+}$ [btpyxa = 2,7-Di-*tert*-butyl-9,9-dimethyl-4,5-bis(2,2′:6′,2′′-terpyrid-4′-yl)xanthene] Driven by a Three-Electron Redox Reaction

Tohru Wada[a] and Koji Tanaka*[a]

Keywords: Electronic structure / O ligands / Oxidation / Reduction / Ruthenium

The bis(chlororuthenium) complex $[Ru_2Cl_2(3,6\text{-}tBu_2sq)_2(btpyxa)](PF_6)_2$ [**1**]$(PF_6)_2$ [3,6-tBu_2sq = 3,6-di-*tert*-butyl-1,2-benzosemiquinone; btpyxa = 2,7-di-*tert*-butyl-9,9-dimethyl-4,5-bis(2,2′:6′,2′′-terpyrid-4′-yl)xanthene] and the oxo-bridged diruthenium complex $[Ru_2(\mu\text{-}O)(3,6\text{-}tBu_2sq)_2(btpyxa)](PF_6)_3$ [**2**]$(PF_6)_3$ were synthesized, and the redox behavior of these complexes, which contain a non-innocent dioxolene ligand, was investigated by electrochemical and electrospectrochemical methods. Dicationic $[\mathbf{1}]^{2+}$ undergoes two successive metal-centered one-electron and a simultaneous two-electron ligand-based redox reaction at $E_{1/2}$ = +0.13 and +0.09 and $E_{1/2}$ = –0.75 V (vs. SCE), respectively, in CH_2Cl_2. The UV/Vis/NIR spectrum of tricationic $[\mathbf{2}]^{3+}$ shows an intervalence-transition (IT) band at 1333 nm (ε = 1.52×10^4 M^{-1} cm^{-1}) in a near-IR region together with two CT bands at 766 (ε = 2.21×10^4 M^{-1} cm^{-1}) and 586 nm (ε = 1.13×10^4 M^{-1} cm^{-1}) in CH_2Cl_2. The mixed-valence complex of $[\mathbf{2}]^{3+}$ with an Ru^{IV}–O–Ru^{III} core is reversibly oxidized and reduced to the Ru^{IV}–Ru^{IV} and Ru^{III}–Ru^{III} oxidation states at $E_{1/2}$ = +0.63 and –0.01 V, respectively, in CH_2Cl_2. On the other hand, three-electron reduction of [**2**]$(PF_6)_3$ is accompanied by the cleavage of the Ru–O–Ru bond at E_p = +0.02 V to give $[\{Ru(OMe)(3,5\text{-}tBu_2sq)\}\{Ru(OH_2)(3,5\text{-}tBu_2sq)\}(btpyxa)]^+$ in MeOH.
(© Wiley-VCH Verlag GmbH & Co. KGaA, 69451 Weinheim, Germany, 2005)

Introduction

Much attention has been paid to transition-metal complexes with non-innocent ligands such as dioxolenes, dithiolenes, and benzoquinonediimines due to their unique electronic,[1] magnetic,[2] and structural[3] properties that derive from pπ–dπ interactions between the metals and such ligands. Ruthenium–dioxolene complexes, in particular, have strong pπ–dπ interactions because of the close orbital energies between the central metal and the dioxolene ligand. Indeed, the electronic structures of ruthenium–dioxolene complexes are characterized in terms of charge distribution due to delocalization of π-electrons over the central metal and the ligand.[4,5] We have demonstrated that the dioxolene ligand in $[Ru(L)(3,5\text{-}tBu_2sq)(trpy)]^{2+}$ [L = OH_2,[6] CO,[7] 3,5-tBu_2sq (3,5-di-*tert*-butyl-1,2-benzosemiquinone), trpy (2,2′:6′,2′′-terpyridine)] exerts an unusually strong influence on the electronic states of the ligand L. For example, an aqua ligand of $[Ru^{III}(OH_2)(3,5\text{-}tBu_2sq)(trpy)]^{2+}$ dissociates two protons under strongly basic conditions to give the corresponding terminal ruthenium oxo complex $[Ru^{II}(O^{\cdot-})(3,5\text{-}tBu_2sq)(trpy)]^0$ without forming a μ-oxo diruthenium complex (Scheme 1).[6] EPR measurements revealed the radical character of the oxo ligand of the resultant oxo complex. Unusual oxyl radical formation results from intramolecular one-electron transfer from the doubly deprotonated aqua ligand of $[Ru^{III}(OH_2)(3,5\text{-}tBu_2sq)(trpy)]^{2+}$ to the Ru^{III}-semiquinone framework. A similar conversion of two hydroxyl ligands into two oxyl radicals in the bis(ruthenium–dioxolene) complex $[Ru_2(OH)_2(3,6\text{-}tBu_2q)_2(btpyan)]^{2+}$ [3,6-tBu_2q = 3,6-di-*tert*-butyl-1,2-benzoquinone, btpyan = 1,8-bis(2,2′:6′,2′′-terpyrid-4′-yl)anthracene], in which two ruthenium-dioxolene frameworks are fixed in a face-to-face conformation by the rigid btpyan ligand, enabled the catalytic four-electron oxidation of water through O–O bond formation by the radical coupling of the two oxyl radical ligands.[8]

We synthesized two new complexes, a bis(chlororuthenium–dioxolene) complex $[\mathbf{1}]^{2+}$ and a μ-oxo-bis(ruthenium–dioxolene) complex $[\mathbf{2}]^{3+}$ bridged by 2,7-di-*tert*-butyl-9,9-dimethyl-4,5-bis(2,2′:6′,2′′-terpyrid-4′-yl)xanthene (btpyxa) in which two terpyridines are linked by a xanthene skeleton (Scheme 2). The two terpyridine units bridged by a xanthene and an anthracene moiety in btpyxa and btpyan, respectively, are not able to rotate freely because of their steric repulsions.[8,9] The distinct difference between btpyxa and btpyan is that the sp^3 carbon and oxygen atoms at the 9- and 10-position of xanthene, respectively, in the former

[a] Institute for Molecular Science and CREST, Japan Science and Technology Agency (JST),
Higashiyama 5-1, Myodaiji, Okazaki, Aichi 444-8787, Japan
E-mail: ktanaka@ims.ac.jp

 © 2005 Wiley-VCH Verlag GmbH & Co. KGaA, Weinheim **DOI: 10.1002/ejic.200500141**

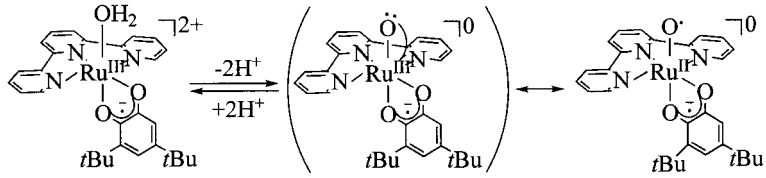

Scheme 1. Acid-base equilibrium of the aqua complex $[Ru(OH_2)(3,5\text{-}tBu_2sq)(trpy)]^{2+}$ and the oxyl radical complex $[Ru(O)(3,5\text{-}tBu_2sq)(trpy)]^{0}$.

give flexibility of the unit, whereas the anthracene in the latter has a rigid planar structure. Complexes $[\mathbf{1}]^{2+}$ and $[\mathbf{2}]^{3+}$ have the same skeleton fixed by btpyxa, but their electronic states and redox behavior are quite different from each other. We will report here the electronic structures of the diruthenium complexes and redox reactions accompanied with the Ru–O–Ru bond cleavage.

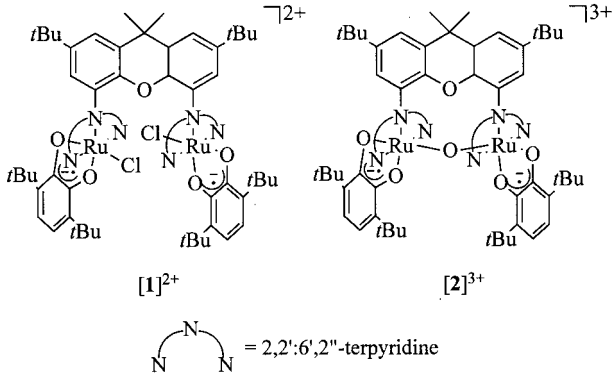

Scheme 2. Schematic structures of $[\mathbf{1}]^{2+}$ and $[\mathbf{2}]^{3+}$.

Results and Discussion

Syntheses and Electronic Structures

The reaction of $[Ru_2Cl_6(btpyxa)]$ with two equivalents of 3,6-di-*tert*-butylcatechol in the presence of *t*BuOK in MeOH gave a purple solution, presumably due to the formation of a bis[ruthenium(II) semiquinone] complex under N_2. The purple solution gradually turned blue upon exposure to air. The crude product was purified by column chromatography on alumina and subsequent treatment with aqueous NH_4PF_6. The product is a dicationic diruthenium complex containing two chloride ligands $\{[\mathbf{1}](PF_6)_2\}$. The UV/Vis/NIR spectrum of $[\mathbf{1}](PF_6)_2$ in CH_2Cl_2 [Figure 1(a)] shows a strong band at 598 nm ($\varepsilon = 1.93 \times 10^4\ M^{-1}cm^{-1}$) assignable to a charge-transfer (CT) band resulting from the $Ru^{III}(sq)$ (sq = semiquinone) framework by analogy with the electronic spectra of the analogous $[Ru^{III}(OH_2)(3,5\text{-}tBu_2sq)(trpy)]$.[6b] The resonance Raman spectrum of $[\mathbf{1}](PF_6)_2$ exhibits two strongly enhanced bands at 1357 and 1158 cm^{-1} upon excitation at 632.8 nm, whereas the intensities of these bands decrease upon excitation at 514.5 nm. In addition, the stretching modes of the semiquinone of $[Ru^{III}(OH_2)(3,5\text{-}tBu_2sq)(trpy)]^{2+}$ are found at 1353 and 1167 cm^{-1}.[6b] The strong absorption band of $[\mathbf{1}]^{2+}$ at 598 nm, therefore, is reasonably assigned to the CT band of the $Ru^{III}(sq)$ core. Thus, two ruthenium-dioxolene frameworks of $[\mathbf{1}]^{2+}$ have the $Ru^{III}(sq)$ oxidation state, although the contribution of an $Ru^{II}(q)$ (q = quinone) framework cannot be ignored in the electronic structure of $[\mathbf{1}]^{2+}$.

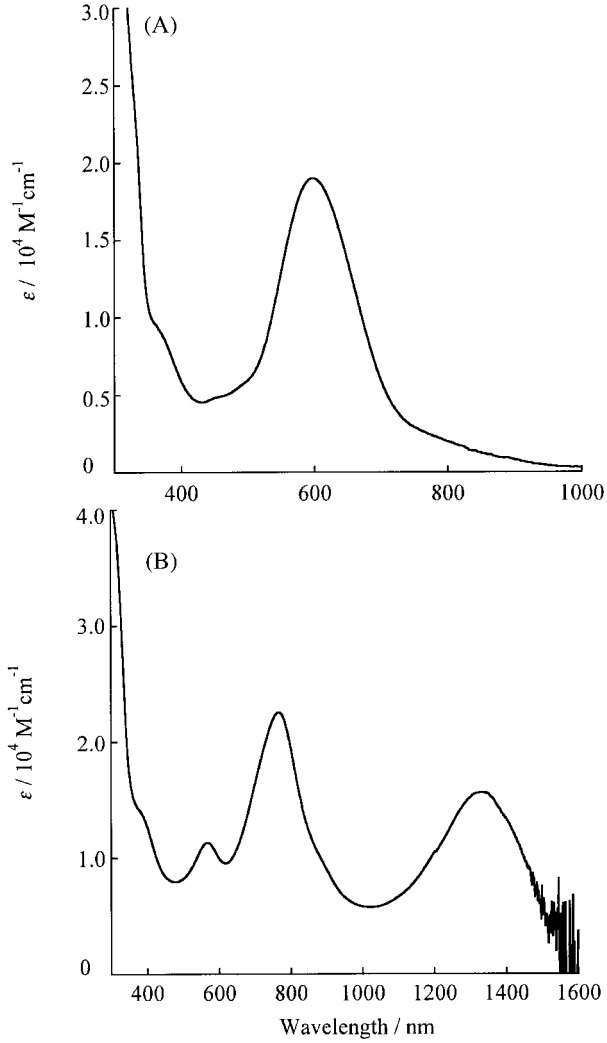

Figure 1. UV/Vis/NIR spectra of (A) $[\mathbf{1}](PF_6)_2$ and (B) $[\mathbf{2}](PF_6)_3$ in CH_2Cl_2.

We noticed the formation of a small amount of an oxo-bridged diruthenium complex $[\mathbf{2}]^{3+}$ as a minor product in the reaction of $[Ru_2Cl_6(btpyxa)]$ with 3,6-di-*tert*-butylcatechol in MeOH. The yield of $[\mathbf{2}](PF_6)_3$ was dependent on

 © 2005 Wiley-VCH Verlag GmbH & Co. KGaA, Weinheim

contamination of water in MeOH, suggesting that the bridging oxygen of $[\mathbf{2}]^{3+}$ comes from H_2O. The reaction of $[Ru_2(\mu\text{-}O)Cl_2(btpyxa)]$ with 3,6-di-*tert*-butylcatechol in the presence of a large excess of KOAc, followed by treatment with $NaPF_6$ in MeOH, gave $[\mathbf{2}](PF_6)_3$ in a low yield of 11%. The fact that no oxo-bridged species (Ru–O–Ru) were detected in the synthesis of the 1,8-bis(terpyridyl)anthracene-bridged complex $[Ru_2(OH)_2(3,6\text{-}t\text{Bu}_2\text{sq})_2(btpyan)]^{2+}$[8] is explained by the greater flexibility of the xanthene skeleton of btpyxa compared with the anthracene in btpyan. The UV/Vis/NIR spectrum of $[\mathbf{2}](PF_6)_3$ [Figure 1(b)] in CH_2Cl_2 shows a strong band at 1333 nm ($\varepsilon = 1.52\times10^4$ M^{-1}cm^{-1}) assigned to the intervalence-transition (IT) band (vide infra) in the near-IR region, with two CT bands at 766 ($\varepsilon = 2.21\times10^4$ M^{-1}cm^{-1}) and 586 nm ($\varepsilon = 1.13\times10^4$ M^{-1}cm^{-1}) in the visible region. The appearance of the IT band at 1333 nm indicates that $[\mathbf{2}]^{3+}$ is a mixed-valence complex. The contribution of $[(sq)Ru^{III}\text{–}O\text{–}Ru^{IV}(sq)]^{3+}$, therefore, is much higher than other resonance forms such as $[(q)Ru^{II}\text{–}O\text{–}Ru^{III}(q)]^{3+}$, $[(cat)Ru^{IV}\text{–}O\text{–}Ru^{IV}(sq)]^{3+}$ (cat = catecholato), etc. in the electronic structure of $[\mathbf{2}]^{3+}$.

Redox Behavior of $[\mathbf{1}]^{2+}$ and $[\mathbf{2}]^{3+}$ in CH_2Cl_2

The cyclic voltammogram (CV) of $[\mathbf{1}](PF_6)_2$ in CH_2Cl_2 shows three pairs of anodic and cathodic waves in a potential range from +0.8 to –1.3 V (vs. SCE; Figure 2).

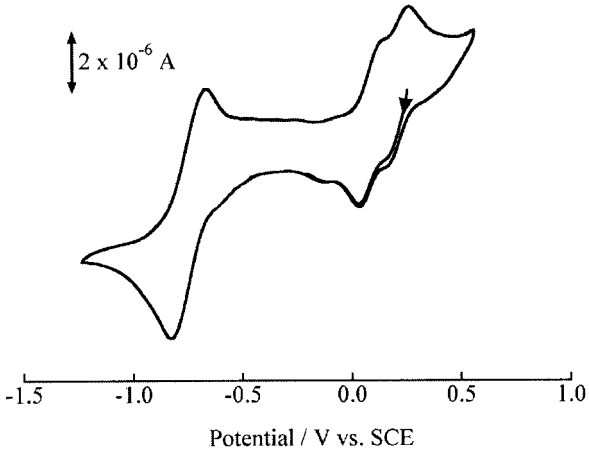

Figure 2. CV of $[\mathbf{1}](PF_6)_2$ in CH_2Cl_2 containing $n\text{Bu}_4NClO_4$ (0.1 M) as an electrolyte under N_2. The arrows indicate the rest potential of the solution and the direction of scan.

Based on the rest potential (+0.26 V) of $[\mathbf{1}]^{2+}$ in CH_2Cl_2, the two quasi-reversible redox couples at $E_{1/2}(1) = +0.13$ and $E_{1/2}(2) = +0.09$ V are associated with the metal-centered redox reactions. The redox couple at $E_{1/2}(3) = -0.75$ V with large peak currents is consistent with a dioxolene-based redox reaction due to its similarity to the redox potential of the analogous monomer [RuCl(3,5-$t\text{Bu}_2$sq)(trpy)].[5] The bulk electrolysis of $[\mathbf{1}]^{2+}$ in CH_2Cl_2 at +0.00 V consumes 2.03 F mol^{-1} of electricity. In addition, 2.01 F mol^{-1} of electricity also passes in the subsequent electrolysis of the resultant solution at –0.75 V.[10] The two redox reactions at $E_{1/2} = +0.13$ and +0.09 V apparently result from a one-electron transfer process because of the similarity of the peak currents of both redox waves (Figure 2). On the other hand, the redox couple at –0.75 V is a simultaneous two-electron transfer. The redox reactions at $E_{1/2}(1) = +0.13$, $E_{1/2}(2) = +0.09$, and $E_{1/2}(3) = -0.75$ V are summarized in Scheme 3.

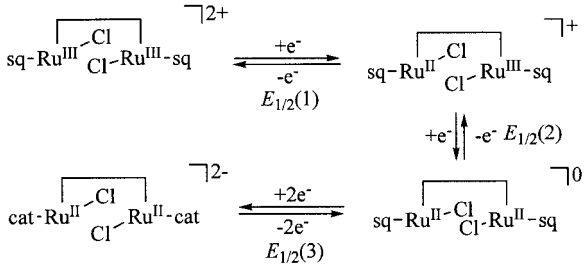

Scheme 3. Redox reactions of $[\mathbf{1}]^{2+}$ in CH_2Cl_2.

The equilibrium constant (K_d) for the disproportionation reaction of $[\mathbf{1}]^+$ is defined by Equations (1) and (2).[11] The K_d calculated from $\Delta E_{1/2} = E_{1/2}(2) - E_{1/2}(1) = -0.04$ V is 0.21, which proves that the mixed-valence complex $[\mathbf{1}]^+$ ($Ru^{II}\text{–}Ru^{III}$) exists as an equilibrium mixture of $[\mathbf{1}]^{2+}$ and $[\mathbf{1}]^0$ in solution.

$$2[\mathbf{1}]^+ \overset{K_d}{\rightleftarrows} [\mathbf{1}]^0 + [\mathbf{1}]^{2+} \quad (1)$$

$$E_{1/2}(2) - E_{1/2}(1) = \frac{RT}{F}\ln K_d \quad (2)$$

Electrospectroscopy of $[\mathbf{1}]^{2+}$ in CH_2Cl_2 (Figure 3) also provides valid information about the $[\mathbf{1}]^{2+}/[\mathbf{1}]^+$ and $[\mathbf{1}]^+/[\mathbf{1}]^0$ redox reactions.

The CT band at 598 nm of $[\mathbf{1}]^{2+}$ decreases by half in the electrochemical reduction at +0.10 V and a new band appears at 882 nm, which is assigned to a CT band resulting from the $Ru^{II}(sq)$ moiety. The 598-nm band disappears completely in the electrolysis at –0.10 V and the 882-nm band is shifted to 866 nm with an increase in its absorbance. The shift of the CT band from 598 nm to 882 nm and then to 866 nm upon the reduction of $[\mathbf{1}]^{2+}$ at +0.10 V and –0.10 V is ascribed to the changes of the electronic structures from $[(sq)ClRu^{III}\text{–}Ru^{III}Cl(sq)]^{2+}$ to $[(sq)ClRu^{III}\text{–}Ru^{II}Cl(sq)]^0$ through $[(sq)ClRu^{II}\text{–}Ru^{III}Cl(sq)]^+$. Further reduction of $[\mathbf{1}]^0$ at –1.0 V completely extinguished the 866-nm band of $[(sq)ClRu^{II}\text{–}Ru^{II}Cl(sq)]^0$. Taking into account that the $Ru^{II}(cat)$ framework, with a fully occupied Ru t_{2g} and π orbital (π* orbital of quinone), has no CT band between Ru and the dioxolene ligand, the $[\mathbf{1}]^0/[\mathbf{1}]^{2-}$ couple at –0.75 V is assigned to the simultaneous two-electron reduction of $[(sq)ClRu^{II}\text{–}Ru^{II}Cl(sq)]^0$ to $[(cat)ClRu^{II}\text{–}Ru^{II}Cl(cat)]^{2+}$. The spectral changes in the redox cycle between $[\mathbf{1}]^{2+}$, $[\mathbf{1}]^+$, $[\mathbf{1}]^0$, and $[\mathbf{1}]^{2-}$ take place reversibly, since re-oxidation of a CH_2Cl_2 solution of $[\mathbf{1}]^{2-}$ at +0.4 V fully restored the spectrum of $[\mathbf{1}]^{2+}$. It is worthy of note that $[\mathbf{1}]^{2+}$ displays two Ru^{II}/Ru^{III} redox couples at $E_{1/2}(1) = +0.13$ and $E_{1/2}(2) = +0.09$ V, while the two semiquinone ligands of $[\mathbf{1}]^0$ are reduced to catecholato ones at the same potential. However,

 © 2005 Wiley-VCH Verlag GmbH & Co. KGaA, Weinheim

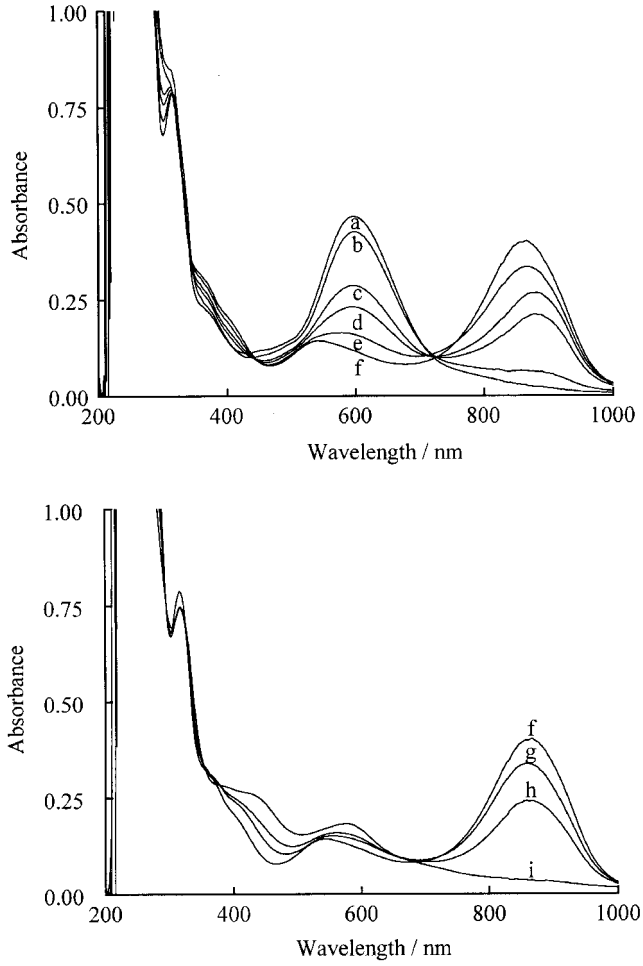

Figure 3. UV/Vis/NIR spectra of $[\mathbf{1}](PF_6)_2$: a) before electrolysis and after electrolysis at b) +0.20 V, c) +0.15 V, d) +0.10 V, e) +0.05 V, f) 0.00 V, g) –0.70 V, h) –0.80 V, and i) –0.90 V in CH_2Cl_2 containing nBu$_4$NClO$_4$ (0.1 M) as an electrolyte.

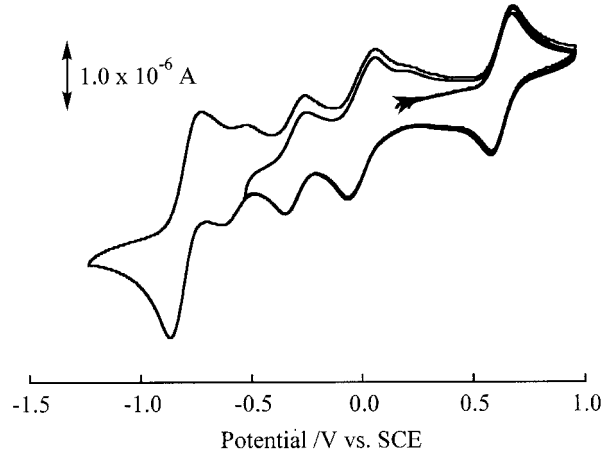

Figure 4. CV of $[\mathbf{2}](PF_6)_3$ in CH_2Cl_2 containing nBu$_4$NClO$_4$ (0.1 M) as an electrolyte under N_2. The arrows indicate the rest potential of the solution and the direction of scan.

the IT band associated with $[\mathbf{1}]^+$, which was generated by the bulk electrolysis of $[\mathbf{1}]^{2+}$ at +0.10 V in CH_2Cl_2, was not detected at all in the region from 500 to 2200 nm. Meyer at al. have demonstrated that electrostatic effects caused by charge differences of dinuclear complexes result in a discrepancy of the redox potentials of two redox sites by about 20–60 mV.[12] The absence of the IT band of $[\mathbf{1}]^{2+}$ and a small potential difference between the two Ru^{II}/Ru^{III} redox couples (ΔE = 40 mV), therefore, may be ascribed to electrostatic effects, although an electronic interaction between the two Ru atoms of the $[(sq)Ru^{II}Cl\ ClRu^{III}(sq)]^+$ framework cannot be ruled out completely.

The oxo-bridged diruthenium complex $[\mathbf{2}]^{3+}$ exhibits a strong IT band at 1333 nm and two strong CT bands at 766 and 578 nm, as described above. The actual electronic structure of $[\mathbf{2}]^{3+}$ is approximated by $[(sq)Ru^{III}–O–Ru^{IV}(sq)]^{3+}$, since the strong electron-donating ability of the μ-oxo group in $[\mathbf{2}]^{3+}$ would stabilize higher oxidation states of Ru. Indeed, the redox behavior of $[\mathbf{2}]^{3+}$ is very different from that of $[\mathbf{1}]^{2+}$ (compare Figures 2 and 4).

The CV of $[\mathbf{2}]^{3+}$ (Figure 4) shows four quasi-reversible redox couples at $E_{1/2}(1)$ = +0.63, $E_{1/2}(2)$ = –0.01, $E_{1/2}(3)$ = –0.30, and $E_{1/2}(4)$ = –0.80 V. The redox reactions at $E_{1/2}(1)$ = +0.63 and $E_{1/2}(2)$ = –0.01 V were assigned to the $[(sq)Ru^{III}–O–Ru^{IV}(sq)]^{3+}/[(sq)Ru^{IV}–O–Ru^{IV}(sq)]^{4+}$ and the $[(sq)Ru^{III}–O–Ru^{IV}(sq)]^{3+}/[(sq)Ru^{III}–O–Ru^{III}(sq)]^{2+}$ couples, respectively, on the basis of the rest potential of the solution (E_{rest} = +0.21 V). The pattern and the potential of the redox couple at $E_{1/2}(1)$ = –0.80 V of $[\mathbf{2}]^{3+}$ are close to those of the simultaneous two-electron reduction of the two semiquinone ligands of $[\mathbf{1}]^{2+}$. Therefore, the redox reaction at $E_{1/2}(3)$ = –0.30 V is correlated with the $[(sq)Ru^{III}–O–Ru^{III}(sq)]^{2+}/[(sq)Ru^{III}–O–Ru^{II}(sq)]^+$ couple. The redox reactions of $[\mathbf{2}]^{3+}$ in CH_2Cl_2 are summarized in Scheme 4.

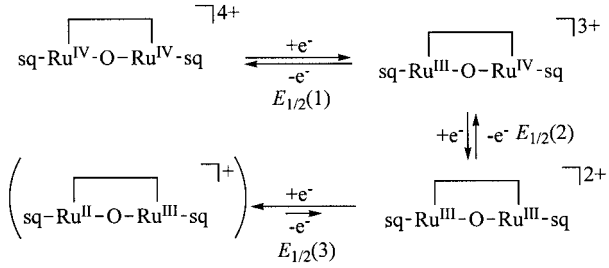

Scheme 4. Redox behavior of $[\mathbf{2}]^{3+}$ in CH_2Cl_2.

The changes of the oxidation states of $[\mathbf{2}]^{3+}$ were followed by UV/Vis/NIR spectroscopy. The one-electron oxidation of $[\mathbf{2}]^{3+}$ at +0.80 V resulted in disappearance of the bands at 1333 and 766 nm and generation of a new band at 656 nm. The electrochemical reduction of $[\mathbf{2}]^{3+}$ at –0.25 V also caused a disappearance of the same bands and the generation of a strong band at 872 nm (Figure 5). These spectral changes between $[\mathbf{2}]^{2+}$, $[\mathbf{2}]^{3+}$, and $[\mathbf{2}]^{4+}$ occur reversibly depending on the electrolysis potentials.

 © 2005 Wiley-VCH Verlag GmbH & Co. KGaA, Weinheim

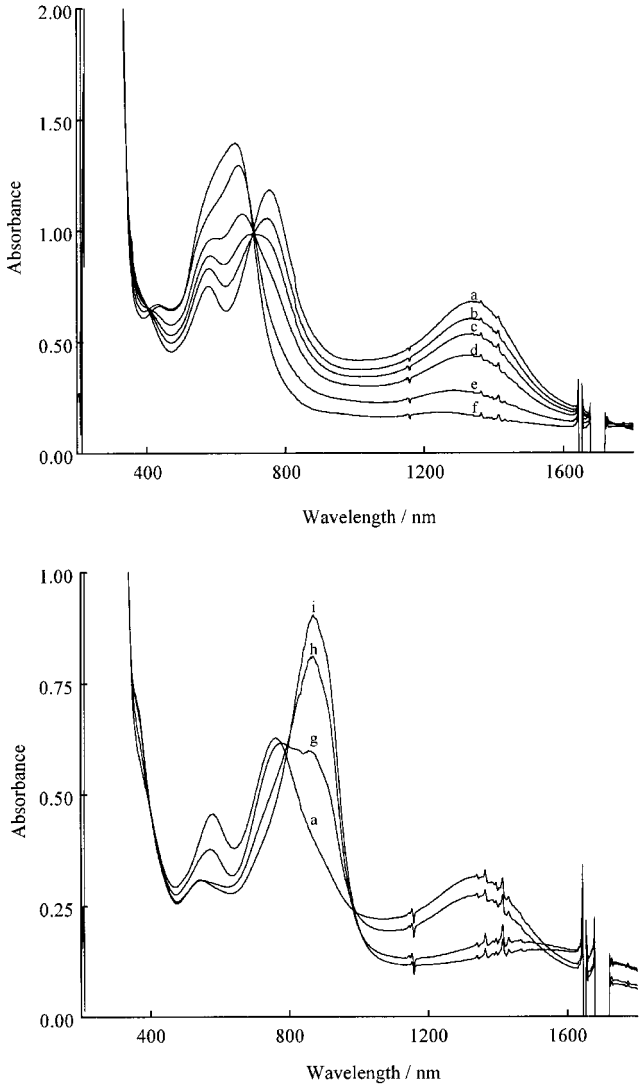

Figure 5. UV/Vis/NIR spectra of [**2**](PF$_6$)$_3$: a) before electrolysis and after electrolysis at b) +0.40 V, c) +0.50 V, d) +0.60 V, e) +0.70 V, f) +0.80 V, g) +0.00 V, h) –0.10 V, and i) –0.25 V in CH_2Cl_2 containing nBu$_4$NClO$_4$ (0.1 M) as an electrolyte.

If [**2**]$^{2+}$ has the [(sq)Ru^{III}–O–Ru^{III}(sq)]$^{2+}$ core, the monocation [**2**]$^{+}$ would also be a mixed-valence metal complex. The controlled potential electrolysis of [**2**]$^{3+}$ at –0.60 V in CH_2Cl_2, however, induced fragmentation reactions of the complex, as re-oxidation of the resultant solution at –0.20 V did not recover the spectrum of [**2**]$^{2+}$.[13] The decomposition of the mixed-valence complex [**2**]$^{+}$ may be caused by the fragility of the Ru^{III}–O–Ru^{II} bond (vide infra). It is worthy of note that the mixed-valence complex [**2**]$^{3+}$, with the [(sq)-Ru^{III}–O–Ru^{IV}(sq)]$^{3+}$ core, is quite stable in solution, since the disproportionation constant of [**2**]$^{3+}$ [Equation (2)] is negligibly small ($K_d = 1.5\times10^{-11}$) in contrast to that of [**1**]$^{+}$ ($K_d = 0.21$).

Redox Behavior of [2]$^{3+}$ in MeOH

The fragility of the highly reduced form of [**2**]$^{3+}$ becomes more prominent in MeOH. In contrast to the CV of [**2**]$^{3+}$ in CH_2Cl_2, the complex exhibits four redox couples in a potential range from +1.0 to –1.0 V in MeOH or CF_3CH_2OH[14] (Figure 6).

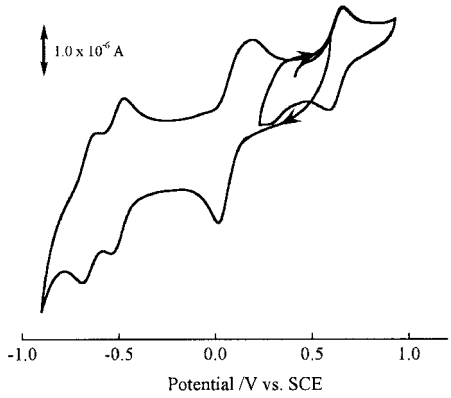

Figure 6. CV of [**2**](PF$_6$)$_3$ in MeOH and CF_3CH_2OH containing nBu$_4$NClO$_4$ (0.1 M) as an electrolyte under N_2. The arrows indicate the rest potentials of the solution and the direction of scan.

The rest potential (E_{rest} = +0.38 V) and the redox potential of the quasi-reversible couple [$E_{1/2}$(1) = +0.66 V] in CF_3CH_2OH are quite close to those in CH_2Cl_2, suggesting the stability of [**2**]$^{4+}$ as well as [**2**]$^{3+}$ in CF_3CH_2OH and MeOH. On the other hand, a peak current of the cathodic wave at E_{pc} = +0.02 V in MeOH is much larger than that of the redox couple at $E_{1/2}$(1) = +0.66 V. Indeed, the controlled potential electrolysis of [**2**]$^{3+}$ at –0.30 V in MeOH consumes 2.96 F mol^{-1} of electricity. Despite the occurrence of such an unusual three-electron reduction of [**2**]$^{3+}$ at E_{pc} = +0.02 V, the pattern of the CV of Figure 6 remained unchanged in multi-potential sweeps in a range of +0.70 V to –0.90 V. We therefore concluded that [**2**]$^{3+}$ undergoes three-electron reduction and oxidation reactions at E_{pc} = +0.02 V and E_{pa} = +0.2 V(broad) in MeOH. The reversible conversion between [**2**]$^{3+}$ and the three-electron oxidation products was also evidenced by the electronic absorption spectra, since the bands of [**2**]$^{3+}$ at 1330 and 766 nm disappeared during the controlled potential electrolysis at –0.30 V in MeOH with generation of two new bands at 848 and 876 nm (Figure 7).

Re-oxidation of the resultant solution at +0.40 V recovered the electronic absorption spectrum of [**2**]$^{3+}$. Taking into account that the three-electron reduction of [**2**]$^{3+}$ takes place at E_{pc} = +0.02 V in MeOH, chemical reduction of [**2**]$^{3+}$ was conducted by treatment with $Na_2S_2O_3$ (excess) in MeOH/H_2O (1:1 v/v) and a dark-purple product was obtained as a PF_6 salt in a 66% yield. The electronic absorption spectra of the product shows two strong CT bands at 848 and 876 nm, suggesting the existence of two types of Ru^{II}(sq) frameworks, and the pattern of the spectrum is fully consistent with that of the electrochemically three-electron-reduced form of [**2**]$^{3+}$ in MeOH. The ESI mass spectra[15] (Figure 8) show a signal at m/z = 738, which corresponds to the summation of the molecular weights of [**2**]^{0} + CH_3OH + H^+ with a composition that is consistent with the elemental analysis of the product.

 © 2005 Wiley-VCH Verlag GmbH & Co. KGaA, Weinheim

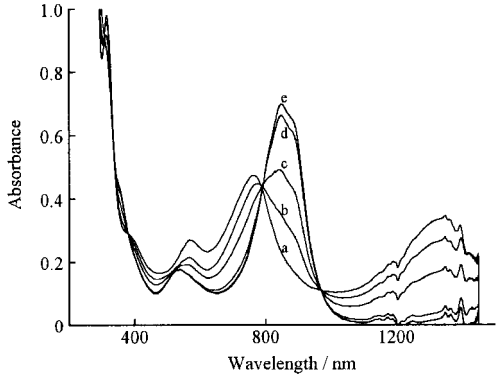

Figure 7. UV/Vis/NIR spectra of [**2**]$(PF_6)_3$: a) before and after electrolysis at b) +0.10 V, c) 0.00 V, d) –0.10 V, and e) –0.20 V in MeOH containing nBu$_4$NClO$_4$ (0.1 M) as an electrolyte under N_2.

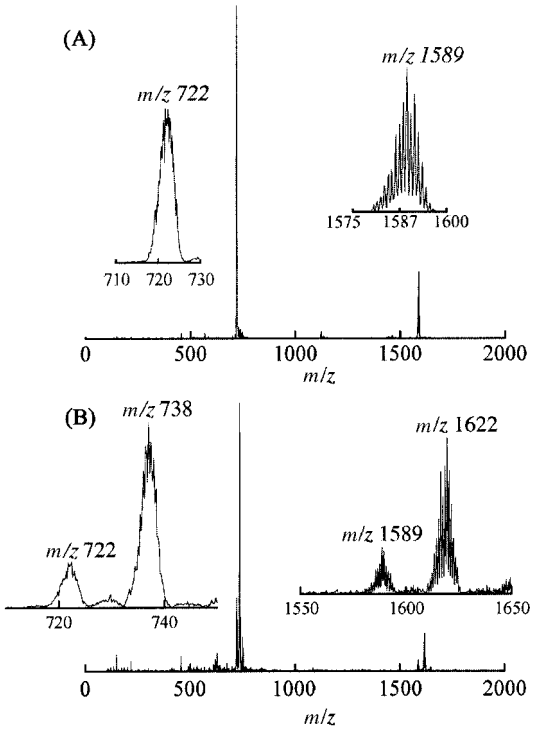

Figure 8. ESI mass spectra of (A) [**2**]$(PF_6)_3$ and (B) [**3**](PF_6) in MeOH.

Based on a combination of the ESI-MS measurements and the UV/Vis/NIR spectra, the most reasonable structure of the product is [{$Ru^{II}(OH_2)$(3,6-tBu$_2$sq)}{Ru^{II}(OMe)(3,6-tBu$_2$sq)}(btpyxa)](PF_6) {[**3**](PF_6)} [Equation (3)].

$$\left[(sq)Ru^{III}\text{–}O\text{—}Ru^{IV}(sq)\right]^{3+} + 3e^- + H^+ + CH_3OH \rightleftharpoons \left[(sq)Ru^{II}(OH_2)\ (MeO)Ru^{II}(sq)\right]^{+} \quad (3)$$

[**2**]$^{3+}$ [**3**]$^{+}$

Chemical reduction of [**2**]$^{3+}$ with a large excess of $Na_2S_2O_3$ in CF_3CH_2OH in place of MeOH gave only [**2**]$^{2+}$ on the basis of ESI-MS and UV/Vis/NIR measurements; the monocationic dimer bearing Ru–OH and Ru–OCH_2CF_3 moieties was not detected at all in the reaction mixtures. The cavity generated by btpyxa may be too small for an attack of CF_3CH_2OH at Ru.

It is worthy of note that the conversion between [**2**]$^{3+}$ and [**3**]$^{+}$ triggered by the three-electron redox reaction takes place reversibly on the CV timescale. Such an unusual reaction can be explained in terms of the fragility of the Ru^{II}–O–Ru^{III} and Ru^{II}–O–Ru^{II} frameworks and the stability of the Ru^{III}–O–Ru^{III} and Ru^{III}–O–Ru^{IV} ones due to the strong electron-donating ability of the μ-oxo ligand. In addition, the flexibility of the btpyxa ligand must play a key role in the smooth μ-oxo bond formation and cleavage reactions. Degradation of the two-electron-reduced form of [**2**]$^{3+}$ ([**2**]$^{+}$) in CH_2Cl_2, therefore, is correlated with the lability of the Ru^{II}–O–Ru^{III} group of [**2**]$^{+}$ in MeOH.

A proposed mechanism for the formation of [**3**]$^{+}$ is depicted in Scheme 5. A one-electron reduction of [**2**]$^{3+}$ at +0.02 V in MeOH will induce protonation of the bridging O atom of [**2**]$^{2+}$, which causes an anodic shift of the reduction potential of the resultant [(sq)Ru^{III}–O(H)–Ru^{III}-(sq)]$^{3+}$. As a result, the latter undergoes further one-electron reduction to generate [(sq)Ru^{II}–O(H)-Ru^{III}(sq)]$^{2+}$ at the same potential. Taking into account that [(sq)Ru^{II}–O–Ru^{III}(sq)]$^{+}$ is not stable in CH_2Cl_2, the Ru–O(H)–Ru bond of [(sq)Ru^{II}–O(H)–Ru^{III}(sq)]$^{2+}$ will be immediately cleaved and the resultant vacant coordination site of Ru attacked by MeOH, which is accompanied by protonation of the Ru–OH group. Such protonation would also cause an anodic shift of the reduction potential of the [{$Ru^{III}(OH_2)$-(sq)}{Ru^{II}(OMe)(sq)}]$^{2+}$ framework. Thus, simultaneous three-electron reduction of [**2**]$^{3+}$ in MeOH is ascribed to a successive one-electron reduction coupled with proton transfer.

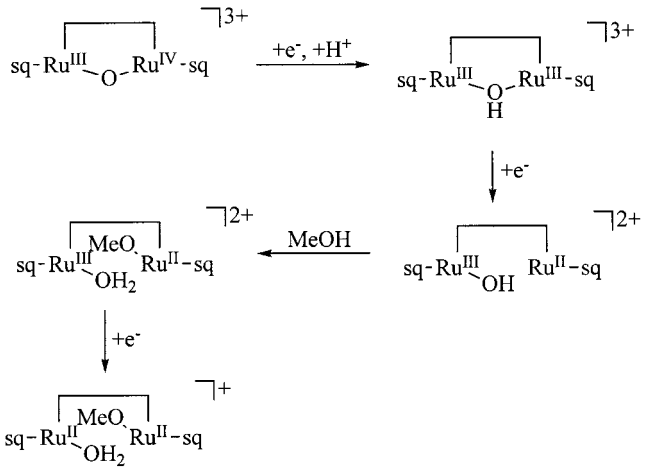

Scheme 5. A proposed mechanism for the reduction of [**2**]$^{3+}$ in MeOH.

The distance between the carbons at the 4- and 5-positions of btpyxa was determined as 4.56 Å by an X-ray structural analysis of [PtCl(btpyxa)]$^{+}$, in which the xanthene skeleton is planar probably due to π-π stacking of two

 © 2005 Wiley-VCH Verlag GmbH & Co. KGaA, Weinheim

trpy planes.[9] On the other hand, the Ru···Ru interatomic distance and the Ru–O–Ru bond angle of the oxo-bridged dimer $[(bpy)_2(OH_2)Ru–O–Ru(OH_2)(bpy)_2]^{4+}$ are 3.708(1) Å and 165.4(3)°.[16] The xanthene framework in the present μ-oxo dimers, therefore, must deviate largely from linear in order to accept two Ru(sq)(trpy) moieties connected by the μ-oxo bond. On the contrary, dinuclear Ru complexes bridged by btpyan, with the rigid anthracene plane, are practically impossible to fit bent Ru–O–Ru bonds. This view reasonably explains why ruthenium dimers bridged by btpyxa form μ-oxo bonds whereas those with btpyan cannot accommodate a bent Ru–O–Ru bond. The unusual simultaneous three-electron redox reaction of $[\mathbf{2}]^{3+}$, which is accompanied by the formation and cleavage of the oxo bridge connecting the two [Ru(trpy)(sq)] frameworks, is therefore ascribed to the synergic effects of participation of proton transfer in the redox reaction, the flexibility of btpyxa, and the high affinity of the μ-oxo bond for high oxidation states of Ru.

Conclusions

Bis(chlororuthenium–semiquinone) $[\mathbf{1}](PF_6)_2$ and μ-oxobis(ruthenium–semiquinone) $[\mathbf{2}](PF_6)_3$ complexes, bridged with btpyxa, have been prepared and their redox behavior investigated. The electronic states of $[\mathbf{1}](PF_6)_2$ and $[\mathbf{2}](PF_6)_3$ were expressed by $[(sq)ClRu^{III}–Ru^{III}Cl(sq)]^{2+}$ and $[(sq)Ru^{III}–O–Ru^{IV}(sq)]^{3+}$, respectively, based on the ESI-MS, elemental analysis, and UV/Vis/NIR spectra. Dicationic $[\mathbf{1}]^{2+}$ undergoes two successive metal-centered one-electron reactions and a ligand-based simultaneous two-electron redox reaction at $E_{1/2}$ = +0.13, +0.09, and –0.75 V (vs. SCE), respectively, in CH_2Cl_2. The mixed-valence state of $[\mathbf{2}]^{3+}$ is quite stable because the ruthenium–semiquinone moieties of $[\mathbf{2}]^{3+}$ interact strongly with each other through the oxo bridge. The mixed-valence complex $[\mathbf{2}]^{3+}$ can be reversibly oxidized and reduced to and from the $Ru^{IV}–Ru^{IV}$ and $Ru^{III}–Ru^{III}$ oxidation states at $E_{1/2}$ = +0.63 and –0.01 V, respectively in CH_2Cl_2. On the other hand, $[\mathbf{2}]^{3+}$ undergoes a three-electron reduction accompanied by cleavage of the Ru–O–Ru bond at E_p = +0.02 V, and $[\{Ru(OMe)(3,5\text{-}tBu_2sq)\}\{Ru(OH_2)(3,5\text{-}tBu_2sq)\}(btpyxa)]^+$ is formed in MeOH. The unusual reversible Ru–O–Ru bond cleavage and formation during the three-electron redox reaction can be ascribed not only to the stability and fragility of the μ-oxo bond at high and low oxidation states of the Ru centers, respectively, but also to the flexibility of btpyxa.

Experimental Section

General Remarks: $RuCl_3·3H_2O$ was purchased from Furuya Metal Co., Ltd., NH_4PF_6 and $Na_2S_2O_3$ from Wako Pure Chemical industries, Ltd. 3,6-Di-*tert*-butylcatechol[17] and btpyxa[9] were synthesized according to literature procedures. All solvents were purified by distillation.

UV/Vis/NIR spectra were recorded on a Shimazu UVPC-3100 UV/Vis/NIR scanning spectrophotometer. ESI mass spectra were measured with a Shimazu LCMS-2010 liquid chromatograph mass spectrometer and Waters Micromass LCT. Elemental analyses were carried out at the Research Center for Molecular-Scale Nanoscience. Cyclic voltammetry (CV) was performed with an ALS/Chi model 660 electrochemical analyzer. CVs were recorded in CH_2Cl_2 or MeOH containing 0.1 mol dm^{-3} of nBu$_4$NClO$_4$ as an electrolyte at a scan rate of 50 mV s^{-1} at 298 K using a glassy carbon disk as the working electrode, a Pt wire as the counter electrode, and Ag/$AgNO_3$ (0.01 M) as the reference electrode. All potentials were converted to SCE ($E_{SCE} = E_{Ag/Ag+} + 0.330$ V). Spectroelectrochemical measurements of UV/Vis/NIR spectra were conducted in CH_2Cl_2 or MeOH containing 0.1 mol dm^{-3} of nBu$_4$NClO$_4$ as an electrolyte using a thin-layer optical cell (path length: 0.5 mm) with a platinum minigrid working electrode sandwiched between the two glass sides of an optical cell, a platinum counter electrode, and an Ag/$AgNO_3$ reference electrode. A Hokuto Denko HA-501 potentiostat and a Shimazu UV-3100PC UV/Vis/NIR scanning spectrophotometer were used. Controlled-potential electrolysis was carried out in CH_2Cl_2 or MeOH at room temperature under N_2 in an electrolysis cell consisting of three compartments: one for the glassy carbon plate (15 mm × 30 mm), the second for a platinum counter electrode (15 mm × 30 mm), which was separated from the working electrode cell by an anion-exchange membrane, and the third for an Ag/$AgNO_3$ reference electrode.

$[Ru_2Cl_6(btpyxa)]$: A dehydrated MeOH solution (30 mL) containing $RuCl_3·3H_2O$ (133 mg, 0.50 mmol) and btpyxa (200 mg, 0.25 mmol) was deoxygenated with a stream of nitrogen gas for 30 min and the solution was then refluxed for 3 h under N_2. The dark brown solid precipitate was filtered off and washed with MeOH (5 mL, three times) and acetone (5 mL, three times) to remove unreacted $RuCl_3$ and btpyxa, and then dried in vacuo. Yield: 204 mg (68%). $C_{53}H_{48}Cl_6N_6ORu_2$ (1199.9): calcd. C 53.05, H 4.03, N 7.00; found C 53.12, H 4.11, N 6.82.

$[Ru_2Cl_2(3,6\text{-}tBu_2sq)_2(btpyxa)](PF_6)_2$ $\{[\mathbf{1}](PF_6)_2\}$: An MeOH suspension (30 mL) containing $[Ru_2Cl_6(btpyxa)]$ (200 mg, 0.17 mmol) and 3,6-di-*tert*-butylcatechol (83 mg, 0.37 mmol) was deoxygenated with a stream of nitrogen gas for 30 min in a 100-mL flask. A deoxygenated MeOH solution (30 mL) of *t*BuOK (124 mg, 1.11 mmol) was then added to the suspension by syringe under N_2 and the reaction mixture was stirred for 24 h at room temperature under N_2. Insoluble $[Ru_2Cl_6(btpyxa)]$ gradually dissolved and the solution became dark-purple. The reaction mixture was then exposed to air. The dark-purple solution turned dark-blue in color in 2 h. After evaporation of the solution to dryness under reduced pressure, the product was purified by column chromatography using Alumina N super-I (ICN Biomedicals GmbH) and acetone/EtOH as an eluent. An aqueous solution of NH_4PF_6 was added to the dark-blue fraction. Concentration of the solution under reduced pressure gave a dark-blue powder, which was separated by filtration and dried in vacuo. Yield: 97 mg (32%). ESI-MS: m/z = 749 ($[\mathbf{1}]^{2+}$). $C_{81}H_{88}Cl_2F_{12}N_6O_5P_2Ru_2$ (1788.6): calcd. C 54.39, H 4.96, N 4.70; found C 54.40, H 5.01, N 4.66.

$[Ru_2(\mu\text{-}O)Cl_4(btpyxa)]·3H_2O$: An MeOH/$H_2O$ (80:20) solution (30 mL) containing $RuCl_3·3H_2O$ (133 mg, 0.50 mmol) and btpyxa (200 mg, 0.25 mmol) was deoxygenated with a stream of nitrogen gas for 30 min, after which time the solution was heated at reflux for 3 h under N_2. The dark-brown hot solution was filtered and evaporated to 10 mL under reduced pressure. The brown solid precipitate was filtered off and washed with cold MeOH (1 mL, three times) to remove unreacted $RuCl_3$ and btpyxa. Yield: 195 mg (65%). $C_{53}H_{54}Cl_4N_6O_5Ru_2$ (1199.0): calcd. C 53.09, H 4.54, N 7.01; found C 52.21, H 4.52, N 6.88.

 © 2005 Wiley-VCH Verlag GmbH & Co. KGaA, Weinheim

$[Ru_2(\mu\text{-}O)(3,6\text{-}t\text{Bu}_2\text{sq})_2(\text{btpyxa})](PF_6)_3$ {[2]$(PF_6)_3$}: An MeOH solution (30 mL) containing $[Ru_2(\mu\text{-}O)Cl_4(\text{btpyxa})]$ (150 mg, 0.13 mmol) and 3,6-di-*tert*-butylcatechol (63 mg, 0.29 mmol) was deoxygenated with a stream of nitrogen gas for 30 min in a 100-mL flask. A deoxygenated MeOH solution (50 mL) of KOAc (852 mg, 8.7 mmol) was then added to the solution by syringe under N_2. The reaction mixture was stirred for 24 h at room temperature under N_2. The reaction mixture gradually turned dark-purple, and it was then exposed to air. The solution's color turned black in 2 h. After evaporation of the solution to dryness under reduced pressure, an aqueous solution of NH_4PF_6 was added to the methanolic solution (5 mL) of the residue. The resultant black powder was filtered and purified by column chromatography using Alumina N super-I (ICN Biomedicals GmbH) and CH_2Cl_2 as the eluent. Evaporation of acetone from the black fraction gave a black powder, which was filtered and dried in vacuo. Yield: 25 mg (11%). ESI-MS: *m*/*z* = 1589 $\{[\mathbf{2}](PF_6)\}^+$, 722 ($[\mathbf{2}]^{2+}$), 481 ($[\mathbf{2}]^{3+}$).[15] $C_{81}H_{88}F_{18}N_6O_6P_3Ru_2$ (1794.6): calcd. C 51.79, H 4.72, N 4.47; found C 51.64, H 4.80, N 4.65.

Chemical Reduction of [2]$(PF_6)_3$: An aqueous solution (5 mL) of $Na_2S_2O_3$ (10 mg, excess) was added to an MeOH solution (5 mL) of [**2**]$(PF_6)_3$ (10 mg, 5.6 μmol) and the solution was stirred for a few minutes. Evaporation of the solution under reduced pressure precipitated a dark-purple powder of [{Ru(OMe)(3,6-$t\text{Bu}_2$sq)}-{Ru(OH_2)(3,6-$t\text{Bu}_2$sq)}(btapyxa)](PF_6) {[**3**](PF_6)}, which was filtered and dried in vacuo. Yield: 6 mg (66%). ESI-MS: *m*/*z* = 1622 $\{[\mathbf{3}](PF_6)\}^+$, 738 ($[\mathbf{3}]^{2+}$).[13] $C_{82}H_{92}F_6N_6O_7PRu_2$ (1620.8): calcd. C 60.73, H 5.78, N 5.18; found C 60.62, H 5.80, N 4.98.

Acknowledgments

We are grateful to Dr. Hideo Kakimi and Dr. Hiroshi Yamasu of Jasco International Co., Ltd. for the ESI-TOF MS measurements.

[1] a) C. R. Pierpont, *Coord. Chem. Rev.* **2001**, *216–217*, 99–125; b) A. B. P. Lever, S. I. Gorelsky, *Coord. Chem. Rev.* **2000**, *208*, 153–167; c) S. I. Gorelsky, E. S. Dodsworth, A. B. P. Lever, A. A. Vlcek, *Coord. Chem. Rev.* **1998**, *174*, 469–494.

[2] a) C. Carbonera, A. Dei, C. Sangregorio, J.-F. Létard, *Chem. Phys. Lett.* **2004**, *396*, 198–201; b) P. Gütlich, A. Dei, *Angew. Chem. Int. Ed. Engl.* **1997**, *36*, 2734–2736; c) D. A. Shultz, in *Magnetism: Molecules to Materials* (Eds.: J. S. Miller, M. Drillon), Wiley-VCH, Weinheim, **2001**, p. 281.

[3] a) K. Yamada, S. Yagishita, H. Tanaka, K. Tohyama, K. Adachi, S. Kaizaki, H. Kumagai, K. Inoue, R. Kitaura, H.-C. Chang, S. Kitagawa, S. Kawata, *Chem. Eur. J.* **2004**, *10*, 2647–2660; b) M. Oh, G. B. Carpenter, D. A. Sweigart, *Acc. Chem. Res.* **2004**, *37*, 1–11; c) W. Paw, J. B. Keister, C. H. Lake, M. R. Churchill, *Organometallics* **1995**, *14*, 767–779.

[4] a) M. Ebadi, A. B. P. Lever, *Inorg. Chem.* **1999**, *38*, 467–474; b) K. Yang, J. A. Martin, S. G. Bott, M. G. Richmond, *Inorg. Chim. Acta* **1997**, *254*, 19–27; c) R. S. da Silva, E. Tfouni, A. B. P. Lever, *Inorg. Chim. Acta* **1995**, *235*, 427–430; d) A. B. P. Lever, H. Masui, R. A. Metcalfe, D. J. Stufkens, E. S. Dodsworth, P. R. Auburn, *Coord. Chem. Rev.* **1993**, *125*, 317–331; e) N. Bag, G. K. Lahiri, P. Basu, A. Chakravorty, *J. Chem. Soc., Dalton Trans.* **1992**, 113–117; f) N. Bag, A. Pramanik, G. K. Lahiri, A. Chakravorty, *Inorg. Chem.* **1992**, *31*, 40–45; g) S. Bhattacharya, C. G. Pierpont, *Inorg. Chem.* **1991**, *30*, 1511–1516; h) H. Masui, A. B. P. Lever, P. R. Auburn, *Inorg. Chem.* **1991**, *30*, 2402–2410; i) P. R. Auburn, E. S. Dodsworth, M. Haga, W. Liu, W. A. Nevin, *Inorg. Chem.* **1991**, *30*, 3502–3512; j) S. R. Boone, C. G. Pierpont, *Polyhedron* **1990**, *9*, 2267–2272; k) M. Haga, K. Isobe, S. R. Boone, C. G. Pierpont, *Inorg. Chem.* **1990**, *29*, 3795–3799; l) D. J. Stufkens, Th. L. Snoeck, A. B. P. Lever, *Inorg. Chem.* **1988**, *27*, 953–956; m) A. B. P. Lever, P. R. Auburn, E. S. Dodsworth, M. Haga, W. Liu, M. Melnik, W. A. Nevin, *J. Am. Chem. Soc.* **1988**, *110*, 8076–8084; n) S. R. Boone, C. G. Pierpont, *Inorg. Chem.* **1987**, *26*, 1769–11773; o) M. Haga, E. S. Dodsworth, A. B. P. Lever, *Inorg. Chem.* **1986**, *25*, 447–453; p) M. Haga, E. S. Dodsworth, A. B. P. Lever, S. R. Boone, C. G. Pierpont, *J. Am. Chem. Soc.* **1986**, *108*, 7413–7414; q) R. B. Salmonsen, A. Abelleira, M. J. Clarke, S. D. Pell, *Inorg. Chem.* **1984**, *23*, 385–387.

[5] a) M. Kurihara, S. Daniele, K. Tsuge, H. Sugimoto, K. Tanaka, *Bull. Chem. Soc. Jpn.* **1998**, *71*, 867–875; b) K. Tsuge, K. Tanaka, *Chem. Lett.* **1998**, 1069–1070; c) K. Tsuge, M. Kurihara, K. Tanaka, *Bull. Chem. Soc. Jpn.* **2000**, *73*, 607–614.

[6] a) K. Kobayashi, H. Ohtsu, T. Wada, K. Tanaka, *Chem. Lett.* **2002**, 868–869; b) K. Kobayashi, H. Ohtsu, T. Wada, T. Kato, K. Tanaka, *J. Am. Chem. Soc.* **2003**, *125*, 6729–6739.

[7] a) H. Sugimoto, K. Tanaka, *J. Organomet. Chem.* **2001**, *622*, 280–285; b) T. Wada, T. Fujihara, M. Tomori, D. Ooyama, K. Tanaka, *Bull. Chem. Soc. Jpn.* **2004**, *77*, 741–749.

[8] a) T. Wada, K. Tsuge, K. Tanaka, *Angew. Chem.* **2000**, *112*, 1542–1545; *Angew. Chem. Int. Ed.* **2000**, *39*, 1479–1482; b) T. Wada, K. Tsuge, K. Tanaka, *Inorg. Chem.* **2001**, *40*, 329–337.

[9] R. Okamura, T. Wada, K. Aikawa, T. Nagata, K. Tanaka, *Inorg. Chem.* **2004**, *43*, 7210–7217.

[10] The difference in the redox potential between the $[\mathbf{1}]^{2+}$/ $[\mathbf{1}]^+$ and $[\mathbf{1}]^+$ /$[\mathbf{1}]^0$ couples ($\Delta E_{1/2}$ = 0.04 V) is too small to form pure $[\mathbf{1}]^+$ in the bulk electrolysis. So, bulk electrolysis was conducted at 0 V. Accordingly, disproportionation of $[\mathbf{1}]^+$ to $[\mathbf{1}]^{2+}$ and $[\mathbf{1}]^0$ [Equation (1)] has no influence on the number of electrons consumed in the electrolysis.

[11] C. L. Bird, A. T. Kuhn, *Chem. Soc. Rev.* **1981**, *10*, 49–82.

[12] R. W. Callahan, G. M. Brown, T. J. Meyer, *Inorg. Chem.* **1975**, *14*, 1443–1453.

[13] The controlled-potential electrolysis of $[\mathbf{2}]^{2+}$ at –0.60 V in CH_2Cl_2 resulted in disappearance of the 872-nm band of $[\mathbf{2}]^{2+}$ and generation of a weak, broad band at 864 nm. Re-oxidation of the solution at –0.25 V, however, did not recover the spectrum of $[\mathbf{2}]^{2+}$ nor produce any strong absorption bands in the visible region. This result implies the dissociation of the dioxolene ligands of $[\mathbf{2}]^+$ during the electrochemical reduction.

[14] CF_3CH_2OH was used as a solvent for the CV of $[\mathbf{2}]^{3+}$ instead of MeOH because MeOH is oxidized above ca. +0.8 V in the conditions of CV.

[15] The trication was not detected in the ESI mass spectrum of [**2**]$(PF_6)_3$ in MeOH or CH_2Cl_2 using a normal electrospray ionization probe because $[\mathbf{2}]^{3+}$ is readily reduced to $[\mathbf{2}]^{2+}$ under the experimental conditions used. The signals of $[\mathbf{2}]^{3+}$ were, however, detected as a cluster ion with solvent at 30 °C by ESI-TOF MS employing a Nanoflow-ESI probe with an orthogonal acceleration time-of-flight (Waters–Micromass). The monocation was not detected in the ESI-mass spectrum of [**3**](PF_6) in MeOH because $[\mathbf{3}]^+$ is readily oxidized to $[\mathbf{3}]^{2+}$, which was detected as the monocation $\{[\mathbf{3}](PF_6)\}^+$.

[16] J. A. Gilbert, D. S. Eggleston, W. R. Murphy Jr., D. A. Geselowitz, S. W. Gersten, D. J. Hodgson, T. J. Meyer, *J. Am. Chem. Soc.* **1985**, *107*, 3855–3864.

[17] I. S. Belostotskaya, N. L. Komissarova, E. V. Dzhuaryan, V. V. Ershov, *Seriya Khimicheskaya* **1972**, *7*, 1594–1596.

Received: February 17, 2005
Published Online: August 17, 2005

 © 2005 Wiley-VCH Verlag GmbH & Co. KGaA, Weinheim

Bifunctional Bioorganometallic Iridium(III)–Platinum(II) Complexes Incorporating Both Intercalative and Covalent DNA Binding Capabilities

Susan Gençaslan[a] and William S. Sheldrick*[a]

Keywords: Iridium / Platinum / Peptides / DNA binding / Bioinorganic chemistry

The DNA binding of bifunctional Ir^{III}–Pt^{II} complexes containing $[(\eta^5\text{-Cp}^*)Ir(dppz)]^{2+}$ and $[Pt(terpy)]^{2+}$ or *trans*-$[PtL_2L']^{2+}$ fragments (L = NH_3, L′ = DMF; L = H_2O, L′ = NH_3) bridged by flexible κ*S*:κ*N*(amino)-coordinated methionine-containing peptides has been studied by UV/Vis and CD spectroscopy. Stable intercalative binding of the Ir^{III} fragment of the complexes $[\{(\eta^5\text{-Cp}^*)Ir(dppz)\}(\mu\text{-peptide-}\kappa S{:}\kappa N)\{Pt(terpy)\}](CF_3SO_3)_4$ (**5**) (peptide = H-Gly-Gly-Phe-Met-OH; H-Gly-OH = glycine, H-Phe-OH = L-phenylalanine, H-Met-OH = L-methionine) and **6** [peptide = H-$(Ala)_4$-Met-OH; H-Ala-OH = L-alanine] is indicated by their steady decrease in absorbance at maxima between 350 and 390 nm on titration with CT DNA and by the bathochromic shifts of these maxima. Binding constants K_b of $1.4(4)\times10^6$ M^{-1} for both **5** and **6** and site sizes *s* of 2.8(1) and 2.2(1), respectively, are in accordance with this monofunctional mode. Both peptide chain length and the site(s) of the labile Pt^{II} substituents DMF or H_2O play an important role in determining the degree of intercalation of the Ir^{III} fragment and the extent of helix distortion caused by simultaneous covalent binding of Pt^{II} centres for the DNA interaction of the complexes $[\{(\eta^5\text{-Cp}^*)Ir(dppz)\}(\mu\text{-peptide-}\kappa S{:}\kappa N)\{trans\text{-}(PtL_2L')\}]^{4+}$ **7**–**10**. Whereas both **9** and **10** (L = H_2O, L′ = NH_3; peptide = H-Gly-Met-OH or H-Gly-Gly-Met-OH) exhibit a high degree of bifunctional binding [**9**, K_b = $1.1(5)\times10^6$ M^{-1}, *s* = 1.3(1); **10**, K_b = $1.4(7)\times10^6$ M^{-1}, *s* = 2.1(1)], CD spectroscopy indicates that a more pronounced reorganisation of the DNA helix is required for the former complex with its shorter peptide. Effective intercalation is also observed for **8** (L = NH_3, L′ = DMF; peptide = H-Gly-Gly-Met-OH) but not for **7** with the analogous Pt^{II} fragment but a shorter bridging peptide (H-Gly-Met-OH).

(© Wiley-VCH Verlag GmbH & Co. KGaA, 69451 Weinheim, Germany, 2005)

Introduction

Multinuclear platinum complexes containing two or more square-planar platinum(II) centres capable of covalent binding to DNA nucleobases represent a relatively new class of anticancer agents.[1–3] They have been shown to exhibit activity in cancer cell lines with intrinsic resistance to cisplatin and can also overcome acquired resistance to this successful antitumor drug, presumably as a result of their participation in long-range interstrand DNA adducts. Length, conformational flexibility, total charge and hydrogen-bonding donor capacity of the linking ligands (e.g. 1, *n*-diaminoalkanes) have been identified by Farrell[1,2] as paramount factors in the design of multinuclear platinum drugs.

A modified approach to the polynuclear concept involves the design of bifunctional complexes with two distinct DNA binding capabilities connected by a rigid or flexible bridging moiety. For instance octahedral ruthenium(II) and square-planar platinum(II) centres have been linked in the heterodinuclear complexes $[\{cis\text{-}RuCl_2(Me_2SO)_3\}(\mu\text{-}H_2N(CH_2)_4NH_2)\{cis\text{-}PtCl_2(NH_3)\}]$[4] and [(terpy)Ru(μ-dtdeg)PtCl]Cl_3 {terpy = 2,2′:6′,2′′-terpyridine, dtdeg = bis[4′-(2,2′:6′,2′′-terpyridyl)]diethyleneglycol ether}.[5] However, the light-sensitive and highly reactive former complex proved to be unsuitable as a DNA binding probe and the latter complex exhibited a lower cytotoxicity towards cisplatin-sensitive cell lines in comparison to $[PtCl(terpy)]\cdot2H_2O$, presumably due to the fact that its ruthenium moiety can only participate in electrostatic DNA interactions. Attempts to improve on the effectiveness of cisplatin have also involved the tethering of intercalating acridine[6,7] and phenazine[8,9] groups to platinum(II) centres. The presence of an intercalative chromophore leads both to a marked increase in the rate of DNA platination and to an altered sequence specificity.[7,9] Metallointercalators such as $[Pt(terpy)]^{2+}$[10,11] or $[Ru(dppz)(phen)_2]^{2+}$ (dppz = dipyrido[3,2-*a*:2′,3′-*c*]phenazine)[12] have also been linked to identical fragments to afford bifunctional complexes with high DNA binding affinities. The use of dppz-containing compounds to promote intercalative DNA binding is well documented.[13]

We have recently demonstrated that bioorganometallic metallointercalators of the type $[(\eta^5\text{-Cp*})Ir(dppz)(peptide)]^{n+}$ (*n* = 1–3)[14] and $[(\eta^6\text{-arene})Ru(dppz)(peptide)]^{n+}$ (*n* = 1–3; arene = C_6H_6, $Me_3C_6H_3$, C_6Me_6)[15] exhibit strong side-on intercalative binding into DNA with equilibration constants K_b of up to 5.5×10^6 M^{-1}. Following initial

[a] Lehrstuhl für Analytische Chemie, Ruhr-Universität Bochum, 44780 Bochum, Germany
Fax: +49-234-32-14742
E-Mail: William.Sheldrick@ruhr-uni-bochum.de

chemospecific κ*S* coordination of the organometallic [(η^5-Cp*)Ir(dppz)]$^{2+}$ or [(η^6-arene)Ru(dppz)]$^{2+}$ fragment in complexes of methionine-containing peptides, a second similar or different metal fragment can be introduced by employing either the terminal amino function or the donor atom of a suitable side chain as the additional binding site. The feasibility of this concept has been demonstrated for [{(η^5-Cp*)Ir(dppz)}$_2$(μ-H-Met-Met-OH-κ*S*:κ*S*′)](CF$_3$SO$_3$)$_4$ and [{(η^5-Cp*)Ir(dppz)}(μ-H-Gly-Met-OH-κ*S*:κ*N*$_G$){Pt(terpy)}](CF$_3$SO$_3$)$_4$.[16] We now extend the design strategy to iridium(III)–platinum(II) complexes exhibiting an intercalating [(η^5-Cp*)Ir(dppz)]$^{2+}$ moiety tethered to a *trans*-[PtL$_2$L′] (L = NH$_3$, H$_2$O;L′ = DMF, NH$_3$) fragment. To the best of our knowledge, such compounds of the type [{(η^5-Cp*)Ir(dppz)}(μ-peptide-κ*S*:κ*N*){*trans*-(PtL$_2$L′)}]$^{4+}$ represent the first examples of bifunctional complexes containing both a metallointercalator and a covalent DNA binding capability.

Results and Discussion

Monofunctional Starting Compounds [(η^5-Cp*)Ir(dppz)(peptide-κ*S*)](CF$_3$SO$_3$)$_2$ 3 and 4

The bioorganometallic starting compounds of the type [(η^5-Cp*)Ir(dppz)(peptide-κ*S*)](CF$_3$SO$_3$)$_2$ [peptide = H-Gly-Met-OH,[16] H-Gly-Gly-Met-OH,[14] H-Gly-Gly-Phe-Met-OH (**3**), H-(Ala)$_4$-Met-OH (**4**)] were prepared as described previously for H-Gly-Met-OH[16] and H-Gly-Gly-Met-OH[14] by initially refluxing [(η^5-Cp*)Ir(acetone)$_3$](CF$_3$SO$_3$)$_2$ (**1**)[17] with dppz in CH$_3$OH/CH$_2$Cl$_2$ for 2 h. Addition of the appropriate peptide in CF$_3$COOH to the resulting [(η^5-Cp*)Ir(acetone)(dppz)](CF$_3$SO$_3$)$_2$ solution leads to formation of the desired complexes [(η^5-Cp*)-Ir(dppz)(peptide-κ*S*)](CF$_3$SO$_3$)$_2$ (Scheme 1). Strongly acidic conditions (CF$_3$COOH) are, however, necessary to achieve chemospecific κ*S* coordination of the methionine side chains in the presence of non-protected terminal amino or carboxylate groups. After stirring at 50 °C for 18 h and volume reduction, the products can be precipitated by addition of diethyl ether. The remaining solution contains a residual quantity of [(η^5-Cp*)Ir(CF$_3$COO)(dppz)](CF$_3$SO$_3$) (**2**), which could be subsequently crystallised in low yield.

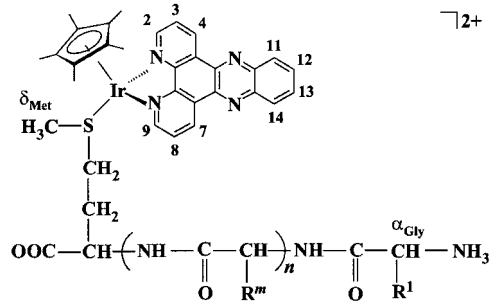

3 $R^3 = CH_2\text{-}C_6H_5$, $R^2 = R^1 = H$ ($n = 2$; $m = 2, 3$)
4 $R^1 - R^4 = CH_3$ ($n = 3$; $m = 2, 3, 4$)

Scheme 1.

As depicted in Figure 1, complex **2** exhibits an interplanar angle of 56.1° between its Cp* and dppz ring systems and contains a κ*O*-coordinated trifluoroacetate ligand with an Ir–O2 distance of 2.156(7) Å. Although individual [(η^5-Cp*)Ir(CF$_3$COO)(dppz)]$^+$ cations dimerise through π–π interactions of their parallel phenanzine ligands in the crystal structure of **2** (Figure 2), more extensive base stacking is prevented by the steric requirements of the Cp* and CF$_3$COO$^-$ ligands. An interplanar distance of 3.48 Å is observed for the dppz ring systems within such cation pairs. Dimerisation of complexes containing the [(η^5-Cp*)-Ir(dppz)]$^{2+}$ fragment will, of course, be expected in solution and also possibly as an external binding mode on the DNA surface for the bifunctional complexes studied in the present work. This prompted us to determine the dimerisation constant K_D for [(η^5-Cp*)Ir(dppz)(H-Gly-Gly-Met-OH-κ*S*)](CF$_3$SO$_3$)$_2$ as a typical monofunctional member of this class of bioorganometallic compounds.

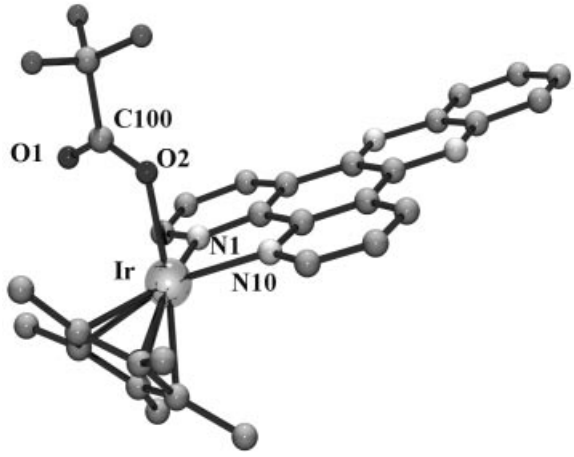

Figure 1. Molecular structure of the cation of [(η^5-Cp*)-Ir(CF$_3$COO)(dppz)](CF$_3$SO$_3$) (**2**): Selected bond lengths [Å] and angles [°]: Ir–N1 2.109(8), Ir–N10 2.106(8), Ir–O2 2.156(7), Ir–C 2.158(4)–2.198(4), C100–O1 1.20(2), C100–O2 1.26(1), N1–Ir–N10 77.4(3), N1–Ir–O2 84.6(3), N10–Ir–O2 82.9(3).

The [(η^5-Cp*)Ir(dppz)(H-Gly-Gly-Met-OH)]$^{2+}$ cation displays two characteristic absorption maxima at 364 and 382 nm for the π–π* transitions of its dppz ligand. At very low concentrations (10 μM or lower) in a 10 mM phosphate buffer at pH = 7.2, the molar absorption coefficients ε_{364} and ε_{382} are independent of the cation concentration, i.e. **2** is present as a monomer. The observed hypochromic shifts in the ε values for the concentration range 10–180 μM (Figure 3) are indicative of increasing intermolecular dipole–dipole interactions between dppz ligands and thereby of dimerisation. Using the equation of Schwarz et al.,[18] a dimerisation constant K_D of 6.4×10^3 M^{-1} was determined on the basis of a regression analysis for ($\varepsilon_M - \varepsilon_{obsd.}$) ($\lambda$ = 382 nm) in the concentration range 10–250 μM. Respective values of 13395 L·mol^{-1}·cm^{-1} and 8894 L·mol^{-1}·cm^{-1} were obtained for the molar absorption constants ε_M and ε_D of the monomer and dimer. These represent a relative decrease in absorption $\Delta A/A$ at 382 nm of 25.4%. The strength of the base stacking for the large planar dppz ligands of [(η^5-Cp*)Ir(dppz)(H-Gly-Gly-Met-OH)]$^{2+}$ is underlined by

 © 2005 Wiley-VCH Verlag GmbH & Co. KGaA, Weinheim

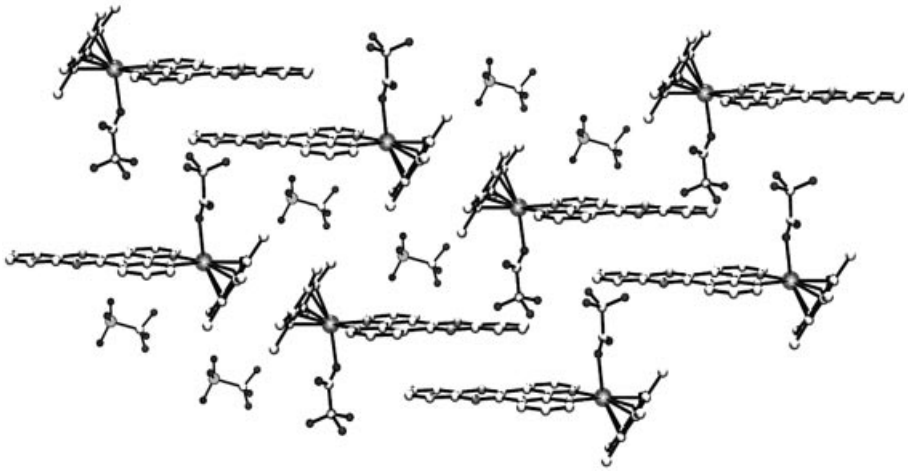

Figure 2. Dimerisation of the $[(\eta^5\text{-Cp*})Ir(CF_3COO)(dppz)]^+$ cations of **2** in the crystal lattice.

comparing its K_D value with the lower values of 4×10^3 and 5×10^2 M^{-1} for [PtCl(terpy)]Cl[19] and proflavine.[18]

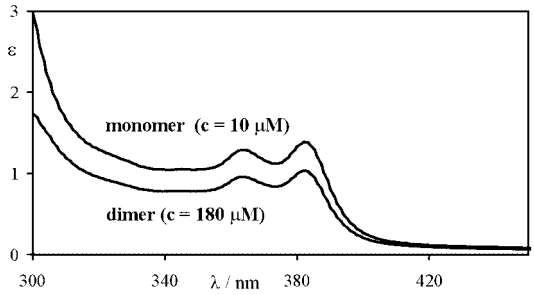

Figure 3. Dimerisation of the $[(\eta^5\text{-Cp*})Ir(dppz)(H\text{-}Gly\text{-}Gly\text{-}Met\text{-}OH)]^{2+}$ cations in a phosphate buffer at pH = 7.2 as demonstrated by the hypochromic shift of the molar absorption coefficients ε ($L \cdot mol^{-1} \cdot cm^{-1}$) in the wavelength range 300–420 nm.

Bifunctional Iridium(III)–Platinum(II) Metallointercalators 5 and 6

The bifunctional iridium(III)–platinum(II) metallointercalators $[\{(\eta^5\text{-Cp*})Ir(dppz)\}(\mu\text{-H-Gly-Gly-Phe-Met-OH-}\kappa S{:}\kappa N_G)\{Pt(terpy)\}](CF_3SO_3)_4$ (**5**) and $[\{(\eta^5\text{-Cp*})Ir(dppz)\}(\mu\text{-H-(Ala)}_4\text{-Met-OH-}\kappa S{:}\kappa N_G)\{Pt(terpy)\}](CF_3SO_3)_4$ (**6**) (Figure 4) are prepared by addition of **3** or **4**, respectively, to an aqueous $[Pt(OH_2)(terpy)](CF_3SO_3)_2$ solution. All four complexes were characterised by elemental analysis, FAB mass spectrometry, ^{1}H and ^{13}C NMR, IR and UV/Vis spectroscopy. Downfield ^{1}H NMR shifts of 0.10 ppm are observed for the signals of the Cp* methyl protons of the κ*S*-coordinated $[(\eta^5\text{-Cp*})Ir(dppz)]^{2+}$ fragments in **3**–**6** in comparison to the δ value of 1.74 for this singlet in a CD_3OD solution of the chloro complex $[(\eta^5\text{-Cp*})Ir(Cl)(dppz)](CF_3SO_3)$.[14] In contrast, the signals of the methionine δ-CH_3 protons adjacent to the coordinated thioether sulfur atoms in the met-containing complexes exhibit a more pronounced opposite upfield shift from typical values of ca. 2.10 ppm in the free peptide to resonance positions in the range δ = 1.79–1.81 ppm. As previously noted for both $[(\eta^5\text{-Cp*})Ir(dppz)]^{2+}$ and $[(\eta^6\text{-arene})Ru(dppz)]^{2+}$ derivatives[14,15] this behaviour represents a striking reversal of the typical positive shift displayed by the signals of the δ-CH_3 protons in analogous half-sandwich organometallic complexes without a chelating aromatic ligand such as dppz.[20,21] The shielding cone of the neighbouring dppz ligand may well be responsible for this anomalous upfield shift in **3**–**6**.

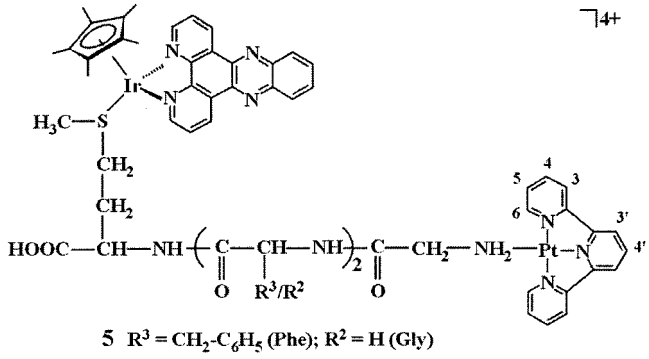

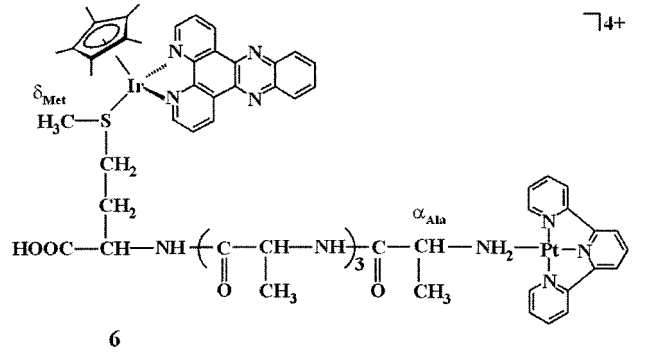

Figure 4. Tetracations of the bifunctional complexes **5** and **6**.

Additional κ*N* coordination of the $[Pt(terpy)]^{2+}$ fragment by the terminal amino group of the peptide ligands in **5** and **6** leads to significant upfield shifts in the δ values of the H6

 © 2005 Wiley-VCH Verlag GmbH & Co. KGaA, Weinheim

and H5 protons from their resonance positions of δ = 9.00 and 7.86 ppm in [PtCl(terpy)]Cl (CD_3OD solution). Respective shifts of δ = 8.83/8.88 and 7.82 ppm are observed for the bifunctional complexes. Further clear evidence for κ*N* coordination is also provided by the characteristic upfield shifts recorded for the signals of the adjacent α proton(s) of the terminal amino acid residue in **5** and **6**. Whereas the α_{Gly1} singlet exhibits only a modest shift from δ = 3.65 ppm in the free peptide to 3.61 ppm upon coordination in **5**, a striking move from δ = 3.94 to 3.72 ppm is observed for signal of the α_{Ala1} proton in **6**.

DNA Binding Studies for 3–6

A pronounced decrease in absorbance at 364 and 382 nm and the bathochromic shifts of these absorption maxima (Figure 5) on UV/Vis titration of 20 μM solution of **3**–**6** with calf thymus DNA (CT DNA) are clearly indicative of dppz intercalation into DNA. In contrast to the hypochromic shifts $-\Delta A/A$ of 32.1–38.7% for **3**–**6** at 382 nm with their associated red shifts of 5 nm, a much smaller decrease in absorbance of only 12.2 or 11.0%, respectively, is observed for the terpyridine ligand at its 343 nm maximum in **5** and **6**, which remains unshifted. As no correction for the increase in DNA absorbance at 343 nm (due to its 15-fold increase in concentration during the UV/Vis titration) was made, it is reasonable to assume that terpyridine intercalation will not be of great significance for the binding of **5** and **6**. Absorption data collected at 382 nm for **3**–**6** were fitted by least squares using the non-cooperative non-specific binding model by Bard and Thorp.[22,23] Best fits were obtained for the intrinsic binding constants K_b and the average binding site sizes *s* listed in Table 1. Both these parameters and the melting temperature shifts ΔT_m for **3** and **4** are closely similar to the values of $1.2(1)\times10^6$ M^{-1} (K_b), 1.6 (*s*) and 6.9 °C (ΔT_m) previously reported for the analogous compound [(η^5-Cp*)Ir(dppz)(H-Gly-Gly-Met-OH-κ*S*)](CF$_3$SO$_3$)$_2$.[14] We chose the longer oligopeptides H-Gly-Gly-Phe-Met-OH and H-(Ala)$_4$-Met-OH in the hope that these might enable long-range bis-intercalation of their bifunctional complexes **5** and **6** into the DNA helix.

However, as simultaneous intercalation of both the aromatic ligands of the [(η^5-Cp*)Ir(dppz)]$^{2+}$ and [Pt(terpy)]$^{2+}$ fragments would be predicted to afford significantly higher binding constants and site sizes [i.e. the average number of nucleobase pairs between the specific or middle binding position of neighbouring mono- or bis-metallointercalators, respectively], the calculated values of 1.4×10^6 M^{-1} and 2.8(1)/2.2(1) for K_b and *s* in **5** and **6** are clearly in accordance with effectively exclusive [(η^5-Cp*)Ir(dppz)]$^{2+}$ mono-intercalation. We have previously reported similar binding constants [$1.5(1)\times10^6$ M^{-1} and $3(3)\times10^6$ M^{-1}] and site sizes (2.6, 2.9) which also indicate only mono-intercalation of the Ir^{III} fragment for two likewise intercalators [{(η^5-Cp*)-Ir(dppz)}$_2$(μ-H-Met-Met-OH-κ*S*:κ*S*′)](CF$_3$SO$_3$)$_4$ and [{(η^5-Cp*)Ir(dppz)}(μ-H-Gly-Met-OH-κ*S*:κ*N*$_G$){Pt(terpy)}]-(CF$_3$SO$_3$)$_4$.[16] These values, taken together with the successful fitting of the UV/Vis data for all complexes in a wide complex/DNA molar ratio {*r* = 0.067–1.0 with [DNA] = M(nucleotide)} indicate that the DNA binding mode of such metallointercalators must be effectively independent of the number of amino acid residues. Whereas the extended aromatic system of dppz preferentially intercalates into DNA, the stabilising role of the smaller terpyridine ligands will presumably be restricted to intermolecular base stacking on the DNA surface. The relatively limited decrease in absorbance at the terpy maximum (λ = 343 nm) observed during UV/Vis titrations is in accordance with this binding description (Figure 5). Interestingly, the highest K_b and *s* values were determined for the H-Gly-Met-OH complex, thereby suggesting that such surface π–π interactions may, indeed, be more favourable for the [Pt(terpy)]$^{2+}$ moiety when bridged to the Ir^{III} fragment by this shorter peptide.

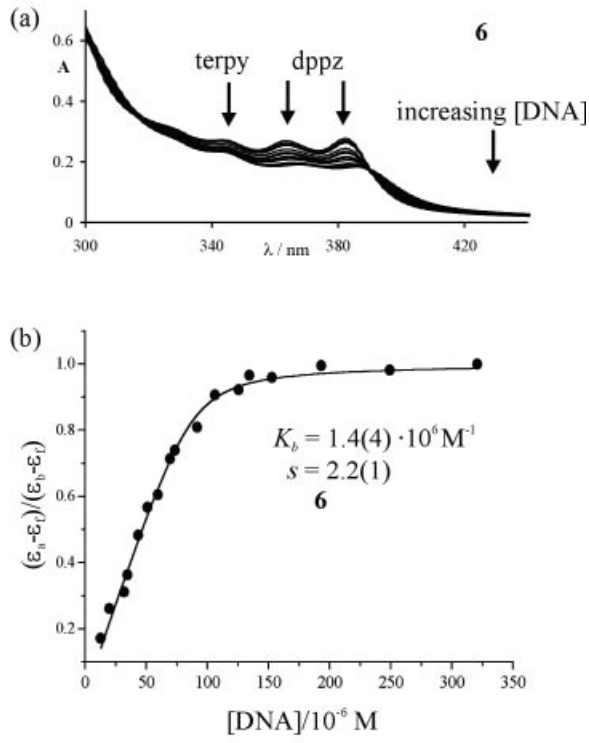

Figure 5. (a) UV/Vis spectra for the titration of [{(η^5-Cp*)Ir(dppz)}-[μ-(Ala)$_4$-Met-OH-κ*S*:κ*N*]{Pt(terpy)}](CF$_3$SO$_3$)$_4$ **6** (20 μM) in a 10 mM phosphate buffer (pH = 7.2) with CT DNA [0–300 μM (nucleotide)]; (b) the best least-squares fit for **6**/DNA to the non-cooperative non-specific binding model by Bard and Thorp.[22,23]

Table 1. Binding constants K_b, site sizes *s* and melting temperature shifts ΔT_m for the interaction of CT DNA with complexes **3**–**6** in a 10 mM phosphate buffer at pH = 7.2.

Complex	K_b [M^{-1}]	s	ΔT_m [°C]
3	$2.3(3)\times10^6$	2.6(1)	5.2
4	$1.0(3)\times10^6$	1.8(1)	5.2
5	$1.4(4)\times10^6$	2.8(1)	7.2
6	$1.4(4)\times10^6$	2.2(1)	8.2
Ref.[14][a]	$1.2(1)\times10^6$	1.6(1)	6.9

[a] For [(η^5-Cp*)Ir(dppz)(H-Gly-Gly-Met-OH-κ*S*)](CF$_3$SO$_3$)$_2$.

 © 2005 Wiley-VCH Verlag GmbH & Co. KGaA, Weinheim

Bifunctional Iridium(III)–Platinum(II) Complexes 7–10 with Both Intercalative and Covalent DNA Binding Capabilities

Treatment of the appropriate monofunctional starting compound $[(\eta^5\text{-Cp*})Ir(dppz)(peptide\text{-}\kappa S)](CF_3SO_3)_2$ with *trans*-$[Pt(DMF)_2(NH_3)_2](NO_3)_2$ in DMF affords the bifunctional complexes $[\{(\eta^5\text{-Cp*})Ir(dppz)\}(\mu\text{-peptide-}\kappa S{:}\kappa N_{G1})(trans\text{-}\{Pt(NH_3)_2DMF\})](CF_3SO_3)_2(NO_3)_2$ (peptide = H-Gly-Met-OH **7**, H-Gly-Gly-Met-OH **8**) shown in Figure 6. The required *trans*-$[Pt(DMF)_2(NH_3)_2](NO_3)_2$ is prepared in situ by addition of 2 equiv. of $AgNO_3$ to *trans*-$[PtCl_2(NH_3)_2]$ in DMF solution followed by filtration of the precipitated AgCl. Retention of the κ*S* coordination mode by the $[(\eta^5\text{-Cp*})Ir(dppz)]^{2+}$ fragment is confirmed by the characteristic ^{1}H NMR upfield shifts of the methionine δ-CH_3 singlets to δ = 1.79 ppm in **7** and **8**. Replacement of the Ir^{III} fragment by *trans*-$[Pt(DMF)(NH_3)_2]$ would, in contrast, lead to a downfield shift for the signals of these protons from δ ≈ 2.10 ppm in the free peptides to a value in the range δ = 2.3–2.5 ppm.[24,25] Coordination of the Pt^{II} moiety by the N-terminal glycine (Gly1) amino function in **7** and **8** is indicated by the pronounced upfield shifts of the α_{Gly1} singlets from δ = 3.72/3.75 ppm in the free peptides to δ = 3.64/3.62 ppm in the bifunctional complexes. The resonances of the *trans*-sited DMF ligand (CD_3OD solution) are observed with appropriate integral values at δ = 2.84, 2.98 (CH_3) and 7.96 (CH) in **7** and 2.85, 2.97 (CH_3) and 7.96 (CH) ppm in **8**.

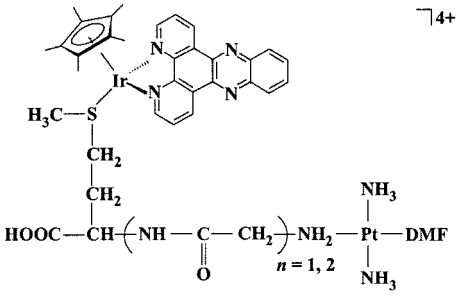

7, n = 1; **8**, n = 2

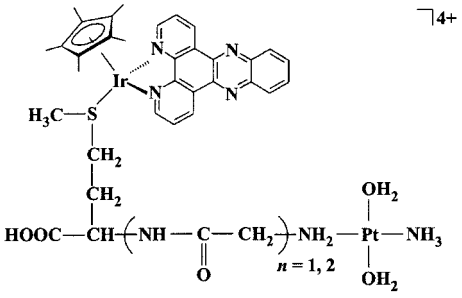

9, n = 1; **10**, n = 2

Figure 6. Tetracations of the bifunctional complexes **7**–**10**.

Bifunctional organometallic compounds of the type $[\{(\eta^5\text{-Cp*})Ir(dppz)\}(\mu\text{-peptide-}\kappa S{:}\kappa N_{G1})(trans\text{-}\{Pt(NH_3)(OH_2)_2\})][Et_4N](CF_3SO_3)_5$ **9** and **10** are prepared by reaction of the starting compounds $[(\eta^5\text{-Cp*})Ir(dppz)(peptide\text{-}\kappa S)](CF_3SO_3)_2$ with $(Et_4N)[PtCl_3(NH_3)]$ in aqueous solution following initial precipitation and removal of AgCl on treatment of the Pt^{II} complex with 3 equiv. of $Ag(CF_3SO_3)$. Although the molecular ions, themselves, could not be detected by FAB mass spectrometry, the bridging μ-1κ*S*:2κN_{Gly1} coordination mode is clearly confirmed for the peptides H-Gly-Met-OH (**9**) and H-Gly-Gly-Met-OH (**10**) by the pronounced ^{1}H NMR upfield shifts of their δ_{Met}-CH_3 and α_{Gly1}–CH_2 singlets to δ = 1.79/3.64 and 1.81/3.64 ppm, respectively. The much stronger *trans* effect of NH_3 in comparison to the aqua ligands (E_t values 200:1)[26] leads to exclusive κ*N* coordination of the peptide amino group in *trans* position to the ammine ligand in **9** and **10**. Sharp singlets for Me α_{Gly1}–CH_2 protons are also in accordance with the presence of only the *trans* isomer.

Before turning in detail to DNA interaction studies of the bifunctional complexes **7**–**10** with their complementary covalent and intercalative binding capabilities, it is necessary to consider possible competitive substitution reactions for the nucleobase nitrogen atoms, i.e. whether Ir^{III} or Pt^{II} will be preferred as coordination partners. The kinetics of nucleobase binding was, therefore, studied by ^{1}H NMR in an exemplary manner for the reaction of **7** with the model purine base 9-ethylguanine at a 1:2 molar ratio in a 10 mM phosphate buffer (pH = 7.2) at T = 298 K (Figure 7). As indicated by the rapid growth in the free DMF CH singlet at δ = 7.94 ppm in comparison to the declining resonance at δ = 7.90 ppm (coordinated DMF), substitution by the hydrogen- or dihydrogenphosphate buffer anions is relatively rapid. The extent of the subsequent slow replacement of the new anionic ligand by κ*N*7-coordinated 9-ethylguanine can be gauged by the integral ratio of the H8 resonances at δ = 8.32 (coordinated) and 7.80 (free) ppm. After 5 d, ca. 90% of **7** is converted into $[\{(\eta^5\text{-Cp*})Ir(dppz)\}(\mu\text{-H-Gly-Met-OH-}\kappa S{:}\kappa N_{G1})[trans\text{-}\{Pt(9\text{-ethylguanine})(NH_3)_2\}]]^{4+}$ (**11**) depicted in Figure 8. Exclusive Pt^{II} coordination is confirmed by the unchanged resonance positions and integral values for the dppz and δ_{Met} protons after this period of time.

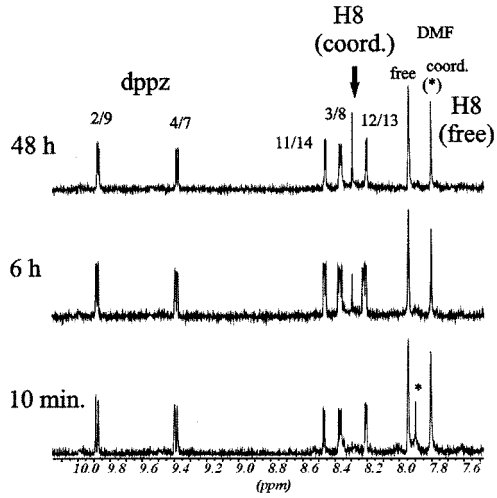

Figure 7. Aromatic region of the ^{1}H NMR spectrum of a 1:2 reaction mixture of **7** (c = 5 mM) and 9-ethylguanine in a 10 mM phosphate buffer at pH = 7.2 and T = 298 K.

 © 2005 Wiley-VCH Verlag GmbH & Co. KGaA, Weinheim

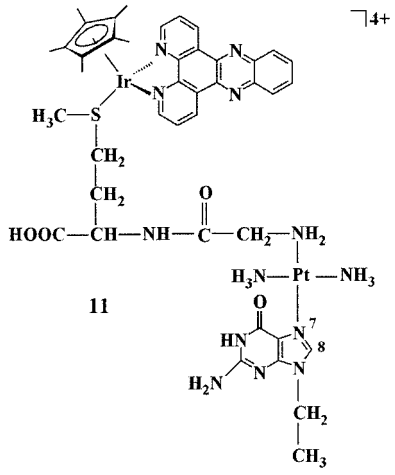

11

Figure 8. Product **11** of the reaction between **7** and 9-ethylguanine.

UV/Vis DNA Binding Studies for 7–10

The interaction of **7**–**10** with CT DNA was studied by UV/Vis titrations, DNA melting temperature determinations and CD spectroscopy. As for **3**–**6**, hypo- and bathochromic shifts were observed for the dppz absorption maxima at 363 and 382 nm on increasing the DNA/complex molar ratio from 1:1 to 15:1. Although ca. 90–95% of the total decrease in absorbance $\Delta A/A$ at 382 nm is achieved within 2 min, it takes between 8 (complex **7**) and 40 h (complex **9**) for the DNA/complex reaction mixtures to reach an equilibrium. This behaviour is in striking contrast to **3**–**6**, for which $-\Delta A/A$ reaches its maximum value within 2 min, and indicates that a slow structural reorganisation and binding optimisation must take place for **7**–**10** following rapid initial intercalation and/or surface base stacking. All UV/Vis spectra employed for the determination of binding constants and site sizes were measured after equilibration, i.e. after no further change in the monitored absorbance at 382 nm was recorded.

DNA binding parameters for **7**–**10** are listed in Table 2. As satisfactory least-squares fits (Figure 9) could be obtained in all cases for the absorption data using the model by Bard and Thorp[22,23] non-cooperative non-specific binding can be assumed for the interaction of the complexes with CT DNA. The low $-\Delta A/A$ value of 27.5% and the physically unrealistic site size (s = 0.9) of less than one base pair between binding sites indicate that only a limited degree of intercalation is achieved by **7** with its dipeptide bridging ligand H-Gly-Met-OH. A comparison of these values with those of the monofunctional complex [(η^5-Cp*)-Ir(dppz)(H-Gly-Met-OH-κ*S*)]$(CF_3SO_3)_2$[27] [$-\Delta A/A$ = 45.1%, $K_b = 1.9(7)\times10^6$ M^{-1}, s = 2.2(1)], for which equilibration is reached within 2 min, suggests that coordination of the Pt^{II} centres by DNA nucleobases must be rapid for **7**. Exclusive initial intercalation of the [(η^5-Cp*)Ir-(dppz)]$^{2+}$ fragment (as observed for the monofunctional complex), followed by a slow increase in κ*N* coordination of the group 10 metal and a concomitant reduction in the degree of intercalation, would otherwise lead to a slow decline in $\Delta A/A$ from a maximum value of ca. 45.1%[27] after 2 min.

Table 2. $-\Delta A/A$ (for λ = 382 nm), binding constants K_b, site sizes s, melting temperature shifts ΔT_m and induced circular dichroism Θ (for λ = 300 nm) for the interaction of CT DNA with complexes **7**–**10** in a 10 mM phosphate buffer at pH = 7.2.

Complex	$-\Delta A/A$ [%]	K_b [M^{-1}]	s	ΔT_m [°C]	[Θ] [deg·cm^2·dmol^{-1}]
7	27.5	$1.1(2)\times10^6$	0.9(1)	8.2	-1.5×10^3
8	35.2	$4(3)\times10^6$	2.4(2)	11.2	-2.9×10^3
9	43.9	$1.1(5)\times10^6$	1.3(1)	17.2	-3.8×10^3
10	38.5	$1.4(7)\times10^6$	2.1(1)	17.2	-3.8×10^3

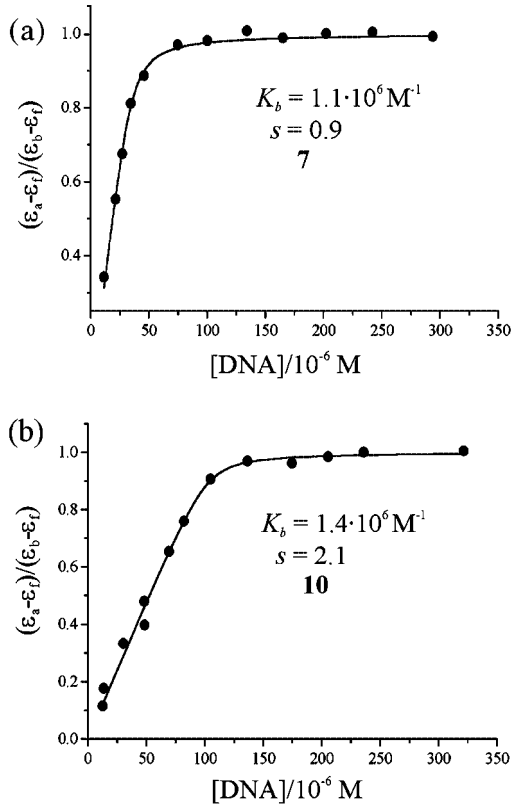

Figure 9. Best least-squares fits to the model by Bard and Thorp[22,23] for complexes **7** and **10**.

Circular Dichroism DNA Binding Studies for 7–10

In contrast to **7**, the much higher $-\Delta A/A$ and s values of 35.2% and 2.4(2), respectively, for **8** indicate that this complex with its longer bridging peptide, H-Gly-Gly-Met-OH, is apparently capable of combining both κ*N* coordination of the DNA nucleobases by the *trans*-[$Pt(NH_3)_2$(peptide-κ*N*)]$^{2+}$ fragment and effective intercalation of the [(η^5-Cp*)-Ir(dppz)(peptide-κ*S*)]$^{2+}$ moiety. Characteristic changes in the observed circular dichroism (CD) spectrum of DNA provide a means of monitoring both conformational changes for the biopolymer and possible intercalation or groove binding of an interacting metal complex.[28,29] As depicted for CT DNA in Figure 10, a negative band at

 © 2005 Wiley-VCH Verlag GmbH & Co. KGaA, Weinheim

246 nm and a positive band at 275 nm due to base stacking are observed for a B-DNA helix. Addition of the metallointercalator [(η^5-Cp*)Ir(dppz)(H-Gly-Gly-Met-OH-κ*S*)](CF_3SO_3)$_2$ at a complex/DNA molar ratio of r = 0.1 leads to a small reduction in the negative Cotton effect at 246 nm and a small hypsochromic shift of 3 nm for the positive band to 272 nm, thereby indicating only minor distortion of the B helix. The additional negative-induced CD band at 300 nm must presumably be caused by the intercalation of the dppz ligands into the DNA helix.[29]

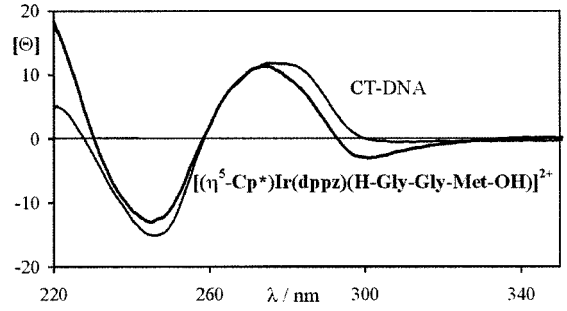

Figure 10. CD spectra of CT DNA and a mixture of [(η^5-Cp*)-Ir(dppz)(H-Gly-Gly-Met-OH-κ*S*)](CF_3SO_3)$_2$ and DNA [molar ratio (1:10)] in a 10 mM phosphate buffer (pH = 7.2) after 48 h incubation at 295 K.

Figure 11 compares the CD spectra of the bifunctional complexes **7** and **8** with CT DNA at a molar ratio of 0.1. The significantly higher degree of intercalation for **8** leads to a molar ellipticity ([Θ] = -2.9×10^3 deg·cm^2·dmol^{-1} for λ = 300 nm) that is almost twice as large as that recorded for the less effective metallointercalator **7** ([Θ] = -1.5×10^3 deg·cm^2·dmol^{-1} for λ = 300 nm). In the case of the former complex, the small but significant increase in [Θ] for the positive CD band at 276 nm may be attributed to additional

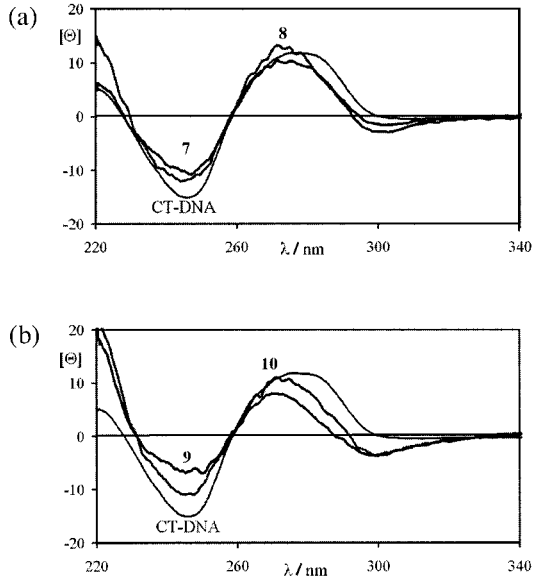

Figure 11. CD spectra of (a) complexes **7** and **8** and (b) complexes **9** and **10** with CT DNA at a complex/[DNA] molar ratio of 1:10 in a 10 mM phosphate buffer (pH = 7.2) at 295 K after 48 h incubation. [Θ] values are given in deg·cm^2·dmol^{-1}·10^3.

stabilisation of base stacking in the helix due to the combination of both dppz intercalation (see Figure 10) and covalent binding of the Pt^{II} centres. In contrast, the decrease in [Θ] for **7** at this wavelength is comparable with that previously reported for [PtCl(dien)]Cl[30] and can, therefore, be regarded as being indicative for monodentate Pt^{II} coordination with a significantly lower degree of intercalation. The large decrease in the negative [Θ] values at 246 nm in both **7** and **8** in comparison to [(η^5-Cp*)Ir(dppz)(H-Gly-Gly-Met-OH-κS)](CF_3SO_3)$_2$ (Figure 10) may be due to the fourfold positive charge of the bifunctional complexes, which could lead to a change in the helical conformation. A schematic illustration of a possible long-range simultaneous covalent and intercalative binding mode for complex **8** with s = 2.0 (calcd. 2.4) is given in Figure 12a.

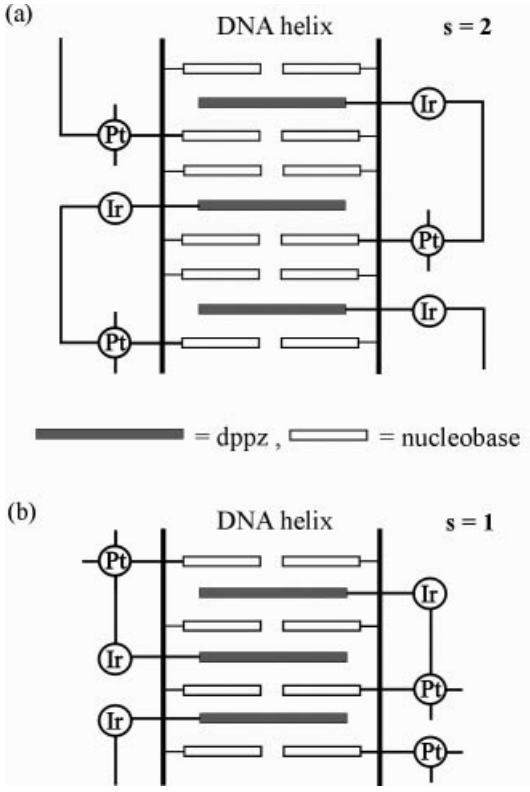

Figure 12. Schematic depictions of possible simultaneous covalent and intercalative binding modes; (a) for **8** with s = 2.0 (calcd. 2.4); (b) for **9** with s = 1.0 (calcd. 1.3).

The *cis* positions of the labile aqua ligands relative to the coordinating amino groups of the peptide ligands in **9** and **10** might be expected to favour a high degree of simultaneous covalent and intercalating DNA binding even for the shorter dipeptide of **9**. Experimental support for this hypothesis is provided by their induced molar ellipticity [Θ] at λ = 300 nm (-3.8×10^3 deg·cm^2·dmol^{-1}) and by the high values of $-\Delta A/A$ (43.9, 38.5%) and K_b (1.1×10^6, 1.4×10^6 M^{-1}) observed for their UV/Vis titrations with CT DNA at 382 nm. The former parameters are particularly interesting for **9**, as they indicate highly effective dppz intercalation for a low average site size of only 1.3 base pairs. In contrast to **10**, for which only the negative band at 247 nm is signifi-

 © 2005 Wiley-VCH Verlag GmbH & Co. KGaA, Weinheim

cantly influenced by metal binding, marked decreases in the intensity are observed for both the positive and negative bands in the CD spectrum recorded for **9**/DNA at a 1:10 molar ratio. The magnitude of these decreases is similar to those observed for *trans*-$[PtCl_2(NH_3)_2]$,[30] which can disturb the DNA helix by participation in *trans*-bidentate binding. However, the characteristic bathochromic shifts of the CD band at maxima for this coordination mode are missing for both **9** and **10**. It can be concluded that **9** and **10** must both exhibit a high degree of simultaneous covalent and intercalative DNA binding and that a more pronounced reorganisation of the DNA conformation is required to achieve this goal with complex **9** with its shorter linking peptide. The high melting temperature shifts ΔT_m of 17.2 °C for the interaction mixtures **9**/DNA and **10**/DNA result presumably from increased electrostatic stabilisation of the double helix due to the presence of an additional $[Et_4N]^+$ cation. The schematic depiction of possible simultaneous covalent and intercalative binding for **9** violates the general rule of the neighbour-exclusion principle,[31] that intercalative binding can only occur at every other base pair ($s \geq 2$). Neighbour-exclusion violating structures are more rigid[32] and support for this type of structure is provided by the pronounced helix distortions evident from the CD spectra of the interaction mixture **9**/DNA (Figure 11b).

The present work, therefore, confirms that bifunctional complexes of the type $[\{(\eta^5\text{-Cp*})Ir(dppz)\}(\mu\text{-peptide-}\kappa S{:}\kappa N)\{trans\text{-}(PtL_2L')\}]^{4+}$ with flexible bridging peptide ligands are capable of simultaneous covalent and intercalative DNA binding. Both the chain length of the peptide backbone and the position of the labile ligands in the square-planar Pt^{II} coordination sphere are shown to exhibit an important influence on the degree of intercalation and the extent of helix distortion.

Experimental Section

General: All manipulations and reactions were performed under argon in carefully dried solvents using standard Schlenk techniques. FTIR: Perkin–Elmer 1760X as KBr discs. CD: Jasco J-715 in the range 220–400 nm for 1:10 complex/[DNA] mixtures [DNA concentration in M(nucleotide)] in a 10 mM phosphate buffer at pH = 7.2. FAB MS: Fisons VG Autospec with 3-nitrobenzyl alcohol as the matrix. ^1H and ^{13}C NMR spectroscopy: Bruker DRX 400 with chemical shifts reported as δ values relative to the signal of the deuterated solvent. ^{13}C NMR signals for the CF_3SO_3 anions are observed in the range δ = 121.8–122.8 (q) ppm and are not listed for individual complexes. Elemental analyses: Vario EL of Elementar Analysensysteme GmbH. $IrCl_3{\cdot}xH_2O$, K_2PtCl_4, *cis*-$[PtCl_2(NH_3)_2]$ and *trans*-$[PtCl_2(NH_3)_2]$ were purchased from Chempur, $Ag(CF_3SO_3)$ and $AgNO_3$ from Acros and peptides, with the exception of H-$(Ala)_4$-Met-OH, from Bachem. The mentioned pentapeptide was prepared by solid-state synthesis, $[\{(\eta^5\text{-Cp*})IrCl\}_2(\mu\text{-Cl})_2]$,[33] [PtCl(terpy)]Cl[34] and dipyrido[3,2-*a*:2′,3′-*c*]-phenazine (dppz)[35] in accordance with literature procedures. Subsequent treatment of an acetone solution of $[\{(\eta^5\text{-Cp*})IrCl\}_2(\mu\text{-Cl})_2]$ with 4 equiv. of $Ag(CF_3SO_3)$ and filtration of the resulting AgCl precipitate afforded the starting compound $[(\eta^5\text{-Cp*})Ir(acetone)_3](CF_3SO_3)_2$ (**1**).[17] $[(\eta^5\text{-Cp*})Ir(dppz)(H\text{-Gly-Met-OH-}\kappa S)](CF_3SO_3)_2$[16] and $[(\eta^5\text{-Cp*})Ir(dppz)(H\text{-Gly-Gly-Met-OH-}\kappa S)](CF_3SO_3)_2$ were prepared from **1** and the relevant peptide in a manner previously described for the latter complex.[14] $(Et_4N)[PtCl_3(NH_3)]$ was obtained according to a literature procedure on treating *cis*-$[PtCl_2(NH_3)_2]$ with $(Et_4N)Cl{\cdot}H_2O$.[36]

$[(\eta^5$-Cp*)Ir(dppz)(H-Gly-Gly-Phe-Met-OH-κS)$](CF_3SO_3)_2$ (3): The ligand dppz (56.5 mg, 0.2 mmol) was added to **1** (159.8 mg, 0.2 mmol) in CH_3OH/CH_2Cl_2 (10 mL) and the resulting solution stirred at reflux for 2 h. After addition of H-Gly-Gly-Phe-Met-OH (82.1 mg, 0.2 mmol) in CF_3COOH (1.5 mL) and stirring at 50 °C for 18 h, the volume was reduced to 3 mL. The product was precipitated by addition of diethyl ether, washed and dried in vacuo. Yield 181.9 mg (69%). $C_{48}H_{51}F_6IrN_8O_{11}S_3$ (1318.3): calcd. C 43.7, H 3.9, N 8.5, S 7.3; found C 43.3, H 3.8, N 8.4, S 7.3. FAB MS: *m*/*z* (%) = 1319 (17) $[M]^+$, 1168 (10) $[M - OTf]^+$, 1019 (44) $[M - 2\ OTf]^+$. ^1H NMR (CD_3OD): δ = 1.79 (s, 3 H, δ Met), 1.84 (s, 15 H, CH_3 Cp*), 1.9–2.1 (mm, 4 H, β and γ Met), 2.93, 3.14 (m, 2 H, β Phe), 3.65, 3.69 (2s, 4 H, α Gly1, α Gly2), 4.29 (m, 1 H, α Phe), 4.36 (m, 1 H, α Met), 7.15 (m, 4 H, Phe), 7.24 (s, 1 H, Phe), 8.11 (m, 2 H), 8.43 (m, 2 H), 8.49 (dd, 2 H), 9.37 (dd, 2 H), 10.04 (dd, 2 H, dppz) ppm. ^{13}C NMR (CD_3OD): δ = 8.6 (CH_3 Cp*), 17.0 (δ Met), 30.6 (β Met), 33.7 (γ Met), 38.2 (β Phe), 41.6, 43.4 (α Gly), 51.0 (α Met), 56.2 (α Phe), 97.2 (Cp*), 127.8, 129.6, 130.3 (Phe), 130.4, 130.9 (dppz), 131.0 (Phe), 133.8, 134.3, 139.2, 140.6, 144.3, 151.3, 155.2 (dppz), 168.1, 171.1, 172.7, 173.6 (COO, NHCO) ppm. IR: $\tilde{\nu}$ = 3436 vs. (NH), 1737, 1675 s (ν CO), 1545, 1499 (δ NH) cm^{-1}.

$[(\eta^5$-Cp*)Ir(dppz)[H-$(Ala)_4$-Met-OH-κS]$](CF_3SO_3)_2$ (4): Preparation as for **3** with H-$(Ala)_4$-Met-OH (86.7 mg, 0.2 mmol). Yield 139.5 mg (52%). $C_{47}H_{56}F_6IrN_9O_{12}S_3$ (1341.4): calcd. C 42.1, H 4.2, N 9.4, S 7.2 (%); found C 42.3, H 3.8, N 9.1, S 6.7 (%). FAB MS: *m*/*z* (%) = 1341 (12) $[M]^+$, 1192 (11) $[M - OTf]^+$, 1042 (10) $[M - 2\ OTf]^+$. ^1H NMR (CD_3OD): δ = 1.33 (mm, 9 H, β Ala), 1.49 (m, 3 H, β Ala), 1.79 (s, 3 H, δ Met), 1.84 (s, 15 H, CH_3 Cp*), 1.9–2.1 (mm, 4 H, β and γ Met), 3.94, 4.10, 4.21 (3m, 3 H, α Ala), 4.35 (m, 2 H, α Ala und α Met), 8.17 (dd, 2 H), 8.44 (m, 2 H), 8.54 (dd, 2 H), 9.39 (m, 2 H), 10.05 (dd, 2 H, dppz) ppm. ^{13}C NMR (CD_3OD): δ = 9.1 (CH_3 Cp*), 17.3 (δ Met), 17.9, 18.1, 18.3, 18.4 (β Ala), 31.4 (β Met), 34.5 (γ Met), 50.4, 50.7, 50.9 (α Ala), 52.6 (α Met), 97.4 (Cp*), 130.8, 131.2, 133.0, 134.3, 138.5, 141.0, 144.6, 151.7, 155.4 (dppz), 167.1, 171.1, 174.9, 175.4, 182.1 (COO, NHCO) ppm. IR: $\tilde{\nu}$ = 3435 s (NH), 1664 (ν CO), 1543, 1499 (δ NH) cm^{-1}.

$[\{(\eta^5$-Cp*)Ir(dppz)$\}(\mu$-H-Gly-Gly-Phe-Met-OH-κS:κN$)\{$Pt-(terpy)$\}](CF_3SO_3)_4$ (5): $Ag(CF_3SO_3)$ (102.8 mg, 0.4 mmol) was added to [PtCl(terpy)]Cl·$2H_2O$ (107.1 mg, 0.2 mmol) in H_2O (10 mL) and stirred in the dark for 24 h. After removal of precipitated AgCl and addition of **3** (263.7 mg, 0.2 mmol), the clear solution was stirred at 50 °C for 18 h. The solvent was removed and the resulting solid redissolved in CH_3OH (3 mL). Following precipitation with diethyl ether, the product was washed and dried in vacuo. Yield 171.8 (42%). $C_{65}H_{62}F_{12}IrN_{11}O_{17}PtS_5$ (2044.9): calcd. C 38.2, H 3.1, N 7.5, S 7.8; found C 38.8, H 3.4, N 7.0, S 7.8. FAB MS: *m*/*z* (%) = 1895 (5) $[M - OTf]^+$, 1319 (13) $[M - 2\ OTf - Pt(terpy)]^+$, 1019 (12) $[M - 4\ OTf - Pt(terpy)]^+$. ^1H NMR (CD_3OD): δ = 1.81 (s, 3 H, δ Met), 1.84 (s, 15 H, CH_3 Cp*), 1.9–2.1 (mm, 4 H, β and γ Met), 3.61, 3.68 (2s, 4 H, α Gly1, α Gly2), 4.32 (m, 1 H, α Phe), 4.39 (m, 1 H, α Met), 7.15 (mm, 5 H, Phe), 7.82 (m, 2 H, terpy H5), 8.11 (m, 2 H, dppz), 8.3–8.5 (mm, 11 H, terpy and dppz), 8.83 (m, 2 H, terpy H6), 9.37 (m, 2 H), 10.03 (dd, 2 H, dppz) ppm. ^{13}C NMR (CD_3OD): δ = 8.5 (CH_3 Cp*), 17.0 (δ Met), 30.5 (β Met), 33.8 (γ Met), 37.1 (β Phe), 41.6, 43.5 (α Gly), 52.5 (α Met), 56.4 (α Phe), 97.2 (Cp*), 125.4, 126.7 (terpy), 127.8,

 © 2005 Wiley-VCH Verlag GmbH & Co. KGaA, Weinheim

129.5, 130.2 (Phe), 130.4, 131.0, 133.8, 134.0, 139.2, 141.0 (dppz), 144.0, 144.2 (terpy), 144.5 (dppz), 148.8 (terpy), 151.6, 155.6 (dppz), 168.3, 170.9 (COO, NHCO) ppm. IR: $\tilde{\nu}$ = 3448 s (NH), 1664 (ν CO), 1543 (δ NH) cm^{-1}.

[{(η⁵-Cp*)Ir(dppz)}(μ-H-(Ala)₄-Met-OH-κ*S*:κ*N*$_{A1}$){Pt(terpy)}](CF₃SO₃)₄ (6): Preparation as for **5** with **4** (268.3 mg, 0.2 mmol). Yield 140.6 mg (34%). $C_{64}H_{67}F_{12}IrN_{12}O_{18}PtS_5$ (2067.9): calcd. C 37.2, H 3.3, N 7.8, S 8.1; found C 37.1, H 3.1, N 8.1, S 8.0. FAB MS: *m*/*z* (%) = 1919 (1) $[M - OTf]^+$, 1042 (17) $[M - 4\ OTf - Pt(terpy)]^+$. ^1H NMR (CD_3OD): δ = 1.32 (mm, 9 H, β Ala), 1.49 (d, 3 H, β Ala), 1.79 (s, 3 H, δ Met), 1.84 (s, 15 H, CH_3 Cp*), 1.9–2.1 (mm, 4 H, β and γ Met), 3.72, 4.10, 4.21 (3m, 3 H, α Ala), 4.35 (m, 2 H, α Ala und α Met), 7.82 (m, 2 H, terpy H5), 8.16 (dd, 2 H, dppz), 8.3–8.6 (mm, 11 H, terpy and dppz), 8.88 (m, 2 H, terpy H6), 9.37 (m, 2 H), 10.05 (dd, 2 H, dppz) ppm. ^{13}C NMR (CD_3OD): δ = 8.5 (CH_3 Cp*), 16.7 (δ Met), 17.6, 17.8, 18.1 (β Ala), 31.4 (β Met), 33.9 (γ Met), 50.2, 50.6, 50.7, 50.8 (α Ala), 51.8 (α Met), 97.2 (Cp*), 123.4, 125.4 (terpy), 130.7, 131.0, 133.6, 134.0, 139.1, 140.5, 144.5 (dppz), 148.7 (terpy), 151.5 (dppz), 151.7 (terpy), 155.7 (dppz), 156.9, 159.1 (terpy), 170.9, 174.5, 175.1 (COO, NHCO) ppm. IR: $\tilde{\nu}$ 3434 vs. (NH), 1742, 1631 (ν CO), 1528 (δ NH) cm^{-1}.

[{(η⁵-Cp*)Ir(dppz)}(μ-H-Gly-Met-OH-κ*S*:κ*N*$_{G1}$)(*trans*-{Pt(NH₃)₂(DMF)})](CF₃SO₃)₂(NO₃)₂ (7): $AgNO_3$ (68.0 mg, 0.4 mmol) was added to *trans*-$[PtCl_2(NH_3)_2]$ (60.0 mg, 0.2 mmol) in DMF (10 mL) and stirred in the dark for 24 h. After removal of precipitated AgCl and addition of [(η⁵-Cp*)Ir(dppz)(H-Gly-Met-OH-κ*S*)]$(CF_3SO_3)_2$ (222.8 mg, 0.2 mmol), the clear solution was stirred at room temperature for 18 h. The solvent was removed and the resulting solid redissolved in CH_3OH (3 mL). Following precipitation with diethyl ether, the product was washed and dried in vacuo. Yield 135.6 mg (44%). $C_{40}H_{52}F_6IrN_{11}O_{16}PtS_3$ (1540.4): calcd. C 31.2, H 3.4, N 10.0, S 6.2; found C 31.3, H 3.3, N 9.8, S 6.3. FAB MS: *m*/*z* (%) = 1043 (41) $[M - 2\ OTf - 2\ NO_3 - DMF]^+$, 1025 (12) $[M - 2\ OTf - 2\ NO_3 - DMF - NH_3]^+$. ^1H NMR (CD_3OD): δ = 1.79 (s, 3 H, δ Met), 1.82 (s, 15 H, CH_3 Cp*), 1.97 (m, 2 H, β Met), 2.16 (m, 2 H, γ Met), 2.84, 2.98 (2s, 6 H, CH_3 DMF), 3.64 (s, 2 H, α Gly), 4.40 (m, 1 H, α Met), 7.96 (s, 1 H, CH DMF), 8.16 (dd, 2 H), 8.45 (m, 2 H), 8.52 (dd, 2 H), 9.39 (m, 2 H), 10.06 (m, 2 H, dppz) ppm. ^{13}C NMR (CD_3OD): δ = 9.1 (CH_3 Cp*), 17.1 (δ Met), 31.0 (β Met), 35.1 (γ Met), 37.4 (CH_3 DMF), 41.4 (α Gly), 52.5 (α Met), 97.6 (Cp*), 130.9, 131.3, 133.4, 134.1, 138.7, 141.1, 144.7, 155.2 (dppz), 168.4, 171.5 (COO, NHCO) ppm. IR: $\tilde{\nu}$ = 3446 vs. (NH), 1684 s (ν CO), 1636 (ν CO DMF), 1496 (δ NH) cm^{-1}.

[{(η⁵-Cp*)Ir(dppz)}(μ-H-Gly-Gly-Met-OH-κ*S*:κ*N*$_{G1}$)(*trans*-{Pt(NH₃)₂(DMF)})](CF₃SO₃)₂(NO₃)₂ (8): Preparation as for **7** with [(η⁵-Cp*)Ir(dppz)(H-Gly-Gly-Met-OH-κ*S*)]$(CF_3SO_3)_2$ (234.2 mg, 0.2 mmol). Yield 147.0 mg (46%). $C_{42}H_{55}F_6IrN_{12}O_{17}PtS_3$ (1597.4): calcd. C 33.8, H 3.5, N 10.5, S 6.0; found C 33.5, H 3.7, N 10.0, S 5.8. FAB MS: *m*/*z* (%) = 1172 (14) $[M - 2\ NO_3 - DMF - Pt(NH_3)_2]^+$, 1022 (6) $[M - OTf - 2\ NO_3 - DMF - Pt(NH_3)_2]^+$. ^1H NMR (CD_3OD): δ = 1.79 (s, 3 H, δ Met), 1.84 (s, 15 H, CH_3 Cp*), 1.9–2.1 (mm, 4 H, β and γ Met), 2.85, 2.97 (2s, 6 H, CH_3 DMF), 3.62 (s, 2 H, α Gly1), 3.88 (s, 2 H, α Gly2), 4.40 (br., 1 H, α Met), 7.96 (s, 1 H, CH DMF), 8.18 (dd, 2 H), 8.45 (m, 2 H), 8.53 (dd, 2 H), 9.37 (dd, 2 H), 10.06 (dd, 2 H, dppz) ppm. ^{13}C NMR (CD_3OD): δ = 9.1 (CH_3 Cp*), 17.6 (δ Met), 30.8 (β Met), 31.9 (CH_3 DMF), 35.6 (γ Met), 37.2 (CH_3 DMF), 41.8, 43.6 (α Gly), 53.4 (α Met), 97.3 (Cp*), 130.7, 131.1, 133.8, 134.1, 139.5, 140.9, 144.6, 151.8, 155.0 (dppz), 165.1 (CH DMF), 171.7, 172.8 (COO, NHCO) ppm. IR: $\tilde{\nu}$ = 3446 vs. (NH), 1636 (ν CO DMF), 1543 (δ NH) cm^{-1}.

[{(η⁵-Cp*)Ir(dppz)}(μ-H-Gly-Met-OH-κ*S*:κ*N*$_{G1}$)(*trans*-{Pt(NH₃)(OH₂)₂})][Et₄N](CF₃SO₃)₅ (9): Preparation as for **7** with $Ag(CF_3SO_3)$ (154.2 mg, 0.6 mmol) and $(Et_4N)[PtCl_3(NH_3)]$ (89.7 mg, 0.2 mmol) in H_2O (10 mL) as starting compounds. Yield 151.3 mg (39%). $C_{48}H_{66}F_{15}IrN_8O_{20}PtS_6$ (1939.7): calcd. C 29.7, H 3.4, N 5.8, S 9.9; found C 29.5, H 2.9, N 5.5, S 9.0. FAB MS: *m*/*z* (%) = 1115 (35) $[M - 3\ OTf - Et_4N - Pt(NH_3)(OH_2)_2]^+$. ^1H NMR (CD_3OD): δ = 1.29 (tt, 12 H, CH_3 Et_4N), 1.79 (s, 3 H, δ Met), 1.84 (s, 15 H, CH_3 Cp*), 1.98 (m, 2 H, β Met), 2.15 (m, 2 H, γ Met), 3.64 (s, 2 H, α Gly), 4.40 (m, 1 H, α Met), 8.18 (dd, 2 H), 8.46 (m, 2 H), 8.54 (dd, 2 H), 9.39 (dd, 2 H), 10.07 (dd, 2 H, dppz) ppm. ^{13}C NMR (CD_3OD): δ = 7.8 (CH_3 Et_4N), 8.7 (CH_3 Cp*), 16.9 (δ Met), 30.3 (β Met), 34.4 (γ Met), 41.8 (α Gly), 52.4 (α Met), 53.5 (CH_2 Et_4N), 97.5 (Cp*), 130.8, 131.2, 133.8, 134.3, 139.4, 141.0, 144.7, 151.8, 155.8 (dppz), 174.3 (COO) ppm. IR: $\tilde{\nu}$ = 3436 vs. (NH), 1629 (ν CO), 1546 (δ NH) cm^{-1}.

[{(η⁵-Cp*)Ir(dppz)}(μ-H-Gly-Gly-Met-OH-κ*S*:κ*N*$_{G1}$)(*trans*-{Pt(NH₃)(OH₂)₂})][Et₄N](CF₃SO₃)₅ (10): Preparation as for **9** with [(η⁵-Cp*)Ir(dppz)(H-Gly-Gly-Met-OH-κ*S*)]$(CF_3SO_3)_2$ (234.2 mg, 0.2 mmol). Yield 171.7 mg (43%). $C_{50}H_{69}F_{15}IrN_9O_{21}PtS_6$ (1996.8): calcd. C 30.1, H 3.5, N 6.3, S 9.6; found C 30.1, H 3.6, N 6.6, S 9.1. FAB MS: *m*/*z* (%) = 1172 (15) $[M - 3\ OTf - Et_4N - Pt(NH_3)(OH_2)_2]^+$, 1022 (29) $[M - 4\ OTf - Et_4N - Pt(NH_3)(OH_2)_2]^+$. ^1H NMR (CD_3OD): δ = 1.29 (tt, 12 H, CH_3 Et_4N), 1.81 (s, 3 H, δ Met), 1.85 (s, 15 H, CH_3 Cp*), 1.9–2.1 (mm, 4 H, β and γ Met), 3.64 (s, 2 H, α Gly1), 3.90 (s, 2 H, α Gly2), 4.39 (br., 1 H, α Met), 8.18 (dd, 2 H), 8.47 (m, 2 H), 8.53 (dd, 2 H), 9.38 (dd, 2 H), 10.06 (dd, 2 H, dppz) ppm. ^{13}C NMR (CD_3OD): δ = 7.9 (CH_3 Et_4N), 8.8 (CH_3 Cp*), 17.2 (δ Met), 30.1 (β Met), 34.1 (γ Met), 41.9, 43.6 (α Gly), 52.1 (α Met), 53.6 (CH_2 Et_4N), 97.5 (Cp*), 130.9, 131.3, 133.9, 134.4, 139.5, 141.2, 144.8, 151.8, 155.8 (dppz), 168.4, 171.7 (COO, NHCO) ppm. IR: $\tilde{\nu}$ = 3436 vs. (NH), 1629 (ν CO), 1499 (δ NH) cm^{-1}.

DNA Binding Studies of 3–10: The thermal denaturation temperature T_m of 1:10 complex/DNA mixtures was determined in a 10 mM phosphate buffer at pH = 7.2. Melting curves were recorded at 260 nm with a Lambda 15 Perkin–Elmer spectrometer connected with a temperature controller (Haake FS thermostat). A ramp rate of 0.25 °C min^{-1} was used over the range 25–97 °C. T_m values were calculated by determining the midpoints of the melting curves from the first-order derivatives. Experimental ΔT_m values are estimated to be accurate within ±1. Concentrations of CT DNA were determined spectrophotometrically using the molar extinction coefficient ε_{260} = 6600 M^{-1} cm^{-1}.[37] All absorption titrations were performed at room temperature. After sonication, buffered solutions of CT DNA gave a ratio of UV absorbance A_{260}/A_{280} of ca. 1.90, indicating that DNA was sufficiently free of protein.[38] 20 μM solutions of the individual metal complexes were treated with DNA over a range of molarities from 20 to 400 μM (nucleotide). All UV/Vis spectra were measured after equilibration, i.e. no further change in monitored absorbance. Titration curves were constructed from the fractional change in the absorbance as a function of DNA concentration according to the model by Bard and Thorp[22,23] for non-cooperative non-specific binding for one type of discrete DNA binding site.

$$(\varepsilon_a - \varepsilon_f)/(\varepsilon_b - \varepsilon_f) = (b - \{b^2 - 2K_b{}^2C_t[\mathrm{DNA}]/s\}^{1/2})/2K_bC_t \quad (1)$$

Equation (1) was used to fit the absorption data by least-squares refinement of binding constants (K_b) and site sizes (s) with $b = 1 + K_bC_t + K_b[\mathrm{DNA}]/2s$, where ε_a is the extinction coefficient observed at a given DNA concentration, ε_f the extinction coefficient of the complex in the absence of DNA, ε_b the extinction coefficient

 © 2005 Wiley-VCH Verlag GmbH & Co. KGaA, Weinheim

of the complex when fully bound to DNA (i.e. no absorption change on further addition of DNA), K_b the equilibrium constant in M^{-1}, C_t the total metal complex concentration, [DNA] the DNA concentration in M(nucleotide), and s the binding site size. Values of ε_b were obtained by extrapolation from the y intercept of plots of $\varepsilon_a/\varepsilon_f$ vs. 1/[DNA]. The K_b and s values of Tables 1 and 2 are those for the best least-squares fits to the individual UV/Vis titration curves using the program ORIGIN 6.0.

X-ray Structural Analysis of 2: $[(\eta^5\text{-Cp*})Ir(CF_3COO)(dppz)](CF_3SO_3)$, $C_{31}H_{25}F_6IrN_4O_5S$, M = 871.8, triclinic, space group $P\bar{1}$ (no. 2), a = 8.701(2), b = 11.535(2), c = 16.603(3) Å, α = 103.60(3), β = 90.93(3), γ = 102.21(3)°, V = 1579.2(5) Å^3, Z = 2, $D_{calcd.}$ = 1.833 g·cm^{-3}, μ(Mo-K_α) = 4.376 mm^{-1}; Siemens P4 diffractometer; graphite-monochromated Mo-K_α radiation (λ = 0.71073 Å). Crystal size: 0.46 × 0.30 × 0.12 mm; ω-scan in the range $2\theta \leq 50°$ ($-10 \leq h \leq 10$, $0 \leq k \leq 13$, $-19 \leq l \leq 19$), 5683 reflections collected, 5406 independent reflections (R_{int} = 0.051); semiempirical absorption corrections with ψ-scans; max./min. transmission 0.716/0.373; 428 parameters refined; R_1 = 0.057 for 4326 reflections with $I > 2\sigma(I)$, $wR_2 = \{[\Sigma w(F_o^2 - F_c^2)^2]/[\Sigma w(F_o)^2]\}^{1/2}$ = 0.136 for all data; min./max. residual electron density 1.82/–1.83 e·Å^{-3}. Anisotropic temperature factors for all non-hydrogen atoms with the exception of the disordered F atoms of the CF_3COO^- ligand, which exhibit s.o.f. values of 0.8 and 0.2.[39]

[1] N. Farrell, Y. Qu, U. Bierbach, M. Valsecchi, E. Mertz, in: *Cisplatin: Chemistry and Biochemistry of a Leading Anticancer Drug* (Ed.: B. Lippert), Wiley-VCH, Weinheim, **1999**, pp. 479–496.

[2] N. Farrell, in: *Platinum-Based Drugs in Cancer Therapy* (Eds.: L. R. Kelland, N. Farrell), Humana Press, Totowa, **2000**, pp: 321–338.

[3] N. J. Wheate, J. G. Collins, *Coord. Chem. Rev.* **2003**, *241*, 133–145.

[4] Y. Qu, N. Farrell, *Inorg. Chem.* **1995**, *34*, 3573–3576.

[5] K. van der Schilden, F. Garcia, H. Kooijman, A. L. Spek, J. G. Haasnoot, J. Reedijk, *Angew. Chem. Int. Ed.* **2004**, *43*, 5786–5788.

[6] B. E. Bowler, K. J. Ahmed, W. I. Sundquist, L. S. Hollis, E. E. Whang, S. J. Lippard, *J. Am. Chem. Soc.* **1989**, *111*, 1299–1306.

[7] M. D. Temple, W. D. McFadyen, R. J. Holmes, W. A. Denny, V. Murray, *Biochemistry* **2000**, *39*, 5593–5599.

[8] L. C. Perrin, C. Cullinane, W. D. McFadyen, D. R. Phillips, *Anti-Cancer Drug Des.* **1999**, *14*, 243–252.

[9] L. C. Perrin, P. D. Prenzler, C. Cullinane, D. R. Phillips, W. A. Denny, W. D. McFadyen, *J. Inorg. Biochem.* **2000**, *81*, 111–117.

[10] W. D. McFadyen, L. P. G. Wakelin, I. A. G. Roos, B. L. Hillcoat, *Biochem. J.* **1986**, *238*, 757–763.

[11] H. Kurosaki, N. Yamakawa, M. Sumimoto, K. Kimura, M. Goto, *Bioorg. Med. Chem. Lett.* **2003**, *13*, 825–828.

[12] B. Önfelt, P. Lincoln, B. Norden, *J. Am. Chem. Soc.* **1999**, *121*, 10846–10847.

[13] K. E. Erkkila, D. T. Odom, J. K. Barton, *Chem. Rev.* **1999**, *99*, 2777–2795.

[14] D. Herebian, W. S. Sheldrick, *J. Chem. Soc. Dalton Trans.* **2002**, 966–974.

[15] A. Frodl, D. Herebian, W. S. Sheldrick, *J. Chem. Soc. Dalton Trans.* **2002**, 3664–3673.

[16] R. Stodt, S. Gençaslan, A. Frodl, C. Schmidt, W. S. Sheldrick, *Inorg. Chim. Acta* **2003**, *355*, 242–253.

[17] C. White, S. J. Thompson, P. M. Maitlis, *J. Organomet. Chem.* **1977**, *127*, 415–421.

[18] G. Schwarz, S. Klose, W. Balthasar, *Eur. J. Biochem.* **1970**, *12*, 454–460.

[19] K. W. Jennette, J. T. Gill, J. A. Sadownick, S. J. Lippard, *J. Am. Chem. Soc.* **1976**, *98*, 6159–6168.

[20] W. S. Sheldrick, S. Heeb, *J. Organomet. Chem.* **1989**, *377*, 357–366.

[21] W. S. Sheldrick, A. Gleichmann, *J. Organomet. Chem.* **1994**, *470*, 183–187.

[22] M. T. Carter, M. Rodriguez, A. J. Bard, *J. Am. Chem. Soc.* **1989**, *111*, 8901–8911.

[23] S. R. Smith, G. A. Neyhart, W. A. Karlsbeck, H. H. Thorp, *New J. Chem.* **1994**, *18*, 397–406.

[24] M. Hahn, M. Kleine, W. S. Sheldrick, *J. Biol. Inorg. Chem.* **2001**, *6*, 556–566.

[25] M. Kleine, D. Wolters, W. S. Sheldrick, *J. Inorg. Biochem.* **2003**, *97*, 354–363.

[26] L. I. Elding, O. Gröning, *Inorg. Chem.* **1978**, *7*, 1872–1880.

[27] S. Gençaslan, *Dissertation*, Ruhr-Universität Bochum, **2004**.

[28] V. Brabec, V. Kleinwächter, J.-L. Butour, N. P. Johnson, *Biophys. Chem.* **1990**, *35*, 129–141.

[29] D. M. Gray, in: *Circular Dichroism and the Conformational Analysis of Biomolecules* (Ed.: G. D. Fasman), Plenum Press, New York, **1996**, pp. 469–500.

[30] J.-P. Macquet, J.-L. Butour, *Eur. J. Biochem.* **1978**, *83*, 375–387.

[31] D. M. Crothers, *Biopolymers* **1968**, *6*, 575–584.

[32] S. N. Rao, P. A. Kollman, *Proc. Nat. Acad. Sci. USA* **1987**, *84*, 5735–5739.

[33] a) J. W. Kang, K. Moseley, P. M. Maitlis, *J. Am. Chem. Soc.* **1969**, *91*, 5970–5977; b) B. L. Booth, R. N. Haszeldine, M. Hill, *J. Chem. Soc. A* **1969**, 1299–1303.

[34] G. Annibale, M. Brandolisio, B. Pitteri, *Polyhedron* **1995**, *3*, 451–453.

[35] M. Yamada, Y. Tanaka, Y. Yoshimoto, *Bull. Chem. Soc. Jpn.* **1992**, *65*, 1006–1011.

[36] M. J. Abrams, C. M. Giandomenico, J. F. Vollano, D. A. Schwartz, *Inorg. Chim. Acta* **1987**, *131*, 3–4.

[37] H.-Q. Liu, T.-C. Cheung, S.-M. Peng, C.-M. Che, *J. Chem. Soc. Chem. Commun.* **1995**, *17*, 1787–1788.

[38] J. Marmur, *J. Mol. Biol.* **1961**, *3*, 208–218.

[39] CCDC-266154 (**2**) contains the supplementary crystallographic data for this paper. These data can be obtained free of charge from The Cambridge Crystallographic Data Centre via www.ccdc.cam.ac.uk/data_request/cif.

Received: March 16, 2005
Published Online: August 4, 2005

 © 2005 Wiley-VCH Verlag GmbH & Co. KGaA, Weinheim

Secondary Periodicity in the Tetrahalogeno Complexes of the Group 13 Elements

Kinga Frąckiewicz,[a] Marian Czerwiński,[b] and Sławomir Siekierski*[a]

Keywords: Quantum calculations / Electronic structure / Group 13 elements / Halogeno complexes / Secondary periodicity

The M–X distances, the charges on the M and X atoms and the natural electron configurations in the hypothetical MX_4^- molecules, where M is a group 13 element and X = F, Cl, Br, I, have been investigated by quantum calculations. The computed distances are compared with the experimental data, mostly in the $Bu_4N[MX_4]$ salts. We found that: (1) down group 13 both the experimental and calculated M–X distances, the charge on the M atom and the sum of the populations of the M valence orbitals show zigzag variations produced by the filled 3d and 4f shells and by the relativistic effects in the 6s and $6p_{1/2}$ orbitals; (2) the experimental distances are shorter than the calculated values due, at least in part, to libration of the MX_4^- anions in the salts; (3) both the charge on M and the sum of the populations of M valence orbitals point to a highly covalent character of the B–X bonds (except for the B–F bond) and much less covalent character of the M–X bonds formed by the heavier members of the group. In the Al–Tl range the covalent character of the M–X bonds oscillates, and it strongly decreases on passing from the MCl_4^- to MF_4^- complexes; (4) the M–X distances (X = Cl, Br, I) are close to the sum of the respective covalent radii, whereas the M–F distances are significantly shorter because of considerable admixture of ionic bonding.

(© Wiley-VCH Verlag GmbH & Co. KGaA, 69451 Weinheim, Germany, 2005)

Introduction

It has been known for a long time that changes in some chemical properties are not uniform down the groups of p-block elements. For instance, despite the general trend of decreasing stability of the highest oxidation state $AsCl_5$ is, in contrast to $SbCl_5$, highly unstable,[1] $HBrO_4$ shows unexpectedly strong oxidizing properties and BrF_7 is, in contrast to IF_7, not known. These and other non-uniform changes in chemical properties, termed secondary periodicity or zigzag behaviour by Biron,[2] result from changes in the valence orbitals. Figure 1 shows for the group 13 elements that the *n*s and *n*p orbital radii and the covalent radius do not increase uniformly down the group but show an oscillatory, saw-tooth or zigzag variation. The orbital radii shown in Figure 1 are those calculated by Desclaux[3] and the covalent radii were taken from the literature.[4] It has been proposed by several authors[5] that the zigzag changes in orbital radii, energies and ionisation potentials of p-block elements result from incomplete shielding of the nuclear charge for valence electrons by the filled 3d shell (the first anomaly at row 4) and by the filled 4f shell (the second anomaly at row 6). Relativistic effects, which for the 6th row were found to be as important as the lanthanide contraction,[5b,5c] additionally shift Tl toward In.

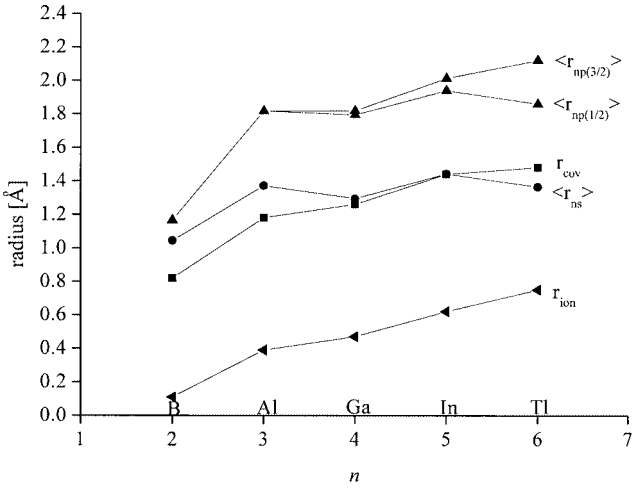

Figure 1. Expectation orbital radii in the atoms, $<r_{nl}>$, M^{3+} ionic radius, r_{ion} (CN = 4), and covalent radius, r_{cov}, for the group 13 elements.

The zigzag changes in the radii of valence orbitals should be more or less reproduced by changes in interatomic distances in compounds formed by the p-block elements. Therefore, one can expect a significant increase in the M–X interatomic distance for the group 13 elements when Al is substituted for B, a decrease or small increase in M–X between Al and Ga, a relatively large increase between Ga and In and again a decrease or small increase between In and Tl. However, such a pattern of changes would only be

[a] Institute of Nuclear Chemistry and Technology,
Dorodna 16, 03-195 Warsaw, Poland
E-mail: ssf@ichtj.waw.pl
[b] Jan Dlugosz University,
Al. Armii Krajowej 13/15, 42-200 Częstochowa, Poland.

 © 2005 Wiley-VCH Verlag GmbH & Co. KGaA, Weinheim **DOI: 10.1002/ejic.200500257**

observed provided the M–X bonds are essentially covalent. That is because the ionic radius, r_{ion} (CN = 4), in contrast to the covalent radius, r_{cov}, shows only a rudimental zigzag behaviour (see Figure 1).

The experimental M–H, M–C and M–Cl distances in the MX_k molecules formed by the elements of groups 13–17 have been compiled and discussed by Haaland.[6] In the above formula the subscript k is equal to one for group 17, two for group 16, three for groups 13 and 15 and four for group 14. The reported distances indeed show zigzag changes, which become less and less conspicuous as one moves from group 13 to group 17, and which seem to be independent of the X atom. The only experimental data which cover all elements of group 13 are those for the M–C bonds in the $M(CH_3)_3$ molecules.[6] These data show a large, very small, relatively large and again a small increase in the M–C distance within the B–Al, Al–Ga, Ga–In and In–Tl pairs, respectively (see Figure 2). Apart from experimental studies on the M–C bond length, the M–X distances in MH, MH_3, MF and MF_3 molecules formed by the group 13 elements have been computed by Schwerdtfeger et al.[7] The computed distances in the MH_3 and MF_3 (also in MH and MF) molecules repeat quite well the zigzag variation found experimentally for the M–C distances (Figure 2). However, in contrast to the M–H and M–C bonds, the M–F bond length in MF_3 (also in MF) increases significantly between Al and Ga (see Figure 2), which may be due to a more ionic character of the M–F bond. That the M–F bond is distinctly more ionic than the M–H bond is shown by the metal charge, q_m, which in TlF_3 is almost twice as large as that in TlH_3.[7] Up to now, variation in the M–X distances down the groups of p-block elements has been studied only for uncharged molecules. Therefore, it was interesting to find out whether the M–X distances in the MX_4^- ions, where M is a group 13 element and X = F, Cl, Br, I, also show a distinct zigzag variation. One could presume that in the MX_4^- ions the negative charge and the coordination

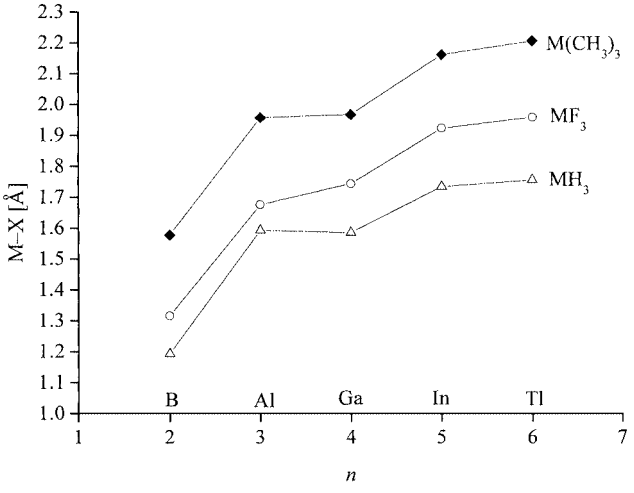

Figure 2. Experimental M–C[6] and calculated M–H and M–F[7] distances in the $M(CH_3)_3$, MH_3 and MF_3 molecules formed by the group 13 elements.

number four would confer considerable ionic character on the M–X bond. This would make the M–X distance depend more on the ionic radius than on the radii of the outermost s and p orbitals. If so, the M–X distance, like r_{ion}, would show only a feeble zigzag variation (see Figure 1). Moreover, one can also presume that this variation would be more distinct for the MI_4^-, MBr_4^- and MCl_4^- than for the MF_4^- complexes. This is because calculations show that the metal charge, q_m, is 0.67 in TlI_3 (TlI_3 is the hypothetical D_{3h} molecule), 1.08 in $TlBr_3$, 1.06 in $TlCl_3$ and 2.03 in MF_4^-,[7] and lower metal charge means less ionic character of the M–X bond. One can expect a similar or even more conspicuous dependence of q_m on X in the MX_4^- ions. In order to check these presumptions we have carried out calculations on the hypothetical gaseous MX_4^- molecules (M = B, Al, Ga, In, Tl and X = F, Cl, Br, I) and compared the calculated M–X distances with the experimental data, mostly in the tetrabutylammonium salts of the MX_4^- anions.

Results and Discussion

M–X Bond Lengths

The experimental M–X distances in the MX_4^- complexes and the computed distances in the hypothetical gaseous MX_4^- molecules (X = F, Cl, Br, I) formed by the group 13 elements are shown in Table 1 and Figure 3. The experimental M–X distances in the tetrabutylammonium salts of $AlBr_4^-$, GaX_4^- (X = Cl, Br, I), InI_4^- and TlX_4^- (X = Cl, Br) are those reported in our previous papers.[8–10] The Al–I, In–X (X = Cl, Br) and Tl–I distances in the tetrabutylammonium salts were taken from other papers.[11–13] Since we have found no data on the $Bu_4N[BX_4]$ and $Bu_4N[AlCl_4]$ salts, the B–Cl and the Al–Cl distances are those in HP(2-methylphenyl)$_3$[BCl_4][14] and $H_2PMe_2[AlCl_4]$.[15] The B–F distance is the average of the distances in $Me_4N[BF_4]$,[16] $Me_3PhN[BF_4]$[17] and $Pr_4N[BF_4]$,[18] whereas the Al–F distance is that in $Ph_4P[AlF_4]$.[19] Comparison of the average Tl–Cl distance in the tetramethylammonium salt[20] with that in the tetrabutylammonium salt[8] (2.416 Å and 2.393 Å, respectively) and of the Al–Cl distance in the $LiAlCl_4$ and $CsAlCl_4$ salts[21] (2.137 Å and 2.119 Å) shows that the effect of the cation on the M–X distance is within about 0.02 Å. This makes it possible to study the secondary periodicity in the M–X distance using the data from MX_4^- salts of different cations. We have also found no experimental data on the B–X distances in the BX_4^- complexes (X = Br, I) and we failed to synthesise the corresponding tetrabutylammonium salts. However, comparison of the data for the $Bu_4N[MX_4]$ salts shows that in the Al–Tl range the differences in the distances |M–Br| – |M–Cl| and |M–I| – |M–Cl|, are independent of M within about 0.015 Å. This allowed us to estimate the B–Br and B–I distances from the experimental B–Cl distance. Since each MX_4^- anion in the $Bu_4N[MX_4]$ salts is surrounded by five Bu_4N^+ cations, which form a highly distorted trigonal bipyramid, the anions are also distorted and show either two pairs of M–

 © 2005 Wiley-VCH Verlag GmbH & Co. KGaA, Weinheim

X distances (orthorhombic system) or four different M–X distances (monoclinic system),[8] with the difference between the longest and shortest M–X distance being about 0.015 Å. In the salts of cations other than the Bu_4N^+ cation the MX_4^- tetrahedra are also distorted. Therefore, the experimental M–X distances collected in Table 1 and the experimental distances in Figures 3, 6 and 7 are average values. Since the hypothetical gaseous tetrahedral MX_4^- molecules are free from any external influence they show only one M–X distance.

Table 1. Experimental and calculated M–X distances [Å] in the MX_4^- complexes.

	M–F		M–Cl		M–Br		M–I	
	exp.	calcd.	exp.	calcd.	exp.	calcd.	exp.	calcd.
B	1.346	1.410	1.856	1.868	1.99[a]	2.037	2.23[a]	2.271
Al	1.647	1.720	2.127	2.166	2.27	2.336	2.522	2.574
Ga		1.822	2.169	2.233	2.307	2.389	2.545	2.617
In		1.966	2.350	2.375	2.479	2.531	2.702	2.758
Tl		2.021	2.393	2.443	2.534	2.606	2.759	2.825

[a] Estimated.

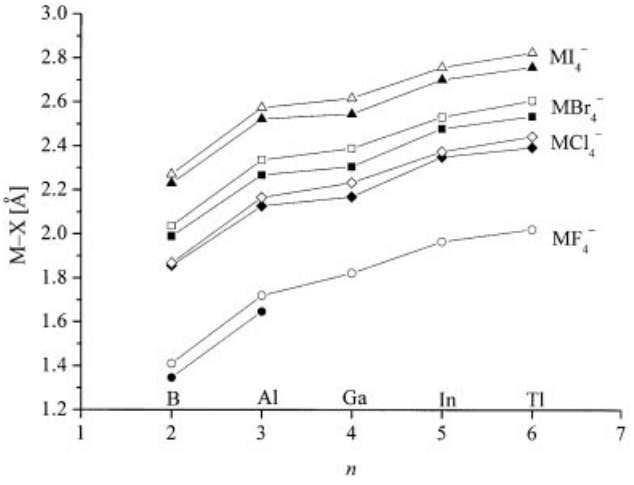

Figure 3. Experimental (filled symbols) and calculated (open symbols) M–X distances in the MX_4^- anions formed by the group 13 elements (X = F, Cl, Br, I).

It follows from the data in Table 1 and Figure 3 that the M–X distances calculated by the MP2/MBW method with the 2d polarisation function are longer than the experimental distances by about 0.05 Å on average. The B–X, Al–X and Ga–X distances (X = F, Cl, Br) calculated by the MP2/6-311+G* method and the M–Cl distance (M = Al, Ga, In, Tl) calculated by the MP2/MBW method with the 2s/2p/1d basis set are also longer than the experimental value by about 0.04 Å. Irrespective of the method, the biggest differences for each X are observed for gallium and thallium. This is because large-core pseudopotential calculations without including core-polarisation effects overestimate the Ga–X and Tl–X distances in particular. Three major factors may be responsible for the difference between the experimental and calculated M–X distances. The first is libration of the MX_4^- anion in the salt, which makes the experimental M–X distance shorter than that in the free MX_4^- molecule[22] that is the subject of the calculations. The second factor is electrostatic interaction in the salt between the MX_4^- anion and the "infinite" number of consecutive coordination shells containing alternately the Bu_4N^+ cations and the MX_4^- anions. This interaction may either expand or shrink the MX_4^- anion, depending on the number of cations and anions in each shell and on the shell radius. Obviously, the first shell, which contains cations, increases the M–X distance because there is a positive charge on the M atom and a negative charge on the X atom. The following shells alternately decrease and increase the M–X distance. However, because of the complex geometry of the system and the great number of shells that must be taken into account, calculation of the final outcome is unfeasible. The third factor may be a systematic error in the M–X distances calculated by the MP2/MBW method. Indeed, a comparison of calculated[7] and experimental[23] distances in the gaseous MH and MF molecules, where M = B, Al and In, shows that the calculated distances are longer than the experimental by about 0.015 Å on average. However, it is important to note that both the experimental and computed distances show a similar zigzag variation down the group, although it is slightly less conspicuous in the calculated distances. This is because, as pointed out above, calculations overestimate the Ga–X and Tl–X distances in particular. In the range from Cl to I the zigzag variation in the M–X bond length seems to be almost independent of the halogen atom and resembles that observed for the MH_3, $M(CH_3)_3$ and MF_3 molecules, (see Figure 2). This similarity shows that the electronegativity of the ligand atom, the number of ligands and the charge on the molecule do not substantially affect the zigzag variation in the M–X distances. However, more detailed examination of changes in the calculated M–X distances (see Table 1 and Figure 3) shows that the zigzag variation in MF_4^- is less conspicuous than in the remaining MX_4^- molecules, which suggests a more ionic character of the M–F bond.

Charges on the Atoms and Natural Electron Configurations

Table 2 shows the calculated atomic charges on the M and X atoms in the MX_4^- molecules, and Figure 4 is a plot of the charge on the metal atom as a function of the row number. The atomic charges were calculated using the B3LYP method with the LANL2DZ basis set. The charge on M and the charge on X, the latter multiplied by four, add almost exactly to –1. Figure 4 shows that the charge on the metal atom, q_m, in each complex increases strongly between B and Al, whereas in the range from Al to Tl it only shows large oscillations. Except for the BCl_4^-/BBr_4^- pair, q_m increases when Br is substituted for I, Cl for Br and F for Cl. The increase in q_m between MCl_4^- and MF_4^- is more than twice as large as that between MI_4^- and MCl_4^-, which points to the singular properties of the fluorine complexes. Table 3 shows the natural electron configurations of the M and X atoms in the MX_4^- molecules; the sum of the populations of the s and p valence orbitals in

 © 2005 Wiley-VCH Verlag GmbH & Co. KGaA, Weinheim

the M atoms, calculated from the electron configurations, is plotted as a function of the row number in Figure 5. Except for boron, the $(n + 1)$s orbitals are practically not occupied and the population of the $(n + 1)$p orbitals is, on average, smaller than 0.03. It is important to note that both q_m and the sum of populations (the latter reflected in the x-axis) show a zigzag variation similar to that in the M–X distance, although it is much more conspicuous. Since both the low value of q_m and the high population of the valence orbitals of the metal atom mean more covalent character of the M–X bonds we conclude that: (1) the B–X bonds are highly covalent, except for the B–F bond, which is significantly less covalent; (2) bonding becomes much less covalent in the Al–Tl range, where the bond character shows strong oscillations. These oscillations are generated by the filled 3d shell (bonding becomes more covalent for Ga than for Al) and by the joint effect of the filled 4f shell and relativistic effects in the 6s and $6p_{1/2}$ orbitals (bonding becomes more covalent for Tl than for In); (3) for each M bonding becomes less covalent on passing from the MI_4^- to MCl_4^- complexes and much less covalent on passing from the MCl_4^- to MF_4^- complexes.

Table 2. Charges on the M (q_m) and X (q_x) atoms in the MX_4^- molecules.

	MF_4^-		MCl_4^-		MBr_4^-		MI_4^-	
	q_m	q_x	q_m	q_x	q_m	q_x	q_m	q_x
B	0.413	–0.353	–0.238	–0.191	–0.154	–0.211	–0.400	–0.150
Al	1.621	–0.655	0.842	–0.460	0.730	–0.432	0.504	–0.376
Ga	1.494	–0.624	0.701	–0.425	0.569	–0.392	0.346	–0.336
In	1.629	–0.657	0.885	–0.471	0.733	–0.433	0.518	–0.379
Tl	1.502	–0.626	0.845	–0.461	0.716	–0.429	0.544	–0.386

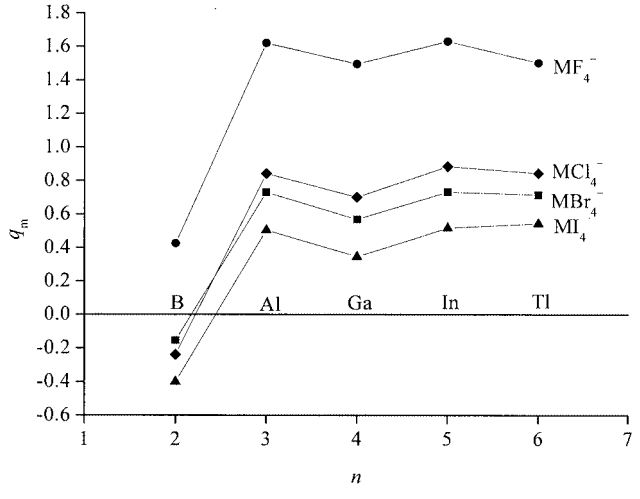

Figure 4. The charge on the group 13 metal atom, q_m, in the MF_4^-, MCl_4^-, MBr_4^- and MI_4^- molecules.

Correlation Between the M–X Distance and the Covalent Radius

Since in the Al–Tl range the ionic radius, r_{ion} (CN = 4), shows only a weak zigzag variation (see Figure 1), one can-

Table 3. Natural electron configurations of the M and X atoms in the MX_4^- molecules.

	MF_4^-		MCl_4^-		MBr_4^-		MI_4^-	
B	$2s^{0.41}\ 2p^{1.19}$	B	$2s^{0.78}\ 2p^{1.85}$	B	$2s^{0.92}\ 2p^{2.09}$	B	$2s^{1.11}2p^{2.42}$
F	$3s^{1.89}\ 3p^{5.69}$	Cl	$3s^{1.83}\ 3p^{5.49}$	Br	$4s^{1.82}\ 4p^{5.40}$	I	$5s^{1.82}\ 5p^{5.27}$
Al	$3s^{0.32}\ 3p^{0.57}$	Al	$3s^{0.60}\ 3p^{1.07}$	Al	$3s^{0.71}\ 3p^{1.24}$	Al	$3s^{0.88}\ 3p^{1.49}$
F	$3s^{1.94}\ 3p^{5.82}$	Cl	$3s^{1.90}\ 3p^{5.68}$	Br	$4s^{1.88}\ 3p^{5.62}$	I	$5s^{1.87}\ 5p^{5.52}$
Ga	$4s^{0.41}\ 4p^{0.57}$	Ga	$4s^{0.74}\ 4p^{1.03}$	Ga	$4s^{0.86}\ 4p^{1.20}$	Ga	$4s^{1.01}\ 4p^{1.44}$
F	$3s^{1.95}\ 3p^{5.80}$	Cl	$3s^{1.91}3p^{5.64}$	Br	$4s^{1.89}\ 4p^{5.58}$	I	$5s^{1.89}\ 5p^{5.49}$
In	$5s^{0.40}\ 5p^{0.49}$	In	$5s^{0.69}\ 5p^{0.90}$	In	$5s^{0.80}\ 5p^{1.02}$	In	$5s^{0.95}\ 5p^{1.20}$
F	$3s^{1.96}\ 3p^{5.81}$	Cl	$3s^{1.93}\ 3p^{5.67}$	Br	$4s^{192}\ 4p^{5.62}$	I	$5s^{1.91}\ 5p^{5.55}$
Tl	$6s^{0.55}\ 6p^{0.43}$	Tl	$6s^{0.89}\ 6p^{0.75}$	Tl	$6s^{1.01}\ 6p^{0.84}$	Tl	$6s^{1.15}\ 6p^{0.99}$
F	$3s^{1.97}\ 3p^{5.78}$	Cl	$3s^{1.94}\ 3p^{5.65}$	Br	$4s^{1.93}\ 4p^{5.60}$	I	$5s^{1.92}\ 5p^{5.54}$

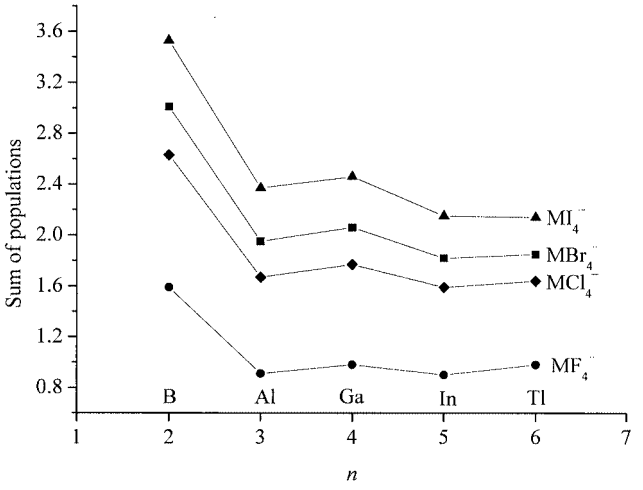

Figure 5. The sum of the populations of metal s and p valence orbitals in the MF_4^-, MCl_4^-, MBr_4^- and MI_4^- molecules of the group 13 elements.

not expect the experimental M–X distance to depend linearly on r_{ion}, as documented in Figure 6. On the other hand, a comparison of the data in Figures 1 and 4 shows that the covalent radius and the average M–X distance in the MX_4^- ions change in a very similar way down group 13, so that a linear correlation between the two can be expected. Figure 7 shows the experimental M–X distance in the MX_4^- complexes as a function of the sum of the covalent radii of the M and X atoms $[r_{cov}(M) + r_{cov}(X)]$. We can see from Figure 7 that for X = Cl, Br, I the experimental M–X distance depends linearly on the sum of the covalent radii. Moreover, the M–X distance is very close to the sum of the respective covalent radii. On the other hand, the experimental B–F and Al–F distances suggest a separate downward-shifted linear plot for the MF_4^- complexes. In order to show that all M–F distances form a separate lower-lying linear branch we have additionally plotted the calculated M–F distances in Figure 7. Since these are greater than the experimental values (as are the calculated M–Cl, M–Br and M–I distances), their position clearly shows that all experimental M–F distances would form a separate

 © 2005 Wiley-VCH Verlag GmbH & Co. KGaA, Weinheim

lower-lying branch. It is worthy to note that the M–C and M–H distances in the $M(CH_3)_3$ and MH_3 molecules[6,7] also form a common linear plot, with the M–X distance close to the sum of the respective covalent radii, whereas the M–F distances in the MF_3 molecules[7] belong to a separate lower-lying branch (see Figure 8). That the length of the M–F bond is considerably shorter than that expected from the sum of the covalent radii results from a significant admixture of ionic bonding. Using somewhat outdated but visual language, one can say that the decrease in the M–F bond length results from the resonance between the covalent and ionic structures.

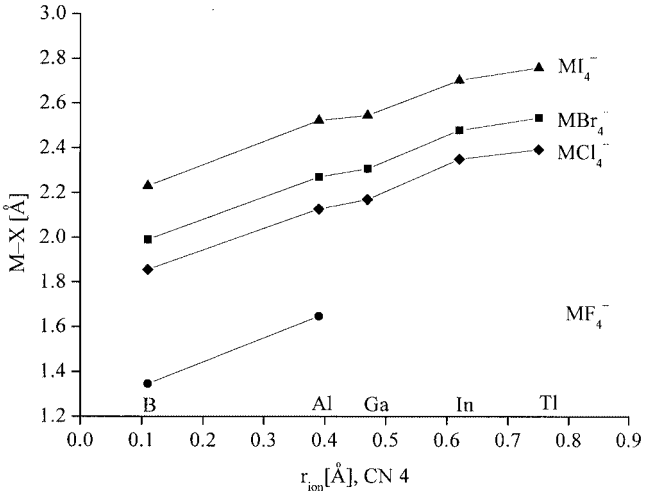

Figure 6. The experimental M–X distance in the MX_4^- anions as a function of the ionic radius, r_{ion} (CN = 4). M is a group 13 element and X = F, Cl, Br, I.

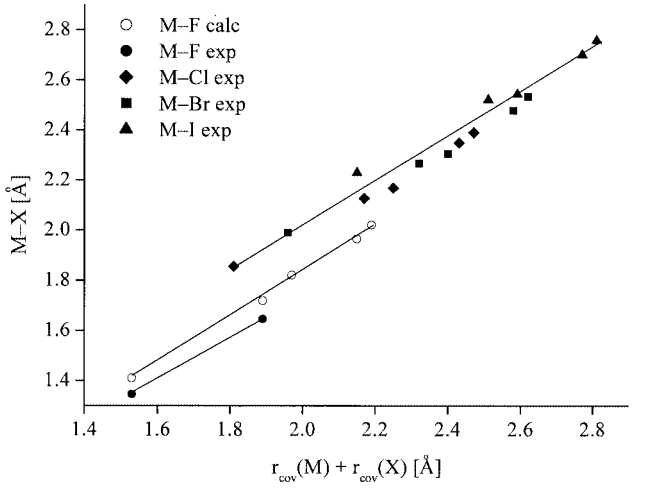

Figure 7. Experimental and calculated M–X distances in the MX_4^- molecules as a function of the sum of the covalent radii [r_{cov}(M) + r_{cov}(X)]. M is a group 13 element and X = F, Cl, Br, I.

Changes in the Unit Cell Volumes

The $Bu_4N[MX_4]$ salts of the group 13 elements studied till now crystallise for each M either in the *Pnna* (X = Cl, Br) or in the $P2_1/n$ (X = I) space groups.[8] Therefore, for a given X the zigzag variation in the M–X distance, i.e. in the volume of the MX_4^- anion, results in a similar variation in the unit cell volume (Figure 9). Because of the interaction between the MX_4^- anion and the five Bu_4N^+ cations from the nearest coordination shell, the zigzag variation in the volume of the anion generates zigzag variation in the anion-to-cation distance, i.e. in the M–N distance. For example, according to the data for the $Bu_4N[MI_4]$ salts,[8] the average M–N distance is equal to 6.584, 6.581, 6.630 and 6.622 Å, for Al, Ga, In and Tl, respectively. Since there is a decrease, an increase and again a decrease in the M–N distance for the consecutive pairs of elements, these data indeed show a distinct zigzag variation in the M–N distance. However, it should be noticed that the overall increase in the M–X distance in the $Bu_4N[MX_4]$ salts between Al and Tl is equal to 0.237 Å, whereas the respective increase in the M–N distance is equal to only 0.037 Å This is because the X atoms are located near the end-atoms of the butyl chains, where

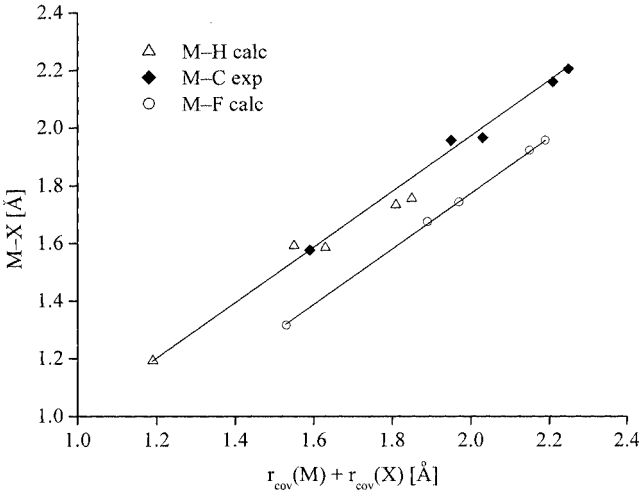

Figure 8. Experimental and calculated M–X distances in the MX_3 molecules[6,7] as a function of the sum of the covalent radii [r_{cov}(M) + r_{cov}(X)]. M is a group 13 element and X = H, C, F.

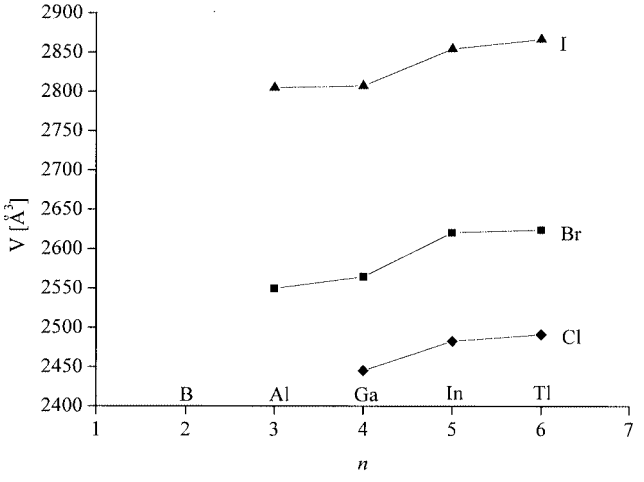

Figure 9. Unit cell volumes of the $Bu_4N[MX_4]$ salts as a function of the row number. M is a group 13 element and X = Cl, Br, I.

 © 2005 Wiley-VCH Verlag GmbH & Co. KGaA, Weinheim

there is enough space for the X atom to change its position without significantly moving the whole Bu_4N^+ cation.

Conclusions

We can draw the following conclusions from our calculations and from the available experimental data.

(1) In group 13 both the experimental M–X distances in the MX_4^- salts (mainly tetrabutylammonium salts) and the computed M–X distances in the hypothetical gaseous MX_4^- molecules (X = F, Cl, Br, I) show almost the same zigzag variation down the group, although slightly less conspicuous in the calculated values. This is because large-core pseudopotential calculations without including core-polarisation effects overestimate the Ga–X and Tl–X distances in particular. The variation in both the experimental and calculated bond length in the MX_4^- ions is similar to those in the MH_3, $M(CH_3)_3$, MF_3, MH and MF molecules. This means that the general pattern of changes in the metal-to-ligand distance down the group 13 is not substantially affected by the electronegativity of the ligand atom, the coordination number of the M atom or the charge on the molecule. However, a comparison of the calculated M–X distances in the MX_4^- molecules shows a less distinct zigzag variation in the M–F distance, which points to a more ionic character of the M–F bonds.

(2) The experimental M–X distances are shorter (on average by about 0.05 Å) than the calculated values. The main reason seems to be libration of the MX_4^- anions in the salts, which is absent in the hypothetical gaseous MX_4^- molecules. Moreover, the MP2/MBW method may slightly overestimate the calculated M–X distances. On the other hand, interaction of the MX_4^- anion with a large number of the coordination shells containing alternately cations and anions may either increase or decrease the experimental M–X distance, i.e. either decrease or increase the difference between the calculated and experimental M–X distances. However, the final outcome for many shells is difficult to calculate.

(3) Both the charge on the M atom, q_m, and the sum of the populations of M valence orbitals show very distinct zigzag variations down group 13, which points to the highly covalent character of the M–X bond formed by boron (except for the B–F bond) and distinctly less covalent for the heavier members of the group. The bond character oscillates strongly in the range from Al to Tl due to the filled 3d shell and to the joint effect of the filled 4f shell and relativistic effects in the 6s and $6p_{1/2}$ orbitals. The covalent character of the bond decreases between the MI_4^- and MCl_4^- complexes for all the group 13 elements and decreases significantly on passing from the MCl_4^- to MF_4^- complexes.

(4) The M–X bond length (X = Cl, Br, I) is close to the sum of the covalent radii. The much greater ionic character of the M–F bond, documented by the high value of q_m, low population of metal valence orbitals and less-conspicuous zigzag variation in the calculated M–F distances, makes the M–F bond length significantly shorter than the sum of the covalent radii.

(5) The M–X distances in the simple MX_k molecules (X = H, CH_3, Cl) formed by the group 14–17 elements show a zigzag variation[6] down each group similar to that in the MX_4^- complexes discussed in this paper. Since we have shown that the zigzag variation in the M–X distance for the MX_4^- complexes correlates with changes in the charge on the central atom and with changes in the population of its valence orbitals, we presume that the contribution from covalent bonding in the MX_k molecules of groups 14–17 changes in a way similar to that found for the MX_4^- complexes of the group 13 elements.

Calculations

In quantum calculations we used the nonrelativistic Hartree–Fock (NRHF) method[24] as well as the Kohn–Sham Density Functional Theory (DFT),[25] and methods which take into account relativistic effects through the use of a relativistic effective core potential (RECP). Calculations carried out in the frame of the NRHF method include electron correlation by Møller–Plesset (MP2)[26] for the 6-311+G* basis set.[27] To take into account relativistic effects we used the Stuttgart/Dresden basis sets and pseudopotentials adjusted to Wood–Boring data (MBW).[28] In the DFT method we chose a hybrid potential of the type B3LYP[29] and carried out calculations for all atoms using the LANL2DZ basis set.[30] Additionally, for all elements we introduced two polarisation functions of the d type whose orbital exponents are given by Huzinaga.[31] In the frame of the methods with pseudopotential we assumed that electrons in the closed shells enter into the core, thereby designating its effective potential. Using the MP2/MBW method with the 2d polarisation function we determined the global optimum geometry with regard to distances and angles for all the MX_4^- molecules, where M = B, Al, Ga, In, Tl and X = F, Cl, Br, I. In order to compare the geometries obtained in this way we carried out calculations using the MP2/6-311+G* method with the basis set which takes into account polarisation and dispersive effects to the greatest possible extent. Because of problems with availability of the 6-311+G* basis sets for heavier atoms, the optimum geometry in this method could only be obtained for the MX_4^- molecules, where M = B, Al, Ga and X = F, Cl, Br. For M = B, Al, Ga, In, Tl and X = Cl we also carried out calculations using the MP2/MBW method and the Stuttgart/Dresden basis sets complemented by the 2s/2p/1d set with one polarisation function of the d type, for which the orbital exponent is given by Huzinaga.[31] Using this method we obtained somewhat better agreement between the calculated and experimental distances in comparison with those obtained by the MP2/MBW method with the 2d polarisation function. However, because of problems with availability of the basis sets we were only able to carry out calculations for the MCl_4^- molecules. For the optimised geometry we calculated the charges on the atoms in the studied molecules by the B3LYP/LANL2DZ method. This method, in contrast to the MP2/MBW method, gives charges on the atoms, which are compatible with changes in the M–X distance and in the occupation of metal valence orbitals. We determined the natural electron configurations of the M and X atoms based on the procedure of natural orbital analysis.[32] The calculations were carried out with the Gaussian 98 package.[33]

[1] a) K. Seppelt, *Z. Anorg. Allg. Chem.* **1977**, *434*, 5–15; b) S. Haupt, K. Seppelt, *Z. Anorg. Allg. Chem.* **2002**, *628*, 729–734.
[2] E. V. Biron, *Zh. Russk. Fiz.-Kim. Obshch.* **1915**, *47*, 964–988.
[3] J. P. Desclaux, *At. Data Nucl. Data Tables* **1973**, *12*, 311–406.

 © 2005 Wiley-VCH Verlag GmbH & Co. KGaA, Weinheim

[4] C. H. Suresh, N. Koga, *J. Phys. Chem. A* **2001**, *105*, 5940–5944.
[5] a) N. N. Greenwood, K. J. Wade, *J. Chem. Soc.* **1956**, 1527–1536; b) P. Pyykkö, *J. Chem. Res.* **1979**, *12*, 380–381; c) P. S. Bagus, Y. S. Lee, K. S. Pitzer, *Chem. Phys. Lett.* **1975**, *33*, 408–411; d) P. Pyykkö, *Chem. Rev.* **1988**, *88*, 563–595.
[6] A. Haaland, *J. Mol. Struct.* **1988**, *97*, 115–128.
[7] P. Schwerdtfeger, G. A. Heath, M. Dolg, M. A. Bennet, *J. Am. Chem. Soc.* **1992**, *114*, 7518–7527.
[8] K. Rudawska-Frąckiewicz, S. Siekierski, *J. Coord. Chem.* **2004**, *57*, 777–784.
[9] K. Rudawska, H. Ptasiewicz-Bąk, *J. Coord. Chem.* **2003**, *56*, 1567–1574.
[10] K. Rudawska, H. Ptasiewicz-Bąk, S. Siekierski, *J. Coord. Chem.* **2002**, *55*, 403–409.
[11] R. D. Rogers, J. C. Backer, J. L. Atwood, *J. Cryst. Spect. Res.* **1984**, *14*, 333–339.
[12] M. A. Khan, D. G. Tuck, *Acta Crystallogr., Sect. B* **1982**, *38*, 803–806.
[13] a) J. Glaser, P. L. Gogin, M. Sandström, V. Lustko, *Acta Chem. Scand. A* **1982**, *36*, 55–62; b) J. Glaser, P. L. Gogin, M. Sandström, V. Lustko, *Acta Chem. Scand. A* **1982**, *37*, 437–438.
[14] J. M. Burke, J. A. K. Howard, T. B. Marder, C. Wilson, *Acta Crystallogr., Sect. C* **2000**, *56*, 1354–1355.
[15] Ch. Aubauer, K. Davidge, T. M. Klapötke, P. Mayer, *Z. Anorg. Allg. Chem.* **2000**, *626*, 1783–1786.
[16] G. Giuseppetti, F. Mazzi, C. Tadini, *Z. Kristallogr.* **1992**, *202*, 81–88.
[17] Th. Wiest, H. Eickmeier, H. Reuter, R. Blachnik, *Z. Kristallogr.* **2000**, *215*, 52–55.
[18] G. Giuseppetti, F. Mazzi, C. Tadini, P. Ferloni, G. Zabinska, S. Torre, *Z. Kristallogr.* **1997**, *212*, 367–371.
[19] M. Ferbinteanu, H. W. Roesky, F. Cimpoesu, M. Atanasov, S. Köpke, R. Herbst-Irmer, *Inorg. Chem.* **2001**, *40*, 4947–4955.
[20] M. Lenck, S.-Q. Dou, A. Weiss, *Z. Naturforsch., Teil A* **1991**, *46*, 777–784.
[21] G. Mairesse, P. Barbier, J. P. Wignacourt, *Acta Crystallogr., Sect. B* **1979**, *35*, 1573–1580.
[22] Y. Ishii, T. Terao, S. Hayashi, *J. Chem. Phys.* **1997**, *107*, 2760–2774.
[23] "Tables of Interatomic Distances and Configurations", in *Molecules and Ions*, The Chemical Society, London, **1958**.
[24] C. C. J. Roothan, *Rev. Mod. Phys.* **1951**, *23*, 69–89.
[25] a) P. Hohenberg, W. Kohn, *Phys. Rev. B* **1964**, *136*, 864–871; b) W. Kohn, L. J. Sham, *Phys. Rev. A* **1965**, *140*, 1133–1138; c) R. G. Parr, W. Yang, *Density-Functional Theory of Atoms and Molecules*, Oxford University Press, Oxford, **1989**.
[26] a) M. Head-Gordon, J. A. Pople, M. J. Frisch, *Chem. Phys. Lett.* **1988**, *153*, 503–506; b) M. J. Frisch, M. Head-Gordon, J. A. Pople, *Chem. Phys. Lett.* **1990**, *166*, 275–280; c) M. J. Frisch, M. Head-Gordon, J. A. Pople, *Chem. Phys. Lett.* **1990**, *166*, 281–289; d) M. Head-Gordon, T. Head-Gordon, *Chem. Phys. Lett.* **1994**, *220*, 122–128; e) S. Saebo, J. Almlof, *Chem. Phys. Lett.* **1989**, *154*, 83–89.
[27] L. A. Curtiss, M. P. McGrath, J. P. Blaudeau, N. E. Davis, R. C. Binning, Jr., L. Radom, *J. Chem. Phys.* **1995**, *103*, 6104–6113.
[28] T. Leininger, A. Nicklass, H. Stoll, M. Dolg, P. Schwerdtfeger, *J. Chem. Phys.* **1996**, *105*, 1052–1059.
[29] C. Lee, W. Yang, R. G. Parr, *Phys. Rev. B* **1988**, *37*, 785–789.
[30] a) T. H. Dunning, Jr., P. J. Hay, in *Modern Theoretical Chemistry* (Ed.: H. F. Schaefer, III), Plenum, New York, **1976**; b) P. J. Hay, W. R. Wadt, *J. Chem. Phys.* **1985**, *82*, 270–283; c) W. R. Wadt, P. J. Hay, *J. Chem. Phys.* **1985**, *82*, 284–298; d) P. J. Hay, W. R. Wadt, *J. Chem. Phys.* **1985**, *82*, 299–310.
[31] S. Huzinaga, *Gaussian Basis Sets for Molecular Calculations*, Elsevier, New York, **1984**.
[32] A. E. Reed, L. A. Curtiss, F. Weinhold, *Chem. Rev.* **1988**, *88*, 899–926.
[33] M. J. Frisch, G. W. Trucks, H. B. Schlegel, G. E. Scuseria, M. A. Robb, J. R. Cheeseman, V. G. Zakrzewski, J. A. Montgomery, Jr., R. E. Stratmann, J. C. Burant, S. Dapprich, J. M. Millam, A. D. Daniels, K. N. Kudin, M. C. Strain, O. Farkas, J. Tomasi, V. Barone, M. Cossi, R. Cammi, B. Mennucci, C. Pomelli, C. Adamo, S. Clifford, J. Ochterski, G. A. Petersson, P. Y. Ayala, Q. Cui, K. Morokuma, D. K. Malick, A. D. Rabuck, K. Raghavachari,; J. B. Foresman, J. Cioslowski, J. V. Ortiz, A. G. Baboul, B. B. Stefanov, G. Liu, A. Liashenko, P. Piskorz, I. Komaromi, R. Gomperts, R. L. Martin, D. J. Fox, T. Keith M. A. Al-Laham, C. Y. Peng, A. Nanayakkara, C. Gonzalez, M. Challacombe, P. M. W. Gill, B. Johnson, W. Chen, M. W. Wong, J. L. Andres, C. Gonzalez, M. Head-Gordon, E. S. Replogle, J. A. Pople, *Gaussian 98*, Revision A.7, Gaussian, Inc., Pittsburgh, PA, **1998**.

Received: March 24, 2005
Published Online: August 29, 2005

 © 2005 Wiley-VCH Verlag GmbH & Co. KGaA, Weinheim

Synthesis, Electronic Characterisation and Significant Second-Order Non-Linear Optical Responses of *meso*-Tetraphenylporphyrins and Their Zn^{II} Complexes Carrying a Push or Pull Group in the β Pyrrolic Position

Elisabetta Annoni,[a] Maddalena Pizzotti,*[a] Renato Ugo,[a] Silvio Quici,[b] Tamara Morotti,[b] Maurizio Bruschi,[c] and Patrizia Mussini[d]

Keywords: Cyclic voltammetry / Nonlinear optics / Porphyrins / UV/Vis spectroscopy / Zinc

This work describes the synthesis and characterisation by electronic absorption spectroscopy, cyclic voltammetry and by a solvatochromic investigation of *meso*-tetraphenylporphyrins and their Zn^{II} complexes substituted at the β pyrrolic position by a pseudo-linear, π-delocalised organic linker carrying either an electron-withdrawing (pull) or electron-donating (push) group. The second-order NLO response of these push-pull porphyrinic chromophores has been investigated by the EFISH technique working with a non-resonant incident wavelength of 1.907 μm. The porphyrin ring substituted at the β pyrrolic position by an electron-acceptor π-system behaves as a significant donor group, comparable to a ferrocenyl group or to a phthalocyanine. Unexpectedly, the porphyrin ring substituted at the β pyrrolic position with an electron-donor π-system shows a larger and significant second-order NLO response.
(© Wiley-VCH Verlag GmbH & Co. KGaA, 69451 Weinheim, Germany, 2005)

Introduction

A wide variety of push-pull organic π-conjugated chromophores have been extensively investigated, both theoretically and experimentally, for their significant second-order optical nonlinearities.[1–3] When compared to organic chromophores, pseudo-linear coordination and organometallic chromophores may offer additional electronic features, acting on the second-order non-linear optical (NLO) response, such as intense charge-transfer transitions (ligand to metal and vice versa) at relatively low energy that are easily tuneable by changing the oxidation state of the metal, its coordination sphere and stereochemistry.[4] Attempts have been made to design two-dimensional push-pull chromophores based on π-delocalised macrocycles such as porphyrins and metalloporphyrins,[5,6] metallophthalocyanines[7a] and subphthalocyanines,[7b,7c] and metallotriazolohemiporphyrazines.[8] Porphyrins and their metal complexes offer some additional advantages, such as good thermal and chemical stability, acceptable solubility for the determination of dipole moments and their second-order molecular NLO response and relatively easy synthetic pathways for the preparation of various architectures.[9] The highly polarisable π ring, with strong π→π* transitions,[10] of push-pull metal porphyrins asymmetrically substituted in the 5- and 15-positions, has been proposed as an excellent linker of the pseudo-linear push-pull chromophore.[11] This latter point was experimentally confirmed by Therien et al.,[6a,6b] Ng et al.[6c] and recently also by some of us.[6d] However, to the best of our knowledge, no-one, with the exception of two rather preliminary communications,[12] has experimentally investigated whether the π system of porphyrins or metalloporphyrins can act as a donor or acceptor group of a pseudo-linear push-pull chromophore. Depending on the number of π electrons, π orbitals, and on the heteroatom electronegativities, heterocyclic rings can act as electron-rich (donor) or electron-poor (acceptor) systems.[13] Pyrrole, with six π electrons and five π orbitals, is an electron-rich π system. Thus, a porphyrinic chromophore with four pyrrole rings may be considered, at first glance, as a π-electron-rich system in which electron-rich and electron-poor carbon atoms may be identified.[14] In order to experimentally prove some interesting theoretical suggestions,[14] we investigated the second-order NLO response of push-pull pseudo-linear chromophores based on a 5,10,15,20-tetraphenylporphyrin, either as free base or as Zn^{II} complex, carrying a push or a pull group linked to the β pyrrolic position through a π-delocalised spacer. One major prob-

[a] Dipartimento di Chimica Inorganica Metallorganica e Analitica dell'Università di Milano, Unità di Ricerca dell' INSTM, Centro di eccellenza CIMAINA dell'Università di Milano, e Istituto di Scienze e Tecnologie Molecolari del CNR (ISTM), Via G.Venezian 21, 20133 Milano, Italy
Fax: +39-02-50314405
E-mail: maddalena.pizzotti@unimi.it
[b] Istituto di Scienze e Tecnologie Molecolari del CNR (ISTM), Via Golgi 19, 20133 Milano, Italy
[c] Dipartimento di Biotecnologie e Bioscienze, Università di Milano Bicocca, Piazza della Scienza 2, 20126 Milano, Italy
[d] Dipartimento di Chimica Fisica ed Elettrochimica dell'Università di Milano, Via Golgi 19, 20133 Milano, Italy

 DOI: 10.1002/ejic.200500292 © 2005 Wiley-VCH Verlag GmbH & Co. KGaA, Weinheim

lem with push-pull π-delocalised macrocycles is the correct determination of their molecular second-order NLO response. The quadratic hyperpolarizability of asymmetric porphyrins and their metal complexes has been measured by HRS (Hyper-Rayleigh Scattering),[6a] Stark effect[6b] and by EFISH (Electric Field Induced Second Harmonic) generation techniques.[5,6c,6d] Depending on the incident wavelength, these measurements can be affected by resonance enhancements[6a,6d] and in the case of the HRS technique also by a fluorescent contribution to the second harmonic.[6a]

In order to avoid both these effects, the second order NLO responses of compounds investigated in this work were measured by the EFISH technique working at a non-resonant incident wavelength of 1.907 μm. In addition, density functional theory (DFT)[15] calculations were carried out in order to confirm experimental dipole moments and to define the best structural geometries using the BP86 functional[16] and an all-electron valence triple-ξ basis set with polarisation functions on all atoms.[17]

Results and Discussion

Synthesis of Porphyrins and Their Zn^{II} Complexes

The asymmetric 5,10,15,20-tetraphenylporphyrins and their Zn^{II} complexes investigated in this work are reported in Figure 1.

Porphyrin **1** was synthesised by reaction of 2-bromo-5,10,15,20-tetraphenylporphyrin, obtained by bromination of 5,10,15,20-tetraphenylporphyrin (TPP) with *N*-bromosuccinimide, first with Ni(acac), then with CuCN[18] to afford the Ni^{II} complex of **1**, and finally by controlled demetallation with concentrated sulfuric acid. Its Zn^{II} complex **2** was obtained by reaction of **1** with $Zn(OAc)_2$.[19] Porphyrin **3** was obtained by reaction of the Zn^{II} complex of TPP with I_2 and $AgNO_3$ to afford **4**,[20] followed by demetallation with concentrated HCl. Complex **6** was obtained by a Sonogashira coupling reaction of the Zn^{II} complex of 2-bromo-5,10,15,20-tetraphenylporphyrin with 4-nitrophenylacetylene in refluxing THF/Et_3N, using $[PdCl_2(PPh_3)_2]$ and CuI as catalysts, followed by demetallation with CF_3COOH in CH_2Cl_2 at room temperature to give porphyrin **5** (Scheme 1).

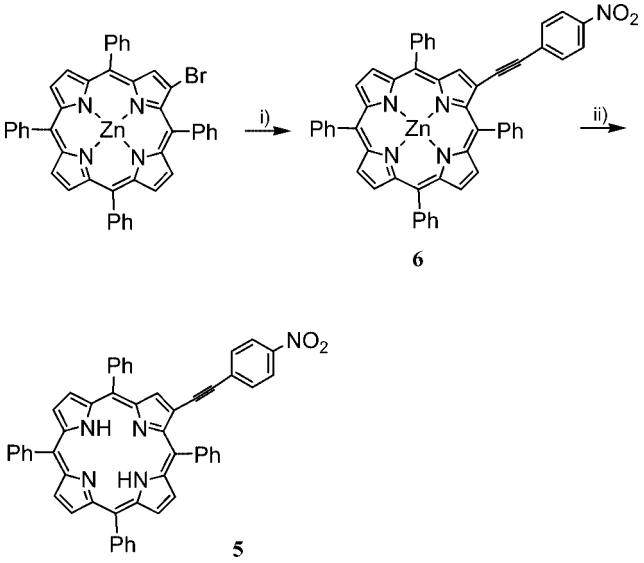

Scheme 1. i) 4-Nitrophenylacetylene, $[PdCl_2(PPh_3)_2]$ (cat), THF/NEt_3, reflux; ii) CF_3COOH, CH_2Cl_2, room temp., 20 h.

Porphyrins **7** and **11**, which are already known,[21] were synthesised by a new and easier method based on the Wittig condensation of 2-formyl-5,10,15,20-tetraphenylporphyrin (**13**) with (4-nitrobenzyl)triphenylphosphonium bromide and [4-(dibutylamino)benzyl]triphenylphosphonium chloride respectively (Scheme 2).

Reactions were carried out in CH_2Cl_2 at room temperature in the presence of solid NaOH as base to afford, after purification by column chromatography, a mixture of (*E*)-

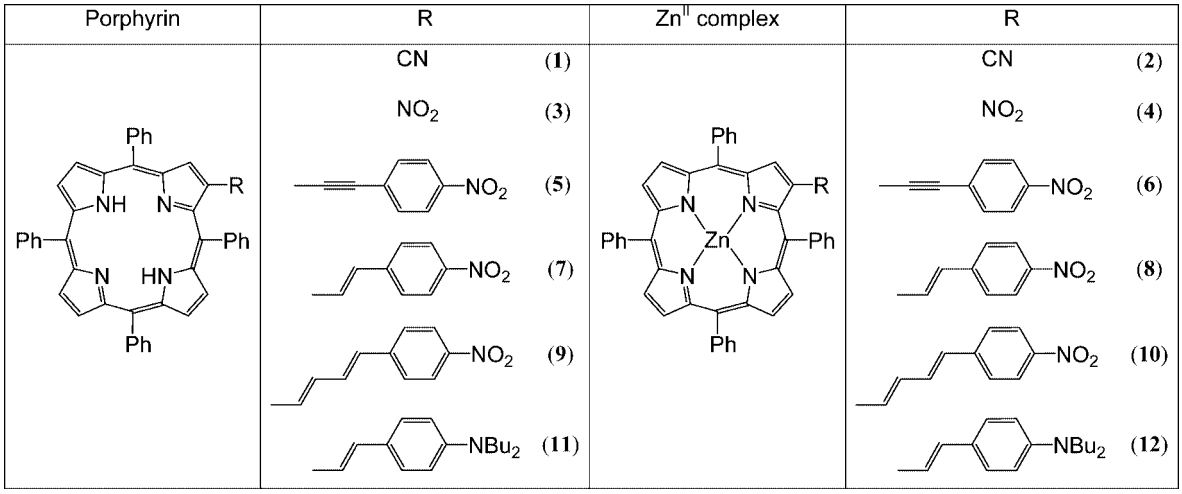

Figure 1. Asymmetrical *meso*-tetraphenylporphyrins and their Zn^{II} complexes with β pyrrolic substitution by electron-withdrawing or -donating groups.

 © 2005 Wiley-VCH Verlag GmbH & Co. KGaA, Weinheim

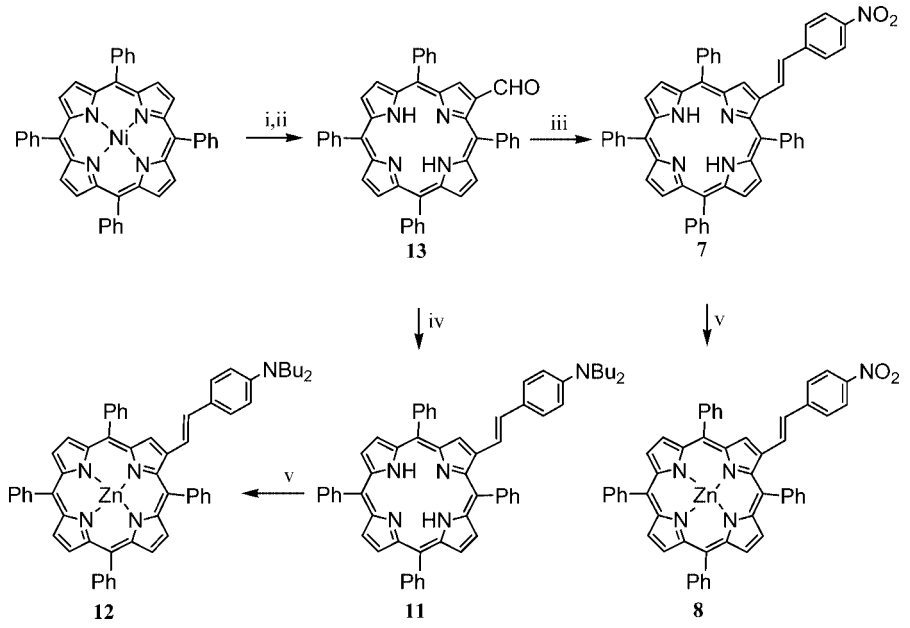

Scheme 2. i) $POCl_3$, DMF, 1,2-dichloroethane, reflux, 24 h; ii) 96% H_2SO_4, CH_3COONa 30% in H_2O; iii) (4-nitrobenzyl)triphenylphosphonium bromide, NaOH, CH_2Cl_2, room temp., 8 h; iv) [4-(dibutylamino)benzyl]triphenylphosphonium chloride, NaOH, CH_2Cl_2, room temp., 4 h; v) $Zn(OAc)_2{\cdot}2H_2O$, $CHCl_3$/MeOH, reflux.

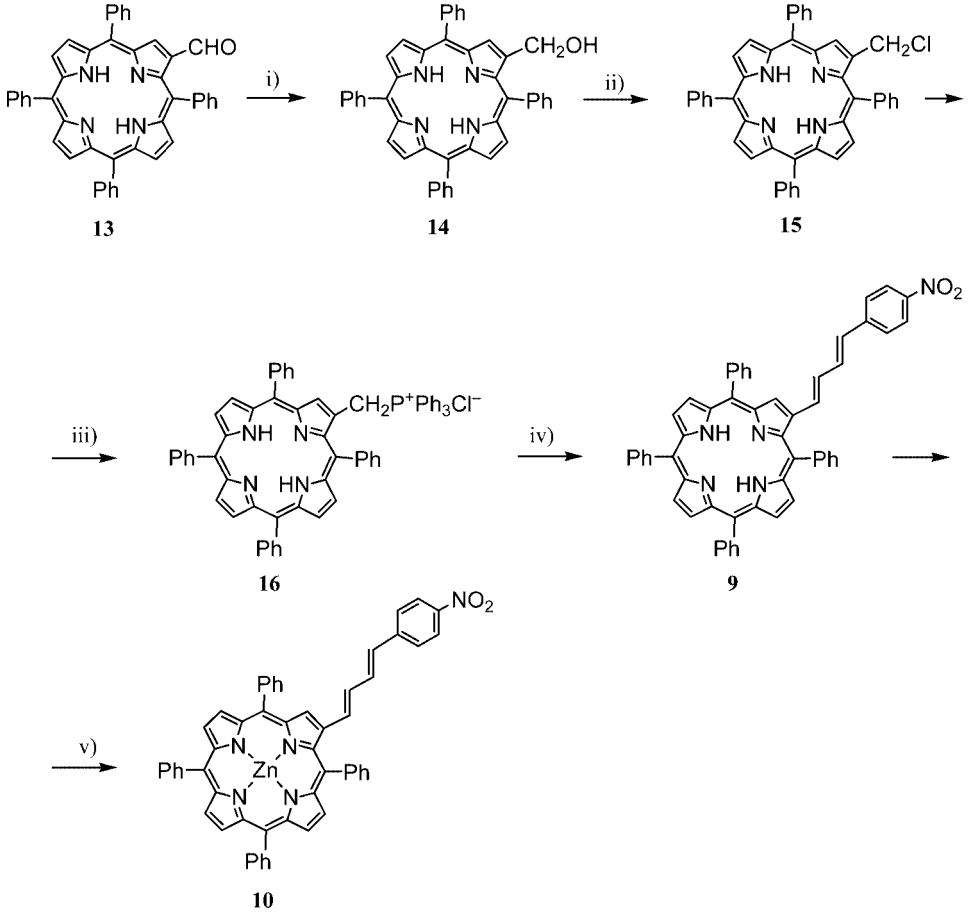

Scheme 3. i) $NaBH_4$, EtOH 96%, reflux, 4 h; ii) $SOCl_2$, pyridine, Et_2O; iii) PPh_3, $CHCl_3$, reflux; iv) 4-nitrocinnamaldehyde, DBU, room temp.; v) $Zn(OAc)_2{\cdot}2H_2O$, $CHCl_3$/MeOH, reflux, 2 h.

 © 2005 Wiley-VCH Verlag GmbH & Co. KGaA, Weinheim

and (*Z*)-isomers. From this mixture the pure (*E*)-isomers **7** and **11** were obtained, in 58% and 69% yields respectively, by repeated crystallisation from CH_2Cl_2/MeOH. Porphyrin **13** was prepared in 70% yield by Vilsmeier formylation of the commercially available Ni complex of TPP (Scheme 2) following a modification of the procedure reported in the literature.[22] (4-Nitrobenzyl)triphenylphosphonium bromide was easily obtained, in quantitative yield, by quaternisation of triphenylphosphane with 4-nitrobenzylbromide in refluxing toluene, while (4-dibutylamino)benzyltriphenylphosphonium chloride was prepared from (4-dibutylamino)benzyl alcohol, obtained by reduction of (4-dibutylamino)benzaldehyde with $NaBH_4$, by adapting a procedure reported in the literature.[23] The Zn^{II} complexes **8** and **12** were obtained in quantitative yield by treating porphyrins **7** and **11**, respectively, with $Zn(OAc)_2$ in $CHCl_3$/MeOH.[19] Porphyrin **9**, bearing a (1*E*,3*E*)-butadiene linker in the β position, was prepared by Wittig condensation of 4-nitrocinnamaldehyde with the phosphonium salt **16** in the presence of 1,8-diazabicyclo[5.4.0]undec-7-ene (DBU) as base (Scheme 3).

The preparation of the phosphonium salt **16** was carried out, starting from the aldehyde **13**, according to the synthetic scheme reported in a preliminary communication by Bonfantini and Officer in 1993.[24] However the detailed experimental procedure was never published, hence a careful description of the synthesis and characterisation of intermediate porphyrins **14**, **15** and **16** is given in the Experimental Section.

Again, treatment of the free porphyrin **9** with $Zn(OAc)_2$ in $CHCl_3$/MeOH at reflux afforded the Zn^{II} complex **10** in quantitative yield. All porphyrins and their Zn^{II} complexes were characterised by elemental analysis, ^1H NMR spectroscopy and mass spectrometry

Electronic Absorption, Emission Spectra and Solvatochromic Behaviour

Metal complexation of tetraarylporphyrins increases the ring microsymmetry from D_{2h} to D_{4h}, with a parallel decrease of the number of Q absorption bands from four to two.[10,25,26] Although the introduction of a substituent in the β pyrrolic position should produce a lowering of the D_{4h} microsymmetry, the usual decrease of the number of Q bands from four to two was reported when comparing porphyrin **7** and its Ni^{II} complex.[21] For porphyrin **1** and its Cu^{II} complex, a decrease of the number of Q bands from four to three was originally published,[18] but later a decrease from four to two was reported when comparing porphyrins **1** and **3** with their Cu^{II} complexes.[25] When comparing porphyrins **1** and **3** with their Zn^{II} complexes **2** and **4**, we observed a decrease of the number of Q bands from four to three, with complete disappearance of the Q_α band above 600 nm but with a weak Q_β band at higher energy still detectable (Table 1 and Figure 2).[27]

A similar decrease of the number of Q bands was observed when comparing porphyrins **5** and **7** with their Zn^{II}

Table 1. Visibile and fluorescence spectra in $CHCl_3$.

Compound[a]	Soret B Half band width $\Delta\nu_{1/2}$ [cm^{-1}][c]	Soret B λ_a [nm] [logε]	Q bands λ_a [nm] [logε]	Fluorescent emission[b] λ_e [nm]
2-Cyano-H_2TPP[d] (**1**)	n.d.	420 [5.29][e]	517 [3.79], 552 [3.21] 593 [3.23], 648 [3.20]	659, 717 (659, 718)
2-Cyano-ZnTPP (**2**)	n.d.	427 [5.62][e]	518 [3.57], 555 [4.20] 593 [4.02]	607.5, 657 (606.5, 656.5)
2-Nitro-H_2TPP (**3**)	2974 (1574)	427 [5.24]	527 [4.14], 560 [3.56] 605 [3.53], 665 [3.88]	716 (706)
2-Nitro-ZnTPP (**4**)	1172 (1874)	425 [5.28]	522 [3.41], 555 [4.00] 598 [3.80]	661 (657)
2-(4-Nitrophenyl)ethynyl-H_2TPP (**5**)	2296 (1675)	430 [5.26]	525 [4.31], 562 [3.83] 601 [3.78], 657 [3.68]	677, 730 (671.5, 730.5)
2-(4-Nitrophenyl)ethynyl-ZnTPP (**6**)	1381 (1474)	431 [5.30]	521 [3.60], 557 [4.25] 594 [4.03]	621, 659.5 (614.5, 660)
(1*E*)-2-(4-Nitrophenyl)ethenyl-H_2TPP (**7**)	1800 (2497)	431 [5.31]	525 [4.34], 569 [4.13] 602 [3.94], 659 [3.47]	671, 732.5 (672, 734)
(1*E*)-2-(4-Nitrophenyl)ethenyl-ZnTPP (**8**)	3216 (2320)	432 [5.20]	526 [3.77], 558 [4.35] 597 [4.13]	617, 664 (616.5, 664.5)
(1*E*,3*E*)-2-(4-Nitrophenyl)buta-1,3-dienyl-H_2TPP (**9**)	3475 (2958)	425 [5.03]	523 [4.21], 572 [4.07] 601 [3.86], 665 [3.51]	668.5 (629, 678)
(1*E*,3*E*)-2-(4-Nitrophenyl)buta-1,3-dienyl-ZnTPP (**10**)	3341 (2741)	430 [4.94]	559 [4.11]; 599 [3.98]	616.5, 666 (616.5, 667)
(1*E*)-2-[4-(Dibutylamino)phenyl]ethenyl-H_2TPP (**11**)	1674 (1102)	422 [5.36]	521 [4.41], 579 [4.16] 603 [4.14], 656 [3.71]	660, 724(sh) (662, 728 sh)
(1*E*)-2-[4-(Dibutylamino)phenyl]ethenyl-ZnTPP (**12**)	1454 (1011)	422 [5.20]	556 [4.08], 601 [3.97]	650 (661)

[a] H_2TPP = 5,10,15,20-tetraphenylporphyrin. [b] Values obtained by irradiation at the Soret wavelength and at the lower energy Q_β band (in parentheses). [c] Values were obtained according to the equation $\Delta\nu_{1/2} = f/4.33\times10^{-9}\cdot\varepsilon$ (F. L. Pilar, *Elementary Quantum Chem.*, McGraw-Hill Book Comp., **1968**) where f is the oscillator strength and ε is the maximum extinction coefficient (values in parentheses are graphically measured[28]). [d] Slightly different values of λ_a are given in ref.[21] [e] An absorption band at 406 nm (logε = 4.65) was also detected for **2**, while **1** showed only a shoulder of the B band at higher energy.

 © 2005 Wiley-VCH Verlag GmbH & Co. KGaA, Weinheim

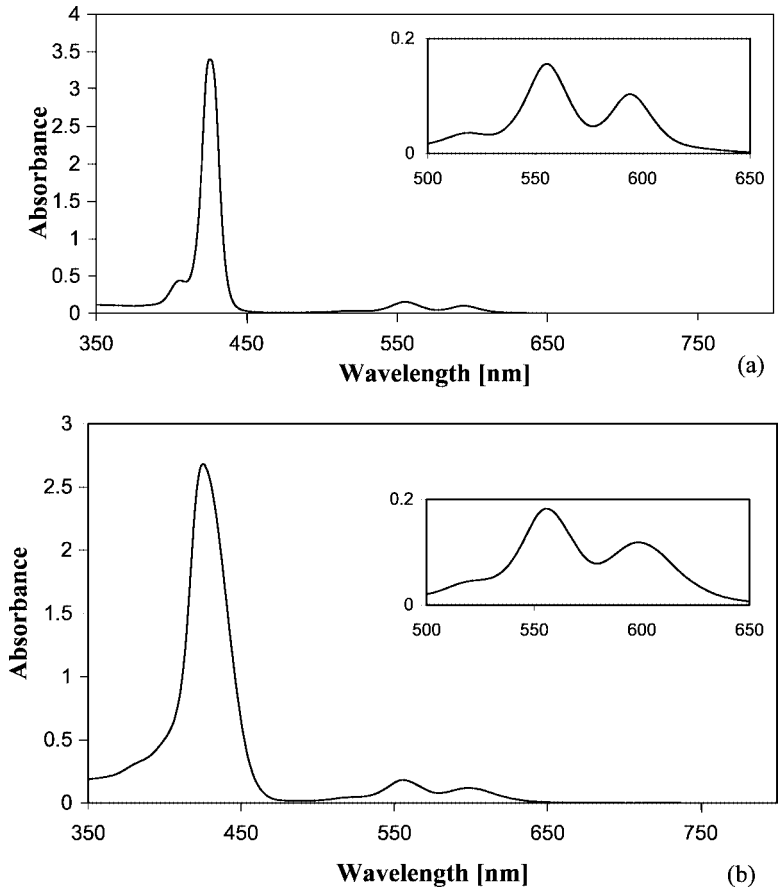

Figure 2. (a) Electronic absorption spectrum of 2-cyano-ZnTPP (**2**) in $CHCl_3$ (8.10×10^{-6} M). (b) Electronic absorption spectrum of 2-nitro-ZnTPP (**4**) in $CHCl_3$ (6.36×10^{-6} M).

complexes **6** and **8**.[27] However, when comparing porphyrin **9** with its Zn^{II} complex **10**, with the electron-withdrawing nitro group further away from the β pyrrolic carbon atom, the number of Q bands decreases from four to two (Table 1 and Figure 4). The above observations would suggest a significant electronic asymmetry of the porphyrin ring when the nitro group is linked to the β pyrrolic position directly or through an arylethenyl or an arylethynyl bridge. This suggestion is also supported by the asymmetry of the B Soret band, with evidence for a shoulder at lower energy (see Figure 3 and Figure 4) and by its bandwidth increase (Table 1).[26]

However, when an electron-donating dibutylamino group is linked to the β pyrrolic position through an arylethenyl linker, the Soret B band remains quite symmetric and its bandwidth does not increase significantly (Table 1). Interestingly, in the spectra of **1** and **2** we also observed an absorption band ($\log\varepsilon = 4.5$) close to the Soret B band but at higher energy (Figure 2 and Table 1) that has not been reported in previous investigations.[25]

The modulation of the π valence orbital levels of porphyrins and metalloporphyrins by substitution at the β pyrrolic position was investigated by a combination of cyclic voltammetry and electronic absorption spectroscopy.[25] A similar approach was later applied when comparing porphyrins **7** and **11** (the latter with a dimethylamino instead of a dibutylamino group) and their Ni^{II} complexes.[21] Electronic transitions from the a_{1u} and a_{2u} HOMO to the e_g LUMO orbitals in porphyrins and their metal complexes cause B and Q absorption bands whose wavelengths and oscillator strengths are defined by the interaction configuration between the a_{1u} and a_{2u} orbitals and therefore by their relative energies.[10] These latter are reported to be affected by substitution at the β pyrrolic position; the effect is more pronounced for the a_{1u} orbital, which has a non-vanishing electron density on both the α and β pyrrolic carbon atoms.[25] For porphyrin **7** and its Ni^{II} complex, with the nitro group not directly linked to the β pyrrolic position, the perturbation of the energy of the a_{1u} orbital has been suggested to be modest.[21] On the contrary, the decrease of Q bands from four to three upon complexation of **7** with Zn^{II}, together with the significant asymmetry of the B band and parallel increased bandwidth, would suggest a significant perturbation of the porphyrin π orbitals. Due to the π delocalised nature of the substituent at the β pyrrolic position, this effect could not be originated only by an inductive perturbation of the energy levels of the a_{1u} and a_{2u} frontier orbitals. As already suggested for porphyrin **7**,[21] this perturbation could be mainly due to the conjugation of the π orbitals of the linker with the π orbitals of the pyrrolic ring, which may induce some charge-transfer character to porphyrin $\pi \rightarrow \pi^*$ transitions that are no longer totally centred

 © 2005 Wiley-VCH Verlag GmbH & Co. KGaA, Weinheim

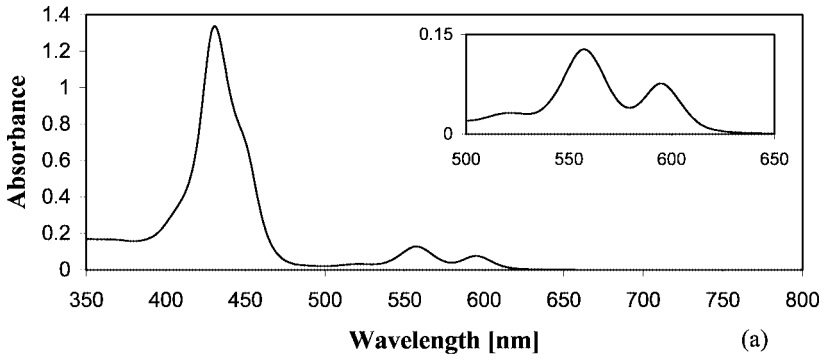

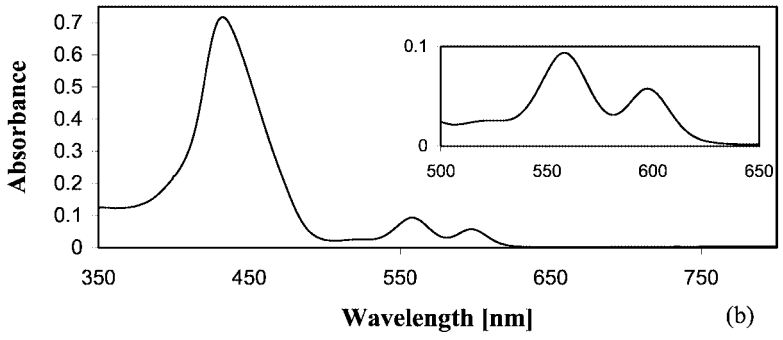

Figure 3. (a) Electronic absorption spectrum of 2-(4-nitrophenyl)ethynyl-ZnTPP (**6**) in $CHCl_3$ (6.25×10^{-6} M). (b) Electronic absorption spectrum of (1*E*)-2-(4-nitrophenyl)ethenyl-ZnTPP (**8**) in $CHCl_3$ (4.52×10^{-6} M).

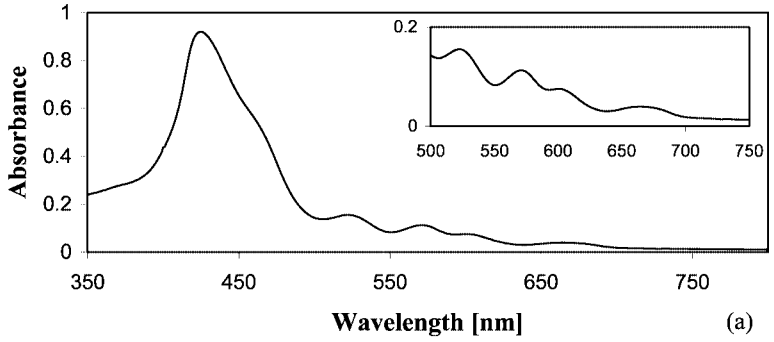

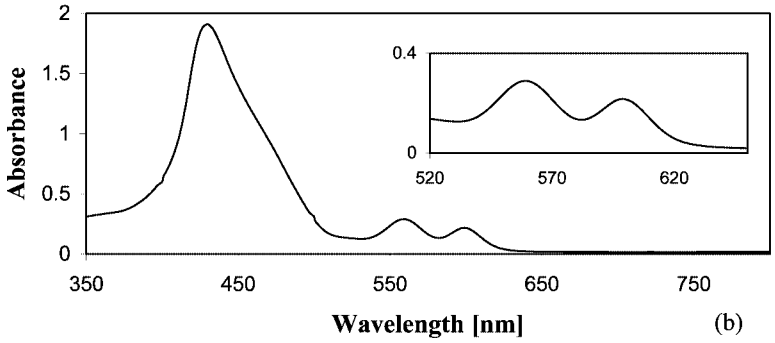

Figure 4. (a) Electronic absorption spectrum of (1*E*,3*E*)-2-(4-nitrophenyl)buta-1,3-dienyl-H_2TPP (**9**) in $CHCl_3$ (8.58×10^{-6} M). (b) Electronic absorption spectrum of (1*E*,3*E*)-2-(4-nitrophenyl)buta-1,3-dienyl-ZnTPP (**10**) in $CHCl_3$ (2.19×10^{-5} M).

 © 2005 Wiley-VCH Verlag GmbH & Co. KGaA, Weinheim

on the porphyrin ring,[28] as supported by the increased bandwidth of the Soret B band.[26] In agreement with this hypothesis, the available structural data indicate, at least for the arylethenyl linker, that the porphyrin core and the styryl group are essentially coplanar,[21,29] a structural feature which should promote a facile interaction of the π orbitals of the linker with the porphyrin π orbitals. Such a nearly planar arrangement was confirmed as the best geometry, by an ab initio DFT method, for the Zn^{II} complexes **8** and **12** and the related porphyrins **7** and **11** (see below).

The effects of substituents upon the relative energies of the frontier orbitals a_{1u} and a_{2u} of metal porphyrin complexes may be evaluated, in a first instance, by the Shelnutt analysis,[28] which correlates the energies of the B and Q_α transitions with the ratio of the square of their transition dipole moments. Shelnutt suggests that the closer in energy the a_{1u} and a_{2u} orbitals are, the smaller the ratio of the square of the transition dipole moments of the Q_α and B transitions, respectively, and the difference in energy $E_B - E_{Q\alpha}$.

The substitution at the β pyrrolic position in the Zn^{II} porphyrin complexes investigated in this work produces a substantial increase of both $E_B - E_{Q\alpha}$ and the ratio of the square of the transition dipole moments of the Q_α and B transition, respectively, with respect to the parent complex ZnTPP (Table 2). Such an increase is more relevant when the π-delocalised substituent carries the strong donor dibutylamino group. This evidence adds further support to a significant perturbation of the energies of the a_{1u} and a_{2u} orbitals, which shift further apart. However, the so-called Shelnutt analysis[28] must be taken with some caution because different linkers may introduce different charge-transfer character to B or Q_α transitions, or to both of them.

In order to produce more evidence for a significant electronic perturbation, we also investigated the trends of a parameter of the electronic absorption spectra of Zn^{II} porphyrin complexes that is independent of the extent of the configurational interaction of the a_{1u} and a_{2u} orbitals. This is the centre of gravity of the B and Q_α bands, defined as $E = ½(E_B + E_{Q\alpha})$, which is an indication of the relative perturbation of the energy levels of the a_{1u} and a_{2u} frontier orbitals.[25] A red shift of the centre of gravity with respect to CuTPP of about 350–700 cm^{-1} has been found for the substitution in the β pyrrolic position with a series of electron-withdrawing groups, while the red shift is much smaller (about 20–400 cm^{-1}) with electron-donating groups.[25] We have found a relevant blue shift of about 1500 cm^{-1} (Table 2) with respect to ZnTPP for complexes **4**, **6**, **8** and **10** carrying a nitro group directly or indirectly bound to the β pyrrolic carbon atom. The centre of gravity appears to be quite independent of the different nature and length of the π linker (Table 2). On the contrary, the centre of gravity of complex **12**, with a π linker carrying an electron-donating dibutylamino substituent, shows a completely different trend with a limited red shift of about 300 cm^{-1} (Table 2). The above observations suggest not only the presence of a perturbation, but also a completely opposite trend when passing from an electron-withdrawing to an electron-donating π delocalised substituent.[25] In conclusion, we have produced a significant and complementary body of evidence for a significant electronic perturbation of the π porphyrin system by β pyrrolic substitution with a π delocalised linker carrying a push or pull group. In order to confirm the role of π conjugation, which should introduce some charge-transfer character to both the B and Q absorption bands, we carried out a solvatochromic investigation using a set of solvents of increasing polarity, excluding those that show strong donor or hydrogen-bonding properties (see Experimental Section), so that mainly the orientational effect of the solvent polarity (and not hydrogen bonding or strong basic ligation) dependency was studied. With this limitation a poor solvatochromic behaviour of the B band of porphyrin complexes was usually reported.[30,31] However, the solvatochromic behaviour of the B band becomes significant for a series of Zn^{II} complexes of various isomers of H_2TPP bearing two NO_2 groups in different β pyrrolic positions.[32]

We have produced clear evidence for a significant solvatochromic behaviour of both B and Q_β (in porphyrins the Q band is at higher energy) bands for porphyrins and their Zn^{II} complexes investigated in this work when carrying a π delocalised linker (Table 3). With the exception of porphyrin **9**, the Soret B band is always shifted to higher energy (blue shift) with increasing polarity of the solvent when a nitro group is linked through a π spacer (Table 3).

The strength of the charge-transfer character, deduced from the absolute value of $\Delta\mu_{eg}$ (difference between excited and ground state dipole moments), which is negative for blue-shifted bands, is relatively small for porphyrins **5**, **7**

Table 2. Some characteristics of the electronic spectra of some 2-substituted Zn(TPP) complexes in $CHCl_3$.

Compound[a]	B band λ_{max} [nm] [r^2_{eg} 10^{-34}][c]	Q_α band λ_{max} [nm] [r^2_{eg} 10^{-36}][c]	Center of gravity[b] [cm^{-1}]	$E_B - E_{Q\alpha}$ [cm^{-1}]
ZnTPP	419 [1.22]	584 [1.16]	20494	5585.0
2-Cyano-ZnTPP (**2**)	427 [n.d.]	593 [n.d.]	21968	6555.8
2-Nitro-ZnTPP (**4**)	425 [0.873]	598 [5.73]	21956	6807.0
2-(4-Nitrophenyl)ethynyl-ZnTPP (**6**)	431 [1.09]	594 [3.67]	21975	6366.8
(1*E*)-2-(4-Nitrophenyl)ethenyl-ZnTPP (**8**)	432 [2.15]	597 [4.96]	21859	6397.7
(1*E*,3*E*)-2-(4-Nitrophenyl)buta-1,3-dienyl-ZnTPP (**10**)	430 [1.15]	599 [3.95]	21975	6561.3
(1*E*)-2-[4-(Dibutylamino)phenyl]ethenyl-ZnTPP (**12**)	422 [0.895]	601 [5.37]	20167	7057.8

[a] H_2TPP is 5,10,15,20-tetraphenylporphyrin. [b] The electronic centre of gravity is defined as $(E_B + E_{Q\alpha})/2$ according to ref.[25] [c] The transition dipole moment r_{eg} is related to the oscillator strength f by the following equation: $r^2_{eg} = 2.13 \times 10^{-30}\, f/\nu_{eg}$, where ν_{eg} is the absorption in cm^{-1} according to ref.[49b]

 © 2005 Wiley-VCH Verlag GmbH & Co. KGaA, Weinheim

Table 3. Solvatochromic behaviour of the Soret B band and of the Q_β band at higher energy.

Compound[a]	Soret B		Q_β	
	$\Delta\mu_{eg}$ [D]	f	$\Delta\mu_{eg}$ [D]	f
ZnTPP		1.36		0.069
2-Cyano-ZnTPP (**2**)	[b]	[b]	–0.09	0.089
2-Nitro-H_2TPP (**3**)	0.7	2.19	1.5	0.068
2-Nitro-ZnTPP (**4**)	[b]	0.96	–0.6	0.061
2-(4-Nitrophenyl)ethynyl-H_2TPP (**5**)	–1.3	1.81	2.32	0.081
2-(4-Nitrophenyl)ethynyl-ZnTPP (**6**)	–5.7	1.19	–4.3	0.063
(1*E*)-2-(4-Nitrophenyl)ethenyl-H_2TPP (**7**)	–2.2	1.59	2.6	0.082
(1*E*)-2-(4-Nitrophenyl)ethenyl-ZnTPP (**8**)	–8.6	2.2	[b]	[b]
(1*E*,3*E*)-2-(4-Nitrophenyl)buta-1,3-dienyl-H_2TPP (**9**)	7.1	1.61	9.3	0.085
(1*E*,3*E*)-2-(4-Nitrophenyl)buta-1,3-dienyl-ZnTPP (**10**)	–19.6	1.26	–5.6	0.062
(1*E*)-2-[4-(Dibutylamino)phenyl]ethenyl-H_2TPP (**11**)	2.86	1.66	11.1	0.22
(1*E*)-2-[4-(Dibutylamino)phenyl]ethenyl-ZnTPP (**12**)	–16.8	0.99	–19.2	0.060

[a] H_2TPP is 5,10,15,20-tetraphenylporphyrin. [b] Not significantly solvatochromic.

and **9** but becomes more relevant for their Zn^{II} complexes **6** and **8**, with an abrupt increase for complex **10** (Table 3). The Q_β band of porphyrins **5**, **7** and **9**, which is only slightly shifted to lower energy (red shift) with increasing polarity of the solvent, becomes blue shifted in the Zn^{II} complexes **6** and **10** or remains unchanged in **8** (Table 3). As already reported,[32] the solvatochromic behaviour becomes insignificant when the nitro group is directly linked to the β pyrrolic position, suggesting that the solvatochromism must be ascribed to a charge-transfer process originated by a significant perturbation of the π frontier orbitals of the porphyrin ring through conjugation with π delocalised substituents (Table 3). Porphyrin **11**, with an arylethenyl linker carrying a dibutylamino group, and its Zn^{II} complex **12** show an unexpectedly significant solvatochromism, blue shifted for **12** and red shifted for **11**, of both B and Q_β bands. In this latter case it is difficult, however, to suggest that this solvatochromic behaviour may be due to a charge-transfer process involving conjugation of the π-delocalised linker and the porphyrin ring, since their B bands are symmetric with no increase of the bandwidth.[26] In this latter case the perturbation of the π system of the porphyrin, which influences the polarity of both the ground and excited states, probably involves the strongly donor dibutylamino group.

All porphyrins and their Zn^{II} complexes investigated in this work show a neat fluorescent emission band when irradiated either at the Soret B band or at the Q_β band. The intensity of the emission for both porphyrins and their Zn^{II} complexes is more relevant when the Soret B band is irradiated. Porphyrin **3** and its Zn^{II} complex **4**, with the nitro group directly bound to the β pyrrolic position, show, as already reported,[33] only one diffuse emission band (Table 1). The same behaviour is shown by the Zn^{II} complex **12**, with a dibutylamino group linked to the β pyrrolic position through an arylethenyl linker. The wavelength of the emission bands of both porphyrins and their Zn^{II} complexes is affected by the length of the π-delocalised linker, while it is not too affected by the substituents (Table 1). As with the absorption B and Q_β bands, the emission bands are also solvatochromic.

In conclusion, our detailed investigation of the electronic spectra and their solvatochromic behaviour has produced strong evidence for a significant perturbation of the π porphyrin ring by β pyrrolic substitution with a π-delocalised linker carrying a donor or acceptor group. This perturbation involves the conjugation of both the π orbital systems, as confirmed by the solvatochromic behaviour of both B and Q_β bands, but the significant excitation processes due to conjugation are different if the π-delocalised linker carries a push or a pull group.

Voltammetric Investigation

The anodic oxidation of porphyrins and their Zn^{II} complexes investigated in this work takes place by two reversible one-electron steps.[34,35] For porphyrin **11** and its Zn^{II} complex **12**, which carry a dibutylamino group, in addition to the two main peaks we noticed a small oxidation prewave located before the second (for **11**) and the first (for **12**) main oxidation peak (Table 4). Porphyrins **5**, **7** and **11**, with a different *para* substituent on the phenyl ring or a different π system connecting the phenyl group to the porphyrin ring, show the following oxidisability sequence for the first oxidation steps: **11** >> **7** > **5** (Table 4).

A significantly lower oxidation potential for the first oxidation step has already been reported for a porphyrin structurally related to **11** that carries a dimethylamino instead of a dibutylamino group.[21] For this latter porphyrin the second oxidation step was reported not to be reversible, while we found that for **11** it is reversible and not at significantly lower oxidation potential with respect to porphyrins **5** and **7** (Table 4). As a consequence, for porphyrin **11** it is better to take into account, when comparing its oxidisability with that of other porphyrins, the second oxidation step, which seems to be centred, as for other porphyrins, on the HOMO energies of the porphyrin π core. In fact, as already suggested,[21] the first step of oxidation of **11** could be centred off the HOMO energies of the porphyrin π core, probably at the dibutylamino functionality. The higher oxidisability of **11** and the slightly lower oxidisability of **5** with respect

 © 2005 Wiley-VCH Verlag GmbH & Co. KGaA, Weinheim

Table 4. Oxidation and reduction peak potentials E_p (V vs. SCE) for three porphyrins and their Zn complexes (glassy carbon electrode, potential scan rate: 0.2 $V s^{-1}$).

	Cathodic peaks[a,b]		Anodic peaks[a,b]	
2-(4-Nitrophenyl)ethynyl-H_2TPP (**5**)	–1.53	–1.170 (–1.055)	*1.105*	*1.255*
(1*E*)-2-(4-Nitrophenyl)ethenyl-H_2TPP (**7**)		–1.180 (–0.955)	*1.075*	*1.225*
(1*E*)-2-[4-(Dibutylamino)phenyl]ethenyl-H_2TPP (**11**)	–1.55	–1.035	*0.655*	(0.935) *1.010*
2-(4-Nitrophenyl)ethynyl-ZnTPP (**6**)		*–1.015*	*0.862*	*1.155*
(1*E*)-2-(4-Nitrophenyl)ethenyl-ZnTPP (**8**)	–1.51	*–1.110*	*0.845*	*1.108*
(1*E*)-2-[4-(Dibutylamino)phenyl]ethenyl-ZnTPP (**12**)	–1.68	–1.28 (–1.0)	(0.390) *0.625*	*0.790*

[a] Reversibile monoelectronic peaks are italicised. [b] Prewaves are in parentheses.

to **7** (Table 4) can be interpreted as an increased stabilisation due to a significant perturbation, produced by the substituents carrying an electron-withdrawing nitro group, on the energy levels of the HOMO electrons, which stabilizes the π core of the porphyrin ring.

This effect is in agreement with a conjugation between the π system of the linker and the π orbitals of the porphyrin ring as proposed above. The slightly higher oxidisability of **7** with respect to **5** can be interpreted in terms of the higher efficiency of the triple bond of the linker in transmitting the perturbation of the electron-withdrawing nitro group to the porphyrin π core.

When a porphyrin ring is complexed to a metal like Zn^{II}, irrespective of the working medium and of the porphyrin structure, a fairly constant difference in the range from –0.31 to –0.16 V between the first oxidation potential of the Zn^{II} complex and that of its parent porphyrin has been reported.[35,36] This range of negative values is shown by two of the three couples investigated in this work: –0.24 V for **6** vs. **5** and –0.23 V for **8** vs. **7** (Table 4). When comparing **12** and **11**, the difference turns out to be –0.27 V only if taking into account the oxidation prewave of the Zn^{II} complex, while when comparing the first "regular" peak the difference (–0.03 V) appears to be anomalously low. However, when taking into account the second oxidation peak, as suggested above, the expected difference of –0.22 V is found. This is additional evidence that the first oxidation peak in porphyrin **11** does not involve the HOMO electrons of the π porphyrin core. The difference $\Delta E_{(ox–red)}$ between the first oxidation and the first reduction process of porphyrins and their Zn^{II} complexes has been reported to be always within 2.25 ± 0.15 V (Kadish's relationship), as expected for a strictly ring-based process of oxidation and reduction.[35] For porphyrins **5** and **7**, the $\Delta E_{(ox–red)}$ values obey Kadish's relationship (2.16 V and 2.26 V respectively), while again for porphyrin **11** this difference is only 1.69 V, if we consider the first "regular" reduction peak. It becomes 2.05 V, as expected, when the second reduction peak is taken into account. For Zn^{II} complexes **6**, **8** and **12** the values of $\Delta E_{(ox–red)}$ deviate from Kadish's relationship (1.88 V for **6**, 1.96 V for **8** and 1.91 V for **12** when taking into account the first oxidation peak; the value becomes 2.07 V for **12** if we consider the second oxidation peak). It thus appears that the π levels of the Zn^{II} porphyrins investigated in this work are quite affected by the perturbation induced by the π system of the linker mainly when it carries a nitro group. Complexation of porphyrins to Zn^{II} results in a significant anticipation, with respect to the parent porphyrin, of both the first and second oxidation potentials, according to a relevant increase of the negative charge on the porphyrin ring (Table 4). However, complexation to Ni^{II} of porphyrin **7** results in only a slight difference of the oxidation potentials with respect to those of the parent porphyrin (e.g. +0.03 V for the first oxidation peak, 0.00 V for the second one),[21] in agreement with the suggestion of Kadish et al.[35] of a higher induction parameter of Ni^{II} (1.8) with respect to Zn^{II} (1.5), resulting in a negative charge on the porphyrin ring that is much less significant for the Ni^{II} complexes. Finally, although the detection of three or four one-electron reduction waves is usually reported for porphyrins and their metal complexes when working with an acceptably broad cathodic window,[37,38] in the present work, due to the less broad window when working in CH_2Cl_2 as solvent, we observed only the first two reduction peaks and only the first one for **6** and **7**. All the potentials but one (namely those of porphyrin **11**) fall within the expected range of 0.42 ± 0.03 V of difference between the first and the second reduction potential, namely 0.42 V for **5** (averaging between the first reduction peak and its shoulder), 0.40 V for **8**, 0.52 V for **11** and 0.40 V for **12**. The first reduction step appears to be clearly monoelectronic and reversible only for Zn^{II} complexes **6** and **8**.

As a conclusion, the voltammetric investigation has confirmed a perturbation of the HOMO levels of the porphyrin π core due to conjugation with the π orbitals of the linker bound to the β pyrrolic position. This perturbation is more significant if the π linker carries a nitro group and if the Zn^{II} ion is complexed to the porphyrin ring. When the π linker carries a donor dibutylamino group the perturbation of the π levels of the porphyrin ring is not only lower, but the HOMO levels are centred on the dibutylamino group.

Dipole Moments

Although the experimental determination of the dipole moment by the Guggenheim method[39] was not reproducible for the push-pull porphyrins and their metal complexes investigated previously, such that it was always calculated by semi-empirical methods,[5,6] we obtained quite reproducible experimental measurements, with the exception of porphyrin **11** and its Zn^{II} complex **12** (see Exp. Sect.). Porphy-

 © 2005 Wiley-VCH Verlag GmbH & Co. KGaA, Weinheim

rins **5**, **7** and **9**, which carry a linker with a nitro group, show a dipole moment comparable to that of their Zn^{II} complexes **6**, **8** and **10**. The nature of the linker, either phenylethynyl, phenylethenyl or even phenylbutan-1,3-dienyl, does not induce a significant effect on the order of magnitude of the experimental dipole moment (Table 5). The best geometries and dipole moments were calculated theoretically by an ab initio approach based on the density functional theory (DFT)[15,16] using an extended basis set[17] (see Experimental Section for details). The calculated optimised geometries always support a quite planar arrangement of the π porphyrin ring and the π system of the organic linker.

Table 5. Experimental and theoretical dipole moments, EFISH β_λ in $CHCl_3$ solution (1.907 μm incident wavelength) and β_0.

Compound[a]	μ_{exp} (μ_{theor}) [D]	$\beta_{1.907}$[b] [10^{-30} esu]	β_0[c] [10^{-30} esu]	$\mu\beta_0$ [10^{-48} esu]
2-Cyano-ZnTPP (**2**)	6.4 (5.43)	9.6[d]	7.30	46.7
2-Nitro-H_2TPP (**3**)	4.5 (5.40)[e]	6.8[d]	5.17	23.3
2-Nitro-ZnTPP (**4**)	6.4 (5.42)	13.4[d]	10.2	65.2
2-(4-Nitrophenyl)ethynyl-H_2TPP (**5**)	6.1 (8.55)[e]	30.1[f]	22.7	138.5
2-(4-Nitrophenyl)ethynyl-ZnTPP (**6**)	7.1 (8.82)	20.4[f]	11.3	80.2
(1*E*)-2-(4-Nitrophenyl)ethenyl-H_2TPP (**7**)	6.6 (8.31) [e]	39.3[f]	19.7	196.0
(1*E*)-2-(4-Nitrophenyl)ethenyl-ZnTPP (**8**)	7.0 (8.69)	29.7[f]	22.4	157
(1*E*,3*E*)-2-(4-Nitrophenyl)buta-1,3-dienyl-H_2TPP (**9**)	6.2 (9.30)[e]	42.8[f]	32.6	202
(1*E*,3*E*)-2-(4-Nitrophenyl)buta-1,3-dienyl-ZnTPP (**10**)	7.1 (9.46)	43.1[f]	32.6	231
(1*E*)-2-[4-(Dibutylamino)phenyl]ethenyl-H_2TPP (**11**)	(5.33)[e][h]	75.7[f][g]	57.9	308.6
(1*E*)-2-[4-(Dibutylamino)phenyl]ethenyl-ZnTPP (**12**)	(5.16)[h]	127.5 [f][g]	97.5	503.1

[a] H_2TPP is 5,10,15,20-tetraphenylporphyrin. [b] Obtained from Equation (2) (see text) omitting the cubic contribution γ(–2ω; ω, ω, 0). [c] Calculated from the two levels model assuming only the B band as the main charge-transfer process [Equation (2)]. [d] The error is ±20–30%. [e] The theoretical value is the semi-sum of the theoretical dipole moments of two isomeric structures. [f] The error is ±10–15%. [g] Using theoretical dipole moment. [h] Theoretical value calculated by an ab initio approach.

Table 6. A comparison of the dipole moments and ^{1}H NMR spectroscopic data of a series of (*E*)-arylethenyl structures.

Compound	μ(D)	H^1 [ppm])[a]	H^2 [ppm][a]	J_{H1-H2} [Hz][a]
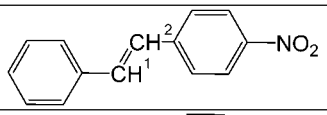	4.56[b]	7.13	7.25	16.2
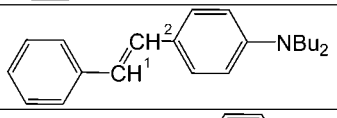	1.07[b]	6.92	7.03	–
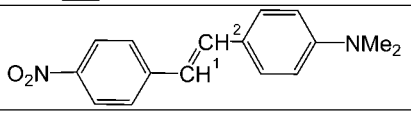	7.42[b]	6.93	7.21	16
[d] 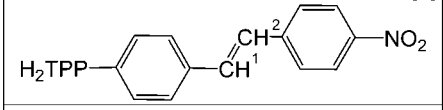	6.6[a] (8.31)[c]	7.11	7.29	16
[d] 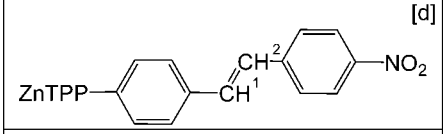	7.0[a] (8.69)[c]	7.18	7.24	16
[d] 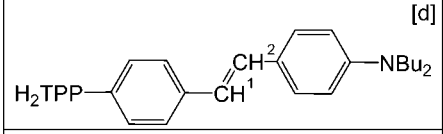	5.33[c]	6.72	7.28	16
[d] 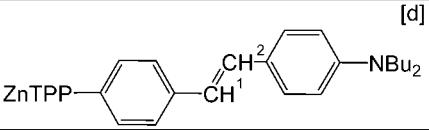	5.16[c]	6.82	7.22	16

[a] In $CHCl_3$ or $CDCl_3$ at 25 °C. [b] In benzene at 25 °C. [c] Calculated by an ab initio approach based on DFT Theory (see Exp. Sect. and Table 5). [d] The stilbene substituent is linked to the β pyrrolic position of the porphyrin ring.

 © 2005 Wiley-VCH Verlag GmbH & Co. KGaA, Weinheim

The calculated dipole moments of the two isomeric structures of asymmetric porphyrins **3**, **5**, **7**, **9** and **11** are quite similar, thus the data reported in Table 5 are mean values. They are in good agreement with the experimental ones with the exception of the couple **9** and **10**. For porphyrin **11** and its Zn^{II} complex **12** the calculated dipole moments are, as expected, rather low and with inversion of polarity (Table 5). In this latter case, complexation to Zn^{II} induces a slight lowering of the dipole moment with respect to the free porphyrin, in agreement with an increased negative charge on the porphyrin ring acting as acceptor. As expected, the opposite effect is calculated and observed experimentally for the couples **5** and **6**, **7** and **8**, and **9** and **10** (Table 5). The order of magnitude of the dipole moments of porphyrins **5**, **7** and **9** and their Zn^{II} complexes **6**, **8** and **10**, with a linker carrying a nitro group, supports a significant electronic asymmetry.

In conclusion, according to theoretical calculations the substitution of the electron-withdrawing nitro group by the strongly electron-donating dibutylamino group introduces a lower electronic asymmetry with a completely opposite polarity. Therefore, we have further evidence that, already in the ground state, the conjugation of the π systems produces a completely opposite electronic effect: the porphyrin ring acts as an electron donor if the linker carries a nitro group, while it acts as an electron acceptor if the linker carries a dibutylamino group. This ambivalent picture of the ground-state electronic density of the porphyrins and their Zn^{II} complexes investigated in this work can be better measured when comparing their dipole moments and ^1H NMR chemical shifts with those of a series of (*E*)-stilbene structures (Table 6).

If compared to the benzene ring, the porphyrin ring, as such or as a Zn^{II} complex, behaves as a much better acceptor and a slightly better donor on the basis of both dipole moments and chemical shifts of the protons of the (*E*)-double bond when linked through the β pyrrolic position. It shows, however, lower donor properties than a benzene ring carrying a dimethylamino group in the *para* position. Therefore, already in the ground state, a porphyrin ring substituted in the β pyrrolic position with a push or pull aryl ethenyl system shows a relevant ambivalent role as donor or acceptor.

Determination of the Quadratic Hyperpolarizability by the EFISH Technique

The EFISH technique[40] allows the determination of the second-order NLO response, γ_{EFISH}, of a solute. In order to avoid resonance enhancement, we worked with an off-resonance incident wavelength of 1.907 μm (see Experimental Section).

In highly π conjugated two dimensional molecules, such as porphyrins and phthalocyanines, the electronic contribution to γ_{EFISH} in Equation (3) (see Experimental Section) cannot, at first instance, be ignored.[5c,41] However, for asymmetrically substituted phthalocyanines, structurally related to our porphyrinic chromophores, carrying an arylethenyl or an arylbutadienyl spacer with a nitro group in the *para* position, the electronic contribution to γ_{EFISH} was evaluated to be much smaller than the dipolar orientational one.[41] In accordance, we neglected the electronic contribution during the evaluation of EFISH $\beta_{1.907}$ from γ_{EFISH}.

Our push-pull porphyrinic chromophores are characterised by a dipole moment axis directed quite parallel to the π linker axis, as confirmed by our DFT calculations on the dipole moments and best geometries. It follows that a charge-transfer process involving the π linker, which may control the second-order NLO response, is probably located quite parallel to this axis, as in traditional two-dimensional, pseudo-linear, organometallic push-pull chromophores.[42] If so, the component of β_{vec} along the dipole moment axis, that is EFISH $\beta_{1.907}$ (see Experimental Section), should be quite coincident with β_{vec}, which is the vectorial part of the quadratic hyperpolarizability tensor. EFISH $\beta_{1.907}$ turns out to be small for porphyrin **3** and for the Zn^{II} complexes **2** and **4**, with the electron-withdrawing group linked directly to the β pyrrolic position (Table 5). The order of magnitude of the quadratic hyperpolarizabilities of **3** and **4** is in agreement with that of a structurally related porphyrin and its Zn^{II} complex but carrying completely fluorinated aromatic rings in *meso* positions, although in this latter case the quadratic hyperpolarizability was measured with the HRS technique (Hyper Raleigh Scattering) working with a resonant incident wavelength of 1.064 μm.[12b] In this latter case, on the basis of solvatochromic evidence the major contribution to the second-order NLO response was attributed to a charge-transfer process from the porphyrin ring (as donor) to the nitro group linked to the β pyrrolic carbon atom (as acceptor) along the dipole moment axis, as assumed above.[43] The very low second-order NLO response of chromophores **2**–**4** is in accordance with the assumption that acceptor groups appended to an electron-rich centre, like the β position of the porphyrin ring, should not produce large NLO responses.[13,14] The values of EFISH $\beta_{1.907}$ increase upon introduction of a π-delocalised linker between the β pyrrolic position of the porphyrin ring and the electron-withdrawing nitro group (Table 5). As in structurally related pseudo-linear, organometallic, push-pull chromophores[42] and in structurally related push-pull phthalocyanines,[41] EFISH $\beta_{1.907}$ increases slightly upon increasing the length of the linker or by substitution of a triple bond with an (*E*)-double bond. We have also shown that EFISH $\beta_{1.907}$ always decreases slightly on going from the free porphyrin to its Zn^{II} complex, with the exception of the couple **9** and **10**, which show comparable values (Table 5).

This limited effect of coordination to Zn^{II} is in agreement with the assumption that the second-order NLO response is controlled by a charge-transfer process, favoured by conjugation, from the occupied π levels of the pyrrolic ring, acting as a push system, to the π* antibonding orbitals of the linker. In fact, this latter process should be scarcely affected by coordination of the porphyrin to Zn^{II}, which mainly influences the energy of the a_{2u} porphyrin orbital, with nodes at the metal centre and little electron density on the *exo* pyrrole positions.[10,25]

 © 2005 Wiley-VCH Verlag GmbH & Co. KGaA, Weinheim

The positive value of the second-order NLO response of porphyrins with a nitro group linked to the β pyrrolic position by a π linker (**5**, **7**, **9** and **6**, **8**, **10**) also supports the role of such a charge-transfer process, which is characterised by the same polarity of the dipole moment.[42]

Interestingly, the values of EFISH $\beta_{1.907}$ of our porphyrinic chromophores **5**–**10** are comparable to that of structurally related chromophores based on the phthalocyanine ring.[41]

A larger and still positive second-order NLO response, confirmed by a series of experimental determinations in two different laboratories (see Experimental Section), was found by substitution of the nitro group with the strongly electron donating dibutylamino group as in porphyrin **11** and its Zn^{II} complex **12**. The second-order NLO response increases by complexation to Zn^{II} (Table 5). This response of both **11** and **12** cannot be due to a charge-transfer process, as above, from the occupied π orbitals of the pyrrolic ring to the π* antibonding orbitals of the π linker, since this process should produce a negative second-order NLO response as its polarity is opposite to that of the calculated dipole moment.[42] It is known that in push-pull NLO molecules the nature of the π conjugation can alter the electron donating ability of push substituents.[13] Thus, we can tentatively propose that the high EFISH $\beta_{1.907}$ values of both **11** and **12** are due to a relevant increase of the electronic effects of the donor properties of the dibutylamino group induced by an extended π system involving the porphyrin ring, possessing π segments that are either electron rich or electron poor.[14] The conjugation process of the overall π system of the linker with the extended π system of the porphyrin ring should stabilize the π* antibonding levels, thus producing a shift of the n→π* transition, which is the main origin of the second order NLO response, to much lower energy. In accordance with this hypothesis, this latter transition, which is usually located around 370–390 nm in *para*-dimethylaminostilbazoles,[42] is absent in the electronic spectra of both **11** and **12**, thus supporting a relevant red shift, probably under the large B band or even under the Q bands at much lower energy. In any case, our experimental observations are in agreement with the suggestion, based on a theoretical approach, of Marks, Ratner et al.[14] that the linkage to the electron-rich β pyrrolic position of a π system carrying a strong electron donating dibutylamino group may be the origin of some depletion of electron density on the donor and thereby of the reduction of the ground-state polarisation with an increase of the effective strength of the donor substituent and thereby of the second-order NLO response.[14] The significant increase of EFISH $\beta_{1.907}$ by coordination of **11** to Zn^{II} is in agreement with this hypothesis because complexation introduces a significant increase of the electron density on the porphyrinic ring, as confirmed by our voltammetric investigation. The significant second-order NLO response cannot be attributed to a aggregation process, which was discarded by a careful spectroscopic investigation carried out over a large range of concentrations.

Finally, the static quadratic hyperpolarizability EFISH, β_0, was calculated with the two-levels model,[44] according to Equation (1), assuming that the major charge-transfer process affecting the second-order NLO response is under the Soret B band.

$$\beta_0 = \beta_{1907}\left[1-\left(\frac{2\lambda_{max}}{1907}\right)^2\right]\left[1-\left(\frac{\lambda_{max}}{1907}\right)^2\right] \quad (1)$$

The dominant role of the Soret B band is supported by its significant charge-transfer character in all our porphyrinic chromophores, as evidenced by the solvatochromic investigation (Table 3) and by its high intensity. Any contribution due to the Q bands, in particular the Q_β band, which is not only slightly solvatochromic, but also of much lower intensity, should be much less relevant.

Obviously, the application of the two-levels model to an extended two-dimensional π system, although already applied to porphyrins[6a,6b] and phthalocyanines,[41] is quite debatable. Therefore, the β_0 values calculated by this approach should be considered only for their order of magnitude.

Conclusions

In this work we have produced, for the first time, clear evidence for a significant perturbation of the energy of the π electron core of the porphyrin ring due to conjugation between the porphyrinic π system, when substituted at the β pyrrolic position with a π delocalised linker carrying a nitro group, and the π system of the linker itself. The asymmetric shape and increased bandwidth of the B band, the Shelnutt analysis,[28] the trend of the centre of gravity of the B and Q_α bands and the sensitivity of the first two voltammetric oxidation steps, which involve the HOMO orbitals, with respect to the nature of the π linker, all support this perturbation, where the porphyrin ring, because of the electron-richness of the β position,[14] acts as an electron donor. This effect seems to be less relevant when the π linker carries a dibutylamino group. In this latter case the HOMO orbitals are centred on this group. Therefore, we have produced clear evidence that, already in the ground state, the porphyrin ring shows an ambivalent character, acting also as an acceptor, as supported, for instance, by the value and polarity of the dipole moments of porphyrin **11** and its Zn^{II} complex **12**, both of which have a linker carrying the strongly electron-donating dibutylamino group.

In the electron excitation process, the significant conjugation of the π levels of both the porphyrin ring and linker facilitates a charge transfer from the occupied π levels of the porphyrin π core, acting as a push group, to the antibonding π* orbitals of the linker carrying the pull nitro group, thus producing positive values of EFISH $\beta_{1.907}$ of the chromophores either as porphyrins (**5**, **7** and **9**) or as their Zn^{II} complexes (**6**, **8** and **10**) (Table 5). Evidence for a charge-transfer process from the porphyrin ring is also provided by the significant solvatochromic behaviour of both B and Q_β bands and by the asymmetric shape and

 © 2005 Wiley-VCH Verlag GmbH & Co. KGaA, Weinheim

increased bandwidth of the B band of chromophores **5**–**10**.

In order to evaluate the unknown push properties of the β position of the porphyrin ring we can compare, for instance, the quadratic hyperpolarizability EFISH $\beta_{1.907}$ of the push-pull chromophore **8** with that of structurally related push-pull chromophores having an organic aryl moiety or an organometallic system like ferrocene as push groups (Figure 5). The EFISH $\beta_{1.907}$ of **8** is comparable to that of the chromophore carrying a ferrocenyl push group[45] but much smaller than the organic chromophore with *para*-dimethylamino as the push group.[46] A similar trend is observed for the porphyrinic chromophore having a butadienyl linker like the Zn^{II} complex **10**, which shows a value of EFISH $\beta_{1.907}$ comparable to that of the structurally related chromophore carrying a push ferrocenyl group,[45] but much smaller than that of the organic chromophore with the *para*-dimethylamino push group.[46] Not very different is the trend with respect to the structurally related organic chromophore when the linker is acetylenic (Figure 5).

Compound	$\beta_{1.907}$ 10^{-30} [esu]
Me_2N–⟨⟩–C≡C–⟨⟩–NO_2	46[a]
(6) ZnTPP–C≡C–⟨⟩–NO_2	20.4[b]
Me_2N–⟨⟩–CH=CH–⟨⟩–NO_2	73[a]
Fe(⟨⟩–CH=CH–⟨⟩–NO_2)(Cp)	31[c]
(8) ZnTPP–⟨⟩–CH=CH–⟨⟩–NO_2	29.7[b]
Me_2N–⟨⟩–CH=CH–CH=CH–⟨⟩–NO_2	107[a]
Fe(⟨⟩–CH=CH–CH=CH–⟨⟩–NO_2)(Cp)	47[c]
(10) ZnTPP–⟨⟩–CH=CH–CH=CH–⟨⟩–NO_2	43.1[b]
[a] Ref. [46]; [b] This work; [c] Ref. [45]	

Figure 5. Quadratic hyperpolarizability ($\beta_{1.907}$) of some organic and organometallic push-pull systems measured in $CHCl_3$ by the EFISH technique at an incident wavelength of 1.907 μm.

Therefore, *meso*-tetraphenylporphyrins and their Zn^{II} complexes, carrying in the β pyrrolic position a π-delocalised linker with an electron-withdrawing nitro group, behave, in a push-pull chromophore, as a push group similar to the ferrocenyl group.

The ambivalent character of the porphyrin ring in the porphyrins and their Zn^{II} complexes investigated in this work is confirmed also by properties involving excited states, like the second-order NLO response. The lack of bandwidth increase of the B band, its symmetry and the lower perturbation of the centre of gravity of the B and Q_α bands for both **11** and **12** do not produce evidence for an excitation process involving a significant charge-transfer from the π porphyrin core to the π linker, as occurs in the series of chromophores **5**–**10**. On the contrary, the significant positive EFISH $\beta_{1.907}$ values of **11** and **12** would suggest an effective screening of the ground-state polarisation induced by the electron-rich β pyrrolic position of the porphyrin ring, which behaves as a kind of acceptor and increases, in the excitation process, the donor properties of the dimethylamino push group.[14]

Experimental Section

All the commercially available solvents and chemicals were of reagent-grade quality and, unless otherwise stated, were used without further purification. Porphyrin **3**,[20] its Zn^{II} complex **4**[20] and 4-nitrophenylacetylene[47] were prepared according to literature methods. ^1H NMR spectra were recorded on a Bruker AC-300 Spectrometer in $CDCl_3$ as solvent. Electronic spectra were obtained in $CHCl_3$ with a Jasco V-530 Spectrometer. Emission spectra were obtained in $CHCl_3$ with a Jasco FP-777 spectrofluorimeter. FAB-MS measurements were performed with an analytical VG 7070 EQ instrument. Elemental analyses were carried out in the Analytical Laboratories of the Department of Inorganic, Metallorganic and Analytical Chemistry of Milan University. Dipole moments were determined in $CHCl_3$ solution with a WTW-DM01 dipolmeter (dielectric constant) coupled with a Pulfrich Zeiss PR2 refractometer (refractive index) according to the Guggenheim method.[39]

Cyclic Voltammetry: Cyclovoltammetric investigations (CV) were carried out on carefully deaerated solutions with a station including an AMEL 2049 potentiostat/galvanostat, an AMEL 568 function generator and a Lynseis LY16100-II *x*/*y* recorder. The working solutions were made up with HPLC-grade CH_2Cl_2 and tetrabutylammonium perchlorate (TBAP; >99% Fluka) at concentrations ranging from 3×10^{-4} M to 7×10^{-4} M. Data were obtained at different potential scan rates (ranging from 0.02 to 0.5 $V\,s^{-1}$) working with two different electrodes: (a) an AMEL glassy carbon disk electrode (GC, 2 mm diameter), and (b) a platinum wire electrode (Pt, 1 cm length, 0.05 cm diameter), using a platinum counter-electrode and a saturated calomel electrode (SCE) as reference. The nearly identical voltammograms indicate that the electrode materials have no catalytic effect on the oxidation process.

The electrochemical reversibility and electron number of each well-defined peak were checked by classical tests,[48] including analysis of the I_p vs. $v^{1/2}$ characteristics, the E_p vs. log*v* characteristics, the ($E_p - E_{p/2}$) vs. log*v* characteristics and the "stationary", step-like waves obtained by convolutive analysis of the original CV characteristics.

 © 2005 Wiley-VCH Verlag GmbH & Co. KGaA, Weinheim

Solvatochromic Investigation: The solvatochromic behaviour of the Soret B and Q_β bands was investigated by using a set of polar, nonprotic and only weakly donor solvents (CH_3CN, acetone, dichloroethane, CH_2Cl_2, THF, ethyl acetate, $CHCl_3$, toluene, CCl_4, cyclohexane, *n*-hexane). The values of $\Delta\mu_{eg}$, the difference between the dipole moments of the excited and of the ground state, were obtained from the Mc Rae equation (2)[49] evaluating the radius of the cavity, *a*, occupied by the solute in the solvent empirically from the molecular weight:

$$\nu_a = \nu_a^{\,g} + A\frac{2(n^2-1)}{a^3(2n^2-1)} + B\left(\frac{\varepsilon-1}{\varepsilon+2} - \frac{n^2-1}{n^2+2}\right); \quad B = \frac{-2\mu\Delta\mu_{eg}}{hca^3} \qquad (2)$$

where ν_a and $\nu_a^{\,g}$ are the frequencies of the absorption maximum in a given solvent and in the gas phase, respectively, μ is the dipole moment, *a* is the radius of the cavity (cm), and ε and *n* are the solvent dielectric constant and refractive index, respectively. Since in the determination of $\Delta\mu_{eg}$ of both B and Q_β bands we were not interested in their absolute value, but only in their order of magnitude and sign, the use of the molecular weight for a rather approximate assignment of the value of *a* (cavity radius) to rather flat molecules, such those studied in this work, may be considered acceptable.

EFISH Measurements: EFISH measurements were performed in our department in $CHCl_3$ solutions, as a function of concentration, working at an incident wavelength of 1.907 μm using a Q-switched Nd:YAG laser with a 60- and 20-ns pulse duration, manufactured by Atalaser. The 1.907 μm fundamental wavelength was obtained by Raman shifting of the 1.064 μm emission of the Q-switched Nd:YAG laser in a high pressure hydrogen cell (60 bar). A liquid cell with thick windows in the wedge configuration was used to obtain the Maker fringe pattern (harmonic intensity variation as a function of liquid cell translation).[40] In the EFISH experiments the incident beam was synchronised with a DC field applied in order to break the centrosymmetry of the solution. The apparatus for the EFISH measurements was a prototype made by SOPRA (France).

From the concentration dependence (10^{-3}–10^{-4} M) of the harmonic signal with respect to that of the pure solvent, the NLO responses EFISH β_λ, were determined from the calculated γ_{EFISH}, according to Equation (3):

$$\gamma_{EFISH} = \frac{\mu\beta_\lambda(-2\omega;\omega,\omega)}{5kT} + \gamma(-2\omega;\omega,\omega,0) \qquad (3)$$

where γ_{EFISH} is the sum of a cubic electronic contribution $\gamma(-2\omega;\ \omega,\ \omega,\ 0)$ and of a quadratic orientational contribution $\mu\beta_\lambda$ $(-2\omega;\ \omega,\ \omega)/5kT$, where μ is the dipole moment and EFISH β_λ is the projection along the dipole moment direction of the vectorial component β_{vec} of the tensorial quadratic hyperpolarizability, β, at the incident wavelength λ.

Computational Methods: The optimised geometry of porphyrins as two geometric isomers and of their Zn^{II} complexes was determined at an ab initio level using the DFT (Density Functional Theory) approach[15] adopting the BP86 functional[16] and an all-electron valence triple-ξ basis set with polarisation functions on all atoms (TZVP).[17] The ab initio DFT approach was undertaken because previous experiences[6d] have shown that semi-empirical Hamiltonians like MNDO or AM1 do not produce optimised geometries for the extended π conjugation when the linker is based on a styryl or phenylbutadienyl structure. A loss of planarity of the π linker and therefore a decrease of the π conjugation is usually the final result.

The final geometry of all the porphyrinic systems investigated, either as the free-base porphyrin or its Zn^{II} complex, shows a good planarity of the π linker with the π system of the porphyrinic moiety. The values of the dipole moments moduli and components were finally computed using the Turbomole suite of programs[50] in connection with the resolution of the identity (RI) approximation.[51]

Synthesis of Porphyrins and Their Zn^{II} Complexes

2-Bromo-5,10,15,20-tetraphenylporphyrinatonickel(II): 2-Bromo-5,10,15,20-tetraphenylporphyrin (205 mg, 0.296 mmol) was dissolved in slightly warmed 1,2-dichloroethane (30 mL) whilst stirring, then $Ni(acac)_2$ (84 mg, 0.326 mmol) was added. After 45 minutes the complete disappearance of the starting porphyrin was evidenced by TLC (*n*-hexane/toluene, 7:3) and by the change of the colour of the reaction mixture from brown to red and finally to orange. After removal of the solvent in vacuo, the crude product was crystallised with CH_2Cl_2/pentane and washed with pentane to afford the complex in quantitative yield.

2-Cyano-5,10,15,20-tetraphenylporphyrin (1): This porphyrin was prepared by demetallation of its Ni^{II} complex, synthesised according to a literature procedure.[18] 2-Cyano-5,10,15,20-tetraphenylporphyrinatonickel(II) (50 mg) was dissolved in 95% H_2SO_4 (2 mL) with magnetic stirring. The green solution was slowly added to a saturated solution of $(NH_4)_2CO_3$ and the dark brown suspension was filtered. The mother liquor was extracted with CH_2Cl_2 (2 × 60 mL), and the organic phase was washed with H_2O, dried with Na_2SO_4 and the solvents evaporated to dryness. The residue was purified by column chromatography (silica gel, CH_2Cl_2/*n*-hexane, 1:1) to afford 43 mg (94%) of pure **1** as a dark brown powder. ^{1}H NMR (300 MHz, $CDCl_3$): δ = –2.80 (br. s, 2 H, NH), 7.71–7.81 (m, 12 H, $H_{m,pPh}$), 8.16–8.19 (m, 8 H, H_{oPh}), 8.74 (s, 2 H, $H_{pyrrolic}$), 8.90–8.98 (m, 4 H, $H_{pyrrolic}$), 9.36 (s, 1 H, $H_{pyrrolic}$) ppm. UV/Vis ($CHCl_3$): λ_{max} (logε) = 420 (5.29), 517 (3.79), 552 (3.21), 605 (3.53), 593 (3.23), 648 (3.20) nm. $C_{45}H_{29}N_5$ (639): calcd. C 84.48, H 4.57, N 10.95; found C 84.40, H 4.73, N 10.94. MS-FAB(+): *m*/*z* = 640 $[M + 1]^+$.

2-Nitro-5,10,15,20-tetraphenylporphyrin (3): A solution of the Zn^{II} complex **4** (68.3 mg, 0.094 mmol) in 50 mL of CH_2Cl_2 was stirred at room temperature with 1.5 mL of concentrated HCl for 5 min, then the pH was raised to 7–8 by addition of NEt_3. The brown solution was transferred into a separating funnel and washed with H_2O, the organic phase was separated, dried with Na_2SO_4, evaporated and the residue purified by column chromatography (silica gel, toluene) to afford pure **3** (quantitative yield) as a violet powder. ^{1}H NMR (300 MHz, $CDCl_3$): δ = –2.58 (br. s, 2 H, NH), 7.71–7.83 (m, 12 H, $H_{m,pPh}$), 8.20–8.29 (m, 8 H, H_{oPh}), 8.91–9.05 (m, 6 H, $H_{pyrrolic}$), 9.07 (s, 1 H, $H_{pyrrolic}$) ppm. UV/Vis ($CHCl_3$): λ_{max} (logε) = 427 (5.24), 527 (4.14), 560 (3.56), 605 (3.53), 665 (3.88) nm. $C_{44}H_{29}N_5O_2$ (659): calcd. C 80.10, H 4.43, N 10.62; found C 80.40, H 4.42, N 10.60. MS-FAB(+): *m*/*z* = 660 $[M + 1]^+$.

2-[2-(4-Nitrophenyl)ethyn-1-yl]-5,10,15,20-tetraphenylporphyrin (5): A solution of Zn^{II} complex **6** (60 mg, 0.073 mmol) and trifluoroacetic acid (1 mL) in CH_2Cl_2 (25 mL) was stirred at room temperature for 12 h. The volatiles were removed in vacuo to afford a dark-green residue which was dissolved in CH_2Cl_2 (100 mL) and carefully washed with a 5% aqueous solution of $NaHCO_3$ (2 × 50 mL) and with H_2O (2 × 50 mL), dried with Na_2SO_4 and the solvents evaporated to dryness. The residue was crystallised from CH_2Cl_2/*n*-hexane to afford 52 mg (94%) of **5** as a red-brown powder. ^{1}H

 © 2005 Wiley-VCH Verlag GmbH & Co. KGaA, Weinheim

NMR (300 MHz, $CDCl_3$): δ = –2.65 (br. s, 2 H, NH), 7.49 (AA′BB′, 2 H, H_{Ar}), 7.60–7.83 (m, 12 H, $H_{m,pPh}$), 8.15–8.22 (m, 10 H, 8H_{oPh}, 2H_{Ar}), 8.78–8.91 (m, 6 H, $H_{pyrrolic}$), 9.13 (s, 1 H, $H_{pyrrolic}$) ppm. UV/Vis ($CHCl_3$): λ_{max} (logε) = 430 (5.26), 525 (4.31), 562 (3.83), 601 (3.78), 657 (3.68) nm. $C_{52}H_{33}N_5O_2$ (759): calcd. C 82.19, H 4.38, N 9.22; found C 81.75, H 4.40, N 8.96. MS-FAB(+): *m*/*z* = 760 $[M + 1]^+$.

2-[(1*E*)-2-(4-Nitrophenyl)ethen-1-yl]-5,10,15,20-tetraphenylporphyrin (7): Solid NaOH (400 mg, 10 mmol) was added to a solution of (4-nitrobenzyl)triphenylphosphonium bromide (596 mg, 1.25 mmol) and 2-formyl-5,10,15,20-tetraphenylporphyrin (**13**; 160 mg, 0.25 mmol) in 30 mL of 1,2-dichloroethane and the resulting suspension was heated at reflux and stirred for 8 h. Then, the reaction mixture was diluted with 150 mL of CH_2Cl_2, washed with 100 mL of H_2O and the organic phase was separated, dried with Na_2SO_4 and the solvents evaporated. The residue was purified by column chromatography (silica gel, CH_2Cl_2) to afford 160 mg of product as a mixture 80:20 of (*E*)- and (*Z*)-isomers. This mixture was purified by crystallisation from CH_2Cl_2/CH_3OH to afford 110 mg (58%) of pure (*E*)-isomer **7**. ^1H NMR (300 MHz, $CDCl_3$): δ = –2.60 (br. s, 2 H, NH), 7.11 (d, *J* = 16.0 Hz, 1 H, $H_{ethenyl}$), 7.29 (d, *J* = 16.0 Hz, 1 H, $H_{ethenyl}$), 7.30 (d, *J* = 8.6 Hz, 2 H, H_{Ar}), 7.74–7.86 (m, 12 H, $H_{m,p}$), 8.14–8.24 (m, 10 H, 8H_{oPh}, 2H_{Ar}), 8.70–8.82 (m, 6 H, $H_{pyrrolic}$), 9.01 (br. s, 1 H, $H_{pyrrolic}$) ppm. UV/Vis ($CHCl_3$): λ_{max} (logε) = 431 (5.31), 525 (4.34), 569 (4.13), 602 (3.94), 659 (3.47) nm. $C_{52}H_{35}N_5O_2$ (761): calcd. C 81.9, H 4.64, N 9.20; found C 81.6, H 4.62, N 9.16. MS-FAB(+): *m*/*z* = 762 $[M + 1]^+$.

2-{(1*E*)-2-[4-(Dibutylamino)phenyl]ethen-1-yl}-5,10,15,20-tetraphenylporphyrin (11): Solid NaOH (480 mg, 12 mmol) was added to a solution of [4-(dibutylamino)benzyl]triphenylphosphonium bromide (258 mg, 0.5 mmol) and 2-formyl-5,10,15,20-tetraphenylporphyrin (**13**; 193 mg, 0,3 mmol) in 25 mL of CH_2Cl_2, and the resulting suspension was stirred at room temperature for 4 h. Then, the reaction mixture was purified by column chromatography (silica gel, CH_2Cl_2) to afford 205 mg of product as a 9:1 mixture of (*E*)- and (*Z*)-isomers. This product was crystallised from CH_2Cl_2/*n*-pentane to give 175 mg (69%) of pure (*E*)-isomer **11**. ^1H NMR (300 MHz, $CDCl_3$): δ = –2.60 (br. s, 2 H, NH), 1.01 (t, *J* = 7.20 Hz, 6 H, $CH_{3\ butyl}$), 1.20–1.70 (m, 4 H, $2CH_{2\ butyl}$), 3.34 (t, *J* = 7.60 Hz, 4 H, NCH_2), 6.60 (d, *J* = 8.80 Hz, 2 H, H_{Ar}), 6.72 (d, *J* = 16.0 Hz, 1 H, $H_{ethenyl}$), 7.12 (d, *J* = 8.80 Hz, 2 H, H_{Ar}), 7.28 (d, *J* = 16.0 Hz, 1 H, $H_{ethenyl}$), 7.65–7.88 (m, 12 H, $H_{m,pPh}$), 8.15–8.30 (m, 8 H, H_{oPh}), 8.65–8.85 (m, 6 H, $H_{pyrrolic}$), 8.96 (s, 1 H, $H_{pyrrolic}$) ppm. UV/Vis ($CHCl_3$): λ_{max} (logε) = 422 (5.36), 521 (4.41), 579 (4.16), 603 (4.14), 660 (3.71) nm. $C_{60}H_{53}N_5$ (843): calcd. C 85.37, H 6.33, N 8.30; found C 85.0, H 6.35, N 8.26. MS-FAB(+): *m*/*z* = 844 $[M + 1]^+$.

2-[(1*E*,3*E*)4-(4-Nitrophenyl)-1,3-butadienyl]-5,10,15,20-tetraphenylporphyrin (9): 1,8-Diazabicyclo[5.4.0]-undec-7-ene (DBU; 509 mg, 3.34 mmol) was added to a solution of the phosphonium salt of the tetraphenylporphyrin **16** (52 mg, 0.0562 mmol) and 4-nitrocinnamaldehyde (12 mg, 0.0674 mmol) in CH_2Cl_2 (5 mL), and the mixture was maintained under magnetic stirring and at room temperature for one hour. The product was isolated by column chromatography (silica gel; toluene/cyclohexane, 9:1) and further purified by crystallisation from CH_2Cl_2/*n*-hexane to afford 38 mg (86%) of pure **9** as a purple solid. ^1H NMR (300 MHz, $CDCl_3$): δ = –2.56 (s, 2 H, NH), 6.40 (d, 1 H, H_{butyl}), 6.74 (d, 2 H, H_{butyl}), 7.17 (m, 1 H, H_{butyl}), 7.54 (d, 2 H, H_{Ar}), 7.78 (m, 12 H, $H_{o,pPh}$), 7.79 (m, 6 H, $H_{pyrrolic}$), 8.15 (d, *J* = 6.98 Hz, 2 H, H_{Ar}), 8.23 (m, 8 H, H_{mPh}), 8.95 (s, 1 H, $H_{pyrrolic}$) ppm. UV/Vis (CH_2Cl_2): λ_{max} (logε) = 425 (5.03), 523 (4.21), 572 (4.07), 601 (3.86), 665 (3.51) nm. $C_{54}H_{37}N_5O_2$ (787): calcd. C 82.32, H 4.73, N 8.89; found C 82.0, H 4.60, N 8.70. MS-FAB(+): *m*/*z* = 788 $[M + 1]^+$.

Synthesis of Zn^{II} Complexes: Zn^{II} complexes **2**, **8**, **10** and **12** were synthesised following the general procedure described in the literature.[19] In a typical preparation, the free porphyrin (100 mg) was dissolved in slightly warmed $CHCl_3$ (50 mL) and a solution of $Zn(OAc)_2{\cdot}2H_2O$ (free porphyrin/metal salt = 1:3) in MeOH (5 mL) was then added. The mixture was heated at reflux for 2 h and the progress of the reaction was monitored by TLC. After removal of the solvent in vacuo, the crude product was purified by crystallisation or by washing with methanol.

2-Cyano-5,10,15,20-tetraphenylporphyrinatozinc(II) (2): The violet powder was crystallised from CH_2Cl_2/*n*-pentane. Yield: 98%. ^1H NMR (300 MHz, $CDCl_3$): δ = 7.60–7.80 (m, 12 H, $H_{m,pPh}$), 8.12–8.20 (m, 8 H, H_{oPh}), 8.87–8.93 (m, 6 H, $H_{pyrrolic}$), 9.46 (br. s, 1 H, $H_{pyrrolic}$) ppm. UV/Vis ($CHCl_3$): λ_{max} (logε) = 427 (5.62), 518 (3.57), 555 (4.20), 593 (4.02) nm. $C_{45}H_{27}N_5Zn$ (702): calcd. C 76.87, H 3.87, N 9.96; found C 76.52, H 3.88, N 9.92. MS-FAB(+): *m*/*z* = 703 $[M + 1]^+$.

2-[(1*E*)-2-(4-Nitrophenyl)ethen-1-yl]-5,10,15,20-tetraphenylporphyrinatozinc(II) (8): The blue-violet powder was washed with *n*-hexane and a small amount of MeOH in order to eliminate the excess of $Zn(OAc)_2$. Yield: 90%. ^1H NMR (300 MHz, $CDCl_3$): δ = 7.18 (d, *J* = 16.0 Hz, 1 H, $H_{ethenyl}$), 7.24 (d, *J* = 16.0 Hz, 1 H, $H_{ethenyl}$), 7.37 (d, *J* = 8.6 Hz, 2 H, H_{Ar}), 7.76- 7.85 (m, 12 H, $H_{m,pPh}$), 8.19–8.28 (m, 10 H, 8H_{oPh}, 2H_{Ar}), 8.82–8.96 (m, 6 H, $H_{pyrrolic}$), 9.16 (br. s, 1 H, $H_{pyrrolic}$) ppm. UV/Vis ($CHCl_3$): λ_{max} (logε) = 432 (5.20), 526 (3.77), 558 (4.35), 597 (4.13) nm. $C_{52}H_{33}N_5O_2Zn$ (824): calcd. C 75.70, H 4.04, N 8.49; found C 75.4, H 4.03, N 8.45. MS-FAB(+): *m*/*z* = 825 $[M + 1]^+$.

2-[(1*E*,3*E*)4-(4-Nitrophenyl)1,3-butadienyl]-5,10,15,20-tetraphenylporphyrinatozinc(II) (10): The dark green powder was washed with *n*-hexane and a small amount of MeOH in order to eliminate the excess of $Zn(OAc)_2$. Yield 90%. ^1H NMR (300 MHz, $CDCl_3$): δ = 6.40 (d, 1 H, H_{butyl}), 6.75 (d, 2 H, H_{butyl}), 7.14 (dd, 1 H, H_{butyl}), 7.55 (d, 2 H, H_{Ar}), 7.78 (m, 12 H, $H_{m,pPh}$), 8.15 (d, 2 H, H_{Ar}), 8.24 (m, 8 H, H_{oPh}), 8.88 (m, 6 H, $H_{pyrrolic}$), 9.07 (br. s, 1 H, $H_{pyrrolic}$) ppm. UV/Vis (CH_2Cl_2): λ_{max} (logε) = 430 (4.94), 559 (4.11), 599 (3.98) nm. $C_{54}H_{35}N_5O_2Zn$ (850): calcd. C 76.20, H 4.14, N 8.23; found C 76.20, H 4.05, N 8.01. MS-FAB(+): *m*/*z* = 851 $[M + 1]^+$.

2-{(*1E*)-2-[4-(Dibutylamino)phenyl]ethen-1-yl}-5,10,15,20-tetraphenylporphyrinatozinc(II) (12): The dark powder was washed with *n*-hexane and a small amount of MeOH in order to eliminate the excess of $Zn(OAc)_2$. Yield: 85%. ^1H NMR [300 MHz, $(CD_3)_2CO$]: δ = 1.02 (t, *J* = 7.2 Hz, 6 H, CH_3), 1.45–1.51 (m, 4 H, CH_2), 1.60–1.73 (m, 4 H, CH_2), 3.41 (t, *J* = 7.2 Hz, 4 H, CH_2N), 6.69 (d, *J* = 8.8 Hz, 2 H, H_{Ar}), 6.82 (d, *J* = 16.0 Hz, 1 H, $H_{ethenyl}$), 7.14 (d, *J* = 8.8 Hz, 2 H, H_{Ar}), 7.22 (d, *J* = 16.0 Hz, 1 H, $H_{ethenyl}$), 7.72- 7.88 (m, 12 H, $H_{m,pPh}$), 8.15–8.30 (m, 8 H, H_{oPh}), 8.70–8.90 (m, 6 H, $H_{pyrrolic}$), 9.01 (s, 1 H, $H_{pyrrolic}$) ppm. UV/Vis ($CHCl_3$): λ_{max} (logε) = 422 (5.20), 556 (4.08), 601 (3.97) nm. $C_{60}H_{51}N_5Zn$ (906): calcd. C 79.47, H 5.63, N 7.73; found C 79.60, H 5.61, N 7.70. MS-FAB(+): *m*/*z* = 907 $[M + 1]^+$.

2-Nitro-5,10,15,20-tetraphenylporphyrinatozinc(II) (4): A solution of $AgNO_3$ (97.8 mg, 0.576 mmol) in 20 mL of CH_3CN and a solution of I_2 (75 mg, 0.295 mmol) in 20 mL of CH_2Cl_2 were rapidly added to a solution of 5,10,15,20-tetraphenylporphyrinatozinc(II) (301 mg, 0.434 mmol) in 80 mL of CH_2Cl_2/CH_3CN (1:1, v/v); the resulting mixture was stirred at room temperature, under nitrogen, in the dark, for two hours. The reaction mixture was filtered, the solvent was evaporated in vacuo and the residue was purified by

 © 2005 Wiley-VCH Verlag GmbH & Co. KGaA, Weinheim

column chromatography (silica gel, CH_2Cl_2) to afford 71.7 mg (22%) of a violet powder. ^1H NMR (300 MHz, $CDCl_3$): δ = 7.67–7.95 (m, 12 H, $H_{m,pPh}$), 8.19–8.22 (m, 8 H, H_{oPh}), 8.98–9.00 (m, 6 H, $H_{pyrrolic}$), 9.22 (s, 1 H, $H_{pyrrolic}$) ppm. UV/Vis ($CHCl_3$): λ_{max} (logε) = 425 (5.28), 522 (3.41), 555 (4.00), 598 (3.80) nm. $C_{44}H_{27}N_5O_2Zn$ (722): calcd. C 73.08, H 3.76, N 9.69; found C 73.20, H 3.89, N 9.80. MS-FAB(+): m/z = 723 $[M + 1]^+$.

2-[2-(4-Nitrophenyl)ethyn-1-yl]-5,10,15,20-tetraphenylporphyrinatozinc(II) (6): A mixture of 2-bromo-5,10,15,20-tetraphenylporphyrinatozinc(II) (150 mg, 0.182 mmol), $[PdCl_2(PPh_3)_2]$ (19 mg, 0.027 mmol), CuI (15.4 mg, 0.0081 mmol), 4-nitrophenylacetylene (61.5 mg, 0.42 mmol) and triethylamine (3 mL) in 40 mL of THF was heated at reflux under nitrogen, in the dark, for 5 h. The solvent was evaporated in vacuo and the residue was purified by column chromatography (silica-gel, toluene/cyclohexane, 1:1) to afford 63 mg (42%) of pure **6** as a dark-violet powder. ^1H NMR (300 MHz, $CDCl_3$): δ = 7.50 (d, J = 8.79 Hz, 2 H, H_{Ar}), 7.61–7.83 (m, 12 H, $H_{m,pPh}$), 8.17–8.22 (m, 10 H, 8H_{oPh}, 2H_{Ar}), 8.65–8.93 (m, 6 H, $H_{pyrrolic}$), 9.27 (br. s, 1 H, $H_{pyrrolic}$) ppm. UV/Vis ($CHCl_3$): λ_{max} (logε) = 431 (5.30), 521 (3.60), 557 (4.25), 594 (4.03) nm. $C_{52}H_{31}N_5O_2Zn$ (822): calcd. C 75.87, H 3.80, N 8.51; found C 76.2, H 3.89, N 8.35. MS-FAB(+): m/z = 823 $[M + 1]^+$.

2-Formyl-5,10,15,20-tetraphenylporphyrin (13): A solution of dimethylformamide (2 mL) and phosphoryl chloride (2 ml) in 10 mL of 1,2-dichloroethane was left at room temperature and stirred magnetically for 30 min. After this time, a solution of tetrakis-5,10,15,20-tetraphenylporphyrinatonickel(II) (300 mg, 0.449 mmol) in 100 mL of 1,2-dichloroethane was added and the reaction mixture was refluxed for 24 h. The dark-green solution was then evaporated to dryness and the residue was treated, while cooling with an ice bath, with 10 mL of 96% H_2SO_4 to afford a green viscous solution, which was diluted with a saturated aqueous solution of CH_3COONa until the pH was basic. The product was extracted with CH_2Cl_2 (3 × 150 mL), the organic phase was washed with aqueous 5% NaOH (100 mL) and then with H_2O (150 mL) and the solvents evaporated in vacuo to afford 320 mg of crude product. Purification by column chromatography (silica gel, CH_2Cl_2) afforded 220 mg (70%) of pure **13** as a purple solid. ^1H NMR (300 MHz, $CDCl_3$): δ = –2.60 (br. s, 2 H, NH), 7.64–7.84 (m, 12 H, $H_{m,pPh}$), 7.95–8.05 (m, 2 H, H_{oPh}), 8.12–8.28 (m, 6 H, H_{oPh}), 8.65–8.81 (m, 2 H, $H_{pyrrolic}$), 8.85–8.87 (m, 4 H, $H_{pyrrolic}$), 9.23 (br. s, 1 H, $H_{pyrrolic}$), 9.42 (s, 1 H, CHO) ppm. UV/Vis ($CHCl_3$): λ_{max} (logε) = 432 (5.47), 526 (4.21), 568 (3.80), 605 (3.70), 664 (3.83) nm. $C_{45}H_{30}N_4O$ (642): calcd. C 84.09, H 4.70, N 8.72; found C 84.35, H 4.83, N 8.79. MS-FAB(+): m/z = 643 $[M + 1]^+$.

2-Hydroxymethyl-5,10,15,20-tetraphenylporphyrin (14): A sample of 2-formyl-5,10,15,20-tetraphenylporphyrin (**13**; 375 mg, 0,583 mmol) was dissolved in 50 mL of refluxing dry tetrahydrofuran, then $NaBH_4$ (609 mg, 16.1 mmol) was added and the suspension was stirred for 15 min. The reaction mixture was cooled to room temperature, 100 mL of H_2O was added in order to eliminate the excess of $NaBH_4$, then the reaction mixture was transferred into a separating funnel and extracted with 100 mL of $CHCl_3$. The organic phase was separated, dried with Na_2SO_4 and evaporated under reduced pressure. The residue was purified by crystallisation with CH_2Cl_2/*n*-hexane to afford 335 mg (89%) of pure **14** as a purple solid. ^1H NMR (300 MHz, $CDCl_3$): δ = –2.75 (br. s, 2 H, NH), 1.95 (t, 1 H, exchange with D_2O), 4.88 (d, J = 5.06 Hz, 2 H, CH_2O), 7.64–7.80 (m, 12 H, $H_{m,pPh}$), 8.08–8.11 (m, 2 H, H_{oPh}), 8.17–8.22 (m, 6 H, H_{oPh}), 8.50–8.61 (m, 2 H, $H_{pyrrolic}$), 8.75 and 8.87 (m, 4 H, $H_{pyrrolic}$), 8.94 (s, 1 H, $H_{pyrrolic}$) ppm. UV/Vis ($CHCl_3$): λ_{max} (logε) = 419 (5.71), 515 (4.27), 549 (3.77), 589 (3.74), 645 (3.50) nm. $C_{45}H_{32}N_4O$ (644): calcd. C 83.83, H 5.00, N 8.69; found C 83.9, H 5.02, N 8.72. MS-FAB(+): m/z = 645 $[M + 1]^+$.

2-(Chloromethyl)-5,10,15,20-tetraphenylporphyrin (15): A solution of thionyl chloride (0.13 g, 1.36 mmol) in 5 mL of Et_2O was slowly added, keeping the temperature in the range 0–5 °C, to a stirred solution of porphyrin **14** (87.5 mg, 0.136 mmol) and pyridine (0.13 g, 1.63 mmol) in 30 mL of Et_2O. Once the addition was complete, the temperature was raised to room temperature and the reaction mixture was stirred for 30 min. The mixture was then transferred into a separating funnel, diluted with 100 mL of CH_2Cl_2 and washed with water (70 mL) and aqueous 5% $NaHCO_3$ (60 mL). The organic phase was dried with Na_2SO_4 and the solvents evaporated in vacuo to afford 95 mg of residue, which was purified by crystallisation from CH_2Cl_2/*n*-pentane to give 85 mg (95%) of a purple solid. ^1H NMR (300 MHz, $CDCl_3$): δ = –2.79 (br. s, 2 H, NH), 4.79 (s, 2 H, CH_2Cl), 7.64- 7.75 (m, 12 H, $H_{m,pPh}$), 8.10–8.25 (m, 8 H, H_{oPh}), 8.65 (d, J = 4.87 Hz, 2 H, $H_{pyrrolic}$), 8.78–8.87 (m, 4 H, $H_{pyrrolic}$), 8.96 (s, 1 H, $H_{pyrrolic}$) ppm. UV/Vis ($CHCl_3$): λ_{max} (logε) = 420 (5.54), 516 (4.26), 550 (3.84), 592 (3.73), 650 (3.81) nm. $C_{45}H_{31}ClN_4$ (662): calcd. C 81.50, H 4.71, N 8.45; found C 81.15, H 4.78, N 8.49. MS-FAB(+): m/z = 663 $[M + 1]^+$, 628 $[M – Cl]^+$.

[2-(5,10,15,20-Tetraphenylporphyrin-2-yl)methylene]triphenylphosphonium Chloride (16): A solution of porphyrin **15** (75.1 mg, 0.113 mmol) and triphenylphosphane (240 mg, 0.9 mmol) in 50 mL of $CHCl_3$ was refluxed under magnetic stirring for 16 h. The solvent was then evaporated in vacuo, the residue was washed with *n*-hexane in order to remove the excess of PPh_3, and the purple solid residue was dried to afford 84 mg (80%) of pure **16**. ^1H NMR (300 MHz, $CDCl_3$): δ = –2.78 (br. s, 2 H, NH), 5.31 (d, J = 15 Hz, 2 H, CH_2P), 7.10- 7.20 (m, 6 H, 3 $H_{m,pPh}$ + 3 $H_{pAr–P}$), 7.22–7.35 (m, 5 H, 3 $H_{o\ Ar–P}$ + 2 H_{oPh}), 7.41 (d, J = 7.2 Hz, 2 H, 2 H_{oPh}), 7.50–7.95 (m, 18 H, 3 $H_{oAr–P}$ + 6 $H_{mAr–P}$ + 9 $H_{m,pPh}$), 8.10–8.20 (m, 4 H, 4H_{oPh}), 8.34 (d, J = 3.6 Hz, 1 $H_{pyrrolic}$), 8.45 (d, J = 4.9 Hz, 1 $H_{pyrrolic}$), 8.70–8.90 (m, 5 $H_{pyrrolic.}$) ppm. UV/Vis (CH_2Cl_2): λ_{max} (logε) = 423 (5.60), 519 (4.26), 556 (3.72), 595 (3.69), 652 (3.70) nm. $C_{63}H_{46}ClN_4P$ (924): calcd. C 81.76, H 5.01, N 6.05; found C 81.50, H 5.03, N 6.10. MS-FAB(+): m/z = 889 $[M – Cl]^+$, 627 $[M – Cl – PPh_3]^+$.

4-(Dibutylamino)benzyl Alcohol: A sample of 4-(dibutylamino)-benzaldehyde (2.33 g, 10 mmol) was dissolved in 100 mL of 96% EtOH. Then, $NaBH_4$ (760 mg, 20 mmol) was added and the suspension was stirred at reflux for 2 h. The reaction mixture was evaporated in vacuo, the residue was taken up into a separating funnel with 60 mL of H_2O and 100 mL of Et_2O and the organic phase was separated. The aqueous phase was extracted with Et_2O (2 × 50 mL). The organic phase was dried with $MgSO_4$ and the solvents evaporated to dryness to afford 2.28 g (97%) of pure product as a thick, colourless oil. ^1H NMR (200 MHz, $CDCl_3$): δ = 0.95 (t, J = 7.2 Hz, 6 H, CH_3), 1.25–1.45 (m, 5 H, CH_2 + OH), 1.45–1.65 (m, 4 H, CH_2), 3.26 (t, J = 7.2 Hz, 4 H, CH_2N), 4.54 (d, J = 5.7 Hz, 2 H, CH_2O), 6.62 (d, J = 8.8 Hz, 2 H, AA′BB′), 7.20 (d, J = 8.8 Hz, 2 H, AA′BB′) ppm.

[4-(Dibutylamino)benzyl]triphenylphosphonium Chloride: A suspension of 4-(dibutylamino)benzyl alcohol (1.18 g, 5 mmol) in 20 mL of CH_3CN, cooled to 0 °C, was saturated with gaseous HCl until a light yellow solution had formed. This solution was heated at reflux and stirred for 40 h. The reaction mixture was evaporated in vacuo, the residue was taken up in a separating funnel with 120 mL of CH_2Cl_2, washed with aqueous 10% Na_2CO_3 (2 × 30 mL) and 50 mL of brine. The organic phase was dried with $MgSO_4$ and the solvents evaporated to dryness to give a white solid residue which

 © 2005 Wiley-VCH Verlag GmbH & Co. KGaA, Weinheim

was ground with Et_2O and filtered to give 2.41 g (93%) of a white solid. ^1H NMR (200 MHz, $CDCl_3$): δ = 0.95 (t, J = 7.2 Hz, 6 H, CH_3), 1.18–1.35 (m, 4 H, CH_2), 1.35–1.55 (m, 4 H, CH_2), 3.16 (t, J = 7.2 Hz, 4 H, CH_2N), 5.14 (d, J = 13 Hz, 2 H, CH_2P^+), 6.36 (d, J = 8.8 Hz, 2 H, AA′BB′), 6.82 (dd, J = 8.8, J = 2.5 Hz, 2 H, AA′BB′), 7.55–7.80 (m, 15 H, H_{phenyl}) ppm.

Acknowledgments

This work was supported by the Ministero dell'Istruzione, dell'Università e della Ricerca (Programma di Ricerca FIRB 2001; Research Title: Nano-organisation of hybrid organic-inorganic molecules with magnetic and non linear optical properties) and by the Consiglio Nazionale delle Ricerche. We thank Dr. Stefania Righetto for help with EFISH measurements and Mr. Pasquale Illiano for NMR measurements.

[1] a) J. Zyss, *Molecular Non-linear Optics: Materials, Physics and Devices*, Academic Press, Boston **1993**; b) I. Ledoux, J. Zyss, *Novel Optical Materials and Application* (Eds.: I. C. Khoo, F. Simoni, C. Venatri), John Wiley and Sons, New York, **1997**.
[2] M. Blanchard-Desce, S. R. Marder, M. Barzoukas, in *Comprehensive Supramolecular Chemistry*, Vol. 10 (Ed.: D. N. Reinhoudt), Pergamon Press, **1996**, p. 833 and references cited therein.
[3] a) D. R. Kanis, M. A. Ratner, T. J. Marks, *Chem. Rev.* **1994**, *94*, 195; b) P. M. Burland, R. D. Miller, C. A. Walash, *Chem. Rev.* **1994**, *94*, 31; c) T. J. Marks, M. A. Ratner, *Angew. Chem. Int. Ed. Engl.* **1995**, *34*, 155.
[4] a) I. R. Whittal, A. M. McDonagh, M. G. Humphrey, *Adv. Organomet. Chem.* **1998**, *42*, 291; b) S. Di Bella, *Chem. Soc. Rev.* **2001**, *30*, 355; c) N. J. Long, *Angew. Chem. Int. Ed. Engl.* **1995**, *34*, 21.
[5] a) K. S. Suslick, C. T. Chen, G. R. Meredith, L. T. Cheng, *J. Am. Chem. Soc.* **1992**, *114*, 6928; b) H. Chou, K. S. Suslick, *J. Phys. Chem.* **1994**, *98*, 383; c) M. Pizzotti, R. Ugo, E. Annoni, S. Quici, I. Ledoux-Rak, G. Zerbi, M. Del Zoppo, P. Fantucci, I. Invernizzi, *Inorg. Chim. Acta* **2002**, *340*, 70–80.
[6] a) S. M. Le Cours, H. W. Guan, S. G. Di Magno, C. H. Wang, M. J. Therien, *J. Am. Chem. Soc.* **1996**, *118*, 1497; b) L. Karki, F. W. Vance, J. H. Hupp, S. M. Le Cours, M. J. Therien, *J. Am. Chem. Soc.* **1998**, *120*, 2606; c) M. Yeung, A. C. H. Ng, M. G. B. Drew, E. Vorpagel, E. M. Breitung, R. J. McMahon, D. K. P. Ng, *J. Org. Chem.* **1998**, *63*, 7143; d) M. Pizzotti, E. Annoni, R. Ugo, S. Bruni, S. Quici, P. Fantucci, M. Bruschi, G. Zerbi, M. Del Zoppo, *J. Porphyrins Phthalocyanines* **2004**, *8*, 1311–1324.
[7] a) G. de La Torre, P. Vázquez, F. Agulló-López, T. Torres, *Chem. Rev.* **2004**, *104*, 3723 and references cited therein; b) C. G. Claessens, D. González-Rodríguez, T. Torres, *Chem. Rev.* **2002**, *102*, 835–853; c) C. G. Claessens, D. González-Rodríguez, T. Torres, G. Martin, F. Agulló-López, I. Ledoux, J. Zyss, V. R. Ferro, J. M. García de la Vega, *J. Phys. Chem. B* **2005**, *109*, 3800–3806.
[8] a) M. A. Diaz-García, I. Ledoux, F. Agulló-López, J. Zyss, *J. Phys. Chem.* **1994**, *98*, 4495; b) F. Fernandez-Lázaro, T. Torres, B. Hanschel, M. Hanack, *Chem. Rev.* **1998**, *98*, 563 and references cited therein.
[9] J. S. Lindsey, in *Metalloporphyrin-Catalysed Oxidations* (Eds.: F. Montanari, L.Casella), Kluwer Academic Publishers, **1994**, p. 49 and references cited therein.
[10] M. Gouterman, in *The Porphyrins*, Vol. III (Ed.: D. Dolphin) Academic Press, New York, **1978**.
[11] S. Priyadarshy, M. J. Therien, D. N. Beratan, *J. Am. Chem. Soc.* **1996**, *118*, 1504.
[12] a) D. N. Quin, T. Wada, H. Sasabe, *Mol. Cryst. Liq. Cryst.* **1992**, *217*, 47; b) A. Sen, P. C. Ray, P. K. Das, V. Krishnan, *J. Phys. Chem.* **1996**, *100*, 19611.
[13] P. R. Varanasi, A. K.-Y. Jen, J. Chandrasekhar, I. N. N. Namboothiri, A. Rathna, *J. Am. Chem. Soc.* **1996**, *118*, 12443.
[14] I. D. L. Albert, T. J. Marks, M. A. Ratner, *Chem. Mater.* **1998**, *10*, 753 and references cited therein.
[15] a) A. D. Becke, *J. Chem. Phys.* **1993**, *98*, 5648; b) C. Lee, W. Yang, R. G. Parr, *Phys. Rev.* **1998**, *37*, 785.
[16] a) A. D. Becke, *Phys. Rev. A* **1988**, *38*, 3098; b) J. P. Perdew, *Phys. Rev. B* **1986**, *33*, 8822.
[17] A. Schafer, C. Huber, R. Ahlrichs, *J. Chem. Phys.* **1994**, *100*, 5829.
[18] H. J. Callot, *Bull. Soc. Chim. Fr.* **1974**, 1492.
[19] a) A. D. Adler, F. R. Longo, F. Kampas, J. Kim, *J. Inorg. Nucl. Chem.* **1970**, *32*, 2443; b) A. R. Menotti, P. Rothemund, *J. Am. Chem. Soc.* **1948**, *70*, 1808.
[20] J. A. Baldwin, M. J. Crossley, J. DeBernardis, *Tetrahedron* **1982**, *38*, 685.
[21] E. E. Bonfantini, A. K. Burrell, D. L. Officer, D. C. W. Reid, M. R. McDonald, P. A. Cocks, K. C. Gordon, *Inorg. Chem.* **1997**, *36*, 6270 and references cited therein.
[22] H. H. Callot, *Tetrahedron* **1973**, *296*, 899.
[23] A. Mylona, J. Nokavouras, I. M. Tekakis, *J. Org. Chem.* **1988**, *53*, 3838.
[24] E. E. Bonfantini, D. L. Officer, *Tetrahedron Lett.* **1993**, *34*, 8531.
[25] R. A. Binstead, M. J. Crossley, N. S. Hush, *Inorg. Chem.* **1991**, *30*, 1259.
[26] J. H. Fuhrhop, *Struc. Bond.* **1974**, *18*, 1.
[27] This latter band cannot be attributed to some impurity of porphyrins **1** or **3** because, taking into consideration the intensity of their Q_β bands at higher energy (Table 1), their concentration should be high enough to be detected by ^1H NMR spectroscopy (signal due to the NH protons). This comment applies also to porphyrins **5** and **7** and their Zn^{II} complexes **6** and **8**.
[28] a) J. A. Shelnutt, *J. Phys. Chem.* **1984**, *88*, 4988; b) J. A. Shelnutt, V. Ortiz, *J. Phys. Chem.* **1985**, *89*, 4733.
[29] A. K. Burrel, D. L. Officer, D. C. Reid, *Angew. Chem. Int. Ed. Engl.* **1995**, *34*, 900.
[30] O. W. Kolling, *J. Phys. Chem.* **1989**, *93*, 3436 and references cited therein.
[31] M. Karlson, K. Pihlaja, T. Tamm, A. Uri, M. C. Zerner, *J. Photochem. Photobiol.* **1995**, *85*, 119.
[32] S. Dahal, V. Krishnan, *J. Photochem. Photobiol.* **1995**, *89*, 105.
[33] K. Takahashi, S. Hase, T. Komura, H. Imanaga, O. Ohno, *Bull. Chem. Soc. Jpn.* **1992**, *65*, 1475.
[34] A. Wolberg, J. Manassen, *J. Am. Chem. Soc.* **1970**, *92*, 2982.
[35] J. H. Fuhrhop, K. M. Kadish, D. G. Davis, *J. Am. Chem. Soc.* **1973**, *95*, 5140.
[36] A. Stanienda, G. Biebl, *Z. Phys. Chem.* **1967**, *52*, 254.
[37] D. W. Clack, N. S. Hush, *J. Am. Chem. Soc.* **1965**, *87*, 4238.
[38] R. H. Felton, H. Linschitz, *J. Am. Chem. Soc.* **1966**, *88*, 1113.
[39] E. A. Guggenheim, *Trans. Faraday Soc.* **1949**, *45*, 203.
[40] a) I. Ledoux, J. Zyss, *Chem. Phys.* **1982**, *73*, 202; b) D. J. Williams, *Angew. Chem. Int. Ed. Engl.* **1984**, *23*, 690 and references cited therein.
[41] G. Rojo, G. de la Torre, J. García-Ruiz, I. Ledoux, T. Torres, J. Zyss, F. Agulló-López, *Chem. Phys.* **1999**, *245*, 27 and references cited therein.
[42] a) D. Roberto, R. Ugo, S. Bruni, E. Cariati, F. Cariati, P. Fantucci, S. Quici, I. Ledoux, J. Zyss, *Organometallics* **2000**, *19*, 1775; b) E. Lucenti, E. Cariati, C. Dragonetti, L. Manassero, F. Tessore, *Organometallics* **2004**, *23*, 687.
[43] P. J. Spellane, M. Gouterman, A. Antipas, S. Kim, Y. C. Liu, *Inorg. Chem.* **1980**, *19*, 386.
[44] a) J. L. Oudar, D. S. Chemla, *J. Chem. Phys.* **1977**, *66*, 2664; b) J. L. Oudar, *J. Chem. Phys.* **1977**, *67*, 446.
[45] D. R. Kanis, M. A. Ratner, T. J. Marks, *J. Am. Chem. Soc.* **1992**, *114*, 10338 and references cited therein.
[46] L. T. Cheng, W. Tam, S. H. Stevenson, G. R. Meredith, G. Rikken, S. R. Marder, *J. Phys. Chem.* **1991**, *95*, 10631.

 © 2005 Wiley-VCH Verlag GmbH & Co. KGaA, Weinheim

[47] S. Takahashi, Y. Kuroyama, K. Sonogashira, N. Hagihara, *Synthesis* **1980**, 627.
[48] A. J.Bard, L. R. Faulkner, *Electrochemical Methods: Fundamentals and Applications*, Wiley, New York, **2002**.
[49] a) E. G. Mc Rae, *J. Phys. Chem.* **1957**, *61*, 562; b) S. Bruni, F. Cariati, E. Cariati, F. A. Porta, S. Quici, D. Roberto, *Spectrochim. Acta, Part A* **2001**, *57*, 1417.
[50] R. Ahlrichs, M. Bar, M. Haser, C. Horn, C. Kolmel, *Chem. Phys. Lett.* **1989**, *162*, 165.
[51] a) K. Eichkorn, O. Treutler, H. Öhm, M. Haser, R. Ahlirchs, *Chem. Phys. Lett.* **1995**, *240*, 283; b) K. Eichkorn, F. Weigend, O. Treutler, R. Ahlirchs, *Theor. Chem. Acc.* **1997**, *97*, 119.
Received: April 6, 2005
Published Online: August 4, 2005

 © 2005 Wiley-VCH Verlag GmbH & Co. KGaA, Weinheim

Nitrate- and Nitrite-Assisted Conversion of an Acetonitrile Ligand Into an Amidato Bridge at an $\{Mo_2(Cp)_2(\mu\text{-}SMe)_3\}$ Core: Electrochemistry of the Amidato Complex $[Mo_2(Cp)_2(\mu\text{-}SMe)_3\{\mu\text{-}\eta^1,\eta^1\text{-}OC(Me)NH\}]^+$

Marc Le Hénanf,[a] Christine Le Roy,[a] François Y. Pétillon,[a] Philippe Schollhammer,[a] and Jean Talarmin*[a]

Keywords: Bridging ligands / Cyclic voltammetry / Electrochemistry / Molybdenum / S ligands

Treatment of $[Mo_2(Cp)_2(\mu\text{-}SMe)_3(MeCN)_2]^+$ (**1**$^+$) with NO_3^- or NO_2^- results in the conversion of one terminally bound acetonitrile ligand into an amidato bridge. The reaction produces $[Mo_2(Cp)_2(\mu\text{-}SMe)_3\{\mu\text{-}\eta^1,\eta^1\text{-}OC(Me)NH\}]^{0/+}$ (**2**$^{0/+}$) and involves the formation of an intermediate, which was detected by cyclic voltammetry but which could not be isolated, and which likely arises from the substitution of the NO_x anion for one MeCN ligand. The electrochemical behaviour of **2**$^+$ was studied by cyclic voltammetry in THF and MeCN. The reduction of **2**$^+$ in the presence of acid (HBF_4/H_2O or HBF_4/Et_2O) in these solvents leads to the release of the amidate bridge. Controlled-potential electrolysis of **2**$^+$ in MeCN in the presence of acid produces **1**$^+$ quantitatively; the charge consumed (>1 F mol^{-1} of **1**$^+$) indicates that electrons are also used to reduce protons. This was confirmed by the formation of **2**$^+$ (in variable amounts depending on the conditions) on treating **2** with acid.

(© Wiley-VCH Verlag GmbH & Co. KGaA, 69451 Weinheim, Germany, 2005)

Introduction

Complexes with the $\{Mo_2(Cp)_2(\mu\text{-}SMe)_3\}$ core have been shown to sustain transformations of various unsaturated substrates.[1–3] The electrochemical reduction of a complex containing a $\mu\text{-}\eta^1,\eta^1$-coordinated phenyldiazene ligand in the presence of acid results in the cleavage of the N=N bond and the release of ammonia and aniline.[2] During this reduction, the nitrogenous moiety undergoes a coordination change, most probably at the hydrazido(1–) stage, from a $\mu\text{-}\eta^1,\eta^1$ to a $\mu\text{-}\eta^1$ geometry.[2] This has been recently confirmed by a theoretical study of the different steps of the reduction process.[4] Similarly, the electrochemical reduction in the presence of protons of a complex bearing a $\mu\text{-}\eta^1,\eta^2$-vinylidene ligand affords a $\mu\text{-}\eta^1$-coordinated carbyne derivative.[3]

These examples, which illustrate the ability of the $\{Mo_2(Cp)_2(\mu\text{-}SMe)_3\}$ entity to adjust to the electronic properties of various unsaturated ligands in different coordination modes, prompted us to examine the possibility of reducing nitrate and nitrite at this site. Nitrate and nitrite are known to adopt various modes of coordination to metal centres,[5–8] including, respectively, $\mu\text{-}\eta^1,\eta^1$-(*O*,*O*) and $\mu\text{-}\eta^1,\eta^1$-(*N*,*O*) binding to bimetallic units. It has been suggested that the nature of the metal-coordinated atom(s) may influence the nature of the reduction products of nitrate and nitrite.[9] In the case of the nitrite ion, the possibility of an asymmetrical $\mu\text{-}\eta^1,\eta^1$-(*N*,*O*) coordination to a bimetallic fragment is particularly attractive since this might allow the reductive cleavage of an N–O bond, with conservation of an M–O bond and *without* the release of NO, which would circumvent the difficulty of re-binding this molecule for further reduction. Several examples of $\mu\text{-}\eta^1,\eta^1$-(*N*,*O*) coordination of NO_2^- have been reported,[5,6,7a] and in some cases the nitrite (nitrate) complex was obtained by substitution of NO_2^- (NO_3^-) for MeCN ligands.[5,6] We therefore examined the reaction of the bis(acetonitrile) complex $[Mo_2(Cp)_2(\mu\text{-}SMe)_3(MeCN)_2]^+$ (**1**$^+$)[10] with nitrate and nitrite. However, these reactions did not produce NO_3^- or NO_2^- derivatives, but the amidato complex, $[Mo_2(Cp)_2(\mu\text{-}SMe)_3\{\mu\text{-}\eta^1,\eta^1\text{-}OC(Me)NH\}]^{0/+}$ (**2**$^{0/+}$), which we already knew to arise from hydration of one acetonitrile ligand in **1**$^+$, and which we fully characterized in a previous study.[11] An example of a nitrite-promoted hydration of acetonitrile has previously been reported.[12] In this case, coordination of the nitrite anion to a $\{Cr(\mu\text{-}OH)_2Cr\}$ core resulted in the cleavage of one hydroxy bridge and attack of this on a non-coordinated acetonitrile molecule. The coordinated nitrite was released upon formation of the amidato bridge.[12]

In this paper, we report the reactions of **1**$^+$ with NO_3^- and NO_2^- as well as the electrochemical behaviour of the reaction product, the amidato complex **2**$^{0/+}$.

[a] UMR CNRS 6521 Chimie, Electrochimie Moléculaires et Chimie Analytique, Université de Bretagne Occidentale,
6 Av. V. Le Gorgeu, CS 93837, 29238 Brest cedex 3, France
E-mail: jean.talarmin@univ-brest.fr

Supporting information for this article is available on the WWW under http://www.eurjic.org or from the author.

Results and Discussion

Reaction of NO_3^- or NO_2^- with $[Mo_2(Cp)_2(\mu\text{-}SMe)_3(MeCN)_2]^+$ ($\mathbf{1}^+$)

The bis(acetonitrile) complex $[Mo_2(Cp)_2(\mu\text{-}SMe)_3(MeCN)_2]^+$ ($\mathbf{1}^+$) undergoes two diffusion-controlled, reversible, one-electron oxidation steps ($E_{1/2}^{ox1}$ = –0.20 V; $E_{1/2}^{ox2}$ = 0.45 V) and an irreversible reduction (E_p^{red} = –2.2 V) in MeCN/$[NBu_4][PF_6]$.[10,13] $\mathbf{1}^+$ is stable in this electrolyte, as shown by control CVs[13] over a period of several hours. Addition of a large excess of NO_3^- to a solution of $\mathbf{1}^+$ in MeCN/$[NBu_4][PF_6]$ leads to drastic changes of the cyclic voltammogram: the two reversible oxidations and the irreversible reduction of $\mathbf{1}^+$ are replaced by two oxidation and two reduction steps, the relative intensities of which change with time. After several minutes, two couples with $E_{1/2}^{ox}$ = 0 V and $E_{1/2}^{red}$ = –0.81 V have developed at the expense of the other two redox systems with $E_{1/2}^{ox}$ = 0.27 V and E_p^{red} = –1.3 V.

In THF/$[NBu_4][PF_6]$, a solution of $\mathbf{1}^+$ instantly turns from red-orange to yellow upon addition of one equivalent of NO_3^-. The CV recorded immediately after mixing (Figure 1a) shows that the reversible oxidations of $\mathbf{1}^+$ ($E_{1/2}^{ox1}$ = –0.25 V; $E_{1/2}^{ox2}$ = 0.37 V in THF/$[NBu_4][PF_6]$) are replaced by two oxidation ($E_{1/2}^{ox}$ = 0.01 V; $E_{1/2}^{ox}$ = 0.24 V) and two reduction steps ($E_{1/2}^{red}$ = –0.80 V; E_p^{red} = –1.37 V), very similar to those observed in MeCN. After about two hours stirring, the redox systems with $E_{1/2}^{ox}$ = 0.24 V and E_p^{red} = –1.37 V have almost completely disappeared (Figure 1b). The metal-containing product, which possesses the same redox potentials as the amidato complex $[Mo_2(Cp)_2(\mu\text{-}SMe)_3\{\mu\text{-}\eta^1,\eta^1\text{-}OC(Me)NH\}]^+$ ($\mathbf{2}^+$; $E_{1/2}^{ox}$ = 0 V; $E_{1/2}^{red}$ = –0.80 V) [11] in THF and MeCN electrolytes, could not be separated from the supporting electrolyte. However, the nature of the product was confirmed by the ^{1}H NMR spectrum of the compound obtained by reaction of $\mathbf{1}^+$ with NO_3^- in THF without supporting electrolyte, and treatment of the reaction mixture with $NaBH_4$ before work-up. The ^{1}H NMR spectrum showed that the reduced amidato complex **2**[11] had formed under these conditions.

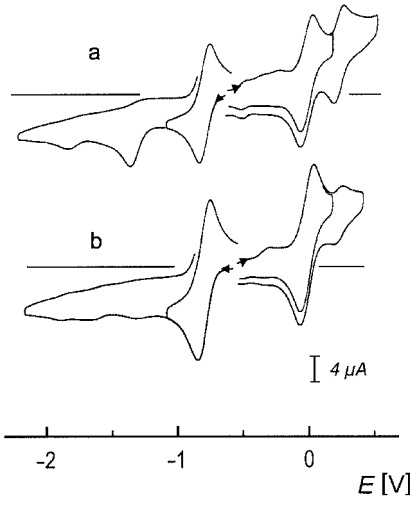

Figure 1. Cyclic voltammetry of $[Mo_2(Cp)_2(\mu\text{-}SMe)_3(MeCN)_2]^+$ ($\mathbf{1}^+$; 1.1 mM) in THF/$[NBu_4][PF_6]$ a) immediately after addition of 1 equiv. of $[NBu_4][NO_3]$, and b) after 2 h stirring (vitreous carbon electrode, v = 0.2 V s^{-1}; potentials are against ferrocene/ferrocenium).

Similar experiments were performed with nitrite (Figure 2). Although the reaction of $\mathbf{1}^+$ with NO_2^- is faster than with NO_3^-, a CV recorded immediately after addition of one equivalent of $\mathbf{1}^+$ to a THF solution of NO_2^- (Figure 2, a) allowed the detection of an intermediate with $E_{1/2}^{ox}$ = 0.21 V and E_p^{red} = –1.39 V, in addition to the final product $\mathbf{2}^+$ (Figure 2, b). Different to the reaction with NO_3^-, the amidato complex formed upon reaction of $\mathbf{1}^+$ with nitrite is present as a mixture of the neutral and cationic forms (**2**/$\mathbf{2}^+$; Figure 2, b). Voltammetry at a rotating disc electrode confirmed this. The nature of the metal product was again ascertained by comparison of the ^{1}H NMR spectrum of the complex isolated (after reduction by $NaBH_4$) from the reaction carried out in THF in the absence of supporting electrolyte, with that of an authentic sample of **2**. The reaction of $\mathbf{1}^+$ with NO_3^- or NO_2^- can be represented as shown in Scheme 1. The CVs in Figures 1b and 2b show that minor co-products, which we have not attempted to characterize, are also present.

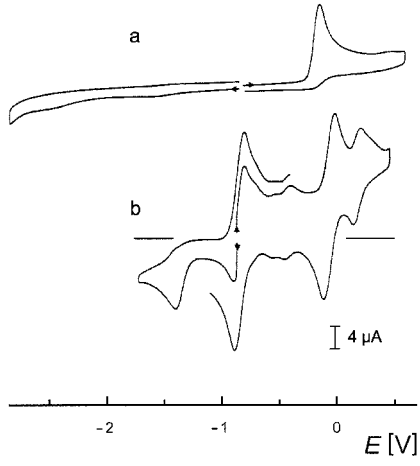

Figure 2. Cyclic voltammetry of a solution of $[NBu_4][NO_2]$ (1 mM) in THF/$[NBu_4][PF_6]$ a) before, and b) immediately after addition of $[Mo_2(Cp)_2(\mu\text{-}SMe)_3(MeCN)_2]^+$ ($\mathbf{1}^+$; 1 mM, 1 equiv.) (vitreous carbon electrode, v = 0.2 V s^{-1}; potentials are against ferrocene/ferrocenium).

In THF, $\mathbf{2}^+$ (or **2**) is not formed from $\mathbf{1}^+$ in the absence of NO_x^- on the timescale of the experiments described above. Therefore, these ions clearly promote the formation of the amidato complex $\mathbf{2}^+$ (or **2**). Two different properties of NO_x^- might explain their role in the reaction. The first possibility is that NO_x^- acts as a ligand, replacing one of the MeCN groups of $\mathbf{1}^+$. Coordination and reduction of nitrate or nitrite ions by oxo transfer to a metal centre have been reported.[14] In the case of transition-metal nitrite complexes, transfer of an oxygen atom to an organic substrate has also been observed, the NO_2^- ligand being N-bound (*nitro* coordination) to the metal.[15] In the present study, the similarity of the redox potentials of the intermediates

 © 2005 Wiley-VCH Verlag GmbH & Co. KGaA, Weinheim

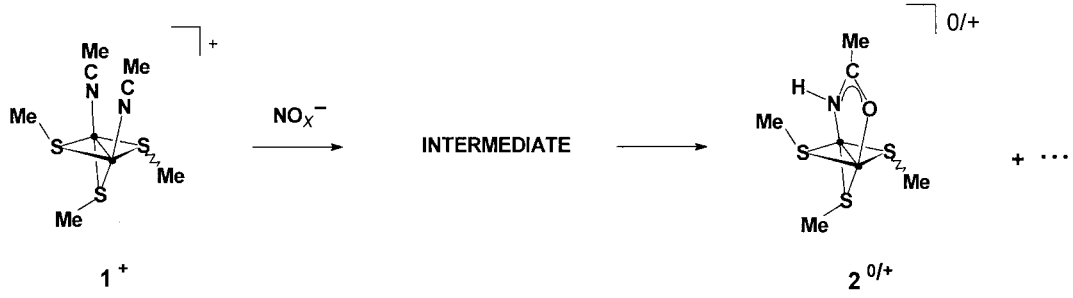

Scheme 1. ● = MoCp; x = 2 or 3.

detected during the course of the reaction of $\mathbf{1}^+$ with either nitrate or nitrite suggests that the intermediates should be similar, that is with a *nitrito* coordination of NO_2^-. The amidato complex would then result from a sequence of reactions that includes the release of an $NO_{(x-1)}$ species (neutral or anionic) and the transfer of a proton or of a H atom from the environment. The release of a nitrite *anion* in the reaction of $\mathbf{1}^+$ with NO_3^- is unlikely since we did not detect the oxidation peak of NO_2^- (see Figure 2, a) by CV after completion of the reaction of $\mathbf{1}^+$ with NO_3^- (Figure 1, b). The fact that $\mathbf{2}^+$ is formed by treating $\mathbf{1}^+$ with NO_3^- while a mixture of $\mathbf{2}/\mathbf{2}^+$ results from the reaction of $\mathbf{1}^+$ with NO_2^- might arise from homogeneous redox steps involving nitrogen oxides released in the reactions.

The second possibility is that the NO_x^- anion acts as a base [HNO_3/NO_3^-: pK_a = 8.89 in MeCN].[16] Since the experiments were not conducted under rigorously anhydrous conditions, residual water in the solvent might be involved. Thus, deprotonation of $[Mo_2(Cp)_2(\mu\text{-}SMe)_3(MeCN)(H_2O)]^+$, a possible precursor of $\mathbf{2}^+$, by nitrate or nitrite would lead to a hydroxo ligand and thus promote the formation of $\mathbf{2}^+$ (or **2**). This would be similar to the postulated mechanism of hydrolytic reactions catalysed by enzymes possessing two metal ions in close proximity at the active site. It is thought that the metal centres in these enzymes act cooperatively, the role of one of them being to modify the pK_a of a bound water molecule, thus generating a hydroxide ligand that attacks the substrate present at the neighbouring metal centre.[17,18] Similar reactions can involve mononuclear complexes. The metal-promoted hydrolysis of a nitrile ligand in the side chain of a tetrazamacrocyclic Cu complex has been reported recently.[19]

If this is the case in our study, the intermediate detected in the reaction of $\mathbf{1}^+$ with NO_x ions would be either a hydroxo complex or a species derived therefrom. However, it is not clear why such an intermediate would be longer-lived when generated by the reaction of $\mathbf{1}^+$ with NO_3^- than when it arises from the reaction of $\mathbf{1}^+$ with nitrite.

In order to discriminate between the above possibilities, we conducted two types of experiments, namely the reaction of $\mathbf{1}^+$ with a base (Et_3N: pK_a = 18.5 in MeCN)[20] and, the reaction of $\mathbf{1}^+$ with a weakly basic, oxygen-containing anion ClO_4^- [$HClO_4/ClO_4^-$: pK_a = 1.6 in MeCN].[21]

The reaction of $\mathbf{1}^+$ with Et_3N (1.2 equiv.) was monitored by cyclic voltammetry in THF/$[NBu_4][PF_6]$. Although the characteristic couples of $\mathbf{1}^+$ were replaced by reversible systems at –0.67 V and 0.67 V on addition of Et_3N, the CV did not show the formation of an intermediate such as the one observed on treatment with nitrate or nitrite. Small reversible couples around –0.8 V and 0 V suggested that only a small amount of the amidato complex might be produced. Therefore, it appears unlikely that $\mathbf{2}^{+/0}$ results from the deprotonation of an aqua precursor. It is worth noting that reaction of $\mathbf{1}^+$ with chloride, the basicity of which is very similar to that of nitrate (HCl/Cl^-: pK_a = 8.94 in MeCN),[16] produces the known $[Mo_2(Cp)_2(\mu\text{-}SMe)_3(\mu\text{-}Cl)]$ complex by the substitution of Cl^- for a MeCN ligand.[10]

The CV of $\mathbf{1}^+$ in MeCN is not affected by the presence of a large excess of ClO_4^- (supporting electrolyte: $[NEt_4][ClO_4]$). On the contrary, the CV of $\mathbf{1}^+$ recorded in THF/$LiClO_4$ or in THF/$[NBu_4][PF_6]$ in the presence of ClO_4^- is totally different from that obtained in the absence of perchlorate. The characteristic redox couples of $\mathbf{1}^+$ are not observed in the presence of ClO_4^-. Instead, redox systems similar to those present after addition of NO_x^- to a solution of $\mathbf{1}^+$ are detected. A small amount of $\mathbf{2}^+$, characterized by a reduction around –0.8 V and an oxidation at 0 V, is present in solution (Figure 3, a), and its concentration increases slowly with time.

The major compound present in a THF solution of $\mathbf{1}^+$ in the presence of ClO_4^- could not be isolated. It clearly arises from a reaction between the metal complex and perchlorate. That the redox potentials of this species ($E_{1/2}^{ox}$ = 0.23 V, E_p^{red} = –1.27 V in THF/Li[ClO_4]; $E_{1/2}^{ox}$ = 0.23 V, E_p^{red} = –1.4 V in THF/$[NBu_4][PF_6]$ + 2 equiv. ClO_4^-) are close to those of the intermediate observed upon addition of NO_x^- to $\mathbf{1}^+$ suggests that the nature of the metal compound responsible for these couples is similar in each case. However, whereas the amidato complex is formed essentially quantitatively from the intermediate observed upon treating $\mathbf{1}^+$ with NO_3^- or with NO_2^- (**2** is also formed in the latter case) within a few minutes (NO_2^-) or a few tens of minutes (NO_3^-), formation of the amidato complex $\mathbf{2}^+$ from the perchlorate intermediate is very much slower, while that of **2** requires an electrochemical reduction step.

The control experiments with Et_3N and ClO_4^- demonstrate that the basic properties of the reactant, that is its ability to deprotonate coordinated water, are not essential to the formation of $\mathbf{2}^{+/0}$. It is therefore unlikely that the residual water of the solvent plays a pivotal part in the pro-

 © 2005 Wiley-VCH Verlag GmbH & Co. KGaA, Weinheim

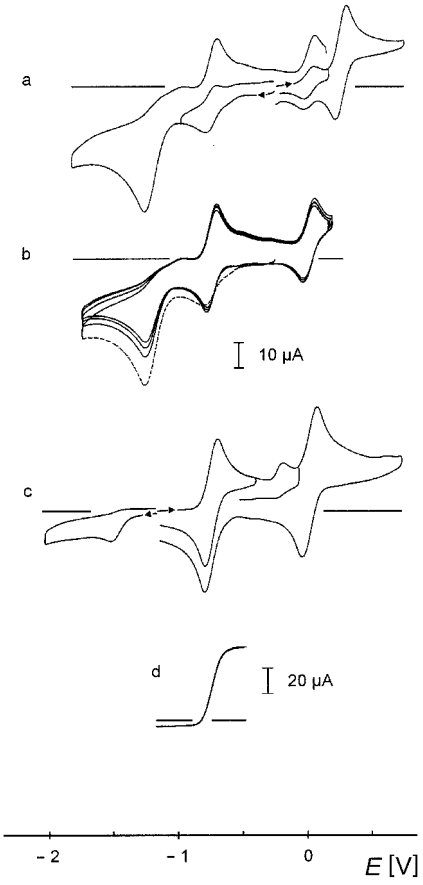

Figure 3. Cyclic voltammetry of $[Mo_2(Cp)_2(\mu\text{-}SMe)_3(MeCN)_2]^+$ ($\mathbf{1}^+$; 2 mM) in THF/$LiClO_4$ recorded immediately after the addition of the metal complex (a); the curve in b) represents repetitive scans in the potential range –1.8/0.2 V and the dashed curve is the first negative-going scan; the cyclic voltammogram in (c) and the RDE voltammogram in (d) were obtained after controlled-potential electrolysis of the solution in b) at –1.4 V on a graphite cathode (n = 2 F per mol of $\mathbf{1}^+$) (vitreous carbon electrode, v = 0.2 V s^{-1}; potentials are against ferrocene/ferrocenium).

cess on the timescale of the electrochemical experiments.That the amidate derivative was obtained upon treatment of $\mathbf{1}^+$ with different oxo anions strongly suggests that the oxygen atom in $\mathbf{2}^{+/0}$ comes from the XO^- moiety bound to a metal centre (X = NO, NO_2 or ClO_3).

Metal complexes containing perchlorate ligands have been reported.[18,22] However, in these compounds ClO_4^- can generally be substituted by a variety of ligands, in contrast to what is observed here: addition of a large excess of acetonitrile has no effect on the CV shown in Figure 3a. Therefore, it is unlikely that the species observed in THF in the presence of perchlorate arises from the simple substitution of ClO_4^- for one MeCN ligand in $\mathbf{1}^+$. Rather, an intermediate such as the one shown in Scheme 2 can be envisaged. The absence of a perchlorate derivative in MeCN/$[NEt_4][ClO_4]$ would then arise from the worse coordinating ability of ClO_4^- as compared to acetonitrile.

The reduced amidato complex **2** is generated from the intermediate formed in the reaction of $\mathbf{1}^+$ with perchlorate by reduction at –1.3 V (Figures 3a and b). This was confirmed by voltammetry of the catholyte after controlled-potential electrolysis (E_{el} = –1.4 V, graphite cathode), as shown in Figures 3c and 3d. However, the charge consumed to produce **2** was between 1.4 and 2 F per mol of $\mathbf{1}^+$, while $\mathbf{2}^+$ was the major product formed after the transfer of about 1 F per mol of $\mathbf{1}^+$. Assuming that the intermediate is as shown in Scheme 2, the formation of $\mathbf{2}^+$ in the early stage of the electrolysis would be consistent with a (one-electron) reductive elimination of X^- (e.g. ClO_3^-) accompanied (or followed) by a protonation step. The reduction of $\mathbf{2}^+$ ($E_{1/2}^{red}$ = –0.8 V) at the electrolysis potential completes the reduction process. A small amount of an unknown product is also present after electrolysis (Figure 3c).

It has been shown that coordinated nitriles can be attacked by carbonate to produce an amide derivative with the release of CO_2.[23] Oxyfunctionalizations of coordinated nitriles with various oxygen-containing substrates have also been reported.[24] A direct attack of XO^- (X = NO, NO_2 or ClO_3) on one of the MeCN ligands of $\mathbf{1}^+$ could also take place. However, this possibility appears less likely on the basis of the experiments carried out in MeCN, since the formation of $\mathbf{2}^+$ from $\mathbf{1}^+$ and NO_3^- is slower than in THF or requires a large excess of nitrate, while no reaction occurred in the presence of ClO_4^-, even when used in very large excess (supporting electrolyte). The fact that the redox potentials of the intermediates detected in the reactions of $\mathbf{1}^+$ with NO_2^-, NO_3^- or ClO_4^- are very similar in THF suggests that they must be closely related. While the intermediate formed by treating $\mathbf{1}^+$ with nitrate and nitrite produces $\mathbf{2}^{+/0}$ within a relatively short time, it appears longer-lived when obtained by reaction of $\mathbf{1}^+$ with perchlorate. As the intermediate could not be isolated from the solution, its nature is not known and the reason for this difference could

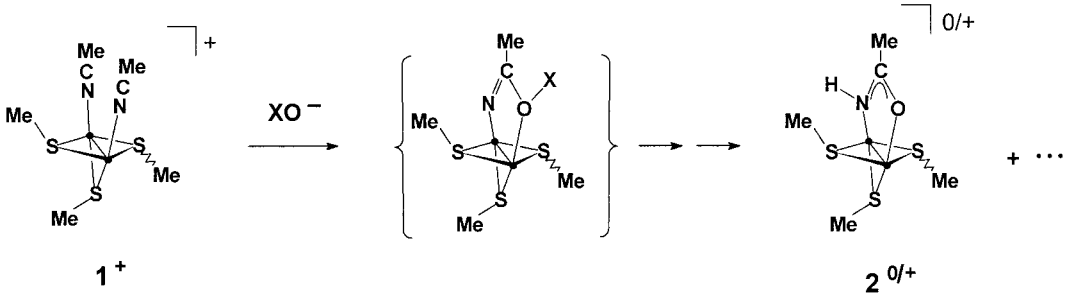

Scheme 2. Postulated intermediate in the reaction of $\mathbf{1}^+$ with XO^- (X = NO_2, NO or ClO_3). ● = MoCp.

 © 2005 Wiley-VCH Verlag GmbH & Co. KGaA, Weinheim

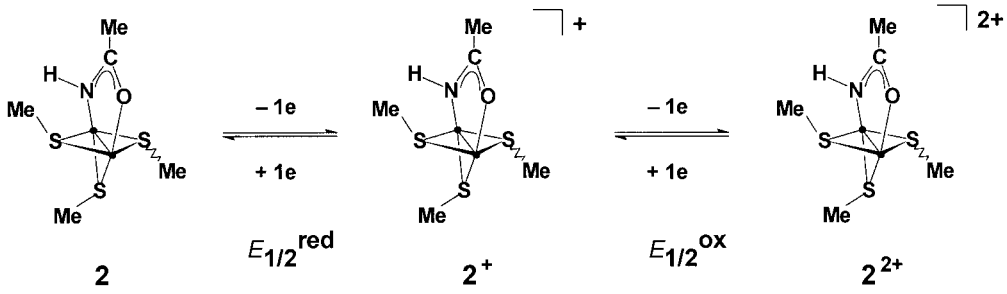

Scheme 3. ● = MoCp.

not be elucidated. However, if the precursor of the amidato complex is as shown in Scheme 2, the different lifetimes might indicate that the X–O bond is stronger for X = Cl than for X = N.

The reactivity of $\mathbf{1}^+$ reveals the occurrence of a bimetallic effect in the $\{Mo_2(Cp)_2(\mu\text{-}SMe)_3\}$ moiety. Treatment of $\mathbf{1}^+$ with chloride or trifluoroacetate produces complexes where the anion occupies a bridging position.[10,32] This indicates that the remaining MeCN ligand in the likely intermediate $[Mo_2(Cp)_2(\mu\text{-}SMe)_3(MeCN)X]$ (X = Cl, CF_3CO_2) is released upon X bridging. Despite the ability of NO_3^- and NO_2^- to adopt bridging coordination modes,[5,6,7a] this was not observed at the $\{Mo_2(Cp)_2(\mu\text{-}SMe)_3\}$ core, and the amidato complex $\mathbf{2}^+$ (and **2**) was obtained instead. Therefore, it appears that the reactivity (the lability) of the acetonitrile bound to one Mo atom is affected by the nature of the ligand present at the adjacent metal centre of the $\{Mo_2(Cp)_2(\mu\text{-}SMe)_3\}$ site.

Electrochemistry of $[Mo_2(Cp)_2(\mu\text{-}SMe)_3\{\mu\text{-}\eta^1,\eta^1\text{-}OC(Me)NH\}]^{0/+}$ ($\mathbf{2}^{0/+}$)

Several compounds containing an amidato ligand are known,[17,18,25] although no electrochemical study of such a complex has been reported so far, to the best of our knowledge. We now report the electrochemistry of $\mathbf{2}^{0/+}$ in THF and MeCN containing $[NBu_4][PF_6]$. We paid special attention to the reduction of $\mathbf{2}^+$ in the presence of acid in order to investigate the mechanism of the release of the amidato ligand as acetamide.[11]

Complex $\mathbf{2}^+$ undergoes diffusion-controlled, one-electron reduction and oxidation steps in both solvents (Scheme 3). Controlled-potential electrolysis at –1.0 V afforded the neutral compound **2** essentially quantitatively[26] after transfer of 1 F per mol of $\mathbf{2}^+$.

The CV of $\mathbf{2}^+$ in MeCN/$[NBu_4][PF_6]$ (Figure 4, a) is strongly affected by the presence of protons, although the changes only concern the reduction step, which becomes irreversible and shifts by about 100 mV towards positive potentials (Figure 4, b). This is indicative of the occurrence of a follow-up reaction (EC process)[13,27,28] under these conditions.

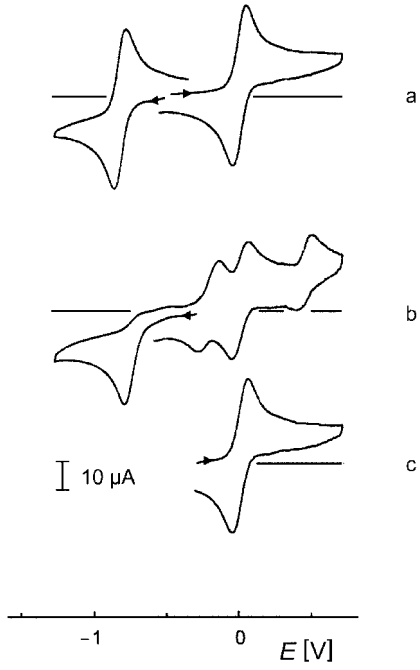

Figure 4. Cyclic voltammetry of $[Mo_2(Cp)_2(\mu\text{-}SMe)_3\{\mu\text{-}\eta^1,\eta^1\text{-}OC(Me)NH\}]^+$ ($\mathbf{2}^+$; 1 mM) in MeCN/$[NBu_4][PF_6]$ a) before, and b) and c) after addition of an excess of HBF_4/H_2O (vitreous carbon electrode, v = 0.2 V s^{-1}; potentials are against ferrocene/ferrocenium).

The reduction of $\mathbf{2}^+$ in the presence of acid in MeCN/$[NBu_4][PF_6]$ affords a product that was identified as $\mathbf{1}^+$ from its redox systems detected on the return scan (Figure 4, b). Controlled-potential electrolysis at –0.9 V effectively produces $\mathbf{1}^+$. However, the CV recorded after the passage of 1 F per mol of $\mathbf{2}^+$ demonstrates that $\mathbf{2}^+$ is still present in solution; conversion of $\mathbf{2}^+$ to $\mathbf{1}^+$ is almost complete (>90%)[26] only after the transfer of about 1.5 F per mol of $\mathbf{2}^+$. While these experiments are entirely consistent with previous ones showing that protonation of **2** in MeCN produces $\mathbf{1}^+$ and acetamide,[11] they also suggest that part of the charge consumed during electrolysis is used to reduce protons. This can be described as shown in Scheme 4.

In contrast to what is observed in MeCN/$[NBu_4][PF_6]$, addition of two equivalents of HBF_4/H_2O to a THF/$[NBu_4][PF_6]$ solution of $\mathbf{2}^+$ did not lead to a significant change of the cyclic voltammogram. However, in the pres-

 © 2005 Wiley-VCH Verlag GmbH & Co. KGaA, Weinheim

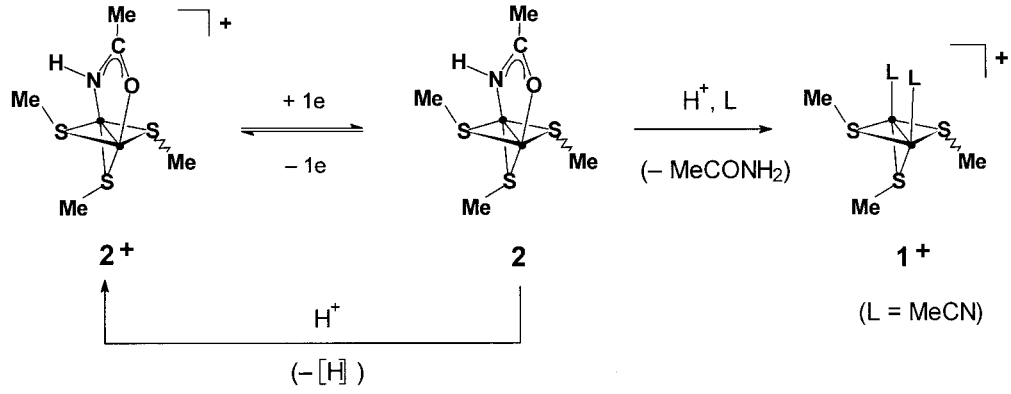

Scheme 4. ● = MoCp.

ence of larger amounts of acid (10–20 equiv. HBF_4/H_2O or HBF_4/Et_2O), the reduction of $\mathbf{2}^+$ in this solvent occurs according to an EC process, as shown by the decrease of the anodic-to-cathodic peak current ratio $[(i_p^a)/(i_p^c)^{red}]$, and by the presence of a product (**3**) detected by its redox steps on the return scan at $E_{1/2}$ = –0.43 V and 0.21 V (Figure 5, b; note that the presence of acid has no effect on the oxidation, cf. Figure 5, c).

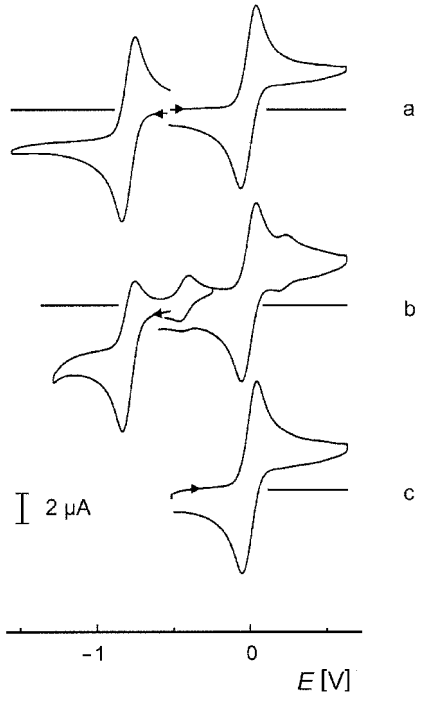

Figure 5. Cyclic voltammetry of $[Mo_2(Cp)_2(\mu\text{-}SMe)_3\{\mu\text{-}\eta^1,\eta^1\text{-}OC(Me)NH\}]^+$ ($\mathbf{2}^+$; 1 mM) in THF/$[NBu_4][PF_6]$ a) before, and b) and c) after addition of a large excess (17 equiv.) of HBF_4/Et_2O (vitreous carbon electrode, v = 0.05 V s^{-1}; potentials are against ferrocene/ferrocenium).

Cyclic voltammetry after controlled-potential reduction of $\mathbf{2}^+$ in the presence of acid (10 equiv. HBF_4/Et_2O) in THF shows that a substantial amount of the starting material $\mathbf{2}^+$ is still present along with product **3** after the passage of 2 and 3 F per mol of $\mathbf{2}^+$ (ca. 60% and 50% $\mathbf{2}^+$ present, respectively).[26] This clearly shows that the charge diverted to reduce protons (see Scheme 4) is larger in THF than in MeCN. Consistent with this, addition of H^+ to an electrogenerated solution of **2** in THF leads to the formation of $\mathbf{2}^+$ along with product **3** (Figure S1c in the Supporting Information). Complex **3** decomposed upon work-up. However, its reaction with acetonitrile affords $\mathbf{1}^+$.[29] This indicates that **3** retains the $\{Mo_2(Cp)_2(\mu\text{-}SMe)_3\}$ core and possesses labile ligand(s) bound to the metal centres. Species such as $[Mo_2(Cp)_2(\mu\text{-}SMe)_3(L)(L')]^+$ (L, L′ = THF and/or H_2O), or a derivative retaining the acetamide ligand, $[Mo_2(Cp)_2(\mu\text{-}SMe)_3(NH_2COMe)(L)]^+$ (L = THF or H_2O), are possible. It should be noted that protonation of $[Mo_2(Cp)_2(\mu\text{-}SMe)_3(\mu\text{-}NH_2)]$ with HBF_4/H_2O in MeCN affords $\mathbf{1}^+$, while a product tentatively assigned as $[Mo_2(Cp)_2(\mu\text{-}SMe)_3(NH_3)(THF)]^+$ [$E_{1/2}^{ox}$ = –0.39 V and 0.31 V] was obtained by protonation with HBF_4/Et_2O in THF.[30]

As mentioned above, a major difference between the CV experiments carried out in THF and in MeCN lies with the detection of **2** in the former solvent, even in the presence of a large excess of acid. The addition of MeCN to an acidic THF solution of $\mathbf{2}^+$ leads to the CV detection of $\mathbf{1}^+$ instead of **3** on the reverse scan (see Figures 6a and b), without a change in the characteristics of the reduction process $[(i_p^c)^{red}, (i_p^a/i_p^c)^{red}]$, that is, without a change in the overall kinetics of the following chemical reaction(s). Therefore, the solvent-dependence of the kinetics of the reduction of $\mathbf{2}^+$ in the presence of acid does not originate in the solvent-binding step itself. This would be consistent with the fact that $\mathbf{1}^+$ is formed from **3**.

Monitoring the course of the reaction of **2** with a large excess of acid by amperometry at a rotating disc electrode (E = –0.6 V, on the plateau of the first oxidation of **2**) indicates[31] the existence of an equilibrium between **2** and a protonated intermediate, which would be shifted by the slower conversion of the intermediate into products [$\mathbf{2}^+$ (with loss of an H atom) and **3** or $\mathbf{1}^+$ (with the release of the amidato bridge upon L binding) in THF or MeCN respectively] (Scheme 5).[32]

The possibility of releasing the amidato bridge upon electrochemical reduction of $\mathbf{2}^+$ in the presence of 10–20 equiv. of acid in THF was confirmed by controlled-potential electrolyses performed in the presence of an excess of substrate

 © 2005 Wiley-VCH Verlag GmbH & Co. KGaA, Weinheim

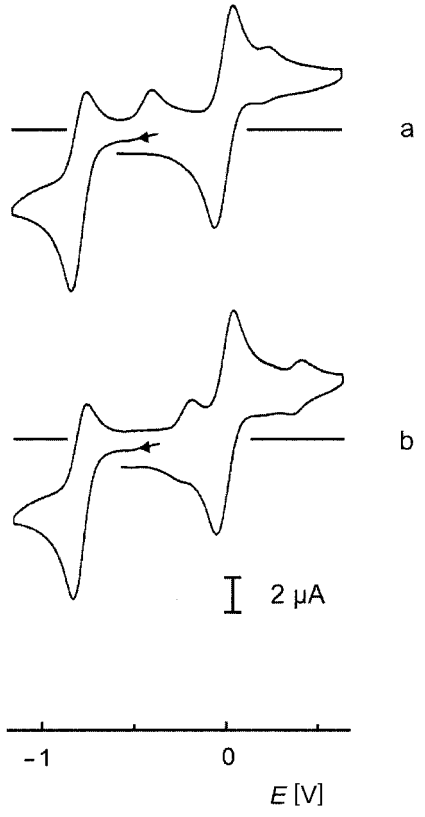

Figure 6. Cyclic voltammetry of $[Mo_2(Cp)_2(\mu\text{-}SMe)_3\{\mu\text{-}\eta^1,\eta^1\text{-}OC(Me)NH\}]^+$ (**2**$^+$; 1 mM) in THF/$[NBu_4][PF_6]$ in the presence of a large excess (17 equiv.) of HBF_4/Et_2O a) before, and b) after addition of MeCN (vitreous carbon electrode, $v = 0.05\ V\,s^{-1}$; potentials are against ferrocene/ferrocenium).

(10 equiv. *t*BuNC). Under these conditions, the bis(isocyanide) analogue of **1**$^+$ was obtained in about 80% yield[26] along with **2**$^+$, after the transfer of more than 2 F per mol of **2**$^+$. The nature of the product was confirmed by comparison of its redox potentials with those of an authentic sample of $[Mo_2(Cp)_2(\mu\text{-}SMe)_3(t\text{BuNC})_2]^+$.[34]

Conclusions

The results reported in this paper illustrate an original oxyfunctionalization of an acetonitrile bound to a bimetallic sulfur core $\{Mo_2(Cp)_2(\mu\text{-}SMe)_3\}$ by oxygen-containing anions, XO^- (X = NO, NO_2, ClO_3), which initially arises from substitution (or less likely direct attack) of MeCN by XO^-, and produces the amidate complex **2**$^{0/+}$.

The electrochemical reduction of **2**$^+$ in the presence of acid demonstrates that the amidate bridge can be released, since **1**$^+$, the precursor of **2**$^+$, is regenerated when the reactions are carried out in MeCN. Because **2**$^+$ is also formed from **1**$^+$ in a wet atmosphere,[11] the present results exemplify the possibility of a cyclic conversion of acetonitrile into acetamide.

Experimental Section

Methods and Materials: All experiments were carried out under an inert atmosphere using Schlenk techniques. THF was purified as described previously.[33] Acetonitrile (Merck, HPLC grade) was used as received. The fluoroboric acid [diethyl ether complex and aqueous solution (Aldrich)], was used as received. The preparation and the purification of the supporting electrolyte $[NBu_4][PF_6]$ and the electrochemical equipment were as described previously.[33] All the potentials quoted in the text and figures are relative to the ferrocene-ferrocenium couple; ferrocene was added as an internal standard at the end of the experiments. ^{1}H NMR spectra were recorded on a Bruker AC300 spectrometer. Shifts are relative to tetramethylsilane as an internal reference. Complexes $[Mo_2(Cp)_2(\mu\text{-}SMe)_3(L)_2]^+$ (L = MeCN, *t*BuNC) were synthesised as described previously.[10,34]

Preparation of $[Mo_2(Cp)_2(\mu\text{-}SMe)_3\{\mu\text{-}\eta^1,\eta^1\text{-}OC(Me)NH\}]$ (2) by treatment of 1$^+$ with NO_x^- (x = 2, 3): In a typical experiment, a

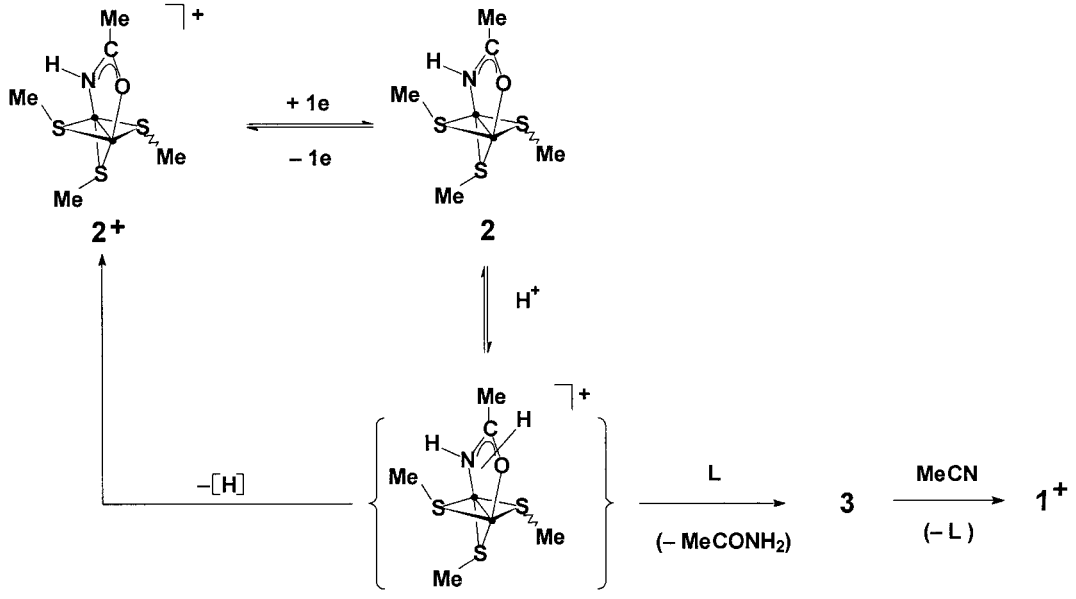

Scheme 5. ● = MoCp; the species in brackets was not detected.

 © 2005 Wiley-VCH Verlag GmbH & Co. KGaA, Weinheim

mixture of $\mathbf{1}^+$ (0.0565 g, 8.9×10^{-5} mol) and $[NBu_4][NO_3]$ (0.1445 g, 4.7×10^{-4} mol, 5.3 equiv.) in 15 mL of THF was stirred under dinitrogen for 3 h. After filtration, the solution was taken to dryness. The solid was dissolved in MeCN and $NaBH_4$ was added in excess (0.017 g, 4.5×10^{-4} mol, 5 equiv.). The solution was stirred for 30 min and then filtered to remove a brown precipitate. The volume of the solution was reduced to 2 mL under reduced pressure, and addition of Et_2O (15 mL) led to the formation of a white precipitate. The latter was removed by filtration, and the solution was taken to dryness. The solid residue was dried under vacuum. The ^1H NMR spectrum of the solid demonstrated that the amidate complex **2** had formed. CV of the NMR sample showed the presence of **2**, with a small amount of $\mathbf{2}^+$ resulting from the oxidation of the neutral complex ($E_{1/2}{}^{ox} = -0.8$ V).

A similar procedure was followed for the reaction of $\mathbf{1}^+$ with nitrite. $[NBu_4][NO_2]$ (0.0182 g, 6.3×10^{-5} mol) and $\mathbf{1}^+$ (0.0418 g, 6.6×10^{-5} mol) were dissolved in THF (15 mL). The solution was stirred for about 1 h, after which time it was taken to dryness. The solid was dissolved in MeCN (10 mL) and an excess of $NaBH_4$ (0.0164 g, 4.3×10^{-4} mol, 6.6 equiv.) was added. After a few minutes stirring, the solvent was evaporated under reduced pressure. Et_2O (10 mL) was added to the residue, and after 10 min stirring the solution was filtered and taken to dryness. The solid was stirred for 10 min in pentane (5 mL), and, after evaporation of the solvent, the solid was dried under vacuum. As above, the ^1H NMR spectrum of the solid demonstrated that the amidate complex **2** had formed.

Acknowledgments

The authors thank CNRS (France), the Université de Bretagne Occidentale and the Conseil Régional de Bretagne (PRIR, operation no. 98CCO9) for financial support. The Conseil Régional de Bretagne is also acknowledged for providing a studentship to M.L.H.

[1] a) F. Y. Pétillon, P. Schollhammer, J. Talarmin, K. W. Muir, *Coord. Chem. Rev.* **1998**, *178–180*, 203–247; b) P. Schollhammer, N. Cabon, J. F. Capon, F. Y. Pétillon, J. Talarmin, K. W. Muir, *Organometallics* **2001**, *20*, 1230–1242; c) N. Cabon, P. Schollhammer, F. Y. Pétillon, J. Talarmin, K. W. Muir, *Organometallics* **2002**, *21*, 448–450; d) P. Schollhammer, B. Didier, N. Le Grand, F. Y. Pétillon, J. Talarmin, K. W. Muir, S. J. Teat, *Eur. J. Inorg. Chem.* **2002**, 658–663.

[2] a) F. Y. Pétillon, P. Schollhammer, J. Talarmin, K. W. Muir, *Inorg. Chem.* **1999**, *38*, 1954–1955; b) N. Le Grand, K. W. Muir, F. Y. Pétillon, C. J. Pickett, P. Schollhammer, J. Talarmin, *Chem. Eur. J.* **2002**, *8*, 3115–3127.

[3] A. Le Goff, N. Cabon, C. Le Roy, F. Y. Pétillon, P. Schollhammer, J. Talarmin, unpublished results.

[4] J. K. Padden Metzker, J. E. McGrady, *Chem. Eur. J.* **2004**, *10*, 6447–6455.

[5] K. B. Shiu, L.-T. Tang, S.-W. Jean, C.-H. Li, R.-R. Wu, J.-C. Wang, L.-S. Liou, M. Y. Chiang, *Inorg. Chem.* **1996**, *35*, 7845–7849.

[6] a) B. K. Hui, W.-T. Wong, *J. Chem. Soc., Dalton Trans.* **1996**, 2177–2178; b) B. K. Hui, W.-T. Wong, *J. Chem. Soc., Dalton Trans.* **1998**, 3977–3985.

[7] a) W. S. Han, S. W. Lee, *Inorg. Chim. Acta* **2003**, *348*, 15–24; b) W. S. Han, S. W. Lee, *J. Organomet. Chem.* **2003**, *678*, 102–107.

[8] a) C. Kimblin, V. J. Murphy, T. Hascall, B. M. Bridgewater, J. B. Bonanno, G. Parkin, *Inorg. Chem.* **2000**, *39*, 967–974; b) S. Ogo, H. Nakai, Y. Watanabe, *J. Am. Chem. Soc.* **2002**, *124*, 597–601; c) P. J. Arnold, S. C. Davies, M. C. Durrant, D. V. Griffiths, D. L. Hughes, P. C. Sharpe, *Inorg. Chim. Acta* **2003**, *248*, 143–149.

[9] F. V. Kudrik, S. V. Makarov, A. Zahl, R. Van Eldik, *Inorg. Chem.* **2003**, *42*, 618–624.

[10] F. Barrière, Y. Le Mest, F. Y. Pétillon, S. Poder-Guillou, P. Schollhammer, J. Talarmin, *J. Chem. Soc., Dalton Trans.* **1996**, 3967–3976.

[11] P. Schollhammer, M. Le Hénanf, C. Le Roy-Le Floch, F. Y. Pétillon, J. Talarmin, K. W. Muir, *J. Chem. Soc., Dalton Trans.* **2001**, 1573–1577.

[12] R. A. Holwerda, *Inorg. Chim. Acta* **1999**, *288*, 211–214.

[13] The parameters i_p and E_p are the peak current and the peak potential of a redox process, respectively; $E_{1/2} = (E_p{}^a + E_p{}^c)/2$; $E_p{}^a$, $i_p{}^a$ and $E_p{}^c$, $i_p{}^c$ are the potential and the current of the anodic and of the cathodic peak of a reversible process, respectively; $\Delta E_p = E_p{}^a - E_p{}^c$; an EC process comprises an electron transfer step (E) followed by a chemical reaction (C). CV stands for cyclic voltammetry; v ($V s^{-1}$) is the scan rate in CV experiments.

[14] a) J. Jiang, R. H. Holm, *Inorg. Chem.* **2005**, *44*, 1068–1072; b) B. A. Moyer, T. J. Meyer, *J. Am. Chem. Soc.* **1979**, *101*, 1326–1328; c) K. Tanaka, M. Honjo, T. Tanaka, *Inorg. Chem.* **1985**, *24*, 2662–2665, and references cited therein.

[15] D. A. Muccigrosso, F. Mares, S. E. Diamond, J. P. Solar, *Inorg. Chem.* **1983**, *22*, 960–965.

[16] I. M. Kolthoff, S. Bruckenstein, M. K. Chantooni Jr., *J. Am. Chem. Soc.* **1961**, *83*, 3927–3935.

[17] a) F. Meyer, E. Kaifer, P. Kircher, K. Heinze, H. Pritzkow, *Chem. Eur. J.* **1999**, *5*, 1617–1630; b) C. D. Bauer, T. E. Concolino, J. L. Eglin, R. D. Rodgers, R. J. Staples, *J. Chem. Soc., Dalton Trans.* **1998**, 2813–2817; c) S. T. Frey, N. N. Murthy, S. T. Weintraub, L. K. Thompson, K. D. Karlin, *Inorg. Chem.* **1997**, *36*, 956–957; d) N. J. Curtis, K. S. Hagen, A. M. Sargeson, *J. Chem. Soc., Chem. Commun.* **1984**, 1571–1573.

[18] E. C. Wilkinson, Y. Dong, L. Que Jr., *J. Am. Chem. Soc.* **1994**, *116*, 8394–8395.

[19] L. Siegfried, A. Comparone, M. Neuburger, T. A. Kaden, *Dalton Trans.* **2005**, 30–36.

[20] E. J. Moore, J. M. Sullivan, J. R. Norton, *J. Am. Chem. Soc.* **1986**, *108*, 2257–2263 and references cited therein.

[21] T. Fujinaga, I. Sakamoto, *J. Electroanal. Chem.* **1977**, *85*, 185–201.

[22] a) M. Hoogenraad, K. Rampkisoensing, W. L. Driessen, H. Kooijman, A. L. Spek, E. Bouwman, J. G. Haasnoot, J. Reedijk, *Inorg. Chim. Acta* **2001**, *320*, 117–126; b) S. C. Chaffee, J. C. Sutton, C. S. Babitt, J. T. Mayer, K. A. Guy, R. D. Pike, G. B. Carpenter, *Organometallics* **1998**, *17*, 5586–5590; c) A. S. Kanmani, S. Vancheesan, *J. Mol. Catal. A: Chem.* **1999**, *150*, 95–104; d) J.-L. Pascal, J. Potier, D. J. Jones, J. Rozière, A. Michalowicz, *Inorg. Chem.* **1985**, *24*, 238–241; e) J.-L. Pascal, J. Potier, D. J. Jones, J. Rozière, A. Michalowicz, *Inorg. Chem.* **1984**, *23*, 2068–2073; f) P. L. Johnson, J. H. Enemark, R. D. Feltham, K. Bizot Swedo, *Inorg. Chem.* **1976**, *15*, 2989–2993.

[23] a) I. I. Creaser, J. MacB. Harrowfield, F. R. Keene, A. M. Sargeson, *J. Am. Chem. Soc.* **1981**, *103*, 3359–3364; b) A. W. Zanella, P. C. Ford, *Inorg. Chem.* **1975**, *14*, 42–47.

[24] a) S. Thomas, P. J. Lim, R. W. Gable, C. G. Young, *Inorg. Chem.* **1998**, *37*, 590–593; b) M. N. Kopylovich, V. Y. Kukushkin, M. Haukka, J. J. R. Frausto da Silva, A. J. L. Pombeiro, *Inorg. Chem.* **2002**, *41*, 4798–4804; c) N. A. Bokach, V. Y. Kukushkin, M. L. Kuznetsov, D. A. Garnovskii, G. Natile, A. J. L. Pombeiro, *Inorg. Chem.* **2002**, *41*, 2041–2053; d) K. V. Luzyanin, V. Y. Kukushkin, M. L. Kuznetsov, D. A. Garnovskii, M. Haukka, A. J. L. Pombeiro, *Inorg. Chem.* **2002**, *41*, 2981–2986; e) N. A. Bokach, A. V. Khripoun, V. Y. Kukushkin, M. Haukka, A. J. L. Pombeiro, *Inorg. Chem.* **2003**, *42*, 896–903.

[25] a) R. A. Michelin, M. Mozzon, R. Bertani, *Coord. Chem. Rev.* **1996**, *147*, 299–338; b) J. L. Eglin, *Comments Inorg. Chem.* **2002**, *23*, 23–43; c) V. Y. Kukushkin, A. J. L. Pombeiro, *Inorg. Chim. Acta* **2005**, *358*, 1–21; d) V. Y. Kukushkin, A. J. L. Pombeiro, *Chem. Rev.* **2002**, *102*, 1771–1802; e) C. S. Chin, D. Chong, B. Lee, H. Jeong, G. Won, Y. Do, Y. J. Park, *Organome-*

 © 2005 Wiley-VCH Verlag GmbH & Co. KGaA, Weinheim

tallics **2000**, *19*, 638–648; f) T. E. Concolino, J. L. Eglin, R. J. Staples, *Polyhedron* **1999**, *18*, 915–921; g) F. A. Cotton, L. M. Daniels, C. A. Murillo, X. Wang, *Polyhedron* **1998**, *17*, 2781–2793; h) A. Erxleben, B. Lippert, *J. Chem. Soc., Dalton Trans.* **1996**, 2329–2333; i) M. B. Hursthouse, M. A. Mazid, S. D. Robinson, A. Sahajpal, *J. Chem. Soc., Dalton Trans.* **1993**, 2835–2839; j) W.-Y. Yeh, S.-M. Peng, L.-K. Liu, *Inorg. Chem.* **1993**, *32*, 2965–2967.

[26] The yield of the reduction of $\mathbf{2}^{+}$ was calculated by comparing the peak current of the reactant to that of the product, assuming identical diffusion coefficients.

[27] a) A. J. Bard, L. R. Faulkner, *Electrochemical Methods. Fundamentals and Applications*, John Wiley & Sons, New York, **1980**, chapter 11, pp 429–485; b) E. R. Brown, R. F. Large, in *Techniques of Chemistry*, vol. I – *Physical Methods of Chemistry*, Part IIA (Ed.: A. Weissberger), John Wiley & Sons, New York, **1971**, chapter 6, pp 423–530.

[28] The variations of the current function $[i_p^{red}(H^+)/v^{1/2}]$ associated with the reduction peak of $\mathbf{2}^{+}$ in the presence of acid $[i_p^{red}(H^+)]$ against scan rate, and the peak current ratio of the reduction in the presence and in the absence of protons $[i_p^{red}(H^+)/i_p^{red} \approx 1.1]$ are consistent with the transfer of a single electron in the reduction in the presence of acid. Also, the fact that the oxidation of $\mathbf{2}^{+}$ is not affected by the presence of H^+ (Figure 4, c) indicates that $\mathbf{2}^{+}$ is not protonated, and that the change in the reduction step arises from the protonation of electrogenerated **2** (EC process).

[29] Addition of MeCN to the solution in Figure S1c (see Supporting Information) results in the conversion of product **3** into $\mathbf{1}^{+}$. This indicates (see part b in Figure 6) that $\mathbf{1}^{+}$ is most probably formed from **3**, with no change in the reduction mechanism due to the presence of MeCN.

[30] F. Y. Pétillon, P. Schollhammer, J. Talarmin, *J. Chem. Soc., Dalton Trans.* **1997**, 4019–4024.

[31] The oxidation current measured at the rotating disc electrode drops to the background level on addition of H^+ to **2** in MeCN, which shows that **2** is removed very rapidly from the solution. In contrast, after an initial abrupt fall of about 30% on adding H^+ to a THF solution of **2**, the oxidation current decreases more slowly.

[32] The mechanism in Scheme 5 was used for CV simulations (VirtualCV 1.0, written by A. Laouénan, is available on the web). The main characteristics of the CVs in Figures 6a and 6b $\{[(i_p^a/i_p^c)^{red}\ \mathbf{2}^{+}]$, $[i_p^a(\mathbf{3})$ or $(\mathbf{1}^{+})/i_p^c(\mathbf{2}^{+})]\}$ were reproduced assuming that $\mathbf{1}^{+}$ is formed from **3**.[29] The solvent-dependence of the overall kinetics (see Figures 4b and 5b) was simulated by an increase of the forward rate constant for protonation, and of the second-order rate constant for the solvent-binding step, on going from THF to MeCN. This is entirely consistent with the fact that HBF_4/H_2O (i.e. H_3O^+) and HBF_4/Et_2O should be stronger acids in MeCN than in THF, and with the properties of MeCN compared to THF as a ligand for the metal sites in this type of complexes. The fact that the amount of $\mathbf{2}^{+}$ formed on reacting **2** with H^+, and that the charge used to reduce protons upon electrolysis of acidic solutions of $\mathbf{2}^{+}$, are larger in THF than in MeCN is assigned to the smaller rate constant of the substrate-binding step (Scheme 5) in the former. This is consistent with the fact that protonation of **2** in MeCN produces $\mathbf{1}^{+}$ with little $\mathbf{2}^{+}$.

[33] M. Le Hénanf, C. Le Roy, K. W. Muir, F. Y. Pétillon, P. Schollhammer, J. Talarmin, *Eur. J. Inorg. Chem.* **2004**, 1687–1700.

[34] N. Cabon, E. Paugam, F. Y. Pétillon, P. Schollhammer, J. Talarmin, K. W. Muir, *Organometallics* **2003**, *22*, 4178–4180.

Received: April 15, 2005
Published Online: August 24, 2005

 © 2005 Wiley-VCH Verlag GmbH & Co. KGaA, Weinheim

Coordination Chemistry of *N*,*N*,*N*′,*N*′-Tetraethylpyridine-2,6-dithiocarboxamide (*S*-dept) – X-ray Crystal Structures and Magnetic Properties of [Co(*S*-dept)X_2] (X = Br, I, and NCS)

Ramesh Kapoor,*[a] Ashok Kataria,[a] Paloth Venugopalan,[a] Pratibha Kapoor,[a] Geeta Hundal,[b] and Montserrat Corbella*[c]

Keywords: *N*,*N*,*N*′,*N*′-Tetraethylpyridine-2,6-dithiocarboxamide / X-ray crystallography / IR / Zero-field splitting / EPR

Mononuclear cobalt(II) complexes [Co(*S*-dept)X_2] [X = Br (**1**), I (**2**) and NCS (**3**)] were synthesized using *N*,*N*,*N*′,*N*′-tetraethylpyridine-2,6-dithiocarboxamide (*S*-dept), and characterised by conductivity, spectral and single-crystal X-ray diffraction studies. These studies reveal that the compounds consist of discrete monomeric molecules in which the cobalt atoms are five-coordinate in an environment that is best described as being distorted square-pyramidal. In dimethylformamide the iodo complex shows significant ionic dissociation (1:1 electrolyte) and its crystal field absorption spectrum is interpretable in terms of an octahedral structure [Co(*S*-dept)$(DMF)_2$I]$^+$. The temperature dependence of the magnetic susceptibility data is indicative of a high-spin compound with an important zero-field splitting. The best fit was obtained with $|D| = 20.5\ cm^{-1}$ and $g = 2.53$ for **1**, $|D| = 14.2\ cm^{-1}$ and $g = 2.38$ for **2** and $|D| = 17.7\ cm^{-1}$ and $g = 2.35$ for **3**. The X-band EPR spectra at low temperature is also characteristic of an $S = 3/2$ state with important zero-field splitting. The most important band appears at low fields (ca. 1200 G).
(© Wiley-VCH Verlag GmbH & Co. KGaA, 69451 Weinheim, Germany, 2005)

Introduction

There has been a growing interest in the development of coordination chemistry of nonmacrocyclic multidentate ligands derived from pyridine-2,6-dicarboxylic acid (I).[1,2] The symmetrical tertiary amide side arms at the 2- and 6-positions of the central pyridine ring provide a variety of novel *ONO*-tridentate receptors for binding to metal ions (II).[2] The inflexibility of the ligand in these systems has been one of the important factors leading to the isolation of low-symmetry five-coordinate complexes of Cu^{II}, Co^{II}, Ni^{II}[3–6] and nine-coordinate complexes of lanthanide ions.[2] Steric and electronic consequences brought by peripheral substitutions to the terminal carboxamide side arms have been well illustrated by Piguet et al.[2] on the complexation of Ln^{III} ions. Recently, we have extended these studies to ligands containing C=S instead of C=O bonds on the side arms at the 2- and 6-positions, i.e., ligands containing an *SNS* set of donor atoms (III).[7,8] Deviations from idealized geometries would be naturally expected because of the bulky alkyl groups on the nitrogen atoms and may cause structural constraints. *N*,*N*,*N*′,*N*′-Tetraethylpyridine-2,6-dithiocarboxamide [R^1, R^2 = Et in (III); *S*-dept] coordinates through the planar *SNS* set of donor atoms. Our recent studies on (*S*-dept)$_2MCl_2$ (M = Co and Cu) complexes have revealed significant structural differences between the two complexes.[7,8] The copper complex is composed of cationic and anionic dimers: $[Cu_2Cl_2(\mu$-*S*-dept$)_2][Cu_2Cl_4(\mu$-Cl$)_2]$. The cationic fragment exhibits an unusual Cu–Cu disposition taking place through bridging sulfur atoms, observed only in a few Cu^{II} complexes.[8] The coordination geometry around each Cu center is approximately distorted square-pyramidal. On the other hand, the cobalt complex[7] is built up of [Co(*S*-dept)(Cl)]$^+$ and $[Co_2Cl_4(\mu\text{-}Cl)_2]^{2-}$ ions. The cobalt ion in the cation has a distorted square-planar geometry. The cationic units are stacked over each other in a staggered manner so that each cobalt ion interacts weakly with a sulfur atom of a unit above and below it.

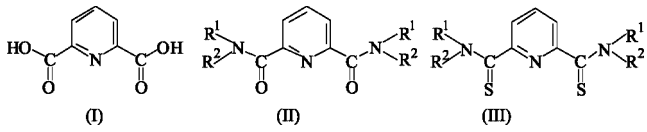

Spectrophotometric, magnetic and electrical conductivity measurements had been reported for a large number of five-coordinate complexes of cobalt(II).[9–27] In most cases, the magnetic moment was only measured at room temperature, in order to determine the spin-sate of the system [high-spin ($S = 3/2$) or low-spin ($S = 1/2$)]. For some compounds the

[a] Department of Chemistry, Panjab University, Chandigarh 160014, India
[b] Department of Chemistry, Guru Nanak Dev University, Amritsar 143005, India
[c] Departament de Química Inorgànica, Facultat de Química, Universitat de Barcelona, 08028 Barcelona, Spain

 © 2005 Wiley-VCH Verlag GmbH & Co. KGaA, Weinheim **DOI: 10.1002/ejic.200500318**

magnetic measurements at different temperatures were reported but not the X-ray crystal structure.[20,21] In other cases, the X-ray crystal structure was reported, but not the study of $\chi_M = f(T)$.[9–13,24,25,27,28]

To the best of our knowledge, very few high-spin five-coordinate Co^{II} complexes are structurally and magnetically characterized. Some of them are polynuclear systems[29–32] and their magnetic properties are due to the interaction between the Co^{II} ions. Only 3 mononuclear complexes are reported in the literature with the structural data and magnetic study (χ vs. T): [Co{(*t*Bu)(Me)salmdptn}],[22] [Co(saloph)(2-MeImd)][23] and $[Co(L^5)_2(H_2O)]$[26] with HL^5 = *N*-(2-chloro-6-methylphenyl)pyridine-2-carboxamide.

In this paper, we describe the crystal structure and magnetic properties of [Co(*S*-dept)X_2] (X = Br, I and NCS) compounds. The present work is aimed to determine the steric influence of the *SNS* set of donor atoms of *S*-dept on the geometry of the complexes. Our studies have revealed significant structural differences between [Co(*S*-dept)-$(NCS)_2$] and its nickel analogue.[33]

Five-coordinated mononuclear Co^{II} (d^7) complexes can be high-spin (S = 3/2), low-spin (S = 1/2) or a temperature-induced spin-transition can be observed. For high-spin Co^{II} complexes the study of the magnetic properties allows to find the value of the zero-field splitting parameters. In this work, we report the temperature dependence of the magnetic susceptibility and the fit of the experimental data allows finding the parameters of the zero-field splitting. The EPR spectra in frozen solution is also reported.

Results and Discussion

These complexes are obtained in good yield by mixing equimolar amounts of *S*-dept and the appropriate salt in anhydrous EtOH. The compounds are air- and moisture-stable and are readily soluble in the common organic solvents such as $CHCl_3$, CH_2Cl_2, and 1,2-dichloroethane. The tridentate nature of the ligand and the fact that the complexes are practically undissociated in chloroform and dichloromethane solutions suggest penta-coordination around the metal ion in these solvents. In CH_3CN and DMF solutions, the iodo complex **2** shows significant dissociation and molar conductivities are in the range typical of 1:1 electrolytes.[35] The complex most probably ionizes to give $[Co(S\text{-dept})I]^+_{solv}$ and I^- in these solutions. The conductivity data clearly show that the dissociation is less extensive for the bromo and thiocyanato complexes and molar conductivities are significantly less than the values expected for 1:1 electrolytes.

The expected positive shifts in position and changes in intensity of the principal IR bands of the pyridine ring are interpreted in favour of the coordination of *S*-dept through the pyridine ring nitrogen atom[36] in the complexes. Bands at 1263, 990, and 818 cm^{-1} may be considered as having significant contribution from C=S vibrations, based on comparison of the spectra of *O*-deap and *S*-dept. These bands show a slight downward shift in frequency in these complexes indicating coordination of the sulfur atoms. The presence of a band at 2062 cm^{-1} in **3** is consistent with *N*-bonded terminal thiocyanato groups.[37] The corresponding ν(CS) modes are obscured by ligand vibrations.[38,39]

The close similarity between the crystal-field spectra of the solid compounds (Br and NCS derivatives) and of their solutions in $CHCl_3$ indicates that these compounds retain the same structure (see Table 4). Compounds **1**, **2**, and **3** each show four distinct bands which are consistent with five-coordinate high-spin cobalt(II) complexes.[14–16] The spectra can be correlated with those of the complexes Co(MABenNEt_2)Cl_2,[17] Co(Et_4dien)X_2 (X = Cl, Br, I, N_3, and NCS),[15] Co(Me_5dien)Cl_2[18,19] and Co(Et_4dien)Cl_2.[11] The complexes **1**–**3** show a common band at ca. 625 nm which is assigned to the $^4A_{2'}(F) \rightarrow {}^4A_{2'}(P)$ transition. This band is characteristic of five-coordinate complexes irrespective of the nature of the donor atoms and the true geometry of the complex.[16] Their electronic spectra also show solvent dependence. In DMF solutions, the spectra are consistent with Co^{II} in an octahedral configuration, probably formed by coordination of DMF. In DMF solution, the iodo complex is, however, strongly conducting, probably one of the iodine atoms is dissociated to give [Co(*S*-dept)$(DMF)_2I]^+$ and free iodide ions. Complexes **1** and **3** are non-conducting in DMF and may be formulated as [Co(*S*-dept)(DMF)X_2] (X = Br and NCS).

Crystal Structures of [Co(S-dept)X_2] [X = Br (1), I (2), and NCS (3)]

The molecular structures and the atom labelling scheme of the complexes are shown in Figures 1, 2, and 3. Selected bond lengths and angles are listed in Table 1. The three complexes consist of monomeric molecules with a five-coordinate stereochemistry resulting from bonding to terdentate *S*-dept ligand and the other two positions are occupied by two X groups (Br, I or terminal *N*-bonded NCS). The geometry about the cobalt atom may be described either as square-pyramidal or trigonal-bipyramidal, depending on the parameter, $\tau = \beta - \alpha/60$ (β is defined as the larger of the basal angles and α is the remaining angle).[39] When τ is 0, the coordination is square-pyramidal; however for a trigonal-bipyramidal configuration τ is 1, and is often reported as a percent value. The τ values for **1** [β = N(1)–Co(1)–Br(2), 159.66(17)° and α = S(2)–Co(1)–S(1), 137.96(9)°], **2** [β = N(1)–Co(1)–I(2), 166.19(12)° and α = S(1)–Co(1)–S(2), 131.58(7)°], and **3** [β = N(5)–Co(1)–N(1), 164.27(18)° and α = S(1)–Co(1)–S(2), 138.76(6)°] are 36.2, 57.7, and 42.5%, respectively. Complexes **1**–**3** may be considered as distorted square-pyramidal. The anions differ in the angles with the metal atom which destroys the two-fold rotational symmetry of the molecules. The torsion angles between the pyridine ring (C1,C2,C3,C4,C5 and N1) and the thioamide planes (C1,C6,S1,N2 and C5,C11,S2,N3) are: 45.4(1) and 35.9(1) for **1**, 38.8(1) and 35.9(1) for **2**, and 38.8(1) and 52.1(1) for **3**. There appears to be no correlation between the angle of rotation of thioamide groups and the pyridine

 © 2005 Wiley-VCH Verlag GmbH & Co. KGaA, Weinheim

ring. However, the conformation of the ligand seems to be dependent on the size of the anion. The conformation of iodide and thiocyanate complexes are almost identical with methyl carbon atoms C13 and C15 being on the same side of the amide group, whereas C8 and C10 are on opposite sides of the plane. In the case of the bromide complex the methyl groups C8 and C10 as well as C13 and C15 are on the opposite sides with respect to the thioamide plane.

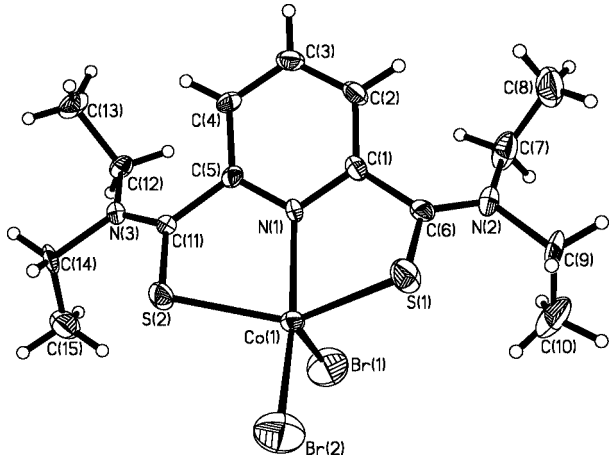

Figure 1. Perspective view of complex **1** with atom numbering scheme (thermal ellipsoids at 50% probability level).

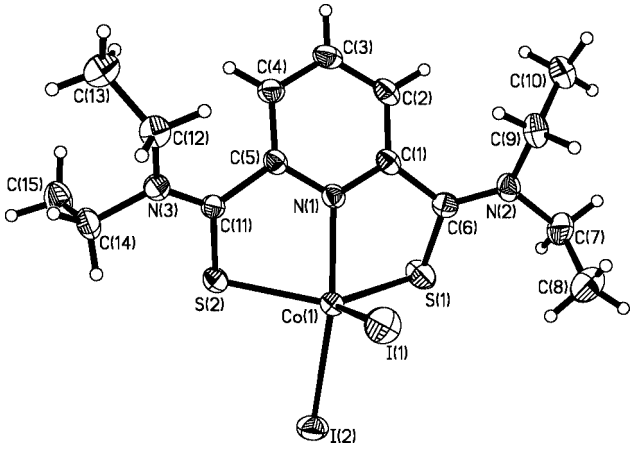

Figure 2. Perspective view of complex **2** with atom numbering scheme (thermal ellipsoids at 50% probability level).

In the structure of **1** the bromine atom Br(1) occupies the apical position and sulfur atoms S(1), S(2), pyridine N(1) and Br(2) form the base of the pyramid. The mean plane through these atoms indicates that the atoms are 0.205, 0.203, –0.238, and –0.170 Å, respectively, above and below the mean plane. The Co ion is –0.607 Å below the mean plane defined by these four atoms. Similarly, in the structure of **2** the iodine atom I(1) occupies the apical position and sulfur atoms S(1), S(2), pyridine N(1) and I(2) form the base of the pyramid. The mean plane through these atoms indicates that the atoms are 0.307, 0.328, –0.396, and –0.239 Å, respectively, above and below the mean plane. The Co ion is –0.599 Å below the mean plane defined by these four atoms.

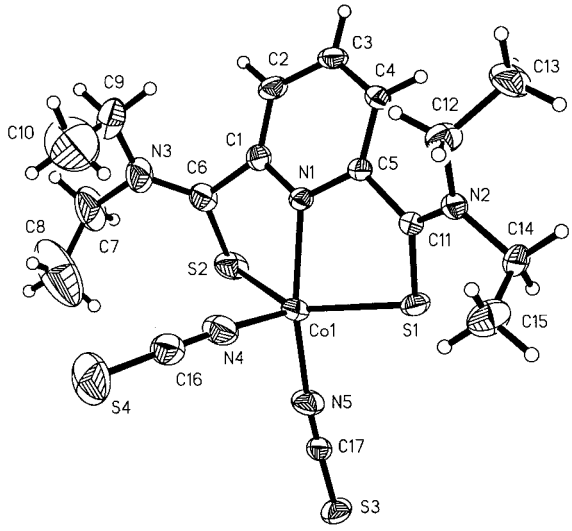

Figure 3. Perspective view of complex **3** with atom numbering scheme (thermal ellipsoids at 50% probability level).

Table 1. Selected bond lengths [Å] and angles [°] for complexes **1**–**3**.

Complex **1**			
Br(1)–Co(1)	2.3985(15)	Br(2)–Co(1)	2.4121(15)
Co(1)–N(1)	2.150(6)	Co(1)–S(2)	2.365(2)
Co(1)–S(1)	2.368(2)	S(1)–C(6)	1.708(8)
S(2)–C(11)	1.696(7)		
N(1)–Co(1)–S(2)	80.14(15)	N(1)–Co(1)–S(1)	81.06(15)
S(2)–Co(1)–S(1)	137.96(9)	N(1)–Co(1)–Br(1)	91.73(16)
S(2)–Co(1)–Br(1)	109.03(7)	S(1)–Co(1)–Br(1)	108.79(8)
N(1)–Co(1)–Br(2)	159.66(17)	S(2)–Co(1)–Br(2)	93.91(6)
S(1)–Co(1)–Br(1)	90.94(7)	Br(1)–Co(1)–Br(2)	108.58(5)
C(6)–S(1)–Co(1)	94.9(2)		
Complex **2**			
I(1)–Co(1)	2.6156(9)	I(2)–Co(1)	2.7065(9)
Co(1)–N(1)	2.137(5)	Co(1)–S(1)	2.3574(18)
Co(1)–S(2)	2.3799(17)	S(1)–C(6)	1.714(6)
S(2)–C(11)	1.709(6)		
N(1)–Co(1)–S(1)	80.17(13)	N(1)–Co(1)–S(2)	79.99(12)
S(1)–Co(1)–S(2)	131.58(7)	N(1)–Co(1)–I(1)	89.55(12)
S(1)–Co(1)–I(1)	107.42(6)	S(2)–Co(1)–I(1)	116.11(5)
N(1)–Co(1)–I(2)	166.19(12)	S(1)–Co(1)–I(2)	98.69(5)
S(2)–Co(1)–I(2)	90.87(4)	I(1)–Co(1)–I(2)	103.83(3)
C(6)–S(1)–Co(1)	95.61(19)	C(11)–S(2)–Co(1)	96.37(19)
Complex **3**			
Co(1)–S(2)	2.3979(16)	Co(1)–S(1)	2.3777(15)
N(4)–Co(1)	1.964(5)	N(5)–Co(1)	2.003(5)
N(1)–Co(1)	2.134(4)	C(17)–S(3)	1.612(5)
C(17)–N(5)	1.147(6)	C(16)–S(4)	1.609(7)
C(16)–N(4)	1.149(7)	C(6)–S(2)	1.682(6)
C(11)–S(1)	1.698(4)		
N(4)–Co(1)–N(5)	102.1(2)	N(4)–Co(1)–N(1)	93.57(18)
N(5)–Co(1)–N(1)	164.27(18)	N(4)–Co(1)–S(1)	114.34(17)
N(5)–Co(1)–S(1)	94.34(14)	N(1)–Co(1)–S(1)	80.03(10)
N(4)–Co(1)–S(2)	103.34(17)	N(5)–Co(1)–S(2)	93.56(15)
N(1)–Co(1)–S(2)	81.56(10)	S(1)–Co(1)–S(2)	138.76(6)
C(11)–S(1)–Co(1)	98.48(16)	C(6)–S(2)–Co(1)	91.50(18)

 © 2005 Wiley-VCH Verlag GmbH & Co. KGaA, Weinheim

The isothiocyanate nitrogen atom N(4) occupies the apical position and sulfur atoms S(1) and S(2), pyridine N(1) and thiocyanate N(5) form the base of the pyramid. The mean plane through N(1), N(5), S(1), S(2) indicates that these atoms are 0.39, 0.52, –0.05, –0.08 Å, respectively, above and below the mean plane. The Co ion is 0.74 Å above the mean plane defined by these four atoms. It is interesting that the Co–NCS linkages in **3** are bent with Co–N(5)–C(17) and Co–N(4)–C(16) angles of 171.0(5) and 167.0(6), respectively. It has been observed by others[40,41] that this linkage may be either linear or angular, with examples of M–N–C angles falling in the range 141–174°. The non-linearity of this type may be attributed to steric factors.[21] It also suggests electron density localisation on the donor nitrogen atom such that a canonical form **I** contributes to the structure.[40,42]

Co

I

It has been known that interactions of cobalt and nickel thiocyanates with terdentate ligands provide complexes of different stereochemistry.[35,43] Our present results provide ample evidence that cobalt has a greater tendency than nickel to give monomeric five-coordinate complexes rather than octahedral complexes.

Extended Hückel Calculations

The compounds reported here show a $CoNS_2X_2$ core, with significant differences in the Co–ligand distances. Compound **3** shows a CoN_3S_2 core, with three short Co–N distances (ca. 2.1 Å) and two long Co–S (ca. 2.4 Å) (*x*-axis) distances (see Scheme 1). Compound **1**, with a $CoNBr_2S_2$ core, has one short Co–N (ca. 2.1) and four long Co–S and Co–Br (ca. 2.4 Å) (*yz*-plane) distances. Finally, for compound **2** with a $CoNI_2S_2$ core, we observe one short Co–N (ca. 2.1 Å), two long Co–S (ca. 2.4 Å) (*x*-axis), and two very long Co–I distances with values in the range ca. 2.6–2.7 Å. Then, from the point of view of bond lengths, compound **3** shows a more regular core, with short Co–L distances, while compound **2** shows the most irregular core, with long Co–L distances.

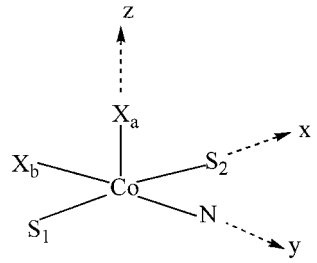

Scheme 1.

Extended Hückel calculations with the crystallographic coordinates of compounds **1**–**3** were carried out with the CACAO program.[44] Due to the absence of symmetry in these complexes a full split of the five d orbitals is obtained and a great delocalisation towards the ligands is observed in all cases. There are at least nine MOs with a cobalt contribution >15%.

High-spin Co^{II} compounds show three singly occupied molecular orbitals (SOMOs). The highest energy SOMO shows a significant contribution of the $x^2 - y^2$ orbital of the cobalt ion and has a σ*-character with the ligands in the basal plane (S_1, N, S_2, and X_b), while the next SOMO is constituted essentially by the z^2 of the cobalt ion and the p orbital of the monodentate ligand in apical position (X_a) (or the non-bonding π_{nb} orbital of the NCS ligand). The lowest energy SOMO shows a significant contribution of the *xz* orbital of the Co^{II} ion and of the p orbitals of S_1 and S_2. In the iodide complex (and in minor proportion in

Table 2. Energy and composition[a] of the three SOMOs for compounds **1**–**3**.

	Energy	% Co	% N	% S1	% S2	Xb	Xa
Compound **1**							
σb*	–10.258	33 (x^2–y^2); 3 (z^2); 3 (*yz*)	15	6	6	14	–
σa*	–11.572	41 (z^2); 6 (*pz*)	2	–	4	–	22
π*	–11.775	28 (*xz*); 8 (*xy*); 4 (*px*)	–	17	19	2	6
Compound **2**							
σb*	–10.430	32 (x^2–y^2); 5 (z^2)	18	4	5	17	2
σa*	–11.646	32 (z^2); 5 (x^2–y^2); 5 (*pz*)	–	8	4	2	26
π*	–11.783	27 (*xz*); 7 (*xy*); 4 (*px*)	–	17	16	3	11
Compound **3**							
σb*	–10.243	38 (x^2–y^2); 7 (z^2)	17	6	5	6	–
σa*	–11.690	46 (z^2); 5 (x^2–y^2); 6 (*pz*)	–	6	7	–	8
π*	–11.878	24 (*xz*); 6 (*xy*); 2 (z^2); 3 (*px*)	–	17	23	–	–

[a] See Scheme 1.

 © 2005 Wiley-VCH Verlag GmbH & Co. KGaA, Weinheim

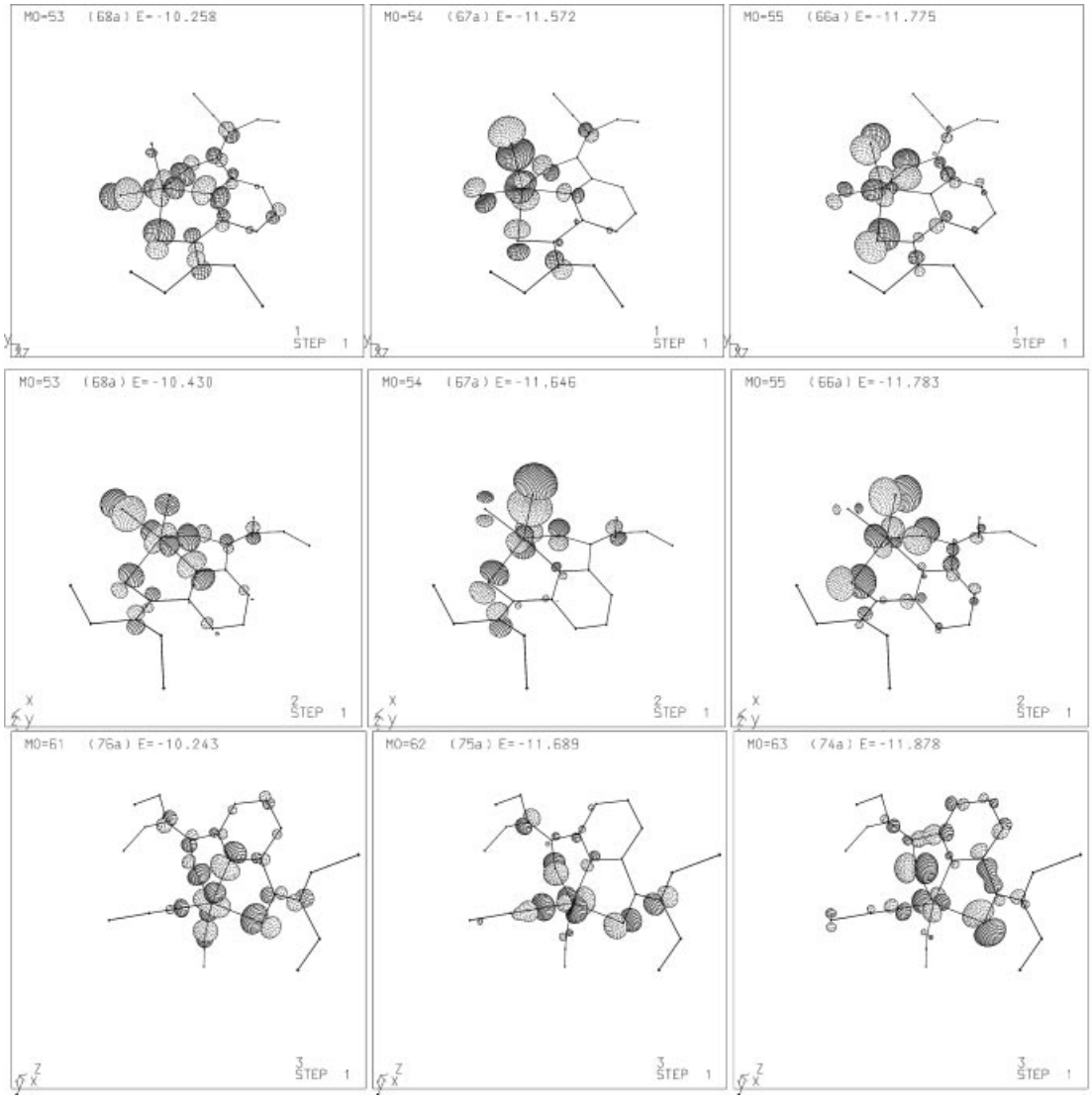

Figure 4. SOMOs for compound **1** (top), **2** (centre), and **3** (bottom).

the bromide complex) a considerable contribution of the apical ligand is also observed (Table 2, Figure 4).

Due to the distortions in the geometry, the *xz*, *yz*, and *xy* orbitals of the Co^{II} ions contribute to several MOs. However, these results confirm the description of the structure of these compounds as a distorted square pyramid. The energy of σ_a* is similar for the three compounds, while σ_b* is more stabilized for compound **2**, which shows a major distortion to the trigonal-bipyramidal geometry, than for **1** and **3** (Figure 5).

One of the limitations of the extended Hückel calculations is the non-inclusion of the inter-electronic repulsions; nevertheless, from a qualitative point of view, we can consider for each compound, a similar pairing energy in each orbital, and from the energy diagram shown in Figure 5, we can find an approximate value for the relative energies of the different excited states (E1–E6). From these results, we can propose, for the three compounds, the presence of several excited states close in energy to the ground state (ca. 5000 cm^{-1}, E1–E3 and E4) (Table 3). These states would

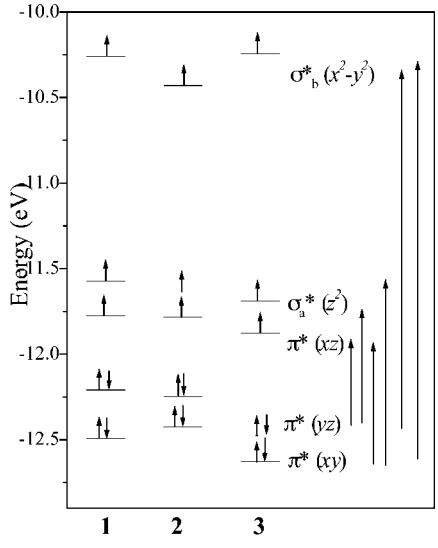

Figure 5. MO energy diagram for compounds **1**–**3**.

 © 2005 Wiley-VCH Verlag GmbH & Co. KGaA, Weinheim

correspond to the different transitions $\pi^* \rightarrow \pi^*$ and $\pi^* \rightarrow \sigma a^*$ (z^2), and the transition $\pi^* \rightarrow \sigma b^*$ ($x^2 - y^2$) should appear at higher energy (ca. 16000 cm^{-1}).

Table 3. Relative Energy [10^{-3} cm^{-1}] of the different excited states proposed for compounds **1**–**3**.

		1	**2**	**3**
$(xy)(yz)^2(xz)(z^2)(x^2–y^2)^2$	E6	17.6	15.8	19.0
$(xy)^2(yz)(xz)(z^2)(x^2–y^2)^2$	E5	15.6	14.6	16.8
$(xy)(yz)^2(xz)(z^2)^2(x^2–y^2)$	E4	7.1	6.1	7.4
$(xy)(yz)^2(xz)^2(z^2)(x^2-y^2)$	E3	5.5	5.0	5.9
$(xy)^2(yz)(xz)(z^2)^2(x^2–y^2)$	E2	5.1	4.8	5.2
$(xy)^2(yz)(xz)^2(z^2)(x^2–y^2)$	E1	3.5	3.7	3.7
$(xy)^2(yz)^2(xz)(z^2)(x^2–y^2)$	E0	0	0	0

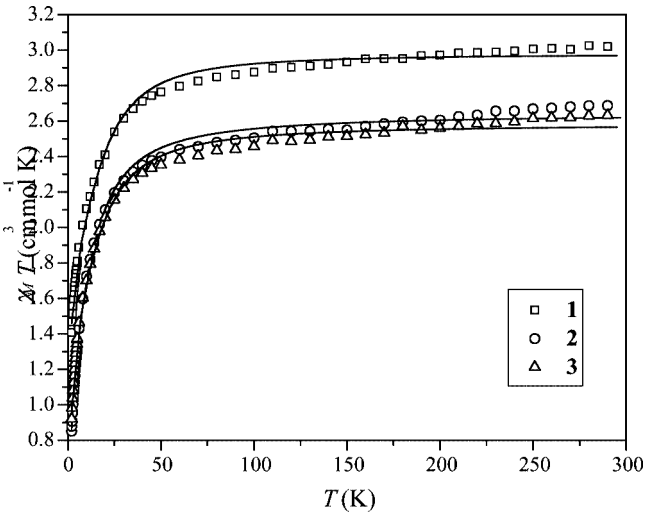

Figure 6. $\chi_M T$ vs. T plot for **1**–**3**. The solid line is the best fit to the experimental data.

Magnetic Properties

The magnetic susceptibility of **1**–**3** was measured in the range 2–300 K (Figure 6). In all cases, the $\chi_M T$ product decreases with the temperature. The shape of the three graphs is similar, but for compound **1**, we found higher $\chi_M T$ values. The room-temperature values of $\chi_M T$ = 3.03 cm^3 mol^{-1} K (for **1**) and 2.7 cm^3 mol^{-1} K (for **2** and **3**) differ from the spin-only value $\chi_M T$ = 1.87 cm^3 mol^{-1} K for S = 3/2 (high-spin Co^{II} complexes) which indicates an orbital contribution to the g-values. On lowering the temperature, $\chi_M T$ decreases, and under 50 K $\chi_M T$ falls drastically. The shape of the $\chi_M T$ vs. T graph is indicative of an important zero-field splitting. Owing to spin-orbit coupling, the S = 3/2 state is split into two Kramer's doublets ($M_s = \pm 1/2, \pm 3/2$), separated by 2D, with D being the axial zero-field splitting parameter. Formally, the magnetic behaviour can be treated as an S = 3/2 spin state under the action of the spin Hamiltonian $H = D[S_z^2 - S(S + 1)/3] + g_{\parallel}\beta Hz S_z + g_{\perp}\beta(H_x S_x + H_y S_y)$. The expression of the magnetic susceptibilities χ_M [with $\chi_M = (\chi_{\parallel} + 2\chi_{\perp})/3$] is derived from this Hamiltonian.[45] With the aim to fit the low-temperature values, it was necessary to modify the equation, including the term of the intermolecular magnetic interactions zJ, where J is the interaction parameter between two nearest neighbour magnetic species and z is the number of nearest neighbours around a given magnetic molecule in the crystal lattice. Then the equation used to fit the experimental data is

$$\chi_M T = \frac{TNg^2\beta^2 F(D,T)}{3kT - zJ \cdot F(D,T)}$$

where

$$F(D,T) = \frac{1}{4}\left[\frac{1+9\exp(-2D/kT)}{1+\exp(-2D/kT)}\right] + 2kT\left(\frac{(\frac{1}{kT}) + \frac{3}{4D} - \frac{3}{4D}\exp(-2D/kT)}{1+\exp(-2D/kT)}\right)$$

The best fits were obtained with $|D|$ = 20.5 cm^{-1}, g = 2.53, zJ = –0.50 cm^{-1} and $R = 1.8 \cdot 10^{-4}$ (**1**); $|D|$ = 14.2 cm^{-1}, g = 2.38, zJ = –1.67 cm^{-1} and R = 2.7 10^{-4} (**2**); $|D|$ = 17.7 cm^{-1}, g = 2.35, zJ = –1.23 cm^{-1} and R = 2.9 10^{-4} (**3**). As it can be seen in Figure 6, compounds **2** and **3** show similar $\chi_M T$ values, while compound **1** shows at room temperature a higher $\chi_M T$ value, indicative of a large g value. The best fit of the experimental data also corresponds to a largeer D value for **1** than for **2** or **3**.

As it has been indicated, very few high-spin five-coordinate Co^{II} complexes are structurally and magnetically characterized. Only three mononuclear complexes are reported in the literature with the structural data and magnetic study (χ vs. T): [Co{(*t*Bu)(Me)salmdptn}] (with D = –38.9 cm^{-1}, E = 1.7 cm^{-1}, g_x = 1.68, g_y = 1.89, g_z = 3.21 and zJ = –1.0 cm^{-1}),[22] [Co(saloph)(2-MeImd)] (with $|D|$ = 22.6 cm^{-1}, g = 2.14),[23] and [Co(L^5)$_2$(H_2O)] with HL^5 = *N*-(2-chloro-6-methylphenyl)pyridine-2-carboxamide (Curie–Weiss law between 80–300 K).[26] The study of the magnetic properties of [Co(Salpad)$_2$(t-MeStpy)] (D = 16.57 cm^{-1}, g = 2.39),[20] [Co(H_2fsa)$_2$(phn)(t-MeStpy)] (spin equilibrium),[20] and [Co(bzimpy)Cl_2] (D = 73.4 cm^{-1}, E = 3.28 cm^{-1}, zJ = –0.205 cm^{-1})[21] are also reported in the literature, but to the best of our knowledge, the crystal structure of these compounds is not published.

In spite of the limited number of mononuclear Co^{II} compounds with five-coordination which have been structurally and magnetically characterized, two facts could be discussed: the stabilization of the spin state S = 3/2 and the magnitude of the zero-field splitting.

Cobalt(II) complexes with Schiff-base ligands could be high-spin or low-spin. In a comparative study of five-coordinate Co^{II} complexes of the types [Co(salen)L] and [Co(saloph)L] reported by Kennedy et al.,[23] the authors note an increase of the out-of-plane displacement of the Co^{II} ion from ca. 0 Å for low-spin complexes to ca. 0.45 Å for the high-spin compounds [Co(saloph)(2-MeImd)] (0.45 Å)[23] and [Co(3-MeOsalen)(H_2O)] (0.43 Å).[28] The three compounds reported in this paper show a high-spin configuration and all of them show an important out-of-plane displacement of the Co^{II} ion of ca. 0.6–0.74 Å. The high value

 © 2005 Wiley-VCH Verlag GmbH & Co. KGaA, Weinheim

Table 4. Comparison of the ZFS parameters and distortions for high-spin five-coordinate Co^{II} complexes.

	Core	$\|D\|$ [cm^{-1}]	g	$-zJ$ [cm^{-1}]	τ[b]	Ref.
[Co(S-dept)Br_2]	$CoNS_2Br_2$	20.5	2.53	0.5	0.36	[c]
[Co(S-dept)I_2]	$CoNS_2I_2$	14.2	2.38	1.67	0.58	[c]
[Co(S-dept)$(NCS)_2$]	$CoNN'_2S_2$	17.7	2.35	1.23	0.43	[c]
[Co(*t*Bu)(Me)(salmdptn)]	CoO_2N_2N'	38.9	2.26[a]	1.0	0.64	[22]
[Co(saloph)(2-MeImd)]	CoO_2N_2N'	22.6	2.14		0.19	[23]

[a] $g = (gx + gy + gz)/3$. [b] $\tau = 1$: trigonal-bipyramid; $\tau = 0$: square pyramid.[38] [c] This work.

of this displacement could be attributed to the different nature of the ligands in the basal plane: N_2O_2 for salen and saloph and NS_2X for compounds **1**–**3**. The presence of a voluminous donor-atom ligand favors the distortion and stabilize the $S = 3/2$ state.

In the same way, Hitchaman showed[46] that increasing distortions from a square-pyramidal geometry could lead to a rapid decrease in the quartet-state energy, especially when $\beta > 102°$ ($\beta = L_{ax}$–Co–N angle). For the three compounds reported in this paper, the largest β angle is found for the iodo complex **2** with $\beta = 107°$ (major distortion to the trigonal-bipyramidal geometry); for **1** and **3** the β angle is slightly more than 90° (91.7° and 93.6°, respectively).

In comparison with the Schiff-base complexes, compounds **1**–**3** show a major distortion in the geometry: the presence of the *S*-dept ligand, with its sulfur atom coordinated to the Co^{II} ion favors the out-of-plane displacement of the metal center. Due to the tridentate character of the *S*-dept ligand, the fourth position of the basal plane is occupied by a monodentate ligand, consequently a major flexibility of the geometry could be attended. The most voluminous monodentate ligand, iodide, leads to a major distortion from the square-pyramidal to the trigonal-bipyramidal geometry. Therefore, in the reported compounds [Co(S-dept)X_2] (**1**–**3**) both ligands, *S*-dept and X, favor the stabilization of the $S = 3/2$ state in preference to the $S = 1/2$ state.

For systems with an $S = 3/2$ state, the magnetic anisotropy due to the non-spherical distribution of the spin density is enhanced by the low symmetry of the five-coordinate chromophore. The D values found for compounds **1**–**3** are of the same order as reported for other five-coordinate Co^{II} complexes with $S = 3/2$. Attempts to correlate the zero-field splitting parameter (D) with the structural distortions are hard, due to the limited number of compounds of this kind reported in the literature. Compounds **1**–**3** show quite smaller D and g values than [Co{(*t*Bu)(Me)salmdptn}][22] and [Co(saloph)(2-MeImd)][23] (Table 4).

It is difficult to interpret the differences in the zero-field splitting parameters for five-coordinate Co^{II} complexes. The magnitude of D and g values is influenced by the second-order spin-orbit coupling, λ and $1/\Delta_i$, where λ is the spin-orbit coupling constant and Δ_i the energy gap between ground state and excited states. The expression of the axial ZFS parameter $D = f(\lambda, 1/\Delta_i)$ for different ions and geometries could be found in a recent review about the zero-field splitting in metal complexes.[47] For Co^{II} ions, the equation for the d^7 ion in a tetrahedral environment is also described in this paper, but not for a five-coordinate complex.

For a free Co^{II} ion $\lambda = -180$ cm^{-1}. But this parameter is sensitive to the covalence of the bond. Compounds **1**–**3** with the *S*-dept ligand must show a greater degree of covalence than the compounds with Schiff-base ligands. Thus, a lower $|\lambda|$ value must be expected for compounds **1**–**3**. Complex **2** with iodide as monodentate ligand, should show a maximum covalence in the Co–X bonds, and consequently the small $|\lambda|$ value must correspond to this compound.

On the other hand, the D value is sensitive to the proximity of excited states with orbital contribution. Several factors influence the energy gaps, Δ_i, such as the bond covalence, the kind of donor atom and the distortions in geometry. In spite of the limitations of the extended Hückel calculations, the presence of several excited states at low energy could be attended. However, the inter-electronic repulsion must be different for the three complexes, due to the presence of different X ligands (Br, I, NCS), and it is not precise to compare the energy values of the excited states postulated in Table 3. The presence of excited states at low energy contributes to the D value, but it is not possible to rationalize their effect.

Compounds formed by voluminous donor ligands such as *S*-dept or iodide, could contribute to diminish the zero-field splitting (small $|D|$ values). Compounds **1**–**3** show lower values than the compounds with Schiff-base ligands.[22,23] Therefore, complex **2** containing S-dept and iodide exhibits the lowest $|D|$ value.

On the other hand, it is difficult to correlate the distortion of the coordination polyhedron with the zero-field splitting parameter. For the two complexes with Schiff-base ligands the compound with major distortion from the square-pyramidal geometry (larger τ) show a larger D value, while for the three complexes reported here with the *S*-dept ligand, the maximum τ value corresponds to compound **2**, with the lowest value of the zero-field splitting parameter.

EPR Spectra

The EPR spectra of powdered samples and of frozen CH_2Cl_2 solution of **1**–**3** were recorded at different temperatures. Only below 100 K was the EPR signal significant, due to the relaxation effects.

The EPR spectra of powdered samples show in all cases a very broad band, with a better resolution at 4 K. The most intense features were found at low field, in the region of 2000 G. In frozen solution the three compounds show very similar spectra (Figure 7) with the most intense feature

 © 2005 Wiley-VCH Verlag GmbH & Co. KGaA, Weinheim

at ca. 1200 G ($g \approx 5.5$). The position of this band is similar for the three compounds (1150 G for **1**, 1250 G for **2**, and 1180 G for **3**). Another small feature was observed at 2760 G. The low-field signal can be attributed to $g_{\perp}$ and the small signal centred at ca. 2800 G to $g_{\|}$. These spectra are characteristic of a high-spin Co^{II} complex, with S = 3/2 and a large zero-field splitting ($D > g\beta H$), as occurs in compounds **1**–**3** whose $|D|$ values are between 14–21 cm^{-1}.

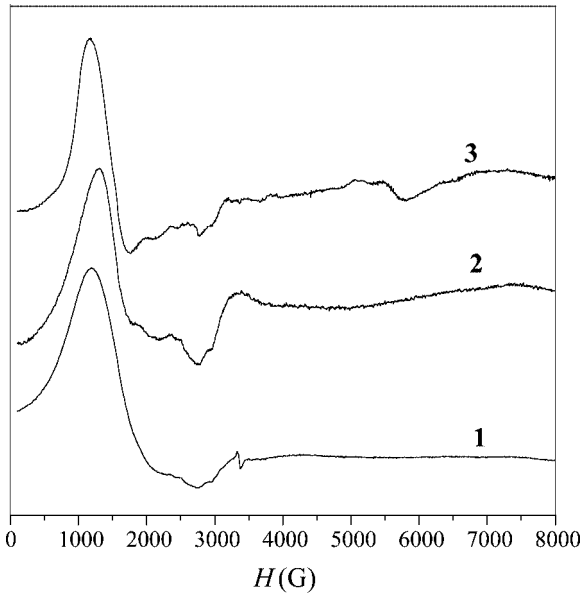

Figure 7. X-band EPR spectra of frozen CH_2Cl_2 solutions of complexes **1**–**3**.

Conclusions

In this work we have reported the synthesis and characterization of three new five-coordinate Co^{II} complexes. In all cases, the coordination polyhedron of the Co^{II} ion is a distorted square pyramid, with an electronic configuration of high-spin. Although there is no correlation between the angle of rotation of thioamide groups and the pyridine ring, the conformation of the ligand is dependent on the size of the anion. The compounds show major distortion in the geometry with a large out-of-plane displacement of the Co^{II} ion of ca. 0.6–0.74 Å. The distortion of the geometry, due to the *S*-dept ligand with voluminous donor atoms, could explain the stabilization of the S = 3/2 state than the S = 1/2 state.

Important zero-filed splitting is observed, as it could be expected for high-spin Co^{II} compounds. The D value seems to be very sensitive to the nature of the ligand. The compounds reported in the literature, with a CoO_2N_2 core show larger $|D|$ values than compounds **1**–**3**, with a $CoNS_2X_2$ core. The smallest value corresponds to compound **2** containing more diffuse donor atoms ($CoNS_2I_2$ core) with maximum covalence of the Co–L bonds.

The EPR spectra at low temperature show two bands, at low fields, characteristic of systems with an S = 3/2 ground state and an important zero-field splitting, as is the case for Co^{II} compounds.

Experimental Section

Materials: All reactions were carried out under anhydrous conditions. Solvents were dried using standard techniques. Absolute ethanol (AR quality, Hayman Ltd.) and pyridine-2,6-dicarboxylic acid (Fluka) were used as supplied. *N*,*N*,*N*′,*N*′-Tetraethylpyridine-2,6-dithiocarboxamide was prepared as described earlier.[7,8]

Synthesis of the Complexes [Co(S-dept)X_2] [X = Br (1), I (2) and NCS (3)]: $CoCl_2$ (3 mmol), dissolved in anhydrous ethanol (20 mL), was added to a solution of KBr or KI or KSCN (each 6 mmol) in ethanol (20 mL). The mixture was refluxed for about 4 h. The white precipitate of KCl was removed by filtration and *S*-dept (3 mmol), dissolved in ethanol (20 mL), was added to the solution. After refluxing for about 4–5 h, **1**, **2** and **3** were obtained as dark green solids on keeping at room temperature. The complexes were crystallized from anhydrous ethanol by slow concentration at room temperature. **1:** Yield 1.36 g (86%). M.p. 210 °C. $C_{15}H_{23}Br_2CoN_3S_2$ (528): calcd. C 34.09, H 4.35, Br 30.3, N 7.95; found C 33.92, H 4.12, Br 29.8, N 8.10. Conductivity (ca. 1 mM solution at 298 K): Λ_M = 32 (MeCN) and 24 (DMF) Ω^{-1} cm^2·mol^{-1} (expected range for 1:1 electrolytes in MeCN and DMF is 120–160 and 65–90 Ω^{-1} cm^2·mol,$^{-1}$ respectively). UV/Vis [10^{-3} cm^{-1}]: λ = 19.8, 17.0, 13.7, 11.0 ($CHCl_3$); 15.7, 14.9 (DMF); 23.5, 16.6, 10.0, 5.9 (solid). Selected IR frequencies (KBr disk [cm^{-1}]): ν̃ = 1600, 1579, 1530, 1463, 1442, 1316, 1310, 1275, 1252, 1186, 1170, 1149, 1097, 1073, 1000, 978, 914, 809, 762, 746, 723, 682, 662, 648, 508, 488, 454. **2:** Yield, 1.79 g (87%). M.p. 242 °C. $C_{15}H_{23}CoI_2N_3S_2$ (622): calcd. C 28.93, H 3.69, I 40.8, N 6.75; found C 28.78, H 3.57, I 40.3, N 6.54. Conductivity (ca. 1 mM solution at 298 K): Λ_M = 95 (MeCN) and 67 (DMF) Ω^{-1} cm^2·mol^{-1}. UV/Vis [10^{-3} cm^{-1}]: λ = 17.4, 15.6, 13.6, 9.3 ($CHCl_3$); 19.0, 15.0 (DMF). Selected IR frequencies (KBr disk [cm^{-1}]): ν̃ = 1600, 1584, 1534, 1463, 1444, 1410, 1314, 1277, 1255, 1186, 1165, 1144, 1097, 1073, 1002, 980, 910, 806, 759, 746, 722, 680, 666, 632, 510, 486, 450. **3:** Yield 1.47 g (87%). M.p. 205 °C. $C_{17}H_{23}N_5S_4Co$ (484): calcd. C 42.14, H 4.75, N 14.46, S 26.4; found C 42.02, H 4.54, N 14.28, S 26.1. Conductivity (ca. 1 mM solution at 298 K): Λ_M = 30 (MeCN) and 25 (DMF) Ω^{-1} cm^2·mol^{-1}. UV/Vis [10^{-3} cm^{-1}]: 17.2, 15.6, 14.2 ($CHCl_3$); 17.2, 16.0 (DMF); 23.5, 17.1, 11.1, 5.9 (solid). Selected IR frequencies (KBr disk [cm^{-1}]): ν̃ = 2062, 1600, 1580, 1530, 1460, 1438, 1410, 1315, 1277, 1259, 1187, 1164, 1144, 1094, 1072, 1010, 980, 909, 812, 722, 668, 640, 562, 478, 456, 424.

Physical Methods: Elemental analyses (C,H,N) were carried out with a Perkin–Elmer model 2400 CHN elemental analyzer at the SAIF, Panjab University. Bromide and iodide anions were determined by precipitation as silver salts and sulfur by precipitation as $BaSO_4$. IR spectra were recorded as KBr pellets with a Perkin–Elmer RX-1 FTIR spectrophotometer. Molar conductances were measured using a Digital conductivity bridge, Model CC601.The UV/Vis spectra were recorded with a JASCO V-530 UV/Vis spectrophotometer in a 1-cm matched quartz cell. The diffuse reflectance spectra of powdered samples were recorded with a Hitachi Model 330 integrating sphere reflectance spectrophotometer in the 185–2600 nm region, using magnesium oxide as reference. Magnetic susceptibility measurements, for polycrystalline samples of **1**–**3**, were performed with a Quantum Design SQUID MPMS-XL susceptometer, working in the range 2–300 K under magnetic fields of 2000 G, at the "Servei de Magnetoquímica" (Universitat de Barcelona). Pascal's constants were used to estimate the diamagnetic

 © 2005 Wiley-VCH Verlag GmbH & Co. KGaA, Weinheim

Table 5. Crystal data and structure refinement parameters for complexes **1**–**3**.

	Complex **1**	Complex **2**	Complex **3**
Emperical formula	$C_{15}H_{23}Br_2CoN_3S_2$	$C_{15}H_{23}I_2CoN_3S_2$	$C_{17}H_{23}CoN_5S_4$
Formula mass	528.23	622.21	484.57
Temperature	293(2) K	293(2) K	293(2) K
Wavelength	0.71073 Å	0.71073 Å	0.70930 Å
Crystal system, space group	triclinic, $P\bar{1}$	monoclinic, $P2_1/c$	triclinic, $P\bar{1}$
Unit-cell dimensions	a = 8.434(1) Å, α = 91.40(1)°	a = 12.824(1) Å, α = 90°	a = 8.6220(9) Å, α = 88.277(6)°
	b = 10.330(1) Å, β = 108.58(1)°	b = 14.967(1) Å, β = 92.88(1)°	b = 11.4370(8) Å, β = 80.842(7)°
	c = 13.220(1) Å, γ = 113.56(1)°	c = 11.092(1) Å, γ = 90°	c = 12.1540(9) Å, γ = 81.312(7)°
Volume	985.34(17) Å^3	2126.3(3) Å^3	1169.63(17) Å^3
Z, calculated density	2, 1.780 Mg/m^3	4, 1.944 Mg/m^3	2, 1.376 Mg/m^3
Absorption coefficient	5.139 mm^{-1}	3.909 mm^{-1}	1.102 mm^{-1}
F(000)	526	1196	502
Crystal size	0.24 × 0.20 × 0.16 mm	0.28 × 0.24 × 0.19 mm	0.2 × 0.2 × 0.1 mm
θ range for data collection	2.18–23.99°	2.09–24.00°	1.69–24.96°
Scan type	2θ-θ	2θ-θ	2θ-θ
Scan speed	variable, 2.0–60.0°/min in ω	variable, 2.0–60.0°/min in ω	variable, 2.0–60.0°/min in ω
Limiting indices	$0 \le h \le 9$	$-14 \le h \le 14$	$0 \le h \le 10$
	$-11 \le k \le 10$	$0 \le k \le 17$	$-13 \le k \le 13$
	$-15 \le l \le 14$	$0 \le l \le 12$	$-14 \le l \le 14$
Reflections collected/unique	3270/3012 [R(int) = 0.0309]	3546/3342 [R(int) = 0.0190]	3602/3602 [R(int) = 0.0147]
Refinement method	Full-matrix least squares on F^2	Full-matrix least squares on F^2	Full-matrix least squares on F^2
Data/restraints/parameters	3012/0/208	3342/0/208	3602/0/244
Goodness-of-fit on F^2	1.012	1.012	1.053
Final R indices [$I > 2\sigma(I)$]	R_1 = 0.0747, wR_2 = 0.2200	R_1 = 0.0383, wR_2 = 0.1093	R_1 = 0.0535, wR_2 = 0.1422
R indices (all data)	R_1 = 0.0804, wR_2 = 0.2275	R_1 = 0.0420, wR_2 = 0.1127	R_1 = 0.0668, wR_2 = 0.1534
Largest difference peak/hole	2.051/–1.579 e·Å^3	0.930/–1.670 e·Å^{-3}	0.765/–0.363 e·Å^{-3}

corrections. The fits were performed by minimizing the function $R = \Sigma[(\chi_M T)_{exp} - (\chi_M T)_{cal}]^2/\Sigma(\chi_M T)_{exp}^2$. EPR spectra for **1**–**3** were recorded at X-band (9.4 GHz) frequency with a Bruker ESP-300E spectrometer from room temperature to 4 K, at the "Servei de Magnetoquímica" (Universitat de Barcelona).

X-ray Crystallography: Crystallization of **1**, **2** and **3** by slow concentration of their saturated ethanolic solutions at room temperature yielded good single crystals. Intensity data were collected with a Siemens P4 single-crystal diffractometer equipped with a molybdenum sealed tube (λ = 0.7173 Å) and highly oriented graphite monochromator. Table 5 shows the unit cell parameters and data measurement details. The parameters associated with the structure of **1** are as follows: Crystal size 0.24 × 0.20 × 0.16 mm. The lattice parameters and standard deviations were obtained by least-squares fit to 40 reflections $10.085° < 2\theta < 30.312°$ The data were collected by the 2θ-θ scan mode with a variable scan speed ranging from 2.0 to a maximum of 60° min^{-1}. Three reflections were used to monitor the stability and orientation of the crystal and were measured after every 97 reflections. Their intensities showed only statistical fluctuations during 40.28 h of X-ray exposure time. The data were collected for Lorentz and polarisation factors and an empirical absorption correction based on the ψ-scan method was applied. The structure was solved by direct methods using SHELX-97[34] and also refined on F^2 using the same one. All non-hydrogen atoms were refined anisotropically. The hydrogen atoms were included in the ideal positions with fixed isotropic U values and were riding on their respective non-hydrogen atoms. A weighting scheme of the form $w = 1/[(\sigma^2F_o^2) + (ap)^2 + bp]$ with a = 0.1606 and b = 8.27 was used. The refinement converged to a final R value of 0.0747 (wR_2 = 0.22 for 3012 reflections) [$I > 2\sigma(I)$]. The final difference map was featureless. The data collection procedure, structure solution and refinement for compounds **2** and **3** were essentially the same as for **1**. The parameters associated with the structures are as follows: **2:** 40 reflections $(0.420° < 2\theta < 30.118°)$ for an accurate cell parameter determination, crystal size 0.28 × 0.24 × 0.19 mm, a total of 46.90 h of X-ray exposure time, R = 0.0383 (wR_2 = 0.1093 for 3342 reflections) [$I > 2\sigma(I)$] with a = 0.0572 and b = 10.73 in weighting scheme. **3:** 40 reflections $(0.420° < 2\theta < 30.118°)$ for an accurate cell parameter determination, crystal size 0.20 × 0.20 × 0.10 mm, a total of 48 h of X-ray exposure time, R = 0.0535 (wR_2 = 0.1422 for 3602 reflections) [$I > 2\sigma(I)$] with a = 0.0811 and b = 1.8505 in above mentioned weighting scheme. A summary of the crystal parameters, experimental details and refinement results are listed in Table 5. CCDC-254292 (**1**), -254293 (**2**), and -254294 (**3**) contain the supplementary crystallographic data for this paper. These data can be obtained free of charge from The Cambridge Crystallographic Data Centre via www.ccdc.cam.ac.uk/data_request/cif.

Acknowledgments

A. K. is grateful to CSIR New Delhi, India for a Senior Research Fellowship. The authors thank MEC of Spain (project BQ2003-00538) for financial support.

[1] S. L. Jain, P. Bhattacharyya, H. L. Milton, A. M. Z. Slawin, J. A. Crayston, J. D. Woollins, *Dalton Trans.* **2004**, 862–871.
[2] a) T. Le Borgne, P. Altmann, N. Andre, J.-C. G. Bunzli, G. Bernardinelli, P. Morgantini, J. Weber, C. Piguet, *Dalton Trans.* **2004**, 723–733; b) T. Le Borgne, J.-M. Benech, S. Floquet, G. Bernardinelli, C. Aliprandini, P. Bettens, C. Piguet, *Dalton Trans.* **2003**, 3856–3868; c) F. Renaud, C. Piguet, G. Bernardinelli, J.-C. G. Bunzli, G. Hopfgartner, *Chem. Eur. J.* **1997**, *3*, 1646–1659.
[3] J. Garcia-Lozano, M. A. Martinez-Lorente, E. Escriva, R. Ballesteros, *Synth. React. Inorg. Met.-Org. Chem.* **1994**, *24*, 365–376.
[4] J. Garcia-Lozano, L. Soto, J. V. Folgado, E. Escriva, *Polyhedron* **1996**, *15*, 4003–4009.
[5] J. G. H. du Preez, B. Van Breeht, *Inorg. Chim. Acta* **1989**, *162*, 49–56.

 © 2005 Wiley-VCH Verlag GmbH & Co. KGaA, Weinheim

[6] J. G. H. du Preez, B. Van Breeht, J. F. de Wet, J. Koorts, *Inorg. Nucl. Chem. Lett.* **1974**, *10*, 935–939.
[7] R. Kapoor, A. Kataria, P. Kapoor, P. Venugopalan, *Trans. Met. Chem.* **2004**, *29*, 425–429.
[8] R. Kapoor, A. Kataria, P. Venugopalan, P. Kapoor, M. Corbella, M. Rodriguez, M. Romero, M. Sola, A. Llobet, *Inorg. Chem.* **2004**, *43*, 6699–6706.
[9] K. R. Justin Thomas, V. Chandrasekhar, S. R. Scott, A. W. Cordes, *Polyhedron* **1995**, *14*, 1607–1613.
[10] C. Arici, D. Veku, R. Kurtaran, K. C. Emergl, O. Atakol, *Z. Kristallogr.* **2003**, *218*, 497–500.
[11] Z. Dori, R. Eisenberg, H. B. Gray, *Inorg. Chem.* **1967**, *6*, 483–486.
[12] E. Goldschmied, N. C. Stephenson, *Acta Crystallogr. Sect. B* **1970**, *26*, 1867–1875.
[13] M. Gerloch, *J. Chem. Soc. A* **1966**, 1317–1325.
[14] L. Sacconi, R. Morassi, S. Midollini, *J. Chem. Soc. A* **1968**, 1510–1515.
[15] Z. Dori, H. B. Gray, *Inorg. Chem.* **1968**, *7*, 889–892.
[16] M. Ciampolini, N. Nardi, *Inorg. Chem.* **1966**, *5*, 41–44; M. Ciampolini, N. Nardi, *Inorg. Chem.* **1966**, *5*, 1150–1154.
[17] L. Sacconi, I. Bertini, R. Morassi, *Inorg. Chem.* **1967**, *6*, 1548–1553.
[18] M. Ciampolini, G. P. Speroni, *Inorg. Chem.* **1966**, *5*, 45–49.
[19] M. Di Vaira, P. L. Orioli, *Chem. Commun.* **1965**, 590.
[20] F. Tuna, L. Patron, E. Rivière, M. Boillot, *Polyhedron* **2000**, *19*, 1643–1648.
[21] D. V. Naik, W. R. Scheidt, *Inorg. Chem.* **1973**, *12*, 272–276; M. G. B. Drew, A. H. bin Othman, S. G. McFall, P. D. A. McIlroy, S. M. Nelson, *J. Chem. Soc. Dalton Trans.* **1977**, 438–446.
[22] R. Boca, H. Elias, W. Haase, M. Hüber, R. Klement, L. Müller, H. Paulus, I. Svoboda, M. Valko, *Inorg. Chim. Acta* **1998**, *278*, 127–135.
[23] B. J. Kennedy, G. D. Fallon, B. M. K. C. Gatehouse, K. S. Murray, *Inorg. Chem.* **1984**,*23*, 580–588.
[24] A. Garoufis, S. Kasselouri, C. P. Raptopoulou, *Inorg. Chem. Commun.* **2000**, *3*, 251–254.
[25] C. Bianchini, G. Mantovani, A. Meli, F. Migliacci, F. Zanobini, F. Laschi, A. Sommazzi, *Eur. J. Inorg. Chem.* **2003**, 1620–1631.
[26] A. K. Patra, M. Ray, R. Mukherjee, *J. Chem. Soc. Dalton Trans.* **1999**, 2461–2466.
[27] T. M. Kooistra, K. F. W. Hekking, Q. Knijnenburg, B. de Bruin, P. H. M. Budzelaar, R. de Gelder, J. M. M. Smits, A. W. Gal, *Eur. J. Inorg. Chem.* **2003**, 648–655.
[28] M. Calligaris, G. Nardin, L. Randaccio, *J. Chem. Soc. Dalton Trans.* **1974**, 1903–1906.
[29] L.-J. Zhang, X.-L. Zhao, P. Cheng, J.-Q. Xu, X. Tang, X.-B. Cui, W. Xu, T.-G. Wang, *Bull. Chem. Soc. Jpn.* **2003**, *76*, 1179–1184.
[30] L.-Y. Wang, B. Zhao, C.-X. Zhang, D. Z. Liao, Z.-H. Jiang, S.-P. Yan, *Inorg. Chem.* **2003**, *42*, 5804–5806.
[31] U. Beckmann, S. Brooker, C. V. Depree, J. D. Ewing, B. Moubaraki, K. S. Murray, *J. Chem. Soc. Dalton Trans.* **2003**, 1308–1313.
[32] T. Whitfield, L.-M. Zheng, X. Wang, A. J. Jacobson, *Solid State Sci.* **2001**, 829–835.
[33] R. Kapoor, A. Kataria, A. Pathak, P. Venugopalan, G. Hundal, P. Kapoor, *Polyhedron* **2005**, *24*, 1221–1231.
[34] G. M. Sheldrick, *SHELX-97, Program for solution and refinement of crystal structures*, University of Göttingen, Göttingen, Germany, **1997**.
[35] W. J. Geary, *Coord. Chem. Rev.* **1971**, *7*, 81–122.
[36] N. N. Greenwood, K. Wade, *J. Chem. Soc.* **1960**, 1130–1141.
[37] P. C. H. Mitchell, R. J. P. Williams, *J. Chem. Soc.* **1960**, 1912–1918; J. Lewis, R. S. Nyholm, P. W. Smith, *J. Chem. Soc.* **1961**, 4590–4599; J. L. Burmeister, *Coord. Chem. Rev.* **1966**, *1*, 205–221; J. L. Burmeister, *Coord. Chem. Rev.* **1968**, *3*, 225–245.
[38] D.-T. Wu, C.-S. Chung, *Inorg. Chem.* **1986**, *25*, 3584–3587.
[39] A. W. Addison, T. N. Rao, J. Reedijk, J. Vm Riju, G. C. Verschoor, *J. Chem. Soc. Dalton Trans.* **1984**, 1349–1356.
[40] S. E. Livingstone, *Q. Rev. Chem. Soc.* **1965**, *19*, 386–425.
[41] L. P. Battaglia, A. Bonamartini Corradi, A. Mangia, *Inorg. Chim. Acta* **1980**, *39*, 211–216.
[42] M. G. B. Drew, A. H. bin Othman, S. M. Nelson, *J. Chem. Soc. Dalton Trans.* **1976**, 1394–1399.
[43] P. Paoletti, M. Ciampolini, *Inorg. Chem.* **1967**, *6*, 64–68.
[44] Package of programs for Molecular Orbital Analysis. C. Mealli, D. M. Proserpio, *J. Chem. Educ.* **1990**, *67*, 399.
[45] O. Kahn, *Molecular Magnetism*, VCH, New York, **1993**.
[46] M. A. Hitchman, *Inorg. Chim. Acta* **1978**, *26*, 237–245.
[47] R. Boca, *Coord. Chem. Rev.* **2004**, *248*, 757–815.

Received: April 17, 2005
Published Online: August 10, 2005

 © 2005 Wiley-VCH Verlag GmbH & Co. KGaA, Weinheim

A Dinuclear Phosphidoplatinum(II) Fragment as a Building Block for Tri-, Tetra-, Hexa-, and Octanuclear Complexes[‡]

Irene Ara,[a] Naima Chaouche,[a,b] Juan Forniés,*[a] Consuelo Fortuño,[a] Abdelaziz Kribii,[b] and Antonio Martín[a]

Keywords: Bridging ligands / Cyanides / P ligands / Platinum / Self-assembly

The dinuclear complex $[(C_6F_5)_2Pt(\mu\text{-}PPh_2)_2Pt(NCCH_3)_2]$ (**1**) is described and fully characterised. Complex **1** reacts with 2,2′-bipyrimidine and *cis*-$[M(C_6F_5)_2(THF)_2]$ to form the di-, tri- and tetranuclear complexes **2**, **3** and **4**, respectively, depending on the ratio of reagents and the type of metal (M = Pt, Pd). Complex **1** reacts with KCN to form the anionic dinuclear complex $[PPh_3(CH_3)]_2[(C_6F_5)_2Pt(\mu\text{-}PPh_2)_2Pt(CN)_2]$ (**6**). Complex **6** acts as a metalloligand towards *cis*-$[M(C_6F_5)_2(THF)_2]$ or **1** to yield the corresponding hexanuclear or octanuclear complexes **7**, **8** and **9**. The structure of $[PPh_3(CH_3)]_4[\{(C_6F_5)_2Pt(\mu\text{-}PPh_2)_2Pt(\mu\text{-}CN)_2Pd(C_6F_5)_2\}_2]$ (**8**) has been established by X-ray diffraction.
(© Wiley-VCH Verlag GmbH & Co. KGaA, 69451 Weinheim, Germany, 2005)

Introduction

The use of transition metal centres and coordination chemistry for directing the formation of complex structures has evolved into one of the most widely used strategies for organizing molecular building blocks into supramolecular arrays.[2–7] The directional-bonding approach, or "molecular library", involves the assembly of large metal-containing structures wherein the metal centres act as highly directional corner or side units in the resulting geometric shapes or polyhedra. This approach uses a blocking ligand to protect coordination sites at the metal centre, thus controlling the positions available for the binding of bridging ligands and enabling the construction of the desired architecture. This type of research began with the use of mononuclear coordination centres, especially Pd^{II} and Pt^{II},[8–10] but considerable success has since been achieved by using dimetallic entities instead.[11,12] In the course of our research in phosphido derivatives we have prepared several polynuclear complexes that contain the "$(C_6F_5)_2Pt(\mu\text{-}PPh_2)_2Pt$" fragment.[13–19] In some cases the precursor for this fragment is the complex $[(C_6F_5)_2Pt(\mu\text{-}PPh_2)_2Pt(S)_2]$[20] (S = solvent) which has been prepared in situ but never isolated. In this paper we describe the isolation of the dinuclear derivative $[(C_6F_5)_2Pt(\mu\text{-}PPh_2)_2Pt(NCCH_3)_2]$ (**1**) and we study its coordination chemistry towards different ligands with the aim of establishing its synthetic potential as a building block for species with predefined geometric shapes.

Results and Discussion

The addition of $AgClO_4$ to an acetone/acetonitrile solution of $[Bu_4N]_2[\{(C_6F_5)_2Pt(\mu\text{-}PPh_2)_2Pt(\mu\text{-}Cl)\}_2]$ (molar ratio 2:1) results in the precipitation of silver chloride; $[(C_6F_5)_2Pt(\mu\text{-}PPh_2)_2Pt(NCCH_3)_2]$ (**1**) is isolated as a white, stable solid from the mother liquors. The ^{19}F NMR spectrum shows a signal with platinum satellites for the *o*-F atoms and the resonances due to *m*- and *p*-F atoms (higher field) appear overlapped, with the expected 2:3 intensity ratio confirming the equivalence of both C_6F_5 groups. The ^{31}P NMR spectrum shows a signal (δ = –143.8 ppm) with platinum satellites for the two equivalent P atoms. The chemical shift appears at high field, indicating that both PPh_2 ligands are supporting two metal centres not involved in M–M bonds [3.443(1) Å]. Two values of $^1J_{Pt,P}$ (1927 and 2454 Hz for Pt^1 and Pt^2, respectively) can be calculated from the platinum satellites (see Scheme 1 for atom numbering). The assignment of each value to Pt^1 or Pt^2 can be carried out considering the great *trans* influence of the C_6F_5 group and comparing the values with those obtained in other similar pentafluorophenyl derivatives.[21] The IR spectrum shows, in the 800 cm^{-1} region, two absorptions of similar intensity due to the X-sensitive mode of the C_6F_5 groups, in agreement with the presence of the "*cis*-$Pt(C_6F_5)_2$" fragment,[22,23] and two absorptions in the 2300 cm^{-1} region due to ν(CN) of the coordinated acetonitrile. All significant spectroscopic data are given in the Exp. Sect.

The crystal structure of complex **1** was determined by X-ray diffraction and is shown in Figure 1. During the resolu-

[‡] Polynuclear Homo- or Heterometallic Palladium(II)-Platinum(II) Pentafluorophenyl Complexes Containing Bridging Diphenylphosphido Ligands, 17. Part 16: Ref.[1]

[a] Departamento de Química Inorgánica, Instituto de Ciencia de Materiales de Aragón, Universidad de Zaragoza-C.S.I.C., 50009 Zaragoza, Spain
Fax: +34-976-761-187
E-mail: juan.fornies@unizar.es
[b] Département de Chimie, Faculté des Sciences, Université Ibn Tofail, B. P. 133, Kenitra, Morocco

 © 2005 Wiley-VCH Verlag GmbH & Co. KGaA, Weinheim **DOI: 10.1002/ejic.200500328**

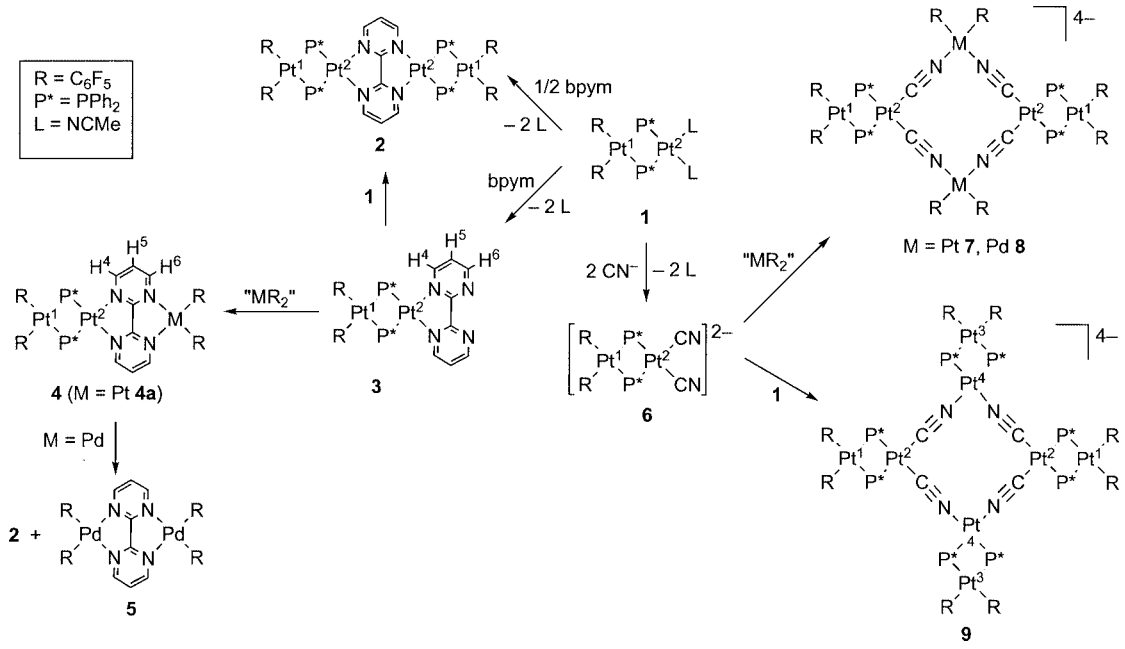

Scheme 1.

tion of the structure, two essentially identical molecules of **1** were found in the asymmetric part of the unit cell and we will discuss only one of them now. Selected bond lengths and angles are listed in Table 1. Complex **1** is a dinuclear complex (Figure 1) in which the two Pt atoms are bridged by two diphenylphosphido ligands. The square-planar environments of the metal centres are completed by two *cis*-pentafluorophenyl groups in the case of Pt(1), and two *cis*-acetonitrile ligands in the case of Pt(2). The two acetonitrile moieties are practically linear, as expected, and the bond lengths and angles fall in the range usually found for this ligand coordinated to Pt.[24–28] The molecular skeleton $C_2PtP_2PtN_2$ is not planar. The angle between the perpendicular lines to the best square planes formed by the Pt atoms and the atoms directly bonded to them is 33.94(4)°.

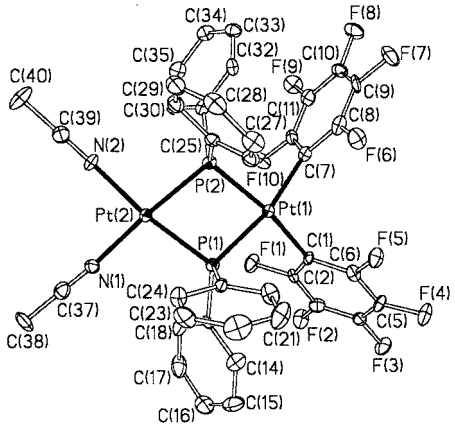

Figure 1. Structure of the complex $[(C_6F_5)_2Pt(\mu\text{-}PPh_2)_2Pt(NCCH_3)_2]$ (**1**).

Table 1. Selected bond lengths [Å] and angles [°] for $[(C_6F_5)_2Pt(\mu\text{-}PPh_2)_2Pt(NCCH_3)_2]\cdot Me_2CO$ (**1**·Me_2CO).

Pt(1)–C(1)	2.061(5)	Pt(1)–C(7)	2.065(5)
Pt(1)–P(2)	2.2844(14)	Pt(2)–N(1)	2.068(5)
Pt(2)–P(2)	2.2641(14)	Pt(2)–P(1)	2.2728(14)
Pt(3)–C(47)	2.070(5)	Pt(3)–P(4)	2.2815(14)
Pt(4)–N(4)	2.083(5)	Pt(4)–N(3)	2.087(5)
Pt(4)–P(4)	2.2702(14)	Pt(4)–P(3)	2.2566(14)
Pt(1)–P(1)	2.2820(14)	Pt(2)–N(2)	2.079(4)
Pt(3)–C(41)	2.070(5)	Pt(3)–P(3)	2.2933(14)
C(1)–Pt(1)–C(7)	92.6(2)	C(1)–Pt(1)–P(1)	98.01(15)
C(7)–Pt(1)–P(1)	167.61(15)	C(1)–Pt(1)–P(2)	169.16(15)
C(7)–Pt(1)–P(2)	93.19(15)	P(1)–Pt(1)–P(2)	75.36(5)
N(1)–Pt(2)–N(2)	87.54(18)	N(1)–Pt(2)–P(2)	175.44(13)
N(2)–Pt(2)–P(2)	96.47(13)	N(1)–Pt(2)–P(1)	100.08(13)
N(2)–Pt(2)–P(1)	172.36(13)	P(2)–Pt(2)–P(1)	75.94(5)
Pt(2)–P(1)–Pt(1)	98.22(5)	Pt(2)–P(2)–Pt(1)	98.40(5)
C(41)–Pt(3)–C(47)	92.77(19)	C(41)–Pt(3)–P(4)	167.51(15)
C(47)–Pt(3)–P(4)	97.61(14)	C(41)–Pt(3)–P(3)	94.46(14)
C(47)–Pt(3)–P(3)	172.27(14)	P(4)–Pt(3)–P(3)	74.88(5)
N(4)–Pt(4)–N(3)	88.36(18)	N(4)–Pt(4)–P(3)	172.82(13)
N(3)–Pt(4)–P(3)	98.47(13)	N(4)–Pt(4)–P(4)	97.29(13)
N(3)–Pt(4)–P(4)	174.06(13)	P(3)–Pt(4)–P(4)	75.82(5)
Pt(4)–P(3)–Pt(3)	100.13(6)	Pt(4)–P(4)–Pt(3)	100.07(5)

The well-known stability of Pt–C_6F_5 bonds and the Pt(μ-PPh_2)$_2$Pt skeleton, and the lability of the Pt–N (acetonitrile) bonds, make complex **1** an excellent dinuclear starting material with a 90° angle between the "open-coordination sites".

Reaction of 1 with 2,2′-Bipyrimidine

In order to explore the potential of complex **1** as a precursor for self-assembly chemistry, we started the study by

 © 2005 Wiley-VCH Verlag GmbH & Co. KGaA, Weinheim

substituting the two acetonitrile ligands in **1** with 2,2′-bipyrimidine (bpym), a ligand with four N donor atoms that can be used as a linker of the building blocks.[29–32] Addition of bpym to an acetone solution of **1** in a 1:2 molar ratio (see Scheme 1) gave the linear tetranuclear complex $[(C_6F_5)_2Pt(\mu\text{-}PPh_2)_2Pt(\mu\text{-}bpym)Pt(\mu\text{-}PPh_2)_2Pt(C_6F_5)_2]$ (**2**). This process is facilitated by both the sp^2 hybridisation at the N atoms, the chelate effect of the ligand and the high insolubility of **2**. Nevertheless, when the ligand is added in a 1:1 molar ratio the dinuclear complex $[(C_6F_5)_2Pt(\mu\text{-}PPh_2)_2Pt(bpym)]$ (**3**) is obtained. The bpym ligand in **3** is coordinated in a terminal chelating mode, and thus the other two N atoms can be used for further coordination. Complex **2** can be obtained by the addition of **1** to solutions of **3** in acetone (1:1 molar ratio).

With the aim of synthesising asymmetric derivatives we added *cis*-$[M(C_6F_5)_2(THF)_2]$ (M = Pt, Pd) to CH_2Cl_2 solutions of **3** (1:1 molar ratio); the results are different for M = Pt or Pd. In the first case the two donor N atoms of **3** coordinate to the added platinum centre and the asymmetric, linear, trinuclear derivative $[(C_6F_5)_2Pt(\mu\text{-}PPh_2)_2Pt(\mu\text{-}bpym)Pt(C_6F_5)_2]$ (**4a**) crystallises from the solution. However, the reaction of **3** with *cis*-$[Pd(C_6F_5)_2(THF)_2]$ does not yield the heteronuclear complex $[(C_6F_5)_2Pt(\mu\text{-}PPh_2)_2Pt(\mu\text{-}bpym)Pd(C_6F_5)_2]$ (**4b**) but rather a mixture of **2** and $[(C_6F_5)_2Pd(\mu\text{-}bpym)(C_6F_5)_2]$ (**5**),[33] which were identified by IR spectroscopy. The two complexes can be easily separated from this solid by dissolving **5** in acetone. The ^1H NMR spectra of **3** and **4a** show, in addition to PPh_2 groups, three resonances due to the H^4, H^5 and H^6 atoms of the bpym ligand, as expected for these asymmetric compounds. The ^{19}F NMR spectra of **3** shows three signals (2 *o*-F, 2 *m*-F, *p*-F) due to the equivalence of both C_6F_5 groups, while complex **4a** shows, as expected, the signals due to both types of inequivalent C_6F_5 groups (see Exp. Sect.). The ^{31}P NMR spectra of **3** and **4a** show the same pattern as **1**.

In the IR spectra of complexes **2** and **3** two absorptions of the same intensity due to the X-sensitive mode of the C_6F_5 groups are observed in the 800 cm^{-1} region, in agreement with the presence of the "*cis*-$M(C_6F_5)_2$" fragment.[22,23] For complex **4a** four absorptions due to the two different "*cis*-$M(C_6F_5)_2$" fragments are observed. In addition, two intense sharp peaks of nearly equal intensity at approximately 1580 and 1560 cm^{-1} (ring stretching modes of bpym) characterise the terminal-chelating mode of the bpym ligand in complex **3**. The presence of the bis(chelating) mode (complexes **2**, **4a** and **5**), however, is indicated either by an asymmetric doublet or a single strong broad feature in the same range.[34]

All our attempts to obtain a single crystal of the tetranuclear complex **2** suitable for X-ray diffraction purposes failed, probably due to its insolubility. Although we obtained single crystals of the asymmetric complex **4a** and collected data for two different crystals, in both cases the value of *R* was not satisfactory, thus the structure of **4a** cannot be fully described. However, the skeleton of the molecule and the connectivity of the atoms are as expected.

Reaction of 1 with Cyanide

The cyanide ligand can act as a linear linker in polynuclear systems that exhibit fascinating structures and properties.[35–41] Although the design of molecular entities has produced large rings, stars, boxes, cages and clusters involving cyanide bridging ligands, only a few examples with platinum centres in their structure have been reported.[42–47] With the aim of synthesising other homo- or heteronuclear square molecules we decided to use the cyanide ligand as: a) it can easily act as a terminal ligand, thus allowing a designed synthesis through a two-pot process; b) although some bent cyanide bridges are known,[48] this group is usually rigid and linear when acting as a bridging ligand; and c) their anionic nature allows the synthesis of anionic molecular squares. Although we have recently reported some examples of anionic heterometallic squares,[42] these molecules are usually neutral or cationic with a high charge.

The addition of KCN to acetone solutions of **1** in a 2:1 molar ratio (a methyltriphenylphosphonium salt was also added to facilitate the crystallisation) yielded the dinuclear complex $[PPh_3(CH_3)]_2[(C_6F_5)_2Pt(\mu\text{-}PPh_2)_2Pt(CN)_2]$ (**6**) in which the cyanide groups act as terminal ligands. The two N atoms of **6** are bonded to other *cis*-blocked metal centres to form the expected squares. The reaction of *cis*-$[M(C_6F_5)_2(THF)_2]$ (M = Pt, Pd) with CH_2Cl_2 solutions of the metalloligand **6** (1:1 molar ratio) gave the hexanuclear anionic macrocycles $[PPh_3(CH_3)]_4[\{(C_6F_5)_2Pt(\mu\text{-}PPh_2)_2Pt(\mu\text{-}CN)_2M(C_6F_5)_2\}_2]$ (M = Pt, **7**; Pd, **8**). Similarly, the reaction of **6** and **1** (1:1 molar ratio) afforded the octanuclear complex $[PPh_3(CH_3)]_4[\{(C_6F_5)_2Pt(\mu\text{-}PPh_2)_2Pt(\mu\text{-}CN)Pt(\mu\text{-}PPh_2)_2Pt(C_6F_5)_2\}_2]$ (**9**; Scheme 1). The ^{19}F NMR spectrum of **6** shows three signals in a 2:2:1 intensity ratio and the low-field signal, due to the *o*-F atoms, shows platinum satellites. This is the expected pattern for **6** in which both C_6F_5 groups are equivalent. In agreement with the formulation given in Scheme 1, the ^{19}F NMR spectrum of **7** exhibits two signals in the *o*-F region (2:2 intensity ratio), two high-field multiplets for the *m*-F (2:2 intensity ratio) and two different signals for the *p*-F atoms (1:1 intensity ratio), thus confirming the presence of two non-equivalent C_6F_5 rings (C_6F_5 *trans* to CN and C_6F_5 *trans* to P). The spectrum of **8** is analogous, but one *m*-F signal appears overlapped with that of the *p*-F one. Moreover, only one signal, with platinum satellites, is observed for the two types of *o*-F atoms (C_6F_5 bonded to platinum or to palladium), thereby indicating that they are isochronous. This was unambiguously confirmed by considering the intensity ratio of the platinum satellites and the central signal (1:10:1). For complex **9**, the two different *o*-F atoms are isochronous and the signals due to *m*-F atoms are overlapped. Nevertheless, the presence of two inequivalent C_6F_5 groups is unambiguously demonstrated by the two well-separated *p*-F signals (see Exp. Sect.). The ^{31}P NMR spectrum of **6** shows one high-field signal with platinum satellites (1:8:17:8:1 intensity ratio) for the P atoms of the diphenylphosphido groups. The two doublets expected for the two isotopomers in which one platinum centre is ^{195}Pt (22.3% abundance each one) are

 © 2005 Wiley-VCH Verlag GmbH & Co. KGaA, Weinheim

overlapped, ;indicating equal coupling constants between the equivalent P atoms and the inequivalent Pt^1 and Pt^2 centres. This is in agreement with the easily observed signals due to the isotopomer in which the two metal centres are ^{195}Pt (11.3% abundance). The same spectral pattern is observed for complexes **7** and **8**, thus indicating that the coordination of the N atoms of the CN ligand in **6** to the metal centre of the "*cis*-$M(C_6F_5)_2$" fragment (M = Pt, Pd) does not perceptibly change the magnetic environment of the Pt^1 and Pt^2 centres. The octanuclear macrocycle **9** shows two different types of diphenylphosphido ligands: the PPh_2 groups bridging Pt^1 and Pt^2 centres, both with two Pt–C bonds (fragment from **6**), and the PPh_2 groups bridging Pt^3 and Pt^4 centres, with two Pt^3–C and two Pt^4–N bonds (fragment from **1**). The ^{31}P NMR spectrum of **9** exhibits, in the high-field region, two signals with platinum satellites. The signal at δ = –161.0 ppm shows a pattern similar to the one observed for **6**–**8** and can be assigned to the P atoms of the "$Pt^1(\mu\text{-}PPh_2)_2Pt^2$" fragment, while two different values of $^1J_{Pt,P}$ (1899 and 2400 Hz) can be extracted from the signal at δ = –157.9 ppm; this signal can be assigned to the P atoms of the "$Pt^3(\mu\text{-}PPh_2)_2Pt^4$" fragment. The assignment of both $^1J_{Pt,P}$ values (see Exp. Sect.) was carried out by comparison with the corresponding values observed in **1**, **3** and **4a**.

The relevant feature of the IR spectra of **6**–**9** is the presence of two sharp absorptions at 2122 and 2113 cm^{-1} in **6** (terminal cyanide), which are assigned to ν(C≡N), and their significant shift towards higher frequencies in the squares **7**, **8** and **9** (bridging cyanide).[49] In all cases the absorptions observed in the 800 cm^{-1} region indicate the presence of "*cis*-$M(C_6F_5)_2$" fragments.[22,23]

Figure 2a shows the structure of the anion in complex **8**. Selected bond lengths and angles are given in Table 2. The X-ray structure establishes the presence of the hexanuclear complex anion $[\{(C_6F_5)_2Pt(\mu\text{-}PPh_2)_2Pt(\mu\text{-}CN)_2Pd(C_6F_5)_2\}_2]^{4-}$ and four $[PPh_3(CH_3)]^+$ cations along with three molecules of acetone and one molecule of *n*-hexane as lattice solvent. The platinum atoms are bonded to two diphenylphosphido ligands, which act as bridges between both metal centres, and to two C_6F_5 ligands in the case of Pt(2) or to two CN bridging ligands in the case of Pt(1). The N atoms of the cyanide are coordinated to the Pd atoms, which complete their coordination with two C_6F_5 groups in *cis* positions. The distances and angles in each coordination sphere are within the expected values. The maximum deviation of the metal atoms with respect to their best least-squares plane is 0.046 Å in the case of Pt(2). The C_6F_5 rings are essentially perpendicular to their coordination planes, with angles ranging from 77.0 to 91.4°. The coordination planes of Pt(1) and Pd(1) are essentially coplanar (4.8°), while the coordination plane of Pt(2) forms an angle of 22.1° with that of Pt(1). The Pt(1) and Pd(1) atoms form an almost perfect square, with edges of 5.19 and 5.21 Å, in which the CN ligands are located, defining an open cavity which is not large enough to accommodate the bulky cations or solvent molecules (see Figure 2b).

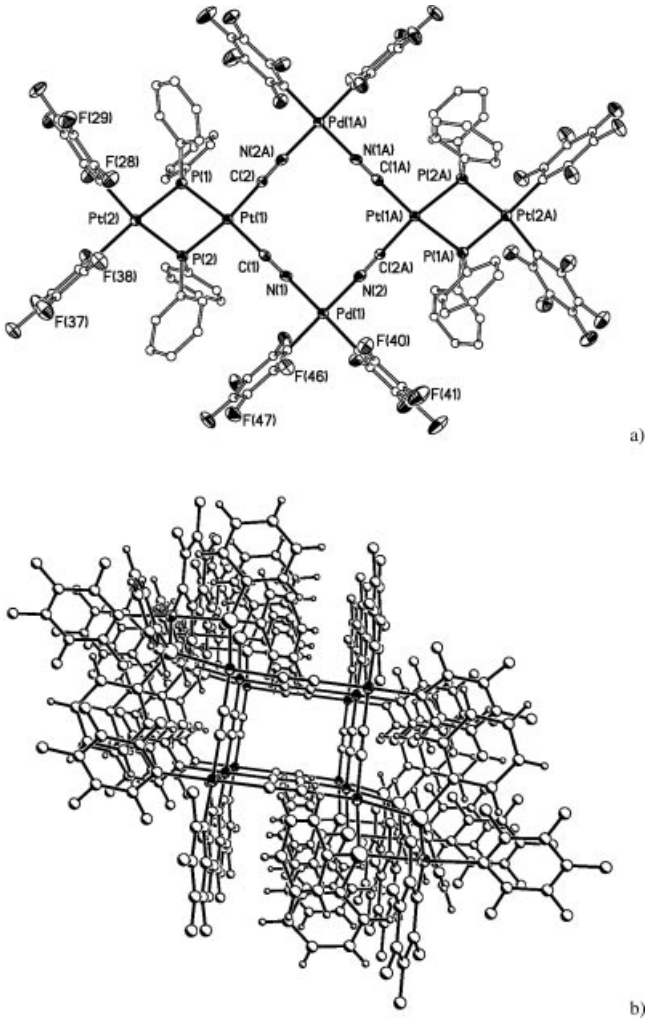

Figure 2. a) Structure of the anion of $[PPh_3Me]_4[\{(C_6F_5)_2Pt(\mu\text{-}PPh_2)_2Pt(\mu\text{-}CN)_2Pd(C_6F_5)_2\}_2]$ (**8**). b) Packing diagram of the anions in **8**, showing how the cores of the molecular squares stack to form an infinite tunnel.

Table 2. Selected bond lengths [Å] and angles [°] for $\{(PPh_3Me)_2[(C_6F_5)_2Pt(\mu\text{-}PPh_2)_2Pt(\mu\text{-}CN)_2Pd(C_6F_5)_2]\}_2\cdot 3Me_2CO\cdot$*n*-hexane (**8**·3$Me_2CO$·*n*-hexane).

Pt(1)–C(2)	1.999(5)	Pt(2)–P(2)	2.3111(14)
Pt(1)–C(1)	2.016(5)	Pd(1)–C(39)	1.990(5)
Pt(1)–P(1)	2.3105(14)	Pd(1)–C(45)	1.993(5)
Pt(1)–P(2)	2.3198(13)	Pd(1)–N(2)	2.045(4)
Pt(2)–C(27)	2.064(5)	Pd(1)–N(1)	2.045(5)
Pt(2)–C(33)	2.069(5)	N(1)–C(1)	1.149(7)
Pt(2)–P(1)	2.2944(13)	N(2)–C(2′)[a]	1.149(6)
C(2)–Pt(1)–C(1)	91.5(2)	C(33)–Pt(2)–P(2)	99.66(14)
C(2)–Pt(1)–P(1)	95.34(14)	P(1)–Pt(2)–P(2)	76.30(5)
C(1)–Pt(1)–P(1)	172.75(14)	C(39)–Pd(1)–C(45)	88.1(2)
C(2)–Pt(1)–P(2)	171.14(14)	C(39)–Pd(1)–N(2)	91.42(18)
C(1)–Pt(1)–P(2)	97.32(14)	C(45)–Pd(1)–N(2)	177.69(19)
P(1)–Pt(1)–P(2)	75.82(5)	C(39)–Pd(1)–N(1)	177.5(2)
C(27)–Pt(2)–C(33)	90.78(19)	C(45)–Pd(1)–N(1)	90.99(18)
C(27)–Pt(2)–P(1)	93.16(14)	N(2)–Pd(1)–N(1)	89.57(16)
C(33)–Pt(2)–P(1)	175.78(14)	Pt(2)–P(1)–Pt(1)	101.85(5)
C(27)–Pt(2)–P(2)	168.51(14)	Pt(2)–P(2)–Pt(1)	101.06(5)

[a] Symmetry transformation used to generate the equivalent atom C(2′): $-x + 1, -y + 1, -z + 1$.

 © 2005 Wiley-VCH Verlag GmbH & Co. KGaA, Weinheim

We also tried to obtain an X-ray structure of complex **9** but unfortunately only poor quality crystals were obtained after many crystallisation attempts. The X-ray data measured with the diffractometer had a very low intensity, which was almost non-existent at 2θ angles $> 40°$. Thus, only a set of poor quality data could be obtained and therefore only the connectivity of the complex was established. The skeleton is rather different to that of **8** since the central core is not planar but angular, as schematized in Figure 3.

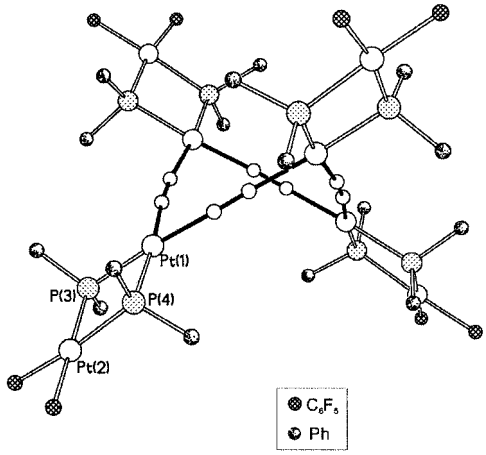

Figure 3. Structure of the anion of $[PPh_3Me]_4[\{(C_6F_5)_2Pt(\mu\text{-}PPh_2)_2Pt(\mu\text{-}CN)_2Pt(\mu\text{-}PPh_2)_2Pt(C_6F_5)_2\}_2]$ (**9**).

Conclusion

Complex **1**, in which the two acetonitrile ligands can be easily replaced, can be considered as a neutral dinuclear building block with "open-coordination sites" at 90°. The study involves the design of one-dimensional complexes with both diphenylphosphido and bpym ligands and two-dimensional molecules with diphenylphosphido and cyanide ligands. The anionic dinuclear complex **6** is used as a metalloligand towards neutral mononuclear or dinuclear species. This is a straightforward route for the preparation of homo- or heterometallic species. The choice of neutral entities,"$(C_6F_5)_2Pt(\mu\text{-}PPh_2)_2Pt$" and "$M(C_6F_5)_2$", and an anionic linker, cyanide, allowed us to synthesize the tetraanionic squares **7**, **8** and **9**, even though the complexes with this molecular architecture that have been reported so far are usually cationic or neutral species.

Experimental Section

General Procedures: C, H and N analysis was performed with a Perkin–Elmer 240B microanalyser. IR spectra were recorded with a Perkin–Elmer Spectrum One spectrophotometer (Nujol mulls between polyethylene plates in the range 4000–350 cm^{-1}). NMR spectra were recorded with a Varian Unity 300 instrument with $SiMe_4$, $CFCl_3$ and 85% H_3PO_4 as external references for ^1H, ^{19}F and ^{31}P, respectively. Conductivities (acetone, $c \approx 5 \times 10^{-4}$ M) were measured with a Philips PW 9509 conductimeter. Literature methods were used to prepare the starting materials $[Bu_4N]_2[\{(C_6F_5)_2Pt(\mu\text{-}PPh_2)_2Pt(\mu\text{-}Cl)\}_2]$[21] and *cis*-$[M(C_6F_5)_2(THF)_2]$ (M = Pt, Pd).[50]

Caution! *Perchlorate salts of metal complexes with organic ligands are potentially explosive. Only small amounts of material should be prepared, and these should be handled with great caution.*

Preparation of $[(C_6F_5)_2Pt(\mu\text{-}PPh_2)_2Pt(NCCH_3)_2]$ (1): $AgClO_4$ (0.150 g, 0.723 mmol) was added to a solution of $[Bu_4N]_2[\{(C_6F_5)_2Pt(\mu\text{-}PPh_2)_2Pt(\mu\text{-}Cl)\}_2]$ (1.000 g, 0.364 mmol) in acetone (10 mL) and acetonitrile (10 mL). The mixture was stirred at room temperature for 4 h, filtered, and the resulting solution was concentrated to ca. 5 mL, whereupon **1** crystallised as a white solid. *i*PrOH (5 mL) was added and the mixture was stirred for 1 h. Complex **1** was collected by filtration and washed with 2 mL of *i*PrOH. Yield: 0.651 g (76%). $C_{40}H_{26}F_{10}N_2P_2Pt_2$ (1176.8): calcd. C 40.82, H 2.22, N 2.38; found C 40.98, H 2.03, N 2.59. IR (nujol mull): $\tilde{\nu}$ = 782 and 774 (X-sensitive C_6F_5 group),[22,23] 2323, 2294 (N≡C) cm^{-1}. ^{19}F NMR (282.4 MHz, [D$_6$]acetone, 22°C): δ = –166.0 (6 *m*- + *p*-F), –114.7 ($^3J_{Pt,F}$ = 301 Hz, 4 *o*-F) ppm. $^{31}P\{^1H\}$ NMR (121.5 MHz, [D$_6$]acetone, 22°C): δ = –143.8 ($J_{Pt^1,P}$ = 1927, $J_{Pt^2,P}$ = 2454 Hz) ppm.

Preparation of $[(C_6F_5)_2Pt(\mu\text{-}PPh_2)_2Pt(\mu\text{-}bpym)Pt(\mu\text{-}PPh_2)_2Pt(C_6F_5)_2]$ (2): 2,2′-bpym (0.013 g, 0.084 mmol) was added, with stirring, to a colourless solution of **1** (0.200 g, 0.169 mmol) in acetone (15 mL) and **2** began to precipitate as a yellow solid. After 45 min stirring, **2** was filtered off, washed with 1 mL of acetone and vacuum-dried. Yield: 0.161 g (81%). $C_{80}H_{46}F_{20}N_4P_4Pt_4$ (2347.6): calcd. C 41.00, H 1.97, N 2.38; found C 41.49, H 1.84, N 2.17. IR (nujol mull): $\tilde{\nu}$ = 784, 776 (X-sensitive C_6F_5 group), 1581 (bpym) cm^{-1}. Complex **2** is not soluble enough in usual organic solvents for NMR studies.

Preparation of $[(C_6F_5)_2Pt(\mu\text{-}PPh_2)_2Pt(bpym)]$ (3): 2,2′-bpym (0.013 g, 0.084 mmol) was added to a colourless solution of **1** (0.100 g, 0.084 mmol) in acetone (15 mL). After 15 h of stirring at room temperature, the orange solution was concentrated almost to dryness and $CHCl_3$ (3 mL) was added while stirring. Complex **3** crystallised as a yellow solid, which was filtered off and washed with 1 mL of $CHCl_3$. Yield: 0.085 g (81%). $C_{44}H_{26}F_{10}N_4P_2Pt_2$ (1252.9): calcd. C 42.14, H 2.07, N 4.47; found C 41.74, H 1.85, N 4.16. IR (nujol mull): $\tilde{\nu}$ = 783, 775 (X-sensitive C_6F_5 group), 1580, 1556 (bpym) cm^{-1}. ^1H NMR (300 MHz, [D$_6$]acetone, 22°C): δ = 7.68 (t, $J_{H^5,H^{4,6}}$ = 5.2 Hz, 2 H^5-bpym), 8.36 (br. d, 2 H^6-bpym), 9.32 (br. d, 2 H^4-bpym) ppm. ^{19}F NMR (282.4 MHz, [D$_6$]acetone, 22°C): δ = –166.1 (2 *p*-F), –165.9 (4 *m*-F), –114.2 ($^3J_{Pt,F}$ = 301 Hz, 4 *o*-F) ppm. $^{31}P\{^1H\}$ NMR (121.5 MHz, [D$_6$]acetone, 22°C): δ = –125.6 ($J_{Pt^1,P}$ = 1859, $J_{Pt^2,P}$ = 2390 Hz) ppm.

Preparation of $[(C_6F_5)_2Pt(\mu\text{-}PPh_2)_2Pt(\mu\text{-}bpym)Pt(C_6F_5)_2]$ (4a): *cis*-$[Pt(C_6F_5)_2(THF)_2]$ (0.053 g, 0.078 mmol) was added to a yellow solution of **3** (0.100 g, 0.079 mmol) in CH_2Cl_2 (10 mL). The colour of the solution changed to brown, while a solid began to crystallise. After 15 min of stirring, the brown solid **4a** was filtered off and washed with 1 mL of CH_2Cl_2. Yield: 0.071 g (50%). $C_{56}H_{26}F_{20}N_4P_2Pt_3$ (1782.1): calcd. C 37.70, H 1.45, N 3.10; found C 37.90, H 1.47, N 2.74. IR (nujol mull): $\tilde{\nu}$ = 816, 808, 782, 774 (X-sensitive C_6F_5 group), 1585 (bpym) cm^{-1}. ^1H NMR (300 MHz, [D$_6$]acetone, 22°C): δ = 8.00 (t, $J_{H^5,H^{4,6}}$ = 5.4 Hz, 2 H^5-bpym), 8.58 (br. d, 2 H$^{6/4}$-bpym), 9.08 (br. d, 2 H$^{4/6}$-bpym) ppm. ^{19}F NMR (282.4 MHz, [D$_6$]acetone, 22°C): δ = –168.0 (6 *m* + *p*-F), –166.0 (4 *m*-F), –163.5 (2 *p*-F), –120.1 ($^3J_{Pt,F}$ = 459 Hz, 4 *o*-F), –116.0 ($^3J_{Pt,F}$ = 300 Hz, 4 *o*-F) ppm. $^{31}P\{^1H\}$ NMR (121.5 MHz, [D$_6$]acetone, 22°C): δ = –128.6 ($J_{Pt^1,P}$ = 1868, $J_{Pt^2,P}$ = 2414 Hz) ppm.

Preparation of $[PPh_3(CH_3)]_2[(C_6F_5)_2Pt(\mu\text{-}PPh_2)_2Pt(CN)_2]$ (6): KCN (0.030 g, 0.460 mmol) was added to a solution of **1** (0.200 g,

 © 2005 Wiley-VCH Verlag GmbH & Co. KGaA, Weinheim

0.170 mmol) in acetone (10 mL) and the mixture was stirred at room temperature for 15 h. $[PPh_3(CH_3)]ClO_4$ (0.128 g, 0.339 mmol) was then added and the mixture was concentrated to dryness. CH_2Cl_2 (10 mL) was added to the white residue and then filtered. The solution was concentrated to ca. 1 mL, *i*PrOH (10 mL) was added and **6** crystallised as a white solid which was filtered off, washed with 2 mL of *i*PrOH and vacuum-dried. Yield: 0.211 g (73%). $C_{76}H_{56}F_{10}N_2P_4Pt_2$ (1701.38): calcd. C 53.65, H 3.31, N 1.64; found C 53.80, H 2.98, N 1.60. IR (nujol mull): $\tilde{\nu}$ = 782, 773 (X-sensitive C_6F_5 group), 2122, 2113 ν(C≡N) cm^{-1}. Λ_M = 91 $\Omega^{-1}cm^2mol^{-1}$. ^{19}F NMR (282.4 MHz, [D$_6$]acetone, 22°C): δ = –166.4 (2 *p*-F), –164.6 (4 *m*-F), –111.7 ($^3J_{Pt,F}$ = 323 Hz, 4 *o*-F) ppm. $^{31}P\{^1H\}$ NMR (121.5 MHz, [D$_6$]acetone, 22°C): δ = –150.3 ($J_{Pt^{1,2},P}$ = 1820 Hz, PPh_2), 27.2 (PPh_3CH_3) ppm.

Preparation of $[PPh_3CH_3]_4[\{(C_6F_5)_2Pt(\mu\text{-}PPh_2)_2Pt(\mu\text{-}CN)_2M(C_6F_5)_2\}_2]$. M = Pt (7): *cis*-$[Pt(C_6F_5)_2(THF)_2]$ (0.060 g, 0.089 mmol) was added to a solution of **6** (0.150 g, 0.088 mmol) in CH_2Cl_2 (10 mL) and the solution was stirred for 1.5 h. The solvent was evaporated to leave 2 mL while a white solid began to crystallise and $CHCl_3$ (5 mL) was added. Complex **7** was filtered off and washed with 1 mL of cold $CHCl_3$. Yield: 0.134 g (68%). $C_{176}H_{112}F_{40}N_4P_8Pt_6$ (4461.2): calcd. C 47.38, H 2.53, N 1.25; found C 47.03, H 2.03, N 1.19. IR (nujol mull): $\tilde{\nu}$ = 810, 800, 783, 773 (X-sensitive C_6F_5 group), 2164 br. ν(C≡N) cm^{-1}. Λ_M = 106 $\Omega^{-1}cm^2mol^{-1}$. ^{19}F NMR (282.4 MHz, [D$_6$]acetone, 22°C): δ = –166.8 (4 *p*-F), –166.6 (4 *p*-F), –166.3 (8 *m*-F), –166.1 (8 *m*-F), –117.7 ($^3J_{Pt,F}$ 505 = Hz, 8 *o*-F), –114.4 ($^3J_{Pt,F}$ = 333 Hz, 8 *o*-F) ppm. $^{31}P\{^1H\}$ NMR (121.5 MHz, [D$_6$]acetone, 22°C): δ = –157.2 ($J_{Pt^{1,2},P}$ = 1831 Hz, PPh_2), 23.1 (PPh_3CH_3) ppm. **M = Pd (8):** This complex was obtained [yield: 0.070 g (56%)] according to a similar procedure to that used for **7** from **6** (0.100 g, 0.058 mmol) and *cis*-$[Pd(C_6F_5)_2(THF)_2]$ (0.034 g, 0.058 mmol). $C_{176}H_{112}F_{40}N_4P_8Pd_2Pt_4$ (4283.8): calcd. C 49.35, H 2.63, N 1.31; found C 49.57, H 2.44, N 1.25. IR (nujol mull): $\tilde{\nu}$ = 797, 784, 774 (X-sensitive C_6F_5 group), 2164, 2157 ν(C≡N) cm^{-1}. Λ_M = 162 $\Omega^{-1}cm^2mol^{-1}$. ^{19}F NMR (282.4 MHz, [D$_6$]acetone, 22°C): δ = –166.0 (4 *p*-F), –164.5 (8 *m*-F), –163.1 (12 *m* + *p*-F), –112.2 (8 *o*-F), –112.2 ($^3J_{Pt,F}$ = 328 Hz, 8 *o*-F) ppm. $^{31}P\{^1H\}$ NMR (121.5 MHz, [D$_6$]acetone, 22°C): δ = –154.8 ($J_{Pt^{1,2},P}$ = 1835 Hz, PPh_2), 26.9 (PPh_3CH_3) ppm.

Preparation of $[PPh_3CH_3]_4[\{(C_6F_5)_2Pt(\mu\text{-}PPh_2)_2Pt(\mu\text{-}CN)\}_4]$ (9): Complex **1** (0.056 g, 0.048 mmol) was added to a solution of **6** (0.080 g, 0.048 mmol) in acetone (10 mL) and the solution was stirred at room temperature for 15 h. The solvent was evaporated to leave ca. 2 mL and $CHCl_3$ (8 mL) was added and the mixture concentrated to ca. 5 mL. Complex **9** crystallised as a white solid which was filtered off and washed with 1 mL of $CHCl_3$. Yield: 0.076 g (57%). $C_{224}H_{152}F_{40}N_4P_{12}Pt_8$ (5592.2): calcd. C 48.12, H 2.70, N 1.00; found C 48.30, H 2.31, N 0.77. IR (nujol mull): $\tilde{\nu}$ = 781, 771 (X-sensitive C_6F_5 group), 2152 br. ν(C≡N) cm^{-1}. Λ_M = 91 $\Omega^{-1}cm^2mol^{-1}$. ^{19}F NMR (282.4 MHz, [D$_6$]acetone, 22°C): δ = –167.5 (4 *p*-F), –167.3 (4 *p*-F), –166.2 (12 *m*-F), –165.6 (4 *m*-F), –114.0 ($^3J_{Pt,F}$ = 317 Hz, 16 *o*-F) ppm. $^{31}P\{^1H\}$ NMR (121.5 MHz, [D$_6$]acetone, 22°C): δ = –161.0 ($J_{Pt^{1,2},P}$ = 1843 Hz, PPh_2), –157.9 ($J_{Pt^{3},P}$ = 1899, $J_{Pt^{4},P}$ = 2400 Hz, PPh_2), 23.0 (PPh_3CH_3) ppm.

Structural Analysis of Complexes 1·Me_2CO and 8·3Me_2CO·*n*-hexane: Crystal data and other details of the structure analysis are presented in Table 3. Single crystals were mounted on quartz fibres in a random orientation and held in place with a fluorinated oil. Data collection was performed at 100 K with a Bruker Smart CCD diffractometer using graphite-monochromated Mo-K_α radiation (λ = 0.71073 Å) with a nominal crystal-to-detector distance of 6.0 cm. Unit-cell dimensions were determined on the basis of the positions of 9622 (**1**) or 7283 (**8**) reflections from the main dataset. For **1**, a hemisphere of data, based on three ω-scans runs (starting ω =

Table 3. Crystal data and structure refinement for $[(C_6F_5)_2Pt(\mu\text{-}PPh_2)_2Pt(NCCH_3)_2]\cdot MeCO$ (**1**·Me2CO) and $\{(PPh_3Me)_2[(C_6F_5)_2Pt(\mu\text{-}PPh_2)_2Pt(\mu\text{-}CN)_2Pd(C_6F_5)_2]\}_2\cdot 3Me_2CO\cdot$*n*-hexane (**8**·3 Me_2CO·*n*-hexane).

	1·Me_2CO	**8**·3Me_2CO·*n*-hexane
Empirical formula	$C_{40}H_{26}F_{10}N_2P_2Pt_2\cdot Me_2CO$	$C_{176}H_{112}F_{40}N_4P_8PdPt_2\cdot 3Me_2CO\cdot$*n*-hexane
Formula mass	1234.83	4544.04
T [K]	100(1)	100(1)
λ [Å]	0.71073	0.71073
Crystal system	monoclinic	triclinic
Space group	$P2_1/n$	$\bar{P}$
a [Å]	12.2295(6)	15.0079(6)
b [Å]	39.6985(18)	19.0293(8)
c [Å]	17.1613(8)	19.1387(8)
α [°]	90	83.089(1)
β [°]	100.560(1)	97.706(11)
γ [°]	90	86.530(1)
V [Å^3]	8190.6(7)	4763.2(3)
Z	8	1
D_c [g cm^{-3}]	2.003	1.584
μ (Mo-K_α) [mm^{-1}]	6.986	3.269
θ range [°]	1.03–25.04	1.73–28.53
Data collected	48272	44051
Independent data (R_{int})	14445 (0.0463)	21666 (0.0306)
Data/restraints/parameters	14445/0/1085	21666/0/1154
Goodness-of-fit on F^2[a]	1.047	0.980
Final R indices [$I > 2\sigma(I)$][b]	R_1 = 0.0315	R_1 = 0.0389
	wR_2 = 0.0697	wR_2 = 0.1001
R indices (all data)	R_1 = 0.0409	R_1 = 0.0551
	wR_2 = 0.0730	wR_2 = 0.1046

[a] Goodness-of-fit = $[\sum w(F_o^2 - F_c^2)^2/(N_{obs} - N_{param})]^{0.5}$. [b] $R_1 = \sum(|F_o| - |F_c|)/\sum|F_o|$; $wR_2 = [\sum w(F_o^2 - F_c^2)^2/\sum w(F_o^2)^2]^{0.5}$.

 © 2005 Wiley-VCH Verlag GmbH & Co. KGaA, Weinheim

–28°) at φ values 0, 90, and 180 with the detector at 2θ = 28°, was collected. At each of these runs, frames (606, 435 and 230 respectively) were collected at 0.3° intervals and 10 s per frame. For **8**, a complete sphere of data was collected based on three ω-scans runs at φ values of 0, 120 and 240. At each of these runs, 606 frames were collected at 0.3° intervals and 30 s per frame. The diffraction frames were integrated using the SAINT package[51] and corrected for absorption with SADABS.[52] Lorentz and polarisation corrections were also applied. The structures were solved by direct methods. All non-hydrogen atoms of the complexes were assigned anisotropic displacement parameters. The hydrogen atoms were constrained to idealised geometries and assigned isotropic displacement parameters equal to 1.2- or 1.5-times the U_{iso} values of their respective parent atoms. After all atoms of the molecules had been located, there still remained some areas of electron density that were modelled as the lattice solvent. Final difference electron density maps showed, only in the case of **8**, some peaks above 1 e Å^{-3} (max. 2.69, largest diff. hole –1.07), most of them close to the heavy metal atoms and with no chemical meaning, others were located in the solvent area. The crystals lost solvent very rapidly and because of this their quality was not good. The structures were refined using the SHELXL-97 program.[53] CCDC-268963 (**1**) and -268963 (**8**) contain the supplementary crystallographic data for this paper. These data can be obtained free of charge from The Cambridge Crystallographic Data Centre via www.ccdc.cam.ac.uk/data_request/cif.

Acknowledgments

We thank the Ministerio de Ciencia y Tecnología y Fondos FEDER (Project BQU2002-03997-C02-02) for financial support and the Agencia Española de Cooperación Internacional (Ministerio de Asuntos Exteriores) for a grant to N.C.

[1] J. Forniés, C. Fortuño, S. Ibáñez, A. Martín, A. C. Tsipis, C. A. Tsipis, *Angew. Chem. Int. Ed.* **2005**, *44*, 2407–2410.
[2] B. J. Holliday, C. A. Mirkin, *Angew. Chem. Int. Ed.* **2001**, *40*, 2022–2043.
[3] M. Fujita, K. Umemoto, M. Yoshizawa, N. Fujita, T. Kusukawa, K. Biradha, *Chem. Commun.* **2001**, 509–518.
[4] S. Leininger, B. Olenyuk, P. J. Stang, *Chem. Rev.* **2000**, *100*, 853–907.
[5] Z. Qin, M. C. Jennings, R. J. Puddephatt, *Inorg. Chem.* **2003**, *42*, 1956–1965.
[6] O. V. Dolomanov, A. J. Blake, N. R. Champness, M. Schröder, C. Wilson, *Chem. Commun.* **2003**, 682–683.
[7] T. Moriuchi, M. Karnikawa, S. Bandoh, T. Hirao, *Chem. Commun.* **2002**, 1476–1477.
[8] P. J. Stang, D. H. Cao, S. Saito, A. M. Arif, *J. Am. Chem. Soc.* **1995**, *117*, 6273–6283.
[9] P. J. Stang, D. H. Cao, K. Chen, G. M. Gray, D. C. Muddiman, R. D. Smith, *J. Am. Chem. Soc.* **1997**, *119*, 5163–5168.
[10] J. A. Whiteford, C. V. Lu, P. J. Stang, *J. Am. Chem. Soc.* **1997**, *119*, 2524–2533.
[11] F. A. Cotton, C. Lin, C. A. Murillo, *Chem. Commun.* **2001**, 11–12.
[12] F. A. Cotton, C. Lin, C. A. Murillo, *Acc. Chem. Res.* **2001**, *34*, 759–771.
[13] E. Alonso, J. Forniés, C. Fortuño, A. Martín, A. G. Orpen, *Organometallics* **2003**, *22*, 2723–2728.
[14] L. R. Falvello, J. Forniés, C. Fortuño, F. Durán, A. Martín, *Organometallics* **2002**, *21*, 2226–2234.
[15] E. Alonso, J. M. Casas, J. Forniés, C. Fortuño, A. Martín, A. G. Orpen, C. A. Tsipis, A. C. Tsipis, *Organometallics* **2001**, *20*, 5571–5582.
[16] E. Alonso, J. M. Casas, F. A. Cotton, X. J. Feng, J. Forniés, C. Fortuño, M. Tomás, *Inorg. Chem.* **1999**, *38*, 5034–5040.
[17] E. Alonso, J. Forniés, C. Fortuño, A. Martín, A. G. Orpen, *Organometallics* **2000**, *19*, 2690–2697.
[18] L. R. Falvello, J. Forniés, C. Fortuño, F. Martínez, *Inorg. Chem.* **1994**, *33*, 6242–6246.
[19] N. Chaouche, J. Forniés, C. Fortuño, A. Kribii, A. Martín, P. Karipidis, A. C. Tsipis, C. A. Tsipis, *Organometallics* **2004**, *23*, 1797–1810.
[20] E. Alonso, J. Forniés, C. Fortuño, M. Tomás, *J. Chem. Soc., Dalton Trans.* **1995**, 3777–3784.
[21] J. Forniés, C. Fortuño, R. Navarro, F. Martínez, A. J. Welch, *J. Organomet. Chem.* **1990**, *394*, 643–658.
[22] R. Usón, J. Forniés, *Adv. Organomet. Chem.* **1988**, *28*, 219–297.
[23] E. J. Maslowsky, *Vibrational Spectra of Organometallic Compounds*, Wiley, New York, **1997**.
[24] B. Longato, G. Bandoli, A. Mucci, L. Schenetti, *Eur. J. Inorg. Chem.* **2001**, 3021–3029.
[25] A. Doppiu, M. A. Cinellu, G. Minghetti, S. Stoccoro, A. Zucca, M. Manassero, M. Sansoni, *Eur. J. Inorg. Chem.* **2000**, 2555–2563.
[26] P. J. J. Albietz, K. Yang, R. Eisenberg, *Organometallics* **1999**, *18*, 2747–2749.
[27] P. Steenwinkel, H. Kooijman, W. J. J. Smeets, A. L. Spek, D. M. Grove, G. van Koten, *Organometallics* **1998**, *17*, 5411–5426.
[28] R. Buchner, J. S. Field, R. J. Haines, C. T. Cunningham, D. R. McMillin, *Inorg. Chem.* **1997**, *36*, 3952–3956.
[29] D. Armentano, G. Munno, F. Lloret, M. Julve, J. Curély, A. M. Babb, J. Y. Lu, *New J. Chem.* **2003**, *27*, 161–165.
[30] J. M. Herrera, D. Armentano, G. Munno, F. Lloret, M. Julve, M. Verdaguer, *New J. Chem.* **2003**, *27*, 128.
[31] L. M. Toma, R. Lescouezec, L. D. Toma, F. Lloret, M. Julve, J. Vaissermann, M. Andruh, *J. Chem. Soc., Dalton Trans.* **2002**, 3171–3176.
[32] S. Triki, F. Thétiot, J.-R. Galán-Mascarós, J. S. Pala, K. R. Dunbar, *New J. Chem.* **2001**, *25*, 954–958.
[33] J. M. Casas, B. Diosdado, J. Forniés, private communication.
[34] F. Bérézovsky, A. A. Hajem, S. Triki, J. Sala-Pala, P. Molinié, *Inorg. Chim. Acta* **1999**, *284*, 8–13.
[35] H. Vahrenkamp, A. Geiss, G. N. Richardson, *J. Chem. Soc., Dalton Trans.* **1997**, 3643–3651.
[36] H. Oshio, M. Yamamoto, T. Ito, *Inorg. Chem.* **2002**, *41*, 5817–5820.
[37] E. Colacio, J. M. Domínguez-Vera, F. Lloret, J. M. Moreno-Sánchez, R. Kivekas, A. Rodríguez, R. Sillanpaa, *Inorg. Chem.* **2003**, *42*, 4209–4214.
[38] R. Lescouezec, F. Lloret, M. Julve, J. Vaissermann, M. Verdaguer, R. Llusar, S. Uriel, *Inorg. Chem.* **2001**, *40*, 2065–2072.
[39] H.-Z. Kou, B. C. Zhou, D.-Z. Liao, R.-J. Wang, Y. Li, *Inorg. Chem.* **2002**, *41*, 6887–6891.
[40] A. Figuerola, C. Díaz, M. S. El-Fallah, J. Ribas, M. Maestro, J. Mahía, *Chem. Commun.* **2001**, 1204–1205.
[41] M. Ohba, H. Okawa, *Coord. Chem. Rev.* **2000**, *198*, 313–328.
[42] J. Forniés, J. Gómez, E. Lalinde, M. T. Moreno, *Chem. Eur. J.* **2004**, *10*, 888–898.
[43] L. R. Falvello, M. Tomás, *Chem. Commun.* **1999**, 273–274.
[44] S.-W. Lai, K.-K. Cheung, M. C.-W. Chan, C.-M. Che, *Angew. Chem. Int. Ed.* **1998**, *37*, 182–184.
[45] R. Usón, J. Forniés, P. Espinet, R. Navarro, M. A. Usón, *Inorg. Chim. Acta* **1979**, *33*, L103–L105.
[46] R. Usón, J. Forniés, P. Espinet, A. Arribas, *J. Organomet. Chem.* **1980**, *199*, 111–118.
[47] R. Usón, J. Forniés, P. Espinet, *Synth. React. Inorg. Met.-Org. Chem.* **1983**, *13*, 513–526.
[48] I. Escorihuela, L. R. Falvello, M. Tomás, *Inorg. Chem.* **2001**, *40*, 636–640.
[49] K. R. Dunbar, R. A. Heintz, *Prog. Inorg. Chem.* **1997**, *45*, 283–391.
[50] R. Usón, J. Forniés, M. Tomás, B. Menjón, *Organometallics* **1986**, *5*, 1581–1584.

 © 2005 Wiley-VCH Verlag GmbH & Co. KGaA, Weinheim

[51] *SAINT-Plus* (version 6.02), 6.02 ed., Bruker Analytical X-ray Systems INC., Madison, USA, Madison, USA, **1999**.
[52] G. M. Sheldrick, *SADABS* (version 2.03), University of Göttingen, Germany, Germany, **1996**.
[53] G. M. Sheldrick, *SHELXL-97*, University of Göttingen, Germany, Germany, **1997**.

Received: April 16, 2005
Published Online: August 29, 2005

 © 2005 Wiley-VCH Verlag GmbH & Co. KGaA, Weinheim

Vertex-Sharing Water Tape Consisting of Cyclic Hexamers

Bao-Qing Ma,*[a] Hao-Ling Sun,[a] and Song Gao*[a]

Keywords: Water aggregates / Cyanides / Hydrogen bonds

A 1D water tape consisting of vertex-sharing cyclic water hexamers has been observed, which represents a subunit of ice structure.

(© Wiley-VCH Verlag GmbH & Co. KGaA, 69451 Weinheim, Germany, 2005)

Introduction

Water is recognized as being essential for life processes, but its actual role in these processes is relatively poorly understood.[1] The obstacle lies in the diversity of hydrogen-bonding associations of water molecules, as reflected by a large number of polymorphous forms of ice. Discrete small clusters, as the basic units of water structure, have been widely investigated both experimentally and theoretically, because their structural information holds considerable promise for the understanding of the behavior of bulk water and processes in biological systems.[2] This realization has prompted enormous studies on the water structures trapped in different environments and great progress has been made regarding structural characterization in hydrate clathrates.[3–7]

One-dimensional water morphologies including chains and tapes constitute an important form of water, which plays a significant role in many fundamental biological processes as "proton wires".[8] Helical water chains have also been observed in crystal hosts.[9] From a structural point of view, the polymeric water morphologies have a close relationship with bulk water, especially those containing a cyclic water hexamer, which is one of the dominant components in liquid water and the building unit of ice I_h. Two-dimensional water layers consisting of hexameric rings with different conformations such as boat, chair, or hybrid chair/boat have been observed in several cases.[10] Although extended tapes containing hexamers have been reported recently, they actually comprise fused tetramers and hexamers[11] rather than sole hexamers. In this context, we report herein a 1D tape-like water structure consisting of vertex-sharing cyclic hexamers, which is hosted within the complex $[Fe(bipy)_2(CN)_2]\cdot 2.5H_2O$ (**1**) (bipy = 2,2′-bipyridine). The tape is a fragment of ice I_h and can be viewed as a simple model of ice structure.

[a] State Key Laboratory of Rare Earth Materials Chemistry and Applications & PKU-HKU, Joint Laboratory on Rare Earth Materials and Bioinorganic Chemistry, College of Chemistry and Molecular Engineering,
Peking University, Beijing 100871, P.R. China
E-mail: mabqing@yahoo.com; gaosong@pku.edu.cn

Results and Discussion

Description of the Structure of 1

An ORTEP view of compound **1** is shown in Figure 1. Selected bond lengths and angles are given in Table 1. The compound consists of one $Fe(bipy)_2(CN)_2$ moiety and two and a half water molecules. The ferricyanide moiety has been widely used for the preparation of molecule-based magnetic materials[12] and recent interest has been focused on the versatile cyanide fragments with capping ligands to diversify the structures and properties.[13] The Fe atom in **1** is coordinated by four N atoms from two chelating 2,2′-bipy molecules [Fe–N1 = 2.004(2); Fe–N2 = 1.978(2); Fe–N3 = 1.987(2); Fe–N4 = 1.962(2) Å] and two C atoms from two *cis* cyanide groups [Fe–C21 = 1.915(2); Fe–C22 = 1.910(2) Å], forming an essentially octahedral coordination environment, which is similar to its analogue, $[Fe(1,10\text{-phen})_2(CN)_2]\cdot 3H_2O$.[14] The corresponding bond lengths are in agreement with those in $[Fe(1,10\text{-phen})_2(CN)_2]\cdot 3H_2O$. The Fe atom and cyanide groups are almost linear, with the Fe–C21–N5 and Fe–C22–N6 bond angles being 176.6(8) and 176.0(8)°, respectively. The C21–Fe–C22 bond angle is

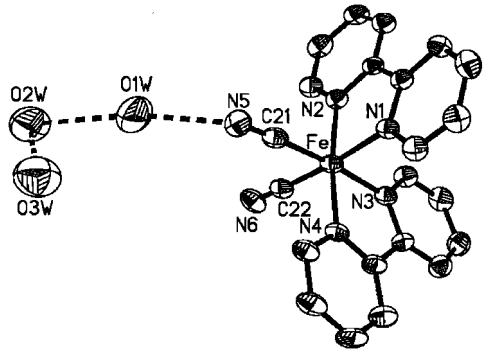

Figure 1. Molecular structure of compound **1**.

 © 2005 Wiley-VCH Verlag GmbH & Co. KGaA, Weinheim DOI: 10.1002/ejic.200500374

87.52°, consistent with that in complex $[Fe(1,10\text{-phen})_2(CN)_2]\cdot 3H_2O$ (88.61°). The dihedral angles between the two pyridine rings of each 2,2′-bipy (N1–N2; N3–N4) are 7.88(62) and 5.17(21)°, respectively, and the two 2,2′-bipy molecules are almost perpendicular, with an intersecting angle of 86.37°.

Table 1. Selected bond lengths [Å] and angles [°] for **1**.

Fe–C(22)	1.9103(18)	Fe–C(21)	1.9154(14)
Fe–N(4)	1.9617(14)	Fe–N(2)	1.9776(14)
Fe–N(3)	1.9867(10)	Fe–N(1)	2.0035(14)
N(5)–C(21)	1.1447(18)	N(6)–C(22)	1.153(2)
C(22)–Fe–C(21)	87.51(7)	C(22)–Fe–N(4)	92.44(7)
C(21)–Fe–N(4)	93.83(6)	C(22)–Fe–N(2)	93.31(7)
C(21)–Fe–N(2)	91.69(6)	N(4)–Fe–N(2)	172.19(5)
C(22)–Fe–N(3)	91.50(6)	C(21)–Fe–N(3)	174.48(7)
N(4)–Fe–N(3)	80.79(5)	N(2)–Fe–N(3)	93.78(5)
C(22)–Fe–N(1)	174.13(7)	C(21)–Fe–N(1)	92.17(6)
N(4)–Fe–N(1)	93.43(6)	N(2)–Fe–N(1)	80.83(6)
N(3)–Fe–N(1)	89.37(5)	N(5)–C(21)–Fe	176.42(17)
N(6)–C(22)–Fe	177.20(17)		

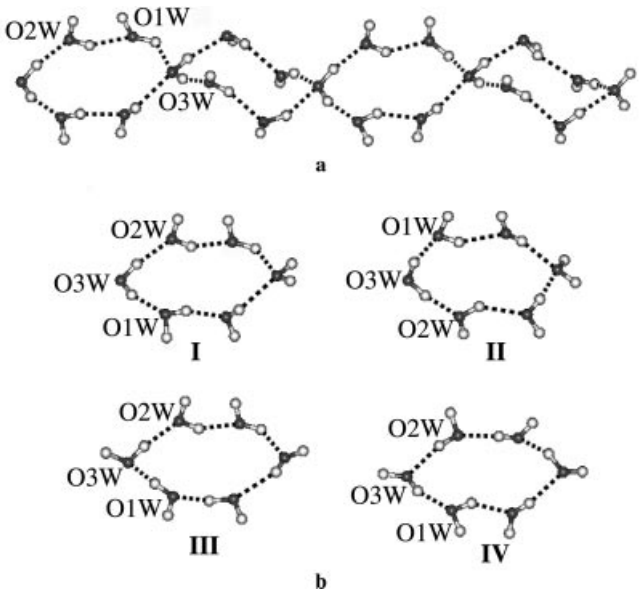

Figure 2. (a) 1D water tape assembled from cyclic hexamers by sharing one vertex. Hydrogen bonds [Å]: O1W···O2W*a* = 2.952(4); O1W···O3W = 2.920(3); O2W···O3W = 2.808(3); $a = -x, -y + 1, -z$. (b) Four different hydrogen-bonding patterns presented in the water tape due to imposed symmetry restriction.

Interestingly, two and a half independent water molecules associated with hydrogen bonds form a cyclic hexamer, which is center-symmetric and adopts a chair conformation (Figure 2a). The average O···O distance of 2.89 Å is close to the value in liquid water (2.85 Å),[15] but longer than that in ice I_h (2.759 Å).[16] Compared with those discrete water hexamers recently observed in the solid states, the distance is slightly shorter than that found in a planar hexamer (2.905 Å)[5b] trapped in an organic compound, however it is longer than that housed in a metal-organic framework.[17] The bond angles in the hexamer vary from 80.5 to 132.9°, which considerably deviates from the corresponding value of 109.3° for preferred tetrahedral geometry in hexagonal ice, implying that the flexibility of hydrogen bonds allows efficient perturbation enforced by the surrounding environments.

Theoretical calculation predicts that hexamer represents the transition from 2D cyclic to 3D cage structure with a cage isomer as a stable configuration.[2a] Other less stable conformers including boat, chair, and quasiplanar, have also been experimentally observed. The chair-shaped hexamers described here are not discrete, but self-assembled into a one-dimensional tape by sharing a vertex, which is located on a twofold axis parallel to the [010] direction (Figure 2a). The adjacent hexamers are tilted with an intersecting angle of 28°. The shared water serves as double hydrogen-bond donors and acceptors with a tetrahedral geometry, which is a quite common configuration for the oxygen atom in ice and liquid water. The remaining two water molecules participate in three hydrogen-bonding interactions as double donors and single acceptor, reminiscent of the water surface or interface, where deficient hydrogen-bonded water molecules are present. Recent spectroscopic experiments also demonstrated that significant numbers of oxygen atoms in liquid water are less than four coordinate.[18] As imposed by the symmetry (space group *C*2/*c*), the hydrogen atoms, except for those bonded to a peripheral host, are disordered, as commonly found in ice structure, and there are four possible hydrogen-bonding patterns, as illustrated in Figure 2b. This reflects the anomalous nature of water due to flexible hydrogen bonds. Four hydrogen atoms related by a twofold axis on O3W have half occupancy. O1W and O2W water molecules each have a full-occupancy hydrogen atom that is hydrogen bonded to the host, while the intratape hydrogen atoms are positionally disordered with half occupancy. The bridging O3W has a typical tetrahedral geometry for a water molecule with O3W···O1W and O3W···O2W distances being 2.904(4) and 2.799(3) Å, respectively.

In contrast to frequently observed discrete water tetrameric, pentameric, and hexameric clusters, the connection of these clusters into a tape-like motif is relatively rare. Very recently, a 1D tape consisting of vertex-sharing water tetramers has been reported[19] and we discovered two water tapes made up of vertex-sharing and edge-sharing pentamers.[6a,20] Water tapes consisting of mixed water rings including fused hexamers and tetramers trapped in an organic compound, 2,4-bimethyl-5-aminobenzo[*b*]-1,8-naphthyridine,[11a] and a metal-organic complex, $[Ag_2(ophen)_2]_2\cdot 6H_2O$ [Hophen = 1*H*-[1,10]phenanthrolin-2-one], have also been observed.[11b] The currently described water tape built from vertex-sharing hexamers represents an important development of this kind of motif. We are unaware of any other reported water tapes made of sole water hexamers, though 1D chains consisting of cyclic hexameric chair conformers linked by metal ions have been reported in the complexes $[M(H_2biim)_2(H_2O)_2](ina)_2\cdot 4H_2O$ (M = Zn, Co; H_2biim = 2,2′-biimidazole; ina = isoniconate).[21] Considering a pivotal position of the hexamer in the water structure, our water tape could provide insight into the mysterious veil

 © 2005 Wiley-VCH Verlag GmbH & Co. KGaA, Weinheim

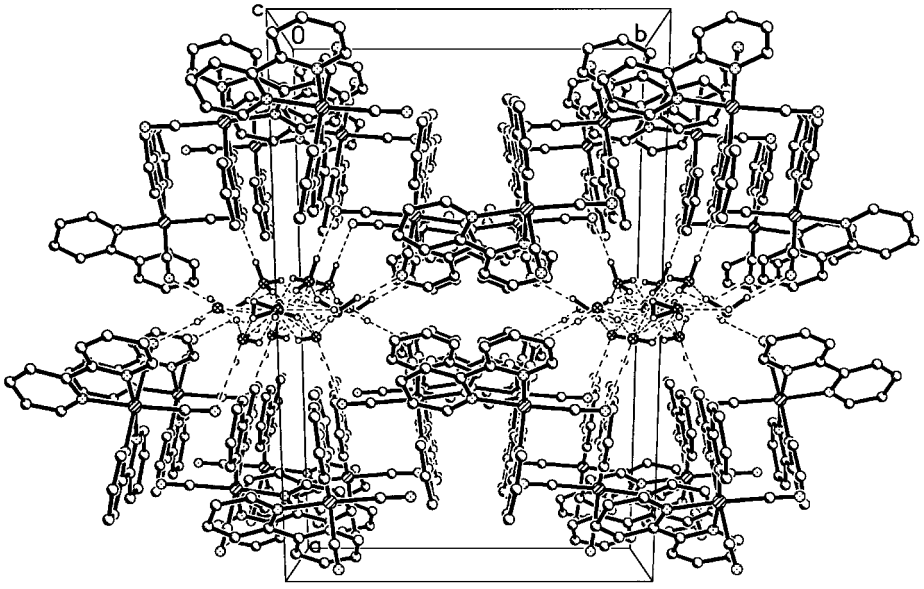

Figure 3. The packing diagram of **1** viewed along crystallographic *c* axis, showing 1D channels in which water tapes are included. Hydrogen atoms on the host are omitted for clarity. Hydrogen bonds [Å]: O1W···N5 = 2.850(3); O2W*a*···N6 = 2.918 (2); *a* = –*x*, –*y* + 1, –*z*.

of water. To simplify the ice structure, one can reduce its dimension to 2D sheet, to 1D tape, to 0D cluster. The 1D tape lies in between 2D sheet and 0D cluster and can be either edge- or vertex-sharing, which not only is a simple model with respect to 2D sheet, but also has close approximation to ice with respect to the discrete hexameric cluster.

These 1D water tapes are anchored within the channels produced by the host packing. The perpendicular arrangement of the two coordinated 2,2′-bipy molecules around the Fe atom in **1** leads to a rectangular channel with approximate dimensions of 5 × 8 Å parallel to the [001] direction (Figure 3). This channel size appears to adapt the water tape well, as opposed to the "armchair" and zigzag water chains which are hosted within the channels of 6.63 × 3.44 Å and 4.80 × 3.02 Å, respectively.[22] By comparison, a linear water trimer cluster is filled within the channel formed in the compound $[Fe(1,10\text{-phen})_2(CN)_2]\cdot 3H_2O$,[14] which has a similar structure to **1**. The small channel size due to the presence of the bulky 1,10-phen ligands prevents further aggregation of water clusters, and no water tape was observed, indicating the influence of the host environment on the water structure. The cyanide groups from $[Fe(2,2'\text{-bipy})_2(CN)_2]$ units point inward to the channels and form hydrogen bonds with the free hydrogen atoms available to O1W and O2W water molecules. The O···N separation from water tapes to cyanide groups are 2.850(3) and 2.918(2) Å, which are comparable to those in the interior of the tape.

Thermogravimetric Analysis

Thermogravimetric analysis was done with an LT-1 model thermobalance. Compound **1** showed a weight loss of 9.59% below 100 °C, which corresponds to the lattice water molecules, in agreement with the calculated value of 9.62%. It also demonstrates that water tapes are loosely anchored within the host. At 220 °C, the complex began to lose the ligands and decomposed completely at 355 °C. The processes of decomposition are very complicated. The final residue (observed 18.84%) is assigned as Fe_2O_3 (calculated 18.20%).

Conclusions

A novel water tape structure featuring vertex-sharing cyclic hexamers has been structurally determined. Characterization of water morphologies in crystal hydrates is rapidly growing into a new field. Although the control of water clusters of different nuclearity is impossible at the current stage, a judicious choice of hosts could be helpful to trap novel water morphologies. This study and our recent finding of an octameric cluster in a cyanide-bridged f-d complex[23] imply that the cyanide compound might be a good promoter to induce water aggregations.

Experimental Section

Synthesis of 1: Compound **1** was prepared by the literature method.[24] Column-shaped single crystals suitable for X-ray diffraction were obtained through recrystallization of **1** in methanol after 2 weeks.

Crystallography: Crystal data and refinement parameters are summarized in Table 2. Data collection was performed with an Enraf–Nonius CAD-4 Mach3 diffractometer with graphite-monochromated Mo-K_α radiation. A dark red single crystal with approximate dimensions of 0.12 × 0.15 × 0.30 mm^3 was chosen. Unit cell was determined from 25 indexed reflections in the range 8.32–14.97°. Intensity data were collected using ω-2θ-scan mode in the range 1.67 ≤ θ ≤ 27.02°. Of the 5793 reflections measured, 4624 were found

 © 2005 Wiley-VCH Verlag GmbH & Co. KGaA, Weinheim

to be unique (R_{int} = 0.1146). An absorption correction based on ψ scan was applied to the data during data reduction. No decay correction was applied. The structure was solved by the heavy atom method and refined by a full-matrix least-squares technique based on F^2 using the SHELXL 97 program[25]. All non-hydrogen atoms were refined anisotropically. Hydrogen atoms on 2,2′-bipy molecules were placed in geometrically calculated positions and refined isotropically. Hydrogen atoms on water molecules were located from difference Fourier maps and refined by fixing the O–H bond length to 0.96 Å and the isotropic temperature factors to a value of 1.5 times that of the oxygen atoms. CCDC-255296 contains the supplementary crystallographic data for this paper. These data can be obtained free of charge from The Cambridge Crystallographic Data Centre via www.ccdc.cam.ac.uk/data_request/cif.

Table 2. Crystal data and structure refinement for **1**.

Formula	$C_{22}H_{21}FeN_6O_{2.5}$
Formula mass	465.30
Crystal system	monoclinic
Space group	*C*2/*c*
a [Å]	23.5045(13)
b [Å]	14.7424(12)
c [Å]	13.2038(10)
β [°]	112.246(5)
V [Å^3]	4234.7(5)
Z	8
$D_{calcd.}$ [Mg/m^3]	1.460
μ [mm^{-1}]	0.747
Unique reflections	4624
Observed reflections [$I > 2(I)$]	2620
Gof	1.069
F(000)	1928
R_1, wR_2 [$I > 2\sigma(I)$]	0.0677/0.1290
R_1, wR_2 [all data]	0.1500/0.1536

Acknowledgments

This work was supported by the National Science Fund for Distinguished Young Scholars (20125104) and NSFC Nos. 20221101, 20490210.

[1] a) G. A. Jeffrey, *An Introduction to Hydrogen Bonding*, Oxford University Press, New York, **1997**; b) G. A. Jeffrey, W. Saenger, *Hydrogen Bonding in Biological Structures*, Springer-Verlag, Berlin, **1991**.

[2] a) K. Liu, M. G. Brown, C. Carter, R. J. Saykally, J. K. Gregory, D. C. Clary, *Nature* **1996**, *381*, 501–503; b) K. Nauta, R. E. Miller, *Science* **2000**, *287*, 293–295; c) F. Weinhold, *J. Chem. Phys.* **1998**, *109*, 367–372; d) J. M. Ugalde, I. Alkorta, J. Elguero, *Angew. Chem. Int. Ed.* **2000**, *39*, 717–721; e) R. Ludwig, *Angew. Chem. Int. Ed.* **2001**, *40*, 1808–1827; f) J. Kim, D. Majumdar, H. M. Lee, K. S. Kim, *J. Chem. Phys.* **1999**, *110*, 9128–9134; g) K. Liu, J. D. Cruzan, R. J. Saykally, *Science* **1996**, *271*, 929–933.

[3] a) J. L. Atwood, L. J. Barbour, T. J. Ness, C. L. Raston, P. L. Raston, *J. Am. Chem. Soc.* **2001**, *123*, 7192–7193; b) L. J. Barbour, G. W. Orr, J. L. Atwood, *Chem. Commun.* **2000**, 859–860; c) L. R. MacGillivray, J. L. Atwood, *J. Am. Chem. Soc.* **1997**, *119*, 2592–2593; d) L. J. Barbour, G. W. Orr, J. L. Atwood, *Nature* **1998**, *393*, 671–673; e) M. Yoshizawa, T. Kusukawa, M. Kawano, T. Ohhara, I. Tanaka, K. Kurihara, N. Niimura, M. Fujita, *J. Am. Chem. Soc.* **2005**, *127*, 2798–2799.

[4] a) K. Liu, M. G. Brown, J. D. Cruzan, R. J. Saykally, *Science* **1996**, *271*, 62–64; b) R. J. Doedens, E. Yohannes, M. I. Khan, *Chem. Commun.* **2002**, 62–63; c) S. K. Ghosh, P. K. Bharadwaj, *Inorg. Chem.* **2004**, *43*, 5180–5182; d) S. Neogi, G. Savitha, P. K. Bharadwaj, *Inorg. Chem.* **2004**, *43*, 3771–3773; e) M. T. Ng, T. C. Deivaraj, W. T. Klooster, G. J. McIntyre, J. J. Vittal, *Chem. Eur. J.* **2004**, *10*, 5853–5859; f) S. K. Ghosh, P. K. Bharadwaj, *Inorg. Chem.* **2004**, *43*, 5180–5182; g) S. K. Ghosh, P. K. Bharadwaj, *Inorg. Chem.* **2004**, *43*, 6887–6889.

[5] a) S. Supriya, S. Manikumari, P. Raghavaiah, S. K. Das, *New J. Chem.* **2003**, *27*, 218–220; b) J. N. Moorthy, R. Natarajan, P. Venugopalan, *Angew. Chem. Int. Ed.* **2002**, *41*, 3417–3420; c) S. K. Ghosh, P. K. Bharadwaj, *Angew. Chem. Int. Ed.* **2004**, *43*, 3577–3580.

[6] a) B. Q. Ma, H. L. Sun, S. Gao, *Chem. Commun.* **2004**, 2220–2221; b) B. Q. Ma, H. L. Sun, S. Gao, *Angew. Chem. Int. Ed.* **2004**, *43*, 1374–1376.

[7] a) C. Janiak, T. G. Scharmann, S. A. Mason, *J. Am. Chem. Soc.* **2002**, *124*, 14010–14011; b) K. Raghuraman, K. K. Katti, L. J. Barbour, N. Pillarsetty, C. L. Barnes, K. V. Katti, *J. Am. Chem. Soc.* **2003**, *125*, 6955–6961; c) L. Infantes, S. Motherwell, *CrystEngComm* **2002**, *4*, 454–461; d) L. Infantes, J. Chisholm, S. Motherwell, *CrystEngComm* **2003**, *5*, 480–486; e) S. Supriya, S. K. Das, *J. Cluster Sci.* **2003**, *14*, 337–366; f) Q. Y. Liu, L. Xu, *CrystEngComm* **2005**, *7*, 87–89.

[8] a) S. Cukierman, *Biophys. J.* **2000**, *78*, 1825–1834; b) K. M. Jude, S. K. Wright, C. Tu, D. N. Silverman, R. E. Viola, D. W. Christianson, *Biochemistry* **2002**, *41*, 2485–2491.

[9] a) B. Sreenivasulu, J. J. Vittal, *Angew. Chem. Int. Ed.* **2004**, *43*, 5769–5772; b) W. Runde, A. C. Bean, B. L. Scott, *Chem. Commun.* **2003**, 1848–1849.

[10] a) K. M. Park, R. Kuroda, T. Iwamoto, *Angew. Chem. Int. Ed. Engl.* **1993**, *32*, 884–886; b) P. Rodríguez-Cuamatzi, G. Vargas-Díaz, H. Höpfl, *Angew. Chem. Int. Ed.* **2004**, *43*, 3041–3044 and reference therein.

[11] a) R. Custelcean, C. Afloroaei, M. Vlassa, M. Polverejan, *Angew. Chem. Int. Ed.* **2000**, *39*, 3094–3096; b) J. P. Zhang, Y. Y. Lin, X. C. Huang, X. M. Chen, *Inorg. Chem.* **2005**, *44*, 3146–3150.

[12] a) H.-Z. Kou, S. Gao, J. Zhang, G.-H. Wen, G. Su, R. K. Zheng, X. X. Zhang, *J. Am. Chem. Soc.* **2001**, *123*, 11809–11810; b) M. Ohba, H. Okawa, N. Fukita, Y. Hashimoto, *J. Am. Chem. Soc.* **1997**, *119*, 1011–1019; c) K. E. Vostrikova, D. Luneau, W. Wernsdorfer, P. Rey, M. Verdaguer, *J. Am. Chem. Soc.* **2000**, *122*, 718–719.

[13] a) S. Wang, J. L. Zuo, S. Gao, Y. Song, H. C. Zhou, Y. Z. Zhang, X. Z. You, *J. Am. Chem. Soc.* **2004**, *126*, 8900–8901; b) Y. Z. Zhang, S. Gao, H. L. Sun, G. Su, Z. M. Wang, S. W. Zhang, *Chem. Commun.* **2004**, 1906–1907; c) R. Lescouezec, F. Lloret, M. Julve, J. Vaissermann, M. Verdaguer, R. Llusar, S. Uriel, *Inorg. Chem.* **2001**, *40*, 2065–2072.

[14] S. Zhan, Q. Meng, X. You, G. Wang, P. Zheng, *Polyhedron* **1996**, *15*, 2655–2658.

[15] A. H. Narten, W. E. Thiessen, L. Blum, *Science* **1982**, *217*, 1033–1034.

[16] D. Eisenberg, W. Kauzmann, *The Structure and Properties of Water*, Oxford University Press, Oxford, **1969**.

[17] S. K. Ghosh, P. K. Bharadwaj, *Inorg. Chem.* **2003**, *42*, 8250–8254.

[18] P. Warnet, D. Nordlund, U. Bergmann, M. Cavalleri, M. Odelius, H. Ogasawara, L. A. Naslund, T. K. Hirsch, L. Ojamae, P. Glatzel, L. G. M. Pettersson, A. Nilsson, *Science* **2004**, *304*, 995–999.

[19] S. Pal, N. B. Sankaran, A. Samanta, *Angew. Chem. Int. Ed.* **2003**, *42*, 1741–1743.

[20] X. Y. Wang, H. Y. Wei, Z. M. Wang, Z. D. Chen, S. Gao, *Inorg. Chem.* **2005**, *44*, 572–583.

[21] B. H. Ye, B. B. Ding, Y. Q. Weng, X. M. Chen, *Inorg. Chem.* **2004**, *43*, 6866–6868.

 © 2005 Wiley-VCH Verlag GmbH & Co. KGaA, Weinheim

[22] L. E. Cheruzel, M. S. Pometun, M. R. Cecil, M. S. Mashuta, R. J. Wittebort, R. M. Buchanan, *Angew. Chem. Int. Ed.* **2003**, *42*, 5452–5455.
[23] B. Q. Ma, H. L. Sun, S. Gao, *Chem. Commun.* **2005**, 2336–2338.
[24] A. A. Schilt, *Inorg. Synth.* **1970**, *12*, 247.
[25] G. M. Sheldrick, *SHELXT 97*, *Program for Crystal Structure Refinement*, University of Göttingen, Germany, **1997**.
Received: April 27, 2005
Published Online: August 29, 2005

 © 2005 Wiley-VCH Verlag GmbH & Co. KGaA, Weinheim

Molecular Recognition – Allosterism Generated by Weak Host–Guest Interactions in Molecular Rectangles

James D. Crowley,[a] Ian M. Steele,[a] and Brice Bosnich*[a]

Keywords: Host–guest systems / Molecular recognition / Allosterism / Self-assembly / Supramolecular chemistry

Two metal-based molecular rectangles that bear two identical binding sites form 1:2 host–guest adducts with a pair of analogous planar Pt^{2+} complexes. The larger of the two guests shows no binding allosterism with either of the two rectangles, but substantial positive allosterism is observed when the smaller guest binds to the rectangles. It is proposed that the smaller guest is better accommodated in the binding sites of the receptor and that this leads to allosterism. Various experiments, including ^{1}H NOESY spectroscopy, support the supposition that the smaller guest is better incarcerated in the receptors.

(© Wiley-VCH Verlag GmbH & Co. KGaA, 69451 Weinheim, Germany, 2005)

1. Introduction

Allosterism is commonly deployed by biological systems for controlling and regulating function. In these systems, the binding of a substrate usually engenders conformational or other changes in the receptor so that the subsequent binding of the same substrate at other identical sites is either of enhanced or of decreased stability. The mechanisms that generate positive or negative allosterism are subtle, and they are poorly understood in complicated systems. There have been numerous model systems developed,[1] starting with the classical experiments of Rebek.[2] Rebek devised several allosteric systems, including **1**.

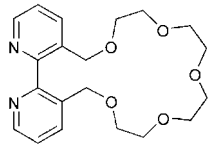

1

The bipyridyl-bound complex [(**1**)W(CO)$_4$] is a (kinetically) stable molecule. Using a U-tube where water is separated by CH_2Cl_2, it was found that the free ligand **1** transported K^+ in preference to Na^+, but that the tungsten complex caused these preferences to be reversed. It was assumed that the transport preference is related to the stability of the alkali ion in the crown-ether site. The bipyridyl that binds to the tungsten generates a different preferred conformation for the crown ether from that adopted by the free ligand **1**. Thus, the tungsten bound to the bipyridyl is mechanically coupled to the crown ether site, leading to different binding affinities of the alkali metals. Following from this work, there have been numerous examples of allosterism involving dinuclear ligands, where the insertion of a metal into one site leads to increased or diminished binding of a second metal in the other site.[1] Some of these systems have been especially sophisticated, some involve allosteric control of catalysis.[1] In some respects, generating allosterism by homo- or heterotopic coordination of metals has a well-understood logic, which relies on the positioning of coordinating ligands for binding to metals with commensurate stereochemical demands. These aspects are cogently presented in Kramer's review.[1]

The next level of complexity in synthetic modeling was in deploying weak (directional) hydrogen bonding for mechanical coupling. The first example of allosterism generated by hydrogen bonding was reported by Hunter[3] who synthesized a host with two identical hydrogen bonding sites for the guest, quinone. In $CHCl_3$ solution, positive allosterism was observed for the two homotopic sites of the host. The allosterism was modest; the successive constants were $K_1 = 14\ M^{-1}$ and $K_2 = 28\ M^{-1}$. Later, a similar hydrogen-bonding homoditopic receptor was found to give positive allosterism for a single guest.[4] More recently, a carefully designed homoditopic system was found capable of giving high positive allosterism for a variety of guests.[5] Differences of 33:1 between the two constants were reported.

As far as we are aware, no examples of allosterism involving weak, poorly directional forces, such as π–π interactions, have been reported.[1e] This paper reports cases where weak molecular recognition forces lead to positive allosterism.

[a] Department of Chemistry, The University of Chicago, 5735 South Ellis Avenue, Chicago, Illinois 60637, USA
E-mail: bos5@uchicago.edu
Fax: +1-773-702-0805

Supporting information for this article is available on the WWW under http://www.eurjic.org or from the author.

2. Receptors and Guests

Molecular rectangles bearing two identical sites were used for investigating allosterism. The molecular cleft **2** is joined by the linkers **3** or **4** to give the molecular rectangles as shown schematically in Equation (1). The three potential metal-containing guests, **5**, **6**, and **7**, were investigated in order to study allosterism. With receptor **2**, both of the guests **5** and **6** form stable 1:1 host–guest complexes in solution.[6,7]

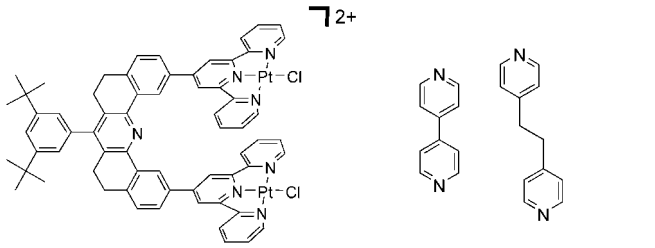

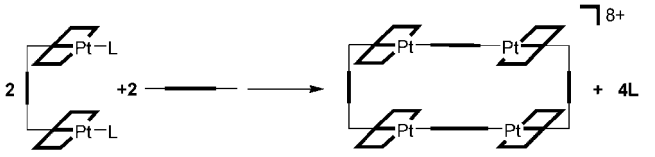

(1)

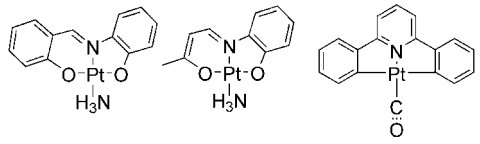

Crystal structures and NOE experiments[6,7] show that the guests **5** and **6** lie within the molecular cleft of **2**. In the solid state, and probably also in solution, the guests **5** and **6** engage in weak Pt–Pt interaction with the receptor **2**. The maximum separation between the face-to-face terpy-Pt-X units of receptor **2** is about 7.2 Å. The crystal structure shows that this interplanar separation is contracted to 6.557 Å in order to accommodate guest **5** in **2**.[6] This contraction is achieved by the concerted rotation of the terpy-Pt-X units about the spacer unit as shown in Scheme 1.

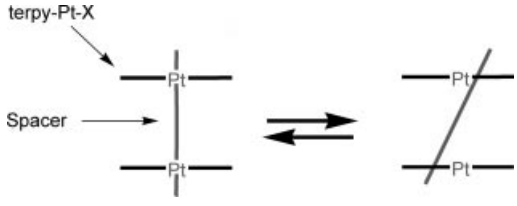

Scheme 1.

Addition of the guests **5** or **6** to solutions of the molecular rectangles will lead to stepwise incarceration of the guests into the molecular clefts. Upon the addition of the first guest, the terpy-Pt-linker unit separation is likely to contract to accommodate the guest. When this happens, the other terpy-Pt-linker unit separation is also likely to contract, because the sites are mechanically coupled by the linkers **3** and **4**. Linker **4** is less rigid than linker **3** and this may lead to less rigid mechanical coupling of the sites. Thus it is conceivable that after the insertion of one guest into a site, the other site may become better organized to accept the second guest because of conformational changes induced by the first adduct formation. If this is the case, then positive allosterism might be observed in host–guest adducts of the rectangles. The reason for including **7**[8] as a guest will become apparent later.

The preparation of the receptor ligand in **2** has been described elsewhere[9] as was the preparation of **5**,[6] **6**,[7] and **7**.[8] Because the reactions of Pt^{2+} complexes are usually kinetically slow, the procedure outlined in Scheme 2 was used for incorporating Pt^{2+} into the two terpy sites of the ligand. The rate of Pt^{2+} incorporation is enhanced by the trans-effect of the olefins and by the fact that presumably labile acetone ligands are being substituted. The reactions are carried out under anhydrous conditions to avoid the formation of nonlabile hydroxo complexes. Solutions of the dipyridine compound **9** and of the two rectangles are kinetically stable at room temperature and below. This behavior contrasts with that of the analogous Pd^{2+} compounds,[10] which are kinetically labile in solution at room temperature. The two rectangles in dimethyl formamide (DMF) solutions give ESI-MS spectra[11] that are devoid of fragmentation and show ion peaks that are consistent with the proposed structures, which, in turn, are confirmed by the peak isotopic distribution of the 2+ ions (Supporting Information). Furthermore, the ^1H NMR spectra of the two rectangles are in full accord with the proposed structures (Supporting Information). There seems little doubt that the molecular rectangles have been correctly identified.

3. Host–Guest Formation

All of the host–guest adduct investigations were carried out in [D_7]DMF solutions at 60 °C. DMF was used because it is a poorly coordinating solvent, and, at 60 °C in this solvent, all of the ^1H NMR spectral peaks are sharp for both the host and the guest. By following the change in chemical shift for certain protons as a function of the mol ratio of host to guest, the stoichiometry of the binding and the binding constants were determined.[12]

As expected, either guest, **5** or **6**, formed 1:1 host–guest adducts with receptor **9** (see Figure 6). The stability constants are listed in Table 1. The smaller value of the stability constant for the **9**–**6** adduct may be related to the smaller π-surface of guest **6**. For both host–guest complexes, complexation-induced chemical shifts are observed for the (internal) H_e but not for the (outer) H_d protons (see Scheme 2), indicating that the guest resides within the molecular cleft. Upon host–guest formation, the color changes

 © 2005 Wiley-VCH Verlag GmbH & Co. KGaA, Weinheim

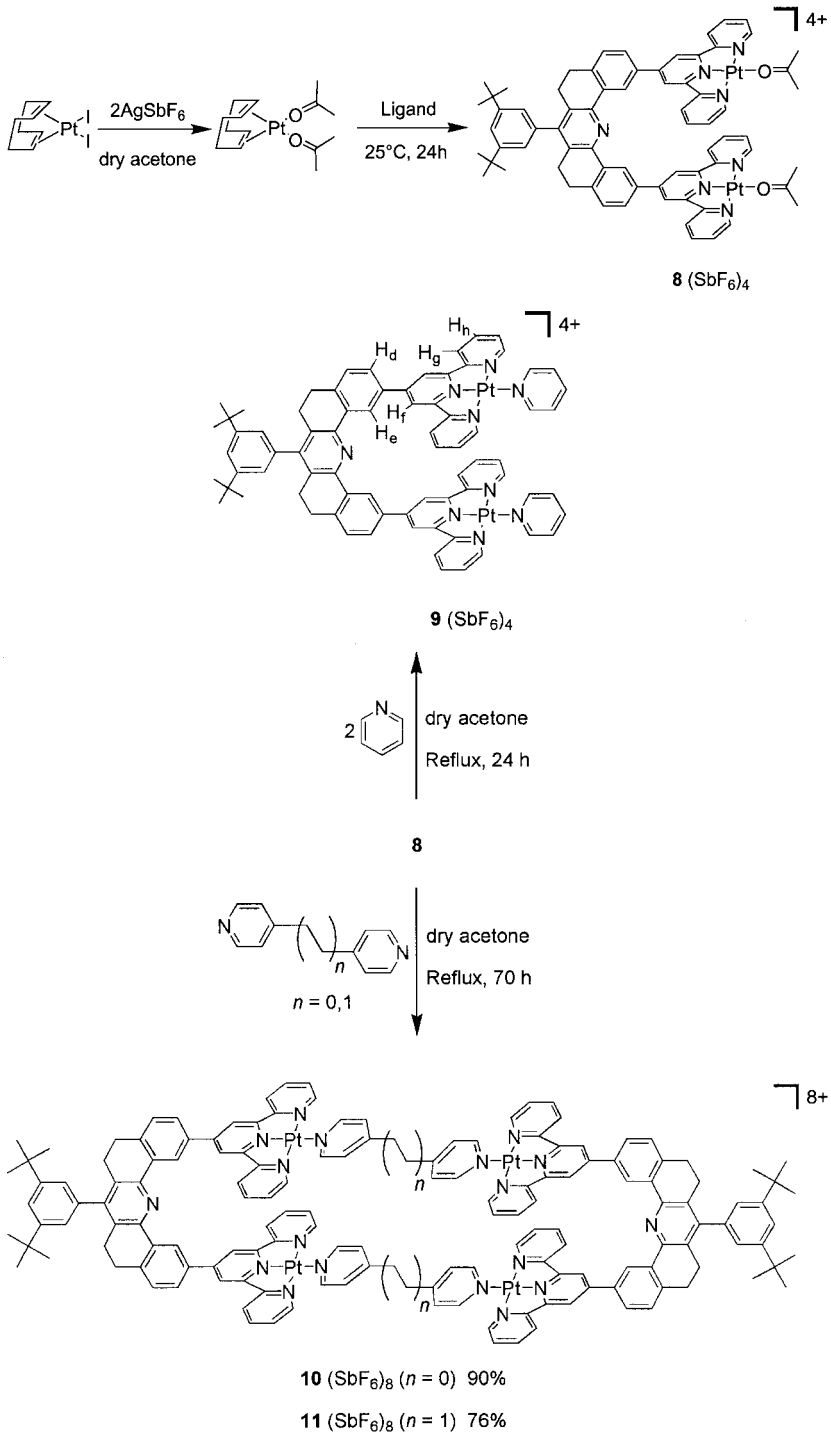

Scheme 2.

to deep red from the light yellow of the components (see Figure 5). The ESI-MS of the host–guest adducts gives peaks for the free receptor, in addition, strong peaks are observed for the 1:1 host–guest adducts formed by **9** with **5** (see Figure 7) and with **6**.

The stabilities of the host–guest adducts **9**–**5** and **9**–**6** should be related in some respects to the first association constants for the two molecular rectangles **10** and **11** (Scheme 2). At 60 °C in [D_7]DMF solution, a 1:2 host–guest complex was found to form between the molecular rectangle **10** and the guest **5** (see Figure 9). As expected, host–guest formation is signaled by the appearance of a deep red color (see Figure 8). ESI-MS of the host–guest adduct, **10**–(**5**)$_2$, provides peaks for the free rectangle, for the receptor with one guest associated, and for the 1:2 host–guest adduct (see Figure 10). Similar ESI-MS data are observed for all rectangle adducts listed in Table 1, and in all cases, host–guest formation is signaled by the appearance

 © 2005 Wiley-VCH Verlag GmbH & Co. KGaA, Weinheim

of red-colored solutions. The two statistically adjusted microscopic stability constants[13] for the adduct are listed in Table 1 together with the ratio of the stability constants, K_2/K_1. No allosterism is observed for this system: the two constants are the same within experimental error. The absence of allosterism for rectangle **10** could be connected with the rigidity of the linker, which may hinder appropriate mechanical coupling between the two sites. Rectangle **11** has a more flexible linker, and this circumstance might allow favorable conformational adjustment at the binding sites. The two microscopic stability constants for the host–guest adduct **11**–(**5**)$_2$ are listed in Table 1. Again, no allosterism is observed within experimental error. Interestingly, the association constants for the adducts **10**–(**5**)$_2$ and **11**–(**5**)$_2$ are the same within experimental error. The absence of allosterism in either of these cases might suggest that the structure of the guest may influence whether or not allosterism is observed. It was supposed that a smaller guest such as **6** might fit better into the molecular clefts of the rectangles, and, as a consequence, better mechanical coupling between the two binding sites may ensue.

The pairs of stability constants for the 1:2 host–guest adducts **10**–(**6**)$_2$ and **11**–(**6**)$_2$ are given in Table 1. Positive allosterism is observed for both adducts, the **11**–(**6**)$_2$ system having the larger cooperative enhancement.

Table 1. Microscopic stability constants (M^{-1}) for host–guest formation in [D_7]DMF at 60 °C.

Adduct	Host–Guest Stoichiometry	K_1 [M^{-1}]	K_2 [M^{-1}]	Ratio K_2/K_1
9–**5**	1:1	3760 ± 600	–	–
9–**6**	1:1	1160 ± 200	–	–
10–(**5**)$_2$	1:2	4100 ± 200	4200 ± 100	1.02
11–(**5**)$_2$	1:2	3800 ± 300	4400 ± 100	1.15
10–(**6**)$_2$	1:2	1450 ± 200	5200 ± 400	3.58
11–(**6**)$_2$	1:2	1250 ± 200	5600 ± 400	4.58

The free energy associated with the first stability constant (K_1) of the adducts **10**–(**6**)$_2$ and **11**–(**6**)$_2$ incorporates the free energy of the conformational rearrangement that leads to allosterism. Thus one might expect that the stability constant for the analogous uncoupled adduct, **9**–**6**, would be larger than the first constants for **10**–(**6**)$_2$ and **11**–(**6**)$_2$. The formation constants for the **9**–**6** adduct and the first association constants (K_1) for the **10**–(**6**)$_2$ and **11**–(**6**)$_2$ adducts are essentially the same (Table 1). Similarly, even though the adducts **10**–(**5**)$_2$ and **11**–(**5**)$_2$ show no allosterism, their first constant (K_1) is essentially the same as the constant (K) found for the 1:1 adduct, **9**–**5**. We discuss these observations later but we can provide no plausible explanation for the results.

The fact that the 1:2 adducts **10**–(**5**)$_2$ and **11**–(**5**)$_2$ show no allosterism whereas the 1:2 adducts **10**–(**6**)$_2$ and **11**–(**6**)$_2$ do may, as we have suggested, be connected with the ability of the receptors to accommodate the smaller guest **6**. ^{1}H NOE experiments suggest that this may be the case.

4. ^{1}H NOE Experiments on the Host–Guest Adducts, 10–(5)$_2$ and 10–(6)$_2$

The ^{1}H NOESY experiments[14] were carried out in [D_7]DMF solutions at 60 °C. The results for the **10**–(**5**)$_2$ and **10**–(**6**)$_2$ host–guest adducts are illustrated in Figure 1 and Figure 2, respectively. Since the rectangles have symmetry operations that interchange the protons H_e and H_d with the corresponding protons of the spacer, the symmetry-related protons are not shown. It will be seen that the two systems (Figures 1 and 2) show different ^{1}H NOESY cross-peaks, but both spectra clearly demonstrate that the guests reside only within the molecular clefts. The two guests **5** within rectangle **10** show cross-peaks between the protons, H_e and H_k, of the rectangle and the "back" (H_s, H_r, H_q, H_p and H_o) and "front" (H_v, NH_3) protons of the guest. The guests are shown in one pair of orientations, but the cross-peaks clearly indicate that several orientations of the guest within the clefts exist for the **10**–(**5**)$_2$ adduct. For the 1:2 host–guest adduct, **10**–(**6**)$_2$, the ^{1}H NOESY data clearly show that the guests exist in one preferred orientation as illustrated in Figure 2, where the ammine ligands of the guests point at the 4,4′-dipyridyl linkers.

It will be noted that for both adducts (Figures 1 and 2) some protons of the guest show no cross-peaks with the host. Given that NOE cross-peaks are generally observed at distances of less than about 3.5 Å,[14] the orientation of the guests in the rectangle **10** is roughly as shown in Figure 1, where the *ortho*-amino phenolate residue probably resides, to some extent, outside of the cleft. The several mutual orientations of the two guests within the rectangular receptor are probably interchanged by intermolecular exchange because scale molecular models suggest that the receptor site does not appear to be large enough to allow for intramolecular rotation of the guest.

Because of the interaction of the *ortho*-protons of the pyridine ligands of the linker with those of the flanking pyridyl ligands of the terpy-Pt unit, the pyridine ligand planes of the linker are expected to lie roughly perpendicular to the terpy-Pt units. The barrier to rotation of the linker pyridine ligands cannot be high, because, even at –90 °C in acetone solution, rapid rotation of the pyridine ligands occurs on a ^{1}H NMR time scale (500 MHz).[10] At 60 °C in [D_7]DMF, the 1:2 host–guest adducts also show rapid rotation of the linker pyridine ligands, but the preferred orientation of the pyridine planes is likely to be perpendicular to the terpy-Pt^{2+} plane. Scale molecular models indicate that when the planes of the linker pyridine ligands lie roughly perpendicular to the terpy-Pt plane, the guests, especially **5**, cannot be fully accommodated within the molecular clefts of the rectangles. It is probable that guest incarceration does not provide sufficient energy to cause the planes of the linker pyridine groups to approach planarity with the terpy-Pt units to open the cleft cavity. Thus, we suggest that the pyridine ligands of the linkers are the main steric impediment to complete incarceration of guest **5**. As shown in Figure 2, guest **6** has only one predominant orientation within the host. Presumably the smaller size of **6** relative to **5** al-

 © 2005 Wiley-VCH Verlag GmbH & Co. KGaA, Weinheim

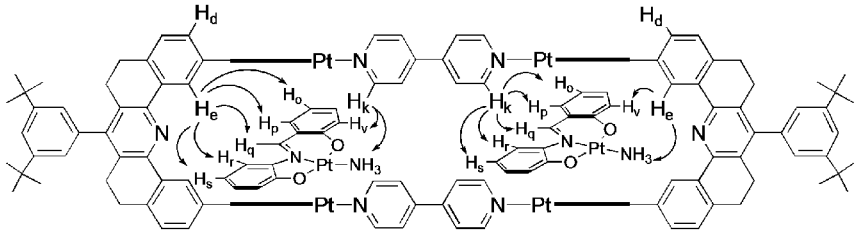

Figure 1. Cross-peaks observed for the 1:2 host–guest adduct **10**–(**5**)$_2$ in [D$_7$]DMF at 60 °C.

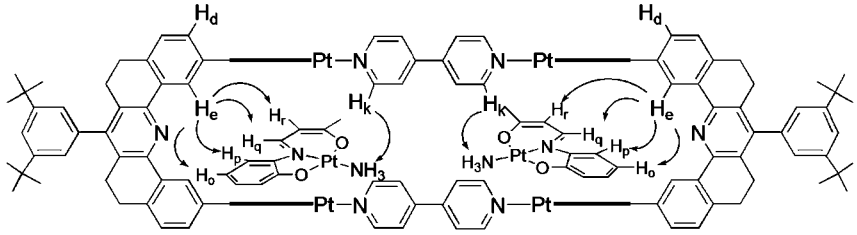

Figure 2. Cross-peaks observed for the 1:2 host–guest adduct **10**–(**6**)$_2$ in [D$_7$]DMF at 60 °C. Possible cross-peaks with the guest methyl group were not investigated.

lows the former to fit better within the cleft. As for the case of the adduct between **2** and **5**,[6] where the guest also has a single orientation and the crystal structure reveals Pt–Pt interaction, it is suggested that Pt–Pt interaction exists for the 1:2 adduct **10**–(**6**)$_2$. These observations suggest that the observed allosterism may depend on how well the guests are accommodated within the hosts, and Pt–Pt interaction may possibly fix the orientation of the guest, which may also contribute to favorable mechanical coupling. The arguments given above depend on the assumption that the disposition of the linker pyridine groups prevents the full accommodation of guests having the dimensions of **5** or larger. Since the barrier to pyridine ligand rotation is unknown, it is possible to argue that the guests could cause the linker pyridine groups to rotate so as to accommodate the guest. This postulate implies that the free energy of host–guest formation is sufficient to overcome the major part of the linker pyridine rotational barrier. In order to explore this matter further, we have studied the host–guest behavior of the much larger guest **7**[8,15] with **10**.

5. Host–Guest Formation of 10 with 7

The receptor **2** forms a bright red 1:2 host–guest complex with the guest **7**, where one guest lies within the molecular cleft and the other guest lies on the outer faces of the terpy-Pt-Cl units.[15] The Pd^{2+} rectangle analogous to **10** forms a red 1:4 host–guest complex with 9-methylanthracene (**12**).[16] In this case, two of the guests lie in the two molecular clefts, and the other two guests are associated with the outer faces of the terpy-Pd-linker units. In [D$_7$]DMF at 60 °C, addition of **7** to the rectangular receptor **10** causes a slightly visible change in color, and ESI-MS data show only ions corresponding to the receptor (Supporting Information). ^{1}H NMR spectral shift titration indicates that a 1:4 host–guest complex is formed (Supporting Information). Inspection of the host protons whose chemical shifts change upon host–guest formation suggests that guest **7** does not occupy the molecular clefts of receptor **10**. This was confirmed by ^{1}H NOESY spectra at 60 °C in [D$_7$]DMF, where only the receptor protons H$_d$ and H$_k$ (but not H$_e$)

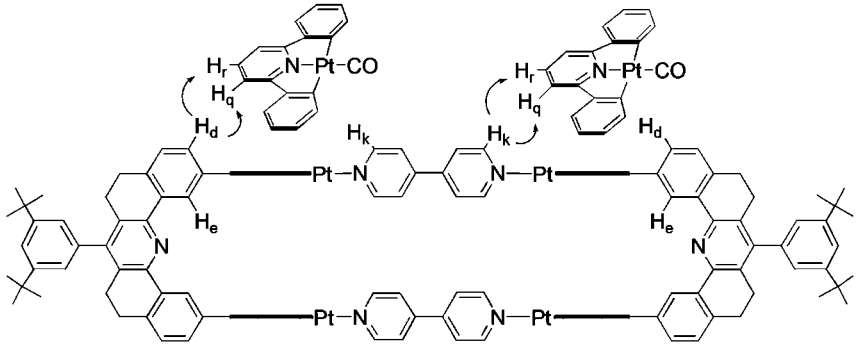

Figure 3. Cross-peaks observed for the 1:4 host–guest adduct **10**–(**7**)$_4$ in [D$_7$]DMF at 60 °C. Only two guests are shown, one for each of the two orientations.

 © 2005 Wiley-VCH Verlag GmbH & Co. KGaA, Weinheim

have cross-peaks to the protons of the guest (Figure 3). The ^{1}H NMR spectrum indicates that the 4,4′-dipyridyl linkers are rapidly rotating so that both of the protons adjacent to the pyridine nitrogen atoms have cross-peaks with the guest. The observed cross-peaks (Figure 3) indicate that the guest adopts two orientations, as evidenced by the interaction of both H_d and H_k with H_r and H_q. Since a 1:4 host–guest complex is formed, it is not possible to obtain the four stability constants, but it is clear that guest **7** does not occupy the molecular clefts of **10** to any significant degree. These data support our supposition that the pyridine ligands of the linkers restrict access to the molecular cleft and that it is possible that a guest of the size of **5** may have difficulty in being fully incarcerated in the clefts. As a consequence, it may be that in such circumstances there is only weak mechanical coupling between the sites.

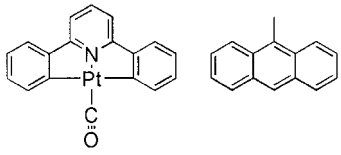

7 **12**

6. X-ray Diffraction Studies

We have attempted to obtain suitable crystals for X-ray diffraction from the host–guest complexes formed by the molecular rectangles **10** and **11** and the two guests **5** and **6** as well as the guest-free rectangles **10** and **11**. Except for crystals formed by the host–guest adduct **10**–(**5**)$_2$, none of the other solids diffracted in a manner suitable for structure determination. The crystals of **10**–(**5**)$_2$ were formed from methyl ethyl ketone by methanol diffusion. The crystals diffracted but they were disordered, and only an outline of the molecular rectangle structure could be obtained. The crystallographic data are listed in Table 2, and the derived structure is shown in Figure 4. The solvent molecules, the SbF_6^- counter ions, the guest molecules, and the di-*tert*-butyl phenyl substituents on the spacers are very disordered and are not shown in Figure 4.

The positions of the guest molecules were indicated by the electron density of the Pt^{2+} ions, which appear in the two molecular clefts and on the outside faces of the four terpy-Pt-linker units of the rectangle. The disorder may arise from this multiple occupancy of these sites. Attempts to crystallize the **10**–(**5**)$_2$ with two extra equivalents of **5** in the hope of occupying all of the guest sites with molecules of **5** failed.

The molecular rectangle is in a *meso* conformation with one spacer in the *R*,*R* and the other in the *S*,*S* configuration. The bonding of the linkers to the Pt^{2+} atoms is not ideal, and the 4,4′-dipyridyl linkers are buckled in order to link to the Pt^{2+} atoms (see lower structure in Figure 4). Presumably this linker strain would be relieved for the rectangle **11** that carries the more flexible 4,4′-dipyridylethane (**4**) linker. The planes of the pyridine groups of the linkers are essentially perpendicular to the plane of the terpy-Pt^{2+} units, a geometry that was inferred from the modeling of the rectangles. Adjacent planes of the terpy-Pt^{2+} units of each cleft are nearly parallel to each other, and the interplanar separation is about 6.9 Å. The "width" of a pyridine (from hydrogen to corresponding hydrogen) is about

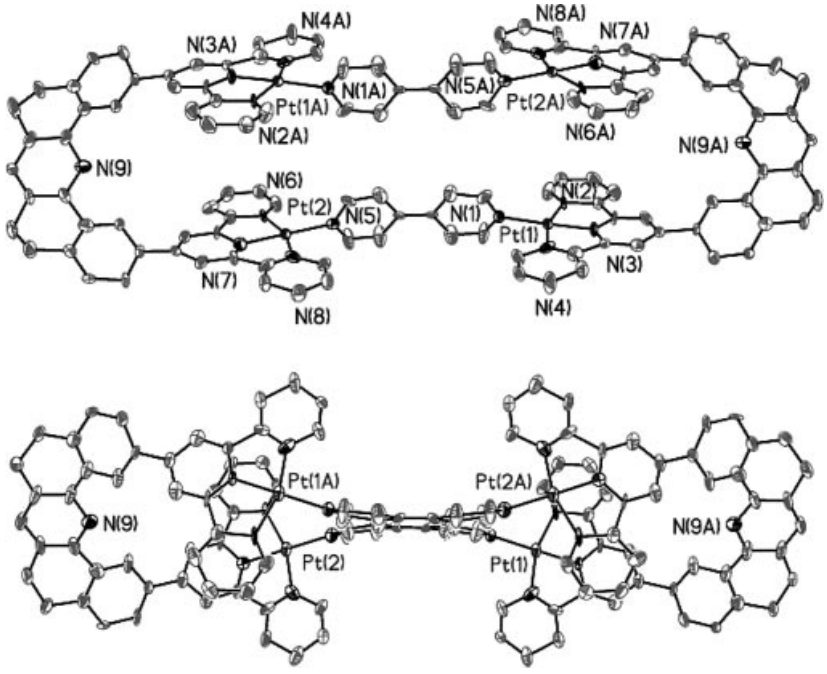

Figure 4. ORTEP diagrams of the "core" of the molecular rectangle. Above, a "side" view, below a "top" view. The disordered guest molecules **5**, the *tert*-butyl-containing phenyl rings of the spacer, the SbF_6^- ions, and the solvents of crystallization have been omitted for clarity. The thermal ellipsoids are shown at 50% probability.

 © 2005 Wiley-VCH Verlag GmbH & Co. KGaA, Weinheim

Table 2. Crystallographic data for the host–guest adduct formed from **10** and **5**.

Compound	**10**–(**5**)$_2$
Formula	$C_{67}N_9Pt_4$ + 3Sb +10F (as refined)
Formula weight	2266.37 (as refined)
space group	$P\bar{1}$
a [Å]	13.886(10)
b [Å]	16.026(11)
c [Å]	35.67(3)
α [deg]	77.126(12)
β, [deg]	85.113(16)
γ, [deg]	67.426(12)
V [Å]^3	7146(9)
Z	2
cryst. size, color, habit	0.20 × 0.15 × 0.15 mm, red, brick
D(calc) [g cm^{-3}]	1.053
μ [mm^{-1}]	4.493
temp [K]	100(5)
Wavelength [Å]	0.71073 (Mo-K_α)
$R(F)$, %[a]	14.84
$R(wF^2)$, %[a]	40.25

[a] Quantity minimized = $R(wF^2) = \Sigma[w(F_o^2 - F_c^2)^2]/\Sigma[(wF_o^2)^2]^{1/2}$; $R = \Sigma\Delta/\Sigma(F_o)$, $\Delta = (F_o - F_c)$; $w = 1/[\sigma^2(F_o^2) + (aP)^2 + bP]$, $P = [2F_c^2 + \mathrm{Max}(F_o, 0)]/3$.

5 Å. Thus, the corresponding pyridine groups of neighboring linkers have nearest approach distances of about 1.9 Å if the pyridine groups of different linkers are aligned as is nearly the case (Figure 4). A separation of this magnitude will not allow a guest to reside between pyridine groups and would not allow a large guest such as **7** to fit into the molecular cleft. The interplanar separation of the terpy-Pt^{2+} units is uncharacteristically large. Usually, this separation is 6.8 Å or less,[17] and the separation in the present system is at the outer limits of π–π stacking distances. There does not seem to be any steric impediment to the contraction of the parallel terpy-Pt^{2+} units to a separation of 6.7 Å. A smaller guest such as **6** may cause this interplanar separation contract more.

7. Discussion

Understanding the origins of allosterism in multimetallic ligand systems and even in hosts bearing hydrogen bonds is relatively simple in outline. This is so for the former because the coordination geometries of metals and the requirements of the ligands are understood. For the latter systems, the geometry of hydrogen bonding with given substrates is usually understood, and, consequently, there are plausible rationalizations that can be advanced on the basis of the directions of the hydrogen bonds. With systems that rely on weak, poorly directional π–π or similar interactions, attempts to rationalize the allosterism are more difficult. This is the case even for the present rectangles that appear to provide a simple mechanism for mechanical coupling between sites. Whereas substantial positive allosterism was observed for the 1:2 host–guest complexes **10**–(**6**)$_2$ (K_2/K_1 = 3.58) and **11**–(**6**)$_2$ (K_2/K_1 = 4.58), the energy differences between the two constants are small. For the former, the free energy difference is 0.65 kcal mol^{-1}, and for the latter the difference is 1.01 kcal mol^{-1}. It is therefore difficult to ascribe these small energy differences to specific interactions of conformational changes for complicated hosts such as the present rectangles. Despite these difficulties, work on allosterism generated by weak interactions is important because biological systems rely on the concerted orchestration of these weak forces.

Experimental Section

Procedures: All reagents were obtained from commercial suppliers and were used without further purification. All reactions were performed under argon, unless otherwise specified. Electronic absorption spectra were obtained with a Perkin–Elmer Lambda 6 UV/Vis spectrophotometer. Elemental analyses were performed by Desert Analytics, Inc., Tucson, Arizona. ^{1}H and ^{13}C NMR spectra were recorded with a Bruker DRX500 Fourier transform spectrometer at 300 K, unless specified otherwise. Proton and carbon chemical shifts, *δ*, are reported in ppm, referenced to TMS. Coupling constants, *J*, are reported in Hertz. APCI-MS and ESI-MS were obtained with an Agilent 1100 MSD LC-MS. Acetonitrile was dried with CaH_2, tetrahydrofuran (THF) was dried with potassium/benzophenone ketyl, diethyl ether (Et_2O) was dried with sodium/benzophenone ketyl, dichloromethane (CH_2Cl_2) was dried with CaH_2, and triethylamine (TEA) was dried with CaH_2. Thin-layer chromatography was carried out using precoated silica gel (Whatman PE SIL G/UV) or precoated aluminum oxide (J. T. Baker, aluminum oxide IB-F). Silica gel 60 Å (Merck, 230–400 mesh) and aluminum oxide 58 Å (either activated, basic, Brockman I or activated, neutral, Brockman I) were used for chromatography as indicated. Celite is J.T. Baker Celite 503. The receptor ligand **L**[9] and the guests **5**,[6] **6**,[7] and **7**[8] were prepared by methods previously described. The linkers 4, 4′-dipyridyl (**3**) and 4, 4′-dipyridylethane (**4**), and [(COD)PtI_2] were obtained from the Sigma–Aldrich Chemical Co. and were used without further purification.

[$LPt_2(Py)_2$][SbF_6]$_4$, Receptor 9: The following procedure must be performed with rigorous exclusion of water. A dried 25-mL flask was charged with $AgSbF_6$ (0.185 g, 0.538 mmol) dissolved in anhydrous acetone (10 mL). To a suspension of [(COD)PtI_2] (0.150 g, 0.269 mmol) in dry acetone (5 mL) was added the colorless solution of the silver salt. Upon addition, the COD complex rapidly dissolved and AgI precipitated. The reaction was stirred for 1 h at room temperature, with brief sonication midway through this period. The AgI was removed by Schlenk filtration through a fine-porosity frit under argon. The receptor ligand **L** (0.126 g, 0.135 mmol) was added to the clear solution. The ligand dissolved rapidly, and the color of the solution changed to orange-yellow. The reaction was stirred at room temperature for 24 h, during which time the color became less orange. Pyridine (0.026 g, 0.028 mL, 0.330 mmol) was added to the solution, and the reaction mixture was heated at reflux (70 °C). The mixture was stirred at this temperature for 24 h. The solvent was then removed under reduced pressure to yield a yellow solid, which was slurried in cold methanol and recovered by filtration. It was washed with cold methanol (1 × 5 mL), ether (1 × 5 mL), and pentane (2 × 5 mL), then dissolved in acetone (5 mL) and filtered through Celite. The product was crystallized by vapor diffusion of diethyl ether into the acetone solution. The receptor **9** was recovered by filtration and was washed with diethyl ether (1 × 5 mL) followed by pentane (2 × 3 mL). Yield = 0.280 g (86%). ^{1}H NMR ([D_6]acetone, 27 °C, 500 MHz): *δ* = 1.41 (s, 18 H), 2.86 (t, *J* = 6.55 Hz, 4 H), 3.16 (t, *J* = 6.75 Hz, 4 H), 7.23 (d, *J* = 1.68 Hz, 2 H), 7.65–7.69 (m, 3 H),

 © 2005 Wiley-VCH Verlag GmbH & Co. KGaA, Weinheim

7.93 (t, J = 6.79 Hz, 4 H), 8.05–8.08 (m, 4 H), 8.15 (d, J = 7.55 Hz, 4 H), 8.48 (t, J = 7.88 Hz, 2 H), 8.57 (t, J = 7.65 Hz, 4 H), 8.89 (d, J = 7.75 Hz, 8 H), 9.17–9.19 (m, 4 H), 9.32 (d, J = 5.09 Hz, 4 H) ppm. $C_{75}H_{65}F_{24}N_9Pt_2Sb_4$ (2425.54): calcd. C 37.14, H 2.70, N 5.20; found C 37.33, H 2.94, N 4.96. ESI-MS: a series of peaks were observed that were consistent with $[M - n(SbF_6)]^{n+}$ (n = 1–4): for example, 370.2 [**9** – 4(SbF_6)]$^{4+}$, 572.3 [**9** – 3(SbF_6)]$^{3+}$, 976.0 [**9** – 2(SbF_6)]$^{2+}$, 2188.9 [**9** – 1(SbF_6)]$^{+}$.

Pt Molecular Rectangle Formed with 4,4′-Dipyridyl (10): The following procedure must be performed with rigorous exclusion of water. A dried 25-mL flask was charged with $AgSbF_6$ (0.185 g, 0.538 mmol) dissolved in anhydrous acetone (10 mL). To a suspension of [(COD)PtI_2] (0.150 g, 0.269 mmol) in dry acetone (5 mL) was added the colorless solution of the silver salt. Upon addition, the COD complex rapidly dissolved and AgI precipitated. The reaction was stirred for 1 h at room temperature, with brief sonication midway through this period. The AgI was removed by Schlenk filtration under argon. The receptor ligand **L** (0.126 g, 0.135 mmol) was added to the clear solution. The ligand dissolved rapidly, and the color of the solution changed to orange-yellow. The reaction was stirred at room temperature for 24 h, during which time the color became less orange. The linker 4,4′-dipyridyl (0.021, 0.135 mmol) was added to the solution, and the reaction mixture was heated at reflux (70 °C). The mixture was stirred at this temperature for 2 d. At the end of this period, the solvent was removed under reduced pressure to yield a yellow solid, which was slurried in cold methanol and recovered by filtration. It was washed with methanol (1 × 5 mL), ether (1 × 5 mL), and pentane (2 × 5 mL), then dissolved in acetone (5 mL) and filtered through Celite. The product was crystallized by vapor diffusion of diethyl ether into the acetone solution. The molecular rectangle was recovered by filtration and was washed with diethyl ether (1 × 5 mL) and pentane (2 × 3 mL). Yield = 0.296 g (91%). ^{1}H NMR ([D_6]acetone, 27 °C, 500 MHz): δ = 1.42 (s, 36 H), 2.84 (t, J = 6.55 Hz, 8 H), 3.10 (t, J = 6.61 Hz, 8 H), 7.23 (d, J = 1.68 Hz, 4 H), 7.65 (t, J = 1.63 Hz, 2 H), 7.68 (d, J = 7.86 Hz, 4 H), 7.86 (t, J = 6.63 Hz, 8 H), 8.02 (d, J = 5.05 Hz, 8 H), 8.14 (dd, J_1 = 1.80 Hz, J_2 = 7.75 Hz, 4 H), 8.65–8.68 (m, 16 H), 8.96 (d, J = 7.95 Hz, 8 H), 9.29 (s, 8 H), 9.36 (d, J = 1.67 Hz, 4 H), 9.65 (d, J = 6.46 Hz, 8 H) ppm. $C_{130}H_{126}F_{48}N_{18}Pt_4Sb_8$ (4847.04): calcd. C 37.17, H 2.62, N 5.20; found C 37.46, H 2.69, N 5.06. ESI-MS: a series of peaks were observed that were consistent with $[M - n(SbF_6)]^{n+}$ (n = 2–6): for example, 571.5 [**10** – 6(SbF_6)]$^{6+}$, 733.2 [**10** – 5(SbF_6)]$^{5+}$, 975.0 [**10** – 4(SbF_6)]$^{4+}$, 1379.1 [**10** – 3(SbF_6)]$^{3+}$, 2187.8 [**10** – 2(SbF_6)]$^{2+}$.

Pt Molecular Rectangle Formed with 4,4′-Dipyridylethane (11): A procedure analogous to that above was used. One equivalent of 4,4′-dipyridylethane (0.025 g, 0.135 mmol) was added to the dry acetone solution formed after the reaction of $AgSbF_6$ with [Pt(COD)I_2], and the reaction mixture was heated at reflux (70 °C). The mixture was stirred at this temperature for 2 d. The solvent was removed under reduced pressure to yield a yellow solid, which was slurried in cold methanol and recovered by filtration. It was washed with methanol (1 × 5 mL), ether (1 × 5 mL), and pentane (2 × 5 mL), then dissolved in acetone (5 mL) and filtered through Celite. The product was crystallized by vapor diffusion of diethyl ether into the acetone solution. The molecular rectangle was recovered by filtration and was washed with diethyl ether (1 × 5 mL) and pentane (2 × 3 mL). Yield = 0.290 g (76%). ^{1}H NMR ([D_6] acetone, 27 °C, 500 MHz): δ = 1.42 (s, 36 H), 2.86 (t, J = 6.83 Hz, 8 H), 3.10 (t, J = 6.44 Hz, 8 H), 3.51 (s, 8 H), 7.23 (d, J = 1.65 Hz, 4 H), 7.66 (t, J = 1.69 Hz 2 H), 7.70 (d, J = 7.80 Hz, 4 H), 7.97–8.00 (m, 8 H), 8.07–8.10 (m, 20 H), 8.25 (dd, J_1 = 1.80 Hz, J_2 = 7.75 Hz, 4 H), 8.60–8.65 (m, 8 H), 8.98 (d, J = 8.06 Hz, 8 H), 9.27 (d, J = 6.43 Hz, 4 H), 9.34 (s, 8 H), 9.42 (d, J = 1.89 Hz, 4 H). $C_{154}H_{134}F_{48}N_{18}Pt_4Sb_8$ (4903.15): calcd. C 37.72, H 2.75, N 5.14; found C 37.42, H 2.49, N 5.05. ESI-MS: a series of peaks were observed that were consistent with $[M - n(SbF_6)]^{n+}$ (n = 2–6): for example, 581.8 [**11** – 6(SbF_6)]$^{6+}$, 745.5 [**11** – 5(SbF_6)]$^{5+}$, 990.3 [**11** – 4(SbF_6)]$^{4+}$, 1399.1 [**11** – 3(SbF_6)]$^{3+}$, 2216.3 [**11** – 2(SbF_6)]$^{2+}$.

Host–Guest Interaction of Receptor 9 with 5: The procedure for stoichiometry determination employed for the host–guest adduct formed between **9** and **5** is representative. A series of solutions of **9** (1.75 mM) in dry [D_7]DMF containing varying amounts of **5** (0.23 mM to 11.4 mM) were prepared and were examined by ^{1}H NMR spectroscopy (60 °C). The host in [D_7]DMF solution is orange, as is the guest. The host–guest mixtures vary in color from orange-red to deep red (Figure 5). The mol ratio method[12] was applied, and the stoichiometry of the association was found to be one guest molecule per one host molecule (Figure 6). The data were analyzed using a curve-fitting procedure,[6] and K_1 was found to be 3670 ± 560 M^{-1}. ESI-MS ([D_7]DMF): a series of peaks were observed that were consistent with $[M - n(SbF_6)]^{n+}$ and $[M{\cdot}G - n(SbF_6)]^{n+}$ (n = 1–4): for example, 370.2 [**9** – 4(SbF_6)]$^{4+}$, 476.6 [**9·5** – 4(SbF_6)]$^{4+}$, 572.3 [**9** – 3(SbF_6)]$^{3+}$, 713.1 [**9·5** – 3(SbF_6)]$^{3+}$, 976.0 [**9** – 2(SbF_6)]$^{2+}$, 1188.4 [**9·5** – 2(SbF_6)]$^{2+}$ (Figure 7).

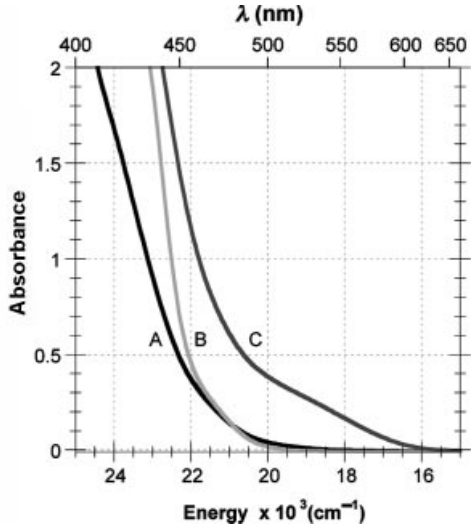

Figure 5. Absorption spectra for **9** (A, 1.75 mM), **5** (B, 2.05 mM), and a 1:1 solution (C) of **9** (1.75 mM) and **5** (1.89 mM). The experiments were performed at 25 °C in dry DMF.

Host–Guest Interaction of Receptor 9 with 6: The procedure was analogous to that used above. The stoichiometry of the association was found to be one guest molecule per one host molecule (Supporting Information). K_1 was found to be 1160 ± 210 M^{-1}. ESI-MS ([D_7]DMF): a series of peaks were observed that were consistent with $[M - n(SbF_6)]^{n+}$ and $[M{\cdot}G - n(SbF_6)]^{n+}$ (n = 1–4): for example, 370.2 [**2** – 4(SbF_6)]$^{4+}$, 467.1 [**9·6** – 4(SbF_6)]$^{4+}$, 572.3 [**9** – 3(SbF_6)]$^{3+}$, 701.5 [**9·6** – 3(SbF_6)]$^{3+}$, 976.0 [**9** – 2(SbF_6)]$^{2+}$, 1170.3 [**9·6** – 2(SbF_6)]$^{2+}$.

Host–Guest Interaction of Molecular Rectangle 10 with 5: The procedure for stoichiometry determination employed for the host–guest adduct formed between **10** and **5** is representative. A series of solutions of **10** (1.65 mM) in dry [D_7]DMF containing varying amounts of **5** (0.25 mM to 23.4 mM) were prepared and were examined by ^{1}H NMR spectroscopy (60 °C). The host in [D_7]DMF solution is orange, as is the guest. The host–guest mixtures vary in

 © 2005 Wiley-VCH Verlag GmbH & Co. KGaA, Weinheim

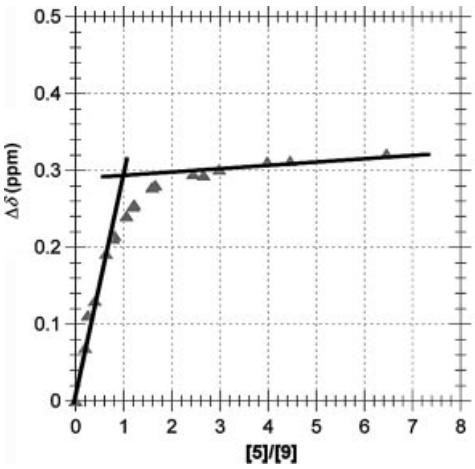

Figure 6. ^{1}H NMR stoichiometry titration for the host–guest complex formed between **9** and **5**. The experiments were performed at 60 °C in [D_7]DMF. The concentration of **9** was held constant at 1.75 mM, and the concentration of **5** was varied between 0.23 mM and 11.4 mM. The plot refers to the proton H_h (see Scheme 2).

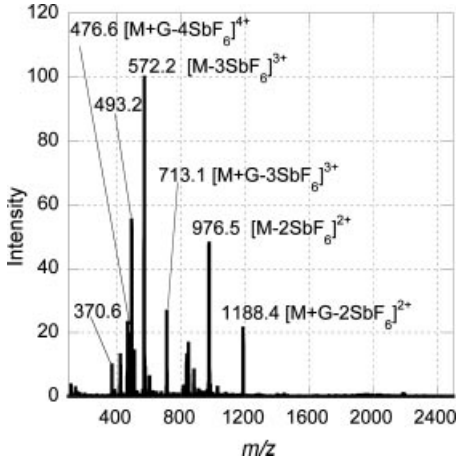

Figure 7. ESI-MS (DMF, 1.75 mM) of the host–guest complex formed between **9** and **5**, *m*/*z* = 370.6 [**9** – 4SbF_6]$^{4+}$, 476.6 [**9·5** – 4SbF_6]$^{4+}$, 572.3 [**9** – 3SbF_6]$^{3+}$, 713.1 [**9·5** – 3SbF_6]$^{3+}$, 976.5 [**9** – 2SbF_6]$^{2+}$, 1188.4 [**9·5** – 2SbF_6]$^{2+}$.

color from orange-red to deep red (Figure 8). The stoichiometry of the association was found to be two guest molecules per one host molecule (Figure 9). Equilibrium constants were determined using a previously described algorithm.[9] The microscopic value of K_1 was found to be 4100 ± 400 M^{-1}, and K_2 was 4200 ± 200 M^{-1}. K_2/K_1 = 1.02. ESI-MS ([D_7]DMF): a series of peaks were observed that were consistent with [M – *n*(SbF_6)]$^{n+}$, [M·G – *n*(SbF_6)]$^{n+}$ and [M·2G – *n*(SbF_6)]$^{n+}$ (*n* = 2–5): for example, 733.1 [**10** – 5(SbF_6)]$^{5+}$, 975.7 [**10** – 4(SbF_6)]$^{4+}$, 1081.3 [**10·5** – 4(SbF_6)]$^{4+}$, 1187.4 [**10**–(**5**)$_2$ – 4(SbF_6)]$^{4+}$, 1379.4 [**10** – 3(SbF_6)]$^{3+}$, 1520.7 [**10·5** – 3(SbF_6)]$^{3+}$, 1662.3 [**10**–(**5**)$_2$ – 3(SbF_6)]$^{3+}$, 2187.5 [**10** – 2(SbF_6)]$^{2+}$ (Figure 10).

Host–Guest Interaction of Molecular Rectangle 11 with 5: The procedure was analogous to that used above. The stoichiometry of the association was found to be two guest molecules per one host molecule (Supporting Information). K_1 was found to be 3800 ± 300 M^{-1}, and K_2 was 4400 ± 200 M^{-1}. K_2/K_1 = 1.15. ESI-MS ([D_7]DMF): a series of peaks were observed that were consistent with [M – *n*(SbF_6)]$^{n+}$, [M·G – *n*(SbF_6)]$^{n+}$ and [M·2G – *n*(SbF_6)]$^{n+}$ (*n* = 2–5): for example, 744.5 [**11** – 5(SbF_6)]$^{5+}$, 990.4 [**11** – 4(SbF_6)]$^{4+}$, 1095.4 [**11·5** – 4(SbF_6)]$^{4+}$, 1201.4 [**11**–(**5**)$_2$ – 4(SbF_6)]$^{4+}$, 1398.2 [**11** – 3(SbF_6)]$^{3+}$, 1539.2 [**11·5** – 3(SbF_6)]$^{3+}$, 1680.7 [**11**–(**5**)$_2$ – 3(SbF_6)]$^{3+}$, 2215.6 [**11** – 2(SbF_6)]$^{2+}$, 2428.1 [**11**–(**5**)$_2$ – 2(SbF_6)]$^{2+}$ (Supporting Information).

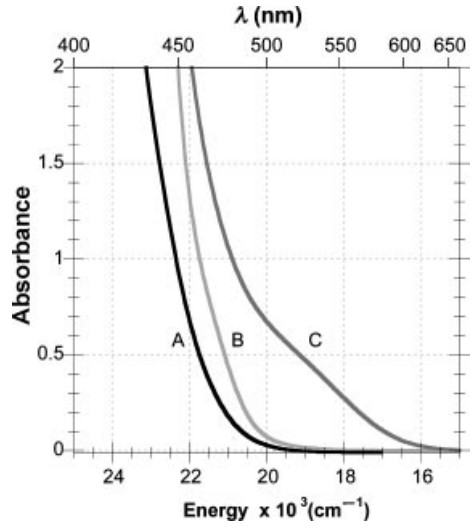

Figure 8. Absorption spectra for **10** (A, 1.65 mM), **5** (B, 3.45 mM), and a 1:2 solution (C) of **10** (1.65 mM) and **5** (3.55 mM). The experiments were performed at 25 °C in dry DMF.

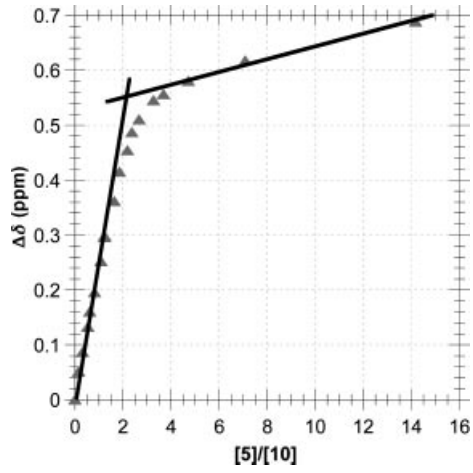

Figure 9. ^{1}H NMR stoichiometry titration for the host–guest complex formed between **10** and **5**. The experiments were performed at 60 °C in [D_7]DMF. The concentration of **10** was held constant at 1.65 mM, and the concentration of **5** was varied between 0.25 mM and 23.4 mM. The plot refers to the proton H_h (see Scheme 2).

Host–Guest Interaction of Molecular Rectangle 10 with 6: The procedure was analogous to those described above. The stoichiometry of the association was found to be two guest molecules per one host molecule (Supporting Information). K_1 was found to be 1450 ± 200 M^{-1}, and K_2 was 5200 ± 400 M^{-1}. K_2/K_1 = 3.58. ESI-MS ([D_7]DMF): a series of peaks were observed that were consistent with [M – *n*(SbF_6)]$^{n+}$ and [M·2G – *n*(SbF_6)]$^{n+}$ (*n* = 3–5): for example, 888.1 [**10**–(**6**)$_2$ – 5(SbF_6)]$^{5+}$, 975.4 [**10** – 4(SbF_6)]$^{4+}$, 1169.2 [**10**–(**6**)$_2$ – 4(SbF_6)]$^{4+}$, 1379.3 [**10** – 3(SbF_6)]$^{3+}$, 1638.0 [**10**–(**6**)$_2$ – 3(SbF_6)]$^{3+}$, 2186.9 [**10** – 2(SbF_6)]$^{2+}$ (Supporting Information).

Host–Guest Interaction of Molecular Rectangle 11 with 6: The procedure was analogous to those described above. The stoichiometry of the association was found to be two guest molecules per one

 © 2005 Wiley-VCH Verlag GmbH & Co. KGaA, Weinheim

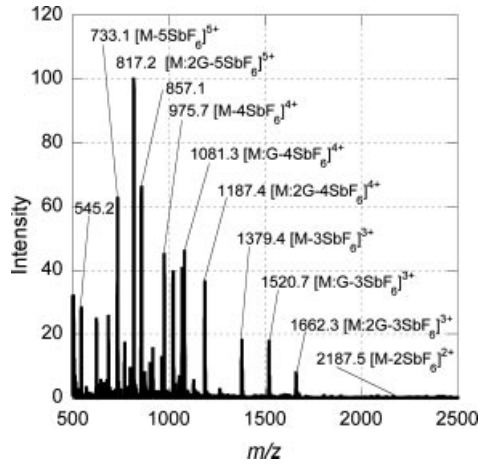

Figure 10. ESI-MS (DMF, 1.65 mM) of the host–guest complex formed between **10** and **5**, 733.1 [**10** – 5(SbF_6)]$^{5+}$, 975.7 [**10** – 4(SbF_6)]$^{4+}$, 1081.3 [**10·5** – 4(SbF_6)]$^{4+}$, 1187.4 [**10**–(**5**)$_2$ – 4(SbF_6)]$^{4+}$, 1379.4 [**10** – 3(SbF_6)]$^{3+}$, 1520.7 [**10·5** – 3(SbF_6)]$^{3+}$, 1662.3 [**10**–(**5**)$_2$ – 3(SbF_6)]$^{3+}$, 2187.5[**10** – 2(SbF_6)]$^{2+}$.

host molecule (Supporting Information). K_1 was found to be 1250 ± 200 M^{-1}, and K_2 was 5600 ± 400 M^{-1}. K_2/K_1 = 4.58. ESI-MS ([D_7]DMF): a series of peaks were observed that were consistent with [M – n(SbF_6)]$^{n+}$, [M·G – n(SbF_6)]$^{n+}$ and [M·2G – n(SbF_6)]$^{n+}$ (n = 3–5): for example, 710.2 [**11**–(**6**)$_2$ – 6(SbF_6)]$^{6+}$, 744.5 [**11** – 5(SbF_6)]$^{5+}$, 929.1 [**11**–(**6**)$_2$ + 2DMF – 5(SbF_6)]$^{5+}$, 990.1 [**11** – 4(SbF_6)]$^{4+}$, 1026.9 [**11** + 2DMF – 4(SbF_6)]$^{4+}$, 1086.4 [**11·6** – 4(SbF_6)]$^{4+}$, 1183.3 [**11**–(**6**)$_2$ – 4(SbF_6)]$^{4+}$, 1398.2 [**11** – 3(SbF_6)]$^{3+}$, 2215.6 [**11** – 2(SbF_6)]$^{2+}$ (Supporting Information).

Host–Guest Interaction of Molecular Rectangle 10 with 7: The procedure was analogous to that used above. The mol ratio method[12] was applied, and the stoichiometry of the association was found to be four guest molecules per one host molecule (Supporting Information). Because of the high host–guest stoichiometry, the binding constants could not be determined. ESI-MS ([D_7]DMF): a series of peaks were observed that were consistent with [M – n(SbF_6)]$^{n+}$(n = 2–6): for example, 571.5 [**10** – 6(SbF_6)]$^{6+}$, 733.2 [**10** – 5(SbF_6)]$^{5+}$, 975.0 [**10** – 4(SbF_6)]$^{4+}$, 1379.1 [**10** – 3(SbF_6)]$^{3+}$, 2187.8 [**10** – 2(SbF_6)]$^{2+}$. No peaks due to the host–guest adducts were observed (Supporting Information).

Crystallographic Structural Determination for the Host–Guest Adduct Formed from 10 and 5: Crystals of the complex were grown by dissolving a 1:2 mixture of host **10** and guest **5** in methyl ethyl ketone and vapor diffusing with methanol for seven days at –4 °C.

Data Collection: A red, brick-shaped fragment (0.20 × 0.15 × 0.15 mm) was selected under a stereomicroscope while immersed in Fluorolube oil to avoid possible reaction with air. The crystal was removed from the oil using a tapered glass fiber that also served to hold the crystal for data collection. The crystal was mounted and centered on a Bruker SMART APEX system at 100 K. Rotation and still images showed the diffractions to be sharp. Frames separated in reciprocal space were obtained and provided an orientation matrix and initial cell parameters. Final cell parameters were obtained from the full data set.

A "full sphere" data set was obtained which samples approximately all of the reciprocal space to a resolution of 0.84 Å using steps of 0.3° in ω and 30-s integration times for each frame. Data were collected at 100 K. Integration of intensities and refinement of cell parameters were performed with SAINT.[18] Absorption corrections were applied using SADABS[18] based on redundant diffractions.

Structure Solution and Refinement: The space group was determined as $P\bar{1}$ on the basis of systematic absences and intensity statistics. Patterson methods were used to locate some Pt atoms and repeated-difference Fourier maps allowed recognition of many carbon atoms. It soon became clear that the expected SbF_6 and other Pt atoms were either not located or located as split atoms. While the C units became obvious, considerable difficulties were encountered in locating some C atoms, particularly those associated with the split Pt atoms or in expected solvent. The F atoms of the SbF_6 groups were either not found or found with poor geometry. It was concluded that there is severe disorder for the anions, solvent, and guest Pt units. Sb and Pt guest positions were usually located and their occupancy refined. Some F atoms were assigned but in general SbF_6 units were not complete. Although anisotropic refinement for the C framework was possible, some terminal C atoms showed poor geometry. No H location was attempted. Final refinement was anisotropic for all C, N, and Pt atoms of the framework. Some thermal parameters were unusual, but overall the framework was consistent with that expected. All ORTEP diagrams have been drawn with 50% probability ellipsoids. The final R value of approximately 14% directly results from the inability to locate the anions and guest molecules.

The CIF file CCDC 267851 [for **10**–(**5**)$_2$] contains the supplementary crystallographic data for this paper. These data can be obtained free of charge from The Cambridge Crystallographic Data Centre via www.ccdc.cam.ac.uk/data_request/cif.

Supporting Information: The Supporting Information contains the ^{1}H NMR stoichiometry plots, ESI-MS, UV/Vis spectra, COSY, and NOESY spectra for the host–guest adducts.

Acknowledgments

This work was supported by grants from the Basic Sciences Division of the Department of Energy.

[1] a) J. Rebek, Jr., *Acc. Chem. Res.* **1984**, *17*, 258–264; b) S. Shinkai, M. Ikeda, A. Sugasaki, M. Takeuchi, *Acc. Chem. Res.* **2001**, *34*, 494–503; c) M. Takeuchi, M. Ikeda, A. Sugasaki, S. Shinkai, *Acc. Chem. Res.* **2001**, *34*, 865–873; d) L. Kovbasyuk, R. Krämer, *Chem. Rev.* **2004**, *104*, 3161–3187. e) Fujita invoked allosterism in the formation of a 1:4 host–guest complex, but this assertion was not supported by stability-constant data; D. Oguro, M. Miyazawa, H. Oka, K. Yamaguchi, K. Ogura, M. Fujita, *Nature* **1995**, *378*, 469–472.
[2] a) J. Rebek, Jr., J. E. Trend, R. V. Wattley, S. Chakravorti, *J. Am. Chem. Soc.* **1979**, *101*, 4333–4337; b) J. Rebek, Jr., R. V. Wattley, *J. Am. Chem. Soc.* **1980**, *102*, 4853–4854.
[3] C. A. Hunter, L. D. Sarson, *Angew. Chem.* **1994**, *106*, 2424–2426; *Angew. Chem. Int. Ed. Engl.* **1994**, *33*, 2313–2316.
[4] a) S.-Y. Chang, H.-Y. Jang, K.-S. Jeong, *Chem. Eur. J.* **2004**, *10*, 4358–4366; b) S.-Y. Chang, M.-C. Um, H. Uh, H.-Y. Jang, K.-S. Jeong, *Chem. Commun.* **2003**, *16*, 2026–2027.
[5] H. Kawai, R. Katoono, K. Nishimura, S. Matsuda, K. Fujiwara, T. Tsuji, T. Suzuki, *J. Am. Chem. Soc.* **2004**, *126*, 5034–5035.
[6] A. J. Goshe, I. M. Steele, B. Bosnich, *J. Am. Chem. Soc.* **2003**, *125*, 444–451.
[7] J. D. Crowley, A. J. Goshe, I. M. Steele, B. Bosnich, *Chem. Eur. J.* **2004**, *10*, 1944–1952.
[8] a) G. W. V. Cave, N. W. Alcock, J. P. Rourke, *Organometallics* **1999**, *18*, 1801–1803; b) G. W. V. Cave, F. P. Fanizzi, R. J. De-

 © 2005 Wiley-VCH Verlag GmbH & Co. KGaA, Weinheim

eth, W. Errington, J. P. Rourke, *Organometallics* **2000**, *19*, 1355–1364.
[9] R. D. Sommer, A. L. Rheingold, A. J. Goshe, B. Bosnich, *J. Am. Chem. Soc.* **2001**, *123*, 3940–3952.
[10] A. J. Goshe, I. M. Steele, C. Ceccarelli, A. L. Rheingold, B. Bosnich, *Proc. Natl. Acad. Sci. USA* **2002**, *99*, 4823–4829.
[11] a) C. A. Schalley, T. Muller, P. Linnartz, M. Witt, M. Schafer, A. Lutzen, *Chem. Eur. J.* **2002**, *8*, 3538; b) C. A. Schalley, *Mass Spectrom. Rev.* **2001**, *20*, 253; c) C. A. Schalley, *Int. J. Mass Spectrom.* **2000**, *194*, 11.
[12] a) A. S. Meyer, G. H. Ayers, *J. Am. Chem. Soc.* **1957**, *79*, 49–53; b) H.-J. Schneider, *Principles and Methods in Supramolecular Chemistry*, John Wiley & Sons, New York, **2000**; c) H. Tsukube, H. Furuta, A. Odani, Y. Takeda, K. Yoshihiro, Y. Inoue, Y. Liu, H. Sakamoto and K. Kimura, *Comprehensive Supramolecular Chemistry* (Eds.: S. E. D. Davies, J. A. Ripmeester), Permagon, Oxford, UK, **1996**, vol. 8, p. 425.
[13] K. A. Connors, *Binding Constants*, John Wiley & Sons, New York, **1987**.
[14] D. Neuhaus, M. P. Williamson, *The Nuclear Overhauser Effect in Structural and Conformational Analysis*, 2nd ed., John Wiley and Sons, New York, **2000**.
[15] J. D. Crowley, I. M. Steele, B. Bosnich, *Inorg. Chem.* **2005**, *44*, 2989–2991.
[16] a) A. J. Goshe, B. Bosnich, *Synlett* **2001**, 941–944; b) J. D. Crowley, B. Bosnich, *Eur. J. Inorg. Chem.* **2005**, 2015–2025.
[17] a) A. J. Goshe, I. M. Steele, B. Bosnich, *Inorg. Chim. Acta* **2004**, *357*, 4544–4551; b) A. J. Goshe, J. D. Crowley, B. Bosnich, *Helv. Chim. Acta* **2001**, *84*, 2971–2985.
[18] G. Sheldrick, *SHELXTL* (version 6.1) Program Library, G. Bruker Analytical X-ray Systems, Madison, WI, **2000**.

Received: May 2, 2005
Published Online: August 4, 2005

 © 2005 Wiley-VCH Verlag GmbH & Co. KGaA, Weinheim

Synthesis and Relaxivity Studies of a Gadolinium(III) Complex of ATP-Conjugated DO3A as a Contrast Enhancing Agent for MRI

S. James Ratnakar[a] and Vedhamonickom Alexander*[a]

Keywords: Gadolinium / Imaging agents / Macrocyclic ligands / N ligands

A gadolinium(III) complex of adenosine 5′-triphosphate (ATP)-appended DO3A has been synthesized in order to attain higher relaxivity and to reduce the in vivo toxicity. DO3A (**2**) was synthesized as the exclusive product by a single step direct trialkylation of cyclen with chloroacetic acid in water (pH 10, –4 °C). ATP was then covalently appended to the DO3A framework through a propyl linker. The 3-bromopropane spacer appended DO3A (**3**) was synthesized by the reaction of DO3A with 1,3-dibromopropane in water/DMF in the presence of triethylamine as proton scavenger. The ATP-appended DO3A (DO3A-Pr-ATP) was synthesized by the reaction of **3** with ATP in water at room temperature. [Gd(DO3A-Pr-ATP)(H_2O)$_2$] (**4**) was synthesized by the reaction of DO3A-Pr-ATP with gadolinium(III) perchlorate hydrate in water. The X- and Q-band EPR spectra of **4** contain a broad band with no hyperfine splitting at both room temperature and liquid nitrogen temperature. The *g*-values are 2.167 and 2.033 at X- and Q-band, respectively. The magnetic moment of **4** is 7.45 BM which is close to the value for free Gd^{III} ion. The longitudinal relaxivity, r_{1p}, of [Gd(DO3A-Pr-ATP)(H_2O)$_2$] is 6.51 $mM^{-1}s^{-1}$ (24 MHz and 35 ± 0.1 °C), which is higher than that of [Gd(DOTA)(H_2O)]$^-$ (r_{1p} = 3.56 $mM^{-1}s^{-1}$, 20 MHz, 39 °C, pH 7.3) and [Gd(DO3A)(H_2O)$_2$] (r_{1p} = 4.8 $mM^{-1}s^{-1}$, 20 MHz, 40 °C). The higher relaxivity of **4** than for other systems with q = 2 is due to the increase in the molecular dimension of the complex by the conjugation of ATP. The relaxivity of **4** at pH 8.4 (TRIS buffer) decreases to 5.64 $mM^{-1}s^{-1}$, probably due to a change in the hydration number by the replacement of the coordinated water molecules by TRIS. The r_{1p} relaxivity of **4** in the presence of β-cyclodextrin is 8.97 $mM^{-1}s^{-1}$ due to the increase in the molecular weight and dimension of the inclusion complex formed by the noncovalent host–guest interaction of the ATP pendant arm with the hydrophobic cavity of β-cyclodextrin. The transverse relaxivity, r_{2p}, of **4** is 7.48 $mM^{-1}s^{-1}$ (24 MHz and 35 ± 0.1 °C). The r_{2p}/r_{1p} ratio of 1.16 indicates that **4** is a T_1-weighted contrast agent. The ATP moiety remains as an extended pendant arm and does not bind with the metal ion, nor does it block the coordination sites for the inner-sphere water molecules.
(© Wiley-VCH Verlag GmbH & Co. KGaA, 69451 Weinheim, Germany, 2005)

Introduction

MRI is a state-of-the-art, noninvasive imaging modality in clinical medicine, as exemplified by the award of the 2003 Nobel Prize for medicine to Professor Paul C. Lauterbur (Biomedical Magnetic Resonance Laboratory, University of Illinois) and Professor Sir Peter Mansfield (University of Nottingham) for their seminal discoveries concerning the use of magnetic resonance to visualize different structures leading to the development of modern MRI.[1] An MRI image is a three dimensional signal intensity map of the spatially encoded proton signal of the in vivo water molecules in a given volume element (voxel). The movement of protons from one position to another during the relaxation experiment alters the signal intensity and therefore the moving blood has no detectable signal. It is common to increase the contrast of the image by administering MRI contrast agents (CAs),[2] which enhance the longitudinal and transverse relaxation rates of the water protons which contribute to the intensity of the MRI signal and thus to the contrast of the image. The first example of a paramagnetic substance used for tissue discrimination in MRI was provided by Lauterbur et al.[3] The in vitro and in vivo chemical results reported by Tweedle et al.[4] support the usefulness of strongly chelated Gd^{III} complexes as CAs, and since then Gd^{III} complexes of polyaminocarboxylate ligands have been widely studied.[2a,2e,2f]

Proton relaxivity by Gd^{III}-based CAs is governed by the magnetic coupling interaction of the unpaired electrons of the metal ion and the water proton nuclei by a through-space dipole–dipole mechanism[5] and is interpreted using the Solomon–Bloembergen–Morgan (SBM) theory.[6] Relaxivity is determined by several parameters,[5d,7] and higher relaxivity may be obtained by increasing the correlation time, τ_c, which modulates the dipole–dipole relaxation mechanism. It depends on the exchange lifetime (k_{ex} = $1/\tau_m$) of the coordinated water molecules, the electronic relaxation times ($T_{1e,2e}$), and the rotational correlation time (τ_R) of the complex. One of the practical approaches to gain higher relaxivity by gadolinium-based contrast agents

[a] Department of Chemistry, Loyola College, Chennai 600034, India
Supporting information for this article is available on the WWW under http://www.eurjic.org or from the author.

 © 2005 Wiley-VCH Verlag GmbH & Co. KGaA, Weinheim **DOI: 10.1002/ejic.200401018**

is increasing τ_R by increasing the size and molecular weight of Gd^{III} chelates by covalent or noncovalent interaction with macromolecules. Examples of Gd^{III} chelates bound to macromolecules include the HSA adduct of the Gd complex of benzyloxy-α-propionic acid substituted DOTA (r_{1p} = 56 $mM^{-1}s^{-1}$),[8] the Gd complex of a *p*-bromobenzyloxy-substituted pyridine macrocycle (r_{1p} = 8.25 $mM^{-1}s^{-1}$), its HSA adduct (r_{1p} = 48 $mM^{-1}s^{-1}$), and its noncovalent adduct with poly-β-cyclodextrin (r_{1p} = 36 $mM^{-1}s^{-1}$),[9] the squaric ester substituted DO3A linked to polyornithine (r_{1p} = 29 $mM^{-1}s^{-1}$),[10] Gd-DTPA-polylysine[11] (r_{1p} = 13 $mM^{-1}s^{-1}$ and 32 $mM^{-1}s^{-1}$ at pH 8), the Gd dendrimer of the DTPA-functionalized second-generation starburst dendrimer (r_{1p} = 234 $mM^{-1}s^{-1}$ at 25 MHz),[12] the Gd complex of *p*-nitrophenyl-substituted DOTA (r_{1p} = 5.4 $mM^{-1}s^{-1}$, 20 MHz, 25 °C, pH 7.3),[13] the HSA adduct of MS-325 (r_{1p} = 50.8 $mM^{-1}s^{-1}$, 20 MHz),[14] the glucitol-conjugated DO3A (r_{1p} = 5.19 $mM^{-1}s^{-1}$),[15] Gd chelates of *p*-bromobenzyl- and *p*-phosphonatomethylbenzanilido-substituted DO3A (r_{1p} = 7.9 $mM^{-1}s^{-1}$ and 10.7 $mM^{-1}s^{-1}$, respectively), and their HSA adducts (r_{1p} = 24.0 $mM^{-1}s^{-1}$ and 21.0 $mM^{-1}s^{-1}$, respectively),[16] and the multiple Gd-DO3A chelates covalently attached to a polysaccharide backbone (r_{1p} = 14.4 $mM^{-1}s^{-1}$ for each Gd, 20 MHz, 39 °C).[17]

The gadolinium(III) chelates approved by the FDA for human imaging are $(NMG)_2[Gd(DTPA)(H_2O)]$[18] (Magnevist, Schering), $(NMG)[Gd(DOTA)(H_2O)]$[19] (Dotarem, Guerbet), $[Gd(DTPA\text{-}BMA)(H_2O)]$[20] (Omniscan, Nycomed), $[Gd(HP\text{-}DO3A)(H_2O)]$[21] (ProHance, Bracco), $[Gd(DO3A\text{-}Butrol)(H_2O)]$[22] (Gadovist, Schering), and $[Gd(BOPTA)(H_2O)]$[23] (MultiHance, Bracco). New classes of MRI contrast agents[24] such as blood pool agents,[25] targeting CAs,[24] and smart contrast agents such as those that are pH-sensitive,[10,25i,26] oxygen-pressure (pO_2) responsive,[27] enzyme responsive,[28] and metal ion concentration dependent[29] are now emerging.

Clinical MRI applications continue to evolve rapidly. This drives the need for more efficient and pathology-specific contrast agents that will increase the potential of MRI as a diagnostic tool. Increasing the molecular weight of a Gd^{III} chelate with two inner-sphere water molecules by conjugating with a biomacromolecule would lead to a biocompatible CA with high relaxivity. Such chelates with high tissue-specific targeting moieties are able to provide improved image contrasts even at a lower concentration than normally required. DO3A is a well-suited ligand framework for functionalization due to the unique secondary amine nitrogen of the macrocyclic ring. Furthermore, biomacromolecule-appended DO3A is expected to exhibit the same stability as that of the parent DO3A. Herein we report the synthesis and relaxivity studies of gadolinium(III) complex of adenosine 5′-triphosphate appended DO3A.

Results and Discussion

Synthesis of the Ligand

1,4,7-Tris(carboxymethyl)-1,4,7,10-tetraazacyclododecane (DO3A) (2)

DO3A was synthesized in a single-step direct N-alkylation of cyclen with chloroacetic acid in a 1:3 molar ratio in 69.58% yield. The reaction was carried out at –4 °C and gradually heated to 50 °C over 4 h. The pH of the medium was maintained at 10 throughout the reaction. DO3A was first synthesized by Tweedle et al.[30] by the reaction of cyclen with chloroacetic acid in water at pH 10. The reaction afforded both DO3A and DOTA and the separation was carried out by ion-exchange chromatography. Tweedle et al.[21a] have also reported the synthesis of DO3A by the alkylation of monoprotected cyclen (*p*-toulenesulfonyl or formyl group) with chloroacetic acid followed by deprotection.

Linker-Appended DO3A (3)

DO3A is a heptadentate ligand with three acetate arms and a unique secondary amine nitrogen on the ring. The bromopropyl linker appended DO3A (**3**) was synthesized by the N-alkylation of DO3A with 1,3-dibromopropane in the presence of triethylamine as proton scavenger in DMF/water at room temperature. The use of triethylamine as a base leads to the formation of its hydrobromide salt along with **3**, which is removed by washing with methanol. The reaction is illustrated in Scheme 1.

ATP-Appended DO3A (DO3A-Pr-ATP)

ATP was appended onto the DO3A framework through the bromopropyl linker by the reaction of **3** with ATP in a

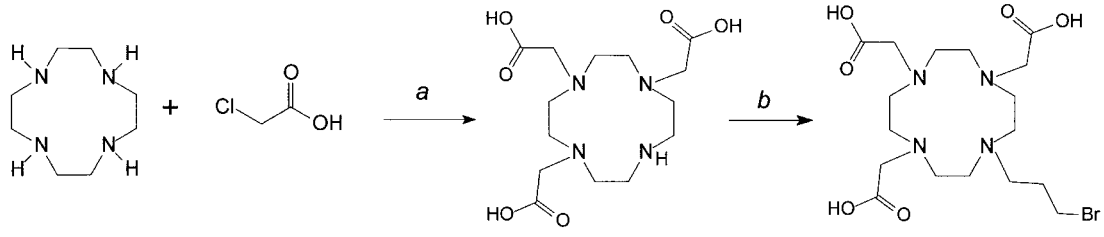

1 **2** **3**

Scheme 1. Synthesis of linker appended DO3A. Reagents and conditions: (a) –4 °C, H_2O, NaOH, pH 10; (b) 1,3-dibromopropane, DMF/water, triethylamine.

 © 2005 Wiley-VCH Verlag GmbH & Co. KGaA, Weinheim

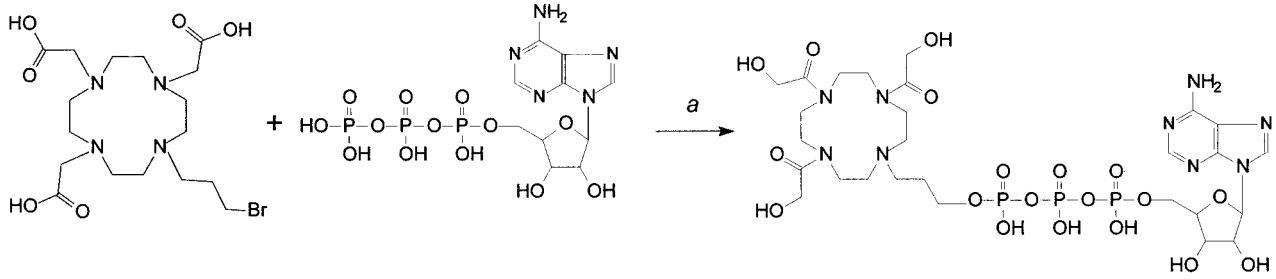

Scheme 2. Synthesis of DO3A-Pr-ATP. Conditions: (a) water, room temp., 36 h.

1:1 molar ratio in water at room temperature (Scheme 2). The reaction of **3** with the commercially available disodium salt of ATP yielded DO3A-Pr-ATP along with sodium bromide as the side product. Since both are soluble in water the isolation of the free ligand becomes difficult. Therefore, the free form of ATP, recovered from its disodium salt by passing an aqueous solution through a cation exchange resin and eluting with water, was reacted with **3**. DO3A-Pr-ATP was isolated as a white solid by adding methanol.

Spectroscopic Studies

Infrared Spectrum

The IR spectrum of DO3A-Pr-ATP shows a broad peak at 3420.1 cm^{-1} assignable to the ν_s(OH) vibration. The peaks at 2926.5 and 1476.8 cm^{-1} are assignable to the ν_s(CH) and δ_s(CH) vibrations, respectively. The sharp peaks at 1700 and 1635.4 cm^{-1} are due to the ν_s(C=O) and δ_s(NH) vibrations, respectively. The sharp peak at 1507.1 cm^{-1} is

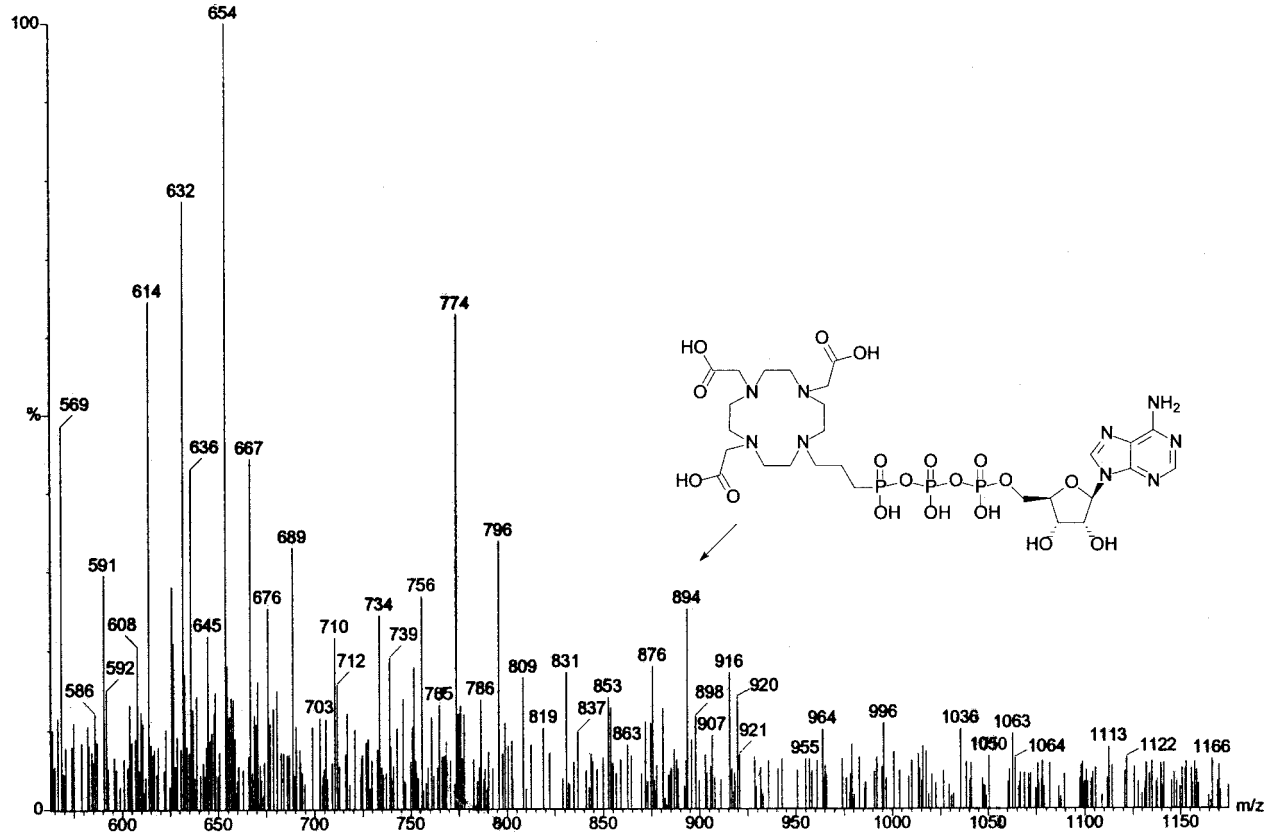

Figure 1. ESI mass spectrum of 10-[3-(adenosine 5′-triphosphate)oxypropyl]-1,4,7-tris(carboxymethyl)-1,4,7,10-tetraazacyclododecane (DO3A-Pr-ATP).

 © 2005 Wiley-VCH Verlag GmbH & Co. KGaA, Weinheim

assigned to the ν_s(C–O) vibration of the ether linkage between the DO3A and ATP. The peak at 1087.6 cm^{-1} is assigned to the ν_s(C–N) vibration. The bands at 1228.4 and 900 cm^{-1} are assigned to the ν_s(P=O) and ν_s(P–O) vibrations, respectively.[31] The IR spectrum of the complex contains the characteristic absorption bands of the ligand except for the OH vibrations of the carboxylic acid. The band at 1608.8 cm^{-1} in the complex is typical of the COO functionality.[32]

ESI Mass Spectrum

The ESI mass spectrum of DO3A-Pr-ATP shows a peak at *m*/*z* = 894 for the molecular ion $[M + 1]^+$ ($C_{27}H_{47}N_9O_{19}P_3$). The peak at *m*/*z* = 756 is assignable to the species $[M - C_5H_7N_5]^+$ ($C_{22}H_{39}N_4O_{19}P_3$) formed by the loss of the adenine moiety of ATP. The peak at *m*/*z* = 654 is assignable to the species $[M - C_9H_{13}N_5O_3]^+$ ($C_{18}H_{33}N_4O_{16}P_3$) formed by the loss of the furan moiety of ATP. The peak at *m*/*z* = 348 is assignable to the species $[M - C_{13}H_{19}N_5O_{13}P_3]^+$ ($C_{14}H_{28}N_4O_6$) formed by the loss of the phosphate group of ATP and the propyl linker group. The ESI mass spectrum of DO3A-Pr-ATP is depicted in Figure 1.

^{1}H NMR Spectrum

The ^{1}H NMR spectrum of DO3A-Pr-ATP in D_2O shows resonances for the methylene protons of the cyclen framework as a multiplet at δ = 3.10–3.4 ppm (12 H, NCH_2CH_2N). The triplet at δ = 3.58–3.63 ppm (*J* = 5.5 Hz, 2 H) is assigned to the OCH_2 protons of the linker that is bonded to ATP. The resonance at δ = 4.37 ppm (6 H, CH_2COO) is assigned to the methylene protons of acetate arms. The triplet centered at δ = 4.25 ppm (1 H) is assigned to the proton of the furan ring of the adenine moiety. The doublet at δ = 4.49–4.65 ppm (2 H) is assigned to the OCH_2 protons of the ATP unit. The signals at δ = 2.25 ppm are assigned to the protons of the propyl linker. The resonances at δ = 8.37, 8.54 (m, 2 H), and 6.07 ppm (m, 1 H) are assigned to the aromatic protons of the adenine moiety. The ^{1}H NMR spectrum of DO3A-Pr-ATP is depicted in Figure 2.

^{13}C NMR Spectrum

The ^{13}C NMR spectrum of DO3A-Pr-ATP in D_2O has a signal at δ = 174.52 ppm assignable to the carboxylic acid carbon. The signals at δ = 152.90–145.57 ppm are assignable to the carbon atoms of the adenine group of ATP. The resonances at δ = 68.43 (OCH_2), 77.38 (OCH_2), and 87.14 ppm are assignable to the C_2, C_3, and C_4 carbons, respectively, of the furan ring. The signal at δ = 34.78 ppm is assignable to the β-CH_2 carbon of the propyl linker. The resonance at δ = 52.99 ppm is due to the methylene carbon of the propyl linker bonded to the nitrogen of the macrocycle. The signal at δ = 68.43 ppm is assigned to the methylene carbon attached to the phosphate group of ATP. The higher chemical shift of this carbon compared to the other two methylene carbons of the linker is indicative of its attachment to the terminal phosphate group of ATP. The signal at δ = 52.99 ppm is assignable to the ethylenic carbon of the macrocyclic framework. The resonance at δ = 57.23 ppm is assignable to the methylene carbon of the acetate arm.

^{31}P NMR Spectrum

The ^{31}P NMR spectrum of DO3A-Pr-ATP in D_2O shows three distinct signals due to the three phosphate groups of ATP in different environments. The signal at δ = 130.20 ppm is assigned to the central phosphate and the signal at δ = 107.35 ppm is assignable to the phosphate attached to the propyl spacer. The signal at δ = 119.30 ppm is assigned to the phosphate that is attached to the furan group of ATP.

Mass Spectrum of [Gd(DO3A-Pr-ATP)(H_2O)$_2$]

The ESI mass spectrum shows a cluster of peaks at *m*/*z* = 1081 assignable to the molecular ion $[M - 2]^+$ $[Gd(C_{27}H_{41}N_9O_{19}P_3)(H_2O)_2]$. The peak at *m*/*z* = 793 is assignable to $[M - C_{11}H_{17}N_5O_5]^+$ $[Gd(C_{17}H_{27}N_4O_{16}P_3)]$, the species formed by the loss of the adenine moiety. The peak at *m*/*z* = 734 is assignable to the species $[M - C_{12}H_{21}N_5O_7]^+$ $[Gd(C_{15}H_{24}N_4O_{14}P_3)]$ formed by the loss of the acetate group. The peak at *m*/*z* = 578 is assignable to the species $[M - Gd(C_{12}H_{20}N_5O_7)]^+$ ($C_{15}H_{25}N_4O_{14}P_3$) formed by the loss of Gd^{III}. The peak at *m*/*z* = 483 is assignable to $[M - Gd(C_{12}H_{20}N_5O_{11}P)]^+$ ($C_{15}H_{25}N_4O_{10}P_2$), the species formed by the loss of one phosphate group. The peak at *m*/*z* = 168 is assignable to $[M - Gd(C_{19}H_{29}N_5O_{21}P_3)]^+$ ($C_8H_{16}N_4$), the species formed by the loss of acetate groups and the propyl linker. The MALDI-TOF mass spectrum shows a peak at *m*/*z* = 1043.80 (100%) assignable to the molecular ion $[M - 2H_2O]^+$ $[Gd(C_{27}H_{41}N_9O_{19}P_3)]$, which further confirms the formation of the complex. The MALDI TOF mass spectrum of [Gd(DO3A-Pr-ATP)(H_2O)$_2$] is given in Figure 3.

EPR Spectra and Magnetic Moment of [Gd(DO3A-Pr-ATP)(H_2O)$_2$]

The X- and Q-band EPR spectra consist of a broad band with no hyperfine splitting at room temperature or at liquid nitrogen temperature. The *g*-value at X-band is 2.167 and at Q-band is 2.0333. The *g*-value at 77 K is 2.103 (X-band). The broad band shows that the dipolar interaction of the metal ion is small. The magnetic moment of [Gd(DO3A-Pr-ATP)(H_2O)$_2$] is 7.5 BM which is close to the value for the free gadolinium(III) ion (7.85 BM).

Relaxivity Studies

Longitudinal Relaxivity (r_{1p})

The ligand DO3A-Pr-ATP has the DO3A framework with an extended ATP pendant arm. It coordinates to the metal ion through four nitrogen donors of the macrocycle and three carboxylate oxygens. Two inner-sphere water molecules complete the coordination geometry. The complex [Gd(DO3A-Pr-ATP)(H_2O)$_2$] (**4**) is expected to have the same coordination geometry as that of [Gd(DO3A)(H_2O)$_2$]. The longitudinal relaxivity of **4** is 6.51 $mM^{-1}s^{-1}$ (normal-

 © 2005 Wiley-VCH Verlag GmbH & Co. KGaA, Weinheim

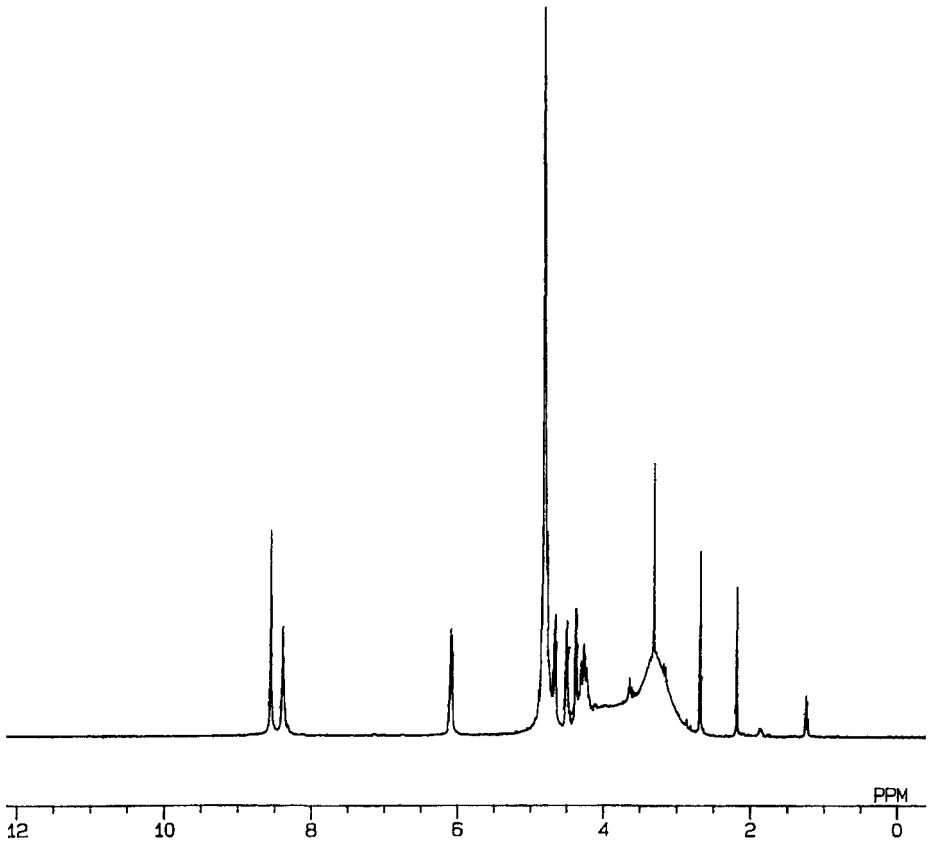

Figure 2. ^{1}H NMR spectrum of 10-[3-(adenosine 5′-triphosphate)oxypropyl]-1,4,7-tris(carboxymethyl)-1,4,7,10-tetraazacyclododecane (DO3A-Pr-ATP).

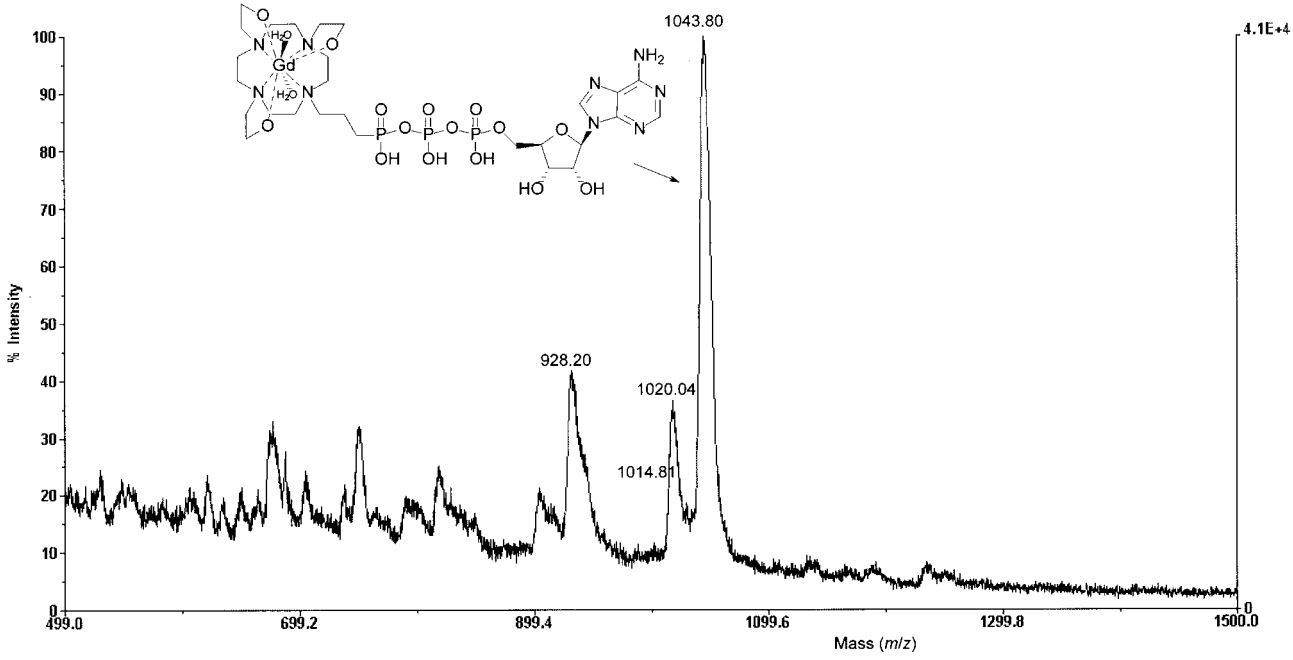

Figure 3. MALDI TOF mass spectrum of [Gd(DO3A-Pr-ATP)(H_2O)$_2$] (**4**).

ized to 1 mM). The contribution by the inner-sphere mechanism to the overall relaxivity is approximately 1.7 mM^{-1} s^{-1} per coordinated water molecule.[2a,2d] The higher longitudinal relaxivity of **4** than that of [Gd(DOTA)(H_2O)]$^-$ (r_{1p} = 3.56 mM^{-1} s^{-1}, 20 MHz, 39 °C, pH 7.3),[15] a q = 1 system, and [Gd(DO3A)(H_2O)$_2$] (r_{1p} = 4.8 mM^{-1} s^{-1} at 20 MHz, 40 °C),[33] a q = 2 system, is attributed not only to the presence of two inner-sphere water molecules bound to the me-

 © 2005 Wiley-VCH Verlag GmbH & Co. KGaA, Weinheim

tal ion, but also to the longer rotational correlation time, τ_R, due to the increase in the molecular dimensions of the complex by the conjugation of ATP. As the molecular tumbling rate is reduced by increasing the molecular dimension, the dipole–dipole interaction between the paramagnetic metal ion and the water proton is efficient and, as a result, a greater paramagnetic effect is transferred to the bulk solvent (water). Tweedle et al.[34] have shown that the relaxivity of Gd^{III} complexes increases with increasing molecular weight. The outer-sphere contribution to overall relaxivity is approximately 2.3–2.5 $mM^{-1}s^{-1}$ deduced on the basis of the relaxivity of Gd^{III} complexes with no inner-sphere water molecules ($q = 0$).[35]

Longitudinal Relaxivity in the Presence of β-Cyclodextrin

The longitudinal relaxivity of $[Gd(DO3A\text{-}Pr\text{-}ATP)(H_2O)_2]$ increases to 8.97 $mM^{-1}s^{-1}$ in the presence of β-cyclodextrin. This is attributed to the formation of an inclusion complex through a nonbonding interaction between the ATP pendant arm and β-cyclodextrin with a concomitant increase in the molecular dimension and τ_R of the complex, which leads to an enhancement in relaxivity. An aqueous solution of β-cyclodextrin (50 mM) under the same experimental conditions does not show enhancement of water proton relaxivity. The concentration of β-cyclodextrin was maintained at 50-times the concentration of the complex to ensure the formation of the inclusion complex. Aime and co-workers[36] have reported that the formation of ternary inclusion complexes between the hydrophobic cavity of β-cyclodextrin and Gd^{III} chelates leads to a 10-fold increase of r_{1p}. Many complexes form inclusion complexes with β-cyclodextrin through noncovalent interactions between the substituent and β-cyclodextrin cavity.[9] The nature of the substituent also plays an important role. Aime et al.[13] have reported a large K_D (dissociation constant) value as a consequence of the poor fit of the substituent into the β-cyclodextrin cavity compared to complexes with no substituent. The presence of the substituent in the *para* position of the phenyl ring is expected to strengthen the binding and favor the formation of the inclusion complex.[37] Thus, the enhancement of the relaxivity of $[Gd(DO3A\text{-}Pr\text{-}ATP)(H_2O)_2]$ in the presence of β-cyclodextrin is attributed to the formation of the inclusion complex by a noncovalent host–guest interaction between the free amine group in the *para* position of the phenyl ring of ATP and the hydrophobic cavity of β-cyclodextrin. A plot of the concentration of $[Gd(DO3A\text{-}Pr\text{-}ATP)(H_2O)_2]$ vs. $1/T_1$ in the presence and absence of β-cyclodextrin is given in Figure 4.

pH Dependence of the Relaxivity

The relaxivity of $[Gd(DO3A\text{-}Pr\text{-}ATP)(H_2O)_2]$ at pH 8.4 (TRIS buffer) is 5.64 $mM^{-1}s^{-1}$, which is one unit lower than the relaxivity of the complex without pH adjustment (pH 5.4). The hydration number of the metal plays an important role on relaxivity. $[Gd(H_2O)_8]^{3+}$ has a q value of 8 or 9 and exhibits a relaxivity of 11.8 $mM^{-1}s^{-1}$. As the q value decreases, the relaxivity also decreases. Sherry et al.[38] have observed that the decrease in relaxivity at higher pH is due to the competition of the hydroxide ion for coordination to the Gd^{III} ion. The decrease in the relaxivity of $[Gd(DO3A\text{-}Pr\text{-}ATP)(H_2O)_2]$ at higher pH may be due to the replacement of bound water molecules by TRIS.

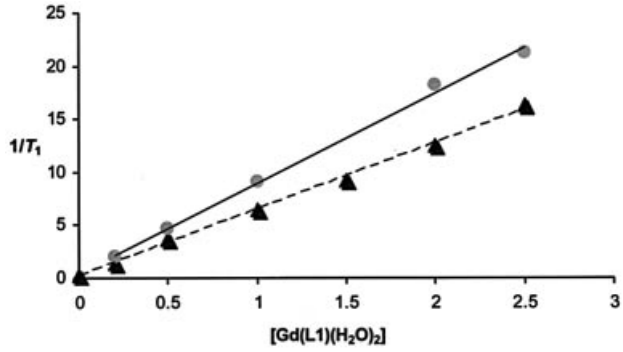

Figure 4. A plot of concentration of $[Gd(DO3A\text{-}Pr\text{-}ATP)(H_2O)_2]$ vs. T_1^{-1} in the presence (●) and in the absence (▲) of β-cyclodextrin.

Transverse Relaxivity (r_{2p})

The transverse relaxivity of $[Gd(DO3A\text{-}Pr\text{-}ATP)(H_2O)_2]$ is 7.48 $mM^{-1}s^{-1}$ (24 MHz and 35 ± 0.1 °C), which is higher than that of $[Gd(DOTA)(H_2O)]^-$ (r_{2p} = 4.57 $mM^{-1}s^{-1}$, 20 MHz). The r_{2p}/r_{1p} ratio for $[Gd(DO3A\text{-}Pr\text{-}ATP)(H_2O)_2]$ is 1.16, showing that the complex is a T_1-weighted contrast agent. The maximum signal intensity attained is determined by the r_{2p}/r_{1p} ratio, with the highest signal intensity occurring when the ratio is unity.

Conclusions

In this work, the synthesis and relaxivity studies of a Gd^{III} complex of adenosine 5′-triphosphate conjugated DO3A has been reported. The increase in the molecular weight of the chelate leads to an increase in the r_{1p} and r_{2p} relaxivities due to the slow tumbling rate of the complex in solution. The covalent attachment of ATP causes the complex to remain intact under different experimental conditions and it is expected to be biocompatible and nontoxic. $[Gd(DO3A\text{-}Pr\text{-}ATP)(H_2O)_2]$ is expected to reduce the in vivo clearance rate due to its noncovalent interaction with blood serum albumin and could be used as an intravascular contrast agent as the persistence of the complex in blood would be higher. Thus, there is a wide scope for studying the interaction and relaxivity of this complex in the presence of blood serum albumin to evaluate its suitability as a blood pool agent. Furthermore, the ATP-conjugated derivative is particularly interesting since the NH_2 group provides a site for further modification of the ligand or covalent attachment of a substituent. The appended ATP does not bind with the central metal ion or block the coordination site of the inner-sphere water molecules and remains as an extended pendant arm. It is worthwhile to study the behavior of this complex in response to biological events such as enzyme action. The advent of attaching metal complexes to larger biological molecules has created a new

 © 2005 Wiley-VCH Verlag GmbH & Co. KGaA, Weinheim

realm of research in the field of bioconjugates. Conjugates of chelates with biological macromolecules that have affinity for specific tissues can be employed to study specific biological processes and physiological function. Design of MRI contrast agents that remain in the body for longer time and target specific tissues is a need for the future.

Experimental Section

Chemicals: Triethylenetetraamine (99%), *p*-toluenesulfonyl chloride, 1,2-dibromoethane, 1,3-dibromopropane, chloroacetic acid, xylenol orange, β-cyclodextrin, Celite, anhydrous potassium carbonate, and TRIS (Fluka) were used as such. Adenosine 5′-triphosphate disodium salt (Aldrich) was converted into the free form by passing through Amberlite IR120 (H^+, strongly acidic) (Aldrich) cation exchange resin and eluting with triply distilled water. The resin was washed with distilled water five times before use. Triethylamine, perchloric acid (Merck, India), sodium hydroxide and potassium hydroxide pellets (Rankem, India), and gadolinium(III) carbonate (Indian Rare Earths Ltd.) were used as such. $Gd(ClO_4)_3 \cdot nH_2O$ was prepared from gadolinium(III) carbonate and perchloric acid in water. The perchlorate salt was recrystallized from triply distilled water prior to use. Cyclen was synthesized by the method of Chavez and Sherry.[39] The solvents were purified by the standard procedures.[40]

Physical Measurements: Infrared spectra were recorded on a Perkin–Elmer Spectrum RX-I FT-IR spectrometer in the range of 4000–400 cm^{-1} using KBr pellets. Potassium bromide (FT IR grade, Aldrich) was used to make pellets. FAB mass spectra were recorded on a Jeol SX-102/DA 6000 mass spectrometer/data system using argon (6 kV, 10 mA) as the FAB gas. The accelerating voltage was 10 kV and the spectra were recorded at room temperature using *m*-nitrobenzyl alcohol as the matrix. Electrospray ionization mass spectra were recorded with a Micromass Quattro-II Triple Quatrapole mass spectrometer. The sample was dissolved in water and introduced into the ESI capillary using a 5-μL syringe pump. The ESI capillary was set at 3.5 kV with a cone voltage of 40 V. CHN microanalyses were carried out using Perkin–Elmer 2400 Series II CHNS/O Elemental Analyzer interfaced with a Perkin–Elmer AD 6 Autobalance. Helium (analytical grade) was used as the carrier gas. Analytical and preparative HPLC analysis were carried out using Varian PrepStar 218 (Varian Instruments Inc., USA) binary gradient solvent delivery module with an inline three channel degasser Model 2000 for solvent delivery. A Rheodyne injector valve (20 μL) was used for the sample injection. HPLC column (250 × 4.6 mm × 1/4 in Valco, Microsorb-MV 100-5 C18) (analytical) and DYNAMAX HPLC column (250 × 10.0 mm, Microsorb 300–10 C18) (preparative) were used. UV/Visible detector Model 345 operating in the range 190–1100 nm was used. The fractions were collected using a Model 704 fraction collector. EPR spectra were recorded on a Jeol instrument at Q-band (34.5 MHz) and X-band (9.4 MHz) with a scan range of 8000 g and the field was set at 12500 T. Magnetic susceptibility measurements were carried out on EG&G PAR Model 155 vibrating sample magnetometer at 25 °C. ^1H NMR spectra were recorded in D_2O and $CDCl_3$ (9.995 atom% D, Aldrich) on a Jeol GSX-400 multinuclear NMR spectrometer working at 400 MHz at 25 °C. The ^{13}C NMR spectra were recorded at 100 MHz using a Jeol GSX-400 instrument. The ^{31}P NMR spectra were recorded at 162 MHz.

Longitudinal Relaxivity (r_{1p}) Measurements: The longitudinal relaxivity of the Gd^{III} complex was determined from the spin-lattice relaxation time, T_1. The T_1 measurements were carried out on a Maran wide line NMR (Resonance Instruments Ltd., UK) operating at 24 MHz and 35 ± 0.1 °C. The temperature was controlled using a temperature console. The complex solutions in triply distilled water were placed in a 10-mm stoppered quartz tube and the instrument parameters were optimized for each T_1 measurement. The T_1 measurements were made using the standard inversion recovery pulse sequence (180°–τ–90°) with phase-sensitive detection[41] with varying τ values ranging from 50 μs to 6 s for each concentration of the complex. The computer program Winfit was used to plot the time vs. signal intensity to get an exponential plot and the T_1 values were calculated from the plot. A delay of at least 5 T_1 was maintained in between successive pulses to allow the complete return of the spin system to equilibrium. The T_1 values for five different concentrations of the complex were measured. A plot of $1/T_1$ vs. concentration of the complex gave a straight line and the slope was taken as the longitudinal relaxivity r_{1p}. The longitudinal relaxivity at pH 8.5 was measured by maintaining the pH by adding TRIS buffer. The longitudinal relaxivity in the presence of β-cyclodextrin was determined by adding aqueous solution of a known amount of β-cyclodextrin and keeping the solution overnight at ambient temperature to attain equilibrium. Six different concentrations (0.2, 0.5, 1.0, 1.5, 2.0, and 2.5 mM) of the complex in water were used for relaxivity measurements.

Transverse Relaxivity (r_{2p}) Measurements: The transverse relaxivity, r_{2p}, was determined from the spin–spin relaxation time T_2. A standard CPMG (Carl–Purcel–Meiboon–Gill) pulse sequence (90°–τ–180°)[42] with a τ value of 50 μs was used to determine T_2. The computer program Winfit was used to plot the time vs. signal intensity to get an exponential curve and T_2 was calculated from the graph. The T_2 values for six different concentrations were measured. The transverse relaxivity was calculated from the slope of the regression line, obtained by the plot of the concentration of the complex vs. $1/T_2$ by a least-squares fitting method. Six different concentrations (0.2, 0.5, 1.0, 1.5, 2.0, and 2.5 mM) of the complex were prepared in triply distilled water.

1,4,7-Tris(carboxymethyl)-1,4,7,10-tetraazacyclododecane (DO3A) (2): Chloroacetic acid (2.820 g, 30 mmol) in 20 mL of water was placed in a double-walled, round-bottomed flask, connected to a cryostat maintained at –4 °C, and aqueous sodium hydroxide (5 N) was added dropwise whilst stirring until the pH reached 5. Cyclen sulfate (3.684 g, 10 mmol) in water (50 mL) was neutralized with 5 N sodium hydroxide and added to the chloroacetic acid solution in the flask whilst stirring at –4 °C. The pH of the mixture was increased to 10 by the addition of 5 N aqueous sodium hydroxide. The solution was maintained at –4 °C with constant stirring whilst maintaining pH 10 by the frequent addition of 5 N aqueous sodium hydroxide for 3 h. The contents of the flask were transferred to another round-bottomed flask, fitted with a double surface condenser, and slowly heated to room temperature for 5 h while maintaining a pH of 10. The solution was further heated to 50 °C over a period of 4 h and the temperature was maintained for 8 h at pH 10. The solution was cooled to room temperature and loaded onto a column containing Amberlite IR 120 (H^+, strongly acidic) cation exchange resin and eluted with deionized water. The solvent was removed under reduced pressure in a rotary evaporator and the resulting white solid was washed with dry acetone and methanol, filtered, and dried in a vacuum desiccator. The purity of DO3A was checked by HPLC (R_f = 3.244, H_2O/CH_3CN 9:1 *v*/*v*); yield 69.58%; m.p. 260 °C. IR (KBr): $\tilde{\nu}$ = 3406.5 cm^{-1} ν_s(OH), 2964.0 ν_s(CH), 1723.0 ν_s(C=O), 1623.6 δ(NH), 1459.8 ν(CH), 1391.6 δ(OH), 1212.3 ν_s(CO), 1087.0 ν_s(CN), 985 δ(CH), 720 δ_r(CH). MS (70 eV, EI): *m*/*z* (%) = 344 (80) $[M - 2]^+$ ($C_{14}H_{24}N_4O_6$),

 © 2005 Wiley-VCH Verlag GmbH & Co. KGaA, Weinheim

329 (50) $[M - NH]^+$ ($C_{14}H_{23}N_3O_6$), 302 $[M - C_2NH_3]^+$ ($C_{12}H_{20}N_3O_6$), 243 (20) $[M - C_4H_7NO_2]^+$ ($C_{10}H_{17}N_3O_4$), 185 (50) $[M - C_6H_9NO_4]^+$ ($C_8H_{15}N_3O_2$), 57 (100) ($C_2H_2O_2$). ^{1}H NMR (400 MHz, D_2O, TMS): δ = 3.21 (m, 12 H, CH_2), 3.39 (m, 4 H, N–CH_2), 3.60 (s, 6 H, CH_2COOH), 3.9 (d, 1 H, J = 5.3 Hz, NH) ppm. ^{13}C NMR (100.34 MHz, D_2O): δ = 42.5 (CH_2), 47.8 (N–CH_2), 52.06 (CH_2COOH), 174.5 (COOH) ppm. $C_{14}H_{26}N_4O_6$ (346.08): calcd. C 48.58, H 7.51, N 16.18; found C 48.14, H 7.43, N 15.94.

10-Bromopropyl-1,4,7-tris(carboxymethyl)-1,4,7,10-tetraazacyclododecane (3): DMF (30 mL) and 5 drops of triethylamine were added, whilst stirring, to a solution of DO3A (3.45 g, 10 mmol) in 60 mL of distilled water in a round-bottomed flask, kept over a rotamantle, and the mixture was heated to 80 °C. The temperature was maintained at 80 °C for 1 h with stirring. 1,3-Dibromopropane (2.01 g, 10 mmol) in 10 mL of DMF was then added slowly and the reaction mixture was stirred for 36 h at 80 °C. The mixture was filtered and the filtrate was evaporated in a rotary evaporator to dryness. The solid compound that separated out was washed with dry methanol to remove triethylamine hydrobromide salt and then with acetone. The white solid was dried in a vacuum desiccator and recrystallized from water. The purity of **3** was checked by HPLC (R_f = 4.20, H_2O/CH_3CN, 3:2 *v*/*v*); yield 67%; m.p. 290 °C (dec). IR (KBr): $\tilde{\nu}$ = 3432.2 cm^{-1} ν_s(OH), 2954.0 ν_s(CH),1692.0 ν_s(C=O), 1460.3 δ(CH), 1385.4 δ(OH), 1214.4 ν_s(CO), 1087.3 ν_s(CN), 980.7 δ(CH), 699.4 δ_r(CH). MS (FAB): *m*/*z* = 466 $[M - 1]^+$ ($C_{17}H_{30}N_4O_6Br$), 341 $[M - C_3H_9Br]^+$ ($C_{14}H_{21}N_4O_6$), 284 $[M - C_5H_{11}O_2Br]^+$ ($C_{12}H_{20}N_4O_4$), 255 $[M - C_7H_{16}O_2Br]^+$ ($C_{10}H_{15}N_4O_4$). ^{1}H NMR (400 MHz, D_2O, TMS): δ = 2.63 (m, 2 H, CH_2), 3.23 (m, 12 H, CH_2), 3.41 (s, 6 H, N–CH_2), 3.84 (CH_2COOH) ppm. ^{13}C NMR (100.34 MHz, D_2O): δ = 36.84 (N-CH$_2$-*C*H$_2$), 52.73 (*C*H$_2$), 58.28 (*C*H$_2$COOH) 174.31 (*C*OOH) ppm. $C_{17}H_{31}BrN_4O_6$ (467.01): calcd. C 43.71, H 6.63, N 11.99; found C 43.18, H 6.33, N 11.53.

10-[3-(Adenosine5′-triphosphate)oxypropyl]-1,4,7-tris(carboxymethyl)-1,4,7,10-tetraazacyclododecane (DO3A-Pr-ATP): Adenosine 5′-triphosphate disodium salt (0.551 g, 1 mmol) was dissolved in 5 mL of water and passed through a column packed with Amberlite IR-120 (H^+, strongly acidic) cation exchange resin and eluted with distilled water. The linker-appended DO3A (**3**; 0.466 g, 1 mmol) in 25 mL of water was added to the eluent, which contains free ATP, and stirred for 24 h at room temperature. The solvent was removed under reduced pressure in a rotary evaporator whilst maintaining the bath temperature below 40 °C. The vitreous solid that separated out became white upon the addition of methanol and was washed with acetone, dried in a vacuum desiccator, and stored in a refrigerator. The purity of DO3A-Pr-ATP was checked by HPLC (R_f = 6.11, H_2O/CH_3CN, 9:5 *v*/*v*); yield 53.4%; m.p. 153 °C (dec). IR (KBr): $\tilde{\nu}$ = 3420.1 cm^{-1} ν_s(OH), 2926.5 ν_s(CH), 1476.8 δ_s(CH), 1700 ν_s(C=O), 1635.4 δ_s(NH), 1507.1 ν_s(C–O), 1087.6 ν_s(C–N), 995 δ(C–H), 719.8 δ_r(C–H), 1228.4 ν_s(P=O), 900 ν_s(P–O). MS (ESI): *m*/*z* = 894 $[M + 1]^+$ ($C_{27}H_{47}N_9O_{19}P_3$), 756 $[M - C_5H_7N_5]^+$ ($C_{22}H_{39}N_4O_{19}P_3$), 654 $[M - C_9H_{13}N_5O_3]^+$ ($C_{18}H_{33}N_4O_{16}P_3$), 348 $[M - C_{13}H_{19}N_5O_{13}P_3]^+$ ($C_{14}H_{28}N_4O_6$). ^{1}H NMR (400 MHz, D_2O, TMS): δ = 2.25 (t, 2 H, N-CH$_2$-CH_2), 3.10–3.4 (m, 12 H, NCH_2CH_2N), 3.58–3.63 (t, J = 5.5 Hz, 2 H; OCH$_2$), 4.25 (t, 1 H), 4.37 (6 H, CH_2COO), 4.49–4.65 (d, J = 7.08 Hz, 2 H), 6.073 (m, 1 H), 8.37, 8.54 (m, 2 H) ppm. ^{13}C NMR (100.34 MHz, D_2O): δ = 34.78 (*C*H$_2$), 52.99 (*C*H$_2$), 57.23 (*C*H$_2$COOH), 68.43 (O*C*H$_2$), 77.38 (O*C*H$_2$), 87.14 (C_2, C_3, and C_4 of furan ring), 174.52 (*C*OOH), 152.90–145.57 (aromatic ring) ppm. ^{31}P NMR (162 MHz, D_2O): δ = 107.35 (*P*–P–P), 119.30 (P–P–*P*), 130.20 (P–*P*–P) ppm. $C_{27}H_{46}N_9O_{19}P_3$ (893.05): calcd. C 36.31, H 5.15, N 14.10; found C 36.14, H 4.96, N 13.94.

[Gd(DO3A-Pr-ATP)(H$_2$O)$_2$] (4): Gadolinium(III) perchlorate hydrate (0.11 g, 0.25 mmol) was added to a solution of DO3A-Pr-ATP (0.22 g, 0.25 mmol) in 30 mL of water and stirred at room temperature for 36 h. Dowex cation exchange resin (10 g) was added to the reaction mixture and stirred for 15 min at room temperature and the absence of uncomplexed Gd^{III} ions was confirmed by testing the solution with xylenol orange indicator.[43] The solution was filtered to remove solid particles and the filtrate was distilled off under reduced pressure in a rotary evaporator to dryness. The white solid was recrystallized from triply distilled water. The purity of the complex was checked by HPLC (single peak, retention time 4.420 (H_2O/CH_3CN, 9:1, *v*/*v*); yield 59.09%; m.p. 175 °C (dec). IR (KBr): $\tilde{\nu}$ = 3303.4 cm^{-1} ν_s(OH), 1608.8 (COO), 1410.6 δ_s(OH), 1238.0 ν_s(P=O), 909 ν_s(P–O). MS (ESI): *m*/*z* = 1081 $[M - 2]^+$ $[Gd(C_{27}H_{41}N_9O_{19}P_3)(H_2O)_2]$, 793 $[M - C_{11}H_{17}N_5O_5]^+$ $[Gd(C_{17}H_{27}N_4O_{16}P_3)]$, 734 $[M - C_{12}H_{21}N_5O_7]^+$ $[Gd(C_{15}H_{24}N_4O_{14}P_3)]$, 578 $[M - Gd(C_{12}H_{20}N_5O_7)]^+$ ($C_{15}H_{25}N_4O_{14}P_3$), 483 $[M - Gd(C_{12}H_{20}N_5O_{11}P)]^+$ ($C_{15}H_{25}N_4O_{10}P_2$), 168 $[M - Gd(C_{19}H_{29}N_5O_{21}P_3)]^+$ ($C_8H_{16}N_4$). $Gd(C_{27}H_{43}N_9O_{19}P_3)(H_2O)_2$ (1083.05): calcd. C 29.94, H 4.33, N 11.63; found C 29.68, H 4.25, N 11.46.

Supporting Information Available (see footnote on the first page of this article): Chart S1. Gadolinium(III) chelates approved by FDA for human imaging. FAB mass spectroscopic data of 10-(3-bromopropyl)-1,4,7-tris(carboxymethyl)-1,4,7,10-tetraazacyclododecane (Figure S1), T_1 values for different concentrations of $[Gd(L1)(H_2O)_2]$ (Table S1), the plot of concentration of $[Gd(L1)(H_2O)_2]$ vs. $1/T_1$ (r_{1p} relaxivity measurements) (Figure S2), T_1 values for different concentrations of $[Gd(L1)(H_2O)_2]$ in the presence of β-cyclodextrin (Table S2), the plot of concentration of $[Gd(L1)(H_2O)_2]$ vs. $1/T_1$ in the presence of β-cyclodextrin (Figure S3), T_1 values for different concentrations of $[Gd(L1)(H_2O)_2]$ at pH 8.4 (Table S3), and a plot of concentration of $[Gd(L1)(H_2O)_2]$ vs. $1/T_1$ (r_{1p} relaxivity measurements at pH 8.4; Figure S4).

Acknowledgments

This research was carried out with the financial support of the Board of Research in Nuclear Sciences (BRNS), Department of Atomic Energy, Government of India. We thank Dr. V. K. Manchanda, Head, Radiochemistry Division, Bhabha Atomic Research Center, Mumbai-400085, for his support. We thank Dr. Venkat Manohar, Measurements Science Division, Unilever Research India, Bangalore, for providing facilities for relaxivity measurements.

[1] The 2003 Nobel Prize in Physiology or Medicine, The Nobel Assembly, Karolinska Institutet, Stockholm, Sweden, October 6, **2003**.

[2] a) P. Caravan, J. J. Ellison, T. J. McMurry, R. B. Lauffer, *Chem. Rev.* **1999**, *99*, 2293–2352; b) M. F. Tweedle, in *Lanthanide Probes in Life, Chemical, and Earth Sciences* (Eds.: J.-C. G. Bunzli and G. R. Choppin), Elsevier, Amsterdam, **1989**; c) R. B. Lauffer, *Chem. Rev.* **1987**, *87*, 901–907; d) K. Kumar, M. F. Tweedle, *Pure Appl. Chem.* **1993**, *65*, 515–520; e) A. E. Merbach, E. Toth, *The Chemistry of Contrast Agents in Medical Magnetic Resonance Imaging*, Wiley-VCH, Weinheim, **2001**; f) J. A. Peters, J. Huskens, D. J. Raber, *Prog. Nucl. Magn. Reson. Spectrosc.* **1996**, *28*, 283–350.

[3] P. C. Lauterbur, M. H. Mendonca-Dias, A. M. Rudin, in *Frontiers of Biological Energetics* (Eds.: P. L. Dutton, L. S. Leigh, A. Scarpa), Academic Press, New York, **1978**.

[4] M. F. Tweedle, G. T. Gaughan, J. Hagan, P. W. Wedeking, P. Sibley, L. J. Wilson, D. W. Lee, *Nucl. Med. Biol.* **1988**, *15*, 31–36.

[5] a) I. Bertini, C. Luchinat, *NMR of Paramagnetic Molecules in Biological Systems*, Benjamin/Cummings Publishing Co.,

 © 2005 Wiley-VCH Verlag GmbH & Co. KGaA, Weinheim

Menlo Park, **1986**; b) D. D. Stark, W. G. Bradley, *Magnetic Resonance Imaging*, The C. V. Mosby Company, St. Louis, Missouri, **1988**; c) L. Banci, I. Bertini, C. Luchinat, *Nuclear and Electron Relaxation*, VCH, Weinheim, Germany, **1991**; d) S. H. Koenig, R. D. Brown III, *Magn. Reson. Med.* **1984**, *1*, 496–501; e) R. Hausser, G. *Z*. Laukien, *Physik* **1959**, *153*, 394; f) R. A. Bernheim, T. H. Brown, H. S. Gutowsky, D. E. Woessner, *J. Chem. Phys.* **1959**, *30*, 950–956; g) L. O. Morgan, A. W. Nolle, *J. Chem. Phys.* **1959**, *31*, 365–368.

[6] a) I. Solomon, *Phys. Rev.* **1955**, *99*, 559–565; b) N. Bloembergen, *J. Chem. Phys.* **1957**, *27*, 572–573; c) N. Bloembergen, *J. Chem. Phys.* **1957**, *27*, 595; d) N. Bloembergen, L. O. Morgon, *J. Chem. Phys.* **1961**, *34*, 842–850.

[7] a) D. H. Powell, O. M. Ni Dhubhghaill, D. Pubanz, L. Helm, Y. S. Lebedev, W. Schlaepfer, A. E. Merbach, *J. Am. Chem. Soc.* **1996**, *118*, 9333–9346; b) S. H. Koenig, *J. Magn. Reson., Ser. A* **1978**, *31*, 1; c) E. Toth, L. Holm, A. E. Merbach, in *The Chemistry of Contrast Agents in Medical Magnetic Resonance Imaging* (Eds.: A. E. Merbach, E. Toth), Wiley-VCH, Weinheim, **2001**.

[8] S. Aime, M. Botta, M. Fasano, S. G. Crich, E. Terreno, *J. Biol. Inorg. Chem.* **1996**, *1*, 312–319.

[9] S. Aime, M. Botta, L. Frullano, S. G. Crich, G. B. Giovenzana, R. Pagliarin, G. Palmisano, M. Sisti, *Chem. Eur. J.* **1999**, *5*, 1253–1260.

[10] a) S. Aime, M. Botta, S. G. Crich, G. Giovenzana, G. Palmisano, M. Sisti, *Chem. Commun.* **1999**, 1577–1578; b) S. Aime, M. Botta, S. G. Crich, G. Giovenzana, G. Palmisano, M. Sisti, *Bioconjugate Chem.* **1999**, *10*, 192–199.

[11] R. C. Brasch, *Magn. Reson. Med.* **1991**, *22*, 282–287.

[12] E. C. Wiener, M. W. Brechbiel, H. Brothers, R. L. Magin, O. A. Gansow, D. A. Tomalia, P. C. Lauterbur, *Magn. Reson. Med.* **1994**, *31*, 1–8.

[13] S. Aime, M. Botta, G. Ermondi, E. Terreno, P. L. Anelli, F. Fedeli, F. Uggeri, *Inorg. Chem.* **1996**, *35*, 2726–2736.

[14] P. Caravan, N. J. Cloutier, M. T. Greenfield, S. A. McDermid, S. A. Dunham, J. W. M. Bulte, J. C. Amedio, R. J. Looby, R. M. Supkowski, W. DeWitt Horrocks Jr, T. J. McMurry, R. B. Lauffer, *J. Am. Chem. Soc.* **2002**, *124*, 3152–3162.

[15] S. Aime, P. L. Anelli, M. Botta, F. Fedeli, M. Grandi, P. Paoli, F. Uggeri, *Inorg. Chem.* **1992**, *31*, 2422–2428.

[16] S. Aime, E. Gianolio, E. Terreno, G. B. Giovenzana, R. Pagliarin, M. Sisti, G. Palmisano, M. Botta, M. P. Lowe, D. Parker, *J. Biol. Inorg. Chem.* **2000**, *5*, 488–497.

[17] T. H. Helbich, A. Gossman, P. A. Mareski, B. Raduchel, T. P. L. Roberts, D. M. Shames, M. Muhler, K. Turetschek, R. C. Brasch, *J. Magn. Reson. Imaging* **2000**, *11*, 694–701.

[18] a) H. J. Weinmann, R. C. Brasch, W. R. Press, G. E. Wesby, *Am. J. Roentgenol.* **1984**, *142*, 619–624; b) M. Laniado, H. J. Weinmann, W. Schorner, R. Felix, U. Speck, *Physiol. Chem. Phys. Med. NMR* **1984**, *16*, 157–166; c) H. J. Weinmann, M. Linado, W. Mutzel, *Physiol. Chem. Phys. Med. NMR* **1984**, *16*, 167–172.

[19] a) M. Magerstadt, O. A. Gansow, M. W. Brechbiel, D. Colcher, L. Baltzer, R. H. Knop, M. E. Girton, M. Naegele, *Magn. Reson. Med.* **1986**, *3*, 808–812; b) R. H. Knop, J. A. Frank, A. J. Dwyer, M. E. Griton, M. Naegela, M. Schrader, *J. Comp. Assist. Tomogr.* **1987**, *11*, 35.

[20] a) M. S. Konings, W. C. Dow, D. B. Love, K. N. Raymond, S. C. Quay, S. M. Rocklage, *Inorg. Chem.* **1990**, *29*, 1488–1491; b) C. A. Chang, *Invest. Radiol.* **1993**, *28*, 21; c) A. Greco, M. T. McNamara, P. Lanthiez, S. C. Quay, G. Michelozzi, *Radiology* **1990**, *176*, 451.

[21] a) D. D. Dischino, E. J. Delaney, J. E. Emswiler, G. T. Gaughan, J. S. Prasad, S. K. Srivastava, M. F. Tweedle, *Inorg. Chem.* **1991**, *30*, 1265–1269; b) M. F. Tweedle, V. M. Runge, *Drugs Future* **1992**, *17*, 187–190; c) K. Kumar, A. Chang, L. C. Francesconi, D. D. Dischino, M. F. Malley, J. Z. Gougoutas, M. F. Tweedle, *Inorg. Chem.* **1994**, *33*, 3567–3575; d) M. F. Tweedle, *Invest. Radiol.* **1992**, *27*, 2–6.

[22] a) J. Platzek, P. Blaszkiewicz, H. Gries, P. Luger, G. Michl, M. A. Fahrnow, B. Raduchel, D. Sulzle, *Inorg. Chem.* **1997**, *36*, 6086–6093; b) H. Vogler, J. Platzek, G. Schuhmann-Giampieri, T. Frenzel, H. J. Weinmann, B. Raduchel, W. R. Press, *Eur. J. Radiol.* **1995**, *21*, 1–10; c) T. Staks, G. Schumann-Giampieri, T. Frenzel, H. J. Weinmann, L. Lange, J. Platzek, *Invest. Radiol.* **1994**, *29*, 709.

[23] a) G. Vittadini, E. Felder, P. Tirone, V. Lorusso, *Invest. Radiol.* **1988**, *23*, 246; b) F. Cavagna, M. Dapra, F. Maggioni, C. De Haen, E. Felder, *Magn. Reson. Med.* **1991**, *22*, 329; c) F. Uggeri, S. Aime, P. L. Anelli, M. Botta, M. Brocchetta, C. De Haen, G. Ermondi, M. Grandi, P. Paoli, *Inorg. Chem.* **1995**, *34*, 633–642.

[24] V. Jacques, J. F. Desreux, *Top. Curr. Chem.* **2002**, *221*, 123–164.

[25] a) A. Bogdanov, Jr., M. Lewin, R. Weissleder, *Adv. Drug Delivery Rev.* **1999**, *37*, 279–293; b) R. B. Lauffer, D. J. Parmelee, H. S. Quellet, R. P. Dolan, H. S. Sajiki, D. M. Scott, P. J. Bernard, *Acad. Radiol.* **1996**, *3*, S356–S358; c) M. V. D. Nguyen, M. E. Brik, B. N. Ouvrard, J. Courtieu, L. Nicolas, A. Gaudemer, *Bull. Soc. Chim. Belg.* **1996**, 105; d) A. Harrison, C. A. Walker, K. A. Pereira, D. Parker, L. Royle, K. Pulukkody, T. J. Norman, *Magn. Reson. Imaging* **1993**, *11*, 761–770; e) K. P. Pulukkody, T. J. Norman, D. Parker, L. Royle, C. J. Broan, *J. Chem. Soc., Perkin Trans. 2* **1993**, 605–620; f) S. K. Kim, M. Pohost, G. A. Elgavish, *Bioconjugate Chem.* **1992**, *3*, 20–26; g) W. C. Baker, M. J. Choi, D. C. Hill, J. L. Thompson, P. A. Petillo, *J. Org. Chem.* **1999**, *64*, 2683–2689; h) C. Glogard, R. Hovland, S. L. Fossheim, A. J. Aasen, J. Klaveness, *J. Chem. Soc., Perkin Trans. 2* **2000**, 1047–1052; i) R. Hovland, C. Glogard, A. J. Aasen, J. Klaveness, *J. Chem. Soc., Perkin Trans. 2* **2001**, 929–933; j) L. J. Guggenberger, E. L. Muetterties, *J. Am. Chem. Soc.* **1976**, *98*, 7221–7225.

[26] a) M. P. Lowe, D. Parker, O. Reany, S. Amie, M. Botta, G. Castellano, E. Gianolio, R. Pagliarin, *J. Am. Chem. Soc.* **2001**, *123*, 7601–7609; b) S. Zhang, K. Wu, A. D. Sherry, *Angew. Chem. Int. Ed.* **1999**, *38*, 3192–3194; c) W. J. L. Hooley, J. Haveman, H. S. Reinhold, *Radiother. Oncol.* **1984**, *2*, 343.

[27] a) L. Burai, E. Toth, S. Seibig, R. Scopelliti, A. E. Merbach, *Chem. Eur. J.* **2000**, *6*, 3761–3770; b) S. Amie, M. Botta, E. Gianolio, E. Terreno, *Angew. Chem. Int. Ed.* **2000**, *39*, 747–750.

[28] a) R. A. Moats, S. E. Fraser, T. J. Meade, *Angew. Chem. Int. Ed. Engl.* **1997**, *36*, 726–728; b) A. Y. Lovie, M. M. Huber, E. T. Arhens, U. Rothbacher, R. A. Moats, R. E. Jacobs, S. E. Fraser, T. J. Meade, *Nature Biotechnol.* **2000**, *18*, 321–325; c) T. J. Meade, *Int. Congr. Ser.* **2000**, *73*, 1205; d) P. L. Anelli, I. Bertini, M. Fragai, L. Lattuada, C. Luchinat, G. Parigi, *Eur. J. Inorg. Chem.* **2000**, *39*, 625–630.

[29] a) W. H. Li, G. Parigi, M. Iragai, C. Luchinat, T. J. Meade, *Inorg. Chem.* **2002**, *41*, 4018–4024; b) W. H. Li, S. E. Fraser, T. J. Meade, *J. Am. Chem. Soc.* **1999**, *121*, 1413–1414.

[30] M. F. Tweedle, G. Gaughan, J. J. Hagen, *U S Patent No. 4,885,363*, **1989**; *Eur. Pat. Appl. EP 232-751-A*, **1986**.

[31] R. M. Silverstein, F. X. Webster, *Spectroscopic Identification of Organic Compounds*, John Wiley & Sons, New York, **1998**.

[32] J. P. Andre, H. R. Macke, E. Toth, A. E. Merbach, *J. Biol. Inorg. Chem.* **1999**, *4*, 341–347.

[33] S. I. Kang, R. S. Ranganathan, J. E. Emswiler, K. Kumar, J. Z. Gougoutas, M. F. Malley, M. F. Tweedle, *Inorg. Chem.* **1993**, *32*, 2912–2918.

[34] R. S. Ranganathan, M. E. Fernandez, S. I. Kang, A. D. Nunn, P. C. Rastep, K. M. R. Pillai, X. Zhang, M. F. Tweedle, *Invest. Radiol.* **1998**, *33*, 779–797.

[35] a) C. F. G. C. Geraldes, A. D. Sherry, W. P. Cacheris, K.-T. Kuan, R. D. Brown, S. H. Koenig, M. Spiller, *Magn. Reson. Med.* **1988**, *8*, 191–199; b) M.-R. Spirlet, J. Rebizant, M.-F. Loncin, J. F. Desreux, *Inorg. Chem.* **1984**, *23*, 4278–4283; c) S. Aime, M. Botta, G. Ermondi, *J. Magn. Reson., Ser. A* **1991**, *92*, 572–580.

 © 2005 Wiley-VCH Verlag GmbH & Co. KGaA, Weinheim

[36] a) S. Aime, F. Benetollo, G. Bombieri, S. Colla, M. Fasano, S. Paoletti, *Inorg. Chim. Acta* **1997**, *245*, 63–70; b) S. Aime, M. Botta, D. Parker, J. A. G. Williams, *J. Chem. Soc., Dalton Trans.* **1995**, 2259–2266; c) S. Aime, M. Botta, M. Panero, M. Grandi, F. Uggeri, *Magn. Reson. Chem.* **1991**, *29*, 923–927.
[37] M. L. Bender, M. Komiyama, in *Cyclodextrin Chemistry*, Springer, Berlin, **1978**.
[38] W. D. Kim, G. E. Kiefre, F. M. K. Maton, R. N. Muller, A. D. Sherry, *Inorg. Chem.* **1995**, *34*, 2233–2243.
[39] F. Chavez, A. D. Sherry, *J. Org. Chem.* **1989**, *54*, 2990–2992.
[40] B. S. Furniss, A. J. Hannaford, V. Rogers, P. W. G. Smith, A. R. Tatchell, *Vogel's Textbook of Practical Organic Chemistry*, 5th ed., Pearson Education, Delhi, **2004**.
[41] R. V. Vold, J. S. Waugh, M. P. Klein, D. E. Phelps, *J. Chem. Phys.* **1968**, *48*, 3831–3832.
[42] S. Meiboom, D. Gill, *Rev. Sci. Instrum.* **1958**, *29*, 688.
[43] G. Brunisholz, M. Randin, *Helv. Chim. Acta* **1959**, *42*, 1927–1938.

Received: December 10, 2004
Published Online: August 15, 2005

 © 2005 Wiley-VCH Verlag GmbH & Co. KGaA, Weinheim

Synthesis, Characterization and Molecular Structures of Yttrium Trifluoroacetate Complexes with O- and N-Donors: Complexation vs. Hydrolysis

Jianyong Zhang,[a] Stéphanie Morlens,[a] Liliane G. Hubert-Pfalzgraf*[a] and Dominique Luneau[b]

Keywords: Carboxylate ligands / Fluorinated ligands / N ligands / Superconductors / Yttrium

Dehydration and complexation reactions of $[Y(TFA)_3(H_2O)_3]$ (**1**; TFA = O_2CCF_3) were investigated with O- and N-donor ligands in order to obtain suitable precursors for MOD (Metal Organic Deposition). Anhydrous adducts such as $[Y_2(\mu,\eta^2\text{-}TFA)_4(\eta^1\text{-}TFA)_2(OHC_2H_4O\textit{i}Pr)_4]$ (**3**), $[Y_2(\mu,\eta^2\text{-}TFA)_4(\eta^1\text{-}TFA)_2(OHC_2H_4OC_2H_4OMe)_2]$ (**4**), or $[Y(TFA)_3(triglyme)]$ (**5**) were isolated. The reactions with N-donor ligands are more complex and afford mixed-ligand derivatives such as $[Y(TFA)_3(H_2O)_2(LL)]_m$ [LL = TMEDA (**9**), $Me_2NC_2H_4NMeC_2H_4NMe_2$ (**10**)] and, in the case of primary amines, yttrium oxohydroxo derivatives such as $[H_3O][Y_3(\mu_3\text{-}OH)(\mu\text{-}O)_3(\eta^1\text{-}TFA)_3(H_2O)_6(en)_3]$ (**6**; en = $NH_2C_2H_4NH_2$). All complexes were characterized by elemental analysis, FT-IR, and by single-crystal X-ray diffraction for **3**, **4**, and **6**. All structurally characterized complexes contain on eight-coordinate Y centers. Perfluorobutyrate and difluoroacetate derivatives were also prepared.

(© Wiley-VCH Verlag GmbH & Co. KGaA, 69451 Weinheim, Germany, 2005)

Introduction

Perfluorocarboxylate derivatives have been used as a source of fluorides by pyrolysis for glasses,[1] as a source of metal films for late transition metals, especially silver, by CVD techniques,[2] and have been considered for high Tc superconductors.[3] Trifluoroacetate (TFA) derivatives are currently used for elaboration of high Tc superconductor coatings by MOD (Metal Organic Deposition),[4a] a low-cost approach by comparison with vacuum approaches such as MOCVD (Metal Organic Chemical Vapour Deposition).[4b] This strategy proceeds via the formation of barium fluoride, thus avoiding the formation of more stable barium carbonate, during the thermal decomposition. However, the synthesis of the Ba, Y and Cu trifluoroacetates in situ starting from commercial acetates has led to lack of reproducibility in the quality of the coatings. This has been attributed to the volatility of the copper(II) derivative during the subsequent thermal treatment as well as to the presence of water. Lanthanide and yttrium trifluoroacetates associated with Al or Zn alkyls have also attracted interest as catalysts in various polymerization processes.[5] Although a large number of lanthanide trifluoroacetate complexes have been reported, often for their luminescence properties, few of them are anhydrous. Most of them are mixed-ligand species such as $[Ln(TFA)_3L_2(H_2O)]$ [L = pyzNO (pyrazine *N*-oxide)[6] or aza (2-azacyclononane)[7]] but species such as $[Ln(TFA)_3(DMF)_2]$ (LL = bipy, *o*-phen)[8] are also known. Structural characterization remains scarce, although such adducts display a large structural diversity, as represented by the $[Ln(TFA)_3(TMSO)_2]$ (TMSO = tetramethylene sulfoxide) derivatives,[9] which form infinite chains of dimers for Ln = La but discrete dimers for Ln = Nd, as well as $[Sm_2(\mu,\eta^2\text{-}TFA)_4(\eta^1\text{-}TFA)_2(aza)_2(H_2O)_2]\cdot 2aza$,[7] ionic compounds for the $Ln(TFA)_3(HMPA)_3$ adducts (Ln = La, Nd, Er) which are not isomorphous and are based on $[Er(\eta^1\text{-}TFA)_2(HMPA)_4]^+$, $[Er(\eta^1\text{-}TFA)_2(HMPA)_2(H_2O)_3]^+$ or $[Nd(\eta^2\text{-}TFA)_2(HMPA)_4]^+$ cations stabilized by a TFA counteranion.[10] Studies on yttrium derivatives remain quite scarce despite their interest in materials science.

We wish to report here the synthesis and characterization of yttrium fluorocarboxylate adducts with O- and N-donor ligands of various denticity. The anhydrous adducts $[Y_2(TFA)_6(OHC_2H_4O\textit{i}Pr)_4]$ (**3**) and $[Y_2(TFA)_6(OHC_2H_4OC_2H_4OMe)_2]$ (**4**) and the ionic hydroxide derivative $[H_3O][Y_3(\mu_3\text{-}OH)(\mu\text{-}O)_3(\eta^1\text{-}TFA)_3(H_2O)_6(en)_3]$ (**6**; en = $NH_2C_2H_4NH_2$) have been structurally characterized.

[a] Université Claude Bernard-Lyon 1, IRC,
2 avenue A. Einstein, 69629 Villeurbanne cédex, France
Fax: +33-4-72-44-5399
E-mail: Hubert@univ-lyon1.fr
[b] Université Claude Bernard-Lyon 1,
Centre de diffractométrie, 69622 Villeurbanne cédex, France

Results and Discussion

The synthetic routes and reactivity of yttrium trifluoroacetate derivatives were investigated. The various compounds were isolated in high yields and characterized by

 DOI: 10.1002/ejic.200500156

elemental analysis and FT-IR and ^{1}H NMR spectroscopy. $[Y_2(TFA)_6(OHC_2H_4OiPr)_4]$ (**3**), $[Y_2(TFA)_6(OHC_2H_4OC_2H_4OMe)_2]$ (**4**), and $[H_3O][Y_3(\mu_3\text{-}OH)(\mu\text{-}O)_3(\eta^1\text{-}TFA)_3(H_2O)_6(en)_3]$ (**6**; en = $NH_2C_2H_4NH_2$) were also characterized by single-crystal X-ray diffraction.

Synthesis of Y Derivatives by Ligand Exchange and Thermal Dehydration

The classical, cost-efficient synthesis of yttrium trifluoroacetate by reacting the oxide with trifluoroacetic acid in refluxing toluene[11] proceeds with formation of water as by-product to afford the hydrate $[Y(TFA)_3(H_2O)_3]$ (**1**). The presence of residual oxide was ascertained by absorption bands at 561 and 461 cm^{-1} in the IR spectrum. Recrystallization of **1** from diethyl ether allowed elimination of Y_2O_3. Attempts to remove the water molecules (48 h, 140 °C, 10^{-4} Torr) were unsuccessful, probably due to the strong hydrogen bonding between the water molecules and the fluorinated ligand.[12] More efficient dehydration of **1** could be achieved at 200 °C in a furnace but some decomposition was observed and the anhydrous $Y(TFA)_3$ is very hygroscopic due to its high Lewis acidity. Methyl orthoformate has been used for the dehydration of $LnCl_3{\cdot}xH_2O$,[13] therefore its potential to dehydrate **1** was evaluated. If the preceding reaction was carried out in the presence of methyl orthoformate (stoichiometry 1:3), a different product was formed. The presence of methanol in the coordination sphere was confirmed by the reaction with $[Y(TFA)_3(H_2O)_3]$ in refluxing methanol, which gives $[Y(TFA)_3(MeOH)_x]$ (20%) and the partially dehydrated adduct $[Y(TFA)_3(MeOH)_x(H_2O)_y]$. Attempts to use acetone as a ligand for access to anhydrous TFA derivatives, as reported for $[Cu_2(TFA)_4]_\infty$,[14] afforded the very hygroscopic species $[Y(TFA)_3(Me_2CO)_3]$ (**2**) in low yield, the major species being a mixture of $[Y(TFA)_3(H_2O)_x(Me_2CO)_y]$ complexes which could not be crystallized out. $[Y(CHF_2CO_2)_3(H_2O)_3]$ was also prepared from the oxide and CHF_2CO_2H but, in contrast to **1**, it was insoluble in THF. Anhydrous perfluorobutyrate $[Y(O_2CC_3F_7)_3]$ (**11**) was prepared from the oxide even in the absence of a dehydrating reagent. However, high yields required long reactions times (3 d) and careful work-up due to its high volatility under vacuum. In contrast, the hydrate $[Y(O_2CC_3F_7)_3(H_2O)_2]$ (**12**) was obtained easily in nearly quantitative yield from $[Y_2(CO_3)_3(H_2O)_3]$ in refluxing toluene.

Ligand-exchange reactions with various polydentate N- or O-donors were more efficient and yielded dehydrated, partially dehydrated, or hydrolyzed adducts in either toluene or THF at room temp. Dissolution of **1** generally required an excess of ligand, especially in toluene. The O- and N-donor ligands behaved quite differently in their potential to give water-free adducts. Exchange reactions with *i*PrOC_2H_4OH, $MeOC_2H_4OC_2H_4OH$, and triglyme ($MeOC_2H_4OC_2H_4OC_2H_4OMe$) provided water-free $[Y_2(TFA)_6(iPrOC_2H_4OH)_4]$ (**3**), $[Y_2(TFA)_6(MeOC_2H_4OC_2H_4OH)_2]$ (**4**), and $[Y(TFA)_3(MeOC_2H_4OC_2H_4OC_2H_4OMe)]$ (**5**), respectively (Scheme 1).

The reactions between $[Y(TFA)_3(H_2O)_3]$ and N-donor Lewis bases (B) were more complex than those with O-donor ligands. Exchange reactions with TMEDA and $Me_2NC_2H_4NMeC_2H_4NMe_2$ provided the partially dehydrated complexes $[Y(TFA)_3(H_2O)_2(Me_2NC_2H_4NMe_2)]$ (**9**) and $[Y(TFA)_3(H_2O)_2(Me_2NC_2H_4NMeC_2H_4NMe_2)]$ (**10**), respectively. However, in the presence of primary amines such as $H_2NC_2H_4NH_2$ (en), $H_2NC_2H_4NMe_2$, $H_2NC_2H_4NHC_2H_4NH_2$, and $H_2NC_2H_4NHC_2H_4OH$, part of the trifluoroacetate ligand was converted into a BH^+TFA^- salt to afford hydrolyzed metallic derivatives. In the case of ethylenediamine, the metallic species corresponds to an anionic trinuclear oxohydroxide $[Y_3(\mu_3\text{-}OH)(\mu\text{-}O)_3(\eta^1\text{-}TFA)_3(H_2O)_6(en)_3]^-$ stabilized by H_3O^+ as counterion, all metals being eight-coordinate (see below). Adducts with similar formulae were obtained with other primary amines, namely the tridentate $NH_2C_2H_4NHC_2H_4X$ (X = NH_2, OH) ligands, although these compounds were devoid of water. The various yttrium oxohydroxide trifluoroacetate complexes were often contaminated by some trifluoroacetate ammonium salts which were difficult to separate by crystallization or by sublimation. These results show that reactions between **1** and tertiary amines afford partially dehydrated adducts, while those with primary amines give

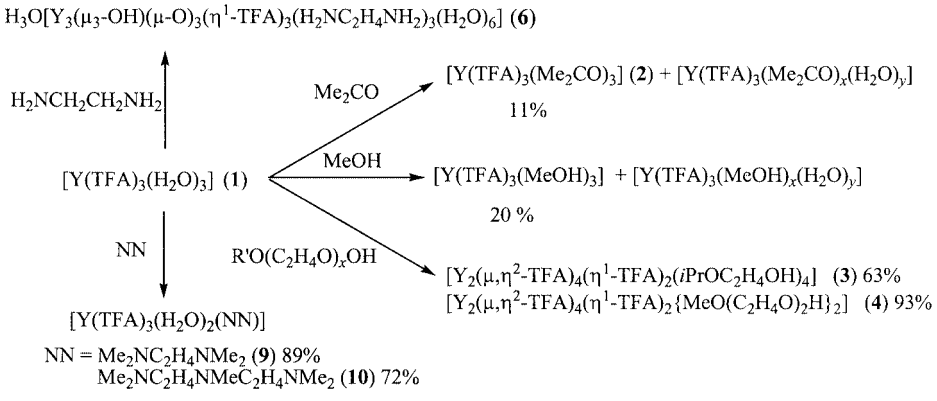

Scheme 1. Reactivity of **1** toward some O- and N-donors (all reactions at room temp.).

 © 2005 Wiley-VCH Verlag GmbH & Co. KGaA, Weinheim

hydrolyzed products. The formation of **6** according to Equation (1) supposes the presence of more water than that resulting from **1**, the additional water molecules being provided either by the solvent or, more likely, by the hygroscopic character of **1**. An hydroxy Pr trifluoroacetate $[Pr_2(TFA)_3(OH)(15\text{-crown-}5)_2][Pr_2(TFA)_8]$ has been reported by treatment of $[Pr(TFA)_3(H_2O)_3]$ with 15-crown-5.[15]

Physical Characteristics and Thermal Behavior

The various complexes display very intense broad absorption bands in their FT-IR spectra − generally two − at around 1290–1100 cm^{-1} corresponding to the C–F vibrations.[16,17] Additional sharp bands due to the coordinated Lewis base are present as well but they are shifted downfield with respect to the free ligand, as illustrated for

$$3\,[Y(TFA)_3(H_2O)_3] + 6\,H_2NC_2H_4NH_2 + 2\,H_2O \longrightarrow H_3O[Y_3(\mu_3\text{-}OH)(\mu\text{-}O)_3(\eta^1\text{-}TFA)_3(H_2O)_6(en)_3] + 3\,[H_3NC_2H_4NH_3](TFA)_2 \quad (1)$$

en = $H_2NC_2H_4NH_2$

Table 1. IR data [cm^{-1}] of the various yttrium fluorocarboxylate adducts.

Compound	$\nu(CO_2)$ $\nu_{as}(CO_2)$	$\nu_s(CO_2)$	ν(M–O)	ν(OH) [ν(NH)]	Observation
$[Y(TFA)_3(H_2O)_3]$ (**1**)	1760 sh, 1732 m, 1671 s, 1652 m, 1623 m, 1601 sh	1482 m, 1462 m	612 w, 523 w, 460 m	3695 m, 3667 w, 3626 w, 3611 w, 3433 br	air-stable.
$[Y(TFA)_3(Me_2CO)_3]$ (**2**)	1682 vs	1456 s	633 w, 613 w, 604 w, 524 m, 500 w, 455 m	–	hygroscopic, gives $Y(TFA)_3(H_2O)_3$ in air.
$[Y_2(TFA)_6(i\text{PrOC}_2H_4OH)_4]$ (**3**)	1738 s, 1674 s	1458 m	615 w, 605 w, 574 w, 522 w, 456 w	3160 br	air-stable for some hours, loses ligands in air; soluble in THF, toluene, EtOH.
$[Y_2(TFA)_6(MeOC_2H_4OC_2H_4OH)_2]$ (**4**)	1747 s, 1674 s	1477 m	617 w, 606 w, 582 w, 537 w, 522 w, 460 w	3144 w, 3115 w	air-stable for some hours, soluble in THF, MeCN, EtOH, insoluble in toluene, hexane.
$[Y(TFA)_3(MeOC_2H_4OC_2H_4OC_2H_4OMe)]$ (**5**)	1749 m, 1681 s	1462 s	653 w, 607 m, 523 m, 456 m	–	soluble in THF, MeOH, DME (comparable), insoluble in toluene, $CHCl_3$.
$[H_3O][Y_3O(OH)_3(TFA)_3(H_2NC_2H_4NH_2)_3(H_2O)_6]$ (**6**)	1682 vs, 1599 s	1405 w	625 m, 599 m, 518 w, 468 m	3606 w, 3375 s, 3336 s, 3298 s, 3175 m	hygroscopic, soluble in THF, EtOH, MeOH, insoluble in $CHCl_3$.
$[H_3O][Y_3O(OH)_3(TFA)_3(H_2NC_2H_4NHC_2H_4NH_2)_3]$ (**7**)	1715 s, 1682 s, 1606 m, 1590 m	1456 m, 1436 w, 1418 w	603 m, 582 m, 501 m, 483 m, 459 w	3344 m, 3293 m, 3234 m, 3171 m	air-stable for some hours, soluble in EtOH, slightly soluble in THF.
$[H_3O][Y_3O(OH)_3(TFA)_3(H_2NC_2H_4NHC_2H_4OH)_3]$ (**8**)	1682 s, 1596 m	1375 w, 1446 m	600 w, 580 m, 552 m, 519 w, 466 m	3375 br, 3319 br, 3288 br. m	soluble in THF, insoluble in Et_2O, toluene, hexane.
$[Y(TFA)_3(H_2O)_2(Me_2NC_2H_4NMe_2)]$ (**9**)	1694 s	1460 s	604 w, 522 m, 453 m	3390 br, 3083 m	hygroscopic, soluble in THF, EtOH, acetone, insoluble in toluene.
$[Y(TFA)_3(H_2O)_2(Me_2NC_2H_4NMeC_2H_4NMe_2)]$ (**10**)	1714 vs	1457 m, 1414 m	602 w, 551 w, 522 m, 453 m	3353 m	hygroscopic, soluble in THF, MeCN, EtOH, insoluble in toluene.
$[Y(O_2CC_3F_7)_3]$ (**11**)	1694 s, 1643 w	1424 w	643 w, 585 w, 532 w, 464 w	–	air-stable, soluble in EtOH, H_2O, slightly soluble in Et_2O, insoluble in toluene.
$[Y(H_2O)_2(O_2CC_3F_7)_3]$ (**12**)	1745 m, 1660 vs	1455 m, 1378 m	639 w, 593 w, 555 w, 530 w, 475 w	3663 br, 3379 br	air-stable, soluble in EtOH, H_2O, slightly soluble in Et_2O; insoluble in toluene.
$[Y(O_2CCHF_2)_3(H_2O)_3]$	1734 m, 1695 m, 1625 s	1483 m, 1421 w	586 m, 484 m	3640 m, 3406 br	air stable, hygroscopic.

 © 2005 Wiley-VCH Verlag GmbH & Co. KGaA, Weinheim

the alcohol adducts **3** and **4**. The absorption bands characteristic of the carboxylate ligands appear generally as several bands for the $\nu_{as}(CO_2)$ stretch, with some around 1740–1715 cm^{-1} and some at lower frequencies around 1680–1600 cm^{-1}, suggesting trifluoroacetate ligands displaying different coordination modes such as bridging or bridging-chelating and monodentate (Table 1). Similar patterns have been observed for $[Sm_2(\mu,\eta^2\text{-TFA})_4(\eta^1\text{-TFA})_2(aza)_4(H_2O)_2]\cdot 2aza$[7] and $[LaCu(bdmmpH)(bdmmp)(\mu\text{-}OH)(TFA)_3]_2$ [bdmmpH = 2,6-bis(dimethylaminomethyl)-4-methylphenol].[18] The absorption band at 1682 cm^{-1} for **6** and **8**, for instance, suggests the presence of monodentate TFA, in agreement with the frequency found for the dangling TFA of $[Y(\eta^1\text{-TFA})_2(H_2O)_6][TFA]$(18-crown-6).[19] The presence of η^1-TFA ligands is also evidenced by the reduction of the intensity of the $\nu_s(CO_2)$ absorption bands around 1403 cm^{-1}. The presence of water molecules in the coordination sphere of the complexes with the N-donor ligands (**9** and **10)** is evidenced by bands between 3350 and 3700 cm^{-1}.

The TGA patterns (N_2, 1 atm) of the perfluorobutyrate derivatives **11** and **12** account for their volatility. They decompose into yttrium fluoride and oxofluoride, respectively. Compound **12** decomposes between 320 and 370 °C after loss of water (up to 210 °C), whereas **11** decomposes between 270 and 310 °C.

Anhydrous metal trifluoroacetate derivatives are less soluble in organic media than their hydrated counterparts, and the yttrium derivatives are also less soluble than the barium derivatives.[17] Complexation with organic ligands improves their solubility and the complexes have good solubility in polar solvents such as THF, DME, and alcohols. All the anhydrous yttrium trifluoroacetate complexes are slightly hygroscopic. As expected, the solubility in organic media also increases with the length of the fluoroalkyl chain, the solubility of $[Y(PFB)_3(H_2O)_2]$ in MeOH, for example, is thus much better than that of $[Y(TFA)_3(H_2O)_3]$. Both compounds are actually more soluble in MeOH than in *i*PrO-C_2H_4OH. The low solubility of the various fluoroacetate compounds in nonpolar solvents precluded access to useful ^1H or ^{19}F NMR spectroscopic data (extensive dissociation was generally observed in CD_3OD).

Molecular Structures of $[Y_2(TFA)_6(R'OH)_x]$ (R' = *i*PrOC$_2$H$_4$, x = 4; R' = MeOC$_2$H$_4$OC$_2$H$_4$, x = 2) and of $[H_3O][Y_3(\mu\text{-}O)_3(\mu_3\text{-}OH)(TFA)_3(en)_3(H_2O)_6]$

Compounds **3**, **4**, and **6** were characterized by low-temperature single-crystal X-ray diffraction. The structures of complexes **3** and **4** with the O-donor ligands are depicted in Figures 1 and 2, respectively. Two independent molecules (**3a** and **3b**) having similar metric parameters are present in the unit cell of **3**. Selected bond lengths and angles are collected in Table 2 and Table 3 for **3** and **4**, respectively. The Y–TFA adducts with O-donor Lewis bases are dinuclear. Their molecular structure is based on a $Y_2(\mu,\eta^2\text{-TFA})_4(\eta^1\text{-TFA})_2$ core, the coordination sphere being completed by neutral ligands in order to achieve eight-coordination for the metals. As a result, the adduct **3** with isopropoxyethanol shows two different coordination modes, namely monodentate η^1- and bidentate η^2- for the alcohol, whereas 2-propoxyethoxyethanol ($HOC_2H_4OC_2H_4OMe$) is tridentate in **4**. The Y–O bond lengths range from 2.280(3) to 2.437(3) Å in **4**. The Y-μ,η^2-O(TFA) bonds [av. 2.329(5) and 2.334(3) Å for **3** and **4**, respectively] are longer than the corresponding Y-η^1-O(TFA) ones [2.301(5) and 2.300(3) Å]. As observed for an η^1-TFA barium derivative, the C–O bonds are slightly elongated by coordination [1.256(3) vs. 1.193(3) Å]. The coordination polyhedra of Y correspond to a square prism and a distorted square antiprism for **3** and **4**, respectively. The Y···Y distances have values of 4.484(2) (av.) and 4.464(5) Å for **3** and **4** respectively. They are thus longer than the Ln···Ln distances in $[Sm_2(\mu,\eta^2\text{-TFA})_4(\eta^1\text{-TFA})_2(aza)_4(H_2O)_2]\cdot 2aza$[7] and $[Nd_2(\mu,\eta^2\text{-TFA})_4(\eta^2\text{-TFA})_2(TMSO)_2]$[9] despite the smaller size of the metal, and also much longer than for $[Y_2(TFA)_6(bdmap)_2]^{2-}$ [bdmap = 1,3-bis(dimethylamino)-2-propoxide {$OCH(CH_2NMe_2)_2$}].[20] The bridging coordination mode of the trifluoroacetate ligand is quite common for homometallic as well as heterometallic compounds such as $[(\mu\text{-}TFA)_2Ln(\mu\text{-}CF_3CHO_2)AlR_2(THF)_2]_2$ (Ln = Nd, Y, Eu). The Y···F distances (>4.5 Å) account for the absence of Y···F interactions in the solid state, in contrast to the lanthanide fluorinated alkoxides.[17b] Octacoordination appears as the preferred coordination number for all structurally characterized yttrium trifluoroacetate derivatives.

Compound **6** crystallizes in the rhombohedral space group $R\bar{3}$ as a trinuclear anion and a H_3O^+ hydroxonium cation with the overall formula $[H_3O][Y_3(\mu_2\text{-}O)_3(\mu_3\text{-}OH)(TFA)_3(en)_3(H_2O)_6]$. The anion has C_3 symmetry, with the O3 oxygen atom (μ_3-OH) and the H_3O^+ ion both located on the C_3 axis, with O3 capping the trinuclear $[Y_3(\mu\text{-}O)_3(\mu_3\text{-}OH)]^{+2}$ unit (Figure 3). Selected bond lengths and angles are collected in Table 4. The Y–O bond lengths spread over the range 2.217(12) to 2.65(2) Å and follow the order Y–μ-O < Y–μ_3-OH < Y–η^1-O(TFA) < Y–Ow(H_2O). For the latter, two types of Y–Ow distances [2.49(2) and 2.64(2) Å] are observed. The Y–η^1-O(TFA) bond lengths of 2.44(2) Å (av.) are much longer than those in **3** and **4** despite the identical coordination numbers. The Y···O distances involving the dangling oxygen atoms have values of 3.636 Å. The Y–N bond distances [2.55(2) Å] are comparable to those observed, for instance, for $[Y_2(thd)_4(\mu,\eta^2\text{-bdmap})_2]$ (thd = 2,2,6,6-tetamethylheptane-3,5-dionate).[20] The Y···Y distance of 3.778(3) Å is in agreement with the data reported for the previous compound or for $[Cp_6Y_3(\mu\text{-}OMe)_3(\mu_3\text{-}H)_2Li_2(THF)_6]$.[21] It is much shorter than for **3** or **4**, where the metals are bridged by the trifluoroacetate ligands, but longer than for most other polynuclear yttrium alkoxides. The TFA and ethylenediamine ligands are located below the Y_3 plane on the same side as the hydroxide ligand, whereas the hydroxonium cation is located on the same side as the water molecules. As for the other derivatives, the structure of **6** displays no short Y···F (>5.127 Å)

 © 2005 Wiley-VCH Verlag GmbH & Co. KGaA, Weinheim

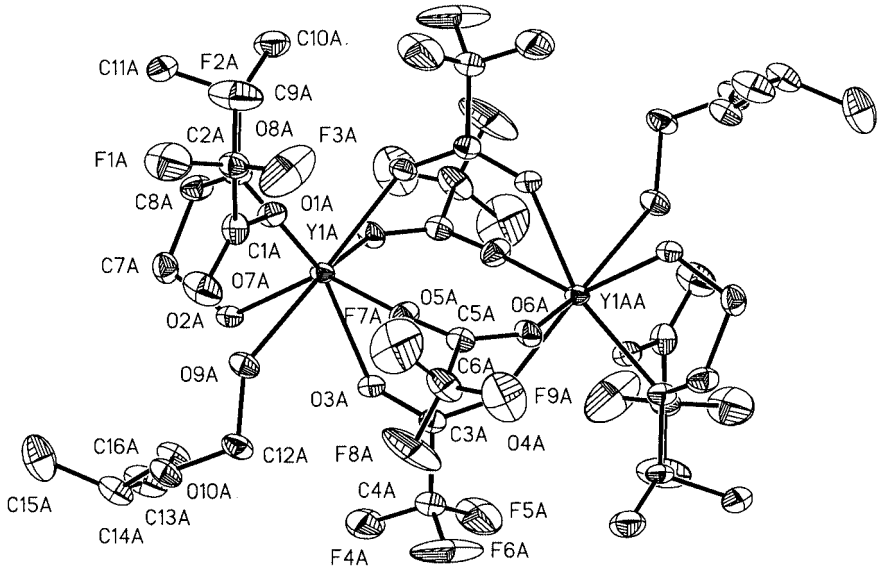

Figure 1. Molecular structure of **3** showing the atom numbering scheme (thermal ellipsoids at 30% probability).

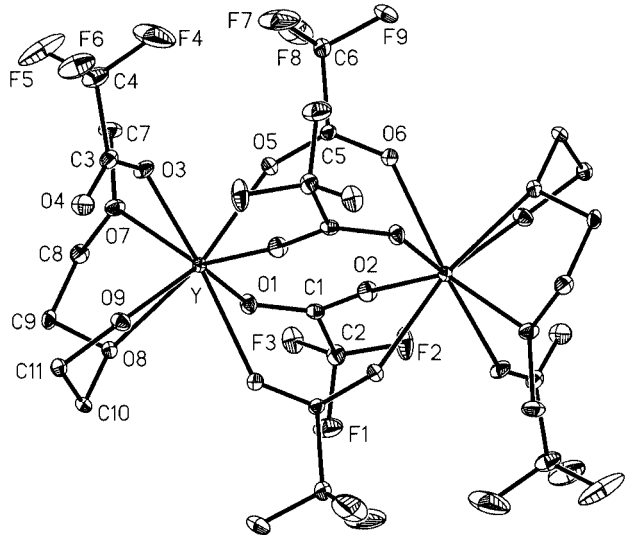

Figure 2. Molecular structure of **4** showing the atom numbering scheme (thermal ellipsoids at 30% probability).

Table 2. Selected bond lengths [Å] for **3a** and **3b** with estimated standard deviations in parentheses.[a]

Y1A–O5A	2.293(5)	Y2A–O1B	2.293(5)
Y1A–O1A	2.200(5)	Y2A–O5B	2.303(5)
Y1A–O4A#1	2.322(4)	Y2B–O4B#2	2.325(5)
Y1A–O3A	2.328(5)	Y2B–O3B	2.344(4)
Y1A–O6A#1	2.366(4)	Y2B–O6B#2	2.359(5)
Y1A–O9A	2.377(4)	Y2B–O7B	2.376(4)
Y1A–O7A	2.388(4)	Y2B–O9B	2.384(5)
Y1A–O8A	2.396(4)	Y2B–O8B	2.396(5)
Y1A···Y1A #1	4.484(2)	Y2B···Y2B#2	4.483(1)

[a] Symmetry transformations used to generate equivalent atoms: #1: *–x*, *–y*, *–z*; #2: *–x* + 1, *–y* + 1, *–z* + 1.

or μ_3-OH···F (>4.44 Å) interactions. In contrast, one observes two quite short N···F interactions, namely N1···F1 and N1···F3, with values of 3.744 and 3.821 Å respectively. These N···F interactions are much shorter than those observed, for instance, for [Ce{OCH$(CF_3)_2\}_4$(tmeda)] (4.137–4.259 Å).[22] The Y···O(H_3O) distance of 4.793(3) Å excludes the presence of ion pairs. The O(H_3O)···O(H_2O, O1w) distance of 3.26 Å shows that no strong hydrogen bonding exists. Metal complexes containing the hydroxonium cation remain scarce. Some examples are represented

Table 3. Selected bond lengths [Å] for **4** with estimated standard deviations in parentheses.[a]

Y–O2#1	2.280(3)	Y–O5	2.297(3)
Y–O3	2.300(3)	Y–O6#1	2.363(3)
Y–O7	2.391(3)	Y–O1	2.397(3)
Y–O9	2.409(3)	Y–O8	2.437(3)
Y···Y #1	4.464 (5)		

[a] Symmetry transformations used to generate equivalent atoms: #1: *–x*, *–y*, *–z*.

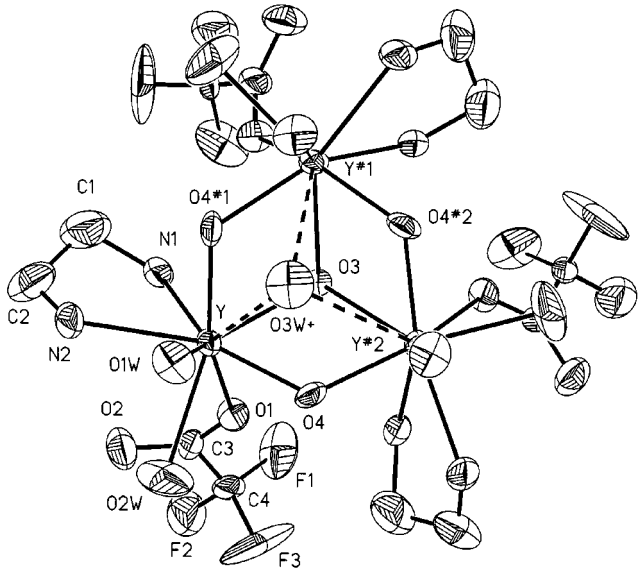

Figure 3. Molecular structure of **6** showing the atom numbering scheme (thermal ellipsoids at 30% probability).

 © 2005 Wiley-VCH Verlag GmbH & Co. KGaA, Weinheim

by $[H_3O][Re_3Cl_{10}(H_2O)_2],5H_2O$[23] and by [18-crown-6]$(H_3O)_2(Hf_2F_{10}\cdot 2H_2O)\cdot 4H_2O$.[24] Trinuclear neutral metal oxocarboxylate cores $[M_3(\mu_3\text{-}O)(TFA)_6(H_2O)_3]$ (M = Fe, Co, Mn, Ni) are quite common and have been used as building blocks for extended arrays.[25] On the other hand, reactions between fluoroacetates and amines are known to form ionic species, as observed, for instance, for bismuth with species such as $[(BH)_2Bi(\eta^1\text{-}TFA)_5]$ (B being pyridine or diamines such as TMEDA or other tertiary diamines) where the cations interact with the dangling oxygen of the trifluoroacetate ligands by H-bonding (Figure 4).[26]

No reaction was observed between Y and Ba trifluoroacetate derivatives, for instance in methanol. This was also confirmed by the fact that the reaction between $[Ba(OH)_2(H_2O)_8]$, yttrium oxide, trifluoroacetic acid, and methyl orthoformate in refluxing toluene gave a mixture of the homometallic species $[Ba(TFA)_2]_m$, $[Y(TFA)_3(H_2O)_3]$ and $[Y(TFA)_3(MeOH)_x(H_2O)_y]$ (IR evidence). In contrast, functional alcohols such as amino alcohols were able to promote the formation of heteronuclear assemblies.[27]

Table 4. Selected bond lengths [Å] and bond angles [°] for **6** with estimated standard deviations in parentheses.[a]

Bond lengths			
Y–O4#1	2.22(1)	Y–O4	2.29(1)
Y–O3	2.39(1)	Y–O1	2.43(2)
Y–N1	2.48(2)	Y–O1W	2.48(2)
Y–N2	2.55(2)	Y–O2W	2.65(2)
O3–Y#1	2.39(1)	O3–Y#2	2.39(1)
O4–Y#2	2.22(1)	Y···Y#1	3.778(3)
Y···Y#2	3.778(3)		
Bond angles			
O4#1–Y–O4	101.8(7)	O4#1–Y–O3	71.6(5)
O4–Y–O3	70.3(5)	O4#1–Y–O1	143.5(7)
O4–Y–O1	89.3(6)	O3–Y–O1	79.9(7)
O4#1–Y–N1	80.1(7)	O4–Y–N1	147.2(6)
O3–Y–N1	79.5(7)	O1–Y–N1	72.5(7)
O4#1–Y–O1W	77.2(7)	O4–Y–O1W	74.6(6)
O3–Y–O1W	126.1(9)	O1–Y–O1W	139.2(6)
N1–Y–O1W	136.4(6)	O4#1–Y–N2	81.0(5)
O4–Y–N2	144.7(8)	O3–Y–N2	140.6(5)
O1–Y–N2	109.5(6)	N1–Y–N2	68.1(8)
O1W–Y–N2	71.8(8)	O4#1–Y–O2W	141.2(8)
O4–Y–O2W	75.9(8)	O3–Y–O2W	137.9(5)
O1–Y–O2W	75.1(8)	N1–Y–O2W	122.8(10)
O1W–Y–O2W	64.7(9)	N2–Y–O2W	80.4(7)
Y–O3–Y#1	104.3(8)	Y–O3–Y#2	104.3(8)
Y#1–O3–Y#2	104.3(8)	Y#2–O4–Y	113.7(6)

[a] Symmetry transformations used to generate equivalent atoms: #1: $-y, x-y-1, z$; #2: $-x+y+1, -x, z$.

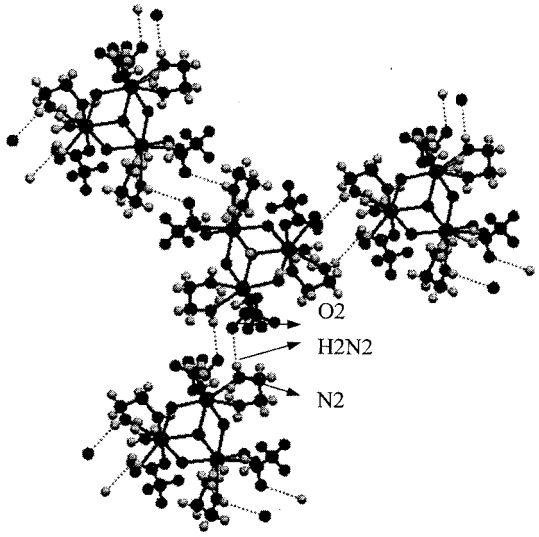

Figure 4. Intermolecular H-bonding for **6** (O2···H2N2 = 2.70 Å, O2···N2 = 3.22 Å, O2···H2N2···N2 = 119.9°).

Experimental Section

All manipulations were routinely performed under argon using Schlenk tubes and vacuum line techniques. Solvents were purified by standard methods. Trifluoroacetic (TFAH), perfluorobutyric (PFBH) and difluoroacetic acids (Aldrich) were stored over molecular sieves. $[Y(TFA)_3(H_2O)_3]$ (**1**) was prepared by reacting the oxide with TFAH in refluxing toluene.[11] IR spectra were recorded as Nujol or as Fluorolub mulls on an IR-FTS 45 spectrometer. Elemental analyses were done at the Centre de Microanalyses du CNRS. IR data and general properties are collected in Table 1.

$[Y(TFA)_3(Me_2CO)_3]$ (2): Complex **1** (0.815 g, 1.69 mmol) was added to acetone (20 mL). Concentration after 2 d gave colorless crystals of **2**. $C_{15}H_{18}F_9O_9Y$ (602.19): calcd. C 29.92, H 3.01, found C 30.03, H 3.10.

$[Y_2(TFA)_6(i\text{PrOC}_2H_4OH)_4]$ (3): $i\text{PrOC}_2H_4OH$ (1.38 mL, 12.0 mmol) was added to a suspension of **1** (0.72 g, 1.5 mmol) in toluene (20 mL). After stirring for 14 h, concentration gave colorless crystals of **3** (0.60 g, 63%). $C_{32}H_{48}F_{18}O_{20}Y_2$ (1272.5): calcd. C 30.20, H 3.80; found C 30.15, H 3.92.

$[Y_2(TFA)_6(MeOC_2H_4OC_2H_4OH)_2]$ (4): $MeOC_2H_4OC_2H_4OH$ (0.43 mL, 3.6 mmol) was added to a suspension of **1** (0.58 g, 1.2 mmol) in toluene (20 mL). After stirring for 14 h, filtration gave a solid, which was redissolved in THF to yield colorless crystals of **4** (0.61 g, 93%). $C_{22}H_{24}F_{18}O_{18}Y_2$ (1096.2): calcd. C 24.11, H 2.21; found C 24.33, H 2.34.

$[Y(TFA)_3(MeOC_2H_4OC_2H_4OC_2H_4OMe)]$ (5): Triglyme (0.5 mL, 2.74 mmol) was added to a solution of **1** (0.658 g, 1.37 mmol) in THF (15 mL). After stirring at room temp. for 14 h, concentration gave colorless crystals of **5** (0.52 g, 63%). $C_{14}H_{18}F_9O_{10}Y$ (606.18): calcd. C 27.74, H 2.99; found C 27.94, H 3.10%.

$[H_3O][Y_3(\mu_3\text{-}OH)(\mu\text{-}O)_3(TFA)_3(H_2NC_2H_4NH_2)_3(H_2O)_6]$ (6): A procedure similar to that of **5** but with ethylenediamine (0.66 mL, 9.92 mmol) and **1** (0.60 g, 1.24 mmol) in THF (15 mL) gave **6** (0.43 g). $C_{12}H_{40}F_9N_6O_{17}Y_3$ (978.18): calcd. C 14.73, H 4.12, N 8.5; found C 16.20, H 4.30, N 9.15. ^1H NMR (CD_3OD): δ = 2.67 (s, 12 H, CH_2), 3.2 (s, Me) ppm. The product was sometimes contaminated with $[H_3NC_2H_4NH_3][TFA]_2$, thus precluding good analytical data.

$[H_3O][Y_3O(OH)_3(TFA)_3(H_2NC_2H_4NHC_2H_4X)_3]$ [X = NH_2 (7) and X = OH (8)]: These complexes were prepared by a procedure similar to **6**.

7: $C_{18}H_{45}F_9N_9O_{11}Y_3$ (1001.3): calcd. C 21.95, H 4.53, N, 12.59; found C 23.48, H 4.12, N 13.20.

8: $C_{18}H_{42}F_9N_6O_{14}Y_3$ (1004.3): calcd. C 21.53, H 4.22, N 8.37; found C 21.72, H 4.35, N 8.55.

 © 2005 Wiley-VCH Verlag GmbH & Co. KGaA, Weinheim

Table 5. Crystal data and structure refinement for **3, 4** and **6**.

	3	**4**	**6**
Empirical formula	$C_{32}H_{48}F_{18}O_{20}Y_2$	$C_{22}H_{24}F_{18}O_{18}Y_2$	$C_{12}H_{40}F_9N_6O_{17}Y_3$
Formula mass	1272.52	1096.23	978.23
Space group	$P\bar{1}$	$P\bar{1}$	$R\bar{3}$
Crystal system	triclinic	triclinic	hexagonal
a [Å]	13.5965(2)	8.7109(1)	20.1921(17)
b [Å]	13.8952(3)	10.2862(2)	20.1921(17)
c [Å]	16.9439(4)	11.5968(2)	22.464(3)
α [°]	66.391(1)	96.221(1)	90
β [°]	68.321(1)	103.231(1)	90
γ [°]	66.182(1)	114.416(1)	120
V [Å^3]	2599.74(9)	896.58(3)	7932.1(14)
Z	2	1	6
Temperature [K]	160(2)	160(2)	163(2)
μ(Mo-$K\alpha$) [mm^{-1}]	2.352	3.388	3.343
θ range [°]	3.07 to 27.47	2.23 to 27.49	1.33 to 27.51
hkl ranges	–16 to 17, –18 to 17, –21 to 18	–11 to 10, –12 to 13, –15 to 13	123 to 20, –20 to 15, –23 to 5
No. of reflections collected	16204	6383	4747
No. of unique reflections (R_{int})	11081 (0.0431)	4078 (0.0217)	4080 (0.0562)
Data/restraints/parameters	11081/0/649	4078/0/271	4080/10/ 159
Goodness-of-fit on F^2	1.062	1.245	1.073
R_1, wR_2 [$I > 2\sigma(I)$][a]	0.0864, 0.2158	0.0409, 0.1165	0.0543, 0.1252
R_1, wR_2 (all data)	0.1153, 0.2403	0.0547, 0.1582	0.0809, 0.1456
Residual electron density	2.038 and –1.033	1.153 and –1.224	0.155 and –0.172

[a] $R_1 = \Sigma||F_o| - |F_c||/\Sigma|F_o|$, w$R_2 = \{\Sigma[w(F_o^2 - F_c^2)^2]/\Sigma[w(F_o^2)^2]\}^{1/2}$.

$[Y(TFA)_3(H_2O)_2(Me_2NC_2H_4NMe_2)]$ (9) and $[Y(TFA)_3(H_2O)_2(Me_2NC_2H_4NMeC_2H_4NMe_2)]$ (10): Prepared by a procedure similar to **4**. Yields: 89% for **9** and 72% for **10**.
9: $C_{12}H_{20}F_9N_2O_8Y$ (580.19): calcd. C 24.84, H 3.47, N 4.93; found C 24.38, H 3.46, N 4.86.
10: $C_{15}H_{27}F_9N_3O_8Y$ (637.29): calcd. C 28.27, H 4.27, N 6.59; found C 28.15, H 4.13, N 6.70.

Treatment of **1** (0.67 g, 1.39 mmol) with $Me_2NC_2H_4NH_2$ (0.46 mL, 4.16 mmol) in toluene or THF (20 mL) gave needles of $Me_2NC_2H_4NH_3$·TFA as the only crystalline species. IR: $\tilde{\nu}$ = 1683 cm^{-1} s, 1586 m, 1518 m, 1463 s, 1424 m; 598 w, 542 w, 520 w. X-ray data: a = 6.427(1), b = 18.124(4), c = 8.753(2) Å, β = 101.58(3)°, V = 998.8 Å^3, space group $P2_1/c$.

$[Y(O_2CC_3F_7)_3]$ (11): Perfluorobutyric acid (1.5 mL, 10.5 mmol) was added to a suspension of Y_2O_3 (0.39 g, 1.74 mmol) in toluene (15 mL). After refluxing for 3 d, filtration and recrystallization from Et_2O gave **11** by condensation into a cold trap during evaporation under vacuum (0.94 g, 75%). $C_{12}F_{21}O_6Y$ (728.00): calcd. C 19.8; found C 19.7.

$[Y(H_2O)_2(O_2CC_3F_7)_3]$ (12): Perfluorobutyric acid (3.3 mL, 25.3 mmol) was added to a suspension of $Y_2(CO_3)_3$·$3H_2O$ (1.74 g, 4.2 mmol) in toluene (30 mL). After refluxing for 24 h, the precipitate was filtered, washed with hexane, and recrystallized from Et_2O to give **12** (6.10 g, 95%). $C_{12}H_4F_{21}O_8Y$ (764.03): calcd. C 18.86, H 0.53, found C 19.05, H 0.62.

$[Y(O_2CCHF_2)_3(H_2O)_3]$ (13): The same procedure as for **1** applied to Y_2O_3 (452 mg, 2.0 mmol) and CHF_2CO_2H (0.4 mL, 6.0 mmol) in refluxing toluene for 32 h. Recrystallization from THF (75%). $C_6H_9F_6O_9Y$ (428.03): calcd. C 16.84, H 2.12, found C 16.92, H 2.22.

All compounds were soluble in polar media (alcohols, THF, DME) but insoluble in $CHCl_3$ or hydrocarbons (aliphatic and aromatic).

X-ray Crystallography of 3, 4, and 6: Suitable crystals of **3**, **4**, and **6** were grown directly from the reaction media. X-ray single-crystal diffraction data were collected with a Nonius Kappa CCD diffractometer. The data were processed with the DENZO reduction software package.[28] An absorption correction (XABS2)[29] was applied to the data of compound **3**. The structures were solved and refined on F^2 using SHELXTL.[30] All non-hydrogen atoms were refined with anisotropic thermal parameters. The hydrogen atoms were included in the final refinement model in calculated positions with isotropic thermal parameters. The distribution of the C–F bond lengths is quite large due to disorder phenomena, which are also illustrated by high thermal factors. Crystal structure and refinement data are summarized in Table 5.
CCDC-227441 (for **3**), -227442 (for **4**), and -244549 (for **6**) contain the supplementary crystallographic data for this paper. These data can be obtained free of charge from The Cambridge Crystallographic Data Centre via www.ccdc.cam.ac.uk/data_request/cif.

Acknowledgments

Financial support from the EEC (G5RDCT 2001 00550) and from the region Rhône Alpes (project Rubis) with a fellowship to SM is acknowledged.

[1] C. Russel, *J. Non-Cryst. Solids* **1993**, *152*, 161.
[2] D. A. Edwards, R. M. Harker, M. F. Mahan, K. C. Molloy, *Inorg. Chim. Acta* **2002**, *328*, 134.
[3] S. A. Krupoder, V. S. Danilovich, A. O. Miller, G. G. Furin, *Zhur. Organi Khimii* **1994**, *30*, 1185.
[4] a) T. Araki, I. Hirabayashi, *Supercond. Sci. Technol.* **2003**, *16*, R71–R94; b) L. G. Hubert-Pfalzgraf, H. Guillon, *Appl. Organomet. Chem.* **1998**, *12*, 321and ref therein.
[5] a) F. Li, Y. Jin, C. Song, Y. Lin, F. Pei, F. Wang, N. Hu, *Appl. Organomet. Chem.* **1996**, *10*, 761; b) C. S. Tan, T. J. Hsu, *Macromolecules* **1997**, *30*, 3147; c) J. Zhang, Z. Gan, Z. Zhong, X. Jing, *Polym. Int.* **1998**, *45*, 60.
[6] F. L. Alencar, J. R. Matos, L. B. Zinner, *J. Alloys Comp.* **1994**, *207–8*, 461.
[7] P. M. Pimentel, V. S. Oliveira, Z. R. Silva, D. M. A. Melo, L. B. Zinner, G. Vicentini, G. Bombieri, *Polyhedron* **2001**, *20*, 2651.
[8] L. B. Zinner, H. F. Brito, *Inorg Chim. Acta* **1985**, *110*, 175.

 © 2005 Wiley-VCH Verlag GmbH & Co. KGaA, Weinheim

[9] E. E. Castellano, G. Oliva, L. B. Zinner, G. Vicentini, *Inorg. Chim. Acta* **1985**, *110*, 77.
[10] G. Bombieri, F. Benetollo, A. Del Pra, V. D. Oliveira, D. M. A. Melo, L. B. Zinner, G. Vicentini, *J. Alloys Comp.* **2001**, *323–324*, 181and references cited therein.
[11] M. Singh, S. N. Misra, *J. Inorg. Nucl. Chem.* **1978**, *40*, 1939.
[12] a) H. Vincent, F. Labrize, L. G. Hubert-Pfalzgraf, *Polyhedron* **1994**, *13*, 3323; b) L. G. Hubert-Pfalzgraf, *Coord. Chem. Rev.* **1998**, *178–180*, 967and references cited therein.
[13] A. Mehrbach, M. N. P. Heloud, P. Jacoud, *Helv. Chim. Acta* **1972**, *55*, 44.
[14] F. A. Cotton, E. V. Dikarev, M. A. Petrukhina, *Inorg. Chem.* **2000**, *39*, 6072.
[15] D. Harrison, A. Giorgetti, J. C. G. Bunzli, *J. Chem. Soc., Dalton Trans.* **1985**, 885.
[16] D. H. Gibson, Y. Ding, R. L. Miller, B. A. Sleadd, M. S. Mashuta, J. F. Richardson, *Polyhedron* **1999**, *18*, 1189.
[17] a) W. A. Wojtczak, P. Atanassova, M. J. Hampden-Smith, E. Duesler, *Inorg. Chem.* **1996**, *35*, 6995; b) W. A. Wojtczak, M. J. Hampden-Smith, E. Duesler, *Inorg. Chem.* **1998**, *37*, 1781.
[18] S. Wang, *Polyhedron* **1998**, *17*, 831.
[19] J. W. Steed, B. J. McCool, P. C. Junk, *J. Chem. Soc., Dalton Trans.* **1998**, 3417.
[20] H. Guillon, L. G. Hubert-Pfalzgraf, J. Vaissermann, *Eur. J. Inorg. Chem.* **2000**, 1243.
[21] a) W. J. Evans, M. S. Sollberger, S. I. Khan, R. Bau, *J. Am. Chem. Soc.* **1988**, *110*, 439; b) W. J. Evans, M. S. Sollberger, J. L. Shreeve, J. M. Olofson, J. H. Hain, J. W. Ziller, *Inorg. Chem.* **1992**, *31*, 2492.
[22] L. G. Hubert-Pfalzgraf, V. Abada, J. Vaissermann, *J. Chem. Soc., Dalton Trans.* **1998**, 3437.
[23] A. Moeller, G. Meyer, *Z. Anorg. Allgem. Chem.* **1993**, *619*, 695.
[24] V. O. Gel'mbol'dt, E. V. Ganin, L. V. Koroeva, M. S. Fonar, Y. A. Simonov, V. K. Kravtsov, Y. Lipkowski, *Zh. Neorg. Khimii* **2001**, *46*, 1833.
[25] K. S. Gravrilenko, A. Vertes, G. Vanko, L. F. Kiss, A. W. Addison, T. Weyhermuller, V. V. Palishchuk, *Eur. J. Inorg. Chem.* **2002**, 3347.
[26] S. R. Breeze, L. Chen, S. Wang, *J. Chem. Soc., Dalton Trans.* **1994**, 2545.
[27] J. Zhang, L. G. Hubert-Pfalzgraf, D. Luneau, *Inorg. Chem. Commun.* **2004**, *7*, 979.
[28] Z. Otwinowski, W. Minor, *Processing of X-ray Diffraction Data collected in oscillation mode*, in *Methods in Enzymology, 276: Macromolecular Crystallography, part A* (Eds.: C. W. Carter Jr., R. M. Sweet), Academic Press, **1997**, pp. 307–326..
[29] S. Parkin, B. Moezzi, H. Hope, *J. Appl. Cryst.* **1995**, *28*, 53.
[30] G. M. Sheldrick, Program for the refinement of crystal structures. University of Göttingen, Germany (Bruker-AXS, Madison, Wisconsin, USA), **1997**.

Received: February 21, 2005
Published Online: August 11, 2005

 © 2005 Wiley-VCH Verlag GmbH & Co. KGaA, Weinheim

Synthesis, Characterization, and Electrochemical Properties of Dinuclear Complexes Assembled from Asymmetric Co^{III} Bis(dioximates) and Boronic Acids

Renata Dreos,*[a] Patrizia Siega,[a] Silvia Scagliola,[a] Lucio Randaccio,*[a] Giorgio Nardin,[a] Claudio Tavagnacco,[a] and Manuela Bevilacqua[a]

Keywords: Boronic acid / Cobalt / Dioximes / Enantioselectivity / Electrochemistry

Bis(methylphenylglyoximate)cobalt(III) complexes exist both as *cis* and *trans* isomers due to the asymmetry of the equatorial ligand, and, when the axial ligands are different, the *trans* isomer is chiral. The reaction of racemic *trans*-$[CH_3Co(mpgH)_2py]$ (**1**) with either 3- or 4-pyridylboronic acid affords dimeric units arranged on a crystallographic symmetry center such that the pyridyl nitrogen of one moiety coordinates to the Co atom of the symmetry-related unit. In principle, three structurally different dimeric species (two homodimers and one heterodimer) can be obtained. Time-resolved ^1H NMR spectra of a 1:1 mixture of racemic **1** and either 3- or 4-pyridylboronic acid in $CDCl_3/CD_3OD$ show that the reaction does not converge toward a unique species in solution. Nevertheless, X-ray structures show that the heterochiral dimers are the only products that crystallize from the reaction mixture. The nature of the dioximate side groups does not affect the geometry of the dimeric arrangements assembled by 4-pyridylboronic acid ("molecular box"). On the contrary, the geometry of the species assembled by 3-pyridylboronic acid varies from the "molecular parallelogram" obtained from the bis(dimethylglyoximates) to the highly squeezed "molecular box" obtained from bis(methylphenylglyoximates). Cyclic voltammetry studies show that the metal centers in the dimeric species do not interact with each other and undergo a simultaneous redox process. However, depending on the geometry of the systems, the redox process involves a single four-electron reduction for **3** and **5** or two consecutive two-electron reduction steps for **4** and **6**.
(© Wiley-VCH Verlag GmbH & Co. KGaA, 69451 Weinheim, Germany, 2005)

Introduction

Organobis(dimethylglyoximato)cobalt(III) complexes {organocobaloximes, $[CH_3Co(dmgH)_2L]$, where L is a neutral ligand} have been extensively studied, mainly for their interest as vitamin B_{12} models,[1] but also for their use as polymerization catalysts[2] and as templates in organic synthesis.[3] Some examples of cobalt complexes with dioximato ligands other than $dmgH_2$, such as glyoximates (gH),[4] dicyclohexylglyoximates (chgH),[5] and diphenylglyoximates (dpgH),[6] are known. Derivatives containing mixed equatorial ligand sets, which include one dpgH and either a dmgH or chgH, have also been reported.[7] To the best of our knowledge, only two reports exist of cobalt complexes with the asymmetric methylphenylglyoximate ligand (mpgH).[8]

Organocobaloximes with either one or both of the intramolecular OHO bridges replaced by organoboryl groups are well known and have recently been reviewed.[9] We have used organobis(dimethylglyoximate)- and organobis(diphenylglyoximate)cobalt(III) complexes as building blocks in the assembly of supramolecular systems.[10] Indeed, functionalized aromatic boronic acids have been shown to efficiently direct the assembly of organocobaloximes through the reaction of the $B(OH)_2$ group with the oxime bridge of one cobaloxime molecule, with simultaneous coordination of the donor atom to the cobalt of another cobaloxime.[10] Products of different nuclearity and geometry have been obtained, depending on the geometry of the boronic acid used as linker (L^1, L^2, and L^3, Scheme 1). The most relevant consequence of replacing the methyl groups by phenyl groups in the equatorial ligand is a change of the nuclearity of the supramolecular species assembled with 3-aminophenylboronic acid (L^3): a molecular triangle was obtained starting from $[CH_3Co(dmgH)_2L]$ (Scheme 1), whereas a dimeric species was obtained from $[CH_3Co(dpgH)_2L]$ (Scheme 2), the trimeric arrangement being prevented by the steric hindrance of the phenyl groups.[11]

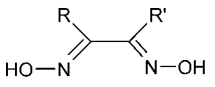

R = R' = CH_3	$dmgH_2$
R = R' = C_6H_5	$dpgH_2$
R = CH_3, R' = C_6H_5	$mpgH_2$
R = R' = C_6H_{11}	$chgH_2$
R = R' = H	gH_2

[a] Dipartimento di Scienze Chimiche, Università di Trieste, Via Licio Giorgieri 1, 34127, Trieste, Italy
Fax: +39-040-558-3903
E-mail: dreos@univ.trieste.it
randaccio@univ.trieste.it
Supporting information for this article is available on the WWW under http://www.eurjic.org or from the author.

 © 2005 Wiley-VCH Verlag GmbH & Co. KGaA, Weinheim **DOI: 10.1002/ejic.200500179**

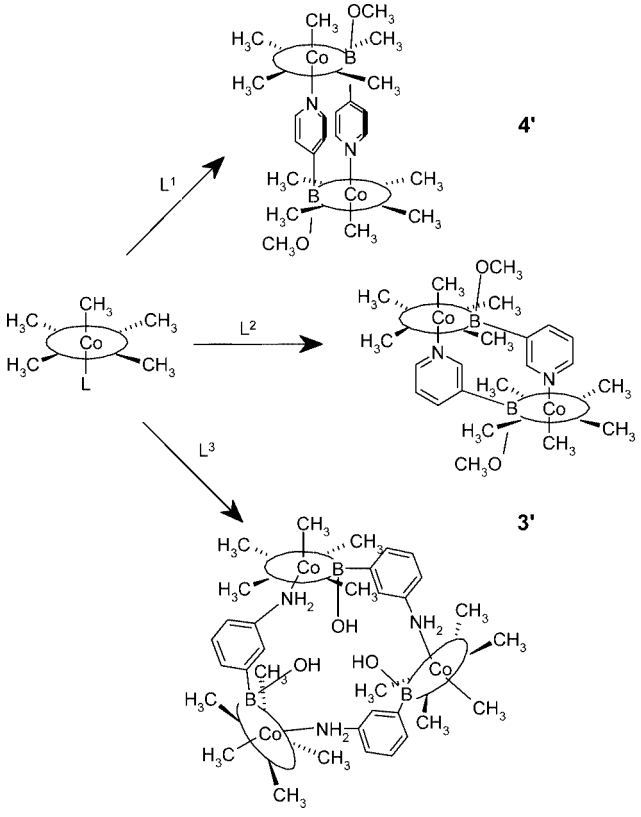

Scheme 1.

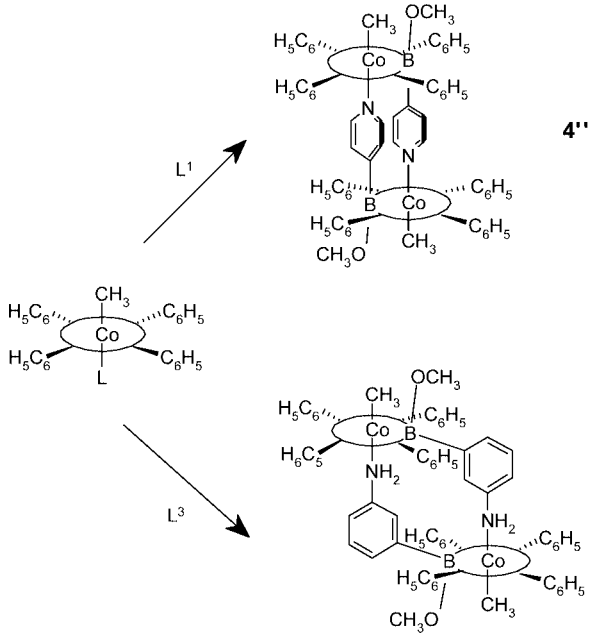

Scheme 2.

In order to systematically study how the steric bulk of the chelate affects the geometry of the assembled species, we have extended our investigation to bis(methylphenylglyoximato) complexes. These complexes exist both as *cis* and *trans* isomers due to the asymmetry of the equatorial ligand, and, when the axial ligands are different, the *trans* isomer is chiral. Therefore *trans*-[CH_3Co(mpgH)py] can be applied as a chiral building block in larger molecular systems.

Here we report a study of the systems assembled from *trans*- and *cis*-[CH_3Co(mpgH)py] with 3- and 4- pyridylboronic acid, which includes the characterization of the dimeric aggregates formed both in solution and in the solid state and an investigation of their electrochemical properties.

Results and Discussion

Synthesis of the Organometallic Complexes

The ligand was prepared by addition of a tenfold excess of hydroxylamine hydrochloride, dissolved in water and neutralized with an equimolar amount of NaOH, to a methanolic solution of 1-phenyl-1,2-propanedione 2-oxime, as shown in Scheme 3.

[ClCo(mpgH)$_2$py] was prepared by direct air oxidation of $CoCl_2$ in the presence of $mpgH_2$ and pyridine (Scheme 4). The ^{1}H NMR spectrum showed that the reaction product is a mixture of the *cis* and *trans* isomers.

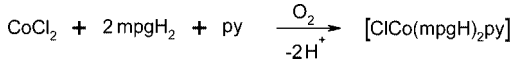

Scheme 4.

Small quantities of the pure isomers could be separated by stratification of *n*-heptane over a $CDCl_3$ solution of the mixture in an NMR tube. After slow diffusion, two different kinds of crystals deposited on the walls of the tube and were manually separated. The ^{1}H NMR spectrum in $CDCl_3$ allowed identification of the *cis* and *trans* isomers, as the *cis* isomer gives rise to two singlets for the nonequivalent oximic protons, whereas only one signal is shown by the *trans* isomer. Integration of the signals of the equatorial methyls in the spectrum of the reaction mixture revealed that the *trans* isomer is the more abundant product of the synthesis. This isomer is chiral and exists in two enantiomeric forms.

The synthesis of the organometallic derivatives was carried out starting from the mixture of the *cis*- and *trans*-[ClCo(mpgH)$_2$py] isomers by reduction with $NaBH_4$ followed by the oxidative addition of CH_3I (Scheme 5). The product always remained a mixture of isomers, but not nec-

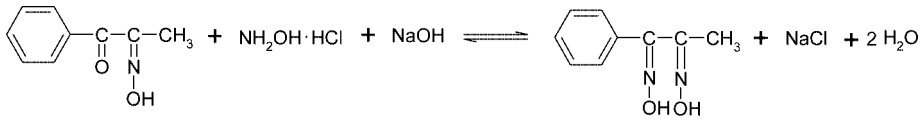

Scheme 3.

 © 2005 Wiley-VCH Verlag GmbH & Co. KGaA, Weinheim

essarily in the same ratio as in the starting mixture. *trans*-[CH_3Co(mpgH)py] (**1**) and *cis*-[CH_3Co(mpgH)py] (**2**) were separated by fractional crystallization from CH_2Cl_2/CH_3OH (1:1) and characterized by ^{1}H NMR spectroscopy and X-ray structural analysis.

$$[ClCo^{III}(pmgH)_2py] \xrightarrow[NaOH]{NaBH_4} [Co^{I}(pmgH)_2py]^-$$

$$[Co^{I}(pmgH)_2py]^- \xrightarrow{CH_3I} [CH_3Co^{III}(pmgH)_2py]$$

Scheme 5.

The chiral *trans* isomer was isolated as a racemic mixture of the A and C enantiomers.[12]

Synthesis of the Supramolecular Species

The reactions were performed in a mixture of solvents (chloroform/methanol, 1:6), because the starting complexes **1** and **2** are poorly soluble in methanol although a hydroxylic solvent is necessary for the formation of hydroxyboronate species containing a tetrahedral boron.[10b] X-ray quality crystals were obtained from solutions containing a racemic mixture of the *trans* derivative **1** and either 3-pyridylboronic acid (**3**) or 4-pyridylboronic acid (**4**). Small crystals, not of X-ray quality, were also obtained from the reactions of the *cis* isomer **2** with 3-pyridylboronic acid and 4-pyridylboronic acid (**5** and **6**, respectively) These were identified by ESI MS and ^{1}H NMR spectroscopy in noncoordinating solvents.

The formation of the supramolecular species from **1** was monitored in solution by ^{1}H NMR spectroscopy. When an equivalent amount of 3-(or 4-)pyridylboronic acid was added to the racemic mixture of *trans*-[CH_3Co(mpgH)py] in $CD_3OD/CDCl_3$ (1:1) at a pH of about 5, the ^{1}H NMR spectrum consisted of a complicated pattern of peaks, which did not simplify on standing for two weeks, attesting to the presence of several species besides **3** (or **4**; Figure S1). Removal of the solvent under vacuum yielded a mixture of products, which was not further characterized. However, if the solvent was left to evaporate slowly from the solution, the crystals deposited on the walls of the NMR tubes consisted of pure **3** (or **4**). Redissolution of **3** (or **4**) in $CD_3OD/CDCl_3$ (1:1) resulted in a partial and slow decomposition of the supramolecular species (Figure S2).

X-ray Structures

ORTEP drawings of **1** and **2** are shown in Figure 1 together with their numbering scheme. Both **1** and **2** crystallize in a centrosymmetric space group with four molecules per unit cell. The equatorial ligand in **1** is nearly planar, the two dioximato moieties (excluding the phenyl side groups) making an interplanar angle of 1.9(3)°. The dioximato moieties in **2** are slightly bent towards the axial methyl group, making an interplanar angle of 6.2(1)°. The axial py ring is oriented with respect to the equatorial ligand in such a way as to nearly bisect the oxime bridges (orientation A) in **1**, whereas in **2** it is rotated by 17° towards N1 with respect to the orientation in **1**. No appreciable differences were detected in the coordination bond lengths and angles. Table 1 shows a comparison of the measured coordination distances with those reported for other methyl derivatives having different dioximate ligands. No evidence of a structural *cis*-influence is apparent.

The crystal of **3** is built up by dimeric units arranged on a crystallographic symmetry center and methanol solvent. The dimeric unit (Figure 2a) is formed by two enantiomeric *trans*-[$CH_3Co(mpgH)_2$] moieties held together by two 3-pyridylboronic acid residues. This arrangement results in a *meso* species whose geometry is similar to that found in the analogous bis(dimethylglyoximato) derivative **3′**.[10a] The C–C_{Me} and C–C_{Ph} units are not coplanar, the C_{Me} and C_{Ph} atoms being about 0.2 Å out of the mean plane of the five-membered rings. In **3′**, the C–C_{Me} bonds are nearly coplanar, with the C_{Me} less than 0.1 Å out of the five-membered rings. The 3-pyridyl residue coordinated to the Co′ atom is tilted by 167° (177° in **3′**) with respect to the equatorial plane, as measured by the Co′–N5–C22 angle. Thus, the two symmetry-related 3-py rings, which are essentially coplanar in **3′**, are still parallel in **3** but displaced by 1.45 Å. As a consequence, the "molecular parallelogram" in **3′** approaches a highly squeezed "molecular box" in **3**. Nevertheless, the dimensions of the Co···B···Co′···B′ parallelogram in **3** are not significantly different from those in **3′**, with a decrease of more than 2° in the B···Co···B′ angle (Table 1). As for **3′**, the 3-py mean plane in **3** is oriented in such a way as to nearly bisect the oxime bridge of the equatorial moiety (orientation A). The coordination bond lengths and angles do not differ significantly from those reported in **3′**. The axial Co–C and Co–N distances are compared in Table 1.

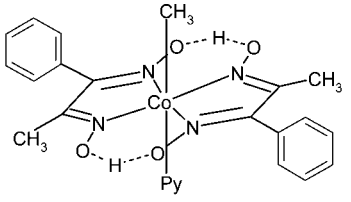

A enantiomer of **1**

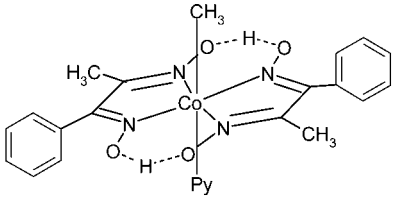

C enantiomer of **1**

 © 2005 Wiley-VCH Verlag GmbH & Co. KGaA, Weinheim

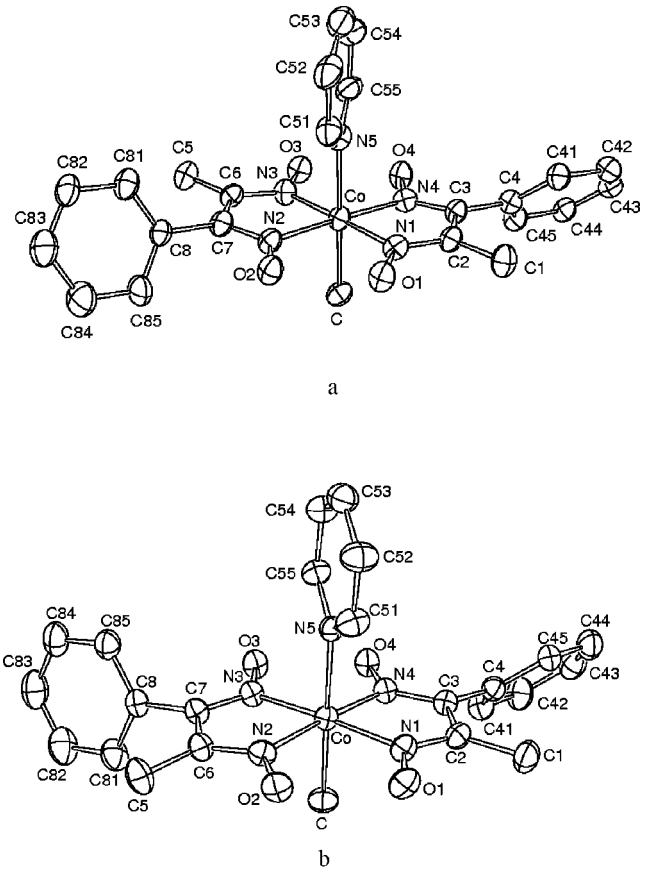

a

b

Figure 1. ORTEP drawing (thermal ellipsoids at 30% probability) and labeling scheme for **1** (a) and **2** (b).

Table 1. Selected bond lengths [Å] of the mononuclear complexes **1** and **2** and the dinuclear complexes **3** and **4** compared with the corresponding distances for other methyl derivatives containing different dioximate ligands.

	Co–C	Co–N	Co–N_{eq} (mean)
1	1.976(6)	2.045(6)	1.872(5)
2	1.994(4)	2.057(3)	1.882(3)
$[CH_3Co(dmgH)_2py]$[13]	1.998(5)	2.068(3)	
$[CH_3Co(dpgH)_2py]$[6b]	1.997(4)	2.053(4)	1.884(3)
3	2.003(3)	2.074(3)	1.875(3)
3′[10a]	1.985(9)	2.069(8)	1.869(8)
4	2.010(9)	2.104(5)	1.884(9)
4′[10b]	2.00(1)	2.08(1)	1.87(1)
4′′[10c]	2.013(4)	2.068(3)	1.879(3)

The crystal of **4** is built up by dimeric units arranged on a crystallographic symmetry center (ORTEP diagram in Figure 2b). The dimer is formed by two enantiomeric *trans*-$[CH_3Co(mpgH)_2]$ moieties held together by two 4-pyridylboronic acid residues as for **3**. This arrangement results in a *meso* species whose geometry is very similar to those found in the analogous derivatives **4′**[10b] and **4′′**,[11] which contain dmgH and dpgH units, respectively. This result shows that the nature of the dioximate side substituents does not affect the geometry of such a dimeric arrangement ("molecular box"); the two symmetry-related 4-py rings face each other at an interplanar distance of about 3.4 Å.

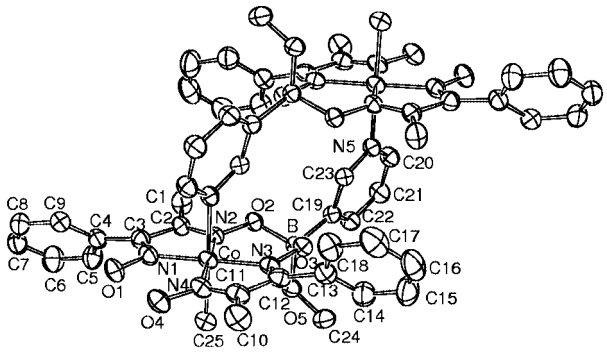

a

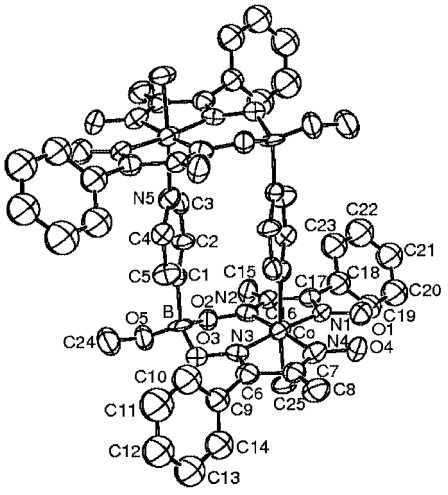

b

Figure 2. ORTEP drawing (thermal ellipsoids at 30% probability) and labeling scheme for **3** (a) and **4** (b).

In all these dinuclear species, the axial 4-py ring nearly bisects the five-membered rings of the equatorial moiety (orientation B, rotated by about 90° with respect to orientation A found in **3** and **3′**). The resulting approximate Co···B···Co′···B′ rectangle in **4** has Co···B and B···Co′ sides of 3.22 and 6.61 Å, respectively, and a B···Co′···B′ angle of 87.3°. A comparison with the corresponding figures in **4′**[10b] and **4′′**[11] show that the side substituents in **4** lead to a more regular rectangle. The coordination bond lengths and angles do not differ appreciably from those found in **4′** and **4′′**; the axial Co–C and Co–N distances are given in Table 1. A comparison of these data shows that the axial Co–N distances are not appreciably affected by the dioximato side substituents in either the mononuclear or in the series of dinuclear compounds. However, it seems that the Co–N_{ax} distance (and possibly that of Co–C) is slightly lengthened in the dinuclear species.

Characterization of the Supramolecular Species in Solution

The ESI mass spectra of the supramolecular species **3**, **4**, **5**, and **6** in CH_2Cl_2/HCOOH (1%) show that the base peaks

 © 2005 Wiley-VCH Verlag GmbH & Co. KGaA, Weinheim

for the molecular ions [M + H^+] correspond to protonated dimeric species held together by two pyridylboronic acids, with the residual B(OH) groups esterified by methanol.

The ^{1}H NMR spectra of **3** and **4** in $CDCl_3$ show similar features except for the signals of pyridine. Only one set of signals is evident, as a consequence of the presence of a symmetry center. The axial methyl, the B(OCH_3), and the residual oximic protons give rise to three singlets, whereas the phenyl protons appear as a multiplet. The two singlets for the equatorial methyls confirm the insertion of a single boryl bridge. The three py protons of **3** give rise to three signals in the range δ = 7.25–8.30 ppm. The signal of the *ortho* NC*H*C(CH)B proton is notably shifted to lower field (δ = 9.6 ppm) with respect to the corresponding proton of free 3-pyridylboronic acid (δ = 8.6 ppm in CD_3OD), due to the deshielding effect of the magnetic anisotropy of the parallel pyridyl ring. The pyridyl protons of **4** appear as four doublets in the range δ = 6.72–7.09 ppm and are all nonequivalent as a consequence of the assembly and of the hindered rotation. The remarkable upfield shift of these protons with respect to the corresponding proton of the free 4-pyridylboronic acid (δ = 8.05 and 8.47 ppm in D_2O)[10b] is due to the shielding effect of the two facing pyridyl rings.

These results are entirely consistent with the solid-state structure, thereby suggesting that **3** and **4** are stable in solution in aprotic solvents − they neither dissociate nor are in equilibrium with species having different nuclearity.

The ^{1}H NMR spectra of **5** and **6** in $CDCl_3$ are very similar to those of **3** and **4**, respectively. The main differences are the presence of only one singlet for the equatorial methyls in both **5** and **6** and the internal equivalence of the *ortho* and the *meta* protons of pyridine in **6**. Both these results are consistent with the presence of a mirror plane bisecting the OHO and the OBO bridges. In the *cis* isomer **2**, the insertion of the boronic acid may occur either in the OHO bridge near to the methyl groups or in that near to the phenyl groups. The close proximity of the resonances of the equatorial methyl groups of **5** and **6** to the resonances of CH_3C=NOB in **3** and **4**, respectively, and the presence of a cross-peak between B(OCH_3) and the equatorial CH_3 group in the ROESY spectrum, strongly support the former hypothesis. The proposed structures for **5** and **6**, very similar to those of **3** and **4**, are depicted in Scheme 6.

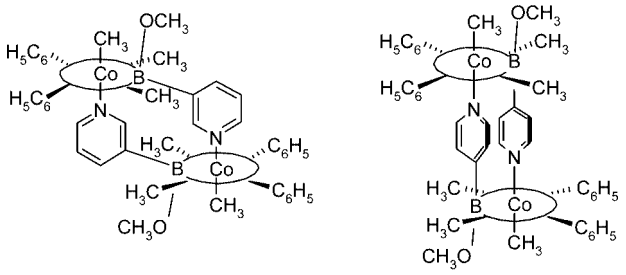

5 **6**

Scheme 6.

Electrochemistry

The electrochemical behavior of both the mononuclear complexes **1** and **2** and the dinuclear species **3**–**6** was investigated by cyclic voltammetry in CH_2Cl_2 containing 0.05 M tetra-*n*-butylammonium perchlorate (TBAP). This solvent proved to be suitably solubilizing for all the compounds and its conductivity is still sufficiently high to allow routine voltammetric studies.[14] This solvent-supporting electrolyte system allows a potential scan from +1.4 to –1.9 V vs. SCE.

The behavior of the *trans*- and *cis*-[CH_3Co(mpgH)$_2$py] isomers is very similar, so the following discussion refers equally to both derivatives. The CV of the mononuclear species **1** and **2** show three signals (Figure 3 and Table 2). The reduction peak **b** (E_{pc} = –1.625 V in both cases, at 100 mV s^{-1} scan rate) shifts toward more negative values at increasing scan rate and has no anodic counterpart up to 1 V s^{-1}. A further peak couple, **a** and **a′**, is visible at more positive potentials and is independent of the reduction peak **b**. In fact, it also develops if the CV is carried out in a range not including peak **b**, such as 0 V → +1.4 V → 0 V. The linear dependence of the height of the peaks **a** and **a′** on the square root of the scan rate, the ratio between the cathodic and the anodic peak current, i_{pa}/i_{pc} (equal to 1), the constancy of (E_{pc} + E_{pa})/2, and the difference E_{pa} – E_{pc} (equal to 110 mV at 100 mV s^{-1}) all show that this peak couple corresponds to a quasi-reversible monoelectronic process.[15] This is assigned to a Co^{III}/Co^{IV} electron transfer in

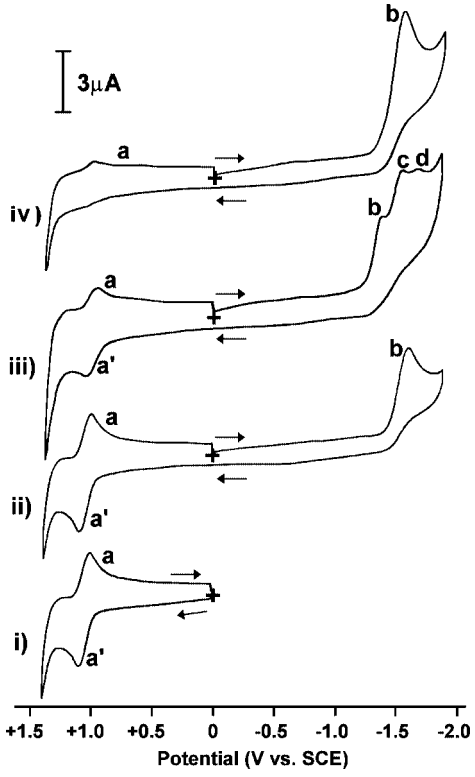

Figure 3. Cyclic voltammetry at a scan rate of 100 mV s^{-1} in CH_2Cl_2 + TBAP (0.05 M) at T = 0.0 °C. i) and ii) complex **2**; iii) complex **6**; iv) complex **5**. Scans are made in the range 0 to 1.4 to 0 V for i) and 0 to –1.9 to +1.4 V to 0 V for ii), iii) and iv).

 © 2005 Wiley-VCH Verlag GmbH & Co. KGaA, Weinheim

which the oxidized species is stable in the CV time range.[16] On the basis of a comparison of the peak currents, the reduction peak **b** is attributed to a dielectronic Co^{III}/Co^{I} reduction, followed by a relatively fast chemical reaction, which gives no more electroactive species (EC mechanism).[15]

Table 2. Summary of E_p potentials at a scan rate of 100 mV s^{-1} in CH_2Cl_2 (TBAP 0.05 M) at 0.0 °C.

Complex	E_{pa}(**a**)	E_{pc}(**a**)	E_{pc}(**b**)	E_{pc}(**c**)	E_{pc}(**d**)
1	+1.08	+0.97	–1.625	–	–
3	+1.05[a]	+0.95	–1.57	–	–
4	–	–	–1.41	–1.60	–
2	+1.09	+0.98	–1.625	–	–
5	+1.05[a]	+0.96	–1.575	–	–
6	+1.04	+0.93	–1.40	–1.56	–1.67

[a] Very low.

The cyclic voltammograms of the dinuclear species assembled with 3-pyridylboronic acid (**3** and **5**) show one cathodic signal **b** (E_{pc} = –1.57 V in both cases at 100 mV s^{-1}) without any anodic counterpart and a couple of low peaks **a** and **a′**, independent of the cathodic peak, at more positive potentials (Table 2 and Figure 3). The cyclic voltammograms of the dinuclear species assembled with 4-pyridylboronic acid (**4** and **6**) both show a couple of cathodic peaks that lack the anodic counterpart at 100 mV s^{-1}: E_{pc} (**b**) = –1.41 and E_{pc} (**c**) = –1.60 V for **4** and E_{pc} (**b**) = –1.40 and E_{pc} (**c**) = –1.56 V for **6**. A very low and scarcely reproducible reduction peak **d** is present in the complex **6** at more negative value, but it was not investigated further. In addition, both species exhibit a further couple of peaks at more positive potential for both of them, but for complex **4** the signals are too low to determine the peak potential.

Therefore, in the dinuclear species, the chemically equivalent and noninteracting metal centers undergo the redox processes simultaneously at the same potential. It is noteworthy that, by comparison of the peak heights and the CV shape,[17] it is possible to attribute two consecutive two-electron reduction steps for **4** and **6** and a single four-electron reduction step for **3** and **5.** It has previously been reported that the electrochemical reduction of a series of organocobaloximes in aprotic solvents, such as dimethyl sulfoxide, dimethylformamide, and acetonitrile, takes place in two separate steps, but in pyridine or in the presence of strong donor species, a single two-electron step is observed.[18] In the present case, 3- and 4-pyridylboronic acids have very similar donor properties, but the orientation of the pyridyl ring in the dinuclear species is different. Indeed, the 3-pyridyl ring has the orientation A in **3** and **5**, whereas the 4-pyridyl ring has the orientation B in **4** and **6**. The latter orientation results in a lengthening of the Co–N bond (Table 1) and, in consequence, an apparent weakening of the electron-donor power of 4-pyridylboronic acid.

The reduction peak potentials of the monomers **1** and **2** are always more negative than that of the supramolecular species **3**–**6**. This behavior can be attributed to the stronger electron-donor power of pyridine with respect to the pyridylboronic acid due to the electron-withdrawing effect of the boron atom on the pyridyl ring.

Conclusion

The reaction of racemic **1** with either 3- or 4-pyridylboronic acid can produce three structurally different dimeric species (two homodimers AA and CC and one heterodimer AC), but only the heterochiral dimers **3** (or **4**) crystallize from the reaction mixture. As the time-resolved ^{1}H NMR spectra of the reaction mixture do not show convergence toward a unique species in solution, the high enantiospecificity of the assembly has to be attributed to a preferential crystallization rather than to an enantiomeric self-recognition in solution.[19] Examples of preferential crystallization have been reported previously and have been attributed to an interplay of enthalpic, entropic, and crystal-packing factors.[20] Furthermore, both **3** and **4** are stable when dissolved in $CDCl_3/CD_3OD$, showing that the dissociation process in solution is quite slow. The slowness of both the formation and the dissociation process reflects the fact that the covalent O–B–O moiety has to be broken in this process.[21]

X-ray structural results show that the nature of the dioximate side substituents does not affect the geometry of the dimeric arrangements assembled by 4-pyridylboronic acid ("molecular box"). On the contrary, the geometry of the species assembled by 3-pyridylboronic acid varies from the "molecular parallelogram" obtained from the bis(dimethylglyoximates) to the highly squeezed "molecular box" obtained from methylphenylglyoximates.

Cyclic voltammetry studies show that the metal centers in the dimeric species do not interact with each other and undergo a simultaneous redox process. However, depending on the geometry of the systems, the redox process involves a single four-electron Co^{III}/Co^{I} step for **3** and **5** or two consecutive two-electron steps Co^{III}/Co^{II} and Co^{II}/Co^{I} for **4** and **6**.

Experimental Section

General Remarks: ^{1}H NMR spectra were recorded with a Jeol EX-400 and referenced to residual solvent protons. Electrospray mass spectra were recorded in positive mode using an API 1 mass spectrometer (Perkin–Elmer). All reagents and solvents were obtained commercially and were used without further purification, unless otherwise stated.

Electrochemical Measurements: Cyclic voltammetry was performed with an Amel 551 potentiostat, equipped with positive feedback, driven by an Amel 568 function generator. The signals were recorded on an Amel 863 x-y recorder with a potential reproducibility of ±3 mV. A three-electrode system was used. The working electrode was a 2-mm-diameter glassy carbon disk (EG&G), which was polished with 0.3 and 0.05 micron Micropolish (Buehler) and sonicated in CH_2Cl_2 solution before any measurement. The reference was an SCE (saturated NaCl) electrode, separated from the solution by a glass frit filled with a 0.05 M solution of TBAP (Fluka) in CH_2Cl_2. The counter electrode was a Pt wire. The mea-

 © 2005 Wiley-VCH Verlag GmbH & Co. KGaA, Weinheim

surements were performed on 1×10^{-3} M solutions of the complexes in CH_2Cl_2 (Carlo Erba). The commercial solvent was shaken with H_2SO_4, water, and $NaHCO_3$ (5% solution) and then distilled from CaH_2 under argon. Dried TBAP (0.05 M) was used as supporting electrolyte. The temperature was maintained at 0 °C and oxygen was removed by bubbling nitrogen that had first been pre-saturated with the solvent.

Synthesis of the Ligand $mpgH_2$: Hydroxylamine hydrochloride (21 g, 30 mmol) was dissolved in water (30 mL) and neutralized with an equimolar amount of NaOH. A methanolic solution of 1-phenyl-1,2-propanedione 2-oxime (5 g, 30 mmol in 80 mL) was added and the mixture was heated under reflux for 3 h. The precipitate was collected by filtration and washed with water and chloroform to give a white product. Yield: 4.25 g (78%). $C_9H_{10}N_2O_2$ (178.19): calcd. C 60.7, H 5.66, N 15.7; found C 60.3, H 5.77, N 15.7. ESI-MS (60 V, CH_3OH): calcd. for $mpgH_2$ 178.188; found 179.1 (100%). ^{1}H NMR (400 MHz, [D$_6$]DMSO, TMS): δ = 2.02 (s, 3 H, C*H*$_3$), 7.14 (d, $^3J_{H,H}$ = 8.3 Hz, 2 H, *ortho* Ph), 7.20–7.43 (m, 3 H, *meta* and *para* Ph), 11.42 (s, 1 H, CH_3C=NO*H*), 11.46 (s, 1 H, PhC=NO*H*) ppm.

Synthesis of [ClCo(mpgH)$_2$py]: The ligand $mpgH_2$ (1.9 g, 11 mmol) was added to a suspension of $CoCl_2 \cdot 6H_2O$ (1.3 g, 5.5 mmol) in ethanol (60 mL). The suspension was heated and stirred in the presence of air for 40 min. After the addition of py (0.9 mL, 11 mmol) to the resulting solution, the mixture was cooled to room temperature in a stream of air. After 2 h, a yellowish microcrystalline precipitate was collected by filtration. The ^{1}H NMR spectrum showed that the precipitate was a mixture of the *cis* and *trans* isomers in a ratio of about 1:1.2. Yield: 2.07 g (71.3%). $C_{23}H_{23}ClCoN_5O_4$ (527.85): calcd. C 52.3, H, 4.39, N 13.2; found C 52.8 H, 4.46, N 12.8. Small quantities of the isomers could be separated by stratification of *n*-heptane over a $CDCl_3$ solution of the mixture in an NMR tube. After slow diffusion, two different kinds of crystals deposited on the walls of the tube and were separated manually. The dark-brown crystals corresponded to the *trans* isomer, whereas the dark-yellow crystals corresponded to the *cis* isomer. ***trans*-[ClCo(mpgH)$_2$py]:** ^{1}H NMR (400 MHz, $CDCl_3$, TMS): δ = 2.32 (s, 6 H, equatorial C*H*$_3$), 7.28 (m, 2 H, *meta* py), 7.45 (m, 10 H, equatorial phenyls), 7.75 (t, $^3J_{H,H}$ = 7.6 Hz, 1 H, *para* py), 8.42 (d, $^3J_{H,H}$ = 5.2 Hz, 2 H, *ortho* py), 18.07 (s, 2 H, O*H*O) ppm. ***cis*-[ClCo(mpgH)$_2$py]:** ^{1}H NMR (400 MHz, $CDCl_3$, TMS): δ = 2.34 (s, 6 H, equatorial C*H*$_3$), 7.26 (m, 2 H, *meta* of py), 7.41 (m, 10 H, equatorial phenyls), 7.75 (t, $^3J_{H,H}$ = 7.6 Hz, 1 H, *para* of py), 8.4 (d, $^3J_{H,H}$ = 5.6 Hz, 2 H, *ortho* of py), 18.32 (s, 1 H, O*H*O), 18.52 (s, 1 H, O*H*O) ppm.

Synthesis of [CH$_3$Co(mpgH)$_2$py]: NaOH (1 pellet in 2 mL of water) and a twofold excess of py (0.18 mL, 1.9 mmol) were added to a suspension of [ClCo(mpgH)$_2$py] (mixture of *cis* and *trans* isomers in a ratio of 1:1.2; 0.50 g, 0.95 mmol) in 130 mL of methanol. The resulting solution was deaerated by bubbling nitrogen. $NaBH_4$ (0.054 g, 1.42 mmol), dissolved in the minimum amount of water, and CH_3I (0.15 mL, 1.89 mmol) were then added in sequence. The solution was stirred at room temperature under nitrogen for 30 min and then the solvent was evaporated in vacuo. The orange crystals were collected by filtration. The ^{1}H NMR spectrum showed that the precipitate was a mixture of the *cis* and *trans* isomers, in a ratio of about 1:1.2. The isomers were separated by fractional crystallization from CH_3OH/CH_2Cl_2 (1:1), exploiting the lower solubility of the *trans* isomer. ***trans*-[CH$_3$Co(mpgH)$_2$py] (1):** Yield: 0.188 g (36%). $C_{24}H_{26}CoN_5O_4$ (507.43): calcd. C 56.8, H 5.16, N 13.8; found C 55.7, H 5.06, N 13.6. ESI-MS (60 V, MeOH): *m*/*z* calcd. for *trans*-[CH$_3$Co(mpgH)$_2$py] 507.428; found 508.0 (60%); further peaks: *m*/*z* (%) = 530.0 (68) [M + Na$^+$], 429.0 (96) [M – py], 451.0 (100) [M + Na$^+$ – py]. ^{1}H NMR (400 MHz, $CDCl_3$, TMS): δ = 1.14 (s, 3 H, axial C*H*$_3$), 2.05 (s, 6 H, equatorial C*H*$_3$), 7.25–7.45 (m, 12 H, *meta* py and equatorial phenyls), 7.79 (t, $^3J_{H,H}$ = 7.6 Hz,

Table 3. Crystallographic data for **1**–**4**.

	1	**2**	**3**	**4**
Empirical formula	$C_{24}H_{26}CoN_5O_4$	$C_{24}H_{26}CoN_5O_4$	$C_{27}H_{35}BCoN_5O_7$	$C_{25}H_{28}BCoN_5O_5$
Formula mass	507.43	507.43	611.34	548.26
Temperature [K]	200(2)	293(2)	150(2)	293(2)
Wavelength [Å]	1.5418	0.71073	0.71073	1.5418
Crystal system, S.G.	monoclinic, $P2_1/c$	monoclinic, $P2_1/n$	monoclinic, $P2_1/n$	triclinic, $P\bar{1}$
a [Å]	14.497(4)	12.432(4)	10.216(3)	7.921(3)
b [Å]	8.607(4)	15.442(4)	15.532(5)	11.777(3)
c [Å]	19.140(6)	13.795(6)	18.584(5)	13.886(3)
α [°]	90	90	90	104.92(2)
β [°]	100.10(3)	115.16(5)	92.26(2)	90.14(2)
γ [°]	90	90	90	94.36(2)
Volume [Å^3]	2351.2(2)	2397.1(2)	2946.5(2)	1247.7(6)
Z, $\rho_{calcd.}$ [Mg m^{-3}]	4, 1.433	4, 1.406	4, 1.378	2, 1.459
μ [mm^{-1}]	6.066	0.756	0.635	5.785
F(000)	1056	1056	1280	570
Crystal size [mm]	0.3 × 0.2 × 0.1	0.3 × 0.3 × 0.3	0.5 × 0.3 × 0.3	0.2 × 0.1 × 0.1
θ range for data collection [°]	5.15 to 57.68	2.24 to 26.45	4.53 to 26.02	6.95 to 62.47
Reflections unique/reflections with $I > 2\sigma(I)$	3108/2534	4930/3017	5756/4731	2248/1361
Refinement method	Full-matrix least squares on F^2	Full-matrix least squares on F^2	Full-matrix least squares on F^2	Full-matrix least squares on F^2
Data/restraints/parameters	3108/0/310	4930/0/310	5756/0/356	2248/0/242
Goodness-of-fit on F^2	0.896	0.714	1.066	0.756
Final *R* indices [$I > 2\sigma(I)$]	R_1 = 0.0693 wR_2 = 0.2020	R_1 = 0.0400 wR_2 = 0.1168	R_1[a] = 0.0574 wR_2[b] = 0.1551	R_1 = 0.0849 wR_2 = 0.2006
R indices (all data)	R_1 = 0.0851 wR_2 = 0.2236	R_1 = 0.0772, wR_2 = 0.1508	R_1 = 0.0685, wR_2 = 0.1627	R_1 = 0.1332, wR_2 = 0.2383
Largest difference peak/hole [e Å^{-3}]	0.315/–0.610	0.328/–0.456	1.036/–0.670	0.294/–0.336

[a] $R_1 = \Sigma||F_o| - |F_c||/\Sigma|F_o|$. [b] $wR_2 = [\Sigma w(|F_o|^2 - |F_c|^2)^2/\Sigma w|F_o^2|^2]^{1/2}$.

 © 2005 Wiley-VCH Verlag GmbH & Co. KGaA, Weinheim

1 H, *para* py), 8.77 (d, $^3J_{H,H}$ = 6.2 Hz, 2 H, *ortho* py), 18.20 (s, 2 H, O*H*O) ppm. ***cis*-[$CH_3Co(mpgH)_2py$] (2):** Yield: 0.124 g (27%). $C_{24}H_{26}CoN_5O_4$ (507.43): calcd. C 56.8, H 5.16, N 13.8; found C 56.7, H 5.40, N 14.0. ESI-MS (60 V, MeOH): *m*/*z* calcd. for *cis*-[$CH_3Co(mpgH)_2py$] 507.428; found 508.0 (24%); further peaks: *m*/*z* (%) = 529.9 (28) [M + Na^+] , 429.1 (80) [M – py], 451.0 (100) [M + Na^+ – py]. ^{1}H NMR (400 MHz, $CDCl_3$, TMS): δ = 1.12 (s, 3 H, axial C*H*$_3$), 2.08 (s, 6 H, equatorial C*H*$_3$), 7.25–7.42 (m, 12 H, *meta* of py and equatorial phenyls), 7.79 (t, $^3J_{H,H}$ = 7.6 Hz, 1 H, *para* of py), 8.75 (d, $^3J_{H,H}$ = 6.2 Hz, 2 H, *ortho* of py), 18.39 (s, 1 H, O*H*O), 18.56 (s, 1 H, O*H*O) ppm.

Synthesis of 3: A solution of 3-pyridylboronic acid (12 mg, 0.098 mmol in 6 mL of MeOH) was added to a solution of *trans*-[$CH_3Co(mpgH)_2py$] (0.050 g, 0.098 mmol in 1 mL $CHCl_3$) The pH was adjusted to 5.5 with concentrated $HClO_4$ and NaOH. The solution was filtered and set aside in a beaker covered with Parafilm. After some days, small orange crystals of **3**, suitable for X-ray analysis, appeared and were collected by filtration. Yield: 33.2 mg (62%). $C_{50}H_{54}B_2Co_2N_{10}O_{10}$ (1094.5): calcd. C 54.8, H 4.97, N 12.8; found C 55.3, H 5.10, N 12.7. ESI-MS (90 V, CH_2Cl_2/HCOOH 1%): *m*/*z* calcd. for **3** 1094.5; found 1095.4 (100%). ^{1}H NMR (400 MHz, $CDCl_3$, TMS: δ = 1.45 (s, 6 H, axial C*H*$_3$), 1.79 (s, 6 H, C*H*$_3$C=NOH), 2.01 (s, 6 H, C*H*$_3$C=NOB), 3.31 (s, 6 H, OC*H*$_3$), 7.12–7.74 (m, 22 H, *meta* of py and equatorial phenyls), 7.90 (d, $^3J_{H,H}$ = 6.8 Hz, 2 H, *ortho* of py), 8.30 (d, $^3J_{H,H}$ = 5.4 Hz, 2 H, *para* of py), 9.60 (s, 2 H, *ortho* of py), 18.54 (s, 2 H, O*H*O) ppm.

Synthesis of 4: The synthesis was performed as described above using 4-pyridylboronic acid instead of 3-pyridylboronic acid. Yield: 17 mg (32%). $C_{50}H_{54}B_2Co_2N_{10}O_{10}$ (1094.5): calcd. C 54.8, H 4.97, N 12.8; found C 54.3, H 5.03, N 12.3. ESI-MS (90 V, CH_2Cl_2/HCOOH 1%): *m*/*z* calcd. for **4** 1094.5; found 1095.4 (100%). ^{1}H NMR (400 MHz, $CDCl_3$, TMS): δ = 1.28 (s, 6 H, axial C*H*$_3$), 2.27 (s, 6 H, C*H*$_3$C=NOH), 2.51 (s, 6 H, C*H*$_3$C=NOB), 3.22 (s, 6 H, OC*H*$_3$), 6.72(d, $^3J_{H,H}$ = 5.4 Hz, 2 H, *meta* of py), 6.83(d, $^3J_{H,H}$ = 5.4 Hz, 2 H, *meta* of py), 7.05 (d, $^3J_{H,H}$ = 5.4 Hz, 2 H, *ortho* of py), 7.09 (d, $^3J_{H,H}$ = 5.4 Hz, 2 H, *ortho* of py), 7.45–7.65 (m, 20 H, phenyls), 17.89 (s, 2 H, O*H*O) ppm.

Synthesis of 5: A solution of 3-pyridylboronic acid (12 mg, 0.098 mmol in 6 mL of MeOH) was added to a solution of *cis*-[$CH_3Co(mpgH)_2py$] (0.050 g, 0.098 mmol in 1 mL of $CHCl_3$) and the pH was adjusted to 5.5. The solution was filtered and allowed to stand in a beaker covered with Parafilm for2 d. Then, the solvent was evaporated under atmospheric pressure and the orange solid collected by filtration. Yield: 22.3 mg (41%). $C_{50}H_{54}B_2Co_2N_{10}O_{10}$ (1094.5): calcd. C 54.8, H 4.97, N 12.8; found C 53.0, H 4.50, N 11.8. ESI-MS (90 V, CH_2Cl_2/HCOOH 1%): *m*/*z* calcd. for **5** 1094.5; found 1095.2 (100%). ^{1}H NMR (400 MHz, $CDCl_3$, TMS: δ = 1.49 (s, 6 H, axial C*H*$_3$), 1.99 (s, 12 H, C*H*$_3$C=NOB), 3.44 (s, 6 H, OC*H*$_3$), 7.30–7.50 (m, 22 H, *meta* of py and equatorial phenyls), 8.09 (d, $^3J_{H,H}$ = 7.1 Hz, 2 H, *ortho* of py), 8.46 (d, $^3J_{H,H}$ = 5.5 Hz, 2 H, *para* of py), 9.72 (s, 2 H, *ortho* of py), 18.56 (s, 2 H, O*H*O) ppm.

Synthesis of 6: A solution of 4-pyridylboronic acid (12 mg, 0.098 mmol in 6 mL of MeOH) was added to a solution of *cis*-[$CH_3Co(mpgH)_2py$] (0.050 g, 0.098 mmol in 1 mL of $CHCl_3$) and the pH was adjusted to 5.5. The solution was filtered and allowed to stand in a beaker covered with Parafilm for 2 d. Then, two drops of water were added and the solvent evaporated under atmospheric pressure. The orange solid was collected by filtration. Yield: 6.3 mg (12%). $C_{50}H_{54}B_2Co_2N_{10}O_{10}$ (1094.5): calcd. C 54.8, H 4.97, N 12.8; found C 53.8, H 5.41, N 11.7. ESI-MS (90 V, CH_2Cl_2/HCOOH 1%): *m*/*z* calcd. for **6** 1094.5; found 1095.4 (80%). ^{1}H NMR (400 MHz, $CDCl_3$, TMS): δ = 1.28 (s, 6 H, axial C*H*$_3$), 2.53 (s, 12 H, C*H*$_3$C=NOB), 3.37 (s, 6 H, OC*H*$_3$), 6.84 (d, $^3J_{H,H}$ = 6.3 Hz, 4 H, *meta* of py), 7.16 (d, $^3J_{H,H}$ = 6.3 Hz, 4 H, *ortho* of py), 7.45–7.55 (m, 20 H, equatorial phenyls), 17.94 (s, 2 H, O*H*O) ppm.

Structure Determinations: Single crystals suitable for X-ray data collection were obtained as reported above. Data for the crystals of compounds **1** and **4**, being of small size and, in the case of **4**, also of poor quality, were collected at 200 K and 293 K, respectively, using a rotating copper-anode generator working at 45 kV and 95 mA, equipped with an Enraf Nonius KCCD diffractometer; 88 images for **1** and 176 for **4** were collected (crystal-to-detector distance of 42 mm) with 6° oscillation and 20 s/° exposure time for CCD image. The data were processed, scaled, and merged with the programs DENZO and SCALE-PACK.[22] Data for the crystals of compounds **2** and **3** were collected at 293 K and 150 K, respectively, with a Nonius DIP 1030 H System, using graphite-monochromated Mo-K_α radiation. For both compounds a total of 30 frames were collected using the Xpress program[23] over half of reciprocal space, with a rotation of 6° about the axis. A Mac Science Image Plate (diameter = 300 mm) was used and the crystal-to-plate distance was fixed at 90 mm. The determination of unit-cell parameters, integration of reflection intensities, and data scaling were performed using the programs DENZO and SCALE-PACK. All structures were solved by direct methods,[24] followed by Fourier syntheses and refined by full-matrix least squares (on F^2) cycles.[25] The H atoms were not refined but were included at calculated positions in the final refinements. A suite of programs[26] was also used for the geometrical and final calculations. Crystal and refinement data are given in Table 3. CCDC-264667 to -264670 (**1**–**4**, respectively) contain the supplementary crystallographic data for this paper. These data can be obtained free of charge from The Cambridge Crystallographic Data Centre via www.ccdc.cam.ac.uk/data_request/cif.

Supporting Information: Time-resolved ^{1}H NMR spectra relative to the formation and decomposition of **3**, ^{1}H NMR spectra of **1**–**6**, and ESI mass spectra of **3**–**6**.

Acknowledgments

This work was supported by MIUR (Prin 2003 no. 2003037580). P. S. acknowledges CIRCMSB (Consorzio Interuniversitario per la Ricerca sui Metalli nei Sistemi Biologici) for a grant. We thank Dr. Fabio Hollan for recording the mass spectra.

[1] a) N. Bresciani Pahor, M. Forcolin, L. G. Marzilli, L. Randaccio, M. F. Summers, P. J. Toscano, *Coord. Chem. Rev.* **1985**, *63*, 1; b) L. Randaccio, N. Bresciani Pahor, E. Zangrando, L. G. Marzilli, *Chem. Soc. Rev.* **1989**, *18*, 225; c) L. Randaccio, *Comments Inorg. Chem.* **1999**, *21*, 327.

[2] A. A. Gridner, S. D. Ittel, *Chem. Rev.* **2001**, *101*, 3611 and references cited therein.

[3] M. E. Welker, *Curr. Org. Chem.* **2001**, *5*, 785 and references cited therein.

[4] B. D. Gupta, R. Yamuna, V. Singh, U. Tiwari, *Organometallics* **2003**, *22*, 226 and references cited therein.

[5] B. D. Gupta, K. Qanungo, R. Yamuna, A. Pandey, U. Tiwari, V. Vijaikanth, V. Singh, T. Barclay, W. Cordes, *J. Organomet. Chem.* **2000**, *608*, 106 and references cited therein.

[6] a) P. J. Toscano, L. Lettko, E. Schermerhorn, J. Waechter, K. Schufon, S. Liu, E. V. Dikarev, J. Zubieta, *Polyhedron* **2003**, *22*, 2809; b) C. López, S. Alvarez, M. Font Bardía, X. Solans, *J. Organomet. Chem.* **1991**, *414*, 245; c) C. López, S. Alvarez, M. Aguiló, X. Solans, M. Font-Altaba, *Inorg. Chim. Acta* **1987**, *127*, 153; d) C. López, S. Alvarez, X. Solans, M. Font-Altaba,

 © 2005 Wiley-VCH Verlag GmbH & Co. KGaA, Weinheim

Inorg. Chem. **1986**, *25*, 2962; e) B. D. Gupta, K. Qanungo, *J. Organomet. Chem.* **1997**, *543*, 125; f) B. D. Gupta, K. Qanungo, *J. Organomet. Chem.* **1998**, *560*, 155.
[7] a) B. D. Gupta, V. Singh, K. Qanungo, V. Vijaikanth, R. Yamuna, T. Barclay, W. Cordes, *J. Organomet. Chem.* **2000**, *602*, 1; b) B. D. Gupta, R. Yamuna, V. Singh, U. Tiwari, T. Barclay, W. Cordes, *J. Organomet. Chem.* **2001**, *627*, 80; c) B. D. Gupta, U. Tiwari, T. Barclay, W. Cordes, *J. Organomet. Chem.* **2001**, *629*, 83.
[8] a) Y. Ohgo, S. Takeuchi, *Chem. Lett.* **1985**, 407; b) A. Uchida, Y. Ohashi, Y. Sasada, Y. Ohgo, *Acta Crystallogr., Sect. C* **1985**, *41*, 25.
[9] H. Höpfl, in *Structure & Bonding*, vol. 103 (Ed.: D. M. P. Mingos), Springer, Berlin, **2002**.
[10] a) R. Dreos, G. Nardin, L. Randaccio, G. Tauzher, S. Vuano, *Inorg. Chem.* **1997**, *36*, 2463; b) R. Dreos, G. Nardin, L. Randaccio, P. Siega, G. Tauzher, V. Vrdoljak, *Inorg. Chem.* **2001**, *40*, 5536; c) R. Dreos, G. Nardin, L. Randaccio, P. Siega, G. Tauzher, *Eur. J. Inorg. Chem.* **2002**, 2885.
[11] R. Dreos, G. Nardin, L. Randaccio, P. Siega, S. Scagliola, G. Tauzher, *Eur. J. Inorg. Chem.* **2004**, 4266.
[12] The stereochemical description of the two enantiomers has been achieved by using the configuration index, the priming convention, and the chirality symbols based on the priority sequence (A/C stereochemical descriptors) [A. von Zelewski, *Stereochemistry of Coordination Compounds*; Wiley, Chichester, **1996**; J. G. Leigh, *Nomenclature of Inorganic Chemistry*, Blackwell, Oxford, **1990**]. For practical purposes, the C_2 axis of the molecule has been chosen as the reference axis with the view from py (having a lower priority number than CH_3) to the metal atom. The complete stereochemical description of the C enantiomer is therefore OC-6-41′-C and that of the A enantiomer OC-6-41′-A.
[13] A. Bigotto, E. Zangrando, L. Randaccio, *J. Chem. Soc., Dalton Trans.* **1976**, 96.
[14] A. E. Kaifer, M. Gomez-Kaifer, *Supramolecular Electrochemistry*, Wiley-VCH, Weinheim, **1999**.
[15] A. J. Bard, L. R. Faulkner, *Electrochemical Methods, Fundamentals and Applications*, John Wiley & Sons, Inc., New York, **1980**.
[16] G. Costa, A. Puxeddu, C. Tavagnacco, R. Dreos-Garlatti, *Inorg. Chim. Acta* **1984**, *89*, 65 and references cited therein.
[17] Due to the closeness of the background discharge to the reduction signals, it was not possible to obtain reproducible coulometric measurements of the number of electrons transferred.
[18] a) G. Costa, A. Puxeddu, C. Tavagnacco, *J. Organomet. Chem.* **1985**, *296*, 161; b) C. Tavagnacco, G. Balducci, G. Costa, K. Täschler, W. von Philipsborn, *Helv. Chim. Acta* **1990**, *73*, 1469.
[19] A. Wu, L. Isaacs, *J. Am. Chem. Soc.* **2003**, *125*, 4831 and references cited therein.
[20] a) P. N. W. Baxter, J. M. Lehn, K. Rissanen, *Chem. Commun.* **1997**, 1323; b) Y. Yamanoi, Y. Sakamoto, T. Kusukawa, M. Fujita, S. Sakamoto, K. Yamaguchi, *J. Am. Chem. Soc.* **2001**, *123*, 980.
[21] S. J. Rowan, S. J. Cantrill, G. R. L. Cousins, J. K. M. Sanders, J. F. Stoddart, *Angew. Chem. Int. Ed.* **2002**, *41*, 898.
[22] Z. Otwinouski, W. Minor, *Methods Enzymol.* **1997**, *276*, 307.
[23] a) B. Schierbeek, Noniusm Delftm The Netherlands, **1998**; b) Collaborative Computational Project, Number 4, *Acta Crystallogr. Sect. A* **1990**, *46*, 467.
[24] *SIR92 – A program for crystal structure solution*: A. Altomare, G. Cascarano, C. Giacovazzo, A. Guagliardi, *J. Appl. Crystallogr.* **1993**, *26*, 343.
[25] G. M. Sheldrick, *SHELXL-97 – Programs for Structure Refinement*, University of Göttingen, Göttingen, Germany, **1998**.
[26] L. J. Farrugia, *J. Appl. Crystallogr.* **1999**, *32*, 837.

Received: February 28, 2005
Published Online: August 4, 2005

 © 2005 Wiley-VCH Verlag GmbH & Co. KGaA, Weinheim

Octahedral Hexahydroxo Rhenium Cluster Complexes $[Re_6Q_8(OH)_6]^{4-}$ (Q = S, Se): Synthesis, Structure, and Properties

Spartak S. Yarovoi,[a] Yuri V. Mironov,[a] Dmitry Y. Naumov,[a] Yuri V. Gatilov,[b] Svetlana G. Kozlova,[a,c] Sung-Jin Kim,[d] and Vladimir E. Fedorov*[a]

Keywords: Rhenium / Hexahydroxo complexes / Cluster compounds / Electronic structure / Luminescence

Two novel rhenium cluster compounds, $K_4[Re_6S_8(OH)_6]\cdot 8H_2O$ (**1**) and $K_4[Re_6Se_8(OH)_6]\cdot 8H_2O$ (**2**), containing octahedral cluster chalcogenide anionic complexes $[Re_6Q_8(OH)_6]^{4-}$ with terminal hydroxo ligands have been synthesized by the reaction of $Re_6Q_8Br_2$ (Q = S, Se) with molten KOH. Two chalcohalide compounds, one known ($Cs_4[Re_6S_8Br_6]\cdot 2H_2O$, **3**) and another new ($Cs_3[Re_6Se_8Cl_6]\cdot 2H_2O$, **4**), were prepared by reactions of **1** and **2** with CsX and HX (X = Br, Cl) in an aqueous solution. Compounds **1**, **2**, and **4** have been characterized by the single-crystal X-ray diffraction method. Compounds **1** and **2** are crystallized in triclinic space group $P\bar{1}$ with one formula unit in the cell of dimensions a = 8.4936(8) Å, b = 8.9101(11) Å, c = 10.5940(13) Å, α = 77.935(11)°, β = 75.933(9)°, γ = 71.244(10)°, V = 728.9(1) Å^3 (compound **1**) and a = 8.613(1) Å, b = 8.996(1) Å, c = 10.057(1) Å, α = 78.587(2)°, β = 77.811(2)°, γ = 71.728(2)°, V = 715.9(2) Å^3 (compound **2**). Compound **4** crystallizes in the monoclinic space group $P2_1/n$ with two formula units in the cell of dimensions a = 9.819(3) Å, b = 12.925(4) Å, c = 11.756(4) Å, β = 113.38(3)°, V = 1369.6(8) Å^3. Compounds **1** and **2** display luminescent properties.

(© Wiley-VCH Verlag GmbH & Co. KGaA, 69451 Weinheim, Germany, 2005)

Introduction

The chemistry of octahedral rhenium cluster complexes with cluster core $\{Re_6Q_8\}^{2+}$ (Q = S, Se, Te) is in a stage of rapid development.[1] Some solids like $Re_6Q_8X_2$ (Q = S, Se; X = Cl, Br)[2] or Re_6Te_{15}[3] containing similar cluster cores prepared by high temperature solid-state reactions are characterized by extended intercluster bonding. A large number of articles have appeared within the last few years that have reported the preparation of molecular cluster complexes of the $Re_6Q_8L_6$ type (L = Cl, Br, I, or different organic ligands).[4] One way of preparing molecular cluster complexes is the excision reaction through interaction of polymeric solids such as $Re_6Q_8X_2$ or Re_6Te_{15} with molten salts. A similar strategy for the preparation of chalcocyanide complexes $[Re_6Q_8(CN)_6]^{4-}$ by reactions of Re_6Te_{15} or $Re_6Q_8X_2$ with molten KCN have been used earlier.[5] Very recently we suggested molten KOH as a new reaction medium: the reaction of $Re_6Se_8Br_2$ with molten KOH at 280 °C results in formation of the unusual cluster core $\{Re_6Se_4O_4\}^{2+}$, found in $Cs_{11}(H_3O)[Re_6Se_4O_4Cl_6]_3\cdot 4H_2O$.[6] Further investigation of reactions of $Re_6Q_8X_2$ with molten KOH results in the preparation of three new cluster compounds: $K_4[Re_6S_8(OH)_6]\cdot 8H_2O$ (**1**), $K_4[Re_6Se_8(OH)_6]\cdot 8H_2O$ (**2**), and $Cs_3[Re_6Se_8Cl_6]\cdot 2H_2O$ (**4**), and one known: $Cs_4[Re_6S_8Br_6]\cdot 2H_2O$ (**3**). All new compounds were characterized by X-ray single-crystal analysis.

Results

Syntheses

Compounds **1** and **2** containing hexahydroxo complexes $[Re_6Q_8(OH)_6]^{4-}$ (Q = S, Se) were obtained from $Re_6S_8Br_2$ (for **1**) and $Re_6Se_8Br_2$ (for **2**) in molten KOH at 280 °C and 200 °C respectively in open vessels following recrystallization of the compounds from water. The only rhenium octahedral cluster complex with OH^- groups as terminal ligands, $[Re_6S_8(OH)_2(H_2O)_4]\cdot 12H_2O$, was described earlier.[7] Compounds **3** and **4** were obtained from aqueous solutions of compounds **1** and **2** by adding CsX and HX and further crystallization. Crystals of diamagnetic compound **3** are orange. Paramagnetic compound **4** crystallizes from the solution as black crystals.

[a] Nikolaev Institute of Inorganic Chemistry, Siberian Branch of Russian Academy of Sciences,
3 Acad. Lavrentiev pr., 630090 Novosibirsk, Russia
Fax: +7-3832-309489
E-mail: yuri@che.nsk.su
[b] Vorozhtsov Institute of Organic Chemistry, Siberian Branch of Russian Academy of Sciences,
9 Acad. Lavrentiev pr., 630090 Novosibirsk, Russia
[c] Boreskov Institute of Catalysis, Siberian Branch of Russian Academy of Sciences,
5 Acad. Lavrentiev pr., Novosibirsk 630090, Russia
[d] Department of Chemistry, Ewha Womans University,
Seoul 120-750, Korea
E-mail: sjkim@ewha.ac.kr

Supporting information for this article is available on the WWW under http://www.eurjic.org or from the author.

Structures

The structures of the cluster anions $[Re_6Q_8(OH)_6]^{4-}$, where Q = S (**1**) or Se (**2**) (Figure 1), are similar to the well-known octahedral complexes of $[Re_6Q_8L_6]^{4-}$ type with L = Cl^-, Br^-, I^-, CN^-. There is a nearly regular Re_6 octahedron residing inside a Q_8 (S, Se) cube with the distances Re–Re in the range 2.5906(9)–2.5846(8) Å (**1**) and 2.6085(6)–2.6155(6) Å (**2**) and Re–(μ_3-Q) in the range 2.407(4)–2.420(3) Å (**1**) and 2.527(1)–2.545(1) Å (**2**). Six terminal OH^- ligands are coordinated to Re atoms with bond lengths Re–O 2.07(1)–2.09(1) Å (**1**) and 2.081(6)–2.088(6) Å (**2**). Whereas the Re–Re and Re–(μ_3-Q) bond lengths increase in the order $Re_6S_8 < Re_6Se_8$, the Re–O bond lengths do not appear to vary.

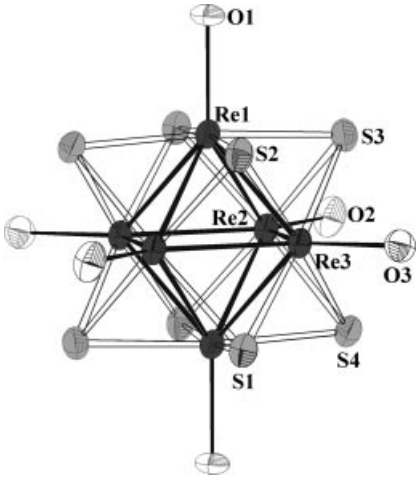

Figure 1. View of the cluster anion $[Re_6(\mu_3\text{-}S)_8(OH)_6]^{4-}$ in **1**. Displacement ellipsoids are drawn at the 50% probability level.

Compound **4** was studied by single-crystal X-ray analysis; the structure of compound **3** was described earlier.[8] The structure of the oxidized cluster anion $[Re_6Se_8Cl_6]^{3-}$ (Figure 2) is also similar to the well-known octahedral complexes $[Re_6Q_8L_6]^{4-}$ where L is a typical acidoligand (Cl^-, Br^-, I^-, CN^-). In the cluster core $\{Re_6Se_8\}$ there is a system of Re–Re and Re–(μ_3-Se) bonds, with lengths in the range 2.606(1)–2.615(1) Å and 2.497(3)–2.525(3) Å, respectively. Six terminal Cl^- ligands are coordinated to Re atoms with bond lengths of 2.414(7)–2.427(6) Å.

To confirm the presence of OH^- groups in the compounds, a solid-state NMR investigation has been carried out at 180 K for $K_4[Re_6Q_8(OH)_6]\cdot 8H_2O$. The wide-line ^1H NMR spectrum was recorded by sweeping the frequency in the neighborhood of 22.8 MHz using a home-made NMR spectrometer with signal accumulation. The experimental NMR spectrum is simulated reasonably by two spectral lines (Figure 3). One line is a classic Pake's line with the parameters: $a = 23.0 \pm 0.5$ kHz and $\beta_1 = 7.4 \pm 0.1$ kHz; these parameters are typical characteristics for H_2O without self-diffusion.[9] The other line is a single one, which can be attributed to H atoms of OH^- groups. This line is simulated

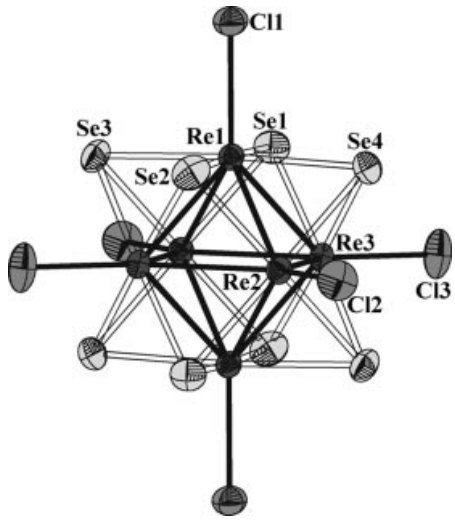

Figure 2. View of the cluster anion $[Re_6(\mu_3\text{-}Se)_8Cl_6]^{3-}$ in **4**. Displacement ellipsoids are drawn at the 50% probability level.

by the Gaussian function with $\beta_2 = 7.5 \pm 0.1$ kHz.[10] The ratio of the integral intensities of the two lines (I_2/I_1) is $R = 0.36 \pm 0.02$, which is very close to the composition of $K_4[Re_6S_8(OH)_6]\cdot 8H_2O$. Analogous results were obtained for $K_4[Re_6Se_8(OH)_6]\cdot 8H_2O$: $a = 24.5 \pm 0.5$ kHz and $\beta_1 = 9.3 \pm 0.1$ kHz; $\beta_2 = 8.4 \pm 0.1$ kHz and $R = 0.30 \pm 0.02$.

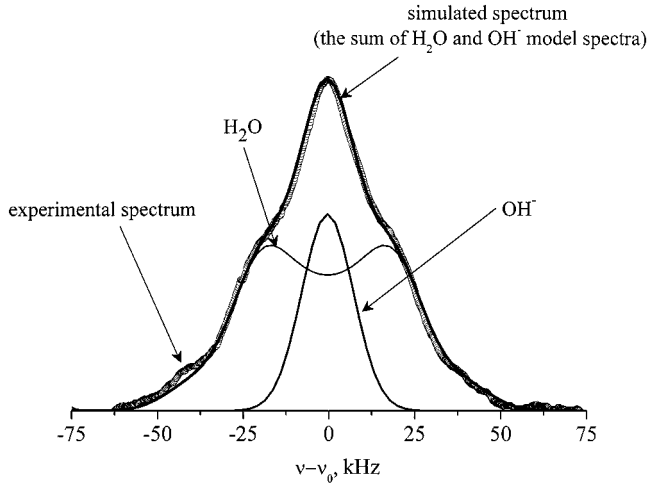

Figure 3. Experimental ^1H NMR absorption at 180 K for $K_4[Re_6S_8(OH)_6]\cdot 8H_2O$ and the calculated spectra for H_2O and OH^- and their sum. For $K_4[Re_6Se_8(OH)_6]\cdot 8H_2O$ the figure is analogous.

The most interesting feature of compound **4** is the oxidized state of the cluster core $\{Re_6Se_8\}^{3+}$, where the number of cluster valence electrons is equal to 23. It is known that diamagnetic complexes $[Re_6Q_8L_6]^{4-}$ containing 24 valence electrons in the Re_6 cluster can be transformed into 23-electron paramagnetic $[Re_6Q_8L_6]^{3-}$ forms. The stability of a sulfur-containing complex in comparable experimental conditions can be explained by its higher electrochemical potential in the redox process. For example, it is known that for chalcocyanide complexes $[Re_6Q_8(CN)_6]^{4-}$ the electrochemi-

 © 2005 Wiley-VCH Verlag GmbH & Co. KGaA, Weinheim

cal potentials of a similar one-electron oxidation reaction are in decreasing order as S > Se > Te; thus for aqueous solutions $E_{1/2}$ are equal to 1.07, 0.82, and 0.53 V respectively for sulfur-, selenium-, and tellurium-containing complexes.[11] Thus, a selenium-containing cluster anion can be oxidized in aqueous solutions rather easily.

The formation of the oxidized anion $[Re_6Se_8Cl_6]^{3-}$ was confirmed by both X-ray analysis (by determination of number of cations in the structure) and magnetic measurements, which showed paramagnetic behavior with one unpaired electron per cluster (see Supporting Information). Simple and high-yield synthesis of this compound opens a path for preparing other compounds containing an oxidized paramagnetic cluster complex. This is rather useful, because oxidized clusters are the most proper starting compounds for the preparation of Re_6 complexes with organic ligands in comparison with rather inert 24-electron complexes.

As seen from our experiments, the hexahydroxo complexes $[Re_6Q_8(OH)_6]^{4-}$ are good precursors for different reactions. They can be transformed into neutral aqua-hydroxo complexes of the type $[Re_6Q_8(OH)_2(H_2O)_4]\cdot nH_2O$. Reactions with halide ions give chalcohalide complexes $[Re_6Q_8L_6]$ where L = Cl, Br, I; in principle, a similar approach for synthesis of chalcohalide complexes may be applied for different variations of μ_3-S or μ_3-Se in the cluster core with terminal Cl, Br, or I ligands. Here we have synthesized only the combinations of S/Br and Se/Cl as the most evident samples in the structure analysis. Beside the substitution of terminal OH^- groups in $[Re_6Q_8(OH)_6]^{4-}$ it is possible to substitute inner μ_3-Q ligands in the cluster core. The first example of a similar reaction is preparation of the compound $Cs_{11}(H_3O)[Re_6Se_4O_4Cl_6]_3\cdot 4H_2O$, containing the cluster core $\{Re_6Se_4O_4\}$.[6] In contrast to easy substitution of terminal OH groups, which is performed in solution, the substitution of inner μ_3-Q ligands in the cluster core requires higher temperatures: for example, substitution of selenium with oxygen was carried out in molten KOH at 280 °C. Finally, selenium-containing complexes can be converted easily in solution in oxidized form.

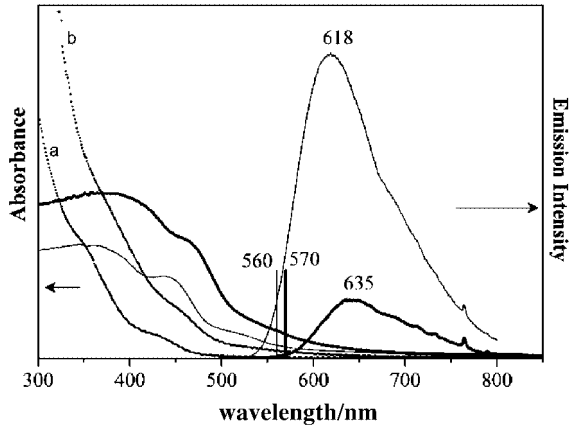

Figure 4. Electronic absorption spectra (at the left) of solids $K_4[Re_6S_8(OH)_6]\cdot 8H_2O$ (thin line), $K_4[Re_6Se_8(OH)_6]\cdot 8H_2O$ (bold line), and their aqueous solutions (dots a and b), and emission luminescent spectra (on the right) of solids $K_4[Re_6S_8(OH)_6]$ (thin line) and $K_4[Re_6Se_8(OH)_6]$ (bold line). Spectral intensities are normalized. Vertical lines show the forbidden transitions.

Luminescence Properties

Luminescence properties of solid samples of **1** and **2** were recorded at room temperature in wavelength range from 500 to 700 nm. Upon excitation at 440 nm, solid samples of **1** and **2** display photoluminescence with λ_{max} at 618 and 635 nm, respectively (Figure 4). The luminescence spectra of aqueous solutions for both compounds are very similar.[12]

Electronic Structure

The optimized calculated values of the geometric parameters of the $[Re_6Q_8L_6]^{n-}$ complexes are in good qualitative agreement with X-ray experimental data. The highest occupied molecular orbitals (HOMO) of diamagnetic $[Re_6S_8(OH)_6]^{4-}$ and $[Re_6Se_8(OH)_6]^{4-}$ complexes are very much alike (Figure 5). The electronic structure of the HOMO ($21e_g$) in the $[Re_6S_8(OH)_6]^{4-}$ cluster anion in general terms corresponds to the quantum calculations of the electronic structure of related complexes, $[Re_6Q_8L_6]^{4-}$ with Q = S, Se and L = Cl, Br, I, CN.[13] The highest occupied orbitals, $18t_{2u}$ and $24e_g$, in the $[Re_6Se_8(OH)_6]^{4-}$ cluster anion have an energy separation of 0.0015 eV. The use of the SAOP GGA functional[14] revealed that the energy separation is 0.019 eV. In this case it is difficult to predict which one of these orbitals is HOMO in reality. It is interesting to note that this is the first example when the HOMO of $Re_6Q_8L_6$ complexes has a t_{2u} symmetry. The LUMO of both clusters have the symmetry eg [22eg (S) and 25eg (Se)]. The similar result for HOMO may be an artifact, but it challenges further wide theoretical and experimental investigations. In particular, it is well known that luminescent properties of $[Re_6Q_8L_6]^{4-}$ complexes are determined by the frontier orbital symmetry.[13e] For these complexes the HOMO (eg)–LUMO (a_{1g} or t_{1g}) transitions are characterized as forbidden electronic dipole transitions. If the HOMO has t_{2u} symmetry, the HOMO–LUMO transition is allowed and decreasing luminescent excitement may be expected. As can be seen from the luminescent properties of **1** and **2** (Figure 4), this prediction takes place here. Notice that the related complexes $[Re_6Se_8(CN)_6]^{4-}$ showed much stronger emissions than $[Re_6S_8(CN)_6]^{4-}$.[15]

The calculated HOMO–LUMO energy gaps are 2.20 and 2.17 eV, the binding energies are –158.0 and –152.3 eV, and ionization potentials (IP) are –6.1 and –5.9 eV for $[Re_6S_8(OH)_6]^{4-}$ and $[Re_6Se_8(OH)_6]^{4-}$ complexes respectively. (IP = –4.5 eV for the $[Re_6Se_8Cl_6]^{4-}$ complex.) The charge distribution of calculated octahedral clusters is presented in Table 1.

 © 2005 Wiley-VCH Verlag GmbH & Co. KGaA, Weinheim

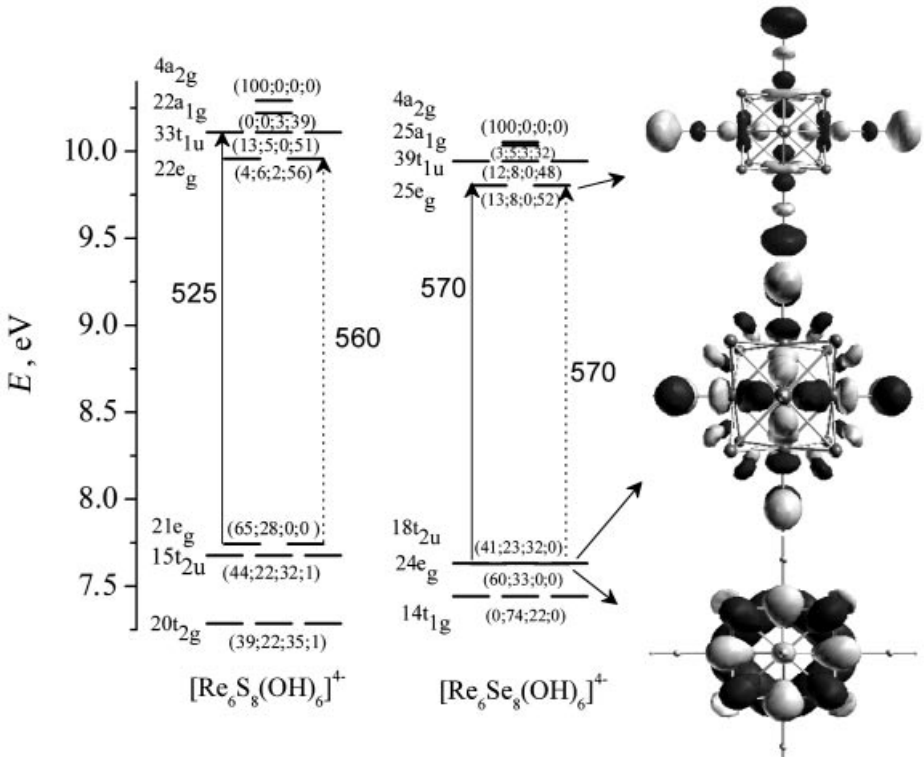

Figure 5. The energy level diagram and schematic figures of MO calculated at the DFT level of theory for $[Re_6S_8(OH)_6]^{4-}$ and $[Re_6Se_8(OH)_6]^{4-}$ complexes. The numbers and symmetry types of the calculated MOs are indicated. Numbers in brackets indicate the percentage of the valent orbitals: 5d Re; 3p S; 4p Se; 2p O; and 1s H, respectively. Arrows show the electronic forbidden (dotted lines) and allowed (solid lines) transitions.

Table 1. The charge distribution in the $[Re_6Q_8L_6]^{4-}$ (Q = S, Se; L = OH, Cl) complexes.

Complex	Re	Q	O; (Cl)	H
$[Re_6S_8(OH)_6]^{4-}$	0.118	–0.283	–0.447	0.039
$[Re_6Se_8(OH)_6]^{4-}$	0.099	–0.276	–0.439	0.041
$[Re_6Se_8Cl_6]^{3-}$	0.069	–0.115	–0.416	–
$[Re_6Se_8Cl_6]^{4-}$	0.054	–0.179	–0.481	–

Experimental Section

$Re_6S_8Br_2$ and $Re_6Se_8Br_2$ were prepared as described.[2] All other reagents were commercially available products of reagent grade quality and were used as purchased. All experiments were performed in an open vessel in air.

$K_4[Re_6S_8(OH)_6]\cdot 8H_2O$ (1) and $K_4[Re_6Se_8(OH)_6]\cdot 8H_2O$ (2): Compounds **1** and **2** were obtained by heating $Re_6Q_8Br_2$ (Q = S, Se) (1 g) and KOH (1.5 g) at 280 °C (**1**) and 200 °C (**2**) in carbon glass vessels for 30 min in air. After cooling, the resulting melt was washed with *i*PrOH (3 × 20 mL portions), dissolved in water (30 mL), filtered, evaporated to 7 mL by heating, and cooled to room temperature. After 12 h red crystals were filtered off and air-dried. Yields: $K_4[Re_6S_8(OH)_6]\cdot 8H_2O$ (0.78 g, 66%), $K_4[Re_6Se_8(OH)_6]\cdot 8H_2O$ (0.9 g, 79%). Electron microprobe analysis (EMA): $K_{4.0}Re_6S_{8.0}$ (**1**), $K_{4.1}Re_6Se_{7.98}$ (**2**).

$Cs_4[Re_6S_8Br_6]\cdot 2H_2O$ (3) and $Cs_3[Re_6Se_8Cl_6]\cdot 2H_2O$ (4): Compounds **3** and **4** were obtained by heating $Re_6Q_8Br_2$ (Q = S, Se) (1 g) and KOH (1.5 g) at 280 °C (**3**) and 200 °C (**4**) in carbon glass vessels for 30 min in air. After cooling, the resulting melt was washed with *i*PrOH (3 × 20 mL portions), dissolved water (50 mL), and filtered. CsBr (1 g, for **3**) or CsCl (1 g, for **4**), and 10 mL of concentrated HBr (for **3**) or HCl (for **4**) were added to the solutions and boiled for 10 min. After this the solutions were filtered and evaporated to 20 mL and cooled to room temperature. After 12 h the orange crystals of **3** or black crystals of **4** were filtered off and air-dried. Yields: $Cs_4[Re_6S_8Br_6]\cdot 2H_2O$ (1.1 g, 70%); $Cs_3[Re_6Se_8Cl_6]\cdot 2H_2O$ (0.91 g, 58%). EMA: $Cs_{4.0}Re_6S_{7.98}Br_{6.1}$ (**3**), $Cs_{3.1}Re_6Se_{7.9}Cl_{6.1}$ (**4**).

X-ray Crystallography: Single-crystal X-ray diffraction data were collected on compounds **1**, **2**, and **4** with the use of graphite-monochromated Mo-K_α radiation (λ = 0.71073 Å) at 273 K (**1** and **4**) and 170 K (**2**) with Enraf Nonius CAD4 (**1**), Bruker Smart CCD with the operating program SMART (**2**) and Siemens P4 (**4**) diffractometers. All structures were solved by direct methods by means of the SHELX-97 program set and were refined by full-matrix least-squares techniques.[16] An empirical absorption correction was applied by measuring three azimuthal scan curves for compound **1**. Face indexed absorption correction was performed numerically with the use of XPREP for compounds **2** and **4**. The program SADABS (**4**) was then employed to make incident beam and decay corrections.

$K_4Re_6S_8(OH)_6\cdot 8H_2O$ (1): M = 1776.26, crystal size 0.25 × 0.20 × 0.15 mm, triclinic space group $P\bar{1}$, a = 8.4936(8) Å, b = 8.9101(11) Å, c = 10.5940(13) Å, α = 77.935(11)°, β = 75.933(9)°, γ = 71.244(10)°, V = 728.9(1) Å^3, Z = 1, $\rho_{calcd.}$ = 4.120 g cm^{-3}, μ = 26.011 mm^{-1}, $2 < \theta < 24.98°$, T = 293(2) K. Reflections: 2746 collected, 2557 unique (R_{int} = 0.0186), 2105 observed [$I > 2\sigma(I)$]; 158 parameters refined with R = 0.0439 [$I > 2\sigma(I)$], wR_2 = 0.1218 (all data), Gof = 1.032, residual electron density: +3.983, –2.509 e Å^{-3}.

$K_4Re_6Se_8(OH)_6\cdot 8H_2O$ (2): (M = 2151.46), crystal size 0.12 × 0.06 × 0.02 mm, triclinic space group $P\bar{1}$, a = 8.613(1) Å, b =

 © 2005 Wiley-VCH Verlag GmbH & Co. KGaA, Weinheim

8.996(1) Å, c = 10.057(1) Å, α = 78.587(2)°, β = 77.811(2)°, γ = 71.728(2)°, V = 715.9(2) Å^3, Z = 1, $\rho_{calcd.}$ = 4.990 g cm^{-3}, μ = 36.058 mm^{-1}, 2.09 < θ < 28.20°, T = 170(2) K. Reflections: 4461 collected, 3174 unique (R_{int} = 0.0186), 2461 observed [$I > 2\sigma(I)$]; 146 parameters refined with R = 0.0329 [$I > 2\sigma(I)$], wR_2 = 0.0941 (all data), Gof = 0.992, residual electron density: + 2.783, –2.382 e Å^{-3}.

$Cs_3[Re_6Se_8Cl_6]\cdot 2H_2O$ (4): (M = 2396.34), crystal size 0.24 × 0.19 × 0.18 mm, monoclinic space group $P2_1/n$, a = 9.819(3) Å, b = 12.925(4) Å, c = 11.756(4) Å, β = 113.38(3)°, V = 1369.6(8) Å^3, Z = 2, $\rho_{calcd.}$ = 5.811 g cm^{-3}, μ = 41.554 mm^{-1}, 2.3 < θ < 29.99°, T = 293(2) K. Reflections: 4202 collected, 3993 unique (R_{int} = 0.0445), 2861 observed [$I > 2\sigma(I)$]; 116 parameters refined with R = 0.0782 [$I > 2\sigma(I)$], wR_2 = 0.2203 (all data), Gof = 1.027, residual electron density: + 5.211, –9.385 e Å^{-3}.

Computational Details: Density functional calculations (DFT) were carried out on $[Re_6Q_8(OH)_6]^{4-}$ models using the ADF2002 code.[14] The local-exchange VWN correlation potential was used for the local density approximation (LDA),[17] and Becke's nonlocal corrections to the exchange energy[18] and Perdew's nonlocal corrections to the correlation energy were added.[19] The zeroth-order relativistic approximation (ZORA) method was used to account for the scalar relativistic effects.[20] The STO basic set without core potentials was used for all atoms (ZORA/TZ2P). The octahedral O_h symmetry was imposed on the full geometry optimization of the ground electronic states for $[Re_6Q_8(OH)_6]^{4-}$ models, a prototype of the analyzed clusters. Calculations of the electronic-binding energy have been performed for the reactions 6 Re + 8 Q + 6 O + 6 H + 4 e^- → $[Re_6Q_8(OH)_6]^{4-}$. The ionization potentials were computed as the energy differences between the $[Re_6Q_8L_6]^{3-}$ and $[Re_6Q_8L_6]^{4-}$, IP = $\Delta E_3 - \Delta E_4$. The atomic net charges for several $[Re_6Q_8(OH)_6]^{n-}$ complexes have been obtained using the Hirshfeld analysis.[21]

Further details of the crystal structure investigations may be obtained from the Fachinformationszentrum Karlsruhe, 76344 Eggenstein-Leopoldshafen, Germany, on quoting the depository CSD-number filenames 415278 (for **1**), 415279 (for **2**), and 415280 (for **4**).

Acknowledgments

This work was supported by the Russian Foundation for Basic Research (grants 05-03-08090 and 05-03-32123), Division of Chemistry and Materials Science of RAS (project No. 15 of Program 4.1), and the International Cooperation Research Program of the Ministry of Science & Technology of Korea. The authors are grateful to V. N. Ikorsky for magnetic measurements.

[1] a) A. Perrin, M. Sergent, *New J. Chem.* **1988**, *12*, 337–356; b) T. Saito, *J. Chem. Soc., Dalton Trans.* **1999**, 97–105; c) Y. V. Mironov, V. E. Fedorov, *J. Struct. Chem. (Engl. Trans.)* **1999**, *40*, 959–974; d) N. G. Naumov, A. V. Virovets, V. E. Fedorov, *J. Struct. Chem. (Engl. Trans.)* **2000**, *41*, 499–520; e) J.-C. P. Gabriel, K. Boubekeur, S. Uriel, P. Batail, *Chem. Rev.* **2001**, *101*, 2037–2066; f) H. D. Selby, B. K. Roland, Z. Zheng, *Acc. Chem. Res.* **2003**, *36*, 933–944.

[2] a) C. Fischer, N. Alonso-Vante, S. Fiechter, H. Tributsch, G. Reck, W. Schulz, *J. Alloys Comp.* **1992**, *178*, 305–314; b) N. L. Speziali, H. Berger, G. Leicht, R. Sanjines, G. Chapuis, F. Levy, *Mater. Res. Bull.* **1988**, *23*, 1597–1604; c) S. S. Yarovoi, Y. I. Mironov, Y. V. Mironov, A. V. Virovets, V. E. Fedorov, U.-H. Paek, S. C. Shin, M.-L. Seo, *Mater. Res. Bull.* **1997**, *32*, 1271–1277.

[3] F. Klaiber, W. Petter, F. Hulliger, *J. Solid State Chem.* **1983**, *46*, 112–120.

[4] Selection of research papers: a) J. R. Long, L. S. McCarty, R. H. Holm, *J. Am. Chem. Soc.* **1996**, *118*, 4603–4616; b) Z. Zheng, J. R. Long, R. H. Holm, *J. Am. Chem. Soc.* **1997**, *119*, 2163–2171; c) Z. Zheng, T. G. Gray, R. H. Holm, *Inorg. Chem.* **1999**, *38*, 4888–4895; d) Y. V. Mironov, J. A. Cody, E. Albrecht-Schmitt, J. A. Ibers, *J. Am. Chem. Soc.* **1997**, *119*, 493–498; e) Y. V. Mironow, M. A. Pell, J. A. Ibers, *Inorg. Chem.* **1996**, *35*, 2709–2710; f) Y. V. Mironov, M. A. Pell, J. A. Ibers, *Angew. Chem. Int. Ed. Engl.* **1996**, *35*, 2854–2856; g) Z.-N. Chen, T. Yoshimura, M. Abe, K. Tsuge, Y. Sasaki, S. Ishizaka, H.-B. Kim, N. Kitamura, *Chem. Eur. J.* **2001**, *7*, 4447–4455; h) A. Itasaka, M. Abe, T. Yoshimura, K. Tsuge, M. Suzuki, T. Imamura, Y. Sasaki, *Angew. Chem. Int. Ed.* **2002**, *41*, 463–466; i) B. K. Roland, C. Carter, Z. Zheng, *J. Am. Chem. Soc.* **2002**, *124*, 6234–6235.

[5] a) A. Slougui, Yu. V. Mironov, A. Perrin, V. E. Fedorov, *Croat. Chem. Acta* **1995**, *68*, 885–890; b) Yu. V. Mironov, A. V. Virovets, V. E. Fedorov, N. V. Podberezskaya, O. V. Shishkin, Yu. T. Struchkov, *Polyhedron* **1995**, *14*, 3171–3173; c) N. G. Naumov, A. V. Virovets, Y. I. Mironov, S. B. Artemkina, V. E. Fedorov, *Ukr. Khim. Zh.* **1999**, *65*, 21–27; d) N. G. Naumov, A. V. Virovets, N. V. Podberezskaya, V. E. Fedorov, *J. Struct. Chem. (Engl. Trans.)* **1997**, *38*, 857–863.

[6] S. S. Yarovoi, Y. V. Mironov, S. F. Solodovnikov, D. Y. Naumov, N. K. Moroz, S. G. Kozlova, A. Simon, V. E. Fedorov, *Chem. Commun.* **2005**, 719–721.

[7] Z. Zheng, H. D. Selby, B. K. Roland, *Acta Crystallogr., Sect. E* **2001**, *57*, i77–i79.

[8] S. S. Yarovoi, S. F. Solodovnikov, Y. V. Mironov, V. E. Fedorov, *J. Struct. Chem. (Engl. Trans.)* **2003**, *44*, 355–358.

[9] G. E. Pake, *J. Chem. Phys.* **1948**, *16*, 327.

[10] A. Abragam, *The Principles of Nuclear Magnetism*, Clarendon Press, Oxford, **1961**.

[11] N. G. Naumov, PhD thesis, Novosibirsk, **2004**.

[12] The emission spectra of the samples were recorded with a UV-Spectrofluorimeter equipped with an ORIEL 77200 monochromator and a Hamamatsu R928 PMT detector. A Xe lamp (ORIEL photomax, 75 W) was used as a light source. The excitation slit width was 1.56 mm and the emission slit width was 60 μm. Both compounds were also measured in aqueous solutions with concentrations in the region of 10^{-5}–10^{-3} mol L^{-1}.

[13] Selection of research papers: a) A. Deluzet, H. Duclusaud, P. Sautet, S. A. Borshch, *Inorg. Chem.* **2002**, *41*, 2537–2542; b) S. G. Kozlova, S. P. Gabuda, K. A. Brylev, Yu. V. Mironov, V. E. Fedorov, *J. Phys. Chem. A* **2004**, *108*, 10565–10567; c) S. A. Baudron, A. Deluzet, K. Boubekeur, P. Batail, *Chem. Commun.* **2002**, 2124–2125; d) R. Arratia-Perez, L. Hernandez-Acevedo, *J. Chem. Phys.* **1999**, *111*, 168–172; e) T. G. Gray, C. M. Rudzinski, E. E. Meyer, R. H. Holm, D. G. Nocera, *J. Am. Chem. Soc.* **2003**, *125*, 4755–4770.

[14] *Amsterdam Density Functional (ADF) program*, Release 2002.02, Vrije Universteit, Amsterdam, The Netherlands, **2002**.

[15] T. Yoshimura, S. Ishizaka, Y. Sasaki, H.-B. Kim, N. Kitamura, N. G. Naumov, M. N. Sokolov, V. E. Fedorov, *Chem. Lett.***1999**, *28*, 1121–1122.

[16] a) G. M. Sheldrick, *SHELXS-97, Program for Crystal Structure Solution*, Universität Göttingen; b) G. M. Sheldrick, *SHELXL-97, Program for Crystal Structure Refinement*, University of Göttingen, Germany.

[17] S. H. Vosko, L. Wilk, M. Nusair, *Can. J. Phys.* **1980**, *58*, 1200–1211.

[18] A. D. Becke, *Phys. Rev. A.* **1988**, *38*, 3098–3100.J. P. Perdew, *Phys. Rev. B.* **1986**, *33*, 8822–8824.E. van Lenthe, A. E. Ehlers, E. J. Baerends, *J. Chem. Phys.* **1999**, *110*, 8943–8951.

[21] F. L. Hirshfeld, *Theor. Chim. Acta* **1977**, *44*, 129–138.

Received: April 2, 2005
Published Online: August 31, 2005

 © 2005 Wiley-VCH Verlag GmbH & Co. KGaA, Weinheim

Synthesis, Crystal Structures and Photophysical Properties of Novel Tetranuclear Cadmium(II) Schiff-Base Complexes

Wing-Kit Lo,[a] Wai-Kwok Wong,*[a,b] Wai-Yeung Wong,[a,b] and Jianping Guo[a]

Keywords: Cadmium / Crystal structures / Phosphorescence / Schiff bases

The synthesis and structural characterisation of some new tetranuclear cadmium(II) Schiff-base complexes were described. Reaction of the hexadentate Schiff-base ligands (H_2L) with an excess of cadmium(II) acetate, $Cd(OAc)_2$, furnished novel tetracadmium complexes of the general formula $[Cd_4(L)_2(OAc)_4]$, which exhibit an interesting three-dimensional cage-like structure of four ligand-supported cadmium atoms. All of the complexes were fully characterised by spectroscopic (FTIR, NMR and FAB MS) methods and their molecular structures were confirmed by single-crystal X-ray analysis. The X-ray crystal structures of these tetranuclear Schiff-base complexes represent the first structurally characterised examples of this kind for the cadmium triad. These new complexes were found to display rich photophysical properties and they all exhibited low-temperature phosphorescence in the frozen state.
(© Wiley-VCH Verlag GmbH & Co. KGaA, 69451 Weinheim, Germany, 2005)

Introduction

Beside supramolecular[1] and bioinorganic studies,[2] cadmium complexes also play an important role in luminescence research.[3] Numerous luminescent polynuclear transition metal complexes of d^{10} transition metals such as Zn^{II}, Cd^{II}, Cu^{I}, Ag^{I}, Au^{I}, and so forth, have been reported.[4] The use of Cd^{II} complexes as luminescence materials has an added advantage because the coordination environment of Cd^{II} is different from other d^{10} transition metals. The coordination number of Zn^{II}, Ag^{I}, Au^{I} and Cu^{I} is usually 4–5 and rarely greater than 6. On the other hand, the coordination number of Cd^{II} lies between 6 and 8, which allows the Cd^{II} complexes to exhibit a special structure and the potential for different structure-related properties, as compared to the other d^{10} metal complexes. Harvesting of the triplet state emission in molecular and polymeric materials has become an important topic nowadays, and metal complexes play an important role in this area. Most of the research is focused on the expensive d-metals (Pt, Ir, Au, etc.) [4,5] and the lanthanide metal complexes.[6] Very recently, phosphorescence has been observed in some Hg^{II} systems.[5d,5e,5f] However, there are relatively few reports on the phosphorescence emission of the analogous cadmium complexes. Schiff-base zinc(II) complexes have been shown to be effective emitters;[7] however, reports on the luminescent properties of Schiff-base cadmium(II) complexes are very rare. In fact, the use of Schiff-base cadmium complexes as potential luminescent materials has great research merits in that they can be prepared on a large scale and are more cost-effective.

Bermejo and co-workers reported the preparation of three-dimensional cage-like Schiff-base Zn complexes by using an electrochemical reaction with hexadentate ligands.[8] In this report, a series of tetranuclear Schiff-base cadmium complexes of the general formula $[Cd_4(L)_2(OAc)_4]$ were prepared by the reaction of the hexadentate Schiff-base ligands H_2L with excess $Cd(OAc)_2$. Under the same reaction conditions, $Zn(OAc)_2$ gave only the mononuclear Schiff-base complexes [ZnL].[9] A possible explanation here is that the coordination number of Zn^{II} ranges normally from 4 to 5, and the inner N_2O_2 cavity of the Schiff-base ligand already provides a tetradentate environment, meaning further extension of the structure from the metal centre is less favourable. On the other hand, the coordination number of Cd^{II} is usually 6–8, and the inner N_2O_2 cavity is only 4, which enables an extension of its structure to the neighbouring complex, forming an interesting tetranuclear cage-like structure.

Results and Discussion

Synthesis and Characterisation

It has been reported that the electrochemical reaction of the cadmium anode with *N*,*N*′-bis(3-hydroxysalicylidene)-ethylene-1,2-diamine (H_4L', L′ = tetraanionic ligand), a potentially hexadentate Schiff base, gave polymeric dinuclear cadmium(II) complexes of the general formula $[Cd_2(L')(H_2O)_2]_n$, whose solid-state structure has not been

[a] Department of Chemistry, Hong Kong Baptist University, Kowloon Tong, Hong Kong, P. R. China
Fax: +852-3411-5862
E-mail: wkwong@hkbu.edu.hk
[b] Centre for Advanced Luminescence Materials, Hong Kong Baptist University, Kowloon Tong, Hong Kong, P. R. China

determined.[8b] However, when the corresponding 3-methoxy derivative *N*,*N*′-bis(3-methoxysalicylidene)ethylene-1,2-diamine H_2L (L = dianionic ligand), also a potentially hexadentate Schiff base, was treated with a threefold excess of cadmium(II) acetate in refluxing absolute ethanol overnight, the resultant clear solution, upon workup, gave yellow, air-stable crystalline tetranuclear Schiff-base cadmium(II) complexes of the general formula $[Cd_4(L)_2(OAc)_4]$ [L = L^1 (**1**), L^2 (**2**), L^3 (**3**)] in around 50% yield (Scheme 1). All attempts to isolate other products from the solution mixture have met with little success so far. Compounds **1**–**3** gave satisfactory elemental analyses and collated spectroscopic data (IR, ^{1}H NMR and FABMS) of these complexes are in good agreement with their formulation. Full details are given in the Exp. Sect. In their FAB (positive mode) mass spectrum, all three compounds exhibit a mass peak corresponding to $[M - OAc]^+$ at *m*/*z* = 1277, 1589 and 1637 for **1**, **2** and **3**, respectively, for ^{79}Br and ^{112}Cd. The complexes are soluble in polar organic solvents such as CH_2Cl_2 and $CHCl_3$. All of them exhibit a broad peak in their ^{1}H NMR spectrum at $\delta \approx 8.4$ for their imino protons (–C*H*=N–). Their solid-state IR spectrum also exhibit strong absorption bands corresponding to $\nu_{C=N}$ and $\nu_{C=O}$ at about 1635 and 1460 cm^{-1}, respectively, which are similar to those reported for the 3-hydroxy analogue.[8b] Conductivity measurements showed that complexes **1**–**3** behave as electrolytes in methanol and non-electrolytes in chloroform. This indicates that these complexes dissociate one or more of their coordinated acetate ligands to form cations in methanol and remain neutral and undissociated in chloroform.

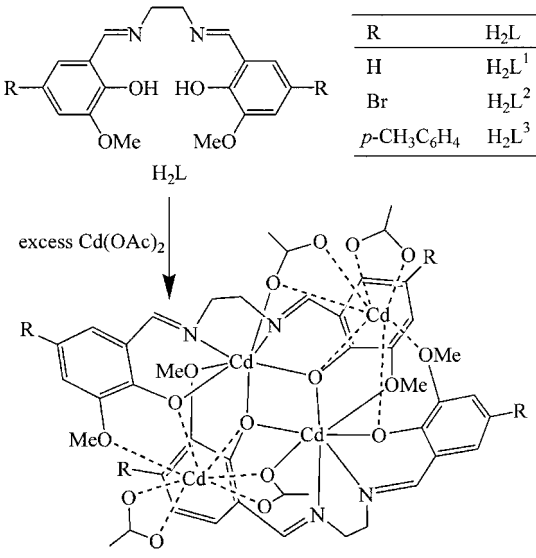

R	H_2L	Complex
H	H_2L^1	**1**
Br	H_2L^2	**2**
p-$CH_3C_6H_4$	H_2L^3	**3**

Scheme 1. Synthesis of compounds **1**–**3**.

The molecular structures of **1** and **3** were ascertained by X-ray crystallography and were found to be structurally very similar. Perspective drawings of **1** and **3** are shown in Figures 1 and 2, respectively, and selected bond lengths and bond angles are given in Tables 1 and 2. Structural analysis revealed that all the Cd atoms of such tetranuclear complex are seven-coordinate and are linked together by the hexadentate Schiff-base ligands. The Cd(1) and Cd(2) atoms form a distorted square base with the two phenolic oxygen atoms [O(2) and O(6)] and each of the latter atoms behaves as a μ_3-O ligand coordinating with the other two Cd atoms [Cd(3) and Cd(4)]. The Cd(1) [or Cd(2)] atom is further linked to the Cd(4) [or Cd(3)] atom by a bridging tridentate acetate ligand. Each of the Cd(3) and Cd(4) atoms is further coordinated to a bidentate acetate ligand to give an overall neutral cage-like tetranuclear structure. The distance between each Cd atom falls in the range of 3.555–5.907 Å, which precludes any significant metal–metal interaction. Presumably, aggregation of the four cadmium atoms in the structures of **1** and **3** is triggered by the use of large cadmium atoms that tend to favour high coordination numbers and the multidentate nature of the Schiff-base ligands in our study. The Cd–N bond lengths lie within 2.324(3)–2.356(3) Å for **1** and 2.294(15)–2.354(11) Å for **3**, which are similar to those reported previously.[10] For **1** and **3**, the Cd–O bond lengths of the two complexes span a wide range of 2.248(3)–2.589(3) Å and 2.229(9)–2.552(9) Å, respectively, and this is probably a manifestation of the difference in the nature of the O-donor group in these complexes.

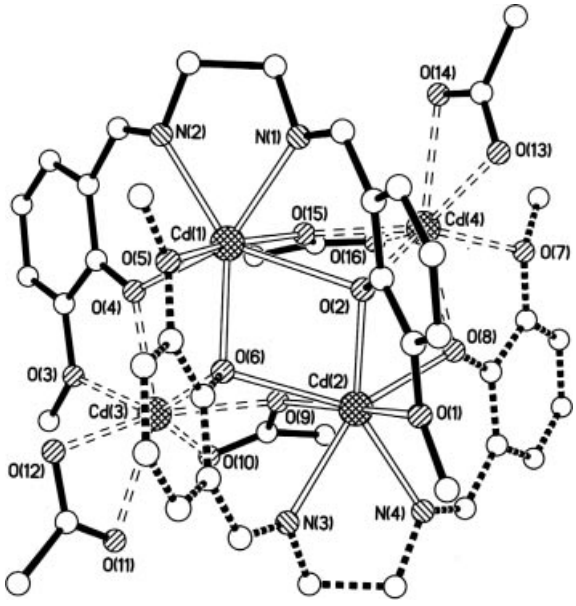

Figure 1. Molecular structure of **1**. Only atoms within the metal coordination core are labelled.

Photophysical Properties

The photophysical properties of **1**–**3** in $CHCl_3$ have been studied and the relevant data are summarised in Table 3. The absorption bands between 240 and 380 nm can be assigned to $\pi \rightarrow \pi^*$ transitions of the Schiff-base ligands. The room-temperature emission of compounds **1**–**3**, with lifetimes (τ) ranging from 0.8 to 1.2 ns and quantum yields (Φ_{em}) of $3.8–5.9 \times 10^{-3}$, can be assigned to the intraligand emission. The absorption, emission and excitation spectra of **1**–**3** are shown in Figures 3, 4 and 5. The room-tempera-

 © 2005 Wiley-VCH Verlag GmbH & Co. KGaA, Weinheim

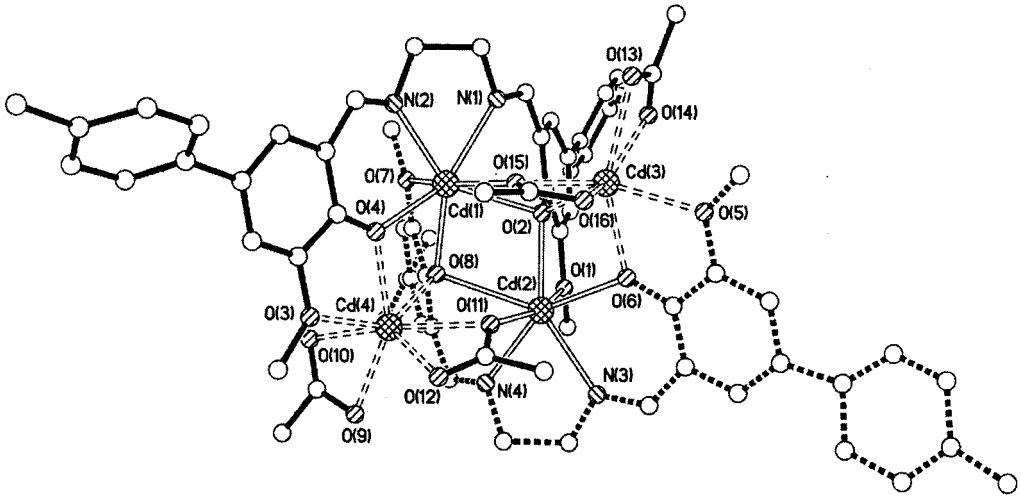

Figure 2. Molecular structure of **3**. Only atoms within the metal coordination core are labelled.

Table 1. Selected bond lengths [Å] and angles [°] for **1**.

Cd(1)–N(1)	2.356(3)	Cd(1)–N(2)	2.324(3)
Cd(2)–N(3)	2.354(3)	Cd(2)–N(4)	2.349(3)
Cd(1)–O(2)	2.589(3)	Cd(2)–O(1)	2.481(3)
Cd(1)–O(4)	2.296(3)	Cd(2)–O(2)	2.266(3)
Cd(1)–O(5)	2.487(3)	Cd(2)–O(6)	2.545(3)
Cd(1)–O(6)	2.292(3)	Cd(2)–O(8)	2.306(3)
Cd(1)–O(15)	2.279(3)	Cd(2)–O(9)	2.301(3)
Cd(3)–O(3)	2.424(3)	Cd(4)–O(2)	2.407(3)
Cd(3)–O(4)	2.248(3)	Cd(4)–O(7)	2.451(3)
Cd(3)–O(6)	2.400(3)	Cd(4)–O(8)	2.282(3)
Cd(3)–O(9)	2.364(3)	Cd(4)–O(13)	2.258(3)
Cd(3)–O(10)	2.450(3)	Cd(4)–O(14)	2.440(4)
Cd(3)–O(11)	2.376(4)	Cd(4)–O(15)	2.262(3)
Cd(3)–O(12)	2.343(4)	Cd(4)–O(16)	2.514(3)
N(1)–Cd(1)–N(2)	73.49(12)	N(1)–Cd(1)–O(2)	69.61(10)
N(2)–Cd(1)–O(4)	78.54(11)	N(3)–Cd(2)–N(4)	72.58(13)
N(3)–Cd(2)–O(6)	70.76(10)	N(4)–Cd(2)–O(8)	78.07(11)

Table 2. Selected bond distances [Å] and angles [°] for **3**.

Cd(1)–N(1)	2.354(11)	Cd(1)–N(2)	2.312(10)
Cd(2)–N(3)	2.332(15)	Cd(2)–N(4)	2.294(15)
Cd(1)–O(2)	2.552(9)	Cd(2)–O(1)	2.424(10)
Cd(1)–O(4)	2.289(10)	Cd(2)–O(2)	2.276(9)
Cd(1)–O(7)	2.472(10)	Cd(2)–O(6)	2.300(11)
Cd(1)–O(8)	2.298(10)	Cd(2)–O(8)	2.525(10)
Cd(1)–O(15)	2.302(14)	Cd(2)–O(11)	2.246(13)
Cd(3)–O(2)	2.428(11)	Cd(4)–O(3)	2.470(10)
Cd(3)–O(5)	2.424(11)	Cd(4)–O(4)	2.229(9)
Cd(3)–O(6)	2.243(10)	Cd(4)–O(8)	2.320(10)
Cd(3)–O(13)	2.502(12)	Cd(4)–O(9)	2.254(12)
Cd(3)–O(14)	2.256(11)	Cd(4)–O(10)	2.383(17)
Cd(3)–O(15)	2.244(11)	Cd(4)–O(11)	2.338(14)
Cd(3)–O(16)	2.502(14)	Cd(4)–O(12)	2.473(18)
N(1)–Cd(1)–N(2)	73.5(4)	N(1)–Cd(1)–O(2)	70.9(4)
N(2)–Cd(1)–O(4)	78.3(4)	N(3)–Cd(2)–N(4)	73.0(5)
N(3)–Cd(2)–O(6)	77.8(5)	N(4)–Cd(2)–O(8)	70.8(4)

ture excitation spectrum of **3** (monitored at 472 nm) is identical to its 77 K excitation spectrum (monitored at 508 nm), indicating that both the room-temperature and 77 K emission features have the same origin. The absorption, excitation and emission bands are slightly red-shifted upon attachment of a bromide or a *p*-tolyl substituent. Figure 6 depicts the 77 K emission spectra of **1**–**3** in a glassy state. Time-resolved spectra and lifetime measurements showed that both ligand-centred singlet (^{1}LC) and triplet (^{3}LC) emissions coexist at 77 K, with the shoulder being the ^{1}LC fluorescence (τ = 3.4–6.0 ns) and the main peak in the lower energy regime being the ^{3}LC phosphorescence (τ = 10.9–44.2 ms). The ^{3}LC emission was not observed at room temperature even in an oxygen-free solvent system. At room temperature, thermal vibrations, which were minimised at 77 K, can efficiently quench the ^{3}LC transition. Comparing the relative intensity of the ^{1}LC with ^{3}LC emission at 77 K, we observe that the intersystem crossing (ISC) efficiency follows the order **3** > **2** > **1**. On the other hand, the ^{1}LC emission quantum efficiency is in the order **1** > **2** > **3**, which shows that an increase in conjugation or the presence of a heavy bromine substituent can enhance the ISC efficiency, and thus effectively suppress the ^{1}LC emission.

Concluding Remarks

To the best of our knowledge, complexes **1**–**3** constitute the first examples of tetranuclear Schiff-base cadmium complexes of this type and these compounds can display strong triplet-state emission induced by the heavy-atom effect of cadmium. Structural characterisations of **1** and **3** are particularly interesting and we were able to build up polymetallic Schiff-base complexes assembled through the high-coordinate large cadmium atoms and the multidentate ligands. Work is in progress to enhance such triplet emission by structural modifications of the Schiff-base ligands. Comparative analyses of these Schiff-base cadmium complexes with their lower zinc(II) congeners are worthy of serious investigations and are expected to give equally interesting results in the area of luminescent metallated materials.

 © 2005 Wiley-VCH Verlag GmbH & Co. KGaA, Weinheim

Table 3. Photophysical properties of **1**, **2** and **3** in $CHCl_3$.

	Absorption at 298 K λ_{max}/nm [log(ε/dm^3 mol^{-1} cm^{-1})]	Excitation at 298 K λ_{max}/nm	Emission at 298 K λ_{max}/nm (τ, $\Phi_{em} \times 10^{-3}$)	Emission at 77 K λ_{max}/nm (τ)
1	360 (4.10), 277 (4.46), 240 (4.71)	359, 281	455 (1.2 ns, 5.9[a])	484 (29.8 ms), 439 sh[b] (6.0 ns)
2	374 (4.16), 275 sh (4.50), 242 (4.94)	372, 280	472 (1.1 ns, 4.7[a])	507 (10.9 ms), 448 sh[b] (3.4 ns)
3	380 (4.14), 275 (5.06)	374, 288	472 (0.8 ns, 3.8[a])	508 (44.2 ms), 458 sh[b] (3.8 ns)

[a] Quantum yield was measured relative to quinine sulfate in 1.0 N H_2SO_4 (Φ_{em} = 0.55). [b] sh = shoulder.

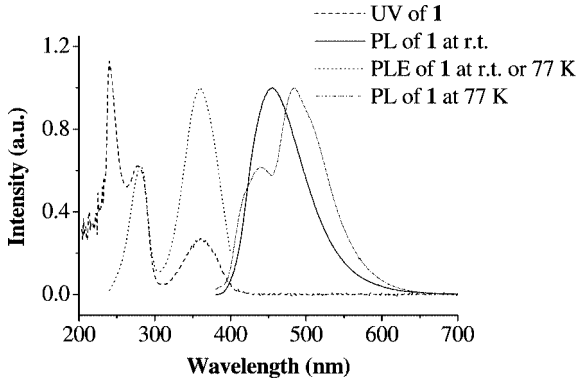

Figure 3. Absorption, photoluminescence excitation (PLE) and photoluminescence (PL) spectra of **1**.

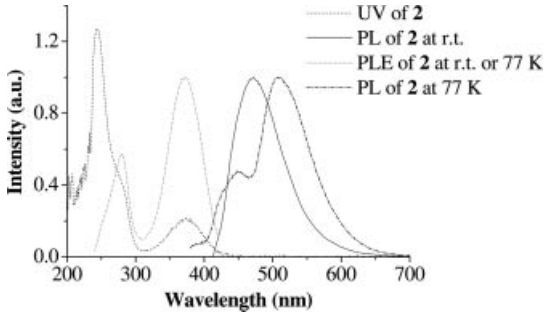

Figure 4. Absorption, photoluminescence excitation (PLE) and photoluminescence (PL) spectra of **2**.

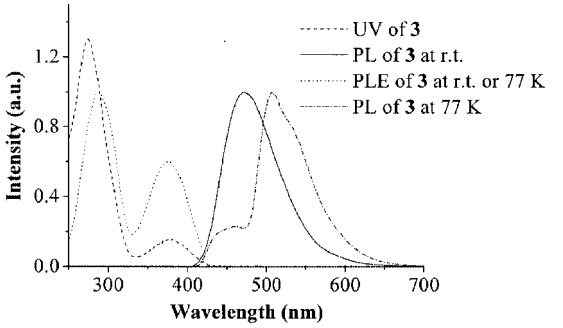

Figure 5. Absorption, photoluminescence excitation (PLE) and photoluminescence (PL) spectra of **3**.

Experimental Section

General Procedures: Solvents and starting materials were purchased commercially and used without further purification unless otherwise stated. The hexadentate Schiff-base ligands H_2L^1, H_2L^2 and H_2L^3 were prepared according to the literature method.[9] Elemental analyses (C, H, N) were performed by the Shanghai Institute of Organic Chemistry, Chinese Academy of Sciences, China. Electronic absorption spectra in the UV/Vis region were recorded with a Hewlett Packard 8453 UV/Vis spectrophotometer, steady-state visible fluorescence and photoluminescence excitation spectra with a Photon Technology International (PTI) Alphascan spectrofluorimeter, and visible decay spectra with a pico-N_2 laser system (PTI Time Master) with λ_{ex} = 337 nm. Quantum yields of visible emissions were computed according to a literature method[11] using quinine sulfate in 0.1 N H_2SO_4 as the reference standard (Φ = 0.55 in air-equilibrated water).[12] Infrared spectra (KBr pellets) were recorded with a Nicolet Nagna-IR 550 spectrometer and NMR spectra with a JEOL EX270 spectrometer. Chemical shifts of ^{1}H and ^{13}C NMR spectra were referenced to internal deuteriated solvents and then recalculated to $SiMe_4$ (δ = 0.00 ppm). Low-resolution mass spectra (LRMS) were obtained with a Finnigan MAT SSQ-710 spectrometer in the positive FAB mode. Conductivity measurements were carried out with a DDS-11 conductivity bridge for 10^{-4} mol dm^{-1} solutions either in CH_3OH or CH_3CN. ***Caution:*** Cadmium complexes are toxic, and all experiments involving these reagents should be carried out in a well-vented hood.

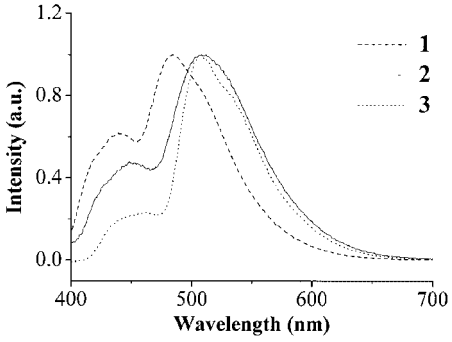

Figure 6. Photoluminescence spectrum of **1**, **2** and **3** at 77 K.

Preparation of $[Cd_4(L^1)_2(OAc)_4]$ (1): Excess $Cd(OAc)_2 \cdot 2H_2O$ (2.80 g, 10.5 mmol) was added to a suspension of H_2L^1 (1.062 g, 3.23 mmol) in absolute ethanol. The resultant reaction mixture was refluxed overnight to give a clear yellow solution. The solution was filtered and the solvents were evaporated to dryness to give a yellow solid. The solid was washed with deionised water, redissolved in a $CHCl_3/CH_3OH$ mixture and the resulting solution was filtered. The filtrate was allowed to concentrate slowly at room temperature to give yellow crystals of $\mathbf{1} \cdot CH_3OH$ in about a week. Yield: 2.214 g (51%). M.p. > 300 °C. ^{1}H NMR ($CDCl_3$): δ = 1.78 (br. s, 12 H, CH_3COO), 3.73 (m, 4 H, NCH_2), 3.80–3.98 (m, 12 H, OCH_3), 4.35 (m, 4 H, NCH_2), 6.37–6.51 (m, 4 H, Ph-*H*), 6.77–6.80 (m, 8 H, Ph-*H*), 8.41 (m, 4 H, C*H*=N) ppm. IR (KBr): $\tilde{\nu}$ = 3423 s, 1633 s, 1558 s, 1450 s, 1415 s, 1288 m, 1215 s, 1099 m, 970 m, 743 m cm^{-1}. FABMS (positive mode): *m*/*z* = 1277 ([M – OAc]$^+$ for ^{112}Cd). $C_{44}H_{48}Cd_4N_4O_{16} \cdot CH_3OH$ (1370.56): calcd. C 39.44, H 3.82, N 4.09; found C 39.13, H 3.78, N 4.05.

Preparation of $[Cd_4(L^2)_2(OAc)_4]$ (2): The synthesis of **2** followed the same procedures as for **1** except that $Cd(OAc)_2 \cdot 2H_2O$ (0.471 g, 1.77 mmol) and H_2L^2 (0.312 g, 0.58 mmol) were used instead. Yel-

 © 2005 Wiley-VCH Verlag GmbH & Co. KGaA, Weinheim

low crystals of **2**·CH_3OH were obtained. Yield: 0.481 g (50%). M.p. > 300 °C. ^{1}H NMR ($CDCl_3$): δ = 1.75 (br. s, 12 H, CH_3COO), 3.70 (m, 4 H, NCH_2), 3.82–3.96 (m, 12 H, OCH_3), 4.28 (m, 4 H, NCH_2), 6.88–6.97 (m, 8 H, Ph-*H*), 8.32 (m, 4 H, C*H*=N) ppm. IR (KBr): $\tilde{\nu}$ = 3423 m, 1635 s, 1542 m, 1456 s, 1401 m, 1286 m, 1233 s, 1211 s, 1094 m, 977 m, 773 m, 688 m cm^{-1}. FABMS (positive mode): *m*/*z* = 1589 ([M – OAc]$^+$ for ^{79}Br and ^{112}Cd). $C_{44}H_{44}Br_4Cd_4N_4O_{16}$·$CH_3OH$ (1686.15): calcd. C 32.05, H 2.87, N 3.32; found 32.53, H 2.85, N 3.45.

Preparation of [$Cd_4(L^3)_2(OAc)_4$] (3): Similarly, a mixture of $Cd(OAc)_2$·$2H_2O$ (0.434 g, 1.78 mmol) and H_2L^3 (0.270 g, 0.53 mmol) was used here to give, after workup, yellow crystals of **3**·$3H_2O$ in 46% yield (0.417 g). M.p. > 300 °C. ^{1}H NMR ($CDCl_3$): δ = 1.81 (br. s, 12 H, CH_3COO), 2.37 (br. s, 12 H, Ph-CH_3), 3.72 (m, 4 H, NCH_2), 3.92–4.06 (m, 12 H, OCH_3), 4.40 (m, 4 H, NCH_2), 6.37–6.51 (m, 4 H, Ph-*H*), 7.03–7.40 (m, 24 H, Ph-*H*), 8.55 (m, 4 H, C*H*=N) ppm. IR (KBr): $\tilde{\nu}$ = 3428 m, 1634 s, 1558 s, 1457 s, 1405 s, 1269 m, 1202 m, 985 m, 815 m, 772 m cm^{-1}. FABMS (positive mode): *m*/*z* = 1637 ([M – OAc]$^+$ for ^{112}Cd). $C_{72}H_{72}Cd_4N_4O_{16}$·$3H_2O$ (1753.07): calcd. C 49.33, H 4.48, N 3.20; found C 49.54, H 4.49, N 3.11.

X-ray Crystallography: Pertinent crystallographic data and other experimental details are summarised in Table 4. Crystals of **1** and **3** suitable for X-ray diffraction studies were grown by slow concentration of a solution of the respective compound in CH_3OH. Intensity data were collected at 293 K with a Bruker Axs SMART 1000 CCD area-detector diffractometer using graphite-monochromated Mo-K_α radiation (λ = 0.71073 Å). The collected frames were processed with the software SAINT[13] and an absorption correction was applied (SADABS)[14] to the collected reflections. The structures of all compounds were solved by direct methods (SHELXTL)[15] and refined against F^2 by full-matrix least-squares analysis. All non-hydrogen atoms were refined anisotropically for these structures. Hydrogen atoms were generated in their idealised positions and allowed to ride on their respective parent carbon atoms. CCDC-241608 (**1**) and -241609 (**3**) contain the supplementary crystallographic data for this paper. These data can be obtained free of charge from The Cambridge Crystallographic Data Centre via www.ccdc.cam.ac.uk/data_request/cif.

Table 4. Crystallographic data for compounds **1** and **3**.

	1·CH_3OH	**3**·$0.5CH_3OH$
Empirical formula	$C_{45}H_{52}Cd_4N_4O_{17}$	$C_{72.5}H_{74}Cd_4N_4O_{16.5}$
Formula mass	1370.51	1714.96
Crystal system	monoclinic	orthorhombic
Space group	$P2_1/n$	$P2_12_12_1$
a [Å]	11.2367(4)	15.9567(17)
b [Å]	16.1250(6)	19.508(2)
c [Å]	27.7456(10)	28.194(3)
β [°]	94.5910(10)	90
V [Å^3]	5011.1(3)	8776.3(16)
Z	4	4
$D_{calcd.}$ [g cm^{-3}]	1.817	1.298
μ(Mo-K_α) [mm^{-1}]	1.748	1.012
F(000)	2712	3444
Reflections collected	24864	44301
Independent reflections	8799	15395
R_{int}	0.0293	0.1611
Observed reflections [$I > 2\sigma(I)$]	7217	6473
Goodness-of-fit on F^2	1.070	0.935
R_1, wR_2 [$I > 2\sigma(I)$]	0.0288, 0.0782	0.0719, 0.1450
R_1, wR_2 [all data]	0.0403, 0.0883	0.2089, 0.1959

Acknowledgments

We would like to thank the Hong Kong Baptist University (FRG/03-04/II-52) and Hong Kong Research Grants Council (HKBU 2038/02P) for financial support.

[1] J. Luo, M. Hong, R. Wang, T. Cao, Q. Shi, J. Weng, *Eur. J. Inorg. Chem.* **2003**, 1778–1784.
[2] J. M. Pérez, V. Cerrillo, A. I. Matesanz, J. M. Millán, P. Navarro, C. Alonso, P. Souza, *ChemBioChem* **2001**, *2*, 119–123.
[3] a) Y. A. Shihadeh, A. Benito, J. M. Lloris, R. Martínez-Máñez, T. Pardo, J. Soto, M. D. Marcos, *J. Chem. Soc., Dalton Trans.* **2000**, 1199–1205; b) H.-K. Fun, S. S. R. Raj, R.-G. Xiong, J.-L. Zuo, Z. Yu, X.-Z. You, *J. Chem. Soc., Dalton Trans.* **1999**, 1915–1916.
[4] a) V. W.-W. Yam, K. K.-W. Lo, *Chem. Soc. Rev.* **1999**, *28*, 323–334 and references cited therein; b) S. Hu, M.-L. Tong, *Dalton Trans.* **2005**, 1165–1167.
[5] a) J. S. Wilson, A. S. Dhoot, A. J. A. B. Seeley, M. S. Khan, A. Köhler, R. H. Friend, *Nature* **2001**, *413*, 828–831; b) M. K. Nazeeruddin, R. Humphry-Baker, D. Berner, S. Rivier, L. Zuppiroli, M. Graetzel, *J. Am. Chem. Soc.* **2003**, *125*, 8790–8797; c) M. A. Baldo, M. E. Thompson, S. R. Forrest, *Pure Appl. Chem.* **1999**, *71*, 2095–2106 and references cited therein; d) W.-Y. Wong, L. Liu, J.-X. Shi, *Angew. Chem. Int. Ed.* **2003**, *42*, 4064–4068; e) W.-Y. Wong, L. Liu, S.-Y. Poon, A. W.-M. Lee, K.-W. Cheah, J.-X. Shi, *Macromolecules* **2004**, *37*, 4496–4504; f) W.-Y. Wong, *J. Inorg. Organomet. Polym. Mater.* **2005**, *15*, 197–219.
[6] J. Kido, Y. Okamoto, *Chem. Rev.* **2002**, *102*, 2357–2368.
[7] a) Y. Ma, H.-Y. Chao, Y. Wu, S. T. Lee, W.-Y. Yu, C.-M. Che, *Chem. Commun.* **1998**, 2491–2492; b) S. Mizukami, H. Houjou, Y. Nagawa, M. Kanesato, *Chem. Commun.* **2003**, 1148–1149.
[8] a) J. Sanmartín, M. R. Bermejo, A. M. García-Deibe, A. L. Llamas-Saiz, *Chem. Commun.* **2000**, 795–796; b) J. Sanmartín, M. R. Bermejo, A. M. García-Deibe, I. M. Rivas, A. R. Fernández, *J. Chem. Soc., Dalton Trans.* **2000**, 4174–4181.
[9] W.-K. Lo, W.-K. Wong, J.-P. Guo, W.-Y. Wong, K.-F. Li, K.-W. Cheah, *Inorg. Chim. Acta* **2004**, *357*, 4510–4521.
[10] a) H.-K. Fun, S. S. R. Raj, R.-G. Xiong, J.-L. Zuo, Z. Yu, X.-Z. You, *J. Chem. Soc., Dalton Trans.* **1999**, 1915–1916; b) A. Jäntti, M. Wagner, R. Suontamo, E. Kolehmainen, K. Rissanen, *Eur. J. Inorg. Chem.* **1998**, 1555–1562.
[11] C. A. Parker, W. T. Rees, *Analyst (London)* **1960**, *85*, 587–600.
[12] S. R. Meech, D. C. Phillips, *J. Photochem.* **1983**, *23*, 193–217.
[13] *SAINT, Reference manual,* Siemens Energy and Automation, Madsion, WI, **1994**–**1996**.
[14] G. M. Sheldrick, *SADABS, Empirical Absorption Correction Program*, University of Göttingen, Germany, **1997**.
[15] G. M. Sheldrick, *SHELXTL*™, Reference manual, version 5.1, Siemens, Madison, WI, **1997**.

Received: April 25, 2005
Published Online: August 29, 2005

Synthesis, Structure, and Properties of Zirconium and Hafnium Complexes Containing η^2-Pyrazolato Ligands

Elena Sebe,[a] Ilia A. Guzei,[a,c] Mary Jane Heeg,[a] Louise M. Liable-Sands,[b] Arnold L. Rheingold,[b,d] and Charles H. Winter*[a]

Keywords: Group-4 transition metals / Zirconium / Hafnium / Pyrazolato ligands / N ligands / Intramolecular hydrogen bond

Treatment of tetrakis(dimethylamido)zirconium with four equiv. of 3,5-dimethylpyrazole, 3,5-di-*tert*-butylpyrazole, or 3,5-diphenylpyrazole in refluxing toluene afforded tetrakis(η^2-3,5-dimethylpyrazolato)zirconium (86%), tetrakis(η^2-3,5-di-*tert*-butylpyrazolato)zirconium (88%), and tetrakis(η^2-3,5-diphenylpyrazolato)zirconium (85%), respectively, as colorless crystalline solids. The analogous hafnium complexes were prepared through treatment of hafnium tetrachloride with four equiv. of the potassium salts of 3,5-dimethylpyrazolate, 3,5-di-*tert*-butylpyrazolate, or 3,5-diphenylpyrazolate in tetrahydrofuran to afford tetrakis(η^2-3,5-dimethylpyrazolato)hafnium (75%), tetrakis(η^2-3,5-di-*tert*-butylpyrazolato)hafnium (58%), and tetrakis(η^2-3,5-diphenylpyrazolato)hafnium·toluene (38%), respectively, as colorless crystalline solids. X-ray crystal structures of representative members of these complexes revealed monomeric species containing four η^2-pyrazolato ligands and approximate dodecahedral geometry about the metal centers. Treatment of tetrakis(η^2-3,5-dimethylpyrazolato)hafnium with 3,5-dimethylpyrazole in a 1:1 molar ratio afforded tris(η^2-3,5-dimethylpyrazolato)(η^1-3,5-dimethylpyrazolato)(η^1-3,5-dimethylpyrazole)hafnium as colorless crystals (84%). Tris(η^2-3,5-dimethylpyrazolato)(η^1-3,5-dimethylpyrazolato)(η^1-3,5-dimethylpyrazole)hafnium contains three η^2-3,5-dimethylpyrazolato, one η^1-3,5-dimethylpyrazolato, and one η^1-3,5-dimethylpyrazole ligands. The η^1-3,5-dimethylpyrazolato and η^1-3,5-dimethylpyrazole ligands are connected through a N–H···N hydrogen bond. Tetrakis(η^2-3,5-dimethylpyrazolato) hafnium did not form an adduct with pyridine or tetrahydrofuran, suggesting that the formation of a hydrogen bond is important to the stability of adducts. Attempted sublimation of all of the new pyrazolato complexes led to some decomposition, as evidenced by the formation of the free pyrazoles in the sublimates and significant amounts of nonvolatile residues. This work greatly expands the number of zirconium and hafnium complexes that contain η^2-pyrazolato ligands.

(© Wiley-VCH Verlag GmbH & Co. KGaA, 69451 Weinheim, Germany, 2005)

Thin films of binary zirconium and hafnium phases are of significant interest, in view of their useful properties and important applications. Hafnium oxide and hafnium silicate have much higher dielectric constants compared to silicon dioxide, and are among the best candidates to replace silicon dioxide as gate dielectric materials in future microelectronics devices.[1] Analogous zirconium phases are also of interest for similar applications.[1] Zirconium nitride (ZrN, Zr_3N_4) and hafnium nitride (HfN, Hf_3N_4) have potential uses that include hard coatings[2] and barrier layers in microelectronics devices.[3] To allow film growth by chemical vapor deposition and related techniques, it is necessary to have volatile complexes that react with additional reagents to afford the desired phases. Since zirconium and hafnium halides have low vapor pressures, there has been considerable investigation of metal–organic and inorganic hafnium complexes with useful vapor pressures. Precursors that have been investigated for the deposition of zirconium and hafnium oxide and related oxide materials contain various ligands that include alkoxide,[4] nitrate,[5] dialkylamido,[6] and others.[7] The growth of zirconium and hafnium nitride films by CVD methods has been much less explored, and has largely employed dialkylamido–based precursors.[8]

Our group and others have been exploring the coordination chemistry of pyrazolato ligands with metals across the periodic table.[9,10] In 1997, we reported the synthesis, structure, and molecular orbital calculations of titanium(IV) complexes that contain terminal η^2-pyrazolato ligands.[10d] In particular, the molecular orbital calculations predicted that filled in-plane nitrogen-based orbitals interact with empty d-orbitals on the titanium(IV) ion. Based upon this

[a] Department of Chemistry, Wayne State University, Detroit, Michigan 48202, USA
Fax: +1-313-577-8289
Tel: +1-313-577-5224
E-mail: chw@chem.wayne.edu
[b] Department of Chemistry, University of Delaware, Newark, Delaware 19716, USA
[c] Current Address: Department of Chemistry, University of Wisconsin, Madison, Wisconsin 53706, USA
[d] Current Address: Department of Chemistry, University of California, San Diego, California 93992, USA

bonding model, η^2-pyrazolato ligand coordination was predicted to be general in a wide variety of metal complexes. Subsequently, we and others have demonstrated η^2-pyrazolato ligand coordination in many transition metal, main group, and lanthanide complexes.[9,10]

As part of our goals related to further exploration of η^2-pyrazolato ligand coordination among the transition metals and the design of new volatile film growth precursors, we set out to explore zirconium and hafnium pyrazolato complexes. Herein we report the synthesis, structure, and properties of a series of monomeric zirconium(IV) and hafnium(IV) complexes that contain η^2-pyrazolato ligands. The thermal stability and volatility of these complexes are described. In addition, tetrakis(η^2-3,5-dimethylpyrazolato) hafnium forms a novel adduct with 3,5-dimethylpyrazole. There have been few reports of zirconium and hafnium pyrazolato complexes.[10c,11,12] Meyer and co-workers reported a homoleptic zirconium complex with four bulky η^2-pyrazolato ligands.[11] We have reported the synthesis and structure of several zirconium and hafnium complexes that contain pyrazolato ligands,[12] but have not published any structural studies of the homoleptic pyrazolato complexes.

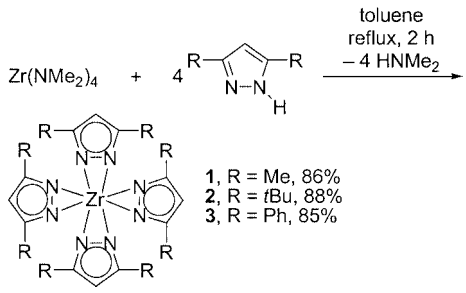

(1)

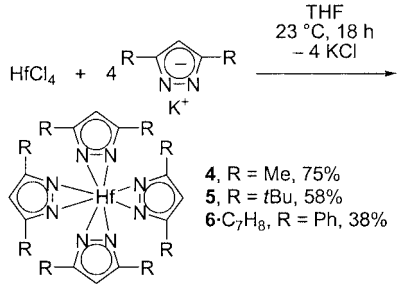

(2)

Results and Discussion

Synthetic Chemistry

Treatment of tetrakis(dimethylamido)zirconium with four equiv. of 3,5-dimethylpyrazole, 3,5-di-*tert*-butylpyrazole, or 3,5-diphenylpyrazole in refluxing toluene afforded tetrakis(η^2-3,5-dimethylpyrazolato)zirconium (**1**, 86%), tetrakis(η^2-3,5-di-*tert*-butylpyrazolato)zirconium (**2**, 88%), and tetrakis(η^2-3,5-diphenylpyrazolato)zirconium (**3**, 85%), respectively, as colorless crystalline solids [Equation (1)]. We have previously reported that treatment of group 4 and 5 metal chlorides with potassium pyrazolato salts constitutes an excellent synthetic route to the corresponding group 4 and 5 pyrazolato complexes.[12,13] Accordingly, salt metathesis routes to hafnium pyrazolato complexes were explored. Treatment of hafnium tetrachloride with 4 equiv. of the potassium salts of 3,5-dimethylpyrazolate,[12b] 3,5-di-*tert*-butylpyrazolate,[13] or 3,5-diphenylpyrazolate[13] in tetrahydrofuran at ambient temperature for 18 h afforded tetrakis(η^2-3,5-dimethylpyrazolato)hafnium (**4**, 75%), tetrakis(η^2-3,5-di-*tert*-butylpyrazolato)hafnium (**5**, 58%), and tetrakis(η^2-3,5-diphenylpyrazolato)hafnium·toluene (**6**·C_7H_8, 38%), respectively, as colorless crystalline solids [Equation (2)]. Complexes **1**–**3** were alternatively prepared by salt metathesis routes similar to those for **4**, **5**, and **6**·C_7H_8. The isolated yields of **1**–**3** were similar to those obtained by protonolysis reactions from tetrakis(dimethylamido)zirconium.

The structural assignments for **1**–**5** and **6**·C_7H_8 were based upon spectral and analytical data. In addition, X-ray crystal structure determinations were carried out for **1**, **3**, **4**, and **6**·C_7H_8, as described below. Complexes **1**, **3**, **4**, and **6**·C_7H_8 are monomeric in the solid state, with four η^2-pyrazolato ligands and eight-coordinate metal centers. They are stable indefinitely at ambient temperature under dry argon or nitrogen. The ^1H and $^{13}C\{^1H\}$ NMR spectra of **1**–**5** and **6**·C_7H_8 are consistent with the solid-state structures, and reveal the expected resonances for one type of pyrazolato ligand. In the dodecahedral structures of **1**–**5** and **6**·C_7H_8, the 3- and 5-substituents on each pyrazolato ligand are in different chemical environments. The fact that only one type of chemical environment is observed in the NMR spectra of **1**–**5** and **6**·C_7H_8 indicates that the pyrazolato ligand substituents are undergoing rapid site exchange on the NMR timescale. Such site exchange probably occurs through a sliding motion of the η^2-pyrazolato ligands across the faces of the dodecahedral molecular structures, which interchanges the two types of sites and is presumably a very low energy process.

During several attempts to crystallize **4** from polar solvents such as tetrahydrofuran or diethyl ether, a new complex was obtained that had a much more complicated ^1H NMR spectrum than that of **4**. A crystal structure determination, as described below, established that this new complex was tris(η^2-3,5-dimethylpyrazolato)(η^1-3,5-dimethylpyrazolato)(η^1-3,5-dimethylpyrazole)hafnium (**7**). Complex **7** probably corresponds to a hydrolysis product of **4**. It is less soluble and more crystalline than **4**, and crystallizes selectively from the polar solvents. Since **7** could only be obtained in low and variable yields by this process, an independent synthesis was developed. Treatment of **4** with one equiv. of 3,5-dimethylpyrazole in hexane at ambient temperature for 18 h afforded **7** in 84% yield as a colorless powder [Equation (3)].

 © 2005 Wiley-VCH Verlag GmbH & Co. KGaA, Weinheim

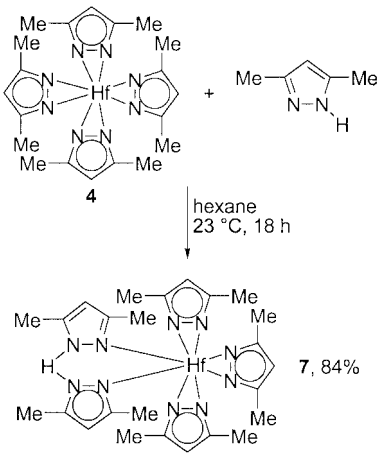

(3)

The structural assignment for **7** was based upon spectral and analytical data, as well as an X-ray crystal structure determination, as described below. Further treatment of **7** with 3,5-dimethylpyrazole or treatment of **4** with 2 or more equiv. of 3,5-dimethylpyrazole did not lead to new complexes, and only **7** and free 3,5-dimethylpyrazole were isolated. Treatment of **1** with 3,5-dimethylpyrazole under conditions similar to the preparation of **7** afforded a species with a ^{1}H NMR spectrum that was similar to that of **7**. However, attempted crystallization of this material afforded only crystals of **1**. Treatment of **4** with pyridine in hexane, followed by crystallization, afforded only **4**. Complex **4** also did not form an isolable adduct with tetrahydrofuran. The ^{1}H NMR spectrum of **4** at ambient temperature in [D_8]toluene in the presence of pyridine (1 equiv.) showed no evidence for the formation of a pyridine adduct. Treatment of **3** or **6**·C_7H_8 with 3,5-diphenylpyrazole (1 equiv.) in [D_8] toluene showed no evidence for adduct formation, and crystallization always afforded pure **3** or **6**·C_7H_8. Similarly, there was no evidence for adduct formation between **2** or **5** and 3,5-di-*tert*-butylpyrazole.

In the solid state, complex **7** contains three η^2-3,5-dimethylpyrazolato, one η^1-3,5-dimethylpyrazolato, and one η^1-3,5-dimethylpyrazole ligands, as described below. The η^1-3,5-dimethylpyrazolato and η^1-3,5-dimethylpyrazole ligands are connected through a N–H···N hydrogen bond. At 20 °C in [D_2]dichloromethane (**7** is much more soluble in this solvent than in toluene), the ^{1}H NMR of **7** exhibited one slightly broad resonance for the methyl groups at δ = 2.17 ppm, one slightly broad resonance at δ = 5.99 ppm for the pyrazolato core C–*H* fragment, and a very broad resonance at δ = 10.3 ppm for the pyrazole N–*H* group. This spectrum indicates that proton exchange between the pyrazole and four pyrazolato ligands and site exchange among the pyrazolato ligands are fast on the NMR timescale at 20 °C. At –93 °C in [D_2]dichloromethane, the ^{1}H NMR was much more complicated. Resonances due to pyrazole N–*H* groups were observed at δ = 16.88, 16.58, 13.70, and 11.19 ppm. If the solid-state structure of **7** is maintained in solution, a single pyrazole N–*H* resonance should be observed. In the pyrazolato core C–*H* resonance region, nine singlets of various intensities were observed between δ = 5.48–6.30 ppm, compared to the five expected resonances if the molecular structure of **7** were maintained in solution. In the methyl resonance region, at least 20 singlets were observed between δ = 0.89–2.35 ppm. The ^{1}H NMR spectrum at –93 °C demonstrates that **7** exists as a mixture of at least several complexes in solution.

Volatility and Thermal Stability Study

Complexes **1**–**7** were evaluated for their volatility and thermal stability in order to assess their potential viability as film growth precursors. Sublimation was observed beginning at about the temperatures at which the free pyrazoles sublime (3,5-dimethylpyrazole, 45 °C/0.05 Torr; 3,5-diphenylpyrazole, 150 °C/0.05 Torr; 3,5-di-*tert*-butylpyrazole, 80 °C/0.05 Torr). For **1**–**5** and **6**·C_7H_8, the sublimed material consisted of the free pyrazole along with smaller amounts of **1**–**5** and **6**·C_7H_8. There were substantial amounts of nonvolatile residues at the conclusion of the sublimations. Sublimation of **7** at 50–60 °C/0.05 Torr afforded 3,5-dimethylpyrazole as the sublimate. This behavior is consistent with thermal decomposition of **1**–**7** during sublimation, and thus these complexes are unlikely to serve as useful film growth precursors under thermal source delivery conditions.

X-ray Crystal Structures

X-ray crystal structures of **1**, **3**, **4**, **6**·C_7H_8, and **7** were determined to establish the geometries about the metal centers and the bonding modes of the pyrazolato ligands. Experimental crystallographic data are summarized in Table 1. Selected bond lengths and angles are given in Table 2. Perspective views of **4** and **7** are presented in Figure 1 and Figure 2. The coordination spheres of **1**, **3**, and **6**·C_7H_8 are similar to that of **4**, so a representative perspective view is only given for **4**.

The molecular structures of **1**, **3**, **4**, and **6**·C_7H_8 consist of monomeric complexes, with four η^2-pyrazolato ligands bonded to each metal center and approximate dodecahedral geometry. The metal–nitrogen distances [**1**, 2.162(5)–2.226(5); **3**, 2.173(2)–2.212(2); **4**, 2.137(8)–2.206(7); **6**·C_7H_8, 2.156(4)–2.191(4) Å] are consistent with idealized η^2-pyrazolato ligand bonding. These bond lengths are comparable for the zirconium and hafnium complexes, due to similar sizes of the zirconium(IV) (r = 0.72 Å for six coordination[14]) and hafnium(IV) (r = 0.71 Å for six coordination[14]) ions. The metal ions in **1**, **3**, **4**, and **6**·C_7H_8 lie approximately in the C_3N_2 planes of the pyrazolato ligand cores, and thus the filled in-plane nitrogen-based orbitals are involved in bonding. The pyrazolato nitrogen–nitrogen bond lengths in **1**, **3**, **4**, and **6**·C_7H_8 vary from 1.37–1.40 Å, while the nitrogen–metal–nitrogen bite angles of the pyrazolato ligands range between 36.3–37.3°.

The molecular structure of **7** consists of monomeric molecules containing three η^2-3,5-dimethylpyrazolato, one

 © 2005 Wiley-VCH Verlag GmbH & Co. KGaA, Weinheim

Table 1. Crystal data and data collection parameters for **1**, **3**, **4**, **6**·C_7H_8, and **7**.

	1	**3**	**4**	**6**·C_7H_8	**7**
Empirical formula	$C_{20}H_{28}N_8Zr$	$C_{60}H_{44}N_8Zr$	$C_{20}H_{28}HfN_8$	$C_{67}H_{52}HfN_8$	$C_{25}H_{36}HfN_{10}$
Formula mass	471.72	968.25	558.99	1147.66	655.13
Space group	$P\bar{1}$	$C2/c$	$P\bar{1}$	$P\bar{1}$	$P\bar{1}$
a [Å]	8.7282(3)	23.9264(7)	8.760(2)	12.428(18)	9.2148(9)
b [Å]	8.7953(3)	16.1975(4)	8.792(3)	13.73(2)	10.3816(11)
c [Å]	16.4224(6)	15.9951(2)	16.410(5)	16.68(3)	17.1557(19)
α [°]	95.269(3)		95.534(5)	74.92(2)	100.493(2)
β [°]	101.460(3)	129.815(2)	101.450(7)	79.48(3)	98.953(2)
γ [°]	90.368(2)		90.138(7)	81.23(3)	112.385(2)
V [Å^3]	1229.95(7)	4761.4(2)	1232.7(6)	2686(7)	1445.7(3)
Z	2	4	2	2	2
T [K]	218(2)	218(2)	295(2)	295(2)	295(2)
λ [Å]	0.71073	0.71073	0.71073	0.71073	0.71073
$\rho_{calcd.}$ [g cm^{-3}]	1.274	1.351	1.506	1.419	1.505
μ [mm^{-1}]	0.467	0.281	4.252	1.993	3.639
$R(F)$[a] (%)	8.13	4.21	4.76	3.75	3.49
$Rw(F)$[a] (%)	17.3	7.65	10.32	7.29	6.25

[a] $R(F) = \Sigma||F_o| - |F_c||/ \Sigma|F_o|$; $R_w(F) = [\Sigma w(F_o^2 - F_c^2)^2/\Sigma w(F_o^2)^2]^{1/2}$ for $I > 2\sigma(I)$.

Table 2. Selected bond lengths [Å] and angles [°] for **1**, **3**, **4**, **6**·C_7H_8, and **7**.

	1	**3**	**4**	**6**·C_7H_8	**7**
M–N(1)	2.183(5)	2.212(2)	2.203(7)	2.156(4)	2.373(4)
M–N(2)	2.220(5)	2.180(2)	2.155(7)	2.176(4)	
M–N(3)	2.202(5)	2.173(2)	2.206(7)	2.164(4)	2.144(3)
M–N(4)	2.164(5)	2.197(2)	2.153(7)	2.179(5)	2.172(3)
M–N(5)	2.226(5)		2.185(8)	2.166(4)	2.251(4)
M–N(6)	2.162(5)		2.137(8)	2.168(4)	2.138(4)
M–N(7)	2.176(5)		2.183(7)	2.191(4)	2.229(4)
M–N(8)	2.204(5)		2.167(7)	2.171(4)	
M–N(9)					2.175(4)
M–N(10)					2.179(4)
N(1)–N(2)	1.373(6)	1.377(3)	1.394(9)	1.367(4)	1.360(5)
N(3)–N(4)	1.385(7)	1.372(3)	1.387(10)	1.365(5)	1.385(5)
N(5)–N(6)	1.394(7)		1.372(10)	1.383(4)	1.377(5)
N(7)–N(8)	1.395(6)		1.380(10)	1.370(5)	1.390(5)
N(9)–N(10)					1.370(5)
N(1)–M–N(2)	36.3(2)	36.52(7)	37.3(2)	36.79(12)	
N(3)–M–N(4)	37.0(2)	36.59(7)	37.1(3)	36.64(12)	37.41(14)
N(5)–M–N(6)	37.0(2)		37.0(3)	37.23(12)	36.45(13)
N(7)–M–N(8)	37.1(2)		37.0(3)	36.62(13)	
N(9)–M–N(10)					36.67(14)

η^1-3,5-dimethylpyrazolato, and one η^1-3,5-dimethylpyrazole ligands bound to each hafnium center. There is an intramolecular hydrogen bond between the hydrogen atom bonded to N(2) of the η^1-3,5-dimethylpyrazole ligand and N(8) of the η^1-3,5-dimethylpyrazolato ligand. The overall geometry about the hafnium center can be considered as pentagonal bipyramidal, with the nitrogen atoms of two η^2-3,5-dimethylpyrazolato and one η^1-3,5-dimethylpyrazolato ligands corresponding to the equatorial plane. The center of the nitrogen–nitrogen bond of the η^2-3,5-dimethylpyrazolato ligand containing N(9) and N(10) and the coordinated nitrogen atom of the 3,5-dimethylpyrazole ligand correspond to the axial groups. The hafnium–nitrogen bond lengths for the η^2-3,5-dimethylpyrazolato ligands fall between 2.138(4)–2.251(3) Å, and these values are similar to those observed in **1**, **3**, and **4**. The η^2-3,5-dimethylpyrazolato ligand containing N(5) and N(6) has slightly asymmetric hafnium–nitrogen bond lengths of 2.138(4) and 2.251(4) Å, respectively. This slight asymmetry may arise from steric interactions between the methyl group containing C(14) and the η^1-3,5-dimethylpyrazole ligand. The hafnium–nitrogen bond lengths for the η^1-3,5-dimethylpyrazolato and 3,5-dimethylpyrazole ligands are 2.229(4) and 2.373(4) Å, respectively. The longer hafnium–nitrogen bond length for the 3,5-dimethylpyrazole ligand is consistent with its assignment as a neutral donor. The nitrogen–nitrogen bond lengths vary from 1.360(5)–1.390(5) Å. The nitrogen–hafnium–nitrogen bite angles of the η^2-3,5-dimethylpyrazolato ligands range between 36.45(13)–37.41(14)°, and are identical to the values for **1**, **3**, **4**, and **6**·C_7H_8.

Comments on 1–7

The results described herein extend our previous studies of homoleptic titanium(IV) pyrazolato complexes[10d,10e] to

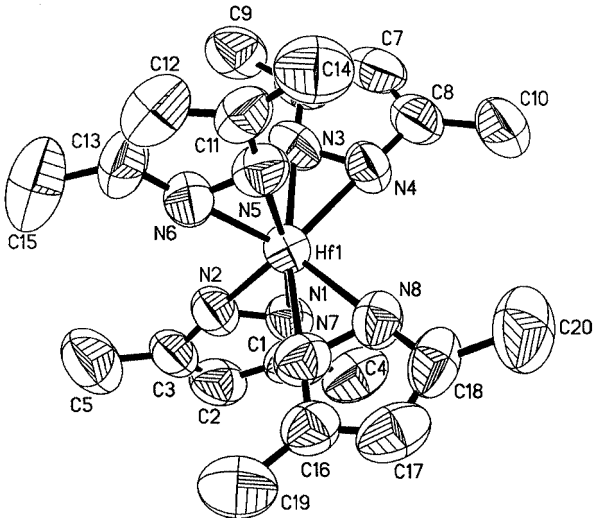

Figure 1. Perspective view of tetrakis(η^2-3,5-dimethylpyrazolato)-hafnium (**4**) with probability ellipsoids at the 50% level.

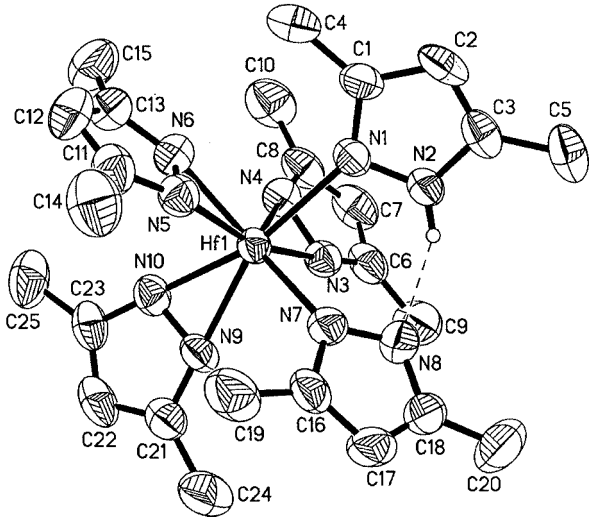

Figure 2. Perspective view of tris(η^2-3,5-dimethylpyrazolato)(η^1-3,5-dimethylpyrazolato)(η^1-3,5-dimethylpyrazole)hafnium (**7**) with probability ellipsoids at the 50% level.

the heavier group 4 elements zirconium and hafnium. $[Zr(R'_2pz)_4]$ (R′ = fluorenylmethyl) is the only other homoleptic heavier group 4 pyrazolato complex that has been structurally characterized.[11] It possesses approximate dodecahedral geometry about each zirconium ion, with zirconium–nitrogen bond lengths that range between 2.158(3)–2.210(3) Å. Thus, in spite of the bulky fluorenylmethyl substituents in the 3- and 5-positions of the pyrazolato ligands in $Zr(R'_2pz)_4$, essentially idealized η^2-pyrazolato ligands are observed. The combined results suggest that η^2-pyrazolato ligand coordination should be very common in zirconium(IV) and hafnium(IV) complexes. Excluding complexes containing tris(pyrazolyl)borate and related ligands (which possess μ–η^1:η^1-pyrazolato ligands), mixed ligand zirconium(IV) and hafnium(IV) pyrazolato complexes that have been structurally characterized to date are consistent with this prediction. For example, $[Cp_2Zr(pz)(THF)]^+BPh_4^-$ contains an η^2-pyrazolato ligand with zirconium–nitrogen bond lengths of 2.182(8) and 2.207(8) Å.[10c] $Hf(tBu_2pz)_3Cl$ contains η^2-pyrazolato ligands with hafnium–nitrogen bond lengths that range between 2.132(5)–2.162(8) Å.[12a] The metal–nitrogen bond lengths in these complexes are very similar to those observed in **1**, **3**, **4**, and **6**·C_7H_8. We have previously carried out molecular orbital calculations on the model pyrazolato complex $Ti(Me_2pz)Cl_3$,[10e] and noted that the η^2-pyrazolato ligand bonding occurs through overlap of filled symmetric and antisymmetric in-plane nitrogen-based orbitals with empty d-orbitals on the titanium center. Thus, the metal ion lies approximately in the C_3N_2 plane to maximize overlap with the in-plane nitrogen-based orbitals. The crystal structures of **1**, **3**, **4**, and **6**·C_7H_8 are consistent with this bonding model.

A surprise that emerged from this study is the formation and unusual structure of **7**. There was spectroscopic evidence in solution for a similar adduct derived from addition of 3,5-dimethylpyrazole to **1**. However, **1** crystallized selectively from these solutions, which indicates that adduct formation with 3,5-dimethylpyrazole is subtly balanced energetically with the crystallization of **1**. There was no evidence for formation of adducts between **4** and pyridine or tetrahydrofuran, either in the solution or the solid state. Accordingly, it appears that the N–H···N hydrogen bond is a key feature of the stability of **7**. Similar pyrazolato-pyrazole adducts bridged by N–H···N hydrogen bonds have been reported.[15]

Experimental Section

General: All manipulations were performed under argon using either glovebox or Schlenk line techniques. Hexane was distilled from P_2O_5, toluene was distilled from sodium, and tetrahydrofuran was distilled from purple solutions of sodium benzophenone ketyl. Tetrakis(dimethylamido)zirconium and hafnium tetrachloride were purchased from Strem Chemicals, Inc. and were used as received. 3,5-Dimethylpyrazole and 3,5-diphenylpyrazole were purchased from Aldrich Chemical Company and were sublimed prior to use. 3,5-Di-*tert*-butylpyrazole[16] and the potassium pyrazolate salts[12b,13] were prepared according to literature procedures. We previously briefly described the synthesis and characterization of **2** and **5**,[12a] but did not describe structural data or reactivity. ^1H and $^{13}C\{^1H\}$ NMR were obtained at 300, 400, 75, or 100 MHz in the indicated solvents. Infrared spectra were obtained using Nujol as the medium. Elemental analyses were performed by Midwest Microlab, Indianapolis, Indiana. Melting points were obtained with a Haake–Buchler HBI digital melting point apparatus and are uncorrected.

Preparation of Tetrakis(η^2-3,5-dimethylpyrazolato)zirconium (1): A 100 mL Schlenk flask was charged with 3,5-dimethylpyrazole (0.288 g, 3.00 mmol), toluene (35 mL), and was fitted with a reflux condenser. A solution of tetrakis(dimethylamido)zirconium (0.200 g, 0.759 mmol) in toluene (2 mL) was injected into the Schlenk flask using a syringe. The reaction mixture was then refluxed for 2 h. Upon cooling to room temperature, the volatile components were removed under reduced pressure to give an off-white solid. This solid was then extracted with hexane (20 mL), and the hexane extract was filtered through a 2-cm pad of Celite on a coarse frit to afford a clear, colorless solution. Removal of the vola-

 © 2005 Wiley-VCH Verlag GmbH & Co. KGaA, Weinheim

tile components under reduced pressure afforded **1** as a white crystalline solid (0.304 g, 86%). An analytical sample was obtained by recrystallization from a hexane solution at –20 °C, which afforded **1** as colorless crystals; m. p. 151–152 °C (dec.). IR (Nujol): $\tilde{\nu}$ = 3108 (w), 1568 (w), 1524 (s), 1440 (s), 1423 (s), 1366 (m), 1341 (w), 1320 (w), 1306 (w), 1262 (w), 1159 (w), 1116 (m), 1035 (w), 1004 (m), 959 (m), 790 (m), 729 (m), 684 (w) cm^{-1}. ^1H NMR ([D$_6$]benzene, 22 °C): δ = 2.17 (s, 24 H, C–C*H*$_3$), 5.97 (s, 4 H, pyrazolato C*H*) ppm. $^{13}C\{^1H\}$ NMR ([D$_6$]benzene, 22 °C): δ = 12.88 (s, C–*C*H$_3$), 112.18 (s, pyrazolato *C*H), 145.82 (s, *C*–CH$_3$) ppm. $C_{20}H_{28}N_8Zr$ (471.72): calcd. C 50.92, H 5.98, N 23.75; found C 50.26, H 5.87, N 23.08.

Preparation of Tetrakis(η^2-3,5-di-*tert*-butylpyrazolato)zirconium (2): In a fashion similar to the preparation of **1**, treatment of tetrakis-(dimethylamido)zirconium (0.200 g, 0.759 mmol) with 3,5-di-*tert*-butylpyrazole (0.540 g, 3.00 mmol) afforded **2** as a white crystalline solid (0.534 g, 88%). An analytical sample was obtained by recrystallization from a hexane solution at –20 °C, which afforded **2** as colorless crystals; m. p. 226 °C (dec.). IR (Nujol): $\tilde{\nu}$ = 3108 (w), 1589 (s), 1570 (s), 1248 (m), 1206 (w), 968 (w), 953 (w), 866 (m), 844 (m), 754 (w), 696 (w) cm^{-1}. ^1H NMR ([D$_6$]benzene, 22 °C): δ = 1.24 [s, 72 H, C(C*H*$_3$)$_3$], 6.34 (s, 4 H, pyrazolato C*H*) ppm. $^{13}C\{^1H\}$ NMR ([D$_6$]benzene, 22 °C): δ = 30.82 [s, C(*C*H$_3$)$_3$], 32.30 [s, *C*(CH$_3$)$_3$], 105.98 (s, pyrazolato *C*H), 159.31 [s, *C*–C(CH$_3$)$_3$] ppm. $C_{44}H_{76}N_8Zr$ (808.37): calcd. C 65.38, H 9.48, N 13.86; found C 63.42, H 9.22, N 12.77.

Preparation of Tetrakis(η^2-3,5-diphenylpyrazolato)zirconium (3): In a fashion similar to the preparation of **1**, treatment of tetrakis(dimethylamido)zirconium (0.200 g, 0.759 mmol) with 3,5-diphenylpyrazole (0.660 g, 3.00 mmol) afforded **3** as a white crystalline solid (0.616 g, 85%). An analytical sample was obtained by recrystallization from a hexane solution at –20 °C, which afforded **3** as colorless crystals; m. p. 240 °C (dec.). IR (Nujol): $\tilde{\nu}$ = 3102 (w), 1407 (w), 1366 (s), 1335 (m), 1262 (m), 1170 (w), 1156 (w), 1101 (m), 1074 (m), 1057 (w), 1023 (m), 971 (m), 918 (w), 804 (m), 761 (s), 723 (s), 691 (s) cm^{-1}. ^1H NMR ([D$_6$]benzene, 22 °C): δ = 6.92 (s, 4 H, pyrazolato C*H*), 6.98 (s, 24 H, *meta*- and *para*-C*H* of C$_6$H$_5$), 7.77 (s, 16 H, *ortho*-C*H* of C$_6$H$_5$) ppm. $^{13}C\{^1H\}$ NMR ([D$_6$] benzene, 22 °C): δ = 109.41 (s, pyrazolato *C*H), 126.69 (s, *para*-*C*H of C$_6$H$_5$), 128.10 (s, *meta*-*C*H of C$_6$H$_5$), 128.72 (s, *ortho*-*C*H of C$_6$H$_5$), 132.18 (s, *ipso*-*C* of C$_6$H$_5$), 150.72 (s, pyrazolato *C*–C$_6$H$_5$) ppm. $C_{60}H_{44}N_8Zr$ (968.25): calcd. C 74.43, H 4.58, N 11.57; found C 74.49, H 4.62, N 11.53.

Preparation of Tetrakis(η^2-3,5-dimethylpyrazolato)hafnium (4): A 100 mL Schlenk flask was charged with hafnium tetrachloride (0.200 g, 0.624 mmol), potassium 3,5-dimethylpyrazolate (0.335 g, 2.50 mmol), and tetrahydrofuran (50 mL). The cloudy colorless reaction mixture was stirred at ambient temperature for 18 h. Then, the volatile components were removed under reduced pressure to give a white solid. This solid was extracted with hexane (80 mL), and the hexane extract was filtered through a 2-cm pad of Celite on a coarse frit to afford a colorless clear solution. Removal of the volatile components under reduced pressure afforded **4** as a white crystalline solid (0.262 g, 75%). An analytical sample was obtained by recrystallization from a hexane solution at –20 °C, which afforded **4** as colorless crystals; m. p. 149–150 °C. IR (Nujol): $\tilde{\nu}$ = 3110 (w), 1524 (m), 1366 (m), 1341 (w), 1323 (w), 1310 (w), 1262 (m), 1170 (w), 1154 (w), 1115 (m), 1037 (w), 1006 (m), 960 (m), 789 (s), 731 (s), 724 (s) cm^{-1}. ^1H NMR ([D$_6$]benzene, 22 °C): δ = 2.16 (s, 24 H, C–C*H*$_3$), 6.08 (s, 4 H, pyrazolato C*H*) ppm. $^{13}C\{^1H\}$ NMR ([D$_6$]benzene, 22 °C): δ = 13.32 (s, C–*C*H$_3$), 112.99 (s, pyrazolato *C*H), 146.15 (s, *C*–CH$_3$) ppm. $C_{20}H_{28}HfN_8$ (558.99): calcd. C 42.97, H 5.05, N 20.05; found C 42.89, H 5.01, N 20.05.

Preparation of Tetrakis(η^2-3,5-di-*tert*-butylpyrazolato)hafnium (5): In a fashion similar to the preparation of **4**, treatment of hafnium tetrachloride (0.200 g, 0.624 mmol) with potassium 3,5-di-*tert*-butylpyrazolate (0.545 g, 2.50 mmol) afforded **5** as a white crystalline solid (0.295 g, 58%). An analytical sample was obtained by recrystallization from a toluene solution at –20 °C, which afforded **5** as colorless crystals; m. p. 202 °C (dec.). IR (Nujol): $\tilde{\nu}$ = 1527 (m), 1509 (m), 1366 (s), 1304 (m), 1260 (s), 1230 (m), 1206 (w), 1094 (s), 1024 (s), 993 (m), 801 (s), 721 (m) cm^{-1}. ^1H NMR ([D$_6$] benzene, 22 °C): δ = 1.23 [s, 72 H, C(C*H*$_3$)$_3$], 6.46 (s, 4 H, pyrazolato C*H*) ppm. $^{13}C\{^1H\}$ NMR ([D$_6$]benzene, 22 °C): δ = 30.71 [s, C(*C*H$_3$)$_3$], 32.22 [s, *C*(CH$_3$)$_3$], 106.02 (s, pyrazolato *C*H), 159.14 [s, *C*–C(CH$_3$)$_3$] ppm. $C_{44}H_{76}HfN_8$ (895.63): calcd. C 59.01, H 8.55, N 12.51; found C 59.14, H 8.46, N 12.32.

Preparation of Tetrakis(η^2-3,5-diphenylpyrazolato)hafnium·Toluene (6·C$_7$H$_8$): In a fashion similar to the preparation of **4**, treatment of hafnium tetrachloride (0.200 g, 0.624 mmol) with [K(Ph$_2$pz)-(THF)]$_6$ (0.645 g, 0.325 mmol) afforded a white crystalline solid. Recrystallization of this solid from a toluene solution at –20 °C afforded **6**·C$_7$H$_8$ as colorless crystals (0.274 g, 38% based upon the potassium pyrazolato reagent); m. p. 239–240 °C (dec; toluene loss observed at 110 °C). IR (Nujol): $\tilde{\nu}$ = 1366 (s), 1303 (w), 1260 (s), 1170 (m), 1153 (m), 1097 (s), 1021 (s), 974 (w), 802 (s), 760 (m), 723 (s) cm^{-1}. ^1H NMR ([D$_6$]benzene, 22 °C): δ = 6.92 (s, 4 H, pyrazolato C*H*), 6.98 (s, 8 H, *para*-C*H* of C$_6$H$_5$), 7.00 (s, 16 H, *meta*-C*H* of C$_6$H$_5$), 7.72 (m, 16 H, *ortho*-C*H* of C$_6$H$_5$) ppm. $^{13}C\{^1H\}$ NMR ([D$_6$]benzene, 22 °C): δ = 109.15 (s, pyrazolato *C*H), 126.62 (s, *para*-*C*H of C$_6$H$_5$), 127.95 (s, *meta*-*C*H of C$_6$H$_5$), 128.34 (s, *ortho*-*C*H of C$_6$H$_5$), 132.08 (s, *ipso*-*C* of C$_6$H$_5$), 150.33 (s, pyrazolato *C*–C$_6$H$_5$) ppm. In addition, resonances due to free toluene were observed in the ^1H and $^3C\{^1H\}$ NMR spectra. $C_{67}H_{52}HfN_8$ (1147.66): calcd. C 70.12, H 4.57, N 9.76; found C 70.09, H 4.64, N 9.47.

Preparation of Tris(η^2-3,5-dimethylpyrazolato)(η^1-3,5-dimethylpyrazolato)(η^1-3,5-dimethyl-pyrazole)hafnium (7): A 100 mL Schlenk flask was charged with **4** (0.254 g, 0.454 mmol), 3,5-dimethylpyrazole (0.044 g, 0.458 mmol), and hexane (50 mL). The colorless mixture was stirred at ambient temperature for 18 h. Then, the solution was filtered through a 2-cm pad of Celite on a coarse frit to afford a clear, colorless solution. The volatile components were removed under reduced pressure to afford **7** as a white crystalline solid (0.250 g, 84%). An analytical sample was obtained by recrystallization from a hexane solution at –20 °C, which afforded **7** as colorless crystals; m. p. 71 °C (dec.). IR (Nujol): $\tilde{\nu}$ = 3248 (m, ν_{NH}), 3205 (m, ν_{NH}), 3135 (m, ν_{NH}), 3110 (m), 3040 (m), 1671 (m), 1622 (m), 1595 (m), 1568 (m), 1524 (m), 1485 (s), 1441 (s), 1418 (s), 1345 (s), 1307 (s), 1260 (s), 1155 (m), 1146 (m), 1112 (s), 1099 (s), 1029 (s), 1016 (s), 1007 (s), 958 (m), 862 (m), 833 (m), 791 (s), 730 (m), 703 (s), 659 (m) cm^{-1}. ^1H NMR ([D$_6$]benzene, 22 °C): δ = 2.12 (broad s, 30 H, C*H*$_3$), 5.89 (broad s, 5 H, pyrazolato and pyrazole C*H*), 13.0 (very broad s, 1 H, N*H*) ppm. $^{13}C\{^1H\}$ NMR ([D$_6$]benzene, 22 °C): δ = 12.56 (s, C–*C*H$_3$), 108.31 (s, pyrazolato and pyrazole *C*H), 144.95 (s, *C*–CH$_3$) ppm. $C_{25}H_{36}HfN_{10}$ (655.13): calcd. C 45.84, H 5.54, N 21.38; found C 45.67, H 5.54, N 21.06.

X-ray Crystallographic Structure Determinations for 1, 3, 4, 6·C$_7$H$_8$, and 7: Crystalline samples of all air sensitive compounds were mounted in sealed thin-walled glass capillaries under nitrogen for X-ray data collection. The single-crystal X-ray diffraction experiments for **1** and **3** were performed with a Siemens P4 diffractometer with Mo-K_α radiation and graphite monochromator. All non-hydrogen atoms were refined with anisotropic displacement parameters. Hydrogen atoms were treated as idealized contributors. Data-

 © 2005 Wiley-VCH Verlag GmbH & Co. KGaA, Weinheim

sets for **4**, **6**·C_7H_8, and **7** were collected at room temperature with a Bruker P4/CCD diffractometer equipped with Mo radiation. For each collection, a full sphere of data was collected at 10 s/frame with 0.2° between each frame. The frame data were integrated with the manufacturer's SMART and SAINT software.[17] Absorption corrections were applied with Sheldrick's SADABS program[17] and each structure was solved and refined using the programs of SHELXL-97.[18] The crystal structures of compounds **4**, **6**·C_7H_8, and **7** consist of discrete monomeric neutral complexes. Complex **4** crystallizes as colorless flat squares. The hydrogen atoms were placed in calculated positions. Complex **6**·C_7H_8 crystallizes as colorless mounds that were grown together. A cut fragment was used for data collection and a dataset was extracted with Sparks' GEMINI software.[17] One molecule of toluene solvent per hafnium ion is present in the model. The hydrogen atoms were placed in calculated positions. Complex **7** crystallizes as colorless blocks. All atoms occupy general positions in the unit cell. The hydrogen atoms were placed in observed and calculated positions.

CCDC-269335 (for **1**), -269336 (for **3**), -269337 (for **4**), -269338 (for **6**·C_7H_8), and -269339 (for **7**) contain the supplementary crystallographic data for this paper. These data can be obtained free of charge on application to CCDC, 12 Union Road, Cambridge CB21EZ, UK; Fax: (+44)-1223-336-033; E-mail: deposit@ccdc.cam.ac.uk.

Acknowledgments

We are grateful to the U. S. National Science Foundation (Grant No. CHE-0314615 to C. H. W.) for support of this research.

[1] Recent leading references: a) J. Robertson, *Solid-State Electron.* **2005**, *49*, 283–293; b) G. B. Rayner Jr., D. Kang, G. Lucovsky, *J. Vac. Sci. Technol. B* **2003**, *21*, 1783–1791.

[2] Recent leading references: a) M. Chhowalla, H. E. Unalan, *Nat. Mater.* **2005**, *4*, 317–322; b) E. Atar, H. Cimenoglu, E. S. Kayali, *Key Eng. Mater.* **2005**, *280–283*, 1459–1462; c) E. Atar, C. Sarioglu, H. Cimenoglu, E. S. Kayali, *Surf. Coat. Technol.* **2005**, *191*, 188–194.

[3] Recent leading references: a) K.-L. Ou, M.-H. Tsai, H.-W. Huang, S.-Y. Chiou, C.-T. Lin, S.-Y. Lee, *Microelectron. Eng.* **2005**, *77*, 184–192; b) C.-S. Chen, C.-P. Liu, H.-G. Yang, C.-Y. A. Tsao, *J. Vac. Sci. Technol. A* **2004**, *22*, 2041–2047; c) C.-S. Chen, C.-P. Liu, H.-G. Yang, C.-Y. A. Tsao, *J. Vac. Sci. Technol. B* **2004**, *22*, 1075–1083.

[4] Recent leading references: a) R. J. Potter, P. R. Chalker, T. D. Manning, H. C. Aspinall, Y. F. Loo, A. C. Jones, L. M. Smith, G. W. Critchlow, M. Schumacher, *Chem. Vap. Deposition* **2005**, *11*, 159–159; b) A. Abrutis, L. G. Hubert-Pfalzgraf, S. V. Pasko, A. Bartasyte, F. Weiss, V. Janickis, *J. Cryst. Growth* **2004**, *267*, 529–537; c) M.-K. Song, S.-W. Kang, S.-W. Rhee, *Thin Solid Films* **2004**, *450*, 272–275; d) M. M. Frank, S. Sayan, S. Dörman, T. J. Emge, L. S. Wielunski, E. Garfunkel, Y. J. Chabal, *Mater. Sci. Eng. B* **2004**, *109*, 6–10; e) A. Baunemann, R. Thomas, M. Winter, R. A. Fischer, P. Ehrhart, R. Waser, A. Devi, *Chem. Commun.* **2004**, 1610–1611.

[5] Recent leading references: a) J. F. Conley, Jr., Y. Ono, D. J. Tweet, R. Solanki, *Appl. Phys. Lett.* **2004**, *84*, 398–400; b) J. F. Conley, Jr., Y. Ono, R. Solanki, G. Stecker, W. Zhuang, *Appl. Phys. Lett.* **2003**, *82*, 3508–3510; c) R. C. Smith, N. Hoilien, J. Roberts, S. A. Campbell, W. L. Gladfelter, *Chem. Mater.* **2002**, *14*, 474–476.

[6] Recent leading references: a) M. K. Song, S. W. Kang, S. W. Rhee, *J. Electrochem. Soc.* **2005**, *152*, C108–C112; b) J. Kim, K. Yong, *J. Cryst. Growth* **2004**, *263*, 442–446; c) R. G. Gordon, D. Haussman, E. Kim, J. Shepard, *Chem. Vap. Deposition* **2003**, *9*, 73–78.

[7] Recent leading references: a) W. H. Nam, S. W. Rhee, *Chem. Vap. Deposition* **2004**, *10*, 201–205; b) W. H. Nam, S. W. Rhee, *Electrochem. Solid-State Lett.* **2004**, *7*, C55–C56; c) J. Niinistö, M. Putkonen, L. Niinistö, K. Kukli, M. Ritala, M. Leskelä, *J. Appl. Phys.* **2004**, *95*, 84–91.

[8] For examples, see: a) W. W. Wang, T. Nabatame, Y. Shimogaki, *Jpn. J. Appl. Phys. Part 2* **2004**, *43*, L1445–L1448; b) J. S. Becker, E. Kim, R. G. Gordon, *Chem. Mater.* **2004**, *16*, 3497–3501; c) D. M. Hoffman, *Polyhedron* **1994**, *13*, 1169–1179.

[9] For reviews of pyrazolato complexes, see: a) F. Nief, *Eur. J. Inorg. Chem.* **2001**, 891–904; b) J. E. Cosgriff, G. B. Deacon, *Angew. Chem. Int. Ed.* **1998**, *37*, 286–287; c) G. LaMonica, G. A. Ardizzoia, *Prog. Inorg. Chem.* **1997**, *46*, 151–238; d) A. P. Sadimenko, S. S. Basson, *Coord. Chem. Rev.* **1996**, *147*, 247–297; e) S. Trofimenko, *Prog. Inorg. Chem.* **1986**, *34*, 115–210; f) S. Trofimenko, *Chem. Rev.* **1972**, *72*, 497–508.

[10] Selected examples of η^2-pyrazolato ligand coordination to metals across the periodic Table: a) C. W. Eigenbrot, Jr., K. N. Raymond, *Inorg. Chem.* **1982**, *21*, 2653–2660; b) J. E. Cosgriff, G. B. Deacon, B. M. Gatehouse, H. Hemling, H. Schumann, *Angew. Chem. Int. Ed. Engl.* **1993**, *32*, 874–875; c) D. Röttger, G. Erker, M. Grehl, R. Frölich, *Organometallics* **1994**, *13*, 3897–3902; d) I. A. Guzei, A. G. Baboul, G. P. A. Yap, A. L. Rheingold, H. B. Schlegel, C. H. Winter, *J. Am. Chem. Soc.* **1997**, *119*, 3387–3388; e) I. A. Guzei, G. P. A. Yap, C. H. Winter, *Inorg. Chem.* **1997**, *36*, 1738–1739; f) D. Pfeiffer, M. J. Heeg, C. H. Winter, *Angew. Chem. Int. Ed.* **1998**, *37*, 2517–2519; g) G. B. Deacon, E. E. Delbridge, C. M. Forsyth, P. C. Junk, B. W. Skelton, A. H. White, *Aust. J. Chem.* **1999**, *52*, 733–739; h) N. C. Mösch-Zanetti, R. Kratzner, C. Lehmann, T. R. Schneider, I. Uson, *Eur. J. Inorg. Chem.* **2000**, 13–16; i) K. R. Gust, J. E. Knox, M. J. Heeg, H. B. Schlegel, C. H. Winter, *Angew. Chem. Int. Ed.* **2002**, *41*, 1591–1594; j) K. R. Gust, J. E. Knox, M. J. Heeg, H. B. Schlegel, C. H. Winter, *Eur. J. Inorg. Chem.* **2002**, 2327–2334.

[11] J. C. Röder, F. Mayer, H. Pritzkow, *Z. Naturforsch. Teil B* **2002**, *57*, 773–776.

[12] Previous reports from our laboratory of zirconium and hafnium complexes that contain η^2-pyrazolato ligands: a) C. Yélamos, M. J. Heeg, C. H. Winter, *Inorg. Chem.* **1999**, *38*, 1871–1878; b) C. Yélamos, K. R. Gust, A. G. Baboul, M. J. Heeg, H. B. Schlegel, C. H. Winter, *Inorg. Chem.* **2001**, *40*, 6451–6462.

[13] C. Yélamos, M. J. Heeg, C. H. Winter, *Inorg. Chem.* **1998**, *37*, 3892–3894.

[14] N. N. Greenwood, A. Earnshaw, *Chemistry of the Elements*, Second Edition, Butterworth-Heinemann, Oxford, **1997**, p. 957.

[15] For selected examples, see: a) M. Cano, J. A. Campo, J. V. Heras, E. Pinilla, C. Rivas, A. Monge, *Polyhedron* **1994**, *13*, 2463–2465; b) G. A. Ardizzoia, G. LaMonica, A. Maspero, M. Moret, N. Masciocchi, *Eur. J. Inorg. Chem.* **1998**, 1503–1512; c) X.-G. Zhou, Z.-E. Huang, R.-F. Cai, L.-B. Zhang, L.-X. Zhang, *Organometallics* **1999**, *18*, 4128–4133; d) N. C. Mösch-Zanetti, M. Ferbinteanu, J. Magull, *Eur. J. Inorg. Chem.* **2002**, 950–956.

[16] J. Elguero, E. Gonzales, R. Jacquier, *Bull. Soc. Chim. Fr.* **1968**, 707.

[17] *APEX-II*, *SMART*, *SAINT*, *GEMINI*, and *SADABS*, *Programs for data collection and data processing*, Bruker AXS Inc., Madison, Wisconsin.

[18] G. M. Sheldrick, *SHELXL-97*, Universität Göttingen, **1997**.

Received: April 28, 2005
Published Online: August 31, 2005

 © 2005 Wiley-VCH Verlag GmbH & Co. KGaA, Weinheim

Zirconium and Hafnium Complexes with (Allylsilyl)(η-amidosilyl)-η^5-cyclopentadienyl Ligands: Synthesis, Structure and Reactivity

Cristina Ramos,[a] Pascual Royo,*[a] Maurizio Lanfranchi,[b] Maria Angela Pellinghelli,[b] and Antonio Tiripicchio[b]

Keywords: Insertion / Isocyanides / Hafnium / Metallocenes / Zirconium

The disubstituted cyclopentadiene $C_5H_4(SiMe_2Cl)[SiMe_2(CH_2CH=CH_2)]$ was isolated by reaction of the lithium salt $[Li\{C_5H_4SiMe_2(CH_2CH=CH_2)\}]$ with $SiMe_2Cl_2$. It was then treated with NH_2tBu and $LiNH(2,6\text{-}Me_2C_6H_3)$ to give the (aminosilyl)cyclopentadienes $C_5H_4[SiMe_2(CH_2CH=CH_2)][SiMe_2(NHR)]$, which were further deprotonated to their dilithium salts $[Li_2\{1\text{-}SiMe_2NR\text{-}3\text{-}SiMe_2(CH_2CH=CH_2)C_5H_3\}]$ (R = *t*Bu, 2,6-$Me_2C_6H_3$). Reactions of the metal halides $ZrCl_4(THF)_2$ and $HfCl_4$ with these dilithium salts, followed by alkylation of the resulting dichloro complexes, afforded the (η^1-amidosilyl)-η^5-cyclopentadienyl complexes $[M\{\eta^5\text{-}C_5H_3(SiMe_2\text{-}\eta^1\text{-}NR)[SiMe_2(CH_2CH=CH_2)]\}X_2]$ (R = *t*Bu, 2,6-$Me_2C_6H_3$; X = Cl, Me, CH_2Ph; M = Zr, Hf). Only the bis(iminoacyl) complexes $[M\{\eta^5\text{-}C_5H_3(SiMe_2\text{-}\eta^1\text{-}Nt\text{Bu})[SiMe_2(CH_2CH=CH_2)]\}\{\eta^2\text{-}CR=N(2,6\text{-}Me_2C_6H_3)\}_2]$ (M = Zr, Hf; R = Me, CH_2Ph) could be isolated when the dialkylzirconium and -hafnium complexes were treated with CN(2,6-$Me_2C_6H_3$); these were slowly transformed into the C–C-coupled diazametallacyclopentene compounds $[M\{\eta^5\text{-}C_5H_3(SiMe_2\text{-}\eta^1\text{-}Nt\text{Bu})[SiMe_2(CH_2CH=CH_2)]\}\{\eta^1\text{-}N(2,6\text{-}Me_2C_6H_3)\text{-}CR=CR\text{-}\eta^1\text{-}N(2,6\text{-}Me_2C_6H_3)\}]$ (R = Me, CH_2Ph, M = Zr; R = Me, M = Hf) when their toluene solutions were heated to 70 °C–80 °C for long periods (2–4 d). The structural characterisation of all of the new compounds is described and the molecular structure of the dimeric dichlorozirconocene $[ZrCl(\mu\text{-}Cl)\{\eta^5\text{-}C_5H_3(SiMe_2\text{-}\eta^1\text{-}Nt\text{Bu})[SiMe_2(CH_2CH=CH_2)]\}]_2$, was determined by X-ray diffraction methods.

(© Wiley-VCH Verlag GmbH & Co. KGaA, 69451 Weinheim, Germany, 2005)

Introduction

Many reports[1–9] have described the dynamics of the ion pairs formed by activation of a precursor metallocene with various Lewis acids, which are assumed to be the species responsible for the metallocene-catalysed alkene polymerisation[5,10–15] and considered to be the cornerstone of its efficiency and stereocontrol. Several strategies have been used to stabilize the intermediate cationic alkyl alkene metallocene[10,16–21] and (η^1-amidosilyl)-η^5-cyclopentadienyl[3,22–30] d^0 group-4 metal complexes. We have reported[31,32] the formation of alkyl alkene metallocene cations through η^2-coordination of the alkene moiety of an allylsilyl group tethered to the cyclopentadienyl ring. In order to study the formation and reactivity of the corresponding (η^1-amidosilyl)-η^5-cyclopentadienyl cationic compounds reported elsewhere, we synthesised and characterised disubstituted (allylsilyl)(amidosilyl)cyclopentadienyl group 4 metal complexes of the type represented in Scheme 1. These compounds are described in this paper, along with the insertion reactions of isocyanides into their metal–alkyl bonds and C–C coupling reactions of the resulting iminoacyl derivatives.

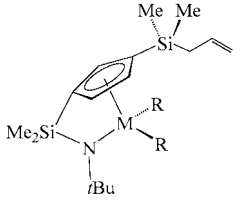

Scheme 1.

Results and Discussion

Successful synthesis of the disubstituted cyclopentadiene containing the two required aminosilyl $[SiMe_2(NHt\text{Bu})]$ and allylsilyl $[SiMe_2(CH_2CH=CH_2)]$ functionalities was achieved by first introducing the allylsilyl group[33] followed by metallation and reaction of the resulting lithium (allylsilyl)cyclopentadienide salt[31,32] with $SiMe_2Cl_2$ to give the disilylated cyclopentadiene $C_5H_4(SiMe_2Cl)[SiMe_2(CH_2CH=CH_2)]$ (**1**, Scheme 2), which was isolated as a yellow liquid.

[a] Departamento de Química Inorgánica, Universidad de Alcalá, Campus Universitario,
28871 Alcalá de Henares, Spain
Fax: +34-91-885-4683
E-mail: pascual.royo@uah.es
[b] Dipartamento di Chimica Generale ed Inorganica, Chimica Analitica, Chimica Fisica, Università di Parma,
Parco Area delle Scienze 17/A, 43100 Parma, Italy
Fax: +39-0521-905-557
E-mail: maurizio.lanfranchi@unipr.it

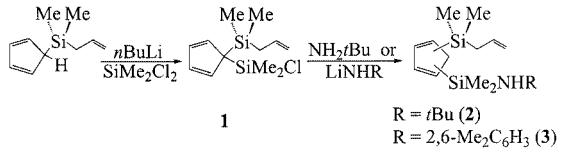

Scheme 2.

Further aminolysis of the chorosilyl derivative **1** by reaction with the primary amine NH_2tBu or metathesis with $LiNH(2,6\text{-}Me_2C_6H_3)$ afforded the disilylated cyclopentadienes $C_5H_4[SiMe_2(CH_2CH{=}CH_2)][SiMe_2(NHR)]$ (R = *t*Bu **2**, 2,6-$Me_2C_6H_3$ **3**), which were isolated as oily yellow and orange liquids, respectively. The chlorosilyl derivative **1** was identified by ^1H NMR spectroscopy as a unique 1,1-isomer. However, formation of the 1,3-isomer is favoured for the aminosilyl compounds **2** and **3** due to the presence of the sterically more demanding amino substituents (see Exp. Sect.).

The mixture of isomers of the disilylcyclopentadienes **2** and **3** was metallated by treatment with 2 equiv. of *n*BuLi to give the dilithium salts, which were isolated as white solids containing one single component and were identified by ^1H NMR spectroscopy as the 1,3-isomer $[Li_2\{1\text{-}SiMe_2NR\text{-}3\text{-}SiMe_2(CH_2CH{=}CH_2)C_5H_3\}]$ (R = *t*Bu **4**, 2,6-$Me_2C_6H_3$ **5**). Their ^1H NMR spectra show the three ring-proton signals expected for an asymmetric molecule, whereas the diastereotopic methyl groups of both silyl fragments and the diastereotopic methylene protons of the allylsilyl fragment are observed as two singlets (see Exp. Sect.).

A direct synthesis based on halide metathesis, when the metal tetrahalides were treated with 1 equiv. of the dilithium salts **4** and **5**, was used to transfer the (amidosilyl)cyclopentadienyl ligand, as shown in Scheme 3. Reaction of **4** with $ZrCl_4(THF)_2$ or $HfCl_4$ in toluene at room temperature yielded the "constrained-geometry" complexes $[MCl(\mu\text{-}Cl)\{\eta^5\text{-}C_5H_3(SiMe_2\text{-}\eta^1\text{-}N\mathit{t}Bu)[SiMe_2(CH_2CH{=}CH_2)]\}]_2$ (M = Zr **6**, Hf **7**), which were isolated in high yield as a yellow crystalline solid (**6**) and an oily orange solid (**7**) and characterised by elemental analysis (**6**), NMR spectroscopy and X-ray diffraction methods (**6**). Analogous reactions using the dilithium salt of the corresponding (2,6-dimethylphenyl) amido ligand **5** were carried out in the hope of obtaining improved crystallinity of the resulting metal compounds.[34] However, the new dichloro complexes $[MCl(\mu\text{-}Cl)\{\eta^5\text{-}C_5H_3[SiMe_2\text{-}\eta^1\text{-}N(2,6\text{-}Me_2C_6H_3)][SiMe_2(CH_2CH{=}CH_2)]\}]_2$ (M = Zr **8**, Hf **9**) were always obtained as oily orange and white solid products, respectively, which easily decomposed with elimination of free amine; consequently, they were difficult to purify, giving rather low yields (lower than 30%) after purification. These compounds were not studied further.

The ^1H and ^{13}C NMR spectra of the silylamido derivatives **6**–**9** show three multiplets (^1H) and five resonances (^{13}C) for the Cp ring protons and carbon atoms and four singlets (^1H and ^{13}C) for the two diastereotopic silylmethyl groups; two of the multiplets were occasionally observed as overlapped signals in the ^1H NMR spectrum. The ^1H NMR

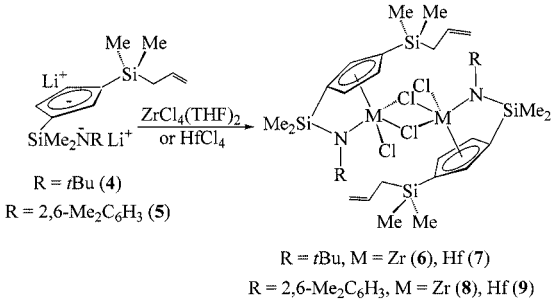

Scheme 3.

spectra of all the complexes show the typical pattern of the allyl substituent, which consists of one high-field multiplet for the $SiCH_2$ protons at δ = 1.7–1.8 ppm, one multiplet at δ = 5.6–5.8 ppm for the internal olefinic proton and one multiplet for the two external olefinic protons at δ = 4.8–4.9 ppm. The ring C_{ipso} resonance for compounds **6**–**9** appears at higher field than those of the other carbon atoms, consistent with the (amidosilyl)cyclopentadienyl ligands adopting a chelate coordination mode with the metal centre.[35] This NMR behaviour may suggest the presence of mononuclear structures of the silylamido derivatives **6**–**9** in solution, for which the enantiotopic 1,3-disilylcyclopentadienyl ring faces are responsible for the asymmetry of these molecules. However, it could also be consistent with a centrosymmetric dimeric diastereoisomer with two equivalent Cp-silylamido systems, which is formed by two mononuclear units held together by a pair of bridging chloro ligands. Both mono- and dinuclear structures exhibit two non-equivalent chloro ligands, one of which is localised under the allyldimethylsilyl substituent of the cyclopentadienyl ligand in the mononuclear structure or is the terminal ligand in the dinuclear compound.

The dimeric structure of complex **6** in the solid state was determined by X-ray diffraction methods on a single crystal obtained from a hexane solution cooled to –35 °C. The same dimeric structure may be tentatively assigned to all of the other complexes **7**–**9** in the solid state, as shown in Scheme 3. Typical signals due to coordinated THF were observed in the ^1H and ^{13}C NMR spectra of the more electron-deficient complex **8** containing the less basic amido ligand.

A view of the molecular structure of complex **6**, together with the atomic labelling scheme, is shown in Figure 1. Selected bond lengths and angles are given in Table 1. The crystal structure consists of discrete chloro-bridged centrosymmetric dimeric molecules of $[ZrCl(\mu\text{-}Cl)\{\eta^5\text{-}C_5H_3(SiMe_2\text{-}\eta^1\text{-}N\mathit{t}Bu)[SiMe_2CH_2CH{=}CH_2]\}]_2$. Each zirconium atom is bound to the cyclopentadienyl ring in a slightly asymmetric fashion [Zr–C bond lengths are in the range 2.441(6)–2.557(7) Å, while the Zr–CT distance is 2.187(8) Å, where CT is the centroid of the ring], to the nitrogen atom of the silylamido moiety [Zr–N = 2.042(6) Å], to a terminal chlorine atom [Zr–Cl2 = 2.457(2) Å] and to two bridging chlorine atoms [Zr–Cl1 = 2.645(2) and Zr–Cl1′ = 2.653(2) Å]. The Zr atom is in a

 © 2005 Wiley-VCH Verlag GmbH & Co. KGaA, Weinheim

four-legged piano-stool arrangement if the centroid of the cyclopentadienyl ring is taken into consideration. The value of the Zr–N bond length is consistent with double-bond character and falls in the range (2.034–2.088 Å) retrieved from the Cambridge Structural Database files for pentacoordinate Zr complexes containing the ZrClCpSiN(amido) moiety.[36–45] The almost equal bridging Zr–Cl distances are significantly longer than the terminal Zr–Cl distance, and this last bond length again falls in the range 2.432–2.529 Å retrieved from the CSD files for similar complexes. To the best of our knowledge, the only chloro-bridged dimeric zirconium complex found in the literature containing a (amidosilyl)cyclopentadienyl moiety is (*R*,*R*)-[ZrCl(μ-Cl)]{η^5:η^1-$C_5Me_4SiMe_2NCH(Me)(Ph)$}$_2$,[39] where the Zr–Cl bridging bond lengths are significantly different. The *trans* influence of the amido nitrogen and chlorine coordinating atoms seem similar in **6**, and the bridging Zr–Cl bond lengths are not significantly different.

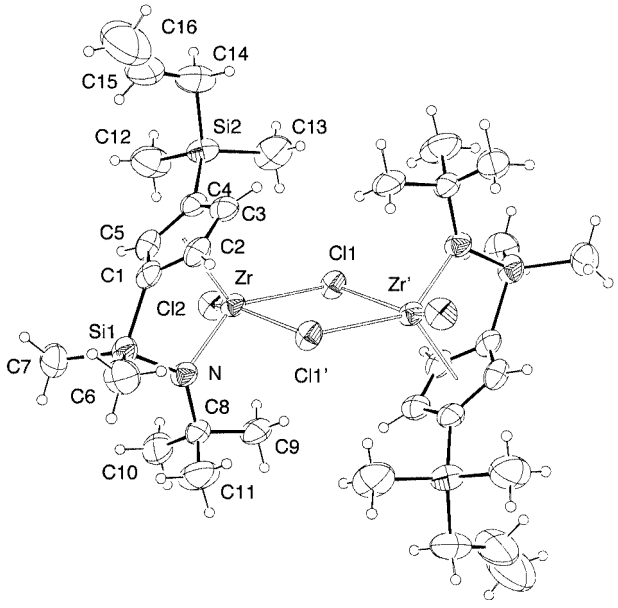

Figure 1. ORTEP drawing of the molecular structure of **6** in the solid state; thermal ellipsoids are drawn at the 30% probability level.

The C1 atom that bears the amidosilyl arm is pyramidally distorted, as shown by the sum of bond angles (350.8°) as in the other chloro(amidosilyl)cyclopentadienyl complexes,[36–45] and in the doubly silylamido-bridged cyclopentadienyltitanium complex,[46] while the C4 atom that bears the allylsilyl arm is weakly pyramidally distorted (the sum of the bond angles is 359.3°). The Si1 and Si2 atoms are out of the Cp plane by –0.845(2) and 0.250(3) Å, respectively.

In spite of having non-equivalent chloro ligands, none of these zirconium and hafnium complexes showed selective reactions when they were treated with alkylating agents. As shown in Scheme 4, reactions of complexes **6** and **7** with 2 equiv. of MgClR (R = Me, CH_2Ph) in hexane at room temperature gave the dialkyl complexes [M{η^5-$C_5H_3(SiMe_2$-η^1-N*t*Bu)[$SiMe_2(CH_2CH{=}CH_2)$]}R_2] (M = Zr, R = Me **10**, CH_2Ph **11**; M = Hf, R = Me **12**, CH_2Ph **13**), which were isolated as brown and orange oily solids, respectively, and identified by elemental analysis and NMR spectroscopy. In addition to the same features discussed above for the precursor dichloro complexes, the non-equivalency of the two alkyl groups of these asymmetric molecules is easily demonstrated by their ^{1}H and ^{13}C NMR spectra. The spectra of the methyl complexes **10** and **12** show two singlets (^{1}H) and two resonances (^{13}C) for the two non-equivalent, metal-bonded methyl groups, whereas four doublets (^{1}H) for the two diastereotopic methylene protons and two resonances (^{13}C) for the methylene carbon atom are observed for each non-equivalent, metal-bonded benzyl group of the benzyl derivatives **11** and **13**.

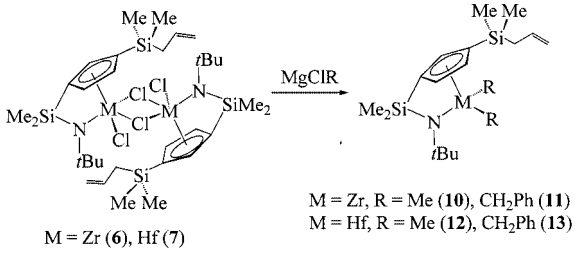

Scheme 4.

Insertion of isocyanide into one of the two non-equivalent metal–alkyl bonds of these dialkyl compounds may afford mixtures of two diastereomers, unless for diastereoselective reactions.[47] However, when 1 equiv. of CN(2,6-$Me_2C_6H_3$) was added to the toluene solutions of the dialkyl(amidosilyl)cyclopentadienyl compounds **10**–**13**, the initially formed 16-electron iminoacyl compounds could not be detected by NMR spectroscopy because they react very easily to give the bis(iminoacyl) complexes by further insertion into the second metal–alkyl bond. This behaviour is in contrast to that observed for metallocene-type complexes for which the monoiminoacyl complexes are 18-electron species, which do not undergo further insertion into the second metal–alkyl bond.

Table 1. Selected bond lengths [Å] and angles [°] for compound **6**.

Zr–Cl(1)	2.645(2)	C(4)–C(5)	1.447(10)
Zr–Cl(1)′	2.653(2)	C(1)–C(5)	1.393(10)
Zr–Cl(2)	2.457(2)	C(1)–Si(1)	1.872(9)
Zr–N	2.042(6)	Si(1)–N	1.743(5)
Zr–CT	2.187(8)	N–C(8)	1.492(9)
C(1)–C(2)	1.418(10)	C(4)–Si(2)	1.890(9)
C(2)–C(3)	1.416(10)	Si(2)–C(14)	1.894(10)
C(3)–C(4)	1.411(10)		
Cl(1)–Zr–Cl(1)′	72.26(7)	N–Zr–Cl(2)	96.6(2)
Cl(2)–Zr–Cl(1)	80.76(7)	N–Zr–Cl(1)	138.2(2)
Cl(2)–Zr–Cl(1)′	145.37(7)	N–Zr–Cl(1)′	89.6(2)
Cl(1)–Zr–CT[a]	120.4(2)	N–Zr–CT	100.3(3)
Cl(2)–Zr–CT[a]	107.9(2)	CT–Zr–Cl(1)′	104.4(2)
Si(1)–N–Zr	108.1(3)	C(8)–N–Zr	123.0(4)
C(8)–N–Si(1)	128.9(5)		

[a] CT is the centroid of the C(1)···C(5) cyclopentadienyl ring. Symmetry transformation used to generate equivalent atoms: –*x*, –*y*, –*z* + 2.

 © 2005 Wiley-VCH Verlag GmbH & Co. KGaA, Weinheim

Therefore these insertion reactions were complete when toluene solutions of the dialkyl complexes **10**–**13** were treated with two equivalents of 2,6-xylyl isocyanide at room temperature to give the corresponding bis(iminoacyl) compounds[48] [M{η^5-C_5H_3($SiMe_2$-η^1-N*t*Bu)[$SiMe_2$(CH_2CH=CH_2)]}{η^2-CR=N(2,6-$Me_2C_6H_3$)}$_2$] (M = Zr, R = Me **14**, CH_2Ph **15**; M = Hf, R = Me **16**, CH_2Ph **17**) which were isolated as red and orange oily products and identified by elemental analysis and NMR and infrared spectroscopy.

As shown in Scheme 5 the bis(iminoacyl) complexes **14**–**16** were slowly converted into the C–C-coupled compounds.[49] This transformation was complete when their toluene solutions were heated at 70 °C–80 °C for long periods (2 d for **18** and **19** and 4 d for **20**) in sealed tubes to give the diazametallacyclopentene complexes [M{η^5-C_5H_3($SiMe_2$-η-N*t*Bu)[$SiMe_2$(CH_2CH=CH_2)]}-{η-N(2,6-$Me_2C_6H_3$)CR=CR-η-N(2,6-$Me_2C_6H_3$)] (R = Me, M = Zr **18**, Hf **19**; R = CH_2Ph, M = Zr **20**). Complexes **18**–**20** were isolated as red (**18**) and brown (**19**, **20**) oily products and identified by NMR and IR spectroscopy. The ^{1}H and ^{13}C NMR spectra of all of these iminoacyl (**14**–**17**) and enediamido (**18**–**20**) compounds correspond to the asymmetric molecules expected from the enantiotopic character of the disilylcyclopentadienyl ligand (see Exp. Sect.). The presence of four methyl resonances (occasionally overlapped) for the [(2,6-dimethylphenyl)imino]acyl groups indicates that rotation around the N–aryl bond is avoided.

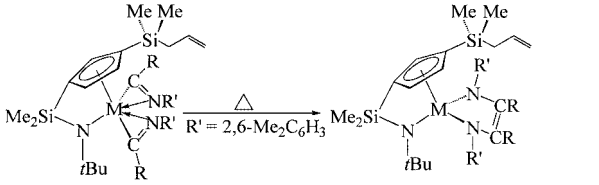

M = Zr, R = Me (**14**), CH_2Ph (**15**)
M = Hf, R = Me (**16**), CH_2Ph (**17**)

M = Zr, R = Me (**18**), CH_2Ph (**19**)
M = Hf, R = Me (**20**)

Scheme 5.

Compounds **14**–**17** contain the iminoacyl ligand η^2-coordinated to the metal centre as shown by their spectroscopic data. The signals observed in the ^{1}H NMR spectra for the alkyl and methylene(benzyl) groups migrated to the inserted aryl isocyanide are shifted downfield (by about 2 ppm) with respect to the values observed for the metal-bonded groups of the precursor dialkyl complexes. In contrast, the ^{13}C NMR resonance of the alkyl carbon atom is shifted to higher field (by about 10 ppm for Zr and 20 ppm Hf) on insertion. The most remarkable feature observed in the NMR spectra of these complexes is the chemical shift of the resonance due to the iminoacyl carbon atoms, which is shifted downfield at δ = 250–268 ppm. Another important spectroscopic feature that allows the assignment of the iminoacyl coordination mode in solution is the stretching ν(C=N) frequency of the iminoacyl bond observed in the IR spectra at 1540–1555 cm^{-1}, which corresponds to the η^2-coordinated iminoacyl ligands.[50] The ^{1}H NMR resonances due to the migrated alkyl groups in the C–C coupled enediamido complexes **18**–**20** are shifted downfield with respect to those observed for the starting bis(iminoacyl) compounds, whereas the ^{13}C NMR signals due to the enediamido sp^2-carbon atoms are observed at δ = 111–112 ppm.

Conclusions

Dichloro- and dialkyl(amidosilyl)cyclopentadienyl zirconium and -hafnium complexes of the type [M{η^5-C_5H_3[$SiMe_2$(CH_2CH=CH_2)]($SiMe_2$-η-NR)}X_2] with the allyldimethylsilyl-substituted cyclopentadienyl ligand have been isolated in high yields by conventional synthetic methods and characterised by NMR spectroscopy and X-ray diffraction methods.

The two non-equivalent chloro and alkyl ligands of these asymmetric molecules do not show diastereoselective reactions, so that alkylation of the dichloro complexes only gives dialkyl derivatives, and insertion of CN(2,6-$Me_2C_6H_3$) into the metal–alkyl bonds only afforded bis(iminoacyl) compounds. Formation of monoalkyl and monoiminoacyl complexes could not be detected in any of these reactions. NMR spectroscopic studies revealed that the iminoacyl ligand is η^2-coordinated in all of these compounds with the nitrogen atom always occupying the internal coordination site. C–C coupling reactions between the two iminoacyl ligands are very slow processes that give quantitative yields of the diazametallacyclopentene complexes after heating the toluene solutions of the bis(iminoacyl) complexes at 70–80 °C for 2–4 d.

Experimental Section

General Considerations: All manipulations were performed under argon using standard Schlenk and high-vacuum line techniques or a glovebox model MO40-2. Solvents were pre-dried and purified by distillation under argon from an appropriate drying agent (sodium for toluene, sodium/potassium alloy for hexane and sodium/benzophenone for diethyl ether and THF) before use. Deuterated solvents were stored over activated molecular sieves (4 Å) in Teflon-valved flasks and previously degassed by several freeze-pump-thaw cycles. NH_2tBu (Aldrich) was dried with sodium and distilled prior to use. $SiMe_2$(CH_2CH=CH_2)Cl (Aldrich), $SiMe_2Cl_2$ (Aldrich), *n*BuLi (Aldrich), $HfCl_4$ (Merck), MgClMe (Aldrich) and MgCl(CH_2Ph) (Aldrich) were purchased from commercial sources and used without further purification. C_5H_5[$SiMe_2$(CH_2CH=CH_2)],[51] [Li{$C_5H_4SiMe_2$(CH_2CH=CH_2)}],[51] and $ZrCl_4(THF)_2$[52] were prepared according to literature procedures. C, H and N microanalyses were performed with a Perkin–Elmer 240B. Unreliable elemental analytical data are not given for some highly soluble and air-sensitive compounds which could not be crystallised and were isolated as spectroscopically pure oily products. NMR spectra, measured at 25 °C, were recorded with a Varian Unity 300 (^{1}H NMR at 300 MHz and ^{13}C NMR at 75 MHz) spectrometer. ^{1}H and ^{13}C chemical shifts are reported in δ units relative to TMS standard.

Synthesis of C_5H_4($SiMe_2$Cl)[$SiMe_2$(CH_2CH=CH_2)] (1): $SiMe_2Cl_2$ (5.7 mL, 47 mmol) was added to a THF (100 mL) solution of [Li{η^5-$C_5H_4SiMe_2$(CH_2CH=CH_2)}] (8.0 g, 47 mmol), cooled to –78 °C and the mixture was stirred at room temperature for 16 h. The solvent was then removed under vacuum and the residue was

 © 2005 Wiley-VCH Verlag GmbH & Co. KGaA, Weinheim

extracted into hexane (2 × 50 mL). After filtration and evaporation of the solvent under reduced pressure, compound **1** was isolated as a yellow liquid (9.81 g, 38.18 mmol, 82% yield). $C_{12}H_{21}ClSi_2$ (256.92): calcd. C 56.10, H 8.24; found C 55.88, H 8.36. ^{1}H NMR (300 MHz, $CDCl_3$, 25 °C): δ = 0.05 (s, 6 H, SiMe_2), 0.23 (s, 6 H, SiMe_2), 1.47 (d, J = 8.1 Hz, 2 H, SiCH_2), 4.86 (m, 2 H, CH=CH_2), 5.65 (m, 1 H, CH=CH_2), 6.57 (m, 2 H, C_5H_4), 6.81 (m, 2 H, C_5H_4) ppm. ^{13}C{^{1}H} NMR (75 MHz, $CDCl_3$, 25 °C): δ = –2.9 (SiMe_2), 1.5 (SiMe_2), 22.8 (SiCH_2), 58.3 (C_5H_4, C_{ipso}), 113.9 (CH=CH_2), 133.1 (C_5H_4), 134.6 (C_5H_4), 134.9 (CH=CH_2) ppm. ^{1}H NMR (300 MHz, C_6D_6, 25 °C): δ = 0.04 (s, 6 H, SiMe_2), 0.10 (s, 6 H, SiMe_2), 1.47 (d, J = 8.1 Hz, 2 H, SiCH_2), 4.86 (m, 2 H, CH=CH_2), 5.63 (m, 1 H, CH=CH_2), 6.40 (m, 2 H, C_5H_4), 6.64 (m, 2 H, C_5H_4) ppm. ^{13}C{^{1}H} NMR (75 MHz, C_6D_6, 25 °C): δ = –2.9 (SiMe_2), 1.7 (SiMe_2), 22.6 (SiCH_2), 58.0 (C_5H_4, C_{ipso}), 113.6 (CH=CH_2), 132.8 (C_5H_4), 134.3 (C_5H_4), 134.7 (CH=CH_2) ppm.

Synthesis of C_5H_4[SiMe$_2$(CH$_2$CH=CH$_2$)][SiMe$_2$(NH*t*Bu)] (2): NH_2tBu (11.5 mL, 109 mmol) was added to a solution of **1** (14 g, 54.5 mmol) in THF at –78 °C. The mixture was slowly warmed to room temperature and stirred for 15 h. After removal of the solvent under vacuum, the residue was extracted into hexane and the ammonium chloride salt was removed by filtration. Product **2** was obtained as a yellow liquid (12.48 g, 42,51 mmol, 78% yield). $C_{16}H_{31}NSi_2$ (293.60): calcd. C 65.46 H, 10.64, N 4.77; found C 64.44, H 10.68, N 4.48. Major isomer: ^{1}H NMR (300 MHz, C_6D_6, 25 °C): δ = –0.14 (s, 3 H, SiMe_2), –0.01 (s, 3 H, SiMe_2), 0.26 (s, 3 H, SiMe_2), 0.36 (s, 3 H, SiMe_2), 0.60 (br. s, 1 H, NH), 1.08 (s, 9 H, CMe_3), 1.45 (m, 2 H, SiCH_2), 3.23 (br. s, 1 H, C_5H_4), 4.93 (m, 2 H, CH=CH_2), 5.69 (m, 1 H, CH=CH_2), 6.60, 6.81, 6.89 (m, 3 H, C_5H_4) ppm. Minor isomer: ^{1}H NMR (300 MHz, C_6D_6, 25 °C): δ = 0.05 (s, 6 H, SiMe_2), 0.07 (s, 6 H, SiMe_2), 0.66 (br. s, 1 H, NH), 1.15 (s, 9 H, CMe_3), 1.74 (m, J = 8.1 Hz, 2 H, SiCH_2), 4.93 (m, 2 H, CH=CH_2), 5.88 (m, 1 H, CH=CH_2), 6.46, 6.72 (m, 3 H, C_5H_4) ppm.

Synthesis of C_5H_4[SiMe$_2$(CH$_2$CH=CH$_2$)][SiMe$_2$NH(2,6-Me$_2$C$_6$H$_3$)] (3): Compound **1** (13 g, 53 mmol) was added at room temperature to a suspension of LiNH(2,6-$Me_2C_6H_3$) (6.7 g, 53 mmol) in hexane (100 ml) and the mixture was stirred for 16 h. LiCl was filtered off and the solvent was removed from the resulting solution to give an orange oil which was identified as **3** (14.5 g, 42.4 mmol, 80% yield). Major isomer: ^{1}H NMR (300 MHz, C_6D_6, 25 °C): δ = –0.20 (s, 3 H, SiMe_2), 0.01 (s, 3 H, SiMe_2), 0.14 (s, 3 H, SiMe_2), 0.34 (s, 3 H, SiMe_2), 1.39 (m, 2 H, SiCH_2), 2.15 (s, 6 H, C_6H_3 Me_2), 2.54 (br. s, 1 H, NH), 3.07 (br. s, 1 H, C_5H_4), 4.92 (m, 2 H, CH=CH_2), 5.68 (m, 1 H, CH=CH_2), 6.40–7.00 (m, C_5H_4 + C_6H_3) ppm. Minor isomer: ^{1}H NMR (300 MHz, C_6D_6, 25 °C): δ = 0.05 (s, 3 H, SiMe_2), 0.10 (s, 3 H, SiMe_2), 0.23 (s, 3 H, SiMe_2), 0.28 (s, 3 H, SiMe_2), 1.70 (m, 2 H, SiCH_2), 2.22 (s, 6 H, C_6H_3 Me_2), 2.54 (br. s, 1 H, NH), 2.92 (br. s, 1 H, C_5H_4), 4.92 (m, 2 H, CH=CH_2), 5.68 (m, 1 H, CH=CH_2), 6.40–700 (m, C_5H_4 + C_6H_3) ppm.

Synthesis of [Li$_2${1-SiMe$_2$N*t*Bu-3-SiMe$_2$(CH$_2$CH=CH$_2$)C$_5$H$_3$}] (4): A 1.6 M solution of *n*BuLi in hexane (17 ml, 28 mmol) was added dropwise to a solution of **3** (4 g, 14 mmol) in diethyl ether at –78 °C. The reaction mixture was warmed to room temperature and stirred for 4 h. The solvent was removed under reduced pressure to yield a solid, which was washed with hexane. The yellow solid was dried under vacuum and was characterised as **3** (3.85 g, 12.6 mmol, 90% yield). $C_{16}H_{29}Li_2NSi_2$ (305.47): calcd. C 62.91, H 9.57, N 4.59; found C 62.19, H 9.78, N 4.04. ^{1}H NMR (300 MHz, C_6D_6, 25 °C): δ = 0.30 (s, 6 H, SiMe_2), 0.46 (s, 6 H, SiMe_2), 1.18 (s, 9 H, CMe_3), 1.83 (m, 2 H, SiCH_2), 4.89 (m, 2 H, CH=CH_2), 6.04 (m, 1 H, CH=CH_2), 6.65 (m, 1 H, C_5H_3), 6.80 (m, 1 H, C_5H_3), 6.90 (m, 1 H, C_5H_3) ppm.

Synthesis of [Li$_2${1-SiMe$_2$N(2,6-Me$_2$C$_6$H$_3$)-3-SiMe$_2$(CH$_2$CH=CH$_2$)-C$_5$H$_3$}] (5): A suspension of **3** (14 g, 41 mmol) in diethyl ether was treated at –78 °C with a 1.6 M hexane solution of *n*BuLi (51 mL, 82 mmol). The mixture was stirred at room temperature for 4 h and the solvent was then removed under vacuum to give a yellow solid which, after being washed with hexane (2 × 50 mL) and dried under vacuum, was identified as the dilithium salt **5** (13 g, 36.9 mmol, 90% yield). $C_{20}H_{29}Li_2NSi_2$ (353.51): calcd. C 67.95, H 8.27, N 3.96; found C 67.18, H 8.02, N 3.95. ^{1}H NMR (300 MHz, C_6D_6, 25 °C): δ = 0.32 (s, 6 H, SiMe_2), 0.57 (s, 6 H, SiMe_2), 1.85 (m, 2 H, SiCH_2), 2.75 (s, 6 H, C_6H_3 Me_2), 4.90 (m, 2 H, CH=CH_2), 6.05 (m, 1 H, CH=CH_2), 6.75–7.45 (m, C_5H_3 + C_6H_3) ppm.

Synthesis of [Zr{η^5-C$_5$H$_3$(SiMe$_2$-η^1-N*t*Bu)[SiMe$_2$(CH$_2$CH=CH$_2$)]}Cl$_2$] (6): Toluene at –78 °C was added to a mixture of **4** (3 g, 9.8 mmol) and $ZrCl_4(THF)_2$ (3.7 g, 9.8 mmol) also cooled to –78 °C. The reaction mixture was warmed to room temperature and was stirred for 16 h. The toluene was removed under vacuum and the residue was extracted into hexane. The solvent volume was reduced and the solution was cooled to –40 °C to give yellow crystals which were isolated by filtration (2.67 g, 5.89 mmol, 60% yield). $C_{16}H_{29}Cl_2NSi_2Zr$ (453.71): calcd. C 42.36, H 6.44, N 3.09; found C 42.90, H 6.42, N 3.05. ^{1}H NMR (300 MHz, $CDCl_3$, 25 °C): δ = 0.33 (s, 6 H, SiMe_2), 0.55 (s, 6 H, SiMe_2), 1.37 (s, 9 H, CMe_3), 1.77 (m, 2 H, SiCH_2), 4.86 (m, 2 H, CH=CH_2), 5.74 (m, 1 H, CH=CH_2), 6.44 (t, 1 H, C_5H_3), 6.58 (t, 1 H, C_5H_3), 7.02 (t, 1 H, C_5H_3) ppm. ^{13}C{^{1}H} NMR (75 MHz, $CDCl_3$, 25 °C): δ = –3.6 (SiMe_2), –3.3 (SiMe_2), 0.5 (SiMe_2), 0.9 (SiMe_2), 23.7 (SiCH_2), 32.5 (CMe_3), 57.1 (CMe$_3$), 111.9 (C_5H_3, C_{ipso}), 113.7 (CH=CH_2), 126.1 (C_5H_3), 127.1 (C_5H_3), 132.9 (C_5H_3, C_{ipso}), 133.5 (CH=CH_2) ppm.

Synthesis of [Hf{η^5-C$_5$H$_3$(SiMe$_2$-η^1-N*t*Bu)[SiMe$_2$(CH$_2$CH=CH$_2$)]}Cl$_2$] (7): Toluene cooled to –78 °C was added to a mixture of **4** (1.5 g, 4.9 mmol) and $HfCl_4$ (1.6 g, 4.9 mmol) also at –78 °C. The reaction mixture was stirred while it was warmed to room temperature. After the solution had been stirred overnight, the toluene was removed under reduced pressure and the residue was extracted into hexane. The solution was filtered and the solvent was removed to give **7** as an orange oil (1.59 g, 2.95 mmol, 60% yield). ^{1}H NMR (300 MHz, $CDCl_3$, 25 °C): δ = 0.32 (s, 3 H, SiMe_2), 0.33 (s, 3 H, SiMe_2), 0.56 (s, 6 H, SiMe_2), 1.31 (s, 9 H, CMe_3), 1.77 (m, 2 H, SiCH$_2$), 4.89 (m, 2 H, CH=CH_2), 5.77 (m, 1 H, CH=CH_2), 6.35 (t, 1 H, C_5H_3), 6.49 (t, 1 H, C_5H_3), 6.97 (t, 1 H, C_5H_3) ppm. ^{13}C{^{1}H} NMR (75 MHz, $CDCl_3$, 25 °C): δ = –3.6 (SiMe_2), –3.3 (SiMe_2), 0.8 (SiMe_2), 1.2 (SiMe_2), 23.7 (SiCH_2), 33.2 (CMe_3), 55.6 (CMe$_3$), 111.8 (C_5H_3, C_{ipso}), 113.7 (CH=CH_2), 124.5 (C_5H_3), 125.6 (C_5H_3), 126.0 (C_5H_3), 131.6 (C_5H_3, C_{ipso}), 133.5 (CH=CH_2) ppm.

Synthesis of [Zr{η^5-C$_5$H$_3$[SiMe$_2$-η^1-N(2,6-Me$_2$C$_6$H$_3$)][SiMe$_2$(CH$_2$-CH=CH$_2$)]}Cl$_2$] (8): Toluene (100 mL) was added at –78 °C to a mixture of solid dilithium salt **5** (2 g, 5.66 mmol) and $ZrCl_4$·2THF (2.13 g; 5.66 mmol) and the mixture was then stirred at room temperature for 16 h. After filtration of the resulting LiCl, the solvent was removed under vacuum and the residue was extracted into hexane (2 × 50 mL). The solution was concentrated by evaporation of the solvent under reduced pressure and cooled to –35 °C to give compound **8** as an orange oily solid (0.91 g, 1.70 mmol, 30% yield). ^{1}H NMR (300 MHz, $CDCl_3$, 25 °C): δ = –0.04 (s, 3 H, SiMe_2), 0.12 (s, 3 H, SiMe_2), 0.38 (s, 3 H, SiMe_2), 0.39 (s, 3 H, SiMe_2), 1.52 (m, 2 H, SiCH_2), 1.80 (t, 4 H, C_2H_4), 2.10 (s, 3 H, C_6H_3 Me_2), 2.24 (s, 3 H, C_6H_3 Me_2), 3.70 (t, 4 H, OC_2H_4), 4.78 (m, 2 H, CH=CH_2), 5.61 (m, 1 H, CH=CH_2), 6.50 (t, 1 H, C_5H_3), 6.77 (t, 1 H, C_5H_3), 6.83 (t, 1 H, C_5H_3), 6.70–7.00 (m, 3 H, C_6H_3) ppm. ^{13}C{^{1}H} NMR (75 MHz, $CDCl_3$, 25 °C): δ = –2.7 (SiMe_2), –2.6 (SiMe_2), –0.4 (SiMe_2), 0.2 (SiMe_2), 20.3 (C_6H_3 Me_2), 20.6 (C_6H_3 Me_2), 24.8

 © 2005 Wiley-VCH Verlag GmbH & Co. KGaA, Weinheim

($SiCH_2$), 25.3 (C_2H_4), 68.5 (OC_2H_4), 113.2 (CH=CH_2), 116.7 (C_5H_3, C_{ipso}), 122.4 (C_5H_3), 124.2 (C_5H_3), 127.8 (C_5H_3), 127.8, 129.8, 130.0, 130.7, 132.4 (C_6H_3), 134.2 (C_5H_3, C_{ipso}), 134.9 (CH=CH_2), 151.2 (C_6H_3, C_{ipso}) ppm.

Synthesis of [Hf{η^5-C_5H_3[$SiMe_2$-η^1-N(2,6-$Me_2C_6H_3$)][$SiMe_2$(CH_2-CH=CH_2)]}Cl_2] (9): Toluene (100 mL) was added at room temperature to a mixture of **5** (2 g, 5.66 mmol) and $HfCl_4$ (1.81 g, 5.66 mmol). The mixture was stirred for 16 h and the solvent was then removed under reduced pressure to give a residue which was extracted into hexane (2 × 50 mL) to separate the LiCl formed. The resulting solution was concentrated and cooled to –35 °C overnight to give a colourless solid identified as **9** (1.0 g, 1.7 mmol, 30% yield). $C_{20}H_{29}Cl_2HfNSi_2$ (589.02): calcd. C 40.78, H 4.96, N 2.38; found C 40.77, H 5.09, N 2.23. ^{1}H NMR (300 MHz, $CDCl_3$, 25 °C): δ = 0.36 (s, 3 H, SiMe_2), 0.39 (s, 3 H, SiMe_2), 0.51 (s, 3 H, SiMe_2), 0.55 (s, 3 H, SiMe_2), 1.80 (m, 2 H, SiCH_2), 2.11 (s, 3 H, C_6H_3 Me_2), 2.14 (s, 3 H, C_6H_3 Me_2), 4.88 (m, 2 H, CH=CH_2), 5.77 (m, 1 H, CH=CH_2), 6.64 (t, 1 H, C_5H_3), 6.80 (t, 1 H, C_5H_3), 7.07 (t, 1 H, C_5H_3), 6.82–7.02 (m, 3 H, C_6H_3) ppm. ^{13}C{^{1}H} NMR (75 MHz, $CDCl_3$, 25 °C): δ = –3.0 (SiMe_2), –2.7 (SiMe_2), 0.1 (SiMe_2), 0.3 (SiMe_2), 19.6 (C_6H_3 Me_2), 19.7 (C_6H_3 Me_2), 24.2 (SiCH_2), 114.3 (CH=CH_2), 117.9 (C_5H_3, C_{ipso}), 123.9 (C_5H_3), 125.6 (C_5H_3), 125.8 (C_5H_3), 126.6–128.6 (C_6H_3), 133.7 (CH=CH_2), 142.5 (C_6H_3, C_{ipso}) ppm.

Synthesis of [Zr{η^5-C_5H_3[$SiMe_2$-η^1-N*t*Bu][$SiMe_2$(CH_2CH=CH_2)]}-Me_2] (10): A solution of MgClMe in THF (3.3 mL, 10 mmol) was added to a solution of **6** (2.3 g, 5.1 mmol) in hexane cooled to –78 °C. The reaction mixture was slowly warmed to room temperature and then stirred for 16 h. The solution was filtered and the solvent was removed under reduced pressure to give **10** as a brown oil (1.3 g, 3.1 mmol, 60% yield). $C_{18}H_{35}NSi_2Zr$ (412.87): calcd. C 52.37, H 8.54, N 3.39; found C 52.74, H 9.13, N 3.04. ^{1}H NMR (300 MHz, C_6D_6, 25 °C): δ = 0.15 (s, 3 H, ZrMe_2), 0.17 (s, 3 H, ZrMe_2), 0.26 (s, 3 H, SiMe_2), 0.27 (s, 3 H, SiMe_2), 0.35 (s, 6 H, SiMe_2), 1.36 (s, 9 H, CMe_3), 1.70 (m, 2 H, SiCH_2), 4.92 (m, 2 H, CH=CH_2), 5.80 (m, 1 H, CH=CH_2), 6.27 (t, 1 H, C_5H_3), 6.36 (t, 1 H, C_5H_3), 6.72 (t, 1 H, C_5H_3) ppm. ^{13}C{^{1}H} NMR (75 MHz, C_6D_6, 25 °C): δ = –2.9 (SiMe_2), –2.7 (SiMe_2), 1.5 (SiMe_2), 2.0 (SiMe_2), 24.9 (SiCH_2), 34.2 (CMe_3), 35.1 (ZrMe_2), 35.7 (ZrMe_2), 55.5 (CMe$_3$, C_{ipso}), 107.1 (C_5H_3, C_{ipso}), 113.9 (CH=CH_2), 122.8 (C_5H_3), 124.8 (C_5H_3), 125.2 (C_5H_3), 126.8 (C_5H_3, C_{ipso}), 134.6 (CH=CH_2) ppm.

Synthesis of [Zr{η^5-C_5H_3[$SiMe_2$-η^1-N*t*Bu][$SiMe_2$(CH_2CH=CH_2)]}-(CH_2Ph)$_2$] (11): A 2 M THF solution of MgClBz (5 mL, 10 mmol) was added at –78 °C to a hexane solution of the dichloro complex **6** (2.3 g, 5.1 mmol). The mixture was stirred for 16 h while it was warmed to room temp. After filtration to separate $MgCl_2$, the solvent was removed under vacuum to give **11** as a brown oil (1.73 g, 3.06 mmol, 60% yield). ^{1}H NMR (300 MHz, C_6D_6, 25 °C): δ = 0.22 (s, 3 H, SiMe_2), 0.24 (s, 3 H, SiMe_2), 0.34 (s, 3 H, SiMe_2), 0.36 (s, 3 H, SiMe_2), 1.11 (s, 9 H, CMe_3), 1.60 (m, 2 H, SiCH_2), 1.50 (d, J = 11.0 Hz, 1 H, CH_2Ph), 1.71 (d, J = 10.3 Hz, 1 H, CH_2Ph), 2.10 (d, J = 11.2 Hz, 1 H, CH_2Ph), 2.15 (d, J = 10.1 Hz, 1 H, CH_2Ph), 4.92 (m, 2 H, CH=CH_2), 5.72 (m, 1 H, CH=CH_2), 6.18 (t, 1 H, C_5H_3), 6.25 (t, 1 H, C_5H_3), 6.52 (t, 1 H, C_5H_3), 6.86–7.18 (m, 10 H, C_6H_5) ppm. ^{13}C{^{1}H} NMR (75 MHz, C_6D_6, 25 °C): δ = –2.7 (SiMe_2), –2.4 (SiMe_2), 1.5 (SiMe_2), 2.1 (SiMe_2), 25.3 (SiCH_2), 33.7 (CMe_3), 54.4 (ZrCH_2), 54.7 (CMe$_3$, C_{ipso}), 57.6 (ZrCH_2), 109.7 (C_5H_3, C_{ipso}), 114.0 (CH=CH_2), 122.4, 124.1, 125.4 (C_5H_3), 126.8, 127.7, 128. 3, 129.6, 129.7 (C_6H_5), 134.4 (CH=CH_2), 145.5, 145.9 (C_6H_5, C_{ipso}) ppm.

Synthesis of [Hf{η^5-C_5H_3[$SiMe_2$-η^1-N*t*Bu][$SiMe_2$(CH_2CH=CH_2)]}-Me_2] (12): A 3 M THF solution of MgClMe (2.9 mL, 8.8 mmol) was added at –78 °C to a solution of the dichloro complex **7** (2.4 g, 4.4 mmol) in hexane. The reaction mixture was stirred for 16 h while it was warmed slowly to room temp. The solution was filtered and the solvent removed under reduced pressure to give complex **12** as an orange oil (1.32 g, 2.64 mmol, 60% yield). $C_{18}H_{35}HfNSi_2$ (500.14): calcd. C 43.23, H 7.05, N 2.80; found C 43.09, H 7.51, N 2.67. ^{1}H NMR (300 MHz, C_6D_6, 25 °C): δ = 0.00 (s, 3 H, HfMe_2), 0.03 (s, 3 H, HfMe_2), 0.24 (s, 3 H, SiMe_2), 0.26 (s, 3 H, SiMe_2), 0.38 (s, 6 H, SiMe_2), 1.32 (s, 9 H, CMe_3), 1.68 (m, 2 H, SiCH_2), 4.91 (m, 2 H, CH=CH_2), 5.78 (m, 1 H, CH=CH_2), 6.20 (t, 1 H, C_5H_3), 6.27 (t, 1 H, C_5H_3), 6.67 (t, 1 H, C_5H_3) ppm. ^{13}C{^{1}H} NMR (75 MHz, C_6D_6, 25 °C): δ = –2.6 (SiMe_2), –2.4 (SiMe_2), 2.0 (SiMe_2), 2.4 (SiMe_2), 25.2 (SiCH_2), 35.1 (CMe_3), 47.1 (HfMe_2), 48.0 (HfMe_2), 55.0 (CMe$_3$, C_{ipso}), 107.9 (C_5H_3, C_{ipso}), 114.3 (CH=CH_2), 122.9 (C_5H_3), 125.2 (C_5H_3), 125.7 (C_5H_3), 126.9 (C_5H_3, C_{ipso}), 134.9 (CH=CH_2) ppm.

Synthesis of [Hf{η^5-C_5H_3[$SiMe_2$-η^1-N*t*Bu][$SiMe_2$(CH_2CH=CH_2)]}-(CH_2Ph)$_2$] (13): The same procedure described to prepare **11** was applied using a 2 M THF solution of MgClBz (4.4 mL, 8.8 mmol) and **7** (2.4 g, 4.4 mmol) to give **13** as an orange oil (1.72 g, 2.64 mmol, 60% yield). $C_{30}H_{43}HfNSi_2$ (652.34): calcd. C 55.24, H 6.64, N 2.15; found C 55.23, H 5.99, N 2.28. ^{1}H NMR (300 MHz, C_6D_6, 25 °C): δ = 0.22 (s, 3 H, SiMe_2), 0.24 (s, 3 H, SiMe_2), 0.38 (s, 3 H, SiMe_2), 0.41 (s, 3 H, SiMe_2), 1.19 (s, 9 H, CMe_3), 1.40 (d, J = 12.5 Hz, 1 H, CH_2Ph), 1.47 (d, J = 11.5 Hz, 1 H, CH_2Ph), 1.63 (m, 2 H, SiCH_2), 1.84 (d, J = 12.5 Hz, 1 H, CH_2Ph), 1.96 (d, J = 11.7 Hz, 1 H, CH_2Ph), 4.83 (m, 2 H, CH=CH_2), 5.69 (m, 1 H, CH=CH_2), 5.91 (t, 1 H, C_5H_3), 6.19 (t, 1 H, C_5H_3), 6.28 (t, 1 H, C_5H_3), 6.77–7.20 (m, 10 H, C_6H_5) ppm. ^{13}C{^{1}H} NMR (75 MHz, C_6D_6, 25 °C): δ = –2.8 (SiMe_2), –2.6 (SiMe_2), 1.4 (SiMe_2), 2.0 (SiMe_2), 25.0 (SiCH_2), 34.5 (CMe_3), 56.4 (CMe$_3$, C_{ipso}), 71.2 (HfCH_2), 73.5 (HfCH_2), 109.2 (C_5H_3, C_{ipso}), 114.0 (CH=CH_2), 122.0, 122.5, 125.3 (C_5H_3), 126.5, 126.7, 128. 2, 128.7, 128.8 (C_6H_5), 134.4 (CH=CH_2), 147.0, 147.3 (C_6H_5, C_{ipso}) ppm.

Synthesis of [Zr{η^5-C_5H_3($SiMe_2$-η^1-N*t*Bu)[$SiMe_2$(CH_2CH=CH_2)]}-{η^2-CMe=N(2,6-$Me_2C_6H_3$)}$_2$] (14): A solution of **10** (1.0 g, 2.42 mmol) in toluene (50 mL) was treated with a toluene (20 mL) solution of CN(2,6-$Me_2C_6H_3$) (0.63 g, 4.84 mmol) at room temperature. The mixture was stirred for 3 h and the solvent was then removed under vacuum. The residue was extracted into pentane (40 mL) and the solution was filtered and concentrated under reduced pressure to give a red oily product identified as compound **14** (1.31 g, 1.94 mmol, 80% yield). ^{1}H NMR (300 MHz, C_6D_6, 25 °C): δ = 0.11 (s, 3 H, SiMe_2), 0.25 (s, 3 H, SiMe_2), 0.70 (s, 6 H, SiMe_2), 1.11 (s, 9 H, CMe_3), 1.62 (m, 2 H, SiCH_2), 1.89 (s, 3 H, N$Me_2C_6H_3$), 1.93 (s, 6 H, N$Me_2C_6H_3$), 1.96 (s, 3 H, N$Me_2C_6H_3$), 2.05 (s, 3 H, CMe_2), 2.12 (s, 3 H, CMe_2), 4.90 (m, 2 H, CH=CH_2), 5.76 (m, 1 H, CH=CH_2), 6.33 (t, 1 H, C_5H_3), 6.53 (t, 1 H, C_5H_3), 6.61 (t, 1 H, C_5H_3), 6.90–7.00 (m, 6 H, C_6H_3) ppm. ^{13}C{^{1}H} NMR (75 MHz, C_6D_6, 25 °C): δ = –2.7 (SiMe_2), –2.5 (SiMe_2), 3.9 (SiMe_2), 4.6 (SiMe_2), 18.4, 18.7, 18.9, 19.6 (N$Me_2C_6H_3$), 24.2 (SiCH_2), 25.5, 25.6 (CMe_2), 35.3 (CMe_3), 55.8 (CMe$_3$, C_{ipso}), 113.4 (CH=CH_2), 114.5 (C_5H_3, C_{ipso}), 119.2, 121.4, 121.7 (C_5H_3), 125.3–129.9 (C_6H_3), 135.1 (CH=CH_2), 146.9, 147.4 (NC), 253.0, 257.1 (CMe$_2$) ppm.

Synthesis of [Zr{η^5-C_5H_3($SiMe_2$-η^1-N*t*Bu)[$SiMe_2$(CH_2CH=CH_2)]}-{η^2-C(CH_2Ph)=N(2,6-$Me_2C_6H_3$)}$_2$] (15): A toluene (10 mL) solution of CN(2,6-$Me_2C_6H_3$) (0.37 g, 2.83 mmol) was added to a solution of **11** (0.80 g, 1.42 mmol) in toluene (40 mL) and the mixture was stirred at room temperature overnight. The solvent was re-

 © 2005 Wiley-VCH Verlag GmbH & Co. KGaA, Weinheim

moved under vacuum and the resulting residue was extracted into pentane (40 mL). The solution was filtered and the solvent was removed under vacuum to give an orange oil identified as compound **15** (0.76 g, 0.92 mmol, 65% yield). ^{1}H NMR (300 MHz, C_6D_6, 25 °C): δ = 0.07 (s, 3 H, SiMe_2), 0.08 (s, 3 H, SiMe_2), 0.64 (s, 3 H, SiMe_2), 0.74 (s, 3 H, SiMe_2), 1.12 (s, 9 H, CMe_3), 1.45 (m, 2 H, SiCH_2), 1.65 (s, 3 H, NMeC$_6$H$_3$), 1.87 (s, 3 H, NMeC$_6$H$_3$), 1.97 (s, 3 H, NMeC$_6$H$_3$), 2.12 (s, 3 H, NMeC$_6$H$_3$), 3.47 (d, J = 14.3 Hz, 1 H, CH_2Ph), 3.60 (d, J = 17.3 Hz, 1 H, CH_2Ph), 3.64 (d, J = 14.6 Hz, 1 H, CH_2Ph), 3.80 (d, J = 17.3 Hz, 1 H, CH_2Ph), 4.85 (m, 2 H, CH=CH_2), 5.63 (m, 1 H, CH=CH$_2$), 6.10 (t, 1 H, C$_5H_3$), 6.21 (t, 1 H, C$_5H_3$), 6.84 (t, 1 H, C$_5H_3$), 6.50–7.40 (m, C$_6H_3$, C$_6H_5$) ppm. ^{13}C{^{1}H} NMR (75 MHz, C_6D_6, 25 °C): δ = –2.1 (SiMe_2), –1.9 (SiMe_2), 4.2 (SiMe_2), 4.6 (SiMe_2), 18.8, 19.0, 20.1, 20.3 (NMeC$_6$H$_3$), 26.2 (SiCH$_2$), 36.1 (CMe_3), 45.7, 46.1 (CH$_2$Ph), 56.4 (CMe$_3$, C$_{ipso}$), 113.6 (CH=CH$_2$), 115.4 (C_5H_3, C$_{ipso}$), 117.1, 121.2, 123.0 (C_5H$_3$), 125.5–130.7 (C_6H$_5$, C_6H$_3$), 135.4 (CH=CH$_2$), 137.7, 137.8, 147.5, 148.3 (C_6H$_5$, C_6H$_3$, C$_{ipso}$), 253.0, 257.1 [C(CH$_2$Ph)$_2$] ppm.

Synthesis of [Hf{η^5-C$_5$H$_3$(SiMe$_2$-η^1-N*t*Bu)[SiMe$_2$(CH$_2$CH=CH$_2$)]}{η^2-CMe=N(2,6-Me$_2$C$_6$H$_3$)}$_2$] (16): A toluene solution (60 mL) of CN(2,6-Me$_2$C$_6$H$_3$) (0.47 g, 3.60 mmol) and **12** (0.90 g, 1.80 mmol) was stirred at room temperature overnight. The solvent was removed under vacuum and the residue was extracted into pentane (40 mL). After filtration and elimination of the solvent under vacuum, compound **16** was obtained as a red oily product (1.37 g, 1.1 mmol, 80% yield). $C_{36}H_{53}HfN_3Si_2$ (762.50): calcd. C 56.71, H 7.01, N 5.51; found C 56.42, H 7.02, N 5.52. ^{1}H NMR (300 MHz, C_6D_6, 25 °C): δ = 0.09 (s, 3 H, SiMe_2), 0.25 (s, 3 H, SiMe_2), 0.67 (s, 3 H, *Si*Me_2), 0.70 (s, 3 H, SiMe_2), 1.08 (s, 9 H, CMe_3), 1.59 (m, 2 H, SiCH$_2$), 1.95 (s, 3 H, NMeC$_6$H$_3$), 1.96 (s, 6 H, NMe_2C$_6$H$_3$), 1.98 (s, 3 H, NMeC$_6$H$_3$), 2.10 (s, 3 H, CMe), 2.19 (s, 3 H, CMe), 4.86 (m, 2 H, CH=CH_2), 5.72 (m, 1 H, CH=CH$_2$), 6.27 (t, 1 H, C$_5H_3$), 6.46 (t, 2 H, C$_5H_3$), 6.95–7.00 (m, 6 H, C$_6H_3$) ppm. ^{13}C{^{1}H} NMR (75 MHz, C_6D_6, 25 °C): δ = –2.8 (SiMe_2), –2.5 (SiMe_2), 4.1 (SiMe_2), 4.6 (SiMe_2), 18.5, 18.6, 18.8, 19.8 (NMeC$_6$H$_3$), 24.6 (SiCH$_2$), 25.7, 25.9 (CMe_2), 35.5 (CMe_3), 55.5 (CMe$_3$, C$_{ipso}$), 113.4 (CH=CH$_2$), 114.1 (C_5H$_3$, C$_{ipso}$), 118.3, 120.3, 120.7 (C_5H$_3$), 125.3–129.5 (C_6H$_3$), 135.1 (CH=CH$_2$), 146.3, 146.8 (NC), 262.3, 268.6 (CMe$_2$) ppm.

Synthesis of [Hf{η^5-C$_5$H$_3$(SiMe$_2$-η^1-N*t*Bu)[SiMe$_2$(CH$_2$CH=CH$_2$)]}{η^2-C(CH$_2$Ph)=N(2,6-Me$_2$C$_6$H$_3$)}$_2$] (17): A toluene (50 mL) solution containing **13** (0.80 g, 1.23 mmol) and CN(2,6-Me$_2$C$_6$H$_3$) (0.32 g, 2.46 mmol) was stirred at room temperature for 2 d. The solvent was removed under reduced pressure and the residue was extracted into pentane (40 mL). After filtration, the solvent was removed under vacuum to give an orange oil identified as compound **17** (0.79 g, 0.86 mmol, 70% yield). $C_{48}H_{61}HfN_3Si_2$ (914.69): calcd. C 63.03, H 6.72, N 4.59; found C 63.00, H 6.55, N 4.50. ^{1}H NMR (300 MHz, C_6D_6, 25 °C): δ = 0.06 (s, 3 H, SiMe_2), 0.09 (s, 3 H, SiMe_2), 0.64 (s, 3 H, SiMe_2), 0.71 (s, 3 H, SiMe_2), 1.11 (s, 9 H, CMe_3), 1.44 (m, 2 H, SiCH_2), 1.72 (s, 3 H, NMeC$_6$H$_3$), 1.89 (s, 3 H, NMeC$_6$H$_3$), 2.00 (s, 3 H, NMeC$_6$H$_3$), 2.11 (s, 3 H, NMeC$_6$H$_3$), 3.54 (d, J = 14.5 Hz, 1 H, CH_2Ph), 3.69 (d, J = 16.8 Hz, 1 H, CH_2Ph), 3.72 (d, J = 14.5 Hz, 1 H, CH_2Ph), 3.86 (d, J = 17.0 Hz, 1 H, CH_2Ph), 4.83 (m, 2 H, CH=CH_2), 5.62 (m, 1 H, CH=CH$_2$), 6.09 (t, 1 H, C$_5H_3$), 6.21 (t, 1 H, C$_5H_3$), 6.72 (t, 1 H, C$_5H_3$), 6.55–7.35 (m, C$_6H_3$, C$_6H_5$) ppm. ^{13}C{^{1}H} NMR (75 MHz, C_6D_6, 25 °C): δ = –2.5 (SiMe_2), –2.3 (SiMe_2), 3.9 (SiMe_2), 4.5 (SiMe_2), 18.6, 19.7, 20.0 (NMeC$_6$H$_3$), 25.9 (SiCH$_2$), 36.0 (CMe_3), 45.8, 46.2 (CH$_2$Ph), 55.7 (CMe$_3$, C$_{ipso}$), 113.3 (CH=CH$_2$), 115.8 (C_5H$_3$, C$_{ipso}$), 120.2, 125.4, 126.7 (C_5H$_3$), 128.5–130.4 (C_6H$_5$, C_6H$_3$), 135.1 (CH=CH$_2$), 137.4, 137.5, 147.0, 147.5 (C_6H$_5$, C_6H$_3$, C$_{ipso}$), 261.2, 265.4 [C(CH$_2$Ph)$_2$] ppm.

Synthesis of [Zr{η^5-C$_5$H$_3$(SiMe$_2$-η^1-N*t*Bu)[SiMe$_2$(CH$_2$CH=CH$_2$)]}{η-N(2,6-Me$_2$C$_6$H$_3$)CMe=CMe-η-N(2,6-Me$_2$C$_6$H$_3$)}] (18): A toluene (50 mL) solution of **14** (0.63 g, 0.93 mmol) was heated at 70 °C for 2 d in a Teflon-valved Schlenk vessel. The solvent was then removed under vacuum and the residue was extracted into pentane (40 mL). After removal of the solvent under vacuum, compound **18** was isolated as a red oil (0.63 g, 0.93 mmol, 100% yield). ^{1}H NMR (300 MHz, C_6D_6, 25 °C): δ = –0.25 (s, 3 H, SiMe_2), –0.12 (s, 3 H, SiMe_2), 0.64 (s, 3 H, SiMe_2), 0.66 (s, 3 H, SiMe_2), 1.10 (s, 9 H, CMe_3), 1.23 (m, 2 H, SiCH_2), 1.59 (s, 3 H, NMeC$_6$H$_3$), 1.62 (s, 3 H, NMeC$_6$H$_3$), 2.04 (s, 3 H, NMeC$_6$H$_3$), 2.09 (s, 3 H, NMeC$_6$H$_3$), 2.45 (s, 3 H, CMe_2), 2.52 (s, 3 H, CMe_2), 4.74 (m, 2 H, CH=CH_2), 5.50 (m, 1 H, CH=CH$_2$), 6.16 (t, 1 H, C$_5H_3$), 6.35 (t, 1 H, C$_5H_3$), 6.53 (t, 1 H, C$_5H_3$), 6.90–7.10 (m, 6 H, C$_6H_3$) ppm. ^{13}C{^{1}H} NMR (75 MHz, C_6D_6, 25 °C): δ = –4.4 (SiMe_2), –3.5 (SiMe_2), 3.4 (SiMe_2), 3.6 (SiMe_2), 16.9, 17.9, 19.8, 19.9 (NMeC$_6$H$_3$), 21.2, 21.7 (CMe_2), 24.5 (SiCH$_2$), 35.7 (CMe_3), 55.5 (CMe$_3$, C$_{ipso}$), 110.8, 111.2 (NC=CN), 113.3 (CH=CH$_2$), 114.5 (C_5H$_3$, C$_{ipso}$), 122.7, 123.4, 124.5 (C_5H$_3$), 125.3–129.5 (C_6H$_3$), 132.3, 133.2, 133.3, 133.8 (C_6H$_3$, C$_{ipso}$), 134.8 (CH=CH$_2$), 149.9, 150.1 (NC) ppm.

Synthesis of [Hf{η^5-C$_5$H$_3$(SiMe$_2$-η^1-N*t*Bu)[SiMe$_2$(CH$_2$CH=CH$_2$)]}{η-N(2,6-Me$_2$C$_6$H$_3$)CMe=CMe-η-N(2,6-Me$_2$C$_6$H$_3$)}] (19): A toluene (50 mL) solution of **15** (0.60 g, 0.79 mmol) was heated at 80 °C for 2 d in a Teflon-valved Schlenk vessel and the solvent was then removed under vacuum. The residue was extracted into pentane (40 mL) and the solvent was removed under vacuum to give compound **19** as a brown oil. (0.60 g, 0.79 mmol, 100% yield). $C_{36}H_{53}HfN_3Si_2$ (762.50): calcd. C 56.71, H 7.01, N 5.51; found C 56.42, H 7.02, N 5.52. ^{1}H NMR (300 MHz, C_6D_6, 25 °C): δ = –0.22 (s, 3 H, SiMe_2), –0.12 (s, 3 H, SiMe_2), 0.65 (s, 3 H, SiMe_2), 0.68 (s, 3 H, SiMe_2), 1.08 (s, 9 H, CMe_3), 1.29 (m, 2 H, SiCH_2), 1.60 (s, 3 H, NMeC$_6$H$_3$), 1.61 (s, 3 H, NMeC$_6$H$_3$), 1.99 (s, 3 H, NMeC$_6$H$_3$), 2.06 (s, 3 H, NMeC$_6$H$_3$), 2.41 (s, 3 H, CMe_2), 2.49 (s, 3 H, CMe_2), 4.79 (m, 2 H, CH=CH_2), 5.53 (m, 1 H, CH=CH$_2$), 6.14 (t, 1 H, C$_5H_3$), 6.46 (t, 1 H, C$_5H_3$), 6.65 (t, 1 H, C$_5H_3$), 6.91–7.08 (m, 6 H, C$_6H_3$) ppm. ^{13}C{^{1}H} NMR (75 MHz, C_6D_6, 25 °C): δ = –4.0 (SiMe_2), –3.3 (SiMe_2), 3.9 (SiMe_2), 4.0 (SiMe_2), 17.0, 18.5, 20.0, 20.2 (NMe_2C$_6$H$_3$), 21.4, 22.6 (CMe_2), 24.7 (SiCH$_2$), 35.6 (CMe_3), 55.7 (CMe$_3$, C$_{ipso}$), 112.0, 112.1 (NC=CN), 113.3 (CH=CH$_2$), 114.9 (C_5H$_3$, C$_{ipso}$), 123.3, 123.4, 124.6 (C_5H$_3$), 125.4–129.5 (C_6H$_3$), 132.0, 132.5, 132.8, 133.2 (C_6H$_3$, C$_{ipso}$), 134.8 (CH=CH$_2$), 149.8, 149.9 (NC) ppm.

Synthesis of [Zr{η^5-C$_5$H$_3$(SiMe$_2$-η^1-N*t*Bu)[SiMe$_2$(CH$_2$CH=CH$_2$)]}{η-N(2,6-Me$_2$C$_6$H$_3$)C(CH$_2$Ph)=C(CH$_2$Ph)-η-N(2,6-Me$_2$C$_6$H$_3$)}] (20): A toluene (50 mL) solution of **16** (0.80 g, 0.97 mmol) was heated at 80 °C for 4 d and the solvent was then removed under vacuum. The residue was extracted into pentane (40 mL) and the solvent was removed under vacuum to give a brown oil identified as compound **20** (0.80 g, 0.97 mmol, 100% yield). ^{1}H NMR (300 MHz, C_6D_6, 25 °C): δ = –0.29 (s, 3 H, SiMe_2), –0.15 (s, 3 H, SiMe_2), 0.63 (s, 3 H, SiMe_2), 0.65 (s, 3 H, SiMe_2), 1.01 (s, 9 H, CMe_3), 1.18 (m, 2 H, SiCH_2), 1.77 (s, 3 H, NMeC$_6$H$_3$), 1.98 (s, 3 H, NMeC$_6$H$_3$), 2.47 (s, 3 H, NMeC$_6$H$_3$), 2.50 (s, 3 H, NMeC$_6$H$_3$), 3.21 (d, J = 15.2 Hz, 1 H, CH_2Ph), 3.61 (d, J = 14.3 Hz, 1 H, CH_2Ph), 3.87 (d, J = 14.5 Hz, 1 H, CH_2Ph), 4.35 (d, J = 15.4 Hz, 1 H, CH_2Ph), 4.76 (m, 2 H, CH=CH_2), 5.50 (m, 1 H, CH=CH$_2$), 6.11 (t, 1 H, C$_5H_3$), 6.20 (t, 1 H, C$_5H_3$), 6.59 (t, 1 H, C$_5H_3$), 6.65–7.15 (m, C$_6H_5$, C$_6H_3$) ppm. ^{13}C{^{1}H} NMR (75 MHz, C_6D_6, 25 °C): δ = –4.7 (SiMe_2), –3.7 (SiMe_2), 3.1 (SiMe_2), 3.9 (SiMe_2), 20.2, 20.3, 21.5, 22.0 (NMeC$_6$H$_3$), 24.5 (SiCH$_2$), 35.6 (CMe_3), 38.3,

 © 2005 Wiley-VCH Verlag GmbH & Co. KGaA, Weinheim

39.2 (CH_2Ph), 55.5 (CMe_3, C_{ipso}), 112.8 (N*C*=*C*N), 113.2 (CH=*C*H_2), 117.3, 119.4 (C_5H_3, C_{ipso}), 123.3, 123.8, 124.8 (C_5H_3), 125.8–129.4 (C_6H_3, C_6H_5), 134.7 (*C*H=CH_2), 138.6, 139.1, 149.4, 149.8 (C_6H_3, C_6H_5, C_{ipso}) ppm.

X-ray Structure Determination of [ZrCl(μ-Cl){η⁵-C_5H_3($SiMe_2$-η¹-N*t*Bu)[$SiMe_2$($CH_2CH=CH_2$)]}]₂ (6): Crystals of compound **6** were obtained by crystallisation from hexane, and a suitably sized crystal in a Lindemann tube was mounted on a Philips PW 1100 diffractometer with graphite-monochromated Mo-K_α radiation (λ = 0.71073 Å). Crystallographic and experimental details are summarised in Table 2. No decay was observed during the data collection. A semi-empirical method of absorption correction was applied (maximum and minimum values for the transmission coefficient were 1.000 and 0.665).[53] The structure was solved by direct methods (SIR97)[54] and refined by least squares against F_o^2 (SHELXL-97).[55] All the non-hydrogen atoms were refined anisotropically and the hydrogen atoms were introduced from geometrical calculations and refined using a riding model. The programs PARST[56] ad ORTEP[57] were also used. CCDC-273336 (**6**) contains the supplementary crystallographic data for this paper. These data can be obtained free of charge from The Cambridge Crystallographic Data Centre via www.ccdc.cam.ac.uk/data_request/cif.

Table 2. Crystal data and structure refinement for **6**.

Empirical formula	$C_{32}H_{58}Cl_4N_2Si_4Zr_2$
Formula mass	907.40
Temperature	293(2) K
Wavelength	0.71073 Å
Crystal system, space group	monoclinic, $P2_1/a$
Unit cell dimensions	a = 14.412(9) Å b = 12.300(6) Å, β = 92.29(2)° c = 12.784(6) Å
Volume	2264(2) Å^3
Z, calculated density	2, 1.331 Mg m^{-3}
Absorption coefficient	0.825 mm^{-1}
F(000)	936
Crystal size	0.45 × 0.25 × 0.20 mm
Theta range for data collection	3.19–24.00°
Limiting indices	$-16 \le h \le 16$, $0 \le k \le 14$, $0 \le l \le 14$
Reflections collected/unique	3729/3563 [R(int) = 0.0971]
Completeness to θ = 24.00	99.8%
Absorption correction	empirical
Max./min. transmission	1.000/0.665
Refinement method	full-matrix least squares on F^2
Data/restraints/parameters	3563/0/199
Goodness-of-fit on F^2	0.857
Final R indices [$I > 2\sigma(I)$]	R_1 = 0.0514, wR_2 = 0.1102
R indices (all data)	R_1 = 0.1346, wR_2 = 0.1372
Largest diff. peak and hole	0.444 and –0.503 e Å^{-3}

Acknowledgments

Financial support of our work by MEC (project MAT2004-02614) and DGU-CM (project GR/MAT/0622/2004) is gratefully acknowledged.

[1] X. M. Yang, C. L. Stern, T. J. Marks, *J. Am. Chem. Soc.* **1991**, *113*, 3623–3625.
[2] M. Bochmann, S. J. Lancaster, M. B. Hursthouse, K. M. A. Malik, *Organometallics* **1994**, *13*, 2235–2243.
[3] X. M. Yang, C. L. Stern, T. J. Marks, *J. Am. Chem. Soc.* **1994**, *116*, 10015–10031.
[4] S. Beck, M. H. Prosenc, H. H. Brintzinger, R. Goretzki, N. Herfert, G. Fink, *J. Mol. Catal. A: Chem.* **1996**, *111*, 67–79.
[5] E. Y. X. Chen, T. J. Marks, *Chem. Rev.* **2000**, *100*, 1391–1434.
[6] S. Beck, S. Lieber, F. Schaper, A. Geyer, H. H. Brintzinger, *J. Am. Chem. Soc.* **2001**, *123*, 1483–1489.
[7] S. Döring, V. V. Kotov, G. Erker, G. Kehr, K. Bergander, O. Kataeva, R. Fröhlich, *Eur. J. Inorg. Chem.* **2003**, 1599–1607.
[8] T. Beringhelli, G. D'Alfonso, D. Maggioni, P. Mercandelli, A. Sironi, *Chem. Eur. J.* **2005**, *11*, 650–661.
[9] D. Maggioni, T. Beringhelli, G. D'Alfonso, L. Resconi, *J. Organomet. Chem.* **2005**, *690*, 640–646.
[10] C. P. Casey, D. W. Carpenetti, H. Sakurai, *J. Am. Chem. Soc.* **1999**, *121*, 9483–9484.
[11] R. F. Jordan, *Adv. Organomet. Chem.* **1991**, *32*, 325–387.
[12] T. J. Marks, *Acc. Chem. Res.* **1992**, *25*, 57–65.
[13] H. H. Brintzinger, D. Fischer, R. Mülhaupt, B. Rieger, R. M. Waymouth, *Angew. Chem. Int. Ed. Engl.* **1995**, *34*, 1143–1170.
[14] M. Bochmann, *J. Chem. Soc., Dalton Trans.* **1996**, 255–270.
[15] L. Resconi, L. Cavallo, A. Fait, F. Piemontesi, *Chem. Rev.* **2000**, *100*, 1253–1345.
[16] Z. Wu, R. F. Jordan, J. L. Petersen, *J. Am. Chem. Soc.* **1995**, *117*, 5867–5868.
[17] C. P. Casey, D. W. Carpenetti, *Organometallics* **2000**, *19*, 3970–3977.
[18] C. P. Casey, S. L. Hallenbeck, D. W. Pollock, C. R. Landis, *J. Am. Chem. Soc.* **1995**, *117*, 9770–9771.
[19] J. F. Carpentier, V. P. Maryin, J. Luci, R. F. Jordan, *J. Am. Chem. Soc.* **2001**, *123*, 898–909.
[20] J. F. Carpentier, Z. Wu, C. W. Lee, S. Stromberg, J. N. Christopher, R. F. Jordan, *J. Am. Chem. Soc.* **2000**, *122*, 7750–7767.
[21] E. J. Stoebenau III, R. F. Jordan, *J. Am. Chem. Soc.* **2003**, *125*, 3222–3223.
[22] Z. T. Xu, K. Vanka, T. Ziegler, *Organometallics* **2004**, *23*, 104–116.
[23] K. Kunz, G. Erker, G. Kehr, R. Fröhlich, H. Jacobsen, H. Berke, O. Blacque, *J. Am. Chem. Soc.* **2002**, *124*, 3316–3326.
[24] G. Lanza, I. L. Fragala, T. J. Marks, *J. Am. Chem. Soc.* **2000**, *122*, 12764–12777.
[25] K. Vanka, M. S. W. Chan, C. C. Pye, T. Ziegler, *Organometallics* **2000**, *19*, 1841–1849.
[26] A. T. Rappe, W. M. Skiff, C. J. Casewit, *Chem. Rev.* **2000**, *100*, 1435–1456.
[27] M. S. W. Chan, K. Vanka, C. C. Pye, T. Ziegler, *Organometallics* **1999**, *18*, 4624–4636.
[28] L. T. Li, T. J. Marks, *Organometallics* **1998**, *17*, 3996–4003.
[29] L. Jia, X. M. Yang, C. L. Stern, T. J. Marks, *Organometallics* **1997**, *16*, 842–857.
[30] P. A. Deck, T. J. Marks, *J. Am. Chem. Soc.* **1995**, *117*, 6128–6129.
[31] J. Cano, P. Gómez-Sal, G. Heinz, G. Martínez, P. Royo, *Inorg. Chim. Acta* **2003**, *345*, 15–26.
[32] M. V. Galakhov, G. Heinz, P. Royo, *Chem. Commun.* **1998**, 17–18.
[33] T. Cuenca, P. Royo, *Coord. Chem. Rev.* **1999**, *195*, 447–498.
[34] M. J. Humphries, M. L. H. Green, R. E. Douthwaite, L. H. Rees, *J. Chem. Soc., Dalton Trans.* **2000**, 4555–4562.
[35] S. Ciruelos, T. Cuenca, R. Gomez, P. Gómez-Sal, A. Manzanero, P. Royo, *Organometallics* **1996**, *15*, 5577–5585.
[36] S. Ciruelos, A. Sebastian, T. Cuenca, P. Gómez-Sal, A. Manzanero, P. Royo, *J. Organomet. Chem.* **2000**, *604*, 103–115.
[37] H. G. Alt, K. Föttinger, W. Milius, *J. Organomet. Chem.* **1998**, *564*, 115–123.
[38] H. G. Alt, K. Föttinger, W. Milius, *J. Organomet. Chem.* **1999**, *572*, 21–30.
[39] W. P. Leung, F. Q. Song, Z. Y. Zhou, F. Xue, T. C. W. Mak, *J. Organomet. Chem.* **1999**, *575*, 232–241.
[40] A. Razavi, U. Thewalt, *J. Organomet. Chem.* **2001**, *621*, 267–276.
[41] Y. Mu, W. E. Piers, D. C. MacQuarrie, M. J. Zaworotko, *Can. J. Chem.* **1996**, *74*, 1696–1703.

 © 2005 Wiley-VCH Verlag GmbH & Co. KGaA, Weinheim

[42] J. Okuda, T. Eberle, T. P. Spaniol, V. Piquet-Faure, *J. Organomet. Chem.* **1999**, *591*, 127–137.
[43] P. Doufou, K. A. Abboud, J. M. Boncella, *J. Organomet. Chem.* **2000**, *603*, 213–219.
[44] K. E. Duplooy, U. Moll, S. Wocadlo, W. Massa, J. Okuda, *Organometallics* **1995**, *14*, 3129–3131.
[45] D. W. Carpenetti, L. Kloppenburg, J. T. Kupec, J. L. Petersen, *Organometallics* **1996**, *15*, 1572–1581.
[46] J. Cano, P. Royo, M. Lanfranchi, M. A. Pellinghelli, A. Tiripicchio, *Angew. Chem. Int. Ed.* **2001**, *40*, 2495.
[47] A. Sebastian, P. Royo, P. Gómez-Sal, C. Ramírez de Arellano, *Eur. J. Inorg. Chem.* **2004**, 3814–3821.
[48] L. Kloppenburg, J. L. Petersen, *Organometallics* **1997**, *16*, 3548–3556.
[49] L. D. Durfee, I. P. Rothwell, *Chem. Rev.* **1988**, *88*, 1059–1079.
[50] L. R. Chamberlain, L. D. Durfee, P. E. Fanwick, L. Kobriger, S. L. Latesky, A. K. McMullen, I. P. Rothwell, K. Folting, J. C. Huffman, W. E. Streib, R. Wang, *J. Am. Chem. Soc.* **1987**, *109*, 390–402.
[51] P. Nicolas, P. Royo, M. V. Galakhov, O. Blacque, H. Jacobsen, H. Berke, *Dalton Trans.* **2004**, 2943–2951.
[52] L. E. Manzer, *Inorg. Synth.* **1982**, *21*, 135–140.
[53] A. C. T. North, D. C. Phillips, F. S. Mathews, *Acta Crystallogr., Sect. A* **1968**, *24*, 351.
[54] A. Altomare, M. C. Burla, M. Camalli, G. L. Cascarano, C. Giacovazzo, A. Guagliardi, A. G. G. Moliterni, G. Polidori, R. Spagna, *J. Appl. Crystallogr.* **1999**, *32*, 115–119.
[55] G. M. Sheldrick, *SHELXL-97*, *Program for the Refinement of Crystal Structures*, Universität Göttingen, Göttingen, Germany, **1997**.
[56] M. Nardelli, *Comput. Chem.* **1983**, *7*, 95–98.
[57] L. Zsolnai, H. Pritzkow, *ZORTEP – ORTEP* original program modified for PC, Universität Heidelberg, Heidelberg, **1994**.

Received: April 28, 2005
Published Online: August 31, 2005

 © 2005 Wiley-VCH Verlag GmbH & Co. KGaA, Weinheim

Pyridine-Ring Alkylation of Cytotoxic *r*-1,*c*-3,*c*-5-Tris[(2-pyridylmethyl)-amino]cyclohexane Chelators: Structural and Electronic Properties of the Mn^{II}, Fe^{II}, Ni^{II}, Cu^{II} and Zn^{II} Complexes

Matt L. Childers,[a] Fan Su,[a] Ann M. Przyborowska,[a] Bimjhana Bishwokarma,[a] Gyungse Park,[a][‡] Martin W. Brechbiel,[b] Suzy V. Torti,[c] Frank M. Torti,[c] Grant Broker,[d] Jacob S. Alexander,[e] Robin D. Rogers,[d] Karin Ruhlandt-Senge,[e] and Roy P. Planalp*[a]

Dedicated to Prof. Dr. Heinrich Vahrenkamp on the occasion of his 65th birthday

Keywords: Antitumor activity / Tripodal ligands / Ligand design / Iron / Zinc / Copper

Effects of pyridyl-ring alkylation on complexation of Mn^{II}, Fe^{II}, Ni^{II}, Cu^{II} and Zn^{II} by chelators based on *r*-1,*c*-3,*c*-5-triaminocyclohexane (tach) have been studied. The chelators studied are *N*,*N*′,*N*′′-tris[(*x*-alkyl-2-pyridyl)methyl] derivatives of tach, where the ring substituents are 3-Me, 4-Me, 5-Me, 6-Me or 6-MeO ("tach-*x*-Rpyr"). Dicationic complexes were synthesized for most combinations of the above five metals and five chelators, using ClO_4^-, NO_3^-, Cl^-, or $CF_3SO_3^-$ as counterions. Their bonding, structure, and aqueous lability were analyzed by UV/Vis/NIR spectroscopy, magnetic moment determination, HPLC, and single-crystal X-ray crystallography. The striking features are seen in the 6-alkylated complexes, where steric repulsions between the 6-substituents at the threefold axis of the pseudo-octahedral coordination sphere result in a substantially weakened metal–ligand interaction. In the $[M(tach\text{-}6\text{-}Rpyr)]^{2+}$ series of divalent Mn, Ni, Cu and Zn, effects of these repulsions include bond angle and length distortions, decrease of the coordination number to five, shifts of d-d electronic transitions to lower energies, and spin-free complexes of the bound metal ion. Aqueous lability studies by HPLC agree with the spectroscopic findings. The bonding properties of the other tach-*x*-Mepyr chelators (x = 3, 4, 5) closely resemble the unalkylated parent tachpyr in solution. Similarly in the X-ray studies, $[Zn(tach\text{-}3\text{-}Mepyr)]^{2+}$ resembles $[Zn(tachpyr)]^{2+}$. The cytotoxicities of the chelators toward human breast cancer cells (MCF7) at a fixed chelator concentration of 16 μM show time-dependent induction of cell death in the order tach-3-Mepyr $>\approx$ tach-4-Mepyr $>$ tach-5-Mepyr $>$ tachpyr, whereas tach-6-Mepyr and tach-6-MeOpyr had no effect on the cells. The depressed cytotoxicities of the latter two are attributed to inability to bind Fe^{II} or Zn^{II} strongly.
(© Wiley-VCH Verlag GmbH & Co. KGaA, 69451 Weinheim, Germany, 2005)

Introduction

The tripodal aminopyridyl chelator tachpyr {*r*-1,*c*-3,*c*-5-tris[(2-pyridylmethyl)amino]cyclohexane} has been shown to readily complex divalent 3d transition metal ions;[1–4] tachpyr and its derivatives are under consideration as chemotherapeutic agents.[5–7] It is strongly cytotoxic to a variety of tumor cells as seen by an IC_{50} of 4.8 μM toward cultured bladder tumor cells. It is also preferentially toxic, showing a sevenfold decrease in IC_{50} in cancer cells relative to normal cells.[8] We have recently shown that it binds Zn^{II} and Fe^{II} in cells, and that the binding of Fe^{II} in vitro is accompanied by redox processes.[9] Metal complexes are well known to promote oxidative damage by catalyzing production of $HO^{\cdot}$, $O_2^{\cdot-}$, or other species collectively termed reactive oxygen species (ROS). We therefore pursue the hypotheses that tachpyr may affect cells by causing depri-

[‡] Current address: School of Science and Technology, Kunsan National University,
68, Miryong-Dong, Kusan, Jeollabuk-Do, Republik of Korea 573-701
[a] Department of Chemistry, University of New Hampshire, Durham, NH 03824-3598, USA
Fax: + 603-862-4278
E-mail: roy.planalp@unh.edu
[b] Radiation Oncology Branch, National Institutes of Health, Bethesda, MD 20892, USA
[c] Departments of Biochemistry and Cancer Biology and the Comprehensive Cancer Center, Wake Forest University Health Sciences,
Winston-Salem, NC 27157, USA
[d] Department of Chemistry, The University of Alabama, Tuscaloosa, AL 35487, USA
[e] Department of Chemistry, Syracuse University, Syracuse, NY 13244, USA
Supporting information for this article is available on the WWW under http://www.eurjic.org or from the author.

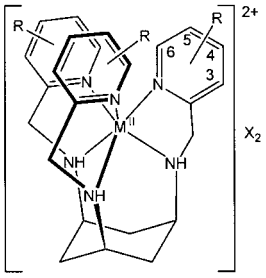

M(II)	tach-3-Mepyr (R = Me)	tach-4-Mepyr (R = Me)	tach-5-Mepyr (R = Me)	tach-6-Mepyr (R = Me)	tach-6-MeOpyr (R = MeO)	tachpyr (R = H)
Mn(II)	–	–	–	**1d** (X=ClO_4^-) **1d'** (X=$CF_3SO_3^-$)	**1e** (X=$CF_3SO_3^-$)	–
Fe(II)[a]	**2a**	**2b**	**2c**	**2d** (X=ClO_4^-)	**2e**	–
Ni(II)[b]	**3a**	**3b**	**3c**	**3d** (X= ClO_4^-) **3d'** (X= NO_3^-)	**3e**	–
Cu(II)[b]	**4a**	**4b**	**4c**	**4d**[3]	**4e**	–
Zn(II)[c]	**5a**	**5b**	**5c**	**5d** (X=NO_3^-) **5d'** (X=ClO_4^-)	**5e**	**5f** (X=$CF_3SO_3^-$)

[a] X = Cl^-(except **2d**); [b] X = ClO_4^- (except **3d'**); [c] X = NO_3^- (except **5d'** and **5f**)

Scheme 1. Structures and numbering of the isolated metal complexes of tach-*x*-Mepyr and tach-6-MeOpyr.

vation of essential biometals and/or that the complexes formed may go on to catalyze oxidative damage, particularly those of redox-active bioavailable metals such as Fe and Cu.

Study of pyridyl-ring-alkylated tachpyr variants appeared appropriate in order to change electronic properties or induce steric hindrance in tachpyr and its derivatives. Herein we focus on the ability of such derivatives to bind divalent biometals as seen from the coordination geometries and the electronic properties of $[M^{II}(tach\text{-}x\text{-}Rpyr)]^{2+}$ (Scheme 1; M = Mn, Fe, Ni, Cu, Zn; R = Me where x = 3–6 and R = MeO where x = 6). The electronic structure in solution has been studied by spectroscopy, and solid-state structures have been studied by single-crystal X-ray crystallography. Aqueous formation processes have been studied by electronic spectroscopy, and the lability of isolated complexes has been investigated by reversed-phase HPLC. Cytotoxicities of tach-*x*-Rpyr in human breast cancer (MCF7) cells are reported and the relationship of metal chelation to biological effects is discussed. In toxicity studies, tach-3-Mepyr, tach-6-Mepyr and tach-6-MeOpyr emerged as most interesting, tach-3-Mepyr due to more rapid onset of toxicity and the tach-6-Rpyr derivatives due to lack of toxicity, hence, these have received greater scrutiny in the present work.

Results and Discussion

Complexation Processes and Products

To investigate steric and electronic effects resulting from variation of the metal ion in the series **1*x***, **2*x***, **3*x***, **4*x*** and **5*x*** and of chelator in the series **#a**, **#b**, **#c**, **#d**, **#e** (Scheme 1), binding of Mn^{II}, Fe^{II}, Ni^{II}, Cu^{II}, and Zn^{II} by tach-*x*-Mepyr (x = 3, 4, 5, and 6) and tach-6-MeOpyr was studied in aqueous and nonaqueous solution. Isolation of complexes proceeded straightforwardly in MeOH by reaction of equimolar amounts of ligands and metal ion salts of counterions Cl^-, ClO_4^-, NO_3^- and $CF_3SO_3^-$ followed by precipitation with Et_2O. The counterion ClO_4^- provided superior material for X-ray study, while the other counterions were preferred for most solution studies due to greater aqueous solubility. Due to the ability of Fe^{II} to mediate oxidation of bound tachpyr,[2] all studies with this metal ion were conducted under anaerobic conditions. To study solution chemistry of alkylated tach chelators, complexation of Fe^{II}, Ni^{II}, Cu^{II} and Zn^{II} ions was carried out generally in water (for all tach-3-Mepyr and tach-6-Mepyr cases and most others; MeOH for a few cases) and the resulting solutions were analyzed. Adequate concentrations for analysis, ca. 5×10^{-2} M were obtained with all counterions except ClO_4^-. The appropriate physical methods were employed including UV/Vis/NIR spectroscopy, ^1H NMR spectroscopy, HPLC and solution magnetic moment determination. The electronic spectra from solution complexation closely resembled those of isolated complexes **2a**–**4e** in MeCN (Table 1 and Exp. Sect.). Mn^{II} complexation was generally not possible in aqueous media, and tach-6-Mepyr complexes were labile under HPLC conditions in some cases (see below). The spectral analyses of the solutions were consistent with six-coordination in all cases except $[Cu(tach\text{-}6\text{-}MeOpyr)]^{2+}$ which is discussed later.

HPLC studies provided good qualitative indications of lability trends and lipophilicities as a function of chelator and metal ion. The method very clearly distinguished metal

 © 2005 Wiley-VCH Verlag GmbH & Co. KGaA, Weinheim

Table 1. UV/Vis/NIR spectroscopic data for tach-*x*-Mepyr complexes.[a]

Complex	ν [cm^{-1}][a]	Assignments[b]	Δ_o [cm^{-1}]	Color
[Fe(tach-3-Mepyr)]Cl_2	22700 (7000)	MLCT	–	bronze
	18200 sh (290)	$^1A_{1g} \rightarrow {}^1T_{1g}$		
[Fe(tach-4-Mepyr)]Cl_2	23100 (6600)	MLCT	–	bronze
	17800 sh (320)	$^1A_{1g} \rightarrow {}^1T_{1g}$		
[Fe(tach-5-Mepyr)]Cl_2	22600 (4200)	MLCT	–	bronze
	17400 sh (290)	$^1A_{1g} \rightarrow {}^1T_{1g}$		
[Fe(tach-6-Mepyr)]$(ClO_4)_2$	28800 (650)	MLCT		
	19600 sh (36.6)	unassigned	11700	red-
	11700 (9.4)	$^5T_{2g} \rightarrow {}^5E_g$		brown
[Fe(tach-6-MeOpyr)]Cl_2	28200 (790)	MLCT		
	11100 (5)	$^5T_{2g} \rightarrow {}^5E_g$	11100	yellow
[Ni(tach-3-Mepyr)]$(ClO_4)_2$	11300 sh (10.8)	$^3A_{2g} \rightarrow {}^1E_g$		
	12900 (15.9)	$^3A_{2g} \rightarrow {}^3T_{2\,g}$	12900	pink
	19700 (11.7)	$^3A_{2g} \rightarrow {}^3T_{1g}$		
[Ni(tach-4-Mepyr)]$(ClO_4)_2$	11300 sh (12.7)	$^3A_{2g} \rightarrow {}^1E_g$		
	12800 (15.9)	$^3A_{2g} \rightarrow {}^3T_{2g}$	12800	pink
	19500 (14.2)	$^3A_{2g} \rightarrow {}^3T_{1g}$		
[Ni(tach-5-Mepyr)]$(ClO_4)_2$	11200 sh (12.7)	$^3A_{2g} \rightarrow {}^1E_g$		
	12800 (17.0)	$^3A_{2g} \rightarrow {}^3T_{2g}$	12800	pink
	19500 (14.2)	$^3A_{2g} \rightarrow {}^3T_{1g}$		
[Ni(tach-6-Mepyr)]$(ClO_4)_2$	10800 (25.4)	$^3A_{2g} \rightarrow {}^3T_{2g}$		
	12400 sh (11.4)	$^3A_{2g} \rightarrow {}^1E_g$	10800	pale
	18100 (9.28)	$^3A_{2g} \rightarrow {}^3T_{1g}$		brown
[Ni(tach-6-MeOpyr)]$(ClO_4)_2$	10900 (17.5)	$^3A_{2g} \rightarrow {}^3T_{2g}$		
	12400 sh (11.4)	$^3A_{2g} \rightarrow {}^1E_g$	10900	violet
	18100 (7.28)	$^3A_{2g} \rightarrow {}^3T_{1g}$		
[Cu(tach-3-Mepyr)]$(ClO_4)_2$	15300 (97.1)	$^2E_g \rightarrow {}^2T_{2g}$	15300	blue
[Cu(tach-4-Mepyr)]$(ClO_4)_2$	15100 (88.3)	$^2E_g \rightarrow {}^2T_{2g}$	15100	blue
[Cu(tach-5-Mepyr)]$(ClO_4)_2$	15000 (68.8)	$^2E_g \rightarrow {}^2T_{2g}$	15000	blue
[Cu(tach-6-Mepyr)]$(ClO_4)_2$[3]	10800 (154.3)	$d_{xz,yz} \rightarrow d_{x^2-y^2}$	–	blue
	14100 (89.5)	$d_{xy} \rightarrow d_{x^2-y^2}$		
	15400 (223.8)	$d_{z^2} \rightarrow d_{x^2-y^2}$		
[Cu(tach-6-MeOpyr)]$(ClO_4)_2$	10400 (117.9)	$d_{xz,yz} \rightarrow d_{x^2-y^2}$	–	blue
	14100 (34.4)	$d_{xy} \rightarrow d_{x^2-y^2}$		
	15300 (174.5)	$d_{z^2} \rightarrow d_{x^2-y^2}$		

[a] All Fe^{II} and Ni^{II} complex spectra measured in MeCN; all Cu^{II} spectra measured in MeOH except [Cu(tach-6-Mepyr)]$(ClO_4)_2$ and [Cu(tach-6-MeOpyr)]$(ClO_4)_2$ which were measured in H_2O. [b] In the case of d-d transitions, assignments of pseudo-octahedral complexes are made in the O_h point group while the square-pyramidal Cu^{II} complexes are given as transitions between individual orbitals according to literature conventions.

complex from metal chelator and was particularly appropriate for study of Zn^{II} and Mn^{II} speciation where Vis/NIR spectroscopy is not available.[1,9] Due to their polarity the metal complexes eluted at 12 to 15 min, whereas free chelator retention times were upwards of 20 min. The separation was improved by isocratic elution with a mobile phase of 90% Et_3N/HOAc buffer and 10% MeOH in order to clearly discriminate complexes of different metal ions with the same chelator.

The Mn^{II} complexes **1d** and **1e** could be prepared in MeOH, but they dissociated completely under HPLC analysis, as expected given the poor match of size and hard–soft acid–base properties as well as the steric effects of 6-substitution of the coordinating pyridine ring. The $[Zn(tach\text{-}6\text{-}Mepyr)]^{2+}$ complex **5d** was also labile, but $[Zn(tach\text{-}3\text{-}Mepyr)]^{2+}$ (**5a**) and $[Zn(tachpyr)]^{2+}$ (**5f**) yielded clean single peaks, indicative of inertness.

Ring alkylation of tachpyr increased lipophilicity of chelators and complexes as shown by RP-HPLC studies in the gradient mode. Thus, the free chelator tachpyr and $[Zn(tachpyr)]^{2+}$ eluted at substantially shorter times (18.8 min and 8.4 min) than the respective alkylated compounds tach-3-Mepyr and $[Zn(tach\text{-}3\text{-}Mepyr)]^{2+}$ (22.9 min and 14.6 min).

^1H NMR spectra of complexes **2a**–**c** and **5a**–**e** are consistent with the octahedral-enforcing nature of tach-framework chelators as previously shown in $[Ni(tachpyr)]^{2+}$, $[Zn(tachpyr)]^{2+}$ and $[Ga(tachpyr)]^{3+}$.[4] Characteristic patterns of proton–proton coupling between cyclohexyl H atoms indicate "closed", complexed tach as opposed to "open" tach.[1] The two methylene protons of the coordinated pendant arms are diastereotopic, indicating that the arms of these complexes are twisted about the metal ion in the Δ or Λ configuration, and Δ–Λ interconversion does not occur on the NMR time-scale at room temperature, also as previously found for $[M(tachpyr)]^{2+}$ (M = Fe^{II}, Zn^{II}, Ga^{III}, In^{III}).[1,2,18]

In total, synthetic and physical studies demonstrate the alkylated derivatives of tachpyr to be effective chelators of Fe^{II}, Ni^{II}, Cu^{II} and Zn^{II}, while Mn^{II} is not bound in aqueous media, and some of the 6-alkylated tachpyr variants are labile in aqueous media.

 © 2005 Wiley-VCH Verlag GmbH & Co. KGaA, Weinheim

Electronic Structure

To examine metal-complex structures in solution and assess effects of pyridyl substituents at various positions, the UV/Vis/NIR spectra of the Fe^{II}, Ni^{II}, and Cu^{II} complexes were measured, assigned, and compared with other amino/pyridyl–metal compounds (Table 1). The spectral assignments for Ni^{II} and Cu^{II} complexes were made as previously reported for their complexes of tachpyr and *N*-alkylated tachpyr derivatives.[1,3] The Fe^{II} complexes **2a**–**c** exhibit a large absorption band at 22600–23100 cm^{-1} with a weak low-energy shoulder at 17400–18200 cm^{-1}. We assign the intense absorption to a metal-to-ligand charge-transfer band ($d\pi \rightarrow p\pi^*$) typical of LS Fe^{II} complexes with π-acceptor ligands.[19–22] This absorption appears to mask all d-d transitions except the low-energy shoulder that is generally assigned as the $^1A_{1g} \rightarrow {}^1T_{1g}$ transition in LS Fe^{II} or Co^{III} complexes.[20,23]

Comparison across the chelate tach-*x*-Mepyr series shows that 6-substituted ligands have weaker field strength toward Fe^{II}, Ni^{II}, and Cu^{II}, while methyl substitution at the 3, 4, and 5 positions on the pyridine rings has no notable effect on the field strength relative to tachpyr. Thus, the 6-substituted Ni^{II} complexes **3d** and **3e** have lower d-d transition energies as compared to the 3-, 4- and 5-substituted compounds **3a**–**c**. In the Fe^{II} series, 6-substitution causes a shift of Fe^{II} from low-spin (LS) to high-spin (HS) state. The Fe^{II} complexes **2d** and **2e** contain a considerably weaker MLCT band around 28500 cm^{-1} with a slight shoulder to lower energy. The MLCT band is weaker as is typical for HS Fe^{II}.[20] Additionally there is a very weak absorption at 11100–11800 cm^{-1}. This absorption is assigned to a $^5T_{2g} \rightarrow {}^5E_g$ transition, as is seen in $[Fe([12]aneN_3py_3)]^{2+}$ and other HS Fe^{II} complexes.[19,20,22]

Alkylation of the pyridyl 6-position leads to a five-coordinate complex in the case of Cu^{II}. The UV/Vis/NIR spectrum of $[Cu(tach\text{-}6\text{-}MeOpyr)]^{2+}$ **4e** displays a low energy shoulder indicative of five-coordination as seen for $[Cu(tach\text{-}6\text{-}Mepyr)]^{2+}$ (**4d**).[3] We obtain a satisfactory fit to three Gaussian peaks (Figure 1) which we assign to the $d_{z^2} \rightarrow d_{x^2-y^2}$, $d_{xy} \rightarrow d_{x^2-y^2}$, and $d_{xy,yz} \rightarrow d_{x^2-y^2}$ transitions in order of increasing energy as has been shown for aqueous $[Cu(tach\text{-}Et_3)(H_2O)_2]^{2+}$ and other square-pyramidal Cu^{II} complexes.[24–26] The molar absorptivities of the component peaks are relatively high, ca. 25–160 M^{-1} cm^{-1} as is typical of d-d transitions of square-pyramidal copper complexes where parity-forbidden Laporte selection rules are relaxed by lowered symmetry.[27]

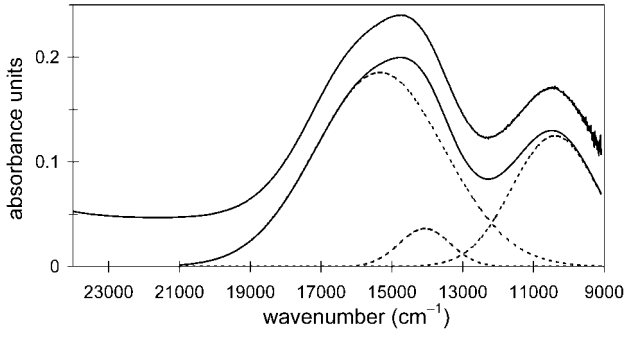

Figure 1. Resolution of the electronic spectrum of $[Cu(tach\text{-}6\text{-}MeOpyr)](ClO_4)_2$ (aq) into bands (L to R, dotted lines): $d_{xz,yz} \rightarrow d_{x^2-y^2}$, $d_{yz} \rightarrow d_{x^2-y^2}$ and $d_{z^2} \rightarrow d_{x^2-y^2}$. The calculated spectrum in the range 21000–9000 cm^{-1} is shown as a solid line and the experimental spectrum at 0.04 absorbance units above.

Overall, the weakened interactions between the 6-substituted ligands and the divalent metal centers that are seen here result in a substantially weakened ligand field as seen from coordination number, spin state, or d-d electronic transitions of the bound metal ion. The effects are due to steric hindrance produced by the methyl or methoxy groups when the pyridyl rings are brought into proximity in the closed conformation of the chelator.

Cytotoxicity Studies

The cytotoxicities of tach-*x*-Mepyr (*x* = 3–6) and of tach-6-MeOpyr were studied against a tachpyr control (Figure 2). Using a fixed concentration of chelator (16 μM), extent of cell death in the first 24 h varied considerably, whereas at the 72 h timepoint all chelators except tach-6-Mepyr and tach-6-MeOpyr had caused loss of 75–80% of cell viability. The lack of toxicity in the 6-substituted chelators is as expected because their metal-binding properties are sterically hindered as demonstrated by the solution UV/Vis spectra. However, there are significant differences in rate of cell killing, in the order tach-3-Mepyr $>\approx$ tach-4-Mepyr $>$ tach-5-Mepyr $>$ tachpyr. There is no corresponding variation in the ligand-field strength as a function of alkylated position on pyridine.

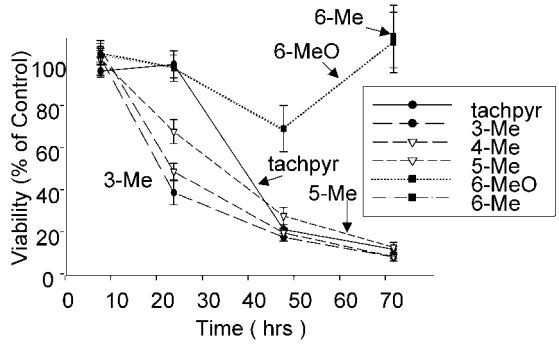

Figure 2. MCF7 cells were treated with 16 μM tach-*x*-Rpyr for the indicated times (8, 24, 48 and 72 h) and viability assessed using an MTT assay as described in Exp. Sect. Viability was expressed as percent survival relative to the control cells, which were untreated. Means and standard errors of 3 independent experiments are shown. In the case of 6-methyl-tachpyridine, only the 72 h timepoint was assessed.

Structural Studies

To elucidate the influences of the metal ion and alkylation of the pyridine rings of tachpyr upon bonding in the complexes, we undertook crystallographic studies of selected complexes. These studies focused on 6-alkylated and

 © 2005 Wiley-VCH Verlag GmbH & Co. KGaA, Weinheim

Table 2. Selected structural parameters of tach-*x*-Rpyr complex cations and reference compounds.

	Metal ion radius [Å]	M–N(amine) bond distance or distance pairs[a] [Å]	M–N(pyridyl) bond distance or distance pairs[a] [Å]	Twist angle or angle pairs,[a] Φ [°]
$[Ni(tach\text{-}6\text{-}Mepyr)]^{2+}$	0.83	2.078(3) 2.099(3) 2.102(3)	2.191(3) 2.203(3) 2.267(3)	55.3(2)
$[Ni(tachpyr)]^{2+}$,[1]	0.83	2.099(4) 2.099(4) 2.107(4)	2.118(4) 2.122(4) 2.127(4)	45.5(2)
$[Cu(tach\text{-}6\text{-}MeOpyr)]^{2+}$	0.87	[2.051(3), 2.008(3)] [2.102(3), 2.045(3)] [2.170(3), 2.172(3)]	[1.994(3), 1.998(3)] [2.012(3), 2.093(3)]	–
$[Zn(tach\text{-}3\text{-}Mepyr)]^{2+}$	0.88	[2.151(3), 2.143(3)] [2.156(3), 2.163(3)] [2.167(3), 2.165(3)]	[2.156(4), 2.158(3)] [2.167(3), 2.170(3)] [2.170(3), 2.183(3)]	[42.8, 41.8]
$[Zn(tach\text{-}6\text{-}Mepyr)]^{2+}$	0.88	[2.128(4), 2.115(5)] [2.133(4), 2.133(5)] [2.135(4), 2.151(5)]	[2.203(4), 2.213(5)] [2.216(4), 2.218(5)] [2.566(5), 2.527(5)]	[53.9(3), 49.5(1)]
$[Zn(tachpyr)]^{2+}$,[4]	0.88	2.160(3) 2.160(3) 2.160(3)	2.165(4) 2.165(4) 2.165(4)	43.7(2)
$[Mn(tach\text{-}6\text{-}Mepyr)]^{2+}$	0.97	[2.235(3), 2.222(4)] [2.247(3), 2.258(3)] [2.262(3), 2.262(3)]	[2.277(3), 2.268(3)] [2.282(3), 2.289(4)] [2.442(3), 2.417(4)]	[52.6(3), 49.6(1)]
$[Mn(tach\text{-}6\text{-}MeOpyr)]^{2+}$	0.97	2.250(2) 2.286(2) 2.300(2)	2.210(2) 2.277(2) 2.306(2)	44.8(2)
$[Mn(tachpyr)]^{2+}$,[1]	0.97	2.2330(17) 2.236(2) 2.245(2)	2.2829(17) 2.2920(18) 2.2992(17)	2.5(1)

[a] In structures with two independent molecules per asymmetric unit, pairs of corresponding distances or angles are given in brackets.

3-alkylated pyridyl derivatives because of their particular influences on lability or biological activity. The salient findings are presented in Table 2, and views of selected complex cations are shown in Figures 3, 4, 5, 6 and 7.

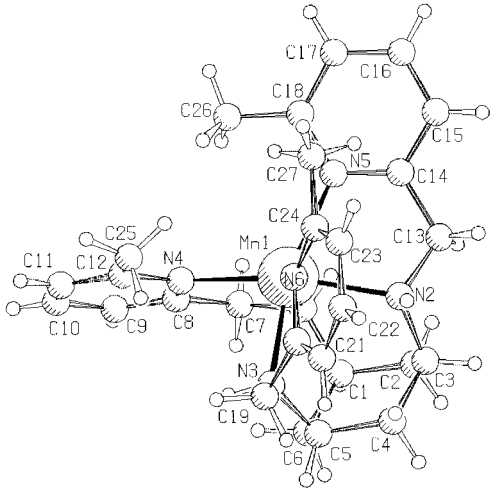

Figure 3. Projection along the N6–Mn bond of one cation in the asymmetric unit of $[Mn(tach\text{-}6\text{-}Mepyr)](ClO_4)_2\cdot 0.5H_2O\cdot 0.5MeOH$ (**1d**·$0.5H_2O$·0.5MeOH) (PLUTO) showing that the pyridyl ring C21•••C24 is not coplanar with the N6–Mn1 bond.

The M–N(amino) bond lengths of the complexes are generally comparable to the unalkylated analogues $[M(tachpyr)]^{2+}$ (M = Ni^{II}, Zn^{II}, Mn^{II})[1] and to other aminopyridyl ligands. They correlate well with the divalent metal ionic radii; as the six-coordinate ionic radius[28,29] increases from Ni^{II} (0.83 Å) to Zn^{II} (0.88 Å) to Mn^{II} (0.97 Å), the M–N bond lengths increase as well.

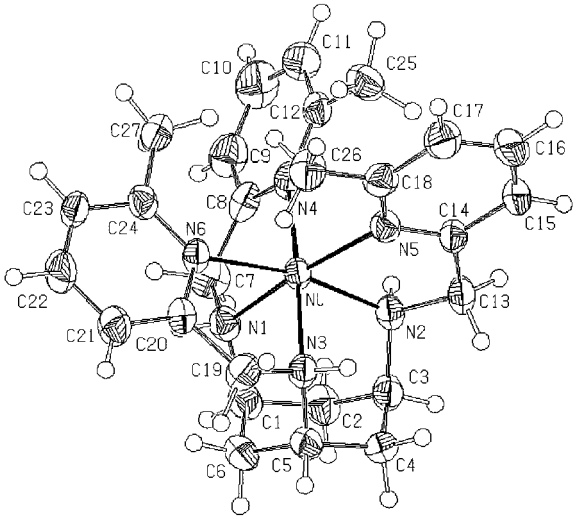

Figure 4. ORTEP view of the complex cation of $[Ni(tach\text{-}6\text{-}Mepyr)](NO_3)_2\cdot 0.5Et_2O$ (**3d′**·$0.5Et_2O$) (50% probability ellipsoids).

From the structural standpoint, 3-alkylation has little effect on complexation geometry in the solid state. The M–N bond lengths and the twist angle of $[Zn(tach\text{-}3\text{-}Mepyr)]^{2+}$ (**5a**) (Figure 6) are very comparable to those of $[Zn(tachpyr)]^{2+}$.[4]

 © 2005 Wiley-VCH Verlag GmbH & Co. KGaA, Weinheim

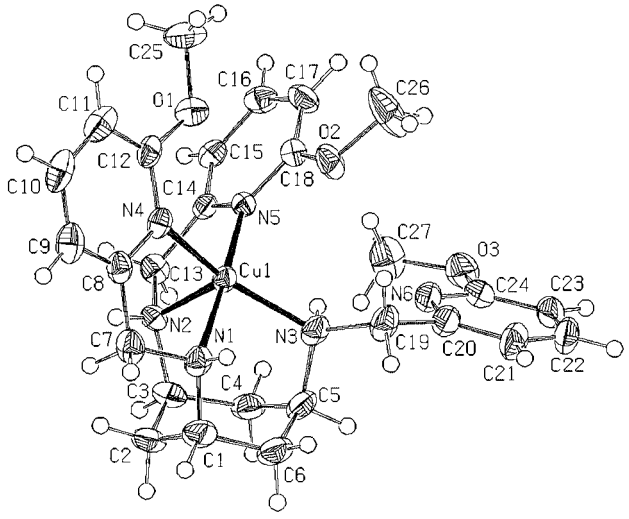

Figure 5. ORTEP view of one molecule in the asymmetric unit of $[Cu(tach\text{-}6\text{-}MeOpyr)](ClO_4)_2$ (**4e**) (50% probability ellipsoids).

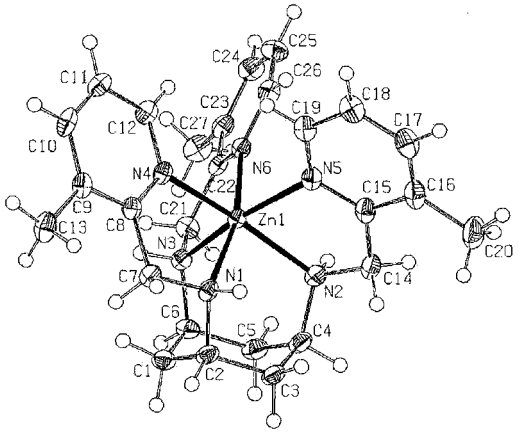

Figure 6. ORTEP view of one molecule in the asymmetric unit of $[Zn(tach\text{-}3\text{-}Mepyr)](NO_3)_2{\cdot}2MeOH{\cdot}0.5H_2O$ (**5a**·2MeOH·0.5H_2O) (50% probability ellipsoids).

However, the M–N(pyridyl) distances vary substantially in the 6-alkylated compounds. Elongations of the $Mn–N_{(py)}$ bond lengths due to steric hindrance may be uniform as seen in the cations $[Ni(tach\text{-}6\text{-}Mepyr)]^{2+}$ (**3d′**) (Figure 4) and $[Mn(tach\text{-}6\text{-}MeOpyr)]^{2+}$ (**1e**) or non-uniform as in $[Zn(tach\text{-}6\text{-}Mepyr)]^{2+}$ (**5d′**) (Figure 7) and $[Mn(tach\text{-}6\text{-}Mepyr)]^{2+}$ (**1d**) (Figure 3). The Ni^{II} complex **3d′** shows a uniform elongation (i.e., $Ni^{II}–N_{(py)}$ distances increase similarly) by roughly 0.11 Å relative to $[Ni(tachpyr)]^{2+}$ for all three $N_{(py)}$ donor atoms. In contrast, the Zn^{II} complex **5d′** shows two lesser elongations (ca. 0.050 Å) of the $Zn–N_{(py)}$ bonds and one very long bond with an elongation of ca. 0.38 Å. In the non-uniform elongation case, it is notable that the plane of the pyridyl ring is not coplanar with the longest $M^{II}–N_{(py)}$ bond; thus, the lone pair of the pyridyl N atom is directed away from the metal center. This is illustrated by a projection of $[Mn(tach\text{-}6\text{-}Mepyr)]^{2+}$ along the (longest) Mn1–N6 bond in Figure 3.

The compound $[Cu(tach\text{-}6\text{-}MeOpyr)](ClO_4)_2$ (**4e**) is five-coordinate in the solid state (Figure 5), consistent with the

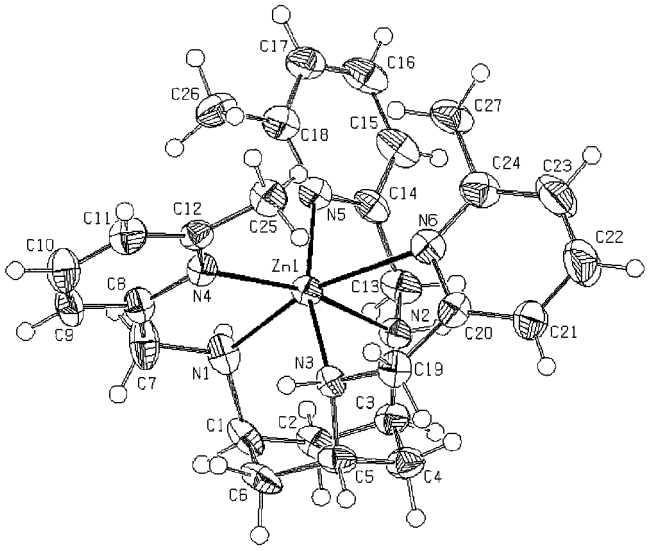

Figure 7. ORTEP view of one molecule in the asymmetric unit of $[Zn(tach\text{-}6\text{-}Mepyr)](ClO_4)_2{\cdot}0.5H_2O{\cdot}0.5MeOH$ (**5d′**·0.5H_2O·0.5MeOH) (50% probability ellipsoids).

assigned aqueous structure. This complex has four shorter bonds and one longer bond as expected in Jahn–Teller-distorted Cu^{II}, and previously observed in $[Cu(tach\text{-}6\text{-}Mepyr)](ClO_4)_2$ (**4d**).[3] The shorter bond lengths of **4e** [range 1.994(3) to 2.102(3) Å] compare favorably to those of **4d** [range 2.001(3)–2.103(3) Å] (Table 2), and the long distances [average of 2.171(3) Å in two molecules in the asymmetric unit] are somewhat shorter than in **4d** [2.216(3) Å]. Sterically crowded Cu^{II} is well known to assume coordination geometries varying from square-based pyramidal to trigonal-bipyramidal. In these cases the coordination geometry may be described by the in-plane angular distortion $\tau = (\beta - \alpha)/60°$, where β and α are the two basal angles formed by the *trans* ligands and the metal ion. The ideal square pyramid is defined by $\tau = 0$ and the trigonal bipyramid by $\tau = 1$.[30] The shape of Cu^{II} compound **4e** is closer to a square-based pyramid with an average $\tau = 0.26$ whereas **4d** has a more distorted intermediate shape, with $\tau = 0.58$.

In the case of Mn^{II}, the 6-substitution of the pyridyl ring makes the trigonal-prismatic geometry less favorable than distorted octahedral, as shown by comparison of trigonal twist angle (Φ) values in $[Mn(tach\text{-}6\text{-}Mepyr)]^{2+}$ (**1d**) and $[Mn(tach\text{-}6\text{-}MeOpyr)]^{2+}$ (**1e**) to $[Mn(tachpyr)]^{2+}$.[1] The Φ value is the angle by which the triangles of pyridyl N atoms and amino N atoms are staggered, as viewed down the pseudo-C_3 axis. The octahedron possesses perfect staggering with an angle $\Phi = 60°$ and the trigonal prism is perfectly eclipsed with $\Phi = 0°$. The value of Φ for $[Mn(tachpyr)]^{2+}$ is 2.5° while values of Φ for **1d** and **1e** are 52.6° and 44.8°, respectively. The drastic change in Φ reflects the closeness of 6-substituents to each other in a trigonal prism. It was observed in $[Mn(tachpyr)]^{2+}$ that extension of the pendant arms into a planar arrangement [i.e., making the N(H)–CH_2–(2-pyridyl) framework planar], to achieve a trigonal-prismatic coordination sphere, allowed the most favorable bite angles for a large metal ion. However, in the trigonal

 © 2005 Wiley-VCH Verlag GmbH & Co. KGaA, Weinheim

prism the groups at the 6-pyridyl position must point directly at each other. Thus, **1d** and **1e** attain larger Φ values because sterics make the trigonal-prismatic geometry unfavorable in this case. Additionally, binding a metal ion into the trigonal-prismatic geometry of an aminopyridyl tach chelator causes severe distortions of the coordination geometry of the tach nitrogen atoms, forcing them into a trigonal-pyramidal geometry (with H at the apex of the pyramid).[1] In **1d** similarly to **5d**, the third arm is forced away from the other two at a greater Mn–N bond length, and it is unable to attain good overlap of the N(py) lone pair with Mn^{II} (Figure 3). In **1e**, steric effects do not seem as great, and the average N(py)–Mn bond length is marginally shorter than that of $[Mn(tachpyr)]^{2+}$ (Table 2).

Conclusions

The 6-position has a considerable effect on metal-binding properties in tach-6-Mepyr due to steric interactions amongst 6-substituents in metal-bound tach-6-Rpyr. On the other hand, there appears to be little electronic effect of 3-, 4-, or 5-alkylation on ligand-field strength in the tach-*x*-Mepyr series, nor any steric effect of 3-alkylation. The biological differences between tach-3-Mepyr and tachpyr appear to derive from other factors such as a difference in rate of metal ion binding, or formation constants of metal–ligand interaction, or other parameters specific to the Fe^{II} complexes. Studies of formation constants and complexation reactivities to compare the interactions of Zn^{II} and Fe^{II} with tach-3-Mepyr and tachpyr are therefore in progress.

Experimental Section

General: Full physical characterization of complexes was carried out with material prepared and isolated using nonaqueous solvents without optimization of yields. Aqueous complexation studies are described by a general procedure for each metal. X-ray crystallography was carried out on the isolated complexes from nonaqueous media. Cytotoxicity studies were performed with phosphate-buffered saline solutions of the free chelators, which were prepared as reported.[3,10]

Materials and Methods: All the materials cited below were of research grade or spectro-quality grade in the highest purity available and were generally obtained from commercial sources and used without further purification except Et_2O. Et_2O was distilled from Na and used immediately. $[D_6]$DMSO was obtained from Cambridge Isotope Laboratories. UV/Vis/NIR solution electronic spectra were measured using a Varian Cary 5 or a Varian Cary 50-Bio UV/Vis spectrometer with 1- or 3-mL quartz cuvettes (1 cm path length). Solid-phase Vis spectra were obtained with a model RSA-HP-53 reflectance spectroscopy attachment (Labsphere, Inc.) to an HP8453 diode-array instrument. All solution UV/Vis/NIR spectra are presented in Table 1; deconvolutions of Cu^{II} spectra were performed using Microcal Origin 6.0 software. Electrospray ionization (ESI) mass spectra in the positive ion detection mode were obtained with a Finnegan LCQ Classic instrument with dual optical Paul traps and Picoview nanospray source. Fast-atom bombardment mass spectra (FAB-MS) were taken with an Extrel 4000 instrument in the positive ion detection mode. Samples were desorbed from mixtures of DMSO and Magic Bullet ("MB"). Calculations from the program developed by Scientific Instrument Services (http://www.sisweb.com/cgi-bin/mass10.pl, accessed August 2, 2004) aided in assignment of peaks. ^{1}H NMR spectra were obtained using a Bruker AM360 instrument or a Varian Mercury 400 MHz instrument. Chemical shifts are reported in ppm on the δ scale relative to TMS. Magnetic moments were determined using Evans' method.[11] Elemental analysis was performed by Atlantic Microlabs (Atlanta, Georgia). Drying was accomplished in air or under reduced pressure (ca. 10^{-2} Torr) with a standard Schlenk line. All work with Fe^{II} was conducted with standard Schlenk or glovebox techniques under prepurified N_2 or Ar due to the oxidation sensitivity of the complexes.[12]

CAUTION: Perchlorate salts can be explosive and should be handled with care. No explosions occurred during the course of this work.

Metal Complex Syntheses

[Mn(tach-6-Mepyr)](ClO$_4$)$_2$·H$_2$O (1d·H$_2$O): A colorless solution of $Mn(ClO_4)_2{\cdot}6H_2O$ (0.0899 g, 2.48×10^{-4} mol) in MeOH (2 mL) was added to a pale yellow solution of tach-6-Mepyr (0.110 g, 2.48×10^{-4} mol) in MeOH (2 mL) affording yellow prisms suitable for X-ray diffraction (shown to be **1d**·1/2MeOH·1/2H$_2$O). The crystals were isolated and dried under reduced pressure giving a pale yellow solid. The solid was washed with MeOH (5 mL) and Et_2O (5 mL) and dissolved in MeCN followed by vapor-phase diffusion of Et_2O generating yellow prisms. The prisms were isolated and dried under reduced pressure affording a yellow solid in 73.9% yield (0.128 g, 1.83×10^{-4} mol). MS (ESI): m/z = 498 [M – 2 ClO_4^- – H^+], 598 [M – ClO_4]. μ_{eff} (DMSO, 25 °C) = 5.79 B.M. $C_{27}H_{38}Cl_2MnN_6O_9$ (715.15): calcd. C 45.26, H 5.35, N 11.73; found C 44.93, H 5.16, N 11.98.

[Mn(tach-6-Mepyr)](CF$_3$SO$_3$)$_2$ (1d′): A solution of $Mn(CF_3SO_3)_2{\cdot}6H_2O$ (0.083 g, 1.8×10^{-4} mol) in MeOH (2 mL) was added to a pale yellow solution of tach-6-Mepyr (0.079 g, 1.8×10^{-4} mol) in MeOH (2 mL) giving a pale yellow solution. Addition of dry Et_2O (20 mL) to this solution gave a pale-yellow oil that was isolated by decantation and triturated to a light tan powder with Et_2O (2 × 20 mL). The powder was dried under reduced pressure, then taken up in MeOH (3 mL) and subjected to vapor-phase diffusion of Et_2O to provide colorless prisms that were isolated and dried under reduced pressure affording a 46% yield (0.066 g, 8.3×10^{-5} mol) of white prisms. HPLC (gradient mode): Identical to free ligand at $R_t \approx$ 21.0 min. MS (FAB/glycerol): m/z = 648 [M – $CF_3SO_3^-$]$^+$. $C_{29}H_{36}F_6MnN_6O_6S_2$ (797.14): calcd. C 43.67, H 4.55, N 10.54; found C 43.62, H 4.51, N 10.50.

[Mn(tach-6-MeOpyr)](CF$_3$SO$_3$)$_2$ (1e): A solution of $Mn(CF_3SO_3)_2{\cdot}6H_2O$ (0.058 g, 1.3×10^{-4} mol) in MeOH (2 mL) was mixed with a pale yellow solution of tach-6-MeOpyr (0.059 g, 1.2×10^{-4} mol) in MeOH (2 mL), giving a pale yellow solution. Addition of dry Et_2O (20 mL) to this solution gave a pale yellow oil that was isolated by decantation and triturated to a white powder with Et_2O (2 × 20 mL). The powder was dried under reduced pressure, then taken up in MeOH (3 mL) and subjected to vapor-phase diffusion of Et_2O to provide colorless prisms (**1e**·MeOH) suitable for X-ray diffraction. The prisms were isolated and dried under reduced pressure affording a 58% yield (0.059 g, 7.0×10^{-5} mol) of white prisms. μ_{eff} (DMSO, 25 °C) = 5.70 B.M. MS (FAB/gly): m/z = 696 [M – $CF_3SO_3^-$]$^+$, 532 [M –2 $CF_3SO_3^-$ – CH_3^+]$^+$. HPLC (gradient mode): identical to free ligand at R_t = 23.7 min. $C_{29}H_{36}F_6MnN_6O_9S_2$ (845.13): calcd. C 41.19, H 4.29, N 9.94; found C 41.03, H 4.33, N 9.86.

 © 2005 Wiley-VCH Verlag GmbH & Co. KGaA, Weinheim

[Fe(tach-3-Mepyr)]Cl_2·1.5H_2O (2a·1.5H_2O): A pale green solution of $FeCl_2$·4H_2O (0.0070 g, 3.53 × 10^{-5} mol) in MeOH (1 mL) was added to a pale yellow solution of tach-3-Mepyr (0.0155 g, 3.48 × 10^{-5} mol) in MeOH (1 mL) producing a brown-yellow solution. Et_2O (2 mL) was added and the solution let stand for 48 h at 10 °C producing clusters of carmine red needles. Product was isolated and dried under reduced pressure affording deep red needles. ^{1}H NMR (400 MHz, [D_6]DMSO, 25 °C): δ = 7.59, 7.15, 6.91 (d, dd, d, 3 H, 3-MeC_5H_3N), 5.29 (br. t, 1 H, N*H*CH_2), 4.23, 4.02 (dd, dd, 2 H, NHC*H*$_2$py, diastereotopic), 2.95 (br. s, 1 H, cyclohexyl methine *H*), 2.37 (s, 3 H, C*H*$_3$py), 2.12 (br. d, 1 H, equatorial cyclohexyl methylene *H*), 1.84 (br. d, 1 H, axial cyclohexyl methylene *H*). $C_{27}H_{39}Cl_2FeN_6O_{1.5}$ (597.19): calcd. C 54.25, H 6.58, N 14.07; found C 54.17, H 6.22, N 13.76.

[Fe(tach-4-Mepyr)]Cl_2·1.5H_2O (2b·1.5H_2O): A pale green solution of $FeCl_2$·4H_2O (0.0110 g, 5.53 × 10^{-5} mol) in MeOH (1 mL) was added to a pale yellow solution of tach-4-Mepyr (0.0244 g, 5.49 × 10^{-5} mol) in MeOH (1 mL) affording a brown-yellow solution. Slow Et_2O diffusion produced several deep red microcrystals. The supernatant was decanted and the microcrystals were dried under reduced pressure. ^{1}H NMR (400 MHz, [D_6]DMSO, 25 °C): δ = 7.42, 7.17, 6.86 (s, d, d, 3 H, 4-MeC_5H_3N), 5.45 (br. t, 1 H, N*H*CH_2), 4.43, 4.19 (dd, dd, 2 H, NHC*H*$_2$py, diastereotopic), 3.21 (br. s, 1 H, cyclohexyl methine *H*), 2.37 (s, 3 H, C*H*$_3$py), 2.02 (br. d, 1 H, equatorial cyclohexyl methylene *H*), 1.79 (br. d, 1 H, axial cyclohexyl methylene *H*). $C_{27}H_{39}Cl_2FeN_6O_{1.5}$ (597.19): calcd. C 54.25, H 6.58, N 14.07; found C 54.56, H 6.16, N 13.86.

[Fe(tach-5-Mepyr)]Cl_2·H_2O (2c·H_2O): A pale green solution of $FeCl_2$·4H_2O (0.0108 g, 5.43 × 10^{-5} mol) in MeOH (1 mL) was added to a pale yellow solution of tach-5-Mepyr (0.0235 g, 5.28 × 10^{-5} mol) in MeOH (1 mL) creating a brown-yellow solution. Addition of Et_2O (ca. 20 mL) produced a slightly cloudy solution that yielded carmine red needles upon standing one week. The supernatant was decanted and the product was allowed to air dry giving deep red needles. ^{1}H NMR (400 MHz, [D_6]DMSO, 25 °C): δ = 7.65, 7.49, 6.78 (d, d, s, 3 H, 5-MeC_5H_3N), 5.57 (br. t, 1 H, N*H*CH_2), 4.43, 4.12 (dd, dd, 2 H, NHC*H*$_2$py), 3.13 (br. s, 1 H, cyclohexyl methine *H*), 2.08 (partially obscured) (s, 3 H, C*H*$_3$py), 2.09 (partially obscured) (br. d, 1 H, equatorial cyclohexyl methylene *H*), 1.81 (br. d, 1 H, axial cyclohexyl methylene *H*). $C_{27}H_{38}Cl_2FeN_6O$: calcd. (588.18) C 55.08, H 6.51, N 14.28; found C 54.73, H 6.45, N 13.88.

[Fe(tach-6-Mepyr)]$(ClO_4)_2$·H_2O (2d·H_2O): A yellow solution of $Fe(ClO_4)_2$·6H_2O (0.0160 g, 4.41 × 10^{-5} mol) in MeOH (1 mL) was added to a pale yellow solution of tach-6-Mepyr (19.5 g, 4.39 × 10^{-5} mol) in MeOH (1 mL) producing a dark red solution. During 24 h at 5 °C red needles precipitated from the solution. Removal of the supernatant and air-drying produced bright red needles. μ_{eff} (DMSO, 25 °C) = 5.46 B.M. at 25 °C. $C_{27}H_{38}Cl_2FeN_6O_9$ (716.14): calcd. C 45.24, H 5.35, N 11.73; found C 45.45, H 5.31, N 11.61.

[Fe(tach-6-MeOpyr)]Cl_2·1.5H_2O (2e·1.5H_2O): A pale green solution of $FeCl_2$·4H_2O (0.0113 g, 5.68 × 10^{-5} mol) in MeOH (1 mL) was added to a pale yellow solution of tach-6-MeOpyr (0.0276 g, 5.61 × 10^{-5} mol) in MeOH (1 mL) producing a yellow solution. Addition of ca. 15 mL of Et_2O produced a slightly cloudy solution that deposited yellow prisms upon standing 48 h. The supernatant was decanted and the product allowed to air-dry resulting in bright yellow prisms. μ_{eff} (DMSO, 25 °C) = 5.77 B.M. at 25 °C. $C_{27}H_{39}Cl_2FeN_6O_{4.5}$ (645.17): calcd. C 50.22, H 6.09, N 13.02; found C 50.21, H 6.10, N 12.84.

[Ni(tach-3-Mepyr)]$(ClO_4)_2$ (3a): A pale green solution of $Ni(ClO_4)_2$·6H_2O (0.0169 g, 4.62 × 10^{-5} mol) in MeOH (1 mL) was added to a pale yellow solution of tach-3-Mepyr (0.0204 g, 4.59 × 10^{-5} mol) in MeOH (1 mL) affording a pale purple-pink solution. Pink needles formed after 24 h. The supernatant was decanted and the solid was washed with Et_2O and dried, producing pale pink needles (0.0191 g, 59.3%). MS (ESI, MeOH): *m*/*z* = 501 = [M – 2 ClO_4^- – H^+], 601 [M – ClO_4^-]. $C_{27}H_{36}Cl_2N_6NiO_8$ (700.13): calcd. C 46.20, H 5.17, N 11.97; found C 46.43, H 5.28, N 12.06.

[Ni(tach-4-Mepyr)]$(ClO_4)_2$ (3b): A pale green solution of $Ni(ClO_4)_2$·6H_2O (0.0159 g, 4.35 × 10^{-5} mol) in MeOH (1 mL) was added to a pale yellow solution of tach-4-Mepyr (0.0197 g, 4.43 × 10^{-5} mol) in MeOH (1 mL) producing a pink solution. Small pink needles were produced by Et_2O diffusion into the MeOH solution. These crystals were isolated, washed with Et_2O, dried under reduced pressure, and taken up in MeOH (1 mL). Et_2O diffusion into the MeOH solution yielded pink needle clusters that were isolated and dried affording a pink solid (0.0184 g, 59.2%). MS (ESI, MeOH): *m*/*z* = 501 [M – 2 ClO_4^- – H^+], 601 [M – ClO_4^-]. $C_{27}H_{36}Cl_2N_6NiO_8$ (700.13): calcd. C 46.20, H 5.17, N 11.97; found C 46.31, H 5.14, N 11.94.

[Ni(tach-5-Mepyr)]$(ClO_4)_2$ (3c): A pale green solution of $Ni(ClO_4)_2$·6H_2O (0.0162 g, 4.42 × 10^{-5} mol) in MeOH (1 mL) was added to a pale yellow solution of tach-5-Mepyr (0.0200 g, 4.50 × 10^{-5} mol) in MeOH (1 mL) producing a purple-pink solution. Slow diffusion of Et_2O produced light pink microcrystals. The microcrystals were isolated, washed with Et_2O, dried under reduced pressure, and taken up in MeOH (1 mL). Diffusion of Et_2O into the MeOH solution produced pink needles that were isolated, washed with Et_2O, and dried producing pink needles (0.0221 g, 70.2%). MS (ESI, MeOH): *m*/*z* 501 [M – 2 ClO_4^- – H^+], 601 [M – ClO_4^-]. $C_{27}H_{36}Cl_2N_6NiO_8$ (700.13): calcd. C 46.20, H 5.17, N 11.97; found C 46.21, H 5.13, N 11.76.

[Ni(tach-6-Mepyr)]$(ClO_4)_2$·H_2O (3d·H_2O): A pale green solution of $Ni(ClO_4)_2$·6H_2O (0.0169 g, 4.62 × 10^{-5} mol) in MeOH (1 mL) was added to a pale yellow solution of tach-6-Mepyr (0.0203 g, 4.57 × 10^{-5} mol) in MeOH (1 mL) affording a dark yellow solution. Small light brown needles along with a yellow-brown oil formed after 24 h. The supernatant was decanted, the needles and oil were washed with Et_2O, and the needles were isolated and dried under vacuum (0.0046 g, 14%). MS (ESI, MeOH): *m*/*z* = 501 [M – 2 ClO_4^- – H^+], 601 [M – ClO_4^-]. μ_{eff} (DMSO, 25 °C) = 3.8 B.M. $C_{27}H_{38}Cl_2N_6NiO_9$ (718.14): calcd. C 45.03, H 5.32, N 11.65; found C 45.37, H 5.32, N 11.63.

[Ni(tach-6-Mepyr)]$(NO_3)_2$ (3d′): A pale yellow solution of tach-6-Mepyr (0.0839 g, 1.89 × 10^{-4} mol in MeOH, 2 mL) was added to a pale green solution of $Ni(NO_3)_2$·6H_2O (0.0549 g, 1.89 × 10^{-4} mol) in MeOH (2 mL) affording a peach solution. After adding Et_2O (12 mL) and standing for 2 h, pale lavender microcrystals formed which were isolated, washed with CH_3CN, and dried under reduced pressure to a pale violet solid. This was dissolved in MeOH followed by vapor diffusion of Et_2O, affording pale violet prisms of an ether adduct (**3d′**·0.5Et_2O) that were suitable for X-ray crystallography. These were isolated and dried to a pale violet solid (0.0828 g, 69.8%). MS (FAB/DMSO/NBA): *m*/*z* = 502 [M – 2 NO_3^-]. UV/Vis/NIR (MeOH): λ_{max} (ε) = 10800 (23.2), 12300 (13.7), 17800 cm^{-1} (7.8 cm^{-1} M^{-1}). μ_{eff} = 3.087 B.M. at 25 °C. $C_{27}H_{36}N_8NiO_6$ (626.21): calcd. C 51.35, H 5.80, N 17.83; found C 51.70, H 5.78, N 17.86.

[Ni(tach-6-MeOpyr)]$(ClO_4)_2$ (3e): A pale green solution of $Ni(ClO_4)_2$·6H_2O (0.0167 g, 4.57 × 10^{-5} mol) in MeOH (1 mL) was added to a pale yellow solution of tach-6-MeOpyr (0.0208 g, 4.23 × 10^{-5} mol) in MeOH (1 mL) producing a pale violet solution. The violet prisms that deposited after 24 h were isolated, washed with

 © 2005 Wiley-VCH Verlag GmbH & Co. KGaA, Weinheim

Et_2O, and dried under vacuum (0.0150 g, 47.3%). MS (ESI, MeOH): *m/z* = 549 [M – 2 ClO_4^- – H^+], 649 [M – ClO_4^-]. μ_{eff} (DMSO, 25 °C) = 3.1 B.M. $C_{27}H_{36}Cl_2N_6NiO_{11}$ (748.12): calcd. C 43.25, H 4.84, N 11.21; found C 43.09, H 4.94, N 11.11.

[Cu(tach-3-Mepyr)](ClO$_4$)$_2$ (4a): A blue solution of $Cu(ClO_4)_2 \cdot 6H_2O$ (0.0267 g, 7.21 × 10^{-5} mol) in MeOH (1 mL) was added to a pale yellow solution of tach-3-Mepyr (0.0315 g, 7.09 × 10^{-5} mol) in MeOH (1 mL). A light indigo-blue precipitate formed that redissolved immediately to a blue solution. Slow Et_2O diffusion into the solution produced shiny blue prisms that were isolated and recrystallized from MeCN (4 mL) by vapor-phase diffusion of Et_2O (0.0419 g, 84.0%). MS (FAB/DMSO/MB): *m/z* = 606 [M – ClO_4^-]. UV/Vis/NIR (solid): λ_{max} = 14700 cm^{-1}. $C_{27}H_{36}Cl_2CuN_6O_8$ (705.13): calcd. C 45.86, H 5.13, N 11.89; found C 45.86, H 5.15, N 11.99.

[Cu(tach-4-Mepyr)](ClO$_4$)$_2$·H$_2$O (4b·H$_2$O): A blue solution of $Cu(ClO_4)_2 \cdot 6H_2O$ (0.0258 g, 6.96 × 10^{-5} mol) in MeOH (1 mL) was added to a pale yellow solution of tach-4-Mepyr (0.0310 g, 6.97 × 10^{-5} mol) in MeOH (1 mL). A blue precipitate formed that immediately redissolved to a blue solution. Slow Et_2O diffusion into the solution formed a blue oil which was triturated to a powder with Et_2O and recrystallized from MeOH by vapor-phase diffusion of Et_2O providing blue plates (0.0240 g, 48.8%). MS (FAB/DMSO/MB): *m/z* = 606 [M – ClO_4^-]. UV/Vis/NIR (solid): λ_{max} = 15100 cm^{-1}. $C_{27}H_{38}Cl_2CuN_6O_9$ (723.14): calcd. C 44.73, H 5.28, N 11.59; found C 44.64, H 5.10, N 11.19.

[Cu(tach-5-Mepyr)](ClO$_4$)$_2$ (4c): A blue solution of $Cu(ClO_4)_2 \cdot 6H_2O$ (0.0264 g, 7.12 × 10^{-5} mol) in MeOH (1 mL) was added to a pale yellow solution of tach-5-Mepyr (0.0322 g, 7.24 × 10^{-5} mol) in MeOH (1 mL). A light blue precipitate formed that immediately redissolved to a blue solution. Slow Et_2O diffusion into the solution formed a blue oil which was triturated to a powder with Et_2O and recrystallized from MeOH by vapor-phase diffusion of Et_2O providing blue needles (0.0376 g, 74.8%). MS (FAB/DMSO/MB): *m/z* = 606 [M – ClO_4^-]. UV/Vis/NIR (solid): λ_{max} = 15200 cm^{-1}. $C_{27}H_{36}Cl_2CuN_6O_8$ (705.13): calcd. C 45.86, H 5.13, N 11.89; found C 46.16, H 5.28, N 11.64.

[Cu(tach-6-MeOpyr)](ClO$_4$)$_2$ (4e): A blue solution of $Cu(ClO_4)_2 \cdot 6H_2O$ (0.0229 g, 6.18 × 10^{-5} mol) in MeOH (1 mL) was added to a pale yellow solution of tach-6-MeOpyr (0.0306 g, 6.22 × 10^{-5} mol) in MeOH (1 mL). A light blue precipitate formed that immediately redissolved to a blue solution. Slow Et_2O diffusion into the solution formed a blue oil which was triturated to a powder with Et_2O and recrystallized from MeCN (2 mL) by vapor-phase diffusion of Et_2O giving shiny blue needles suitable for X-ray crystallography (0.0365 g, 78.3%). MS (FAB/DMSO/MB): *m/z* = 654 [M – ClO_4^-], 493 (free tach-6-MeOpyr). UV/Vis/NIR (solid): λ_{max} = 10204, 15060 cm^{-1}. $C_{27}H_{36}Cl_2CuN_6O_{11}$ (753.11): calcd.C 42.95, H 4.81, N 11.13; found C 43.12, H 4.80, N 11.17.

[Zn(tach-3-Mepyr)](NO$_3$)$_2$·2H$_2$O (5a·2H$_2$O): A solution of $Zn(NO_3)_2 \cdot 6H_2O$ (0.0335 g, 1.126 × 10^{-4} mol) in MeOH (2 mL) was mixed with a pale yellow solution of tach-3-Mepyr (0.0502 g, 1.129 × 10^{-4} mol) in MeOH (2 mL) with no obvious change observed. Diffusion of Et_2O into the solution overnight gave clusters of colorless needles. The product was isolated, washed with Et_2O, and dried under reduced pressure affording white needles (0.0364 g, 5.74 × 10^{-5} mol, 51.0%). Suitable crystals for X-ray diffraction (shown to be **5a**·2MeOH·0.5H_2O) were grown from MeOH by vapor-phase diffusion of Et_2O. ^{1}H NMR (360 MHz, [D$_6$]DMSO, 25 °C): δ = 7.91, 7.76, 7.42 (d, d, dd, 3 H, 3-MeC_5H_3N), 4.41 (br. t, 1 H, N*H*CH_2), 4.05, 3.95 (dd, dd, 2 H, MepyCH_2N, diastereotopic), 3.29 (br. s, 1 H, cyclohexyl methine *H*), 2.32 (partially obscured) [s, 3 H, (CH_3)py], 2.34 (partially obscured) (br. d, 1 H, equatorial cyclohexyl methylene *H*), 1.88 (br. d, 1 H, axial cyclohexyl methylene *H*). MS (ESI): *m/z* = 507 [M – 2 NO_3^- – H^+], 570 [M – NO_3^-]. HPLC (gradient mode): R_t = 14.6 min (free ligand R_t = 22.9 min). $C_{27}H_{40}N_8O_8Zn$ (668.23): calcd. C 48.40, H 6.02, N 16.72; found C 48.15, H 6.06, N 16.66.

[Zn(tach-4-Mepyr)](NO$_3$)$_2$ (5b): A solution of $Zn(NO_3)_2 \cdot 6H_2O$ (0.0284 g, 6.16 × 10^{-5} mol) in MeOH (1 mL) was mixed with a pale yellow solution of tach-4-Mepyr (0.0278 g, 6.25 × 10^{-5} mol) in MeOH (1 mL), giving a pale yellow solution. Diffusion of Et_2O overnight gave colorless needle clusters. The product was isolated, washed with Et_2O, and dried under reduced pressure affording white needles (0.0235 g, 3.71 × 10^{-5} mol, 60.2%). ^{1}H NMR (360 MHz, [D$_6$]DMSO, 25 °C): δ = 7.68, 7.46, 7.34 (d, s, dd, 3 H, 4-MeC_5H_3N), 4.60 (br. t, 1 H, N*H*CH_2), 4.07 (m, 2 H, MepyCH_2N, diastereotopic), 3.26 (br. s, 1 H, cyclohexyl methine *H*), 2.48 (s, 3 H, CH_3py), 2.32 (br. d, 1 H, equatorial cyclohexyl methylene *H*), 1.86 (br. d, 1 H, axial cyclohexyl methylene *H*). MS (FAB/DMSO/MB): *m/z* = 507 [M – 2 NO_3^- – H^+], 570 [M – NO_3^-]. $C_{27}H_{36}N_8O_6Zn$ (632.20): calcd. C 51.15, H 5.72, N 17.68; found C 51.11, H 5.75, N 17.61.

[Zn(tach-5-Mepyr)](NO$_3$)$_2$·3H$_2$O (5c·3H$_2$O): A solution of $Zn(NO_3)_2 \cdot 6H_2O$ (0.0203 g, 6.82 × 10^{-5} mol) in MeOH (1 mL) was mixed with a pale yellow solution of tach-5-Mepyr (0.0301 g, 6.77 × 10^{-5} mol) in MeOH (1 mL), giving a colorless solution. Diffusion of Et_2O into the solution overnight gave a colorless oil. Trituration produced a white precipitate. The product was isolated, washed with Et_2O, and dried under reduced pressure affording a white powder (0.0345 g, 5.44 × 10^{-5} mol, 80.4%). ^{1}H NMR (360 MHz, [D$_6$]DMSO, 25 °C): δ = 7.95, 7.60, 7.52 (d, s, d, 3 H, 5-MeC_5H_3N), 4.59 (br. t, 1 H, N*H*CH_2), 4.07 (qd, 2 H, MepyCH_2N, diastereotopic), 3.23 (br. s, 1 H, cyclohexyl methine *H*), 2.29 (partially obscured) (s, 3 H, CH_3py), 2.33 (partially obscured) (br. d, 1 H, equatorial cyclohexyl methylene *H*), 1.86 (br. d, 1 H, axial cyclohexyl methylene *H*). MS (FAB/gly): *m/z* = 507 [M – 2 NO_3^- – H^+], 570 [M – NO_3^-]. $C_{27}H_{42}N_8O_9Zn$ (686.24): calcd. C 47.14, H 6.15, N 16.29; found C 47.18, H 6.11, N 15.96.

[Zn(tach-6-Mepyr)](NO$_3$)$_2$·H$_2$O (5d·H$_2$O): A solution of $Zn(NO_3)_2 \cdot 6H_2O$ (0.0423 g, 1.42 × 10^{-4} mol) in MeOH (2 mL) was mixed with a pale yellow solution of tach-6-Mepyr (0.0614 g, 1.38 × 10^{-4} mol) in MeOH (2 mL), giving a pale yellow solution. Adding Et_2O directly into the solution and waiting 18 h gave a white solid. The product was isolated, washed with Et_2O, and dried under reduced pressure affording a white solid (0.0143 g, 2.26 × 10^{-5} mol, 16.3%). ^{1}H NMR (360 MHz, [D$_6$]DMSO, 25 °C): δ = 7.89, 7.37, 7.31 (t, d, d, 3 H, 6-MeC_5H_3N), 4.23 (br. m, 1 H, N*H*CH_2), 4.20, 4.09 (d, d, 2 H, MePyCH_2N, diastereotopic), 3.08 (br. s, 1 H, cyclohexyl methine *H*), 2.16 (s, 3 H, C$H_3C_5H_3$N), 2.10 (br. d, 1 H, equatorial cyclohexyl methylene *H*), 1.82 (br. d, 1 H, axial cyclohexyl methylene *H*). MS (FAB/NBA/DMSO): *m/z* = 570 [M – NO_3^-], 507 [M – 2 NO_3^- – H^+]. HPLC (gradient): labile, identical to free tach-6-Mepyr at $R_t \approx$ 21.3 min. $C_{27}H_{38}N_8O_7Zn$ (650.22): calcd. C 49.74, H 5.87, N 17.19; found C 49.30, H 5.91, N 17.15.

[Zn(tach-6-Mepyr)](ClO$_4$)$_2$·H$_2$O (5d′·H$_2$O) and [Zn(tach-6-Mepyr)](ClO$_4$)$_2$·0.5MeOH·0.5H$_2$O (5d′·0.5MeOH·0.5H$_2$O): A pale yellow solution of tach-6-Mepyr (0.0540 g, 1.22 × 10^{-4} mol) in MeOH (4 mL) was added to a solution of $Zn(ClO_4)_2 \cdot 6H_2O$ (0.0493 g, 1.22 × 10^{-4} mol) in EtOH (4 mL) affording a white precipitate. After standing for 1 h, the precipitate was isolated and washed with Et_2O and MeOH. This was dried under reduced pressure affording a white solid in 60.3% yield (0.0569 g, 8.05 × 10^{-5} mol). Single crystals suitable for X-ray crystallography (shown to be

 © 2005 Wiley-VCH Verlag GmbH & Co. KGaA, Weinheim

5d′·1/2MeOH·1/2H_2O) were obtained by Et_2O diffusion into an MeOH solution of the complex. ^1H NMR ([D_6]DMSO, 25 °C): δ = 7.89, 7.36, 7.34 (t, d, d, 3 H, $CH_3C_5H_3N$), 4.22, 4.05 (m, d, 3 H, diastereotopic methylene H's of MePyCH_2N and NHCH_2), 3.07 (br. s, cyclohexyl methine *H*), 2.15 (s, 3 H, CH_3C$_5$H$_3$N), 2.13 (br. d, 1 H, equatorial cyclohexyl methylene *H*), 1.82 (br. d, 1 H, axial cyclohexyl methylene *H*). MS (FAB/glycerol): *m*/*z* = 507 [M – 2 ClO_4^- – H^+]. $C_{27}H_{38}Cl_2N_6O_9Zn$(724.14): calcd. C 44.61, H 5.27, N 11.56; found C 44.58, H 5.41, N 11.74.

[Zn(tach-6-MeOpyr)](NO$_3$)$_2$ (5e): A solution of $Zn(NO_3)_2$·$6H_2O$ (0.0212 g, 7.13 × 10^{-5} mol) in MeOH (1 mL) was mixed with a colorless solution of tach-6-Mepyr (0.0364 g, 7.39 × 10^{-5} mol) in MeOH (1 mL) giving a colorless solution. Diffusion of Et_2O overnight produced colorless needles that were isolated, washed with Et_2O, and dried under reduced pressure affording white needles (0.0232 g, 3.36 × 10^{-5} mol, 47.1%). ^1H NMR (360 MHz, [D_6]DMSO, 25 °C): δ = 7.99, 7.10, 6.92 (t, d, d, 3 H, 6-OMeC$_5$H$_3$N), 4.39 (d, 1 H, NHCH_2), 4.14, 3.95 (dd, dd, 2 H, MeOpyCH_2N), 3.28 (s, 3 H, CH_3O), 3.13, (br. s, 1 H, cyclohexyl methine *H*), 2.24 (br. d, 1 H, equatorial cyclohexyl methylene *H*), 1.81 (br. d, 1 H, axial cyclohexyl methylene *H*). MS (FAB//NBA/DMSO): *m*/*z* = 618 [M – NO_3^-]. $C_{27}H_{36}N_8O_9Zn$ (680.19): calcd. C 47.56, H 5.32, N 16.43; found C 47.30, H 5.24, N 16.17.

[Zn(tachpyr)](CF$_3$SO$_3$)$_2$ (5f): A solution of $Zn(CF_3SO_3)_2$ (0.063 g, 1.7 × 10^{-4} mol) in MeOH (2 mL) was mixed with a pale yellow solution of tachpyr (0.070 g, 1.7 × 10^{-4} mol) in MeOH (2 mL), giving a pale yellow solution. Vapor-phase diffusion of Et_2O into this solution gave colorless needles after 18 h, which were isolated by decantation of solvent, washed with Et_2O and dried under reduced pressure affording an 82% yield (0.110 g, 1.4 × 10^{-4} mol) of white needles. ^1H NMR ([D_6]DMSO, 25 °C): MS (ESI, MeOH): *m*/*z* = 617 [M – $CF_3SO_3^-$], 469 [M – 2 $CF_3SO_3^-$ + H^+]$^+$. HPLC (gradient mode): R_t = 8.4 min (free ligand R_t = 18.8 min). HPLC (isocratic mode): R_t = 5.0 min. $C_{26}H_{30}F_6N_6O_6S_2Zn$ (764.09): calcd. C 40.76, H 3.95, N 10.97; found C 40.92, H 3.87, N 10.96.

Solution-Phase Complexation: Solution complexation studies for Fe^{II}, Ni^{II}, and Cu^{II} were carried out by combining aqueous or methanolic M^{II} and ligand solutions followed by spectroscopic analysis as described below; tach-*x*-Mepyr (*x* = 3, 4, 5 and 6) were easily dissolved in water while acidic conditions were required for tach-6-MeOpyr to dissolve (6 equiv. HCl). M^{II} (aq) was added to the chelator solution resulting in immediate complexation except in the case of tach-6-MeOpyr where 6 equiv. of NaOH was needed. Their spectra agreed well with those of the isolated metal complexes in MeCN (Table 1).

Fe^{II} Complexes: Complexation by tach-3-Mepyr and tach-6-Mepyr was studied in H_2O and solution reactions for all other chelators were run in MeOH. $FeCl_2$ (10 μL of 0.1 M aqueous) was added to tach-3-Mepyr (10 μL of 0.1 M aqueous) affording a bronze solution. Aqueous $FeCl_2$ (30 μL of 0.1 M) was added to tach-6-Mepyr (30 μL of 0.1 M) resulting in a red-brown solution. Each solution was brought to 1 mL with water producing solutions adequate for analysis. $FeCl_2$ (10 μL of 0.1 M methanolic solution) was added to tach-*x*-Mepyr or tach-6-MeOpyr (10 μL of 0.1 M methanolic solution) producing a bronze solution when *x* = 3, 4 or 5, a red-brown solution when *x* = 6 and a yellow solution for tach-6-MeOpyr. MeOH (980 μL) was added to the reactions producing solutions suitable for UV/Vis spectroscopic analysis.

Ni^{II} Complexes: Aqueous $NiCl_2$ (100 μL, 0.05 M) was added to aqueous tach-*x*-Mepyr or tach-6-MeOpyr, (100 μL of a 0.05 M solution) producing a clear pink solution with tach-*x*-Mepyr (*x* = 3, 4, 5), a clear yellow solution with tach-6-Mepyr, and a violet-white precipitate with tach-6-MeOpyr. Water (800 μL) was added to the reactions and the solutions were warmed (60 °C, 1 min) affording the appropriate pink, brown, and violet solutions for UV/Vis spectroscopic analysis.

Cu^{II} Complexes: All solution reactions for Cu^{II} complexes were run in water. $Cu(ClO_4)_2$ (60 μL of 0.05 M solution) was added to tach-*x*-Mepyr (*x* = 3, 4, 5) or tach-6-MeOpyr (120 μL of 0.025 M solution) producing a pale blue precipitate in all the reactions. Applying heat (50 °C, 30 s) and adding water (820 μL) produced bright blue solutions appropriate for analysis. Aqueous $Cu(ClO_4)_2$ (100 μL of 0.05 M solution) was added to aqueous tach-6-Mepyr (100 μL of 0.05 M solution) affording a pale blue precipitate. Water (800 μL) was added to the reaction producing a blue solution for UV/Vis spectroscopic analysis.

HPLC Studies: HPLC analyses of $[Fe(tach\text{-}3\text{-}Mepyr)]^{2+}$, $[Zn(tachpyr)]^{2+}$,[1] $[Zn(tach\text{-}6\text{-}Mepyr)]^{2+}$, $[Zn(tach\text{-}6\text{-}MeOpyr)]^{2+}$, $[Mn(tachpyr)]^{2+}$,[1] $[Mn(tach\text{-}6Mepyr)]^{2+}$ and $[Mn(tach\text{-}6MeOpyr)]^{2+}$ were conducted. Chromatograms in the gradient elution mode (RP-HPLC) were obtained with a Waters 600E/486/746 dual-pump system with UV detection at 254 nm. A Beckman Ultrasphere 4.6 × 25 cm RP-18 column was eluted with a gradient of 100% 0.05 M Et_3N·HOAc buffer (pH = 5.5) to 100% MeOH over 25 min. Chromatograms in the isocratic mode (RP-HPLC) were obtained on a Perkin–Elmer 250 dual-pump system with UV detection at 254 nm. A Beckman Ultrasphere 4.6 × 25 cm RP-18 column was eluted with 90% 0.05 M Et_3N·HOAc buffer (pH = 5.5) and 10% MeOH over 20 min. All complexes of tach-6-Mepyr and tach-6-MeOpyr, and also $[Mn(tachpyr)]^{2+}$, produced signals attributed to the free ligand and were therefore determined to be labile under gradient elution conditions. The complex $[Zn(tachpyr)]^{2+}$ was found inert as described previously,[1] and $[Fe(tach\text{-}3\text{-}Mepyr)]^{2+}$ showed a broad set of peaks indicative of imine formation previously observed for iron complexes of tach derivatives.[2,12] Under isocratic elution, the separation of $[Fe(tach\text{-}3\text{-}Mepyr)]^{2+}$ oxidation products improved sufficiently that the progressive transformations into higher imino species were observed.

Attempted Aqueous Reaction of tachpyr with Mg^{II} and Ca^{II}: These reactions were conducted in D_2O and analyzed by ^1H NMR spectroscopy; tachpyr (500 μL of 0.0241 M, 1.20 × 10^{-5} mol) was added to excess $MgBr_2$·$6H_2O$ (0.0180 g, 6.20 × 10^{-5} mol) or $CaCl_2$ (6.8 × 10^{-3} g, 6.1 × 10^{-5} mol); tachpyr remained unbound in both reactions.

X-ray Data Collection, Structure Solution and Refinement: See Tables 3 and 4) Single crystals of the various solvates of **1d**, **1e**, **3d**, **4e**, **5a**, and **5d′** were grown as described. The crystals were removed from the supernatant under a stream of N_2 and immediately covered with a layer of viscous hydrocarbon oil (Paratone N, Exxon). A suitable crystal was selected under the microscope, attached to a glass fiber, and immediately placed in the low-temperature nitrogen stream of the diffractometer. All data sets were collected using a Bruker SMART system, complete with 3-circle goniometer and CCD detector operating at –54 °C. The data sets were collected using a Cryojet low-temperature device from Oxford Instruments by employing graphite-monochromated Mo-K_α radiation (λ = 0.71073 Å). Crystal decay was monitored by repeating the initial frames at the end of the data collection and analyzing the duplicate reflections. In all cases, no decay was observed. The crystal structures of all compounds were solved by direct methods, as included in the SHELX program package.[13] Absorption corrections were made with SADABS.[14] Missing atoms were located in subsequent difference Fourier maps and included in the refinement. The structures were refined by full-matrix least-squares refinement on F^2.

 © 2005 Wiley-VCH Verlag GmbH & Co. KGaA, Weinheim

Hydrogen atoms were placed geometrically and refined using a riding model, including free rotation about C–C bonds for methyl groups. Thermal parameters for hydrogen atoms were refined with U_{iso} constrained at 1.2 (for non-methyl groups), and 1.5 (for methyl groups) times U_{eq} of the carrier C atom. All non-hydrogen atoms, with the exception of some disordered or restrained positions were refined anisotropically. The twist angles Φ were calculated by first determining the centroid in each of the triangles of the three cyclohexylamino nitrogen atoms [N(tach); designated as X1] and of the three ethylamino nitrogen atoms [N(en); designated as X2]. Then, the torsion angles N(tach)–X1–X2–N(en), each involving the two nitrogen atoms of the same chelate arm, were calculated and averaged. ORTEP drawings were made with SHELXTL[13] and ORTEP-3.[15,16] The ORTEP plots of **1d**·1/2H_2O·1/2MeOH and **1e** are available as Supporting Information. CIF files for the structural analyses of **1d**·1/2H_2O·1/2MeOH, **1e**, **3d′**·0.5Et_2O, **4e**, **5a**·2MeOH·0.5H_2O, and **5d′**·0.5H_2O·0.5MeOH have been deposited with the Cambridge Crystallographic Data Centre. CCDC-

Table 3. Crystal data and structure refinement parameters for **1d**·0.5H_2O·0.5MeOH, **1e**·MeOH and **3d′**·0.5Et_2O.

	1d·0.5H_2O·0.5MeOH	**1e**·MeOH	**3d′**·0.5Et_2O
Empirical formula	$C_{27.50}H_{37.50}Cl_2MnN_6O_9$	$C_{30}H_{39}F_6MnN_6O_{10}S_2$	$C_{29}H_{41}N_8NiO_{6.50}$
Formula mass	721.97	876.73	664.41
Crystal system	triclinic	monoclinic	monoclinic
Space group	$P\bar{1}$	$P2_1/c$	$P2_1/n$
a [Å]	9.4981(4)	14.490(8)	12.0745(4)
b [Å]	17.6530(7)	15.655(8)	16.6907(5)
c [Å]	19.2146(7)	17.015(9)	15.0261(5)
α [°]	96.521(3)	90	90
β [°]	95.382(1)	104.461(10)	92.280(1)
γ [°]	94.633(1)	90	90
V [Å^3]	3173.1(2)	3737(3)	3025.8(2)
Z	4	4	4
Color	colorless	colorless	pale violet
Crystal shape	fragment	fragment	fragment
Crystal dimensions [mm]	0.14 × 0.20 × 0.27	0.05 × 0.12 × 0.21	0.24 × 0.35 × 0.40
$D_{calcd.}$ [g cm^{-3}]	1.515	1.558	1.458
μ [mm^{-1}]	0.646	0.557	0.700
Λ [Å]	0.71073	0.71073	0.71073
Refl. collected/unique	20018/8601	16755/4080	18825/3830
θ range [°]	1.07–27.88	1.79–23.29	1.82–27.88
Parameters	883	512	419
GOF	0.996	1.040	1.054
Final R indices [$I > 2\sigma(I)$]	R = 0.0625	R = 0.0343	R = 0.0710
	R_w = 0.1518	R_w = 0.0898	R_w = 0.1473
$\Delta\rho_{max.}$ [e·Å^{-3}]	1.601	0.552	0.715

Table 4. Crystal data and structure refinement parameters for **4e**, **5a**·2MeOH·0.5H_2O and **5d′**·0.5H_2O·0.5MeOH.

	4e	**5a**·2MeOH·0.5H_2O	**5d′**·0.5H_2O·0.5MeOH
Empirical formula	$C_{27}H_{36}Cl_2CuN_6O_{11}$	$C_{58}H_{72}N_{16}O_{17}Zn_2$	$C_{55}H_{72}Cl_4N_{12}O_{18}Zn_2$
Formula mass	755.06	1396.06	730.91
Crystal system	monoclinic	monoclinic	triclinic
Space group	$P2_1/n$	$P2_1/c$	$P\bar{1}$
a [Å]	20.450(4)	16.3245(10)	9.4081(4)
b [Å]	16.643(4)	18.9702(12)	17.6239(8)
c [Å]	21.223(5)	20.9807(13)	19.1521(8)
α [°]	90	90	96.581(1)
β [°]	118.293(4)	92.3000(10)	95.722(1)
γ [°]	90	90	95.383(1)
V [Å^3]	6360(2)	6492.0(7)	3121.1(2)
Z	8	4	2
Color	blue	colorless	colorless
Crystal shape	fragment	needle	fragment
Crystal dimensions [mm]	0.03 × 0.09 × 0.31	0.30 × 0.30 × 0.55	0.06 × 0.08 × 0.49
$D_{calcd.}$ [g cm^{-3}]	1.577	1.428	1.563
μ [mm^{-1}]	0.924	0.819	1.021
Λ [Å]	0.71073	0.71073	0.71073
Refl. collected/unique	28509/5763	34815/8774	19752/7146
θ range [°]	1.14–23.29	1.45–25.00	1.08–27.97
Parameters	868	839	883
GOF	0.813	1.022	1.027
Final R indices [$I > 2\sigma(I)$]	R = 0.0378	R = 0.0538	R = 0.0698
	R_w = 0.0812	R_w = 0.1427	R_w = 0.1346
$\Delta\rho_{max.}$ [e·Å^{-3}]	0.704	1.499	0.986

 © 2005 Wiley-VCH Verlag GmbH & Co. KGaA, Weinheim

268824 to -268829 contain the supplementary crystallographic data for this paper. These data can be obtained free of charge from The Cambridge Crystallographic Data Centre via www.ccdc.cam.ac.uk/data_request/cif.

Cytotoxicity Assays: MCF-7, a breast cancer cell line, was obtained from the ATCC and was grown in Dulbecco's Modified Eagle medium containing 10% fetal bovine serum in a humidified chamber containing 5% CO_2. 5×10^3 cells were plated in 96-well tissue culture dishes and allowed to attach overnight before test compounds were added. Six replicate cultures were used for each point. After 8, 24, 48 and 72 h (8 and 72 h in the case of tach-6-Mepyr), viability was assessed using an MTT assay, in which 3-(4,5-dimethylthiazol-2-yl)-2,5-diphenyltetrazolium bromide was added to the medium and the formation of a reduced product assayed by measuring the optical density at 560/650 nm after 3 h. Color formation is proportional to viable cell number.[17] Assays of all compounds were repeated at least three times.

Acknowledgments

We thank the NIH for the support of this work (Grant DK-57781-R01 to S. V. T.). Research at The University of Alabama is supported by the Division of Chemical Sciences, Office of Basic Energy Sciences, Office of Research, U. S. Department of Energy (Grant DE-FG02-96ER14673). Purchase of the X-ray equipment at Syracuse University was made possible with generous support from the National Science Foundation (CHE-95-27898), Syracuse University and the W. M. Keck Foundation.

[1] G. Park, A. M. Przyborowska, N. Ye, N. Tsoupas, C. B. Bauer, G. A. Broker, R. D. Rogers, M. W. Brechbiel, R. P. Planalp, *Dalton Trans.* **2003**, 318.
[2] G. Park, F. Lu, N. Ye, M. Brechbiel, S. Torti, F. Torti, R. Planalp, *J. Biol. Inorg. Chem.* **1998**, *3*, 449.
[3] G. Park, E. Dadachova, A. Przyborowska, S.-J. Lai, D. Ma, G. Broker, R. Rogers, R. Planalp, M. Brechbiel, *Polyhedron* **2001**, *20*, 3155.
[4] G. Park, N. Ye, R. Rogers, M. Brechbiel, R. Planalp, *Polyhedron* **2000**, *19*, 1155.
[5] S. V. Torti, R. P. Planalp, M. W. Brechbiel, G. Park, F. M. Torti, in: *Molecular Biology of Hematopoiesis* (Ed.: N. G. Abraham), Kluwer/Plenum Press, New York, **1999**, vol. 6 , pp. 381.
[6] N. Le, D. Richardson, *Biochim. Biophys. Acta* **2002**, *1603*, 31.
[7] J. Easmon, *Expert Opin. Ther. Pat.* **2002**, *12*, 789.
[8] S. V. Torti, F. M. Torti, S. P. Whitman, M. W. Brechbiel, G. Park, R. P. Planalp, *Blood* **1998**, *92*, 1384.
[9] R. Zhao, R. P. Planalp, R. Ma, B. Greene, B. Jones, M. Brechbiel, F. M. Torti, S. V. Torti, *Biochem. Pharmacol.* **2004**, *67*, 1677.
[10] D. Ma, F. Lu, T. Overstreet, D. E. Milenic, M. W. Brechbiel, *Nucl. Med. Biol.* **2002**, *29*, 91.
[11] D. F. Evans, *J. Chem. Soc.* **1959**, 2003.
[12] G. Lu, D. P. Kennedy, S. Lai, G. Park, A. M. Przyborowska, M. W. Brechbiel, G. A. Broker, R. D. Rogers, R. Ma, F. M. Torti, S. V. Torti, R. P. Planalp, *Inorg. Chem.*, submitted for publication.
[13] G. M. Sheldrick, *SHELXTL*, version 5.05, Siemens Analytical X-ray Instruments Inc., **1996**.
[14] G. M. Sheldrick, *Program for Semiempirical Absorption Correction of Area Detector Data*, University of Göttingen, Germany, **1996**.
[15] M. Burkitt, *Methods Enzymol.* **1994**, *234*, 66.
[16] L. J. Farrugia, *J. Appl. Crystallogr.* **1997**, *30*, 565.
[17] T. Mosmann, *J. Immunol. Methods* **1983**, *65*, 55.
[18] K. A. Hilfiker, R. D. Rogers, M. W. Brechbiel, R. P. Planalp, *Inorg. Chem.* **1997**, *36*, 4600.
[19] H. L. Chum, J. A. Vanin, M. I. D. Holanda, *Inorg. Chem.* **1982**, *21*, 1146.
[20] H. Toftlund, S. Yde-Andersen, *Acta Chem. Scand., Series A* **1981**, *35*, 575.
[21] K. Wieghardt, E. Schoeffmann, B. Nuber, J. Weiss, *Inorg. Chem.* **1986**, *25*, 4877.
[22] L. J. Wilson, D. Georges, M. A. Hoselton, *Inorg. Chem.* **1975**, *14*, 2968.
[23] R. D. Hancock, G. J. McDougall, *J. Chem. Soc. Dalton Trans.* **1977**, 67.
[24] G. Park, J. Shao, F. H. Lu, R. D. Rogers, N. D. Chasteen, M. W. Brechbiel, R. P. Planalp, *Inorg. Chem.* **2001**, *40*, 4167.
[25] M. Duggan, N. Ray, B. Hathaway, G. Tomlinson, P. Brint, K. Pelin, *J. Chem. Soc. Dalton Trans.* **1980**, 1342.
[26] K. D. Karlin, J. C. Hayes, S. Juen, J. P. Hutchinson, J. Zubieta, *Inorg. Chem.* **1982**, *21*, 4106.
[27] B. Figgis, *Introduction to ligand fields*, Wiley, New York, **1966**.
[28] R. D. Shannon, C. T. Prewitt, *Acta Crystallogr. Sect. B* **1969**, *25*, 925.
[29] R. Shannon, *Acta Crystallogr., Sect. A* **1976**, *32*, 751.
[30] B. Hathaway, R. Gillard, J. McCleverty, in: *Comprehensive Coordination Chemistry* (Eds.: G. Wilkinson, R. Gillard, J. McCleverty), Pergamon, Oxford, **1987**, vol. 5, chapter 53.4.

Received: April 28, 2005
Published Online: August 24, 2005

 © 2005 Wiley-VCH Verlag GmbH & Co. KGaA, Weinheim

Indium(I) Hexafluoropnictates ($InPnF_6$; Pn = P, As, Sb)

Zoran Mazej*[a]

Keywords: Fluorides / Indium / Pnictides / Raman spectroscopy / Structure elucidation

The colourless compounds $InPnF_6$ (Pn = P, As, Sb), with In^I in a solely fluorine environment, were prepared by reacting In metal with PnF_5 (Pn = P) and displacement of the weaker Lewis acid BF_3 from $InBF_4$ by a stronger one, PnF_5 (Pn = As, Sb), in anhydrous hydrogen fluoride (aHF). The X-ray powder diffraction analyses show that $InPF_6$ crystallises in cubic unit cell with a = 8.07(2) Å, while $InAsF_6$ crystallises in a rhombohedral unit cell with a = 7.58(2) and c = 7.90(1) Å. The Raman spectra of $InPnF_6$ (Pn = P, As, Sb) confirm the formation of PnF_6^- salts. An attempt to prepare InF and In_2F_4 ($In^IIn^{III}F_4$) by reaction of CsF with $InSbF_6$ in aHF or by metathetical reaction of $InSbF_6$ with $CsInF_4$ in aHF, respectively, failed. Instead of InF and In_2F_4, respectively, a mixture of In and InF_3 was obtained.
(© Wiley-VCH Verlag GmbH & Co. KGaA, 69451 Weinheim, Germany, 2005)

Introduction

The main oxidation state of group 13 elements (B, Al, Ga, In, Tl) is trivalent, although on going from lighter to heavier elements the univalent state becomes more stable. The occurrence of the latter is often described as an inert-pair effect.[1] In contrast to thallium, univalent indium compounds are not common. All thallium monohalides are well characterised, whereas only InCl, InBr and InI are known in the condensed phase.[2] Unstable InF has only been observed in the gas phase.[2–5] Furthermore, reports of complex fluorides with In^+ in a solely fluorine environment are also scarce.[6,7] One rare example is $InBF_4$, which has been prepared by reaction of elemental In with BF_3 in anhydrous hydrogen fluoride (aHF).[6] In the second case the authors erroneously claimed that they made $InBF_4$ for the first time.[7]

In the present work, two aims were followed: to prepare and characterise new ternary compounds with In^+ in a solely fluorine environment and to exploit the possibility of preparing indium(I) fluoride (InF) and a mixed-valence In^I/In^{III} fluoride ($In^IIn^{III}F_4$).

Discussion

Synthesis

The previously known BF_4^- salt of In^+ was prepared by the reaction of In metal with an excess of BF_3 in anhydrous hydrogen fluoride (aHF).[6] The same approach is not applicable to other Lewis acids (i.e., AsF_5, SbF_5) because they oxidize elemental In to In^{3+} to yield InF_3 (with AsF_5) or a mixture of $InF_3{\cdot}3SbF_5$[8] and $SbF_3{\cdot}nSbF_5$ (with SbF_5). For that reason, a different approach has to be used.

The displacement of the weaker Lewis acid BF_3 from $InBF_4$ by the stronger acid, AsF_5 or SbF_5, in the highly acidic solvent aHF, was successful. When a stoichiometric amount of Lewis acid (AsF_5, SbF_5) was added to a colourless solution of $InBF_4$ in aHF, a colourless precipitate formed immediately. Colourless $InAsF_6$ and $InSbF_6$ were obtained after decanting the liquid phase and removing the remaining traces of volatiles under vacuum at ambient temperature, see Equation (1).

$$InBF_4 + PnF_5 \xrightarrow[298\ K]{aHF} InPnF_6\ (Pn = As, Sb) + BF_3 \quad (1)$$

Use of an excess of AsF_5 or SbF_5 caused oxidation of In^+ to In^{3+} to give InF_3 or a mixture of $InF_3{\cdot}3SbF_5$/$SbF_3{\cdot}nSbF_5$, respectively. In the course of this study it was also found that $InAsF_6$, prepared by the reaction of $InBF_4$ with AsF_5 in aHF [Equation (1)], should be isolated immediately after its precipitation. When the reaction was left to proceed for a longer time, In^+ was slowly oxidized to In^{3+} to give $InAsF_6$ contaminated with InF_3. Its oxidation was complete in a few days and only InF_3 was recovered from the reaction mixture.

Compared with AsF_5 or SbF_5, PF_5 and BF_3 are weak Lewis acids (MF_x; x = 4 when M = B and x = 6 when M = P, As, Sb). A good measure of the strength of their Lewis acidity is the reaction enthalpy $\Delta H(MF_x + F^- = [MF_{x+1}]^-)$, i.e. fluoride ion affinity (FIA).[9] The main driving forces for the formation of $InPnF_6$ compounds [Equation (1)] are the difference in fluoride ion affinities (FIA) of BF_3 (347.7 kJ mol^{-1})[9] and PnF_5 (Pn = P: 397.1 kJ mol^{-1}; As =

[a] Department of Inorganic Chemistry and Technology, Jožef Stefan Institute,
Jamova 39, 1000 Ljubljana, Slovenia
Fax: +386-1-477-3155
E-mail: zoran.mazej@ijs.si

 DOI: 10.1002/ejic.200500481 © 2005 Wiley-VCH Verlag GmbH & Co. KGaA, Weinheim

443.1 kJ mol^{-1}; Sb = 503.3 kJ mol^{-1})[9] and the lattice energy differences between the starting $InBF_4$ and the resulting $InPnF_6$ salts. The lattice potential energies of $InMF_x$ salts have been estimated by Jenkins and Passmore et al. from a generalized volume-based Kapustinskii equation, see Equation (2).[10,11]

$$U_{POT}(InMF_x) = 2I\cdot[a\cdot V_m(InMF_x)^{-1/3} + \beta] \quad (2)$$

where a = 117.3 kJ mol^{-1} nm, β = 51.9 kJ mol^{-1} and the lattice ionic strength, I, is 1 for $InMF_x$ salts. Using values of $V_m(InMF_x) = V_{unit\ cell}/Z$ from the crystallographic data of $InBF_4$[6] and $InPnF_6$ (Pn = P, As), their lattice potential energies were estimated to be 616 kJ mol^{-1} ($InBF_4$) and about 566 kJ mol^{-1} ($InPF_6$, $InAsF_6$). The smaller lattice energy of $InAsF_6$ in comparison to $InBF_4$ is offset by a better fluoride ion acceptor ability of AsF_5 against BF_3, which makes the reaction $InBF_4 + AsF_5$ thermodynamically more favourable. In the contrast to AsF_5, the FIA of PF_5 is insufficient to compensate the poorer lattice energy of $InPF_6$ in comparison to $InBF_4$ and the reaction with the latter does not proceed.

As mentioned previously, In metal is oxidized to In^{3+} by the excess of AsF_5 or SbF_5 in aHF. However, the reaction between In metal and an excess of PF_5 in aHF proceeded in a different manner. Indium metal was slowly oxidized to In^+ to yield a colourless powder and cubic-shaped single crystals of $InPF_6$. Even after several days the reaction was not completed. During the isolation the powdery $InPF_6$ material turned grey and the smooth transparent surface of the crystals became rough and opaque.

The attempt to prepare In^I hexafluorobismuthate by the reaction of $InBF_4$ with BiF_5 in aHF failed. The yellowish solid isolated immediately after its precipitation was found to consist of InF_3 and $BiF_3\cdot nBiF_5$.[12]

Crystal Structures

Hexafluoropnictates ($MPnF_6$, Pn = As, Sb, Bi) of the heavier univalent metals (M = Tl, Rb, Cs) crystallise in a rhombohedral unit cell with the $KOsF_6$ structure type.[13] The only exceptions are hexafluorophosphates, which have cubic lattices at room temperature.[14] The expectation that PnF_6^- salts of In^+ should crystallise in a similar manner were confirmed by X-ray powder analyses.

The X-ray powder data of $InPF_6$, obtained at 298 K, were indexed with the Dicvol91 program[15] as a cubic unit cell (Table 1) with a = 8.07(2) Å and V = 524.9 Å^3. The isomorphic $CsPF_6$ has a cubic unit cell with a = 8.228(5) Å, V = 557(1) Å^3 and Z = 4.[14,16]

The X-ray powder pattern of $InAsF_6$ obtained at 298 K is very similar to that of $CsAsF_6$. The isostructurality of both compounds was confirmed after indexing the X-ray powder data of $InAsF_6$ in a rhombohedral unit cell (Table 2) with a = 7.58(2) Å, c = 7.90(1) Å and V = 393.3 Å^3. Isomorphic $CsAsF_6$ has a rhombohedral unit cell with a = 7.723(1) Å, c = 8.0503(10) Å, V = 415.8 Å^3 and Z = 3.[17]

Table 1. X-ray powder data for $InPF_6$ with a cubic unit cell.[a]

I/I_o	d (obsd.)	d (calcd.)	h	k	l
1	4.685	4.657	1	1	1
10	4.030	4.033	2	0	0
9	2.848	2.852	2	2	0
9	2.432	2.432	3	1	1
5	2.324	2.329	2	2	2
1	2.020	2.017	4	0	0
2	1.851	1.851	3	3	1
5	1.805	1.804	4	2	0
5	1.645	1.647	4	2	2
2	1.552	1.552	3	3	3
		1.552	5	1	1
1	1.427	1.426	4	4	0
2	1.345	1.344	4	4	2
		1.344	6	0	0
1	1.274	1.275	6	2	0
1	1.215	1.216	6	2	2

[a] a = 8.07(2) Å and V = 524.9 Å^3.

Table 2. X–ray powder data for $InAsF_6$ with a rhombohedral unit cell.[a]

I/I_o	d (obsd.)	d (calcd.)	h	k	l
10	3.772	3.791	1	1	0
10	3.373	3.385	1	0	2
1	2.624	2.633	0	0	3
4	2.521	2.525	2	0	2
4	2.355	2.368	2	1	1
4	2.190	2.189	3	0	0
9	2.100	2.101	2	1	2
5	1.891	1.891	1	0	4
2	1.692	1.692	2	0	4
2	1.653	1.654	3	1	2
2	1.548	1.545	2	1	4
2	1.517	1.516	4	0	2
2	1.437	1.433	4	1	0
2	1.406	1.407	3	2	2
1	1.339	1.339	3	1	4
1	1.264	1.264	3	3	0

[a] a = 7.58(2) Å, c = 7.90(1) Å and V = 393.3 Å^3.

In the case of $InSbF_6$ the obtained X-ray powder photographs showed no lines, thereby indicating that the isolated $InSbF_6$ was of very low crystallinity. This couldn't be improved even after recrystallisation of $InSbF_6$ from its saturated solution in aHF.

Vibrational Spectra

The Raman spectra of $InPnF_6$ (Pn = P, As, Sb) are shown in Figure 1 and given in Table 3. They are in agreement with the presence of regular PnF_6^- octahedra.

Attempted Synthesis of InF and $InInF_4$

Preparation of InF has previously been attempted by thermal decomposition of $InBF_4$ at 373 K.[6] On the basis of the results of X-ray powder analysis, it was claimed that the grey product contains, along with In metal, another phase which couldn't be identified. However, the X-ray

 © 2005 Wiley-VCH Verlag GmbH & Co. KGaA, Weinheim

Table 3. Raman spectra of $InPnF_6$ (Pn = P, As, Sb) and the literature data for corresponding Cs^+ salts.

$InPF_6$	$CsPF_6$ [14,16]	$InAsF_6$	$CsAsF_6$ [18]	$InSbF_6$	$CsSbF_6$[19]	Assignment[a]
738(100)	744(100)	677(100)	685(100)	641(100)	650(100)	ν_1
568(5)	578(5)	561(20)	576(30)	555(20)	570(13)	ν_2
470(5)	476(16)	365(25)	372(30)	283(15)	283(40)	ν_5
				272(15)	276(26)	ν_5

[a] Assignments are made for octahedral symmetry although in the solid state the actual symmetry could be lower.

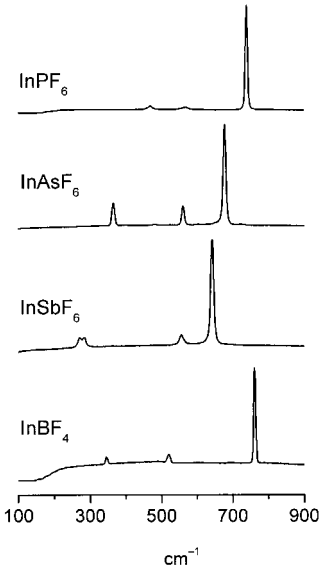

Figure 1. Raman spectra of indium(I) hexafluoropnictates and Raman spectrum of $InBF_4$ [761(100), 519(10), 346(10)].

powder diffraction pattern of this phase didn't match that of InF_3 nor could it be assigned to a high-ordered room-temperature form of TlF or to the NaCl structural type which is expected for InF.[6]

Our attempt to prepare InF slightly above the melting point of aHF (189.4 K) by reaction between $InSbF_6$ and CsF in aHF, expecting that the $CsSbF_6$ would precipitate and leave InF dissolved in aHF, failed. At this temperature all the insoluble solid was greyish. Colourless CsF reacted with $InSbF_6$ to form a mixture of colourless $CsSbF_6$ and InF_3 and finely powdered grey In metal.

Several phases have been isolated and characterised in the TlF/TlF_3 system (i.e., $Tl_2F_3 \equiv Tl^{I}_3\,Tl^{III}F_6$, $Tl_3F_5 \equiv Tl^{I}_2\,Tl^{III}F_5$, $TlF_2 \equiv Tl^{I}Tl^{III}F_4$, $Tl_3F_7 \equiv Tl^{I}Tl^{III}_2F_7$).[20,21] An attempt to prepare the indium analogue of TlF_2 (i.e., $InF_2 \equiv In^{I}In^{III}F_4$) by a metathetical reaction between $InSbF_6$ and $CsInF_4$ in aHF failed. Nothing happened at 243 K, and when the reaction mixture was brought to ambient temperature and left for one hour, a dark solid formed. This insoluble dark solid was separated from the colourless solution. The former consisted of a mixture of In and InF_3 still contaminated with $CsSbF_6$, while the colourless solid isolated from the decanted solution corresponded to $CsSbF_6$.

Experimental Section

CAUTION: Anhydrous HF and some of the fluorides below are highly toxic and must be handled using appropriate apparatus and protective gear.

Apparatus and Reagents: Volatile materials (PF_5, AsF_5, SbF_5, BF_3, aHF) were manipulated in an all-PTFE vacuum line equipped with PTFE valves. Non-volatile materials were manipulated in a dry box (M. Braun). The residual water in the atmosphere within the dry box never exceeded 1 ppm. The reactions were carried out in translucent fluorocarbon polymer (FEP, tetrafluoroethylene-hexafluoropropylene copolymer) reaction vessels (height 250–300 mm with inner diameter 15.5 mm and outer diameter 18.75 mm) equipped with PTFE body valves and PTFE-coated stirring bars. Reaction vessels made from two FEP tubes in a T-shape manner and equipped with PTFE body valves were used in some experiments. Each reaction vessel was pre-treated with F_2 (to about 1 bar) for several hours before use.

Pieces of In metal (Alfa Aesar, 99.99%) were treated with concentrated HCl prior to use to remove the oxide layer. BF_3 (Union Carbide Austria GmbH, 99.5%), CsF (Ventron, 99.9%) and InF_3 (Aldrich, 99.9) were used as supplied. Anhydrous HF (Praxair, 99.9%) was treated with K_2NiF_6 (Ozark-Mahoning, 99%) for several hours prior to use. PF_5, AsF_5, SbF_5 and BiF_5, were synthesised by pressure fluorination of phosphorus pentoxide (Aldrich, 99.99%), arsenic trioxide (Fluka, 99.5%), antimony trifluoride (Alfa Aesar, 99%) or bismuth trifluoride (ABCR, 99.5%), respectively, with elemental fluorine in a nickel reactor at 573 K.[22]

$InBF_4$ was synthesised from In metal and BF_3 in aHF as described.[6] $CsInF_4$ was prepared by annealing a stoichiometric mixture of CsF and InF_3.[23]

Instrumentation: Raman spectra were recorded with a Renishaw Raman Imaging Microscope System 1000, with He-Ne laser with wavelength 632.8 nm. X-ray powder diffraction photographs were obtained using the Debye–Scherrer technique with Ni-filtered Cu-K_α radiation. The positions of the lines were measured by visual inspection. Samples were loaded into 0.3-mm i.d. quartz capillaries in a dry-box, which were temporarily stoppered with halocarbonic grease and sealed outside in the H_2/O_2 flame.

Chemical Analyses: The amount of total fluoride ion was determined after total decomposition of the sample using a fluoride ion selective electrode.[24,25] The amount of indium was determined by complexometric titration with EDTA,[26] the amount of antimony by redox titration,[27] and the amount of AsF_6^- ion gravimetrically by precipitation with tetraphenylarsonium chloride.[28,29] The results of chemical analyses are given in mass percents.

Syntheses – General Procedure: Nonvolatile reactants were loaded into FEP reaction vessels in a glove box. Anhydrous hydrogen fluoride (aHF) and, when necessary, PF_5, AsF_5 or SbF_5 were con-

 © 2005 Wiley-VCH Verlag GmbH & Co. KGaA, Weinheim

densed onto the solid reactants at 77 K. The reaction vessels were brought to ambient temperature. The reaction mixtures were vigorously agitated and, after some time, the volatiles were pumped off. Isolated products were characterised by mass balance, chemical analysis, vibrational spectroscopy and/or X-ray powder diffraction analyses.

Reaction Between $InBF_4$ and PF_5 in aHF: Reaction mixture: 0.544 g (2.70 mmol) of $InBF_4$ and 0.340 g (2.70 mmol) of PF_5 in 2 mL aHF. After 2 d only a colourless clear solution was visible. An excess of PF_5 (ca. 1.00 g) was then added. The Raman spectrum of the isolated solid showed only bands which could be assigned to $InBF_4$ (Figure 1).

Synthesis of $InPF_6$: Reaction mixture: 0.340 g (2.96 mmol) of In metal and approximately 1.00 g of PF_5 in 4 mL of aHF. After 7 d pieces of In metal were still present. Cubic shaped crystals and a colourless powdered solid were observed beside unreacted In metal. After isolation the colourless powdered solid turned grey. Under microscopic observation it was found that single crystals also decomposed on the surface.

Synthesis of $InAsF_6$: Reaction mixture: 0.443 g (2.32 mmol) of $InBF_4$ and 0.480 g (2.44 mmol) of AsF_5 in 6 mL of aHF. A white precipitate formed immediately and the reaction was left to proceed for 10 min. To decrease the loss of $InAsF_6$ because of its solubility in aHF the reaction vessel was cooled to 243 K and, whilst cold, the solution was decanted to remove any possible traces of $InBF_4$. Yield of $InAsF_6$: 0.706 g (100% based on $InBF_4$). $InAsF_6$ (303.74): calcd. In 37.80, F 37.53, AsF_6 62.20; found In 37.6, F 37.1, AsF_6 62.5. X-ray powder diffraction analysis and Raman spectroscopy excluded the presence of $InBF_4$ or InF_3.

When the reaction mixture was left for a longer time the isolated product consisted of $InAsF_6$ and InF_3 (after 2 d) or only InF_3 (after 9 d).

When In metal or $InBF_4$ were treated with an excess of AsF_5 in aHF the final product consisted only of InF_3.

Synthesis of $InSbF_6$: Reaction mixture: 0.450 g (2.23 mmol) of $InBF_4$ and 0.398 g (2.23 mmol) of SbF_5 in 5 mL of aHF. A white precipitate formed immediately. After 1 d the volatiles were pumped off. Yield of $InSbF_6$: 0.794 g (100% based on $InBF_4$). $InSbF_6$ (350.56): calcd. In 32.75, F 32.52, Sb 34.73; found In 33.0, F 32.1, Sb 34.5.

The reaction between In metal or $InBF_4$ and an excess of SbF_5 in aHF yielded a mixture of $InF_3{\cdot}3SbF_5$[8] and $SbF_3{\cdot}nSbF_5$, as found by Raman spectroscopy. A detailed characterisation of the latter is beyond the scope of this study.

Reaction Between $InBF_4$ and BiF_5 in aHF: Reaction mixture: 0.569 g (2.82 mmol) of $InBF_4$ and 0.857 g (2.82 mmol) of BiF_5 in 10 mL of aHF. A white, very dense suspension was obtained. The liquid phase was decanted away and the remaining volatile components pumped off. The isolated solid was yellowish. The Raman spectrum [587 (100), 570 (sh), 535 (20), 493 (10), 231 (5) 125 (5)] indicated the formation of $BiF_3{\cdot}nBiF_5$.[12] A detailed characterisation of this adduct is beyond the scope of this study.

Attempt to Prepare InF: A mixture of $InSbF_6$ (0.84 mmol) and CsF (0.84 mmol) was loaded into the double T-shaped apparatus. After condensation of aHF onto the sample at 77 K, the reaction vessel was warmed slightly to the melting point of aHF (ca. 190 K). At that temperature the insoluble solid was greyish in aHF. The reaction vessel was allowed to reach room temperature and left for 0.5 h. The colourless liquid was decanted and aHF condensed back onto the insoluble solid. After repeating this procedure several times, the volatile materials were pumped off at ambient temperature. The X-ray powder diffraction pattern of the grey isolated solid showed lines that could be assigned to InF_3 still contaminated with $CsSbF_6$, while the Raman spectrum of the colourless solid isolated from the decanted solution corresponded to that of $CsSbF_6$.

Attempt to Prepare In_2F_4: A mixture of $InSbF_6$ (0.239, 0.68 mmol) and $CsInF_4$ (0.221 g, 0.68 mmol) was loaded into the double T-shaped apparatus. After condensation of aHF onto the sample at 77 K, the reaction vessel was warmed to 243 K. A clear solution was visible above the insoluble colourless solid. Since no visible change was observed after 1 h, the reaction vessel was brought to ambient temperature and left for 0.5 h. The colour of the insoluble solid turned to grey-black. The colourless liquid was decanted and aHF condensed back onto the insoluble solid. After repeating this procedure several times, the volatile materials were pumped off at ambient temperature. The X-ray powder diffraction pattern of the grey isolated solid showed lines which could be assigned to InF_3, while the Raman spectrum of the colourless solid isolated from the decanted solution corresponded to $CsSbF_6$.

Acknowledgments

The author gratefully acknowledges the Slovenian Research Agency (ARRS) for the financial support of the present study within the research program: P1-0045 Inorganic Chemistry and Technology. I am also grateful to Dr. Maja Ponikvar for the chemical analysis.

[1] F. A. Cotton, G. Wilkinson, *Advanced Inorganic Chemistry*, John Wiley & Sons, New York, **1988**, p. 208.
[2] N. N. Greenwood, A. Earnshaw, *Chemistry of the Elements*, Pergamon Press, Oxford, **1984**, pp. 270–272.
[3] J. Hoeft, K. P. R. Nair, *Z. Phys. D* **1994**, *29*, 203–207.
[4] T. Karkanis, M. Dulick, Z. Morbi, J. B. White, P. F. Bernath, *Can. J. Phys.* **1994**, *72*, 1213–1217.
[5] K. D. Hensel, M. C. L. Gerry, *J. Chem. Soc., Faraday Trans.* **1997**, *93*, 1053–1059.
[6] H. Fitz, B. G. Müller, *Z. Anorg. Allg. Chem.* **1997**, *623*, 579–582.
[7] C. L. B. Macdonald, A. M. Corrente, C. G. Andrews, A. Taylor, B. D. Ellis, *Chem. Commun.* **2004**, 250–251.
[8] Z. Mazej, P. Benkič, in *Proceedings of the 13th European Symposium on Fluorine Chemistry*, Bordeaux, **2001**, p. B3 (abstract) .
[9] K. O. Christe, D. A. Dixon, D. McLemore, W. W. Wilson, J. A. Sheehy, J. A. Boatz, *J. Fluorine Chem.* **2000**, *101*, 151–153.
[10] H. D. B. Jenkins, H. K. Roobottom, J. Passmore, L. Glasser, *Inorg. Chem.* **1999**, *38*, 3609–3620.
[11] L. Glasser, H. D. B. Jenkins, *J. Am. Chem. Soc.* **2000**, *122*, 632–638.
[12] K. O. Christe, W. W. Wilson, E. C. Curtis, *Inorg. Chem.* **1979**, *18*, 2578–2586.
[13] C. Röhr, R. Kniep, *Z. Naturforsch. Teil B* **1994**, *49*, 650–654.
[14] K. Kitashita, R. Hagiwara, Y. Ito, O. Tamada, *J. Fluorine Chem.* **2000**, *101*, 173–179.
[15] A. Boultif, D. Luoer, *J. Appl. Cryst.* **1991**, *24*, 987–993.
[16] R. B. English, A. M. Heyns, *J. Cryst. Spec. Res.* **1984**, *14*, 531–541.
[17] S. Loss, C. Roehr, *Z. Naturforsch. B* **1998**, *B53*, 75–80.
[18] G. M. Begun, A. C. Rutenberg, *Inorg. Chem.* **1967**, *6*, 2212–2216.
[19] W. H. J. de Beer, A. M. Heyns, *J. Solid State Chem.* **1980**, *33*, 283–288.
[20] J. Grannec, L. Lozano, J. Portier, P. Hagenmuller, *Z. Anorg. Allg. Chem.* **1971**, *385*, 26–32.

 © 2005 Wiley-VCH Verlag GmbH & Co. KGaA, Weinheim

[21] J. Grannec, J. Portier, *C. R. Acad. Sci. Paris Ser. C* **1971**, *272*, 942–944.
[22] A. Jesih, B. Žemva, *Vestn. Slov. Kem. Drus.* **1986**, *33*, 25–28.
[23] J. Grannec, J. C. Champarnaud-Mesjard, J. P. Costy, J. C. Cousseins, B. Gaudreau, *Rev. Chim. Miner.* **1972**, *9*, 569–580.
[24] M. Ponikvar, B. Sedej, B. Pihlar, B. Žemva, *Anal. Chim. Acta* **2000**, *418*, 113–118.
[25] M. Ponikvar, B. Žemva, J. F. Liebman, *J. Fluorine Chem.* **2003**, *123*, 217–220.
[26] G. Schwarzenbach, H. Flaschka, *Complexometric Titrations*, Methuen, London, **1969**, 275–277.
[27] M. Ponikvar, B. Pihlar, B. Žemva, *Talanta* **2002**, *58*, 803–810.
[28] M. Ponikvar, B. Pihlar, B. Žemva, *J. Fluorine Chem.* **2003**, *122*, 215–217.
[29] H. M. Dess, R. W. Parry, *J. Am. Chem. Soc.* **1957**, *79*, 1589–1591.

Received: May 27, 2005
Published Online: August 24, 2005

 © 2005 Wiley-VCH Verlag GmbH & Co. KGaA, Weinheim

EurJIC
European Journal of Inorganic Chemistry

Issue 20/2005

Pages 3993–4228

Papers available ahead of print in Early View at www.interscience.wiley.com

Earliest available Table of Contents:
Automatically, free of charge by e-mail through
www.interscience.wiley.com/alerts

COVER PICTURE

The cover picture shows the concept of operating a homogeneous catalyst under continuous operation conditions: The recycling of molecular-weight-enlarged transition-metal complexes by suitable filtration methods and equipment in order to combine the advantages of both classical homogeneous and heterogeneous catalysis. Various aspects of molecular-weight enlargement and immobilization of catalysts, and recent developments, are reported in the Microreview by D. Vogt et al. on p. 4011 ff.

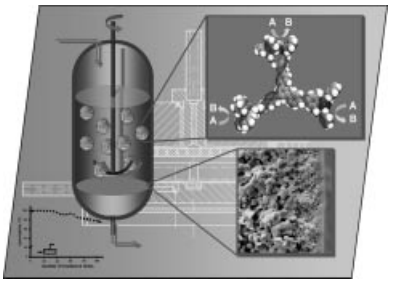

MICROREVIEW

Contents

4011 **C. Müller, M. G. Nijkamp, D. Vogt***

Continuous Homogeneous Catalysis

Keywords: Homogeneous catalysis / Membrane reactor / Soluble support / Recycling / Immobilisation / Nanofiltration

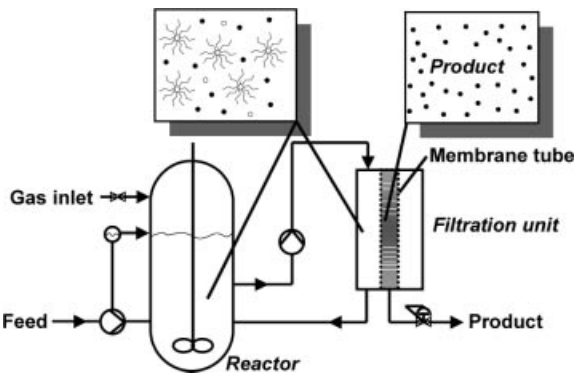

 © 2005 Wiley-VCH Verlag GmbH & Co. KGaA, Weinheim

SHORT COMMUNICATIONS

4023 **M. Scheer,* J. Bai, B. P. Johnson, R. Merkle, A. V. Virovets, C. E. Anson**

Fullerene-Like Nanoballs Formed by Pentaphosphaferrocene and CuBr

Keywords: Polyphosphorus ligands / Fullerene-like molecules / Iron / Phosphorus / Cluster / Nanochemistry

4027 **J. D. E. T. Wilton-Ely,* D. Solanki, G. Hogarth***

Multifunctional Dithiocarbamates as Ligands Towards the Rational Synthesis of Polymetallic Arrays: An Example Based on a Piperizine-Derived Dithiocarbamate Ligand

Keywords: Dithiocarbamates / Piperazine / Multimetallic arrays / Ruthenium complexes / Coordination chemistry

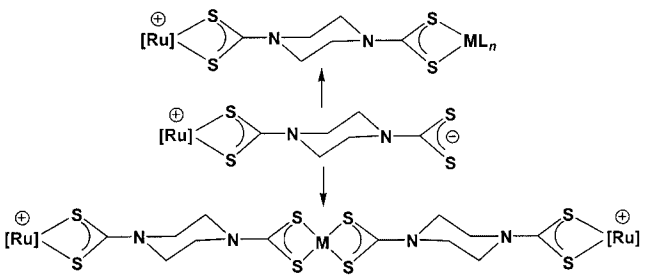

4031 **J. Wan, Z. Wang, X. Chen, L. Mu, Y. Qian***

Shape-Induced Enhanced Luminescent Properties of Red Phosphors: $Sr_2MgSi_2O_7:Eu^{3+}$ Nanotubes

Keywords: Nanotubes / Silicates / Hydrothermal synthesis / Photoluminescence

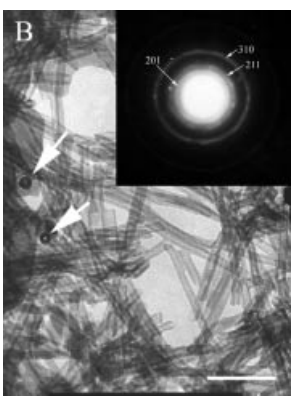

FULL PAPERS

4035 **S. Chou, F. Cheng, J. Chen***

Electrochemical Deposition of $Ni(OH)_2$ and Fe-Doped $Ni(OH)_2$ Tubes

Keywords: Nickel hydroxide / Iron doping / Tubes / Electrochemical deposition / Template

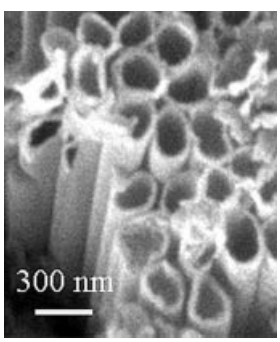

 © 2005 Wiley-VCH Verlag GmbH & Co. KGaA, Weinheim

4040 **R. Bosque,* F. Maseras**

A Theoretical Assessment of the Thermodynamic Preferences in the Cyclopalladation of Amines

Keywords: Density functional calculations / Metallacycles / N ligands / Palladium

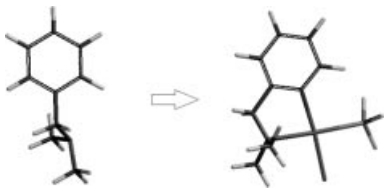

4048 **M. Riondato,* D. Camporese, D. Martín, J. Suades, A. Alvarez-Larena, U. Mazzi**

Synthesis and Characterisation of $[Re(CO)_3(SS)(P)]$ Complexes: A [2+1] Concept for ^{99m}Tc- and ^{188}Re-Radiopharmaceutical Applications

Keywords: Carbonyl ligands / P ligands / Rhenium / S ligands / Technetium

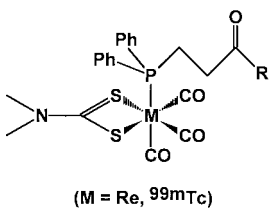

4056 **D. Gudat, V. K. Jain, A. Klein,* T. Schurr, S. Záliš**

On the Borderline between *cis* and *trans* in Organometallic (Phosphane)platinum(II) Complexes

Keywords: Density functional calculations / Isomers / NMR spectroscopy / Phosphane ligands / Platinum

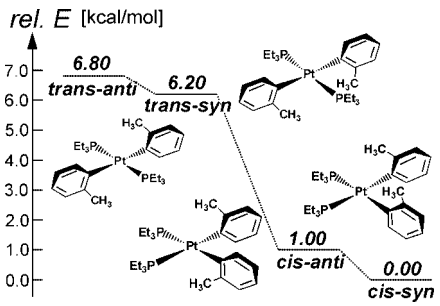

4064 **M. Schulz-Dobrick, M. Panthöfer, M. Jansen***

Supramolecular Arrangement of C_{60} and Phenol into a Square Packing Arrangement of π-π Interacting and Hydrogen-Bonded Rods in $C_{60}\cdot 5C_6H_5OH$

Keywords: Fullerenes / Supramolecular chemistry / Pi interactions / Hydrogen bonds

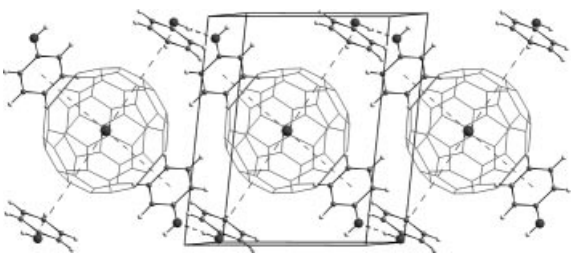

4070 **M. M. Ibrahim, G. He, J. Seebacher, B. Benkmil, H. Vahrenkamp***

Biomimetic Thiolate Alkylation with Zinc Pyrazolylbis(thioimidazolyl)borate Complexes

Keywords: Bioinorganic chemistry / Enzyme models / N,S ligands / Thiolates / Zinc

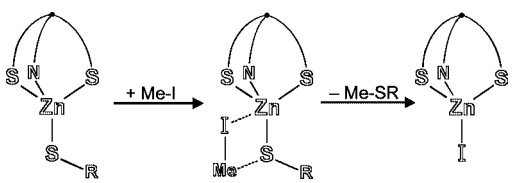

4078 **D. Scheschkewitz, P. Amseis, G. Geiseler, W. Massa, M. Hofmann, A. Berndt***

Classical 1,2,4-Triboracyclopentanes and Their Rearrangement into Nonclassical 2-Boryl-1,3-diboracyclobutanes: Intramolecular C−H Bond Activation by a B−B Moiety

Keywords: Ab initio computations / Boron heterocycles / Three-centre, two-electron bonds

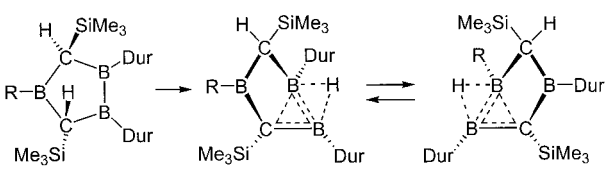

 © 2005 Wiley-VCH Verlag GmbH & Co. KGaA, Weinheim

4086 A. Goswami, T. H. Staeb, F. Rominger, R. Gleiter, W. Siebert*

Reactivity of the [η^2-Bis(*tert*-butylsulfonyl)-acetylene](carbonyl)(η^5-cyclopentadienyl)cobalt Complex Towards Electron-Rich and -Poor Acetylenes

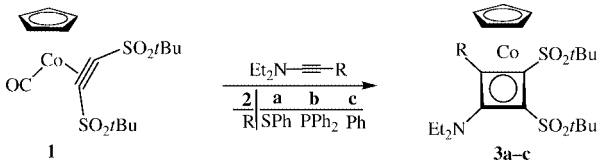

Keywords: Alkynes / Cobalt / Cyclopentadienyl ligands / N ligands

4090 T. H. Staeb, J. Chávez, R. Gleiter,* B. Nuber

The Role of [η^2-Bis(*tert*-butylsulfonyl)acetylene]-(carbonyl)(η^5-cyclopentadienyl)cobalt(I) as an Intermediate in the Alkyne Dimerisation

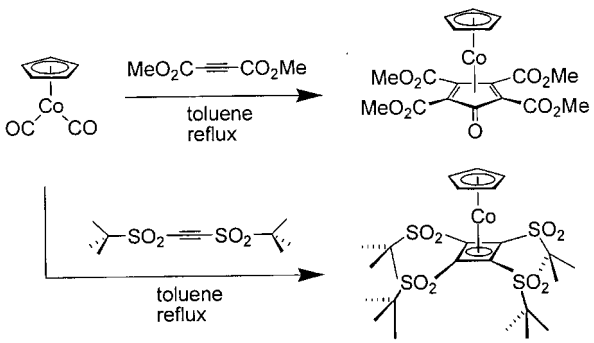

Keywords: Alkynes / Cobalt / Cyclobutadiene / Cyclopentadienyl ligands

4094 C. Krinninger, S. Wirth, J. C. G. Ruiz, P. Klüfers, H. Nöth, I.-P. Lorenz*

Reactivity of 1-Nitroso-2-naphthol Towards the Carbonyl Complexes $XRe(CO)_5$ (X = Cl, Br, I): Molecular Structures of *cis*-[η^2-{*N*,*O*-$C_{10}H_6ON(O)$}$Re(CO)_4$] and *fac*-[η^2-{*N*,*O*-$C_{10}H_6ON(H)$}$Re(CO)_3X$]

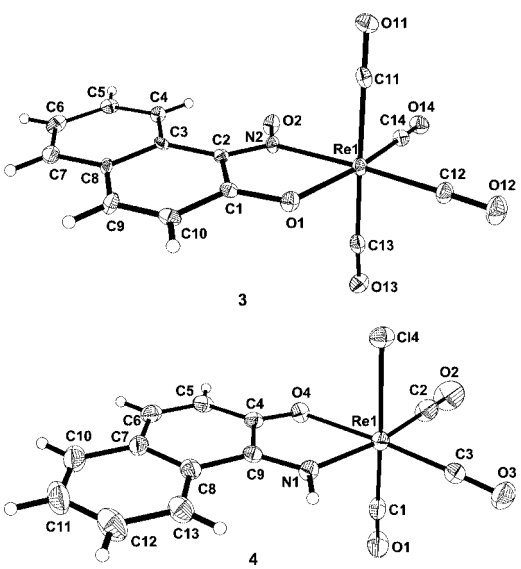

Keywords: 1-Nitroso-2-naphtholate ligand / 1,2-Naphthaquinone-2-imine ligand / Chelates / Rhenium complexes / Redox chemistry / CO_2 elimination

4099 V. V. Zhivonitko, A. Yu. Makarov, I. Yu. Bagryanskaya, Y. V. Gatilov, M. M. Shakirov, A. V. Zibarev*

New Polysulfur-Nitrogen Heterocycles by Thermolysis of 1,3$\lambda^4\delta^2$,2,4-Benzodithiadiazines in the Hydrocarbon and Fluorocarbon Series

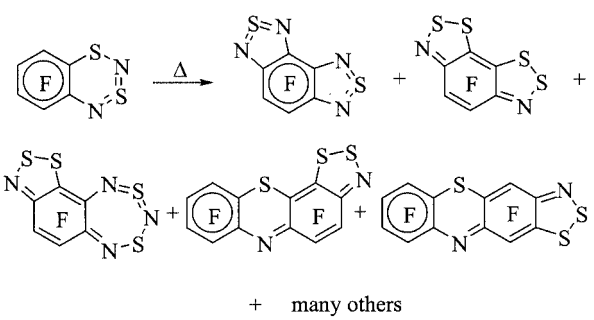

Keywords: Fluorescence / Fluorine / Nitrogen heterocycles / Radicals / Sulfur heterocycles / Thermolysis

 © 2005 Wiley-VCH Verlag GmbH & Co. KGaA, Weinheim

4109 **Y.-Z. Zheng, M.-L. Tong,* X.-M. Chen**

Synthesis, Structure and Photoluminescent Studies of Two Novel Layered Uranium Coordination Polymers Constructed from UO(OH) Polyhedra and Pyridinedicarboxylates

Keywords: Carboxylate ligands / Coordination polymers / Photoluminescence / Uranium

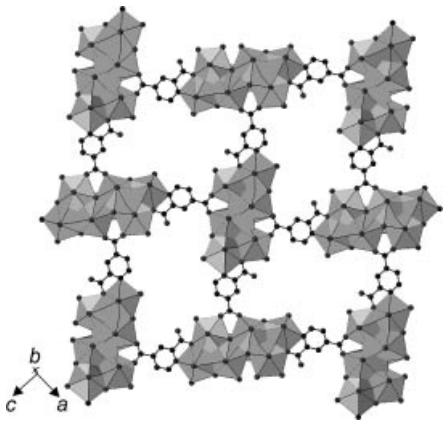

4118 **D. Bayot, M. Devillers, D. Peeters***

Vibrational Spectra of Eight-Coordinate Niobium and Tantalum Complexes with Peroxo Ligands: A Theoretical Simulation

Keywords: Density functional calculations / IR spectroscopy / Niobium / Tantalum / Peroxo ligands / Raman spectroscopy

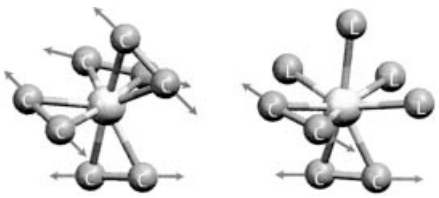

4124 **S. Lei, K. Tang,* Q. Yang, H. Zheng**

Solvothermal Synthesis of Metastable γ-MnS Hollow Spheres and Control of Their Phase

Keywords: Manganese / Nanostructures / Semiconductors / Solvothermal synthesis

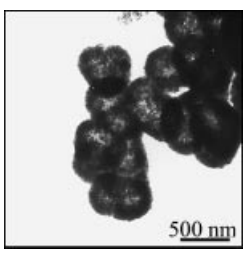

4129 **R. Pavithran, M. L. P. Reddy,* S. A. Junior, R. O. Freire, G. B. Rocha, P. P. Lima**

Synthesis and Luminescent Properties of Novel Europium(III) Heterocyclic β-Diketone Complexes with Lewis Bases: Structural Analysis Using the Sparkle/AM1 Model

Keywords: Europium / Lewis bases / Luminescence / O ligands / Sparkle/AM1 model

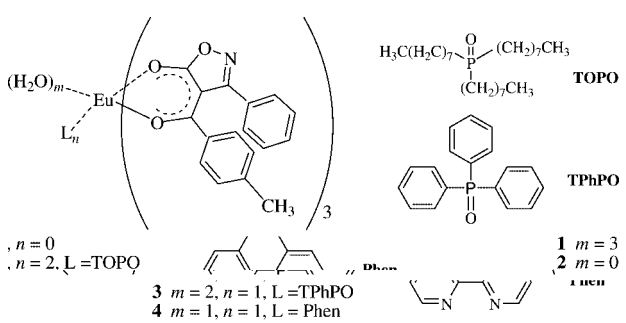

 © 2005 Wiley-VCH Verlag GmbH & Co. KGaA, Weinheim

4138 **M. L. Cole, G. B. Deacon, P. C. Junk,* K. M. Proctor, J. L. Scott, C. R. Strauss**

Direct Syntheses and Structural Novelty of Lanthanoid Aryloxides with Flexible Radial Arms

Keywords: Lanthanoids / Aryloxides / Benzyl group / π-Donors / Phenolates / X-ray crystal structures

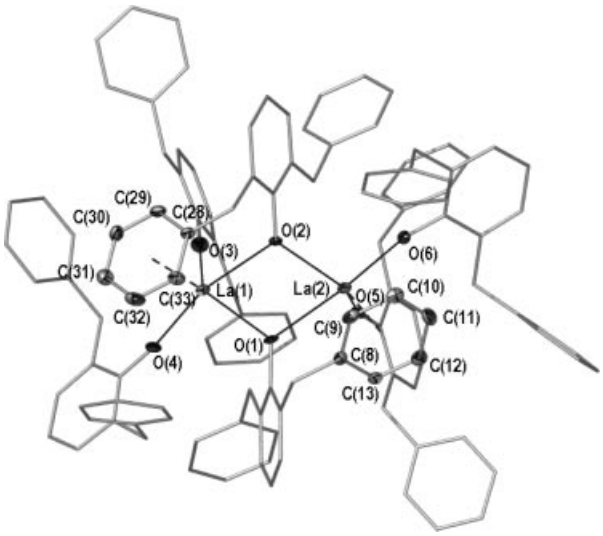

4145 **J. Liu, Q. Wu,* Y. Ding***

Self-Assembly and Fluorescent Modification of Hydroxyapatite Nanoribbon Spherulites

Keywords: Fluorescence / Hydroxyapatite / Nanostructures / Self-assembly

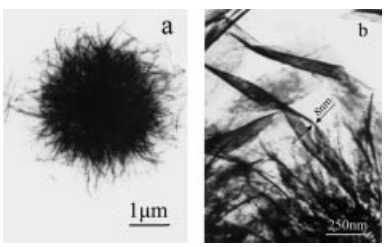

4150 **C.-Y. Sun, X.-J. Zheng, S. Gao, L.-C. Li, L.-P. Jin***

Multiple Regulated Assembly, Crystal Structures and Magnetic Properties of Porous Coordination Polymers with Flexible Ligands

Keywords: Cobalt / Coordination polymers / Magnetic properties / Nickel / Porous materials

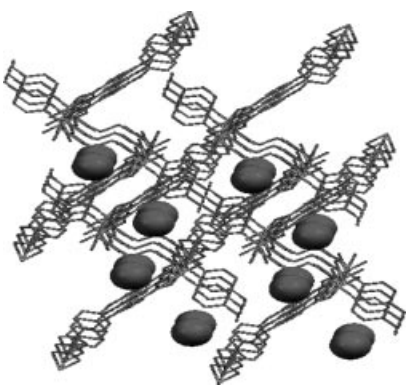

4160 **A. Eichhöfer,* G. Buth**

Synthesis and Structure of the Group 12 Pyrimidinethiolate Complexes $^{3}_{\infty}[Zn(S\text{-}2\text{-}N_2C_4H_3)_2]$, $^{2}_{\infty}[Cd(S\text{-}2\text{-}N_2C_4H_3)_2]$, $[Hg(S\text{-}2\text{-}N_2C_4H_3)_2]$ and $[Cd(S\text{-}2\text{-}N_2C_4H_3)_2(tmeda)]$

Keywords: Cadmium / IR spectroscopy / Mercury / N,S ligands / Zinc

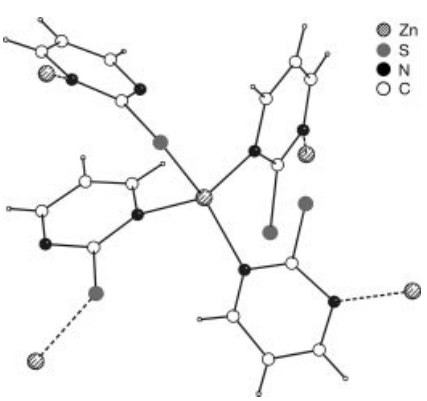

 © 2005 Wiley-VCH Verlag GmbH & Co. KGaA, Weinheim

4168 **V. Patroniak,* A. R. Stefankiewicz, J.-M. Lehn, M. Kubicki**

Self-Assembly and Characterization of Grid-Type Copper(I), Silver(I), and Zinc(II) Complexes

Keywords: Copper / Silver / Zinc / Supramolecular chemistry / Self-assembly

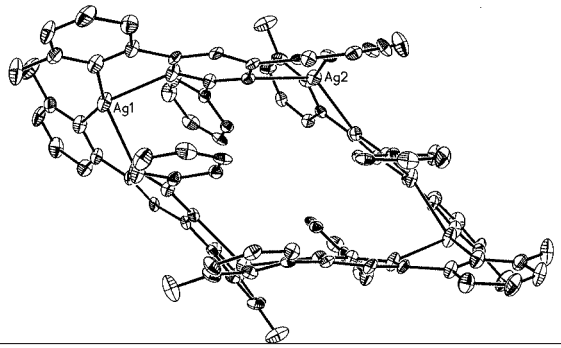

4174 **M. Westerhausen,* M. Krofta, P. Mayer, H. Piotrowski**

The Influence of the Neutral Coligand on the Spectroscopic Properties and Crystal Structures of Lithium Tri(*tert*-butyl)silylarsanides of the Type [(L)LiAs(H)Si*t*Bu$_3$] (L = DME, THF)

Keywords: Arsanes / Arsanides / Lithium / Lithiation / Pnicogens

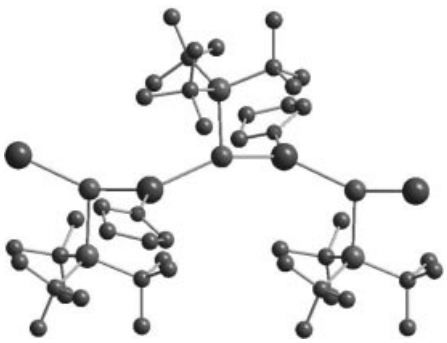

4179 **E. S. Peters, C. J. Carmalt,* I. P. Parkin, D. A. Tocher**

Aerosol-Assisted Chemical Vapor Deposition of NbS_2 and TaS_2 Thin Films from Pentakis(dimethylamido)metal Complexes and 2-Methylpropanethiol

Keywords: Niobium disulfide / Tantalum sulfide / Thin film / Aerosol-assisted CVD

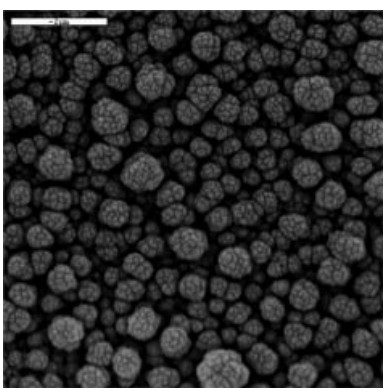

4186 **G. Zhang, S. Wang, Q. Gan, Y. Zhang, G. Yang,* J. S. Ma, H. Xu**

A Stable Trinuclear Zinc Cluster Assembled from a Thiazolylazo Dye and Zinc Acetate: Preparation, Structural Characterization and Spectroscopic Studies

Keywords: Azo compounds / Pi interactions / UV/Vis spectroscopy / Zinc

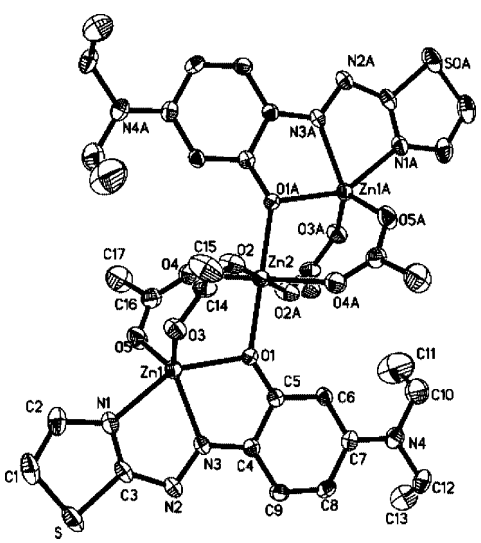

 © 2005 Wiley-VCH Verlag GmbH & Co. KGaA, Weinheim

4193 **J. G. Planas, C. Viñas, F. Teixidor,* M. E. Light, M. B. Hursthouse, H. R. Ogilvie**

B-Substituted (Arene)ruthenacarborane−Sulfonium, −Thioether and −Mercaptan Complexes: Mild Single and Double Dealkylation and Structural Implications in the Antipodal Distance

Keywords: Antipodal effect / (Arene)ruthenacarboranes / Carboranes / Charge-compensated ligands / Dealkylation

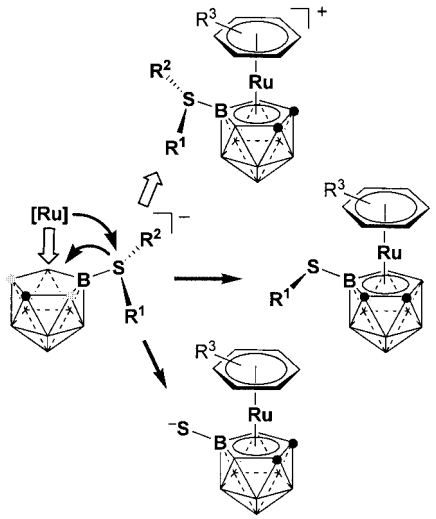

4206 **S. Dagorne,* S. Bellemin-Laponnaz,* A. Maisse-François, M.-N. Rager, L. Jugé, R. Welter**

Synthesis and Structure of Neutral and Cationic Gallium Complexes Incorporating Bis(oxazolinato) Ligands

Keywords: Cations / Gallium / Lewis acids / N ligands

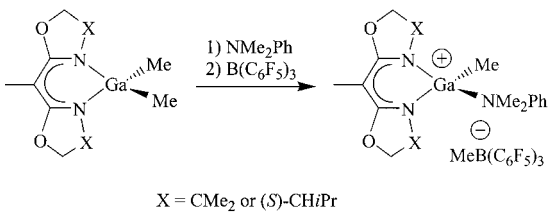

4215 **D. H. Nguyen, G. Laurenczy, M. Urrutigoïty, P. Kalck***

A Hydride Route for the Palladium-Catalysed Cyclocarbonylation of Monoterpenes

Keywords: Carbonylation / Hydrides / Palladium / Terpenes

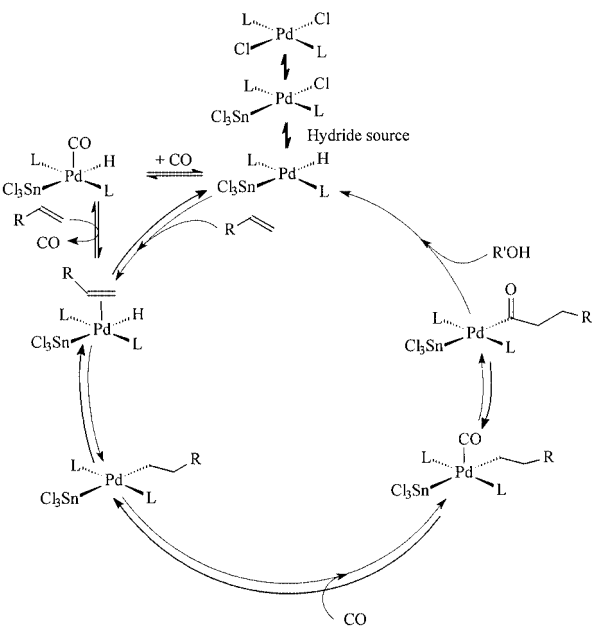

Continuous Homogeneous Catalysis

Christian Müller,[a] Marije G. Nijkamp,[a] and Dieter Vogt*[a]

Keywords: Homogeneous catalysis / Membrane reactor / Soluble support / Recycling / Immobilisation / Nanofiltration

This review article illustrates possible aspects for molecular-weight enlargement and immobilisation of transition-metal complexes that have been developed for bridging the gap between homogeneous and heterogeneous catalysis. The recycling of homogeneous catalysts can be performed using different types of supports, such as dendrimers, hyperbranched polymers, nanostructured materials or stabilized nanoparticles in combination with suitable filtration methods and equipments. Continuous homogeneous catalysis is ideally performed in a continuously operated membrane reactor. A general overview of molecular-weight enlargement along with selected examples and recent developments in continuous homogeneous catalysis is provided.

(© Wiley-VCH Verlag GmbH & Co. KGaA, 69451 Weinheim, Germany, 2005)

Introduction

The contribution of soluble transition-metal complexes as selective homogeneous catalysts for a number of chemical transformations under mild reaction conditions has increased significantly during the last decades. A number of important large-scale processes, such as the production of adiponitrile, α-olefins (SHOP process), acetic acid and acetic anhydride, and butanal are nowadays based on homogeneous catalysis.[1] A notorious drawback, however, is the tedious separation of the catalyst from the reaction products, a problem not encountered with typical heterogeneous catalysts and often accompanied by thermal strain on reactants and products. For large-scale industrial processes, individual solutions have been developed for catalyst separation and recovery in each case.

In most cases, the development of materials combining the advantages of classical homogeneous and heterogeneous catalysts has remained an elusive goal. However, molecular-weight enlargement and immobilisation of transition-metal complexes in combination with filtration methods offers the possibility to still operate the catalyst under homogeneous reaction conditions, hence maintaining the intrinsically high selectivity and activity, while avoiding mass-transfer limitations.[2] Furthermore, low energy consumption of the separation step and the potential for continuous homogeneous catalysis is provided. However, the synthesis of molecular-weight-enlarged catalyst systems is strongly related to the development of new membranes and reactors, which are compatible with homogeneous reaction conditions.

[a] Laboratory of Homogeneous Catalysis and Inorganic Chemistry, Schuit Institute of Catalysis, Eindhoven University of Technology,
P. O. Box 513, 5600 MB Eindhoven, The Netherlands
Fax: +31-40-245-5054
E-mail: d.vogt@tue.nl

The Concept: Molecular-Weight Enlargement of Transition-Metal Complexes

A prerequisite for the application of filtration methods is a significant difference in molecular size of the catalyst, the reactants and products, as well as a suitable filtration unit. Different methods have been developed for the molecular-weight enlargement of transition-metal complexes in order to make them amenable to filtration methods. A general overview is given below, while specific examples will be given later on.

The first examples of the concept of binding catalytically active metal complexes to soluble supports were reported in the 1970s, when Rh-containing soluble polymers were successfully applied as hydrogenation catalysts.[3] Since then, functionalised soluble polystyrenes (**A**),[4] poly(ethylene glycol)s (**B**),[5] poly(methyl methacrylate)s (**C**),[6] poly(vinylpyrrolidine)s,[6] polyethylene oligomers,[6] poly(vinylchloride)s,[6] hyperbranched polymers[7] or polyelectrolytes (**D**)[8] have been applied as soluble polymeric supports for transition-metal complexes (Figure 1).[9]

MICROREVIEWS: This feature introduces the readers to the authors' research through a concise overview of the selected topic. Reference to important work from others in the field is included.

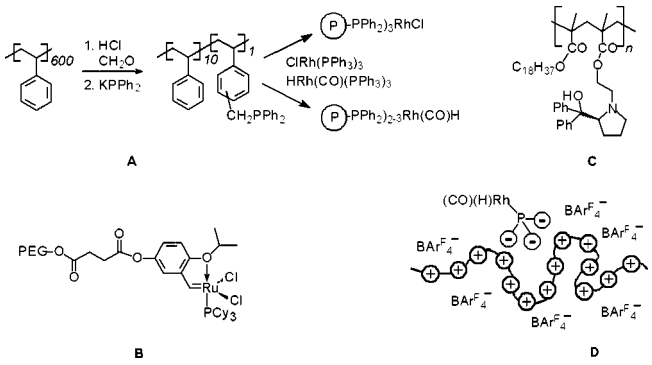

Figure 1. Functionalised polymeric supports.

Dendrimer-based systems are more defined soluble support structures. Most commonly, carbosilane (**1**), polyphenylene, poly(benzyl ether), DAB, PANAM (**2**) and PPI dendrimers have been applied for the immobilisation of transition-metal complexes.[10]

More recently, carbosilane dendrimers have been attached to polyhedral oligosilsesquioxane cages (POSS) (**3**).[11] In a different approach, this POSS cage has been used as the molecular-weight enlargement unit and directly linked to arylphosphane or aryl phosphite ligands (**4**).[12]

POSS-enlarged systems provide the unique properties of being rigid, three-dimensional and mostly kinetically and thermodynamically stable compounds whose size can easily be adjusted by the choice of the substituents attached to the silicon atoms.

In the above-mentioned examples, the transition-metal complexes, which are the catalytically active sites, are either covalently tethered to the support or through ionic interactions. A different approach is the stabilisation of catalytically active metal clusters on soluble supports, such as polyglycerols, polyamides or dendrimers (Figure 2). Metal atoms constituting nanoparticles can be generated in the presence of such a protecting agent, which forms a shell that prevents agglomeration of the particles into larger, and therefore less active, clusters. The protectors can be divided into two categories: those providing electrostatic and those providing steric stabilisation. Popular steric agents are polymers, poly(vinylpyrrolidone), cyclodextrins and dendrimers. Ionic surfactants protect nanoparticles by both electrostatic and steric mechanisms (Figure 2).

Membranes for Catalyst–Product Separations

Filtration processes can be classified into micro-, ultra-, nanofiltration and reversed osmosis, depending on the size of the particles that are retained by the membrane (Figure 3). In most cases ultra- or nanofiltration is used for catalyst separation and recycling.

An important parameter of a membrane is the molecular weight cut-off (MWCO), which is defined as the molecular weight at which 90% of the solutes are retained by the membrane. However, the pore size of many ultra- and nano-

Christian Müller was born in Germany in 1972. He studied Chemistry at the University of Bielefeld and the University of Michigan, Ann Arbor (USA). He received his Ph.D. under the supervision of Prof. Dr. P. Jutzi at the University of Bielefeld in 2000 and was awarded a fellowship of the Deutsche Forschungsgemeinschaft (DFG) to work with Prof. Dr. W. D. Jones at the University of Rochester, New York (USA). Afterwards he accepted a postdoctoral position in the group of Prof. Dr. P. W. N. M. van Leeuwen at the University of Amsterdam (The Netherlands). In February 2003 he joined the group of Prof. D. Vogt at Eindhoven University of Technology and was appointed Lecturer in 2004. His research interests are centred around the subjects "molecular weight enlarged systems for continuous homogeneous catalysis", "low-coordinate phosphorus ligands", "nanocatalysts" and "combinatorial approaches for ligand (catalyst) synthesis and testing".

Marije Nijkamp was born in 1973 in Paramaribo, Surinam. She finished her masters thesis in Inorganic Chemistry and Heterogeneous Catalysis at Utrecht University in 1998. In the same year she started her Ph.D. on Hydrogen Storage using physisorption, modified carbon nanofibres and related materials at Utrecht University with Prof. Dr. Krijn de Jong. In 2003 and 2004 she worked on a postdoctoral research project at Eindhoven University of Technology with Prof. Dr. Dieter Vogt where she investigated the use of polyglycerol- and polyamide-stabilized palladium colloids in continuous homogeneous catalysis. Currently she is employed by Engelhard De Meern B.V.

Dieter Vogt was born in Germany in 1962. He received his Ph.D. from the RWTH Aachen under the supervision of Prof. Dr. W. Keim in 1992 and continued with a Habilitation at the Institute of Industrial Chemistry and Petrochemistry of the RWTH Aachen. In 1999 he was appointed to full Professor of Inorganic Chemistry and Coordination Chemistry at the Eindhoven University of Technology, The Netherlands. Since 2001 he is chairman of the Schuit Institute of Catalysis and director of the Institute of Catalysis and Inorganic Chemistry. His main research interests are in the field of homogeneous catalysis. Ligand design for selectivity control in intermediate synthesis and fine chemicals, catalyst recycling, and new materials for application in catalysis, continuous miniplant operation, and kinetics of homogeneous catalytic processes, C1 building blocks, and renewable feed stocks are present research topics.

 © 2005 Wiley-VCH Verlag GmbH & Co. KGaA, Weinheim

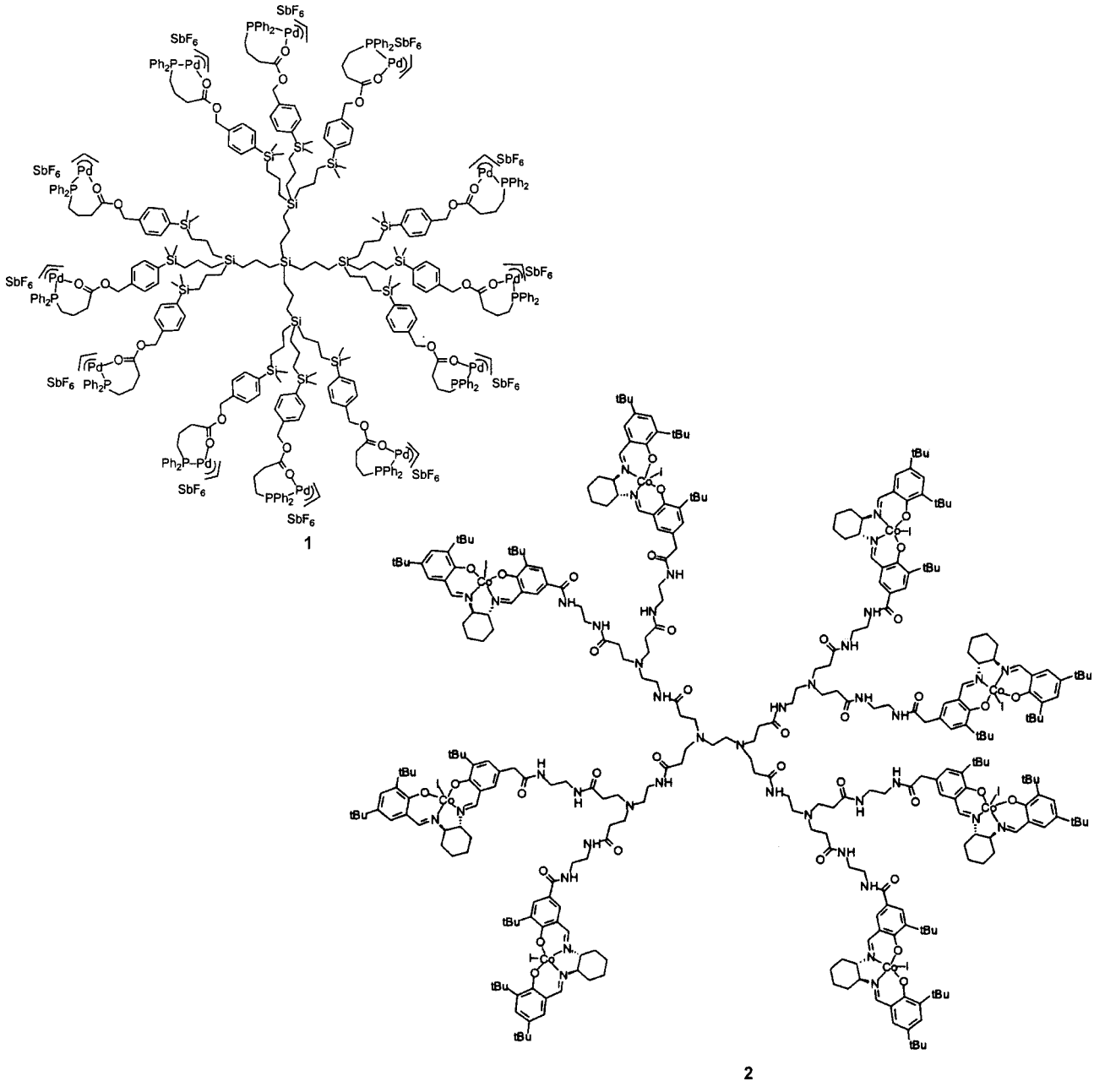

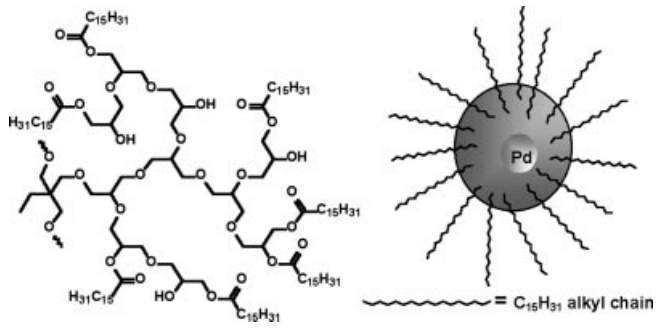

Figure 2. Stabilisation of metal clusters by soluble supports.

filtration membranes is greatly influenced by the reaction conditions, such as temperature and solvent, and should be taken into account.

As for the membrane material itself, basically two types of membranes are frequently used: organic (polymer) membranes and inorganic (ceramic) membranes. The most widely applied commercial organic membrane is the MPF series of Koch Int., which are basically silicon-derived membranes in the MWCO range of 400–700 Da (Figure 4, **a**).[13] Due to their polymeric nature, the MWCO is highly dependent on the solvent used.[14] Another common membrane is the STARMEM series from MET (polyimide-based), with MWCOs in the range of 200–400 Da.[15] Ceramic membranes are much less common, and published

 © 2005 Wiley-VCH Verlag GmbH & Co. KGaA, Weinheim

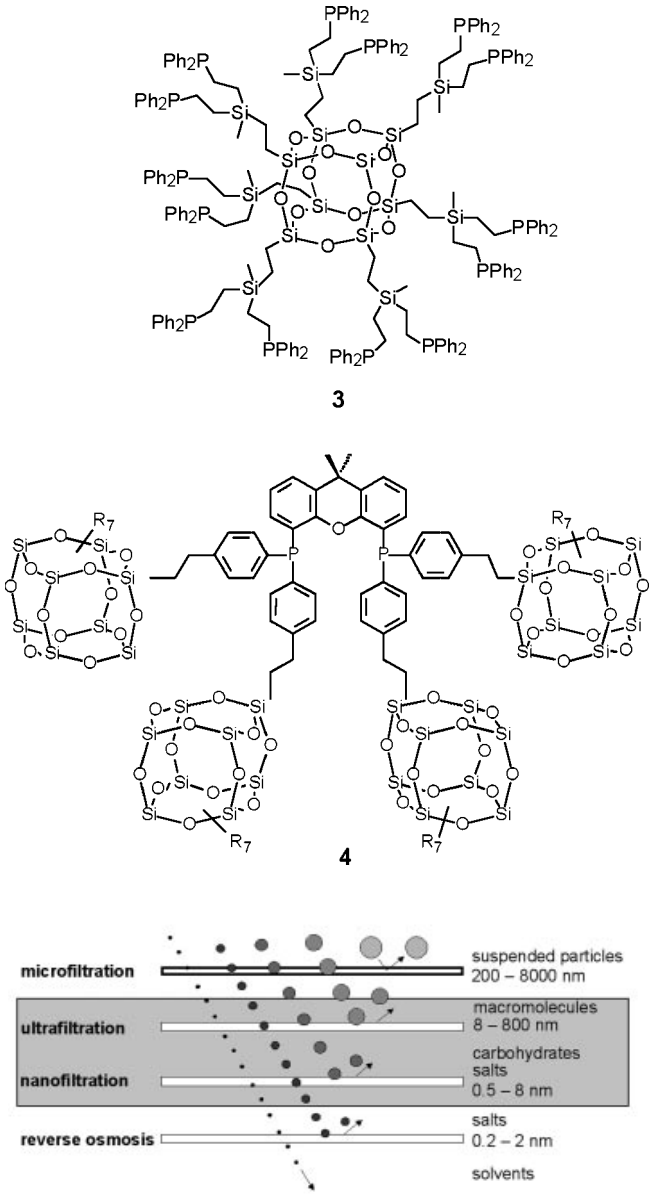

Figure 3. Classification of filtration types.

results are only available for the tubular microporous silica membranes provided by ECN (Petten, The Netherlands).[16] These membranes have pore sizes between 0.5 and 0.8 nm and consist of several support layers of α- and γ- alumina, while the selective top layer at the outer wall of the tube is made of amorphous silica (Figure 4, **b**).[17]

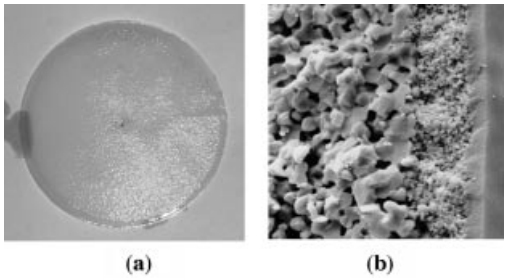

Figure 4. Organic (a) and ceramic (b) membranes.

Reactors for Continuous Homogeneous Catalysis

Decoupling of the residence times of the catalyst and the reactants by means of membrane technology provides the opportunity to control homogeneously catalysed processes by means of reaction engineering − an essential advantage largely restricted to heterogeneous catalysis to date. This is particularly desirable in the case of possible consecutive reactions, which can result in large amounts of undesired by-products. Such control of homogeneous catalysis would represent the break of a paradigm in fine chemicals production, where generally only batch processes are used nowadays.

For initial investigation of catalyst performance, a simple laboratory-scale dead-end ultrafiltration unit (Figure 5, a) with a commercially available flat membrane can be employed. Dead-end filtration means that the product flow is perpendicular to the surface of the membrane. This eventually is a disadvantage because concentration polarisation can occur. The dead-end filtration setup in Figure 5 was developed by us for applications at high pressures and used for the hydrovinylation of styrene (vide infra). In this reaction, ethylene was used as a solution in dichloromethane, prepared separately in a stainless-steel tank, while the second substrate (styrene), dissolved in dichloromethane, was pumped with a second HPLC pump into the reactor. The catalyst solution, on the other hand, was introduced via an HPLC injection valve. Products and unreacted compounds cross the membrane and leave the reactor on top.[18]

In a cross-flow filtration setup (Figure 5, **b**), the product flow is parallel to the membrane surface, which requires a separation unit next to the actual reactor and an additional pump to provide a rapid circulation across the membrane. A special type of cross-flow reactor has been developed in our laboratories to handle continuous gas/liquid reactions. The challenge in the reactor design was the combination of efficient gas/liquid mixing, liquid level control in the reactor, turbulent flow across the membrane and efficient gas/liquid separation to avoid gas contacting the membrane, which would lead to a shunt of gas. Ceramic membrane tubes (HITK) with higher temperature stability and much better solvent resistance are used.

Selected Examples of Continuous Homogeneous Catalysis

1) Polymer-Enlarged Homogeneous Catalysts

The use of homogeneous catalysts bound to soluble polymeric supports[19] in continuously operating membrane reactors was pioneered by Wandrey and co-workers as well as Kragl and Dreisbach. The catalyst consists of a soluble polymeric support − a copolymer of 2-hydroxyethyl methacrylate and octadecyl methacrylate − combined with α,α-

 © 2005 Wiley-VCH Verlag GmbH & Co. KGaA, Weinheim

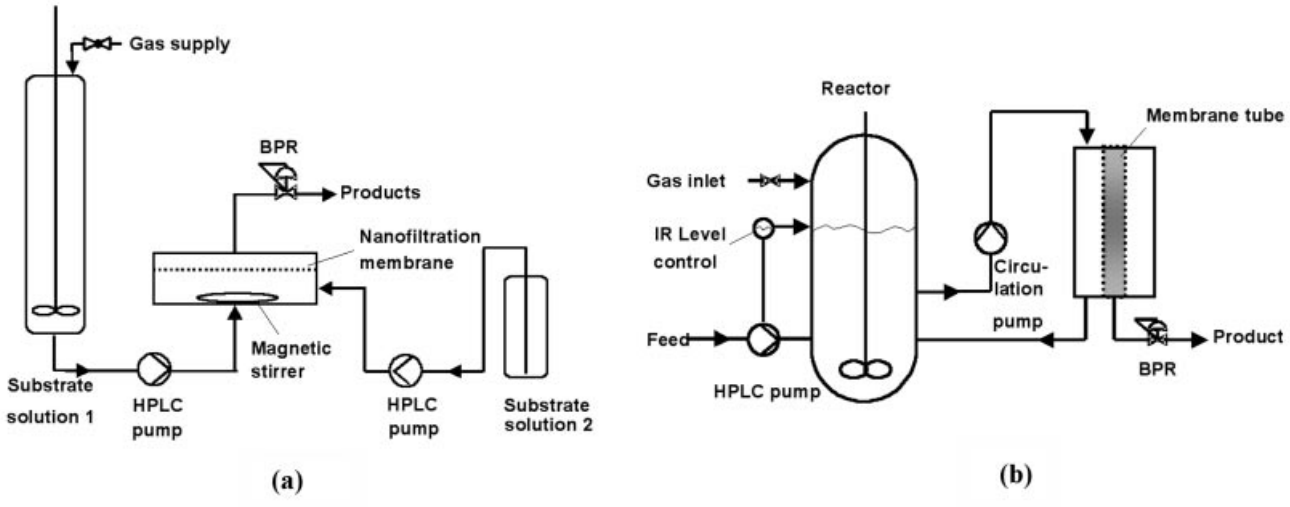

Figure 5. A dead-end filtration reactor (**a**) and cross-flow filtration reactor (**b**) described by Vogt et al.[18]

diphenyl-L-prolinol as the active organocatalytic site (see C), which was used for the enantioselective addition of diethylzinc to benzaldehyde [Equation (1)].

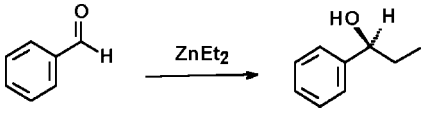

(1)

The reaction was carried out in a continuous way by using an ultrafiltration membrane (Hoechst-Nadir-UF-PA20). A retention of the polymeric support of more than 99.8% was observed. Even though the *ee* achieved with the molecular-weight-enlarged catalyst was lower (80%) than with the non-supported analogue (97%) the proof of principle to run the reaction in a continuous way was shown. Interestingly, the total turnover number (tTON) of the chiral organocatalyst under continuous conditions could be raised by a factor of 10, to 500. After seven days, no deactivation of the catalyst could be observed.[20]

Plenio et al. have used a polymer-enlarged catalyst formed from $(1\text{-Ad})_2$P-substituted poly(methylstyrene) (Scheme 1), a suitable palladium source {$[PdCl_2(PhCN)_2]$, $Pd(OAc)_2$, or $Pd(dba)_2$} and a base ($HNiPr_2$ or K_3PO_4).[21] This system was used to efficiently mediate carbon–carbon coupling reactions of the Suzuki, Sonagashira and Heck type for aryl bromides and aryl chlorides. Such catalysts were also studied in nanofiltration separation experiments. The linear 5000 Da polymer backbone [poly(*p*-methylstyrene)] is sufficiently large to be retained quantitatively by a PMDS nanofiltration membrane. The leaching of the catalyst into the product-containing permeate is very small (<0.05%). The catalyst was reused up to nine times by using the catalyst-containing retentate after filtration from the product. Further evidence for the recyclability of the catalyst was derived from the constant and high yields in the Sonogashira and Suzuki reactions and from the unchanged TOF. In the Heck reaction, the highly polar and aprotic solvents are detrimental to the integrity of the polymeric membranes. It is therefore impossible to draw conclusions on the suitability of using this catalyst in repeated Heck coupling reactions. A disadvantage of the system is the multistep synthesis of the polymer. The polymer is prepared by anionic polymerisation of *p*-methylstyrene and then treated with Br_2 to convert up to 18% of the CH_3 groups into CH_2Br. Subsequently, a phosphane group is loaded onto the polymer (Scheme 1) and the Pd catalyst is formed in situ. This multi-step synthesis makes such a polymer relatively expensive and therefore less suitable for industrial applications. Also, it should be noted that the catalyst was employed in a batch reaction and after completion of the reaction was recycled by nanofiltration. These experiments were not performed in a continuous manner.

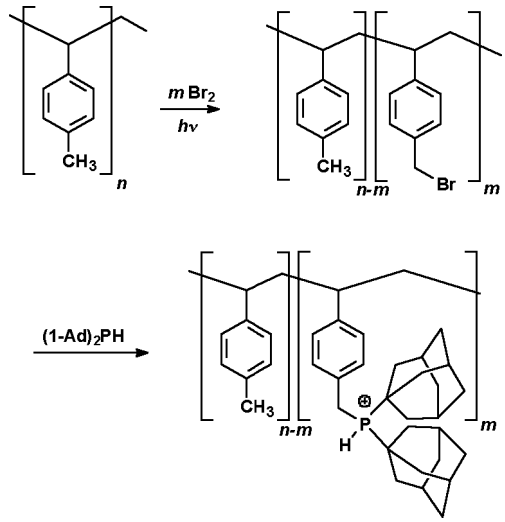

Scheme 1. Preparation of a polymer-supported phosphonium salt.

2) Dendrimers as a Soluble Support

Dendrimers have attracted considerable attention since the pioneering work by Vögtle et al. on these systems.[22]

 © 2005 Wiley-VCH Verlag GmbH & Co. KGaA, Weinheim

While (perfectly branched) dendrimers provide a well-defined structure, their syntheses are usually tedious and expensive and, correspondingly, commercial applications of dendrimers are scarce. Dendrimers differ in the position of the catalytic site(s). Surface-functionalised dendrimers lead to catalysts that are sufficiently large to be retained by membranes. However, detailed studies on the macromolecular structure of dendrimers have revealed that they do not always adopt the ideal spherical structures their drawings suggest − amphiphilic dendrimers, in particular, have structures that are far from spherical.[23]

In principle, dendritic catalysts can show the kinetic behaviour and thus the activity and selectivity of a conventional homogeneous catalyst. The transition metals on the outer sphere are directly available for the substrate, which allows for reaction rates that are comparable with homogeneous systems. On the other hand, these periphery-functionalised systems contain multiple reaction sites and ligands, which results in extremely high local catalyst and ligand concentrations. For example, a second-generation carbosilane dendrimer functionalised with 36 terminal phosphanes results, theoretically, in local concentrations of 8 M of ligand and 4 M of catalyst. In reactions where excess ligand is required to stabilize the catalyst this local-concentration effect can indeed result in stable systems. However, several deactivation processes can operate by a bimetallic mechanism. Examples of these are ruthenium-catalysed metathesis,[24] palladium-catalysed reductive coupling of benzene and chlorobenzene[25] and reactions that involve radicals.[26]

A difficult problem in the use of dendrimers is leaching. Two forms of leaching are known: leaching of the dendritic catalyst through the membrane and metal leaching from the dendrimer into the solution and further leaching of the active metal through the membrane, usually in the form of small homogenized complexes. For industrial applications, the overall retention of the dendritic catalyst must be extremely good to keep a high activity in a continuous reactor for longer reaction times. The required retention obviously depends on the application, since processes for the bulk industry generally require more efficient catalyst recycling (higher TONs) than those for fine chemicals. Generally, a retention of at least 99.99% is required to obtain a catalyst system that remains in the reactor for a prolonged period of time, even for fine chemical production processes.

The groups of van Koten and van Leeuwen have reported G_0 and G_1 carbosilane dendrimers functionalised with up to 12 pincer NCN-nickel(II) groups (**5**).[27] These dendrimers were then applied as catalysts for the Kharasch addition of CX_3Y to alkenes [Equation (2)]. While being used in a continuous membrane reactor the compound showed decomposition, which has been ascribed to hydrolysis of the Si–O bond of the linker between the ligand and the carbosilane backbone. In a further modification of the system, the NCN ligands were attached directly to the carbosilane backbone of **5**.

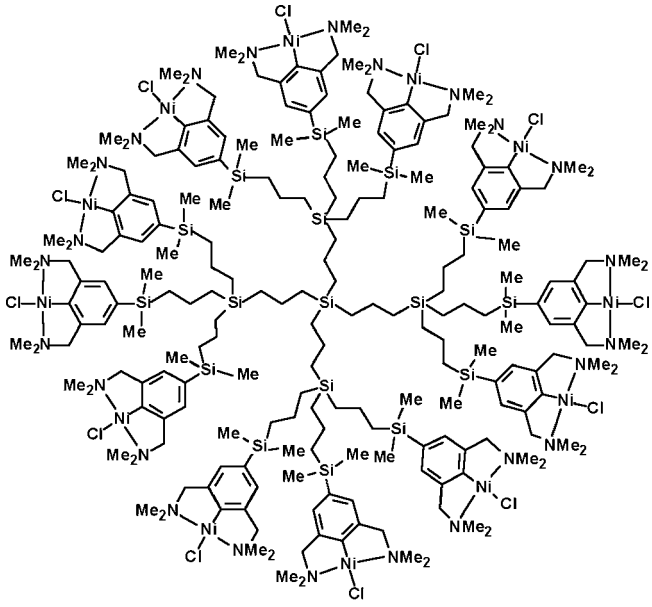

5

While retentions of the molecular-weight-enlarged systems of up to 99.75% were observed, the formation of insoluble purple species occurred under continuous flow conditions. Addition of Bu_4NBr prevented catalyst precipitation but a fast decrease in conversion was detected: after 45 cycles, the activity of the catalyst dropped to almost zero, most likely due to the formation of inactive Ni^{III} species (Figure 6). Furthermore, the carbosilane support plays a pivotal role in the accessibility of the active sites: surface congestion can lead to the formation of mixed-valence Ni^{II}/Ni^{III} complexes on the dendrimer periphery that compete for reactions with substrate radicals.

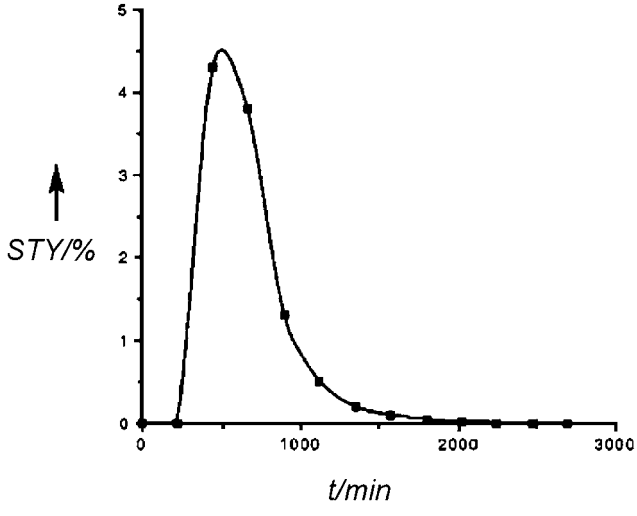

Figure 6. A continuous Kharasch addition (reprinted with permission from ref.[27d] Copyright 2000 American Chemical Society.

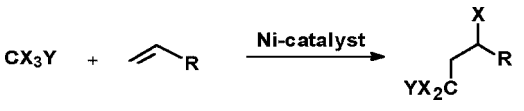

(2)

Commercially available fourth- and fifth-generation DAB dendrimers have been functionalised with diphenylphosphanyl groups at the periphery by Reetz and Kragl and their respective co-workers.

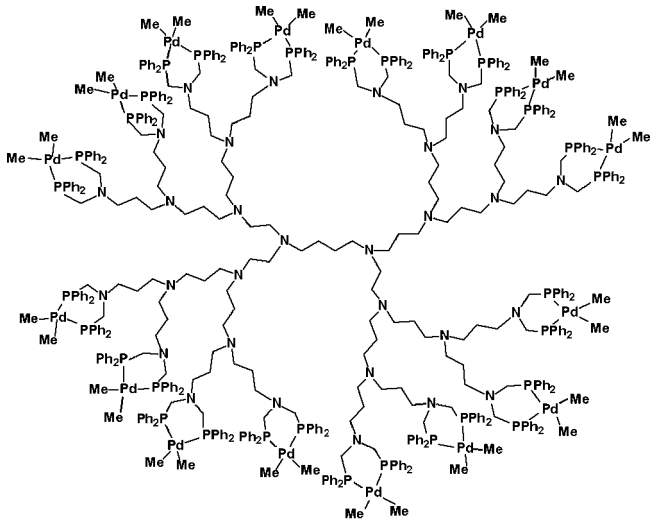

6

The corresponding Pd complexes (**6**) were used for the Pd-catalysed allylic amination to yield *N*-[3-phenyl-2-propenyl]morpholine in a continuously operating dead-end filtration [Equation (3)].

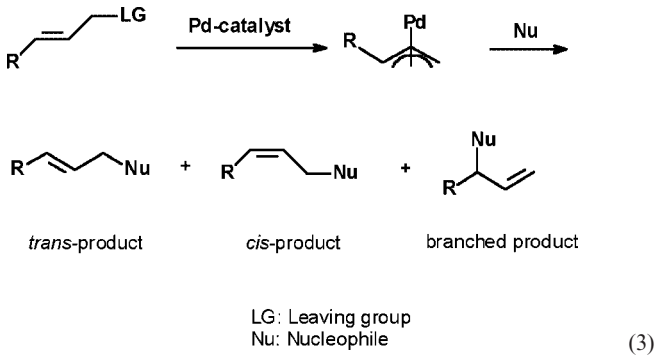

(3)

A conversion of 100% was obtained in the beginning but a 20% decrease was observed after 100 h, as well as palladium leaching of between 0.07 and 0.14% per residence time. The soluble support, on the other hand, was completely retained in the membrane reactor.[28] Several studies on the use of these types of palladium-functionalised dendrimers for allylic substitution reactions have all shown significant loss of activity during the reaction. In all cases, the leaching of the dendrimer through the membrane was much smaller than the observed loss in activity. These results suggest that the catalyst decomposes during the course of the reaction and leaches through the membrane as small soluble metal clusters.[28,29] The leaching gives rise to two problems, loss of expensive catalyst or active metal and contamination of the product with this metal. In some cases it can be economically acceptable to compensate for the loss in activity by addition of the active metal to the feed solution. However, the contamination of the product should be limited to an acceptable amount.

Van Koten et al. and ourselves have reported on shape-persistent multi-NCN-palladium and/or platinum complexes exhibiting one-, two- and three-dimensional geometries. These were subjected to nanofiltration experiments to investigate the influence of rigidity and geometry on the retention of these molecules by MPF membranes. A clear relationship between the dimensions calculated by molecular modelling and the retention rates of the synthesised complexes was observed. Furthermore, similar sized complexes with zero- and first-generation flexible dendrimers were compared and it was found that a high degree of rigidity in the backbone of the macromolecular complexes indeed leads to more efficient retention by the membrane.

In a later study, a very shape-persistent dendrimer, the dodecakis[NCN-Pd^{II}-aqua](BF$_4$)$_{12}$ complex **7** was synthesised and employed as a Lewis acid catalyst in the double Michael addition reaction between methyl vinyl ketone and ethyl α-cyanoacetate. The efficiency of the reaction was significantly enhanced, as the TON was increased by a factor of more than 40. After prolonged reaction times (>25 h) a small decrease in activity was observed, which can be completely ascribed to slow leaching of the catalyst. The retention of the reaction was 99.5%.[30]

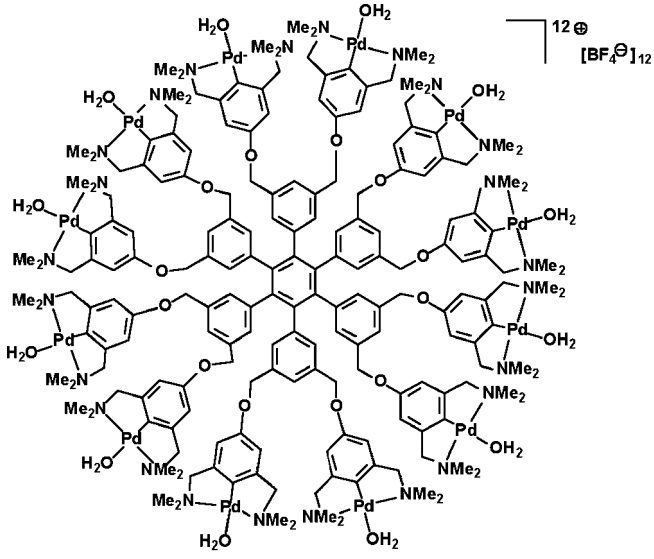

7

This shows that very shape-persistent dendrimers can be used in continuous homogeneous catalytic reactions. However, even under these optimised circumstances, the retention is still lower than desired (99.99%). Recycling of the catalyst by microporous filtration showed no significant loss of activity or selectivity during five consecutive runs. This is promising for use in a continuous process, but more experiments have still to be performed.

 © 2005 Wiley-VCH Verlag GmbH & Co. KGaA, Weinheim

The above-mentioned examples describe catalytic reactions in which only liquid components participate in the chemical transformation. The situation becomes more complicated when one of the reactants is a gas. Typical reactors and membranes are not designed for use with certain organic solvents, high temperature and/or high pressure, and only a few examples of continuous catalytic gas/liquid reactions have been reported in the literature up to now. Therefore, C–H and C–C linkage reactions involving the consumption of one or more gases are usually performed in a batch-wise process with subsequent filtration through a membrane in order to separate the molecular-weight-enlarged catalyst from the product. In case of hydrogenation reactions, the saturation of the solvent with hydrogen is in most cases sufficient to run the reaction in a continuous way. However, the design of suitable reactors for applications under more drastic reaction conditions (e.g. elevated temperatures and pressures) is less obvious.

A pressure membrane reactor has been developed by us for the co-dimerisation of ethylene and styrene [the hydrovinylation reaction, Equation (4)] under continuous reaction conditions.

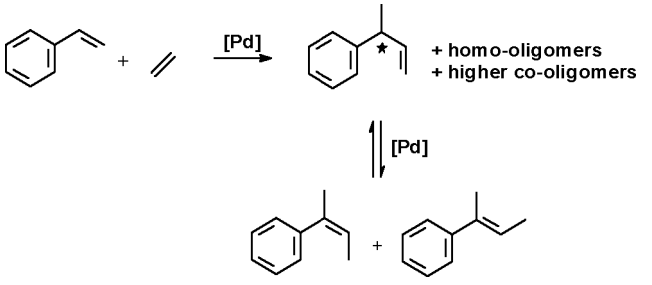

(4)

Molecular-weight-enlarged carbosilane dendrimers (such as **1**), functionalised with four or 12 P–O ligands on the periphery have been used as catalysts in this reaction. Interestingly, the reaction runs almost without any isomerisation of the products to a mixture of the (*E*)- and (*Z*)-isomers of 2-phenyl-2-butenes or formation of any side products, which are usually observed at high conversions. The maximum productivity was reached after an induction period of about nine hours, followed by a steady decrease of activity (Figure 7). However, catalyst deactivation was also observed (precipitation of palladium on the membrane).[18]

The core-functionalised dendritic dppf analogue **8** (dppf = diphenylphosphanylferrocene) was synthesised by van Leeuwen et al. While the corresponding rhodium complex could only be applied in a batch-wise hydroformylation reaction [the hydroformylation reaction is typically performed at elevated temperature (40–80 °C) as well as under a syngas pressure of 10–20 bar], the hydrogenation of dimethyl itaconate could be performed under continuous reaction conditions. Interestingly, no deactivation of the catalyst occurred during the catalytic experiment, which has often been observed in continuous palladium-catalysed reactions. The drop in conversion (77% after 35 exchanged reactor volumes) could fully be explained by the retention of the dendritic system (99.8%).[31]

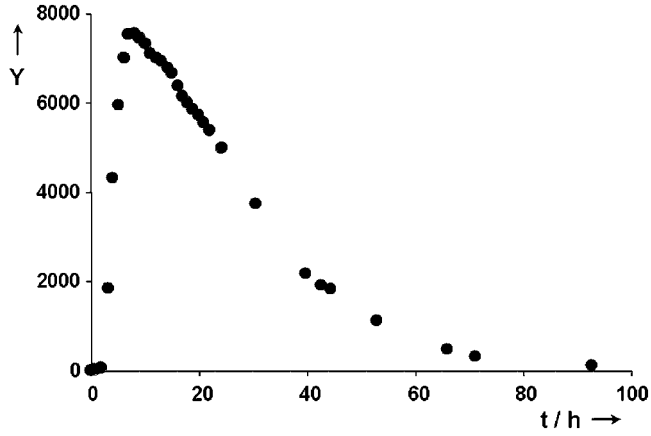

Figure 7. A continuous hydrovinylation experiment (reprinted with permission from ref.[18b] Copyright 2000 American Chemical Society.

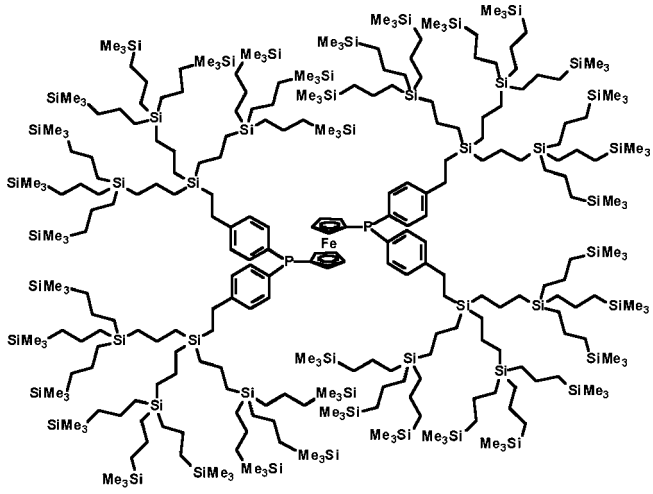

8

3) Nanocolloids: Metal Nanoclusters Stabilized in Dendrimers

Dendrimers can also be used as templates for the preparation of precise metal nanoclusters within their interior. Hydroxy-terminated poly(amido amine) dendrimers have been found to be particularly good for this purpose.[32] While high catalytic activity of metal clusters is well known, they tend to aggregate into larger and, therefore less-active, systems under catalytic conditions. Precise construction of nanocomposites in the cavities of dendrimers might lead to both cluster stability and full control over size and size distribution, while the dendrimer branches still allow substrate access to the catalytically active clusters. Additionally, dendrimers could enhance the solubility of the metal clusters, as they have good solubilities in a wide range of solvents. A water-soluble and stable G4-OH(Pd_{40}) dendrimer, for example, exhibits high activity for the hydrogenation of alkenes in water. It was reported to be sufficiently stable for recycling and reuse, although the actual data of such

experiments were not provided.[32a] The use of a dendrimer gives a more reproducible and more robust backbone than the use of polymers, but the preparation of a dendrimer is infinitely more time consuming and expensive, while the sizes of the palladium particles are similar those which are stabilized by branched polyglycerols and polyamides.

4) Metal Nanoparticles Stabilized with Hyperbranched Polyglycerols and Polyamides

Catalytically active metal nanoparticles can also be confined by utilizing the structure of easily accessible, compartmented amphiphilic (statistically branched) hyperbranched polymers. Recently, a one-step synthesis allowing a convenient access to hyperbranched polyglycerols of controlled, narrow molecular weight distributions was found.[33] Partial esterification of the OH groups with long-chain fatty acids yields amphiphilic molecules (Scheme 2; $M_w/M_n < 1.7$), which can function as nanocapsules for the incorporation of individual hydrophilic dye molecules as guests.[34]

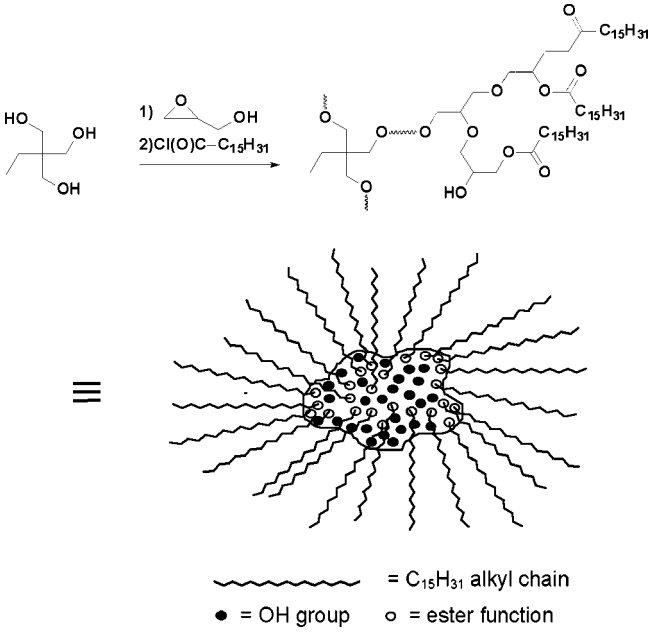

Scheme 2. Schematic representation of the preparation and structure of a hyperbranched amphiphilic polyglycerol.

Solubilisation of metal salts by such well-defined polymers and subsequent reduction (H_2, CO or thermally) can yield stable solutions of metal colloid/polymer hybrids, while the metal-particle sizes (ranging from 1 to ≥20 nm) increase with increasing polymer molecular weight.[35] A large portion of the individual metal particles appears to be confined in a single branched macromolecule. Such metal nanoparticle/hyperbranched polymer hybrid materials display a remarkable catalytic activity and stability in cyclohexene hydrogenation as a model reaction.[36] A total of 7×10^4 turnover over 30 h and well-behaved kinetics were observed at 1 atm hydrogen pressure. Further investigations have shown these materials to be stable in small-scale ultrafiltration experiments.

In order to achieve a better membrane performance, a loop filtration module was employed rather than the commonly used dead-end filtration cell (Figure 5, b). In this way, much more reliable and reproducible data, also with a view to possible applications, were obtained. The use of tubular membranes enables a facile scale-up and membrane surface enlargement.

With polyglycerols of different molecular weights (M_n = 2000–20000 g mol^{-1}) as a scaffold, functionalised polymers with varying degrees of substitution can be prepared. Apart from palmitoyl moieties, other lipophilic groups (e.g. bulky adamantoyl moieties or aromatic residues) and other linking units (e.g. ether instead of ester functions) were investigated. Thus, hyperbranched polymers of low polydispersity and controlled, variable hydrophilic-hydrophobic balance were produced.

The polymeric molecule environment of the metal particles can control the approach of substrates to the metal particles and the reactivity of the metal surface atoms. Hydrogenation reactions employing substrates differing in polarity and steric bulk serve as initial simple model reactions. For instance, cyclohexene has been hydrogenated to cyclohexane and the reaction was performed in a continuous membrane reactor with good retentions observed (R = 99.8%).[37] Eventually, C–C coupling reactions, such as Heck, Suzuki and Stille reactions, will be particularly intriguing. Such reactions are important for the preparation of fine chemicals, and are employed, for example, for the production of pharmaceuticals and other biologically active substances.

Hyperbranched poly(ethylene imine) amides have been prepared by amidation of different carboxylic acid amide derivatives.[34,36,38,39] These poly(ethylene imine) amides proved more suited for structural investigations. The hyperbranched polyamine core binds metal precursors and consequently solubilises them in apolar organic solvents much more effectively than the polyether-polyol scaffold of polyglycerol, as expected. Silver nitrate (insoluble in toluene in the absence of the polymers) was found to be well suited as a model compound for structural investigations. For poly(ethylene imine) amides, the concept of solubilisation of a metal salt in a polymeric inverted unimolecular micelle, and formation of a metal particle in the micelle upon reduction, indeed proved to be applicable. Also, by contrast to unmodified poly(ethylene imine), the amphiphilic derivatives are not washed out by water.

Heck reactions have been studied with amphiphilic polyglycerol-stabilized colloids. Reaction conditions were studied extensively with respect to appropriate combinations of colloid stabilisation, solvent, substrates, base and temperature. Pivaloyl-modified polyglycerols were found to stabilize palladium colloids in dimethylacetamide effectively. With 4-bromoacetophenone and butylacrylate as substrates, potassium carbonate was found to be particularly suited as a base. The reaction solutions were filtered and the filtrates were found to contain small amounts of

 © 2005 Wiley-VCH Verlag GmbH & Co. KGaA, Weinheim

palladium, as determined by ICP-AAS, and to be very active upon reuse for a further Heck reaction. This points towards smaller species than the original metal nanoparticles as the active species.

5) Continuous Homogeneous Catalysis in Supercritical Fluids

As an example of a continuous-flow approach to the separation of homogeneous catalysts, the use of supercritical fluids should be mentioned.[40] As a clear advantage, the catalyst always stays in its active state inside the reactor. Additionally, high throughputs can be obtained from relatively small-sized reactors. Webb and Cole-Hamilton have reported on the rhodium-catalysed hydroformylation of long-chain alkenes.[41] This process can be carried out as a continuous process using a supercritical fluid–ionic liquid biphasic system. The authors observed reaction rates that were comparable to those obtained in the commercially performed rhodium-catalysed hydroformylation of propene. Furthermore, very low rhodium leaching (0.012 ppm in the recovered product) was observed. The catalyst was formed in situ from [3-methyl-1-propylimidazolium][$Ph_2PC_6H_4SO_3$] and [$Rh(acac)(CO)_2$] in [3-methyl-1-octylimidazolium][bis-trifluoromethylsulfonyl amide], and supercritical CO_2 was used as the transport vector. The linear-to-branched ratio of the products could be improved from 3:1 to 40:1 by using a ligand based on the Xantphos backbone.[42] The major drawback of the system is that the overall pressure must be very high (200 bar) in order to extract the aldehyde from the ionic liquid in which it is soluble. However, the pressure can be reduced to 125 bar by omitting the ionic liquid and operating in such a way that the reaction product(s) is the solvent.[41b]

6) Continuous Homogeneous Catalysis Applying Zeolite Membranes

Molecular-weight enlargement of a homogeneous catalyst is not the only way to achieve a significant difference in molecular size of the catalyst, the reactants and products. Zeolite membranes, for example, have been developed by Turlan et al., with pore sizes in the 0.3 to 0.8 nm range.[43] For this work, silicalite was chosen with pores of 0.55 nm, well below the size of the homogeneous catalyst, but still able to permeate certain solvents and products.

The membranes were grown on the inner side of porous stainless-steel tubular supports.[44] Only separation experiments were carried out with model mixtures containing a Pd complex plus solvent and a possible reaction product. The reaction studied was the Heck reaction of 4-bromobenzonitrile with methyl acrylate. The chosen catalyst was [$Pd(\mu\text{-}Cl)(PPh_3)_2]_2(BF_4)_2$. This is a well-known Heck catalyst with a molecular diameter of 1.22 nm, which is considerably larger than the zeolite pores. The permeation rates were extremely low when DMA was used as a solvent, which suggests strong adsorption of the DMA in the zeolite pores, thus preventing permeation of catalyst and product. With the use of dichloromethane as solvent, complete catalyst retention was observed. Also, the permeation fluxes across the membrane were high. This shows the possibility to retain homogeneous catalysts of the right size behind very good membranes, without the need to molecularly enlarge their size. However, in order to truly evaluate these membranes, they have to be used in real continuous catalytic reactions and not to separate approximated reaction mixtures.

Conclusions

There is definitely not only one option for continuous homogeneous catalysis. Although many approaches exist to immobilize homogeneous catalysts, appropriate polymeric supports are not as readily available commercially. Furthermore, multi-step synthetic procedures are typically necessary to prepare the required ligand and the corresponding catalyst. Catalyst degradation and ligand oxidation have to be taken into account, especially when continuous processes are applied. Dendrimers have the advantage of high reproducibility and can be combined with a large variety of ligands and metals, which makes their catalytic scope very versatile. Also, they can be prepared with a very rigid backbone. In combination with a suitable filtration unit their retentions can be sufficiently high to be used in a broad range of utilisations. Similar to soluble polymeric supports, however, catalyst stability and their multistep synthesis is a major drawback and makes them relatively expensive and therefore less suitable for industrial applications. This also holds for the use of dendrimers as stabilizing agents for colloids.

Metal nanoparticles stabilized by polymers of different sizes and shapes can be more easily synthesised than dendrimers. They have proven their usefulness in hydrogenations and several types of C–C coupling reactions. The retentions are close to the desired amount for industrial purposes, so their future looks promising.

In general, both polymeric and ceramic membranes are used in these continuous processes and high retentions can be achieved with both options. The drawback of polymeric membranes is their solvent-sensitivity and their limited temperature resistance. Ceramic membranes can tolerate a wide range of solvents and higher temperatures, and the zeolite membranes are of special interest. Their very small pore diameters makes it possible to directly use some types of homogeneous catalyst without molecular-weight enlargement. Of course, such a small diameter also limits the possibilities for solvents and products, since they have to be able to penetrate the membrane.

The design of new membranes and reactors that are compatible with homogeneous reaction conditions is required to develop the fascinating area of continuous homogeneous catalysis to its full potential.

[1] a) B. Cornils, W. A. Herrmann, *Applied Homogeneous Catalysis with Organometallic Compounds*, 2nd Ed., Wiley-VCH,

 © 2005 Wiley-VCH Verlag GmbH & Co. KGaA, Weinheim

Weinheim, Germany, **2002**; b) D. Vogt, in *Aqueous Phase Organometallic Catalysis − Concepts and Application* (Eds.: B. Cornils, W. A. Herrmann), 2nd completely revised and enlarged ed., Wiley-VCH, Weinheim, Germany, **2004**, pp. 541–547.
[2] a) D. J. Cole-Hamilton, *Science* **2003**, *299*, 1702–1706; b) J. T. Scarpello, D. Nair, L. M. Freitas dos Santos, L. S. White, A. G. Livingston, *J. Membr. Sci.* **2002**, *203*, 71–85; c) J. Wöltinger, K. Drauz, A. S. Bommarius, *Appl. Catal. A: General* **2001**, *221*, 171–185; d) Q.-H. Fan, Y.-M. Li, A. S. C. Chan, *Chem. Rev.* **2002**, *102*, 3385–3466.
[3] a) J. Manassen, *Platinum Met. Rev.* **1971**, *15*, 142–143; b) E. Bayer, V. Schurig, *Angew. Chem. Int. Ed. Engl.* **1975**, *14*, 493–494.
[4] a) C. A. McNamara, M. J. Dixon, M. Bradley, *Chem. Rev.* **2002**, *102*, 3275–3300; b) D. E. Bergbreiter, C. Li, *Org. Lett.* **2003**, *5*, 2445–2447.
[5] a) Q. Yao, *Angew. Chem. Int. Ed.* **2000**, *39*, 3896–3898; b) R. Annunziata, M. Benaglia, M. Cinquini, F. Cozzi, M. Pitillo, *J. Org. Chem.* **2001**, *66*, 3160–3166.
[6] D. E. Bergbreiter, *Chem. Rev.* **2002**, *102*, 3345–3384.
[7] a) C. Bolm, N. Derrien, A. Seger, *Synlett* **1996**, 387; b) C. Bolm, C. L. Dinter, A. Seger, H. Höcker, J. Brozio, *J. Org. Chem.* **1999**, *64*, 5730; c) C. Schlenk, A. W. Kleij, H. Frey, G. van Koten, *Angew. Chem. Int. Ed.* **2000**, *39*, 3445–3447.
[8] E. Schwab, S. Mecking, *Organometallics* **2001**, *20*, 5504–5506.
[9] C. Müller, D. Vogt, in *Multiphase Homogeneous Catalysis*, Wiley-VCH, Weinheim, Germany, **2005**, chapter 7.4.1.
[10] a) H. P. Dijkstra, G. P. M. van Klink, G. van Koten, *Acc. Chem. Res.* **2002**, *35*, 798–810; b) R. van Heerbeek, P. C. J. Kamer, P. W. N. M. van Leeuwen, J. N. H. Reek, *Chem. Rev.* **2002**, *102*, 3717–3756; c) G. E. Oosterom, J. N. H. Reek, P. C. J. Kamer, P. W. N. M. van Leeuwen, *Angew. Chem. Int. Ed.* **2001**, *40*, 1828–1849; d) H. Frey, C. Schlenk, in *Topics in Current Chemistry*, Springer-Verlag, Berlin, Heidelberg, **2000**, vol. 210, p. 69–129.
[11] L. Ropartz, K. J. Haxton, D. F. Foster, R. E. Morris, A. M. Z. Slawin, D. J. Cole-Hamilton, *J. Chem. Soc., Dalton Trans.* **2002**, 4323.
[12] C. Müller, D. Vogt, unpublished results.
[13] a) Koch Membrane Systems, Wilmington, USA, http://www.kochmembrane.com; b) C. Linder, M. Nemas, M. Perry, R. Katraro, U. S. patent no. 5,265,734.
[14] E. Gibbins, M. D'Antonio, D. Nair, L. S. White, L. M. S. dos Santos, I. F. J. Vankelecom, A. G. Livingston, *Desalination* **2002**, *147*, 307–313.
[15] Membrane Extraction Technology, London, U. K., http://www.membrane-extraction-technology.com.
[16] E. L. V. Goetheer, A. W. Verkerk, L. J. P. van den Broeke, E. de Wolf, B.-J. Deelman, G. van Koten, J. T. F. Keurentjes, *J. Catal.* **2003**, *219*, 126–133.
[17] M. K. Koukou, N. Papayannakos, N. C. Markatos, M. Bracht, H. M. Van Veen, A. Roskam, *J. Membr. Sci.* **1999**, *155*, 241–259.
[18] a) N. J. Hovestad, E. B. Eggeling, H. J. Heidbüchel, J. T. B. H. Jastrzebski, U. Kragl, W. Keim, D. Vogt, G. van Koten, *Angew. Chem. Int. Ed.* **1999**, *38*, 1655–1658; b) E. B. Eggeling, N. J. Hovestad, J. T. B. H. Jastrzebski, D. Vogt, G. van Koten, *J. Org. Chem.* **2000**, *65*, 8857–8865.
[19] S. Bräse, F. Lauterwasser, R. E. Ziegert, *Adv. Synth. Catal.* **2003**, *345*, 869–929.
[20] a) U. Kragl, D. Gygax, O. Ghisalba, C. Wandrey, *Angew. Chem. Int. Ed. Engl.* **1991**, *30*, 827–828; b) U. Kragl, C. Dreisbach, *Angew. Chem. Int. Ed. Engl.* **1996**, *35*, 642–644; c) J. Wöltinger, A. S. Bommarius, K. Drauz, C. Wandrey, *Org. Process Res. Dev.* **2001**, *5*, 241–248.
[21] A. Datta, K. Ebert, H. Plenio, *Organometallics* **2003**, *22*, 4685–4691.
[22] E. Buhleier, W. Wehner, F. Vögtle, *Synthesis* **1978**, 155–158.
[23] A. P. H. J. Schenning, C. Elissen-Roman, J. W. Weener, M. W. P. L. Baars, S. J. van der Gaast, E. W. Meijer, *J. Am. Chem. Soc.* **1998**, *120*, 8199–8208.
[24] M. Ulman, R. H. Grubbs, *J. Org. Chem.* **1999**, *64*, 7202–7207.
[25] S. Mukhopadhyah, G. Rothenberg, D. Gitis, Y. Sasson, *J. Org. Chem.* **2000**, *65*, 3107–3110.
[26] L. A. van de Kuil, D. M. Grove, R. A. Gossage, J. W. Zwikker, L. W. Jenneskens, W. Drenth, G. van Koten, *Organometallics* **1997**, *16*, 4985–4994.
[27] a) J. W. Knapen, A. W. van der Made, J. C. Wilde, P. W. N. M. van Leeuwen, P. Wijkens, D. M. Grove, G. van Koten, *Nature* **1994**, *372*, 659–663; b) G. van Koten, J. T. B. H. Jastrzebski, *J. Mol. Catal. A: Chem.* **1999**, *146*, 317–323; c) A. W. Kleij, R. A. Gossage, J. T. B. H. Jastrzebski, J. Boersma, G. van Koten, *Angew. Chem. Int. Ed.* **2000**, *39*, 176–178; d) A. W. Kleij, R. A. Gossage, R. J. M. Klein Gebbink, N. Brinkmann, E. J. Reijerse, U. Kragl, M. Lutz, A. L. Spek, G. van Koten, *J. Am. Chem. Soc.* **2000**, *122*, 12112–12124.
[28] N. Brinkmann, D. Giebel, G. Lohmer, M. T. Reetz, U. Kragl, *J. Catal.* **1999**, *183*, 163.
[29] D. de Groot, E. B. Eggeling, J. C. de Wilde, H. Kooijman, R. J. van Haaren, A. W. van der Made, A. L. Spek, D. Vogt, J. N. H. Reek, P. C. J. Kramer, P. W. N. M. van Leeuwen, *Chem. Commun.* **1999**, 1623–1624.
[30] a) H. P. Dijkstra, N. J. Ronde, G. P. M. van Klink, D. Vogt, G. van Koten, *Adv. Synth. Catal.* **2003**, *345*, 364; b) H. P. Dijkstra, C. A. Kruithof, N. Ronde, R. van de Coevering, D. J. Ramon, D. Vogt, G. P. M. van Klink, G. van Koten, *J. Org. Chem.* **2003**, *68*, 675–685.
[31] G. E. Oosterom, S. Steffens, J. N. H. Reek, P. C. J. Kamer, P. W. N. M. van Leeuwen, *Top. Catal.* **2002**, *19*, 61–73.
[32] a) M. Zhao, L. Sun, R. M. Crooks, *Polym. Mater. Sci. Eng.* **1999**, *217*, 28–30; b) L. Balogh, D. A. Tomalia, *J. Am. Chem. Soc.* **1998**, *120*, 7355–7356.
[33] A. Sunder, R. Hanselmann, H. Frey, R. Mülhaupt, *Macromolecules* **1999**, *32*, 4240–4246.
[34] a) A. Sunder, M. Krämer, R. Hanselmann, R. Mülhaupt, H. Frey, *Angew. Chem. Int. Ed.* **1999**, *38*, 3552–3554; b) S.-E. Stiriba, H. Kautz, H. Frey, *J. Am. Chem. Soc.* **2002**, *124*, 9698–9699.
[35] S. Mecking, U. Schlotterbeck, M. Stieger, M. Soddemann, W. Richtering, H. Kautz, *Polym. Mater. Sci. Eng.* **2001**, *84*, 511–512.
[36] S. Mecking, R. Thomann, H. Frey, A. Sunder, *Macromolecules* **2000**, *33*, 3958–3960.
[37] M. G. Nijkamp, D. Vogt, unpublished results.
[38] R. Sablong, U. Schlotterbeck, D. Vogt, S. Mecking, *Adv. Synth. Catal.* **2003**, *345*, 333–336.
[39] C. Aymonier, U. Schlotterbeck, L. Antonietti, P. Zacharias, R. Thomann, J. C. Tiller, S. Mecking, *Chem. Commun.* **2002**, 3018–3019.
[40] N. J. Meehan, A. J. Sandee, J. N. H. Reek, P. C. J. Kamer, P. W. N. M. van Leeuwen, M. Poliakoff, *Chem. Commun.* **2000**, 1497.
[41] a) P. B. Webb, M. F. Sellin, T. E. Kunene, S. M. Williamson, A. M. Z. Slawin, D. J. Cole-Hamilton, *J. Am. Chem. Soc.* **2003**, *125*, 15577; b) P. B. Webb, D. J. Cole-Hamilton, *Chem. Commun.* **2004**, 612–613.
[42] P. B. Webb, T. E. Kunene, D. J. Cole-Hamilton, *Green Chem.* **2005**, *7*, 373.
[43] D. Turlan, E. P. Urriolabeitia, R. Navarro, C. Royo, M. Menéndez, J. Santamaria, *Chem. Commun.* **2001**, 2608–2609.
[44] E. Piera, J. Coronas, M. Menéndez, J. Santamaria, *Chem. Commun.* **1999**, 1309–1310.

Received: May 23, 2005
Published Online: August 24, 2005

 © 2005 Wiley-VCH Verlag GmbH & Co. KGaA, Weinheim

Fullerene-Like Nanoballs Formed by Pentaphosphaferrocene and CuBr

Manfred Scheer*[a] Junfeng Bai,[b] Brian P. Johnson,[a] Roger Merkle,[a] Alexander V. Virovets,[c] and Christopher E. Anson[d]

Dedicated to Professor H. W. Roesky on the occasion of his 70th birthday

Keywords: Polyphosphorus ligands / Fullerene-like molecules / Iron / Phosphorus / Cluster / Nanochemistry

Reaction of [$Cp^xFe(\eta^5\text{-}P_5)$] {$Cp^x = \eta^5\text{-}C_5Me_5$ (**1a**), $\eta^5\text{-}C_5Me_4Et$ (**1b**)} with CuBr leads to the fullerene-like nanoballs [{$Cp^xFe(\eta^5{:}\eta^1{:}\eta^1{:}\eta^1{:}\eta^1\text{-}P_5)$}$_{12}${CuBr}$_{10}${$Cu_2Br_3$}$_5${Cu($CH_3CN$)$_2$}$_5$] {$Cp^x = \eta^5\text{-}C_5Me_5$ (**5a**), $\eta^5\text{-}C_5Me_4Et$ (**5b**)} comprising a cluster core of 90 non-carbon atoms. In contrast to previous results by variation of stoichiometry and concentration conditions, the formation of polymeric product was hindered, and exclusive formation of the spherical cage compound was achieved. The cluster **5b** possesses an inside diameter of 1.29 nm and an outside diameter of 2.37 nm. Definitive evidence for encapsulation of a [$Cp^xFe(\eta^5\text{-}P_5)$] unit (**1b**) within the inner cavity of the nanocluster **5b** is shown by X-ray crystallographic results.

(© Wiley-VCH Verlag GmbH & Co. KGaA, 69451 Weinheim, Germany, 2005)

Introduction

Large spherical molecules and clusters are a fascinating field in contemporary chemistry. Established areas like the borane cages have recently been augmented by the discovery of low-valent aluminium and gallium metalloid clusters,[1] and within the growing area of giant clusters the chalcogeno-bridged copper and silver clusters[2] as well as the giant polyoxomolybdates establishing wheels and balls[3] are of the largest structurally characterised clusters so far. Among others an inorganic "superfullerene" $[Mo_{132}O_{372}(CH_3CO_2)_{30}(H_2O)_{72}]^{42-}$ has been reported reflecting a pentagonal-shaped symmetry.[4,5] Fullerene-like molecules based on carbon-free elements exist so far only in the solid state Zintl phases $Na_{172}In_{197}M_2$ (M = Ni, Pd, or Pt) with a C_{60}-like polyhedron of $In_{48}Na_{12}$ moieties, whereas an In_{74} fullerene-like unit with D_{3h} symmetry was found within $Na_{96}In_{97}M_2$.[6,7]

Within our efforts to study the coordination chemistry of naked P_n ligand complexes to form well-oriented supramolecular assemblies as well as one-dimensional (1D) and two-dimensional (2D) polymers, we used pentaphosphaferrocene **1a** as a starting material. Thus, the reaction of **1a** with Cu^I bromide and iodide led to the quantitative formation of 2D polymeric frameworks of **2a**,**b**.[8] However, when CuCl was used, the reaction yielded **3** as a linear 1D polymer in a maximum of about 50% yield.[8] As the soluble product of the latter reaction complex **4** was formed revealing a spherical fullerene-like molecule containing 90 non-carbon core atoms.[9] In continuation of these investigations the question arises whether it would be possible selectively to obtain such soluble nano-scaled spherical aggregates for the other Cu^I halides. We have now found that depending on the stoichiometry of the starting materials and the concentration conditions it is possible to obtain exclusively soluble spherical molecules of the formula [{$Cp^xFe(\eta^5{:}\eta^1{:}\eta^1{:}\eta^1{:}\eta^1\text{-}P_5)$}$_{12}${CuBr}$_{10}${$Cu_2Br_3$}$_5${Cu($CH_3CN$)$_2$}$_5$] {$Cp^x = \eta^5\text{-}C_5Me_5$ (**5a**), $\eta^5\text{-}C_5Me_4Et$ (**5b**)} by the reaction of **1a,b** with CuBr. This fullerene-like molecule possesses 90 non-carbon atoms. Furthermore, for the first time we have structural evidence of the existence of encapsulated molecules of **1b** in the ball of **5b**, results we are reporting herein.[10]

[$Cp^xFe(\eta^5\text{-}P_5)$] {$Cp^x = \eta^5\text{-}C_5Me_5$ (**1a**), $\eta^5\text{-}C_5Me_4Et$ (**1b**)} [$CuX\{Cp^*Fe(\eta^5{:}\eta^1{:}\eta^1\text{-}P_5)\}]_\infty$ (**2a**: X = Br, **2b**: X = I) [$CuCl\{Cp^*Fe(\eta^5{:}\eta^1\text{-}P_5)\}]_\infty$ (**3**)

[a] Institut für Anorganische Chemie der Universität Regensburg, 93040 Regensburg, Germany
Fax: +49-941-943-4439
E-mail: mascheer@chemie.uni-regensburg.de
[b] Present address: Coordination Chemistry Institute & the State Key Laboratory of Coordination Chemistry, Nanjing University,
210093 Nanjing, P. R. China
E-mail: bjunfeng@netra.nju.deu.cn
[c] Nikolaev Institute of Inorganic Chemistry, Siberian Division of RAS,
Acad. Lavrentyev str. 3, Novosibirsk 630090 (Russia)
Fax: +7-3833-309489
E-mail: a_v_virovets@yahoo.com
[d] Institut für Anorganische Chemie der Universität Karlsruhe, Engesserstr. 15, 76128 Karlsruhe, Germany
Fax: +49-721-608-8142
E-mail: anson@chemie.uni-karlsruhe.de

$[\{Cp^*Fe(\eta^5{:}\eta^1{:}\eta^1{:}\eta^1{:}\eta^1\text{-}P_5)\}_{12}\{CuCl\}_{10}\{Cu_2Cl_3\}_5\{Cu(CH_3CN)_2\}_5]$ (**4**)

Results and Discussion

Complexes **5a,b** were obtained by the reaction of **1a,b** with CuBr in mixed solvents of CH_3CN and CH_2Cl_2 at ambient temperature. In comparison with the reactions leading to the 2D polymers **2a**,[8] the increase of the dilution (15 mmol/L to 7.5 mmol/L)[11] leads to the formation of the soluble products. However the polymer **2a** is still formed in yields up to 50%. With a more dilute solution (3.75 mmol/L) coupled with a stoichiometry of 2:1 CuBr/**1a**, as required for the composition of the spherical molecules of **5**, the formation of polymer was essentially negligible. Using the 2:1 stoichiometry without diluting the reaction mixture from 15 mmolar still resulted in formation of significant quantities of the polymer **2a**. Thus, the decisive criteria for the exclusive (polymer-free) formation of **5** are both the correct stoichiometry of 2:1 and a larger dilution of the reaction components ($\leq$ 3.75 mmol/L).

The black crystals of **5a**,**b** are stable under nitrogen and soluble in mixtures of CH_2Cl_2/CH_3CN. They exhibit broad ^{31}P NMR chemical shifts at about 66 and 68 ppm, respectively.

5b has been characterised by X-ray diffraction analysis.[12] The unit cell contains two crystallographically independent molecules of **5b** both lying on the mirror plane of the space group *Cm*. The molecular structure of **5b** is similar to the chlorine analog **4** (Figure 1).[9] All P atoms of the *cyclo*-P_5 ring of $[Cp^xFe(\eta^5\text{-}P_5)]$ coordinate to the copper atoms of CuBr, which are further coordinated by P atoms of other *cyclo*-P_5 rings, leading to the formation of six-membered P_4Cu_2 rings around the central *cyclo*-P_5 ring (Figure 1, a). The five- and six-membered ring alternation is similar to that seen in the fullerenes, with the difference that due to the distorted tetrahedral coordination sphere of the Cu^I ions, the six-membered rings are not planar and folded along the Cu···Cu axis (folding angle between 132.7 and 141.9°). The thus formed pseudo-hemispherical $[Cu_{10}Br_{10}\{Cp^xFe(\eta^5\text{-}P_5)\}_6]$ half-shells (Figure 1, a) are joined by five $[Cu_2Br_3]^-$ as well as by five $[Cu(CH_3CN)_2]^+$ units (Figure 1, b). Thus, ideal symmetry of the $[Cu_{25}Br_{25}(FeP_5)_{12}]$ core, consisting of 90 non-carbon atoms, is D_{5h} but the presence of ethyl groups at the cyclopentadienyl ligands reduces symmetry of the whole molecule to C_s or even C_1. All copper atoms have a tetrahedral P_3Br, P_2Br_2 or P_2N_2 environment. The Cu–Br bond lengths are 2.328(3)–2.379(3) Å (av. 2.351 Å) and 2.446(3)–2.472(4) Å (av. 2.462 Å) for terminal and bridging Br atoms, respectively. All *cyclo*-P_5 rings are nearly planar. The P–P distances, varying from 2.075(8) to 2.130(5) Å (av. 2.102 Å), are in good agreement with 2.088(3)–2.108(3) Å (av. 2.096 Å) found for the starting material **1b**.[13] The Cu–P bonds vary from 2.284(4) to 2.324(7) Å (av. 2.304 Å). This is also in good agreement with the values found in **4**

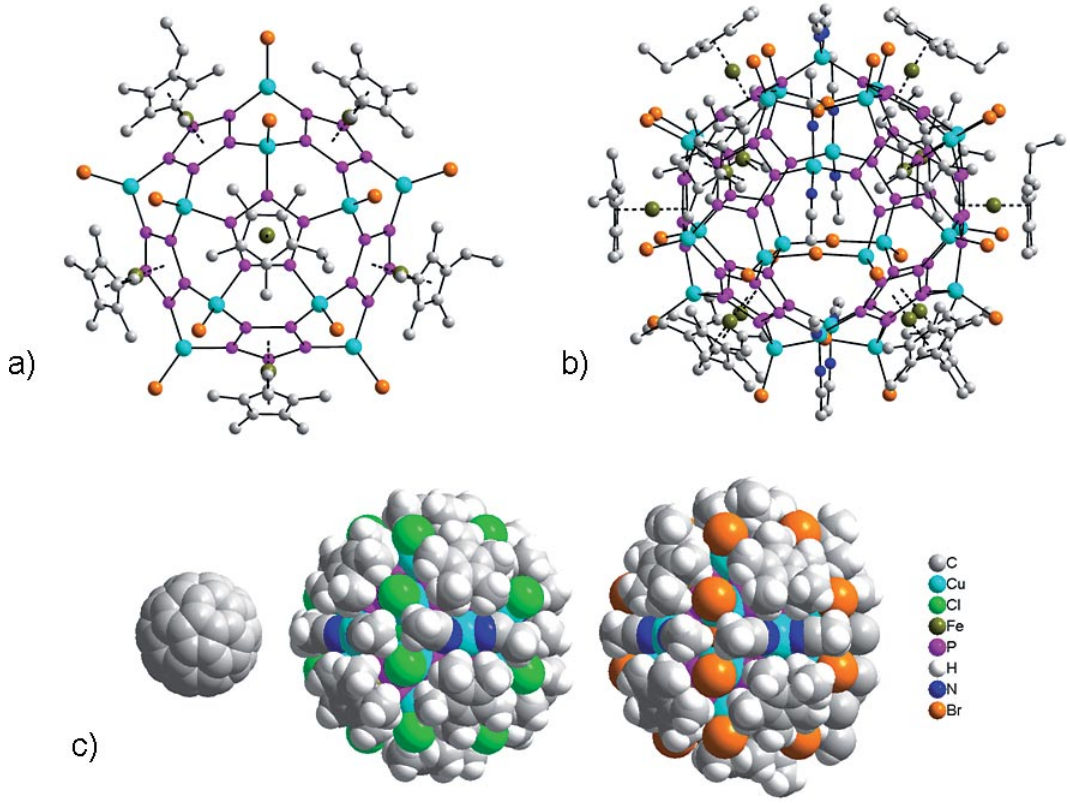

Figure 1. a) View of a half shell of a molecule of **5b**; b) Complete ball-and-stick structure of a molecule of **5b**; c) Size comparison of the spherical molecules of C_{60}, **4** and **5b** (space-filing model).

 © 2005 Wiley-VCH Verlag GmbH & Co. KGaA, Weinheim

[2.294(6)–2.353(6) Å].[9] Due to the longer Cu–Br–Cu bridges [compare **4**: 2.294(6)–2.353(6) Å], which link the two half shells together, and the presence of Et groups at the Cp^x ligands the spherical body of **5b** is in comparison with **4** slightly larger and more elongated. It possesses an inside diameter of 12.9 Å (**4**: 12.2 Å) and an outside diameter of 21.4/23.7 Å (**4**: 21.4 Å), which is about three times larger than that of C_{60} (Figure 1, c).[14] Whereas for **4** we had only weak experimental data for the existence of an encapsulated [Cp*Fe(η^5-P_5)] (**1a**) moiety in every second ball, in **5b** we have much better structural data for the existence of an encapsulated molecule **1b** in each ball of **5b**, which is disordered in two directions with no special preference to the five-membered rings of the half-shells.

The results have shown that both stochiometry and dilution conditions are decisive for the exclusive formation of non-carbon containing nanoballs. Thus, while heterofullerenes are known containing only a few boron, nitrogen[15] and phosphorus atoms,[16] the complexes **4** and **5** exhibit a complete heteroatom composition and therefore represent a novel class of fullerene-like molecules.

Experimental Section

General Remarks: All manipulations were carried out under an atmosphere of dinitrogen using standard Schlenk techniques. All solvents were dried using standard procedures and distilled freshly before use. [$Cp^xFe(\eta^5$-$P_5)$] {Cp^x = η^5-C_5Me_5 (**1a**), η^5-C_5Me_4Et (**1b**)}[13] were prepared according to the literature.

[{$Cp^xFe(\eta^5$:η^1:η^1:η^1:η^1-$P_5)$}$_{12}${CuBr}$_{10}${Cu_2Br_3}$_5${$Cu(CH_3CN)_2$}$_5$] {Cp^x = η^5-C_5Me_5 (5a), η^5-C_5Me_4Et (5b)}: A solution of CuBr (21.5 mg, 0.15 mmol) in 5 mL of CH_3CN and 5 mL of CH_2Cl_2 was layered onto a solution of [$Cp^xFe(\eta^5$-$P_5)$] (**1a**: 26 mg, 0.075 mmol; **1b**: 27 mg, 0.075 mmol) in 10 mL of CH_2Cl_2 at room temperature. After complete diffusion of the phases (about one week), the solution was decanted into a fresh Schlenk tube and layered with 20 mL of hexane. This mixture was kept for two further weeks and black crystals of **5** were formed. The mother liquor was decanted and the obtained black crystals were dried under high vacuum. **5a**: 10 mg, 20% (based on **1a**); **5b**: 8 mg, 15% (based on **1b**).

5a: $^{31}P\{^1H\}$ NMR (162 MHz, CD_2Cl_2, 300 K): δ = 66 ppm (br., $\omega_{1/2}$ = 1000 Hz).

5b: $^{31}P\{^1H\}$ NMR (162 MHz, CD_2Cl_2, 300 K): δ = 68 ppm (br., $\omega_{1/2}$ = 850 Hz).

Acknowledgments

This work was comprehensively supported by the Deutsche Forschungsgemeinschaft and the Fonds der Chemischen Industrie.

[1] H.-G. Schnöckel, H. Köhnlein, *Polyhedron* **2002**, *21*, 489–502; H.-G. Schnöckel, A. Schnepf, *Angew. Chem.* **2002**, *114*, 3682–3703; *Angew. Chem. Int. Ed. Angew. Chem. Int Ed.* **2002**, *41*, 3532–3552.

[2] a) S. Dehnen, A. Eichhöfer, J. F. Corrigan, D. Fenske, "Synthesis and Characterization of Ib-IV Nanoclusters", in: G. Schmid (Ed.): *Nanoparticles*, Wiley-VCH, Weinheim, **2003**; b) D. Fenske, C. Persau, S. Dehnen, C. E. Anson, *Angew. Chem.* **2004**, *116*, 309–313; *Angew. Chem. Int. Ed.* **2004**, *43*, 305–309.

[3] L. Cronin, E. Diemann, A. Müller, "Polyoxomolybdate Clusters: Nanoscopic Wheels and Balls" in: *Inorganic Experiments* (Ed.: J. D. Woollins), Wiley-VCH, Weinheim, **2003**, pp. 340–346; A. Müller, S. Roy, "Oxomolybdates: From Structures to Functions, in: a New Era of Nanochemistry" in: *The Chemistry of Nanomaterials: Synthesis Properties and Applications*, vol. II (Eds.: C. N. R. Rao, A. Müller, A. K. Cheetham), Wiley-VCH, Weinheim, **2004**, pp. 452–475.

[4] A. Müller, E. Krickemeyer, H. Bögge, M. Schmidtmann, F. Peters, *Angew. Chem.* **1998**, *110*, 3567–3571; *Angew. Chem. Int. Ed.* **1998**, *37*, 3360–3363.

[5] A. Müller, E. Krickemeyer, H. Bögge, M. Schmidtmann, S. Roy, A. Berkle, *Angew. Chem.* **2002**, *114*, 3756–3761; *Angew. Chem. Int. Ed.* **2002**, *41*, 3603–3609.

[6] S. C. Sevov, J. D. Corbet, *Science* **1993**, *262*, 880–883.

[7] S. C. Sevov, J. D. Corbet, *J. Solid State Chem.* **1996**, *123*, 344–370.

[8] J. Bai, A. V. Virovets, M. Scheer, *Angew. Chem.* **2002**, *114*, 1808–1811; *Angew. Chem. Int. Ed.* **2002**, *41*, 1737–1740.

[9] J. Bai, A. V. Virovets, M. Scheer, *Science* **2003**, *300*, 781–783.

[10] Several intensive attempts to obtain soluble products with CuI failed.

[11] Concentrations discussed here refer to the overall concentrations of complexes **1**, as calculated using the total volume obtained after layering with the CuBr solutions.

[12] Since the single crystals of **5a** unfortunately proved to be very weakly diffracting, only the unit cell could be roughly determined at T = 100 K as a monoclinic unit cell with: a = 23.22(6) Å, b = 23.21(6) Å, c = 31.67(5) Å, β = 91.32(10), V = 17138 (105) Å^3. Crystal structure analysis of a single crystal of **5b** was carried out at 100 K on a Bruker SMART Apex CCD diffractometer using graphite-monochromated Mo-K_α radiation (λ = 0.71073 Å). The data were corrected for absorption using the SADABS program.[17a] The structure was solved by direct methods and refined by full-matrix least-squares methods using SHELX-97 program set.[17b]

{(Cp^xFeP_5)⊂[$Cu_{25}Br_{25}(Cp^xFeP_5)_{12}(CH_3CN)_{10}$]}·0.5$CH_3CN$·2$CH_2Cl_2$ (Cp^x = η^5-C_5Me_4Et): $C_{166}H_{256.5}Br_{25}Cl_4Cu_{25}Fe_{13}N_{10.5}P_{65}$, M = 8866.47, crystal dimensions 0.30 × 0.25 × 0.08 mm^3, monoclinic, space group *C*m (No. 8), a = 37.4766(14) Å, b = 23.8734(9) Å, c = 37.3372(14) Å, β = 98.313(1)°, T = 100(1) K, Z = 4, V = 33054(2) Å^3, D_c = 1.782 Mg/m^3, μ(Mo-K_α) = 5.524 mm^{-1}. 82792 data measured to $2\theta_{max}$ = 56.04°, 68911 unique (R_{int} = 0.0562). 2726 parameters, wR_2 = 0.2315, R_1 = 0.1141 (all data), R_1 = 0.0877 [51811 with $I > 2\sigma(I)$].

There are two crystallographically independent molecules of **5b** in the unit cell both lying on mirror plane of the *Cm* space group. When all atoms of main molecules were localized the electron density ($\Delta\rho$) map contained a few peaks inside both of the spheres. Accurate analysis led us to a conclusion that each sphere contains a [$Cp^xFe(\eta^5$-$P_5)$] molecule located almost in the center. Each molecule is disordered over two positions with an opposite orientation and relative shift by 2.23–2.29 Å. Two positions of Cp^x ligand are overlapped. The iron and phosphorus atoms of disordered molecules were localized directly from the $\Delta\rho$ map and refined anisotropically with variable site occupancy factors. Then the positions of disordered Cp^x ligands were fitted from an idealized model to the largest $\Delta\rho$-peaks and included into refinement with fixed coordinates and U_{iso} = 0.04 Å^2. The final $\Delta\rho$ map contained one CH_3CN and four CH_2Cl_2 solvent molecules outside the ball-like structure. There were also some peaks probably corresponding to severely disordered CH_2Cl_2 molecules but several attempts to include them into refinement failed. Finally the structure was refined in anisotropic approximation for all non-hydrogen atoms except for carbon atoms of disordered [$Cp^xFe(\eta^5$-$P_5)$]

 © 2005 Wiley-VCH Verlag GmbH & Co. KGaA, Weinheim

molecules inside the balls and two CH_2Cl_2 solvent molecules. Hydrogen atoms were refined geometrically. Site occupancy factors of disordered [$Cp^xFe(\eta^5\text{-}P_5)$] molecules were set as 0.70/0.30 and 0.60/0.40.

CCDC-267819 contains the supplementary crystallographic data for this paper. These data can be obtained free of charge from the Cambridge Crystallographic Data Centre via www.ccdc.cam.ac.uk/conts/retrieving.html [or from the Cambridge Crystallographic Data Centre, 12 Union Road, Cambridge CB2 1EZ, UK; Fax: +44-1223-336033; E-mail: deposit@ccdc.cam.ac.uk].

[13] O. J. Scherer, T. Brück, G. Wolmershäuser, *Chem. Ber.* **1988**, *121*, 935–938.

[14] Sizes reported refer to interatomic distances without regard to van-der-Waals radii.

[15] A. Hirsch, B. Nuber, *Acc. Chem. Res.* **1999**, *32*, 795.

[16] C. Möschel, M. Jansen, *Z. Anorg. Allg. Chem.* **1999**, *625*, 175.

[17] a) G. M. Sheldrick, SADABS (the Siemens Area Detector Absorption Correction), University of Göttingen, **1996**; b) G. M. Sheldrick, SHELXTL 5.1, Bruker AXS Inc., 6300 Enterprise Lane, Madison, WI 53719-1173, USA, **1997**.

Received: April 14, 2005
Published Online: September 8, 2005

 © 2005 Wiley-VCH Verlag GmbH & Co. KGaA, Weinheim

Multifunctional Dithiocarbamates as Ligands Towards the Rational Synthesis of Polymetallic Arrays: An Example Based on a Piperizine-Derived Dithiocarbamate Ligand

James D. E. T. Wilton-Ely,*[a] Dina Solanki,[a] and Graeme Hogarth*[a]

Keywords: Dithiocarbamates / Piperazine / Multimetallic arrays / Ruthenium complexes / Coordination chemistry

The zwitterionic piperazine-derived dithiocarbamate complex $[(dppm)_2Ru(S_2CNC_4H_8NCS_2)]$ has been prepared and utilised in the synthesis of multimetallic arrays incorporating a wide range of transition metal centres.

(© Wiley-VCH Verlag GmbH & Co. KGaA, 69451 Weinheim, Germany, 2005)

Introduction

Dithiocarbamates are extremely versatile ligands which form complexes with all the transition metals, leading to the stabilisation of a wide range of oxidation states.[1] Since their complexes are easily prepared and manipulated, a wide range of applications have been developed in areas as diverse as materials science, medicine and agriculture. Given this versatility, their well-defined architecture and the bountiful metal-centred electrochemistry shown by these complexes,[2] it is surprising that they have found little use in the burgeoning area of supramolecular chemistry. Recently, however, Beer and co-workers have started to address this issue, preparing a range of exciting new supramolecular architectures based on multifunctional dithiocarbamate ligands, many of which show interesting structural-redox properties.[3] It is clear from this work that dithiocarbamates have the potential to be utilised to a far greater extent than found currently in the areas of supramolecular chemistry and materials science. With this in mind we have focused our initial efforts on the development of multidentate dithiocarbamate ligands for the synthesis of multimetallic arrays. Such arrays could be one, two or three-dimensional in nature, the dimensionality being easily controlled as a function of the properties of both the metal and ligand. We envisage that these materials will show novel physical properties in their own right and will be explored as precursors to the synthesis of well-defined nanoparticulates in a manner developed extensively by O'Brien and co-workers.[4]

Results and Discussion

A simple strategy for the synthesis of multimetallic wires is outlined below (Scheme 1). It centres on the use of a molecule containing two secondary amine centres. Such species react with CS_2 to afford a zwitterionic product,[5,6] whereby one of the amines acts as a nucleophile and the second as a base. Under the right conditions, only small amounts of the symmetrical double salt $[S_2CN(X)NCS_2][H_2N(X)NH_2]$ (X = spacer) are formed, which is a key advantage of this approach as this allows one end of the amine to be extended selectively by reaction with carbon disulfide. Reaction of the zwitterionic product, $[H_2NC_4H_8NCS_2]$, with a metal complex results in the formation of a new metal-amine compound, which in turn can react with further CS_2 to generate a new metal-containing dithiocarbamate ligand. In this manner multimetallic arrays can be constructed in a modular, step-wise fashion (Scheme 1). This approach, which is demonstrated by the reactions shown in Scheme 2, can be extended using tri- and tetradentate amines to incorporate further dimensionality.

As a proof of concept, we have used cheap and commercially available piperazine in order to demonstrate the ease and potential of such an approach. We have used the ruthenium(II) complex *cis*-$[RuCl_2(dppm)_2]$[7] to provide a *cis*-$Ru(dppm)_2$ moiety as the initial metal fragment. This choice was based on our observation that *cis*-$[RuCl_2(dppm)_2]$ reacts cleanly with a wide range of dithiocarbamate salts to afford the cations $[Ru(S_2CNR_2)(dppm)_2]^+$ in high yield. These complexes are easily characterised by a range of spectroscopic techniques, of which ^{31}P NMR spectroscopy proves particularly useful.

Addition of CS_2 to piperazine in water results in the formation of the zwitterion, $H_2NC_4H_8NCS_2$ (**1**), which is readily isolated (Scheme 2). Addition of one equivalent of *cis*-$[RuCl_2(dppm)_2]$ to this zwitterion, followed by an excess of $NaBF_4$ affords $[(dppm)_2Ru(S_2CNC_4H_8NH_2)][BF_4]_2$ (**2**) in high yield,[8] which is then converted into the new complex, $[(dppm)_2Ru(S_2CNC_4H_8NCS_2)]$ (**3**), upon sequential addition of two equivalents of base and CS_2. The latter is a

[a] Department of Chemistry, University College London, 20 Gordon Street, London, WC1H 0AJ, UK
E-mail: j.wilton-ely@ucl.ac.uk
g.hogarth@ucl.ac.uk

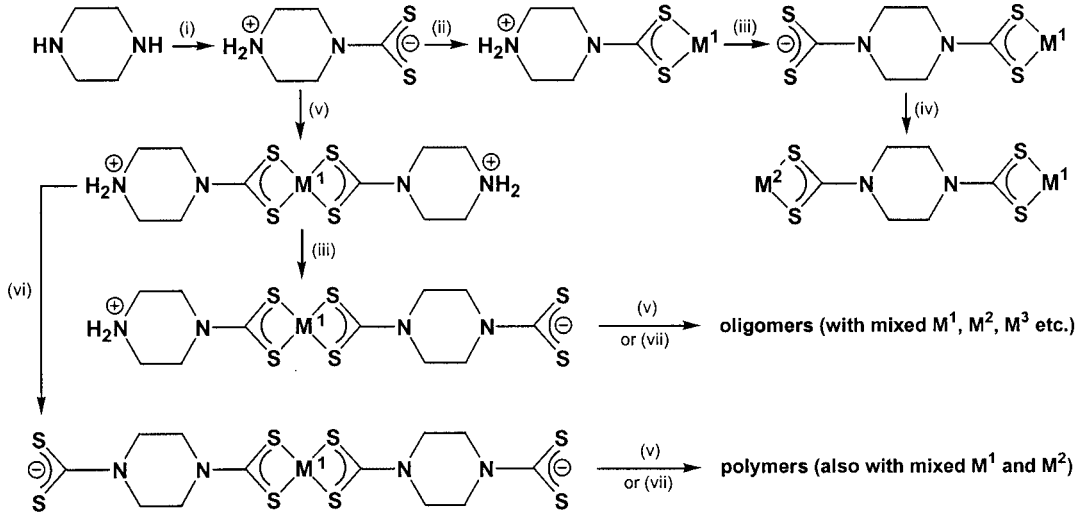

Scheme 1. (i) CS_2; (ii) M^1X; (iii) $2NEt_3$, CS_2; (iv) M^2X; (v) M^1X_2; (vi) $4NEt_3$, $2CS_2$; (vii) M^2X_2.

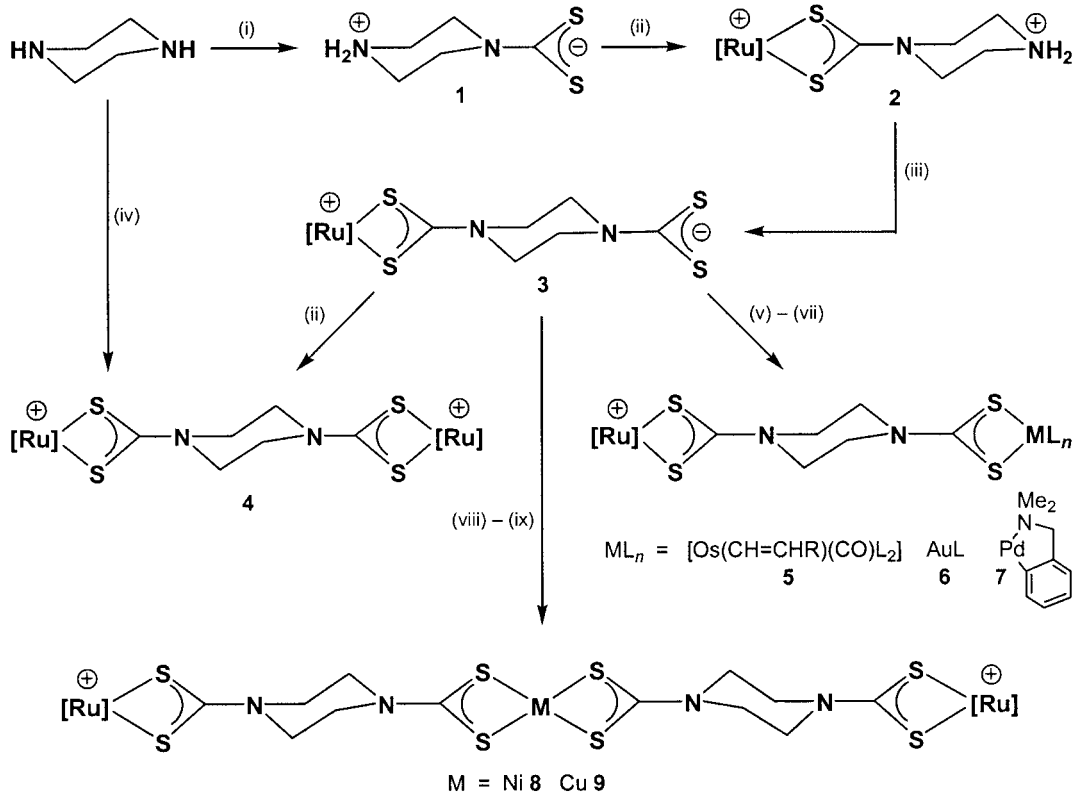

Scheme 2. [M] = $Ru(dppm)_2$;L = PPh_3; R = C_6H_4Me-4; (i) CS_2; (ii) *cis*-$[RuCl_2(dppm)_2]$, $2NaBF_4$; (iii) $2NEt_3$, CS_2; (iv) $2NEt_3$, $2CS_2$; 2*cis*-$[RuCl_2(dppm)_2]$; (v) $[Os(CH{=}CHR)Cl(CO)(BTD)L_2]$ (BTD = 2,1,3-benzothiadiazole); (vi) ClAuL; (vii) $[Pd(C_6H_4CH_2NMe_2)Cl]_2$; (viii) $Ni(OAc)_2$; (ix) $Cu(OAc)_2$.

key building block and can be considered to be a metallodithiocarbamate. In order to demonstrate its utility we treated this compound with a second equivalent of *cis*-$[RuCl_2(dppm)_2]$ to afford (after salt metathesis) the binuclear complex $[(dppm)_2Ru(S_2CNC_4H_8NCS_2)Ru(dppm)_2][BF_4]_2$ (**4**).[9] The same complex is also produced in a one-step reaction upon addition of $Na_2[S_2CNC_4H_8NCS_2]$ to two equivalents of *cis*-$[RuCl_2(dppm)_2]$ followed by salt metathesis. In order to confirm the bridging nature of the dithiocarbamate, a crystallographic study of **4** was performed (Figure 1).[10] The bridging dithiocarbamate mode found in **4** is rare but not unique; Shaver and co-workers having recently prepared a related diruthenium complex, $[Cp(PPh_3)Ru(S_2CNC_6H_4NCS_2)Ru(PPh_3)Cp]$, from the unusual reaction of two equivalents of $[CpRu(PPh_3)_2SH]$ with *para*-phenylenediisothiocyanate.[11] A dinuclear tin complex has

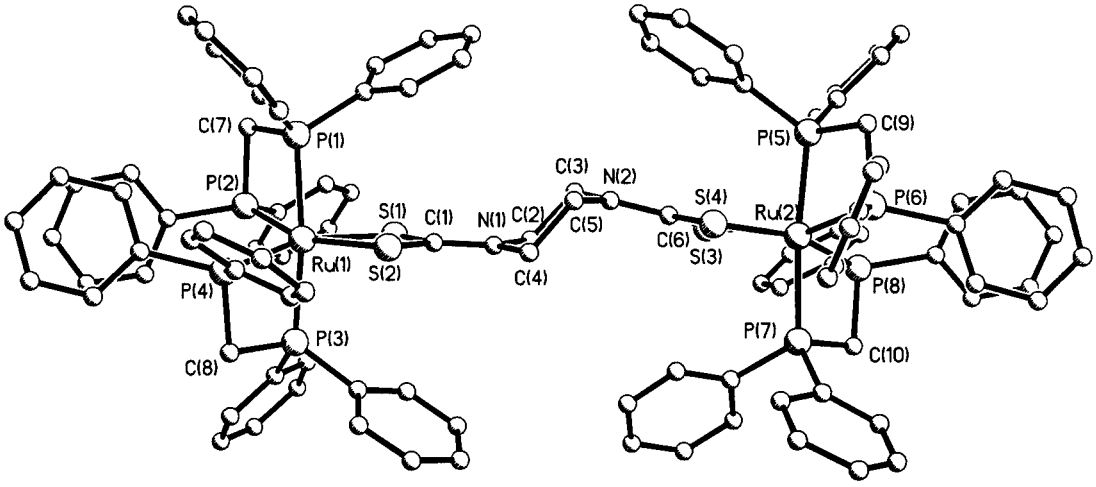

Figure 1. Structure of the cation in $[\{Ru(dppm)_2\}_2(S_2CNC_4H_8NCS_2)][BF_4]_2$ (**4**).

also been reported.[6a] Zwitterion **3** can be employed to prepare a wide range of dithiocarbamate-bridged binuclear metal complexes as we have illustrated with the formation of **5**–**7**,[9] in which osmium,[8] gold and palladium centres, respectively, are coordinated using suitable reagents.

In each of the cases described above, the added metal centre binds only a single dithiocarbamate ligand. Trimetallic units based on two bidentate dithiocarbamate ligands result from the addition of metals with two dithiocarbamate-binding sites. In order to illustrate this, we treated **3** with nickel and copper acetate to quantitatively afford $[\{(dppm)_2Ru(S_2CNC_4H_8NCS_2)\}_2M][BF_4]_2$ [M = Ni (**8**), Cu (**9**)] (Scheme 2).[9] These examples illustrate the ease of incorporation of diamagnetic and paramagnetic centres which show well-defined and understood redox properties into these arrays. We have extended this strategy to the formation of tetranuclear complexes upon coordination of zwitterion **3** to Fe^{III}, Co^{III} and La^{III} centres and are currently using methyl-substituted piperazines to prepare chiral materials. We have also begun work using 1,4,7-triazacyclononane and 1,4,8,11-tetraazacyclotetradecane (cyclam) as a building block to prepare multidentate dithiocarbamate ligands with the aim of preparing magnetic 2D sheet-like structures with large cavities.

Conclusions

The piperazine-based dithiocarbamate complexes reported here demonstrate how the construction of multimetallic arrays can be achieved in a controlled, stepwise manner. This approach has great potential for the fabrication of materials incorporating a wide range of metal centres whose properties (e. g., redox, CVD, host-guest chemistry) can be tailored.

Acknowledgments

We gratefully acknowledge the Ramsay Memorial Trust for provision of a Fellowship (J. D. E. T. W.-E.) and the EPSRC for a Case studentship (D. S.). We also thank the Department of Chemistry, UCL, The Central Research Fund, the UCL Graduate School and Cognis Ltd for funding and Johnson Matthey Ltd for a generous loan of ruthenium salts.

[1] G. Hogarth, *Prog. Inorg. Chem.* **2005**, *53*, 71–561.
[2] A. M. Bond, R. L. Martin, *Coord. Chem. Rev.* **1984**, *54*, 23–98.
[3] a) P. D. Beer, N. G. Berry, A. R. Cowley, E. J. Hayes, E. C. Oates, W. W. H. Wong, *Chem. Commun.* **2003**, 2408–2409; b) W. W. H. Wong, D. Curiel, A. R. Cowley, P. D. Beer, *Dalton Trans.* **2005**, 359–364; c) P. D. Beer, A. G. Cheetham, M. G. B. Drew, O. D. Fox, E. J. Hayes, T. D. Rolls, *Dalton Trans.* **2003**, 603–611; d) P. D. Beer, N. Berry, M. G. B. Drew, O. D. Fox, M. E. Padilla-Tosta, S. Patell, *Chem. Commun.* **2001**, 199–200; e) M. E. Padilla-Tosta, O. D. Fox, M. G. B. Drew, P. D. Beer, *Angew. Chem. Int. Ed.* **2001**, *40*, 4235–4239; f) O. D. Fox, M. G. B. Drew, P. D. Beer, *Angew. Chem. Int. Ed.* **2000**, *39*, 135–140.
[4] a) T. Trindade, P. O'Brien, *J. Mater. Chem.* **1996**, *6*, 343–347; b) M. Green, P. O'Brien, *Chem. Commun.* **1999**, 2235–2241; c) T. Trindade, P. O'Brien, N. L. Pickett, *Chem. Mater.* **2001**, *13*, 3843–3858.
[5] J. Dunderdale, T. A. Watkins, *Chem. Ind. (London)* **1956**, 174–175 and references cited therein.
[6] Some metal complexes of piperazine dithiocarbamates have been reported: a) K. S. Siddiqi, F. R. Zaidi, S. A. A. Zaidi, *Synth. React. Inorg. Met.-Org. Chem.* **1980**, *10*, 569–578; b) G. Marcotrigiano, G. C. Pellacani, C. Preti, G. Tosi, *Bull. Chem. Soc. Jpn.* **1975**, *48*, 1018–1020; c) A. Hulanicki, L. Shishkova, *Chem. Anal. (Warsaw)* **1965**, *10*, 837–845.
[7] B. P. Sullivan, T. J. Meyer, *Inorg. Chem.* **1982**, *21*, 1037–1040.
[8] Representative syntheses: a) Zwitterion **1** (26 mg, 0.161 mmol) and $NaBF_4$ (23 mg, 0.210 mmol) were suspended in methanol (20 mL) and *cis*-$[RuCl_2(dppm)_2]$ (100 mg, 0.106 mmol) added as a dichloromethane (10 mL) solution. The reaction was heated at reflux for 10 min and then stirred for 2 h. All solvent was removed and the residue was taken up in a minimum amount of dichloromethane and filtered through diatomaceous earth. Addition of ethanol (30 mL) and reduction of solvent volume by rotary evaporation yielded complex **2** (93 mg, 73%). b) Complex **2** (100 mg, 0.083 mmol) was dissolved in dichloromethane (10 mL) and treated with NEt_3 (5 drops, excess) and stirred for 5 min. Carbon disulfide (3 drops, excess) was added and the reaction stirred for 5 min to generate complex **3**. $[Os(CH=CHC_6H_4Me\text{-}4)Cl(CO)(BTD)(PPh_3)_2]$ (86 mg, 0.083 mmol) was added as a dichloromethane solution (10 mL) and the reaction was stirred for 1 h. All solvent was removed

 © 2005 Wiley-VCH Verlag GmbH & Co. KGaA, Weinheim

and the residue was taken up in a minimum amount of dichloromethane and filtered through diatomaceous earth. Addition of ethanol (30 mL) and reduction of solvent volume by rotary evaporation yielded complex **5** (121 mg, 71%).

[9] Characterisation data for new complexes. **1**: IR (KBr/nujol): $\tilde{\nu}$ = 1601 [ν(CS)], 1580, 1265, 1227, 1207, 1134, 1119, 1015, 966, 897 cm^{-1}. ^{1}H NMR ($CDCl_3$): δ = 2.88 (m, 4 H, $H_2CNH_2CH_2$), 4.30 (s, 2 H, NH_2), 4.31 [m, 4 H, $H_2CN(CS_2)CH_2$] ppm. MS(EI): *m*/*z* = 162 [M]$^+$. $C_5H_{10}N_2S_2$ (162.28): calcd. C 37.0, H 6.2, N 17.3; found C 37.7, H 6.5, N 17.5. **2**: IR (KBr/nujol): $\tilde{\nu}$ = 1585, 1574, 1312, 1269, 1236, 1190, 1161, 1057 [ν(BF)], 918, 849 cm^{-1}. ^{31}P{^{1}H} NMR ($CDCl_3$): δ = –3.8, –17.3 [2 t, J_{PP} = 34.4 Hz, dppm] ppm. ^{1}H NMR ($CDCl_3$): δ = 2.35 [br. s, 2 H, NH_2], 3.04, 3.88 [2m, 2×4 H, NC_4H_8N], 4.53, 4.91 [2 m, 2×2 H, PCH_2P], 6.48–7.57 [6 m, 40 H, C_6H_5] ppm. FAB-MS: *m*/*z* (abundance) = 1030 (100) [M]$^+$. $C_{55}H_{53}BF_4N_2P_4RuS_2{\cdot}0.5CH_2Cl_2$ (1160.41): calcd. C 57.5, H 4.7, N 2.4; found C 57.8, H 4.6, N 2.5 (this recrystallised material was analysed as the deprotonated monotetrafluoroborate salt, [dppm$_2$Ru($S_2CNC_4H_8NH$)]BF_4). **4**: IR (KBr/nujol): $\tilde{\nu}$ = 1614, 1574, 1310, 1278, 1219, 1057 [ν(BF)], 918, 849 cm^{-1}. ^{31}P{^{1}H} NMR ($CDCl_3$): δ = –4.1, –16.8 [2 t, J_{PP} = 34.2 Hz, dppm] ppm. ^{1}H NMR ($CDCl_3$): δ = 3.51, 3.62 [2 d, J_{HH} = 9.5 Hz, 8 H, ax/eq-NC_4H_8N], 4.56, 4.91 [2 m, 2×4 H, PCH_2P], 6.50, 6.93, 7.03, 7.26, 7.38, 7.63 [6 m, 80 H, C_6H_5] ppm. FAB-MS: *m*/*z* (abundance) = 2063 (20) [M + BF_4]$^+$, 1976 (13) [M]$^+$. $C_{106}H_{96}B_2F_8N_2P_8Ru_2S_4{\cdot}CH_2Cl_2$ (2234.68): calcd. C 57.5, H 4.4, N 1.3; found C 57.3, H 4.6, N 1.3. **5:** IR (KBr/nujol): $\tilde{\nu}$ = 1898 [ν(CO)], 1614, 1310, 1217, 1188, 1057 [ν(BF)], 918, 847 cm^{-1}. ^{31}P{^{1}H} NMR ($CDCl_3$): δ = 9.3 [s, PPh_3], –4.4, –17.1 [2 t, J_{PP} = 34.4 Hz, dppm] ppm. ^{1}H NMR ($CDCl_3$): δ = 2.21 (s, 3 H, CH_3), 2.78–3.33 (m br., 8 H, NC_4H_8N), 4.64, 4.97 (2 m, 2×2 H, PCH_2P), 5.59 [d, J_{HH} = 17.1 Hz, 1 H, Hβ], 6.36, 6.81 [$(AB)_2$, J_{AB} = 8.0 Hz, 4 H, C_6H_4], 6.52, 6.93, 6.96, 7.26, 7.61 [5m, 70 H, C_6H_5], 8.28 [dt, J_{HH} = 17.1, J_{HP} = 2.6 Hz, 1 H, Hα] ppm. FAB-MS: *m*/*z* (abundance) = 1967 (38) [M]$^+$. $C_{102}H_{91}BF_4N_2OOsP_6RuS_4{\cdot}CH_2Cl_2$ (2137.97): calcd. C 57.9, H 4.4, N 1.3; found C 57.7, H 4.5, N 1.3. **6**: IR (KBr/nujol): $\tilde{\nu}$ = 1585, 1572, 1310, 1277, 1207, 1155, 1055 [ν(BF)], 912, 849 cm^{-1}. ^{31}P{^{1}H} NMR ([D_6]acetone): 37.5 [br. s, PPh_3], –3.0, –18.0 [2 t, J_{PP} = 34.5 Hz, dppm] ppm. ^{1}H NMR ([D_6]-acetone): δ = 3.73, 3.92, 4.14, 4.23 (4 m, 8 H, NC_4H_8N), 4.75, 5.36 (2 m, 2×2 H, PCH_2P), 6.69, 7.00, 7.24, 7.40, 7.60, 7.63 (6 m, 55 H, C_6H_5) ppm. FAB-MS: *m*/*z* (abundance) = 1566 (3) [M]$^+$. $C_{74}H_{67}AuBF_4N_2P_5RuS_4$ (1652.33): calcd. C 53.8, H 4.1, N 1.7; found C 54.0, H 4.0, N 1.6. **7**: IR (KBr/nujol): $\tilde{\nu}$ = 1574, 1308, 1278, 1219, 1157, 1055 [ν(BF)], 907, 849 cm^{-1}. ^{31}P{^{1}H} NMR ($CDCl_3$): δ = –4.2, –16.9 (2 t, J_{PP} = 34.2 Hz, dppm) ppm. ^{1}H NMR ($CDCl_3$): δ = 2.92 [s, 6 H, CH_3], 3.71, 3.79 (2 m, 8 H, NC_4H_8N), 4.01 (s, 2 H, CCH_2), 4.64, 4.96 (2 m, 2×2 H, PCH_2P), 6.53, 6.94, 7.03, 7.17, 7.31, 7.62 (6 m, 40 H + 4 H, C_6H_5 + C_6H_4) ppm. FAB-MS: *m*/*z* (abundance) = 1346 (12) [M]$^+$. $C_{65}H_{64}BF_4N_3P_4PdRuS_4{\cdot}0.5CH_2Cl_2$ (1476.16): calcd. C 53.3, H 4.4, N 2.9; found C 53.1, H 5.0, N 3.2. **8**: IR (KBr/nujol): $\tilde{\nu}$ = 1614, 1559, 1308, 1279, 1221, 1192, 1057 [ν(BF)], 910, 849 cm^{-1}. ^{31}P{^{1}H} NMR ($CDCl_3$): δ = –4.2, –16.8 (2 t, J_{PP} = 34.5 Hz, dppm) ppm. ^{1}H NMR ($CDCl_3$): δ = 3.58 (m, 16 H, NC_4H_8N), 4.64, 4.98 (2m, 2×4 H, PCH_2P), 6.52, 6.94, 7.03, 7.18, 7.26, 7.38, 7.61 (7 m, 80 H, C_6H_5) ppm. FAB-MS: *m*/*z* (abundance) = 2271 (9) [M]$^+$. $C_{112}H_{104}B_2F_8N_4NiP_8Ru_2S_8$ (2444.84): calcd. C 55.0, H 4.3, N 2.3; found C 55.4, H 4.2, N 2.2. **9**: IR (KBr/nujol): $\tilde{\nu}$ = 1585, 1572, 1310, 1279, 1221, 1157, 1057 [ν(BF)], 910, 849 cm^{-1}. ^{31}P{^{1}H} NMR ($CDCl_3$): δ = –4.2, –16.8 (2t, J_{PP} = 34.3 Hz, dppm) ppm. ^{1}H NMR ($CDCl_3$): δ = 4.61, 4.96 (2 br. s, 2×4 H, PCH_2P), 6.52, 6.93, 7.03, 7.32, 7.62 [5 br. s, 80 H, PC_6H_5] ppm (NC_4H_8N not observed due to effect of paramagnetism). FAB-MS: *m*/*z* (abundance) = 2276 (3) [M]$^+$. $C_{112}H_{104}B_2CuF_8N_4P_8Ru_2S_8{\cdot}CH_2Cl_2$ (2534.63): calcd. C 53.6, H 4.2, N 2.2; found C 53.4, H 4.2, N 2.2.

[10] Single crystals of **4** were grown by slow evaporation of a concentrated solution of the complex in chloroform. Crystal data for **4**: [{Ru(dppm$_2$($S_2CNC_4H_8NCS_2$)][BF_4]$_2{\cdot}3CHCl_3$, $C_{109}H_{99}B_2Cl_9F_8N_2P_8Ru_2S_4$, *M* = 2507.71, monoclinic, space group $P2_1/n$, *a* = 22.2606(14), *b* = 22.2816(14), *c* = 22.5341(14) Å, β = 80.1650(10)°, *U* = 11012.7(12) Å^3, *Z* = 4, *T* = 150(2) K, μ(Mo-K_α) = 0.747 mm^{-1}, $D_{calcd.}$ = 1.512 g cm^{-3}, 26374 independent reflections measured, 10556 $I \geq 2\sigma(I)$, R_1 = 0.1020, R_w = 0.1675. Data reduction and refinement were carried using the SHELXTL PLUS V6.10 program package. The supplementary crystallographic data for this structure, CCDC-266476 contains the supplementary crystallographic data for this paper. These data can be obtained free of charge from The Cambridge Crystallographic Data Centre via www.ccdc.cam.ac.uk/data_request/cif.

[11] I. Kovács, A.-M. Lebuis, A. Shaver, *Organometallics* **2001**, *20*, 35–41.

Received: May 15, 2005
Published Online: August 17, 2005

 © 2005 Wiley-VCH Verlag GmbH & Co. KGaA, Weinheim

Shape-Induced Enhanced Luminescent Properties of Red Phosphors: $Sr_2MgSi_2O_7:Eu^{3+}$ Nanotubes

Junxi Wan,[a] Zhenghua Wang,[a] Xiangying Chen,[a] Li Mu,[a] and Yitai Qian*[a]

Keywords: Nanotubes / Silicates / Hydrothermal synthesis / Photoluminescence

$Sr_2MgSi_2O_7:Eu^{3+}$ nanotubes with red phosphor luminescent properties were successfully synthesized via a low-temperature hydrothermal route in order to understand the underlying relationship between shape and luminescent properties. The one-dimensional shape results in an obvious improvement of color purity. From emission spectra, the relative intensity of $^5D_0\rightarrow{}^7F_2$ to $^5D_0\rightarrow{}^7F_1$ transitions in tubular phosphors is higher than that of bulk material. The better color purity results from the more distorted lattices and relatively lower crystal symmetry around Eu^{3+} ions, which ascribes to the large surface area due to synthesize it in the form of nanotubes. Furthermore, the as-synthesized tubular red phosphor has shorter fluorescent lifetime and blue-shift phenomenon in excitation spectra than that of the bulk counterpart. Based on these results, shape-induced luminescent properties improvement is proposed as an efficient way to obtain red phosphors with high color purity.

(© Wiley-VCH Verlag GmbH & Co. KGaA, 69451 Weinheim, Germany, 2005)

Introduction

Since decades, phosphors doped with rare earth ions have attracted great interest.[1–4] Among those rare earth ions, the Eu^{3+} ion as a red luminescent activator in many host materials[5–10] has been studied intensively. Major emissions are centered at 590 nm ($^5D_0\rightarrow{}^7F_1$) and 616 nm ($^5D_0\rightarrow{}^7F_2$), corresponding well to orange and red color, respectively. So, the relative intensities of $^5D_0\rightarrow{}^7F_2$ to $^5D_0\rightarrow{}^7F_1$ transitions in phosphors are important for their applications. In order to obtain red phosphors with high color purity, it is necessary to increase the relative intensity of $^5D_0\rightarrow{}^7F_2$ to $^5D_0\rightarrow{}^7F_1$ transitions. It is well known that the relative intensities of the $^5D_0\rightarrow{}^7F_2$ to $^5D_0\rightarrow{}^7F_1$ transitions strongly depend on the local symmetry of Eu^{3+} ions.[11–13] The peak at 616 nm is due to the forced electric dipole transition ($^5D_0\rightarrow{}^7F_2$), which is allowed on condition that the europium ion occupies a site without an inverse center. Its intensity is hypersensitive to crystal environments. A relatively strong $^5D_0\rightarrow{}^7F_2$ transition is associated with a relatively low local symmetry of Eu^{3+} ions. The better color purity might result from the more distorted lattices and relatively lower crystal symmetry. Consequently, a change of the crystal structure of host materials can produce a good red phosphor.[14] However, shape and size are now regarded as particularly important factors influencing the chemical and physical properties of the materials.[11–13,15–21] If materials were fabricated in the form of a one-dimensional nanostructure, they would be expected to be highly functionalized materials as a result of both shape-specific and quantum confinement effects, acting as optically functional host materials. Based on this viewpoint, a possible way to improve the performance of current phosphors is to synthesize them in the form of 1D nanostructures. Nanotubes possess especially large surface area and high surface energy owing to their inner and outer surfaces, which could lead to a high degree of disorder and correspondent lower symmetry of crystal field around Eu^{3+} ions.[16,17] This lower symmetry of the crystal field will result in a higher relative intensity of $^5D_0\rightarrow{}^7F_2$ to $^5D_0\rightarrow{}^7F_1$ transitions. Therefore, it is favorable to get red phosphors with high color purity while the host materials are fabricated in the form of nanotubes. Only few efforts have been made to test and apply this idea and to develop new red phosphors.

We have synthesized a tubular Eu^{3+}-doped $Sr_2MgSi_2O_7$ red phosphor via a hydrothermal route. The as-synthesized phosphor has better color purity, which illustrates the validity and practicability of the idea that shape influences the improvement of luminescent properties. To our best knowledge, this is the first report about hydrothermal synthesis of Eu^{3+}-doped $Sr_2MgSi_2O_7$ nanotubes.

Results and Discussion

The phase purity and phase structure of as-prepared samples were characterized by the X-ray powder diffraction (XRD) patterns, using a Philips X′pert X-ray diffractometer equipped with graphite-monochromatized Cu-

[a] Hefei National Laboratory for Physical Sciences at Microscale and Department of Chemistry, University of Science and Technology of China,
Hefei, Anhui 230026, People's Republic of China
Fax: +86-551-3607402
E-mail: ytqian@ustc.edu.cn

Kα radiation (λ = 1.54178 Å). Samples for XRD analysis were prepared by dispersing the as-synthesized phosphors into absolute ethanol, then spreading several drops of this suspension on a clear silicon wafer, and then letting the solvent evaporate slowly at room temperature. The transmission electron microscopy (TEM) images and corresponding selected area electron diffraction (SAED) pattern were performed with a Hitachi H-800 transmission electron microscope using an accelerating voltage of 200 kV. Photoluminescence (PL) spectra and luminescent decay curve were recorded on a Fluorolog-3-TAU fluorescence spectrophotometer with an Hg lamp at room temperature.

Figure 1 shows the XRD patterns of as-synthesized Eu^{3+}-doped $Sr_2MgSi_2O_7$ red phosphors. All the diffraction peaks can readily be indexed to a pure tetragonal structured $Sr_2MgSi_2O_7$ with cell constants of a = 7.993 Å, and c = 5.158 Å, which are in good agreement with the values in the literate (JCPDS card No. 75–1736, a = 7.996 Å, and c = 5.152 Å). No obvious impurity phase can be detected. Compared to the XRD patterns of bulk phosphor (Figure 1, a) and as-synthesized sample (Figure 1, b), the intensity of the XRD peaks from as-synthesized sample is weaker than that of the bulk phosphor. Some weak peaks in Figure 1 (b) are nearly invisible. The intensification of peaks from bulk phosphor would result in improved luminescent intensity due to the increase of crystallinity. Table 1 shows representative comparisons of half-width and relative intensities of the XRD peaks from bulk and as-prepared sample. In Table 1, only the eight strongest peaks of both XRD patterns are listed. The differences of the eight strongest peaks of both XRD patterns are sufficient to demonstrate the fine-structural differences in the bulk and as-prepared phosphors. The differences of relative intensities of the XRD peaks indicate that the as-synthesized sample has a tendency to grow only in one direction. The increase of half-width of XRD peaks from as-prepared sample indicates the nanometer-scale sizes of sample. These differences in XRD peaks would lead to enhanced luminescent properties of phosphors. These results are further evidenced by the following TEM images and luminescent spectra.

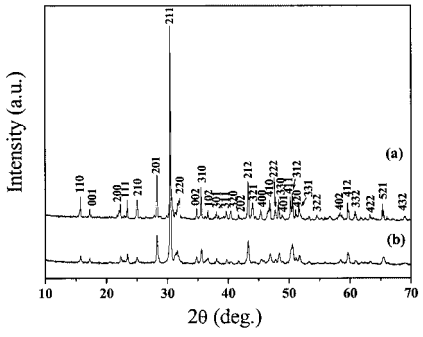

Figure 1. XRD patterns of the as-synthesized (a) bulk $Sr_2MgSi_2O_7$:Eu^{3+} and (b) $Sr_2MgSi_2O_7$:Eu^{3+} nanotubes.

TEM analysis has provided further insight into the microstructural details of these nanotubes. As shown in Figure 2, all samples dispersed on to the TEM copper grids have uniform nanotube morphologies with open ends. The as-synthesized nanotubes have diameters of about 15 nm and lengths up to several hundreds of nanometer. Figure 2 (b) shows two $Sr_2MgSi_2O_7$ nanotubes (the white arrows shown) parallel to the electron beam, from which the hollow structure features can be clearly seen with an inner diameter of about 10 nm and an outer diameter of about 20 nm. The electron diffraction patterns (inset in Figure 2, b), taken from bundles of $Sr_2MgSi_2O_7$ nanotubes, indicate that the nanotubes are crystalline. This result is in agreement with that of XRD pattern.

Table 1. Comparisons of eight strongest peaks in XRD patterns from bulk $Sr_2MgSi_2O_7$:Eu^{3+} and $Sr_2MgSi_2O_7$:Eu^{3+} nanotubes, respectively.

Indexing peaks	Bulk $Sr_2MgSi_2O_7$:Eu^{3+}		$Sr_2MgSi_2O_7$:Eu^{3+} nanotubes	
	Relative intensity	Half-width [mm]	Relative intensity	Half-width [mm]
110	12%	0.161		
201	23%	0.123	26%	0.191
211	100%	0.120	100%	0.196
310	17%	0.121	14%	0.286
212	20%	0.020	22%	0.260
330	10%	0.135	11%	0.297
411	11%	0.129	14%	0.279
312	13%	0.125	18%	0.271
412			12%	0.201

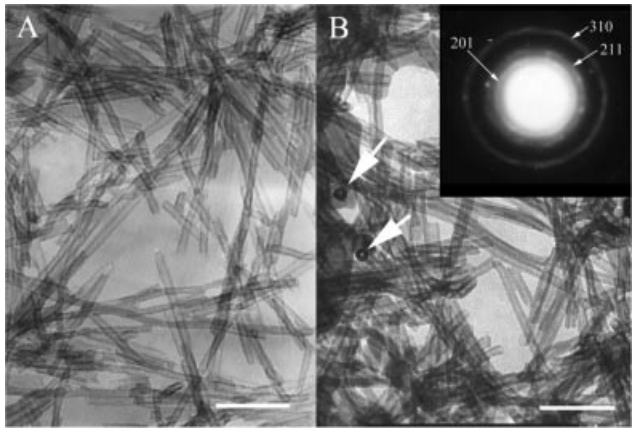

Figure 2. Representative TEM images and SAED pattern of synthesized samples; length of bar: 100 nm.

The excitation spectra of Eu^{3+}-doped $Sr_2MgSi_2O_7$ nanotubes and bulk phosphor for the emission at 616 nm are shown in Figure 3. The broad band on the excitation spectra is excitation from the ground state of the 4f shell to an Eu–O charge transfer state.[22] Moreover, the CTS (charge transfer state absorption) peak position of $Sr_2MgSi_2O_7$ nanotubes shows a blue-shift phenomenon compared with the bulk counterpart. The CTS peaks of the nanotubes and bulk phosphor center at 250 nm and 261 nm, respectively. A similar observation was reported in nanometer Y_2O_3:Eu phosphor.[19] The sharp absorption peaks on excitation

 © 2005 Wiley-VCH Verlag GmbH & Co. KGaA, Weinheim

spectra is a characteristic of rare earth ions as a result of transitions within the 4f shell, which is shielded from environmental effects by the outer shell electrons.[23] Thus, these peaks position are consistent.

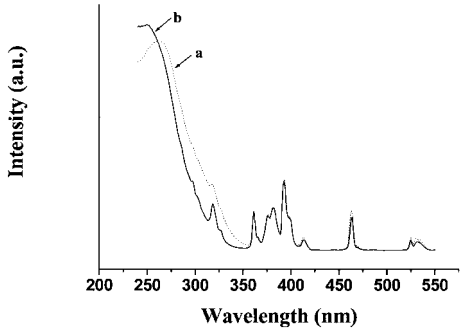

Figure 3. Excitation spectra of (a) bulk $Sr_2MgSi_2O_7$:Eu^{3+} phosphor, (b) $Sr_2MgSi_2O_7$:Eu^{3+} nanotubes.

Figure 4 shows the emission spectra of as-synthesized Eu^{3+}-doped $Sr_2MgSi_2O_7$ nanotubes and bulk phosphor. Both of them consist of two main peaks centered at 590 nm and 616 nm, which come from the transitions of $^5D_0 \rightarrow {}^7F_1$ and $^5D_0 \rightarrow {}^7F_2$, respectively. The most intense emission is the $^5D_0 \rightarrow {}^7F_2$ transition located in 616 nm, corresponding to the red emission, in good accordance with the Judd–Ofelt theory.[24] Compared with the bulk phosphor, the luminescent properties of as-synthesized $Sr_2MgSi_2O_7$ nanotubes are obviously enhanced. The emission intensity of the $^5D_0 \rightarrow {}^7F_2$ transition is 3.2 times that of the $^5D_0 \rightarrow {}^7F_1$ transition. However, the ratio only is 1.7 for bulk phosphor. Only the emission peak located at 616 nm of $Sr_2MgSi_2O_7$ nanotubes has a remarkable enhancement than that of bulk phosphor. This phenomenon indicates that more Eu^{3+} occupy sites with relatively low local symmetry. These results prove the idea that red phosphors with high color purity can be obtained by changing the shape of host materials.

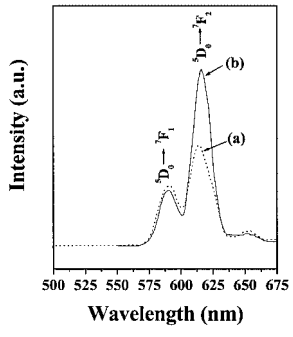

Figure 4. Emission spectra of (a) bulk $Sr_2MgSi_2O_7$:Eu^{3+} phosphor, (b) $Sr_2MgSi_2O_7$:Eu^{3+} nanotubes.

The decay time of Eu^{3+} fluorescence of Eu^{3+}-doped $Sr_2MgSi_2O_7$ nanotubes and bulk phosphor were measured at room temperature. Figure 5 shows the results that the lifetime values are 1.2 ms of $Sr_2MgSi_2O_7$ nanotubes and 2.3 ms of bulk phosphor, respectively. Similar phenomena was observed in nanometer ZnS:Mn^{2+}[25] and Y_2O_3:Eu^{3+} phosphors.[26] The shorter lifetime value can be attributed to the fact that the $Sr_2MgSi_2O_7$ nanotubes have relatively more defects, which results from the increase of the surface/volume ratio in the nanotubes. The shorter decay time is beneficial to PDP (plasma display panel) applications. With further optimization, Eu^{3+}-doped $Sr_2ZnSi_2O_7$ may serve as good red phosphor candidates. Further research is underway.

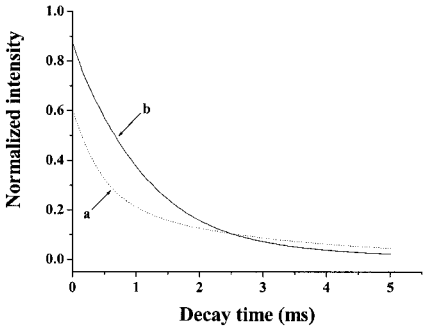

Figure 5. Normalized decay curve of (a) bulk $Sr_2MgSi_2O_7$:Eu^{3+} phosphor, (b) $Sr_2MgSi_2O_7$:Eu^{3+} nanotubes.

Conclusions

In summary, we have successfully synthesized pure tetragonal phased $Sr_2MgSi_2O_7$:Eu^{3+} nanotubes via a low-temperature hydrothermal route at 200 °C for 2 days. The resulting tubular red phosphor has a shorter decay time than that of the bulk counterpart. A close study of the excitation spectra points to a blue-shift phenomenon for the $Sr_2MgSi_2O_7$:Eu^{3+} nanotubes. The emission spectra show that the as-prepared tubular red phosphor has a better color purity than the bulk counterpart. The improvement of luminescent properties was analyzed and the influence of shape on luminescence was explored. Based on these results, shape-induced luminescent properties improvement is a simple and efficient way to obtain red phosphors with high color purity. This idea provides helpful guidance for the application of the $Sr_2MgSi_2O_7$:Eu^{3+} red phosphor. Furthermore, this strategy may also be applied to other rare earth ion-doped phosphors.

Experimental Section

All reagents were purchased from Shanghai Chemical Reagent Co. and used without further purification. Distilled water and absolute ethanol, degassed with N_2 for one hour, were used. In a typical procedure, 2 mmol of $Sr(NO_3)_2$, 1 mmol of $Mg(NO_3)_2 \cdot 6H_2O$, and 0.1 mmol of $EuCl_3$ were dissolved in a mixture of 5 mL of distilled water and 30 mL of absolute ethanol whilst stirring in a Teflon liner of 60 mL capacity. Then an aqueous solution of 2 mmol of $Na_2SiO_3 \cdot 9H_2O$ dissolved in 5 mL of distilled water was slowly added. After about 10 minutes, the aqueous solution of 1 g of NaOH dissolved in 5 mL of distilled water and 2 mL of 85% $N_2H_4 \cdot H_2O$ were added whilst stirring. Hydrazine hydrate was used to prevent reduction of Eu^{3+}. Finally, the mixture was degassed with N_2 for another one hour. Then, the liner was sealed in a stainless steel autoclave, first aged at 90 °C for 12 h, and then maintained at 220 °C for 2 days. After cooled to room temperature naturally,

 © 2005 Wiley-VCH Verlag GmbH & Co. KGaA, Weinheim

the resulting white solid products were filtered off, washed with distilled water and absolute ethanol for several times, respectively, and finally calcined in air at 800 °C for 6 h. For comparison, Eu^{3+}-doped $Sr_2MgSi_2O_7$ red phosphor was also prepared via solid-state reaction at 1300 °C for 3 h in air according to the literature.[27] The as-synthesized sample was finely ground to give a powder that was used for further characterization.

Acknowledgments

This work was supported by the National Natural Science Foundation of China and the 973 Project of China.

[1] G. Wakefield, E. Holland, P. J. Dobson, J. L. Hutchison, *Adv. Mater.* **2001**, *13*, 1557–1560.
[2] H. Lin, E. Y. B. Pun, X. J. Wang, X. R. Liu, *J. Alloys Compd.* **2005**, *390*, 197–201.
[3] A. N. Georgobiani, A. N. Gruzintsev, C. Barthou, P. Benalloul, *Inorg. Mater.* **2004**, *40*, 840–844.
[4] Y. Liu, C. N. Xu, *Appl. Phys. Lett.* **2004**, *84*, 5016–5018.
[5] Q. L. Liu, Y. Bando, F. F. Xu, C. C. Tang, *Appl. Phys. Lett.* **2004**, *85*, 4890–4892.
[6] O. Lehmann, K. Kompe, M. Haase, *J. Am. Chem. Soc.* **2004**, *126*, 14935–14942.
[7] Y. Zhang, Y. D. Li, *J. Alloys Compd.* **2004**, *370*, 99–103.
[8] S. S. Yi, J. S. Bae, B. K. Moon, J. H. Jeong, J. H. Kim, *Appl. Phys. Lett.* **2005**, *86*, 071921.
[9] A. Huignard, V. Buissette, A. C. Franville, T. Gacoin, J. P. Boilot, *J. Phys. Chem. B* **2003**, *107*, 6754–6759.
[10] J. H. Kang, W. B. Im, D. C. Lee, J. Y. Kim, D. Y. Jeon, Y. C. Kang, K. Y. Jung, *Solid State Commun.* **2005**, *133*, 651–656.
[11] Z. G. Wei, L. D. Sun, C. S. Liao, J. L. Yin, X. C. Jiang, C. H. Yan, *J. Phys. Chem. B* **2002**, *106*, 10610–10617.
[12] Z. G. Wei, L. D. Sun, C. S. Liao, X. C. Jiang, C. H. Yan, *J. Appl. Phys.* **2003**, *93*, 9783–9788.
[13] Z. G. Wei, L. D. Sun, X. C. Jiang, C. S. Liao, C. H. Yan, Y. Tao, J. Zhang, T. D. Hu, Y. N. Xie, *Chem. Mater.* **2003**, *15*, 3011–3017.
[14] C. J. Jia, L. D. Sun, F. Luo, X. C. Jiang, L. H. Wei, C. H. Yan, *Appl. Phys. Lett.* **2004**, *84*, 5305–5307.
[15] X. C. Jiang, L. D. Sun, C. H. Yan, *J. Phys. Chem. B* **2004**, *108*, 3387–3390.
[16] G. S. Wu, Y. Lin, X. Y. Yuan, T. Xie, B. C. Cheng, L. D. Zhang, *Nanotechnology* **2004**, *15*, 568–571.
[17] C. F. Wu, W. P. Qin, G. S. Qin, D. Zhan, J. S. Zhang, S. H. Huang, S. Z. Lu, H. Q. Liu, H. Y. Lin, *Appl. Phys. Lett.* **2003**, *82*, 520–522.
[18] Y. He, Y. Tian, Y. F. Zhu, *Chem. Lett.* **2003**, *32*, 862–863.
[19] T. Igarashi, M. Ihara, T. Kusunoki, K. Ohno, T. Isobe, M. Senna, *Appl. Phys. Lett.* **2000**, *76*, 1549–1551.
[20] D. K. Williams, H. Yuan, B. M. Tissue, *J. Lumin.* **1999**, *83–84*, 297–300.
[21] G. Wang, Z. D. Wang, Y. X. Zhang, G. T. Fei, L. D. Zhang, *Nanotechnology* **2004**, *15*, 1307–1311.
[22] M. Yin, W. Zhang, S. Xia, J.-C. Krupa, *J. Lumin.* **1996**, *68*, 335–339.
[23] G. Blasse, *Handbook on the Physics and Chemistry of Rare Earths*, vol. 4, North Holland, Amsterdam, **1976**.
[24] B. R. Judd, *Phys. Rev.* **1962**, *127*, 750–761.
[25] R. N. Bhargava, D. Gallagher, X. Hong, A. Nurmikko, *Phys. Rev. Lett.* **1994**, *72*, 416–419.
[26] W. W. Zhang, W. P. Zhang, P. B. Xie, M. Yin, H. T. Chen, L. Jing, Y. S. Zhang, L. R. Lou, S. D. Xia, *J. Colloid Interface Sci.* **2003**, *262*, 588–593.
[27] Y. H. Lin, C. W. Nan, X. S. Zhou, J. B. Wu, H. F. Wang, D. P. Chen, S. M. Xu, *Mater. Chem. Phys.* **2003**, *82*, 860–863.

Received: June 4, 2005
Published Online: September 12, 2005

 © 2005 Wiley-VCH Verlag GmbH & Co. KGaA, Weinheim

Electrochemical Deposition of $Ni(OH)_2$ and Fe-Doped $Ni(OH)_2$ Tubes

Shulei Chou,[a] Fangyi Cheng,[a] and Jun Chen*[a]

Keywords: Nickel hydroxide / Iron doping / Tubes / Electrochemical deposition / Template

Arrays of $Ni(OH)_2$ and Fe-doped $Ni(OH)_2$ tubes were successfully prepared by electrochemical deposition in porous alumina membranes under ambient conditions. Extensive analysis of the tubes was carried out by X-ray diffraction (XRD), scanning electron microscopy (SEM), transmission electron microscopy (TEM) and high-resolution transmission electron microscopy (HRTEM) equipped with energy dispersive spectroscopy (EDS), and X-ray photoelectron spectroscopy (XPS). The results show that the electrodeposition method yielded uniform $Ni(OH)_2$ and Fe-doped $Ni(OH)_2$ tubes with inner diameters of 150–180 nm, wall thicknesses of 20–30 nm, and lengths of about 60 μm. This template-based electrochemical deposition method can be extended to the synthesis of other similar materials such as micro- or nanotubes, -wires, and -rods. Furthermore, the $Ni(OH)_2$ and Fe-doped $Ni(OH)_2$ tubes may have promising applications in alkaline rechargeable batteries and electrocatalytic electrolysis for the production of hydrogen.
(© Wiley-VCH Verlag GmbH & Co. KGaA, 69451 Weinheim, Germany, 2005)

Introduction

A variety of 1D nanomaterials including nanotubes, nanorods, nanowires, and nanobelts have become a symbol of the new and fast-developing research area of nanoscience and nanotechnology.[1,2] As members of an important class of 1D nanomaterials, inorganic nanotubes[3–5] such as WS_2,[6] MoS_2,[7] BN,[8] Au,[9] Bi,[10] SiO_2,[11] VO_x,[12] and $NiCl_2$[13] have attracted much attention owing to their special properties. Substantial progress has been achieved in the synthesis of inorganic nanotubes by various methods. For example, the template synthesis,[14–16] in which a template membrane serves as a scaffold for other materials to be assembled with a morphology similar (or complementary) to that of the template pore, is a simple approach to the preparation of inorganic nanotubes such as Au,[9] Si,[17] MoS_2,[18] GaN,[19] and Bi_2O_3.[20]

Nickel hydroxide is the active material in the positive electrodes of alkaline rechargeable batteries such as nickel/cadmium (Ni/Cd), nickel/iron (Ni/Fe), nickel/metal hydride (Ni/MH), and nickel/zinc (Ni/Zn).[21] The capacities of these batteries are usually limited by the positive electrodes for reasons of proper recombination reactions and battery safety. It follows that increasing the energy density of the nickel hydroxide electrode is essential for raising the energy density of such batteries. To improve the characteristics of the nickel hydroxide electrode, much work has been focused on the development of spherical $Ni(OH)_2$ powder and related composite materials.[22–25] On one hand, spherical nickel hydroxide particles exhibit superior electrochemical behavior and higher proton diffusion coefficients.[26,27] On the other hand, the core of the spherical nickel hydroxide powder is still inactive at high-rate and high-temperature charge/discharge because of the diffusion barrier, which can be improved by using $Ni(OH)_2$ tubes.[28]

Electrolysis is an attractive process for hydrogen production from alkaline solutions when cheap solar power is available. A potentially more important application of Fe-doped $Ni(OH)_2$ tubes is their use as oxygen-evolving anodes for the electrolytic production of hydrogen. This is due to their low overpotential and stability in alkaline solution.[29] The tubelike Fe-doped $Ni(OH)_2$, which has a high specific surface area, could be very useful in hydrogen production in the future.

Electrochemical deposition, which is a convenient method to control the thickness of the deposited product, has already been used to prepare $Ni(OH)_2$ and Fe-doped $Ni(OH)_2$ thin films for a few years.[30–32] Four possible mechanisms of electrochemical deposition of $Ni(OH)_2$ from nickel nitrate solution have been proposed by MacArthur.[33] Furthermore, electrochemical deposition in Al_2O_3 templates has recently been used to prepare inorganic micro- or nanotubes of Au,[34] Co, Fe,[35] Ni,[36] Cu,[37] Pt,[38] CdS,[39] and TiO_2.[40] The process of electrochemical deposition of metal nanotubes under low-current-density conditions occurs by simultaneous deposition along the holes of the membranes.[41] However, to the best of our knowledge, the synthesis of metal hydroxide tubes or nanotubes by electrochemical deposition in templates is limited.

Here we report on the preparation of $Ni(OH)_2$ and Fe-doped $Ni(OH)_2$ tubes by electrochemical deposition in the pores of alumina membranes. The results show that the wall

[a] Institute of New Energy Material Chemistry, Nankai University,
Tianjin 300071, P.R. China
E-mail: chenabc@nankai.edu.cn

thickness of the $Ni(OH)_2$ and Fe-doped $Ni(OH)_2$ tubes is easily controlled by adjusting the reaction conditions. This method can be extended to the synthesis of other similar micro- or nanotubes, -wires, and -rods.

Results and Discussion

Figure 1 shows the XRD patterns of the α-$Ni(OH)_2$ (Figure 1a) and Fe-doped α-$Ni(OH)_2$ tubes (Figure 1b). The peaks in Figure 1a can be indexed as a hexagonal structure of α-$Ni(OH)_2$·$0.75H_2O$ with the lattice parameters a = 3.08 Å and c = 23.41 Å, which are in good agreement with the standard value (ICDD-JCPDS card 38–0715). The broadening of the peaks in the XRD pattern indicates that the product consists of nanocrystallites, in which amorphous particles may coexist. Figure 1b shows the XRD pattern of Fe-doped α-$Ni(OH)_2$ tubes. The 2θ value of each peak is in accordance with α-$Ni(OH)_2$·$0.75H_2O$ as shown in Figure 1a. However, the relative intensities of the peaks at 11.70° and 23.58° in Figure 1b are higher than those in Figure 1a. This might arise from the Fe-doping. That is, the incorporation of Fe in the Ni lattice sites of α-$Ni(OH)_2$ might have caused the intensity changes. Therefore, a further investigation by XPS was used to verify the existence and form of Fe present.

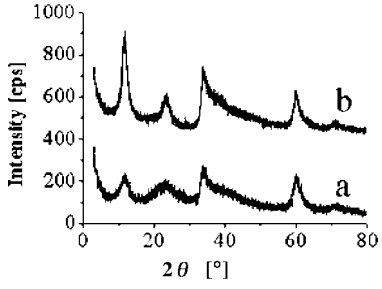

Figure 1. X-ray diffraction patterns of the α-$Ni(OH)_2$ tubes (a) and Fe-doped α-$Ni(OH)_2$ tubes (b).

Figure 2 shows the XPS spectra of the Fe-doped α-$Ni(OH)_2$ tubes. Figure 2a shows that the sample contains Fe, Ni and O. Figure 2b shows that a binding energy of 855.8 eV is assigned to Ni $2p_{3/2}$ in $Ni(OH)_2$. Figure 2c shows the Fe 2p spectrum of the tubes produced. The Fe-doped $Ni(OH)_2$ tubes contain only Fe^{III} because two binding energies of 725.3 eV and 711.1 eV were detected, which are assigned to Fe $2p_{1/2}$ and Fe $2p_{3/2}$ in Fe_2O_3, respectively.[42] Balasubramanian et al.[32] reported that cathodic codeposition of Fe^{II} with Ni^{II} led to the incorporation of Fe in the Ni lattice sites of α-$Ni(OH)_2$ and these Fe ions were present as Fe^{III}. Our XPS and XRD studies have confirmed this report and have shown that the Fe-doped $Ni(OH)_2$ tubes are Fe^{III}-doped α-$Ni(OH)_2$·$0.75H_2O$. The quantitative XPS study of Fe-doped $Ni(OH)_2$ tubes shows that the atomic ratio of Fe to Ni is 1:3.7. Since Corrigan's study shows that iron/nickel hydrous oxides with this atomic ratio are very useful in lowering the Tafel slope for catalyzing the oxygen evolution reaction,[29] we believe that the Fe^{III}-doped α-$Ni(OH)_2$·$0.75H_2O$ tubes have potential uses as electrocatalysts for alkaline electrolysis to produce hydrogen.

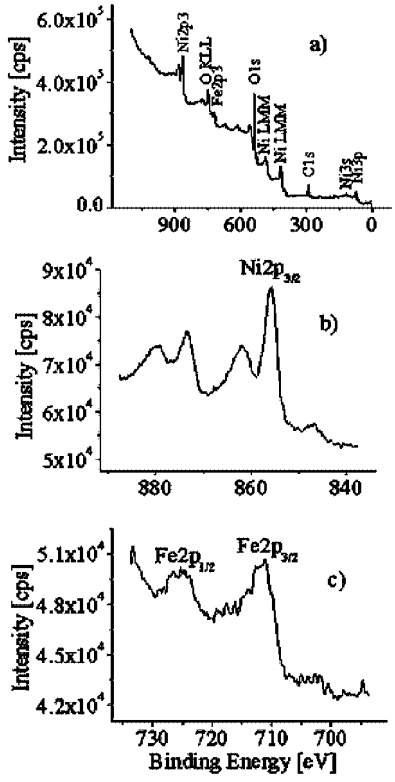

Figure 2. XPS spectra of Fe-doped $Ni(OH)_2$ tubes in the binding energy range of (a) 0–1100 eV, (b) 840–890 eV, and (c) 695–735 eV.

Figure 3 shows the SEM images of the $Ni(OH)_2$ (Figure 3a–c) and Fe-doped $Ni(OH)_2$ tubes (Figure 3d and e) at different magnifications. Figure 3a is an overall view of the $Ni(OH)_2$ tubes, which shows that bundles of standing or lying $Ni(OH)_2$ tubes were obtained. The length of the $Ni(OH)_2$ tube bundles is approximately 60 μm, which corresponds to the thickness of the template membrane employed in the synthetic process. In Figure 3a shorter and broken bundles can also be found, which may arise from the weakness of the tubes. Figure 3b shows that the $Ni(OH)_2$ tubes are arranged roughly parallel to one another with a smooth-surface alignment. This might be due to a remaining trace of the alumina matrix rather than any kind of self-organization. Figure 3c is the high-magnification SEM image of the bundle tips of the $Ni(OH)_2$ tubes which shows their open-ended character. The $Ni(OH)_2$ tubes are cylinders with a wall thickness of 20–30 nm. There is a distribution of diameters of the tubes around 200 nm because of the pore-diameter distribution of the template. Figure 3d and Figure 3e show the SEM images of Fe-doped $Ni(OH)_2$ tubes at different magnifications. Figure 3d shows a bundle of Fe-doped $Ni(OH)_2$ tubes, which is not as uniform as the $Ni(OH)_2$ tubes. Figure 3e, which is the enlargement of the square marked in Figure 3d, shows a clear view of the Fe-doped $Ni(OH)_2$ tubes with open-ended tips. It should be noted that when we removed Fe-doped $Ni(OH)_2$ tubes from the alumina membranes, almost all of them were broken.

 © 2005 Wiley-VCH Verlag GmbH & Co. KGaA, Weinheim

Thus, the Fe-doped $Ni(OH)_2$ tubes are not as long as the $Ni(OH)_2$ tubes. This may be due to the Fe doping.

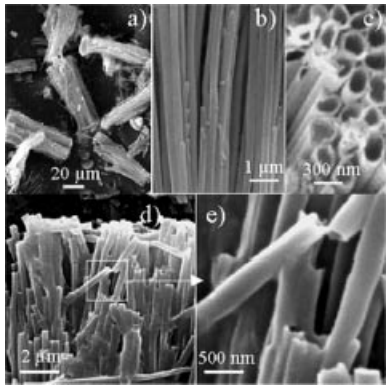

Figure 3. Typical SEM images of the $Ni(OH)_2$ (a, b, c) and Fe-doped $Ni(OH)_2$ tubes (d, e). $Ni(OH)_2$ tubes: (a) overall view, (b) walls of the tube bundles, and (c) tube bundle tips at high magnification. Fe-doped $Ni(OH)_2$ tubes: (d) low magnification and (e) enlargement of the square marked in (d).

To understand the structure in further detail, the $Ni(OH)_2$ and Fe-doped $Ni(OH)_2$ tubes were inspected with TEM (Figure 4). Figure 4a shows the TEM image of the $Ni(OH)_2$ tubes at a lower magnification. In addition to the tubes there are some particles in the product. This phenomenon arises from the strong supersonic vibrations used in the sample preparation for TEM analysis, that is, some of the tubes were broken down into shorter ones and then into particles. Figure 4b shows a TEM image of an open-ended $Ni(OH)_2$ tube. The centers of the mesostructures are bright in contrast to their edges, confirming their hollow-tube nature. The inner diameters are about 150–160 nm, and the wall thickness is about 20–30 nm. Figure 4c shows the TEM image of the tube wall. It can be seen that the surface of the tube is smooth with an amorphous structure. This is consistent with the XRD analysis. Figure 4d shows that most of the Fe-doped $Ni(OH)_2$ tubes have similar wall thickness, and there is also an interesting branchlike structure which simply reflects the structure of alumina templates. That is, the template contains not only aligned pores but also some abnormal structures that look like branches. This phenomenon also means that, if we have the template, we can also prepare some complex tubular structures by this method. A view of the open-ended Fe-doped $Ni(OH)_2$ tubes is shown in Figure 4e, from which we can estimate that the tubes have an inner diameter of about 170–180 nm. EDS analysis in Figure 5 shows that the tubes in Figure 4e contain three elements, Fe, Ni, and O, and two other elements, Cu and C, which come from the carbon-coated copper grid. This is consistent with the XRD and XPS studies. The TEM image in Figure 4f shows that the Fe-doped $Ni(OH)_2$ tubes are needlelike structures with wall thicknesses of about 20–30 nm. The needlelike structure of Fe-doped $Ni(OH)_2$ tubes is weaker than the smooth-surface structure of $Ni(OH)_2$ tubes, so it might not be easy to prepare long bundles of Fe-doped $Ni(OH)_2$ tubes like the $Ni(OH)_2$ tubes under the same conditions.

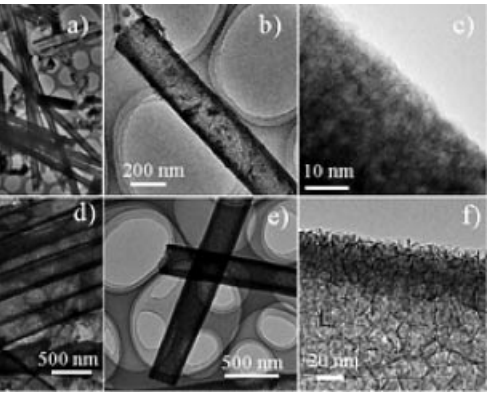

Figure 4. Representative TEM images of the $Ni(OH)_2$ (a, b, c) and Fe-doped $Ni(OH)_2$ tubes (d,e,f).

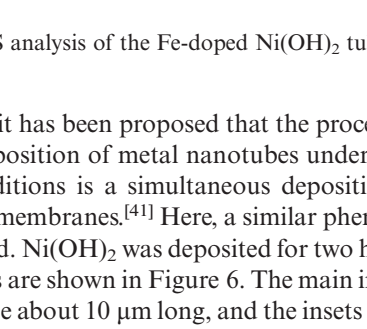

Figure 5. EDS analysis of the Fe-doped $Ni(OH)_2$ tubes taken from Figure 4e.

Recently, it has been proposed that the process of electrochemical deposition of metal nanotubes under low-current-density conditions is a simultaneous deposition along the holes of the membranes.[41] Here, a similar phenomenon was also observed. $Ni(OH)_2$ was deposited for two hours, and the TEM images are shown in Figure 6. The main image shows a $Ni(OH)_2$ tube about 10 μm long, and the insets (a, b, c and d) are the corresponding magnifications marked on the tube. The wall thickness of the $Ni(OH)_2$ tubes are different on the Au side of the membrane. It can be clearly seen from Figure 6 that the wall thickness decreases from Figure 6d to Figure 6a. This is especially evident as shown in Figure 6d where the

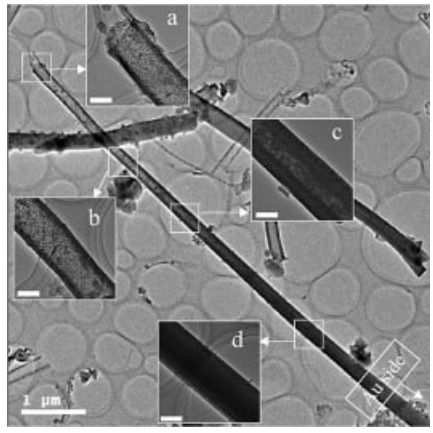

Figure 6. TEM images of $Ni(OH)_2$ deposited in the template for 2 h. The insets (a, b, c, and d) are the corresponding magnifications marked on the tube. Scale bars in the insets represent 100 nm.

 © 2005 Wiley-VCH Verlag GmbH & Co. KGaA, Weinheim

tubes are already completely filled. Therefore, when we use electrochemical deposition in templates to prepare tubular semiconductors, attention must be paid to control the deposition time. Depositing for quite a long time such as 10 h leads to wire- or rodlike semiconductors. Figure 7 shows the TEM images of $Ni(OH)_2$ rods which were deposited for 10 h. Figure 7a shows several $Ni(OH)_2$ rods which are about 6 μm long and about 200 nm in outer diameter. Figure 7b shows the smooth-surface structure which is consistent with the structure of the $Ni(OH)_2$ tubes above.

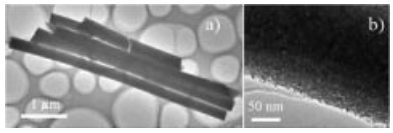

Figure 7. TEM images of the $Ni(OH)_2$ rods prepared by electrochemical deposition for 10 hours at low (a) and high (b) magnification.

Conclusions

Arrays of α-$Ni(OH)_2 \cdot 0.75H_2O$ and Fe^{III}-doped α-$Ni(OH)_2 \cdot 0.75H_2O$ tubes were prepared by electrochemical deposition in porous alumina membranes. The smooth-surface α-$Ni(OH)_2 \cdot 0.75H_2O$ tubes are more uniform and stronger than the needlelike Fe-doped α-$Ni(OH)_2 \cdot 0.75H_2O$ tubes. Nanostructures of tubes to wires or rods can be obtained by controlling the depositing conditions. It is obvious that this method of template-based electrochemical deposition can be extended for the synthesis of other similar materials such as micro- or nanotubes, -wires, and -rods.

Experimental Section

Electrochemical Deposition: A thin Au layer was evaporated onto one side of the pore walls of the alumina membranes (Whatman, Φ47 mm with 0.2-μm pores and 60 μm thickness), which was used as the working electrode for the electrochemical deposition. The Au-coated side of the alumina membrane was pasted on a Ni sheet with electric adhesive tape and the rest of the Ni tape was covered with insulated adhesive tape. The face and the side of the working electrode are schematically shown in Figure 8. The counter electrode was a nickel plate about 1.0 cm^2. The conditions for the electrochemical deposition of pure $Ni(OH)_2$ tubes and Fe-doped $Ni(OH)_2$ tubes are summarized in Table 1. Before the electrochemical deposition, the working electrode was submerged in the electrolyte, which was stirred by an electromagnetic blender, for 2 hours in order to make the electrolyte penetrate into the membranes. The electrochemical deposition was done in a plating bath under constant current and controlled temperature.

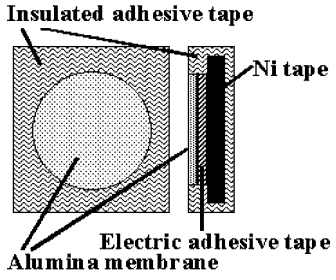

Figure 8. Schematic diagram showing the working electrode for electrochemical deposition of pure $Ni(OH)_2$ and Fe-doped $Ni(OH)_2$ tubes.

Table 1. The electrochemical deposition conditions for preparing pure $Ni(OH)_2$ and Fe-doped $Ni(OH)_2$ tubes.

Tubes	Electrolyte composition	Temp. (°C)	Curr. dens. ($mA\,cm^{-2}$)	Time (min)
$Ni(OH)_2$	0.05 M $Ni(NO_3)_2 \cdot 6H_2O$	20	10	10
Fe-doped $Ni(OH)_2$	0.05 M $Ni(NO_3)_2 \cdot 6H_2O$	20	5	20
	0.001 M $Fe(NH_4)_2(SO_4)_2 \cdot 6H_2O$			

Instrumental Analyses: The alumina membranes with the prepared samples were peeled off the Ni tape and immersed in 2 M NaOH for 4 h to remove the alumina template. After careful rinsing with deionized water, the samples were characterized using a combination of the following techniques: XRD, SEM, TEM and HRTEM equipped with EDS, and XPS.

XRD analysis was carried out with a Rigaku INT-2000 X-ray generator. The X-ray intensity was measured over a diffraction 2θ angle from 3° to 80° with a velocity of 0.02°/step and 2°/min. Specimens for SEM were collected on an electric adhesive tape and allowed to air-dry before the measurement. The electric adhesive tape with the sample was fixed to a piece of glass, which was attached to a SEM stub and then sputtered with a 2-nm layer of gold. Images were taken with a Philips XL-30 scanning electron microscope working at an accelerating voltage of 20 kV. Samples for TEM were put into an alcohol-water sonicator for about 5 min. Then the samples were collected on a carbon-coated copper grid and allowed to air-dry before the measurement. Images were obtained with a Philips Tecnai F20 TEM working at an accelerating voltage of 200 kV. EDS was performed in the microscope with use of a Kevex Super 8000 detector. The composition of the Fe-doped $Ni(OH)_2$ tubes was examined with an XPS (ESCA-3400, Shimadzu Electron) using monochromatic Mg–K_α radiation (1253.6 eV). The binding energy values were referenced to the carbon C 1*s* core peak at 284.7 eV.

Acknowledgments

This work was supported by the NSFC (20325102 and 90406001) and MoE (104055 and 2004164).

[1] T. Braun, A. P. Schubert, R. N. Kostoff, *Chem. Rev.* **2000**, *100*, 23–37.
[2] L. Hueso, N. Mathur, *Nature* **2004**, *427*, 301–304.
[3] C. N. R. Rao, M. Nath, *Dalton Trans.* **2003**, 1–24.
[4] a) G. R. Patzke, F. Krumeich, R. Nesper, *Angew. Chem. Int. Ed.* **2002**, *41*, 2446–2461; b) R. Tenne, *Angew. Chem. Int. Ed.* **2003**, *42*, 5124–5132.
[5] M. Remskar, *Adv. Mater.* **2004**, *16*, 1497–1504.
[6] R. Tenne, L. Margulis, M. Genut, G. Hodes, *Nature* **1992**, *360*, 444–446.
[7] Y. Feldman, E. Wasserman, D. J. Srolovitz, T. Tenne, *Science* **1995**, *267*, 222–225.
[8] N. G. Chopra, R. G. Luyken, K. Cherrey, V. H. Crespi, M. L. Cohen, S. G. Louie, A. Zettl, *Science* **1995**, *269*, 966–967.
[9] J. C. Hutleen, K. B. Jirage, C. R. Martin, *J. Am. Chem. Soc.* **1998**, *120*, 6603–6604.
[10] a) Y. D. Li, J. W. Wang, Z. X. Deng, Y. Y. Wu, X. M. Sun, D. P. Yu, P. D. Yang, *J. Am. Chem. Soc.* **2001**, *123*, 9904–9905; b) B. Yang, C. Li, H. Hu, X. Yang, Q. Li, Y. T. Qian, *Eur. J. Inorg. Chem.* **2003**, 3699–3702.

 © 2005 Wiley-VCH Verlag GmbH & Co. KGaA, Weinheim

[11] H. Nakamura, Y. Matsui, *J. Am. Chem. Soc.* **1995**, *117*, 2651–2652.
[12] M. E. Spahr, P. Bitterli, R. Nesper, M. Muller, F. Krumeich, H. U. Nissen, *Angew. Chem. Int. Ed.* **1998**, *37*, 1263–1265.
[13] Y. R. Hacohen, E. Grunbaum, R. Tenne, J. Sloan, J. L. Hutchison, *Nature* **1998**, *395*, 336–337.
[14] C. R. Martin, *Science* **1994**, *266*, 1961–1966.
[15] F. Schuth, *Angew. Chem. Int. Ed.* **2003**, *42*, 3604–3622.
[16] K. J. C. van Bommel, A. Friggeri, S. Shinkai, *Angew. Chem. Int. Ed.* **2003**, *42*, 980–999.
[17] J. Sha, J. Niu, X. Ma, J. Xu, X. Zhang, D. Yang, *Adv. Mater.* **2002**, *14*, 1219–1221.
[18] C. M. Zelenski, P. K. Dorhout, *J. Am. Chem. Soc.* **1998**, *120*, 734–742.
[19] J. Goldberger, R. He, Y. Zhang, S. Lee, H. Yan, H. J. Choi, P. Yang, *Nature* **2003**, *422*, 599–602.
[20] B. Yang, M. Mo, H. Hu, C. Li, X. Yang, Q. Li, Y. T. Qian, *Eur. J. Inorg. Chem.* **2004**, 1785–1787.
[21] D. Linden, *Handbook of Batteries*, 3rd ed., McGraw-Hill, New York, **2002**.
[22] M. Oshitani, M. Watada, T. Tanaka, T. Iida, in *Hydrogen and Metal Hydride Batteries*, vol. 94 (Eds.: P. D. Bennett, T. Sakai), The Electrochemistry Society, Pennington, NJ, **1994**, p. 303.
[23] B. Liu, X. Y. Wang, H. T. Yuan, Y. S. Zhang, D. Y. Song, Z. X. Zhou, *J. Appl. Electrochem.* **1999**, *29*, 855–860.
[24] M. Fojas, E. Murphy, P. Stroeve, *Ind. Eng. Chem. Res.* **2002**, *41*, 2662–2667.
[25] I. Zhitomirsky, *J. Appl. Electrochem.* **2004**, *34*, 235–240.
[26] E. David, J. Alvin, R. Peter, T. Xiao, *J. Power Sources* **1997**, *65*, 231–233.
[27] X. Wang, H. Luo, P. V. Parkhutik, A. C. Millan, E. Matveeva, *J. Power Sources* **2003**, *115*, 153–160.
[28] F. S. Cai, G. Y. Zhang, J. Chen, X. L. Gou, H. K. Liu, S. X. Dou, *Angew. Chem. Int. Ed.* **2004**, *43*, 4212–4216.
[29] A. Corrigan, *J. Electrochem. Soc.* **1987**, *134*, 377–384.
[30] H. Bode, K. Dehmelt, J. Witte, *Electrochim. Acta* **1966**, *11*, 1079–1087.
[31] Oliva, J. Leonardi, J. F. Laurent, *J. Power Sources* **1982**, *8*, 229–255.
[32] M. Balasubramanian, C. A. Melendres, S. Mini, *J. Phys. Chem. B* **2000**, *104*, 4300–4306.
[33] D. M. MacArthur, *J. Electrochem. Soc.* **1970**, *117*, 422–425.
[34] C. J. Brumlik, C. R. Martin, *J. Am. Chem. Soc.* **1991**, *113*, 3174–3175.
[35] G. Tourillon, L. Pontonnier, J. P. Levy, V. Langlais, *Electrochem. Solid-State Lett.* **2000**, *3*, 20–23.
[36] J. Bao, C. Tie, Z. Xu, Q. Zhou, D. Shen, Q. Ma, *Adv. Mater.* **2001**, *13*, 1631–1633.
[37] Y. H. Wang, C. H. Ye, X. S. Fang, L. D. Zhang, *Chem. Lett.* **2004**, *33*, 166–167.
[38] Y. Zhao, Y. G. Guo, Y. L. Zhang, K. Jiao, *Phys. Chem. Chem. Phys.* **2004**, *6*, 1766–1768.
[39] S. M. Zhou, Y. S. Feng, L. D. Zhang, *Eur. J. Inorg. Chem.* **2003**, 1794–1797.
[40] P. Hoyer, *Langmuir* **1996**, *12*, 1411–1413.
[41] W. C. Yoo, J. K. Lee, *Adv. Mater.* **2004**, *16*, 1097–1101.
[42] J. F. Moulder, W. F. Stickle, P. E. Sobol, K. D. Bomben, in *Handbook of X-ray Photoelectron Spectroscopy* (Ed.: J. Chastain), Perkin–Elmer Corporation, Wellesley, MA, **1992**.

Received: January 25, 2005
Published Online: September 9, 2005

 © 2005 Wiley-VCH Verlag GmbH & Co. KGaA, Weinheim

A Theoretical Assessment of the Thermodynamic Preferences in the Cyclopalladation of Amines

Ramón Bosque*[a] and Feliu Maseras[b,c]

Keywords: Density functional calculations / Metallacycles / N ligands / Palladium

The factors affecting the cyclopalladation of amines are explored by a comparison of the energy differences between the cyclopalladated amine and the free ligand for a series of compounds. Four factors are considered: the substituents in the nitrogen atom (primary vs. tertiary amines), the hybridization (sp^2 or sp^3) of the metalated carbon atom, the number of members in the metallacycle ring (four, five, or six), and the presence of electron-donor or -acceptor groups. The trends that arise from these calculations, performed at the B3LYP level of theory, are compared with the experimental data available.

(© Wiley-VCH Verlag GmbH & Co. KGaA, 69451 Weinheim, Germany, 2005)

Introduction

The activation of C–H bonds is among the most important topics in organometallic chemistry. One of the ways that it can be achieved is by means of the so-called cyclometallation reaction, which can be defined as the formation of a bond between a transition metal and a carbon atom of one of its ligands, giving rise to a cycle that contains the metal atom (Scheme 1).[1] The most widely used metal is palladium, and to a lesser extent platinum, gold, manganese, rhodium, and ruthenium. As for the heteroatom E that attaches the ligand to the metal, most of the published work deals with N-donor systems, although there are examples with phosphorus, sulfur, oxygen, and arsenic. The mechanism of this reaction depends on the nature of the metallic atom; for example, cobalt(II) and palladium(II) react through an electrophilic pathway, while other late transition elements follow a nucleophilic pathway, which can also be regarded as an oxidative addition. On the other hand, early transition metals react via a multicentered pathway, which can be formally written as a nucleophilically assisted electrophilic reaction.[2]

There are many examples in the literature of the use of cyclometallated complexes in organic synthesis,[3] catalysis,[4] and medicine;[5] these substances can also be used as liquid crystals[6] or even as nanoscale devices.[7] Due to the importance of this cyclometallation reaction, a large amount of experimental work has been published, both presenting new features of the reaction and trying to elucidate which factors play a dominant role in its mechanism.[8,9] The work from Cope and Friedrich[8] regarding the cyclopalladation of N-donor ligands has achieved a seminal importance. These authors undertook the cyclopalladation of aromatic amines. By comparing the relative ease with which the reaction occurs, the authors postulated some empirical rules (the so-called Cope rules), that can be summarized as follows: (a) the stability of the cyclometallated species is greatest when the cycle has five members; (b) the reaction occurs more easily when the amine nitrogen is tertiary; (c) the mechanism is based on an electrophilic substitution. Although there are some exceptions in the literature,[10] these rules provide a useful guide for the rationalization of the products of the reaction in polyfunctional substracts. More recently, Ryabov[2] has reviewed the most important features of the mechanism based on kinetic measurements.

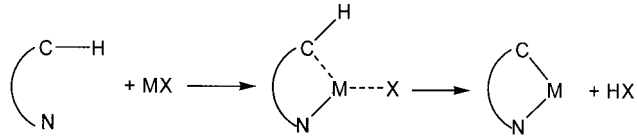

Scheme 1.

In contrast with the abundance of experimental results, the theoretical work published is scarce: although some articles about the reactivity of these species have appeared in the literature,[11] to the best of our knowledge the theoretical basis for the Cope rules has not been analyzed. In the bibliography there are several examples of theoretical studies of C–H activation;[12] however, none of them deals with cyclometallation reactions. The aim of this work is to start filling this void by presenting a first approach to the factors

[a] Department de Química Inorgànica, Universitat de Barcelona, Martí i Franquès 1–11, 08028 Barcelona, Spain
E-mail: ramon.bosque@qi.ub.es
[b] Institute of Chemical Research of Catalonia (ICIQ), Av. Països Catalans s/n, 43007 Tarragona, Spain
[c] Unitat de Química Física, Edifici Cn, Universitat Autònoma de Barcelona, 08193 Bellaterra, Spain

Supporting information for this article is available on the WWW under http://www.eurjic.org or from the author.

influencing the mechanism of the cyclopalladation reaction from the thermodynamic point of view.

Results and Discussion

The cyclopalladation reaction is the most important example of cyclometallation that follows an electrophilic pathway.[2] It is also the most widely studied from an experimental point of view, beginning with the work of Cope and Friedrich that resulted in the empirical Cope rules.[8] In order to find the eventual thermodynamic basis for these rules, we have studied the variations in energy between the free amines and the cyclopalladated complexes (**1a**–**24a** and **1b**–**24b** respectively; Scheme 2). In the first stage, we performed the calculations on a series of aromatic amines (**1a**–**12a**). In order to discern the influence of the hybridization of the metalated carbon atom, we also studied a series of alkenylamines (**13a**–**18a**), as well as alkylamines (**19a**–**24a**). The role of the basicity of the nitrogen atom was evaluated by using either hydrogen or methyl as the substituent R^1 on nitrogen. On the other hand, modification of the number *n* of methylene groups allowed us to study the influence of the size of the metallacycle (from four to six members). In the case of five-membered rings derived from tertiary benzylamines, either acceptor or donor groups were added in order to evaluate their effect.

According to the proposed mechanism, the reaction takes place in two stages:[2] first, the palladium coordinates to the nitrogen atom, and then the electrophilic substitution of hydrogen occurs. Usually a dimeric compound, with halogen or acetate bridging ligands, depending on the starting palladium derivative, is obtained; subsequent treatment with a Lewis base affords the corresponding monomer (Scheme 3). It is worth noting that this ligand usually occupies a position *cis* to the metalated carbon; this is the so-called transphobia effect.[13] To simplify the calculations, we only considered the free ligand and the cyclometallated monomer with a phosphane ligand. As all the other species involved in the process are the same for all the reactions, the differences in energy between the metalated complexes and the corresponding free amines allowed us to define a simple scale of relative energies; the energy associated with the cyclopalladation of *N*,*N*-dimethylbenzylamine (**4a**), which features the formation of a five-membered metallacycle with an aromatic metalated carbon, a tertiary nitrogen, and with hydrogen as the only substituent in the remaining carbon atoms, was chosen as reference and assigned the value of 0 kcal mol^{-1}.

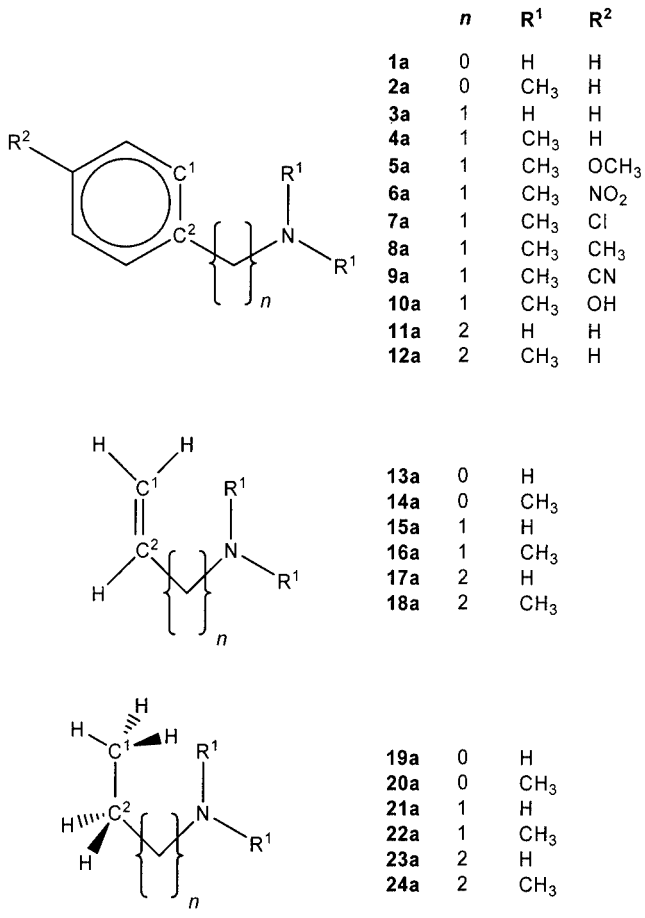

Scheme 2.

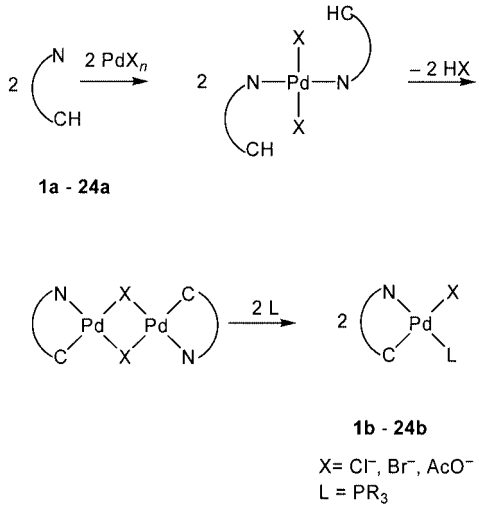

Scheme 3.

Geometry Optimizations

In order to obtain accurate values for the energies corresponding to the different species, the geometries of the free amines and the cyclometallated species were optimized without imposing any symmetry restriction. The most important geometric parameters for the amines that can give rise to four-membered metallacycles are listed in Table 1; the data for all the remaining ligands are included as Supporting Information. In these systems a possible problem of conformation arises from the free rotation around the single bonds. For this reason, several conformations were calculated for the different systems, and in each case only the most stable one was taken into account. In the case of the amines **11a**, **12a**, **17a**, and **18a**, which have larger chains,

 © 2005 Wiley-VCH Verlag GmbH & Co. KGaA, Weinheim

a systematic search of conformers was performed at the semi-empirical AM1 level;[14] the most stable one for each ligand was then re-optimized at the DFT level.

Table 1. Selected optimized geometric parameters for the amines leading to four-membered metallacycles. Lengths are given in angstroms and angles in degrees.

	C1–C2	C2–N	C1–C2–N
1a	1.405	1.398	120.7
2a	1.413	1.394	121.3
13a	1.339	1.394	126.7
14a	1.330	1.431	122.7
19a	1.526	1.468	110.4
20a	1.529	1.464	113.5

The geometrical parameters corresponding to the cyclopalladated compounds are given in Table 2. The geometric distortions are apparent in the four-membered rings, with C(1)–Pd–N angles (see Scheme 2 for the atom numbering) of less than 70°, rather than the 90° that would correspond to a nonstressed, square-planar geometry. It is also worth mentioning the values of the C–N–Pd angles (87–92°, compared to a range of 105–110° for the five-membered rings and 114–120° for the six-membered metallacycles) and the C(2)–C(1)–Pd angles (93–99°, compared with 106–117° and 108–125° for the five- and six-membered rings); this angle is also smaller in the metallacycles that feature a metalated carbon atom with sp^3 hybridization.

The environment around the palladium atom changes as a function of the substituents in the nitrogen atom. Thus, in the tertiary amines the Pd–P and Pd–Cl distances are larger, while the palladium–carbon bonds are shorter than in the primary ones. On the other hand, the variation in the nitrogen–palladium bond-length also depends on the size of the metallacycle: the bonds in the five- and six-membered rings are much longer for the tertiary amines, while in the four-membered rings the observed trend is the opposite.

The variation in the size of the rings also modifies the environment of the palladium atom. The Pd–P and Pd–Cl distances increase upon incrementing the number of members of the ring. The palladium–carbon bond-length shows a less definite trend: for the non-aromatic sp^2 and sp^3 carbon atoms, the distance is smallest for the five-membered rings and largest for the six-membered systems, whereas for the aromatic derivatives the distance is smallest for the four-membered rings, while for the larger rings it depends also on the nature of the nitrogen atom. Finally, no clear trend arises for the variation of the palladium–nitrogen distances.

The changes of the hybridization of the carbon atom also result in some variations of the distances between the palladium atom and its neighbors. However, the only clear trend arises from the palladium–carbon bond length, which increases in the following order: d[Pd–C(sp^2), non aromatic] < d[Pd–C(sp^2), aromatic] < d[Pd–C(sp^3)]. As for the C(1)–Pd–N bite angle, this parameter is larger in nearly all cases for the C(sp^3) systems, as would be expected from the increment in the C(1)–C(2) distance that takes place upon changing the bond between these atoms from double to single; an exception is the six-membered ring with a tertiary nitrogen (**24b** vs. **12b** and **18b**): in this case the angle is nearly constant due to the flexibility of the aliphatic chain. The increment of the bite angle for the four- and five-membered metallacycles involves a decrease of the strain around the palladium atom due to the fact that it is smaller than

Table 2. Optimized geometric parameters for the cyclopalladated systems **1b**–**24b**. Lengths are given in angstroms and angles in degrees.

	C1–C2[a]	C1–Pd	N–Pd	P–Pd	Cl–Pd	P–Pd–N	C–Pd–Cl	Cl–Pd–N	P–Pd–C	C–N–Pd	C2–C1–Pd	C–C–N	C–Pd–N
1b	1.393	2.019	2.214	2.254	2.421	169.7	171.8	105.4	103.4	87.5	97.8	108.4	66.3
2b	1.393	2.015	2.198	2.267	2.423	171.1	168.8	102.0	104.3	87.5	97.3	108.3	66.9
3b	1.416	2.033	2.125	2.280	2.434	177.5	173.9	92.9	100.7	108.4	112.9	108.0	81.1
4b	1.413	2.030	2.177	2.283	2.454	177.4	176.5	96.5	99.7	105.3	113.0	110.0	81.9
5b	1.401	2.031	2.177	2.282	2.456	177.2	176.5	96.6	100.0	105.1	112.8	109.8	81.9
6b	1.415	2.029	2.178	2.285	2.440	178.0	176.5	96.2	99.8	105.8	113.3	110.3	81.9
7b	1.413	2.030	2.177	2.284	2.447	177.6	176.6	96.4	100.0	105.5	113.1	110.0	81.9
8b	1.413	2.030	2.179	2.282	2.456	177.5	176.5	96.5	99.7	105.2	112.8	109.9	81.9
9b	1.414	2.030	2.177	2.286	2.441	177.6	176.5	96.3	100.1	105.6	113.2	110.1	81.9
10b	1.412	2.030	2.177	2.284	2.447	177.6	176.6	96.4	100.0	105.5	113.1	110.0	81.9
11b	1.409	2.031	2.152	2.280	2.449	172.9	176.3	86.5	95.6	119.4	117.4	111.9	90.1
12b	1.408	2.039	2.216	2.287	2.486	170.0	172.7	92.6	94.2	114.7	120.6	113.1	93.2
13b	1.330	2.016	2.198	2.259	2.421	169.2	171.3	106.0	104.0	87.2	99.2	108.4	65.3
14b	1.330	2.015	2.191	2.268	2.426	170.4	169.2	103.6	104.8	87.0	98.6	108.9	65.6
15b	1.342	2.012	2.132	2.272	2.432	178.6	174.4	93.8	98.0	110.5	115.4	108.3	80.7
16b	1.340	2.006	2.180	2.274	2.454	178.2	177.1	96.7	97.1	107.3	115.4	110.0	81.4
17b	1.339	2.017	2.129	2.283	2.451	174.3	177.8	87.1	94.8	117.0	126.0	111.4	90.8
18b	1.336	2.014	2.202	2.282	2.488	174.1	173.4	93.0	92.7	115.8	125.2	115.3	93.0
19b	1.531	2.072	2.140	2.273	2.438	171.2	171.9	103.0	102.3	92.3	94.3	103.4	68.9
20b	1.528	2.070	2.148	2.279	2.442	171.7	169.7	100.9	102.9	90.9	93.4	103.4	68.8
21b	1.536	2.077	2.140	2.272	2.443	179.0	175.1	92.3	96.3	109.7	107.2	107.1	83.1
22b	1.532	2.070	2.183	2.273	2.466	178.9	178.3	94.5	95.4	106.9	106.7	109.8	84.0
23b	1.529	2.081	2.150	2.275	2.459	174.8	176.8	86.9	94.4	114.6	111.3	111.7	90.2
24b	1.528	2.077	2.216	2.276	2.491	175.3	174.4	93.2	93.9	113.4	108.8	115.9	90.3

[a] See Scheme 2 for the atom numbering.

 © 2005 Wiley-VCH Verlag GmbH & Co. KGaA, Weinheim

Table 3. Relative energies [kcal mol^{-1}] for the metalation of amines **1a**–**24a**.

Ring size	N substituent	Benzylamines R^2 subst.	Aromatic		Alkenylamines		Alkylamines	
4	H	(H)[a]	**1a**	14.1	**13a**	13.1	**19a**	4.9
4	CH_3	(H)[a]	**2a**	11.7	**14a**	6.7	**20a**	5.7
5	H	(H)[a]	**3a**	–3.3	**15a**	–6.0	**21a**	–4.3
5	CH_3	(H)[a]	**4a**	0.0[b]	**16a**	–2.5	**22a**	–1.9
5	CH_3	OCH_3	**5a**	1.2				
5	CH_3	NO_2	**6a**	1.8				
5	CH_3	Cl	**7a**	–5.6				
5	CH_3	CH_3	**8a**	0.4				
5	CH_3	CN	**9a**	1.5				
5	CH_3	OH	**10a**	–5.4				
6	H	(H)[a]	**11a**	–3.2	**17a**	–7.4	**23a**	–1.1
6	CH_3	(H)[a]	**12a**	0.4	**18a**	–2.2	**24a**	3.6

[a] Only applicable to aromatic amines. [b] Value taken as reference.

90° in all cases. The influence of the presence of donor or acceptor groups upon the environment of the palladium is small.

Factors Affecting the Cyclopalladation Reaction

In order to compare the factors that affect the stability of the palladacycles, the relative increment in energy corresponding to the metalation of the amines was calculated. We took into account the difference of energy between the cyclometallated species and the free amine, and the results were referenced to the formation of compound **4b** (five-membered ring with an aromatic metalated carbon, a tertiary nitrogen and without donor or acceptor groups bonded to the remaining carbon atoms), which was taken as 0.0 kcal mol^{-1}. The results are shown in Table 3.

Hybridization of the Metalated Carbon

The first factor that we took into account was the nature of the metalated carbon: C(sp^2, aromatic), C(sp^2, non-aromatic), or C(sp^3). Cope and Friedrich[8] worked only with benzylamine derivatives, and nearly all the published articles deal with the metalation of aromatic carbons; however, there are examples of the activation of C(sp^3)–H bonds in imines where there are aromatic carbons available.[15] This result is more remarkable considering that, in this case, the reaction yields a six-membered ring, while the activation of the C(sp^2)–H bond would yield a five-membered metallacycle, which is regarded as the most favored ring size. In this case, however, there are other factors that must be considered, especially the position of the C=N double bond: the systems in which this bond is included in the metallacycle (endocyclic) are formed more easily than those with the bond outside the metallacycle (exocyclic).[16] Minghetti and co-workers[17] have compared the aliphatic vs. aromatic C–H activation in the reaction of 6-substituted 2,2′-bipyridines with Na_2PdCl_4 in order to obtain five- or six-membered metallacycles. The reaction depends strongly on the substituent of the 2,2′-bipyridine, often in an unpredictable way. Dunina and co-workers[18] have studied the activation of C(sp^3)–H and C(sp^2)–H bonds in the reaction of *N*-methyl-α-*tert*-butylbenzylamine with palladium(II). In this secondary amine, weak palladating agents such as Li_2PdCl_4 favor the formation of C(sp^3)–Pd bonds, while under more drastic reaction conditions the C(sp^2)–H bond is activated. However, in the related tertiary amine *N*,*N*′-dimethyl-α-*tert*-butylbenzylamine only the palladation of the aromatic carbon is observed. There are other examples of four-[19] and five-membered[20] metallacycles with C(sp^3) metalated atoms, but they are prepared by oxidative addition and not by means of the cyclometallation reaction. A five-membered metallacycle with an aliphatic metalated carbon and a negative charge has also been postulated as an intermediate in the palladium-catalyzed internal phenylation of *N*,*N*-dialkylallylamines,[21] while an intermediate in the intramolecular Heck reaction of a pyrrolidine that features a five-membered aliphatic ring has recently been isolated and characterized.[22]

Finally, there are some examples of five-membered metallacycles where the metalated carbon has sp^2 hybridization although it is not aromatic,[23] and thus they are formally similar to our system **16b**. However, they are not prepared by the cyclopalladation reaction of the corresponding tertiary allylamine, but via the chloropalladation of substituted alkynes.

In view of this experimental evidence, we found it interesting to study the behavior of three different types of carbon center. The first of them was a phenyl, as in benzylamine (systems **1**–**12**), which represents the most usual case of aromatic carbons. The second one was a saturated alkyl (systems **19**–**24**), in line with the more recent results. We also introduced alkenyl in the comparison (systems **13**–**18**), with the idea that, if the energetics were similar, it could be a more computationally accessible model for a phenyl group. The relative energies from the calculations presented in Table 3 allow a series of comparisons between the behaviors of the three types of carbon hybridization. In order for the comparison to be fair, one must take a series of compounds where only the nature of the carbon changes and the rest of characteristics, that is, the substituents R^1 at nitrogen and the number, *n*, of carbons in the chain remain the same. A number of phenyl/alkenyl/alkyl series can be

 © 2005 Wiley-VCH Verlag GmbH & Co. KGaA, Weinheim

defined following this concept, namely, **1/13/19**, **2/14/20**, **3/15/21**, **4/16/22**, **11/17/23**, and **12/18/24**. The corresponding relative energies are 14.1/13.1/4.9, 11.7/6.7/5.7, –3.3/–6.0/–4.3, 0.0/–2.5/–1.9, –3.2/–7.5/–1.1, and 0.4/–2.2/3.6 kcal mol^{-1}, respectively. It is worth noting that the first number of the series, corresponding to phenyl, is in no case the lowest (or the most negative). Thus, it can be concluded that the abundance of aromatic carbons in cyclopalladated compounds cannot be attributed to a thermodynamic preference because in no case is this the favored reaction. A second observation is that there is no special similarity between the first (phenyl) and the second (alkenyl) number of each series. Finally, concerning the particular numbers being presented, it can be seen that the larger differences (up to 10 kcal mol^{-1}) appear in the first two series (**1/13/19** and **2/14/20**), while for the other four groups the differences are 6 kcal mol^{-1} at most. This can be easily explained by the geometric strain of the four-membered rings in the first two sequences. The C–C–Pd angles are smaller than 100° in **1b**, **13b**, and **19b**, and this is more easily tolerated by sp^3 carbons than by their sp^2 counterparts.

Substituents on the Nitrogen Atom

The second factor considered was the variation in the nitrogen substituents. It is commonly assumed that M–N bonds are weaker in tertiary than in primary or secondary amines.[2] This effect is attributed, among other factors, to the steric hindrance of tertiary amines, as well as to the decrease in the outer-sphere solvation energy induced by N-alkylation;[24] however, it has been found that, in some cases, N-alkylation can stabilize coordination complexes in the gas phase.[25] Cope[8] was able to cyclometallate only tertiary amines, and nearly all the published work about the cyclopalladation of amines deals with tertiary nitrogen. Several explanations have been proposed for this fact: the greater coordinating ability of primary and secondary amines, which makes the subsequent C–H bond cleavage by the palladium atom via an electrophilic attack more difficult,[8] steric factors, which lead to a smaller internal entropy decrease in the cyclometallation of tertiary amines;[26] and, finally, the weaker bond between the palladium and the tertiary nitrogen atoms in the coordination intermediates, which facilitate the formation of unsaturated species that subsequently undergo Pd–C bond formation.[2] However, under carefully controlled experimental conditions, it is possible to prepare cyclopalladated compounds with primary[27] or secondary[27f,28] amines. Recently, the mechanism of the cyclometallation of primary amines has been investigated,[29] and it has been found that the choice of the solvent is critical in order to perform this reaction.

In our calculations we examined two limiting cases: primary amines, with two hydrogen substituents at nitrogen, and tertiary amines, with two methyl substituents. In this case, there are as many as nine primary/tertiary pairs of relative energies in Table 3 that can be compared. These are **1/2**, **3/4**, **11/12**, **13/14**, **15/16**, **17/18**, **19/20**, **21/22**, and **23/24**. The corresponding relative energies are 14.1/11.7, –3.3/0.0, –3.2/0.4, 13.1/6.7, –6.0/–2.5, –7.5/–2.2, 4.9/5.7, –4.3/–1.9, and –1.1/3.6 kcal mol^{-1}. In all but two pairs (**1/2** and **13/14**) the first number is smaller than the second, indicating that the reaction of primary amines is thermodynamically favored. The only two exceptions correspond to four-membered rings, which have their own characteristics associated with the large steric strain. Our calculations therefore indicate that cyclometallation tends to be favored when the nitrogen is primary; the energy differences between the metalation of primary and tertiary amines are between 2 and 5 kcal mol^{-1} for the five- and six-membered rings. The reasons for this can be electronic and/or steric; in this regard, the comparison of the Pd–N distances shows a shortening of the bond in the primary amines as compared to the tertiary ones. Also, we cannot rule out the presence of an interaction between the hydrogen of the primary amine and the chlorine atom. This interaction could lead to a stabilization of those metallacycles that feature primary nitrogen.

The experimental observation that the primary amines are so difficult to cyclopalladate is thus not due to a lack of thermodynamic stability of the product. In fact, it has been proposed from experimental data that an intermediate complex with two amines coordinated is too stable in this case, thus precluding the cyclometallation.[2] However, a definite answer can only be obtained after a thorough computational study of all the intermediates corresponding to the cyclopalladation reaction.

Size of the Metallacyle

The number of members in the formed metallacycle is considered to be a crucial factor in this reaction. In their original work, Cope and Friedrich tried the reaction of lithium tetrachloropalladate with *N*,*N*′-dimethylbenzylamine, *N*,*N*′-dimethyl-1-ethyl-2-phenylamine and *N*,*N*′-dimethyl-3-phenyl-1-propylamine in order to obtain five-, six-, and seven-membered rings, respectively, but they were successful only in the first case.[8] However, there are some recent examples of six-membered rings with primary benzyl-[10,30] and ferrocenylamines,[27e] and also with heterocycles.[31] Five- or six-membered rings can be obtained in the cyclopalladation of imines depending on the reaction conditions;[15,32] however, examples with six-membered metallacycles are less common than their five-membered counterparts.[1]

In order to test the importance of the ring size we performed calculations with four-, five-, and six-membered rings, both for primary and for tertiary amines (Table 3). In this case, we can form six series of relative energies corresponding to four/five/six-membered rings with identical settings for the other variables. The series are **1/3/11**, **2/4/12**, **13/15/17**, **14/16/18**, **19/21/23**, and **20/22/24**, and the corresponding relative energies are 14.1/–3.3/–3.2, 11.7/0.0/0.4, 13.1/–6.0/–7.5, 6.7/–2.5/–2.2, 4.9/–4.3/–1.1, and 5.7/–1.9/3.6 kcal mol^{-1}, respectively. As could be expected, the first number of the triad is always the highest, indicating that the formation of four-membered palladacycles is always the least thermodynamically favored, with differences larger than 10 kcal mol^{-1} in a number of cases. The reason for this

 © 2005 Wiley-VCH Verlag GmbH & Co. KGaA, Weinheim

is the greater strain associated with four-membered rings, as can be seen in the comparison of the bond angles in the metallacycles (Table 2).

The comparison between five- and six-membered systems shows that the cyclopalladation is more favored for the former in nearly all the cases, with the only exception being the tertiary alkenylamines. Due to the lack of reaction between lithium tetrachloropalladate and *N*,*N*-dimethyl-1-ethyl-2-phenylamine,[8] it could be anticipated that the formation of six-membered rings would be less favored than in the five-membered systems. However, our calculations show that the difference in energy is small, mainly in the case of the aromatic amines, where it is smaller than 0.5 kcal mol^{-1}.

In order to ascertain the transferability of the results of these calculations, we analyzed the combined effect of the nature of the metalated atom and the size of the metallacycle on the 2-methylbenzylamine system depicted in Figure 1, which can produce the two different cyclometallation products shown. The calculation indicates that the isomer on the left-hand side, which features an aromatic metalated carbon atom and a five-membered metallacycle, is 5.9 kcal mol^{-1} more stable than the one on the right-hand side, which contains an aliphatic metalated carbon atom and a six-membered metallacycle. This compares well with the numbers in Table 3, where the reaction associated to an alkyl compound with a tertiary amine leading to a six-membered cyclometallated complex (**24a**) is 3.6 kcal mol^{-1} disfavored with respect to that of an aryl compound with a tertiary amine leading to a five-membered cyclometallated complex (**4a**). The minor difference between both energy differences can be easily explained by the presence of some sp^2 carbons in the six-membered ring of our test compound that are absent in model species **24b**.

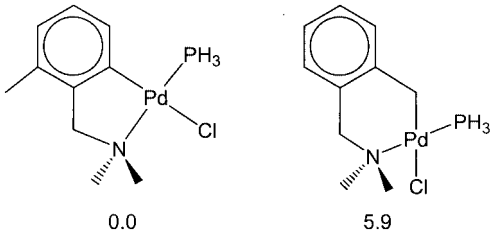

Figure 1. Relative energies [kcal mol^{-1}] of the two possible isomers that arise from the cyclopalladation of *N*,*N*-dimethyl(*o*-tolyl)methylamine.

We thus see that four-membered rings are indeed greatly disfavored from a thermodynamic point of view, and that five-membered rings are slightly more favored than six-membered rings. Therefore, it seems that the Cope rule concerning the size of the rings being formed can be explained by the thermodynamic stability of the product.

Electron-Donor or -Acceptor Groups in the Aromatic Ring

The last factor that was taken into account was the presence of electron-donor or -acceptor groups in the aryl ring. If the reaction has an electrophilic character, donors will favor it, while acceptors will render it more difficult. An example of this is the cyclopalladation of substituted azobenzenes, where the ring with electron-donating groups is preferentially metalated.[33] As for the tertiary benzylamines, Cope and Friedrich[8] metalated the 4-methoxy and 3,5-dimethoxy derivatives, with yields very similar to the unsubstituted tertiary amine, but were unsuccessful with the 4-NO_2 analog; this compound needs stronger palladating agents, such as palladium(II) acetate.[34] Kinetic measurements for the cyclometallation reaction of substituted *N*,*N*-dimethylbenzylamines[9a] or *N*-benzyltriamines[9d] show that there is a linear correlation between the logarithm of the rate constant and the Hammett parameter, σ_m, of the substituents, thus confirming that the reaction takes place through an electrophilic attack of the Pd^{II} center on the carbon atom.

In order to test the importance of the ring substituents we performed calculations on several substituted *N*,*N*′-dimethylbenzylamines of general formula 4-R-$C_6H_4CH_2N(CH_3)_2$, where R = -OCH_3 (**5a**), -NO_2 (**6a**), -Cl (**7a**), -CH_3 (**8a**), -CN (**9a**), and –OH (**10a**). They are depicted in Scheme 2. In addition to **5a** and **6a**, the cyclopalladated derivatives of **7a** and **8a** have been prepared previously,[9a] while, to the best of our knowledge, there are no examples of simple cyclopalladated derivatives of the hydroxy- and cyano-substituted tertiary benzylamines.

The relative energies corresponding to the cyclopalladation reactions, taking the unsubstituted tertiary benzylamine **4a** as reference, are shown in Table 3. There is not a perfect relationship between the electron-donor or -acceptor character of the R groups and the stability of the resulting palladacycles, but some trends are apparent. Acceptor groups, such as NO_2 (+1.8 kcal mol^{-1}) and CN (+1.5 kcal mol^{-1}), seem to render the metallacycles more unstable, whereas donor groups, such as OH (–5.4 kcal mol^{-1}), tend to stabilize the palladacycles, as would be expected from the electrophilic substitution mechanism indicated by the Cope rules. Donor groups making the reaction more difficult, as is the case with OCH_3 (+1.2 kcal mol^{-1}) and CH_3 (+0.4 kcal mol^{-1}), is somehow in disagreement with the rule, but can be attributed to their *meta* arrangement with respect to carbon C1. Finally, the chloro-substituted benzylamine **7a**, with a relative reaction energy of –5.6 kcal mol^{-1}, has a similar behavior to the electron donor OH. However, it has been reported that, at least in azobenzenes, a chloro substituent renders the substrate less reactive towards cyclopalladation than a hydrogen atom,[35] which would be in disagreement with this result.

It seems clear from these results that our simplified analysis fails to reproduce the experimental reactivity trends associated with the effect of electron-donor and electron-acceptor substituents. A subsequent study of the reaction mechanism could shed some light on the effect of these groups on the reaction kinetics.

Conclusions

A comparison of the relative energies of a series of amines and those of the corresponding cyclometallated

 © 2005 Wiley-VCH Verlag GmbH & Co. KGaA, Weinheim

compounds allows a relatively simple computational evaluation of the correlation between the nature of the amine and the thermodynamic change involved in the cyclopalladation reaction. If these thermodynamic trends reproduced the experimental observations on the easiness of the reaction, this would be an efficient approach for the prediction of the likeliness of cyclometallation for a given compound and for the identification of the preferred product when more than one is possible. Unfortunately, our results indicate that this is not always the case.

The empirical rules proposed initially by Cope, and confirmed by a variety of experimental data afterwards, predict that cyclometallation is favored in the case of five-membered-ring products, tertiary amines, and in the presence of electron donors. Of these three rules, only the first of them, concerning the size of the rings, has an undisputable thermodynamic basis. Four-membered rings are strongly disfavored by the large steric strain, and products with five-membered rings are also preferred over their six-membered counterparts. The second rule, concerning the nature of the substituents at both the nitrogen and the carbon atoms, does not have a thermodynamic origin. It must therefore be associated to kinetics. The third rule, related to the nature of the substituents at the carbon atoms, seems to have a certain thermodynamic basis, but there are exceptions for some substituents, thus suggesting a significant kinetic contribution. The theoretical evaluation of kinetics requires a detailed knowledge of the reaction mechanism, with location of intermediates, transition states, and their associated energies. Further understanding of these empirical rules, as well as computational predictions on cyclometallation, will thus require the performance of a much more elaborate computational study.

Computational Details

All calculations were carried out with the Gaussian 98[36] package of programs at the B3LYP computational level.[37] The basis set was chosen as follows: an effective core potential was used to replace the 36 innermost electrons of Pd and the 10 innermost electrons of P and Cl; for these atoms, the LANL2DZ basis[38] was used, and in the case of phosphorus and chlorine, polarization functions were added. For carbon, hydrogen, oxygen, and nitrogen the 6-31G(d,p) basis including polarization functions[39] was used. Some conformational searches were carried out at the AM1 computational level[14] using the Spartan program.[40]

Acknowledgments

We are indebted to the Spanish Ministerio de Ciencia y Tecnología (grant nos. BQU2003-00906 and BQU2002-04110-CO2-02) and to the Generalitat de Catalunya (grant nos. SGR-2001-00054 and SGR-2001-00179) for financial support. FM thanks DURSI as well as the ICIQ foundation for financial support.

[1] I. Omae, *Organometallic Intramolecular Coordination Compounds*; Elsevier Science Publications, Amsterdam, **1986**.
[2] A. D. Ryabov, *Chem. Rev.* **1990**, *90*, 403–424.
[3] a) J. Spencer, M. Pfeffer, *Adv. Met-Org. Chem.* **1998**, *6*, 103–144; b) M. Pfeffer, *Recl. Trav. Chim. Pays-Bas* **1990**, *109*, 567–576.
[4] a) M. Ohff, A. Ohff, D. Milstein, *Chem. Commun.* **1999**, 357–358; b) Y. J. Wu, J. J. Hou, H. Y. Yun, X. L. Cui, R. J. Yuan, *J. Organomet. Chem.* **2001**, *637*, 793–795; c) J. Dupont, M. Pfeffer, J. Spencer, *Eur. J. Inorg. Chem.* **2001**, 1917–1927; d) R. B. Bedford, *Chem. Commun.* **2003**, 1787–1796.
[5] a) D. M. Fan, C. T. Yang, J. D. Ranford, J. J. Vittal, P. F. Lee, *Dalton Trans.* **2003**, 3376–3381; b) A. Gómez Quiroga, C. Navarro Ranninger, *Coord. Chem. Rev.* **2004**, *248*, 119–133.
[6] a) M. Ghedini, D. Pucci, G. Barberio, *Liq. Cryst.* **2000**, *27*, 1277–1283; b) L. Diez, P. Espinet, J. A. Miguel, M. B. Ros, *J. Mater. Chem.* **2002**, *12*, 3694–3698.
[7] M. Albrecht, M. Lutz, A. L. Spek, G. van Koten, *Nature* **2000**, *406*, 970–974.
[8] A. C. Cope, E. C. Friedrich, *J. Am. Chem. Soc.* **1968**, *90*, 909–913.
[9] a) A. D. Ryabov, I. K. Sakodinskaya, A. K. Yatsimirsky, *J. Chem. Soc., Dalton Trans.* **1985**, 2629–2638; b) J. M. Valk, J. Boersma, G. van Koten, *Organometallics* **1996**, *15*, 4366–4372; c) S. T. Lin, H. S. Cheo, L. S. Liu, J. C. Wang, *Organometallics* **1997**, *16*, 1803–1805; d) T. Yagyu, S. Aizawa, S. Funahashi, *Bull. Chem. Soc. Jpn.* **1998**, *71*, 619–629; e) P. Steenwinkel, R. A. Gossage, G. van Koten, *Chem. Eur. J.* **1998**, *4*, 759–762; f) J. Campora, J. A. Lopez, P. Palma, P. Valerga, E. Spillner, E. Carmona, *Angew. Chem. Int. Ed.* **1999**, *38*, 147–151; g) J. Vicente, I. Saura-Llamas, J. Turpin, M. C. Ramirez de Arellano, P. G. Jones, *Organometallics* **1999**, *18*, 2683–2693; h) G. Zhao, Q. C. Yang, T. C. W. Mak, *Organometallics* **1999**, *18*, 3623–3636; i) M. Albrecht, P. Dani, M. Lutz, A. L. Spek, G. van Koten, *J. Am. Chem. Soc.* **2000**, *122*, 11822–11833; j) J. Albert, J. Granell, R. Tavera, *Polyhedron* **2003**, *22*, 287–291.
[10] J. Vicente, I. Saura-Llamas, J. Cuadrado, M. C. Rodríguez de Arellano, *Organometallics* **2003**, *22*, 5513–5517.
[11] a) P. de Vaal, A. Dedieu, *J. Organomet. Chem.* **1994**, *478*, 121; b) S. A. Macgregor, E. Wenger, *Organometallics* **2002**, *21*, 1278–1289.
[12] a) S. Niu, M. B. Hall, *Chem. Rev.* **2000**, *100*, 353; b) D. Musaev, K. Morokuma, *J. Am. Chem. Soc.* **1995**, *117*, 799–805; c) A. Dedieu, *Chem. Rev.* **2000**, *100*, 543–600; d) A. C. Cooper, E. Clot, J. C. Huffman, W. E. Streib, F. Maseras, O. Eisenstein, K. G. Caulton, *J. Am. Chem. Soc.* **1999**, *121*, 97–106.
[13] J. Vicente, A. Arcas, D. Bautista, P. G. Jones, *Organometallics* **1997**, *16*, 2127–2138.
[14] M. J. S. Dewar, E. G. Zoebisch, E. F. Heal, J. J. P. Stewart, *J. Am. Chem. Soc.* **1985**, *107*, 3902–3909.
[15] J. Albert, M. Gomez, J. Granell, J. Sales, X. Solans, *Organometallics* **1990**, *9*, 1405–1413.
[16] a) C. López, R. Bosque, X. Solans, M. Font-Bardia, J. Silver, G. Fern, *J. Chem. Soc., Dalton Trans.* **1995**, 4053–4058; b) M. Gómez, J. Granell, M. Martinez, *Eur. J. Inorg. Chem.* **2000**, 217–224.
[17] A. Zucca, M. A. Cinellu, M. V. Pinna, S. Stoccoro, G. Minghetti, M. Manassero, M. Sansoni, *Organometallics* **2000**, *19*, 4295–4304.
[18] V. V. Dunina, O. N. Gorunova, E. B. Averina, Y. K. Grishin, L. G. Kuzmina, J. A. K. Howard, *J. Organomet. Chem.* **2000**, *603*, 138–151.
[19] R. Arnek, K. Zetterberg, *Organometallics* **1987**, *6*, 1230–1235.
[20] a) A. C. Cope, J. M. Kliegman, E. C. Friedrich, *J. Am. Chem. Soc.* **1967**, *89*, 287–291; b) R. A. Holton, R. A. Kjonaas, *J. Am. Chem. Soc.* **1977**, *99*, 4177–4179; c) R. McCrindle, G. Ferguson, M. A. Khan, A. J. McAlees, B. L. Ruhl, *J. Chem. Soc., Dalton Trans.* **1981**, 986–991; d) J. W. Suggs, K. S. Lee, *J. Organomet. Chem.* **1986**, *299*, 297–309; e) R. A. Holton, J. R. Zoeller, *J. Am. Chem. Soc.* **1985**, *107*, 2124–2131; f) J. Dupont, R. A. P. Halfen, R. Schenato, A. Berger, M. Horner, A. Bortoluzzi, C. Maichle-Mössmer, *Polyhedron* **1996**, *15*, 3465–3468.

 © 2005 Wiley-VCH Verlag GmbH & Co. KGaA, Weinheim

[21] K. Olofsson, H. Sahlin, M. Larhed, A. Hallberg, *J. Org. Chem.* **2001**, *66*, 544–549.
[22] B. Clique, C.-H. Fabritius, C. Couturier, N. Monteiro, G. Balme, *Chem. Commun.* **2003**, 272–273.
[23] a) E. L. S. Gomes, M. Hörner, V. G. Young Jr., J. Dupont, V. Caliman, O. L. Casagrande Jr., *Organometallics* **1999**, *18*, 3898–3903; b) M. L. Zanini, M. R. Meneghetti, G. Ebeling, P. R. Livotto, F. Rominger, J. Dupont, *Polyhedron* **2003**, *22*, 1665–1671; c) M. L. Zanini, M. R. Meneghetti, G. Ebeling, P. R. Livotto, F. Rominger, J. Dupont, *Inorg. Chim. Acta* **2003**, *350*, 527–536.
[24] D. Meyerstein, *Coord. Chem. Rev.* **1999**, *185–186*, 141–147.
[25] H. Deng, P. Kebarle, *J. Am. Chem. Soc.* **1998**, *120*, 2925–2931.
[26] B. L. Shaw, *J. Organomet. Chem.* **1980**, *200*, 307–318.
[27] a) A. Avshu, R. D. O'Sullivan, A. W. Parkins, N. W. Alcock, R. M. Countryman, *J. Chem. Soc., Dalton Trans.* **1983**, 1619–1624; b) J. Vicente, I. Saura-Llamas, P. G. Jones, *J. Chem. Soc., Dalton Trans.* **1993**, 3619–3624; c) J. Albert, J. Granell, A. Luque, J. Minguez, R. Moragas, M. Font-Bardia, X. Solans, *J. Organomet. Chem.* **1996**, *522*, 87–95; d) Y. Fuchita, K. Yoshinaga, Y. Ikeda, J. Kinoshita-Kawasima, *J. Chem. Soc., Dalton Trans.* **1997**, 2495–2499; e) R. Bosque, C. López, *Polyhedron* **1999**, *18*, 135–143; f) Y. Fuchita, K. Yoshinaga, H. Kawano, J. Kinoshita-Nagaoka, *J. Organomet. Chem.* **1999**, *580*, 273–281.
[28] a) V. V. Dunina, O. A. Zalevskaya, V. M. Potapov, *Z. Obsch. Khim.* **1984**, *54*, 389–397; b) Y. Fuchita, H. Tsuchiya, *Inorg. Chim. Acta* **1993**, *209*, 229–230.
[29] S. A. Kurzeev, G. M. Kazankov, A. D. Ryabov, *Inorg. Chim. Acta* **2002**, *340*, 192–196.
[30] J. Vicente, I. Saura-Llamas, M. G. Palin, P. G. Jones, M. C. Ramirez de Arellano, *Organometallics* **1997**, *16*, 826–833.
[31] a) K. Hiraki, Y. Fuchita, K. Takechi, *Inorg. Chem.* **1981**, *20*, 4316–4320; b) M. Nonoyama, *Transition Met. Chem.* **1982**, *7*, 281–284; c) D. J. de Geest, B. J. O'Keefe, P. J. Steel, *J. Organomet. Chem.* **1999**, *579*, 97–105.
[32] L. Kind, A. J. Klaus, P. Rys, *Helv. Chim. Acta* **1998**, *81*, 307–316.
[33] a) H. Takahashi, J. Tsuji, *J. Organomet. Chem.* **1967**, *10*, 511–517; b) M. I. Bruce, B. L. Goodall, F. G. A. Stone, *J. Chem. Soc., Dalton Trans.* **1978**, 687–694.
[34] A. D. Ryabov, A. K. Yatsimirsky, *Inorg. Chem.* **1984**, *23*, 789–790.
[35] G. W. Parshall, *Acc. Chem. Res.* **1970**, *3*, 139–144.
[36] Gaussian 98 (Revision A11), M. J. Frisch, G. W. Trucks, H. B. Schlegel, G. E. Scuseria, M. A. Robb, J. R. Cheeseman, V. G. Zakrzewski, J. A. Montgomery, R. E. Stratmann, J. C. Burant, S. Dapprich, J. M. Millam, A. D. Daniels, K. Kudin, M. C. Strain, O. Farkas, J. Tomasi, V. Barone, M. Cossi, R. Cammi, B. Mennucci, C. Pomelli, C. Adamo, S. Clifford, J. Ochterski, G. A. Petersson, P. Y. Ayala, Q. Cui, K. Morokuma, D. K. Malick, A. D. Rabuck, K. Raghavachari, J. B. Foresman, J. Cioslowski, J. V. Ortiz, B. B. Stefanov, G. Liu, A. Liashenko, P. Piskorz, I. Komaromi, R. Gomperts, R. L. Martin, D. J. Fox, T. Keith, M. A. Al-Laham, C. Y. Peng, A. Nanayakkara, C. Gonzalez, M. Challacombe, P. M. W. Gill, B. G. Johnson, W. Chen, M. W. Wong, J. L. Andres, E. Head-Gordon, E. S. Replogle, J. A. Pople, Gaussian Inc., Pittsburgh PA, **1998**.
[37] a) A. D. Becke, *J. Chem. Phys.* **1993**, *98*, 5648–5652; b) C. Lee, W. Yang, R. G. Parr, *Rev. Phys. B* **1988**, *37*, 785–789.
[38] a) W. R. Wadt, P. J. Hay, *J. Chem. Phys.* **1985**, *82*, 284; b) P. J. Hay, W. R. Wadt, *J. Chem. Phys.* **1985**, *82*, 299–310.
[39] a) W. J. Hehre, R. Ditchfield, J. A. Pople, *J. Chem. Phys.* **1972**, *56*, 2257–2261; b) P. C. Hariharan, J. A. Pople, *Theor. Chim. Acta* **1973**, *28*, 213–222.
[40] Spartan, version 5.0. Wavefunction, Inc. 18401 Von Karman Avenue, Suite 370, Irvine CA 92612, USA.

Received: February 22, 2005
Published Online: September 8, 2005

 © 2005 Wiley-VCH Verlag GmbH & Co. KGaA, Weinheim

Synthesis and Characterisation of [Re(CO)$_3$(SS)(P)] Complexes: A [2+1] Concept for ^{99m}Tc- and ^{188}Re-Radiopharmaceutical Applications

Mattia Riondato,*[a] Davide Camporese,[a] David Martín,[b] Joan Suades,[b] Angel Alvarez-Larena,[c] and Ulderico Mazzi[a]

Keywords: Carbonyl ligands / P ligands / Rhenium / S ligands / Technetium

A new (SS)(P) coordination set based on the concurrent use of a dithiocarbamate and a functionalised phosphane is reported. The (SS)(P) fashion is achieved by applying the [2+1] mixed-ligand concept and makes it possible to obtain stable rhenium tricarbonyl complexes without employing tripodal bifunctional chelating agents (BFCAs). The coordination chemistry of the simple sodium *N*,*N*-dimethyldithiocarbamate and new functionalised phosphanes **L1**–**L3** [**L1** = $Ph_2PCH_2CH_2C(O)OCH_3$, **L2** = $Ph_2PCH_2CH_2C(O)NHCH_2C(O)OCH_3$, **L3** = $Ph_2PCH_2CH_2C(O)NHCH_2CH_2C(O)OCH_3$] was studied by reaction with the rhenium complex $[NEt_4]_2[fac\text{-}Re(CO_3)Br_3]$. The rhenium tricarbonyl core was found to be stabilised by the SS chelation of dithiocarbamate and by the P coordination of the phosphane. Two synthetic pathways leading to the complexes [*fac*-Re(CO)$_3$(L)(MDTC)] (L = **L1**, **L2**, **L3**; MDTC = *N*,*N*-dimethyldithiocarbamate) are described. The structural characterisation of the isolated complexes by spectroscopic methods is reported, including X-ray crystallographic analysis for rhenium complexes with ligands **L1** and **L3**. The homologous Tc-99m compounds with the same (SS)(P) coordination set were prepared at tracer level with the **L2** and **L3** ligands, and characterised by HPLC methods.

(© Wiley-VCH Verlag GmbH & Co. KGaA, 69451 Weinheim, Germany, 2005)

Introduction

The most important goal of radiopharmacy is the application of radiolabelled compounds in medicine for non-invasive diagnostic and therapeutic purposes. Technetium-99m is a γ-emitter with optimal characteristics that is widely employed in nuclear medicine for imaging and is readily available as pertechnetate from the ^{99}Mo/^{99m}Tc generator.[1] Rhenium-188 appears to be promising as a candidate for the treatment of neoplasia for its β^- emission and is available as perrhenate from a commercially available ^{188}W/^{188}Re generator, proposed by Oak Ridge National Laboratory (USA).[2]

For the development of site-directed diagnostic and therapeutic radiopharmaceuticals, a biomolecule (hormones, peptides) with high affinity for a receptor target should be labelled to deliver the radionuclide in a specific body region.[3] However, labelling a biomolecule might give an important alteration of its biological properties due to the link with transition metals such as Tc or Re. Hence, the most successfully employed procedure at present is the "bifunctional approach". This consists of a chelating system (bifunctional chelating agent, BFCA) that is able to stabilise and keep the metal far from the target molecule.[4]

In recent years, Tc and Re radiopharmaceutical chemistry with the cation *fac*-$[M(H_2O)_3(CO)_3]^+$ has been intensely stimulated by the fundamental contributions of Alberto, Schibli and Schubiger with the development of novel and simple methods for preparing the aqua ions *fac*-$[^{99m}Tc(H_2O)_3(CO)_3]^+$ and *fac*-$[^{188}Re(H_2O)_3(CO)_3]^+$.[5] The interest in the design of radiopharmaceuticals with carbonyl ligands results from their high thermodynamic stability, small size, kinetic inertia and in vivo stability.[6] Furthermore, the $[M(CO)_3]^+$ moiety allows the use of a wide range of ligand systems, therefore many different chelating sets have been tested.[7]

In this context, several research groups are currently looking for an "ideal building block" with an optimised in vitro and in vivo behaviour. In the last few years, these complexation studies have been principally focused on the development of tridentate BFCAs to obtain a tripodal mode of coordination (Scheme 1). Nevertheless, tricoordination can also be achieved by using a mixture of two ligands, one bidentate L_2 and one monodentate L_1 to produce an $[M(L_2)(L_1\text{-Biomol})(CO)_3]$ complex by means of a [2+1] mixed-ligand approach (Scheme 1).[8] A recent paper has reported the use of this "[2+1]" approach to prepare new *fac*-M(CO)$_3$ compounds for radiopharmaceutical use from a dithiocarbamate and a monodentate isocyanide ligand.[9]

[a] Department of Pharmaceutical Sciences, University of Padova, Via Marzolo 5, 35131 Padova, Italy
[b] Department of Chemistry, Universitat Autònoma de Barcelona, 08193 Bellaterra, Spain
[c] X-ray Diffraction Service, Universitat Autònoma de Barcelona, 08193 Bellaterra, Spain

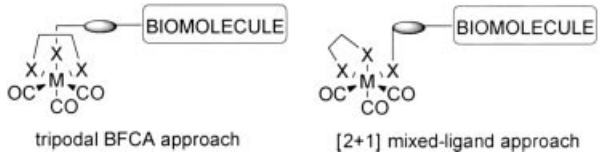

Scheme 1. Two different approaches for the stabilisation of a tricarbonylrhenium or -technetium core (M = Re/Tc).

Here, we report an investigation where we propose a suitable chelating system for the stabilisation of the *fac*-[M(CO)$_3$]$^+$ moiety by the [2+1] mixed-ligand approach, based on the simple *N*,*N*-dimethyldithiocarbamate (MDTC) as bidentate ligand and a functionalised phosphane as monodentate ligand. The phosphane acts as a bifunctional agent because it contains an anchor group that is useful for the conjugation with the biological vector, while MDTC acts as a co-ligand as it is able to neutralise and stabilise the metal system.

Phosphane ligands are well known for their capability to form very stable and inert bonds with organometallic fragments. Succinimidyl 3-diphenylphosphanylpropionate was selected as the BFCA because it can be simultaneously linked to a metal centre and to a biomolecule (Scheme 2).[10,11]

To evaluate the viability of this new [2+1] mixed-ligand approach we synthesised phosphane derivatives with aminoacid methyl esters following the above reaction. These ligands can simulate the presence of a conjugated targeting biomolecule and test the potential application of the new [2+1] mixed-ligand system in the presence of a biomolecule anchored to the monodentate ligand.

The coordination chemistry of the phosphane derivatives and sodium MDTC was studied by reaction with "cold" [NEt$_4$]$_2$[Re(CO$_3$)Br$_3$].[12] Rhenium complexes are structural models of technetium complexes due to the lanthanide contraction that ensures that the analogous complexes display very similar coordination parameters and physical properties.[13]

This study presents the syntheses and structural characterisation of three phosphane ligands and the [2+1] rhenium complexes obtained by combining the prepared phosphanes and sodium MDTC with the [Re(CO)$_3$]$^+$ moiety.

Results and Discussion

Synthesis of the Ligands

The synthesis and characterisation of the phosphane ester ligand **L1** has been reported previously.[14,15] We obtained the same compound using an alternative preparation starting from succinimidyl 3-diphenylphosphanylpropionate. The new functionalised phosphanes **L2** and **L3** were prepared by reaction of the same activated ester with the amino acid derivatives glycine methyl ester (**L2**) and β-alanine methyl ester (**L3**; Scheme 2) using modifications of the published procedures.[10,16] All these results are consistent with the ability of succinimidyl 3-diphenylphosphanylpropionate to act as a synthon for preparing phosphane-derivatised compounds. All ligands were obtained in good yields (70–75%) after purification by flash column chromatography as pale-yellow pure oils (air-sensitive compounds) and were characterised by NMR (^{1}H, ^{13}C, ^{31}P) and FT-IR spectroscopy and ESI mass spectrometry.

The collected data are consistent with the proposed structures and can be compared with the characterisation reported for similar ligands.[11,16] The ^{31}P NMR spectra of **L1**–**L3** show a sole singlet in the range δ = –13.9/–14.4 ppm characteristic of a ligand containing a diphenylphosphane group. The formation of the amide bond in **L2** and **L3** is evidenced by the IR spectra, which show a strong band near 1650 cm^{-1}, and by the proton signals of the amide group observed at δ = 6.12 (**L2**) and 6.03 ppm (**L3**) in the ^{1}H NMR spectra. The presence of a methyl ester group in **L1**–**L3** was evidenced in the IR spectra by a strong absorption between 1738–1752 cm^{-1} and by a singlet in the ^{1}H NMR spectra at around δ = 3.65 ppm. The ^{1}H and ^{13}C NMR

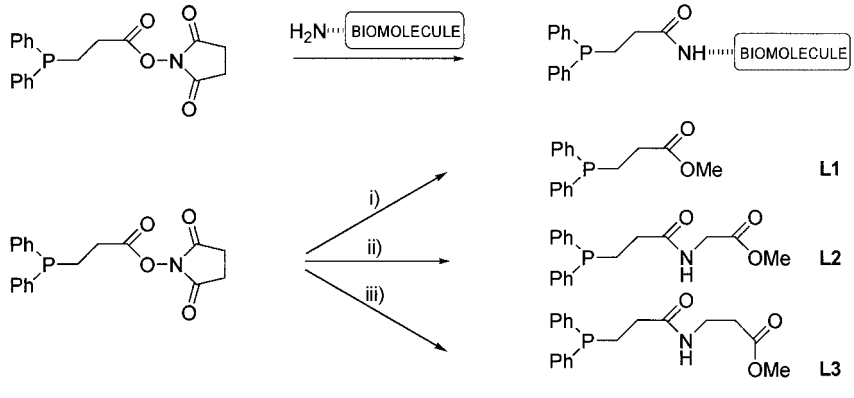

Scheme 2. General syntheses for biomolecule-functionalised phosphanes and synthesis of the phosphane ligands **L1**–**L3**.

 © 2005 Wiley-VCH Verlag GmbH & Co. KGaA, Weinheim

spectra display the signals of all organic groups involved in ligands **L1**–**L3**. Finally, the identities of **L1**–**L3** were confirmed by the positive ion ESI mass spectra, which display an intense signal assigned to the $[M + H]^+$ cation.

Complexation Studies

The great capability of phosphorus(III) to form stable complexes with transition metals in low oxidation states is well known, and coordination studies employing phosphanes with the Re^I tricarbonyl core have been carried out and reported in the literature.[17–20] Benak et al. have demonstrated that the reaction between $[Re(CO)_5Cl]$ and a diphenylphosphane ester affords the mononuclear tricarbonyl complexes *fac*-$[Re(CO)_3ClL_2]$ (L = phosphane) with the metal centre stabilised by the two phosphorus ligands.[18] Santos et al. have explored the coordination ability of tridentate hetero-functionalised diphenylphosphanes and obtained mainly PO or PN bicoordinated complexes.[19,20] In both cases tricoordination is generally not achieved, and the last position of the metal coordination sphere is occupied by a halogen. Furthermore, the formation of different isomers is often observed when bidentate ligands are employed.[21]

The use of sodium MDTC and diphenylphosphane in the [2+1] strategy has the potential advantage of producing monomeric and neutral tricoordinate complexes. Only one phosphane coordinates to rhenium in a monodentate fashion to produce minimal steric impact between the aliphatic chain and the metal sphere.

The rhenium(I) tricarbonyl complexes **C1**–**C3** were prepared in two different ways, as shown in Scheme 3. In the two-step pathway, or "indirect synthesis", complexes **C1**–**C3** were formed from an intermediate dithiocarbamate complex. This complex was synthesised in the first step by simple addition of sodium MDTC to a solution of the rhenium tricarbonyl precursor $[Re(CO)_3Br_3]^{2-}$ in methanol. The resulting product was not characterised; however, we suppose that a neutral soluble monomeric SS-bicoordinated species is formed, as reported by Gorshkov et al. for similar dithiocarbamates with the $[Re(CO)_3]^+$ moiety.[9] The simple substitution of a coordinated methanol by a monodentate phosphane ligand (**L1**–**L3**) blocks the coordination vacancy and leads to the target complexes (**C1**–**C3**) in good yields after purification by flash chromatography. The solid compounds are remarkably inert and stable to air and moisture, even in solution (organic solvents). No decomposition was observed after many weeks.

The presence of the *fac*-$[Re(CO)_3]$ fragment in complexes **C1**–**C3** was revealed by the three characteristic CO stretching bands (**C1**: 2016, 1921 and 1890 cm^{-1}) observed in the IR spectra.[18–21] This technique also supplies useful information about the coordination of the dithiocarbamate ligand, since a single, strong band at 1522–1526 cm^{-1} was observed, which was assigned to the C–N stretching of a symmetrical bidentate dithiocarbamate.[22] The C=O stretching vibrations of the ester and amide groups are similar to those of the free ligand, and were accorded to the exclusion of these groups from the participation in the metal sphere.

The ^{31}P NMR spectra of complexes **C1**–**C3** show the complete absence of the corresponding free ligand, and display a sole signal in the range δ = 5–8 ppm, thus confirming the absence of isomers. A significant downfield shift with respect to the resonance of the free ligands (δ = –14 to –16 ppm) was observed, in agreement with the formation of a phosphorus–metal bond. The coordination of the phosphane ligand is also evidenced by the ^{13}C NMR spectra, which show an important increase of the $^1J_{P,C}$ and $^2J_{P,C}$ couplings of the methylene groups with respect to the values observed in the free ligands. These data are in accordance with literature reports.[11,17,18] Furthermore, the simultaneous presence of MDTC and phosphane ligands with the rhenium tricarbonyl core is also consistent with the ^1H NMR, ^{13}C NMR and ESI-MS data, supporting the (SS)(P) coordination to the fragment *fac*-$[Re(CO)_3]^+$.

Single crystals of complexes **C1** and **C3** were obtained by recrystallisation and their structures were determined by X-ray methods. Perspective views of both molecules are displayed in Figures 1 and 2, respectively. Selected bond lengths and angles are collected in Table 1. The simultaneous coordination of the chelated dithiocarbamate and the phosphane to the *fac*-$[Re(CO)_3]^+$ fragment confirms the proposed structure and therefore the formation of the target [2+1] mixed-ligand rhenium tricarbonyl complexes. The coordination geometry around the metal atom can be described as a slightly distorted octahedron. The principal distortion comes from the bite angle of the chelated dithiocarbamate ligand, which forces the S–Re–S angles to be near 70°, a common value in other metal complexes with chelated dithiocarbamates.[23] The almost identical Re–S dis-

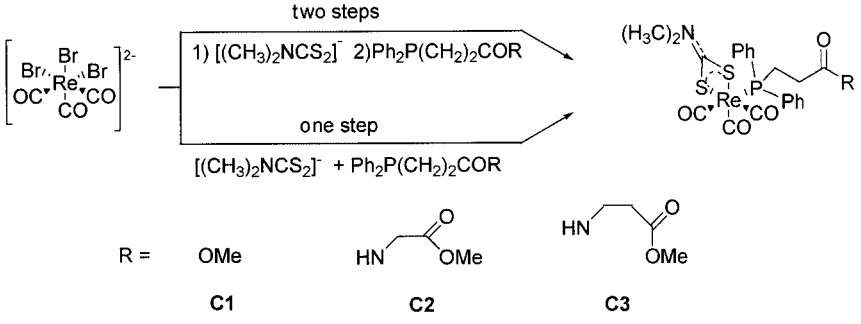

Scheme 3. Syntheses of the complexes **C1**–**C3** by the one-step and two-step approaches.

 © 2005 Wiley-VCH Verlag GmbH & Co. KGaA, Weinheim

tances indicate that the dithiocarbamate ligand links to rhenium in a symmetrical bidentate mode in both complexes. The SCS plane of the dithiocarbamate is nearly coincident with the SReS plane, with S42–Re–S41 and S41–C43–S42 angles of 2.2(4)° and 4.7(5)° for **C1** and **C3**, respectively Consequently, the metal atom, the dithiocarbamate and the two carbonyl ligands *trans* to sulfurs lie in a slightly distorted plane. The third carbonyl and the Re–P bond are arranged almost perpendicular to this plane, and the Re–P distances for both **C1** and **C3** are in the range observed for other diphenylphosphanyl–metal complexes. It should be pointed out that the ester and amido groups of the functionalised phosphanes are located away from the metal atom. This result is relevant with regard to radiopharmaceutical applications since the amino acid fragment linked to the phosphane is not affected by the coordination to the metal. Another interesting point concerns the similar Re–C distances observed in the *fac*-Re(CO)$_3$ fragments despite the different electronic characteristics of the ligands located in the *trans* position (dithiocarbamate or phosphane). The Re–C distances of carbonyl ligands *trans* to phosphane are comparable with the carbonyls *trans* to dithiocarbamate both for **C3** and **C1**. This fact could be related to the capability of phosphane and dithiocarbamate ligands to form similar strong bonds with rhenium and to the observed experimental stability and kinetic inertia of the studied complexes.[22]

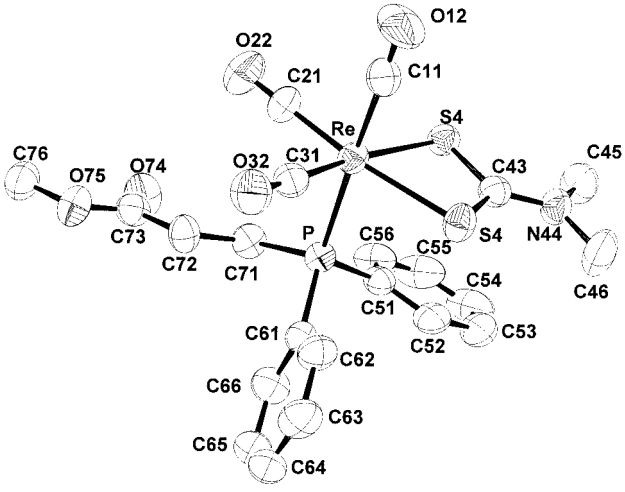

Figure 1. ORTEP diagram of **C1** showing 50% probability ellipsoids (hydrogen atoms omitted for clarity).

The one-step synthesis of complexes **C1**–**C3** by direct reaction between the rhenium precursor [Re(CO)$_3$Br$_3$]$^{2-}$ and an equimolecular mixture of dithiocarbamate and phosphane was studied in order to evaluate whether the characterised complexes are the main products by this pathway (Scheme 3). This reaction can be regarded as a test at macroscopic concentrations of the viability for future development of a [2+1] mixed-ligand kit for radiopharmaceutical applications.[24] Complexes **C1**–**C3** were obtained in good yields (68–75%) by this direct pathway and they display identical spectroscopic and analytical parameters to

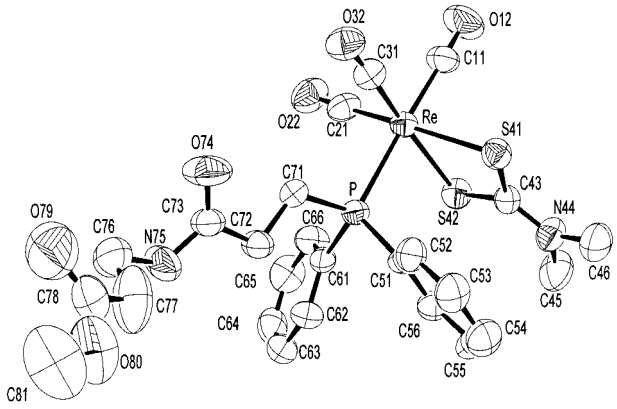

Figure 2. ORTEP diagram of **C3** showing 50% probability ellipsoids (hydrogen atoms omitted for clarity).

Table 1. Selected bond lengths [Å] and angles [°] for **C1** and **C3**.

	C1	**C3**
Re–P	2.495(2)	2.492(2)
Re–C11	1.911(8)	1.943(10)
Re–C21	1.929(6)	1.905(10)
Re–C31	1.898(6)	1.913(9)
Re–S41	2.508(2)	2.516(2)
Re–S42	2.511(2)	2.507(2)
S41–C43	1.715(6)	1.733(8)
S42–C43	1.718(6)	1.710(8)
C43–N44	1.327(7)	1.313(10)
S41–Re–S42	70.18(5)	70.00(7)
P–Re–S41	88.63(5)	88.86(7)
P–Re–S42	88.16(5)	84.08(7)
C11–Re–C21	89.1(3)	87.6(4)
C21–Re–C31	89.8(3)	89.0(4)
C11–Re–C31	89.0(3)	88.5(4)
C11–Re–P	177.5(2)	178.1(3)
S41–Re–C31	100.3(2)	99.9(3)
S42–Re–C21	99.8(2)	101.3(3)
S41–C43–S42	114.3(4)	113.6(5)

the complexes synthesised by the two-step method. On comparing the two methods, the yields seem to be independent of the reaction path, but in the second case the product is obtained in a simple one-step reaction. In the reaction with a ligand mixture, the main product was still the tricoordinate monomeric neutral complex. The absence of significant quantities of phosphane complexes or dithiocarbamate complexes (or bidentate complexes in general) as by-products is a relevant result since it could be related to the peculiar thermodynamic stability of the tripodal (SS)(P) donor set for the metal tricarbonyl core.

Labelling Studies with ^{99m}Tc

The preparations of the homologous radioactive complexes were studied under no-carrier-added conditions by ligand substitution with the precursor *fac*-[^{99m}Tc(H$_2$O)$_3$(CO)$_3$]$^+$ and checked by HPLC analysis. The labile water ligands can easily be replaced by more stable and inert ligands. This reaction has been explored with DMTC[9] and phosphane ligands.[20,25,26]

 © 2005 Wiley-VCH Verlag GmbH & Co. KGaA, Weinheim

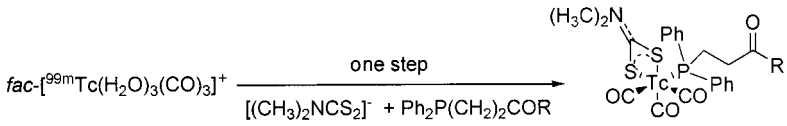

R = $HNCH_2COOCH_3$ (**C4**), $HN(CH_2)_2COOCH_3$ (**C5**)

Scheme 4. Syntheses of the radio complexes **C4** and **C5** by the one-step approach.

We used the representative ligands **L2** and **L3** to simulate the presence of a biomolecule conjugated to the phosphorus atom of the phosphane (Scheme 4). The one-step synthesis was used to evaluate the (SS)(P) approach because it is the more attractive method for preparing radiopharmaceuticals. So, we added the dithiocarbamate and the phosphane ligand at the same time. The lipophilic character of diphenylphosphanes justified the use of ethanol to prepare the mixed-ligand solution. HPLC analysis showed that the addiction of the ligand mixture to the precursor *fac*-$[^{99m}Tc(H_2O)_3(CO)_3]^+$ led to the formation of a major compound in both cases. The retention times between the two ^{99m}Tc compounds (13.27 min for **C4** and 13.44 min for **C5**) and the analogous Re complexes (13.39 and 13.54 min for **C2** and **C3**, respectively) are almost identical (Figure 3). These results are consistent with the structure of the $Re(CO)_3$(SS)(P) coordination system for the radio complexes **C4** and **C5**.

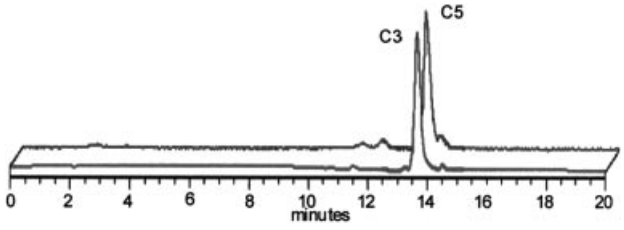

Figure 3. HPLC UV trace of the rhenium complex **C3** and γ-trace of the radioactive ^{99m}Tc complex **C5**.

The labelling reactions were also studied under different reaction conditions (pH temperature, reaction time, reagents' concentration and ratio) in order to obtain the optimised protocols. Reaction of a 4:1 mixture of MDTC and phosphane ligands at 80 °C for 60 min was found to give the best results in terms of yields.

To confirm the [2+1] coordination set, the precursor was reacted under the same conditions, but with only dithiocarbamate or with only phosphane ligands in the reaction mixture. The labelling mixtures were analysed by HPLC to determine the retention times of the products. DMTC reacts with the tricarbonyl radioactive moiety to give a unique peak at 14.21 min, while the reaction with the phosphane ligands gave two peaks at 10.98/11.57 min (**L2**) and 11.38/12.12 min (**L3**). These results support the formation of (SS)(P) coordination to $^{99m}Tc(CO)_3^+$ as the main product because these signals were observed as minor products in the reaction with the simultaneous addition of the dithiocarbamate and the phosphane ligand.

Conclusions

The coordinating chelating system (SS)(P) appears to be promising for a future medical application since complexes with the $[Re(CO)_3]^+$ moiety can easily be prepared in a one-step synthesis (useful in the design of a commercial kit), with good yields, and the synthesised products are very stable. The achieved tricoordination presented in this paper is very versatile and offers the possibility to link a wide range of target molecules to the monodentate phosphane. Furthermore, the chemistry of dithiocarbamates is well understood, and it is relatively easy to synthesise derivatives with different residues to modulate the hydro- or lipophilic characteristics of the desired complexes. Indeed, this [2+1] integrated approach with a symmetric bidentate chelating agent also avoids the formation of stereoisomers, which are often detected when using non-symmetric bidentate ligands or tridentate BFCA. The isomer formation influences the specific receptor binding because of the different metal–ligand orientation and may produce labelled species with different affinity for the same target, principally for small biomolecules.[27] From the perspective of developing a new drug, single and chemically stable products are essential for FDA approval.[8a]

Tc-99m labelling studies using the one-step method have confirmed the capability to produce (SS)(P) radio complexes. The next step will be to test the stability and kinetic inertia of the prepared compounds in order to evaluate their application for the formulation of new radiopharmaceuticals.

We conclude that the present [2+1] complex fashion could be a useful building block in the design and development of new target-specific ^{99m}Tc and $^{186/188}Re$ radiopharmaceuticals based on the tricarbonyl concept.

Experimental Section

Materials and Analytical Methods: All reactions were performed under nitrogen using standard Schlenk tube techniques. Solvents were degassed and tested for peroxides prior to use. All chemicals and solvents were reagent grade and were used without further purification. Infrared spectra were recorded with a Perkin–Elmer 1710 FT spectrometer as KBr pellets. The NMR spectra were recorded by the Servei de Ressonància Magnètica Nuclear de la Universitat Autònoma de Barcelona with a Bruker AM400 instrument. The ^{31}P chemical shifts are reported in ppm up-field from external 85% H_3PO_4. The ^1H and ^{13}C chemical shifts are expressed in ppm up-field from TMS.

 © 2005 Wiley-VCH Verlag GmbH & Co. KGaA, Weinheim

Succinimidyl 3-diphenylphosphanylpropionate was provided by Argus Spechem S.a.s. (Prato, Italy) and the precursor $[NEt_4]_2[Re(CO_3)Br_3]$ was prepared by published procedures.[12] Microanalyses were performed at the Servei d'Anàlisi Química de la Universitat Autònoma de Barcelona. Electrospray ionisation mass spectra (ESI-MS) were obtained with an Applied Mariner System 5220 mass spectrometer (PerSeptive Biosystems Inc., Framingham, MA) in the positive-ion mode after dissolving the samples in acetonitrile (10^{-3} M).

The diffraction measurements were recorded by the X-ray Diffraction Service of the Universitat Autònoma de Barcelona.

Analytical thin-layer chromatography (TLC) was performed on Merck (Darmstadt, Germany) silica gel 60-F_{254} plates using the following elution systems: (a): *n*-hexane/EtOAc (3:2); (b): *n*-hexane/AcOEt (1:3); visualisation was accomplished by UV detection at 254 nm. Flash chromatography was carried out using silica gel 230–400 Mesh (Merck, Darmstadt, Germany) according to the method of Still.[28]

RP-HPLC analyses were performed on a Waters chromatography system (Waters, Milford, MA) controlled with a binary Waters 510 programmable gradient pump of the Department of Pharmaceutical Sciences, University of Padova. The analyses were monitored with a Waters 486 tunable absorbance detector set at 215 nm and a Bioscan-γ-detector B-FC 3200 (Milano, Italy). A Hamilton C18 reverse-phase column (10 μm, 250×4.6 mm, Alltech Italia, Sedriano, Milano) was used and the solvents were water with 0.1% trifluoroacetic acid (A) and acetonitrile with 0.05% trifluoroacetic acid (B). The HPLC gradient system started at 50% A/50% B, which was maintained for 5 min, rising to 100% B in 5 min with a linear gradient. It was maintained at a maximum of B for 8 min before returning to initial conditions in 2 min. The flow rate was 1 mL min^{-1}.

$Na^{99m}TcO_4$ was eluted from a commercial Drytec Sorin ^{99}Mo/^{99m}Tc Nycomed Amersham Sorin generator (Saluggia, Vercelli, Italy) using a 0.9% saline solution. The radioactive precursor *fac*-$[^{99m}Tc(H_2O)_3(CO)_3]^+$ was prepared with an IsoLink kit purchased from Mallinckrodt Med. B.V. (Pettern, Netherland).

All manipulations were carried out as approved for low-level radioactivity use.

Methyl 3-Diphenylphosphanylpropionate (L1): A solution of succinimidyl 3-diphenylphosphanylpropionate (1.41 mmol) in methanol (20 mL) was added dropwise to a stirred solution of (benzotriazol-1-yloxy)tripyrrolidinophosphonium hexafluorophosphate (PyBOP, 1.41 mmol) in the same solvent (20 mL). The mixture was left stirring for 6 h at room temperature, then the solvent was removed under vacuum. The oily residue containing product **L1** was purified by silica gel flash column chromatography (a) and concentrated to obtain a pale-yellow oil. Yield: 268 mg (70%). TLC (a): R_f = 0.8. HPLC: R_t = 14.63 min. FT-IR (KBr): $\tilde{\nu}$ = 1744 cm^{-1} (C=O, ester). ^{1}H NMR ($CDCl_3$): δ = 2.35–2.41 (m, 4 H, PCH_2CH_2), 3.64 (s, 3 H, OCH_3), 7.32–7.43 (m, 10 H, ArH) ppm. ^{13}C NMR ($CDCl_3$, except phenyl resonances): δ = 22.7 (d, $^1J_{C,P}$ = 12.5 Hz, P*C*H$_2$), 30.3 (d, $^2J_{C,P}$ = 19.2 Hz, PCH$_2$*C*H$_2$), 52.5 (s, OCH$_3$), 173.2 (d, $^3J_{C,P}$ = 15.3 Hz, *C*OOMe) ppm. ^{31}P NMR ($CDCl_3$): δ = –14.4 ppm. ESI-MS: *m*/*z* = 273 [M + H]$^+$.

Methyl [3-(Diphenylphosphanyl)propionylamino]acetate (L2): Triethylamine (2.39 mmol) was added to a suspension of glycine methyl ester hydrochloride (1.59 mmol) in anhydrous CH_2Cl_2 (50 mL). The solution was stirred for 30 min and then succinimidyl 3-(diphenylphosphanyl)propionate (1.59 mmol) was added. The mixture was stirred for 3 h and the solvent was then removed under vacuum. The oily crude containing product **L2** was purified by silica gel flash column chromatography (b) and concentrated to obtain a pale-yellow oil. Yield: 368 mg (70%). TLC (b): R_f = 0.8. HPLC: R_t = 9.90 min. FT-IR (KBr): $\tilde{\nu}$ = 1752 cm^{-1} (C=O, ester), 1654 (C=O, amide). ^{1}H NMR ($CDCl_3$): δ = 2.31–2.41 (m, 4 H, PCH_2CH_2), 3.72 (s, 3 H, OCH$_3$), 3.98 (d, $^3J_{CH,NH}$ = 6.3 Hz, 2 H, -NHCH_2), 6.12 (br., 1 H, NH), 7.30–7.45 (m, 10 H, ArH) ppm. ^{13}C NMR ($CDCl_3$, except phenyl resonances): δ = 23.3 (d, $^1J_{C,P}$ = 10.6 Hz, P*C*H$_2$), 32.5 (d, $^2J_{C,P}$ = 17.3 Hz, PCH$_2$*C*H$_2$), 41.5 (s, *C*H$_2$COOMe), 52.5 (s, OCH$_3$), 170.3 (s, *C*OOMe), 171.4 (d, $^3J_{C,P}$ = 13.4 Hz, *C*ONH) ppm. ^{31}P NMR ($CDCl_3$): δ = –13.9 ppm. ESI-MS: *m*/*z* = 330 [M + H]$^+$

Methyl [3-(Diphenylphosphanyl)propionylamino]propionate (L3): Triethylamine (2.68 mmol) was added to a suspension of β-alanine methyl ester hydrochloride (1.79 mmol) in anhydrous CH_2Cl_2 (50 mL). The resulting solution was stirred for 30 min and succinimidyl 3-(diphenylphosphanyl)propionate (1.79 mmol) was added. The mixture was stirred for 4 h and the solvent was then removed under vacuum. The oily crude residue containing product **L3** was purified by silica gel flash column chromatography (b) and concentrated to obtain a pale-yellow oil. Yield: 442 mg (72%). TLC (b): R_f = 0.75. HPLC: R_t = 9.98 min. FT-IR (KBr): $\tilde{\nu}$ = 1738 cm^{-1} (C=O, ester), 1652 (C=O, amide). ^{1}H NMR ($CDCl_3$): δ = 2.15–2.23 (m, 2 H, PCH_2), 2.32–2.35 (m, 2 H, PCH$_2$CH_2), 2.43 (t, ^3J = 6.3 Hz, 2 H, CH_2COOMe), 3.35–3.41 (dt, ^3J = 6.3, $^3J_{CH,NH}$ = 6.0 Hz, 2 H, -NHCH_2), 3.59 (s, 3 H, OCH$_3$), 6.03 (t, $^3J_{CH,NH}$ = 6.0 Hz, 1 H, NH), 7.22–7.36 (m, 10 H, ArH) ppm. ^{13}C NMR ($CDCl_3$, except phenyl resonances): δ = 23.1 (d, $^1J_{C,P}$ = 11.5 Hz, P*C*H$_2$), 32.4 (d, $^2J_{C,P}$ = 18.2 Hz, PCH$_2$*C*H$_2$), 33.5 (s, *C*H$_2$COOMe), 34.7 (s, HN*C*H$_2$), 51.5 (s, OCH$_3$), 171.9 (d, $^3J_{C,P}$ = 13.2 Hz, CONH), 172.1 (s, 1C, *C*OOMe) ppm. ^{31}P NMR ($CDCl_3$): δ = –14.3 ppm. ESI-MS: *m*/*z* = 344 [M + H]$^+$.

Synthesis of Rhenium Complexes. Two-Step Method: A solution of sodium *N*,*N*-dimethyldithiocarbamate (0.35 mmol) dissolved in methanol (20 mL) was added dropwise to a solution of rhenium tricarbonyl precursor $[NEt_4]_2[Re(CO_3)Br_3]$ (0.35 mmol) in the same solvent (20 mL). The obtained mixture was stirred for 30 min. A methanolic solution (20 mL) of phosphane ligand (0.35 mmol) was then added dropwise to the resulting pale yellow-green solution, and stirred for 90 min. The solvent was removed under vacuum and the oily residue containing the complex was purified by silica gel flash column chromatography (elution system a for **C1** and b for **C2** and **C3**). The solvents were then evaporated under vacuum. The obtained oil was taken up with 5 mL of Et_2O and then 50 mL of *n*-hexane was added to precipitate the product. The white powder was filtered off and dried under vacuum.

One-Step Method: A solution of *N*,*N*-dimethyldithiocarbamate (0.28 mmol) and phosphane ligand (0.28 mmol) dissolved in methanol (40 mL) was added dropwise to a solution of rhenium tricarbonyl precursor $[NEt_4]_2[Re(CO_3)Br_3]$ (0.28 mmol) in the same solvent (20 mL). The obtained mixture was stirred for 60 min and the solvent was removed under vacuum. The crude product containing the complex was purified by silica gel flash column chromatography (elution system a for **C1** and b for **C2** and **C3**). The solvents were evaporated under vacuum. The obtained oil was taken up with 5 mL of Et_2O and then 50 mL of *n*-hexane was added to precipitate the product. The white solid was filtered off and dried under vacuum.

[Re(CO)$_3$(L1)(*N*,*N*-dimethyldithiocarbamate)] (C1): Two-step method: Yield: 172 mg (76%). One-step method: Yield: 132 mg (73%). TLC (a): R_f = 0.4. HPLC: R_t = 14.94 min. FT-IR (KBr): $\tilde{\nu}$ = 2016 cm^{-1}, 1921, 1890 (C≡O), 1733 (C=O, ester), 1523 (C–N,

 © 2005 Wiley-VCH Verlag GmbH & Co. KGaA, Weinheim

S_2CNMe_2). ^1H NMR ($CDCl_3$): δ = 2.31–2.39 (m, 2 H, PCH_2), 2.86 [s, 6 H, N(CH_3)$_2$], 2.89–2.97 (m, 2 H, PCH_2CH_2), 3.61 (s, 3 H, OCH_3), 7.26–7.55 (m, 10 H, ArH) ppm. ^{13}C NMR ($CDCl_3$, except phenyl resonances): δ = 22.7 (d, $^1J_{C,P}$ = 28.7 Hz, PCH_2), 30.1 (d, $^2J_{C,P}$ = 43.3 Hz, PCH_2CH_2), 38.2 [s, N(CH_3)$_2$], 51.6 (s, OCH_3), 172.6 (d, $^3J_{C,P}$ = 16.4 Hz, *C*OOMe), 190.1–193.6 [m, Re(CO)$_3$], 206.6 (s, NCS_2) ppm. ^{31}P NMR ($CDCl_3$): δ = 5.2 ppm. $C_{22}H_{23}NO_5PReS_2$: calcd. C 39.77, H 3.50, N 2.11, S 9.68; found C 39.66, H 3.65, N 2.08, S 9.42. ESI-MS: *m*/*z* = 664 [M + H]$^+$.

[Re(CO)$_3$(L2)(*N*,*N*-dimethyldithiocarbamate)] (C2): Two-step method: Yield: 165 mg (68%). One-step method: Yield: 146 mg (75%). TLC (b): R_f = 0.5. HPLC: R_t = 13.39 min. FT-IR (KBr): $\tilde{\nu}$ = 2016 cm^{-1}, 1919, 1890 (C≡O), 1750 (C=O, ester), 1654 (C=O, amide) 1522 (C–N, S_2CNMe_2). ^1H NMR ($CDCl_3$): δ = 2.25–2.33 (m, 2 H, PCH_2), 2.85 [s, 6 H, N(CH_3)$_2$], 2.94–3.02 (m, 2 H, PCH_2CH_2), 3.74 (s, 3 H, OCH_3), 3.96 (d, $^3J_{CH,NH}$ = 5.1 Hz, 2 H, -NHCH_2), 5.88 (br., 1 H, NH), 7.37–7.55 (m, 10 H, ArH) ppm. ^{13}C NMR ($CDCl_3$, except phenyl resonances): δ = 24.1 (d, $^1J_{C,P}$ = 28.7 Hz, PCH_2), 30.2 (d, $^2J_{C,P}$ = 43.0 Hz, PCH_2CH_2), 38.2 [s, N(CH_3)$_2$], 41.4 (s, CH_2COOMe), 52.4 (s, OCH_3), 170.16 (s, *C*O-OMe), 171.48 (d, $^3J_{C,P}$ = 14.7 Hz, CONH), 189.2–193.3 [m, Re(CO)$_3$], 212.4 (s, NCS_2) ppm. ^{31}P NMR ($CDCl_3$): δ = 6.7 ppm. $C_{24}H_{26}N_2O_6PReS_2$: calcd. C 40.05, H 3.64, N 3.89, S 8.91; found C 39.97, H 3.75, N 3.65, S 8.62. ESI-MS: *m*/*z* = 721 [M + H]$^+$.

[Re(CO)$_3$(L3)(*N*,*N*-dimethyldithiocarbamate)] (C3): Two-step method: Yield: 192 mg (77%). One-step method: Yield: 147 mg (73%). TLC (b): R_f = 0.5. HPLC: R_t = 13.54 min. FT-IR (KBr): $\tilde{\nu}$ = 2015 cm^{-1}, 1920, 1889 (C≡O), 1734 (C=O, ester), 1652 (C=O, amide) 1526 (C–N, S_2CNMe_2). ^1H NMR ($CDCl_3$,): δ = 2.20–2.27 (m, 2 H, PCH_2CH_2), 2.40 (t, ^3J = 6.1 Hz, 2 H, Ala-CH_2-COOMe), 2.85 [s, 6 H, N(CH_3)$_2$], 2.93–3.00 (m, 2 H, PCH_2CH_2), 3.42–3.49 (dt, ^3J = 6.3, $^3J_{CH,NH}$ = 5.0 Hz, 2 H, Ala-NH-CH_2), 3.70 (s, 3 H, OCH_3), 5.97 (t, $^3J_{CH,NH}$ = 5.0 Hz, 1 H, NH), 7.41–7.57 (m, 10 H, ArH) ppm. ^{13}C NMR ($CDCl_3$, except phenyl resonances): δ = 24.3 (d, $^1J_{C,P}$ = 28.8 Hz, PCH_2), 30.0 (d, $^2J_{C,P}$ = 47.0 Hz, PCH_2CH_2), 31.9 (s, CH_2COOMe), 34.9 (s, HNCH_2), 38.4 [s, N(CH_3)$_2$], 51.5 (s, OCH_3), 171.5 (d, $^3J_{C,P}$ = 14.4 Hz, CONH), 172.5 (s, *C*OOMe), 189.2–193.4 [m, Re(CO)$_3$], 212.2 (s, NCS_2) ppm. ^{31}P NMR ($CDCl_3$): δ = 7.7 ppm. $C_{25}H_{28}N_2O_6PReS_2$: calcd. C 40.92, H 3.85, N 3.82, S 8.74; found C 40.87, H 3.93, N 3.71, S 8.70. ESI-MS: *m*/*z* = 735 [M + H]$^+$.

Synthesis of Technetium-99m Complexes. General Procedure: Technetium-99m labelling was performed by addiction of 15 μL of an ethanolic solution of *N*,*N*-dimethyldithiocarbamate (0.8 mM, 0.012 μmol) and phosphane ligand (0.2 mM, 0.003 μmol) to 85 μL of a freshly prepared solution of *fac*-[^{99m}Tc(H$_2$O)$_3$(CO)$_3$]$^+$ (15 MBq), pH 7.4. The mixture was incubated at 80 °C and stirred for 1 h. Analysis by HPLC equipped with a γ-radiometric detector showed a main peak for all experiments. Data are expressed as means of ±SD of three experiments.

Comparative *fac*-[^{99m}Tc(H$_2$O)$_3$(CO)$_3$]$^+$ labelling reactions with the only presence of *N*,*N*-dimethyldithiocarbamate or phosphane ligand were carried out under the same conditions and analysed by HPLC.

[^{99m}Tc(CO)$_3$(L2)(*N*,*N*-dimethyldithiocarbamate)] (C4): HPLC: R_t = 13.27 min. Labelling yield = 83 ± 1.7%. (HPLC: R_t [^{99m}Tc(CO)$_3$ with DMTC] = 14.29 min, R_t [^{99m}Tc(CO)$_3$ with L2] = 10.98 min, 11.57 min).

[^{99m}Tc(CO)$_3$(L3)(*N*,*N*-dimethyldithiocarbamate)] (C5): HPLC: R_t = 13.44 min. Labelling yield = 83 ± 1.7%. (HPLC: R_t [^{99m}Tc(CO)$_3$ with DMTC] = 14.29 min, R_t [^{99m}Tc(CO)$_3$ with L3] = 11.38 min, 12.12 min).

X-ray Crystallography: Colourless single crystals were obtained from methanol at –30 °C (**C1**) or by slow diffusion of *n*-hexane into a solution of the compound in ethyl acetate at room temperature (**C3**). Crystal data and selected information on data collection and structure determination are given in Table 2. Data were collected on a Bruker SMART CCD area-detector diffractometer at room temperature. Graphite-monochromated Mo-K_α radiation (λ = 0.71073 Å) was used. Lorentz-polarisation and absorption corrections were applied using Bruker SAINT and SADABS software. The structures were solved by direct methods and refined by full-matrix least-squares on F^2 for all unique measured data with weighting $w^{-1} = \sigma^2(F_o^2) + (aP)^2 + bP$, where $P = (F_o^2 + 2F_c^2)/3$.[29] Non-hydrogen atoms were refined anisotropically. Hydrogen atoms were included with riding model constraints and isotropic displace-

Table 2. Crystal data and structure refinement parameters for **C1** and **C3**.

	C1	**C3**
Empirical formula	$C_{22}H_{23}NO_5PReS_2$	$C_{25}H_{28}N_2O_6PReS_2$
Formula mass	662.70	733.78
Crystal system	monoclinic	monoclinic
Space group	*C*2/*c*	$P2_1/c$
a [Å]	22.6340(16)	10.6473(8)
b [Å]	10.6284(7)	29.191(2)
c [Å]	21.2346(14)	9.1776(7)
β [°]	103.212(1)	92.566 (2)
V [Å^3]	4973.1(6)	2849.6(4)
Z	8	4
$\rho_{calcd.}$ [Mg m^{-3}]	1.770	1.710
Absorption coefficient [mm^{-1}]	5.152	4.508
F(000)	2592	1448
Crystal size [mm]	0.22 × 0.18 × 0.08	0.22 × 0.10 × 0.05
Theta range for data collection	1.85 to 28.26	1.40 to 28.22
Reflections collected/unique	15196/5601 (R_{int} = 0.0445)	17896/6380 (R_{int} = 0.0560)
Max. and min. transmission	0.66 and 0.32	0.80 and 0.37
Data/restraints/parameters	5601/12/292	6380/12/337
Goodness-of-fit on F^2	1.056	1.068
$R(F)$, $R_w(F^2)$ [$I > 2\sigma(I)$]	0.0457, 0.0899	0.0603, 0.1120
$R(F)$, $R_w(F^2)$ (all data)	0.0636, 0.0960	0.0989, 0.1275

 © 2005 Wiley-VCH Verlag GmbH & Co. KGaA, Weinheim

ment parameters 1.5 (methyl H) or 1.2 (the rest) times the U_{eq} values of the corresponding carbon or nitrogen atoms.
CCDC-258371 (for **C1**) and -258372 (for **C3**) contain the supplementary crystallographic data for this paper. These data can be obtained free of charge from the Cambridge Crystallographic Data Centre via www.ccdc.cam.ac.uk/data_request/cif.

Acknowledgments

The authors would like to thank the COST action B12, the C.I.R.C.MSB. (Bari, Italy), the Italian Ministero dell'Universitá e della Ricerca Scientifica e Tecnologica and the Spanish Dirección General de Investigación for financial support.

[1] a) K. Schwochau, *Technetium, Chemistry and Radiopharmaceutical Application*, Wiley-VCH, Weinheim, Germany, **2000**; b) J. Steigman, W. C. Eckelman, *The Chemistry of Technetium in Medicine*, Nuclear Science Series, National Academic Press, Washington DC, **1992**.
[2] a) S. Jurisson, D. Berning, W. Jia, D. Ma, *Chem. Rev.* **1993**, *93*, 1137–1156; b) F. F. Knapp Jr., A. L. Beet, S. Guhlke, *Anticancer Res.* **1997**, *17*, 1783–1796.
[3] a) C. J. Smith, G. L. Sieckman, N. K. Owen, D. L. Hayes, D. G. Mazuru, R. Kannan, W. A. Volkert, T. J. Hoffman, *Cancer Res.* **2003**, *63*, 4082–4088; b) R. La Bella, E. Garcia-Garayoa, M. Langer, P. Bläuenstein, A. G. Beck-Sickinger, P. A. Schubiger, *Nucl. Med. Biol.* **2002**, *29*, 553–560.
[4] a) S. Liu, D. S. Edwards, *Chem. Rev.* **1999**, *99*, 2235–2268; b) S. S. Jurisson, J. F. Lydon, *Chem. Rev.* **1999**, *99*, 2205–2218.
[5] a) R. Alberto, K. Ortner, N. Wheatley, R. Schibli, A. P. Schubiger, *J. Am. Chem. Soc.* **2001**, *123*, 3135–3136; b) R. Schibli, R. Schwarzbach, R. Alberto, K. Ortner, H. Schmalle, C. Dumas, A. Egli, P. A. Schubiger, *Bioconjugate Chem.* **2002**, *13*, 750–756.
[6] a) R. Alberto, R. Schibli, R. Waibel, U. Abram, A. P. Schubiger, *Coord. Chem. Rev.* **1999**, 190–192; R. Alberto, R. Schibli, R. Waibel, U. Abram, A. P. Schubiger, *Coord. Chem. Rev.* **1999**, 901–919; b) W. A. Volkert, T. J. Hoffman, *Chem. Rev.* **1999**, *99*, 2269–2292.
[7] a) J. K. Pak, P. Benny, B. Spingler, K. Ortner, R. Alberto, *Chem. Eur. J.* **2003**, *9*, 2053–2061; b) R. Schibli, K. V. Katti, C. Higginbotham, W. A. Volkert, R. Alberto, *J. Nucl. Med. Biol.* **1999**, *26*, 711–716; c) J. Bernard, K. Ortner, B. Spingler, H. J. Pietzsch, R. Alberto, *Inorg. Chem.* **2003**, *42*, 1014–1022.
[8] a) R. Alberto, *Eur. J. Nucl. Med. Mol. Imaging* **2003**, *30*, 1299–1302; b) S. Mundwiler, M. Kündig, K. Ortner, R. Alberto, *Dalton Trans.* **2004**, *9*, 1320–1328; c) R. Alberto, J. K. Pak, D. Van Staveren, S. Mundwiler, P. Benny, *Biopolymers* **2004**, *76*, 324–333.
[9] N. I. Gorshkov, R. Schibli, A. P. Schubiger, A. A. Lumpov, A. E. Miroslavov, D. N. Suglobov, *J. Organomet. Chem.* **2004**, *689*, 4757–4763.
[10] G. W. Anderson, J. E. Zimmerman, F. M. Callahan, *J. Am. Chem. Soc.* **1964**, *86*, 1839–1842.
[11] R. Visentin, R. Rossin, M. C. Giron, A. Dolmella, G. Bandoli, U. Mazzi, *Inorg. Chem.* **2003**, *42*, 950–959.
[12] R. Alberto, R. Schibli, P. A. A. Egli, P. A. Schubiger, W. A. Hermann, G. Artus, U. Abram, T. A. Kaden, *J. Organomet. Chem.* **1995**, *493*, 119–127.
[13] a) C. J. Davidson, L. Lock, in *Comprehensive Coordination Chemistry*, vol. 4 (Eds.: H. G. Wilkinson, R. D. Gillard, J. A. McCleverty), Pergamon Press, Oxford **1987**; b) R. Dilworth, S. J. Parrott, *Chem. Soc. Rev.* **1998**, *27*, 43–55.
[14] D. A. Blinn, R. S. Button, V. Farazi, M. K. Neeb, C. L. Tapley, T. E. Trehearne, S. D. West, T. L. Kruger, B. N. Storhoff, *J. Organomet. Chem.* **1990**, *393*, 143–152.
[15] K. Heesche-Wagner, T. N. Mitchell, *J. Organomet. Chem.* **1994**, *468*, 99–106.
[16] D. Osella, P. Pollone, M. Ravera, M. Salmain, G. Jaouen, *Bioconjugate Chem.* **1999**, *10*, 607–612.
[17] R. Schibli, K. V. Katti, W. A. Volkert, C. L. Burnes, *Inorg. Chem.* **2001**, *40*, 2358–2362.
[18] K. R. Benak, B. N. Storhoff, *J. Coord. Chem.* **1995**, *36*, 303–309.
[19] J. D. G. Correia, A. Domingos, I. Santos, R. Alberto, K. Ortner, *Inorg. Chem.* **2001**, *40*, 5147–5151.
[20] a) T. Kniess, J. D. G. Correia, A. Domingos, E. Palma, I. Santos, *Inorg. Chem.* **2003**, *42*, 6130–6135; b) E. Palma, J. D. G. Correia, A. Domingos, I. Santos, R. Alberto, A. Spies, *J. Organomet. Chem.* **2004**, *689*, 4811–4819.
[21] A. A. Marti, G. Mazei, L. Maldonado, G. Paralitici, R. G. Raptis, J. L. Colon, *Eur. J. Inorg. Chem.* **2005**, *1*, 118–124.
[22] a) J. F. Rowbottom, G. Wilkinson, *J. Chem. Soc., Dalton Trans.* **1974**, *1*, 684–689; b) E. Lindner, R. Grimmer, *J. Organomet. Chem.* **1970**, *25*, 493–501.
[23] J. D. Dilworth, D. V. Griffiths, S. J. Parrott, Y. Zheng, *J. Chem. Soc., Dalton Trans.* **1997**, *17*, 2931–2936.
[24] D. L. Nosco, A. J. Tofe, T. J. Dunn, L. R. Lyle, R. G. Wolfangel, M. J. Bushman, G. D. Grummon, D. E. Helling, M. E. Marmion, K. M. Miller, D. W. Pipes, T. W. Strubel, D. W. Wester, in *Technetium and Rhenium in Chemistry and Nuclear Medicine, 3* (Eds.: M. Nicolini, G. Bandoli, U. Mazzi), Cortina International, Verona, Raven Press, New York, pp. 381–392, **1990**.
[25] K. K. Kothari, N. K. Pillarsetty, K. V. Katti, W. A. Volkert, *Radiochim. Acta* **2003**, *91*, 53–57.
[26] C. J. Smith, G. L. Sieckman, N. K. Owen, D. L. Hayes, D. G. Mazuru, R. Kannan, W. A. Volkert, T. J. Hoffman, *Cancer Res.* **2003**, *63*, 4082–4088.
[27] Wüst, M. B. Skaddan, P. Leibnitz, H. Spies, J. A. Katzenellenbogen, B. Johannsen, *Bioorg. Med. Chem.* **1999**, *7*, 1827–1835.
[28] W. C. Still, M. Kahn, A. Mitra, *J. Org. Chem.* **1978**, *43*, 2923–2925.
[29] G. M. Sheldrick, *SHELXS97*/*SHELXL97*, University of Göttingen, Germany.

Received: March 22, 2005
Published Online: September 8, 2005

 © 2005 Wiley-VCH Verlag GmbH & Co. KGaA, Weinheim

On the Borderline between *cis* and *trans* in Organometallic (Phosphane)platinum(II) Complexes

Dietrich Gudat,[a] Vimal K. Jain,[b] Axel Klein,*[c] Thilo Schurr,[c] and Stanislav Záliš[d]

Keywords: Density functional calculations / Isomers / NMR spectroscopy / Phosphane ligands / Platinum

The borderline between the *cis* and *trans* configurations in square-planar diarylplatinum(II) complexes with triethylphosphane ligands $[Pt(Ar)_2(PEt_3)_2]$ [Ar = 2,4,6-trimethylphenyl (mesityl), 2,6-dimethylphenyl, 2-methylphenyl, 3-methylphenyl, 4-methylphenyl and phenyl] has been investigated by a combination of multinuclear (^1H, ^{13}C, ^{31}P and ^{195}Pt) NMR spectroscopy, X-ray crystallography and quantum chemical (DFT) calculations. When formed under thermodynamic conditions, the complexes show a clear cut-off between *cis* (tolyl and phenyl complexes) and *trans* (2,6-xylyl and mesityl complexes). The *syn* and *anti* stereoisomers were identified for the 2-methylphenyl and 3-methylphenyl derivatives. Calculated data (structural isomers or NMR) are in excellent agreement with experimental findings.
(© Wiley-VCH Verlag GmbH & Co. KGaA, 69451 Weinheim, Germany, 2005)

Introduction

The stability of the *cis* or *trans* conformation of square-planar complexes with a d^8 configuration is usually governed by an interplay of steric and electronic factors:[1,2] bulky ligands tend to avoid each other, and the presence of two of them usually leads to a *trans* configuration, whereas strong donor ligands prefer a *cis* orientation towards other strong ligands due to the *trans* influence. The latter should not be confused with the *trans* effect. The former is responsible for ground state-properties (structure, thermodynamic stability etc.), whereas the latter governs the behaviour in chemical reactions.[1] Both the *trans* influence and the *trans* effect are of high importance since both stability and formation reactions predetermine the occurrence of *cis* and *trans* configurations in such complexes, which is very often crucial for their applications. This is of enhanced importance for platinum(II) complexes, since in the series of d^8-configured transition metals like Rh^I, Ir^I, Ni^{II}, Pd^{II}, Pt^{II} and Au^{III} platinum(II) derivatives are markedly more resistant to isomerisation reactions than others.[1–3] The most prominent example of the different behaviour of two isomeric platinum(II) complexes is probably diamminedichloroplatinum $[PtCl_2(NH_3)_2]$: the *cis* derivative is an effective anti-cancer drug ("cisplatin") with sales of around 2 million € a year, whereas the *trans* derivative is inactive in that respect.[4–6]

Phosphane ligands have been explored in organoplatinum complexes for more than half a century.[2,7–9] Besides their numerous applications in organometallic catalysis, they have been found to be ideally suited for the determination of their configurations or configurational equilibria since the ^{31}P–^{195}Pt coupling constants are very sensitive to the *trans* and *cis* influence of further co-ligands.[10,11] Aryl ligands can be used to probe the subtle interplay of steric and electronic factors of the configuration since they are (i) strongly donating ligands; (ii) their electronic properties can be tuned by various substituents and the observed changes can be easily rationalised in terms of inductive or mesomeric influences; (iii) they can be easily introduced by established metathesis reactions;[9] (iv) their steric demand can be varied almost deliberately;[12] and (v) since their ring planes are usually oriented almost perpendicular with respect to the binding plane they allow discrimination of the two hemispheres above and below the binding plane, for example by unsymmetrical aryl ligands like 2-R,6-R′-C_6H_4 that give rise to further isomerism.[13]

We therefore decided to prepare a series of (triethylphosphane)platinum complexes $[Pt(Ar)_2(PEt_3)_2]$ [Ar = 2,4,6-trimethylphenyl (Mes), 2,6-dimethylphenyl (Xyl), 2-methylphenyl (2-Tol), 3-methylphenyl (3-Tol), 4-methylphenyl (4-Tol) and phenyl (Ph)] with various alkyl substitution patterns on the aryl ligands.

A similar study was undertaken by Rieger and coworkers some years ago[14] and some of the compounds (Ar = Ph, 2-Tol, 4-Tol) were reported in 1959 by Chatt and Shaw.[9] However, their preparation routes, involving me-

[a] Institut für Anorganische Chemie, Universität Stuttgart, Pfaffenwaldring 55, 70569 Stuttgart, Germany
E-mail: gudat@iac.uni-stuttgart.de
[b] Novel Materials and Structural Chemistry Division, Bhabha Atomic Research Centre, Mumbai 400 085, India
E-mail: jainvk@apsara.barc.ernet.in
[c] Institut für Anorganische Chemie, Universität zu Köln, Greinstraße 6, 50939 Köln, Germany
E-mail: axel.klein@uni-koeln.de
[d] J. Heyrovsky Institute of Physical Chemistry, Academy of Sciences of the Czech Republic, Dolejškova 3, 18 000 Prague 8, Czech Republic
E-mail: stanislav.zalis@jh-inst.cas.cz

 © 2005 Wiley-VCH Verlag GmbH & Co. KGaA, Weinheim **DOI: 10.1002/ejic.200500251**

tathesis reactions between *cis*- or *trans*-[$PtCl_2(PEt_3)$] and an appropriate Grignard reagent, did not allow synthesis of the sterically highly crowded dimesityl or bis(2,6-xylyl) derivatives and often led to mixtures of isomers.[9,14] To prevent this we have chosen a different preparation route to ensure the thermodynamically controlled selective formation of only one isomer. To this end we applied ligand-exchange reactions at elevated temperatures using the DMSO precursor complexes [$Pt(Ar)_2(DMSO)_2$] to obtain isomerically pure compounds.

Results and Discussion

Preparation

The preparation of the complexes was performed as shown in Scheme 1 from the corresponding DMSO derivatives [$Pt(Ar)_2(DMSO)_2$][15] by ligand-exchange reactions at elevated temperatures (boiling toluene, see Exp. Sect.). With the exception of [$Pt(2\text{-Tol})_2(PEt_3)_2$], where ^1H and ^{31}P NMR spectra showed the presence of two isomers, we observed in all cases the formation of only one isomer in the crude reaction product as well as in the recrystallised products.

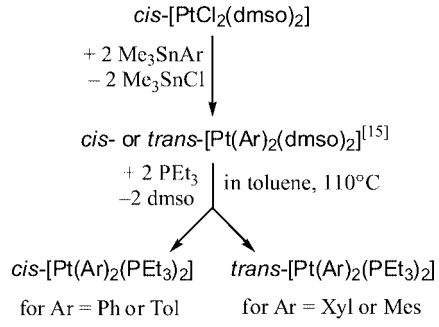

Scheme 1. Preparation of the platinum complexes [$Pt(Ar)_2(PEt_3)_2$].

NMR Spectroscopy

The thoroughly recrystallised complexes were submitted to multinuclear (^1H, ^{13}C, ^{31}P and ^{195}Pt) NMR studies. Selected data for the determination of the structure by NMR spectroscopy are summarised in Table 1 together with ADF/BP calculated data. Full NMR spectroscopic data can be found in the Experimental Section.

From the NMR spectroscopic data, especially from the $^1J_{Pt,P}$ and $^1J_{Pt,C(1)}$ coupling constants (Table 1), a clear line can be drawn between the Ph and Tol derivatives on one side and the Xyl and Mes derivatives on the other side. The $^1J_{Pt,P}$ coupling constants of the former are markedly smaller and the $^1J_{Pt,C(1)}$ couplings markedly larger than the values found for the more substituted derivatives. Both findings are indicative of shorter Pt–P and longer Pt–C(1) bonds, and thus the less substituted derivatives are assigned to have *cis* configurations whereas the more substituted ones are *trans*-configured. The calculated $^1J_{Pt,C}$ coupling constants are in excellent agreement with the experimental ones and clearly support the assignment of *cis* and *trans* configurations. Due to the simplification of the phosphane ligand (PMe_3 instead of PEt_3), the calculated $^1J_{Pt,P}$ coupling constants reflect the *cis*/*trans* variation only qualitatively.

Two sets of signals (ca. 2:1 ratio) were found for the 2-Tol derivative (Figure 1), both clearly showing a *cis* configuration. The two isomers correspond to species with a *syn* (C_S symmetry) and *anti* (C_2 symmetry) orientation of the two *ortho*-methyl groups (above and below the coordination plane), as has been reported previously for these systems[14] and related ditolyl complexes.[16,17] Detailed NMR experiments, including ^1H gsNOESY, ^1H,^{13}C HMQC and ^1H,^{195}Pt HMQC experiments, allowed the assignment of all signals to the two stereoisomers. Furthermore, the absence of exchange correlations in the ^1H NOESY spectra disclosed that the stereoisomers do not undergo any mutual exchange on a second time-scale, even in the presence of additional PEt_3. This stands in contrast to similar results

Table 1. Experimental[a] and calculated (DFT)[b] NMR spectroscopic data for complexes [$Pt(Ar)_2(PEt_3)_2$].

Ar	$^1J_{Pt,C(1)}$ exp. [Hz]	$^1J_{Pt,C}$ calcd. [Hz]	$^1J_{Pt,P}$[c] exp. [Hz]	$^1J_{Pt,P}$ calcd. [Hz]	$\delta_{^{195}Pt}$ [ppm]	Conformation from NMR spectroscopic data
Ph	879	*cis*: 840.1 *trans*: 512.1	1775	*cis*: 1093.8 *trans*: 2575.3	–4568	*cis*
2-Tol (*syn*)	844	*cis*: 888.8 *trans*: 541.6	1751	*cis*: 942.2 *trans*: 2566.8	–4471	*cis-syn*
2-Tol (*anti*)	832	*cis*: 874.7 *trans*: 514.8	1739	*cis*: 933.9 *trans*: 2566.9	–4466	*cis-anti*
3-Tol	812	*cis*: 856.0 *trans*: 537.6	1754	*cis*:1005.8 *trans*: 2455.4	–4570	*cis*
4-Tol	1090	*cis*: 846.7 *trans*: 517.8	1762	*cis*: 959.8 *trans*: 2346.9	–4566	*cis*
Xyl	591	*cis*: 937.4 *trans*: 526.8	2835	*cis*: 985.1 *trans*: 2595.5	–4311	*trans*
Mes	536	*cis*: 922.7 *trans*: 530.2	2841	*cis*: 875.1 *trans*: 2737.8	–4306	*trans*

[a] As measured in $CDCl_3$ at 303 K. [b] Calculated for [$Pt(Ar)_2(PMe_3)_2$]. [c] From ^{31}P NMR measurements.

 © 2005 Wiley-VCH Verlag GmbH & Co. KGaA, Weinheim

with the related DMSO complexes *cis*-[Pt(2-Tol)$_2$(DMSO)$_2$], where *syn*/*anti* isomerisation takes place presumably by a dissociative pathway.[15] Analogous stereoisomers were expected for the 3-Tol derivative. However, we found only one set of signals in the NMR spectra at ambient temperature (298 K). Recently, Hashemi and Rashidi have reported line-broadening on related bis(3-Tol) and bis(4-Tol) complexes, thus indicating fluxional behaviour.[16] We therefore performed quantum-chemical calculations on the energy barrier of *syn*/*anti* isomerisation of the 2-Tol and 3-Tol derivatives. The barrier calculated for [Pt(2-Tol)$_2$(PMe$_3$)$_2$] (111.7 kcal mol^{-1}) turns out to be much larger than for [Pt(3-Tol)$_2$(PMe$_3$)$_2$] (34.1 kcal mol^{-1}), which seems to be reasonable. However, both numbers indicate the occurrence of *syn* and *anti* isomers for 2-Tol as well as for 3-Tol. We therefore examined the 3-Tol derivative at low temperatures (223 and 193 K) and found two sets of signals in the ^{1}H, ^{13}C, ^{31}P and ^{195}Pt NMR spectra. Due to the rather small splitting of the corresponding signals of the two isomers (some signals are just broadened; see, for example, Tables 6 and 7) and signal ratios of approximately 1:1, we could not assign either the *syn* or *anti* isomers or calculate the energy difference. We also refrained from measuring exact coalescence temperatures since the two measurements (at 223 and 193 K) indicated already that different coalescence temperatures will be found for the various signals.

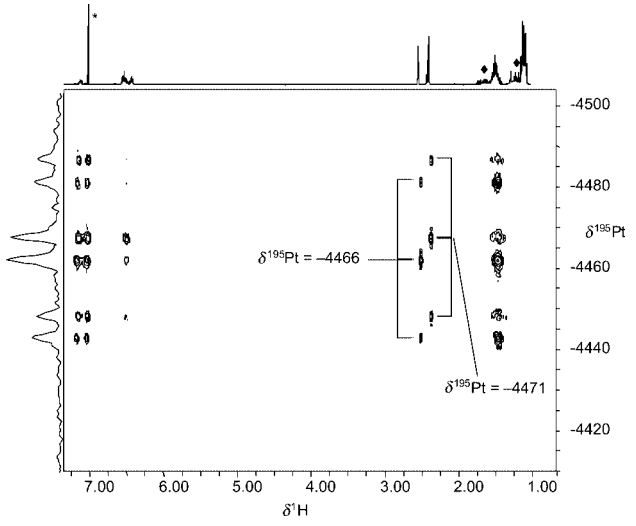

Figure 1. Magnitude-mode two-dimensional ^{1}H,^{195}Pt gs-HMQC spectrum (defocusing time 8.3 ms), showing various long-range correlations between the protons in the 2-Tol and PEt$_3$ groups and the metal atom, and the ^{1}H NMR spectrum (top projection; the solvent signal is denoted by * and the resonances of an impurity of OPEt$_3$ by ♦) of a mixture of the *syn* and *anti* stereoisomers of *cis*-[Pt(2-Tol)$_2$(PEt$_3$)$_2$]. The *F*1 projection (left) shows the ^{195}Pt signals of both isomers as interleaved triplets split by $^1J_{Pt,P}$.

Comparing the *syn*/*anti* ratios for the 2-Tol and 3-Tol derivatives we found a ratio of approx. 1:1 for 3-Tol, whereas for the 2-Tol derivative the ratio is about 2:1. This ratio is reversed (*syn*/*anti* = 1:2) in the precursor complex *cis*-[Pt(2-Tol)$_2$(DMSO)$_2$].[15] Since for the DMSO derivative we found isomerisation already at ambient temperature (NMR), we assume that the *syn* derivative of the DMSO precursor complex is more reactive than the *anti*, which is (thermodynamically) slightly more stable. It is also worthwhile mentioning that the PEt$_3$ complexes retain the *cis* or

Table 2. Crystallographic and structure refinement data of complexes [(PEt$_3$)$_2$Pt(Ar)$_2$].[a]

Ar	Ph (*cis*)	3-Tol (*cis*)	4-Tol (*cis*)	Xyl (*trans*)	Mes (*trans*)
Empirical formula	$C_{24}H_{40}P_2Pt$	$C_{26}H_{44}P_2Pt$	$C_{26}H_{44}P_2Pt$	$C_{28}H_{48}P_2Pt$	$C_{30}H_{52}P_2Pt$
Formula mass	585.59	613.64	613.64	641.69	669.75
Crystal system	monoclinic	monoclinic	monoclinic	triclinic	orthorhombic
Space group	*Cc*	$P2_1/c$	$P2_1/n$	$P\bar{1}$	$Pca2_1$
a [Å]	20.411(5)	15.951(3)	13.3174(15)	8.8835(18)	22.885(5)
b [Å]	9.8288(14)	10.111(2)	14.8753(19)	10.314(2)	9.2381(18)
c [Å]	15.3942(17)	17.737(4)	14.5993(18)	15.804(3)	14.246(3)
α [°]	90	90	90	90.54(3)	90
β [°]	124.411(13)	104.37(3)	99.662(9)	91.09(3)	90
γ [°]	90	90	90	104.44(3)	90
V [Å^3]	2547.9(7)	2771.1(10)	2851.1(6)	1401.9(5)	3011.8(10)
Z	4	4	2	2	4
$\rho_{calcd.}$ [g cm^{-3}]	1.527	1.471	1.430	1.520	1.477
μ [mm^{-1}]/*F*(000)	5.639/1168	5.189/1232	5.043/1232	5.132/648	4.781/1360
Limiting indices	$0 \le h \le 27$	$-17 \le h \le 20$	$0 \le h \le 17$	$-10 \le h \le 11$	$-1 \le h \le 30$
	$0 \le k \le 13$	$-8 \le k \le 13$	$0 \le k \le 19$	$-13 \le k \le 13$	$-1 \le k \le 12$
	$-21 \le l \le 17$	$-23 \le l \le 22$	$-18 \le l \le 18$	$-20 \le l \le 20$	$-1 \le l \le 18$
Reflections collected/unique	3463/3463	6596/6371	6423/6162	7200/6769	4718/4054
R_{int}	0.0639	0.0614	0.0460	0.0388	0.0369
Data/restraints/parameters	3463/2/250	6371/11/306	6160/0/270	6769/0/293	4054/1/322
Goof. on F^2	1.031	1.050	1.007	1.179	1.212
Final indices: R_1	0.0323	0.0691	0.0650	0.0295	0.0364
$[I > 2\sigma(I)]$ wR_2	0.0730	0.1425	0.1326	0.0824	0.0758
R value all data: R_1	0.0417	0.1270	0.1416	0.0398	0.0528
wR_2	0.0769	0.1718	0.1617	0.0919	0.0822
Largest diff. peak/hole [e Å^{-3}]	1.505/–1.427	1.976/–2.538	3.419/–2.313	1.122/–1.445	1.378/–1.069

[a] Measurement temperature: 173(2) K; radiation wavelength: 0.71073 Å; refinement method: full-matrix least squares on F^2; absorption correction: empirical, ψ-scans.

 © 2005 Wiley-VCH Verlag GmbH & Co. KGaA, Weinheim

trans configuration of their DMSO precursors. This is not trivial, since the DMSO precursor complexes may undergo facile isomerisation, which comprises not only *syn*/*anti* (vide supra) but also *cis*/*trans* isomerisation, for example during the formation of the *cis*-configured (diimine)platinum complexes *cis*-[Pt(Ar)$_2$($\widehat{NN}$)] ($\widehat{NN}$ = α-diimine; Ar = Mes or Xyl) from *trans*-configured DMSO precursor complexes.[18–20]

Crystal Structures

The crystal and molecular structures of [Pt(Ph)$_2$(PEt$_3$)$_2$], [Pt(3-Tol)$_2$(PEt$_3$)$_2$], [Pt(4-Tol)$_2$(PEt$_3$)$_2$], [Pt(Xyl)$_2$(PEt$_3$)$_2$] and [Pt(Mes)$_2$(PEt$_3$)$_2$] were determined from single-crystal XRD experiments. The structures of the *syn* and *anti* isomers of *cis*-[Pt(2-Tol)$_2$(PEt$_3$)$_2$] have been reported previously by Rieger et al.[14] The results of the structure determinations are summarised in Table 2, with bond lengths and angles given in Table 3. The first three compounds crystallise in monoclinic space groups, the Xyl derivative is found in triclinic $P\bar{1}$ and the Mes compound in orthorhombic $Pca2_1$. No significant intermolecular contacts were found in any of the crystal structures.

The molecular structures confirm the conclusions drawn from spectroscopic studies in solution: The Ph, 3-Tol and 4-Tol derivatives exhibit a *cis* conformation (Figure 2) as has been found before for the 2-Tol derivative.[14] The Xyl and Mes derivatives show a *trans* orientation of the two aryl groups (Figure 3), and the platinum atom lies on a centre of symmetry for Ar = Xyl. The 3-Tol derivative shows a *syn* orientation of the two methyl substituents. All structures show nearly perfect planar arrangements of ligands around the platinum atom, as can be seen from the sum of angles and the small CCPt/PPPt tilt angles (Table 3).

The bond lengths and angles around the platinum atom in the series of complexes nicely reflect the *trans* influence.[1] For instance, the Pt–P distances are slightly longer for the *cis*-configured compounds while the Pt–C distances are markedly shorter. The bond lengths and angles of the previously reported *syn* and *anti* isomers of *cis*-[Pt(2-Tol)$_2$(PEt$_3$)$_2$][14] fit nicely into our series. Interestingly, Osakada et al.[21] have recently reported the structure of the *trans*-

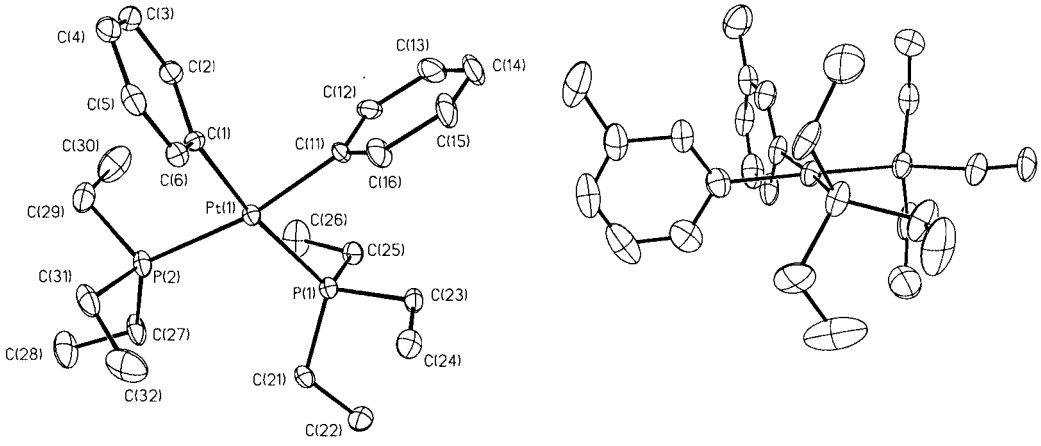

Figure 2. Molecular structures (30% thermal ellipsoids) of *cis*-[(Pt(Ar)$_2$(PEt$_3$)$_2$] with Ar = Ph (left, with full numbering) and 3-Tol (right). H atoms omitted for clarity.

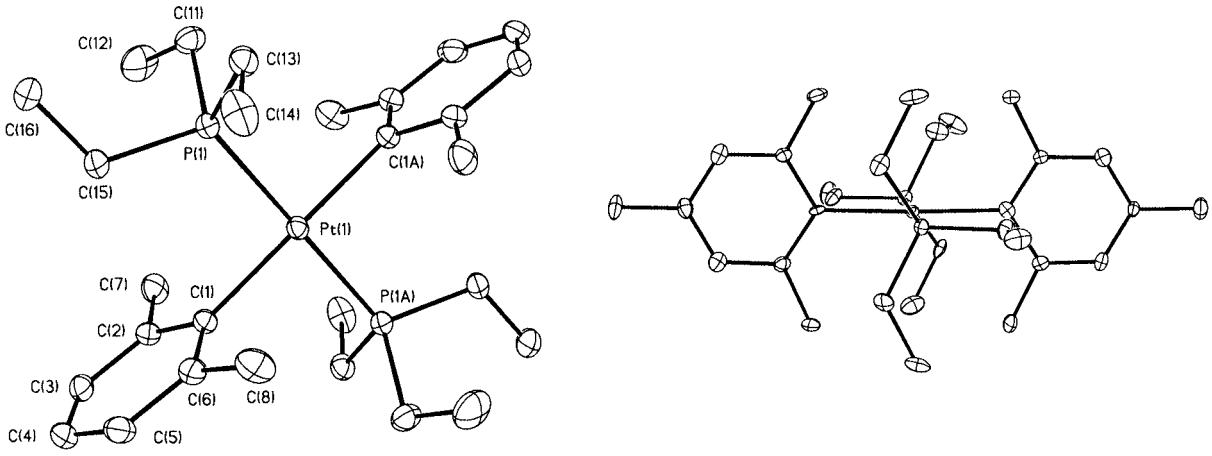

Figure 3. Molecular structures (30% thermal ellipsoids) of *trans*-[(Pt(Ar)$_2$(PEt$_3$)$_2$] with Ar = Xyl (left) or Mes (right). H atoms omitted for clarity.

 © 2005 Wiley-VCH Verlag GmbH & Co. KGaA, Weinheim

Table 3. Selected bond lengths [Å] and bond angles [°] of complexes $[(PEt_3)_2Pt(Ar)_2]$.[a]

	Ph (*cis*)	4-Tol (*cis*)	3-Tol (*cis*)	Xyl (*trans*) (1)[b]	Xyl (*trans*) (2)[b]	Mes (*trans*)
Pt–P(1)	2.318(2)	2.309(3)	2.301(3)	2.2991(12)	2.2954(13)	2.296(2)
Pt–P(2)	2.328(2)	2.324(4)	2.316(3)	2.2991(12)	2.2954(13)	2.290(2)
Pt–C(1)	2.061(9)	2.057(12)	2.067(12)	2.113(4)	2.104(3)	2.101(8)
Pt–C(11)	2.073(8)	2.057(9)	2.083(11)	2.113(4)	2.104(3)	2.104(7)
Pt–C(7/17)	–	–	–	3.346(5)	3.360(4)	3.319(7), 3.375(7)
Pt–C(8/18)	–	–	–	3.377(5)	3.367(3)	3.336(8), 3.377(8)
P–Pt–P	103.72(8)	99.32(11)	102.12(11)	180.00(7)	180.00(6)	179.66(10)
C–Pt–C	84.3(3)	83.4(4)	84.2(5)	180.0(3)	180.0(2)	178.1(6)
C(1)–Pt–P(1)	86.2(2)	90.2(3)	88.3(3)	90.45(11)	91.58(10)	90.5(2)
C(1)–Pt–P(2)	169.1(2)	170.2(3)	169.1(3)	89.55(11)	88.42(10)	89.7(2)
C(11)–Pt–P(2)	86.3(2)	87.3(3)	85.6(3)	90.45(11)	91.58(10)	90.7(3)
C(11)–Pt–P(1)	169.1(2)	172.4(4)	171.8(3)	89.55(11)	88.42(10)	89.1(3)
Sum of angles	360.52	360.22	360.22	360.00	360.00	360.00
Tilt CCPt/PPPt	6.7	4.8	4.5	0.00 [c]	0.00 [c]	1.9 [c]
CCPtPP/aryl	86.0, 76.3	89.9, 83.4	80.3, 86.6	89.3	88.7	85.5, 89.9

[a] Numbering scheme employed in figures and text is as shown in Scheme 2. [b] Two molecules (1) and (2) were found for Ar = Xyl, each with a centre of inversion on the platinum atom. [c] Tilt angles PCPt/PCPt.

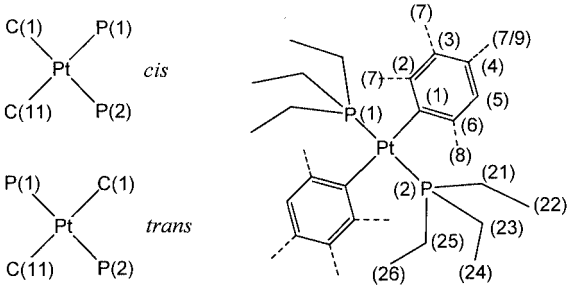

Scheme 2. Numbering scheme.

configured complex $[Pt(4\text{-}CF_3Ph)_2(PEt_3)_2]$, which they obtained by an oxidative addition/reductive elimination sequence using $[PtBr(PEt_3)_3]BF_4$ and the silanol 4-$CF_3PhSi(Me)_2OH$. The Pt–C bonds are markedly longer [2.089(8) Å] and the Pt–P bonds slightly shorter [2.287(3) Å] than what we found for the *cis*-4-Tol derivative.

The distances between the *ortho*-methyl groups and the platinum atoms in compounds Ar = Xyl or Mes range from 3.32 to 3.38 Å, with the upper value representing approximately the sum of the van der Waals radii of Pt and CH_3,[17] values which have also been found for the series of phosphane(2-Tol)platinum complexes reported by Rieger et al.[14] They are slightly lower for the (diimine)platinum complexes *cis*-$[Pt(Ar)_2(\widehat{NN})]$ ($\widehat{NN}$ = α-diimine; 3.2–3.3 Å),[19,20] probably caused by shorter Pt–C(1) bond lengths due to the weaker *trans* influence of the diimine ligands. The tilt angles between the aryl rings and the CCPtPP coordination plane range from 76 to 90° for the *cis* derivatives but are almost 90° for the two *trans*-configured analogues. Since 90° is the optimum value for steric reasons, this is remarkable. We have previously made a similar observation for related *cis*-configured (diimine)platinum complexes (angles around 70°) and have ascribed this effect to an optimisation of ligand-to-metal overlap in conjunction with a metal-mediated ligand-to-ligand interaction.[19] Such interactions seem to be absent for the *trans*-configured compounds.

Essential structural data marking the differences between *cis* and *trans* conformers are summarised in Table 4 together with DFT-calculated energies for possible isomers.

Table 4. Experimental and ADF/BP calculated structural data for complexes $[Pt(Ar)_2(PEt_3)_2]$.

	Exp. structure from single-crystal XRD	Lowest-energy structure[a]/ stabilisation energy [kcal mol^{-1}]
$[Pt(Ph)_2(PEt_3)_2]$	*cis* (173 K)	*cis*/10.7
$[Pt(2\text{-}Tol)_2(PEt_3)_2]$ (*syn*)	*cis-syn* (293 K)[b]	*cis-syn*/6.2
$[Pt(2\text{-}Tol)_2(PEt_3)_2]$ (*anti*)	*cis-anti* (293 K)[b]	*cis-anti*/5.8
$[Pt(3\text{-}Tol)_2(PEt_3)_2]$ (*syn*)	*cis-syn* (173 K)	*cis-syn*/3.5
$[Pt(3\text{-}Tol)_2(PEt_3)_2]$ (*anti*)	–	*cis-anti*/3.5
$[Pt(4\text{-}Tol)_2(PEt_3)_2]$	*cis* (173 K)	*cis*/3.0
$[Pt(Xyl)_2(PEt_3)_2]$	*trans* (173 K)	*trans*/4.7
$[Pt(Mes)_2(PEt_3)_2]$	*trans* (173 K)	*trans*/7.3

[a] Calculated data for $[Pt(Ar)_2(PMe_3)_2]$ model systems, stabilisation energy calculated as the energy difference between the highest and lowest bonding energies of the corresponding *cis* and *trans* isomers. [b] Data for *cis*-$[Pt(2\text{-}Tol)_2(PEt_3)_2]$ (*cis-syn*: monoclinic $P2_1/n$, *cis-anti*: monoclinic $P2_1/c$) from ref.[14]

The ADF/BP calculated ground-state molecular structures agree fully with the experimental structures The *syn* isomer was calculated to be slightly more stable (1 kcal mol^{-1}) for the *cis*-2-Tol complex, which is in agreement with the observed ratio of *syn*/*anti* stereoisomers of approximately 2:1 in solution (see NMR). The calculated difference in bond energy for the *syn* and *anti* isomers of the 3-Tol derivative is negligible, which fully agrees with the approximate 1:1 ratio found in the low-temperature NMR spectra. The fact that we found the *syn* form for the 3-Tol derivative in the crystal structure determination can thus not be ascribed to its higher stability; it might instead be due to a higher tendency to crystallise.

 © 2005 Wiley-VCH Verlag GmbH & Co. KGaA, Weinheim

Conclusions

The combination of structural and spectroscopic data with quantum chemical calculations on diarylplatinum complexes with triethylphosphane ligands has revealed that the borderline between *cis*- and *trans*-configured ground-state geometries is crossed when two *ortho*-methyl groups are introduced on the aryl ligands. Under the applied preparation conditions (high-temperature ligand exchange using the $[Pt(Ar)_2(DMSO)_2]$ precursor complexes) we found the selective formation of either the *cis* (Ph or Tol) or *trans* (Xyl or Mes) isomers. In case of the 2-Tol and the 3-Tol derivatives, the formation of a mixture of the *syn* and *anti* stereoisomers was observed. Detailed NMR experiments allowed the structural assignment of the individual isomers and within these experiments we did not observe any isomerisation reaction. Therefore, we postulate that our chosen reaction conditions are appropriate to obtain the thermodynamically most stable forms. The results of quantum chemical calculations are in excellent agreement with the findings, even in predicting the relative energies of *syn* or *anti* stereoisomers with relatively small energy differences.

Experimental Section

General: The precursor complexes $[Pt(Ar)_2(DMSO)_2]$ (Ar = Ph, 2-Tol, 3-Tol, 4-Tol, 2,6-Xyl or Mes) were prepared according to literature methods.[15,18] Triethylphosphane was obtained from Aldrich. All reactions were carried out under argon in dry and distilled analytical-grade solvents. One-dimensional ^1H, $^{13}C\{^1H\}$, $^{31}P\{^1H\}$, and $^{195}Pt\{^1H\}$ NMR spectra were recorded with a Bruker DPX-300 NMR spectrometer (^1H: 300.13; ^{13}C: 75.47; ^{31}P: 121.49; ^{195}Pt: 64.52 MHz). Chemical shifts are relative to the internal chloroform peak at δ = 7.26 ppm for ^1H and δ = 77.0 ppm for ^{13}C, external 85% H_3PO_4 for ^{31}P and Na_2PtCl_6 in D_2O for ^{195}Pt. A 90° pulse was used in every case. NMR measurements for the assignment of the *syn* and *anti* conformations of $[Pt(2\text{-}Tol)_2(PEt_3)_2]$ were carried out with a Bruker DPX 400 spectrometer (^1H: 400.13 MHz; ^{195}Pt: 86.01 MHz; ^{13}C: 100.3 MHz) in $CDCl_3$ at 303(1) K; for $[Pt(3\text{-}Tol)_2(PEt_3)_2]$ these measurements were performed in CD_2Cl_2 at 223(5) or 193(5) K; chemical shifts were referenced to external TMS (^1H, ^{13}C) or K_2PtCl_6 (Ξ = 21.496784 MHz, ^{195}Pt). The assignment of ^{13}C and ^{195}Pt resonances was obtained from two-dimensional gradient selected (gs) $^1H,^{13}C$ HMQC and HMBC and $^1H,^{195}Pt$ HMQC spectra. Conformational assignments and the analysis of dynamic properties were derived from two-dimensional ^1H gs-NOESY NMR spectra using mixing times of between 500 and 750 ms. All 2D NMR spectra were obtained by using standard pulse sequences from the Bruker pulse program library.

Synthesis of the Complexes $[Pt(Ar)_2(PEt_3)_2]$: An excess of triethylphosphane (1 mmol) was added to a stirred toluene (20 mL) solution of $[Pt(Ar)_2(DMSO)_2]$ (Ar = Ph, 2-Tol, 3-Tol, 4-Tol, Xyl, Mes; typically 0.28 mmol). The mixture was stirred with refluxing for 24 h. The solvent, DMSO and the excess of PEt_3 were distilled off and the residue washed with cold pentane. The colourless products were dried in vacuo. Recrystallisation of the products from warm pentane gave colourless crystals. Yields and elemental analyses are given in Table 5, and full NMR spectroscopic data in Tables 6, 7 and 8.

Table 5. Yields and analytical data of complexes $[Pt(Ar)_2(PEt_3)_2]$.

Ar	Yield [mg]	Yield [%]	Calculated [%]	Found [%]
Ph	105	64	C 49.22, H 6.89	C 50.01, H 6.90
2-Tol	167	97	C 50.89, H 7.23	C 50.93, H 7.28
3-Tol	168	98	C 50.89, H 7.23	C 50.90, H 7.24
4-Tol	165	96	C 50.89, H 7.23	C 50.94, H 7.27
Xyl	154	86	C 52.41, H 7.54	C 52.53, H 7.58
Mes	161	86	C 53.80, H 7.83	C 53.83, H 7.83

Crystallography: Single crystals of $[Pt(Ar)_2(PEt_3)_2]$ (Ar = Ph, 3-Tol, 4-Tol, 2,6-Xyl or Mes) were obtained by slow evaporation of the solvent from saturated solutions in CH_2Cl_2 or pentane. The X-ray data of these complexes were collected at 173(2) K with a Siemens P4 or P3 diffractometer, using graphite-monochromated Mo-K_α radiation (λ = 0.71073 Å) and employing Wyckoff scans. The structures for Ar = Xyl or Mes were solved by direct methods; for all others the Patterson method was employed, in each case using the SHELXTL package,[22] while refinement was carried out with SHELXL97 employing full-matrix least-squares methods on F^2 with $F_o^2 \geq 2\sigma(F_o^2)$.[23] All non-hydrogen atoms were refined aniso-

Table 6. ^1H NMR spectroscopic data of complexes $[Pt(Ar)_2(PEt_3)_2]$.[a]

Ar	H(2)	H(6)	H(3)	H(5)	H(4)	δ ($J_{H,Pt}$) $CH_3(o)$	$CH_3(m)$	$CH_3(p)$	CH_2(Et)	CH_3(Et)
Ph	7.31 (55.5)	7.31 (55.5)	6.84 (21.6)	6.84 (21.6)	6.63	–	–	–	1.50	1.08
2-Tol (*syn*)[b]	–	7.4 (56.0)	6.77	6.67	6.77	2.45 (5.7)	–	–	1.47	1.07
2-Tol (*anti*)[b]	–	7.37 (54.5)	6.77	6.67	6.77	2.60 (5.9)	–	–	1.47	1.07
3-Tol (303 K)	7.16 (56.7)	7.10 (56.8)	–	6.74 (25.2)	6.46	–	2.15	–	1.48	1.07
3-Tol (193 K)	7.00 (br)	6.95 (br)	–	6.63/ 6.60	6,33 (br)	–	1.98/ 2.01	–	1.27 (br)	0.88 (br)
4-Tol	7.16 (56.9)	7.16 (56.9)	6.68	6.68	–	–	–	2.10	1.51	1.07
Xyl	–	–	6.80	6.80	6.80	2.60 (5.1)	–	–	1.32	0.89
Mes	–	–	6.64	6.64	–	2.54 (4.7)	–	2.17	1.29	0.89

[a] Chemical shifts in ppm ($J_{H,Pt}$ in Hz), as measured in CD_2Cl_2. [b] Measured in $CDCl_3$.

 © 2005 Wiley-VCH Verlag GmbH & Co. KGaA, Weinheim

Table 7. ^{13}C NMR spectroscopic data of complexes $[Pt(Ar)_2(PEt_3)_2]$.[a]

Ar	C(1)	C(2)	C(6)	C(3)	C(5)	δ ($J_{C,Pt}$) C(4)	CH_3(*o*)	CH_3(*p*)	CH_2(Et)	[b]	CH_3(Et)
Ph	155.1	127.1	127.1	136.8	136.8	121.0	–	–	15.9		8.2
	(878.9)	(63.5)	(63.5)	(34.1)	(34.1)	(12.3)			(26.4)	(29.1)	(17.6)
2-Tol (*syn*)	162.5	127.6	123.8	142.2	135.8	121.0	27.5	–	15.8		8.0
	(844.0)	(43.0)	(62.4)	(25.4)	(24.3)	(9.6)	(74.6)				
2-Tol (*anti*)	161.4	128.2	123.7	142.6	136.8	120.9	25.9	–	15.8		8.0
	(832.2)	(40.0)	(62.7)	(20.4)	(37.9)	(9.2)	(67.3)				
3-Tol (303 K)[c]	164.4	137.1	133.4	135.2	126.3	121.2		21.7	15.4		7.7
	(812)	(34.6)	(32.9)	(63.4)	(66.1)	(11.5)		[d]	(21.8)		(17.4)
3-Tol (193 K)[c]	166.6/	136.9/	133.0/	135.6	126.3	121.0/	21.6/		14.6		8.1
	166.5	137.2	133.1	(br)	(br)	121.0	21.6		(br)		
4-Tol	160.8	127.7	127.7	135.8	135.8	129.1	–	20.9	15.6		8.2
	(1090)	(66.2)	(66.2)	(35.4)	(35.4)	(5.8)			(25.6)	(28.6)	(17.7)
Xyl	160.2	125.2	125.2	145.0	145.0	121.9	26.6	–	15.0		7.83
	(591.1)	(24.9)	(24.9)				(55.5)		(32.9)	(41.0)	(16.24)
Mes	155.5	126.3	126.3	144.7	144.7	131.1	26.4	20.8	15.0		7.87
	(536.0)						(59.0)		(33.5)	(39.6)	(17.7)

[a] Chemical shifts in ppm ($J_{C,Pt}$ in Hz), as measured in $CDCl_3$. [b] Further coupling $^2J_{CH_2,P}$ (Hz). [c] In CD_2Cl_2. [d] *m*CH_3.

Table 8. ^{31}P NMR and ^{195}Pt NMR spectroscopic data of complexes $[Pt(Ar)_2(PEt_3)_2]$.[a]

Ar	$\delta_{^{31}P}$	$\delta_{^{195}Pt}$
Ph	5.4 (t, $^1J_{P,Pt}$ = 1775 Hz)	–4568 (t, $^1J_{P,Pt}$ = 1790 Hz)[b]
2-Tol (*syn*)	0.8 (t, $^1J_{P,Pt}$ = 1751 Hz)	–4471 (t, $^1J_{P,Pt}$ = 1751 Hz)
2-Tol (*anti*)	1.0 (t, $^1J_{P,Pt}$ = 1739 Hz)	–4466 (t, $^1J_{P,Pt}$ = 1739 Hz)
3-Tol (303 K)	3.9 (t, $^1J_{P,Pt}$ = 1754 Hz)	–4570 (t, $^1J_{P,Pt}$ = 1764 Hz)
3-Tol (193 K)[c]	2.42 ($^1J_{P,Pt}$ = 1754 Hz)	–4587 (t, $^1J_{P,Pt} \approx$ 1.77 kHz)
	2.45 ($^1J_{P,Pt}$ = 1754 Hz)	–4589 (t, $^1J_{P,Pt} \approx$ 1.77 kHz)
4-Tol	4.0 (t, $^1J_{P,Pt}$ = 1762 Hz)	–4566 (t, $^1J_{P,Pt}$ = 1780 Hz)
Xyl	1.1 (t, $^1J_{P,Pt}$ = 2845 Hz)	–4311 (t, $^1J_{P,Pt}$ = 2848 Hz)
Mes	1.8 (t, $^1J_{P,Pt}$ = 2841 Hz)	–4306 (t, $^1J_{P,Pt}$ = 2841 Hz)

[a] Chemical shifts in ppm ($J_{P,Pt}$ in Hz), as measured in $CDCl_3$. [b] Measured in $(CD_3)_2CO$. [c] In CD_2Cl_2.

tropically, including the disordered C atoms of the ethyl groups in the compounds Ar = 3-Tol or Mes. Hydrogen atoms were introduced using appropriate riding models. An empirical absorption correction was performed using ψ-scans. CCDC-266186 for $[Pt(Ph)_2(PEt_3)_2]$, -266187 for $[Pt(3\text{-}Tol)_2(PEt_3)_2]$, -266188 for $[Pt(4\text{-}Tol)_2(PEt_3)_2]$, -266189 for $[Pt(2,6\text{-}Xyl)_2(PEt_3)_2]$ and -266190 for $[Pt(Mes)_2(PEt_3)_2]$ contain the supplementary crystallographic data for this paper. These data can be obtained free of charge from The Cambridge Crystallographic Data Centre via www.ccdc.cam.ac.uk/data_request/cif.

Quantum Chemical Calculations: Ground-state electronic structure calculations were performed by density-functional theory (DFT) methods using the ADF2004.01 program package.[24] Nuclear spin-spin coupling constants were calculated with the CPL module[25] within ADF2004.01. The calculations were performed on the model systems $[Pt(Ar)_2(PMe_3)_2]$ due to the size of the $[Pt(Ar)_2(PEt_3)_2]$ complexes. Slater-type orbital (STO) basis sets of triple-ζ quality with one polarisation function (TZ2P)[24b] for Pt and two polarisation functions (TZP)[24b] for the remaining atoms were employed for geometry optimisation. The inner shells were represented by the frozen-core approximation (1s for C, 2p for P and 1s–4d for Pt were kept frozen). Core electrons were included for the calculation of NMR parameters, and here the quadruple-ζ with four polarisation functions (QZ4P)[24b] basis set was used for Pt. The calculations were carried out with the functional including Becke's gradient correction[26] to the local exchange expression in conjunction with Perdew's gradient correction[27] to the local correlation (BP86). The scalar relativistic (SR) zero-order regular approximation (ZORA) was used within this study. The energy barriers of *syn*/*anti* isomerisation within $[Pt(2\text{-}Tol)_2(PMe_3)_2]$ and $[Pt(3\text{-}Tol)_2(PMe_3)_2]$ model complexes were calculated as the lowest energy rotation barrier associated with the rotation of one 2-Tol or 3-Tol group, respectively.

Acknowledgments

Dr. M. Bader and Dr. M. Niemeyer (University of Stuttgart) are thanked for collecting single-crystal XRD data. Support for this work under the Indo-German bilateral program from the BMBF (Project No. IND 99/060) and the COST D14 action is also acknowledged. We are also grateful for a loan of K_2PtCl_4 by Johnson Matthey. S. Z. also acknowledges financial support by the Grant Agency of the Academy of Sciences of the Czech Republic (grant 1ET400400413).

[1] F. R. Hartley, *The Chemistry of Platinum and Palladium*, John Wiley & Sons, New York, **1973**.
[2] J. N. Harvey, K. M. Heslop, A. G. Orpen, P. G. Pringle, *Chem. Commun.* **2003**, 278–279 and references cited therein.
[3] G. K. Anderson, R. J. Cross, *Chem. Soc. Rev.* **1980**, *9*, 185–215.
[4] G. A. Petsko, *Nature* **1995**, *377*, 580–581.
[5] P. J. Sadler, *Adv. Inorg. Chem.* **2000**, *49*, 183–306.
[6] *Cisplatin – Chemistry and Biochemistry of a Leading Anticancer Drug* (Ed.: B. Lippert), 1st ed., Helvetica Chimica Acta (Zürich), Wiley-VCH (Weinheim), **1999**.
[7] J. Chatt, R. G. Wilkins, *J. Chem. Soc.* **1952**, 273–278.
[8] J. Chatt, R. G. Wilkins, *J. Chem. Soc.* **1952**, 4300–4306.
[9] J. Chatt, B. L. Shaw, *J. Chem. Soc.* **1959**, 4020–4033.
[10] T. G. Appleton, M. A. Bennett, *Inorg. Chem.* **1978**, *3*, 738–747.
[11] R. Romeo, M. R. Plutino, L. M. Scolaro, S. Stoccoro, *Inorg. Chim. Acta* **1997**, *265*, 225–233.
[12] P. Power, *J. Organomet. Chem.* **2004**, *689*, 3904–3919.

 © 2005 Wiley-VCH Verlag GmbH & Co. KGaA, Weinheim

[13] M. C. Biagini, M. Ferrari, M. Lanfranchi, L. Marchio, M. A. Pellinghelli, *J. Chem. Soc., Dalton Trans.* **1999**, 1575–1580.
[14] A. L. Rieger, G. B. Carpenter, P. H. Rieger, *Organometallics* **1993**, *12*, 842–847.
[15] A. Knödler, T. Schurr, A. Klein, W. Kaim, V. K. Jain, K.-W. Klinkhammer, D. Gudat, S. Záliš, *Organometallics* **2005**, *24*, 4125–4131.
[16] M. Hashemi, M. Rashidi, *J. Organomet. Chem.* **2005**, *690*, 982–989.
[17] A. T. Hutton, P. G. Pringle, B. L. Shaw, *J. Chem. Soc., Dalton Trans.* **1985**, 1677–1682.
[18] C. Eaborn, K. Kundu, A. Pidcock, *J. Chem. Soc., Dalton Trans.* **1981**, 933–938.
[19] A. Klein, J. van Slageren, S. Záliš, *Eur. J. Inorg. Chem.* **2003**, 1917–1938.
[20] W. Kaim, A. Klein, *Organometallics* **1995**, *14*, 1176–1186.
[21] N. Mintcheva, Y. Nishihara, M. Tanabe, K. Hirabayashi, A. Mori, K. Osakada, *Organometallics* **2001**, *20*, 1243–1246.
[22] G. M. Sheldrick, *SHELXTL*, Bruker Analytical X-ray Systems, Madison, Wisconsin, USA, **1998**.
[23] G. M. Sheldrick, *SHELXL-97: A program for Crystal Structure Determination*, Universität Göttingen, Göttingen, Germany, **1997**.
[24] a) G. te Velde, F. M. Bickelhaupt, S. J. A. van Gisbergen, C. Fonseca Guerra, E. J. Baerends, J. G. Snijders, T. Ziegler, *J. Comput. Chem.* **2001**, *22*, 931–967; b) ADF2004.01, SCM, Theoretical Chemistry, Vrije Universiteit, Amsterdam, The Netherlands, http://www.scm.com.
[25] a) J. Autschbach, T. Ziegler, *J. Chem. Phys.* **2000**, *113*, 936–947; b) J. Autschbach, T. Ziegler, *J. Chem. Phys.* **2000**, *113*, 9410–9418.
[26] A. D. Becke, *Phys. Rev. A* **1988**, *38*, 3098–3100.
[27] J. P. Perdew, *Phys. Rev. B* **1986**, *33*, 8822–8824.

Received: March 23, 2005
Published Online: September 5, 2005

 © 2005 Wiley-VCH Verlag GmbH & Co. KGaA, Weinheim

Supramolecular Arrangement of C_{60} and Phenol into a Square Packing Arrangement of π-π Interacting and Hydrogen-Bonded Rods in C_{60}·5C_6H_5OH

Martin Schulz-Dobrick,[a] Martin Panthöfer,[a] and Martin Jansen*[a]

Keywords: Fullerenes / Supramolecular chemistry / Pi interactions / Hydrogen bonds

The supramolecular adduct C_{60}·5C_6H_5OH was obtained as single crystals by the slow hydrolysis of a solution of C_{60} in triphenylphosphite. The crystal structure was determined with atomic resolution by single-crystal X-ray diffraction [triclinic, space group $P\bar{1}$, a = 1003.52(14) pm, b = 1011.71(14) pm, c = 1264.17(17) pm, α = 88.566(2) °, β = 84.026(2) °, γ = 83.485(2) °, V = 1.2681(3) nm^3, Z = 1]. The overall structure can be described as a distorted square packing pattern of hydrogen-bonded and π-π interacting rods, $^1_\infty$[C_{60}(C_6H_5OH)$_4$]. The fullerene molecules are fully ordered and the C–C bond lengths exhibit remarkably small variations within the 6:6 and 6:5 subsets. The results are discussed in the context of an analysis of reliable crystal structure data for several different fullerene co-crystal compounds.
(© Wiley-VCH Verlag GmbH & Co. KGaA, 69451 Weinheim, Germany, 2005)

Introduction

Fullerenes are promising candidates for the generation of novel materials due to their electron acceptor capabilities, and the interesting electronic and magnetic properties of chemically reduced fullerene species, e.g. A_3C_{60} (A = alkaline metal[1]), [Cr(C_7H_8)$_2$]C_{60},[2] TDAE-C_{60},[3] and the ability of fullerenes to form adducts with π-donors. A variety of supramolecular π-donor-fullerene arrangements have been crystallographically characterized, including donors like porphyrins[4,5], calixarenes,[6] tetrachalcogenefulvalenes[7] and various aromatic donors.[8,9] In order to provide a sufficiently strong interaction, the donor molecules should be able to complement the spherical shape of the fullerene species. This may be realized by large molecules exhibiting an intrinsic concave or even bowl-like shape, as well as by the supramolecular organization of small donor molecules into a network that gives rise to spherical voids of the appropriate size. The latter case was observed in the crystal structure of C_{60}·3HOC_6H_4OH,[10] where the hydroquinone molecules form a hydrogen-bonded network in which the fullerenes are encapsulated by bowl-shaped moieties. The primary motivation behind these efforts has been to study the electronic and structural response of the fullerenes to the supramolecular interactions. However, in many cases crystal structure analysis has been hampered by severe orientational and librational disorder of the fullerene sub-structure.

In this work, we present the synthesis and structural characterization of a supramolecular adduct of C_{60} and phenol, where the hydrogen-bonded arrangement of the phenol molecules is strong, yet at the same time flexible enough to give rise to strong π-π interactions and a full ordering of the C_{60} molecules, thus enabling an extraordinary accurate determination of the molecular structure of the fullerene moieties (Figure 1).

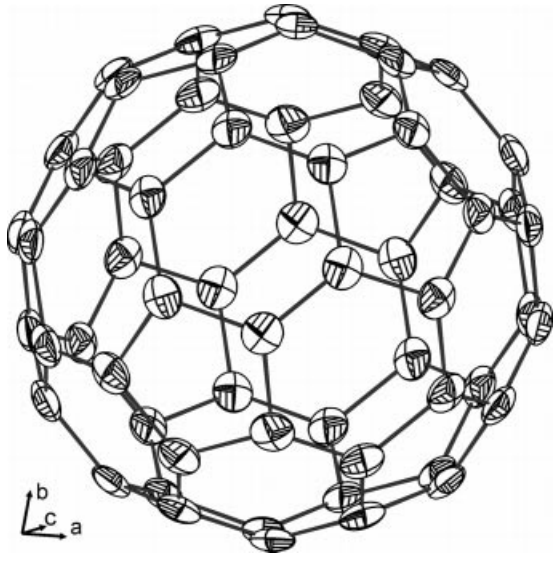

Figure 1. Molecular structure of the fullerene C_{60} moiety (probability density function corresponds to the 50% probability level).

Results and Discussion

The supramolecular adduct C_{60}·5C_6H_5OH was obtained as red, plate-shaped crystals by the slow hydrolysis (with

[a] Max Planck Institute for Solid State Research,
Heisenbergstraße 1, 70569 Stuttgart, Germany
Fax: +49-711-689-1502
E-mail: M.Jansen@fkf.mpg.de

water vapor) of a solution of C_{60} in triphenylphosphite and the in-situ generation of phenol, which acts as a co-crystallization agent as well as a precipitation agent. This method (in-situ formation of the precipitation agent) has not been employed in the synthesis of fullerene co-crystals before. The majority of fullerene co-crystals, as reported in the literature, were obtained from solutions containing both the fullerene and the co-crystallization agent, either by the slow evaporation of the solvent or by vapor diffusion methods. It is particularly advantageous for precipitation to occur from a homogeneous solution by the slow chemical evolution of the co-crystallization agent, as in case of $C_{60}{\cdot}5C_6H_5OH$, as this allows crystal growth to proceed under low and almost constant super-saturation conditions, leading to well grown crystals of an appropriate size.

$C_{60}{\cdot}5C_6H_5OH$ crystallizes in the triclinic space group $P\bar{1}$ with one formula unit in the unit cell. The fullerene C_{60} molecule is located on a centre of symmetry (Wyckoff position 1*f,* ½ 0 ½). Despite the low crystallographic symmetry, the symmetry of the molecular structure of the C_{60} molecule is very close to I_h [rms = 0.48 pm^2, module molsym, Platon[11]]. While the C_{60} and two of the phenol molecules are fully ordered, orientational disorder is observed for the third phenol molecule, which is also located on a centre of symmetry (1*e,* ½ ½ 0). A TLS analysis of the ordered part of the molecular structure converges at convincing reliability factors (R_1 = 0.043, Platon) and points toward a slight rigid body librational motion of the fullerene molecule [$(\lambda/°)^2$ = (7.68, 7.04, 4.49)]. Corrections to the C–C bond lengths due to librational shortening ($\langle\Delta d$ = 0.28 pm$\rangle$) are of the same order of magnitude as the corresponding estimated standard deviations and were regarded negligible.

As a general feature, the intramolecular C–C bond lengths of the C_{60} molecule separate into a set of short 6:6 bonds and a set of long 6:5 bonds, exhibiting a remarkably sharp distribution, as measured by the total span ($d_{max.}$ – $d_{min.}$) and the standard deviation within each set (see Table 1 and the discussion below).

Each fullerene molecule is coordinated to four phenol molecules (see part a in Figure 2). The centre-to-centre distances are 660.5 pm (C_{60}–Phenol-0, 2×) and 673.8 pm (C_{60}–Phenol-1, 2×). The phenol molecules coordinate to different structural moieties, i.e. Phenol-0 to a hexagon [C(10), C(11), C(22), C(23), C(24), C(30)] and Phenol-1 to a pentagon [C(14), C(15), C(16), C(28), C(29)] with the closest phenol carbon to hexagon- and pentagon-plane approaches being 311(1) pm and 325(1) pm, respectively. The phenol and C_{60} rings have a virtual co-planar orientation [∠(Phenol-0 ···Hexagon) = 13.63(5) °, ∠(Phenol-1···Pentagon) = 8.95(5) °]. These distance values are shorter than the interlayer separation in graphite [d = 335.6(4) pm[12]], and lie in the range typically found in fullerene to arene π-π-interacting species (300 pm – 350 pm). Thus, π-π complex units, $[C_{60}(C_6H_5OH)_4]$, are present, and may be regarded as the basic building unit of this structure.

The hydroxyl groups of the phenol molecules are connected via almost linear, medium strength hydrogen bonds (d[O(100)-H(100)···O(110)] = 273.9(2) pm, ∠ = 174(2) °). Remarkably, these hydrogen-bonds do not appear between phenol molecules of the same complex unit, $[C_{60}(C_6H_5OH)_4]$, but in a pair wise manner with the phenol molecules of the neighboring complex units along the [100] and [$\bar{1}$00] directions. The Hydrogen-bonds between the complex units are the strongest intermolecular interactions present in this structure. The π-π complex units are connected via hydrogen-bonds to give $^1_\infty[C_{60}(C_6H_5OH)_4]$ rods along [100] (see part b of Figure 2). The overall structure is a distorted square packing of rods[13] in (100) plane. The remaining phenol molecules (Phenol-2) fill voids within the packing, which are located at a centre of symmetry.

Two symmetry equivalent Phenol-0 molecules, belonging to two different $^1_\infty[C_{60}(C_6H_5OH)_4]$ rods along the [011] diagonal

Table 1. Data for selected, reliable crystal structure analyses of C_{60} co-crystals, spans, statistical mean values, and standard deviations for the 6:6 and 6:5 sets of C–C bond lengths, and the results of thermal motion analyses of the structure models.

Compound	C_{60}·triphenyl-benzene· C_6H_5Cl	C_{60}·Ag(OEP)·C_6H_6	C_{60}·Ni(OEP)·C_6H_6	C_{60}·TMPDA	C_{60}·Pt(OEP)·C_6H_6	C_{60}·5 C_6H_5OH
CCDC number	195338	168839	182460	213452	198536	267147
Reference	[8]	[21]	[22]	[23]	[24]	this work
$\langle d_{6:6}\rangle$ /pm	138.94(41)	139.12(42)	139.04(36)	138.81(43)	138.73(40)	138.74(28)
$d_{6:6}$: min., max.; Δ /pm	138.3, 140.0; 1.7	138.1, 140.0; 1.9	138.2, 139.8; 1.6	138.0, 139.7; 1.7	137.9, 139.6; 1.7	138.3, 139.5; 1.2
$\langle d_{6:6}\rangle$ /pm	144.70(54)	145.03(56)	145.18(33)	144.72(44)	145.09(41)	144.83(25)
$d_{5:6}$: min., max.; Δ /pm	143.6, 145.6; 2.0	143.7, 146.3; 2.6	144.3, 145.9; 1.6	143.7, 145.4; 1.7	144.0, 146.1; 2.1	144.3, 145.3; 1.0
Temperature /K	110	83	92	90	90	100
Space group	$P\bar{1}$	$P\bar{1}$	$P\bar{1}$	$P2_1/c$	$P\bar{1}$	$P\bar{1}$
Position of C_{60}	1*e* ($\bar{1}$)	general	general	2*a* ($\bar{1}$)	general	1*f* ($\bar{1}$)
Parameters	507	1018	1026	328	1018	478
Restraints	0	0	0	0	0	0
No. of refl. (all)	14107	14049	44245	17750	43336	10841
No. of refl. (unique)	9328	14040	19789	4512	19865	5623
No. of refl. ($I > 2\sigma$)	6297	12595	16575	2396	18705	3584
R_{int}	0.037	0.030	0.022	0.092	0.019	0.028
wR_2	0.272	0.130	0.107	0.158	0.054	0.108
TLS R_1	0.055	0.091	0.030	0.072	0.035	0.043
TLS $\lambda_1/\lambda_2/\lambda_3$ /(°)^2	6.69/5.08/3.90	8.44/5.65/4.76	7.82/5.76/4.11	5.75/4.34/3.81	9.37/6.08/4.98	7.68/7.04/4.49

 © 2005 Wiley-VCH Verlag GmbH & Co. KGaA, Weinheim

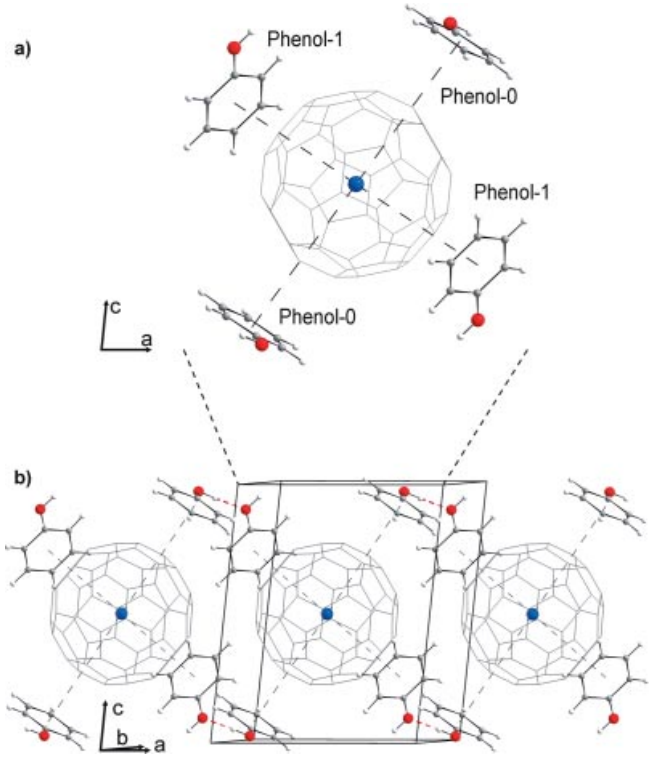

Figure 2. a) Coordination of C_{60} to four phenol molecules to give the supramolecular building unit $[C_{60}(C_6H_5OH)_4]$, and b) interconnection of these units via hydrogen bonds to give $^1_\infty[C_{60}(C_6H_5OH)_4]$ strands along [100]. Blue dots indicate the centers of gravity of the C_{60} molecules, and hydrogen bonds are emphasized in red.

of the square packing pattern, are found to be potential hydrogen-bond acceptors for different, but symmetry equivalent, orientations of the Phenol-2 molecules (d[O(120)···O(100)] = 275.9(3) pm, ∠ = 172(2) °). Thus, the orientational disorder of this particular phenol molecule is a consequence of the requirements of the supramolecular self assembly of the $^1_\infty[C_{60}(C_6H_5OH)_4]$ rods, and the comparably strong hydrogen-bond donor and acceptor capability of phenol.

The shortest intermolecular distances between fullerene molecules within this supramolecular arrangement, with d = 1003.5(1) pm, are observed along [100], i.e. the propagation direction of the $^1_\infty[C_{60}(C_6H_5OH)_4]$ rods, and are found to be significantly higher than those in pristine C_{60} (d = 992.8 pm[14]). While the fullerene-to-fullerene distances along [010] are only slightly higher [d = 1011.7(1) pm], the ones observed along [001] are significantly larger [d = 1264.2(2) pm]. This is due to the spatial requirements of the herring-bone like arrangement of the Phenol-0 and Phenol-1 molecules in the distorted square packing of the $^1_\infty[C_{60}(C_6H_5OH)_4]$ rods, and the occupation of the voids at symmetry site 1e by the orientationally disordered Phenol-2 molecules (Figure 3).

Despite the considerable effort made in determining reliable experimental values for the 6:6 and 6:5 bond lengths, reference data is still subject to review. For comparison, we have selected a set of reliable crystal structure analyses of fullerene co-crystals on the basis of the overall quality, span and standard deviation of the bond length distribution, and

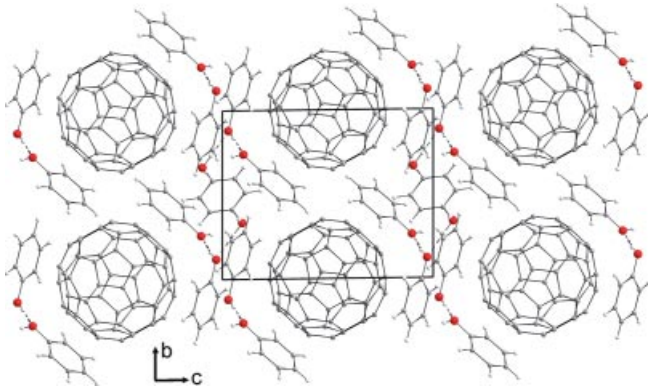

Figure 3. Distorted square packing of the $^1_\infty[C_{60}(C_6H_5OH)_4]$ strands in the (100) plane, the filling of the voids at 1e by further disordered phenol molecules is also shown.

the results of thermal motion analyses in context of the TLS formalism.[15] The data presented in Table 1 and Figure 4 include the overall statistical mean values of the corresponding bond sets within the range of the individual statistical standard deviations. From consideration of the span, as well as the standard deviation, of the reported 6:6 and 6:5 sets of bond lengths, the structure data in this work have to be regarded as the most precise.

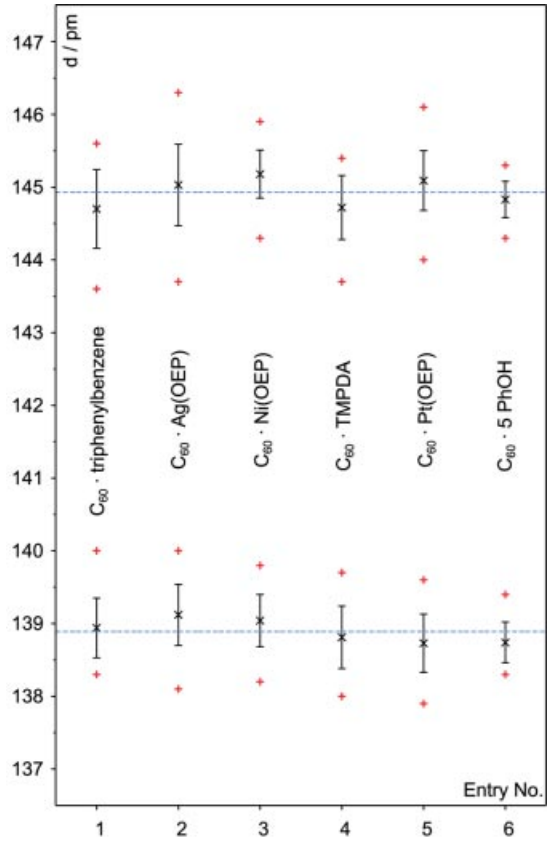

Figure 4. Spans (red), mean values and standard deviations (black) for the selected crystal structure data (Blue dashed lines correspond to the overall mean values of 138.9 pm and 144.9 pm; entry numbers correspond to the appearances of the compound in Table 1).

 © 2005 Wiley-VCH Verlag GmbH & Co. KGaA, Weinheim

The kinds of interaction, e.g. pure π-π interactions, multipolar π interactions, and dipole–multipole interactions, and the strength of interaction differ between the various co-crystals. The strength of the overall interaction may be estimated by means of the mean square liberation amplitudes (λ_i, see Table 1). Surprisingly, the reported values do not differ significantly. There is no significant experimental evidence to indicate a change in the molecular structure of C_{60} upon alteration of the nature of a co-crystallization agent. Furthermore, the selected data are, despite the varying spans and standard-deviations, virtually identical and exhibit a significantly higher reliability than the data reported for pristine C_{60}.[14] The mean values are $\langle d_{6:6}\rangle$ = 138.9 pm and $\langle d_{6:5}\rangle$ = 144.9 pm.

Conclusions

Precipitation of $C_{60}{\cdot}5C_6H_5OH$ from a homogeneous solution of C_{60} in triphenylphosphite yields single crystals of high quality. The combination of hydrogen-bonding and π-π interactions leads to a distorted square packing of $^1_\infty[C_{60}(C_6H_5OH)_4]$ strands, in which the fullerene molecules are fully ordered. The 6:6- and 6:5-bond lengths were determined to be 138.74(28) pm and 144.83(25) pm, respectively. A careful analysis of selected, reliable structure data for C_{60}-co-crystals hints to i) no significant influence of the co-crystallization agent, and ii) $\langle d_{6:6}\rangle$ = 138.9 pm and $\langle d_{6:5}\rangle$ = 144.9 pm for the 6:6 and 6:5 bond lengths, respectively.

Experimental Section

Commercially available C_{60} (5 mg, 99.9%, MER Corporation, USA) was dissolved in triphenylphosphite (10 mL, >97% purity, Fluka). The violet solution was hydrolyzed slowly by exposure to water vapor under ambient conditions. During a period of ten days, the solution turned brown and then red, and plate-shaped crystals of $C_{60}{\cdot}5\ C_6H_5OH$ had formed. The crystals could be stored without any sign of decomposition in the mother liquid at 35 °C, which was necessary to prevent the crystallization of the phenol. Upon separation from the mother liquid, the crystals turned black within hours, this color change was accompanied by total loss of crystallinity.

A crystal suitable for X-ray diffraction was transferred into inert oil, picked with a loop and cooled rapidly to 100 K. Intensity data were collected on a SMART-APEX CCD X-ray diffractometer (Bruker) at 100 K with graphite-monochromated Mo-K_α radiation. A total of 1800 frames were collected with an exposure time of 30 s/frame. The reflection intensities were integrated using the SAINT[16] subprogram in the SMART[17] software package. Intensities were corrected for absorption effects by the application of a semi-empirical method (SADABS[18]). A total of 10841 reflections were measured, 5623 of which were independent, and 3584 of which had intensities greater than 2σ. The crystal structure was solved by direct methods and subsequent Fourier syntheses (SHELXS[19]). All non-hydrogen atoms were refined anisotropically (SHELXL[19]). Hydrogen atoms were located from the residual electron density map and refined individually with isotropic thermal parameters fixed to 1.2 and 1.5 times that of the equivalent isotropic displacement parameter of the carbon or oxygen atom to which it is bound. The disordered hydrogen atom, H(121), was fixed using the HFIX command.

In order to elucidate the nature of the disorder of the phenol-2 molecule, the structure was also solved and refined in space group $P1$. Two oxygen atoms at the 1,4 positions of the phenol-2 molecule (in $P\bar{1}$) were located in the residual electron density maps, and refined to a occupancy of ½, i.e. refined as an orientationally disordered phenol molecule, but not as a hydroquinone molecule. The

Table 2. Crystal and refinement parameters for $C_{60}{\cdot}5C_6H_5OH$.

Chemical moiety	$C_{60}{\cdot}5C_6H_5OH$
Molecular formula	$C_{90}H_{30}O_5$
Molecular mass /g mol^{-1}	1191.14
Temperature /K	100(2)
Wavelength /pm	71.073
Crystal system, space group	triclinic, $P\bar{1}$
Cell parameters /pm, °	a = 1003.52(14), α = 88.566(2) b = 1011.71(14), β = 84.026(2) c = 1264.17(17), γ = 83.485(2)
Cell volume /nm^3	1.2681(3)
Z, density (calcd.) /Mg·m^{-3}	1, 1.560
Absorption coefficient /mm^{-1}	0.096
F(000)	610
Crystal size /mm	0.3 × 0.1 × 0.03
θ Range /°	2.03–28.42
Range (H)	$-12 \le h \le 12$ $-12 \le k \le 12$ $-16 \le l \le 16$
Reflections measured / unique / observed	10841 / 5623 / 3584
$R_{int.}$, R_σ	0.028, 0.056
Completeness to θ = 28.42°	88.1%
Absorption correction	empirical (SADABS[18])
Refinement method	full-matrix least-squares on F^2 (SHELXL[19])
Data / restraints / parameter	5623 / 0 / 478
$S(F^2)$	1.002
Residuals (obsd.)	R_1 = 0.043, wR_2 = 0.092
Residuals (all)	R_1 = 0.085, wR_2 = 0.108
$\Delta\rho_{min.}$, $\Delta\rho_{max.}$ /10^{-6} e pm^{-3}	–0.25(5), 0.24(5)

 © 2005 Wiley-VCH Verlag GmbH & Co. KGaA, Weinheim

Table 3. Selected bond lengths [pm] and angles [°] for C_{60}·$5C_6H_5OH$.

Fullerene C_{60}	6:6 bonds		
C13–C14	138.3(3)	C19–C20	138.8(3)
C3–C15	138.4(3)	C22–C30[a]	138.8(3)
C1–C9	138.5(3)	C25–C26	138.8(3)
C21–C29[a]	138.5(3)	C16–C17	138.9(3)
C27–C28	138.5(3)	C2–C12	139.1(3)
C10–C11	138.6(3)	C4–C18	139.1(3)
C23–C24	138.7(3)	C5–C6	139.5(3)
C7–C8	138.8(3)		
	6:5 bonds		
C17–C30	144.3(3)	C7–C27[a]	144.9(3)
C19–C23[a]	144.3(3)	C8–C9	144.9(3)
C26–C27	144.4(3)	C10–C22	144.9(3)
C28–C29	144.5(3)	C12–C13	144.9(3)
C2–C3	144.6(3)	C18–C19	144.9(3)
C11–C12	144.6(3)	C4–C5	145.0(3)
C15–C16	144.6(3)	C8–C21	145.0(3)
C16–C29	144.7(3)	C11–C24	145.0(3)
C20–C26[a]	144.7(3)	C14–C15	145.0(3)
C1–C5	144.8(3)	C24–C25	145.0(3)
C6–C7	144.8(3)	C3–C4	145.1(3)
C6–C20	144.8(3)	C14–C28	145.1(3)
C9–C10	144.8(3)	C17–C18	145.1(3)
C23–C30[a]	144.8(3)	C21–C22	145.2(3)
C1–C2	144.9(3)	C13–C25	145.3(3)
Phenol-0		Phenol-1	
O100–C101	136.7(2)	O110–C111	137.4(2)
O100–H100	94(3)	O110–H110	89(3)
C101–C102	138.4(3)	C111–C112	138.0(3)
C101–C106	138.5(3)	C111–C116	138.2(3)
C102–C103	138.3(3)	C112–C113	138.0(3)
C103–C104	138.5(3)	C113–C114	137.9(3)
C104–C105	138.3(3)	C114–C115	138.2(3)
C105–C106	138.6(3)	C115–C116	138.1(3)
Phenol-2			
C121–C122	138.2(3)	C123–C122[b]	138.7(3)
C121–C123	138.6(3)	C121–O120	132.6(4)
D–H···A	*d*(D–H)	*d*(D···A)	∠(DHA)
O100–H100···O110[c]	94(3)	273.9(2)	174(2)
O120–H120···O100[d]	91(4)	275.0(3)	172(4)

[a] Symmetry operators: $1-x, -y, 1-z$. [b] Symmetry operators: $1-x, 1-y, -z$. [c] Symmetry operators: $-x, -y, 1-z$. [d] Symmetry operators: $1-x, -y, -z$.

implementation of this disorder model, as well as the application of an inversion-twin law, enabled the refinement to converge to virtually the same residuals as the refinement of the structure model in space group $P\bar{1}$, but the model in *P*1suffered from strong pair wise correlation of positional and anisotropic displacement parameters for all the atoms, and exhibited esd values about four times higher for the C–C bond lengths than for the disordered structure model in $P\bar{1}$. Furthermore, no indications to the presence of a superstructure or modulation were observed. Thus, we conclude C_{60}·$5C_6H_5OH$ crystallizes in space group $P\bar{1}$ with phenol-2 being orientationally disordered, due to the structural boundary conditions set by the supramolecular motif. Further details of the structure analysis and selected bond lengths are given in Table 2 and Table 3.

CCDC-267147 contains the supplementary crystallographic data for this paper. These data can be obtained free of charge from The Cambridge Crystallographic Data Centre via www.ccdc.cam.ac.uk/data_request/cif.

Raman spectra were recorded on individual single-crystals, which were protected by a thin layer of the mother liquid, with a microscope laser Raman system (Jobin–Yvon, LabRam) operating at an excitation wavelength of 784.7 nm at 20 mW. Bands corresponding exclusively to C_{60} were observed (270, 432, 492, 772, 1424, 1468 cm^{-1}). The deviations from the resonances of pristine C_{60}[20] are not larger than 3 cm^{-1}, which is expected for non-ionic molecular crystals.

Acknowledgments

The authors want to thank Hanne Nuss for single crystal X-ray measurements, Armin Schulz for Raman-spectroscopic measurements and the Fonds der Chemischen Industrie for financial support.

[1] A. F. Hebard, M. J. Rosseinsky, R. C. Haddon, D. W. Murphy, S. H. Glarum, T. T. M. Palstra, A. P. Ramirez, A. R. Kortan, *Nature* **1991**, *350*, 600–601.

 © 2005 Wiley-VCH Verlag GmbH & Co. KGaA, Weinheim

[2] A. Hönnerscheid, L. van Wüllen, M. Jansen, J. Rahmer, M. Mehring, *J. Chem. Phys.* **2001**, *115*, 7161–7165.
[3] P. W. Stephens, D. Cox, J. W. Lauher, L. Mihaly, J. B. Wiley, P. M. Allemand, A. Hirsch, K. Holczer, Q. Li, J. D. Thompson, F. Wudl, *Nature* **1992**, *355*, 331–332.
[4] D. V. Konarev, I. S. Neretin, Y. L. Slovokhotov, E. I. Yudanova, N. V. Drichko, Y. M. Shul′ga, B. P. Tarasov, L. L. Gumanov, A. S. Batsanov, J. A. K. Howard, R. N. Lyubovskaya, *Chem. Eur. J.* **2001**, *7*, 2605–2616.
[5] M. M. Olmstead, D. A. Costa, K. Maitra, B. C. Noll, S. L. Phillipps, P. M. van Calcar, A. L. Balch, *J. Am. Chem. Soc.* **1999**, *121*, 7090–7097.
[6] J. L. Atwood, L. J. Barbour, M. W. Heaven, C. L. Raston, *Angew. Chem. Int. Ed.* **2003**, *42*, 3254–3257.
[7] A. Izuoka, T. Tachikawa, T. Sugawara, Y. Suzuki, M. Konno, Y. Saito, H. Shinohara, *Chem. Commun.* **1992**, 1472–1473.
[8] A. L. Litvinov, D. V. Konarev, A. Y. Kovalevsky, I. S. Neretin, Y. L. Slovokhotov, P. Coppens, R. N. Lyubovskaya, *CrystEngComm* **2002**, 618–622.
[9] G. Waidmann, M. Jansen, *Z. Naturforsch. B: Chem. Sci.* **1998**, *53*, 161–164.
[10] O. Ermer, *Helv. Chim. Acta* **1991**, *74*, 1339–1351.
[11] A. L. Spek, Utrecht University, **2005**.
[12] P. Trucano, R. Chen, *Nature* **1975**, *258*, 136–137.
[13] M. O'keeffe, S. Andersson, *Acta Crystallog. A* **1977**, *33*, 914–923.
[14] W. I. F. David, R. M. Ibberson, J. C. Matthewman, K. Prassides, T. J. S. Dennis, J. P. Hare, H. W. Kroto, R. Taylor, D. R. M. Walton, *Nature* **1991**, *353*, 147–149.
[15] V. Schomaker, K. N. Trueblood, *Acta Crystallogr. B* **1968**, *24*, 63–76.
[16] Version 6.45, Bruker AXS, Madison, WI, USA, **2003**.
[17] Version 5.618, Bruker AXS, Madison, WI, USA, **1997**.
[18] G. M. Sheldrick, version 2.10, Bruker AXS, Madison, WI, USA, **2003**.
[19] G. M. Sheldrick, version 6.10, Bruker AXS, Madison, WI, USA, **2000**.
[20] M. S. Dresselhaus, G. Dresselhaus, P. C. Eklund, *J. Raman Spectrosc.* **1996**, *27*, 351–371.
[21] T. Ishii, N. Aizawa, R. Kanehama, M. Yamashita, H. Matsuzaka, T. Kodama, K. Kikuchi, I. Ikemoto, *Inorg. Chim. Acta* **2001**, *317*, 81–90.
[22] H. M. Lee, M. M. Olmstead, T. Suetsuna, H. Shimotani, N. Dragoe, R. J. Cross, K. Kitazawa, A. L. Balch, *Chem. Commun.* **2002**, 1352–1353.
[23] D. V. Konarev, A. Y. Kovalevsky, A. L. Litvinov, N. V. Drichko, B. P. Tarasov, P. Coppens, R. N. Lyubovskaya, *J. Solid State Chem.* **2002**, *168*, 474–485.
[24] M. M. Olmstead, A. de Bettencourt-Dias, H. M. Lee, D. Pham, A. L. Balch, *Dalton Trans.* **2003**, 3227–3232.

Received: March 24, 2005
Published Online: September 5, 2005

 © 2005 Wiley-VCH Verlag GmbH & Co. KGaA, Weinheim

Biomimetic Thiolate Alkylation with Zinc Pyrazolylbis(thioimidazolyl)borate Complexes

Mohamed M. Ibrahim,[a] Guosen He,[a] Jan Seebacher,[a] Boumahdi Benkmil,[a] and Heinrich Vahrenkamp*[a]

Keywords: Bioinorganic chemistry / Enzyme models / N,S ligands / Thiolates / Zinc

The NS_2ZnX coordination in thiolate-alkylating zinc enzymes is reproduced in (tripod)ZnX complexes with substituted pyrazolylbis(thioimidazolyl)borate tripod ligands. Intermediate (tripod)Zn nitrates and perchlorates are converted into (tripod)Zn thiolates, including the biologically relevant homocysteinate. Methylation with CH_3I converts these to (tripod)ZnI and the corresponding thioethers CH_3SR, including methionine. A kinetic investigation has shown the alkylations to be intramolecular S_N2 processes that take place at the zinc-bound thiolates. They are considerably faster for the $(NS_2)Zn$ thiolates than for the (N_2S)- and $(N_3)Zn$-thiolates with similar pyrazolylborate-derived tripod ligands, in agreement with Nature's choice of an NS_2 donor set for zinc.

(© Wiley-VCH Verlag GmbH & Co. KGaA, 69451 Weinheim, Germany, 2005)

Introduction

In two classes of zinc enzymes, a subgroup of the alcohol dehydrogenases and a subgroup of the thiolate alkylating enzymes, the zinc ion is in the unusual $(NS_2)ZnX$ coordination, with N representing histidine, S representing cysteinate, and X being the catalytic site.[1,2] Thus, as a complex the $(NS_2)ZnX$ unit is an uncharged molecular species, and the reacting substrates (alkoxides or thiolates) convert this into an anionic complex upon coordination to zinc. Obviously, this is of advantage for the reactions to be catalyzed (removal of a hydride from the α-carbon of the alkoxide or attack of the alkylating agent at the zinc-bound thiolate) due to the enhanced electron density at the substrates.

On the other hand, it is difficult to reproduce these bonding situations and chemical reactions in coordination compounds of zinc.[3] At present, alcohol dehydrogenase modeling has not gone beyond structural mimics, and thiolate alkylation has not yet been achieved for a thiolate bound to zinc in an anionic complex. Thiolate alkylation in other types of zinc complexes has, however, been performed in a number of cases. Thus, thiolates bound to ZnN_2O,[4,5] ZnN_2S,[5–7] $ZnNS_2$,[8] and ZnS_3 units[9] have been subjected to alkylations by our competitors in this field. The only anionic thiolate complex used for such reactions, $Zn(SPh)_4^{2-}$,[10] was found to dissociate prior to alkylation.

Our own contributions to this field have involved zinc thiolates with bidentate N_2[11] and tridentate N_2S ligands,[12] as well as the tris(pyrazolyl)borate as N_3 tripods.[13] During these studies it became obvious that the tripods of the pyrazolylborate type are the best substitutes for the biological ligand environment of zinc, as observed before,[14] due to their synthetic variability, which allows the encapsulation of the metal in a favorable way. It therefore seemed promising to us to use sulfur-containing pyrazolylborate ligands for studies of this kind, that is, to investigate the alkylation of **L**·Zn-SR complexes in which the ligands **L** are pyrazolylborate-derived tripods with N_2S, NS_2, and S_3 donor sets. A complete series of such ligands with substituted thioimidazolyl groups as sulfur donors is available now: after Reglinski's discovery of the tris(thioimidazolyl)borates,[15] Parkin[16] and ourselves[17] introduced the pyrazolylbis(thioimidazolyl)borates, and very recently we added the final member, the bis(pyrazolyl)(thioimidazolyl)borates.[18]

Following our introductory study on the alkylation of tris(pyrazolyl)boratozinc thiolates,[13] in the second part of the investigation we used the bis(pyrazolyl)(thioimidzolyl)-boratozinc thiolates.[19] The major, and unexpected, observation of this study was that the thiolate alkylations are slower than those of the tris(pyrazolyl)boratozinc thiolates, despite the increased electron density of the complexes. It remained to be demonstrated, however, that the trend continued for the (pyrazolyl)bis(thioimidazolyl)boratozinc thiolates. This is the subject of the present study, which is the third in the series. Work on part four, concerning the tris(thioimidazolyl)boratozinc thiolates, is in progress.

The zinc thiolate complexes of the present study, representing the $(NS_2)Zn$-SR ligand environment, are the closest structural models of the thiolate-alkylating zinc enzymes so far.[2,3] We chose $\mathbf{L^1}$ and $\mathbf{L^2}$ as the NS_2 ligands. The substitution pattern on their pyrazolyl and thioimidazolyl groups

[a] Institut für Anorganische und Analytische Chemie der Universität Freiburg,
Albertstr. 21, 79104 Freiburg, Germany
Fax: +49-761-203-6001
E-mail: vahrenka@uni-freiburg.de

was meant to provide encapsulation of the zinc ion in a hydrophobic pocket. This was achieved for the pyrazolyl units in the usual way[14] by 3-phenyl-5-methyl substitution. The thioimidazolyl units bear *N*-phenyl groups with *ortho* substituents. This was found to be favorable for encapsulation as it induces the phenyl substituents that point away from the zinc centers to rotate such that their *ortho* positions get placed nearer to the metal.[20]

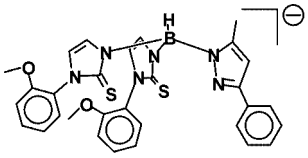

L¹

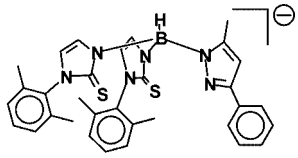

L²

Ligands L¹ and L²

L¹ has been described by us previously,[17] and **L²** was prepared by the same procedure from equimolar amounts of the thioimidazole and the pyrazole together with KBH_4 in boiling toluene. In order to purify **L²** it had to be subjected to column chromatography over silica gel. As a result of this the anionic ligand was protonated and isolated as the molecular species **HL²**. This is not unprecedented in the chemistry of the tris(pyrazolyl)borates.[21,22] We are, however, not aware of the existence of the protonated form of a pyrazolylborate-based heteroscorpionate like **HL²**. After isolating **HL²** it was straightforward to convert it into K**L²**, the standard form of all these tripod ligands, by treating it with KOH in methanol.

The identity of **HL²** was revealed by an X-ray structure determination (Figure 1). Compound **HL²** can be considered a zwitterion, with the positive charge on the protonated pyrazole nitrogen and the negative charge on boron. Although the pyrazole nitrogen is the only reasonable position for protonation, the NH hydrogen could not be located with certainty or refined freely. The geometry around the boron atom is close to ideally tetrahedral, and the B–N bond lengths are in the normal range for pyrazolylborates.[22] Unlike in the complexes of such ligands where the N and S donor atoms are locked in place by coordination to the metal, they seem to be locked in this free ligand by weak hydrogen bonds. One of these attaches one of the thioimidazole sulfur atoms to the oxygen atom of a co-crystallized methanol molecule, and the other links the pyrazole nitrogen atom with the other thioimidazole sulfur atom. This latter hydrogen bond serves as a reminder that the proton in question may actually be bound to sulfur rather than to nitrogen.

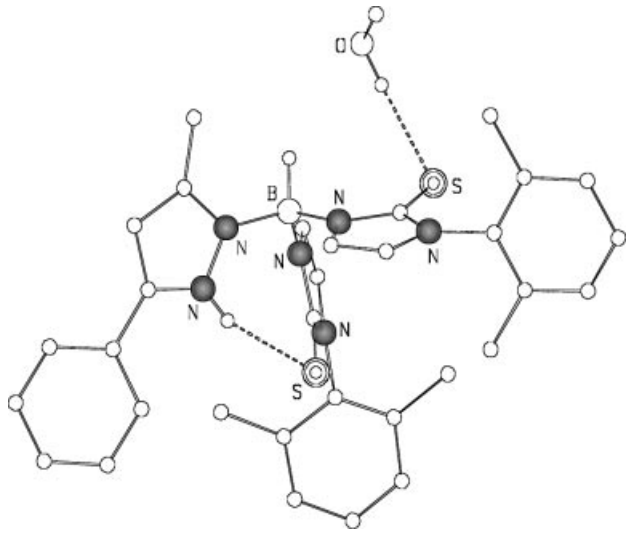

Figure 1. Molecular structure of **HL²**. Relevant distances [Å] and angles [°]: B–N 1.555, 1.534 and 1.550(4), C–S 1.677 and 1.695(3); N–B–N 108.1, 110.2, and 111.7(3); S···N 3.10; S···O 3.27.

Basic Complexes

While with the tris(pyrazolyl)borate ligands the starting point for all functional zinc complexes are the Zn–OH compounds,[14] these compounds have not been isolated yet with the pyrazolylbis(thioimidazolyl)borate ligands.[17] Instead, perchlorate and nitrate were found to be labile enough to be displaced from zinc by even weakly coordinating donors. Therefore, in addition to complexes **1a** and **1b** already described for ligand **L¹**,[17] the corresponding complexes **2a** and **2b** were prepared here for ligand **L²**. They resulted from the reaction of **HL²** with the zinc salts in methanol. It can be assumed that **2a** and **2b**, just like **1a** and **1b**,[17] contain the oxoanions attached to zinc through one of their oxygen atoms. As considerable amounts of complexes **1** and **2** are lost in the isolation process, further reactions with them were usually carried out by using them in situ.

When doing reactions with complexes **1** and **2**, or when trying to prepare further **L**Zn-X complexes by combining K**L** and ZnX_2, we observed many times, as before,[17] that these systems have a very high tendency to dismutate into ZnL_2 and ZnX_2. This is one of the reasons why the desired **L**Zn–OH complexes have evaded us so far and why the derivative chemistry with **L**Zn units is not nearly as rich as that of the tris(pyrazolyl)boratozinc units. For example, the attempted syntheses of **L²**Zn acetate from **HL²** and zinc acetate resulted in **3b**. The structure of **3b** (see Table 1 below and data deposited under CCDC-268609) complements those of other related ZnL_2 complexes.[16,17]

$L^1Zn\text{-}ONO_2$	$L^1Zn\text{-}OClO_3$	$L^2Zn\text{-}ONO_2$	$L^2Zn\text{-}OClO_3$
1a	**1b**	**2a**	**2b**

 © 2005 Wiley-VCH Verlag GmbH & Co. KGaA, Weinheim

ZnL^1_2 ZnL^2_2

3a **3b**

On the other hand, halides coordinate readily to these **L**Zn units. Like other such **L**Zn halide complexes,[17] the iodides **4a** and **4b** were prepared here from the ligands and ZnI_2. They were fully characterized, including structure determinations for reference purposes, as they are one of the products of each of the alkylation reactions described below.

L^1Zn-I L^2Zn-I

4a **4b**

The structure of **4b** is shown in Figure 2, mainly for comparison with the structure of the free ligand in Figure 1. The tetrahedral coordination of zinc (bond angles 104–113°) and the Zn–N, Zn–S, and Zn–I bond lengths correspond to those reported for related **L**ZnI complexes.[17,23] One can say that in HL^2 the proton of the N–H···S hydrogen bond has the same role as the zinc ion in **4b** in fixing the orientation of the pyrazole and one thioimidazole of the ligand, but that in **4b** coordination to zinc overcomes the tendency of the second thioimidazole to point away from the center of the molecule. This comparison offers one explanation for the high tendency of formation of the ZnL_2 complexes, in which also only two donor units of the tripod are fixed, while the third is free and pointing away from the complex center.

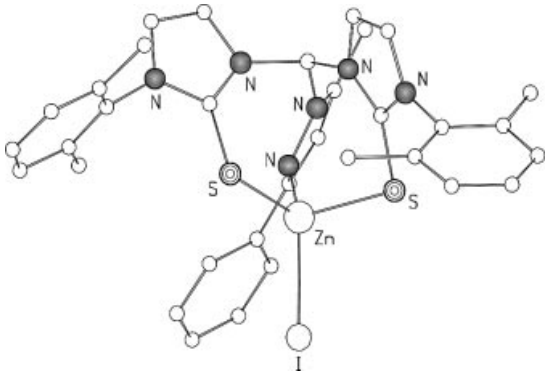

Figure 2. Molecular structure of L^2ZnI (**4b**). Relevant bond lengths [Å]: Zn–N 2.039(3), Zn–S 2.338 and 2.320(2), Zn–I 2.533(2).

Thiolates

While the preparation of (tripod)ZnSR complexes for the tris(pyrazolyl)borate[13] and bis(pyrazolyl)(thioimidazolyl)-borate tripods[18] is straightforward, in this case it required careful control of the reaction conditions. The high tendency of formation of the bis(ligand)complexes **3** and the oligomeric zinc bis(thiolates) prevented the isolation of most of the desired thiolate complexes with tripod L^2, and it allowed the isolation of the alkyl- and benzylthiolate complexes of tripod L^1 only when carefully controlling the reaction conditions. Only with the least electron-rich *p*-nitrothiophenolates was it easy to obtain the **L**ZnSR complexes.

Complexes **5a**–**c** and **6d** were prepared from the perchlorates **1b** and **2b** and the corresponding thiolates. Complex **5d** could be obtained in a one-pot synthesis from *p*-nitrothiophenol, $NaOCH_3$, $Zn(NO_3)_2{\cdot}6H_2O$, and KL^1. Likewise, the homocysteine derivative **5e**, which is the closest representation of the reactive intermediate in the synthesis of methionine from homocysteine by cobalamine-independent methionine synthase[2] reported so far, was prepared from *N*-acetylhomocysteine ethyl ester, NaOH, $Zn(NO_3)_2{\cdot}6H_2O$, and KL^1 in methanol. As mentioned above, **5a** and **5b** are very labile, dismutating in solution to $[Zn(SR)_2]_n$ and the ZnL_2 complex **3a**.

L^1Zn-SR L^2Zn-SR

5a-e **6d**

a: R = C_2H_5, **b**: R = $CH_2C_6H_5$, **c**: R = C_6H_5,

d: R = C_6H_4-p-NO_2, **e**: R = $CH_2CH_2CH(COOEt)NHAc$

The structures of the two most stable thiolate complexes (**5d** and **6d**) were determined. They are closely related, making it sufficient to display only the structure of **6d** in Figure 3. The coordination of zinc is severely distorted tetrahedral, with the largest angle (ca. 123°) being that between the pyrazole nitrogen and the thiolate sulfur and the smallest angle (ca. 101°) being that between the pyrazole nitrogen and one of the thioimidazolyl sulfurs. The Zn–N and Zn–S distances concerning the tripod ligand compare well with those in the other pyrazolylbis(thioimidazolyl)boratozinc complexes (this work and ref.[17]). The Zn–S (thiolate) bond lengths of 2.28 Å in both **5d** and **6d** are not much different

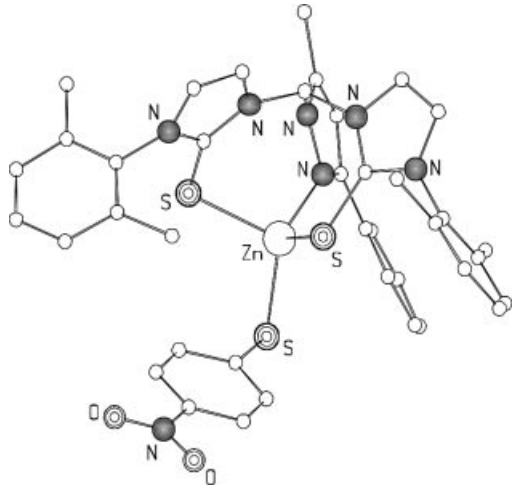

Figure 3. Molecular structure of the thiolate complex **6d**. Relevant bond lengths [Å]: Zn–S (tripod) 2.362(1) and 2.341(1), Zn–S (thiolate) 2.285(1), Zn–N 2.038(3).

 © 2005 Wiley-VCH Verlag GmbH & Co. KGaA, Weinheim

from those in the related zinc *p*-nitrothiophenolate complexes of a tris(pyrazolyl)borate[13] and a bis(pyrazolyl)-(thioimidazolyl)borate ligand[19] [2.25 and 2.25 Å (av.) respectively]. A notable feature of the structure of **6d** is the orientation of one of the *o*-dimethylphenyl rings. As anticipated, it is rotated to such a degree that one of the methyl groups contributes to the encapsulation of the zinc ion in a similar way as the phenyl substituent on the pyrazole ring.

Methylation Reactions

As before for the N_3- and N_2S-ligated zinc thiolates,[13,19] all thiolate complexes **5** and **6** were subjected to methylation with methyl iodide in chloroform. In each case the reactions proceeded according to Equation (1) and, according, to ^{1}H NMR spectroscopy, they were quantitative. The solid reaction products **L**ZnI (**4a** and **4b**) were isolated, and the thioethers CH_3SR were identified by NMR spectroscopy; there were no other reaction products in the solutions.

$$\mathbf{L}ZnSR + CH_3I \rightarrow \mathbf{L}ZnI + CH_3SR \quad (1)$$

The ethyl and benzyl thiolates **5a** and **5b** reacted within minutes, whereas the phenyl and homocysteinyl thiolates **5c** and **5e** needed about an hour. Even the methylations of the *p*-nitrothiophenolates **5d** and **6d** came to completion within a few hours. This is in marked contrast to the reactions of the N_3- and N_2S-ligated zinc-*p*-nitrothiophenolates. Those of the tris(pyrazolyl)borates were found not to proceed at all at room temperature,[13] and those of the bis(pyrazolyl)-(thioimidazolyl)borates took weeks to come to completion. These observations lead to the rough estimate that the NS_2-ligated zinc thiolates react about two orders of magnitude faster than the N_3- and N_2S-ligated ones. Further work is needed to quantify this statement.

The popular alternative alkylating agent trimethylphosphate was also used here. We had found before that, under forcing conditions (i.e. in boiling DMSO), it does lead to methylation of neocuproinzinc bis(thiolates)[11] and of zinc thiolates bearing a tridentate N_2S ligand.[12] Yet, even under these forcing conditions, it reacted extremely slowly with the zinc thiolates bearing tripodal N_2S ligands.[19] This was now observed for complex **5d** too. In boiling DMSO it took three days to methylate about one third of the thiolate with $PO(OMe)_3$. While this is again about one to two orders of magnitude faster than the corresponding methylation of the complex ligated with a bis(pyrazolyl)(thioimidazolyl)borate,[19] it demonstrates again that zinc thiolate model complexes are not nearly as reactive as the thiolate-alkylating zinc enzymes, which employ such mild alkylating agents as methyl tetrahydrofolate.[2]

Kinetic data were obtained for the methylations of **5d** and **6d** with methyl iodide in $CDCl_3$ at 300 K. We found it convenient to record the intensity of the ^{1}H NMR signal of the SCH_3 group of the resulting *p*-nitrothioanisole during the kinetic runs. Complexes **5d** and **6d** were treated under pseudo-first-order conditions with a four- to tenfold excess of CH_3I. From the SCH_3 signal intensities, recorded for at least five $t_{½}$ intervals (see Figure 4), the pseudo-first-order rate constants were obtained according to $\ln(I_t - I_0) = \ln(I_\infty - I_0) - k_{obs} \times t$.

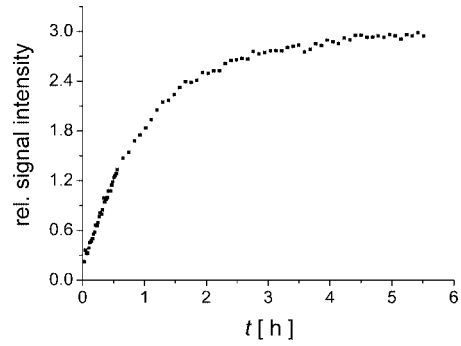

Figure 4. Intensities of the CH_3 ^{1}H NMR signals of $CH_3SC_6H_4$-*p*-NO_2 resulting from the reaction of **5d** with a sixfold excess of CH_3I.

The log plots for five different excess concentrations of CH_3I were linear with correlation coefficients greater than 0.995. The resulting k_{obs} values, plotted against the CH_3I concentrations (see Figure 5), define regression lines passing through the origin with correlation coefficients greater than 0.998. The second-order rate constants of the thiolate alkylations, taken from the slopes of these regression lines, are $8.5(1) \times 10^{-3}$ M^{-1} s^{-1} for **5d** and $1.5(1) \times 10^{-3}$ M^{-1} s^{-1} for **6d**.

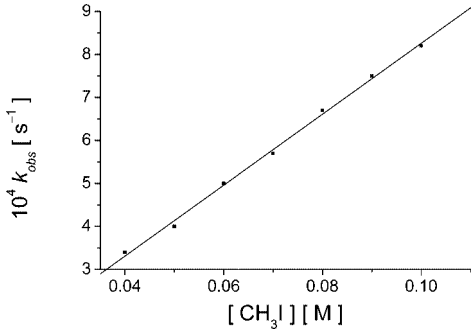

Figure 5. Plot of the pseudo-first-order rate constants against the CH_3I concentration for the methylation of **5d**.

Again, the clean second-order reactions support the statement that the alkylations occur at the zinc-bound thiolates, as proposed for the enzymes.[2,3] At present their rates can be compared only to one another, as comparable rates for other *p*-nitrothiophenolate complexes are not available. The fact that **5d** reacts faster than **6d** can be explained by electronic as well as steric effects: due to the *o*-methoxy substituents **5d** is slightly more electron-rich than **6d**, and the better encapsulation of the reactive center of **6d** (see discussion above) renders the latter less reactive. The fact that the thiolate complexes of this study are considerably more reactive than the previously studied ones with N_3[13] and N_2S tripods[19] certainly relates to the fact that sulfur donor ligands render the zinc ion, and hence the thiolate attached to it, more electron-rich.

 © 2005 Wiley-VCH Verlag GmbH & Co. KGaA, Weinheim

Conclusions

The present study, the third in our series on thiolate alkylations of zinc complexes with pyrazolylborate-derived ligands, has yielded model complexes in which the (NS_2) ZnSR ligand environment of the zinc ion correctly reproduces that in the thiolate alkylating zinc enzymes like cobalamin-independent methionine synthase. The simple alkanethiolate complexes are labile, indicating that the electron-richness in these systems is reaching a borderline, comparable to the situation in the $Zn(SR)_4^{2-}$ species, among which the alkanethiolates have been inaccessible to date. Nevertheless, the homocysteinate complex could be prepared and methylated to yield methionine, which is the closest reproduction so far of the last step of enzymatic methionine synthesis.

The mechanistic investigation of the alkylation reactions has shown them to be second order and probably intramolecular again. They are significantly faster than the alkylations of the Zn-SR complexes with N_3 and N_2S tripod ligands, as expected due to their increased electron-richness. This relates well with Nature's choice of an NS_2 donor set for zinc in the thiolate-alkylating enzymes.

Nature, however, also uses a $Zn(SR)_4^{2-}$ system to dealkylate phosphate esters in the Ada repair protein.[24] Thus, model systems in the form of zinc complexes with an (S_3) Zn-SR composition are also a valuable subject of investigation. We are at present studying such a model system employing the tris(thioimidazolyl)boratozinc thiolates. The results of this study are to be published as the fourth part of our series on tripod-zinc thiolate complexes.

Experimental Section

General: For the general working and measuring procedures, see ref.[25] Ligand **L¹**,[17] 5-methyl-3-phenylpyrazole,[26] and *N*-(*o*-dimethylphenyl)thioimidazole[27] were prepared according to the published procedures. All other starting materials were commercially available. The methyl thioethers resulting from the methylations,[28–31] including *N*-acetylmethionine ethyl ester,[13] have been described and were identified by their ^{1}H NMR spectra, which are also reported in ref.[13]

A frequent problem with the elemental analyses of this kind of complexes is that the carbon values are outside the accepted range. When this was the case here, at least one additional analysis value (S or Zn) was determined.

Ligand HL²: a) HL²: A mixture of 5-methyl-3-phenylpyrazole (4.20 g, 26.5 mmol), *N*-(2,3-dimethylphenyl)-2-thioimidazole (5.42 g, 26.5 mmol), and KBH_4 (0.72 g, 13.3 mmol) was finely ground and heated to 100 °C in vacuo for 2 h. Then, 400 mL of freshly distilled toluene were added and the mixture refluxed at 160 °C in an oil bath for a week. The solvent was then removed in vacuo, the residue dissolved in dichloromethane, and filtered through celite. Chromatography through a 3 × 30 cm silica gel column with a gradient solvent system (dichloromethane/acetone, 200:0 → 200:4) yielded raw **HL²**. Repeating the chromatography yielded 5.32 g (69%) of **HL²** as a colorless powder, m.p. 194 °C. $C_{32}H_{33}BN_6S_2$ (576.60): calcd. C 66.78, H 5.60, N 14.60, S 11.14; found C 66.69, H 5.93, N 13.95, S 10.49. ^{1}H NMR ($CDCl_3$): δ = 2.25 [s, 6 H, Me(Ph)], 2.29 [s, 6 H, Me(Ph)], 2.92 [s, 3 H, Me(pz)], 6.78 [s, 1 H, H(pz)], 6.80 [d, J = 2.2 Hz, 2 H, H(im)], 7.20 [d, J = 2.2 Hz, 2 H, H(im)], 7.29 (m, 1 H, Ar), 7.33 (s, 3 H, Ar), 7.42 (m, 2 H, Ar), 7.64 (m, 3 H, Ar), 7.96 (m, 2 H, Ar) ppm.

b) KL²: 20 mL of a 0.1 M solution of KOH in methanol (2.00 mmol) was added dropwise to a solution of **HL²** (1.15 g, 2.00 mmol) in 20 mL of methanol. The solvent was removed in vacuo, the residue dissolved in dichloromethane, and the product precipitated by addition of petroleum ether (50–70 °C). Recrystallization from dichloromethane/heptane by slow evaporation yielded 0.71 g (58%) of **KL²** as a colorless powder, m.p. 240 °C (dec.). $C_{32}H_{32}BKN_6S_2$ (614.69): calcd. C 62.53, H 5.25, N 13.67, S 10.43; found C 62.75, H 5.42, N 13.28, S 10.14. ^{1}H NMR ($CDCl_3$): δ = 1.92 [s, 6 H, Me(Ph)], 1.96 [s, 6 H, Me(Ph)], 2.16 [s, 3 H, Me(pz)], 6.24 [s, 1 H, H(pz)], 6.43 [s, 2 H, H(im)], 6.47 [s, 2 H, H(im)], 6.98 (s, 1 H, Ar), 7.05 (m, 5 H, Ar), 7.30 (m, 2 H, Ar), 7.62 (m, 3 H, Ar) ppm.

Complex 2a: A solution of **HL²** (0.057 g, 0.10 mmol) in 20 mL of methanol was added with stirring to a solution of $Zn(NO_3)_2{\cdot}6H_2O$ (0.030 g, 0.10 mmol) in 20 mL of methanol. After stirring for 15 h the solvent was removed in vacuo and the residue dissolved in 20 mL of dichloromethane. After washing with water the dichloromethane solution was filtered through celite. The filtrate was then reduced to 5 mL in vacuo. Slow diffusion of *n*-pentane into the solution yielded 32 mg (46%) of **2a** as colorless crystals, m.p. 215 °C (dec.). $C_{32}H_{32}BN_7O_3S_2Zn$ (702.98): calcd. C 54.67, H 4.59, N 13.95, S 9.12; found C 54.98, H 4.49, N 13.36, S 8.73. ^{1}H NMR ($CDCl_3$): δ = 1.89 [s, 6 H, Me(Ph)], 1.93 [s, 6 H, Me(Ph)], 2.43 [s, 3 H, Me(pz)], 6.36 [s, 1 H, H(pz)], 6.77 [d, J = 2.1 Hz, 2 H, H(im)], 7.01 [d, J = 2.1 Hz, 2 H, H(im)], 7.04 (s, 2 H, Ar), 7.13–7.31 (m, 2 H, Ar), 7.45 (m, 6 H, Ar), 7.75 (s, 1 H, Ar) ppm.

Complex 2b: Prepared as **2a** from **HL²** (0.115 g, 0.20 mmol) in 50 mL of methanol and $Zn(ClO_4)_2{\cdot}6H_2O$ (0.074 g, 0.20 mmol) in 40 mL of methanol. Yield: 67 mg (45%) of **2a** as colorless crystals, m.p. 194 °C. $C_{32}H_{32}BClN_6O_4S_2Zn$ (740.43): calcd. C 51.91, H 4.36, N 11.35, S 8.66; found C 52.26, H 4.83, N 11.20, S 8.65. ^{1}H NMR ($CDCl_3$): δ = 1.70 [s, 3 H, Me(Ph)], 1.77 [s, 3 H, Me(Ph)], 1.83 [s, 3 H, Me(Ph)], 1.86 [s, 3 H, Me(Ph)], 2.45 [s, 3 H, Me(pz)], 6.59 [s, 1 H, H(pz)], 6.79 [s, br, 2 H, H(im)], 6.95 [s, br, 2 H, H(im)], 7.00 (s, 2 H, Ar), 7.10 (m, 4 H, Ar), 7.48 (m, 3 H, Ar), 7.87 (m, 2 H, Ar) ppm.

Complex 3b: This complex formed during an attempted synthesis of **L²Zn** acetate. It was prepared as **2a** from **HL²** (0.115 g, 0.20 mmol) and $Zn(OAc)_2{\cdot}6H_2O$ (0.044 g, 0.20 mmol). Workup yielded 144 mg (59%) of **3b** as colorless crystals, m.p. 210 °C (dec.). $C_{64}H_{64}B_2N_{12}S_4Zn$ (1216.6): calcd. C 63.19, H 5.30, N 13.82, S 10.54; found C 62.76, H 5.37, N 13.71, S 10.48. ^{1}H NMR ($CDCl_3$): δ = 1.60 [s, 3 H, Me(Ph)], 1.79 [s, 3 H, Me(Ph)], 1.83 [s, 3 H, Me(Ph)], 1.88 [s, 3 H, Me(Ph)], 2.66 [s, 3 H, Me(pz)], 6.28 [s, 1 H, H(pz)], 6.43 [d, J = 2.1 Hz, 2 H, H(im)], 6.49 [d, J = 2.1 Hz, 2 H, H(im)], 6.99 (s, 1 H, Ar), 7.02 (m, 2 H, Ar), 7.06 (s, 1 H, Ar), 7.17 (m, 3 H, Ar), 7.28 (m, 2 H, Ar), 7.84 (m, 2 H, Ar) ppm.

Complex 4a: A solution of **KL¹** (301 mg, 0.49 mmol) in 50 mL of methanol was slowly added dropwise, with stirring, to a solution of anhydrous ZnI_2 (155 mg, 0.49 mmol) in 30 mL of methanol. The resulting colorless precipitate was filtered off and the filtrate was reduced in vacuo to 20 mL to produce a precipitate of raw **4a**. Slow diffusion of toluene into a solution of raw **4a** in dichloromethane yielded 257 mg (69%) of **4a** as colorless crystals, m.p. 230 °C (dec.). $C_{30}H_{28}BIN_6O_2S_2Zn$ (771.83): calcd. C 46.69, H 3.66, N 10.89, S 8.31; found C 45.79, H 3.95, N 10.75, S 8.25. ^{1}H NMR ($CDCl_3$): δ = 2.49 [s, 3 H, Me(pz)], 3.85 (s, 6 H, OMe), 6.15 [s, 1 H, H(pz)], 6.91–7.95 [m, 17 H, H(im) + Ar] ppm.

 © 2005 Wiley-VCH Verlag GmbH & Co. KGaA, Weinheim

Complex 4b: Prepared as **2a** from **HL²** (57 mg, 0.10 mmol) and anhydrous ZnI_2 (52 mg, 0.16 mmol). Yield: 37 mg (48%) of **4b** as colorless crystals, m.p. 240 °C (dec.). $C_{32}H_{32}BIN_6S_2Zn$ (767.88): calcd. C 50.05, H 4.20, N 10.94, S 8.35; found C 49.84, H 3.96, N 10.95, S 8.03. ^{1}H NMR ($CDCl_3$): δ = 1.93 [s, 6 H, Me(Ph)], 2.08 [s, 6 H, Me(Ph)], 2.40 [s, 3 H, Me(pz)], 6.32 [s, 1 H, H(pz)], 6.73 [d, J = 2.1 Hz, 2 H, H(im)], 7.01 [d, J = 2.1 Hz, 2 H, H(im)], 7.11 (m, 3 H, Ar), 7.19 (s, 2 H, Ar), 7.30 (m, 3 H, Ar), 7.40 (m, 3 H, Ar) ppm.

Complex 5a: A solution of 33 μL (28 mg, 0.45 mmol) of ethanethiol in 5 mL of methanol was deprotonated by addition of 1.8 mL (0.45 mmol) of a 0.25 M solution of $NaOCH_3$ in methanol. A solution of $Zn(ClO_4)_2{\cdot}6H_2O$ (112 mg, 0.30 mmol) in 15 mL of methanol and then a solution of **KL¹** (186 mg, 0.30 mmol) in 40 mL of methanol were added dropwise to this solution with stirring. After stirring for 4 d the volume of the solution was reduced to 15 mL in vacuo. Filtration yielded raw **5a**, which was dissolved in dichloromethane. Slow diffusion of *n*-hexane into this solution precipitated 126 mg (59%) of **5a** as a colorless powder, m.p. 215 °C (dec.). $C_{32}H_{33}BN_6O_2S_3Zn{\cdot}0.25CH_2Cl_2$ (706.05 + 21.23): calcd. C 53.26, H 4.64, N 11.56, S 13.23; found C 53.27, H 4.43, N 11.76, S 13.01. ^{1}H NMR ($CDCl_3$): δ = 1.32 [t, J = 7.4 Hz, 3 H, CH_3(SEt)], 2.48 [s, 3 H, Me(pz)], 2.54 [q, J = 7.4 Hz, 2 H, CH_2(SEt)], 3.71 (s, 6 H, OMe), 5.29 (s, 0.5 H, CH_2Cl_2), 6.31 [s, 1 H, H(pz)], 6.69–6.85 (m, 2 H, Ar), 6.91 [d, J = 2.0 Hz, 2 H, H(im)], 6.99 [d, J = 2.0 Hz, 2 H, H(im)], 7.02–7.05 (m, 4 H, Ar), 7.34 (m, 2 H, Ar), 7.36–7.58 (m, 3 H, Ar), 7.95 (d, J = 7.0 Hz, 2 H, Ar) ppm.

Complex 5b: Prepared as **5a** from 54 μL (56 mg, 0.45 mmol) of benzylmercaptan, $Zn(ClO_4)_2{\cdot}6H_2O$ (112 mg, 0.30 mmol), and **KL¹** (186 mg, 0.30 mmol). Yield: 128 mg (55%) of **5b** as a colorless powder, m.p. 190 °C (dec.). $C_{37}H_{35}BN_6O_2S_3Zn$ (768.12): calcd. C 57.86, H 4.59, N 10.94, S 12.52; found C 57.26, H 4.59, N 11.87, S 11.63. ^{1}H NMR ($CDCl_3$): δ = 2.36 [s, 3 H, Me(pz)], 3.62 (s, 6 H, OMe), 3.38 [s, 2 H, CH_2(Bz)], 6.31 [s, 1 H, H(pz)], 6.69–6.76 (m, 2 H, Ar), 6.90 [d, J = 2.2 Hz, 2 H, H(im)], 6.96 [d, J = 2.2 Hz, 2 H, H(im)], 7.01–7.05 (m, 4 H, Ar), 7.19 (m, 2 H, Ar), 7.30 (m, 2 H, Ar), 7.34 (m, 1 H, Ar), 7.39 (d, J = 1.8 Hz, 2 H, Ar), 7.52 (m, 3 H, Ar), 7.91 (d, J = 7.0 Hz, 2 H, Ar) ppm.

Complex 5c: A solution of thiophenol (45 mg, 0.41 mmol) in 15 mL of methanol was deprotonated by addition of a 0.25 M solution of $NaOCH_3$ in methanol (1.64 mL, 0.41 mmol). This solution was added dropwise with stirring to a solution of **1b** (306 mg, 0.41 mmol) in 40 mL of chloroform. After stirring for 12 h the solvent was removed in vacuo and the residue treated with 20 mL of dichloromethane. The dichloromethane extract was filtered and the filtrate evaporated to dryness. Recrystallization from dichloromethane/methanol (1:1) yielded 194 mg (63%) of **5c** as a colorless powder, m.p. 225 °C (dec.). $C_{36}H_{33}BN_6O_2S_3Zn$ (754.09): calcd. C 57.34, H 4.41, N 11.14, S 12.76; found C 56.87, H 4.36, N 10.85, S 12.63. ^{1}H NMR ($CDCl_3$): δ = 2.48 [s, 3 H, CH_3(pz)], 3.79 (s, 6 H, OMe), 6.34 [s, 1 H, H(pz)], 6.72 (m, 2 H, Ar), 6.82 [d, J = 2.0 Hz, 2 H, H(im)], 6.97 [d, J = 2.0 Hz, 2 H, H(im)], 7.22 (m, 2 H, Ar), 7.29 (m, 2 H, Ar), 7.36 (d, J = 1.8 Hz, 2 H, Ar), 7.39 (m, 1 H, Ar], 7.50–7.60 (m, 5 H, Ar), 7.92 (m, 2 H, Ar) ppm.

Complex 5d: A solution of *p*-nitrothiophenol (125 mg, 0.81 mmol) in 30 mL of methanol was treated with 5.0 mL of a 0.25 M solution of NaOH in methanol (1.25 mmol), thereby turning red. A solution of $Zn(ClO_4)_2{\cdot}6H_2O$ (240 mg, 0.81 mmol) in 15 mL of methanol was slowly added dropwise, with stirring, to the red solution, which turned yellow. Finally, a solution of **KL¹** (500 mg, 0.81 mmol) in 50 mL of methanol was slowly added with stirring, upon which a yellow precipitate formed. Filtration and drying in vacuo yielded 279 mg (43%) of **5d** as a yellow powder, m.p. 200 °C. $C_{36}H_{32}BN_7O_4S_3Zn$ (799.09): calcd. C 54.11, H 4.04, N 12.27, S 12.04; found C 54.68, H 4.24, N 12.60, S 10.75. ^{1}H NMR ($CDCl_3$): δ = 2.51 [s, 3 H, Me(pz)], 3.82 (s, 6 H, OMe), 6.31 [s, 1 H, H(pz)], 6.92 [d, J = 2.1 Hz, 2 H, H(im)], 7.01 [d, J = 2.1 Hz, 2 H, H(im)], 7.35 (m, 11 H, Ar), 7.55 (d, J = 8.8 Hz, 2 H, $C_6H_4NO_2$), 7.83 (m, 2 H, Ar), 8.11 (d, J = 8.8 Hz, 2 H, $C_6H_4NO_2$) ppm.

Complex 5e: Prepared as **5d** from *N*-acetylhomocysteine ethyl ester (168 mg, 0.82 mmol), NaOH (21.7 mg, 0.82 mmol), $Zn(NO_3)_2{\cdot}4H_2O$ (214 mg, 0.82 mmol), and **KL¹** (506 mg, 0.82 mmol). Yield: 390 mg (56%) of **5e** as a colorless powder, m.p. 200 °C (dec.). $C_{38}H_{42}BN_7O_5S_3Zn$ (849.19): calcd. C 53.75, H 4.98, N 11.55, S 11.33; found C 53.62, H 4.84, N 11.75, S 11.46. ^{1}H NMR ([D_6]DMSO): δ = 1.15 [t, J = 6.8 Hz, 3 H, CH_3(Et)], 1.69–1.93 (m, 2 H, CH_2), 1.85 [s, 3 H, CH_3(Ac)], 2.45 [s, 3 H, CH_3(pz)], 2.65–2.76 (m, 2 H, CH_2), 3.78 (s, 6 H, OMe), 4.07 [q, J = 6.8 Hz, 2 H, CH_2(Et)], 4.31 (m, 1 H, CH), 6.47 [s, 1 H, H(pz)], 6.75–7.66 [m, 15 H, H(im) + Ar], 7.91 (m, 2 H, Ar), 8.13 (m, 1 H, NH) ppm.

Complex 6d: A solution of *p*-nitrothiophenol (33 mg, 0.20 mmol) in 30 mL of methanol was deprotonated with 0.8 mL of a 0.25 M solution of NaOH in methanol (0.20 mmol). This solution was slowly added dropwise, with stirring, to a solution of **KL²** (123 mg, 0.20 mmol) in 50 mL of methanol. The resulting yellow precipitate was filtered off and dried in vacuo to yield 81 mg (51%) of **6d** as a yellow powder, m.p. 225 °C (dec.). $C_{38}H_{36}BN_7O_2S_3Zn$ (795.15): calcd. C 57.40, H 4.56, N 12.33, S 12.10; found C 57.41, H 4.68, N 12.37, S 11.98. ^{1}H NMR ($CDCl_3$): δ = 1.89 [s, 6 H, Me(Ph)], 2.07 [s, 6 H, Me(Ph)], 2.43 [s, 3 H, Me(pz)], 6.34 [s, 1 H, H(pz)], 6.75 [d, J = 2.1 Hz, 2 H, H(im)], 6.93 (d, J = 9.0 Hz, 2 H, $C_6H_4NO_2$), 7.02 [d, J = 2.1 Hz, 2 H, H(im)], 7.09 (s, 1 H, Ar), 7.13 (s, 1 H, Ar), 7.19 (m, 7 H, Ar), 7.36 (m, 2 H, Ar), 7.46 (d, J = 9.0 Hz, 2 H, $C_6H_4NO_2$) ppm.

Methylation Reactions: Methyl iodide was used as a 1 M solution in chloroform. Equimolar amounts (0.1–0.2 mmol) of methyl iodide and one of the complexes **5** or **6** were combined in 5 mL of chloroform (for **5e** DMSO was used as the solvent). Reactions were followed by ^{1}H NMR spectroscopy and were found to produce the resulting thioethers quantitatively. After 10 min (**5a**, **5b**), 2 h (**5c, 5e**), or 1 d (**5d**, **6d**) the solvent was removed in vacuo. The residue was washed with two 3-mL portions of diethyl ether and then dried in vacuo. The remaining solid was pure **4a** or **4b**, as seen from the ^{1}H NMR spectrum. Of the resulting thioethers, CH_3SEt was found in the condensate and the others in the diethyl ether extracts, which also contained part of the iodide complexes **4**.

Complex **5a** (44 mg, 0.062 mmol) gave 45 mg (94%) of **4a**.

Complex **5b** (48 mg, 0.062 mmol) gave 43 mg (89%) of **4a**.

Complex **5c** (87 mg, 0.12 mmol) gave 70 mg (79%) of **4a**.

Complex **5d** (88 mg, 0.11 mmol) gave 54 mg (64%) of **4a**.

Complex **5e** (5.1 mg, 006 mmol) gave 2.5 mg (55%) of **4a**.

Complex **6d** (72 mg, 0.09 mmol) gave 33 mg (48%) of **4b**.

Kinetic Measurements: The standard solutions of complexes **5d** and **6d** and of methyl iodide in $CDCl_3$ (99.8%) were kept in the dark. All reagents and the cavity of the NMR spectrometer were thermostatted to 300.0 K before the measurements. The reagents were combined immediately prior to the measurements. The intensities of the ^{1}H NMR resonance of the SCH_3 protons of the resulting *p*-nitrothioanisole were recorded automatically every 100 s and stored for digital data processing. Each kinetic run was repeated once, and the averaged data were used for the calculations.

 © 2005 Wiley-VCH Verlag GmbH & Co. KGaA, Weinheim

Table 1. Crystallographic details.

	HL²	**3b**	**4a**	**4b**	**5d**	**6d**
Empirical formula	$C_{32}H_{33}BN_6S_2 \cdot CH_3OH$	$C_{64}H_{64}B_2N_{12}S_4Zn \cdot 2H_2O$	$C_{30}H_{28}BIN_6O_2S_2Zn$	$C_{32}H_{32}BIN_6S_2Zn \cdot CH_2Cl_2$	$C_{36}H_{32}BN_7O_4S_3Zn \cdot \frac{1}{2}CH_3OH$	$C_{38}H_{36}BN_7O_2S_3Zn$
Molecular mass	576.60 + 32.04	1216.57 + 36.03	771.78	767.88 + 84.93	799.09 + 13.96	795.15
Crystal size [mm]	0.2×0.2×0.2	0.4×0.2×0.2	0.2×0.1×0.1	0.2×0.2×0.2	0.2×0.1×0.1	0.4×0.2×0.2
Space group	$P2_12_12_1$	$P\bar{1}$	$P2_1/c$	$P\bar{1}$	$P\bar{1}$	$P\bar{1}$
Z	4	2	4	2	4	2
a [Å]	13.630(3)	13.522(2)	11.662(3)	10.112(9)	12.863(2)	10.163(3)
b [Å]	14.235(3)	14.939(2)	13.804(3)	11.852(10)	13.359(3)	11.762(4)
c [Å]	16.681(4)	16.844(3)	20.201(5)	17.166(14)	23.601(5)	17.824(6)
α [°]	90	80.214(3)	90	90.30(1)	95.950(4)	90.908(6)
β [°]	90	83.039(3)	95.976(4)	105.71(1)	100.031(4)	102.198(7)
γ [°]	90	74.849(3)	90	108.49(1)	100.469(4)	110.860(6)
V [Å^3]	3236(1)	3226(1)	3234(1)	1869(2)	3888(1)	1936(1)
d(calcd.) [g cm^{-3}]	1.24	1.29	1.59	1.49	1.39	1.38
μ(Mo-K_α) [mm^{-1}]	0.20	0.56	1.88	1.77	0.84	0.84
hkl range	h: –17 to 18	h: –17 to 17	h: –15 to 15	h: –13 to 13	h: –15 to 15	h: –13 to 11
	k: –19 to 19	k: –19 to 20	k: –18 to 18	k: –15 to 16	k: –15 to 15	k: –15 to 15
	l: –21 to 22	l: –22 to 21	l: –26 to 26	l: –22 to 22	l: –28 to 28	l: –22 to 23
Measured reflections	29296	29306	28220	16947	28935	11567
Independent reflections	7863	15099	7780	8763	13656	8225
Observed refl. [$I > 2\sigma(I)$]	4858	6692	3014	5308	5949	3719
Parameters	396	801	388	415	954	469
Refined reflections	7863	15099	7780	8763	13656	8225
R_1 (obsd. reflections)	0.061	0.063	0.063	0.042	0.075	0.054
wR_2 (all reflections)	0.175	0.198	0.242	0.121	0.246	0.125
Resid. e$^-$ density [e Å^{-3}]	+0.6/–0.4	+0.9/–0.6	+0.8/–1.4	+1.1/–1.0	+1.7/–0.6	+0.6/–0.6

The initial concentration of **5d** was adjusted to 0.010 M for all seven measurements, during which the concentrations of CH_3I were 0.040, 0.050, 0.060, 0.070, 0.080, 0.090, and 0.100 M. The resulting k_{obs} values for these concentrations were 3.4, 4.0, 5.0, 5.7, 6.7, 7.5, and 8.2×10^{-4} s^{-1}, respectively.

The initial concentration of **6d** was adjusted to 0.033 for all five measurements, during which the concentrations of CH_3I were 0.167, 0.209, 0.251, 0.293, and 0.335. The resulting k_{obs} values for these concentrations were 2.3, 2.9, 3.7, 4.2, and 4.9×10^{-4} s^{-1}, respectively.

Structure Determinations:[32] Crystals of **HL²**, **3b**, and **5d** were obtained by cooling saturated CH_2Cl_2/CH_3OH solutions, those of **4a** by diffusion of toluene into a CH_2Cl_2 solution, and those of **4b** and **6d** by cooling saturated CH_2Cl_2/*n*-pentane solutions. Diffraction data were recorded at room temp. with a Bruker Smart CCD diffractometer. Empirical absorption corrections (SADABS) were applied. The structures were solved by direct methods and refined anisotropically using the SHELX program suite.[33] Hydrogen atoms were included with fixed distances and isotropic temperature factors 1.2-times those of their attached atoms. Parameters were refined against F^2. Drawings were produced with SCHAKAL.[34] Table 1 lists the crystallographic details.

Acknowledgments

This work was supported by the Deutsche Forschungsgemeinschaft and the Fonds der Chemischen Industrie. We are indebted to Drs. W. Deck and H. Brombacher for help with the structure determinations and to Mrs. P. Klose for assistance in the laboratory.

[1] S. Ramaswamy, H. Eklund, B. V. Plapp, *Biochemistry* **1994**, *33*, 5230–5237 and references cited therein.
[2] R. G. Matthews, *Acc. Chem. Res.* **2001**, *34*, 681–689.
[3] G. Parkin, *Chem. Rev.* **2004**, *104*, 699–767.
[4] B. S. Hammes, C. J. Carrano, *Inorg. Chem.* **2001**, *40*, 919–927.
[5] B. S. Hammes, C. R. Warthen, D. C. Crans, C. J. Carrano, *J. Biol. Inorg. Chem.* **2001**, *6*, 82–90.
[6] C. A. Grapperhaus, T. Tuntulani, J. H. Reibenspies, M. Y. Darensbourg, *Inorg. Chem.* **1998**, *37*, 4052–4058.
[7] M. Machuqueiro, T. Darbre, *J. Inorg. Biochem.* **2003**, *94*, 193–196.
[8] S. J. Chiou, C. G. Riordan, A. L. Rheingold, *Proc. Natl. Acad. Sci. USA* **2003**, *100*, 3695–3700.
[9] B. M. Bridgewater, T. Fillebeen, R. A. Friesner, C. Parkin, *J. Chem. Soc., Dalton Trans.* **2000**, 4494–4496.
[10] J. J. Wilker, S. Lippard, *Inorg. Chem.* **1997**, *36*, 969–978.
[11] J. Seebacher, M. Ji, H. Vahrenkamp, *Eur. J. Inorg. Chem.* **2004**, 409–417.
[12] M. Ji, H. Vahrenkamp, *Eur. J. Inorg. Chem.* **2005**, 1398–1405.
[13] U. Brand, M. Rombach, J. Seebacher, H. Vahrenkamp, *Inorg. Chem.* **2001**, *40*, 6151–6157.
[14] H. Vahrenkamp, *Acc. Chem. Res.* **1999**, *32*, 589–596.
[15] M. Garner, J. Reglinski, I. Cassidy, M. D. Spicer, A. R. Kennedy, *Chem. Commun.* **1996**, 1975–1976.
[16] C. Kimblin, B. M. Bridgewater, D. G. Churchill, T. Hascall, G. Parkin, *Inorg. Chem.* **2000**, *39*, 4240–4243.
[17] M. Shu, R. Walz, B. Wu, J. Seebacher, H. Vahrenkamp, *Eur. J. Inorg. Chem.* **2003**, 2502–2511.
[18] B. Benkmil, M. Ji, H. Vahrenkamp, *Inorg. Chem.* **2004**, *43*, 8212–8214.
[19] M. Ji, B. Benkmil, H. Vahrenkamp, *Inorg. Chem.* **2005**, *44*, 3518–3523.
[20] M. M. Ibrahim, M. Shu, H. Vahrenkamp, *Eur. J. Inorg. Chem.* **2005**, 1388–1397.
[21] A. Looney, G. Parkin, A. L. Rheingold, *Inorg. Chem.* **1991**, *30*, 3099–3101.
[22] S. Trofimenko, *Scorpionates*, Imperial College Press, London, **1999**.
[23] C. Kimblin, T. Hascall, G. Parkin, *Inorg. Chem.* **1997**, *36*, 5680–5681.
[24] L. C. Myers, M. P. Terranova, A. E. Ferentz, G. Wanger, G. L. Verdine, *Science* **1993**, *261*, 1164–1167.

 © 2005 Wiley-VCH Verlag GmbH & Co. KGaA, Weinheim

[25] M. Förster, R. Burth, A. K. Powell, T. Eiche, H. Vahrenkamp, *Chem. Ber.* **1993**, *126*, 2643–2648.
[26] A. Rheingold, R. L. Ostrander, B. S. Haggerty, S. Trofimenko, *Inorg. Chem.* **1994**, *33*, 3666–3676.
[27] A. L. Johnson, J. C. Kauer, D. C. Sharma, R. I. Dorfmen, *J. Med. Chem.* **1969**, *12*, 1024–1028.
[28] P. Bonviccini, A. Levi, V. Lucchini, G. Scorrano, *J. Chem. Soc., Perkin Trans. 2* **1972**, 2267–2269.
[29] D. Villemin, M. Hachemi, *Synth. Commun.* **1996**, *26*, 2449–2460.
[30] R. C. Chambers, C. L. Hill, *J. Am. Chem. Soc.* **1990**, *112*, 8427–8433.
[31] T. Okajima, Z. H. Wang, Y. Fukazawa, *Chem. Lett.* **1991**, *1*, 37–40.
[32] CCDC-268614 (for **HL^2**), -268609 (for **3b**), -268610 (for **4a**), -268611 (for **4b**), -268612 (for **5d**) and -268613 (for **6d**) contain the supplementary crystallographic data for this paper. These data can be obtained free of charge from The Cambridge Crystallographic Data Center via www.ccdc.cam.ac.uk/data_request/cif.
[33] *SHELXTL* program package for the Bruker Smart CCD diffractometer, version 5.1, **2002**.
[34] E. Keller, *SCHAKAL* for Windows, University of Freiburg, **2001**.

Received: March 30, 2005
Published Online: September 8, 2005

 © 2005 Wiley-VCH Verlag GmbH & Co. KGaA, Weinheim

Classical 1,2,4-Triboracyclopentanes and Their Rearrangement into Nonclassical 2-Boryl-1,3-diboracyclobutanes: Intramolecular C–H Bond Activation by a B–B Moiety

David Scheschkewitz,[a] Peter Amseis,[a] Gertraud Geiseler,[a] Werner Massa,[a] Matthias Hofmann,[b] and Armin Berndt*[a]

Keywords: Ab initio computations / Boron heterocycles / Three-centre, two-electron bonds

1,2,4-Triboracyclopentanes **1a–c** in solution spontaneously transform into their nonclassical isomers **2a–c**. These have been characterised by NMR spectroscopy and X-ray structural analyses. Compounds **2a–c** are strongly distorted when compared with the five-membered ring of **1a**, the structure of which was determined for comparison. In addition, the pattern of the substituents at the boron centres in **2a**,**b** is different from that in **1a**,**b**. This can be rationalised on the basis of a rapid topomerisation in **2c** as determined by analysis of its temperature dependent ^{13}C NMR spectra. The environment of the boron centres B1 and B3 is exchanged by transforming the two 3c–2e bonds which both involve B1 into a B2–H and a B1–C 2c–2e bond. This leads to the 2-boryl-1,3-diboracyclobutane **4c** and formation of corresponding new 3c–2e bonds employing B3 gives the topomer of **2c**. The low barrier of this topomerisation reveals that **2a–c** may also be regarded as nonclassical isomers of the 2-boryl-1,3-diboracyclobutanes **4a–c**. Ab initio computations of models at the MP4SDTQ/6-311+G**// MP2/6-311+G** levels support this interpretation. In addition, they show that the transformation of **1u** to **2u** occurs by an intramolecular C–H bond activation process initiated by the B–B moiety. Derivatives of the type **1** and **2** described here represent the first examples of 1,2-diboron heterocycles which can be isolated as classical as well as nonclassical isomers.

(© Wiley-VCH Verlag GmbH & Co. KGaA, 69451 Weinheim, Germany, 2005)

Introduction

Classical forms of unsubstituted 1,2-diboron heterocycles of type **I–III** (Scheme 1) have been computed to be considerably higher in energy than their nonclassical forms **IV–VI**.[1,2] This is due to the two-electron aromaticity of **IV** and homoaromaticity of **V** and **VI**, respectively. The electron deficiency at the boron atoms in **I–III** is reduced in **IV–VI** by formation of two three-centre, two-electron (3c–2e) bonds. Experimentally, derivatives are known for nonclassical **IV**[3] and **V**[2] as well as for classical **II**[4] and **III**.[5] While the boron atoms of all nonclassical species bear only weakly donating substituents, those of the experimentally known classical ones carry amino substituents which strongly reduce the electron deficiency at these boron atoms. As a consequence, isomerisation of the classical compounds **II** or **III** into nonclassical compounds of type **V** or **VI** has not been observed so far. Recently, 1,2,4-triboracyclopentanes with only weakly donating substituents at the boron atoms became accessible in their classical form **1**.[6]

In this paper we show that 1,2,4-triboracyclopentanes **1a–c** (Scheme 2) isomerise into nonclassical isomers **2a–c**. Ab initio computations at the MP2/6-311+G** level[7] for the prototypes **1u** and **2u** (Scheme 3) reveal that these transformations are intramolecular C–H bond activations by B–B moieties. However, **2a**,**b** are isomers of the products to be expected from these C–H bond activations in **1a**,**b**. This discrepancy can be rationalised by an additional rearrangement via **4a**,**b** (Scheme 4) which shows up in **2c** as a topomerisation via **4c**. Therefore, compounds of type **2** may be regarded equally well as nonclassical 1,2,4-triboracyclopentanes and as nonclassical 2-boryl-1,3-diboracyclobutanes.

Results and Discussion

Syntheses and NMR Characterisation

Details of the preparation of 1,2,4-triboracyclopentanes **1a**,**b**[6] and **1d**[6] are described in the experimental section. Compound **1d** does not react with duryllithium to yield **1c** which, finally, was synthesised by oxidation of its dianion $\mathbf{1c^{2-}}$. This can be obtained by addition of duryllithium to the borenate **3**.[6] In $CDCl_3$ solution, **1a**,**b** transform into their nonclassical isomers **2a**,**b** within four and nine days, respectively. Isomerisation of **1c** into **2c** requires only 2 h in diethyl ether. Interestingly, $CDCl_3$ solutions of the stereo-

[a] Fachbereich Chemie der Universität Marburg,
Hans-Meerwein-Strasse, 35032 Marburg
Fax: +49-6421-2828917
E-mail: berndt@chemie.uni-marburg.de
[b] Anorganisch-Chemisches Institut der Universität Heidelberg,
Im Neuenheimer Feld 270, 69120 Heidelberg

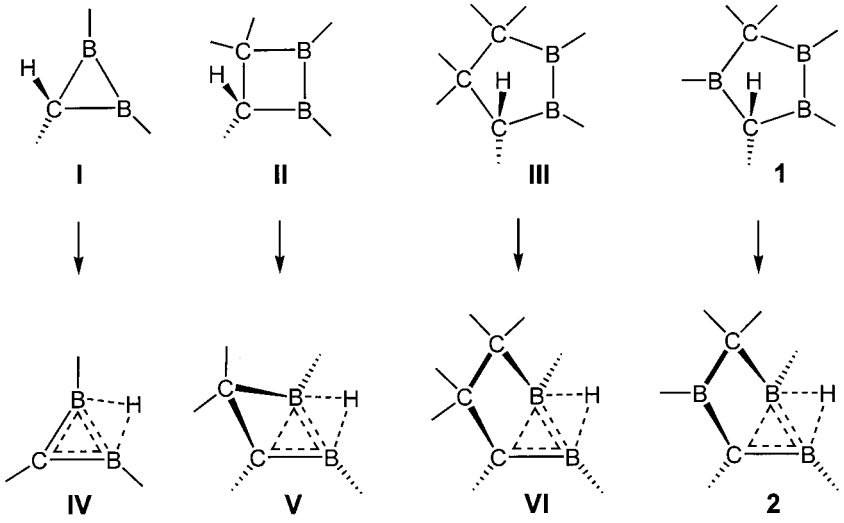

Scheme 1.

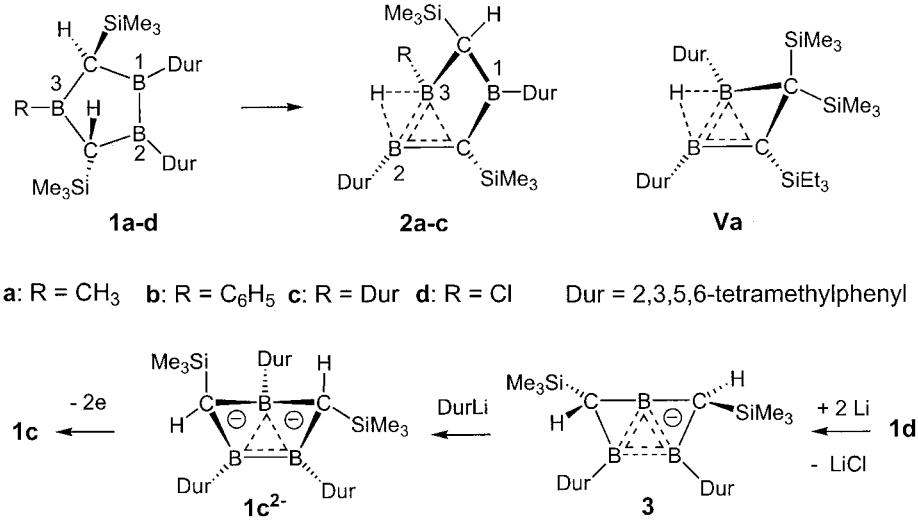

Scheme 2.

isomers of **1a**,**b** having the trimethylsilyl substituents in *cis* positions[8] do not show any isomerisation over a period of three months.

Compounds **2a–c** were characterised by ^{1}H, ^{13}C and ^{11}B NMR spectroscopy. The chemical shifts of the skeleton atoms of **2a**,**b** are in good agreement with those computed for **2u** at the IGLO/II/MP2/6-31+G* level and resemble those of **Va** (see Table 1).

Table 1. Selected NMR chemical shifts [ppm] of **2a**–**c**, **Va** (exp.) and **2u** (calcd. at IGLO/II/MP2/6-31+G*).

	2a	**2b**	**2c**	**2u**	**Va**
δ^{11}B B3[a]	0	–2	ca. 30[b]	–6.0	3[c]
δ^{11}B B2[a]	48	42	ca. 47[b]	46.9	
δ^{11}B B1[a]	56	57	ca. 47[b]	48.5	48[d]
δ^{13}C C1[a]	74.6	70.7	105	72.6	68.2[e]
δ^{13}C C2[a]	27.6	26.8	24.8	16.6	32.1[f]

[a] Numbering as in Figures 1, 2, 3 and 4. [b] Broad signal. [c] B1. [d] B2. [e] C3. [f] C4.

These chemical shifts are characteristic for homoaromatic species containing a 3c–2e bond between one carbon and two boron atoms. Compounds **2a–c** are rare examples of homoaromatics having two-membered homobridges. The boron centres B1 of **2a**,**b**, which are not part of the 3c–2e bond, are considerably shielded (48, 42 ppm) compared with those of **1a**,**b** (88, 82 ppm). This can be explained mainly by the interactions of the formally empty p orbital at B1 with the 3c–2e bond between B2, B3 and C1 (see NBO analysis of **2u** in section "Ab initio computations").

The substitution patterns at the boron atoms of **2a**,**b** are different from those of the precursors **1a**,**b**. While the boron centres between two carbon atoms carry a methyl or phenyl group in **1a**,**b**, it is a duryl group in **2a**,**b**. The methyl and phenyl substituents are found at a boron atom *adjacent* to a boron atom in **2a**,**b**. This was demonstated for **2a**,**b** by the X-ray structure analyses discussed below and for **2a** in solution by a selectively ^{11}B-decoupled ^{13}C NMR spectrum.

 © 2005 Wiley-VCH Verlag GmbH & Co. KGaA, Weinheim

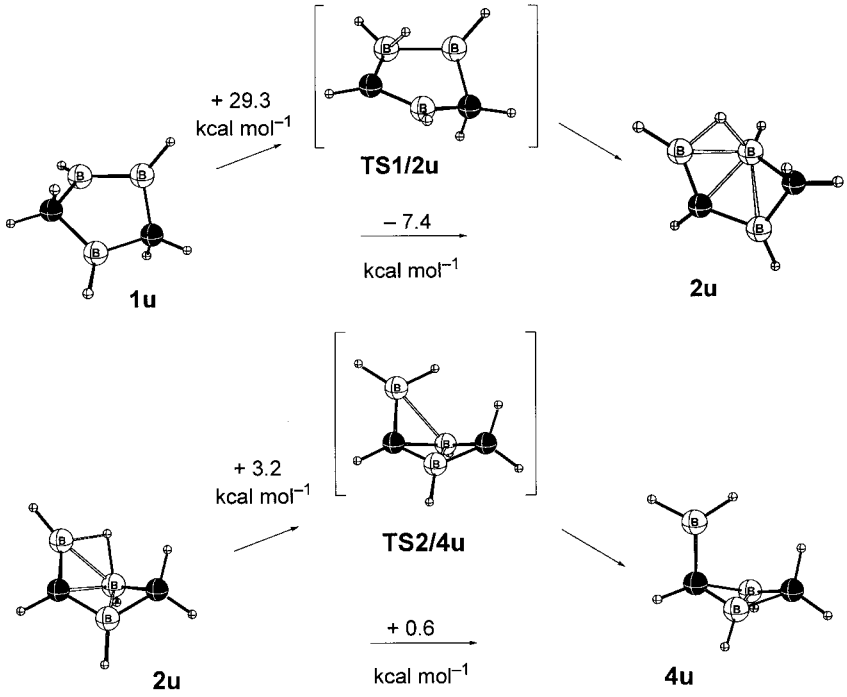

Scheme 3.

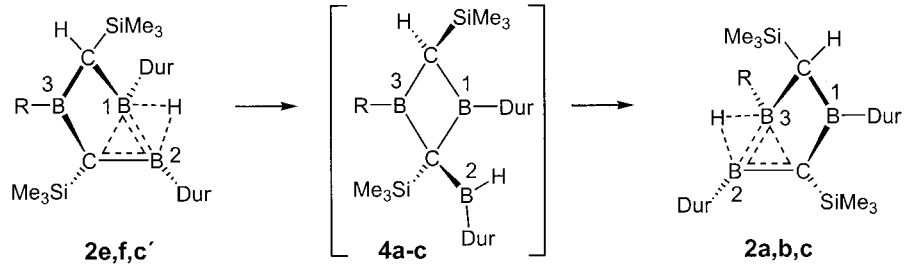

a,e: R = CH_3 **b,f**: R = C_6H_5 **c,c′**: R = Dur

Scheme 4.

Decoupling using the frequency corresponding to the chemical shift $\delta^{11}B = -2$ ppm strongly sharpens the ^{13}C NMR signal of the boron bound methyl group at 4.9 ppm. This indicates this methyl group to be bound to the pentacoordinate boron atom. Computations for **2u** (see below) clearly support the assignment of the most shielded boron atom to that of the highest coordination number.

The chemical shifts of the skeleton atoms of **2c** are distinctly different from those of **2a**,**b**. There is no sharp ^{11}B signal at about $\delta = 0$ for a pentacoordinate boron atom but only a broad shoulder at about 30 ppm of a very broad signal at about 47 ppm. The ^{13}C NMR spectrum of **2c** at ambient temperature shows signals for only two different kinds of duryl substituents and not for three as would be expected from its asymmetric structure which has been unambiguously deduced from the X-ray analysis described below. However, at –90 °C signals for three different duryl substituents can be observed which broaden at higher temperatures and show coalescence between –70 and –60 °C, respectively. From the chemical shift differences $\delta\nu$ of corresponding signals and their coalescence temperatures T_c, the following $\Delta G^{\#}$ values can be calculated using Equation (1): 9.2, 10.0, 9.7 and 10.0 kcal mol^{-1}.

$$\Delta G^{\#} = 4.57 \cdot T_c \cdot [9.97 + \log (T_c/\delta\nu)] \quad (1)$$

On average, a barrier of exchange of 9.7 kcal mol^{-1} can be obtained. We have assigned this barrier to the enantiomerisation of **2c′** to **2c** which arises through opening of the 3c–2e bonds in **2c′** to form the 2-boryl-1,3-diboracyclobutane **4c** and the corresponding new 3c–2e bonds employing the C1–B3 and B2–H bond. These transformations lead to **2c**, the enantiomer of planar-chiral **2c′**. The enantiomerisation of **2c** can be observed by NMR spectroscopy because it includes a topomerisation of two duryl substituents.

On the basis of the topomerisation of **2c′**, the unexpected pattern of substituents in **2a**,**b** can easily be explained by

 © 2005 Wiley-VCH Verlag GmbH & Co. KGaA, Weinheim

the corresponding process leading to isomerisation instead of topomerisation. Opening of both 3c–2e bonds in the primarily formed **2e**,**f** generates the classical 2-boryl-1,3-diboretanes **4a**,**b.** If the ring boron centre carrying the sterically less demanding substituent is employed in reforming the corresponding 3c–2e bonds, **2a**,**b** are obtained which are isomers of **2e**,**f**.

Crystal Structures

Figures 1, 2, 3 and 4 show the structures of **1a** and **2a–c** in the crystal. Characteristic distances and angles of **2a–c** and **1a** are compared with those computed for **2u** (Table 2).

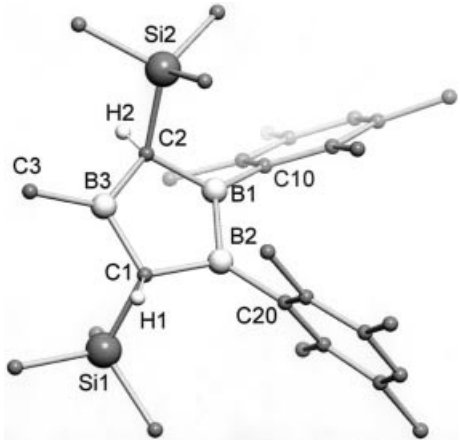

Figure 1. Structure of **1a** in the crystal. Most of the hydrogen atoms have been omitted for clarity. Selected bond lengths [pm] and angles [°] (completing Table 2): C1–B3 156.6(3), B3–C2 157.5(3), C2–B1 156.0(2), C1–Si1 189.8(2), B1–C10 158.0(2), C2–Si2 191.6(2), B2–C20 157.6(2); B1–C2–B3 107.6(1).

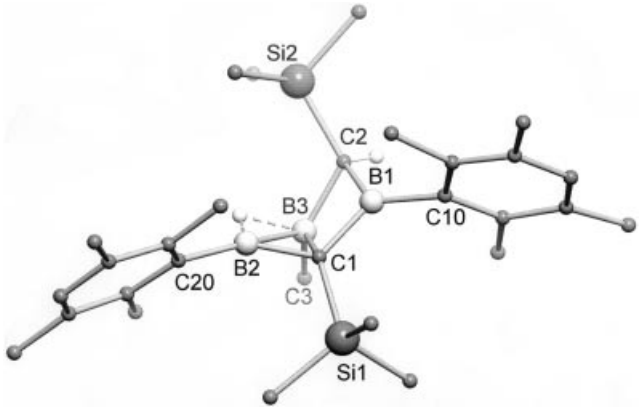

Figure 2. Structure of **2a** in the crystal. Most of the hydrogen atoms have been omitted for clarity. Selected bond lengths [pm] and angles [°] (completing Table 2): C1–B1 156.7(5), B1–C2 156.2(5), C2–B3 160.8(5), C1–Si1 188.3(3), B1–C10 159.0(5), C2–Si2 185.8(4), B3–C3 158.1(5), B2–C20 155.6(5); C1–B1–C2 106.6(3), B1–C2–B3 78.2(3).

The five-membered rings of **2a–c** are strongly distorted in comparison with that in **1a**. This can be demonstrated, inter alia, by the much shorter transannular C1···B3 distances in **2a–c** [178.0(5), 179.6(3) and 219.9(7) pm, respectively] compared with the shortest in **1a** [C2···B2 = 261.6(3) pm]. The bonding distances and angles of the C1B2B3 moiety of **2a**,**b** resemble those of the corresponding part of homoaromatic **Va**[3] (Table 2). Elongation of C1···B3 in **2a**,**b** relative to **Va** can be explained by weakening of the 3c–2e bond due to interaction with the formally empty orbital at B1 (see computations). For **2c**, the transannular B···C distance (219.9 pm) is about midway between those of **2a**,**b** and **1a**. In **2a** the C1,B1,B3 plane is folded towards the C1,B2,B3 and B1,C2,B3 planes by angles of 48 and 25°, respectively. In **2c** the corresponding angles are only 39 and 6°. Clearly, the sterically demanding duryl substituent at B3 in **2c** prevents the strong folding present in **2a,b** and **2u**, all of which lack a large substituent at the boron centre B3.

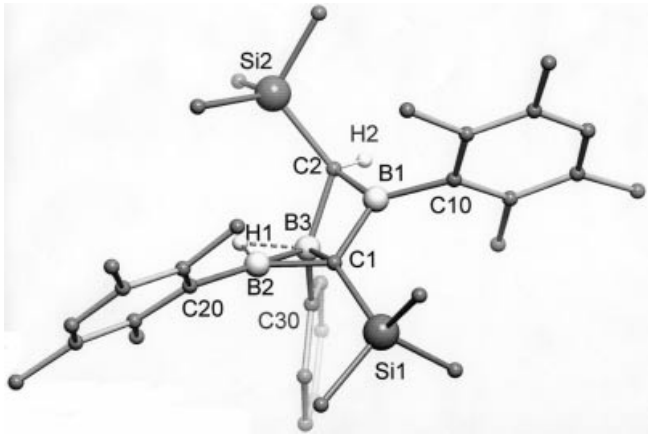

Figure 3. Structure of **2b** in the crystal. Most of the hydrogen atoms have been omitted for clarity. Selected bond lengths [pm] and angles [°] (completing Table 2): C1–B1 156.9(3), B1–C2 155.8(3), C2–B3 160.8(3), C1–Si1 189.3(2), B1–C10 157.9(3), C2–Si2 185.8(2), B3–C30 158.1(3), B2–C20 155.3(3); C1–B1–C2 107.9(2), B1–C2–B3 76.8(1).

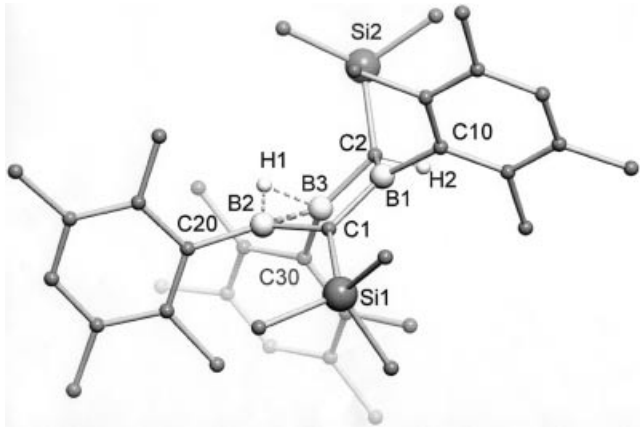

Figure 4. Structure of one of the two independent molecules **2c** in the crystal structure of **2c**·pentane. Most of the hydrogen atoms have been omitted for clarity. Selected bond lengths [pm] and angles [°] (completing Table 2): C1–B1 151.8(8), B1–C2 160.5(8), C2–B3 153.3(8), C1–Si1 189.2(6), B1–C10 159.3(7), C2–Si2 186.9(6), B3–C30 156.6(8), B2–C20 155.5(7); C1–B1–C2 109.7(4), B1–C2–B3 92.7(4).

 © 2005 Wiley-VCH Verlag GmbH & Co. KGaA, Weinheim

Table 2. Comparison of characteristic distances [pm] and angles [°] of **2a–c**, **Va**, **1a** (exp.) and **2u** (calcd. at MP2/6-311+G**).

	2u	**2a**	**2b**	**2c**·pentane	**Va**	**1a**
B2–B3	180.3	186.9(6)	187.2(3)	192.4(9)	179.9(3)[a]	175.9(2)[b]
C1–B2	147.1	149.5(5)	147.8(3)	146.5(7)	147.2(3)[c]	156.0(2)
C1···B3	180.5	178.0(5)	179.6(3)	219.9(9)	172.3(3)[d]	263.2(2)[e]
B1···B3	193.1	200.0(5)	196.8(3)	227.3(8)	–	252.9(3)[f]
C1–B2–B3	66.0	62.7(2)	63.6(1)	79.7(4)	62.7(1)[g]	104.8(1)[h]
B2–C1–B3	65.9	69.0(2)	69.0(1)	59.4(4)	68.0(1)[i]	106.6(1)
C1–B3–B2	48.1	48.3(2)	47.5(1)	41.0(3)	49.3(1)[j]	111.9(1)[k]
B2–B3–C1–B1	–145.3	–131.9(3)	–133.6(2)	–140.7(5)	133.7(2)[l]	158.6(2)[m] 163.5(2)[n]

[a] B2–B1. [b] B1–B2. [c] C3–B2. [d] C3···B1. [e] C1···B1. [f] B3···B2. [g] B1–B2–C3. [h] B1–B2–C1. [i] B2–C3–B1. [j] C3–B1–B2. [k] C1–B3–C2. [l] B2–B1–C3–C4, positive sign since the corresponding enantiomer was used. [m] B2–B1–C1–B3. [n] B1–B2–C2–B3.

Ab Initio Computations

Energies and geometries of model compounds **1u** and **2u** were computed at the MP2/6-311+G** level.[7] Bond lengths and angles obtained for **2u** are in good agreement (Table 2) with the corresponding data from the X-ray crystal structure determinations of **2a**,**b**. Chemical shifts computed at the IGLO/II/MP2/6-31+G* level for **2u** agree (Table 1) with the experimental data of **2a**,**b** but not with those of **2c**. This indicates the structure of **2c** to be different from those of **2a**,**b** in solution as well.

NBO analyses for **2u** reveal a 3c–2e bond between the neighbouring boron atoms and the formally tricoordinate carbon atom occupied by 1.84 electrons. The 0.26 electrons in the p orbital of the boron centre between carbon atoms indicate its interaction with the CB_2 3c–2e bond and explain the NMR shielding of the boron atom of the two-membered homo bridge. This interaction is essential for the stabilisation of **2u** relative to **1u** by 7.4 kcal mol^{-1}: the related nonclassical **VIu** with CH_2 instead of BH in the two-membered homo bridge is only 0.5 kcal mol^{-1} lower in energy than the classical C_s symmetric **IIIu**.[2,9]

The transition state **TS1/2u** for the transformation of **1u** into **2u** was computed to be 29.3 kcal mol^{-1} higher in energy than **1u**. **TS1/2u** has a short C–B distance (151.8 pm), a very long C–H (159.9 pm) distance as well as short (130.9 pm) and long (158.1 pm) B–H distances. According to an NBO analysis it contains a 3c–2e C–H–B bridge occupied by 1.79 electrons (29% at C, 24% at B and 37% at H). Only 4 and 7% of the two electrons are found in the p orbitals of the adjacent boron centres. This transition state thus describes the activation of a C–H bond by a neighbouring B–B moiety. The five-membered ring of the transition state is still considerably less distorted than that of the product **2u**.

Computations also revealed that classical **4u** is only 0.6 kcal mol^{-1} higher in energy than nonclassical **2u** and that the barrier for the **2u** → **4u** rearrangement via transition state **TS2/4u** is only 3.2 kcal mol^{-1}**.**

Compound **4u** is considerably stabilised by C–B hyperconjugation as revealed by an NBO analysis which showed the formally empty orbitals of the boron atoms to be occupied by 0.145 and 0.163 electrons at the boryl and ring boron centres, respectively. This stabilisation is certainly reduced by the substituents in **4a–c** and, as a result, the barrier from **2e**,**f**,**c′** to **2a**,**b**,**c** can be expected to be larger.

Conclusions

Classical and nonclassical 1,2,4-triboracyclopentanes **1a–c** and **2a–c** are the first representatives of 1,2-diboron heterocycles which can be isolated as classical as well as nonclassical isomers. Isomerisation of **1a**,**b** can be easily observed and computations for models reveal an intramolecular C–H bond activation by a B–B moiety as the mechanism for this process. Nonclassical 1,2,4-triboracyclopentanes **2a–c** are only slightly lower in energy than the corresponding classical 2-boryl-1,3-diboretanes **4a–c** which are considerably stabilised by C–B hyperconjugation, the general alternative to stabilisation by formation of 3c–2e bonds. Compounds of type **2** may therefore be regarded as nonclassical 2-boryl-1,3-diboracyclobutanes as well as nonclassical 1,2,4-triboracyclopentanes.

Experimental Section

General: Reactions were carried out under dry argon or nitrogen using standard Schlenk techniques. Solvents were dried, distilled and saturated with nitrogen. Glassware was dried with a heat gun under high vacuum. ^{1}H, ^{13}C NMR spectroscopy: Bruker DRX 200 and Bruker AC 500 instruments, ^{11}B NMR: Bruker DRX 200 instrument. The NMR references used were Me_4Si and BF_3·Et_2O. Melting points (uncorrected) were measured under argon.

4-Methyl-1,2-bis(2′,3′,5′,6′-tetramethylphenyl)-*trans*-3,5-bis(trimethylsilyl)-1,2,4-triboracyclopentane (1a): MeLi solution (Et_2O, 1.6 M, 4.20 mL) was added by syringe to a solution of **1d** (3.45 g, 6.8 mmol) in Et_2O (50 mL) at –78 °C. The solution was then allowed to reach –10 °C over 1 h with stirring. Stirring was then suspended to allow the salts to settle and the solution was decanted through a precooled reversed frit (–15 °C, about 4 cm diameter). All solvents were removed at –10 °C. The yellow residue consisted of spectroscopically pure **1a** which was used for subsequent reactions immediately after preparation. Yield: 3.31 g (99%) of deeply yellow **1a**, m.p. 105–106 °C (dec.) ^{1}H NMR (300 MHz, $CDCl_3$, 25 °C): δ = 6.88 (s, 2 H, Dur-H), 3.31 (s, 2 H, BCH), 2.12–1.98 (br., 24 H in total), 1.10 (s, 3 H, BCH_3), 0.03 (s, 18 H, $SiMe_3$) ppm. ^{13}C{^{11}B}NMR (125 MHz, $CDCl_3$, –10 °C): δ = 149.2 (s, *i*-C), 132.8, 131.5 (both s, *o*- and *m*-C), 130.0 (d, *p*-C), 66.4 [d, ^1J(C,H)

= 107 Hz, BCH], 20.5, 19.5 (both q, Dur-CH_3), 13.9 [br. q, ^1J(C,H) = 120 Hz, BCH_3], 2.8 (q, $SiMe_3$) ppm. ^{11}B NMR (96 MHz, $CDCl_3$, 25 °C): δ = 104 (2B), 88 (1B) ppm.

4-Phenyl-1,2-bis(2′,3′,5′,6′-tetramethylphenyl)-*trans*-3,5-bis(trimethylsilyl)-1,2,4-triboracyclopentane (1b): PhLi solution (cyclohexane/Et_2O, 1.85 M, 2.05 mL) was added to a solution of **1d** (1.91 g, 3.8 mmol) in Et_2O (50 mL) at –78 °C. The mixture was allowed to reach room temperature over 2 h and stirring was continued for 1 h at this temperature. The solvents were removed in vacuo and the residue was digested with pentane (50 mL). The salts were separated from the deep yellow solution by filtration with a reversed frit and washed with pentane (10 mL). The filtrates were reduced to dryness in vacuo yielding spectroscopically pure **1b**. Yield: 2.04 g (99%) of deep yellow **1b**, m.p. 99 °C (dec.). For spectroscopic data see ref.[6]

4-Chloro-1,2-bis(2′,3′,5′,6′-tetramethylphenyl)-*trans*-3,5-bis(trimethylsilyl)-1,2,4-triboracyclopentane (1d): $B(OMe)_3$ (9.15 g, 88.0 mmol, 10 mL) was added slowly by syringe to a suspension of dilithium-2,3-bis(2′,3′,5′,6′-tetramethylphenyl)-1,4-bis(trimethylsilyl)-2,3-diboratabuta-1,3-diene[6] (13.4 g, 21.5 mmol) in pentane (200 mL) at –78 °C. The mixture was allowed to reach room temperature during which time it gradually became yellow. Stirring was continued overnight and the solvents were then removed in vacuo. The viscous residue was thoroughly dried in vacuo for 2 h and was then digested with pentane (200 mL) and cooled again to –78 °C. After addition of BCl_3 (30 g, 256 mmol) with a syringe, the mixture was warmed to room temperature over 2 h and stirring was continued for 30 min at this temperature. All volatile materials were then removed in vacuo and the solid residue digested with pentane (200 mL). The salts were filtered through a reversed frit and washed with pentane (2×20 mL). The combined filtrates were reduced to dryness in vacuo and thoroughly dried thereafter. The deep yellow residue was of almost spectroscopic purity. Crystallisation from pentane (50 mL) at –30 °C yielded **1d** as yellow crystals. Yield: 8.17 g (75%) of bright-yellow **1d**, m.p. 134 °C (dec.). For spectroscopic data see ref.[6]

1-Methyl-2,4-bis(2′,3′,5′,6′-tetramethylphenyl)-3,5-bis(trimethylsilyl)-μ(1,2)-hydro-3-dehydro-1,2,4-triboracyclopentane (2a): A solution of freshly prepared **1a** (3.00 g, 6.17 mmol) in $CDCl_3$ (20 mL) was stored for 4 d at room temperature and the solution was monitored frequently by ^{1}H NMR spectroscopy. After completion of the reaction all volatile materials were removed in vacuo. The white residue consisted of essentially pure **2a** which could be crystallised at –30° from toluene. Yield: 2.97 g (99%) of white **2a**, m.p. 113 °C. ^{1}H NMR (500 MHz, $CDCl_3$, –40 °C): δ = 7.21, 6.99 (both s, 1 H each, Dur-H), 6.72 (br. s, 1 H, B–H–B), 2.49, 2.43, 2.37, 2.31, 2.28, 2.19 (all s, 24 H in total, Dur-CH_3), 1.10 (s, 1 H, CHSi), 0.66 (s, 3 H, BCH_3), 0.01, –0.26 (both s, 9 H each, $SiMe_3$) ppm. ^{13}C NMR (125 MHz, $CDCl_3$, –40 °C): δ = 146.7, 133.9 (each br. s, *i*-C), 140.0, 138.4, 134.0, 133.1, 133.05, 132.9, 132.8, 131.8 (each s, *o*- and *m*-C), 134.9, 129.6 (both d, *p*-C), 74.6 (s, B_2C), 27.6 [d, ^1J(C,H) = 116 Hz, B_2CH], 20.6, 20.5, 20.3, 20.1, 19.6, 19.3 (all q, Dur-CH_3), 4.9 [br. q, ^1J(C,H) = 117 Hz, BCH_3], 0.9, 0.2 (both q, $SiMe_3$) ppm. ^{11}B NMR (96 MHz, $CDCl_3$, 25 °C): δ = 56, 48, 0 (each 1B) ppm.

1-Phenyl-2,4-bis(2′,3′,5′,6′-tetramethylphenyl)-3,5-bis(trimethylsilyl)-μ(1,2)-hydro-3-dehydro-1,2,4-triboracyclopentane (2b): A solution of **1b** (5.67 g, 10.3 mmol) in $CDCl_3$ (25 mL) was stored for 9 d at room temperature and was monitored frequently by ^{1}H NMR spectroscopy. All volatile materials were then removed in vacuo and the residue was dissolved in a 1:1-mixture of Et_2O and pentane (30 mL). After four days at –30 °C **2b** precipitated as a white solid which was contaminated with approx. 5% of a product of unknown constitution. Yield: 1.97 g (35%) of white **2b**, m.p. 128 °C. ^{1}H NMR (500 MHz, $CDCl_3$, 25 °C): δ = 7.5 (br., BHB, located by ^{1}H/^{1}H COSY to d at 1.43), 7.5, 7.4 (br.s, 6 H in total, Ph–H and B–H–B), 7.17, 6.91 (both s, 1 H each, Dur-H), 2.61, 2.32, 2.28, 2.20, 2.2 (br.), 1.7 (br) (all s, 24 H in total, Dur-Me), 1.43 [d, ^3J(H,H) = 4.6 Hz, 1 H, CHSi, identified by a cross peak to δ^{13}C = 26.8 in a C,H correlated spectrum], 0.09, –0.12 (both s, 9 H each, $SiMe_3$) ppm. ^{1}H NMR (500 MHz, $CDCl_3$, –40 °C) 7.7–7.6 (br., 6 H in total, Ph–H and B–H–B), 7.24, 6.99 (both s, 1 H each, Dur-H), 2.65, 2.36, 2.31, 2.29, 2.28, 2.18, 2.02, 1.67 (all s, 3 H each, Dur-Me), 1.51 [d, ^3J(H,H) = 4.6 Hz, 1 H, CHSi], 0.09, –0.12 (both s, 9 H each, $SiMe_3$) ppm. ^{13}C NMR (75 MHz, $CDCl_3$, 25 °C): δ = 146.8 (br. s, *i*-C), 140.8, 139.8, 134.0, 133.5, 132.9, 132.5 (all s, Dur-*o*- and *m*-C), 136.7, 127.3 (both d, Ph-*o*- or *m*-C), 135.5, 130.0 (both d, Dur-*p*-C), 128.3 (d, Ph-*p*-C), 71.9 (br. s, B_2C), 26.8 [d, ^1J(C,H) = 113 Hz, B_2CH], 21.1, 20.3, 20.2, 20.0, 19.55, 19.50 (all q, Dur-CH_3), 1.6, 0.8 ppm (both q, $SiMe_3$), Ph-*i*-C and one Dur-*i*-C not observed. ^{13}C NMR (125 MHz, $CDCl_3$, –40 °C): δ = 146.5, 139.2 (both br., Dur-*i*-C′s), 141.0, 139.7, 133.9, 133.4, 133.0,. 132.9, 132.6, 132.3 (Dur-*o*- and *m*-C′s), 136.6, 127.2 (br., Ph-*o*- or *m*-C′s), 135.5, 129.7 (Dur-*p*-C′s), 133.1 (br., Ph-*i*-C), 128.2 (Ph-*p*-C), 70.7 (B_2C), 26.4 (B_2CH), 21.0, 20.6, 20.4, 20.3, 20.0, 19.9, 19.6, 19.5 (Dur-CH_3), 1.4, 0.6 ($SiMe_3$) ppm. ^{11}B NMR (160 MHz, $CDCl_3$, 25 °C): δ = 57, 42, –2 ppm (each 1B).

1,2,4-Tris(2′,3′,5′,6′-tetramethylphenyl)-3,5-bis(trimethylsilyl)-μ(1,2)-hydro-3-dehydro-1,2,4-triboracyclopentane (2c): A mixture of **1d** (5.5 g, 10.85 mmol) and lithium powder (0.25 g) in diethyl ether (70 mL) was stirred at room temperature and monitored frequently by ^{11}B NMR spectroscopy until the signals of **1d** were replaced by those of **3** at δ = 24 and 21 ppm (about 1 h). After cooling to –78 °C, duryllithium (1.53 g, 10.85 mmol) was added with stirring. Formation of the dianion of **1c** during warming to room temperature was indicated by the presence of a ^{11}B NMR signal at δ = –16 ppm. After disappearance of the signals of **3** and cooling to –78 °C, 2,3-dibromo-2,3-dimethylbutane (2.6 g, 10.85 mmol) was added and the mixture allowed to warm to room temperature with stirring for an additional 1 h. ^{11}B NMR signals at δ = 97 and 80 ppm unambiguously indicated the formation of **1c**. All volatile materials were removed in vacuo and the residue was dissolved in pentane (50 mL). The salts were separated by filtration with a reversed frit and washed further with pentane (10 mL). The filtrate was reduced to dryness in vacuo yielding yellow **2c** which could be crystallised at –30 °C from pentane**.** Yield: 6.2 g (84%) of yellow **2c**, m.p. 134 °C. ^{1}H NMR (500 MHz, CD_2Cl_2, 25 °C): δ = 7.87 (br., 1 H, BHB), 7.02, 6.98 (both s, 1H and 2 H, respectively, *p*-H), 2.30, 2.26, 2.20, 2.10, 1.95 (all s, 36 H in total, Dur-Me), 1.17 (d, ^1J = 6.2 Hz, 1 H, CHSi), 0.06, –0.15 (both s, 9 H each, $SiMe_3$) ppm. ^{13}C NMR (125 MHz, CD_2Cl_2, 25 °C): δ = 143.4 (br. s, *i*-C), 136.9, 133.9, 133.6, 133.4 (all s, Dur-*o*- and *m*-C), 132.6, 131.0 (all d, 1C and 2C, *p*-C), 102.3 (br. s, B_2C), 25.0 (br. B_2CH), 21.1, 19.9, 19.7, 19.6 (all q, Dur-CH_3), 1.6, 0.9 (both q, $SiMe_3$) ppm. ^{13}C NMR (125 MHz, CD_2Cl_2, –90 °C): δ = 149.0, 146.0, 142.3, 137.5, 136.0, 135.6, 135.0, 134.5, 133.3,. 132.5, 132.1, 131.6 (*o*- *m*- and *i*-C′s), 131.6, 130.1, 129.1 (*p*-C), 89.1 (B_2C), 21.6 (B_2CH), 22.2, 21.6, 21,4, 20.3, 20.2, 20.1, 19.1, 18.7, 18.1 (Dur-CH_3), –0.01, –0.21 ($SiMe_3$) ppm. ^{11}B NMR (96 MHz, $CDCl_3$, 25 °C): δ = ca. 47 (2B), ca. 30 ppm (1B).

X-ray Crystal Structure Analyses of 1a, 2a, 2b and 2c·pentane: Single crystals were grown from toluene/Et_2O at 0 °C for **2a** and pentane at –30 °C for **2b** and **2c**. Those of **1a** were obtained from diethyl ether at –30 °C. The crystals were investigated on imaging plate systems (IPDS Stoe) using graphite monochromated Mo-K_α radiation at 193 K. The space groups were determined from the

 © 2005 Wiley-VCH Verlag GmbH & Co. KGaA, Weinheim

Table 3. Crystal and experimental data for the structure determinations of **1a**, **2a**, **2b** and **2c**·pentane.

			1a	**2a**	**2b**	**2c**·pentane
Empirical formula			$C_{29}H_{49}B_3Si_2$	$C_{29}H_{49}B_3Si_2$	$C_{34}H_{51}B_3Si_2$	$C_{43}H_{71}B_3Si_2$
Formula mass			486.29	486.29	548.36	676.61
Measuring temperature			193 K	193 K	193 K	193 K
Crystal system			monoclinic	triclinic	monoclinic	triclinic
Space group			$P2_1/c$	$P\bar{1}$	$P2_1/c$	$P\bar{1}$
Unit cell	*a*	[pm]	1187.1(1)	877.8(1)	2036.4(1)	15.985(2)
	b	[pm]	1427.7(1)	1131.1(2)	1121.6(1)	16.758(2)
	c	[pm]	1905.1(1)	1725.1(3)	1596.7(1)	17.223(2)
	α	[°]	90	96.37(1)	90	77.21(1)
	β	[°]	104.45(1)	97.65(1)	110.49(1)	79.31(2)
	γ	[°]	90	109.46(1)	90	89.87(2)
Volume [Å^3]			3126.7(4)	1578.3(4)	3416.2(4)	4417.5(9)
Z			4	2	4	4
Calculated density [g cm^{-3}]			1.033	1.023	1.066	1.017
Absorption coefficient [mm^{-1}]			0.128	0.127	0.124	0.107
F(000)			1064	532	1192	1488
crystal size [mm]			0.55 × 0.40 × 0.10	0.30 × 0.30 × 0.05	0.30 × 0.25 × 0.15	0.45 × 0.30 × 0.05
Θ_{max} [°]			25.02	24.97	25.98	25.96
Index range			–14/14, –16/16, –22/22	–10/10, –13/13, –20/20	–25/24, –13/13, –19/19	–19/19, –20/20, –21/21
Scan type			ω-scans	ω-scans	φ-scans	φ-scans
No. of reflections			23617	14411	23778	42952
Unique refl., (R_{int})			5467 (0.0399)	5408 (0.0905)	6647 (0.0624)	16051 (0.1418)
Observed refl. [$I > 2\sigma(I)$]			4529	2878	3669	4713
Parameters, data/param. ratio			331, 16.5	330, 16.4	374, 17.8	916, 17.5
Goodness-of-fit (F^2)			1.071	0.904	0.814	0.852
R [$I > 2\sigma(I)$]			0.0375	0.0588	0.0403	0.0771
wR_2 (all refl.)			0.1140	0.1572	0.0879	0.1829
Largest diff. peak/hole [e Å^{-3}]			+0.173/–0.214	+0.303/–0.234	+0.259/–0.212	+0.462/–0.259

systematic absences and intensity statistics, no absorption corrections were applied. The structures were solved by direct methods and refined against all F^2 data using full-matrix least-squares and difference Fourier techniques [SHELX programmes[10,11]]. Most hydrogen atoms were kept riding in calculated positions with isotropic displacement factors taken as 1.2 times (1.5 times for CH_3) the U_{eq} value of the corresponding C atom. The hydrogen atoms at the central ring were located and refined with individual isotropic displacement factors. For all heavier atoms, anisotropic displacement parameters were used. The structure of **2c**·pentane showed two independent molecules and, in addition, two strongly vibrating or disordered pentane molecules in the asymmetric unit. The solvent molecules were refined with restraints in geometry and in the anisotropy of the displacement factors. Due to this problem and the weak data set [29% of reflections $> 4\sigma(F)$ only] the precision of the structural data is reduced. Details of the experimental and crystal data are summarised in Table 3. Crystallographic data (excluding structure factors) for the structures reported in this paper have been deposited with the Cambridge Crystallographic Data Centre as supplementary publication no. CCDC-245202 (for **1a**), -245204 (for **2a**), -245203 (for **2b**) and -245205 (for **2c**). Copies of the data can be obtained free of charge on application to CCDC, 12 Union Road, Cambridge CB2 1EZ, UK [Fax: +44-1223-336-033; E-mail: deposit@ccdc.cam.ac.uk]

Acknowledgments

This work was supported by the Deutsche Forschungsgemeinschaft (SPP Polyeder) and the Fonds der Chemischen Industrie.

[1] K. Sorger, P. von Ragué Schleyer, *J. Mol. Struct. (Theochem.)* **1995**, *338*, 317–346 and literature cited therein.; S. Fau, G. Frenking, *J. Mol. Struct. (Theochem.)* **1995**, *338*, 117–130.

[2] D. Steiner, C. Balzereit, H.-J. Winkler, N. Stamatis, M. Hofmann, P. von Ragué Schleyer, W. Massa, A. Berndt, *Angew. Chem.* **1994**, *106*, 2391–2394; *Angew. Chem. Int. Ed. Engl.* **1994**, *33*, 2303–2306.

[3] M. Menzel, D. Steiner, H.-J. Winkler, D. Schweikart, S. Mehle, S. Fau, G. Frenking, W. Massa, A. Berndt, *Angew. Chem.* **1995**, *107*, 368–370; *Angew. Chem. Int. Ed. Engl.* **1995**, *34*, 327–329.

[4] A. Krämer, J.-K. Uhm, S. E. Garner, H. Pritzkow, W. Siebert, *Z. Naturforsch.* **1990**, *45b*, 1019–1021.

[5] a) G. E. Herberich, C. Ganter, L. Wesemann, *Chem. Ber.* **1990**, *123*, 49–51; b) G. Knörzer, H. Seyffer, W. Siebert, *Z. Naturforsch., Teil B* **1990**, *45*, 1136–1138.

[6] D. Scheschkewitz, A. Ghaffari, P. Amseis, M. Unverzagt, G. Subramanian, M. Hofmann, P. von Ragué Schleyer, H. F. Schaefer III, G. Geiseler, W. Massa, A. Berndt, *Angew. Chem.* **2000**, *112*, 1329–1332; *Angew. Chem. Int. Ed.* **2000**, *39*, 1272–1275.

[7] All structures were optimized at the MP2(fc)/6-311+G** level and relative energies were determined at the MP4SDTQ/6-311+G**//MP2(fc)/6-311+G** + 0.93 ZPE[MP2(fc)/6-311+G**] level using Gaussian 98: M. J. Frisch, G. W. Trucks, H. B. Schlegel, G. E. Scuseria, M. A. Robb, J. R. Cheeseman, V. G. Zakrzewski, J. A. Montgomery Jr., R. E. Stratmann, J. C. Burant, S. Dapprich, J. M. Millam, A. D. Daniels, K. N. Kudin, M. C. Strain, O. Farkas, J. Tomasi, V. Barone, M. Cossi, R. Cammi, B. Mennucci, C. Pomelli, C. Adamo, S. Clifford, J. Ochterski, G. A. Petersson, P. Y. Ayala, Q. Cui, K. Morokuma, D. K. Malick, A. D. Rabuck, K. Raghavachari, J. B. Foresman, J. Cioslowski, J. V. Ortiz, B. B. Stefanov, G. Liu, A. Liashenko,

 © 2005 Wiley-VCH Verlag GmbH & Co. KGaA, Weinheim

P. Piskorz, I. Komaromi, R. Gomperts, R. L. Martin, D. J. Fox, T. Keith, M. A. Al-Laham, C. Y. Peng, A. Nanayakkara, C. Gonzalez, M. Challacombe, P. M. W. Gill, B. Johnson, W. Chen, M. W. Wong, J. L. Andres, C. Gonzalez, M. Head-Gordon, E. S. Replogle, J. A. Pople, *Gaussian 98*, Revision A.6, Gaussian, Inc., Pittsburgh PA, **1998**.

[8] M. Unverzagt, G. Subramanian, M. Hofmann, P. von Ragué Schleyer, S. Berger, K. Harms, G. Geiseler, W. Massa, A. Berndt, *Angew. Chem.* **1997**, *109*, 1567–1569; *Angew. Chem. Int. Ed. Engl. Ed.* **1997**, *36*, 1469–1472.

[9] At the MP2/6-31G* level nonclassical **VIu** is more stable than classical **III** by 2.5 kcal mol^{-1}: ref.[2].

[10] G. M. Sheldrick, *SHELXS-97, Program for the Solution of Crystal Structures*, University of Göttingen, **1997**.

[11] G. M. Sheldrick, *SHELXL-97, Program for the Refinement of Crystal Structures*, University of Göttingen, **1997**.

Received: March 31, 2005
Published Online: August 17, 2005

 © 2005 Wiley-VCH Verlag GmbH & Co. KGaA, Weinheim

Reactivity of the [η^2-Bis(*tert*-butylsulfonyl)acetylene](carbonyl)(η^5-cyclopentadienyl)cobalt Complex Towards Electron-Rich and -Poor Acetylenes

Avijit Goswami,[a] Tobias H. Staeb,[b] Frank Rominger,[b] Rolf Gleiter,[b] and Walter Siebert*[a]

Dedicated to Prof. Günter Helmchen on the occasion of his 65th birthday

Keywords: Alkynes / Cobalt / Cyclopentadienyl ligands / N ligands

The electron-rich aminoacetylenes Et_2NC_2R (**2a**–**c**, R = SPh, PPh_2, and Ph, respectively) react smoothly with [η^2-bis(*tert*-butylsulfonyl)acetylene](carbonyl)(η^5-cyclopentadienyl)cobalt (**1**) to form the donor–acceptor stabilized (η^4-cyclobutadiene)cobalt complexes **3a**–**c** in good yields. However, treatment of the electron-poor borylacetylenes **2d**–**f** with the cobalt complex **1** does not lead to the expected (η^4-cyclobutadiene)cobalt complexes. Analogously, the reaction of bis(1-phenylethynyl)sulfide (**2g**) with two equivalents of **1** gives rise to the sulfur-bridged bis[η^4-(cyclobutadiene)cobalt] complex **3g**. The new cobalt complexes were characterized by NMR spectroscopy, mass spectrometry, and by X-ray structure analysis for **3a**, which reveals almost equal C–C bond lengths within the cyclobutadiene ring.
(© Wiley-VCH Verlag GmbH & Co. KGaA, 69451 Weinheim, Germany, 2005)

Introduction

Di(carbonyl)(η^5-cyclopentadienyl)cobalt [$CpCo(CO)_2$] is a very convenient and efficient reagent for the di- and trimerization of alkynes.[1] The CpCo-supported oligomerization of unsymmetrical alkynes generally leads to isomers, which is one of the major disadvantages of that reaction. This might be overcome if oligomerization could be carried out in a stepwise fashion. Lee and Brintzinger[2] have been able to demonstrate by means of IR spectroscopy that, on irradiation of [$CpCo(CO)_2$] in the presence of diphenylacetylene, a new complex with only one CO ligand must be present. In order to contribute to the clarification of the mechanism of dimerization and trimerization of alkynes, Krebs et al.[3,4] reported the first generation of a mono(alkyne)cobalt complex by reacting the highly strained alkyne 3,3,6,6-tetramethyl-1-thiacycloheptyne[3] with [$CpCo(CO)_2$]. More recently, Gleiter et al.[5] have synthesized the mono(alkyne)cobalt complex **1** by the replacement of one of the carbonyl groups in di(carbonyl)(η^5-cyclopentadienyl) cobalt with bis(*tert*-butylsulfonyl)acetylene,[6] which was found to be a strong electrophile. In the course of their study, a large number of electron-rich, chalcogen-substituted acetylenes as well as alkyl- and aryl-substituted acetylenes were allowed to react with **1** to form a new class of stable (cyclobutadiene)cobalt complexes.[7] They found that the more electron-rich acetylenes react faster with **1** under mild conditions, whereas carbon-substituted acetylenes require heating to initiate the reactions. We have studied electron-poor borylacetylenes with respect to oligomerization and therefore tested the possibility whether electron-poor acetylenes can react with **1** under drastic conditions. Furthermore, we were interested to find out whether other heteroatom-substituted acetylenes (such as nitrogen and phosphorus) are also able to act in the same way as chalcogen-substituted alkynes. In this paper, we will address the scope and limitations of the replacement of the CO group in **1** by the triple bonds of the electron-rich and -poor acetylenes.

[a] Anorganisch-Chemisches Institut der Universität,
Im Neuenheimer Feld 270, 69120 Heidelberg, Germany
Fax: +49-6221-545-609
E-mail: walter.siebert@urz.uni-heidelberg.de
[b] Organisch-Chemisches Institut der Universität,
Im Neuenheimer Feld 270, 69120 Heidelberg, Germany
Fax: +49-6221-544-205
E-mail: rolf.gleiter@urz.uni-heidelberg.de

Results and Discussion

Treatment of Cobalt Complex 1 with Electron-Rich and -Poor Acetylenes

The reactions between the cobalt complex **1** and the electron-rich aminoacetylenes **2a**–**c** were carried out in toluene at room temperature to afford the (η^4-cyclobutadiene)cobalt complexes **3a**–**c**, respectively, in good yields (Scheme 1). On the other hand, reactions of the cobalt complex **1** with the "push-pull" 1-boryl-2-aminoacetylene **2d** as well as electron-poor borylacetylenes **2e** and **2f** in refluxing

 DOI: 10.1002/ejic.200500308

toluene were unsuccessful, and only the starting materials were recovered from the reaction mixtures. This indicates that electron-poor borylacetylenes have no tendency to react with the powerful electrophile **1**, even when applying drastic reaction conditions.

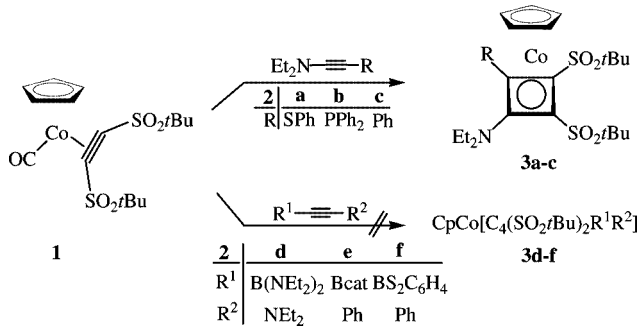

Scheme 1.

The cobalt complexes were isolated by column chromatography on silica gel and characterized by ^{1}H and ^{13}C NMR spectroscopy, mass spectrometry, and by X-ray structure analysis for **3a**. The ^{1}H NMR spectra of **3a**–**c** show two singlets in the region δ = 1.2–1.5 ppm for the *tert*-butyl groups in addition to the Cp resonance (δ = 5.0–5.3 ppm). In general, the characteristic feature of the ^{13}C NMR spectra is the chemical shift of the cyclobutadiene ring atoms, which have values of between δ = 75 and 85 ppm.[7a–7c] However, compounds **3a**,**b** exhibit low-field resonances (δ = 55–75 ppm) for the cyclobutadiene ring atoms. In the ^{13}C NMR spectra of **3a**–**c**, the signals for C_5H_5 (δ = 82–84 ppm) were detected along with the aryl carbon atoms (δ = 125.0–138.9 ppm). EI-MS data confirmed the formation of complexes **3a**–**c** by the appearance of the molecular-ion peaks with the expected isotopic pattern.

The molecular structure of the mononuclear (cyclobutadiene)cobalt complex **3a** is shown in Figure 1. In the solid-state, **3a** crystallizes with toluene. The conformation is highly influenced by the bulky *tert*-butylsulfonyl groups, which point away from the metal center, as does the phenyl group bound to the sulfur atom. This behavior allows an almost parallel orientation of the C_5 and C_4 rings. The space group ($P2_1/c$) of complex **3a** clearly indicates the presence of a racemic mixture.

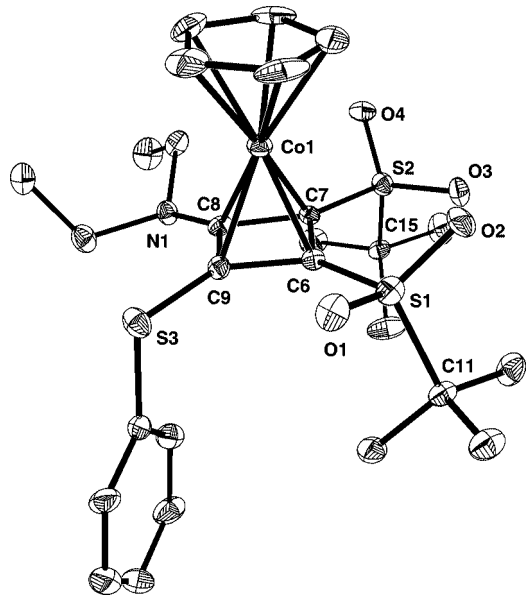

Figure 1. Molecular structure of **3a** in the solid state; hydrogen atoms have been omitted for the sake of clarity. Selected bond lengths [Å] and bond angles [°]: C6–S1 1.769(5), C7–S2 1.755(5), C6–C7 1.494(6), C7–C8 1.484(7), C8–C9 1.459(7), C6–C9 1.476(7), C8–N1 1.360(6), C9–S3 1.741(5); C9–C6–C7 88.8(4), C8–C7–C6 89.8(4), C9–C8–C7 89.9(4), C8–C9–C6 91.5(4).

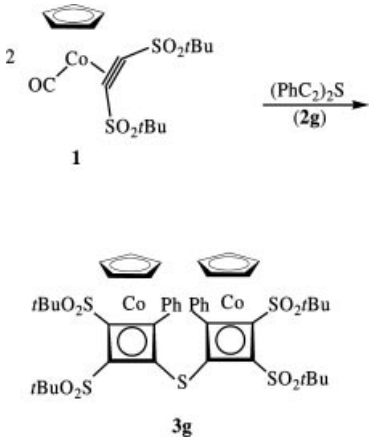

Scheme 2.

Sulfur-Bridged Dinuclear Cobalt Complex 3g

The sulfur-bridged bis[(η^4-cyclobutadiene)cobalt] complex **3g** was prepared in moderate yield by treating $(PhC_2)_2S$ (**2g**) with two equivalents of **1** (Scheme 2). No evidence for the mononuclear cobalt complex was found.

This reaction reveals an interesting route to a sulfur-bridged bis[(η^4-cyclobutadiene)cobalt] complex, which is important especially because the introduction of a heteroatom between two metal-stabilized cyclobutadiene rings is still difficult. The method used by Wadepohl et al.[8] leads to the mononuclear (η^4-cyclobutadiene)cobalt complex from the reaction of two equivalents of $(Me_3SiC_2)_2S$ with $[CpCo(CO)_2]$.

The brown oil **3g** was purified by column chromatography on silica gel and characterized by ^{1}H and ^{13}C NMR spectroscopy as well as by mass spectrometry. The ^{1}H NMR spectrum of **3g** shows the expected multiplets (δ = 6.9–7.1 ppm) for the aryl hydrogens in addition to two singlets (δ = 1.19 and 1.27 ppm) for the *tert*-butyl groups and the Cp resonance (δ = 5.01 ppm). In the ^{13}C NMR spectrum, the signals (δ = 58.6–75.2 ppm) for the cyclobutadiene ring are found along with the Cp resonance at δ = 83.5 ppm. The molecular-ion peak of **3g** was detected with the correct isotopic distribution in the mass spectrum.

 © 2005 Wiley-VCH Verlag GmbH & Co. KGaA, Weinheim

Conclusions

We have shown that the electron-rich aminoacetylenes **2a**–**c** react smoothly (as do the chalcogen-substituted acetylenes) with complex **1** to form CpCo-stabilized η^4-cyclobutadiene complexes **3a**–**c**, respectively However, the CO group in the mono(alkyne)cobalt complex **1** cannot be replaced by the "push-pull" borylacetylene **2d** or by the electron-poor borylacetylenes **2e** and **2f**. This result may be explained by considering the electronic nature of complex **1**. The electron-poor bis(*tert*-butylsulfonyl)acetylene in **1** reduces the back bonding between the Co atom and the CO ligand, which means that CO is easily replaced by the electron-rich acetylenes **2a**–**c**; the electron-poor monoborylacetylenes **2d**–**f** have weaker donor capabilities and thus do not react with **1**. Interestingly, the sulfur-bridged bis[(η^4-cyclobutadiene)cobalt] complex **3g** can be prepared by treating complex **1** with $(PhC_2)_2S$ (**2g**). The cobalt complexes **3a**–**c** and **3g** are stable at room temperature and resistant to light, oxygen, and moisture.

Experimental Section

General: All reactions were performed under nitrogen using standard Schlenk techniques. Solvents were dried with the appropriate drying agents and distilled under nitrogen. Glassware was dried with a heat gun under high vacuum. ^{1}H, ^{11}B, and ^{13}C NMR: Bruker AC 200 spectrometer; ^{1}H and ^{13}C spectra were referenced to $(CH_3)_4Si$. IR spectra were recorded on a Bruker IFS 28 FT spectrometer. Mass spectra were obtained on a Finnigan MAT 8230 plus spectrometer using the EI technique. Elemental analyses were carried out by the Mikroanalytisches Laboratorium der Universität Heidelberg. Melting points (uncorrected) were obtained on a Büchi apparatus, using capillaries which were filled under nitrogen and sealed. Complex (**1**),[9] 2-(diethylamino)-1-phenylthioacetylene (**2a**),[10] 2-(diethylamino)-1-(diphenylphosphanyl)acetylene (**2b**),[11] 2-(diethylamino)-1-phenylacetylene (**2c**),[12] 1-(diethylamino)-2-bis(diethylaminoboryl)acetylene,[13] 1-catecholboryl-2-phenylacetylene,[12] 1-dithiocatecholboryl-2-phenylacetylene,[12] and $(PhC_2)_2S$ (**2g**)[14] were prepared according to literature procedures.

General Procedure for the Synthesis of 3a–c and 3g: The mono(alkyne)cobalt complex **1** was dissolved in 30 mL of toluene and the appropriate acetylene was added. The reaction mixture was stirred for 2 d at room temperature. After completion of the reaction, the solvent was removed to dryness and the crude product was purified by column chromatography on silica gel (THF/toluene, 2:1). Cobalt complex **3a** was recrystallized from a solution of toluene at –20 °C.

[η^4-1,2-Bis(*tert*-butylsulfonyl)-4-(diethylamino)-3-phenylthiocyclobutadiene](η^5-cyclopentadienyl)cobalt (3a): Starting material: 0.25 g (1.21 mmol) of **2a**, 0.50 g (1.21 mmol) of **1**. Yield: 0.55 g (0.92 mmol; 76%), orange solid, m.p. 132–133 °C. ^{1}H NMR (200.1 MHz, $CDCl_3$): δ = 1.03 (t, 6 H, CH_2CH_3), 1.38, 1.47 [2s, 2×9 H, $C(CH_3)_3$], 3.1, 3.4 (2m, 2×2 H, CH_2CH_3), 5.21 (s, 5 H, Cp), 7.0–7.3 (m, 5 H, SPh) ppm. ^{13}C NMR (50.3 MHz, $CDCl_3$): δ = 11.05 (CH_2CH_3), 24.32, 24.89 [$C(CH_3)_3$], 42.25 (CH_2CH_3), 61.77, 62.62 [$C(CH_3)_3$], 54.90, 58.34, 65.79, 74.87 (C_{4ring}), 83.24 (Cp-C), 125.1, 125.4, 128.9, 138.9 (SPh) ppm. MS (70 eV, EI): *m*/*z* (%) = 595 (30) [M^+], 475 (20) [$M^+ - SO_2tBu$], 353 (45) [$M^+ - 2SO_2tBu$], 124 (15) [CpCo]. MS (70 eV, HR-EI): *m*/*z* (%) = 595.1277 (95) [M^+; $^{12}C_{27}{}^1H_{38}{}^{14}N^{16}O_4{}^{32}S_3{}^{59}Co$: 595.1295]; Δmmu = –1.8.

[η^4-1,2-Bis(*tert*-butylsulfonyl)-4-diethylamino-3-diphenylphospanylcyclobutadiene](η^5-cyclopentadienyl)cobalt (3b): Starting material: 0.34 g (1.21 mmol) of **2b**, 0.50 g (1.21 mmol) of **1**. Yield: 0.48 g (0.71 mmol; 58%), orange oil. ^{1}H NMR (200.1 MHz, $CDCl_3$): δ = 0.85 (t, 6 H, CH_2CH_3), 1.45, 1.49 [2s, 2×9 H, $C(CH_3)_3$], 3.0, 3.3 (2m, 2×2 H, CH_2CH_3), 5.03 (s, 5 H, Cp), 7.2–7.7 (m, 10 H, PPh_2) ppm. ^{13}C NMR (50.3 MHz, $CDCl_3$): δ = 11.87 (CH_2CH_3), 24.32, 24.89 [$C(CH_3)_3$], 44.02 (CH_2CH_3), 61.77, 62.64 [$C(CH_3)_3$], 65.84, 67.24, 69.79, 72.85 (C_{4ring}), 84.03 (Cp-C), 125.0, 128.1, 129.3, 135.2 (PPh_2) ppm. MS (70 eV, EI): *m*/*z* (%) = 671 (5) [M^+], 550 (60) [$M^+ - SO_2tBu$], 429 (50) [$M^+ - 2SO_2tBu$], 124 (5) [CpCo]. MS (70 eV, HR-EI): *m*/*z* (%) = 671.1688 (51) [M^+; $^{12}C_{33}{}^1H_{43}{}^{14}N^{16}O_4{}^{31}P^{32}S_2{}^{59}Co$: 671.1704]; Δmmu = –1.6.

[η^4-1,2-Bis(*tert*-butylsulfonyl)-4-diethylamino-3-phenylcyclobutadiene](η^5-cyclopentadienyl)cobalt (3c): Starting material: 0.062 g (0.035 mmol) of **2c**, 0.15 g (0.035 mmol) of **1**. Yield: 0.16 g (0.028 mmol; 80%), orange solid, m.p. 127–128 °C. ^{1}H NMR (200.1 MHz, $CDCl_3$): δ = 0.95 (t, 6 H, CH_2CH_3), 1.18, 1.45 [2s, 2×9 H, $C(CH_3)_3$], 2.9, 3.2 [2m, 2×2 H, CH_2CH_3], 5.35 (s, 5 H, Cp), 7.2, 7.6 (2m, 5 H, Ph) ppm. ^{13}C NMR (50.3 MHz, $CDCl_3$): δ = 11.33 (CH_2CH_3), 24.43, 24.85 [$C(CH_3)_3$], 43.62 (CH_2CH_3), 61.57, 62.17 [$C(CH_3)_3$], 82.70 (Cp-C), 127.5, 128.2, 129.0, 132.48 (Ph) ppm; C_{4ring} not found. MS (70 eV, EI): *m*/*z* (%) = 563 (10) [M^+], 442 (25) [$M^+ - SO_2tBu$]. MS (70 eV, HR-EI): *m*/*z* (%) = 563.1584 (68) [M^+; $^{12}C_{27}{}^1H_{38}{}^{16}O_4{}^{32}S_2{}^{59}Co$: 563.1574]; Δmmu = 1.0. $C_{27}H_{38}CoO_4S_2$ (563.66): calcd. C 57.53, H 6.80, N 2.48; found C 57.65, H 6.88, N 2.54.

Bis[(η^4-cyclobutadiene)]cobalt Complex 3g: Starting material: 0.25 g (1.06 mmol) of $(PhC_2)_2S$ (**2g**), 0.89 g (2.12 mmol) of **1**. Yield: 0.47 g (0.46 mmol; 43%), brown oil. ^{1}H NMR (200.1 MHz, $CDCl_3$): δ = 1.19, 1.27 [2s, 2×18 H, $C(CH_3)_3$], 5.01 (s, 10 H, Cp), 7.0–7.3 (m, 10 H, C_6H_5) ppm. ^{13}C NMR (50.3 MHz, $CDCl_3$): δ = 24.62, 25.19 [$C(CH_3)_3$], 62.07, 62.92 [$C(CH_3)_3$], 55.20, 58.64, 66.09, 75.17

Table 1. Crystal data and structure refinement for **3a**.

Empirical formula	$C_{27}H_{38}CoNO_4S_3 \cdot C_7H_8$
Formula mass	687.83
Crystal system	monoclinic
Space group	$P2_1/c$
a [Å]	14.7043(8)
b [Å]	8.9725(5)
c [Å]	26.3058(6)
α [°]	90
β [°]	99.080(2)
γ [°]	90
Volume [Å^3]	3427.1(3)
Z	4
$D_{calcd.}$ [g cm^{-3}]	1.33
μ [mm^{-1}]	0.72
F(000)	1456
Crystal size [mm]	0.30×0.08×0.04
Θ_{max}(°)	21.5
Index ranges	–15/15, –9/9, –27/27
Reflections collected	20502
Reflections independent (R_{int})	3940 (0.1512)
Reflections observed [$I > 2\sigma(I)$]	2243
Parameters	397
Goodness-of-fit on F^2	0.99
R_1 [$I > 2\sigma(I)$]	0.048
wR_2 [$I > 2\sigma(I)$]	0.071
T [K]	200(2)
Residual electron density [e Å^{-3}]	0.38/–0.35

 © 2005 Wiley-VCH Verlag GmbH & Co. KGaA, Weinheim

(C_{4ring}), 83.54 (Cp-C), 125.5, 125.7, 129.3, 135.4 (Ph) ppm. MS (70 eV, EI): *m*/*z* (%) = 1014 (10) [M^+], 941 (15) [$M^+ - t$BuO]. MS (70 eV, HR-EI): *m*/*z* (%) = 1014.1307 (100) [M^+; $^{12}C_{46}{}^{1}H_{56}{}^{16}O_8{}^{32}S_5{}^{59}Co_2$: 1014.1243]; Δmmu = 6.4.

X-ray Crystal Structure Determination of 3a: Crystal data and details of the structure determination are listed in Table 1. Reflections were collected with a Bruker-AXS SMART 1000 diffractometer (Mo-K_α radiation, λ = 0.71073 Å, graphite monochromator, ω-scan). An empirical absorption correction was applied. The structure was solved by direct methods and refined by least-squares methods based on F^2 with all measured reflections (SHELXTL 5.1).[15] All non-hydrogen atoms were refined anisotropically.
CCDC-268675 (for **3a**) contains the supplementary crystallographic data for this paper. These data can be obtained free of charge from The Cambridge Crystallographic Data Center via www.ccdc.cam.ac.uk/data_request/cif.

Acknowledgments

This work was supported by the Deutsche Forschungsgemeinschaft (SFB 623) and the Fonds der Chemischen Industrie.

[1] a) J. P. Collman, L. S. Hegedus, J. R. Norton, R. G. Finke, *Principles and Applications of Organotransition Metal Chemistry*, University Science Books, Mill Valley, California, **1987**; b) R. D. W. Kemmit, D. R. Russell, in *Comprehensive Organometallic Chemistry* (Eds: F. G. A. Stone, E. W. Abel), Pergamon Press, Oxford, **1982**, vol. 5, p. 248.
[2] W. S. Lee, H. H. Brintzinger, *J. Organomet. Chem.* **1977**, *127*, 93.
[3] A. Krebs, J. Wilke, *Top. Curr. Chem.* **1983**, *109*, 189.
[4] B. Jessel, Dissertation, Universität Hamburg, **1984**; see ref.[3]
[5] C. Benisch, J. Chavez, R. Gleiter, B. Nuber, H. Irngartinger, T. Oeser, H. Pritzkow, F. Rominger, *Eur. J. Inorg. Chem.* **1998**, 629–632.
[6] A. Riera, M. Marti, A. Moyano, M. A. Pericas, J. Santamaria, *Tetrahedron Lett.* **1990**, *31*, 2169–2172.
[7] a) C. Benisch, R. Gleiter, T. H. Staeb, B. Nuber, T. Oeser, H. Pritzkow, F. Rominger, *J. Organomet. Chem.* **2002**, *641*, 102–112; b) C. Benisch, D. B. Werz, R. Gleiter, F. Rominger, T. Oeser, *Eur. J. Inorg. Chem.* **2003**, 1099–1112; c) D. B. Werz, R. Gleiter, F. Rominger, *Eur. J. Inorg. Chem.* **2004**, 4021–4027.
[8] H. Wadepohl, A. Wolf, H. Pritzkow, *J. Organomet. Chem.* **1996**, *506*, 287–292.
[9] C. Benisch, J. Chavez, R. Gleiter, B. Nuber, H. Irngartinger, T. Oeser, H. Pritzkow, F. Rominger, *Eur. J. Inorg. Chem.* **1998**, 629–632.
[10] T. Nakai, K. Tanaka, N. Ishikawa, *Chem. Lett.* **1976**, *11*, 1263.
[11] G. Himbert, M. Regitz, *Chem. Ber.* **1974**, *107* 2513.
[12] L. Brandsma, *Preparative Acetylene Chemistry*, Elsevier, **1971**, *p.* 89.
[13] A. Goswami, C.-J. Maier, H. Pritzkow, W. Siebert, *Eur. J. Inorg. Chem.* **2004**, 2635–2645.
[14] M. Herres, O. Walter, H. Lang, R. Hosch, J. Hahn, *J. Organomet. Chem.* **1994**, *466*, 237–240.
[15] SHELXTL 5.1, Bruker AXS, Madison, WI, USA, **1997**.
Received: April 14, 2005
Published Online: August 24, 2005

 © 2005 Wiley-VCH Verlag GmbH & Co. KGaA, Weinheim

The Role of [η^2-Bis(*tert*-butylsulfonyl)acetylene](carbonyl)(η^5-cyclopentadienyl)cobalt(I) as an Intermediate in the Alkyne Dimerisation

Tobias H. Staeb,[a] Jorge Chávez,[a] Rolf Gleiter,*[a] and Bernhard Nuber[b]

Dedicated to Prof. Dr. Günter Helmchen on the occasion of his 65th birthday

Keywords: Alkynes / Cobalt / Cyclobutadiene / Cyclopentadienyl ligands

Dicarbonyl(η^5-cyclopentadienyl)cobalt(I) (**1**) reacts with the electron-poor alkyne bis(*tert*-butylsulfonyl)acetylene to give the corresponding cyclobutadiene complex **6**, whereas the reaction of [$CpCo(CO)_2$] with dimethyl acetylenedicarboxylate yields the cyclopentadienone complex **7** under the same conditions. The cyclobutadiene complex **6** could not be obtained by the treatment of [η^2-bis(*tert*-butylsulfonyl)acetylene](carbonyl)(η^5-cyclopentadienyl)cobalt(I) [**3(H)**] with an excess of bis(*tert*-butylsulfonyl)acetylene. The same holds for the treatment of **3(H)** with dimethyl acetylenedicarboxylate and bis(catecholatoboryl)acetylene. With these results we assume that the monoalkyne complex **3(H)** is not an intermediate in the alkyne oligomerisation of electron-poor alkynes, as was shown for electron-rich ones.
(© Wiley-VCH Verlag GmbH & Co. KGaA, 69451 Weinheim, Germany, 2005)

Introduction

The $CpCo^I$-mediated dimerisation of alkynes to cyclobutadiene (cbd) complexes is a well-known reaction.[1–4] There are two suggested mechanisms in the literature for the formation of these complexes, one by Brintzinger et al.[5,6] and the other based on work by Bergman, Vollhardt, Yamazaki and others.[6,7] Both mechanisms are shown in Scheme 1.

Brintzinger assumed that the reaction of two equivalents of dicarbonyl(η^5-cyclopentadienyl)cobalt(I) {[$CpCo(CO)_2$], **1**} leads to complex **A**, which can form complexes **B** and **C** by the reaction with alkynes (mechanism **a** in Scheme 1). These intermediates have been isolated and characterised.[6,8] The cyclobutadiene (cbd) complex **F** can arise from both precursors. The second mechanism (**b** in Scheme 1) involves intermediates with only one cobalt nucleus. Complex **1** yields a monoalkyne complex **D** by loss of one CO ligand and subsequent reaction with one equivalent of alkyne. Addition of another alkyne forms the cobaltol species **E**.[9] Dissociation of the second CO unit and subsequent reductive elimination gives the cbd complexes **F**. The second mechanism has also been investigated by theoretical means.[10–12] The first experimental evidence of a monoalkyne species **D** was provided by Brintzinger by means of IR spectroscopy.[5] Later, Krebs et al. were able to isolate the first monoalkyne complex **2** by reaction of 3,3,6,6-tetramethyl-1-thiacycloheptyne[13] with [$CpCo(CO)_2$] (Scheme 2).[14]

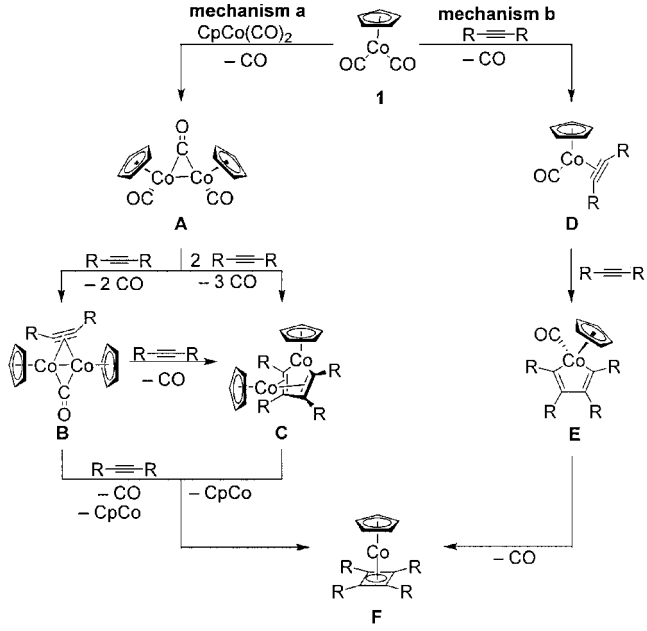

Scheme 1. Abridged version of mechanisms to rationalize the formation of cyclobutadiene CpCo complexes according to Brintzinger et al. (**a**) and based on the work by Bergman, Vollhardt, Yamazaki and others (**b**).

The second class of complexes of type **D** were synthesised in our laboratory by the reaction of bis(*tert*-butylsulfonyl)acetylene[15] with [$CpRCo(CO)_2$] derivatives.[16] The

[a] Organisch-Chemisches Institut der Universität Heidelberg
Im Neuenheimer Feld 270, 69120 Heidelberg, Germany
Fax: +49-6221-544-205
E-mail: rolf.gleiter@urz.uni-heidelberg.de
[b] Anorganisch-Chemisches Institut der Universität Heidelberg
Im Neuenheimer Feld 270, 69120 Heidelberg, Germany

 © 2005 Wiley-VCH Verlag GmbH & Co. KGaA, Weinheim DOI: 10.1002/ejic.200500394

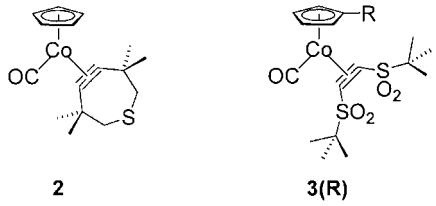

Scheme 2. Isolated monoalkyne Co^{I} complexes.

obtained complexes **3(R)** (Scheme 2) were treated with different alkynes to yield the corresponding cyclobutadiene complexes, as shown in Scheme 3.[17–19]

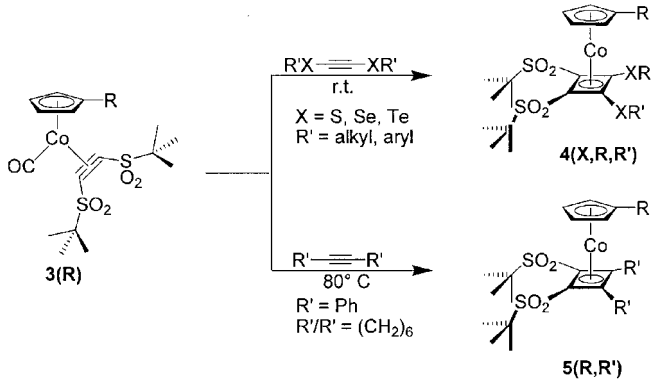

Scheme 3.

We showed that the electrophilic complexes **3(R)** react readily with electron-rich alkynes at room temperature to the corresponding cyclobutadiene complexes **4(X,R,R′)** in good yields. The reaction with alkynes that have no strong donor substituents, for example diphenylacetylene or cyclooctyne, needs higher temperatures to form the complexes **5(R,R′)**. These experiments provide strong evidence that the monoalkyne complexes **3(R)** are intermediates in the cyclobutadiene formation. In this paper we present the reactions of electron-poor alkynes with $[CpCo(CO)_2]$ and **3(H)**.

Results and Discussion

As electron-poor alkynes we chose bis(*tert*-butylsulfonyl)-acetylene (BTSA) and dimethyl acetylenedicarboxylate (DMAD). They react quite differently towards $[CpCo(CO)_2]$ in refluxing toluene. As shown in Scheme 4, BSTA forms the cbd complex **6** in 19% yield in refluxing toluene, whereas the reaction of **1** with an excess of DMAD gives the cyclopentadienone complex **7** (5% yield). A further electron-poor alkyne derivative, bis(catecholatoboryl)acetylene (BCBA),[20] yielded the hexakis-substituted benzene derivative **8** with **1**.[21]

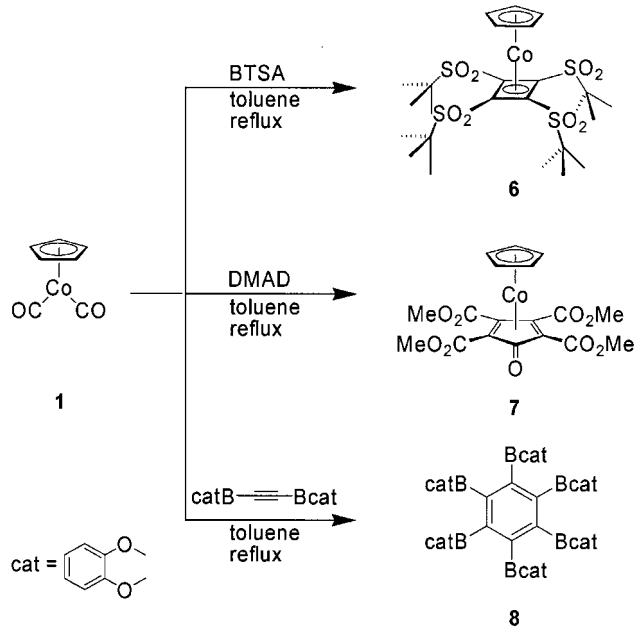

Scheme 4.

Following our previous studies, we reacted the monoalkyne complex **3(H)** with BTSA, DMAD, and BCBA by heating **3(H)** and the corresponding alkynes in toluene. The anticipated products were not obtained (Scheme 5).

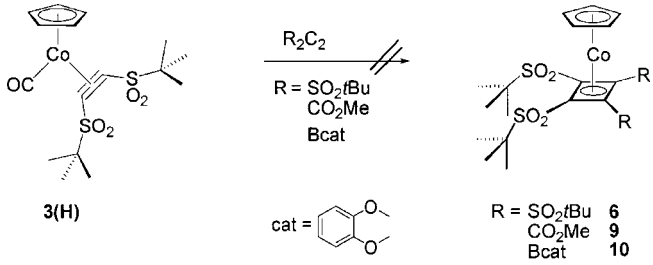

Scheme 5.

These results suggest that the nucleophilic monoalkyne complex **3(H)** is not an intermediate in the alkyne oligomerisation for electron-poor alkynes, as postulated in mechanism **b** (Scheme 1), and it seems more likely that this reaction has dinuclear Co^{I} intermediates, in analogy to the Brintzinger mechanism (cf. Scheme 1).[5,6]

Structural Investigations

In the case of **6** we were able to obtain single crystals which were investigated by X-ray techniques. Figure 1 shows the molecular structure of **6** (Table 1).

 © 2005 Wiley-VCH Verlag GmbH & Co. KGaA, Weinheim

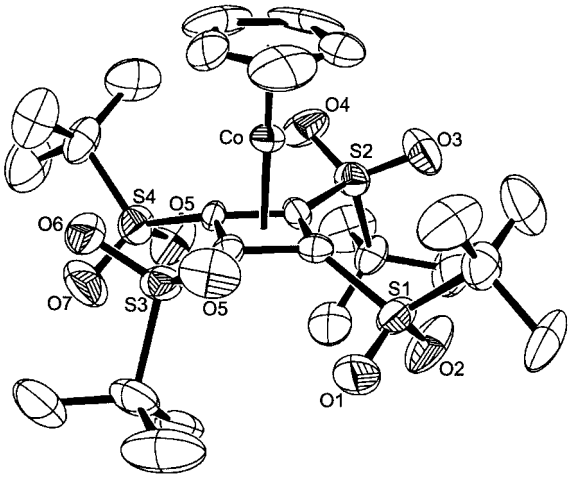

Figure 1. Molecular structure of **6** (ORTEP plot; thermal ellipsoids at 50% probability level; H atoms have been omitted for clarity).

Table 1. Selected bond distances and angles in the molecular structure of **6**.

d(C–C) Cbd [pm]	*d*(Cp_{centre}–Co) [pm]	*d*(Co_{centre}–Cbd) [pm]	*α* (CpCoCbd) [°]
145	168	169	2.3
147			
145			
147			

Two opposite *tert*-butyl groups point away from the cyclopentadiene ring, whereas the other two groups point towards the Cp ring. This conformation reduces the steric strain and the overall dipole moment of the molecule arising from the sulfonyl groups. The two ring ligands are nearly parallel to each other (2.3° distortion). No bond alternation is found within the cyclobutadiene ring.

Conclusions

The products obtained from the reaction of [CpCo(CO)$_2$] and electron-poor alkynes are highly dependent on the electronic properties of the alkynes. The BTSA monoalkyne complex **3(H)** is not an intermediate in the cyclobutadiene formation with electron-poor alkynes, whereas it is with electron-rich ones.

Experimental Section

Starting Materials: Dicarbonyl(η^5-cyclopentadienyl)cobalt(I),[22] and bis(*tert*-butylsulfonyl)acetylene[11] were prepared according to literature methods. Dimethyl acetylenedicarboxylate (98%) was purchased from ACROS.

General Remarks: All melting points are uncorrected. Elemental analyses were carried out by the Mikroanalytisches Laboratorium der Universität Heidelberg. UV absorption data were recorded with a Hewlett–Packard 8452A spectrometer. IR spectra were recorded with a Bruker Vector 22. The NMR spectra were measured with a Bruker Avance 500 spectrometer (^{1}H NMR at 500 MHz and ^{13}C NMR at 125 MHz) using the solvent as internal standard (*δ*). FAB mass spectra refer to data from a Jeol JMS-700 instrument. *m*-Nitrobenzyl alcohol was used as the matrix for the FAB experiments. All reactions were carried out in dry glassware under argon in dry, oxygen-free solvents.

[η^4-Tetrakis-(*tert*-butylsulfonyl)cyclobutadiene](η^5-cyclopentadienyl)cobalt(I) (6): Dicarbonyl(η^5-cyclopentadienyl)cobalt(I) (200 mg, 1.1 mmol) and bis(*tert*-butylsulfonyl)acetylene (BTSA; 700 mg, 2.6 mmol) were dissolved in toluene (40 mL) and the mixture was stirred for 5 h at 120 °C. The product was purified by column chromatography (SiO_2, *n*-hexane/diethyl ether). Yield: 129 mg (19%) of a yellow solid (dec. 167 °C). ^{1}H NMR (500 MHz, $CDCl_3$): *δ* = 1.56 (s, 36 H, CH_3), 5.73 (s, 5 H, CH) ppm. ^{13}C NMR (125 MHz, $CDCl_3$): *δ* = 25.3 [C(CH_3)$_3$], 65.2 [C(CH$_3$)$_3$], 82.2 (Cbd-C), 89.1 (Cp-C) ppm. MS (FAB+): *m*/*z* (%) = 679 [M + Na]$^+$, 656 [M$^+$], 583 [M – *t*BuO]$^+$. IR (KBr): $\tilde{\nu}$ = 2978, 2934, 1311, 1189, 1129 cm^{-1}. UV/Vis (CH_2Cl_2): λ_{max} (log *ε*) = 254 nm (4.36), 304 (4.12), 334 (3.73), 352 (3.65), 388 (3.25). HRMS (FAB+): calcd. for $C_{25}H_{41}CoO_8S_4$ [M$^+$] 656.0989; found 656.1016; calcd. for $C_{25}H_{41}CoNaO_8S_4$ [M$^+$ + Na] 679.0896; found 679.0914. $C_{25}H_{41}CoO_8S_4$: calcd. C 59.77, H 8.13, S 11.00; found, C 59.65, H 8.08, S 10.98.

(η^5-Cyclopentadienyl)[η^4-2,3,4,5-tetrakis(methoxycarbonyl)cyclopentadienone]cobalt(I) (7): Dicarbonyl(η^5-cyclopentadienyl)cobalt(I) (2.0 mg, 11.0 mmol) and dimethyl acetylenedicarboxylate (DMAD; 700 mg, 2.6 mmol) were dissolved in toluene (40 mL) and the mixture was stirred for 5 h at 120 °C. The product was purified by column chromatography (SiO_2, *n*-hexane/diethyl ether and diethyl ether/methanol). Yield: 212 mg (5%) of a red solid (m.p. 112 °C). ^{1}H NMR (500 MHz, CH_3OD): *δ* = 3.82 and 3.85 (s, 6 H, CO_2CH_3), 5.41 (s, 5 H, Cp-CH) ppm. ^{13}C NMR (125 MHz, CH_3OD): *δ* = 53.5 (CO_2CH_3), 54.2 (CO_2CH_3), 72.0 (Cpd-C), 84.4 (Cpd-C), 88.2 (Cp-C), 156.1 (Cpd-CO), 165.5 (CO_2CH_3), 166.2 (CO_2CH_3) ppm. MS (FAB+): *m*/*z* (%) = 459 [M + Na]$^+$, 437 [M + H]$^+$, 436 [M$^+$]. IR (KBr): $\tilde{\nu}$ = 2955, 1733, 1634, 1447, 1234 cm^{-1}. UV/Vis (CH_2Cl_2): λ_{max} (log *ε*) = 264 nm (4.03), 300 (4.01), 374 (3.49), 430 (2.97). HRMS (FAB+): calcd. for $C_{18}H_{18}CoO_9$ [M + H]$^+$ 437.0282; found 437.0256; calcd. for $C_{18}H_{17}O_9CoNa$ [M + Na]$^+$ 459.0102; found 459.0085.

X-ray Diffraction Analyses: The reflections of **6** were collected with a Syntex R3 diffractometer (Mo-K_α radiation, graphite monochromator). Intensities were corrected for Lorentz and polarisation effects, and an empirical absorption correction (psi-scans) was applied. The structure was solved by direct methods. The structural parameters of the non-hydrogen atoms were refined anisotropically according to a full-matrix least-squares technique (F^2). The hydrogen atoms were calculated according to stereochemical aspects. Structure solution and refinement were carried out with the SHELXTL-PLUS (5.10) software package.[23] ORTEP drawings were obtained using the ORTEP-3 program for Microsoft Windows® by Farrugia.[24] Table 2 contains the crystallographic data and details of the data collection and refinement procedure.
CCDC-269077 (for **6**) contains the supplementary crystallographic data for this paper. These data can be obtained free of charge from The Cambridge Crystallographic Data Centre via www.ccdc.cam.ac.uk/data_request/cif.

Acknowledgments

This work was supported by the Deutsche Forschungsgemeinschaft (SFB 623) and the Fonds der Chemischen Industrie. We are grate-

Table 2. Structural data of **6**.

	6
Empirical formula	$C_{25}H_{41}CoO_8S_4$
Formula weight	656.792
Crystal system	monoclinic
Space group	$P2_1/n$
Z	4
a [Å]	11.261(9)
b [Å]	19.086(11)
c [Å]	14.223(7)
β [°]	91.21(5)
V [Å^3]	3056(3)
$D_{calcd.}$ [g cm^{-3}]	1.43
μ [mm^{-1}]	0.878
Crystal shape	cube
Crystal size [mm^3]	0.40 × 0.40 × 0.30
Temperature [K]	293
Θ [°]	1.8 to 24.1
Index ranges	$0 \le h \le 12$
	$0 \le k \le 21$
	$-16 \le l \le 16$
Reflections collected	4829
Independent reflections	4829
Observed reflections [$I > 2\sigma(I)$]	2861
Max. and min. transmission	1.00, 0.92
Parameters	357
Goodness-of-fit on F^2	1.08
Final R indices [$I > 2\sigma(I)$]	
R_1	0.085
wR_2	0.129
$(\Delta\rho)_{max.}$ $(\Delta\rho)_{min.}$ [e Å^{-3}]	0.46, –0.37

ful to Prof. Dr. Walter Siebert for useful discussions and to Avijit Goswami for providing BCBA.

[1] A. Nakamura, N. Hagihara, *Bull. Chem. Soc. Jpn.* **1961**, *34*, 452–453.
[2] H. Sakurai, J. Hayashi, *J. Organomet. Chem.* **1974**, *70*, 85–87.
[3] J. P. Collman, L. S. Hegedus, J. R. Norton, R. G. Finke, *Principles and Applications of Organotransition Metal Chemistry*, University Science Books, Mill Valley, California, **1987**.
[4] R. D. W. Kemmit, D. R. Russel, in *Comprehensive Organometallic Chemistry* (Eds.: F. G. A. Stone, E. W. Abel), Pergamon Press, Oxford, **1982**, vol. 5, p. 1–276.
[5] W.-S. Lee, H. H. Brintzinger, *J. Organomet. Chem.* **1977**, *127*, 87–92.
[6] W.-S. Lee, H. H. Brintzinger, *J. Organomet. Chem.* **1977**, *127*, 93–103.
[7] K. P. C. Vollhardt, *Acc. Chem. Res.* **1977**, *10*, 1–8; H. Yamazaki, N. Hagihara, *J. Organomet. Chem.* **1970**, *21*, 431–443; D. R. McAlister, J. E. Bercaw, R. G. Bergman, *J. Am. Chem. Soc.* **1977**, *99*, 1668–1669.
[8] H. Sakurai, J. Hayashi, *J. Organomet. Chem.* **1972**, *39*, 365–370.
[9] Y. Wakatsuki, O. Nomura, K. Kitaura, K. Morokuma, H. Yamazaki, *J. Am. Chem. Soc.* **1983**, *105*, 1907–1912; R. Diercks, B. E. Eaton, S. Gürtzgen, S. Jalisatgi, A. J. Matzger, R. H. Radde, K. P. C. Vollhardt, *J. Am. Chem. Soc.* **1998**, *120*, 8247–8248.
[10] J. H. Hardesty, J. B. Koerner, T. A. Albright, G.-Y. Lee, *J. Am. Chem. Soc.* **1999**, *121*, 6055–6067.
[11] L. F. Veiros, G. Dazinger, K. Kirchner, M. J. Calhorda, R. Schmid, *Chem. Eur. J.* **2004**, *10*, 5860–5870.
[12] K. Kirchner, M. J. Calhorda, R. Schmid, L. F. Veiros, *J. Am. Chem. Soc.* **2003**, *125*, 11721–11729.
[13] A. Krebs, J. Wilke, *Top. Curr. Chem.* **1983**, *109*, 189–233.
[14] B. Jessel, *Dissertation*, University of Hamburg, **1984**.
[15] A. Riera, F. Cabré, A. Moyano, M. A. Pericàs, J. Santamaria, *Tetrahedron Lett.* **1990**, *31*, 2169–2172.
[16] C. Benisch, J. Chávez, R. Gleiter, B. Nuber, H. Irngartinger, T. Oeser, H. Pritzkow, F. Rominger, *Eur. J. Inorg. Chem.* **1998**, 629–632.
[17] C. Benisch, R. Gleiter, T. H. Staeb, B. Nuber, T. Oeser, H. Pritzkow, F. Rominger, *J. Organomet. Chem.* **2002**, *641*, 102–112.
[18] C. Benisch, D. B. Werz, R. Gleiter, F. Rominger, T. Oeser, *Eur. J. Inorg. Chem.* **2003**, 1099–1112.
[19] D. B. Werz, R. Gleiter, F. Rominger, *Eur. J. Inorg. Chem.* **2004**, 4021–4027.
[20] H. Schulz, G. Gabbert, H. Pritzkow, W. Siebert, *Chem. Ber.* **1993**, *126*, 1593–1595.
[21] C. Ester, A. Maderna, H. Pritzkow, W. Siebert, *Eur. J. Inorg. Chem.* **2000**, 1177–1184.
[22] T. S. Piper, F. A. Cotton, G. Wilkinson, *J. Inorg. Nucl. Chem.* **1955**, *1*, 165–167.
[23] G. M. Sheldrick, Bruker Analytical X-ray-Division, Madison, WI, **1997**.
[24] L. J. Farrugia, *Appl. Crystallogr.* **1997**, *30*, 565.

Received: May 3, 2005
Published Online: September 8, 2005

 © 2005 Wiley-VCH Verlag GmbH & Co. KGaA, Weinheim

Reactivity of 1-Nitroso-2-naphthol Towards the Carbonyl Complexes $XRe(CO)_5$ (X = Cl, Br, I): Molecular Structures of *cis*-[η^2-{*N*,*O*-$C_{10}H_6ON(O)$}$Re(CO)_4$] and *fac*-[η^2-{*N*,*O*-$C_{10}H_6ON(H)$}$Re(CO)_3X$]

Christoph Krinninger,[a] Stefan Wirth,[a] Juan C. Galvez Ruiz,[b] Peter Klüfers,[a] Heinrich Nöth,[a] and Ingo-Peter Lorenz*[a]

Keywords: 1-Nitroso-2-naphtholate ligand / 1,2-Naphthaquinone-2-imine ligand / Chelates / Rhenium complexes / Redox chemistry / CO_2 elimination

The halogeno complexes $(CO)_5ReX$ (**1a–c**) (X = Cl, Br, I) react with 1-nitroso-2-naphthol $C_{10}H_6N(O)OH$ (**2**) in refluxing CH_2Cl_2 to give the substitution product *cis*-$(CO)_4Re\{C_{10}H_6ON(O)\}$ (**3**) via HX and CO elimination in good yield. Compound **3** is coordinated to the Re centre by the bidentate chelate ligand via the N-atom of the nitroso and O-atom of the naphtholato groups. The same reaction in refluxing toluene, however, gave no HX elimination but instead, the *fac*-$(CO)_3XRe\{C_{10}H_6ON(H)\}$ (**4–6**) complexes are formed, which contain the rare, *N*,*O*-chelating ligand 1,2-naphthaquinone-2-imine. The nitroso function of **2** has been reduced to the imine function by an intermolecular redox process, which was confirmed by the detection of CO_2 generated during the reaction. The new compounds **3–6** have been characterised by their IR, ^1H and ^{13}C NMR, UV/Vis and mass spectra, as well as by X-ray structure analyses. The Re^I centres show a distorted octahedral coordination of the CO and X (in **4–6**) ligands and the almost planar aromatic (**3**) or quinoid (**4–6**) *N*,*O* chelating ligands.

(© Wiley-VCH Verlag GmbH & Co. KgaA, 69451 Weinheim, Germany, 2005)

Introduction

Metal complexes with *C*-nitroso ligands have attracted great attention for several reasons. The *C*-nitroso group is isoelectronic with dioxygen and like dioxygen can form adducts with metalloproteins[1–6] and metalloporphyrins.[6] Some metal complexes with *C*-nitroso compounds have also been proposed as reaction intermediates,[6–9] for example in the cytochrome-P450-dependent oxidative metabolism of amphetamines and other amino derivatives.[10]

Recently, we reported the synthesis of the dinuclear μ_2-(η^2-*NO*)-nitrosoaniline complexes of rhenium(I) of the type $[\{(CO)_3ReX\}_2ONC_6H_4NR_2]$ (X = Cl, Br, I; R = Me, Et).[11,12] The single crystals of all six compounds exhibit a pronounced linear dichroism. This surprising property may be due to the *C*-nitroso group which lies together with the planar phenyl- and NC_2-moieties (of NR_2) almost exactly within the symmetry plane of the dinuclear complexes.[11,12] Therefore, we tried to synthesise analogous complexes of $XRe(CO)_5$ (X = Cl, Br, I) with the sterically more demanding 1-nitroso-2-naphthol. Instead of the desired analogous dinuclear complexes mentioned above, we obtained new monomeric complexes of the type $[Re(CO)_3X\{C_{10}H_6ON(H)\}]$ (X = Cl, Br, I), whereby the nitroso group of the naphthol-derivative has been reduced to an imino-function by a CO-ligand, resulting in the new bidentate ligand 1,2-naphthaquinone-2-imine. Using milder reaction conditions we were also successful in isolating and characterising the intermediate product $[Re(CO)_4\{C_{10}H_6ON(O)\}]$, where the *C*-nitroso group remains intact.

Metal complexes which contain 1,2-naphthoquinone-monoimines are of interest because they are widely used for analytical purposes.[13,14] Metal complexes derived from 1,2-naphthoquinone-monoimines can also be employed as starting reagents in the synthesis of a wide variety of organic compounds.[15–17]

It is well known that nitro and nitroso compounds can be reduced to give products via the formation of imido intermediates. In 1975 Saarinen et al. published the X-ray structure of a copper complex with the 1-nitroso-2-naphthol ligand, which was followed by a report by Charalambous et al. in 1983.[18–20] Recently, Wong et al. prepared complexes with 1-nitroso-2-naphthol ligands and characterised a ruthenium complex as a by-product, where the nitroso group had been reduced to an imino function in very low yields.[21,22] N–O bond cleavage reactions of oximes have been recently documented by their oxidative addition reactions with suitable Re complexes to give the corresponding imine complexes.[23–25] Whereas Pombeiro et al.[23] report

[a] Ludwig-Maximilians-Universität, Department of Chemistry and Biochemistry,
Butenandtstr. 5–13, 81377 München, Germany
Fax: +49-89-2180-77867
E-mail: ipl@cup.uni-muenchen.de
[b] Departamento de Ciencias Quimico-Biologicas, Universidad de Sonora,
Sonora, Mexico

oxygen transfer only to the metal, Zubieta et al.[24] and Chakravorty et al.[25] observe its transfer to both metal and oxophilic co-ligands like phosphanes. In this work we present the first report on the formation of the 1,2-nitrosonaphtholato-*O*,*N* complex **3** which appears to be an intermediate in the reaction of $XRe(CO)_5$ (X = Cl, Br, I) with 1-nitroso-2-naphthol, because complexes **4**–**6** which are obtained by the same reaction in refluxing toluene, possess the 1,2-naphthochinone-2-imine-*N*,*O* ligand, which is generated by an intramolecular redox process.

Results and Discussion

The addition of one equivalent of 1-nitroso-2-naphthol to $XRe(CO)_5$ (X = Cl, Br, I) in CH_2Cl_2 or toluene followed by heating of this solution to 40 °C for 30 min leads to a colour change from yellow to orange. After 40 h, the orange product $[Re(CO)_4\{C_{10}H_6ON(O)\}]$ (**3**) was isolated by column chromatography (CH_2Cl_2, Scheme 1). When the same reaction was repeated in toluene with $XRe(CO)_5$ (X = Cl, Br, I) at 100 °C the colour changed initially to orange, then to green and finally to blue. After purifying the blue product by column chromatography (3 cm column, CH_2Cl_2), blue crystals of the compounds $[Re(CO)_3X\{C_{10}H_6ON(H)\}]$ (X = Cl, Br, I) (**4**–**6**) could be isolated. In compounds **4**–**6** no nitroso function was observed as it had been reduced to an imine function. Our first assumption that the overall redox reaction can only occur when a CO ligand is oxidised to CO_2 has been proven experimentally, as a white precipitate of $BaCO_3$ formed when the gas atmosphere in the reaction tube was connected with a solution of $Ba(OH)_2$ in H_2O (Scheme 1).

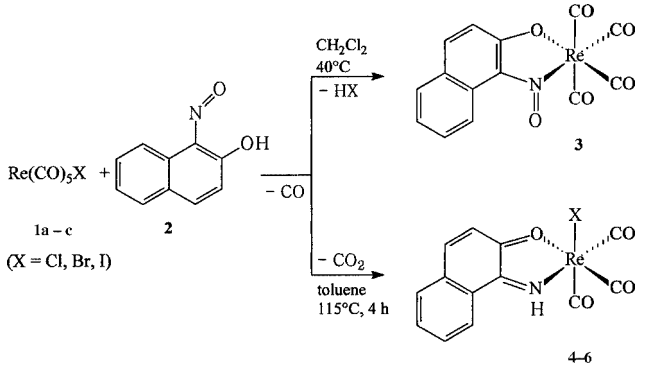

Scheme 1. Synthesis of **3**–**6**.

Compounds **3**–**6** are stable in air for some days, and are soluble in THF, acetone, $CHCl_3$, CH_2Cl_2 and even toluene, but nearly insoluble in nonpolar solvents like pentane or hexane. The orange (**3**) and blue solutions (**4**–**6**) can be stored in air for some days without decomposition. In the UV/Vis spectrum ($CHCl_3$) of **3** two broad absorptions at λ_1 = 260–315 nm and λ_2 = 360–440 nm due to ligand-to-metal CT bands ([NO–Re^I] and [O–Re^I]) are observed. For **4**–**6** two absorptions were also observed at lower frequencies in comparison to those observed for **3** at 380–395 and 570–670 nm (**4**), 380–420 and 570–670 nm (**5**), 450–500 and 590–690 nm (**6**) corresponding to [NH–Re^I] and [O–Re^I]. The position of these absorptions depends on the halogen and increases from X = Cl to X = I. In comparison with the corresponding electronic transition (π-π* NO) of the free ligand **2**, the absorption bands of the complexes **3**–**6** are shifted to lower frequencies.

The IR spectra (in CH_2Cl_2 and KBr) of the tetracarbonyl derivative **3** show four ν(CO)-absorptions at 2113 (A_1), 2017 (A_1), 2002 (B_2) and 1957 cm^{-1} (B_2) due to the pseudo-C_{2v} symmetry. The IR spectra of the facial tricarbonyl derivatives **4**–**6** in CH_2Cl_2 show three absorptions due to their lower symmetry (C_1) at 2031–2032 (*A*), 1923–1925 (*A*) and 1945–1951 cm^{-1} (*A*). The corresponding IR spectra (in KBr) show only two broad absorptions instead of the three observed in CH_2Cl_2 for compounds **4** and **5**. The NO group of **3** is found to absorb at 1380 cm^{-1}, indicating that the absorption of the NO bond of 1-nitroso-2-naphthol is shifted to lower wavenumbers on complexation. Depending on the halogen present, the ν(NH) absorptions of **4**–**6** are found at 3162 (**4**), 3175(**5**) and 3192 cm^{-1} (**6**).

The ^{1}H NMR spectrum of **3** shows three doublets for each proton at δ = 7.04, 7.82, 9.26 ppm and a triplet at δ = 7.49 ppm. The other three aromatic protons were only observed as a multiplet between 7.62–7.65 ppm. The ^{1}H NMR spectra of compounds **4**–**6** are very similar and display a double-doublet at δ = 7.05 (**4**), 7.10 (**5**) and 7.16 ppm (**6**). A further aromatic proton of **4**–**6** is detected at δ = 8.05 ppm, in addition to two multiplets at δ = 7.70–7.78 and 8.28–8.49 ppm. Only **5** shows an additional signal for the NH-group at δ = 14.47. All of the signals of **4**–**6** are generally shifted to a lower field in comparison to **3**.

In the ^{13}C NMR spectra of **3**–**6** the aromatic carbon atoms can be found between δ = 123.0–134.4 ppm, and the *N*-bonded carbon atom at δ = 156.3 (**3**), 160.1 (**4**), 166.4 (**5**) and 165.0 ppm (**6**). Compounds **4** and **6** show an additional signal for a quaternary carbon-atom at δ = 150.4 (**4**) and 148.0 ppm (**6**). The signals for the CO ligands and carbonyl groups appear between δ = 181.2–183.4 ppm. In comparison with the starting material **2**, all of the signals of complexes **4**–**6** are shifted to a lower field.

In the mass spectra (DEI-MS) of **3**–**6** the parent peaks are observed, as well as peaks corresponding to fragments resulting from the successive loss of up to three (**4**–**6**) and four CO ligands (**3**).

The stoichiometry and structures of complexes **3**–**6** were confirmed by X-ray structure analyses (Table 1).[26] In all cases, single crystals were obtained by the diffusion of pentane into solutions of **3**–**6** in $CHCl_3$. The molecular structures and selected bond lengths and angles are given in Figures 1, 2, 3 and 4.

All four compounds show the same distorted octahedral arrangement of the Re^I centre with O–Re–N angles between 73 and 75° [75.20 (**3**), 73.33 (**4**), 73.70 (**5**) and 73.07° (**6**)]. The O–Re–X and N–Re–X angles of **4**–**6** increase within the series **4** < **5** < **6** (84.65, 86.96 < 86.09, 87.40 < 88.20, 88.24°) depending on the size of the halogen atom. The Re–N bonds of **3** and **6** are approximately 2.115 Å and are significantly shorter than the corresponding Re–O bonds [2.155 (**3**) and 2.129 Å (**6**)]. However, in compounds **4** and **5**, the Re–O dis-

 © 2005 Wiley-VCH Verlag GmbH & Co. KGaA, Weinheim

Table 1. X-ray structure analysis of compounds **3**–**6**.[26]

	3	**4**	**5**	**6**
Empirical formula	$C_{14}H_6NO_6Re$	$C_{13}H_7ClNO_4Re$	$C_{13}H_7BrNO_4Re$	$C_{13}H_7INO_4Re$
Formula mass [g mol^{-1}]	470.40	462.85	507.31	554.31
Crystal size [mm]	0.20 × 0.06 × 0.03	0.23 × 0.27 × 0.27	0.18 × 0.06 × 0.04	0.150 × 0.07 × 0.05
Crystal colour, habit	orange, plate	black, platelet	black, platelet	black, platelet
Crystal system	triclinic	monoclinic	monoclinic	monoclinic
Space group	$P\bar{1}$	$C2/c$	$C2/c$	$C2/c$
a [Å]	7.1437(14)	10.222(2)	10.4446(7)	10.925(2)
b [Å]	8.9999(18)	22.302(5)	22.0422(15)	21.687(4)
c [Å]	11.475(2)	12.480(9)	12.4732(9)	12.809(3)
α [°]	75.17(3)	90	90	90
β [°]	78.76(3)	107.03(3)	106.768(8)	107.45(3)
γ [°]	68.91(3)	90	90	90
Volume [Å^3]	661.1(2)	2720.4(9)	2749.5(3)	2895.3(10)
Z	2	8	8	8
Density, calcd. [g cm^{-3}]	2.363	2.260	2.451	2.543
Absorption coefficient [mm^{-1}]	9.221	9.140	11.756	10.537
F(000)	440	1728	1872	2016
Index ranges	$-8 \le h \le 8$	$-11 \le h \le 0$	$-13 \le h \le 13$	$-13 \le h \le 13$
	$-12 \le k \le 11$	$-25 \le k \le 0$	$-28 \le k \le 29$	$-28 \le k \le 29$
	$-7 \le l \le 15$	$-13 \le l \le 14$	$-16 \le l \le 16$	$-16 \le l \le 16$
θ range [°]	2.48–29.04	2.45–23.96	2.24–27.97	3.33–25.01
Reflections collected	3408	2260	11836	18221
Independent reflections	2585	2131	3301	2554
Observed reflections	2424	1848	2444	2238
Parameter/restrains	200/0	182/0	185/0	182/0
R_1/wR_2 (all data)	0.0526/0.1314	0.0246/0.0416	0.0656/0.1165	0.0424/0.0924
R_1/wR_2 (final)	0.0546/0.1340	0.0168/0.0390	0.0468/0.1112	0.0349/0.0878
Goodness of fit	1.074	1.077	0.953	1.061
Min./max. ρ_e (e Å^3)	–4.492/5.558	–0.451/0.466	–5.939/2.138	–2.356/1.247
Temperature [K]	200	293	200	200
Diffractometer used	Siemens CCD Area-Detector	Nonius Mach 3	Nonius Kappa CCD	Nonius Kappa CCD
Scan type	area detection	area detection	area detection	area detection
Solution, software	SHELXS-97	SHELXS-97	SHELXS-97	SHELXS-97
Refinement, software	SHELXS-97	SHELXS-97	SHELXS-97	SHELXS-97
CCDC number	259837	258934	258935	258936

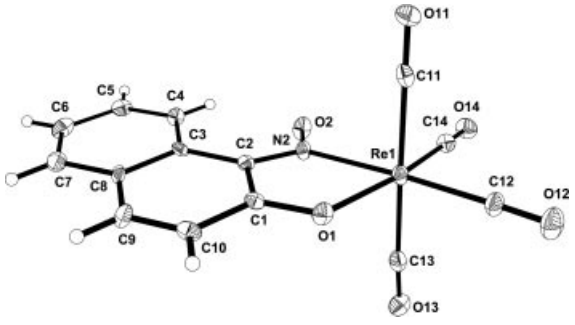

Figure 1. Molecular structure of **3**. Selected bond lengths [Å] and angles [°]: Re(1)–N(2) 2.155(7), Re(1)–O(1) 2.117(6), N(2)–O(2) 1.246(11), Re(1)–C(11) 2.015(10), Re(1)–C(12) 1.972(9), Re(1)–C(13) 1.983(11), Re(1)–C(14) 1.931(8), O(1)–C(1) 1.297(9), N(2)–C(2) 1.358(10); O(1)–Re(1)–N(2) 75.2(2), C(13)–Re(1)–N(2) 91.6(3), C(11)–Re(1)–N(2) 89.5(3), C(11)–Re(1)–O(1) 90.1(3), C(13)–Re(1)–C(11) 178.3(2), C(2)–N(2)–Re(1) 116.1(5), C(1)–O(1)–Re(1) 115.7(5).

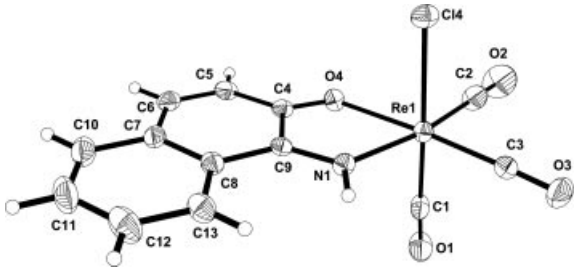

Figure 2. Molecular structure of **4**. Selected bond lengths [Å] and angles [°]: Re(1)–N(1) 2.109(3), Re(1)–O(4) 2.152(3), Re(1)–Cl(4) 2.4807(12), Re(1)–C(1) 1.916(5), Re(1)–C(2) 1.926(5), Re(1)–C(3) 1.903(5), O(4)–C(4) 1.245(5), N(1)–C(9) 1.290(5); N(1)–Re(1)–O(4) 73.33(12), N(1)–Re(1)–Cl(4) 86.96(9), O(4)–Re(1)–Cl(4) 84.65(8), C(1)–Re(1)–N(1) 94.27(16), C(1)–Re(1)–O(4) 93.57(16), C(1)–Re(1)–Cl(1) 177.46(15), C(4)–O(4)–Re(1) 117.8(3), C(9)–N(1)–Re(1) 119.8(3).

tances [2.152 (**4**), 2.149 Å (**5**)] are longer than the Re–N bonds [2.109 (**4**), 2.105 Å (**5**)]. The C(4)/C(9)–O(4) bond lengths increase from **4** to **6** [1.245 (**4**), 1.267 (**5**), 1.301 Å (**6**)] and C(1)–O(1) in compound **3** is approximately 1.297 Å, therefore they all lie between normal C–O (1.43 Å) and C=O (1.19 Å) bonds. In the case of **3**, this observation can be rationalised by considering two mesomeric forms of 1-nitroso-2-naphthol (Scheme 2).

The short C–N bond lengths of **4**–**6** can be explained as a result of the reduction due to CO forming the quinoid sys-

 © 2005 Wiley-VCH Verlag GmbH & Co. KGaA, Weinheim

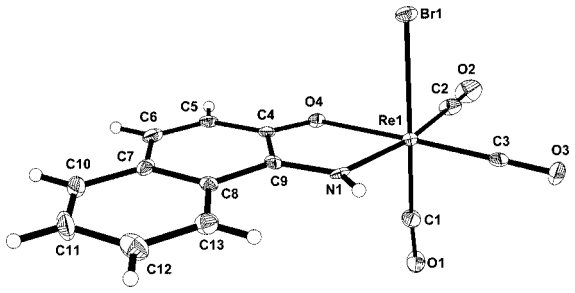

Figure 3. Molecular structure of **5**. Selected bond lengths [Å] and angles [°]: Re(1)–N(1) 2.105(8), Re–O(4) 2.149(6), Re–Br 2.6118(10), Re–C(1) 1.921(10), Re–C(2) 1.908(10), Re–C(3) 1.908(18), O(4)–C(4) 1.267(11), N–C(9) 1.311(12); N–Re–O(4) 73.7(3), N–Re–Br 87.40(18), O(4)–Re–Br 86.09(16), C(1)–Re–N 94.4(4), C(1)–Re–O(4) 93.0(4), C(1)–Re–Br 177.7(3), C(4)–O(4)–Re 117.5(6), C(9)–N–Re 119.0(6).

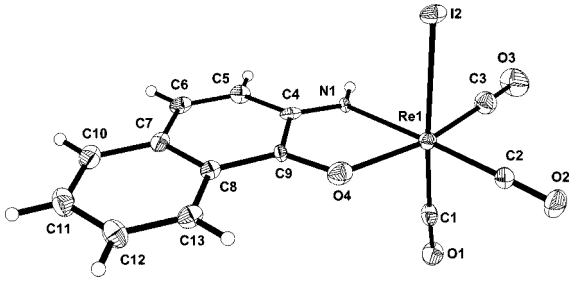

Figure 4. Molecular structure of **6**. Selected bond lengths [Å] and angles [°]: Re(1)–N(1) 2.129(4), Re(1)–O(4) 2.113(5), Re(1)–I(2) 2.7940(9), Re(1)–C(1) 1.912(8), Re(1)–C(2) 1.902(8), Re(1)–C(3) 1.939(8), O(4)–C(9) 1.301(9), N(1)–C(4) 1.238(8), N(1)–Re(1)–O(4) 73.07(18), N(1)–Re(1)–I(2) 88.24(12), C(1)–Re(1)–N(1) 95.2(2), C(1)–Re(1)–O(4) 95.2(2), C(1)–Re(1)–I(2) 175.7(2), C(9)–O(4)–Re(1) 120.1(4), C(4)–N(1)–Re(1) 119.2(4).

tem. In addition **4** and **5** have significantly shorter C–O bonds than **3**.

The N–O distance of the nitroso group in **3** is 1.246 Å, which is within the range of most metal complexes with *N*-bonded nitroso groups, for example in [Cu{η²-N(O)$C_{10}H_6O$}[PPh_3]$_2$] (1.287 Å)[17] and *cis*-[Ru{η²-N(O)$C_{10}H_6O$}$_2$($CO)_2$] (1.258 Å).[21] The dihedral angles N(1)–C(9)–C(4)–O(4) and N(1)–C(9)–C(8)–C(13) (for **4** and **5**) as well as N(1)–C(4)–C(9)–O(4) and N(1)–C(4)–C(5)–C(6) (for **6**) are less than 1.3°, which means that the quinone-imine in **4**–**6** is planar. In contrast to **4**–**6**, the 1-nitroso-naphthol ligand of **3** is slightly twisted out of the Re–O plane [N(2)–C(2)–C(1)–O(1) = 5.42°, N(2)–C(2)–C(3)–C(4) = 8.47°].

Experimental Section

All operations were carried out in an oxygen free atmosphere under Ar in dry and Ar-saturated solvents.[27] $Re(CO)_5X$ (X = Cl, Br, I) was prepared according to the literature procedure.[28] 1-Nitroso-2-naphthol was used as purchased from Alfa Aesar. NMR spectra were recorded with a Jeol EX 400 spectrometer (^{1}H: 399.78 MHz and ^{13}C: 100.54 MHz) and with a Jeol 270 spectrometer (^{1}H: 270.17 MHz, ^{13}C: 67.93 MHz) in [D_8]THF or CD_2Cl_2. Mass spectra were obtained with a Jeol Mstation JMS 700. IR and UV/Vis spectra were measured with a Perkin–Elmer Spectrum One FT-IR and a Perkin–Elmer UV Lambda 16 spectrometer, respectively. Elemental analyses were performed with a Heraeus Elementar Vario EL.

Tetracarbonyl-1-nitroso-naphtholato-*N*,*O*-rhenium(I) (3): Compounds **1b** (99.7 mg, 0.246 mmol) and **2** (46.9 mg, 0.271 mmol) were dissolved in CH_2Cl_2 (20 mL) and heated under reflux for 40 h, whereby the solution turned deep orange. The solvent was evaporated, and the orange residue was purified by column chromatography (CH_2Cl_2). The same product was obtained in similar yields when the appropriate quantities of **1a** or **1c** are used instead of **1b**. Yield: orange crystals (97.6 mg, 0.207 mmol, 72%), m.p. 184 °C (dec.). ^{1}H NMR (399.78 MHz, $CDCl_3$): δ = 7.04 (d, 1 H, ^3J = 9.40 Hz, $CH_{arom.}$), 7.49 (t, 1 H, ^3J = 7.86 Hz, $CH_{arom.}$), 7.62–7.65 (m, 2 H, $CH_{arom.}$), 7.82 (d, 1 H, ^3J = 9.40 Hz, $CH_{arom.}$), 9.26 (d, 1 H, ^3J = 8.35 Hz, $CH_{arom.}$) ppm. ^{13}C NMR (100.53 MHz, $CDCl_3$): δ = 123.0 ($CH_{arom.}$), 124.1 ($CH_{arom.}$), 125.0 ($CH_{arom.}$), 127.1 ($CH_{arom.}$), 128.0 ($CH_{arom.}$), 129.1 ($CH_{arom.}$), 133.4 ($CH_{arom.}$), 144.9 ($CH_{arom.}$), 156.3 ($C_{q,arom.}$), 183.4 ($C_{q,arom.}$), 190.9 ($C_{q,carbonyl}$) ppm. IR (KBr) : $\tilde{\nu}$ = 3121 (w), 3065 (w), 2962 (m), 2926 (m), 2854 (w), 2753 (w), 2687 (w), 2644 (w), 2584 (w), 2456 (w), 2421 (w), 2338 (w), 2114 (vs), 2017 (vs), 1994 (vs), 1958 (vs), 1820 (w), 1790 (w), 1726 (w), 1647 (m), 1619 (m), 1608 (s), 1599 (s), 1554 (s), 1517 (vs), 1482 (m), 1454 (w), 1422 (w), 1380 (s), 1357 (vs), 1323 (s), 1311 (s), 1266 (s), 1214 (s), 1139 (m), 1024 (m), 970 (w), 878 (w), 832 (w), 821 (s), 803 (m), 755 (s), 739 (m), 712 (w), 683 (w), 664 (m), 625 (s), 590 (w), 565 (m) cm^{-1}. IR (CH_2Cl_2): $\tilde{\nu}$ = 2113 (vs), 2017 (vs), 2002 (vs), 1957 (vs) cm^{-1}. UV/Vis ($CHCl_3$) λ_{max} (log ε): 299 (13705), 323 (5836), 419 (13612) nm. $C_{14}H_6NO_5Re$ (470.40): calcd. C 35.63, H 1.50, N 2.97; found C 35.27, H 1.20, N 2.67. MS (DEI): *m*/*z* (%) = 470.7 (60) [M]$^+$, 442.8 (22) [M – CO]$^+$, 414.8 (7) [M – 2 CO]$^+$, 386.8 (35) [M – 3 CO]$^+$, 358.9 (100) [M – 4 CO]$^+$, 328.9 (47) [M – 4 CO, – NO]$^+$.

Synthesis of 4–6. General Procedure: $Re(CO)_5X$ (**1a**–**c**) and 1-nitroso-2-naphthol (**2**) were dissolved in toluene (20 mL) and heated to 115 °C for 4 h, whereby the solution turned deep blue. The solvent was evaporated, and the blue residue was purified by column chromatography (CH_2Cl_2, 3 cm column).

Tricarbonyl-chloro-(1-imino-*1H*-naphthalene-2-one)rhenium(I) (4): Complex **1a** (143 mg, 0.397 mmol) and **2** (68.4 mg, 0.397 mmol). Yield: blue crystals (104 mg, 0.225 mmol, 57%), m.p. 234 °C (dec.). ^{1}H NMR (270.16 MHz, [D_8]THF): δ = 7.05 (dd, 1 H, ^3J = 9.80, ^4J = 1.34 Hz, $CH_{arom.}$), 7.70–7.76 (m, 3 H, $CH_{arom.}$), 8.05 (d, 1 H, ^3J = 9.94 Hz, $CH_{arom.}$), 8.47–8.49 (m, 1 H, $CH_{arom.}$) ppm. ^{13}C NMR (67.94 MHz, [D_8]THF): δ = 125.4 ($CH_{arom.}$), 127.7 ($CH_{arom.}$), 128.7 ($CH_{arom.}$), 132.3 ($CH_{arom.}$), 132.3 ($CH_{arom.}$), 132.5 ($CH_{arom.}$), 134.2

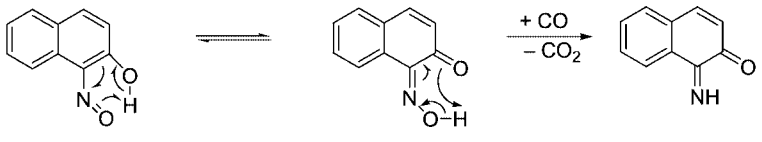

Scheme 2. Tautomerisation of 1-nitroso-2-naphthol and its reduction to form 1,2-naphtaquinone-2-imine.

 © 2005 Wiley-VCH Verlag GmbH & Co. KGaA, Weinheim

($CH_{arom.}$), 150.4 ($C_{q,arom.}$), 160.1 ($C_{q,arom.}$), 182.4 ($C_{q,arom.}$), 195.7 ($C_{q,carbonyl}$) ppm. IR (KBr): $\tilde{\nu}$ = 3162 (w), 2026 (vs), 1937 (vs), 1911 (vs), 1605 (m), 1555 (w), 1517 (w), 1409 (w), 1463 (w), 1409 (m), 1381 (w), 1356 (w), 1314 (w), 1288 (w), 1275 (w), 1213 (w), 1169 (w), 1139 (w), 1094 (w), 1023 (w), 959 (w), 907 (w), 846 (w), 755 (w), 692 (w), 637 (w), 604 (w), 582 (w), 547 (w) cm^{-1}. IR (CH_2Cl_2): $\tilde{\nu}$ = 2031 (vs), 1945 (s), 1932 (vs) cm^{-1}. UV/Vis ($CHCl_3$) λ_{max} (log ε): 307 (5002), 388 (2040), 630 (8209) nm. $C_{13}H_7ClNO_4Re$ (462.85): calcd. C 33.70, H 1.51, N 3.02; found C 33.51, H 1.90, N 2.76. MS (DEI): *m/z* (%): 463.0 (8) $[M]^+$, 435.1 (17) $[M - CO]^+$, 407.1.1 (12) $[M - 2\ CO]^+$, 379.1 (88) $[M - 3\ CO]^+$.

Bromo-tricarbonyl-(1-imino-1*H*-naphthalene-2-one)rhenium(I) (5): Complex **1b** (242 mg, 0.596 mmol) and **2** (104 mg, 0.596 mmol). Yield: blue crystals (197 mg, 0.387 mmol, 65%), m.p. 242 °C (dec.). ^1H NMR (399.78 MHz, [D$_8$]THF): δ = 7.10 (dd, 1 H, ^3J = 9.67, ^4J = 1.32 Hz, $CH_{arom.}$), 7.72–7.76 (m, 3 H, $CH_{arom.}$), 8.07 (d, 1 H, ^3J = 10.11 Hz, $CH_{arom.}$), 8.47–8.48 (m, 1 H, $CH_{arom.}$), 14.47 (s, 1 H, NH) ppm. ^{13}C NMR (100.53 MHz, [D$_8$]THF): δ = 125.5 ($CH_{arom.}$), 127.6 ($CH_{arom.}$), 128.6 ($CH_{arom.}$), 132.3 ($CH_{arom.}$), 132.5 ($CH_{arom.}$), 132.6 ($CH_{arom.}$), 134.1 ($CH_{arom.}$), 166.4 ($C_{q,arom.}$), 181.7 ($C_{q,arom.}$), 194.9 ($C_{q,carbonyl}$), 197.9 ($C_{q,carbonyl}$) ppm. IR (KBr): $\tilde{\nu}$ = 3175 (m), 3053 (w), 2924 (w), 2853 (w), 2028 (vs), 1930 (vs), 1914 (vs), 1736 (w), 1604 (s), 1559 (w), 1480 (m), 1461 (m), 1408 (s), 1380 (w), 1315 (w), 1229 (w), 1169 (w), 1141 (w), 1092 (w), 1020 (w), 974 (w), 902 (w), 844 (w), 804 (w), 755 (w), 717 (w), 653 (w), 581 (w), 547 (w) cm^{-1}. IR (CH_2Cl_2): $\tilde{\nu}$ = 2032 (vs), 1951 (s), 1925 (s) cm^{-1}. UV/Vis ($CHCl_3$) λ_{max} (log ε): 300 (5021), 407 (2741), 637 (10960) nm. $C_{13}H_7BrNO_4Re$ (507.31): calcd. C 30.75, H 1.38, N 2.76; found C 30.83, H 1.35, N 2.74. MS (DEI): *m/z* (%): 506.7 (17) $[M]^+$,478.7 (33) $[M - CO]^+$, 450.7 (16) $[M - 2\ CO]^+$, 422.7 (66) $[M - 3\ CO]^+$, 342.8 (17) $[M - 3\ CO, - Br]^+$.

Tricarbonyl-iodo-(1-imino-*1H*-naphthalene-2-one)rhenium(I) (6): Complex **1c** (102 mg, 0.225 mmol) and **2** (42.0 mg, 0.247 mmol). Yield: blue crystals (81.1 mg, 0.146 mmol, 65%), m.p. 247 °C (dec.). ^1H NMR (399.78 MHz, [D$_8$]THF): δ = 7.16 (dd, 1 H, ^3J = 9.65, ^4J = 1.34 Hz, $CH_{arom.}$), 7.74–7.78 (m, 3 H, $CH_{arom.}$), 8.03 (d, 1 H, ^3J = 9.65 Hz, $CH_{arom.}$), 8.28 (m, 1 H, $CH_{arom.}$) ppm. ^{13}C NMR (100.53 MHz, [D$_8$]THF): δ = 124.4 ($CH_{arom.}$), 127.4 ($CH_{arom.}$), 128.3 ($CH_{arom.}$), 132.0 ($CH_{arom.}$), 132.3 ($CH_{arom.}$), 133.7 ($CH_{arom.}$), 134.4 ($CH_{arom.}$), 148.0 ($CH_{arom.}$), 165.0 ($C_{q,arom.}$), 181.2 ($C_{q,arom.}$), 193.2 ($C_{q,carbonyl}$), 196.9 ($C_{q,carbonyl}$) ppm. IR (KBr): $\tilde{\nu}$ = 3192 (m), 2148 (w), 2025 (vs), 1935 (vs), 1919 (vs), 1626 (w), 1603 (m), 1533 (w), 1480 (w), 1454 (w), 1406 (m), 1315 (m), 1289 (w), 1271 (w), 1231 (w), 1168 (w), 1108 (w), 1022 (w), 887 (w), 838 (w), 805 (w), 754 (w), 692 (w), 632 (w), 581 (w) cm^{-1}. IR (CH_2Cl_2): $\tilde{\nu}$ = 2032 (vs), 1955 (s), 1931 (s) cm^{-1}. UV/Vis ($CHCl_3$) λ_{max} (log ε): 483 (3856), 638 (6337) nm. $C_{13}H_7INO_4Re$ (554.31): calcd. C 28.14, H 1.26, N 2.53; found C 27.78, H 1.53, N 2.41. MS (DEI): *m/z* (%): 554.6 (19) $[M]^+$, 526.7 (26) $[M - CO]^+$, 498.7 (12) $[M - 2\ CO]^+$, 470.7 (46) $[M - 3\ CO]^+$, 343.9 (15) $[M - 3\ CO, - I]^+$.

CCDC-259837 (for **3**), -258934 (for **4**), -258935 (for **5**) and -258936 (for **6**) contain the supplementary crystallographic data for this paper. These data can be obtained free of charge from The Cambridge Crystallographic Data Centre via www.ccdc.cam.ac.uk/data_request/cif.

[1] F. Jung, *Biochem. Z.* **1940**, *305*, 248.
[2] D. Keilin, E. F. Hartree, *Nature* **1943**, *151*, 390.
[3] W. Scheler, *Acta Biol. Med. Ger.* **1960**, *5*, 382.
[4] Q. H. Gibson, *Biochem. J.* **1960**, *77*, 519.
[5] *M*. Murayama, *J. Biol. Chem.* **1960**, *235*, 1024.
[6] D. Mansuy, P. Battioni, J. C. Chottard, M. Lange, *J. Am. Chem. Soc.* **1977**, *99*, 6441.
[7] K. Mertis, G. Wilkinson, *J. Chem. Soc. Dalton Trans.* **1976**, 1488.
[8] G. Gervasio, R. Rossetti, P. L. Stanghellini, *J. Chem. Soc. Chem. Commun.* **1977**, 387.
[9] A. R. Middleton, G. Wilkinson, *J. Chem. Soc. Dalton Trans.* **1980**, 1888.
[10] D. Mansuy, P. Battioni, J. C. Chottard, M. Lange, *Biochem. Pharmacol.* **1976**, *25*, 609.
[11] R. Wilberger, C. Krinninger, H. Piotrowski, P. Mayer, I.-P. Lorenz, *Eur. J. Inorg. Chem.* **2004**, 2488–2492.
[12] C. Krinninger, C. Högg, J. C. G. Ruiz, P. Mayer, O. Burkacky, A. Zumbusch, I.-P. Lorenz, *Chem. Eur. J.* **2005**, in press.
[13] O. K. Borggaard, H. E. M. Christensen, S. P. Lund, *Analyst* **1984**, *109*, 1179–1182.
[14] O. K. Borggaard, H. E. M. Christensen, T. K. Nielsen, M. Willems, *Analyst* **1982**, *107*, 1479–1483.
[15] H. Barjesteh, E. G. Brain, J. Charalambous, P. Gaganatsou, T. A. Thomas, *J. Chem. Res. (S)* **1995**, 454.
[16] A. Mc Killop, T. S. B. Sayer, *J. Org. Chem.* **1976**, *41*, 1079–1080.
[17] R. G. Buckley, J. Charalambous, M. J. Kensett, M. MacPartlin, D. Mukerjee, E. G. Brain, J. M. Jenkins, *J. Chem. Soc. Perkin Trans.* **1983**, 693–697.
[18] R. G. Buckley, J. Charalambous, E. G. Brain, *J. Chem. Soc. Perkin Trans.* **1982**, 1075–1078.
[19] H. Saarinen, J. Korvenranta, *Acta Chem. Scand.* **1975**, *A29*, 409–413.
[20] J. Korvenranta, H. Saarinen, *Acta Chem. Scand.* **1975**, *A29*, 861–865.
[21] K. Ka-Hong Lee, Wing-Tak Wong, *J. Chem. Soc. Dalton Trans.* **1997**, 2987–2995.
[22] K. Ka-Hong Lee, Wing-Tak Wong, *J. Organomet. Chem.* **1997**, *547*, 329–335.
[23] C. M. P. Ferreira, M. F. C. Guedes da Silva, V. Y. Kukushkin, J. J. R. Frausto da Silva, A. J. L. Pombeiro, *J. Chem. Soc. Dalton Trans.* **1998**, 325–326.
[24] X. Chen, F. J. Femia, J. W. Babich, J. Zubieta, *Inorg. Chim. Acta* **2000**, *306*, 112–115.
[25] I. Chakraborty, B. K. Panda, J. Gangopadhyay, A. Chakravorty, *Bioinorg. Chem. Appl. Inorg. Chem.* **2005**, *44*, 1054–1060.
[26] CCDC-259837 (for **3**), -258934 (for **4**), -258935 (for **5**) and -258936 (for **6**) contain the supplementary crystallographic data for this paper. These data can be obtained free of charge from The Cambridge Crystallographic Data Centre via www.ccdc.cam.ac.uk/data_request/cif..
[27] *Trocknen im Labor*, brochure from the series "Reagenzien", Merck, Darmstadt.
[28] G. Brauer, *Handbuch der Präparativen Anorganischen Chemie*, Ferdinand Enke, Verlag, Stuttgart, vol. III, 3rd ed., **1981**, 1951–1952.

Received: April 15, 2005
Published Online: September 8, 2005

 © 2005 Wiley-VCH Verlag GmbH & Co. KGaA, Weinheim

New Polysulfur-Nitrogen Heterocycles by Thermolysis of 1,3λ⁴δ²,2,4-Benzodithiadiazines in the Hydrocarbon and Fluorocarbon Series

Vladimir V. Zhivonitko,[a,b] Alexander Yu. Makarov,[a] Irina Yu. Bagryanskaya,[a] Yuri V. Gatilov,[a] Makhmut M. Shakirov,[a] and Andrey V. Zibarev*[a,c]

Keywords: Fluorescence / Fluorine / Nitrogen heterocycles / Radicals / Sulfur heterocycles / Thermolysis

In contrast to thermolysis of 1,3λ⁴δ²,2,4-benzodithiadiazine (**1**) and its 5,6,7,8-tetrafluoro derivative **2** in dilute (10^{-3} M) hydrocarbon solutions, which leads to persistent 1,2,3-benzodithiazolyls in nearly quantitative yields, the thermolysis of **1** and **2** (the 6-6 bicyclic system) in concentrated (0.5 M) solutions at 150–170 °C results in complex mixtures of various polysulfur-nitrogen heterocycles, in particular differently fused 5-5-6, 5-6-7 and 5-6-6-6 polycyclic systems that were previously unknown. The products were isolated by column chromatography, and the structures of the 5-5-6 (**11**, **12**), 5-6-7 (**5**, **13**), and 5-6-6-6 (**6**, **14**, **15**) polycyclic systems, as well as the 6-7 (**4**) and 5-6 (**16**) bicyclic derivatives, confirmed by X-ray diffraction. The crystal packing of **6** and **11**–**16** is discussed with special emphasis on π-stacking interactions. The fluorescent properties of the 5-6-6-6 systems synthesized are reported. An alternative approach to the linear 5-6-6-6 system **15** based on self-condensation of an R–N=PPh_3 precursor (R = 4,5,6,7-tetrafluoro-1,2,3-benzodithiazol-2-yl) is described, and the free-radical character of this new reaction is proved.
(© Wiley-VCH Verlag GmbH & Co. KGaA, 69451 Weinheim, Germany, 2005)

Introduction

Hyperelectronic (π- and σ-excessive) 1,3λ⁴δ²,2,4-benzodithiadiazine[1] and its carbocyclic substituted derivatives[2–5] (Scheme 1), including polyfluorinated versions, reveal some features of weak 12π-electron antiaromaticity[5–7] combined with moderate thermo- and photostability.[8–11] Mild thermolysis[8,9,11] or photolysis[10,11] of their dilute (10^{-3} M) hydrocarbon solutions results in persistent 1,2,3-benzodithiazolyls (Scheme 1), which are promising building blocks in the design and synthesis of organic molecular magnets and/or organic molecular conductors.[12,13] The key intermediates of this transformation are R–S–N: ↔ R–S≡N nitrenoids (R = 1,2,3-benzodithiazol-2-yl), which can be identified under matrix isolation conditions.[10]

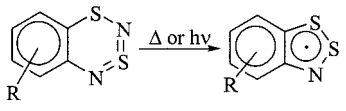

Scheme 1.

The traditional synthetic approach to 1,2,3-benzodithiazolyls is the reduction of 1,2,3-benzodithiazolium chlorides (Herz salts). It should be emphasized that the thermolysis of 1,3λ⁴δ²,2,4-benzodithiadiazines affords 1,2,3-benzodithiazolyls for which the corresponding 1,2,3-benzodithiazoliums, for example fluoro-containing ones, are unknown.[8,9]

With dilute solutions of 1,3λ⁴δ²,2,4-benzodithiadiazines, the yields of radicals estimated by means of ESR measurements are nearly quantitative. It is therefore of obvious interest to investigate whether the thermolysis of 1,3λ⁴δ²,2,4-benzodithiadiazines can be a preparative approach to 1,2,3-benzodithiazolyls.

The present article deals with further investigation of the solution thermolysis of 1,3λ⁴δ²,2,4-benzodithiadiazines in both hydrocarbon and fluorocarbon series with special emphasis on concentrated solutions. It will be shown that under thermolysis conditions and in concentrated hydrocarbon solutions all the aforementioned species are seemingly involved in further transformations to give complex mixtures of products including several new and unusual polysulfur-nitrogen heterocyclic systems. Despite very low yields, the latter were isolated and unambiguously characterized by means of X-ray diffraction. Selected spectral properties of the new polysulfur-nitrogen heterocycles synthesized, including fluorescent properties, are also reported.

Results and Discussion

Thermal Transformations

Under argon, the thermolysis of 0.5 M solutions of 1,3λ⁴δ²,2,4-benzodithiadiazine (**1**) and its 5,6,7,8-tetra-

[a] Institute of Organic Chemistry, Russian Academy of Sciences, 630090 Novosibirsk, Russia
Fax: +7-3832-309-752
E-mail: zibarev@nioch.nsc.ru
[b] Department of Natural Sciences, Novosibirsk State University, 630090 Novosibirsk, Russia
[c] Department of Physics, Novosibirsk State University, 630090 Novosibirsk, Russia

fluoro derivative **2** in hydrocarbons (squalane, decane) at 150–170 °C leads to complex mixtures of various polysulfur-nitrogen heterocycles, including previously unknown polycyclic systems (Schemes 2 and 3). In particular, the 6-6 bicyclic system of **1** and **2** transforms into differently fused 5-5-6, 5-6-7, and 5-6-6-6 polycyclic systems. The latter are identified for the first time. Thus, compound **1** affords 2,1,3-benzothiadiazole (**3**), benzopentathiepine (**4**), [1,2,3]dithiazolo[5,4-*g*][2λ^{4}δ^2,4,1,3,5]benzodithiatriazepine (**5**), and [1,2,3]dithiazolo[4,5-*c*]phenothiazine (**6**), which were isolated by column chromatography of the reaction mixtures; 1,2,3-benzothiadiazole (**7**), benzotrithiol (**8**), 1,2,4λ^{4}δ^2,3,5-benzotrithiadiazepine (**9**), and elemental sulfur were also identified in the reaction mixtures by GLC-MS and/or ^{1}H NMR techniques (Scheme 2), and NH_3 was detected in the gas phase.

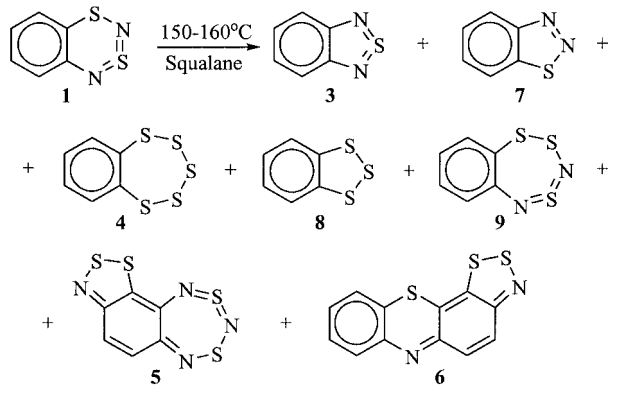

Scheme 2.

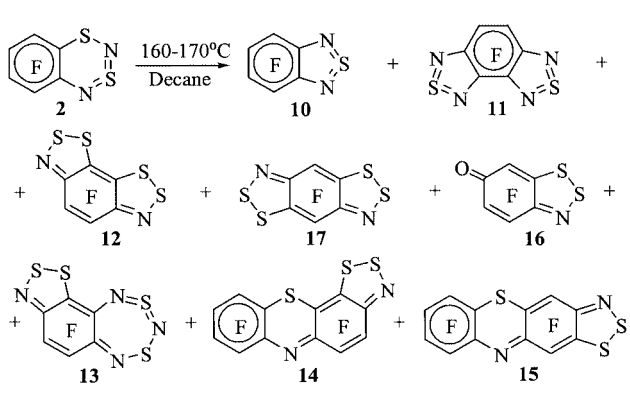

Scheme 3.

The thermolysis of compound **2** gives 4,5,6,7-tetrafluoro-2,1,3-benzothiadiazole (**10**), 7,8-difluorobenzo[1,2-*c*:3,4-*c*′]-bis[1,2,5]thiadiazole (**11**), 4,5-difluorobenzo[1,2-*d*:4,3-*d*′]-bis[1,2,3]dithiazole (**12**), 6,7-difluoro[1,2,3]dithiazolo-[5,4-*g*][2λ^{4}δ^2,4,1,3,5]benzodithiatriazepine (**13**), 4,5,7,8,9,10-hexafluoro[1,2,3]dithiazolo[4,5-*c*]phenothiazine (**14**), 4,6,7,8,9,11-hexafluoro[1,2,3]dithiazolo[5,4-*b*]phenothiazine (**15**), and 4,5,7-trifluoro-6-oxo-1,2,3-benzodithiazole (**16**), which were isolated by column chromatography (Scheme 3). Additionally, 4,8-difluorobenzo[1,2-*d*:4,5-*d*′]bis[1,2,3]dithiazole (**17**) was detected in the reaction mixture by ^{19}F NMR spectroscopy and GLC-MS (Scheme 3; the structure was assigned tentatively by comparison with isomeric **12**). In contrast to the thermolysis of **1**, evolution of acidic gases was observed.

In both cases the major isolated products are 2,1,3-benzothiadiazoles **3** and **10** (Schemes 2 and 3) as transformation of 12π-electron antiaromatic compounds **1** and **2** into 10π-electron aromatic derivatives **3** and **10** is thermodynamically attractive.

The thermal transformations of **1** also proceed in boiling 1-butanol (which does not react nucleophilically with either **1** or **2**) at 117 °C, i.e. at much lower temperature than in the hydrocarbons (Scheme 4). In this case only compound **6** was isolated from the reaction mixture, which also contained also small amounts of compounds **3**, **4**, **7**, **9** and elemental S according to the GLC-MS data.

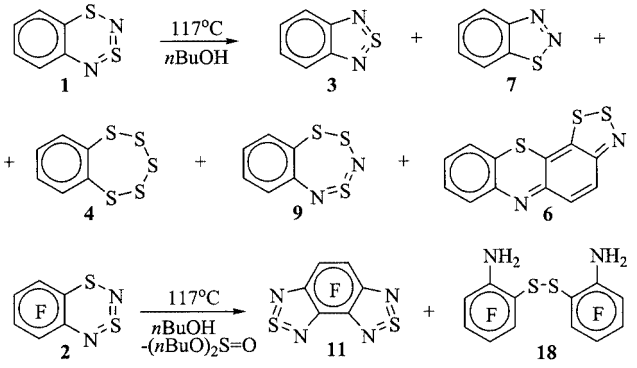

Scheme 4.

In the case of **2**, di-*n*-butyl sulfite and 2,2′-diamino-3,3′,4,4′,5,5′,6,6′-octafluorodiphenyl disulfide (**18**) were isolated as major products along with minor compound **11** (Scheme 4). Formation of $(n\text{BuO})_2\text{S=O}$ (not observed in the case of **1**) can be explained by an acid-catalyzed (traces of HF) dehydration of *n*BuOH, 1:1 addition of released H_2O to **2**,[14] and further reaction of the addition product with *n*BuOH. Compound **18** can also be considered to be a hydrolysis product (see ref.[3]). Thus, in this case acid-initiated hydrolysis seemingly dominates thermal transformations.

The structures of compounds **4**–**6** and **11**–**16** were confirmed by X-ray crystallography (see below).

Thus, the final products of the thermal transformations of 1,3λ^{4}δ^2,2,4-benzodithiadiazines appear to depend strongly upon the reaction conditions employed (this work and refs.[8,9,11]).

Formation of the same 5-6-7 and 5-6-6-6 polycyclic systems in both the hydrocarbon (**5**, **6**) and fluorocarbon (**13**, **14**) series indicates that the required carbocyclic substitution is not electrophilic or nucleophilic in character, as is typical of hydrocarbon and fluorocarbon aromatics, respectively. Rather, we are dealing with radical and nitrenoid processes − a conclusion which is in agreement with previous observations.[8–11] Thus, tetracyclic compounds **6**, **14**, and **15** can formally be considered the products of condensation of the corresponding 1,2,3-benzodithiazolyls accompanied by elimination of H_2S or SF_2 in the hydrocarbon and fluorocarbon series, respectively (Scheme 5).

 © 2005 Wiley-VCH Verlag GmbH & Co. KGaA, Weinheim

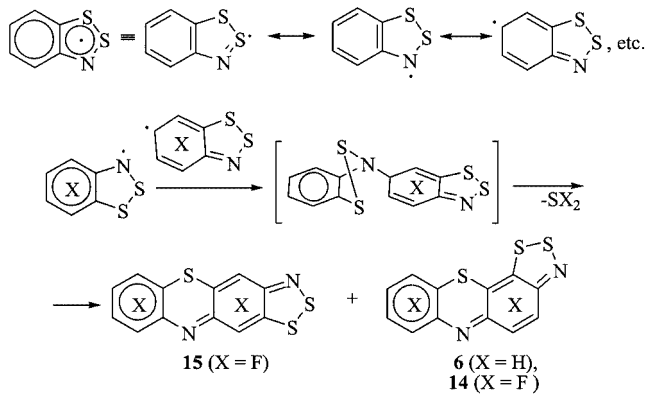

Scheme 5.

The formation of 2,1,3- (**3**, **10**) and 1,2,3-benzothiadiazoles (**7**) can be explained by oxidative imination of the S atoms of **1** and **2** by R–S–N: nitrenoids followed by splitting of the initial adducts (cf. the ability of $1,3\lambda^4\delta^2$,2,4-benzodithiadiazines to undergo oxidative imination with S^{II} and P^{III} derivatives).[4,15] Compound **7** is known to react with elemental sulfur to give benzopentathiepine **4**, which reversibly eliminates S to afford benzotrithiol **8**.[16] Compound **16** could be formed by reaction of 4,5,6,7-tetrafluoro-1,2,3-benzodithiazolyl with dioxygen.

Crystal and Molecular Structures

According to the X-ray diffraction data (Tables 2–4 and Figures 1, 2, and 3), the polysulfur-nitrogen heterocyclic molecules **6** and **11**–**16** are perfectly planar in the crystal. The standard deviations from the mean plane are 0.039, 0.014, 0.011, 0.023, 0.064, 0.064, and 0.018 Å for **6**, **11**, **12**, **13**, **14**, **15**, and **16**, respectively.

Generally, the crystal packing of **6** and **11**–**16** demonstrates numerous shortened contacts[17,18] between the heteroatoms of neighboring molecules, especially S···S (**4**, **12**, **13**, **16**), S···N (**6**, **11**–**13**), S···O (**16**), S···F (**12**–**16**), and F···F (**15**) contacts.

The crystal structures of **6**, **13**, and **15** reveal π-stacks with a slipped-parallel arrangement of the neighboring molecules. The molecules of **6** and **13** are arranged in a head-to-tail fashion, whilst those of **15** are packed in a head-to-head mode. The separation between the planes of π-stacked molecules is 3.67, 3.33–3.37, and 3.44 Å for **6**, **13**, and **15**, respectively (see Figures 4, 5, and 6, respectively), whereas their inclination varies from 0° for **15** to 2.8° for **6**. The crystal packing of **15** reveals shortened intermolecular F···F contacts of 2.74–2.79 Å.

In the crystal lattice of **12** (Figure 7), one of two crystallographically independent molecules is involved in S···π interactions (S···ring centroid distance: 3.46 Å) leading to columnar stacks, whilst another one is involved in π–π interactions that form dimeric pairs (interplanar separation: 3.51 Å). Both stacks and pairs are arranged in a head-to-tail fashion. For the hydrocarbon analog of **12**, a slipped π-stack structure with a head-to-head orientation of neighboring molecules is observed.[19]

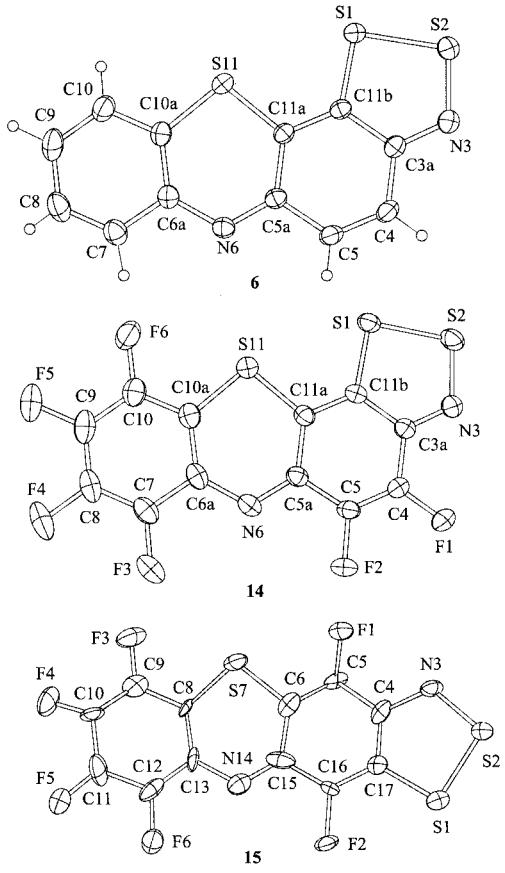

Figure 1. Molecular structures of **6**, **14**, and **15**. Selected bond lengths [Å] and bond angles [°]: **6**: C3a–N3 1.308(3), N3–S2 1.644(2), S2–S1 2.0934(9), S1–C11b 1.747(2), S11–C10a 1.752(2), S11–C11a 1.740(2), N6–C5a 1.312(3), C4–C5 1.342(3), C11a–C11b 1.365(3); C3a–N3–S2 116.0(2); N3–S2–S1 98.56(8), S2–S1–C11b 91.39(8). **14**: C3a–N3 1.303(4), N3–S2 1.627(3), S2–S1 2.0998(19), S1–C11b 1.747(3), S11–C10a 1.749(3), S11–C11a 1.749(3), N6–C5a 1.308(4), C4–C5 1.328(4), C11a–C11b 1.366(4); C3a–N3–S2 115.9(2), N3–S2–S1 98.57(11), S2–S1–C11b 91.50(11). **15** (averaged over four crystallographically independent molecules): C17–S1 1.73(2), S1–S2 2.114(7), S2–N3 1.66(2), N3–C4 1.32(2), N14–C13 1.42(2), N14–C15 1.27(2), S7–C8 1.766(7), S7–C6 1.73(2); C17–S1–S2 91.3(6), S1–S2–N3 97.9(6), S2–N3–C4 115.5(12), C13–N14–C15 119.4(12), C6–S7–C8 101.5(6).

The structure of **5**, a non-fluorinated analog of **13**, was reported earlier.[20] Previously, compound **5** was obtained in ca. 1% yield from an unsuccessful attempt to prepare the benzobis($1,3\lambda^4\delta^2$,2,4-dithiadiazine) system.[20] The crystal packing, with a π-stacked head-to-tail arrangement of neighboring molecules, features an interplanar separation of 3.39 Å that is closely reminiscent of that of **13** (Figure 5).

In contrast to **6**, the neighboring molecules in its fluorinated analog **14** are oriented in a head-to-head manner, whilst their enlarged offset leads to F···π interactions rather than normal π-stacking interactions (Figure 8). The dihedral angle between molecular planes is 6° and the F···π separation is 3.44–3.53 Å (Figure 8). As above, the different orientation of the molecules for **6** and **14** can be attributed to S···N interactions in the lattice of **6** (S···N contacts: 3.10 and 3.06 Å) and to S···F interactions in that of **14** (S···F contacts: 3.07 and 2.90 Å).

 © 2005 Wiley-VCH Verlag GmbH & Co. KGaA, Weinheim

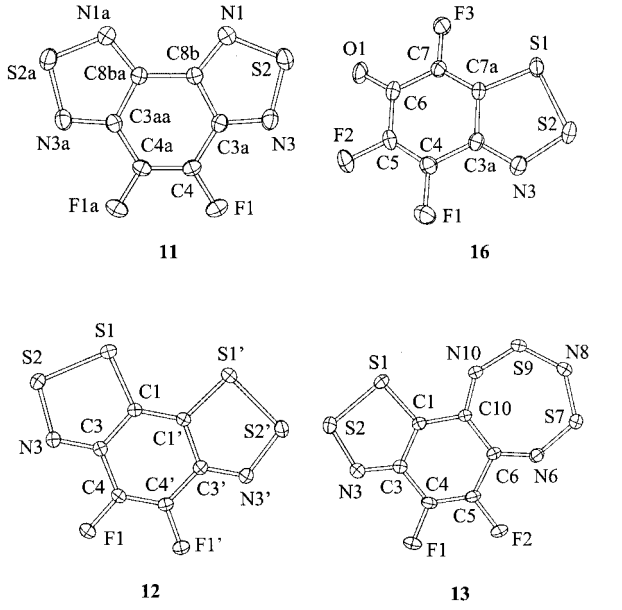

Figure 2. Molecular structures of **11**–**13** and **16**. Selected bond lengths [Å] and bond angles [°]: **11**: C3a–N3 1.330(2), N3–S2 1.628(2), S2–N1 1.625(2); C3a–N3–S2 106.0(1), N3–S2–N1 100.10(8), S2–N1–C8b 106.5(1). **12** (two crystallographically independent parts of molecule): C1–S1 1.743(2), 1.741(2), S1–S2 2.0944(9), 2.083(1), S2–N3 1.643(2), 1.645(2), C3–N3 1.310(3), 1.307(3); C1–S1–S2 91.04(8), 90.81(8), S1–S2–N3 99.10(8), 99.46(8), S2–N3–C3 115.2(2), 114.8(2). **13**: C6–N6 1.308(4), N6–S7 1.576(3), S7–N8 1.621(3), S9–N8 1.568(3), S9–N10 1.539(3), C10–N10 1.350(4), C1–S1 1.700(3), S1–S2 2.055(1), S2–N3 1.614(3), C3–N3 1.304(4); C6–N6–S7 137.0(2), N6–S7–N8 117.6(1), S7–N8–S9 130.3(2), N8–S9–N10 120.8(2), C10–N10–S9 135.6(2), C1–S1–S2 91.8(1), S1–S2–N3 99.0(1), S2–N3–C3 115.3(2). **16**: S1–S2 2.064(1), S2–N3 1.617(2), N3–C3a 1.314(3), S1–C7a 1.723(2), C6–O1 1.234(3); S1–S2–N3 99.19(8), S2–N3–C3a 115.7(2), S2–S1–C7a 92.07(9), S1–C7a–C3a 113.5(2), N3–C3a–C7a 119.6(2).

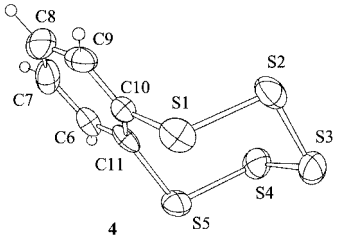

Figure 3. Molecular structure of **4**. Selected bond lengths [Å] and bond angles [°] (averaged over two crystallographically independent molecules): C10–S1 1.806(9), S1–S2 2.044(4), S2–S3 2.050(4), S3–S4 2.043(4), S4–S5 2.041(4), S5–C11 1.808(10); C11–C10–S1 123.2(8), C10–S1–S2 103.6(3), S1–S2–S3 104.1(1), S2–S3–S4 102.5(1), S3–S4–S5 104.3(2), S4–S5–C11 103.5(3), S5–C11–C10 122.7(7).

The crystal packing of **11** and **16** reveals a typical herringbone pattern. In contrast to **11**, columnar π-stacks and molecular layers are formed in the crystal structure of its non-fluorinated analog. Additionally, shortened S···N contacts give rise to a ribbon-like quasi-polymeric structure.[21]

For compound **4**, which was structurally defined previously[22] (see ref.[16] for derivatives), a new polymorph is observed. The hetero rings of two crystallographically independent molecules have the chair-twist-chair (TC) confor-

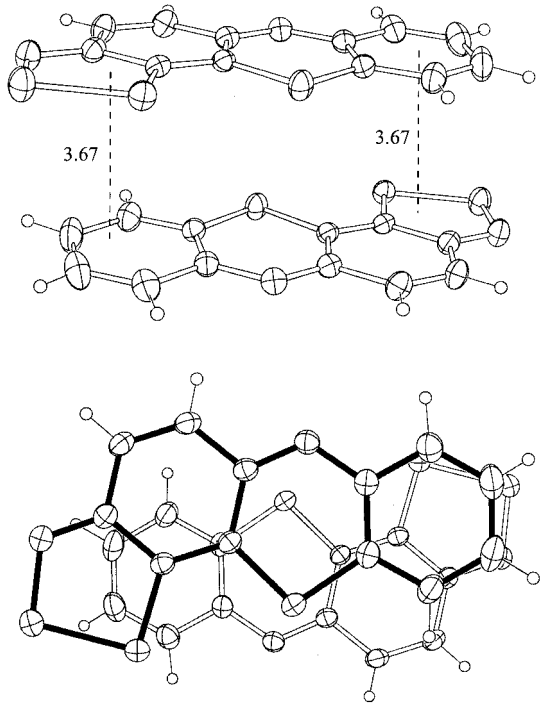

Figure 4. Orientation of neighboring molecules in the crystal lattice of **6**.

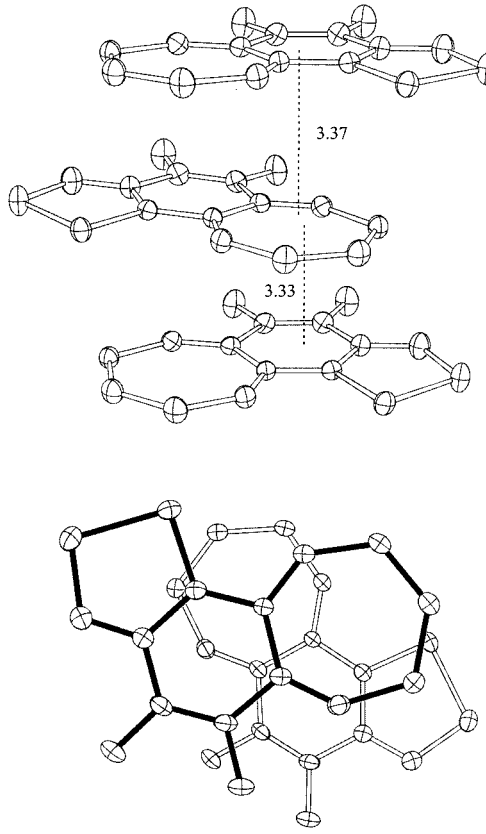

Figure 5. Orientation of neighboring molecules in the crystal lattice of **13**.

 © 2005 Wiley-VCH Verlag GmbH & Co. KGaA, Weinheim

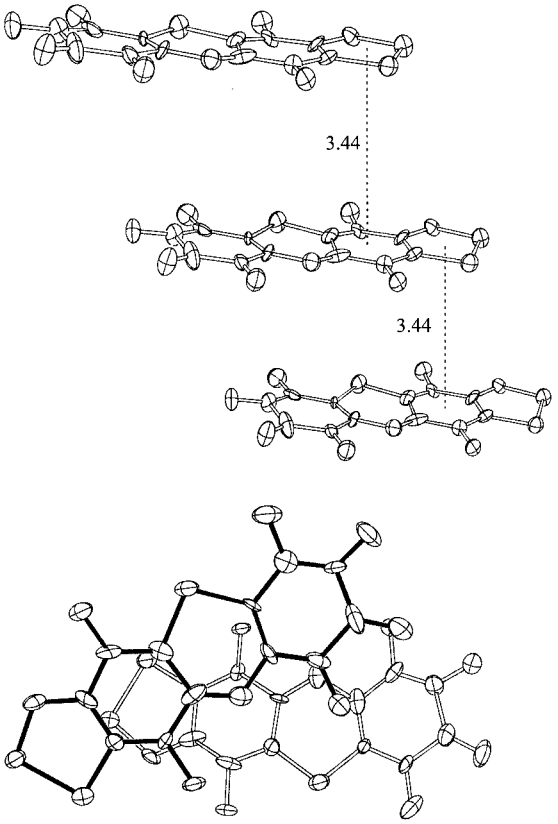

Figure 6. Orientation of neighboring molecules in the crystal lattice of **15**.

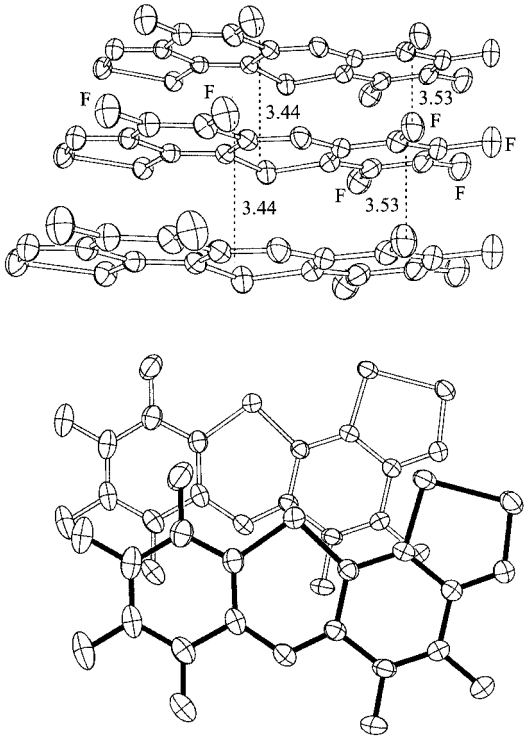

Figure 8. Orientation of neighboring molecules in the crystal lattice of **14**.

mation with C_2 symmetry. The molecules are involved in π-stacking interactions with a separation of 3.52–3.57 Å between neighboring benzene rings (Figure 9). Overall, the stacks form a layered structure.

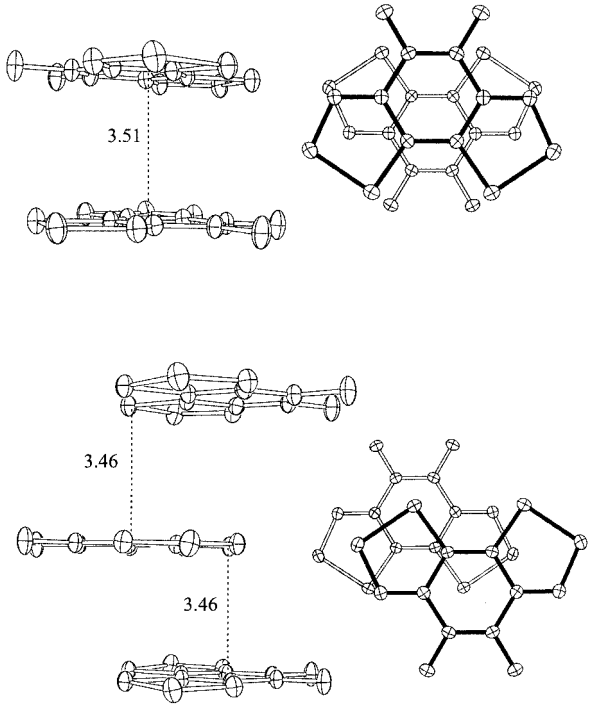

Figure 7. Orientation of neighboring molecules in the crystal lattice of **12**.

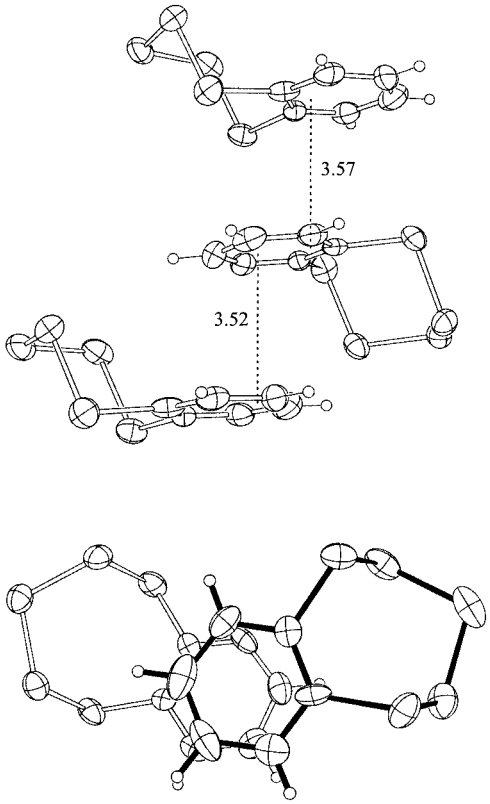

Figure 9. Orientation of neighboring molecules in the crystal lattice of **4**.

 © 2005 Wiley-VCH Verlag GmbH & Co. KGaA, Weinheim

In the previously observed crystal lattice,[22] π-stacked dimers can be identified (separation of benzene rings: 3.41 Å) that are combined into stacks by S···π interactions (ring centroid···S atom distance: 3.48 Å). Overall, the stacks form a herringbone structure.[22]

Selected Spectral Properties

For **1** and its carbocyclic substituted derivatives, the maxima of the weak ($\log \varepsilon \approx 2.4$–$2.8$) long-wavelength absorptions in the UV/Vis spectra are in the range of ca. 610–635 nm.[1–5] The 5-5-6 (**12** and its hydrocarbon analog[19]), 5-6-7 (**5**, **13**), and angular 5-6-6-6 (**6**, **14**) systems reveal strong ($\log \varepsilon \approx 3.9$–$4.2$) absorptions in about the same range of ca. 570–635 nm, whereas the linear 5-6-6-6 system **15** absorbs at shorter wavelengths (Table 1), with only a weak dependence of the corresponding π→π* transitions in extended polyheteroatom π-systems upon substitution of fluorine for hydrogen. Additionally, the 5-6-6-6 systems (**6**, **14**, **15**) demonstrate strong fluorescence in the range of ca. 660–680 nm (Table 1). The Stokes shifts are very different for angular (ca. 40–60 nm for **6**, **14**) and linear (ca. 140 nm for **15**) derivatives (Table 1). Taking into account the solubility of the discussed compounds in organic solvents, their thermal stability, and their stability towards moisture (in sharp contrast to starting 1,3λ^{4}δ^2,2,4-benzodithiadiazines),[3,14] it is possible to believe that the polysulfur-nitrogen heterocycles synthesized here can be considered as potential fluorescent dyes. Furthermore, the spectral properties of compound **15** are very similar to those of novel nondoping organic light-emitting diodes (OLEDs).[23]

Alternative Approaches to 5-6-6-6 Systems

Due to the potential of the 5-6-6-6 systems as fluorescent dyes, rational approaches to their preparation are of interest. These can probably be designed based on phenothiazine systems in both the hydrocarbon and fluorocarbon series.

Meanwhile, it was found that compound **15**, the most interesting in the context of OLEDs, can be obtained in moderate yield as the final product of a spontaneous transformation of R–N=PPh$_3$ (**19**; R = 4,5,6,7-tetrafluoro-1,2,3-benzodithiazol-2-yl) in $CHCl_3$ solution (Scheme 6). The ^{19}F and ^{31}P NMR spectra of the reaction mixture reveal formation of Ph_3PF_2 [$\delta_{^{19}F}$ = 121.9 ppm (d, $J_{F,P}$ = 660 Hz); $\delta_{^{31}P}$ = –54.5 ppm (t, $J_{P,F}$ = 660 Hz); cf. ref.[24]] and, tentatively, Ph_3P=N–H [$\delta_{^{31}P}$ = 22.0 (s); cf. ref.[25]] as by-products. At the same time, Ph_3P=S[26] and $(SN)_4$[27] are not observed in the ^{31}P and ^{14}N NMR spectra, respectively. The reaction is solvent-dependent and does not proceed, for example, in toluene.

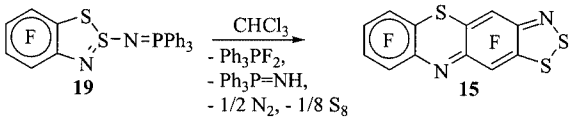

Scheme 6.

We found by ESR spectroscopy that in $CHCl_3$ solution (but not in toluene) and at ambient temperature, compound **19** spontaneously produces 1,2,3-benzodithiazolyl (**20**; Scheme 7; see refs.[8,9] for the ESR spectrum), seemingly by reversible homolytic splitting of the exocyclic S–N bond. At the same time, the second product of such splitting − the

Table 1. Spectroscopic data for compounds **5**, **6**, and **11**–**16**.

	NMR, δ [ppm] ^{1}H	^{19}F[a]	^{13}C	^{14}N	UV/Vis λ_{max} [nm] (log ε)	Fluorescence $\lambda_{max}/\lambda_{exit.}$ [nm]
5	7.60 (d)[b], 7.11 (d)[b]				625 (4.0), 582 (4.0)[20]	
6	7.48 (d, 1 H), 7.41 (d, 1 H), 7.23 (m, 2 H), 7.18 (td, 1 H), 7.14 (ddd, 1 H)				610 (4.02), 579 (4.02), 337 (4.15), 253 (4.23)	667/330
11		15.8	148.2, 144.6, 142.3	334	315 (3.89; sh.), 286 (4.44)	
12		17.9	149.6, 142.8, 123.7	295	589 (4.23), 340 (4.17), 234 (3.84)[c]	
13		31.3, 0.8[d]			635 (3.95), 587 (4.02), 363 (4.09)	
14		23.9, 20.7, 19.4, 17.3, 8.7, 4.8	148.8, 145.2, 144.9, 143.8, 143.5, 141.9, 140.1, 132.5, 126.3, 105.7, 103.4		615 (3.88; sh.), 585 (3.90), 394 (3.70), 349 (3.92), 255 (4.10)	657/340
15		42.0, 40.9, 18.8, 16.5, 7.4, 4.5			533 (4.68), 268 (4.70), 235 (4.49)	675/335
16		32.8, 20.6, 17.8[d]			482 (3.97), 348 (3.80), 253 (3.47)	

[a] C_6F_6 as standard; the chemical shift of C_6F_6 with respect to $CFCl_3$ is –162.2 ppm. [b] J = 10 Hz. [c] Cf. Hydrocarbon analog (in CH_2Cl_2): 572 (4.2), 329 (4.0).[19] [d] In [D_8]toluene.

 © 2005 Wiley-VCH Verlag GmbH & Co. KGaA, Weinheim

$Ph_3P{=}N^{\cdot}$ radical − was not observed, very likely due to fast decay by hydrogen abstraction from the $CHCl_3$ solvent. Thus, the equilibrium shown in Scheme 7 might be shifted towards radical **20** and an explanation of the self-condensation of **19** into **15** can be suggested, including the role of the $CHCl_3$ solvent (Scheme 7).

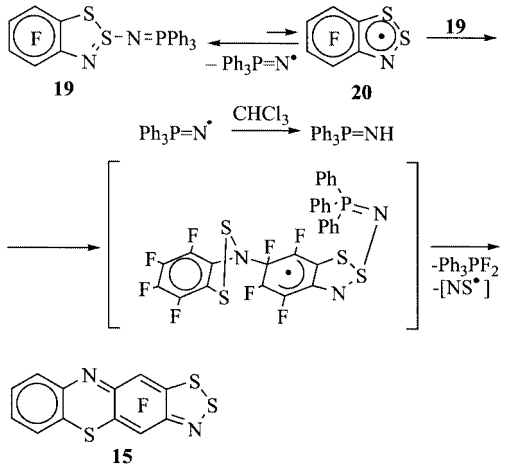

Scheme 7.

A postulated $SN^{\cdot}$ by-product (Scheme 7) is very unstable and undetectable by ESR spectroscopy in the condensed phase due to strong *g*-anisotropy (see ref.[28] and references therein).

Conclusions

In contrast to thermolysis in dilute solutions, which leads to persistent 1,2,3-benzodithiazolyls (which are promising building blocks in the design and synthesis of organic molecular magnets and/or organic molecular conductors) in nearly quantitative yields, the thermal transformations of 1,3λ^{4}δ^2,2,4-benzodithiadiazines **1** and **2** (the 6-6 bicyclic system) in concentrated solutions results in complex mixtures of various polysulfur-nitrogen heterocycles, in particular differently fused 5-5-6, 5-6-7, and 5-6-6-6 polycyclic systems that were previously unknown. Despite very low yields, the products were isolated and unambiguously identified by X-ray diffraction. The polycyclic π-functional molecules prepared engage in anisotropic intermolecular interactions in the solid state and are therefore of interest for materials science.[29] In both hydrocarbon and fluorocarbon series, the polycyclic systems synthesized demonstrate strong long-wavelength absorption and fluorescence and can be considered as potential fluorescent dyes. All the aforementioned properties motivate the elaboration of rational approaches to the discussed compounds, and this can be a direction for further investigations in this field. The transformation of the R–N=PPh_3 derivative **19** (R = 4,5,6,7-tetrafluoro-1,2,3-benzodithiazol-2-yl) into the 5-6-6-6 system **15**, which was discovered and explained in the present work, can be considered promising in this context.

Experimental Section

General: Compounds **1**[1] and **2**[2] were prepared by known methods. Their thermolysis was carried out under argon in absolute solvents, with stirring. The concentration of residual water in *n*BuOH was controlled by gas chromatography to be 0.02 M. The chromatographic separations of the products were performed with silica columns. The physical and analytical data for the compounds synthesized are listed in Tables 4 and 5. Compound **19**[15] was prepared in 60% yield by an improved procedure, the details of which will be given elsewhere.[30]

The ^{1}H, ^{13}C, ^{14}N, and ^{31}P NMR spectra were measured with a Bruker DRX-500 spectrometer at frequencies of 500.13, 125.76, 36.13, and 202.46 MHz, respectively, with TMS, NH_3 (liq.) and 85% H_3PO_4 as standards; the ^{19}F NMR spectra were recorded with a Bruker AC-200 machine at a frequency of 188.28 MHz with C_6F_6 as the standard; solutions in $CDCl_3$ were used unless otherwise indicated.

The high-resolution mass spectra (EI, 70 eV) were recorded with a Finnigan MAT MS-8200 instrument.

The UV/Vis spectra were recorded on Specord M40 and Hewlett–Packard 8453 spectrophotometers for solutions in $CHCl_3$. The fluorescent spectra were measured with a Kontron SFM-25 spectrofluorimeter for MeCN solutions.

The GLC-MS determinations were performed with a Hewlett–Packard G1800A GDC apparatus. The GC measurements were carried out with a Hewlett–Packard 5890 instrument.

The ESR measurements were carried out on a Bruker ESP-300 spectrometer (MW power: 265 mW; modulation frequency: 100 kHz; modulation amplitude: 0.005 mT) for a $CHCl_3$ solution of **19**. The spectral integration and simulation were performed with the Winsim 32 program.

Crystallographic Analysis: The single-crystal structure determinations (Tables 2, 3, and 4) were carried out on Bruker P4 (**4**–**6**, **11**–**14**, **16**) and Syntex $P2_1$ (**15**) diffractometers with graphite-monochromated Mo-K_α (λ = 0.71073 Å) and Cu-K_α (λ = 1.54178 Å) radiation, respectively. The structures were solved by direct methods by use of the SHELXS-97 program[31] and refined by the least-squares method in the full-matrix anisotropic (isotropic for H atoms) approximation by use of the SHELXL-97 program.[31] Hydrogen atoms were located geometrically. The structures obtained were analyzed for shortened contacts between non-bonded atoms with the PLATON program.[32,33]
For compounds **4** and **15**, available single crystals were very small (Tables 2 and 4) and reflections could only be measured to θ = 22.5° and θ = 57°, respectively. The structure of **15** was refined with AFIX and EADP restraints applied to selected geometrical and anisotropic parameters, respectively: the C_6F_4 moiety was restrained to be a right hexagon with all C–F bond distances of 1.35 Å, for each C–F bond of the molecule thermal parameters of the F atom were fixed at corresponding values of the C atom.
CCDC-268796 (for **4**), -268797 (for **6**), -268798 (for **11**), -268799 (for **12**), -268800 (for **13**), -268801 (for **14**), -268802 (for **15**), and -268803 (for **16**) contain the supplementary crystallographic data for this paper. These data can be obtained free of charge from The Cambridge Crystallographic Data Centre via www.ccdc.cam.ac.uk/data_request/cif. For **5**, the data obtained in this work are in full agreement with those published previously.[20]

Identification of Known Compounds: The isolated compounds **3**,[34] **5**,[20] **10**,[35] and **18**,[3] described previously, were identified by comparison of reported m.p.'s, unit cell (XRD) and spectral (^{1}H and

 © 2005 Wiley-VCH Verlag GmbH & Co. KGaA, Weinheim

Table 2. Crystal data and structure refinement for compounds **4**, **6**, and **11**.

Compound	**4**	**6**	**11**
Empirical formula	$C_6H_4S_5$	$C_{12}H_6N_2S_3$	$C_6F_2N_4S_2$
Formula mass	236.39	274.37	230.22
Temperature [K]	298(2)	296(2)	296(2)
Crystal system	monoclinic	monoclinic	orthorhombic
Space group	$P2_1/c$	$C2/c$	$Pnma$
a [Å]	7.729(1)	12.9236(7)	9.2356(6)
b [Å]	9.457(1)	12.8240(8)	16.856(1)
c [Å]	25.453(3)	15.214(1)	5.1668(4)
β [°]	95.06(1)	114.964(5)	90
Volume [Å^3]	1853.3(4)	2285.9(3)	804.33(9)
Z	8	8	4
$D_{calcd.}$ [Mg m^{-3}]	1.694	1.594	1.901
Absorption coefficient [mm^{-1}]	1.179	0.622	0.654
Crystal size [mm^3]	0.20 × 0.15 × 0.05	0.70 × 0.20 × 0.15	0.80 × 0.34 × 0.05
θ range for data collection [°]	2.30–22.50	2.35–25.00	2.42–30.00
Index ranges	$-8 \le h \le 0$	$0 \le h \le 15$	$-12 \le h \le 0$
	$0 \le k \le 10$	$-15 \le k \le 0$	$0 \le k \le 23$
	$-27 \le l \le 27$	$-18 \le l \le 16$	$-7 \le l \le 0$
Reflections collected	2627	2096	1212
Independent reflections	2417 [$R_{(int)}$ = 0.0466]	2017 [$R_{(int)}$ = 0.0205]	1212 [$R_{(int)}$ = 0.0]
Completeness to θ [%]	99.8	100.0	100.0
Absorption correction	empirical	empirical	integration
Min. and max. transmission	0.73 and 0.88	0.96 and 0.99	0.78 and 0.97
Data/restraints/parameters	2417/0/199	2017/0/154	1212/0/64
Goodness-of-fit on F^2	0.885	1.062	1.044
Final R indices [$I > 2\sigma(I)$]	R_1 = 0.0572, wR_2 = 0.1319	R_1 = 0.0329, wR_2 = 0.0843	R_1 = 0.0381, wR_2 = 0.0923
R indices (all data)	R_1 = 0.1163, wR_2 = 0.1487	R_1 = 0.0420, wR_2 = 0.0894	R_1 = 0.0616, wR_2 = 0.1033

Table 3. Crystal data and structure refinement for compounds **12**–**14**.

Compound	**12**	**13**	**14**
Empirical formula	$C_6F_2N_2S_4$	$C_6F_2N_4S_4$	$C_{12}F_6N_2S_3$
Formula mass	266.32	294.34	382.32
Temperature [K]	296(2)	296(2)	296(2)
Crystal system	monoclinic	monoclinic	monoclinic
Space group	$C2/m$	$P2_1/c$	$P2_1/n$
a [Å]	7.818(2)	8.513(3)	7.292(6)
b [Å]	23.204(5)	16.677(6)	4.700(4)
c [Å]	10.124(2)	6.690(2)	37.29(3)
β [°]	102.45(1)	97.71(1)	94.27(5)
Volume [Å^3]	1793.4(6)	941.2(6)	1274.7(19)
Z	8	4	4
$D_{calcd.}$ [Mg m^{-3}]	1.973	2.077	1.992
Absorption coefficient [mm^{-1}]	1.043	1.011	0.653
Crystal size [mm^3]	0.80 × 0.28 × 0.20	0.70 × 0.34 × 0.10	0.90 × 0.44 × 0.02
θ range for data collection [°]	2.06–27.50	2.41–27.51	2.19–25.00
Index ranges	$0 \le h \le 9$	$-10 \le h \le 11$	$0 \le h \le 8$
	$0 \le k \le 30$	$-21 \le k \le 0$	$0 \le k \le 5$
	$-13 \le l \le 12$	$-8 \le l \le 0$	$-44 \le l \le 44$
Reflections collected	2243	2337	2421
Independent reflections	2094 [$R_{(int)}$ = 0.0323]	2158 [$R_{(int)}$ = 0.0822]	2229 [$R_{(int)}$ = 0.0348]
Completeness to θ [%]	98.7	99.9	98.8
Absorption correction	integration	integration	integration
Min. and max. transmission	0.77 and 0.84	0.72 and 0.91	0.84 and 0.99
Data/restraints/parameters	2094/0/128	2158/0/145	2229/0/208
Goodness-of-fit on F^2	1.036	1.049	1.038
Final R indices [$I > 2\sigma(I)$]	R_1 = 0.0383, wR_2 = 0.1039	R_1 = 0.0546, wR_2 = 0.1451	R_1 = 0.0383, wR_2 = 0.0974
R indices (all data)	R_1 = 0.0412, wR_2 = 0.1061	R_1 = 0.0653, wR_2 = 0.1551	R_1 = 0.0563, wR_2 = 0.1068

^{19}F NMR, UV/Vis, MS) parameters with those obtained in this work. Di-*n*-butyl sulfite was identified by GLC-MS. Compounds **7**,[34] **8**,[16] and **9**[36] were identified without isolation by means of GLC-MS and ^{1}H NMR techniques by comparison with the authentic samples.

See Table 5 for spectroscopic data for compounds **5**, **6**, and **11**–**16**.

Thermolysis of 1,3λ^{4}δ^2,2,4-Benzodithiadiazine (1) in Squalane. Formation of Compounds 3–6: A solution of 0.34 g (2 mmol) of **1** in 3 mL of squalane was stirred at 150–160 °C for 3 h, cooled to

 © 2005 Wiley-VCH Verlag GmbH & Co. KGaA, Weinheim

Table 4. Crystal data and structure refinement for compounds **15** and **16**.

Compound	**15**	**16**
Empirical formula	$C_{12}F_6N_2S_3$	$C_6F_3NOS_2$
Formula mass	382.32	223.19
Temperature [K]	296(2)	296(2)
Crystal system	monoclinic	monoclinic
Space group	*Cc*	$P2_1/n$
a [Å]	11.310(2)	5.1828(7)
b [Å]	11.311(2)	9.706(1)
c [Å]	39.884(8)	14.298(2)
β [°]	97.97(2)	95.85(1)
Volume [Å^3]	5052.7(18)	715.5(2)
Z	16	4
$D_{calcd.}$ [Mg m^{-3}]	2.010	2.072
Absorption coefficient [mm^{-1}]	6.119	0.749
Crystal size [mm^3]	0.13 × 0.13 × 0.03	0.80 × 0.20 × 0.08
θ range for data collection [°]	2.24–57.43	2.54–24.99
Index ranges	$0 \le h \le 12$	$-6 \le h \le 0$
	$0 \le k \le 12$	$0 \le k \le 11$
	$-43 \le l \le 43$	$-16 \le l \le 16$
Reflections collected	4151	1398
Independent reflections	3688 [$R_{(int)}$ = 0.1374]	1250 [$R_{(int)}$ = 0.0186]
Completeness to *θ* [%]	100.0	99.9
Absorption correction	empirical	empirical
Min. and max. transmission	0.46 and 0.82	0.87 and 0.98
Data/restraints/parameters	3688/38/544	1250/0/118
Goodness-of-fit on F^2	1.051	1.065
Final *R* indices [$I > 2\sigma(I)$]	R_1 = 0.0739, wR_2 = 0.1679	R_1 = 0.0329, wR_2 = 0.0939
R indices (all data)	R_1 = 0.1311, wR_2 = 0.2071	R_1 = 0.0387, wR_2 = 0.0980

Table 5. Characterization of compounds **5**, **6**, and **11**–**16**.

	M.p. [°C]	Formula	MS: M^+ (*m*/*z*) measured (calculated)
5	269–271	$C_6H_4N_4S_4$	257.9154 (257.9162)
6	206–208	$C_{12}H_6N_2S_3$	273.9724 (273.9693)
11	175–176[a]	$C_6F_2N_4S_2$	229.9542 (229.9533)
12	230–232[a]	$C_6F_2N_2S_4$	265.8918 (265.8912)
13	280–282[a]	$C_6F_2N_4S_4$	293.8972 (293.8974)
14	216–217	$C_{12}F_6N_2S_3$	381.9133 (381.9128)
15[b]	234–236	$C_{12}F_6N_2S_3$	381.9152 (381.9128)
16	210–212	$C_6F_3NOS_2$	222.9371 (222.9374)

[a] In a sealed capillary. [b] Correct elemental analyses for C, F, N, S.

20 °C, filtered and chromatographed. Elution with hexane gave 50 mg of a red oil consisting (GLC-MS, ^{1}H NMR) of compounds **9** (33%), **4** (31%), **8** (13%), **3** (3%), **7** (1.5%), elemental S (0.6%), and squalane (5%). Compound **4** (5 mg) was isolated by low-temperature crystallization from hexane as pale-yellow crystals (m.p. 55–56 °C). Elution with toluene gave 30 mg (10% yield) of compound **3**[34] as colorless crystals. Elution with 1:1 CH_2Cl_2/ethyl acetate followed by crystallization of the product from 10:1 hexane/toluene gave compound **6** (4 mg) as black crystals. The reaction precipitate was refluxed in toluene and the solution formed was chromatographed. Elution with toluene followed by recrystallization of the product from the same solvent gave compound **5** (2 mg) as black crystals. The gases evolved during the thermolysis were absorbed by dilute HCl. Photometrical analysis with Nessler's reagent revealed NH_3 in 3% yield.

Thermolysis of 5,6,7,8-Tetrafluoro-1,3λ^{4}δ^2,2,4-benzodithiadiazine (2) in Decane. Formation of Compounds 10–16: A solution of 0.96 g (4 mmol) of **2** in 8 mL of decane was stirred at 160–170 °C for 6 h, cooled to 20 °C, filtered and chromatographed (hexane). Compound **10**[35] (36 mg; 5%) was obtained as colorless crystals. The reaction precipitate was sublimed at 170 °C/2 mm and the sublimate chromatographed. Elution with toluene gave blue and red zones. Sublimation of the product from the blue zone at 110 °C/2 mm gave a mixture of **12**, **14**, and **17**. Compound **14** (6 mg) was obtained as black crystals by further chromatography of this mixture (1:1 hexane/toluene) followed by crystallization from hexane. Compound **12** (3 mg) was obtained as black crystals by crystallization of its mixture with isomeric **17** from 4:1 hexane/toluene. The mother liquor contained residual **12** (GLC-MS: *m*/*z* = 226 [M^+]; ^{19}F NMR: *δ* = 17.9 ppm) and **17** (GLC-MS: *m*/*z* = 226 [M^+]; ^{19}F NMR: *δ* = 40.7 ppm; the structure was assigned tentatively). Crystallization (toluene) of the non-volatile residue from sublimation gave **13** (3 mg) as black crystals. Sublimation of the product from the red zone at 120 °C/2 mm gave **15** (1 mg) as black crystals. Elution with 10:1 toluene/ethyl acetate gave **11** and **16**, which were purified by sublimation at 120 °C/2 mm. Compound **11** (12 mg) was obtained as colorless crystals and compound **16** (6 mg) as black crystals.

Thermolysis of Compound 1 in 1-Butanol. Formation of Compound 6: A solution of 0.17 g (1 mmol) of **1** in 1 mL of *n*BuOH was refluxed for 3.5 h, cooled to 20 °C and chromatographed. Elution with CH_2Cl_2 gave ca. 4 mg of a mixture (GLC-MS data) of compounds **3** (20%), **4** (traces), **7** (40%), **9** (20%), and elemental S (20%). Elution with 10:1 CH_2Cl_2/ethyl acetate gave compound **6**. The latter was repeatedly chromatographed under the same conditions and recrystallized from 10:1 hexane/toluene to give black crystals (1 mg).

Thermolysis of Compound 2 in 1-Butanol. Formation of Compounds 11 and 18: A solution of 0.48 g (2 mmol) of **2** in 2 mL of *n*BuOH was refluxed for 4 h, cooled to 20 °C, and chromatographed (hexane) to give ca. 0.17 g of di-*n*-butyl sulfite, compound **11**, and compound **18**. Compound **11** (4 mg) was obtained as colorless crystals

 © 2005 Wiley-VCH Verlag GmbH & Co. KGaA, Weinheim

by sublimation at 120 °C/2 mm followed by recrystallyzation from hexane. Compound **18**[3] (54 mg) was obtained as yellow crystals by sublimation at 130 °C/2 mm followed by recrystallization from hexane.

Spontaneous Transformation of Compound 19 in Chloroform Solution. Formation of Compound 15: A solution of 0.10 g (0.2 mmol) of **19** in 0.5 mL of $CHCl_3$ was kept for 7 d at ambient temperature and then evaporated. The residue was chromatographed (benzene) to give compound **15** (12 mg, 30%) as black crystals.

According to the ESR measurements, the radical **20** appeared immediately upon dissolving precursor **19** and was detectable for a few days. For the ^{19}F and ^{31}P NMR measurements, the preparation was performed in $CDCl_3$ solution.

Acknowledgments

The authors are grateful to Dr. Vladimir V. Koval and Dr. Irina G. Irtegova for measurements of fluorescent and ESR spectra, respectively, to the Siberian Division of the Russian Academy of Sciences for access to instrumental facilities at the Collective Chemical Center of the Division, and to the Russian Foundation for Basic Research for access to the Cambridge Crystallographic Database (grant 02-07-90322) and the STN International databases via STN Center at the Institute of Organic Chemistry, Novosibirsk, Russia (grant 00-03-32721).

[1] A. W. Cordes, M. Hojo, H. Koenig, M. C. Noble, R. T. Oakley, W. T. Pennington, *Inorg. Chem.* **1986**, *25*, 1137–1145.
[2] A. V. Zibarev, Yu. V. Gatilov, A. O. Miller, *Polyhedron* **1992**, *11*, 1137–1141.
[3] I. Yu. Bagryanskaya, Yu. V. Gatilov, A. Yu. Makarov, A. M. Maksimov, A. O. Miller, M. M. Shakirov, A. V. Zibarev, *Heteroat. Chem.* **1999**, *10*, 113–124.
[4] A. Yu. Makarov, I. Yu. Bagryanskaya, Yu. V. Gatilov, T. V. Mikhalina, M. M. Shakirov, L. N. Shchegoleva, A. V. Zibarev, *Heteroat. Chem.* **2001**, *12*, 563–576.
[5] A. Yu. Makarov, I. Yu. Bagryanskaya, F. Blockhuys, C. Van Alsenoy, Yu. V. Gatilov, V. V. Knyazev, A. M. Maksimov, T. V. Mikhalina, V. E. Platonov, M. M. Shakirov, A. V. Zibarev, *Eur. J. Inorg. Chem.* **2003**, 77–87.
[6] F. Blockhuys, S. L. Hinchley, A. Yu. Makarov, Yu. V. Gatilov, A. V. Zibarev, J. D. Woollins, D. W. H. Rankin, *Chem. Eur. J.* **2001**, *7*, 3592–3602.
[7] A. R. Turner, F. Blockhuys, C. Van Alsenoy, H. E. Robertson, S. L. Hinchley, A. V. Zibarev, A. Yu. Makarov, D. W. H. Rankin, *Eur. J. Inorg. Chem.* **2005**, 572–578.
[8] V. A. Bagryansky, I. V. Vlasyuk, Yu. V. Gatilov, A. Yu. Makarov, Yu. N. Molin, V. V. Shcherbukhin, A. V. Zibarev, *Mendeleev Commun.* **2000**, 5–7.
[9] I. V. Vlasyuk, V. A. Bagryansky, N. P. Gritsan, Yu. N. Molin, A. Yu. Makarov, Yu. V. Gatilov, V. V. Shcherbukhin, A. V. Zibarev, *Phys. Chem. Chem. Phys.* **2001**, *3*, 409–415.
[10] N. P. Gritsan, V. A. Bagryansky, I. V. Vlasyuk, Yu. N. Molin, A. Yu. Makarov, M. S. Platz, A. V. Zibarev, *Russ. Chem. Bull., Int. Ed.* **2001**, *50*, 2064–2070.
[11] A. Yu. Makarov, S. N. Kim, N. P. Gritsan, I. Yu. Bagryanskaya, Yu. V. Gatilov, A. V. Zibarev, *Mendeleev Commun.* **2005**, 14–16.
[12] J. M. Rawson, G. D. McManus, *Coord. Chem. Rev.* **1999**, *189*, 135–168.
[13] J. M. Rawson, F. Palacio, *Struct. Bond. (Berlin)* **2001**, *100*, 93–128.
[14] A. Yu. Makarov, I. Yu. Bagryanskaya, Yu. V. Gatilov, M. M. Shakirov, A. V. Zibarev, *Mendeleev Commun.* **2003**, 19–21.
[15] A. V. Zibarev, Yu. V. Gatilov, I. Yu. Bagryanskaya, A. M. Maksimov, A. O. Miller, *J. Chem. Soc., Chem. Commun.* **1993**, 298–299.
[16] a) L. S. Konstantinova, O. A. Rakitin, C. W. Rees, *Chem. Rev.* **2004**, *104*, 2617–2630; b) R. Sato, *Heteroat. Chem.* **2002**, *13*, 419–423; c) R. Steudel, K. Hassenberg, V. Munchow, O. Schumann, J. Pickardt, *Eur. J. Inorg. Chem.* **2000**, 921–928.
[17] a) A. Bondi, *J. Phys. Chem.* **1964**, *68*, 441–451; b) R. S. Rowland, R. Taylor, *J. Phys. Chem.* **1996**, *100*, 7384–7391.
[18] a) Yu. V. Zefirov, P. M. Zorky, *Usp. Khim.* **1989**, *58*, 713–746; b) Yu. V. Zefirov, M. A. Porai-Koshits, *Z. Strukt. Khim.* **1980**, *21*, 150–151; c) L. N. Kuleshova, M. Yu. Antipin, *Russ. Chem. Rev.* **1999**, *68*, 1–18.
[19] T. M. Barclay, A. W. Cordes, R. T. Oakley, K. E. Preuss, R. W. Reed, *Chem. Mater.* **1999**, *11*, 164–169.
[20] P. W. Codding, H. Koenig, R. T. Oakley, *Can. J. Chem.* **1983**, *61*, 1562–1566.
[21] A. Gieren, H. Betz, T. Hubner, V. Lamm, R. Neidlen, D. Droste, *Z. Naturforsch. B* **1984**, *39*, 485–496.
[22] F. Feher, B. Engelen, *Z. Anorg. Allg. Chem.* **1979**, *452*, 37–42.
[23] Q. Fang, B. Xu, B. Jiang, H. Fu, X. Chen, A. Cao, *Chem. Commun.* **2005**, 1468–1470.
[24] K. M. Doxsee, E. M. Hanawalt, T. J. R. Weakley, *Inorg. Chem.* **1992**, *31*, 4420–4421.
[25] H. J. Cristau, L. Chiche, J. Kadoura, E. Torreilles, *Tetrahedron Lett.* **1988**, *29*, 3931–3934.
[26] *Phosphorus-31 NMR spectroscopy. Principles and Applications* (Ed.: D. G. Gorenstein), Academic Press, Orlando, **1984**, pp. 549–588.
[27] T. Chivers, *Chem. Rev.* **1985**, *85*, 341–365.
[28] K. V. Shuvaev, V. A. Bagryansky, N. P. Gritsan, A. Yu. Makarov, Yu. N. Molin, A. V. Zibarev, *Mendeleev Commun.* **2003**, 178–179.
[29] P. Batail, *Chem. Rev.* **2004**, *104*, 4887–4890 (and other articles of this special issue dedicated to molecular conductors).
[30] a) V. V. Zhivonitko, A.Yu. Makarov, A. V. Zibarev, to be published; b) V. V. Zhivonitko, Diploma Work, Novosibirsk State University, Novosibirsk, **2005**.
[31] G. M. Sheldrick, *SHELX-97 – Programs for Crystal Structure Analysis (Release 97-2)*, Institute for Inorganic Chemistry, University of Göttingen, Göttingen, Germany.
[32] A. L. Spek, *PLATON – A Multipurpose Crystallographic Tool (Version 10M)*, Utrecht University, Utrecht, The Netherlands.
[33] A. L. Spek, *J. Appl. Crystallogr.* **2003**, *36*, 7–13.
[34] M. Weinstock, I. Shinkai, in *Comprehensive Heterocyclic Chemistry*, *vol. 6* (Ed.: K. T. Potts), Pergamon Press, Oxford, **1984**, pp. 513–544 (and references cited therein).
[35] A. V. Zibarev, A. O. Miller, *J. Fluorine Chem.* **1990**, *50*, 359–363.
[36] A. Yu. Makarov, M. M. Shakirov, K. V. Shuvaev, I. Yu. Bagryanskaya, Yu. V. Gatilov, A. V. Zibarev, *Chem. Commun.* **2001**, 1774–1775.

Received: April 29, 2005
Published Online: September 8, 2005

 © 2005 Wiley-VCH Verlag GmbH & Co. KGaA, Weinheim

Synthesis, Structure and Photoluminescent Studies of Two Novel Layered Uranium Coordination Polymers Constructed from UO(OH) Polyhedra and Pyridinedicarboxylates

Yan-Zhen Zheng,[a] Ming-Liang Tong,*[a] and Xiao-Ming Chen[a]

Keywords: Carboxylate ligands / Coordination polymers / Photoluminescence / Uranium

Two new uranium coordination polymers have been obtained from the hydrothermal reaction of $(UO_2)(CH_3COO)_2{\cdot}2H_2O$ with 3,4-pyridinedicarboxylic acid (3,4-pydaH$_2$) or 2,4-pyridinedicarboxylic acid (2,4-pydaH$_2$). $[(UO_2)_3(\mu_3\text{-}O)(\mu_3\text{-}OH)_2(3,4\text{-pydaH})(3,4\text{-pyda})_{0.5}]_n$ (**1**) crystallizes in the orthorhombic space group *Pccn* with a = 18.168(2), b = 12.635(1), c = 16.149(1) Å, V = 3707.0(5) Å^3, and Z = 8. $[(UO_2)_3(\mu_3\text{-}O)(\mu_3\text{-}OH)(\mu_2\text{-}OH)(2,4\text{-pyda})(H_2O)_2]_n{\cdot}nH_2O$ (**2**) is in the orthorhombic space group *Pbcn* with a = 22.788(2), b = 7.1468(5), c = 21.627(1) Å, V = 3522.1(4) Å^3, and Z = 8. Complex **1** features a wave-like 2D layer that is constructed by connecting the 1D UO(OH) ribbons by the V-shaped 3,4-pyda or 3,4-pydaH ligands. Complex **2** is a rare hexameric species amongst uranium compounds and features a (4,4) planar "open-layer", which is constructed by the 4-connected hexameric UO(OH) polyhedra and the 2-connected 2,4-pyda ligands. The fluorescence emission (521 nm) of **2** is red-shifted by about 13 nm (emission) and about 40 nm (excitation) compared to that of **1**, and the lifetimes increase with the polymerization of UO(OH) polyhedra (145 μs for **1** compared to 24.4 μs for **2**).
(© Wiley-VCH Verlag GmbH & Co. KGaA, 69451 Weinheim, Germany, 2005)

Introduction

In the area of inorganic-organic hybrid materials, metal-organic coordination polymers built from nano-sized MO(OH) clusters and multi-functional carboxylates are of current interest driven partially by their intriguing molecular topologies and crystal packing motifs as well as the fact that they may be designed with a variety of functionalities in mind, such as photoelectronics, separation, magnetism, ion exchange, gas storage, and catalysis.[1–7] In addition to being robust and thermally stable, some possess photoluminescent properties, a feature that has contributed to the closed-shell d^{10} metal compounds, including 3d^{10} copper(I) and zinc(II), 4d^{10} silver(I) and cadmium(II), and 5d^{10} gold(I) and mercury(II) complexes, being widely investigated for new materials.[8–11] In fact, the highest valent actinide elements have similar 5d^{10} electrons in spite of the shielding of the outer 6s^{2}6p^6 electrons, therefore they are also good candidates for luminescent materials. However, the luminescent properties of solid-state actinide compounds are relatively less studied compared to other transition metal compounds.[12] Uranium is the most representative element of the actinides and therefore has been investigated most.[12–15] Several groups are endeavoring to obtain functional uranium oxide and oxyfluoride materials and have made much progress; so far, a wide range of uranyl phosphates, nitrates, perchlorates, sulfates, selenates, and iodates have been successfully synthesized and characterized.[12a,12b,13,14] These uranium compounds can be classified as "uranium-inorganic frameworks" (UIFs), in which the frameworks are merely constructed by the inorganic UO(F) polyhedra, and the role of the organic component is just charge-balancing and/or space-filling. In contrast, the term "uranium-organic frameworks" (UOFs) means that the uranium–organic connectivity is interrupted by a bridging organic spacer.[1c] Unlike UIFs, UOFs were hardly known before 2003, and were not rapidly developed until recently by O'Hare, Cahill, You, and Chen.[12c,12d,15] The emergence of UOFs is meaningful because diverse organic components can be incorporated, and therefore the construction and functionalities of this kind of uranium coordination polymer are getting more intriguing.[12c,12d,15]

The heterofunctional pyridinedicarboxlic acids are optimal ligands not only due to their "antenna effect",[16] which can occur through an energy transfer from the excited π orbitals of the pyridine ring to the uranium metal center,[12c,12d,16] but also due to their ability to incorporate the MO(OH) clusters into the metal–organic frameworks.[17] Our previous studies of 3d^{10} and 4d^{10} photoluminescent compounds revealed that the formation of MO(OH) cores can significantly increase the emission lifetime,[11] which is important for luminescent materials. We have now extended our research to 5d^{10} actinides to search for new photolumi-

[a] School of Chemistry and Chemical Engineering & State Key Laboratory of Optoelectronic Materials and Technologies, Sun Yat-Sen University,
Guangzhou 510275, China
Fax: +86-20-8411-2245
E-mail: cestml@zsu.edu.cn
Supporting information for this article is available on the WWW under http://www.eurjic.org or from the author.

nescent materials containing MO(OH) clusters, and report herein two novel layered UOFs constructed from UO(OH) polyhedra and pyridinedicarboxylates, namely $[(UO_2)_3(\mu_3\text{-}O)(\mu_3\text{-}OH)_2(3,4\text{-pydaH})(3,4\text{-pyda})_{0.5}]_n$ (**1**) and $[(UO_2)_3(\mu_3\text{-}O)(\mu_3\text{-}OH)(\mu_2\text{-}OH)(2,4\text{-pyda})(H_2O)_2]_n{\cdot}nH_2O$ (**2**).

Results and Discussion

Synthesis and Characterization

The hydrothermal method has been proved to be very effective for the synthesis of uranium coordination polymers.[12–15] It is well known that changing the hydrothermal conditions, such as the temperature, reaction time, pH value, and molar ratio of the reactants, can significantly influence the final reaction products. In previous explorations of the synthesis of metal-cluster-based coordination polymers containing mixed organic ligands under typical hydrothermal conditions (i.e. 120–180 °C and 2–7 days), we and others have found that pH 8–9 is most suitable for the formation of metal–hydroxy(oxy) clusters,[11,17] although uranium–hydroxy(oxy) species can be formed at a rather lower pH value of 3–4, which was used in the preparation of uranylhydroxy(oxy) clusters **1** and **2**.

Crystal Structures

X-ray structural analysis showed that compound **1** crystallizes in the orthorhombic space group *Pccn*. Each asymmetric unit in **1** contains three crystallographically unique uranyl ions, one μ_3-oxo (O_7), two μ_3-hydroxo groups (O_8, O_9), and one 3,4-pydaH, all of which lie on a general position, and one 3,4-pyda which lies across a twofold axis. Selected bond lengths and angles are listed in Table 1. Bond-valence sum (BVS) calculations with U–O and U–N bond-valence parameters taken from the literature[13a,18] confirm that the uranium centers are unambiguously U^{VI} with values of 6.10, 6.08, and 6.11 in **1**. Owing to the presence of the heavy uranium atoms, hydrogen atoms can hardly be located in the difference map, so we distinguished the μ_3-oxo and μ_3-hydroxo oxygen atoms by comparing the U–O bond lengths and U–O–U angles with corresponding ones of related compounds containing $(UO_2)_4(\mu_3\text{-}OH)_2$[13a–13c] and $(UO_2)_3(\mu_3\text{-}O)$[15c] cores as well as by BVS calculations on the oxygen atoms.[13a,14c,18] Each uranium center is bound to two axial oxides to form a uranyl unit $[UO_2]^{2+}$. The $U\text{–}O_{uranyl}$ bond lengths range between 1.75(1) and 1.79(1) Å, in good agreement with the reported average uranyl bond length of 1.758(4) Å.[13a] Each uranyl unit is coordinated to five equatorial oxides to form a $[UO_7]$ pentagonal bipyramid (Figure 1, a) with U–O(μ_3-oxo), U–O(μ_3-hydroxo), and U–O (carboxylate) bonds lengths of 2.21(1)–2.264(9), 2.39(1)–2.54(1), and 2.38(1)–2.46(1) Å, respectively, which are all in the normal range of U–O distances reported in the literature.[12–15] Interestingly, no pyridyl nitrogen atoms from the pyda and pydaH ligands are coordinated to the uranyl units in **1**, therefore the polymerization of the uranyl cations extends in the [100] direction by edge-sharing the adjacent pentagonal bipyramids to form infinite $[(UO_2)_3(\mu_3\text{-}O)(\mu_3\text{-}OH)_2]_n^{2n+}$ ribbons. The one-dimensional ribbons are connected by 3,4-pyda and 3,4-pydaH bridges into wave-like sheets with a dihedral angle of 77.8° between the U–O ribbons (Figure 1, b). The coordination mode of the 3,4-pyda ligands in **1** is different from those found in other coordination polymers containing 3,4-pyda ligands.[17a,17b]

Each crystallographically independent unit of **1** contains one $[(UO_2)_3(\mu_3\text{-}O)(\mu_3\text{-}OH)_2]^{2+}$, one $(3,4\text{-pydaH})^-$, and one half of $3,4\text{-pyda}^{2-}$. The proton on the pyridyl nitrogen could not be located from the difference map owing to the presence of the heavy uranium ion. However, the distances [N···O = 2.85(2)–3.00(2) Å] between the pyridyl nitrogen and three uranyl oxygen atoms indicate the presence of a trifurcated hydrogen-bonding interaction, which means that the pyridyl nitrogen should be protonated and the net charge of the $(pydaH)^-$ moiety can be assigned as –1 (Figure 1, c). Moreover, C5 can be distinguished from N1 by considering their hydrogen-bonding environment. The C···O distance between C5 and O3A is 3.10(2) Å, with a C–H···O angle of 173.5°, which suggests a typical C–H···O interaction.[19] However, the N2 and C11 atoms of another pyda ligand are not distinguishable because this pyda moiety lies on a twofold axis.

Compound **2** crystallizes in the orthorhombic space group *Pbcn*. Each asymmetric unit in **1** contains three crystallographically unique uranyl ions, one μ_3-oxo(O_1), one μ_2-hydroxo(O_2), one μ_3-hydroxo(O_3), one 2,4-pyda, and two aqua ligands, all of which lie on a general position (Figure 2, a). Selected bond lengths and angles are listed in Table 2. BVS calculations confirm that the uranium centers are U^{VI}, with values of 6.05, 6.05, and 6.03 in **2** for U(1), U(2), and U(3), respectively.[13a,18] There are two kinds of uranium pentagonal bipyramids in **2**, namely a $[UO_7]$ and a $[UO_6N]$ unit, with mean U=O, U–O(μ_3-oxo), U–O(hydroxo), U–O(carboxylate), U–O(aquo), and U–N(pyridyl) bonds lengths of 1.775(7), 2.213(7), 2.397(7), 2.464(8), 2.389(8), and 2.617(9) Å, respectively. All these distances are also within the normal range of U–O or U–N bonds.[12–15] In contrast to **1**, the pyridyl nitrogen atom and one 2-position carboxylate oxygen atom of each 2,4-pyda ligand chelate to a uranium atom, while the other carboxylate end bridges two uranyl units in a μ_2-carboxylato-*O*,*O*′ mode. This coordination mode has recently been found in the 3D coordination polymer $\alpha\text{-}[Cd_2(\mu_3\text{-}OH)_2(2,4\text{-pyda})]$.[17c] The pyridyl ring is efficiently driven by this chelating coordination mode to be coplanar with the uranyl pentagonal equatorial plane. Each hexameric uranyl cluster is surrounded by four 2,4-pyda ligands, which means that further polymerization of uranyl in the plane is inevitably interrupted. As shown in part b of Figure 2, the resulting open framework is a 2D (4,4) square grid by considering the hexameric uranyl clusters as the 4-connected nodes and the 2,4-pyda ligands as the connections between the 4-connected nodes. The lattice water molecules are situated be-

 © 2005 Wiley-VCH Verlag GmbH & Co. KGaA, Weinheim

Table 1. Selected bond lengths [Å] and angles [°] for **1**.[a]

Compound **1**			
U(1)–O(11)	1.75(1)	U(3)–O(14)	1.76(1)
U(1)–O(10)	1.76(1)	U(3)–O(7)	2.21(1)
U(1)–O(7)	2.26(1)	U(3)–O(1)	2.38(1)
U(1)–O(2a)	2.39(1)	U(3)–O(9c)	2.44(1)
U(1)–O(5)	2.39(1)	U(3)–O(4b)	2.45(1)
U(1)–O(8)	2.49(1)	U(3)–O(8)	2.50(1)
U(1)–O(9)	2.50(1)	U(1)–U(2)	3.8498(8)
U(2)–O(13)	1.77(1)	U(1)–U(3)	3.8678(8)
U(2)–O(12)	1.79(1)	U(2)–U(3)	3.8190(9)
U(2)–O(7)	2.21(1)	U(2)–U(3a)	3.9301(8)
U(2)–O(8a)	2.39(1)	N(1)···O(15d)	2.85(2)
U(2)–O(6a)	2.41(1)	N(1)···O(12e)	3.00(2)
U(2)–O(4b)	2.46(1)	N(1)···O(10e)	2.95(2)
U(2)–O(9)	2.54(1)	C(5)···O(3d)	3.10(2)
U(3)–O(15)	1.75(1)		
O(11)–U(1)–O(10)	178.3(6)	O(4b)–U(2)–O(9)	135.9(4)
O(11)–U(1)–O(7)	90.6(5)	O(15)–U(3)–O(14)	177.5(5)
O(10)–U(1)–O(7)	90.9(5)	O(15)–U(3)–O(7)	88.6(5)
O(11)–U(1)–O(2a)	87.9(5)	O(14)–U(3)–O(7)	93.7(5)
O(10)–U(1)–O(2a)	90.5(5)	O(15)–U(3)–O(1)	91.0(5)
O(7)–U(1)–O(2a)	142.5(4)	O(14)–U(3)–O(1)	87.8(5)
O(11)–U(1)–O(5)	91.1(5)	O(7)–U(3)–O(1)	143.5(4)
O(10)–U(1)–O(5)	88.2(5)	O(15)–U(3)–O(9c)	86.3(5)
O(7)–U(1)–O(5)	139.9(4)	O(14)–U(3)–O(9c)	91.3(5)
O(2a)–U(1)–O(5)	77.6(4)	O(7)–U(3)–O(9c)	137.2(4)
O(11)–U(1)–O(8)	93.4(5)	O(1)–U(3)–O(9c)	79.1(4)
O(10)–U(1)–O(8)	87.8(5)	O(15)–U(3)–O(4b)	95.5(5)
O(7)–U(1)–O(8)	68.7(4)	O(14)–U(3)–O(4b)	86.3(5)
O(2a)–U(1)–O(8)	148.7(4)	O(7)–U(3)–O(4b)	68.7(4)
O(5)–U(1)–O(8)	71.2(4)	O(1)–U(3)–O(4b)	75.0(4)
O(11)–U(1)–O(9)	91.3(5)	O(9c)–U(3)–O(4b)	154.1(4)
O(10)–U(1)–O(9)	88.6(5)	O(15)–U(3)–O(8)	94.5(5)
O(7)–U(1)–O(9)	68.8(4)	O(14)–U(3)–O(8)	85.4(4)
O(2a)–U(1)–O(9)	73.8(4)	O(7)–U(3)–O(8)	69.3(4)
O(5)–U(1)–O(9)	151.2(4)	O(1)–U(3)–O(8)	147.0(4)
O(8)–U(1)–O(9)	137.3(3)	O(9c)–U(3)–O(8)	68.9(4)
O(13)–U(2)–O(12)	175.0(5)	O(4b)–U(3)–O(8)	136.4(4)
O(13)–U(2)–O(7)	94.5(5)	U(3b)–O(4)–U(2b)	102.2(4)
O(12)–U(2)–O(7)	89.2(5)	U(2)–O(7)–U(3)	119.3(5)
O(13)–U(2)–O(8a)	85.8(5)	U(2)–O(7)–U(1)	118.8(4)
O(12)–U(2)–O(8a)	89.2(5)	U(3)–O(7)–U(1)	119.7(5)
O(7)–U(2)–O(8a)	137.5(4)	U(2c)–O(8)–U(1)	131.7(5)
O(13)–U(2)–O(6a)	92.7(5)	U(2c)–O(8)–U(3)	107.2(4)
O(12)–U(2)–O(6a)	86.8(5)	U(1)–O(8)–U(3)	101.9(4)
O(7)–U(2)–O(6a)	138.0(4)	U(3a)–O(9)–U(1)	131.7(5)
O(8a)–U(2)–O(6a)	84.2(4)	U(3a)–O(9)–U(2)	104.4(4)
O(13)–U(2)–O(4b)	87.5(5)	U(1)–O(9)–U(2)	99.8(4)
O(12)–U(2)–O(4b)	97.0(5)	U(2)···U(3)···U(2c)	129.36(17)
O(7)–U(2)–O(4b)	68.5(4)	U(1)···U(3)···U(2c)	69.53(16)
O(8a)–U(2)–O(4b)	153.6(4)	U(3)···U(2)···U(3a)	130.45(17)
O(6a)–U(2)–O(4b)	70.6(4)	U(1)···U(2)···U(3a)	70.723(16)
O(13)–U(2)–O(9)	85.9(5)	U(2)···U(1)···U(3)	59.318(16)
O(12)–U(2)–O(9)	92.3(5)	N(1)–H(1A)···O(15d)	125.2
O(7)–U(2)–O(9)	68.7(4)	N(1)–H(1A)···O(12e)	132.7
O(8a)–U(2)–O(9)	69.0(3)	N(1)–H(1A)···O(10e)	122.1
O(6a)–U(2)–O(9)	153.2(4)	C(5)–H(5)···O(3d)	173.5

[a] Symmetry codes: a) $-x + 1$, $y + 1/2$, $-z - 1/2$; b) $-x + 3/2$, $-y + 3/2$, z; c) $-x + 1$, $y - 1/2$, $-z - 1/2$; d) $-x + 3/2$, y, $z + 1/2$; e) $x + 1/2$, $y - 1/2$, $-z$.

tween the wave-like coordination layers and form water···oxo [O···O: 2.89(1)–3.05(1) Å; O–H–O: 145(13)–174(16)°] and water···hydroxo [O···O: 2.68(1) Å; O–H–O: 164.6°] hydrogen-bonding interactions with the upper and lower layers, respectively. These may make some contributions to the bending of the hexameric U–O polyhedra, with an angle of 142.6°, and disturb the further equatorial polymerization in **2**. It should be noted that **2** is the first hexameric species of uranium(VI) compounds, although hexameric uranium(IV) compounds have been found.[13d,13e] As far as we know, the majority of U^{6+} phases prefer to adopt a structure that is based upon infinite sheets of poly-

 © 2005 Wiley-VCH Verlag GmbH & Co. KGaA, Weinheim

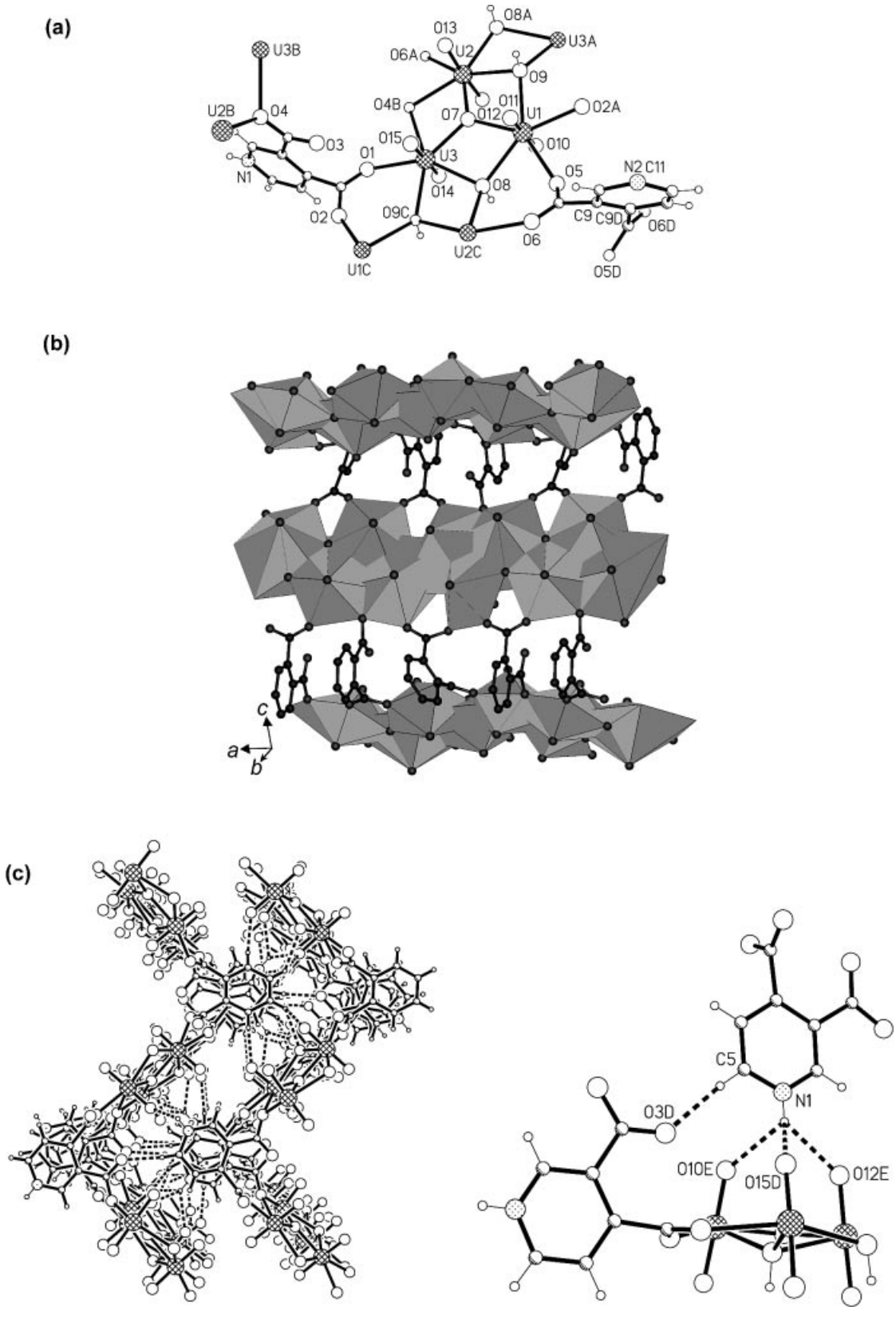

Figure 1. (a) Coordination environment in **1**. (b) A view of the 2D wave-like sheet in **1** with the UO_7 pentagonal bipyramids shown in gray. (c) Left: crystal packing between the wave-like layers in **1**; Right: an illustration of the trifurcated N–H···O and C–H···O hydrogen bonds between the adjacent layers in **1**.

 © 2005 Wiley-VCH Verlag GmbH & Co. KGaA, Weinheim

hedra or a 1D chain (either trimeric, dimeric, or mononuclear).[13–15]

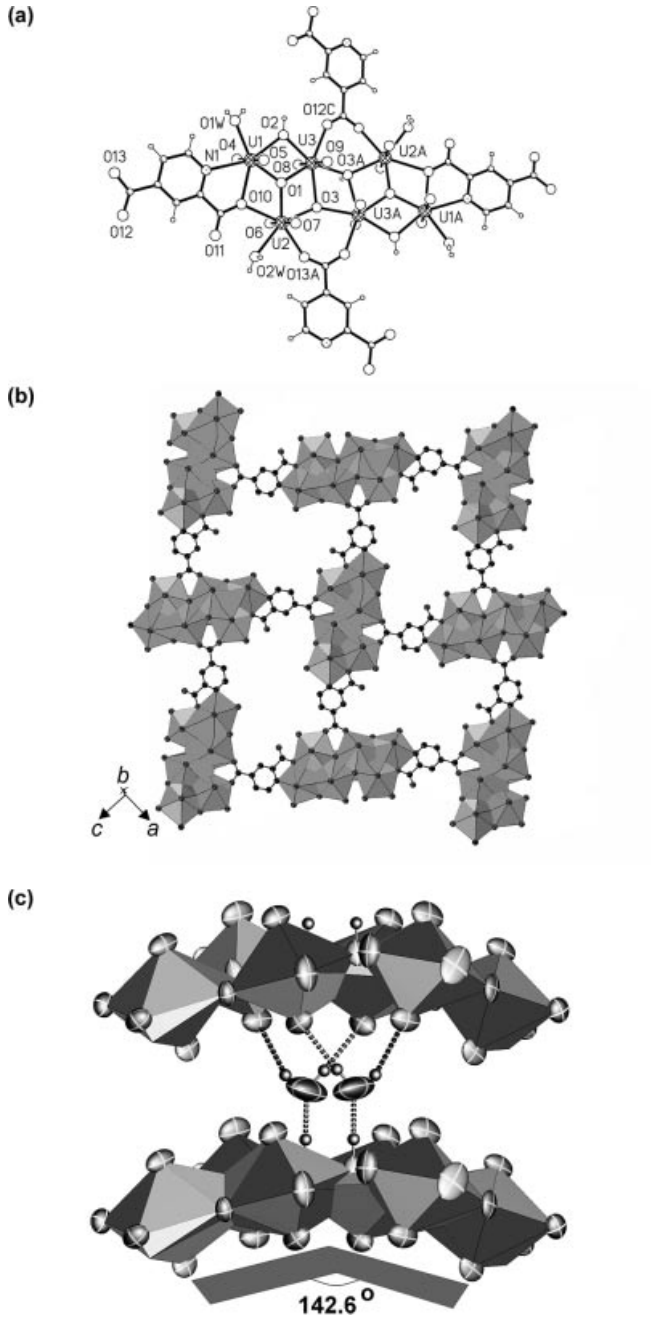

Figure 2. (a) Coordination environment in **2**. (b) A view of the 2D open-framework of **2**. (c) An illustration of the hydrogen bonding between the water molecules and the adjacent layers in **2** (atoms are shown as 50% probability displacement ellipsoids).

It is interesting to compare the dimensions and densities of compounds **1** and **2** with other recently reported UOFs and UIFs. As listed in Table 3, the representative UOFs are mainly based on uranium carboxylate coordination polymers, including the zero-dimensional metallamacrocycles constructed with (2*R*,3*R*,4*S*,5*S*)-tetrahydrofuran-tetracarboxylic acid,[15d] the one-dimensional chains constructed with glutaric acid,[15a] isophthalic acid,[15a] or adipic acid,[15b] the two-dimensional layers constructed with 1-oxo-4-cyanopyridine,[12c] ethyl (*S*)-lactic acid,[12c] or 3,5-pyrazoledicarboxylic acid,[12d] and the three-dimensional networks constructed with succinic acid,[15a] adipic acid,[15b] or quinolinic acid.[15c,15e] If we sort the order as the density, **1** and **2** are the densest UOFs and are even denser than some UIFs. These results may be due to the following two facts. Firstly, these two compounds adopt a close-packing style *ABAB*... in order to fill the hollow space as much as possible, and secondly, the inorganic uranyl ions are highly polymerized with the O^{2-} or OH^{-} ions, which can enhance the density of the entire compounds. Although both zero-dimensional (0D) UOFs and UIFs have the lowest density, it is hard to determine the relationship between density and dimensions because there is no appropriate example (such as supramolecular isomers) in the reported UOFs and UIFs.

Luminescent Properties

The fluorescence spectra (Figure 3) of **1** and **2** were measured for crushed single-crystalline powder samples, which are were pure phases, as confirmed by an XRD study (Figure S1 in the Supporting Information). Interestingly, the well-known characteristic emission fine-structure of UO_2^{2+} is observed in **1,** featuring a main peak (λ = 521 nm) and three shoulder peaks (λ = 503, 542, and 568 nm), while the emission fine-structure of **2** is inconspicuous and only a broad peak is observed (λ = 534 nm). In contrast, the highest emission peak of **2** is red-shifted by 13 nm compared to **1**, and the peaks (λ = 362, 478 nm) in the excitation spectrum of **2** are all red-shifted by 40 nm relative to **1** (λ = 322, 438 nm). It should be noted that the fluorescence spectra of free 2,4-pydaH$_2$ and 3,4-pydaH$_2$ display very weak photoluminescent properties (Supporting Information, Figure S2). Despite the weak intensity of the free ligands, the wavelengths of the excitation peaks (λ = 364 nm in 3,4-pydaH$_2$ and 343 nm in 2,4-pydaH$_2$) resemble the peaks of **1** and **2**, which indicates that the aromatic ligands may contribute to the related absorption bands in the excitation spectra of **1** and **2**, therefore ligand-to-metal charge transfer (LMCT) may occur between the 5d orbital of U^{6+} and the chromophoric pyridine-containing ligands,[20] and the component of LMCT in the emission peak may contribute to the single peak nature of **2**,[20] in which the pyridine nitrogen atom coordinates directly to the U^{6+} center. It is noteworthy that the exited-state lifetime (ca. 145 μs) of **1** is about six times that (ca. 24.4 μs) of **2** (see Figure S3; data were fitted with a single exponential decay function). This result is consistent with the long lifetime nature of the actinide ions.[12] Several reasons may account for this difference. Firstly, the enhancement of the lifetime in **1** may be caused by the effect of infinite UO(OH) ribbons, which is consistent with our previous studies of 3d^{10} and 4d^{10} compounds[11] as well as an aqueous fluorescence study of uranyl hydrolysis.[21] Secondly, the chromophoric 2,4-pyda li-

 © 2005 Wiley-VCH Verlag GmbH & Co. KGaA, Weinheim

Table 2. Selected bond lengths [Å] and angles [°] for **2**.[a]

Compound **2**			
U(1)–O(5)	1.766(8)	U(3)–O(1)	2.234(8)
U(1)–O(4)	1.779(7)	U(3)–O(3b)	2.390(7)
U(1)–O(1)	2.209(7)	U(3)–O(2)	2.403(7)
U(1)–O(1w)	2.355(8)	U(3)–O(12c)	2.440(9)
U(1)–O(2)	2.390(8)	U(3)–O(3)	2.510(7)
U(1)–O(10)	2.447(8)	U(1)···U(3)	3.7875(5)
U(1)–N(1)	2.617(9)	U(1)···U(2)	3.8865(6)
U(2)–O(6)	1.758(8)	U(2)···U(3)	3.8211(6)
U(2)–O(7)	1.795(7)	O(3)···O(3w)	2.68(1)
U(2)–O(1)	2.197(7)	O(3w)···O(7d)	3.05(1)
U(2)–O(13a)	2.357(7)	O(3w)···O(9a)	2.89(1)
U(2)–O(3)	2.406(7)	O(2)···O(5e)	3.36(1)
U(2)–O(2w)	2.422(9)	O(2w)···O(7f)	2.83(1)
U(2)–O(10)	2.612(7)	O(1w)···O(2g)	2.64(1)
U(3)–O(9)	1.772(7)	O(1w)···O(8e)	2.74(1)
U(3)–O(8)	1.778(7)		
O(5)–U(1)–O(4)	176.2(4)	O(7)–U(2)–O(10)	89.5(3)
O(5)–U(1)–O(1)	91.9(4)	O(1)–U(2)–O(10)	66.4(3)
O(4)–U(1)–O(1)	91.9(4)	O(13a)–U(2)–O(10)	147.5(3)
O(5)–U(1)–O(1w)	84.1(3)	O(3)–U(2)–O(10)	136.9(2)
O(4)–U(1)–O(1w)	92.7(3)	O(2w)–U(2)–O(10)	72.5(3)
O(1)–U(1)–O(1w)	149.5(3)	O(9)–U(3)–O(8)	178.1(4)
O(5)–U(1)–O(2)	90.8(3)	O(9)–U(3)–O(1)	90.2(4)
O(4)–U(1)–O(2)	90.7(3)	O(8)–U(3)–O(1)	91.6(3)
O(1)–U(1)–O(2)	69.5(3)	O(9)–U(3)–O(3b)	89.5(3)
O(1w)–U(1)–O(2)	80.3(3)	O(8)–U(3)–O(3b)	88.7(3)
O(5)–U(1)–O(10)	89.3(3)	O(1)–U(3)–O(3b)	134.9(2)
O(4)–U(1)–O(10)	91.8(3)	O(9)–U(3)–O(2)	86.1(3)
O(1)–U(1)–O(10)	69.4(3)	O(8)–U(3)–O(2)	95.2(3)
O(1w)–U(1)–O(10)	140.4(3)	O(1)–U(3)–O(2)	68.9(3)
O(2)–U(1)–O(10)	138.9(2)	O(3b)–U(3)–O(2)	155.9(2)
O(5)–U(1)–N(1)	90.5(3)	O(9)–U(3)–O(12c)	89.8(3)
O(4)–U(1)–N(1)	86.7(3)	O(8)–U(3)–O(12c)	89.1(3)
O(1)–U(1)–N(1)	133.8(3)	O(1)–U(3)–O(12c)	144.3(3)
O(1w)–U(1)–N(1)	76.6(3)	O(3b)–U(3)–O(12c)	80.8(3)
O(2)–U(1)–N(1)	156.6(3)	O(2)–U(3)–O(12c)	75.4(3)
O(10)–U(1)–N(1)	64.5(3)	O(9)–U(3)–O(3)	93.0(3)
O(6)–U(2)–O(7)	176.7(4)	O(8)–U(3)–O(3)	87.2(3)
O(6)–U(2)–O(1)	92.1(4)	O(1)–U(3)–O(3)	68.1(2)
O(7)–U(2)–O(1)	90.5(4)	O(3b)–U(3)–O(3)	66.9(3)
O(6)–U(2)–O(13a)	89.2(4)	O(2)–U(3)–O(3)	137.0(3)
O(7)–U(2)–O(13a)	87.5(4)	O(12c)–U(3)–O(3)	147.6(3)
O(1)–U(2)–O(13a)	145.9(3)	U(3)···U(1)···U(2)	59.71(1)
O(6)–U(2)–O(3)	84.3(3)	U(3)···U(2)···U(1)	58.86(1)
O(7)–U(2)–O(3)	94.7(3)	U(1)···U(3)···U(2)	61.43(1)
O(1)–U(2)–O(3)	70.6(3)	O(3)–H(3a)···O(3w)	164.6
O(13a)–U(2)–O(3)	75.6(3)	O(3w)–H(3wa)···O(7d)	145(13)
O(6)–U(2)–O(2w)	89.0(4)	O(3w)–H(3wb)···O(9a)	174(16)
O(7)–U(2)–O(2w)	90.3(3)	O(2)–H(2a)···O(5e)	148.6
O(1)–U(2)–O(2w)	138.9(3)	O(2w)–H(2wa)···O(7f)	163(11)
O(13a)–U(2)–O(2w)	75.2(3)	O(1w)–H(1wa)···O(2g)	152(10)
O(3)–U(2)–O(2w)	150.1(3)	O(1w)–H(1wb)···O(8e)	163(10)
O(6)–U(2)–O(10)	93.4(4)		

[a] Symmetry codes: a) $-x + 3/2, -y + 3/2, z + 1/2$; b) $-x + 1, y, -z + 1/2$; c) $x - 1/2, -y + 3/2, -z$; d) $x, 1 + y, z$; e) $-x, 1 + y, -z + 0.5$; f) $-x + 1.5, y + 0.5, z$; g) $-x, y + 2, -z + 0.5$.

gand, which is a strong π-donor ligand that coordinates directly to the uranyl in the equatorial plane, would correlate well with the low luminescence quantum yield.[12,20] Thirdly, the presence of the protonated pyridyl ring could enhance energy transfer from pyridinium to uranyl moieties in **1**.[12] Finally, the existence of the lattice water molecules could partially quench the excited state in **2**.[12,20]

Conclusions

Two new layered uranium–organic photoluminescent coordination polymers of 3,4- and 2,4-pyridinedicarboxylates, which contain infinite and finite UO(OH) polyhedra, respectively, have been hydrothermally synthesized and crystallographically characterized. This work reveals that

 © 2005 Wiley-VCH Verlag GmbH & Co. KGaA, Weinheim

Table 3. A comparison of the densities and dimensions of representative UIFs and UOFs.

	Compounds	Dimensions	D_c [g cm^{-3}]	Ref.
UOFs	$(C_7H_{16}N)_6[(UO_2)(C_8H_4O_9)]_3 \cdot 9H_2O$	0D	1.346	[15d]
	$(C_6H_{16}N)_8[(UO_2)(C_8H_4O_9)]_4 \cdot 2(CH_3OH) \cdot 2H_2O$	0D	1.633	[15d]
	$[UO_2F(C_5H_6O_4)] \cdot 2H_2O$	1D	2.324	[15a]
	$[(UO_2)_{1.5}(C_8H_4O_4)_2]_2[CH_3NCOH_2] \cdot H_2O$	1D	2.400	[15a]
	$[UO_2(C_4H_4O_4)] \cdot H_2O$	3D	3.442	[15a]
	$UO_2(C_6H_4NO_3)_2$	2D	2.551	[12c]
	$UO_2(C_3H_5O_3)_2$	2D	2.898	[12c]
	$UO_2(C_6H_8O_4)(H_2O)_2$	1D	2.729	[15b]
	$UO_2(C_6H_8O_4)$	3D	3.106	[15b]
	$(ZnO_2)_2(UO_2)_3(C_6H_4NO_2)_4(CH_3CO_2)_2$	3D	2.918	[15c]
	$UO_2Cu(C_5H_2N_2O_4)_2(H_2O)_2$	2D	2.954	[12d]
	$UO_2(C_5H_2N_2O_4)_2(H_2O)$	2D	3.548	[12d]
	$[Ni_2(H_2O)_2(C_7H_3NO_4)_2(C_{10}H_8N_2)U_5O_{14}(H_2O)_2(C_2H_3O_2)_2] \cdot 2H_2O$	3D	2.723	[15e]
	$[(UO_2)_3(O)(OH)_2(C_7H_4NO_4)(C_7H_3NO_4)_{0.5}]$	2D	3.968	this work
	$[(UO_2)_3(O)(OH)_2(C_7H_3NO_4)(H_2O)_2] \cdot H_2O$	2D	4.071	this work
UIFs	$(C_4H_{12}N_2)UO_2F_4 \cdot 3H_2O$[a]	0D	2.622	[14j]
	$(C_4H_{12}N_2)UO_2F_4 \cdot 3H_2O$[b]	0D	2.643	[14j]
	$(C_4H_{12}N_2)_2U_2F_{12} \cdot H_2O$	1D	2.922	[14j]
	$(C_4H_{12}N_2)_2(U_2O_4F_5)_4 \cdot 11H_2O$	2D	3.792	[14j]
	$(C_4H_{12}N_2)U_2O_4F_6$	3D	3.977	[14j]
	$[(CH_3)_4N][(C_5H_5NH)_{0.8}[(CH_3)_3NH]_{0.2}]U_2Si_9O_{23}F_4$	3D	2.759	[14a]
	$(C_6H_{14}N_2)[UO_2(H_2O)(SO_4)]$	2D	2.78	[14d]
	$(C_5H_{14}N_2)[UO_2(H_2O)(SO_4)]$	1D	2.80	[14d]
	$(C_4H_{12}N_2)[UO_2(H_2O)(SO_4)]$	1D	2.95	[14d]
	$(C_5H_6N)UO_2F_3$	1D	3.220	[12a]
	$(C_3H_5N_2)UO_2F_3$	1D	3.481	[12a]
	$(C_5H_{14}N_2)U_2O_4F_6$	1D	3.624	[12a]
	$(C_3H_5N_2)U_2O_4F_5 \cdot 1.75H_2O$	1D	3.834	[14k]
	$(C_5H_6N)U_2O_4F_5$	2D	4.020	[14k]
	$(C_6H_{14}N_2)_2[(UO_2)_6(H_2O)_2F_2(PO_4)_2(HPO_4)_4] \cdot 4H_2O$	3D	3.557	[14h]
	$[(UO_2)_3(PO_4)O(OH)(H_2O)_2] \cdot H_2O$	3D	5.092	[14b]
	$UO_2(IO_3)_2(H_2O)$	2D	5.300	[12b]
	$UO_2(IO_3)_2$	1D	5.786	[12b]
	$Cs_3[(UO_2)_3O_2(OH)_3]_2Cl(H_2O)_3$	3D	5.590	[14c]
	$(NH_4)_3(H_2O)_2\{[(UO_2)_{10}O_{10}(OH)][(UO_4)(H_2O)_2]\}$	3D	6.252	[14c]
	$Cs[(UO_2)_3(HIO_6)(OH)(O)(H_2O)] \cdot 1.5H_2O$	3D	5.711	[14g]

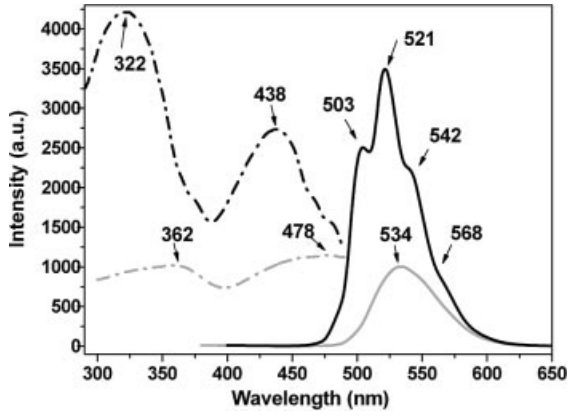

Figure 3. The emission spectra (solid line) and excitation spectra (dash-dot line) of **1** (black) and **2** (gray).

the multitopic ligand has an important effect on the structures of uranium–organic coordination polymers and the lifetimes evidently increase with the polymerization of the UO(OH) polyhedra.

Experimental Section

General Remarks: The reagents and solvents employed were commercially available and used as received without further purification. The C, H, and N microanalyses were carried out with an Elementar Vario-EL CHNS elemental analyzer. The FT-IR spectra were recorded from KBr pellets in the range 4000–400 cm^{-1} on a Bio-Rad FTS-7 spectrometer. X-ray powder diffraction (XRD) intensities for **1** and **2** were measured at 293 K on a Rigaku D/max-IIIA diffractometer (Cu-K_α, λ = 1.54056 Å). The crushed, single-crystalline powder samples were prepared by crushing the crystals and scanned from 4–65° with a step of 0.1° s^{-1}. Calculated patterns for **1** and **2** were generated with PowderCell 2.3. The emission/excitation spectra were recorded on an F-4500 fluorescence spectrophotometer and the lifetimes were measured on an Edinburgh FLS-920 spectrophotometer equipped with a continuous Xe-900 Xenon lamp or a μF900 microsecond flash lamp. Crushed single-crystalline powder samples of **1** and **2** and powder samples of the free ligands 2,4-pydaH$_2$ and 3,4-pydaH$_2$ were used for the photoluminescence measurements.

Synthesis: Complexes **1** and **2** were synthesized by heating a mixture of $(UO_2)(CH_3COO)_2 \cdot 2H_2O$ (0.203 g, 0.5 mmol), 3,4-pydaH$_2$ [or 2,4-pydaH$_2$ (0.083 g, 0.5 mmol)], and deionized water (9 mmol) in a molar ratio of 1:1:1000 in a 23-mL, Teflon-lined autoclave at

 © 2005 Wiley-VCH Verlag GmbH & Co. KGaA, Weinheim

Table 4. Crystal and structure refinement data for compounds **1** and **2**.

Compound	**1**	**2**
Empirical formula	$C_{10.5}H_8N_{1.5}O_{15}U_3$	$C_7H_{11}NO_{16}U_3$
Formula mass	1109.26	1079.26
Temperature [K]	293(2)	293(2)
Wavelength [Å]	0.71073	0.71073
Crystal system	orthorhombic	orthorhombic
Space group	*Pccn* (no. 56)	*Pbcn* (no. 60)
a [Å]	18.168(2)	22.788(2)
b [Å]	12.635(1)	7.1468(5)
c [Å]	16.149(1)	21.627(1)
V [Å^3]	3707.0(5)	3522.1(4)
Z	8	8
$D_{calcd.}$ [mg m^{-3}]	3.968	4.071
Absorption coefficient [mm^{-1}]	22.229	27.603
F(000)	3804	3712
Crystal size [mm]	0.10 × 0.08 × 0.02	0.08 × 0.08 × 0.02
θ range for data collection [°]	1.96 to 27.50	1.79 to 27.50
Limiting indices	$-21 \le h \le 23$, $-16 \le k \le 15$, $-17 \le l \le 20$	$-29 \le h \le 17$, $-9 \le k \le 9$, $-27 \le l \le 28$
Reflections collected/unique	20920/4238 [R_{int} = 0.0850]	19029/4002 [R_{int} = 0.0513]
Completeness	99.2% (θ_{max} = 27.50°)	98.9% (θ_{max} = 27.50°)
Absorption correction	Multi-scan (*SADABS*; Bruker, 2002)	Multi-scan (*SADABS*; Bruker, 2002)
Max. and min. transmission	0.6220 and 0.1790	0.6082 and 0.2162
Refinement method	Full-matrix least-squares on F^2	Full-matrix least-squares on F^2
Data/restraints/parameters	4238/342/271	4002/9/262
Goodness-of-fit on F^2	1.048	1.070
Final *R* indices [$I > 2\sigma(I)$]	R_1 = 0.0618, wR_2 = 0.1331[a]	R_1 = 0.0411, wR_2 = 0.1002[a]
R indices (all data)	R_1 = 0.0833, wR_2 = 0.1436[a]	R_1 = 0.0507, wR_2 = 0.1050[a]
Extinction coefficient	none	none
Largest diff. peak and hole [e Å^{-3}]	2.756 and –2.523	4.887 and –1.495

[a] $R_1 = \Sigma||F_o| - |F_c||/\Sigma|F_o|$, $wR_2 = [\Sigma w(F_o^2 - F_c^2)^2/\Sigma w(F_o^2)^2]^{1/2}$.

180 °C for 3 d. After slowly cooling down to room temperature within 12 h, yellow needle-like crystals of **1** (yield: 0.166 g, ca. 90% based on U) or yellow plate-like crystals of **2** (yield: 0.160 g, ca. 87% based on U) were filtered, washed with deionized water, and dried in the air.

1: $C_{10.5}H_8N_{1.5}O_{15}U_3$: calcd. C 11.37, H 0.73, N 1.89; found C 11.41, H 0.71, N 1.90. IR: $\tilde{\nu}$ = 911 cm^{-1} U=O; 1374, 1427, 1551, 1582 C=$C_{(py)}$ or C=$N_{(py)}$; 1643, 1680 C=O; 2881, 3000, 3058, 3077 C–H or N–H; 3438, 3547 cm^{-1} O–H.

2: $C_7H_{11}NO_{16}U_3$: calcd. C 7.79, H 1.03, N 1.30; found C 7.81, H 1.01, N 1.29. IR: $\tilde{\nu}$ = 930 cm^{-1} U=O; 1322, 1384, 1479, 1542 C=$C_{(py)}$ or C=$N_{(py)}$; 1596, 1635 C=O; 2850, 2916, 3067 C–H; 3424, 3535, 3623 cm^{-1} O–$H_{(H_2O)}$ (for details, see Figure S4 in the Supporting Information).

X-ray Crystallographic Study: Diffraction intensities of **1** and **2** were collected on a Bruker Apex CCD area-detector diffractometer (Mo-K_α, λ = 0.71073 Å). Absorption corrections were applied by using the multiscan program SADABS.[22] The structures were solved by direct methods and refined with a full-matrix least-squares technique with the SHELXTL program package.[23] Anisotropic thermal parameters were applied to all non-hydrogen atoms. The organic hydrogen atoms were generated geometrically (C–H = 0.96 Å), as were the hydroxy oxygen atoms (O–H = 0.85 Å); the aqua hydrogen atoms were located from difference maps. For **1**, the proton on the pyridyl nitrogen of (3,4-pydaH)$^-$ was added in a geometrically idealized position. The disordered atoms of N2 and C11 were treated as each having an occupation of 50%. The crystallographic data for **1** and **2** are listed in Table 4.

CCDC270938 (for **1**) and -270939 (for **2**) contain the supplementary crystallographic data for this paper. These data can be obtained free of charge from The Cambridge Crystallographic Data Centre via www.ccdc.cam.ac.uk/data_request/cif.

Supporting Information Available: IR spectra, powder X-ray diffraction patterns, fluorescence spectra and lifetime spectra (with fitting results).

Acknowledgments

This work was supported by the NSFC (20131020 and 20471069), the FANEDD of China (200122), the Scientific and Technological Project of Guangdong Province (04205405), and Sun Yat-Sen University. Special thanks are offered to one of the reviewers who pointed out that compound **2** is the first hexameric species in U(VI) compounds. Z.-Y. Zheng thanks Prof. R. D. Rogers and Prof. Ling-Kang Liu for their help in collecting the references.

[1] a) M. Eddaoudi, D. B. Moler, H. Li, B. Chen, T. M. Reineke, M. O'Keeffe, O. M. Yaghi, *Acc. Chem. Res.* **2001**, *34*, 319–330; b) P. J. Hagrman, D. Hagrman, J. Zubieta, *Angew. Chem. Int. Ed.* **1999**, *38*, 2638–2684; c) C. Janiak, *Dalton Trans.* **2003**, 2781–2804.

[2] B. Moulton, M. J. Zaworotko, *Chem. Rev.* **2001**, *101*, 1629–1658.

[3] O. R. Evans, W. Lin, *Acc. Chem. Res.* **2002**, *35*, 511–522.

[4] S. Kitagawa, R. Kitaura, S.-i. Noro, *Angew. Chem. Int. Ed.* **2004**, *43*, 2334–2375.

[5] C. N. R. Rao, S. Natarajan, R. Vaidhyanathan, *Angew. Chem. Int. Ed.* **2004**, *43*, 1466–1496.

[6] a) A. K. Cheetham, G. Férey, T. Loiseau, *Angew. Chem. Int. Ed.* **1999**, *38*, 3268–3292; b) G. Ferey, *Chem. Mater.* **2001**, *13*, 3084–3098.

[7] a) L. Pan, H. Liu, X. Lei, X. Huang, D. H. Olson, N. J. Turro, J. Li, *Angew. Chem. Int. Ed.* **2003**, *42*, 542–546; b) L. Pan, K. M. Adams, H. E. Hernandez, X. Wang, C. Zheng, Y. Hattori, K. Kaneko, *J. Am. Chem. Soc.* **2003**, *125*, 3062–3067.

 © 2005 Wiley-VCH Verlag GmbH & Co. KGaA, Weinheim

[8] a) L. Hiltunen, M. Leskelä, M. Mäkelä, L. Niinistö, *Acta Chem. Scand., Sect. A* **1987**, *41*, 548–555; b) H. Kunkely, A. Vogler, *J. Chem. Soc., Chem. Commun.* **1990**, 1204–1205; c) R. Bertoncello, M. Betinelli, M. Casarin, A. Gulino, E. Tondello, A. Vittadini, *Inorg. Chem.* **1992**, *31*, 1558–1565; d) M. Weidenbruch, M. Herrndorf, A. Schafer, S. Pohl, W. Saak, *J. Organomet. Chem.* **1989**, *361*, 139–145; e) T. Konno, Y. Kageyama, K. I. Okamoto, *Bull. Chem. Soc. Jpn.* **1994**, *67*, 1957–1960.

[9] a) J.-C. Dai, X.-T. Wu, Z.-Y. Fu, C.-P. Cui, S.-M. Wu, W.-X. Du, L.-M. Wu, H.-H. Zhang, R.-Q. Sun, *Inorg. Chem.* **2002**, *41*, 1391–1396; b) W. Chen, J.-Y. Wang, C. Chen, Q. Yue, H.-M. Yuan, J.-S. Chen, S.-N. Wang, *Inorg. Chem.* **2003**, *42*, 944–946; c) J.-H. Luo, M.-C. Hong, R.-H. Wang, R. Cao, L. Han, Z.-Z. Lin, *Eur. J. Inorg. Chem.* **2003**, 2705–2710; d) Z.-F. Chen, R.-G. Xiong, J. Zhang, J.-L. Zuo, X.-Z. You, C.-M. Che, H.-K. Fun, *J. Chem. Soc., Dalton Trans.* **2000**, 4010–4012; e) S.-T. Wang, Y. Hou, E.-B. Wang, Y.-G. Li, L. Xu, J. Peng, S.-X. Liu, C.-W. Hu, *New J. Chem.* **2003**, 1144–1147.

[10] a) C.-F. Lee, K.-F. Chin, S.-M. Peng, C.-M. Che, *J. Chem. Soc., Dalton Trans.* **1993**, 467–470; b) K.-Y. Ho, W.-Y. Yu, K.-K. Cheung, C.-M. Che, *Chem. Commun.* **1998**, 2491–2492; c) R.-G. Xiong, J.-L. Zuo, X.-Z. You, B. F. Abrahams, Z.-P. Bai, C.-M. Che, H.-K. Fun, *Chem. Commun.* **2000**, 2061–2062.

[11] a) J. Tao, M.-L. Tong, J.-X. Shi, X.-M. Chen, S. W. Ng, *Chem. Commun.* **2000**, 2043–2044; b) J. Tao, J.-X. Shi, M.-L. Tong, X.-X. Zhang, X.-M. Chen, *Inorg. Chem.* **2001**, *40*, 6328–6330; c) M.-L. Tong, X.-M. Chen, B.-H. Ye, L.-N. Ji, *Angew. Chem. Int. Ed.* **1999**, *38*, 2237–2240; d) L.-Y. Zhang, G.-F. Liu, S.-L. Zheng, B.-H. Ye, X.-M. Zhang, X.-M. Chen, *Eur. J. Inorg. Chem.* **2003**, 2965–2971; e) S.-L. Zheng, M.-L. Tong, S.-D. Tan, Y. Wang, J.-X. Shi, Y.-X. Tong, H.-K. Lee, X.-M. Chen, *Organometallics* **2001**, *20*, 5319–5325; f) S.-L. Zheng, J.-P. Zhang, X.-M. Chen, Z.-L. Huang, Z.-Y. Lin, W.-T. Wong, *Chem. Eur. J.* **2003**, *9*, 3888–3896; g) J.-H. Yang, W. Li, S. L. Zheng, Z.-L. Huang, X.-M. Chen, *Aust. J. Chem.* **2003**, *56*, 1175–1178; h) S.-L. Zheng, J.-H. Yang, X.-L. Yu, X.-M. Chen, W.-T. Wong, *Inorg. Chem.* **2004**, *43*, 830–838.

[12] a) P. M. Almond, C. E. Talley, A. C. Bean, S. M. Peper, T. E. Albrecht-Schmitt, *J. Solid State Chem.* **2000**, *154*, 635–641; b) A. C. Bean, S. M. Peper, T. E. Albercht-Schmitt, *Chem. Mater.* **2001**, *13*, 1266–1272; c) Y.-R. Xie, H. Zhao, X.-S. Wang, Z.-R. Qu, R.-G. Xiong, X. Xue, Z. Xue, X.-Z. You, *Eur. J. Inorg. Chem.* **2003**, 3712–3715; d) M. Frisch, C. L. Cahill, *Dalton Trans.* **2005**, 1518–1523.

[13] a) P. C. Burns, R. C. Ewing, F. C. Hawthorne, *Can. Mineral.* **1997**, *35*, 1551–1570; b) P. C. Burns, M. L. Miller, R. C. Ewing, *Can. Mineral.* **1996**, *34*, 845–880; c) P. C. Burns, *Rev. Mineral.* **1999**, *38*, 23–90; d) L. M. Mokry, S. N. Dean, C. J. Carrano, *Angew. Chem. Int. Ed. Engl.* **1996**, *35*, 1497–1499; e) G. Lundgren, *Arkiv. Kemi.* **1952**, *5*, 349–352.

[14] a) X. Wang, J. Huang, A. Jacobson, *J. Am. Chem. Soc.* **2002**, *124*, 15190–15191; b) P. C. Burns, C. M. Alexopoulos, P. J. Hotchkiss, A. J. Locock, *Inorg. Chem.* **2004**, *43*, 1816–1818; c) Y. Li, C. L. Cahill, P. C. Burns, *Chem. Mater.* **2001**, *13*, 4026–4031; d) A. J. Norquist, P. M. Thomas, M. B. Doran, D. O'Hare, *Chem. Mater.* **2002**, *14*, 5179–5184; e) P. M. Almond, M. L. Mckee, T. E. Albrecht-Schmitt, *Angew. Chem. Int. Ed.* **2002**, *41*, 3426–3427; f) P. M. Almond, T. E. Albrecht-Schmitt, *Inorg. Chem.* **2002**, *41*, 1177–1183; g) T. A. Sullens, R. A. Jensen, T. Y. Shvareva, T. E. Albrecht-Schmitt, *J. Am. Chem. Soc.* **2004**, *126*, 2676–2677; h) M. B. Doran, C. L. Stuart, A. J. Norquist, D. O'Hare, *Chem. Mater.* **2004**, *16*, 565–566; i) R. J. Francis, P. S. Halasyamani, D. O'Hare, *J. Am. Chem. Soc.* **1999**, *121*, 1609–1610; j) S. M. Walker, P. S. Halasyamani, S. Allen, D. O'Hare, *J. Am. Chem. Soc.* **1999**, *121*, 10513–10521; k) C. E. Talley, A. C. Bean, T. E. Albrecht-Schmitt, *Inorg. Chem.* **2000**, *39*, 5174–5175; l) A. J. Norquist, M. B. Doran, P. M. Thomas, D. O'Hare, *Dalton Trans.* **2003**, 1168–1175; m) M. J. Sarsfield, M. Helliwell, *J. Am. Chem. Soc.* **2004**, *126*, 1036–1037.

[15] a) J.-Y. Kim, A. J. Norquist, D. O'Hare, *Dalton Trans.* **2003**, 2813–2814; b) L. A. Borkowski, C. L. Cahill, *Inorg. Chem.* **2003**, *42*, 7041–7045; c) W. Chen, H.-M. Yuan, J.-Y. Wang, Z.-Y. Liu, J.-J. Xu, M. Yang, J.-S. Chen, *J. Am. Chem. Soc.* **2003**, *125*, 9266–9267; d) C. V. Thuéry, J. Jaud, M. Ephritikhine, B. Masci, *J. Am. Chem. Soc.* **2004**, *126*, 6838–6839; e) Z.-T. Yu, Z.-L. Liao, Y.-S. Jiang, G.-H. Li, G.-D. Li, J.-S. Chen, *Chem. Commun.* **2004**, 1814–1815; f) J. Leciejewicz, N. W. Alcock, T. J. Kemp, *Struct. Bond. (Berlin)* **1995**, *82*, 43–84.

[16] A. M. Klonkowski, S. Lis, M. Pietraszkiewicz, Z. Hnatejko, K. Czarnobaj, M. Elbanowski, *Chem. Mater.* **2003**, *15*, 656–663.

[17] a) M.-L. Tong, L.-J. Li, K. Mochizuki, H.-C. Chang, X.-M. Chen, Y. Li, S. Kitagawa, *Chem. Commun.* **2003**, 428–429; b) M.-L. Tong, J. Wang, S. Hu, *J. Solid State Chem.* **2005**, *178*, 1518–1525; c) M.-L. Tong, S. Hu, J. Wang, S. Kitagawa, S. W. Ng, *Cryst. Growth Des.* **2005**, *5*, 837–839; d) X. Wang, C. Qin, E. Wang, Y. Li, N. Hao, C. Hu, L. Xu, *Inorg. Chem.* **2004**, *43*, 1850–1856.

[18] a) B. N. E. Brese, M. O'Keeffe, *Acta Crystallogr., Sect. B* **1991**, *47*, 192–197; b) B. I. D. Brown, D. Altermatt, *Acta Crystallogr., Sect. B* **1985**, *41*, 244–247.

[19] a) G. R. Desiraju, *Acc. Chem. Res.* **1996**, *29*, 441–449; b) T. Steiner, *Angew. Chem. Int. Ed.* **2002**, *41*, 48–76.

[20] a) B. Valeur, *Molecular Fluorescence: Principles and Applications*, Wiley-VCH, Weinheim, **2002**; b) A. W. Adamson, P. D. Fleischauer, *Concepts of Inorganic Photochemistry*, John Wiley & Sons, New York, **1975**; c) *Photochemistry and Photophysics of Coordination Compounds* (Eds.: H. Yersin, A.Vogler), Springer-Verlag, Berlin, **1987**.

[21] P. Zanonato, P. D. Bernardo, A. Bismondo, G. Liu, X. Chen, L. Rao, *J. Am. Chem. Soc.* **2004**, *126*, 5515–5522.

[22] G. M. Sheldrick, *SADABS 2.05*, University of Göttingen.

[23] *SHELXTL 6.10*, Bruker Analytical Instrumentation, Madison, Wisconsin, USA, **2000**.

Received: May 4, 2005
Published Online: September 5, 2005

 © 2005 Wiley-VCH Verlag GmbH & Co. KGaA, Weinheim

Vibrational Spectra of Eight-Coordinate Niobium and Tantalum Complexes with Peroxo Ligands: A Theoretical Simulation

Daisy Bayot,[a] Michel Devillers,[a] and Daniel Peeters*[b]

Keywords: Density functional calculations / IR spectroscopy / Niobium / Tantalum / Peroxo ligands / Raman spectroscopy

A theoretical interpretation of the experimental observations made by vibrational IR and Raman spectroscopy on eight-coordinate peroxo complexes of niobium(V) and tantalum(V) is carried out. The theoretical study, realised on stoichiometric models of general formula $[M(O_2)_4]^{3-}$, $[M(O_2)_3L_2]^{x-}$, *cis*- and *trans*-$[M(O_2)_2L_4]^{y-}$ and $[M(O_2)L_6]^{z-}$ (M = Nb^V or Ta^V), provides the normal modes of vibrations involving peroxo ligands, their corresponding calculated frequency and their activity in IR and/or Raman spectroscopy. The theoretical results from the model complexes are compared with experimental IR and Raman spectroscopic data.

(© Wiley-VCH Verlag GmbH & Co. KGaA, 69451 Weinheim, Germany, 2005)

Introduction

In the last decades, peroxo species of transition metals have attracted considerable attention because of their extended coordination chemistry as well as their role in several challenging domains. Peroxo species of d^0 transition metals, for example V^V, Ti^{IV}, Mo^{VI}, W^{VI} and Nb^V, are potential oxygen donors to organic substrates in the liquid phase.[1–5] They can act as stoichiometric oxidants or as catalysts in the presence of oxidizing agents, such as H_2O_2 or *t*BuOOH, that are used to regenerate the starting peroxo metal species in situ. Such peroxo complexes can oxidize some electrophilic species and a large variety of nucleophilic substrates, such as phosphanes, sulfides, alcohols, olefins, enolates, imines, amides, etc.[3]

A further interest in peroxo complexes results from the important role they play in biological systems. For example, peroxovanadium(V) complexes have been found to have anti-tumour and insulin mimetic activities, while others have been studied as functional models for the vanadium haloperoxidase enzymes.[6,7] Finally, because such peroxo-type coordination compounds are most of the time soluble in water, they are also of great interest as precursors for the preparation of oxide materials and, more particularly, multimetallic oxides involving highly polarizing d^0 transition metals like Ti^{IV}, Zr^{IV}, Nb^V or Ta^V, for which the availability of water-soluble compounds is very limited.[8–13] This "peroxo way" has recently been shown to be a valuable approach for the synthesis of mixed oxides containing niobium and/or tantalum from well-defined and pre-isolated complexes.[14,15]

The peroxo compounds of transition metals correspond either to homoleptic complexes or to heteroleptic ones. In the heteroleptic compounds, one to three coordinated peroxo groups are associated with one or more monodentate or polydentate ligands. The various ways in which a peroxo group is expected to coordinate to metals are illustrated in Figure 1, but the most common type, observed for d^0 transition metals, is the so-called side-bonded peroxo ligand, complexed in an η^2 mode.

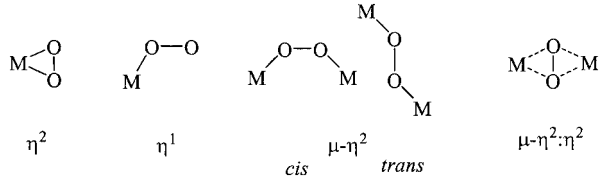

Figure 1. Coordination modes of peroxo groups to metal atoms.

The coordination polyhedra in heteroleptic peroxo compounds are fairly predictable. For the heavy group five elements niobium and tantalum, for example, coordination number 8 with dodecahedral geometry has invariably been observed. Several structural analyses of such heteroleptic complexes have been carried out, revealing the actual coordination spheres in each case.[14,16–21] However, most of the time no crystal structure could be obtained, and the determination of the metal environment in the complex is ambiguous. In that context, vibrational spectroscopy is still essential to characterise complexes containing coordinated peroxo groups. In the case of side-bonded peroxo ligands, two types of vibrational modes are expected: the peroxo stretch-

[a] Unité de Chimie des Matériaux Inorganiques et Organiques, Université Catholique de Louvain,
Place Louis Pasteur 1, 1348 Louvain-la-Neuve, Belgium
[b] Unité de Chimie Structurale et des Mécanismes Réactionnels, Université Catholique de Louvain,
Place Louis Pasteur 1, 1348 Louvain-la-Neuve, Belgium
Fax: +32-10-472-707
E-mail: peeters@chim.ucl.ac.be

Supporting information for this article is available on the WWW under http://www.eurjic.org or from the author.

ing, ν(O–O), and the metal–peroxo stretching, ν[M(O_2)]. As far as niobium and tantalum compounds are concerned, the determination of the number of peroxo ligands present around the metal atom in heteroleptic complexes can be deduced from the number of ν(O–O) bands, occurring near 850 cm^{-1}, by using an empirical rule which states that the presence of two or three ν(O–O) bands in the IR spectrum indicates the formation of a diperoxo or triperoxo complex, respectively.[22] As far as homoleptic $[M(O_2)_4]^{3-}$ (M = Nb^V or Ta^V) complexes are concerned, one broad or two ν(O–O) bands are observed in the IR and two such bands in the Raman spectra.[23–26] A recent study reported the vibrational spectra of tetraperoxotantalate compounds with several different counterions, $(A^I)_3[Ta(O_2)_4]$ (A^I = K^+, Rb^+, Cs^+). The authors determined the different vibrational modes of the O–O and Ta–O stretching vibrations from the site-group analysis of the $[Ta(O_2)_4]^{3-}$ anion (site group symmetry D_{2d}).[26]

The present work deals with the theoretical simulation of the experimental observations made by vibrational IR and Raman spectroscopy on eight-coordinate peroxo complexes of niobium(v) and tantalum(v). This study will provide the normal modes of vibrations involving peroxo ligands, their corresponding frequency and their activity in IR and/or Raman spectroscopy and so constitute a guide to interpret experimental spectra. By validating the empirical rules mentioned so far for the interpretation of the vibrational spectra of eight-coordinate peroxo complexes, this work provides important tools to develop the coordination chemistry of such compounds.

Results and Discussion

Theoretical calculations were performed at the DFT level using various functionals for five stoichiometric models corresponding to tetra-, tri-, di- and monoperoxo species, of general formula $[M(O_2)_4]^{3-}$, $[M(O_2)_3L_2]^{x-}$, *cis*- and *trans*-$[M(O_2)_2L_4]^{y-}$ and $[M(O_2)L_6]^{z-}$, respectively. The metal, M, chosen for the simulation is niobium(v) and L corresponds to the oxygen atoms of oxalate, which mimics a coordinated atom from one or several mono- or polydentate ligand(s). More details about the methodologies used and the choices made for the computations are explicitly presented in the Computational Details section (Figure 2).

The symmetry obtained after geometry optimisation for the various compounds $[M(O_2)_4]^{3-}$, $[M(O_2)_3L_2]^{x-}$, *cis*- or *trans*-$[M(O_2)_2L_4]^{y-}$ and $[M(O_2)L_6]^{z-}$ is D_{2d}, C_s, C_{2v} or D_2 and C_1, respectively. For the diperoxo species, their relative stability is small and the results depend on the chosen methodology. As mentioned in the Computational Details section, the C_{2v} symmetry (*cis* configuration) is more stable at the Hartree–Fock level but the opposite is the case at the DFT level. More details about those structures are given in the Supporting Information. For each one, a normal mode analysis was realised at the harmonic level in order to obtain vibration frequencies and to identify the normal modes involving the peroxo functions.

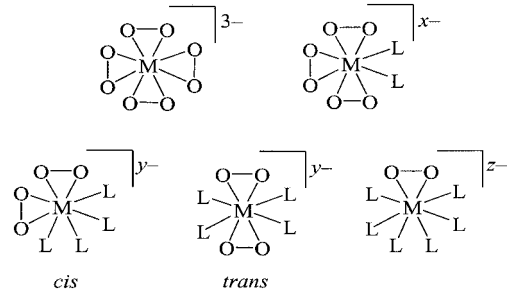

Figure 2. Schematic representation of model stoichiometries considered for the theoretical study (M = Nb^V and L = oxygen atom from an oxalate ligand).

The theoretical values were compared with those of corresponding complexes described in the literature for each of the tetra-, tri- and *cis*-diperoxo species studied. Because the experimental vibrational data of peroxotantalum(v) complexes are quite close to those of their niobium(v) equivalents, some of them are also taken into account in this study and compared to the calculated values. The stoichiometries of the selected representative Nb and Ta complexes are given in Table 1. As far as monoperoxo and *trans*-diperoxo species are concerned, no such compounds with an eight-fold coordination have been described so far in the literature. The IR data from complexes listed in Table 1 have already been reported,[14,16,17,22,27,28] while little information from Raman spectroscopy is available.

Table 1. Stoichiometries of the peroxo complexes of niobium(v) and tantalum(v) described in the literature and used in this work for comparison (ox = oxalate, *o*-phen = 1,10-phenanthroline, picO = picolinate *N*-oxide, tart = tartrate, edtaO_2 = ethylenediaminetetraacetate *N*,*N*′-dioxide).

		Stoichiometry	Ref.
tetraperoxo	1	$(NH_4)_3[Nb(O_2)_4]$	[14]
	2	$(gu)_3[Nb(O_2)_4]$	[14]
	3	$(gu)_3[Ta(O_2)_4]$	[17]
triperoxo	4	$K_3[Nb(O_2)_3(ox)]$	[22]
	5	$K_3[Nb(O_2)_3(o\text{-phen})]$	[27]
	6	$K_3[Ta(O_2)_3(o\text{-phen})]$	[27]
	7	$(gu)_2[Nb(O_2)_3(picO)]$	to be published
cis–diperoxo	8	$K_3[Nb(O_2)_2F_4]$	[28]
	9	$(NH_4)_3[Nb(O_2)_2(ox)_2]$	[14]
	10	$(gu)_5[Nb_2(O_2)_4(Htart)(tart)]\cdot 4H_2O$	[18]
	11	$(gu)_3[Nb(O_2)_2(edtaO_2)]\cdot 2H_2O$	[16]
	12	$(gu)_3[Ta(O_2)_2(edtaO_2)]\cdot 2H_2O$	[17]

Tables 2–6 present the theoretical results obtained for each of the five species considered and compare them to the experimental results from IR and Raman spectroscopy reported in the literature or obtained in the present work. These tables list, for each normal mode, its corresponding vibrational motion, its activity in IR and/or Raman (R), its

 © 2005 Wiley-VCH Verlag GmbH & Co. KGaA, Weinheim

calculated frequency (in cm^{-1}) and finally its frequency (in cm^{-1}) observed experimentally on the spectra.

In the tetraperoxometallate anion, the stretching vibrations of the peroxo groups, ν(O–O), belong to the A_1, B_2 and E modes. The first one is only Raman active and is due to the total symmetric vibration where all four peroxo groups vibrate in phase. The second one is only IR active, while the third one is active in IR as well as in Raman. These theoretical results are in agreement with the experimental IR and Raman spectra of complexes **1**–**3**, which each display two ν(O–O) bands beyond 800 cm^{-1} (see Table 2). Haeuseler et al. have observed only one ν(O–O) band in the IR spectrum of corresponding tantalum compounds with several counterions. This band was attributed to the ν(O–O) belonging to the E mode. As far as the metal–peroxo stretching ν[$M(O_2)$] vibrations are concerned, two modes occur and correspond to E and A_1 species; the first one is active in both techniques while the second one is only Raman active. These bands are observed near 550 and 530 cm^{-1}, respectively, in the experimental spectra of complexes **1**–**3** (see Table 2).

Table 2. Theoretical results for the tetraperoxo species $[M(O_2)_4]^{3-}$ compared to the experimental results for compounds **1**–**3**.

Schematic representation of the normal mode		Activity		Calculated frequency[a] [cm^{-1}]	Observed frequency [cm^{-1}] 1	2	3
A_1	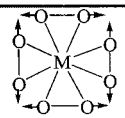	IR		886	849	849	840
		R	✓				
B_2	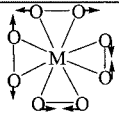	IR	✓	860	818	825	817
		R					
E[b]	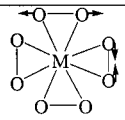	IR	✓	861	813	818	810
		R	✓		812	822	814
E[b]	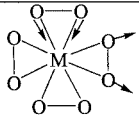	IR	✓	502	540	554	551
		R	✓		534	539	550
A_1	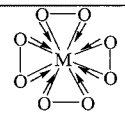	IR		483	520	527	536
		R	✓				

[a] The theoretical frequencies obtained at the B3LYP/6-31+G(d) level cannot be directly compared to the experimental ones but must be scaled by some empirical factor. [b] Doubly degenerate vibrational mode.

In the case of the heteroleptic tri- and *cis*-diperoxo complexes, the theoretical results confirmed the empirical rule which states that the presence of two or three ν(O–O) bands in the IR spectrum indicates the formation of a diperoxo or triperoxo complex, respectively.[22] Moreover, according to the theoretical results obtained, the same rule can be applied in the case of Raman spectroscopy.

The triperoxo species $[M(O_2)_3L_2]^{x-}$ shows three vibration modes which involve the O–O stretching and which are all active in both IR and Raman spectroscopy. This result is in agreement with the experimental spectra illustrated in Figure 3 in the case of $(gu)_2[Nb(O_2)_3(picO)]$ (**7**), which each display three ν(O–O) bands near 850 cm^{-1}. The additional bands occurring in the IR spectrum of compound **7** in that zone (871 and 811 cm^{-1}) are due to the bending vibration of the *N*-oxide group, δ(N–O), present in the picolinato ligand. The triperoxo complex also shows two ν[$M(O_2)$] vibrations which are both IR and Raman active, as confirmed by the experimental observations (see Figure 2). As illustrated in Table 3, the first ν[$M(O_2)$] mode implies the presence of two peroxo ligands, while the second one implies the presence of only one.

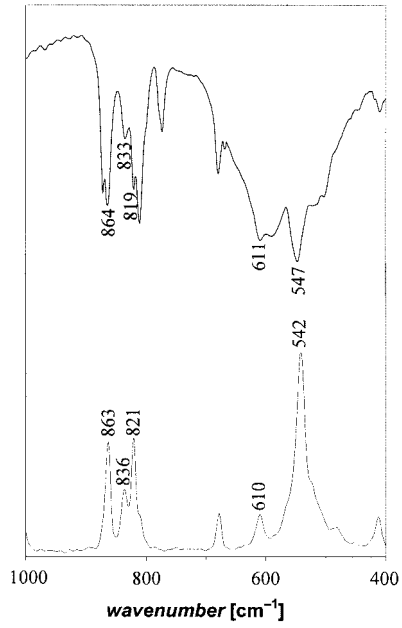

Figure 3. Experimental IR (top) and Raman (bottom) spectra of $(gu)_2[Nb(O_2)_3(picO)]$ (**7**).

As far as the *cis*-diperoxo species $[M(O_2)_2L_4]^{y-}$ is concerned, the theoretical calculations provide two ν(O–O) vibrations. As shown in Table 4, in the first mode, of B_1 symmetry, the peroxo ligands vibrate out of phase, while in the second one, of symmetry A_1, they vibrate in phase. The diperoxo complex also displays two ν[$M(O_2)$] vibrations, which are both active in IR and Raman spectroscopy. The theoretical results are in agreement with the experimental ones, which are illustrated in Figure 4 in the case of $(NH_4)_3[Nb(O_2)_2(ox)_2]$ (**9**).

As illustrated in Table 5, the *trans*-diperoxo model compound shows two peroxo stretching modes. The antisymmetric mode is active in both IR and Raman spectroscopy while the symmetric one is only Raman active. This species also displays four metal–peroxo stretching vibrations, ν[$M(O_2)$], which belong to the B_1, B_3, B_2 and A modes, respectively. Only the first and third ones show a fair ac-

 © 2005 Wiley-VCH Verlag GmbH & Co. KGaA, Weinheim

Table 3. Theoretical results for the triperoxo species $[M(O_2)_3L_2]^{x-}$ compared to the experimental results for compounds **4**–**7**.

Schematic representation of the normal mode		Activity		Calculated frequency[a] [cm^{-1}]	Observed frequency [cm^{-1}] **4**	**5**	**6**	**7**
A'	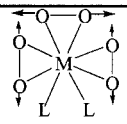	IR	✓	911	852	865	865	864
		R	✓		–[b]	–	–	863
A'	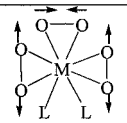	IR	✓	884	834	815	805	833
		R	✓		–	–	–	836
A"	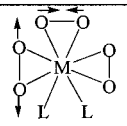	IR	✓	881	825	800	795	819
		R	✓		–	–	–	821
A"	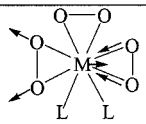	IR	✓	567	568	–	–	603
		R	✓		–	–	–	611
A'	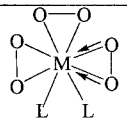	IR	✓	559	513	–	–	547
		R	✓		–	–	–	542

[a] The theoretical frequencies obtained at the B3LYP/6-31+G(d) level cannot be directly compared to the experimental ones but must be scaled by some empirical factor. [b] Unreported value.

Table 4. Theoretical results realised for the *cis*-diperoxo species $[M(O_2)_2L_4]^{y-}$ compared to the experimental results for compounds **8**–**12**.

Schematic representation of the normal mode		Activity		Calculated frequency[a] [cm^{-1}]	Observed frequency [cm^{-1}] **8**	**9**	**10**	**11**	**12**
B_1	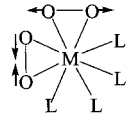	IR	✓	905	880	874	866	872	873
		R	✓		–[b]	871	868	873	875
A_1	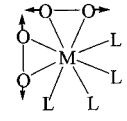	IR	✓	895	860	851	850	857	857
		R	✓		–	850	851	854	861
B_1	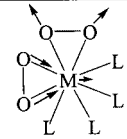	IR	✓	583	550	570	571	642	643
		R	✓		–	573	570	638	636
A_1	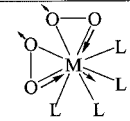	IR	✓	542	500	537	536	554	544
		R	✓		–	532	531	559	555

[a] The theoretical frequencies obtained at the B3LYP/6-31+G(d) level cannot be directly compared to the experimental ones but must be scaled by some empirical factor. [b] Unreported value.

tivity in IR spectroscopy, while the A mode is Raman active. No comparison can be made in this case with experimental data because such complexes have not been described in the literature so far.

Finally, in the case of the monoperoxo species $[M(O_2)L_6]^{z-}$, the results are quite simple because only one ν(O–O) mode and two ν[$M(O_2)$] vibrations − the symmetric and antisymmetric ones − are obtained (see Table 6). These three vibrational modes are all active in IR and Raman spectroscopy. Here also no comparison with the literature can be made because such compounds with an eightfold coordination are not yet known.

Conclusions

Theoretical interpretations of the experimental observations made by vibrational IR and Raman spectroscopy on eight-coordinate peroxo complexes of niobium(v) and tantalum(v) have been carried out. This study provides the normal modes of vibrations involving peroxo ligands, their corresponding calculated frequency and their activity in IR and/or Raman spectroscopy. This work thus validates the empirical rules mentioned so far for the interpretation of the vibrational spectra of eight-coordinate heteroleptic peroxo complexes, and provides important tools to develop the

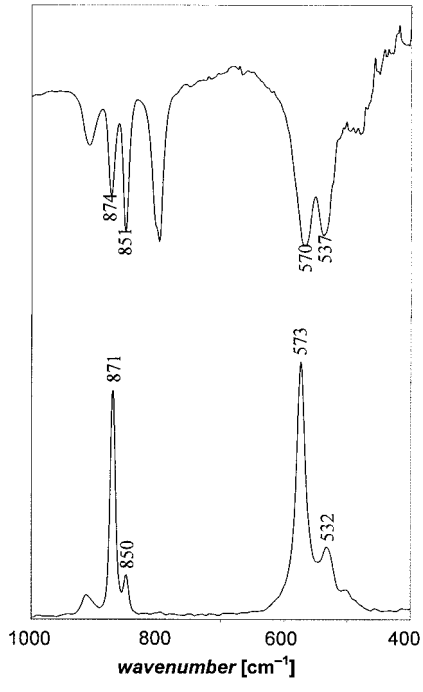

Figure 4. Experimental IR (top) and Raman (bottom) spectra of $(NH_4)_3[Nb(O_2)_2(ox)_2]$ (**9**).

 © 2005 Wiley-VCH Verlag GmbH & Co. KGaA, Weinheim

Table 5. Theoretical results obtained for the *trans*-diperoxo species $[M(O_2)_2L_4]^{y-}$.

Schematic representation of the normal mode	Activity		Calculated frequency [cm^{-1}]
B_1 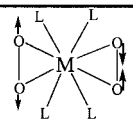	IR	✓	948
	R	✓	
A 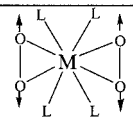	IR		947
	R	✓	
B_1 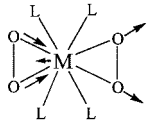	IR	✓	588
	R		
B_3 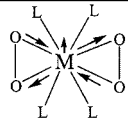	IR	[a]	568
	R		
B_2 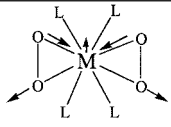	IR	✓	566
	R		
A 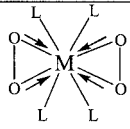	IR		523
	R	✓	

[a] The theoretical computation gives a very small IR activity.

Table 6. Theoretical results for the monoperoxo species $[M(O_2)L_6]^{z-}$.

Schematic representation of the normal mode	Activity		Calculated frequency [cm^{-1}]
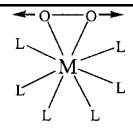	IR	✓	937
	R	✓	
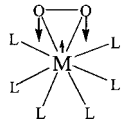	IR	✓	598
	R	✓	
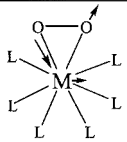	IR	✓	481
	R	✓	

coordination chemistry of peroxo species as it could be extended to equivalent complexes of other transition metals.

Experimental Section

General: The Nb^V and Ta^V complexes **1**–**3** and **9**–**12** (see Table 1) were prepared according to procedures described elsewhere.[14,16–18] The IR spectrum of compound **7** was recorded with an FTS-135 Bio-RAD spectrometer, using KBr pellets containing ca. 1 wt.-% of the powder. FT-Raman spectra of complexes **1**–**3**, **7** and **9**–**12** were recorded with a Bruker spectrometer (type RFS100/S) at a wavelength of 1064 nm. Measurements were carried out on powders sampled on an aluminium support.

Computational Details: Theoretical calculations were performed at the Hartree–Fock and DFT levels for five stoichiometric models corresponding to tetra-, tri-, di- and monoperoxo species, of general formula $[M(O_2)_4]^{3-}$, $[M(O_2)_3L_2]^{x-}$, *cis*- and *trans*-$[M(O_2)_2L_4]^{y-}$ and $[M(O_2)L_6]^{z-}$, respectively. The metal, M, chosen for the simulation is niobium(v) and L corresponds to the oxygen atoms of oxalate, which mimic a coordinated atom from one or several mono- or polydentate ligand(s). For the central metal atom, an effective core potential was used to represent all but the valence n*d* and (*n*+1)*s* and outer core n*s* and n*p* electrons. The latter were described with a double-zeta basis set, this combination being referred to as the LANL2DZ basis set. In order to check the functional dependence of the obtained results, the computations were completed using Becke's three-parameter hybrid functional (B3LYP), the Perdew 86 functional (P86) and finally the Perdew–Burke–Ernzerhof (PBE) hybrid functional. These anionic complexes require fairly good basis sets to obtain reliable results. In particular, polarisation functions are needed on the ligands to introduce enough flexibility into the wave function. The introduction of diffuse orbitals also improves the long-range spatial distribution required by the presence of negative charges. To check this point, we used two basis sets to represent the non-metal atoms, namely. the standard 6-31G(d) basis as starting point, completed afterwards by 6-31+G(d), which introduces diffuse functions on each atom. These basis sets are those available in the Gaussian series of programs.[29] Concerning the geometry optimisation, trial structures of the selected species were taken from available crystallographic data to yield the starting points for full optimisation. All structures were optimised without any symmetry constraints and the point group was deduced from the optimised geometries. A single minimum was obtained for all *n* values except when *n* equals two, where two minima appear. Within numerical precision, the symmetry deduced for the various compounds $[M(O_2)_4]^{3-}$, $[M(O_2)_3L_2]^{x-}$, *cis*- or *trans*-$[M(O_2)_2L_4]^{y-}$ and $[M(O_2)L_6]^{z-}$ is D_{2d}, C_s, C_{2v} or D_2 and C_1, respectively, regardless of the method or basis set being used. These structures are, of course, "gas-phase" structures that do not consider the nature of the counterion or the incidence of the solid-state environment. We report the relative stabilities obtained for the diperoxo species in Table 7. While B3LYP gives no significant energy difference between both structures, Hartree–Fock results give a C_{2v} symmetry (*cis* configuration) that is some 27 kJ mol^{-1} more stable than the D_2 symmetry (*trans* configuration). Finally, the P86 and PBE functional favour the D_2 structure slightly. A normal mode analysis was realised at the harmonic level for each obtained structure in order to obtain vibrational frequencies and to identify the normal modes involving the peroxo functions. At this level of methodology, the theoretical frequencies cannot be directly compared to the experimental ones but must be scaled by an empirical factor. As it is not useful to give all the results here, Table 8 gives an example of

 © 2005 Wiley-VCH Verlag GmbH & Co. KGaA, Weinheim

the wavenumbers obtained for $[M(O_2)_3L_2]^{3-}$ at all levels of methodology. They show that the numbers obtained at the B3LYP and P86 levels are close to the experimental values and that even though a slight improvement is obtained with the diffuse basis set, it is not really significant. Hartree–Fock results, as is well known, are overestimated by some 20%, but the PBE functional does not behave very well as it overestimates the frequencies by about 10%. As the best fit was obtained with the B3LYP and P86 functionals using the diffuse basis functions, the data referred to in the above discussion are those obtained at the B3LYP level. The optimised XYZ coordinates of the niobium complexes are given in the Supporting Information (see footnote on the first page of this article). The reported data contain the DFT/B3LYP level results obtained with a LANL2DZ pseudopotential for Nb and the 6-31+G(d) basis sets for C and O atoms.

Table 7. Relative stability [kJ mol^{-1}] between *cis*- and *trans*-$[M(O_2)_2L_4]^{3-}$.

Method	6-31G(d)	With diffuse functions
B3LYP	0.3	–3.7
P86	–12.0	–16.1
PBE	–6.0	–13.6
HF	27.0	27.0

Table 8. Comparison between a selected experimental and various theoretically[a] obtained wavenumbers of $[M(O_2)_3L_2]^{x-}$ [cm^{-1}].

Exp	B3LYP	P86	PBE	HF
513	551 (553)	525 (534)	567 (572)	641 (634)
568	559 (568)	535 (544)	579 (583)	642 (644)
825	881 (900)	844 (863)	931 (947)	1015 (1025)
834	884 (902)	845 (864)	933 (948)	1024 (1032)
852	911 (928)	870 (888)	959 (974)	1053 (1061)

[a] 6-31+G(d) and 6-31G(d) (in parentheses) basis sets.

Acknowledgments

The authors thank the Belgian National Fund for Scientific Research (FNRS) for the research fellowship allotted to D. B. and financial support.

[1] V. Conte, F. DiFuria, S. Moro, *J. Phys. Org. Chem.* **1996**, *9*, 329–336.
[2] K. A. Jorgensen, *Chem. Rev.* **1989**, *89*, 431–458.
[3] R. Noyori, M. Aoki, K. Sato, *Chem. Commun.* **2003**, *16*, 1977–1986.
[4] R. A. Sheldon, *Top. Curr. Chem.* **1993**, *164*, 21–43.
[5] R. A. Sheldon, I. W. C. E. Arends, A. Dijksman, *Catal. Today* **2000**, *57*, 157–166.
[6] D. C. Crans, J. J. Smee, E. Gaidamauskas, L. Q. Yang, *Chem. Rev.* **2004**, *104*, 849–902.
[7] K. H. Thompson, J. H. McNeill, C. Orvig, *Chem. Rev.* **1999**, *99*, 2561–2571.
[8] H. Ichinose, M. Taira, S. Furuta, H. Katsuki, *J. Am. Ceram. Soc.* **2003**, *86*, 1605–1608.
[9] V. T. Kalinnikov, O. G. Gromov, G. B. Kunshina, A. P. Kuz'min, E. P. Lokshin, V. I. Ivanenko, *Inorg. Mater.* **2004**, *40*, 411–414.
[10] Y. Narendar, G. L. Messing, *Chem. Mater.* **1997**, *9*, 580–587.
[11] N. Uekawa, T. Kudo, F. Mori, Y. J. Wu, K. Kakegawa, *J. Colloid Interface Sci.* **2003**, *264*, 378–384.
[12] Y. Yoshikawa, K. Uchino, *J. Am. Ceram. Soc.* **1996**, *79*, 2417–2421.
[13] Y. F. Gao, Y. Masuda, H. Ohta, K. Koumoto, *Chem. Mater.* **2004**, *16*, 2615–2622.
[14] D. Bayot, B. Tinant, M. Devillers, *Catal. Today* **2003**, *78*, 439–447.
[15] D. Bayot, M. Devillers, *Chem. Mater.* **2004**, *16*, 5401–5407.
[16] D. Bayot, B. Tinant, B. Mathieu, J. P. Declercq, M. Devillers, *Eur. J. Inorg. Chem.* **2003**, 737–743.
[17] D. Bayot, B. Tinant, M. Devillers, *Inorg. Chem.* **2004**, *43*, 5999–6005.
[18] D. Bayot, B. Tinant, M. Devillers, *Inorg. Chem.* **2005**, *44*, 1554–1562.
[19] G. Mathern, R. Weiss, *Acta Crystallogr, Sect. B* **1971**, *27*, 1598–1609.
[20] G. Mathern, R. Weiss, *Acta Crystallogr, Sect. B* **1971**, *27*, 1572–1581.
[21] G. Mathern, R. Weiss, *Acta Crystallogr, Sect. B* **1971**, *27*, 1582–1597.
[22] R. N. Shchelokov, E. N. Traggeim, M. A. Michnik, K. I. Petrov, *Russ. J. Inorg. Chem.* **1972**, *17*, 1270–1272.
[23] A. C. Dengel, W. P. Griffith, *Polyhedron* **1989**, *8*, 1371–1377.
[24] K. I. Selezneva, L. A. Nisel'son, *Russ. J. Inorg. Chem.* **1968**, *13*, 45–47.
[25] R. N. Shchelokov, E. N. Traggeim, M. A. Michnik, *Russ. J. Inorg. Chem.* **1971**, *16*, 211–213.
[26] G. Haxhillazi, H. Haeuseler, *J. Solid State Chem.* **2004**, *177*, 3045–3051.
[27] C. Djordjevic, N. Vuletic, *Inorg. Chem.* **1968**, *7*, 1864–1868.
[28] N. Vuletic, C. Djordjevic, *J. Less-Common Met.* **1976**, *45*, 85–89.
[29] M. J. Frisch, G. W. Trucks, H. B. Schlegel, G. E. Scuseria, M. A. Robb, J. R. Cheeseman, V. G. Zakrzewski, J. A. Montgomery, Jr., R. E. Stratmann, J. C. Burant, S. Dapprich, J. M. Millam, A. D. Daniels, K. N. Kudin, M. C. Strain, O. Farkas, J. Tomasi, V. Barone, M. Cossi, R. Cammi, B. Mennucci, C. Pomelli, C. Adamo, S. Clifford, J. Ochterski, G. A. Petersson, P. Y. Ayala, Q. Cui, K. Morokuma, D. K. Malick, A. D. Rabuck, K. Raghavachari, J. B. Foresman, J. Cioslowski, J. V. Ortiz, A. G. Baboul, B. B. Stefanov, G. Liu, A. Liashenko, P. Piskorz, I. Komaromi, R. Gomperts, R. L. Martin, D. J. Fox, T. Keith, M. A. Al-Laham, C. Y. Peng, A. Nanayakkara, C. Gonzalez, M. Challacombe, P. M. W. Gill, B. Johnson, W. Chen, M. W. Wong, J. L. Andres, C. Gonzalez, M. Head-Gordon, E. S. Replogle, J. A. Pople, *Gaussian 98*, revision A.7, Gaussian, Inc., Pittsburgh PA, 1998.

Received: May 11, 2005
Published Online: September 5, 2005

 © 2005 Wiley-VCH Verlag GmbH & Co. KGaA, Weinheim

Solvothermal Synthesis of Metastable γ-MnS Hollow Spheres and Control of Their Phase

Shuijin Lei,[a,b] Kaibin Tang,*[a,b] Qing Yang,[a,b] and Huagui Zheng[b]

Keywords: Manganese / Nanostructures / Semiconductors / Solvothermal synthesis

A solvothermal route has been developed to prepare metastable wurtzite-structure γ-MnS hollow spheres from anhydrous manganese chloride, sulfur powder, and potassium borohydride in ethylene glycol at 150–180 °C. The metastable γ-MnS and stable α-MnS were characterized by X-ray diffraction, X-ray photoelectron spectroscopy, field-emission scanning electronic microscopy, scanning electron microscopy, transmission electron microscopy, and photoluminescence. Experiments show that the reaction temperature, the solvent, and the concentration and reducibility of the reductant are the crucial factors affecting the phase of the product. A possible growth mechanism for the hollow sphere is proposed.

(© Wiley-VCH Verlag GmbH & Co. KGaA, 69451 Weinheim, Germany, 2005)

Introduction

In recent years, inorganic and inorganic–organic hybrid hollow spheres of nanometer or submicrometer size have attracted considerable attention because of their potential applications in a broad range of areas, such as delivery vehicles for the controlled release of various substances, for example drugs, cosmetics, dyes, and inks, and for the protection of biologically active macromolecules, artificial cells, catalysts, fillers, coatings, pigments, light-weight structural or low density materials, and waste removal owing to their low density, large specific area, mechanical and thermal stability, and surface permeability.[1–5] A variety of chemical and physicochemical approaches have been employed to prepare hollow spheres, for example polymer, oxide, glass, and ceramic materials, including nozzle systems to dispense individual liquid droplets of uniform size (e.g. spray drying or pyrolysis),[6] emulsion/phase separation techniques (usually associated with sol-gel processing),[7] emulsion/interfacial polymerization strategies,[8] and self-assembly routes.[9]

Manganese sulfide (MnS), is a VIIB–VIA dilute magnetic semiconductor with a wide gap [bandgap energy: E_g (T = 0) ≈ 3.7 eV],[10] which has potential applications in solar cells, as a window/buffer material, and in short-wavelength optoelectronic materials. MnS usually has three polymorphs:[11] α-MnS, with a rock-salt structure, and the metastable phases β-MnS, with a zincblende structure, and γ-MnS, with a wurtzite structure. During equilibrium growth techniques, MnS crystallizes in the stable α phase. Both of the latter phases are antiferromagnetic, with Néel temperatures of 152 K (β-phase) and 90 K (γ-phase), and are transformed irreversibly into stable α-MnS upon heating.[12–16]

In previous studies, MnS is usually prepared by the direct reaction of manganese (Mn) and sulfide in an evacuated tube at high temperatures (above 800 °C).[17] β- and γ-MnS bulk phases have been prepared in polycrystalline form by low temperature chemical synthesis or evaporation.[18,19] The direct synthesis of polycrystalline β- and γ-MnS has also been reported by gas source molecular-beam epitaxy (MBE).[13,14] Metastable MnS thin films, which consist of nanocrystallite domains with mixed cubic and hexagonal phases, have been prepared by adopting a chemical bath deposition (CBD) method,[20,21] and recently a solvothermal route has been used to grow stable α-MnS and rod-like metabstable β- and γ-MnS nanocrystallites.[22] α-MnS nanocrystallites have also been prepared by a colloidal synthesis route by the reaction of $MnCl_2$ and $S[Si(CH_3)_3]_2$ in trioctylphosphane oxide,[23] and α-MnS nanorods have been prepared by a hydrothermal method from the elements (manganese and sulfur powder).[24] However, to the best of our knowledge, the metastable γ-MnS hollow sphere structure has not been reported.

In this paper, metastable γ-MnS hollow spheres are prepared by a developed solvothermal reaction at 150–180 °C from anhydrous manganese chloride ($MnCl_2$), sulfur powder, and potassium borohydride (KBH_4) as the reactants and ethylene glycol (EG) as the solvent. The phase of the as-formed MnS crystallites is influenced by the solvent, the reaction temperature, and the concentration and reducibility of the reductant.

[a] Nanomaterial and Nanochemistry, Hefei National Laboratory for Physical Sciences at Microscale, University of Science and Technology of China,
Hefei, Anhui 230026, P. R. China
Fax: +86-551-360-1791
E-mail: kbtang@ustc.edu.cn
[b] Department of Chemistry, University of Science and Technology of China,
Hefei, Anhui 230026, P. R. China

 © 2005 Wiley-VCH Verlag GmbH & Co. KGaA, Weinheim DOI: 10.1002/ejic.200500442

Results and Discussion

Figure 1 shows the XRD patterns of as-prepared MnS powders. The samples shown in parts a–d of Figure 1 were prepared in EG. The diffraction peaks in Figure 1a can be indexed as the hexagonal γ-MnS with lattice constants a = 3.981 and c = 6.423 Å, which are close to those reported for γ-MnS [Joint Committee on Powder Diffraction Standards (JCPDS), Powder Diffraction File No. 40-1289: a = 3.979 and c = 6.446 Å]. The average crystallite size of γ-MnS is about 30 nm, as calculated from the Debye–Scherrer formula. Figure 1 (parts b–d) are the XRD patterns of the samples in which α-MnS and γ-MnS are coexistent. The peak marked by an asterisk in part c of Figure 1 is derived from $MnCO_3$. In Figure 1 (e), the XRD pattern of the product synthesized in $N_2H_4{\cdot}H_2O$, can be indexed as the cubic α-MnS (RS) with a = 5.216 Å (JCPDS, Powder Diffraction File No. 06-0518: a = 5.224 Å). We found that α-MnS gradually becomes the dominant phase with an increase of the reaction temperature, the concentration, and reducibility of the reductant, or the complexing ability of the solvent.

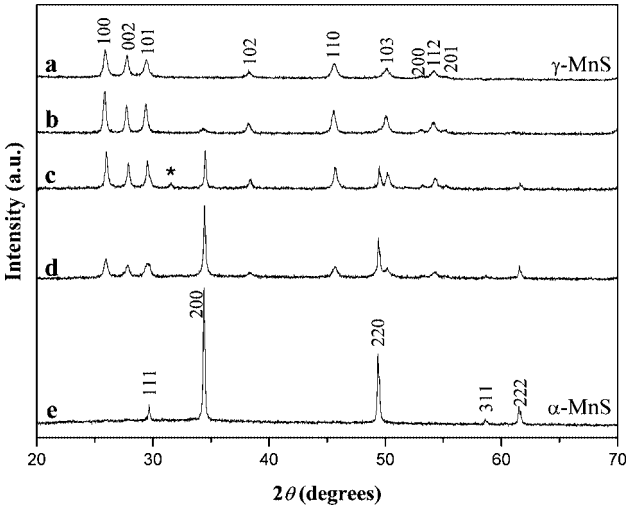

Figure 1. XRD patterns of the as-prepared MnS samples with different phase(s) synthesized: (a) in EG at 180 °C with a 3:5 molar ratio of S and KBH_4; (b) in EG at 240 °C with a 3:5 molar ratio of S and KBH_4; (c) in EG at 260 °C with a 3:10 molar ratio of S and KBH_4; (d) in EG at 260 °C with a 3:20 molar ratio of S and KBH_4; (e) in EA at 180 °C.

Figure 2 shows the XPS spectrum of as-synthesized γ-MnS. The binding energies of Mn $2p_{3/2}$ and S 2p were found to be 641.3 and 161.3 eV, respectively, which is consistent with the values reported in the literature.[25] There are also peaks for C reference and O impurity, due to the surface absorption of the samples exposed to air during processing of the samples. Direct elemental analysis for the composition of the sample was provided by ICP-AES, which gave an Mn/S molar ratio of 1:1.034. These results show that the product is stoichiometric.

Figure 3 (parts a and b) shows TEM images of the as-prepared γ-MnS, which reveal that the product consists of hollow spheres 300–500 nm in diameter; the wall thickness around the shell is about 50 nm. The strong contrast between the dark edges and pale centers is evidence of their hollow structures.[1d,2b,26,27] The direct observation of a broken sphere, as shown in Figure 3b, provides the most powerful proof of the hollow nature. The corresponding SAED pattern of the γ-MnS hollow sphere in Figure 3 (a) shows seven diffuse diffraction rings, which can be characterized as the (100), (002), (101), (102), (110), (103), and (112) planes from inner to outer (Figure 3, c) and further reveals the hexagonal γ-MnS polycrystals. The morphology of the sample synthesized in EG at 260 °C with a 3:10 molar ratio of S to KBH_4 was also examined. It consists of γ-MnS hollow spheres and α-MnS cubes. Figure 3 (d) presents the hollow and solid-sphere image of γ-MnS that was prepared using manganese chloride tetrahydrate ($MnCl_2{\cdot}4H_2O$) instead of anhydrous $MnCl_2$. The hollow spheres are clearly far fewer than the solid spheres. Figure 3 (e) gives the TEM image of α-MnS solid spheres prepared in EA at 180 °C. If the solvent is changed to EN, then α-MnS aggregates consisting of many micron-sized rods are obtained. Figure 3 (f) presents the TEM image of an individual rod aggregate. The corresponding ED pattern of a single rod (marked by an arrow) reveals that the as-prepared sample is well crystallized (see the inset).

Figure 4 shows the FE-SEM image of the γ-MnS broken hollow sphere. From this image, we can observe that the hollow sphere is structured with a lot of smaller particles, which are about 30–40 nm in size. Figure 4 (b) is the SEM image of γ-MnS hollow spheres and solid spheres. According to the difference of the hollow and solid sphere images, it can also be determined that the hollow spheres are in a very minor amount. The SEM photographs shown in Figures 4c and 4d are α-MnS solid sphere and α-MnS rod aggregates, respectively, which correspond to the samples of Figure 3 (parts e and f, respectively).

Figure 5 shows the room temperature PL spectra of the as-prepared γ-MnS hollow spheres (Figure 5, a) and α-MnS rod aggregates (Figure 5, b) with the same excitation wavelength of 365 nm (a filter with 500 nm wavelength was needed for γ-MnS). Figure 5 (a) exhibits a relatively strong and wide emission band peaking at about 720 nm (1.7 eV). In Figure 5 (b), an emission peaking at 435 nm (2.8 eV) can be observed, which is similar to the bandgap of the bulk counterpart.[23]

Table 1 summarizes the experiments and the effects of changing the solvent, the reaction temperature, and the concentration and reducibility of the reductant on the phase of the product.

From the results above, it can be seen that the optimum reaction temperature is 150–180 °C. When the reaction was performed in EG at 180 °C with a 3:5 molar ratio of S and KBH_4, γ-MnS hollow spheres were formed after five hours, whereas if the reaction temperature was reduced to 150 °C, then the reaction time had to be prolonged to 20 hours to produce pure γ-MnS. In this reaction system, KBH_4 is vital to prepare γ-MnS, and if the reaction temperature was increased above 200 °C, α-MnS appeared. In the range of 200–260 °C, the higher the temperature the greater the amount of α-MnS is present in the product. In this reaction

 © 2005 Wiley-VCH Verlag GmbH & Co. KGaA, Weinheim

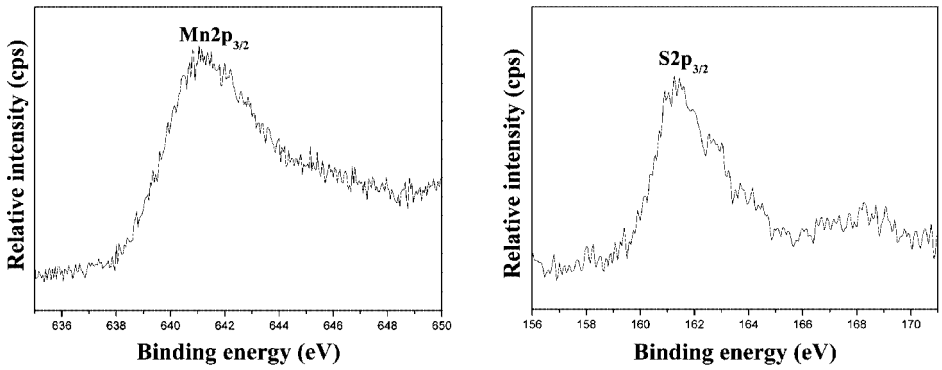

Figure 2. XPS spectra of the as-synthesized γ-MnS hollow spheres.

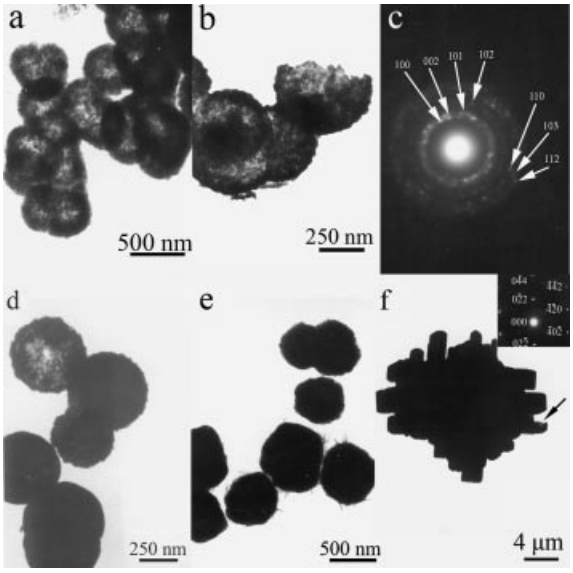

Figure 3. TEM images of as-prepared samples: (a) γ-MnS hollow spheres with anhydrous $MnCl_2$ as the reactant; (b) γ-MnS broken hollow sphere; (c) ED pattern for (a); (d) γ-MnS hollow spheres and solid spheres with $MnCl_2{\cdot}4H_2O$ as the reactant; (e) α-MnS spheres with EA as the solvent; (f) α-MnS rod aggregates with EN as the solvent (inset: the corresponding ED pattern of the single rod marked by an arrow).

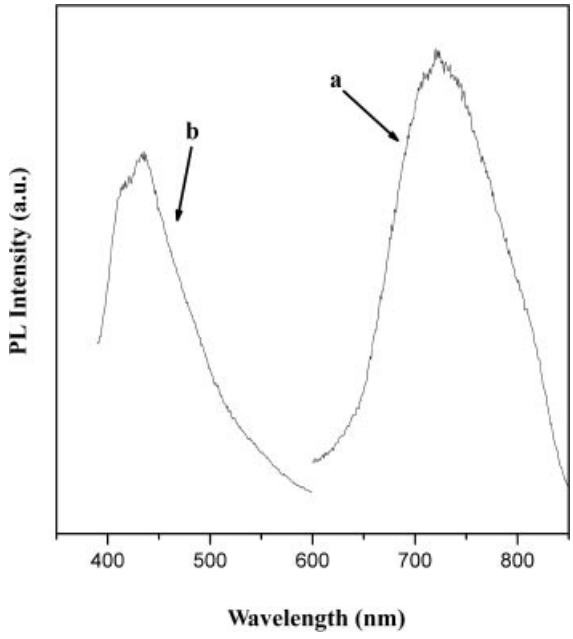

Figure 5. PL spectrum (λ_{ex} = 365 nm) of the as-synthesized samples for: (a) γ-MnS hollow spheres, and (b) α-MnS rod aggregates with EN as the solvent.

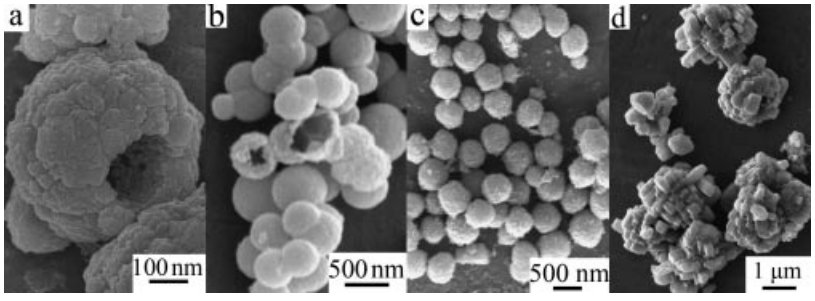

Figure 4. (a) FE-SEM image of γ-MnS broken hollow sphere and SEM images; (b) γ-MnS hollow spheres and solid spheres when $MnCl_2{\cdot}4H_2O$ was used as the reactant; (c) α-MnS solid spheres when EA was used as the solvent; (d) α-MnS rod aggregates when EN was used as the solvent.

system, the γ phase is readily obtained at low temperature and the α phase at high temperature as at higher reaction temperatures the metastable γ-MnS is transformed into stable α-MnS.

When the system was maintained at an appropriate reaction temperature above 200 °C, and the amount of KBH_4 was increased gradually, we also found that the content of α-MnS in the product increased. It must be pointed out

 © 2005 Wiley-VCH Verlag GmbH & Co. KGaA, Weinheim

Table 1. Effects of the solvent, the reaction temperature, and the concentration and reducibility of the reductant on the phase of product.

Reaction temperature [°C]	Solvent[a]	Molar ratio of $MnCl_2/KBH_4$ or the amount of $N_2H_4{\cdot}H_2O$	Reaction time [h]	Product[b]
150	EG	3:5	>20	γ-MnS
180	EG	3:5	>5	γ-MnS
220–240	EG	3:5	12	γ-MnS*, α-MnS
250–260	EG	3:10~15	12	γ-MnS, α-MnS
250–260	EG	3:20	12	γ-MnS, α-MnS*
180	EG	5 mL of $N_2H_4{\cdot}H_2O$	12	γ-MnS, α-MnS*
180	EG	10 mL of $N_2H_4{\cdot}H_2O$	12	α-MnS
180	EA	3:5	12	α-MnS
180	EN	3:5	12	α-MnS

[a] EG stands for ethylene glycol, EA for ethanol amine, and EN for ethylenediamine. [b] * indicates the dominant phase in the product.

that a large excess of KBH_4 (e.g. 10–20 mol) and a high reaction temperature (e.g. 240–260 °C) also resulted in the appearance of $MnCO_3$. If KBH_4 was replaced by the stronger reductant $N_2H_4{\cdot}H_2O$, α-MnS was obtained easily along with a small quantity of γ-MnS; an increase of the amount of $N_2H_4{\cdot}H_2O$ gave pure α-MnS. These results reveal that a stronger reductant and higher concentration are beneficial for the formation of α-MnS.

The influence of the solvent on the phase of the product was also studied. If EA and EN were used as the solvent, keeping the other conditions identical, the sample obtained was α-MnS. The amido groups in EA and EN, which have a strong N-chelation ability, form a relatively stable Mn^{2+} complex, which is favorable for the transformation to the stable form. $N_2H_4{\cdot}H_2O$ also has an amido group, so when it was used as the reductant α-MnS also formed.

Scheme 1 illustrates the possible mechanism for the formation of γ-MnS hollow spheres. In the detailed procedure, solid-state sulfur powder could be transformed into tiny spherical sulfur liquid droplets dispersed in the EG solvent to form a heterogeneous liquid–liquid two-phase mixture on account of the surface tension[28,29] at temperatures above the melting point of sulfur (120 °C at normal atmosphere) in the autoclave. Sulfur acts as the template for the fabrication of γ-MnS hollow spheres, as well as the sulfur source. Around the sulfur liquid droplets, BH_4^- and Mn^{2+} dissolved in EG react with them on the surface. BH_4^- can readily serve as a hydride and electron transfer agent,[30] which reduces elemental S to S^{2-} and forms MnS with Mn^{2+}. Experiments showed that elemental S can be reduced to S^{2-} by BH_4^- even in the absence of Mn^{2+} ions in this system, although Mn^{2+} ions could shift the redox reaction equilibrium to the forward reaction direction. The interface reaction results in the consumption of liquid sulfur droplets and the formation of γ-MnS hollow spheres. With the increase of the reaction temperature and the amount of KBH_4, α-MnS cubes were simultaneously obtained besides γ-MnS hollow spheres. The anisotropy of hexagonal γ-MnS should support the aggregation of the γ-MnS nanoparticles into spheres, while the formation of α-MnS cubes is maybe due to the growth character based on the cubic structure of α-MnS. In addition, compared with γ-MnS, α-MnS is high-temperature phase, and its nucleation velocity is smaller, so it is relatively difficult to be aggregated and tends to form bigger crystals.

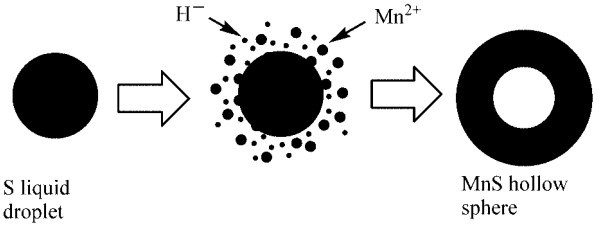

Scheme 1. Schematic illustration of the possible growth mechanism for γ-MnS hollow spheres.

The crystallization water of the reactant evidently affects the morphology of the final product. When $MnCl_2{\cdot}4H_2O$ was used without prior dehydration, then γ-MnS solid spheres and a small number of hollow spheres were obtained, as shown in Figure 3 (c) and Figure 5 (a). In the presence of the crystallization water, the reaction was accelerated owing to hydrolysis of BH_4^- with the generation of hydrogen. This reaction even occurs very rapidly at room temperature. What's more, the higher the water temperature and the smaller the ratio of water to borohydride, the more rapid the hydrolysis.[31–34] In this system most of the sulfur probably reacts with BH_4^- and Mn^{2+} before the formation of the tiny liquid sulfur droplets.

$$4S_{(s)} + BH_4^- + 2H_2O \rightarrow BO_2^- + 4S^{2-} + 8H^+$$

$$S^{2-} + Mn^{2+} \rightarrow MnS$$

This causes the fabrication of the γ-MnS solid spheres. With an increase of temperature, the remaining sulfur forms the liquid droplets that act as the template for the formation of γ-MnS hollow spheres.

Sulfur is readily soluble in EA or EN therefore the liquid sulfur droplets can't form and hence the γ-MnS hollow spheres aren't obtained.

Conclusions

In summary, metastable γ-MnS submicrometer hollow spheres and α-MnS spheres have been successfully synthesized by a solvothermal method. The reaction temperature, the solvent, and the concentration and reducibility of the reductant strongly influence the phase(s) of the product. The photoluminescence of the γ-MnS hollow spheres and α-MnS rod aggregates has been investigated at room temperature using the same excitation line at 365 nm. A possible growth mechanism for the hollow structure has also

 © 2005 Wiley-VCH Verlag GmbH & Co. KGaA, Weinheim

been tentatively proposed on the basis of the experimental results. A further exploration of the growth mechanism for the hollow structure, the control of the reaction kinetics, and the morphology of α-MnS are underway.

Experimental Section

All the chemical reagents were of analytical grade and were purchased from Shanghai Chemical Reagent Company and used without further purification. Anhydrous $MnCl_2$ was obtained by the dehydration of $MnCl_2·4H_2O$ with thionyl chloride as dehydrating agent.

Preparation of Metastable γ-MnS Hollow Spheres: Typically, a slight excess of anhydrous $MnCl_2$ (0.4 g) was dissolved in 20 mL of EG. Sulfur powder (0.096 g) and KBH_4 (0.27 g) with a 3:5 molar ratio, together with the above solution, were put into a 60-mL Teflon-lined autoclave, which was then filled with EG up to 85% of the total volume. The autoclave was sealed quickly and maintained at 150–180 °C for 5–24 h, and then cooled to room temperature naturally. The products were filtered off, washed with absolute ethanol and distilled water several times to remove impurities, and dried in vacuo at 60 °C for 4 h.

When 10 mL of 80% (wt.) hydrazine hydrate ($N_2H_4·H_2O$) solution was used instead of KBH_4, or the solvent EG was replaced by ethanol amine (EA) or ethylenediamine (EN), then α-MnS was obtained.

Sample Characterization: The X-ray powder diffraction (XRD) patterns were recorded on a Philips X'pert PRO SUPER diffractometer with Cu-K_α radiation (λ = 1.541874 Å). The X-ray photoelectron spectra (XPS) were recorded on a VGESCALAB MK II X-ray photoelectron spectrometer, using Mg-K_α radiation as the excitation source. Field-emission scanning electronic microscopy (FE-SEM) measurements were recorded with a field-emission microscope (JEOL, 7500B) operating at an acceleration voltage of 10 kV. The scanning electron microscopy (SEM) images were taken with an X-650 scanning electronic microanalyzer. The transmission electron microscopy (TEM) images and selected area electron diffraction (SAED) patterns were obtained with a Hitachi H-800 transmission electron microscope, using an accelerating voltage of 200 kV. Photoluminescence (PL) spectra of the sample were obtained on a Hitachi F-4500 fluorescence spectrophotometer at room temperature.

Acknowledgments

Financial support by the National Natural Science Foundation of China, the 973 Projects of China, and the Program for New Century Excellent Talents in Universities (NCET) is gratefully acknowledged.

[1] a) D. L. Wilcox, M. Berg, T. Bernat, D. Kellerman, J. K. Cochran, *Hollow and Solid Spheres and Microspheres: Science and Technology Associated with Their Fabrication and Application*, Materials Research Society Proceedings, MRS, Pittsburgh, PA, **1995**, p372; b) J. K. Cochran, *Curr. Opin. Solid State Mater. Sci.* **1998**, *3*, 474; c) H. Huang, E. E. Remsen, *J. Am. Chem. Soc.* **1999**, *121*, 3805; d) C. E. Fowler, D. Khushalani, S. Mann, *J. Mater. Chem.* **2001**, *11*, 1968.
[2] a) F. Caruso, *Chem. Eur. J.* **2000**, *6*, 413; b) F. Caruso, R. A. Caruso, H. Möhwald, *Science* **1998**, *282*, 1111.
[3] Z. Zhong, Y. Yin, B. Gates, Y. Xia, *Adv. Mater.* **2000**, *12*, 206.
[4] A. B. Bourlinos, M. A. Karakassides, D. Petridis, *Chem. Commun.* **2001**, *16*, 1518.
[5] K. H. Rhodes, S. A. Davis, F. Caruso, B. Zhang, S. Mann, *Chem. Mater.* **2000**, *12*, 2832.
[6] a) P. Tartaj, T. González-Carreño, C. J. Serna, *Adv. Mater.* **2001**, *13*, 1620; b) M. R. Al-Ubaidi, J. Anno, *Fusion Technol.* **1989**, *16*, 464; c) P. J. Bruinsma, A. Y. Kim, J. Liu, S. Baskarn, *Chem. Mater.* **1997**, *9*, 2507; d) Y. Lu, H. Fan, A. Stump, T. L. Ward, T. Rieker, C. J. Brinker, *Nature* **1999**, *398*, 223; e) M. Iida, T. Sasaki, M. Watanabe, *Chem. Mater.* **1998**, *10*, 3780.
[7] a) S. Schacht, Q. Huo, I. G. Voigt-Martin, G. D. Stucky, F. Schüth, *Science* **1996**, *273*, 768; b) K. J. Pekarek, J. S. Jacob, E. Mathiowitz, *Nature* **1994**, *367*, 258; c) J. G. Liu, D. L. Wilcox, *J. Mater. Res.* **1995**, *10*, 84.
[8] a) J. Hotz, W. Meier, *Langmuir* **1998**, *14*, 1031; b) K. B. Thurmond, T. Kowalewski, K. L. Wooley, *J. Am. Chem. Soc.* **1997**, *119*, 6656; c) M. Okubo, Y. Konishi, H. Minami, *Colloid Polym. Sci.* **1998**, *276*, 638.
[9] a) B. M. Discher, Y.-Y. Won, D. S. Ege, J. C.-M. Lee, F. S. Bates, D. E. Discher, D. A. Hammer, *Science* **1999**, *284*, 1143; b) M. Zhao, L. Sun, R. M. Crooks, *J. Am. Chem. Soc.* **1998**, *120*, 4877; c) M. S. Wendland, S. C. Zimmerman, *J. Am. Chem. Soc.* **1999**, *121*, 1389; d) K. B. Thurmond, *Biointerfaces* **1999**, *16*, 45; e) S. A. Jenekhe, X. L. Chen, *Science* **1998**, *279*, 1903.
[10] O. Goede, W. Heimbrodt, *Phys. Status Solidi B* **1988**, *146*, 11.
[11] C. Sombuthawee, S. B. Bonsall, F. A. Hummel, *J. Solid State Chem.* **1978**, *25*, 391.
[12] O. Goede, W. Heimbrodt, V. Weinhold, *Phys. Status Solidi B* **1987**, *143*, 511.
[13] M. Okajima, T. Tohda, *J. Cryst. Growth* **1992**, *117*, 810.
[14] B. J. Skromme, Y. Zhang, D. J. Smith, *Appl. Phys. Lett.* **1995**, *67*, 2690.
[15] L. Wang, S. Sivananthan, R. Sporken, *Phys. Rev. B* **1996**, *54*, 2718.
[16] S. W. Kennedy, K. Harris, E. Summerville, *J. Solid State Chem.* **1980**, *31*, 355.
[17] H. Wiedemeier, A. G. Sigal, *J. Cryst. Growth* **1969**, *6*, 67.
[18] O. Goede, W. Heimbrodt, V. Weinhold, *Phys. Status Solidi B* **1986**, *136*, K49.
[19] W. Heimbrodt, *Phys. Status Solidi B* **1989**, *154*, 405.
[20] M. A. Akhter, *Thin Solid Films* **1988**, *158*, 83.
[21] C. D. Lokhande, A. Ennaoui, P. S. Patil, *Thin Solid Films* **1998**, *330*, 70.
[22] J. Lu, P. F. Qi, Y. Y. Peng, Z. Y. Meng, Z. P. Yang, W. C. Yu, Y. T. Qian, *Chem. Mater.* **2001**, *13*, 2169.
[23] S. H. Kan, I. Felner, U. Banin, *Isr. J. Chem.* **2001**, *41*, 55.
[24] C. H. An, K. B. Tang, X. M. Lin, F. Q. Li, G. E. Zhou, Y. T. Qian, *J. Cryst. Growth* **2003**, *252*, 575.
[25] G. E Muilenberg, C. D. Wagner, W. M. Riggs, L. E. Davis, J. F. Moulder, *Handbook of X-ray Photoelectron Spectroscopy*, Physical Electronics Division, Perkin–Elmer Corp., New York, **1979**, p. 74.
[26] P. V. Braun, S. I. Stupp, *Mater. Res. Bull.* **1999**, *34*, 463.
[27] S. Dieluweit, D. Pum, U. B. Sleytr, *Supramol. Sci.* **1998**, *5*, 15.
[28] G. M. Barrow, *Physical Chemistry*, McGraw-Hill, New York, **1979**, ch. 21.
[29] R. B. Heslop, P. L. Robinson, *Inorganic Chemistry*, Elsevier, Amsterdam, **1963**, ch. 22.
[30] F. A. Cotton, G. Wilkinson, *Advanced Inorganic Chemistry*, 5th ed., Jonh Wiley & Sons, New York, **1988**, pp. 190–192.
[31] H. I. Schlesinger, H. C. Brown, A. E. Finholt, J. R. Gilbreath, H. R. Hoekstra, E. K. Hyde, *J. Am. Chem. Soc.* **1953**, *75*, 215.
[32] G. N. Glavee, K. J. Klabunde, C. M. Sorensen, G. C. Hadjipanayis, *Inorg. Chem.* **1995**, *34*, 28.
[33] G. N. Glavee, K. J. Klabunde, C. M. Sorensen, G. C. Hadjipanayis, *Langmuir* **1993**, *9*, 162.
[34] G. N. Glavee, K. J. Klabunde, C. M. Sorensen, G. C. Hadjipanayis, *Langmuir* **1994**, *10*, 4726.

Received: May 16, 2005
Published Online: September 5, 2005

 © 2005 Wiley-VCH Verlag GmbH & Co. KGaA, Weinheim

Synthesis and Luminescent Properties of Novel Europium(III) Heterocyclic β-Diketone Complexes with Lewis Bases: Structural Analysis Using the Sparkle/AM1 Model

Rani Pavithran,[a] M. L. P. Reddy,*[a] Severino A. Junior,[b] Ricardo O. Freire,[b] Gerd B. Rocha,[b] and Patricia P. Lima[b]

Keywords: Europium / Lewis bases / Luminescence / O ligands / Sparkle/AM1 model

Tris(β-diketonato)europium(III) complexes of general formula $[Eu(TPI)_3{\cdot}L]$, with chelating ligands such as 3-phenyl-4-(4-toluoyl)-5-isoxazolone (HTPI) and adduct-forming reagents [L = H_2O, tri-*n*-octylphosphane oxide (TOPO), triphenylphosphane oxide (TPhPO), 1,10-phenanthroline], have been synthesized and characterized by elemental analysis and FT-IR, ^1H NMR, and photoluminescence spectroscopy. The coordination geometries of the complexes were calculated using the Sparkle/AM1 (Sparkle model for the calculation of lanthanide complexes within the Austin model 1) model. The ligand–Eu^{3+} energy-transfer rates were calculated using a model of intramolecular energy transfer in lanthanide coordination complexes reported in the literature. The room-temperature PL spectra of the europium(III) complexes are composed of the typical Eu^{3+} red emission, assigned to transitions between the first excited state ($^5D_0$) and the multiplet ($^7F_{0-4}$). The results clearly show that the substitution of water molecules by TOPO leads to greatly enhanced quantum yields (i.e., 1.3 % vs. 49.5 %) and longer $^5D_0$ lifetimes (220 vs. 980 μs). This can be ascribed to a more efficient ligand-to-metal energy transfer and a less efficient nonradiative $^5D_0$ relaxation process. The theoretical quantum yields are in good agreement with the experimental quantum yields, which highlights that the present theoretical approach can be a powerful tool for the a priori design of highly luminescent lanthanide complexes.
(© Wiley-VCH Verlag GmbH & Co. KGaA, 69451 Weinheim, Germany, 2005)

Introduction

Eu^{III} complexes have been regarded as attractive for use in electroluminescent devices for light-emitting diodes,[1,2] phosphors,[3] contrast agents for medical magnetic resonance imaging,[4] luminescent probes for analytes,[5] and light-emitting sensors in fluoroimmunoassays[6] because of their red emissions. The characteristic emissions of Eu^{III} complexes mainly come from electric dipole transitions. Transition from the 4f inner shell of free Eu^{III} is forbidden because it does not correlate with the change of parity. However, transitions that are forbidden by odd parity become partially allowed by mixing 4f and 5d states through ligand-field effects of designed Eu^{III} complexes.[7] Unfortunately, the lanthanide ions are characterized by very low absorption coefficients ($\varepsilon < 1\ M^{-1}cm^{-1}$), which make direct excitation of the emitting levels impossible. Furthermore, coordination of solvent molecules to the lanthanide ions has dramatic effects on their excited state decay, because this decay is mainly governed by nonradiative processes. When solvents containing OH groups are coordinated to lanthanide ions, efficient nonradiative deactivations take place by vibronic coupling with the vibrational states of the OH oscillators.[8] A way to circumvent these difficulties is to use ligands bearing suitable chromophores that are capable of forming thermodynamically stable complexes with lanthanide ions. These ligands would play the antenna role, absorbing light and transferring excitation energy to the emitting ion. Additionally, when the Ln^{3+} cation is coordinatively unsaturated by the original ligands, an additional neutral ligand coordinates to the lanthanide center to form a highly coordinated complex, thereby excluding the coordination of solvent molecules. Recently, a large number of highly coordinated complexes of lanthanide tris(β-diketonates) containing several nitrogen ligands such as 1,10-phenanthroline, 2,2′-bipyridine, and 2,2′:6′,6′′-terpyridine have been reported.[9,10] The central Eu^{3+} ion coordinated with β-diketonato ligands gives stronger luminescence than that of the parent compounds, especially when β-diketonato ligands with aromatic or fluorinated substituents are present.[9] Phosphane oxide ligands in the europium(III) tris(β-diketonate) complex can produce a square-antiprismatic structure that promotes faster radiation rates and an increased quantum yield because of an increase in the $^5D_0$–$^7F_2$ emissions (electric dipole transitions), related to odd parity. Furthermore, increased quantum yields of the Eu^{3+} complexes can be expected because coordination of the

[a] Chemical Sciences Division, Regional Research Laboratory (CSIR),
Thiruvananthapuram 695019, India
E-mail: mlpreddy@yahoo.co.uk
[b] Departmento de Química Fundamental – UFPE,
50670-901 Recife, PE, Brazil

phosphane oxide molecule prevents coordination of water or solvent molecule and lowers vibrations.[7] The above factors prompted us to utilize a novel heterocyclic β-diketone, namely 3-phenyl-4-(4-toluoyl)-5-isoxazolone, for the preparation of coordinatively saturated Eu^{III} tris(isoxazolonate) complexes with Lewis bases such as trioctylphosphane oxide, triphenylphosphane oxide, or 1,10-phenanthroline (Figure 1). The synthesized Eu^{3+} complexes have been characterized by various spectroscopic techniques and their photophysical properties investigated.

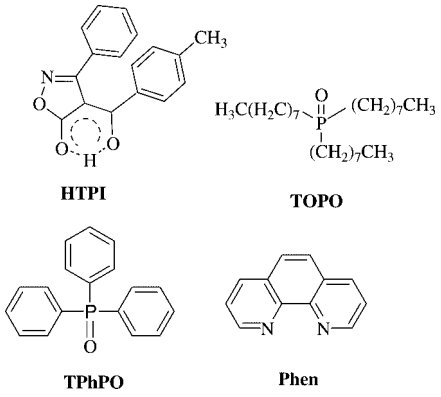

Figure 1. Structures of ligands used for the synthesis of Eu^{III} complexes.

Theoretical Approach

Sparkle Model Geometries

The ground-state geometries of all Eu^{III} complexes were calculated with the new version of the Sparkle/AM1 model[14] implemented in the MOPAC93r2 package.[15] The MOPAC keywords used in all Sparkle/AM1 calculations were: GNORM = 0.25, SCFCRT = 1.D-10 (in order to increase the SCF convergence criterion), and XYZ (the geometry optimizations were performed in Cartesian coordinates). Recently, Freire et al.[14] have improved the Sparkle model by presenting a much more accurate parameterization. This new parameterization, named Sparkle/AM1, yields an unsigned mean error for all interatomic distances between the Eu^{3+} ion and the ligand atoms of the first sphere of coordination for 96 different Eu^{3+} complexes of 0.09 Å, an improvement over the value of 0.28 Å for the second version SMLCII[16] and the value of 0.68 Å for the original version SMLC.[17]

INDO/S-CI Electronic Structures

For all calculated ground-state geometries, we predicted their singlet and triplet excited states using the intermediate neglect of differential overlap/spectroscopic configuration interaction (INDO/S-CIS) method[18,19] implemented in the ZINDO program.[20] We used a point charge of +3e to represent the trivalent europium ion. The CIS space was gradually increased until there were no further meaningful changes in the calculated transitions. In contrast, the energy levels of the Eu^{3+} metal ions were considered as being those of the free ion in the intermediate coupling scheme.[21] The INDO/S accuracy is about 1000 cm^{-1}.[18]

Energy-Transfer Rates

According to the theoretical model developed by Malta et al.,[22,23] the following expression was obtained for the ligand–lanthanide ion energy-transfer (ET) rate, W_{ET} [Equation (1)].

$$W_{ET} = W_{ET}^{mm} + W_{ET}^{em} \quad (1)$$

The first term, W_{ET}^{mm}, corresponds to the energy-transfer rate obtained from the multipolar mechanism and Equations (2) and (3)

$$W_{ET}^{mm} = W_{ET}^{mp} + W_{ET}^{dd} \quad (2)$$

$$\text{where } W_{ET}^{mp} = \frac{2\pi}{\eta}\frac{e^2 S_L}{(2J+1)G} F \sum_{\lambda} \gamma_{\lambda} \left\langle \alpha' J' \middle\| U^{(\lambda)} \middle\| \alpha J \right\rangle^2 \quad (3)$$

which correspond to the dipole–2^{λ} pole mechanism (λ = 2, 4, and 6), and Equation (4)

$$W_{ET}^{dd} = \frac{4\pi}{\eta}\frac{e^2 S_L}{(2J+1)G R_L^6} F \sum_{\lambda} \Omega_{\lambda}^{e,d} \left\langle \alpha' J' \middle\| U^{(\lambda)} \middle\| \alpha J \right\rangle^2 \quad (4)$$

corresponding to the dipole–dipole mechanism (λ = 2, 4, and 6).

The second term of Equation (1), W_{ET}^{em}, corresponds to the energy-transfer rate obtained from the exchange mechanism. This term is calculated from Equation (5)

$$W_{ET}^{em} = \frac{8\pi}{3\eta}\frac{e^2 (1-\sigma_0)^2}{(2J+1)R_L^4} F \left\langle \alpha' J' \middle\| S \middle\| \alpha J \right\rangle^2 \sum_m \left| \left\langle \phi \middle| \sum_k \mu_Z(k)\, s_m(k) \middle| \phi' \right\rangle \right|^2 \quad (5)$$

In the above equations, J represents the total angular momentum quantum number of the lanthanide ion, G is the degeneracy of the ligand initial state, a specifies a given 4f spectroscopic term, and S_L is the electric dipole strength associated with the $\varphi \rightarrow \varphi'$ transition in the ligand. The quantities are reduced matrix elements $U^{(\lambda)}$, and R_L is the distance from the lanthanide ion nucleus to the region of the ligand molecule in which the ligand donor (or acceptor) state is localized. In Equation (3), S is the total spin operator of the lanthanide ion, μ_z is the z component of the electric dipole operator and s_m (m = 0, ±1) is a spherical component of the spin operator, both for the ligand electrons, and σ_0 is a distance-dependent screening factor.

The quantities F and γ_{λ} are given by Equation (6)

 © 2005 Wiley-VCH Verlag GmbH & Co. KGaA, Weinheim

$$F = \frac{1}{\eta\gamma_L}\sqrt{\frac{\ln 2}{\pi}}\,exp\left[-\left(\frac{\Delta}{\eta\gamma_L}\right)^2 \ln 2\right] \quad (6)$$

where γ_L is the ligand-state band width at half-height and Δ is the difference between the donor and acceptor transition energies involved in the transfer process [Equation (7)].

$$\gamma_\lambda = (\lambda+1)\frac{\langle r^\lambda\rangle^2}{(R_L^{\lambda+2})^2}\langle 3\|C^{(\lambda)}\|3\rangle^2(1-\sigma_\lambda)^2 \quad (7)$$

where $\langle r^2\rangle$ is the radial expectation value of r^λ for 4f electrons, $\langle 3\|C^{(2)}\|3\rangle$ is a reduced matrix element of the Racah tensor operator $C^{(\lambda)}$,[24] and the σ_λ values are screening factors due to the 5s and 5p filled sub-shells of the lanthanide ion.

The selection rules that can be derived from the above equations are the following: $J + J' \geq \lambda \geq |J - J'|$, for the mechanisms expressed by Equations (1) and (2), and $\Delta J = 0, \pm 1$, for the exchange mechanism; in both cases $J' = J = 0$ is excluded. From the ligand side, the selection rules can be derived from the electric dipole strength, S_L, and the matrix element of the coupled operators μ_z and S_m in Equation (3). The theoretical procedures for using the above equations and the corresponding selection rules have been discussed in detail elsewhere.[25]

The numerical solution of the rate equations describing the kinetics of the 4f–4f luminescence was carried out according to this model.[23] These numerical solutions of the rate equations yield the time dependence of the energy level populations, which reach the steady-state regime after 10^{-6}–10^{-5} s. These steady-state populations were then used to calculate the emission quantum yield, which is given by Equation (8)

$$q = \frac{A_T\eta_2}{\phi\eta_1} \quad (8)$$

where the subscripts 1 and 2 indicate the ground state and the emitting level ($^5D_0$), respectively, in the complex, A_T is the sum of the coefficients of spontaneous emission for the $^5D_0 \rightarrow {}^7F_{0,1,2,4}$ transitions, and φ is the pumping rate.

The microanalyses of complexes **1**–**4** show that the Eu^{3+} ion has reacted with 3-phenyl-4-(4-toluoyl)-5-isoxazolone in a metal/ligand molar ratio of 1:3. The IR spectrum of complex **1** shows a broad absorption in the region 3000–3500 cm^{-1}, which indicates the presence of H_2O molecules in the complex. The existence of water molecules in lanthanide complexes with heterocyclic β-diketones such as 4-acyl-3-methyl-1-phenylpyrazolones is well documented.[26,27] The presence of water molecules was also noticed in the complexes **3** and **4**. The disappearance of the broad band in the region 3000–3500 cm^{-1} for complex **2**, which is associated with the coordinated water molecules in the neat complex **1**, suggests that water molecules have been displaced by the insertion of TOPO as a coordinating unit. The carbonyl stretching frequency of 3-phenyl-4-(4-toluoyl)-5-isoxazolone (1706 cm^{-1}) is shifted to lower wavenumbers in complexes **1**–**4** (1640 cm^{-1} in **1**, 1643 cm^{-1} in **2**, 1679 cm^{-1} in **3**, and 1639 cm^{-1} in **4**), thus indicating the involvement of the carbonyl oxygen atom in the complex formation with Eu^{3+}. Further, a shift in the P=O stretching frequency of the phosphane oxide molecules in complexes **2** (from 1143 to 1132 cm^{-1}) and **3** (from 1182 to 1155 cm^{-1}) shows the involvement of the phosphoryl oxygen atom in complex formation with Eu^{3+}. Vibration bands at 1608, 1574, 1476, 1445, and 1384 cm^{-1} in complex **4** are characteristic of 1,10-phenanthroline.

The ^1H NMR spectrum of complex **1** shows all expected signals for the 3-phenyl-4-(4-toluoyl)-5-isoxazolone protons. The integration of the bands is in accordance with the proposed formula. A clear indication of complex formation is given by the absence of the enolic OH peak of the free ligand HTPI. Signals for water protons were also noticed in the complex **1**, as evidenced from the IR spectroscopic data. The signals of the phenyl protons are shifted upfield upon coordination with the metal ion in the complex (from δ = 6.93–7.36 ppm in HTPI to δ = 4.99–6.57 ppm in **1**). The signal of the CH_3 group in the HTPI complex is also shifted upfield (from δ = 2.31 ppm in HTPI to δ = 2.13 ppm in **1**) upon coordination with Eu^{3+}.

Figures 2, 3, 4, and 5 show the optimized molecular structures of the Eu^{III} complexes **1**–**4**, respectively, obtained using the Sparkle/AM1 model. The Eu^{3+} ion in complexes **1**, **3**, and **4** is nine-coordinate and the coordination polyhedron can be approximately described as a tricapped trigonal prism. On the other hand, the Eu^{3+} ion in complex **2** is eight-coordinate and the coordination polyhedron can be described as a square antiprism. The spherical coordinates on the bonded oxygen atoms with respect to a coordinate system centered around the Eu^{3+} ion are given in Tables 1 and 2. These structural data are consistent with a very low symmetry of the chemical environment around the Eu^{3+} ion. An interesting point that is predicted by the present structure optimization is that the TOPO oxygen atoms are considerably closer to the Eu^{3+} ion than the H_2O oxygen atoms in the case of the hydrated compound **1**. Further, the two Eu–O bonds with TOPO ligands (2.32 and 2.33 Å) are shorter than the six Eu–O bonds with HTPI ligands (2.40–2.42 Å), as observed in the X-ray single-crystal structure (Eu–O bonds with TPhPO ligands: 2.31–2.32 Å; Eu–O bonds with hexafluoroacetylacetone ligand: 2.39–2.44 Å) of the complex tris-(hexafluoroacetylacetonato)europium(III) with phosphane oxide.[7] This clearly highlights that TOPO ligands interact more strongly with the Eu^{3+} ion in complex **2**. Similarly, the TPhPO oxygen atoms are also found to be closer to the Eu^{3+} ion than those of the water molecules in the hydrated complex. Another interesting phenomenon observed from the Sparkle/AM1 model prediction data for complex **4** is that the phenanthroline nitrogen atoms (Eu–N: 2.52 Å) are considerably further away from the Eu^{3+} ion than the HTPI oxygen atoms. This is again in good agreement with the recently reported X-ray single-crystal data

 © 2005 Wiley-VCH Verlag GmbH & Co. KGaA, Weinheim

for the complex [Eu(HFNH)$_3$] with phenanthroline [Eu–N: 2.59 and 2.61 Å; Eu–O bonds with 4,4,5,5,6,6,6-heptafluoro-1-(2-naphthyl)hexane-1,3-dione (HFNH): 2.34–2.40 Å].[28]

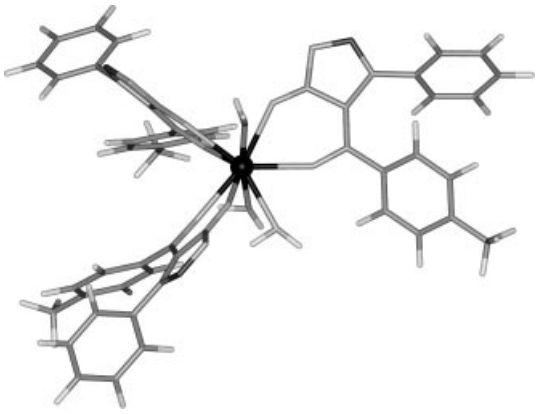

Figure 2. Optimized molecular structure of [Eu(TPI)$_3$·3H$_2$O] obtained from the Sparkle/AM1 model.

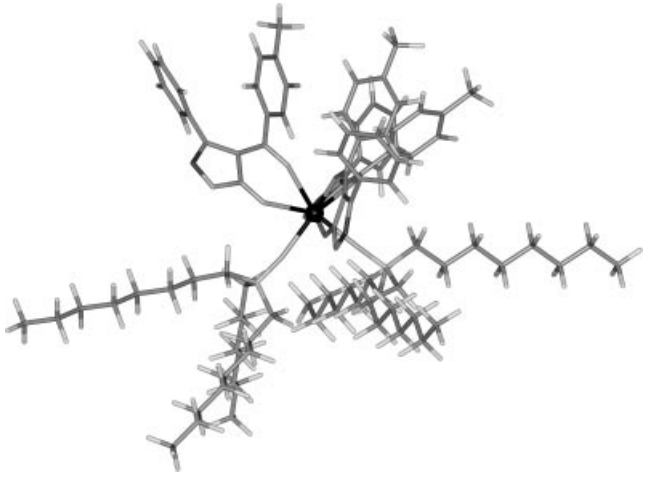

Figure 3. Optimized molecular structure of [Eu(TPI)$_3$·2TOPO] obtained from the Sparkle/AM1 model.

The excitation spectrum of the $^5D_0$ emission of Eu^{3+} in [Eu(TPI)$_3$·3H$_2$O] at 14 K is shown in Figure 6. It consists of two broad bands in the UV region, with maxima at 265, 325, and 387 nm, and 4f–4f excitation lines. The excitation spectrum suggests an efficient ligand-to-metal energy transfer, since the most intense feature is a broad band that corresponds to transitions populating ligand-centered excited states. The typical excitation spectrum of [Eu(TPI)$_3$·2TOPO] (**2**) at 300 K, depicted in Figure 7, exhibits a large, broad band between 270 and 400 nm, with a maximum around 294 nm, corresponding to ligand excitations. This strongly suggests an efficient sensitization process between the ligands and the metal ion, with the ligand unit acting as an antenna.

The room-temperature emission spectra of europium complexes **1**–**4** (in the solid state) are shown in Figures 8, 9, 10, and 11, respectively. Comparing the emission spectra of the complexes, a significant change in the profile and in the splitting of the $^5D_0 \rightarrow {}^7F_{0-4}$ transitions (essentially in the

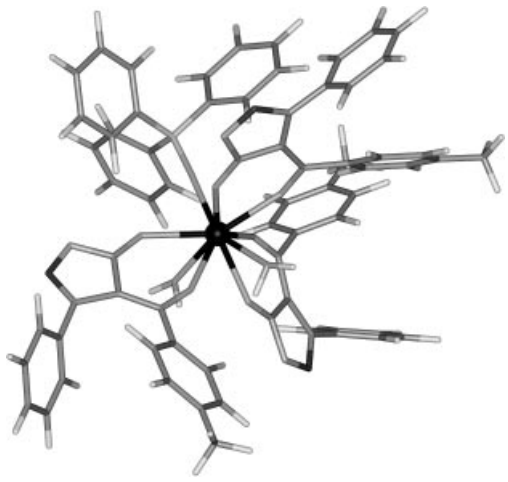

Figure 4. Optimized molecular structure of [Eu(TPI)$_3$·TPhPO·2H$_2$O] obtained from the Sparkle/AM1 model.

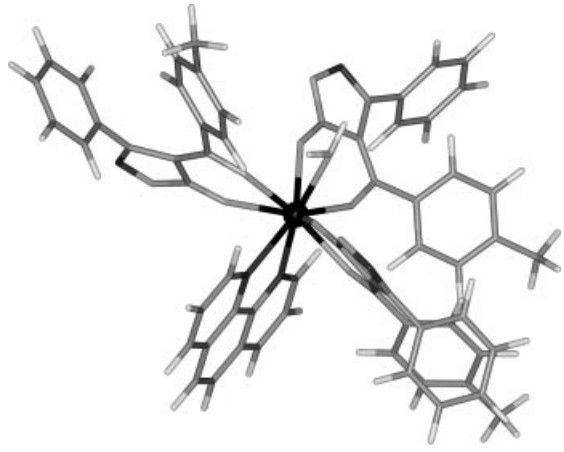

Figure 5. Optimized molecular structure of [Eu(TPI)$_3$·Phen·H$_2$O] obtained from the Sparkle/AM1 model.

Table 1. Spherical coordinates of the oxygen atoms bonded to the Eu^{3+} ion in complexes **1** and **2**.

Complex	Spherical coordinates		
	R [Å]	θ [°]	φ [°]
1	2.389	127.950	168.082
HTPI oxygen atoms	2.405	65.610	187.161
	2.403	75.196	101.320
	2.387	92.089	39.061
	2.407	59.321	295.129
	2.392	114.529	262.421
H$_2$O oxygen atoms	2.397	168.275	334.592
	2.393	10.984	113.529
	2.393	108.741	338.302
2	2.395	53.306	136.984
HTPI oxygen atoms	2.419	18.392	256.820
	2.401	108.903	74.190
	2.422	148.912	2.842
	2.398	132.205	159.055
	2.418	95.530	217.622
TOPO oxygen atoms	2.325	65.617	11.825
	2.318	98.986	288.886

 © 2005 Wiley-VCH Verlag GmbH & Co. KGaA, Weinheim

Table 2. Spherical coordinates of the nitrogen and oxygen atoms bonded to the Eu^{3+} ion in complexes **3** and **4**.

Complex	Spherical coordinates		
	R [Å]	θ [°]	φ [°]
3	2.395	34.831	245.927
HTPI oxygen atoms	2.418	90.190	209.375
	2.418	70.557	325.000
	2.406	130.082	351.408
	2.413	70.863	127.890
	2.398	90.788	65.669
TPhPO oxygen atom	2.316	151.175	150.726
H_2O oxygen atoms	2.403	101.427	269.854
	2.397	32.257	32.746
4	2.391	69.381	193.726
HTPI oxygen atoms	2.411	52.648	266.381
	2.414	89.858	125.151
	2.395	98.767	61.811
	2.413	125.792	253.769
	2.391	138.067	342.370
N (Phen)	2.520	22.017	85.750
	2.522	63.305	353.118
H_2O oxygen atom	2.396	134.142	172.751

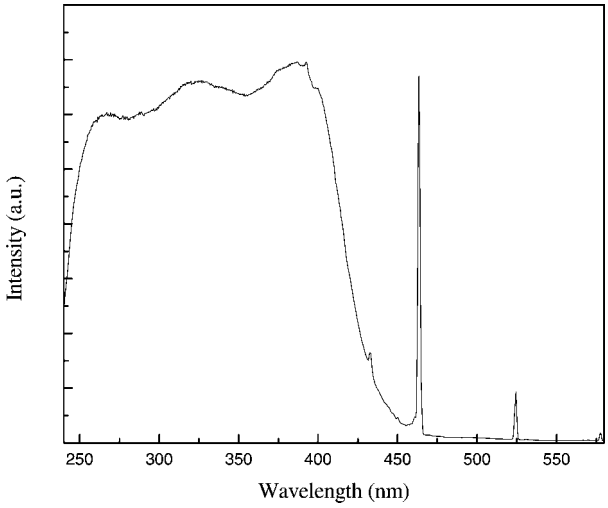

Figure 6. The excitation spectrum of $^5D_0$ emission (λ_{em} = 614 nm) of Eu^{3+} in $[Eu(TPI)_3{\cdot}3H_2O]$ (**1**) at 14 K.

$^5D_0 \rightarrow {}^7F_2$ lines) can be observed upon substitution of water molecules in **1** by Lewis bases such as TOPO, TPhPO, and Phen. The emission spectra of the complexes display characteristic sharp peaks in the 575–725 nm region associated with the $^5D_0 \rightarrow {}^7F_J$ transitions of the Eu^{3+} ion. The five expected Stark components of the $^5D_0 \rightarrow {}^7F_{0-4}$ transitions are well resolved and the hypersensitive $^5D_0 \rightarrow {}^7F_2$ transition is very intense, pointing to a highly polarizable chemical environment around the Eu^{3+} ion, and is responsible for the brilliant red emission color of these complexes.[29] The emission spectra of the complexes show only one peak for the $^5D_0 \rightarrow {}^7F_0$ transition, thus indicating the presence of a single chemical environment around the Eu^{3+} ion, and also show that the Eu^{3+} ion occupies a low symmetry site. Further, the emission band at 525 nm, corresponding to the emission from the lowest triplet state of the ligand, is not observed

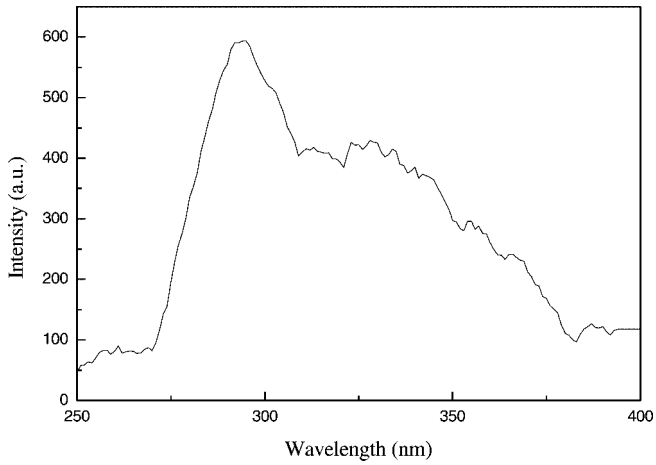

Figure 7. The excitation spectrum of $^5D_0$ emission (λ_{em} = 614 nm) of Eu^{3+} in $[Eu(TPI)_3{\cdot}2TOPO]$ (**2**) at 300 K.

in these Eu^{3+} complexes, thus indicating that energy transfer from the lowest triplet state of 4-toluoyl-5-isoxazolone to the Eu^{3+} ion is efficient.

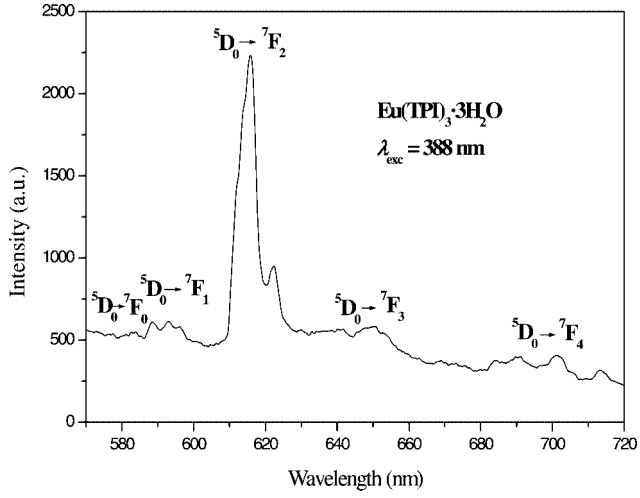

Figure 8. Room-temperature PL spectrum of compound **1** excited at 388 nm.

The experimental intensity parameters Ω_2 and Ω_4 were determined from the emission spectra (Figures 8–11) based on the $^5D_0 \rightarrow {}^7F_2$ and $^5D_0 \rightarrow {}^7F_4$ electronic transitions, respectively, and by expressing the emission intensity $I = \hbar\bar{\omega}A_{RAD}N$ in terms of the surface under the emission curve. Here $\hbar\bar{\omega}$ is the transition energy, A_{RAD} is the corresponding coefficient of spontaneous emission, and N is the population of the emitting level $^5D_0$. The magnetic dipole allowed $^5D_0 \rightarrow {}^7F_1$ transition was taken as the reference.[30,31] The A_{RAD} values are given by Equation (9)[32]

$$A_{RAD} = \frac{4e^2\omega^3}{3\eta c^3}\chi\sum_{\lambda}\Omega_\lambda\left\langle {}^7F_J\left\|U^{(\lambda)}\right\|{}^5D_0\right\rangle^2\frac{1}{2J+1} \quad (9)$$

where, λ = 2 and 4, χ is the Lorentz local field correction term that is given by $n(n^2 + 2)^2/9$, with a refraction index, n,

 © 2005 Wiley-VCH Verlag GmbH & Co. KGaA, Weinheim

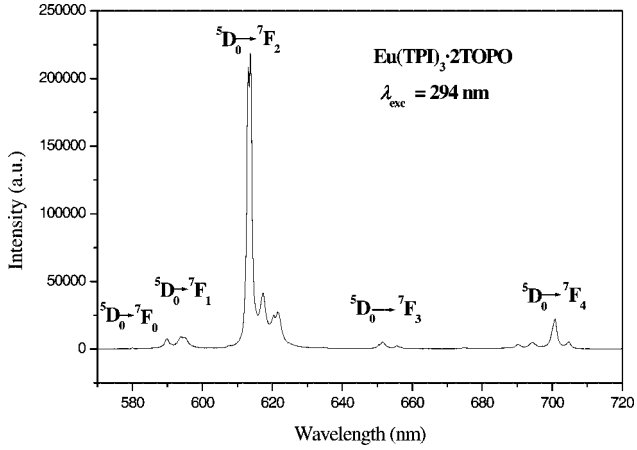

Figure 9. Room-temperature PL spectrum of compound **2** excited at 294 nm.

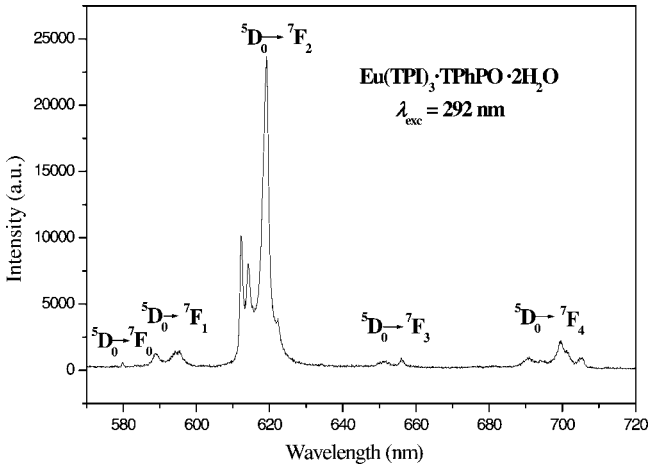

Figure 10. Room-temperature PL spectrum of compound **3** excited at 292 nm.

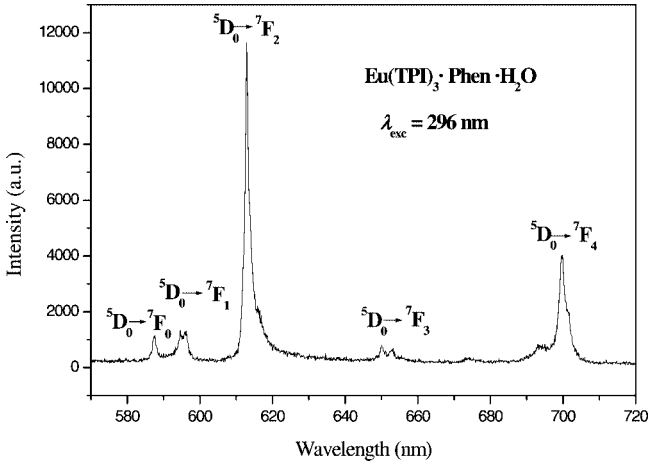

Figure 11. Room-temperature PL spectrum of compound **4** excited at 296 nm.

of 1.5, and $\langle {}^5D_0 \| U^{(2)} \| {}^7F_J \rangle^2$ are the squared reduced matrix elements whose values are 0.0032 and 0.0023 for $J = 2$ and 4, respectively.[21] Table 3 presents the values of Ω_2 and Ω_4 for complexes **1**–**4** at room temperature (300 K) and the values at 14 K for complex **1**. The high values of Ω_2 for complexes **1**–**3** might be interpreted as a consequence of the hypersensitive behavior of the $^5D_0 \rightarrow {}^7F_2$ transition,[33] suggesting that dynamic coupling mechanism is quite operative in these complexes.

Table 3. Experimental intensity parameters, radiative (A_{RAD}) and nonradiative decay rates (A_{NR}), experimental (q_{exp}) and theoretical emission quantum yields (q_{theo}), $^5D_0$ lifetime (τ), and quantum efficiency (ε) for complexes **1**–**4** at 300 K.

	Ω_2 ($\times 10^{-20}$) [cm^2]	Ω_4 ($\times 10^{-20}$) [cm^2]	A_{RAD} [s^{-1}]	A_{NR} [s^{-1}]	q_{exp} [%]	q_{theo} [%]	τ [ms]	ε [%]
1	8.10	5.76	381	2952	1.3	10.80	0.30	13
1[a]	11.93	11.28	580	2277	–	–	0.35	20
2	20.72	6.42	773	242	49.5	52.53	0.98	76
3	17.55	5.76	658	1265	8.3	23.00	0.52	34
4	6.02	6.99	335	1304	5.5	14.02	0.61	20

[a] Measured at 14 K.

By comparing the values of the Ω_2 parameter determined for the complexes at room temperature, it can be concluded that the polarizability is in the order [Eu(TPI)$_3$·Phen·H$_2$O] (**4**) < [Eu(TPI)$_3$·3H$_2$O] (**1**) < [Eu(TPI)$_3$·TPhPO·2H$_2$O] (**3**) and [Eu(TPI)$_3$·2TOPO] (**2**). As pointed out by Reisfeld and Jørgensen,[34] the intensity parameter Ω_2 can be correlated to the degree of covalency experienced by the lanthanide ion, greater values being obtained in more covalent surroundings (e.g., 1.2×10^{-20} cm^2 for LaF_3:Eu; 1×10^{-19} cm^2 for Y_2O_3:Eu). Therefore, the high value of Ω_2 obtained for complex **2** in the present investigations indicates that the covalent contribution is larger for the complex containing the TOPO ligand, which may be ascribed to stronger bonding. It can be argued that this is expected to increase the ligand–Eu^{3+} ion energy-transfer rate,[35] since a stronger bond causes the ligand–metal ion distances to be shorter, thus increasing electric-dipole interactions and wavefunction overlap.

The lifetime values (τ) of the $^5D_0$ level were determined from the luminescence decay profiles for the complexes at room temperature by fitting with a mono-exponential curve; they are listed in Table 3. The relatively shorter lifetimes obtained for complex **1** may be due to dominant nonradiative decay channels associated with vibronic coupling due to the presence of water molecules, as has been documented in many hydrated europium β-diketonate complexes.[25] A longer lifetime value has been observed for complex **2** as compared to complexes **3** and **4**. This may also be due to the presence of water molecules in complexes **3** and **4**.

The nonradiative rates, A_{NR}, can be obtained from the calculated A_{RAD} rates and the experimental decay rates by Equation (10).[35]

$$\tau^{-1} = A_T = A_{RAD} + A_{NR} \quad (10)$$

It is clear from Table 3 that complexes **1**, **3**, and **4**, which have water molecules in the coordination sphere, exhibit lower quantum efficiencies and lifetimes. This is due to the

 © 2005 Wiley-VCH Verlag GmbH & Co. KGaA, Weinheim

presence of O–H oscillators in these systems, which effectively quench the luminescence of the Eu^{3+} ion. On the other hand, complex **2**, which does not contain any water molecule in its coordination sphere, as is also evident from the molecular structure analysis with the Sparkle/AM1 model, exhibits high quantum efficiency and lifetime values. The experimental and theoretical quantum yields of these complexes increase in the order **1** < **4** < **3** < **2**. The theoretical quantum yield of complex **2** is in good agreement with the experimental value. On the other hand, the degree of agreement between the theoretical and experimental quantum yields in the case of **1**, **3**, and **4** is not promising. This may be due to the fact that the model for quantum yield does not take into account the suppression by vibronic coupling with coordinated water molecules. Another factor contributing towards the error could be the phenomenon of nonradiative deactivation via a charge-transfer state involving the metal and the ligand.

The energy-transfer rates from the ligand triplet state T to the $^5D_1$ and $^5D_0$ levels and energy-transfer rates from the singlet state S to the $^5D_4$ level are presented in Table 4. We assumed a singlet→triplet intersystem crossing rate of 10^8 s^{-1}, a triplet state decay rate of 10^5 s^{-1}, and a nonradiative decay rate of 10^6 s^{-1}.[9] The theoretical energies of the singlet and triplet were used in the calculation of the energy-transfer rates. We considered an average of the three singlet and triplet excited states where the difference of the energy between the average values of the triplet states of the ^5D_J levels is smaller than 9.000 cm^{-1}. The average values of the singlet excited states were chosen because these values are closer to the values of the experimental singlet excited state of the complexes. The values for the theoretical triplet excited states were also chosen in the same way. An energy level diagram for the compound [$Eu(TPI)_3$·2TOPO] is shown in Figure 12. The symbols S_0, T, and S_1 shown in Figure 12 refer to the ground singlet, lowest energy triplet, and first excited singlet, respectively. The theoretical energies of the singlet and triplet were used in this diagram.

Table 4. Predicted values of intramolecular energy-transfer rates in compounds **1**–**4**. The back transfer rates were calculated by multiplying the direct transfer rates by the Boltzmann factor $e^{-|\Delta|/kT}$ at room temperature.

Compound	Levels	Transfer rate [s^{-1}]	Back transfer rate [s^{-1}]
1	$S_1 \rightarrow {}^5D_4$	1.386×10^5	1.924×10^{-5}
	$T \rightarrow {}^5D_1$	3.933×10^8	3.400×10^{-1}
	$T \rightarrow {}^5D_0$	8.353×10^7	9.757×10^{-6}
2	$S_1 \rightarrow {}^5D_4$	7.698×10^4	8.703×10^{-8}
	$T \rightarrow {}^5D_1$	1.703×10^8	4.121×10^{-4}
	$T \rightarrow {}^5D_0$	2.541×10^7	8.298×10^{-9}
3	$S_1 \rightarrow {}^5D_4$	4.311×10^4	7.148×10^{-9}
	$T \rightarrow {}^5D_1$	1.028×10^8	1.738×10^{-5}
	$T \rightarrow {}^5D_0$	1.306×10^7	2.982×10^{-10}
4	$S_1 \rightarrow {}^5D_4$	6.757×10^5	5.010×10^{-1}
	$T \rightarrow {}^5D_1$	1.169×10^8	7.086×10^{-5}
	$T \rightarrow {}^5D_0$	1.604×10^7	1.313×10^{-9}

According to the selection rules for the process of energy transfer, in the case of the ion Eu^{3+}, levels $^5D_2$, $^5L_6$, $^5G_6$, and $^5D_4$ are good candidates for the multipolar mechanism, while for the exchange mechanism a strong candidate is level $^5D_1$.[36] Therefore for the complexes in this work, the predominant process in the transfer of energy is the exchange mechanism. In accordance with Table 4, the values of the energy-transfer rate indicate that the energy transfer is predominant from the triplet state of the ligand to the $^5D_1$ and $^5D_0$ levels of the Eu^{3+} ion.

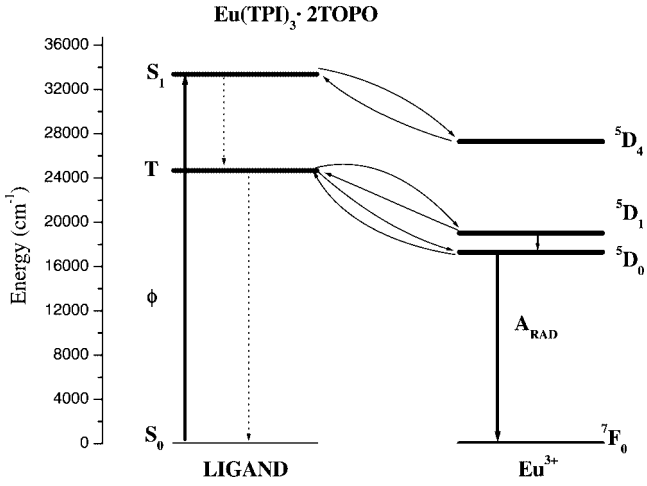

Figure 12. The energy level diagram of ligands and Eu^{3+} ion in [$Eu(TPI)_3$·2TOPO].

Conclusions

In the present study, various new 3-phenyl-4-(4-toluoyl)-5-isoxazolonate complexes of Eu^{3+} with Lewis bases such as tri-*n*-octylphosphane oxide, triphenylphosphane oxide, and 1,10-phenanthroline have been synthesized and characterized by various spectroscopic techniques. Their ground-state geometries have been calculated using the Sparkle/AM1 model. Experimental and theoretical results on ligand-field parameters, 4f–4f intensities, and intramolecular energy-transfer processes have been described. The photophysical properties of the above complexes have been determined and compared with the theoretical predictions.

The characteristic emission spectra of Eu^{3+} complexes **1**–**4** show a very high intensity for the hypersensitive $^5D_0 \rightarrow {}^7F_2$ transition, pointing to a highly polarizable chemical environment around the Eu^{3+} ion. The theoretically predicted values of intramolecular energy-transfer rates of complexes **1**–**4** clearly indicate that the energy transfer is predominant from the triplet state of the ligand to the $^5D_1$ and $^5D_0$ levels of the Eu^{3+} ion. Higher quantum yields (49.5%) and lifetime values (980 μs) are observed for complex **2** than for complexes **1**, **3**, and **4**, and this can be ascribed to a more efficient ligand-to-metal energy transfer and less efficient nonradiative $^5D_0$ relaxation process in the former case. This is also in accordance with the strong coordination between the oxygen atom of TOPO and the Eu^{3+} ion, as predicted by the Sparkle model. It is also important to point out that there is a good agreement between the experimental and the theoretical quantum yields, especially for complex **2**, thus

 © 2005 Wiley-VCH Verlag GmbH & Co. KGaA, Weinheim

showing that the theoretical estimation of quantum yields can be a valuable tool for developing efficient light conversion molecular devices (LCMDs). The luminescent properties observed in the Eu–heterocyclic β-diketonate complexes indicate that 3-phenyl-4-aroyl-5-isoxazolones form a promising class of antenna molecules that can be employed in the design of new LCMDs.

Experimental Section

Materials and Methods: The commercially available chemicals europium(III) nitrate hexahydrate, 99.9% (Acros Organics); 3-phenyl-5-isoxazolone, 98% (Aldrich), 4-toluoyl chloride, 98% (Aldrich), trioctylphosphane oxide, 99% (Aldrich), triphenylphosphane oxide, 98% (Aldrich), and 1,10-phenanthroline, 99.5% (Merck) were used without further purification. All the other chemicals used were of analytical reagent grade. C, H and N analyses were performed with a Perkin–Elmer Series 2 Elemental Analyser 2400. A Nicolet FT-IR 560 Magna Spectrometer (KBr, neat) was used to obtain IR spectroscopic data and a Bruker 300 MHz NMR spectrometer was used to obtain ^{1}H NMR spectra of the compounds in $CDCl_3$ or [D_6]acetone. Photoluminescence (PL) spectra were recorded with a Jobin Yvon Spex spectrometer (HR, 460) coupled to an R928 Hamamatsu photomultiplier. A Xe arc lamp (150 mW) coupled to a Jobin Yvon Spex monochromator (TRIAX 180) was used as the excitation source. All the spectra were corrected for the response of the detector. The lifetime measurements were taken using a pulsed Xe arc lamp (5 mJ/pulse, 3 ms bandwidth) coupled to a Kratos GM-252 monochromator and a Spex 1934 C phosphorimeter. The emission quantum yield, q_x, of the $^5D_0$ emission band of the Eu^{III} complexes, defined as the ratio between the number of photons emitted by the Eu^{3+} ion and the number of photons absorbed by the ligand, was determined from the following formula:

$$q_x = \left(\frac{1-r_{st}}{1-r_x}\right)\left(\frac{\Delta\Phi_x}{\Delta\Phi_{st}}\right)q_{st}$$

where r_{st} and r_x are the amounts of exciting radiation reflected by the standard phosphor and by the sample, respectively, and q_{st} is the quantum yield of the standard phosphor. The terms $\Delta\Phi_x$ and $\Delta\Phi_{st}$ give the integrated photon flux (photons per second) for the sample and the standard phosphor, respectively. A detailed description of this method has been presented elsewhere.[11,12]

Synthesis of 3-Phenyl-4-(4-toluoyl)-5-isoxazolone (HTPI): A mixture of 3-phenyl-5-isoxazolone (3 g, 18 mmol), $Ca(OH)_2$ (2.7 g, 27 mmol), and dioxane (30 mL) was heated at 50 °C for 0.5 h. 4-Toluoyl chloride (2.88 g, 18 mmol) was then added dropwise and the mixture stirred for 6 h (Scheme 1). The crude product was filtered, dried, and recrystallized from ethyl acetate.[13] The synthesized 3-phenyl-4-(4-toluoyl)-5-isoxazolone was identified by elemental analyses and IR and ^{1}H NMR spectroscopic data.

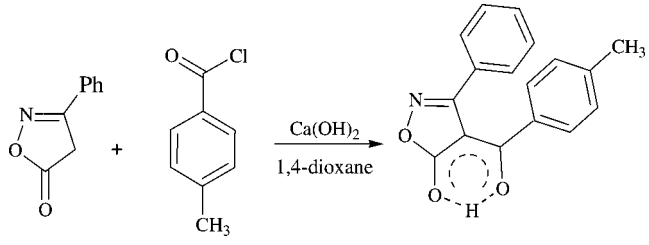

Scheme 1.

HTPI: M.p. 145 °C. ^{1}H NMR: δ = 6.93–7.37 (m, 9 H, phenyl), 2.31 (3 H, methyl) ppm. The peak observed at δ = 4.08 ppm corresponds to the enolic OH group in the compound, which was found to undergo exchange on addition of D_2O, thus confirming the existence of this compound in the enolic form. The absence of a peak at δ = 3.8 ppm corresponding to the methylene proton at position 4 of the isoxazolone ring further confirms the existence of HTPI quantitatively in the enolic form. IR: $\tilde{\nu}$ = 2600, 1706, 1613, 1600, 830 cm^{-1}. $C_{17}H_{13}NO_3$ (279): calcd. C 73.12, H 4.66, N 5.02; found C 73.52, H 4.73, N 5.31.

[Eu(TPI)$_3$·3H$_2$O] (1): An aqueous solution of $Eu(NO_3)_3·6H_2O$ (0.5 mmol) was added to a solution of HTPI (1.5 mmol) in ethanol in the presence of NaOH (1.5 mmol). Precipitation took place immediately and the reaction mixture was stirred at room temperature for 10 h (Scheme 2). It was then filtered, washed with ethanol, water and then with ethanol, and dried and stored in a desiccator. $C_{51}H_{42}EuN_3O_{12}$ (1040.0): calcd. C 58.84, H 4.04, Eu 14.61, N 4.04; found C 58.63, H 4.27, Eu 14.59, N 4.4. IR (KBr): $\tilde{\nu}_{max}$ = 3300, 2919, 1640, 1606, 1441, 1387, 1189, 917, 771 cm^{-1}.

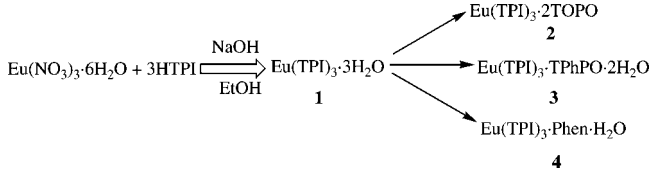

Scheme 2.

[Eu(TPI)$_3$·2TOPO] (2): An aqueous solution of $Eu(NO_3)_3·6H_2O$ (0.5 mmol) was added to a mixture of HTPI (1.5 mmol) and TOPO (1.0 mmol) in ethanol in the presence of NaOH (1.5 mmol). Precipitation took place immediately and the reaction mixture was stirred at room temperature for 10 h (Scheme 2). It was then filtered, washed with ethanol, water and then with ethanol, dried, and stored in a desiccator.$C_{99}H_{138}EuN_3O_{11}P_2$ (1759.3): calcd. C 67.53, H 7.84, Eu 8.64, N 2.39; found C 67.57, H 8.16, Eu 8.61, N 2.59. IR (KBr): $\tilde{\nu}_{max}$ = 2925, 2839, 1643, 1603, 1570, 1483, 1380, 1132, 909, 767 cm^{-1}.

[Eu(TPI)$_3$·TPhPO·2H$_2$O] (3): An aqueous solution of $Eu(NO_3)_3·6H_2O$ (0.25 mmol) was added to a mixture of HTPI (0.75 mmol) and TPhPO (0.5 mmol) in ethanol in the presence of NaOH (0.75 mmol). Precipitation took place immediately and the reaction mixture was stirred at room temperature for 10 h (Scheme 2). It was then filtered, washed with ethanol, water and then with ethanol, dried, and stored in a desiccator.$C_{69}H_{55}EuN_3PO_{12}$ (1300.3): calcd. C 63.67, H 4.23, Eu 11.68, N 3.23; found C 63.69, H 3.64, Eu 11.64, N 3.44. IR (KBr): $\tilde{\nu}_{max}$ = 3400, 2912, 2853, 1679, 1640, 1606, 1480, 1381, 1155, 910, 771 cm^{-1}.

[Eu(TPI)$_3$·Phen·H$_2$O] (4): An aqueous solution of $Eu(NO_3)_3·6H_2O$ (0.5 mmol) was added to a mixture of HTPI (1.5 mmol) and 1,10-phenanthroline (0.5 mmol) in ethanol in the presence of NaOH (1.5 mmol). Precipitation took place immediately and the reaction mixture was stirred at room temperature for 10 h (Scheme 2). It was then filtered, washed with ethanol, water and then with ethanol, dried, and stored in a desiccator. $C_{63}H_{46}EuN_5O_{10}$ (1184.2): calcd. C 63.84, H 3.88, Eu 12.83, N 5.91; found C 64.08, H 3.92, Eu 12.80, N 5.09. IR (KBr): $\tilde{\nu}_{max}$ = 3402, 2919, 1639, 1608, 1574, 1476, 1445, 1384, 1180, 916, 844, 766 cm^{-1}.

 © 2005 Wiley-VCH Verlag GmbH & Co. KGaA, Weinheim

Acknowledgments

The authors would like to acknowledge the financial support from the Council of Scientific and Industrial Research and Defence Research and Development Organization, India. The authors also wish to thank Prof. T. K. Chandrashekar, Director, Regional Research Laboratory, Trivandrum, for constant encouragement. The authors acknowledge CNPq, CAPES, FACEPE (Brazilian agencies), PRONEX, PROFIX, Instituto do Milênio de Materiais Complexos, and Programa Primeiros Projetos for financial support, and CENAPAD (Brazilian institution) for providing the computational facilities.

[1] J. Kido, Y. Okamoto, *Chem. Rev.* **2002**, *102*, 2357–2368.
[2] Y. Hasegawa, Y. Wada, S. Yanagida, *J. Photochem. Photobiol. C: Photochem. Rev.* **2004**, *5*, 183–202.
[3] T. Justel, H. Nikol, C. Ronda, *Angew. Chem. Int. Ed.* **1998**, *37*, 3084–3103.
[4] P. Caravan, J. J. Ellison, T. J. McMurry, R. B. Lauffer, *Chem. Rev.* **1999**, *99*, 2293–2352.
[5] D. Parker, *Coord. Chem. Rev.* **2000**, *205*, 109–130.
[6] J. C. G. Bünzli, C. Piguet, *Chem. Rev.* **2002**, *102*, 1897–1928.
[7] Y. Hasegawa, M. Yamamuro, Y. Wada, N. Kanehisa, Y. Kai, S. Yanagida, *J. Phys. Chem. A* **2003**, *107*, 1697–1702.
[8] N. Sabbatini, M. Guardigli, J. M. Lehn, *Coord. Chem. Rev.* **1993**, *123*, 201–228.
[9] G. F. de Sa, O. L. Malta, C. de Mello Donegá, A. M. Simas, R. L. Longo, P. A. Santa-Cruz, E. F. da Silva, Jr., *Coord. Chem. Rev.* **2000**, *196*, 165–195.
[10] A. Bellusci, G. Barberio, A. Crispini, M. Ghedini, M. La Deda, D. Pucci, *Inorg. Chem.* **2005**, *44*, 1818–1825.
[11] C. de Mello Donegá, S. J. L. Ribeiro, R. R. Gonçalves, G. Blasse, *J. Phys. Chem. Solids* **1996**, *57*, 1727–1734.
[12] C. de Mello Donegá, S. A. Junior, G. F. de Sa, *Chem. Commun.* **1996**, 1199–1200.
[13] R. Pavithran, M. L. P. Reddy, *Radiochim. Acta* **2004**, *92*, 31–38.
[14] R. O. Freire, G. B. Rocha, A. M. Simas, *Inorg. Chem.* **2005**, *44*, 3299–3310.
[15] J. J. P. Stewart, *MOPAC 93.00 Manual*, Fujitsu Limited: Tokyo, Japan, **1993**.
[16] G. B. Rocha, R. O. Freire, N. B. da Costa, Jr., G. F. de Sa, A. M. Simas, *Inorg. Chem.* **2004**, *43*, 2346–2354.
[17] A. V. M. Andrade, N. B. da Costa, Jr., A. M. Simas, G. F. de Sa, *Chem. Phys. Lett.* **1994**, *227*, 349–353.
[18] J. E. Ridley, M. C. Zerner, *Theor. Chim. Acta* **1976**, *42*, 223–236.
[19] M. C. Zerner, G. H. Loew, R. F. Kirchner, U. T. Mueller-Westerhoff, *J. Am. Chem. Soc.* **1980**, *102*, 589–599.
[20] M. C. Zerner, *ZINDO manual*, **1990**, QTP, University of Florida, Gainesville, FL. 32611.
[21] W. T. Carnall, H. M. Crosswhite, *Energy levels, Structure and Transition Probabilities of the Trivalent Lanthanides in LaF_3*, Argonne National Laboratory Illinois, **1977**.
[22] O. L. Malta, F. R. Gonçalves e Silva, *Spectrochim. Acta A* **1998**, *54*, 1593–1599.
[23] O. L. Malta, F. R. Gonçalves e Silva, R. Longo, *Chem. Phys. Lett.* **1999**, *307*, 518–526.
[24] B. R. Judd, *Operator Techniques in Atomic Spectroscopy*, 2nd ed., McGraw-Hill Book Company, New York, USA, **1998**.
[25] O. L. Malta, H. F. Brito, J. F. S. Menezes, F. R. Gonçalves e Silva, S. Alves, Jr., F. S. Farias, Jr., A. M. V. de Andrade, *J. Lumin.* **1997**, *75*, 255–268.
[26] C. Pettinari, F. Marchetti, A. Cingolann, A. Drozdov, I. Timokhin, S. I. Troyanov, V. Tsaryuk, V. Zolin, *Inorg. Chim. Acta* **2004**, *357*, 4181–4190.
[27] D. Zhou, Q. Li, C. H. Huang, G. Yao, S. Umetani, M. Matsui, L. Ying, A. Yu, X. Zhao, *Polyhedron* **1997**, *16*, 1381–1389.
[28] J. Yu, L. Zhou, H. Zhang, Y. Zheng, H. Li, R. Deng, Z. Peng, Z. Li, *Inorg. Chem.* **2005**, *44*, 1611–1618.
[29] N. Sabbatini, M. Guardigli, I. Manet, in *Handbook on the Physics and Chemistry of Rare Earths, 21* (Eds.: K. A. Gschneidner, Jr., L. Eyring), Elsevier Science B. V., North Holland, **1996**, p. 69–119.
[30] O. L. Malta, M. A. C. dos Santos, L. C. Thompson, N. K. Ito, *J. Lumin.* **1996**, *69*, 77–84.
[31] O. L. Malta, H. F. Brito, J. F. S. Menezes, F. R. Gonçalves e Silva, S. Alves, Jr., F. S. Farias, Jr., A. V. M. de Andrade, *J. Lumin.* **1997**, *75*, 255–268.
[32] B. R. Judd, *Phys. Rev.* **1962**, *127*, 750–761.
[33] R. D. Peacock, *Struct. Bond.* **1975**, *22*, 83–121.
[34] R. Reisfeld, C. K. Jørgensen, in *Handbook on the Physics and Chemistry of Rare Earths* (Eds.: K. A. Gschneidner, Jr., L. Eyring), Elsevier Science B. V., North Holland, **1987**, chapter 58.
[35] C. de Mello Donegá, S. Alves, Jr., G. F. de Sá, *J. Alloys Compd.* **1997**, *250*, 422– 426.
[36] O. L. Malta, *J. Lumin.* **1997**, *71*, 229–236.

Received: May 20, 2005
Published Online: September 12, 2005

 © 2005 Wiley-VCH Verlag GmbH & Co. KGaA, Weinheim

Direct Syntheses and Structural Novelty of Lanthanoid Aryloxides with Flexible Radial Arms

Marcus L. Cole,[a][‡] Glen B. Deacon,[a] Peter C. Junk,*[a,b] Kathryn M. Proctor,[b] Janet L. Scott,[b] and Christopher R. Strauss[b]

Keywords: Lanthanoids / Aryloxides / Benzyl group / π-Donors / Phenolates / X-ray crystal structures

Direct treatment of excess lanthanum, europium or ytterbium metal with 2,6-dibenzylphenol (HOdbp) at 150 °C afforded $[La_2(Odbp)_6]$, $[Eu_2(Odbp)_4]$ and $[Yb(Odbp)_2]_n$, respectively, in high yields. Alternatively, treatment of Yb metal with excess HOdbp gave an ytterbium(III) species $[Yb_2(Odbp)_6]$, similar to the lanthanum analogue. X-ray crystal structures were obtained for $[La_2(Odbp)_6]$, $[Eu_2(Odbp)_4]$ and $[Yb_2(Odbp)_6]$. $[La_2(Odbp)_6]$ and $[Yb_2(Odbp)_6]$ are pseudo-centrosymmetric dimers with two terminal and four bridging $Odbp^-$ ligands and $[Eu_2(Odbp)_4]$ crystallizes as a centrosymmetric dimer with further organization in a polymeric form through supramolecular interactions. All three structurally characterized compounds achieve coordination saturation by Ln–π-arene interactions.
(© Wiley-VCH Verlag GmbH & Co. KGaA, 69451 Weinheim, Germany, 2005)

Introduction

Lanthanoid aryloxides are accessible by a wide array of synthetic routes and exhibit an enormous structural variety.[1] Use of bulky aryloxides has provided a range of exciting low-coordinate complexes for both Ln^{II} and Ln^{III} oxidation states.[1] Whilst most of these have additional neutral ligands, e.g. $[Ln(OAr)_3(THF)_n]$ (n = 1–3), (where OAr = 2,6-diphenylphenolate,[2] 2,6-diisopropylphenolate,[3] 3,5-dimethyl-2,6-diphenylphenolate,[4a] 3,5-di-*tert*-butyl-2,6-diphenylphenolate[4a] and 3,5-di-*tert*-butylphenolate[4b]), there has been increasing interest in homoleptic complexes, both neutral $[Ln(OAr)_n]$ (n = 2 or 3, where OAr = 2,6-diphenylphenolate[5] and 2,6-di-*tert*-butylphenolates[6]) and anionic $[Ln(OAr)_4]^-$ (where OAr = 2,6-diphenylphenolate[5a,7] 2,6-diisopropylphenolate,[8,9] 2,6-di-*tert*-butyl-4-methylphenolate[10]). Homoleptic complexes of the bulkiest aryloxides (OAr = $OC_6H_2tBu_2$-2,6-X-4, where X = H, Me) are normally coordinatively and sterically saturated with solely oxygen donors. However, less bulky phenolates, e.g. OAr = $OC_6H_3Ph_2$-2,6,[5,7] $OC_6H_3iPr_2$-2,6,[8,9] give rise to additional π-arene–Ln interactions ranging from η^1 to η^6. These can involve either the pendant groups as with $OC_6H_3Ph_2$-2,6[5,7] or the central arene as with $OC_6H_3iPr_2$-2,6.[8,9] Use of more flexible side arms presents opportunities for optimal π-arene–Ln coordination geometry provided that the interaction is strong enough to overcome the capacity of the aryl group to rotate away. We now report novel lanthanoid complexes obtained from the direct reactions of La, Eu or Yb metal with 2,6-dibenzylphenol (HOdbp) and find extensive π-arene–Ln interactions in the solid state. These are the first lanthanoid benzylphenolates to show such interactions, which do not appear to be exhibited by related calixarenes.[11]

Results and Discussion

Direct treatment of excess lanthanum, europium or ytterbium metal with 2,6-dibenzylphenol (HOdbp), in an evacuated Carius tube at 170 °C for 4 d, afforded crystalline material comprising $[Ln(Odbp)_n]_2$ [Ln = La, n = 3 (**1**); Ln = Eu, n = 2 (**2**)] or $[Yb(Odbp)_2]_n$ (**3**) [Equations (1) and (2)]. Initially, several drops of mercury were added to the reaction mixture to form a reactive lanthanoid amalgam. In previous related syntheses,[4,5] this was found to be essential for complete reaction. However, subsequently, it was found that the reactions occurred cleanly and in significant but lower yield without mercury for **1** and **2**, but not for **3** or **4**. In all cases crystals were obtained directly from the reaction tube. Low solubility in non-coordinating solvents (e.g. hexane and toluene) necessitated separation of crystalline products from excess metal by hand-picking under a microscope. In an attempt to improve the method of isolation, experiments were performed in the presence of excess ligand (rather than metal), followed by sublimation or washing out of the residual ligand from the product. In the cases of compounds **1** and **2**, this presented no apparent problems, but

[a] School of Chemistry, Box 23, Monash University, Clayton, Victoria 3800, Australia
Fax: +61-3-9905-4597
[b] Special Research Centre for Green Chemistry, Monash University, Clayton, Victoria 3800, Australia
E-mail: peter.junk@sci.monash.edu.au
[‡] Current address: Department of Chemistry, University of Adelaide, South Australia 5005, Australia

 DOI: 10.1002/ejic.200500530

for Ln = Yb, a Yb^{III} species, $[Yb_2(Odbp)_6]$ (**4**), was obtained rather than the Yb^{II} compound **3**. This is not surprising since previously we have found that excess lanthanoid metal in redox transmetallation reactions,[12] as well as in direct Ln metal/phenol reactions,[5a] aids in formation of the lower oxidation state product. Excess metal acts as a reductant if any Ln^{III} species is formed for Ln = Yb. The formation of compound **4** rather than **3** contrasts with the chemistry of compound **2**, where the Eu^{II} species is obtained when either excess metal or ligand is used. The results are consistent with Eu having the most stable divalent state of the lanthanoids.

$$Ln_{(metal)} + 2n\,HOdbp \xrightarrow{170^{o}C} [Ln(Odbp)_n]_2 + n\,H_2$$

Ln = La, n = 3 (**1**); Ln = Eu, n = 2 (**2**)
Ln = Yb, n = 3 (**4**) (1)

$$Yb_{(metal)} + 2n\,HOdbp \xrightarrow{170^{o}C} [Yb(Odbp)_2]_n + n\,H_2 \quad (2)$$

The infrared spectra of all compounds showed the absence of an OH stretching band at around 3560 cm^{-1} establishing complete deprotonation of the phenol. Furthermore, in the ^1H NMR spectrum (C_6D_6) of compounds **1** and **3**, there was no appreciable resonance at $\delta \approx 4.6$ ppm for the OH protons (however, products consistently showed small amounts of phenol detectable in the IR and NMR spectra perhaps arising from slight decomposition during measurement). Unfortunately, compounds **2** and **4** were too insoluble in C_6D_6 to afford reasonable ^1H NMR spectroscopic data. The low solubility of all compounds in the same solvent precluded recording of ^{13}C NMR spectra. The ^1H NMR spectra of compounds **1** and **3** had reasonably sharp peaks. The methylene resonances were slightly shifted in both compounds, from $\delta = 4.0$ ppm in the parent phenol, to $\delta = 3.78$ and 3.72 ppm in compounds **1** and **3**, respectively. Compounds **1**–**4** were all analytically pure based on lanthanoid analyses as determined by complexometric titrations. For compounds **1**, **2** and **4**, crystals suitable for X-ray crystal structure determination were obtained directly from the reaction tube, however, for compound **3** no such crystals resulted; nor could crystals be grown from non-coordinating solvents such as toluene or hexane due to insolubility. The aggregation of compound **3** is therefore unknown.

Compound **1** crystallizes in the triclinic space group $P\bar{1}$ with one whole dimer comprising the asymmetric unit. Aside from La–π-arene interactions (see below) each La center is four-coordinate, being bound by two terminal and two bridging phenolate ligands. The $La–O_{(bridging)}$ distances range from 2.402(4) to 2.565(5) Å, while the $La–O_{(terminal)}$ distances [range 2.172(6)–2.227(5) Å] are expectedly shorter than the former and comparable with those of mononuclear $[La(OC_6H_3Ph_2\text{-}2,6)_3]$,[5b] which exhibits solely terminal $OC_6H_3Ph_2$-2,6 ligands (though there are additional π-arene–Ln interactions). The La···La distance of 4.031(4) Å rules out any metal–metal interactions, being well in excess of the sum of the ionic radii of two four-coordinate La^{3+} ions.[13] Compared with monomeric $[La(OC_6H_3Ph_2\text{-}2,6)_3]$,[5b] the presence of the methylene linker in compound **1** allows for increased steric freedom about the metal center owing to the rotational ability about the $Ph–CH_2$ bond as well as the ability of the Ph group to swing away from the metal centres about the CH_2 linker. This creates more space about the La centers resulting in dimerisation, and a higher O-donor coordination number.

To compensate for the coordinatively unsaturated four-coordinate La center in compound **1**, the metal atom is also involved in La···π-arene interactions. This mode of interaction has been a common feature of other lanthanoid aryloxide chemistry that we have presented previously,[2,5,7] and the possibility arises due to the synthesis being performed in a donor-solvent-free manner. Thus, each La center interacts with an adjacent aromatic ring of an *O*-bridged ligand in an η^6-fashion through carbon atoms C(28) to C(33) for La(1) and C(8) to C(13) for La(2) (see Figure 1a). Therefore, the four-coordination about La (O only) expands to a formal coordination number of seven. If the centroid of the η^6-attachment is regarded as a coordination site, then the geometry about La is a distorted square pyramid with the arene ring seated at the apex (see Figure 1a). The La···C distances [for La(1) 3.057(8) to 3.277(8), for La(2) 3.043(8) to 3.300(8) Å] are all within the parameters defined for $[La(OC_6H_3Ph_2\text{-}2,6)_3]$[5b] (>3.5 Å is considered non-bonding for this compound) and similar to those in $[La_2(OC_6H_3iPr\text{-}2,6)_6]$[3b] (av. La···C 3.06 Å) where there are η^6-π-arene bridges. Thus, given there is only a small spread in La···C(π-arene) interactions for this compound, and there is no obvious cut-off in La···C distances, the interactions can only be regarded as η^6-binding. The π-arene bridges are from *O*-bridging ligands which thus bind in a $\mu\text{-}\eta^6\text{:}\eta^1\text{:}\eta^1$-manner and contrast the arrangement in $La(OC_6H_3Ph_2\text{-}2,6)_3$ where an arene arm from one terminal ligand binds in an η^6-fashion whilst a Ph from another binds η^3 to the metal atom.

Compound **4** is structurally similar to compound **1** in that it is also a dimer with Yb–π-arene interactions. Unfortunately, all attempts to determine a high-precision X-ray crystal structure were thwarted by consistent twinning of crystals. However, the low-precision structure leaves no doubt as to the connectivity of the compound, and the structure is similar to that of its La analogue **1**. One pertinent and clear feature of the structure is a reduction in coordination number about the metal center through reduced π-arene connectivity. In compound **3**, Yb(1) is bound in an η^3-manner, while Yb(2) is η^2-bound (Figure 2), lowered from $\eta^6\text{:}\eta^6$ in **1**. For Yb(1) there are three $Yb\cdots C_{arene}$ distances of 2.719(13), 2.997(12) and 3.174(13) Å, while there is a drastic increase (well outside error limits) to the next closest carbon atom on the same aromatic ring [Yb(1)–C(33) 3.610(12) Å], and for Yb(2) there are two $Yb\cdots C_{arene}$ distances of 2.837(12) and 2.894(12) Å, and the next closest approach is Yb(2)–C(10), 3.358(12) Å, thus defining a cut-off for potential bonding. These "bonding" distances compare well with previously established $Yb^{III}\cdots C$ bond lengths

 © 2005 Wiley-VCH Verlag GmbH & Co. KGaA, Weinheim

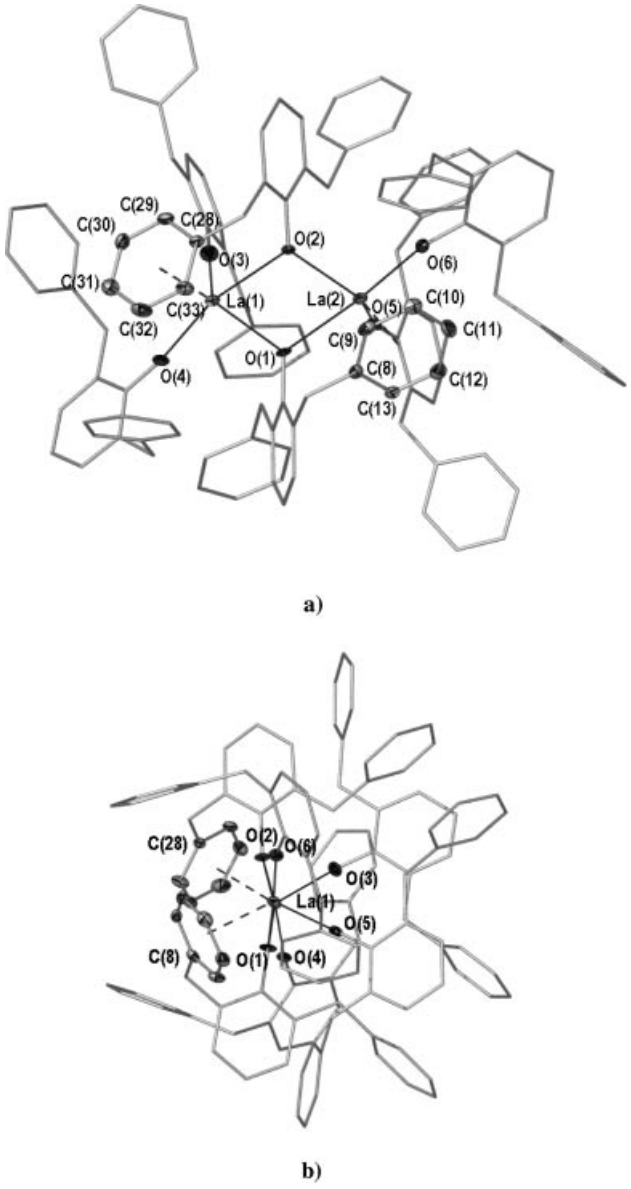

Figure 1. Molecular structure of [{La(μ-Odbp)(Odbp)$_2$}$_2$] (**1**) (40% thermal ellipsoids): all hydrogen atoms omitted for clarity and non-coordinating hydrocarbon groups depicted as wireframes. a) Normal to La_2O_2 fragment and b) along the La···La vector. Selected bond lengths [Å] and angles [°]: La(1)–O(1) 2.402(4), La(1)–O(2) 2.565(5), La(1)–O(3) 2.172(6), La(1)–O(4) 2.218(5), La(1)···C(28) 3.057(8), La(1)···C(29) 3.058(8), La(1)···C(30) 3.182(8), La(1)···C(31) 3.277(8), La(1)···C(32) 3.258(9), La(1)···C(33) 3.127(9), La(2)–O(1) 2.549(5), La(2)–O(2) 2.417(4), La(2)–O(5) 2.189(6), La(2)–O(6) 2.227(5), La(2)···C(8) 3.043(8), La(2)···C(9) 3.080(8), La(2)···C(10) 3.216(8), La(2)···C(11) 3.300(8), La(2)···C(12) 3.236(7), La(2)···C(13) 3.100(7); O1–La1–O2 69.90(16), O(1)–La(1)–O(3) 114.37(19), O(1)–La(1)–O(4) 95.18(17), O(2)–La(1)–O(3) 84.36(18), O(2)–La(1)–O(4) 165.07(16), O(3)–La(1)–O(4) 103.1(2), O(1)–La(2)–O(2) 69.94(16), O(1)–La(2)–O(5) 87.17(18), O(1)–La(2)–O(6) 174.38(16), O(2)–La(2)–O(5) 120.47(17), O(2)–La(2)–O(6) 104.52(17), O(5)–La(2)–O(6) 96.72(19).

in [Yb(OC$_6$H$_3$Ph$_2$-2,6)$_3$] and are consistent (after allowance for ionic radius differences) with the more extensive data for Yb^{II}···arene interactions.[2,5a,14] A consequence of this binding is that the capping aromatic ring does not sit flatly above the Ln center but is rather much more angled. Thus, in compound **1** the La–centroid–C_{ipso} angles are 85.0° and 84.3° for La(1) and La(2), while in compound **4** the corresponding angles are much more acute, at 72° and 69° for Yb(1) and Yb(2), respectively. The Yb–O(bridging) distances are asymmetric with two short [Yb(1)–O(1) 2.198(7) and Yb(2)–O(1) 2.209(8) Å] and two long [Yb(1)–O(2) 2.317(8) and Yb(2)–O(1) 2.378(7) Å] interactions, as is observed in compound **1**. In each case, the longer Ln–O bond is *cisoid* to a bonding phenyl group.

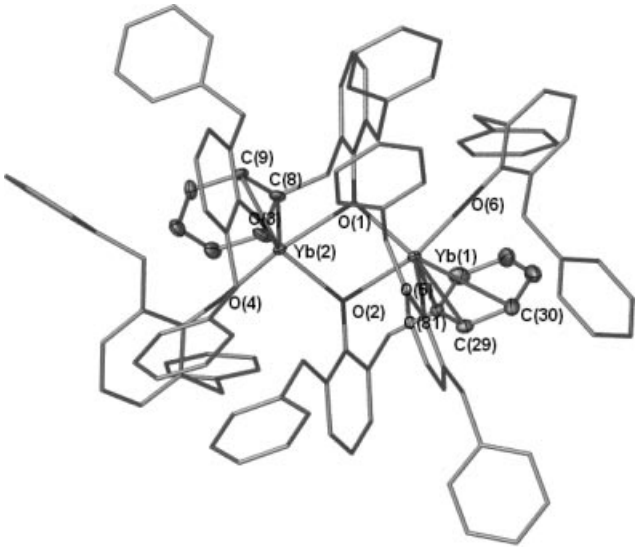

Figure 2. Molecular structure of [{Yb(μ-Odbp)(Odbp)$_2$}$_2$] (**4**) showing η^3-coordination to Yb(1) and η^2-coordination to Yb(2); all hydrogen atoms omitted for clarity. Selected bond lengths [Å] and angles [°]: Yb(1)–O(1) 2.198(7), Yb(1)–O(2) 2.317(8), Yb(1)–O(5) 2.031(9), Yb(1)–O(6) 2.055(10), Yb(2)–O(1) 2.378(7), Yb(2)–O(2) 2.209(8), Yb(2)–O(3) 2.056(8), Yb(2)–O(4)2.049(10), Yb(1)–C(28) 2.997(12), Yb(1)–C(29) 2.719(13), Yb(1)–C(30)3.174(13), Yb(2)–C(8) 2.894(12), Yb(2)–C(9) 2.837(12); O(1)–Yb(1)–O(2) 73.1(3), O(1)–Yb(1)–O(5) 121.3(3), O(1)–Yb(1)–O(6) 92.4(3), O(2)–Yb(1)–O(5) 89.2(3), O(2)–Yb(1)–O(6) 163.0(4), O(5)–Yb(1)–O(6) 106.2(4), O(1)–Yb(2)–O(2) 71.7(3), O(1)–Yb(2)–O(3) 90.5(3), O(1)–Yb(2)–O(4) 168.0(3), O(2)–Yb(2)–O(3) 120.6(3), O(2)–Yb(2)–O(4) 99.3(3), O(3)–Yb(2)–O(4) 101.0(4), Yb(1)–O(1)–Yb(2) 105.4(3), Yb(1)–O(2)–Yb(2) 107.1(3).

Compound **2** crystallizes in the triclinic space group $P\bar{1}$ with two unique half dimers in the asymmetric unit. Each unique europium(II) center is bound by oxygen atoms of a terminal and two bridging phenolate groups, thereby giving an oxygen donor coordination number about Eu^{II} of three. The Eu–O bond lengths (av. 2.46 Å for bridging and av. 2.29 Å for terminal) are unexceptional, being similar to Eu–O bridging and terminal distances of 2.48 (av.) and 2.361(3) Å, respectively, in [Eu(OC$_6$H$_3$Ph$_2$-2,6)$_2$]$_2$ where there are only one terminal and three bridging ligands.[5a] The longer Eu–$O_{terminal}$ distance in [Eu(OC$_6$H$_3$Ph$_2$-2,6)$_2$]$_2$ is consistent with a lower coordination number in compound **2**. Each dimer is structurally similar but with some significant differences, one being a discrete dimer and the other a polymer of dimers, involving extended nuclearity through inter- and intramolecular Eu–π-arene interactions (see below) that increase the coordination number of Eu

 © 2005 Wiley-VCH Verlag GmbH & Co. KGaA, Weinheim

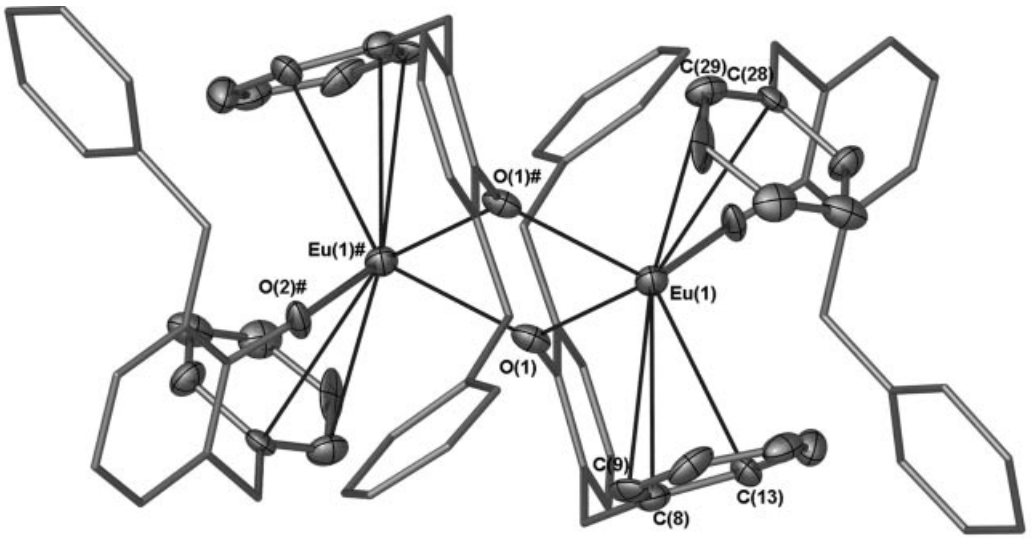

a)

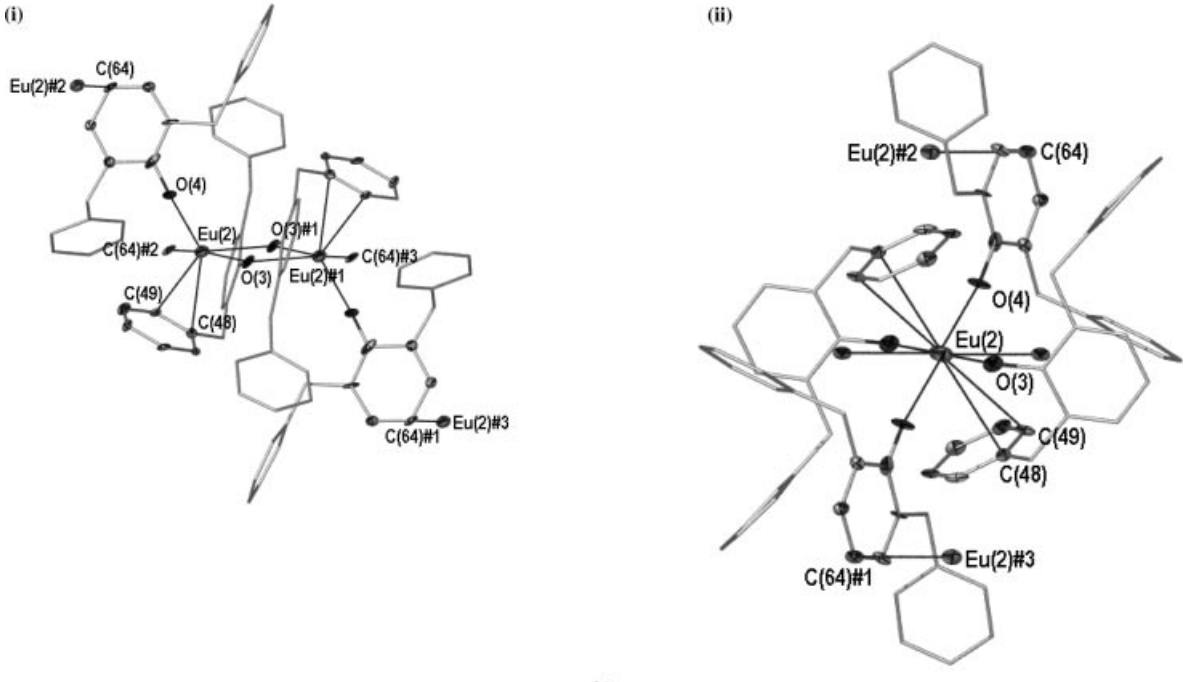

b)

Figure 3. Molecular structure of $[\{Eu(\mu\text{-}Odbp)(Odbp)\}_2]/[\{Eu(\mu\text{-}Odbp)(Odbp)\}_2]_\infty$ (**2**) (40% thermal ellipsoids); all hydrogen atoms omitted for clarity and non-coordinating hydrocarbon groups depicted as wireframes. a) $[\{Eu(\mu\text{-}Odbp)(Odbp)\}_2]$ normal to Eu_2O_2 metallacycle; b) $[\{Eu(\mu\text{-}Odbp)(Odbp)\}_2]_\infty$ (i) side-on and (ii) along Eu···Eu vector. Selected bond lengths [Å] and angles [°]: Eu(1)–O(2) 2.287(10), Eu(1)–O(1) 2.463(11), Eu(1)–O(1)#1 2.491(12), Eu(1)–C(8) 3.130(16), Eu(1)–C(9) 3.150(17), Eu(1)–C(13) 3.187(16), Eu(1)–C(28) 3.171(16), Eu(1)–C(29) 3.153(19), Eu(2)–O(3) 2.446(10), Eu(2)–O(3)#2 2.461(11), Eu(2)–O(4) 2.294(10), Eu(2)–C(49) 3.196(16), Eu(2)–C(48) 3.197(15), Eu(2)–C(64)#3 3.136(16); O(1)–Eu(1)–O(2) 90.5(4), O(1)–Eu(1)–O(1)#1 71.7(4), O(2)–Eu(1)–O(1)#1 117.4(4), O(3)–Eu(2)–O(3)#2 69.6(4), O(3)–Eu(2)–O(4) 97.3(4), O(4)–Eu(2)–O(3)#2 119.0(4), Eu(1)–O(1)–Eu(1)#1 108.3(4), Eu(2)–O(3)–Eu(2)#2 110.4(4). Symmetry transformations used to generate equivalent atoms: #1: $-x + 1, -y + 1, -z$; #2: $-x + 1, -y + 2, -z + 1$; #3: $-x, -y + 2, -z + 1$.

 © 2005 Wiley-VCH Verlag GmbH & Co. KGaA, Weinheim

significantly. In the true dinuclear molecule the Eu centers are capped on two sides by an η^2- and an η^3-bound arene ring arising from one terminal and one bridging ligand (Figure 3a). In the other molecule, each Eu has one η^2-bound π-arene interaction with an arene group from *only* the bridging group of the dimer while an arene from the terminal groups (involved in π-interactions in the true dimer) swings away from the Eu atom with a closest Eu···C distance of 4.72(1) Å. This leaves a vacancy in the coordination sphere of Eu(2) which allows a further π-arene interaction between Eu(2) and (symmetry-generated) C(64)#1 of 3.136(16) Å [C(64) is the *p*-C atom of the central (phenolate) group of a terminal ligand rather than a radial group]. This forms a single-stranded polymer, where "dimers" are linked by Eu(2)···C(64)(arene) interactions (Figure 3b). This structure is drastically different from the stoichiometrically related $[Eu_2(OC_6H_3Ph_2\text{-}2,6)_4]$ which possesses a remarkable three bridging phenolate groups and one terminal phenolate ligand.

Conclusion

The direct reaction of lanthanoid metals (Ln = La, Eu, Yb) with 2,6-dibenzylphenol at 170°C provides the corresponding homoleptic lanthanoid phenolates in good yield. For Ln = Yb, use of either excess metal or excess phenol gives Yb^{II} or Yb^{III} complexes. All structures feature oxygen-bridged dimeric units with coordination saturation effected by intra- or intermolecular π-phenyl···Ln coordination.

Experimental Section

General: 2,6-Dibenzylphenol (HOdbp) was prepared by a literature method.[15] The lanthanoid metals used were purchased either from Strem chemicals, Tianjiao (Baotou, China), Rhône–Poulenc or Santoku, either as fine powders or as metal ingots, which were manually filed under an inert gas into metal powder for use in reactions. Toluene and hexane were dried with sodium/benzophenone and freeze-thaw-degassed prior to use. All manipulations were performed using conventional Schlenk or glovebox techniques under high-purity argon or dinitrogen in flame-dried glassware. Infrared spectra were recorded as Nujol mulls using sodium chloride plates with a Nicolet Nexus FTIR spectrophotometer. ^{1}H NMR spectra were recorded at 300.13 MHz using a Bruker BZH 300/52 spectrometer and chemical shifts were referenced to the residual ^{1}H resonances of the deuteriobenzene solvent employed. NMR and IR spectra of compounds **1** and **3** showed slight impurities of phenol due to decomposition of the rare earth phenolate compounds in the process of measurement. Compounds **2** and **4** had insufficient solubility in common non-coordinating solvents to obtain NMR spectra. Melting points were determined in sealed glass capillaries under dinitrogen. The metal analyses were adapted from the method described in a previous paper.[16]

$[La_2(Odbp)_6]$ (1). Method A: 2,6-Dibenzylphenol (0.60 g, 2.19 mmol) was treated directly with lanthanum metal (0.10 g, 0.73 mmol) in the presence of 2 drops of mercury and sealed under vacuum in a Carius tube. After 4 d of heating at 170 °C, a white crystalline material formed upon cooling. Unreacted ligand was removed by sublimation. Crystals suitable for XRD analysis were obtained. Yield: 0.58 g (82%). M.p. 184–187 °C. $C_{60}H_{51}LaO_3$ (958.92): calcd. La 14.48; found La 14.30. ^{1}H NMR (C_6D_6): δ = 3.78 (s, 12 H, CH_2), 6.67–6.70 (m, 3 H, ArH), 6.73–6.87 (m, 6 H, ArH), 6.88–7.12 (m, 30 H, ArH) ppm. IR (Nujol, cm^{-1}): $\tilde{\nu}$ = 1589 m, 1452 s, 1262 s, 1191 m, 1081 s, 1029 m, 937 w, 859 m, 819 w, 754 s, 697 s, 559 w, 515 w.

$[La(Odbp)_3]_2$. Method B (Without Mercury): HOdbp (0.25 g, 0.91 mmol) was treated with excess lanthanum metal (0.10 g, 0.72 mmol) in an evacuated sealed glass Carius tube. The reaction mixture was heated at 250 °C for 5 d, forming a clear glassy solid upon cooling. Unreacted ligand was removed by a hexane wash. The product was identical to the compound **1** synthesised in the presence of mercury. Yield: 0.12 g (41%). M.p.183–187 °C. IR (Nujol, cm^{-1}): $\tilde{\nu}$ = 1601 m, 1453 s, 1260 s, 1202 m, 1074 s, 1029 m, 950 w, 869 m, 820 w, 755 s, 698 s, 601 w, 515 w.

$[La(Odbp)_3]_2$. Method C (Excess Ligand): HOdbp (0.60 g, 2.18 mmol) and lanthanum metal (0.08 g, 0.55 mmol) were sealed under vacuum in the presence of 2 drops of mercury in a glass Carius tube. A white oil formed after heating at 210 °C for 2 d and all of the lanthanum metal was consumed. The remaining (excess) ligand was sublimed to one end of the tube (HOdbp sublimes at 240 °C). The product was identical with that obtained in Methods A and B above. Yield: 0.35 g (66%). M.p. 184–186 °C. IR (Nujol, cm^{-1}): $\tilde{\nu}$ = 1594 m, 1456 s, 1259 s, 1200 m, 1072 s, 1029 m, 950 w, 865 m, 819 w, 755 s, 699 s, 600 w, 510 w.

$[Eu_2(Odbp)_4]$ (2). Method A: 2,6-Dibenzylphenol (0.53 g, 1.93 mmol) was treated directly with europium metal (0.15 g, 0.97 mmol) in the presence of 2 drops of mercury in an evacuated Carius tube. After 4 d of heating at 170 °C, an orange molten/crystalline material formed upon cooling. Unreacted excess ligand was removed by sublimation. Crystals suitable for XRD analysis were obtained. Yield: 0.56 g (83%). M.p. 198–200 °C. $C_{40}H_{34}EuO_2$ (698.63): calcd. Eu 22.81; found Eu 22.58. IR (Nujol, cm^{-1}): $\tilde{\nu}$ = 1587 m, 1458 s, 1310 m, 1286 m, 1258 m, 1231 s, 1200 m, 1157 m, 1081 m, 1028 m, 933 w, 885 w, 854 m/w, 815 w, 748 s, 698 s, 601 w.

$[Eu(Odbp)_2]_2$ (2). Method B (Without Mercury): HOdbp (0.30 g, 1.09 mmol) was treated with excess europium metal (0.11 g, 0.72 mmol) in an evacuated glass Carius tube. The reaction was heated for 5 d at 250 °C, forming a glassy orange solid upon cooling. The residue was washed with hexane to remove any unreacted ligand. The product was identical to compound **2** from Method A. Yield: 0.19 g (49%). M.p. 197–200 °C. IR (Nujol, cm^{-1}): $\tilde{\nu}$ = 1586 m, 1458 s, 1305 m, 1281 m, 1252 m, 1230 s, 1155 m, 1078 m, 1026 m, 971 w, 888 w, 850 m/w, 754 s, 696 s, 595 w.

$[Eu(Odbp)_2]_2$ (2). Method C (Excess Ligand): HOdbp (0.50 g, 1.82 mmol) and europium metal (0.09 g, 0.61 mmol) were sealed under vacuum in the presence of 2 drops of mercury in a glass Carius tube. An orange oil formed after heating at 210 °C overnight. All of the europium metal had reacted; the remaining excess ligand was sublimed to one end of the tube (HOdbp sublimes at 240°). The product was identical with that obtained from Methods A and B above. Yield: 0.32 g (77%). M.p. 197–200 °C. IR (Nujol): $\tilde{\nu}$ = 1600 m, 1453 s, 1347 m, 1286 m, 1231 m, 1200 m, 1150 m, 1075 m, 1026 m, 934 w, 885 w, 852 m/w, 755 s, 698 s, 590 w.

$[Yb(Odbp)_2]$ (3): 2,6-Dibenzylphenol (0.60 g, 2.19 mmol) was treated directly with excess ytterbium metal (0.40 g, 2.30 mmol) in the presence of 2 drops of mercury in a sealed, evacuated Carius tube. After 4 d of heating at 170 °C, a red glassy material formed upon cooling. Yield: 0.53 g (67%). M.p. 125–128 °C. $C_{40}H_{34}O_2Yb$ (719.75): calcd. Yb 23.99; found Yb 23.80. ^{1}H NMR (C_6D_6): δ =

 © 2005 Wiley-VCH Verlag GmbH & Co. KGaA, Weinheim

3.72 (s, 8 H, CH_2), 6.72–6.77 (m, 2 H, ArH), 6.82–6.87 (m, 4 H, ArH), 6.89–7.13 (m, 20 H, ArH) ppm. IR (Nujol, cm^{-1}): $\tilde{\nu}$ = 1601 m, 1456 s, 1363 s, 1230 s, 1074 w, 1028 w, 1006 w, 950 m, 923 m, 889 w, 830 w, 820 w, 794 w, 755 s, 698 s. Attempts to form this compound in the absence of mercury with heating up to 250 °C (2,6-dibenzylphenol slowly decomposes above 260 °C, so was not heated any further) resulted in the isolation of unreacted starting material.

$[Yb_2(Odbp)_6]$ (4): 2,6-Dibenzylphenol (0.30 g, 1.09 mmol) was treated directly with ytterbium metal (0.04 g, 0.23 mmol) in the presence of 2 drops of mercury. The reactants were sealed under vacuum in a glass Carius tube. After 2 d of heating at 150 °C, deep orange/red crystals were grown upon cooling. Unreacted ligand was removed by a hexane wash and the remaining material characterised. Yield: 0.18 g (78%). M.p. 78–80 °C. $C_{60}H_{51}O_3Yb$ (993.05): calcd. Yb 17.42; found 18.11. IR (Nujol, cm^{-1}): $\tilde{\nu}$ = 1601 m, 1459 s, 1365 s, 1230 s, 1074 w, 1029 w, 950 m, 923 m, 889 w, 829 w, 820 w, 794 w, 755 s, 698 s. Attempts to form this compound in the absence of mercury with heating up to 250 °C (2,6-dibenzylphenol slowly decomposes above 260 °C, so was not heated any further) resulted in the isolation of unreacted starting material.

X-ray Crystallography: Crystalline samples of compounds **1**, **2** and **4** were mounted on glass fibres in viscous paraffin oil at –150 °C (123 K). Crystal data were obtained using an Enraf–Nonius Kappa CCD. An empirical absorption correction (SORTAV)[17] was applied to all data. Structural solution and refinement were carried out using SHELXL-97[18] and SHELXS-97[19] utilising the graphical interface X-Seed.[20] Crystal data and refinement parameters for all complexes are compiled below.

$[La_2(Odbp)_6]$ (1): $C_{120}H_{102}La_2O_6$, M = 1917.84, 0.25 × 0.20 × 0.20 mm, triclinic, space group $P\bar{1}$ (No. 2), a = 13.4374(5), b = 13.9358(5), c = 26.7937(12) Å, α = 98.976(1), β = 95.312(2), γ = 108.065(4)°, V = 4658.3(3) Å^3, Z = 2, D_c = 1.367 g/cm^3, F_{000} = 1968, Nonius Kappa CCD, Mo-K_α radiation, λ = 0.71073 Å, T = 123(2) K, $2\theta_{max}$ = 56.5°, 53379 reflections collected, 21478 unique (R_{int} = 0.2204). Final *GooF* = 0.872, R_1 = 0.0748, wR_2 = 0.1217, R indices based on 7518 reflections with $I > 2\sigma(I)$ (refinement on F^2), 1147 parameters, 0 restraints. Lp and absorption corrections applied, μ = 0.963 mm^{-1}.

$[Eu_2(Odbp)_4]$ (2): $C_{80}H_{68}Eu_2O_4$, M = 1397.26, 0.10 × 0.10 × 0.10 mm, triclinic, space group $P\bar{1}$ (No. 2), a = 10.0458(12), b = 13.136(2), c = 23.773(3) Å, α = 103.448(11), β = 94.188(9), γ = 94.379(7)°, V = 3028.9(8) Å^3, Z = 2, D_c = 1.532 g/cm^3, F_{000} = 1412, Nonius Kappa CCD, Mo-K_α radiation, λ = 0.71073 Å, T = 123(2) K, $2\theta_{max}$ = 55.9°, 19023 reflections collected, 10992 unique (R_{int} = 0.1653). Final *GooF* = 0.930, R_1 = 0.0993, wR_2 = 0.2022, R indices based on 4255 reflections with $I > 2\sigma(I)$ (refinement on F^2), 775 parameters, 66 restraints. Lp and absorption corrections applied, μ = 2.106 mm^{-1}.

$[Yb_2(Odbp)_6]$ (4): $C_{120}H_{102}O_6Yb_2$, M = 1986.10, orange, rectangular, 0.20 × 0.10 × 0.10 mm, triclinic, space group $P\bar{1}$ (No. 2), a = 13.364(3), b = 13.475(3), c = 26.927(5) Å, α = 98.44(3), β = 97.42(3), γ = 104.68(3)°, V = 4569.2(16) Å^3, Z = 2, D_c = 1.444 g/cm^3, F_{000} = 2020, Nonius Kappa CCD, Mo-K_α radiation, λ = 0.71073 Å, T = 123(2) K, $2\theta_{max}$ = 56.5°, 57274 reflections collected, 21355 unique (R_{int} = 0.0743). Final *GooF* = 1.108, R_1 = 0.0993, wR_2 = 0.2751, R indices based on 16207 reflections with $I > 2\sigma(I)$ (refinement on F^2), 1153 parameters, 42 restraints. Lp and absorption corrections applied, μ = 2.094 mm^{-1}.

CCDC-274466 (**1**), -274467 (**2**) and -274468 (**3**) contain the supplementary crystallographic data for this paper. These data can be obtained free of charge from The Cambridge Crystallographic Data Centre via www.ccdc.cam.ac.uk/data_request/cif.

Acknowledgments

The authors acknowledge the ARC Special Research Centre for Green Chemistry at Monash University for financial support and postgraduate scholarship (K. M. P.), and CSIRO for supporting C. R. S. on secondment.

[1] D. C. Bradley, R. C. Mehrotra, I. P. Rothwell, A. Singh, *Alkoxo and Aryloxo Derivatives of Metals*, Academic Press, San Diego, **2001**.
[2] G. B. Deacon, S. Nickel, P. MacKinnon, E. R. T. Tiekink, *Aust. J. Chem.* **1990**, *43*, 1245–1257.
[3] a) D. M. Barnhart, D. L. Clark, J. C. Gordon, J. C. Huffman, R. L. Vincent, J. G. Watkin, B. D. Zwick, *Inorg. Chem.* **1994**, *33*, 3487–3497; b) R. J. Butcher, D. L. Clark, S. K. Grumbine, R. L. Vincent-Hollis, B. L. Scott, J. G. Watkin, *Inorg. Chem.* **1995**, *34*, 5468–5476.
[4] a) G. B. Deacon, P. E. Fanwick, A. Gitlits, I. P. Rothwell, B. W. Skelton, A. H. White, *Eur. J. Inorg. Chem.* **2001**, 1505–1514; b) G. B. Deacon, C. M. Forsyth, R. Harika, P. C. Junk, J. W. Ziller, W. J. Evans, *J. Mater. Chem.* **2004**, *14*, 3144–3149.
[5] a) G. B. Deacon, C. M. Forsyth, P. C. Junk, B. W. Skelton, A. H. White, *Chem. Eur. J.* **1999**, *5*, 1452–1459; b) G. B. Deacon, T. Feng, C. M. Forsyth, A. Gitlits, D. C. R. Hockless, Q. Shen, B. W. Skelton, A. H. White, *J. Chem. Soc., Dalton Trans.* **2000**, 961–966.
[6] a) H. D. Amberger, H. Reddmann, C. Guttenberger, B. Unrecht, L. Zhang, C. Apostolidis, O. Walter, B. Kanellokopulos, *Z. Anorg. Allg. Chem.* **2003**, *629*, 1522–1534; b) H. A. Stecher, A. Sen, A. L. Rheingold, *Inorg. Chem.* **1988**, *27*, 1130–1132; c) M. F. Lappert, A. Singh, R. G. Smith, *Inorg. Synth.* **1990**, *27*, 164–168; d) P. B. Hitchcock, M. F. Lappert, A. Singh, *J. Chem. Soc., Chem. Commun.* **1983**, 1499–1501; e) P. B. Hitchcock, M. F. Lappert, R. G. Smith, *Inorg. Chim. Acta* **1987**, *139*, 183–184; f) J. R. van den Hende, P. B. Hitchcock, M. F. Lappert, *J. Chem. Soc., Chem. Commun.* **1994**, 1413–1414; g) J. R. van den Hende, P. B. Hitchcock, S. A. Holmes, M. F. Lappert, *J. Chem. Soc., Dalton Trans.* **1995**, 1435–1440.
[7] a) G. B. Deacon, T. Feng, P. C. Junk, B. W. Skelton, A. H. White, *J. Chem. Soc. Dalton Trans.* **1997**, 1181–1186; b) G. B. Deacon, A. Gitlits, P. C. Junk, B. W. Skelton, A. H. White, *Z. Anorg. Allg. Chem.* **2005**, *631*, 861–865.
[8] D. L. Clark, J. G. Watkin, J. C. Huffman, *Inorg. Chem.* **1992**, *31*, 1554–1556.
[9] a) D. L. Clark, R. V. Hollis, B. L. Scott, J. G. Watkin, *Inorg. Chem.* **1996**, *35*, 667–674; b) D. L. Clark, G. B. Deacon, T. Feng, R. V. Hollis, B. L. Scott, B. W. Skelton, J. G. Watkin, A. H. White, *J. Chem. Soc., Chem. Commun.* **1996**, 1729–1730.
[10] L.-L. Zhang, Y.-M. Yao, Y.-J. Luo, Q. Shen, J. Sun, *Polyhedron* **2000**, *19*, 2243–2247.
[11] P. Thuery, M. Nierlich, J. Harrowfield, M. Ogden, *Phenoxide Complexes of f-Elements*, in: *Calixarenes* (Eds.: Z. Asfari, V. Bohmer, J. Harrowfield, J. Vicens), Kluwer Academic Publishers, Netherlands, **2001**, p. 561–582.
[12] G. B. Deacon, C. M. Forsyth, S. Nickel, *J. Organomet. Chem.* **2002**, *647*, 50–60.
[13] R. D. Shannon, *Acta Crystallogr., Sect. A* **1976**, *32*, 751–767.
[14] a) M. Niemeyer, *Eur. J. Inorg. Chem.* **2001**, 1969–1981; b) G. B. Deacon, C. M. Forsyth, P. C. Junk, *Eur. J. Inorg. Chem.* **2005**, 817–821.
[15] a) E. C. Horning, *J. Org. Chem.* **1945**, *10*, 263–266; b) M. L. Cole, L. T. Higham, P. C. Junk, K. M. Proctor, J. L. Scott, C. R. Strauss, *Inorg. Chim. Acta*, in press.
[16] J. E. Cosgriff, G. B. Deacon, B. M. Gatehouse, *Aust. J. Chem.* **1993**, *46*, 1881–1896.

 © 2005 Wiley-VCH Verlag GmbH & Co. KGaA, Weinheim

[17] R. H. Blessing, *Acta Crystallogr., Sect. A* **1995**, *51*, 33–37.
[18] G. M. Sheldrick, *SHELXL-97*, University of Göttingen, Germany, **1997**.
[19] G. M. Sheldrick, *SHELXS-97*, University of Göttingen, Germany, **1997**.
[20] L. J. Barbour, *J. Supramol. Chem.* **2001**, *1*, 189–191.
Received: June 15, 2005
Published Online: September 9, 2005

 © 2005 Wiley-VCH Verlag GmbH & Co. KGaA, Weinheim

Self-Assembly and Fluorescent Modification of Hydroxyapatite Nanoribbon Spherulites

Jinku Liu,[a] Qingsheng Wu,*[a] and Yaping Ding*[b]

Keywords: Fluorescence / Hydroxyapatite / Nanostructures / Self-assembly

Hydroxyapatite nanoribbon spherulites have been successfully synthesized, with the bioactive eggshell membrane as directing template and in the presence of ethylenediamine, in a one-step reaction under mild conditions. The spherulites are about 2.5 μm in diameter and the extended nanoribbon about 1.1 μm long. The spherulites were modified with fluorescein to obtain a fluorescent probe material with strong luminescence.
(© Wiley-VCH Verlag GmbH & Co. KGaA, 69451 Weinheim, Germany, 2005)

Introduction

Assembly of nanocrystals to form ordered structures is of great interest in the area of materials science. The ability to synthesize uniformly assembled nanospheres with diameters ranging from nano- to microscale dimensions is especially desirable[1] as these structures can be used in therapeutic, storage, and catalytic fields[2,3] etc.[4] Ribbon-shaped nanomaterials or nanostructures have attracted a great deal of attention since the discovery of zinc oxide nanobelts in 2001 by Wang,[5] and the assembly of materials/structures is still an important objective. Up to now, the obtained inorganic nanobelts/nanoribbons mainly include oxides,[5–7] elementary substances,[8–10] sulfides,[11,12] etc.,[13–16] and no study has been reported on the formation of hydroxyapatite nanoribbons. On the other hand, although various spherical nano-/micromaterials have been reported, they are mainly solid[17–22] or hollow.[23–33]

In this paper, a novel assembly method for nanomaterials, which includes a bioactive eggshell membrane[34] template approach with the cooperative effect of ethylenediamine, is developed that gives hydroxyapatite nanoribbon spherulites in a single-step reaction at room temperature. The obtained spherulites can be modified with fluorescein to form spherical fluorescent probe materials with strong luminescence. The hydroxyapatite spherulites have attracted a good deal of attention as a delivery system because of their special physical and chemical properties, high surface-interaction properties, and their biocompatibility. Therefore, these nanoribbon spherulites have potential value in biology, medicine, and drug fields etc.

[a] Department of Chemistry, Tongji University, Shanghai 200092, China
Fax: +86-021-6598-2287
E-mail: qswu@mail.tongji.edu.cn
[b] Department of Chemistry, Shanghai University, Shanghai 200444, China
E-mail: ypding@mail.shu.edu.cn

Results and Discussion

All the XRD diffraction patterns in Figure 1 can be readily indexed to a hydroxyapatite [$Ca_5(PO_4)_3(OH)$] phase, and there is an obvious indication of the crystal growth direction in the XRD pattern. The XRD analysis was repeated several times with similar results: the 002 diffraction looks rather sharp and intense, indicating a non-nanoscale and good crystallization at the 002 crystal face, while the other diffractions look broad, indicating a nanoscale and a poorer crystallization. According to the product's morphology and XRD results, the most likely growth direction of the nanoribbons is on the [002] crystal face.

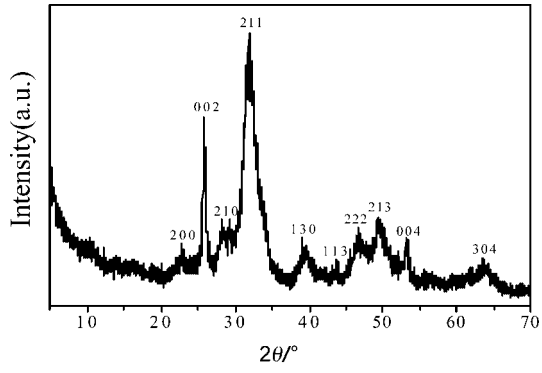

Figure 1. The XRD pattern of hydroxyapatite nanoribbon spherulites.

Figure 2 also shows a similar widening in the FT-IR absorption peaks. The ν_{P-O} vibration of the hydroxyapatite nanoribbon spherulites in Figure 2 (b) is at almost the same wavelength as that of hydroxyapatite bulk materials in Figure 2 (a) (1040 cm^{-1}), although it is obviously wider. This may be because the small-size effects and interface effects of nanomaterials change the ν_{P-O} vibration energy.

 DOI: 10.1002/ejic.200500207 © 2005 Wiley-VCH Verlag GmbH & Co. KGaA, Weinheim

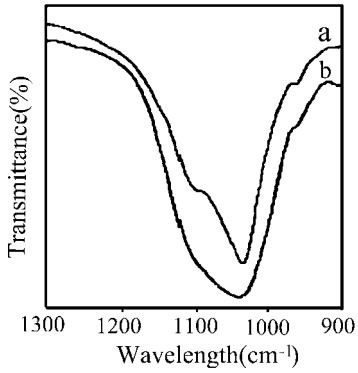

Figure 2. The FT-IR spectrum of products (a: bulk materials; b: spherulites).

The hydroxyapatite nanoribbon spherulites are different from hollow spherulites and solid spheres as the spherulites are in fact built from interlaced nanoribbons. Figure 3 (see part a) shows a typical TEM image of the products, which shows that they are spherulites with a diameter of about 2.5 μm. The high magnification TEM image in Figure 3 (part b) indicates that the spherulites consist of a large number of nanoribbons, the thickness and width of which are about 8 nm and 200 nm respectively; the length of the extended nanoribbons is about 1.1 μm. The electron diffraction (ED) lattice of a selected region suggests that the nanoribbons are single crystals (Figure 3, c). The obtained spherulites are porous structures composed of nanoribbons. They have a large surface area that contains a large number of hydroxy groups. With such a structure, they can easily combine with organic fluorescent compounds that contain carboxyl or hydroxy groups.

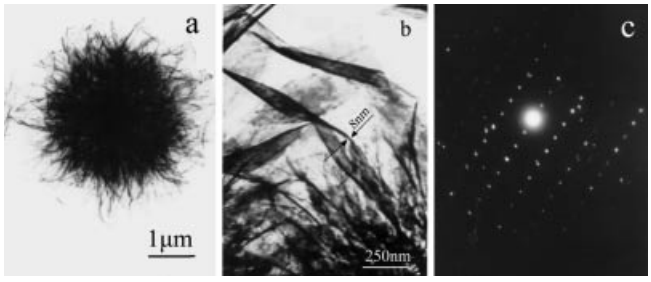

Figure 3. TEM and ED images of the products.

When irradiated with an electron beam, the hydroxyapatite nanoribbon spherulites change into a solid sphere. Figure 4 (a) shows the TEM image of a spherulite with a diameter of about 2.5 μm before irradiation. After irradiation with an electron beam for several seconds the product changes into a solid sphere with a diameter of 2.3 μm (Figure 4, b) consisting of melted hydroxyapatite. This can be explained by the fact that hydroxyapatite has a high chemical stability,[35] therefore decomposition cannot occur at the irradiation temperature of the electron beam[36] and it only melts.

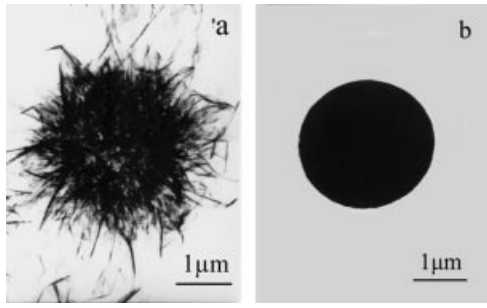

Figure 4. TEM images of the products (a: nanoribbon spherulite; b: solid sphere).

The growth processes of hydroxyapatite spherulites were determined by examining different stages of their formation. As shown in Figure 5a, nanoribbons with lengths ranging from 200 to 250 nm have formed after 0.5 h of aging, and they distributed randomly. After aging for 4 h, the products are approximately spherical with a diameter of 1.9 μm, as shown in part b of Figure 5, which suggests that the nanoribbons are not yet completely assembled and the spherulites are rather loose. When the aging time was further increased to 10 h, integrated spherical hydroxyapatite appeared, but the extended nanoribbons were still a little longer. They continued to become larger and more compact with time, and when the aging time reached two days, very compact spherulites had formed whose extended nanoribbons are shorter (200 nm; Figure 5, d). Even after aging for four days (further aging leads to the decomposition of the eggshell membrane), the final products were still hydroxyapatite nanoribbon spherulites similar to that in Figure 5, part d; no solid spherulite was obtained. These results indicate that shorter nanoribbons form at first, and then these assemble gradually to form many spherulite cores. Thereafter, the nanoribbons continue to assemble around the cores to form many large and compact spherulites.

The most suitable temperature for the formation of spherical hydroxyapatite is 37 °C, which is approximately physiological temperature. When the reaction was performed at a lower temperature (0 °C for 10 h) spherical hydroxyapatite also formed, as shown in Figure 6, but with a diameter of about 1.6 μm, far smaller than that at 37 °C. This may be explained by considering that the low temperature slows down diffusion of the ions and therefore assembly of the nanoribbons, and the eggshell membrane has lower activity at 0 °C than at physiological temperature, whichl weakens its inducing ability foro the formation of spherical hydroxyapatite.

The hydroxyapatite nanoribbons assemble into spherulites by an organic direction process.[22,23,37–39] This process is induced under the cooperative effect of the eggshell membrane and ethylenediamine. A TEM image in which the spherulites and the intermediate products exist simultaneously was taken during the experiment, as shown in Figure 7, from which a conjecture can be made that the spherulite cores marked with an arrow are assembled from a small

 © 2005 Wiley-VCH Verlag GmbH & Co. KGaA, Weinheim

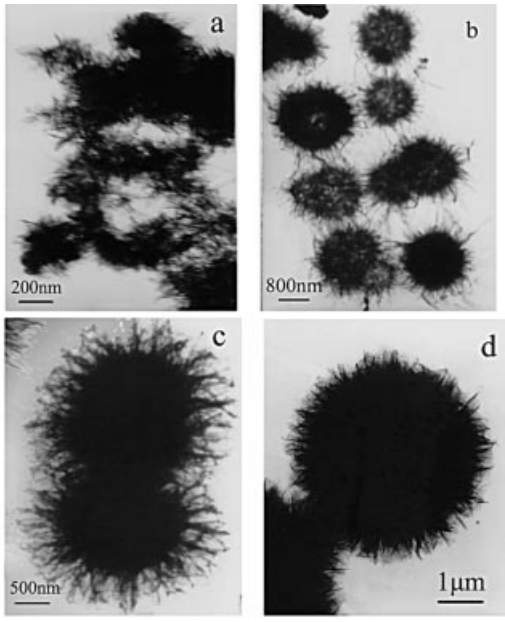

Figure 5. TEM images of the products [aging time: 1 h (a); 4 h (b); 10 h (c); 2 d (d)].

Figure 6. TEM pattern of the products obtained at 0 °C (aging for 10 h).

quantity of nanoribbons formed during the first step, and then these spherulite cores assemble into nanoribbon spherulites. Figure 8 shows a typical scanning electron microscopy (SEM) image of the eggshell membrane. The eggshell membrane is a microporous network with diameters of 1.5–10 μm, which is composed of interlaced protein fibers with an average diameter of about 2 μm. The eggshell membrane mainly contains collagens, glycoproteins, and proteoglycans. These macromolecules contain a large amount of amido, carboxy, and hydroxy groups, and have both hydrophilic and hydrophobic domains located at their ends.[40] The hydrophobic domains extend onto the surface of the crystal and block diffusion of the lattice ions to the crystal surface. The ethylenediamine acts as an additional template due to hydrogen-bonding effects between its NH_2 groups and the surface groups of the eggshell membrane such as COOH and NH_2. The products are obtained on either side of the eggshell membrane, which indicates that the products fall randomly from the template.

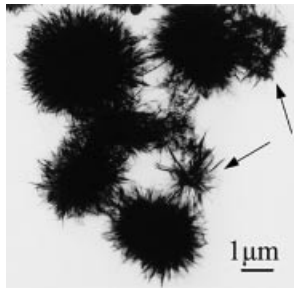

Figure 7. The SEM pattern of spherulites and intermediate products (after aging for 2 d).

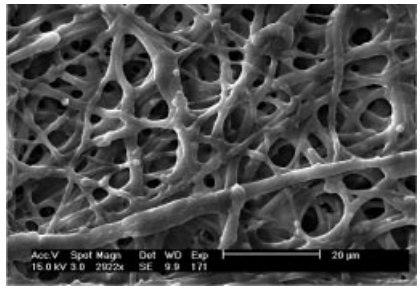

Figure 8. The SEM pattern of eggshell membrane.

As a template, the eggshell membrane has an effect in three aspects. Firstly, it can control the transport of ions due to its semi-permeable structure. Secondly, it not only can alone induce the formation of products, but can also interact with ethylenediamine through hydrogen bonds and consequently control the growth of products. Finally, the eggshell membrane offers a physical site in the hole channels of which the two kinds of ions meet, react, aggregate to form a crystal nucleus, and then grow under the control of the eggshell membrane and ethylenediamine to form the products. Moreover, it must be emphasized that the template used in this paper is not a simple flat structure. Rather, it is composed of macromolecules on the surface of curving hole channels of the eggshell membrane and ethylenediamine, which cooperatively form a spherical template and control the growth of hydroxyapatite nanoribbon spherulites. The nanoribbon spherulites can't be obtained in the absence of the eggshell membrane (Figure 9, a).

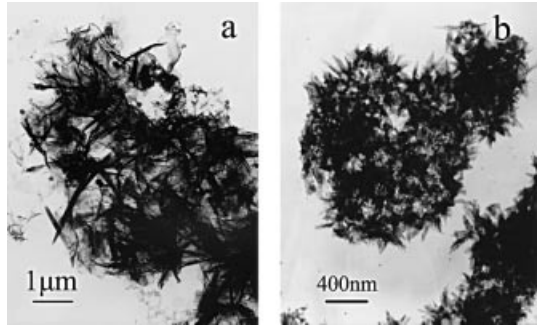

Figure 9. TEM images of the products (a: when the eggshell membrane is absent; b: when KOH was added to adjust the pH to 7.4).

 © 2005 Wiley-VCH Verlag GmbH & Co. KGaA, Weinheim

The organic base ethylenediamine is employed here to modulate the pH value to 7.4 and spherical products were obtained. When potassium hydroxide was used instead, the products were sparse flakes of hydroxyapatite about 300 nm long, as shown in part b of Figure 9. This indicates that the organic base plays an important role in the controllable assembly of spherical products. The morphological difference in the presence of inorganic and organic base is because, besides the adjusting pH value, ethylenediamine also acts as an accessorial template due to hydrogen-bonding effects between its NH_2 groups and the surface groups of the eggshell membrane such as COOH, NH_2.

The hydroxyapatite nanoribbon spherulites form as follows. First, the two reacting ions meet and react in the hole channels of the eggshell membrane. The formed $Ca_5(PO_4)_3$-OH molecules then aggregate to form a crystal nucleus, which grows under the cooperative control of the eggshell membrane and ethylenediamine on the surface of the eggshell membrane to form hydroxyapatite nanoribbon spherulites. The formed nanoribbon spherulites fall from the eggshell membrane into the solution due to the pressure of the diffused reaction ions, the newly formed products, gravity, and thermal motion.

The hydroxyapatite nanoribbon spherulites were treated with fluorescein, $C_{20}H_{12}O_5$, which is a fluorescent molecule whose structural formula is shown in Scheme 1. The TEM images of the resulting fluorescent probe materials (Figure 10, a) indicate that they are spherical with a diameter of about 2.1 μm, which is less than that of the unmodified products. This can be explained by supposing that the close combination of fluorescein and hydroxyapatite nanoribbon spherulites, mainly through two kinds of strong effects, reduces the diameter. As the hydroxyapatite nanoribbon spherulite is a porous structure composed of interlaced nanoribbons, one of these effect is likely to be hydrogen bonding between the hydroxy groups in the hydroxyapatite spherulite and the COOH, OH, and C=O groups of fluorescein. The other is the strong surface adsorption ability of hydroxyapatite spherulites to fluorescein molecules due to its large surface area. It is these two effects that combine the fluorescein and nanoribbon spherulite tightly. The TEM images show that the nanoribbons have almost disappeared, the surface is smooth, and there is appreciable darkness in the center, as indicated by the arrow in Figure 10 (b), which suggests that, instead of just adhering to the spherulite surface, fluorescein is embedded inside the spherulites.

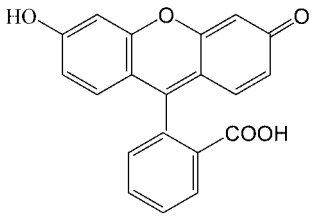

Scheme 1. Structure of fluorescein.

The modified products were rinsed several times with ethanol to exclude the possibility that fluorescein just clings

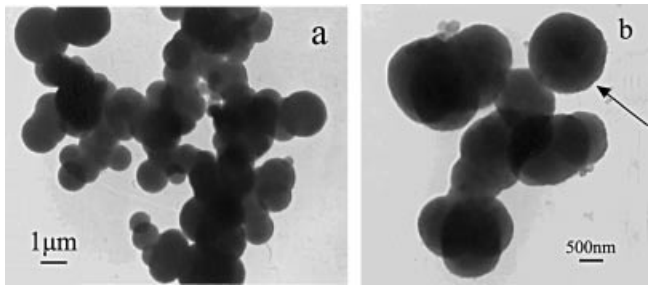

Figure 10. The TEM pattern of products modified with fluorescein.

to the surface of the fluorescent probe materials. The fluorescence spectra of unmodified and modified products indicate that nanoribbon spherulites are not photoluminescent, as shown in Figure 11 (c), whereas Figure 11 (b) shows that the luminescence of the modified products is very strong. At an excitation wavelength of 314 nm, the fluorescent probe materials emit green lighty of 514 nm (Figure 11, b), slightly different from the emission wavelength of the nanoribbon spherulites (511nm; Figure 11, a). This is because the interaction between the nanoribbons and fluorescein changes the ligand field of fluorescein and thus alters the electron distribution in the conjugated system of fluorescein molecules, which results in a change of the transition bandgaps of the electrons. Moreover, the XRD pattern of the modified product (Figure 12, a) shows that it is also a

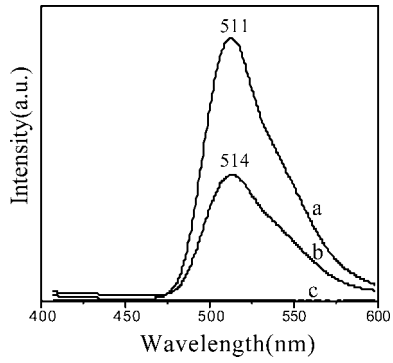

Figure 11. The fluorescence spectra of the products (a: fluorescein; b: fluorescent probe materials; c: nanoribbon spherulites. Excitation wavelength: 383 nm).

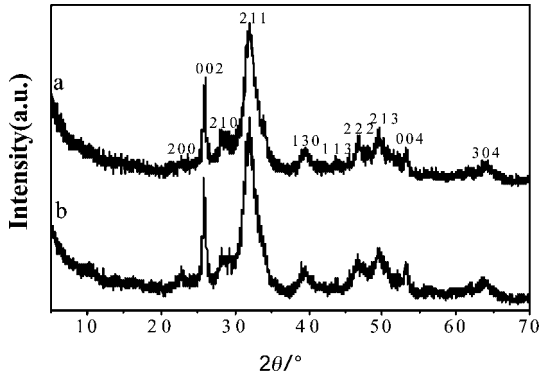

Figure 12. The XRD pattern of modified products (a: modified products; b: nanoribbon spherulites).

 © 2005 Wiley-VCH Verlag GmbH & Co. KGaA, Weinheim

hydroxyapatite structure, which indicates that hydroxyapatite combines with the fluorescein through nonchemical bonds, such as hydrogen bonds.

Conclusion

Hydroxyapatite spherulites assembled from long nanoribbons have been synthesized in a one-step reaction at room temperature with a novel bioactive eggshell membrane as the template and in the presence of ethylenediamine. This porous spherulite can be transformed into a solid one by electron beam irradiation. It can also combine with some organic compounds through hydrogen bonding and surface adsorption effects. Based on these properties, a fluorescent probe material with hydroxyapatite nanoribbons spherulites as substrates has been successfully prepared, and it provides a novel idea for the application of assembling nanoribbon spherulites in medical, biological, and industrial fields.

Experimental Section

The eggshell membrane was taken from a fresh eggshell after removing the outer shell and washing with deionized water. It was then fastened in a container to separate it into two horizontal compartments into which 20 mL of 0.1 M $CaCl_2$ and 20 mL of 0.06 M KH_2PO_4 were added, respectively. Ethylenediamine was put in both sides of the membrane to modulate the pH value to 7.4. All reagents used were of analytical purity. Thereafter, the reaction container was kept at 37 °C for ten hours. The obtained products were separated in a centrifuge at 1500 rpm and washed with deionized water and alcohol several times, one after the other, until no Ca^{2+} and ethylenediamine could be detected. The washed products were collected and dried in a desiccator to give the final products.

A sample of the above products (0.5 g) was put in 50 mL of a 2% aqueous fluorescein solution, the system was vibrated ultrasonically for 20 min, and then separated. The precipitates were rinsed with ethanol to remove the excessive fluorescein until the ethanol solution showed no fluorescence by fluorescent spectroscopy. Then, the washed products were collected and dried in a desiccator to obtain the final modified products.

The morphologies of the products were observed by transmission electron microscopy (TEM). The crystal phase and structure of the products were determined by X-ray powder diffraction (XRD) using a Shimadzu XD-3A diffractometer with graphite-monochromated Cu-K_α radiation (50 kV, 100 mA). The optical properties of the products were studied by FT-IR spectroscopy and fluorescent spectroscopy (Perkin–Elmer LS-55).

Acknowledgments

This work was supported by the National Natural Science Foundation of China (grant nos. 20471042 and 20131030), the Nano Foundation of Shanghai (grant nos. 0452nm075 and 0352nm129), and the Doctoral Program Foundation of the Ministry of Education of China (grant no. 20040247045).

[1] J. K. Yuan, K. Laubernds, Q. H. Zhang, S. L. Suib, *J. Am. Chem. Soc.* **2003**, *125*, 4966.
[2] F. Caruso, R. A. Caruso, H. Mohwald, *Science* **1998**, *282*, 1111.
[3] H. W. Duan, D. Y. Chen, M. Jiang, W. J. Gan, S. J. Li, M. Wang, J. Gong, *J. Am. Chem. Soc.* **2001**, *123*, 12097.
[4] C. F. Wang, S. Y. Xie, S. C. Lin, X. Cheng, X. H. Zhang, R. B. Huang, L. S. Zheng, *Chem. Commun.* **2004**, *15*, 1766.
[5] Z. W. Pan, Z. R. Dai, Z. L. Wang, *Science* **2001**, *291*, 1947.
[6] X. L. Li, Y. D. Li, *Chem. Eur. J.* **2003**, *9*, 2726.
[7] A. Maiti, J. A. Rodriguez, M. Law, P. Kung, J. R. Mckinney, P. D. Yang, *Nano Lett.* **2003**, *3*, 1025.
[8] X. B. Cao, Y. Xie, S. Y. Zhang, F. Q. Li, *Adv. Mater.* **2004**, *16*, 649.
[9] Y. G. Sun, B. Mayers, Y. N. Xia, *Nano. Lett.* **2003**, *3*, 675.
[10] A. Swami, A. Kumar, P. R. Selvakannan, S. Mandal, R. Pasricha, M. Sastry, *Chem. Mater.* **2003**, *15*, 17.
[11] J. Zhang, F. H. Jiang, L. D. Zhang, *J. Phys. Chem. B* **2004**, *108*, 7002.
[12] Z. P. Liu, S. Peng, Q. Xie, Z. K. Hu, Y. Yang, S. Y. Zhang, Y. T. Qian, *Adv. Mater.* **2003**,*15*, 936.
[13] C. Ma, Y. Ding, D. Moore, X. D. Wang, Z. L. Wang, *J. Am. Chem. Soc.* **2004**, *126*, 708.
[14] H. T. Shi, L. M. Qi, J. M. Ma, H. M. Cheng, B. Y. Zhu, *Adv. Mater.* **2003**,*15*, 1647.
[15] Y. Jiang, X. M. Meng, W. C. Yiu, J. Liu, J. X. Ding, C. S. Lee, S. T. Lee, *J. Phys. Chem. B* **2004**, *108*, 784.
[16] X. T. Zhang, J. Zhang, Z. F. Liu, C. Robinson, *Chem. Commun.* **2004**, *16*, 1852.
[17] S. H. Yu, H. Cölfen, A. W. Xu, W. F. Dong, *Cryst. Growth Des.* **2004**, *4*, 33.
[18] L. E. Euliss, T. M. Trnka, T. J. Deming, G. D. Stucky, *Chem. Commun.* **2004**, *15*, 1736.
[19] C. Z. Wu, Y. Xie, D. Wang, J. Yang, T. W. Li, *J. Phys. Chem. B* **2003**, *107*, 13583.
[20] S. H. Rheel, J. Tanaka, *Biomaterials* **1999**, *20*, 2155.
[21] M. S. Fleming, T. K. Mandal, D. R. Walt, *Chem. Mater.* **2001**, *13*, 2210.
[22] X. M. Sun, Y. D. Li, *Angew. Chem. Int. Ed.* **2004**, *43*, 597.
[23] Q. Peng, Y. J. Dong, Y. D. Li, *Angew. Chem. Int. Ed.* **2003**, *42*, 3027.
[24] J. X. Huang, Y. Xie, B. Li, Y. Liu, Y. T. Qian, S. Y. Zhang, *Adv. Mater.* **2000**, *12*, 808.
[25] B. Liu, H. C. Zeng, *J. Am. Chem. Soc.* **2004**, *126*, 8124.
[26] N. Bowden, A. Terfort, J. Carbeck, G. M. Whitesides, *Science* **1997**, *276*, 233.
[27] H. Cölfen, S. Mann, *Angew. Chem. Int. Ed.* **2003**, *42*, 2350.
[28] J. C. Love, A. R. Urbach, M. G. Prentiss, G. M. Whitesides, *J. Am. Chem. Soc.* **2003**, *125*, 12696.
[29] G. M. Whitesides, B. Grzybowski, *Science* **2002**, *295*, 2418.
[30] K. P. Velikov, C. G. Christova, R. P. A. Dullens, V. A. Blaaderen, *Science* **2002**, *296*, 106.
[31] P. Yang, *Nature* **2003**, *425*, 243.
[32] S. Park, J. H. Lim, S. W. Chung, C. A. Mirkin, *Science* **2004**, *303*, 348.
[33] M. Antonietti, M. Breulmann, C. G. Göltner, H. Cölfen, K. K. W. Wong, D. Walsh, S. Mann, *Chem. Eur. J.* **1998**, *4*, 2493.
[34] D. Yang, L. M. Qi, J. M. Ma, *Adv. Mater.* **2002**, *14*, 1543.
[35] T. Hirai, M. Hodono, I. Komasawa, *Langmuir* **2000**, *16*, 955.
[36] Y. D. Li, J. W. Wang, Z. X. Deng, Y. Y. Wu, X. M. Sun, D. P. Yu, P. D. Yang, *J. Am. Chem. Soc.* **2001**, *123*, 9904.
[37] C. Pacholski, A. Kornowski, H. Weller, *Angew. Chem. Int. Ed.* **2002**, *41*, 1188.
[38] X. W. Lou, H. C. Zeng, *J. Am. Chem. Soc.* **2003**, *125*, 2697.
[39] H. T. Shi, L. M. Qi, J. M. Ma, H. M. Cheng, *Chem. Commun.* **2002**, *16*, 1704.
[40] P. K. Ajikumar, R. Lakshminarayanan, B. T. Ong, S. Valiyaveettil, R. M. Kini, *Biomacromolecules* **2003**, *4*, 1321.

Received: March 8, 2005
Published Online: September 13, 2005

 © 2005 Wiley-VCH Verlag GmbH & Co. KGaA, Weinheim

Multiple Regulated Assembly, Crystal Structures and Magnetic Properties of Porous Coordination Polymers with Flexible Ligands

Chang-Yan Sun,[a] Xiang-Jun Zheng,[a] Song Gao,[b] Li-Cun Li,[c] and Lin-Pei Jin*[a]

Keywords: Cobalt / Coordination polymers / Magnetic properties / Nickel / Porous materials

Four novel coordination polymers of Ni^{II} and Co^{II} with flexible ligands, namely $[Ni(oba)(bpe)]_n \cdot nH_2O$ (**1**), $[Co(oba)(bpe)]_n$ (**2**), $[Ni_2(oba)_2(bpy)_2(H_2O)_2]_n \cdot n$bpy (**3**), and $[Co(oba)(bpy)_{1/2}]_n$ (**4**) [H_2oba = 4,4′-oxybis(benzoic acid), bpe = 1,2-bis(4-pyridyl)ethane, bpy = 4,4′-bipyridine] were synthesised by hydrothermal reactions and characterised by single-crystal X-ray diffraction, elemental analysis and IR spectroscopy. The Ni^{II} ions in complex **1** are linked by flexible oba and bpe ligands to form square-grid-like corrugated sheets. These sheets are interpenetrated with each other, resulting in the formation of a 3D porous network with lattice water molecules in the channels. The variable temperature X-ray diffraction analysis shows that the framework is stable up to 300 °C despite the complete removal of the lattice water molecules during the heat treatment. Complex **2** can be regarded as possessing a α-polonium-related topology. Triple interpenetration occurs to form a nonporous structure. In complex **3**, the oba and bpy ligands link Ni^{II} ions into 1D train-like boxes. These boxes are entangled, with the aid of hydrogen bonds, leading to the formation of a 3D porous supramolecular architecture. Free bpy ligands reside in the channels. The Co^{II} ions in complex **4** are linked by oba and bpy ligands to form a complicated 3D coordination polymer. The lattice water molecules in complex **1** and free bpy ligands in complex **3** can be regarded as templates that play an important role in the formation of the porous structures of complexes **1** and **3**. The magnetic properties of complexes **1**, **2**, and **4** have also been investigated.
(© Wiley-VCH Verlag GmbH & Co. KGaA, 69451 Weinheim, Germany, 2005)

Introduction

Porous coordination polymers are of current interest in the fields of supramolecular chemistry and crystal engineering not only because of the intriguing variety of architectures and topologies but also because of their potential applications in gas storage,[1] separation,[2] sensors[3] and catalysis.[4] The most commonly used synthetic strategy is to select appropriate ligands to bridge metal ions, with the aid of hydrogen bonds, metal–metal bonds, π-π stacking, van der Waals and electrostatic interactions, to form the desired extended network under mild conditions.[5] It is well-known that the topology of porous coordination polymers depends both on the coordination behaviour of the organic ligands and on the selection of the coordination geometry of the metal centres. Thus far, porous coordination polymers have centred on the assembly of linear rigid polycarboxylates, especially dicarboxylates,[6,7] and d-block metal ions, as these metal ions have low coordination numbers and are easily linked to form grid,[8] honeycomb,[9] brick-wall[10] and other geometries.[11] Long flexible ligands, because of their easy interpenetration, are seldom used in the construction of porous coordination polymers, although with ingenious design, interpenetrated networks can give novel topologies and useful properties.[12] More and more interest has focused on long flexible ligands recently, and how to avoid, or make use of, their interpenetration to construct porous coordination polymers is an interesting challenge. 4,4′-Oxybis(benzoic acid) (H_2oba) is the typical example of a long, V-shaped, flexible ligand. As far as we know, its coordination chemistry has been studied and several coordination polymers have been obtained.[13] Of these coordination polymers, only one complex, $[Zn_2(oba)_2(DMF)_2] \cdot 2DMF$, possesses a porous structure.[13f] In this complex, the DMF molecules act as guests, thus preventing interpenetrating. It is supposed that appropriate molecules may function as guests occupying the pores and consequently promote the formation of large pores,[14] and the introduction of ancillary ligands, such as the N-containing ligands 1,2-bis(4-pyridyl)ethane (bpe) and 4,4′-bipyridine (bpy), often has a significant effect on the formation and dimension of the resulting structures. With this idea in mind, we chose H_2oba as a bridging ligand to react with the d-block metal ions Ni^{II} and Co^{II}. The neutral ligands bpe and bpy were introduced into the M^{II}/oba system, and four novel coordination polymers, namely $[Ni(oba)(bpe)]_n \cdot nH_2O$ (**1**),

[a] Department of Chemistry, Beijing Normal University, Beijing 100875, China
Fax: +86-10-5880-2075
E-mail: lpjin@bnu.edu.cn
[b] State Key Laboratory of Rare Earth Materials Chemistry and Applications, College of Chemistry and Molecular Engineering, Peking University, Beijing, 100871, China
[c] Department of Chemistry, Nankai University, Tianjin 300071, China

 © 2005 Wiley-VCH Verlag GmbH & Co. KGaA, Weinheim **DOI: 10.1002/ejic.200500217**

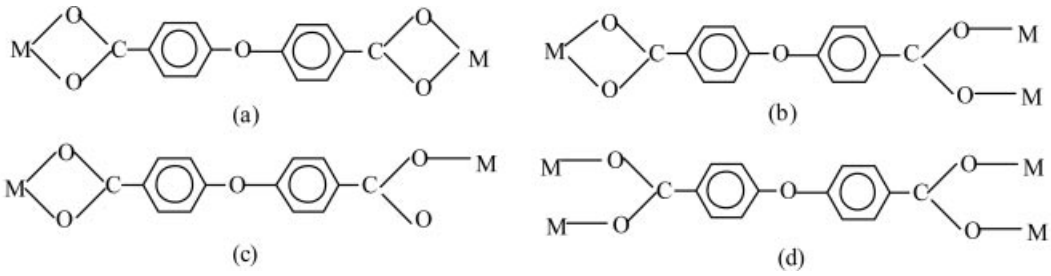

Scheme 1. The coordination modes of the oba ligands in complexes **1**–**4**.

$[Co(oba)(bpe)]_n$ (**2**), $[Ni_2(oba)_2(bpy)_2(H_2O)_2]_n \cdot n$bpy (**3**) and $[Co(oba)(bpy)_{1/2}]_n$ (**4**) were obtained. The details of their synthesis, structure and magnetic properties are reported below.

Results and Discussion

Description of the Structures

The oba ligands in complexes **1**–**4** are completely deprotonated and are significantly bent at the ether-oxygen sites [C–O–C = 115.9(3)–119.2(7)°]. They afford four kinds of coordination modes (see Scheme 1). All bpe ligands are in an *anti* conformation.

[Ni(oba)(bpe)]$_n$·nH$_2$O (1)

In the asymmetrical unit of complex **1**, there is one Ni^{II} ion, one oba ligand, one bpe ligand and one lattice water molecule. The Ni^{II} ion is located in a slightly distorted octahedral geometry and is coordinated to four oxygen atoms of two oba ligands and two nitrogen atoms of two bpe ligands, as shown in Figure 1. The average Ni–N bond length is 2.051 Å and the Ni–O bond lengths are in the range 2.010(2)–2.312(3) Å. The details are depicted in Table 1. Each oba ligand adopts a bis(chelating bidentate) mode, linking two Ni^{II} ions [see Scheme 1 (a)].

The Ni^{II} ions are linked by oba and bpe ligands into square-grid-like corrugated sheets with grid dimensions of about 13×13 Å^2 in the *bc* plane, as shown in Figure 2 (a) (based on the separation of the metal ions). It is noteworthy that all the metal ions in the layer of complex **1** are not coplanar, but are present in a stair-like fashion. These stair-like layers are interpenetrated with each other, resulting in the formation of the 3D network. Although interpenetration occurs in complex **1**, there are still channels in the 3D network [see Figure 2 (b)], and lattice water molecules are accommodated in the channels. Hydrogen bonds are formed between the lattice water molecules and the carboxylate groups {*d*[O(6)···O(2)i] = 3.005 Å (symmetry code i: *x* + 1, *y*, *z*), *d*[O(2)i···H(6B)] = 2.562 Å and *θ*[O(6)–H(6B)

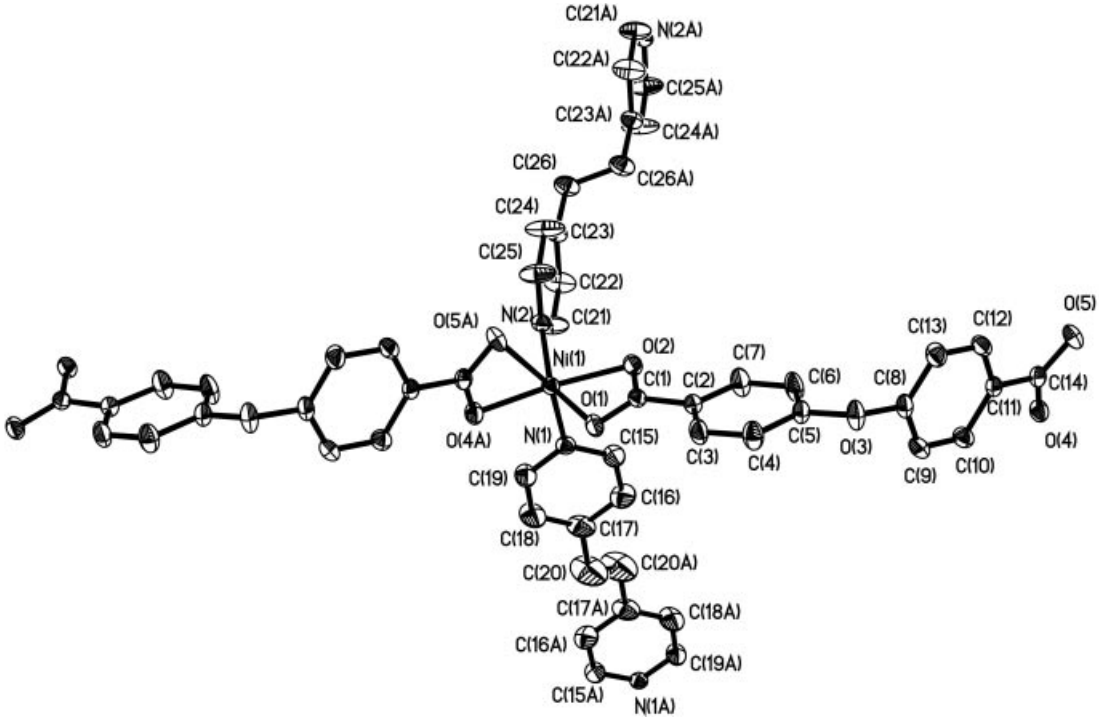

Figure 1. The coordination environment of the Ni^{II} ion in complex **1** with 30% thermal ellipsoids. All hydrogen atoms and lattice water molecules have been omitted for clarity.

 © 2005 Wiley-VCH Verlag GmbH & Co. KGaA, Weinheim

Table 1. Selected bond lengths [Å] and angles [°] for **1** and **2**.

1[a]			
Ni(1)–O(1)	2.169(3)	Ni(1)–O(5)#1	2.312(3)
Ni(1)–O(2)	2.073(2)	Ni(1)–N(1)	2.050(3)
Ni(1)–O(4)#1	2.010(2)	Ni(1)–N(2)	2.053(3)
O(1)–Ni(1)–O(5)#1	86.89(9)	N(1)–Ni(1)–O(1)	96.67(1)
O(2)–Ni(1)–O(1)	61.79(9)	N(1)–Ni(1)–O(2)	96.14(1)
O(2)–Ni(1)–O(5)#1	107.86(9)	N(1)–Ni(1)–O(5)#1	154.26(1)
O(4)#1–Ni(1)–O(1)	97.82(1)	N(1)–Ni(1)–N(2)	98.24(1)
O(4)#1–Ni(1)–O(2)	158.11(1)	N(2)–Ni(1)–O(1)	150.66(1)
O(4)#1–Ni(1)–O(5)#1	60.22(9)	N(2)–Ni(1)–O(2)	91.53(1)
O(4)#1–Ni(1)–N(1)	94.05(1)	N(2)–Ni(1)–O(5)#1	90.47(1)
O(4)#1–Ni(1)–N(2)	106.13(1)		
2[b]			
Co(1)–O(1)	2.020(2)	Co(1)–O(5)#3	2.232(2)
Co(1)–O(2)#1	2.026(2)	Co(1)–N(1)	2.164(3)
Co(1)–O(4)#3	2.170(2)	Co(1)–N(2)#2	2.147(3)
O(1)–Co(1)–O(2)#1	112.46(8)	O(2)#1–Co(1)–N(1)	90.17(8)
O(1)–Co(1)–O(4)#3	151.03(8)	O(2)#1–Co(1)–N(2)#2	89.76(8)
O(1)–Co(1)–O(5)#3	91.35(9)	N(1)–Co(1)–O(4)#3	87.64(9)
O(1)–Co(1)–N(1)	87.89(9)	N(2)#2–Co(1)–O(4)#3	88.73(9)
O(1)–Co(1)–N(2)#2	95.52(9)	N(2)#2–Co(1)–N(1)	176.34(8)
O(2)#1–Co(1)–O(4)#3	96.17(8)		

[a] Symmetry transformations used to generate equivalent atoms: #1 x, $y-1$, $z+1$. [b] Symmetry transformations used to generate equivalent atoms: #1 $-x+1$, $-y$, $-z+1$; #2 $x+1$, y, $z+1$; #3 $x+1$, $-y+1/2$, $z-1/2$.

···O(2)i] = 111.69°}, which enhances the stability of the open framework.

[Co(oba)(bpe)]$_n$ (2)

In complex **2**, one carboxylate group of an oba ligand adopts a chelating bidentate mode while the other adopts a bridging bidentate mode, which means that every oba ligand links three Co^{II} ions [see Scheme 1 (b)]. There is only one crystallographically unique Co^{II} centre, which is coordinated to four carboxylate oxygen atoms of three oba ligands and two nitrogen atoms of two bpe ligands (see Figure 3). The average Co–N bond length is 2.155 Å and the Co–O bond lengths are in the range 2.020(2)–2.232(2) Å. Thus, the Co^{II} centre displays a distorted octahedral geometry with one [CoO_4N_2] unit. Two such [CoO_4N_2] units are connected together by two carboxylate groups, leading to the formation of a binuclear secondary building unit (SBU) in which the Co···Co distance is 4.298 Å. The oba ligands link the SBUs into 2D layers with rhombus-shaped cavities of about 13 × 15 Å^2. Although this framework motif is common, the bent oba structure provides a new aspect in the cavity shape, and it has seldom been reported that this motif contains concertinaed corners.[15] These layers are pillared by bpe ligands with a Co–N coordination bond, resulting in the formation of a 3D net that can be regarded as possessing an α-polonium-related topology [see Figure 4 (a)]. There are large channels (13 × 15 Å^2) in the open sub-framework (named net), but triple interpenetration occurs, as shown in Figure 4 (b). The nodes of the second and third nets are located, equally spaced, along the rhombohedral diagonal of the first net, and each rhombic "window" has a rod from each of the adjacent two nets passing through it, giving a complicated nonporous structure.

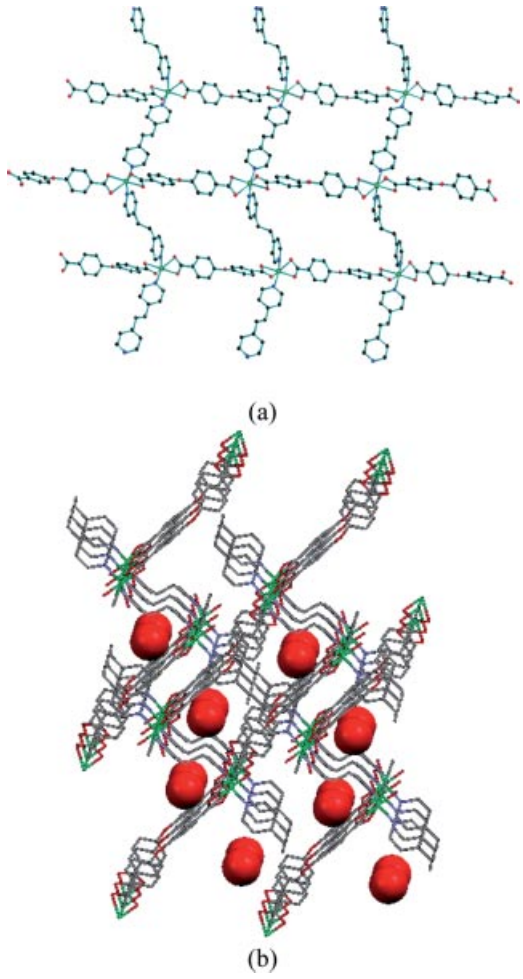

Figure 2. (a) Square-grid-like sheet of complex **1** in the *bc* plane. (b) The 3D porous network of complex **1,** with lattice water molecules in the channels, viewed along the *a* axis.

[Ni$_2$(oba)$_2$(bpy)$_2$(H$_2$O)$_2$]$_n$·nbpy (3)

There are two kinds of metal coordination environments in complex **3**, as shown in Figure 5. Ni(1) and Ni(2) are both six-coordinate and their coordination geometries can be described as distorted octahedral. Both Ni^{II} ions are coordinated to three oxygen atoms of two oba ligands, two nitrogen atoms of two bpy ligands and one oxygen atom of one water molecule. However, the corresponding bond lengths and bond angles are different. The Ni(1)–O bond lengths are in the range 1.992(4)–2.143(5) Å and the average value is 2.095 Å, while for Ni(2) the bond lengths range from 2.026(4) Å to 2.195(4) Å and the average value is 2.091 Å. The details are depicted in Table 2. In complex **3**, one carboxylate group of an oba ligand coordinates to a Ni^{II} ion in a monodentate mode while the other adopts a chelating-bidentate mode. Thus, every oba ligand links two Ni^{II} ions [see Scheme 1 (c)]. Ni(1) and Ni(2) are bridged by a bpy ligand with a distance of 11.129 Å, which can be regarded as a binuclear SBU. Such SBUs are linked together

 © 2005 Wiley-VCH Verlag GmbH & Co. KGaA, Weinheim

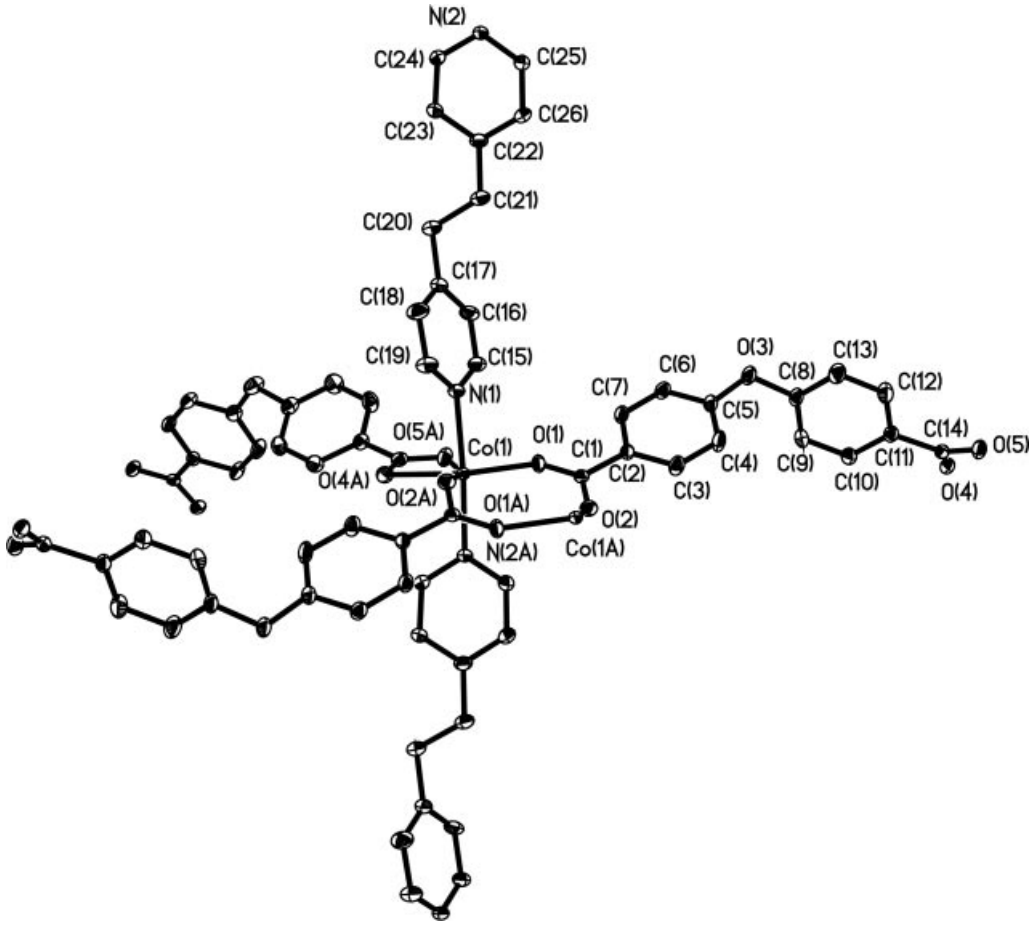

Figure 3. The coordination environment of the Co^{II} ion in complex **2** with 30% thermal ellipsoids. All hydrogen atoms have been omitted for clarity.

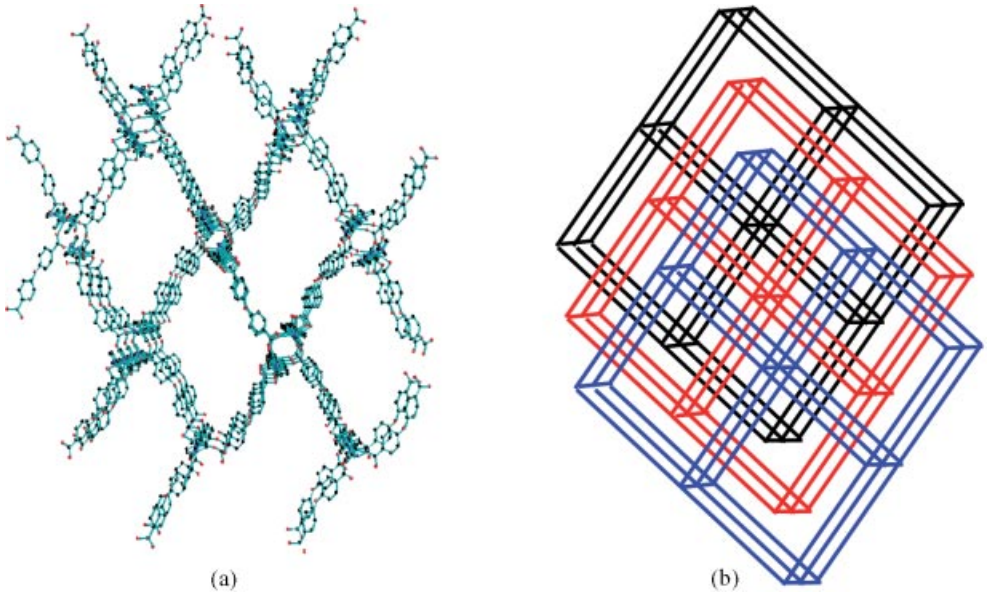

Figure 4. (a) The 3D framework of complex **2** with channels viewed along the [101] direction. (b) A simplified representation of the interpenetrating framework of complex **2**, the alternating frameworks are shown in black, red and blue.

 © 2005 Wiley-VCH Verlag GmbH & Co. KGaA, Weinheim

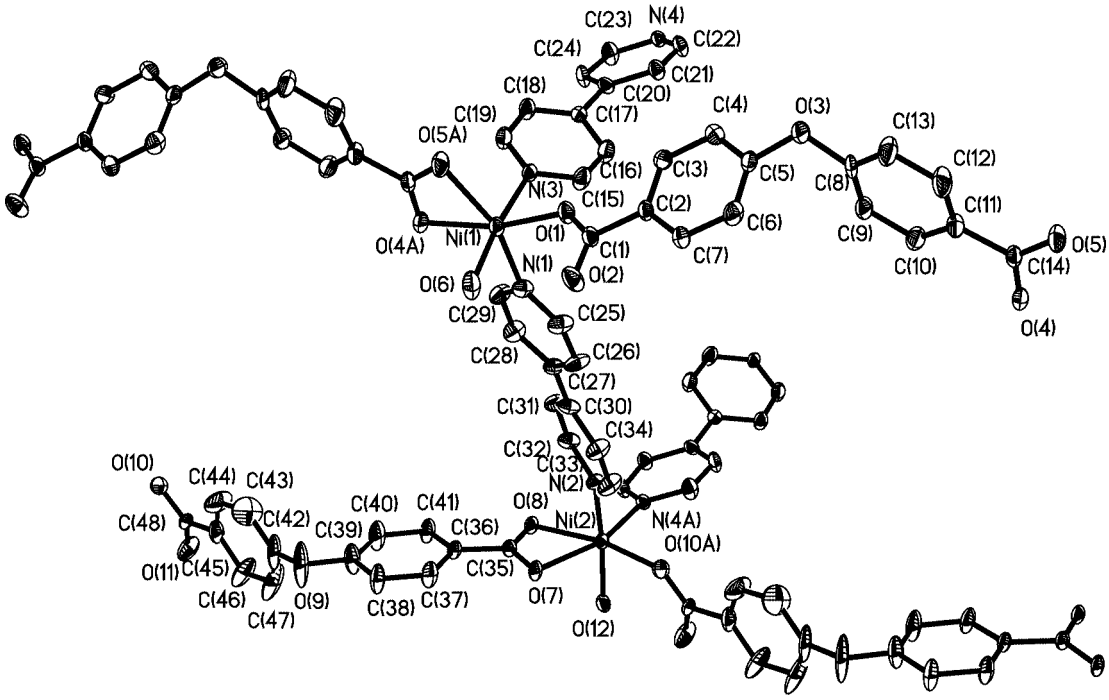

Figure 5. The coordination environments of the Ni^{II} ions in complex **3** with 30% thermal ellipsoids. All hydrogen atoms and free bpy ligands have been omitted for clarity.

Table 2. Selected bond lengths [Å] and angles [°] for **3** and **4**.

3[a]			
Ni(1)–O(1)	1.992(4)	Ni(2)–O(7)	2.195(4)
Ni(1)–O(4)#1	2.054(4)	Ni(2)–O(8)	2.112(4)
Ni(1)–O(5)#1	2.143(5)	Ni(2)–O(10)#2	2.026(4)
Ni(1)–O(6)	2.081(5)	Ni(2)–O(12)	2.030(4)
Ni(1)–N(1)	2.053(6)	Ni(2)–N(2)	2.060(5)
Ni(1)–N(3)	2.137(5)	Ni(2)–N(4)#3	2.059(5)
O(1)–Ni(1)–O(4)#1	165.4(2)	O(8)–Ni(2)–O(7)	60.77(2)
O(1)–Ni(1)–O(5)#1	103.88(2)	O(10)#2–Ni(2)–O(7)	103.92(2)
O(1)–Ni(1)–O(6)	90.76(2)	O(10)#2–Ni(2)–O(8)	164.60(2)
O(1)–Ni(1)–N(3)	85.10(2)	O(10)#2–Ni(2)–O(12)	88.67(2)
O(4)#1–Ni(1)–O(5)#1	61.81(2)	O(10)#2–Ni(2)–N(2)	90.83(2)
O(4)#1–Ni(1)–O(6)	92.89(2)	O(10)#2–Ni(2)–N(4)#3	96.43(2)
O(4)#1–Ni(1)–N(3)	92.18(2)	O(12)–Ni(2)–O(7)	88.91(2)
O(6)–Ni(1)–O(5)#1	93.5(2)	O(12)–Ni(2)–O(8)	89.29(2)
O(6)–Ni(1)–N(3)	174.03(2)	O(12)–Ni(2)–N(2)	172.71(2)
N(1)–Ni(1)–O(4)#1	94.8(2)	O(12)–Ni(2)–N(4)#3	93.75(2)
N(1)–Ni(1)–O(5)#1	156.5(2)	N(2)–Ni(2)–O(7)	84.15(2)
N(1)–Ni(1)–O(6)	89.1(2)	N(2)–Ni(2)–O(8)	89.27(2)
N(1)–Ni(1)–N(3)	87.3(2)	N(4)#3–Ni(2)–O(7)	159.54(2)
		N(4)#3–Ni(2)–O(8)	98.94(2)
		N(4)#3–Ni(2)–N(2)	93.5(2)
4[b]			
Co(1)–O(1)	2.077(3)	Co(1)–O(5)#1	1.976(3)
Co(1)–O(2)#2	2.000(3)	Co(1)–N(1)	2.084(3)
Co(1)–O(4)#3	2.020(3)		
O(1)–Co(1)–N(1)	170.89(2)	O(4)#3–Co(1)–N(1)	88.85(2)
O(2)#2–Co(1)–O(1)	85.31(1)	O(5)#1–Co(1)–O(1)	88.94(1)
O(2)#2–Co(1)–O(4)#3	141.82(2)	O(5)#1–Co(1)–O(2)#2	112.92(2)
O(2)#2–Co(1)–N(1)	87.87(1)	O(5)#1–Co(1)–O(4)#3	104.97(1)
O(4)#3–Co(1)–O(1)	100.25(1)	O(5)#1–Co(1)–N(1)	88.15(1)

[a] Symmetry transformations used to generate equivalent atoms: #1 $x, y + 1, z$; #2 $x, y - 1, z$; #3 $-x + 1, -y + 1, -z + 2$. [b] Symmetry transformations used to generate equivalent atoms: #1 $-x + 2, -y + 1, -z + 2$; #2 $-x + 2, y, -z + 3/2$; #3 $x, y - 1, z$.

by the oba ligands, resulting in 1D train-like boxes that contain free bpy ligands (see Figure 6). Each box is entangled with another two adjacent boxes. There are hydrogen bonds between the water molecules and the carboxylate groups {d[O(6)···O(2)] = 2.669 Å, d[O(2)···H(6A)] = 2.128 Å and θ[O(6)–H(6A)···O(2)] = 113.19°; d[O(12)···O(11)i] = 2.553 Å (symmetry code i: $x, y - 1, z$), d[O(11)i···H(12B)] = 2.027 Å and θ[O(12)–H(12B)···O(11)i] = 119.37°}, which leads to the formation of a 3D porous supramolecular architecture.

The Structure of [Co(oba)(bpy)$_{1/2}$]$_n$ (4)

The coordination environment of the Co^{II} ions in complex **4** is shown in Figure 7. The Co^{II} ion is five-coordinate, with four oxygen atoms from four oba ligands and one nitrogen atom from one bpy ligand. The coordination geometry of the Co^{II} ion can best be described as a distorted triangular bipyramid. The Co–N bond length is 2.084(3) Å and the Co–O bond lengths are in the range 1.976(3)–2.077(3) Å. Every oba ligand in complex **4** adopts a bis(bridging-bidentate) mode and links four Co^{II} ions [see Scheme 1 (d)]. The Co^{II} ions are bridged by the carboxylate groups of oba ligands into 1D chains along the c axis, in which the adjacent Co···Co distances are alternately 3.288 Å and 4.238 Å. These chains are further bridged by the bent oba ligands to produce 2D regular metal-organic layers. When viewed along the c axis, these 2D layers can be regarded as sine- and cosine-type curves intersecting at the zero points. The bpy ligands connect the Co^{II} ions in these 2D layers into a 3D structure.

Effect of the Metal Ions on the Molecular Structure

It is interesting that, although they are bound to the same ligands, Ni^{II} and Co^{II} give completely different pro-

 © 2005 Wiley-VCH Verlag GmbH & Co. KGaA, Weinheim

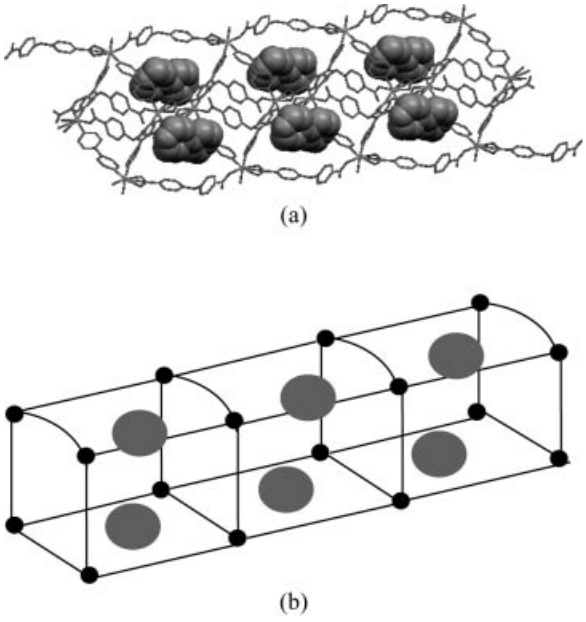

Figure 6. (a) The 1D train-like box in complex **3** (space-filling diagrams represent free bpy ligands). (b) A simplified representation of the 1D train-like box in complex **3** (nodes represent Ni^{II} ions and the balls represent free bpy ligands).

ducts, as shown in Scheme 2. We found from the structural analysis of complexes **1**–**4** that the two Ni^{II} complexes **1** and **3** possess a 3D open supramolecular architecture while the two Co^{II} complexes **2** and **4** have a 3D non-porous structure. Taking **1** and **2** as examples, the Ni^{II} and Co^{II} ions are both six-coordinate and in distorted octahedral geometries, but their coordination environments are different. In complex **1**, there are two oba ligands and two bpe ligands around each Ni^{II} ion, while in complex **2**, there are three oba ligands and two bpe ligands around each Co^{II} ion. More ligands are around each Co^{II} ion than each Ni^{II} ion. This is consistent with the fact that the radius of Co^{II} ion is larger than that of Ni^{II} ion. Furthermore, the coordination modes of the oba ligands in the two complexes are different. The oba ligands adopt a bis(chelating-bidentate) mode in complex **1** and a chelating-bridging mode in complex **2** (see parts a and b in Scheme 1), which results in the different structures of the corresponding complexes. Similar results are found for complexes **3** and **4**. This may also be attributed to the different size of the metal ions. Lower-dimensional nets are usually less likely to interpenetrate because there are more possible ways to maximize the packing efficiency.[16] So, after the stacking of 2D layers, complex **1** possesses 3D porous structure, while triple interpenetration occurs in complex **2**, as shown in Figure 6, to give a non-porous structure. A rational assembly of metal ions and flexible ligands is critical for the formation of a porous structure.

Effect of the Ligand on the Molecular Structure

Although the bpe and bpy ligands are both N-containing spacers, they are quite different. For example, bpe has *anti* and *gauche* conformations and is more flexible than bpy. When the bpe ligand is in the *anti* conformation, the distance between the two nitrogen atoms is larger than that of the bpy ligand, therefore *anti*-bpe is a longer spacer than bpy. When the bpe ligand is introduced into the M^{II}/H_2oba system, we obtain 2D square-grid-like sheets for Ni^{II} and a 3D α-polonium-related framework for Co^{II}, while with bpy we obtain 1D train-like boxes for the Ni^{II} complex and a complicated 3D framework for the Co^{II} complex. The oba ligands in the four complexes adopt four different coordination modes, as shown in Scheme 1, so for a special M^{II}/H_2oba system, the ancillary ligand has a significant effect on the formation and structure of the coordination polymers. In order to construct porous coordination polymers, it is a feasible method to introduce ancillary ligands.

Effect of Guest Molecules on the Molecular Structure

From the structural descriptions above, we know that lattice water molecules are accommodated in the channels of

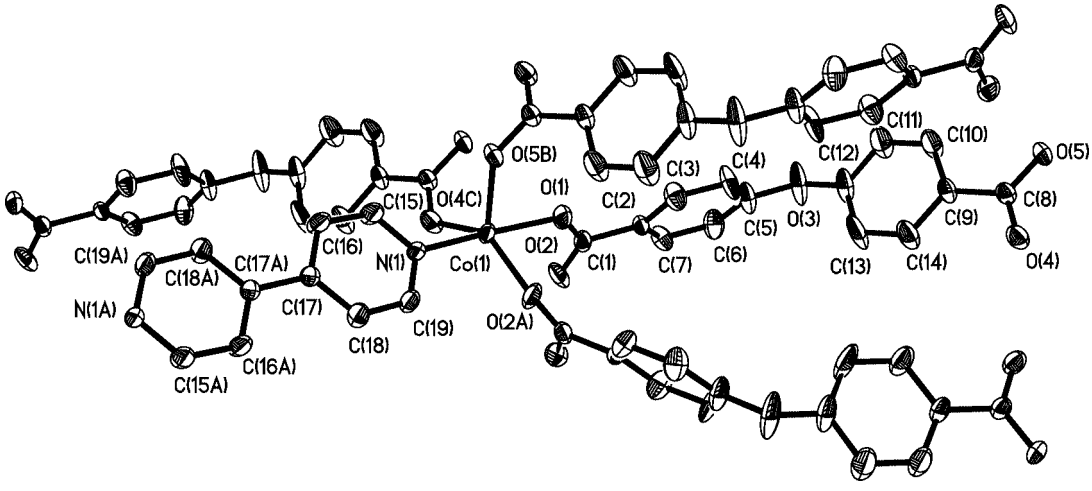

Figure 7. The coordination environment of the Co^{II} ion in complex **4** with 30% thermal ellipsoids. All hydrogen atoms have been omitted for clarity.

 © 2005 Wiley-VCH Verlag GmbH & Co. KGaA, Weinheim

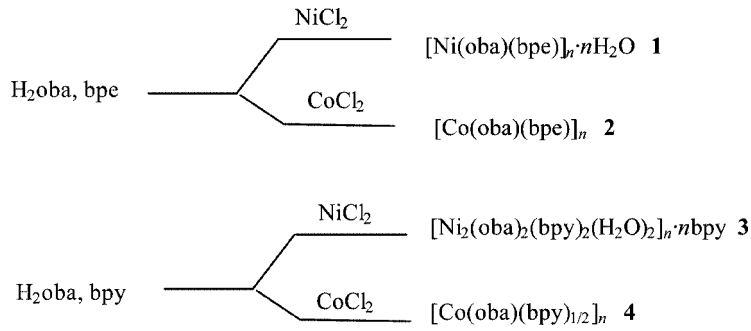

Scheme 2. Self-assembly of the coordination polymers.

complex **1** and free bpy ligands reside in the channels of complex **3**. The presence of lattice water molecules and free bpy ligands may be one of the more important factors for constructing the porous structures of complexes **1** and **3** as they occupy the pores and function as templates, thus preventing further interpenetration. This provides a valuable approach for constructing porous coordination polymers. If the potential pore walls are formed by the hydrophobic parts of ligand molecules, we can introduce hydrophobic molecules to function as guest molecules and occupy the pores through hydrophobic interactions with the ligands;[2b,14] on the other hand, if the potential pore walls are formed by the hydrophilic parts of ligand molecules, we can introduce hydrophilic molecules.[17] It can be expected that the presence of these guest molecules promotes the formation of large pores.

Thermal Stability Analysis of Complex 1

The thermal analysis of complex **1** is consistent with the crystallographic observations. The TG curve shows that the first weight loss of 3.7% from 75 °C to 290 °C corresponds to the loss of the lattice water molecules (calcd. 3.5%), leaving a framework of [Ni(oba)(bpe)]. This framework remains stable beyond 300 °C and it begins to decompose at 390 °C. This further decomposition finishes at 550 °C, leaving a powder of NiO. It is the interpenetrated nature of the structure that causes the higher thermal stability of complex **1**.

To further test the thermal stability of complex **1**, powder samples were examined by powder X-ray diffraction analysis. Corresponding to the TG analysis, powder XRD patterns were recorded at 20, 100, 300 and 450 °C (see Figure 8). It can be seen from Figure 8 that the XRD patterns at 100 °C and 300 °C are similar to that at room temperature, but not the same, indicating that the framework is able to survive. However, there are changes in the XRD patterns at 20, 100, and 300 °C, which are probably due to the contraction of the structure upon removal of the water molecules and the presence of the flexible ligands. At 450 °C, the XRD pattern changes completely, revealing the collapse of the framework, which is in accordance with the result of the thermogravimetric analysis.

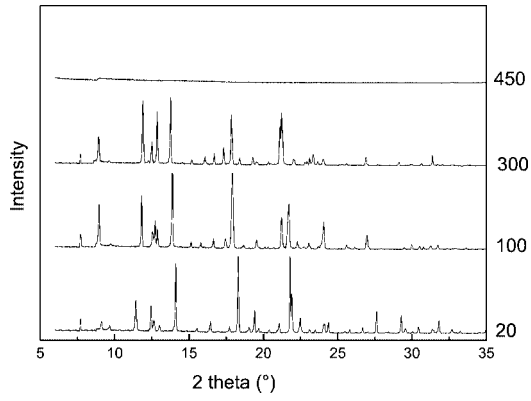

Figure 8. The powder X-ray diffraction patterns of complex **1** at different temperatures.

Magnetic Properties

Because the bridging ligands oba, bpe and bpy are quite long in complexes **1** and **3**, and thus the Ni···Ni distances are very long too, the magnetic interactions transferred by these ligands should be very weak. The magnetic properties of complexes **1** and **3** can be regarded as those of a single metal ion anisotropy. Here, we only give the magnetic property of complex **1** as an example.

Complex 1

The magnetic properties of complex **1** in the form of χ_M and μ_{eff} vs. T plots (χ_M is the molar magnetic susceptibility and μ_{eff} is the effective magnetic moment) are shown in Figure 9. Data were collected in the range 2–300 K in a magnetic field of 5 kOe. The μ_{eff} value for complex **1** is 3.15 μ_B at 300 K and it is practically constant in the temperature range analysed. It only starts to decrease at around 10 K, reaching a minimum value of 2.83 μ_B at 2 K, which should be mainly attributed to the zero-field splitting of Ni^{II} ions.

The experimental susceptibility data were fitted to the equation that considers only non-interacting $S = 1$ ions in the presence of a single ion anisotropy. The magnetic susceptibility is given in Equation (1).[18]

$$\chi_M = \frac{2Ng^2\beta^2}{3kT} \times \frac{2x^{-1} - 2\exp(-x)x^{-1} + \exp(-x)}{1 + 2\exp(-x)} \quad (1)$$

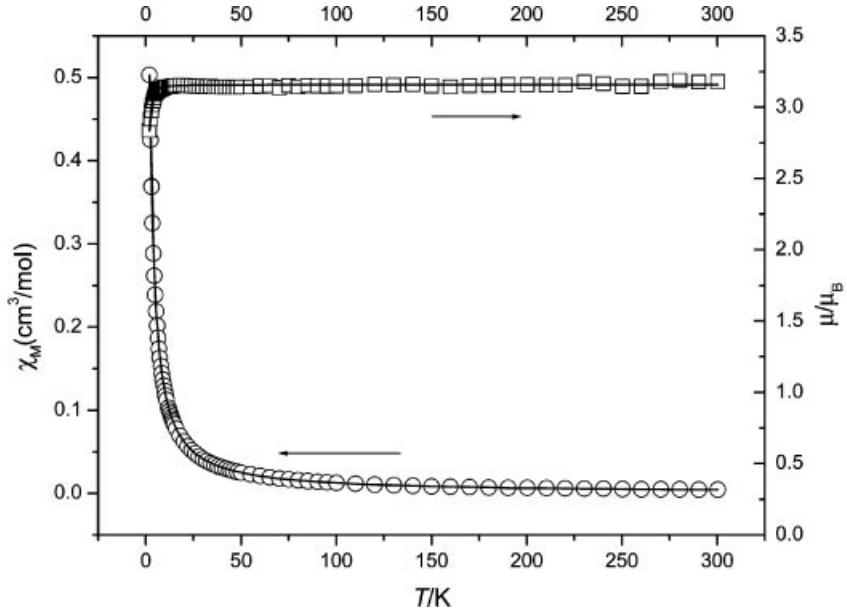

Figure 9. Plots of χ_M (○) and μ_{eff} (□) vs. T for complex **1**; the solid lines are theoretical fits based on Equation (1).

where $x = D/kT$. The best fit is given by the parameters $g = 2.23$, $D = 2.62\ cm^{-1}$, with an agreement factor, R, of 2.03×10^{-4} $\{R = \Sigma[(\chi_M)_{obs} - (\chi_M)_{calc}]^2/\Sigma[(\chi_M)_{calc}]^2\}$.

Complex 2

The magnetic susceptibility data of complex **2** in the form of $1/\chi_M$ and μ_{eff} vs. T plots are given in Figure 10. They were measured in the range 2–300 K in a magnetic field of 1 kOe. It can be seen that the μ_{eff} value decreases very gradually upon cooling and the μ_{eff} value at 300 K is 4.25 μ_B, which is larger than that expected for the spin-only case of Co^{II} (μ_{eff} = 3.87 μ_B), indicating an unquenched orbital contribution. The magnetic data above 30 K can be fitted to the Curie–Weiss law with $C = 2.268(5)\ cm^3\,mol^{-1}\,K$ and $\theta = -1.8$ K. The C value corresponds to $g = 2.20$ with $S = 3/2$. These results suggest a possible very weak antiferromagnetic coupling.

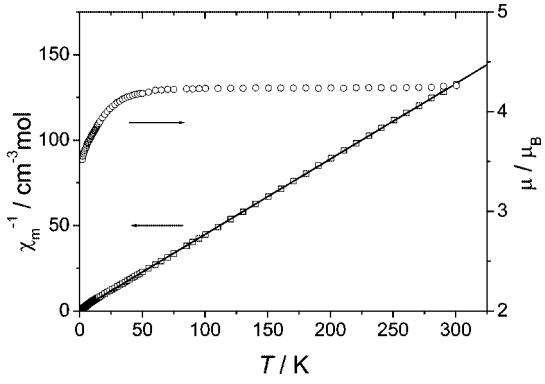

Figure 10. Plots of $1/\chi_M$ (□) and μ_{eff} (○) vs. T for complex **2**; the solid line is the theoretical fit based on the Curie–Weiss law.

Complex 4

Figure 11 shows the magnetic properties of complex **4** in the form of $1/\chi_M$ and μ_{eff} vs. T plots in the range 2–300 K measured at 1 kOe. It can be seen that the μ_{eff} value decreases very gradually upon cooling and the μ_{eff} value at 300 K is 4.71 μ_B, which is obviously larger than the expected spin-only value of 3.87 μ_B for a Co^{II} ion with S = 3/2, thus showing an unquenched orbital contribution. The magnetic data above 50 K can be fitted to the Curie–Weiss law with $C = 2.836(6)\ cm^3\,mol^{-1}\,K$ and $\theta = -7.3(1)$ K. The C value corresponds to $g = 2.46$ with $S = 3/2$. These results suggest a weak antiferromagnetic interaction.

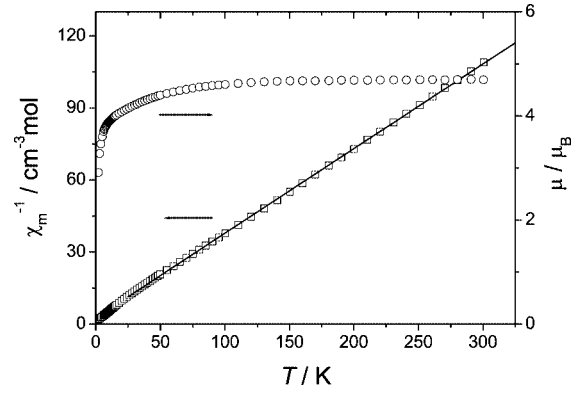

Figure 11. Plots of $1/\chi_m$ (□) and μ_{eff} (○) vs. T for complex **4**; the solid line is the best fit based on the Curie–Weiss law.

Conclusions

We have successfully obtained four novel coordination polymers of Ni^{II} and Co^{II}, namely $[Ni(oba)(bpe)]_n \cdot nH_2O$

 © 2005 Wiley-VCH Verlag GmbH & Co. KGaA, Weinheim

(**1**), $[Co(oba)(bpe)]_n$ (**2**), $[Ni_2(oba)_2(bpy)_2(H_2O)_2]_n \cdot n$bpy (**3**) and $[Co(oba)(bpy)_{1/2}]_n$ (**4**), with different dimensionalities. Comparing the structures of complexes **1** and **2**, and complexes **3** and **4**, it has been found that the different size of the metal ions has a significant effect on the formation and dimensions of the resulting structures. Furthermore, comparing the structures of complexes **1** and **3**, and complexes **2** and **4**, we can see that the neutral ancillary ligand is very important for the formation of coordination polymers. The presence of guest molecules can promote the formation of larger pores.

Experimental Section

General Remarks: All reagents were used as received without further purification. The C, H and N microanalyses were carried out with a Vario EL elemental analyzer. The IR spectra were recorded with a Nicolet Avatar 360 FT-IR spectrometer using the KBr pellet technique. Thermogravimetric curves were measured on a Perkin–Elmer TGA-7 (USA) at a heating rate of 5 °C min^{-1} from room temperature to 600 °C under nitrogen. The magnetic susceptibilities were obtained on crystalline samples using a Quantum Design MPMS SQUID magnetometer. The experimental susceptibilities were corrected for the sample holder and the diamagnetism contributions estimated from Pascal's constants. The powder X-ray diffraction patterns were recorded on a Bruker AXS D8 ADVANCE diffractometer.

Synthesis of $[Ni(oba)(bpe)]_n \cdot nH_2O$ (1): A mixture of H_2oba (0.1 mmol), $NiCl_2 \cdot 6H_2O$ (0.1 mmol), bpe (0.1 mmol) and 5 mL of deionised water was placed in a Teflon-lined stainless vessel (25 mL) and 0.2 mL of a 0.65 M aqueous NaOH solution was added whilst stirring. The vessel was then sealed and heated to 180 °C for 72 h under autogenous pressure, and then cooled slowly to room temperature. Single crystals were obtained by filtration, washed with deionized water and ethanol, and dried in air. Yield: 0.042 g (81.2%) $C_{26}H_{22}NiN_2O_6$ (517.17): calcd. C 60.33, H 4.25, N 5.41; found C 60.44, H 3.91, N 5.53. IR data (KBr pellet): $\tilde{\nu}$ = 3449 cm^{-1} (m), 3063 (w), 2929 (w), 1616 (m), 1596 (s), 1534 (m), 1504 (m), 1417 (s), 1226 (m), 1165 (m), 1098 (w), 1071 (w), 1025 (w), 876 (m), 835 (w), 781 (m), 662 (w), 548 (w).

Synthesis of $[Co(oba)(bpe)]_n$ (2): The synthesis of complex **2** followed the same procedure as complex **1** except that the volume of aqueous NaOH solution added was 0.3 mL. Yield: 0.04 g (80.1%) $C_{26}H_{20}CoN_2O_5$ (499.37): calcd. C 62.48, H 4.00, N 5.61; found C 62.70, H 4.13, N. 5.50. IR data (KBr pellet): $\tilde{\nu}$ = 3445 cm^{-1} (m), 3058 (w), 2971 (w), 2928 (w), 1616 (m), 1596 (s), 1538 (m), 1503 (m), 1417 (s), 1227 (s), 1163 (m), 1094 (w), 1049 (w), 1025 (w), 875 (m), 836 (w), 781 (m), 662 (w), 546 (w).

Synthesis of $[Ni_2(oba)_2(bpy)_2(H_2O)_2]_n \cdot n$bpy (3): A mixture of H_2oba (0.1 mmol), $NiCl_2 \cdot 6H_2O$ (0.1 mmol), bpy (0.1 mmol) and 5 mL of deionised water was placed in a Teflon-lined stainless vessel (25 ml) and 0.2 mL of a 0.65 M aqueous NaOH solution was added whilst stirring. The vessel was then sealed and heated to 180 °C for 72 h under autogenous pressure, and then cooled slowly to room temperature. Single crystals were obtained by filtration, washed with deionized water and ethanol, and dried in air. Yield: 0.024 g (42.3%). $C_{58}H_{44}N_6Ni_2O_{12}$ (1134.4): calcd. C 61.35, H 3.88, N 7.40; found C 61.20, H 3.74, N 7.04. IR data (KBr pellet): $\tilde{\nu}$ = 3444 cm^{-1} (m), 1595 (s), 1540 (m), 1496 (w), 1420 (s), 1381 (s), 1300 (w), 1248 (m), 1232 (m), 1158 (w), 875 (w), 808 (w), 784 (w), 659 (w), 635 (w).

Synthesis of $[Co(oba)(bpy)_{1/2}]_n$ (4): The synthesis of complex **4** was similar to that of complex **3**. Yield: 0.027 g (68.7%) $C_{19}H_{12}CoNO_5$ (393.23): calcd. C 57.98, H 3.05, N 3.56; found C 57.95, H 3.03, N 4.01. IR data (KBr pellet): $\tilde{\nu}$ = 3436 cm^{-1} (w), 3063 (w), 2924 (w), 1594 (s), 1551 (m), 1499 (m), 1393(s), 1299 (w), 1240 (s), 1221 (m), 1159 (m), 1013 (w), 877 (m), 779 (m), 675 (w), 565 (w), 514 (w).

X-ray Crystallographic Study: Diffraction intensities for the four complexes were collected at 293 K on a Bruker SMART 1000 CCD diffractometer employing graphite-monochromated Mo-K_α radiation (λ = 0.71073 Å). A semi-empirical absorption correction was applied using the SADABS program.[19] The structures were solved by direct methods and refined by full-matrix least-squares on F^2 using the SHELXS 97 and SHELXL 97 programs, respectively.[20,21] Non-hydrogen atoms were refined anisotropically and hydrogen atoms were placed in geometrically calculated positions. The crystallographic data for complexes **1**–**4** are listed in Table 3, and selected bond lengths and angles are listed in Tables 1 and 2. CCDC-265220–265223 (for **1**–**4**, respectively) contain the supplementary crystallographic data for this paper. These data can be

Table 3. Crystal data and structure refinement parameters for **1**–**4**.

	1	**2**	**3**	**4**
Chemical formula	$C_{26}H_{22}N_2NiO_6$	$C_{26}H_{20}CoN_2O_5$	$C_{58}H_{44}N_6Ni_2O_{12}$	$C_{19}H_{12}CoNO_5$
Crystal system	triclinic	monoclinic	triclinic	monoclinic
Space group	$P\bar{1}$	$P2_1/c$	$P\bar{1}$	$C2/c$
Formula mass	517.17	499.37	1134.41	393.23
a [Å]	9.254(3)	10.466(6)	12.375(5)	22.376(7)
b [Å]	11.512(4)	18.575(13)	14.886(6)	13.685(5)
c [Å]	12.298(4)	12.637(7)	15.858(7)	12.770(4)
α [°]	69.890(6)	90	88.144(7)	90
β [°]	80.995(6)	108.47(6)	73.229(7)	116.207(6)
γ [°]	86.981(6)	90	69.927(7)	90
V [Å^3]	1215.1(7)	2330(2)	2620.0(19)	3508(2)
Z	2	4	2	8
F(000)	536	1028	1172	1600
D_c [mg m^{-3}]	1.413	1.423	1.438	1.489
T [K]	293(2)	293(2)	293(2)	293(2)
θ range [°]	1.88–26.45	2.02–26.50	2.57–25.01	2.03–25.01
Goodness-of-fit on F^2	1.019	1.084	1.015	1.000
R_{int} [$I > 2\sigma(I)$]	R_1 = 0.0494 wR_2 = 0.1069	R_1 = 0.0415 wR_2 = 0.1003	R_1 = 0.0799 wR_2 = 0.1812	R_1 = 0.0613 wR_2 = 0.1071

 © 2005 Wiley-VCH Verlag GmbH & Co. KGaA, Weinheim

obtained free of charge from The Cambridge Crystallographic Data Centre via www.ccdc.cam.ac.uk/data_request/cif.

Acknowledgments

This work was supported by the National Natural Science Foundation of China (20331010).

[1] a) S. Noro, S. Kitagawa, M. Kondo, K. Seki, *Angew. Chem. Int. Ed.* **2000**, *39*, 2081–2084; b) M. Eddaoudi, J. Kim, N. L. Rosi, D. T. Vodak, J. Wachter, M. O'Keeffe, O. M. Yaghi, *Science* **2002**, *295*, 469–472; c) G. Férey, M. Latriche, C. Serre, F. Millange, T. Loiseau, A. Percheron-Guégan, *Chem. Commun.* **2003**, 2976–2977; d) L. Pan, M. B. Sander, X. Y. Huang, J. Li, M. Smith, E. Bittner, B. Bochrath, J. K. Johnson, *J. Am. Chem. Soc.* **2004**, *126*, 1308–1309.

[2] a) K. S. Min, M. P. Suh, *Chem. Eur. J.* **2001**, *7*, 303–313; b) K. Uemura, S. Kitagawa, M. Kondo, K. Fukui, R. Kitaura, H. C. Chang, T. Mizutani, *Chem. Eur. J.* **2002**, *8*, 3587–3600; c) D. N. Dybtsev, H. Chun, S. H. Yoon, D. Kim, K. Kim, *J. Am. Chem. Soc.* **2004**, *126*, 32–33.

[3] a) M. Albrecht, M. Lutz, A. L. Spek, G. van Koten, *Nature* **2000**, *406*, 970–974; b) L. G. Beauvais, M. P. Shores, J. R. Long, *J. Am. Chem. Soc.* **2000**, *122*, 2763–2772.

[4] a) M. Fujita, Y. J. Kwon, S. Washizu, K. Ogura, *J. Am. Chem. Soc.* **1994**, *116*, 1151–1152; b) T. Sawaki, Y. Aoyama, *J. Am. Chem. Soc.* **1999**, *121*, 4793–4798; c) J. S. Seo, D. Whang, H. Lee, S. I. Jun, J. Oh, Y. Jeon, K. Kim, *Nature* **2000**, *404*, 982–986; d) L. Pan, H. M. Liu, X. G. Lei, X. Y. Huang, D. H. Olson, N. J. Turro, J. Li, *Angew. Chem. Int. Ed.* **2003**, *42*, 542–546.

[5] a) H. L. Li, M. Eddaoudi, T. L. Groy, O. M. Yaghi, *J. Am. Chem. Soc.* **1998**, *120*, 8571–8572; b) K. S. Min, M. P. Suh, *J. Am. Chem. Soc.* **2000**, *122*, 6834–6840; c) R. Cao, D. F. Sun, Y. C. Liang, M. C. Hong, K. Tatsumi, Q. Shi, *Inorg. Chem.* **2002**, *41*, 2087–2094; d) C. D. Wu, C. Z. Lu, W. B. Yang, S. F. Lu, H. H. Zhuang, J. S. Huang, *Eur. J. Inorg. Chem.* **2002**, 797–800; e) Y. G. Li, N. Hao, Y. Lu, E. B. Wang, Z. H. Kang, C. W. Hu, *Inorg. Chem.* **2003**, *42*, 3119–3124; f) X. J. Zheng, L. P. Jin, S. Gao, *Inorg. Chem.* **2004**, *43*, 1600–1602.

[6] a) T. M. Reineke, M. Eddaoudi, M. O'Keeffe, O. M. Yaghi, *Angew. Chem. Int. Ed.* **1999**, *38*, 2590–2594; b) M. Eddaoudi, H. Li, O. M. Yaghi, *J. Am. Chem. Soc.* **2000**, *122*, 1391–1397; c) D. T. Vodak, M. E. Braun, J. Kim, M. Eddaoudi, O. M. Yaghi, *Chem. Commun.* **2001**, 2534–2535; d) M. Eddaoudi, J. Kim, M. O'Keeffe, O. M. Yaghi, *J. Am. Chem. Soc.* **2002**, *124*, 376–377.

[7] a) M. Kondo, T. Okubo, A. Asami, S. Noro, T. Yoshitomi, S. Kitagawa, T. Ishii, H. Matsuzaka, K. Seki, *Angew. Chem. Int. Ed.* **1999**, *38*, 140–143; b) D. F. Sun, R. Cao, Y. C. Liang, Q. Shi, W. P. Su, M. C. Hong, *J. Chem. Soc., Dalton Trans.* **2001**, 2335–2340; c) K. Barthelet, J. Marrot, D. Riou, G. Férey, *Angew. Chem. Int. Ed.* **2002**, *41*, 281–284; d) X. M. Zhang, M. L. Tong, M. L. Gong, X. M. Chen, *Eur. J. Inorg. Chem.* **2003**, 138–142.

[8] a) M. Eddaoudi, D. B. Moler, H. Li, B. Chen, T. M. Reineke, M. O'Keeffe, O. M. Yaghi, *Acc. Chem. Res.* **2001**, *34*, 319–330; b) M. E. Braun, C. D. Steffek, J. Kim, P. G. Rasmussen, O. M. Yaghi, *Chem. Commun.* **2001**, 2532–2533; c) C. Ruiz-Pérez, P. Lorenzo-Luis, M. Hernández-Molina, M. M. Laz, F. S. Delgado, P. Gili, M. Julve, *Eur. J. Inorg. Chem.* **2004**, 3873–3879.

[9] a) B. Q. Ma, P. Coppens, *Chem. Commun.* **2003**, 2290–2291; b) M. Liang, Q. L. Wang, L. H. Yu, D. Z. Liao, Z. H. Jiang, S. P. Yan, P. Cheng, *Polyhedron* **2004**, *23*, 2203–2208; c) E. Coronado, J. R. Galán-Mascarós, C. J. Gómez-García, E. Martínez-Ferrero, S. V. Smaalen, *Inorg. Chem.* **2004**, *43*, 4808–4810.

[10] a) M. Oh, G. B. Carpenter, D. A. Sweigart, *Angew. Chem. Int. Ed.* **2003**, *42*, 2025–2028; b) F. A. A. Paz, J. Klinowski, *Inorg. Chem.* **2004**, *43*, 3882–3893.

[11] a) J. Tao, M. L. Tong, X. M. Chen, *J. Chem. Soc., Dalton Trans.* **2000**, 3669–3674; b) S. A. Bourne, J. Lu, A. Mondal, B. Moulton, M. J. Zaworotko, *Angew. Chem. Int. Ed.* **2001**, *40*, 2111–2113; c) J. Sun, L. Weng, Y. Zhou, J. Chen, Z. Chen, Z. Liu, D. Zhao, *Angew. Chem. Int. Ed.* **2002**, *41*, 4471–4473; d) J. F. Ma, J. Yang, G. L. Zheng, L. Li, J. F. Liu, *Inorg. Chem.* **2003**, *42*, 7531–7534; e) D. N. Dybtsev, H. Chun, K. Kim, *Angew. Chem. Int. Ed.* **2004**, *43*, 5033–5036.

[12] X. L. Wang, C. Qin, E. B. Wang, L. Xu, Z. M. Su, C. W. Hu, *Angew. Chem. Int. Ed.* **2004**, *43*, 5036–5040.

[13] a) J. Tao, J. X. Shi, M. L. Tong, X. X. Zhang, X. M. Chen, *Inorg. Chem.* **2001**, *40*, 6328–6330; b) X. M. Chen, G. F. Liu, *Chem. Eur. J.* **2002**, *8*, 4811–4817; c) G. F. Liu, Z. P. Qiao, H. Z. Wang, X. M. Chen, G. Yang, *New J. Chem.* **2002**, *26*, 791–795; d) Y. Z. Zheng, G. F. Liu, B. H. Ye, X. M. Chen, *Z. Anorg. Allg. Chem.* **2004**, *630*, 296–300; e) Y. B. Wang, Z. M. Wang, C. H. Yan, L. P. Jin, *J. Mol. Struct.* **2004**, *692*, 177–186; f) M. Kondo, Y. Irie, Y. Shimizu, M. Miyazawa, H. Kawaguchi, A. Nakamura, T. Naito, K. Maeda, F. Uchida, *Inorg. Chem.* **2004**, *43*, 6139–6141.

[14] E. Y. Choi, K. Park, C. M. Yang, H. Kim, J. H. Son, Y. H. Lee, D. Min, Y. U. Kwon, *Chem. Eur. J.* **2004**, *10*, 5535–5540.

[15] F. A. A. Paz, Y. Z. Khimyak, A. D. Bond, J. Rocha, J. Klinowski, *Eur. J. Inorg. Chem.* **2002**, 2823–2828.

[16] S. R. Batten, B. F. Hoskins, B. Moubaraki, K. S. Murray, R. Robson, *Chem. Commun.* **2000**, 1095–1096.

[17] a) J. W. Ko, K. S. Min, M. P. Suh, *Inorg. Chem.* **2002**, *41*, 2151–2157; b) H. Kumagai, C. J. Kepert, M. Kurmoo, *Inorg. Chem.* **2002**, *41*, 3410–3422.

[18] V. Ramon, E. Albert, S. Xavier, F. B. Mercé, *Inorg. Chim. Acta* **1996**, *248*, 59–65.

[19] G. M. Sheldrick, *SADABS, A Program for Empirical Absorption Correction of Area detector Data*, University of Göttingen, Germany, **1997**.

[20] G. M. Sheldrick, *SHELXS 97, Program for Crystal Structure Solution*, University of Göttingen, Germany, **1997**.

[21] G. M. Sheldrick, *SHELXL 97, Program for Crystal Structure Refinement*, University of Göttingen, Germany, **1997**.

Received: March 12, 2005
Published Online: September 5, 2005

 © 2005 Wiley-VCH Verlag GmbH & Co. KGaA, Weinheim

Synthesis and Structure of the Group 12 Pyrimidinethiolate Complexes $^{3}_{\infty}$[Zn(S-2-$N_2C_4H_3$)$_2$], $^{2}_{\infty}$[Cd(S-2-$N_2C_4H_3$)$_2$], [Hg(S-2-$N_2C_4H_3$)$_2$] and [Cd(S-2-$N_2C_4H_3$)$_2$(tmeda)]

Andreas Eichhöfer*[a] and Gernot Buth[b]

Keywords: Cadmium / IR spectroscopy / Mercury / N,S ligands / Zinc

The pyrimidinethiolate complexes $^{3}_{\infty}$[Zn(S-2-$N_2C_4H_3$)$_2$], $^{2}_{\infty}$[Cd(S-2-$N_2C_4H_3$)$_2$] and [Hg(S-2-$N_2C_4H_3$)$_2$] have been prepared by reaction of MCl_2 (M = Zn, Cd, Hg) with 2 equiv. of Me_3SiS-2-$N_2C_4H_3$ in organic solvents, whilst [Cd(S-2-$N_2C_4H_3$)$_2$(tmeda)] was obtained by recrystallisation of $^{2}_{\infty}$[Cd(S-2-$N_2C_4H_3$)$_2$] in TMEDA at 40 °C. The structures of the complexes were determined by single-crystal X-ray crystallography, which shows that the different metal atoms each have different coordination environments. The zinc atom in $^{3}_{\infty}$[Zn(S-2-$N_2C_4H_3$)$_2$] exhibits a tetrahedral coordination with one sulfur and three nitrogen atoms from pyrimidinethiolate ligands, whereas the cadmium atoms in $^{2}_{\infty}$[Cd(S-2-$N_2C_4H_3$)$_2$] and [Cd(S-2-$N_2C_4H_3$)$_2$(tmeda)] are six-coordinate with either three sulfur and three nitrogen atoms or two sulfur and four nitrogen atoms. In contrast, the mercury atoms in [Hg(S-2-$N_2C_4H_3$)$_2$] display a distorted square-planar coordination to a pair of chelating $^{-}$S-2-$N_2C_4H_3$ ligands with additional weak Hg–S interactions to adjacent molecules. While known cadmium and zinc pyrimidinethiolate complexes consist of one-dimensional chains, $^{3}_{\infty}$[Zn(S-2-$N_2C_4H_3$)$_2$] and $^{2}_{\infty}$[Cd(S-2-$N_2C_4H_3$)$_2$] form either three- or two-dimensional polymeric networks of metal atoms.
(© Wiley-VCH Verlag GmbH & Co. KGaA, 69451 Weinheim, Germany, 2005)

Introduction

There has been considerable interest in the past in the synthesis and coordination properties of chalcogenolates, comprising an amine-based heterocyclic ring, towards group 12 transition metal elements. Heterocyclic thiols, like pyridinethiol or pyrimidinethiol, are some of the most versatile sulfur donor ligands as they can act as monodentate or chelating ligands in the neutral form or as monodentate, chelating and bridging ligands between two or three metal atoms when anionic to yield oligo- or polymeric species.[1,2] Several factors determine the degree of aggregation. [Cd(S-2-NC_5H_4)$_2$][3] and [Zn{S-4,6(CH_3)$_2$-2-N_2C_4H}$_2$],[4] for example, are polymeric, while the additional presence of pyridine in the case of the zinc complex leads to the isolation of the monomeric species [Zn{S-4,6(CH_3)$_2$-2-N_2C_4H}$_2$(NC_5H_5)].[5] Additional bonding of bulky groups near the donor atoms in cadmium complexes leads to a reduction of aggregation, as can be seen in [Cd{S-4,6(CH_3)$_2$-2-N_2C_4H}$_2$]$_6$,[6] which is hexanuclear, and the dimeric [Cd{S-3(CH_3)$_3$Si–NC_5H_4}$_2$]$_2$,[7] which contains the more bulky trimethylsilyl substituent close to the sulfur donor atom. However, [Cd(S-4-CH_3-6-CF_3-2-N_2C_4H)$_2$] is also found to consist of polymeric chains containing octahedrally *cis*-coordinated cadmium atoms.[8] Further influence on the aggregation behaviour also arises from the coordination chemistry of the different metal ions, with mercury preferring lower coordination numbers, as, for example, in [Hg(C_5H_4NS)$_2$][9] and [Hg{S-4,6-(CH_3)$_2$-2-N_2C_4H}$_2$].[10] As well as their rich structural chemistry, additional interest in these ligands also arises from their relationship to pyridine and pyrimidine bases and their nucleosides and nucleotides, which have important roles in living systems, with zinc being bonded to several enzymes and proteins, as well as the search for new antidotes to mercury poisoning.[10] Finally, their also exists a materials aspect to this chemistry as related complexes of cadmium with the general formula [Cd(E-2-NC_5H_6)$_2$]$_n$ (E = S,[11] Se[12]) have been found to be volatile CVD precursors for 12/16 semiconductors.

As a result of our general interest in structural studies of group 12 metal chalcogenide complexes,[13–17] we started studies on the ligand $^{-}$S-4-$N_2C_4H_3$, which has been reported to yield [M(S-2-$N_2C_4H_3$)$_2$] (M = Zn, Cd) in an electrochemical synthesis.[18] However, crystal structures have not been reported to date. Herein, the structures of [M(S-2-$N_2C_4H_3$)$_2$]$_n$ (M = Zn, Cd, Hg) are reported and the complexes synthesised by an organometallic approach.

Results and Discussion

The pyrimidinethiolate complexes $^{3}_{\infty}$[Zn(S-2-$N_2C_4H_3$)$_2$] (**1**), $^{2}_{\infty}$[Cd(S-2-$N_2C_4H_3$)$_2$] (**2**) and [Hg(S-2-$N_2C_4H_3$)$_2$] (**3**)

[a] Institut für Nanotechnologie, Forschungszentrum Karlsruhe, Postfach 3640, 76021 Karlsruhe, Germany
Fax: +49-7247-82-6368
E-mail: eichhoefer@int.fzk.de
[b] Institut für Synchrotronstrahlung, Forschungszentrum Karlsruhe, Postfach 3640, 76021 Karlsruhe, Germany

were prepared as crystalline precipitates by reaction of anhydrous MCl_2 (M = Zn, Cd, Hg) with 2 equiv. of $(CH_3)_3$-SiS-2-$N_2C_4H_3$ in organic solvents according to Scheme 1. Recrystallisation of **2** from TMEDA at room temperature yielded [Cd(S-2-$N_2C_4H_3)_2$(tmeda)] (**4**) nearly quantitatively along with some remaining **2**. Completion of this reaction was achieved by storing the suspension at 40 °C in a dry oven for one week.

MCl_2 + 2 $(CH_3)_3SiS$-2-$N_2C_4H_3$ M = Zn, Cd, Hg

– 2 $ClSiMe_3$ ↓ organic solvent/r.t.

$^3_\infty$[Zn(S-2-$N_2C_4H_3)_2$] (**1**)

$^2_\infty$[Cd(S-2-$N_2C_4H_3)_2$] (**2**)

[Hg(S-2-$N_2C_4H_3)_2$] (**3**)

$^2_\infty$[Cd(S-2-$N_2C_4H_3)_2$] (**2**)

↓ TMEDA/40 °C

[Cd(S-2-$N_2C_4H_3)_2$(tmeda)] (**4**)

Scheme 1.

Complex **1** crystallises in the orthorhombic space group $Pna2_1$. The zinc atoms in **1** are bridged in three dimensions by pyrimidinethiolate ligands to form an infinite network (Figure 1b). A view of a mononuclear fragment is given in Figure 1a, which shows a distorted tetrahedral coordination environment around the zinc atom formed by three nitrogen atoms [N(1), N(3) and N(4)] and one sulfur atom [S(1)]. These atoms belong to two differently coordinating $^-$S-2-$N_2C_4H_3$ ligands in either coordination mode **D** or **E** (Scheme 2). One of them, formed by C(1)–C(4), N(1), N(2) and S(1), bridges a neighbouring zinc atom through the sulfur atom and one nitrogen atom of the ligand, while the additional nitrogen atom N(2) is not involved in further coordination. The other pyrimidinethiolate ligand, consisting of C(5)–C(8), N(3), N(4) and S(2), bridges two adjacent zinc atoms through two of its nitrogen atoms [N(3) and N(4)] whilst the sulfur atom S(2) remains uncoordinated. Neither bridging mode has been observed before in related zinc and cadmium pyrimidinethiolate complexes, which usually comprise a bidentate chelating coordination mode of the ligands towards the metal atoms through a sulfur and a nitrogen atom, as found in [Zn{S-4,6$(CH_3)_2$-2-N_2C_4H}$_2$][4] or [Zn{S-4,6$(CH_3)_2$-2-N_2C_4H}$_2$$(NC_5H_5)$].[5] However, the Zn–N (205.3–209.8 pm) and Zn–S (234.4 pm) bond lengths in **1** are comparable to the related distances observed in theses complexes. The three-dimensional network in **1** is formed by helical chains of alternating zinc atoms and pyrimidinethiolate ligands in bridging mode **D** arranged along the crystallographic *c*-axis (2_1 symmetry) which are themselves further crosslinked through $^-$S-2-$N_2C_4H_3$ ligands in the coordination mode **E** (Figure 1b). This differs from known structures formed by pyrimidine- and pyridinethiolates with group 12 transition elements, such as [Cd(S-2-$NC_5H_4)_2$],[3] [Zn{S-4,6$(CH_3)_2$-2-N_2C_4H}$_2$],[4] [Cd(S-4-CH_3-6-CF_3-2-$N_2C_4H)_2$][8] and [$Hg(C_5H_4NS)_2$],[9] which all consist of chain structures.

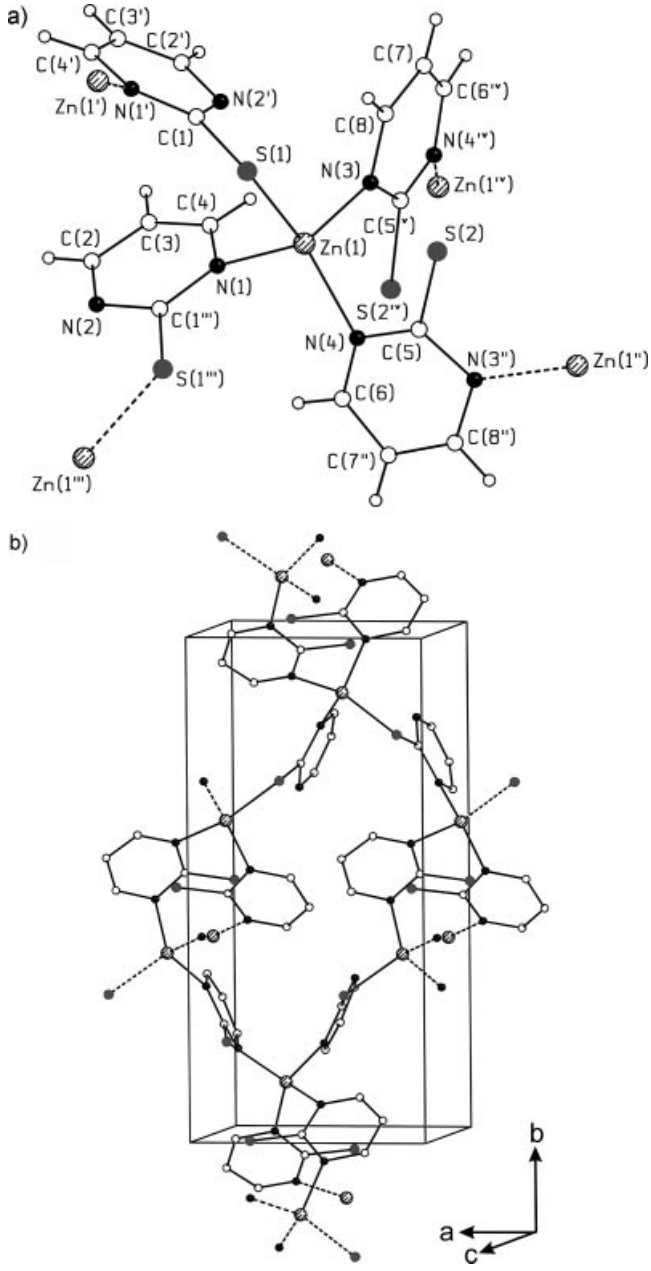

Figure 1. a) View of the coordination sphere of the zinc atom in [Zn(S-2-$N_2C_4H_3)_2$] (**1**). b) Section of the three-dimensional polymeric network in **1**. Symmetry transformation for generation of equivalent atoms [I]: $x + 1/2, -y + 3/2, z$; [II]: $-x, -y + 1, z + 1/2$; [III]: $x - 1/2, -y + 3/2, z$; [IV]: $-x, -y + 1, z - 1/2$. Selected bond lengths [pm] and angles [°]: Zn(1)–N(4) 205.3 (10), Zn(1)–N(3) 206.5(11), Zn(1)–N(1) 209.8(12), Zn(1)–S(1) 234.4(4); N(4)–Zn(1)–N(3) 106.1(4), N(4)–Zn(1)–N(1) 107.0(4), N(3)–Zn(1)–N(1) 104.7(4), N(4)–Zn(1)–S(1) 127.2(3), N(3)–Zn(1)–S(1) 109.1(3), N(1)–Zn(1)–S(1) 100.7(3).

Complex **2** crystallises in the orthorhombic space group *Pbca*. Figure 2 shows a view of the coordination sphere of the cadmium atom (Cd1) in **2**, which is six-coordinate with

 © 2005 Wiley-VCH Verlag GmbH & Co. KGaA, Weinheim

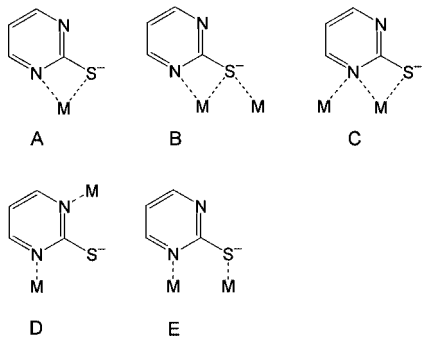

Scheme 2. Schematic drawing of the coordination modes of the pyrimidinethiolate ligand ($^{-}$S-2-$N_2C_4H_3$) found in **1**–**4**.

three sulfur [S(1), S(2) and S(2′)] and three nitrogen atoms [N(1)–N(3)]. Two pairs of sulfur and nitrogen atoms [S(2′), N(3) and S(1), N(1)] belong to two $^{-}$S-2-$N_2C_4H_3$ ligands that chelate the cadmium atom with bite angles of 59° and 61.6(1)° for N(3)–Cd(1)–S(2′) and N(1)–Cd(1)–S(1), respectively. These values are comparable to those found in the monomeric complex [Cd(S-2-$N_2C_4H_3)_2$(phen)].[18] However, further coordination of each of the pyrimidine-2-thiolate ligands is different, with one of the ligands coordinating additionally through the sulfur atom [S(2′)] to a neighbouring cadmium atom [Cd(1′)] to form an asymmetric μ_2-S-2-$N_2C_4H_3$ bridge and the other additionally binding through the free nitrogen atom [N(2′′)] to another neighbouring cadmium atom [Cd(1′′)]. Whilst the Cd–S bond of the pure chelating μ_2-S-2-$N_2C_4H_3$ ligand [Cd(1)–S(1): 261.2(2)] is comparable to that found in the monomeric complex [Cd(S-2-$N_2C_4H_3)_2$(phen)], the Cd–S bonds of the other pyrimidine-2-thiolate ligand, which acts as both a bidentate and a μ_2-bridging ligand, exhibit one shorter [Cd(1)–S(2): 260.3(2) pm] and one longer distance [Cd(1)–S(2′) 292.6(2) pm]. This effect of a weakening of the Cd–S chelating bond upon formation of additional μ_2-bridges has also been observed to a different extent in other complexes that contain heterocyclic thiolates as ligands, such as [Cd(S-2-$NC_5H_4)_2$],[3] [Cd{S-4,6-$(CH_3)_2$-2-N_2C_4H}$_2$]$_6$,[6] [Cd{S-3-$(CH_3)_3SiNC_5H_4$}$_2$]$_2$[7] and [Cd(S-4-CH_3-6-CF_3-2-$N_2C_4H)_2$].[8] The Cd–N bond lengths, which range from 233.3(5) to 248.0(6) pm, are also comparable to those found for the six-coordinate cadmium complexes mentioned above. In the crystal structure (Figure 2b), each cadmium atom is therefore linked to a total of three other cadmium atoms. One connection consists of two μ_2-S-2-$N_2C_4H_3$ bridges, each of which additionally chelates one of the two cadmium atoms, and the other two linkages are each formed by a single $^{-}$S-2-$N_2C_4H_3$ ligand in two inverted coordination forms. In one case the ligand chelates the central cadmium atom and acts as a monodentate ligand through the other nitrogen atom towards the neighbouring metal atom and in the other case the other way round. In this way **2** forms a distorted two-dimensional honeycomb network in the 011 plane which is in contrast to related structures in the literature which consist of one-dimensional polymeric structures.

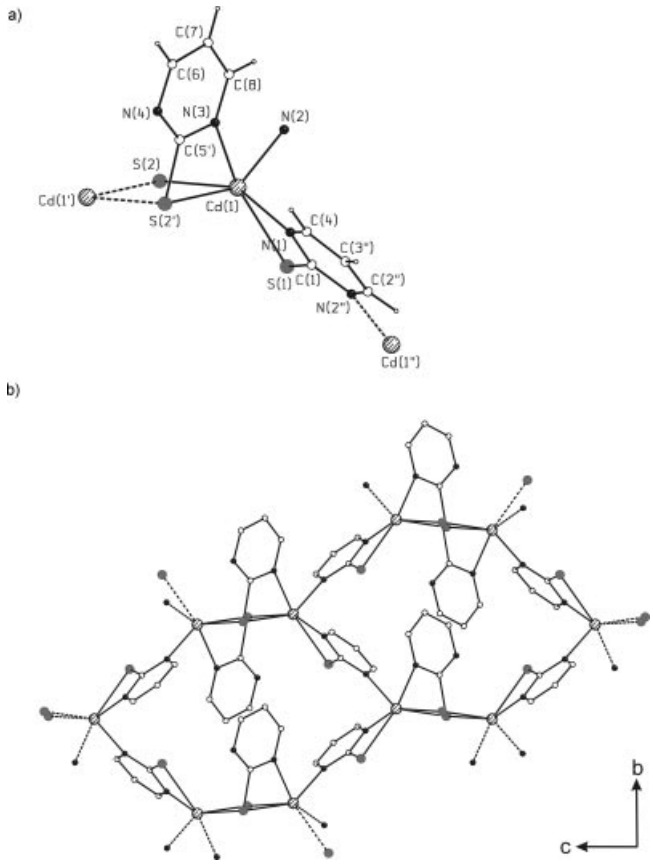

Figure 2. a) View of the coordination sphere of the cadmium atoms in [Cd(S-2-$N_2C_4H_3)_2$] (**2**). b) Section of the two-dimensional polymeric network in **2** viewed along *a*. Symmetry transformation for generation of equivalent atoms ^{I}: $-x$, $-y$, $-z + 1$; ^{II}: $-x$, $y + 1/2$, $-z + 3/2$; ^{III}: $-x$, $y - 1/2$, $-z + 3/2$. Selected bond lengths [pm] and angles [°]: Cd(1)–N(1) 248.0(6), Cd(1)–N(2) 240.2(5), Cd(1)–N(3) 233.3(5), Cd(1)–S(1) 261.2(2), Cd(1)–S(2) 260.3(2), Cd(1)–S(2′ 292.7(2); N(3)–Cd(1)–N(2) 90.4(2), N(3)–Cd(1)–N(1) 95.3(2), N(2)–Cd(1)–N(1) 113.3(2), N(3)–Cd(1)–S(2) 96.5(2), N(2)–Cd(1)–S(2) 91.9(1), N(1)–Cd(1)–S(2) 152.1(1), N(3)–Cd(1)–S(1) 156.5(1), N(2)–Cd(1)–S(1) 95.0(1), N(1)–Cd(1)–S(1) 61.6(1), S(2)–Cd(1)–S(1) 106.1(1), N(3)–Cd(1)–S(2)′ 59.0(1), N(2)–Cd(1)–S(2)′ 148.5(1), N(1)–Cd(1)–S(2)′ 79.4(1), S(2)–Cd(1)–S(2)′ 85.3(1), S(1)–Cd(1)–S(2)′ 115.9(1).

Complex **3** crystallises in the monoclinic space group $P2_1/n$ with two independent molecules **3a** and **3b**, which differ slightly in their geometry, in the asymmetric unit (Figure 3). In both molecules the mercury atoms are four-coordinate and are chelated by two $^{-}$S-2-$N_2C_4H_3$ ligands in a bidentate fashion through the sulfur atom and one nitrogen atom, with S–Hg–N bite angles ranging from 59.65° to 61.35° (coordination mode **A** in Scheme 2). Molecule **3a** [Hg(2), S(3), S(4), N(5)–N(8), C(9)–C(16)] (Figure 3a) exhibits an almost square-planar coordination of the mercury atom with a maximum deviation of 0.151(4) pm for S(4) from the molecular plane and a torsion angle along C(9)–S(3)–S(4)–C(13) of 176.9°. In molecule **3b** [Hg(1), S(1), S(2), N(1)–N(4), C(1)–C(8); (Figure 3b)], the pyrimidinethiolate ligands are twisted from this plane to give a torsion angle of 151.9° along C(1)–S(1)–S(2)–C(5). Mean Hg–S bond lengths of around 235.4 pm as well as mean Hg–N separa-

 © 2005 Wiley-VCH Verlag GmbH & Co. KGaA, Weinheim

tions around 287.9 pm are comparable to those found in similar compounds like $[Hg(C_5H_4NS)_2]$[9] and $[Hg\{S\text{-}4,6\text{-}(CH_3)_2\text{-}2\text{-}N_2C_4H\}_2]$.[10] Additional weaker Hg–S separations with a mean value of 329.9 pm lead to the formation of one-dimensional chains for both forms of **3a** and **3b** (shown only for **3b** in Figure 3b). While the mercury thiopyridine structure also contains mercury(II) ions in a square-planar environment with a similar chain structure, the pyrimidinethiolate derivative exhibits five-coordinate metal atoms, which leads in the crystal structure to the formation of a helix-like polymer chain of the molecular units.

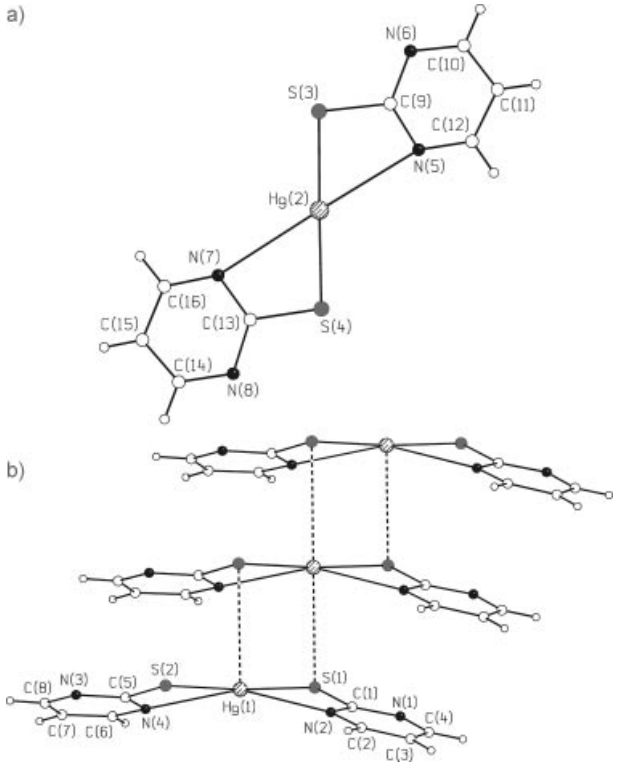

Figure 3. Molecular structures of the two independent molecules in $[Hg(S\text{-}2\text{-}N_2C_4H_3)_2]$ (**3a**/**3b**) with a drawing of the chain structure formed by weak intermolecular Hg–S interactions (dotted lines). Selected bond lengths [pm] and angles [°]: Hg(1)–S(2) 235.0(2), Hg(1)–S(1) 236.0(2), Hg(1)–N(4) 290.7(7), Hg(1)–N(2) 281.5(6), Hg(2)–S(4) 234.9(2), Hg(2)–S(3) 235.5(2), Hg(2)–N(5) 286.0(6), Hg(2)–N(7) 293.5(6); S(2)–Hg(1)–S(1) 176.06(7), S(1)–Hg(1)–N(2) 61.4(1), S(2)–Hg(1)–N(4) 60.1(1), N(4)–Hg(1)–N(2) 157.1(1), S(4)–Hg(2)–S(3) 178.7(1), S(4)–Hg(2)–N(7) 59.7(1), S(3)–Hg(2)–N(5) 60.8(1), N(5)–Hg(2)–N(7) 177.3(1). Weak intermolecular Hg–S interactions [pm]: Hg(1)···S(1) 322.9, Hg(1)···S(2) 338.8, Hg(2)···S(3) 331.1, Hg(2)···S(4) 326.7.

Monomeric **4** crystallises in the monoclinic space group $P2_1/n$ (Figure 4) and exhibits a highly distorted octahedral coordination around the cadmium atom. The coordination sphere involves two nitrogen atoms [N(5) and N(6)] from the bidentate TMEDA ligand, and one sulfur atom [S(1) and S(2)] and one nitrogen atom [N(1) and N(3)] belonging to each of two pyrimidine-2-thiolate ligands. The bond lengths and bite angles of the three bidentate ligands are similar to those found in $[Cd(S\text{-}2\text{-}N_2C_4H_3)_2(phen)]$[18] and **2** as discussed above.

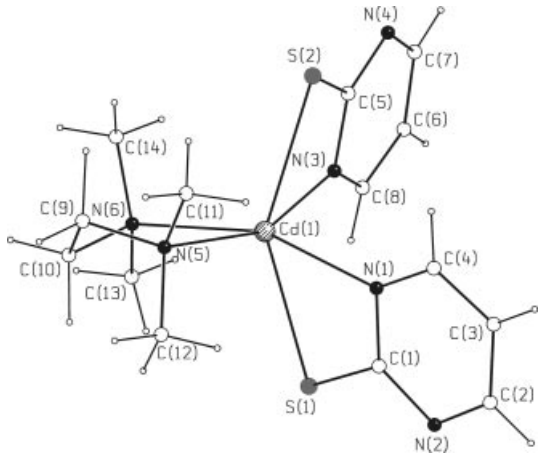

Figure 4. Molecular structure of $[Cd(S\text{-}2\text{-}N_2C_4H_3)_2(tmeda)]$ (**4**). Selected bond lengths [pm] and angles [°]: Cd(1)–N(6) 240.0(2), Cd(1)–N(5) 240.4(2), Cd(1)–N(1) 244.0(2), Cd(1)–N(3) 245.1(2), Cd(1)–S(1) 260.7(1), Cd(1)–S(2) 260.9(1); N(6)–Cd(1)–N(5) 76.1(1), N(6)–Cd(1)–N(1) 158.6(1), N(5)–Cd(1)–N(1) 91.5(1), N(6)–Cd(1)–N(3) 90.4(1), N(5)–Cd(1)–N(3) 158.9(1), N(1)–Cd(1)–N(3) 106.0(1), N(6)–Cd(1)–S(1) 102.3(1), N(5)–Cd(1)–S(1) 101.3(1), N(1)–Cd(1)–S(1) 62.7(1), N(3)–Cd(1)–S(1) 97.4(1), N(6)–Cd(1)–S(2) 103.7(1), N(5)–Cd(1)–S(2) 104.7(1), N(1)–Cd(1)–S(2) 96.2(1), N(3)–Cd(1)–S(2) 62.3(1), S(1)–Cd(1)–S(2) 146.8(1).

A comparison of the powder diffraction patterns of the crystalline precipitates of **1**–**4** with the calculated pattern of the crystals investigated by single-crystal X-ray analysis displays a good agreement, which proves, together with the elemental analysis, the purity of the compounds (Figure 5). Small deviations in intensity and reflection position at higher angles might be due to the fact that the powder measurements were done at room temperature in contrast to 190 K for the single-crystal measurement, and that needle-like crystals (e.g. **3**) preferably align in the capillary vertical to the beam.

The IR spectra of **1**–**3** (Figure 6) differ from that of the neutral thiol $HS\text{-}2\text{-}N_2C_4H_3$, in agreement with coordination of the monoanion $^-S\text{-}2\text{-}N_2C_4H_3$ to the metal atoms. Additionally, there are differences between the spectra of **1**–**3** due to the different coordination modes of the pyrimidinethiolate ligand towards the metal atoms. As IR data for complexes of monoanionic pyridine- and pyrimidinethiolate ligands are rare and have not been assigned in full detail, the discussion mostly refers to the spectra of the neutral thiol $HS\text{-}2\text{-}N_2C_4H_3$[19,20] and a study of several metal complexes of pyridinethiol.[21] In solution, pyrimidines and pyridines that are substituted at the 2- or 4-position by thiol groups can exist in two tautomeric forms **I** (thiol) and **II** (thione; Scheme 3).[22] In the solid state, 2-mercaptopyridine and 4-mercaptopyridine have been found to exist as H-bonded dimers of the thione form.[23,24] Similarly, it might be assumed that 2-mercaptopyrimidine also exists in the solid state as an H-bonded dimer, displayed in Scheme 3 as form **III**. Evidence for this in the IR spectrum of $HS\text{-}2\text{-}N_2C_4H_3$ is a broad band around 2633 cm^{-1}, which can be assigned to the stretching of the N–H bonds being strongly hydrogen-bonded in the solid state, and the three bands

 © 2005 Wiley-VCH Verlag GmbH & Co. KGaA, Weinheim

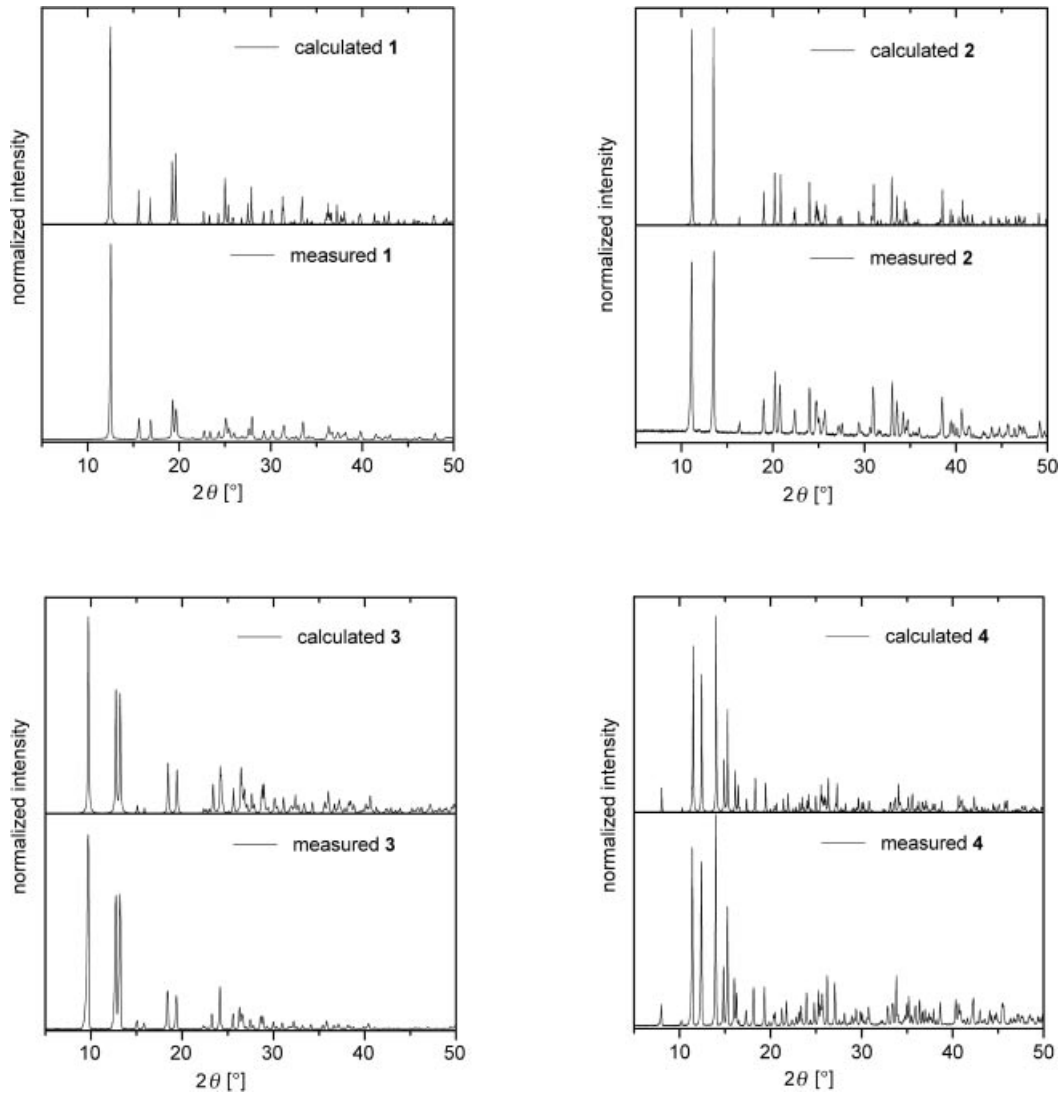

Figure 5. Calculated (top) and measured (bottom) powder XRD pattern of $[Zn(S\text{-}2\text{-}N_2C_4H_3)_2]$ (**1**), $[Cd(S\text{-}2\text{-}N_2C_4H_3)_2]$ (**2**), $[Hg(S\text{-}2\text{-}N_2C_4H_3)_2]$ (**3**) and $[Cd(S\text{-}2\text{-}N_2C_4H_3)_2(tmeda)]$ (**4**).

near 2000 cm^{-1}, which can be assigned as a result of Fermi resonances and overtones of the ν(N–H) mode. Both these features are absent from the IR spectra of **1**–**3** because of the anionic character of the ligand. However, one can see the peaks that result from the C–H stretching vibrations of the aromatic pyrimidine rings between 3100 and 3000 cm^{-1}. The aromatic ring stretching vibrations (C=C and C=N), which fall in the region from 1600 to 1500 cm^{-1}, show a characteristic two-band structure with slightly shifted peak positions in **1**–**3**, especially when compared to the ligand spectrum. In the region further down to 1250 cm^{-1}, a strong and broad peak around 1370 cm^{-1}, which probably consists of several vibrations, is visible in all three group 12 metal pyrimidinethiolates rather than the three separate peaks at 1492, 1424 and 1333 cm^{-1} in the free thiol, which are assigned to ring stretching and C–H bending vibrations. This is followed by a pair of strong peaks (three peaks for **1**) at around 1200 cm^{-1}. These bands are interpreted as being due to C–H bending and C–S stretching vibrations in the neutral ligand. Interestingly, Kennedy et al. have found that extensive coupling within the ring system, as indicated, for example, by an ^{18}O study of 2-hydroxypyridine,[25] precludes the identification of any band definitively assigned to a C–S stretching vibration.[21] Two peaks in the spectrum of pyrimidinethiol at 1051 and 983 cm^{-1} have been assigned as ring breathing vibrations.[20] These are significantly altered in the spectra of the three metal complexes **1**–**3** of the anionic pyrimidine-2-thiolate ligand. A shift in the ring breathing mode in simple pyridine–metal complexes is used as a guide to metal coordination.[26] However, for metal complexes of 2-pyridinethiol and 4-pyridinethiol it has been found that changes in energy of these bands are indicative of a change in coordination but not informative concerning the mode of the coordination.[21] Further down, the neutral ligand displays two peaks at 793 and 751(sh) cm^{-1}, characteristic of a mono-substituted aromatic ring, which have been assigned to C–H bending and a combination of C–S stretching, C–H bending and ring deformation modes,

 © 2005 Wiley-VCH Verlag GmbH & Co. KGaA, Weinheim

respectively. While one observes a similar group in **1**, consisting of a single peak at 810 cm^{-1} and a second peak at 750 cm^{-1} with a shoulder at 768 cm^{-1}, this second peak splits in **2** and **3** to give two well-separated peaks at either 767 and 746 cm^{-1} or 769 and 743 cm^{-1}, respectively. Four more peaks can be identified down to 300 cm^{-1} for HS-2-$N_2C_4H_3$, which are assigned to either ring deformation (625 cm^{-1}) and/or C–S bending and stretching modes (486, 472 cm^{-1} and 406 cm^{-1}). This area displays the most visible changes in the IR spectra for **1**–**3**, indicative of the different coordination modes of the anionic pyrimidinethiolate ligand towards the metal atoms. New bands arise in the spectra of **1**–**3** compared to the neutral ligand in the far-IR region below 300 cm^{-1}. For complexes of the type $[MX_2L_2]$ (M = Zn, Cd, Hg; X = Cl, Br and L = Py-2-SH, Py-4-SH), bands between 198 and 235 cm^{-1} have been assigned as M–L vibrational modes.[21] In pyridine complexes like $[Zn(py)_2X_2]$, M–Py vibrations have been assigned by the isotope technique in the region of 200 to 225 cm^{-1}.[27,26] Interestingly, **3** displays only one strong peak in this region at 254 cm^{-1}, probably due to the symmetric square-planar coordination environment of the metal atom, while the spectra of **1** and **2** contain several peaks.

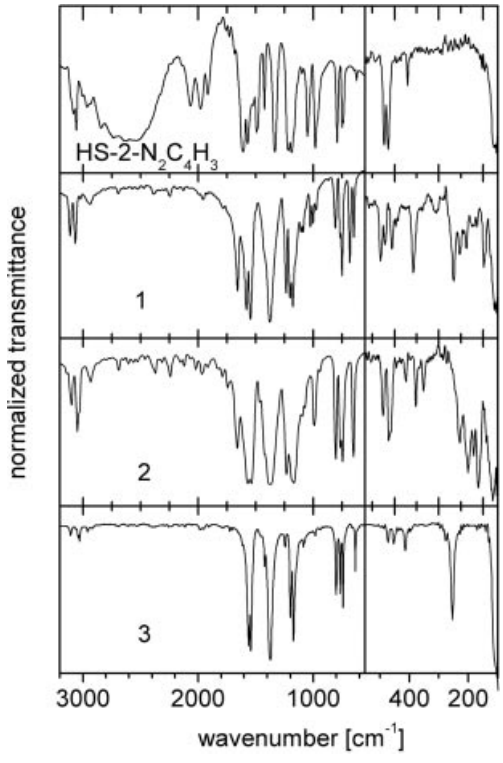

Figure 6. Comparison of the IR spectra of HS-2-$N_2C_4H_3$ (top), $[Zn(S\text{-}2\text{-}N_2C_4H_3)_2]$ (**1**), $[Cd(S\text{-}2\text{-}N_2C_4H_3)_2]$ (**2**) and $[Hg(S\text{-}2\text{-}N_2C_4H_3)_2]$ (**3**) measured as a CsI pellets.

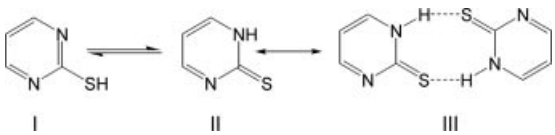

Scheme 3.

The UV/Vis spectra in the solid state display a shift in the absorption onset on going from **1** (450 nm) to **2** (430 nm) to **4** (395 nm) to **3** (366 nm) in such a way that the zinc complex **1** absorbs at higher wavelengths (lower energy) than the other complexes **2**, **3**, **4**. Apart from the spectrum of **1**, which shows a shoulder at 375 nm followed by a broad peak at 285 nm, and **4**, which displays a shoulder at 325 nm followed by a peak at 285 nm, the spectra of **1**–**4** are almost featureless.

The ^1H and ^{13}C NMR spectra of the complexes in dimethyl sulfoxide display similar peak patterns for the pyrimidinethiolate ligand to those observed for the precursor compound $(CH_3)_3S\text{-}2\text{-}N_2C_4H_3$, with only slightly shifted positions of the signals. In contrast to the situation found in the crystalline state, the equivalence of the two hydrogen and carbon atoms in the *meta* position indicates a symmetric coordination of the ligand in solution that is probably generated by a complex equilibrium with fast exchange between different coordination modes.

Experimental Section

Physical Measurements: ^1H and ^{13}C NMR spectra were recorded with a Bruker DPX Avance 300. ^{29}Si NMR spectra were measured with a Bruker Avance 400. UV/Vis absorption spectra of cluster molecules in solution were measured with a Varian Cary 500 spectrophotometer in quartz cuvettes. Solid-state reflection spectra were measured as micron-sized crystalline powders between quartz plates with a Labsphere integrating sphere. IR and FIR spectra were measured with a Perkin–Elmer Spectrum GX as CsI pellets in the region from 4000 to 30 cm^{-1}.

Synthesis: Standard Schlenk techniques were employed throughout the syntheses using a double-manifold vacuum line with high-purity dry nitrogen. The solvent diethyl ether was dried with sodium/benzophenone and distilled under nitrogen. Anhydrous DMF ($H_2O < 0.005\%$) and pyridine ($H_2O < 0.01$) obtained from Aldrich were degassed, freshly distilled and stored over molecular sieves under nitrogen. Anhydrous $ZnCl_2$, $CdCl_2$ and $HgCl_2$ were purchased from Aldrich. $(2\text{-}N_2C_4H_3)SSiMe_3$ was prepared according to a general procedure for silylthiopyrimidines.[28] Thus, $(2\text{-}N_2C_4H_3)SH$ [6 g (0.0535 mol)] was dissolved in a mixture of 130 mL of hexamethyldisilazane (HDMS) and 50 mL of dioxane and heated under reflux for 24 h. Excess HDMS and dioxane were removed by distillation and the remaining oil distilled under vacuum (1×10^{-3} mbar) to yield $(2\text{-}N_2C_4H_3)SSiMe_3$ as a yellow oily liquid (b.p. 70 °C). Yield: 8.93 g (90.6%). ^1H NMR (300 MHz, C_6D_6): $\delta = 0.52$ [s, $Si(CH_3)_3$, 9 H], 6.54 (t, $^3J_{H,H} = 4.9$ Hz, *para*-C*H*, 1 H), 8.18 (d, $^3J_{H,H} = 4.9$ Hz, *meta*-C*H*, 2 H) ppm. $^{13}C\{^1H\}$NMR (75 MHz, C_6D_6): $\delta = 1.4$ [s, $Si(CH_3)_3$], 117.1 (s, *meta*-*C*H), 157.3 (s, *para*-*C*H), 172.9 (s, *C*SSi) ppm. ^{29}Si NMR (79.5 MHz, C_6D_6): $\delta = 15.7$ [s, $Si(CH_3)_3$] ppm.

$[Zn(S\text{-}2\text{-}N_2C_4H_3)_2]$ (1): $ZnCl_2$ (0.14 g, 1.03 mmol) was dissolved in 20 mL of DMF. $(2\text{-}N_2C_4H_3)SSiMe_3$ (0.4 mL, 2.18 mmol) was then added at 0 °C and the resulting yellow solution slowly warmed to room temperature. After a short time, **1** started to precipitate as a pale-yellow crystalline powder. The crystallisation was completed by layering the reaction solution with diethyl ether by evaporation and condensation from a connected flask. Yield: 0.25 g (84.5%). $C_8H_6N_4S_2Zn$ (287.7): calcd. C 33.4, H 2.1, N 19.5, S 22.3; found C 33.5, H 2.4, N 19.5, S 21.5. Small but suitable crystals for single-

 © 2005 Wiley-VCH Verlag GmbH & Co. KGaA, Weinheim

crystal X-ray analysis were found in carefully layered DMF solutions of **1** with diethyl ether or directly in carefully warmed up reaction solutions. IR (CsI): $\tilde{\nu}$ = 3111 (m), 3066 (m), 3021 (w), 2940 (w, br), 2693 (w), 2389 (w), 2245 (w), 1956 (w, br), 1782 (w), 1657 (s), 1580 (vs), 1545 (vs), 1377 (vs, br), 1235 (s), 1202 (vs), 1178 (vs), 1106 (m), 1088 (m), 1025 (m), 1001 (m), 976 (w), 810 (m), 750 (s, sh), 684 (s), 648 (m), 498 (m), 483 (m), 459 (m), 446 (w), 386 (m), 250 (m), 230 (m), 207 (m), 187 (w, sh), 170 (w), 148 (m) cm^{-1}. UV/Vis (nujol): λ_{max} = 375 (sh), 285 (vbr) nm. ^1H NMR (300 MHz, $(CD_3)_2SO$]: δ = 6.9 (t, $^3J_{H,H}$ = 4.9 Hz, *para*-C*H*, 1 H), 8.3 (d, $^3J_{H,H}$ = 4.9 Hz, *meta*-C*H*, 2 H) ppm. $^{13}C\{^1H\}$ NMR [75 MHz, $(CD_3)_2SO$]: δ = 114.9 (s, *meta*-*C*H), 157.6 (s, *para*-*C*H), 182.6 (s, *C*SSi) ppm.

[Cd(S-2-$N_2C_4H_3$)$_2$] (2): $CdCl_2$ (0.4 g, 2.18 mmol) was dissolved in 55 mL of DMF. (2-$N_2C_4H_3$)$SSiMe_3$ (0.8 mL, 4.36 mmol) was then added at 0 °C and the resulting yellow solution warmed to room temperature. After a short time, **2** precipitated as a white crystalline powder. Yield: 0.53 g (73%). $C_8H_6CdN_4S_2$ (334.7): calcd. C 28.7, H 1.8, N 16.7, S 19.2; found C 28.8, H 1.9, N 16.1, S 19.2. Crystals suitable for single-crystal X-ray analysis were grown upon layering DMF/pyridine (1:1) solutions of **2** with diethyl ether. IR (CsI): $\tilde{\nu}$ = 3098 (m), 3048 (s), 2932 (w), 2688 (w), 2371 (w, sh), 2242 (w, sh), 1966 (w, b), 1789 (w), 1744 (w), 1659 (s), 1569 (vs), 1540 (vs), 1373 (vs, b), 1232 (vs), 1169 (vs, sh), 994 (s), 806 (s), 765 (s), 746 (s), 652(s), 488 (m), 465 (s), 412 (w), 378 (m), 352 (w), 229 (s), 201 (s), 182 (s), 167 (s) cm^{-1}. UV/Vis (nujol): λ_{max} = 350 (sh), 292 (vbr) nm. ^1H NMR (300 MHz, $(CD_3)_2SO$]: δ = 6.9 (t, $^3J_{H,H}$ = 4.9 Hz, *para*-C*H*, 1 H), 8.2 (d, $^3J_{H,H}$ = 4.9 Hz, *meta*-C*H*, 2 H) ppm. $^{13}C\{^1H\}$ NMR [75 MHz, $(CD_3)_2SO$]: δ = 114.6 (s, *meta*-*C*H), 157.3 (s, *para*-*C*H), 183.5 (s, *C*SSi) ppm.

[Hg(S-2-$N_2C_4H_3$)$_2$] (3): $HgCl_2$ (0.21 g, 0.78 mmol) was dissolved in 25 mL of acetonitrile. (2-$N_2C_4H_3$)$SSiMe_3$ (0.3 mL, 1.62 mmol) was then added at 0 °C which resulted immediately in the formation of a white and fluffy precipitate of **3**. After warming up to room temperature, **3** was filtered and washed twice with diethyl ether. Yield: 0.3 g (90.9%). $C_8H_6HgN_4S_2$ (422.9): calcd. C 22.7, H 1.4, N 13.3, S 15.2; found C 23.2, H 1.5, N 13.7, S 15.4. Crystals suitable for single-crystal X-ray analysis were grown by recrystallisation of ca. 30 mg of **3** from 10 mL of hot CH_3CN/DMF (10:2). IR (CsI): $\tilde{\nu}$ = 3108 (w), 3029 (w,sh), 2959 (w), 1726 (w), 1704 (w), 1560 (vs), 1542 (vs), 1423 (m), 1372 (vs), 1242 (w, sh), 1200 (s), 1173 (vs), 1087 (w, sh), 983 (w, sh), 803 (m), 769 (m), 743 (s), 635 (m), 473 (w), 454 (w), 414 (w), 279 (w), 254 (s) cm^{-1}. UV/Vis (nujol): λ_{max} = 280 (vbr) nm. ^1H NMR [300 MHz, $(CD_3)_2SO$]: δ = 7.2 (t, $^3J_{H,H}$ = 4.9 Hz, *para*-C*H*, 1 H), 8.5 (d, $^3J_{H,H}$ = 4.9 Hz, *meta*-C*H*, 2 H) ppm. $^{13}C\{^1H\}$ NMR [75 MHz, $(CD_3)_2SO$]: δ = 117.7 (s, *meta*-*C*H), 158.3 (s, *para*-*C*H), 176.5 (s, *C*SSi) ppm.

[Cd(S-2-$N_2C_4H_3$)$_2$(tmeda)] (4): Complex **1** (0.05 g, 0.15 mmol) was suspended in 15 mL of TMEDA for 2 min in an ultrasonic bath. Then, the flask was sealed with a Teflon screw tap and placed in a dry oven at 35 °C for one week to yield **4** as a white crystalline powder. Yield: 0.066 g (98%). $C_{14}H_{22}CdN_6S_2$ (450.9): calcd. C 37.3, H 4.9, N 18.6, S 14.2; found C 37.1, H 4.9, N 19.4, S 14.6. Crystals suitable for single-crystal X-ray analysis were grown by allowing the solution to stand at room temperature. IR (CsI): $\tilde{\nu}$ = 3097 (w), 3044 (w, sh), 2980 (m), 2956 (m), 2874 (m, br), 2847 (m), 2800 (m), 1730 (w), 1538 (vs), 1569 (vs), 1463 (s), 1426 (s), 1372 (vs), 1298 (m), 1239 (s), 1211 (s), 1181 (vs), 1134 (w), 1103 (w), 1068 (m), 1036 (m), 1019 (m), 983 (m), 953 (s), 791 (s, sh), 770 (s), 744 (s), 646 (m), 584 (w), 485 (m), 462 (s), 447 (w, sh), 433 (m), 401 (w), 377 (w, sh), 244 (w), 203 (s, sh), 181 (m, br), 171 (w, sh), 152 (m, sh), 142 (w), 135 (w) cm^{-1}. UV/Vis (nujol): λ_{max} = 325 (sh) 285 (br) nm. ^1H NMR [300 MHz, $(CD_3)_2SO$]: δ = 2.3 (s, N*C*H_3, 12 H), 2.5 (s, *C*H_2N, 4 H), 6.9 (t, $^3J_{H,H}$ = 4.9 Hz, *para*-C*H*, 1 H), 8.3 (d, $^3J_{H,H}$ = 4.9 Hz, *meta*-C*H*, 2 H) ppm. $^{13}C\{^1H\}$ NMR [75 MHz, $(CD_3)_2SO$]: δ = 47.0 (s, N*C*H_3), 57.1 (s, *C*H_2N), 114.8 (s, *meta*-*C*H), 157.5 (s, *para*-*C*H), 183.5 (s, *C*SSi) ppm.

Crystallography: Crystals suitable for single-crystal X-ray diffraction were taken directly from the reaction solution of the compound and then selected in perfluoroalkylether oil. Single-crystal X-ray diffraction data of **2**–**4** were collected using graphite-monochromated Mo-K_α radiation (λ = 0.71073 Å) with a STOE IPDS

Table 1. Crystallographic data for $^3_\infty$[Zn(S-2-$N_2C_4H_3$)$_2$] (**1**), $^2_\infty$[Cd(S-2-$N_2C_4H_3$)$_2$] (**2**), [Hg(S-2-$N_2C_4H_3$)$_2$] (**3**) and [Cd(S-2-$N_2C_4H_3$)$_2$(tmeda)] (**4**).

	1	**2**	**3**	**4**
Formula mass	287.7	334.7	422.9	450.9
Crystal system	orthorhombic	orthorhombic	monoclinic	monoclinic
Space group	$Pna2_1$	$Pbca$	$P2_1/n$	$P2_1/n$
a [Å]	7.812(2)	15.858(3)	19.300(4)	12.317(3)
b [Å]	16.526(3)	7.969(2)	3.963(1)	10.785(2)
c [Å]	7.861(2)	16.775(3)	29.367(6)	15.130(3)
β [°]	90	90	108.82(3)	109.77(3)
V [Å^3]	1014.8(4)	2119.8(7)	2126.2(7)	1891.4(7)
Z	4	8	8	14
T [K]	180	180	190	190
$D_{calcd.}$ [g cm^{-3}]	1.883	2.097	2.642	1.583
μ(Mo-K_α) [mm^{-1}]	2.798	2.422	14.839	1.382
F(000)	576	1296	1552	912
$2\theta_{max}$ [°]	51	54	54	54
Measured reflections	3895	13987	15340	9890
Unique reflections	1304	2337	4650	3993
R_{int}	0.1193	0.0624	0.09	0.0597
Reflections with $I > 2\sigma(I)$	1181	1925	3458	3365
Refined parameters	137	136	271	296
R_1 [$I > 2\sigma(I)$][a]	0.0657	0.0502	0.0441	0.0370
wR_2 (all data)[b]	0.1727	0.1539	0.1398	0.1183
Absolute structure parameter	0.54(5)	–	–	–

[a] $R_1 = \Sigma||F_o| - |F_c||/\Sigma|F_o|$. [b] $wR_2 = \{\Sigma[w(F_o^2 - F_c^2)^2]/\Sigma[w(F_o^2)^2]\}^{1/2}$.

 © 2005 Wiley-VCH Verlag GmbH & Co. KGaA, Weinheim

II (Imaging Plate Diffraction System) equipped with a Schneider rotating anode. Single-crystal X-ray diffraction data of **1** were collected using synchrotron radiation (λ = 0.80 Å) with a STOE IPDS II (Imaging Plate Diffraction System) at the ANKA synchrotron source in Karlsruhe. The structures were solved with the direct-methods program SHELXS[29] of the SHELXTL PC suite of programs, and were refined with the use of the full-matrix least-squares program SHELXL (Table 1).[29] Molecular diagrams were prepared using SCHAKAL 97[30] and DIAMOND.[31] All Cd, Zn, S, N and C atoms were refined with anisotropic displacement parameters whilst H atoms were calculated in fixed positions. CCDC-266974 (**1**), -266975 (**2**), -266976 (**3**) and -266977 (**4**) contain the supplementary crystallographic data for this paper. These data can be obtained free of charge from The Cambridge Crystallographic Data Centre via www.ccdc.cam.ac.uk/data_request/cif. X-ray powder diffraction patterns (XRD) were measured with a STOE STADI P diffractometer (Cu-$K_{\alpha 1}$ radiation, germanium monochromator, Debye–Scherrer geometry) in sealed glass capillaries. A theoretical powder diffraction pattern for **1** was calculated on the basis of the atom coordinates obtained from single-crystal X-ray analysis by using the program package STOE WinXPOW.[32]

Acknowledgments

This work was supported by the Deutsch–Israelisches Programm (DIP) and the Deutsche Forschungsgemeinschaft (centre for functional nanostructures CFN). A. E. is grateful to Prof. Dr. D. Fenske for helpful discussions and for providing excellent working conditions, E. Tröster for her invaluable assistance in the practical work, Dr. E. Matern for the measurement of the ^{29}Si NMR spectra and Dr. Dale Cave for careful revision of the manuscript.

[1] E. S. Raper, *Coord. Chem. Rev.* **1996**, *153*, 199–255.
[2] E. S. Raper, *Coord. Chem. Rev.* **1997**, *165*, 475–567.
[3] M. B. Hursthouse, O. F. Z. Kahn, M. Mazid, M. Motevalli, P. O'Brien, *Polyhedron* **1990**, *9*, 541–544.
[4] M. L. Godino-Salido, M. D. Gutiérrez-Valero, R. López-Garzón, J. M. Moreno-Sánchez, *Inorg. Chim. Acta* **1994**, *221*, 177–181.
[5] R. Castro, J. A. Garcia-Vazquez, J. Romero, A. Sousa, W. Hiller, J. Strähle, *Polyhedron* **1994**, *13*, 273–279.
[6] R. Castro, J. A. Garcia-Vazquez, J. Romero, A. Sousa, R. Pritchard, C. A. McAuliffe, *J. Chem. Soc., Dalton Trans.* **1994**, 1115–1120.
[7] R. Castro, J. A. Garcia-Vazquez, J. Romero, A. Sousa, A. Castineiras, W. Hiller, J. Strähle, *Inorg. Chim. Acta* **1993**, *211*, 47–54.
[8] J. Romero, J. A. Garcia-Vazquez, A. Sousa, J. Zubieta, Y. Chang, *Polyhedron* **1996**, *15*, 2741–2745.
[9] S. Wang, J. P. Fackler, Jr., *Inorg. Chem.* **1989**, *28*, 2615–2619.
[10] A. K. Das, S. Seth, *J. Inorg. Biochem.* **1997**, *65*, 207–218.
[11] M. B. Hursthouse, O. F. Z. Kahn, M. Mazid, M. Motevalli, P. O'Brien, *Polyhedron* **1990**, *9*, 541–544.
[12] Y. Cheng, T. J. Emge, J. G. Brennan, *Inorg. Chem.* **1994**, *33*, 3711–3714.
[13] A. Eichhöfer, P. Deglmann, *Eur. J. Inorg. Chem.* **2004**, 349–355.
[14] A. Eichhöfer, O. Hampe, M. Blom, *Eur. J. Inorg. Chem.* **2003**, 1307–1314.
[15] A. Eichhöfer, A. Aharoni, U. Banin, *Z. Anorg. Allg. Chem.* **2002**, *628*, 2415–2421.
[16] V. Soloviev, A. Eichhöfer, D. Fenske, U. Banin, *J. Am. Chem. Soc.* **2001**, *123*, 2354–2364.
[17] S. Behrens, M. Bettenhausen, A. C. Deveson, A. Eichhöfer, D. Fenske, A. Lohde, U. Woggon, *Angew. Chem.* **1996**, *108*, 2360–2363; *Angew. Chem. Int. Ed. Engl.* **1996**, *35*, 2215–2218.
[18] R. Castro, M. L. Duran, J. A. Garcia-Vazquez, J. Romero, A. Sousa, A. Castineiras, W. Hiller, J. Strähle, *Z. Naturforsch. B* **1992**, *47*, 1067–1074.
[19] M. J. Nowak, H. Rostkowska, L. Lapinski, J. Leszczynski, J. S. Kwiatkowski, *Spectrochim. Acta, Part A* **1991**, *47*, 339–353.
[20] D. N. Sathyanarayana, S. V. Kasimir Raja, *Spectrochim. Acta, Part A* **1985**, *41*, 809–813.
[21] B. P. Kennedy, A. B. P. Lever, *Can. J. Chem.* **1972**, *50*, 3488–3507.
[22] S. Stoyanov, I. Petkov, L. Antonov, T. Stoyanova, *Can. J. Chem.* **1990**, *68*, 1482–1489.
[23] B. R. Penfold, *Acta Crystallogr.* **1953**, *6*, 707–713.
[24] H. T. Flakus, A. Tyl, P. G. Jones, *Spectrochim. Acta, Part A* **2002**, *58*, 299–310.
[25] G. H. Keller, L. Bauer, C. L. Bell, *Can. J. Chem.* **1968**, *46*, 2475–2479.
[26] D. A. Thornton, *Coord. Chem. Rev.* **1990**, *104*, 251–295.
[27] Y. Saito, M. Cordes, K. Nakamoto, *Spectrochim. Acta, Part A* **1972**, *28*, 1459–1466.
[28] H. Vorbrüggen, P. Strehlke, *Chem. Ber.* **1973**, *106*, 3039–3061.
[29] G. M. Sheldrick, *SHELXTL, An Integrated System for Solving, Refining, and Displaying Crystal Structures from Diffraction Data*, PC version 5.1, Bruker Analytical X-ray Systems, Karlsruhe, **2000**.
[30] E. Keller, *SCHAKAL 97, A Computer Program for the Graphic Representation of Molecular and Crystallographic Models*, University of Freiburg, **1997**.
[31] K. Brandenburg, *DIAMOND*, version 2.1d, Visual Crystal Structure Information System, Bonn, **2000**.
[32] *STOE WinXPOW*, STOE & Cie GmbH, Darmstadt, **2000**.

Received: March 23, 2005
Published Online: September 7, 2005

 © 2005 Wiley-VCH Verlag GmbH & Co. KGaA, Weinheim

Self-Assembly and Characterization of Grid-Type Copper(I), Silver(I), and Zinc(II) Complexes

Violetta Patroniak,*[a,b] Artur R. Stefankiewicz,[a,b] Jean-Marie Lehn,[b] and Maciej Kubicki[a]

Dedicated to Professor Bogdan Marciniec on the occasion of his 65th birthday

Keywords: Copper / Silver / Zinc / Supramolecular chemistry / Self-assembly

The reactions of ligand **L**, which comprises two bidentate binding units, with copper(I), silver(I), and zinc(II) lead to the self-assembly of the expected supramolecular architectures **1**–**3**, respectively, of the [2×2] grid type, containing four ions in tetrahedral coordination sites. The grid-type structures are assigned on the basis of the spectroscopic data in solution, and confirmed in the solid state in the case of complex **2** by X-ray crystallography.
(© Wiley-VCH Verlag GmbH & Co. KGaA, 69451 Weinheim, Germany, 2005)

Introduction

Metal-directed self-assembly is a powerful synthetic methodology for supramolecular architectures that may exhibit novel physical and chemical properties with potential applications in supramolecular engineering, nanotechnology, biomedical inorganic chemistry, biological catalysis, and in the area of sensors. A variety of architectural types are known, such as, for example, inorganic double,[1–5] triple,[4,5] and quadruple[6] helicates, rotaxanes,[7–9] clusters,[10–12] racks,[13] cages,[14–16] grids[17–28] etc., based on ligand design and on the application of suitable coordination geometries for the assembly process. Among them, there is an increasing interest in grid-shaped complexes based on ligands containing oligopyridine-type groups and various transition metal ions. These grids are thermodynamically most stable when metal ions of tetrahedral coordination geometry are combined with a planar ligand containing bidentate binding subunits.[17,18,29–40] The first [2×2] grid type was obtained with copper(I) ions,[17] and copper(I) grid complexes have recently attracted much attention because of their well-defined supramolecular architectures and their interesting properties, such as special optical,[35] magnetic,[36] and electrochemical features or the atypical geometry of the grid structure.[37] Silver(I) has also been used as an assembling ion and, thanks to the flexibility of its coordination sphere, has yielded sophisticated coordination architectures such as [3×3][29] and $[(2\times5)_2]$[6] multinuclear grids. Such compounds form supramolecular systems that self-assemble into monolayer or bilayer crystalline films, which are of potential interest for microelectronics and nanotechnology.[38–41] Zinc is one of the most abundant metals in the human body, and fluorescent imaging has been proven to be the most suitable technique for its monitoring in vivo.[42,43]

One aim of our studies has been to explore further the possibilities of the self-assembly of supramolecular structures, in particular multinuclear grids from N-heterocyclic ligands. In this paper, we describe the synthesis and structural characterization of some polynuclear metal complexes prepared from the tetradentate ligand **L**, which contains pyridine and pyrimidine nitrogen donor atoms. The investigation of the complexation of ligand **L** with metal ions of preferred tetrahedral coordination geometry, such as Cu^{I}, Ag^{I}, and Zn^{II}, has revealed that the ligand is adequately preorganised for the assembly of tetranuclear [2×2] grid type complexes.

Results and Discussion

Synthesis of Ligand L

Ligand **L** possesses two N,N bidentate binding subunits for the complexation of ions with tetrahedral coordination geometry. It contains heterocyclic pyrimidine and pyridine units and was synthesised as outlined in Scheme 1.

2-Methyl-6-(trimethylstannyl)pyridine was obtained from 2-bromo-6-methylpyridine by a halogen/lithium exchange protocol at low temperature in THF with *n*-butyllithium, followed by quenching the pyridyllithium interme-

[a] Faculty of Chemistry, Adam Mickiewicz University, Grunwaldzka 6, 60780 Poznań, Poland
E-mail: violapat@amu.edu.pl
[b] ISIS, Université Louis Pasteur, 8, Allée Gaspard Monge, BP 70028, 67083 Strasbourg, France

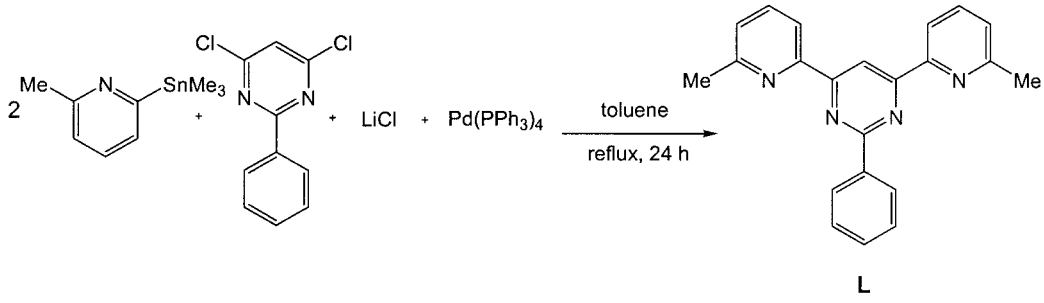

L

Scheme 1. Reaction scheme for the synthesis of ligand **L**.

diate with $ClSnMe_3$.[44,45] 4,6-Dichloro-2-phenylpyrimidine was prepared by treatment of $POCl_3$ with 2-phenylpyrimidine-4,6-diol.[46] The twofold Stille-type[47] coupling reaction of 2-methyl-6-(trimethylstannyl)pyridine with 4,6-dichloro-2-phenylpyrimidine in toluene using $[Pd(PPh_3)_4]$ as a catalyst furnished **L** in 54% yield after workup. The structure of ligand **L** was confirmed by NMR spectroscopy, FAB mass spectrometry, and elemental analysis. It was also structurally characterized by X-ray crystallography (Figure 1).

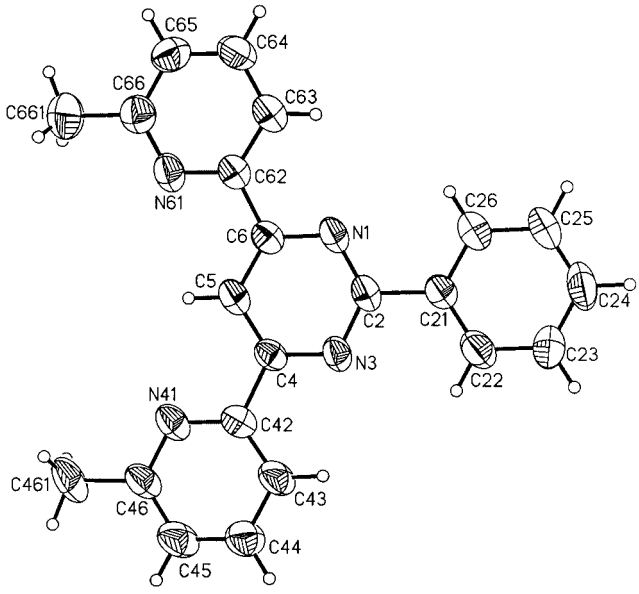

Figure 1. Anisotropic-ellipsoid representation of molecule **L** together with the numbering scheme. The ellipsoids are drawn at the 50% probability level; hydrogen atoms are represented by spheres of arbitrary radii.

Crystallographic Characterization of Ligand L

The crystal structure of the ligand molecule **L** shows that it is approximately planar (Figure 1). The four constituent rings are planar within the experimental error [maximum deviation from the least-squares plane is 0.012(3) Å], and the dihedral angles between their planes are small, up to 6.7(2)°. The mean values of aromatic C_{ar}–C_{ar} [1.373(9) Å], single C_{ar}–C_{ar} [1.489(6) Å], C_{ar}–C_{sp^3} [1.506(4) Å], and C_{ar}–N [1.340(4) Å] bond lengths are very close to typical values. The bond-angle pattern is also typical, with distortions from the ideal (120°) caused by the presence of heteroatoms and substituents. In the crystal structure, the principal intermolecular interaction is probably π-stacking between neighbouring molecules (approximately along the [610] direction); the mean distance between the π systems is 3.44 Å.

Synthesis and Characterization of the Complexes

Multitopic ligands with N,N-type donor sets allow the metal ion-directed assembly of coordination architectures. Thus, ligand **L** leads to the generation of the [2×2] grid architectures **1**–**3** with Cu^I, Ag^I, and Zn^{II}, respectively (Scheme 2).

The self-assembly of these complexes was achieved by reaction of **L** in acetonitrile, at room temperature, with tetrakis(acetonitrile)copper(I) hexafluorophosphate or the silver(I) and zinc(II) triflates. The complexation reactions were followed by ESI mass spectrometry and NMR spectroscopy.

The ^1H NMR spectra of the complexes show strongly shifted signals, as expected, and are strongly supportive of the grid-type structures. The signals of the symmetrically coordinated ligand in a single chemical and magnetic environment are in agreement with this type of structure. Interestingly, significant coordination-induced shifts of the signals are observed when the spectra of the complexes are compared to those of the uncomplexed ligand **L**.

ESI mass spectrometry is a highly sensitive and accurate analytical tool, which has been found to be particularly suitable for the identification of large metallosupramolecular architectures in solution, in which multiply charged ions are generated by sequential loss of counterions, resulting in characteristic isotopic patterns in the spectrum. The ESI-MS investigation of all complexes was performed with acetonitrile solutions at approximately 10^{-4} M. For example, the ESI mass spectrum of **2** shows peaks corresponding to multiply charged species at m/z = 785 (80%, $[AgL_2]^+$), 447 (100%, $[Ag_4L_4]^{4+}$), 339 (45%, $[L]^+$). These data confirm the presence of grid **2** in solution. The spectra of all the complexes include signals for $[ML_2]^{n+}$, $[M_4L_4]^{n+}$, and $[L]^+$, which means that significant dissociation of the grid complexes to mononuclear species and ligand molecules occurs in solution.

 © 2005 Wiley-VCH Verlag GmbH & Co. KGaA, Weinheim

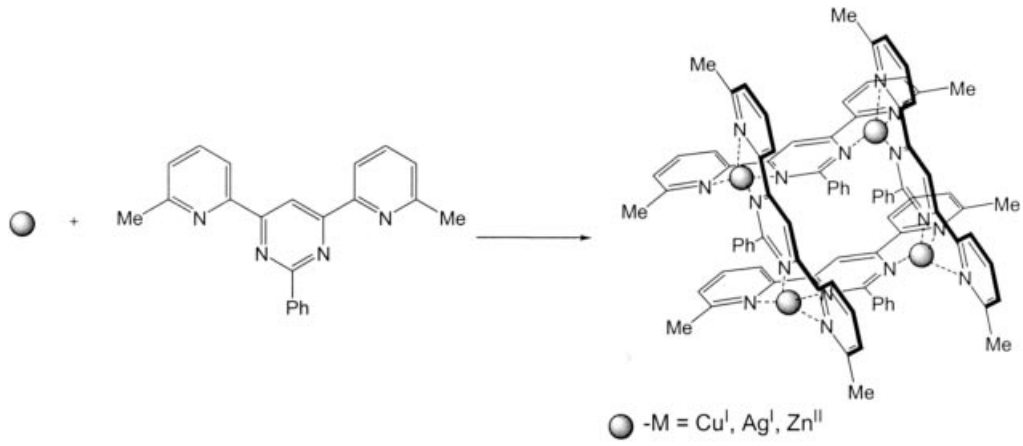

Scheme 2. Reaction scheme for the assembly of the [2×2] grid complexes **1**–**3**.

Solid-State Molecular Structure of Complex 2

Crystals of complex **2** were obtained by diffusion of diisopropyl ether into a solution of the complex in acetonitrile. The molecular structure of complex **2** was determined by X-ray crystallography at both 291 K and 100 K. It shows that it is of [2×2] grid-type (Figure 2), and is stable from 100 K to at least room temperature. We will discuss the low temperature structure here, but this discussion is equally valid for the structure determined at room temperature.

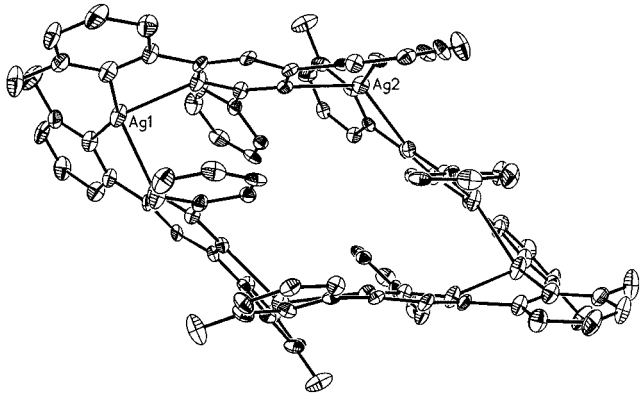

Figure 2. Anisotropic-ellipsoid representation of molecule **2** together with numbering scheme. The ellipsoids are drawn at the 50% probability level; hydrogen atoms are represented by spheres of arbitrary radii. The counterions, diisopropyl ether, and ligand molecules have been omitted for clarity.

The unit cell contains, besides the grid molecules, also the free ligand, counterion (triflate), and disordered solvent (diisopropyl ether) molecules. The grid is highly symmetrical: two independent silver ions, which lie on two different twofold axes, occupy the special positions of the space group *Ccca*. One of them occupies the Wyckoff position *e* (twofold axis along *x*), while the other occupies the Wyckoff position *f* (twofold axis along *y*). Thus, the symmetry-independent part of the grid contains two halves of silver ions and one ligand, and the rest is produced by symmetry operations. The free ligand molecule occupies yet another special position, that on the third twofold axis along the *z*-direction (atoms C2, C21, C24, and C5 lie at Wyckoff positions *g*).

Due to its symmetry, the grid is of rhombic shape and its size is within nanoscopic scale − the lengths of the diagonals are 1.18 and 1.92 nm. The formation of the grid causes significant changes in the shape of the ligand molecule. The free ligand molecule present in the crystal has a structure similar to that determined for **L**, with a maximum value of the dihedral angle between the least-squares of the aromatic planes of 9.9°. In contrast, the molecule in the complex is fairly folded. The dihedral angles between the planes of the central ring and terminal rings are 13.0°, 22.6°, and 40.0°, and the dihedral angles between the planes of the terminal rings are as large as 56.9°.

The Ag^{I} ions show distorted tetrahedral coordination, and the Ag···Ag distances are in the range 6.640–12.087 Å. The Ag–N distances can be divided into two classes: shorter [2.276(4) Å and 2.219(3) Å], to pyrimidine nitrogen atoms, and longer [2.449(5) Å and 2.471(5) Å], to pyridine nitrogen atoms. Selected bond lengths and angles are listed in Table 1.

Table 1. Selected geometrical parameters of the [2×2] grid-type complex **2**.[a]

Ag1–N1A	2.449(5)
Ag1–N61A	2.276(4)
Ag2–N41A	2.219(3)
Ag2–N3A	2.471(5)
$<(C–C)_{ar}>$	1.387(14)
$<(C–N)_{ar}>$	1.349(14)
N61A–Ag1–N61A^{i}	150.4(2)
N61A–Ag1–N1A^{i}	133.2(1)
N1A–Ag1–N61A	70.7(1)
N1A–Ag1–N1A^{i}	92.6(2)
N41A–Ag2–N41A^{ii}	164.3(2)
N3A–Ag2–N41A	72.2(2)
N41A–Ag2–N3A^{ii}	114.9(2)
N3A–Ag2–N3A^{ii}	130.1(2)

[a] Symmetry codes: ^{i} 1 – *x*, *y*, 1/2 – *z*; ^{ii} *x*, 1/2 – *y*, 1/2 – *z*.

The triflate anions are situated between the grid molecules and are held there by relatively strong and linear C–H···O hydrogen bonds (Table 2, Figure 3). Approximately

 © 2005 Wiley-VCH Verlag GmbH & Co. KGaA, Weinheim

planar, free ligand molecules lie between the grids, and interact with the aromatic rings by π-stacking interactions (the distance between the mean planes of the rings is about 3.4 Å). This intercalation occurs between two different grid fragments; an analogous intra-grid intercalation of the free ligand is observed, for example, in the copper(I) biphenanthroline grid structure.[33] There is additional free space in the crystal structure that is filled by disordered diisopropyl ether solvent molecules.

Table 2. Hydrogen bond data for **2** (low-temperature data).

D	H	A	D–H [Å]	H···A [Å]	D···A [Å]	D–H···A [°]
C461	H46C	O3^{i}	0.96	2.34	3.242(7)	157
C65A	H65A	O2^{ii}	0.93	2.34	3.275(7)	176
C661	H66B	O3^{ii}	0.96	2.48	3.429(7)	172
C5A	H5A	O1	0.92	2.48	3.380(6)	168
C43A	H43A	O1	0.92	2.46	3.303(7)	153

[a] Symmetry codes: ^{i} 1 – *x*, *y*, 1/2 – *z*; ^{ii} *x*, 1/2 – *y*, 1/2 – *z*.

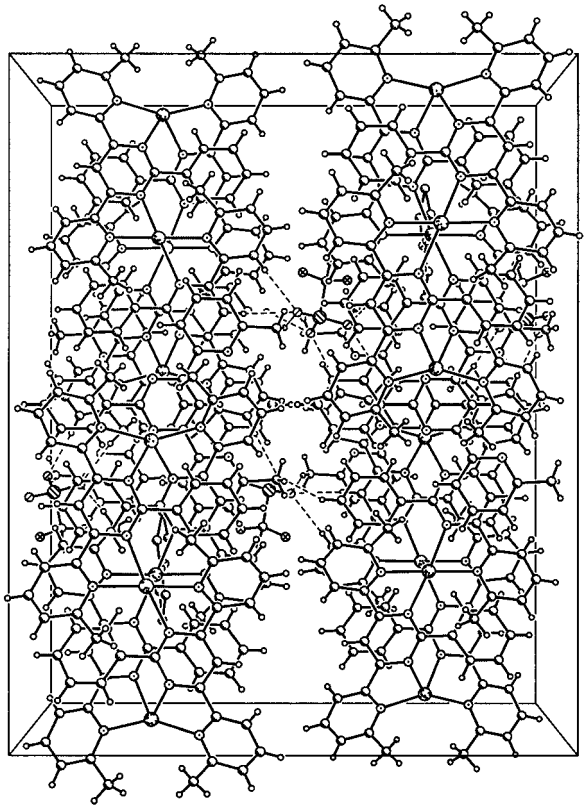

Figure 3. The content of the unit cell as seen approximately along the *a* direction (*z* across, *b* down). Weak hydrogen bonds are drawn as dashed lines.

Conclusions

The novel ligand **L** containing two bidentate N,N-binding subunits has been prepared and its solid state conformational properties characterized by X-ray crystallography. The reaction of **L** with Cu^{I}, Ag^{I}, and Zn^{II} results in the clean and quantitative formation of [2×2] grid-type complexes, which were characterized in solution on the basis of ESI mass spectrometry and ^{1}H NMR spectroscopy. The molecular structure of the Ag^{I} complex **2** was also investigated by X-ray crystallography, which confirmed that it indeed has a [2×2] grid-type architecture, with each metal ion tetrahedrally coordinated by two N,N donors.

The present results detail a particularly facile and rapid synthetic protocol for the preparation of [2×2] grid-type coordination scaffolds with Cu^{I}, Ag^{II}, and Zn^{II}. Related ligands and coordination arrays may be envisioned for the generation of various metallosupramolecular architectures.

Experimental Section

General: CH_3CN was freshly distilled under argon over CaH_2. 2-Methyl-6-(trimethylstannyl)pyridine[44,45] and 4,6-dichloro-2-phenylpyrimidine[46] were prepared according to the literature. The metal salts were used without further purification as supplied by Aldrich. NMR spectroscopic data were recorded on a Varian Gemini 300 MHz spectrometer, and were calibrated against the residual protonated solvent signal ($CDCl_3$: δ = 7.24 ppm; CD_3CN: δ = 1.94 ppm) and are given in ppm. Mass spectra were determined by FAB^{+} using a ZAB-HF VG apparatus in a *m*-nitrobenzyl alcohol matrix and a Waters Micromass ZQ spectrometer in acetonitrile. The electronic absorption spectrum for ligand **L** in acetonitrile was measured on a Shimadzu UV 2401 PC spectrometer, with λ_{max} in nm and ε ($\times 10^4$) in $M^{-1}\,cm^{-1}$. The luminescence spectrum for ligand **L** in CH_3CN was recorded using a Perkin–Elmer MPF-3 spectrofluorimeter. Microanalyses were obtained using a Perkin–Elmer 2400 CHN microanalyzer. Melting points were recorded on an Electrothermal Digital melting point apparatus.

4,6-Bis(6-methylpyridin-2-yl)-2-phenylpyrimidine (L): 2-Methyl-6-(trimethylstannyl)pyridine (2.0 g, 8 mmol) and degassed toluene (25 mL) were added consecutively, by syringe, to a mixture of 4,6-dichloro-2-phenylpyrimidine (0.6258 g, 3 mmol), $[Pd(PPh_3)_4]$ (0.10 g, 0.9 mmol), and LiCl (0.68 g, 16 mmol) under argon. The reaction was refluxed and stirred at 120 °C for 24 h, and the toluene evaporated in a water bath under reduced pressure. The residue was then purified by column chromatography on alumina and eluted with dichloromethane/*n*-hexane (4:6); yield: 0.50 g (54%). ^{1}H NMR (300 MHz, $CDCl_3$): δ = 9.27 (s, 1 H, H-5), 8.72 (t, *J* = 7.9 Hz, 1 H, H-4′′′), 8.50 (d, *J* = 7.6 Hz, 2 H, H-2′′′,6′′′), 7.79 (t, *J* = 7.6 Hz, 2 H, H-4′,4′′), 7.54 (m, *J* = 5.2 Hz, 4 H, H-3′,3′′,5′,5′′), 7.20 (t, *J* = 7.9 Hz, 2 H, H-3′′′,5′′′), 2.66 (s, CH_3) ppm. ^{13}C NMR (DEPT, 75 MHz, $CDCl_3$): δ = 164.4, 163.9, 158.4, 154.1, 138.0 (CH), 137.2 (CH), 130.6, 128.5 (CH), 128.4 (CH), 124.9 (CH), 119.0 (CH), 111.6 (CH), 24.6 (CH_3). FAB-MS: *m*/*z* (%) = 339.2 (100) [L + H]. UV/Vis (CH_3CN): λ = 233, 272.5, 281.5, 318 nm. Luminescence: $\lambda_{ex.}$ = 298 nm, $\lambda_{em.}$ = 356 nm. $C_{22}H_{18}N_4$ (338.4): calcd. C 78.08, H 5.36, N 16.56; found C 77.99, H 5.33, N 16.42. M.p. 170 °C.

Cu Complex 1: An equimolar mixture of $[Cu(CH_3CN)_4]PF_6$ (11.0 mg, 30 μmol) and ligand **L** (10.0 mg, 30 μmol) in MeCN (5 mL) was stirred at room temperature for 24 h. The solvent was then evaporated under reduced pressure to give a quantitative yield of **1** as a purple-violet powder. ^{1}H NMR (300 MHz, CD_3CN): δ = 9.16 (s, 1 H, H-5), 8.71 (t, 1 H, H-4′′′), 8.59 (d, 2 H, H-2′′′,6′′′), 8.01 (t, 2 H, H-4′,4′′), 7.55 (m, 4 H, H-3′,3′′,5′,5′′), 7.26 (t, 2 H, H-3′′′,5′′′), 2.68 (s, CH_3) ppm. ESI-MS: *m*/*z* = 739 $[CuL_2]^{+}$, 401 $[Cu_4L_4]^{4+}$, 339 $[L]^{+}$. $Cu_4(L)_4(PF_6)_4$ (2187.7): calcd. C 48.31, H 3.32, N 10.24; found C 49.01, H 3.33, N 9.98.

 © 2005 Wiley-VCH Verlag GmbH & Co. KGaA, Weinheim

Ag Complex 2: A solution of ligand **L** (10.0 mg, 30 μmol) and $Ag(CF_3SO_3)$ (7.6 mg, 30 μmol) in MeCN (5 mL) was stirred at room temperature for 24 h. The white complex **2** was isolated in quantitative yield by evaporation of the solvent. ^1H NMR (300 MHz, $CDCl_3$): δ = 9.21 (s, 1 H, H-5), 8.73 (t, 1 H, H-4′′′), 8.55 (d, 2 H, H-2′′′,6′′′), 7.91 (t, 2 H, H-4′,4′′), 7.58 (m, 4 H, H-3′,3′′,5′,5′′), 7.45 (t, 2 H, H-3′′′,5′′′), 2.69 (s, CH_3) ppm. ESI-MS: *m*/*z* = 785 $[Ag\mathbf{L}_2]^+$, 447 $[Ag_4\mathbf{L}_4]^{4+}$, 339 $[\mathbf{L}]^+$. $Ag_4(\mathbf{L})_4(CF_3SO_3)_4 \cdot 2\mathbf{L} \cdot C_6H_{14}O$ (3160.4): calcd. C 53.97, H 3.89, N 10.64, S 4.06; found C 54.39, H 3.83, N 10.65, S 4.10.

Zn Complex 3: An equimolar mixture of $Zn(CF_3SO_3)_2$ (13.3 mg, 39 μmol) and ligand **L** (14.2 mg, 39 μmol) in MeCN (5 mL) was stirred at room temperature for 24 h. The solvent was evaporated under reduced pressure to yield a pale-green complex **3** in quantitative yield. ESI-MS: *m*/*z* = 889 $\{[Zn(\mathbf{L})_2](CF_3SO_3)\}^+$, 553 $\{[Zn_4(\mathbf{L})_4](CF_3SO_3)_4\}^{4+}$, 371 $[Zn(\mathbf{L})_2]^{2+}$, 339 $[\mathbf{L}]^+$, 254 $\{[Zn_4(\mathbf{L})_4](CF_3SO_3)\}^{7+}$. ^1H NMR (300 MHz, CD_3CN): δ = 9.32 (s, 1 H, H-5), 8.64 (t, 1 H, H-4′′′), 8.52 (d, 2 H, H-2′′′,6′′′), 7.99 (t, 2 H, H-4′,4′′), 7.83 (m, 4 H, H-3′,3′′,5′,5′′), 7.60 (t, 2 H, H-3′′′,5′′′), 2.75 (s, CH_3) ppm. $Zn_4(\mathbf{L})_4(CF_3SO_3)_8$ (2807.7): calcd. C 41.07, H 2.58, N 7.98, S 9.14; found C 41.12, H 2.49, N 7.77, S 9.28.

Crystal Structure Determination of Ligand and Complex 2: Diffraction data for **L** were collected at 291(1) K and for **2** at both 291(1) and 100(1) K by the ω-scan technique up to $2\theta = 60°$, on a KUMA-KM4CCD diffractometer[48] with graphite-monochromated Mo-K_α radiation (λ = 0.71073 Å). The temperature was controlled by an Oxford Instruments Cryosystems cooling device. The data were corrected for Lorentz-polarization effects,[49] as well as for absorption, with SORTAV.[50] Unit-cell parameters were determined by the least-squares fit of 2258 (**L**), 4514 (**2**-RT), and 3783 (**2**-LT) reflections of highest intensity, chosen from the whole experiment. The structures were solved with SHELXS97[51] and refined with the full-matrix least-squares procedure on F^2 by SHELXL97.[52] Scattering factors incorporated in SHELXL97 were used. All non-hydrogen atoms were refined anisotropically; hydrogen atoms were placed geometrically in idealized positions and refined as rigid groups, with U_{iso} of the hydrogen atoms set as 1.2 (1.3 for CH_2 and CH_3 groups) times U_{eq} of the appropriate carrier atom. Relevant crystal data are listed in Table 3, together with refinement details.

Table 3. Crystal data, data collection, and structure refinement.

Compound	**L**	**2**
Formula	$C_{22}H_{18}N_4$	$C_{142}H_{122}Ag_4F_{12}N_{24}O_{13}S_4$
Formula mass	338.40	3160.35
Crystal system	orthorhombic	orthorhombic
Space group	$P2_12_12_1$	*Ccca*
a [Å]	4.2565(8)	17.4365(9)
b [Å]	16.8939(16)	30.4319(18)
c [Å]	24.1686(17)	24.5520(13)
V [Å^3]	1737.9(4)	13027.9(12)
Z	4	2
$D_{calcd.}$ [g cm^{-3}]	1.293	1.585
F(000)	712	6288
μ [mm^{-1}]	0.079	0.7471
Crystal size [mm]	0.5 × 0.08 × 0.07	0.15 × 0.08 × 0.08
Θ range [°]	2.94–29.44	2.82–29.57
hkl range	$-5 \le h \le 2$	$-23 \le h \le 21$
	$-23 \le k \le 23$	$-40 \le k \le 40$
	$-33 \le l \le 33$	$-33 \le l \le 20$
Reflections collected	11688	27152
Reflections unique (R_{int})	2576 (0.074)	8263 (0.094)
Final $R(F)$ [$I > 2\sigma(I)$]	0.058	0.065
Final $wR(F^2)$ [all data]	0.096	0.095
Goodness of fit	1.060	0.967
Max/min $\Delta\rho$ [e Å^{-3}]	0.14/–0.14	0.87/–0.51

CCDC-264396 (for **1**), -264397 (for **2**-RT), and -264398 (for **2**-LT) contain the supplementary crystallographic data for this paper. These data can be obtained free of charge from The Cambridge Crystallographic Data Centre via www.ccdc.cam.ac.uk/data_request/cif.

Acknowledgments

This work was partly supported by the Polish Ministry of Scientific Research and Information Technology (grant No. 4 T09A 049 24).

[1] J.-M. Lehn, A. Rigault, J. Siegel, J. Harrowfield, B. Chevrier, D. Moras, *Proc. Natl. Acad. Sci. USA* **1987**, *84*, 2565–2569.
[2] M. Barboiu, G. Vaughan, N. Kyritsakas, J.-M. Lehn, *Chem. Eur. J.* **2003**, *9*, 763–769.
[3] J. E. Aguado, M. J. Calhorda, P. J. Costa, O. Crespo, V. Félix, M. C. Gimeno, P. G. Jones, A. Laguna, *Eur. J. Inorg. Chem.* **2004**, 3038–3047.
[4] C. Piguet, G. Bernardinelli, G. Hopfgartner, *Chem. Rev.* **1997**, *97*, 2005–2062; M. Albrecht, *Chem. Rev.* **2001**, *101*, 3457–3497.
[5] R. Krämer, J.-M. Lehn, A. DeCian, J. Fischer, *Angew. Chem. Int. Ed. Engl.* **1993**, *32*, 703–706.
[6] P. N. W. Baxter, J.-M. Lehn, G. Baum, D. Fenske, *Chem. Eur. J.* **2000**, *6*, 4510–4517.
[7] P. N. W. Baxter, H. Sleiman, J.-M. Lehn, K. Rissanen, *Angew. Chem. Int. Ed. Engl.* **1997**, *36*, 1294–1296.
[8] H. Sleiman, P. N. W. Baxter, J.-M. Lehn, K. Airola, K. Rissanen, *Inorg. Chem.* **1997**, *36*, 4734–4742.
[9] M. C. Jimenez-Molero, Ch. Dietrich-Buchecker, J.-P. Sauvage, *Chem. Eur. J.* **2002**, *8*, 1455–1466.
[10] L. J. Ashfield, A. R. Cowley, J. R. Dilworth, P. S. Donelly, *Inorg. Chem.* **2004**, *43*, 4121–4123.
[11] A. L. Pickering, D.-L. Long, L. Cronin, *Inorg. Chem.* **2004**, *43*, 4953–4961.
[12] F. Bramsen, A. D. Bond, C. J. McKenzie, R. G. Hazell, B. Moubaraki, K. S. Murray, *Chem. Eur. J.* **2005**, *11*, 825–831.
[13] R. L. Paul, S. M. Couchman, J. C. Jeffery, J. A. McCleverty, Z. R. Reeves, M. D. Ward, *J. Chem. Soc., Dalton Trans.* **2000**, 845–851.
[14] A. M. Garcia, D. M. Bassani, J.-M. Lehn, G. Baum, D. Fenske, *Chem. Eur. J.* **1999**, *5*, 1234–1238.
[15] M. Yoshizawa, T. Kusukawa, M. Fujita, S. Sakamoto, K. Yamaguchi, *J. Am. Chem. Soc.* **2001**, *123*, 10454–10459.
[16] M. Yoshizawa, Y. Takeyama, T. Kusukawa, M. Fujita, *Angew. Chem. Int. Ed.* **2002**, *41*, 1347–1349.
[17] M.-T. Youinou, N. Rahmouni, J. Fischer, J. A. Osborn, *Angew. Chem. Int. Ed. Engl.* **1992**, *31*, 733–735.
[18] P. N. W. Baxter, J.-M. Lehn, K. Rissanen, *Chem. Commun.* **1997**, 1323–1324.
[19] J. Rojo, M. Ruben, E. Breuning, J.-P. Giesselbrecht, J.-M. Lehn, *Angew. Chem. Int. Ed.* **2000**, *39*, 4139–4142.
[20] E. Breuning, M. Ruben, J.-M. Lehn, F. Renz, Y. Garcia, V. Ksenofontov, P. Gütlich, E. Wegelius, K. Rissanen, *Angew. Chem. Int. Ed.* **2000**, *39*, 2504–2505.
[21] H. Oshio, H. Onodera, O. Tamada, H. Mizutani, T. Hikichi, T. Ito, *Chem. Eur. J.* **2000**, *6*, 2523–2530.
[22] P. N. W. Baxter, R. G. Khoury, J.-M. Lehn, G. Baum, D. Fenske, *Chem. Eur. J.* **2000**, *6*, 4140–4148.
[23] A. Marquis, J.-P. Kintzinger, R. Graff, P. N. W. Baxter, J.-M. Lehn, *Angew. Chem. Int. Ed.* **2002**, *41*, 2760–2764.
[24] J. P. Plante, P. D. Jones, D. R. Powell, T. E. Glass, *Chem. Commun.* **2003**, 336–337.
[25] M. Ruben, E. Breuning, M. Barboiu, J.-P. Gisselbrecht, J.-M. Lehn, *Chem. Eur. J.* **2003**, *9*, 291–299.
[26] J. Hausmann, G. B. Jameson, S. Brooker, *Chem. Commun.* **2003**, 2992–2993.

 © 2005 Wiley-VCH Verlag GmbH & Co. KGaA, Weinheim

[27] V. Patroniak, P. N. W. Baxter, J.-M. Lehn, M. Kubicki, M. Nissinen, K. Rissanen, *Eur. J. Inorg. Chem.* **2003**, 4001–4009.
[28] L. H. Uppadine, J.-P. Gisselbrecht, J.-M. Lehn, *Chem. Commun.* **2004**, 718–719.
[29] P. N. W. Baxter, J.-M. Lehn, J. Fisher, M.-T. Youinou, *Angew. Chem. Int. Ed. Engl.* **1994**, *33*, 2284–2287.
[30] P. N. W. Baxter, J.-M. Lehn, B. O. Kneisel, D. Fenske, *Chem. Commun.* **1997**, 2231–2232.
[31] P. N. W. Baxter, J.-M. Lehn, B. O. Kneisel, D. Fenske, *Angew. Chem. Int. Ed. Engl.* **1997**, *36*, 1978–1981.
[32] S. Toyota, C. R. Woods, M. Benaglia, R. Haldimann, K. Wärnmark, K. Hardcastle, J. S. Siegel, *Angew. Chem. Int. Ed.* **2001**, *40*, 751–754.
[33] A. Marquis, J.-P. Kintzinger, R. Graff, P. N. W. Baxter, J.-M. Lehn, *Angew. Chem. Int. Ed.* **2002**, *41*, 2760–2764.
[34] R. Ziessel, L. Charbonnière, M. Cesario, T. Prangé, H. Nierengarten, *Angew. Chem. Int. Ed.* **2002**, *41*, 975–979.
[35] R. Hoogenboom, G. Kickelbick, U. S. Schubert, *Eur. J. Org. Chem.* **2003**, 4887–4896.
[36] Y. Lan, D. K. Kennepohl, B. Moubaraki, K. S. Murray, J. D. Cashion, G. B. Jameson, S. Brooker, *Chem. Eur. J.* **2003**, *9*, 3772–3784.
[37] J. R. Nitschke, M. Hutin, G. Bernardinelli, *Angew. Chem. Int. Ed.* **2004**, *43*, 6724–6727.
[38] I. Weissbuch, P. N. W. Baxter, S. Cohen, H. Cohen, K. Kjaer, P. B. Howes, J. Als-Nielsen, G. S. Hanan, U. S. Schubert, J.-M. Lehn, L. Leiserowitz, M. Lahav, *J. Am. Chem. Soc.* **1998**, *120*, 4850–4860.
[39] I. Weissbuch, P. N. W. Baxter, I. Kuzmenko, H. Cohen, S. Cohen, K. Kjaer, P. B. Howes, J. Als-Nielsen, J.-M. Lehn, L. Leiserowitz, M. Lahav, *Chem. Eur. J.* **2000**, *6*, 725–734.
[40] M. Ruben, J. Rojo, F. J. Romero-Salguero, L. H. Uppadine, J.-M. Lehn, *Angew. Chem. Int. Ed.* **2004**, *43*, 3644–3662.
[41] B. Wiley, Y. Sun, B. Mayers, Y. Xia, *Chem. Eur. J.* **2005**, *11*, 454–463.
[42] P. Jiang, Z. Guo, *Coord. Chem. Rev.* **2004**, *248*, 205–229.
[43] N. C. Lim, H. C. Freake, C. Brückner, *Chem. Eur. J.* **2005**, *11*, 38–49.
[44] P. Jutzi, U. J. Gilge, *J. Organomet. Chem.* **1983**, *246*, 163–168.
[45] G. V. Long, S. E. Boyd, M. M. Harding, I. E. Buys, T. W. Hambley, *J. Chem. Soc., Dalton Trans.* **1993**, 3175–3180.
[46] K. Burdeska, H. Fuhrer, G. Kabas, A. E. Siegriest, *Helv. Chim. Acta* **1981**, *64*, 113–152.
[47] J. K. Stille, *Angew. Chem. Int. Ed. Engl.* **1986**, *25*, 508–524.
[48] Oxford Diffraction (**2003**). *CrysAlisCCD*, User Guide v.171. Oxford Diffraction Poland Sp., Wrocław, Poland.
[49] Oxford Diffraction (**2003**). *CrysAlisRed*, CCD data reduction GUI v.171. Oxford Diffraction Poland Sp., Wrocław, Poland.
[50] R. H. Blessing, *J. Appl. Crystallogr.* **1989**, *22*, 396.
[51] G. M. Sheldrick, *Acta Crystallogr., Sect. A* **1990**, *46*, 467–476.
[52] G. M. Sheldrick, *SHELX97 – Programs for Crystal Structure Analysis* (Release 97-2). Institut für Anorganische Chemie der Universität, Tammanstrasse 4, 3400 Göttingen, Germany, **1998**.

Received: April 15, 2005
Published Online: September 8, 2005

 © 2005 Wiley-VCH Verlag GmbH & Co. KGaA, Weinheim

The Influence of the Neutral Coligand on the Spectroscopic Properties and Crystal Structures of Lithium Tri(*tert*-butyl)silylarsanides of the Type [(L)LiAs(H)Si*t*Bu$_3$] (L = DME, THF)

Matthias Westerhausen,*[a] Mathias Krofta,[b] Peter Mayer,[b] and Holger Piotrowski[b]

Keywords: Arsanes / Arsanides / Lithium / Lithiation / Pnicogens

The reaction of [(dme)LiAsH$_2$] with F$_3$CSO$_3$Si*t*Bu$_3$ yields tri(*tert*-butyl)silylarsane (**1**). The reaction of **1** with *n*-butyllithium in 1,2-dimethoxyethane gives [(dme)LiAs(H)Si*t*Bu$_3$]$_2$ (**2**), whereas the lithiation of **1** in THF leads to the formation of the one-dimensional polymer [(THF)LiAs(H)Si*t*Bu$_3$]$_\infty$ (**3**). The Li–As bond lengths of both of these compounds show a similar value of approximately 260 pm. However, the smaller coordination number of the lithium atom in **3** leads to a short Li–O distance of 190 pm, whereas in **2**, which has a tetracoordinate lithium atom, an average bond length of 199 pm is observed.

(© Wiley-VCH Verlag GmbH & Co. KGaA, 69451 Weinheim, Germany, 2005)

Introduction

Silylphosphanes and their lithiated derivatives have aroused the interest of many research groups over several decades[1–5] because these compounds are valuable synthons for a wide variety of novel compounds such as phosphaalkenes and phosphaalkynes.[6] However, the homologous silylated arsanes, as well as their lithium derivatives, have been investigated far less extensively, although the synthesis and the structure of DME complexes of LiAsH$_2$ have been published[7,8] and have led to a moderate development of arsanide chemistry. The huge preference for phosphorus chemistry stems from the NMR-sensitive ^{31}P nucleus, which allows a spectroscopic follow-up of reactions prior to isolation of new compounds. Furthermore, the comparable van der Waals radii of phosphorus (1.85 Å) and arsenic (1.9 Å) due to the contraction of the d-block elements suggest a similar chemical behaviour of homologous compounds, whereas nitrogen (1.55 Å) and antimony (2.2 Å) differ more drastically. In addition, the structures of silylated amines also show planar-coordinated and sp^2-hybridized nitrogen atoms, whereas the heavy pnicogen atoms in silylated phosphanes, arsanes and stibanes display a pyramidal environment and avoid hybridisation.[5]

After the first synthesis of [LiAs(SiMe$_3$)$_2$] by Becker and co-workers 25 years ago,[9] the crystal structures of the DME[10] and THF adducts[11] were reported. The growing interest in these compounds, for example as precursors for element III/V semiconductors, finally led to the publication of slightly modified and improved preparation procedures.[12,13] Modifications of the substitution pattern of tris(triorganylsilyl)arsanes were also investigated.[14] Whereas the reaction of E(SiMe$_3$)$_3$ with an alkyllithium yields [LiE(SiMe$_3$)$_2$] (E = P, As, Sb), the monosubstituted trimethylsilylated phosphanes undergo redistribution reactions with the formation of a mixture of LiPH$_2$, [LiP(H)SiMe$_3$] and [LiP(SiMe$_3$)$_2$].[15] In order to prevent these redistribution reactions larger groups such as Si*i*Pr$_3$ and Si*t*Bu$_3$ have to be employed, and even the bulkiness of the triisopropylsilyl substituents enforces an almost planar environment at the pnicogen atoms in E(Si*i*Pr$_3$)$_3$ (E = P, As, Sb).[16]

The synthesis of H$_2$AsSi*i*Pr$_3$ succeeded smoothly by the reaction of [(dme)LiAsH$_2$][7] with chlorotriisopropylsilane.[17] Metallation reactions led to the formation of triisopropylsilylarsanediides, which can be part of a cluster[18] or trapped between two metal fragments.[17] Monometallated triisopropylsilylarsanes have been published for the alkaline-earth metals;[19] however, there are no detailed investigations on the key compounds [(L)$_n$LiAs(H)SiR$_3$] with bulky trialkylsilyl substituents. There are only sporadic investigations on lithiated easily accessible primary arsanes, even though reports on [LiAs(H)R] were published as far back as 1964/65 (R = *t*Bu)[20] and 1977 (R = Ph).[21] The helical structure of [(THF)$_2$LiAs(H)Ph]$_\infty$ was determined more than two decades later.[22]

[a] Institute of Inorganic and Analytic Chemistry, Friedrich-Schiller-Universität Jena,
August-Bebel-Str. 2, 07743 Jena, Germany
Fax: +49-3641-948-102
E-mail: m.we@uni-jena.de
[b] Department of Chemistry and Biochemistry, Ludwig-Maximilians-Universität München,
Butenandtstr. 9 (Haus D), 81377 München, Germany

Results and Discussion

Synthesis and NMR Spectroscopy

Whereas the metallation of tri(*tert*-butyl)silylphosphane has already been reported,[23] there are no reports on the homologous arsane. The metathesis reaction of [(dme)LiAsH$_2$] with tBu$_3$SiO$_3$SCF$_3$ in DME yields tri(*tert*-butyl)silylarsane (**1**) and lithium trifluoromethanesulfonate in large quantities according to Equation (1). This primary arsane shows no tendency to undergo dismutation or redistribution reactions. The AsH$_2$ moiety is clearly detected by the symmetric and asymmetric stretching vibrations at 2100 and 2091 cm^{-1} in the IR spectrum.

$$(\text{dme})\text{LiAsH}_2 + \text{F}_3\text{C}-\overset{\overset{\text{O}}{\|}}{\underset{\underset{\text{O}}{\|}}{\text{S}}}-\text{OSi}t\text{Bu}_3 \xrightarrow[-\text{DME}]{-\text{LiO}_3\text{S-CF}_3} t\text{Bu}_3\text{Si-AsH}_2 \quad \mathbf{1} \qquad (1)$$

The stoichiometric metallation of H$_2$AsSitBu$_3$ with alkyllithium leads to the monolithiated arsanides according to Equation (2). The solvent determines which solvate is formed during the metallation reaction. These complexes are very sensitive to moisture and air.

$$\text{H}_2\text{As-Si}t\text{Bu}_3 + n\text{BuLi} \xrightarrow[-n\text{BuH}]{\text{L}} [(\text{L})\text{LiAs(H)Si}t\text{Bu}_3] \quad \text{L = DME (}\mathbf{2}\text{), THF (}\mathbf{3}\text{)} \qquad (2)$$

The deprotonation (lithiation) shifts the As–H stretching vibrations to lower energies. These frequencies, as well as the NMR parameters, are listed in Table 1. Several general trends can be deduced from the NMR spectroscopic parameters dependent on the pnicogen atom and the substitution of hydrogen by a lithium atom (higher negative charge on the pnicogen atom). The heavier pnicogen atom causes the E–H vibration to lie at lower wavenumbers and the ^{1}H NMR resonance at higher field. Furthermore, the ^{29}Si{^{1}H} NMR shift is observed at lower field for the arsenic derivatives. Similar trends are observed for the substitution of an H atom by a lithium atom: the trialkylsilylphosphanides and -arsanides show lower E–H stretching energies, a high-field shift of the proton in the NMR spectra, and a low-field shift for the silicon nuclei. The substitution of the triisopropylsilyl groups by the bulkier tri(*tert*-butyl)silyl substituents leads to larger δ values of the silicon nucleus.

Molecular Structures

The tetracoordinate pnicogen atoms in the lithium tri(*tert*-butyl)silylarsanides discussed above are bonded to a silicon, a hydrogen and two lithium atoms. The structure of the DME adduct is shown in Figure 1. The central structural motif is a four-membered Li$_2$As$_2$ cycle with an alkali metal in a distorted tetrahedral environment.

Table 1. Spectroscopic properties of H$_2$AsSitBu$_3$ (**1**) and the lithium tri(*tert*-butyl)silylarsanides of the type [(L)LiAs(H)SiR$_3$] [L = DME (**2**), THF (**3**)]. For comparison reasons the values of the homologous phosphorus derivatives H$_2$PSitBu$_3$ (**A**) and [(dme)LiP(H)SitBu$_3$]$_2$ (**B**) are also included.

	A	**B**	**1**	**2**	**3**
$\tilde{\nu}$	2295 2395	2261	2091 2100	2065	2042
δ(E*H*)	0.94[a]	–2.11[b]	1.15	–2.83	–2.48
δ(SiC*Me*)	1.09	1.10	1.10	1.42	1.47
δ(Si*C*)	23.1	23.6	23.4	24.1	23.9
δ(SiCMe)	30.7	31.5	30.6	32.2	32.0
δ(Si)	24.1	33.6	31.2	39.2	38.2
Ref.	[24]	[23]			

[a] $^1J_{P,H}$ = 185.6 Hz; $\delta_{^{31}P}$ = –263.8 ppm. [b] $^1J_{P,H}$ = 165.9 Hz; $\delta_{^{31}P}$ = –322.2 ppm.

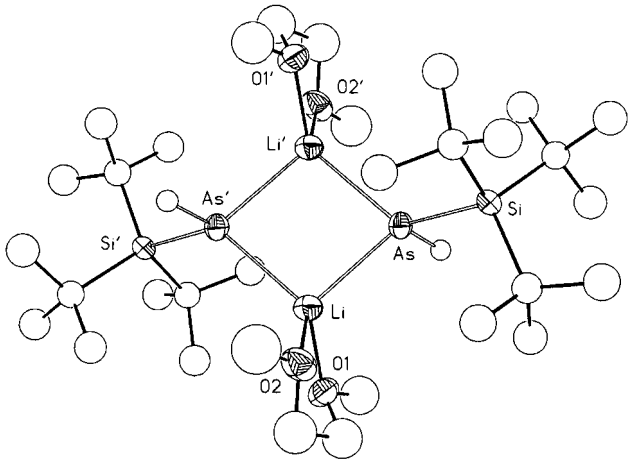

Figure 1. Molecular structure of **2**. The hydrogen atoms have been omitted for clarity, with the exception of the arsenic-bound H atom. Symmetry-related atoms (x, $-y$ + 1, $-z$ + 1) are marked with an apostrophe. Selected bond lengths [pm]: As–Li 260.9(3), As–Li′ 259.7(3), As–Si 231.49(5), As–H 154(2), Li–O1 201.0(4), Li–O2 197.2(4), Si–C1 194.6(2), Si–C5 194.9(2), Si–C9 195.3(2); angles [°]: Si–As–Li 122.61(8), Si–As–Li′ 123.90(8), Li–As–Li′ 85.2(1), Si–As–H 96(1), Li–As–H 111(1), Li′–As–H 120(1), As–Li–As′ 94.8(1).

The THF complex **3** crystallises as an infinite polymeric strand. Part of the chain is represented in Figure 2. Although the four-membered Li$_2$E$_2$ cycle (E = P, As), which can annelate into ladder-type structures, is the main structural feature, infinite chains of alternating lithium and pnicogen atoms have also been observed for [(dme)LiPH$_2$]$_\infty$[25,26] and [(THF)$_2$LiAs(H)Ph]$_\infty$.[22]

Selected structural parameters of the ether complexes of lithium tri(*tert*-butyl)silylarsanide are listed in Table 2 together with those of other phosphanides and arsanides of lithium. Bis(triisotriisopropylsilyl)phosphane[27] and tris(triisopropylsilyl)phosphane and -arsane[16] are included for comparison reasons as well. The anionic charge on the pnicogen atom leads to a shortening of the E–Si bond of approximately 6 pm due to an additional electrostatic attraction between the pnicogen and the silicon atoms. The Li–E distances are scattered widely between 247 and 262 pm for the phosphanides and between 258 and 273 pm for the arsanides. These values depend on the coordination

 © 2005 Wiley-VCH Verlag GmbH & Co. KGaA, Weinheim

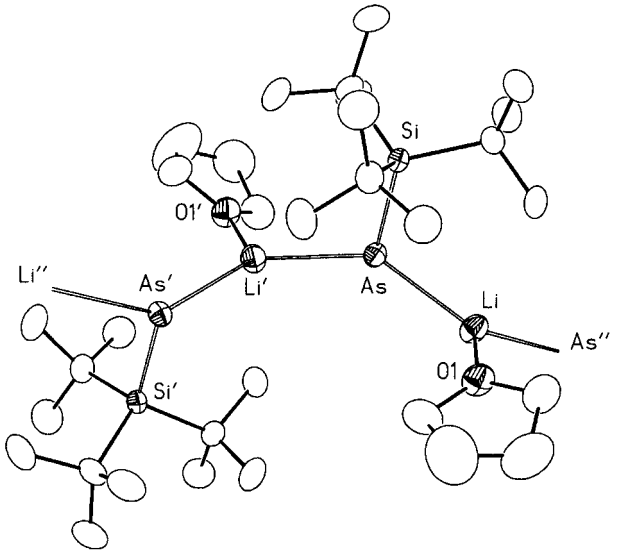

Figure 2. Structure model of **3**. All hydrogen atoms have been omitted for clarity. Symmetry-related atoms are marked with one (x + 1, y – 1/2, $–z$ + 1/2) or two apostrophes (x + 1, y + 1/2, $–z$ + 1/2). Selected bond lengths [pm]: As–Si 233.83(6), As–Li 258.1(4), As–Li′ 260.8(4), Li–O1 190.4(4), Si–C1 194.9(2), Si–C2 195.3(2), Si–C3 194.8(2); angles [°]: Si–As–Li 104.9(1), Si–As–Li′ 107.8(1), Li–As–Li′ 141.81(4), As–Li–As″ 128.4(1).

numbers of the alkali metal and the pnicogen atoms. Thus, the smallest Li–P bond lengths were observed for a phosphanide with a two-coordinate lithium atom and the shortest Li–As bonds were found for arsanides with three-coordinate alkali metals. Intramolecular steric repulsion leads to an enhancement of these bonds. The Li–O distances follow a similar pattern: triply coordinated lithium atoms show smaller distances, whereas a coordination number of four leads to an elongation of this bond. Furthermore, monodentate ethers display shorter Li–E bonds than the bidentate 1,2-dimethoxyethane ligand.

The smallest angle is observed at the alkali metal atom in four-membered Li_2E_2 ring systems. This fact is a consequence of repulsive forces between the large pnicogen atoms. If the four-membered cycle is opened to a one-dimensional strand, Li–E–Li′ angles of more than 140° are realized, whereas in polymeric $[(dme)LiPH_2]_\infty$ a nearly linear Li–P–Li′ fragment is found. A linear E–Li–E′ moiety is never found because additional agostic interactions enhance the coordination number, especially of the low-coordinate alkali metal atoms.

Summary

Lithiated primary arsanes do not undergo redistribution reactions if large trialkylsilyl groups are bonded at the arsenic atom. The bidentate 1,2-dimethoxyethane ligand leads to a dimeric molecule whereas the smaller and monodentate tetrahydrofuran molecule favours the crystallisation of a one-dimensional coordination polymer. These compounds are valuable synthons for arsenide-transfer reactions and further deprotonation reactions (formation of arsanedides).

Experimental Section

General: All experiments and manipulations were carried out under an atmosphere of argon. Reactions were performed by using standard Schlenk techniques and in dried and thoroughly deoxygenated solvents. $[(dme)LiAsH_2]$[7] as a DME solution and F_3CSO_3Si-tBu$_3$[24] were prepared according to a literature procedure. The NMR spectroscopic data were obtained at room temperature from [D$_6$]benzene solutions. For the IR spectra the crystalline compounds were dissolved in Nujol and measured between CsBr windows.

***t*Bu$_3$SiAsH$_2$ (1):** A solution of $[(dme)LiAsH_2]$ (80.0 mmol) in 100 mL of 1,2-dimethoxyethane was cooled to –50 °C. Then,

Table 2. Comparison of selected structural parameters of lithium trialkylsilylphosphanides and -arsanides of the type $[(L)_nLiE(H)SiR_3]$ (E = P, As) with $HP(Si\mathit{i}Pr_3)_2$[26] and $E(Si\mathit{i}Pr_3)_3$.[16]

	Li–E	E–Si	Li–O	LiELi′	ELiE′	Ref.
$HP(Si\mathit{i}Pr_3)_2$	–	226.5	–	–	–	[27]
$P(Si\mathit{i}Pr_3)_3$	–	226.5	–	–	–	[16]
$[(THF)_2LiP(H)Si\mathit{i}Pr_3]_2$	258.0	219.5	196.5	83.8	96.2	[28]
$[(dme)LiP(H)Si\mathit{t}Bu_3]_2$	253.1	221.3	200.8	81.6	98.4	[23]
$[(dme)LiP(SiMe_3)_2]_2$	255.9	220.5	201.9	75.7	104.3	[26]
$[(THF)_2LiP(SiMe_3)_2]_2$	262	219.5	198	80.0	100.0	[29]
$[LiP(SiPh_3)_2]_2$	247.2	219.3	–	72.9	107.0	[30]
$[(dme)LiPH_2]_\infty$	256.7	–	203.2	176.5	117.8	[25,26]
$As(Si\mathit{i}Pr_3)_3$	–	237.3	–	–	–	[16b]
2	260.3	231.5	199.1	85.2	94.8	
3	259.5	233.8	190.4	141.8	128.4	
$[(1,4\text{-dioxane})_3LiAsPh_2]$	266	–	194	–	–	[31]
$[(THF)_2LiAs(H)Si\mathit{i}Pr_3]_2$	263	229.7	195	86	94	[28]
$[(dme)LiAs(SiMe_3)_2]_2$	259	230.7	210	81	99	[10]
$[(THF)_2LiAs(SiMe_3)_2]_2$	269	228.6	196	81.8	98.2	[11]
$[(Et_2O)_2LiAsPh_2]_2$	273.3	–	198.6	89.5	90.3	[31]
$[(THF)LiAs(\mathit{t}Bu)As\mathit{t}Bu_2]_2$	258	–	189	79.4	100.6	[32]
$[LiAs\{CH(SiMe_3)_2\}_2]_3$	260	–	–	102	138	[33]
$[(THF)_2LiAs(H)Ph]_\infty$	270	–	194	143.4	116	[22]

 © 2005 Wiley-VCH Verlag GmbH & Co. KGaA, Weinheim

$F_3CSO_3SitBu_3$ (13.9 g, 40.0 mmol) dissolved in 25 mL of DME was added dropwise. After complete addition the reaction solution was heated to reflux for 5 h. Thereafter all volatile materials were removed in vacuo at room temp. and the residue redissolved in 100 mL of *n*-pentane. This solution was decanted from the precipitate. After removal of the solvent 8.84 g of tri(*tert*-butyl)silylarsane (**1**; 32.0 mmol, 80%) remained as a slightly yellow solid which was very sensitive towards moisture and air. M.p. 207 °C. ^1H NMR: δ = 1.10 ($SitBu_3$), 1.15 (AsH_2) ppm. $^{13}C\{^1H\}$ NMR: δ = 23.4 (SiC), 30.6 ($SiCMe_3$) ppm. $^{29}Si\{^1H\}$ NMR: δ = 31.20 ($SitBu_3$) ppm. IR: $\tilde{\nu}$ = 2292 cm^{-1} w, 2177 w, 2100 vs, 2091 vs, 1478 vs, 1441 w, 1423 w, 1390 vs, 1366 s, 1260 w, 1189 w, 1178 w, 1096 w, 1049 w, 1013 s, 956 m, 932 m, 913 w, 816 vs, 745 w, 695 vw, 648 m w, 624 s, 609 m, 587 m, 565 s, 495 vs, 450 s, 407 w, 378 w. $C_{12}H_{29}AsSi$ (276.37): calcd. C 52.15, H 10.58; found C 51.07, H 10.59.

[(dme)LiAs(H)Si*t*Bu$_3$] (2): Tri(*tert*-butyl)silylarsane (**1**; 0.42 g, 1.5 mmol) was dissolved in 10 mL of DME at –78 °C. Then, 1.5 mmol of *n*-butyllithium in hexane (0.6 ml of 2.5 M solution) was added dropwise. Whilst warming to room temp. the solution turned yellow. All volatile materials were removed at room temp. in vacuo and the residue was extracted with pentane. From this solution 0.44 g of **2** (0.6 mmol, 78%) precipitated at 0 °C in the shape of slightly blue prisms; decomp. above 135 °C. ^1H NMR: δ = –2.83 (LiAsH), 1.42 ($SitBu_3$), 3.11 (DME), 3.25 (DME) ppm. $^7Li\{^1H\}$ NMR: δ = 3.9 ppm. $^{13}C\{^1H\}$ NMR: δ = 24.1 (SiC), 32.2 ($SiCMe_3$), 58.5 (DME), 71.6 (DME) ppm. $^{29}Si\{^1H\}$ NMR: δ = 39.2 ($SitBu_3$) ppm. IR: $\tilde{\nu}$ = 2065 cm^{-1} vs, 1478 vs, 1444 m, 1407 vw, 1390 s, 1366 m, 1354 w, 1271 s, 1262 s, 1242 m, 1192 s, 1180 s, 1162 m, 1123 vs, 1107 vs, 1086 vs, 1046 s, 1032 s, 1014 vs, 956 w, 932 m, 869 s, 838 m, 814 vs, 644 m, 623 m, 592 s, 564 s, 539 m, 497 vs, 451 s, 410 m, 380 m, 354 w, 347 w, 343 w, 331 w, 325 w, 300 w. $C_{32}H_{76}As_2Li_2O_4Si_2$ (744.85): calcd. C 51.60, H 10.28; found C 51.03, H 10.28.

[(THF)LiAs(H)Si*t*Bu$_3$] (3): A 2.5 M solution of *n*-butyllithium in hexane (15 mL) was added dropwise to a solution of tri(*tert*-butyl)silylarsane (**1**; 0.58 g, 2.1 mmol) in 15 mL of THF at 0 °C. Whilst warming up to room temp. the solution turned greenish. Recrystallisation from benzene gave **3** (0.53 g, 1.5 mmol, 71%) as colourless prisms; decomp. above 127 °C. ^1H NMR: δ = –2.48 (LiAsH), 1.39 (THF), 1.47 ($SitBu_3$), 3.66 (THF) ppm. $^7Li\{^1H\}$ NMR: δ = 4.9 ppm. $^{13}C\{^1H\}$ NMR: δ = 23.9 (SiC), 25.2 (THF), 32.0 ($SiCMe_3$), 68.4 (THF) ppm. $^{29}Si\{^1H\}$ NMR: δ = 38.2 ($SitBu_3$) ppm. IR: $\tilde{\nu}$ = 2042 cm^{-1} s, 1495 w, 1477 s, 1444 m, 1388 m, 1381 s, 1359 m, 1354 m, 1316 w, 1293 vw, 1261 vw, 1246 vw, 1193 m, 1184 m, 1049 s, 1013 s, 973 m, 932 m, 917 m, 892 m, 817 vs, 729 s, 695 m, 673 w, 636 w, 621 m, 593 s, 563 s, 497 vs, 463 s, 454 s, 410 s, 393 s, 386 s, 348 m, 320 m, 308 m, 299 w. $C_{16}H_{36}AsLiOSi$ (354.40): calcd. C 54.22, H 10.24; found C 53.71, H 9.93.

Crystal Structure Determinations of 2 and 3: The data sets were collected on a STOE-IPDS diffractometer (operating at –73 °C) with graphite-monochromated Mo-K_α radiation (λ = 0.71073 Å) using oil-coated, rapidly cooled single crystals.[34] Crystallographic parameters, details of data collection and refinement procedures are summarised in Table 3. The structures were solved by direct methods with the program SIR97[35] and refined with the software packages SHELXL-93 and SHELXL-97.[36] Neutral scattering factors were taken from Cromer and Mann[37] and for the hydrogen atoms from Stewart et al.[38] The hydrogen atoms were considered with a riding model under the restriction of ideal tetrahedral symmetry at the corresponding carbon atoms. The arsenic-bound H atoms were taken from the residual electron density maps and refined isotropically.

CCDC-269668 (for **2**) and -269669 (for **3**) contain the supplementary crystallographic data for this paper. These data can be obtained free of charge from The Cambridge Crystallographic Data Centre via www.ccdc.cam.ac.uk/data_request/cif.

Table 3. Crystallographic data and details of the refinement procedures for the lithium tri(*tert*-butyl)silylarsanides of the type [(L)-LiAs(H)SiR_3] [L = DME (**2**), THF (**3**)].

	2	**3**·½C_6H_6
Empirical formula	$C_{16}H_{38}AsLiO_2Si$	$C_{19}H_{38}AsLiOSi$
Mol. mass	372.420	392.453
Temp. [K]	200(3)	200(3)
Crystal system	monoclinic	monoclinic
Space group[33]	$P2_1/n$ (no. 14)	$P2_1/c$ (no. 14)
a [pm]	856.00(5)	1187.79(7)
b [pm]	2234.95(15)	873.01(4)
c [pm]	1167.09(7)	2245.39(16)
β [°]	105.427(7)	104.685(8)
V [Å^3]	2152.3(2)	2252.3(2)
Z	4	4
$\rho_{calcd.}$ [g cm^{-3}]	1.1493	1.1574
μ [mm^{-1}]	1.636	1.564
$F(000)$	800	840
No. of measured data	11393	15521
No. of independent data (N_o (R_{int})	4055 (0.0396)	4127 (0.0421)
Abs. correction	numerical	numerical
T_{min}/T_{max}	0.567/0.774	0.666/0.811
Restraints	0	0
No. of parameters N_p	194	217
N_o/N_p	20.9/1	19.0/1
wR_2 (all data, on F^2)[a]	0.0604	0.0704
No. of data with $I > 2\sigma(I)$	3239	3163
wR_2 [$I > 2\sigma(I)$ on F^2]	0.0585	0.0675
R_1 [$I > 2\sigma(I)$]	0.0251	0.0284
Goodness of fit, s,[b] on F^2	0.926	0.942
Residual density [e Å^{-3}]	0.260/–0.277	0.541/–0.368

[a] $R_1 = (\Sigma||F_o| - |F_c||)/\Sigma|F_o|$; w$R_2 = \{\Sigma[w(F_o^2 - F_c^2)^2]/\Sigma[w(F_o^2)^2]\}^{1/2}$ with $w^{-1} = \sigma^2(F_o^2) + (aP)^2$. [b] $s = \{\Sigma[w(F_o^2 - F_c^2)^2]/(N_o - N_p)\}^{1/2}$.

Acknowledgments

This work was generously supported financially by the German Research Foundation (Deutsche Forschungsgemeinschaft DFG, Bonn/Germany). We also thank Dr. H. Görls for his valuable support.

[1] a) G. Fritz, *Comments Inorg. Chem.* **1982**, *1*, 329–360; b) G. Fritz, *Adv. Inorg. Chem.* **1987**, *31*, 171–214; c) G. Fritz, P. Scheer, *Chem. Rev.* **2000**, *100*, 3341–3401.
[2] W. Levason, C. A. McAuliffe, *Coord. Chem. Rev.* **1976**, *19*, 173–185.
[3] K. Izod, *Adv. Inorg. Chem.* **2000**, *50*, 33–107.
[4] F. Pauer, P. P. Power, in *Lithium Chemistry: A Theoretical and Experimental Overview* (Eds.: A.-M. Sapse, P. von Ragué Schleyer), John Wiley & Sons, New York, **1995**; chapter 9, p. 295–392.
[5] E. Lukevics, O. Pudova, R. Sturkovich, *Molecular Structures of Organosilicon Compounds*, Ellis Horwood, Chichester, **1989**; chapter 3.5, p. 93–171.
[6] K. B. Dillon, F. Mathey, J. F. Nixon: *Phosphorus: A Carbon Copy*, Wiley, Chichester, **1998**.
[7] G. Becker, D. Käshammer, O. Mundt, M. Westerhausen, in *Synthetic Methods of Organometallic and Inorganic Chemistry* (Ed.: H. Karsch), Thieme, Stuttgart, **1996**, vol. 3, p. 189–193.

 © 2005 Wiley-VCH Verlag GmbH & Co. KGaA, Weinheim

[8] G. Becker, B. Eschbach, O. Mundt, M. Reti, E. Niecke, K. Issberner, M. Nieger, V. Thelen, H. Nöth, R. Waldhör, M. Schmidt, *Z. Anorg. Allg. Chem.* **1998**, *624*, 469–482.
[9] G. Becker, G. Gutekunst, H. J. Wessely, *Z. Anorg. Allg. Chem.* **1980**, *462*, 113–129.
[10] G. Becker, C. Witthauer, *Z. Anorg. Allg. Chem.* **1982**, *492*, 28–36.
[11] L. J. Jones, A. T. McPhail, R. L. Wells, *J. Coord. Chem.* **1995**, *34*, 119–127.
[12] G. Becker, H. Freudenblum, O. Mundt, M. Reti, M. Sachs, in *Synthetic Methods of Organometallic and Inorganic Chemistry* (Ed.: H. Karsch), Thieme, Stuttgart, **1996**, vol. 3, p. 193–198.
[13] R. L. Wells, M. F. Self, J. D. Johansen, J. A. Laske, S. R. Aubuchon, L. J. Jones, *Inorg. Synth.* **1997**, *31*, 150–158.
[14] R. A. Baldwin, H. Rahbarnoohi, L. J. Jones, A. T. McPhail, R. L. Wells, P. S. White, A. L. Rheingold, G. P. A. Yap, *Heteroatom Chem.* **1996**, *7*, 409–416.
[15] M. Wieneke, M. Westerhausen, in *Organosilicon Chemistry IV – From Molecules to Materials* (Eds.: N. Auner, J. Weis), Wiley-VCH, Weinheim, **2000**, p. 281–286.
[16] a) M. Driess, K. Merz, C. Monsé, *Z. Anorg. Allg. Chem.* **2000**, *626*, 2264–2268; b) C. v. Hänisch, *Z. Anorg. Allg. Chem.* **2001**, *627*, 1414–1416.
[17] M. Westerhausen, M. Wieneke, W. Schwarz, *J. Organomet. Chem.* **1999**, *572*, 249–257.
[18] M. Driess, R. E. Mulvey, M. Westerhausen, in *Molecular Clusters of the Main Group Elements* (Eds.: M. Driess, H. Nöth), Wiley-VCH, Weinheim, **2004**; chapter 3.6, p. 391–424. See also: C. v. Hänisch, D. Nikolova, *Z. Anorg. Allg. Chem.* **2004**, *630*, 345–346 (see Erratum: ibid. **2004**, *630*, 763) and C. v. Hänisch, B. Rolli, *Z. Anorg. Allg. Chem.* **2002**, *628*, 2255–2258.
[19] a) M. Westerhausen, C. Birg, H. Piotrowski, *Eur. J. Inorg. Chem.* **2000**, 2173–2178; b) M. Westerhausen, C. Birg, H. Piotrowski, T. Habereder, M. Suter, H. Nöth, *Z. Anorg. Allg. Chem.* **2001**, *627*, 882–890.
[20] a) A. Tzschach, G. Pacholke, *Chem. Ber.* **1964**, *97*, 419–425; b) A. Tzschach, W. Deylig, *Z. Anorg. Allg. Chem.* **1965**, *336*, 36–41.
[21] K. Issleib, A. Balszuweit, P. Thorausch, *Z. Anorg. Allg. Chem.* **1977**, *437*, 5–9.
[22] M. A. Beswick, Y. G. Lawson, P. R. Raithby, J. A. Wood, D. S. Wright, *J. Chem. Soc., Dalton Trans.* **1999**, 1921–1922.
[23] M. Westerhausen, S. Weinrich, B. Schmid, S. Schneiderbauer, M. Suter, H. Nöth, H. Piotrowski, *Z. Anorg. Allg. Chem.* **2003**, *629*, 625–633.
[24] a) N. Wiberg, H. Schuster, *Chem. Ber.* **1991**, *124*, 93–95; b) N. Wiberg, A. Wörner, H.-W. Lerner, K. Karaghiosoff, D. Fenske, G. Baum, A. Dransfeld, P. von Ragué Schleyer, *Eur. J. Inorg. Chem.* **1998**, 833–841.
[25] R. A. Jones, S. U. Koschmieder, C. M. Nunn, *Inorg. Chem.* **1987**, *26*, 3610.
[26] G. Becker, H.-M. Hartmann, W. Schwarz, *Z. Anorg. Allg. Chem.* **1988**, *577*, 9–22.
[27] M. Westerhausen, R. Löw, W. Schwarz, *J. Organomet. Chem.* **1996**, *513*, 213–229.
[28] M. Westerhausen, N. Makropoulos, unpublished results.
[29] E. Hey, P. B. Hitchcock, M. F. Lappert, A. K. Rai, *J. Organomet. Chem.* **1987**, *325*, 1–12.
[30] M. Driess, H. Pritzkow, *Z. Anorg. Allg. Chem.* **1996**, *622*, 1524–1530.
[31] R. A. Bartlett, H. V. Rasika Dias, H. Hope, B. D. Murray, M. M. Olmstead, P. P. Power, *J. Am. Chem. Soc.* **1986**, *108*, 6921–6926.
[32] A. M. Arif, R. A. Jones, K. B. Kidd, *J. Chem. Soc., Chem. Commun.* **1986**, 1440–1441.
[33] P. B. Hitchcock, M. F. Lappert, S. J. Smith, *J. Organomet. Chem.* **1987**, *320*, C27–C30.
[34] a) T. Kottke, D. Stalke, *J. Appl. Crystallogr.* **1993**, *26*, 615–619; b) D. Stalke, *Chem. Soc. Rev.* **1998**, *27*, 171–178.
[35] A. Altomare, M. C. Burla, M. Camalli, G. L. Cascarano, C. Giacovazzo, A. Guagliardi, A. G. G. Moliterni, G. Polidori, R. Spagna, *J. Appl. Crystallogr.* **1999**, *32*, 115–119.
[36] G. M. Sheldrick, *SHELXL-93*, University of Göttingen, **1993**; *SHELXL-97*, University of Göttingen, **1997**.
[37] D. T. Cromer, J. B. Mann, *Acta Crystallogr.* **1968**, *24*, 321–324.
[38] R. F. Stewart, E. R. Davidson, W. T. Simpson, *J. Chem. Phys.* **1965**, *42*, 3175–3187.

Received: April 22, 2005
Published Online: September 5, 2005

 © 2005 Wiley-VCH Verlag GmbH & Co. KGaA, Weinheim

Aerosol-Assisted Chemical Vapor Deposition of NbS_2 and TaS_2 Thin Films from Pentakis(dimethylamido)metal Complexes and 2-Methylpropanethiol

Emily S. Peters,[a] Claire J. Carmalt,*[a] Ivan P. Parkin,[a] and Derek A. Tocher[a]

Keywords: Niobium disulfide / Tantalum sulfide / Thin film / Aerosol-assisted CVD

Thin films of NbS_2 and TaS_2 have been produced from $[M(NMe_2)_5]$ (M = Nb, Ta) and *t*BuSH by aerosol-assisted chemical vapor deposition on glass. Gold-colored, reflective films were obtained and deposition took place at 250–350 °C for NbS_2 and 225–450 °C for TaS_2 using dichloromethane or hexanes as solvent. The niobium and tantalum sulfide films were analyzed by Raman spectroscopy, scanning electron microscopy (SEM), X-ray powder diffraction, energy dispersive analysis of X-rays (EDAX) and X-ray photoelectron spectroscopy (XPS). In order to identify possible compounds present in the aerosol mist, the solution phase reaction of $[M(NMe_2)_5]$ and five equivalents of *t*BuSH in toluene at room temperature was carried out. Yellow crystals of the partially substituted tantalum thiolate $[Ta(S\text{-}tBu)_2(NMe_2)_3]$ were isolated. The X-ray structure of $[Ta(S\text{-}tBu)_2(NMe_2)_3]$ has been determined.
(© Wiley-VCH Verlag GmbH & Co. KGaA, 69451 Weinheim, Germany, 2005)

The layered transition-metal dichalcogenides, which include tantalum disulfide and niobium disulfide, exhibit a number of interesting properties as a result of their structure. Thus, the layered structure has resulted in transition-metal dichalcogenides having diverse applications, such as high-temperature lubricants, catalysts and also in photovoltaic cells.[1–3] Tantalum disulfide in particular has been tested for use in lithium ion batteries, while NbS_2 has been shown to be an effective humidity sensor, in addition to uses as a catalyst in hydrotreating petroleum cuts.[4–9] These applications require a high surface area for optimum performance suggesting that thin film formation would be favorable. However, there are only limited reports of thin film formation of either NbS_2 or TaS_2.[3,10–15]

Physical deposition of NbS_2 films has been achieved by dipping the substrate into a NbS_2 powder layer, lying at the interface between water and an organic solvent.[5,10] This produced films with the basal planes parallel to the substrate's surface. Chemical vapor deposition (CVD) from single-source precursors of the form $[NbCl_4(S_2R_2)_2][NbCl_6]$ [R = CH_3 or $CH(CH_3)_2$] produced mixed NbS_2/Nb_2O_5 films.[11] However, the films formed were very thin (≤1000 Å) due to insufficient volatility of the precursors. Niobium monosulfide (NbS) films were deposited by low-pressure CVD from the homoleptic niobium thiolate $[Nb(SC_6H_3Me_2\text{-}2,6)_5]$.[12] We have recently reported the formation of NbS_2 films by atmospheric pressure CVD from the reaction of $NbCl_5$ with a range of sulfur precursors.[13] It was found that reaction of $NbCl_5$ with sulfides $[S(SiMe_3)_2$ or $tBu_2S_2]$ produced a new 1T-NbS_2 polytype. Conversely, reaction of $NbCl_5$ with thiols [*t*BuSH or $HS(CH_2)_2SH$] produced the known 3R-NbS_2 polytype. Reports of TaS_2 films have been limited to physical deposition routes.[14,15]

To the best of our knowledge, this paper represents the first thin film growth of TaS_2 by CVD and a novel aerosol-assisted (AA)CVD route to MS_2 (M = Nb, Ta) from $[M(NMe_2)_5]$ and *t*BuSH. Different and unique morphologies of films can be obtained by AACVD due to the influence of the solvent on the deposition, which could potentially lead to improved properties. Furthermore, thin films can be deposited under AACVD conditions at low temperatures and require only minimal amounts of precursor (ca. 0.1 g). In this study, niobium and tantalum thiolates were generated in situ from the reaction of $[M(NMe_2)_5]$ and *t*BuSH in hexanes or dichloromethane. An aerosol of this reaction mixture was then passed over a heated glass substrate, which resulted in the deposition of thin films of niobium and tantalum sulfide. The synthesis and crystal structure of the tantalum thiolate precursor $[Ta(S\text{-}tBu)_2(NMe_2)_3]$, prepared from the solution phase reaction of $[Ta(NMe_2)_5]$ and *t*BuSH, is also reported. Previous reports of the reaction of transition-metal amides with thiols suggest that complete substitution of the amide ligands is not achieved.[16,17] For example, the reaction of $[Ta(NMe_2)_5]$ with an excess of 2,6-dimethylthiophenol resulted in the substitution of four thiolate ligands forming $[Ta(SC_6H_3Me_2\text{-}2,6)_4(NMe_2)]$.[17]

Results and Discussion

Aerosol-Assisted Chemical Vapor Deposition

Gold-colored, reflective films have been deposited on glass from the dual-source AACVD reaction of

[a] Department of Chemistry, University College London, 20 Gordon Street, London, WC1H 0AJ, UK
E-mail: c.j.carmalt@ucl.ac.uk

 DOI: 10.1002/ejic.200500400 © 2005 Wiley-VCH Verlag GmbH & Co. KGaA, Weinheim

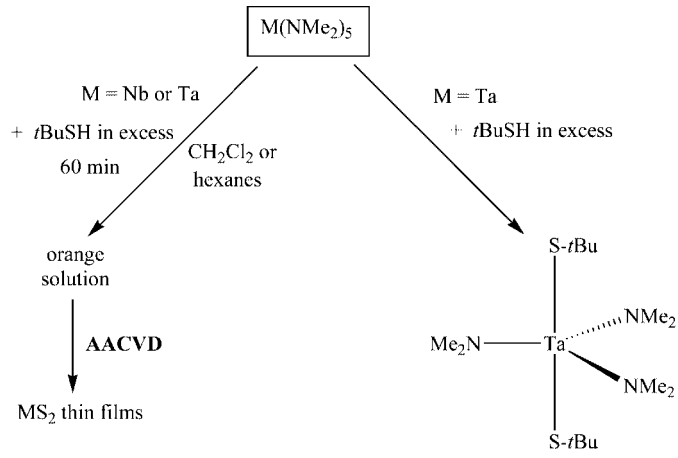

Scheme 1.

$[M(NMe_2)_5]$ (M = Nb, Ta) and *t*BuSH (Scheme 1). The reaction of $[M(NMe_2)_5]$ (M = Nb, Ta) and excess *t*BuSH in hexanes or dichloromethane was assumed to generate in situ the homoleptic metal thiolate, $[M(S\text{-}tBu)_5]$. However, solution phase studies (vida supra) indicate that this reaction could be incomplete and the bubbler would probably comprise of a mixture of $[M(S\text{-}tBu)_x(NMe_2)_{5-x}]$ (x = 0–5). Deposition was observed on both the top plate and the substrate due to larger particles formed by gas phase nucleation being unable to diffuse through the boundary layer at the substrate surface. However, the films deposited on the top plate correspond to those on the substrate but at a lower (50–75 °C) temperature (as measured). Niobium sulfide films were deposited between 250 and 350 °C and tantalum sulfide films were deposited between 225 and 450 °C (Table 1). The films deposited at the higher temperatures were localized towards the front of the substrate, which is an effect of fast film-growth kinetics. As the temperature was reduced complete substrate coverage was achieved. The gold color of the films is consistent with NbS_2 films grown by dual-source CVD routes at atmospheric pressure.[13] The films were adherent to the substrate, passing the Scotch Tape test. However, they were readily scratched by a brass or stainless steel stylus. The films remained unchanged after immersion in toluene, dichloromethane, THF, ether or acetonitrile for 1 month. The tantalum sulfide films were also unchanged by immersion in HCl for 1 month although the niobium sulfide films dissolved after one day. However, the niobium and tantalum sulfide films dissolved within minutes on immersion in HNO_3.

The reflectance and transmission spectra indicated that the gold-colored niobium sulfide films had good reflectance and minimal transmission (approx. 5%) in the region 400–1000 nm. The reflectance was fairly low in the visible region (approx. 15–20%) but increased to approx. 35% in the IR region. Four-point probe measurements suggest that the niobium sulfide films are metallic conductors at room temperature, as expected. Accurate readings could not be obtained as the films were scratched by the probe causing the reading to fluctuate. The tantalum sulfide films did not transmit at any wavelength and had a low reflectance (max. 15%).

Table 1. Deposition conditions and analysis of the films grown from the AACVD of $[M(NMe_2)_5]$ (M = Nb, Ta) and *t*BuSH.

Precursors	T [°C]	Solvent	EDXA
$Nb(NMe_2)_5$/*t*BuSH	350	dichloromethane	$NbS_{2.0}$
$Nb(NMe_2)_5$/*t*BuSH	300	dichloromethane	$NbS_{1.9}$
$Nb(NMe_2)_5$/*t*BuSH	250	dichloromethane	$NbS_{1.8}$
$Nb(NMe_2)_5$/*t*BuSH	300	hexanes	$NbS_{1.9}$
$Nb(NMe_2)_5$/*t*BuSH	250	hexanes	$NbS_{1.6}$
$Ta(NMe_2)_5$/*t*BuSH	450	dichloromethane	$TaS_{2.1}$
$Ta(NMe_2)_5$/*t*BuSH	350	dichloromethane	$TaS_{1.6}$
$Ta(NMe_2)_5$/*t*BuSH	450	hexanes	$TaS_{2.0}$
$Ta(NMe_2)_5$/*t*BuSH	400	hexanes	$TaS_{2.1}$
$Ta(NMe_2)_5$/*t*BuSH	350	hexanes	$TaS_{1.9}$
$Ta(NMe_2)_5$/*t*BuSH	300	hexanes	$TaS_{2.1}$
$Ta(NMe_2)_5$/*t*BuSH	250	hexanes	$TaS_{2.1}$
$Ta(NMe_2)_5$/*t*BuSH	225	hexanes	$TaS_{2.0}$

The niobium and tantalum sulfide films were characterized using a range of techniques. EDAX analysis shows the films are homogeneous and have a metal to sulfur ratio close to 1:2 over a number of spots (Table 2). The deviations from the MS_2 stoichiometry occurred primarily for the films deposited at lower temperatures, which were thinner meaning that a significant amount of the underlying glass was incorporated in the quantification. XPS of the niobium peaks in the NbS_2 films show that there is a single niobium environment with binding energies of 207.9 and 210.7 eV for $3d_{5/2}$ and $3d_{3/2}$, respectively. This matches well with the previously reported $3d_{5/2}$ value of 207.7 eV for bulk NbS_2.[19] However, ca. 2 atom-% nitrogen contamination was found by XPS in the films suggesting that complete reaction of the niobium amide with thiol to afford the homoleptic niobium thiolate had not occurred. Carbon and oxygen were found on the surface of the films by XPS, but these were removed by sputtering to leave the bulk of the film consisting of niobium and sulfur. The XPS of the tantalum in the TaS_2 films gave peaks at 23.5 and 25.4 eV corresponding to Ta $4f_{7/2}$ and $4f_{5/2}$ (Figure 1), which match well with published values for TaS_2 ($4f_{7/2}$, 23.8 eV; $4f_{5/2}$,

 © 2005 Wiley-VCH Verlag GmbH & Co. KGaA, Weinheim

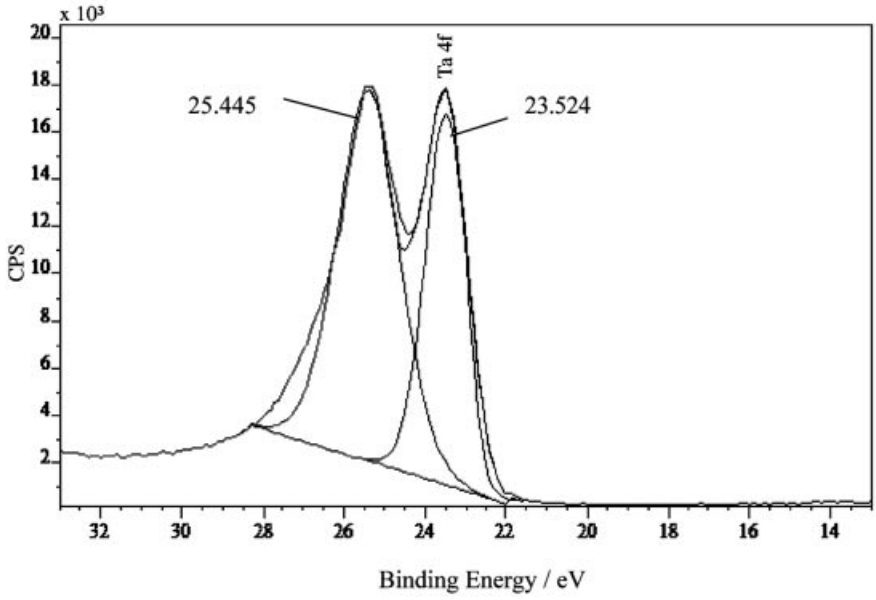

Figure 1. XPS of the Ta 4f peaks from a film deposited by AACVD from the in situ reaction of $[Ta(NMe_2)_5]$ and *t*BuSH at 450 °C.

25.7 eV).[20] Again, carbon and oxygen were found on the surface of the films by XPS but these were removed by sputtering to leave the bulk of the film comprised of tantalum and sulfur. The XPS of the TaS_2 films shows that there is also only one sulfur environment present with binding energies of 161.3 and 162.5 eV, corresponding to S $2p_{3/2}$ and $2p_{1/2}$, respectively.

All the films deposited were amorphous to X-rays even at the highest deposition temperatures. In comparison, NbS_2 films grown at 350–600 °C by atmospheric-pressure CVD from $NbCl_5$ and *t*BuSH were nanocrystalline; films deposited below 350 °C were amorphous.[13] The Raman pattern obtained for the NbS_2 films formed in this study (AACVD of $[Nb(NMe_2)_5]$/*t*BuSH) had a series of poorly separated peaks between 191 and 320 cm^{-1}, in addition to a peak at 543 cm^{-1} (Figure 2). The pattern is similar to that reported previously for 2H-NbS_2.[21] The Raman pattern obtained for the TaS_2 films had a large peak between 233 and 301 cm^{-1} and a second broad peak at 365 cm^{-1}. This Raman pattern does not correspond with any reported for TaS_2. However, the Raman pattern is similar to that obtained for 3R-NbS_2, suggesting that the 3R-TaS_2 polytype has been formed. Furthermore, Raman spectroscopy of the niobium and tantalum disulfide films indicated the absence of graphitic carbon in the films despite the use of a carbon-containing solvent being used to create the aerosol.

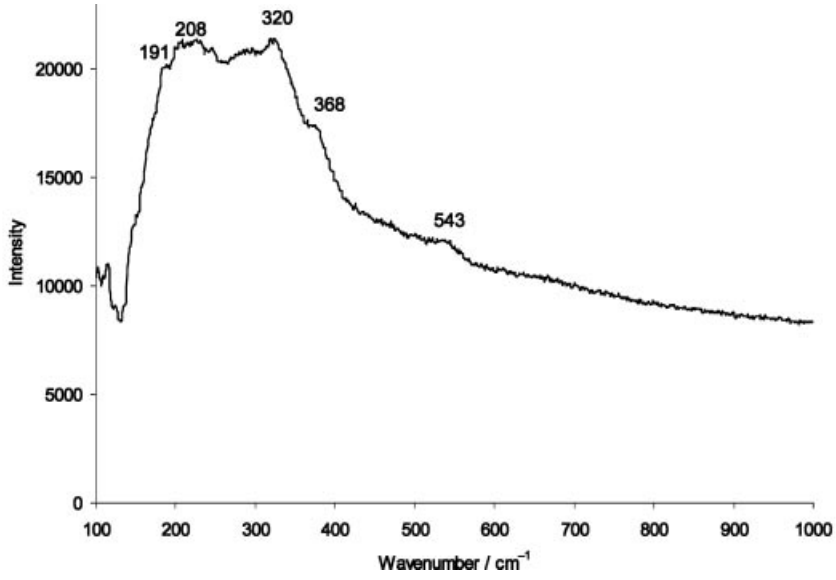

Figure 2. Raman pattern obtained for the film formed on glass from the AACVD reaction of $[Nb(NMe_2)_5]$ and *t*BuSH in dichloromethane at 300 °C.

 © 2005 Wiley-VCH Verlag GmbH & Co. KGaA, Weinheim

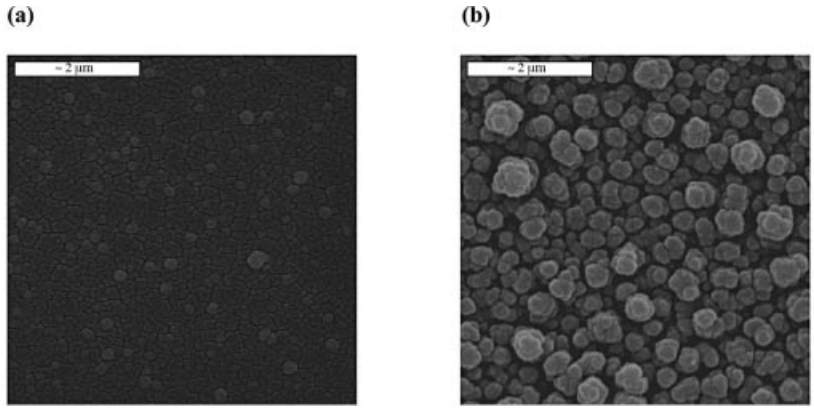

Figure 3. SEM images for films deposited by AACVD from the in situ reaction of $[Nb(NMe_2)_5]$ and *t*BuSH (**a**) in hexanes at 250 °C and (**b**) in dichloromethane at 350 °C.

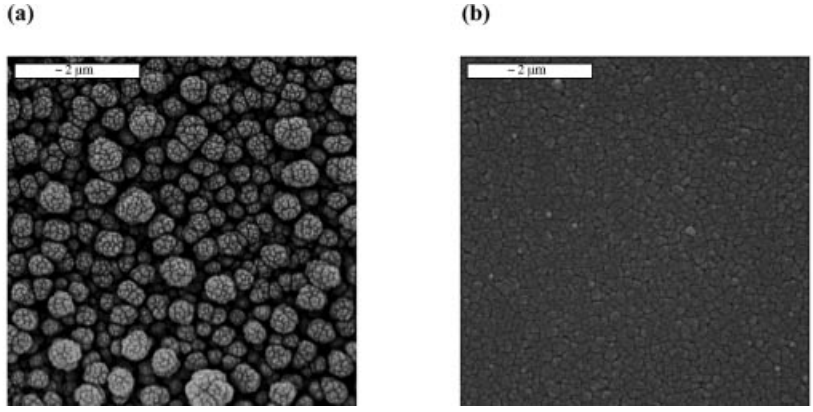

Figure 4. SEM images for films deposited by AACVD at 350 °C from the in situ reaction of $[Ta(NMe_2)_5]$ and *t*BuSH in (**a**) hexanes and (**b**) dichloromethane.

The film morphology was studied using SEM, which showed that the NbS_2 and TaS_2 films grew by an island growth-type mechanism. Individual clusters are clearly visible in the NbS_2 images with cluster size of 0.6 μm and 0.4 μm for films deposited from dichloromethane and hexanes, respectively (Figure 3). The NbS_2 films deposited from hexanes were more uniform than when dichloromethane was used as the solvent. However, the reverse was observed for TaS_2, with films deposited from dichloromethane being more uniform with clusters of 0.4 μm in diameter in comparison with those using hexanes, which had a diameter of 0.8 μm (Figure 4).

The successful formation of NbS_2 and TaS_2 thin films from the in situ AACVD reaction of $[M(NMe_2)_5]$ and *t*BuSH indicates that there is no need to prepare, isolate and purify a metal thiolate single-source precursor, such as $[M(S\text{-}tBu)_5]$. The use of excess *t*BuSH in the AACVD reactions resulted in little oxygen contamination and pre-treating the coater led to more adherent and uniform films. The mechanism for the deposition process was not investigated. However, the decomposition of $[Ti(S\text{-}tBu)_4]$ to TiS_2 has been described previously, and it is likely that the formation of MS_2 (M = Nb, Ta) films described herein would follow a similar mechanism.[22] Thus, the byproducts formed during the deposition of TiS_2 from $[Ti(S\text{-}tBu)_4]$ were principally isobutylene and *tert*-butyl thioalcohol, along with smaller amounts of isobutene, di-*tert*-butyl disulfide, H_2S and di-*tert*-butyl sulfide. The formation of these byproducts was thought to be the result of both β-hydrogen abstraction and a proton-transfer mechanism.[22] In the absence of a sulfur precursor, $[M(NMe_2)_5]$ produces amorphous metal carbonitride coatings.[23] Therefore, the decomposition of $[M(NMe_2)_5]$ can be considered to be the baseline in terms of the coating produced. The reaction of *t*BuSH with $[M(NMe_2)_5]$ results in facile elimination of Me_2NH either via gas phase or surface reactions, due to the presence of the acidic hydrogen in *tert*-butyl thiol. Notably the coatings produced from these reactions contained minimal nitrogen incorporation and even at low substrate temperatures formed MS_2 films with no MN_xC_y incorporation. We attribute this to the fact that the decomposition of $[M(NMe_2)_5]$ is slower than its reaction with *tert*-butyl thiol.

Synthesis

In order to gain an insight into compounds present in the aerosol mist of the AACVD reactions described above, the reaction of $[Ta(NMe_2)_5]$ with five equivalents of *t*BuSH was carried out in toluene at room temperature. An immediate color change from pale yellow to bright orange occurred. After work-up a dark orange oil resulted, which

 © 2005 Wiley-VCH Verlag GmbH & Co. KGaA, Weinheim

produced large yellow crystals, on cooling a concentrated dichloromethane solution to –20 °C, in a 47% yield. $^1H/^{13}C$ NMR spectroscopic data obtained from solutions of these crystals were consistent with the formation of the neutral species $[Ta(S\text{-}tBu)_2(NMe_2)_3]$ (Scheme 1). The structure of $[Ta(S\text{-}tBu)_2(NMe_2)_3]$ was confirmed by X-ray crystallography, the results of which are shown in Figure 5. Selected bond lengths and angles are detailed in Table 2. The structure of $[Ta(S\text{-}tBu)_2(NMe_2)_3]$ is monoclinic and crystallizes in the *C*2/*c* space group with the metal on a twofold axis. The tantalum centre in $[Ta(S\text{-}tBu)_2(NMe_2)_3]$ adopts a distorted trigonal bipyramidal geometry with a S–Ta–S bond angle of 166°. Therefore, the two thiolate ligands take up axial positions, with the equatorial sites occupied by the three NMe_2 groups. The Ta–S bonds are 2.47 Å in length and are comparable to those in the reported tantalum thiolate $[Ta(S\text{–}2,6\text{-}Me_2C_6H_3)_4(NMe_2)]$ (2.39–2.43 Å).[17] Ta–N bonds lengths are in the range 1.94–1.97 Å and again compare well with those in $[Ta(S\text{-}2,6\text{-}Me_2C_6H_3)_4(NMe_2)]$ (1.92 Å). The formation of $[Ta(S\text{-}tBu)_2(NMe_2)_3]$ suggests that in the AACVD reaction a mixture of $[M(S\text{-}tBu)_x(NMe_2)_{5-x}]$ (x = 0–5) may be present. However, it is worth noting that a larger excess of thiol is present in the AACVD reaction and so the formation of the homoleptic metal thiolate is possible.

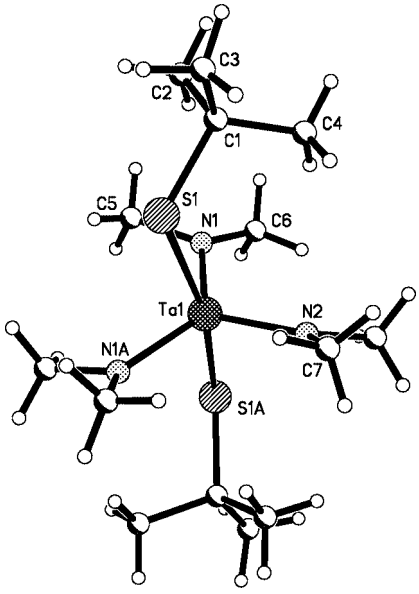

Figure 5. The molecular structure of $[Ta(S\text{-}tBu)_2(NMe_2)_3]$.

Table 2. Selected bond lengths [Å] and angles [°] for $[Ta(S\text{-}tBu)_2(NMe_2)_3]$.

Ta(1)–N(2)	1.939(9)	Ta(1)–S(1)	2.4698(19)
Ta(1)–N(1)	1.968(7)		
N(2)–Ta(1)–N(1)	116.0(2)	N(1A)–Ta(1)–N(1)	128.1(4)
N(2)–Ta(1)–S(1)	96.88(5)	N(1A)–Ta(1)–S(1)	80.4(2)
N(1)–Ta(1)–S(1)	93.5(2)	S(1)–Ta(1)–S(1A)	166.24(10)

Further evidence for the formation of a mixture of complexes in the AACVD reaction was obtained from the reaction of $[Nb(NMe_2)_5]$ with five equivalents of *t*BuSH in toluene at room temperature. After work-up a red/brown oil resulted which was shown by ^1H and ^{13}C NMR to consist of a mixture of products. Thus, in the ^1H NMR of the red/brown oil a number of peaks were observed for each proton environment (*t*Bu, NMe_2) suggesting the formation of a mixture of products of the type $[Nb(S\text{-}tBu)_x(NMe_2)_{5-x}]$ (x = 0–5). The formation of $[Nb(S\text{-}tBu)_x(NMe_2)_{5-x}]$ is in agreement with previous reports of the reaction which suggest that complete substitution of the metal amide ligands by thiolate groups is not achieved.[16,17] Attempts to purify the red/brown oil by recrystallization and distillation were unsuccessful.

Conclusions

Thin films of NbS_2 and TaS_2 can be grown from $[M(NMe_2)_5]$ and *t*BuSH under AACVD conditions. This represents the first deposition of TaS_2 by CVD and the first AACVD formation of NbS_2 and TaS_2 films. Furthermore, the in situ reaction of $[M(NMe_2)_5]$ and *t*BuSH eliminates the need for the synthesis, isolation and purification of a single-source metal thiolate precursor. The solution phase reaction of $[Ta(NMe_2)_5]$ and *t*BuSH resulted in the isolation of $[Ta(S\text{-}tBu)_2(NMe_2)_3]$, which has been structurally characterized. The formation of $[Ta(S\text{-}tBu)_2(NMe_2)_3]$ suggests that a mixture of species of the type $[M(S\text{-}tBu)_x(NMe_2)_{5-x}]$ may be present in the aerosol bubbler. However, due to the large excess of thiol present in the AACVD reactor, it is possible that the homoleptic metal thiolate forms in solution.

Experimental Section

Depositions were carried out under dinitrogen (99.99% from BOC). Precursors were placed in a round-bottomed glass bubbler and a mist was created using a PIFCO HEALTH ultrasonic humidifier (product no. 1077). The solvent mist was transported in a flow of cold nitrogen from the bubbler in an 8-mm gauge pipe to a mixing chamber and then to a horizontal bed, cold-wall reactor with a carbon-heating block containing two Whatman cartridge heaters. Aerosol droplet sizes were calculated to be 50–60 μm.[18] A top plate was suspended 0.5 cm above the glass substrate to ensure a laminar flow. Films were deposited on pieces of 150 mm × 47 mm × 4 mm SiCO-coated float glass (SiCO is a coating containing Si, O and C. It is an effective blocking layer that prevents diffusion of ions in the glass into the coating). The transition metal thiolate complex was generated in situ from the reaction of $[M(NMe_2)_5]$ with excess *t*BuSH (0.3 g $[M(NMe_2)_5]$, M = Ta (0.74 mmol), Nb (0.96 mmol), *t*BuSH 1.0 mL, 8.87 mmol) in solvent (80 mL). Pentakis(dimethylamido)tantalum $[Ta(NMe_2)_5]$ was supplied by Epichem Ltd. and used without further purification, $[Nb(NMe_2)_5]$ was prepared using literature procedures.[16] *t*BuSH was purchased from Aldrich, dried with molecular sieves and degassed. Excess thiol was used in order to minimize the risk of producing partially oxidized films. The reagents were left to react for 1 h prior to the start of each deposition. The *t*BuSH was placed in solvent (60 mL) and the coater was pre-treated with the thiol (1.0 mL) for 20 minutes prior to deposition. Depositions were carried out in either dichloromethane or hexanes at a flow rate of 1.0 $Lmin^{-1}$ over a range of substrate temperatures (225–450 °C).

 © 2005 Wiley-VCH Verlag GmbH & Co. KGaA, Weinheim

Dichloromethane was distilled from CaH_2 prior to use; hexanes and toluene were dried using sodium/benzophenone. The experiment was contained in a fume cupboard and the exhaust gases passed through three bleach bubblers. At the end of the deposition the bubbler line was closed and nitrogen was passed over the substrate. The glass substrate was cooled to ca. 60 °C before it was removed. The substrates were cut into ca. 4 cm × 1 cm strips for analysis by SEM, XPS, Raman and UV studies. 3 cm × 2 cm strips were used for X-ray diffraction. Film adherence to the glass was assessed using the Scotch tape test and by scratching the surface using brass and steel.

X-ray powder diffraction patterns were measured with a Siemens D5000 diffractometer using monochromated Cu-$K_{\alpha1}$ radiation (λ_1 = 1.5406 Å). The diffractometer used glancing incident radiation (1.5°). EDXA was obtained with a JOEL 35CF and SEM was obtained with a Hitachi S570 instrument using the KEVEX system. X-ray photoelectron spectra were recorded using a VG ESCALAB 220i XL instrument using focused (300 μm spot) monochromatic Al-K_α radiation at a pass energy of 20 eV. Scans were acquired with steps of 50 meV. A flood gun was used to control charging and the binding energies were referenced to an adventitious C 1s peak at 284.8 eV. Depth profile measurements were obtained by using argon beam sputtering. Reflectance and transmission spectra were recorded between 300 and 1200 nm by a Zeiss minature spectrometer. Reflectance measurements were standardized relative to a rhodium mirror and transmission relative to air. Raman spectra were acquired with a Renishaw Raman System 1000 using a helium-neon laser of wavelength 632.8 nm. The Raman system was calibrated against the emission lines of neon. NMR spectra were recorded with a Bruker AMX400 spectrometer at UCL, referenced to CD_2Cl_2, which was dried and degassed over molecular sieves prior to use. ^1H and ^{13}C chemical shifts are reported relative to $SiMe_4$ (δ, 0.00). Single-crystal X-ray data were collected with a Bruker SMART APEX CCD diffractometer.

AACVD Reaction of [Nb(NMe$_2$)$_5$] and *t*BuSH: *t*BuSH (1.0 mL, 8.87 mmol) was placed in 60 mL of solvent in the AACVD bubbler and used to pre-treat the reactor for 5 min before the addition of the niobium precursor. After pre-treating the reactor, [Nb(NMe$_2$)$_5$] (0.3 g, 0.96 mmol) in 15 mL of solvent was added to the bubbler. An orange solution formed immediately, and the mixture was reacted for 60 minutes before each deposition was started.

AACVD reaction of [Ta(NMe$_2$)$_5$] and *t*BuSH: The experimental procedure was the same as for the AACVD reaction of [Nb(NMe$_2$)$_5$] and *t*BuSH but [Ta(NMe$_2$)$_5$] (0.3 g, 0.74 mmol) was used in place of [Nb(NMe$_2$)$_5$].

Reaction of [Nb(NMe$_2$)$_5$] and *t*BuSH: 2-Methylpropanethiol (0.4 mL, 1.60 mmol) was added to a stirred solution of [Nb(NMe$_2$)$_5$] (0.2 g, 0.64 mmol) in toluene (30 mL). An immediate color change from pale orange to deep red occurred on addition of the thiol. Stirring was continued for 4 h and the solution was concentrated in vacuo to give a dark red/brown oil. ^1H NMR (CD_2Cl_2): δ = 1.2 [s, (CH_3)$_3$CS], 1.3 [s, (CH_3)$_3$CS], 1.4 [s, (CH_3)$_3$CS], 1.6 [s, (CH$_3$)$_3$CS*H*], 3.45 (s, N*Me*$_2$), 3.55 (s, N*Me*$_2$) ppm. $^{13}C\{^1H\}$ NMR (CD_2Cl_2): δ = 30.7 [(*C*H$_3$)$_3$CS], 31.7 [(*C*H$_3$)$_3$CS], 34.6 [(CH$_3$)$_3$CSH], 35.0 [(CH$_3$)$_3$*C*S], 35.7 [(*C*H$_3$)$_3$CS], 49.0 (s, N*Me*$_2$), 50.6 (s, N*Me*$_2$) ppm.

Synthesis of [Ta(S-*t*Bu)$_2$(NMe$_2$)$_3$]: 2-Methylpropanethiol (0.14 mL, 1.25 mmol) was added to a stirred solution of [Ta(NMe$_2$)$_5$] (0.1 g, 0.25 mmol) in toluene (20 mL). Stirring was continued for 16 h resulting in a dark orange solution. The solvent was removed in vacuo to give an orange-brown oil. This oil was redissolved in ca. 2 mL of hexanes and cooled to –20 °C. Large, rectangular, pale yellow crystals (0.06 g, 47%) suitable for X-ray analysis were formed. ^1H NMR (CD_2Cl_2): δ = 1.25 [s, 18 H, (CH_3)$_3$CS], 3.45 (s, 18 H, N*Me*$_2$) ppm. $^{13}C\{^1H\}$ NMR (CD_2Cl_2): δ = 36.0 [(*C*H$_3$)$_3$CS], 42.0 [(CH$_3$)$_3$*C*S], 47.3 (N*Me*$_2$) ppm. $C_{14}H_{36}N_3TaS_2$ (491): calcd. C 34.2, H 7.38, N 8.55; found C 34.1, H 7.5, N 8.1. M.p. 105 °C.

Caution: It should be noted that the AACVD reaction of [M(NMe$_2$)$_2$] (M = Nb, Ta) and *t*BuSH could conceivably produce H_2S. Care should be taken to conduct all experiments in a fume cupboard.

X-ray Crystallography: Crystals of [Ta(S-*t*Bu)$_2$(NMe$_2$)$_3$] were grown from hexanes at –20 °C. Yellow rectangular crystals 0.50 × 0.50 × 0.10 mm, M_r = 491.53, monoclinic, *C*2/*c*, *a* = 10.2460(14), *b* = 15.052(2), *c* = 13.2966(18) Å, β = 92.855(2)°, *V* = 2048.1(5) Å^3, ρ(calcd.) = 1.594 g cm^{-3}, *Z* = 4, Mo-K_α (λ = 0.71073 Å), 150 K, 7531 reflections measured, 2376 independent, μ(Mo-K_α) = 5.567 mm^{-1}, T_{max} –0.600, T_{min} = 0.1673, structure solved by direct methods (SHELXS) and refined on F^2 (SHELXL97), 98 parameters, all non-hydrogen atoms anisotropic, hydrogen atoms refined with riding model, R = 0.0578, wR_2 = 0.1376 (all data), R = 0.0551, wR_2 = 0.1353 [$I > 2\sigma(I)$], largest residual 3.6 e Å^3, close to the metal atom.

CCDC-256491 contains the supplementary crystallographic data for this paper. These data can be obtained free of charge from The Cambridge Crystallographic Data Centre via www.ccdc.cam.ac.uk/data_request/cif.

Acknowledgments

I. P. P. thanks the EPSRC for grant GR/M82592 for purchase of the Renishaw Raman microscope. E. S. P. thanks the EPSRC for a studentship. Epichem Ltd. is thanked for supplying [Ta(NMe$_2$)$_5$].

[1] S. Whittingham, *Prog. Solid State Chem.* **1978**, *12*, 41.
[2] K. Ellmer, C. Stock, K. Diesner, I. Sieber, *J. Cryst. Growth* **1997**, *182*, 389.
[3] M. Regula, C. Ballif, J. H. Moser, F. Levy, *Thin Solid Films* **1995**, *289*, 67.
[4] L. Hernan, J. Morales, L. Sánchez, J. L. Tirado, *Electrochim. Acta* **1994**, *39*, 2665.
[5] W. M. R. Divigalpitiya, R. F. Frindt, S. R. Morrison, *J. Phys. D: Appl. Phys.* **1990**, *23*, 966.
[6] C. Geantet, J. Afonso, M. Breyesse, N. Allali, M. Danot, *Catal. Today* **1996**, *28*, 23.
[7] V. Gaborit, N. Allali, C. Geantet, M. Breysse, M. Vrinat, M. Danot, *Catal. Today* **2000**, *57*, 267.
[8] P. Afanasiev, L. Fischer, F. Beauchesne, M. Danot, V. Gaborit, M. Breysse, *Catal. Lett.* **2000**, *64*, 59.
[9] N. Allali, E. Prouzet, A. Michalowicz, V. Gaborit, A. Nadiri, M. Danot, *Appl. Catal. A* **1997**, *159*, 333.
[10] W. M. R. Divigalpitya, R. F. Frindt, S. R. Morrison, *Science* **1989**, *246*, 369.
[11] P. J. McKarns, M. J. Heeg, C. H. Winter, *Inorg. Chem.* **1998**, *37*, 4743.
[12] C. J. Carmalt, C. W. Dinnage, I. P. Parkin, A. J. P. White, D. J. Williams, *Inorg. Chem.* **2002**, *41*, 3668.
[13] C. J. Carmalt, T. D. Manning, I. P. Parkin, E. S. Peters, A. L. Hector, *J. Mater. Chem.* **2004**, *14*, 290.
[14] T. Shimada, F. S. Ohuchi, A. Koma, *Surf. Sci.* **1993**, *291*, 57.
[15] H. Enomoto, T. Kawano, M. Kawaguchi, Y. Takano, K. Sekizawa, *Jpn. J. Appl. Phys. Lett.* **2004**, *43*, L123.
[16] D. C. Bradley, P. A. Hammersley, *J. Chem. Soc. (A)* **1967**, 1894.
[17] C. J. Carmalt, C. W. Dinnage, I. P. Parkin, A. J. P. White, D. J. Williams, *J. Chem. Soc. Dalton Trans.* **2001**, 2554.

 © 2005 Wiley-VCH Verlag GmbH & Co. KGaA, Weinheim

[18] R. J. Lang, *J. Acoustical Soc. Am.* **1962**, *34*, 6.
[19] G. E. McGuire, G. K. Schweitzer, T. A. Carlson, *Inorg. Chem.* **1973**, *12*, 2451.
[20] K. Dartigeas, L. Benoist, D. Gonbeau, G. Pfister-Guillouzo, G. Ouvrard, A. Levasseur, *J. Electron Spectrosc. Relat. Phenom.* **1997**, *83*, 45.
[21] W. G. McMullan, J. C. Irwin, *Solid State Commun.* **1983**, *45*, 557.
[22] J. Cheon, J. E. Gozum, G. S. Girolami, *Chem. Mater.* **1997**, *9*, 1847.
[23] R. Fix, R. Gordon, D. M. Hoffman, *Chem. Mater.* **1990**, *2*, 235.

Received: May 4, 2005
Published Online: September 9, 2005

 © 2005 Wiley-VCH Verlag GmbH & Co. KGaA, Weinheim

A Stable Trinuclear Zinc Cluster Assembled from a Thiazolylazo Dye and Zinc Acetate: Preparation, Structural Characterization and Spectroscopic Studies

Guoqi Zhang,[a] Shuangqing Wang,[a] Quan Gan,[a] Yongfang Zhang,[a] Guoqiang Yang,*[a] Jin Shi Ma,[a] and Huijun Xu[a]

Keywords: Azo compounds / Pi interactions / UV/Vis spectroscopy / Zinc

A thiazolylazo dye, 5-(diethylamino)-2-(2-thiazolylazo)phenol (H**L**), containing potential tridentate binding sites was synthesized in high yield and well characterized. In solution, the reaction of zinc acetate and the deprotonated ligand, $\mathbf{L}^-$, results in the instantaneous formation of the supramolecular trinuclear species $[Zn_3\mathbf{L}_2(OAc)_4]$ (**1**). UV/Vis and ^{1}H NMR spectroscopic titration experiments in solution confirmed that the ligand and zinc salt interact spontaneously with each other and produce exclusively the polymetallic complex with the metal-to-ligand ratio of 3:2. The crystal structures of both the ligand and coordination complex are reported in this paper. The aromatic part of H**L** is planar and, significantly, the intermolecular C–H···π hydrogen bonds and thiazo ring-S···π weak interactions observed here should be responsible for the orthorhombic space group $P2_12_12_1$. The structure of **1** reveals a linear trinuclear zinc cluster. The two $\mathbf{L}^-$ units are linked to three zinc atoms in an N_2O tridentate mode, and the four acetate anions are chelated to three metal centers as bridges to result in two pentacoordinate and one hexacoordinate zinc centers. The resulting bridging Zn1–Zn2–Zn1A array is linear by symmetry, with a nonbonding Zn···Zn distance of 3.390 Å and a Zn1···Zn2···Zn1A angle of 180.0°.
(© Wiley-VCH Verlag GmbH & Co. KGaA, 69451 Weinheim, Germany, 2005)

Introduction

Aromatic azo derivatives are widely used in the dyestuff industry, in analytical chemistry as acid-base, redox, and metallochromic indicators,[1,2] and also, more recently, in the field of optical data storage and nonlinear optics.[3,4] The structure of azo dyes has also attracted considerable attention over the years in view of their wide applicability as optical materials.[5,6] While numerous publications have focused on the industrial applications of azo dyes, the structural characterization and studies of the metal-chelating properties of substituted azo compounds remain sparse in the literature.[7–9]

Metal-chelating azo derivatives are considered to be some of the most promising optical materials.[8,9] Coordination of transition metals to aromatic azo dyes not only results in a rich variety of supramolecular structures, but also in a significant enhancement of their nonlinearity, both of which are potentially useful in a wide range of optical devices. Hence, it is greatly promising to develop new functionalized azo-metal chelates. Goswami and co-workers have systematically studied metal coordination compounds of one class of pyridine-containing phenylazo ligands.[10] Divalent transition metals such as Zn^{II}, Cd^{II}, Hg^{II}, Ni^{II}, Pd^{II}, and Pt^{II}, or trivalent metals like Cr^{III}, In^{III}, etc., have been widely used to coordinate to the azo ligands. Accordingly, mononuclear or binuclear metallized azo complexes were obtained depending on the different nature of the metal ions. Their crystal structures, reactivity, and optical properties have also been investigated in detail.[10]

Recently, we became interested in the investigation of a new class of azo derivative, namely 5-(diethylamino)-2-(2-thiazolylazo)phenol (H**L**), and its transition metal chelates (Scheme 1).[8] The azo compound H**L** has several coordination sites and displays versatile chelating properties toward transition metal ions. The spectroscopic properties and third-order nonlinearity of certain transition metal complexes of H**L** have been investigated very recently. These results showed that the third-order nonlinearity is remarkably enhanced and size-tunable in nanoparticles of a nickel(II) complex of H**L**.[8e]

Inspired by these interesting results on the nonlinearity and optical spectroscopic properties of this class of metallized thiazolylazo dyes as optical recording materials, we report here the synthetic procedure, solution properties, and structural characterization of the azo ligand H**L** and its zinc(II) complex. Both the ligand and complex display an ordered molecular arrangement in the solid state and significant intermolecular interactions are observed. The formation of the resultant trinuclear Zn^{II} cluster, as confirmed by both solution studies and X-ray diffraction analysis, is

[a] CAS Key Laboratory of Photochemistry, Institute of Chemistry, Chinese Academy of Sciences,
Beijing 100080, P. R. China
E-mail: gqyang@iccas.ac.cn
Supporting information for this article is available on the WWW under http://www.eurjic.org or from the author.

 © 2005 Wiley-VCH Verlag GmbH & Co. KGaA, Weinheim **DOI: 10.1002/ejic.200500451**

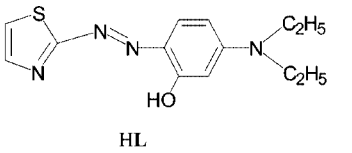

HL

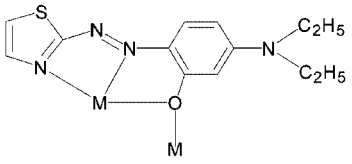

Bridging multi-metallic coordination of $\mathbf{L}^-$

Scheme 1. The structure of the azo ligand and its bridging multimetallic binding mode.

the first example of an azo-based polymetallic cluster. Both compounds were characterized by microanalysis, TGA analysis, mass spectrometry, FT-IR, ^{1}H NMR, and UV/Vis spectroscopy, and single-crystal X-ray diffraction analysis.

Results and Discussion

Synthesis and Characterization

The thiazolylazo ligand **HL** was readily synthesized in high yield. The 2-aminothiazo precursor was diazotized with solid $NaNO_2$ in 85% phosphoric acid at 0–5 °C to give the diazonium salt, which was then added dropwise to the coupling component 3-diethylaminophenol in ethanol. After filtration, the azo dye was separated as a bright red solid. Block-like, deep-red crystals were obtained by slow evaporation of a MeOH/EtOH solution of the ligand. The azo dye is well soluble in common organic solvents like MeOH, EtOH, CH_2Cl_2, CH_3CN, THF, etc. It is a potentially tridentate N,N,O-donor ligand for transition metal complexes, with the thiazoimine-N, azo-N, and phenoxo-O atoms providing the coordination sites, which can lead to versatile coordination models with different metal ions. Accordingly, the reaction of **HL** with zinc acetate hydrate resulted in the quantitative separation of an unusual trinuclear complex **1**. This needle-like complex is dark-red and also has excellent solubility in CH_2Cl_2, $CHCl_3$, and THF, etc. The structures of both the ligand and trinuclear zinc complex were confirmed by mass spectrometry, ^{1}H NMR, IR, and UV/Vis spectroscopy, and elemental analysis. X-ray diffraction analysis unambiguously confirmed the solid-state structures of both compounds.

UV/Vis Titration with Zn^{2+}

The formation of the zinc complex in solution was monitored by a UV/Vis titration experiment. Figure 1 shows the changes in the absorption spectra of the azo ligand **HL** upon increasing the concentration of Zn^{2+} in methanol. The inset presents the plot of the absorbance at 540 nm as a function of the $[Zn^{2+}]/[\mathbf{HL}]$ ratio. In methanol, the absorption spectrum of the free ligand exhibits a band with a maximum at 500 nm characteristic of the π–π* transition. The absorbance of this band decreases and a new band appears at around 540 nm upon increasing the $[Zn^{2+}]/[\mathbf{HL}]$ ratio. An apparent isosbestic point appears at 512 nm, indicating the formation of a metal–ligand coordination compound. Furthermore, the inset shows a maximum at [metal]/[ligand] = 1.5, which indicates the formation of a 2:3 complex in solution.

X-ray Structural Analysis

An ORTEP view of **HL**, including the atomic numbering scheme, is shown in part a of Figure 2; selected bond lengths and angles are given in Table 1. The azo ligand crystallizes in the orthohombic space group $P2_12_12_1$ with the Flack parameter refined to be 0.28(6), indicating the ligand crystallizes as a racemic twin. Overall, the conjugated aromatic part of the azo molecule is planar (part b, Figure 2); the dihedral angle of the two ring planes is only 4.0°. Interestingly, in the crystal packing of **HL** (part c, Figure 2), both intermolecular C–H···π hydrogen bonding and weak thiazo ring-S···π interactions are observed. While C–H···π hydrogen bonding is prevalent and also one of the most important intermolecular forces in the crystal packing of multi-aromatic systems,[11] the thio···π weak interaction reported here is a new class of aromatic–aromatic interaction. It is well-known that the ability of the π-cloud of aromatic ring to interact with positively polarized atoms is not limited to C–H···π interactions,[12] and electron-deficient cations can interact with aromatic systems, even biological macromolecules. In contrast, an interaction between electron-rich donors and/or anions with aromatic π-clouds is usually unexpected. A few papers are devoted to theoretical and experimental studies on this interaction.[12] Hence, the observed interaction of an electron-rich thiazolyl S atom with a phenyl ring is reasonable, albeit unusual, on the basis of the similar reports.

The moderately strong C–H···π hydrogen bond has a separation of 3.082 Å for H···π-ring center and an angle of 146.3° for C–H···π-ring center,[13] while the weak S_{thiazo}···π interaction has a short separation of 3.569 Å and a dihedral angle of 64.7° between the phenol and thiazo ring planes, comparable to the common distances of strong π···π interactions.[14]

The neutral complex with a formula of $[Zn_3\mathbf{L}_2(OAc)_4]$ (**1**) was obtained by reaction of two equivalents of azo ligand with three equivalents of zinc(II) acetate hydrate in CH_2Cl_2/MeOH solution, according to the results of the UV/Vis titration. Complex **1** crystallizes in the monoclinic space group $P2_1/c$. Its ORTEP structure is shown in Figure 3, in which two deprotonated ligand molecules $\mathbf{L}^-$ are linked with three zinc atoms, and two of three zinc atoms (Zn1 and Zn1A) are located in the thiazolylazo chelate moieties in a five-coordinate ZnN_2O_3 environment, with a thi-

 © 2005 Wiley-VCH Verlag GmbH & Co. KGaA, Weinheim

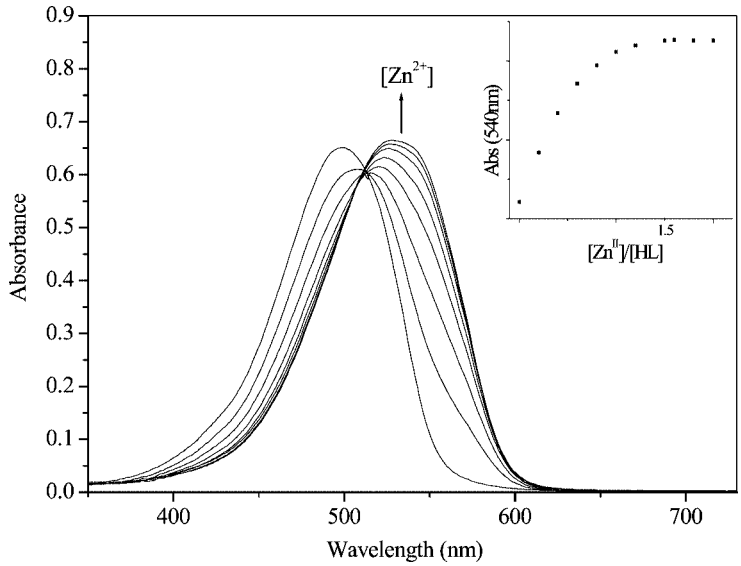

Figure 1. Change of absorption spectra of HL in methanol (1×10^{-5} M) upon addition of different concentrations of Zn^{2+}. Inset: plot of absorbance at 540 nm vs. the $[Zn^{2+}]/[HL]$ ratio.

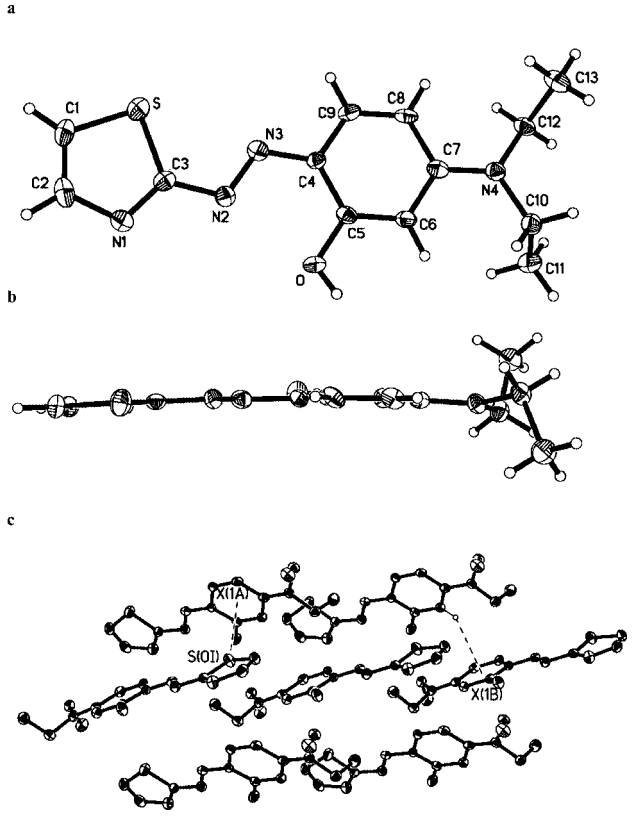

Figure 2. (a) ORTEP structure (30% probability level) and atom labeling scheme for azo ligand HL. (b) View along the plane of the azo moiety. (c) Crystal packing model showing the novel intermolecular S···π interaction and C–H···π hydrogen bonding.

azo nitrogen, an azo nitrogen, a phenoxo oxygen, and two oxygens from two acetate ions. The μ-phenoxo oxygen atoms (O1 and O1A), together with four acetate oxygen atoms, coordinate further to Zn2 at the inversion center to form a ZnO_6 octahedral geometry. Four μ-acetato ligands bind to three zinc centers (bridging Zn1–Zn2 and Zn1A–Zn2) and saturate the coordination numbers of zinc atoms, meaning that the whole charge of the complex is neutral. Thus, the resulting bridging Zn1–Zn2–Zn1A array is linear by symmetry. The nonbonding Zn···Zn distance is 3.390 Å, with a Zn1···Zn2···Zn1A angle of 180.0°, which indicates a weak interaction between the three zinc centers. The Zn–O bond lengths are in the range of 1.946(2)–2.128(2) Å, and the Zn–N bond lengths are 2.094(3) Å and 2.162 Å, respectively (see Table 1), comparable to other known zinc complexes.[15–17]

Table 1. Selected bond lengths [Å] and angles [°] for HL and **1**.[a]

HL			
S–C(1)	1.709(4)	S–C(3)	1.733(4)
O–C(5)	1.352(4)	N(1)–C(3)	1.303(4)
N(1)–C(2)	1.379(6)	N(2)–N(3)	1.303(4)
N(2)–C(3)	1.391(5)	N(3)–C(4)	1.351(4)
C(1)–S–C(3)	89.4(2)	C(3)–N(1)–C(2)	109.2(4)
N(3)–N(2)–C(3)	111.7(3)	N(2)–N(3)–C(4)	116.5(3)
C(7)–N(4)–C(12)	123.0(4)	C(7)–N(4)–C(10)	121.6(3)
C(12)–N(4)–C(10)	115.1(3)		
1			
Zn(1)–O(5)	1.946(2)	Zn(1)–O(3)	1.948(2)
Zn(1)–O(1)	2.094(2)	Zn(1)–N(3)	2.094(3)
Zn(1)–N(1)	2.162(3)	Zn(2)–O(1)	2.0753(19)
Zn(2)–O(1)$^{\#1}$	2.0753(19)	Zn(2)–O(4)	2.098(3)
Zn(2)–O(4)$^{\#1}$	2.098(3)	Zn(2)–O(2)	2.128(2)
Zn(2)–O(2)$^{\#1}$	2.128(2)		
O(5)–Zn(1)–N(3)	117.94(11)	O(3)–Zn(1)–N(3)	125.03(10)
O(1)–Zn(1)–N(3)	76.95(9)	O(5)–Zn(1)–N(1)	96.45(11)
O(3)–Zn(1)–N(1)	95.53(10)	O(1)–Zn(1)–N(1)	150.37(10)
N(3)–Zn(1)–N(1)	73.76(11)	O(5)–Zn(1)–O(3)	116.78(11)
O(5)–Zn(1)–O(1)	101.08(10)	O(3)–Zn(1)–O(1)	97.60(9)
O(1)–Zn(2)–O(2)$^{\#1}$	91.55(8)	O(1)$^{\#1}$–Zn(2)–O(2)$^{\#1}$	88.45(8)
O(4)–Zn(2)–O(2)$^{\#1}$	86.97(11)	O(2)–Zn(2)–O(2)$^{\#1}$	180.000(1)

[a] Symmetry transformations used to generate equivalent atoms: $^{\#1}$ $-x + 1, -y, -z + 2$.

 © 2005 Wiley-VCH Verlag GmbH & Co. KGaA, Weinheim

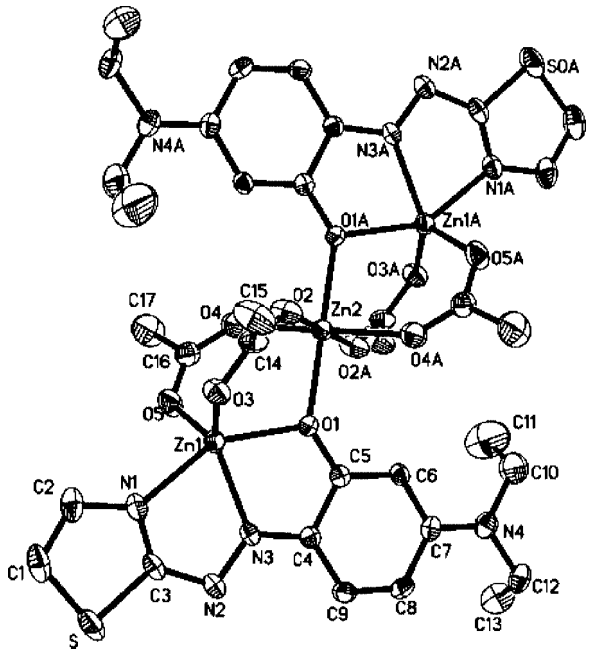

Figure 3. ORTEP structure (30% probability level) and atom-numbering scheme for trinuclear zinc cluster **1**. Hydrogen atoms have been omitted for clarity.

In addition, due to the good planarity and conjugation of the whole supramolecular complex, significant intermolecular π···π stacking interactions are observed in the crystal packing of **1** along the crystallographic *c* axis. (Figure 4) The aromatic planes of adjacent molecules are parallel, and the shortest C···C and C···N separations of π···π interactions are 3.426(4) Å and 3.455(4) Å, respectively, thus falling in the range of strong π···π interactions.[14] It is worth mentioning that the reported metal complexes based on azo ligands usually adopt mono- or binuclear structures,[10] therefore the trinuclear cluster structure depicted herein is surely the first example of an azo-based polynuclear Zn^{II} complex, although polynuclear cluster structures are not uncommon. Moreover, this observation may provide new references for designing other novel polynuclear metal complexes with special functional properties.

Spectroscopic Studies and Thermal Analysis

The infrared spectra (see Exp. Section) of ligand H**L** and complex **1** reveal the stretching vibration of the N=N band at 1431 and 1304 cm^{-1}. These values are indicative of the metal chelating behavior and are very similar to previous results.[10d] The thioazole ν(C=N) (1527 cm^{-1}) vibration appears as a very strong band which, upon complex formation, shifts to lower frequency (1501 cm^{-1}) with a reduction in its intensity.

The UV/Vis absorption spectra of both the free ligand H**L** and complex **1** were measured in various solvents. The π–π* transition band of H**L** is slightly solvent-dependent, the absorption maxima varied from 489 to 500 nm upon increasing the polarity of the solvent from ethyl acetate to methanol. (Table 2) The spectra of two forms of the conjugated base and protonated salt of H**L** show a pronounced bathochromic shift, relative to that of H**L** in methanol, which was attributed to the formation of conjugated species. In contrast, the UV/Vis spectra of complex **1** show a remarkable solvent effect (see Supporting Information). In methanol, the spectrum exhibits a single peak at around 530 nm, while in other solvents like ethyl acetate, chloroform, and toluene etc. this single band splits into two or three fine peaks between 400 and 600 nm, indicating that this complex is very sensitive to the solvent environment.

In contrast, some salicylideneimine ligands usually form mononuclear or binuclear metal complexes depending on the substituents or the reaction conditions.[17,18] As discussed previously, however, the [Zn(**L**$^-$)] unit readily assembles spontaneously to give the stable 2:3 complex in excellent yield. The ^{1}H NMR titration experiment confirmed the cooperative formation and stability of the unique trinuclear complex [Zn_3**L**$_2$(OAc)$_4$] in solution. (see Supporting Information) The ^{1}H NMR spectra of the reaction were monitored by varying the amount of zinc(II) in $CDCl_3$/CD_3OD (1:1), and the results clearly indicated that a single species, [Zn_3**L**$_2$(OAc)$_4$], was formed very cooperatively upon the addition of a 1.5-fold amount of zinc(II).

The crystalline solid of complex **1** is stable up to 220 °C. The TGA curve exhibits an important weight loss from ca. 220 °C to 324 °C, assigned to the removal of four bridging acetate ions, with a weight decrease of 24.08% (calcd. 24.14%). Further heating leads to the degradation of the compound, which might be attributed to the elimination of azo ligand moieties (see Supporting Information).

Conclusions

In summary, we have synthesized and characterized a thiazolylazo dye and its zinc(II) complex. X-ray structure analysis showed the interesting intermolecular interactions, i.e. C–H···π hydrogen bonds and thiazo ring-S···π weak interactions, present in the crystal of H**L**, which are believed to play a crucial role in stabilizing the crystalline solid. A stable 2:3 complex was confirmed both in solution and in the solid state by UV/Vis, ^{1}H NMR, and FT-IR spectroscopy, elemental analysis, TGA measurements, and X-ray crystal diffraction. Spectroscopic studies showed that the formation of the trinuclear complex is highly efficient. The trinuclear zinc cluster complex obtained here is significant for building supramolecular arrays with novel optical properties. Further, the formation of the trinuclear complex from a multidentate azo-based chelate is interesting for the study of coordination-driven molecular assembly by introduction of various metal ions (transition metal or lanthanide ions), and also opens up new pathways for the design of more complicated and polynuclear metallosupramolecules by changing the appropriate substituent groups (and/or binding sites) on the azo ligand.

 © 2005 Wiley-VCH Verlag GmbH & Co. KGaA, Weinheim

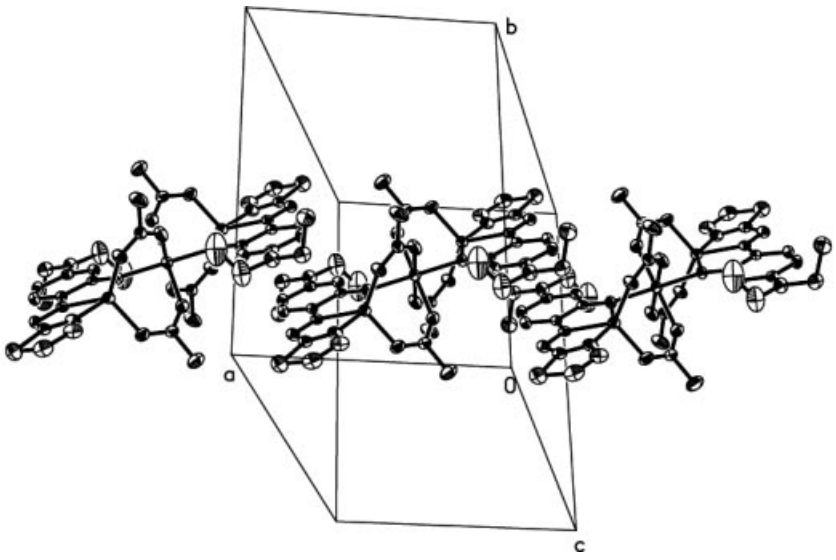

Figure 4. The crystal packing model of complex **1** along the crystallographic *c* axis showing the intermolecular π···π interaction.

Table 2. Spectroscopic data.

	Solvent	UV/Vis λ_{max} [nm] (ε [$M^{-1}\,cm^{-1}$])	Chemical shift in ppm ($CDCl_3$) O–H	thiazolyl proton	aromatic proton	IR $\tilde{\nu}$ [cm^{-1}]
	MeOH	500 (65456)	13.36(s)	7.78(d), 7.16(d)	7.53(d), 6.44(q)	ν(N=N) 1431
HL	$CHCl_3$	496 (58581)			6.15(d)	ν(C=N) 1527
	EtOAc	489 (62019)				
	C_7H_8	491 (56261)				
L^{-}[a]	MeOH	508 (58374)				
$[H_2L]ClO_4$	MeOH	540 (83294), 515[b](70404)				
1	MeOH	530 (56898)		7.54(d), 7.21(d)	7.60(d), 6.47(q)	ν(N=N)1304
	$CHCl_3$	534 (43990), 563[b] (42089)			6.10(s)	ν(C=N) 1501
	EtOAc	520 (35120), 562[b] (25697)				
	C_7H_8	513 (31002), 566[b] (23796)				

[a] The conjugated base, L^{-}, was generated in situ by the addition of NEt_3 to a solution of HL in methanol. [b] Shoulder.

Experimental Section

Materials and Synthesis: All reagents and solvents for syntheses and analyses were of analytical grade and were used as received. Solvents for spectral measurements were purchased as spectrophotometric grade. 2-Aminothiazole, 3-diethylaminopheno,l and zinc acetate hydrate were purchased from Aldrich and used without further purification.

Synthesis of 5-(Diethylamino)-2-(2-thiazolylazo)phenol (HL). Diazotization of 2-Aminothiazole: 2-Aminothiazole (1.0 g, 0.01 mol) was dissolved in 15 mL of 85% phosphoric acid. The solution was cooled to 0–5 °C in an ice-brine bath and maintained at this temperature. Solid sodium nitrite (0.75 g, 0.011 mol, 10% excess) was added to the solution over 30 min and stirring was continued for 3 h, keeping the temperature in the range of 0–5 °C. Urea (50 mg) was then added to destroy the excess nitrous acid.

Coupling with 3-(Diethylamino)phenol: 3-(Diethylamino)phenol (1.65 g, 0.01 mol) was dissolved in 25 mL of ethanol and the solution was cooled to 0–5 °C in an ice-brine bath. The above diazonium solution was added portionwise to the coupling component, and maintained at 0–5 °C for 3 h. Then, 30 mL of water was added, stirring was continued for another 3 h, and the solution was allowed to stand overnight while the temperature rose spontaneously to room temperature. After filtration, 1.09 g of crude dye was obtained (yield 39.4%). The crude dye was purified by column chromatography on neutral aluminum oxide using chloroform as eluent. Deep brown single crystals suitable for X-ray structure analysis were grown from a MeOH/EtOH solution of the azo dye. M.p.: 140–141 °C. MALDI-TOF-MS ($C_{13}H_{16}N_4OS$): *m*/*z* = 277 [M + 1]$^+$, 299 [M + Na]$^+$. FT-IR (KBr pellet): $\tilde{\nu}$ = 3410 cm^{-1}, 2972, 2361, 1636, 1527, 1474, 1431, 1336, 1272, 1181, 1137, 1008, 949, 807, 729, 683, 629. ^{1}H NMR ($CDCl_3$): δ = 1.26 (t, *J* = 7.14 Hz, 6 H), 3.47 (q, *J* = 7.14 Hz, 4 H), 6.15 (d, *J* = 2.61 Hz, 1 H), 6.44 (q, *J* = 9.30 Hz, 1 H), 7.16 (d, *J* = 3.33 Hz, 1 H), 7.53 (d, *J* = 9.30 Hz, 1 H), 7.78 (d, *J* = 3.33 Hz, 1 H), 13.36 (s, 1 H) ppm. $C_{13}H_{16}N_4OS$ (276.1): calcd. C 56.50, H 5.84, N 20.27, S 11.60; found C 56.11, H 5.70, N 20.26, S 11.72.

Synthesis of Complex 1: The 5-(diethylamino)-2-(2-thiazolylazo) phenol dye (55.2 mg, 0.2 mmol) was dissolved in 10 mL of dichloromethane and a 5 mL methanol solution of zinc acetate hydrate (65.9 mg, 0.3 mmol) was added. The solution was stirred at room temperature for 2 h, then allowed to stand at 5 °C for two weeks. During this period dark-red needle-like crystals appeared and were collected by filtration, washed with diethyl ether, and dried under vacuum. Yield: 51.8 mg (53.0%). MALDI-TOF-MS: *m*/*z* = 859.21 [M – 2OAc$^-$], 741.1 [M – 4OAc$^-$]. FT-IR (KBr pellet): $\tilde{\nu}$ = 2975 cm^{-1}, 2353, 1605, 1501, 1420, 1304, 1211, 1127, 1078, 1011, 949, 874, 826, 795, 665. ^{1}H NMR ($CDCl_3$): δ = 1.24 (t, *J* = 7.04 Hz, 12 H), 2.01 (s, 12 H), 3.50 (q, *J* = 7.08 Hz, 8 H), 6.10 (s, 2 H), 6.47 (q, *J* = 9.88 Hz, 2 H), 7.21 (d, *J* = 3.50 Hz, 2 H), 7.54 (d, *J* =

 © 2005 Wiley-VCH Verlag GmbH & Co. KGaA, Weinheim

3.50 Hz, 2 H), 7.60 (d, J = 9.81 Hz, 2 H) ppm. $C_{34}H_{42}N_8O_{10}S_2Zn_3$ (978.0): calcd. C 41.54, H 4.31, N 11.40; found C 41.83, H 4.32, N 11.30.

Physical Measurements: Melting points were determined on a Yanaco MP-500 micro-melting point apparatus. MALDI-TOF MS measurements were carried out on a Bruker APEX II and KYKY-ZHP-5 spectrometer. FT-IR spectra were recorded on a BIO-RAD FT-165 IR spectrometer. Samples for C, H, N, and S analyses were dried under vacuum and the analysis were performed with a Carlo Erba-1106 elemental analyzer. Thermogravimetric analysis was performed with a Dupont 951 thermogravimetric analyzer under nitrogen atmosphere, with a heating rate of 10 °C min^{-1}. ^{1}H NMR spectra were measured with a Bruker dmx400 MHz NMR spectrometer at room temperature in $CDCl_3$ with tetramethylsilane as the internal reference. UV/Vis absorption spectra and solution titration measurement were obtained on a Hitachi UV-3010 absorption spectrophotometry. UV/Vis spectrophotometric titration experiments were carried out as follows: a solution of H**L** in MeOH (original concentration 1×10^{-5} M) was titrated directly in 10 mL volumetric flasks by successive addition of methanol solutions of zinc acetate hydrate. A concentrated $Zn(OAc)_2 \cdot H_2O$ (0.01 M) solution was added in 2 to 20-μL aliquots using a microliter syringe. The absorption spectra were obtained by monitoring the spectra between 350 and 750 nm after transfer of the solution to a 1-cm quartz cell. The total volume change during the titration was negligible; the titration process was readily repeatable.

X-ray Crystallography: Crystals suitable for X-ray diffraction studies were obtained by solvent evaporation at 5 °C. Accurate unit-cell parameters were determined by a least-squares fit of 2θ values, measured for 200 strong reflections, and intensity data sets were measured on Rigaku Raxis Rapid IP diffractometer with Mo-K_α radiation (λ = 0.71073 Å) at room temperature. The intensities were corrected for Lorentz and polarization effects, but no corrections for extinction were made. All structures were solved by direct methods. The non-hydrogen atoms were located in successive difference Fourier synthesis. The final refinement was performed by full-matrix least-squares methods with anisotropic thermal parameters for non-hydrogen atoms on F^2. The hydrogen atoms were added theoretically as riding on the concerned atoms. Crystallographic data and experimental details for structure analyses are summarized in Table 3. Selected bond lengths and angles data are listed in Table 1. CCDC-272172 (for H**L**) and -272173 (for **1**) contain the supplementary crystallographic data for this paper. These data can be obtained free of charge from The Cambridge Crystallographic Data Center via www.ccdc.cam.ac.uk/data_request/cif.

Table 3. Crystallographic data for compounds H**L** and **1**.

	H**L**	**1**
Empirical formula	$C_{13}H_{16}N_4OS$	$C_{17}H_{21}N_4O_5SZn_{1.5}$
Mol. mass	276.36	491.49
Color	Deep brown	Dark red
Crystal system	orthohombic	monoclinic
Space group	$P2_12_12_1$	$P2_1/c$
T [K]	293(2)	293(2)
λ [Å]	0.71073	0.71073
a [Å]	7.6375(4)	10.0649(3)
b [Å]	8.8561(6)	15.9702(5)
c [Å]	19.9822(9)	14.0015(10)
α [°]	90.00	90.00
β [°]	90.00	110.1030(14)
γ [°]	90.00	90.00
V [Å^3]	1351.57(13)	2113.47(9)
Z	4	4
F(000)	584	1008
$\rho_{calcd.}$ [g cm^{-3}]	1.358	1.545
Crystal dimensions [mm^3]	0.51 × 0.11 × 0.11	0.37 × 0.22 × 0.22
Reflections collected	1785	4711
Unique reflections	793	2922
μ [mm^{-1}]	0.237	1.849
R[a]	0.0411	0.0408
wR_2[b]	0.0697	0.0898

[a] $R = \Sigma(F_o - F_c)/\Sigma(F_o)$. [b] $wR_2 = \Sigma w[(F_o^2 - F_c^2)^2/\Sigma w(F_o^2)^2]^{1/2}$.

Supporting Information: Thermogravimetric analysis curve for complex **1**, absorption spectra for H**L**, $\mathbf{L}^-$, and $[H_2\mathbf{L}][ClO_4]$ in methanol, solvent-dependent absorption spectra for H**L** and **1**, and ^{1}H NMR titration spectra (Figures S1–S5).

Acknowledgments

We would like to express our sincere thanks to the Major State Basic Research Development Program of China (grant no. G2000078100) and the National Natural Science Foundation of China for the financial support (grant no. 50303019).

[1] H. Rau, *Photochromism. Molecules and Systems* (Eds.: H. Dürr, H. Bouas-Laurent), Elsevier, Amsterdam, **1990**, chapter 4, p. 165.
[2] H. Zollinger, *Color Chemistry, Syntheses, Properties and Applications of Organic Dyes and Pigments*, VCH Publishers, New York, **1987**, p. 92.
[3] R. J. H. Clark, R. E. Hester, *Advances in Materials Science Spectroscopy*, John Wiley & Sons, New York, **1991**.
[4] a) H. Bach, K. Anderle, Th. Fuhrmann, J. H. Wendorff, *J. Phys. Chem.* **1996**, *100*, 4135–4140; b) Z. Liu, C. Zhao, M. Tang, S. Cai, *J. Phys. Chem.* **1996**, *100*, 17337–17344; c) K. Taniike, T. Matsumoto, T. Sato, Y. Ozaki, K. Nakashima, K. Iriyama, *J. Phys. Chem.* **1996**, *100*, 15508–15516.
[5] a) P. S. Ramanujam, S. Hvilsted, F. Andruzzi, *Appl. Phys. Lett.* **1993**, *62*, 1041–1043; b) G. J. Lee, D. Kim, M. Lee, *Appl. Opt.* **1995**, *34*, 138–143; c) P. S. Ramanujam, S. Hvilsted, I. Zebger, H. W. Siesler, *Macromol. Rapid Commun.* **1995**, *16*, 455–461; d) S. Hvilsted, F. Andruzzi, P. S. Ramanujam, *Opt. Lett.* **1992**, *17*, 1234–1236; e) I. Willner, S. Rubin, *Angew. Chem. Int. Ed. Engl.* **1996**, *35*, 367–385.
[6] N. Biswas, S. Umapathy, *J. Phys. Chem. A* **2000**, *104*, 2734–2745.
[7] a) M. Shivakumar, K. Pramanik, I. Bhattacharyya, A. Chakravorty, *Inorg. Chem.* **2000**, *39*, 4332–4338; b) A. C. G. Hotze, A. H. Velders, F. Ugozzoli, M. Biagini-Cingi, A. M. Manotti-Lanfredi, J. G. Haasnoot, J. Reedijk, *Inorg. Chem.* **2000**, *39*, 3838–3844; c) P. Gupta, R. J. Butcher, S. Bhattacharya, *Inorg. Chem.* **2003**, *42*, 5405–5411; d) A. Dogan, B. Sarkar, A. Klein, F. Lissner, T. Schleid, J. Fiedler, S. Záliš, V. K. Jain, W. Kaim, *Inorg. Chem.* **2004**, *43*, 5973–5980.
[8] a) S. Wang, S. Shen, H. Xu, D. Gu, J. Yin, X. Tang, *Dyes Pigm.* **1999**, *42*, 173–177; b) S. Wang, S. Shen, H. Xu, D. Gu, J. Yin, X. Dong, *Mater. Sci. Eng., B* **2001**, *79*, 45–48; c) S. Wang, S. Shen, H. Xu, *Dyes Pigm.* **2000**, *44*, 195–198; d) S. Wu, W. Qian, Z. Xia, Y. Zou, S. Wang, S. Shen, H. Xu, *Chem. Phys. Lett.* **2000**, *330*, 535–540; e) Z. Tian, W. Huang, D. Xiao, S. Wang, Y. Wu, Q. Gong, W. Yang, J. Yao, *Chem. Phys. Lett.* **2004**, *391*, 283–287.
[9] a) P. Gopalan, H. K. Katz, D. J. McGee, C. Erben, T. Zielinski, D. Bousquet, D. Müller, J. Grazul, Y. Olsson, *J. Am. Chem. Soc.* **2004**, *126*, 1741–1747 and references cited therein; b) N. Ertan, P. Gürkan, *Dyes Pigm.* **1997**, *33*, 137–147.
[10] a) K. K. Kamar, A. Saha, A. Castiñeiras, C.-H. Hung, S. Goswami, *Inorg. Chem.* **2002**, *41*, 4531–4538; b) S. Das, A. Saha, C.-H. Hung, G.-H. Lee, S.-M. Peng, S. Goswami, *Inorg. Chem.*

 © 2005 Wiley-VCH Verlag GmbH & Co. KGaA, Weinheim

2003, *42*, 198–204; c) S. Das, C.-H. Hung, S. Goswami, *Inorg. Chem.* **2003**, *42*, 5153–5157; d) S. Das, C.-H. Hung, S. Goswami, *Inorg. Chem.* **2003**, *42*, 8592–8597; e) K. K. Kamar, S. Das, C.-H. Hung, A. Castiñeiras, M. D. Kuz'min, C. Rillo, J. Bartolomé, S. Goswami, *Inorg. Chem.* **2003**, *42*, 5367–5375.

[11] a) M. A. Viswamitra, R. Radhakrishnan, J. Bandekar, G. R. Desiraju, *J. Am. Chem. Soc.* **1993**, *115*, 4868–4869; b) W. L. Jorgensen, D. L. Severance, *J. Am. Chem. Soc.* **1990**, *112*, 4768–4774; c) D. A. Evans, K. T. Chapman, D. T. Hung, A. T. Kawaguchi, *Angew. Chem. Int. Ed. Engl.* **1987**, *26*, 1184–1186; d) D. Braga, F. Grepioni, E. Tedesco, *Organometallics* **1998**, *17*, 2669–2672.

[12] S. Demeshko, S. Dechert, F. Meyer, *J. Am. Chem. Soc.* **2004**, *126*, 4508–4509 and references cited therein.

[13] T. Steiner, *Angew. Chem. Int. Ed.* **2002**, *41*, 48–76.

[14] C. Janiak, *J. Chem. Soc., Dalton Trans.* **2000**, 3885–3896.

[15] P. de Hoog, L. D. Pachón, P. Gamez, M. Lutz, A. L. Spek, J. Reedijk, *Dalton Trans.* **2004**, *17*, 2614–2615.

[16] J. Reglinski, S. Morris, D. E. Stevenson, *Polyhedron* **2002**, *21*, 2175–2182.

[17] S. Akine, T. Taniguchi, T. Nabeshima, *Inorg. Chem.* **2004**, *43*, 6142–6144.

[18] S. Mizukami, J. Houjou, Y. Nagawa, M. Kanesato, *Chem. Commun.* **2003**, 1148–1149.

Received: May 18, 2005
Published Online: September 8, 2005

 © 2005 Wiley-VCH Verlag GmbH & Co. KGaA, Weinheim

B-Substituted (Arene)ruthenacarborane–Sulfonium, –Thioether and –Mercaptan Complexes: Mild Single and Double Dealkylation and Structural Implications in the Antipodal Distance

José Giner Planas,[a] Clara Viñas,[a] Francesc Teixidor,*[a] Mark E. Light,[b] Michael B. Hursthouse,[b] and Helen R. Ogilvie[b]

Keywords: Antipodal effect / (Arene)ruthenacarboranes / Carboranes / Charge-compensated ligands / Dealkylation

Reactions of $[RuCl_2(\eta^6\text{-arene})]_2$ (arene = benzene, *p*-cymene) with *nido*-[7-R-10-L-7,8-$C_2B_9H_9$]$^-$ in THF at room temperature for 3 d give the (arene)ruthenacarborane complexes *closo*-[3-Ru(η^6-arene)-1-R-8-L-1,2-$C_2B_9H_9$]$^+$ {arene = benzene, R = H [L = Me_2S (**1a**), THT (**1b**), EtPhS (**1c**)], R = Me [L = Me_2S (**2a**)]; arene = *p*-cymene, R = H [L = Me_2S (**3a**)]} and mercaptan *closo*-[3-Ru(η^6-arene)-1-R-8-HS-1,2-$C_2B_9H_9$] [arene = benzene, R = H (**4**), Me (**5**); arene = *p*-cymene, R = H (**6**)] in yields of 20–40 % and 22–29 %, respectively. The asymmetric ligand *nido*-[9-Me_2S-7,8-$C_2B_9H_{10}$]$^-$ leads to the thioether complex *closo*-[3-Ru(η^6-benzene)-7-MeS-1,2-$C_2B_9H_{10}$] (**8**) in 34 % yield under the same reaction conditions. The crystal structure of **1a** is described and compared with those of **4** and **8**. The fully assigned ^{11}B NMR spectroscopic data for a whole series of ruthenacarboranes having *B*-substituted sulfonium, thioether and mercaptan groups are presented. These data show a relation between antipodal cluster atom distances (antipodal distance) and antipodal effect (AE) in the crystal structures of these complexes and for other families of heteroboranes such as *closo*-[$EB_{11}H_{11}$] and *closo*-[EB_9H_9].

(© Wiley-VCH Verlag GmbH & Co. KGaA, 69451 Weinheim, Germany, 2005)

Introduction

Metal complexes having the dicarbollide ligand *nido*-[7-R-8-R^1-7,8-$C_2B_9H_9$]$^{2-}$ constitute the most widely studied class of metallacarboranes since they were first reported by Hawthorne in the 1960s.[1] These dicarbollide ligands have planar binding faces and are isolobal and isoelectronic analogues of the cyclopentadienide ligand $[C_5H_5]^-$ (Cp), both behaving as 6-electron donors in transition metal complexes.[1,2] Introduction of substituents such as amines, ethers, sulfides and phosphanes etc. at the boron atoms reduces the cluster charge, thereby producing "charge-compensated" ligands such that a better comparison with the classical (Cp)metal complexes can be made.[3] In particular, sulfides are widely used as substituents in polyhedral *B*-substituted carboranes affording "charge-compensated" ligands of the type *nido*-[9- or 10-L-7,8-R$R^1$$C_2B_9H_8$]$^-$ (L = SR^2R^3).[4] Interestingly, whereas nearly 500 structures of icosahedral cages of the type *closo*-[3,1,2-MC_2B_9] have been determined by X-ray crystallography, only 33 of those contain a sulfur atom attached to a boron atom.[5] Of these, only 5 correspond to ruthenacarboranes all having a "charge-compensated" ligand, i.e. *closo*-[3-Ru(Cp*)-7-Me_2S-1-R-2-R^1-1,2-$C_2B_9H_8$] (R/R^1 = H/H, H/Ph, Ph/H),[3g] *closo*-[3-Ru(η^6-benzene)-7-Me_2S-1,2-$C_2B_9H_{10}$][6] and *closo*-[3-Ru-3-H-3,3-$(PPh_3)_2$-8-Me_2S-1,2-$C_2B_9H_{10}$].[3i] The latter type of (phosphane)ruthenacarborane complexes have proven to be very efficient catalysts in various types of olefin-related catalytic reactions surpassing, in some cases, the Cp-type complexes.[7] As part of our systematic work on monoanionic *o*-carboranes as alternatives to the cyclopentadienide ligand in transition metal complex catalysts,[7] we became interested in the synthesis of (arene)ruthenacarborane complexes. Here we report the syntheses and characterisation of the new symmetrically *B*-substituted (arene)ruthenacarborane–sulfonium complexes *closo*-[3-Ru(η^6-arene)-1-R-8-L-1,2-$C_2B_9H_9$]$^+$ {arene = benzene, R = H [L = Me_2S (**1a**), THT (**1b**), EtPhS (**1c**)], R = Me [L = Me_2S (**2a**)]; arene = *p*-cymene, R = H [L = Me_2S (**3a**)]} and of the unprecedented (arene)ruthenacarborane–mercaptan complexes *closo*-[3-Ru(η^6-arene)-1-R-8-HS-1,2-$C_2B_9H_9$] {arene = benzene, R = H (**4**), Me (**5**); arene = *p*-cymene, R = H (**6**)} and the asymmetric thioether complex *closo*-[3-Ru(η^6-benzene)-7-MeS-1,2-$C_2B_9H_{10}$] (**8**), formed by double and single dealkylation of the sulfonium groups in the starting *nido*-carboranes, respectively. A pathway for the dealkylation reaction is proposed. The structure for [**1a**]PF_6 is now reported and compared with those of complexes **4** and **8**

[a] Institut de Ciència de Materials de Barcelona (CSIC), Campus de la U.A.B,
08193 Bellaterra, Spain
Fax: +34-935805729
E-mail: teixidor@icmab.es
[b] School of Chemistry, University of Southampton, Highfield, Southampton SO17 1BJ, UK
Fax: +44-2380596723
E-mail: M.B.Hursthouse@soton.ac.uk

which were published in a preliminary communication.[8] We present here the fully assigned ^{11}B NMR spectroscopic data for a whole series of ruthenacarboranes having *B*-substituted sulfonium, thioether and mercaptan groups. The study reveals clear trends in the ^{11}B NMR spectra and the antipodal effect (AE)[9] which, to date, had only been related to NMR spectroscopic data. We have found that the AE can be clearly observed in the crystal structures for the new complexes and other previously reported heteroboranes of the type $EB_{11}H_{11}$ and EB_9H_9. We have adopted in this work the carborane numbering system shown in Scheme 1.

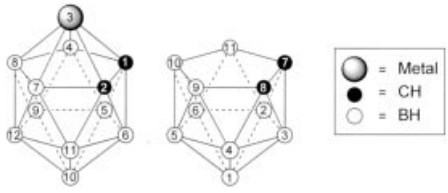

Scheme 1. Carborane numbering.

Results

1. Reactions of $[RuCl_2(\eta^6\text{-arene})]_2$ with Charge-Compensated Carboranes *nido*-[7-R-10-L-7,8-$C_2B_9H_9$]$^-$ and *nido*-[9-Me_2S-7,8-$C_2B_9H_{10}$]$^-$

According to protocols established in our group, *t*BuOK was employed as the base for in situ deprotonation of the neutral "charge-compensated" *o*-carboranes *nido*-[7-R-10-L-7,8-$C_2B_9H_{10}$] (R = H, L = Me_2S, THT, EtPhS; R = Me, L = Me_2S) (THT = tetrahydrothiophene) affording the potassium salt of the anionic "charge-compensated" *o*-carboranes *nido*-[7-R-10-L-7,8-$C_2B_9H_9$]$^-$.[10] Exclusive deprotonation of the bridge BHB proton is confirmed by disappearance of its resonance signal in the $^1H\{^{11}B\}$ NMR spectrum. The $^{11}B\{^1H\}$ NMR spectra show the typical highfield displacement of the antipodal boron B-1 signal after hydrogen bridge deprotonation (see Figure 1 for one example). Treatment of the *nido*-[7-R-10-L-7,8-$C_2B_9H_9$]$^-$ compounds with a suspension of the (arene)ruthenium complexes $[RuCl_2(\eta^6\text{-arene})]_2$ (arene = benzene, *p*-cymene) in THF at room temperature for 3 d afforded the new cationic ruthenacarborane complexes *closo*-[3-Ru(η^6-arene)-1-R-8-L-1,2-$C_2B_9H_9$]$^+$ Cl^- (**1**–**3**) as insoluble solids (Scheme 2). A Cl^- exchange reaction in **1**–**3** using PF_6^- afforded the readily soluble complexes *closo*-[3-Ru(η^6-arene)-1-R-8-L-1,2-$C_2B_9H_9$][PF_6] (**1a**–**c** and **3a**) in yields of 20–40% but only traces of **2a** were obtained. Detailed analysis of the remaining solution showed, in all cases, the presence of starting anionic "charge-compensated" *o*-carboranes *nido*-[7-R-10-L-7,8-$C_2B_9H_9$]$^-$ which could be recovered. In addition, we unexpectedly found that (mercaptan)ruthenacarborane complexes of the type *closo*-[3-Ru(η^6-arene)-1-R-8-HS-1,2-$C_2B_9H_9$] (**4**–**6**) were also formed in yields of 22–29% (Scheme 2). Although yields for the latter complexes were low, their formation is remarkable since they are the result of double dealkylation of all sulfonium salt derivatives under very mild conditions regardless of the nature of the substituents at the sulfur atom. Small amounts of sandwich complexes of the type *closo*-[3,3′-Ru-(8-L-1,2-$C_2B_9H_{10})_2$] were also detected in the reaction mixtures in some cases. Synthesis of the latter has been reported in a separate paper.[11] As an example, the sandwich complex *closo*-[3,3′-Ru-(8-Me_2S-1,2-$C_2B_9H_{10})_2$] was obtained in 8% yield after workup of the reaction mixture of *nido*-[10-Me_2S-7,8-$C_2B_9H_{10}$]$^-$ with (benzene)ruthenium dichloride. Fortunately, the latter type of sandwich complexes could, in most cases, be easily removed by column chromatography (see Exp. Sect.). The reactions shown in Scheme 2 have been conclusively established by spectroscopic (^{11}B, ^1H and ^{13}C NMR) and analytical characterisation of all compounds and crystallographic characterisation of [**1a**]PF_6 and **4**.

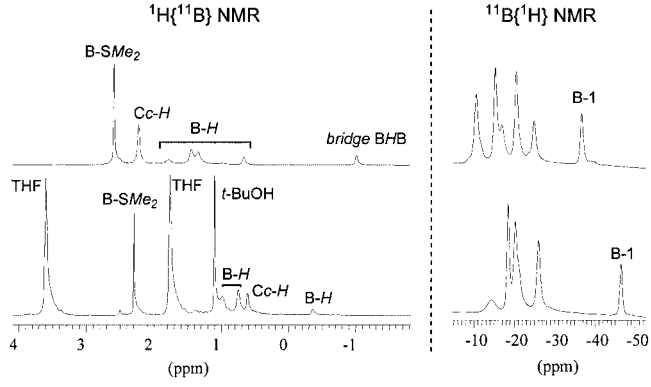

Figure 1. NMR monitoring for the deprotonation of *nido*-[10-Me_2S-7,8-$C_2B_9H_{11}$]: (top) NMR spectra before addition of *t*BuOK (1.0 M solution in THF); (bottom) after addition of 1 equiv. of *t*BuOK (>99% *nido*-K[10-Me_2S-7,8-$C_2B_9H_{10}$]).

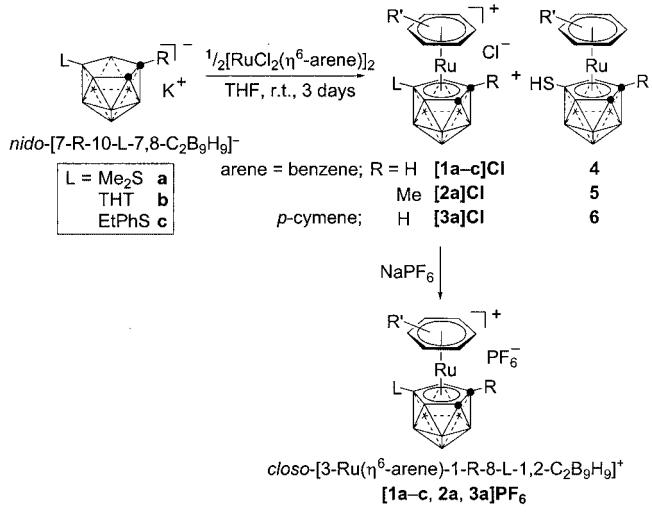

Scheme 2. Syntheses of new (arene)ruthenacarborane complexes.

Interestingly, the asymmetric isomer of **1a**, namely *closo*-[3-Ru(η^6-benzene)-7-Me_2S-1,2-$C_2B_9H_{10}$]$^+$ (**7**), has been previously reported in an analogous reaction of $[RuCl_2(\eta^6$-benzene)]$_2$ with the anionic *nido*-[9-Me_2S-7,8-$C_2B_9H_{10}$][Na] in

 © 2005 Wiley-VCH Verlag GmbH & Co. KGaA, Weinheim

44% yield but no other species were reported to be formed.[6] Based on our present results, we have examined this reaction in more detail in order to determine whether C–S bond cleavage of Me_2S was also possible in this case. We found that the new soluble neutral complex *closo*-[3-Ru(η^6-benzene)-7-MeS-1,2-$C_2B_9H_{10}$] (**8**) is formed, in addition to the previously reported **7**, in 34% yield [Equation (1)]. Complex **8** has been identified by ^{11}B, ^1H and $^{13}C\{^1H\}$ NMR spectroscopy and structurally characterised by X-ray diffraction.

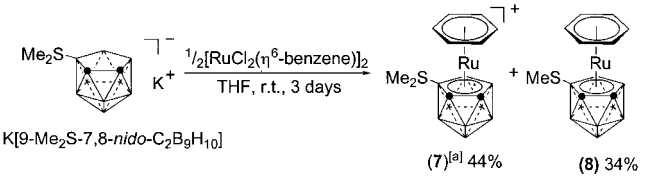

K[9-Me_2S-7,8-*nido*-$C_2B_9H_{10}$] (**7**)[a] 44% (**8**) 34%

[a] From ref.[6]

(1)

2. Characterisation of the New Complexes

a. closo-[3-Ru(η^6-arene)-1-R-8-L-1,2-$C_2B_9H_9$]$^+$

The ^1H NMR spectra for all cationic complexes **1**–**3** (anion for all cationic complexes throughout the text is PF_6^-, unless otherwise noted) show diagnostic signals for coordinated (η^6-arene) fragments to Ru at δ = 6.62–6.82 ppm.[12] Signals for the cage C–H protons (C_c–H) appear as broad resonances at δ = 4.61–4.67 ppm for the unsubstituted carborane compounds (**1** and **3**) and at δ = 4.97 ppm for the methylcarborane complex **2a**, all data being consistent with those of other (arene)ruthenacarborane complexes.[6,13] The $^{13}C\{^1H\}$ NMR spectra for all complexes also show characteristic peaks for the benzene or *p*-cymene ligands, two cage-carbon vertices and the L groups (see Exp. Sect.). The $^{11}B\{^1H\}$ NMR spectra for all complexes are consistent with a *closo*-icosahedral geometry for the cage and are similar to those found for related metallacarborane species.[3i,11] The fully coupled ^{11}B NMR spectra of these complexes show a singlet for the L–B boron vertex whereas the rest of the boron atoms appear as doublets due to ^{11}B-^1H coupling. For example, complex **1a** displays six resonances in a 1:1:2:2:2:1 ratio in its ^{11}B NMR spectrum at δ = 7.1 (s, B-8), 1.9 (d, $^1J_{B,H}$ = 148 Hz, B-10), –6.9 (d, $^1J_{B,H}$ = 153 Hz, B-4,7), –9.8 (d, $^1J_{B,H}$ = 144 Hz, B-9,12), –17.5 (d, $^1J_{B,H}$ = 155.1 Hz, B-5,11), –22.0 (d, $^1J_{B,H}$ = 169 Hz, B-6) ppm. The assignments for each boron atom have been unequivocally determined by 2D $^{11}B\{^1H\}$-$^{11}B\{^1H\}$ COSY for all complexes. These data are consistent with C_s symmetry for the complexes as shown in Scheme 2. However, the symmetry is disrupted in complexes **1c** and **2a** due the presence of the compensating EtPhS group at B(8) and a methyl group at one of the carbon cage vertexes. Thus, the $^{11}B\{^1H\}$ NMR spectrum for **1c** displays seven resonances with relative intensities of 1:1:2:1:1:2:1. The asymmetry can also be observed in the $^{13}C\{^1H\}$ NMR spectrum which shows two different C_c–H resonances (two broad singlets at δ = 49.2 and 49.9 ppm). The asymmetry of **2a** results in all the B signals being inequivalent such that extensive overlap can be observed. In addition, all cationic complexes [**1**–**3**]PF_6 show typical septuplets in their ^{31}P NMR spectra at $\delta \approx$ –143 to –146 ppm, due to $^1J_{P,F}$ coupling (ca. 710 Hz).

b. closo-[3-Ru(η^6-arene)-1-R-8-HS-1,2-$C_2B_9H_9$]

The ^{11}B NMR spectrum for the neutral mercaptan derivative **4** closely resembles that of **1a** with an even larger downfield resonance for the B–SH vertex (δ = 14.3 ppm). The corresponding ^1H NMR spectrum shows a broad resonance at δ = 0.87 ppm which is consistent with an SH group, a situation similar to that found in the related (mercaptan)cobaltacarborane complex *closo*-[3-Co(Cp)-8-HS-1,2-$C_2B_9H_{10}$].[14] In addition, the ^1H and $^{13}C\{^1H\}$ NMR signals for the η^6-benzene moiety and the cage C_c–H for this complex appear at higher field than in the cationic complex **1** and are consistent with other neutral ruthenacarborane complexes.[13a] Complexes **5** and **6** exhibited very similar NMR characteristics to **4** so that their multinuclear NMR spectroscopic data were assigned accordingly.

c. closo-[3-Ru(η^6-benzene)-7-MeS-1,2-$C_2B_9H_{10}$]

The resonance for the substituted B atom in the ^{11}B NMR spectrum is more shielded than in **4** (δ = 6.4 ppm) and, unlike the latter, a signal for an MeS fragment can be observed in the ^1H and $^{13}C\{^1H\}$ NMR spectra. These data are in agreement with cleavage of only one of the C–S bonds of the Me_2S moiety affording the new neutral thioether complex **8** as outlined in Equation (1). The asymmetry of the complex is also evident in the ^1H and $^{13}C\{^1H\}$ NMR spectra which display two resonances for the C_c–H atoms.

3. Crystal Structures

The structures for [**1a**]PF_6, **4** and **8** have been unequivocally established by X-ray crystallography (Figures 2, 3 and 4). The Exp. Sect. contains the crystal and data collection parameters for [**1a**]PF_6. Figure 2 clearly shows that the ruthenium atom in **1a** is sandwiched between the benzene and *nido*-[10-Me_2S-7,8-$C_2B_9H_{10}$]$^-$ ligands giving the cluster the expected *closo*-[3,1,2-MC_2B_9] geometry. The Ru–(C_2B_3 plane) and Ru–(C_6 plane) distances are 1.629 and 1.724 Å, respectively, and these values are similar to those of the dicarbollide-containing neutral complex *closo*-[3-Ru(η^6-benzene)-1,2-$C_2B_9H_{11}$].[13c] Interestingly, the C_6 benzene ring and C_2B_3 plane angle is 1.59° in **1a** which is significantly smaller than that for the related complex *closo*-[3-Ru(η^6-benzene)-1,2-$C_2B_9H_{11}$] (4.1°).[13c] Notably the C1–C2 distance is 1.637(4) Å which is similar to that in other *closo* structures.[3] The B8–S1 distance of 1.899(2) Å is consistent with that in other *B*-substituted sulfonium salts.[15]

 © 2005 Wiley-VCH Verlag GmbH & Co. KGaA, Weinheim

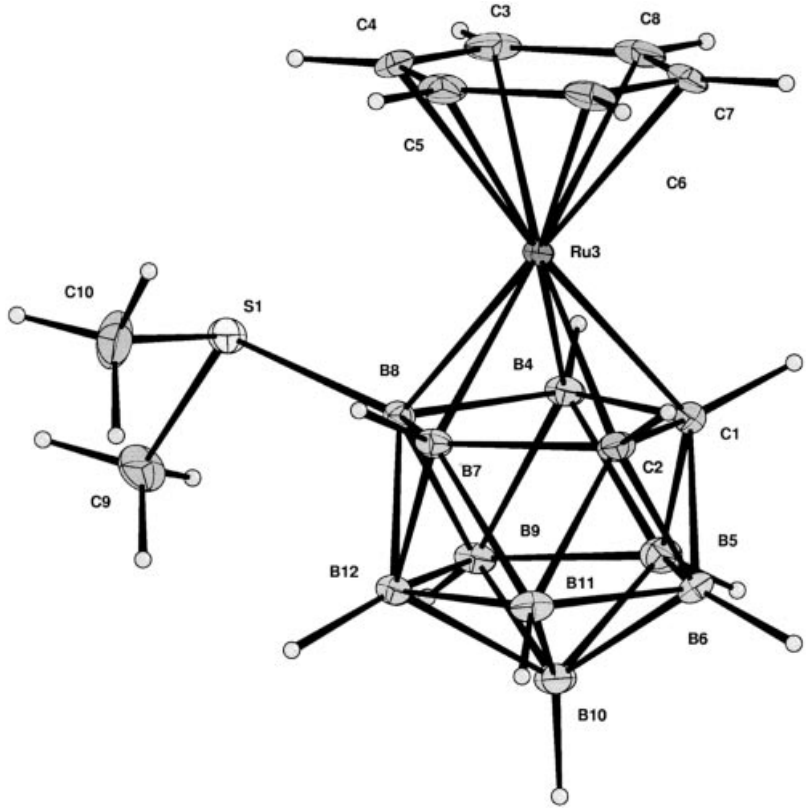

Figure 2. Molecular structure of [**1a**]PF_6 (thermal ellipsoids shown at the 50% probability level). The PF_6^- anion has been omitted for clarity. Selected interatomic distances [Å]: Ru3–C1 2.169(2), Ru3–C2 2.177(2), Ru3–B4 2.212(2), Ru3–B7 2.215(2), Ru3–B8 2.217(2), Ru3–C3 2.219(2), Ru3–C4 2.218(2), Ru3–C5 2.228(2), Ru3–C6 2.236(2), Ru3–C7 2.230(2), Ru3–C8 2.226(2), C1–C2 1.637(4), C2–B7 1.719(3), B7–B8 1.798(3), B4–B8 1.794(3), B8–S1 1.899(2).

The neutral complex **4** also displays a *closo*-[3,1,2-MC_2B_9] geometry for the cluster (Figure 3). The ruthenium atom is sandwiched between the benzene and *nido*-[10-HS-7,8-$C_2B_9H_{10}]^-$ ligands, thus supporting the structure for the complex in solution and confirming that double demethylation occurs from the starting charge-compensated ligand. The average Ru–(C_2B_3 plane) and Ru–(C_6 plane) distances are similar to those in **1a** (1.613 and 1.718 Å). The C_6 benzene ring and the C_2B_3 planes are nearly parallel, the dihedral angle of 2.74° is slightly larger than that for the sulfonium derivative **1a**. The C1–C2 distance is 1.644(4) Å and the B8–S1 bond [1.836(3) Å] is shorter than that of **1a** thereby being consistent with a thiol fragment attached to a boron atom.[16]

As can be seen in Figure 4, the structure of **8** exhibits a similar sandwich-type geometry with the ruthenium atom flanked both by the benzene ring and the C_2B_3 face of the *nido*-[9-MeS-7,8-$C_2B_9H_{10}]^-$ cage. The Ru–(C_2B_3 plane) and Ru–(C_6 plane) distances are 1.719 and 1.606 Å, respectively, the angle between planes of 3.68° is similar to that for the related complex *closo*-[3-Ru(η^6-benzene)-7-Me_2S-1,2-$C_2B_9H_{10}]^+$ (**7**) (4.4°).[6] The C1–C2 [1.627(3) Å] and B4–S1 distances [1.855(3) Å] are also consistent with the above data.

Discussion

1. Reactions of [$RuCl_2(\eta^6$-arene)]$_2$ with Charge-Compensated Carboranes *nido*-[7-R-10-L-7,8-$C_2B_9H_9]^-$ and *nido*-[9-Me_2S-7,8-$C_2B_9H_{10}]^-$

The yields of the new cationic (arene)ruthenacarborane complexes **1**–**3** (Scheme 2) and the reported **7**[6] [Equation (1)] are usually below 50% (Table 1). As demonstrated in this work, these low yields can be partially accounted for by the formation of the (mercaptan)ruthenacarborane complexes **4**–**6** in the case of the symmetric ligands *nido*-[7-R-10-L-7,8-$C_2B_9H_9]^-$ (*isomer-10*) or the thioether complex **8** for the related asymmetric ligand *nido*-[9-Me_2S-7,8-$C_2B_9H_{10}]^-$ (*isomer-9*). Since the starting (arene)ruthenium dichloride and *isomer-10* ligand were also detected during workup of the reactions, we initially thought that insolubility of the benzene(chloro)ruthenium dimer was responsible for the low yields of the complexes (Table 1, Entries 1–2 and 4–5). However, yields for the cationic complexes did not increase when using the more soluble chloro(*p*-cymene) ruthenium dimer (Table 1, Entry 3). Heating was avoided to minimise the formation of the unwanted sandwich complexes *closo*-[3,3′-Ru-(8-L-1,2-$C_2B_9H_{10})_2$] mentioned earlier.[11]

 © 2005 Wiley-VCH Verlag GmbH & Co. KGaA, Weinheim

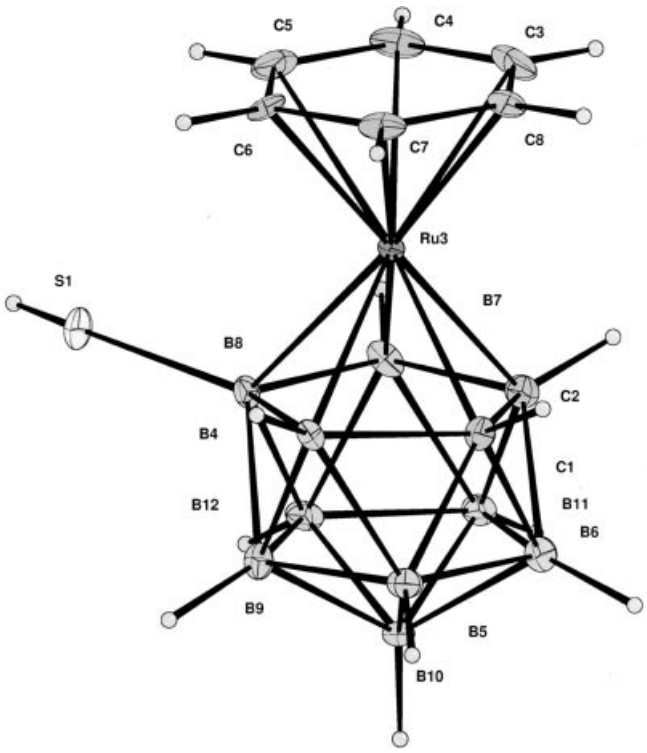

Figure 3. Molecular structure of **4** (thermal ellipsoids shown at the 50% probability level). Selected interatomic distances [Å]: Ru3–C1 2.157(3), Ru3–C2 2.164(3), Ru3–B4 2.202(3), Ru3–B7 2.198(3), Ru3–B8 2.215(3), Ru3–C3 2.242(3), Ru3–C4 2.229(4), Ru3–C5 2.206(3), Ru3–C6 2.197(3), Ru3–C7 2.221(4), Ru3–C8 2.238(3), C1–C2 1.644(4), C2–B7 1.727(4), B7–B8 1.810(4), B4–B8 1.808(4), B8–S1 1.836(3).

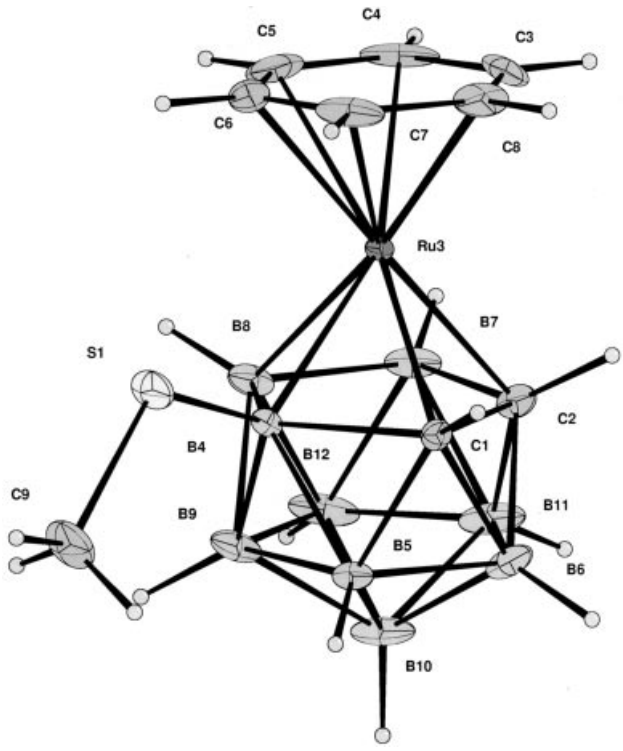

Figure 4. Molecular structure of **8** (thermal ellipsoids shown at the 50% probability level). Selected interatomic distances [Å]: Ru3–C1 2.153(2), Ru3–C2 2.163(2), Ru3–B4 2.202(3), Ru3–B7 2.198(3), Ru3–B8 2.215(3), Ru3–C3 2.228(3), Ru3–C4 2.199(3), Ru3–C5 2.188(3), Ru3–C6 2.199(3), Ru3–C7 2.214(3), Ru3–C8 2.235(3), C1–C2 1.627(3), C2–B7 1.721(4), B7–B8 1.801(4), B4–B8 1.815(4), B4–S1 1.855(3), C9–S1 1.810(3).

Table 1. Yield distribution of *closo*-[3-Ru(η^6-arene)-1-R-8-L-1,2-$C_2B_9H_9$]$^+$ (**1**–**3**) and *closo*-[3-Ru(η^6-arene)-1-R-8-HS-1,2-$C_2B_9H_9$] (**4**–**6**) formed for each reaction.

Entry	R	L	Arene	**1**–**3** [%]	**4**–**6** [%]
1	H	Me_2S	benzene	40 (**1a**)	22 (**4**)
2	Me	Me_2S	benzene	<1 (**2a**)	29 (**5**)
3	H	Me_2S	*p*-cymene	40 (**3a**)	–[a] (**6**)
4	H	THT	benzene	20 (**1b**)	26 (**4**)
5	H	EtPhS	benzene	17 (**1c**)	28 (**4**)

[a] Spectroscopically characterised (see Exp. Sect. for details).

Formation of complexes **4**–**6** is remarkable since they are the result of double dealkylation of any of the sulfonium derivatives at room temperature regardless of the nature of the groups attached to the sulfur atom. This was further confirmed by detection of MeCl (Entry 1 in Table 1), $Cl(CH_2)_4Cl$ (Entry 4) or PhCl and EtCl (Entry 5) during the formation of **4**. Elimination of the alkyl or aryl halides suggests that C–S bond cleavage takes place by means of nucleophilic addition of Cl^- to the organic fragments of the L groups. Similar yields for complexes **4**–**6**, regardless of the starting sulfonium salt derivative, indicate that neither the electronic nor the steric nature of the carbon substituents at the sulfur atom have an important role in the C–S bond cleavage. Although this type of C–S bond activation has been previously reported in thioethers coordinated to electron-withdrawing W or Pt centres, cleavage of only one C–S bond (single dealkylation) was observed in those cases.[17] Double demethylation has only been observed in polyhedral boranes having the charge-compensated Me_2S group but, in this case, a large excess of Li was needed as the reducing agent.[18] Two crucial questions then arise: (i) Does the C–S bond cleavage take place prior to or after coordination of Ru to the open face of the monoanionic carboranes and (ii) does Ru participate in the double C–S bond cleavage? In order to address these points, we first attempted the reaction of complex [**1a**]PF_6 with a Cl^- source such as $[Bu_4N]Cl$. The latter did not cleave any C–S bond. The only reaction observed was a single anion exchange reaction as shown in Equation (2). On the other hand, addition of an excess of the same Cl^- source during the reaction of $[RuCl_2(\eta^6\text{-benzene})]_2$ with *nido*-[10-Me_2S-7,8-$C_2B_9H_{10}]^-$ (Scheme 2) did not affect the ratio of species formed. These two observations are consistent with the cationic complexes not being intermediates of the dealkylation reaction, a fact which is further supported by in situ NMR spectroscopic studies of the formation of [**1a**]Cl and **4** (see Exp. Sect.). In fact, the (arene)ruthenacarborane complexes are so stable that they could be subjected to heating under reflux or photolysis for days without alteration. This clearly suggests that the Cl^- anion itself is not the nucleophile and that Ru must play some role in the cleavage reaction.

 © 2005 Wiley-VCH Verlag GmbH & Co. KGaA, Weinheim

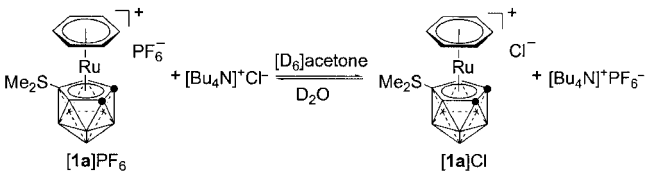

(2)

All the above data support the suggestion that cleavage of the C–S bond in the sulfonium fragments takes place prior to coordination of Ru to the open face of the cluster. Since addition of an external Cl^- source did not affect the dealkylation reaction, formation of alkyl halides could then only be explained by the occurrence of some type of nucleophilic addition of Cl^- bonded to Ru. Taking into account all experimental evidence, we propose the following pathway for the dealkylation reactions: thioether–*exo*-*nido*-carboranes could be formed first (Scheme 3, proposed intermediate **B**) with release of 1 equiv. of either an alkyl or aryl halide. In this way, only Cl^- anions attached to Ru are able to cleave the C–S bond by some type of sulfonium–Ru interaction like that proposed in **A**. The first stepwise single dealkylation is supported by the isolation and crystallographic characterisation of the neutral methyl thioether complex *closo*-[3-Ru(η^6-benzene)-7-MeS-1,2-$C_2B_9H_{10}$] (**8**). Observation of a resonance at δ = –4.27 ppm in the ^{1}H NMR spectrum during the double dealkylation reaction provides evidence for the participation of some type of B–H→Ru agostic interaction like that postulated in **B**.[19] We have previously reported a series of *exo*-cluster monothioether and monophosphanyl complexes having these types of B–H→M (M = Rh, Ru) agostic bonds (Scheme 4, **I** and **IVa**).[20] Carbon–sulfur bond cleavage in (thioether)Ru complexes, as could be the case in intermediate **B**, is known to happen by means of π-back-donation from the metal to the thioether C–S σ*-orbitals.[21] Thus, further dealkylation by C–S bond cleavage in the thioether **B** would follow liberation of a second equivalent of the halide and an *exo*-cluster *S*-bonded (thiolato)ruthenium intermediate like **C** could be formed (Scheme 3). Decoordination of the *S*-bonded thiolato complex **C** could then take place[22] thus forming the more stable (η^5-C_2B_3)ruthenacarborane complex which becomes protonated to give the mercaptan complex.

The stability of the thioether complex **8** towards further cleavage to the corresponding (mercaptan)ruthenacarborane derivative could be related to the different electronic nature of this isomer with regard to its symmetrical analogue. Calculation of Mulliken charges at the Hartree-Fock 3-21G level clearly confirms that charge distribution is affected by the position of C atoms in the C_2B_3 open face of the *nido*-[10-MeS-7,8-$C_2B_9H_9$]$^{2-}$ and *nido*-[9-MeS-7,8-$C_2B_9H_9$]$^{2-}$ carboranes as shown in Scheme 5. It is noteworthy that whereas both hydrogen atoms in the BH vertexes besides the BSMe group are negatively charged in *isomer-10* (both have hydridic B–H hydrogen atoms), those for the asymmetric *isomer-9* have different charges (a hydridic B–H and a protic C–H hydrogen atom). The necessary condition for B–H→M agostic interactions to take place is the existence of electron-enriched B–H bonds such as those in the open-face (C_2B_3) boron atoms of *nido*-C_2B_9 clusters.[20d] Therefore, existence of two hydridic B–H hydrogen atoms in the postulated *exo*-*nido* intermediate **B** (Scheme 3), which could interact indistinctly with Ru, might prevent fast isomerisation of **B** to the thioether and facilitate the second dealkylation to give the observed mercaptan complex **4** (Schemes 2 and 5 left). In the presence of only one hydridic hydrogen atom, the related *isomer-9* might isomerise faster from *exo*-*nido* to *closo* than its symmetrical analogue precluding the Ru from cleaving the second C–S bond (Scheme 5, right). Such isomerisation has been shown to take place in related Rh complexes of the type **IV** at room temperature in $CHCl_3$ solution (Scheme 3).[20d] Removal of the bridging H in the *nido*-carborane in **II** also favours the formation of the *closo* tautomer **III**.[23]

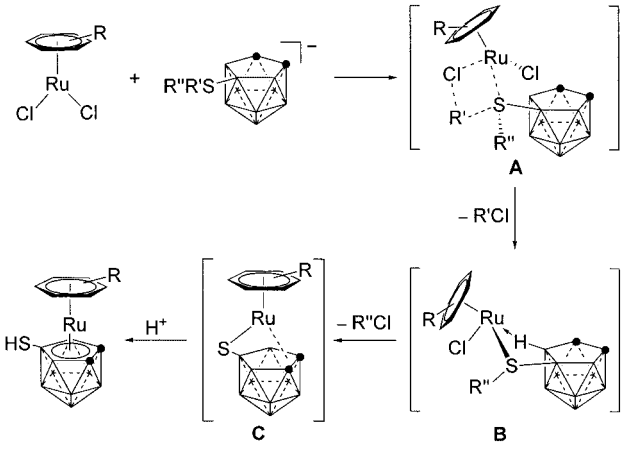

Scheme 3. Proposed pathway for the double dealkylation reaction.

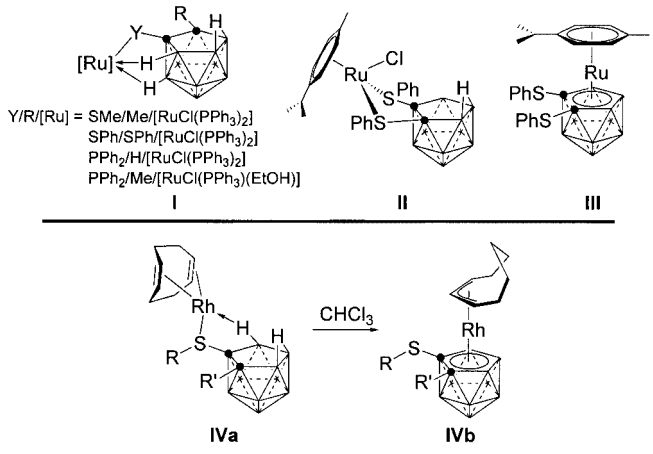

Scheme 4. Other selected ruthenium complexes and reactions.

2. Trends in ^{11}B NMR Spectroscopy for the Ruthenacarboranes

All compounds reported in this paper exhibit a *closo*-[3,1,2-RuC_2B_9] geometry; thus, it is possible to compare the differences in the boron chemical shifts caused by the dif-

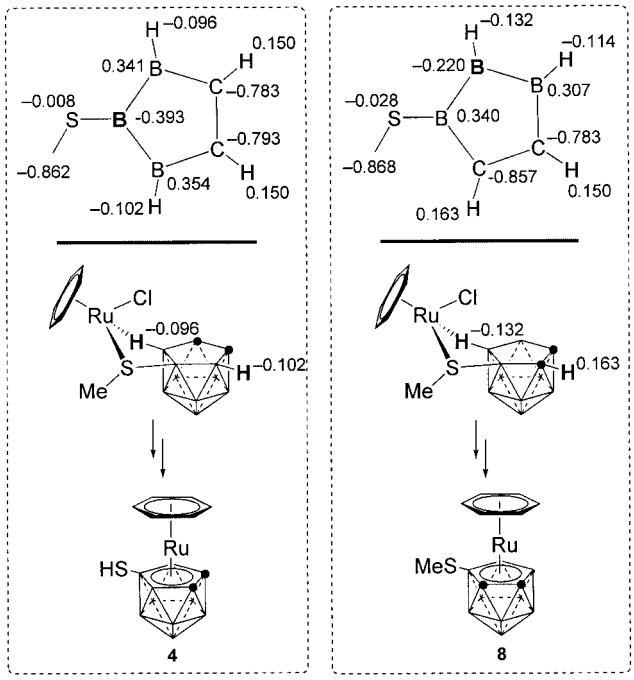

Scheme 5. Representation of the C_2B_3 faces of the *nido*-[10-MeS-7,8-$C_2B_9H_{10}]^{2-}$ (left) and *nido*-[9-MeS-7,8-$C_2B_9H_{10}]^{2-}$ ligands (right) and corresponding postulated *exo-nido* Ru species prior to the dealkylation reaction (below bold lines). Boron atoms in bold correspond to the B-8 vertex in the *closo*-ruthenacarborane complexes.

ferent substituents at the boron atoms. Cationic **1**–**3** and **7** as well as the neutral ruthenacarborane complexes **4**–**6** and **8** can be considered as resulting from substitution of a hydride ion in *closo*-[3-Ru(η^6-benzene)-1,2-$C_2B_9H_{11}$] by sulfonium and thioether or thiol fragments, respectively. Figure 5 shows a comparison of the neutral *closo*-[3-Ru(η^6-benzene)-1,2-$C_2B_9H_{11}$] which is taken as the reference, with substituted Me_2S and HS at B-8 (Table 2; Entries 1, 2 and 7).

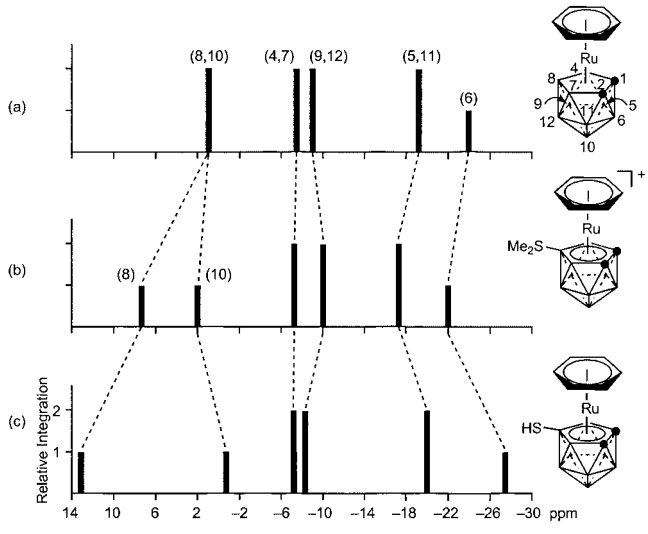

Figure 5. Representation of the $^{11}B\{^1H\}$ NMR spectra for complexes: (a) *closo*-[3-Ru(η^6-benzene)-1,2-$C_2B_9H_{11}$] (showing boron assignment); (b) [**1a**]PF_6; (c) **4**.

{Although the ruthenacarborane complex *closo*-[3-Ru(η^6-benzene)-1,2-$C_2B_9H_{11}$] has been previously reported,[13a] assignment of the cluster ^{11}B NMR spectroscopic data was not published; the present assignments were made by $^{11}B\{^1H\}$-$^{11}B\{^1H\}$ COSY spectrosopy ([D_6]acetone): δ = 1.3 (m, 2 B, B-8 and -10), –7.4 (d, $^1J_{B,H}$ = 117 Hz, 2 B, B-4 and -7), –8.7 (d, $^1J_{B,H}$ = 117 Hz, 2 B, B-9 and -12), –18.9 (d, $^1J_{B,H}$ = 152 Hz, 2 B, B-5 and -11) and –23.7 [d, $^1J_{B,H}$ = 176 Hz, 1 B, B-6] ppm.} The most apparent effect observed in Figure 5 is a large downfield displacement of chemical shifts for the substituted B-8 with respect to our reference complex, that of the HS derivative being larger than that of the Me_2S derivative. Whereas the signal for the Me_2S–B boron atom in **1a** is shifted downfield by about 7 ppm, that for the HS-B boron atom in **4** is displaced by 13 ppm. A second significant effect apparent from Figure 5 is the so-called antipodal effect (AE)[9] to the substituted boron atom (B-6). Whereas the chemical shift for the boron atom antipodal to Me_2S has moved downfield (Figure 5b), that of the boron atom antipodal to HS is displaced upfield (Figure 5c). These two main effects have good precedent.[9,18] As expected, smaller antipodal effects can also be observed in the asymmetric complexes *closo*-[3-Ru(η^6-benzene)-7-Me_2S-1,2-$C_2B_9H_{10}]^+$ (**7**) and *closo*-[3-Ru(η^6-benzene)-7-MeS-1,2-$C_2B_9H_{10}$] (**8**) due to the lack of a plane of symmetry crossing both the substituted and antipodal vertex[9] {compound/δ(B-5): *closo*-[3-Ru(η^6-benzene)-1,2-$C_2B_9H_{11}$]/–18.9 ppm, **7**/–18.7 ppm,[6] **8**/–17.0 ppm}.

Other minor effects include a downfield/upfield butterfly effect (BE)[9] analogous to the AE in our system (signals for B-5, -10 and -11 have moved downfield with respect to the reference in the case of the Me_2S-substituted species **1a** but those for the HS analogue **4** are displaced upfield) and the neighbouring effect (NE)[9] which only affects B-9 and -12 in the Me_2S-substituted **1a**.

3. Crystal Structures and Antipodal Effect

The empirically observed AE has been previously explained through cooperation of atomic orbitals on antipodally interacting vertices.[9] It is noteworthy that although the AE has been extensively studied using calculations[24] and by comparing various series of compounds,[9] the comparison has always been related to the ^{11}B chemical shifts as the only experimental evidence. Surprisingly, even though such a hypothesis involves the transfer of part of the electrons between antipodal boron atoms and, therefore, through some type of interaction between atomic orbitals, no other experimental evidence has ever been obtained apart from NMR chemical shifts.

We were curious to see whether the AE obtained by NMR spectroscopy, for neutral and cationic ruthenacarboranes, has any influence on their X-ray structures. A comparison of the X-ray structures of the complexes *closo*-[3-Ru(η^6-benzene)-1,2-$C_2B_9H_{11}$] (the reference compound) with *closo*-[3-Ru(η^6-benzene)-8-Me_2S-1,2-$C_2B_9H_{10}]^+$ (**1a**) and *closo*-[3-Ru(η^6-benzene)-8-HS-1,2-$C_2B_9H_{10}$] (**4**)

 © 2005 Wiley-VCH Verlag GmbH & Co. KGaA, Weinheim

Table 2. Comparison of ^{11}B NMR chemical shifts for *closo*-[3-Ru(η^6-arene)-1-R-8-L-1,2-$C_2B_9H_{10}$][PF_6] (above bold line) and *closo*-[3-Ru(η^6-arene)-1-R-8-HS-1,2-$C_2B_9H_9$] (below bold line).[a]

Entry	Arene	L	R	Complex	B-8	B-10	B-4/B-7	B-9/B-12	B-5/B-11	B-6
1	benzene	H	H	–	1.3	1.3	–7.4	–8.7	–18.9	–23.7
2	benzene	Me_2S	H	1a	7.1	1.9	–6.9	–9.8	–17.5	–22.0
3	benzene	THT	H	1b	6.2	1.2	–8.0	–10.7	–19.0	–23.3
4	benzene	EtPhS	H	1c	7.1	2.1	–6.6	–9.2/–9.6	–17.6	–21.7
5	benzene	Me_2S	Me	2a	6.1	1.7		–4.5 to –18.5		–22.9
6	*p*-cymene	Me_2S	H	3a	7.2	1.2	–5.7	–9.8	–17.6	–21.6
7	benzene	HS	H	4	14.3	–1.1	–6.9	–8.5	–20.0	–27.5
8	benzene	HS	Me	5	15.0	0.0	–3.5 to –9.4		–15.1/-18.6	–22.0
9	*p*-cymene	HS	H	6	13.6	–2.9	–7.7	–7.7	–20.9	–27.9

[a] See Scheme 1 for numbering.

(Table 3, polyhedral type V) shows a significant shortening of the distance between the substituted B atom and its antipodal boron atom (A_d: antipodal distance) in the sulfonium salt derivative **1a** with respect to the reference complex (0.061 Å). A smaller shortening can be observed for the neutral complex **4** (0.023 Å). The same situation can be observed when comparing the structures of the related substituted polyhedral boranes *closo*-[1-L-$B_{12}H_{11}$]$^{z-}$ with the reference *closo*-[$B_{12}H_{12}$]$^{2-}$ molecule (Table 3, polyhedral type VII). In this case the shortening of A_d is slightly larger (0.093 Å) than in the related ruthenacarborane structures. In contrast, the shortening of A_d is hardly seen in the asymmetric *closo*-[3-Ru(η^6-benzene)-7-L-1,2-$C_2B_9H_{10}$]$^+$ (Table 3, polyhedral type VI) which is consistent with a smaller AE for these complexes as expected from the lack of symmetry.[9] It is remarkable that the shortening of the antipodal distance (A_d) is observed in those compounds having strong electron-attracting substituents attached to boron atoms. According to the accepted hypothesis,[9] such substituents are believed to decrease the electron density at the antipodal boron atom with the consequent downfield shift of the chemical shift of the signal of this boron atom. Although the magnitudes of both the downfield chemical shift and the shortening of A_d are quite small in our complexes, a relation between AE and the shortening of A_d can be clearly seen when analysing the X-ray structures for the polyhedral heteroboranes *closo*-$EB_{11}H_{11}$ and *closo*-EB_9H_9 (Table 4).[25] The latter complexes are known to exhibit AE of at least one order of magnitude larger than the examples in Table 3.[8] The data summarised in table 4 clearly show that the downfield AE and the shortening of A_d both follow the same order, E = $MeAl^{2-}$ < HB^{2-} < HC^- < HN, i.e. with decreasing electron density at the E vertex. The shortening of the antipodal distances A_d is really significant. The difference between the first compound in the *closo*-$EB_{11}H_{11}$ series ($MeAl^{2-}$) and the last (HC^-) is 0.637 Å (Table 4)! The shortening of A_d is clearly not driven by the charges on the clusters, since *closo*-[$MeAlB_{11}H_{11}$]$^{2-}$ and *closo*-[$B_{12}H_{12}$]$^{2-}$ already show a significant shortening. To the best of our knowledge, this correlation has not been previously observed.

Table 3. Antipodal distances (A_d) for *closo*-[3-Ru(η^6-benzene)-8-L-1,2-$C_2B_9H_{10}$]$^+$ (polyhedral type V), *closo*-[3-Ru(η^6-benzene)-7-L-1,2-$C_2B_9H_{10}$]$^+$ (type VI) and *closo*-[$LB_{12}H_{11}$]$^{z-}$ (type VII).

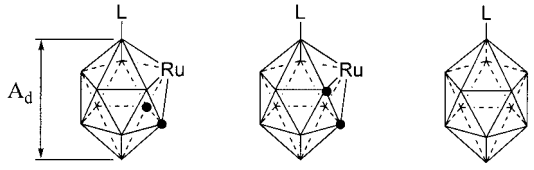

Polyhedral type	L	Compound charge	A_d [Å]
V	H	0	3.439[a]
	HS (**4**)	0	3.416[b]
	Me_2S (**1a**)	+1	3.378[c]
VI	H	0	3.387[a]
	MeS (**8**)	0	3.405[b]
	Me_2S	+1	3.354[c]
VII	H	–2	3.391[d]
	MeS	–2	3.374[e]
	Me_2S	–1	3.298[f]

[a] Value measured from the structure in ref.[13c] [b] From ref.[8] [c] This work. [d] From ref.[26] [e] From ref.[18a] [f] From ref.[15a]

Table 4. Antipodal distances (A_d) for *closo*-$EB_{11}H_{11}$ (polydedral type VIII) and *closo*-EB_9H_9 (type IX).[a]

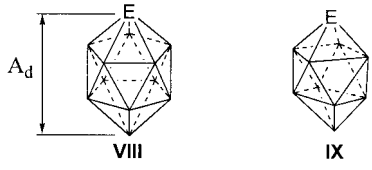

Polyhedral type	E	Cluster charge	δ[b]	A_d [Å]
VIII	MeAl	–2	–25.5	3.893
	HB	–2	–15.3	3.391
	HC	–1	–7.0	3.256
IX	HB	–2	–2.0	3.697
	HC	–1	28.4	3.387
	HN	0	61.0	3.303

[a] A_d values were measured from the structures in ref.[25] [b] ^{11}B NMR chemical shift for antipodal B atoms taken from ref.[9]

Conclusion

In this study, we describe the formation of cationic ruthenacarborane complexes *closo*-[3-Ru(η^6-arene)-1-R-8-L-

1,2-$C_2B_9H_9]^+$ (L = Me_2S, THT, EtPhS) (**1**–**3**) and neutral mercaptan *closo*-[3-Ru(η^6-arene)-1-R-8-HS-1,2-$C_2B_9H_9$] (**4**–**6**) and *closo*-[3-Ru(η^6-benzene)-7-MeS-1,2-$C_2B_9H_{10}$] (**8**). The neutral complexes are the result of double or single dealkylation of L groups in mono-anionic "charge-compensated" *o*-carborane derivatives at room temperature. Such facile C–S bond activations are unprecedented in polyhedral carborane chemistry and open a new route to mercaptan metallocarboranes. A pathway for the dealkylation reactions is proposed. The findings also show, for the first time, a relation between the empirical antipodal effect (AE) and the structural antipodal distance (A_d) in the crystal structures for the new complexes and other previously reported 12- and 10-vertex heteroboranes. We are currently working on an extension of this correlation to other *closo*-heteroboranes.

Experimental Section

General: All manipulations were carried out under N_2. Chemicals were prepared as follows: THF was distilled from Na/benzophenone; acetone was distilled from P_2O_5; *t*BuOK (95%, Aldrich or 1.0 M solution in THF) and $NaPF_6$ (98%, Aldrich) were used as received. The following were prepared by literature procedures: *nido*-[9-Me_2S-7,8-$C_2B_9H_{11}$],[4a] *nido*-[7-R-10-L-7,8-$C_2B_9H_{10}$] (R = H, L = Me_2S, THT, EtPhS; R = H, L = Me_2S)[4] and [$RuCl_2$(η^6-arene)]$_2$ (arene = benzene, *p*-cymene).[12] NMR spectra were acquired with a Bruker ARX 300 MHz spectrometer and referenced to the solvent (^{1}H, residual signals of [D_5]acetone, [D_2]acetonitrile or [D_7]THF; ^{13}C signals of [D_6]acetone or [D_3]acetonitrile),[26] BF_3·OEt_2 (^{11}B NMR) or PPh_3 (^{31}P NMR; a C_6D_6 solution in an internal sealed capillary, δ = –5.00 ppm). Chemical shifts are reported in ppm and coupling constants in Hz. Multiplet nomenclature is as follows: s, singlet; d, doublet; t, triplet; sept, septuplet; br., broad; m, multiplet. Chromatography was carried out using ACROS silica gel (0.035–0.070 mm, pore diameter ca. 6 nm). Microanalyses were conducted with a Carlo Erba EA1108 instrument. The mass spectra were recorded in the negative ion mode using a Bruker Biflex MALDI-TOF instrument [N_2 laser; λ_{exc} = 337 nm (0.5 ns pulses); voltage ion source 20.00 kV (Uis1) and 17.20 kV (Uis2)]. Photochemical reactions were performed in a quartz Schlenk vessel equipped with a magnetic bar and condenser. The unfiltered output of an in-house 76.8 W medium-pressure mercury lamp was used as a light source.

***closo*-[3-Ru(η^6-benzene)-8-Me_2S-1,2-$C_2B_9H_{10}$]$^+$ (1a) and *closo*-[3-Ru(η^6-benzene)-8-HS-1,2-$C_2B_9H_{10}$] (4). General Procedure:** A Schlenk flask was charged with *nido*-[10-Me_2S-7,8-$C_2B_9H_{11}$] (95.1 mg, 0.489 mmol), *t*BuOK (0.550 mL, 1.0 M) and THF (10 mL). The mixture was stirred at room temperature for 30 min giving a clear pale yellow solution. The flask was then charged with [$RuCl_2$(η^6-benzene)]$_2$ (122.4 mg, 0.245 mmol) and the resultant heterogeneous brown mixture was stirred at room temperature for 3 d. Workup for **1a** and **4** was as follows:

1a: A solid residue was separated from the supernatant orange solution and transferred into another Schlenk vessel for further isolation of **4** (vide infra). The solid residue remaining in the flask was dried by oil-pump vacuum to give **[1a]**Cl and KCl as a pale brown powder. Addition of an aqueous solution of $NaPF_6$ (176.7 mg, 1.052 mmol) to the heterogeneous brown mixture of **[1a]**Cl in ethanol (10 mL) resulted in the formation of a tan precipitate. After stirring for at room temperature for 1 h, the remaining ethanol was removed under reduced pressure and the resultant suspension was allowed to settle without stirring in the refrigerator for 1 h. The aqueous solution was separated by cannula and the residue was washed with H_2O (1 mL) and extracted with CH_2Cl_2 which was then evaporated and the residue dried by oil-pump vacuum to afford **[1a]**PF_6 as a tan powder (101.3 mg, 0.196 mmol, 40%). $C_{10}H_{22}B_9F_6PRuS$: calcd. C 23.20, H 4.28, S 6.19; found C 22.92, H 3.92, S 5.86. MALDI-TOF *m*/*z* (%) = 373.53 (100) [M], 311.46 (43) [M – Me_2S].

[1a]Cl: ^{1}H NMR ([D_3]acetonitrile): δ = 6.58 (s, 6 H, η^6-C_6H_6), 4.50 (br. s, 2 H, C_c-*H*), 2.45 (s, 6 H, Me_2S) ppm. ^{1}H{^{11}B} NMR ([D_3]acetonitrile; only signals due to B-H protons are given): δ = 2.92 (br. s, 2 H), 1.90–1.60 (m, 6 H) ppm. ^{11}B NMR ([D_3]acetonitrile): δ = 6.9 (s, 1 B, B-8), 1.7 (d, $^1J_{B,H}$ = 154 Hz, 1 B, B-10), –7.1 (d, $^1J_{B,H}$ = 150 Hz, 2 B, B-4 and -7), –10.0 (d, $^1J_{B,H}$ = 144 Hz, 2 B, B-9 and -12), –17.6 (d, $^1J_{B,H}$ = 162 Hz, 2 B, B-5 and -11), –22.0 (d, $^1J_{B,H}$ = 175, 1 B, B-6) ppm. ^{13}C{^{1}H} NMR ([D_3]acetonitrile): δ = 93.3 (s, η^6-benzene), 50.8 (br. s, C_c-H), 25.7 (s, Me_2S) ppm.

[1a]PF_6: ^{1}H NMR ([D_6]acetone): δ = 6.80 (s, 6 H, η^6-benzene), 4.64 (br. s, 2 H, C_c-*H*), 2.63 (s, 6 H, Me_2S) ppm. ^{1}H{^{11}B} NMR ([D_6]acetone; only signals due to B-H protons are given): δ = 3.40 (br. s, 1 H), 3.02 (br. s, 2 H), 1.86 (br. s, 2 H), 1.70 (m, 3 H) ppm. ^{11}B NMR ([D_6]acetone): δ = 7.1 (s, 1 B, B-8), 1.9 (d, $^1J_{B,H}$ = 148 Hz, 1 B, B-10), –6.9 (d, $^1J_{B,H}$ = 153 Hz, 2 B, B-4 and -7), –9.8 (d, $^1J_{B,H}$ = 144 Hz, 2 B, B-9 and -12), –17.5 (d, $^1J_{B,H}$ = 155 Hz, 2 B, B-5 and 11), –22.0 (d, $^1J_{B,H}$ = 169 Hz, 1 B, B-6) ppm. ^{13}C{^{1}H} NMR ([D_6]acetone): δ = 92.6 (s, η^6-benzene), 49.4 (br. s, C_c-H), 24.5 (s, Me_2S) ppm. ^{31}P NMR ([D_6]acetone): δ = –143.7 (sept, $^1J_{P,F}$ = 708 Hz, PF_6) ppm.

4: Concentration of the above-mentioned supernatant orange THF solution afforded a mixture of **4** and *closo*-[3,3′-Ru-(8-Me_2S-1,2-$C_2B_9H_{10}$)$_2$] as an orange residue. Chromatographic separation on silica gel using THF as the eluent afforded *closo*-[3,3′-Ru-(8-Me_2S-1,2-$C_2B_9H_{10}$)$_2$] (R_f = 0.63) as a yellow-orange solid (10.0 mg, 0.020 mmol, 8%) and **4** (R_f = 0.50) as a yellow solid after washing with cold CH_2Cl_2 (36.4 mg, 0.106 mmol, 22%). $C_8H_{17}B_9RuS$ (343.65): calcd. C 27.96, H 4.99, S 9.33; found C 28.09, H 4.74, S 8.39. ^{1}H NMR ([D_6]acetone): δ = 6.38 (s, 6 H, η^6-benzene), 4.31 (br. s, 2 H, C_c-*H*), 0.87 (br. m, 1 H, S*H*) ppm. ^{1}H{^{11}B} NMR ([D_6]acetone; only signals due to B-H protons are given): δ = 3.09 (br. s, 1 H), 2.91 (br. s, 2 H), 1.99 (br. s, 2 H), 1.53 (br. s, 2 H), 1.31 (br. s, 1 H) ppm. ^{11}B NMR ([D_6]acetone): δ = 14.3 (s, 1 B, B-8), –1.1 (d, $^1J_{B,H}$ = 140 Hz, 1 B, B-10), –6.9 (d, $^1J_{B,H}$ = 144 Hz, 2 B, B-4 and -7), –8.5 (d, $^1J_{B,H}$ = 160 Hz, 2 B, B-9 and -12), –20.0 [d, $^1J_{B,H}$ = 155 Hz, 2 B, B-5 and -11), –27.5 (d, $^1J_{B,H}$ = 170 Hz, 1B, B-6) ppm. ^{13}C{^{1}H} NMR ([D_6]acetone): δ = 92.1 (s, η^6-benzene), 46.2 (br. s, C_c-H) ppm.

The synthesis was repeated in a modified form to identify the volatile by-product MeCl. A Schlenk flask was charged with 10-Me_2S-7,8-*nido*-$C_2B_9H_{11}$ (294.0 mg, 1.513 mmol), *t*BuOK (1.65 mL, 1.0 M) and THF (20 mL). The mixture was stirred at room temperature for 30 min affording a clear pale-yellow solution. The flask was then charged with [$RuCl_2$(η^6-benzene)]$_2$ (369.9 mg, 0.740 mmol), closed with a rubber stopper and the resultant heterogeneous brown mixture was stirred at room temperature for 3 d. MeCl gas was detected using gas chromatography by comparing the retention time with that of an authentic sample. ^{1}H NMR identification was also carried out (see in situ NMR studies below).

***closo*-[3-Ru(η^6-benzene)-8-THT-1,2-$C_2B_9H_{10}$]$^+$ (1b) and 4:** The general procedure described above was applied using *nido*-[10-THT-7,8-$C_2B_9H_{11}$] (103.9 mg, 0.471 mmol), *t*BuOK (0.48 mL, 1.0 M),

 © 2005 Wiley-VCH Verlag GmbH & Co. KGaA, Weinheim

THF (5 mL), $[RuCl_2(\eta^6\text{-benzene})]_2$ (116.9 mg, 0.234 mmol) and $NaPF_6$ (165 mg, 0.982 mmol) to give **[1b]PF_6** (51.0 mg, 0.094 mmol, 20%). The neutral complex **4** was separated and purified by chromatography as described above (41.7 mg, 0.121 mmol, 26%).

[1b]Cl: ^{1}H NMR ([D$_3$]acetonitrile): δ = 6.53 (s, 6 H, η^6-benzene), 4.42 (br. s, 2 H, C$_c$-*H*), 3.45 [m, 2 H, S(C*H*H′CH′′H′′′)$_2$], 3.03 [m, 2 H, S(CH*H*′CH′′H′′′)$_2$], 2.12 [br. t, $^3J_{H,H}$ = 7.5 Hz, 2 H, S(CHH′C*H*′′H′′′)$_2$], 2.10 ppm [br. t, $^3J_{H,H}$ = 7.8 Hz, 2 H, S(CHH′CH′′*H*′′′)$_2$]. ^{11}B NMR ([D$_3$]acetonitrile): δ = 7.4 (s, 1 B, B-8), 2.2 (d, $^1J_{B,H}$ = 144 Hz, 1 B, B-10), –6.7 [d, $^1J_{B,H}$ = 151 Hz, 2 B, B-4 and -7), –9.7 (d, $^1J_{B,H}$ = 145 Hz, 2 B, B-9 and -12), –17.8 (d, $^1J_{B,H}$ = 160 Hz, 2 B, B-5 and -11), –22.1 (d, $^1J_{B,H}$ = 183 Hz, 1 B, B-6) ppm. ^{13}C{^{1}H} NMR ([D$_3$]acetonitrile): δ = 93.4 (s, η^6-benzene), 51.0 (s, *C*$_c$-H), 44.5 [s, S(*C*H$_2$CH$_2$)$_2$], 30.4 [s, S(CH$_2$*C*H$_2$)$_2$] ppm.

[1b]PF_6: $C_{12}H_{24}B_9F_6PRuS$ (543.72): calcd. C 26.51, H 4.45, S 5.90; found C 26.72, H 4.46, S 6.00. MALDI-TOF: *m*/*z* (%) = 397.9 (74) [M + 1], 309.8 (100) [M + 1 – (CH$_2$)$_4$S]. ^{1}H NMR ([D$_6$]acetone): δ = 6.82 (s, 6 H, η^6-benzene), 4.67 (br. s, 2 H, C$_c$-*H*), 3.72 [m, 2 H, S(C*H*H′CH′′H′′′)$_2$], 3.20 [m, 2 H, S(CH*H*′CH′′H′′′)$_2$], 2.22 [br. t, $^3J_{H,H}$ = 7.5 Hz, 2 H, S(CHH′C*H*′′H′′′)$_2$], 2.20 ppm [br. t, $^3J_{H,H}$ = 6.6 Hz, 2 H, S(CHH′CH′′*H*′′′)$_2$]. ^{1}H{^{11}B} NMR ([D$_6$]acetone; only signals due to B-H protons are given): δ = 3.42 (br. s, 1 H), 3.06 (br. s, 2 H), 1.78 (br. s, 2 H), 1.68 (br. s, 3 H) ppm. ^{11}B NMR ([D$_6$]acetone): δ = 6.2 (s, 1 B, B-8), 1.2 (d, $^1J_{B,H}$ = 147 ppm, 1 B, B-10), –8.0 (d, $^1J_{B,H}$ = 152 Hz, 2 B, B-4 and -7), –10.7 (d, $^1J_{B,H}$ = 144 Hz, 2 B, B-9 and -12), –19.0 (d, $^1J_{B,H}$ = 156 Hz, 2 B, B-5 and -11), –23.3 (d, $^1J_{B,H}$ = 174 Hz, 1 B, B-6) ppm. ^{13}C{^{1}H} NMR ([D$_6$] acetone): δ = 92.4 (s, η^6-benzene), 49.3 (s, *C*$_c$-H), 45.7 [s, S(*C*H$_2$CH$_2$)$_2$], 43.2 [s, S(CH$_2$*C*H$_2$)$_2$] ppm. ^{31}P{^{1}H} NMR ([D$_6$]acetone): δ = –146.0 (sept, $^1J_{P,F}$ = 705 Hz, PF_6) ppm.

***closo*-[3-Ru(η^6-benzene)-8-EtPhS-1,2-$C_2B_9H_{10}$]$^+$ (1c) and 4:** The general procedure described above was applied using *nido*-[10-EtPhS-7,8-$C_2B_9H_{11}$] (116.6 mg, 0.431 mmol), *t*BuOK (0.47 mL, 1.0 M), THF (15 mL), $[RuCl_2(\eta^6\text{-benzene})]_2$ (107.9 mg, 0.216 mmol) and $NaPF_6$ (82.9 mg, 0.494 mmol) to afford **[1c]**PF_6 (44.0 mg, 0.074 mmol, 17%). The neutral complex **4** (41.7 mg, 0.121 mmol, 28%) was isolated by chromatography as in the previous procedure.

[1c]Cl: ^{1}H NMR ([D$_3$]acetonitrile): δ = 7.80–7.50 (m, 5 H, S*Ph*), 6.34 (s, 6 H, η^6-benzene), 4.35 (br. s, 2 H, C$_c$-*H*), 3.40–3.15 [m, 2 H, S(C*H*$_2$CH$_3$)], 1.14 [t, $^3J_{H,H}$ = 7.2 Hz, 3 H, S(CH$_2$C*H*$_3$)] ppm.[27] ^{11}B NMR ([D$_3$]acetonitrile): δ = 7.0 (s, 1 B, B-8), 2.1 (d, $^1J_{B,H}$ = 170 Hz, 1 B, B-10), –6.7 (d, $^1J_{B,H}$ = 139 Hz, 2 B, B-4 and -7), –9.4 (d, $^1J_{B,H}$ = 133 Hz, 1 B, B-9 or -12), –9.9 (d, $^1J_{B,H}$ = 122 Hz, 1 B, B-12 or -9), –17.6 (d, $^1J_{B,H}$ = 162 Hz, 2 B, B-5 and -11), –21.8 (d, $^1J_{B,H}$ = 190 Hz, 1 B, B-6) ppm. ^{13}C{^{1}H} NMR ([D$_3$]acetonitrile): δ = 134.2, 133.0, 131.7 (3 s, *o*-, *m*- and *p*-S*Ph*), 93.2 (s, η^6-benzene), 49.9 (s, *C*$_c$-H), 49.3 (s, *C*$_c$′-H), 38.7 [s, S(*C*H$_2$CH$_3$)], 11.5 [s, S(CH$_2$*C*H$_3$)] ppm.

[1c]PF_6: MALDI-TOF: *m*/*z* (%) = 448.95 (77) [M], 310.93 (100) [M – EtPhS]. ^{1}H NMR ([D$_6$]acetone): δ = 7.80 (d, $^3J_{H,H}$ = 6.9 Hz 2 H, *o*-S*Ph*), 7.80 (d, $^3J_{H,H}$ = 7.2 Hz, 1 H, *p*-S*Ph*), 7.73 (t, $^3J_{H,H}$ = 6.9 Hz, 2 H, *m*-S*Ph*), 6.62 (s, 6 H, η^6-benzene), 4.61 (br. s, 2 H, C$_c$-*H*), 3.50 [dq, $^2J_{H,H}$ = 13.2 Hz, $^3J_{H,H}$ = 7.3 Hz, 1 H, S(C*H*H′CH$_3$)], 3.41 [dq, $^2J_{H,H}$ = 13.2 Hz, $^3J_{H,H}$ = 7.3 Hz, 1 H, S(CH*H*′CH$_3$)], 1.27 [t, $^3J_{H,H}$ = 7.3 Hz, 3 H, S(CHH′C*H*$_3$)] ppm.[28] ^{11}B NMR ([D$_6$] acetone): δ = 7.1 (s, 1 B, B-8), 2.1 (d, $^1J_{B,H}$ = 148 Hz, 1 B, B-10), –6.6 (d, $^1J_{B,H}$ = 145 Hz, 2 B, B-4 and -7), –9.2 (d, $^1J_{B,H}$ = 141 Hz, 1 B, B-9 or -12), –9.9 (d, $^1J_{B,H}$ = 132 Hz, 1 B, B-12 or -9), –17.6 (d, $^1J_{B,H}$ = 154 Hz, 2 B, B-5 and -11), –21.7 (d, $^1J_{B,H}$ = 172 Hz, 1 B, B-6) ppm. ^{13}C{^{1}H} NMR ([D$_6$]acetone): δ = 133.3, 132.1, 130.7 (3 s, *o*-, *m*- and *p*-S*Ph*), 124.4 (s, *i*-S*Ph*), 92.5 (s, η^6-benzene), 49.9 (s, *C*$_c$-H), 49.2 (s, *C*$_c$′-H), 37.6 [s, S(*C*H$_2$CH$_3$)], 10.7 [s, S(CH$_2$*C*H$_3$)] ppm. ^{31}P{^{1}H} NMR ([D$_6$]acetone): δ = –142.7 (sept, $^1J_{P,F}$ = 708 Hz, PF_6) ppm.

The reaction was repeated in a modified fashion to identify the by-products PhCl and EtCl. 10-Me$_2$S-7,8-*nido*-$C_2B_9H_{11}$ (14.8 mg, 0.055 mmol), [D$_8$]THF (0.50 mL) and a THF solution of *t*BuOK (0.066 mL, 1.0 M) were placed into an NMR tube. The clear solution rapidly turned light yellow. After 20 min, the solution was transferred under N_2 by syringe to another NMR tube containing $[RuCl_2(\eta^6\text{-benzene})]_2$ (13.4 mg, 0.026 mmol). PhCl [δ = 7.34–7.18 (m) ppm] and EtPhS [δ = 7.30–7.35 (m, 5 H, *Ph*), 2.95 (q, $^3J_{H,H}$ = 7.5 Hz, 2 H, *Et*), 1.26 (t, $^3J_{H,H}$ = 7.5 Hz, 3 H, *Et*) ppm] were detected by ^{1}H NMR spectroscopy. Signals for THF prevented identification of EtCl due to overlapping of signals (proton resonances for terminal B-H groups appear as broad unresolved peaks in the range $\delta \approx$ 3.5–1.0 ppm).

***closo*-[3-Ru(η^6-benzene)-1-Me-8-Me$_2$S-1,2-$C_2B_9H_9$]$^+$ (2a) and *closo*-[3-Ru(η^6-benzene)-1-Me-8-HS-1,2-$C_2B_9H_9$] (5):** The general procedure described above was applied using *nido*-[10-Me$_2$S-7-Me-8-$C_2B_9H_{10}$] (104.8 mg, 0.502 mmol), *t*BuOK (0.55 mL, 1.0 M), THF (10 mL), $[RuCl_2(\eta^6\text{-benzene})]_2$ (125.7 mg, 0.251 mmol) and $NaPF_6$ (114.0 mg, 0.665 mmol) to afford traces of **[2a]**PF_6. The neutral complex **5** was purified by chromatography as described above (52.0 mg, 0.145 mmol, 29%).

[2a]PF_6: Selected NMR spectroscopic data are given: ^{1}H NMR ([D$_6$]acetone): δ = 6.82 (s, 6 H, η^6-benzene), 4.97 (br. s, 1 H, C$_c$-*H*), 2.25 (s, 3 H, C$_c$-*Me*), 2.66 (s, 3 H, S*Me*$_2$), 2.60 (s, 3 H, S*Me*$_2$) ppm. ^{11}B NMR ([D$_6$]acetone): δ = 6.1 (s, 1 B, B-8), 1.7 (d, $^1J_{B,H}$ = 156 Hz, 1 B, B-10), –4.5 to –18.5 (m, 6 B, B-4, -5, -7, -9, -11 and -12), –22.1 (d, $^1J_{B,H}$ = 177 Hz, 1 B, B-6) ppm. ^{31}P{^{1}H} NMR ([D$_6$] acetone): δ = –142.6 (sept, $^1J_{P,F}$ = 707 Hz, PF_6) ppm.

5: $C_9H_{19}B_9RuS$ (357.68): calcd. C 30.22, H 5.35, S 8.96; found C 30.15, H 5.20, S 9.10. ^{1}H NMR ([D$_6$]acetone): δ = 6.40 (s, 6 H, η^6-benzene), 4.60 (br. s, 1 H, C$_c$-*H*), 2.17 (s, 3 H, C$_c$-*Me*), 0.87 (br. m, 1 H, S*H*) ppm. ^{1}H{^{11}B} NMR ([D$_6$]acetone; only signals due to B-H protons are given): δ = 3.17 (br. s, 2 H), 3.02 (br. s, 1 H), 2.07 (br. s, 2 H), 1.82 (br. s, 1 H), 1.62 (br. s, 2 H) ppm. ^{11}B NMR ([D$_6$] acetone): δ = 15.0 (s, 1 B, B-8), 0.0 (d, $^1J_{B,H}$ = 143 Hz, 1 B, B-10), –3.5 to –9.4 (4 B, B-4, -7, -9 and -12) (these signals can be clearly observed in the ^{11}B{^{1}H } NMR spectrum as singlets for 1 B each at δ = –4.2, –5.5, –7.8, –8.6 ppm), –15.1 (d, $^1J_{B,H}$ = 155 Hz, 1 B, B-5 or -11), –18.6 (d, $^1J_{B,H}$ = 156 Hz, 1 B, B-11 or -5), –22.0 (d, $^1J_{B,H}$ = 172 Hz, 1 B, B-6) ppm. ^{13}C{^{1}H} NMR ([D$_6$]acetone): δ = 93.02 (s, η^6-benzene), 68.40 (br. s, *C*$_c$-Me), 55.03 (br. s, *C*$_c$-H), 35.15 (s, C$_c$-*Me*) ppm.

***closo*-[3-Ru(η^6-*p*-cymene)-8-Me$_2$S-1,2-$C_2B_9H_{10}$]$^+$ (3a) and *closo*-[3-Ru(η^6-*p*-cymene)-8-HS-1,2-$C_2B_9H_{10}$] (6):** The general procedure described above was applied using *nido*-[10-Me$_2$S-7,8-$C_2B_9H_{11}$] (90.5 mg, 0.466 mmol), *t*BuOK (0.51 mL, 1.0 M), THF (15 mL), $[RuCl_2(\eta^6\text{-}p\text{-cymene})]_2$ (143.1 mg, 0.234 mmol) and $NaPF_6$ (78.8 mg, 0.469 mmol) to afford **[3a]**PF_6 (107.3 mg, 0.187 mmol, 40%). From the procedure described above, a brown-orange oily mixture, which was found to include the neutral complexes **6** (R_f = 0.69) and *closo*-[3,3′-Ru-(8-Me$_2$S-1,2-$C_2B_9H_{10}$)$_2$] (R_f = 0.63), was obtained and characterised spectroscopically.

[3a]Cl: ^{1}H NMR ([D$_3$]acetonitrile): δ = 6.38 (d, $^2J_{H,H}$ = 6.6 Hz, 2 H, *m*- of *p*-cymene), 6.33 (d, $^2J_{H,H}$ = 6.6 Hz, 2 H, *o*- of *p*-cymene), 4.30 (br. s, 2 H, C$_c$-*H*), 2.98 (sept, $^3J_{H,H}$ = 6.6 Hz, 1 H, MeC$_6$H$_4$C*H*Me$_2$), 2.46 (s, 6 H, *Me*$_2$S), 2.42 (S, 3 H, *Me*C$_6$H$_4$CHMe$_2$), 1.32 (d, $^3J_{H,H}$ = 6.9 Hz, 6 H, MeC$_6$H$_4$CH*Me*$_2$)

 © 2005 Wiley-VCH Verlag GmbH & Co. KGaA, Weinheim

ppm. $^1H\{^{11}B\}$ NMR ([D$_3$]acetonitrile; only signals due to B-H protons are given): δ = 3.31 (br. s, 1 H), 2.64 (br. s, 2 H), 2.50–2.30 (m, 2 H), 1.79 (br. s, 1 H), 1.66 (br. s, 2 H) ppm. ^{11}B NMR ([D$_3$] acetonitrile): δ = 7.0 (s, 1 B, B-8), 1.0 (d, $^1J_{B,H}$ = 138 Hz, 1 B, B-10), –5.8 (d, $^1J_{B,H}$ = 146 Hz, 2 B, B-4 and 7), –9.9 (d, $^1J_{B,H}$ = 144 Hz, 2 B, B-9 and -12), –17.7 (d, $^1J_{B,H}$ = 165 Hz, 2 B, B-5 and -11), –21.7 (d, $^1J_{B,H}$ = 169 Hz, 1 B, B-6) ppm. $^{13}C\{^1H\}$ NMR ([D$_3$] acetonitrile): δ = 115.7 (s, *C*CHMe$_2$), 106.4 (s, Me*C*), 92.1 (s, *o*- of *p*-cymene), 89.5 (s, *m*- of *p*-cymene), 49.5 (s, C_c-H), 31.3 (s, MeC$_6$H$_4$*C*HMe$_2$), 24.8 (s, S*Me*$_2$), 21.8 (s, *Me*C$_6$H$_4$CHMe$_2$), 18.0 (s, MeC$_6$H$_4$CH*Me*$_2$) ppm.

[3a]PF$_6$: $RuC_{14}H_{30}B_9SPF_6$ (573.79): calcd. C 29.31, H 5.27, S 5.59; found C 29.56, H 5.29, S 5.47. MALDI-TOF: *m*/*z* (%) = 429.00 (100) [M], 363.97 (22) [M – Me$_2$S – 3 H]. ^1H NMR ([D$_6$]acetone): δ = 6.63 (d, $^2J_{H,H}$ = 6.6 Hz, 2 H, *m*- of *p*-cymene), 6.58 (d, $^2J_{H,H}$ = 6.6 Hz, 2 H, *o*- of *p*-cymene), 4.49 (br. s, 2 H, C_c-*H*), 3.11 (sept, $^3J_{H,H}$ = 6.8 Hz, 1 H, MeC$_6$H$_4$C*H*Me$_2$), 2.65 (s, 6 H, *Me*$_2$S), 2.53 (S, 3 H, *Me*C$_6$H$_4$CHMe$_2$), 1.38 (d, $^3J_{H,H}$ = 6.9 Hz, 6 H, MeC$_6$H$_4$CH*Me*$_2$) ppm. $^1H\{^{11}B\}$ NMR ([D$_6$]acetone; only signals due to B-H protons are given): δ = 3.38 (br. s, 1 H), 2.80–2.50 (br. s, 2 H), 1.86 (br. s, 2 H), 1.69 (br. s, 3 H) ppm. ^{11}B NMR ([D$_6$] acetone): δ = 7.2 (s, 1 B, B-8), 1.2 (d, $^1J_{B,H}$ = 144 Hz, 1 B, B-10), –5.7 (d, $^1J_{B,H}$ = 146 Hz, 2 B, B-4 and -7), –9.8 (d, $^1J_{B,H}$ = 142 Hz, 2 B, B-9 and -12), –17.6 (d, $^1J_{B,H}$ = 159 Hz, 2 B, B-5 and -11), –21.6 (d, $^1J_{B,H}$ = 195 Hz, 1 B, B-6) ppm. $^{13}C\{^1H\}$ NMR ([D$_6$]acetone): δ = 116.0 (s, *C*CHMe$_2$), 106.8 (s, Me*C*), 92.5 (s, *o*- of *p*-cymene), 89.9 (s, *m*- of *p*-cymene), 49.5 (s, C_c-H), 31.7 (s, MeC$_6$H$_4$*C*HMe$_2$), 24.9 (s, *Me*$_2$S), 22.1 (s, *Me*C$_6$H$_4$CHMe$_2$), 18.2 (s, MeC$_6$H$_4$CH*Me*$_2$) ppm. $^{31}P\{^1H\}$ NMR ([D$_6$]acetone): δ = –145.6 (sept, $^1J_{P,F}$ = 708 Hz, PF$_6$) ppm.

6: ^1H NMR ([D$_6$]acetone): δ = 6.17 (d, $^2J_{H,H}$ = 6.5 Hz, 2 H, *m*- of *p*-cymene), 6.10 (d, $^2J_{H,H}$ = 6.5 Hz, 2 H, *o*- of *p*-cymene), 4.19 (br. s, 2 H, C_c-*H*), 3.02 (sept, $^3J_{H,H}$ = 7.2 Hz, 1 H, MeC$_6$H$_4$C*H*Me$_2$), 2.43 (s, 3 H, *Me*C), 1.35 (d, $^3J_{H,H}$ = 6.9 Hz, 6 H, MeC$_6$H$_4$CH*Me*$_2$) ppm. ^{11}B NMR ([D$_6$]acetone): δ = 13.6 (s, 1 B, B-8), –2.9 (d, $^1J_{B,H}$ = 143 Hz, 1 B, B-10), –7.7 (d, $^1J_{B,H}$ = 137 Hz, 4 B, B-4, -7, -9 and -12), –20.9 (d, $^1J_{B,H}$ = 154 Hz, 2 B, B-5 and -11), –27.9 (d, $^1J_{B,H}$ = 183 Hz, 1 B, B-6) ppm. $^{13}C\{^1H\}$ NMR ([D$_6$]acetone): δ = 113.2 (s, *C*CHMe$_2$), 104.1 (s, Me*C*), 92.9 (s, *o*- of *p*-cymene), 89.7 (s, *m*- of *p*-cymene), 46.1 (s, C_c-H), 31.5 (s, MeC$_6$H$_4$*C*HMe$_2$), 22.1 (s, *Me*C$_6$H$_4$CHMe$_2$), 18.0 (s, MeC$_6$H$_4$CH*Me*$_2$) ppm.

***closo*-[3-Ru(η^6-benzene)-7-MeS-1,2-C$_2$B$_9$H$_{10}$] (8):** A Schlenk flask was charged with *t*BuOK (52.5 mg, 0.408 mmol), *nido*-[9-Me$_2$S-7,8-C$_2$B$_9$H$_{11}$] (64.9 mg, 0.334 mmol), THF (10 mL) and CH$_3$CN (1.0 mL). The mixture was stirred at room temperature for 30 min giving a clear pale yellow solution. The flask was then charged with [RuCl$_2$(η^6-benzene)]$_2$ (81.5 mg, 0.167 mmol) and the resultant heterogeneous brown mixture was stirred at room temperature for 3 d. The supernatant orange solution was filtered using a cannula and transferred into another Schlenk vessel. The remaining solid residue was washed with further THF (2×5 mL) and combined with the orange solution. The orange residue obtained after evaporation of the THF was then filtered through a short silica gel column using CH$_2$Cl$_2$ as eluent. Concentration of the eluate gave a yellow-orange solid which was washed with Et$_2$O (2×5 mL) to eliminate of the remaining 9-Me$_2$S-7,8-*nido*-C$_2$B$_9$H$_{11}$ and complex **8** was obtained as a yellow solid (40.8 mg, 0.114 mmol, 34%). $C_8H_{17}B_9RuS$ (343.65): calcd. C 30.22, H 5.35, S 8.96; found C 30.24, H 5.37, S 8.71. ^1H NMR ([D$_6$]acetone): δ = 6.34 (s, 6 H, η^6-benzene), 4.51 (br. s, 1 H, C_c-*H*), 4.30 (br. s, 1 H, C_c-*H*′), 1.87 ppm (s, 3 H, *Me*S). $^1H\{^{11}B\}$ NMR ([D$_6$]acetone; only signals due to B-H protons are given): δ = 3.22 (br. s, 1 H), 2.98 (br. s, 1 H), 2.49 (br. s, 1 H), 1.64 (br. s, 2 H), 1.38 (br. m, 3 H) ppm. ^{11}B NMR ([D$_6$]acetone): δ = 6.4 (s, 1 B, B-7), 4.91 (d, $^1J_{B,H}$ = 114 Hz; this resonance overlaps partially with the signal at δ = 6.36 ppm so that the coupling constant is an estimate, 1 B, B-8), 1.2 (d, $^1J_{B,H}$ = 127 Hz, 1 B, B-10), –6.6 (d, $^1J_{B,H}$ = 159 Hz, 2 B, B-4 and -12), –8.3 (d, $^1J_{B,H}$ = 171 Hz, 1 B, B-9), –17.0 (d, $^1J_{B,H}$ = 159 Hz, 1 B, B-5), –20.2 (d, $^1J_{B,H}$ = 169 Hz, 1 B, B-11), –22.1 (d, $^1J_{B,H}$ = 197 Hz, 1 B, B-6) ppm. $^{13}C\{^1H\}$ NMR ([D$_6$]acetone): δ = 91.0 (s, η^6-benzene), 51.0 (br. s, C_c-H), 47.3 (br. s, C'_c-H), 14.7 (s, *Me*S) ppm.

Reaction of *closo*-[3-Ru(η^6-benzene)-8-Me$_2$S-1,2-C$_2$B$_9$H$_{10}$][PF$_6$] ([1a]PF$_6$) with [Bu$_4$N]Cl: A 5-mm NMR tube was charged with solid [**1a**]PF$_6$ (22.9 mg, 0.044 mmol), [Bu$_4$N]Cl (13.6 mg, 0.046 mmol) and [D$_6$]acetone (0.50 mL). A beige precipitate was observed after a few minutes and a remaining pale yellow solution. After 1 h, ^1H and ^{11}B NMR spectra showed no change in the chemical shifts for all species but the ratio of [**1a**]$^+$/[Bu$_4$N]$^+$ was found to be 1:2. Addition of D$_2$O (0.50 mL) was followed by dissolution of the precipitate and the ratio between the latter species was restored to 1:1. Whereas [**1a**]PF$_6$ and [Bu$_4$N]Cl are readily soluble in [D$_6$]acetone, [**1a**]Cl is only partially soluble. The NMR experiment can be explained by a simple anion exchange reaction as shown in Equation (2).

Reaction of [RuCl$_2$(η^6-benzene)]$_2$ with *nido*-[10-Me$_2$S-7,8-C$_2$B$_9$H$_{10}$][K]. In situ NMR Studies: An analogous procedure for the deprotonation of the carborane was applied: *nido*-[10-Me$_2$S-7,8-C$_2$B$_9$H$_{11}$] (10.7 mg, 0.055 mmol), [D$_8$]THF (0.50 mL) and a THF solution of *t*BuOK (0.07 mL, 1.0 M) were mixed. The clear solution rapidly turned light yellow. After 20 min, ^1H and ^{11}B NMR spectra showed 100% conversion of *nido*-[10-Me$_2$S-7,8-C$_2$B$_9$H$_{11}$] to *nido*-K[10-Me$_2$S-7,8-C$_2$B$_9$H$_{10}$] with concomitant formation of *t*BuOH. The solution was then transferred by syringe to another NMR tube containing [RuCl$_2$(η^6-benzene)]$_2$ (13.7 mg, 0.028 mmol) under N$_2$. NMR spectra of the heterogeneous mixture were frequently recorded over a period of 6 d. Due to low solubility of the ruthenacarborane [**1a**]Cl, no quantitative measure of concentration of the species was obtained. However, the experiment clearly showed a gradual and constant increase in **1a** and **4**, whereas *nido*-K[10-Me$_2$S-7,8-C$_2$B$_9$H$_{10}$] decreased. A small amount of reprotonation of the latter was observed, probably due to moisture in the solvent. MeCl (δ = 3.06 ppm) was also detected by ^1H NMR spectroscopy and a broad resonance at low field (δ = – 4.27 ppm) was observed during the experiment which could be due to a B–H→Ru agostic interaction. NMR spectroscopic data for *nido*-K[10-Me$_2$S-7,8-C$_2$B$_9$H$_{10}$]: ^1H NMR ([D$_8$]THF): δ = 2.37 (s, 6 H, *Me*$_2$S), 0.85 (br. s, 2 H, C_c-*H*) ppm. $^1H\{^{11}B\}$ NMR ([D$_6$]acetone; only signals due to B-H protons are given): δ = 1.59 (br. s, 1 H), 1.0–0.6 (m, 6 H), –0.16 (br. s, 1 H) ppm. ^{11}B NMR ([D$_8$]THF, 96 MHz): δ = –14.1 (br. s, 1 B, B-8), –18.2 (d, $^1J_{B,H}$ = 135 Hz, 3 B), –19.6 (d, $^1J_{B,H}$ = 135 Hz, 2 B), –25.4 (d, $^1J_{B,H}$ = 132 Hz, 2 B), –45.9 (d, $^1J_{B,H}$ = 134 Hz, 1 B, B-10) ppm.

Photolysis of *closo*-[3-Ru(η^6-arene)-8-Me$_2$S-1,2-C$_2$B$_9$H$_{10}$][PF$_6$]: An acetonitrile solution (8.0 mL) of the benzene complex [**1a**]PF$_6$ (36.4 mg, 0.070 mmol) or *p*-cymene complex [**3a**]PF$_6$ (40.7 mg, 0.071 mmol) was irradiated with stirring for 3–5 d. Evaporation of the solvent afforded unreacted starting material.

Calculation Details: The geometries for *nido*-[10- and 9-MeS-7,8-C$_2$B$_9$H$_{10}$]$^{2-}$ were obtained from the X-ray structures of *nido*-[10- and 9-Me$_2$S-7,8-C$_2$B$_9$H$_{11}$].[4c,28] Geometries were then optimised with AM1 semiempirical methods and a single-point UHF calculation at the 3-21G level using Hyperchem Release 7 for Windows (Hypercube Inc.). A summary of selected charges is outlined in Scheme 5.

 © 2005 Wiley-VCH Verlag GmbH & Co. KGaA, Weinheim

Crystallography: Colourless crystals of **[1a]**PF_6 were obtained from acetone at room temperature. Cell parameters and intensity data were collected with a Bruker Nonius Kappa CCD diffractometer mounted at the window of a molybdenum rotating anode according to standard procedures. Crystal data for **1a**: Colourless block, $0.38 \times 0.36 \times 0.20$ mm, $C_{10}H_{22}B_9F_6PRuS$, M_r = 517.67, T = 120(2) K, monoclinic, $P2_1/c$, a = 6.6900(3), b = 30.6880(14), c = 9.4050(3) Å, β = 92.916(2)°, V = 1928.37(14) Å^3, Z = 4, $\rho_{calcd.}$ = 1.783 g cm^{-3}, $2\theta_{max}$ = 27.47°, Mo-K_α (0.71073 Å) radiation, φ and ω scans used to fill the asymmetric unit, 13685 reflections measured, 4324 independent reflections used in the refinement, R_{int} = 0.0253, Lorentz polarisation corrections were made using Scalepack,[29] a multi-scan absorption correction was applied using SADABS[30] (μ = 1.054 mm^{-1}, min/max transmission factor ratio = 0.811856), the structure was solved by direct methods and refined using full-matrix least squares with SHELX-97,[31] 253 parameters were refined and hydrogen atoms were placed in calculated positions and refined using a riding model, final R indices [$I > 2\sigma(I)$]: R_1 = 0.0267, wR_2 = 0.0818, R indices (all data): R_1 = 0.0323. wR_2 = 0.0860, largest difference peak/hole: 0.508/–0.486 e Å^{-3}. CCDC-264406 contains the supplementary crystallographic data for this paper. These data can be obtained free of charge from The Cambridge Crystallographic Data Centre via www.ccdc.cam.ac.uk/data_request/cif.

Acknowlegments

We thank CICYT (Project MAT2004-01108), Generalitat de Catalunya (2001/SGR/00337), CSIC (I3P contract to J. G. P.), and the UK EPSRC for support.

[1] a) M. F. Hawthorne, D. C. Young, P. A. Wegner, *J. Am. Chem. Soc.* **1965**, *87*, 1818–1819; b) M. F. Hawthorne, D. C. Young, T. D. Andrews, D. V. Howe, R. L. Pilling, A. D. Pitts, M. Reintjes, L. F. Warren, Jr., P. A. Wegner, *J. Am. Chem. Soc.* **1968**, *90*, 879–896; c) M. F. Hawthorne, *Pure Appl. Chem.* **1973**, *33*, 475; d) K. P. Callahan, M. F. Hawthorne, *Adv. Organomet. Chem.* **1976**, *14*, 145; e) R. N. Grimes, in: *Comprehensive Organometallic Chemistry*, vol. 1 (Eds.: G. Wilkinson, F. G. A. Stone, E. W. Abel), Pergamon, New York, **1982**, pp. 459–537; f) R. N. Grimes, in: *Comprehensive Organometallic Chemistry II*, vol. 1 (Eds.: E. W. Abel, F. G. A. Stone, G. Wilkinson), Pergamon, New York, **1995**, pp. 373–425.

[2] D. M. P. Mingos, *J. Chem. Soc., Dalton Trans.* **1977**, 602–610.

[3] a) F. N. Tebbe, P. M. Garret, M. F. Hawthorne, *J. Am. Chem. Soc.* **1968**, *90*, 869–879; b) D. C. Young, D. V. Howe, M. F. Hawthorne, *J. Am. Chem. Soc.* **1969**, *91*, 859–862; c) J. Plešek, Z. Janousek, S. Heřmánek, *Collect. Czech. Chem. Commun.* **1978**, *43*, 2862–2868; d) H. C. Kang, S. S. Lee, C. B. Knobler, M. F. Hawthorne, *Inorg. Chem.* **1991**, *30*, 2024–2031; e) G. M. Rosair, A. J. Welch, A. S. Weller, S. K. Zahn, *J. Organomet. Chem.* **1997**, *536*, 299–308; f) G. M. Rosair, A. J. Welch, A. S. Weller, *Organometallics* **1998**, *17*, 3227–3235; g) S. Dunn, R. M. Garrioch, G. M. Rosair, L. Smith, A. J. Welch, *Collect. Czech. Chem. Commun.* **1999**, *64*, 1013–1027; h) O. Tutusaus, R. Nuñez, C. Viñas, F. Teixidor, I. Mata, E. Molins, *Inorg. Chem.* **2004**, *43*, 6067–6074; i) R. Nuñez, O. Tutusaus, F. Teixidor, C. Viñas, R. Sillanpää, R. Kivekäs, *Organometallics* **2004**, *23*, 2273–2280.

[4] a) J. Plešek, Z. Janousek, S. Heřmánek, *Inorg. Synth.* **1983**, *22*, 239; b) J. Plešek, T. Jelínek, F. Mares, S. Heřmánek, *Collect. Czech. Chem. Commun.* **1993**, *58*, 1534–1547; c) Y.-K. Yan, D. M. P. Mingos, T. E. Müller, D. J. Willians, M. Kurmoo, *J. Chem. Soc., Dalton Trans.* **1994**, 1735–1741; d) O. Tutusaus, F. Teixidor, R. Núñez, C. Viñas, R. Sillanpää, R. Kivekäs, *J. Organomet. Chem.* **2002**, *657*, 247–255.

[5] A search of the February 2005 release of the Cambridge Structural Database revealed 498 examples of *closo*-[3-M-1,2-C_2B_9] metallacarboranes, 33 of those having a *B*-attached sulfonium group. With regards to the related ruthenacarboranes, 59 *closo*-[3-Ru-1,2-C_2B_9] structures were found, 5 of which have a *B*-attached sulfonium group.

[6] A. R. Kudinov, D. S. Perekalin, P. V. Petrovskii, G. V. Grintselev-Knyazev, *Russ. Chem. Bull.* **2002**, *51*, 1928–1930.

[7] a) O. Tutusaus, S. Delfosse, A. Demonceau, A. F. Noels, C. Viñas, F. Teixidor, *Tetrahedron Lett.* **2003**, *44*, 8421–8425; b) O. Tutusaus, S. Delfosse, F. Simal, A. Demonceau, A. F. Noels, R. Nuñez, C. Viñas, F. Teixidor, *Tetrahedron Lett.* **2002**, *43*, 983–987; c) C. Viñas, O. Tutusaus, R. Nuñez, F. Teixidor, A. Demonceau, S. Delfosse, A. F. Noels, I. Mata, E. Molins, *J. Am. Chem. Soc.* **2003**, *125*, 11830–11831.

[8] J. G. Planas, C. Viñas, F. Teixidor, M. B. Hursthouse, M. E. Light, *Dalton Trans.* **2004**, 2059–2061.

[9] See for example: a) S. Heřmánek, J. Plešek, B. Štíbr, 2nd IMEBORON, Leeds, 25–29 March **1974**, abstract no. 38; b) A. R. Siedle, G. M. Bodner, A. R. Garber, D. C. Beer, L. J. Todd, *Inorg. Chem.* **1974**, *13*, 2321–2324; c) F. Teixidor, C. Viñas, R. W. Rudolph, *Inorg. Chem.* **1986**, *25*, 3339–3345; d) S. Heřmánek, *Chem. Rev.* **1992**, *92*, 325–362; S. Heřmánek, *Inorg. Chim. Acta* **1999**, *289*, 20–44; e) J. M. Oliva, C. Viñas, *J. Mol. Struct.* **2000**, *556*, 33–42; f) C. Viñas, G. Barberà, J. M. Oliva, F. Teixidor, A. J. Welch, G. M. Rosair, *Inorg. Chem.* **2001**, *40*, 6555–6562.

[10] C. Viñas, J. Pedrajas, J. Bertran, F. Teixidor, R. Kivekäs, R. Sillanpää, *Inorg. Chem.* **1997**, *36*, 2482–2486.

[11] R. Núñez, O. Tutusaus, F. Teixidor, C. Viñas, R. Sillanpää, R. Kivekäs, *Chem. Eur. J.* **2005**, *11*, 1933–1941.

[12] M. A. Bennett, A. K. Smith, *J. Chem. Soc., Dalton Trans.* **1974**, 233–241.

[13] a) T. P. Hanusa, J. C. Huffman, L. J. Todd, *Polyhedron* **1982**, *1*, 77–82; b) T. P. Hanusa, J. C. Huffman, T. L. Curtis, L. J. Todd, *Inorg. Chem.* **1985**, *24*, 787–792; c) M. P. Garcia, M. Green, F. G. A. Stone, R. G. Somerville, A. J. Welch, C. E. Briant, D. N. Cox, M. P. Mingos, *J. Chem. Soc., Dalton Trans.* **1985**, 2343–2348.

[14] J. Plešek, S. Heřmánek, *Collect. Czech. Chem. Commun.* **1978**, *43*, 1325–1331.

[15] a) E. J. M. Hamilton, G. T. Jordan, E. A. Meyers, S. G. Shore, *Inorg. Chem.* **1996**, *35*, 5335–5341; b) S. Du, J. A. Kautz, T. D. McGrath, F. G. A. Stone, *J. Chem. Soc., Dalton Trans.* **2001**, 2791–2800; c) A. Franken, C. A. Kilner, M. Thornton-Pett, J. D. Kennedy, *Collect. Czech. Chem. Commun.* **2002**, *67*, 869–912; d) O. Tutusaus, C. Vinas, R. Kivekäs, R. Sillanpää, F. Teixidor, *Chem. Commun.* **2003**, 2458–2459.

[16] a) W. Schwarz, H. D. Hausen, H. Hess, J. Mandt, W. Schmelzer, B. Krebs, *Acta Crystallogr., Sect. B* **1973**, *29*, 2029–2031; b) H. Nakai, M. Komura, M. Shiro, *Acta Crystallogr., Sect. C* **1987**, *43*, 1420–1422; c) H. Brunner, G. Gehart, B. Nuber, J. Wachter, M. L. Ziegler, *Angew. Chem. Int. Ed. Engl.* **1992**, *31*, 1021–1023; d) M. Ito, N. Tokitoh, R. Okazaki, *Organometallics* **1997**, *16*, 4314–4319.

[17] a) R. J. Angelici, *Polyhedron* **1997**, *16*, 3073–3088 and references cited therein; b) L. R. Hanton, K. Lee, *Inorg. Chem.* **1999**, *38*, 1634–1637.

[18] a) R. G. Kultyshev, J. Liu, E. A. Meyers, S. G. Shore, *Inorg. Chem.* **2000**, *39*, 3333–3341; b) R. G. Kultyshev, S. Liu, S. G. Shore, *Inorg. Chem.* **2000**, *39*, 6094–6099.

[19] a) R. T. Baker, R. E. King III, C. Knobler, C. A. O'Con, M. F. Hawthorne, *J. Am. Chem. Soc.* **1978**, *100*, 8266–8267; b) M. Green, J. A. K. Howard, A. P. James, A. N. de M. Jelfs, C. M. Nunn, F. G. A. Stone, *J. Chem. Soc., Chem. Commun.* **1985**, 1778–1780; c) I. T. Chizhevsky, I. A. Lobanova, V. I. Bregadze, P. V. Petrovskii, V. A. Antonovich, A. V. Polyakov, A. I. Yanovskii, Y. T. Struchkov, *J. Chem. Soc. Mendeleev Commun.* **1991**, 47.

[20] a) F. Teixidor, C. Viñas, J. Casabó, A. M. Romerosa, J. Rius, C. Miravitlles, *Organometallics* **1994**, *13*, 914–919; b) F. Teixidor,

 © 2005 Wiley-VCH Verlag GmbH & Co. KGaA, Weinheim

M. A. Flores, C. Viñas, R. Kivekas, R. Sillanpää, *Angew. Chem.* **1996**, *108*, 2388; *Angew. Chem. Int. Ed. Engl.* **1996**, *35*, 2251–2253; c) C. Viñas, R. Nuñez, M. A. Flores, F. Teixidor, R. Kivekäs, R. Sillanpää, *Organometallics* **1995**, *14*, 3952–3957; C. Viñas, R. Nuñez, M. A. Flores, F. Teixidor, R. Kivekäs, R. Sillanpää, *Organometallics* **1996**, *15*, 3850–3858; d) F. Teixidor, M. A. Flores, C. Viñas, R. Kivekäs, R. Sillanpää, *Organometallics* **1998**, *17*, 4675–4679; e) F. Teixidor, M. A. Flores, C. Viñas, R. Kivekäs, R. Sillanpää, *J. Am. Chem. Soc.* **2000**, *122*, 1963–1973.

[21] G. E. D. Mullen, M. J. Went, S. Wocadlo, A. K. Powell, P. J. Blower, *Angew. Chem. Int. Ed. Engl.* **1997**, *36*, 1205–1207.

[22] Y. Ohki, H. Sadohara, Y. Takikawa, K. Tatsumi, *Angew. Chem. Int. Ed.* **2004**, *43*, 2290–2293.

[23] F. Teixidor, C. Viñas, M. A. Flores, G. M. Rosair, A. J. Welch, A. S. Weller, *Inorg. Chem.* **1998**, *37*, 5394–5395.

[24] See for example: a) J. Plešek, D. Hnyk, Z. Havlas, *J. Chem. Soc., Chem. Commun.* **1989**, 1859–1861; b) T. P. Fehlner, P. T. Czech, R. F. Fenske, *Inorg. Chem.* **1990**, *29*, 3103–3109; c) M. Bühl, P. V. R. Schleyer, Z. Havlas, S. Heřmánek, *Inorg. Chem.* **1991**, *30*, 3107–3111.

[25] a) $MeAlB_{11}H_{11}$: T. D. Getman, S. G. Shore, *Inorg. Chem.* **1988**, *27*, 3439–3440 (GEZGEX); b) $B_{12}H_{12}$; A_d was taken from two structures (average of 10 B–B bonds): G. Shoham, D. Schomburg, W. N. Lipscomb, *Cryst. Struct. Commun.* **1980**, *9*, 429 (ETADCB); K. Hofmann, B. Albert, *Z. Anorg. Allg. Chem.* **2001**, *627*, 1055 (VIRQOC); c) $HCB_{11}H_{11}$: A. S. Larsen, J. D. Holbrey, F. S. Tham, C. A. Reed, *J. Am. Chem. Soc.* **2000**, *122*, 7264–7272 (IBEDUO, IBEGAX); d) $B_{10}H_{10}$; A_d is the average of 11 structures: E. S. Shubina, I. A. Tikhonova, E. V. Bakhmutova, F. M. Dolgushin, M. Yu. Antipin, V. I. Bakhmutov, I. B. Sivaev, L. N. Teplitskaya, I. T. Chizhevsky, I. V. Pisareva, V. I. Bregadze, L. M. Epstein, V. B. Shur, *Chem. Eur. J.* **2001**, *7*, 3783–3790 (ACERAB, ACEREF); Yu. N. Mikhailov, A. S. Kanishcheva, L. A. Zemskova, V. E. Mistryukov, N. T. Kuznetsov, K. A. Solntsev, *Zh. Neorg. Khim.* **1982**, *27*, 2343 (BOVRAF); Z. Yongmao, C. Zhaoping, C. Zhiwei, P. Kezhen, L. Jiaxi, Z. Guomin, Z. Hong, *Jiegou Huaxue* **1982**, *1*, 45 (BUBCUW); D. J. Fuller, D. L. Kepert, B. W. Skelton, A. H. White, *Aust. J. Chem.* **1987**, *40*, 2097 (FUDHIV, FUDHOB); E. A. Malinina, K. A. Solntsev, L. A. Butman, N. T. Kuznetsov, *Koord. Khim.* **1989**, *15*, 1039 (JIJNUL); A. V. Virovets, N. N. Vakulenko, V. V. Volkov, N. V. Podberezskaya, *Zh. Strukt. Khim.* **1994**, *35*, 72 (POCHOE); S. Chitsaz, H. Folkerts, J. Grebe, T. Grob, K. Harms, W. Hiller, M. Krieger, W. Massa, J. Merle, M. Mohlen, B. Neumuller, K. Dehnicke, *Z. Anorg. Allg. Chem.* **2000**, *626*, 775 (QEYKUA); A. M. Orlova, V. N. Mustyatsa, L. V. Goeva, S. B. Katser, K. A. Solntsev, N. T. Kuznetsov, *Zh. Neorg. Khim.* **1996**, *41*, 1956 (REBRUL); S. B. Katser, E. A. Malinina, V. N. Mustyatsa, K. A. Solntsev, N. T. Kuznetsov, *Koord. Khim.* **1992**, *18*, 387 (WAKXIP); e) $HCB_{10}H_{10}$: K. Nestor, B. Stibr, J. D. Kennedy, M. Thornton-Pett, T. Jelinek, *Collect. Czech. Chem. Commun.* **1992**, *57*, 1262–1268 (JOXCUU); f) $HNB_{10}H_{10}$: L. Schneider, U. Englert, P. Paetzold, *Z. Anorg. Allg. Chem.* **1994**, *620*, 1191 (WIHKED).

[26] H. E. Gottlieb, V. Kotlyar, A. Nudelman, *J. Org. Chem.* **1997**, *62*, 7512–7515.

[27] P. M. Boorman, X. Gao, J. F. Fait, M. Parvez, *Inorg. Chem.* **1991**, *30*, 3886–3893.

[28] J. Cowie, E. J. M. Hamilton, J. C. V. Laurie, A. J. Welch, *Acta Crystallogr., Sect. C* **1998**, *54*, 1648–1650.

[29] Z. Otwinowski, W. Minor, "Processing of X-ray diffraction data collected in oscillation mode", in *Macromol. Crystallogr., Part A* **1997**, *276*, 307.

[30] *SADABS, Area-Detector Absorption Correction*, Siemens Industrial Automation, Inc., Madison, WI, **1996**.

[31] G M Sheldrick, *SHELX97, Programs for Crystal Structure Analysis*, release 97-2, Universität Göttingen, Germany, **1998**.

Received: May 24, 2005
Published Online: September 5, 2005

 © 2005 Wiley-VCH Verlag GmbH & Co. KGaA, Weinheim

Synthesis and Structure of Neutral and Cationic Gallium Complexes Incorporating Bis(oxazolinato) Ligands

Samuel Dagorne,*[a] Stéphane Bellemin-Laponnaz,*[b] Aline Maisse-François,[b] Marie-Noëlle Rager,[c] Lauriane Jugé,[c] and Richard Welter[d]

Keywords: Cations / Gallium / Lewis acids / N ligands

The bis(oxazolinato)dimethylgallium complexes [{BOX-Me_2}$GaMe_2$] (**2a**) and [{BOX-(*S*)-*i*Pr}$GaMe_2$] (**2b**) are easily obtained in nearly quantitative yield by a methane elimination reaction between $GaMe_3$ and the corresponding bis(oxazoline) ligands {BOX-Me_2}H (**1a**) and {BOX-(*S*)-*i*Pr}H (**1b**). Compound **2a** was also synthesized by a salt metathesis involving the formation of the dichloro complex [{BOX-Me_2}$GaCl_2$] by reaction of [(BOX-Me_2)Li] with $GaCl_3$, followed by its in situ methylation with MeMgBr. The neutral complexes **2a** and **2b** are rapidly ionized by $B(C_6F_5)_3$ to cations **3a**$^+$ and **3b**$^+$, respectively, which are either three-coordinate methylgallium cations or four-coordinate Ga solvent adducts, as their $MeB(C_6F_5)_3^-$ salts. These cationic species exhibit a limited stability and decompose in solution within several hours at room temperature. However, stable four-coordinate Ga-NMe_2Ph cations (**4a**$^+$ and **4b**$^+$) are isolated in good yield when these ionization reactions are performed in the presence of a Lewis base such as NMe_2Ph. Unlike that of $B(C_6F_5)_3$, the reaction of [{BOX-Me_2}$GaMe_2$] with $[Ph_3C][B(C_6F_5)_4]$ quantitatively affords an unusual bis(imine)-dimethylgallium cation {H_2C=C(OX-Me_2)$_2$}$GaMe_2^+$ (**5a**$^+$) in a reaction that proceeds via a hydride abstraction occurring at the Me group located at the back of the bis(oxazolinato) ligand chelated to the Ga center in **2a**. Overall, the reactivity and structural trends observed for the Ga derivatives are closely related to those of the Al analogs, with the Ga compounds being more stable.

(© Wiley-VCH Verlag GmbH & Co. KGaA, 69451 Weinheim, Germany, 2005)

Introduction

Cationic group 13 complexes have been the subject of several studies over the past few years since the enhanced Lewis acidity at the metal center, which is a result of its cationic charge, renders these species potentially interesting as Lewis acid catalysts.[1] As such, they have already found applications in isobutene,[2] ethylene,[3] alkene oxide,[4] and D,L-lactide[5] polymerization catalysis. In this regard, three- and four-coordinate cationic group 13 complexes of the general type $[(LX)MR]^+$ and $[(LX)M(R)(L)]^+$ (L labile), readily accessible by reaction of neutral precursors $[(LX)MR_2]$ with strong Lewis acids such as $[Ph_3C][B(C_6F_5)_4]$ and $B(C_6F_5)_3$, have appeared as appealing targets because they incorporate a cationic and low-coordinate metal center; accordingly, these cations behave like potent Lewis acids.[6,7] Thus far, most of the investigations in this area have concerned aluminum derivatives, where it has been found that the structure and the stability of the formed Al cations are greatly dependent upon the steric properties of the ancillary LX^- bidentate ligand and the nature of the counterion.[7] More specifically, the presence of an extremely bulky LX^- ligand and the use of an inert counterion $[B(C_6F_5)_4^-$ or $MeB(C_6F_5)_3^-]$ are required to obtain, in some cases, reasonably stable Al cations. However, the frequent poor stability of these highly reactive alkylaluminum species may limit the scope of their applications in catalysis.

Although much less studied than their Al counterparts, low-coordinate cationic alkylgallium complexes are expected to exhibit an increased stability as a result of the less polar character of the Ga–C vs. Al–C bond,[8] while still remaining reactive due to the presence of an electron-deficient metal center. Thus, cationic Ga derivatives may well represent a reasonable balance of reactivity and stability, which is a required feature for catalysis involving polar substrates and/or media.

We are interested in the design and synthesis of stable low-coordinate cationic group 13 complexes of the type $[(LX)MR]^+$ and $[(LX)M(R)(L)]^+$ for applications in catalysis. To this purpose, we have recently focused our attention toward the synthesis of $[(LX)AlR]^+$ and $[(LX)Al(R)(L)]^+$

[a] Laboratoire de Chimie Organométallique, UMR CNRS 7576, Ecole Nationale Supérieure de Chimie de Paris,
11 rue Pierre et Marie Curie, 75231 Paris Cedex 05, France
Fax: +33-1-43260061
E-mail: samuel-dagorne@enscp.fr
[b] Laboratoire de Chimie Organométallique et de Catalyse, UMR 7513, Institut Le Bel, Université Louis Pasteur,
4 rue Blaise Pascal, 67000 Strasbourg, France
E-mail: bellemin@chimie.u-strasbg.fr
[c] NMR Service, Ecole Nationale Supérieure de Chimie de Paris, 11 rue Pierre et Marie Curie, 75231 Paris Cedex 05, France
[d] Laboratoire DECMET, UMR 7513, Institut Le Bel, Université Louis Pasteur,
4 rue Blaise Pascal, 67000 Strasbourg, France

cations bearing either an *N*,O-aminophenolate or an *N*,*N*-bis(oxazolinato) bidentate ligand (**A** and **B**, Scheme 1).[9,10] In particular, the use of a chiral C_2-symmetric *N*,*N*-bis(oxazolinato) ligand has provided access to chiral cationic alkylaluminum complexes, which are of potential interest in asymmetric catalysis.[10] However, the instability of the Al cations incorporating **B**, especially in catalytic conditions, prompted us toward the synthesis of the Ga analogs, which are expected to be more stable. Thus, as part of our continuous studies of cationic and chiral group 13 alkyl complexes, we here report the synthesis and structure of neutral and cationic bis(oxazolinato)methylgallium complexes.

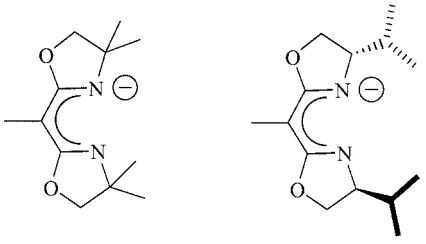

A **B**

Scheme 1.

Results and Discussion

Bis(oxazolinato)dimethylgallium compounds were synthesized by the classical alkane elimination route involving a reaction between the appropriate bis(oxazoline) ligand and $GaMe_3$. This pathway was found to be the most straightforward and efficient method to access such compounds.

Thus, the reaction of the bis(oxazoline) ligands (BOX-Me_2)H (**1a**) and {BOX-(*S*)-*i*Pr}H (**1b**; Scheme 2) with an equimolar amount of $GaMe_3$ in pentane at –35 °C yields the bis(oxazolinato)dimethylgallium compounds [(BOX-Me_2)$GaMe_2$] (**2a**) and [{BOX-(*S*)-*i*Pr}$GaMe_2$] (**2b**; Scheme 2), respectively, which were isolated in nearly quantitative yields (>95% yield) as air-stable colorless solids. Alternatively, the achiral Ga derivative **2a** was also obtained by a salt metathesis pathway, although this approach was less efficient. Thus, the reaction of the bis(oxazolinato)lithium salt [(BOX-Me_2)Li], generated by deprotonation of bisoxazoline **1a** with *t*BuLi at –78 °C, with an equimolar amount of $GaCl_3$ (18 h, room temp.) yields [(BOX-Me_2)-$GaCl_2$], as observed by ^{1}H NMR spectroscopy. The in situ methylation of the dichlorogallium derivative with two equivalents of MeMgBr affords [(BOX-Me_2)$GaMe_2$] (**2a**) in moderate yield (48%).

The molecular structures of the Ga complexes **2a** and **2b** were determined by X-ray crystallography analysis, thus establishing their monomeric nature as well as the effective chelation of one bis(oxazolinato) ligand (Figures 1 and 2 and Table 1). As expected, both Ga species exhibit very similar structural features in the solid state and these will only discussed for the chiral derivative **2b**.

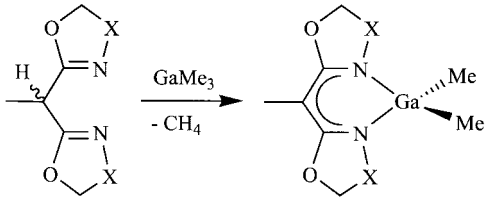

1a: X = CMe_2 **2a**: X = CMe_2
1b: X = (*S*)-CH*i*Pr **2b**: X = (*S*)-CH*i*Pr

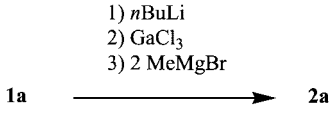

Scheme 2.

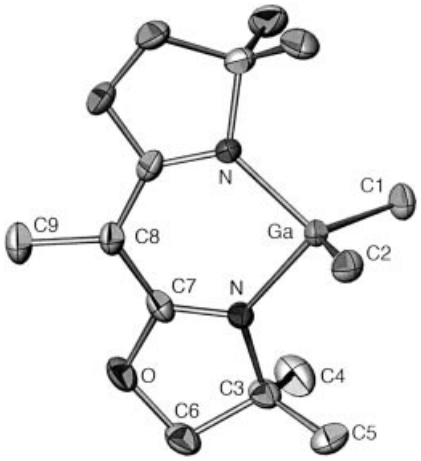

Figure 1. Molecular structure of complex **2a**. The H atoms have been omitted for clarity.

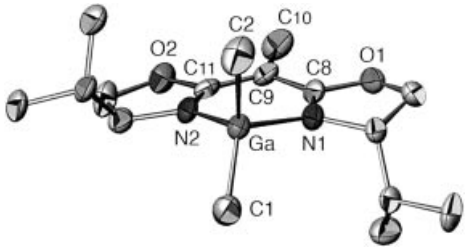

Figure 2. Molecular structure of chiral complex **2b**. The H atoms have been omitted for clarity. Selected torsion angles [°]: N(1)–C(8)–C(9)–C(11) = 5.8(15), Ga–N(2)–C(11)–C(10) = 3.2(4), Ga–N(2)–C(11)–C(9) = 2.5(11).

The Ga metal center in **2b** adopts a slightly distorted tetrahedral geometry with a chelate bite angle [N(1)–Ga–N(2) = 91.1(2)°] similar to that in the related β-diketiminatodimethylgallium complex [HC{C(Me)N(C_6H_3-2,6-*i*Pr_2)}-$GaMe_2$] [93.92(7)°], which also contains a six-membered C_3N_2Ga metallacycle.[11] The Ga–N and Ga–C bond lengths in **2b** [1.966(9) Å and 1.98(1) Å average, respectively] are similar to those observed in related {LX}$GaMe_2$

 © 2005 Wiley-VCH Verlag GmbH & Co. KGaA, Weinheim

Table 1. Selected bond lengths [Å] and angles [°] for **2a** and **2b**.

2a		**2b**	
Ga–N	1.9677(17)	Ga–N(1)	1.967(6)
Ga–C(1)	1.970(3)	Ga–N(2)	1.966(6)
Ga–C(2)	1.970(3)	Ga–C(1)	1.963(9)
N–C(7)	1.320(3)	Ga–C(2)	2.004(10)
C(7)–C(8)	1.395(3)	N(1)–C(8)	1.333(8)
		N(2)–C(11)	1.306(9)
		C(8)–C(9)	1.384(11)
		C(9)–C(11)	1.386(10)
N–Ga–N	91.33(10)	N(1)–Ga–N(2)	91.1(2)
N–Ga–C(2)	109.38(8)	C(1)–Ga–N(2)	111.8(4)
N–Ga–C(1)	111.85(8)	C(1)–Ga–N(1)	113.5(3)
C(1)–Ga–C(2)	119.47(14)	C(1)–Ga–C(2)	119.9(4)

species such as [HC{C(Me)N(C_6H_3-2,6-*i*Pr_2)}$GaMe_2$],[11] [{PhC($NPh)_2$}$GaMe_2$],[12] and [{*t*BuC($NCy)_2$}$GaMe_2$].[13]

The six-membered C_3N_2Ga metallacycle in [{BOX-(*S*)-*i*Pr}$GaMe_2$] (**2b**) is nearly planar (C–C–Ga–N < 6°) with the carbon and nitrogen atoms adopting a trigonal-planar geometry (sum of angles ca. 360°). The planarity of the six-membered C_3N_2Ga backbone in **2b** contrasts with the folding of the C_3N_2Ga ring observed in [HC{C(Me)N(C_6H_3-2,6-*i*Pr_2)}$GaMe_2$], in which the Ga metal center lies significantly out of the C_3N_2 plane (0.76 Å). This structural difference presumably results from much weaker steric interactions between the Ga metal center and the chelating ligand in **2b** compared to [HC{C(Me)N(C_6H_3-2,6-*i*Pr_2)}-$GaMe_2$].[11] The C–C bond lengths within the C_3N_2 moiety [1.38(1) Å average] in **2b** are close to the C–C bond length in aromatic systems (1.395 Å), while the C–N bond lengths [1.32(1) Å average] lie between the C=N double-bond length in imines (1.28 Å) and the C(sp^2)–N single-bond length (1.47 Å). Altogether, these structural data are consistent with significant π-delocalization of the bis(oxazolinato) ligand backbone, resulting in a nearly C_2 symmetry for **2b** in the solid state. Similar structural features have been observed for the Al analogs.[10]

The NMR spectroscopic data for the Ga complexes **2a** and **2b** at room temperature are consistent with these species adopting overall C_{2v} and C_2 symmetry, respectively, in solution. These NMR spectroscopic data are therefore in agreement with the solid-state structures of **2a** and **2b** being retained in solution under the conditions studied here. For example, the ^{1}H NMR spectrum of **2b** (C_6D_6, room temp.) exhibits one Ga*Me*$_2$ resonance, one N-C*H* resonance and two Me-*i*Pr resonances, which is in agreement with a C_2-symmetric complex.

Reaction of Bis(oxazolinato)dimethylgallium Complexes 2a and 2b with $B(C_6F_5)_3$

Cationic alkylgallium complexes could be obtained by reaction of the neutral dimethylgallium derivatives with the strong Lewis acid $B(C_6F_5)_3$, which is known to readily abstract a methyl anion from the metal center of group 13 [{LX}MMe_2] species. Thus, the reaction of [{BOX}$GaMe_2$] (**2a**,**b**) with one equivalent of $B(C_6F_5)_3$ (C_6D_5Br, room temp., 10 min) results in the nearly quantitative formation of the cations [{BOX-Me_2}GaMe]$^+$ (**3a**$^+$) and [BOX-(*S*)-*i*Pr}GaMe]$^+$ (**3b**$^+$), respectively, as their $MeB(C_6F_5)_3^-$ salts, as observed by ^{1}H, ^{13}C, and ^{19}F NMR spectroscopy (Scheme 3). As expected, the Ga cations **3a**,**b**$^+$ are more stable than their Al counterparts; however, they slowly decompose at room temp. in C_6D_5Br ($t_{1/2} \approx 10$ h) to yield unidentified species, which precluded their isolation in a pure form. Initial attempts (by ^{1}H NMR) to observe cations **3a**,**b**$^+$ by carrying out the reaction on an NMR-tube scale in CD_2Cl_2 were unsuccessful, presumably due to fast decomposition of the desired cations in CD_2Cl_2.

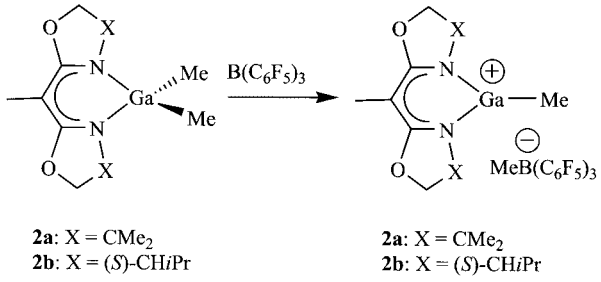

Scheme 3.

The ^{1}H, ^{13}C and ^{19}F NMR spectroscopic data for the [**3a**,**b**][$MeB(C_6F_5)_3$] salt species are consistent with weak interactions between the cation and the anion down to –30 °C in C_6D_5Br solution. In particular, the *Me*$B(C_6F_5)_3^-$ resonance (δ = 0.97 ppm) in the ^{1}H NMR spectra of [**3a**,**b**]-[$MeB(C_6F_5)_3$] is characteristic of a free $MeB(C_6F_5)_3^-$ anion in solution at room temp. (Figure 3).[14] The NMR spectroscopic data for the Ga cations **3a**$^+$ and **3b**$^+$ are essentially unchanged between –30 °C and room temp. and agree with effective C_{2v}- and C_2-symmetric species for **3a**$^+$ and **3b**$^+$, respectively, under these conditions. For instance, as illustrated in Figure 3, the ^{1}H NMR spectrum of [**3a**][$MeB(C_6F_5)_3$] only exhibits four resonances for cation **3a**$^+$ (Ga*Me*$^+$, C*Me*$_2$, O-C*H*$_2$, and C*Me*), which is in agreement with a C_{2v}-symmetric complex. In addition, the Ga*Me*$^+$ resonance in **3a**$^+$ (δ = 0.40 ppm) is shifted dramatically downfield relative to the Ga*Me*$_2$ resonance of the neutral precursor **2a** (δ = –0.17 ppm) as a result of the cationic charge on Ga. Overall, on the basis of NMR spectroscopic data, the Ga cations **3a**,**b**$^+$ are most likely either three-coordinate "base-free" cationic species or four-coordinate cationic Ga solvent adducts (i.e. C_6D_5Br adducts) with a fast coordination/decoordination process on the NMR scale down to –30 °C. The latter proposal is based on the fact that a solid-state structure of a four-coordinate cationic Ga-ClPh adduct has been reported recently.[15]

The Lewis acidic Ga cation **3a**$^+$ reacts rapidly with an excess of propylene oxide (PO; 200 equiv., –20 °C, 5 min) to yield atactic oligomers with a broad polydispersity (40% conversion, M_n = 448, M_w/M_n = 2.38). A longer reaction time did not yield higher conversion, which strongly suggests a fast decomposition of cation **3a**$^+$ (within 5 min at –20 °C) to inactive species in the presence of excess PO.

 © 2005 Wiley-VCH Verlag GmbH & Co. KGaA, Weinheim

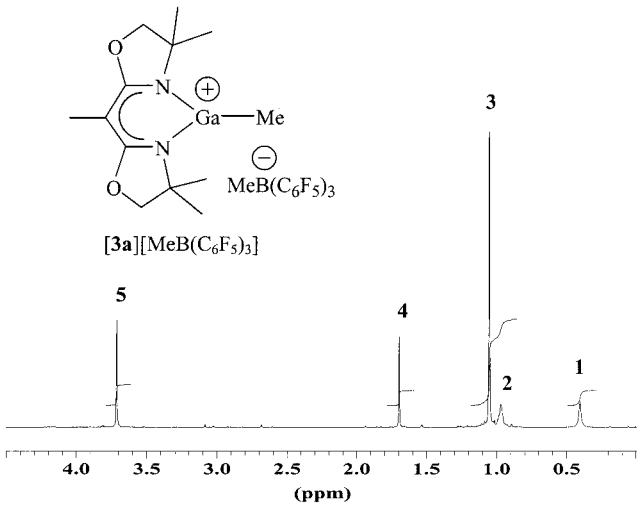

Figure 3. ^{1}H NMR spectrum of [**3a**][MeB(C_6F_5)$_3$] (C_6D_5Br, room temp.): δ = 0.40 (**1**, Ga*Me*), 0.97 (**2**, *Me*B), 1.05 (**3**, C*Me*$_2$), 1.70 (**4**, *Me*CCN), 3.71 (**5**, OCH_2) ppm.

Synthesis and Structure of Four-Coordinate Methylgallium Cations (4a,b$^+$)

The lack of stability of cations **3a**,**b**$^+$ prompted us to generate them in the presence of a Lewis base such as NMe_2Ph, which is expected to trap the Ga cations to yield stable four-coordinate Ga–NMe_2Ph cationic adducts. Thus, the reaction of the bis(oxazolinato)dimethylgallium complexes (**2a**,**b**) with one equivalent of B(C_6F_5)$_3$ in the presence of one equivalent of NMe_2Ph (CH_2Cl_2, room temp., 10 min) yields the quantitative formation of the four-coordinate cations [{BOX-Me_2}Ga(Me)(NMe_2Ph)]$^+$ (**4a**$^+$) and [{BOX-(*S*)-*i*Pr}Ga(Me)(NMe_2Ph)]$^+$ (**4b**$^+$), respectively, as their MeB(C_6F_5)$_3^-$ salts (Scheme 4). The salt compounds [**4a**,**b**][MeB(C_6F_5)$_3$] are stable for days at room temperature in CH_2Cl_2 and could thus be isolated in a pure form as colorless solids in good yields. To the best of our knowledge, cation **4b**$^+$ in [**4b**][MeB(C_6F_5)$_3$] is the first example of a chiral cationic alkylgallium complex.

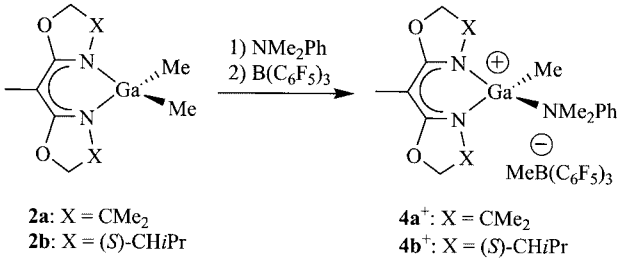

Scheme 4.

Compounds [**4a**,**b**][MeB(C_6F_5)$_3$] are dissociated species down to –30 °C in CD_2Cl_2 with weakly interacting **4a**,**b**$^+$ cations and MeB(C_6F_5)$_3^-$. The ^{1}H NMR spectra of the cationic NMe_2Ph adducts **4a**,**b**$^+$ both contain a Ga*Me*$^+$ resonance that is significantly downfield shifted as compared to the Ga*Me*$_2$ resonances in the neutral precursors **2a**,**b**, which is indicative of a cationic Ga center. Likewise, the ^{1}H and ^{13}C NMR resonances of **4a**,**b**$^+$ assigned to the coordinated NMe_2Ph are strongly downfield shifted relative to those in free NMe_2Ph, which is consistent with an effective coordination of NMe_2Ph to the Ga center. Overall, the NMR spectroscopic data at room temp. agree with effective C_{2v}- and C_2-symmetric solution structures for cations **4a** and **4b**$^+$, respectively, thereby indicating a fast face-exchange of NMe_2Ph on the NMR timescale. To probe this issue further, low temperature ^{1}H and ^{13}C NMR experiments were carried out to reach a slow NMe_2Ph exchange process. Thus, the NMR spectroscopic data for cations **4a**$^+$ and **4b**$^+$ recorded at –25 °C and –35 °C in CD_2Cl_2, respectively, exhibit an overall C_s symmetry for **4a**$^+$ and a C_1 symmetry for chiral **4b**$^+$. These data are consistent with a slow face-exchange of NMe_2Ph on the NMR timescale for both cations (see Exp. Sect.). For comparison, the labile coordination of NMe_2Ph to Ga observed here for **4a**,**b**$^+$ at room temperature contrasts with the nonlabile coordination of this amine to Al in the cationic Al analogs under identical conditions, which may reflect a more Lewis acidic cationic Al vs. Ga center.[10]

The Lewis acid character of the Ga–NMe_2Ph adduct **4a**$^+$ was also tested with PO. Like **3a**$^+$, cation **4a**$^+$ oligomerizes PO (200 equiv. of PO, room temp., 15 min) to afford low molecular weight oligomers in high conversion (85% conversion, M_n = 339, M_w/M_n = 1.25). The oligomerization process is clearly multimodal, as deducted from size exclusion chromatographic data, thus suggesting the presence of several active species.

Solid-State Structure of the Cationic Adduct 4a$^+$

While a few examples of X-ray characterized low-coordinate Al cations are known, solid-state structures of Ga analogs are rather scarce,[1,7a,16] and, to date, none of the type [{LX}Ga(R)(L)]$^+$ have been reported.

The molecular structure of the salt species [**4a**][MeB(C_6F_5)$_3$] was confirmed by X-ray crystallography analysis (Tables 2 and 3). It crystallizes as discrete **4a**$^+$ cations and MeB(C_6F_5)$_3^-$ anions, with no cation–anion interaction. As shown in Figure 4, cation **4a**$^+$ is an NMe_2Ph-stabilized four-coordinate methylgallium cation in which the Ga center adopts a distorted tetrahedral structure with a chelate bite angle N(1)–Ga–N(2) [96.98(7)°] similar to that in the neutral precursor **2a**. Unlike the nearly planar six-membered C_3N_2Ga metallacycle in complexes **2a**,**b**, that in **4a**$^+$ is significantly distorted from planarity, with the Ga center being displaced by 0.33(2) Å from the N(2)–C(6)–N(1)–C(9) average plane toward the coordinated NMe_2Ph. This distortion may well be to minimize steric interactions between the Ga-NMe_2Ph moiety and the bis(oxazolinato) ligand. The Ga–N bond lengths within the chelate-Ga entity [1.9018(19) and 1.9100(16) Å] are rather short as compared to those in **2a** [1.966(9) Å], due to the stronger ionic character of these bonds in **4a**$^+$ vs. **2a**, a result of the cationic charge, whereas the Ga–N_{amine} bond length [Ga–N(3) = 2.124(3) Å] is considerably longer and is comparable to those observed in neutral bulky gallium amine adducts such

 © 2005 Wiley-VCH Verlag GmbH & Co. KGaA, Weinheim

as $[Me_3Ga(tBuNH_2)]$ [2.12(1) Å].[17] Due to the enhanced Lewis acidity of Ga in **4a**$^+$ vs. $[Me_3Ga(tBuNH_2)]$, a shorter Ga–N(3) bond length in **4a**$^+$ vs. $Me_3Ga(tBuNH_2)$ would be expected from an electronic point of view; this rather long Ga–N distance for **4a**$^+$ may be to minimize steric interactions between the aniline and the chelating ligand.

Table 2. Selected bond lengths [Å] and angles [°] for [**4a**][$MeB(C_6F_5)_3$] and [**5a**][$B(C_6F_5)_4$].

4a$^+$		**5a**$^+$	
Ga–N(1)	1.9018(19)	Ga–C(2)	1.953(2)
Ga–N(2)	1.9100(16)	Ga–C(1)	1.956(2)
Ga–C(1)	1.944(3)	Ga–N(1)	2.0171(17)
Ga–N(3)	2.124(2)	Ga–N(2)	2.0191(17)
N(1)–C(9)	1.331(2)	N(2)–C(10)	1.282(3)
N(2)–C(6)	1.339(3)	N(1)–C(3)	1.285(3)
C(7)–C(9)	1.395(3)	C(8)–C(9)	1.329(3)
C(7)–C(6)	1.383(3)	C(8)–C(3)	1.466(3)
		C(8)–C(10)	1.470(3)
N(1)–Ga–N(2)	96.98(7)	C(1)–Ga–C(2)	122.76(11)
N(1)–Ga–N(3)	103.06(8)	N(1)–Ga–N(2)	90.18(8)
C(1)–Ga–N(3)	108.60(11)	C(1)–Ga–N(1)	107.28(10)
N(2)–Ga–C(1)	123.12(12)	C(1)–Ga–N(2)	110.12(10)

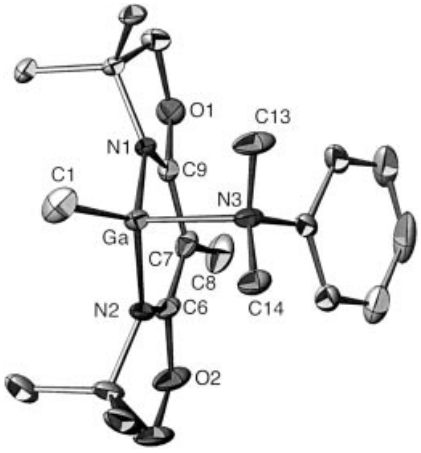

Figure 4. Molecular structure of the Ga cation **4a**$^+$. The H atoms have been omitted for clarity. Selected torsion angles [°]: N(2)–Ga–N(1)–C(9) = 13.54(14),; N(1)–Ga–N(2)–C(6) = 15.36(15), N(1)–C(9)–C(7)–C(6) = 13.0(3).

Reaction of [{BOX-Me_2}$GaMe_2$] (2a) with [Ph_3C][$B(C_6F_5)_4$]

As stated in the introduction, the trityl salt [Ph_3C][$B(C_6F_5)_4$] is the other landmark reagent, along with $B(C_6F_5)_3$, that is used to generate group-13 alkyl cations of the type [{LX}MMe]$^+$ from [{LX}MMe_2] by a Me^- abstraction at the metal center. We thus decided to study the reaction between [{BOX-Me_2}$GaMe_2$] (**2a**) and [Ph_3C][$B(C_6F_5)_4$].

The reaction of [{BOX-Me_2}$GaMe_2$] (**2a**) with one equivalent of [Ph_3C][$B(C_6F_5)_4$] (CH_2Cl_2, room temp., 10 min) yields the quantitative formation of the bis(imine)-dimethylgallium cation [{H_2C=C(OX-Me_2)$_2$}$GaMe_2$]$^+$ (**5a**$^+$) as a $B(C_6F_5)_4^-$ salt, along with one equivalent of Ph_3CH (Scheme 5). Thus, instead of abstracting a Me^- from the Ga center of **2a**, Ph_3C^+ abstracts a hydride from the Me group located at the back of the bis(oxazolinato) ligand in compound **2a** to afford cation **5a**$^+$. The outcome of this reaction confirms a reactivity already observed with the Al analog [{BOX-Me_2}$AlMe_2$], which has been found to yield a similar bis-imine cation when treated with [Ph_3C][$B(C_6F_5)_4$].[10] Nevertheless, the observed reactivity, i.e. a hydride abstraction at a group rather far away from the metal center, contrasts with the usual reactivity of Ph_3C^+ with alkyl metal complexes. Typically, hydride abstractions by Ph_3C^+ at such dialkyl species occur either at the C_α of the metal-bonded alkyl group or at the C_β, both of which, in any case, are in the vicinity of the metal center.[18]

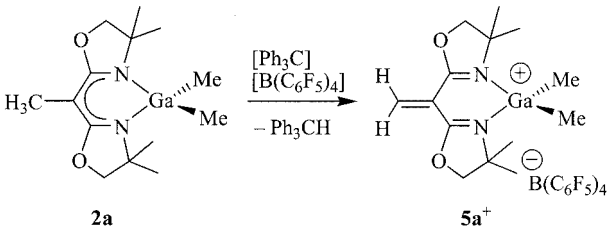

Scheme 5.

The salt compound [**5a**][$B(C_6F_5)_4$], which is stable for days at room temp. in CH_2Cl_2, was obtained as an analytically pure colorless solid in good yield (see Exp. Sect.). Its molecular structure, as determined by X-ray crystallography, shows that [**5a**][$B(C_6F_5)_4$] crystallizes as **5a**$^+$ cations and $B(C_6F_5)_4^-$ anions with no cation–anion interaction in the solid state. The cationic species **5a**$^+$can be seen as a dimethylgallium cation in which the $GaMe_2^+$ moiety is chelated by the neutral bisoxaline H_2C=C(OX-Me_2)$_2$ (Figure 5). Accordingly, the bonding parameters within the C_3N_2 ligand backbone in **5a**$^+$ are consistent with a π-localized structure: the C(3)–N(1) and C(10)–N(2) bond lengths [1.285(3) and 1.282(3) Å] compare with the typical value for C(sp^2)=N double bonds (1.30 Å) while the C(8)–C(9) bond length [1.329(3) Å] is consistent with that of a C=C double

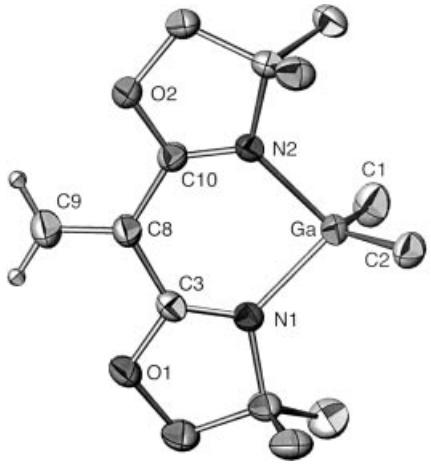

Figure 5. Molecular structure of the Ga cation **5a**$^+$. The H atoms have been omitted for clarity. Selected torsion angles [°]: N(1)–Ga–N(2)–C(10) = 12.53(19), N(2)–C(10)–C(8)–C(3) = 3.7(3), N(2)–C(10)–C(8)–C(9) = 3.0(3).

bond (1.337 Å). In addition, the Ga–N bond lengths in **5a**$^+$ [2.018(1) Å average] are comparable to those observed in neutral Ga imine complexes, e.g. in dimethyl-(*N*-methylsalicylaldiminato)gallium, Ga–N = 2.019 Å,[19] as expected for a bis-imine gallium complex such as **5a**$^+$. All other structural parameters are very similar to those in the neutral precursor **2a**.

As for the solution structure of **5a**$^+$, the NMR spectroscopic data agree with the solid-state structure being retained in solution and with no association between **5a**$^+$ and its counterion in CD_2Cl_2 solution at room temp. In particular, the ^1H and ^{13}C NMR spectra of **5a**$^+$ both contain one characteristic resonance at δ = 7.30 and 143.7 ppm, respectively, which can be assigned to the H_2C=C group of the chelating bis(oxazoline).

Summary and Conclusions

Bis(oxazolinato)dimethylgallium complexes of the type [{BOX}$GaMe_2$] (**2a**,**b**) can be obtained in high yield by reaction of $GaMe_3$ with the desired neutral bis(oxazoline) via methane elimination. These neutral dimethylgallium precursors react rapidly with $B(C_6F_5)_3$, via a Me^- abstraction, to yield the Ga cations **3a**,**b**$^+$, which are either three-coordinate methylgallium cations of the type [{BOX}GaMe]$^+$ or four-coordinate cationic Ga-solvent adducts. Although more stable than their Al counterparts, cations **3a**,**b**$^+$ decompose over the course of several hours to give unidentified species. The lack of stability of the [{BOX}GaMe]$^+$ methyl cations reported here contrasts with the stability of the three-coordinate Al cation [HC{C(Me)N(C_6H_3-2,6-*i*Pr_2)}AlMe]$^+$, which also incorporates a six-membered Al metallacycle. The greater steric crowding provided at the metal center by HC{C(Me)N(C_6H_3-2,6-*i*Pr_2)}$^-$ vs. {BOX-Me_2}$^-$ or {BOX-(*S*)-*i*Pr}$^-$ may be responsible for this difference of stability.

When the ionization of [{BOX}$GaMe_2$] (**2a**,**b**) with $B(C_6F_5)_3$ is performed in the presence of an external Lewis base such as NMe_2Ph, the corresponding four-coordinate cationic Ga adducts [{BOX}Ga(Me)(NMe_2Ph)]$^+$ (**4a**,**b**$^+$) are isolated in good yield, the cation **4b**$^+$ being of particular interest as a chiral cationic derivative. Finally, [{BOX-Me_2}$GaMe_2$] (**2a**) reacts with [Ph_3C][$B(C_6F_5)_4$] to yield an unusual cationic bis(imino)gallium adduct [{H_2C=C(OX-Me_2)$_2$}$GaMe_2$]$^+$ (**5a**$^+$) via a hydride abstraction at the back of the bis(oxazolinato) ligand.

Cations **3a**$^+$ and **4a**$^+$ were found to rapidly olygomerize PO at low temperature, thereby illustrating the Lewis acid character of these species. However, the broad polydispersity of the obtained oligomers suggests a poor stability of these species in catalytic conditions.

Further studies will focus on the synthesis and use of bulkier and chiral LX^- ligands for coordination to group 13 metals.

Experimental Section

General Procedures: All experiments were carried out under N_2 using standard Schlenk techniques or in an Mbraun Unilab glovebox. Toluene, pentane, and THF were distilled from Na/benzophenone and stored over activated molecular sieves (4 Å) in a glovebox prior to use. CH_2Cl_2 and CD_2Cl_2, were distilled from CaH_2 and stored over activated molecular sieves (4 Å) in a glovebox prior to use. C_6D_6 was degassed under an N_2 flow and stored over activated molecular sieves (4 Å) in a glovebox prior to use. $B(C_6F_5)_3$ was purchased from Strem Chemicals and was extracted with dry pentane prior to use. [Ph_3C][$B(C_6F_5)_4$] was purchased from Asahi Glass Europe and used as received. CD_2Cl_2, C_6D_6, and C_6D_5Br were purchased from Eurisotop. All other chemicals were purchased from Aldrich and were used as received. The bisoxazoline ligands **1a**,**b** were synthesized according to a literature procedure.[10] All NMR spectra were recorded at room temperature (unless otherwise indicated) on a Bruker Avance 300 MHz or 400 MHz spectrometer. ^1H and ^{13}C chemical shifts are reported relative to $SiMe_4$ and were determined by reference to the residual ^1H and ^{13}C solvent peaks. ^{11}B and ^{19}F chemical shifts are reported relative to $BF_3{\cdot}Et_2O$ in CD_2Cl_2 and $CFCl_3/CDCl_3$, respectively. SEC analysis was carried out on a system equipped with 4 PL Gel columns (250 mm length × 7.5 mm inner diameter) in series and with THF as solvent. A Shimadzu SPD10Avp UV detector coupled with a Shimadzu RID6A refractometer was employed. The apparatus was calibrated using a POE standard from Polymer Laboratories. Elemental analyses for [**4a**,**b**][$MeB(C_6F_5)_3$] and [**5a**][$B(C_6F_5)_4$] were performed by the Mikroanalytisches Labor Pascher, Remagen-Bandorf, Germany, while those for compounds **2a**,**b** were performed by the microanalysis laboratory of the Université Pierre et Marie Curie, Paris, France.

For the compounds listed below, the assignment of all ^1H and $^{13}C\{^1H\}$ NMR resonances was possible using DEPT experiments combined, when necessary, with HMQC experiments.

[{BOX-Me_2}$GaMe_2$] (2a) by Methane Elimination: In a glovebox, a pentane solution (3 mL) of $GaMe_3$ (285 mg, 2.48 mmol), previously cooled to –35 °C in a freezer, was slowly added with a Pasteur pipette to a pentane solution (7 mL) of bisoxazoline **1a** (557 mg, 2.48 mmol), also precooled to –35 °C. The resulting colorless solution was then allowed to warm to room temperature. Upon warming to room temperature, a slight bubbling was observed, as expected for methane formation. After stirring the solution for 2 h at room temperature, it was then evaporated to dryness under vacuum to yield pure **2a** as a colorless solid in nearly quantitative yield (785 mg, 98% yield). ^1H NMR (400 MHz, C_6D_6): δ = 0.03 (s, 6 H, Ga*Me*$_2$), 1.02 (s, 12 H, C*Me*$_2$), 2.26 (s, 3 H, *Me*CCN), 3.41 (s, 4 H, OC*H*$_2$) ppm. ^1H NMR (400 MHz, CD_2Cl_2): δ = –0.38 (s, 6 H, Ga*Me*$_2$), 1.29 (s, 12 H, C*Me*$_2$), 1.70 (s, 3 H, *Me*CCN), 3.95 (s, 4 H, OC*H*$_2$) ppm. ^1H NMR (400 MHz, C_6D_5Br): δ = –0.17 (s, 6 H, Ga*Me*$_2$), 1.11 (s, 12 H, CMe$_2$), 1.99 (s, 3 H, *Me*CCN), 3.64 (s, 4 H, OC*H*$_2$) ppm. $^{13}C\{^1H\}$ NMR (100 MHz, C_6D_6): δ = –2.8 (Ga*Me*$_2$), 10.3 (*Me*CCN), 27.7 (C*Me*$_2$), 62.3 (Me*C*CN), 63.7 (*C*Me$_2$), 78.7 (O*C*H$_2$), 170.2 (O*C*N) ppm. $C_{14}H_{25}GaN_2O_2$ (323.08): calcd. C 52.05, H 7.80; found C 52.14, H 7.72.

[{BOX-Me_2}$GaMe_2$] (2a) by Salt Metathesis: On a nitrogen-filled vacuum line, *t*BuLi (0.550 mL of a 1.7 M pentane solution, 0.934 mmol) was added dropwise, from a syringe, to a THF solution (10 mL) of bisoxazoline **1a** (209 mg, 0.934 mmol) that had been cooled to –78 °C in an acetone/dry ice bath. Upon addition of *t*BuLi, the initial colorless solution turned bright yellow. After the addition, the resulting yellow solution was allowed to warm to room temperature and was stirred for 3 h. Evaporation of the volatiles under reduced pressure yielded a yellow sticky residue which was washed twice with cold pentane (2 × 10 mL cooled to –35 °C) to afford a colorless solid. In a glovebox, this solid was dissolved

 © 2005 Wiley-VCH Verlag GmbH & Co. KGaA, Weinheim

in toluene (10 mL) in a small Schlenk flask and cooled to –35 °C in a freezer for 1 h. After this time, the cold colorless solution was taken out of the freezer and stirred vigorously. A toluene solution (5 mL) of $GaCl_3$ (164 mg, 0.934 mmol), also precooled to –35 °C, was then quickly added to this solution and the resulting mixture was allowed to warm to room temperature. Upon warming to room temperature, the initial solution turned into a colorless suspension (indicating the formation of LiCl), which was left stirring overnight at room temperature. The reaction mixture was then filtered through a glass frit and the resulting filtrate evaporated under vacuum to yield crude **2a** as a sticky colorless solid. Recrystallization of this crude product from a 1:1 Et_2O/pentane solution cooled to –35 °C afforded pure **2a** as colorless crystals (145 mg, 48% yield).

[{BOX-(*S*)-*i*Pr}$GaMe_2$] (2b): The chiral dimethylgallium compound **2b** was synthesized by methane elimination using the same procedure as for **2a**, using an equimolar amount of {BOX-(*S*)-*i*Pr}H (300 mg, 1.19 mmol) and $GaMe_3$ (136 mg, 1.19 mmol) to afford pure **2b** as a colorless solid in high yield (401 mg, 96% yield). ^{1}H NMR (300 MHz, C_6D_6): δ = 0.00 (s, 6 H, Ga*Me*$_2$), 0.49 (d, $^3J_{H,H}$ = 7.0 Hz, 6 H, *Me*-*i*Pr), 0.74 (d, $^3J_{H,H}$ = 6.8 Hz, 6 H, *Me*-*i*Pr), 1.91 (d of septet, $^3J_{H,H\ doublet}$ = 3.3, $^3J_{H,H\ septet}$ = 6.9 Hz, 2 H, C*H*-*i*Pr), 2.21 (s, 3 H, *Me*CCN), 3.56–3.66 (m, 4 H, OCH_2), 3.68–3.75 (m, 2 H, C*H*N) ppm. ^{1}H NMR (300 MHz, CD_2Cl_2): δ = –0.45 (s, 6 H, Ga*Me*$_2$), 0.80 (d, $^3J_{H,H}$ = 6.8 Hz, 6 H, *Me*-*i*Pr), 0.89 (d, $^3J_{H,H}$ = 7.0 Hz, 6 H, *Me*-*i*Pr), 1.68 (s, 3 H, *Me*CCN), 1.96 (d of septet, $^3J_{H,H\ doublet}$ = 3.4, $^3J_{H,H\ septet}$ = 6.9 Hz, 2 H, C*H*-*i*Pr), 3.96–4.01 (m, 2 H, C*H*N), 4.06–4.11 (dd, $^2J_{H,H}$ = 8.4, $^3J_{H,H}$ = 8.4 Hz, 2 H, OCH_2), 4.17–4.23 (dd, $^2J_{H,H}$ = 8.4, $^3J_{H,H}$ = 9.2 Hz, 2 H, OCH_2) ppm. ^{1}H NMR (300 MHz, C_6D_5Br): δ = –0.19 (s, 6 H, Ga*Me*$_2$), 0.66 (d, $^3J_{H,H}$ = 7.0 Hz, 6 H, *Me*-*i*Pr), 0.73 (d, $^3J_{H,H}$ = 6.8 Hz, 6 H, *Me*-*i*Pr), 1.90 (d of septet, $^3J_{H,H\ doublet}$ = 3.3, $^3J_{H,H\ septet}$ = 6.9 Hz, 2 H, C*H*-*i*Pr), 1.96 (s, 3 H, *Me*CCN), 3.84–3.92 (m, 6 H, OCH_2 and C*H*N) ppm. ^{13}C{^{1}H} NMR (100 MHz, C_6D_6): δ = –6.4 (Ga*Me*$_2$), 10.4 (*Me*CCN), 14.5 (*Me*-*i*Pr), 18.9 (*Me*-*i*Pr), 30.0 (*C*H-*i*Pr), 61.4 (Me*C*CN), 66.5 (*C*HN), 66.9 (O*C*H$_2$), 171.1 (O*C*N) ppm. $C_{16}H_{29}GaN_2O_2$ (351.14): calcd. C 54.73, H 8.32; found C 54.42, H 8.17.

[{BOX-Me_2}GaMe][MeB(C_6F_5)$_3$] ([3a][MeB(C_6F_5)$_3$]): In a glovebox, an equimolar amount of **2a** (30.0 mg, 0.093 mmol) and B(C_6F_5)$_3$ (47.5 mg, 0.093 mmol) were charged in a J-Young NMR tube and 0.75 mL of C_6D_5Br was added. The NMR tube was vigorously shaken to yield a colorless solution and a ^{1}H NMR spectrum was immediately recorded, showing the nearly quantitative formation of [**3a**][MeB(C_6F_5)$_3$] as a fully dissociated salt species, along with minor impurities. Due to the relatively poor stability of [**3a**][MeB(C_6F_5)$_3$], the ^{13}C{^{1}H} NMR spectrum was recorded at –25 °C to ensure good data. ^{1}H NMR (400 MHz, C_6D_5Br): δ = 0.40 (s,3 H, Ga*Me*), 0.97 (br. s, 3 H, *Me*B), 1.05 (s, 12 H, C*Me*$_2$), 1.70 (s, 3 H, *Me*CCN), 3.71 (s, 4 H, OCH_2) ppm. ^{13}C{^{1}H} NMR (100 MHz, C_6D_5Br, 248 K): δ = –4.6 (Ga*Me*), 9.3 (*Me*CCN), 11.7 (br., *Me*B), 28.2 (C*Me*$_2$), 64.4 (*C*Me$_2$), 71.3 (Me*C*CN), 79.4 (O*C*H$_2$), 137.2 (dm, $^2J_{C,F}$ = 256 Hz, *o*- or *m*-C_6F_5), 137.9 (dm, $^2J_{C,F}$ = 243 Hz, *p*-C_6F_5), 148.8 (dm, $^2J_{C,F}$ = 237 Hz, *o*- or *m*-C_6F_5), 171.0 (O*C*N) ppm.

[{BOX-(*S*)-*i*Pr}GaMe][Me(BC_6F_5)$_3$] ([3b][MeB(C_6F_5)$_3$]): The chiral salt compound [**3b**][MeB(C_6F_5)$_3$] was generated on an NMR scale using the same procedure as that for [**3a**][MeB(C_6F_5)$_3$], with an equimolar amount of **2b** (15 mg, 0.043 mmol) and B(C_6F_5)$_3$ (21.9 mg, 0.043 mmol). ^{1}H NMR (400 MHz, C_6D_5Br, 298 K): δ = 0.36 (s,3 H, Ga*Me*), 0.57 (d, $^3J_{H,H}$ = 6.8 Hz, 6 H, Me-*i*Pr), 0.63 (d, $^3J_{H,H}$ = 6.9 Hz, 6 H, Me-*i*Pr), 0.97 (br. s, 3 H, *Me*B), 1.57 (d of septet, $^3J_{H,H\ doublet}$ = 3.1, $^3J_{H,H\ septet}$ = 6.6 Hz, 2 H, C*H*-*i*Pr), 1.74 (s, 3 H, *Me*CCN), 3.77–3.83 (m, 4 H, OCH_2), 3.90–3.95 (m, 2 H, NC*H*) ppm. ^{13}C{^{1}H} NMR (100 MHz, C_6D_5Br, 248 K): δ = –4.1 (Ga*Me*), 9.9 (*Me*CCN), 11.7 (br., *Me*B), 15.2 (*Me*-*i*Pr), 18.7 (*Me*-*i*Pr), 33.1 (*C*H-*i*Pr), 65.9 (*C*HN), 69.7 (*C*H$_2$O), 71.9 (Me*C*CN), 137.2 (dm, $^2J_{C,F}$ = 256 Hz, *o*- or *m*-C_6F_5), 137.9 (dm, $^2J_{C,F}$ = 243 Hz, *p*-C_6F_5), 148.8 (dm, $^2J_{C,F}$ = 237 Hz, *o*- or *m*-C_6F_5), 172.3 (O*C*N) ppm.

[{BOX-Me_2}Ga(Me)(NMe_2Ph)][MeB(C_6F_5)$_3$] ([4a][MeB(C_6F_5)$_3$]): In a glovebox, the dimethylgallium derivative **2a** (200 mg, 0.619 mmol) was charged in a Schlenk flask and dissolved in CH_2Cl_2 (5 mL). NMe_2Ph (78.5 µL, 0.620 mmol) was then first added from a syringe to the colorless solution, followed by the addition of B(C_6F_5)$_3$ (317 mg, 0.619 mmol) all at once. The resulting mixture was stirred for 1 h at room temperature and, after this time, evaporated to dryness under vacuum to yield a colorless foamy residue. Trituration of this residue with cold pentane (precooled to –35 °C) caused the precipitation of a colorless solid, which, after passing the solution through a glass frit nd further drying in vacuo, was found to be the salt species [**4a**][MeB(C_6F_5)$_3$] in a pure form (479 mg, 81% yield). ^{1}H NMR (400 MHz, CD_2Cl_2): δ = 0.39 (s, 3 H, Ga*Me*), 0.48 (*Me*B), 1.13 (br., 12 H, C*Me*$_2$), 1.73 (s, 3 H, *Me*CCN), 2.96 (s, 6 H, N*Me*$_2$Ph), 4.05 (br., 4 H, OCH_2), 7.00–7.41 (br., 5 H, NMe$_2$*Ph*) ppm. ^{1}H NMR (400 MHz, CD_2Cl_2, 253 K): δ = 0.36 (s, 3 H, Ga*Me*), 0.42 (*Me*B), 0.92 (s, 6 H, C*Me*$_2$), 1.11 (s, 6 H, C*Me*$_2$), 1.67 (s, 3 H, *Me*CCN), 2.93 (s, 6 H, N*Me*$_2$Ph), 3.81 (br. d, $^2J_{H,H}$ = 8.2 Hz, 2 H, OCH_2), 4.16 (br. d, $^2J_{H,H}$ = 8.2 Hz, 2 H, OCH_2), 7.20 (d, $^3J_{H,H}$ = 7.2 Hz, 2 H, NMe$_2$*Ph*), 7.33 (br., 1 H, NMe$_2$*Ph*), 7.44 (br., 2 H, NMe$_2$*Ph*) ppm. ^{13}C{^{1}H} NMR (100 MHz, CD_2Cl_2): δ = –10.2 (Ga*Me*), 8.3 (*Me*CCN), 9.1 (br., *Me*B), 26.8 (br., C*Me*$_2$), 45.2 (br., N*Me*$_2$Ph), 63.6 (*C*Me$_2$), 67.4 (Me*C*CN), 78.4 (O*C*H$_2$), 118.5 (br., NMe$_2$*Ph*), 129.0 (br., NMe$_2$*Ph*), 129.5 (NMe$_2$*Ph*), 136.7 (d, $^1J_{C,F}$ = 233 Hz, *m*-C_6F_5), 137.9 (d, $^1J_{C,F}$ = 238 Hz, *p*-C_6F_5), 148.6 (d, $^1J_{C,F}$ = 233 Hz, *o*-C_6F_5), 171.7 (O*C*N) ppm. ^{13}C{^{1}H} NMR (100 MHz, CD_2Cl_2, 263 K): δ = –10.7 (Ga*Me*), 8.1 (*Me*CCN), 9.4 (br., *Me*B), 23.8 (C*Me*$_2$), 27.6 (C*Me*$_2$), 45.8 (br., N*Me*$_2$Ph), 63.2 (*C*Me$_2$), 69.0 (Me*C*CN), 77.9 (O*C*H$_2$), 119.6 (*o*-*Ph*NMe$_2$), 127.2 (*p*-*Ph*NMe$_2$), 129.4 (*m*-*Ph*NMe$_2$), 136.7 (d, $^1J_{C,F}$ = 233 Hz, *m*-C_6F_5), 137.9 (d, $^1J_{C,F}$ = 238 Hz, *p*-C_6F_5), 145.1 (C_{ipso}-*Ph*NMe$_2$), 148.6 (d, $^1J_{C,F}$ = 233 Hz, *o*-C_6F_5), 171.2 (O*C*N) ppm. $C_{40}H_{36}BF_{15}GaN_3O_2$ (956.24): calcd. C 50.24, H 3.79; found C 49.91, H 3.47.

[{BOX-(*S*)-*i*Pr}Ga(Me)(NMe_2Ph)][MeB(C_6F_5)$_3$] ([4b][MeB(C_6F_5)$_3$]): The chiral salt species [**4b**][MeB(C_6F_5)$_3$] was generated following the same procedure as that for [**4a**][MeB(C_6F_5)$_3$], using equimolar amounts of compound **2b** (72.0 mg, 0.205 mmol), NMe_2Ph (26 µL, 0.205 mmol), and B(C_6F_5)$_3$ (105 mg, 0.205 mmol). It was isolated as an analytically pure colorless solid in a similar yield (151 mg, 75% yield). ^{1}H NMR (400 MHz, CD_2Cl_2): δ = 0.37 (s,3 H, Ga*Me*), 0.48 (br. s, 3 H, *Me*B), 0.60–0.98 (br., 12 H, *Me*-*i*Pr), 1.65 (br., 2 H), 1.72 (s, 3 H, *Me*CCN), 1.78 (br., 1 H), 3.00 (s, 3 H, N*Me*$_2$Ph), 3.80–4.40 (6 H, CH_2O and C*H*N), 7.24 (d, $^3J_{H,H}$ = 7.3 Hz, 2 H, *o*-*Ph*NMe$_2$), 7.31 (br., 1 H, *p*-*Ph*NMe$_2$), 7.51 (t, $^3J_{H,H}$ = 7.8 Hz, 2 H, *m*-*Ph*NMe$_2$) ppm. ^{1}H NMR (400 MHz, CD_2Cl_2, 243 K): δ = 0.33 (s,3 H, Ga*Me*), 0.40 (br. s, 3 H, *Me*B), 0.44 (br. d, 3 H, Me-*i*Pr), 0.46 (br. d, 3 H, Me-*i*Pr), 0.99 (br. d, 3 H, Me-*i*Pr), 1.02 (br. d, 3 H, Me-*i*Pr), 1.29 (br., 1 H, C*H*-*i*Pr), 1.65 (s, 3 H, *Me*CCN), 1.70 (br., 1 H, C*H*-*i*Pr), 1.81 (br., 1 H, C*H*N), 2.88 (s, 3 H, N*Me*$_2$Ph), 3.00 (s, 3 H, N*Me*$_2$Ph), 3.81 (t, $J_{H,H}$ = 8.7 Hz, 1 H, CH_2O), 4.02 (br., 1 H, C*H*N), 4.12 (t, $J_{H,H}$ = 8.6 Hz, 1 H, CH_2O), 4.30 (t, $J_{H,H}$ = 8.7 Hz, 1 H, CH_2O), 4.41 (t, $J_{H,H}$ = 8.6 Hz, 1 H, CH_2O), 7.30 (br., 2 H, *o*-*Ph*NMe$_2$), 7.42 (br., 1 H, *p*-*Ph*NMe$_2$), 7.52 (br., 2 H, *m*-*Ph*NMe$_2$) ppm. ^{13}C{^{1}H} NMR (100 MHz, CD_2Cl_2, 243 K): δ = –11.3 (Ga*Me*), 8.6 (*Me*CCN), 9.5 (br., *Me*B), 12.8 (*Me*-*i*Pr), 14.5

 © 2005 Wiley-VCH Verlag GmbH & Co. KGaA, Weinheim

Table 3. Crystal data and refinements details for compounds **2a**, **2b**, [**4a**][$MeB(C_6F_5)_3$], and [**5a**][$B(C_6F_5)_4$].

	2a	**2b**	[**4a**][$MeB(C_6F_5)_3$]	[**5a**][$B(C_6F_5)_4$]
Formula	$C_{14}H_{25}GaN_2O_2$	$C_{16}H_{29}GaN_2O_2$	$C_{21}H_{33}GaN_3O_2$, $C_{19}H_3BF_{15}$	$C_{14}H_{24}GaN_2O_2$, $C_{24}BF_{20}$
Formula mass	323.08	351.13	956.25	1001.12
Crystal system	orthorhombic	monoclinic	triclinic	monoclinic
Space group	*Pnma*	$P2_1$	$P\bar{1}$	$P2_1/c$
a [Å]	11.7380(10)	9.3270(4)	10.397(5)	12.843(2)
b [Å]	11.0420(10)	11.5310(6)	13.441(5)	19.380(3)
c [Å]	12.249(2)	9.5600(7)	15.762(5)	15.829(2)
α [°]	90.00	90.00	73.66(5)	90.00
β [°]	90.00	116.8500(19)	80.66(5)	97.85(5)
γ [°]	90.00	90.00	73.90(5)	90.00
V [Å^3]	1587.6(3)	917.33(9)	2022.3(14)	3902.9(10)
Z	4	2	2	4
Density [g cm^{-3}]	1.352	1.271	1.570	1.704
μ (Mo-K_α) [mm^{-1}]	1.734	1.506	0.790	0.840
F(000)	680	372	968	1992
Data collection				
Temperature [K]	173(2)	173(2)	173(2)	173(2)
θ min./max.	2.40/30.03	2.39/30.00	1.35/30.01	1.60/30.04
Data set [*h*,*k*,*l*]	–16/14, –15/14, –16/17	–13/11, 0/16, 0/13	–14/14, –17/18, 0/22	–18/17, 0/27, 0/22
Total, unique data, *R*(int)	2445, 1898, 0.0615	2780, 1699, 0.0000	11773, 8935, 0.0000	11395, 7624, 0.0000
Observed data	$I > 2\sigma(I)$	$I > 2\sigma(I)$	$I > 2\sigma(I)$	$I > 2\sigma(I)$
Refinement				
No. of reflections, parameters	2445, 94	2780, 190	11773, 559	11395, 577
R_2, R_1, wR_2, wR_1, Goof	0.0715, 0.0456, 0.0856, 0.0800, 1.074	0.0961, 0.0457, 0.1525, 0.1026, 0.951	0.0617, 0.0417, 0.1184, 0.1089, 1.063	0.0728, 0.0404, 0.1188, 0.1000, 0.929
Flack *x*	–	0.04(3)	–	–
Min., max. residual electron density [e Å^{-3}]	–0.477, 0.378	–0.855, 0.691	–0.607, 0.365	0.002, 0.000

(*Me*-*i*Pr), 17.3 (*Me*-*i*Pr), 19.7 (*Me*-*i*Pr), 31.0 (*C*H-*i*Pr), 31.2 (*C*H-*i*Pr), 43.1 (N*Me*$_2$Ph), 47.0 (N*Me*$_2$Ph), 64.2 (N*C*H), 65.2 (N*C*H), 65.9 (Me*C*CN), 67.0 (*C*H$_2$O), 67.5 (*C*H$_2$O), 119.2 (*o*-*Ph*NMe$_2$), 127.3 (*p*-*Ph*NMe$_2$), 129.8 (*m*-*Ph*NMe$_2$), 136.7 (d, $^1J_{C,F}$ = 233 Hz, *m*-C_6F_5), 137.9 (d, $^1J_{C,F}$ = 238 Hz, *p*-C_6F_5), 145.3 (C_{ipso}-*Ph*NMe$_2$), 148.6 (d, $^1J_{C,F}$ = 233 Hz, *o*-C_6F_5), 170.9 (O*C*N), 172.0 (O*C*N) ppm. $C_{42}H_{40}BF_{15}GaN_3O_2$ (984.29): calcd. C 51.25, H 4.10; found C 51.03, H 3.88.

[{H$_2$C=C(OX-Me$_2$)$_2$}GaMe$_2$][B(C$_6$F$_5$)$_4$] ([5a][B(C$_6$F$_5$)$_4$]): In a glovebox, stoichiometric amounts of [{BOX-Me$_2$}GaMe$_2$] (50 mg, 0.155 mmol) and [Ph_3C][$B(C_6F_5)_4$] (143 mg, 0.155 mmol) were charged in a 25-mL round-bottomed flask and dissolved in CH_2Cl_2 (2 mL). While under vigorous stirring at room temperature, the initial bright-red solution turned pale yellow within seconds, indicating the total consumption of the trityl salt. The mixture was stirred for 1 h at room temperature, after which it was evaporated to dryness under vacuum. Addition of cold pentane (precooled to –35 °C) provoked the precipitation of a colorless solid. The mixture was then filtered through a glass frit and the obtained colorless residue washed three times with cold pentane to remove any remaining Ph_3CH. Further drying of the residue in vacuo afforded the salt species [**5a**][$B(C_6F_5)_4$] as an analytically pure colorless solid (136 mg, 88% yield). ^{1}H NMR (400 MHz, CD_2Cl_2): δ = –0.01 (s, 6 H, Ga*Me*$_2$), 1.53 (s, 12 H, C*Me*$_2$), 4.44 (s, 4 H, OC*H*$_2$), 7.30 (s, 2 H, C*H*$_2$=C) ppm. ^{13}C{^{1}H} NMR (100 MHz, CD_2Cl_2): δ = –4.3 (Ga*Me*$_2$), 26.8 (C*Me*$_2$), 69.3 (*C*Me$_2$), 80.6 (O*C*H$_2$), 118.4 (H$_2$C=*C*), 136.7 (dm, $^1J_{C,F}$ = 243 Hz, *C*$_6$F$_5$), 138.6 (dm, $^1J_{C,F}$ = 243 Hz, *C*$_6$F$_5$), 143.7 (H$_2$*C*=C), 148.5 (dm, $^1J_{C,F}$ = 239 Hz, *C*$_6$F$_5$), 162.6 (O*C*=N) ppm. $C_{38}H_{24}BF_{20}GaN_2O_2$ (1001.11): calcd. C 45.59, H 2.42; found C 45.95, H 2.37.

X-ray Structure Analysis of Complexes 2a,b, [4a][MeB(C$_6$F$_5$)$_3$] and [5a][B(C$_6$F$_5$)$_4$]: Single crystal of **2a**, **2b**, [**4a**][$MeB(C_6F_5)_3$], and [**5a**][$B(C_6F_5)_4$] were mounted on a Nonius Kappa-CCD area detector diffractometer (Mo-K_α radiation; λ = 0.71073 Å). The complete conditions of data collection (Denzo software)[20] and structure refinements are given in Table 3. The cell parameters were determined from reflections taken from one set of 10 frames (1.0° steps in phi angle), each at 20 s exposure. The structures were solved by direct methods (SHELXS97) and refined against F^2 using the SHELXL97 software.[21] The absorption was not corrected. All non-hydrogen atoms were refined anisotropically. Hydrogen atoms were generated according to stereochemistry and refined using a riding model in SHELXL97.

CCDC-273080 (for **2a**), -273081 (for **2b**), -273082 (for [**4a**][$MeB(C_6F_5)_3$]), and -273083 (for [**5a**][$MeB(C_6F_5)_3$]) contains the supplementary crystallographic data for this paper. These data can be obtained free of charge from The Cambridge Crystallographic Data Centre via www.ccdc.cam.ac.uk/data_request/cif.

Acknowledgments

We thank the French Ministry of Research for financial support through an ACI grant (no. JC4045). We also thank Dr. A. De Cian for the X-ray diffraction studies.

[1] D. A. Atwood, *Coord. Chem. Rev.* **1998**, *176*, 407–430.
[2] M. Bochmann, D. M. Dawson, *Angew. Chem. Int. Ed. Engl.* **1996**, *35*, 2226–2228.

 © 2005 Wiley-VCH Verlag GmbH & Co. KGaA, Weinheim

[3] a) M. P. Coles, R. F. Jordan, *J. Am. Chem. Soc.* **1997**, *119*, 8125–8126; b) M. Bruce, V. C. Gibson, C. Redshaw, G. A. Solan, A. J. P. White, *Chem. Commun.* **1998**, 2523–2524.
[4] a) D. A. Atwood, J. A. Jegier, D. Rutherford, *J. Am. Chem. Soc.* **1995**, *117*, 6779–67780; b) J. A. Jegier, D. A. Atwood, *Inorg. Chem.* **1997**, *36*, 2034–2039.
[5] N. Emig, H. Nguyen, H. Krautscheid, R. Réau, J.-B. Cazaux, G. Bertrand, *Organometallics* **1998**, *17*, 3599–3608.
[6] For two structurally characterized "base-free" three-coordinate group 13 alkyls, see: a) C. E. Radzewich, M. P. Coles, R. F. Jordan, *J. Am. Chem. Soc.* **1999**, *121*, 8673–8674; b) A. H. Cowley, Z. Lu, J. N. Jones, J. A. More, *J. Organomet. Chem.* **2004**, *689*, 2562–2564.
[7] a) S. Dagorne, I. A. Guzei, M. P. Coles, *J. Am. Chem. Soc.* **2000**, *122*, 274–289; b) A. V. Korolev, E. Ihara, I. A. Guzei, V. G. Young, Jr., R. F. Jordan, *J. Am. Chem. Soc.* **2001**, *123*, 8291–8309; c) P. A. Cameron, V. C. Gibson, C. Redshaw, J. A. Segal, G. A. Solan, A. J. P. White, D. J. Williams, *J. Chem. Soc., Dalton Trans.* **2001**, 1472–1476; d) P. A. Cameron, V. C. Gibson, C. Redshaw, J. A. Segal, A. J. P. White, D. J. Williams, *J. Chem. Soc., Dalton Trans.* **2002**, 415–422; e) D. Pappalardo, C. Tedesco, C. Pellechia, *Eur. J. Inorg. Chem.* **2002**, 621–628; f) J. A. R. Schmidt, J. Arnold, *Organometallics* **2002**, *21*, 2306–2313; g) D. Pappalardo, M. Mazzeo, P. Montefusco, C. Tedesco, C. Pellechia, *Eur. J. Inorg. Chem.* **2004**, 1292–1298.
[8] Several cationic methylgallium complexes are stable in water due to the high stability of the $GaMe^{2+}$ moiety. For examples, see: a) D. F. Shriver, R. W. Parry, *Inorg. Chem.* **1962**, *1*, 835–838; b) R. S. Tobias, M. J. Sprague, G. E. Glass, *Inorg. Chem.* **1968**, *7*, 1714–1721.
[9] a) S. Dagorne, L. Lavanant, R. Welter, C. Chassenieux, P. Haquette, G. Jaouen, *Organometallics* **2003**, *22*, 3732–3741; b) S. Dagorne, I. Janowska, R. Welter, J. Zakrzewski, G. Jaouen, *Organometallics* **2004**, *23*, 4706–4710.
[10] S. Dagorne, S. Bellemin-Laponnaz, R. Welter, *Organometallics* **2004**, *23*, 3053–3061.
[11] M. Stender, B. E. Eichler, N. J. Hardman, P. P. Power, J. Prust, M. Noltemeyer, H. W. Roesky, *Inorg. Chem.* **2001**, *40*, 2794–2799.
[12] J. Barker, N. C. Blacker, P. R. Phillips, N. W. Alcock, W. Errington, M. G. H. Wallbridge, *J. Chem. Soc., Dalton Trans.* **1996**, 431–437.
[13] S. Dagorne, R. F. Jordan, V. J. Young, *Organometallics* **1999**, *18*, 4619–4623.
[14] The ^1H NMR resonance of the $MeB(C_6F_5)_3^-$ anion (δ = 0.97 ppm) at room temp. in C_6D_5Br is close to that of the ammonium salt $[NBu_3(CH_2Ph)][MeB(C_6F_5)_3]$ (δ = 1.01 ppm).
[15] A. V. Korolev, F. Delpech, S. Dagorne, I. A. Guzei, R. F. Jordan, *Organometallics* **2001**, *20*, 3367–3369.
[16] D. A. Atwood, R. A. Jones, A. H. Cowley, S. G. Bott, J. L. Atwood, *J. Organomet. Chem.* **1992**, *425*, C1–C3.
[17] D. A. Atwood, R. A. Jones, A. H. Cowley, S. G. Bott, J. L. Atwood, *J. Organomet. Chem.* **1992**, *434*, 143–150.
[18] For a H^- abstraction by Ph_3C^+ at a C_α metal-bonded alkyl group, see, for example: P. Jernakoff, N. J. Cooper, *Organometallics* **1986**, *5*, 747–751. For a recent example of an abstraction at a C_β metal-bonded alkyl group, see: P. Mehrkhodavanti, R. R. Schrock, *J. Am. Chem. Soc.* **2001**, *123*, 10746–10747.
[19] V. I. Bregadze, N. G. Furmanova, L. M. Golubiskaya, O. Y. Kompan, Y. T. Struchkov, *J. Organomet. Chem.* **1980**, *192*, 1–15.
[20] *Kappa CCD Operation Manual*; Nonius B. V.: Delft, The Netherlands, **1997**.
[21] G. M. Sheldrick, *SHELXL97*, *Program for the refinement of crystal structures*, University of Göttingen, Germany, **1997**.

Received: May 26, 2005
Published Online: September 8, 2005

 © 2005 Wiley-VCH Verlag GmbH & Co. KGaA, Weinheim

Hydride Route for the Palladium-Catalysed Cyclocarbonylation of Monoterpenes

Duc Hanh Nguyen,[a] Gábor Laurenczy,[b] Martine Urrutigoïty*[a] and Philippe Kalck*[a]

Keywords: Carbonylation / Hydrides / Palladium / Terpenes

This paper focuses on the mechanism by which a monoterpene undergoes a cyclocarbonylation reaction catalysed by a palladium complex. Evidence is provided, based on intermediate species observed under pressure or with various ligands, that the catalytic cycle follows a hydride route starting from $[Pd(H)(SnCl_3)L_2]$. The $[Pd(H)(SnCl_3)L_2]$ complexes (L = PPh_3 or PCy_3) have been observed for the first time by multinuclear NMR spectroscopy. Cationic hydride complexes or palladium(0) precursors show either no or poor reactivity. Studies related to model platinum complex chemistry have detected an acylplatinum species. Most of the observations have been done on the cyclocarbonylation of isopulegol, dihydromyrcenol or isolimonene into the corresponding lactones or cyclopentanones. The use of dihydromyrcene allowed us to observe the acylplatinum complex and the corresponding elusive acylpalladium species. The co-catalytic role of $SnCl_2$ is also demonstrated.

(© Wiley-VCH Verlag GmbH & Co. KGaA, 69451 Weinheim, Germany, 2005)

Introduction

Palladium chemistry is currently the workhorse of organic chemistry and is a versatile tool to perform carbon–carbon coupling.[1] When appropriate building blocks are introduced the substrate can follow a multistep functionalisation so that tandem reactions open the way for the preparation of rather sophisticated organic molecules.[2] A number of interesting compounds that show biological activity contain a lactone moiety.[3] During the last few years we have explored the introduction of a CO building block into an unsaturated substrate to obtain such a backbone in a one-pot synthesis.[4] We chose to follow an hemisynthetic way starting from an abundant and cheap raw material like monoterpenes. Thus, we functionalised isopulegol and dihydromyrcenol into the corresponding lactones,[4] and then extended this type of tandem reaction to the cyclocarbonylation of isolimonene, which produces a cyclopentanone.[5] All these reactions are an extension of the classical alkoxycarbonylation reaction by which a terminal alkene is carbonylated in the presence of an alcohol to provide an ester. Generally, this reaction is catalysed by a palladium complex containing a phosphane or a diphosphane ligand, and most often the $[PdCl_2L_2]$ precursor is introduced into the medium. These reactions are promoted by the addition of a Lewis acid such as $SnCl_2$. Two catalytic pathways have been considered, and are still proposed in the literature: the first one involves an alkoxycarbonylpalladium intermediate [Pd-COOR] to which the alkene coordinates and finally a *cis*-migration produces an alkylpalladium moiety containing the ester group,[6] whereas the second one starts from an intermediate palladium hydride species [Pd–H] which gives an alkylpalladium intermediate by successive coordination of the alkene and subsequent hydride transfer.[1,7] The copolymerisation of ethylene and carbon monoxide catalysed by the cationic $[Pd(diphos)]^{2+}$ complexes in the presence of methanol perfectly interconnects the two catalytic pathways[8] such that polymers with $-CH_2COOCH_3$ and $-CH_2CH_3$ terminal functions are produced in equal proportions. For the alkoxycarbonylation reaction of an alkene, Knifton has reported the $[PdCl_2(PPh_3)_2]/SnCl_2$ catalytic system, with which he detected the presence of a ν(Pd–H) stretching frequency.[7] In the literature, several papers deal with evidence that the palladium hydride pathway operates preferentially.[9,10] Particularly, in recent studies Heaton and co-workers have synthesised cationic Pd^{II} hydride complexes containing both a diphosphane ligand and a coordinated solvent molecule, $[Pd(H)(dtbpx)(MeOH)]^+$ [dtbpx = 1,2-$(CH_2P\mathit{t}Bu_2)_2C_6H_4$].[10] They demonstrated that this complex is an essential intermediate in the catalytic system for the formation of methyl propanoate by carbonylation of ethene in methanol.

The present study is concerned with spectroscopic evidence obtained for various $[Pd(H)(X)L_2]$ and $[Pd(H)L_3]^+$

[a] Laboratoire de Catalyse, Chimie Fine et Polymères, Ecole Nationale Supérieure des Ingénieurs en Arts Chimiques et Technologiques,
118 route de Narbonne, 31077 Toulouse Cedex 04, France
Fax: +33-5-6288-5600,
E-mail: Philippe.Kalck@ensiacet.fr; Martine.Urrutigoity@ensiacet.fr
[b] Ecole polytechnique fédérale de Lausanne, Institut des sciences et ingénierie chimiques,
BCH-LCOM, 1015 Lausanne, Switzerland

complexes under normal conditions or under CO pressure. We demonstrate that the essential active species in the cyclocarbonylation reaction is $[Pd(H)(SnCl_3)L_2]$.

Results and Discussion

Carbonylation of isopulegol **A** or isolimonene **B**, under a CO pressure of 40 bar, in the presence of $[PdCl_2L_2]/SnCl_2$ provides the lactone **C** or the cyclopentanone **D**, irrespective of whether the medium contains methanol or not (Scheme 1).[4,11,12]

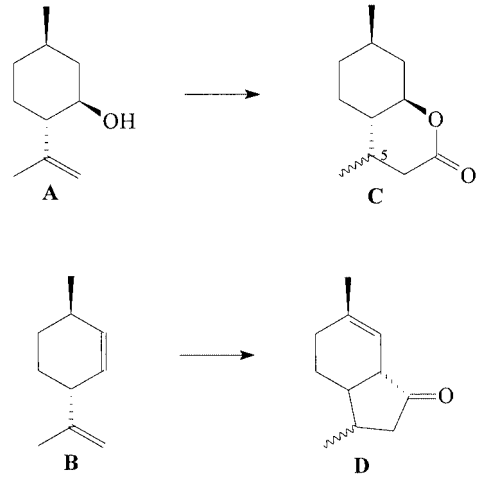

Scheme 1. Cyclocarbonylation of isopulegol **A** and isolimonene **B**.

After catalysis, we never detected any alkoxycarbonylpalladium complex containing the isopulegyl moiety among the organometallic compounds. However, starting from isolimonene, small amounts of dehydro-**D** have previously been identified corresponding to a cyclopentenone resulting from the sacrificial formation of the palladium hydride species.[5,11,13]

During the present study, we carefully analysed the products resulting from the cyclocarbonylation of isopulegol by GC/MS and we identified small amounts of the unsaturated lactone dehydro-**C**, which leads to Equation (1). In order to gain direct evidence of the involvement of this catalytic hydride route, we prepared a series of neutral and cationic palladium hydride complexes, whose characterisation is described below.

Synthesis of $[Pd(H)(X)L_2]$ and $[Pd(H)(L_3)]^+$ Complexes

Complexes $[PdCl_2L_2]$ were prepared in high yields by addition of PPh_3, PCy_3 or the diphosphane dCypb [dCypb = bis(dicyclohexylphosphanyl)butane] to the complex $[PdCl_2(PhCN)_2]$ according to the published procedures.[12,14,15] Addition of ten equivalents of the silane $HSiPh_3$ to these dichloro-, PPh_3- or PCy_3-containing compounds gave the corresponding hydrido complexes $[Pd(H)(Cl)L_2]$ (L = PPh_3 **1**, PCy_3 **2**) in 40% yields after crystallisation.[16a] For the tricyclohexylphosphane ligand, better yields can be obtained when $[Pd(PCy_3)_2]$ is synthesised by reduction of $[PdCl_2(PCy_3)_2]$. Subsequent addition of one equivalent of anhydrous HCl in diethyl ether affords **2** in 80% yield as a crystalline material.[16b] We did not succeed in preparing [Pd(H)(Cl)(dCypb)] (**3**) by reduction of one chloro ligand in $[PdCl_2(dCypb)]$ by $HSiPh_3$, since in all experiments palladium black precipitated. As our attempts with other diphosphanes also resulted in the precipitation of abundant quantities of black materials, we suspect that this absence of stability is due to the *trans*-position of the incoming hydride ligand to a phosphorus atom. However, starting from $[Pd(PCy_3)_2]$ we succeeded in the exchange of ligand dCypb, and addition in an NMR tube at 183 K of one equivalent of HCl (in Et_2O solution) produced the corresponding hydride [Pd(H)(Cl)(dCypb)] (**3**), which shows a hydride signal at δ = –8.0 ppm (Table 1), a doublet of doublets due to the coupling with a phosphorus in the *trans*-position ($^2J_{^1H,^{31}P_{trans}}$ = 200 Hz) and another one in the *cis*-position ($^2J_{^1H,^{31}P_{cis}}$ = 10 Hz). However, we could not isolate the hydride in the solid state.

Addition of one equivalent of $SnCl_2$ to $[D_8]$THF solutions of **1** or **2** gives $[Pd(H)(SnCl_3)L_2]$ (L = PPh_3 **4**, PCy_3 **5**). As shown in Table 1, these two derivatives are characterised in their ^1H NMR spectra by a hydride signal at δ = –6.90 and –8.50 ppm, respectively, flanked by two satellites due to $^2J_{^1H,^{119}Sn}$ coupling (944 Hz and 1760 Hz, respectively). The ^1H-^{31}P coupling is too small to be detected. The coupling between ^1H and ^{119}Sn was confirmed by a 2D-HMQC sequence and is shown in Figure 1.

The ^{31}P NMR spectra show a broad singlet at δ = 33.80 ppm for **4** and a singlet at δ = 52.26 ppm for **5** flanked by the two satellites due to the coupling with ^{119}Sn ($^2J_{^{31}P,^{119}Sn}$ = 138 Hz). In these compounds, the two phosphane ligands are in mutual *trans* positions and the exchange of a Cl for an $SnCl_3$ ligand results in a decrease of nearly 6 ppm for the chemical shift of the hydride ligand

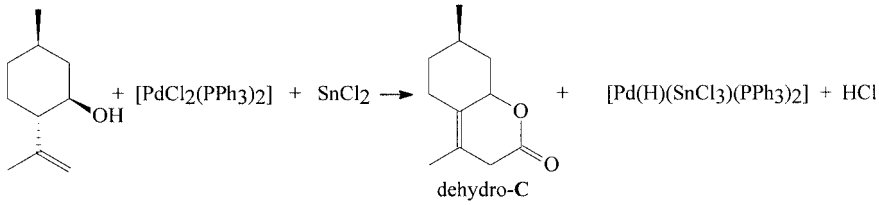

(1)

 © 2005 Wiley-VCH Verlag GmbH & Co. KGaA, Weinheim

Table 1. NMR spectroscopic data for hydridopalladium [Pd(H)(X)L_2] complexes.[a]

Compound	Hydridopalladium complex	^{1}H NMR δ	$^2J_{^1H,^{31}P}$	^{31}P NMR δ	$^2J_{^{31}P,^{119}Sn}$	^{119}Sn NMR δ	$^2J_{^1H,^{119}Sn}$
1*	*trans*-[Pd(H)(Cl)(PPh_3)$_2$]	–13.12	–	30.75			
2*	*trans*-[Pd(H)(Cl)(PCy_3)$_2$]	–14.32	3	45.63			
3	*cis*-[Pd(H)(Cl)(dCypb)]	–8.00	10; 200				
4	*trans*-[Pd(H)($SnCl_3$)(PPh_3)$_2$]	–6.90	–	33.80	–	–	944
5	*trans*-[Pd(H)($SnCl_3$)(PCy_3)$_2$]	–8.50	–	52.30	138	154	1760

[a] T = 183 K (*: T = 298 K); solvent: [D_8]THF; δ in ppm and J in Hz.

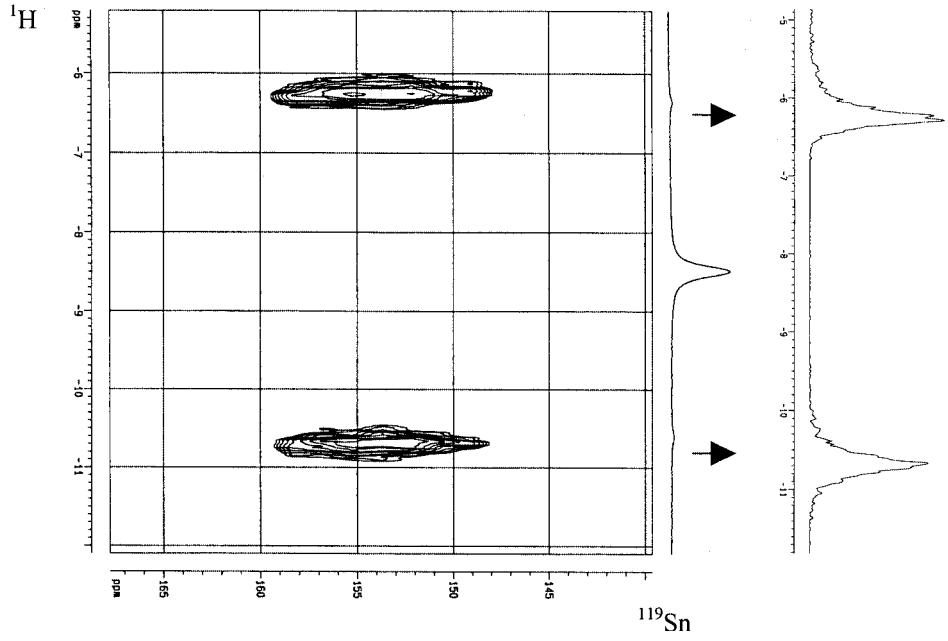

Figure 1. {^{1}H-^{119}Sn} HMQC spectra of complex **5** with an expansion of the two satellite signals on the right-hand side.

(6.22 ppm between **1** and **4** and 5.82 ppm between **2** and **5**), thus showing that the addition of $SnCl_2$ has a dramatic effect. Such a shift is certainly related to significant changes and decreases in the electron density at the H ligand and thus its hydride character. Recent studies on [Mo(H)(NO)(dmpe)$_2$] [dmpe = bis(dimethylphosphanyl)ethane] have shown that the hydridic character of the hydride ligand is largely influenced by the nitrosyl ligand in the *trans* position. As a consequence, this complex presents a high propensity to undergo hydride-transfer reactions.[17]

The ^{1}H NMR spectrum of complex **5** at 183 K shows the additional presence of a small amount of complex **2** (Figure 2). Increasing the temperature to 203 K leads to a large increase in the concentration of **2** due to decoordination of $SnCl_2$, complex **5** becoming the minor species. This observation does not mean that under the catalytic conditions (348–373 K, P_{CO} = 30–100 bar) only the chloro complex is operative. Indeed, the NMR spectra at room temperature (under inert atmosphere) still show the presence of **5** but a fluxional process occurs, as detected by the broadening of its hydride signal, whereas that of **2** remains sharp. We did not observe the possible intermediates, i.e. the *cis*-isomer of **5** or a pentacoordinate species arising from the coordination of $SnCl_2$ to **2**.

It is worth mentioning that addition of $SnCl_2$ to complex **3**, even at 183 K, does not result in the formation of the expected Pd-$SnCl_3$ species. The hydride signal of **3** disappears, and several unassigned signals are detected in the ^{31}P NMR spectrum. Decomposition into an orange material occurs rapidly. Table 1 lists all the NMR spectroscopic data for complexes **1**–**5**.

The synthesis of complexes containing the Pd(H)($SnBu_3$) core was attempted in order to introduce another Lewis acid into the coordination sphere of palladium. The synthetic procedure is to add $HSnBu_3$ directly to a palladium(0) species. In fact, [$Pd(PPh_3)_n$] (n = 2, 3, 4 in solution) reacts sluggishly, and at room temperature gives mainly the complex [Pd($SnBu_3$)$_2$(PPh_3)$_2$] ($\delta_{^{31}P}$ = 34.30 ppm, $^2J_{^{31}P,^{119}Sn}$ = 113 Hz). Nevertheless, a ν(Pd–H) absorption is detected at 2046 cm^{-1} in the IR spectrum, which belongs presumably to [Pd(H)($SnBu_3$)(PPh_3)$_2$]. The reaction proceeds cleanly with [$Pd(PCy_3)_2$], [Pd(diphos)(PCy_3)] [diphos = 1,2-bis(dicyclohexylphosphanyl)ethane (dCype)], 1,4-bis(dicyclohexylphosphanyl)butane or 1,6-bis(diphenylphosphanyl)hexane

 © 2005 Wiley-VCH Verlag GmbH & Co. KGaA, Weinheim

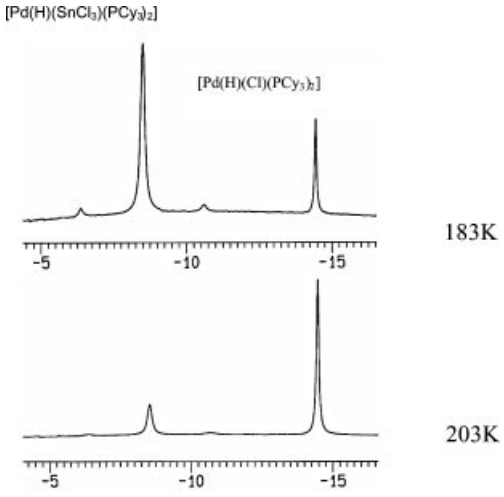

Figure 2. Evidence for a dynamic equilibrium between **2** and **4**.

(dpph) to give, according to ^{1}H and ^{31}P NMR analysis, $[Pd(H)(SnBu_3)(PCy_3)_2]$ (**6**), $[Pd(H)(SnBu_3)(dCype)]$ (**7**), $[Pd(H)(SnBu_3)(dCypb)]$ (**8**) or $[Pd(H)(SnBu_3)(dpph)]$ (**9**), respectively, in which the two hydrido and $SnBu_3$ ligands are in mutual *trans* (**6**) or *cis* (**7**–**9**) positions. Indeed, the hydride signal of **6** is at δ = –14.32 ppm due to the large *trans* influence of the $SnBu_3$ ligand. For **7**–**9**, the hydride signals are at δ = –2.67, –3.84 and –4.06 ppm, respectively. All NMR spectroscopic data are displayed in Table 2. Similarly, the platinum analogue $[Pt(H)(SnBu_3)(PPh_3)_2]$ (**10**) was prepared from $[Pt(PPh_3)_4]$. Here also addition of $HSnBu_3$ provides $[Pt(SnBu_3)_2(PPh_3)_2]$ directly, which was characterised by ^{31}P NMR spectroscopy ($\delta_{^{31}P}$ = 18.0 ppm). However, as already described in the literature[18] for the preparation of $[Pt(H)(SnMe_3)(PPh_3)_2]$, bubbling dihydrogen through the solution allows the isolation of **10**.

Comparison between the two $SnCl_3$ and $SnBu_3$ ligands shows immediately that the *trans* influence of the tributyltin ligand is significantly stronger than that of $SnCl_3$ and is rather similar to that of the chloro ligand. The hydridic character decreases significantly when $SnCl_2$ is introduced into the coordination sphere (the chemical shift is δ = –8.5 ppm for **5**, whereas it is δ = –14.32 ppm for **2** and δ = –14.53 ppm for **6**). When we consider complex **8**, in which the hydrido and $SnBu_3$ ligands are in mutual *cis* positions, the situation is more contrasted. Indeed, the hydride signal is found at δ = –3.84 ppm, i.e. roughly 10 ppm to lower field than in **6**. Provided the steric effects are ignored, the phosphorus atom P_A in the *trans* position to $SnBu_3$ [$\delta_{^{31}P}$ = 27.36 ppm (t, $J_{^{31}P,^{119}Sn}$ = 1402 Hz] receives more electron density from the metal centre than the second phosphorus atom P_B *trans* to the hydride [$\delta_{^{31}P}$ = 43.96 ppm (t, $^2J_{^{31}P,^1H}$ = 166 Hz], which is not significantly affected by the presence of the $SnBu_3$ in the *trans* position. In the paragraph devoted to catalysis, these electronic effects will be taken into account to explain the various catalytic activities observed.

Variable-temperature ^{1}H and ^{31}P NMR studies of complex **8** (Figure 3) show that a stereochemical non-rigidity phenomenon occurs, and the square-planar complex does not lose the $SnBu_3$ ligand. The ^{1}H NMR signal at room temperature is consistent with a hydride ligand coupled to two equivalent phosphorus atoms and to tin. A fast isomerisation process makes the P_A and P_B phosphorus atoms equivalent. A similar phenomenon has recently been reported for $[Pd(H)(SiR_3)(dCype)]$.[19] In addition, sophisticated ^{1}H-^{119}Sn{^{31}P} 2D-HMQC NMR experiments unambiguously show the ^{119}Sn chemical shift at δ = 7.50 ppm.

Some authors consider that the main role of adding $SnCl_2$ is to provide the $SnCl_3^-$ counterion, but this hypothesis has been essentially confirmed in platinum chemistry.[20] We prepared the cationic hydrido complexes $[Pd(H)L_3]^+$ in the presence of weakly coordinating anions such as CF_3COO^- **a**, BF_4^- **b**, and $TolSO_3^-$ **c**. Table 3 displays all the NMR spectroscopic data related to the complexes that were isolated and characterised by ^{1}H and ^{31}P NMR spectroscopy. They obey the general formula $[Pd(H)(PCy_3)L_2]^+$, except for $[Pd(H)(PCy_3)_2]^+$ (**11**), for which the hydride signal appears at δ = –18.8 ppm as a triplet with a small hydride–phosphorus coupling of 3.5 Hz, consistent with a 14-electron palladium complex having the two PCy_3 ligands in *trans* positions and the hydrogen atom *cis* to each phosphorus atom.[9i–9k,21] For the 16-electron complexes $[Pd(H)(PCy_3)L_2]^+$ {L_2 = dCype **12**, [1,2-bis(diphenylphosphanyl)ethane] (dppe) **13**, [1,3-bis(diphenylphosphanyl)propane] (dppp) **14**, [1,4-bis(diphenylphosphanyl)butane] (dppb) **15**, [1,1′-bis(diphenylphosphanyl)ferrocene] (dppf) **16**}, the nature of the counterion is almost insignificant. For instance, when L_2 = dppp, $\delta_{^1H}$ = –6.62 ppm with CF_3COO^- or –6.84 ppm with BF_4^-. Variation of L_2 (**13**–**16**) induces larger effects. For example, for **13a**, **14a**, **15a** and **16a** the shifts are δ = –5.58, –6.62, –6.12 and –7.87 ppm, respectively. The geometry is presumably square planar, with the PCy_3 ligand being *cis* to the hydride ligand. The

Table 2. NMR spectroscopic data for the $[Pd(H)(SnBu_3)L_2]$ complexes.[a]

Compound	Hydridopalladium complex	^{1}H NMR δ	$^2J_{^1H,^{31}P}$	$^2J_{^1H,^{119}Sn}$	^{31}P NMR δ	$^2J_{^{31}P,^{119}Sn}$	^{119}Sn NMR δ
6	*trans*-$[Pd(H)(SnBu_3)(PCy_3)_2]$	–14.5	5.5	2494	48.30		
7	*cis*-$[Pd(H)(SnBu_3)(dCype)]$	–2.67	177	310	25.10, 45.20		
8*	*cis*-$[Pd(H)(SnBu_3)(dCypb)]$	–3.84	8, 166	200	27.36, 43.96	1402	7.50
9	*cis*-$[Pd(H)(SnBu_3)(dpph)]$	–4.01	200		40.70	–	–

[a] T = 298 K; solvent: C_7D_8; *: a coupling constant is observed between the two phosphorus atoms ($^2J_{^{31}P_A,^{31}P_B}$ = 20 Hz).

 © 2005 Wiley-VCH Verlag GmbH & Co. KGaA, Weinheim

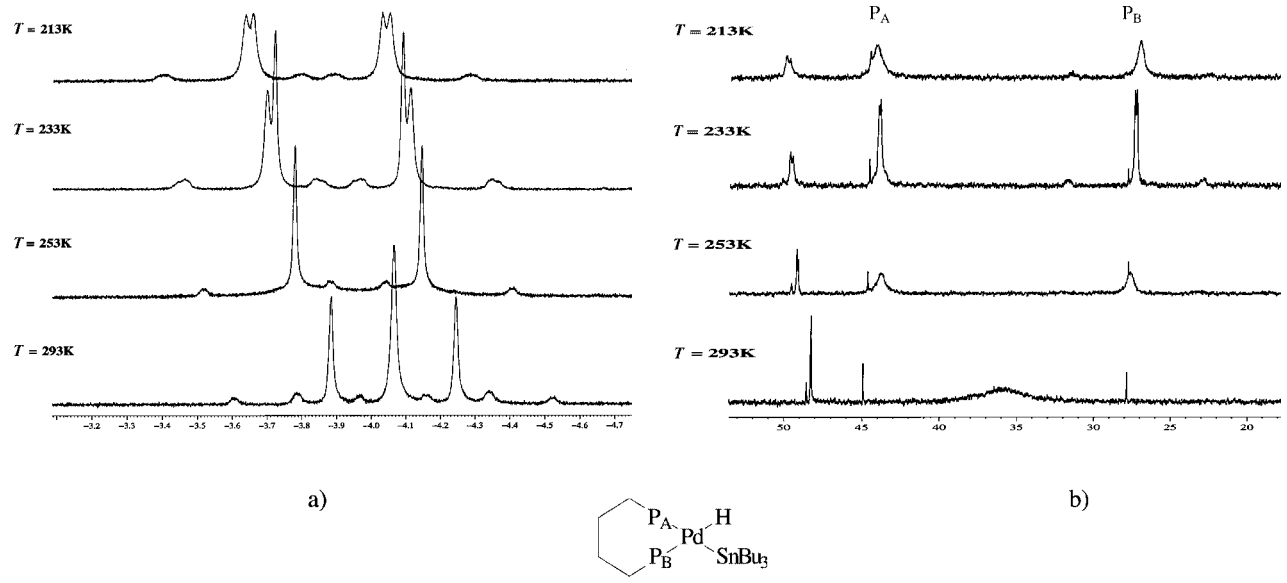

Figure 3. a) Hydride section of the variable temperature ^{1}H NMR spectra measured for **8**; b) Variable temperature ^{31}P NMR spectra measured for **8**.

Table 3. NMR spectroscopic data of $[Pd(H)(PCy_3)_2]^+(X)^-$ and $[Pd(H)(PCy_3)L_2]^+(X)^-$.

Complexes $[Pd(H)(PCy_3)_2]^+$	δ (^{1}H) [ppm][a]	$^{2}J_{^{1}H,^{31}P}$ [Hz]	δ (^{31}P) [ppm]	$^{2}J_{^{31}P,^{31}P}$ [Hz]
11a	–18.20	3.5	39.40	–
11b	–18.84	3.7	–	–
11c	–18.71	–	45.7	–
$[Pd(H)(PCy_3)(L_2)]^+(X)^-$				
12a	–6.29	7, 13, 179	86.95, 65.43, 49.68	311, 18, 18
12b	–6.15*	–	–	–
12c	–6.12	9, 12, 177	–	–
13a	–5.58	20, 196	–	–
14a	–6.62	28, 189	51.18, 9.16, 3.58	306, 48, 22
14b	–6.90	12, 75	49.87, 7.66, 3.97	315, 51, 21
15a	–6.12	13, 185	–	–
16a	–7.87	10, 179	52.57, 24.94, 20.15	337, 31, 27

[a] T = 298 K; *: broad signal due to exchange phenomena at room temperature.

diphos ligand shows two phosphorus atoms in different magnetic environments, giving rise to an AMX system (Table 3).

Catalytic Activity in Carbonylation of Isopulegol

The catalytic activity of $[Pd(H)(SnCl_3)(PPh_3)_2]$ {formed from $[Pd(H)(Cl)(PPh_3)_2]$ by addition of an excess of $SnCl_2$ in situ with a P/Pd ratio of 4} was examined in the cyclocarbonylation of isopulegol in toluene, exclusively with CO as a reactant (**A** giving **C** in Scheme 1). Conversion of the substrate is 100% within 16 h at 60 °C (see Table 4, run R1). One more experiment was carried out at the same pressure but at lower temperature (40 °C, run R2): the yield was 62%. The effect of the temperature appears to be prominent, since when the pressure was decreased from 30 bar to 20 bar and even 10 bar the yields were not affected (compare runs R1, R3 and R4 at 60 °C).

Table 4. Catalytic activity for cyclocarbonylation of isopulegol in the presence of $[Pd(H)(Cl)L_2/SnCl_2/L]$.

Test	t [h]	P_{CO} [bar]	T [°C]	Yield [%]	(5*R*)-C [%]	(5*S*)-C [%]	*de*[a] [%]
R1	16	30	60	100	60	40	20
R2	16	30	40	62	35	27	13
R3	40	20	60	100	60	40	20
R4	16	10	60	100	66	44	22
R5	68	10	50	68	45	23	22
R6[b]	16	10	60	100	78	22	56

[a] de = {R(%) – S(%)}/{R(%) + S(%)}. [b] dppb was used as ligand.

The two diastereomers of lactone **C** were obtained in a nearly 60:40 proportion (runs R1, R3 and R4). In fact, as noted by Knifton in his early studies, the promoting role of the $SnCl_2$ co-catalyst is essentially to increase the regioselectivity of the alkoxycarbonylation of the terminal alkene into the corresponding linear ester.[7] In the present case, the re-

 © 2005 Wiley-VCH Verlag GmbH & Co. KGaA, Weinheim

action with $[Pd(H)(Cl)(PPh_3)_2]$ is slower and less diastereoselective.[11] Increasing the electron density on palladium by substituting the PPh_3 ligands with PCy_3 results in the complete absence of reactivity under the same reaction conditions irrespective of whether the complex is prepared and isolated or generated in situ. Formation of $[Pd(H)(SnCl_3)(dppb)]$ from $[Pd(H)(Cl)(PPh_3)_2]$ (**1**), dppb and $SnCl_2$ leads to lower reaction rates but improved diastereomeric ratios (78:22). On the contrary, producing the cationic hydrido precursor **15a** by direct addition of CF_3COOH to $[Pd(PCy_3)(dppb)]$ gives a poor yield of **C** (17%). Similarly, $[Pd(H)(PCy_3)(dppf)]^+[CF_3COO]^-$ (**16a**) leads to a 21% yield. All the other prepared cationic complexes were examined in the carbonylation of isopulegol: the results are similarly deceiving.

Moreover, the effect of the introduction of $SnBu_3$ in the coordination sphere of palladium was analysed. In the presence of $[Pd(H)(SnBu_3)(PPh_3)_2]$, prepared in situ by addition of $HSnBu_3$ to $[Pd(PPh_3)_n]$, or *cis*-$[Pd(H)(SnBu_3)(dCypb)]$, the carbonylation reaction gives only traces of lactone. The important difference in the chemical shift − δ = –14.50 ppm for **6** and δ = –8.50 ppm for **5** − is presumably related to the significant differences in reactivity of the two complexes. Indeed, **6** presents a high hydridic character and its intrasphere nucleophilic attack of the olefin should be easy, this transfer producing the alkyl species, but the coordination of the olefin to the metal centre is presumably retarded. Moreover, we cannot exclude that in the subsequent step the CO migratory insertion could be disfavoured due to the steric hindrance of $SnBu_3$ and/or the electronic effects on palladium.

Mechanistic Proposal

Characterisation of an Acylplatinum Species

Platinum complexes are often used to mimic the reactivity of palladium because they are less labile and they lead to more stable pentacoordinate species. The complex *trans*-$[Pt(H)(SnCl_3)(PPh_3)_2]$ (**17**) was therefore prepared from *cis*-$[PtCl_2(PPh_3)_2]$[22] and treated with dihydromyrcene at 100 °C under a CO pressure of 40 bar. Microcrystalline material precipitated at the end of the reaction. After separation and dissolution of the solid, analysis by multinuclear NMR showed that its structure corresponds to the square-planar acyl complex *trans*-$[PtCl\{C(O)CH_2CH_2CH(CH_3)CH_2CH_2CHC(CH_3)_2\}(PPh_3)_2]$ (**18**), as shown in Equation (2).

A signal with two satellites is observed in the ^{31}P NMR spectrum at δ = 23.18 ppm due to the coupling with ^{195}Pt ($^1J_{^{31}P,^{195}Pt}$ = 3186 Hz), and a triplet is observed for the ^{195}Pt signal at δ = –3933 ppm due to the coupling with two equivalent phosphorus atoms. Furthermore, in the ^{13}C NMR spectrum the acyl carbon atom appears as a triplet at δ = 219.45 ppm ($^2J_{^{31}P,^{13}C}$ = 6 Hz) flanked by satellites with $^1J_{^{195}Pt,^{13}C}$ = 458 Hz. A similarly high chemical shift value of δ = 243.9 ppm has been found for the C(O)Me carbon in the anionic acylplatinum(II) complex [Li][(η^2-Tp′)Pt(CO-Me)(Me)] [Tp′ = hydridotris(3,5-dimethylpyrazolyl)borate].[23]

Thus, under a CO atmosphere the platinum complex that separates from the medium as a solid contains the acyl moiety *trans* to the chloro atom. We supposed that, in fact, the formation of the $SnCl_3$ ligand is reversible, so we decided to add one equivalent of $SnCl_2$ to the acyl chloro complex. All the analyses show that we unambiguously produced the acylplatinum $SnCl_3$ complex *trans*-$[Pt(SnCl_3)\{C(O)CH_2CH_2CH(CH_3)CH_2CH_2CHC(CH_3)_2\}(PPh_3)_2]$ (**19**), as given by Equation (3).

The ^{31}P NMR spectrum of this complex shows that the two phosphane ligands are equivalent and give a signal, with two satellites, at δ = 18.95 ppm ($^1J_{^{195}Pt,^{31}P}$ = 3186 Hz). The ^{195}Pt NMR signal at δ = –4466 ppm is a triplet due to the coupling with the two equivalent phosphorus atoms. The ^{119}Sn NMR spectrum contains a signal at δ = 55.61 ppm (t) with a ^{31}P-^{119}Sn coupling constant of 296 Hz that we obtained from ^{31}P-^{119}Sn INEPTND and ^{31}P-^{119}Sn HMQC experiments. Finally, the ^{13}C NMR spectrum presents an acyl signal at δ = 224.80 ppm (t), with $^2J_{^{13}C,^{31}P}$ = 5 Hz, the $^2J_{^{13}C,^{195}Pt}$ coupling constant being difficult to determine due to the low signal-to-noise ratio.

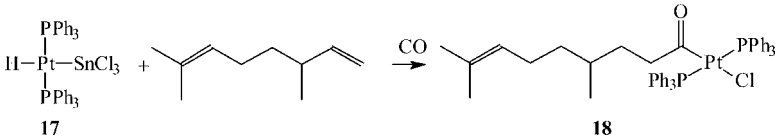

(2)

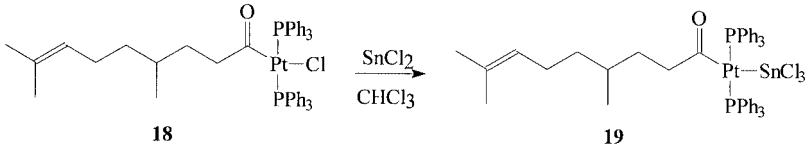

(3)

Observations by ^{1}H NMR carried out over a period of several days showed that the acyl complex **19** evolves toward the starting complex [Pt(H)($SnCl_3$)(PPh_3)$_2$] (**17**). Dihydromyrcene was also unambiguously detected. Thus, we can deduce that the equilibrium between these two complexes involves the intermediate alkyl species **20** shown in Figure 4. Indeed, decarbonylation of complex **19** would give **20**, which produces the pentacoordinate species [Pt(H)($SnCl_3$)(dihydromyrcene)(PPh_3)$_2$] by β-elimination. This latter complex would give **17** by loss of dihydromyrcene.

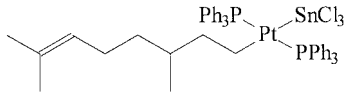

20

Figure 4. Alkylplatinum species **19** resulting from the addition of dihydromyrcene.

In situ Characterisation of Palladium Species under CO Pressure

Zudin and al.[24] have previously shown that the cationic hydridopalladium complex [Pd(H)(PPh_3)$_3$]$^+$[CF_3COO]$^-$, prepared in situ, reacts with CO to afford the dinuclear complex [Pd_2(μ-H)(μ-CO)(PPh_3)$_4$]$^+$[CF_3COO]$^-$ in which the hydrido and carbonyl ligands occupy the two bridging positions. A similar monocationic dinuclear complex has been prepared with the diphosphane ligand 1,3-bis[di(isopropyl)-phosphanyl]propane.[25] Moreover, Elsevier and Tóth started from the mononuclear neutral acyl complex [Pd(Cl)(COMe)(bdppp)] [bdppp is (2*S*,4*S*)-2,4-bis(diphenylphosphanyl)pentane] and observed that a methanolysis reaction occurs under a CO atmosphere to provide the elusive intermediate [Pd(H)(Cl)(bdppp)], which leads to a mixture of [$PdCl_2$(bdppp)] and [Pd_2(μ-H)(μ-CO)(bdppp)$_2$]$^+$-[Cl]$^-$.[26]

Introduction of $SnCl_2$ into the Palladium Hydride Coordination Sphere

[Pd(H)($SnCl_3$)(PCy_3)$_2$] (**5**), prepared in situ in an NMR tube by addition of one equivalent of $SnCl_2$ to [Pd(H)(Cl)(PCy_3)$_2$] (**2**), was pressurised with 3 bar ^{13}CO. The ^{1}H NMR spectra present a broad signal at δ = –8.70 ppm and even at 183 K no ^{1}H-^{31}P nor ^{1}H-^{119}Sn coupling constants could be determined due to an exchange phenomenon. However, the ^{13}C NMR spectra clearly reveal a triplet at δ = 232.4 ppm with a $^2J_{^{13}C,^{31}P}$ coupling constant of 3.7 Hz, the CO ligand thus being *cis* to two equivalent phosphorus atoms. The same spectra also show two satellites due to ^{13}C-^{119}Sn coupling (^2J = 144.6 Hz), such a value being in agreement with a mutual *cis* arrangement of the CO and $SnCl_3$ ligands. In the ^{31}P NMR spectrum, a signal is detected at δ = 50.80 ppm with two satellites due to a small coupling with ^{119}Sn (^2J = 148 Hz), consistent with the $SnCl_3$ ligand being *cis* with regard to the two equivalent phosphorus atoms. Thus, we can assign to this pentacoordinate species either the trigonal bipyramid geometry **21a** or the square-planar pyramid structure **21b** represented in Figure 5.

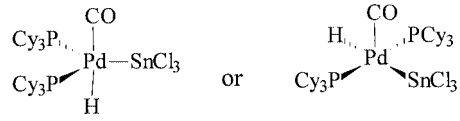

21a **21b**

Figure 5. Two possible geometries for the pentacoordinate species [Pd(H)($SnCl_3$)(CO)(PCy_3)$_2$] (**21a**) and **21b**.

The hydrido and carbonyl ligands in **21a** occupy the axial positions of the tbp geometry. Although such pentacoordinate hydrido species have already been proposed in the literature,[27] no such characterisation has been reported in palladium chemistry. However, it is worth mentioning that a palladium atom with five ligands in tbp or sp environments is known for [Pd(CH_2CMe_2-*o*-C_6H_4)-(PMe_3)$_2$(SO_2)],[28] or for a cationic palladium complex containing a triphosphane ligand and an imine ligand in the *o*-position of an aryl group.[29a]

Although we did not reach the slow exchange limit for complex **21a**, we suggest that a Berry pseudo-rotation mechanism occurs in solution which exchanges the axial and equatorial ligands. In this way the dynamic equilibrium shown in Figure 6 should occur. In this case, the second tbp isomer contains the CO and $SnCl_3$ ligands in mutual *cis* positions with regard to the two PCy_3 ligands (Figure 6).

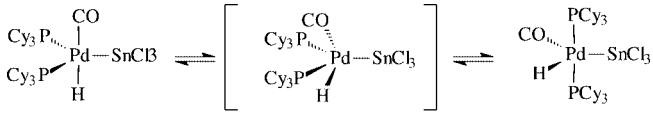

21a **21a'**

Figure 6. Axial–equatorial ligand exchange in [Pd(H)($SnCl_3$)(CO)(PCy_3)$_2$] (**21a**).

In addition to these observations, we detected a weak signal in the ^{1}H NMR spectrum at δ = –14.5 ppm corresponding to a weak signal in the ^{13}C NMR spectrum at δ = 194.6 ppm. Such a value for the hydride ligand recalls the shift of [Pd(H)(Cl)(PCy_3)$_2$] (**2**) ($\delta_{^1H}$ = –14.32 ppm) and we suggest that these signals should correspond to the species [Pd(H)(CO)(Cl)(PCy_3)$_2$] (**22**) (**21**/**22** = 65:35). As we previously observed (see above) the equilibrium between [Pd(H)($SnCl_3$)(PCy_3)$_2$] (**5**) and [Pd(H)(Cl)(PCy_3)$_2$] (**2**) + $SnCl_2$, and since removing $SnCl_2$ from a pentacoordinate species is rather uncommon, we propose that the complex [Pd(H)(Cl)(CO)(PCy_3)$_2$] (**22**) results from the direct coordination of a CO ligand to the square-planar complex [Pd(H)(Cl)(PCy_3)$_2$] (**2**).

NMR Monitoring of the Reactivity of the Substrate with [Pd(H)($SnCl_3$)(PCy_3)$_2$] (5)

We carried out the same type of experiments, maintaining the same temperature and concentrations, but now four equivalents of dihydromyrcene were added and the ^{13}CO/^{12}CO pressure was increased to 10 bar. In less than one hour, still at 183 K, the main hydride peak at δ =

 © 2005 Wiley-VCH Verlag GmbH & Co. KGaA, Weinheim

–8.7 ppm and the weak signal at δ = –14.5 ppm disappeared, presumably due to the formation of the corresponding alkyl species. In the ^{13}C NMR spectrum two CO signals were detected at δ = 232.6 ppm (complex **23**) and δ = 194.7 ppm (complex **24**) as two triplets with relative intensities of 70:30 and $^{2}J_{^{13}C,^{31}P}$ coupling constants of 4.5 and 3.2 Hz, respectively; this ratio was found to be 75:25 for the hydride signals of $[Pd(H)(SnCl_3)(PCy_3)_2]$ (**5**) and $[Pd(H)(Cl)(PCy_3)_2]$ (**2**) in the ^1H NMR spectrum. The proximity of the two chemical shifts and the coupling constants for **21a** and **23** led us to propose that we observe the pentacoordinate species in which CO is coordinated as shown in Figure 7. Similarly, we propose that **24**, with the chloro ligand, is characterised by the shift at δ = 194.7 ppm. Pentacoordinated platinum species have previously been described in which the coordination sphere contains the diphosphane dppe, CO, methyl and methoxy ligands.[29b]

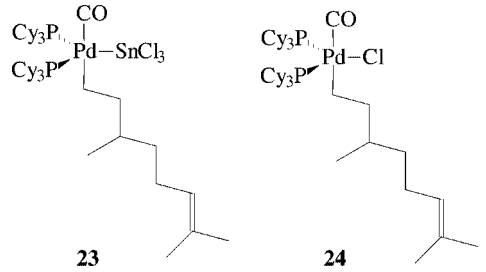

Figure 7. Representation of the two pentacoordinate acyl species **23** and **24** observed under CO pressure in HP/NMR spectroscopy.

The CO migratory insertion is presumably the rate-determining step, since at 183 K the coordination of the alkene followed by the hydride transfer are relatively fast steps. Such an observation parallels the reactivity of $[Pd(H)(SnCl_3)(PPh_3)_2]$ (**4**) in catalytic tests, since at 40 °C and 30 bar the conversion rate is near to 60% in 16 h, whereas at 60 °C and even at 10 bar the reaction reaches completion overnight (see Table 4).

Conclusions

In this paper, the identification of various neutral, cationic, square-planar and pentacoordinate (under CO pressure) hydridopalladium complexes has been described. It appears that the co-catalyst role of $SnCl_2$ is crucial because it produces an active palladium–$SnCl_3$ species. Preparation of $[Pd(H)(SnCl_3)(PPh_3)_2]$, as shown by multinuclear NMR spectroscopy, leads to an active complex which catalyses the alkoxycarbonylation reaction of an alkene efficiently. Thus, we propose a catalytic cycle exclusively based on the hydride route, with the two L phosphorus ligands in *trans* positions (Figure 8).

Recent studies reported by van Leeuwen and Heaton[30] are consistent with the coordination of methanol to explain the last step of the alcoholysis, provided the two phosphane

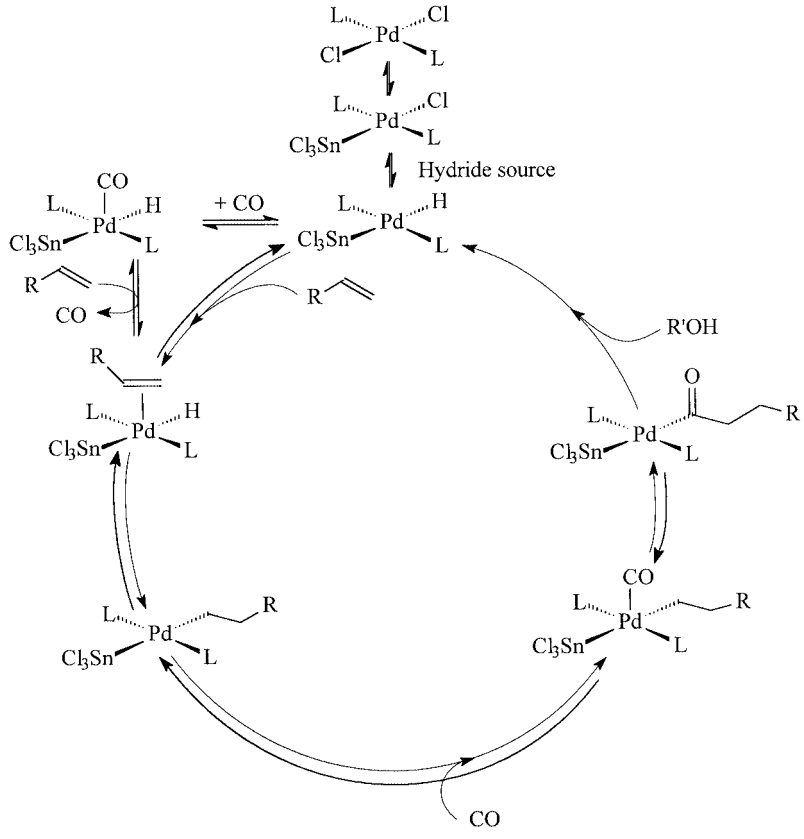

Figure 8. Proposed hydridopalladium route for alkoxycarbonylation reaction.

 © 2005 Wiley-VCH Verlag GmbH & Co. KGaA, Weinheim

ligands are mutually *cis*. Our preliminary observations that isomerisation occurs for the monophosphane ligands prompted us to explore and investigate the final step of the catalytic reaction in the present system.

Experimental Section

General Considerations: All reactions and manipulations were carried out in dried and distilled solvents under argon using standard Schlenk techniques. All NMR measurements were performed on Bruker AM250, AMX400 or DRX400 spectrometers using 5-mm triple resonance inverse probes with a dedicated ^{31}P channel. All chemical shifts for ^{1}H and ^{13}C are relative to TMS using ^{1}H (residual) or ^{13}C chemical shifts of the solvent as a secondary standard. The chemical shifts were referenced to external H_3PO_4 (85%) for ^{31}P, $SnMe_4$ for ^{119}Sn and H_2PtCl_6 for ^{195}Pt. High-pressure NMR experiments in situ were carried out in special sapphire tubes with a diameter of 10 mm (for more details concerning the setup and procedure see ref.[31]). IR spectra were recorded on a Perkin–Elmer 1710 FT-IR spectrophotometer. Gas chromatography analyses were performed on a Perkin–Elmer instrument equipped with a DB-5GC column (30 m × 0.25 mm × 0.25 μm) and a flame ionisation detector. Mass spectrometric measurements were performed at the Service de Spectrométrie de Masse de l'Université Paul Sabatier on a NERMAG R 10-10 apparatus for organometallic compounds and on a Perkin–Elmer TURBO MASS instrument equipped with a DB-5MS 30 m × 0.25 mm × 0.25 μm column for organic products. Elemental analysis (C,H,O) was performed at the Ecole Nationale Supérieure des Ingénieurs en Arts Chimiques et Technologiques de Toulouse. Several compounds are unstable, so mass spectrometry or elemental analyses were not always possible.

All the chemical products were purchased from Aldrich Chemical Co., except for the following complexes, which were prepared by the methods reported in the literature: $[PdCl_2(PhCN)_2]$,[15] *cis*-$[PdCl_2(dppb)]$,[12,15] *cis*-$[PdCl_2(dCypb)]$,[12,15] *trans*-$[Pt(H)(SnBu_3)(PPh_3)_2]$ (**6**),[18] *cis*-$[PtCl_2(PPh_3)_2]$,[22] *trans*-$[Pt(H)(SnCl_3)(PPh_3)_2]$ (**17**),[22] *trans*-$[PdCl_2(PPh_3)_2]$,[14] *trans*-$[PdCl_2(PCy_3)_2]$,[12,32] $[Pd(PPh_3)_n]$,[14] $[Pd(PCy_3)_2]$.[32] ^{12}CO and ^{13}CO (99%) were purchased from Air Liquide.

Catalytic Tests: A mixture of triphenylphosphane (0.4 mmol) and tin(II) chloride (0.5 mmol) was introduced into a 150 mL stainless steel autoclave with magnetic stirring. A nitrogen-saturated mixture of palladium complex [chlorobis(triphenylphosphanyl)palladium(II) hydride or dichlorobis(triphenylphosphanyl)palladium (0.2 mmol)] and isopulegol (10 mmol) in toluene (10 mL) was introduced into the evacuated autoclave by aspiration. It was heated (40–60 °C) under pressure (10–30 bar) of carbon monoxide. After 16 h, the autoclave was cooled and then slowly depressurized. The obtained solution was analysed by gas chromatography.

Synthesis of $[Pd(H)(Cl)L_2]$ (L = PPh_3 1; PCy_3 2): A 100 mL benzene solution of $[PdCl_2L_2]$ (0.57 mmol) and $HSiPh_3$ (11.44 mmol) was heated at 70–80 °C for 2 h. The resultant red solution was concentrated to ca. 30 mL, and addition of hexane afforded a powder of *trans*-$[Pd(H)(Cl)L_2]$ which was dissolved in benzene and precipitated with hexane three times; the final product was white and was isolated in 40% yield.

Alternative Method for the Synthesis of 2: A pale-green solution of $[Pd(PCy_3)_2]$ (1 mmol) in 10 mL of toluene was slowly treated with one equivalent of 2 M HCl in diethyl ether solution at room temperature. The resultant pale-yellow solution was evaporated under reduced pressure. The obtained solid was washed three times with diethyl ether; the final product was pale yellow and was isolated in 80% yield.

$[Pd(H)(Cl)(PPh_3)_2]$ (1): IR: ν(Pd–H) = 2050 cm^{-1}. ^{1}H NMR (250 MHz, 293 K, $CDCl_3$): δ = –13.12 ppm. ^{31}P NMR (250 MHz, 293 K, $CDCl_3$): δ = 30.75 ppm.

$[Pd(H)(Cl)(PCy_3)_2]$ (2): IR: ν(Pd–H) = 2046 cm^{-1}. ^{1}H NMR (250 MHz, 293 K, $CDCl_3$): δ = –14.32 ppm. ^{31}P NMR (250 MHz, 293 K, $CDCl_3$): δ = 46.63 ppm.

Preparation of [Pd(H)(Cl)(dCypb)] (3): A solution of $[Pd(PCy_3)_2]$ (0.1 mmol) in 1 mL of $[D_8]$THF was treated with 0.1 mmol of 1,4-bis(dicyclohexylphosphanyl)butane at room temperature. After 1 h, one equivalent of HCl (in Et_2O solution) was added and the solution was stirred for 1 h at 183 K. Then, ^{1}H NMR spectra were recorded, and revealed the presence of [Pd(H)(Cl)(dCypb)] (**3**) along with small amounts of $[Pd(H)(Cl)(PCy_3)_2]$ (**2**) and traces of unidentified hydridopalladium complexes. ^{1}H NMR (400.13 MHz, 183 K): δ = –8.0 ppm ($^{2}J_{^{1}H,^{31}P}$ = 10 and 200 Hz). From the integration of the ^{1}H signals, the yield of **3** was estimated to be 40%.

Preparation of $[Pd(H)(SnCl_3)L_2]$ (L = PPh_3, 4; PCy_3, 5): A solution of $[Pd(H)(Cl)L_2]$ (0.1 mmol) in 1 mL of $[D_8]$THF was treated with one equivalent of anhydrous $SnCl_2$ at 183 K for 2 h, and the ^{1}H, ^{31}P and ^{119}Sn NMR spectra were recorded; the spectra indicated the presence of a mixture of $[Pd(H)(SnCl_3)L_2]$ and $[Pd(H)(Cl)L_2]$ with relative intensities **1/4** = 20:80 and **2/5** = 75:25.

$[Pd(H)(SnCl_3)(PPh_3)_2]$ (4): ^{1}H NMR (400.13 MHz, 183 K): δ = –6.90 ppm ($^{2}J_{^{1}H,^{119}Sn}$ = 944 Hz). $^{31}P\{^{1}H\}$ NMR (161.98 MHz, 183 K): δ = 33.80 ppm.

$[Pd(H)(SnCl_3)(PCy_3)_2]$ (5): ^{1}H NMR (400.13 MHz, 183 K): δ = –8.50 ppm. $^{31}P\{^{1}H\}$ NMR (161.98 MHz, 183 K): δ = 52.3 ppm ($^{2}J_{^{31}P,^{119}Sn}$ = 138.1 Hz). ^{1}H-^{119}Sn HMQC NMR (400.13 MHz, 149.21 MHz, 183 K): δ = 154 ppm ($^{2}J_{^{1}H,^{119}Sn}$ = 1760 Hz).

Synthesis of $[Pd(H)(SnBu_3)(dCypb)]$ (8): A solution of $[Pd(PCy_3)_2]$ (0.2 mmol) in 5 mL of toluene was treated with 0.2 mmol of 1,4-bis(dicyclohexylphosphanyl)butane at room temperature. After 1 h, one equivalent of tri(*n*-butyl)tin hydride was added and the solution was stirred for 1 h. Then, the solvent was removed under reduced pressure and the remaining solid with 75% yield was dissolved in C_7D_8 for characterisation by NMR spectroscopy. ^{1}H NMR (400.13 MHz, 213 K): δ = –3.84 ppm ($^{2}J_{^{1}H,^{31}P_{cis}}$ = 8.4, $^{2}J_{^{1}H,^{31}P_{trans}}$ = 165.9, $^{2}J_{^{1}H,^{119}Sn}$ = 110 Hz). ^{1}H-^{119}Sn {^{31}P} HMQC NMR (400.13 MHz, 149.22 MHz, 253 K): δ = 7.50 ppm. $^{31}P\{^{1}H\}$ NMR (161.99 MHz, 233 K): δ = 27.36 ppm ($^{31}P_A$, $^{2}J_{^{31}P_A,^{119}Sn}$ = 1402 Hz), 43.96 ($^{31}P_B$, $^{2}J_{^{31}P_B,^{119}Sn} < 20$ Hz).

Identification of Neutral and Cationic Complexes: A similar procedure to the preceding one was adopted. A solution of $[Pd(PCy_3)_2]$ (0.1 mmol) in 2 mL of $[D_8]$toluene was treated with 0.1 mmol of ligand L (L = dCype, dppe, dppp, dCypb, dppb, dpph, dppf) at room temperature. After 1 h, one equivalent of HX (HX = $HSnBu_3$, CF_3COOH, HBF_4, $TolSO_3H$) was added and the solution was stirred for 1 h. The solution was filtered and transferred to a 5-mm NMR tube for NMR measurements. Only the most relevant shifts are given below. In addition, after removal of the solvent, the resulting solids were tested in cyclocarbonylation reaction.

$[Pd(H)(SnBu_3)(PCy_3)_2]$ (6): ^{1}H NMR: δ = –14.5 ppm ($^{2}J_{^{1}H,^{31}P}$ = 5.5, ($^{2}J_{^{1}H,^{119}Sn}$ = 2494 Hz). ^{31}P NMR: δ = 48.30 ppm.

$[Pd(H)(SnBu_3)(dCype)]$ (7): ^{1}H NMR: δ = –2.67 ppm ($^{2}J_{^{1}H,^{119}Sn}$ = 310, $^{2}J_{^{1}H,^{31}P_{trans}}$ = 177 Hz). ^{31}P NMR: δ = 25.10 ppm, 45.20 ($^{2}J_{^{1}H,^{31}P_{trans}}$ = 200 Hz), 40.70.

 © 2005 Wiley-VCH Verlag GmbH & Co. KGaA, Weinheim

[Pd(H)(SnBu$_3$)(dpph)] (9): ^{1}H NMR: δ = –4.01 ppm (exchange phenomena at room temperature).

[Pd(H)(PCy$_3$)(dCype)]$^+$(CF$_3$COO)$^-$ (12a): ^{1}H NMR: δ = –6.29 ppm ($^2J_{^1H,^{31}P}$ = 7, 13, 179 Hz). ^{31}P NMR: δ = 86.95, 65.43, 49.68 ppm ($^2J_{^{31}P,^{31}P}$ = 18, 311 and 18 Hz).

[Pd(H)(PCy$_3$)(dCype)]$^+$(BF$_4$)$^-$ (12b): ^{1}H NMR: δ = –6.15 ppm. (exchange phenomena at room temperature).

[Pd(H)(PCy$_3$)(dCype)]$^+$(TolSO$_3$)$^-$ (12c): ^{1}H NMR: δ = –6.12 ppm ($^2J_{^1H,^{31}P}$ = 9, 12 and 177 Hz).

[Pd(H)(PCy$_3$)(dppe)]$^+$(CF$_3$COO)$^-$ (13a): ^{1}H NMR: δ = –5.58 ppm ($^2J_{^1H,^{31}P}$ = 20, 196 Hz.

[Pd(H)(PCy$_3$)(dppp)]$^+$(CF$_3$COO)$^-$ (14a): ^{1}H NMR: δ = –6.62 ppm ($^2J_{^1H,^{31}P}$ = 28, 189 Hz). ^{31}P NMR: δ = 51.18, 9.16, 3.58 ppm $^2J_{^{31}P,^{31}P}$ = 306, 48 and 22 Hz).

[Pd(H)(PCy$_3$)(dppp)]$^+$(BF$_4$)$^-$ (14b): ^{1}H NMR: δ = –6.90 ppm ($^2J_{^1H,^{31}P}$ = 12, 75 Hz). ^{31}P NMR: δ = 49.87, 7.66, 3.97 ppm ($^2J_{^{31}P,^{31}P}$ = 315, 51 and 21 Hz).

[Pd(H)(PCy$_3$)(dppb)]$^+$(CF$_3$COO)$^-$ (15a): ^{1}H NMR: δ = –6.12 ppm ($^2J_{^1H,^{31}P}$ = 13, 185 Hz).

[Pd(H)(PCy$_3$)(dppf)]$^+$(CF$_3$COO)$^-$ (16a): ^{1}H NMR: δ = –7.87 ppm ($^2J_{^1H,^{31}P}$ = 10, 179 Hz). ^{31}P NMR: δ = 52.57, 24.94, 20.15 ppm ($^2J_{^{31}P,^{31}P}$ = 337, 27, 31 Hz). FAB$^+$/MS: *m*/*z* = 941.3; mode FAB$^-$/MS: *m*/*z* = 113.1.

Synthesis of [(CH$_3$)$_2$C=CH(CH$_2$)$_2$CH(CH$_3$)CH$_2$CH$_2$C(O)-PtCl(PPh$_3$)$_2$] (18): Complexes **18** and **19** were prepared according to the methods previously reported by Gómez et al.[27] A mixture of *trans*-[Pt(H)(Cl)(PPh$_3$)$_2$] (0.473 g, 0.5 mmol), PPh$_3$ (0.118 g, 0.45 mmol), dihydromyrcene (6.90 g, 50.0 mmol) and ethanol (25 mL) was charged in an autoclave. The autoclave was purged of air under reduced pressure and was then pressurised with 50 bar of CO, heated to 100 °C and stirred for 4 h. Then, the reactor was cooled to room temperature and depressurised. The resulting green solution was cooled to –30 °C to give **18** as a white solid, which was washed three times with cool ethanol, diethyl ether and finally dried under vacuo. Yield: 55%.

18: ^{31}P{^{1}H} NMR (161.98 MHz, CDCl$_3$, 298 K): δ = 23.2 ppm ($^2J_{^{31}P,^{195}Pt}$ = 3510.7 Hz). ^{195}Pt{^{1}H} NMR (85.68 MHz, CDCl$_3$, 298 K): δ = –3933 ppm. ^{13}C{^{1}H}bb+{^{31}P} NMR (100.63 MHz, CDCl$_3$, 298 K): δ = 219.4 ($^2J_{^{13}C,^{31}P}$ = 6, $^1J_{^{13}C,^{195}Pt}$ = 457.8 Hz), 135.4, 134.5, 131.3, 131.3, 130.8, 125.4, 57.1, 37.4, 32.1, 31.4, 26.2, 25.9, 19.5, 15.7 ppm.

Synthesis of [(CH$_3$)$_2$C=CH(CH$_2$)$_2$CH(CH$_3$)CH$_2$CH$_2$C(O)-Pt(SnCl$_3$)(PPh$_3$)$_2$] (19): A mixture of complex **18** (0.0922 g, 0.10 mmol), SnCl$_2$ (0.019 g, 0.1 mmol) and CHCl$_3$ (2 mL) was placed in a Schlenk tube and stirred for 15 min at room temperature. The solution was filtered and multinuclear NMR analysis was carried out. After removal of the solvent **19** was obtained as a yellow compound in 50% yield. ^{31}P-^{119}Pt HMQCND {^{1}H}bb NMR (161.98 MHz, 85.63 MHz, CDCl$_3$, 233 K) and ^{31}P{^{1}H} NMR (161.98 MHz, CDCl$_3$, 233 K): δ = 18.9 ppm ($^2J_{^{31}P,^{119}Sn}$ = 296 Hz). ^{31}P-^{119}Sn INEPTND {^{1}H}bb NMR: δ = 55.6 ppm. ^{31}P-^{195}Pt HMQCND {^{1}H}bb NMR, ^{195}Pt{^{1}H,^{31}P} NMR (85.68 MHz, CDCl$_3$, 233 K) and ^{31}P-^{195}Pt INEPTND {^{1}H}bb NMR: δ = –4466 ppm ($^1J_{^{195}Pt,^{31}P}$ = 3185.6 Hz). ^{13}C NMR: δ = 224.8, 135.1, 134.2, 132.5, 132.2, 129.9, 125.1, 37.3, 32.0, 30.5, 26.6, 25.7, 18.5, 15.1 ppm.

Observation of Mixtures of [Pd(H)(^{13}CO)(SnCl$_3$)(PCy$_3$)$_2$] (21) and [Pd(H)(^{13}CO)(Cl)(PCy$_3$)$_2$] (22): A solution of [Pd(H)(Cl)L$_2$] (0.1 mmol) in 2 mL of [D$_8$]THF was treated with one equivalent of anhydrous SnCl$_2$ at 183 K. After 2 h, this solution was transferred to a sapphire tube and the solution was charged with 3 bar of ^{13}CO at the same temperature. The ^{1}H, ^{31}P and ^{13}C spectra indicated the presence of [Pd(H)(^{13}CO)(SnCl$_3$)(PCy$_3$)$_2$] (**21**; 65%) and [Pd(H)(^{13}CO)(Cl)(PCy$_3$)$_2$] (**22**; 35%).

[Pd(H)(^{13}CO)(SnCl$_3$)(PCy$_3$)$_2$] (21): ^{1}H NMR: δ = –8.70 ppm. ^{31}P NMR: δ = 50.80 ppm ($^2J_{^{31}P,^{119}Sn}$ = 148 Hz). ^{13}C NMR: δ = 232.4 ppm (CO; $^2J_{^{13}C,^{31}P}$ = 3.7, $^2J_{^{13}C,^{119}Sn}$ = 144.6 Hz).

[Pd(H)(^{13}CO)(Cl)(PCy$_3$)$_2$] (22): ^{1}H NMR: δ = –14.50 ppm. ^{13}C NMR: δ = 194.6 ppm (CO).

Observation of Mixtures of [Pd(Alkyl)(CO)(SnCl$_3$)(PPh$_3$)$_2$] (23) and [Pd(Alkyl)(CO)(Cl)(PPh$_3$)$_2$] (24): A solution of [Pd(H)(Cl)L$_2$] (0.1 mmol) in 2 mL of [D$_8$]THF was treated with one equivalent of anhydrous SnCl$_2$ at 183 K. After 2 h, this solution was transferred to a sapphire tube and the solution was charged with four equivalents of dihydromyrcene and 3 bar of ^{13}CO at the same temperature. Multinuclear NMR analyses indicated the formation of a mixture of **23** and **24**, with a **23/24** ratio of 70:30. **23:** ^{13}C NMR: δ = 232.6 ppm ($^2J_{^{13}C,^{31}P}$ = 4.5 Hz). **24:** ^{13}C NMR: δ = 194.7 ppm ($^2J_{^{13}C,^{31}P}$ = 3.2 Hz).

Characterisation of Compound (5*R*)-C: MS: *m*/*z* (%) = 95(100), 81 (62), 96(41), 122 (30), 183 (18) [M + 1], 138 (7). ^{1}H NMR (250.13 MHz, CDCl$_3$): δ = 3.75 (ddd, *J* = 4.2, 10.5 and 10.5 Hz, 1 H, H1), 2.55 (dd, *J* = 6.8 and 18 Hz, 1 H, H4$_{ax}$), 1.96 (dd, *J* = 9.4 and 17.8 Hz, 1 H, H4$_{eq}$), 1.8 (m, 1 H, H10$_{eq}$), 1.84 (m, 1 H, H7$_{eq}$), 1.54 (m, 1 H, H8$_{ax}$), 1.45 (m, 1 H, H5), 1.34 (m, 1 H, H9), 1.10 (m, 1 H, H7$_{ax}$), 0.92 (m, 1 H, H8$_{eq}$), 0.82 (d, *J* = 6.2 Hz, 3 H, CH$_3$ 11), 0.80 (m, 1 H, H6), 0.77 (d, *J* = 6.5 Hz, 3 H, CH$_3$ 12) ppm. ^{13}C NMR (62.9 MHz, CDCl$_3$): δ = 171.3 (C3), 82.3 (C1), 44.6 (C6), 40.4 (C10), 38.0 (C4), 33.7 (C8), 31.7 (C5), 30.9 (C9), 27.7 (C7), 21.8 (C12), 19.0 (C11) ppm.

Characterisation of Compound (5*S*)-C: MS: *m*/*z* (%) = 96 (100), 81 (85), 122 (31), 183 (12) [M + 1], 138 (6). ^{1}H NMR (250.13 MHz, CDCl$_3$): δ = 4.13 (ddd, *J* = 4.3, 11, and 11 Hz, 1 H, H1), 2.69 (dd, *J* = 6.6 and 17.6 Hz, 1 H, H4$_{ax}$), 2.41 (dd, *J* = 2.8 and 17.6 Hz, 1 H, H4$_{eq}$), 2.13 (ddd, *J* = 1.6, 12, and 12 Hz, 1 H, H10$_{eq}$), 2.07 (m, 1 H, H5), 1.73 (m, 2 H, H8$_{ax}$ and H8$_{eq}$), 1.66 (m, 1 H, H7$_{eq}$), 1.60 (m, 1 H, H6), 1.48 (m, 1 H, H9), 1.27 (ddd, *J* = 3.5, 12.9, and 12.9 Hz, 1 H, H7$_{ax}$), 1.16 (ddd, *J* = 3.0, 12, and 12 Hz, 1 H, H10$_{ax}$), 1.00 (d, *J* = 7.2 Hz, 3 H, CH$_3$ 11), 0.97 (d, *J* = 6.6 Hz, 3 H, CH$_3$ 12). ^{13}C NMR (62.9 MHz, CDCl$_3$): δ = 171.2 (C3), 77.8 (C1), 41.7 (C6), 40.9 (C10), 38.9 (C4), 33.9 (C8), 30.8 (C9), 28.8 (C5), 27.2 (C7), 21.7 (C12), 14.7 (C11) ppm. C$_{11}$H$_{18}$O$_2$ (182.12): calcd. C 71.5, H 10, O 17.6; found C 71.8, H 9.8, O 18.3.

Characterisation of Dehydro-C: MS: *m*/*z* (%) = 181 (14) [M + 1], 138 (12), 123 (40), 109 (13), 95 (66), 81 (100), 67 (69), 55 (30), 41 (55), 29 (13).

[1] a) H. M. Colquhoun, D. J. Thompson, M. V. Twigg, *Carbonylation*, Plenum Press, New York, **1991**; b) J. Tsuji, *Palladium Reagents and Catalysis*, John Wiley & Sons, Chichester, New York, **1999**; c) B. El Ali, H. Alper, *Transition Metals for Organic Synthesis*, vol. 1 (Eds.: M. Beller, C. Bolm), Wiley-VCH, Weinheim, Germany, **1998**, 49–66; d) I. Ojima, *Catalytic Asymmetric Synthesis*, Wiley-VCH, Weinheim, Germany, **2000**.

[2] a) K. C. Nicolaou, E. J. Sorensen, *Classics in Total Synthesis*, Wiley Verlag GmbH, Weinheim, Germany, **1996**; b) *Transition Metals for Organic Synthesis, Building Blocks and Fine Chemicals* (Eds.: M. Beller, C. Bolm), vol. 1–2, Wiley-VCH, Weinheim, Germany, **1998**; c) P. J. Teisseire, *Chimie des Substances Odorantes*, Lavoisier, Paris, **1991**.

[3] a) E. J. Corey, K. C. Nicolaou, *J. Am. Chem. Soc.* **1974**, *96*, 5614; b) E. J. Corey, K. C. Nicolaou, L. S. Melvin, *J. Am.*

 © 2005 Wiley-VCH Verlag GmbH & Co. KGaA, Weinheim

Chem. Soc. **1975**, *97*, 653; c) Y. S. Rao, *Chem. Rev.* **1976**, *76*, 5; d) S. Masamune, G. S. Bates, J. W. Corcoran, *Angew. Chem. Int. Ed. Engl.* **1977**, *16*, 585; e) B. El Ali, H. Alper, *J. Org. Chem.* **2000**, *65*, 4131; f) K. A. D. Swift, *Top. Catal.* **2004**, *27*, 143.

[4] a) D. H. Nguyen, F. Hebrard, J. Duran, A. Polo, M. Urrutigoïty, P. Kalck, *Appl. Organomet. Chem.* **2005**, *19*, 30; b) G. Lenoble, R. Naigre, T. Chenal, M. Urrutigoïty, J. C. Daran, P. Kalck, *Tetrahedron: Asymmetry* **1999**, *10*, 929; c) G. Lenoble, M. Urrutigoïty, P. Kalck, *Tetrahedron Lett.* **2001**, *42*, 3697; d) G. Lenoble, M. Urrutigoïty, P. Kalck, *J. Organomet. Chem.* **2002**, *643*, 12.

[5] R. Naigre, T. Chenal, I. Ciprès, P. Kalck, J. C. Daran, J. Vaissermann, *J. Organomet. Chem.* **1994**, *480*, 91.

[6] a) R. F. Heck, *J. Am. Chem. Soc.* **1969**, *91*, 6707; b) D. M. James, J. K. Stille, *J. Am. Chem. Soc.* **1976**, *98*, 1810; c) H. Alper, J. B. Woell, B. Despeyroux, D. J. H. Smith, *J. Chem. Soc., Chem. Commun.* **1983**, 1270; d) K. Bittler, N. Kutepov, D. Neubauer, H. Reis, *Angew. Chem. Int. Ed. Engl.* **1968**, *7*, 329; e) D. M. Fenton, *J. Org. Chem.* **1973**, *38*, 3192; f) G. Cavinato, L. Toniolo, *J. Organomet. Chem.* **1990**, *398*, 187; g) G. Cavinato, L. Toniolo, *J. Organomet. Chem.* **1993**, *444*, C65.

[7] a) J. F. Knifton, *J. Org. Chem.* **1976**, *41*, 2885; b) J. F. Knifton, *J. Am. Oil Chem. Soc.* **1978**, *55*, 496.

[8] a) E. Drent, P. H. M. Budzelaar, *Chem. Rev.* **1996**, *96*, 663; b) R. I. Pugh, E. Drent, *Adv. Synth. Catal.* **2002**, *344*, 837; c) J. Liu, B. T. Heaton, J. A. Iggo, R. Whyman, *Angew. Chem. Int. Ed.* **2004**, *43*, 90; d) C. Bianchini, H. M. Lee, A. Meli, W. Oberhauser, M. Peruzzini, F. Vizza, *Organometallics* **2002**, *21*, 16; e) C. Bianchini, A. Meli, G. Müller, W. Oberhauser, E. Passaglia, *Organometallics* **2002**, *21*, 4965.

[9] a) G. Cavinato, A. Vavasori, L. Toniolo, F. Benetollo, *Inorg. Chim. Acta* **2003**, *343*, 183; b) G. Cavinato, L. Toniolo, A. Vavasori, *J. Mol. Catal.* **2004**, *219*, 233; c) R. P. Tooze, K. Whiston, A. P. Malyan, M. J. Taylor, N. W. Wilson, *J. Chem. Soc., Dalton Trans.* **2000**, 3441; d) G. R. Easthman, R. P. Tooze, M. Kilner, D. F. Foster, D. J. Cole-Hamilton, *J. Chem. Soc., Dalton Trans.* **2002**, 1613; e) V. V. Grushin, *Chem. Rev.* **1996**, *96*, 2011 and references cited therein; f) I. del Rio, C. Claver, P. W. N. M. van Leeuwen, *Eur. J. Inorg. Chem.* **2001**, 2719; g) K. Kudo, Y. Oida, K. Mitsuhashi, S. Mori, K. Komatsu, N. Sugita, *Bull. Chem. Soc. Jpn.* **1996**, *69*, 1337; h) C. Benedek, G. Szalontai, A. Gömöry, S. Tõrös, B. Heil, *J. Organomet. Chem.* **1999**, *579*, 147; i) J. Gironès, J. Duran, A. Polo, J. Real, *Chem. Commun.* **2003**, 1776; j) V. N. Zudin, V. D. Chinakov, V. M. Nekipelov, V. A. Rogov, V. A. Likhoilobov, Y. I. Yermakov, *J. Mol. Catal.* **1989**, *52*, 27; k) G. Verspui, I. I. Moiseev, R. A. Sheldon, *J. Organomet. Chem.* **1999**, *586*, 196.

[10] a) G. R. Eastham, B. T. Heaton, J. A. Iggo, R. P. Tooze, R. Whyman, S. Zacchini, *Chem. Commun.* **2000**, 609; b) W. Clegg, G. R. Eastham, M. R. J. Elsegood, B. T. Heaton, J. A. Iggo, R. P. Tooze, R. Whyman, S. Zacchini, *Organometallics* **2002**, *21*, 1832; c) W. Clegg, G. R. Eastham, M. R. J. Elsegood, B. T. Heaton, J. A. Iggo, R. P. Tooze, R. Whyman, S. Zacchini, *J. Chem. Soc., Dalton Trans.* **2002**, 3300; d) J. Wolowska, G. R. Eastham, B. T. Heaton, J. A. Iggo, C. Jacob, R. Whyman, *Chem. Commun.* **2002**, 2784.

[11] R. Naigre, PhD Thesis **1993**, INP Toulouse.

[12] G. Lenoble, C. Lacaze-Dufaure, M. Urrutigoïty, C. Mijoule, P. Kalck, *Eur. J. Inorg. Chem.* **2004**, 791.

[13] T. Chenal, R. Naigre, I. Ciprès, P. Kalck, J. C. Daran, J. Vaissermann, *J. Chem. Soc., Chem. Commun.* **1993**, 747.

[14] D. R. Coulson, L. C. Satek, S. O. Orim, *Inorg. Synth.* **1972**, *13*, 121.

[15] J. M. Jenkins, J. C. Verkade, *Inorg. Synth.* **1968**, *11*, 108.

[16] a) T. Tanase, T. Ohizumi, K. Kobayashi, Y. Yamamoto, *Organometallics* **1996**, *15*, 3404; b) M. L. H. Green, H. Munakata, *J. Chromatogr. A* **1971**, 469.

[17] F. Liang, H. W. Schmalle, T. Fox, H. Berke, *Organometallics* **2003**, *22*, 3382.

[18] M. Akhatar, H. C. Clark, *J. Organomet. Chem.* **1970**, *22*, 233.

[19] R. C. Boyle, J. T. Mague, M. J. Fink, *J. Am. Chem. Soc.* **2003**, *125*, 3228.

[20] a) A. Scrivanti, A. Berton, L. Toniolo, C. Botteghi, *J. Organomet. Chem.* **1986**, *314*, 369; b) S. C. Tang, L. Kim, *J. Mol. Catal.* **1982**, *14*, 231; c) E. Paumard, A. Mortreux, F. Petit, *J. Chem. Soc., Chem. Commun.* **1989**, 1380.

[21] a) D. Braga, M. Sabatino, C. Di Bugno, P. Leoni, M. Pasquali, *J. Organomet. Chem.* **1987**, *334*, C46; b) C. Di Bugno, M. Pasquali, P. Leoni, P. Sabatino, D. Braga, *Inorg. Chem.* **1989**, *28*, 1390; c) P. Leoni, M. Sommovigo, M. Pasquali, S. Midollini, D. Braga, P. Sabatino, *Organometallics* **1991**, *10*, 1038.

[22] J. C. Bailar, Jr., H. Itatani, *Inorg. Chem.* **1965**, *4*, 161.

[23] S. Reinartz, M. Brookhart, J. L. Templeton, *Organometallics* **2002**, *21*, 247.

[24] a) V. N. Zudin, V. D. Chinakov, V. M. Nekipelov, V. A. Likhoilobov, Y. I. Yermakov, *J. Organomet. Chem.* **1985**, *289*, 425; b) V. N. Zudin, V. D. Chinakov, V. M. Nekipelov, V. A. Rogov, V. A. Likhoilobov, Y. I. Yermakov, *J. Mol. Catal.* **1989**, *52*, 27.

[25] P. J. Perez, J. C. Calabrese, E. E. Bunel, *Organometallics* **2001**, *20*, 337.

[26] I. Tóth, C. J. Elsevier, *Organometallics* **1994**, *13*, 2118.

[27] M. Gómez, G. Muller, D. Sainz, J. Sales, *Organometallics* **1991**, *10*, 4036.

[28] J. Cámpora, J. A. López, P. Palma, D. del Rio, E. Carmona, P. Valerga, C. Graiff, A. Tiripicchio, *Inorg. Chem.* **2001**, *40*, 4116.

[29] a) J. M. Vila, M. T. Pereira, J. M. Ortigueira, J. J. Fernández, A. Fernández, M. L. Torres, *Organometallics* **1999**, *18*, 5484; b) H. E. Bryndza, *Organometallics* **1985**, *4*, 1686.

[30] a) P. W. N. M. van Leeuwen, M. A. Zuideveld, B. H. G. Swennenhuis, Z. Freixa, P. C. J. Kamer, K. Goubitz, J. Fraanje, M. Lutz, A. L. Spek, *J. Am. Chem. Soc.* **2003**, *125*, 5523; b) J. Liu, B. T. Heaton, J. A. Iggo, R. Whyman, *Chem. Commun.* **2004**, 1326.

[31] a) G. Laurenczy, F. Joó, L. Nádasdi, *Inorg. Chem.* **2000**, *39*, 5083; b) G. Laurenczy, F. Lukacs, R. Roulet, *Anal. Chim. Acta* **1998**, *359*, 275.

[32] V. V. Grushin, C. C. Bensimon, H. Alper, *Inorg. Chem.* **1994**, *33*, 4808.

Received: February 16, 2005
Published Online: September 5, 2005

 © 2005 Wiley-VCH Verlag GmbH & Co. KGaA, Weinheim

EurJIC
European Journal of Inorganic Chemistry

Issue 21/2005

Pages 4229–4448

Papers available ahead of print in Early View at www.interscience.wiley.com

Earliest available Table of Contents: Automatically, free of charge by e-mail through www.interscience.wiley.com/alerts

COVER PICTURE

The cover picture shows the self-assembly of two selected terpy-type ligands by π-π stacking around the Zn^{2+} ion to form isolated "heterodimers" (top left with terpy and a bis-Schiff-base ligand), 2D layers (bottom right with a hydrazone bis-pyridine ligand and a bis-Schiff-base ligand) and a double helix (on the diagonal, with only bis-Schiff-base ligands). In addition a 1D stacked layer could be synthesized. Further details may be found in the article by M. Barboiu et al. on p. 4255ff.

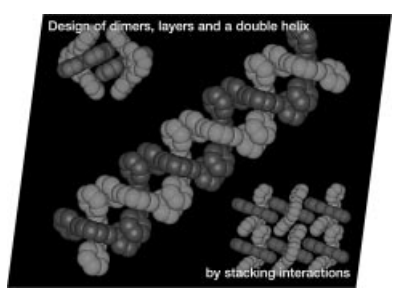

MICROREVIEW

Contents

4245 **J. M. Bollinger Jr.,* J. C. Price, L. M. Hoffart, E. W. Barr, C. Krebs***

Mechanism of Taurine: α-Ketoglutarate Dioxygenase (TauD) from *Escherichia coli*

Keywords: Bioinorganic chemistry / Metalloenzymes / Reaction intermediates / Oxygen activation / Iron

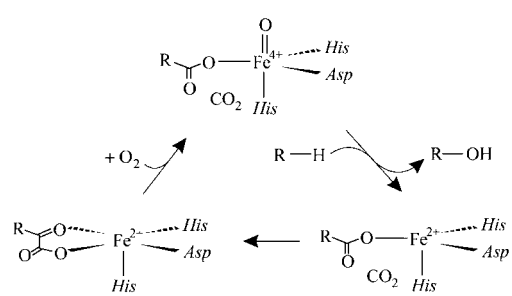

 © 2005 Wiley-VCH Verlag GmbH & Co. KGaA, Weinheim

FULL PAPERS

4255 **F. Dumitru, E. Petit, A. van der Lee, M. Barboiu***

Homo- and Heteroduplex Complexes Containing Terpyridine-Type Ligands and Zn^{2+}

Keywords: Crystal engineering / N ligands / Supramolecular chemistry / Ternary complexes / Zinc

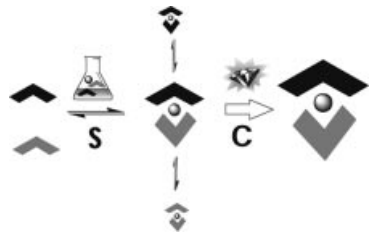

4263 **H. Stolzenberg, B. Weinberger, W. P. Fehlhammer,* F. G. Pühlhofer, R. Weiss**

Free and Metal-Coordinated (*N*-Isocyanimino)-triphenylphosphorane: X-ray Structures and Selected Reactions

Keywords: Chromium / Isocyanide ligands / Isomerisation / Phosphoranes / Tungsten / Quantum chemical calculations

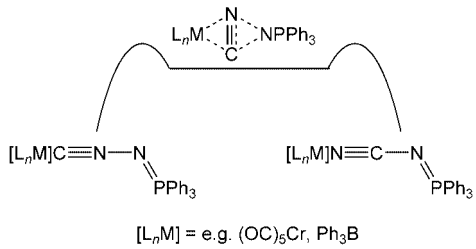

4272 **R. Ferreira, H. García, B. de Castro, C. Freire***

(Salen)nickel-Catalysed Epoxidations in the Homogeneous and Heterogeneous Phase: The Implications of Oxygen on the Efficiency and Product Selectivity

Keywords: Alkenes / Epoxidation / Heterogeneous catalysis / N,O ligands / Nickel / Zeolites

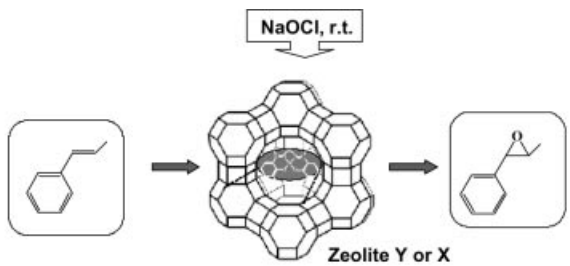

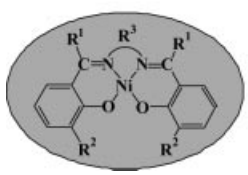

O_2 present	↑ conversion	↓ epoxide selectivity
O_2 absent	↓ conversion	↑ epoxide selectivity

4280 **U. García-Couceiro, O. Castillo,* A. Luque,* J. P. García-Terán, G. Beobide, P. Román**

One-Dimensional Oxalato-Bridged Metal(II) Complexes with 4-Amino-1,2,4-triazole as Apical Ligand

Keywords: Chain structures / Oxalato bridging ligand / Triazole / X-ray diffraction / Structure–magnetism relationships

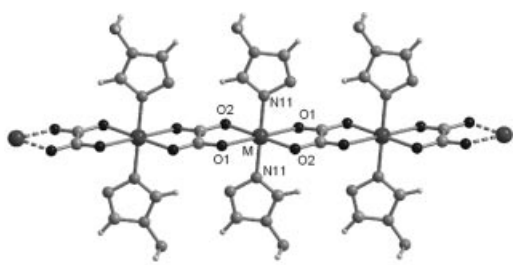

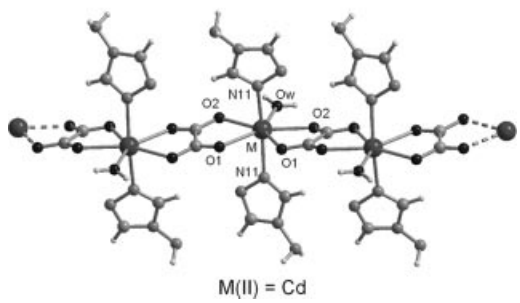

 © 2005 Wiley-VCH Verlag GmbH & Co. KGaA, Weinheim

4291 **T. Tajima, N. Takeda, T. Sasamori, N. Tokitoh***

Generation and Reactions of Overcrowded Diaryldilithiostannane and Diaryldipotassiostannane

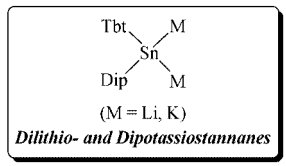

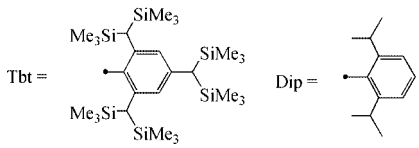

Keywords: Group 14 elements / Tin / Anions / Lithium / Potassium / Solid-state structures

4301 **R. Aucejo, J. Alarcón, E. García-España,* J. M. Llinares, K. L. Marchin, C. Soriano, C. Lodeiro, M. A. Bernardo, F. Pina,* J. Pina, J. Seixas de Melo**

A New Zn^{II} Tweezer Pyridine-Naphthalene System − An Off-On-Off System Working in a Biological pH Window

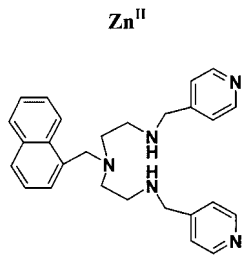

Keywords: Luminescence / N ligands / Sensors / Zinc

4309 **M. C. Haberecht, M. Bolte, H.-W. Lerner, M. Wagner***

An Approach Towards Functional Dendrimers Based on the Hydroboration Reaction and Spontaneous Boron−Nitrogen Bond Formation

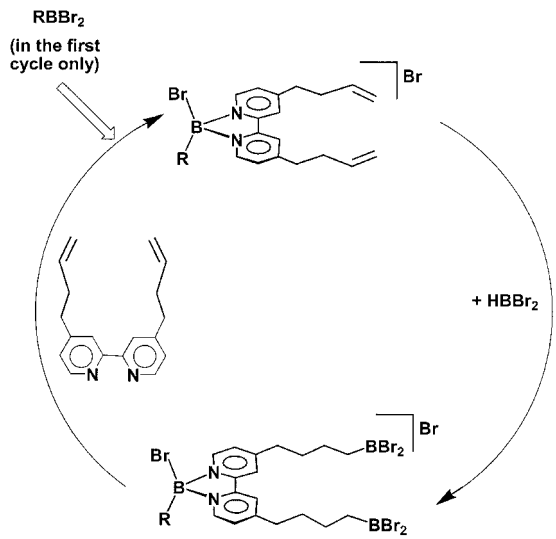

Keywords: Boranes / Dendrimers / Hydroboration / N ligands

4317 **A. Küsel, J. Zhang, M. Alvariño Gil, A. C. Stückl, W. Meyer-Klaucke, F. Meyer,* U. Diederichsen***

Metal Binding Within a Peptide-Based Nucleobase Stack with Tuneable Double-Strand Topology

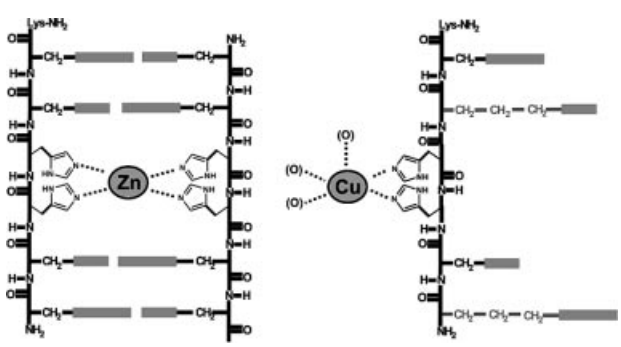

Keywords: EXAFS spectroscopy / Molecular recognition / Nucleic acids / Peptides / Protein models

 © 2005 Wiley-VCH Verlag GmbH & Co. KGaA, Weinheim

4325 **B. Modec,* J. V. Brenčič**

Anions of 1,3,5-Benzenetricarboxylic and Heptanedioic Acids Serving as Bridges between Dimolybdenum(v) Metal−Metal Bonded Units: Preparation and Structural Characterization of Dinuclear and Tetranuclear Complexes

Keywords: Molybdenum / Carboxylato complexes / 1,3,5-Benzenetricarboxylate / Heptanedioate

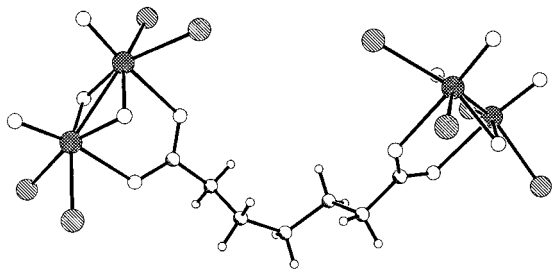

4335 **Y. Albo, E. Maimon,* I. Zilbermann, M. Saphier, H. Cohen, D. Meyerstein***

The Redox Chemistry of (N^1-[3-(2-aminoethylimino)-1,1-dimethylbutyl]ethane-1,2-diamine)-nickel(II) Perchlorate, $Ni^{II}L^1(ClO_4)_2$, in Aqueous Solutions − A Pulse Radiolytic and an Electrochemical Study

Keywords: Nickel complexes / Pulse radiolysis / Electrochemistry

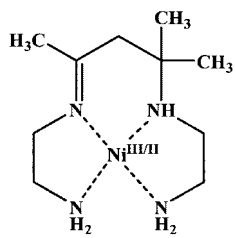

4341 **M. Gómez,* S. Jansat, G. Muller, G. Aullón, M. A. Maestro**

Ruthenium Complexes Containing Chiral N-Donor Ligands as Catalysts in Acetophenone Hydrogen Transfer − New Amino Effect on Enantioselectivity

Keywords: Ruthenium / Chiral N-donors / Asymmetric catalysis / NMR spectroscopy / Density functional calculations

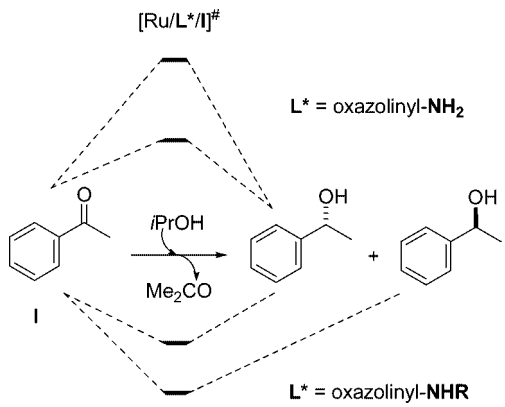

4352 **A. J. Deeming,* C. S. Forth, M. I. Hyder, S. E. Kabir, E. Nordlander,* F. Rodgers, B. Ullmann**

Mechanisms of Concurrent Hydride Migration Processes in a Triruthenium Cluster Capped by a Phenylphosphinidene (PPh) Ligand

Keywords: Ruthenium / Clusters / Hydrides / Dynamic mobility / Kinetics

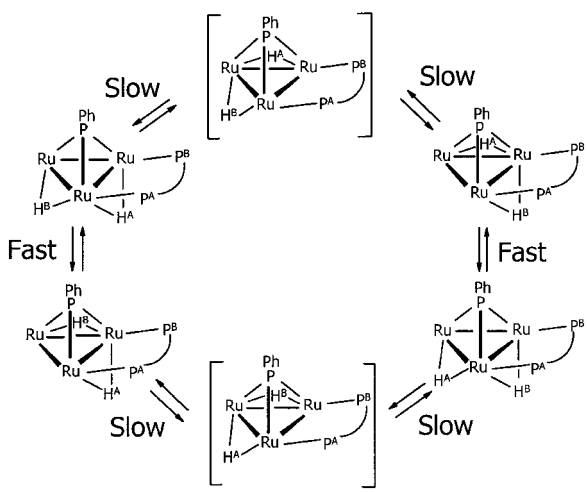

 © 2005 Wiley-VCH Verlag GmbH & Co. KGaA, Weinheim

4361 **A. M. Fonseca,* M. M. M. Raposo, A. R. C. Sousa, G. Kirsch, M. Beley**

Synthesis and Electrochemical and Spectroscopic Properties of Molybdenum Complexes Bearing 5-Alkoxythiophene or -bithiophene Groups

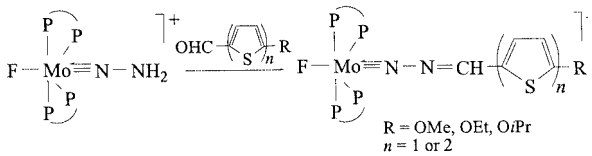

Keywords: Sulfur heterocycles / Molybdenum / N ligands / Conjugated systems

4366 **B. Tang,* J. Ge, L. Zhuo, G. Wang, J. Niu, Z. Shi, Y. Dong**

A Facile and Controllable Synthesis of γ-Al_2O_3 Nanostructures without a Surfactant

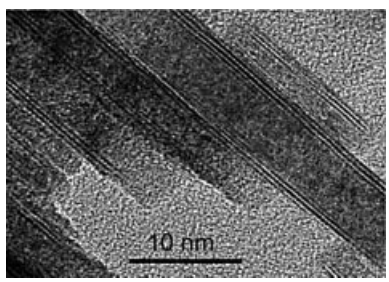

Keywords: γ-Alumina / Materials science / Nanostructures / Solvothermal synthesis

4370 **M. L. Gallego, M. Cano,* J. A. Campo, J. V. Heras, E. Pinilla, M. R. Torres, P. Cornago, R. M. Claramunt***

Cationic Silver Coordination Compounds of Polydentate Ligands: Supramolecular Structures of $[Ag(Pz^{bp2}Py)_2(OSO_2CF_3)]$ and $[Ag_2(Pz^{bp2}Py)_2(OSO_2CF_3)_2]$ {$Pz^{bp2}Py$ = 2-[3,5-Bis(4-butoxyphenyl)pyrazol-1-yl]pyridine}

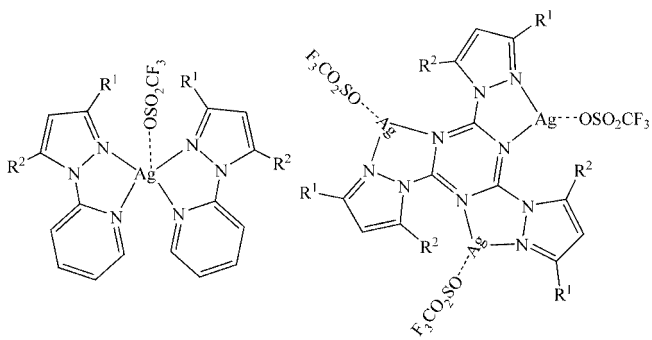

Keywords: N ligands / NMR spectroscopy / Silver / Supramolecular chemistry

4382 **T. Irrgang,* R. Kempe***

Early and Late Transition Metal Complexes Stabilised by Imidazopyridazine-Substituted Bisamido Ligands

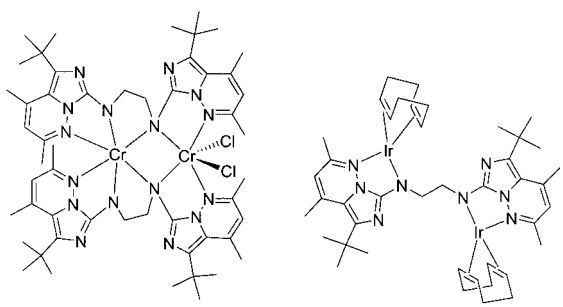

Keywords: Amido ligands / Imidazo[1,5-*b*]pyridazines / N ligands / Chromium / Iridium / Rhodium / Titanium / Zirconium

4393 **V. K. Sharma, P. Á. Szilágyi, Z. Homonnay,* E. Kuzmann, A. Vértes**

Mössbauer Investigation of Peroxo Species in the Iron(III)−EDTA−H_2O_2 System

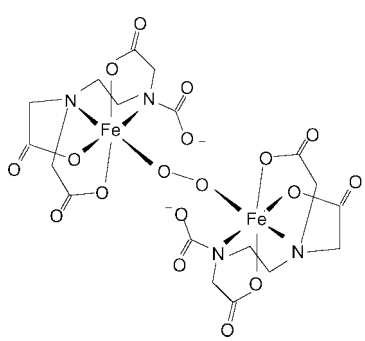

Keywords: Chelates / EDTA / Iron / Mössbauer spectroscopy / Peroxo ligands

 © 2005 Wiley-VCH Verlag GmbH & Co. KGaA, Weinheim

4401 **D. G. Calatayud, E. López-Torres, M. A. Mendiola,* C. J. Pastor, J. R. Procopio**

Structural Trends in Divalent Benzil Bis(thiosemicarbazone) Complexes

Keywords: Copper / N ligands / S ligands / Thiosemicarbazone complexes / Zinc

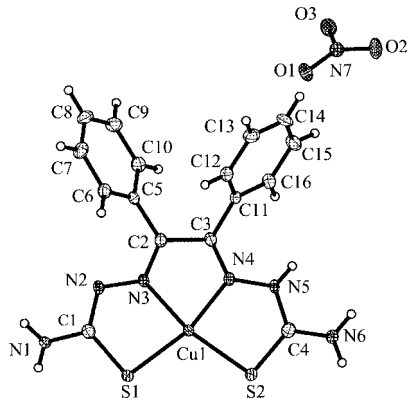

4410 **A. Varela, M. Parras, J. M. González-Calbet***

Influence of Na Content on the Chemical Stability of Nanometric Layered Na_xRhO_2 ($0.7 \leq x \leq 1.0$)

Keywords: Na_xRhO_2 nanoparticles / Layered oxides / High resolution electron microscopy

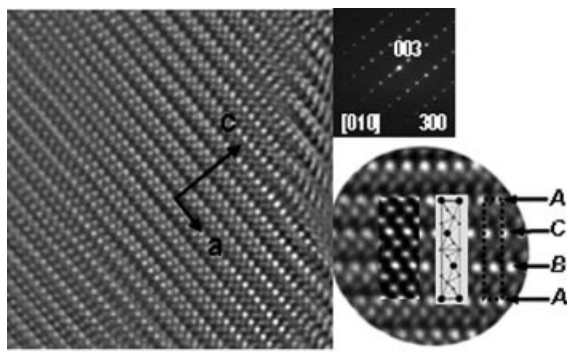

4417 **O. Jarjayes,* F. Mortini, A. du Moulinet d'Hardemare, C. Philouze, G. Serratrice**

Tuning pGa with Chelating Agents Related to (*o*-Hydroxybenzyl)iminodiacetic Acid

Keywords: Carboxylate ligands / Gallium / N ligands / Potentiometry / Stability constants

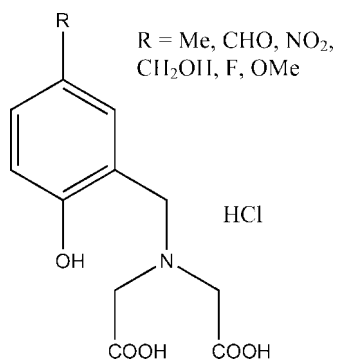

4425 **P. Álvarez-Boo, J. S. Casas, M. D. Couce, V. Fernández-Moreira, E. Freijanes, E. García-Martínez, J. Sordo, E. Vázquez-López**

Formation of 3-Sulfanylcoumarins by $SnPh_3OH$-Promoted Cyclization of 3-Aryl-2-Sulfanylpropenoic Acids

Keywords: Tin / Triphenyltin complexes / 3-(2-hydroxyphenyl)-2-sulfanylpropenoic acids / 3-sulfanylcoumarin / X-ray diffraction

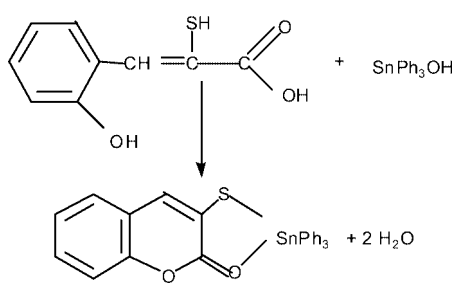

 © 2005 Wiley-VCH Verlag GmbH & Co. KGaA, Weinheim

4430 **M. Arroyo, Á. López-Sanvicente, D. Miguel, F. Villafañe***

Pyrazolylamidino- and Bis(pyrazole)manganese(I) Complexes

Keywords: Manganese / N ligands / Pyrazole / Pyrazolylamidino ligands

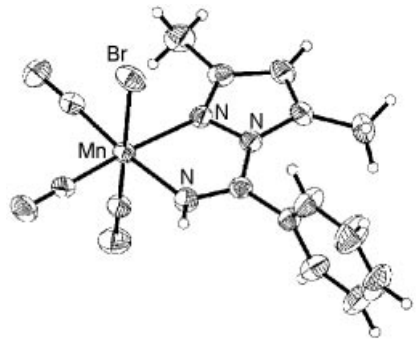

4438 **F. Feil, S. Harder***

Guanidinate Complexes of Heavier Alkaline-Earth Metals (Ca, Sr): Syntheses, Structures, Styrene Polymerization and Unexpected Reaction Behaviour

Keywords: Alkaline earth metals / Amides / Amidinates / Guanidinates / Polystyrene

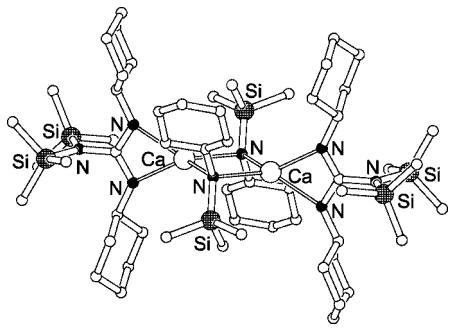

CORRECTION

4445 **W.-Z. Shen, X.-Y. Chen, P. Cheng,* S.-P. Yan, B. Zhai, D.-Z. Liao, Z.-H. Jiang**

A Structural and Magnetic Investigation of Ferromagnetically Coupled Copper(II) Isophthalates

Keywords: Copper / Magnetic properties / N ligands / Organic-inorganic hybrid composites

Mechanism of Taurine: α-Ketoglutarate Dioxygenase (TauD) from *Escherichia coli*

J. Martin Bollinger Jr.,*[a,b] John C. Price,[a] Lee M. Hoffart,[a] Eric W. Barr,[a] and Carsten Krebs*[a,b]

Keywords: Bioinorganic chemistry / Metalloenzymes / Reaction intermediates / Oxygen activation / Iron

The iron(II)- and α-ketoglutarate-dependent dioxygenases comprise enzymes that catalyze a variety of important reactions in biology, including steps in the biosynthesis of collagen and antibiotics, the degradation of xenobiotics, the repair of alkylated DNA, and the sensing of oxygen and response to hypoxia. In these reactions, the reductive activation of oxygen is coupled to hydroxylation of the substrate and decarboxylation of the co-substrate, α-ketoglutarate. It is believed that a single, conserved mechanistic pathway for formation of a high-valent iron intermediate that attacks the substrate is operant in all members of this family. Application of a combination of rapid kinetic and spectroscopic techniques to the reaction of taurine/α-ketoglutarate dioxygenase (TauD), one member of this large enzyme family, has led to the detection of two reaction intermediates. The first intermediate, which is termed **J**, is a high-spin Fe^{IV}-oxo complex. Decay of **J** exhibits a large, normal C1 deuterium kinetic isotope effect, demonstrating that it is the species activating the C–H bond for hydroxylation. The second intermediate is an Fe^{II}-containing product(s) complex.
(© Wiley-VCH Verlag GmbH & Co. KGaA, 69451 Weinheim, Germany, 2005)

1. Introduction

The Fe^{II}- and α-ketoglutarate (αKG)-dependent dioxygenases are a large and functionally diverse family of enzymes that employ a structurally conserved, mononuclear, non-heme Fe^{II} center.[1–4] The Fe^{II} center is facially coordinated by three protein ligands, two histidines and one aspartate or glutamate.[5,6] These residues are organized in a His-Xxx-(Asp/Glu)-$(Xxx)_n$-His sequence motif.[3] The Fe^{II} center is used to activate dioxygen to effect (1) the decarboxylation of the co-substrate, αKG, and (2) a two-electron oxidation of the substrate. In most cases the substrate oxidation is a hydroxylation of an unactivated carbon atom, although other two-electron oxidations, such as desaturation and cyclization reactions, are effected by some family members.[3,4]

The αKG-dependent dioxygenases catalyze a wide variety of reactions with diverse biological functions, which have recently been summarized by Hausinger.[3] They catalyze reactions involved in the degradation of xenobiotics,[7] and the biosyntheses of connective tissue,[8,9] various antibiotics,[10–12] and a wide variety of plant secondary metabolites, including flavonoids, gibberellins, and alkaloids (see ref.[3] and references cited therein). In addition, the dysfunction of members of the αKG-dependent dioxygenase family has been implicated in the etiology of several disease states.[13]

Recently, several additional reactions of importance to human biochemistry have been found to be catalyzed by αKG-dependent dioxygenases. The first involves repair of alkylated DNA and RNA by the enzyme AlkB.[14,15] Studies on AlkB from *E. coli* have demonstrated that it can hydroxylate the N-linked carbon of alkyl groups on 1-alkyladenine and 3-alkylcytosine residues in DNA and RNA, leading to elimination of the potentially mutagenic substituent and repair of the base.[14–16] Eight putative homologues of AlkB have been identified in humans, but they are less well studied than *E. coli* AlkB.[14,17]

The second involves control of oxygen homeostasis by the transcription factor, hypoxia inducible factor (HIF).[18,19] When oxygen levels drop, an adaptive response is initiated by the HIF-mediated transcriptional activation of genes that, for example, direct synthesis of new blood vessels (angiogenesis) and production of red blood cells

[a] Department of Biochemistry and Molecular Biology, The Pennsylvania State University,
University Park, PA 16802, USA
Fax: +1-814-863-7024
E-mail: jmb21@psu.edu
ckrebs@psu.edu
[b] Department of Chemistry, The Pennsylvania State University,
University Park, PA 16802, USA

MICROREVIEWS: This feature introduces the readers to the authors' research through a concise overview of the selected topic. Reference to important work from others in the field is included.

(erythropoiesis) to combat hypoxia.[20] HIF activity is controlled by posttranslational hydroxylation of specific amino acid residues in its α-subunit. These reactions are catalyzed by two αKG-dependent dioxygenases. Because molecular oxygen is a co-substrate, the activities of the enzymes provide the mechanism by which oxygen levels are sensed by cells. The first enzyme is the HIF-specific prolyl-4-hydroxylase, which hydroxylates Pro564 of the HIFα-protein.[18,19] Hydroxylated HIFα forms a complex with the von Hippel-Lindau (VHL) tumor suppressor protein, is ubiquitinated, and consequently is subject to proteasomal degradation. The second enzyme catalyzes the hydroxylation of a specific asparagine, Asn803.[21,22] This enzyme has been termed FIH, *f*actor *i*nhibiting *H*IF. Hydroxylation of Asn803 prevents binding of HIFα to the transcriptional coactivator, p300, rendering it (HIFα) inactive. These processes play important roles in the pathophysiology of human diseases, including cancer, cardiovascular, and pulmonary diseases.[20,23] Manipulation of these processes is thus considered a promising strategy for drug design.[24,25]

The third process contributes to iron homeostasis by controlling the activity of the iron regulatory protein 2 (IRP2). It is known that IRP2 is posttranslationally modified, and that modified IRP2 is subject to ubiquitination and proteasomal degradation.[26,27] This process is remarkably similar to the constitutive degradation of the HIFα-protein in oxygen homeostasis. Current evidence suggests that the posttranslational modification of IRP2 is also carried out by a αKG-dependent dioxygenase.[28,29]

2. Mechanism

It is thought that the αKG-dependent dioxygenases use a conserved mechanistic pathway to activate O_2 and form a high-valent iron intermediate that attacks the substrate, leading to hydroxylation or a related two-electron oxidation.[3,4,30] The consensus mechanism for hydroxylation was first formulated by Hanauske-Abel and Günzler solely on the basis of theoretical considerations.[31] Nevertheless, it has thus far held up to the experimental and computational scrutiny of the enzymes and inorganic models of them that has since been carried out. A modified version of this mechanism, adapted for the specific case of the enzyme taurine/αKG dioxygenase (TauD) from *E. coli*, is shown in Scheme 1. The first step in the mechanism is binding of αKG in a chelating mode to the binary enzyme·Fe^{II} complex, a step that gives rise to a weak ($\varepsilon \approx 200\ M^{-1}\,cm^{-1}$) absorption feature in the visible regime (with a peak at 530 nm in TauD). Solomon and co-workers demonstrated for the enzyme clavaminate synthase by a combination of UV/Visible absorption, CD, and MCD spectroscopy and computational studies that this feature arises from a metal-to-ligand charge transfer (MLCT) transition involving the coordinated αKG ligand.[32] The iron site in the ternary enzyme·Fe^{II}·αKG complex is six-coordinate (6C), nearly octahedral, and in the high-spin configuration. The next step in the consensus mechanism is binding of substrate to the ternary enzyme·Fe^{II}·αKG complex.[33] Substrate binds in the vicinity of the Fe^{II} center, but not directly as a ligand, causing changes in the CD and MCD spectra that are indicative of conversion to a five-coordinate (5C) square-pyramidal Fe^{II} site.[32] Hausinger and co-workers have shown that, for TauD, binding of substrate results in a shift of the peak of the MLCT band from 530 nm to 520 nm.[34] Que and co-workers studied the ternary enzyme·Fe^{II}·αKG and quaternary enzyme·Fe^{II}·αKG·substrate complexes of TauD, as well as model complexes for them, by resonance Raman spectroscopy.[35] The bidentate binding mode of the co-sub-

Lee M. Hoffart (left) obtained his Bachelor of Science in Biochemistry, Genetics, and Mathematics in 2003 from Texas A&M University and joined the Department of Biochemistry and Molecular Biology at Penn State as a graduate student in 2003. He continues the work on the α-ketoglutarate dioxygenases under the supervision of Professors Bollinger and Krebs.

Eric W. Barr (second from left) obtained his Bachelor of Science degree in Biochemistry in 1998 from Temple University. He joined Professor Bollinger's group in 2001 as a research assistant and works on the mechanism of oxygen activation by the enzyme taurine/α-ketoglutarate dioxygenase.

John C. Price (middle) obtained his Bachelor of Arts in Chemistry in 2001 from Utah State University, where he worked under the supervision of Professor Lisa Berreau. He joined the Department of Biochemistry and Molecular Biology at Penn State as a graduate student in 2001. His thesis work, which he carries out under the supervision of Professors Bollinger and Krebs, is on the mechanism of oxygen activation by the enzyme taurine/α-ketoglutarate dioxygenase.

Carsten Krebs (second from right) received his Diploma in Chemistry in 1994 and his Ph.D. in Chemistry in 1997 from the Ruhr-University of Bochum, Germany, under the supervision of Professor Karl Wieghardt. In 1997 he joined the group of Professor Boi Hanh (Vincent) Huynh in the Department of Physics at Emory University, Atlanta. In 2002, he joined the Department of Biochemistry and Molecular Biology at the Pennsylvania State University as Assistant Professor. In 2004 he was appointed to the Department of Chemistry at Penn State. His research interest is the determination of the reaction mechanisms of iron-containing enzymes.

J. Martin Bollinger Jr. (right) received his Bachelor of Science degree in Chemistry from Penn State University in 1986 and his Ph.D. degree in Chemistry in 1993 from the Massachusetts Institute of Technology, where he worked under the direction of Professor JoAnne Stubbe. After an N.I.H. post-doctoral fellowship with Professor Christopher Walsh at Harvard Medical School, Professor Bollinger joined the department of Biochemistry and Molecular Biology at Penn State in 1995. He was promoted to Associate Professor in 2002 and appointed to the Department of Chemistry in 2004. His work focuses on enzyme reaction mechanisms, particularly those of iron-dependent oxygenases.

 © 2005 Wiley-VCH Verlag GmbH & Co. KGaA, Weinheim

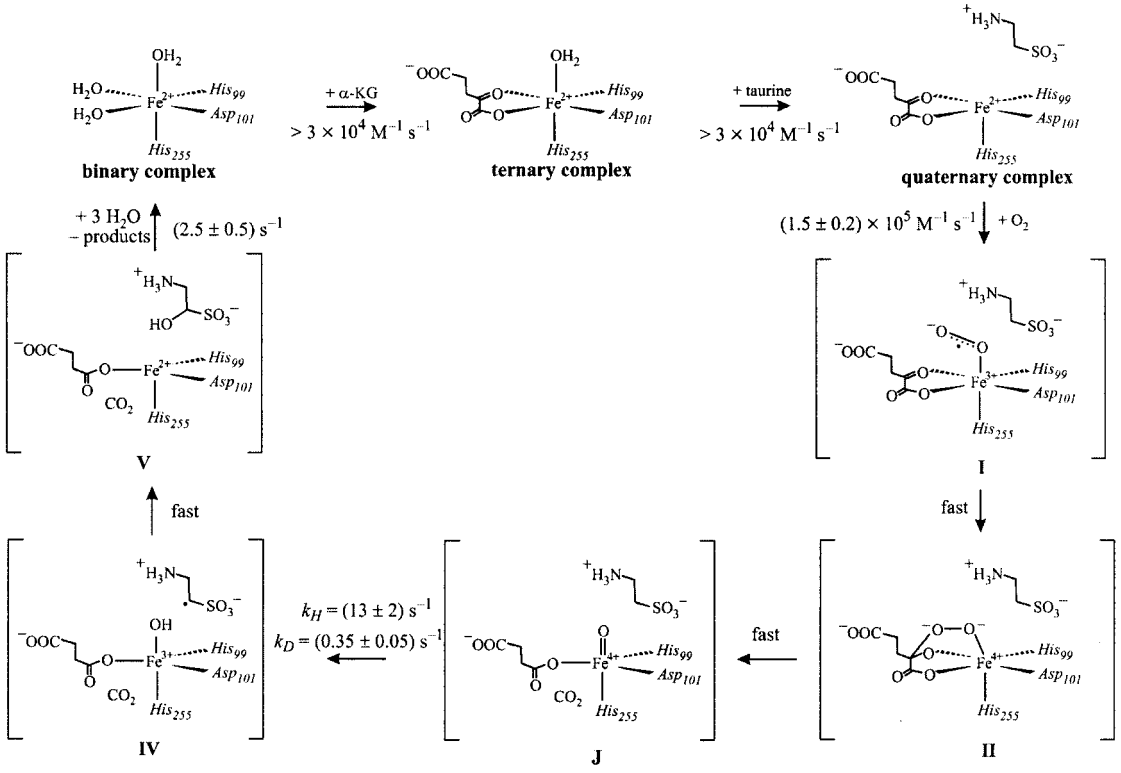

Scheme 1. Consensus mechanism for the Fe^{II}- and α-ketoglutarate-dependent dioxygenases, adapted for the specific case of taurine/α-ketoglutarate dioxygenase. The assignment of rate constants at 5 °C to individual steps of the mechanism is based on refs.[39,61,68,72,78]

strate, αKG, has also been demonstrated by X-ray crystallographic studies of a number of αKG-dependent dioxygenases (see ref.[3] and references cited therein). The structures reveal that the carbonyl group of αKG binds *trans* to the protein carboxylate ligand, whereas the C1 carboxylate group of αKG binds opposite to one of the histidine residues. Interestingly, it can bind either *trans* to the histidine of the His-Xxx-Asp/Glu-motif, which is termed "in line" binding mode, or it can bind *trans* to the histidine more distant in sequence ("off line" binding mode).[3] There is X-ray crystallographic evidence for flexibility of αKG-binding in some of the enzymes. For example, in clavaminate synthase, αKG binds "in line" when the substrate analogue deoxyguanidinoproclavaminate is bound, and it binds "off line" when NO as an analogue of oxygen coordinates to the Fe center of the deoxyguanidinoproclavaminate complex.[36] Another example is the enzyme alkyl sulfatase, for which "in line" coordination of αKG to the Fe^{II} center is observed, whereas "off line" binding is observed when the Fe^{II} is substituted with Na^+.[37] In addition, αKG binding is stabilized by the ionic interaction of its C5 carboxylate group with an arginine or lysine residue.

The dissociation of the water ligand creates an open coordination site, and it is proposed that this is the site to which oxygen adds.[4,30] Indeed, it has been shown that binding of the substrate increases reactivity toward O_2 many-fold.[38,39] Thus, the enzymes have evolved what amounts to a conformational "trigger" for O_2 activation, which serves to favor the formation of reactive intermediates only in the presence of the target substrate, thereby minimizing the potentially inactivating self-oxidation reactions that have been demonstrated to occur in a number of the enzymes when the ternary enzyme·Fe^{II}·αKG complex reacts with O_2 in the absence of substrate.[40–42] Addition of oxygen to the coordinatively unsaturated Fe^{II} center of the quaternary complex yields intermediate **I**, in which the O_2 moiety is proposed to coordinate end-on to the Fe center. **I** is a $\{FeOO\}^8$ complex, and computational studies from the Solomon group suggest that it should be described as a Fe^{III}-superoxo species.[43] These calculations were calibrated by correlating experimental and computational data for the related $\{FeNO\}^7$ complexes,[43] which have been prepared by addition of NO to the Fe^{II} forms of a number of different mononuclear non-heme enzymes[44,45] and models thereof.[46,47] The postulated Fe^{III}-superoxo complex **I** is proposed to react by a nucleophilic attack of the uncoordinated O atom on C2 of αKG, thereby forming the bicyclic species, **II**. The next step in the proposed mechanism is decarboxylation of αKG and cleavage of the O–O bond to yield an Fe^{IV}-oxo, intermediate, **J**.[48] Alternative structures for the Fe^{IV}-oxo intermediate have been proposed. These include a mixed anhydride of carbonic and succinic acids, in which the O atom is inserted into the C1–C2 bond of αKG.[3] The products of decarboxylation of αKG are succinate and CO_2. Importantly, the mechanism predicts that one O atom of succinate should derive from O_2, and this has been verified for several of the enzymes by use of $^{18}O_2$ (see ref.[3] and references cited therein). In the next step, the Fe^{IV}-oxo intermediate is proposed to abstract a H atom from the substrate, yielding **IV**, which consists of a Fe^{III}–

 © 2005 Wiley-VCH Verlag GmbH & Co. KGaA, Weinheim

OH complex and a substrate radical. Although **IV** has never been detected directly, evidence for the formation of a substrate radical was obtained by Begley and co-workers in their study of prolyl-4-hydroxylase (P4H) from *Paramecium bursaria Chlorella virus* 1.[49] P4H-directed oxidation of a peptide substrate containing 5-oxaproline was shown to result in conversion of the proline analogue to aspartate in a process that is likely to involve rearrangement of the expected substrate radical intermediate. In the normal catalytic processes, "oxygen rebound" of the Fe^{III}–OH complex of **IV** with the substrate radical generates the hydroxylated product and a Fe^{II} center. Thus, the mechanism also predicts that the O atom incorporated into the substrate should be derived from dioxygen, and this has also been verified by isotopic labeling experiments. Importantly, incorporation of ^{18}O from O_2 has been shown for some enzymes to be less than stoichiometric, suggesting that the O atom in **J** or **IV** (or both) may exchange with solvent (see ref.[3] and references cited therein). Alternatively, the oxo group may be protonated and a coordinated hydroxide ligand may become deprotonated and be incorporated into the product. This mechanism was named "ferryl-flip".[3] The hydroxide ligand required for this mechanism is not shown in Scheme 1, but coordination of a hydroxide ligand in addition to the ligands shown is entirely possible, especially considering that **J** and **IV** are depicted as having only five ligands.

Significant insight into the mechanism was also obtained from studies on inorganic model complexes.[4] Fe^{IV}-oxo complexes have been synthesized and characterized spectroscopically,[50–54] and oxygen activation by Fe^{II} centers coordinated by α-ketoacids has been investigated in detail.[35,55–59] These studies revealed that the α-ketoacid can bind as a monodentate or bindentate ligand, but only the latter exhibits the diagnostic MLCT band. Decarboxylation is accelerated by electron-withdrawing substituents on the α-ketoacid, consistent with the proposed nucleophilic attack of the superoxo species of **I** on the α-ketone carbonyl.[57]

Although the aforementioned studies provided support for the consensus mechanism, until very recently none of the proposed intermediates (enclosed in brackets in Scheme 1) had been directly detected for any enzyme in the family. In 2002, we selected one member of this enzyme family, TauD, which catalyzes hydroxylation of C1 of taurine (2-aminoethane-1-sulfonic acid) and other organosulfonates to initiate elimination of sulfite for sulfur acquisition,[60] for kinetic studies designed finally to reveal intermediates in this important reaction cycle. Several characteristics made it an ideal choice for such studies.[34] It is relatively small (32 kDa), soluble to high concentration, thermally stable, and readily obtained in large quantity by overexpression in *E. coli*.[34] In addition, its substrate, taurine, is chemically simple, making analogues with chemical or isotopic substitutions designed to perturb the reaction kinetics or mechanism synthetically accessible.

Investigation of the TauD reaction by rapid kinetic (stopped-flow and freeze-quench) and spectroscopic methods (UV/Visible, Mössbauer, EPR, resonance Raman, X-ray absorption) led to the detection of two intermediates in the catalytic cycle not previously detected for any member of the family. These studies are summarized in the following sections.

3. Detection of Two Intermediates in the TauD Reaction

The first evidence for the accumulation of two intermediates was obtained from stopped-flow absorption experiments.[61] Changes in the spectrum after mixing of the quaternary TauD·Fe^{II}·αKG·taurine complex with an oxygenated buffer solution (but not after a control mix with O_2-free buffer) were shown to be dominated by a positive feature at 318 nm, which reaches maximum intensity after approximately 20 ms (Figure 1, A), and a negative feature associated with loss of the chromophoric reactant complex, which develops fully only after the 318 nm feature has decayed (inset to Figure 1, A). These observations were rationalized by a minimal kinetic mechanism involving two accumulating intermediate states, the 318-nm absorbing first intermediate, **J**, which also absorbs into the visible regime to partially compensate for the loss of the absorption from the reactant complex, and a second species lacking both UV and visible absorption that accumulates prior to regeneration of the reactant complex. Rate constants of 1.5×10^5 M^{-1} s^{-1} for formation of **J**, 13 s^{-1} for decay of **J** to the second intermediate, and 2.5 s^{-1} for conversion of this intermediate back to the reactant quaternary complex were shown to accommodate the data well. Kinetic traces at 318 nm and 520 nm illustrate the three-step sequence clearly (Figure 1, B).

Although revealing their accumulation, the stopped-flow absorption experiments provided no clues as to the structures of the two intermediates, nor their positions within the catalytic cycle. Rapid freeze-quench (RFQ) Mössbauer spectroscopy provided the first such clues.[61] Mixing of the quaternary complex, which has a spectrum typical of a high-spin Fe^{II} species (Figure 1, C, top), with O_2-containing buffer results in a new Mössbauer absorption line at +0.75 mm/s (Figure 1, C). With increasing reaction time, the new peak was found to decay (Figure 1, D, filled circles) with the same time-dependence predicted for **J** (Figure 1, D, solid line), thereby establishing that the Mössbauer absorption at +0.75 mm/s is associated with **J**. Analysis of the experimental spectra revealed that **J** exhibits a quadrupole doublet (solid line shown above the spectrum of the 20-ms sample in Figure 1, D) with unusual parameters, an isomer shift (δ) of 0.31 mm/s and a quadrupole splitting parameter (ΔE_Q) of 0.88 mm/s. In general, the reduced isomer shift of **J** suggested that it is an oxidized species, but the value did not allow assignment of oxidation state, because it is higher than any of the isomer shifts reported for Fe^{IV} complexes[51,62–66] but also at the low extreme for high-spin Fe^{III}. Indeed, a trigonal bipyramidal high-spin Fe^{III} model complex reported by MacBeth et al. has the same isomer

 © 2005 Wiley-VCH Verlag GmbH & Co. KGaA, Weinheim

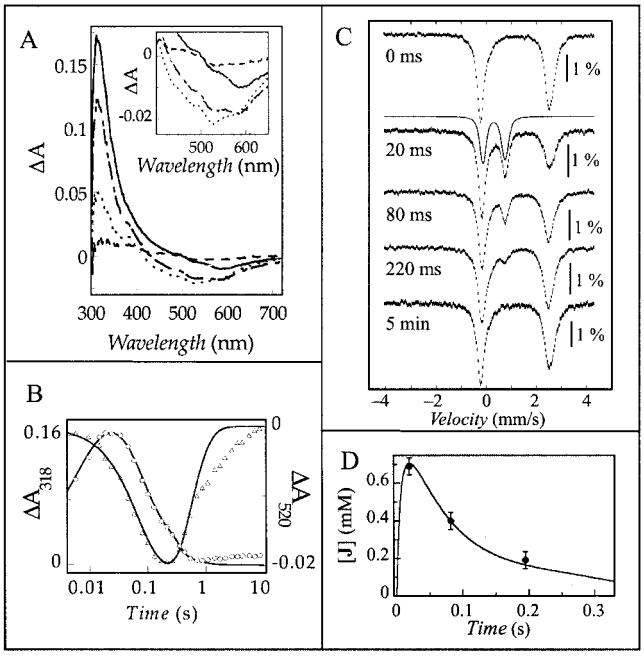

Figure 1. (**A**) UV/Visible absorption spectroscopic changes recorded 20 ms (solid lines), 68 ms (dot-dashed lines), 210 ms (dotted lines), and 10 s (dashed lines) after equal-volume mixing at 5 °C of a solution of 2.4 mM TauD, 2.2 mM Fe^{II}, 10 mM αKG, and 10 mM taurine with O_2-saturated buffer. The inset is a magnification of the absorbance changes in the 500-nm region. (**B**) Absorbance kinetic traces at 318 nm (circles) and 520 nm (triangles). The solid lines are simulations according to the rate constants shown in Scheme 1. (**C**) 4.2-K/40-mT Mössbauer spectra of RFQ samples from the reaction of the TauD·Fe^{II}·αKG·taurine complex with O_2. The reaction times are shown. A simulation of the spectrum of **J** (δ = 0.31 mm/s, ΔE_Q = 0.88 mm/s) is shown as solid line. (**D**) Concentration of **J** determined from RFQ Mössbauer spectroscopy (circles) and a simulation according to Scheme 1 (solid line). All figures are adapted from Price et al.[61]

shift, 0.31 mm/s.[67] Exposure of samples containing high levels of **J** to γ-irradiation at 77 K (cryoreduction) monitored by EPR and Mössbauer spectroscopy was shown to convert it to one (or more) high-spin Fe^{III} complex, establishing the formal oxidation state of **J** as +IV.[61]

Decay of **J** is accompanied by an increase of the intensity of the high-energy line (at ≈ 2.7 mm/s) of the Mössbauer quadrupole doublet of the high-spin Fe^{II} species, demonstrating that the second intermediate contains Fe^{II}.[39]

4. Placement of the Intermediates within the Catalytic Cycle and Integration of the Kinetic and Chemical Mechanisms

The stopped-flow absorption and freeze-quench Mössbauer data by themselves established neither the identities nor the positions within the catalytic cycle of the two intermediates. The formal +IV oxidation state of **J** and +II state of the second intermediate suggested that the former occurs before taurine hydroxylation and the latter after, but the lack of good precedents for intermediates in the catalytic cycle precluded more definitive assignment by simple comparison of Mössbauer and optical properties. For example, it is possible to depict both **I** and **II** (in addition to **J**) with "resonance structures" having the Fe in the +IV oxidation state. Similarly, the second intermediate might be either a product(s) complex or the TauD·Fe^{II} binary complex awaiting rebinding of substrates. Additional kinetic experiments resolved these issues.

4.1 J is the Hydroxylating Intermediate

The position of **J** in the catalytic cycle was resolved by testing for substrate deuterium kinetic isotope effects (KIEs) on formation and decay of the intermediate. 1,1-$[^2H]_2$-taurine and the (control) unlabeled substrate were synthesized and used to prepare the reactant quaternary complex for reaction with O_2. A large normal KIE ($k_H/k_D \approx 37$) on decay of **J**, but no KIE on its formation, were observed. This result was shown both by stopped-flow absorption measurements (Figure 2, A) and by RFQ Mössbauer (Figure 2, B).[68] The result suggests that **J** is responsible for cleavage of the C1-$[^{1,2}H]$ bond, making the most likely identity of the complex the Fe^{IV}-oxo species in Scheme 1. This conclusion was subsequently confirmed by resonance Raman and X-ray absorption spectroscopic experiments (see below).

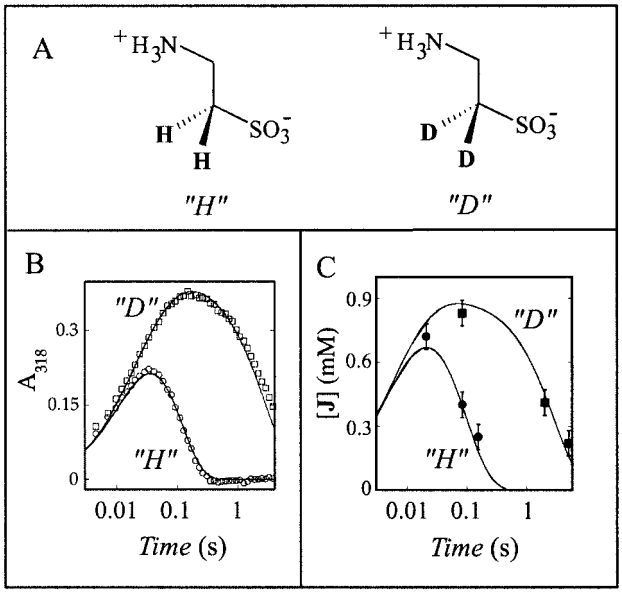

Figure 2. (**A**) Structures of 1,1-$[^1H]_2$-taurine and 1,1-$[^2H]_2$-taurine. Kinetics of **J** monitored by (**B**) stopped-flow absorption and (**C**) RFQ Mössbauer spectroscopy. The circles and squares represent the experimental data obtained using 1,1-$[^1H]_2$-taurine and 1,1-$[^2H]_2$-taurine, respectively. The solid lines are simulations for **J** according to the rate constants shown in Scheme 1. In **B**, a solution containing 2.0 mM TauD, 1.8 mM Fe^{II}, 17 mM αKG and 17 mM taurine was mixed with air-saturated buffer in a volume ratio of 2:5 at 5 °C. In **C**, a solution containing 4 mM TauD, 3.6 mM $^{57}Fe^{II}$, 10 mM αKG, and 10 mM taurine was mixed with an equal volume of O_2-saturated buffer at 5 °C. Adapted from Price et al.[68]

 © 2005 Wiley-VCH Verlag GmbH & Co. KGaA, Weinheim

4.2 An Integrated Kinetic/Chemical Mechanism: Verification of its Predictions

The identity of **J** and the apparent failure of precursors to accumulate suggested that **J** forms rapidly after the initial slower addition of O_2 to the quaternary complex. The demonstration of a first-order dependence of the kinetics of formation of **J** on the concentration of O_2 proved this point[69] and allowed an upper limit to be established for the quantity of a precursor that can accumulate.[39] The demonstration by chemical quenched-flow experiments that loss of CO_2 from αKG correlates with formation of **J** established a second important prediction of the integrated mechanism and provided support for the structure assigned to **J**. The large C1 deuterium KIE on conversion of **J** to an Fe^{II} complex, again apparently without accumulation of intervening intermediates (e.g., **IV** in Scheme 1), indicates that the postulated "radical rebound" to the C1 radical is rapid compared to the preceding H atom abstraction. The implication that decay of **J** should be kinetically correlated with formation of product has been verified by chemical quenched-flow experiments quantifying sulfite released by the immediate product, 1-hydroxytaurine. All that remained was to establish the nature of the second intermediate and define the steps involved in its rate-limiting conversion back to the reactant quaternary complex.

4.3 Assignment of the Second Intermediate as a Product Complex

The initial transient-kinetic study on TauD had reported that binding of αKG to the TauD·Fe^{II} binary complex is relatively slow (2–6 s^{-1} at 4 °C) and, somewhat surprisingly for an association reaction, of kinetic order zero in αKG.[34] This report implicated a unimolecular step associated with formation of the TauD·Fe^{II}·αKG complex as the rate-limiting step and suggested that the second intermediate might be the binary complex. Resolution of the Mössbauer spectrum of the second intermediate showed that it is distinct from that of the TauD·Fe^{II} complex and also different from those of the TauD·Fe^{II}·αKG and TauD·Fe^{II}·αKG·taurine complexes.[39] Re-examination of αKG binding by stopped-flow absorption experiments monitoring development of the MLCT band at 530 nm showed that formation of the complex is remarkably complex, but much faster overall than the rate-limiting conversion of the second intermediate back to the reactant complex (Figure 3, A).[39] Taurine binding to the TauD·Fe^{II}·αKG complex is fast, but prior binding of taurine impedes binding of αKG (Figure 3, B), consistent with the preferred or obligatory order of substrate binding that has been seen in the reactions of other members of this family and providing a rationale for inhibition by taurine of both steady-state turnover and quaternary complex re-formation. The demonstration that formation of **J** upon mixing of TauD·Fe^{II} simultaneously with all three substrates is only slightly slower than upon mixing of the quaternary complex with O_2 (and much faster than the 2.5 ± 0.5 s^{-1} decay of the second intermediate) ruled out the possibility that steps involved in substrate binding contribute to the rate-limiting conversion of the second intermediate to the quaternary complex. This conclusion left only steps involved in product dissociation as candidates for the rate-limiting step and implied that the second intermediate is a product(s) complex. Support for these inferences came from examining the dependence of k_{cat} on solvent viscosity. With 1,1-[^{1}H]$_2$-taurine, the significant reduction of k_{cat} by increasing viscosity is consistent with rate-limiting diffusion of product from the active site. By contrast, with 1,1-[^{2}H]$_2$-taurine as substrate, the large KIE renders H atom abstraction rate-limiting, leading to a much less pronounced solvent-viscosity effect.[39]

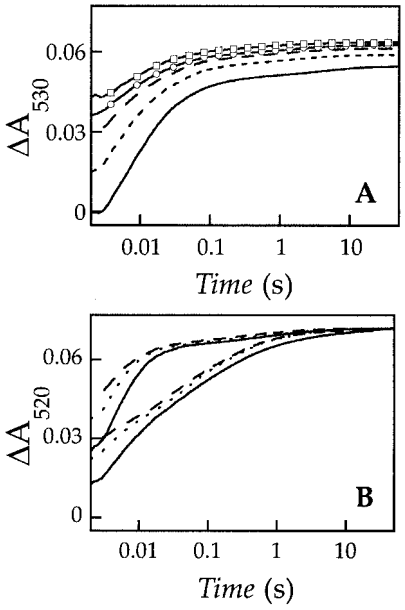

Figure 3. Absorbance-vs.-time traces monitoring binding of αKG in the absence (**A**) and presence (**B**) of taurine. In **A**, TauD containing 0.69 equivalents of Fe^{II} was mixed at 5 °C in the absence of O_2 with solutions of αKG to give final concentrations of 0.49 mM TauD and 1.5 mM (solid trace), 3 mM (dotted trace), 6 mM (dashed trace), 9 mM (solid trace with open circles), or 15 mM (solid trace with open squares) αKG. In **B**, both sets of traces are from experiments in which TauD containing 0.69 equivalents of Fe^{II} was mixed with a solution of αKG to give final concentrations of 0.49 mM TauD and 3 mM (solid traces), 6 mM (dotted traces), or 9 mM (dashed traces) αKG. For the lower three traces, taurine was present in the TauD·Fe^{II} solution such that [taurine] was 5 mM after mixing. In the upper three traces, taurine was present in the αKG solution, also giving 5 mM taurine after mixing. Adapted from Price et al.[39]

5. Structural Characterization of J

The results described in Sections 3 and 4 established that **J** contains a (formally) Fe^{IV} center and that it cleaves the C1–H bond of taurine to initiate its hydroxylation. In the consensus mechanism, the C1–H abstracting species is an Fe^{IV}-oxo species. Characterization of **J** by a variety of spectroscopic and computational methods described in the following sections demonstrated that **J** is indeed the long-pos-

 © 2005 Wiley-VCH Verlag GmbH & Co. KGaA, Weinheim

tulated Fe^{IV}-oxo complex. Interestingly, the Fe center of **J** is in the high-spin ($S = 2$) configuration.

5.1 Mössbauer Spectroscopy

Mössbauer spectra of **J** recorded in varying external magnetic fields allowed for the determination of the spin state of the Fe center and the associated zero-field splitting (ZFS) parameters, D and E/D. The facts that **J** gives rise to a quadrupole doublet in a weak (40-mT) magnetic field but displays increasing magnetic splitting with increasing externally applied magnetic field is typical of paramagnetic complexes with (almost) axial integer-spin electronic ground states and $D > 0$. The 8-T spectrum of **J** exhibits six sharp lines with peak separations that reflect an effective magnetic field of about 24 T experienced by the ^{57}Fe nucleus, corresponding to an internal magnetic field of ca. 32 T oriented antiparallel to the externally applied 8-T field (Figure 4, A).[61] The magnitude of the internal magnetic field is much larger than those experimentally observed for the many low-spin ($S = 1$) heme and non-heme Fe^{IV}-oxo compounds,[50–52,62,70] suggesting that S of the Fe^{IV} site in **J** is larger than 1. To illustrate this point, a simulation of the spectrum of a low-spin ($S = 1$) non-heme Fe^{IV}-oxo complex is shown in part B of Figure 4 for comparison.[51] Analysis of the field-dependent spectra under the assumption that the Fe^{IV} site of **J** is in the high-spin ($S = 2$) configuration yielded $D = 10.5\ cm^{-1}$, $E/D = 0.03$, $g = (2.0, 2.0, 2.0)$ (fixed), $\delta = 0.31$ mm/s, $\Delta E_Q = -0.88$ mm/s, $\eta = 0$ (fixed), and $A/g_N\beta_N = (-18\ T, -18\ T,$ not determined).[71] Interestingly, these parameters are similar to those observed for the high-spin Fe^{IV} site of intermediate **X** from *E. coli* ribonucleotide reductase,[65] thereby corroborating the assignment of **J** as a high-spin Fe^{IV} species.

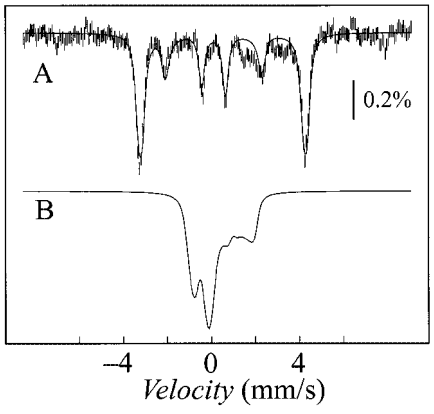

Figure 4. (**A**) 4.2-K/8-T Mössbauer reference spectrum of **J**. The solid line is a spin Hamiltonian simulation according to parameters given in the text. (**B**) Theoretical simulation of the spectrum of the low-spin Fe^{IV}-oxo complex reported by Rohde et al.: $S = 1$, $D = 29\ cm^{-1}$, $E/D = 0$, $g = (2.3, 2.3, 2.0)$, $\delta = 0.17$ mm/s, $\Delta E_Q = 1.24$ mm/s, $\eta = 0.5$, $A/g_N\beta_N = (-22.5, -18.2, -2.9)$ T.[51]

5.2 Resonance Raman Spectroscopy

The assignment of **J** as an Fe^{IV}-oxo complex was to this point based solely on chemical precedent and intuition. Resonance Raman experiments by Proshlyakov et al. provided the first direct evidence for the assignment.[72] One of the spectroscopic hallmarks of the Fe^{IV}-oxo unit is a vibrational frequency in the 800 cm^{-1} region which is downshifted by approximately 35 cm^{-1} for the ^{18}O isotopomer.[73] This downshift is close to the value predicted for a Fe–O diatomic harmonic oscillator. Proshlyakov et al.[72] succeeded in obtaining the stretching frequency of the Fe^{IV}-oxo unit of **J** by using continuous flow of reactants (quaternary complex and O_2) at low temperature (- 38 °C) to generate the intermediate and collecting at a distance from the mixer corresponding to a reaction time of 150 ms. This time was selected on the basis of absorption data recorded under the same experimental conditions, which suggested that the concentration of **J** would be at its maximum then. Resonance Raman difference spectra, which were obtained from the reaction carried out with either $^{16}O_2$ or $^{18}O_2$, revealed bands at 821 cm^{-1} ($^{16}O_2$) and 789 cm^{-1} ($^{18}O_2$). The energies of these bands are close to those observed in resonance Raman spectra of Fe^{IV}-oxo units found in heme enzymes and heme and non-heme model complexes.[51,73] Consequently, these features were attributed to the Fe=O stretching frequency.

In addition to the vibration of the Fe^{IV}-oxo unit, the authors observed a second O isotope-sensitive feature at 583 cm^{-1} ($^{16}O_2$) and 555 cm^{-1} ($^{18}O_2$). Because Fe^{IV}-oxo species do not exhibit a band in this region, the authors reasoned that it originates from a different intermediate. Interestingly, terminally coordinated Fe^{III}-superoxo oxyhemoglobins exhibit the Fe–O stretching frequency in this region, in addition to the O–O stretching frequency in the 1130 cm^{-1} region.[74] The authors did indeed observe a derivative band in the 1100 to 1160 cm^{-1} spectral region, but it overlaps with an intense solvent band, hence not allowing for its unambiguous assignment. This raises the possibility that the features at 583 (555) cm^{-1} may also emanate from a Fe^{III}-superoxo species, e.g. structure **I** of Scheme 1. Whereas this assignment is plausible, the vast quantities of protein required and the inflexibility of the apparatus necessitated by the extraordinary technical demands of the experiment prevented the crucial demonstration of the expected time-dependent decrease in the ratio of intensities of the 583/555 cm^{-1} band of the putative precursor and the 821/789 cm^{-1} band of **J**. If the lower energy feature does indeed arise from a precursor to **J**, the complex should be detectable by RFQ Mössbauer experiments carried out with similar reaction conditions, because it should have an integer-spin ground state, give rise to a quadrupole doublet at 4.2 K in a small externally applied magnetic field, and, therefore, be detectable even at relatively modest concentrations.

5.3 X-ray Absorption Spectroscopy

The second prominent characteristic of the Fe^{IV}-oxo group is a short (ca. 1.65 Å) Fe–O bond.[51,52,70,75–77] Because of the high reactivity of the Fe^{IV}-oxo unit, the bond

 © 2005 Wiley-VCH Verlag GmbH & Co. KGaA, Weinheim

length generally cannot be determined using X-ray crystallography. The recent report of the first X-ray structure of a Fe^{IV}-oxo non-heme model complex is a remarkable exception.[51] For the case of **J**, the Fe–O distance was determined by X-ray absorption spectroscopy.[78] These experiments required that the Fe^{IV}-oxo complex be the predominant species in the sample. Accumulation of **J** to 80% of the Fe in the sample was made possible by the use of 1,1-$[^2H]_2$-taurine and the large deuterium KIE on decay of **J**.[68] X-ray absorption spectra of samples containing primarily **J** were shown to exhibit the hallmarks of a Fe^{IV}-oxo unit. First, the edge energy is significantly higher than that of the quaternary TauD·Fe^{II}·αKG·taurine complex, suggesting that **J** is in a high oxidation state. Second, the pre-edge feature caused by the 1s→3d transitions is intense, which is caused by the less centrosymmetric ligand environment of the Fe center imposed by the oxo ligand. Third, fitting of the EXAFS region of the spectra requires the assumption of a short, 1.62 Å, interaction between the Fe and one of its ligands. Importantly, the coordination number for this short interaction was found to range from 0.5 to 0.8, in agreement with the fraction of **J** in the sample determined independently by Mössbauer spectroscopy. On the basis of the extensive precedent, the 1.62 Å interaction was assigned to the Fe^{IV}-oxo unit.

5.4 Proposed Structure of J

The data indicate that **J** has an Fe^{IV}-oxo unit with the iron in high-spin configuration. To the best of our knowledge, the only other example of a high-spin Fe^{IV}-oxo unit is a dinuclear model complex.[79] Importantly, the large number of characterized mononuclear heme and non-heme Fe^{IV}-oxo species all have a low-spin (S = 1) Fe^{IV}-oxo group.[50–52,62,70] In a trigonal bipyramidal ligand field the d-orbitals split into two low-lying *e*-sets and one orbital high in energy (d_{z^2}). To evaluate the possibility that the four low-lying orbitals can accommodate four unpaired electrons, resulting in the experimentally observed S = 2 configuration, density functional calculations on the trigonal bipyramidal model of **J** shown in Figure 5 were conducted.[71] This model contains two imidazole ligands (one axial and one equatorial), two equatorial carboxylate ligands, and the axial oxo ligand. The three protein ligands derived from the $(His)_2$-$(Asp)_1$ triad are represented by the two imidazole ligands and one of the carboxylate ligands. They coordinate the Fe center facially. The second equatorial carboxylate ligand mimics one of the products of the reaction, succinate. The other product of the decarboxylation reaction, CO_2, has not been included in this model, although interactions of CO_2 with the Fe center have been reported. Coordination of CO_2, derived from hydrogencarbonate in the buffer, to the Fe^{II} center opposite to the more distant (in sequence) histidine has been detected by X-ray crystallography for deacetoxycephalosporin C synthase,[80] and by perturbation of the Fe^{III}-catecholate chromophore in TauD, which is obtained by the self-hydroxylation of tyrosine 73 followed by coordination of the catecholate to the iron.[40] Geometry optimization of the model of **J** does not result in significant structural changes and yields a lower energy for the S = 2 state, suggesting that the trigonal bipyramidal geometry is one way of rationalizing the high-spin state of the Fe^{IV} center of **J**.

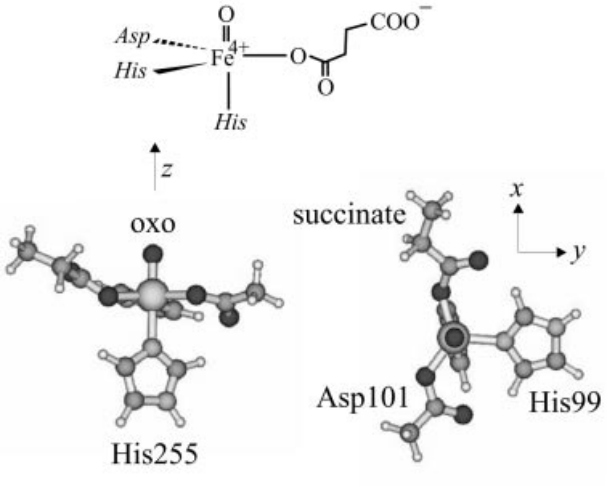

Figure 5. Structural model of intermediate **J** in TauD obtained by DFT calculations. Adapted from Krebs et al.[71]

As noted, the Mössbauer isomer shift of **J** is unusually high, approaching values observed for high-spin Fe^{III} complexes.[67] Because DFT methods can predict Mössbauer parameters with considerable accuracy,[81–84] the comparison of calculated and experimental parameters provides a means of validating structural models for reactive intermediates of unknown structure. Although the Mössbauer isomer shift of the trigonal bipyramidal model calculated by this approach (0.22 mm/s) is lower than the experimentally observed isomer shift of **J** (0.31 mm/s), the deviation is still within the uncertainty of the method (0.10 mm/s).[81] Although further calculations, in particular those taking into account the effect of the protein, are clearly warranted to more rigorously evaluate potential structures for **J**, the agreement between theory and experiment suggests that **J** may have a trigonal bipyramidal structure with an axial oxo ligand.

6. Conclusion and Outlook

Two intermediates detected in the reaction of the quaternary TauD·Fe^{II}·αKG·taurine complex with oxygen have been assigned by a combination of rapid kinetic and spectroscopic methods as a high-spin Fe^{IV}-oxo species, **J**, which abstracts H from C1 of taurine, and a product(s) complex, **V** in Scheme 1, that releases product in the rate-limiting step of the catalytic cycle. Other intermediates in the consensus mechanism are kinetically masked, and therefore do not accumulate. Current efforts are directed towards accumulation of these intermediate states for their spectroscopic characterization. For example, the resonance Raman spectroscopic studies by Proshlyakov et al. suggest that in-

 © 2005 Wiley-VCH Verlag GmbH & Co. KGaA, Weinheim

termediate **I** or **II** may accumulate when the reaction is carried out at low temperature (–35 °C).[72] Perturbation of the reaction kinetics by the use of substrate analogues, variant proteins, or both may also allow for accumulation and characterization of additional complexes in the cycle.

Acknowledgments

We thank our collaborators and co-workers, whose work is reported in this article. This work has been supported by the Pennsylvania State University (startup funds to C. K.) and grant from the National Institutes of Health (NIH-GM 69657 to J. M. B. and C. K.).

[1] R. Y. N. Ho, L. Que Jr., *Chem. Rev.* **1996**, *96*, 2607–2624.
[2] M. J. Ryle, R. P. Hausinger, *Curr. Opin. Chem. Biol.* **2002**, *6*, 193–201.
[3] R. P. Hausinger, *Crit. Rev. Biochem. Mol. Biol.* **2004**, *39*, 21–68.
[4] M. Costas, M. P. Mehn, M. P. Jensen, L. Que Jr., *Chem. Rev.* **2004**, *104*, 939–986.
[5] L. Que Jr., *Nature Struct. Biol.* **2000**, *7*, 182–184.
[6] K. D. Koehntop, J. P. Emerson, L. Que Jr., *J. Biol. Inorg. Chem.* **2005**, *10*, 87–93.
[7] R. P. Hausinger, F. Fukumori, D. A. Hogan, T. M. Sassanella, Y. Kamagata, H. Takami, R. E. Saari, in: *Microbial Diversity and Genetics of Biodegradation* (Eds.: K. Horikoshi, M. Fukuda, T. Kudo,); Japan Scientific Press: Tokyo, **1997**, pp. 35–51.
[8] J. J. Hutton Jr., A. L. Tappel, S. Udenfriend, *Biochem. Biophys. Res. Commun.* **1966**, *24*, 179–184.
[9] K. I. Kivirikko, T. Pihlajaniemi, *Adv. Enzymol. Rel. Areas Mol. Biol.* **1998**, *72*, 325–398.
[10] M. D. Lloyd, K. D. Merritt, V. Lee, T. J. Sewell, B. Wha-Son, J. E. Baldwin, C. J. Schofield, S. W. Elson, K. H. Baggaley, N. H. Nicholson, *Tetrahedron* **1999**, *55*, 10201–10220.
[11] R. W. Busby, M. D. T. Chang, R. C. Busby, J. Wimp, C. A. Townsend, *J. Biol. Chem.* **1995**, *270*, 4262–4269.
[12] J. E. Baldwin, R. M. Adlington, J. B. Coates, M. J. C. Crabbe, N. P. Crouch, J. W. Keeping, G. C. Knight, C. J. Schofield, H. H. Ting, C. A. Vallejo, M. Thorniley, E. P. Abraham, *Biochem. J.* **1987**, *245*, 831–841.
[13] A. G. Prescott, M. D. Lloyd, *Nat. Prod. Rep.* **2000**, *17*, 367–383.
[14] T. Duncan, S. C. Trewick, P. Koivisto, P. A. Bates, T. Lindahl, B. Sedgwick, *Proc. Natl. Acad. Sci. U. S. A.* **2002**, *99*, 16660–16665.
[15] S. C. Trewick, T. F. Henshaw, R. P. Hausinger, T. Lindahl, B. Sedgwick, *Nature* **2002**, *419*, 174–178.
[16] P. A. Aas, M. Otterlei, P. O. Falnes, C. B. Vagbo, F. Skorpen, M. Akbari, O. Sundheim, M. Bjoras, G. Slupphaug, E. Seeberg, H. E. Krokan, *Nature* **2003**, *421*, 859–863.
[17] M. A. Kurowski, A. S. Bhagwat, G. Papaj, J. M. Bujnicki, *BMC Genomics* **2003**, *4*, 48.
[18] M. Ivan, K. Kondo, H. Yang, W. Kim, J. Valiando, M. Ohh, A. Salic, J. M. Asara, W. S. Lane, W. G. Kaelin Jr., *Science* **2001**, *292*, 464–468.
[19] P. Jaakkola, D. R. Mol, Y.-M. Tian, M. I. Wilson, J. Gielbert, S. J. Gaskell, A. von Kriegsheim, H. F. Hebestreit, M. Mukherji, C. J. Schofield, P. H. Maxwell, C. W. Pugh, P. J. Ratcliffe, *Science* **2001**, *292*, 468–472.
[20] C. J. Schofield, P. J. Ratcliffe, *Nat. Rev. Mol. Cell Biol.* **2004**, *5*, 343–354.
[21] K. S. Hewitson, L. A. McNeill, M. V. Riordan, Y.-M. Tian, A. N. Bullock, R. W. Welford, J. M. Elkins, N. J. Oldham, S. Bhattacharya, J. M. Gleadle, P. J. Ratcliffe, C. W. Pugh, C. J. Schofield, *J. Biol. Chem.* **2002**, *277*, 26351–26355.
[22] P. C. Mahon, K. Hirota, G. L. Semenza, *Genes Dev.* **2001**, *15*, 2675–2686.
[23] G. L. Semenza, *Nature Rev. Cancer* **2003**, *3*, 721–732.
[24] K. S. Hewitson, C. J. Schofield, *Drug Discovery Today* **2004**, *9*, 704–711.
[25] K. S. Hewitson, L. A. McNeill, C. J. Schofield, *Curr. Pharm. Des.* **2004**, *10*, 821–833.
[26] K. Iwai, R. D. Klausner, T. A. Rouault, *EMBO J.* **1995**, *14*, 5350–5357.
[27] K. Iwai, S. K. Drake, N. B. Wehr, A. M. Weissman, T. Lavaute, N. Minato, R. D. Klausner, R. L. Levine, T. A. Rouault, *Proc. Natl. Acad. Sci. U. S. A.* **1998**, *95*, 4924–4928.
[28] E. S. Hanson, M. L. Rawlins, E. A. Leibold, *J. Biol. Chem.* **2003**, *278*, 40337–40342.
[29] J. Wang, G. Chen, M. Muckenthaler, B. Galy, M. W. Hentze, K. Pantopoulos, *Mol. Cell. Biol.* **2004**, *24*, 954–965.
[30] E. I. Solomon, T. C. Brunold, M. I. Davis, J. N. Kemsley, S.-K. Lee, N. Lehnert, F. Neese, A. J. Skulan, Y.-S. Yang, J. Zhou, *Chem. Rev.* **2000**, *100*, 235–349.
[31] H. M. Hanauske-Abel, V. Günzler, *J. Theor. Biol.* **1982**, *94*, 421–455.
[32] E. G. Pavel, J. Zhou, R. W. Busby, M. Gunsior, C. A. Townsend, E. I. Solomon, *J. Am. Chem. Soc.* **1998**, *120*, 743–753.
[33] In contrast, for the enzyme prolyl-4-hydroxylase, it was reported that binding of oxygen occurs prior to binding of substrate (R. Myllylä, L. Tuderman, K. I. Kivirikko, *Eur. J. Biochem.* **1977**, *80*, 349–357; M. Rundgren, *J. Biol. Chem.* **1977**, *252*, 5094–5099).
[34] M. J. Ryle, R. Padmakumar, R. P. Hausinger, *Biochemistry* **1999**, *38*, 15278–15286.
[35] R. Y. N. Ho, M. P. Mehn, E. L. Hegg, A. Liu, M. J. Ryle, R. P. Hausinger, L. Que Jr., *J. Am. Chem. Soc.* **2001**, *123*, 5022–5029.
[36] Z. Zhang, J.-s. Ren, K. Harlos, C. H. McKinnon, I. J. Clifton, C. J. Schofield, *FEBS Lett.* **2002**, *517*, 7–12.
[37] I. Müller, A. Kahnert, T. Pape, G. M. Sheldrick, W. Meyer-Klaucke, T. Dierks, M. Kertesz, I. Usón, *Biochemistry* **2004**, *43*, 3075–3088.
[38] M. J. Ryle, A. Liu, R. B. Muthukumaran, R. Y. N. Ho, K. D. Koehntop, J. McCracken, L. Que Jr., R. P. Hausinger, *Biochemistry* **2003**, *42*, 1854–1862.
[39] J. C. Price, E. W. Barr, L. M. Hoffart, C. Krebs, J. M. Bollinger Jr., *Biochemistry* **2005**, *44*, 8138–8147.
[40] M. J. Ryle, K. D. Koehntop, A. Liu, L. Que Jr., R. P. Hausinger, *Proc. Natl. Acad. Sci. U. S. A.* **2003**, *100*, 3790–3795.
[41] A. Liu, R. Y. N. Ho, L. Que Jr., M. J. Ryle, B. S. Phinney, R. P. Hausinger, *J. Am. Chem. Soc.* **2001**, *123*, 5126–5127.
[42] T. F. Henshaw, M. Feig, R. P. Hausinger, *J. Inorg. Biochem.* **2004**, *98*, 856–861.
[43] G. Schenk, M. Y. M. Pau, E. I. Solomon, *J. Am. Chem. Soc.* **2004**, *126*, 505–515.
[44] D. M. Arciero, A. M. Orville, J. D. Lipscomb, *J. Biol. Chem.* **1985**, *260*, 14035–14044.
[45] V. J. Chen, A. M. Orville, M. R. Harpel, C. A. Frolik, K. K. Surerus, E. Münck, J. D. Lipscomb, *J. Biol. Chem.* **1989**, *264*, 21677–21681.
[46] K. Pohl, K. Wieghardt, B. Nuber, J. Weiss, *J. Chem. Soc. Dalton Trans.* **1987**, 187–192.
[47] M. Ray, A. P. Golombek, M. P. Hendrich, G. P. A. Yap, L. M. Liable-Sands, A. L. Rheingold, A. S. Borovik, *Inorg. Chem.* **1999**, *38*, 3110–3115.
[48] Footnote, We called the Fe^{IV}-oxo complex previously **III**. Results obtained by us and others allowed assignment of the intermediate **J** to this structure.
[49] M. Wu, H.-S. Moon, T. P. Begley, J. Myllyharju, K. I. Kivirikko, *J. Am. Chem. Soc.* **1999**, *121*, 587–588.
[50] C. A. Grapperhaus, B. Mienert, E. Bill, T. Weyhermüller, K. Wieghardt, *Inorg. Chem.* **2000**, *39*, 5306–5317.
[51] J.-U. Rohde, J.-H. In, M. H. Lim, W. W. Brennessel, M. R. Bukowski, A. Stubna, E. Münck, W. Nam, L. Que Jr., *Science* **2003**, *299*, 1037–1039.

 © 2005 Wiley-VCH Verlag GmbH & Co. KGaA, Weinheim

[52] M. H. Lim, J.-U. Rohde, A. Stubna, M. R. Bukowski, M. Costas, R. Y. N. Ho, E. Münck, W. Nam, L. Que Jr., *Proc. Natl. Acad. Sci. U. S. A.* **2003**, *100*, 3665–3670.
[53] J. Kaizer, M. Costas, L. Que Jr., *Angew. Chem. Int. Ed.* **2003**, *42*, 3671–3673.
[54] A. Decker, J.-U. Rohde, L. Que Jr., E. I. Solomon, *J. Am. Chem. Soc.* **2004**, *126*, 5378–5379.
[55] E. H. Ha, R. Y. N. Ho, J. F. Kisiel, J. S. Valentine, *Inorg. Chem.* **1995**, *34*, 2265–2266.
[56] Y.-M. Chiou, L. Que Jr., *J. Am. Chem. Soc.* **1995**, *117*, 3999–4013.
[57] M. P. Mehn, K. Fujisawa, E. L. Hegg, L. Que Jr., *J. Am. Chem. Soc.* **2003**, *125*, 7828–7842.
[58] S. Hikichi, T. Ogihara, K. Fujisawa, N. Kitajima, M. Akita, Y. Moro-oka, *Inorg. Chem.* **1997**, *36*, 4539–4547.
[59] Y.-M. Chiou, L. Que Jr., *Inorg. Chem.* **1995**, *34*, 3577–3578.
[60] E. Eichhorn, J. R. van der Ploeg, M. A. Kertesz, T. Leisinger, *J. Biol. Chem.* **1997**, *272*, 23031–23036.
[61] J. C. Price, E. W. Barr, B. Tirupati, J. M. Bollinger Jr., C. Krebs, *Biochemistry* **2003**, *42*, 7497–7508.
[62] P. G. Debrunner, *Phys. Bioinorg. Chem. Ser.* **1989**, *4*, 137–234.
[63] S. K. Lee, B. G. Fox, W. A. Froland, J. D. Lipscomb, E. Münck, *J. Am. Chem. Soc.* **1993**, *115*, 6450–6451.
[64] K. E. Liu, D. Wang, B. H. Huynh, D. E. Edmondson, A. Salifoglou, S. J. Lippard, *J. Am. Chem. Soc.* **1994**, *116*, 7465–7466.
[65] B. E. Sturgeon, D. Burdi, S. Chen, B. H. Huynh, D. E. Edmondson, J. Stubbe, B. M. Hoffman, *J. Am. Chem. Soc.* **1996**, *118*, 7551–7557.
[66] D. Lee, B. Pierce, C. Krebs, M. P. Hendrich, B. H. Huynh, S. J. Lippard, *J. Am. Chem. Soc.* **2002**, *124*, 3993–4007.
[67] C. E. MacBeth, A. P. Golombek, V. G. Young Jr., C. Yang, K. Kuczera, M. P. Hendrich, A. S. Borovik, *Science* **2000**, *289*, 938–941.
[68] J. C. Price, E. W. Barr, T. E. Glass, C. Krebs, J. M. Bollinger Jr., *J. Am. Chem. Soc.* **2003**, *125*, 13008–13009.
[69] P. K. Grzyska, M. J. Ryle, G. R. Monterosso, J. Liu, D. P. Ballou, R. P. Hausinger, *Biochemistry* **2005**, *44*, 3845–3855.
[70] T. Wolter, W. Meyer-Klaucke, M. Müther, D. Mandon, H. Winkler, A. X. Trautwein, R. Weiss, *J. Inorg. Biochem.* **2000**, *78*, 117–122.
[71] C. Krebs, J. C. Price, J. Baldwin, L. Saleh, M. T. Green, J. M. Bollinger Jr., *Inorg. Chem.* **2005**, *44*, 742–757.
[72] D. A. Proshlyakov, T. F. Henshaw, G. R. Monterosso, M. J. Ryle, R. P. Hausinger, *J. Am. Chem. Soc.* **2004**, *126*, 1022–1023.
[73] T. Kitagawa, Y. Mizutani, *Coord. Chem. Rev.* **1994**, *135/136*, 685–735.
[74] T. K. Das, M. Couture, Y. Ouellet, M. Guertin, D. L. Rousseau, *Proc. Natl. Acad. Sci. U. S. A.* **2001**, *98*, 479–484.
[75] M. Chance, L. Powers, T. Poulos, B. Chance, *Biochemistry* **1986**, *25*, 1266–1270.
[76] J. E. Penner-Hahn, K. Smith Eble, T. J. McMurry, M. Renner, A. L. Balch, J. T. Groves, J. H. Dawson, K. O. Hodgson, *J. Am. Chem. Soc.* **1986**, *108*, 7819–7825.
[77] J.-U. Rohde, S. Torelli, X. Shan, M. H. Lim, E. J. Klinker, J. Kaizer, K. Chen, W. Nam, L. Que Jr., *J. Am. Chem. Soc.* **2004**, *126*, 16750–16761.
[78] P. J. Riggs-Gelasco, J. C. Price, R. B. Guyer, J. H. Brehm, E. W. Barr, J. M. Bollinger Jr., C. Krebs, *J. Am. Chem. Soc.* **2004**, *126*, 8108–8109.
[79] H. Zheng, S. J. Yoo, E. Münck, L. Que Jr., *J. Am. Chem. Soc.* **2000**, *122*, 3789–3790.
[80] H.-J. Lee, M. D. Lloyd, K. Harlos, I. J. Clifton, J. E. Baldwin, C. J. Schofield, *J. Mol. Biol.* **2001**, *308*, 937–948.
[81] F. Neese, *Inorg. Chim. Acta* **2002**, *337*, 181–192.
[82] F. Neese, *Curr. Opin. Chem. Biol.* **2003**, *7*, 125–135.
[83] Y. Zhang, J. Mao, N. Godbout, E. Oldfield, *J. Am. Chem. Soc.* **2002**, *124*, 13921–13930.
[84] V. Vrajmasu, E. Münck, E. L. Bominaar, *Inorg. Chem.* **2003**, *42*, 5974–5988.

Received: May 25, 2005
Published Online: September 16, 2005

 © 2005 Wiley-VCH Verlag GmbH & Co. KGaA, Weinheim

Homo- and Heteroduplex Complexes Containing Terpyridine-Type Ligands and Zn^{2+}

Florina Dumitru,[a,b] Eddy Petit,[a] Arie van der Lee,[a] and Mihail Barboiu*[a]

Keywords: Crystal engineering / N ligands / Supramolecular chemistry / Ternary complexes / Zinc

We describe a study of the equilibrium binding of Zn^{2+} to binary mixtures of tridentate terpy-type ligands **1**–**3**, which leads to the formation of a dynamic mixture of homo (**4**–**6**) and hetero (**7**–**9**) coordination compounds. We report the crystal structures of five such complexes (**4**, **5**, **7**–**9**) which assemble into complementary duplex compounds that further self-organize into double helical- or lamellar-type architectures in the solid state. The ligand exchange between homoduplex complexes in solution leads to the preferential formation of the heteroduplex complexes. As might be expected, these processes display a statistical distribution of homoduplex:heteroduplex:homoduplex complexes of 1:2:1 for the mixtures resulting from **4**:**6** and **5**:**6** ligands. However, complex **8** is preferred in a **4**:**5** mixture which presents a composition of 1:4:1 (amplification factor of about 33 %). The X-ray structural determinations of selected single crystals resulting from the stoichiometric mixtures of homoduplex complexes show unique heteroduplex superstructures **7**–**9** in the solid state. The present results present the solid-state structures of homo- and heterocomplexes resulting from terpyridine-type ligands **1**–**3** and Zn^{2+} metal ions. The heteroduplex Zn^{2+} complexes **7**–**9** are quantitatively crystallized in the solid state by statistical (**7**, **9**) and structural (**8**) driven selection in solution from a binary mixture of the terpyridine-type complexes and then trapped by crystallization in the solid state.

(© Wiley-VCH Verlag GmbH & Co. KGaA, 69451 Weinheim, Germany, 2005)

Introduction

Under biological and environmental conditions, multiligand-multimetal equilibria dominate homonuclear interactions and mixed- or higher-order complexes are formed.[1] Thus it becomes understandable why the mixed complexes have been studied extensively during the last four decades. The most simple of these species − the ternary (heteroduplex) complexes − consist of a metal ion and two different ligands. The driving forces leading to the formation of such complexes are statistical events, and non-covalent forces like charge and hydrophobic or π-π stacking interactions.[2]

The self-organization of metallosupramolecular entities may be directed by design and is based on the implementation of ligands containing specific molecular information stored in the arrangement of suitable binding sites and of metal ions reading out the structural information through the algorithm defined by their coordination geometry. The design of the ligand is crucial, and bipyridine, terpyridine, etc. derivatives have been extensively used.[3] The synthesis of such ligands is very challenging and other simple procedures are much sought-after as they may provide a more direct access to these systems by using or imine and hydrazone mimics, which are useful building blocks for the generation of grid-type, cage, helical architectures, etc.[4–7]

Coordination complexes based on terpyridine-type ligands **1** and octahedrally coordinated metal ions are of special interest as they reveal a range of interesting structural and physicochemical properties.[5] Other terpyridine-type (terpy) tridentate ligands like the bis-Schiff-base **2**[6] and the hydrazone bis-pyridine **3**[7] give easy synthetic access to similar systems (Scheme 1). Addition of Zn^{2+} to the binary mixture of terpy-type ligands **1**–**3** should cause the appropriate recruitment of two ligands in a pairwise mode and might be controlled by the coordination behavior and internal interactions between different aromatic moieties of these compounds. Specifically, it is of interest to investigate whether the coordination behavior of these systems on the addition of octahedral Zn^{2+} ions can be selectively expressed in the formation of ternary complexes.

We describe in this paper a study of the equilibrium binding of Zn^{2+} to binary mixtures of tridentate terpy-type ligands **1**–**3**, which leads to the formation of a dynamic mixture of homo- (**4**–**6**) and hetero- (**7**–**9**) coordination compounds. We report the crystal structures of five such complexes (**4**, **5**, **7**–**9**), which assemble into complementary duplex compounds that further self-organize into double helical- or lamellar-type architectures in the solid state.

[a] Institut Européen des Membranes − IEM-CNRS 5635,
Place Eugène Bataillon, CC 47, 34095 Montpellier, Cedex 5, France
Fax: +33-467-14-91-19
E-mail: barboiu@iemm.univ-montp2.fr
[b] Department of Inorganic Chemistry, University Politehnica of Bucharest,
1, Polizu st., 011061 Bucharest, Romania

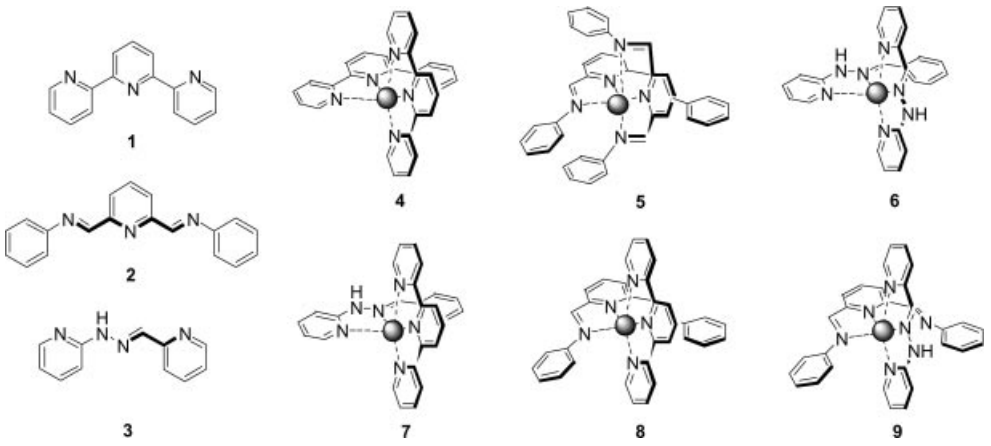

Scheme 1. Structures of the terpyridine-type ligands **1**–**3** and the combinatorial library of resulting homo- (**4**–**6**) and heteroduplex (**7**–**9**) metallosupramolecular complexes.

Result and Discussions

Synthesis and Characterization of Ligands 2 and 3

Ligands **2** and **3** were synthesized in EtOH by condensation of one equivalent of 2,6-pyridinedicarboxaldehyde with two equivalents of aniline and of one equivalent of 2-pyridinecarboxaldehyde with one equivalent of hydrazinopyridine, respectively. The solutions of **2** and of **3** in $CDCl_3$ give sharp ^1H NMR spectra with a strong deshielding of the *meta* protons of the central pyridine (**2**) and of the iminopyridine (**3**) rings, consistent with the *transoid* conformation[8] of the –N=C–C=N– moiety. As expected, a strong deshielding is observed for the *meta* pyridine hydrogens, thus indicating a tight contact with the neighboring imine nitrogen atoms; this effect agrees with an unwrapped conformation of compounds **2** and **3**.

Two-Component Self-Assembly, Generation and Interconversion of the Zn^{2+} Complexes Formed by Ligands 1–3

The formation of homoduplex Zn^{2+} complexes from terpyridine-type ligands **1**–**3** has been studied in detail because it is a very common prototype for coordination self-assembly processes and because of the physicochemical properties and functions that such materials may possess.[2–9] One may consider the formation of these complexes to result from the "reading" of the steric and binding information of the ligands by the Zn^{2+} ions following their octahedral coordination geometry.

Of particular interest, both as a control of the ligand selection and due to the formation of novel mixed species, would be the generation of the heteroduplex complexes from two different terpy-type ligands **1**–**3** and Zn^{2+} ions. Considering that Zn^{2+} ions, which display hexacoordination geometry, bind two terpy units in a octahedral geometry, one might expect that the exchange of different terpy-type ligands in the metal coordination sphere would result in the interconversion of all possible combinations. The rate of such exchange depends on the coordination behavior and on the specific interactions between ligands, therefore it should be possible to form mixtures from which a ternary architecture[10] can be amplified by favorable attractive interactions, including stacking[11] or hydrophobic[12] interactions, between the ligands, while minimizing the ligand–solvent interactions.[8]

As a step towards this goal, we decided to investigate the formation and interconversion of the Zn^{2+} duplex complexes that may result from the binding of Zn^{2+} ions to stoichiometric ratios (1:1) of binary mixtures of ligands **1**–**3**. Such systems form by self-assembly under mild conditions and are readily amenable to solution studies by ^1H NMR spectroscopy and ESI mass spectrometry.

The ^1H NMR spectra of homoduplex complexes **4**–**6** (Scheme 1) consist of a series of sharp peaks, indicating high symmetry (Figure 1). The spectra can be interpreted as ligands **1**–**3** in one magnetic environment and show a deshielding of the protons of the pyridine moieties due to the Zn^{2+} ion complexation. Tridentate metal ion coordination converts the *transoid* form of the free ligand to the *cisoid* one, corresponding to a terpy-type complexation site. The proton signals of the phenyl moieties of complex **5** are overall strongly shielded ($\Delta\delta$ = 0.5 ppm) with respect to ligand **2**, thus suggesting strong intramolecular attractive π-π stacking interactions between the phenyl and central pyri-

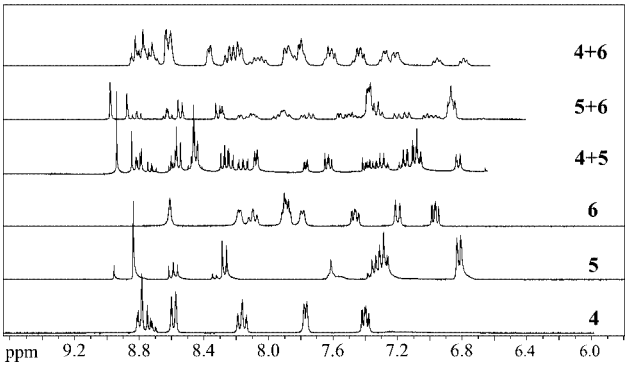

Figure 1. ^1H NMR spectra of the homoduplex complexes **4**–**6** in CD_3CN and of species resulting from the combination of stoichiometric binary mixtures of **4**:**5**, **5**:**6**, and **4**:**6** in a 1:1 molar ratio.

 © 2005 Wiley-VCH Verlag GmbH & Co. KGaA, Weinheim

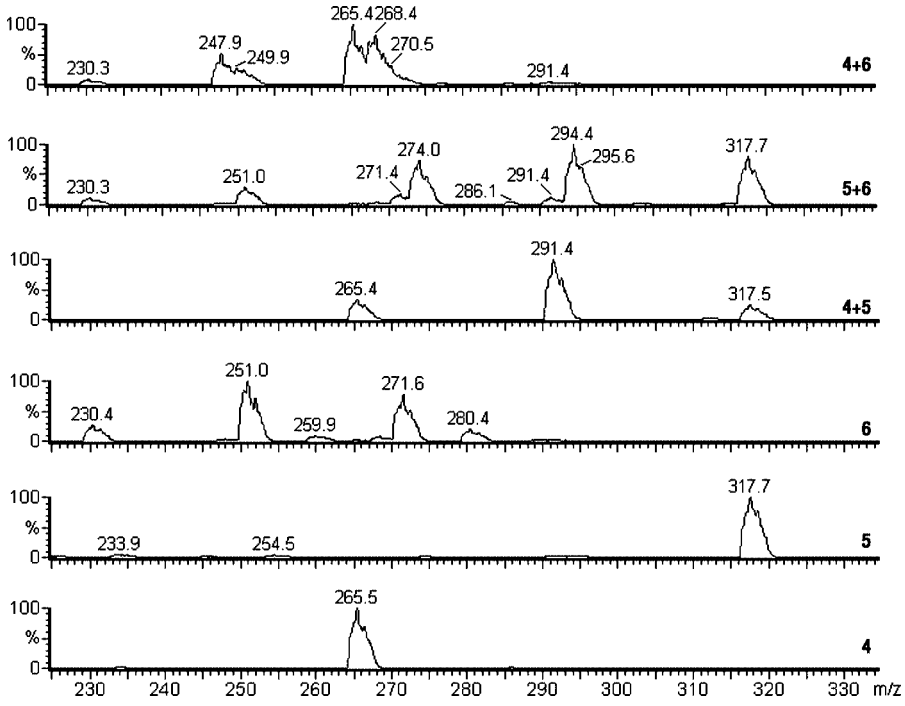

Figure 2. ESI mass spectra of the homoduplex complexes **4**–**6** in CH_3CN and of species resulting from the combination of stoichiometric binary mixtures of **4**:**5**, **5**:**6**, and **4**:**6** in a 1:1 molar ratio.

dine moiety. The ESI mass spectra of homoduplex Zn^{2+} complexes **4**–**6** show strong doubly charged molecular peaks at M/2 (**4**, **5**) or at (M + $n$$CH_3CN$)/2 ($n$ = 0–2, **6**; Figure 2).

The ligand exchange between Zn^{2+} complexes **4**–**6** was studied in the reaction of stoichiometric binary mixtures (**4**:**5**, **4**:**6**, **5**:**6**, 1:1, mol:mol) of homoduplex complexes. In all reactions the signals of symmetrical complexes as well as those of the cross-products were monitored by ^1H NMR spectroscopy (Figure 1) and ESI mass spectrometry (Figure 2). The same results were obtained by mixing two different ligands in a 1:1 ratio and by subsequently adding the stoichiometric amount of metal ions. The ^1H NMR spectra of the binary mixtures show three sets of sharp proton resonances and consist of the two initial homoduplex complexes together with the heteroduplex mixed species. We did not detect any N-exchange reaction between the bis-Schiff-base **2** and the hydrazone bis-pyridine **3** ligands; the core Zn^{2+}–ligand units, despite their kinetic lability, are thermodynamically very stable species in solution.

The ^1H NMR signals of heteroduplex complexes **7**–**9** show an overall shielding of the pyridine protons with respect to the homoduplex species, thereby suggesting an enhanced coordination power when two different ligands are coordinated. Moreover, the proton signals of the phenyl moieties of the heteroduplex complex **8** are overall strongly shielded ($\Delta\delta$ = 0.4 ppm) with respect to the homoduplex complex **5** (Figure 1). This suggests that intramolecular attractive π-π stacking interactions play an important role in the formation of the heteroduplex complexes **7**–**9**.

The ligand exchange was also monitored by ESI mass spectrometry; in all reactions, the mass spectra showed the preferential formation of the cross-products **7**–**9** after a rapid equilibration of the 1:1 solutions of the homoduplex complexes **4**–**6** (Figure 2). The composition of the binary mixtures was determined on the basis of the NMR signals of the imine, phenyl, and pyridine protons of the homo- and heteroduplex complexes **4**–**9**. As might be expected, these processes display a statistical distribution of homoduplex:heteroduplex:homoduplex complexes of 1:2:1 for the mixtures resulting from **4**:**6** and **5**:**6** ligands. However, complex **8** is preferred in a **4**:**5** mixture, which has a composition of 1:4:1. Considering the statistical distribution of 1:2:1 and the NMR detection limit error under the experimental conditions used is about 1%, the formation of **8** must display an amplification factor of about 33%.

Solid-State Structures of the Homoduplex (4, 5) and Heteroduplex (7–9) Zn^{2+} Complexes

The crystal structures of the complexes were determined from crystals obtained from acetonitrile/diisopropyl ether (**4**, **5**, **8**, **9**) and acetonitrile/benzene (**7**) solutions at room temperature. The molecular and the crystal packing structures are presented below. In all structures the Zn^{2+} ion is fully coordinated by two ligands and presents an octahedral coordination geometry. The average Zn^{2+}–$N_{Pyridine}$ Zn^{2+}–N_{imine}, and Zn^{2+}–$N_{hydrazone}$ distances are 2.07 or 2.20 (depending on the nature and the position of the pyridine moiety), 2.25, and 2.15 Å, respectively.

Surprisingly, only one crystal structure containing the $Zn(terpy)_2^{2+}$ [13a] duplex (with the peroxodisulfate counterion) was found in the Cambridge Structural Database (Feb-

 © 2005 Wiley-VCH Verlag GmbH & Co. KGaA, Weinheim

ruary 2005).[13b] The unit cell of the new crystal structure of **4** was found to contain four homoduplex complexes together with eight triflate counterions. Each $Zn(terpy)_2^{2+}$ duplex has the two terpyridines arranged into two orthogonal planes (Figure 3a), associated by offset face-to-face (***off***)[5a] pyridine–pyridine interactions with average π-π stacking centroid–centroid distances of 3.90 Å.[12a] In the crystal lattice, the homoduplex cations of **4** pack in one direction into parallel layers that are alternatively stratified. In the adjacent layers, the terpyridine ligand planes on either side of the layer interface are rotated by 45° to each other (Figure 3b). The triflate anions and the cations are in van der Waals contact, thus disrupting the classical two-dimensional motif of "terpyridine embrace"[5a] and filling the interstices so that all available space is filled.

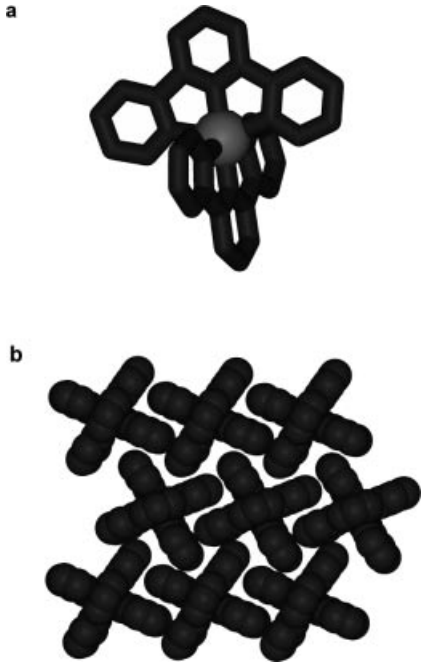

Figure 3. Crystal structure of the homoduplex complex **4**: a) side view in stick representation (the Zn^{2+} ion is shown as a gray sphere); b) space-filling representation of the crystal packing.

The unit cell of complex **5** was found to contain two homoduplex complexes together with four triflate counterions and four acetonitrile molecules. The two ligands of the duplex are arranged into two intertwined strands that are held together in double-helix form (0.5 turns per duplex) by the Zn^{2+} cation (Figure 4, a). As expected from the solution studies, the relative position of the duplex ligands allow an internal overlap between the phenyl moieties and the central pyridine moiety, with an average distance of 3.8 Å corresponding to a van der Waals contact. Each duplex of one helical sense is π-π stacked with two duplexes of the same helical sense (Figure 4, b). Each duplex present a tight contact with the two neighboring ones by stacking of the terminal phenyl moieties (average distance of 3.68 Å). This pattern generates infinite double helix stacks of units of one helical sense, with a helical pitch of about 15.3 Å. The crystal contains spontaneously resolved domains of alternate helicity. Accordingly, chiral double helical channels are generated in the solid state with an interior void of about 1.8 Å (considering a projection in a plane and taking into account the van der Waals radii of diagonally located N and C-H sites). The zinc ions are arranged into an approximately linear array that fits tightly into the central cavity of the double helical channel. The double helical entity is reminiscent of other terpyridine–Ag^+ complexes[5e] or of the double stranded dinuclear Ag^+ helicates[12b] described earlier.

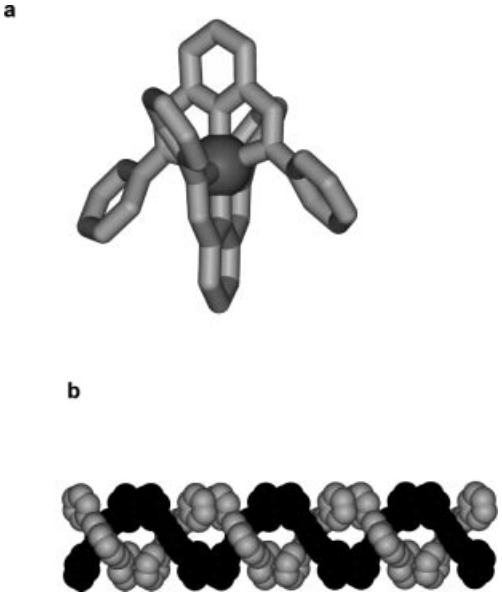

Figure 4. Crystal structure of the homoduplex complex **5**: a) side view in stick representation (the Zn^{2+} ion is shown as a gray sphere); b) space-filling representation of the crystal packing.

All attempts to crystallize complex **6** failed, and only tiny single crystals too small for X-ray analysis could be obtained from different solution-diffusion experiments.

Layering such solutions of stoichiometric binary mixtures (1:1, mol:mol) of homoduplex complexes **4**–**6** in acetonitrile with a non-solvent resulted in a unique set of crystals for each experiment. The X-ray structural determinations of selected single crystals resulting from these stoichiometric binary mixtures revealed that such complexes present unique heteroduplex superstructures **7**–**9** in the solid state. Redissolution of the crystals in CD_3CN results in regeneration of the reaction mixture prior to crystal growth. These features are similar to other dynamic processes operating in mixtures of coordination complexes from which a single member may be trapped by crystallization.[14]

The unit cell of complex **7** was found to contain four heteroduplex complexes together with eight triflate counterions and four benzene molecules. The two different ligands of the duplex are arranged into two orthogonal planes (Figure 5, a). Each duplex of **7** associates in the crystal lattice by terpyridine–terpyridine offset-face-to-face (***off***)[5a] interactions. They are restricted to one direction (average π-π stacking centroid–centroid distances of 3.75 Å), thus forming parallel layers that are alternatively stratified (Figure 5, b). Interactions in the other direction are disrupted, and the

 © 2005 Wiley-VCH Verlag GmbH & Co. KGaA, Weinheim

hydrazone bis-pyridine ligands are not involved in pyridine–pyridine π-π stacking interactions (average centroid–centroid distances of 4.60 Å).

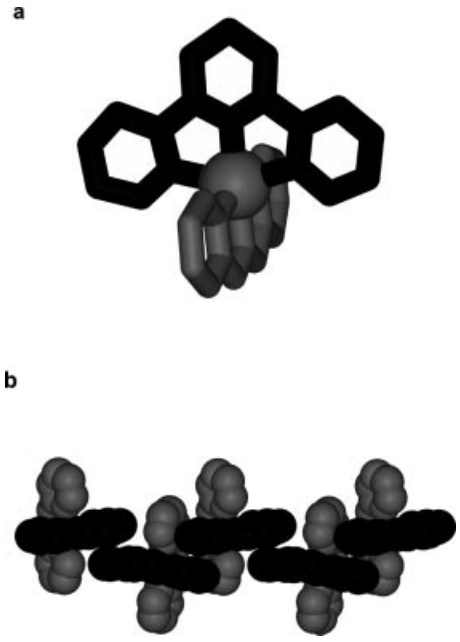

Figure 5. Crystal structure of the heteroduplex complex **7**: a) side view in stick representation (the Zn^{2+} ion is shown as a gray sphere); b) space-filling representation of the crystal packing.

The unit cell of complex **8** was found to contain four heteroduplex complexes together with eight triflate counterions and four acetonitrile molecules. The two different ligands of the duplex are arranged into two orthogonal planes (Figure 6, a). The relative flexibility of ligand **2** allows an internal overlap between the phenyl moieties and the central pyridine moiety of the terpyridine **1** with an average distance (3.98 Å) corresponding to a van der Waals contact. This is consistent with the NMR results and suggests that intramolecular attractive π-π stacking interactions play an important role in the preferential formation and amplification of the heteroduplex **8** from a stoichiometric mixture of **4** and **5**. Each heteroduplex of **8** associates two by two in the crystal lattice by terpyridine–terpyridine ***off*** interactions (average π-π stacking centroid–centroid distances of 3.75 Å), resulting in the formation of dimeric species that are alternatively stratified in the crystal lattice (Figure 6, b).

The unit cell of complex **9** was found to contain four heteroduplex complexes together with eight triflate counterions and four acetonitrile molecules. The two different ligands of the duplex are arranged into two orthogonal planes. The replacement of the central pyridine group by a hydrazone group in ligand **3** results in the disruption of the internal π-π stacking between the phenyl and pyridine moiety; in the heterocomplex **9** the phenyl substituents are perpendicularly twisted with the respect to the ligand **3** plane (Figure 7, a). In the crystal lattice, the heteroduplex cations of **9** associate by ***off*** interactions between the lateral pyridine moieties of ligand **3** (average π-π stacking centroid–centroid distances of 3.80 Å), forming parallel layers (Figure 7, b). In the other direction, each layer is alternatively stratified above another by stacking of the terminal phenyl moieties of the ligand **2**, such that each layer is in van der Waals contact (average distance of 4.05 Å).

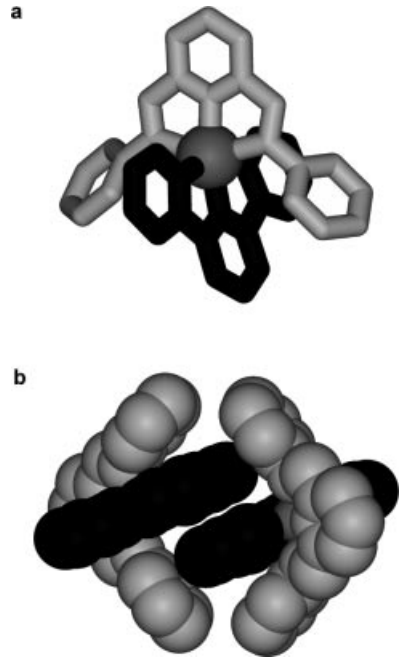

Figure 6. Crystal structure of the heteroduplex complex **8**: a) side view in stick representation (the Zn^{2+} ion is shown as a gray sphere); b) space-filling representation of the crystal packing.

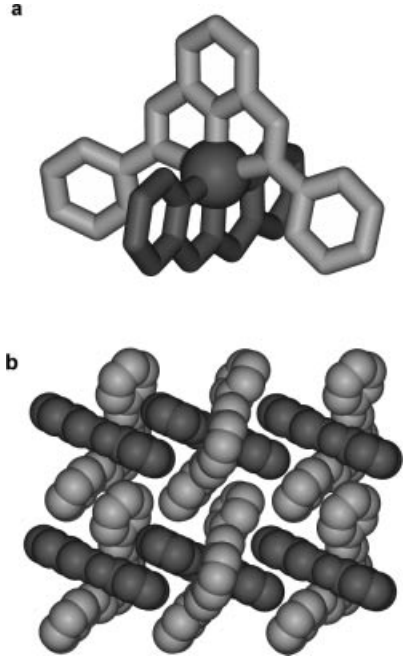

Figure 7. Crystal structure of the heteroduplex complex **9**: a) side view in stick representation (the Zn^{2+} ion is shown as a gray sphere); b) space-filling representation of the crystal packing.

The X-ray crystallographic results allow the following conclusions to be made. In term of specific self-assembly, the homo- and heteroduplex Zn^{2+} complexes of the terpyri-

 © 2005 Wiley-VCH Verlag GmbH & Co. KGaA, Weinheim

dine-type ligands **1**–**3** self-organize in the solid state into 1D or 2D stacked layers (**4**, **7**, **9**), double-helix (**5**), or dimeric (**8**) architectures as a function of synergetic intra- and intermolecular π-π stacking interactions between different constitutional ligands. In terms of specific self-organization, the heteroduplex architectures **7**–**9** represent an attractive example of solid-state structures resulting from the synergistic effects of statistical (**7**, **9**) and structural-driven (**8**) binding of two different ligands by the Zn^{2+} metal ions.

Conclusions

This paper present the solid-state structures of homo- and heterocomplexes resulting from terpyridine-type ligands **1**–**3** and Zn^{2+} metal ions. The heteroduplex Zn^{2+} complexes **7**–**9** are quantitatively crystallized in the solid state by statistical (**7**, **9**) and structural (**8**) driven selection in solution from a binary mixture of the terpyridine-type complexes and are then trapped by crystallization in the solid state (Scheme 2).

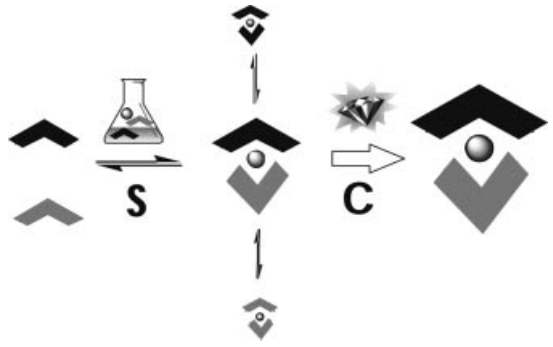

Scheme 2. Statistical pre-amplification in solution (**S**) and solid-state selection process (**C**) of the heteroduplex complexes **7**–**9**.

The crystal structures and their packing present common features with many other similar architectures reported up to now.[5] However, their structural concept − octahedral Zn^{2+} coordination, positioning two ligands in an orthogonal position such that they further interact by π-π stacking in the crystal − allows us to obtain different 1D or 2D stacked layers (**4**, **7**, **9**), double-helix (**5**), or dimeric (**8**) architectures.

A further step toward such nanosystems could involve side-by side formation of "dynamic ligands" by correct selection of their specific components by reversible interconnections. We are currently extending this approach to such optical, magnetic, etc. dynamic combinatorial nanosystems.

Experimental Section

General Methods: 2,6-Pyridinedicarboxaldehyde, 2,2′:6′,2′′-terpyridine (**1**), 2-pyridinecarboxaldehyde, and 2-pyridylhydrazine were purchased from Aldrich and used as received. All other reagents were obtained from commercial suppliers and used without further purification. All organic solutions were routinely dried over sodium sulfate (Na_2SO_4).

^{1}H NMR, COSY, and ROESY spectra were recorded on an ARX 300 MHz Bruker spectrometer in $CDCl_3$ and CD_3CN, with the use of the residual solvent peak as reference. Mass spectrometric studies were performed in the positive-ion mode using a quadrupole mass spectrometer (Micromass, Platform 2+). Samples were dissolved in acetonitrile and were continuously introduced into the mass spectrometer at a flow rate of 10 mL min^{-1} with a Waters 616HPLC pump. The temperature (60 °C) and the extraction cone voltage (5–10 V) were usually set to avoid fragmentations. The numerotations used for the assignments of the ^{1}H NMR signals (according to the corresponding COSY and ROESY spectra) are given below.

Synthesis of Ligands and Complexes: The pyridine-based ligands **2**[6] and **3**[7] were prepared according to the procedures described in the literature. Their NMR, ESI-mass spectra, and elemental analyses are consistent with analytically pure compounds.

General Procedure for the Preparation of Zn^{II} Homoduplex Complexes 4–6: The reactions were performed typically on a 10-mg scale of ligand. The ligands **1–3** (0.035 mmol) and $Zn(CF_3SO_3)_2$ (0.0175 mmol) were dissolved in CD_3CN (1 mL), and stirred overnight at 60 °C.

$[Zn(1)_2](CF_3SO_3)_2$ (4): ^{1}HNMR (300 MHz, CD_3CN): δ = 8.81–8.78 (d, ^1J = 6.6 Hz, 4 H, H^b), 8.75–8.73 (t, ^2J = 6.6 Hz, 2 H, H^a), 8.60–8.57 (d, ^1J = 7.91 Hz, 4 H, H^4), 8.19-8.13 (td, ^2J = 7.91 Hz, 4 H, H^3), 7.78–7.76 (d, ^1J = 4.71 Hz, 4 H, H^1), 7.42–7.37 (td, ^2J = 5.28 Hz, 4 H, H^2) ppm. MS (ESI): *m*/*z* (%) = 265.5 (100) $[Zn(\mathbf{1})_2]^{2+}$.

$[Zn(2)_2](CF_3SO_3)_2$ (5): ^{1}HNMR (300 MHz, CD_3CN): δ = 8.81 (s, 4 H, H^1), 8.61–8.55 (t, ^2J = 8.1, J = 7.5 Hz, 2 H, H^a), 8.27–8.24 (d, ^1J = 7.8 Hz, 4 H, H^b), 7.36–7.26 (m, 12 H, H^{3+4}), 6.82–6.79 (d, ^1J = 3.6 Hz, 8 H, H^2) ppm. MS (ESI): *m*/*z* (%) = 317.7 (100) $[Zn(\mathbf{3})_2]^{2+}$.

$[Zn(3)_2](CF_3SO_3)_2$ (6): ^{1}HNMR (300 MHz, CD_3CN): δ = 8.61 (s, 2 H, H^5), 8.19–8.17 (d, ^1J = 4.52 Hz, 2 H, H^1), 8.12–8.07 (t, ^2J = 7.72 Hz, 2 H, H^3), 7.92-7.86 (m, 4 H, H^{8+4}), 7.80–7.78 (d, ^1J = 4.71 Hz, 2 H, H^{10}), 7.49–7.44 (td, ^2J = 5.27 Hz, 2 H, H^2), 7.21-7.19 (d, ^1J = 8.48 Hz, 2 H, H^7), 6.99–6.95 (td, ^1J = 4.53 Hz, 2 H, H^9) ppm. MS (ESI): *m*/*z* (%) = 230.4 (25) $[Zn(\mathbf{3})_2]^{2+}$, 251.0 (100) $[Zn(\mathbf{3})_2 + CH_3CN]^{2+}$, 259.9 (10) $[Zn(\mathbf{3})_2 + CH_3CN + H_2O]^{2+}$, 271.6 (75) $[Zn(\mathbf{3})_2 + 2\ CH_3CN]^{2+}$, 280.4 (20) $[Zn(\mathbf{3})_2 + 2\ CH_3CN + 2\ H_2O]^{2+}$.

General Procedure for the Preparation of Zn^{II} Homo and Heteroduplex Complex Combinatorial Libraries: Stoichiometric binary solu-

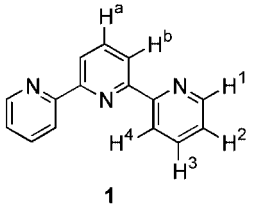

1

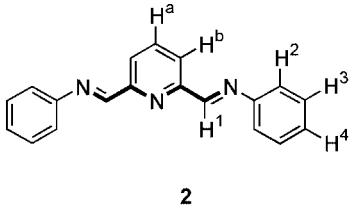

2

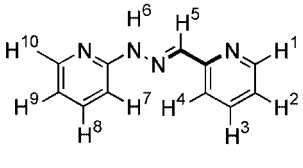

3

 © 2005 Wiley-VCH Verlag GmbH & Co. KGaA, Weinheim

Table 1. Crystallographic data for complexes **4**, **5**, **7**, **8**, and **9**.

	4	**5**	**7**	**8**	**9**
Formula	$C_{32}H_{22}F_6N_6O_6S_2Zn$	$C_{44}H_{36}F_6N_8O_6S_2Zn$	$C_{65}H_{49}F_{12}N_{14}O_{12}S_4Zn_2$	$C_{38}H_{29}F_6N_7O_6S_2Zn$	$C_{34}H_{27}F_6N_8O_6S_2Zn$
M_r	830	1016	1705	923	887
Space group	*Pnca*	$P22_12_1$	$P\bar{1}$	$P2_1/n$	$P2_1/c$
a [Å]	9.0838(3)	8.2081(3)	13.8360(10)	10.9922(7)	10.1927(8)
b [Å]	16.8483(7)	14.5003(5)	14.022(2)	25.3050(10)	20.5260(10)
c [Å]	21.2904(7)	18.7227(7)	21.774(2)	14.3410(9)	17.6730(10)
α [°]	90	90	80.985(9)	90	90
β [°]	90	90	83.609(9)	93.642(5)	91.976(6)
γ [°]	90	90	61.970(10)	90	90
V [Å^3]	3258.4(2)	2228.37(14)	3679.3(8)	3981.0(4)	3695.3(4)
Z	4	2	2	4	4
Crystal size [mm]	0.20×0.22×0.24	0.17×0.25×0.38	0.08×0.26×0.40	0.11×0.13×0.50	0.08×0.10×0.32
Solvent	acetonitrile/ diisopropyl ether	acetonitrile/ diisopropyl ether	acetonitrile/ benzene	acetonitrile/ diisopropyl ether	acetonitrile/ diisopropyl ether
ρ [g cm^{-3}]	1.692	1.520	1.539	1.540	1.595
θ_{max} [°]	32.39	32.38	32.35	32.35	32.39
N_{ref}(tot)	63659	42552	67244	75361	70056
N_{ref} unique [$I > 2\sigma(I)$]	1884	5195	3432	2368	1843
N_{par}	242	304	380	246	229
R_1	0.0244	0.0362	0.1155	0.0676	0.0570
wR_2	0.0405	0.0387	0.1838	0.0950	0.0603

tions (1:1, molar ratio) of homoduplex complexes **4**–**6** in CD_3CN were mixed and stirred overnight at 60 °C. Stoichiometric binary solutions (1:1, molar ratio) of binary mixtures of ligands **1**–**3** in CD_3CN were mixed with the stoichiometric amount of metal ions and stirred overnight at 60 °C. These solutions were monitored by ^{1}H NMR spectroscopy and ESI mass spectrometry.

X-ray Crystallographic Data for Complexes 4, 5, 7, 8, and 9: All X-ray diffraction data were collected on an Xcalibur-I diffractometer (Oxford Diffraction) with graphite-monochromated Mo-K_α radiation (λ = 0.71073 Å) at the joint X-ray scattering service of the Institut Européen des Membranes and the Institut Charles Gerhardt of the Université de Montpellier II. All measurements were carried out at 173 K using ω-scans after having placed the crystals in oil. All structures were solved using SIR2002;[15a] refinements were carried out using CRYSTALS[15b] against $|F|$ on data having $I > 2\sigma(I)$; R-factors are based on these data. Hydrogen atoms were partly located from difference Fourier synthesis, partly placed based on geometrical arguments, and in general not refined. Non-hydrogen atoms were in general refined anisotropically, except where the data-to-parameter ratio did not allow us to do this. Details of the refinements and data collections can be found in Table 1.

CCDC-266698–266702 (for **4**, **5**, **7**, **8**, and **9**, respectively) contain the supplementary crystallographic data for this paper. These data can be obtained free of charge from The Cambridge Crystallographic Data Centre via www.ccdc.cam.ac.uk/data_request/cif.

Acknowledgments

This research was supported by the European Science Foundation (EURYI Award 2004) and by the CNRS. D.F. acknowledges the generous support of Agence Universitaire Francophone (AUF). We thank Dr. René Astier for the X-ray measurements.

[1] Z. Guo, P. J. Sadler, *Angew. Chem.* **1999**, *111*, 1610–1630; *Angew. Chem. Int. Ed.* **1999**, *38*, 1512–1531.

[2] For a general review of ternary complexes see: H. Sigel, *Angew. Chem.* **1975**, *87*, 391–398; *Angew. Chem. Int. Ed.* **1999**, *38*, 394–401 and references cited therein.

[3] For recent reviews on metal-ion-metal self-assembly, see: a) S. Leininger, B. Olenyuk, P. J. Stang, *Chem. Rev.* **2000**, *100*, 853–908; b) G. F. Swiegers, T. F. Malfetese, *Chem. Rev.* **2000**, *100*, 3483–3538; c) B. J. Holliday, C. A. Mirkin, *Angew. Chem. Int. Ed.* **2001**, *40*, 2022–2043; d) S. R. Seidel, P. J. Stang, *Acc. Chem. Res.* **2002**, *35*, 972–983; e) M. Fujita, K. Umemoto, M. Yoshizawa, N. Fujita, T. Kusukawa, K. Biradha, *Chem. Commun.* **2001**, 509–518.

[4] For recent papers on generation of metallosupramolecular complexes by self-assembly, see: a) J. R. Nitschke, J.-M. Lehn, *Proc. Natl. Acad. Sci. USA* **2003**, *100*, 11970–11974; b) V. Goral, M. I. Nelen, A. V. Eliseev, J.-M. Lehn, *Proc. Natl. Acad. Sci. USA* **2001**, *98*, 1347–1352; c) P. N. W. Baxter, R. G. Khoury, J.-M. Lehn, G. Baum, D. Fenske, *Chem. Eur. J.* **2000**, *6*, 4140–4148; d) M. Barboiu, G. Vaughan, R. Graff, J.-M. Lehn, *J. Am. Chem. Soc.* **2003**, *125*, 10257–10265; e) K.-W. Chi, C. Addicott, A. M. Arif, P. J. Stang, *J. Am. Chem. Soc.* **2004**, *126*, 16569–16574; f) D. M. Epstein, S. Choudhary, M. R. Churchill, K. M. Keil, A. V. Eliseev, J. R. Morrow, *Inorg. Chem.* **2001**, *40*, 1591–1596.

[5] For recent reviews and papers on terpyridine–metal complexes, see: a) M. L. Scudder, H. A. Goodwin, I. G. Dance, *New J. Chem.* **1999**, *23*, 695–705; b) H. Hofmeier, U. S. Schubert, *Chem. Soc. Rev.* **2004**, *33*, 373–399; c) J.-F. Gohy, B. G. G. Lohmeijer, U. S. Schubert, *Chem. Eur. J.* **2003**, *9*, 3472–3479; d) U. S. Schubert, C. Eschbaumer, O. Hein, P. R. Andres, *Tetrahedron Lett.* **2001**, *42*, 4705–4707; e) M. J. Hannon, C. L. Painting, E. A. Plummer, L. J. Childs, N. A. Alcock, *Chem. Eur. J.* **2002**, *8*, 2225–2238; f) U. Siemeling, J. Vor der Bruggen, U. Vorfeld, B. Neumann, A. Stammler, H.-G. Stammler, A. Brockhinke, R. Plessow, P. Zanello, F. Laschi, F. Fabrizi de Biani, M. Fontani, S. Steenken, M. Stapper, G. Gurzadyan, *Chem. Eur. J.* **2003**, *9*, 2819–2833; g) U. S. Schubert, C. Eschbaumer, P. Andres, H. Hofmeier, C. H. Weidl, E. Herdtweck, E. Dulkeith, A. Morteani, N. E. Hecker, J. Feldmann, *Synth. Met.* **2001**, *121*, 1249–1252.

[6] a) A. L. Vance, N. A. Alcock, J. A. Heppert, D. H. Busch, *Inorg. Chem.* **1998**, *37*, 6912–6920; b) F. Lions, K. V. Martin, *J.*

 © 2005 Wiley-VCH Verlag GmbH & Co. KGaA, Weinheim

Am. Chem. Soc. **1957**, *79*, 2733–2738; c) B. de Bruin, E. Bill, E. Bothe, T. Weyhermüller, K. Wieghardt, *Inorg. Chem.* **2000**, *39*, 2936–2947.
[7] a) J. F. Geldard, F. Lions, *Inorg. Chem.* **1963**, *2*, 270–282; b) F. Lions, K. V. Martin, *J. Am. Chem. Soc.* **1958**, *80*, 3858–3865; c) M. Ruben, J.-M. Lehn, G. Vaughan, *Chem. Commun.* **2003**, 1338–1339.
[8] M. S. Goodman, V. Jubian, B. Linton, A. W. Hamilton, *J. Am. Chem. Soc.* **1995**, *117*, 11610–11611.
[9] For *transoid* conformation see: M. Barboiu, J.-M. Lehn, *Proc. Natl. Acad. Sci. USA* **2002**, *99*, 5201–5206.
[10] B. Hasenknopf, J.-M. Lehn, G. Baum, D. Fenske, *Proc. Natl. Acad. Sci. USA* **1996**, *93*, 1397–1400.
[11] J. R. Nitschke, M. Hutin, G. Bernardinelli, *Angew. Chem.* **2004**, *116*, 6892–6895; *Angew. Chem. Int. Ed.* **2004**, *43*, 6724–6727.
[12] a) C. Janiak, *J. Chem. Soc., Dalton Trans.* **2000**, 3885–3896; b) M. Barboiu, G. Vaughan, N. Kyritsakas, J.-M. Lehn, *Chem. Eur. J.* **2003**, *9*, 763–769.
[13] a) M. A. Harvey, S. Baggio, A. Ibanez, R. Baggio, *Acta Crystallogr., Sect. C* **2004**, *60*, m375–m381; b) F. H. Allen, *Acta Crystallogr., Sect. B* **2002**, *58*, 380–388.
[14] a) P. N. W. Baxter, J.-M. Lehn, K. Rissanen, *Chem. Commun.* **1997**, 1323–1324; b) P. N. W. Baxter, J.-M. Lehn, B. O. Kneisel, D. Fenske, *Chem. Commun.* **1997**, 2231–2232.
[15] a) M. C. Burla, M. Camalli, B. Carrozzini, G. L. Cascarano, C. Giacovazzo, G. Polidori, R. Spagna, *J. Appl. Crystallogr.* **2003**, *36*, 1103; b) P. W. Betteridge, J. R. Carruthers, R. I. Cooper, K. Prout, D. J. Watkin, *J. Appl. Crystallogr.* **2003**, *36*, 1487.

Received: May 20, 2005
Published Online: September 12, 2005

 © 2005 Wiley-VCH Verlag GmbH & Co. KGaA, Weinheim

Free and Metal-Coordinated (*N*-Isocyanimino)triphenylphosphorane: X-ray Structures and Selected Reactions

Heribert Stolzenberg,[a][‡] Bernd Weinberger,[a] Wolf Peter Fehlhammer,*[b,c] Frank G. Pühlhofer,[d][‡‡] and Robert Weiss[d][‡‡]

Keywords: Chromium / Isocyanide ligands / Isomerisation / Phosphoranes / Tungsten / Quantum chemical calculations

An improved procedure for the synthesis of (*N*-isocyanimino)-triphenylphosphorane, C≡N–N=PPh_3 (**3**), is described. The X-ray structure analysis reveals an unusually small N–N=P angle [115.2(2)°] and an N–N bond order of only about 1.5, which indicates considerable C≡N–N^-–P^+ participation and electronically more-isolated functional groups (CN, P=N) in the isocyanide than, for example, in the isomeric N≡C–N=PPh_3 (**4**) [C–N=P = 123.0(4)°, C–N bond order = 2.0]. In order to gain insight into the stereochemical consequences of metal coordination of **3**, an X-ray structural study of [Cr-$(CO)_5$C≡N–N=PPh_3] (**5**) was also undertaken. Surprisingly, the central bond lengths (C–N, N–N) and angles (C–N–N) remain practically unchanged with noticeable coordination effects occurring only at the periphery of **5**, with the N–N–P angle [112.3(2)°] further decreased by 15σ, the elongated (by 7σ) P–N bond, the somewhat shortened (by 4σ) P–C(Ph) bonds and even shorter C–H(Ph) bonds on the one side, and the well-known Cr–$C(O)_{trans}$ contraction on the other. Treatment of **5** or its tungsten derivative with anhydrous Brønstedt and Lewis acids such as CF_3COOH, HCl, COS, phosgene or, most efficiently, [$PdCl_2$(1,5-COD)] causes CN→NC isomerisation to give [$M(CO)_5$N≡C–N=PPh_3] [M = Cr (**6**), W (**7**)]. In solution, [$PdCl_2(CNNPh_3)_2$] and $Ph_3BCNNPPh_3$ (**8**) slowly isomerize even without additional acid to give both free and Pd-coordinated **4** and $Ph_3BNCNPPh_3$ (**9**), respectively. In the presence of catalytic amounts of [$PdCl_2$(1,5-COD)], **3** is converted into **4** and the dimer Ph_3PN–C(CN)=N–$NPPh_3$ (**10**) in an almost 1:1 ratio. The optimised geometries of the methyl derivatives of **3** and **4**, namely Me_3P=N–N≡C (**3c**) and Me_3P=N–C≡N (**4c**), are in excellent agreement with the experimental data; major differences between the isomers (P–N–N angle, N–N bond length) are explained by the higher electronegativity of the isocyano group as compared to the CN substituent, which, in turn, is a better π-acceptor). The reaction path of the isomerisation of **3** to **4** (**3c** to **4c**) has also been studied computationally and been found to proceed via an [(P)=N^A–N≡C^A(N^A–C^A)] cyclic transition state. The overall process is exothermic by 50 kcal mol^{-1}.
(© Wiley-VCH Verlag GmbH & Co. KGaA, 69451 Weinheim, Germany, 2005)

Introduction

Despite occasional reports for almost 100 years now, *N*-isocyanides, i.e. species with the structural element C≡N–N, still remain an exotic class of compounds. This holds particularly true of the parent molecule, isodiazomethane, C≡N–NH_2 (**1**).[1] Its mere naming as something which it is *not*, viz. diazomethane, reflects the uncertainties and difficulties connected with the discovery and understanding of this very labile substance.[2] Staudinger, in search of diisocyan, CN–NC, obviously was the first to get hold of **1**, and very remarkably assigned it the correct structure of an isocyanoamine.[3] Later, for more than 30 years, alternative constitutions were favoured, and it was not until 1968 that Müller et al. returned to Staudinger's formula.[2,4] In the mid-1970s, the first metal complexes of **1** were synthesised in our laboratory both from Müller's isodiazomethane solutions and, much more elegantly, from a stable, storable derivative, Wiberg's C≡N–N($SiMe_3$)$_2$ (**2**), by hydrolysis at the protecting metal.[5,6] The only disadvantage of **2** was its problematic accessibility, requiring many steps and costly low-temperature techniques. In 1980 we reported a novel precursor of **1** which is synthesised in a one-step procedure from cheap starting materials and actually proved to be a key substance in *N*-isocyanide chemistry.[7,8] In the following we present an improved preparation of C≡N–$NPPh_3$ (**3**), its X-ray structure in comparison with that of its pentacarbonylchromium complex, and its metal-catalysed CN/NC-isomerisation and dimerisation reactions. In addition, quantum chemical calculations have been carried out to get more insight into the electronic and structural properties of

[a] Institut für Anorganische Chemie der Universität Erlangen-Nürnberg,
Egerlandstraße 1, 91054 Erlangen, Germany
[b] Institut für Anorganische und Analytische Chemie der Freien Universität Berlin,
Fabeckstraße 34–36, 14195 Berlin, Germany
[c] Present address: Department Chemie und Biochemie der Ludwig-Maximilians-Universität München,
Butenandtstr. 5–13, 81377 München, Germany
E-mail: wpfehlhammer@gmx.de
[d] Institut für Organische Chemie der Universität Erlangen-Nürnberg,
Henkestraße 42, 91054 Erlangen, Germany
[‡] X-ray structure determinations.
[‡‡] Quantum chemical computations.
Supporting information for this article is available on the WWW under http://www.eurjic.org or from the author.

 DOI: 10.1002/ejic.200500196 © 2005 Wiley-VCH Verlag GmbH & Co. KGaA, Weinheim

compounds **3** and **4** and the reaction path of their respective isomerisation.

Results

(*N*-Isocyanimino)triphenylphosphorane: Synthesis and X-ray Structure

The title compound was prepared by reaction of *N*-formyl hydrazine with two equivalents of Appel's three-component reagent, which serves two purposes, viz. dehydration of the formamido group and masking of the primary amine function [Equation (1)].[7]

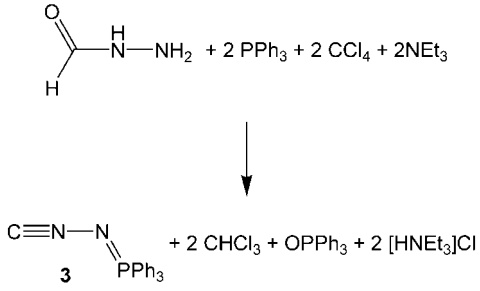

(1)

Repetition of the procedure as published, however, turned out to be difficult, and in only a few cases could yields of the claimed order of magnitude be reached. As reasons presumably responsible for this problem we have identified an incomplete reaction and decomposition of the desired product during work-up (vide infra). Taking this into account, in the modified procedure refluxing of the reaction mixture is prolonged and immediately followed by basic hydrolysis (with aqueous Na_2CO_3) of the highly acidic phosphorus(v) intermediates (e.g. $Ph_3PCl^+Cl^-$) and separation of the organic layer (containing **3**) from the aqueous one (see Experimental Section).

Single crystals suitable for an X-ray structure analysis were grown by slowly cooling a solution of **3** in warm ethanol. The molecule shows the expected bent structure at the imino nitrogen N1 (Figure 1). Structural investigations of iminophosphoranes generally reveal a considerable flexibility of this nitrogen as regards its hybridisation. P=N–X angles ranging from 119° up to 137° indicate that this is primarily sp^2 with a tendency to higher *s* participation. The unusually small angle in **3** [115.2(2)°] conversely points to more *p*-character (i.e. some $C^-{\equiv}N^+{-}N^-{-}P^+Ph_3$ form), which causes the phosphorus and the isocyano nitrogen atoms to get as close as 2.494 Å which is actually the shortest nonbonding distance between non-hydrogen atoms in this crystal structure.

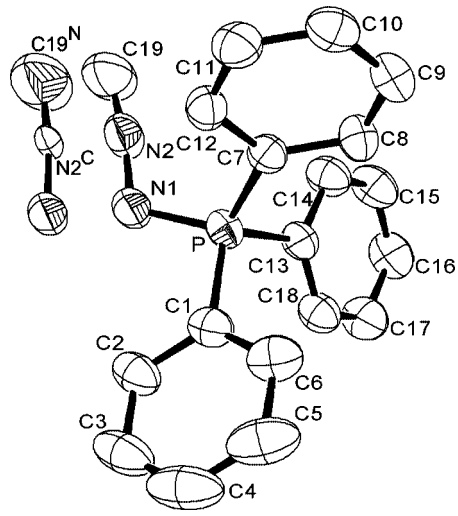

Figure 1. ORTEP drawing of the molecular structure of **3** (30% probability). The effect on the thermal ellipsoids of the functional group of a refinement cycle with interchanged scattering factors for C19 and N2 ("CN/NC test") is also shown. Both the abnormal blowing up of C19 (treated as an N atom) and the odd shrinkage of N2 (calculated as C) clearly exclude the cyanide form of **3**, as does the *R* value which increased by 0.34%. Selected bond lengths [Å] and angles [°]: P–N1 1.604(2), P–$C_{av.}$ 1.797, N2–N1 1.345(4), N2–C19 1.154(4); P–N1–N2 115.2(2), N1–N2–C19 173.4(3).

Interestingly, the corresponding P=N–C angle [123.0(4)°] in the isomeric cyanoiminophosphorane **4** (Scheme 1) is much wider, while the C≡N and P=N bond lengths are identical with those in **3** within one or two standard deviations.[9] Furthermore, the CN distances agree perfectly with the rated value for an ideal CN triple bond, and both PN bonds come very close to a true PN double bond (1.57 Å) as derived from experimental data.[10] Another major difference occurs in the remaining bonds, however. The N1–N2 bond distance in **3** [1.345(4) Å] lies halfway between an NN single (1.44 Å) and an NN double bond (1.24 Å), while the C–N(imine) bond in **4**, which is formally a single bond, is only slightly longer than a typical CN double bond (1.27 Å). The two functional groups (C≡N and P=N) are thus electronically more isolated in the isocyanide **3** than in the cyano isomer **4**, an observation which has been made many times in systems of the type C≡N(N≡C)–X=Y. A more realistic description of the bonding in **4** – although not in **3** (!) – might therefore make use of a further resonance formula such as **4a**.

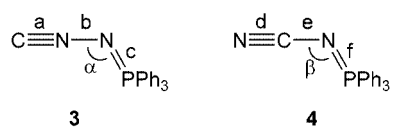

Scheme 1. Schematic formulae with selected bonding parameters (bond lengths in Å): *a* = 1.154(5), *b* = 1.345(4), *c* = 1.604(2) Å, *α* = 115.2(2)°; *d* = 1.151(9), *e* = 1.301(7), *f* = 1.595(4) Å, *β* = 123.0(4)°.

Deviations from a tetrahedral configuration at the P atom in **3** are marginal. The phenyl rings show the well-known propeller-like arrangement with dihedral angles rel-

 © 2005 Wiley-VCH Verlag GmbH & Co. KGaA, Weinheim

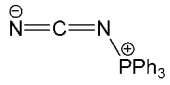

4a

ative to the P–N1–N2–C19 plane of 18.3° (Ph1), 69.8° (Ph2) and –69.6° (Ph3).

The intermolecular contacts (≤ 3.5 Å) were also calculated. With the exception of a weak N···H–C bridge between a phenyl hydrogen and N1, which also shows strong intramolecular interactions with two hydrogen atoms, none of the contacts lies substantially below the sum of the corresponding van der Waals radii.

X-ray Structure of Pentacarbonyl[(*N*-isocyanimino)-triphenylphosphorane]chromium (5): Stereochemical Consequences of Metal Coordination

Metal coordination of a stable isocyanide is routine, and C≡N–N=PPh_3 (**3**) is no exception. Preparation of the chromium complex **5** proceeds by substitution of THF in the photolytic intermediate [$Cr(CO)_5$THF];[7,8] suitable crystals for the X-ray study were obtained from dichloromethane.

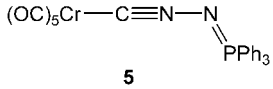

5

Figure 2 presents the overall geometry as expected for the combination of the functional *N*-isocyanide ligand **3** and the metal complex fragment $Cr(CO)_5$, together with selected bonding parameters. The first point of interest is the stereochemistry of the $Cr(CO)_5$ entity, which reflects the ligand properties of the incoming group. While all of the CO ligands experience the donating capacity of a typical isocyanide ligand, it is the *trans*-CO ligand which has to take the lion's share of the electronic charge transported onto the metal. In the present case the result is particularly striking: the Cr–$(CO)_{trans}$ bond in **5** is shortened to 1.861(3) Å as compared, for example, to that in $Cr(CO)_6$ (1.918 Å) or those of $Cr(CO)_5$ adducts of several other functional isocyanides such as [$Cr(CO)_5CNCH_2C(Me)(CH_2NC)_2$] [1.882(2) Å],[11] [$Cr(CO)_5CNC{\equiv}N$] [1.913(4) Å],[12] [$Cr(CO)_5$-CNC(=O)Ph] [1.899(3) Å][13] and [$Cr(CO)_5CNC{\equiv}CPh$] [1.896(4) Å],[14] while the average Cr–$(CO)_{cis}$ distance in **5** only drops to 1.895 Å. A much less significant effect, yet one pointing in the same direction, is the corresponding lengthening of the C–O bonds, which again is more pronounced for $(C–O)_{trans}$ [1.140(4) Å] than for the averaged $(C–O)_{cis}$ (1.135 Å).

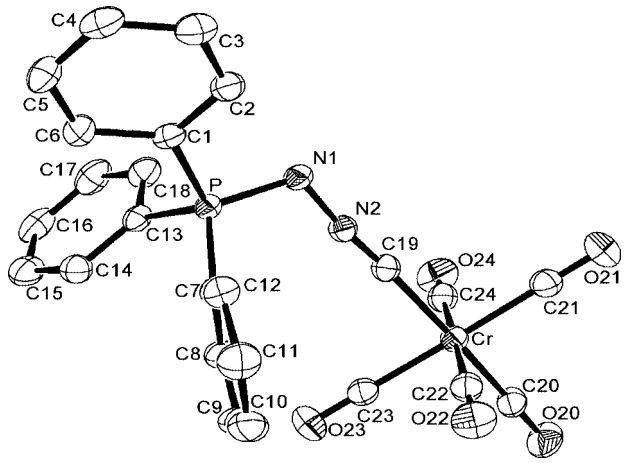

Figure 2. ORTEP drawing of the molecular structure of **5** (30% probability). The isocyanide nature of the ligand was ascertained by a "CN/NC test" (cf. caption of Figure 1), which resulted in unrealistic temperature factors and an increase of the *R* value by 0.66%. Selected bond lengths [Å] and angles [°]: P–N1 1.618(2), $P–C_{av.}$ 1.787, N2–N1 1.345(3), N2–C19 1.151(4), Cr–C19 2.031(3), Cr–$C20_{trans}$ 1.861(3), $(Cr–C_{cis})_{av.}$ 1.895, $(C20–O20)_{trans}$ 1.140(4), $(C–O)_{cis,av.}$ 1.135; P–N1–N2 112.3(2), N1–N2–C19 174.2(2), Cr–C19–N2 176.9(2).

The Cr–CN bond length is 2.031(3) Å, which fits well into the range of 2.00–2.05 Å determined so far for pentacarbonyl(*N*-isocyanide)chromium complexes. This is long in comparison with the corresponding values for [$Cr(CO)_5$(*C*-isocyanide)] complexes [*d*(Cr–CNC) < 2.00 Å] and clearly indicates a lower degree of π back-bonding.

Turning to the new ligand itself, which, according to what we know from the stereochemistry of the CrC_6 surrounding, is a markedly better donor than common *C*-isocyanides, we were surprised to find its central skeleton practically unchanged: the C≡N and N–N bond lengths are absolutely identical in **3** and **5**, and the 3σ deviation in the quasi-linearity of the C–N–N atomic sequence is insignificant; again, coordination effects are noticed only at the periphery of $CNNPPh_3$ [as they appeared – most distinctly – at the other end of the molecule, namely the remote *trans*-CO ligand (see above)]: the more acute N–N–P angle of 112.3(2)° [–2.9° (15σ)], which brings the P and N2 atoms even closer together, the slight elongation [by 0.014 Å (7σ)] of the P–N bond and, remarkably, the somewhat shortened P–C(Ph) bonds [–0.010 Å (4σ)]. All these data point to a considerable $Ph_3P^+–N^––N^+C[M^–]$ participation in the overall bonding in **5** by which extra electronic charge is transferred to $M(CO)_5$. Obviously, the N–N bond is not as insulating as inferred from a comparison with the nitrile **4** (**4a**) earlier on. These findings are perhaps best understood in terms of Gutmann's "pile up" and "spill over" effects accompanying Lewis acid–Lewis base interactions.[15]

Selected Reactions

CN/NC Isomerisations of (N-Isocyanimino)-triphenylphosphorane Complexes

The action of aqueous trifluoroacetic acid on $CNNPPh_3$ coordinated to pentacarbonyl–group VI metal fragments

 © 2005 Wiley-VCH Verlag GmbH & Co. KGaA, Weinheim

proceeds with hydrolysis of the (imino)N–P bond to give isodiazomethane complexes, occasionally in excellent yield (group VI metal = chromium).[7,8] A totally different reaction occurs, however, when $[Cr(CO)_5CNNPPh_3]$ (**5**) is treated with anhydrous acids: when allowed to stand for 1–2 days a solution of **5** in dichloromethane containing a few drops of CF_3COOH undergoes complete conversion of the isocyanide ligand into its nitrile isomer to form **6**.

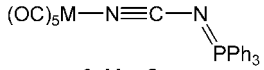

6: M = Cr
7: M = W

The same effect can be achieved by passing a stream of dry HCl through a solution of **5**. While protic acids seem not to prompt the corresponding tungsten complex to isomerize, Lewis acids like COS and $COCl_2$ are effective with both metal complexes. Even more sophisticated Lewis acids such as $[PdCl_2(1,5\text{-COD})]$ work if the reaction is carried out under a CO atmosphere. Thus, under 1 bar of CO **5** isomerizes quantitatively within 3–4 days, whereas in a rotating autoclave under a CO pressure of 10 bar the transformation is complete in 24 h. Without carbon monoxide, Pd metal separates slowly from the solution, which then turns deep green. Complexes **6** and **7** were adequately characterised by their analytical and IR spectroscopic data (see Experimental Section); the data of **6** are in full agreement with the data reported for the compound which has earlier been synthesised directly by photolysis of hexacarbonylchromium in the presence of $NCNPPh_3$.[16]

At palladium(II), **3** isomerizes without the need for any additional acid. After two weeks two strong new bands appear at 2230 and 2180 cm^{-1} in the IR spectrum of a solution of $[PdCl_2(CNNPPh_3)_2]$[8] in dichloromethane in place of the very weak original ν(CN) (2200 cm^{-1}). Of these, the absorption at 2180 cm^{-1} can unambiguously be assigned to the free $NCNPPh_3$, while the band at 2230 cm^{-1} fits into the range of palladium-coordinated nitrile species.

With equimolar amounts of triphenylboron, **3** forms an almost colourless crystalline adduct **8** which is air-stable and soluble in chlorinated hydrocarbons. In the IR spectrum, the weak CN stretch of the free ligand at 2067 cm^{-1} has been replaced by a new weak band at much higher wavenumbers (2230 cm^{-1}). As frequency shifts even of this order of magnitude are quite possible for isocyanide–BPh_3 adducts − for the corresponding (*N*-isocyanodialkylamine)triphenylboron species $Ph_3B–CN–NR_2$, $\Delta\nu(CN)$ $[\nu(CN)_{complex} - \nu(CN)_{free}]$ amounts to 135 cm^{-1}[17] − we can be sure that we are still dealing with the isocyanide isomer. In the end, this was unequivocally confirmed by its slow conversion in chloroform into **9**, which exhibits a very strong IR absorption at even higher wavenumbers (2280 cm^{-1}).

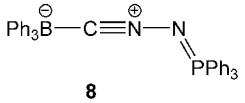

8

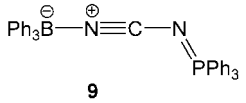

9

CN ⇌ NC isomerisations in both directions are by no means rare.[18] What is surprising here, though, is how spontaneously and smoothly they occur under the applied mild reaction conditions. It is true that these kinds of isomerisations are very common in cyanometal coordination polymers and are known to happen immediately by what has been termed a "flip-over" mechanism, however, the organic synthesis of nitriles by isomerisation of free *C*-isocyanides requires severe heating over a longer period.[19] Obviously, the involvement of at least one metal (or metalloid, e.g. $SiMe_3$[18,20]) is essential for the activation energy to be sufficiently small. Strangely enough, this is particularly born out by the functional *N*-isocyanide under consideration, which, as a free ligand, cannot be transformed into its isomer at all, either thermally, say by refluxing in THF or chloroform, or by protonation.

If we accept a synchronous mechanism with a "rotating" C≡N species between the fixed metal and $NPPh_3$ groups, or, which comes down to the same thing, a migration of these groups about a stationary C≡N, perhaps via some bicyclic transition state of the type **A**, it seems plausible that the addition of an acid (Brønsted or Lewis) to the imino nitrogen greatly enhances the (less pronounced) migration tendency of the iminophosphorane group (as $HN{=}PPh_3$). At any rate, in the absence of an acid the $[M(CO)_5CNNPPh_3]$ complexes do not show any sign of isomerisation even after standing for weeks in various solvents.

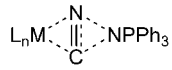

A

A closely related case of a CN → NC isomerisation to the one presented here is the rearrangement of a coordinated fulminate into an isomeric isocyanate ligand. This reaction occurred on attempted protonation of difulminatobis(triphenylphosphane)platinum to produce the then unknown isofulminic acid (C≡N–OH) stabilized in a complex.[21] Later, we studied the spontaneous isomerisation of $[W(C{\equiv}N–O)(CO)_5]^-$ and found it to be strongly solvent-dependent.[22]

Catalytic Isomerisation and Dimerisation of 3

From the findings discussed above, it was obvious that we should study the possibility of a catalytic isomerisation of **3** with traces of a metal component. As such, $[PdCl_2(1,5\text{-COD})]$ was chosen and found to produce complete disappearance of the weak ν(CN) band at 2067 cm^{-1} within 20 h at ambient temperature. What appeared, however, were two absorptions at 2180 and 2220 cm^{-1} instead of the only one expected. Work-up finally resulted in two products: the isomeric (*N*-cyanoimino)triphenylphosphorane (**4**), which has already been synthesised by Appel and co-workers and was identified on the basis of its elementary analysis, its melting point and its IR data,[23,24] and a second pale -yellow compound **10**, which was recrystallised from dichloromethane/diethyl ether and showed the same analytical composition but double the molecular mass. The IR spectrum with a

 © 2005 Wiley-VCH Verlag GmbH & Co. KGaA, Weinheim

weak to medium intensity band at 2200 cm^{-1} [ν(C≡N)], a ν(C=N) absorption at 1520 cm^{-1} and two ν(P=N) features at 1110 [ν(P=N–N)] and 1300 cm^{-1} [ν(P=N–C)], as well as the ^{31}P NMR spectrum, which contains two singlets at δ = 24 and 11 ppm, are in perfect agreement with the suggested structure for **10**.

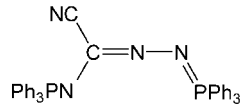

10

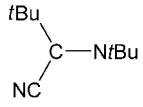

11

A catalytic dimerisation of isocyanides has so far only been reported in one case, that of *tert*-butyl isocyanide with trace amounts of BF_3 to give **11**.[25] On the other hand, there are numerous examples of stoichiometric C-C couplings of *C*-bonded species in the ligand spheres of metal complexes,[26] with Lippard's reductive dimerisation of *tert*-butyl isocyanide ligands in $[Mo(CNtBu)_6I]I$ to give **B** being among the first.[27] Still, for the case at hand it seems most plausible to assume a mechanism **C** in analogy to that of the well-known metal-catalysed α-additions to isocyanides (or isocyanide insertions), which proceed via a primary nucleophilic attack at the metal-bonded isocyano carbon.[28] Actually, all the necessary "instruments" are there: thus, we have shown that *N*-isocyanides are prone to nucleophilic attack even in less activating metal complexes,[8,29] **3** carries a strong nucleophile in the form of the imino nitrogen, and N–N cleavage is a common occurrence in *N*-isocyanide chemistry.[17,30,31]

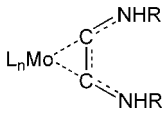

B (R = *t*Bu)

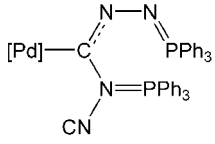

C

Computational Section

Quantum chemical calculations were performed to gain a detailed insight into the electronic and structural properties of the compounds **3** and **4**. To simplify the problem, the phenyl substituents in **3** and **4** were replaced by methyl groups, and the geometries of the resulting compounds **3c** and **4c** were optimised at the B3LYP/6-311+G** level of theory. ZPEs were determined at the same level. The frequencies were also analysed at this level to confirm that the optimised geometries correspond to minima (NIMAG = 0) or first-order transition states (NIMAG = 1). A transition-state search was performed using the QST3 method. NBO analyses were performed at the above-mentioned level of theory. All computations were run using the Gaussian98W suite of programs and NBO 3.1, as implemented in G98W.[32]

Discussion

Table 1 contains selected stereochemical parameters of compounds **3**, **3c**, **4** and **4c**. In general, the differences between the bond lengths and angles of the phenyl-substituted systems **3** and **4**, as obtained from X-ray analyses, and the data computed for the corresponding methyl species (**3c** and **4c**) are minor and easily explained by the exchange at P1 of phenyl for methyl (cf. Figure 3 and Table 1). Thus, the elongation of the P1–N1 bonds in **3c** and **4c** is clearly a consequence of the decreased electron-acceptor capacity of the trimethylphosphonio moiety. Other points of interest are the deviations between **3c** and **4c** (**3** and **4**, respectively), especially those of the P1–N1–X angles (**3**, **3c**: X = NC; **4**, **4c**: X = CN).

Table 1. Comparison of the experimental bonding parameters of **3** and **4** with those obtained from geometry optimisation (B3LYP/6-311+G**) (**3c**, **4c**).

Bond length [Å]	**3**	**3c** (*Cs*)	**4**	**4c** (*Cs*)
P1–N1	1.604	1.620	1.595	1.600
N1–N2	1.345	1.342		
N1–C1			1.301	1.318
C1–N2	1.154	1.176	1.151	1.167
Bond angle [°]				
P1–N1–N2	115.2	114.5		
P1–N1–C1			123.0	121.8

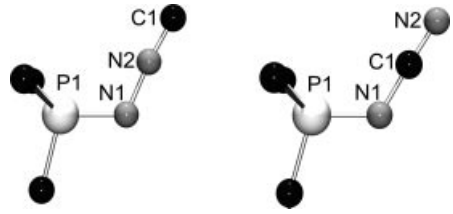

Figure 3. Representative structural elements in **3** (**3c**) (left) and **4** (**4c**) (right).

The exchange of N2 by the less electronegative C1 in **3c** (to give **4c**) changes the electronic nature of N1. NBO analyses assume N1 in both compounds to carry a lone pair of *p*-character oriented perpendicular to the symmetry plane of **3c** and **4c**. This results in an overall hybridisation of sp^2 for the remaining three substituents of N1 in this plane: the PMe_3 group, the second lone pair and the -NC (**3c**) or -CN (**4c**) group. The specific breakdown of the overall sp^2 hybridisation into the contributions of N1 to each bond results in the data listed in Table 2. The most noticeable changes are obviously caused by very different hybridisations of the lone pair and the bond to the (iso)cyano group, whereas the hybridisation of the N1–P1 bond remains nearly unchanged. The former can easily be explained by Bent's rule:[33] electronegative substituents force the central atom (N1) to increase the *p*-character of the corresponding bond. The isocyano substituent in **3c** is clearly more electronegative than the cyano function in **4c**, which results in the very different orbital hybridisations of N1 in the two N1–X bonds (Table 2). As a result, the P1–N1–N2

 © 2005 Wiley-VCH Verlag GmbH & Co. KGaA, Weinheim

angle in **3c** is smaller than the P1–N1–C1 angle in **4c**. In **3c**, both bonds (P1–N1 and N1–N2) have contributions from N1 hybridisations with *p* coefficients close to 3.0, hence the P1–N1–N2 angle is expected to be way below 120° (computed: 114.5°). In **4c**, the average hybridisation of the respective two bonds is $sp^{2.1}$ (cf. Table 2), which should give rise to an angle of about 120° (computed: 122°). These values are in excellent agreement with the corresponding X-ray data of the phenyl derivatives **3** (115°) and **4** (123°; Table 1).

Table 2. Orbital hybridisation of N1 based on NBO analyses (B3LYP/6-311+G**).

	3c (X = NC)	**4c** (X = CN)
N1–PMe_3	$sp^{2.8}$	$sp^{2.5}$
N1–X	$sp^{2.9}$	$sp^{1.7}$
Lone pair (in plane)	$sp^{1.1}$	$sp^{1.9}$

As described above, the N1–N2 bond in **3** lies halfway between an N-N single and an N-N double bond, whereas the N1–C1 bond in **4** is much closer to a C-N double bond. The same observations are made in the case of the computed structures **3c** and **4c**, and can again be explained on the basis of NBO analyses: both lone pairs of N1 interact with the two mutually perpendicular π*-orbitals of the C1–N2 bond. Since the π-bonds between C1 and N2 are polarized towards the nitrogen atom, the π*-orbitals have larger coefficients at C1, and hence the cyano group in **4c** is a much better π-acceptor than the isocyano function in **3c**. The respective donor–acceptor interactions were computed at the B3LYP/6-311+G** level resulting to be about 63 kcal mol^{-1} for **4c** and 33 kcal mol^{-1} for **3c**. The experimentally observed pronounced multiple-bond character of the N1–CN bond in **4** is thus confirmed computationally.

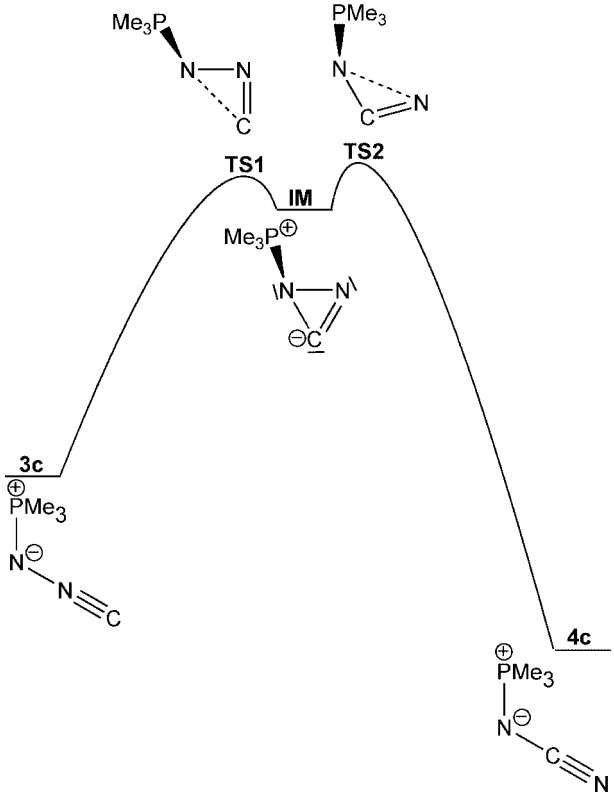

Figure 4. Reaction profile of the isomerisation of **3c** to **4c** at the B3LYP/6-311+G** level (including uncorrected ZPE at the same level).

Finally, the reaction path of the isomerisation of **3** to **4** (**3c** to **4c**) was studied computationally using the QST3 method as implemented in Gaussian98W. The reaction profile is shown qualitatively in Figure 4, quantitative details are given in Table 3, and geometric parameters of TS1, TS2 and IM are given in Figure 5 (see also Supporting Information).

Table 3. Relative energies of the species in Figure 3 (B3LYP/6-311+G** incl. uncorrected ZPE).

	Relative energy [kcal mol^{-1}]
3c	+50.3
TS1	+81.7
IM	+79.8
TS2	+82.1
4c	±0.0

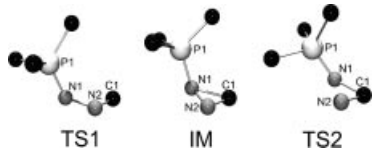

Figure 5. Geometrical data of TS1, IM and TS2 (bond lengths in Å). TS1: P1–N1 1.631, N1–N2 1.556, N1–C1 2.018, N2–C1 1.215; N1–N2–C1 92.7°. IM: P1–N1 1.646, N1–N2 1.613, N1–C1 1.681, N2–C1 1.234; N1–N2–C1 71.0°, N1–C1–N2 65.1°. TS2: P1–N1 1.629, N1–N2 1.861, N1–C1 1.597, N2–C1 1.215; N1–C1–N2 81.7°.

As shown in Figure 4, the reaction proceeds with formation of a new σ-bond between the $2p_z$ lone pair at N1 and the terminal carbon atom, via the transition state TS1 (E_a = 31.4 kcal mol^{-1}), to the cyclic intermediate IM. The latter reacts with cleavage of the N–N bond via TS2 (E_a = 2.3 kcal mol^{-1}) to the rearrangement product **4c**. The overall process is exothermic by 50.3 kcal mol^{-1} (cf. Table 3).

The experimentally observed lowering of the activation energy for the isomerisation by addition of Lewis acids can also be explained on this basis: the formation of donor–acceptor complexes between the intermediate IM and Lewis acids stabilizes the former by decreasing the repulsive interactions of lone pairs (see Figures 4 and 5).

Experimental Section

General Remarks: All experiments were performed under argon in dry, argon-saturated solvents. The (*N*-isocyanimino)triphenylphosphorane metal complexes [$M(CO)_5CNNPPh_3$] [M = Cr (**5**), W] and [$PdCl_2(CNNPPh_3)_2$] were prepared according to literature procedures.[7,8] IR spectra were recorded on a Perkin–Elmer 621 or a Beckman IR 12 spectrometer. NMR spectra (^{31}P) were recorded on a Jeol JNM-PS-100. Mass spectra were recorded on a Varian CH-5 (excitation energy 70 eV). Microanalyses (C,H,N) were obtained with a Heraeus CHN Rapid-Elementanalysator. Molecular

 © 2005 Wiley-VCH Verlag GmbH & Co. KGaA, Weinheim

weights were determined in CH_2Cl_2 solution using a Knauer Dampfdruck Osmometer, and melting or decomposition points were determined with a Büchi Model 510 melting point apparatus and are uncorrected.

Preparation of (*N*-Isocyanimino)triphenylposphorane (3). Revised Procedure: CH_2Cl_2 (600 mL), PPh_3 (157.4 g, 0.6 mol), NEt_3 (freshly distilled from KOH; 50.6 g, 0.5 mol) and formylhydrazine (dried in high-vacuum at 45 °C; 15.3 g, 0.25 mol) were placed in a reaction flask which had been dried with a heat-gun under high-vacuum. The slurry was then heated to 50–60 °C, and CCl_4 (77.0 g, 0.5 mol) was added dropwise over a period of about 30 min. The mixture was kept at 50–60 °C for at least 5–6 h. After cooling to room temp., 250 mL of a saturated aqueous Na_2CO_3 solution was added, the layers were separated, and the aqueous layer was washed with two 50-mL portions of CH_2Cl_2. The combined organic phases were dried with Na_2SO_4 and filtered. After evaporation of the solvent, the residue was dried under high vacuum, pulverised, stirred in 200 mL of ethanol/water (1:1.5) and collected on a frit. Recrystallisation from hot ethanol yielded 30.2 g (40%) of an orange-brown crystalline material (m.p. 159–160 °C, dec.). IR (KBr): $\tilde{\nu}$ = 2067 cm^{-1} w [ν(CN)]; 1117 s, 1099 sh [ν(PN)]. $C_{19}H_{15}N_2P$ (302.32): calcd. C 75.49, H 5.00, N 9.27; found C 75.69, H 4.99, N 9.40.

CN/NC-Isomerisation of Pentacarbonyl[(*N*-isocyanimino)triphenylphosphorane]chromium (5) with Protic Acids and COS: A few drops (8–10) of CF_3COOH were added, with stirring, to a solution of $[Cr(CO)_5CNNPPh_3]$ (**5**; 1.48 g, 3.0 mmol) in dry CH_2Cl_2 (25 mL). After standing for 48 h at room temp. the volatile components were removed under high vacuum and the residue was dissolved in a small amount of CH_2Cl_2 and chromatographed on silica gel in *n*-hexane (3.5 × 20 cm column) with a CH_2Cl_2/*n*-hexane (3.5:1) eluent. Slow evaporation of the bright yellow phase resulted in the cyano isomer **6** as yellow to green crystals.

Similar results were obtained by (a) passing a rapid stream of dry HCl through the above solution for a few seconds and keeping it at room temp. for 14 h, and (b) by treating a solution of $[Cr(CO)_5CNNPPh_3]$ (1.48 g, 3.0 mmol) in THF (30 mL) with an excess of COS at 45 °C for 24 h and applying the same work-up procedure to the reaction mixtures. The yields (non-optimised) varied between 30 and 70% (see also below).

CN/NC-Isomerisation of Pentacarbonyl[(*N*-isocyanimino)triphenylphosphorane]chromium (5) with $[PdCl_2(1,5\text{-COD})]$. Preparation of Pentacarbonyl[(*N*-cyanimino)triphenylphosphorane]chromium (6): (a) $[Cr(CO)_5CNNPPh_3]$ (**5**; 990 mg, 2 mmol) and $[PdCl_2(1,5\text{-COD})]$ (290 mg, 1 mmol) were dissolved in 90 mL of toluene/CH_2Cl_2 (2:1) under a CO atmosphere and stirred for one week at room temp. Every two days the CO atmosphere was renewed. After evaporation of the solvent, the residue was extracted with diethyl ether. The extract was filtered and concentrated, and the product **6** crystallised on cooling to about –35 °C as yellow-green crystals. Yield: 60%.

(b) A mixture of **5** (1.98 g, 4.0 mmol) and $[PdCl_2(1,5\text{-COD})]$ (580 mg, 2.0 mmol) in 60 mL of toluene/CH_2Cl_2 (2:1) was placed in a 500-mL rotation autoclave and reacted under a CO pressure of 10 atm for 2 d. The work-up procedure was the same as in (a) and yielded 1.4 g (71%) of yellow-green crystalline **6**, m.p. 107 °C (dec.; ref.[16] 102–106 °C). IR (KBr): $\tilde{\nu}$ = 2240 cm^{-1} s [ν(NC)]; 2065 s, 1920 vs, 1870 sh [ν(CO)]; 1260 s, br. [ν(PN)]. $C_{24}H_{15}CrN_2O_5P$ (494.4): calcd. C 58.31, H 3.06, N 5.67; found C 58.49, H 3.07, N 5.55.

CN/NC-Isomerisation of Pentacarbonyl[(*N*-isocyanimino)triphenylphosphorane]tungsten. Preparation of 7: $COCl_2$ (30 mL of a 0.1 M solution in THF) was added to a solution of $[W(CO)_5CNNPPh_3]$ (940 mg, 1.5 mmol) in 30 mL of CH_2Cl_2. After stirring for 2 h at room temp., the solvent was removed in vacuo and the raw product was dissolved in a few millilitres of CH_2Cl_2. Cooling to about –35 °C gave 432 mg (48%) of **7** as yellow-green crystals, m.p. 125 °C (dec.). IR (KBr): $\tilde{\nu}$ = 2230 cm^{-1} s [ν(NC)]; 2060 m, 1905 vs, br., 1870 sh [ν(CO)]; 1280 s, br. [ν(PN)]. $C_{24}H_{15}N_2O_5PW$ (626.22): calcd. C 46.03, H 2.41, N 4.47; found C 45.89, H 2.39, N 4.62.

CN/NC-Isomerisation of (*N*-Isocyanimino)triphenylphosphorane at BPh_3

Preparation of [(*N*-Isocyanimino)triphenylphosphorane]triphenylborane (8): A solution of $CNNPPh_3$ (**3**; 906 mg, 3.0 mmol) in 35 mL of CH_2Cl_2 was added dropwise to a solution of BPh_3 (730 mg, 3.0 mmol) in 30 mL of CH_2Cl_2 at 0 °C. After stirring for 1.5 h at 0 °C the product was precipitated with petroleum ether and stored overnight at –18 °C to give **8** (1.2 g, 74%) as off-white crystals, m.p. 153 °C (dec.). IR (KBr): $\tilde{\nu}$ = 2225 cm^{-1} w [ν(CN)]; 1190 sh, 1150 sh, 1120 vs, br. [ν(PN)]. $C_{37}H_{30}BN_2P$ (544.5): calcd. C 81.63, H 5.55, N 5.15; found C 81.63, H 5.87, N 4.88. Compound **8** is thermally stable in the solid state and can be kept under nitrogen at room temp.

CN/NC Isomerisation of [(*N*-Isocyanimino)triphenylphosphorane]triphenylborane. Preparation of [(*N*-Cyanimino)triphenylphosphorane]-triphenylborane (9): A solution of **8** (1.09 g, 2.0 mmol) in 10 mL of $CHCl_3$ was stored for 2 weeks at room temp. After evaporation of the solvent the crude material was treated with ethanol. The insoluble white powder (**9**) was filtered off and dried in high vacuum. Yield: ca. 600 mg (55%). IR (KBr): $\tilde{\nu}$ = 2280 cm^{-1} vs, 2085 sh [ν(NC)]; 1350 s, 1320 sh [ν(PN)]. $C_{37}H_{30}BN_2P$ (544.5): calcd. C 81.63, H 5.55, N 5.15; found C 80.03, H 5.80, N 5.14.

Catalytic Isomerisation and Dimerisation of (*N*-Isocyanimino)triphenylphosphorane (3). Preparation of (*N*-Cyanimino)triphenylphosphorane (4) and $(CNNPPh_3)_2$ (10): A catalytic amount of $[PdCl_2(1,5\text{-COD})]$ (29 mg, 0.1 mmol) was added, with stirring, to a solution of $CNNPPh_3$ (**3**; 3.25 g, 10.75 mmol) in 40 mL of CH_2Cl_2. Stirring was continued for 20 h at room temp., after which time the solvent was removed in vacuo and the residue stirred in 30 mL of ethanol for 1 h. The insoluble yellow product was filtered off and recrystallised from CH_2Cl_2/Et_2O to give 1.6 g (50%) of pure **10**, m.p. 221 °C (dec.). IR (KBr): $\tilde{\nu}$ = 2220 cm^{-1} w [ν(NC)]; 1300 s, br., 1275 sh, 1130 sh, 1110 s, br. [ν(PN)]; 1540 s, 1480 w, 1140 s, 1040 sh, 1030 s. $C_{38}H_{30}N_4P_2$ (604.60): calcd. C 75.49, H 5.00, N 9.27, P 10.25; found C 75.81, H 5.05, N 9.21, P 10.14. Mol. mass calibrated against PPh_3: 616.

The brown ethanolic solution was evaporated to dryness and the solid residue was dissolved in 10 mL of warm CH_2Cl_2. Compound **4** (1.45 g, 45%) separated in the form of a light-brown powder at 0 °C, m.p. 188 °C (dec.). [ref.[23,24] 192–196 °C (dec.)]. IR (KBr): $\tilde{\nu}$ = 2180 cm^{-1} vs [ν(NC)]; 1270 s, br. [ν(PN)]. $C_{19}H_{15}N_2P$ (302.3): calcd. C 75.49, H 5.00, N 9.27; found C 74.73, H 5.07, N 9.18.

X-ray Structure Determinations: Single crystals of **3** were obtained by slowly cooling a warm ethanol solution of **3**; those of **5** were grown from dichloromethane. Crystallographic data of **3** and **5** were collected on a Philips PW1100 diffractometer in the ω–2θ scan mode using Ag-K_α radiation (λ = 0.5596 Å) and a graphite monochromator (Table 4). The phase problem in **3** was solved by direct methods, and that of **5** by applying the heavy atom approach. Neither absorption nor extinction corrections were carried out. In both cases, all hydrogen positions could be obtained from ΔF syntheses yet were not included in the final cycles of refinement. All calculations were carried out using the program system SHELX-76[34] with scattering factors for neutral atoms taken from the literature.[35] The molecular plots were produced with the ORTEP program.[36]

 © 2005 Wiley-VCH Verlag GmbH & Co. KGaA, Weinheim

Table 4. Crystal data and structure refinement of **3** and **5**.

	3	**5**
Empirical formula	$C_{19}H_{15}N_2P$	$C_{24}H_{15}CrN_2O_5P$
Formula mass	302.3	494.4
Crystal size [mm]	0.4×0.3×0.15	0.4×0.3×0.2
Crystal system	monoclinic	monoclinic
Space group	$P2_1/n$	$P2_1/a$
a [Å]	9.680(2)	12.817(5)
b [Å]	16.602(4)	15.431(3)
c [Å]	10.356(2)	12.536(4)
β [°]	110.55(1)	116.03(4)
V [Å^3]	1558.38	2227.86
Z	4	4
$\rho_{calcd.}$ [Mg m^{-3}]	1.288	1.473
$\mu_{(Ag\text{-}K_\alpha)}$ [cm^{-1}]	0.94	2.80
$F(000)$	632	1008
Temperature [K]	293	233
2θ range for data collection [°]	13.62–49.42	3.10–47.64
Reflections collected	9661	10721
Independent reflections	2180	4921
R_{int} [%]	0.0511	0.0419
Observed reflections	1835 [$I \geq 2.5\sigma(I)$]	3691 [$I \geq 2.5\sigma(I)$]
Weighting scheme	$w = 1/[\sigma^2(F_o) + 9\times10^{-5}F_o^2]$	$w = 1/[\sigma^2(F_o) + 10^{-6}F_o^2]$
R_1/wR_2 [$F > 4\sigma(F)$]	0.0439/0.0426	0.0409/0.0397

CCDC-279551 (for **3**) and -279552 (for **5**) contain the supplementary crystallographic data for this paper. These data can be obtained free of charge from The Cambridge Crystallographic Data Centre via www.ccdc.cam.ac.uk/data_request/cif.

Supporting Information: Gaussian98W archive entries and cartesian coordinates of all computed species.

Acknowledgments

Financial support for this work by the Fonds der Chemischen Industrie, the Deutsche Forschungsgemeinschaft and the BAYER AG is gratefully acknowledged. We also thank Professor Joachim Fuchs of the Institut für Anorganische und Analytische Chemie der Freien Universität Berlin for his assistance in the X-ray structure determinations and Professor Wolfgang Beck from the Department Chemie und Biochemie der Ludwig-Maximilians-Universität München for helpful discussions.

[1] J.-P. Anselme, *J. Chem. Educ.* **1966**, *43*, 596–598; J.-P. Anselme, *J. Chem. Educ.* **1977**, *54*, 296–297.
[2] E. Müller, H. Disselhoff, *Justus Liebigs Ann. Chem.* **1934**, *512*, 250–263; E. Müller, W. Kreutzmann, *Justus Liebigs Ann. Chem.* **1934**, *512*, 264–275; E. Müller, D. Ludsteck, *Chem. Ber.* **1954**, *87*, 1887–1895; E. Müller, W. Rundel, *Chem. Ber.* **1957**, *90*, 1302–1309; E. Müller, *Newer Perspectives in Organic Chemistry*, 2nd ed., Springer, Berlin, **1957**, p. 454.
[3] H. Staudinger, O. Kupfer, *Ber. Dtsch. Chem. Ges.* **1912**, *45*, 501–509.
[4] E. Müller, P. Kästner, R. Beutler, W. Rundel, H. Suhr, B. Zeeh, *Justus Liebigs Ann. Chem.* **1968**, *713*, 87–95; E. Müller, R. Beutler, B. Zeeh, *Justus Liebigs Ann. Chem.* **1968**, *719*, 72–79.
[5] W. P. Fehlhammer, P. Buraças, K. Bartel, *Angew. Chem.* **1977**, *89*, 752–753; *Angew. Chem. Int. Ed. Engl.* **1977**, *16*, 707–708.
[6] N. Wiberg, G. Hübler, *Z. Naturforsch., Teil B* **1976**, *31*, 1317–1321.
[7] B. Weinberger, W. P. Fehlhammer, *Angew. Chem.* **1980**, *92*, 478–479; *Angew. Chem. Int. Ed. Engl.* **1980**, *19*, 480–481.
[8] W. P. Fehlhammer, *Nachr. Chem. Tech. Lab.* **1982**, *30*, 187–189; B. Weinberger, W. P. Fehlhammer, *Chem. Ber.* **1985**, *118*, 42–50; B. Weinberger, F. Degel, W. P. Fehlhammer, *Chem. Ber.* **1985**, *118*, 51–65; B. Weinberger, G. Zinner, W. P. Fehlhammer, in *Organometallic Syntheses* (Eds.: R. B. King, J. J. Eisch), Elsevier, Amsterdam **1988**, *4*, 87–91.
[9] J. Kaiser, H. Hartung, R. Richter, *Z. Anorg. Allg. Chem.* **1980**, *469*, 188–196.
[10] D. E. C. Corbridge, *The Structural Chemistry of Phosphorus*, Elsevier, Amsterdam, **1974**.
[11] F. E. Hahn, M. Tamm, *Chem. Ber.* **1992**, *125*, 119–121.
[12] G. Christian, H. Stolzenberg, W. P. Fehlhammer, *J. Chem. Soc., Chem. Commun.* **1982**, 184–185.
[13] P. J. Le Marouille, P. Caillet, *Acta Crystallogr., Sect. B* **1982**, *38*, 267–269.
[14] R. Kunz, W. P. Fehlhammer, *Angew. Chem.* **1994**, *106*, 331–333; *Angew. Chem. Int. Ed. Engl.* **1994**, *33*, 330–332.
[15] V. Gutmann, *The Donor–Acceptor Approach*, Plenum Press, New York, **1978**, p. 37.
[16] H. Bock, H. tom Dieck, *Z. Anorg. Allg. Chem.* **1966**, *345*, 9–22.
[17] W. P. Fehlhammer, R. Metzner, W. Sperber, *Chem. Ber.* **1994**, *127*, 631–637.
[18] W. P. Fehlhammer, M. Fritz, *Chem. Rev.* **1993**, *93*, 1243–1280.
[19] Review: Ch. Rüchardt, M. Meier, K. Haaf, J. Pakusch, E. K. A. Wolber, B. Müller, *Angew. Chem.* **1991**, *103*, 907–915; *Angew. Chem. Int. Ed. Engl.* **1991**, *30*, 893–901.
[20] F. Beck, PhD Thesis, University of Erlangen-Nürnberg, Germany, **1980**.
[21] W. Beck, *Organomet. Chem. Rev. Sect. A* **1971**, *7*, 159–190; W. Beck, K. Schorpp, C. Oetker, *Chem. Ber.* **1974**, *107*, 1380–1388.
[22] F. Beck, W. P. Fehlhammer, W. Beck, *J. Organomet. Chem.* **1985**, *279*, C22–C24.
[23] I. Ruppert, R. Appel, *Chem. Ber.* **1978**, *111*, 751–758. See also: H. Köhler, B. Kotte, *Z. Chem.* **1973**, *13*, 350.
[24] See also: G. Zinner, G. Beck, W. P. Fehlhammer, N. Wiberg, *J. Organomet. Chem.* **1989**, *368*, 23–30.
[25] H.-J. Kabbe, *Angew. Chem.* **1968**, *80*, 406; *Angew. Chem. Int. Ed. Engl.* **1968**, *7*, 389.
[26] In the SciFinder Scholar **2004** edition (ACS), 354 references were found containing the concept carbon–carbon coupling and metal complexes.
[27] C. T. Lam, P. W. R. Corfield, S. J. Lippard, *J. Am. Chem. Soc.* **1977**, *99*, 617–618.
[28] E. M. Badley, J. Chatt, R. L. Richards, *J. Chem. Soc., Chem. Commun.* **1969**, 1322–1323; E. M. Badley, J. Chatt, R. L. Rich-

ards, *J. Chem. Soc. A* **1971**, 21–25; *Isonitrile Chemistry* (Ed.: I. Ugi), Academic Press, New York, **1971**; K. R. Dixon, A. C. Dixon, in *Comprehensive Organometallic Chemistry II* (Eds.: E. W. Abel, F. G. A. Stone, G. Wilkinson), Elsevier, Oxford, **1995**, *9*, p. 193.
[29] W. P. Fehlhammer, R. Metzner, P. Luger, Z. Dauter, *Chem. Ber.* **1995**, *128*, 1061–1068.
[30] W. P. Fehlhammer, R. Metzner, R. Kunz, *Chem. Ber.* **1994**, *127*, 321–327.
[31] W. P. Fehlhammer, R. Metzner, W. Sperber, *Chem. Ber.* **1994**, *127*, 829–833.
[32] M. J. Frisch, G. W. Trucks, H. B. Schlegel, G. E. Scuseria, M. A. Robb, J. R. Cheeseman, V. G. Zakrzewski, J. A. Montgomery Jr., R. E. Stratmann, J. C. Burant, S. Dapprich, J. M. Millam, A. D. Daniels, K. N. Kudin, M. C. Strain, O. Farkas, J. Tomasi, V. Barone, M. Cossi, R. Cammi, B. Mennucci, C. Pomelli, C. Adamo, S. Clifford, J. Ochterski, G. A. Petersson, P. Y. Ayala, Q. Cui, K. Morokuma, D. K. Malick, A. D. Rabuck, K. Raghavachari, J. B. Foresman, J. Cioslowski, J. V. Ortiz, A. G. Baboul, B. B. Stefanov, G. Liu, A. Liashenko, P. Piskorz, I. Komaromi, R. Gomperts, R. L. Martin, D. J. Fox, T. Keith, M. A. Al-Laham, C. Y. Peng, A. Nanayakkara, C. Gonzalez, M. Challacombe, P. M. W. Gill, B. Johnson, W. Chen, M. W. Wong, J. L. Andres, M. Head-Gordon, E. S. Replogle, J. A. Pople, *Gaussian 98*, Revision A.7, Gaussian, Inc., Pittsburgh PA, **1998**.
[33] H. A. Bent, *Chem. Rev.* **1961**, *61*, 275–311.
[34] G. M. Sheldrick, *SHELX-76 Program*, Univ. of Cambridge, UK, **1976**.
[35] D. T. Cromer, J. T. Waber, *International Tables for X-ray Crystallography*, Kynoch Press, Birmingham, UK, **1974**, vol.4.
[36] C. K. Johnson, *ORTEP*, Rep. ORNL-5138, Oak Ridge National Laboratory, Oak Ridge, TN, USA, **1976**.

Received: March 4, 2005
Published Online: September 19, 2005

 © 2005 Wiley-VCH Verlag GmbH & Co. KGaA, Weinheim

(Salen)nickel-Catalysed Epoxidations in the Homogeneous and Heterogeneous Phase: The Implications of Oxygen on the Efficiency and Product Selectivity

Rita Ferreira,[a][‡] Hermenegildo García,[b] Baltazar de Castro,[a] and Cristina Freire*[a]

Keywords: Alkenes / Epoxidation / Heterogeneous catalysis / N,O ligands / Nickel / Zeolites

The catalytic activity of several nickel(II) complexes with salen-type ligands and their zeolite-immobilised analogues is assessed in the epoxidation of *trans*-β-methylstyrene by NaOCl, in the absence and in the presence of oxygen. The complexes were immobilised in zeolites X and Y using the "ship-in-a-bottle" procedure, and the resulting materials were characterised by chemical analysis, XPS and IR, and UV/Vis diffuse reflectance spectroscopy. The loading and the distribution of the complexes in the materials were found to be dependent on the ligand. All (salen)nickel complexes proved to be active in the homogeneous and heterogeneous epoxidation of *trans*-β-methylstyrene by NaOCl. The immobilised complexes gave lower conversions and their catalytic activity is dependent on the loading and distribution of the complexes within the zeolites. In both homogeneous and heterogeneous systems, the alkene conversion is influenced by oxygen. Removing oxygen from the reaction media results in lower alkene conversion but higher epoxide selectivity. Based on these results, two competitive mechanisms are proposed for the epoxidation reaction, one implying the formation of free radicals and other involving the binding of the substrate to a (oxo)metal intermediate.
(© Wiley-VCH Verlag GmbH & Co. KGaA, 69451 Weinheim, Germany, 2005)

Introduction

The use of transition metal complexes as catalysts for the epoxidation of alkenes has been a subject of interest in the past few decades due to the increasing use of epoxides in agro- and pharmacological chemistry.[1] A large number of publications concern the use of the (salen)Mn complexes developed by Katsuki and Jacobsen as highly enantioselective catalysts in the epoxidation of alkenes.[2–4] In these studies, oxidants such as *tert*-butyl hydroperoxide and iodosylbenzene are often employed, although lately the use of environmentally more friendly oxidants such as H_2O_2 and NaOCl has been pursued.

Although (salen)nickel(II) complexes have not been as widely investigated as their manganese analogues, earlier studies by Burrows and co-workers, and later by Kureshy, proved that nickel complexes with cyclam and salen ligands are also active catalysts in the epoxidation of alkenes.[5–10]

The immobilisation of transition metal complexes in solid supports has intrinsic practical advantages, namely the heterogenised catalysts are easy to handle and can be reused.[11,12] Transition metal complexes can be immobilised in several supports such as zeolites,[13] activated carbon[14] and pillared clays.[15] Recently, we demonstrated that (salen)-manganese complexes immobilised in carbon and pillared clays can be used as heterogeneous catalysts in epoxidation reactions without significant loss in their catalytic activity upon re-use.[16–18]

The immobilisation and employment of (salen)nickel complexes in heterogeneous catalysis has not been extensively explored. Some examples include the use of (salen)-Ni-type complexes in faujasites for the oxidation of phenol with H_2O_2[19] and for the epoxidation of cyclohexene and 1-hexene by NaOCl.[20,21] A more recent study concerned the use of [Ni(salen)] immobilised in several solid supports as a catalyst for hydrogenation reactions.[22]

This paper exploits the use of (salen)Ni^{II} complexes as homogeneous catalysts and, after immobilisation in zeolites X and Y, as heterogeneous catalysts in the epoxidation of *trans*-β-methylstyrene by NaOCl. Zeolites X and Y have a crystalline faujasite-type structure composed of small pores (diameter 7 Å), which access internal cavities with a diameter of 13 Å. This topology originates two special properties: (i) zeolites can act as molecular sieves, and (ii) they can be hosts by accommodating and restricting molecules inside the cavities. When considering the potential use of zeolites as supports for catalysts, the above characteristics can result in very important features such as reactant/product size-and-shape selectivity and the possibility to host metal complexes that have proved to be good catalysts in solution. Nevertheless, it is noteworthy that the catalyst performance

[a] REQUIMTE/Departamento de Química,
Rua do Campo Alegre, 4169-007 Porto, Portugal
Fax: +351-22-608-2959
E-mail: acfreire@fc.up.pt
[b] Instituto de Tecnología Química, UPV-CSIC,
Av. de los Naranjos s/n, 46022 Valencia, Spain
[‡] Present address: ESTG-Instituto Politécnico de Viana do Castelo,
Av. do Atlântico, 4900-348 Viana do Castelo, Portugal
E-mail: rferreira@estg.ipvc.pt

 © 2005 Wiley-VCH Verlag GmbH & Co. KGaA, Weinheim **DOI: 10.1002/ejic.200500314**

can be affected by the immobilisation in a solid material with its own physical and chemical properties.

Four different (salen)Ni^{II} complexes (Scheme 1) were encapsulated in both zeolites X and Y using the "ship-in-a-bottle" procedure[23] accomplished by the "flexible ligand" approach. This two-step synthesis consists of (i) the introduction of Ni^{II} cations by ion exchange and (ii) solvent-free diffusion of the ligands, followed by complexation with the nickel ions. The four (salen)nickel(II) complexes meet the requirements needed for this method of immobilisation because their ligands have a suitable size to diffuse through the pores and reach the cavities containing the metal ions.

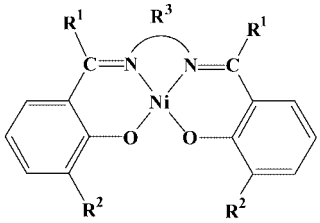

		R^1	R^2	R^3
1	[Ni(salen)]	H	H	CH_2CH_2
2	[Ni(salhd)]	H	H	*cyclo*-C_6H_{10} (*cis*/*trans* mixture)
3	[Ni(α,α′-Me_2salen)]	CH_3	H	CH_2CH_2
4	[Ni(3-MeOsalen)]	H	CH_3O	CH_2CH_2

Scheme 1. Structure of (salen)nickel(II) complexes.

The catalytic activity of the materials was then tested in the epoxidation of *trans*-β-methylstyrene by NaOCl and compared with the results obtained for the complexes in the homogeneous phase. In order to understand the effect of molecular oxygen, a possible co-oxidant, all the reactions were performed in the presence and in the absence of oxygen. These experiments have enabled us to obtain insights into the mechanism of the alkene epoxidation by nickel complexes.

Results and Discussion

Materials Characterisation

The ship-in-a-bottle synthesis resulted in an efficient loading of the nickel complexes inside the zeolites. The loading of the complexes and their distribution within the material was deduced from the nickel content determined by bulk chemical analysis and from XPS. Table 1 presents the nickel content of the materials (wt.-% Ni) obtained by chemical bulk analysis and the Ni/Si ratio obtained by chemical analysis and by XPS.

Table 1. Nickel content (% weight) obtained by chemical analysis (CA) and Ni/Si ratios obtained by chemical analysis (CA) and XPS for the immobilised (salen)nickel(II)complexes.

Catalyst	wt.-% Ni (CA)	Ni/Si CA	Ni/Si XPS
[Ni(salen)]@X	1.0	0.040	0.176
[Ni(salhd)]@X	1.9	0.053	0.142
[Ni(α,α′-Me_2salen)]@X	1.0	0.033	0.196
[Ni(3-MeOsalen)]@X	1.8	0.050	0.161
[Ni(salen)]@Y	1.0	0.019	0.101
[Ni(salhd)]@Y	1.3	0.055	0.074
[Ni(α,α′-Me_2salen)]@ Y	0.4	0.011	0.117
[Ni(3-MeOsalen)]@Y	1.5	0.031	0.074

The results in Table 1 show that the amount of complex and its distribution within the solids differs with the size of the complex and with the zeolite type. Loadings between 0.4 and 1.8 wt.-% Ni were obtained, but generally zeolite X presents a slightly higher complex content than zeolite Y. This is explained by the higher number of exchangeable cations present in the parent NaX (Na/Si = 0.7) when compared with NaY (Na/Si = 0.4), which results in a higher number of Ni^{II} cations in the cavities and, consequently, a higher complex loading.

In both zeolites X and Y, the complexes [Ni(3-MeOsalen)] and [Ni(salhd)] have a higher content inside the zeolites. Also, the distribution of the complexes depends on the ligand type. All the complexes show a higher Ni/Si ratio by XPS than by chemical analysis, pointing to a preferential location of the complexes in the outer layers. This difference is more significant for [Ni(salen)] and [Ni(α,α′-Me_2salen)], suggesting that these complexes occupy more the surface layers while [Ni(3-MeOsalen)] and [Ni(salhd)] are more uniformly distributed.

The preferential location in the outer layers could be due to diffusion of the complexes out of the inner cavities, probably during the extraction step.

The IR spectra of the solids were recorded and compared with the IR spectra of the corresponding free complexes. Figures 1a and 1b show the IR spectra of [Ni(salen)]@X and [Ni(salen)]@Y, respectively, in the region 2000–1000 cm^{-1}. For comparison, the spectra of the parent materials, NiX, NiY, and of [Ni(salen)] are also included. All the materials present intense bands in this region due to zeolite lattice vibrations (1200–1000 cm^{-1}) and a large band centred at 1620 cm^{-1} attributed to adsorbed water.[24]

The characteristic bands of the complex are observed in the region between 1600 and 1200 cm^{-1}, where the zeolites do not absorb, and represent the ν(C=N), ν(C=C), ν(C–C) and ν(C–O) vibrations. The frequencies of these vibrations are practically coincident with those of the complexes, thus providing evidence for their presence inside the zeolites without significant interaction with the matrixes.

The encapsulation of the complexes was also confirmed by UV/Vis diffuse reflectance. Figures 2a and b display typical UV/Vis diffuse reflectance spectra of [Ni(salen)]@X and [Ni(salen)]@Y, respectively. The spectra of the corresponding original materials, NiX and NiY, and of [Ni(salen)] are included for comparison.

 © 2005 Wiley-VCH Verlag GmbH & Co. KGaA, Weinheim

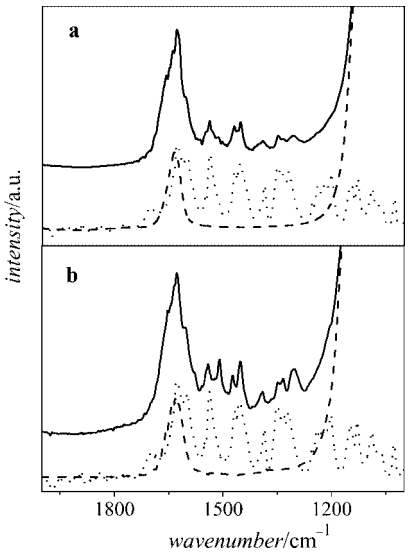

Figure 1. a) IR spectra of [Ni(salen)]@X (solid line), [Ni(salen)] free complex (dotted line) and the parent NiX (dashed line), and b) IR spectra of [Ni(salen)]@Y (solid line), [Ni(salen)] free complex (dotted line) and the parent NiY (dashed line).

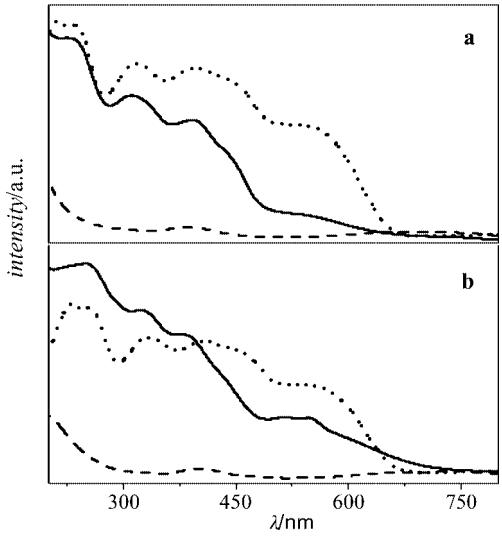

Figure 2. a) UV/Vis solid-state diffuse reflectance spectra of [Ni(salen)]@X (solid line), [Ni(salen)] (dotted line) and NiX (dashed line), and b) UV/Vis solid-state diffuse reflectance spectra of [Ni(salen)]@Y (solid line), [Ni(salen)] (dotted line) and NiY (dashed line).

All the materials exhibit bands in the range λ = 300–700 nm. The bands with $\lambda_{max} < 450$ nm were attributed to charge-transfer bands. Characteristic d-d bands appear at 510–560 nm in the spectra of the free complexes as well as in the spectra of the zeolite-immobilised complexes. However, the materials show slight shifts of the transition bands in relation to the free complexes, thus suggesting some degree of distortion around the metal centre, probably induced by the immobilisation.

Homogeneous Catalysis

The catalytic activity of the four (salen)nickel(II) complexes was first studied in the homogeneous phase (substrate/catalyst ratio = 0.025:1, in dichloromethane) with NaOCl as oxidant. The experiments were run in the presence and in the absence of oxygen. Figure 3 shows the alkene conversion as a function of the reaction time for the epoxidation of *trans*-β-methylstyrene catalysed by [Ni(salen)], [Ni(salhd)], [Ni(α,α′-Me$_2$salen)] and [Ni(3-MeOsalen)] in the presence of oxygen. It is clear from this figure that all complexes are active catalysts in the reaction. The conversion follows a sigmoid curve with an induction period of about 1 h, and reaches maximum conversion after 10 h. The presence of an induction period suggests that the oxidant efficiency is limited.[25]

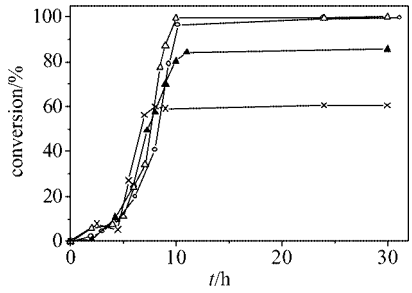

Figure 3. Conversion vs. time plot of the epoxidation of *trans*-β-methylstyrene with NaOCl catalysed by [Ni(salen)] (Δ), [Ni(salhd)] (○), [Ni(α,α′-Me$_2$salen)] (▲) and [Ni(3-MeOsalen)] (×) in the presence of oxygen.

Figure 4 shows the alkene conversion as a function of the reaction time obtained in the epoxidation of *trans*-β-methylstyrene catalysed by [Ni(salen)], [Ni(salhd)], [Ni(α,α′-Me$_2$salen)] and [Ni(3-MeOsalen)], in the absence of oxygen. All the complexes are also active in the absence of oxygen and the evolution with time pursues a similar pattern as observed in the presence of oxygen: a sigmoidal curve with an induction period, although the reaction is slower and the time needed to reach the maximum conversion is about 20 h. The induction period is higher in this case, and dependent on the complex. Table 2 summarises the results obtained after 24 h for the reactions catalysed by the nickel(II) complexes in the homogeneous phase under aerobic or anaerobic conditions.

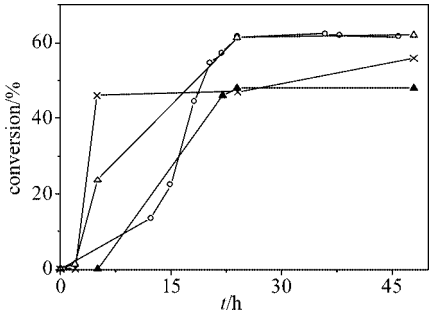

Figure 4. Conversion vs. time plot of the epoxidation of *trans*-β-methylstyrene with NaOCl catalysed by [Ni(salen)] (Δ), [Ni(salhd)] (○), [Ni(α,α′-Me$_2$salen)] (▲) and [Ni(3-MeOsalen)] (×) in the absence of oxygen.

Alkene conversions of between 61 and 100% were obtained in the presence of oxygen and between 47 and 65%

 © 2005 Wiley-VCH Verlag GmbH & Co. KGaA, Weinheim

Table 2. Epoxidation reactions with the free complexes in the presence and absence of oxygen.[a]

Catalyst	O_2[b]	Conv. [%][c]	Selectivity [%] (Yield [%])		
			Epoxide[d]	Benzaldehyde	Others
[Ni(salen)]	present	100	54 (54)	9 (1)	37 (4)
[Ni(salhd)]	present	99	54 (54)	11 (11)	35 (3)
[Ni(α,α′-Me_2salen)]	present	84	58 (49)	11 (9)	31 (26)
[Ni(3-MeOsalen)]	present	61	52 (32)	12 (7)	36 (22)
[Ni(salen)]	absent	62	60 (37)	8 (5)	32 (20)
[Ni(salhd)]	absent	65	65 (42)	15 (10)	20 (13)
[Ni(α,α′-Me_2salen)]	absent	48	69 (33)	9 (4)	22 (11)
[Ni(3-MeOsalen)]	absent	47	47 (22)	9 (4)	44 (21)

[a] Solvent: CH_2Cl_2; alkene/catalyst ratio = 1.0:0.025; results after 24 h. [b] Oxygen is present as in normal atmosphere (1 atm). For the conditions in the absence of oxygen, see Exp. Sect. [c] Conversion (as disappearance of alkene) determined by GC using *n*-decane as internal standard. [d] Obtained as 100% *trans*-epoxide.

in its absence; epoxide was the major product but benzaldehyde and other products were also obtained.[26]

In the presence of oxygen, the reactions catalysed by [Ni(salen)] and [Ni(salhd)] show the highest conversion, reaching almost 100%. The introduction of two methyl groups at the α-imine carbon atom in [Ni(α,α′-Me_2salen)] decreases the conversion but does not affect the epoxide selectivity. The effect of an electron-donor group in the third position of the aldehyde fragment is more significant: the methoxy group in [Ni(3-MeOsalen)] decreases the conversion significantly (61%), although the epoxide selectivity is not affected. No significant changes were observed when the aliphatic imine bridge was substituted by a cyclohexyl bridge, as in [Ni(salhd)]. In general, the selectivity of the products does not seem to be dependent on the ligand: [Ni(α,α′-Me_2salen)] shows the highest value for the epoxide selectivity (58%) whereas [Ni(3-MeOsalen)] has the lowest value (52%).

For the reactions in the absence of oxygen, the alkene conversion is lower when compared with reactions under aerobic conditions (Table 2), but the complexes [Ni(salen)] and [Ni(salhd)] still present the highest values (62 and 65%, respectively) followed by [Ni(α,α′-Me_2salen)] (48%) and finally [Ni(3-MeOsalen)] (47%). On the other hand, the epoxide selectivity increases for all complexes except for the [Ni(3-MeOsalen)]-catalysed reaction. As observed for the reactions in the presence of oxygen, the highest epoxide selectivity was obtained for [Ni(α,α′-Me_2salen)], whereas [Ni(3-MeOsalen)] shows the lowest value. The dependency of the epoxide selectivity on the ligand is noteworthy, and is more significant when oxygen is absent.

Overall, the alkene conversion is higher and the reaction faster in the presence of oxygen, although the epoxide selectivity is higher in the absence of oxygen.

Reaction Mechanism

Salen-type complexes have been used in epoxidation reactions owing to their special coordination environment, which, like porphyrins, provides a square-planar geometry around the metal atom that allows reactants and/or oxidant to access the active centre. Although the oxidation mechanism through which the metal complexes act in an oxidation reaction is not completely understood, it is known that the reaction selectivity depends on how the oxygen atom is transferred to the alkene. A rebound mechanism involving the formation of a (oxo)metal intermediate and alkyl radicals has been proposed for Cytochrome P450, a (porphyrin)iron compound.[27] Recently, it has been proved that these short-lived radicals are mainly free in solution rather than being bound to the (oxo)metal species.[28]

The involvement of an (oxo)metal species of high oxidation state (M^{n+}=O; n = 3, 4 or 5) has also been proved for (salen)manganese- and -chromium-catalysed epoxidations.[29] In the case of the (salen)nickel-catalysed epoxidations, the formation of an (oxo)metal intermediate is consistent with the dependency of the alkene conversion with the ligand type, although, as suggested by Burrows and coworkers, another intermediate with a radical character can also be formed, namely Ni^{III}–O$^{\cdot}$. This species can instigate the formation of free radicals that compete in the oxidation of the substrate and, therefore, result in reactions with low epoxide selectivity (Scheme 2, mechanism A).[6,9] Alternatively, the alkene can bind to the (oxo)metal intermediate and different paths can then follow (Scheme 2, mechanism B).[30] In the case of epoxidations catalysed by (cyclam) nickel complexes, two main pathways have been suggested for the subsequent steps: (1) a concerted mechanism in which the substrate–(oxo)metal intermediate suffers a heterolytic cleavage leading to the desired epoxide, and (2) a stepwise pathway implying the formation of a carbocation or a carbon radical, which forms the product by homolytic cleavage. The heterolytic cleavage is known to afford high yields of epoxide, while the other preferably performs allylic oxidations;[31] both are summarised in Scheme 2.

On the basis of the catalytic results obtained in the absence and presence of oxygen, the formation of free radicals (mechanism A) cannot be excluded. Free radicals can capture oxygen and consequently enhance the reaction rate and alkene conversion;[32,33] therefore, a free-radical mechanism would explain the higher rates and alkene conversions observed for the reactions run under oxygen. On the other hand, the dissimilarity in product selectivity obtained with different complexes in the absence of oxygen points to the involvement of a substrate–(oxo)metal intermediate (mechanism B), which, through a concerted or a stepwise

 © 2005 Wiley-VCH Verlag GmbH & Co. KGaA, Weinheim

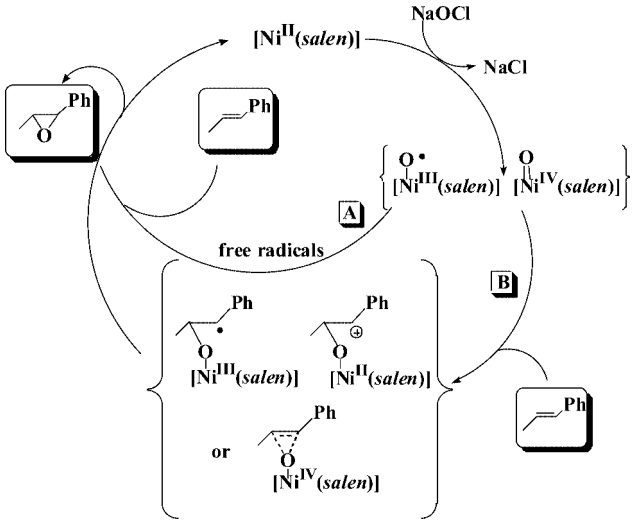

Scheme 2. Proposed mechanism for the *trans*-β-methylstyrene epoxidation by NaOCl with (salen)nickel(II) complexes.

mechanism, allows a good proximity of the substrate to the ligand. Also, as the carbon radical formed in the stepwise pathway in mechanism B is expected to be very sensitive to the presence of O_2, resulting in highly oxidised products (such as benzaldehyde), this mechanism could explain the lower epoxide selectivity observed in the reactions run in the presence of oxygen.

The substantially lower epoxide selectivity obtained with the complex that bears electron-donor substituents, [Ni(3-MeOsalen)], in the absence of oxygen is noteworthy. Studies on the epoxidation of alkenes by (salen)chromium complexes have shown that complexes bearing methoxy groups in the *ortho*-position to the hydroxy group of the salicylaldehyde moiety are easily destroyed by the oxidant.[34]

In this context, our results support the occurrence of two competitive mechanisms (Scheme 2): a mechanism where the (oxo)metal species originates free radicals that, in the presence of oxygen, cause higher and faster alkene conversions but indistinguishable epoxide selectivity (mechanism A), and a mechanism involving binding of the substrate to the (oxo)metal intermediate that, through a concerted or a stepwise pathway, results in lower conversions, but higher epoxide selectivity (mechanism B).

Mechanism A is favoured in the presence of oxygen, while mechanism B is favoured in its absence.

Heterogeneous Catalysis

To study the catalytic activity of the immobilised nickel(II) complexes, the epoxidation of *trans*-β-methylstyrene by NaOCl was carried out using the prepared materials as heterogeneous catalysts. The reactions were run under the same conditions as described for the homogeneous phase, using an amount of zeolite corresponding to the same substrate/catalyst ratio (1:0.025) in dichloromethane (see Exp. Sect.). As in the homogeneous phase, the reactions were performed in the presence and in the absence of oxygen.

Table 3 summarises the results obtained in the heterogeneous phase using the nickel complexes immobilised in zeolites X and Y, in the presence of oxygen.

Table 3. Results obtained for the heterogeneous catalysis in the presence of oxygen.[a]

Catalyst	Conv. [%][b]	Selectivity [%] (Yield [%])		
		Epoxide[c]	Benzaldehyde	Others
[Ni(salen)]@X	71	40 (28)	23 (16)	37 (26)
[Ni(salhd)]@X	27	28 (8)	27 (7)	45 (12)
[Ni(α,α′-Me_2salen)]@X	88	53 (47)	15 (13)	32 (28)
[Ni(3-MeOsalen)]@X	19	22 (4)	36 (7)	42 (8)
[Ni(salen)]@Y	30	34 (10)	16 (5)	50 (15)
[Ni(salhd)]@Y	44	48 (21)	23 (10)	28 (12)
[Ni(α,α′-Me_2salen)]@Y	62	45 (28)	22 (14)	33 (20)
[Ni(3-MeOsalen)]@Y	19	25 (5)	60 (11)	15 (3)

[a] Solvent: CH_2Cl_2; alkene/catalyst ratio = 1.0:0.025; results after 48 h. [b] Conversion (as disappearance of alkene) determined by GC using *n*-decane as internal standard. [c] Obtained as 100% *trans*-epoxide.

The reaction time increased significantly and thus the results in Table 3 refer to values obtained after 48 h. The results show that all the immobilised complexes are active in the epoxidation of the alkene, but the catalytic activity is lower than in the homogeneous reactions. The reactions catalysed by zeolites with [Ni(α,α′-Me_2salen)], which reached conversions close to those obtained in the homogeneous phase, are excluded from this conclusion. In fact, the maximum conversion (88%) among the heterogeneous catalysts was observed for [Ni(α,α′-Me_2salen)]@X, together with the highest epoxide selectivity.

Lower conversions and longer reactions times are usually observed on going from solution to immobilised catalysts due to the diffusion constraints imposed by the pore network.[18] Although the solid support can constitute a protective environment around the metal atom, the physical restrictions imposed by the zeolite can make the access of reactants to the metal centre more difficult and, as a result, the activity decreases.

In this case, a correlation between the catalytic activity of the complexes and their distribution within the solids confirms the effect of diffusion constraints: the complexes localised in the outer layers of the zeolites (see above), which therefore can be more easily accessed by the reactants, give higher catalytic activities.

Surprisingly, the epoxide selectivity was lower in all the heterogeneous reactions than in the homogeneous phase, resulting in higher benzaldehyde selectivity. The chemical microenvironment imposed by the zeolites could be the cause of this result. Epoxide ring opening in acidic media forms benzaldehyde, thus the acid character of the zeolites contributes to the lowering of the epoxide selectivity. Again, the zeolites that bear complexes closer to the surface, such as [Ni(α,α′-Me_2salen)]@X and [Ni(α,α′-Me_2salen)]@Y, are less affected by the zeolite characteristics and present nearly the same epoxide selectivity as in the homogeneous phase.

The effect of the zeolites' acidity in the reaction selectivity can be noted by comparing the epoxide selectivity ob-

 © 2005 Wiley-VCH Verlag GmbH & Co. KGaA, Weinheim

tained for a complex immobilised in zeolite X with the same complex immobilised in zeolite Y (Table 3). Apart from the other factors already discussed in this paper, the complexes in zeolite X have a higher epoxide selectivity than the complexes in Y, a zeolite with more acidic sites.

The activity of the immobilised catalysts was also evaluated in the absence of oxygen and the results are collected in Table 4. As observed for the homogeneous phase, the absence of oxygen results in lower conversions and higher epoxide selectivity, except for [Ni(3-MeOsalen)], which registers an increase in the conversion when compared with the reaction run under oxygen. Once more, as observed for the homogeneous system, this is the complex with the lowest epoxide selectivity, due to its fast decomposition in the reaction media.

Table 4. Results obtained for the heterogeneous catalysis in the absence of oxygen.[a]

Catalyst	Conv. [%][b]	Selectivity [%] (Yield [%])		
		Epoxide[c]	Benzaldehyde	Others
[Ni(salen)]@X	62	60 (37)	13 (8)	28 (17)
[Ni(salhd)]@X	13	41 (5)	7 (1)	52 (7)
[Ni(α,α′-Me_2salen)]@X	62	59 (37)	12 (7)	29 (18)
[Ni(3-MeOsalen)]@X	39	46 (18)	14 (5)	40 (16)
[Ni(salen)]@Y	48	60 (29)	18 (9)	22 (11)
[Ni(salhd)]@Y	43	59 (25)	14 (6)	27 (12)
[Ni(α,α′-Me_2salen)]@Y	64	64 (41)	16(10)	20 (13)
[Ni(3-MeOsalen)]@Y	32	38 (12)	31 (10)	31 (10)

[a] Solvent: CH_2Cl_2; alkene/catalyst ratio = 1.0:0.025; results after 48 h. [b] Conversion (as disappearance of alkene) determined by GC using *n*-decane as internal standard. [c] Obtained as 100% *trans*-epoxide.

The catalytic activity in the heterogeneous phase follows the same pattern as the homogeneous-phase reactions, hence we propose that the conclusions concerning the reaction mechanism drawn for the homogeneous system can be extended to the heterogeneous counterpart. In this context, the two mechanisms presented above are also competing in the heterogeneous reaction: a mechanism involving the formation of free radicals and a mechanism occurring through a substrate–(oxo)metal intermediate.

Re-Use of Heterogeneous Catalysts

The possibility to re-use [Ni(3-MeOsalen)]@X and [Ni(3-MeOsalen)]@Y was evaluated in the subsequent way: after the first run, the catalysts were filtered from the solution, washed with copious amounts of dichloromethane, dried and re-used according to the general procedure described for the heterogeneous reactions. The results of the re-utilisation and the relation with the first use are illustrated in Figure 5.

For [Ni(3-MeOsalen)]@X, the conversion is similar to that obtained in the first use (19%), but the epoxide selectivity shows a significant increase from 22% to 53%. In the case of [Ni(3-MeOsalen)]@Y, an increase in both conversion (from 19 to 30%) and epoxide selectivity (from 25 to 46%) was observed.

The immobilised catalysts show similar conversions in their re-use compared to their first utilisation: the conversion is equal or even higher than in the first use and there is an increase in the epoxide selectivity. These positive results can be attributed to a change in the overall chemical environment around the complex. In the first use the materials are in contact with NaOCl and a chemical modification from acidic to more basic environment might have occurred. This effect is more significantly reflected in the reactions catalysed by the zeolite with higher initial acidity (zeolite Y). Also, a possible migration of the complex to the outer surface layers of the zeolites cannot be excluded; this decreases the diffusion constraints and therefore favours an increase in conversion.

However, as [Ni(3-MeOsalen)] suffers decomposition in both homogeneous and heterogeneous media, additional experiments should be performed to reach safer conclusions about the catalysts' re-utilisation.

Conclusions

All the (salen)nickel(II) complexes are active catalysts in the epoxidation of *trans*-β-methylstyrene by NaOCl in homogeneous media, both in the presence and in the ab-

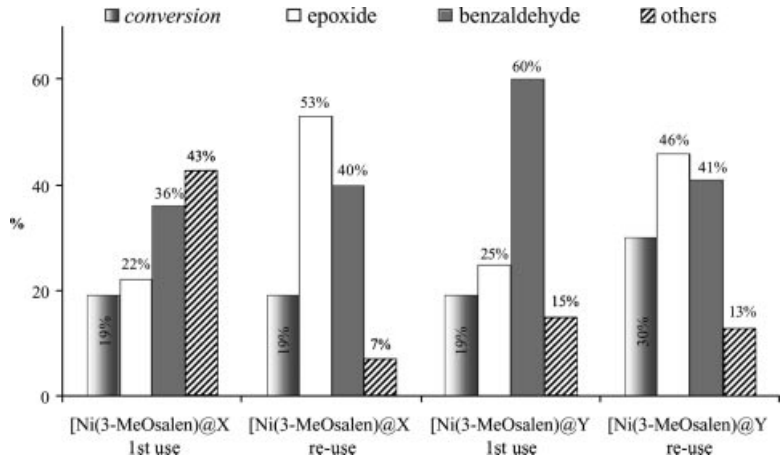

Figure 5. Conversion and selectivity obtained in the first use and in the re-use of [Ni(3-MeOsalen)]@X and of [Ni(3-MeOsalen)]@Y in the epoxidation of *trans*-β-methylstyrene by NaOCl.

 © 2005 Wiley-VCH Verlag GmbH & Co. KGaA, Weinheim

sence of oxygen. Conversions of up to 100% and epoxide selectivity of around 54% are obtained in the presence of oxygen. However, in the absence of oxygen, the reaction is slower, with lower conversions but with higher epoxide selectivity.

These results lead to a proposal of two simultaneous mechanisms for this reaction: a mechanism implying the formation of free radicals, which is favoured in the presence of oxygen, in competition with a mechanism where the substrate binds to an (oxo)metal intermediate. The first would lead to higher alkene conversions but lower and indistinguishable epoxide selectivity, while the other would result in higher epoxide selectivity dependent on the ligand, but lower conversions.

The immobilisation of the four nickel complexes in zeolites X and Y results in materials with different loading and distribution of the complexes. Complexes [Ni(salhd)] and [Ni(3-MeOsalen)] have higher loadings than [Ni(α,α′-Me_2-salen)] and [Ni(salen)]. The former are also more uniformly distributed than the latter, which are preferentially localised in the surface layers of the zeolites.

All the materials are active catalysts in the epoxidation of *trans*-β-methylstyrene by NaOCl, both in the presence of oxygen and in its absence, but the conversions are lower than in the homogeneous phase. The zeolites bearing the metal complexes closer to the surface give higher conversions than those having higher loadings, but a more uniform distribution of the complexes. These results can be explained by the physical restrictions imposed by the zeolite pore network, which makes the access of the reactants to the metal centre more difficult, resulting in lower activities. Furthermore, the zeolite chemical environment, namely its acidic character, influences the selectivity of the reaction. Nevertheless, the zeolites can constitute an important protective environment around the ligand and an opportunity to improve the catalyst life, i.e., by catalyst re-utilisation.

Experimental Section

Reagents and Solvents: The solvents used in the preparation of the complexes were of reagent grade and were used as received. Dichloromethane used in the epoxidation reactions was HPLC grade. An aqueous solution of NaOCl (available chlorine 10–13%, Aldrich) was used as oxidant. Salicylaldehyde, 2-hydroxy-3-methoxybenzaldehyde, 2′-hydroxyacetophenone and the diamines 1,2-cyclohexanediamine (as *cis*/*trans* mixture) and ethylenediamine were purchased from Aldrich. The substrate *trans*-β-methylstyrene was also purchased from Aldrich and *n*-decane was obtained from Fluka. Nickel acetate, nickel nitrate pentahydrate and sodium hydrogen phosphate were obtained from Merck. All reagents were used with no further purification, except the diamines, which were distilled prior to use. The GC standard epoxide was prepared by epoxidation of *trans*-β-methylstyrene with *m*-chloroperbenzoic acid (*m*-CPBA) at 4 °C and stored at that temperature. The phase-transfer catalyst benzyltributylammonium bromide was obtained from Fluka. The zeolites in their sodium form, NaY and NaX, were kindly provided by Grace GmbH (Germany) and were calcinated at 600 °C under oxygen before use.

Instrumentation: Silicon, aluminium, sodium and nickel contents were determined by Kingston Analytical Services (UK) by ICP-AES. The samples were previously treated by fusion with $LiBO_2$ and the mixture dissolved in nitric acid. Surface chemical analysis of the materials was performed by X-ray photoelectron spectroscopy at the Centro de Materiais da Universidade do Porto (Portugal) in a VG Scientific ESCALAB 200A spectrometer, using Mg-K_α radiation (1253.6 eV). Electronic spectra were recorded with a Shimadzu UV/3101PC spectrophotometer equipped with a $BaSO_4$ sphere and using the same salt as reference. FTIR spectra were recorded from KBr pellets of the materials or complexes with a JASCO FT/IR-460 Plus spectrometer. GC analysis was carried out with a Varian 3400 CX equipped with a fused silica Chrompack capillary column (30 m × 0.53 mm) and a TCD detector. The column temperature was programmed from 60 °C (3 min) to 170 °C, at a rate of 5 °C min^{-1}, and the injection temperature was 200 °C.

General Procedure for the Synthesis of Nickel Complexes: The ligands H_2salen, H_2(salhd), H_2(α,α′-Me_2salen) and H_2(3-MeOsalen) and the respective nickel(II) complexes *N*,*N*′-bis(salicylidene)-1,2-diamine, [Ni(salen)] (**1**), *N*,*N*′-bis(salicylidene)-1,2-cyclohexenediamine, [Ni(salhd)] (**2**), *N*,*N*′-bis(α-methylsalicylidene)-1,2-diamine [Ni(α,α′-Me_2salen)] (**3**) and *N*,*N*′-bis(3-methoxysalicylidene)-1,2-diamine, [Ni(3-MeOsalen)] (**4**) (Scheme 1) were prepared and fully characterised in refs.[35,36] according to standard procedures.[37]

General Procedure for the Preparation of the Immobilised Catalysts: The preparation of the immobilised (salen)nickel complexes followed the "ship-in-a-bottle" procedure[23] using the "flexible ligand" method. In a typical preparation, a suspension of calcinated NaY or NaX (10 g) in an aqueous solution containing $Ni(NO_3)_2$ (6 mmol) was heated at 70–80 °C for 24 h. The solid was then filtered and dried at 120 °C under vacuum, and the ion-exchanged zeolite (2 g; NiY or NiX) was mixed with the corresponding ligand (metal/ligand molar ratio = 1:2) and heated to 130–150 °C for 2 h. A change in the colour of the material from pale green (characteristic of hexahydrated Ni^{II}) to orange-brown [typical of (salen)Ni^{II} complexes] confirmed complex formation. The solids were then purified by solid-liquid Soxhlet extraction with appropriate solvents (dichloromethane or ethanol) to remove unreacted ligands and surface-bound complexes. The materials were denoted as [Ni(salen)]@X, [Ni(salhd)]@X, [Ni(α,α′-Me_2salen)]@X [Ni(3-MeOsalen)]@X, [Ni(salen)]@Y, [Ni(salhd)]@Y, [Ni(α,α′-Me_2salen)]@Y and [Ni(3-MeOsalen)]@Y.

General Procedure for the Epoxidation Reactions: In a typical experiment, a solution of the oxidant (5 mL) buffered to pH = 11 (with a solution of Na_2HPO_4) was stirred at room temperature in a solution of dichloromethane (5 mL) enriched with *trans*-β-methylstyrene (2 mmol), the nickel catalyst (0.05 mmol) (substrate/catalyst = 1:0.025) and benzyltributylammonium bromide (0.06 mmol), used as phase-transfer agent. A similar procedure was employed for the heterogeneous reactions using an amount of material corresponding to a substrate/nickel complex ratio of 1:0.025. In this case the catalysts were first activated at 120 °C for 2 h just before use and no phase-transfer agent was employed. The reactions were run at room temperature with continuous magnetic stirring and were followed by GC using *n*-decane as internal standard. For the reactions carried out in the absence of oxygen, the solvent was first deoxygenated with argon for some minutes in a Schlenk tube, and the reaction was run under argon.

Acknowledgments

This work was partially funded by Fundação para a Ciência e a Tecnologia (FCT) and FEDER, through the project ref. POCTI/

CTM/45449/2002. R. F. acknowledges FCT for a PhD fellowship. We are indebted to Dr. M. J. Sabater (Valencia) for helpful discussions.

[1] L. Canali, D. C. Sherrington, *Chem. Soc. Rev.* **1999**, *28*, 85–93.
[2] E. N. Jacobsen, A. Pfaltz, H. Yamamoto, *Comprehensive Asymmetric Catalysis*, Springer, Berlin, **1999**, vol. III.
[3] H. Nishikori, C. Ohta, T. Katsuki, *Synlett* **2000**, 1557–1560.
[4] M. J. Sabater, A. Corma, A. Domenech, V. Fornés, H. García, *Chem. Commun.* **1997**, 1285–1286.
[5] J. F. Kinneary, T. R. Wagner, C. J. Burrows, *Tetrahedron Lett.* **1988**, *29*, 877–880.
[6] J. F. Kinneary, J. S. Albert, C. J. Burrows, *J. Am. Chem. Soc.* **1988**, *110*, 6124–6129.
[7] R. I. Kureshy, N. H. Khan, S. H. R. Abdi, P. Iyer, A. K. Bhatt, *J. Mol. Catal. A: Chem.* **1998**, *130*, 41–50.
[8] R. I. Kureshy, N. H. Khan, S. H. Abdi, S. t. Patel, P. Iyer, E. Suresh, P. Dastidar, *J. Mol. Catal. A: Chem.* **2000**, *160*, 217–227.
[9] H. Yoon, C. J. Burrows, *J. Am. Chem. Soc.* **1988**, *110*, 4087–4089.
[10] H. Yoon, T. R. Wagner, K. J. O'Connor, C. J. Burrows, *J. Am. Chem. Soc.* **1990**, *112*, 4568–4570.
[11] R. A. Sheldon, R. S. Downing, *Appl. Catal. A* **1999**, *189*, 163–183.
[12] J. M. Thomas, T. Maschmeyer, B. F. G. Johnson, D. S. Shepard, *J. Mol. Catal. A: Chem.* **1999**, *141*, 139–144.
[13] R. Ferreira, M. Silva, C. Freire, B. de Castro, J. L. Figueiredo, *Microporous Mesoporous Mater.* **2000**, *38*, 391–401.
[14] A. R. Silva, M. Martins, M. M. A. Freitas, J. L. Figueiredo, C. Freire, B. de Castro, *Eur. J. Inorg. Chem.* **2004**, 2027–2035.
[15] R. Ferreira, C. Freire, B. de Castro, A. P. de Carvalho, J. Pires, M. Brotas de Carvalho, *Eur. J. Inorg. Chem.* **2002**, 3032–3038.
[16] I. Kuzniarska-Biernacka, A. R. Silva, R. Ferreira, A. P. de Carvalho, J. Pires, M. Brotas de Carvalho, C. Freire, B. de Castro, *New J. Chem.* **2004**, *28*, 853–858.
[17] A. R. Silva, J. L. Figueiredo, C. Freire, B. de Castro, *Microporous Mesoporous Mater.* **2004**, *68*, 83–89.
[18] A. R. Silva, C. Freire, B. de Castro, *Carbon* **2004**, *42*, 3003–3042.
[19] M. R. Maurya, S. J. J. Titinchi, S. Chand, *J. Mol. Catal. A: Chem.* **2003**, *201*, 119–130.
[20] D. Chatterjee, A. Mitra, *J. Mol. Catal. A: Chem.* **1999**, *144*, 363–367.
[21] D. Chatterjee, S. Mukherjee, A. Mitra, *J. Mol. Cat. A: Chem.* **2000**, *154*, 5–8.
[22] V. Ayala, A. Corma, M. Iglesias, J. A. Rincón, F. Sanchez, *J. Catal.* **2004**, *224*, 170–177.
[23] A. Corma, H. García, *Eur. J. Inorg. Chem.* **2004**, 1143–1164.
[24] V. Crupi, D. Majolino, V. Venuti, *J. Phys. Condens. Matter* **2004**, *16*, S5297–S5316.
[25] V. Ramaswamy, M. Sivarama, K. Krishnan, A. V. Ramaswamy, *J. Mol. Catal. A* **2002**, *181*, 81–89.
[26] Mainly chlorinated and allyclic hydroxylation products (identified by GC-MS).
[27] J. T. Groves, G. A. McClusky, *J. Am. Chem. Soc.* **1976**, *98*, 859–861.
[28] S. Shaik, S. Cohen, S. P. de Visser, P. K. Sharma, D. Kumar, S. Kozuch, F. Ogliaro, D. Danovich, *Eur. J. Inorg. Chem.* **2004**, 207–226.
[29] C. T. Dalton, K. M. Ryan, V. M. Wall, C. Bousquet, D. G. Gilheany, *Top. Catal.* **1998**, *5*, 75–91.
[30] A. M. Daly, M. F. Renehan, D. G. Gilheany, *Org. Lett.* **2001**, *3*, 663.
[31] W. Adam, K. J. Roschmann, C. R. Saha-Möller, D. Seebach, *J. Am. Chem. Soc.* **2002**, *124*, 5068–5073.
[32] For this reason, in certain oxidations using peroxides, such as the Fenton reaction, H_2O_2 is often seen as an initiator rather than an oxidant because it contributes only to initiate the formation of radicals from O_2. It is therefore interesting to explore the catalytic activity of the complexes in the absence of oxygen.
[33] W. R. Sanderson, *Pure Appl. Chem.* **2000**, *72*, 1289–1304.
[34] K. M. Ryan, C. Bousquet, D. G. Gilheany, *Tetrahedron Lett.* **1999**, *40*, 3613–3616.
[35] C. Freire, B. de Castro, *J. Chem. Soc., Dalton Trans.* **1998**, 1491–1497.
[36] C. Freire, B. de Castro, *Polyhedron* **1998**, *17*, 4227–4235.
[37] R. H. Holm, G. W. Everett Jr., A. Chakravorty, in *Progress in Inorganic Chemistry* (Ed.: F. A. Cotton), John Wiley and Sons, New York, **1966**, vol. 7, p. 183.

Received: April 15, 2005
Published Online: September 21, 2005

 © 2005 Wiley-VCH Verlag GmbH & Co. KGaA, Weinheim

One-Dimensional Oxalato-Bridged Metal(II) Complexes with 4-Amino-1,2,4-triazole as Apical Ligand

Urko García-Couceiro,[a] Oscar Castillo,*[a] Antonio Luque,*[a] Juan P. García-Terán,[a] Garikoitz Beobide,[a] and Pascual Román[a]

Keywords: Chain structures / Oxalato bridging ligand / Triazole / X-ray diffraction / Structure–magnetism relationships

The synthesis, chemical characterization, thermal behavior and magnetic properties of six new one-dimensional oxalato-bridged metal(II) complexes of formula $[M(\mu\text{-ox})(4atr)_2]_n$ [M^{II} = Cu (**1**), Ni (**2**), Co (**3**), Zn (**4**), Fe(**5**)] and $[Cd(\mu\text{-ox})(4atr)_2(H_2O)]_n$ (**6**) (ox = oxalato dianion, 4atr = 4-amino-1,2,4-triazole) are reported. The crystal structures of **1** and **6** have been solved by single-crystal X-ray diffraction, whereas the remaining compounds have been studied by means of X-ray powder diffraction methods. Compounds **1**–**5** are isomorphous and crystallize in the triclinic space group $P\bar{1}$ with unit cell parameters for **1** of a = 5.538(1) Å, b = 7.663(1) Å, c = 7.711(2) Å, α = 62.21(1)°, β = 73.91(1)°, γ = 86.11(1)°, and Z = 1. The crystal structures are comprised of one-dimensional linear chains in which the *trans*-$[M(4atr)_2]^{2+}$ units are sequentially bridged by bis(bidentate) oxalato ligands, resulting in an octahedral O_4N_2 donor set. Cryomagnetic susceptibility measurements show the occurrence of antiferromagnetic intrachain interactions for **2**, **3**, and **5**, whereas compound **1** exhibits a weak ferromagnetic coupling in agreement with the out-of-plane exchange pathway involved. The magnetic behavior of **1** and **2** is analyzed and discussed in the light of the available magneto-structural data for analogous systems. Cd^{II} complex crystallizes in the monoclinic space group $C2/c$ with unit cell parameters of a = 16.128(2) Å, b = 6.757(1) Å, c = 11.580(2) Å, β = 104.46(1)°, and Z = 4. Its crystal structure contains one-dimensional chains in which metal centers are heptacoodinated to four oxygen atoms from two symmetry-related bis(bidentate) oxalato bridges, two endocyclic nitrogen atoms of *trans*-coordinated triazole ligands and one water molecule, to give a $CdO_4O_wN_2$ pentagonal-bipyramidal geometry. Thermoanalytical and variable-temperature X-ray powder diffraction analyzes show that compound **6** undergoes a reversible dehydration–hydration process in which the anhydrous residue crystallizes with a different crystal lattice retaining the dimensionality of the oxalato–metal framework.
(© Wiley-VCH Verlag GmbH & Co. KGaA, 69451 Weinheim, Germany, 2005)

Introduction

In recent years the area of inorganic crystal engineering[1] has become one of intense research activity due to the growing need for novel solid-state architectures with potential applications as functional materials in fields such as catalysis, conductivity, zeolitic behavior and magnetism.[2] The judicious choice of the metal ion, a well understanding of the coordination preferences of the bridging entities, and a careful selection of the terminal ligands are key steps for the rational design of metal-organic coordination polymers with novel topologies and specific chemical and physical properties.[3] In this context, the oxalato dianion, essentially as bridging ligand, has appeared as a very appealing tecton in constructing a great diversity of homo- and heterometallic compounds with interesting physical properties (magnetic, electric, or optical).[4] The prevalence of its rigid bis(chelating) bridging mode provides a degree of predictability with regard to the structural motifs, and architectures reported for oxalato coordination networks range from discrete oligonuclear species to high dimensionality (one-, two-, and three-dimensional) systems.[5] The formation of these structures largely depends on the shape of the templating counterions and/or the features of the auxiliary ligands used to complete the metal coordination sphere.

Without being exhaustive, 2D honeycomb-layered structures of general formula $[M^{II}M^{III}(ox)_3]^-$ (M^{II} = V, Cr, Mn, Fe, Co, Ni, Cu, Zn; M^{III} = V, Cr, Fe) are obtained with voluminous cations such as $[XR_4]^+$ (X = N, P; R = phenyl, *n*-propyl, *n*-butyl, *n*-pentyl), decamethylferrocenium, and tetrathiafulvalene derivatives.[6] The use of tris(chelated) transition-metal diimine complexes $[M(L)_3]^{m+}$ (L = 2,2-bipyridine or phenanthroline, m = 2, 3) leads to helical 3D networks of formula $[M^{II}_2(ox)_3]^{2-}$, $[M^{II}M^{III}(ox)_3]^-$, and $[M^{I}M^{III}(ox)_3]^{2-}$ where cation and anion exhibit inverted chirality.[7] Discrete species are obtained by using polydentate N- and/or O-donor ligands that block most of the coordination sites around the metal center which precludes the formation of extended polymeric oxalato–metal systems of higher di-

[a] Departamento de Química Inorgánica, Facultad de Ciencia y Tecnología, Universidad del País Vasco,
Apartado 644, 48080 Bilbao, Spain
Fax: (internat) +34-94601-3500
E-mail: qipcacao@lg.ehu.es
qipluara@lg.ehu.es

Supporting information for this article is available on the WWW under http://www.eurjic.org or from the author.

mensionality.[8] Interestingly, in a series of previous papers, we have demonstrated that zigzag or linear one-dimensional complexes of formula $[M(\mu\text{-ox})(L)_x]_n$ (M^{II} = Cu, Ni, Co) can be obtained by utilizing aromatic pyridyl moieties as monodentate terminal/axial ligands, which permits the polymerization process of the oxalato–metal framework.[9–11] This work aims (a) to develop standard synthesis routes (nature of reactants and synthetic conditions) to achieve a straight-forward design of one-dimensional oxalato–metal frameworks, (b) to study the influence of the structural features of these compounds on the magnetic interactions transmitted through the oxalato ligand, (c) to analyze the role of the terminal ligands in the type and magnitude of the crystalline interactions (essentially, hydrogen bonds and other non-covalent interactions between the aromatic systems of the pyridine rings), which ensure the cohesiveness of the crystal structure, and finally (d) to obtain analogous 1D systems with biological molecules such as nucleobases and other N-containing rings as terminal ligands. Indeed, our synthesis efforts have recently been successful with the isolation of a new family of 1D oxalato-bridged complexes in which the pyridinic bases are replaced by nucleobases such as purine and adenine, which behave as N-monodentate ligands.[12]

As a continuation of our research program concerning the use of structure-directing N-containing ligands in the synthesis of 1D oxalato network structures, herein we report the synthesis, crystal structures, and the magnetic behavior of a new family of complexes of formula $[M(\mu\text{-ox})(4atr)_2]_n$, where M = Cu^{II}, Ni^{II}, Co^{II}, Fe^{II}, Zn^{II}, and $[Cd(\mu\text{-ox})(4atr)_2(H_2O)]_n$ with the 4-amino-1,2,4-triazole ligand (4atr) acting as apical ligand with a quite unusual monodentate coordination mode. The use of the 1,2,4-triazole moiety as a part of ligand systems has gained considerable attention in recent years mainly because of the fact that it represents a hybrid of pyrazole and imidazole with regard to the arrangement of its heteroatoms, thus promising a rich and versatile coordination chemistry.[13]

Results and Discussion

$[M(\mu\text{-ox})(4atr)_2]$ [M = Cu (1), Ni (2), Co (3), Zn (4), Fe (5)]

Compounds **1**–**5** are isomorphous and crystallize in the triclinic space group $P\bar{1}$. Crystal parameters and details of the final refinements are summarized in Tables 1 and 2. Compounds **2**–**5** crystallize as poor-quality specimens, and therefore X-ray powder diffraction methods have been performed to obtain structural information (for Supporting Information see footnote on the first page of this article). The observed, calculated and difference X-ray powder diffraction patterns of compound **2** are shown in Figure 1. The

Table 1. Single-crystal data and structure refinement details of the compound $[Cu(\mu\text{-ox})(4atr)_2]_n$ (**1**).

Empirical formula	$C_6H_8CuN_8O_4$	Z	1
Formula mass	319.74	$\rho_{calcd.}$ [g cm^{-3}]	1.914
Crystal system	triclinic	$\rho_{obsd.}$ [g cm^{-3}]	1.91(1)
Space group	$P\bar{1}$ (no. 2)	μ [mm^{-1}]	1.997
a [Å]	5.538(1)	Reflections collected	1689
b [Å]	7.663(1)	Unique data/parameters	1610/94
c [Å]	7.711(2)	R_{int}	0.0283
α [°]	62.21(1)	Reflections with $I \geq 2\sigma(I)$	1451
β [°]	73.91(1)	Goodness of fit (S)	1.048
γ [°]	86.11(1)	R_1/wR_2 [$I \geq 2\sigma(I)$]	0.0685/0.1800
V [Å^3]	277.4(1)	R_1/wR_2 [all data]	0.0758/0.1841

$R_1 = \Sigma(|F_o| - |F_c|)/\Sigma|F_o|$. $wR_2 = [\Sigma w(F_o^2 - F_c^2)^2/\Sigma w(F_o^2)^2]^{1/2}$; $w = 1/[\sigma^2(F_o^2) + (0.1572P)^2]$ with $P = (|F_o|^2 + 2|F_c|^2)/3$.

Table 2. X-ray powder crystal data for compounds **2**–**4**.

Compound	**2**	**3**	**4**
Empirical formula	$C_6H_8N_8NiO_4$	$C_6H_8CoN_8O_4$	$C_6H_8N_8O_4Zn$
Formula mass	314.87	315.11	321.57
Crystal system	triclinic	triclinic	triclinic
Space group	$P\bar{1}$ (no. 2)	$P\bar{1}$ (no. 2)	$P\bar{1}$ (no. 2)
a [Å]	5.386(1)	5.461(1)	5.455(1)
b [Å]	7.716(1)	7.741(1)	7.769(1)
c [Å]	7.946(1)	7.978(1)	8.002(1)
α [°]	60.87(1)	60.96(1)	60.93(1)
β [°]	76.54(1)	76.33(1)	76.34(1)
γ [°]	89.66(1)	89.62(1)	89.64(1)
V [Å^3]	278.3(1)	284.2(1)	285.7(1)
Z	1	1	1
$\rho_{obsd.}$ [g cm^{-3}]	1.87(1)	1.84(1)	1.86(1)
$\rho_{calcd.}$ [g cm^{-3}]	1.878	1.841	1.868
R_f/R_b [%]	9.95/8.70	9.13/9.25	5.47/9.87
R_p/R_{wp} [%]	9.57/13.29	8.88/11.76	10.06/13.72
χ^2	2.37	5.50	6.30

$R_f = \Sigma|(I_{obsd.})^{1/2} - (I_{calcd.})^{1/2}|/\Sigma(I_{obsd.})^{1/2}$; $R_b = \Sigma|I_{obsd.} - I_{calcd.}|/\Sigma I_{obsd.}$; $R_p = \Sigma|yi_{obsd.} - yi_{calcd.}|/\Sigma yi_{obsd.}$; $R_{wp} = [\Sigma wi|yi_{obsd.} - yi_{calcd.}|^2/\Sigma wi(yi_{obsd.})^2]^{1/2}$.

 © 2005 Wiley-VCH Verlag GmbH & Co. KGaA, Weinheim

XRPD pattern of **5** shows preferred orientation effects and it has only allowed a structureless pattern matching analysis giving a centric triclinic unit cell with a = 5.685(1) Å, b = 7.773(1) Å, c = 8.110(1) Å, α = 61.27(2)°, β = 72.16(2)°, γ = 87.29(1)°, and V = 297.0(1) Å^3.

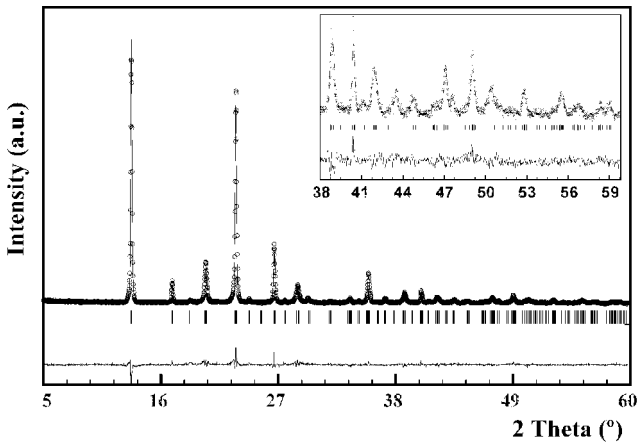

Figure 1. Final Rietveld plot for compound **2**. The observed data are shown by the dots, the calculated pattern by the solid line, and the lower trace corresponds to the difference between observed and calculated patterns.

The crystal structures of **1**–**4** are built up of *trans*-$[M(4atr)_2]^{2+}$ units joined sequentially by centrosymmetric bis(bidentate) oxalato ligands to form polymeric linear chains running parallel to the *a*-axis. The separation of the M^{II} atoms along the chains varies from 5.386(1) Å (**2**) to 5.538(1) Å (**1**). The metal atoms, located on crystallographic inversion centers, are coordinated to four oxygen atoms of two bridging oxalato ligands, and two endocyclic nitrogen atoms from two crystallograhically related 4atr molecules, resulting in octahedral MO_4N_2 donor sets. A perspective view of the polymeric chain of **1** is given in Figure 2, whereas selected bond lengths and angles are gathered in Table 3.

Table 3. Selected bond lengths [Å] and angles [°] for $[M(\mu\text{-ox})(4atr)_2]_n$ [M = Cu (**1**), Ni (**2**), Co (**3**) and Zn (**4**)].

	Cu (**1**)	Ni (**2**)	Co (**3**)	Zn (**4**)
M–O1 × 2	1.986(3)	2.10(1)	2.15(1)	2.14(1)
M–O2 × 2	2.307(3)	2.06(1)	2.07(1)	2.07(1)
M–N11 × 2	2.003(3)	2.16(1)	2.26(1)	2.31(1)
O1–M–O2	77.5(1)	80.8(1)	79.5(1)	79.6(1)
O1–M–N11	89.8(1)	93.8(1)	86.4(1)	89.5(1)
O1–M–N11a	90.2(1)	86.2(1)	93.6(1)	90.5(1)
O1–M–O1a	180(–)	180(–)	180(–)	180(–)
O1–M–O2a	102.5(1)	99.2(1)	100.5(1)	100.4(1)
O2–M–N11	90.3(1)	85.3(1)	89.9(1)	87.3(1)
O2–M–N11a	89.7(1)	94.7(1)	90.1(1)	92.7(1)
O2–M–O2a	180(–)	180(–)	180(–)	180(–)
N11–M–N11a	180(–)	180(–)	180(–)	180(–)

Symmetry code: (a) $-x$, $-y$, $2-z$

The most striking difference between the polymeric chains is the expected tetragonal Jahn–Teller elongation of the copper(II) octahedron in **1**, with two *trans* axial bond lengths [Cu–O2: 2.307(3) Å] substantially longer than the equatorial ones (ca. 2.00 Å). The difference of the Cu–O bond lengths (0.31 Å) involving the bis(bidentate) oxalato ligand is similar to those observed in other six-coordinate copper(II) complexes based on asymmetrically coordinated oxalato bridges.[14–16] The atoms involved in the four short bonds (O1, O1a, N11, N11a) define the equatorial plane of the MO_4N_2 chromophore that forms a dihedral angle of 83.5° with the oxalato bridging ligand.

Compounds **2**, **3** and **4** exhibit a rather typical octahedral metal(II) coordination with $M–O_{ox}$ bond lengths similar to those found in other oxalato-bridged metal(II) complexes (Ni: 1.960–2.152 Å; Co: 2.051–2.212 Å; Zn: 2.011–2.271 Å) registered in the Cambridge Structural Database (CSD, March 2005 release).[17] The triazole ligand is coordinated to the metal atom through the endocyclic N11 atom of the pentagonal ring[18] and it is perpendicular to the oxalato–metal framework (ca. 89°). The rings are arranged along the growing axis of the polymeric chain owing to an intra-

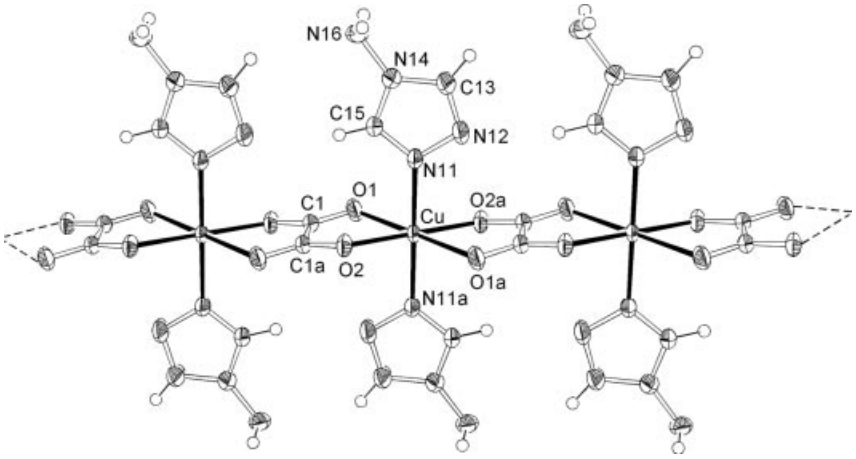

Figure 2. Perspective drawing of the polymeric chain of **1**. Thermal ellipsoids are drawn at the 50% probability level. Symmetry code: (a) $-x$, $-y$, $2-z$.

 © 2005 Wiley-VCH Verlag GmbH & Co. KGaA, Weinheim

molecular C–H···N hydrogen bond that is established between two consecutive 4atr ligands of the same side of the chain [C15···N12: 3.381(5) Å, C15–H15···N12: 166° for compound **1**]. The hydrogen atoms of the exocyclic amino group of the apical ligands are projected forward to the outside of the chains which allows their involvement in an extended network of N–H···O_{ox} hydrogen bonds with the oxalato oxygen atoms belonging to adjacent chains which sustains the supramolecular 3D structure of the complexes (Figure 3). The hydrogen-bonded chains are related by crystallographic inversion centers with a chain···chain distance coincident with the *c* parameter of the unit cell [from 7.711(2) Å for **1** to 8.002(1) Å for **4**]. Crystal building of these compounds can be alternatively described as a pillar-layered structure based on sheets of neutral oxalato–metal chains along the *ab* plane and triazole ligands perpendicularly inserted in the interlamellar region. Each organic molecule serves as pillar to link adjacent inorganic sheets. It is directly bound to a metal center of a sheet and its hydrogen-bonding donor is attached to the adjacent one supporting the cohesiveness of the layered structure.

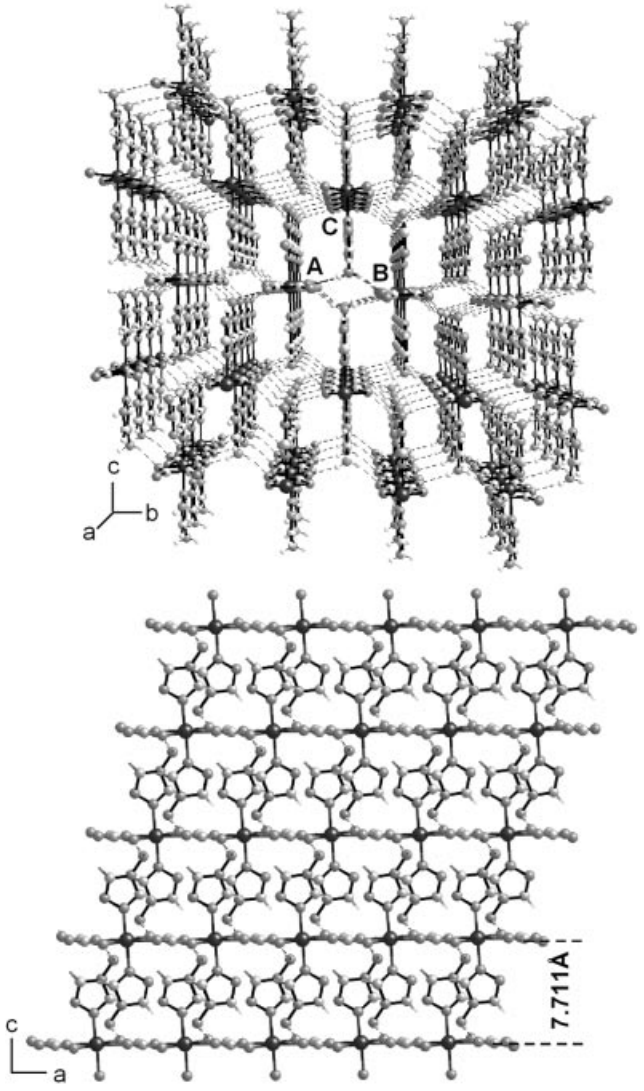

Figure 3. Views of the crystal packing of compound **1** showing the hydrogen bonds (dashed lines) and the layered structure. Intrachain distances [Å]: A···B = 7.663(1) (*b* parameter of the unit cell); A···C = 7.711(2) (*c* parameter).

The thermal degradation of compounds **1**–**5**, deduced from their TG and DTA curves in synthetic air (see Supporting Information), clearly indicates that the overall supramolecular three-dimensional architecture of all compounds is quite stable. The metal-organic framework of **1** retains its rigidity and stability up to 200 °C after which three exothermic processes take place to give copper(II) oxide as a final black powdery product above 500 °C. The three-dimensional cohesiveness of the remaining crystal structures is more robust and they undergo a first exothermic degradation process with an on-set temperature of approximately 325 °C for **2**, 310 °C for **3**, 250 °C for **4**, and 255 °C for **5**. In all the cases, the thermal degradation is completed above 500 °C to yield the metal(II) oxide (**2** and **4**) or M_2O_3 (**3** and **5**) as final products.

The temperature dependence of the $\chi_M T$ product (χ_M is the magnetic susceptibility per copper atom) and the variation of the inverse susceptibility (χ_M^{-1}) for compound **1** are shown in Figure 4. The $\chi_M T$ values increase continuously, upon cooling, from 0.418 cm^3 mol^{-1} K at room temperature up to a value of 0.920 cm^3 mol^{-1} K at 2.0 K. Above 15 K, thermal variation of χ_M^{-1} is well described by the Curie–Weiss law with a θ value of +4.12 K. That is indicative of the predominance of ferromagnetic interactions between the metal centers. The magnetic data were successfully fitted by a numerical expression proposed for uniform copper(II) chains with ferromagnetic[19] intrachain interactions derived through the Hamiltonian $H = -J\Sigma S_i S_{i+1}$. The best-fitted values were $J = +2.18\ cm^{-1}$, $g = 2.16$ and $R = 2.0 \times 10^{-5}$. The agreement factor R is defined as $\Sigma_i[(\chi_M T)_{obsd.}(i) - (\chi_M T)_{calcd.}(i)]^2/\Sigma_i[(\chi_M T)_{obsd.}(i)]^2$.

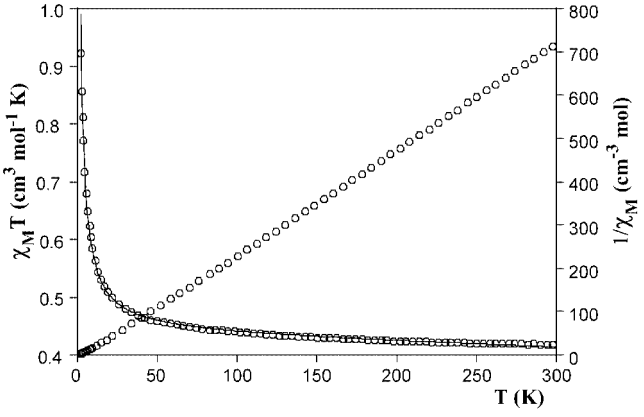

Figure 4. Thermal dependence plots of $\chi_M T$ and $1/\chi_M$ for compound **1**. (−) best theoretical fit (see text).

For oxalato-bridged Cu^{II} complexes it has been found[9–12,20] that the value and type of the magnetic coupling is essentially governed by the magnitude of the overlap between the symmetry-adapted highest occupied molecular orbitals (HOMOs, σ symmetry) of the oxalato ligand and the metal-centered magnetic orbitals (mainly, a $d_{x^2-y^2}$-type

 © 2005 Wiley-VCH Verlag GmbH & Co. KGaA, Weinheim

orbital in square-pyramidal or tetragonally elongated octahedral geometries) which are defined by the short equatorial (or basal) copper–ligand bonds. The strongest antiferromagnetic coupling (values of J ranging from –260 to –400 cm^{-1})[12,20,21] result when the oxalato bridge is symmetrically coordinated with two short bonds to each copper(II) center in such a way that it is coplanar with the singly occupied molecular orbitals (SOMOs) of the copper atoms. But when one copper–bridge distance is long (i.e., oxalato bridge is asymmetrically coordinated), the two metal-centered magnetic orbitals are parallel to each other and perpendicular to the bridging ligand (Scheme 1), the interaction between the d magnetic orbitals through the oxalato ligand is poor, and a weak anti- or ferromagnetic (when the overlap is zero, accidental orthogonality)[9–11,14,20,22–25] coupling results, as occurs in **1**.

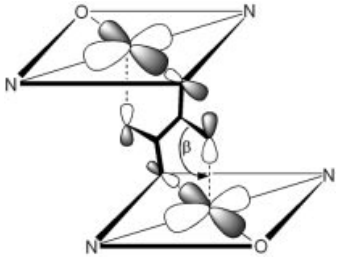

Scheme 1.

The magnetostructural data which are listed in Table 4 correspond to copper(II) complexes with an out-of-plane exchange pathway (perpendicular orbital arrangement). It shows that the value of the bond angle C–O–Cu involving the apical oxalate oxygen atom (β) is the main structural factor governing the nature of the magnetic interaction for the perpendicular topology between the oxalato and the copper(II) magnetic plane represented in Scheme 1. Compounds with $\beta \leq 109.5°$ show ferromagnetic interactions, whereas for $\beta > 109.5°$ the magnetic coupling between copper(II) ions is antiferromagnetic. This angle seems to be related to the overlap between the two metal-centered SOMOs and as a consequence to the sign of the magnetic exchange for the perpendicular topology. This magnetostructural result could be used to anticipate the magnetic interaction for new structurally characterized compounds based on oxalato-bridged copper(II) frameworks. For example, the two-dimensional $[Cu_3(\mu\text{-ox})_3(\mu\text{-bpy})_2(bpy)]_n$ polymer consists of sheets in which oxalato–copper(II) chains are crosslinked by bridging bidentate 4,4′-bypyridine ligands. The magnetic measurements show the occurrence of weak ferromagnetic interactions ($J = +0.6\ cm^{-1}$) transmitted through two asymmetrically coordinated oxalato bridges with $\beta < 108.3°$.[26]

Figure 5 shows the magnetic behavior of compounds **2**, **3** and **5**. The thermal dependence of the molar magnetic susceptibility, χ_M, of compound **2** shows a maximum at 44 K which is characteristic of antiferromagnetic interactions between the nickel(II) centers. The magnetic data of compound **2** were fitted by numerical expressions proposed for $S = 1$ chains with uniform antiferromagnetic interactions.[27] The results of the best fits were $J = -23.7\ cm^{-1}$, $g = 2.10$, $\rho = 0.010$ and $R = 4.0 \times 10^{-5}$. The percentage of paramagnetic impurities per mol of nickel atom is ρ (assuming that the molecular weight of the impurity is the same as that of the investigated compound). Previous magnetostructural studies of dinuclear oxalato-bridged Ni^{II} complexes have revealed that the magnitude of the exchange coupling constant is strongly dependent on the nature of the donor atoms in the peripheral ligands: the less electronegative they are, the greater the antiferromagnetic coupling is. This effect is more marked when the less electronegative donor atoms are coplanar with the bridging oxalato ligand.[9,28] The observed J value for compound **2** ($-23.7\ cm^{-1}$) compares well with that reported for the

Table 4. Selected magnetostructural data ([Å], [°], [cm^{-1}]) for oxalato-bridged copper(II) complexes having out-of-plane exchange pathway.

Compound[a]	Cu–O_{ax}	Cu···Cu	h(Cu)	γ	β	J	Ref.
$[Cu_2(\mu\text{-ox})(bpcam)_2(H_2O)_2]$	2.44	5.68	0.00	101.8	106.6	+0.8	[23]
$[Cu_2(\mu\text{-ox})(bpca)_2(H_2O)_2]$	2.41	5.63	0.05	80.7	106.9	+1.0	[25]
$[Cu(\mu\text{-ox})(2apy)_2]_n$	2.38	5.63	0.02	75.6	107.8	+2.0	[9]
$[Cu(\mu\text{-ox})(4atr)_2]_n$	2.31	5.54	0.00	83.5	108.0	+2.2	this work
$[Cu(\mu\text{-ox})(py)_2]_n$	2.27	5.46	0.00	80.8	108.0	+1.4	[15]
$\{[Cu(\mu\text{-ox})(bpy)]\cdot 2H_2O\}_n$[b]	2.31	5.55	0.03	83.4	108.5	+2.4	[14]
	2.32	5.56		83.4	108.3		
$\{[Cu(\mu\text{-ox})(tmen)]\cdot 4H_2O\}_n$[b]	2.35	5.60	0.01	81.2	108.3	+0.3	[16]
	2.38	5.66		78.4	108.7		
$[Cr_2Cu_2(\mu\text{-ox})_5(bpy)_4]\cdot 2H_2O$	2.25	5.44	0.03	81.7	108.8	+2.0	[24]
$[Cu(\mu\text{-ox})(pyOH)_2]_n$	2.28	5.55	0.00	81.9	109.2	+1.3	[10]
$[Cu(\mu\text{-ox})(isq)_2]_n$	2.23	5.48	0.06	88.5	109.5	+0.6	[11]
$[Cu(\mu\text{-ox})(4apy)_2]_n$	2.35	5.66	0.00	88.7	109.7	–1.1	[9]
$\{[Cu(\mu\text{-ox})(3apy)_2]\cdot 1.5H_2O\}_n$	2.21	5.46	0.00	85.2	111.0	–1.3	[9]
$[Cu_2(\mu\text{-ox})(bpmen)_2](ClO_4)_2$	2.18	5.49	0.00	88.2	111.6	–2.1	[8a]

[a] Abbreviations used: Cu–O_{ax}: copper–oxalate oxygen axial bond. Cu···Cu: copper–copper separation across the bridging oxalato ligand. h(Cu): Displacement of the copper atom out of the basal plane. γ: dihedral angle between the equatorial and oxalato mean planes. β: C–O–Cu angle involving the apical oxalato oxygen atom. bpy = 2,2-bipyridine; 2apy = 2-aminopyridine; py = pyridine; pyOH = 3-hydroxypyridine; isq = isoquinoline; tmen = *N*,*N*,*N*′,*N*′-tetramethylethylenediamine; 4apy = 4-aminopyridine; 3apy = 3-aminopyridine; bpmen = *N*,*N*′-bis(2-pyridylmethyl)-*N*,*N*′-dimethyl-1,2-ethanediamine; bpca = bis(2-pyridylcarbonyl)amidate; bpcam = bis(2-pyrimidylcarbonyl)-amidate. [b] The compound presents two crystallographically independent oxalato bridges.

 © 2005 Wiley-VCH Verlag GmbH & Co. KGaA, Weinheim

1D-[Ni(μ–ox)(4apy)$_2$]$_n$ (4apy = 4-aminopyridine) (J = –24.4 cm^{-1})[9] that also shows a *trans*-NiO_4N_2 chromophore, but it is somewhat lower than those reported for other one-dimensional complexes with a *cis*-NiO_4N_2 environment (J varies between –26.8 and –31.3 cm^{-1}).[9,11]

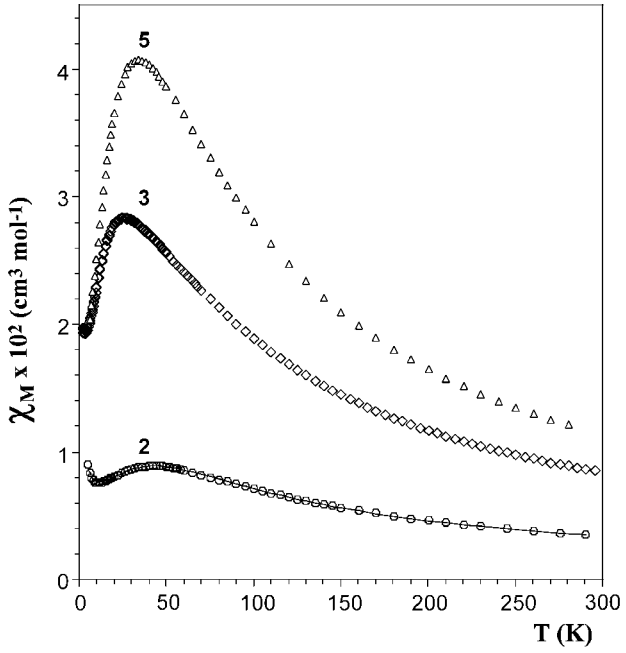

Figure 5. Thermal dependence plots of χ_M for the nickel(II) (**2**), cobalt(II) (**3**), and iron(II) (**5**) compounds; (–) best theoretical fit for **2** (see text).

The molar magnetic susceptibility (χ_M) values of compounds **3** and **5** increase when the temperature decreases, reaching a maximum at approximately 26 (**3**) and 35 K (**5**), with values of 2.83×10^{-2} for **3** and 4.07×10^{-2} cm^3 mol^{-1} for **5**, and then decreases very quickly. The $\chi_M T$ curves exhibit a continuous decrease upon cooling. This behavior suggests the presence of a moderate antiferromagnetic coupling between the magnetic centers through the bridging oxalato ligand. The experimental effective magnetic moments at room temperature of 5.00 (**3**) and 5.64 μ_B (**5**) are larger than the spin-only values of 3.87 μ_B for an uncoupled high-spin cobalt(II) ion (S = 3/2) and 4.90 μ_B for a high spin Fe^{II} center (S = 2). This behavior is typical of cobalt(II) and iron(II) ions in distorted octahedral geometries and a large orbital contribution to the magnetic moment should be considered.[9,11,24,29]

The quantitative analysis of the magnetic properties for systems involving ions with a significant orbital contribution is a difficult task. All our attempts to reproduce the experimental data of the compounds **3** and **5** by using the classical spin Heissenberg chain model[30] with S = 3/2 (Co) and S = 2 (Fe) or by fitting the low-temperature data (for **3**) as collections of Ising chains S = 1/2 effective spins with antiferromagnetic interactions were unsuccessful.[9,31,32] However, it is necessary to note that the magnetism curves and the χ_{max} and T_{max} values for complexes **3** and **5** are similar to those reported for polynuclear oxalato-bridged metal(II) complexes containing these paramagnetic centers with J values up to –25 cm^{-1} (Co)[8a,32] and –10 cm^{-1} (Fe).[32a,33] There are no known examples where the oxalate ion mediates a ferromagnetic interaction.

[Cd(μ-ox)(4atr)$_2$(H$_2$O)]$_n$ (6)

Crystal parameters and refinement results for compound **6** are summarized in Table 5. Its crystal structure consists of zigzag polymeric chains in which the Cd^{II} centers are sequentially bridged by bis(bidentate) oxalato ligands. The intrachain Cd···Cd distance across the oxalato bridge is 6.068(1) Å with a Cd···Cd···Cd angle between three consecutive atoms of 145(1)°. A detailed picture of a one-dimensional fragment is shown in Figure 6. Values of selected bond lengths and angles are reported in Table 6. The distorted pentagonal-bipyramidal coordination about each Cd^{II} center is completed by a water molecule [Cd–O3w: 2.431(9) Å] in the equatorial plane and the N11 endocyclic nitrogen atoms of two triazole ligands [2.321(6) Å] in the apical positions with an N11–Cd–N11a angle of 168.4(4)°, to give a $CdO_4O_wN_2$ donor set with a twofold axis along the Cd–O3w bond. The centrosymmetric oxalato bridge is coordinated with two similar Cd–O distances [Cd–O1: 2.331(6) Å, Cd–O2: 2.422(6) Å]. These values are typical of Cd^{II} complexes based on bis(bidentate) oxalato ligands.[34] The bite angle O1–Cd–O2 [70.1(2)°] is similar to those reported for oxalato-bridged cadmium(II) complexes with a pentagonal-bipyramidal coordination (range from 66 to 71°), but it is lower than the octahedral ones (72–74°).[17] The two symmetry-related oxalato ligands around the metal

Table 5. Single-crystal data and final refinement details of the compound [Cd(μ-ox)(4atr)$_2$(H$_2$O)]$_n$ (**6**).

Empirical formula	$C_6H_{10}CdN_8O_5$	Z	4
Formula mass	386.62	$\rho_{calcd.}$ [g cm^{-3}]	2.102
Crystal system	monoclinic	$\rho_{obsd.}$ [g cm^{-3}]	2.09(1)
Space group	*C*2/*c* (no. 15)	μ [mm^{-1}]	1.825
a [Å]	16.128(2)	Reflections collected	4581
b [Å]	6.757(1)	Unique data/parameters	1185/101
c [Å]	11.580(2)	R_{int}	0.0730
α [°]	90	Reflections with $I \geq 2\sigma(I)$	787
β [°]	104.46(1)	Goodness of fit [*S*]	1.068
γ [°]	90	R_1/wR_2 [$I \geq 2\sigma(I)$]	0.0428/0.0882
V [Å^3]	1222.0(3)	R_1/wR_2 [all data]	0.0815/0.0988

$R_1 = \Sigma(|F_o| - |F_c|)/\Sigma|F_o|$; $wR_2 = [\Sigma w(F_o^2 - F_c^2)^2/\Sigma w(F_o^2)^2]^{1/2}$; $w = 1/[\sigma^2(F_o^2) + (0.0442P)^2]$ with $P = (|F_o|^2 + 2|F_c|^2)/3$.

 © 2005 Wiley-VCH Verlag GmbH & Co. KGaA, Weinheim

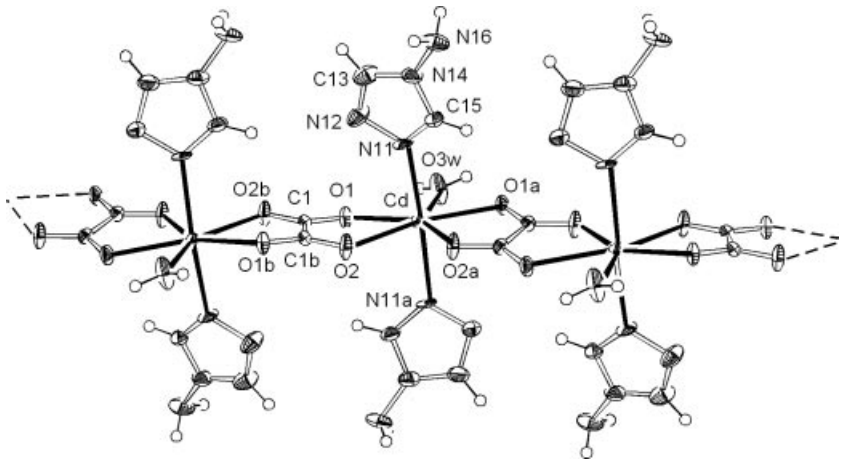

Figure 6. ORTEP drawing of a fragment of the polymeric chain of compound **6**. Symmetry code: (a) 1 – *x*, *y*, 3/2 + *z*; (b) 1 – *x*, –*y*, 2 – *z*.

atom are essentially planar and they are twisted to each other by 11.5(3)°. The cadmium atoms are displaced 0.39(1) Å out of the oxalate plane. The *trans*-coordinated triazole ligands are nearly parallel to the propagation direction of the chain (7.8°) and they are tilted with respect to each other and to the metal equatorial mean plane by 26.9 and 80.5°, respectively.

Table 6. Selected bond lengths [Å] and angles [°] for compound **6**.

Cd–O1 × 2	2.331(6)	Cd–O2 × 2	2.422(6)
Cd–O3w	2.431(9)	Cd–N11 × 2	2.321(6)
O1–Cd–O2	70.1(2)	O2–Cd–O3w	142.6(1)
O1–Cd–O3w	72.6(2)	O2–Cd–N11	84.2(2)
O1–Cd–N11	93.7(2)	O2–Cd–O2a	74.8(3)
O1–Cd–O1a	145.3(3)	O2–Cd–N11a	86.7(2)
O1–Cd–O2a	144.6(2)	O3w–Cd–N11	95.8(2)
O1–Cd–N11a	89.8(2)	N11–Cd–N11a	168.4(4)

Symmetry code: (a) 1 – *x*, *y*, 3/2 – *z*

The polymeric chains grow along the *c*-axis of the unit cell, and each coordinated water molecule forms two hydrogen bonds, related by a twofold axis, with the O2 oxygen atom from two consecutive oxalato bridges belonging to a neighboring chain with an interchain Cd···Cd distance of 6.757(1) Å (*b* parameter). These O_w–H_w···O_{ox} interactions give rise to sheets, which are spreading out along the crystallographic *bc* plane (Figure 7). The triazole rings are pointing in a direction almost perpendicular to the layers (in the inter-lamellar region) and crosslink adjacent sheets by means of the N–H···O_{ox} hydrogen bonds involving the exocyclic amino group and the oxalato oxygen atoms belonging to two adjacent chains with Cd···Cd and chain···chain distances of 8.813 and 8.064 Å, respectively.

The analysis of the crystal packing clearly shows that the coordinated water molecules are located in unobstructed microchannels along the *c*-axis. This arrangement is able to facilitate the reversible transport of the water molecules along the channels and allows an understanding of why the dehydration temperature of the compound **6** falls within the lower range of values reported for the loss of coordinated water molecules.[35] Thermogravimetric curves (TG/DTA) of compound **6** are portraited in Figure 8. The release of

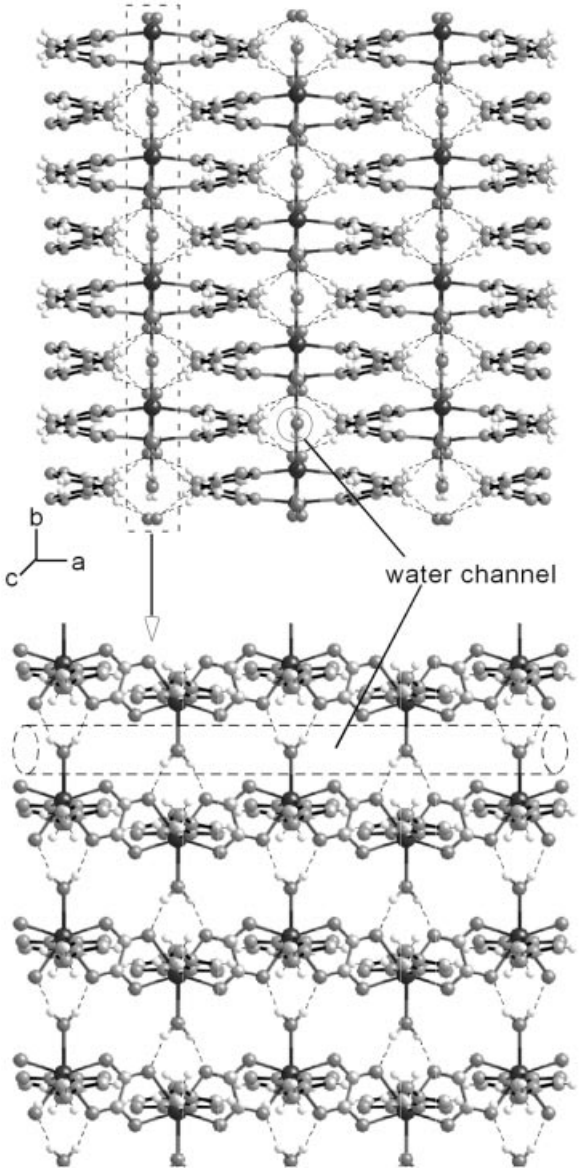

Figure 7. Crystal packing of compound **6** (hydrogen bonds are indicated by dashed lines).

 © 2005 Wiley-VCH Verlag GmbH & Co. KGaA, Weinheim

the water molecule is an endothermic process that starts at 90 °C and is completed by about 110 °C (DTA peak: 100 °C; weight loss: exp. 4.70%, calcd. 4.66%). The anhydrous compound **7** is stable up to 290 °C and then it undergoes three successive exothermic processes (DTA peaks: 310, 380 and 515 °C) leading to CdO above 520 °C, with a total weight loss of 67.60% (calcd. 66.79%).

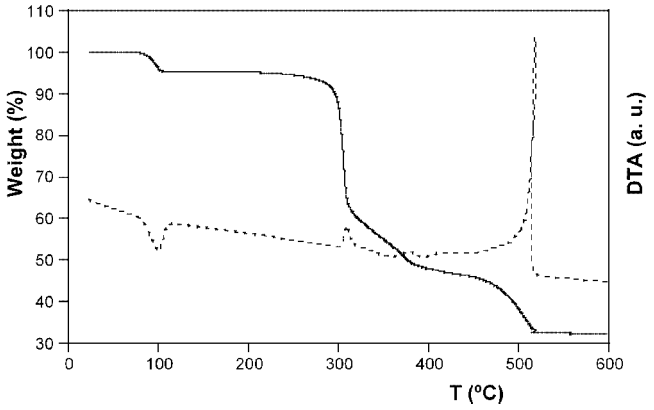

Figure 8. Thermogavimetric curves (TG/DTA) of compound **6** from room temperature to 600 °C.

Although crystal shape and size seem to be initially retained during the loss of the coordinating water molecule, single crystals of **6** lose gradually luster and become effectively a polycrystalline powder, precluding the in-situ structure determination from single-crystal diffraction techniques. Nevertheless, variable-temperature X-ray powder diffraction measurements (XRPD) revealed that the sample remains crystalline (Figure 9). The XRPD profile at 135 °C of **7** is not only substantially different than that obtained for the original compound, but also shows marked differences with the ones of the above-described compounds **1**–**5** (Figure 10). In a first approach, the powder pattern of **7** has been indexed in the orthorhombic space group *Pnmn* with unit cell parameters of a = 5.915(2) Å, b = 7.408(4) Å, c = 14.210(2) Å. These values are comparable to those found for the one-dimensional $[Mn(\mu\text{-ox})(4atr)_2]_n$ compound[36] except for a significant elongation of the crystallographic parameter a.

The Mn^{II} complex contains linear one-dimensional chains similar to those described for the triclinic compounds **1**–**4** where the M···M distance across the oxalato bridge also coincides with the repeat distance of the a-axis [5.599(1) Å for Mn]. The subtle difference between the Mn^{II} crystal structure and those of the above described compounds is the greater parallel displacement of the neighboring chains of the Mn^{II} compound. The hydrogen-bonded polymeric chains are related through a symmetry center in compounds **1**–**5**, whereas they are related through twofold axes in the Mn^{II} complex in such a way that the observed value of 5.915(2) Å for the fully anhydrous compound might be the Cd···Cd intrachain distance, and it is within the range found for other oxalato-bridged Cd^{II} complexes (5.827–6.213 Å).[17] Therefore, the Mn complex and the dehydrated Cd^{II} compound seem to be isostructural and it is

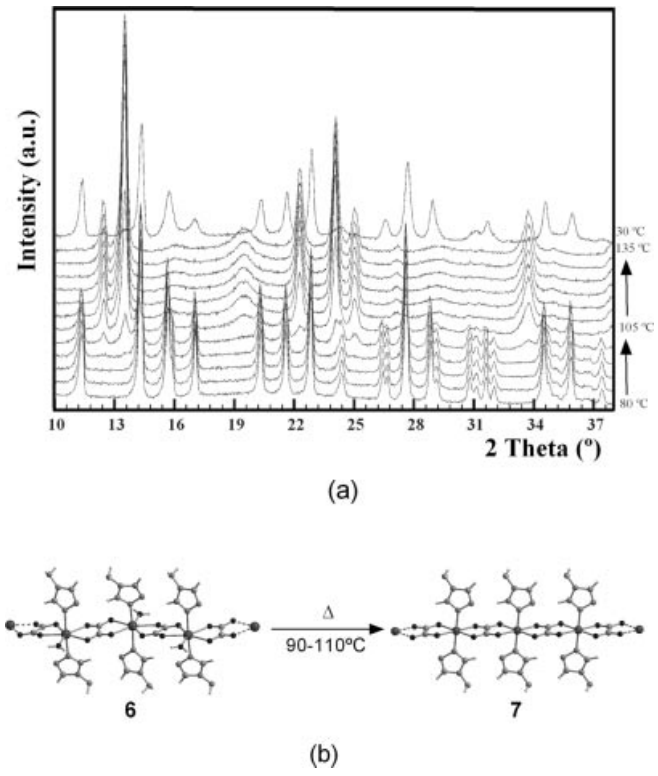

Figure 9. (a) Variable-temperature XRPD patterns of compound **6**. The last one was performed at room temperature 12 h after cooling. (b) Drawing of the polymeric chains of compounds **6** and the tentative structure of the anhydrous one (**7**) above 110 °C.

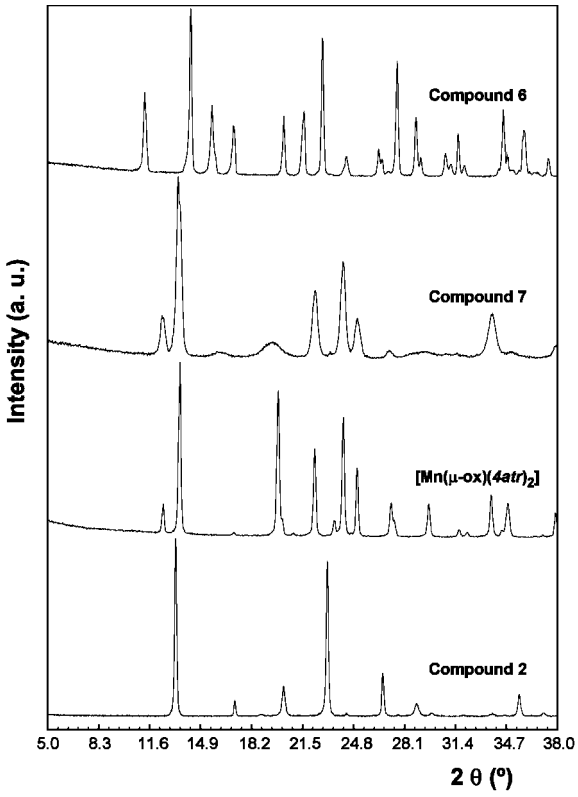

Figure 10. Diffraction patterns for compounds **2**, **6**, **7** and the analogous $[Mn(\mu\text{-ox})(4atr)_2]_n$.

 © 2005 Wiley-VCH Verlag GmbH & Co. KGaA, Weinheim

likely that the loss of the coordinated water molecule provides an octahedral coordination environment around the Cd^{II} atoms with a slight distortion of the oxalato–metal framework, but the initial overall 1D structure of the polymeric chain is retained without a drastic structural rearrangement (Figure 9b). In addition, thermogravimetric and X-ray powder crystallographic analyses indicate that the dehydration process is reversible. Upon exposure of **7** to air at room temperature for 12 h, it changed back to the initial aqua form, and the crystallinity was again retained. The system does not suffer any noticeable fatigue after repeating several **6** ↔ **7** cycles. It deserves to note that the references in the literature concerning the reversible loss of coordinated water molecules with no loss of crystallinity are scarce.[37] Usually, the residue is poorly crystalline (even amorphous) or its anhydrous crystal lattice shows a substantial rearrangement of the structural units that precludes the reversibility of the process.

Conclusions

Complexes **1**–**6** are examples of crystal engeneering, because we show how the 4-amino-1,2,4-triazole can be used as terminal ligand towards oxalato–metal frameworks to afford one-dimensional architectures, as previously thought. The analysis of structural and magnetic data of compound **1** and another related oxalato-bridged copper(II) complexes with an out-of-plane exchange pathway clearly evidences the influence of the C–O–Cu angle on the type of the magnetic coupling. This trend would provide a useful tool to predict the behavior of new magnetic compounds. The Cd complex is one of the few examples that shows a reversible release of coordination water molecules, the anhydrous compound remains crystalline but with a different phase.

Experimental Section

Reagents: All chemicals were of reagent grade and were used as commercially obtained. Standard literature procedures were used to prepare the starting materials Co(ox)·$2H_2O$, Ni(ox)·$2H_2O$, K_2[Cu(ox)$_2$]·$2H_2O$ and Cd(ox)·$3H_2O$.[38]

Physical Measurements: Elemental analyses (C, H, N) were performed with a Perkin–Elmer 2400 microanalytical analyser. Metal content was determined by absorption spectrometry. The purity and homogeneity of the polycrystalline samples of **1**–**6** used for physical measurements were checked by IR spectroscopy, elemental analysis, and X-ray powder diffraction methods.[39] The IR spectra (KBr pellets) were recorded with a Nicolet 740 FT-IR spectrometer in the 4000–400 cm^{-1} spectral region. Magnetic measurements were performed on polycrystalline samples of the complexes taken from the same uniform batches used for the structural determinations with a Quantum Design SQUID susceptometer covering the temperature range 2.0–300 K at a magnetic field of 1000 G. The susceptibility data were corrected for the diamagnetism estimated from Pascal's tables,[40] the temperature-independent paramagnetism and the magnetization of the sample holder. Thermal analyses (TG/DTA) were performed with a TA Instruments SDT 2960 thermal analyser in synthetic air (79% N_2/21% O_2) with a heating rate of 5 °C min^{-1}. A prismatic blue crystal of **1** (0.15 × 0.06 × 0.06 mm) and a prismatic colorless crystal of **6** (0.10 × 0.10 × 0.06 mm) were selected for the structural analysis. Diffraction data were collected at 293(2) K with Enraf–Nonius CAD4 automatic four-circle (**1**) and Oxford Diffraction Xcalibur (**6**) diffractometers with graphite-monochromated Mo-K_α radiation (λ = 0.71069 Å). Unit-cell parameters and orientation matrix of **1** were determined by least-squares treatment of the setting angles of 25 reflections on the range $4° < \theta < 13°$. Indexation and unit-cell refinement of **6** were based on all observed reflections from 10 frames collected with an oscillation range of 1°/frame and an exposure time of 3 min/frame. The data reduction was done with the XCAD[41] and CrysAlis RED[42] programs for compounds **1** and **6**, respectively. Both structures were solved by direct methods using the SIR92 program[43] and refined by full-matrix least squares on F^2 including all reflections (SHELXL93).[44] All calculations were performed using the WINGX crystallographic software package.[45] The final geometrical calculations and the graphical manipulations were carried out with the PARST95[46] and PLATON[47] programs. The X-ray powder diffraction (XRPD) patterns of compounds **2**–**5** were collected with a Phillips X'PERT powder diffractometer with Cu-K_α radiation over the range $5° < 2\theta < 60°$ with a fixed-time counting of 6–25 s at 25 °C. Indexation of the diffraction profiles of compounds **2**–**5** was made by means of the FULLPROF program (pattern-matching analysis)[48] on the basis of the space group and the cell parameters found for compound **1**. The atomic coordinates of **1** have been used as starting values for a least-squares refinement based on fitting the calculated and observed intensity profiles of an XRPD pattern of compounds **2**–**4**. Crystallographic data for compounds **1**–**4** and **6** have been deposited with the Cambridge Crystallographic Data Centre as supplementary publication nos. CCDC-269268 (**1**), -282657 (**2**), -282658 (**3**), -282659 (**4**), and -269269 (**6**). These data can be obtained free of charge at www.ccdc.cam.ac.uk/conts/retrieving.html [or from the CCDC, 12 Union Road, Cambridge CB2 1EZ, UK; Fax: +44-1223-336-033; E-mail: deposit@ccdc.cam.ac.uk]. Thermodiffractometry measurements of the Cd^{II} compound **6** were run under ambient atmosphere in the range $9° < 2\theta < 38°$ with a step size of 0.03° and an acquisition time of 2.5 s per step. The compound was heated to 80 °C with a heating rate of 10 °C min^{-1} and after that diagrams were collected every 5 °C with a heating rate of 1 °C min^{-1} up to 140 °C. Finally, the sample was allowed to cool for 12 h and a new diffraction profile was collected at 30 °C.

Synthesis of [Cu(μ-ox)(4atr)$_2$]$_n$ (1): Single crystals of **1** were grown by layering a methanol solution of 4-amino-1,2,4-triazole (0.200 g, 2.5 mmol) onto an aqueous solution of K_2[Cu(ox)$_2$]·$2H_2O$ (0.175 g, 0.5 mmol) and K_2ox·H_2O (0.061 g, 0.33 mmol). After allowing the solution to stand for 2 weeks, the crystals were isolated in 80% yield by filtration. They were washed with cold water and diethyl ether, and dried in air. $C_6H_8CuN_8O_4$ (319.74): calcd. C 22.54, H 2.52, N 35.05, Cu 19.87; found C 22.48, H 2.52, N 34.99, Cu 19.82. Main IR features (KBr pellet): $\tilde{\nu}$ = 3295 s, 3175 s for ν(N–H); 3115 s for ν(C–H); 1655 vs. for $\nu_{as}(CO_2)$; 1615 s for $\delta(NH_2)$; 1540 m, 1465 m for ν_{as}(C=N); 1360 m, 1310 s for $\nu_s(CO_2)$; 1220 m, 1200 m, 1075 s for δ_{ip}(C–H); 1035 m, 1015 m for ν_s(CO); 970 m for δ_{ring}; 890 m, 850 w δ_{op}(C–H); 800 s for $\delta(CO_2)$; 690 w, 625 s for τ_{ring}; 500 m, 415 m for ν(M–O, M–N) cm^{-1}.

Synthesis of [Ni(μ-ox)(4atr)$_2$]$_n$ (2): An aqueous solution (10 mL) of 4-amino-1,2,4-triazole (0.168 g, 2.00 mmol) was added dropwise to an aqueous solution (30 mL) containing Ni(ox)·$2H_2O$ (0.080 g, 0.44 mmol) and K_2ox·H_2O (0.442 g, 2.4 mmol). Immediately, a green precipitate corresponding to compound **2** appeared. Yield 90%. $C_6H_8N_8NiO_4$ (314.87): calcd. C 22.89, H 2.56, N 35.59, Ni

 © 2005 Wiley-VCH Verlag GmbH & Co. KGaA, Weinheim

18.64; found C 22.92, H 2.55, N 35.55, Ni 18.62. Main IR features (KBr pellet): $\tilde{\nu}$ = 3305 m, 3215 m for ν(N–H); 3105 m for ν(C–H); 1655 sh for $\nu_{as}(CO_2)$; 1615 vs for $\delta(NH_2)$; 1535 w, 1470 w for ν_{as}(C=N); 1360 m, 1315 m for $\nu_s(CO_2)$; 1230 m, 1205 m, 1070 m for δ_{ip}(C–H); 1020 m for ν_s(CO); 970 m for δ_{ring}; 890 w, 855 w δ_{op}(C–H); 800 m for $\delta(CO_2)$; 685 w, 620 m for τ_{ring}; 490 m, 420 m for ν(M–O, M–N) cm^{-1}.

Synthesis of $[Co(\mu\text{-ox})(4atr)_2]_n$ (3): The preparation of **3** is analogous to that described for **2** but using $Co(ox)\cdot 2H_2O$ (0.080 g, 0.44 mmol), $K_2ox\cdot H_2O$ (0.737 g, 4.00 mmol) and 4-amino-1,2,4-triazole (0.168 g, 2.0 mmol). A pink polycrystalline powder of **3** was obtained almost immediately. Yield 90%. $C_6H_8CoN_8O_4$ (315.11): calcd. C 22.87, H 2.56, Co 18.70, N 35.56; found C 22.88, H 2.56, Co 18.68, N 35.60. Main IR features (KBr pellet): $\tilde{\nu}$ = 3295 m, 3215 m for ν(N–H); 3105 m for ν(C–H); 1655 sh for $\nu_{as}(CO_2)$; 1615 vs for $\delta(NH_2)$; 1535 m, 1465 w for ν_{as}(C=N); 1365 m, 1320 m for $\nu_s(CO_2)$; 1220 m, 1205 m, 1075 m for δ_{ip}(C–H); 1010 w for ν_s(CO); 965 m for δ_{ring}; 895 m, 855 w δ_{op}(C–H); 800 m for $\delta(CO_2)$; 680 w, 625 m for τ_{ring}; 495 m, 415 m for ν(M–O, M–N) cm^{-1}.

Synthesis of $[Zn(\mu\text{-ox})(4atr)_2]_n$ (4): 10 mL of a water solution containing $H_2C_2O_4\cdot 2H_2O$ (0.034 g, 0.2 mmol) was added dropwise to an aqueous solution (25 mL) of 4-amino-1,2,4-triazole (0.069 g, 1.00 mmol) and $ZnCl_2$ (0.054 g, 0.40 mmol). Immediately, a white polycrystalline powder of **4** appeared. The precipitate was separated from the mother liquor and it was washed with cold water and diethyl ether, and dried in air. Yield 90%. $C_6H_8N_8O_4Zn$ (321.57): calcd. C 22.41, H 2.51, N 34.85, Zn 20.33; found C 22.43, H 2.52, N 34.82, Zn 20.35. Main IR features (KBr pellet): $\tilde{\nu}$ = 3295 s, 3210 s for ν(N–H); 3100 s for ν(C–H); 1655 sh for $\nu_{as}(CO_2)$; 1615 vs for $\delta(NH_2)$; 1540 m, 1465 m for ν_{as}(C=N); 1370 m, 1320 s for $\nu_s(CO_2)$; 1220 m, 1205 m, 1075 m for δ_{ip}(C–H); 1015 m for ν_s(CO); 970 m for δ_{ring}; 895 m, 850 w for δ_{op}(C–H); 800 s for $\delta(CO_2)$; 685 w, 625 s for τ_{ring}; 500 m, 410 m for ν(M–O, M–N) cm^{-1}.

Synthesis of $[Fe(\mu\text{-ox})(4atr)_2]_n$ (5): Orange polycrystalline samples of compound **5** were prepared as **4** but using $FeSO_4\cdot 7H_2O$ (0.064 g, 0.2 mmol). Yield 90%. $C_6H_8FeN_8O_4$ (312.02): calcd. C 23.09, H 2.58, N 35.91, Fe 17.90; found C 23.05, H 2.57, N 35.95, Fe 17.96. Main IR features (KBr pellet): $\tilde{\nu}$ = 3340 m, 3300 m, 3215 m for ν(N–H); 3110 m for ν(C–H); 1620 vs for $\delta(NH_2)$; 1530 m, 1460 w for ν_{as}(C=N); 1360 w, 1325 m for $\nu_s(CO_2)$; 1215 m, 1200 m, 1075 m for δ_{ip}(C–H); 1005 m for ν_s(CO); 960 m for δ_{ring}; 885 w, 860 w δ_{op}(C–H); 800 m for $\delta(CO_2)$; 680 w, 620 m for τ_{ring}; 495 m, 410 m for ν(M–O, M–N) cm^{-1}.

Synthesis of $[Cd(\mu\text{-ox})(4atr)_2(H_2O)]_2$ (6): Prismatic colorless crystals appropriate for the X-ray diffraction were obtained using an analogous method to that described for **2** but using $Cd(ox)\cdot 3H_2O$ (0.072 g, 0.28 mmol), $K_2(ox)\cdot H_2O$ (1.182 g, 5.0 mmol) and 4atr (0.087 g, 1.0 mmol). Yield 60%. $C_6H_{10}CdN_8O_5$ (386.62): calcd. C 18.64, H 2.61, Cd 29.08, N 28.98; found C 18.59, H 2.60, Cd 29.10, N 29.01. Main IR features (KBr pellet): $\tilde{\nu}$ = 3435 s for ν(O–H); 3330 s, 3275 m, 3225 m for ν(N–H); 3130 m, 3105 m for ν(C–H); 1680 m, 1630 sh for $\nu_{as}(CO_2)$; 1610 vs. for $\delta(NH_2)$; 1530 m, 1460 w for ν_{as}(C=N); 1385 w, 1315 m for $\nu_s(CO_2)$; 1200 m, 1070 m for δ_{ip}(C–H); 1005 m, 990 sh for ν_s(CO); 960 w for δ_{ring}; 880 m for δ_{op}(C–H); 790 m for $\delta(CO_2)$; 685 w, 620 m for τ_{ring}; 505 w, 420 w for ν(M–O, M–N) cm^{-1}.

Supporting Information: XRPD patterns of compounds **2**–**7**. Final Rietveld plots of compounds **3**–**4**. Thermoanalytical (TG/DTA) curves for compounds **1**–**6**. Views of the crystal packing of compound $[Mn(\mu\text{-ox})(4atr)_2]_n$. Magnetostructural parameters for oxalato-bridged nickel(II) compounds.

Acknowledgments

This work was supported by the Ministerio de Ciencia y Tecnología (MAT2002-03166) and the Universidad del País Vasco/Euskal Herriko Unibertsitatea (9/UPV 00169.310-15329/2003). U. G-C. thanks the latter institution for a predoctoral fellowship.

[1] a) L. Brammer, *Chem. Soc. Rev.* **2004**, *33*, 476–489; b) D. Braga, L. Brammer, N. R. Champness, *Cryst. Eng. Comm.* **2005**, *7*, 1–19.

[2] a) S. L. James, *Chem. Soc. Rev.* **2003**, *32*, 276–288; b) C. Janiak, *Dalton Trans.* **2003**, 2781–2804.

[3] a) B. J. Hollyday, C. A. Mirkin, *Angew. Chem. Int. Ed.* **2001**, *40*, 2022–2043; b) D. Braga, G. R. Desiraju, J. S. Miller, A. G. Orpen, S. L. Price, *CrystEngComm.* **2002**, *4*, 500–509.

[4] a) P. Day, *Supramolecular Engineering of Synthetic Metallic Materials*, Nato Asi Series, vol. C518 (Eds: J. Vecina, C. Rovira, D. B. Amabilino), Kluwer Academic Publishers, Dordrecht, The Netherlands, **1999**; b) M. Verdaguer, *Polyhedron* **2001**, *20*, 1115–1128; c) E. Coronado, P. Day, *Chem. Rev.* **2004**, *104*, 5419–5448.

[5] a) M. Pilkington, S. Decurtins, *Comprehensive Coordination Chemistry II*, vol. 7 (Eds: J. A. McCleverty, T. J. Meyer), Elsevier, University of Berna, Switzerland, **2004**, p. 214–229; b) C. N. R. Rao, S. Natarajan, R. Vaidhyanathan, *Angew. Chem. Int. Ed.* **2004**, *43*, 1466–1496.

[6] a) L. O. Atovmyan, G. V. Shilov, R. N. Lyubovskaya, N. S. Ovanesyan, Y. G. Moronov, S. I. Pirumova, I. G. Gusakovskaya, *JETP Lett.* **1993**, *58*, 818–821; b) S. G. Carling, C. Mathoniere, P. Day, K. M. A. Malik, S. J. Coles, M. B. Hursthouse, *J. Chem. Soc. Dalton Trans.* **1996**, 1839–1843; c) E. Coronado, J. R. Galán-Mascarós, C. J. Gómez-García, J. Ensling, P. Gütlich, *Chem. Eur. J.* **2000**, *6*, 552–563; d) E. Coronado, J. R. Galán-Mascarós, C. J. Goméz-García, V. Laukhin, *Nature* **2000**, *408*, 447–449; e) L. Martin, S. S. Turner, P. Day, P. Guionneau, J. A. K. Howard, D. E. Hibbs, M. E. Light, M. B. Hursthouse, M. Uruichi, K. Yakushi, *Inorg. Chem.* **2001**, *40*, 1363–1371; f) E. Coronado, J. R. Galán-Mascarós, C. J. Gómez-García, E. Martínez-Ferrero, S. van Smaalen, *Inorg. Chem.* **2004**, *43*, 4808–4810.

[7] a) S. Decurtins, H. W. Schmalle, P. Schneuwly, H. R. Oswald, *Inorg. Chem.* **1993**, *32*, 1888–1892; b) S. Decurtins, H. W. Schmalle, R. Pellaux, P. Schneuwly, A. Hauser, *Inorg. Chem.* **1996**, *35*, 1451–1460; c) E. Coronado, J. R. Galán-Mascarós, C. J. Gómez-García, J. M. Martínez-Agudo, *Inorg. Chem.* **2001**, *40*, 113–120; d) R. Andrés, M. Brissard, M. Gruselle, C. Train, J. Vaissermann, B. Malézieux, J.-P. Jamet, M. Verdaguer, *Inorg. Chem.* **2001**, *40*, 4633–4640; e) G. Ballester, E. Coronado, C. Giménez-Saiz, F. M. Romero, *Angew. Chem. Int. Ed.* **2001**, *40*, 792–795.

[8] a) J. Glerup, P. A. Goodson, D. J. Hodgson, K. Michelsen, *Inorg. Chem.* **1995**, *34*, 6255–6264; b) I. Muga, J. M. Gutiérrez-Zorrilla, P. Vitoria, A. Luque, M. Insausti, P. Román, F. Lloret, *Eur. J. Inorg. Chem.* **2000**, 2541–2547; c) H. Xiang, T.-B. Lu, S. Chen, Z.-W. Mao, X.-L. Feng, K.-B. Yu, *Polyhedron* **2001**, *20*, 313–319; d) L. J. Farrugia, S. Lopinski, P. A. Lovatt, R. D. Peacock, *Inorg. Chem.* **2001**, *40*, 558–559; e) F. Tuna, G. I. Pascu, J.-P. Sutter, M. Andruh, S. Golhen, J. Guillevic, H. Pritzkow, *Inorg. Chim. Acta* **2003**, *342*, 131–138.

[9] O. Castillo, A. Luque, P. Román, F. Lloret, M. Julve, *Inorg. Chem.* **2001**, *40*, 5526–5535.

[10] O. Castillo, A. Luque, M. Julve, F. Lloret, P. Román, *Inorg. Chim. Acta* **2001**, *315*, 9–17.

[11] O. Castillo, A. Luque, F. Lloret, P. Román, *Inorg. Chim. Acta* **2001**, *324*, 141–148.

[12] J. P. García-Terán, O. Castillo, A. Luque, U. García-Couceiro, P. Román, F. Lloret, *Inorg. Chem.* **2004**, *43*, 5761–5770.

 © 2005 Wiley-VCH Verlag GmbH & Co. KGaA, Weinheim

[13] a) J. G. Haasnoot, *Coord. Chem. Rev.* **2000**, *200–202*, 131–185; b) M. H. Klingele, S. Broker, *Coord. Chem. Rev.* **2003**, *241*, 119–132.
[14] a) W. Fitzgerald, J. Foley, D. McSweeney, N. Ray, D. Sheahan, S. Tyagi, *J. Chem. Soc. Dalton Trans.* **1982**, 1117–1121; b) H. Oshio, U. Nagashima, *Inorg. Chem.* **1992**, *31*, 3295–3301.
[15] J. Suárez-Varela, J. M. Domínguez-Vera, E. Colacio, J. C. Avila-Rosón, M. A. Hidalgo, D. Martín-Ramos, *J. Chem. Soc. Dalton Trans.* **1995**, 2143–2146.
[16] C. S. Hong, H. Yoon, Y. S. You, *Inorg. Chem. Commun.* **2005**, *8*, 310–318.
[17] F. H. Allen, *Acta Crystallogr. Sect. B* **2002**, *58*, 380–388.
[18] a) L. Yi, J. Y. Du, S. Liu, X. X. Wang, *J. Chem. Res.* **2004**, 29–31; b) N. V. Podberezskaya, N. V. Pervukhina, V. P. Doronina, *J. Struct. Chem.* **1991**, *32*, 34–39.
[19] G. A. Baker, G. S. Rushbrooke, H. E. Gilbert, *Phys. Rev.* **1964**, *135*, A1272–A1277.
[20] a) J. Cabrero, N. Ben Amor, C. de Graaf, F. Illas, R. Caballol, *J. Phys. Chem. A* **2000**, *104*, 9983–9989; b) J. Cano, P. Alemany, S. Alvarez, M. Verdaguer, E. Ruiz, *Chem. Eur. J.* **1998**, *4*, 476–484; c) S. Alvarez, M. Julve, M. Verdaguer, *Inorg. Chem.* **1990**, *29*, 4500–4507.
[21] a) M. Julve, J. Faus, M. Verdaguer, A. Gleizes, *J. Am. Chem. Soc.* **1984**, *106*, 8306–8308; b) A. Bencini, C. Fabretti, C. Zanchini, P. Zannini, *Inorg. Chem.* **1987**, *26*, 1445–1449; c) A. Gleizes, M. Julve, M. Verdaguer, J. A. Real, J. Faus, X. Solans, *J. Chem. Soc. Dalton Trans.* **1992**, 3209–3216.
[22] Z. Smekal, Z. Travnicek, F. Lloret, J. Marek, *Polyhedron* **1999**, *18*, 2787–2793.
[23] D. Cangussu, H. O. Stumpf, H. Adams, J. A. Thomas, F. Lloret, M. Julve, *Inorg. Chim. Acta* **2005**, *358*, 2292–2302.
[24] E. Coronado, M. C. Giménez, C. J. Gómez-García, F. M. Romero, *Polyhedron* **2003**, *22*, 3115–3122.
[25] M. L. Calatayud, I. Castro, J. Sletten, F. Lloret, M. Julve, *Inorg. Chim. Acta* **2000**, *300–302*, 846–854.
[26] O. Castillo, J. Alonso, U. García-Couceiro, A. Luque, P. Román, *Inorg. Chem. Comm.* **2003**, *6*, 803–806.
[27] a) C. Y. Weng, Ph. D. Thesis, Carnegie Institute of Technology, **1968**; b) A. Meyer, A. Gleizes, J. J. Girerd, M. Verdaguer, O. Kahn, *Inorg. Chem.* **1982**, *21*, 1729–1739.
[28] a) P. Román, C. Guzmán-Miralles, A. Luque, J. I. Beitia, J. Cano, F. Lloret, M. Julve, S. Alvarez, *Inorg. Chem.* **1996**, *35*, 3741–3751; b) A. Escuer, R. Vicente, M. S. El Fallah, J. Jaud, *Inorg. Chim. Acta* **1995**, *232*, 151–156; c) P. Vitoria, I. Muga, J. M. Gutiérrez-Zorrilla, A. Luque, P. Román, L. Lezama, F. J. Zúñiga, J. I. Beitia, *Inorg. Chem.* **2003**, *42*, 960–969.
[29] a) M. E. Lines, *J. Chem. Phys.* **1971**, *55*, 2977–2984; b) G. de Munno, M. Julve, F. Lloret, J. Faus, A. Caneschi, *J. Chem. Soc. Dalton Trans.* **1994**, 1175–1183; c) L.-M. Zheng, X. Fang, K.-H. Lii, X.-Q. Xin, H.-K. Fun, K. Chinnakali, I. A. Razak, *J. Chem. Soc. Dalton Tans.* **1999**, 2311–2316.
[30] a) M. E. Fisher, *J. Math. Phys.* **1963**, *4*, 124–135; b) M. E. Fisher, *Am. J. Phys.* **1964**, *32*, 343.
[31] O. Kahn, *Molecular Magnetism*, VCH, New York, **1993**.
[32] a) M. B. Hursthouse, M. E. Light, D. J. Price, *Angew. Chem. Int. Ed.* **2004**, *43*, 472–475; b) U. García-Couceiro, O. Castillo, A. Luque, G. Beobide, P. Román, *Inorg. Chim. Acta* **2004**, *357*, 339–344.
[33] a) D. Armentano, G. De Munno, F. Lloret, M. Julve, J. Curely, A. M. Babb, J. Y. Lu, *New J. Chem.* **2003**, *27*, 161–165; b) D. J. Price, A. K. Powell, P. T. Wood, *Dalton Trans.* **2003**, 2478–2482.
[34] a) P. Orioli, B. Bruni, M. Di Vaira, L. Messori, F. Piccioli, *Inorg. Chem.* **2002**, *41*, 4312–4314; b) R. A. Prasad, S. Neeraj, R. Vaidhyanathan, S. Natarajan, *J. Solid State Chem.* **2002**, *166*, 128–141; c) S.-Q. Xia, S.-M. Hu, J.-C. Dai, X.-T. Wu, Z.-Y. Fu, J.-J. Zhang, W.-X. Du, *Polyhedron* **2004**, *23*, 1003–1009.
[35] a) S. Petit, G. Coquerel, *Chem. Mater.* **1996**, *8*, 2247–2258; b) O. Castillo, A. Luque, S. Iglesias, P. Vitoria, P. Román, *New J. Chem.* **2000**, *24*, 771–775.
[36] U. García-Couceiro, D. Olea, O. Castillo, A. Luque, P. Román, P. J. de Pablo, J. Gómez-Herrero, F. Zamora, *Inorg. Chem*, in press, **2005**.
[37] a) V. Neil, A. L. Thompson, M. C. Muñoz, A. Galet, A. E. Goeta, J. A. Real, *Angew. Chem. Int. Ed.* **2003**, *42*, 3760–3763; b) C.-H. Lin, S.-L. Wang, *Chem. Mater.* **2002**, *14*, 96–102; c) J. Greve, I. Jeb, C. Näther, *J. Solid State Chem.* **2003**, *175*, 328–340; d) C.-C. Wang, C.-H. Yang, S.-M. Tseng, G.-H. Lee, H.-S. Sheu, K. W. Phyu, *Inorg. Chim. Acta* **2004**, *357*, 3759–3764.
[38] a) H. Remy, *Treatise on Inorganic Chemistry*, VCH, Weinheim, Germany, **1956**; b) S. Kirschner, *Inorganic Synthesis*, vol. 4 (Ed.: E. G. Rochow), McGraw-Hill Book Co., New York, **1960**.
[39] K. Iron, W. Jeitschko, E. Parthe, *LAZY PULVERIX*, Laboratoire de Crystallographie aux Rayons-X, Universtité of Genève, Switzerland, **1977**.
[40] A. Earnshaw, *Introduction to Magnetochemistry*, Academic Press, London, **1968**.
[41] K. Harm, S. Wocadlo, *XCAD*, CAD4 Data Reduction, University of Marburg, Germany, **1995**.
[42] *CrysAlis RED*, version 1.170, Oxford Diffraction, Wroclaw, Poland, **2003**.
[43] A. Altomare, M. Cascarano, C. Giacovazzo, A. Guagliardi, *J. Appl. Crystallogr.* **1993**, *26*, 343–350.
[44] G. M. Sheldrick, *SHELXL93, Program for the Solution of Crystal Structures*, University of Göttingen, Germany, **1993**.
[45] L. J. Farrugia, *WINGX, A Windows Program for Crystal Structure Analysis*, University of Glasgow, Great Bretain, **1998**.
[46] M. Nardelli, *J. Appl. Crystallogr.* **1995**, *28*, 659.
[47] A. L. Spek, *Acta Crystallogr. Sect. A* **1990**, *46*, C34.
[48] J. Rodríguez-Carvajal, *FULLPROF, Program for Rietveld Pattern Matching Analysis of Powder Patterns*, Laboratoire Leon Brillouin, Saclay, France, **1997**.

Received: April 20, 2005
Published Online: September 12, 2005

 © 2005 Wiley-VCH Verlag GmbH & Co. KGaA, Weinheim

Generation and Reactions of Overcrowded Diaryldilithiostannane and Diaryldipotassiostannane

Tomoyuki Tajima,[a] Nobuhiro Takeda,[a] Takahiro Sasamori,[a] and Norihiro Tokitoh*[a]

Keywords: Group 14 elements / Tin / Anions / Lithium / Potassium / Solid-state structures

Exhaustive reduction of an overcrowded dibromostannane bearing two bulky aromatic substituents, Tbt(Dip)$SnBr_2$ {Tbt = 2,4,6-tris[bis(trimethylsilyl)methyl]phenyl; Dip = 2,6-diisopropylphenyl}, with an excess amount of lithium naphthalenide in THF at –78 °C gave the corresponding dilithiostannane, Tbt(Dip)$SnLi_2$, the generation of which was confirmed by trapping experiments with some electrophiles together with ^{119}Sn and ^{7}Li NMR spectroscopy. The diaryldilithiostannane was found to be stable in solution under an inert gas below –25 °C. The potassium analogue, Tbt(Dip)-SnK_2, was also generated by the reduction of the dibromostannane in THF at –78 °C by the use of KC_8 as a reductant. The reactions of dilithiostannane and dipotassiostannane obtained with *o*-dibromobenzene did not give a stannacyclopropabenzene derivative but an unexpected cyclization product, a stannacyclobutabenzene derivative, in contrast to the reactions of the corresponding dilithiosilane and dilithiogermane, Tbt(Dip)ELi_2 (E = Si, Ge), with *o*-dibromobenzene leading to the formation of the corresponding metallacyclopropabenzenes as stable crystalline compounds. A preliminary result of the synthesis of a tin–tellurium double-bond compound from the dilithiostannane is also presented.
(© Wiley-VCH Verlag GmbH & Co. KGaA, 69451 Weinheim, Germany, 2005)

Introduction

One of the most important classes of organometallic compounds is probably that of organolithium compounds, which are now recognized as very powerful synthetic tools in organic chemistry. Among them, the chemistry of lithium compounds of heavier group 14 elements has attracted considerable interest in recent years,[1] and some dilithiosilane and dilithiogermane derivatives have been structurally characterized and successfully applied to the construction of novel bondings and/or structures of heavier group 14 elements.[2] By contrast, there are very few reports on tin dianion species. Saito and his co-workers have recently reported the spectroscopic observation of a stannole dianion.[3] Although Schmidt et al. have proposed the formation of $(C_6H_5)_2SnLi_2$ in the reaction of $(C_6H_5)_2SnCl_2$ with 4 molar amounts of Li,[4,5] the yields of the trapping reactions are not high and the generation of dilithiodiphenylstannane was not evidenced by ^{119}Sn and ^{7}Li NMR spectroscopy. More recently, Egorov et al. reported the ^{119}Sn and ^{13}C NMR studies of Et_2SnLi_2 and $(C_6H_5)_2SnLi_2$.[6] The chemistry of tin-dianion species has recently gained more and more attention.

Meanwhile, the study of three-membered ring compounds containing a heavier group 14 element is one of the most fascinating research areas in main group element chemistry.[7,8] Recently, we have also succeeded in the synthesis and isolation of the first stable sila-[9] and germacyclopropabenzenes,[10] **2a** and **2b**, by reactions of the corresponding overcrowded dilithiosilane **1a**[11] and dilithiogermane **1b**[2g,10] with *o*-dibromobenzene, respectively. Although there have been many reports on the syntheses and characterization of Si- and Ge-containing three-membered ring compounds, investigations of their tin analogues, stannacyclopropanes and stannacyclopropenes,[8] are quite rare. To the best of our knowledge, only one report has so far appeared on the synthesis of stannacyclopropenes.[8c]

In this article, we report the generation of overcrowded, diaryl-substituted dilithiostannane and dipotassiostannane together with their attempted applications to the synthesis of a hitherto unknown stannacyclopropabenzene **2c** and a tin–tellurium double-bond compound,[12] stannanetellone (Scheme 1).

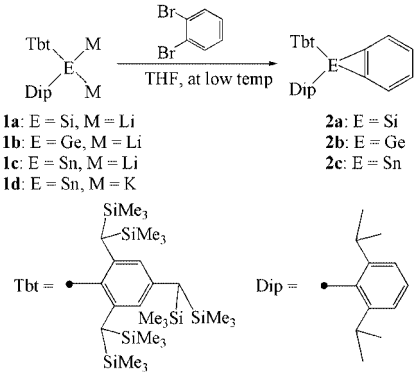

Scheme 1. Synthesis of metallacyclopropabenzenes using dianion species of group 14 elements.

[a] Institute for Chemical Research, Kyoto University, Gokasho, Uji, Kyoto 611-0011, Japan
Fax: +81-774-38-3209
E-mail: tokitoh@boc.kuicr.kyoto-u.ac.jp

Results and Discussion

Dibromostannane **4** was prepared by a method similar to that for the synthesis of Tbt(Mes)$SnBr_2$,[13] as shown in Scheme 2. Tbt-substituted trihalostannane was synthesized by the reaction of $SnCl_4$ with TbtLi. Tbt- and Dip-substituted stannane, Tbt(Dip)SnH_2 (**3**), was prepared by the nucleophilic displacement reaction of the Tbt-substituted trihalostannane using DipMgBr, followed by reduction with $LiAlH_4$. Bromination reaction of **3** using Br_2 in ether afforded the corresponding dibromostannane **4**.

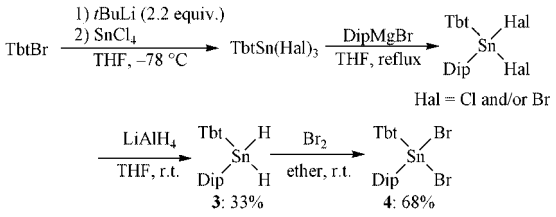

Scheme 2. Synthesis of dibromostannane **4**.

Tbt(Dip)$SnLi_2$ (**1c**) was generated by the exhaustive reduction of the overcrowded diaryldibromostannane **4** with an excess amount of lithium naphthalenide (5 equiv.) in dry THF at –78 °C under argon. The reaction mixture was stirred at the same temperature for 1 h, and then treated with an excess amount of MeI to afford Tbt(Dip)$SnMe_2$ (**5**) in 96% yield. The addition of DCl to the solution of **1c** at –78 °C resulted in the formation of Tbt(Dip)SnD_2 (**3a**) in 96% yield (D content: 93%) (Scheme 3). The formation of **3a** and **5** in the trapping experiments in high yields is most likely interpreted in terms of the almost quantitative generation of dilithiostannane **1c** as a stable compound in THF at –78 °C.

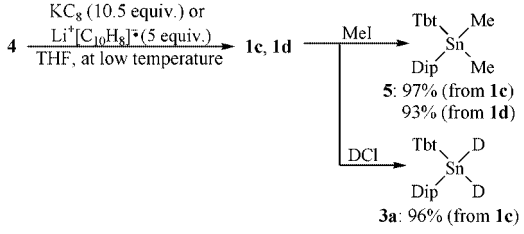

Scheme 3. Generation of overcrowded dilithiostannane **1c** and dipotassiostannane **1d**.

The ^{119}Sn NMR spectrum of **1c** in THF at –80 °C showed a broad signal at δ = –362.2 ppm, which is observed at a much higher field than that of Tbt(Dip)$SnBr_2$ (**4**: δ = –162.0 ppm in THF at –80 °C).[14] In the ^{7}Li NMR spectrum, only one singlet signal was observed at δ = 0.6 ppm, suggesting the rapid exchange of lithium cations between **1c** and LiBr. After the NMR sample was left at room temperature for a few days, the remeasurement of the ^{119}Sn NMR spectrum was performed. The ^{119}Sn NMR signal of **1c** disappeared and a new signal appeared at 1856.8 ppm, the chemical shift of which is close to those of stannylene species reported so far.[16]

Meanwhile, we have already succeeded in the generation of dilithiosilane **1a**[11] and dilithiogermane **1b**[2g,10] bearing Tbt and Dip groups on the silicon and germanium atoms, respectively. The thermal stability of **1a** and **1b** in THF solutions has been investigated by the trapping experiments using D_2O, which revealed that dilithiosilane **1a** was stable below –78 °C and dilithiogermane **1b** was stable below –25 °C. When the solutions of **1a** and **1b** were warmed above these temperatures, they underwent intramolecular proton abstraction from one of the *o*-$CH(SiMe_3)_2$ units of the Tbt group to give the corresponding lithium migration products **6a** and **6b**, respectively (Scheme 4).[10,11] Treatment of the intermediates such as **6a** and **6b** with D_2O afforded **7a** and **7b**, respectively. Similarly, thermal stability of **1c** was studied by the trapping reactions using MeI at various temperatures. The isolated yields of **5** in these reactions were 97% at –78 °C, 97% at –25 °C, and 45% at 0 °C, suggesting that dilithiostannane **1c** could be stable at least below –25 °C.

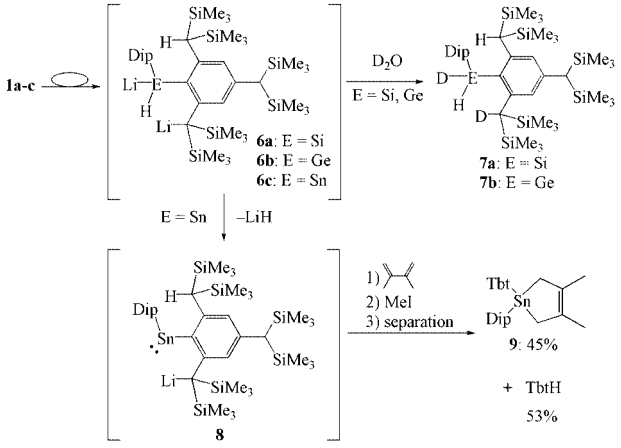

Scheme 4. Stability of **1a**, **1b**, and **1c**.

Trapping reactions of the decomposed compound from **1c** were performed. Treatment of the THF solution of **1c** with 2,3-dimethyl-1,3-butadiene at room temperature followed by the addition of MeI afforded TbtH and **9** (Scheme 4). The trapping experiment and the ^{119}Sn NMR studies suggest that dilithiostannane **1c** is initially formed and then it undergoes an intramolecular lithium migration reaction giving a lithium-migrated compound **6c** as in the case of **6a** and **6b**. However, the stability of **6c** is considered to be different from that of **6a** and **6b**. The formation of **9** strongly indicates that stannylene **8** is generated from **6c** by the elimination of LiH.

The reduction of **4** was alternatively performed with KC_8 in THF at –110 °C to give the corresponding dipotassiostannane **1d**, the generation of which was confirmed by the trapping experiment with MeI, giving **5** in 93% yield (Scheme 3). Dianion species **1d** was unstable at higher temperatures, and its purple solution in THF rapidly turned yellow at room temperature within a few minutes. The addition of H_2O to the yellow solution resulted in the formation of TbtH, DipH, and **10**[17] (Scheme 5). As this 1,3-silicon rearrangement product **10** was reportedly obtained from TbtLi above –30 °C in THF,[20] these results strongly suggest the initial formation of TbtK and DipK at low tem-

 © 2005 Wiley-VCH Verlag GmbH & Co. KGaA, Weinheim

perature in this reaction. Although we attempted the reactions of **4** with other reductants (Li, K, *t*BuLi, and *n*BuLi), the generation of the corresponding dianion species (**1c** or **1d**) was not confirmed.

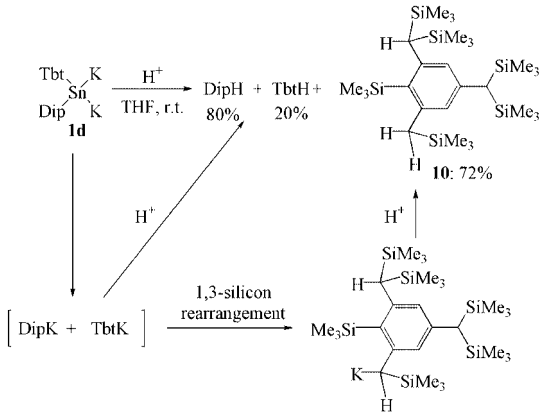

Scheme 5. Stability of **1d**.

With the evidence for the formation of dilithiostannane **1c** and dipotassiostannane **1d** in hand, we next attempted the synthesis of stannacyclopropabenzene **2c** by the method similar to those for the syntheses of **2a**[9] and **2b**.[10] However, the reactions of **1c** or **1d** with *o*-dibromobenzene gave an unexpected cyclic compound **11** as stable colorless crystals (16% yield from **1c** and 26% yield from **1d**) instead of the expected product **2c** (Scheme 6). The structure of the cyclic product **11** was satisfactorily confirmed by mass spectrometry, elemental analysis, and NMR spectroscopy, and the molecular structure of **11** was finally determined by X-ray crystallographic analysis. In Figure 1 the ORTEP drawing of stannacyclobutabenzene **11** is shown.[18] The deformation from the normal sp^2 configuration is larger on the C1 atom than the C6 atom, as judged by the bond angles of Sn1–C1–C6 [92.6(3)°] and C1–C6–C7 [114.4(4)°]. Additionally, the bond lengths of Sn1–C1 [2.144(4) Å] and C7–C6 [1.522(6) Å] are slightly shorter than those reported for stannabutabenzene [Sn1–C1 2.185(5) Å, C7–C6 1.588(8) Å].[18] All carbon–carbon bond lengths in the central benzene ring of **11** are almost equal.

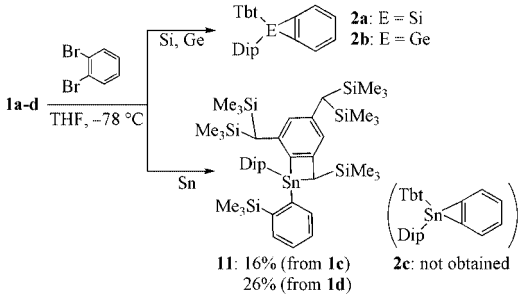

Scheme 6. Reaction of **1a**–**d** with *o*-dibromobenzene.

Although the detailed formation mechanism for **11** is not clear at present, compound **13** might be formed as an initial intermediate by the mechanism similar to those in the reactions of **1a** and **1b**; thus, the dilithiostannane **1c** or dipotassiostannane **1d** reacts with *o*-dibromobenzene to give

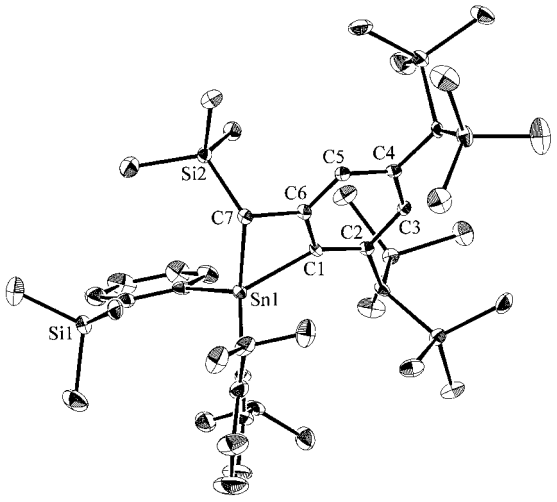

Figure 1. ORTEP drawing of **11** (50% probability). Hydrogen atoms are omitted for clarity. Selected bond lengths [Å] and angles [°]: Sn1–C1 2.144(4), Sn1–C7 2.205(4), C7–C6 1.522(6), C1–C2 1.398(6), C2–C3 1.397(6), C3–C4 1.411(6), C4–C5 1.402(6), C5–C6 1.379(6), C6–C1 1.407(6), C1–Sn1–C7 67.62(16), Sn1–C7–C6 87.2(3), C1–C6–C7 114.4(4), Sn1–C1–C6 92.6(3), C1–C2–C3 117.8(4), C2–C3–C4 122.5(4), C3–C4–C5 118.0(4), C4–C5–C6 120.3(4), C5–C6–C1 121.0(4), C6–C1–C2 120.3(4).

Tbt(Dip)SnMBr (M = Li, K) (**12**) and 1-bromo-2-metallabenzene by the M–Br exchange reaction, and then the resulting **12** adds to benzyne generated from 1-bromo-2-metallabenzene to afford the *o*-stannylated phenyl anion **13**. The intermediacy of **13** in these reactions is strongly supported by the fact that a small amount of Tbt(Dip)SnBr(Ph) (**14**; 6%) was obtained along with **11** (7%) when the reaction mixture was quenched by the addition of water after stirring for 3 h.

For the transformation of the anionic intermediate **13** into the final product **11**, we propose here two possible mechanisms as shown in Scheme 7. In the first mechanism, the intramolecular cyclization of **13** may give stannacyclopropabenzene **2c**, and the subsequent ring-opening reaction of the three-membered ring in **2c** results in the formation of cyclic compound **11** along with the 1,6-migration of a trimethylsilyl group (path A).[19] The other is the direct nucleophilic attack of the anionic center of **13** toward one of the trimethylsilyl groups followed by the ring-closure reaction giving **11** (path B).

In our previous works, there was no evidence of the formation of silicon or germanium analogues of the anionic intermediate **13** under any conditions for the reactions of dilithiosilane or dilithiogermane with *o*-dibromobenzene. In fact, these anionic species were not detected by quenching reactions using D_2O.[9,10] These results suggest that these anionic species of silicon and germanium readily undergo intramolecular cyclization reactions giving metallacyclopropabenzenes, **2a** and **2b**. Thus, the different results among the reactions of **1a**, **1b**, **1c**, and **1d** with *o*-dibromobenzene are most likely interpreted in terms of much lower reactivity of **13** in the intramolecular cyclization to give **2c** than that of the silicon and/or germanium analogues or instability of the strained stannacyclopropene ring of **2c**.

 © 2005 Wiley-VCH Verlag GmbH & Co. KGaA, Weinheim

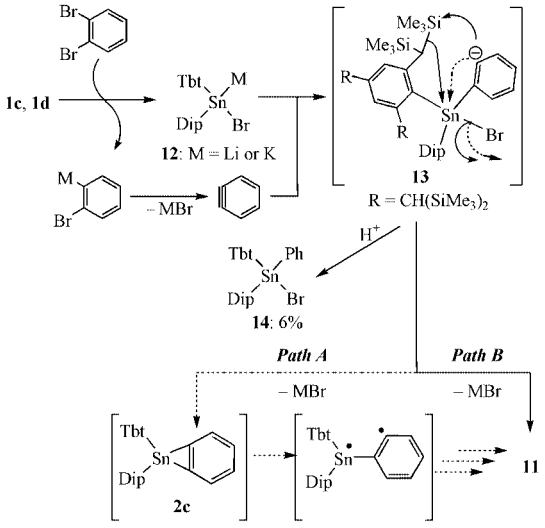

Scheme 7. Possible formation mechanism for **11**.

On the other hand, it is well known that dilithiosilanes and dilithiogermanes are useful for the preparation of double-bond compounds of heavier group 14 elements.[2] Recently, we reported the synthesis of silanetellone and germanetellone by the reactions of overcrowded dilithiometallanes **1a** and **1b** with tellurium(II) dichloride, respectively.[2g,20] Taking these results into account, the dilithiostannane should be a good precursor for the synthesis of a tin–tellurium double-bond compound **16**.[12] We reported that tin–chalcogen double-bond compounds having Tbt and 2,4,6-triisopropylphenyl (Tip) groups on the tin atom easily underwent self-dimerization, giving 1,3,2,4-dichalcogenastannetanes at room temperature.[13] In order to stabilize a stannanethione and stannanesellone effectively, it was necessary to use a combination of extremely bulky ligands such as 2,2′′-diisopropylphenyl-*m*-terphenyl-2′-yl (Ditp) and the Tbt group.[21] Therefore, we tried the synthesis of stannanetellone having Tbt and Ditp groups.

Interestingly, treatment of a THF solution of Tbt(Ditp)-$SnLi_2$ (**1e**)[22] with tellurium(II) dichloride[23] at –78 °C afforded a unique cyclic compound **18** (8%) along with TbtTeTeTbt (**19**; 11%), DitpH (**20**; 70%), and TbtH (73%), (Scheme 8). Orange crystals of **18** are stable under air for at least several weeks. The ^{119}Sn NMR signals of the cyclic compound, spirobi(ditelluradistannetane) **18**, were observed at δ = –149, –384, and –387 ppm in C_6D_6. The ^{125}Te NMR chemical shift of **18** was observed at δ = 762.9, 765.0, 766.0, and 771.3 ppm in C_6D_6. The molecular structure of **18** was finally determined by X-ray crystallographic analysis (Figure 2). Both ditelluradistannetane rings were found to be nearly planar (the sums of interior bond angles are about 359.99° and 359.91°, respectively). The three tin atoms are situated in a linear alignment (angle of Sn2–Sn1–Sn3: 179.9°). All Sn–Te bond lengths [2.7445(13)–2.7661(13)] Å are in the range reported for 1,3,2,4-ditelluradistannetanes, $[(Dis)_2SnTe]_2$ [Dis = –$CH(SiMe_3)_2$] [2.756(1) and 2.771(1) Å][24a] and $(tBu_2SnTe)_2$ [2.754(1) and 2.758(1) Å].[24b]

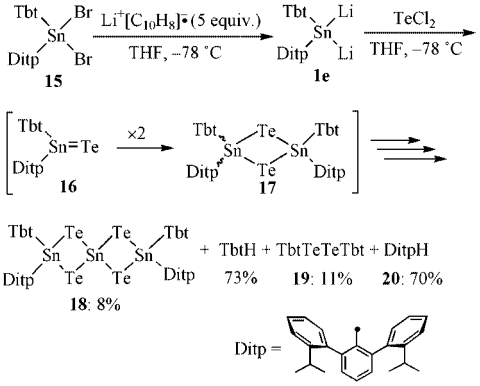

Scheme 8. Reaction of **1e** with tellurium(II) dichloride.

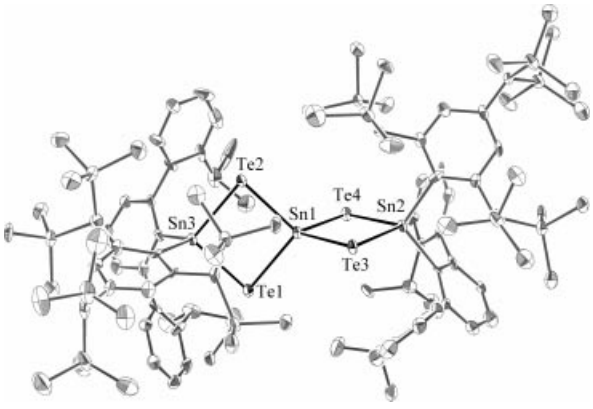

Figure 2. ORTEP drawing of **18**·1.5(toluene) (50% probability). Hydrogen atoms and solvated toluene molecules are omitted for clarity. Tbt and Ditp groups are described with gray lines for clarity. Selected bond lengths [Å] and angles [°]: Sn1–Te1 2.7445(13), Sn1–Te4 2.7526(13), Sn1–Te3 2.7536(13), Sn1–Te2 2.7574(13), Sn2–Te3 2.7577(13), Sn2–Te4 2.7657(13), Te1–Sn3 2.7661(13), Te2–Sn3 2.7627(13), Te4–Sn1–Te3 94.95(4), Te1–Sn1–Te2 95.03(4), Te3–Sn2–Te4 94.56(4), Sn1–Te1–Sn3 85.36(4), Sn1–Te2–Sn3 85.18(4), Te2–Sn3–Te1 94.42(4), Sn1–Te3–Sn2 85.27(4), Sn1–Te4–Sn2 85.13(4).

Although the formation mechanism of **18** is not clear at present, the formation of **18** can be explained in terms of a mechanism similar to the case of the formation of a spirobi(dithiasiletane) in the reaction of a silylene with S_8 through the corresponding silanethione and silanethione dimer.[25] Based on this report, the self-dimerization of stannanetellone **16**, which is generated in the reaction of dilithiostannane **1e** with tellurium(II) dichloride, afforded stannanetellone dimer **17** and the subsequent reactions of **17** result in the formation of cyclic compound **18**. The formation of **18** indicates that some amount of stannanetellone **16** might be generated in the reaction of **1e** with tellurium(II) dichloride; however, on the other hand, it suggests that stannanetellones are much less stable and much more difficult to isolate than the silicon and germanium analogues such as silanetellones and germanetellones and the lighter chalcogen analogues (e.g., stannanethiones and stannanesellones), because of the longer Sn–Te bonds and larger energy gaps between σ- and π-bond energies than those of the lighter element(s) analogues. In order to isolate a stable stannane-

 © 2005 Wiley-VCH Verlag GmbH & Co. KGaA, Weinheim

tellone, it is necessary to introduce a much more crowded combination of the protection groups than that in Tbt(Ditp)Sn=Te.

Conclusions

By taking advantage of a bulky substituent, Tbt group, we succeeded in the generation of diaryldimetallastannanes **1c**, **1d**, and **1e** by the exhaustive reduction of overcrowded diaryldibromostannanes **4** and **15**. We found that the reactions of **1c** and **1d** with *o*-dibromobenzene resulted in the formation of an unexpected compound **11** instead of the expected stannacyclopropabenzene **2c**. The reaction of **1e** with tellurium(II) dichloride afforded a novel cyclic compound **18**. As **1c** and **1d** were found to have enough stability in solution at low temperature, further investigation of their synthetic application toward a variety of tin-containing new chemical species is currently in progress.

Experimental Section

General: All experiments were performed under argon unless otherwise noted. THF was dried by standard methods and freshly distilled prior to use. ^{1}H NMR (300 MHz), ^{13}C NMR (75 MHz), ^{119}Sn NMR (111 MHz), and ^{125}Te NMR (94 MHz) spectra were measured in $CDCl_3$ or C_6D_6 with a JEOL JNM AL-300 spectrometer. ^{1}H and ^{13}C NMR chemical shifts were recorded in ppm relative to tetramethylsilane (δ = 0 ppm) and were referenced internally with respect to the residual proton impurity ($CHCl_3$: δ = 7.26 ppm, benzene: δ = 7.15 ppm) and the ^{13}C resonance of the solvent ($CDCl_3$: δ = 77.2 ppm, [D_6]benzene: δ = 128.0 ppm), respectively. ^{119}Sn NMR chemical shifts were referenced with tetramethylstannane (δ = 0 ppm) as an external standard. ^{125}Te NMR chemical shifts were referenced with diphenylditelluride (δ = 450 ppm) as an external standard. Fast atom bombardment (FAB) mass spectrometric data were obtained with a JEOL JMS-700 spectrometer. Mass spectrometric data (EI) were obtained with a Shimadzu QP-5000. Preparative gel permeation liquid chromatography (GPLC) was performed with an LC-918 apparatus (Japan Analytical Industry Co., Ltd.) equipped with JAIGEL 1H and 2H columns (eluent: $CHCl_3$ or toluene). Preparative thin-layer chromatography (PTLC) was performed with Merck Kieselgel 60 PF254. All melting points were determined with a Yanaco micro melting point apparatus and are uncorrected. IR spectra were measured at room temperature with a JASCO FT/IR-460 plus. Elemental analyses were carried out at the Microanalytical Laboratory of the Institute for Chemical Research, Kyoto University. 1-Bromo-2,4,6-tris[bis(trimethylsilyl)-methyl]benzene (TbtBr),[26] 1-bromo-2,6-diisopropylbenzene (DipBr),[27] and 2′-iodo-2,2′′-diisopropyl-1,1′:3′1′′-terphenyl (DitpI)[21] were prepared according to reported procedures.

Tbt(Dip)SnH$_2$ (3): *t*BuLi (2.30 N solution in pentane, 35.2 mL, 81.0 mmol) was added to a solution of TbtBr (22.5 g, 35.6 mmol) in THF (380 mL) at –78 °C. After the reaction mixture was stirred at the same temperature for 30 min, $SnCl_4$ (5.0 mL, 42.7 mmol) and LiCl (34.4 g, 0.81 mol) were added at –78 °C. The mixture was warmed to room temperature, and then the solvents were evaporated. After removal of the insoluble inorganic salts by filtration through Celite®, the reaction mixture was concentrated to give colorless crystals. Recrystallization from CH_3CN/$CHCl_3$ afforded a mixture of TbtSn(Hal)$_3$ (Hal = Cl and/or Br) (16.4 g). A THF solution (50 mL) of DipMgBr (5.78 g, 21.8 mmol), which was prepared by the reaction of Mg (602 mg, 24.8 mmol) and DipBr (5.25 g, 21.8 mmol), was added to a THF solution (100 mL) of the mixture of TbtSn$Cl_{3-n}Br_n$ (n = 0–3) (10.1 g) at room temperature. After the solution was stirred under reflux conditions for 16 h, the reaction mixture was cooled to room temperature. $LiAlH_4$ (6.00 g, 19.5 mmol) was added to the reaction mixture at 0 °C and then the mixture was stirred for 5 h. After quenching by an ice-cold 15% NaOH solution (100 mL) and the subsequent filtration to remove the insoluble inorganic salts, the organic layer was extracted. After extraction with hexane (50 mL), the organic layers were combined, washed with H_2O, and then dried with Na_2SO_4. After the removal of the solvent, the mixture was purified by column chromatography (SiO_2/hexane) to afford Tbt(Dip)SnH_2 (**3**) as colorless crystals. Yield: 4.0 g (33%). M.p. 155.5 °C (dec.). $C_{39}H_{78}Si_6Sn$ (834.26): calcd. C 56.15, H 9.42; found C 56.06, H 9.51. FAB-MS: *m*/*z* calcd. for $C_{39}H_{78}Si_6{}^{120}Sn$ 834 [M$^+$], found 834 [M$^+$]. ^{1}H NMR (300 MHz, C_6D_6, 25 °C): δ = 0.30 (s, 9 H, $SiMe_3$), 0.32 (s, 36 H, $SiMe_3$), 0.35 (s, 9 H, $SiMe_3$), 1.34 (d, $^3J_{HH}$ = 5.5 Hz, 6 H, CH_3), 1.51 (d, $^3J_{HH}$ = 5.5 Hz, 6 H, CH_3), 1.61 (s, 1 H, *p*-BnH for Tbt), 2.15 (br. s, 1 H, *o*-BnH for Tbt), 2.45 (br. s, 1 H, *o*-BnH for Tbt), 2.91 (sept, $^3J_{HH}$ = 5.5 Hz, 2 H, BnH for Dip), 6.38 (s, $^1J_{^{117}SnH}$ = 1769.4, $^1J_{^{119}SnH}$ = 1855.2 Hz, 2 H, SnH_2), 6.73 (br. s, 1 H, *m*-PhH for Tbt), 6.87 (br. s, 1 H, *m*-PhH for Tbt), 7.14–7.50 (m, 3 H, *m*- and *p*-PhH for Dip) ppm. ^{13}C NMR (75 MHz, C_6D_6, 25 °C): δ = 0.6 (q), 1.0 (q), 1.2 (q), 25.1 (q), 30.6 (d), 33.3 (d), 37.5 (d × 2), 122.1 (d), 123.1 (d), 127.0 (d), 130.1 (d), 135.6 (s), 140.1 (s), 143.9 (s), 151.74 (s), 151.83 (s), 155.4 (s) ppm. ^{119}Sn{^{1}H} NMR (111 MHz, C_6D_6, 25 °C): δ = –345.6 ppm. IR (KBr): $\tilde{\nu}$ = 1863.9 [ν(Sn–H)] cm^{-1}.

Tbt(Dip)SnBr$_2$ (4): A solution of **3** (3.70 g, 4.43 mmol) and Br_2 (0.50 mL, 9.76 mmol) in Et_2O (130 mL) was stirred at room temperature for 2 h. The solution was washed with an aqueous solution of NaOH and then with a saturated aqueous solution of NaCl. The organic layer was dried with Na_2SO_4. After the removal of the solvent, the residue was recrystallized from $CHCl_3$ and EtOH to afford **4** as colorless crystals. Yield: 2.98 g (68%). M.p. 188.4–192.5 °C. $C_{39}H_{76}Br_2Si_6Sn$ (992.05): calcd. C 47.22, H 7.72; found C 47.24, H 7.82. FAB-MS: *m*/*z* calcd. for $C_{39}H_{76}{}^{79}Br_2Si_6{}^{120}Sn$ 992 [M$^+$], found 992 [M$^+$]. ^{1}H NMR (300 MHz, $CDCl_3$, 25 °C): δ = 0.03 (s, 36 H, $SiMe_3$), 0.05 (s, 18 H, $SiMe_3$), 1.16 (s, 1 H, *p*-BnH for Tbt), 1.33 (d, $^3J_{HH}$ = 6.6 Hz, 12 H, CH_3), 2.13 (br. s, 1 H, *o*-BnH for Tbt), 2.43 (br. s, 1 H, *o*-BnH for Tbt), 3.36 (sept, $^3J_{HH}$ = 6.6 Hz, 2 H, BnH for Dip), 6.37 (br. s, 1 H, *m*-PhH for Tbt), 6.47 (br. s, 1 H, *m*-PhH for Tbt), 7.20–7.42 (m, 3 H, *m*- and *p*-PhH for Dip) ppm. ^{13}C NMR (75 MHz, $CDCl_3$, 25 °C): δ = 1.2 (q), 1.8 (q), 2.0 (q), 26.4 (q), 31.1 (d), 31.8 (d), 37.4 (d × 2), 123.6 (d), 125.4 (d), 128.4 (d), 131.6 (d), 133.7 (s), 137.5 (s), 143.8 (s), 146.7 (s), 151.0 (s), 154.5 (s) ppm. ^{119}Sn NMR (111 MHz, $CDCl_3$, 25 °C): δ = –171.0 ppm.

Generation of Tbt(Dip)SnM$_2$ (M = Li, K) and Preparation of Tbt(Dip)SnMe$_2$ (5). Method A (M = Li): Lithium naphthalenide (2.33 N solution in THF, 0.14 mL, 0.33 mmol, 5 molar amounts) was added to a THF solution (1.0 mL) of **4** (62.4 mg, 62.9 μmol) at –78 °C. The reaction mixture was stirred at the same temperature for 1 h, and then an excess amount of MeI (0.1 mL, 1.6 mmol) was added to the reaction mixture. After the removal of the solvent, the residue was extracted with hexane several times. Insoluble inorganic salts were removed by filtration through Celite®. The residue was subjected to GPLC ($CHCl_3$) followed by PTLC (hexane) to afford **5** as colorless crystals. Yield: 52.7 mg (97%). **Method B (M = K):** KC_8 (98.0 mg, 0.72 mmol) was added to a THF solution (1.0 mL) of **4** (68.0 mg, 68.5 μmol) at –110 °C. The reaction mixture was stirred vigorously at the same temperature for 1 h, and

 © 2005 Wiley-VCH Verlag GmbH & Co. KGaA, Weinheim

then an excess of MeI (0.1 mL, 1.6 mmol) was added to the mixture. A similar workup procedure mentioned above afforded **5** as colorless crystals. Yield: 63.5 mg (93%). M.p. 167.9–174.3 °C. $C_{41}H_{82}Si_6Sn$ (862.31): calcd. C 57.11, H 9.58; found C 56.96, H 9.59. FAB-MS: *m*/*z* calcd. for $C_{41}H_{82}Si_6{}^{120}Sn$ 863 [M$^+$], found 863 [M$^+$]. ^{1}H NMR (300 MHz, $CDCl_3$, 25 °C): δ = –0.05 (s, 18 H, $SiMe_3$), –0.01 (s, 18 H, $SiMe_3$), 0.02 (s, 18 H, $SiMe_3$), 0.64 (s, $^2J_{HSn}$ = 48.3 Hz, 6 H, SnMe), 1.23 (d, $^3J_{HH}$ = 5.5 Hz, 12 H, CH_3), 1.31 (s, 1 H, *p*-BnH for Tbt), 1.68 (br. s, 1 H, *o*-BnH for Tbt), 1.84 (br. s, 1 H, *o*-BnH for Tbt), 2.99 (sept, $^3J_{HH}$ = 5.5 Hz, 2 H, BnH for Dip), 6.25 (br. s, 1 H, *m*-PhH for Tbt), 6.38 (br. s, 1 H, *m*-PhH for Tbt), 7.18–7.40 (m, 3 H, *m*- and *p*-PhH for Dip) ppm. ^{13}C NMR (75 MHz, C_6D_6, 25 °C): δ = 0.9 (q), 1.2 (q), 1.5 (q), 3.7 (q), 26.0 (q), 30.0 (d), 30.7 (d), 30.9 (d), 36.5 (d), 122.1 (d), 123.1 (d), 127.0 (d), 128.9 (d), 131.8 (s), 137.2 (s), 143.0 (s), 143.9 (s), 151.3 (s), 155.4 (s) ppm. ^{119}Sn NMR (111 MHz, $CDCl_3$, 25 °C): δ = –126.4 ppm.

Generation of Tbt(Dip)SnLi$_2$ and the Trapping Reaction with DCl: Lithium naphthalenide (1.26 N solution in THF, 0.22 mL, 0.28 mmol, 5 molar amounts) was added to a THF solution (1.0 mL) of **4** (58.6 mg, 59.1 μmol) at –78 °C. The reaction mixture was stirred at the same temperature for 1 h. After stirring for 30 min, DCl (1.0 N solution in Et_2O, 75 μL) was added to the reaction mixture. After the removal of the solvent, the mixture was extracted with hexane several times. The extracts were combined, filtered through Celite®, and the solvents evaporated. The residue was subjected to GPLC (toluene) to give Tbt(Dip)SnD_2 (**3a**) as colorless crystals. Yield: 47.5 mg [96% (deuterium content: 93%)]. M.p. 154.8 °C (dec.). High-resolution FAB-MS: *m*/*z* calcd. for $C_{39}H_{76}D_2Si_6{}^{120}Sn$ 836.3865 [M$^+$], found 836.3894 [M$^+$]. ^{1}H NMR (300 MHz, C_6D_6, 25 °C): δ = 0.30 (s, 9 H, $SiMe_3$), 0.32 (s, 36 H, $SiMe_3$), 0.35 (s, 9 H, $SiMe_3$), 1.34 (d, $^3J_{HH}$ = 5.5 Hz, 6 H, CH_3), 1.51 (d, $^3J_{HH}$ = 5.5 Hz, 6 H, CH_3), 1.61 (s, 1 H, *p*-BnH for Tbt), 2.15 (br. s, 1 H, *o*-BnH for Tbt), 2.45 (br. s, 1 H, *o*-BnH for Tbt), 2.91 (sept, $^3J_{HH}$ = 5.5 Hz, 2 H, BnH for Dip), 6.73 (br. s, 1 H, *m*-PhH for Tbt), 6.87 (br. s, 1 H, *m*-PhH for Tbt), 7.14–7.50 (m, 3 H, *m*- and *p*-PhH for Dip) ppm. ^{13}C NMR (75 MHz, C_6D_6, 25 °C): δ = 0.6 (q), 1.0 (q), 1.2 (q), 25.1 (q), 30.6 (d), 33.3 (d), 37.5 (d × 2), 122.1 (d), 123.1 (d), 127.0 (d), 130.1 (d), 135.6 (s), 140.1 (s), 143.9 (s), 151.74 (s), 151.83 (s), 155.4 (s) ppm. ^{119}Sn NMR (111 MHz, C_6D_6, 25 °C): δ = –346.8 (quint, $^1J_{SnD}$ = 280.7 Hz) ppm. IR (KBr): $\tilde{\nu}$ = 1317.1 [ν(Sn–D)] cm^{-1}.

Generation of Tbt(Dip)SnLi$_2$ (1c) and the Trapping Reaction of the Decomposed Compounds with 2,3-Dimethyl-1,3-butadiene and MeI: Lithium naphthalenide (1.03 N solution in THF, 0.25 mL, 0.26 mmol, 5 molar amounts) was added to a THF solution (1.0 mL) of **4** (50.2 mg, 50.0 μmol) at –78 °C. The reaction mixture was stirred at the same temperature for 1 h. After additional stirring at room temperature for 30 min, 2,3-dimethyl-1,3-butadiene (0.1 mL, 82.0 μmol) was added. After stirring for 30 min, an excess of MeI (0.1 mL, 1.6 mmol) was added to the reaction mixture. After the removal of the solvent, hexane was added to the residue. Insoluble inorganic salts were removed by filtration through Celite® and the filtrate was concentrated. The residue was subjected to GPLC ($CHCl_3$) followed by PTLC (hexane) to give TbtH (14.7 mg, 53%) and **9** (20.4 mg, 45%). M.p. 164.2–166.4 °C. FAB-MS: *m*/*z* calcd. for $C_{45}H_{87}Si_6{}^{120}Sn$ 915 [M + H]$^+$, found 915 [M + H]$^+$. High-resolution FAB-MS: *m*/*z* calcd. for $C_{45}H_{87}Si_6{}^{120}Sn$ 915.4445 [M + H]$^+$, found 915.4456 [M + H]$^+$. ^{1}H NMR (300 MHz, $CDCl_3$, 25 °C): δ = –0.05 (br. s, 18 H, $SiMe_3$), –0.24 (br. s, 18 H, $SiMe_3$), 0.03 (s, 18 H, $SiMe_3$), 1.19 (d, $^3J_{HH}$ = 6.6 Hz, 9 H, CH_3 for Dip), 1.19 (br. s, 1 H, *p*-BnH for Tbt), 1.28 (d, $^3J_{HH}$ = 6.6 Hz, 3 H, CH_3 for Dip), 1.68 (s, 1 H, *o*-BnH for Tbt), 1.74 (br. s, 6 H, CH_3), 1.79 (s, 1 H, *o*-BnH for Tbt), 2.09 (d, ^2J = 17.0 Hz, 2 H, CH_2), 2.14 (d, ^4J = 17.0 Hz, 2 H, CH_2), 3.02 (sept, $^3J_{HH}$ = 6.6 Hz, 1 H, BnH for Dip), 3.12 (sept, $^3J_{HH}$ = 6.6 Hz, 1 H, BnH for Dip), 6.27 (br. s, 1 H, *m*-PhH for Tbt), 6.41 (s, 1 H, *m*-PhH for Tbt), 7.12 (d, $^3J_{HH}$ = 7.5 Hz, 2 H, *m*-PhH for Dip), 7.23 (t, $^3J_{HH}$ = 7.5 Hz, 1 H, *p*-PhH for Dip) ppm. ^{13}C NMR (75 MHz, $CDCl_3$, 25 °C): δ = 0.8 (q), 1.1 (q), 1.3 (q), 21.4 (q), 24.9 (q), 25.8 (q), 30.1 (d), 31.1 (d), 31.5 (d × 2), 32.6 (t), 37.9 (d), 122.0 (d), 123.1 (d), 124.6 (d), 128.9 (d), 131.7 (s), 137.7 (s), 141.2 (s), 142.9 (s), 145.7 (s), 151.2 (s), 154.7 (s) ppm. ^{119}Sn NMR (111 MHz, $CDCl_3$, 25 °C): δ = –110.2 ppm.

Generation of Tbt(Dip)SnK$_2$ and the Trapping Reaction of the Decomposed Compounds with H$_2$O at Room Temperature: KC_8 (129 mg, 0.95 mmol) was added to a THF solution (1.5 mL) of **4** (101 mg, 0.10 mmol) at –110 °C. The reaction mixture was stirred vigorously at the same temperature for 1 h, and then warmed to room temperature. After additional stirring at the same temperature for 1 h, the reaction mixture was exposed to air. After the removal of the solvent, the mixture was extracted with hexane several times. Insoluble inorganic salts were removed by filtration through Celite® and the filtrate was concentrated. The residue was subjected to GPLC ($CHCl_3$) followed by PTLC (hexane) to give TbtH (12.1 mg, 20%), **10** (39.7 mg, 72%), and DipH (14.1 mg, 80%).[17]

Stannacyclobutabenzene (11). Method A: Lithium naphthalenide (1.56 N solution in THF, 0.67 mL, 5 molar amounts) was added to a THF solution (5.0 mL) of **4** (205 mg, 0.21 mmol) at –78 °C. After stirring at the same temperature for 1 h, *o*-dibromobenzene (25 μL, 0.21 mmol) was added to the reaction mixture. The solution was slowly warmed to room temperature over 10 h. After the removal of the solvent, hexane was added to the residue. Insoluble inorganic salts were removed by filtration through Celite® and the filtrate was concentrated. The residue was subjected to GPLC ($CHCl_3$) followed by PTLC (hexane) to give **11** as colorless crystals. Yield: 30.1 mg (16%). **Method B:** KC_8 (150 mg, 1.11 mmol) was added to a THF solution (3.0 mL) of Tbt(Dip)$SnBr_2$ (**4**) (170 mg, 0.17 mmol) at –78 °C. After stirring at the same temperature for 1 h, *o*-dibromobenzene (25 μL, 0.21 mmol) was added to the reaction mixture. The solution was slowly warmed to room temperature over 10 h, and **11** was separated and purified by a procedure similar to that described above. Yield: 40.1 mg (26%). M.p. 99.4 °C (dec.). $C_{45}H_{80}Si_6Sn$ (908.34): calcd. C 59.50, H 8.88; found C 59.53, H 8.63. FAB-MS: *m*/*z* calcd. for $C_{45}H_{80}Si_6{}^{120}Sn$ 908 [M$^+$], found 908 [M$^+$]. ^{1}H NMR (300 MHz, $CDCl_3$, 25 °C): δ = –0.26 (s, 9 H, $SiMe_3$), –0.16 (s, 9 H, $SiMe_3$), 0.02 (s, 9 H, $SiMe_3$), 0.04 (s, 9 H, $SiMe_3$), 0.15 (s, 9 H, $SiMe_3$), 0.17 (s, 9 H, $SiMe_3$), 0.86 (br. s, 6 H, Me), 1.24 (br. s, 6 H, Me), 1.34 (s, 1 H, BnH), 1.57 (s, 1 H, BnH), 2.94 (s, $^2J_{HSn}$ = 64 Hz, 1 H, BnH), 3.29 (br. s, 2 H, BnH for Dip), 6.39 (br. s, 1 H, *m*-PhH for Tbt), 6.45 (s, 1 H, *m*-PhH for Tbt), 7.07 (d, $^3J_{HH}$ = 7.2 Hz, 2 H, *m*-PhH for Dip), 7.20–7.27 (m, 2 H, PhH), 7.30 (t, $^3J_{HH}$ = 7.2 Hz, 1 H, *p*-PhH for Dip), 7.60 (dd, $^3J_{HH}$ = 7.2, $^4J_{HH}$ = 2.1 Hz, 1 H, PhH), 7.93 (dd, $^3J_{HH}$ = 7.2, $^4J_{HH}$ = 2.1 Hz, 1 H, PhH) ppm. ^{13}C NMR (75 MHz, $CDCl_3$, 50 °C): δ = 0.2 (q), 0.39 (q), 0.44 (q), 0.5 (q), 0.6(q), 1.1 (q), 24.9 (br. q), 30.2 (d), 30.4 (d), 37.1 (d), 39.7 (d), 121.8 (br. d), 123.2 (d), 123.4 (d), 127.5 (d), 128.0 (d), 129.5 (d), 135.8 (d), 138.0 (d), 143.9 (s), 145.0 (s), 145.1 (s), 147.5 (s), 147.7 (s), 154.6 (s), 155.0 (s), 155.8 (s) ppm. ^{119}Sn{^{1}H} NMR (111 MHz, $CDCl_3$, 25 °C): δ = –83.4 ppm.

Tbt(Dip)Sn(Ph)Br (14): Lithium naphthalenide (1.30 N solution in THF, 1.87 mL, 5 molar amounts) was added to a THF solution (10 mL) of **4** (479 mg, 0.48 mmol) at –78 °C. After stirring at the same temperature for 1 h, *o*-dibromobenzene (65 μL, 0.54 mmol)

 © 2005 Wiley-VCH Verlag GmbH & Co. KGaA, Weinheim

was added to the reaction mixture. The solution was stirred for 3 h, and then the mixture was separated by the procedure similar to that described above to afford **11** (29.0 mg, 7%) and **14** (29.6 mg, 6%). M.p. 155.8 °C (dec.). FAB-MS: *m*/*z* calcd. for $C_{45}H_{81}{}^{79}BrSi_6{}^{120}Sn$ 988 [M$^+$], found 988 [M$^+$]. High-resolution FAB-MS: *m*/*z* calcd. for $C_{45}H_{81}{}^{79}BrSi_6{}^{120}Sn$ 988.3159 [M$^+$], found 988.3193 [M$^+$]. ^{1}H NMR (300 MHz, $CDCl_3$, 25 °C): δ = –0.16 (s, 27 H, $SiMe_3$), –0.13 (s, 9 H, $SiMe_3$), –0.07 (s, 9 H, $SiMe_3$), –0.06 (s, 9 H, $SiMe_3$), 0.83 (d, $^3J_{HH}$ = 6.3 Hz, 6 H, Me), 1.20 (d, $^3J_{HH}$ = 6.3 Hz, 6 H, Me), 1.23 (s, 1 H, *p*-BnH for Tbt), 1.97 (br. s, 1 H, *o*-BnH for Tbt), 2.02 (br. s, 1 H, *o*-BnH for Tbt), 3.18 (sept, $^3J_{HH}$ = 6.3 Hz, 2 H, BnH for Dip), 6.24 (br. s, 1 H, *m*-PhH for Tbt), 6.36 (br. s, 1 H, *m*-PhH for Tbt), 7.05–7.13 (m, 2 H, PhH), 7.20–7.28 (m, 4 H, PhH), 7.59–7.82 (m, 2 H, PhH) ppm. ^{13}C NMR (75 MHz, $CDCl_3$, 25 °C): δ = 0.8 (q), 1.0 (q), 1.7 (q), 1.9 (q), 24.3 (q), 27.2 (q), 30.5 (d), 31.1 (d), 31.5 (d), 36.8 (d), 122.9 (d), 124.6 (d), 127.2 (d), 128.3 (d), 129.2 (d), 130.3 (d), 136.5 (d), 138.4 (s), 140.2 (s), 144.9 (s), 147.0 (s), 151.2 (s), 154.6 (s), 155.2 (s) ppm. ^{119}Sn{^{1}H} NMR (111 MHz, $CDCl_3$, 25 °C): δ = –102.2 ppm.

Synthesis of Tbt(Ditp)SnH$_2$: A THF solution (20 mL) of $TbtSn(Hal)_3$ (2.31 g) was added to a THF solution of DitpLi, prepared from DitpI (1.49 g, 3.37 mmol) and *t*BuLi (2.32 M in pentane, 3.2 mL, 7.41 mmol) at –78 °C in THF (20 mL), at –78 °C, and then the mixture was stirred at room temperature for 2 h. After the removal of the solvent, hexane was added to the residue. Insoluble inorganic salts were removed by filtration through Celite®. The filtrate was concentrated and subjected to GPLC ($CHCl_3$) to afford a mixture containing $Tbt(Ditp)Sn(Hal)_2$ (1.48 g) as colorless crystals. $LiAlH_4$ (734 mg, 19.3 mmol) was added to a THF solution (50 mL) of the mixture containing $Tbt(Ditp)Sn(Hal)_2$ (1.28 g) at 0 °C. The mixture was stirred at room temperature for 3 h. After quenching by an ice-cold 15% NaOH solution (30 mL) and subsequent filtration to remove the insoluble inorganic salts, the organic layer was extracted. After extraction with hexane (50 mL), the organic layers were combined, and washed with H_2O, and then dried with Na_2SO_4. After removal of the solvents, the mixture was purified by column chromatography (SiO_2/benzene) to afford $Tbt(Ditp)SnH_2$ as colorless crystals. Yield 962 mg (29%). M.p. 155.5 °C (dec.). FAB-MS: *m*/*z* calcd. for $C_{51}H_{87}Si_6{}^{118}Sn$ 985 [M + H]$^+$, found 985 [M + H]$^+$. ^{1}H NMR (300 MHz, C_6D_6, 25 °C): δ = 0.09 (s, 36 H, $SiMe_3$), 0.20 (s, 18 H, $SiMe_3$), 0.95 (d, $^3J_{HH}$ = 5.1 Hz, 6 H, Me), 1.40 (d, $^3J_{HH}$ = 5.1 Hz, 6 H, Me), 1.43 (s, 1 H, *p*-BnH for Tbt), 1.71 (br. s, 1 H, *o*-BnH for Tbt), 1.85 (br. s, 1 H, *o*-BnH for Tbt), 3.01 (sept, $^3J_{HH}$ = 5.1 Hz, 2 H, BnH for Ditp), 5.66 (s, $^1J_{^{117}SnH}$ = 1768.6, $^1J_{^{119}SnH}$ = 1851.7 Hz, 2 H, SnH), 6.41 (br. s, 1 H, *m*-PhH for Tbt), 6.53 (br. s, 1 H, *m*-PhH for Tbt), 7.09–7.26 (m, 9 H, ArH for Ditp), 7.52 (d, $^3J_{HH}$ = 6.6 Hz, 2 H, ArH for Ditp) ppm. ^{13}C NMR (75 MHz, C_6D_6, 25 °C): δ = 1.1 (q), 1.7 (q), 22.4 (q), 24.8 (q), 30.2 (d), 30.4 (d), 32.4 (d × 2), 122.5 (d), 125.4 (d), 125.7 (d), 126.2 (d), 128.9 (d), 129.4 (d), 129.7 (d), 135.3 (d), 139.0 (s), 141.2 (s), 143.2 (s), 143.7 (s) 147.2 (s), 149.8 (s), 151.2 (s) 151.3 (s) ppm. ^{119}Sn{^{1}H} NMR (111 MHz, C_6D_6, 25 °C): δ = –342.9 ppm. IR (KBr): $\tilde{\nu}$ = 1841.7 [ν(Sn–H)] cm^{-1}.

Synthesis of Tbt(Ditp)SnBr$_2$ (15): A solution of $Tbt(Ditp)SnH_2$ (734 mg, 0.74 mmol) and Br_2 (0.21 mL, 0.84 mmol) in Et_2O (40 mL) was stirred at room temperature for 30 min. The solution was washed with a saturated aqueous solution of Na_2SO_3 and then with a saturated aqueous solution of NaCl. The organic layer was dried with Na_2SO_4. After the removal of the solvent, the residue was recrystallized from $CHCl_3$ and EtOH to afford **15** as colorless crystals. Yield: 621 mg (73%). M.p. 278.5–279.6 °C. $C_{51}H_{84}Br_2Si_6Sn$ (1144.24): calcd. C 53.53, H 7.40; found C 53.52, H 7.46. FAB-MS: *m*/*z* calcd. for $C_{51}H_{84}{}^{79}Br_2Si_6{}^{120}Sn$ 1144 [M$^+$], found 1144 [M$^+$]. ^{1}H NMR (300 MHz, C_6D_6, 25 °C): δ = 0.19 (br. s, 36 H, $SiMe_3$), 0.21 (br. s, 18 H, $SiMe_3$), 1.03 (d, $^3J_{HH}$ = 6.3 Hz, 6 H, Me), 1.39 (d, $^3J_{HH}$ = 6.3 Hz, 6 H, Me), 1.51 (br. s, 1 H, *p*-BnH for Tbt), 1.80 (br. s, 1 H, *o*-BnH for Tbt), 2.82 (br. s, 1 H, *o*-BnH for Tbt), 2.96 (sept, $^3J_{HH}$ = 6.3 Hz, 2 H, BnH for Ditp), 6.37–6.75 (m, 2 H, *m*-PhH for Tbt), 7.01–7.35 (m, 9 H, ArH for Ditp), 7.45 (d, $^3J_{HH}$ = 7.2 Hz, 2 H, ArH for Ditp) ppm. ^{13}C NMR (75 MHz, C_6D_6, 25 °C): δ = 0.6 (q), 1.9 (q), 2.4 (q), 2.6 (q), 23.2 (q), 25.2 (q), 30.0 (d), 31.1 (d), 32.8 (d), 33.1 (d), 123.4 (d), 123.9 (d), 126.3 (d), 126.9 (d), 128.8 (d), 129.4 (d), 129.7 (d), 135.3 (d), 141.1 (s × 2), 142.9 (s), 146.1 (s), 146.4 (s) 147.7 (s), 148.8 (s), 153.5 (s) ppm. ^{119}Sn{^{1}H} NMR (111 MHz, $CDCl_3$, 25 °C): δ = –192.5 ppm.

Generation of Tbt(Ditp)SnLi$_2$ and Preparation of Tbt(Ditp)SnMe$_2$: Lithium naphthalenide (1.30 N solution in THF, 0.15 mL, 0.20 mmol, 5 molar amounts) was added to a THF solution (1.0 mL) of **15** (45.6 mg, 39.8 μmol) at –78 °C. The reaction mixture was stirred at the same temperature for 1 h, and then MeI (0.1 mL, 1.6 mmol) was added to the reaction mixture. After the removal of the solvent, hexane was added to the residue. Insoluble inorganic salts were removed by filtration through Celite®. The filtrate was concentrated and subjected to GPLC ($CHCl_3$) followed by PTLC (hexane) to afford $Tbt(Ditp)SnMe_2$ as colorless crystals. Yield: 38.1 mg (93%). M.p. 265.3–265.7 °C. $C_{53}H_{90}Si_6Sn$ (1014.50): calcd. C 62.75, H 8.94; found C 62.67, H 9.05. High-resolution FAB-MS: *m*/*z* calcd. for $C_{53}H_{90}Si_6{}^{120}Sn$ 1014.4680 [M$^+$], found 1014.4697 [M$^+$]. ^{1}H NMR (300 MHz, $CDCl_3$, 25 °C): δ = –0.45 (s, $^2J_{HSn}$ = 51.0 Hz, 6 H, SnMe), –0.04 (br. s, 36 H, $SiMe_3$), –0.09 (s, 18 H, $SiMe_3$), 1.04 (d, $^3J_{HH}$ = 6.6 Hz, 6 H, Me), 1.15 (d, $^3J_{HH}$ = 6.6 Hz, 6 H, Me), 1.27 (s, 1 H, *p*-BnH for Tbt), 1.32 (br. s, 2 H, *o*-BnH for Tbt), 2.71 (sept, $^3J_{HH}$ = 6.6 Hz, 2 H, BnH for Ditp), 6.25 (br. s, 1 H, *m*-PhH for Tbt), 6.40 (br. s, 1 H, *m*-PhH for Tbt), 6.98 (t, $^3J_{HH}$ = 7.2 Hz, 1 H, PhH for Ditp), 7.13 (d, $^3J_{HH}$ = 7.2 Hz, 2 H, PhH for Ditp), 7.21–7.39 (m, 8 H, PhH for Ditp) ppm. ^{13}C NMR (75 MHz, $CDCl_3$, 25 °C): δ = –0.4 (q, $^1J_{^{117}SnC}$ = 339.6, $^1J_{^{119}SnC}$ = 346.0 Hz), 1.0 (q), 1.9 (q), 2.2 (q), 22.8 (q), 24.9 (q), 29.2 (d × 2), 29.8 (d), 31.1 (d), 121.9 (d), 122.5 (d), 125.4 (d), 125.8 (d), 126.8 (d), 127.7 (d), 128.9 (d), 130.0 (d, $^3J_{SnC}$ = 37.7 Hz), 140.1 (s), 142.3 (s), 143.1 (s), 143.7 (s), 147.3 (s), 148.2 (s), 150.3 (s), 150.7 (s) ppm. ^{119}Sn{^{1}H} NMR (111 MHz, $CDCl_3$, 25 °C): δ = –114.9 ppm.

Reaction of Tbt(Ditp)SnLi$_2$ (1e) with Tellurium(II) Dichloride: Lithium naphthalenide (1.24 N solution in THF, 0.38 mL, 0.47 mmol, 5 molar amounts) was added to a THF solution (1.0 mL) of **15** (108 mg, 94.0 μmol) at –78 °C. After stirring at the same temperature for 1 h, tellurium(II) dichloride (20.2 mg, 101 μmol) was added to the reaction mixture. The solution was slowly warmed to room temperature over 10 h. After the removal of the solvent, hexane was added to the residue. Insoluble inorganic salts were removed by filtration through Celite® and the solvents evaporated. The residue was subjected to GPLC (toluene) to give TbtH (37.8 mg, 73%), **18** (19.6 mg, 8%), **19** (20.2 mg, 11%), and **20** (20.6 mg, 70%). **18:** Orange crystals. M.p. 129.7 °C (dec.). $C_{102}H_{168}Si_{12}Sn_3Te_4$·1.5(toluene) (2736.22): calcd. C 49.38, H 6.63; found C 49.03, H 6.85. FAB-MS: *m*/*z* calcd. for $C_{51}H_{84}Si_6{}^{120}Sn_2{}^{130}Te_3$ 1488 [{M – Tbt(Ditp)SnTe}$^+$], found 1488 [{M – Tbt(Ditp)SnTe}$^+$], $C_{51}H_{84}Si_6{}^{120}Sn{}^{130}Te$ 1115 [{M – $Tbt(Ditp)Sn_2Te_3$}$^+$], found 1115 [{M – $Tbt(Ditp)Sn_2Te_3$}$^+$]. ^{1}H NMR (300 MHz, C_6D_6, 70 °C): δ = 0.17 (br. s, 36 H, $SiMe_3$), 0.24 (s, 36 H, $SiMe_3$), 0.26 (s, 36 H, $SiMe_3$), 1.17 (d, $^3J_{HH}$ = 6.9 Hz, 6 H, Me), 1.25 (d, $^3J_{HH}$ = 6.9 Hz, 6 H, Me), 1.46 (d, $^3J_{HH}$ = 6.9 Hz, 6 H, Me), 1.55 (s, 2 H, *p*-BnH for Tbt), 1.58 (d, $^3J_{HH}$ = 6.9 Hz, 6 H, Me), 2.93 (sept, $^3J_{HH}$ = 6.9 Hz, 2 H, BnH for Ditp), 2.98 (sept, $^3J_{HH}$ = 6.9 Hz, 2 H, BnH for Ditp), 3.64 (br. s, 2 H, *o*-BnH for

 © 2005 Wiley-VCH Verlag GmbH & Co. KGaA, Weinheim

Tbt), 4.31 (br. s, 2 H, *o*-BnH for Tbt), 6.67 (br. s, 4 H, *m*-ArH for Tbt), 6.88–7.11 (m, 16 H, PhH for Ditp), 7.24 (t, $^3J_{HH}$ = 7.8 Hz, 2 H, PhH for Ditp), 7.35 (d, $^3J_{HH}$ = 7.8 Hz, 2 H, PhH for Ditp), 7.43 (d, $^3J_{HH}$ = 7.8 Hz, 2 H, PhH for Ditp) ppm. ^{13}C NMR (75 MHz, C_6D_6, 70 °C): δ = 1.05 (q), 1.09 (q), 3.3 (q), 24.5 (q), 24.9 (q), 25.6 (q), 26.0 (q), 29.8 (d), 30.2 (d × 2), 30.9 (d), 31.1 (d), 125.9 (d), 126.2 (d), 126.8 (d), 127.2 (d), 127.6 (d), 128.4 (d), 128.6 (d), 128.8 (d), 128.9 (d), 129.0 (d), 131.2 (d), 131.9 (d × 2), 133.7 (s), 140.0 (s), 141.1 (s), 141.3 (s), 144.3 (s), 147.3 (s), 148.5 (s), 149.6 (s), 150.0 (s), 150.7 (s), 151.0 (s) ppm. ^{119}Sn{^{1}H} NMR (54 MHz, C_6D_6, 25 °C): δ = –384.1, –386.8, –149.0 ppm. ^{125}Te{^{1}H} NMR (94 MHz, C_6D_6, 25 °C): δ = 762.9, 765.0, 766.0, 771.3 ppm. The coupling constant between ^{119}Sn and ^{125}Te could not be determined because of low solubility of **18**. **19:** Green crystals. M.p. 253.2 °C (dec.). High-resolution FAB-MS: *m*/*z* calcd. for $C_{54}H_{118}Si_{12}{}^{128}Te_2$ 1358.4554 [M$^+$], found 1358.4556 [M$^+$]. ^{1}H NMR (300 MHz, $CDCl_3$, 60 °C): δ = 0.08 (br. s, 36 H, $SiMe_3$), 0.14 (br. s, 72 H, $SiMe_3$), 3.64 (s, 2 H, *p*-BnH for Tbt), 2.88 (br. s, 4 H, *o*-BnH for Tbt), 6.51 (br. s, 4 H, *m*-PhH for Tbt) ppm. ^{13}C NMR (75 MHz, $CDCl_3$, 60 °C): δ = 0.8 (q × 2), 1.1 (q), 30.6 (d × 2), 38.1 (d), 120.7 (d), 125.5 (d), 144.4 (s), 147.5 (s), 149.8 (s), 153.3 (s) ppm. ^{125}Te{^{1}H} NMR (94 MHz, $CDCl_3$, 60 °C): δ = 225.4 ppm. **20:** Colorless liquid. EI-MS: *m*/*z* calcd. for $C_{24}H_{26}$ 314 [M$^+$], found 314 [M$^+$]. ^{1}H NMR (300 MHz, C_6D_6, 25 °C): δ = 1.09 (d, $^2J_{HH}$ = 6.9 Hz, 12 H, Me), 3.26 (sept, $^2J_{HH}$ = 6.9 Hz, 2 H, BnH), 7.08 (t, $^3J_{HH}$ = 7.5 Hz, 1 H, ArH), 7.19 (d, $^3J_{HH}$ = 7.5 Hz, 2 H, ArH), 7.20–7.29 (m, 8 H, ArH), 7.38 (s, 1 H, ArH) ppm. ^{13}C NMR (75 MHz, C_6D_6, 25 °C): δ = 24.3 (d), 29.8 (q), 125.7 (d), 125.8 (d), 128.1 (d), 128.7 (d), 129.6 (d), 130.3 (d), 130.8 (d), 141.4 (s), 142.4 (s), 146.5 (s) ppm.

NMR Measurement of Tbt(Dip)SnLi$_2$ (1c): Lithium naphthalenide (1.33 N THF solution, 0.38 mL, 0.51 mmol) was added to a THF solution (0.5 mL) of **4** (99.2 mg, 0.1 mmol) at –78 °C in a 5-mm NMR glass tube. After it was sealed and the reaction mixture kept at –78 °C for 30 min, the ^{119}Sn NMR of this solution was measured at –80 °C.

X-ray Crystallography: Single crystals of **11** and **18**·1.5(toluene) were grown by the slow concentration of their saturated solutions in acetone and toluene, respectively, at room temperature. The sample preparation consisted of coating the crystal with hydrocarbon oil, mounting it on a glass fiber, and placing it under a cold stream of N_2 on the diffractometer. The intensity data of **11** and **18**·1.5(toluene) were collected with a Rigaku/MSC Mercury CCD diffractometer with graphite-monochromated Mo-K_α radiation (λ = 0.71071 Å) to $2\theta_{max}$ = 50° at 103 K (Table 1). All structures were solved by Patterson methods (DIRDIF)[28] and refined by full-matrix least-squares procedures on F^2 for all reflections (SHELXL-97).[29] All hydrogen atoms except for 0.5(toluene) of **18**·1.5(toluene) were placed using AFIX instructions; hydrogen atoms of 0.5(toluene) were not placed. All the other atoms were refined anisotropically. In the case of **18**·1.5(toluene), the over-

Table 1. Crystallographic data for **11** and **18**·1.5(toluene).

	11	**18**·1.5(toluene)
Empirical formula	$C_{45}H_{80}Si_6Sn$	$C_{112.50}H_{176}Si_{12}Sn_3Te_4$
Formula mass	908.32	2732.08
Crystal color	colorless	orange
Crystal dimensions [mm]	0.20 × 0.10 × 0.10	0.20 × 0.10 × 0.02
Crystal system	triclinic	triclinic
Space group	$P\bar{1}$(#2)	$P\bar{1}$(#2)
Unit cell dimensions		
a [Å]	12.395(6)	13.767(4)
b [Å]	13.847(8)	21.023(6)
c [Å]	15.867(9)	22.299(7)
α [°]	105.633(11)	95.993(7)
β [°]	90.095(9)	90.455(4)
γ [°]	91.121(8)	94.119(7)
V [Å^3]	2622(2)	6401(3)
Z	2	2
$D_{calcd.}$ [g·cm^{-3}]	1.151	1.417
μ [mm^{-1}]	0.651	1.628
F(000)	968	2754
Radiation	Mo-K_α (λ = 0.71070 Å)	Mo-K_α (λ = 0.71070 Å)
Temperature [K]	103(2)	103(2)
θ range [°]	4.82–25.00	2.36–25.00
h,*k*,*l* range	$-14 \le h \le 14$	$-12 \le h \le 16$
	$-16 \le k \le 16$	$-24 \le k \le 24$
	$-18 \le l \le 18$	$-26 \le l \le 26$
No. of reflections measured	16732	41931
No. of unique reflections	8940 (R_{int} = 0.0864)	22042 (R_{int} = 0.0689)
Completeness to θ	96.9%	97.7%
Max./min. transmission	0.9377/0.8808	0.9682/0.7367
Refinement method	full-matrix least squares on F^2	full-matrix least squares on F^2
No. of data/restraints/parameter	8940/0/469	22042/73/1210
Goodness-of-fit	1.034	1.025
Final *R* indices [$I > 2\sigma(I)$]	R_1 = 0.058	R_1 = 0.075
	wR_2 = 0.108	wR_2 = 0.170
R indices (all data)	R_1 = 0.090	R_1 = 0.121
	wR_2 = 0.117	wR_2 = 0.207
Largest diff. peak/hole [e·Å^{-3}]	0.696/–0.596	1.967/–0.822

 © 2005 Wiley-VCH Verlag GmbH & Co. KGaA, Weinheim

lapped and disordered toluene molecules were restrained to be identical to each other using DFIX, SADI, SAME, and SIMU instructions. The *ipso*-carbon atom of the Ditp group was restrained using ISOR instruction. The residual electron densities of **18**·1.5(toluene) that are larger than 1.0 can be assigned to the heavy elements (Si, Sn, and Te atoms) of a minor disordered molecule (about 2%). However, the peaks for the carbon atoms of the disordered molecule could not be found. CCDC-265559 (**11**) and -276174 [**18**·1.5(toluene)] contain the supplementary crystallographic data for this paper. These data can be obtained free of charge from The Cambridge Crystallographic Data Center via www.ccdc.cam.ac.uk/data_request/cif.

Acknowledgments

This work was partially supported by Grants-in-Aid for the COE Research on Elements Science (No.12CE2005), Scientific Research (Nos. 14078213, 14204064, and 16000754), and the 21st Century COE on Kyoto University Alliance for Chemistry (Novel Organic Materials Creation & Transformation Project), and Nanotechnology Support Project from the Ministry of Education, Culture, Sports, Science, and Technology of Japan. T. T. thanks Research Fellowships of the Japan Society for the Promotion of Science for Young Scientists.

[1] For recent reviews, see: a) P. D. Lickiss, C. M. Smith, *Coord. Chem. Rev.* **1995**, *145*, 75–124; b) K. Tamao, A. Kawachi, *Adv. Organomet. Chem.* **1995**, *38*, 1–62; c) J. Belzner, U. Dehnert, in: *The Chemistry of Organic Silicon Compounds* (Eds.: Z. Rappoport, Y. Apeloig), Wiley, Chichester, **1998**, vol. 2, pp. 779–825; d) A. Sekiguchi, V. Y. Lee, M. Nanjo, *Coord. Chem. Rev.* **2000**, *210*, 11–45.

[2] Dilithiometallanes are now useful reagents in organometallic chemistry, see: a) A. Sekiguchi, M. Ichinohe, S. Yamaguchi, *J. Am. Chem. Soc.* **1999**, *121*, 10231–10232; b) A. Sekiguchi, R. Izumi, S. Ihara, M. Ichinohe, V. Y. Lee, *Angew. Chem. Int. Ed.* **2002**, *41*, 1598–1600; c) A. Sekiguchi, R. Izumi, V. Y. Lee, M. Ichinohe, *J. Am. Chem. Soc.* **2002**, *124*, 14822–14823; d) A. Sekiguchi, R. Izumi, V. Y. Lee, M. Ichinohe, *Organometallics* **2003**, *22*, 1483–1486; e) N. Nakata, R. Izumi, V. Y. Lee, M. Ichinohe, A. Sekiguchi, *J. Am. Chem. Soc.* **2004**, *126*, 5058–5059; f) N. Nakata, R. Izumi, V. Y. Lee, M. Ichinohe, A. Sekiguchi, *Chem. Lett.* **2005**, *34*, 582–583; g) N. Tokitoh, T. Sadahiro, K. Hatano, T. Sasaki, N. Takeda, R. Okazaki, *Chem. Lett.* **2002**, *31*, 34–35.

[3] a) M. Saito, R. Haga, M. Yoshioka, *Chem. Commun.* **2002**, 1002–1003; b) M. Saito, R. Haga, M. Yoshioka, *Chem. Lett.* **2003**, *32*, 912–913; c) M. Saito, R. Haga, M. Yoshioka, *Phosphorus, Sulfur Silicon Relat. Elem.* **2004**, *179*, 703–705.

[4] H. Schumann, K. F. Thom, M. Schmidt, *J. Organomet. Chem.* **1964**, *2*, 97–98.

[5] Very recently, Saito et al. reported that reduction of $(C_6H_5)_2SnCl_2$ with excess of lithium, followed by treatment with methyl iodide, gave $(C_6H_5)_3SnMe$, $(C_6H_5)_2SnMe_2$, and $[(C_6H_5)_2SnMe]_2$. They proposed that the intermediates of this reaction were $[(C_6H_5)_2SnLi]_2$ and $(C_6H_5)_3SnLi$, which were characterized by ^{119}Sn and ^{13}C NMR spectroscopy. M. Saito, Y. Okamoto, M. Yoshioka, *Appl. Organomet. Chem.* **2005**, *19*, 894–897.

[6] P. A. Chugunov, N. A. Troitskii, K. S. Nosov, M. P. Egorov, O. M. Nefedov, *Russ. Chem. Bull. Int. Ed.* **2004**, *53*, 2327–2329.

[7] For recent reviews, see: a) A. Sekiguchi, V. Y. Lee, in *Organosilicon Chemistry V, From Molecules to Materials* (Eds.: N. Auner, J. Weis), Wiley-VCH, Weinheim, **2003**, pp. 92–100; b) V. Y. Lee, A. Sekiguchi, in *The Chemistry of Organic Germanium, Tin and Lead Compounds* (Eds.: Z. Rappoport, Y. Apeloig), John Wiley & Sons Ltd., New York, **2002**, vol. 2, chapter 14, pp. 903–933; c) E. Roskamp, C. Roskamp, in *Comprehensive Heterocyclic Chemistry II* (Eds.: A. R. Katritzky, C. W. Rees, E. F. V. Scriven), Pergamon, New York, **1996**, vol. 1A, pp. 305–331.

[8] a) J. Fu, W. Neumann, *J. Organomet. Chem.* **1984**, *272*, C5–C9; b) S. Masamune, L. R. Sita, *J. Am. Chem. Soc.* **1985**, *107*, 6390–6391; c) L. R. Sita, R. D. Bickerstaff, *J. Am. Chem. Soc.* **1988**, *110*, 5208–5209; d) L. R. Sita, I. Kinoshita, *Organometallics* **1990**, *9*, 2865–2867; e) L. Baiget, H. Ranaivonjatovo, J. Escudié, H. Gornitka, *J. Am. Chem. Soc.* **2004**, *126*, 11792–11793.

[9] a) K. Hatano, N. Tokitoh, N. Takagi, S. Nagase, *J. Am. Chem. Soc.* **2000**, *122*, 4829–4830; b) T. Tajima, K. Hatano, T. Sasaki, T. Sasamori, N. Takeda, N. Tokitoh, N. Takagi, S. Nagase, *J. Organomet. Chem.* **2003**, *686*, 118–126; c) T. Tajima, K. Hatano, T. Sasaki, T. Sasamori, N. Takeda, N. Tokitoh, *Chem. Lett.* **2003**, *32*, 220–221.

[10] N. Tokitoh, K. Hatano, T. Sasaki, T. Sasamori, N. Takeda, N. Takagi, S. Nagase, *Organometallics* **2002**, *21*, 4309–4311.

[11] N. Tokitoh, K. Hatano, T. Sadahiro, R. Okazaki, *Chem. Lett.* **1999**, *28*, 931–932.

[12] Synthesis and isolation of thermodynamically stabilized tin–tellurium double-bond compounds have been reported: a) T. Chivers, D. J. Eisler, *Angew. Chem. Int. Ed.* **2004**, *43*, 6686–6689; b) T. Chivers, T. J. Clark, M. Krahn, M. Parvez, G. Schatte, *Eur. J. Inorg. Chem.* **2003**, 1857–1860; c) W.-P. Leung, W.-H. Kwok, Z.-Y. Zhou, T. C. W. Mak, *Organometallics* **2000**, *19*, 296–303.

[13] Y. Matsuhashi, N. Tokitoh, R. Okazaki, M. Goto, S. Nagase, *Organometallics* **1993**, *12*, 1351–1358.

[14] It is well known that ^{119}Sn NMR chemical shifts of halostannanes are extremely sensitive towards solvent influence, concentration, and sometimes temperature. However, such a drastic change was not observed in the case of **4** (δ = –166.0 to –165.6 ppm: 0.11 to 2.8×10^{-2} M THF solution at 25 °C; δ = –162.0 ppm: 0.11 M THF solution at –80 °C). Dibromostannane **4** is considered to exist as a monomer in solution, probably because bulky Tbt and Dip groups prevent the intermolecular coordination of the halogen atoms to the tin atom constructing halogen-bridged structures.[15]

[15] a) K. C. Molloy, K. Quill, I. W. Nowell, *J. Organomet. Chem.* **1985**, *289*, 271–279; b) P. Ganis, G. Valle, D. Furlani, G. Tagliavini, *J. Organomet. Chem.* **1986**, *302*, 165–170; c) M. M. Amini, E. M. Holt, J. J. Zuckerman, *J. Organomet. Chem.* **1987**, *327*, 147–155.

[16] We previously reported the ^{119}Sn NMR spectra of Tbt(Tip)Sn**:** (Tip = 2,4,6-triisopropylphenyl) in [D_8]toluene showed only one signal at δ = 2208 ppm between –30 and 60 °C: a) M. Saito, N. Tokitoh, R. Okazaki, *J. Am. Chem. Soc.* **1993**, *115*, 2065–2066. 2,2,5,5-Tetrakis(trimethylsilyl)-1-stannacyclopentane-1,1-diyl[16b] and bis[bis(trimethylsilyl)methyl]stannylene[16c] have been reported to show the ^{119}Sn NMR signals at δ = 2323 (no temperature dependence) and 2315 ppm ([D_8]toluene, 102 °C), respectively: b) M. Kira, R. Yauchibara, R. Hirano, C. Kabuto, H. Sakurai, *J. Am. Chem. Soc.* **1991**, *113*, 7785–7787; c) K. W. Zilm, G. A. Lawless, R. M. Merrill, J. M. Millar, G. G. Webb, *J. Am. Chem. Soc.* **1987**, *109*, 7236–7239.

[17] This reaction proceeded cleanly, and the ^1H NMR spectrum of the crude mixture showed only signals assigned to the three compounds. DipH, which was purified by GPLC, was identified by the comparison of the ^1H NMR and GC-MS spectra with those of an authentic sample. Spectral data for **10** are identical with those reported previously, see: N. Tokitoh, T. Matsumoto, H. Suzuki, R. Okazaki, *Tetrahedron Lett.* **1991**, *32*, 2049–2052.

[18] To the best of our knowledge, there is only one report on the X-ray crystallographic analysis of a stannacyclobutabenzene: M. Weidenbruch, K. Schäfers, J. Schlaefke, K. Peters, H. G. von Schnering, *J. Organomet. Chem.* **1991**, *415*, 343–348.

 © 2005 Wiley-VCH Verlag GmbH & Co. KGaA, Weinheim

[19] The thermal reaction of germacyclopropabenzene with $[Mn_2(CO)_{10}]$ afforded a germacyclobutabenzene derivative by a radical pathway, see: T. Tajima, T. Sasaki, T. Sasamori, N. Takeda, N. Tokitoh, *Appl. Organomet. Chem.* **2005**, *19*, 570–577.

[20] For reviews on double-bond compounds between heavier group 14 and group 16 elements, see: a) N. Tokitoh, Y. Matsuhashi, K. Shibata, T. Matsumoto, H. Suzuki, M. Saito, K. Manmaru, R. Okazaki, *Main Group Met. Chem.* **1994**, *17*, 55–65; b) N. Tokitoh, T. Matsumoto, R. Okazaki, *Bull. Chem. Soc. Jpn.* **1999**, *72*, 1665–1684; c) R. Okazaki, N. Tokitoh, *Acc. Chem. Res.* **2000**, *33*, 625–630; d) N. Tokitoh, R. Okazaki, *Adv. Organomet. Chem.* **2001**, *47*, 121–166.

[21] a) M. Saito, N. Tokitoh, R. Okazaki, *J. Am. Chem. Soc.* **2004**, *126*, 15572–15582; b) M. Saito, N. Tokitoh, R. Okazaki, *J. Am. Chem. Soc.* **1997**, *119*, 11124–11125.

[22] An exhaustive reduction of the overcrowded Tbt(Ditp)$SnBr_2$ (**15**) with an excess amount of lithium naphthalenide (THF solution) gave the corresponding dilithiostannane **1e**. Generation of **1e** was confirmed by a trapping experiment using MeI, giving Tbt(Ditp)$SnMe_2$ in an almost quantitative yield.

[23] R. C. Paul, A. Arneja, S. P. Narula, *Inorg. Nucl. Chem. Lett.* **1969**, *5*, 1013–1015.

[24] a) J. J. Schneider, J. Hagen, O. Heinemann, J. Bruckmann, C. Krüger, *Thin Solid Films* **1997**, *304*, 144–148; b) H. Puff, G. Bertram, B. Ebeling, M. Franken, R. Gattermayer, R. Hundt, W. Schuh, R. Zimmer, *J. Organomet. Chem.* **1989**, *379*, 235–245.

[25] M. Haaf, A. Schmiedl, T. A. Schmedake, D. R. Powell, A. J. Millevolte, M. Denk, R. West, *J. Am. Chem. Soc.* **1998**, *120*, 12714–12719.

[26] R. Okazaki, N. Tokitoh, T. Matsumoto, in *Synthetic Methods of Organometallic and Inorganic Chemistry* (Ed.: W. A. Herrmann; Volume Eds.: N. Auner, U. Klingebiel), Thieme, New York, **1996**, vol. 2, pp. 260–269, and references therein.

[27] R. R. Schrock, M. Wesolek, A. H. Liu, K. C. Wallace, J. C. Dewan, *Inorg. Chem.* **1988**, *27*, 2050–2054.

[28] P. T. Beurskens, G. Beurskens, R. de Gelder, S. Garcia-Granda, R. O. Gould, R. Israel, J. M. M. Smits, *The DIRDIF-99 program system*, Crystallography Laboratory, University of Nijmegen, The Netherlands, **1999**.

[29] G. M. Sheldrick, *SHELXL-97, Program for the Refinement of Crystal Structures*, University of Göttingen, Göttingen, Germany, **1997**.

Received: April 28, 2005
Published Online: September 23, 2005

 © 2005 Wiley-VCH Verlag GmbH & Co. KGaA, Weinheim

A New Zn^{II} Tweezer Pyridine-Naphthalene System – An Off-On-Off System Working in a Biological pH Window

Ricardo Aucejo,[a] Javier Alarcón,[a] Enrique García-España,*[a] José M. Llinares,[b] Katherine L. Marchin,[a] Conxa Soriano,[b] Carlos Lodeiro,[c] M. Alexandra Bernardo,[c,d] Fernando Pina,*[c] João Pina,[e] and J. Seixas de Melo[e]

Keywords: Luminescence / N ligands / Sensors / Zinc

The synthesis, protonation behaviour and Zn^{2+} coordination chemistry of a new photoactive polyamine exhibiting "off-on-off" fluorescence is presented. Addition of Zn^{2+} reduces the width of the fluorescence window, which is centred around physiological pH, and sharply enhances the emission intensity.
(© Wiley-VCH Verlag GmbH & Co. KGaA, 69451 Weinheim, Germany, 2005)

Introduction

The concept of pH windows leading to "off-on-off" fluorescence was discussed by A. P. de Silva and co-workers a few years ago.[1] Their basic idea consisted of the connection of an amine to a fluorophoric anthracene unit on one side and to a pyridine moiety on the other. At acidic pH values the amino and the pyridine groups are protonated and a photoinduced electron transfer (PET) occurs from the π-π* excited state of the anthracene to the protonated pyridinium unit, leading to quenching of the fluorescence. However, at high pH values, where the amino group is not protonated, PET alternatively takes place from the amine lone pair to the same excited state of the fluorophore, yielding the same inhibitory effect on the fluorescence. Between these two pH values, there is a pH window where PET does not take place and fluorescence emission is observed. Based on this idea, A. P. de Silva et al. have developed several related "off-on-off" fluorescent systems combining anthracene, pyridine and amino groups.[2,3] On the same lines, S. A. de Silva et al. have reported a system containing two pyridine units and one anthracene fluorophore, all of them connected to a tertiary nitrogen through methylenic groups, that is able to display on-off-on behaviour in the presence of Zn^{2+} in methanol/water.[4] Fabbrizzi et al.[5] have also reported a related tweezer that has anthracene and a two-amine, two-pyridine system which displays off-on-off fluorescent behaviour in water/acetonitrile both when free and when coordinated to Zn^{2+}. More recently, S. A. de Silva has shown the influence of sodium and protons on the on-off-on behaviour of a system built up by a 15-membered crown ether, anthracene and anabasine in methanol. The on state is only achieved when the system is monoprotonated in the presence of Na^+.[6]

In this paper, we present a tweezer system that works in water and exhibits an optimised pH window. With this purpose, we have prepared a compound consisting of a triamine chain functionalised at both of its termini with 4-picolyl units and at its central nitrogen with a methylnaphthyl fragment (L, Scheme 1). The binding of metal ions like

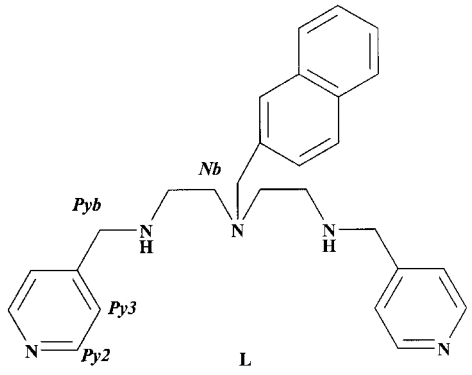

Scheme 1. Drawing of the ligands relevant to the discussion of this work. L is studied here.

[a] Departament de Química Inorgànica, Facultat de Química, Universitat de València,
Burjassot, Spain
Fax: +34-96-354-4879
E-mail: Enrique.Garcia-es@uv.es
[b] Departament de Química Orgánica, Facultat de Farmacia, Universitat de València,
Burjassot, Spain
[c] REQUIMTE, Departamento de Química, Faculdade de Ciências e Tecnologia, Universidade Nova de Lisboa,
Lisboa, Portugal
Fax: +351-21-294-8550
E-mail: fjp@dq.fct.unl.pt
[d] Instituto Superior de Ciências da Saúde-Sul, Cooperativa de Ensino Superior Egas Moniz, Campus Universitário,
Quinta da Granja, 2829-511 Monte de Caparica, Portugal
[e] Departamento de Química, Universidade de Coimbra,
3004-535 Coimbra, Portugal
Supporting information for this article is available on the WWW under http://www.eurjic.org or from the author.

Zn^{2+} to the polyamine chain can give rise to metal complexes that are able to present fluorescence pH windows with improved "off-on-off" performance and a narrower pH range. In addition, Zn^{2+} is a very interesting metal ion from a biochemical point of view due to its presence in the active site of many hydrolytic enzymes and its involvement in processes that take place in the central nervous system.[7–13] Thus, the ability to sense Zn^{2+} at physiological pH is an attractive goal. As the characteristics of the system reported here make it a promising candidate in this respect, we have explored this possibility.

Results and Discussion

Synthesis

L was synthesised in a four-step procedure (Scheme 2) that includes: i) protection of N^1-(2-aminoethyl)ethane-1,2-diamine with phthalate groups to avoid the alkylation of the secondary amino groups,[14] ii) alkylation of the central nitrogen by nucleophilic attack with (bromomethyl)naphthalene,[12–16] iii) deprotection of the phthalate groups with hydrazine in ethanol to give the free alkylated polyamine, which precipitated as its hydrochloride salt, and iv) condensation of the polyamine with 4-pyridinecarbaldehyde in a 1:2 ratio to obtain the imine of L, which was reduced in situ with $NaBH_4$. Finally, L was precipitated as its hydrochloride salt by addition of aqueous HCl to an ethanolic solution of L.

Protonation Behaviour

The protonation constants of tweezer L at 298.1 ± 0.1 K in 0.15 M NaCl by pH-metric titration, determined using the program HYPERQUAD,[17] are shown in Table 1. There are several points of interest to be noted. First, the number of protonation constants found (five) indicates that all the protonable groups in the compound undergo protonation in the pH range of study. As discussed below, the first two protonation processes, which mainly affect the secondary amino groups, are rather low in comparison with saturated triamines like 1,4,7-triazaheptane (dien)[18] or with respect to analogous polyamines functionalised with benzene rings at both of their termini instead of pyridine.[19] This detrimental effect on the basicity can be ascribed to the electron-withdrawing characteristics of pyridine, which cause the adjacent nitrogen atoms to be less negatively charged. On the other hand, it is well-known that tertiary nitrogen atoms are less basic in water than secondary ones due to solvation effects.[20] Therefore, the presence of the methylnaphthyl group at the central nitrogen also contributes to the low overall basicity displayed by L.

Table 1. Protonation constants of L determined in 0.15 M NaCl at 298.1 ± 0.1 K.

Reaction	pK_a
$H^+ + L \rightleftharpoons [HL]^+$	8.33(1)[a]
$[HL]^+ + H^+ \rightleftharpoons [H_2L]^{2+}$	7.06(1)
$[H_2L]^{2+} + H^+ \rightleftharpoons [H_3L]^{3+}$	4.41(1)
$[H_3L]^{3+} + H^+ \rightleftharpoons [H_4L]^{4+}$	3.37(1)
$[H_4L]^{4+} + H^+ \rightleftharpoons [H_5L]^{5+}$	2.14(1)
log β	25.31

[a] Values in parentheses are standard deviations in the last significant figure.

The pH-dependent absorption spectra of compound L are presented in Figure 1A. The two contributions from the pyridine and naphthalene chromophores can easily be detected: the pyridine shows an absorption band at around

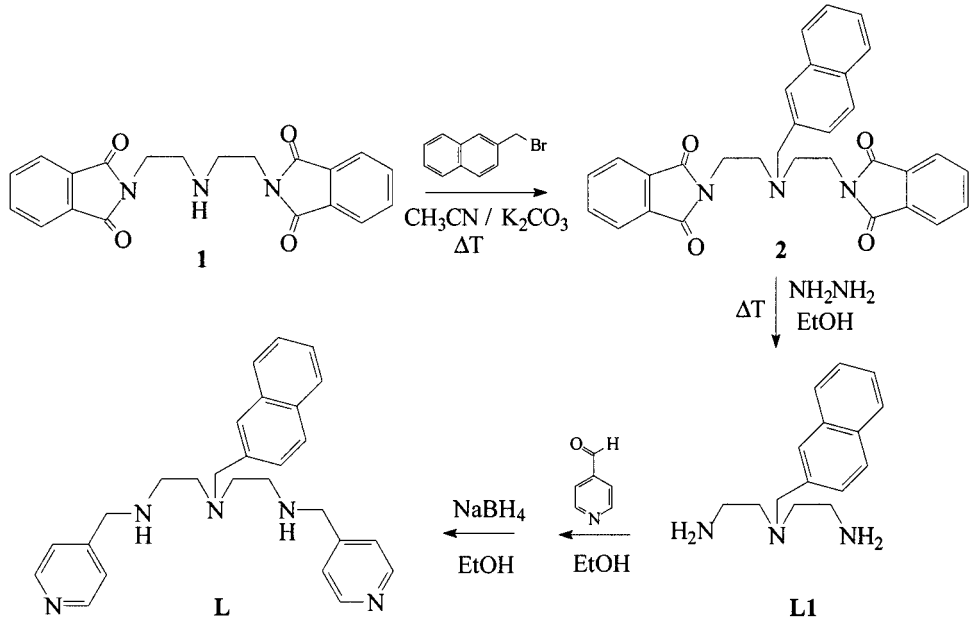

Scheme 2. Synthetic pathway to L.

 © 2005 Wiley-VCH Verlag GmbH & Co. KGaA, Weinheim

255 nm whose intensity increases upon protonation, whereas the naphthalene contribution is pH independent and appears as a maximum at approximately 275 nm. Observation of Figure 1A shows that there is little broadening (or extended tail) of the naphthalene absorption (above 300 nm). This presumably suggests little formation (but not absence) of a pre-formed charge-transfer complex (CT complex, also commonly know as an electron donor–acceptor complex),[21] which would result from the interaction between the electron-donating moiety (pyridine) and the electron-accepting species (naphthalene).

Fluorescence emission spectra as a function of pH are shown part B of Figure 1. As mentioned above, protonation of the pyridine units leads to an increase of the absorption intensity. Since there are five basic centres in L, all of them − the two secondary amino groups, the tertiary one at the centre of the chain and both pyridine nitrogens − will be protonated in H_5L^{5+}. The spectroscopic data suggest that both pyridine units are also protonated in H_4L^{4+}, and that even in H_3L^{3+} the proton should still interact with the pyridine units as no significant decrease in the absorption maximum is observed for the three more protonated species. The ^{1}H NMR spectroscopic data also support this average protonation sequence, since the greatest downfield shifts of the pyridine protons Py2 and particularly Py3 (see Scheme 1 for the labelling; $\Delta\delta$ = 0.1 and 0.5 ppm, respectively) occur from pH 6.0 to 4.0, corresponding to the protonation of H_2L^{2+} to give H_3L^{3+} (see Figure S1A in the Supporting Information).

However, the most remarkable aspect to note in the emission spectra of compound L (Figure 1, B) is the additional band at longer emitting wavelengths. In fact, this emission exhibits the well-known characteristics of an exciplex as it is broad, structureless and red-shifted. The existence of a double exponential law (see below) is compatible with the existence of a "monomer" species (naphthalene emission) in equilibrium with an exciplex-like structure involving the naphthalene and one of the pyridine units. This is likely to be the case, because in a similar previously studied compound we found the coexistence of the emission of a monomer and an excimer formed by two naphthalenes.[22] In that case the macrocyclic structure studied also possessed pyridine units, yet the maximum emission wavelength occurred at 400 nm. This is in contrast with the 443 nm maximum found with the present system. It also excludes intermolecular interactions as the origin of this band. Moreover, since there is no formal difference between a relaxed CT excited state of an electron donor–acceptor complex and an exciplex, it is not easy sometimes to distinguish between the two.[21] However, in systems where CT contributions are reported, the presence of CT band leads to a visible colour of the solutions in contrast with colourless solutions where CT is absent,[21] which is reflected by the appearance of a tail at longer wavelengths. In the present case no such band is observed. Moreover, it can be seen that the absorption tail does not display a significant change with the pH, which clearly points to a lower contribution of a CT state.

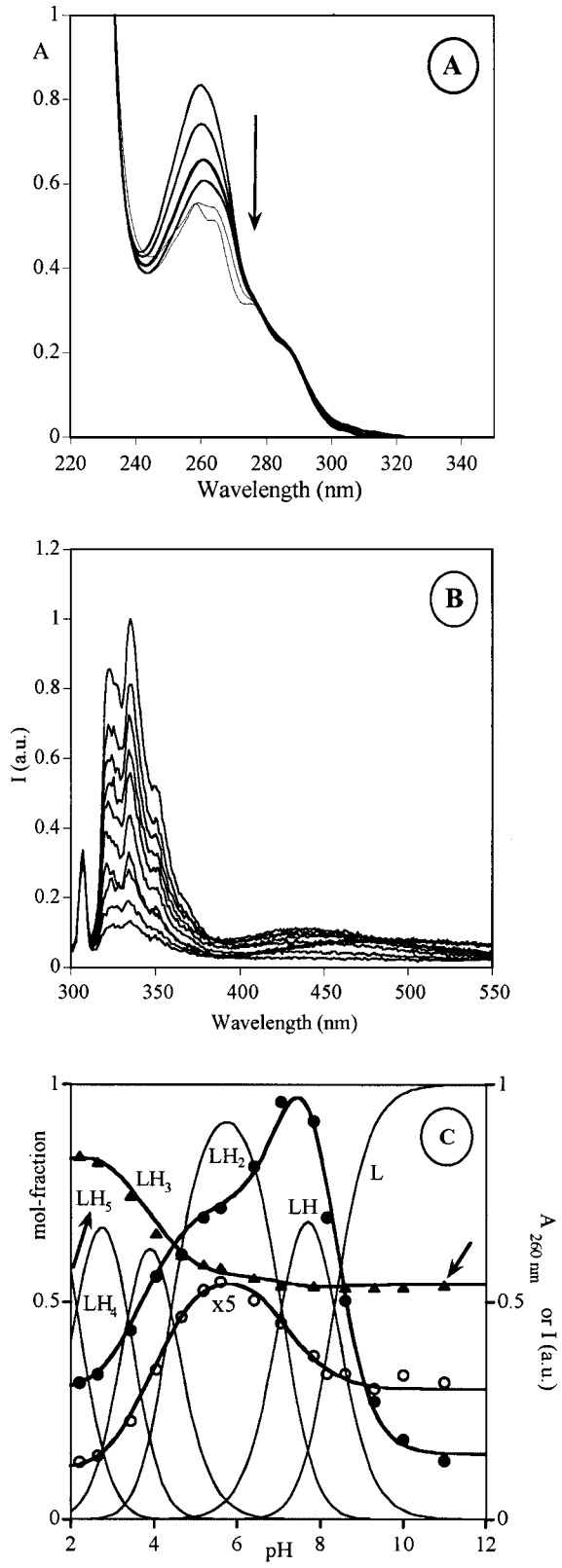

Figure 1. Absorption (A) and emission spectra (B) as function of pH of L (λ_{exc} = 280 nm at pH 2.20, 3.45, 4.05, 4.65, 6.40 and 11.0. [L] = 2.50×10^{-5} M; [NaCl] = 0.15 M). Fluorescence emission and absorption titration curves of L: emission [λ_{exc} = 280 nm, λ_{em} = 335 nm (●) and λ_{em} = 443 nm (○); absorption λ_{abs} = 260 nm (▲)] [L] = 2.5×10^{-5} M, superimposed on the respective mol-fraction distribution of the different species present in solution.

 © 2005 Wiley-VCH Verlag GmbH & Co. KGaA, Weinheim

The possibility of formation of a charge-transfer excited state, as observed, for instance, in dendrimers functionalised at the periphery with naphthylsulfonamide units,[23] between the excited naphthalene and the amine units could potentially explain the emission of this structureless long-emission band. However, this is not likely to explain the present situation, since a similar band is not observed with analogous compounds containing a single naphthalene unit and an amine chain.[24,25] In fact, macrocyclic structures possessing a single naphthalene unit and polyaminic chains (with different sizes) have been shown to display only the naphthalene monomer emission.[24] Based on the considerations above, we therefore felt confident enough to attribute the long-wavelength emission band as being due to an exciplex-type species.

Inspection of part C of Figure 1 shows that the decrease in the absorption (deprotonation of the pyridines) and the increase in the fluorescence emission occur simultaneously. This result can be ascribed to an electron transfer quenching from the excited naphthalene to the protonated pyridine rings.[1–6] On the other hand, the sharp decrease of fluorescence observed at higher pH values can be explained by the well-established quenching by electron transfer from the lone pairs of the amines to the naphthalene fluorophore.[24] It is interesting to note that although a higher fluorescence emission intensity should, in principle, be expected for the H_2L^{2+}species, the most emissive species is HL^+. One plausible explanation could be that the two protons in H_2L^{2+}, due to their mutual repulsion, should be principally located at the two terminal nitrogens.[20,26] Therefore, the central nitrogen will be free at this stage for the quenching of the neighbouring excited naphthalene. However, the proton in HL^+ will be more shared between the secondary and the tertiary nitrogens due to the absence of charge–charge repulsion. The ^{1}H NMR spectroscopic data support this explanation. First, although the signal of the proton labelled as Pyb, which is placed in the α-position with respect to the secondary amino groups,[9] shifts downfield throughout all the pH range, it experiences its greatest downfield shift in the pH range 9–7, where the first two protonations occur ($\Delta\delta$ = 0.3 ppm). This supports the involvement of the secondary amino groups in such protonation steps. On the other hand, the ^{1}H signal of Nb also undergoes a slight downfield shift ($\Delta\delta$ = 0.12 ppm) on going from pH 9.0 to 7.5, corresponding to the first protonation step, which suggests that the first proton binding L is also shared by the tertiary nitrogen atom.

The off-on-off behaviour of L is depicted in Scheme 3. This "off-on-off" behaviour of the fluorescence emission of compound L, however, presents some disadvantages as the fluorescence emission quantum yields are very low and the pH width of the window is very large. A much better performance can be achieved with the Zn^{II} complexes of compound L (see below).

The speciation studies for the system Zn^{2+}-L carried out by pH-metric titration at 298.1 ± 0.1 K show a very simple model in which three species of stoichiometries $[ZnL]^{2+}$, $[ZnL(OH)]^+$ and $[ZnL(OH)]_2$ are formed. The stability constants for these species are collected in Table 2 and the distribution of the species with pH is shown in Figure 2.

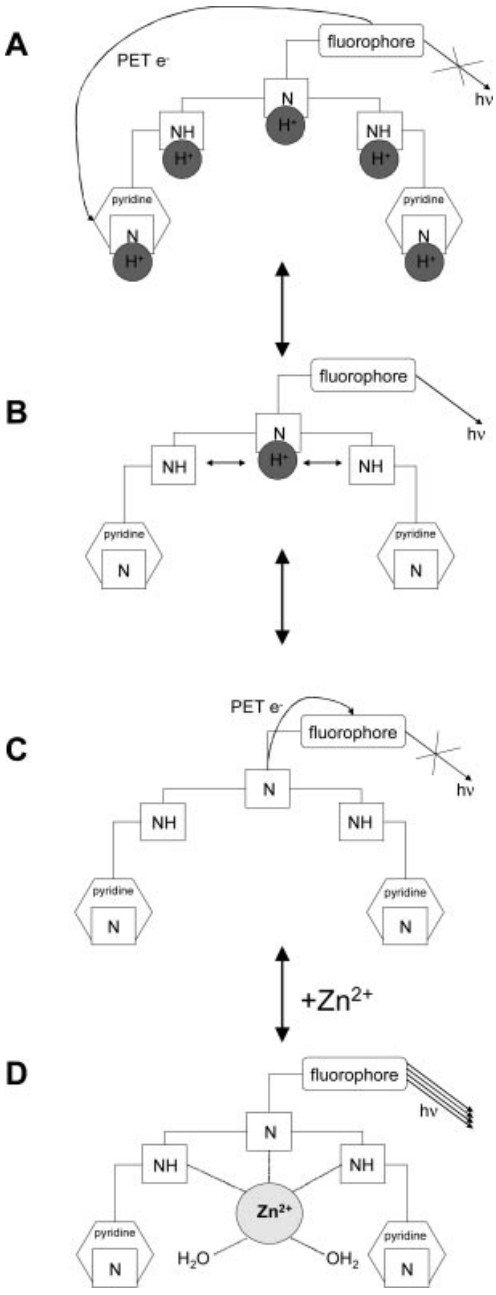

Scheme 3. Representation of the changes in fluorescence of L with pH and upon addition of Zn^{2+}. A) Fully protonated L. B) Monoprotonated L; the proton is shared to some extent between the three nitrogens of the chain. C) Deprotonated L. D) Emission of the $[ZnL]^{2+}$ complex.

The most noticeable observation is the low stability displayed by these complexes. The stability constant of the $[ZnL]^{2+}$ complex is clearly lower than that presented by the open-chain polyamine 1,4,7-triazaheptane (log K = 8.8)[18] or that of a related ligand with both of its terminal nitrogens functionalised with naphthylmethyl groups (log K =

 © 2005 Wiley-VCH Verlag GmbH & Co. KGaA, Weinheim

Table 2. Stability constants for the formation of Zn^{2+} complexes of **L** determined in 0.15 M NaCl at 298.1 ± 0.1 K.

Species	log K[a]
$Zn^{2+} + L \leftrightharpoons [ZnL]^{2+}$	4.72(1)
$Zn^{2+} + L + H_2O \leftrightharpoons [ZnL(OH)]^{+} + H^{+}$	–4.22(2)
$Zn^{2+} + L + 2H_2O \leftrightharpoons [ZnL(OH)_2] + 2H^{+}$	–12.89(1)
$[ZnL]^{2+} + H_2O \leftrightharpoons [ZnL(OH)_2]^{+} + H^{+}$	–8.94
$[ZnL(OH)]^{+} + H_2O \leftrightharpoons [ZnL(OH)_2] + H^{+}$	–8.66(1)

[a] Values in parentheses are standard deviations in the last significant figure.

8.25).[27] This low stability can be ascribed to the electron-withdrawing characteristics of the pyridine rings and to the poor σ-donor character of the central tertiary nitrogens. This low constant leads to a ready hydroxylation of two water molecules that would serve to complete the coordination sphere of the metal ion. In fact, the pH range of formation of the dihydroxylated species overlaps that of the monohydroxylated and of the neutral species. This low stability also means that, as might be expected, the pyridine rings do not participate in the coordination of the Zn^{2+} ion.

The pH-dependent absorption and emission spectra of compound L in the presence of equimolar amounts of Zn^{2+} are shown in Figure 2. A comparison of the absorption spectra in the absence and presence of metal does not show any significant difference. However, the fluorescence emission exhibits a much higher intensity, and the shape of the fluorescence emission titration curve presents a much narrower pH-dependent fluorescence window (Figure 2, C). The mol-fraction distribution of the various species in solution are also represented superimposed on the fluorescence emission titration curve in part C of Figure 2. Inspection of this figure shows the background emission from the free ligand up to pH 6.0, and for more basic pH values an emission whose shape and position can be attributed to the $[ZnL]^{2+}$ species. In this species the metal is bonded to the polyamine chain, thus preventing the PET from occurring (see Scheme 3).

No interaction of the metal with the pyridine units is observed. This is confirmed by the lack of changes in the absorption spectra and absence of fluorescence quenching, which is expected when Zn^{2+} is bonded to pyridine units. The ^1H NMR signals of Py2 and Py3 in the system Zn^{2+}-L do not experience any shift with respect to the free ligand from pH 2.0 to 6.0, thus supporting this point (see Figure S2).

At higher pH values the formation of hydroxo species leads to a quenching effect, as reported previously,[28] which explains the bell shape of the titration curve. One of the most remarkable aspects is the great increase in the intensity of the fluorescence emission when Zn^{2+} is complexed to L (see Figure 3), which exceeds the maximum intensity of the free ligand 10-fold.

The fluorescence decays of ligand L were obtained at the shorter and longer wavelength bands at different pH values. The data resulting from the best fitting, obtained with global or independent analysis of the decays (Table 3) show

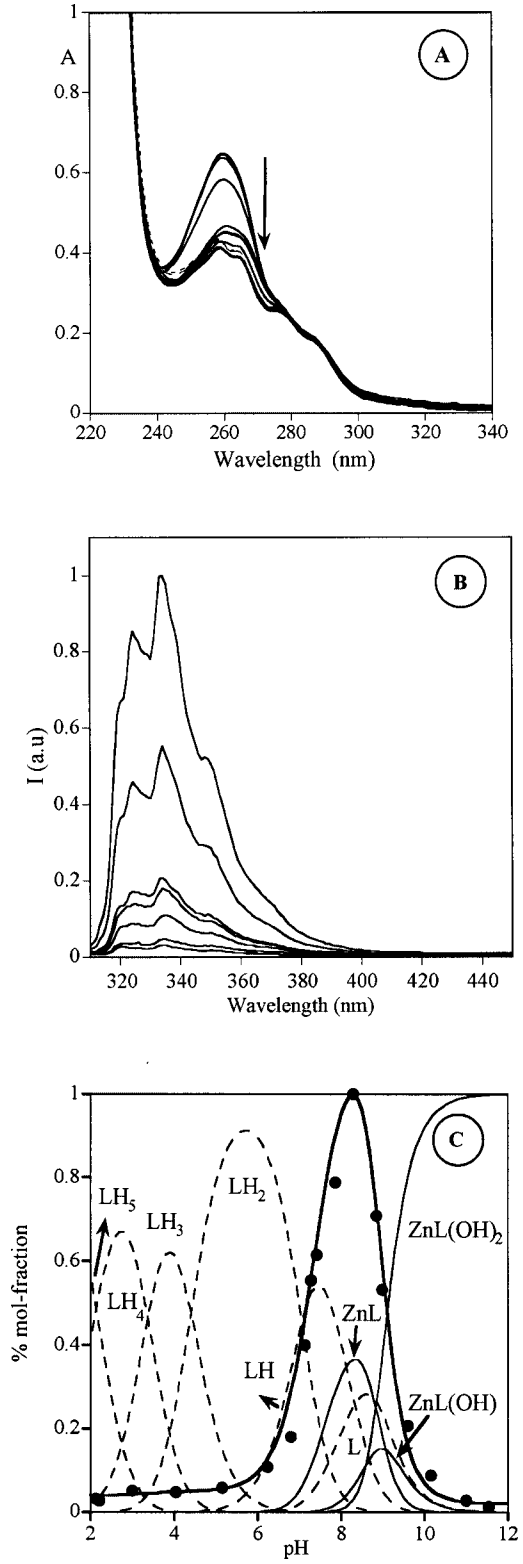

Figure 2. Absorption (A) and emission spectra (B) of the complex ZnL as a function of pH. (λ_{exc} = 280 nm, [ZnL] = 2.50×10^{-5} M, [NaCl] = 0.15 M). Fluorescence emission titration curve of the complex ZnL (C) (λ_{exc} = 280 nm, λ_{em} = 335 nm (●), [ZnL] = 2.50×10^{-5} M, [NaCl] = 0.15 M) superimposed on the respective mol-fraction distribution of the different species present in solution.

 © 2005 Wiley-VCH Verlag GmbH & Co. KGaA, Weinheim

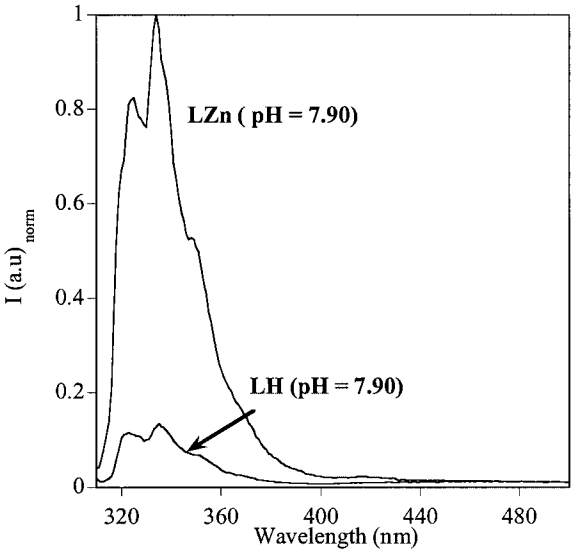

Figure 3. Comparison between the fluorescence of free L and its Zn^{2+} complex at pH 7.9.

that the decays are properly fitted with double-exponential laws, according to:

$$I_\lambda(t) = a_{i1}e^{-t/\tau_1} + a_{i2}e^{-t/\tau_2}$$

where $i = 1$ for $\lambda_{em} = 335$ nm and $i = 2$ for $\lambda_{em} = 450$ nm.

According to Table 3, the shorter-lifetime component remains approximately constant with the pH (with an averaged value of ca. 3.4 ns) and the longer-lifetime component increases up to pH 7.0–8.0, decreasing thereafter. As reported in Figure 1, the emission at pH values above 8.0 is due to the deprotonated HL and L species. In this situation the lone electron pairs of the deprotonated amines are able to effectively quench the emission of compound L.[29] This is revealed both by the decrease in the lifetime of this component as well as by the decrease of the total fluorescence emission, as shown in Figure 1, B. Analysis of the lifetime data points to another important observation: the absence of a rise-time (negative pre-exponential) is associated with the shorter lifetime at $\lambda_{em} = 450$ nm. The lack of a rise-time (see below) might indicate that this new emission band should, presumably, possess some (small) CT degree; with improved time-resolution (ours is presently limited to 150 ps) it could be the case that a faster component, with a rising component, is present. However, with our current time resolution we were unable to visualize such a component. Based on our present data, this again presumably indicates that the 443 nm (maxima) emissive species (exciplex) results from a small CT degree contribution. In fact, exciplex formation due to CT interactions can involve excited- and ground-state molecules and be the driving force for its formation. However, based on our current data, we believe that we have a complex (presumably with some ground-state contribution) with CT character.

However, even if the formation of the exciplex-type species (emission at 443 nm) does not show a strong dependence on the exciting light, it is clearly dependent on the pH of the medium. This can be viewed by the observation of the ratio of the emission at 335 nm vs. 443 nm, where it can be seen that this attains two maxima at pH 2.0 and pH 8.0.

In summary, the analysis of the fluorescence data (steady-state and time-resolved) suggest that the 443 nm emitting species can be interpreted as a charge-transfer complex A^-D^+ which is stabilised by electron transfer form the donor (pyridine unit) to the acceptor (naphthalene) that is not totally unstable in its ground-state. In fact, it is unlikely, based on the arguments discussed above, that this equilibrium is only formed once the excited state is formed, but rather that it is already present (to some degree) in the ground state. Therefore, the off-on-off system is mainly due to the pH of the media and less to the action of light, contrary to other related systems previously studied by our groups.[25]

Table 3. Fluorescence decay times and pre-exponential factors (τ_i and a_{ij}) for compound L in water as a function of pH. The data were obtained with excitation at 290 nm and emission at 335 nm and 440 nm. Also presented are the chi-squared values for a better judgment of the quality of the fits.

pH	λ_{em}	τ_1	τ_2	a_{i1}	a_{i2}	χ^2	Type of analysis[a]
3	335	2.44	13.16	0.600	0.40	1.29	i
	440	2.95	10.34	0.702	0.297	1.28	i
5.1	335	2.44	12.78	0.560	0.440	1.10	i
	440	3.08	11.88	0.829	0.171	1.19	i
6.2	335	2.86	12.92	0.784	0.216	1.06	g
	440			0.87	0.13	1.33	
7.1	335	3.82	14.74	0.904	0.096	0.97	g
	440			0.897	0.103	1.06	
8.4	335	3.97	14.65	0.873	0.127	1.14	g
	440			0.909	0.091	1.01	
9.5	335	3.53	13.05	0.704	0.296	1.07	g
	440			0.882	0.118	0.83	
10.6	335	3.53	12.56	0.625	0.375	1.06	g
	440			0.88	0.12	1.03	
Zn:L pH 8.2	335	3.84	24.74	0.411	0.584	0.95	i

[a] i: Independent analysis; g: global analysis.

 © 2005 Wiley-VCH Verlag GmbH & Co. KGaA, Weinheim

Off-On-Off Behaviour

According to the data reported in Figure 2 (C), Zn^{2+} can be detected by the fluorescence emission intensity of its complex with tweezer L, in a very narrow pH window centred at around pH 8.0. In order to characterise the narrowness of the bell shape titration curve, it is useful to measure the width at half of the maximum of the fluorescence intensity. In the present system it is 1.9 pH units. This value compares with a value of about 3 for the system previously reported by A. P. de Silva.[1] Another aspect concerns the central pH value of the window, which is pH 8.2 in our system and about 6.5 in the one previously described by de Silva.

Different to previously reported systems, our system presents the advantage of being soluble and therefore operative in aqueous 0.15 M NaCl solutions. This ionic strength is close to that found in biological fluids.

Experimental Section

The synthesis of **1** was carried out as described previously.[12]

3-Naphthylmethyl-1,5-Diphthalimido-3-azapentane (2):[15,16] 1,5-Diphthalimido-3-azapentane (**1**; 10.1 g, 36.2 mmol), 2-(bromomethyl)naphthalene (10.0 g, 45.2 mmol) and K_2CO_3 (6.4 g, 45.2 mmol) were dissolved in 200 mL of CH_3CN and the mixture was refluxed for 24 h under nitrogen. After filtration, the solvent was removed under reduced pressure. The resulting residue was mixed with 50 mL of water and extracted with dichloromethane (3 × 50 mL). The organic phase was dried with anhydrous sodium sulfate and the solvent was evaporated to yield a light-yellow oil. The oil was taken up in EtOH and precipitated as a solid, which was filtered to give **2**. Yield: 6.85 (38%).^{1}H NMR ($CDCl_3$): δ = 2.87 (t, J = 6 Hz, 4 H), 3.79 (t, J = 6 Hz, 4 H), 3.80 (s, 2 H), 7.16 (d, J = 8 Hz, 1 H), 7.20 (d, J = 8 Hz, 1 H), 7.23–7.36 (m, 2 H), 7.45–7.48 (m, 1 H), 7.51 (s, 1 H), 7.58–7.61 (m, 1 H), 7.62–7.69 (m, 8 H) ppm. ^{13}C NMR (D_2O): δ = 36.2, 52.2, 58.8, 123.3, 125.7, 126.1, 127.5, 127.9, 128.0, 128.0, 132.7, 132.9, 133.5, 134.0, 136.8, 168.5 ppm.

4-(2-Napthylmethyl)-1,4,7-triazaheptane Tris(hydrochloride) (L1·3HCl): Compound **2** (6.9 g, 13.6 mmol) and hydrazine monohydrate (13.6 g 272 mmol) were dissolved in 400 mL of EtOH and the mixture was refluxed for 1 d under nitrogen. The precipitate was removed by filtration and the solvent was evaporated until the sample was dry. The resulting residue was dissolved in 300 mL of $CHCl_3$ and the solution was stirred for 12 h under nitrogen. The solution was vacuum evaporated to dryness to give the crude product. This product was dissolved in EtOH and was precipitated with aqueous HCl to obtain L as its hydrochloride salt (1.98 g, 42%). M.p. 223–224 °C. ^{1}H NMR (D_2O): δ = 3.30–3.34 (m, 4 H), 3.35–3.42 (m, 4 H), 4.43 (s, 2 H), 7.49 (d, J = 8 Hz, 1 H), 7.51–7.57 (m, 2 H), 7.89–797 (m, 4 H) ppm. ^{13}C NMR (D_2O): δ = 34.8, 50.1, 59.0, 127.4, 127.6, 127.7, 128.0, 128.2, 128.5, 129.8, 131.3, 133.2, 133.7 ppm. $C_{15}H_{24}Cl_3N_3$ (352.8): calcd. C 51.5, H 6.9, N 11.9; found C 50.9, H 7.0, N 11.8.

1,7-Bis(4-methylpyridine)-4-(2-napthylmethyl)-1,4,7-triazaheptane Pentahydrochloride (L·5HCl): 4-Pyridinecarbaldehyde (1.28 g, 11.9 mmol) dissolved in 100 mL of EtOH was added to a solution of L1 (1.30 g, 5.96 mmol) in EtOH. $NaBH_4$ (0.56 g, 15 mmol) was then added portionwise. The mixture was stirred for 2 h at room temperature and the solvent was then vacuum evaporated to dryness. The residue was treated with 50 mL of water and extracted with CH_2Cl_2 (3 × 40 mL). The organic phase was dried with anhydrous sodium sulfate and the solvent evaporated to dryness. The resulting oil was dissolved in EtOH and L was precipitated as its pentahydrochloride salt with aqueous HCl (1.55 g, 43%). M.p. 177–178 °C. ^{1}H NMR (D_2O): δ = 2.95 (t, J = 6 Hz, 4 H), 3.15 (t, J = 6 Hz, 4 H), 3.73 (s, 2 H), 4.16 (s, 4 H), 7.33–7.40 (m, 4 H), 7.60–7.63 (m, 3 H), 7.70 (d, J = 7 Hz, 4 H), 8.52 (d, J = 7 Hz, 4 H) ppm. ^{13}C NMR (D_2O): δ = 45.1, 49.4, 50.4, 59.3, 127.9, 128.1, 128.3, 129.3, 129.5, 133.0, 133.2, 133.5, 142.1, 151.3 ppm. $C_{27}H_{40}Cl_5N_5O_2$ (644.1): calcd. C 50.5, H 6.3, N 10.9; found C 50.6, H 6.4, N 10.8.

Emf Measurements: The potentiometric titrations were carried out at 298.1 ± 0.1 K with 0.15 M NaCl as the supporting electrolyte. The experimental procedure (burette, potentiometer, cell, stirrer, microcomputer, etc.) has been fully described elsewhere.[30] The acquisition of the emf data was performed with the computer program PASAT.[31] The reference electrode was an Ag/AgCl electrode in saturated KCl solution. The glass electrode was calibrated as a hydrogen-ion concentration probe by titration of previously standardised amounts of HCl with CO_2-free NaOH solutions and the equivalent point determined by Gran's method,[32] which gives the standard potential, $E°'$, and the ionic product of water [pK_w = 13.73(1)].

The computer program HYPERQUAD was used to calculate the protonation and stability constants.[30] The pH range investigated was 2.5–11.0 and the concentration of the metal ions and of the ligand ranged from 1×10^{-3} to 5×10^{-3} M with M:L molar ratios varying from 2:1 to 1:2 The different titration curves for each system (at least two) were treated either as a single set or as separate curves without significant variations in the values of the stability constants. Finally, the sets of data were merged together and treated simultaneously to give the final stability constants.

Spectrophotometric and Spectrofluorimetric Measurements: Absorption spectra were recorded on a Shimadzu UV-2501PC spectrophotometer and fluorescence emission on a Horiba–Jobin–Yvon SPEX Fluorolog 3.22 spectrofluorimeter at 25 °C. HCl and NaOH were used to adjust the pH values, which were measured on a Metrohm 713 pH meter. All measurements were made in 0.15 M NaCl.

Fluorescence decays were measured using a home-built TCSPC apparatus with an N_2-filled IBH 5000 coaxial flashlamp as excitation source, Jobin–Yvon monochromators, Philips XP2020Q photomultiplier, and Canberra instruments TAC and MCA. Alternate measurements (1000 c.p.c.) of the pulse profile at 285 nm and the sample emission were performed until $1–2 \times 10^4$ counts at the maximum were reached.[33] The fluorescence decays were analysed using the modulating functions method of Striker with automatic correction for the photomultiplier "wavelength shift".[34]

Supporting Information: As supporting information we include plots of the variations with pH of the ^{1}H NMR chemical shifts of protons labelled as py2, py3 (Figure S1A), Nb and pyb (Figure S1B). Figure S2 plots the variations with pH of the chemical shifts of protons py2 and py3 in the absence and presence of Zn^{2+}.

Acknowledgments

Financial support from the Spanish Dirección General de Enseñanza Superior (projects BQ2003-0215-CO3 and GV-Grupos-03/196 and GV04B-225), the Portuguese Fundaçao para a Ciência e a Tecnologia MCT-ES (project POCTI/QUI/97357/2002 FCT-FEDER)

 © 2005 Wiley-VCH Verlag GmbH & Co. KGaA, Weinheim

is acknowledged. R. A. thanks the MECD for a PhD grant (AP2002-1382) and K. M. the Fulbright Commission for a grant.

[1] A. P. de Silva, H. Q. N. Gunaratne, C. P. McCoy, *Chem. Commun.* **1996**, *21*, 2399–2400.
[2] A. P. de Silva, H. Q. N. Gunaratne, T. T. Gunnlaugsson, A. J. M. Huxley, C. P. McCoy, J. T. Rademacher, T. E. Rice, *Chem. Rev.* **1997**, *97*, 1515–1566.
[3] A. P. de Silva, H. Q. N. Gunaratne, P. L. M. Lynch, *J. Chem. Soc., Perkin Trans. 2* **1995**, 685–690.
[4] S. A. de Silva, A. Zavaleta, D. E. Baron, O. Allam, E. V. Isidor, N. Kashimura, J. M. Percarpio, *Tetrahedron Lett.* **1997**, *38*, 2237–2240.
[5] L. Fabbrizzi, F. Gatti, P. Pallavicini, L. Parodi, *New J. Chem.* **1998**, *22*, 1403–1407.
[6] S. A. de Silva, B. Amorelli, D. C. Isidor, K. C. Loo, K. E. Crooker, Y. E. Pena, *Chem. Commun.* **2002**, 1360–1361.
[7] Y. V. Li, C. J. Hough, J. M. Savey, *Sci. STKE* **2003**, *182*, 19.
[8] L. Aniksztejn, G. Charton, Y. Ben-Ari, *Brain Res.* **1987**, *404*, 58–64.
[9] S. Y. Assaf, S. H. Chung, *Nature* **1984**, *308*, 734–736.
[10] G. A. Howell, M. G. Welch, C. J. Frederickson, *Nature* **1984**, *308*, 736–738.
[11] S. Peters, J. Koh, D. W. Choi, *Science* **1987**, *236*, 589–593.
[12] E. H. Buhl, T. S. Otis, I. Mody, *Science* **1996**, *271*, 369–373.
[13] Y. Li, C. J. Hough, C. J. Frederickson, J. M. Sarvey, *J. Neurosci.* **2001**, *21*, 8015–8025.
[14] P. L. Anelli, L. Lunazzi, F. Montanari, S. Quici, *J. Org. Chem.* **1984**, *49*, 4197–4203.
[15] G. H. Searle, S. F. Lincoln, S. G. Teague, D. G. Rowe, *Aust. J. Chem.* **1979**, *32*, 519.
[16] C. Yuen Ng, R. J. Motekaitis, A. E. Martell, *Inorg. Chem.* **1979**, *18*, 2982–2986.
[17] P. Gans, A. Sabatini, A. Vacca, *Talanta* **1996**, *43*, 1739–1753.
[18] a) A. E. Martell, R. M. Smith, *Critical Stability Constants*, Plenum, New York, **1975**; b) R. J. Motekaitis, *NIST Critically Selected Stability Constants of Metal Complexes Database*, NIST Standard Reference Database, version 4, **1997**.
[19] M. A. Bernardo, J. A. Guerrero, E. García-España, J. M. Llinares, F. Pina, J. A. Ramírez, C. Soriano, *J. Chem. Soc., Perkin Trans. 2* **1996**, 2335–2342.
[20] A. Bencini, A. Bianchi, E. García-España, M. Micheloni, J. A. Ramírez, *Coord. Chem. Rev.* **1999**, *88*, 97–156.
[21] F. Brouwer, *Structural Aspects of Exciplex Formation, in Conformational Analysis of Molecules in Excited States* (Ed.: J. Waluk), Wiley-VCH, New York, **2000**.
[22] J. Seixas de Melo, J. Pina, F. Pina, C. Lodeiro, A. J. Parola, J. C. Lima, M. T. Albelda, M. P. Clares, E. Garcia-España, *J. Phys. Chem. B* **2003**, *107*, 11307–11318.
[23] F. Pina, M. Maestri, V. Balzani, F. Vogtle, *ChemPhysChem.* **2004**, *5*, 473–480.
[24] F. Pina, J. C. Lima, C. Lodeiro, J. Seixas de Melo, P. Díaz, M. T. Albelda, E. García-España, *J. Phys. Chem. A* **2002**, *106*, 8207–8212.
[25] M. T. Albelda, M. A. Bernardo, P. Díaz, E. García-España, J. Seixas de Melo, F. Pina, C. Soriano, S. V. Luis, *Chem. Commun.* **2001**, 1520–1521.
[26] J. E. Sarneski, H. L. Surprenant, F. K. Molen, C. N. Reiley, *Anal. Chem.* **1975**, *47*, 2116.
[27] J. Alarcón, R. Aucejo, M. T. Albelda, S. Alves, M. P. Clares, E. García-España, C. Lodeiro, K. L. Marchin, J. Parola, F. Pina, J. Seixas de Melo, C. Soriano, *Supramol. Chem.* **2004**, *16*, 573–580.
[28] a) A. Bencini, A. Bianchi, C. Lodeiro, A. Masotti, A. J. Parola, F. Pina, J. Seixas de Melo, B. Valtancolo, *Chem. Commun.* **2000**, 1639–1640; b) C. Lodeiro, A. J. Parola, F. Pina, C. Bazzicalupi, A. Bencini, A. Bencini, C. Giorgi, A. Masotti, B. Valtancoli, *Inorg. Chem.* **2001**, *40*, 2968–2975; c) M. P. Clares, J. Aguilar, R. Aucejo, C. Lodeiro, M. T. Albelda, F. Pina, J. C. Lima, A. J. Parola, J. Pina, S. Seixas de Melo, C. Soriano, E. García-España, *Inorg. Chem.* **2004**, *43*, 6114–6122.
[29] B. Valeur, *Molecular Fluorescence*, Wiley-VCH, Weinheim, **2002**.
[30] E. García-España, M. J. Ballester, F. Lloret, J. M. Moratal, J. Faus, A. Bianchi, *J. Chem. Soc., Dalton Trans.* **1988**, 101–104.
[31] M. Fontanelli, M. Micheloni, *Proceedings of the I Spanish-Italian Congress on Thermodynamics of the Metal Complexes*, Diputación de Castellón, Castellón, Spain, **1990**. Program for the automatic control of microburette and the acquisition of the electromotive force readings.
[32] a) E. Gran, *Analyst (London)* **1952**, *77*, 661; b) F. J. C. Rossotti, H. Rossotti, *J. Chem. Educ* **1965**, *42*, 375.
[33] J. Seixas de Melo, P. F. Fernandes, *J. Mol. Struct.* **2001**, *565*, 69–78.
[34] G. Striker, V. Subramaniam, C. A. M. Seidel, A. Volkmer, *J. Phys. Chem. B.* **1999**, *103*, 8612–8617.

Received: May 4, 2005
Published Online: September 8, 2005

 © 2005 Wiley-VCH Verlag GmbH & Co. KGaA, Weinheim

An Approach Towards Functional Dendrimers Based on the Hydroboration Reaction and Spontaneous Boron–Nitrogen Bond Formation

Monika C. Haberecht,[a] Michael Bolte,[a] Hans-Wolfram Lerner,[a] and Matthias Wagner*[a]

Keywords: Boranes / Dendrimers / Hydroboration / N ligands

The reaction of 1,4-bis- or 1,3,5-tris(bromoboryl)benzenes **4** and **6**, respectively, with 2 or 3 equiv. of 4,4′-bis(but-3′′-enyl)-2,2′-bipyridyl (**2**) leads to the corresponding 2,2′-bipyridylboronium cations **5** and **7** in almost quantitative yield. Using the monocation $[(MeC_6H_4)B(Br)\{4,4'$-bis(but-3′′-enyl)-2,2′-bipyridyl$\}]^+$ (**3Br**) as a model system, it is shown that the olefinic side-chains of such compounds are readily transformed into alkyldibromoborane functionalities by hydroboration with $HBBr_2$. Subsequent addition of 4,4′-dimethyl-2,2′-bipyridyl leads to the formation of a branched system of three 2,2′-bipyridylboronium cations (**9Br**). The species **5** and **7** can be regarded as generation zero (G_0) 2,2′-bipyridylboronium dendrimers, and the hydroboration/B–N adduct formation sequence offers a convenient route for the assembly of higher generations.

(© Wiley-VCH Verlag GmbH & Co. KGaA, 69451 Weinheim, Germany, 2005)

Introduction

Dendrimers are macromolecules with well-defined molecular architectures derived from a central atom or core with multiple branches. They are gaining great attention due to their potential applications in, for example, biology, catalysis and materials science. Apart from purely organic dendrimers, metallodendrimers[1–3] and heteroatom-based dendrimers[4–6] represent an important area of research. In 1994, Puddephatt reported organometallic dendrimers featuring (2,2′-bipyridyl)Pt^{IV} chelates in every generation.[7,8] Since then, numerous dendrimers incorporating (polypyridyl)metal complexes have been synthesised, mainly with the aim of studying photoinduced energy transfer and multielectron redox processes.[9]

Research in our group focuses on the chemistry of main group chelates of the 2,2′-bipyridyl (bipy) ligand, particularly on 2,2′-bipyridylboronium cations **A** (Figure 1), which are relatives of the organic electron acceptor Diquat (**B**; Figure 1) and thus behave as reversible two-electron redox systems.[10–15]

Cations **A** form spontaneously and under very mild conditions upon treatment of haloboranes XBR_2 (X = Cl, Br) with 2,2′-bipyridyl. For example, starting from 1,1′,3,3′-tetrakis(bromoboryl)ferrocene, the ferrocene derivative **C** (Figure 1) bearing four redox-active 2,2′-bipyridylboronium units has been synthesised in almost quantitative yield.[16] Compound **C**, which possesses an unusual deep-purple colour due to charge-transfer interactions between the ferrocene backbone and its Diquat-like substituents,[15] acts as a fully reversible nine-electron redox system in DMF solution.[16] In an attempt to generate larger aggregates, we initially employed 1,1′-diborylated ferrocenes and bridging 2,2′-bipyridyl derivatives (e.g. quaterpyridine) with the hope of obtaining polymeric materials. However, macrocyclic dimers (e.g. **D**; Figure 1) always formed as the sole reaction products irrespective of the experimental conditions applied.[17] In our second approach, we tried to link ferrocene-1,1′-diylbis(2,2′-bipyridylboronium) cations via their boron atoms by introducing oxygen bridges between them. In contrast to our expectations, no polymeric species were formed but *ansa*-bridged complexes **E** (Figure 1) were obtained as the result of an intramolecular reaction.[12]

We therefore developed a new concept for the preparation of macromolecules containing larger numbers of 2,2′-bipyridylboronium cations and thus possessing the potential to act as electron storage media. Our synthetic methodology is based on a two-reaction sequence using a spontaneous B–N adduct formation in combination with a hydroboration reaction (Scheme 1).

To start, multiply borylated core units are required. Ferrocene and benzene are particularly well-suited candidates since they can easily be borylated up to four (ferrocene)[18] or up to three times (benzene).[19] In the present study, *p*-(dibromoboryl)toluene together with 1,4-bis- and 1,3,5-tris-(dibromoboryl)benzene will be employed. The other building blocks are 4,4′-bis(but-3′′-enyl)-2,2′-bipyridyl (**2**) and dibromoborane, $HBBr_2$, which may either be purchased as its dimethyl sulfide adduct or prepared in situ from tribromoborane and triethylsilane[20,21] in dichloromethane solution. In order to build the desired macromolecules, we will follow a divergent reaction sequence (Scheme 1): First, the

[a] Institut für Anorganische Chemie, Johann Wolfgang Goethe-Universität Frankfurt am Main,
Marie-Curie-Straße 11, 60439 Frankfurt, Germany
Fax: +49-69-798-29260
E-mail: Matthias.Wagner@chemie.uni-frankfurt.de

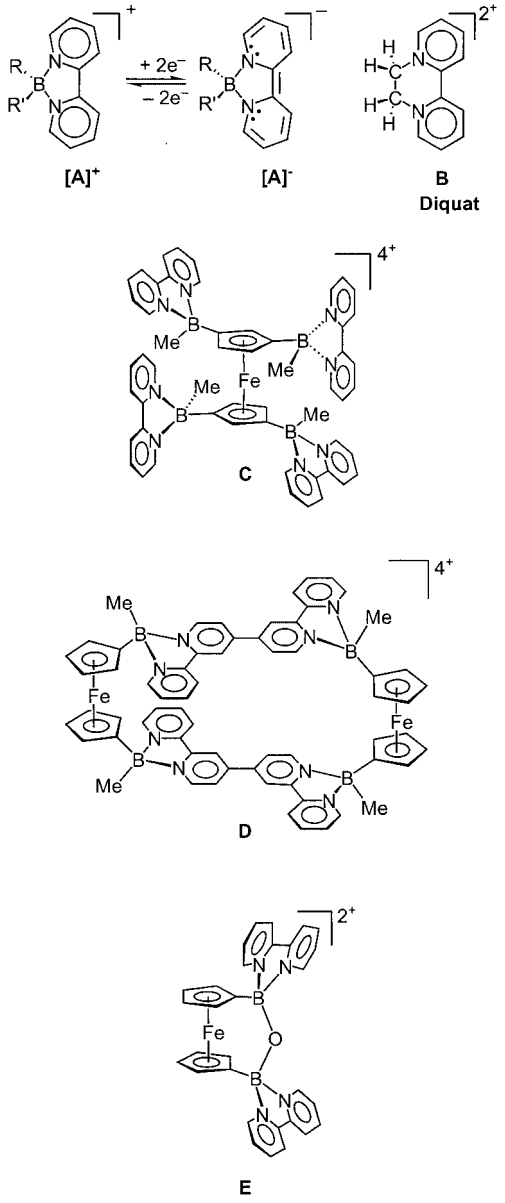

Figure 1. 2,2′-Bipyridylboronium cation (**A**), Diquat (**B**), ferrocene **C** bearing four 2,2′-bipyridylboronium substituents, macrocyclic dinuclear ferrocene complex **D**, and *ansa*-ferrocene **E**.

core unit is treated with the appropriate amount of substituted 2,2′-bipyridyl to prepare the zeroth generation (G_0) of the dendrimer. Second, the G_0 2,2′-bipyridylboronium cation is hydroborated with $HBBr_2$ at its peripheral olefin substituents to generate a molecule bearing alkyldibromoborane side-chains. In the third step, addition of the functionalised 2,2′-bipyridyl gives access to the G_1 dendrimer. The reaction cycle may then be repeated to attach further 2,2′-bipyridylboronium cations and to obtain higher generation dendrimers. The purpose of this paper is (i) to present an optimised procedure for the hydroboration of bipyridylboronium cations with olefinic side-chains, (ii) to prove that up to three bipyridylboronium substituents can be grouped around a benzene ring such that it qualifies as a core unit

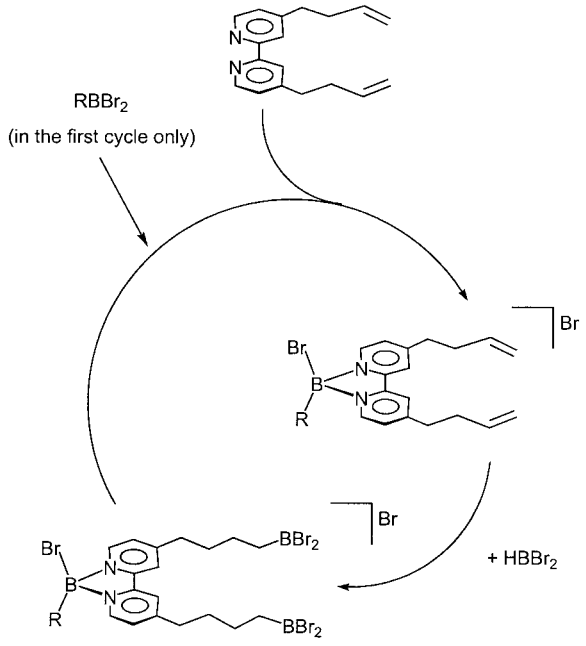

Scheme 1. Concept for the synthesis of branched 2,2′-bipyridylboronium cations by hydroboration with dibromoborane.

for further dendrimer syntheses, and (iii) to describe our first results regarding the synthesis of G_1 dendrimers.

Results and Discussion

Syntheses

Treatment of *p*-(dibromoboryl)toluene (**1Br**)[19] with tetramethylstannane or diethyl ether gives *p*-[bromo(methyl)boryl]toluene (**1Me**) and *p*-[bromo(ethoxy)boryl]toluene (**1OEt**), respectively (Scheme 2). Addition of **1Br**, **1Me** or **1OEt** to the 2,2′-bipyridyl derivative **2**[22] in toluene or dichloromethane at ambient temperature leads to the formation of **3Br**, **3Me** and **3OEt**, respectively, in excellent yields. Compound **3Br**, bearing a bromo substituent at the boron atom, closely mimics the reaction intermediates encountered during the hydroboration/adduct formation cycle (cf. Scheme 1). However, B–Br bonds are prone to hydrolysis and it was therefore desirable to have also the moisture-stable methyl derivative **3Me** at hand. The ethoxy-2,2′-bipyridylboronium cation **3OEt** is described here because it gave crystals suitable for X-ray crystal structure analysis. Most importantly, the bromo substituent of **3Br** can be replaced by a methoxy group (**3OMe**; Scheme 2) when **3Br** is dissolved in dry methanol in the presence of stoichiometric amounts of triethylamine. This reaction proceeds cleanly and quantitatively, and thus offers a convenient way to transform the primary products of future dendrimer syntheses into air- and moisture-stable materials.

 © 2005 Wiley-VCH Verlag GmbH & Co. KGaA, Weinheim

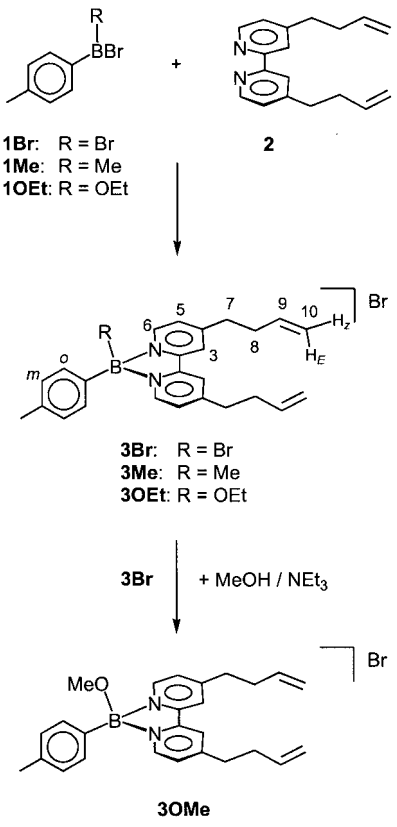

Scheme 2. Synthesis of the 2,2′-bipyridylboronium bromides **3Br**, **3Me**, **3OEt** and **3OMe**.

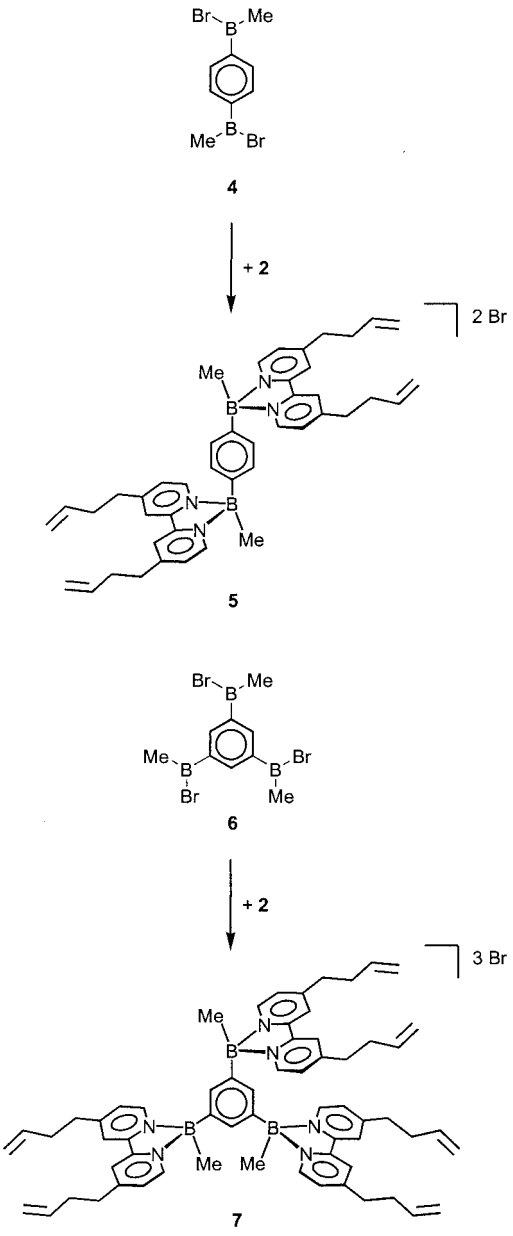

Scheme 3. Synthesis of the bis- and tris(2,2′-bipyridylboronium) bromides **5** and **7**.

The bromo(methyl)boryl-substituted benzenes **4** and **6**, which are accessible from $SnMe_4$ and 1,4-bis(dibromoboryl)benzene or 1,3,5-tris(dibromoboryl)benzene,[19] respectively, in a way similar to the synthesis of **1Me**, readily react with ligand **2** in dichloromethane to form the di- and trications **5** and **7**, respectively (Scheme 3). For purification, the reaction products were precipitated from their dichloromethane solutions by the addition of hexane.

The crucial hydroboration step was carried out using the bromo-substituted monocation **3Br**, since it is the least complex system available but nevertheless contains all the functional groups of a growing dendrimer according to Scheme 1. At the beginning we relied on $HBBr_2{\cdot}SMe_2$ as the hydroboration reagent, but it soon turned out that the in situ generation of $HBBr_2$ from equimolar amounts of triethylsilane and boron tribromide[20,21] gives better results. In the optimised procedure, a mixture of **3Br** and triethylsilane in dichloromethane is added dropwise at –78 °C to a solution of tribromoborane in the same solvent. The reaction is usually complete after warming to ambient temperature. Note that 3 equiv. of BBr_3 are required since 1 equiv. coordinates the bromide counterion of **3Br** to form tetrabromoborate $[BBr_4]^-$. As expected, the hydroboration of **3Br** is not fully regioselective such that isomers $\mathbf{8^t}$ (t = terminal) and $\mathbf{8^i}$ (i = internal) with a BBr_2 substituent attached to C-10 and C-9, respectively, are obtained [approx. ratio (^{1}H NMR spectroscopy): $\mathbf{8^t/8^i}$ = 4:1; see below] (Scheme 4). In order to increase the regioselectivity, we extended our studies to a derivative of **3Br** bearing methyl groups at both its C-9 atoms. In this case, however, C-9 becomes a chiral atom after hydroboration and a mixture of diastereomers is obtained.

Apart from the regioselectivity problem, the crude product **8** is sufficiently pure for further reaction with 2,2′-bipyridyls. A sample of **8** was thus treated with 4,4′-dimethyl-2,2′-bipyridyl in dichloromethane and subsequently with methanol/triethylamine to synthesise the G_1 trication **9OMe**. Attempts to isolate the regioisomers of **9OMe** by reversed-phase HPLC failed since a satisfactory separation could not be achieved.

As already mentioned above, tetrabromoborate is created as a new counterion in the hydroboration reaction. This causes additional problems, since $[BBr_4]^-$ reacts stoichio-

 © 2005 Wiley-VCH Verlag GmbH & Co. KGaA, Weinheim

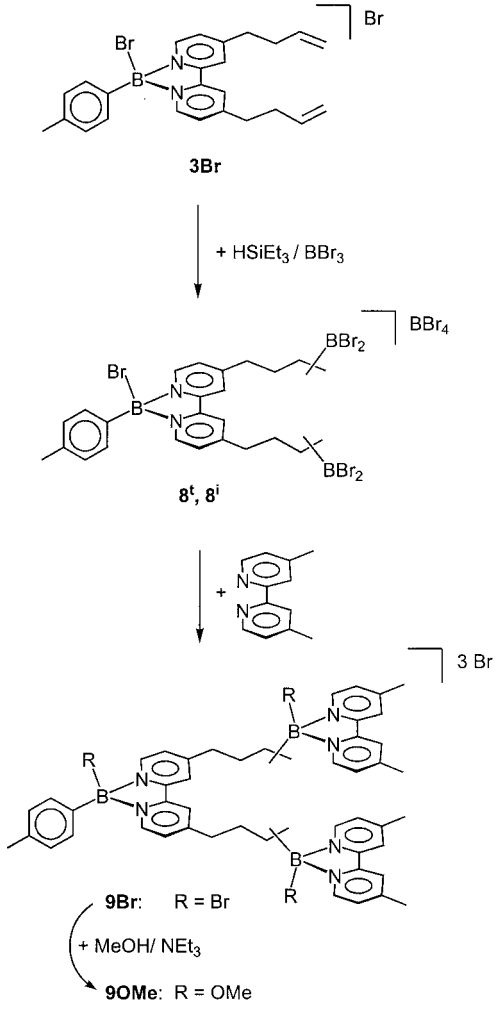

Scheme 4. Hydroboration of **3Br**, subsequent formation of the branched cation **9Br**, and transformation of **9Br** into the moisture-stable derivative **9OMe**.

metrically with 2,2′-bipyridyl similar to the alkyldibromoborane side-chains of **8**. As a consequence, the preparation of the first generation dendrimer **9Br** requires 3 rather than 2 equiv. of the ligand to achieve quantitative conversion. In our search for more suitable counterions, we finally found that $[B(C_6F_5)_4]^-$ is not affected by BBr_3/$HSiEt_3$, which makes it the counterion of choice for further dendrimer syntheses.

NMR Spectroscopy

The ^{11}B NMR shifts of the 2,2′-bipyridylboronium cations appear in the range between δ = 9.8 (**3OMe**) and 6.5 ppm (**3Br**, **7**), thus indicating the presence of tetracoordinate boron nuclei.[23] Very similar ^1H NMR spectra are observed for the monocations **3Br**, **3Me**, **3OEt** and **3OMe**. In all these compounds, the position of the H-3 resonance is strongly dependent on the nature of the counterion and the choice of solvent [cf. **3Me**: δ(H-3) = 10.31 (Br^-/$CDCl_3$), 8.87 (Br^-/CD_3OD), 7.16 ($[B(C_6H_5)_4]^-$/$CDCl_3$), 8.88 ppm ($[PF_6]^-$/$CDCl_3$)]. This effect may therefore be attributed to the formation of contact ion pairs, an interpretation also supported by the structure of **3OEt** in the solid state in which the two C-3–H-3 vectors act as "chelating hydrogen-bond donors" towards the bromide ion (corresponding H···Br contacts in the range between 2.80 and 3.00 Å (Figure 2; for the theoretical treatment of a related system, see ref.[24]). Hydroboration of **3Br** leads to the disappearance of the signals for the olefinic protons [δ(H-9) = 5.81, δ(H-10_E) = 5.05, δ(H-10_Z) = 4.99 ppm] and carbon atoms [δ(C-9) = 135.6, δ(C-10) = 117.1 ppm] and the appearance of new signals in the aliphatic region of the spectrum [**8^t**: δ(H-9) = 1.80, δ(H-10) = 1.71 ppm; δ(C9) = 26.4, δ(C-10) = 36.2 ppm]. Moreover, the ^{11}B NMR spectrum of **8** now reveals two resonances possessing chemical shift values typical of four- and three-coordinate boron nuclei [δ(Bbipy) = 6.5, δ(BBr_2) = 57.3 ppm; integral ratio ≈ 1:2]. Upon addition of 2 equiv. of 4,4′-dimethyl-2,2′-bipyridyl to **8**, the signal at δ = 57.3 ppm disappears and an extremely broad signal occurs at δ ≈ 7 ppm, which clearly shows that all former BBr_2 groups are now tetracoordinate.[23] There are three possible regioisomers of **9OMe**, containing between two and three different kinds of 2,2′-bipyridyl fragments. As a consequence, both the ^1H and the ^{13}C NMR spectra of **9OMe** are poorly resolved and very complex. It is therefore not possible to assign resonances to individual atoms

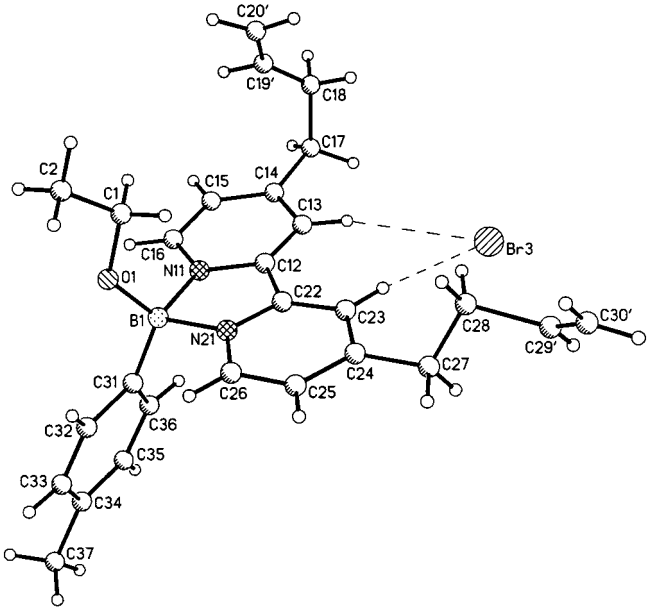

Figure 2. Ball-and-stick model of **3OEt** in the solid state. For clarity, only one of the three crystallographically independent molecules within the asymmetric unit is shown. Selected bond lengths [Å], angles [°] and torsion angles [°]: B(1)–O(1) 1.416(12), B(1)–C(31) 1.539(16), B(1)–N(11) 1.635(13), B(1)–N(21) 1.666(11), N(11)–C(12) 1.369(10), C(12)–C(22) 1.473(11), N(21)–C(22) 1.334(11); O(1)–B(1)–C(31) 114.7(8), O(1)–B(1)–N(11) 111.2(9), O(1)–B(1)–N(21) 110.2(7), C(31)–B(1)–N(11) 114.6(8), C(31)–B(1)–N(21) 111.9(8), N(11)–B(1)–N(21) 92.0(6), C(1)–O(1)–B(1) 123.1(8), C(12)–N(11)–B(1) 115.0(6), C(22)–N(21)–B(1) 113.9(7), N(11)–C(12)–C(22) 108.1(7), N(21)–C(22)–C(12) 110.8(7), C(13)–C(12)–C(22) 129.7(8), C(12)–C(22)–C(23) 127.1(8); N(11)–C(12)–C(22)–N(21) –3.4(12).

 © 2005 Wiley-VCH Verlag GmbH & Co. KGaA, Weinheim

in this case. However, the proposed molecular structure of **9OMe** was clearly proven by mass spectrometry.

Mass Spectrometry

Low resolution electrospray mass spectra (ESI) in the positive-ion mode were recorded for the G_0 compounds **3Me**, **3OMe**, **3OEt**, **5** and **7**. The spectra of the 2,2′-bipyridylboronium salts **3Me**, **3OMe**, **3OEt** reveal exclusively peaks of the free monocations [**3Me** – Br]$^+$, [**3OMe** – Br]$^+$, and [**3OEt** – Br]$^+$ at *m*/*z* values of 381, 397 and 411, respectively. A similar result was obtained for the diborylated species **5**, which gave rise to only one peak assignable to the free dication [**5** – 2 Br]$^{2+}$ (*m*/*z* = 328). In the case of the trisubstituted benzene derivative **7**, two peaks with an integral ratio of 100 (*m*/*z* = 512):95 (*m*/*z* = 315) appear in the mass spectrum, which correspond to the di- and trications [**7** – 2 Br]$^{2+}$ and [**7** – 3 Br]$^{3+}$. An ESI mass spectrum was also recorded for **9OMe**. Again, the most intense peaks (*m*/*z* = 465, 284) by far may be assigned to the cations [**9OMe** – 2 Br]$^{2+}$ and [**9OMe** – 3 Br]$^{3+}$.

X-ray Crystallography

Single crystals of **3OEt** (triclinic, space group $P\bar{1}$) grew slowly from an oily sample at room temperature. There are three crystallographically independent molecules in the asymmetric unit. Since their structure parameters are equal within experimental error, the data of only one of the three molecules are discussed here. As already deduced from the NMR spectra, the compound contains a tetracoordinate boron centre chelated by a 2,2′-bipyridyl ligand [B(1)–N(11) = 1.635(13) Å, B(1)–N(21) = 1.666(11) Å; N(11)–B(1)–N(21) = 92.0(6)°]. Chelation of the small boron atom leads to a slight distortion of the 2,2′-bipyridyl moiety such that the angles C(13)–C(12)–C(22) and C(12)–C(22)–C(23) on the outer frame of the aromatic system are stretched to values of 129.7(8)° and 127.1(8)°, respectively. The terminal atoms C(19′), C(20′), C(29′) and C(30′) of the butenyl chains are disordered. Although a model with two different conformations has been employed, the anisotropic displacement parameters of C(19′) and C(20′) are still rather large.

Conclusions

This paper reports a novel strategy for the generation of dendritic macromolecules consisting of redox-active 2,2′-bipyridylboronium cations. 1,4-Di- and 1,3,5-triborylated benzenes are chosen as core units and a hydroboration/B–N adduct formation sequence is suggested for the assembly of the individual branches.

To prove the suitability of the benzene core unit, we first synthesised the air- and moisture-stable benzene derivatives **5** and **7** bearing two and three 4,4′-bis(but-3′′-enyl)-2,2′-bipyridylboronium substituents in their 1,4- and 1,3,5-positions. The reactions proceed cleanly and quantitatively, which leads to the conclusion that there is sufficient space along the periphery of a benzene ring to attach up to three branching subunits. Compounds **5** and **7** may therefore be regarded as generation zero (G_0) dendrimers.

In order to optimise the hydroboration reaction, the monocation **3Br**, derived from *p*-(dibromoboryl)toluene (**1Br**) and 4,4′-bis(but-3′′-enyl)-2,2′-bipyridyl (**2**), was employed as a model system. Quantitative conversion of both its olefinic side-chains into alkyldibromoboryl substituents was achieved under mild conditions with BBr_3/$HSiEt_3$ as hydroborating reagent. The regioselectivity of the hydroboration reaction is high (ratio of terminal vs. internal hydroboration ≈ 4:1). Introduction of methyl groups into the β-positions of the terminal alkenes eliminates the regioselectivity problem (NMR spectroscopic control) but leads to an inseparable mixture of diastereomers after hydroboration.

Apart from the fact that **8** was found to be a mixture of isomers **8**$^{\mathbf{t}}$ and **8**$^{\mathbf{i}}$, the sample obtained was sufficiently pure for further derivatisation with 4,4′-dimethyl-2,2′-bipyridyl. This reaction requires 3 rather than 2 equiv. of bipyridyl ligand; the third equivalent is consumed by the $[BBr_4]^-$ counterion of **8**. Bromo-substituted 2,2′-bipyridylboronium cations are sensitive towards hydrolysis, therefore **9Br** was transformed into the air- and moisture-stable derivative **9OMe** by treatment with methanol/triethylamine. The successful synthesis of **9OMe** was proven by ESI mass spectrometry.

Overall, the general synthetic concept outlined in this paper has successfully passed its first evaluation. However, the following modifications are required: (1) Despite numerous efforts, we have not been able to separate the different regioisomers of **9OMe** by HPLC or GPC techniques. Apart from the fact that the solubilities, polarities etc. of these isomers are obviously similar, the alkyl(bipyridyl)boronium cations within the dendrimer branches appear to be less stable than the aryl(bipyridyl)boronium cations formed with the core unit. We therefore decided to abandon the hydroboration step in future syntheses and to look for an alternative reaction that leads to more stable aryl(bipyridyl)-boronium ions and does not suffer from any regioselectivity problems. All these requirements are met by the system (trimethylsilyl)arene/BBr_3, which gives aryldibromoboranes and bromotrimethylsilane (in fact, this reaction has already been employed for the synthesis of our di- and triborylated core units[19]). Since we already have the 2,2′-bipyridyl derivative **10** (Figure 3) at our disposal,[22] there should be no major problem on switching from the hydroboration reaction to the Si/B exchange protocol. (2) During the hydro-

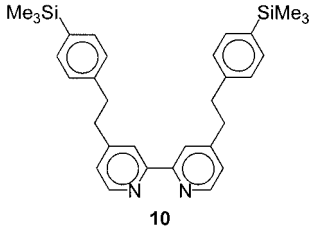

10

Figure 3. 2,2′-Bipyridyl ligand **10** bearing 2-[(trimethylsilyl)aryl)]-ethyl groups.

 © 2005 Wiley-VCH Verlag GmbH & Co. KGaA, Weinheim

boration step, a $[BBr_4]^-$ ion is created, which is reactive towards 2,2′-bipyridyls. Since the perfluorated tetraphenylborate anion $[B(C_6F_5)_4]^-$ turned out to be inert under the reaction conditions applied, it is advantageous to replace the Br^- ion by $[B(C_6F_5)_4]^-$ in future syntheses {e.g. by treatment with $Tl[B(C_6F_5)_4]$ or $Ag[B(C_6F_5)_4]$}.

Experimental Section

General Remarks: All reactions were carried out under oxygen-free argon or nitrogen using standard Schlenk techniques. Solvents were distilled under argon from sodium/benzophenone (toluene, *n*-hexane, *n*-pentane, triethylamine, methanol) or passed through a 4 Å molecular sieves column (CH_2Cl_2, $CHCl_3$) prior to use; the syntheses of *p*-(dibromoboryl)toluene (**1Br**),[19] 1,4-bis(dibromoboryl)benzene,[19] 1,3,5-tris(dibromoboryl)benzene[19] and 4,4′-bis(but-3′′-enyl)-2,2′-bipyridyl (**2**)[22] have been described elsewhere. NMR spectra were recorded with Bruker AMX 250, DPX 250 or Avance 400 spectrometers. Chemical shifts are referenced to residual solvent peaks (^1H, $^{13}C\{^1H\}$); ^{11}B NMR chemical shifts are reported relative to external $BF_3{\cdot}Et_2O$. Low resolution electrospray mass spectra (ESI) were recorded in the positive-ion mode with a Fisons VG Platform II spectrometer.

1Me: Tetramethylstannane (4.699 g, 26.27 mmol) was added dropwise, at ambient temperature, to **1Br** (6.543 g, 25.00 mmol) in *n*-pentane (15 mL), and the mixture was stirred for 5 h. After the solvent had been evaporated, the residue was kept at 50 °C in vacuo for 3 h. Subsequent vacuum distillation gave pure **1Me** as a colourless liquid. Yield: 3.498 g (70%). ^1H NMR (250.1 MHz, $CDCl_3$, 25 °C): δ = 7.99 (d, $^3J_{H,H}$ = 8.0 Hz, 2 H, H-Ar$_o$), 7.25 (d, $^3J_{H,H}$ = 8.0 Hz, 2 H, H-Ar$_m$), 2.39 (s, 3 H, CH_3-Ar), 1.49 (s, 3 H, CH_3B) ppm. ^{11}B NMR (128.4 MHz, $CDCl_3$, 25 °C): δ = 70.5 ($h_{1/2}$ = 250 Hz) ppm. ^{13}C NMR (62.9 MHz, $CDCl_3$, 25 °C): δ = 146.8 (C-Ar$_p$), 138.0 (C-Ar$_o$), 129.0 (C-Ar$_m$), 22.1 (CH_3-Ar) ppm; C-Ar$_i$, CH_3B not observed.

1OEt: Diethyl ether (1.495 g, 20.17 mmol) was added with a syringe to **1Br** (5.235 g, 20.00 mmol) in toluene (40 mL). After the solution had been stirred at room temperature for 5 d, the solvent was evaporated to give **1OEt** as an off-white oil, which was used without further purification. Yield: 3.993 g (88%). ^1H NMR (250.1 MHz, $CDCl_3$, 25 °C): δ = 8.16 (d, $^3J_{H,H}$ = 7.8 Hz, 2 H, H-Ar), 7.13 (d, $^3J_{H,H}$ = 7.8 Hz, 2 H, H-Ar), 4.18 (q, $^3J_{H,H}$ = 7.1 Hz, 2 H, OCH_2), 2.16 (s, 3 H, CH_3-Ar), 1.13 (t, $^3J_{H,H}$ = 7.1 Hz, 3 H, OCH_2CH_3) ppm. ^{11}B NMR (128.4 MHz, $CDCl_3$, 25 °C): δ = 38.4 ($h_{1/2}$ = 200 Hz) ppm. ^{13}C NMR (62.9 MHz, $CDCl_3$, 25 °C): δ = 137.9, 135.9, 128.9 (C-Ar), 66.0 (OCH_2), 21.4 (CH_3-Ar), 16.1 (OCH_2CH_3) ppm; C-Ar$_i$ not observed.

3Br: A solution of **1Br** (0.393 g, 1.50 mmol) in toluene (2.5 mL) was added dropwise to a solution of **2** (0.397 g, 1.50 mmol) in toluene (5 mL). The reaction mixture immediately turned yellow and **3Br** precipitated as a yellow oil. This oil was isolated, washed with *n*-hexane and dried in vacuo to give the pure product as a yellow foam. Yield: 0.602 g (76%). ^1H NMR (250.1 MHz, $CDCl_3$, 25 °C): δ = 10.25 (br., 2 H, H-3), 8.45 (d, $^3J_{H,H}$ = 6.0 Hz, 2 H, H-6), 7.76 (dd, $^3J_{H,H}$ = 6.0, $^4J_{H,H}$ = 1.4 Hz, 2 H, H-5), 7.15 (d, $^3J_{H,H}$ = 8.3 Hz, 2 H, H-Ar$_o$), 7.09 (d, $^3J_{H,H}$ = 8.3 Hz, 2 H, H-Ar$_m$), 5.81 (ddt, $^3J_{H,H}$ = 17.1, 10.3, 6.6 Hz, 2 H, H-9), 5.05 (d, $^3J_{H,H}$ = 17.1 Hz, 2 H, H-10$_E$), 4.99 (d, $^3J_{H,H}$ = 10.3 Hz, 2 H, H-10$_Z$), 3.20 (t, $^3J_{H,H}$ = 7.4 Hz, 4 H, H-7), 2.67 (m, 4 H, H-8), 2.27 (s, 3 H, CH_3-Ar) ppm. ^{11}B NMR (128.4 MHz, $CDCl_3$, 25 °C): δ = 6.5 ($h_{1/2}$ = 400 Hz) ppm. ^{13}C NMR (62.9 MHz, $CDCl_3$, 25 °C): δ = 164.7 (C-4), 144.6 (C-2), 142.3 (C-6), 140.0 (C-Ar$_p$), 135.6 (C-9), 132.2 (C-Ar$_o$), 129.4 (C-Ar$_m$), 129.0 (C-5), 126.8 (C-3), 117.1 (C-10), 35.3 (C-7), 33.1 (C-8), 21.2 (CH_3-Ar) ppm; C-Ar$_i$ not observed.

3Me: A solution of **1Me** (0.591 g, 3.00 mmol) in dichloromethane (5 mL) was added dropwise, at ambient temperature, to **2** (0.793 g, 3.00 mmol) in dichloromethane (10 mL). The solvent volume was reduced to approximately 5 mL and *n*-hexane added dropwise, whereupon **3Me** precipitated as a pale-yellow oil. Yield: 1.211 g (88%). ^1H NMR (400.1 MHz, $CDCl_3$, 25 °C): δ = 10.31 (br., 2 H, H-3), 8.22 (d, $^3J_{H,H}$ = 5.9 Hz, 2 H, H-6), 7.59 (dd, $^3J_{H,H}$ = 5.9, $^4J_{H,H}$ = 1.4 Hz, 2 H, H-5), 7.06 (d, $^3J_{H,H}$ = 7.8 Hz, 2 H, H-Ar$_m$), 6.91 (d, $^3J_{H,H}$ = 7.8 Hz, 2 H, H-Ar$_o$), 5.85 (ddt, $^3J_{H,H}$ = 17.1, 10.3, 6.7 Hz, 2 H, H-9), 5.07 (d, $^3J_{H,H}$ = 17.1 Hz, 2 H, H-10$_E$), 5.01 (d, $^3J_{H,H}$ = 10.3 Hz, 2 H, H-10$_Z$), 3.20 (t, $^3J_{H,H}$ = 7.5 Hz, 4 H, H-7), 2.69 (m, 4 H, H-8), 2.27 (s, 3 H, CH_3-Ar), 0.61 (s, 3 H, CH_3B) ppm. ^{11}B NMR (128.4 MHz, $CDCl_3$, 25 °C): δ = 7.5 ($h_{1/2}$ = 350 Hz) ppm. ^{13}C NMR (62.9 MHz, $CDCl_3$, 25 °C): δ = 161.5 (C-4), 145.1 (C-2), 141.3 (C-6), 138.1 (C-Ar$_p$), 135.7 (C-9), 131.1 (C-Ar$_o$), 129.0 (C-Ar$_m$), 128.3 (C-5), 125.3 (C-3), 116.5 (C-10), 34.8 (C-7), 33.2 (C-8), 20.9 (CH_3-Ar), 6.9 (CH_3B) ppm; C-Ar$_i$ not observed. ESI-MS: *m*/*z* (%) = 381 (100) [M^+ – Br]. $C_{26}H_{30}BBrN_2$ (461.25): calcd. C 67.70, H 6.56, N 6.07; found C 67.11, H 6.51, N 5.91.

3OEt: Compound **2** (2.247 g, 8.50 mmol) was dissolved in toluene (20 mL) and a solution of **1OEt** (1.929 g, 8.50 mmol) in toluene (20 mL) was added dropwise at ambient temperature, whereupon the reaction mixture became cloudy and the product precipitated as a red-brown oil. The solvent was decanted and the oil washed with *n*-hexane. Yield: 3.645 g (87%). ^1H NMR (250.1 MHz, $CDCl_3$, 25 °C): δ = 10.18 (br., 2 H, H-3), 8.27 (d, $^3J_{H,H}$ = 5.8 Hz, 2 H, H-6), 7.67 (dd, $^3J_{H,H}$ = 5.8, $^4J_{H,H}$ = 1.4 Hz, 2 H, H-5), 7.00 (m, 4 H, H-Ar), 5.81 (ddt, $^3J_{H,H}$ = 17.2, 10.3, 6.8 Hz, 2 H, H-9), 5.02 (d, $^3J_{H,H}$ = 17.2 Hz, 2 H, H-10$_E$), 4.96 (d, $^3J_{H,H}$ = 10.3 Hz, 2 H, H-10$_Z$), 3.17 (t, $^3J_{H,H}$ = 7.6 Hz, 4 H, H-7), 2.92 (q, $^3J_{H,H}$ = 6.9 Hz, 2 H, OCH_2), 2.65 (m, 4 H, H-8), 2.23 (s, 3 H, CH_3-Ar), 1.06 (t, $^3J_{H,H}$ = 6.9 Hz, 3 H, OCH_2CH_3) ppm. ^{11}B NMR (128.4 MHz, $CDCl_3$, 25 °C): δ = 9.1 ($h_{1/2}$ = 350 Hz) ppm. ^{13}C NMR (62.9 MHz, $CDCl_3$, 25 °C): δ = 163.6 (C-4), 145.2 (C-2), 141.7 (C-6), 138.7 (C-Ar$_p$), 135.7 (C-9), 131.0 (C-Ar$_o$), 129.0 (C-Ar$_m$), 128.5 (C-5), 126.0 (C-3), 116.8 (C-10), 58.2 (OCH_2), 35.1 (C-7), 33.3 (C-8), 21.2 (CH_3-Ar), 17.4 (OCH_2CH_3) ppm; C-Ar$_i$ not observed. ESI-MS: *m*/*z* (%) = 411 (100) [M^+ – Br]. $C_{27}H_{32}BBrN_2O$ (491.27): calcd. C 66.01, H 6.57, N 5.70; found C 65.74, H 6.47, N 5.59.

3OMe: Compound **3Br** (0.789 g, 1.50 mmol) was dissolved in dry methanol (5 mL), treated with dry triethylamine (0.152 g, 1.50 mmol) from a syringe and the resulting reaction mixture was stirred at ambient temperature for 2 h. The solvent was evaporated and the residue dissolved in dichloromethane (5 mL). Addition of a few drops of *n*-hexane made the product precipitate as a light brown oil, which was isolated by decantation and washed with a mixture of dichloromethane and *n*-hexane. Yield: 0.635 g (89%). ^1H NMR (250.1 MHz, $CDCl_3$, 25 °C): δ = 10.18 (br., 2 H, H-3), 8.26 (d, $^3J_{H,H}$ = 5.8 Hz, 2 H, H-6), 7.67 (dd, $^3J_{H,H}$ = 5.8, $^4J_{H,H}$ = 1.5 Hz, 2 H, H-5), 7.02 (d, $^3J_{H,H}$ = 8.0 Hz, 2 H, H-Ar$_m$), 6.97 (d, $^3J_{H,H}$ = 8.0 Hz, 2 H, H-Ar$_o$), 5.81 (ddt, $^3J_{H,H}$ = 17.1, 10.4, 6.9 Hz, 2 H, H-9), 5.03 (d, $^3J_{H,H}$ = 17.1 Hz, 2 H, H-10$_E$), 4.97 (d, $^3J_{H,H}$ = 10.4 Hz, 2 H, H-10$_Z$), 3.18 (t, $^3J_{H,H}$ = 7.5 Hz, 4 H, H-7), 2.86 (s, 3 H, OCH_3), 2.66 (m, 4 H, H-8), 2.23 (s, 3 H, CH_3-Ar) ppm. ^{11}B NMR (128.4 MHz, $CDCl_3$, 25 °C): δ = 9.8 ($h_{1/2}$ = 400 Hz) ppm. ^{13}C NMR (62.9 MHz, $CDCl_3$, 25 °C): δ = 163.7 (C-4), 145.2 (C-2), 141.7 (C-6), 138.8 (C-Ar$_p$), 135.7 (C-9), 131.0 (C-Ar$_o$), 129.0 (C-Ar$_m$), 128.6 (C-5), 126.0 (C-3), 116.8 (C-10), 50.4 (OCH_3), 35.1 (C-

7), 33.2 (C-8), 21.2 (CH_3-Ar) ppm; C-Ar_i not observed. ESI-MS: *m/z* (%) = 397 (100) [M^+ – Br]. $C_{26}H_{30}BBrN_2O$ (477.25): calcd. C 65.43, H 6.34, N 5.87; found C 64.80, H 6.33, N 5.62.

4: 1,4-Bis(dibromoboryl)benzene (2.295 g, 5.50 mmol) was dissolved in chloroform (15 mL) and tetramethylstannane (1.967 g, 11.00 mmol) was added dropwise at ambient temperature. The reaction mixture was stirred overnight, the solvent was evaporated, bromotrimethylstannane removed at 50 °C in vacuo, and the residue vacuum-sublimed to give pure **4** as a colourless solid. Yield: 0.854 g (54%). ^{1}H NMR (250.1 MHz, $CDCl_3$, 25 °C): δ = 8.14 (s, 4 H, H-Ar), 1.55 (s, 6 H, CH_3B) ppm. ^{11}B NMR (128.4 MHz, $CDCl_3$): δ = 72.3 ($h_{1/2}$ = 400 Hz) ppm. ^{13}C NMR (62.9 MHz, $CDCl_3$, 25 °C): δ = 135.5 (C-Ar) ppm; C-Ar_i, CH_3B not observed.

5: A solution of **4** (0.431 g, 1.50 mmol) in dichloromethane (5 mL) was added dropwise, at ambient temperature, to **2** (0.793 g, 3.00 mmol) in dichloromethane (10 mL). After the addition was complete, the solvent volume was reduced to approximately 5 mL and *n*-hexane added dropwise, which made **5** precipitate as a pale-yellow oil. Yield: 1.084 g (89%). ^{1}H NMR (250.1 MHz, $CDCl_3$, 25 °C): δ = 9.88 (br., 4 H, H-3), 8.31 (d, $^3J_{H,H}$ = 5.9 Hz, 4 H, H-6), 7.76 (dd, $^3J_{H,H}$ = 5.9, $^4J_{H,H}$ = 1.4 Hz, 4 H, H-5), 6.89 (s, 4 H, H-Ar), 5.81 (ddt, $^3J_{H,H}$ = 17.0, 10.3, 6.6 Hz, 4 H, H-9), 5.04 (d, $^3J_{H,H}$ = 17.0 Hz, 4 H, H-10$_E$), 4.98 (d, $^3J_{H,H}$ = 10.3 Hz, 4 H, H-10$_Z$), 3.15 (t, $^3J_{H,H}$ = 7.5 Hz, 8 H, H-7), 2.63 (m, 8 H, H-8), 0.58 (s, 6 H, CH_3B) ppm. ^{11}B NMR (128.4 MHz, $CDCl_3$, 25 °C): δ = 7.7 ($h_{1/2}$ = 580 Hz) ppm. ^{13}C NMR (62.9 MHz, $CDCl_3$, 25 °C): δ = 161.8 (C-4), 145.2 (C-2), 141.4 (C-6), 135.9 (C-9), 131.5 (C-Ar), 128.6 (C-5), 125.5 (C-3), 116.9 (C-10), 35.1 (C-7), 33.4 (C-8) ppm; C-Ar_i, CH_3B not observed. ESI-MS: *m/z* (%) = 328 (100) [M^{2+} – 2 Br]. $C_{44}H_{50}B_2Br_2N_4$ (816.34): calcd. C 64.74, H 6.17, N 6.86; found C 64.29, H 6.07, N 6.66.

6: Preparation and purification was achieved as described for **4**. 1,3,5-Tris(dibromoboryl)benzene (2.348 g, 4.00 mmol), tetramethylstannane (2.217 g, 12.40 mmol), chloroform (20 mL). Yield: 0.674 g (43%). ^{1}H NMR (250.1 MHz, $CDCl_3$, 25 °C): δ = 9.02 (s, 3 H, H-Ar), 1.34 (s, 9 H, CH_3B) ppm. ^{11}B NMR (128.4 MHz, $CDCl_3$, 25 °C): δ = 72.0 ($h_{1/2}$ = 350 Hz) ppm. ^{13}C NMR (62.9 MHz, $CDCl_3$, 25 °C): δ = 149.0 (C-Ar) ppm; C-Ar_i, CH_3B not observed.

7: Compound **6** (0.863 g, 2.20 mmol) was dissolved in dichloromethane (10 mL) and added dropwise to a solution of **2** (1.718 g, 6.50 mmol) in dichloromethane (20 mL). The reaction mixture became yellow. After the addition was complete, *n*-hexane was added, which made **7** precipitate as a yellow oil. Yield: 2.086 g (80%). ^{1}H NMR (400.1 MHz, $CDCl_3$, 25 °C): δ = 8.89 (br., 6 H, H-3), 8.81 (d, $^3J_{H,H}$ = 5.9 Hz, 6 H, H-6), 8.13 (dd, $^3J_{H,H}$ = 5.9, $^4J_{H,H}$ = 1.3 Hz, 6 H, H-5), 6.62 (s, 3 H, H-Ar), 5.80 (ddt, $^3J_{H,H}$ = 17.1, 10.4, 6.6 Hz, 6 H, H-9), 5.05 (d, $^3J_{H,H}$ = 17.1 Hz, 6 H, H-10$_E$), 5.01 (d, $^3J_{H,H}$ = 10.4 Hz, 6 H, H-10$_Z$), 3.07 (m, 12 H, H-7), 2.56 (m, 12 H, H-8), 0.45 (s, 9 H, CH_3B) ppm. ^{11}B NMR (128.4 MHz, CD_3OD, 25 °C): δ = 6.5 ($h_{1/2}$ = 600 Hz) ppm. ^{13}C NMR (62.9 MHz, $CDCl_3$, 25 °C): δ = 160.4 (C-4), 144.5 (C-2), 143.9 (C-6), 135.6 (C-9), 134.3 (C-Ar), 129.8 (C-5), 123.2 (C-3), 117.0 (C-10), 35.2 (C-7), 33.6 (C-8), 7.6 (CH_3B) ppm; C-Ar_i not observed. ESI-MS: *m/z* (%) = 512 (100) [M^{2+} – 2 Br], 315 (95) [M^{3+} – 3 Br]. $C_{63}H_{72}B_3Br_3N_6$ (1185.45): calcd. C 63.83, H 6.12, N 7.09; found C 63.39, H 6.08, N 6.85.

8: An intensely yellow solution of **3Br** (0.395 g, 0.75 mmol) and Et_3SiH (0.262 g, 2.25 mmol) in dichloromethane (5 mL) was added dropwise at –78 °C to BBr_3 (0.564 g, 2.25 mmol) in dichloromethane (5 mL) and the mixture then warmed to room temperature. Addition of *n*-hexane (5 mL) made **8** precipitate as a pale-yellow oil, which was isolated and vacuum-dried to give a colourless foam. According to the NMR spectra the conversion was quantitative. Major isomer **8^t**: ^{1}H NMR (400.1 MHz, CD_2Cl_2, 25 °C): δ = 8.87 (s, 2 H, H-3), 8.60 (d, $^3J_{H,H}$ = 6.0 Hz, 2 H, H-6), 7.86 (dd, $^3J_{H,H}$ = 6.0, $^4J_{H,H}$ = 1.4 Hz, 2 H, H-5), 7.27 (d, $^3J_{H,H}$ = 7.8 Hz, 2 H, H-Ar$_o$), 7.17 (d, $^3J_{H,H}$ = 7.8 Hz, 2 H, H-Ar$_m$), 3.15 (t, $^3J_{H,H}$ = 7.6 Hz, 4 H, H-7), 2.32 (s, 3 H, CH_3-Ar), 1.94 (m, 4 H, H-8), 1.80 (m, 4 H, H-9), 1.71 (m, 4 H, H-10) ppm. ^{11}B NMR (126.8 MHz, CD_2Cl_2, 25 °C): δ = 57.3 (BBr_2, $h_{1/2}$ = 530 Hz), 6.5 (Bbipy, $h_{1/2}$ = 650 Hz), –24.1 ($[BBr_4]^-$, $h_{1/2}$ = 260 Hz) ppm. ^{13}C NMR (100.6 MHz, CD_2Cl_2, 25 °C): δ = 165.5 (C-4), 144.6 (C-2), 143.7 (C-6), 140.5 (C-Ar$_p$), 132.9 (C-Ar$_o$), 130.0 (C-5), 129.7 (C-Ar$_m$), 124.4 (C-3), 36.5 (C-7), 36.2 (C-10), 31.8 (C-8), 26.4 (C-9), 21.4 (CH_3-Ar) ppm; C-Ar_i not observed.

9OMe: Compound **8** (0.840 g, 0.75 mmol) was dissolved in dichloromethane (5 mL) and a solution of 4,4′-dimethyl-2,2′-bipyridyl (0.415 g, 2.25 mmol) in dichloromethane (5 mL) added dropwise with stirring. Upon addition, the solution adopted an intense yellow colour. After the reaction mixture had been stirred at ambient temperature for 2 h, the solvent was evaporated and the solid residue redissolved in methanol (5 mL). Et_3N (0.227 g, 2.25 mmol) was added with a syringe, the reaction mixture was stirred for 2 h, and the volatiles were removed in vacuo. All attempts to isolate **9OMe** from the solid residue obtained applying reversed-phase HPLC techniques [stationary phase: ReproSil-Pur C18-AQ (10 μm, 250 × 20 mm); eluent: methanol or methanol/acetonitrile] failed. However, ESI mass spectrometry proved the presence of **9OMe** in the crude product. ESI-MS: *m/z* = 284 [M^{3+} – 3 Br], 465 [M^{2+} – 2 Br].

Crystal Structure Determination: $C_{27}H_{32}BBrN_2O$, M = 491.27, triclinic, space group $P\bar{1}$, a = 13.154(2), b = 14.371(2), c = 23.377(5) Å, α = 87.329(15)°, β = 87.113(15)°, γ = 63.314(12)°, V = 3941.9(12) Å^3, Z = 6, D_c = 1.242 Mg m^{-3}, F(000) = 1536, Mo-K_α radiation (λ = 0.71073 Å), T = 173(2) K; crystal size 0.24 × 0.23 × 0.16 mm, ω-scan mode, measurement range ($-16 \le h \le 15$, $-17 \le k \le 17$, $-28 \le l \le 26$, $3.58 \le \theta \le 25.92$), 15100 independent reflections, μ = 1.584 mm^{-1}. The structure was solved by direct methods[25] and full-matrix least-squares refinement was carried out against F^2 using the SHELXL-97 program,[26] 905 parameters, R_1 = 0.1833 (all data), wR_2 = 0.2230 (all data), max./min. residual electron density +0.580/–0.512 e Å^{-3}. CCDC-271402 contains the supplementary crystallographic data for this paper. These data can be obtained free of charge from The Cambridge Crystallographic Data Centre via www.ccdc.cam.ac.uk/data_request/cif.

[1] C. Gorman, *Adv. Mater.* **1998**, *10*, 295.
[2] P. A. Chase, R. J. M. Klein Gebbink, G. van Koten, *J. Organomet. Chem.* **2004**, *689*, 4016.
[3] G. R. Newkome, E. He, C. N. Moorefield, *Chem. Rev.* **1999**, *99*, 1689.
[4] J.-P. Majoral, A.-M. Caminade, *Chem. Rev.* **1999**, *99*, 845.
[5] H. Frey, C. Lach, K. Lorenz, *Adv. Mater.* **1998**, *10*, 279.
[6] M. Dasgupta, M. B. Peori, A. K. Kakkar, *Coord. Chem. Rev.* **2002**, *233–234*, 223.
[7] S. Achar, R. J. Puddephatt, *Angew. Chem. Int. Ed. Engl.* **1994**, *33*, 847.
[8] S. Achar, R. J. Puddephatt, *J. Chem. Soc., Chem. Commun.* **1994**, 1895.
[9] S. Serroni, S. Campagna, F. Puntoriero, C. Di Pietro, N. D. McClenaghan, F. Loiseau, *Chem. Soc. Rev.* **2001**, *30*, 367.
[10] S. Hünig, I. Wehner, *Heterocycles* **1989**, *28*, 359.
[11] L. Ding, K. Ma, M. Bolte, F. Fabrizi de Biani, P. Zanello, M. Wagner, *J. Organomet. Chem.* **2001**, *637–639*, 390.
[12] L. Ding, K. Ma, F. Fabrizi de Biani, M. Bolte, P. Zanello, M. Wagner, *Organometallics* **2001**, *20*, 1041.

 © 2005 Wiley-VCH Verlag GmbH & Co. KGaA, Weinheim

[13] K. Ma, M. Scheibitz, S. Scholz, M. Wagner, *J. Organomet. Chem.* **2002**, *652*, 11.
[14] K. Ma, F. Fabrizi de Biani, M. Bolte, P. Zanello, M. Wagner, *Organometallics* **2002**, *21*, 3979.
[15] M. D. Thomson, M. Novosel, H. G. Roskos, T. Müller, M. Scheibitz, M. Wagner, F. Fabrizi de Biani, P. Zanello, *J. Phys. Chem. A* **2004**, *108*, 3281.
[16] F. Fabrizi de Biani, T. Gmeinwieser, E. Herdtweck, F. Jäkle, F. Laschi, M. Wagner, P. Zanello, *Organometallics* **1997**, *16*, 4776.
[17] L. Ding, K. Ma, G. Dürner, M. Bolte, F. Fabrizi de Biani, P. Zanello, M. Wagner, *J. Chem. Soc., Dalton Trans.* **2002**, 1566.
[18] A. Appel, F. Jäkle, T. Priermeier, R. Schmid, M. Wagner, *Organometallics* **1996**, *15*, 1188.
[19] M. C. Haberecht, J. B. Heilmann, A. Haghiri, M. Bolte, J. W. Bats, H.-W. Lerner, M. C. Holthausen, M. Wagner, *Z. Anorg. Allg. Chem.* **2004**, *630*, 904.
[20] R. Soundararajan, D. S. Matteson, *J. Org. Chem.* **1990**, *55*, 2274.
[21] R. Soundararajan, D. S. Matteson, *Organometallics* **1995**, *14*, 4157.
[22] M. C. Haberecht, M. Bolte, J. W. Bats, H.-W. Lerner, M. Wagner, *Z. Naturforsch. Teil B* **2005**, *60*, 745.
[23] H. Noeth, B. Wrackmeyer, *NMR: Basic Principles and Progress*, Springer, Berlin, **1978**.
[24] V. S. Bryantsev, B. P. Hay, *J. Am. Chem. Soc.* **2005**, *127*, 8282.
[25] G. M. Sheldrick, *Acta Crystallogr. Sect. A* **1990**, *46*, 467.
[26] G. M. Sheldrick, University of Göttingen, Germany, **1997**.

Received: May 9, 2005
Published Online: September 21, 2005

 © 2005 Wiley-VCH Verlag GmbH & Co. KGaA, Weinheim

Metal Binding Within a Peptide-Based Nucleobase Stack with Tuneable Double-Strand Topology

Andrea Küsel,[a] Jinhua Zhang,[a] Miguel Alvariño Gil,[b] A. Claudia Stückl,[b] Wolfram Meyer-Klaucke,[c] Franc Meyer,*[b] and Ulf Diederichsen*[a]

Keywords: EXAFS spectroscopy / Molecular recognition / Nucleic acids / Peptides / Protein models

Peptide nucleic acid (PNA) oligomers with linear topology are synthesised with histidines at the central positions in order to provide metal-ion coordination sites within the water shielded and non-polar environment of a nucleobase stack that emerges upon duplex formation. Variation of the linker length used for attachment of the nucleobases to the regular peptide backbone allows for fine tuning of the distances and coordination environment at the metal binding site. The effect of zinc and copper incorporation into the modified alanyl-PNA scaffolds on duplex stability was probed by temperature-dependent UV spectroscopy, and additional insight was gained from EPR spectroscopy and EXAFS. Whenever four histidines (two per oligomer strand) are available, addition of Zn^{2+} significantly enhances double-strand stability, thus supporting coordination of Zn^{2+} by the histidine-N and incorporation of the metal ion within the base stack. In contrast to Zn^{2+}, however, Cu^{2+} ions do not induce double-strand formation of an alanyl/norvalyl-PNA oligomer, as confirmed by EPR and EXAFS, which reveal a mixed $\{N_2O_x\}$ donor environment. While metal-ion binding to histidine-modified alanyl-PNA oligomers (and homologues) is apparently feasible, a proper matching of the binding-site geometry and the stereoelectronic requirements of the specific metal ion are essential in order to mediate double-strand formation. This might offer new options for alternative pairing schemes in alanyl-PNA chemistry in which metal coordination substitutes the common base-pair H-bonding pattern, and for metal-dependent regulation of alanyl-PNA duplex formation.
(© Wiley-VCH Verlag GmbH & Co. KGaA, 69451 Weinheim, Germany, 2005)

Introduction

Artificial DNA, in which one or multiple nucleosides is replaced by so-called "ligandosides" capable of metal-ion binding, is receiving increasing attention.[1–3] Inter alia, metal-mediated base pairing is exploited in order to increase the thermal stability of the DNA duplex, to extend the genetic alphabet for DNA-based information storage, or to develop novel nanostructured metal-containing architectures with interesting physical properties.[4] Peptide nucleic acids (PNAs) are synthetic analogues of nucleic acids with a non-natural polyamide backbone, most commonly based on *N*-(2-aminoethyl)glycine.[5] Their particularly attractive properties comprise self-recognition, high chemical and biological stability, and strong binding to target DNA or RNA sequences. Recently, some high affinity metal-binding sites such as porphyrins,[6] bipyridines[7,8] or chelating amines[9–11] and organometallic moieties[12] have been appended to PNA, and these metal complex/PNA conjugates have been probed in the context of sequence-specific DNA/RNA cleavage and detection,[6,8,13] DNA-templated catalysis,[10] and for the development of new antisense drugs.[14] In most of these systems the ligand site for metal binding is attached to one end of the PNA strand, but it has also been shown that metal incorporation in the middle of complementary *N*-(2-aminoethyl)glycine PNA strands that have been modified by bipyridine is indeed feasible and leads to preservation of the helical duplex structure.[7]

In the present contribution we probe hitherto unexplored metal incorporation into alanyl peptide nucleic acids (alanyl-PNA). Alanyl-PNA is structurally based on a regular peptide composed of alanyl amino acids with alternating configuration and nucleobases covalently linked to methylene side-chains.[15–17] Double strands are formed by two complementary alanyl-PNA strands based on base-pair recognition, stacking and solvation. The duplexes need to adopt a linear double-strand topology since the distance between consecutive side-chains in an extended peptide is close to the ideal base-pair stacking distance. The resulting alanyl-PNA double strand with linear topology is well defined regarding nucleobase orientation and distances and it is limited with respect to conformational freedom. Further-

[a] Institut für Organische und Biomolekulare Chemie, Georg-August-Universität Göttingen,
Tammannstraße 2, 37077 Göttingen, Germany
Fax: +49-551-392-944
E-mail: udieder@gwdg.de
[b] Institut für Anorganische Chemie, Georg-August-Universität Göttingen,
Tammannstraße 4, 37077 Göttingen, Germany
Fax: +49-551-393-063
E-mail: franc.meyer@chemie.uni-goettingen.de
[c] European Molecular Biology Laboratory, Outstation Hamburg, Notkestraße 85, 22603 Hamburg, Germany

more, chromophores incorporated within the nucleobase stack are known to be significantly shielded from aqueous solution.[18]

Coordination of metal ions within the nucleobase stack is especially interesting, since the non-polar environment inside the base stack should have unique consequences for the stability and geometry of metal coordination. The alanyl-PNA framework offers the particular advantage of being able to use natural amino acids such as histidine as biomimetic metal binding sites at different positions of the strand. Metal ions in such a metalloenzyme-inspired water-shielded environment might be useful for, inter alia, catalytic applications, while the alanyl-PNA backbone and nucleobases offer additional possibilities for specific substrate recognition via hydrogen-bonding interactions. This investigation might also be of interest to establish specific metal-mediated recognition next to hydrogen bonding in double-strand interactions. Finally, homologation of the side-chains in alanyl-PNA might allow for fine tuning of the distances and geometries of the metal binding sites or even the possibility to introduce dinuclear metal arrays.

Here, various alanyl-PNAs and side-chain homologous oligomers with central histidine metal binding sites are presented and investigated with respect to their ability to stabilize double-strand formation mediated by metal ions. It should be noted that in the absence of high-affinity ligands the amide groups in the PNA backbone and the nucleobases may act as competing binding sites for metal ion complexation,[19] and various spectroscopic and analytical tools are thus required in order to clearly characterise metal incorporation into the modified PNA duplexes.

Results and Discussion

Double-strand formation of an alanyl-PNA hexamer based on Watson–Crick pairing of six G-C base pairs is

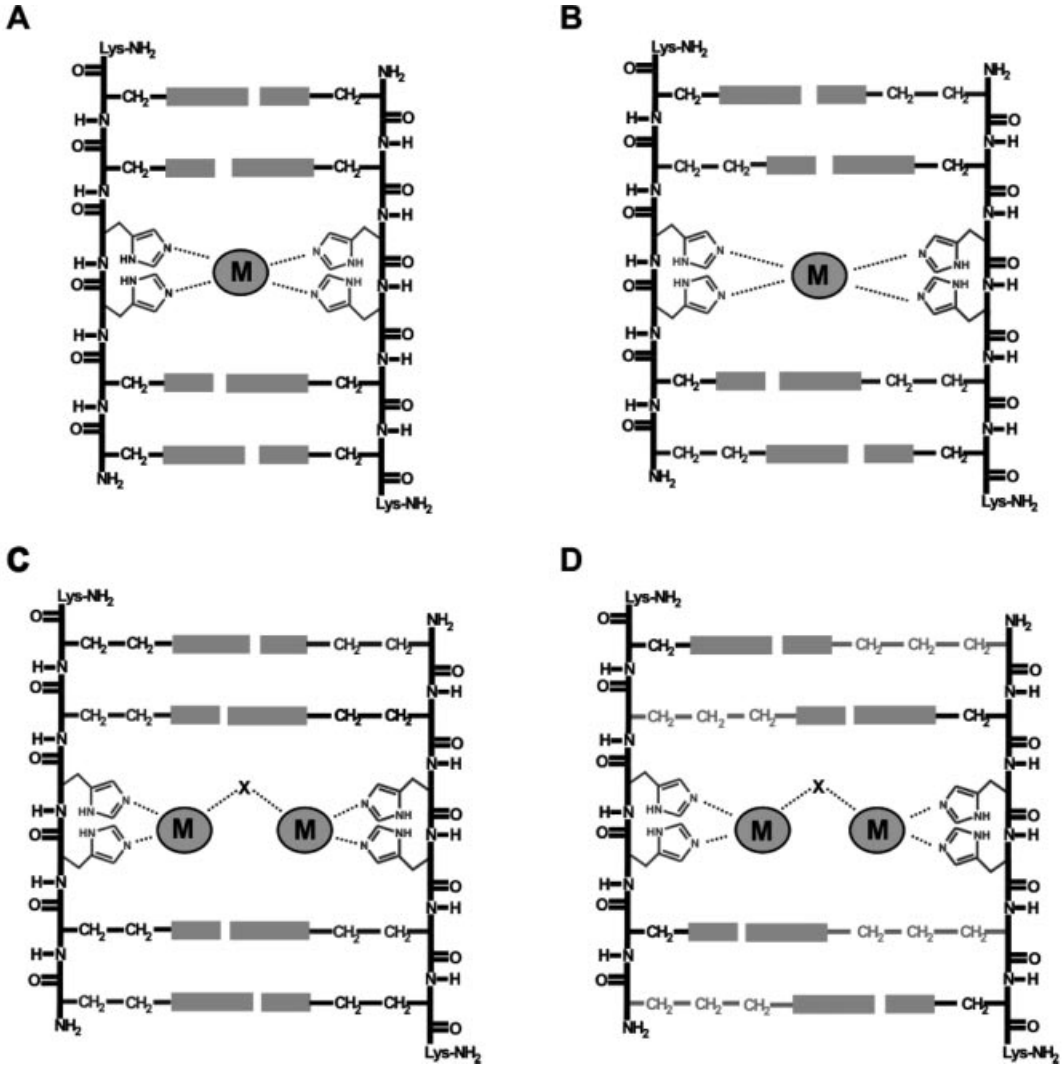

Figure 1. Idealized representation of double strands with a linear topology based on a peptide backbone with alternating amino acid configuration, four G-C base pairs and central histidines as metal ion coordination sites. Alanyl-peptide nucleic acids (alanyl-PNAs) should allow for coordination of one metal ion (**A**) as should alanyl/homoalanyl mixed PNAs (**B**). The distance of histidine coordination sites in homoalanyl-PNA might allow incorporation of two metal ions (**C**); the metal binding geometry in mixed alanyl/norvalyl-PNAs should be comparable (**D**). X might be a small bridging ligand such as HO^-, Cl^- or AcO^-.

 © 2005 Wiley-VCH Verlag GmbH & Co. KGaA, Weinheim

known to be quite stable (T_m = 58 °C).[16] Therefore, it was likely that an exchange of the central two G-C base pairs for histidine side-chains would retain the ability for duplex formation. In alanyl-PNA and mixed alanyl/homoalanyl-PNA double strands with four central histidines, coordination of one metal ion can be expected based on a backbone distance of about 14–15 Å (Figure , A and B). The backbone distance is extended to about 16.5 Å by further side-chain homologation, possibly allowing for two metal coordination sites. Therefore, homoalanyl-PNA and alanyl/norvalyl-PNA with central histidines were prepared (Figure 1, C and D).

Alanyl-PNA oligomers **1**–**3** as well as the side-chain homologous alanyl/homoalanyl-PNAs **4**–**6**, homoalanyl-PNAs **7** and **8** and alanyl/norvalyl-PNA oligomers **9** and **10** (Table 1) were prepared by manual solid-phase peptide synthesis based on a Boc strategy.[20] The respective nucleobase-substituted amino acids were assembled on an MBHA polystyrene support using HATU as the coupling reagent. The oligomers were purified by HPLC and characterised by mass spectrometry.

Double-strand formation was investigated by temperature-dependent UV spectroscopy. This method relies on a sigmoidal increase of UV absorption with higher temperatures caused by a cooperative destacking of the nucleobases. It was adapted from oligonucleotide chemistry and has been used successfully for the characterisation of PNA double strands.

Alanyl-PNA Oligomers

In the alanyl-PNA series enantiomeric oligomers provide tridentate G-C Watson–Crick pairing, as has been shown for an equimolar mixture of hexamers **1** and ***ent*-1** (T_m = 58 °C).[16] In contrast, nucleo amino acids with a different configuration form the less stable G-C reverse Watson–Crick base pair (self pairing of **1**: T_m = 42 °C).[16] Therefore, the enantiomeric oligomers **2** and ***ent*-2** were prepared, both of which feature two histidines in central positions. Watson–Crick self-pairing as well as equimolar pairing of enantiomers **2** and ***ent*-2** turned out not to be stable enough for detection of double-strand formation. Nevertheless, in the presence of Zn^{2+} ions UV melting curves clearly indicate self-pairing of **2** and pairing of enantiomeric oligomers **2** and ***ent*-2**, both with a stability of about 15 °C (Figure 2, A). Zinc ions obviously interact with the respective oligomers in order to overcome the low double-strand stability.

Table 1. Synthesized peptide nucleic acid oligomers with their double-strand stabilities in the absence or presence of Zn^{2+} ions.

Oligomers[a]	No.	T_m	T_m with Zn^{2+}
H-(AlaG-AlaG-AlaC-AlaG-AlaC-AlaC)-Lys Lys-(AlaC-AlaC-AlaG-AlaC-AlaG-AlaG)-H	**1** ***ent*-1**	58 °C[b]	
H-(AlaG-AlaC-**His**-**His**-AlaG-AlaC)-Lys Lys-(AlaC-AlaG-**His**-**His**-AlaC-AlaG)-H	**2**	< 0 °C[b]	15 °C[b]
H-(AlaG-AlaC-**His**-**His**-AlaG-AlaC)-Lys Lys-(AlaC-AlaG-**His**-**His**-AlaC-AlaG)-H	**2** ***ent*-2**	< 0 °C[b]	15 °C[b]
H-(AlaG-AlaC-**His**-**Gly**-AlaG-AlaC)-Lys Lys-(AlaC-AlaG-**Gly**-**His**-AlaC-AlaG)-H	**3**	13 °C[b]	13 °C[b]
H-(AlaG-AlaC-**His**-**His**-AlaG-AlaC)-Lys Lys-(AlaC-AlaG-**Gly**-**His**-AlaC-AlaG)-H	**2** **3**	15 °C[b]	14 °C[b]
H-(AlaC-HalC-AlaG-HalC-AlaG-HalG)-Lys Lys-(HalG-AlaG-HalC-AlaG-HalC-AlaC)-H	**4**	52 °C[b]	
H-(HalG-AlaC-**His**-**His**-HalG-AlaC)-Lys Lys-(AlaC-HalG-**His**-**His**-AlaC-HalG)-H	**5**	< 0 °C[b] < 0 °C[c]	17 °C[b] 12 °C[c]
H-(AlaC-HalC-AlaG-**His**-**His**-HalC-AlaG-HalG)-Lys Lys-(HalG-AlaG-HalC-**His**-**His**-AlaG-HalC-AlaC)-H	**6**	12 °C[c]	24 °C[c]
H-(HalG-HalG-HalC-HalG-HalC-HalC)-Lys Lys-(HalC-HalC-HalG-HalC-HalG-HalG)-H	**7** ***ent*-7**	32 °C[b]	
H-(HalG-HalC-**His**-**His**-HalG-HalC)-Lys Lys-(HalC-HalG-**His**-**His**-HalC-HalG)-H	**8**	< 0 °C[b] < 0 °C[c]	15 °C[b] 8 °C[c]
H-(AlaG-NvaG-AlaC-NvaG-AlaC-NvaC)-Lys Lys-(NvaC-AlaG-NvaG-AlaC-NvaG-AlaG)-H	**9** ***ent*-9**	16 °C[b]	
H-(AlaC-NvaC-AlaG-**His**-**His**-NvaC-AlaG-NvaG)-Lys Lys-(NvaG-AlaG-NvaC-**His**-**His**-AlaG-NvaC-AlaC)-H	**10**	11 °C[b] 17 °C[c]	22 °C[c]
H-(AlaC-NvaC-AlaG-**His**-**His**-NvaC-AlaG-NvaG)-Lys Lys-(NvaG-AlaG-NvaC-**His**-**His**-AlaG-NvaC-AlaC)-H	**10** ***ent*-10**	15 °C[b] 21 °C[c]	27 °C[c]

[a] AlaG = β-(9-guaninyl)alanine, AlaC = β-(1-cytosinyl)alanine, HalG = γ-(9-guaninyl)homoalanine, HalC = γ-(1-cytosinyl)homoalanine, NvaG = δ-(9-guaninyl)norvaline, NvaC = δ-(1-cytosinyl)norvaline; nucleobase-substituted amino acids with a D-configuration are underlined. [b] Phosphate buffer (0.01 M Na_2HPO_4/H_3PO_4, 0.1 M NaCl, pH 7). [c] HEPES buffer (0.01 M HEPES, 0.1 M NaCl, pH 7).

 © 2005 Wiley-VCH Verlag GmbH & Co. KGaA, Weinheim

In the absence of zinc, however, the non-coordinating histidines seem to suppress double-strand formation, presumably because of charge repulsion of the protonated side-chains at physiological pH; one should note that double-strand formation with considerable stability is known for G-C alanyl-PNA tetramers.[16]

Oligomer **3**, which features a histidine next to a glycine in the central position, was synthesised with the intention to test oligomers with lower potential for zinc coordination. Interestingly, self-pairing was now provided with a stability of T_m = 13 °C and it was not possible to increase this stability by zinc addition. First of all, this is an argument for the charge repulsion of neighbouring histidines hampering formation of double strands in the case of oligomer **2**. Furthermore, the lack of double-strand stabilisation upon addition of zinc to oligomer **3** is in agreement with two histidines not being sufficient for incorporation of zinc. Coordination at the nucleobases can be excluded as a reason for the stabilisation of double strands formed by oligomers **2** and ***ent*-2**, which only occurs in the presence of zinc ions. This result was confirmed by homochiral Watson–Crick pairing of oligomers **2** and **3** providing a potential zinc binding centre of three histidines: in agreement with the more stable pairing mode and possible charge repulsion of neighbouring histidines, the double strand **2** + **3** without zinc ions was formed only with slightly higher stability (T_m = 15 °C) than self-pairing of oligomer **3**, whereas addition of zinc had no effect on the overall stability (T_m = 14 °C).

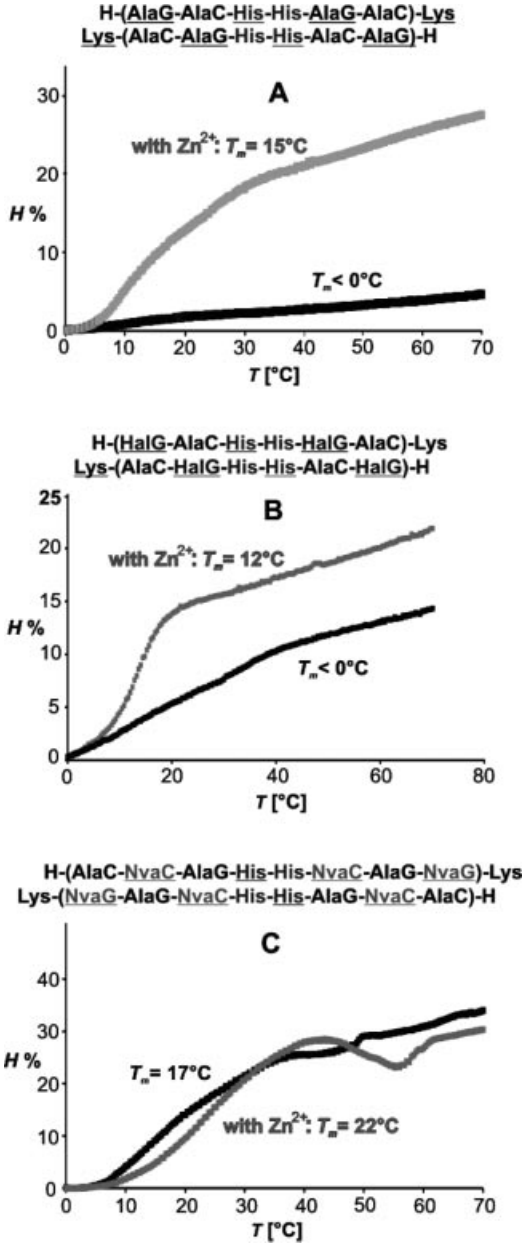

Figure 2. UV melting curves of alanyl-PNA (**2**) in phosphate buffer (A) and of alanyl/homoalanyl-PNA (**5**; B) as well as alanyl/norvalyl-PNA (**10**; C) in HEPES buffer in the absence (dark curves) or presence (light curves) of Zn^{2+}.

Mixed Alanyl/Homoalanyl-PNA Oligomers

Peptide nucleic acid double strands composed of alternating alanyl and homoalanyl nucleo amino acids provide a backbone distance that is about 1 Å larger than alanyl-PNA duplexes. This should significantly influence metal coordination by the central histidines. Furthermore, in the mixed alanyl/homoalanyl-PNA series the more stable Watson–Crick G-C base pairs are formed with self-pairing homodimers.[20] A stability of T_m = 52 °C was found for the homodimer of hexamer **4**. Like in alanyl-PNA, the exchange of the central G-C base pairs for four histidines in the double strand of oligomer **5** prevents double-strand formation. Addition of zinc ions to oligomer **5** leads to stabilisation (T_m = 17 °C) of the same order of magnitude as observed for the respective alanyl-PNA **2**.

Since a possible application of the metal/PNA conjugates will be the catalysis of, inter alia, phosphodiester hydrolysis, the double-strand stabilities were also investigated in HEPES buffer instead of the more common phosphate buffer in order to evaluate the effect of the medium. In HEPES buffer double-strand formation of oligomer **5** was again not observed and zinc ions turned out to be essential for stabilisation (T_m = 12 °C; Figure 2, B). However, the change from phosphate to HEPES buffer resulted in a 5 °C decrease of stability.

With the aim of providing double strands with a higher overall stability, the mixed alanyl/homoalanyl-PNA oligomer **6**, which features six nucleo amino acids and two central histidines, was prepared. The low double-strand stability of the homodimer **6** (T_m = 13 °C) resembles the effect of four non-coordinating histidines in the central region, as mentioned already in the alanyl-PNA series. Addition of zinc ions leads to a significant increase in stability (T_m = 25 °C) even in HEPES buffer, which makes this system a promising candidate for further studies.

Homoalanyl-PNA and Mixed Alanyl/Norvalyl-PNA Oligomers

Both homoalanyl-PNA as well as mixed alanyl/norvalyl-PNA double strands provide a distance between the peptide

 © 2005 Wiley-VCH Verlag GmbH & Co. KGaA, Weinheim

backbones that is determined by the base-pair size extended by overall four methylene units (Figure 1, C and D). This might open the possibility for coordination of two zinc ions within the centre of a linear PNA double strand. In the homoalanyl-PNA series, double-strand formation with nucleobases having the same configuration (homochiral base pairing) leads to the more stable G-C Watson–Crick pairing.[20] The double strand of homoalanyl-PNA enantiomers **7** and ***ent*-7** with six G-C base pairs provides a stability of T_m = 32 °C. The drop of stability compared to the alanyl and alanyl/homoalanyl-PNAs **1** and **4** is caused by higher side-chain flexibility and lower stacking contributions.[20] As a consequence, double-strand formation of homoalanyl-PNA **8** was not observed since it would only be based on four poorly stacked reverse Watson–Crick G-C base pairs with four histidine amino acids in the centre. Considering the poor situation for self-pairing, it is even more remarkable that addition of zinc ions to oligomer **8** induced duplex formation with a similar order of stability as observed for alanyl/homoalanyl oligomer **5** (T_m = 15 °C in phosphate and T_m = 8 °C in HEPES buffer).

The stabilities of the G-C Watson–Crick pairing homoalanyl-PNA hexamer double strand **7** + ***ent*-7** (T_m = 32 °C) and the respective alanyl/norvalyl-PNA duplex **9** + ***ent*-9** (T_m = 16 °C) are quite different despite a similar overall double-strand geometry.[20] The lower degree of side-chain preorganisation in the case of the norvalyl amino acids seems to be responsible for this effect. In analogy to oligomer **6**, the alanyl/norvalyl-PNA oligomers **10** and ***ent*-10**, with six nucleo amino acids and two central histidines, were prepared for the investigation of zinc binding. Reverse Watson–Crick pairing was provided with a stability of T_m = 17 °C in the absence of zinc, whereas the stability of the mixture of enantiomers **10** and ***ent*-10** forming the more stable Watson–Crick base pairs was even higher at T_m = 22 °C. The larger backbone distance in alanyl/norvalyl-PNA provides reduced charge interaction for opposed central histidines. In contrast to oligomers **2** and **5**, this allows for stable duplex formation without zinc binding. For both alanyl/norvalyl-PNA oligomers **10** and **10** + ***ent*-10** the addition of zinc leads to a significant increase in double-strand stability of 5 or 6 °C, respectively.

In order to provide additional information on the metal ion binding potential of oligomer **10**, this particular system was studied in more detail by spectroscopic methods in solution. Since Zn^{2+} is spectroscopically silent, Cu^{2+} was used instead. It should be noted, though, that according to the temperature-dependent UV spectra, double-strand formation was not induced by the addition of copper salts to oligomer **10** (data not shown).

EPR spectroscopy was used as a qualitative probe to verify the binding of Cu^{2+} by PNA **10**. Part a of Figure 3 shows the X-band EPR spectra of a solution of Cu^{2+} only (top) and of a solution of oligomer **10** with 1 equiv. of Cu^{2+} (bottom) in HEPES-buffered water/glycerine (3:1). A much smaller value for $A_z(^{63,65}Cu)$ in the presence of oligomer **10** is clearly discernible, thus confirming coordination of Cu^{2+}. Both the g_z and A_z values are within the range expected

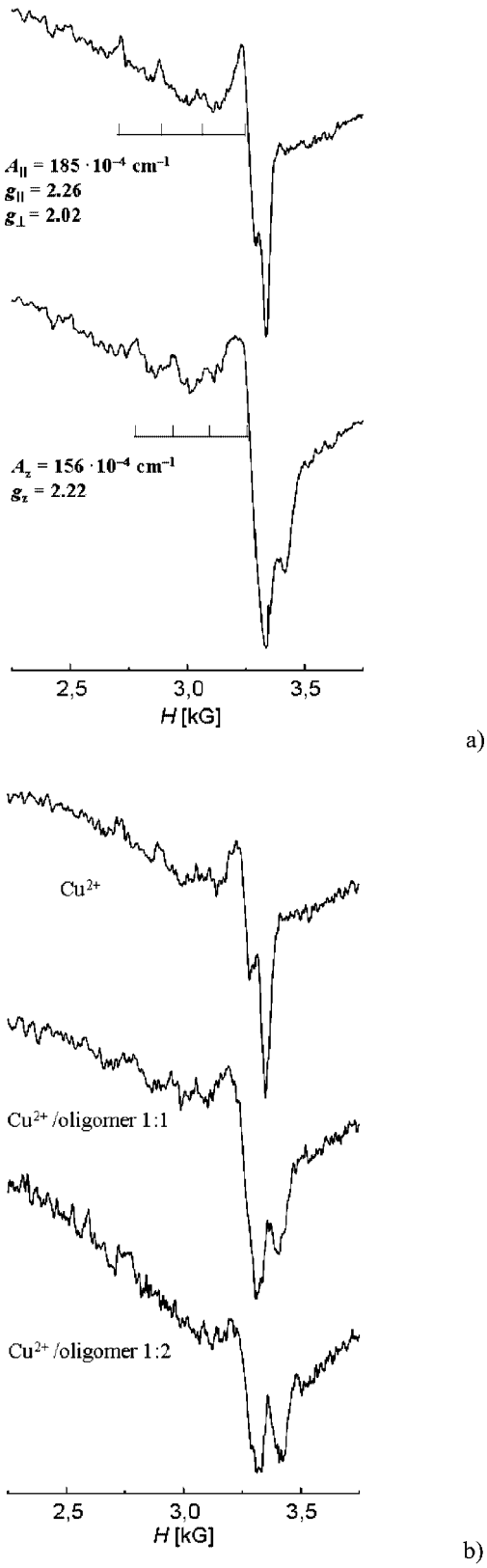

Figure 3. a) EPR spectra of Cu^{2+} in the absence or presence of **10**: H_2O/glycerin (3:1), HEPES pH 7, 150 K; only Cu^{2+} (top) or Cu^{2+}/**10** (1:1, bottom). b) EPR spectra of Cu^{2+} in the absence or presence of **10**: H_2O, HEPES pH 7.4, 150 K; only Cu^{2+} (top), Cu^{2+}/**10** (1:1, middle) or Cu^{2+}/**10** (1:2, bottom).

 © 2005 Wiley-VCH Verlag GmbH & Co. KGaA, Weinheim

for some mixed $\{N_xO_y\}$ ligation,[21] but no ^{14}N hyperfine coupling could be detected and no satisfactory simulation of the data could be achieved because of, inter alia, a relatively low signal-to-noise ratio.[22] In addition, the spectra in water at different ratios of Cu^{2+} to PNA **10** (Figure 3, b) indicated the possible presence of several species, leaving the EPR confirmation of metal ion binding by oligomer **10** only a qualitative one.

Cu^{2+} coordination by the histidine N-atoms of PNA **10** was further substantiated by X-ray absorption spectroscopy conducted on a frozen sample of oligomer **10**/Cu^{2+}. X-ray absorption spectroscopy allows the element-specific characterisation of metal environments and thus yields information about the type and distances of coordinating ligands. Ligands with a rather linear arrangement of the backscattering atoms lead to special features in the spectrum due to multiple scattering of the photoelectron wave that is created upon absorption of photons with energies larger than the edge energy. Here, a flat plateau at $k \approx 4.5$ Å^{-1} indicates the presence of imidazole groups coordinating the metal ion. This was further supported by the Fourier transform of the spectrum. The intense contribution at about 4 Å arises from scattering events at the remote atoms of the imidazole rings. Their intensity was increased due to the multiple scattering events including the metal coordinating nitrogen atom. The first coordination shell has a typical distance of about 2.0 Å and its high intensity indicates a homogeneous coordination by light atoms (C/N or O).

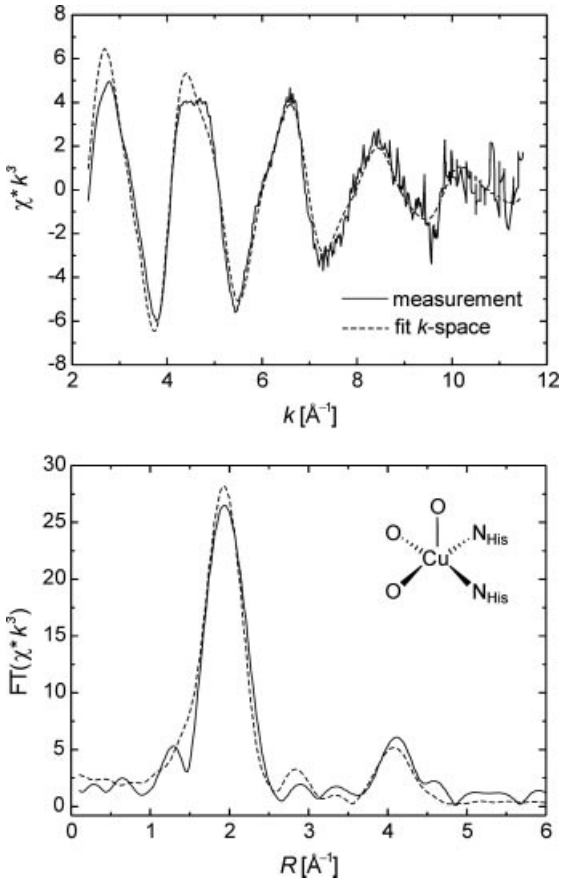

Figure 4. EXAFS and corresponding Fourier transform for the PNA **10**/Cu^{2+} complex (black). The best fit to the data is shown in dashed lines and represents coordination by two imidazole groups and three oxygen atoms.

With this in mind, different combinations of O and imidazole ligands were modelled to the data. The final model given in Figure 4 comprises two imidazole groups and three oxygen ligands at a distance of 1.98 Å. In order to keep the number of free parameters as low as possible the distances for these ligands as well as their Debye–Waller factors ($2\sigma^2 = 0.021$ Å^2) were constrained. Thus, the measurement is not resembled in all details, but any over-interpretation of data is prevented. Typical errors for the coordination number are in the range of 20%, whereas the distances have an error of less than 1% for the first coordination sphere.

Conclusions

A series of alanyl-, homoalanyl- and norvalyl-PNA hexamers or octamers has been prepared in which two central nucleobase-substituted amino acids are replaced by histidines. While the incorporation of histidine residues is shown to drastically lower the tendency for self-pairing compared to the parent PNAs, double-strand formation is still observed for properly chosen systems that provide at least six G-C pairs framing the central histidines (such as in **6**, **10** or **10**/***ent*-10**). As soon as four histidines (two per oligomer strand) are placed at the centre of PNA double strands, addition of Zn^{2+} significantly enhances the duplex stability, thus supporting the coordination of Zn^{2+} by the histidine-N and incorporation of the metal ion within the base stack (Figure 5). Metal ion binding to the histidine-N of the modified alanyl/norvalyl-PNA oligomers is further supported by ESR and EXAFS spectroscopy on the corresponding Cu^{2+} hybrid of **10**. In contrast to Zn^{2+}, however, Cu^{2+} ions do not induce double-strand formation, in accordance with the mixed $\{N_2O_x\}$ donor environment that was deduced from EPR and EXAFS experiments (Figure 5). One might speculate that the different geometric preferences of Zn^{2+} and Cu^{2+} upon binding to four histidine-N (tetrahedral for Zn^{2+}, square planar for Cu^{2+}) give rise to these different effects. It should be noted that for modified DNA it has also been observed that duplex formation is mediated by only specific metal ions.[3]

The present findings thus confirm the anticipated metal ion binding capabilities of histidine-modified alanyl-PNA oligomers (and homologues), i.e. metal binding to conjugates of alanyl-PNA and natural amino acids. However, proper organisation of the metal binding site is essential in order to match the stereoelectronic requirements of the specific metal ion upon double-strand formation. This might offer new options for alternative pairing schemes in alanyl-PNA chemistry in which metal coordination substitutes the common base-pair H-bonding pattern, and for metal-dependent regulation of alanyl-PNA duplex formation.

 © 2005 Wiley-VCH Verlag GmbH & Co. KGaA, Weinheim

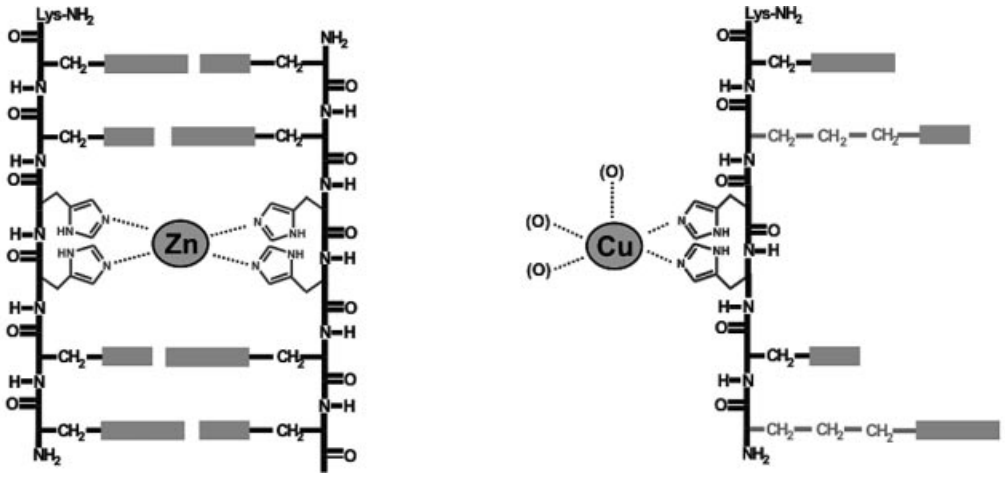

Figure 5. Likely binding modes of Zn^{2+} and Cu^{2+} to histidine-modified alanyl-PNA.

Experimental Section

General Remarks: All reagents were of analytical grade and used as supplied. Solvents were of the highest grade available. Synthesis and analytical data of *N*-Boc-AlaG-OH, *N*-Boc-AlaC(*Z*)-OH, *N*-Boc-HalG-OH, *N*-Boc-HalC(*Z*)-OH, *N*-Boc-NvaG-OH and *N*-Boc-NvaC(*Z*)-OH were performed as described previously.[20] (*S*)-*N*-Boc-His(Bom)-OH and (*R*)-*N*-Boc-His(Bom)-OH were purchased from Bachem.

ESI mass spectra were recorded with a TSQ 700 Finnigan spectrometer and high resolution mass spectra with a Bruker Apex IV FT-ICR MS instrument. HPLC was done on a Pharmacia Äkta Basic using YMC-Pack ODS, RP-C18 with a linear gradient of A (0.1% TFA in water) to B (0.1% TFA in acetonitrile/water, 9:1). Oligomers were purified using 250 × 20 mm, 5 μm, 120 Å for preparative and 250 × 4.6 mm, 5 μm, 120 Å columns for analytical samples. UV melting curves were measured with a Perkin–Elmer UV/Vis Lambda 10 with a Peltier temperature programmer PTP 1 or a Jasco V-550 UV/Vis spectrometer equipped with a Jasco ETC-505S/ETC-505T temperature controller. The oligomer concentration was determined by taking the extinction coefficient at 80 °C as being the sum of the extinction coefficients of all nucleo amino acids.[20] Complex formation was achieved by heating to 85 °C, followed by slow cooling over a period of three hours to 0 °C and equilibration for at least three hours at 0 °C. EPR spectra were measured on a Bruker ELEXSYS E500 spectrometer, equipped with a digital temperature control system ER 4131 VT using nitrogen as coolant. All spectra at 150 K were recorded at about 9.4 GHz microwave frequency, 5–9 G field modulation amplitude, 100 kHz field modulation frequency, and around 10 mW microwave power. Glycerine was added to some of the samples to improve their freezing behaviour. To induce complex formation, the same procedure was used as in the case of UV/Vis spectroscopy immediately before recording the spectra.

General Method for Solid-Phase Peptide Synthesis (SPPS) of the Oligomers: Oligomerisation was performed as a solid-phase peptide synthesis on a 4-methylbenzhydrylamine (MBHA)-polystyrene resin loaded with (*S*)-*N*-*tert*-butoxycarbonyl-lysine(2-Cl-Z)-OH (0.43 mmol/g) or (*R*)-*N*-Boc-lysine(*Z*)-OH (0.57 mmol/g) in a small column. For each step, 5 equiv. of *N*-Boc-protected amino acid was used and activated by 4.5 equiv. of *N*-(7-azabenzotriazol-1-yl)-1,1,3,3-tetramethyluronium hexafluorophosphate (HATU) and 5 equiv. of 1-hydroxy-7-azabenzotriazol (HOAt) in DMF (600–1000 μL). After 3 min, 10 equiv. of *N*,*N*-diisopropylethylamine was added.

After swelling the resin for 1 h in CH_2Cl_2, the following strategy was repeated for every amino acid unit: 1) Deprotection: The resin was washed with TFA/*m*-cresol (95:5, 2 mL) and then treated with TFA/*m*-cresol (95:5, 2 mL) for 5 min. 2) Washing: CH_2Cl_2/DMF (1:1; 5 × 2 mL) followed by pyridine (2 × 2 mL). 3) Coupling: The reaction column was gently moved for 30–90 min with the coupling reagents (30 min for natural amino acids, 45 min for cytosine-containing amino acids, 90 min double coupling for guanine-containing amino acids). 4) Washing: CH_2Cl_2/DMF (1:1; 5 × 2 mL), DMF/piperidine (9:1; 5 × 2 mL), CH_2Cl_2/DMF (1:1; 5 × 2 mL). 5) Capping: 2 × 5 min with Ac_2O/NEt_3/DMF (1:1:8; 2 mL). 6) Washing: CH_2Cl_2/DMF (1:1; 5 × 2 mL), DMF/piperidine (9:1; 5 × 2 mL), CH_2Cl_2/DMF (1:1, 5 × 2 mL). Finally, the resin was washed with MeOH and dried for 3 h over KOH. Cleavage from the solid support was carried out within 2 h using trifluoromethanesulfonic acid/*m*-cresol/TFA (1:1:8; 2 mL). The dark brown solution was concentrated to 300 μL and the peptide nucleic acids were precipitated with diethyl ether (10–20 mL) as a white solid. The PNA was separated using a centrifuge, followed by purification with HPLC (RP-C18).

H-(AlaG-AlaC-His-His-AlaG-AlaC)-Lys-NH_2 (2): HPLC (gradient: 5–30% B in 30 min): t_R = 11.54 min. ESI-MS: *m*/*z* = 1220.7 $[M + H]^+$, 611.2 $[M + 2H]^{2+}$. HRMS: calcd. for $C_{48}H_{61}N_{29}O_{11}$ $[M + 2H]^{2+}$ 610.76254; found 610.76220.

H-(AlaG-AlaC-His-His-AlaG-AlaC)-Lys-NH_2 (*ent*-2): HPLC (gradient: 5–30% B in 30 min): t_R = 11.67 min. ESI-MS: *m*/*z* = 1220.8 $[M + H]^+$, 611.2 $[M + 2H]^{2+}$. HRMS: calcd. for $C_{48}H_{61}N_{29}O_{11}$ $[M + 3H]^{3+}$ 407.51079; found 407.51079.

H-(AlaG-AlaC-His-Gly-AlaG-AlaC)-Lys-NH_2 (3): HPLC (gradient: 5–30% B in 30 min): t_R = 10.19 min. ESI-MS: *m*/*z* = 1140.6 $[M + H]^+$, 571.4 $[M + 2H]^{2+}$. HRMS: calcd. for $C_{44}H_{57}N_{27}O_{11}$ $[M + 2H]^{2+}$ 570.74382; found 570.74371.

H-(HalG-AlaC-His-His-HalG-AlaC)-Lys-NH_2 (5): HPLC (gradient: 5–30% B in 30 min): t_R = 12.50 min. ESI-MS: *m*/*z* = 1276.9 $[M + H]^+$, 639.2 $[M + 2H]^{2+}$. HRMS: calcd. for $C_{52}H_{69}N_{29}O_{11}$ $[M + 2H]^{2+}$ 638.79384; found 638.79362.

H-(AlaC-HalC-AlaG-His-His-HalC-AlaG-HalG)-Lys-NH_2 (6): HPLC (gradient: 5–25% B in 20 min): t_R = 14.19 min. ESI-MS:

 © 2005 Wiley-VCH Verlag GmbH & Co. KGaA, Weinheim

m/z = 1662.8 $[M + H]^+$, 832.2 $[M + H]^{2+}$. HRMS: calcd. for $C_{66}H_{83}N_{39}O_{15}$ $[M + 3H]^{3+}$ 554.90497; found 554.90492.

H-(HalG-HalC-His-His-HalG-HalC)-Lys-NH_2.(8): HPLC (gradient: 5–30% B in 30 min): t_R = 12.50 min. ESI-MS: *m/z* =1276.6 $[M + H]^+$, 639.5 $[M + 2H]^{2+}$.

H-(AlaC-NvaC-AlaG-His-His-NvaC-AlaG-NvaG)-Lys-NH_2 (10): HPLC (gradient: 5–25% B in 20 min): t_R = 13.55 min. ESI-MS: *m/z* =853.2 $[M + H]^{2+}$, 569.3 $[M + 2H]^{3+}$. HRMS: calcd. for $C_{69}H_{89}N_{39}O_{15}$ $[M + 3H]^{3+}$ 568.92062; found 568.92063.

H-(AlaC-NvaC-AlaG-His-His-NvaC-AlaG-NvaG)-Lys-NH_2 (*ent*-10): HPLC (gradient: 5–25% B in 20 min): t_R = 13.69 min. ESI-MS: *m/z* =1705.7 $[M + H]^+$, 853.2 $[M + H]^{2+}$, 569.3 $[M + 2H]^{3+}$. HRMS: calcd. for $C_{69}H_{89}N_{39}O_{15}$ $[M + 4H]^{4+}$ 426.94228; found 426.94228.

EXAFS Measurements: An X-ray absorption spectrum at the Cu-*K* edge for oligomer **10** was recorded in fluorescence mode at the EMBL beamline D2 (DESY, Hamburg, Germany) equipped with a Si(111) double crystal monochromator, a focusing mirror and a 13 element Ge solid-state fluorescence detector (Canberra). The Cu-peptide solution was filled into plastic sample holders covered with polyimide windows, frozen in liquid nitrogen, and kept at 30 K during the experiment. Harmonic rejection was achieved by a focusing mirror with a cut-off energy of 21 keV and a monochromator detuning to 70% of peak intensity. A dead-time correction was applied. Saturation was not observed because the dead-time was always below 20%. The energy axis of each scan was calibrated by using the Bragg reflections of a static Si(220) crystal in back reflection geometry.[23] Averaging of 12 scans and data reduction was performed with the EXPROG software package (C. Hermes and H. F. Nolting, EMBL, Hamburg) using $E_{0,Cu}$ = 8979 eV. The EXAFS spectrum was analysed with EXCURV98.[24]

Acknowledgments

Generous support from the Deutsche Forschungsgemeinschaft (SFB 416, project A14) is gratefully acknowledged.

[1] a) K. Tanaka, M. Shionoya, *J. Org. Chem.* **1999**, *64*, 5002–5003; b) K. Tanaka, A. Tengeiji, T. Kato, N. Toyama, M. Shiro, M. Shionoya, *J. Am. Chem. Soc.* **2002**, *124*, 12494–12498; c) K. Tanaka, A. Tengeiji, T. Kato, N. Toyama, M. Shionoya, *Science* **2003**, *299*, 1212–1213.

[2] a) H. Weizman, Y. Tor, *Chem. Commun.* **2001**, 453–454; b) H. Weizman, Y. Tor, *J. Am. Chem. Soc.* **2001**, *123*, 3375–3376.

[3] a) E. Meggers, P. L. Holland, W. B. Tolman, F. E. Romesberg, P. G. Schultz, *J. Am. Chem. Soc.* **2000**, *122*, 10714–10715; b) S. Atwell, E. Meggers, G. Spraggon, P. G. Schultz, *J. Am. Chem. Soc.* **2001**, *123*, 12364–12367; c) N. Zimmermann, E. Meggers, P. G. Schultz, *J. Am. Chem. Soc.* **2002**, *124*, 13684–13685; d) L. Zhang, E. Meggers, *J. Am. Chem. Soc.* **2005**, *127*, 74–75.

[4] a) H.-A. Wagenknecht, *Angew. Chem.* **2003**, *115*, 3322–3324; *Angew. Chem. Int. Ed.* **2003**, *42*, 3204–3206; b) M. Shionoya, K. Tanaka, *Curr. Opin. Chem. Biol.* **2004**, *8*, 592–597.

[5] a) P. E. Nielsen, M. Egholm, O. Buchardt, *Bioconjugate Chem.* **1994**, *5*, 3–7; b) B. Hyrup, P. E. Nielsen, *Bioorg. Med. Chem.* **1996**, *4*, 5–23; c) P. E. Nielsen, M. Egholm, *Curr. Issues Mol. Biol.* **1999**, *1*, 89–104.

[6] P. Bigey, S. H. Sönnichsen, B. Meunier, P. E. Nielsen, *Bioconjugate Chem.* **1997**, *8*, 267–270.

[7] D.-L. Popescu, T. J. Parolin, C. Achim, *J. Am. Chem. Soc.* **2003**, *125*, 6354–6355.

[8] A. Whitney, G. Gavory, S. Balasubramanian, *Chem. Commun.* **2003**, 36–37.

[9] A. Mokhir, R. Stiebing, R. Krämer, *Bioorg. Med. Chem. Lett.* **2003**, *13*, 1399–1401.

[10] a) J. Brunner, A. Mokhir, R. Krämer, *J. Am. Chem. Soc.* **2003**, *125*, 12410–12411; b) F. H. Zelder, J. Brunner, R. Krämer, *Chem. Commun.* **2004**, 902–903.

[11] O. Kornyushyna, A. J. Stemmler, D. M. Graybosch, I. Bergenthal, C. J. Burrows, *Bioconjugate Chem.* **2005**, *16*, 178–183.

[12] a) A. Hess, N. Metzler-Nolte, *Chem. Commun.* **1999**, 885–886; b) R. Hamzavi, T. Happ, K. Weitershaus, N. Metzler-Nolte, *J. Organomet. Chem.* **2004**, *689*, 4745–4750.

[13] a) F. H. Zelder, A. A. Mokhir, R. Krämer, *Inorg. Chem.* **2003**, *42*, 8618–8620; b) A. Mokhir, R. Krämer, H. Wolf, *J. Am. Chem. Soc.* **2004**, *126*, 6208–6209.

[14] K. S. Schmidt, M. Boudvillain, A. Schwartz, G. A. van der Marcel, J. H. van Boom, J. Reedijk, B. Lippert, *Chem. Eur. J.* **2002**, *8*, 5566–5570.

[15] U. Diederichsen, *Angew. Chem.* **1996**, *108*, 458–461; *Angew. Chem. Int. Ed. Engl.* **1996**, *35*, 445–448.

[16] U. Diederichsen, *Angew. Chem.* **1997**, *109*, 1966–1969; *Angew. Chem. Int. Ed. Engl.* **1997**, *36*, 1886–1889.

[17] U. Diederichsen, in *Bioorganic Chemistry − Highlights and New Aspects* (Eds.: U. Diederichsen, T. Lindhorst, L. A. Wessjohann, B. Westermann), Wiley-VCH, Weinheim, **1999**, pp. 255–261.

[18] U. Diederichsen, D. Weicherding, *Synlett* **1999**, *S1*, 917–920.

[19] a) J. Brasuń, P. Ciapetti, H. Kozlowski, S. Oldziej, M. Taddei, D. Valensin, G. Valensin, N. Gaggelli, *J. Chem. Soc., Dalton Trans.* **2000**, 2639–2644; b) J. Brasuń, S. Oldziej, M. Taddei, H. Kozlowski, *J. Inorg. Biochem.* **2001**, *85*, 79–87.

[20] For the preparation of alanyl, homoalanyl and norvalyl nucleo amino acids and their oligomerisation, see: U. Diederichsen, D. Weicherding, N. Diezemann, *Org. Biomol. Chem.* **2005**, *3*, 1058–1066.

[21] J. Peisach, W. E. Blumberg, *Arch. Biochem. Biophys.* **1974**, *165*, 691–708.

[22] The sample solution was prepared from 14.2 μL of 10^{-3} M $Cu(ClO_4)_2$ in H_2O/HEPES and a stoichiometric amount of the investigated oligomer. The low concentrations led to significant problems with regard to the signal-to-noise ratio. In addition, aging of the samples could be observed during repeated measurements as well as a slight temperature dependence of the peak intensities in the range from 8 to 180 K (spectra were recorded using the helium temperature control system ER4112HV; not depicted). The latter finding could be a hint of an increased mobility quenching within the glassy samples at lower temperatures (see also: M. F. Ottaviani, F. Montalti, N. Turro, D. A. Tomalia, *J. Phys. Chem. B* **1997**, *101*, 158–166.). A dependence on the pH values of the actual solution is to be expected but was not tested due to the small amount of sample.

[23] R. F. Pettifer, C. Hermes, *J. Appl. Crystallogr.* **1985**, *18*, 404–412.

[24] N. Binsted, R. W. Strange, *Biochemistry* **1992**, *31*, 12117–12125.

Received: May 22, 2005
Published Online: September 12, 2005

 © 2005 Wiley-VCH Verlag GmbH & Co. KGaA, Weinheim

Anions of 1,3,5-Benzenetricarboxylic and Heptanedioic Acids Serving as Bridges between Dimolybdenum(V) Metal–Metal Bonded Units: Preparation and Structural Characterization of Dinuclear and Tetranuclear Complexes

Barbara Modec,*[a] and Jurij V. Brenčič[a]

Keywords: Molybdenum / Carboxylato complexes / 1,3,5-Benzenetricarboxylate / Heptanedioate

$(PyH)_5[MoOCl_4(H_2O)]_3Cl_2$ and $(PyH)[MoOBr_4]$ reacted with the anions of 1,3,5-benzenetricarboxylic acid ($btcH_3$) and heptanedioic acid ($hdaH_2$) to afford a series of novel carboxylato complexes based on the $\{Mo_2O_4\}^{2+}$ structural core: $(PyH)_4[Mo_2O_4Cl_4(\mu_2\text{-}btcH_2)]Cl$ (**1**), $(PyH)_4[Mo_2O_4Br_4(\mu_2\text{-}btcH_2)]Br$ (**2**), $[(Mo_2O_4Py_3)_2(\mu_3\text{-}btcH)_2]\cdot 6Py$ (**3**), $(PyH)_6[(Mo_2O_4Cl_4)_2(\mu_4\text{-}hda)]\cdot 2CH_3CN$ (**4**), and $(PyH)_{10}[(Mo_2O_4Cl_4)_2(\mu_4\text{-}hda)][MoOCl_5]Cl_2$ (**5**) {Py = pyridine, C_5H_5N; PyH^+ = pyridinium cation, $C_5H_5NH^+$; $btcH_2^-$ = $(HOOC)_2C_6H_3COO^-$; $btcH^{2-}$ = $(HOOC)C_6H_3(COO)_2^{2-}$ and hda^{2-} = $^-OOC(CH_2)_5COO^-$}. A pair of isostructral compounds **1** and **2** contains dinuclear anions $[Mo_2O_4X_4(\mu_2\text{-}btcH_2)]^{3-}$ (X = Cl, Br) in which the $btcH_2^-$ ligand is bonded to the $\{Mo_2O_4\}^{2+}$ core via one carboxylate group in a *syn-syn* bidentate bridging manner. In **3**, two $btcH^{2-}$ ligands link two $\{Mo_2O_4\}^{2+}$ cores into a loop-like structure. Each $btcH^{2-}$ ligand is coordinated via two carboxylate groups, with one in the *syn-syn* bidentate bridging manner and with another in a monodentate manner. The linkage of two dinuclear subunits was also realized in $[(Mo_2O_4Cl_4)_2(\mu_4\text{-}hda)]^{6-}$, the anion in **4** and **5**, where both carboxylate groups of the hda^{2-} ligand bind in the *syn-syn* bidentate-bridging manner to $\{Mo_2O_4\}^{2+}$ cores. The title compounds were characterized by X-ray crystallography and infrared spectroscopy.
(© Wiley-VCH Verlag GmbH & Co. KGaA, 69451 Weinheim, Germany, 2005)

Introduction

The use of labile metal cations and polyfunctional organic molecules in the assembly of supramolecular arrays has emerged as an area of great interest.[1] In this context, di- and tricarboxylates constitute one of the most commonly employed classes of organic ligands.[2] The anions of 1,3,5-benzenetricarboxylic acid with three symmetrically arranged carboxylate groups form rigid, planar linkers.[3] By contrast, the ligands derived from dicarboxylic acids such as heptanedioic acid possess flexibility, an advantageous property in certain cases.[4] The metal cations such as Cu^{II}, Cd^{II}, Zn^{II}, Co^{II}, and Ni^{II} often do not impose a strong preference for a given geometry, leading to the lack of predictability over the stoichiometry and the structure of the product. On the contrary when dimolybdenum(II) precursors were used, both the number of coordinative sites and their locations could be suitably chosen in order to produce in combination with organic linkers a variety of supramolecular complexes.[5] Our quest has been the preparation of complexes containing a dinuclear $\{Mo_2O_4\}^{2+}$ structural core (Scheme 1). The core consists of two metal atoms, each with a strongly bound terminal oxygen atom, and a pair of bridging oxygen atoms. A single metal–metal bond between molybdenum atoms with a typical separation of 2.5–2.6 Å contributes to the cohesion of the unit.[6] Its six sites open for further coordination are not equivalent: the two which are in *trans* positions relative to the terminal oxo groups are subject to their labilizing *trans* influence and consequently bonding of the ligands at these sites is weaker when compared to the four equatorial sites. Various supramolecular complexes, encompassing discrete species[7] and infinite 1D or 2D arrays[8–10] could be prepared by combining the reactive $\{Mo_2O_4\}^{2+}$ precursors and multidentate ligands. Unfortunately, the control over the reaction outcome cannot be gained solely by tuning the ligand-to-molybdenum ratio. When the amount of the ligand was small, a necessary condition for the formation of polymeric phases, the metal centres attained the coordination saturation through the self-assembly of $\{Mo_2O_4\}^{2+}$ cores, enabled by the ability of oxo groups to participate in μ_3- and μ_4-bridging interactions.[7a] The latter process is the reason for the scarcity of polymeric $\{Mo_2O_4\}^{2+}$ complexes with multidentate ligands. The literature reports on only three structurally characterized $\{Mo_2O_4\}^{2+}$ species of this type: an oxalate-bridged $[Mo_2O_4(\mu_2\text{-}C_2O_4)Cl_2]_n^{2n-}$, a phosphate-bridged $[Mo_2O_4(C_2O_4)_2(\mu_2\text{-}H_2PO_4)]_n^{3n-}$, both with an infinite chain structure, and a phosphate-bridged $[Mo_2O_4(PO_4)(HPO_4)]_n^{3n-}$ with an infinite layer structure.[8–10] No preferential binding pattern of multidentate ligands over the six coordination sites of the $\{Mo_2O_4\}^{2+}$ core could be dis-

[a] Department of Chemistry and Chemical Technology, University of Ljubljana, Aškerčeva 5, 1000 Ljubljana, Slovenia
Fax: +386-1-2419-220
E-mail: barbara.modec@guest.arnes.si
Supporting information for this article is available on the WWW under http://www.eurjic.org

cerned. A normally favoured, chelating coordination of the ligand was observed only in $[Mo_2O_4(\mu_2\text{-}C_2O_4)Cl_2]_n^{2n-}$. We were interested to see how different multidentate ligands, in particular the carboxylate-based ligands with a well-known tendency towards the chelating coordination, coordinate to the $\{Mo_2O_4\}^{2+}$ core. Herein we report the preparation and the structural characterization of a novel anionic tetranuclear heptanedioato complex, $[(Mo_2O_4Cl_4)_2(\mu_4\text{-hda})]^{6-}$, and three 1,3,5-benzenetricarboxylato complexes: anionic dinuclear $[Mo_2O_4X_4(\mu_2\text{-btcH}_2)]^{3-}$ (X = Cl, Br) and a neutral tetranuclear $[(Mo_2O_4Py_3)_2(\mu_3\text{-btcH})_2]$.

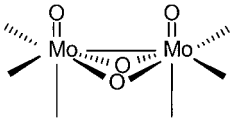

Scheme 1. The $\{Mo_2O_4\}^{2+}$ structural core.

Results and Discussion

Solid State Structures

The structures of $(PyH)_4[Mo_2O_4Cl_4(\mu_2\text{-btcH}_2)]Cl$ (**1**) and $(PyH)_4[Mo_2O_4Br_4(\mu_2\text{-btcH}_2)]Br$ (**2**) will be discussed concurrently because of their structural similarity. A dinuclear anion $[Mo_2O_4X_4(\mu_2\text{-btcH}_2)]^{3-}$, depicted in Figure 1a, occu-

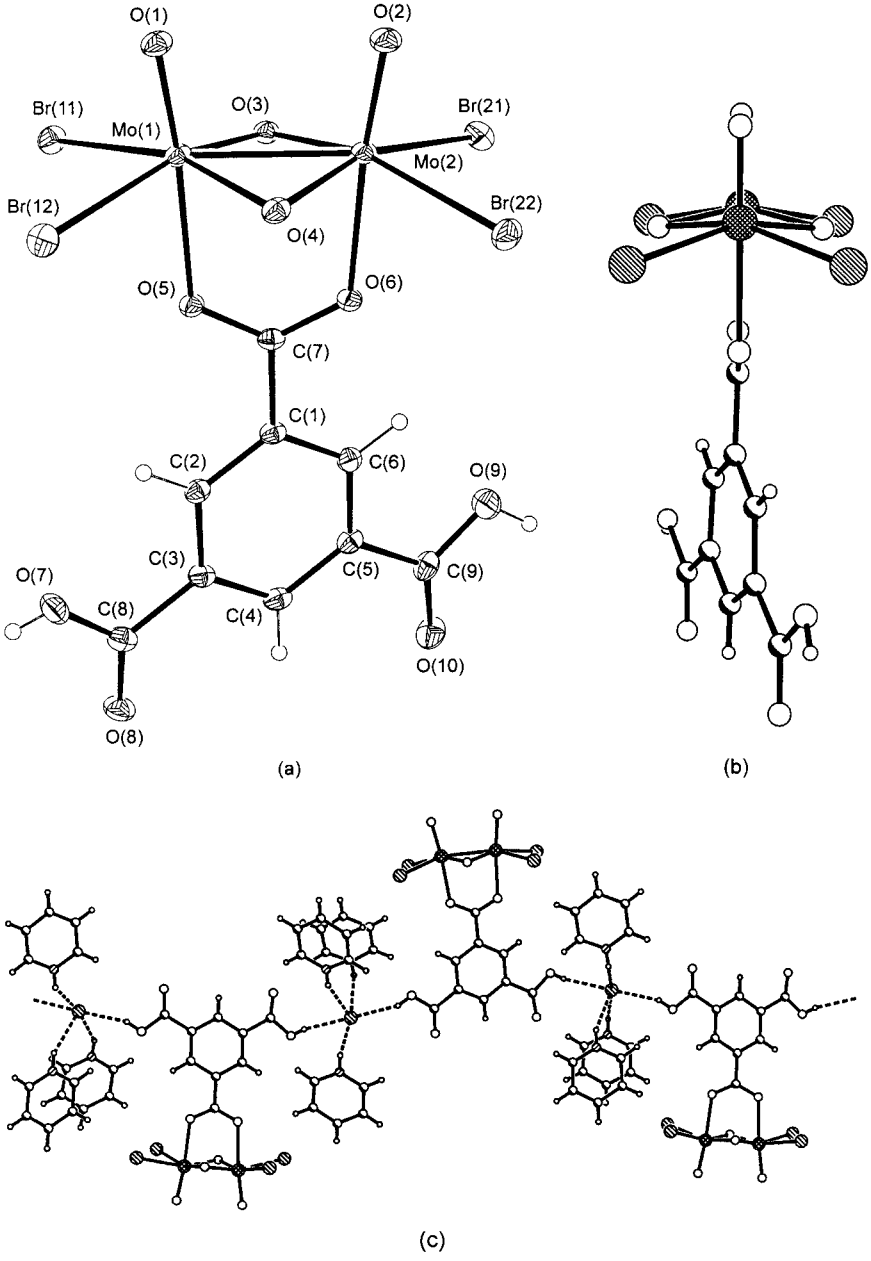

Figure 1. (a) Molecular structure of the anion $[Mo_2O_4Br_4(\mu_2\text{-btcH}_2)]^{3-}$ in **2** with displacement ellipsoids drawn at the 30% probability level. (b) A view along the metal–metal bond vector of the anion in **2** illustrating the orientation of the $btcH_2^-$ ligand. (c) Hydrogen bonds occurring between COOH groups and halide counteranions in **1** and **2** result in infinite chains.

 © 2005 Wiley-VCH Verlag GmbH & Co. KGaA, Weinheim

pies a general position within the unit cell of the monoclinic space group $P2_1/n$. Associated with each dinuclear anion are four protonated pyridine molecules and one halide counteranion. Geometric parameters of the basic $\{Mo_2O_4\}^{2+}$ core are very similar to those determined in related compounds:[6] (i) a short distance between molybdenum atoms, 2.5962(4) Å for **1** and 2.5856(3) Å for **2**, typical for a single metal–metal bond; and (ii) a buckled $Mo(\mu_2\text{-}O)_2$-Mo ring with the metal atoms above and the bridging oxygen atoms below the mean plane. The dihedral angle between the two $Mo(\mu_2\text{-}O)_2$ planes, 159.85(5)° for **1** and 159.37(4)° for **2**, is greater than the angles observed for $\{Mo_2O_4\}^{2+}$ compounds without the third bridging ligand. A distorted octahedral coordination of each metal centre of the $\{Mo_2O_4\}^{2+}$ core is completed by a pair of halides and an oxygen from the carboxylate group. An exhaustive list of bond lengths is given in Table 1. The carboxylato ligand, the anion of 1,3,5-benzenetricarboxylic acid with two non-ionized carboxylic groups, is coordinated to the metal centres of the $\{Mo_2O_4\}^{2+}$ core, as will be shown presently, in the usual manner, i.e., through both oxygen atoms of the carboxylate group to a pair of molybdenum atoms. This type of carboxylate coordination will be denoted throughout this paper as a *syn-syn* bidentate bridging mode.[11] The carboxylate group thereby serves as a third bridge between a pair of molybdenum atoms. Taking into account that the carboxylate group occupies a pair of *trans* positions relative to Mo=O bonds and is, therefore, subject to their well-documented *trans* influence, the molybdenum-to-carboxylate oxygen bond lengths are relatively short, 2.269(2) and 2.281(2) Å for **1** and 2.270(2) and 2.292(2) Å for **2**. It has been observed that the extent to which the *trans* influence is expressed within a certain species differs from one case to another.[12] Table 2 lists some $\{Mo_2O_4\}^{2+}$ complexes with different carboxylates. In all, the carboxylato ligand occupies a pair of *trans* positions within the $\{Mo_2O_4\}^{2+}$ unit. It can be seen that the Mo–O distances span a wide range and that they can exceed 2.40 Å. The carboxylate group in all listed complexes in Table 2 is invariably almost coplanar with the plane defined by a pair of molybdenyl groups. The same observation pertains to the coordinated carboxylate moiety in the anions of **1** and **2**, whereas the benzene ring of the $btcH_2^-$ ligand with both carboxylic groups is slightly rotated away (Figure 1b). The protonated carboxylate groups and pyridinium cations, which can act as donors of hydrogen bonds, are matched with the halide counteranions and the doubly-bridging oxygen atoms as the acceptors. The hydrogen bonding interactions between the carboxylic groups and halide counteranions result in infinite chains that propagate along the [10–1] unit cell direction (Figure 1c). The corresponding O(7)···X and O(9)···X distances are 2.920(3) and 2.938(3) Å for **1** and 3.084(3) and 3.093(2) Å for **2**. The halide counteranion also forms hydrogen bonds to three protonated pyridine molecules with the N···X distances ranging from 3.112(3) to 3.291(3) Å for **1** and from 3.240(3) to 3.415(3) Å for **2**. Protonated pyridine

Table 1. Selected interatomic distances [Å] for compounds **1** and **2**.[a]

	1	**2**
Mo(1)–Mo(2)	2.5962(4)	2.5856(3)
Mo(1)–O(1)	1.683(2)	1.679(2)
Mo(2)–O(2)	1.681(2)	1.678(2)
Mo(1)–O(3)	1.952(2)	1.952(2)
Mo(1)–O(4)	1.977(2)	1.973(2)
Mo(2)–O(3)	1.952(2)	1.954(2)
Mo(2)–O(4)	1.975(2)	1.970(2)
Mo(1)–X(11)	2.4426(8)	2.5901(3)
Mo(1)–X(12)	2.4695(9)	2.6320(4)
Mo(2)–X(21)	2.4528(8)	2.5994(4)
Mo(2)–X(22)	2.4555(9)	2.6160(4)
Mo(1)–O(5)	2.281(2)	2.292(2)
Mo(2)–O(6)	2.269(2)	2.270(2)
C(7)–O(5)	1.272(4)	1.267(3)
C(7)–O(6)	1.267(4)	1.263(3)
C(8)–O(7)	1.326(4)	1.321(4)
C(8)–O(8)	1.213(4)	1.213(3)
C(9)–O(9)	1.321(4)	1.326(4)
C(9)–O(10)	1.208(4)	1.212(4)

[a] Same labelling scheme pertains to compounds **1** and **2**.

Table 2. Selected geometric parameters [Å, °] for some carboxylate molybdenum(v) complexes with the $\{Mo_2O_4\}^{2+}$ core.

Compound	Mo–Mo	Fold angle[a]	Mo–O(carboxylate)[b]
1	2.5962(4)	159.85(5)	2.269(2), 2.281(2)
2	2.5856(3)	159.37(4)	2.270(2), 2.292(2)
3	2.5410(3)	160.4(1)	2.209(2), 2.343(2)
	2.5326(3)	160.1(1)	2.233(2), 2.325(2)
4	2.5824(3)	159.9(1)	2.274(2), 2.320(2)
$[Mo_2O_4Cl_4(\mu_2\text{-maleH})]^{3-}$ [12][c]	2.5916(3)	156.49(9)	2.380(2), 2.438(2)
	2.5951(3)	158.3(1)	2.371(2), 2.377(2)
$[Mo_2O_4Br_4(\mu_2\text{-maleH})]^{3-}$ [12][c]	2.5724(4)	156.44(6)	2.316(2), 2.413(2)
$[Mo_2O_4(SCN)_4(\mu_2\text{-}OOCCH_3)]^{3-}$ [13][d]	2.560(1)		2.277(7), 2.335(6)
$[Mo_2O_4(\mu_2\text{-}OOCH)(OOCH)_4]^{3-}$ [14]	2.5490(5)	162.6	2.302(2)[e]
$[\{Mo_2O_4(mal)_2\}_2(\mu_4\text{-mal})]^{6-}$ [15][f]	2.555	161	2.321[g]

[a] A dihedral angle between the $Mo(\mu_2\text{-}O)_2$ planes of the $\{Mo_2O_4\}^{2+}$ core. [b] The distance pertains to the carboxylate bonded in the *syn-syn* bidentate bridging manner. [c] maleH = hydrogen maleate ion. [d] Fold angle was not reported. [e] The monodentate terminal formate ions bind to molybdenum with bond lengths of 2.085(2) and 2.130(2) Å. [f] mal = $CH_2(COO)_2^{2-}$. [g] The chelating malonate ions bind to molybdenum with bond lengths of 2.081 Å.

 © 2005 Wiley-VCH Verlag GmbH & Co. KGaA, Weinheim

molecules are engaged in another type of interaction. These occur with both doubly bridging oxo groups of the $\{Mo_2O_4\}^{2+}$ core. Their lengths are 2.711(4)–2.802(4) Å for **1** and 2.708(3)–2.844(3) Å for **2**.[16]

The structure of **3** consists of neutral, tetranuclear molecules with the $[(Mo_2O_4Py_3)_2(\mu_3\text{-btcH})_2]$ composition and pyridine solvent molecules. Two $\{Mo_2O_4\}^{2+}$ moieties are linked by two carboxylato ligands to form a tetranuclear molecule (Figure 2a). Both carboxylato ligands, each with a nonionized carboxylic group and two deprotonated ones, are bound in the same way: with one carboxylate group in the usual *syn-syn* bidentate bridging mode to a pair of metal atoms of the $\{Mo_2O_4\}^{2+}$ unit in the asymmetric manner [2.209(2) vs. 2.343(2) and 2.233(2) vs. 2.325(2) Å] and with the other carboxylate group in a monodentate manner to molybdenum from the other dinuclear unit (Figure 2b) with bond lengths of 2.068(2) and 2.070(2) Å. The asymmetric carboxylate coordination finds precedence in several other complexes (see Table 2). No adequate explanation could be provided in either case.[12] The $\{Mo_2O_4\}^{2+}$ core with the *syn-syn* bidentately bridging carboxylato ligand resembles the anions of **1** and **2**. The carboxylate group is coplanar

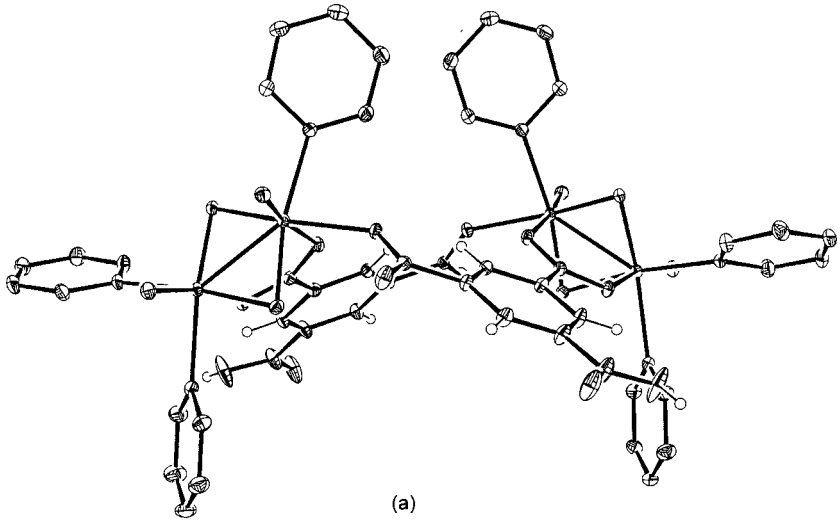

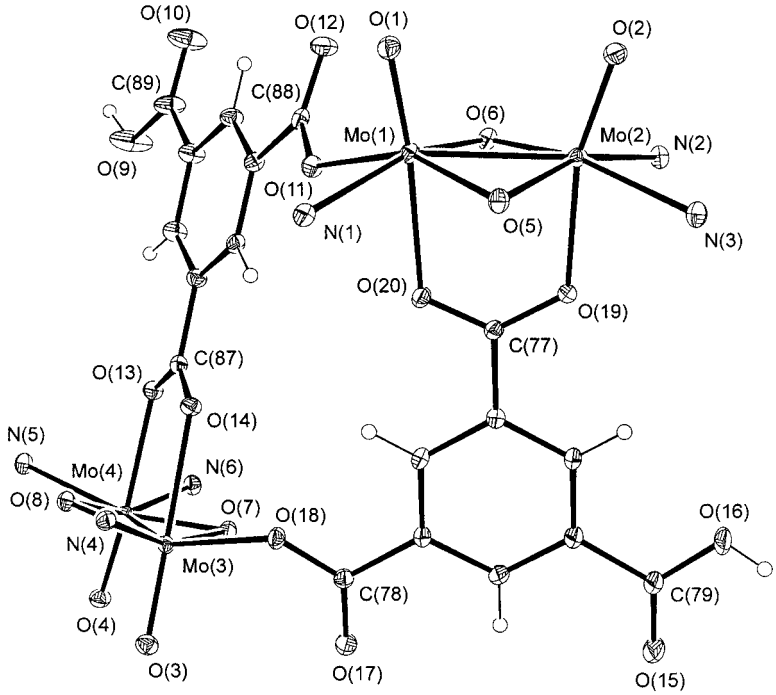

(b)

Figure 2. (a) Molecular structure of $[(Mo_2O_4Py_3)_2(\mu_3\text{-btcH})_2]$ in **3** with displacement ellipsoids drawn at the 30% probability level. Pyridine hydrogen atoms have been omitted for clarity. (b) The tetranuclear complex of **3** in a different orientation. Pyridine carbon and hydrogen atoms have been omitted.

 © 2005 Wiley-VCH Verlag GmbH & Co. KGaA, Weinheim

with the plane of two molybdenyl groups, while the remaining part of the ligand is rotated away from this plane. The misalignment of the two planes is smaller in complex **3** than in the anions of **1** and **2**, as shown by the values of the corresponding dihedral angles, 5.42(7) and 8.99(7)° for **3** vs. 17.79(6) for **1** and 20.80(5)° for **2**. The participation of $btcH^{2-}$ ligands in **3** in a monodentate coordination via another carboxylate group may well be responsible for such a conformation of the ligand. Each $btcH^{2-}$ ligand thus connects three molybdenum atoms: a pair of metal atoms from one $\{Mo_2O_4\}^{2+}$ unit is connected via a long bridge with molybdenum from another dinuclear unit. The separations between the molybdenum atoms are in the range 8.1894(9)–11.0690(4) Å. The geometric parameters of the $\{Mo_2O_4\}^{2+}$ moieties are: (i) separations between molybdenum atoms of 2.5410(3) and 2.5326(3) Å; and (ii) fold angles of 160.4(1) and 160.1(1)°. A distorted octahedral environment of molybdenum atoms in **3** is completed by pyridine ligands. The rather short length of the metal–metal bonds in **3** may be explained in terms of the high content of pyridine ligands whose nature is electron-donating. As a rule, longer metal–metal bonds occur in complexes with the electron-withdrawing ligands such as chloro or bromo ligands. Although the entire tetranuclear molecule of **3** is the crystallographic asymmetric unit, it comes very close to having C_2 symmetry with the C_2 axis going through the centre of the loop delineated by Mo(1), a $btcH^{2-}$ ligand, Mo(3) and another $btcH^{2-}$ ligand. As far as the bonding pattern in the distorted octahedral environment of each molybdenum atom is concerned, the pairwise equivalences demanded by the C_2 symmetry are very closely approximated. An exhaustive list of bond lengths is given in Table 3. The nonionized carboxylic group of each $btcH^{2-}$ ligand is engaged in hydrogen bonding interaction with a pyridine solvent molecule. The corresponding O···N distances are 2.646(4) and 2.657(4) Å.

Table 3. Selected interatomic distances [Å] for **3**.

Mo(1)–Mo(2)	2.5410(3)	Mo(3)–Mo(4)	2.5326(3)
Mo(1)–O(1)	1.681(2)	Mo(3)–O(3)	1.678(2)
Mo(2)–O(2)	1.689(2)	Mo(4)–O(4)	1.694(2)
Mo(1)–O(5)	1.947(2)	Mo(3)–O(7)	1.927(2)
Mo(1)–O(6)	1.926(2)	Mo(3)–O(8)	1.950(2)
Mo(2)–O(5)	1.930(2)	Mo(4)–O(7)	1.934(2)
Mo(2)–O(6)	1.940(2)	Mo(4)–O(8)	1.930(2)
Mo(1)–N(1)	2.260(2)	Mo(3)–N(4)	2.249(2)
Mo(2)–N(2)	2.235(3)	Mo(4)–N(5)	2.254(2)
Mo(2)–N(3)	2.251(2)	Mo(4)–N(6)	2.233(3)
Mo(1)–O(20)	2.343(2)	Mo(3)–O(14)	2.325(2)
Mo(2)–O(19)	2.209(2)	Mo(4)–O(13)	2.233(2)
Mo(1)–O(11)	2.068(2)	Mo(3)–O(18)	2.070(2)
C(77)–O(19)	1.274(4)	C(87)–O(13)	1.274(4)
C(77)–O(20)	1.258(3)	C(87)–O(14)	1.258(3)
C(78)–O(18)	1.294(3)	C(88)–O(11)	1.300(3)
C(78)–O(17)	1.227(4)	C(88)–O(12)	1.226(4)
C(79)–O(16)	1.320(4)	C(89)–O(9)	1.306(4)
C(79)–O(15)	1.211(4)	C(89)–O(10)	1.209(4)

The ionic structure of **4** consists of tetranuclear anions with the $[(Mo_2O_4Cl_4)_2(\mu_4\text{-hda})]^{6-}$ composition (Figure 3), protonated pyridine molecules as countercations and solvent molecules of acetonitrile. The linkage of two basic $\{Mo_2O_4\}^{2+}$ cores to produce a tetranuclear structure is achieved via a quadridentate hda^{2-} ligand whose two carboxylate groups occupy *trans* positions within both $\{Mo_2O_4\}^{2+}$ cores. Each carboxylate group of the hda^{2-} ligand is coordinated in the *syn-syn* bidentate bridging manner and serves as a third bridge between a pair of metal–metal bonded atoms whose separation, 2.5824(3) Å, falls in the normally observed range. The hda^{2-} ligand thus connects four molybdenum atoms: two pairs are connected via a long bridge consisting of the whole hda^{2-} ligand. The resulting separations between the molybdenum atoms from different dinuclear subunits are in the 8.9043(4)–11.6186(4) Å range. The molybdenum-to-carboxylate bond lengths, subject to the labilizing *trans* influence of the Mo=O bonds, reveal an asymmetric bonding pattern, 2.274(2) vs. 2.320(2) Å. The tetranuclear anion has a twofold rotation symmetry. The anion sits with the central carbon atom of the alkyl chain on a special position within the *C*2/*c* space group, on a twofold rotation axis. The pattern of hydrogen bonds in **4** is typical for anionic $\{Mo_2O_4\}^{2+}$ complexes with protonated pyridine molecules as the countercations: each doubly-bridging oxygen from the $\{Mo_2O_4\}^{2+}$ core is linked to a pyridinium cation. The corresponding N···O distances are 2.710(3) and 2.732(3) Å. The remaining two pyridinium cations participate in another type of hydrogen bonding interaction: each forms a relatively short hydrogen bond with one of the four coordinated chloro ligands, N(2)···Cl(21) = 3.071(3) Å, leading to a nonequivalence of the molybdenum-to-chlorine bond lengths. As expected, the respective bond length is longer than the others. A list of bond lengths is given in Table 4.

In spite of the wide use of 1,3,5-benzenetricarboxylate anions in coordination chemistry, the literature reports on only one molybdenum(v) complex with this ligand, a cyclic $[Mo_{12}S_{12}O_{12}(OH)_{12}(\mu_6\text{-btc})]^{3-}$ anion.[17] The dodecanuclear complex consists of six $\{Mo_2O_2(\mu_2\text{-}S)_2\}^{2+}$ moieties arranged around the central btc^{3-} anion which is coordinated with each of its carboxylate groups in the *syn-syn* bidentate bridging manner. The btc^{3-} anion serves on the whole as a μ_6-ligand with the molybdenum-to-carboxylate oxygen bond lengths in the 2.350(10)–2.425(10) Å range. The ability of inorganic rings with the general formula $[Mo_nO_nS_n(OH)_n]$ (n = 8, 10, 12) to encapsulate in their centres organic templates was further exploited in the preparation of $[Mo_{12}S_{12}O_{12}(OH)_{12}(\mu_6\text{-hda})]^{2-}$, the only structurally characterized molybdenum(v) heptanedioato complex prior to this study.[18] Each carboxylate group of the ligand is coordinated to three molybdenum atoms as follows: one oxygen atom is bonded to the metal atom of the $\{Mo_2O_2(\mu_2\text{-}S)_2\}^{2+}$ moiety, while the other oxygen binds to the other metal atom of the same dinuclear core and also to molybdenum from the neighbouring dinuclear core. The heptanedioate thus serves as a μ_6-ligand with the molybdenum-to-carboxylate oxygen bond lengths in the 2.341(12)–2.440(9) Å range. Both ring structures are essentially planar. The most apparent difference between them is the shape of

 © 2005 Wiley-VCH Verlag GmbH & Co. KGaA, Weinheim

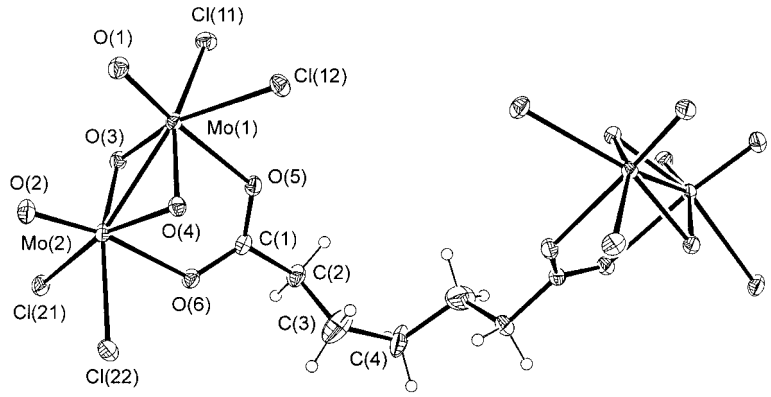

Figure 3. Molecular structure of the anion $[(Mo_2O_4Cl_4)_2(\mu_4\text{-hda})]^{6-}$ in **4** with displacement ellipsoids drawn at the 30% probability level.

Table 4. Selected interatomic distances [Å] for **4**.

Mo(1)–Mo(2)	2.5824(3)
Mo(1)–O(1)	1.682(2)
Mo(2)–O(2)	1.685(2)
Mo(1)–O(3)	1.952(2)
Mo(1)–O(4)	1.959(2)
Mo(2)–O(3)	1.947(2)
Mo(2)–O(4)	1.944(2)
Mo(1)–Cl(11)	2.4467(7)
Mo(1)–Cl(12)	2.4598(6)
Mo(2)–Cl(21)	2.4947(6)
Mo(2)–Cl(22)	2.4840(7)
Mo(1)–O(5)	2.320(2)
Mo(2)–O(6)	2.274(2)
C(1)–O(5)	1.255(3)
C(1)–O(6)	1.275(3)

the ring: a perfect cycle for the btc^{3-} complex and an oval ring for the hda^{2-} complex.

Although the carboxylate group is known to coordinate in several different ways,[11] a survey of molybdenum(V) carboxylate complexes reveals that a number of possible coordination modes reduces to only two: (i) a monodentate terminal mode; and (ii) a *syn-syn* bidentate bridging mode. Speaking in terms of distances, the carboxylato ligand spans in the latter case distances between metal atoms as short as 2.5–2.6 Å and at the other extreme, as long as 3.850 Å as exemplified by $[Mo_4O_6(\mu_2\text{-}OOCCH_3)_6Cl_2]$.[19] It is pertinent to note that in no instance was a chelating coordination of carboxylate encountered among molybdenum(V) complexes. The X-ray structures of two thiobenzoato complexes, $[Mo_2O_2S_2(OSCC_6H_5)_2Py_2]$ and $[Mo_2O_2S_2(OSCC_6H_5)_2(4\text{-MePy})_2]$ (4-MePy = 4-methylpyridine), demonstrate that thio derivatives of carboxylato ligands are capable of chelating coordination.[20] The same binding scheme emerges upon inspection of the rare di- and tricarboxylato molybdenum(V) complexes. In addition to the above-described coordination modes, only two new ones are displayed: (i) the coordination of each carboxylate group of the hda^{2-} ligand to three metal atoms in $[Mo_{12}S_{12}O_{12}(OH)_{12}(\mu_6\text{-hda})]^{2-}$;[18] and (ii) the chelating coordination of malonate ions in $[\{Mo_2O_4(mal)_2\}_2(\mu_4\text{-mal})]^{6-}$ via two oxygen atoms, each belonging to a different carboxylate group.[15] The binding modes adopted by the $btcH_2^-$, $btcH^{2-}$, and hda^{2-} ligands in the title complexes add further validity to the observed binding scheme of carboxylato ligands in complexes with molybdenum(V).

In contrast to numerous oligonuclear complexes obtained upon the self-assembly of $\{Mo_2O_4\}^{2+}$ cores,[6] species where two or more dinuclear subunits are linked covalently solely by multidentate ligands are extremely rare. Apart from the three polymeric species, already mentioned in the introduction, that leaves to the best of our knowledge two tetranuclear anions, $[\{Mo_2O_4(\eta^2\text{-}C_2O_4)_2\}_2(\mu_4\text{-}C_2O_4)]^{6-}$[21] and $[\{Mo_2O_4(mal)_2\}_2(\mu_4\text{-mal})]^{6-}$,[15] where the linkage is achieved via quadridentate oxalate and malonate, respectively. Their structural analogy to $[(Mo_2O_4Cl_4)_2(\mu_4\text{-hda})]^{6-}$, the anion in **4**, is obvious: pairs of dinuclear subunits are linked covalently by dicarboxylates, differing in the number of carbon atoms between the carboxylate groups. It is to be noted that a class of related $\{Mo_2O_2(\mu_2\text{-}S)_2\}^{2+}$ species also reveals tetranuclear anions of this type, $[\{Mo_2O_2S_2(\eta^2\text{-}C_2O_4)_2\}_2(\mu_4\text{-}C_2O_4)]^{6-}$[22] and $[\{Mo_2O_2S_2(\eta^2\text{-}SO_4)_2\}_2(\mu_4\text{-}SO_4)]^{6-}$.[23] The X-ray structure analysis of $[\{Mo_2O_4(\eta^2\text{-}$

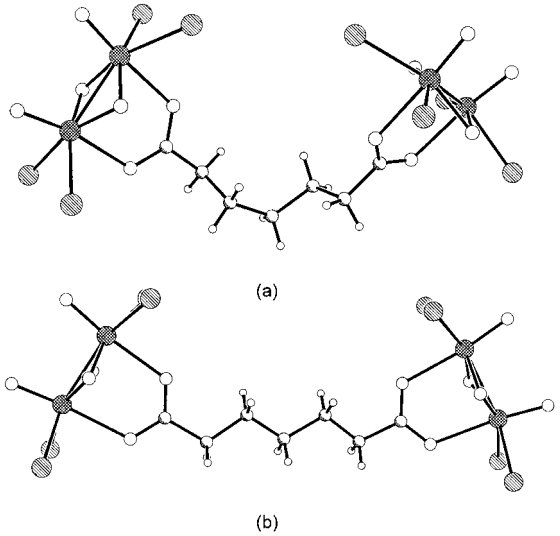

Figure 4. Two different conformations of the $[(Mo_2O_4Cl_4)_2(\mu_4\text{-hda})]^{6-}$ anion as found in **4** (a) and **5** (b).

 © 2005 Wiley-VCH Verlag GmbH & Co. KGaA, Weinheim

$C_2O_4)_2\}_2(\mu_4\text{-}C_2O_4)]^{6-}$ revealed the μ_4-oxalate in a complete staggered conformation, whereas the μ_4-oxalate in $[\{Mo_2O_2S_2(\eta^2\text{-}C_2O_4)_2\}_2(\mu_4\text{-}C_2O_4)]^{6-}$ adopted the usual planar form. With dicarboxylates that contain alkyl chains, the existence of complexes with different chain conformations in the solid state seems very likely. The $[(Mo_2O_4Cl_4)_2(\mu_4\text{-hda})]^{6-}$ anion, found in **4** and **5**, presents such a case. The alkyl chain in the anion of **5** is straighter than in **4** (Figure 4). Consequently, the separations between molybdenum atoms from the two $\{Mo_2O_4\}^{2+}$ moieties in **5** are larger than in **4**. The $[(Mo_2O_4Cl_4)_2(\mu_4\text{-hda})]^{6-}$ anions in **4** and **5** also differ in the mutual orientations of the metal–metal bond vectors. Unfortunately, the low-quality X-ray data of **5** does not allow any further discussion of its structural parameters. The linkage of two dinuclear subunits with the agency of $btcH^{2-}$ ligands in $[(Mo_2O_4Py_3)_2(\mu_3\text{-}btcH)_2]$ (**3**) finds no precedence.

Infrared Spectroscopy

The positions of asymmetric and symmetric ν(COO) vibrations can be used to diagnose the carboxylate binding mode: large Δ values, defined as $\nu_{asym}(COO) - \nu_{sym}(COO)$, are observed for the monodentate binding mode, while *syn-syn* bidentate bridging carboxylates display Δ values which are close to those observed for ionic compounds.[24] Accordingly, the bands at 1538 and 1410 cm^{-1} in the spectrum of **4** can be attributed to $\nu_{asym}(COO)$ and $\nu_{sym}(COO)$, respectively. The calculated Δ value, 128 cm^{-1}, is in line with the *syn-syn* bidentate bridging coordination. With at least two carboxylate groups of the 1,3,5-benzenetricarboxylate anions in **1**, **2**, and **3** engaged in different binding modes, no unambiguous assignations can be made. The spectra of **1** and **2** are very similar to each other. An absorption band at 1718 cm^{-1} for **1** and bands at 1722 and 1708 cm^{-1} for **2** are indicative of nonionized carboxylic groups in the $btcH_2^-$ ligand. The region of asymmetric and symmetric ν(COO) vibrations displays a number of strong bands, at 1618, 1554, 1539, 1433, and 1365 cm^{-1} for **1** and at 1617, 1537, 1435, and 1365 cm^{-1} for **2**. The spectrum of **3**, with all carboxylate groups distinctly different, displays a band at 1711 cm^{-1} which is associated with the C=O stretching vibration of the carboxylic group and several bands in the region of asymmetric [at 1649, 1607, and 1545 cm^{-1}] and symmetric ν(COO) vibrations [at 1449 and 1406 cm^{-1}]. For comparison, several bands were also observed for $[Cd_{1.5}(btc)(bpe)(H_2O)_2]\cdot H_2O$ [bpe = 1,2-bis(4-pyridyl)ethane] where two carboxylate groups are bound in a chelating manner and the third one is bound monodentately.[3d] Δ values of 122 and 255 cm^{-1} were calculated from their positions.

Synthetic Considerations

The composition of the heptanedioato complex $[(Mo_2O_4Cl_4)_2(\mu_4\text{-hda})]^{6-}$, the anion in **4** and **5**, is as anticipated. Acetonitrile was used as a solvent for its low coordinating ability towards molybdenum(v) and since both, the molybdenum(v) starting material and the tetrabutylammonium heptanedioate, display a good acetonitrile solubility. The substitution of the labile aqua and halo ligands in acetonitrile usually does not proceed beyond the formation of the $\{Mo_2O_4\}^{2+}$ core and so species with a high content of unsubstituted halo ligands can be isolated.[12] The carboxylate groups of the heptanedioate coordinated to two $\{Mo_2O_4\}^{2+}$ cores, resulting in a tetranuclear anion $[(Mo_2O_4Cl_4)_2(\mu_4\text{-hda})]^{6-}$. The successful isolation of $(PyH)_6[(Mo_2O_4Cl_4)_2(\mu_4\text{-hda})]\cdot 2CH_3CN$ (**4**) required a substantial reduction of the volume of the reaction mixture. When too much solvent was removed, a product with a different composition, $(PyH)_{10}[(Mo_2O_4Cl_4)_2(\mu_4\text{-hda})][MoOCl_5]Cl_2$ (**5**), crystallized from the concentrate. The composition of **5** is intriguing for two reasons. Although a sufficient amount of the hda^{2-} ligand was used, its coordination to molybdenum(v) was not quantitative. The identity of the uncomplexed species turned out to be $[MoOCl_5]^{2-}$, giving evidence for the transformation of $[MoOCl_4(H_2O)]^-$ into $[MoOCl_5]^{2-}$.

The compositions of the 1,3,5-benzenetricarboxylato complexes, the $[Mo_2O_4X_4(\mu_2\text{-}btcH_2)]^{3-}$ anions, and the neutral $[(Mo_2O_4Py_3)_2(\mu_3\text{-}btcH)_2]$, didn't meet expectations. Although fully neutralized salt of 1,3,5-benzenetricarboxylic acid was used in the case of **1** and **2**, the protonation of two carboxylate groups by pyridinium cations, introduced into the reaction mixture via the molybdenum(v) starting materials, prevented their ligation to two more $\{Mo_2O_4\}^{2+}$ units. The only carboxylate group of the 1,3,5-benzentricarboxylate capable of coordination attached to the $\{Mo_2O_4\}^{2+}$ core in the usual manner. Because of the greater lability of bromo vs. chloro ligands, the crystallization of **2** was not as straightforward as that of **1**, it took longer and the yield was significantly smaller. An important role for the solvent was observed. When methanol or ethanol was used in place of acetonitrile, the coordination of alcohol and alkoxide to the $\{Mo_2O_4\}^{2+}$ core took place first, followed by the assembly of two $\{Mo_2O_4\}^{2+}$ units into a tetranuclear $\{Mo_4O_4(\mu_3\text{-}O)_2(\mu_2\text{-}O)_2(\mu_2\text{-}OR)_2\}^{2+}$ core. The composition of the final products as $(PyH)_2[Mo_4O_8(OR)_2(ROH)_2X_4]$ (R = Me, Et; X = Cl, Br) was established on the basis of their infrared spectra.[25–26] Carrying out the reaction between (PyH)[$MoOBr_4$] and 1,3,5-benzenetricarboxylic acid in pyridine, a solvent with a strong coordinating ability, at 115 °C resulted in the coordination of both ligands and a neutral complex $[(Mo_2O_4Py_3)_2(\mu_3\text{-}btcH)_2]$ (**3**) was isolated. By using the oxobromomolybdate(v) starting material, the number of labile sites in the molybdenum(v) coordination sphere was increased. The $btcH^{2-}$ ligand with two carboxylate groups is capable of coordination to two $\{Mo_2O_4\}^{2+}$ cores, yet in $[(Mo_2O_4Py_3)_2(\mu_3\text{-}btcH)_2]$ (**3**) the coordination of both in the *syn-syn* bidentate bridging manner was not realized. Namely, one carboxylate group coordinated monodentately. The large amount of the ligand used explains the formation of a discrete species.

Conclusions

A series of 1,3,5-benzenetricarboxylato and heptanedioato molybdenum(v) complexes based on the $\{Mo_2O_4\}^{2+}$

 © 2005 Wiley-VCH Verlag GmbH & Co. KGaA, Weinheim

structural core was prepared. The carboxylate group usually binds to a pair of metal atoms of the $\{Mo_2O_4\}^{2+}$ core in the *syn-syn* bidentate bridging manner. Coordination of two carboxylate groups of either 1,3,5-benzenetricarboxylate or heptanedioate results in the formation of tetranuclear clusters.

Experimental Section

General Remarks: All manipulations and procedures were conducted in air. Chemicals were purchased from Aldrich and used as received. $(PyH)_5[MoOCl_4(H_2O)]_3Cl_2$ and $(PyH)[MoOBr_4]$ were prepared as reported.[26–27] The solvothermal reactions were carried out in sealed glass tubes under autogenous pressure. The IR spectra were measured on solid samples as Nujol or poly(chlorotrifluoroethylene) mulls using a Perkin–Elmer 2000 series FT-IR spectrometer. Elemental analyses were performed by the Chemistry Department service at the University of Ljubljana.

Preparation of the Acetonitrile Solution of $(n\mathrm{Bu_4N})_3$btc: 1,3,5-benzenetricarboxylic acid (2.1 g, 0.010 mol) was dissolved in methanol (35 mL), followed by the addition of a methanol solution (1.0 M) of $n\mathrm{Bu_4NOH}$ (30 mL, 0.030 mol). Methanol was removed by careful pumping on the vacuum line. Acetonitrile was added (20 mL) to the oily residue. Each gram of the resulting solution contained 0.315 mmol of $(n\mathrm{Bu_4N})_3$btc.

Preparation of the Acetonitrile Solution of $(n\mathrm{Bu_4N})_2$hda: Heptanedioic acid (w = 0.98, 1.429 g, 8.74 mmol) was dissolved in methanol (10 mL) followed by the addition of a methanol solution (1.0 M) of $n\mathrm{Bu_4NOH}$ (17.5 mL, 17.5 mmol). Methanol was removed by careful pumping on the vacuum line. Acetonitrile (30 mL) was added to the oily residue. Each gram of the resulting solution contained 0.355 mmol of $(n\mathrm{Bu_4N})_2$hda.

$(PyH)_4[Mo_2O_4Cl_4(\mu_2\text{-btcH}_2)]Cl$ (1): $(PyH)_5[MoOCl_4(H_2O)]_3Cl_2$ (450 mg, 1.05 mmol of Mo) was dissolved in acetonitrile (20 mL). A weighted amount of the acetonitrile solution of $(n\mathrm{Bu_4N})_3$btc (0.647 mmol) was added dropwise with constant stirring. The reaction mixture was left to stand at 8 °C in the refrigerator. The orange, block-shaped crystals of **1** that formed after three days were collected by filtration and washed with the hexanes. Yield: 53% (269 mg). $C_{29}H_{29}Cl_5Mo_2N_4O_{10}$ (962.7): calcd. C 36.18, H 3.04, N 5.82; found C 36.44, H 3.27, N 6.11. IR: $\tilde{\nu}$ = 3228 (w), 3156 (w), 3134 (w), 3090 (w), 3059 (w), 1718 (vvs), 1635 (s), 1618 (vs), 1554 (s), 1539 (vs), 1488 (vvs), 1458 (w), 1433 (vs), 1365 (vs), 1245 (m), 1201 (s), 1183 (vvs), 1163 (vs), 1108 (w), 1097 (w), 1048 (w), 1000 (w), 957 (vvs), 940 (s), 893 (w), 766 (s), 750 (vvs), 694 (m), 678 (vs), 665 (vvs), 649 (vvs), 606 (vvs), 513 (s), 488 (s), 428 (m), 397 (m), 384 (s), 373 (vs), 330 (vvs), 310 (s), 299 (vvs), 292 (vvs), 272 (vs) cm^{-1}.

$(PyH)_4[Mo_2O_4Br_4(\mu_2\text{-btcH}_2)]Br$ (2): $(PyH)[MoOBr_4]$ (540 mg, 1.06 mmol) was dissolved in acetonitrile (20 mL). A weighted amount of the acetonitrile solution of $(n\mathrm{Bu_4N})_3$btc (0.647 mmol) was added dropwise with constant stirring. The volume of the reaction mixture was reduced on the following day to ca. one half by pumping on the vacuum line. The solution was allowed to stand at ambient conditions. The orange, block-shaped crystals of **2** which formed after six days were collected by filtration and washed with the hexanes. Yield: 19% (119 mg). $C_{29}H_{29}Br_5Mo_2N_4O_{10}$ (1185.0): calcd. C 29.40, H 2.47, N 4.73; found C 29.23, H 2.52, N 4.70. IR: $\tilde{\nu}$ = 3219 (w), 3132 (w), 3057 (w), 1722 (vvs), 1708 (s), 1636 (m), 1617 (s), 1537 (s), 1487 (vvs), 1435 (s), 1365 (s), 1246 (w), 1201 (w), 1173 (vs), 1162 (vs), 1107 (w), 1058 (w), 1049 (w), 1026 (w), 1001 (w), 958 (vvs), 941 (s), 893 (w), 748 (vvs), 721 (w), 697 (m), 677 (vvs), 664 (vs), 635 (w), 605 (s), 510 (m), 477 (m), 424 (w), 397 (w), 379 (m), 357 (s), 325 (m), 264 (m), 252 (m) cm^{-1}.

$[(Mo_2O_4Py_3)_2(\mu_3\text{-btcH})_2]\cdot 6Py$ (3): A glass tube was charged with $(PyH)[MoOBr_4]$ (120 mg, 0.235 mmol), 1,3,5-benzenetricarboxylic acid (220 mg, 1.05 mmol) and pyridine (4 mL). The tube was sealed and heated for 90 h in an electric oven maintained at 115 °C. After cooling to room temperature, the reaction mixture consisted of a clear, orange solution and colourless, crystalline material. Red, block-shaped crystals of **3** which formed after one month were separated manually from the colourless phase. Yield: 55% (61 mg). Note: The crystals lost interstitial solvent and turned powdery immediately upon removal from the mother liquor. IR: $\tilde{\nu}$ = 3112 (w), 3078 (w), 1958 (w), 1711 (m), 1649 (vs), 1633 (m), 1607 (vs), 1573 (w), 1545 (s), 1486 (m), 1449 (vs), 1436 (m), 1406 (m), 1319 (s), 1291 (s), 1271 (vs), 1234 (m), 1218 (vs), 1161 (m), 1102 (w), 1071 (s), 1046 (s), 1016 (m), 1007 (m), 966 (vvs), 942 (vs), 758 (vvs), 742 (vvs), 718 (vs), 694 (s), 641 (m), 626 (m), 570 (s), 524 (w), 474 (w), 452 (m), 436 (m), 410 (w), 371 (m), 317 (s), 277 (s), 256 (w) cm^{-1}.

$(PyH)_6[(Mo_2O_4Cl_4)_2(\mu_4\text{-hda})]\cdot 2CH_3CN$ (4): $(PyH)_5[MoOCl_4(H_2O)]_3Cl_2$ (450 mg, 1.05 mmol of Mo) was dissolved in acetonitrile (20 mL). A weighted amount of the acetonitrile solution of $(n\mathrm{Bu_4N})_2$hda (0.65 mmol) was added dropwise with constant stirring. The solution was concentrated on the following day on the vacuum line to ca. one half of the initial volume. The resulting solution was left to stand at ambient conditions overnight. The yellow, plate-shaped crystals of **4** were collected by filtration and washed with the hexanes. Yield: 26% (105 mg). $C_{41}H_{52}Cl_8Mo_4N_8O_{12}$ (1516.3): calcd. C 32.48, H 3.46, N 7.39; found C 32.42, H 3.53, N 7.12. IR: $\tilde{\nu}$ = 3223 (w), 3160 (w), 3130 (w), 2249 (m), 1634 (m), 1612 (s), 1538 (vvs), 1486 (vvs), 1410 (vs), 1273 (w), 1250 (m), 1202 (m), 1163 (m), 1048 (m), 1024 (m), 1002 (m), 960 (vvs), 938 (vvs), 879 (w), 758 (vvs), 740 (vvs), 708 (vvs), 682 (vvs), 663 (w), 639 (w), 604 (s), 517 (m), 483 (m), 448 (w), 398 (w), 379 (s), 292 (vvs), 262 (vs) cm^{-1}.

$(PyH)_{10}[(Mo_2O_4Cl_4)_2(\mu_4\text{-hda})][MoOCl_5]Cl_2$ (5): The same procedure was used as for **4**, only the initial solution was concentrated to ca. 2 mL and left to stand at ambient conditions. Large, yellow-orange, block-like crystals of **5** deposited from the solution overnight. Yield: 11% (51 mg). ***Note:*** The crystals decompose in air.

X-ray Crystallographic Study: Crystals were mounted on the tip of a glass fibre with a small amount of silicon grease and transferred to a goniometer head. Data were collected with a Nonius Kappa CCD diffractometer. Data reduction and integration were performed with the software package DENZO-SMN.[28] Averaging of the symmetry-equivalent reflections largely compensated for the absorption effects. For all compounds, the coordinates of some or all of the non-hydrogen atoms were found via direct methods using the structure solution program SHELXS.[29] The positions of the remaining non-hydrogen atoms were located by use of a combination of least-squares refinement and difference Fourier maps in the SHELXL-97 program. The carboxylic hydrogen atoms in **1** and **2**, located in the final stages of refinement from the difference Fourier maps, were refined with isotropic displacement parameters. The remaining hydrogen atoms were added in calculated positions. Although the R_1 and wR_2 residuals for the least-squares refinement of **5** are large (R_1 almost 10%), its composition, determined to be $(PyH)_{10}[(Mo_2O_4Cl_4)_2(\mu_4\text{-hda})][MoOCl_5]Cl_2$, is unquestionable. Unfortunately, repeated attempts to obtain crystals with better diffraction data have not been successful. Therefore, we only report some basic crystal data (triclinic, space group $P1$, a = 9.9381(2), b = 14.3948(2), c = 15.5022(3) Å, α = 69.9388(8), β = 86.5969(7), γ = 89.1332(7)°, V = 2079.44(6) $Å^3$, Z = 1, T = 150(2) K, 29834 mea-

 © 2005 Wiley-VCH Verlag GmbH & Co. KGaA, Weinheim

Table 5. Crystallographic data for compounds **1**, **2**, **3**, and **4**.

	1	**2**	**3**	**4**
Empirical formula	$C_{29}H_{29}Cl_5Mo_2N_4O_{10}$	$C_{29}H_{29}Br_5Mo_2N_4O_{10}$	$C_{78}H_{68}Mo_4N_{12}O_{20}$	$C_{41}H_{52}Cl_8Mo_4N_8O_{12}$
Formula mass	962.69	1184.99	1877.20	1516.27
Crystal system	monoclinic	monoclinic	orthorhombic	monoclinic
Space group	$P2_1/n$	$P2_1/n$	$Pcab$	$C2/c$
T [K]	150(2)	150(2)	150(2)	150(2)
a [Å]	15.0672(2)	14.9928(1)	17.8525(1)	35.2318(3)
b [Å]	14.0299(2)	14.1363(1)	29.1533(2)	9.2980(1)
c [Å]	17.3771(3)	18.1821(2)	29.9545(2)	20.9025(2)
α [°]	90	90	90	90
β [°]	99.5378(5)	98.5988(4)	90	126.0046(5)
γ [°]	90	90	90	90
V [Å^3]	3622.59(9)	3810.25(6)	15590.1(2)	5539.30(9)
Z	4	4	8	4
λ [Å]	0.71073	0.71073	0.71073	0.71073
μ [mm^{-1}]	1.120	5.958	0.709	1.334
Collected reflections	16036	16750	29052	11882
Unique reflections, R_{int}	8240, 0.0194	8696, 0.0167	15213, 0.0187	6291, 0.0160
Observed reflections	6730	7470	12384	5700
R_1 [$I > 2\sigma(I)$]	0.0359	0.0265	0.0362	0.0267
wR_2 [all data]	0.0966	0.0641	0.1192	0.0826

sured reflections, 16997 unique (R_{int} = 0.056), R_1 [$I > 2\sigma(I)$] = 0.0987 and wR_2 [all data] = 0.2826) and the most relevant geometric parameters of the $[(Mo_2O_4Cl_4)_2(\mu_4\text{-hda})]^{6-}$ anion [Mo–Mo = 2.572(2) and 2.578(2) Å, Mo–Cl = 2.444(5)–2.483(4) Å, Mo–O(hda^{2-} ligand) = 2.291(10)–2.389(10) Å, Mo···Mo (from different $\{Mo_2O_4\}^{2+}$ moieties) = 11.538(2)–14.098(2) Å] and of the $[MoOCl_5]^{2-}$ anion [Mo–O = 1.685(13), Mo–Cl = 2.368(5)–2.533(4) Å]. All the calculations were performed using the WinGX System Version 1.64.05.[30] Figures depicting the structures were prepared using ORTEP3[31] and SHELXTL.[32] Cell parameters and refinement results are summarized in Table 5.

CCDC-271782 (for **1**), -271783 (for **2**), -271784 (for **3**), -271785 (for **4**), and -276050 (for **5**) contain the supplementary crystallographic data for this paper. These data can be obtained free of charge at www.ccdc.ac.uk/conts/retrieving.html [or from the Cambridge Crystallographic Data Centre, 12 Union Road, Cambridge CB2 1EZ, UK; Fax: +44-1223/336-033; E-mail: deposit@ccdc.cam.ac.uk].

Supporting Information (see also footnote on the first page of this article): Contains infrared spectra of compounds **1**–**4** (Figures S1–S12).

Acknowledgments

The work was supported by the Ministry of Higher Education, Science and Technology of the Republic of Slovenia through research grant P1-0134.

[1] S. L. James, *Chem. Soc. Rev.* **2003**, *32*, 276–288.
[2] a) B.-H. Ye, M. L. Tong, X.-M. Chen, *Coord. Chem. Rev.* **2005**, *249*, 545–565; b) D. A. Dickie, M. C. Jennings, H. A. Jenkins, J. A. C. Clyburne, *Inorg. Chem.* **2005**, *44*, 828–830; c) C. Serre, J. Marrot, G. Ferey, *Inorg. Chem.* **2005**, *44*, 654–657; d) E. Y. Choi, Y.-U. Kwon, *Inorg. Chem.* **2005**, *44*, 538–545; e) A. C. Sudik, A. P. Cote, O. M. Yaghi, *Inorg. Chem.* **2005**, *44*, 2998–3000; f) A. D. Burrows, A. S. Donovan, R. W. Harrington, M. F. Mahon, *Eur. J. Inorg. Chem.* **2004**, 4686–4695; g) P. S. Mukherjee, D. Ghoshal, E. Zangrando, T. Mallah, N. R. Chaudhuri, *Eur. J. Inorg. Chem.* **2004**, 4675–4680.
[3] a) S. Konar, P. S. Mukherjee, E. Zangrando, M. G. B. Drew, C. Diaz, J. Ribas, N. R. Chaudhuri, *Inorg. Chim. Acta* **2005**, *358*, 29–35; b) M. Pascu, F. Lloret, N. Avarvari, M. Julve, M. Andruh, *Inorg. Chem.* **2004**, *43*, 5189–5191; c) K. E. Holmes, P. F. Kelly, M. R. J. Elsegood, *Dalton Trans.* **2004**, 3488–3494; d) F. A. A. Paz, J. Klinowski, *Inorg. Chem.* **2004**, *43*, 3948–3954; e) M. Riou-Cavellec, C. Albinet, J.-M. Greneche, G. Ferey, *J. Mater. Chem.* **2001**, *11*, 3166–3171.
[4] a) C. Livage, C. Egger, M. Nogues, G. Ferey, *C. R. Acad. Sci. Paris, Chimie/Chemistry* **2001**, *4*, 221–226; b) C. Bazzicalupi, A. Bencini, A. Bianchi, V. Fusi, E. Garcia-Espana, C. Giorgi, J. M. Llinares, J. A. Ramirez, B. Valtancoli, *Inorg. Chem.* **1999**, *38*, 620–621; c) M. McCann, J. F. Cronin, M. Devereux, G. Fergusson, *Polyhedron* **1995**, *14*, 2379–2387; d) G. A. Van Albada, J. G. Haasnoot, J. Reedijk, M. Biagini-Cingi, A. M. Manotti-Lanfredi, F. Ugozzoli, *Polyhedron* **1995**, *14*, 2467–2473.
[5] a) F. A. Cotton, J. P. Donahue, C. Lin, C. A. Murillo, *Inorg. Chem.* **2001**, *40*, 1234–1244; b) F. A. Cotton, C. Lin, C. A. Murillo, *Inorg. Chem.* **2001**, *40*, 575–577; c) F. A. Cotton, L. M. Daniels, C. Lin, C. A. Murillo, *J. Am. Chem. Soc.* **1999**, *121*, 4538–4539; d) F. A. Cotton, C. Lin, C. A. Murillo, *Inorg. Chem.* **2001**, *40*, 478–484; e) F. A. Cotton, L. M. Daniels, C. Lin, C. A. Murillo, *Chem. Commun.* **1999**, 841–842.
[6] a) H. K. Chae, W. G. Klemperer, T. A. Marquart, *Coord. Chem. Rev.* **1993**, *128*, 209–224; b) B. Modec, J. V. Brenčič, *J. Cluster Sci.* **2002**, *13*, 279–302.
[7] a) B. Modec, J. V. Brenčič, E. M. Burkholder, J. Zubieta, *Dalton Trans.* **2003**, 4618–4625; b) M. J. Manos, A. D. Keramidas, J. D. Woollins, A. M. Z. Slawin, T. A. Kabanos, *J. Chem. Soc., Dalton Trans.* **2001**, 3419–3420; c) M. J. Manos, J. D. Woollins, A. M. Z. Slawin, T. A. Kabanos, *Angew. Chem. Int. Ed.* **2002**, *41*, 2801–2805; d) E. Dumas, C. Sassoye, K. D. Smith, S. C. Sevov, *Inorg. Chem.* **2002**, *41*, 4029–4032.
[8] B. Modec, J. V. Brenčič, D. Dolenc, J. Zubieta, *J. Chem. Soc., Dalton Trans.* **2002**, 4582–4586.
[9] M.-Y. Lee, S.-L. Wang, *Chem. Mater.* **1999**, *11*, 3588–3594.
[10] L. A. Mundi, R. C. Haushalter, *Inorg. Chem.* **1990**, *29*, 2879–2881.
[11] R. L. Rardin, W. B. Tolman, S. J. Lippard, *New J. Chem.* **1991**, *15*, 417–430.
[12] B. Modec, J. V. Brenčič, *Inorg. Chem. Commun.* **2004**, *7*, 516–520.
[13] T. Glowiak, M. Sabat, H. Sabat, M. F. Rudolf, *J. Chem. Soc., Chem. Commun.* **1975**, 712.

 © 2005 Wiley-VCH Verlag GmbH & Co. KGaA, Weinheim

[14] B. Kamenar, M. Penavič, B. Markovič, *Acta Crystallogr., Sect. C* **1987**, *43*, 2275–2277.
[15] T. Shibahara, H. Kuroya, K. Matsumoto, S. Ooi, *Inorg. Chim. Acta* **1981**, *54*, L75–L81.
[16] The corresponding sums of the van der Waals radii are 3.27, 3.37, 3.30, 3.40, and 3.07 Å for O+Cl, O+Br, N+Cl, N+Br, and N+O, respectively. Data were taken from B. Douglas, D. McDaniel, J. Alexander, *Concepts and Models of Inorganic Chemistry*, 3rd ed., John Wiley & Sons, Inc., New York, **1994**, p. 102.
[17] A. Dolbecq, E. Cadot, F. Secheresse, *C. R. Acad. Sci. Paris, Serie llc, Chimie/Chemistry* **2000**, *3*, 193–197.
[18] B. Salignac, S. Riedel, A. Dolbecq, F. Secheresse, E. Cadot, *J. Am. Chem. Soc.* **2000**, *122*, 10381–10389.
[19] B. Kamenar, B. Korpar-Čolig, M. Penavič, *J. Chem. Soc., Dalton Trans.* **1981**, 311–313.
[20] M. Cindrič, V. Vrdoljak, B. Prugovečki, B. Kamenar, *Polyhedron* **1998**, *17*, 3321–3325.
[21] B. Modec, J. V. Brenčič, J. Koller, *Eur. J. Inorg. Chem.* **2004**, 1611–1620.
[22] A. Dolbecq, B. Salignac, E. Cadot, F. Secheresse, *Bull. Pol. Acad. Sci. Chem.* **1998**, *46*, 237–271.
[23] C. G. Kim, D. Coucouvanis, *Inorg. Chem.* **1993**, *32*, 2232–2233.
[24] a) K. Nakamoto, *Infrared and Raman Spectra of Inorganic and Coordination Compounds. Part B: Applications, in: Coordination, Organometallic, and Bioinorganic Chemistry*, 5th ed., John Wiley & Sons, Inc., New York, **1997**, p. 59–62; b) G. B. Deacon, R. J. Phillips, *Coord. Chem. Rev.* **1980**, *33*, 227–250.
[25] B. Modec, J. V. Brenčič, J. Zubieta, *J. Chem. Soc., Dalton Trans.* **2002**, 1500–1507.
[26] B. Modec, J. V. Brenčič, *Eur. J. Inorg. Chem.* **2005**, 1698–1709.
[27] G. R. Hanson, A. A. Brunette, A. C. McDonell, K. S. Murray, A. G. Wedd, *J. Am. Chem. Soc.* **1981**, *103*, 1953–1959.
[28] Z. Otwinowski, W. Minor, *Methods Enzymol.* **1997**, *276*, 307–326.
[29] G. M. Sheldrick, *SHELXS-97* and *SHELXL-97*, Universität Göttingen, **1997**.
[30] *WinGX*. L. J. Farrugia, *J. Appl. Crystallogr.* **1999**, *32*, 837–838.
[31] *ORTEP3* for Windows. L. J. Farrugia, *J. Appl. Crystallogr.* **1997**, *30*, 565.
[32] G. M. Sheldrick, *SHELXTL*, Bruker Analytical Instruments, Madison, Version 5.1, **1997**.

Received: May 24, 2005
Published Online: September 8, 2005

 © 2005 Wiley-VCH Verlag GmbH & Co. KGaA, Weinheim

The Redox Chemistry of (N^1-[3-(2-aminoethylimino)-1,1-dimethylbutyl]ethane-1,2-diamine)nickel(II) Perchlorate, $Ni^{II}L^1(ClO_4)_2$, in Aqueous Solutions – A Pulse Radiolytic and an Electrochemical Study

Yael Albo,[a] Eric Maimon,*[a,b] Israel Zilbermann,[a,b] Magal Saphier,[a,b] Haim Cohen,[a,c] and Dan Meyerstein*[a,c]

Keywords: Nickel complexes / Pulse radiolysis / Electrochemistry

The ligand (N^1-[3-(2-aminoethylimino)-1,1-dimethylbutyl]-ethane-1,2-diamine), L^1, induces a high ligand field on the central Ni^{II} ion. Thus it is relatively easy to oxidize $(Ni^{II}L^1)^{2+}$. However, the kinetic stability of the $Ni^{III}L^1$ complexes is considerably lower than that of their analogous macrocyclic complexes. This difference in stabilities is attributed to the less rigid ligand framework, which facilitates the oxidation of ligand.
(© Wiley-VCH Verlag GmbH & Co. KGaA, 69451 Weinheim, Germany, 2005)

Introduction

The thermodynamic and kinetic stabilization of uncommon oxidation states of transition metal ions has been studied extensively. It has been suggested that for tetraaza aliphatic ligands a macrocyclic ligand frame sets the condition for the acceptance of high oxidation states,[1–3] which are not achievable in the case of the open tetraamine analogues. As a result there is not much information regarding the redox properties of transition metal complexes with open tetraamine ligands in aqueous solutions. Thus, there is an interest in expanding the knowledge of the ability of such ligands to stabilize uncommon oxidation states of transition metal ions. Herein the redox properties of the linear tetraamine Ni complex $Ni^{II}L^1(ClO_4)_2$ are investigated in aqueous solutions, and are compared to those of the tetraaza macrocyclic analogue $Ni^{II}L^2(ClO_4)_2$.

Results and Discussion

Characterization of $NiL^1(ClO_4)_2$

The complex was characterized by X-ray diffraction and by UV/Vis spectrophotometry. Spectral data of the complex at pH = 6.0 are summarized in Table 1. Spectral data of the $NiL^2(ClO_4)_2$ are included in the Table for comparison. It is interesting to note that the d-d bands of both complexes have the same λ_{max}, i.e. the two ligands impose the same ligand field on the central nickel ion. The electronic configuration of both complexes is low spin, i.e. the ligands impose a strong ligand field.

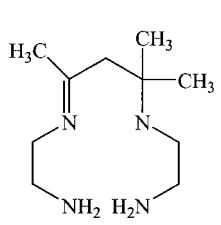

L^1

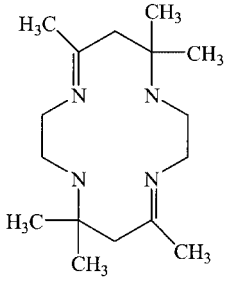

L^2

Table 1. UV/Vis spectrophotometric data for the $Ni^{II}L^1(ClO_4)_2$ and $Ni^{II}L^2(ClO_4)_2$ complexes.

	λ_{max} [nm]	ε [$M^{-1}cm^{-1}$]
$Ni^{II}L^1(ClO_4)_2$	436	70
	268	2000
	208	15000
$Ni^{II}L^2(ClO_4)_2$[18]	436	104
	238	7900
	213	17000

Crystal Structure

The ORTEP view of $[NiL^1(ClO_4)_2]$ is provided in Figure 1 and relevant geometric details are listed in Table 2. The complex is isolated as its perchlorate salt, and the Ni^{II} ion has a typical square-planar coordination geometry, as the bond angles N^1–Ni–N^4 and N^1–Ni–N^3 are 91.7° and 176°, respectively. The two perchlorate counterions are above and below the coordination plane, beyond bonding

[a] Chemistry Department, Ben Gurion University of the Negev, Beer Sheva, Israel
[b] Nuclear Research Centre Negev, Beer Sheva, Israel
E-mail: emymon@bgu.ac.il
[c] Biological Chemistry Department, College of Judea and Samaria, Ariel, Israel

distance. There is a hydrogen bonding interaction between the perchlorate counterions and the amines' hydrogen atoms of two neighboring complexes. These intermolecular interactions stabilize the structure of the complex. The Ni–N^3_{imine} bond length, 1.899 Å, is slightly shorter than the Ni–N^2_{amine} bond length. This is probably due to some back donation to the π system. The relative Ni–N bond lengths are clearly also affected by the N–H···O–Cl hydrogen bonds between the perchlorate anions and the N^1, N^2 and N^4 amines. The same effect was observed for the analogous macrocyclic complexes.[4]

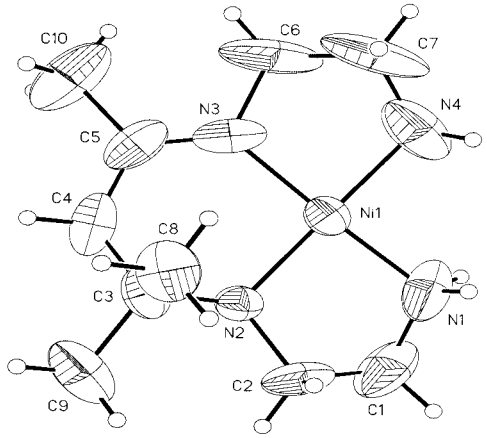

Figure 1. ORTEP view of $[NiL^1(ClO_4)_2]$, with displacement.

Table 2. Bond lengths [Å] and angles [°].

Ni(1)–N(1)	1.875(7)
Ni(1)–N(3)	1.899(8)
Ni(1)–N(2)	1.911(5)
Ni(1)–N(4)	1.910(7)
N(1)–Ni(1)–N(3)	176.6(4)
N(1)–Ni(1)–N(2)	87.6(3)
N(3)–Ni(1)–N(2)	95.0(3)
N(1)–Ni(1)–N(4)	91.7(4)
N(3)–Ni(1)–N(4)	85.7(4)
N(2)–Ni(1)–N(4)	179.3(4)

The small ellipsoids and the high order of the crystallographic structure indicate that only the R chiralic isomer was obtained, and not a racemic mixture of the two possible isomers.

Electrochemistry

A cyclic voltammetric study of $(NiL^1)^{2+}$ in aqueous solutions containing perchlorate and/ or sulfate ions was performed. The complex displays a quasi-reversible wave in the cyclic voltamogramm associated with the $Ni^{III/II}$ redox process. The redox potential of the couple in 0.1 M $NaClO_4$ is cathodically shifted by 250 mV relative to its tetraaza macrocyclic analogue,[5] $(NiL^2)^{2+}$, thus displaying a better ability of the open ligand frame to thermodynamically stabilize the trivalent state. This observation is probably due to contributions of the following factors:

a) The macrocyclic ligand contains two iminic bonds and is thus a softer base.

b) The macrocyclic complex has less hydrogen bonds with the solvent, i.e. is more hydrophobic.[6–9]

c) The open ligand is less rigid and thus has a better ability to satisfy the electronic and stereochemical demands of the central metal ion.

The redox potential in neutral solutions containing only $NaClO_4$ (0.1 M) is 950 mV vs. SCE. The complex is thermodynamically stabilized by sulfate ions (Figure 2), due to ligation of the anion to the complex $(NiL^1)^{3+}$. From the dependence of the redox potential on $[SO_4^{2-}]$ the slope of the plot of E vs. $\log[SO_4^{2-}]$ is 57 mV, thus it is concluded that the complex formed is $Ni^{III}L^1(SO_4)^+$ with an apparent stability constant $K_{app} = [(NiL^1SO_4)^+]/[(NiL^1)^{3+}][SO_4^{2-}] = 490 \pm 50\ M^{-1}$. This equilibrium constant was determined at pH = 6.0, as the divalent complex is unstable at lower pH values in sulfate containing solutions. The equilibrium constant for the macrocyclic complex $K = [\{NiL^2(SO_4)_2\}^-]/[(NiL^2)^{3+}][SO_4^{2-}]^2 > 10^5\ M^{-2}$ was obtained at pH = 1.2.[5] The lower value of the apparent equilibrium constant of the open complex probably stems from the higher pH value at which it was determined, as the equilibrium constant is pH dependent, as shown by the following relations:

$$NiL^1(H_2O)^{3+} \rightleftharpoons NiL^1OH^{2+}_{(aq)} + H^+_{(aq)}$$

$$K_1 = \frac{[(NiL^1OH)^{2+}][H^+]}{[(NiL^1)^{3+}]}$$

$$(NiL^1)^{3+}_{(aq)} + SO_4^{2-}{}_{(aq)} \rightleftharpoons NiLSO_4^+{}_{(aq)}$$

$$K_2 = \frac{[(NiL^1SO_4)^+]}{[(NiL^1)^{3+}][SO_4^{2-}]}$$

Combining the two equations:

$$K_2 = \frac{[(NiL^1SO_4)^+]K_1}{[SO_4^{2-}][(NiL^1OH)^{2+}][H^+]}$$

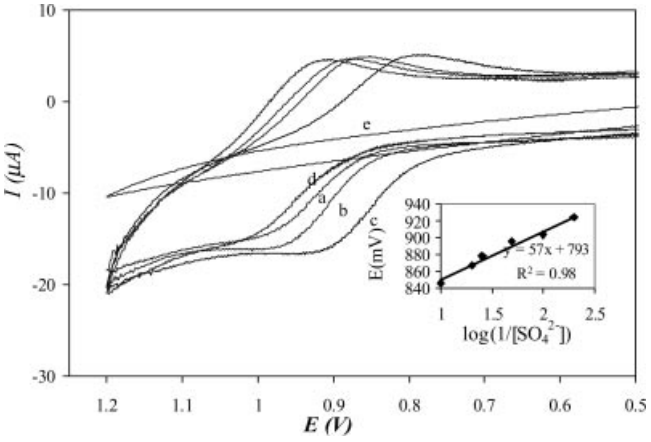

Figure 2. Cyclic voltammograms of the couple $Ni^{III/II}L^1$ in sulfate-containing solutions. Conditions: working electrode glassy carbon, reference SCE, scan rate 150 mV/s, ionic strength regulated with $NaClO_4$: $1 \cdot 10^{-3}$ M $Ni^{II}L^1$(a–d), 0.005 M Na_2SO_4 (a), 0.01 M Na_2SO_4 (b), 0.04 M Na_2SO_4 (c), 0.15 M $NaClO_4$ (d), 0.1 M Na_2SO_4 (e), pH = 6, I = 0.15.

The observation that two sulfate ions ligate to the macrocyclic complex, in comparison to the open complex, to

 © 2005 Wiley-VCH Verlag GmbH & Co. KGaA, Weinheim

which only one sulfate ion ligates might be attributed to the fact that the less rigid open ligand enables a tetragonal bipyramid conformation which is not possible for the macrocyclic complex.

Pulse Radiolysis Studies

The redox properties of the complex were further investigated using the pulse radiolysis technique. N_2O-saturated solutions in the presence and absence of bromide ions were irradiated.

Oxidation of the Complex by Hydroxyl Radicals

When N_2O-saturated solutions containing $(2–25)\cdot10^{-5}$ M $Ni^{II}L^1(ClO_4)_2$ are irradiated three consecutive reactions are observed. The rate of the formation of the first trivalent transient obeys a pseudo-first order rate law, Figure 3. From the linear dependence of the observed rate on $[(Ni^{II}L^1)^{2+}]$, a rate constant of $(5.0\pm1.0)\cdot10^9$ $M^{-1}s^{-1}$ is determined. The trivalent complex is obtained via:[10]

$$H_2O \xrightarrow{e,\gamma} e^-_{aq}(2.65), H^{\cdot}(0.60), {}^{\cdot}OH(2.65), H_2(0.45), H_2O_2(0.75)$$

where the values in parentheses give the relative yields of the primary products, number of molecules formed per 100 eV absorbed in the solution.

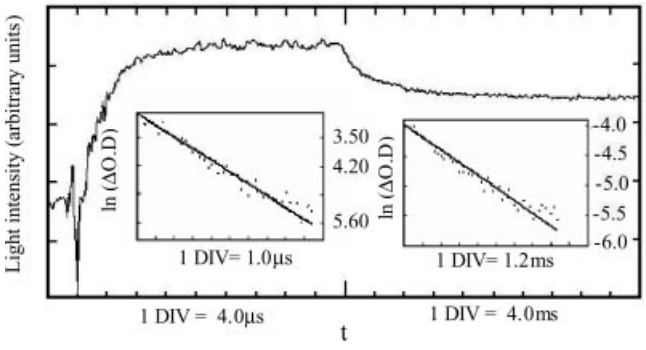

Figure 3. The formation and isomerization kinetics of $Ni^{III}L^1$. Conditions: $5.0\cdot10^{-5}$ M $(Ni^{II}L^1)^{2+}$, pH = 3.8, λ = 525 nm, N_2O-satd., pulse intensity 8.1 Gy.

$$e^-_{aq} + N_2O + H_2O \rightarrow N_2 + {}^{\cdot}OH + OH^- \quad (1)$$
$$k_1 = 8.7\cdot10^9\ M^{-1}s^{-1}[11]$$

$$Ni^{II}L^1 + {}^{\cdot}OH \rightarrow Ni^{III}L^1{}_{aq} + OH^- \quad (2)$$
$$k_2 = 5.0\cdot10^9\ M^{-1}s^{-1}$$

(The rate of the analogous reaction for the macrocyclic complex is $9\cdot10^9$ $M^{-1}s^{-1}$.[12]) The second reaction, which obeys a first order rate law with a rate which is independent of the complex concentration, causes a significant change in the spectrum of the $Ni^{III}L^1{}_{aq}$ complex (Figure 4). This reaction is attributed to the isomerization of the complex from a pentacoordinated geometry to an octahedral geometry in analogy[12] to the observations for $Ni^{III}L^2{}_{(aq)}$.

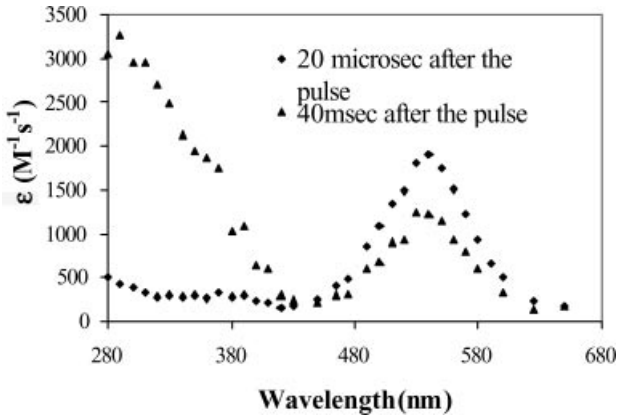

Figure 4. Spectra of $Ni^{III}L^1$ and $(Ni^{III}L^1)_R$. Conditions: $1\cdot10^{-4}$ M $(Ni^{II}L^1)^{2+}$, pH = 4.0 N_2O-satd., pulse intensity: 7.2 Gy.

The absorbance of the product of reaction (3), $(Ni^{III}L^1)_R$, depends on the pH value (Figure 5). The results indicate a pK_a of 4.3 ± 0.2 for the complex formed after the first reaction, reaction (2). It is suggested that this pK_a is due to equilibrium (4). The pK_a value for the complex with the macrocyclic ligand is lower (3.4).[12] The strong absorption band of $Ni^{III}L^1(OH)^{2+}$ at 540 nm is attributed to a d-d transition in the highly unsymmetrical $Ni^{III}L^1(OH)^{2+}$ complex. It is thus found that the basic complex $Ni^{III}L^1(OH)^{2+}$ does not isomerize. Again this finding is analogous to that reported earlier for $Ni^{III}L^2(OH)^{2+}$.[12]

$$Ni^{III}L^1\ aq \rightarrow (Ni^{III}L^1aq)_R \quad (3)$$
$$k_3 = 190\ s^{-1}$$

$$(Ni^{III}L^1)_{aq}{}^{3+} \rightleftharpoons Ni^{III}L(OH)^{2+} + H_3O^+ \quad (4)$$

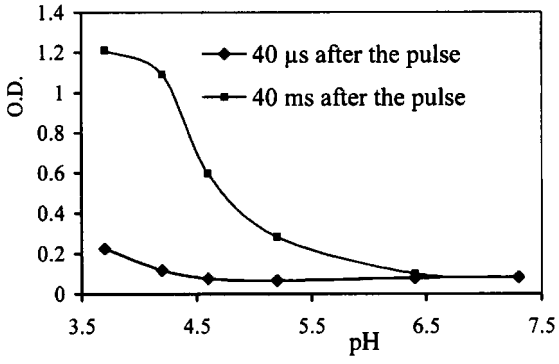

Figure 5. Optical densities of transient as a function of the pH value. Conditions: $2.5\cdot10^{-4}$ M $(Ni^{II}L^1)^{2+}$, λ = 300 nm, N_2O-satd., pulse intensity 32 Gy.

Clearly the formation of the red Ni^{III} transient in this study is not due to the macrocyclic effect and not to the favorable preorientation of the donor atoms in the 14-membered tetraaza macrocyclic ligand as proposed in the literature.[13]

The third reaction occurs on a time scale of seconds, obeys a second order rate law and is base catalyzed. This reaction results in the disappearance of the spectrum of the in-

 © 2005 Wiley-VCH Verlag GmbH & Co. KGaA, Weinheim

termediate and is attributed to the decomposition of the trivalent complex. It is proposed that the decomposition mechanism is as described in reaction (5).

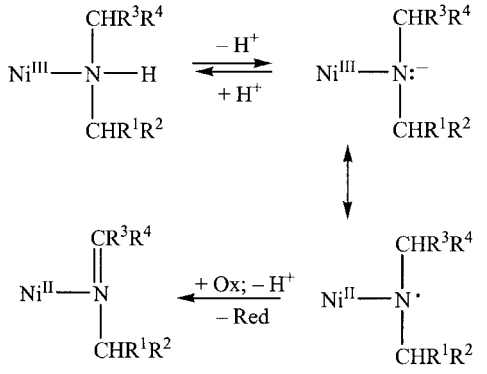

(5)

A linear dependence of the observed second-order rate constant on [OH^-] is observed, but the slope is 0.25 (Figure 6), i.e. considerably smaller than a slope of 1 which is expected according to this mechanism. This discrepancy is attributed to the pK_a of the tervalent complex, reaction (4) and probably to another pK_a i.e. to the formation of $Ni^{III}L^1(OH)_2^+$. Alternatively there is another decomposition mechanism, which does not require the loss of a proton.

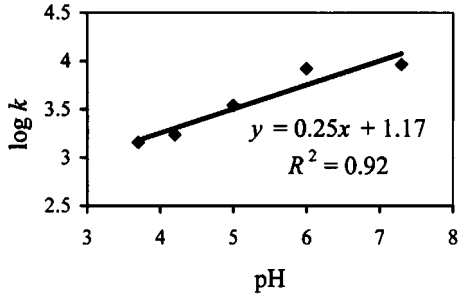

Figure 6. Decomposition rate constant as a function of the pH value. Conditions: $2.5\cdot10^{-4}$ M $(Ni^{II}L^1)^{2+}$, N_2O-satd., pulse intensity: 7.2 Gy.

The oxidation mechanism by the hydroxyl radicals and the mechanism of decomposition of the trivalent complex and its products are similar to those of its macrocyclic analogue.[12] However the oxidation product of $(Ni^{II}L^1)^{2+}$ is less stable.

Oxidation of the Complex by $Br_2^{\cdot-}$ Ion Radicals

As hydroxyl radicals might, at least partially, react also via hydrogen abstraction from the organic ligands it was decided to use also $Br_2^{\cdot-}$ as an oxidizing agent [$E^0(Br_2^{\cdot-}/2Br^-)$ = +1.63 V vs. N.H.E[11]]. N_2O-saturated solutions containing 0.01–0.1 M NaBr, $(0.1–2.0)\cdot10^{-4}$ M $Ni^{II}L^1(ClO_4)_2$ were irradiated. The first reaction observed obeys a first order rate law, with a rate proportional to $[(Ni^{II}L^1)^{2+}]$. The spectrum of the transient formed in this reaction differs considerably from that of $(Ni^{III}L^1)^{3+}$, Figure 7 and 4, and therefore it is proposed that $Ni^{III}LBr^{2+}$ is formed in this reaction, see (8).

$$^{\cdot}OH + Br^- \rightleftharpoons OHBr^{\cdot-} \quad (6)$$

$$OHBr^{\cdot-} + Br^- + H^+ \rightarrow Br_2^{\cdot-} + H_2O \quad (7)$$

$k > 10^9$ M^{-1}s^{-1} at pH $\leq$ 9.5

$$(Ni^{II}L^1)^{2+} + Br_2^{\cdot-} \rightarrow (Ni^{III}L\text{–}Br)_{aq}^{2+} + Br^- \quad (8)$$

$k = (7.5\pm2.0)\cdot10^9$ M^{-1}s^{-1}

(The rate of the analogous reaction for the macrocyclic complex is $2.5\cdot10^9$ M^{-1}s^{-1}.[12])

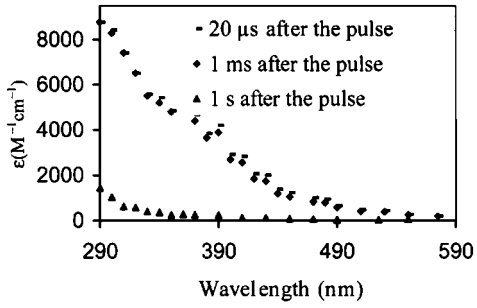

Figure 7. Spectra at different times after the pulse in the bromide-containing system. Conditions: $1\cdot10^{-4}$ M $(Ni^{II}L^1)^{2+}$, 0.1 M NaBr (for the micro- and milliseconds time scales), 0.01 M NaBr (1 second after the pulse), pH = 3.8, N_2O-satd., pulse intensity 8.2 Gy.

The second reaction observed also obeys a first order rate law and its rate is proportional to [Br^-], Figure 8; the large intercept suggests that this is an equilibrium process, see (9).

$$(Ni^{III}L^1Br)^{2+}_{(aq)} + Br^- \rightleftharpoons Ni^{III}L^1Br_2^+ \quad (9)$$

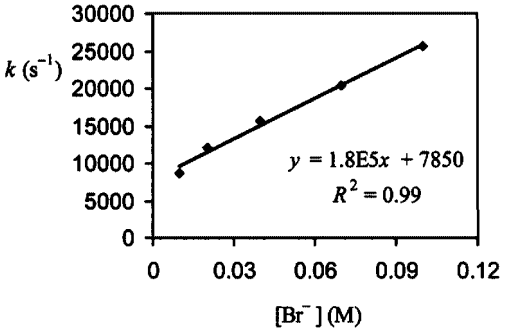

Figure 8. Observed rate as a function of [Br^-]. Conditions: $1\cdot10^{-4}$ M $(Ni^{II}L^1)^{2+}$, (0.01–0.1) M NaBr, pH = 3.8, ionic strength of 0.1 M adjusted by $NaClO_4$, N_2O-satd., pulse intensity 7.1 Gy, λ = 500 nm.

The spectrum of the product of the transient formed in reaction (9) is very similar to that formed in reaction (8), Figure 7. This is reasonable as the major band observed is clearly due to a LMCT transition. The slight shift to the blue is attributed to the lowering of the redox potential of the $Ni^{III/II}$ couple by the binding of a second bromide. From the slope and intercept in Figure 8 one obtains $k_9 = (1.8\pm0.2)\cdot10^5$ M^{-1}s^{-1} and $K_9 = 23\pm10$ M^{-1}.

The oxidation mechanism by the $Br_2^{\cdot-}$ ion radicals of the macrocyclic complex is different. In this case only one bromide ion ligates as an axial ligand, and the number of reac-

 © 2005 Wiley-VCH Verlag GmbH & Co. KGaA, Weinheim

tions occurring and the reaction rate constants are pH-dependent.[12]

The decomposition reaction of $Ni^{III}L^1Br_2^+$ obeys a second order rate law, with a rate independent on the divalent complex concentration and weakly dependent on pH and bromide concentration [k = $9.9\cdot10^5$ $M^{-1}s^{-1}$, $2\cdot10^{-4}$ M $(Ni^{II}L^1)^{2+}$, 0.01 M NaBr, pH = 3.8; k = $9.8\cdot10^5$ $M^{-1}s^{-1}$, $1\cdot10^{-4}$ M $(Ni^{II}L^1)^{2+}$, 0.01 M NaBr, pH = 3.8; k = $3.6\cdot10^6$ $M^{-1}s^{-1}$, $1\cdot10^{-4}$ M $(Ni^{II}L^1)^{2+}$, 0.1 M NaBr, pH = 3.8; k = $1.7\cdot10^4$ $M^{-1}s^{-1}$, $1\cdot10^{-4}$ M $(Ni^{II}L^1)^{2+}$, 0.01 M NaBr, pH = 7.0]:

$$2\ Ni^{III}L^1Br_2^{+} \longrightarrow \begin{cases} 2\ (Ni^{II}L^1)^{2+} + Br_2 + 2\ Br^- \ (Br^- + BrO^-) \\ (Ni^{II}L^1)^{2+} + Ni^{II}L_{-2H}^{2+} + 4\ Br^- + H^+ \end{cases} \quad (10)$$

The mechanism of decomposition of the trivalent macrocyclic complexes in the presence of bromide differs considerably. Comparison of the decomposition reaction shows that the rate of decomposition in the case of the open ligand is slightly higher at acidic pH values, and is much higher in neutral solutions than that of the analogous macrocyclic complex. The dependence of the rate on the bromide concentration is smaller in the case of the open ligand frame, both in acidic and neutral solutions. For the open ligand the decomposition reaction is second order in the whole pH range, while it is first order in neutral solution in the macrocyclic system. The difference in the kinetic stabilities of the two complexes is attributed to the less rigid frame of the open ligand. The formation of $Ni^{II}L_{-2H}^{2+}$ requires the formation of a C–N double bond, i.e. a significant change in geometry, which is facilitated by the less rigid open ligand.[14] This conclusion is in agreement with the observation that the stabilities of the isomers of Ni^{III}(5,7,7,12,14,14-hexamethyl-1,4,8,11-tetraaazacyclotetradecane) differ considerably.[15]

Concluding Remarks

In conclusion it was found that the less rigid open ligand has a better ability to adjust itself to the structure of each valence, and as such it thermodynamically stabilizes the trivalent state better than its macrocyclic analogue, although the oxidation product is less kinetically stable.

Experimental Section

Materials: All the chemicals used were of AR grade and were used without further treatment. All solutions were prepared with deionized water, which was further purified by passing through a Millipore Milli-Q water purification system, the final resistance being above 10 MΩ

Synthesis of $NiL^1(ClO_4)_2$: 0.2 mol $Ni(ClO_4)_2\cdot6H_2O$ and 0.4 mol of ethylenediamine were added to an excess of acetone (as the solvent). The solution was stirred and heated under reflux for 4 days. The first crude orange crystals formed were filtered and washed in methanol. Single crystals suitable for X-ray diffraction were obtained from recrystalization in methanol.

The tetrachlorozincate salt of this complex was synthesized by Curtis and House using a different procedure.[16]

Electrochemical Measurements: Electrochemical studies were carried out using an EG&G Princeton Applied Research potentiostat/galvanostat, Model 263, operated by a Research Electrochemistry software EG&G PARC, using a three electrode assembly consisting of a glassy carbon electrode (A = 0.07 cm^2), a Pt wire auxiliary electrode and a SCE as the reference electrode. The solutions were purged with argon.

Pulse Radiolysis: The solutions were handled by the syringe technique. Deaeration was performed by bubbling N_2O through the solutions.

The experiments were carried out at the linear electron accelerator facility of the Hebrew University of Jerusalem; 0.5–1.5 μs, 5 MeV and 200 mA pulses were used. The dose per pulse was in the range of 7–32 Gy/pulse. The experimental setup and the techniques used for evaluating the results have been described elsewhere in detail.[17]

X-ray Structure Determination: The data were collected on a Bruker SMART system with 1 K CCD detector. Mo-$K\alpha$ radiation was used with a graphite monochromator. The data were reduced using SAINT, absorption corrections were performed using SADABS, and then solved with SHELXL and refined using SHELXL. The non-hydrogen atoms were located from the difference map and refined anisotropically. The hydrogen atoms were located from the difference map and then allowed to refine using a riding model. An ORTEP view of the molecules is provided in Figure 1, and geometry details are listed in Table 2.

***C*rystal and Structure Refinement Data:** Crystal data $[NiL^1(ClO_4)_2]$: $C_{10}H_{24}Cl_2N_4NiO_8$ (457.92), monoclinic, space group $P21/c$, a = 10.3442(17), b = 12.540(2), c = 14.381(2) Å, $\alpha = \gamma$ = 90°, β = 101.795(5)°, V = 1826.1(5) $Å^3$, D_c (Z = 4) = 1.658 g/cm^3, crystal size $0.97\times0.77\times0.41$ mm^3, hkl range –8 to 13, –16 to 16, –19 to 19, N = 14613, N_{ind} = 4538 (R_{int} = 0.0412), residuals $R_1(F)$ 0.0674, wR_2 = 0.2067, GoF(all) = 1.307, Dr (min./max.) = 0.964/–0.664 $e\cdot A^3$.

CCDC-238587 contains the supplementary crystallographic data for this paper. These data can be obtained free of charge from the Cambridge Crystallographic Data Center via www.cccdc.cam.ac.uk/data_request/cif.

Acknowledgments

We thank Dr. Janice Rubin-Preminger for her X-ray structure determination. This study was supported in part by a grant from the Budgeting and Planning Committee of the Council of Higher Education and the Israel Atomic Energy Commission. D. M. wishes to express his thanks to Mrs. Irene Evens for her ongoing interest and support.

[1] I. Zilbermann, G. Golub, H. Cohen, D. Meyerstein, *J. Chem. Soc., Dalton Trans.* **1997**, *2*, 141–143.
[2] F. V. Lovecchio, E. S. Gore, D. H. Busch, *J. Am. Chem. Soc.* **1974**, *96*, 3109–3118.
[3] A. Bencini, L. Fabbrizzi, A. Poggi, *Inorg. Chem.* **1981**, *20*, 2544–2549.
[4] D. J. Szalda, E. Fujita, *Acta Crystalografica, Sect. C: Crystal Structure Communications* **1992**, *48*, 1767–1771.
[5] E. Zeigerson, G. Ginzburg, *J. Electroanal. Chem.* **1981**, *127*, 113–126.

 © 2005 Wiley-VCH Verlag GmbH & Co. KGaA, Weinheim

[6] I. Zilbermann, E. Maimon, H. Cohen, D. Meyerstein, *Chem. Rev.* **2005**, *105*, *2609*–2625.
[7] D. Meyerstein, *Coord. Chem. Rev.* **1999**, *186*, 141–147.
[8] G. Golub, H. Cohen, P. Paoletti, A. Bencini, A. Messory, I. Bertini, D. Meyerstein, *J. Am. Chem. Soc.* **1995**, *117*, 8353–8361.
[9] T. Clark, M. Hennemann, R. van Eldik, D. Meyerstein, *Inorg. Chem.* **2002**, *41*, 2927–2935.
[10] L. J. Kirschenbaum, D. Meyerstein, *Inorg. Chem.* **1980**, *19*, 1973.
[11] G. V. Buxton, C. L. Greenstock, W. P. H. Helman, A. R. Ross, *J. Phys. Chem. Ref. Data* **1988**, *17*, 513.
[12] M. Jaacobi, D. Meyerstein, J. Lillie, *Inorg. Chem.* **1979**, *18*, 429–433.
[13] G. De Santis, L. Fabbrizzi, A. Poggi, A. Taglietti, *Inorg. Chem.* **1994**, *33*, 134–139.
[14] D. Shamir, I. Zilbermann, E. Maimon, D. Meyerstein, *Eur. J. Inorg. Chem.* **2004**, 4002–4005.
[15] E. Zeigerson, G. Ginzburg, J. Y. Becker, L. J. Kirschenbaum, H. Cohen, D. Meyerstein, *Inorg. Chem.* **1981**, *20*, 3988–3992.
[16] D. A. House, N. F. Curtis, *J. Am. Chem. Soc.* **1962**, *84*, 3248–3250.
[17] S. Goldstein, G. Czapski, H. Cohen, D. Meyerstein, *Inorg. Chem.* **1992**, *31*, 2439–2444.
[18] E. Zeigerson, Ph. D. Thesis, Ben-Gurion Gurion University of the Negev, Beer-Sheva, **1980**

Received: June 6, 2005
Published Online: September 13, 2005

 © 2005 Wiley-VCH Verlag GmbH & Co. KGaA, Weinheim

Ruthenium Complexes Containing Chiral N-Donor Ligands as Catalysts in Acetophenone Hydrogen Transfer – New Amino Effect on Enantioselectivity

Montserrat Gómez,*[a] Susanna Jansat,[a] Guillermo Muller,[a] Gabriel Aullón,[a] and Miguel Angel Maestro[b]

Keywords: Ruthenium / Chiral N-donors / Asymmetric catalysis / NMR spectroscopy / Density functional calculations

New *p*-cymene ruthenium species containing chiral amino alcohols (**1**–**3**), primary (**4**–**7**) and secondary (**8**, **9**) amino-oxazolines, were tested as catalysts in the hydrogen transfer of acetophenone, using 2-propanol as the hydrogen source. A remarkable effect on the enantioselectivity, but also on the activity, was observed depending on the amino-type oxazoline, Ru/**8** and Ru/**9** being low active and nonselective catalytic systems, in contrast to their primary counterpart Ru/**5**. Complexes containing amino-oxazolines (**10**–**12**) were prepared and fully characterized, both in solution and in solid state. The X-ray structure was determined for (S_{Ru},R_C)-**10**. The diastereomeric ratios observed for complexes **10** and **11** were determined by ^{1}H NMR and confirmed by means of structural modeling (semi-empirical PM3(tm) level). DFT theoretical calculations for the transition states involved in the hydrogen transfer process proved the important differences in their relative populations, which could justify the enantioselectivity divergences observed between primary and secondary amino-oxazoline ruthenium systems.

(© Wiley-VCH Verlag GmbH & Co. KGaA, 69451 Weinheim, Germany, 2005)

Introduction

Chiral hydrogen transfer of prochiral ketones catalyzed by transition metals has emerged as a convenient methodology to give enantiomerically pure secondary alcohols, based on the simplicity of the process and the safety of the reagents.[1]

From a mechanistic point of view, three alternatives have been proposed for metal-catalyzed hydrogen transfer of ketones (Scheme 1): i) direct transfer of a hydrogen atom of the alcohol to the carbonyl carbon through a concerted process involving a six-membered cyclic transition state (**a**), a mechanism accepted for Al-catalyzed Meerwein-Ponndorf-Verley reductions and generally for main group elements;[2] ii) stepwise mechanism through the formation of a hydride metal intermediate and the migratory insertion of a C=O into a M–H bond (**b**), a mechanism suggested for rhodium(I) and ruthenium free-arene systems;[3] and iii) a concerted mechanism where a proton and a hydride are simultaneously transferred to the unsaturated substrate (**c**), a mechanism proposed by Noyori for the Ru arene derivatives.[4]

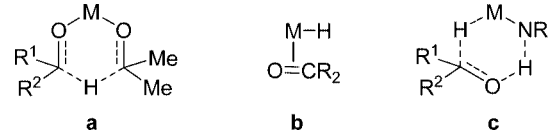

Scheme 1. Key species involved in the three main mechanisms [concerted (**a**) and (**c**), and stepwise (**b**)] of metal-catalyzed hydrogen transfer (spectator ligands on the metal have been omitted for clarity).

The efficient catalytic system described by Noyori and co-workers, Ru/TsDPEN (TsDPEN=*N*-(*p*-tolylsulfonyl)-1,2-diphenylethylendiamine), suggests the requirement of amino groups in order to achieve high activities.[4,5] Other related works showed similar trends.[6] In order to understand the reaction pathway, theoretical studies have been reported on the basis of the ruthenium complex structures and their reactivity, for systems containing primary and secondary amines.[7] These systems are in agreement with a metal–ligand bifunctional mechanism.

We previously tested *p*-cymene ruthenium systems containing chiral bis(oxazolines) as catalysts in the acetophenone reduction processes, in particular in hydrogenation transfer.[8] Moderated enantiomeric excesses were obtained (*ee* up to 38%), and the best chiral auxiliaries were found among those containing two carbon spacers between both oxazoline fragments. As stated above, the presence of NH_2 or NH groups in the auxiliaries is fundamental for catalytic reactivity.[4b] For that reason, and following our research with oxazoline ligands,[9] we proposed to use primary (**4**–**7**)

[a] Departament de Química Inorgànica, Universitat de Barcelona, Martí I Franquès 1-11, 08028 Barcelona, Spain
Fax: +34-93-4907725
E-mail: montserrat.gomez@qi.ub.es
[b] Departamento de Química Fundamental, Universidade da Coruña,
Campus da Zapateira, s/n, 15071 A Coruña, Spain

and secondary (**8**–**9**) amino-oxazolines in order to improve the results previously obtained (Figure 1). The amino alcohol precursors of the corresponding oxazolines were also tested (**1**–**3**). In order to rationalize the catalytic results found, a structural study of ruthenium complexes was carried out, both in solution (by means of NMR spectroscopy) and in solid state (by means of X-ray diffraction). The diastereomeric distributions observed in solution were confirmed by structural modeling (PM3(tm) level). In addition, a theoretical study (DFT level) was also carried out concerning the relative energies of the corresponding transition states responsible for the hydrogen transfer from catalytic species to the prochiral ketone.

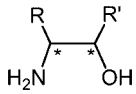

(*R*)-**1**, R = Et, R' = H
(*S*)-**2**, R = *i*Pr, R' = H
(*S,S*)-**3**, R = CH_2OH, R' = Ph

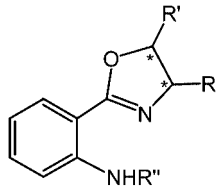

(*R*)-**4**, R = Et, R' = R" = H
(*S*)-**5**, R = *i*Pr, R' = R" = H
(*S,S*)-**6**, R = CH_2OH, R' = Ph, R" = H
(*S,S*)-**7**, R = CH_2OSiMe_3, R' = Ph, R" = H
(*S*)-**8**, R = *i*Pr, R' = H, R" = *p*-tolylsulfonyl
(*S*)-**9**, R = *i*Pr, R' = H, R" = Me

Figure 1. Chiral amino alcohols (**1**–**3**) and amino-oxazolines (**4**–**9**).

Results and Discussion

Synthesis of Chiral Amino-Oxazoline Ligands

The optically pure amino-oxazolines **4** and **5** recently reported in the literature were prepared in one and three steps, respectively.[10] The standard Zn-catalyzed condensation of anthranilonitrile with the appropriated amino alcohol, followed for the synthesis of **4**,[10b] gave low yields for **5** and **6** (less than 30% after three days of reaction). But better results were obtained when the cyclization process took place under basic conditions in a mixture of glycerol and ethylenglycol in a one-step process (Scheme 2),[11] in contrast to the three-step synthetic route from isatoic anhydride.[10c] The one-pot synthesis gave a mixture of the expected oxazoline and the corresponding amide (oxazoline/amide 85:15 for **5** and 1:1 for **6**), which were separated by aqueous extractions (the oxazoline remains in the organic phase). The pure amide derived from L-valinol can be transformed to the corresponding oxazoline **5** by substitution of the hydroxyl group with *p*-tolylsulfonyl chloride and cyclization under basic conditions (0.5 M NaOH, in H_2O/MeOH 1:1) at room temperature for two days. The oxazoline **7** was easily obtained by silylation of **6** with $SiClMe_3$ in excellent yield. The secondary amine ligands, **8** and **9**, were obtained in two different synthetic ways. Ligand **8** was prepared from the primary amino-oxazoline **5** following the procedure described previously in the literature.[12] But analogous methodology using methyl iodide in place of *p*-toluenesulfonyl chloride failed to give **9**, which was isolated in good yield

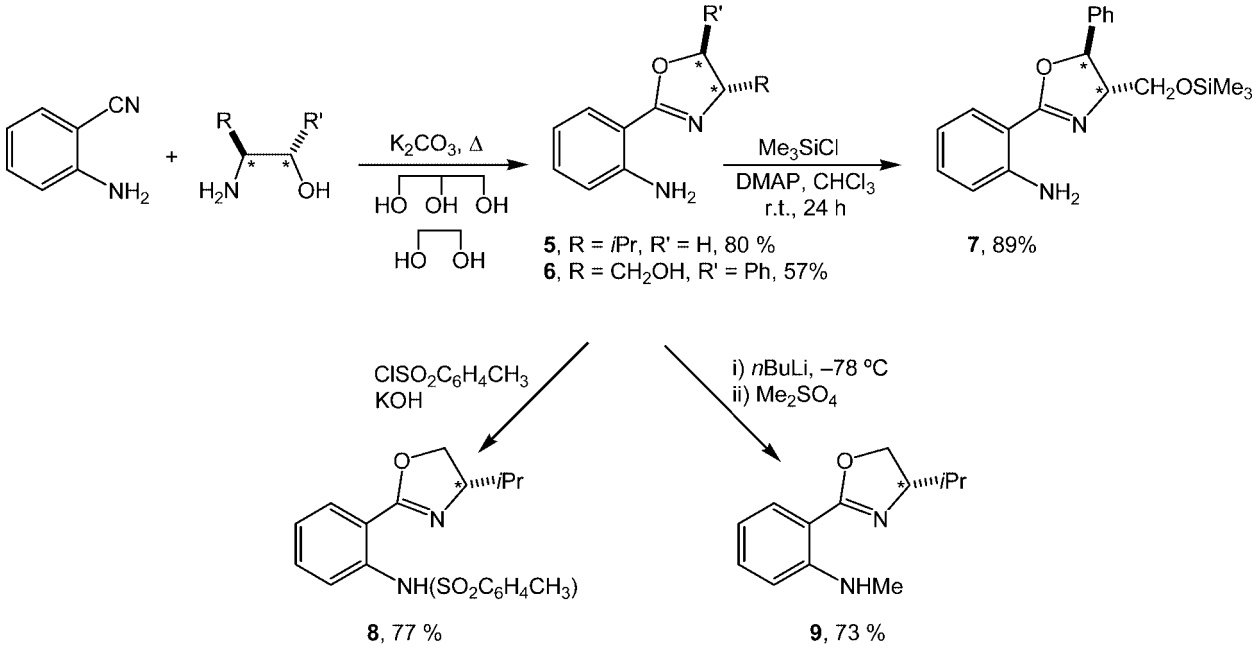

Scheme 2. Synthesis of primary (**5**–**7**) and secondary (**8**–**9**) chiral amino-oxazolines.

 © 2005 Wiley-VCH Verlag GmbH & Co. KGaA, Weinheim

in two steps, reacting dimethyl sulfate with the lithium derivative of **5** (Scheme 2).

Ruthenium Complexes

The cationic complexes **10**, **11** and **12**, of general formula [RuCl(*p*-cymene)(κ²-*N,N*-L)]Cl (where L = **4**, **5** and **8**, respectively) were synthesized from the dimeric *p*-cymene precursor and the appropriated amino-oxazoline (Scheme 3). Complexes **10** and **11** were obtained as a mixture of two diastereomers, since the ruthenium chiral center formed upon coordination of optically pure oxazoline ligand: (S_{Ru},R_C)- + (R_{Ru},R_C)-**10** and (S_{Ru},S_C)- + (R_{Ru},S_C)-**11**, as observed for analogous arene Ru complexes containing pyridino-oxazolines.[13] In solution, complex **12** shows at least three isomers, probably due to the N stereocenter. The complexes were fully characterized both in solid state and solution.

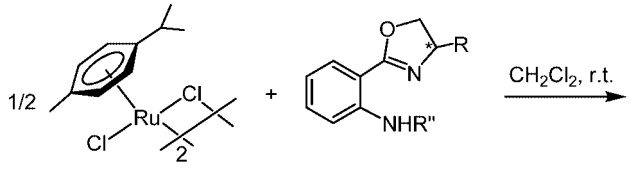

4, R = Et, R" = H
5, R = *i*Pr, R" = H
8, R = *i*Pr, R" = *p*-tolylsulfonyl

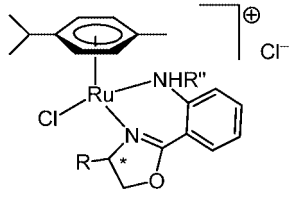

10, R = Et, R" = H
11, R = *i*Pr, R" = H
12, R = *i*Pr, R" = *p*-tolylsulfonyl

Scheme 3. Synthesis of ruthenium complexes (**10**–**12**) containing amino-oxazolines (**4**, **5**, **8**).

Single crystals of **10** were obtained by slow diffusion of hexane over a chloroform/dichloromethane solution of the complex (Figure 2). Selected bond lengths and angles are listed in Table 1. The absolute configuration of the ruthenium stereocenter is S_{Ru} [according to the priority sequence η⁶-arene > Cl > N_{ox}(1) > N_{amino}(2)].[14] The complex adopts a distorted three-legged "piano stool" geometry. The ruthenium atom is η⁶-coordinated to the *p*-cymene unit (calculated distance between the planar arene group and metal is 1.66 Å), and the other three positions are occupied by the two nitrogen (from the bidentated ligand) and chlorine atoms. The bond distances and angles are quite similar to those for the known analogous ruthenium complexes.[15] It is interesting to note the short intramolecular nonbonded distances of one amino hydrogen atom (H1B) with the oxazoline nitrogen and chlorine atoms: N_{amino}(1)–H(1B)···Cl(1) = 2.62 Å and N_{amino}(1)–H(1B)···N_{ox}(2) = 2.79 Å, shorter than the expected van der Waals separations (3.0 Å),[16] and consistent with hydrogen bonds.[17,18] These distances are significantly shorter than for H(1A): N_{amino}(1)–H(1A)···Cl(1) = 2.85 Å and N_{amino}(1)–H(1A)···N_{ox}(2) = 3.30 Å (the hydrogen positions were calculated, not found in the difference Fourier map). It is also significant that the nitrogen–axial hydrogen distance (N–H(1B) = 0.862 Å) is shorter than the nitrogen–equatorial hydrogen one (N–H(1A) = 0.869 Å), as observed for other related compounds.[5b]

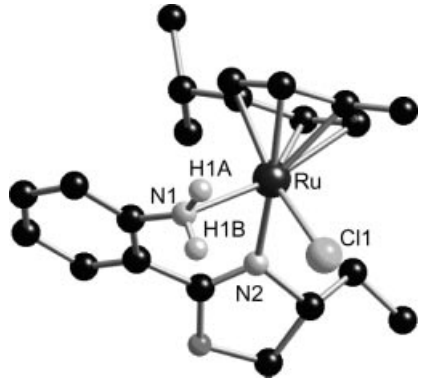

Figure 2. Molecular structure and atom labeling scheme for the cation of (S_{Ru},R_C)-**10**. Hydrogen atoms, except H1A, H1B, and the chloride contra-anion have been omitted for clarity.

Table 1. Selected bond lengths [Å] and angles [°] for (S_{Ru},R_C)-**10** (with esd's in parentheses).

Ru(1)–N(2)	2.110(7)
Ru(1)–N(1)	2.135(6)
Ru(1)–Cl(1)	2.401(2)
Ru(1)–C(17)	2.168(8)
Ru(1)–C(13)	2.177(8)
Ru(1)–C(16)	2.184(8)
Ru(1)–C(14)	2.209(8)
Ru(1)–C(15)	2.212(8)
Ru(1)–C(12)	2.225(9)
N(2)–Ru(1)–N(1)	80.5(3)
N(2)–Ru(1)–Cl(1)	83.2(2)
N(1)–Ru(1)–Cl(1)	83.7(2)

Conductivity measurements in acetonitrile for complexes **10** and **11** show the existence of 1:1 electrolytes in solution (about 50 $\Omega^{-1}cm^2mol^{-1}$).[19] The highest peak of positive FAB mass spectra corresponds to the cation [RuCl(*p*-cymene)L]⁺ (L = **4** for **10**; L = **5** for **11**).

^{1}H NMR spectra for both ruthenium complexes indicate the existence of two isomers in about 5:1 and 2:1 ratios for **10** and **11**, respectively. For complex **10** many signals appeared overlapped and consequently a complete assignment for both isomers was not possible, in contrast to complex **11** (see Experimental section for NMR spectroscopic data). The N_{amino}-coordination of the oxazoline ligand in **11** is proven by the different chemical shifts of the two N–H protons, for each isomer, analogously to Ru arene complexes containing amino alcohols.[20] The difference between both chemical shifts (more than 5 ppm) stands out, due to the intramolecular hydrogen bond between one N–H and the

 © 2005 Wiley-VCH Verlag GmbH & Co. KGaA, Weinheim

chlorine atom coordinated to the metal (see above, X-ray discussion). As mentioned above, the diastereomers are due to the two chiral centers, the oxazoline carbon stereocenter (*R* or *S* for **4** or **5**, respectively), and the Ru atom. These isomers are exchanged at a low rate in solution, because no isomeric composition change was observed in the noncoordinating solvent ($CDCl_3$) in the temperature range studied (223–298 K). When a 2-propanol solution of **11** was treated at 60 °C for three hours, slight changes in the diastereomeric composition were detected (ratio of both isomers about 2.5:1).

The ^{1}H NMR spectrum for **12** shows the existence of at least three isomers in a ratio of about 4:1:1 at room temperature. A complete assignment could be done only for the major isomer. At lower temperatures (temperature range studied: 298–233 K), the signals corresponding to the minor isomers became larger and the relative ratio could not be determined. Upon coordination of the amino nitrogen atom (NHR, R = *p*tolylsulfonyl) to the ruthenium, a new stereocenter is formed, which could be the factor responsible for the presence of more isomers: (S_{Ru},S_C,R_N)-**12**, (S_{Ru},S_C,S_N)-**12**, (R_{Ru},S_C,R_N)-**12**, and (R_{Ru},S_C,S_N)-**12**.

In order to evaluate the relative isomer stability for complexes **10** and **11**, semi-empirical optimizations [PM3(tm) level] were carried out for both isomers of each complex.[21] The energy difference between the two diastereomers is 1.029 and 0.685 kcal mol^{-1} for **10** and **11**, respectively, the most stable isomers being (R_{Ru},R_C)-**10** and (S_{Ru},S_C)-**11**. The Boltzmann species distribution (about 6:1 and 3:1 for **10** and **11**, respectively, at 298 K) is in good accordance with the ratio observed in the ^{1}H NMR spectra (see above). For both cases, the most stable diastereomer corresponds to the configuration at the Ru atom, that leads to the oxazoline substituent at the stereocenter pointing away from the arene group. To prove the steric hindrance between *p*-cymene and the remaining ligands, the rotation effect around the Ru-arene axis has been considered for both diastereomers. In Figure 3, calculated formation enthalpies versus the dihedral angle defined by C(methyl of *p*-cymene)–*p*-cymene ring–ruthenium–chlorine are plotted for both isomers of each complex **10** and **11**. For the epimer in which the ethyl or isopropyl oxazoline group points toward the arene [(S_{Ru},R_C)-**10** and (R_{Ru},S_C)-**11**, respectively], higher energy intermediates are observed than for the other isomer [(R_{Ru},R_C)-**10** and (S_{Ru},S_C)-**11**, respectively]. In addition, these hills show higher energy for (R_{Ru},S_C)-**11** than for (S_{Ru},R_C)-**10**, due to the more important steric hindrance of the isopropyl than the ethyl group.

Ru-Catalyzed Enantioselective Hydrogen Transfer of Acetophenone

The Ru/amino alcohol (**1**–**3**) and Ru/amino-oxazoline (**4**–**9**) catalytic systems were tested in the asymmetric transfer hydrogenation of acetophenone (**I**), using 2-propanol as the hydrogen source under basic conditions (Scheme 4).[22] The catalytic results are summarized in Table 2. The catalyses were performed with in situ prepared catalyst precursor, [Ru_2Cl_4(*p*-cymene)$_2$], and the corresponding chiral ligand, in a Ru/**L*** ratio 1:2. In the absence of *t*BuOK, Ru/**L*** systems were inactive. Conversions of acetophenone (**I**) and enantiomeric excesses of 1-phenylethanol (**II**) were monitored during the catalytic reaction by GC.

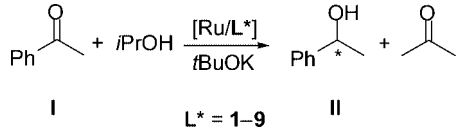

Scheme 4. Hydrogen transfer of acetophenone (**I**) catalyzed by Ru/**L*** systems (**L*** = **1**–**9**).

Concerning the catalytic behavior of Ru/amino alcohols (entries 1–5), the β-monosubstituted amino alcohols, **1** and **2**, are more active than the α,β-disubstituted one, **3** (entries

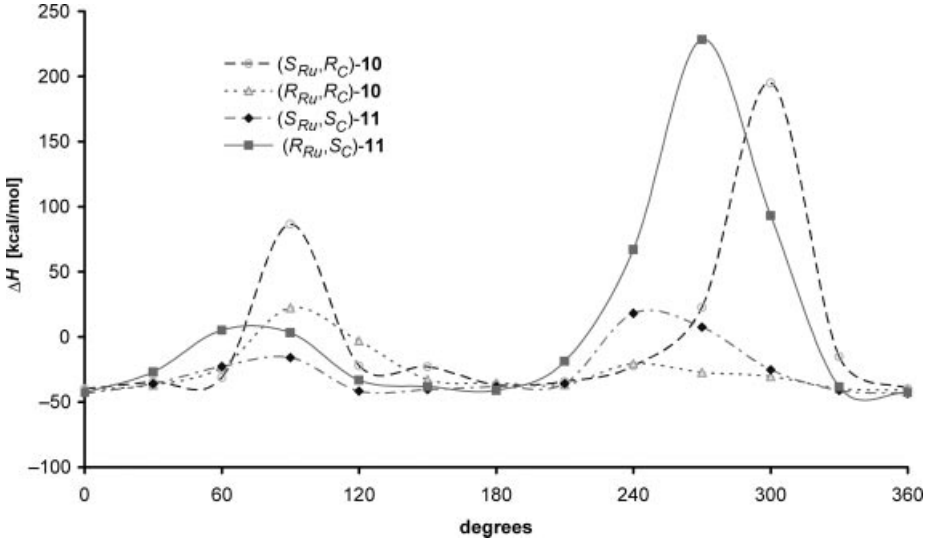

Figure 3. Plot of calculated enthalpies (kcal mol^{-1}) vs dihedral angle "C(methyl of *p*-cymene)–*p*-cymene ring–ruthenium–chlorine" [°] for complexes **10** and **11**.

 © 2005 Wiley-VCH Verlag GmbH & Co. KGaA, Weinheim

Table 2. Asymmetric hydrogen transfer of acetophenone catalyzed by chiral ruthenium systems, Ru/**L*** (**L*** = **1**–**9**).[a]

Entry	L*	**I**/Ru	Time (h)	Conv. (%)[b]	*ee* **II** (%)[b]	TOF (h^{-1}) (%)
1	1	100/1	1.5	89	12 (*R*)	59
2	2	100/1	1.5	80	32 (*S*)	53
3	2	20/1	0.5	92	32 (*S*)	37
4	3	100/1	24	0	–	–
5	3	20/1	72	17	33 (*S*)	0.2
6[c]	4	20/1	24	20	43 (*R*)	0.2
7	5	20/1	1.5	53	45 (*S*)	7.0
8	5	20/1	24	75	45 (*S*)	0.6
9	5	20/1	72	33	79 (*S*)	0.1
10	6	20/1	1.5	9	n.d.	
11[c]	6	20/1	24	41	2.0	1.2
12[c]	7	20/1	1.5	95	71 (*S*)	0.3
13	8	20/1	1.5	3	nd	0
14	8	20/1	24	63	0	0.5
15[c]	8	20/1	72	92	0	0.3
16	9	20/1	1.5	12	0	1.6
17[c]	9	20/1	24	42	0	0.3

[a] Results from duplicated experiments. Ru/**L***/*t*BuOK 1:2:3. See Scheme 4. [b] Conversions based on the substrate **I** and enantiomeric excesses (absolute configuration in parenthesis) determined by GC. [c] Reaction monitored up to 120 h, being conversion and enantioselectivity constants.

1 and 2 vs 4 and 5), in contrast to the results observed with α,β-dialkyl-substituted amino alcohols.[20] In our case the introduction of a second alcohol function leads to a dramatic activity decrease, but with an asymmetric induction similar to ligand **2** (entries 2 and 5). The selectivity of Ru/**1** and Ru/**2** systems is independent of the acetophenone/ruthenium ratio (entries 2 and 3). When the ruthenium-to-ligand ratio was 1:1, the catalytic behavior did not change, proving that the catalytic species are active without the ligand excess in the reaction medium that was observed previously for other ligands.[23]

Amino-oxazolines **4** and **5** are less active but more selective than the corresponding amino alcohols **1** and **2** (entries 6 and 7 vs 1 and 2, respectively). Also, oxazoline **6** is more selective than **3** (entry 11 vs 5), and, in turn, the silyl oxazoline **7** is more active than **6** (entry 12 vs 10 and 11), the Ru/**7** system being the most active oxazoline catalyst tested. These results indicate a "poison" effect of the alcohol group, both for the amino alcohol **3** and the oxazoline derivative **6**. In addition, we observe that the catalytic activity and selectivity are highly influenced by the substitution degree of the oxazoline heterocycle (**7**, α,β-disubstituted oxazoline, is more active and affords better enantiomeric excesses than **4** and **5**, β-monosubstituted oxazolines), as reported for α,β-dialkyl-substituted amino alcohols.[20]

We note that only the Ru/**5** catalytic system leads to an increase of enantiomeric excess (up to 79%) at long reaction times, together with a conversion decrease (entries 8 and 9). This proves the reversibility of the transfer hydrogenation, as stated by Noyori.[4a,24] In order to verify this kinetic resolution, the dehydrogenative oxidation of *rac*-**II** with acetone was carried out under similar conditions as those described above for the direct process (Scheme 5). After 48 h at room temperature, 46% of acetophenone was formed, achieving an enantiomeric excess for 1-phenylethanol up to 50% (*S*); then (*R*)-**II** dehydrogenates faster than the (*S*)-**II** enantiomer.

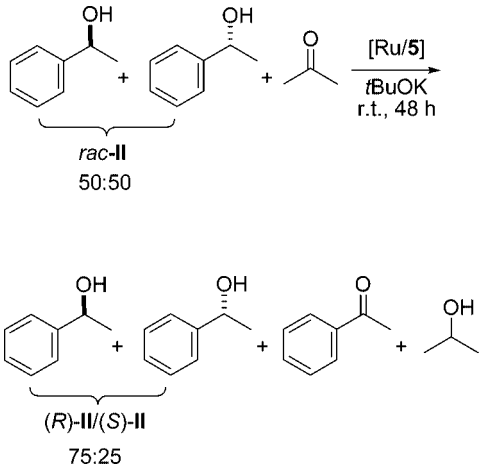

Scheme 5. Dehydrogenative oxidation of *rac*-**II** catalyzed by the Ru/**5** system.

Secondary amino-oxazolines, *N*-(*p*-tolylsulfonyl)- and *N*-methyl-amino-oxazoline (**8** and **9**, respectively), were somewhat less active than the analogous primary amino-oxazoline **5** (entries 14 and 17 vs 8), and what is more significant, they did not induce asymmetry (entries 13–17). Then a primary amine moiety and not a secondary amine function in the ligand appears essential for the enantioselectivity. This is something that has not been observed before and is only mentioned for indanol amino alcohol derivatives.[6c]

Theoretical Calculations

Assuming that the Ru-catalyzed hydrogen transfer process involves a concerted transfer of both proton and hydride, a six-membered transition state may be responsible for the ketone reduction by means of a double hydrogen transfer from Ru–H and N–H bonds towards the prochiral substrate, as postulated by Noyori.[7a,25] This concerted

 © 2005 Wiley-VCH Verlag GmbH & Co. KGaA, Weinheim

mechanism for Ru complexes containing bidentated N-donor ligands, in particular oxazolinyl (N_{ox})-amino(NHR) ligands, is represented in Figure 4.

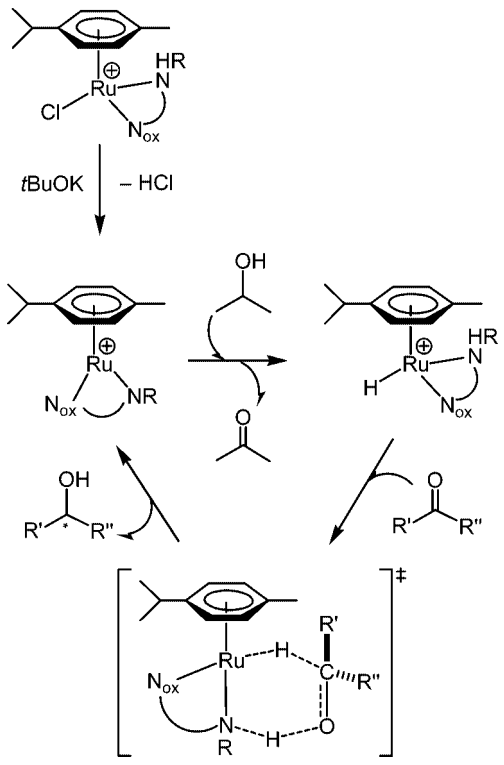

Figure 4. Catalytic cycle for Ru-catalyzed hydrogen transfer of ketones through a concerted mechanism.

For prochiral substrates, like the acetophenone, the enantiomeric enhancement of the chiral alcohol formed depends on the way that the ketone enantioface approaches the metal–hydride intermediate (see transition states depicted in Figure 5). In order to understand the enantioselectivity differences observed with our catalytic systems containing substituted (NHR for ligands **8** and **9**) and nonsubstituted (NH_2 for **4**–**7**) amino groups, theoretical calculations at DFT level were carried out for the corresponding transition states (see below). In the hydride model structure **13** (Figure 5), the substituent on the oxazoline stereocenter is a methyl group with *S* absolute configuration. The energy difference between both optimized diastereomers was 0.59 kcal mol^{-1} (Boltzmann distribution, 73:27), the S_{Ru} being the most stable isomer, where the oxazoline substituent at the stereocenter points away from the arene group, analogously to the related prepared chloro complexes **10** and **11** (see above).

The calculated transition states are labeled as **TS**-R_{II}-**13** or **TS**-S_{II}-**13** depending on the 1-phenylethanol enantiomer afforded (Figure 5). Their relative stability of four transition states are determined by an equilibrium between weak hydrogen interactions of the type C–H···Ar. Our calculations show that the two most stable states produce the *R* alcohol (relative energies are 0.0 and +1.2 kcal mol^{-1}), whereas the relative *S* alcohol states are higher in energy (+1.6 and +2.5 kcal mol^{-1}). Concerning the transition states related to the **13** hydride species, the Boltzmann distribution (298 K) for their four transition states leads to a calculated enantiomeric excess for the secondary alcohol **II** of about 40% in the *R* isomer (Figure 6), in agreement with the catalytic results obtained with the analogous amino-oxazolines con-

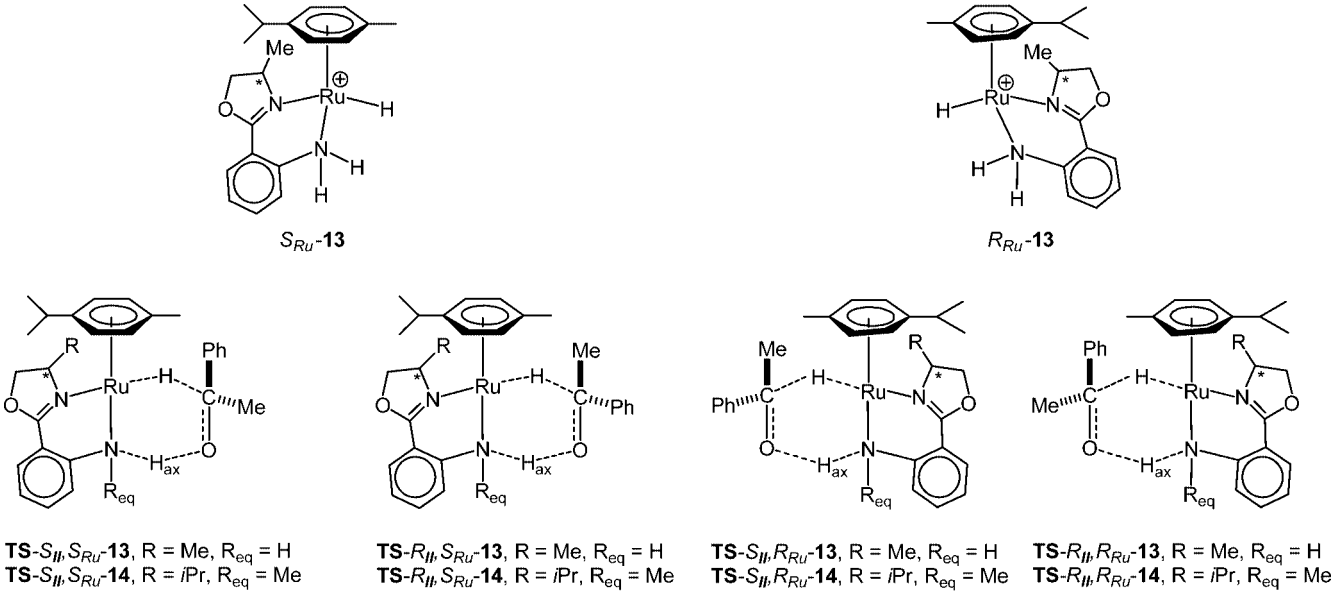

Figure 5. Optimized hydride species **13** (S_{Ru}-**13** and R_{Ru}-**13**) and the transition states involved in the hydrogenation of acetophenone used in the DFT study.

 © 2005 Wiley-VCH Verlag GmbH & Co. KGaA, Weinheim

taining an ethyl and isopropyl instead of the methyl group (ligands **4** and **5**).

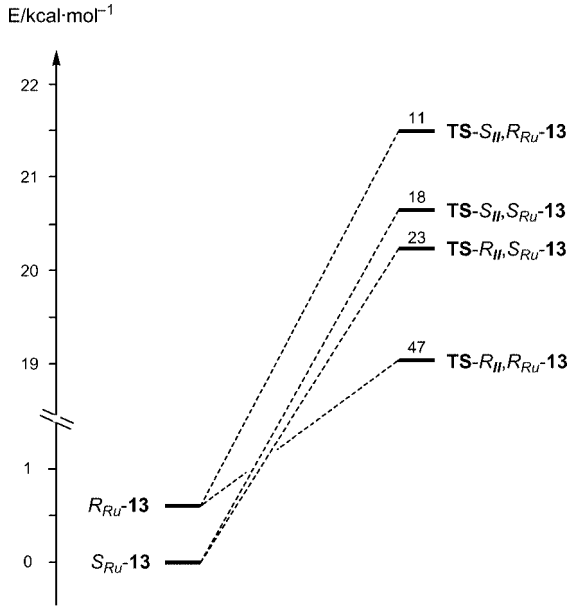

Figure 6. Energy profile for minima of compound model **13**, and their generated transition states (Figure 5) for the reaction with acetophenone, depending on the relative orientation of prochiral ketone. Relative populations of transition states are shown according to the Boltzmann distribution at 298 K.

The good correlation observed between experimental and calculated data for the Ru systems containing primary amino ligands led us to calculate the relative population of the transition states involved with Ru species containing secondary amino-oxazoline **9** (transition states labeled as **14** in Figure 5). For these states, only the two axial related species were taken into account because of the topological arrangement for hydrogen transfer to the prochiral ketone in the transition state (Figure 5). As depicted in Figure 7, the isomers **TS**-S_{Ru}-**14** are less stable than the other two, possibly due to steric repulsions, having an energy higher than 10 kcal mol^{-1} and higher than the related **TS**-R_{Ru}-**14**. For this reason they do not play any role in our catalytic system (Figure 8). Consequently, only the lowest transition states, **TS**-R_{II},R_{Ru}-**14** and **TS**-S_{II},R_{Ru}-**14**, participate in the hydrogenation reaction and the small energy gap between the two forms is responsible for a decrease of enantiomeric excess (calculated *ee* = 26%). In contrast, in the related transition states of **13**, the largest populations corresponded to the transition states loading to the *R* enantiomers, explaining the selectivity trends observed for Ru catalytic systems containing primary and secondary amino-oxazolines (see Catalytic section).

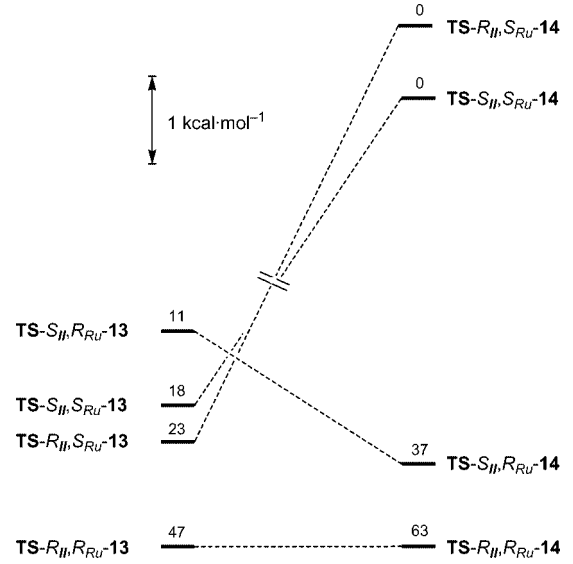

Figure 7. Relative stabilities of Ru transition states involved in the acetophenone hydrogen transfer containing primary (**13**) and secondary (**14**) oxazolinyl-amines. Relative populations are shown as Figure 5 and zero level is taken from the **TS**-R_{II},R_{Ru} isomer.

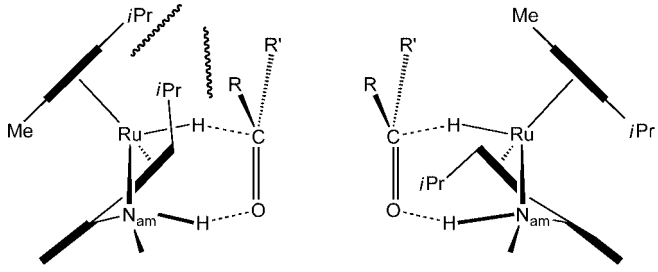

Figure 8. Schematic representation of the transition states **TS-14**. The steric repulsions between hydrocarbon groups for **TS**-S_{Ru}-**14** (left) are missing in analogous **TS**-R_{Ru}-**14** (right).

Conclusions

We used modular chiral N-donor ligands in order to study the fine effects on the transfer hydrogenation of acetophenone catalyzed by Ru arene systems. An important influence on selectivity was found to depend on the nature of the amino group: secondary amino ligands (**8**–**9**) do not induce enantioselectivity, in contrast to their analogous primary derivative (**5**). In order to rationalize these results, a structural and mechanistic study was proposed. The synthesis and full characterization of complexes containing primary (**10** and **11**) and secondary (**12**) oxazolinyl-amino ligands was carried out. The NMR spectroscopic data show the presence of isomers due to the new sterocenters (Ru and also N for **12**) generated upon coordination of the ligands (**4**, **5**, and **8**) to the metal. The relative populations found by modeling structures (PM3(tm) level) are in agreement with the diastereomeric ratios observed by NMR spectroscopy. The enantioselectivity loss observed for secondary amines relative to the analogous primary ligands can be justified by the theoretical data obtained (DFT studies) for the transition states proposed for the arene ruthenium systems involved in the hydrogen transfer of prochiral ketones.

 © 2005 Wiley-VCH Verlag GmbH & Co. KGaA, Weinheim

Experimental Section

General Remarks: All compounds were prepared under purified nitrogen using standard Schlenk and vacuum-line techniques. The solvents were purified by standard procedures and distilled under nitrogen.[26] (*R*)-(+)-2-Aminobutanol (Fluka), L-valinol (Aldrich), and [RuCl(*p*-cymene)(μ-Cl)]$_2$ (Aldrich) were used without previous purification. Ligand **4**[10b] was prepared as described previously. NMR spectra were recorded with Varian XL-500 (^{1}H, standard $SiMe_4$), Varian Gemini (^{1}H, 200 MHz; ^{13}C, 50 MHz; standard $SiMe_4$), Bruker DRX 250 (^{13}C, 62.9 MHz, standard $SiMe_4$), and Mercury 400 (^{1}H, 400 MHz; ^{13}C, 100 MHz, standard $SiMe_4$) spectrometers, using $CDCl_3$ as solvent, unless stated otherwise. Chemical shifts were reported downfield from standards. IR spectra were recorded with a Nicolet 520 FTIR spectrometer. FAB mass chromatograms were obtained on a Fisons V6-Quattro instrument. The GC analyses were performed on a Hewlett–Packard 5890 Series II gas chromatograph (50 m Ultra 2 capillary column) with a FID detector. Enantiomeric excesses were determined by GC on a FS-cyclodex-β-I/P column. Optical rotations were measured on a Perkin–Elmer 241MC spectropolarimeter. Conductivities were obtained on a Radiometer CDM3 conductimeter. Elemental analyses were carried out by the *Serveis Cientifico-Tècnics de la Universitat de Barcelona* in an Eager 1108 microanalyzer.

(+)-(4′*S*)-2-(4′-Isopropyl-3′,4′-dihydrooxazol-2′-yl)aniline (5): L-Valinol (0.743 g, 7.20 mmol), 2-aminobenzonitrile (0.500 g, 4.23 mmol), and potassium carbonate (0.054 g, 0.39 mmol) were successively introduced in a Schlenk, followed by a solution of glycerol (5 mL) in dry ethylene glycol (9 mL). The resulting mixture was brought to 105 °C under nitrogen. The disappearance of the nitrile was followed by thin-layer chromatography (hexane/ethyl acetate, 3:1). After 24 h, the reaction was complete. Two new spots appeared on the thin layer, which were further identified as the amide for the high R_f and the oxazoline for the low R_f one (15:85 respectively, determined by GC analysis). The mixture was cooled to room temperature and then poured over crushed ice. The resulting white solid was filtered, dissolved in dichloromethane and, after several extractions with water, the organic phases were dried with anhydrous Na_2SO_4. Solvent elimination under low pressure gave the product as a white solid. Yield: 0.860 g (80%). IR (KBr): $\tilde{\nu}$ = 3395 (N–H), 3261 (N–H), 1640 (C=N), 1255 (C–O) cm^{-1}. ^{1}H NMR (250 MHz, $CDCl_3$; multiplicity, coupling constants in Hz, and relative integration in parentheses): 7.67 (pdd, 8.8, 1.6, 1 H), 7.19 (pt, 7.4, 1 H), 6.69 (m, 2 H), 6.13 (br. s, 2 H), 4.32 (ppd, 8.6, 7, 1 H), 4.11 (m, 1 H), 4.00 (t, 7.3, 1 H), 1.81 (m, 1 H), 1.03 (d, 6.8, 3 H), 0.93 (d, 6.8, 3 H) ppm. ^{13}C NMR (50 MHz, $CDCl_3$): 163.4 (C), 148.5 (C), 131.8 (C), 129.5 (CH), 115.9 (CH), 115.5 (CH), 109.1 (CH), 72.9 (CH), 68.7 (CH_2), 33.2 (CH), 19.1 (CH_3), 18.6 (CH_3) ppm. $C_{12}H_{16}N_2O$ (204): calcd. C 70.58, H 7.84, N 13.72; found C 70.29, H 8.02, N 13.74. MS (FAB positive) *m*/*z* 204 ([M]$^+$). Melting point: 103 °C. $[\alpha]_D^{25}$ (1×10^{-3} M, $CHCl_3$) = +19.8.

(+)-(3′*S*,4′*S*)-2-(3′-Phenyl-4′-hydroxymethyl-3′,4′-dihydrooxazol-2′-yl)aniline (6): (1*S*,2*S*)-2-Amino-1-phenyl-1,3-propanediol (1.201 g, 7.20 mmol), 2-aminobenzonitrile (0.500 g, 4.23 mmol), and potassium carbonate (0.054 g, 0.39 mmol) were successively introduced in a Schlenk, followed by a solution of glycerol (5 mL) in dry ethylene glycol (9 mL). The resulting mixture was brought to 105 °C under nitrogen. The disappearance of the nitrile was followed by thin-layer chromatography (hexane/ethyl acetate, 3:1). The reaction was complete after 36 h. Two new spots appeared on the thin layer, which were further identified as the amide for the high R_f and the oxazoline for the low R_f one (1:1 respectively, determined by GC analysis). The mixture was cooled to room temperature and washed with a saturated aqueous solution of NH_4Cl and extracted with dichloromethane (3 × 15 mL). The organic extracts were dried with anhydrous Na_2SO_4. Solvent elimination under low pressure gave the product as a yellow oil. Yield: 0.640 g (57%). IR (NaCl): $\tilde{\nu}$ = 3466 (N–H), 3415 (O–H), 3309 (N–H), 1633 (C=N), 1261 (C–O) cm^{-1}. ^{1}H NMR (200 MHz, $CDCl_3$; multiplicity, coupling constants in Hz, and relative integration in parentheses): 7.81 (dd, 7.9, 0.6, 1 H), 7.24 (m, 3 H), 6.70 (m, 5 H), 6.07 (br. s, 2 H), 4.39 (d, 7, 1 H), 4.26 (pq, 3.6, 1 H), 3.94 (pdd, 11.5, 3.7, 1 H), 3.74 (dd, 11.2, 4.0, 1 H), 2.61 (br. s, 1 H) ppm. ^{13}C NMR (50 MHz, $CDCl_3$): 164.8 (C), 148.6 (C), 140.8 (C), 132.4 (CH), 129.9 (CH), 128.8 (CH), 128.2 (CH), 125.6 (CH), 116.4 (CH), 115.9 (CH), 108.8 (C), 80.9 (CH), 64.1 (CH_2) ppm. MS (FAB positive) *m*/*z* 267 ([M – H]$^+$). $[\alpha]_D^{25}$ (1×10^{-3} M, $CHCl_3$) = +59.3.

(+)-(3′*S*,4′*S*)-2-(3′-Phenyl-4′-trimethylsilyloxymethyl-3′,4′-dihydrooxazol-2′-yl)aniline (7): Compound **6** (0.330 g, 1.23 mmol), imidazole (0.175 g, 2.58 mmol), DMAP (6.6 mg, 5.3×10^{-2} mmol), and $SiClMe_3$ (0.132 g, 1.22 mmol) were successively introduced in a Schlenk. The solids were dissolved in 50 mL of freshly distilled chloroform, and the resulting mixture was stirred for 24 h at room temperature. The evolution of the reaction was followed by thin-layer chromatography (hexane/ethyl acetate, 2:1). When the reaction was over, the organic phase was treated successively with 10 mL of saturated aqueous solution of sodium hydrogenocarbonate and 10 mL of a saturated aqueous solution of brine, and the organic extracts were then dried with anhydrous Na_2SO_4. After solvent evaporation, the resulting oil was purified by column chromatography on silica using a mixture of hexane/ethyl acetate (2:1) as eluent. The product was obtained as a white solid. Yield: 0.372 g (89%). IR (KBr): $\tilde{\nu}$ = 3408 (N–H), 3276 (N–H), 1635 (C=N), 1261 (C–O) cm^{-1}. ^{1}H NMR (200 MHz, $CDCl_3$; multiplicity, coupling constants in Hz, and relative integration in parentheses): 7.67 (pdd, 7.9, 1.5, 2 H), 7.16 (m, 4 H), 6.58 (d, 8.6, 2 H), 6.54 (pt, 7.6, 1 H), 5.97 (br. s, 2 H), 5.29 (d, 6.0, 1 H), 4.15 (m, 1 H), 3.83 (dd, 10.4, 4.2, 1 H), 3.55 (pdd, 10.1, 7.3, 1 H), –0.02 (s, 9 H) ppm. ^{13}C NMR (50 MHz, $CDCl_3$): 164.2 (C), 148.8 (C), 141.5 (C), 132.2 (CH), 129.8 (CH), 128.6 (CH), 127.9 (CH), 125.0 (CH), 116.0 (CH), 115.6 (CH), 108.9 (C), 81.6 (CH), 77.2 (CH), 64.9 (CH_2), 0.1 (CH_3) ppm. $C_{19}H_{25}N_2O_2Si$ (341.5): calcd. C 67.03, H 7.05, N 8.23; found C 67.69, H 7.11, N 8.30. MS (FAB positive) *m*/*z* 340 ([M]$^+$). Melting point: 153 °C. $[\alpha]_D^{25}$ (1×10^{-3} M, $CHCl_3$) = +30.7.

(+)-(4′*S*)-2-(4′-Isopropyl-3′,4′-dihydrooxazol-2′-yl)-*N*-(*p*-tolylsulfonyl)aniline (8): Stirring a solution of **5** (0.100 g, 0.49 mmol) and *p*-tolylsulfonyl chloride (0.160 g, 0.84 mmol) in dichloromethane with an aqueous solution of KOH (0.049 g, 0.89 mmol) for 8 h gave a white solid, which was filtered off and purified by column chromatography on silica using hexane/ethyl acetate (5:1) as eluent. Yield: 0.134 g (77%). IR (KBr): $\tilde{\nu}$ = 3389 (N–H), 1637 (C=N), 1341 (S=O), 1163 (S=O) cm^{-1}. ^{1}H NMR (200 MHz, $CDCl_3$; multiplicity, coupling constants in Hz, and relative integration in parentheses): 12.54 (br. s, 1 H), 7.66 (d, 8.2, 2 H), 7.62 (m, 2 H), 7.26 (ptd, 7.8, 1.4, 2 H), 6.91 (ptd, 7.9, 1.0, 1 H), 4.28 (dd, 8.6, 7.4, 1 H), 4.06 (m, 1 H), 3.98 (m, 1 H), 2.26 (s, 3 H), 1.73 (m, 1 H), 0.98 (d, 6.6, 3 H), 0.88 (d, 6.6, 3 H) ppm. ^{13}C NMR (50 MHz, $CDCl_3$): 164.8 (C), 142.5 (C), 137.8 (C), 135.4 (C), 132.3 (CH), 129.4 (CH), 129.1 (CH), 127.1 (CH), 122.1 (CH), 117.6 (CH), 72.3 (CH), 69.5 (CH_2), 33.1 (CH), 18.8 (CH_3), 18.6 (CH_3) ppm. $C_{19}H_{22}N_2O_2S$ (342): calcd. C 63.68, H 6.14, N 7.81; found C 63.78, H 6.53, N 7.60. MS (FAB positive) *m*/*z* 340 ([M]$^+$). Melting point : 129 °C. $[\alpha]_D^{25}$ (1×10^{-3} M, $CHCl_3$) = +82.1.

(4′*S*)-2-(4′-Isopropyl-3′,4′-dihydrooxazol-2′-yl)-*N*-(methyl)aniline (9): Compound **5** (0.150 g, 0.73 mmol) was dissolved in 10 mL of

 © 2005 Wiley-VCH Verlag GmbH & Co. KGaA, Weinheim

THF. The resulting mixture was cooled to –78 °C under nitrogen. After 30 min, *n*BuLi (0.55 mL, 0.88 mmol) was introduced in the Schlenk, followed by a solution of Me_2SO_4 (0.111 g, 0.88 mmol) in THF (3 mL). The resulting mixture was warmed to room temperature. The reaction was complete after 18 h. Two new spots appeared on the thin layer, which were further identified as the product for the high R_f and the oxazoline **5** for the low R_f one (70:30 respectively, determined by GC analysis). The mixture was dissolved in dichloromethane and after several extractions with an aqueous saturated solution of NH_4Cl and water, the organic phases were dried with anhydrous Na_2SO_4. The resulting oil was purified by column chromatography on silica using hexane/ethyl acetate (20:1) as eluent. Solvent elimination under low pressure gave the product as a yellow oil. Yield: 0.116 g (73%). IR (KBr) = 3265 (N–H), 3171 (N–H), 2959 (C–H), 1636 (C=N), 1253 (C–O) cm^{-1}. ^1H NMR (200 MHz, $CDCl_3$; multiplicity, coupling constants in Hz, and relative integration in parentheses): 8.31 (br. s, 1 H), 7.63 (dd, 7.9, 1.8, 1 H), 7.23 (m, 1 H), 6.53 (m, 2 H), 4.21 (dd, 8.4, 7.0, 1 H), 4.03 (m, 1 H), 3.90 (q, 7.0, 1 H), 2.85 (d, 4.8, 3 H), 1.69 (m, 1 H), 0.94 (d, 6.6, 3 H), 0.84 (d, 6.6, 3 H) ppm. ^{13}C NMR (50 MHz, $CDCl_3$): 163.6 (C), 149.8 (C), 132.2 (CH), 129.6 (CH), 113.9 (CH), 109.6 (CH), 108.3 (C), 72.8 (CH), 68.3 (CH_2), 33.1 (CH), 29.4 (CH_3), 19.0 (CH_3), 18.5 (CH_3) ppm. MS (FAB positive) *m*/*z* 218 ($[M]^+$).

Chloro-(η⁶-*p*-cymene)-[(4′*R*)-2-(4′-ethyl-3′,4′-dihydrooxazol-2′-yl)-aniline-*N*,*N*]ruthenium(II) Chloride (10): $[RuCl(p\text{-cymene})(\mu\text{-}Cl)]_2$ (102 mg, 0.166 mmol) and **4** (63.5 mg, 0.33 mmol) were dissolved in dichloromethane (18 mL) and stirred at room temperature for 8 h. The solvent was then removed and the residue washed with diethyl ether. The product was recrystallized from dichloromethane and diethyl ether, giving an orange solid. Yield: 0.156 g (95%). IR (KBr) = 3414 (N–H), 3052 (N–H), 1630 (C=N), 1293 (C–O) cm^{-1}. ^1H NMR (250 MHz, $CDCl_3$, 233 K; multiplicity, coupling constants in Hz, and relative integration in parentheses) δ = *major isomer*: 9.84 (d, 10.0, 1.6, 2 H), 8.61 (d, 7.5, 1 H), 7.60 (m, 2 H), 7.31 (m, 1 H), 5.78 (br. s, 2 H), 5.69 (br. s, 2 H), 5.58 (br. s, 2 H), 4.86 (pt, 11.2, 1 H), 4.68 (br. s, 1 H), 4.29 (m, 1 H), 2.28 (br. s, 1 H), 2.07 (br. s, 1 H), 1.64 (s, 3 H), 0.95 (m, 9 H) ppm. δ *minor isomer*: 8.52 (d, 12.5, 1 H), 7.74 (d, 7.5, 1 H), 5.05 (m, 1 H), 2.54 (m, 1 H) ppm. ^{13}C NMR (63 MHz, $CDCl_3$) δ = *major isomer*: 163.9 (C), 135.1 (CH), 129.7 (CH), 126.8 (CH), 123.6 (CH), 119.4 (CH), 107.1 (CH), 97.9 (CH), 83.8 (CH), 81.3 (CH), 73.9 (CH), 67.9 (CH_2), 31.0 (CH), 26.9 (CH_2), 18.2 (CH_3), 9.9 (CH_3) ppm. $C_{21}H_{28}Cl_2N_2ORu$ (496.4): calcd. C 50.70, H 5.63, N 5.63, Cl 14.26; found C 50.94, H 5.49, N 5.78, Cl 14.20. MS (FAB positive): *m*/*z* calcd. for $C_{21}H_{28}ClN_2ORu$ $[M^+]$: 460.2; found 460.3. Melting point: 232 °C. Molar conductivity (*c* = 0.001 M, acetonitrile): 47 $\Omega^{-1}\,cm^2\,mol^{-1}$.

Chloro-(η⁶-*p*-cymene)-[(4′*S*)-2-(4′-isopropyl-3′,4′-dihydrooxazol-2′-yl)aniline-*N*,*N*]ruthenium(II) Chloride (11): $[RuCl(p\text{-cymene})(\mu\text{-}Cl)]_2$ (102 mg, 0.166 mmol) and **5** (67.9 mg, 0.33 mmol) were dissolved in dichloromethane (18 mL) and stirred at room temperature for 8 h. The solvent was then removed and the residue washed with diethyl ether. The product was recrystallized from dichloromethane and diethyl ether, giving an orange solid. Yield: 0.161 g (95%). IR (KBr) = 3427 (N–H), 3045 (N–H), 1631 (C=N), 1394 (C–O) cm^{-1}. ^1H NMR (500 MHz, $CDCl_3$, 298 K; multiplicity, coupling constants in Hz, and relative integration in parentheses) δ = *major isomer*: 10.31 (d, 10.0, 1 H), 8.77 (d, 8.0, 1 H), 7.58 (m, 1 H), 7.54 (dd, 7.2, 1.5, 1 H), 7.27 (t, 7.5, 1 H), 5.98 (m, 2 H), 5.76 (d, 5.5, 1 H), 5.62 (d, 6.0, 2 H), 4.58 (dd, 8.0, 6.0, 1 H), 4.52 (m, 2 H), 4.45 (dd, 10.0, 8.0, 1 H), 4.34 (d, 10.0, 1 H), 2.51 (m, 1 H), 2.42 (m, 1 H), 1.92 (s, 3 H), 1.04 (pt, 7.2, 6 H), 0.98 (pt, 7.0, 6 H) ppm. δ *minor isomer*: 9.91 (d, 11.0, 1 H), 8.57 (d, 8.0, 1 H), 7.79 (dd, 7.2, 1.5, 1 H), 7.58 (m, 1 H), 7.30 (t, 7.5, 1 H), 5.89 (br. s, 2 H), 5.79 (d, 6.0, 1 H), 5.65 (d, 6.0, 1 H), 5.01 (d, 11.0, 1 H), 4.86 (pt, 9.5, 1 H), 4.70 (m, 1 H), 4.52 (m, 2 H), 2.84 (m, 1 H), 2.60 (m, 1 H), 1.84 (s, 3 H), 0.93 (d, 7.5, 3 H), 0.59 (d, 6.5, 3 H) ppm. ^{13}C NMR ($CDCl_3$, 100 MHz) δ = *major isomer*: 164.2 (C), 142.1 (C), 134.7 (C), 128.7 (CH), 126.7 (CH), 124.7 (CH), 119.4 (CH), 107.2 (CH), 84.4 (CH), 84.1 (CH), 81.1 (CH), 80.6 (CH), 71.4 (CH_2), 69.4 (CH_2), 31.2 (CH), 28.3 (CH), 22.1 (CH), 21.2 (CH), 19.7 (CH_3), 18.2 (CH_3), 15.0 (CH_3) ppm. δ *minor isomer*: 163.3 (C), 142.7 (C), 134.7 (C), 130.8 (CH), 126.8 (CH), 123.7 (CH), 118.7 (CH), 97.2 (CH), 84.0 (CH), 79.0 (CH), 78.3 (CH), 77.5 (CH), 69.5 (CH_2), 66.0 (CH_2), 30.9 (CH), 28.8 (CH), 23.3 (CH), 19.8 (CH_3), 18.1 (CH_3), 14.9 (CH_3) ppm. $C_{22}H_{30}Cl_2N_2ORu$ (475): calcd. C 51.76, H 5.88, N 5.49, Cl 13.90; found C 51.29, H 6.00, N 5.25, Cl 13.40. MS (FAB positive): *m*/*z* calcd. for $C_{22}H_{30}ClN_2ORu$ $[M^+]$: 439.6; found 439.0. Melting point: 243 °C. Molar conductivity (*c* = 0.001 M, acetonitrile): 50 $\Omega^{-1}\,cm^2\,mol^{-1}$.

Chloro-(η⁶-*p*-cymene)-[(4′*S*)-2-(4′-isopropyl-3′,4′-dihydrooxazol-2′-yl)-*N*-(*p*-tolylsulfonyl)aniline-*N*,*N*]ruthenium(II) Chloride (12): $[RuCl(p\text{-cymene})(\mu\text{-}Cl)]_2$ (9.6 mg, 0.015 mmol) and **8** (11.3 mg, 0.031 mmol) were dissolved in dichloromethane (4 mL) and stirred at room temperature for 8 h. The solvent was then removed and the residue washed with diethyl ether. The product was recrystallized from dichloromethane and diethyl ether, giving an orange solid. Yield: 0.019 g (99%). IR (KBr) = 3245 (N–H), 1634 (C=N), 1267 (SO_2), 1099 (SO_2) cm^{-1}. ^1H NMR (500 MHz, $CDCl_3$, 298 K; multiplicity, coupling constants in Hz, and relative integration in parentheses) δ = *major isomer*: 9.49 (br. s, 1 H), 8.30 (d, 8.0, 1 H), 7.60 (d, 7.0, 1 H), 7.58 (t, 7.8, 1 H), 7.37 (d, 6.5, 2 H), 7.32 (m, 1 H), 7.23 (q, 6.7, 2 H), 6.84 (m, 3 H), 6.26 (m, 3 H), 6.25 (d, 6.0, 1 H), 6.10 (d, 5.5, 1 H), 5.37 (d, 4.5, 1 H), 5.22 (d, 4.5, 1 H), 4.30 (t, 12.2, 1 H), 4.23 (d, 11.5, 1 H), 4.13 (d, 10.0, 1 H), 3.94 (d, 12.0, 1 H), 2.31 (m, 1 H), 1.23 (s, 3 H), 1.24 (m, 1 H), 0.98 (d, 6.5, 6 H), 0.85 (d, 6.0, 6 H), 0.29 (s, 3 H) ppm. $C_{29}H_{36}Cl_2N_2O_3RuS$ (664.6): calcd. C 52.41, H 5.45, N 4.21, S 4.82; found C 52.80, H 5.60, N 4.00, S 4.95. MS (FAB positive): *m*/*z* calcd. for $C_{29}H_{36}ClN_2O_3RuS$ $[M^+]$: 629.20; found 629.00.

Ruthenium-Catalyzed Hydrogen Transfer of Acetophenone: The precursor ($[Ru(p\text{-cymene})Cl(\mu\text{-}Cl)]_2$, 1.8 mg, 3×10^{-3} mmol) and ligand (12×10^{-3} mmol) were dissolved in a solution (2 mL, 0.012 M) of *t*BuOK in 2-propanol at room temperature for 30 min. Then a solution of acetophenone in 2-propanol (2 mL, 0.06 M) was added. The reaction was performed at room temperature under nitrogen, monitored by GC. When the Ru/substrate ratio was 1:100, the precursor (1.8 mg, 3×10^{-3} mmol) and ligand (12×10^{-3} mmol) were dissolved in a solution of *t*BuOK in 2-propanol (10 mL, 0.012 M) at room temperature for 30 min. Then a solution of acetophenone in 2-propanol (10 mL, 0.06 M) was added. The reaction was performed at room temperature under nitrogen, monitored by GC.

Ruthenium-Catalyzed Dehydrogenation of *rac*-1-Phenylethanol: The precursor (1.8 mg of $[Ru(p\text{-cymene})Cl(\mu\text{-}Cl)]_2$, 3×10^{-3} mmol) and ligand **5** (25 mg, 12×10^{-3} mmol) were dissolved in a solution of *t*BuOK in 2-propanol (2 mL, 0.012 M) at room temperature for 30 min. Then an equimolar solution of *rac*-1-phenylethanol and acetone in 2-propanol (2 mL, 0.06 M) was added. The reaction was performed at room temperature under nitrogen, monitored by GC.

X-ray Crystallographic Study: An orange block of **10** was selected and mounted on a Bruker SMART CCD area detector single-crystal diffractometer with graphite monochromatized Mo-K_α radiation (λ = 0.71073 Å) operating at room temperature. Crystal data are summarized in Table 3.

 © 2005 Wiley-VCH Verlag GmbH & Co. KGaA, Weinheim

Table 3. Crystal data for (S_{Ru},R_C)-**10**.

	(S_{Ru},R_C)-**10**
Empirical formula	$C_{23}H_{29}Cl_8N_2ORu$
Molecular mass	734.15
Crystal size [mm]	$0.39\times0.09\times0.08$
Temperature [K]	298(2)
Crystal system	orthorhombic
Space group	$P2_12_12_1$
a (Å)	8.881(1)
b (Å)	18.102(2)
c (Å)	20.231(2)
V [Å^3]	3252.6(5)
Z	4
Density (calculated) [Mg m^{-3}]	1.499
Absorption coefficient [mm^{-1}]	1.158
θ range for data collection [°]	1.51–26.37
Reflections collected ($I \geq 2\sigma(I)$)	19013
Independent reflections	6599
Final R indices [$I > 2\sigma(I)$][a]	R_1 = 0.0643
Final wR_2 indices (all data)[a]	wR_2 = 0.1547
Gof on F^2	1.018
Abs. structure parameter[b]	0.05(8)
Largest diff. peak and hole [e Å^{-3}]	0.565 and –0.481

[a] $R_1 = \Sigma||F_o| - |F_c|| / \Sigma|F_o|$ and $wR_2 = \{\Sigma[w(F_o^2 - F_c^2)^2] / \Sigma[w(F_o^2)^2]\}^{1/2}$. [b] H. D. Flack, *Acta Crystallogr. Sect. A* **1983**, *39*, 876.

Preliminary unit cell constants were calculated with a set of 45 narrow-frame (0.3° in ω) scans. A total of 1271 frames of data were collected using the phi–omega scan method. The first 50 frames were recollected at the end of data collection to monitor for decay. The crystal used for the diffraction study showed no decomposition during data collection. Absorption corrections were applied by using the SADABS program[27] (maximum and minimum transmission coefficients 0.9130 and 0.6608). The structure was solved by direct methods using the SHELXS-97 computer program[28] for crystal structure determination and refined by full-matrix least-squares method on F^2, with the SHELXL-97 computer program.[29] 6599 reflections were included in the refinement and no restraints were applied to the 310 parameters. Hydrogen atoms were included in calculated positions and refined in riding mode. The weighting scheme employed was $w = [\sigma^2(F_o^2 + (0.0997P)^2 + 0.4457P]$ and $P = (|F_o|^2 + 2|F_c|^2)/3$.

CCDC-274550 contains the supplementary crystallographic data for this paper. These data can be obtained free of charge from The Cambridge Crystallographic Data Centre via www.ccdc.cam.ac.uk/data_request/cif.

Computational Details: Calculations were carried out using the GAUSSIAN98 package.[30] The hybrid density function method known as B3LYP was applied.[31] Relativistic effective core potentials (ECP) from the Stuttgart–Dresden group were used to represent the innermost electrons of the ruthenium atoms.[32] The basis set for the main group elements was split-valence and included a polarization function in all atoms (abbreviated as SVP).[33] The geometries for the minima **13** and **14** were fully optimized in all the isomers. The search for transition states failed, and in an attempt to evaluate their relative stability we decided to make a partial optimization, which was performed by keeping the distances of the Ru···H···C fragment fixed at 1.75 and 1.38 Å, respectively.[7] Some changes in these parameters were introduced without major changes in the relative stability of each family of compounds.

Acknowledgments

The authors thank Prof. Santiago Álvarez for constructive discussions. The authors also wish to thank the Ministerio de Educación y Ciencia (CTQ2004-01546/BQU and 2002-04033/BQU) and the Generalitat de Catalunya for financial support. The installation of the SMART CCD Single-Crystal Diffractometer at the University of A Coruña was supported by the Xunta de Galicia (XUGA INFRA-97).

[1] For reviews see: a) D. Carmona, M. P. Lamata, L. A. Oro, *Eur. J. Inorg. Chem.* **2002**, 2239; b) M. J. Palmer, M. Wills, *Tetrahedron: Asymmetry* **1999**, *10*, 2045; c) G. Zassinovich, G. Mestroni, *Chem. Rev.* **1992**, *92*, 1051.
[2] C. F. de Graauw, J. A. Peters, H. van Bekkum, J. Huskens, *Synthesis* **1994**, 1007.
[3] a) M. Bernard, V. Guiral, F. Delbecq, F. Fache, P. Sautet, M. Lemaire, *J. Am. Chem. Soc.* **1998**, *120*, 1441; b) J.-E. Backwall, R. L. Chowdhuri, U. Karlsson, G. Z. Wang, in *Perspectives in Coordination Chemistry* (Eds.: A. F. Williams, C. Floriani, G. Merbach), Verlag Helvetica Chimica Acta, Basel, Switzerland, **1992**, p. 463.
[4] a) R. Noyori, S. Hashiguchi, *Acc. Chem. Res.* **1997**, *30*, 97; b) K.-J. Haack, S. Hashiguchi, A. Fujii, T. Ikariya, R. Noyori, *Angew. Chem. Int. Ed. Engl.* **1997**, *36*, 285.
[5] a) J.-X. Gao, T. Ikariya, R. Noyori, *Organometallics* **1996**, *15*, 1087; b) S. Hashiguchi, A. Fujii, S.-I. Inoue, T. Ikariya, R. Noyori, *J. Chem. Soc., Chem. Commun.* **1996**, 233.
[6] a) P. Gamez, F. Fache, M. Lemaire, *Tetrahedron: Asymmetry* **1995**, *6*, 705; b) Y.-T. Jiang, Q.-Z. Jiang, X.-M. Zhang, *J. Am. Chem. Soc.* **1998**, *120*, 3817; c) M. Palmer, T. Walsgrove, M. Wills, *J. Org. Chem.* **1997**, *62*, 5226; d) Y.-B. Zhou, F.-Y. Tang, H.-D. Xu, X.-Y. Wu, J.-A. Ma, Q.-L. Zhou, *Tetrahedron: Asymmetry* **2002**, *13*, 469.
[7] a) M. Yamakawa, H. Ito, R. Noyori, *J. Am. Chem. Soc.* **2000**, *122*, 1466; b) D. A. Alonso, P. Brandt, S. J. M. Nordin, P. G. Andersson, *J. Am. Chem. Soc.* **1999**, *121*, 9580.
[8] M. Gómez, S. Jansat, G. Muller, M. C. Bonnet, J. A. J. Breuzard, M. Lemaire, *J. Organomet. Chem.* **2002**, *659*, 197.
[9] Selected recent contributions: a) D. Franco, M. Gómez, F. Jiménez, G. Muller, M. Rocamora, M. A. Maestro, J. Mahía, *Organometallics* **2004**, *23*, 3197; b) J. A. Brito, M. Gómez, G. Muller, H. Teruel, J.-C. Clinet, E. Duñach, M. A. Maestro, *Eur. J. Inorg. Chem.* **2004**, 4278; c) M. Gómez, S. Jansat, G. Muller, M. A. Maestro, J. Mahía, *Organometallics* **2002**, *21*, 1077; d) M. A. Pericàs, C. Puigjaner, A. Riera, A. Vidal-Ferran, M. Gómez, F. Jiménez, G. Muller, M. Rocamora, *Chem. Eur. J.* **2002**, *8*, 4164.
[10] a) M. K. Button, R. A. Gossage, *J. Heterocyclic Chem.* **2003**, *40*, 513; b) J. Castro, S. Cabaleiro, P. Pérez-Lourido, J. Romero, J. García-Vázquez, A. Sousa, *Polyhedron* **2001**, *20*, 2329; c) N. End, L. Macko, M. Zehnder, A. Pfaltz, *Chem. Eur. J.* **1998**, *4*, 818.
[11] J. M. Canal, M. Gómez, F. Jiménez, M. Rocamora, G. Muller, E. Duñach, D. Franco, A. Jiménez, F. H. Cano, *Organometallics* **2000**, *19*, 966.
[12] S. Cabaleiro, P. Pérez-Lourido, J. Castro, J. Romero, J. García-Vázquez, A. Sousa, *Transition Met. Chem.* **2001**, *26*, 709.
[13] A. J. Davenport, D. L. Davies, J. Fawcett, S. A. Garratt, D. R. Russell, *J. Chem. Soc., Dalton Trans.* **2000**, 4432.
[14] a) K. Stanley, M. C. Baird, *J. Am. Chem. Soc.* **1975**, *97*, 6598; b) R. S. Cahn, C. K. Ingold, V. Prelog, *Angew. Chem. Int. Ed. Engl.* **1966**, *5*, 385.
[15] H. Brunner, B. Nuber, M. Prommesberger, *Tetrahedron: Asymmetry* **1998**, *9*, 3223.
[16] A. Bondi, *J. Phys. Chem.* **1964**, *68*, 441.
[17] M. D. Fryzuk, C. D. Montgomery, *Organometallics* **1991**, *10*, 467.

 © 2005 Wiley-VCH Verlag GmbH & Co. KGaA, Weinheim

[18] G. Aullón, D. Bellamy, L. Brammer, E. A. Bruton, A. G. Orpen, *Chem. Commun.* **1998**, 653.
[19] W. J. Geary, *Coord. Chem. Rev.* **1971**, *7*, 81.
[20] M. Henning, K. Püntener, M. Scalone, *Tetrahedron: Asymmetry* **2000**, *11*, 1849.
[21] MACSPARTAN PRO Version 1.0.4. WaveFunction, Inc., 18401 Von Karman Avenue, suite 370, Irvine, CA 92612, U.S.A.
[22] Blank tests using HCOOH/NEt_3 as hydrogen donor system showed that the amino-oxazoline ligands are not stable under these conditions.
[23] D. G. I. Petra, P. C. J. Kamer, P. W. N. M. van Leeuwen, K. Goubitz, A. M. van Loon, J. G. de Vries, H. E. Schoemaker, *Eur. J. Inorg. Chem.* **1999**, 2335.
[24] S. Hashiguchi, A. Fujii, K.-J. Haack, K. Matsumura, T. Ikariya, R. Noyori, *Angew. Chem. Int. Ed. Engl.* **1997**, *36*, 288.
[25] R. Noyori, M. Tamakawa, S. Hashiguchi, *J. Org. Chem.* **2001**, *66*, 7931.
[26] W. L. F. Armarego, D. D. Perrin, *Purification of Laboratory Chemicals*, 4th ed., Butterworth-Heinemann, Oxford, UK, **1996**.
[27] G. M. Sheldrick, SADABS, a program for empirical absorption correction of area detector data, University of Göttingen, Germany, **1996**. Based on the method of Robert Blessing: R. H. Blessing, *Acta Crystallogr., Sect. A* **1995**, *51*, 33.
[28] G. M. Sheldrick, SHELXS 97, a computer program for crystal structure determination, University of Göttingen, **1997**.
[29] G. M. Sheldrick, SHELXL 97, a computer program for crystal structure refinement, University of Göttingen, **1997**.
[30] M. J. Frisch, G. W. Trucks, H. B. Schlegel, G. E. Scuseria, M. A. Robb, J. R. Cheeseman, V. G. Zakrzewski, J. A. Montgomery Jr., R. E. Stratmann, J. C. Burant, S. Dapprich, J. M. Millam, A. D. Daniels, K. N. Kudin, M. C. Strain, O. Farkas, J. Tomasi, V. Barone, M. Cossi, R. Cammi, B. Mennucci, C. Pomelli, C. Adamo, S. Clifford, J. Ochterski, G. A. Petersson, P. Y. Ayala, Q. Cui, K. Morokuma, P. Salvador, J. J. Dannenberg, D. K. Malick, A. D. Rabuck, K. Raghavachari, J. B. Foresman, J. Cioslowski, J. V. Ortiz, A. G. Baboul, B. B. Stefanov, G. Liu, A. Liashenko, P. Piskorz, I. Komaromi, R. Gomperts, R. L. Martin, D. J. Fox, T. Keith, M. A. Al-Laham, C. Y. Peng, A. Nanayakkara, M. Challacombe, P. M. W. Gill, B. Johnson, W. Chen, M. W. Wong, J. L. Andres, C. Gonzalez, M. Head-Gordon, E. S. Replogle, J. A. Pople, Gaussian98 (Revission A.11), Gaussian Inc., Pittsburgh, PA, **2001**.
[31] a) A. D. Becke, *J. Chem. Phys.* **1993**, *98*, 5648; b) C. Lee, W. Yang, R. G. Parr, *Phys. Rev. B* **1988**, *37*, 785.
[32] D. Andrae, U. Haeussermann, M. Dolg, H. Stoll, H. Preuss, *Theor. Chim. Acta* **1990**, *77*, 123.
[33] A. Schafer, H. Horn, R. Ahlrichs, *J. Chem. Phys.* **1992**, *97*, 2571.

Received: June 8, 2005
Published Online: September 21, 2005

 © 2005 Wiley-VCH Verlag GmbH & Co. KGaA, Weinheim

Mechanisms of Concurrent Hydride Migration Processes in a Triruthenium Cluster Capped by a Phenylphosphinidene (PPh) Ligand

Antony J. Deeming*[a] Caroline S. Forth,[a] Md. Iqbal Hyder,[b] Shariff E. Kabir,*[b] Ebbe Nordlander*[c] Fiona Rodgers[a] and Bettina Ullmann[c]

Keywords: Ruthenium / Clusters / Hydrides / Dynamic mobility / Kinetics

Two methods were used to synthesise $[Ru_3(\mu\text{-}H)_2(\mu_3\text{-}PPh)(CO)_7(\mu\text{-}dppm)]$ (**3**) (dppm = $Ph_2PCH_2PPh_2$), the subject of this paper. Treatment of $[Ru_3(CO)_{10}(\mu\text{-}dppm)]$ (**1**) with phenylphosphane in refluxing THF gave both $[Ru_3(\mu\text{-}H)(\mu\text{-}PHPh)(CO)_8(\mu\text{-}dppm)]$ (**2**) and $[Ru_3(\mu\text{-}H)_2(\mu_3\text{-}PPh)(CO)_7(\mu\text{-}dppm)]$ (**3**). Cluster **2** converts to **3** in refluxing THF. Alternatively the phenylphosphinidene cluster $[Ru_3(\mu\text{-}H)_2(\mu_3\text{-}PPh)(CO)_9]$ (**4**), prepared by the reported method of treating $[Ru_3(CO)_{12}]$ with phenylphosphane, reacts with dppm to produce cluster **3**. The single-crystal X-ray structures of **2** and **3** are reported. Hydride mobility in $[Ru_3(\mu\text{-}H)_2(\mu_3\text{-}PPh)(CO)_7(\mu\text{-}dppm)]$ (**3**) was analysed by variable-temperature ^1H and $^{31}P\{^1H\}$ NMR methods. The variations in the spectra with temperature could not be interpreted by a single process, several of which were explored and which gave inadequately matching computed and experimental spectra. However, the spectra were successfully analysed by two concurrent processes, both involving the migration of hydride ligands between Ru–Ru edges. The faster process leads to the exchange of the nonequivalent phosphorus nuclei but not hydride exchange, whereas the hydrides are also exchanged in the slower process. Both processes require hydride ligand migration from one Ru–Ru edge to a vacant one. The hydride ligand bridging the same pair of ruthenium atoms as the dppm ligand is the slower to migrate.

(© Wiley-VCH Verlag GmbH & Co. KGaA, 69451 Weinheim, Germany, 2005)

Introduction

Hydride migration between edge-bridging, face-bridging and terminal sites in transition-metal clusters has been commonly observed.[1] It is possible to probe these migrations by NMR coalescence and other classical methods if the hydride ligands are inequivalent, by changes in the appearance of coupling patterns to the metal centres if there is a spin-active metal nucleus, or by exchanges in sites within another ligand that result from hydride migration. The phosphinidene-capped cluster $[Ru_3(\mu\text{-}H)_2(\mu_3\text{-}PPh)(CO)_9]$[2–4] (**4**) presumably has mobile hydride ligands which can undergo degenerate migrations from either of the two occupied edges to the vacant one. To the best of our knowledge this has never been demonstrated although in related clusters, such as $[Os_3(\mu\text{-}H)_2(\mu_3\text{-}S)(CO)_9]$, this type of process has been investigated.[5] By introducing phosphane ligands into $[Ru_3(\mu\text{-}H)_2(\mu_3\text{-}PPh)(CO)_9]$ (**4**), the hydrides may become inequivalent and distinguishable hydride migrations of different rate might occur. The hydride ligands will preferentially occupy some sites rather than others, in particular the bridging sites between the most electron-rich metal centres. Migration of hydrides out of electron-rich sites into electron-poor sites is likely to be slow.

In this paper we will describe in detail the fluxional behaviour of the cluster $[Ru_3(\mu\text{-}H)_2(\mu_3\text{-}PPh)(CO)_7(\mu\text{-}dppm)]$ (**3**) which has C_1 symmetry. There are inequivalent hydrides and three inequivalent ^{31}P nuclei so that NMR analysis of the fluxional behaviour is straightforward.

Results and Discussion

Synthesis and Characterisation of Compounds

We used two different methods to synthesise compound **3** from $[Ru_3(CO)_{12}]$ as shown in Scheme 1. The introduction of the diphosphane (dppm) ligand first followed by treatment of $[Ru_3(CO)_{10}(dppm)]$ (**1**)[6] with Ph_2PH in refluxing THF, gave both $[Ru_3(\mu\text{-}H)(\mu\text{-}PHPh)(CO)_8(\mu\text{-}dppm)]$ (**2**) and $[Ru_3(\mu\text{-}H)_2(\mu_3\text{-}PPh)(CO)_7(\mu\text{-}dppm)]$ (**3**), which were easily separated and characterised. There was no improvement in the reaction of **1** with $PhPH_2$ when Me_3NO was employed to remove CO ligands by oxidation. Thermal treatment of **2** in refluxing THF leads to **3**, and presumably this is the route by which **3** is formed as shown in Scheme 1.

Alternatively, the PPh ligand may be introduced in the first step to form $[Ru_3(\mu\text{-}H)_2(\mu_3\text{-}PPh)(CO)_9]$ **4** from Ph_2PH and $[Ru_3(CO)_{12}]$ by known methods.[2–4] Cluster **4** may then

[a] Department of Chemistry, University College London, 20 Gordon Street, London, UK WC1H 0AJ
E-mail: a.j.deeming@ucl.ac.uk
[b] Department of Chemistry, Jahangirnagar University, Savar, Dhaka 1342, Bangladesh
[c] Inorganic Chemistry, Center for Chemistry and Chemical Engineering, Lund University, Box 124, 22100 Lund, Sweden

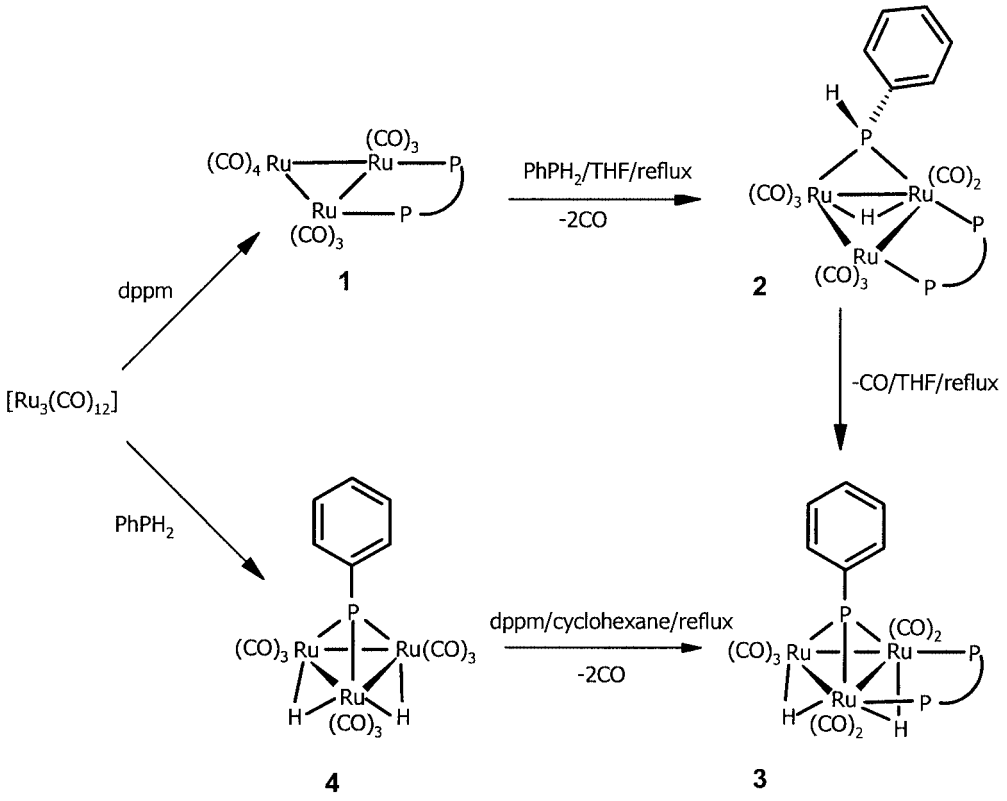

Scheme 1.

be substituted by dppm. This substitution was attempted unsuccessfully by preparing MeCN derivatives of the type $[Ru_3(\mu\text{-}H)_2(\mu_3\text{-}PPh)(CO)_{9-x}(MeCN)_x]$ (x = 1 or 2), followed by treatment of these in situ with dppm. Likewise a photochemical procedure (UV) for the reaction of $[Ru_3(\mu\text{-}H)_2(\mu_3\text{-}PPh)(CO)_9]$ (**4**) with dppm was attempted. Neither of these methods gave much product. However, direct thermal treatment of **4** with dppm leads to the two products: $[Ru_3(\mu\text{-}H)_2(\mu_3\text{-}PPh)(CO)_7(\mu\text{-}dppm)]$ (**3**) and a minor yellow band which gave $[Ru_3(\mu\text{-}H)_2(\mu_3\text{-}PPh)(CO)_8(\mu\text{-}dppm)]$. The latter complex readily looses CO to form **3**, and we have been unable to characterise it fully. We believe it contains a monodentate dppm ligand. This was indicateded by its IR spectrum around 2000 cm^{-1}, which is very closely similar to that of monodentate phosphane derivatives such as $[Ru_3(\mu\text{-}H)_2(\mu_3\text{-}PPh)(CO)_8(PMe_2Ph)]$.[7,8]

Characterisation of Compound 2

The single-crystal XRD structure of cluster **2** is shown in Figure 1. Crystal data are in Table 1 and some selected geometric data are in Table 2. The framework of the compound corresponds to that of $[Ru_3(\mu\text{-}H)(\mu\text{-}PHPh)(CO)_{10}]$ with the H and the PHPh ligands spanning the same Ru–Ru edge.[2] The hydride ligand was located from diffraction data. The dppm ligand, however, bridges one of the other two Ru–Ru edges, unlike the structure of $[Os_3(\mu\text{-}H)_2(CO)_8(\mu\text{-}dppm)]$ in which the three bridging ligands are at the same Os–Os edge.[9] The structure of **2** is essentially as expected for this arrangement of ligands but there are some bond lengths worth noting. Atom Ru(3) is the most heavily substituted by P-donors but is associated with the shorter Ru–P bonds. For the PHPh ligand, Ru(3)–P(1) [2.3069(12) Å] is shorter than Ru(1)–P(1) [2.3490(12) Å] and for dppm, Ru(3)–P(2) [2.2998(11) Å] is shorter than Ru(2)–P(3) [2.3245(12) Å]. If, as one would expect, Ru(3) is the most electron-rich centre, the bond lengths could be explained by greater π donation by that atom to the phosphorus ligands. One should also note that Ru–CO distances *trans* to the μ-PHPh ligand are long and Ru–CO distances *trans* to μ-H are short with respect to the other related distances in this molecule. The bridging dppm has negligible impact on the length of the Ru–Ru bond compared to the unbridged edge; 2.8494(10) Å compared with 2.8509(8) Å.

In the light of this structure, there are some problems in accounting for the ^1H NMR spectra. The IR and mass spectra are completely consistent with the solid-state structure but the NMR spectrum seems to indicate higher symmetry than that in the crystal. The hydride appears as a 1:2:1 triplet at δ = –16.30 ppm and the CH_2 hydrogen atoms appear as a single triplet at δ = 4.26 ppm. Neither of these observations are predicted from the XRD structure. The spectra at –50 °C as well as at 27 °C show these features so we believe the compound is non-fluxional. The CH_2 triplet must be due to accidental isochronicity and the observed triplet for the hydride signal is probably due to similar coupling to the two non-equivalent ^{31}P nuclei at Ru(3)

 © 2005 Wiley-VCH Verlag GmbH & Co. KGaA, Weinheim

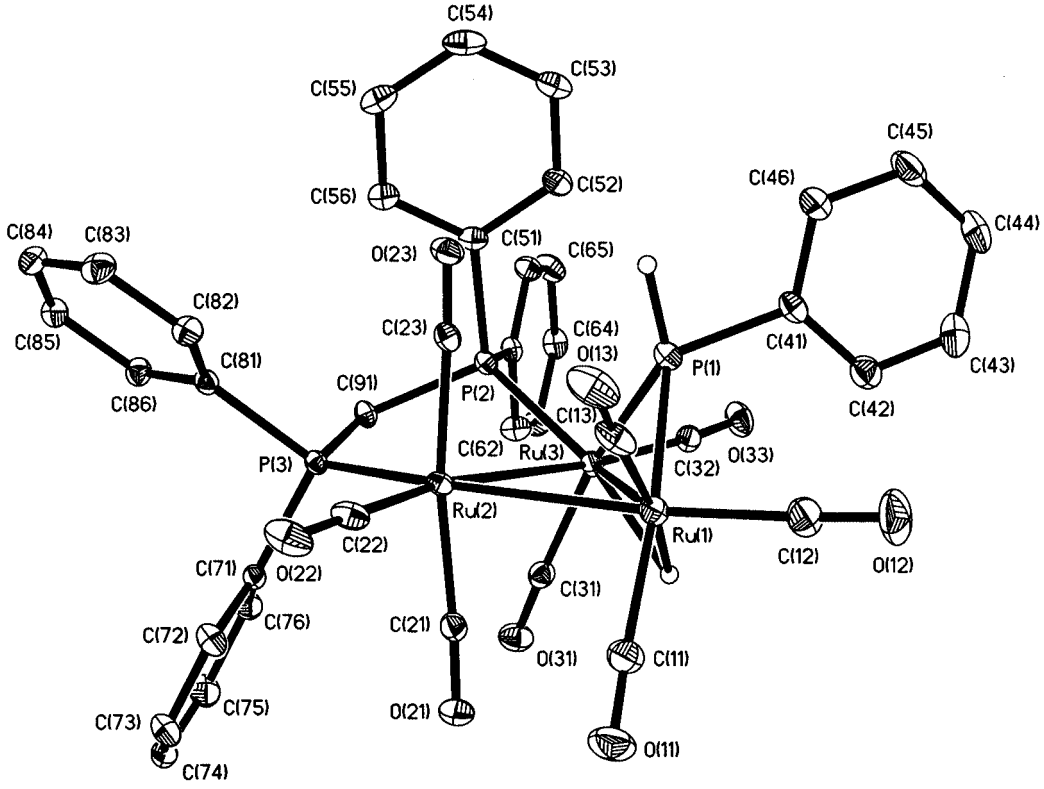

Figure 1. Molecular structure of $[Ru_3(\mu\text{-H})(\mu\text{-PHPh})(CO)_8(\mu\text{-dppm})]$ (**2**). H atoms on phenyl rings were omitted.

Table 1. Crystal data and structure refinement for the clusters $[Ru_3(\mu\text{-H})(\mu\text{-PHPh})(CO)_8(\mu\text{-dppm})]$ (**2**) and $[Ru_3(\mu\text{-H})_2(\mu_3\text{-PPh})(CO)_7(\mu\text{-dppm})]$ (**3**).

	2	**3**
Chemical formula	$C_{39}H_{29}O_8P_3Ru_3$	$C_{38}H_{29}O_7P_3Ru_3$
Formula mass	1021.74	993.73
Temperature [K]	150(2)	293(2)
Crystal system, space group	triclinic, $P\bar{1}$	monoclinic, $P2_1/n$
a [Å]	11.524(4)	17.4429(12)
b [Å]	12.337(4)	12.8386(9)
c [Å]	15.278(6)	17.7454(12)
α [°]	112.940(5)	90
β [°]	92.037(6)	92.1310(10)
γ [°]	106.155(6)	90
Cell volume [Å^3]	1895.6(12)	3971.2(5)
Z	2	4
Calcd. density [g cm^{-3}]	1.790	1.662
Abs. coeff. μ [mm^{-1}]	1.359	1.293
$F(000)$	1008	1960
Crystal colour	orange-red	yellow
Crystal size [mm]	0.46 × 0.13 × 0.11	0.43 × 0.33 × 0.23
θ range for data collection [°]	1.47 to 28.41	1.61 to 28.30
Index ranges	h –15/15, k –16/16, l –19 /19	h –22/22, k –17/17, l –23/23
Completeness to θ	91.5% to 28.41	99.9% to 26.00°
Reflections collected	16773	34723
Independent reflections	8740 (R_{int} = 0.0231)	9530 (R_{int} = 0.0211)
Reflections with $F^2 > 2\sigma$	7935	8382
Min. and max. transmission	0.5744 and 0.8705	0.6070 and 0.7571
Structure solution	Patterson synthesis	Direct methods
Weighting parameters a, b	0.0337, 4.9084	0.0401, 1.3354
Data/restraints/parameters	8740/0/484	9530/0/466
Final R indices [$F^2 > 2\sigma$]	R_1 = 0.0384, wR_2 = 0.0921	R_1 = 0.0315, wR_2 = 0.0752
R indices (all data)	R_1 = 0.0427, wR_2 = 0.0946	R_1 = 0.0376, wR_2 = 0.0784
Goodness-of-fit on F^2	1.073	1.061
Largest and mean shift/su	0.001 and 0.000	0.004 and 0.000
Largest diff. peak and hole [e·Å^{-3}]	2.716 and –1.515	0.486 and –0.332

 © 2005 Wiley-VCH Verlag GmbH & Co. KGaA, Weinheim

Table 2. Selected bond lengths [Å] and angles [°] for the compound $[Ru_3(\mu\text{-H})(\mu\text{-PHPh})(CO)_8(\mu\text{-dppm})]$ (**2**).

Ru(1)–Ru(2)	2.8509(8)	Ru(1)–P(1)–Ru(3)	77.62(4)
Ru(1)–Ru(3)	2.9183(10)	Ru(2)–Ru(3)–P(2)	86.22(3)
Ru(2)–Ru(3)	2.8494(10)	Ru(3)–Ru(2)–P(3)	92.38(3)
Ru(1)–P(1)	2.3490(12)	P(1)–Ru(3)–P(2)	101.91(4)
Ru(3)–P(1)	2.3069(12)	P(1)–Ru(1)–C(13)	92.68(13)
Ru(3)–P(2)	2.2998(11)	Ru(1)–Ru(2)–P(3)	153.74(3)
Ru(2)–P(3)	2.3245(12)	Ru(1)–Ru(3)–P(2)	136.40(3)

which are not resolved, together perhaps with virtual coupling effects.

Characterisation of $[Ru_3(\mu\text{-H})_2(\mu_3\text{-PPh})(CO)_7(\mu\text{-dppm})]$ (3)

The single-crystal XRD structure of cluster **3** is shown in Figure 2 and some selected geometric data are listed in Table 3. The structure is based on that known for $[Ru_3(\mu\text{-H})_2(\mu_3\text{-PPh})(CO)_9]$.[2] The dppm ligand bridges in equatorial sites at Ru(1) and Ru(2) with all three P nuclei on the same side of the Ru_3 plane. The hydride ligands are located on the Ru(1)–Ru(2) and Ru(1)–Ru(3) edges consistent with these bonds being longer than Ru(2)–Ru(3). ^{1}H NMR spectroscopic data at 233 K and $^{31}P\{^1H\}$ NMR spectroscopic data at 213 K show all three ^{31}P nuclei are in different environments and that the hydrides are non-equivalent. The P nuclei of the dppm ligand both lie equatorially (*cis* to the PPh ligand) and it is the hydride locations that make the dppm unsymmetrical.

Analysis of VT ^{1}H and $^{31}P\{^1H\}$ NMR spectra for $[Ru_3(\mu\text{-H})_2(\mu_3\text{-PPh})(CO)_7(\mu\text{-dppm})]$ (3)

Figure 3 shows that the $^{31}P\{^1H\}$ NMR spectrum for $[Ru_3(\mu\text{-H})_2(\mu_3\text{-PPh})(CO)_7(\mu\text{-dppm})]$ (**3**) at 213 K contains a double doublet at δ = 277.75 for the phosphinidene ligand and two doublets of doublets at δ = 25.20 and 27.70 ppm for the inequivalent dppm phosphorus nuclei. Changes oc-

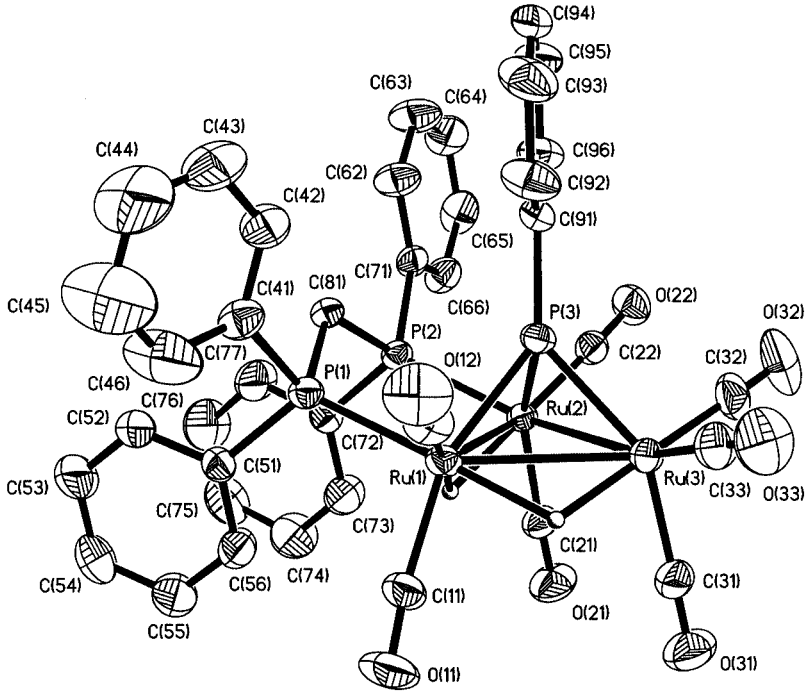

Figure 2. Molecular structure of $[Ru_3(\mu\text{-H})_2(\mu_3\text{-PPh})(CO)_7(\mu\text{-dppm})]$ (**3**). H atoms on phenyl rings were omitted.

Table 3. Selected bond lengths [Å] and angles [°] for the compound $[Ru_3(\mu\text{-H})_2(\mu_3\text{-PPh})(CO)_7(\mu\text{-dppm})]$ (**3**).

Ru(1)–Ru(2)	2.9351(3)	Ru(1)–P(3)–Ru(2)	79.40(2)
Ru(1)–Ru(3)	2.9428(4)	Ru(1)–P(3)–Ru(3)	79.21(2)
Ru(2)–Ru(3)	2.8317(3)	Ru(2)–P(3)–Ru(3)	76.55(2)
Ru(1)–P(3)	2.3196(7)	Ru(1)–Ru(2)–P(2)	93.724(18)
Ru(2)–P(3)	2.2750(7)	Ru(2)–Ru(1)–P(1)	90.406(18)
Ru(3)–P(3)	2.2964(7)	P(1)–Ru(1)–P(3)	96.36(2)
Ru(1)–P(1)	2.3205(7)	P(2)–Ru(2)–P(3)	99.35(2)
Ru(2)–P(2)	2.3140(7)		

 © 2005 Wiley-VCH Verlag GmbH & Co. KGaA, Weinheim

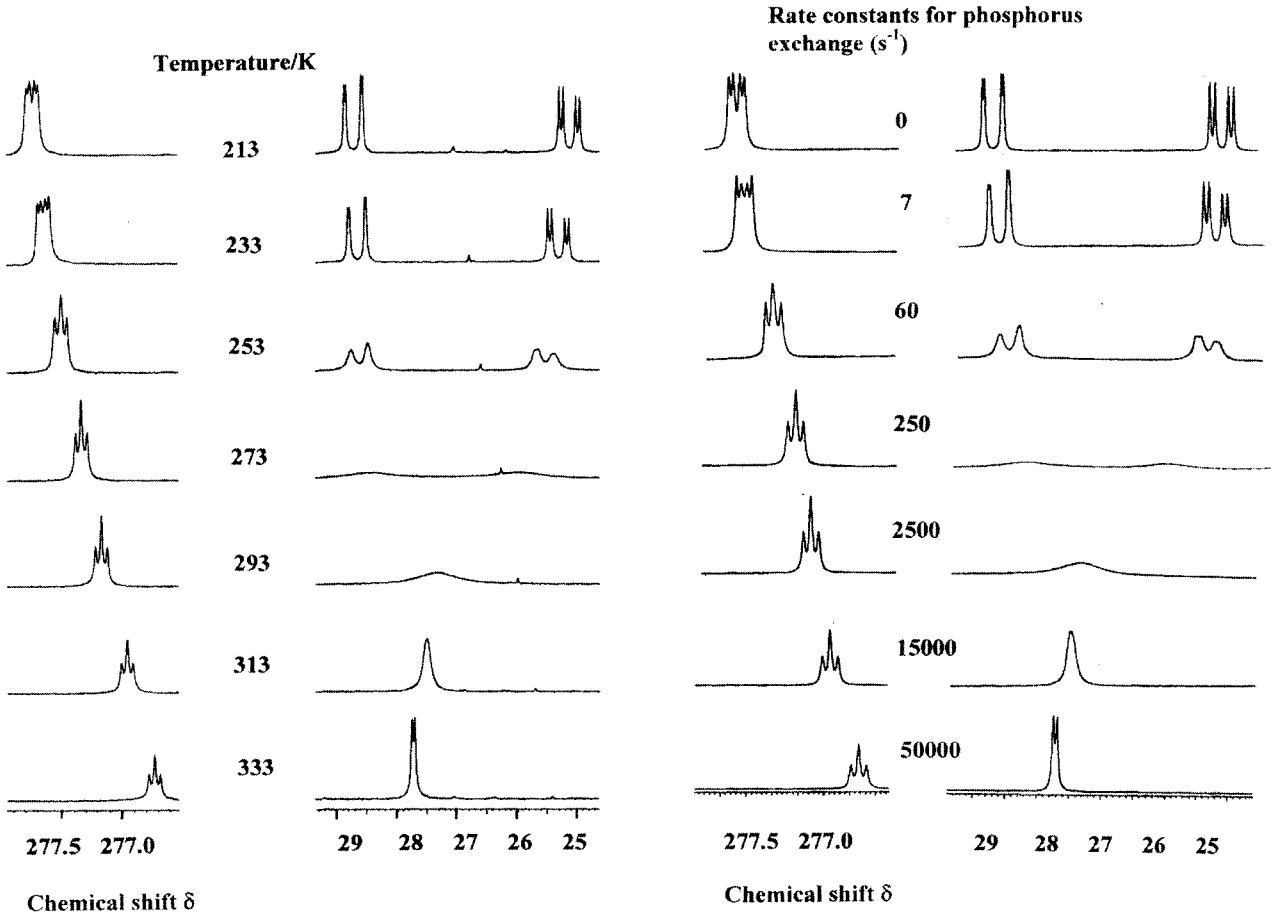

Figure 3. Spectra on left: observed 202.5 MHz $^{31}P\{^1H\}$ NMR spectra of $[Ru_3(\mu\text{-}H)_2(\mu_3\text{-}PPh)(CO)_7(\mu\text{-}dppm)]$ (**3**) in $CDCl_3$ recorded at the various temperatures given. Spectra on right: corresponding $^{31}P\{^1H\}$ NMR spectra of **3** simulated using gNMR at the given rate constants for phosphorus–phosphorus exchange.

cur as the temperature is raised. The dppm signals broaden and coalesce at about 260 K forming a doublet at 333 K. The phosphinidene converts from a double doublet to a 1:2:1 triplet over the same temperature range. These observations are consistent with the exchange of the phosphorus atoms of the dppm resulting from hydride mobility. This was confirmed by a accurate simulation of the $^{31}P\{^1H\}$ NMR spectra (using gNMR[10]) also shown in Figure 3 which gives the rates used to simulate the spectra. It was also necessary to change the chemical shifts somewhat with temperature to produce an accurate simulation. The simplest intramolecular process to account for the observations is shown in Scheme 2.

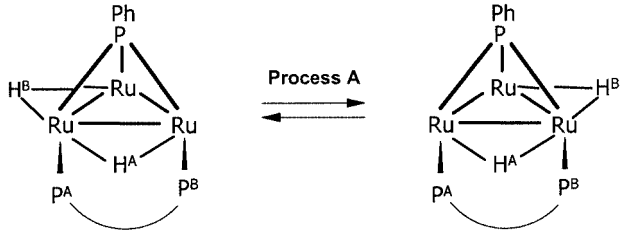

Scheme 2.

Process A does not lead to hydride exchange. This wastested by recording the hydride spectrum over a temperature range (Figure 4). The ^1H NMR spectrum for the hydrides of $[Ru_3(\mu\text{-}H)_2(\mu_3\text{-}PPh)(CO)_7(\mu\text{-}dppm)]$ at 333 K is a single doublet (with an indication of a small triplet pattern at each branch of the doublet). The crystal structure indicates that the hydrides should be non-equivalent, and at 233 K the hydride spectrum appears as a complex multiplet (at least 10 peaks resolved) (see Figure 4). We were able to model this multiplet satisfactorilly by two overlapping multiplets for the non-equivalent hydride ligands at δ = –18.450 and –18.466 ppm, and the NMR shifts and coupling constants used in these simulations are given in Table 4. By using the data in Table 4 we obtained good agreement between observed and calculated spectra at the low-temperature limit (233 K for ^1H and 213 K for ^{31}P). The overlap of hydride signals made it difficult to follow coalescence. We attempted to simulate the spectra on the basis of various exchange processes. Figure 4 shows spectra predicted by process A in Scheme 2. Clearly the hydrides are not exchanging so two overlapping multiplets are found even at the highest rates. Hydride exchange is required to give the observed high-temperature spectra. Figure 4 show the spec-

 © 2005 Wiley-VCH Verlag GmbH & Co. KGaA, Weinheim

tra expected on the basis of the exchange of hydride nuclei alone without any other exchange occurring. A single resonance is obtained but very different from that observed. We also simulated spectra on the basis of process B shown in Scheme 3. The central configuration with a plane of symmetry is not detectably populated at any time and is not observed in the low-temperature spectra. Hence we cannot descriminate process B from one in which there is synchro-

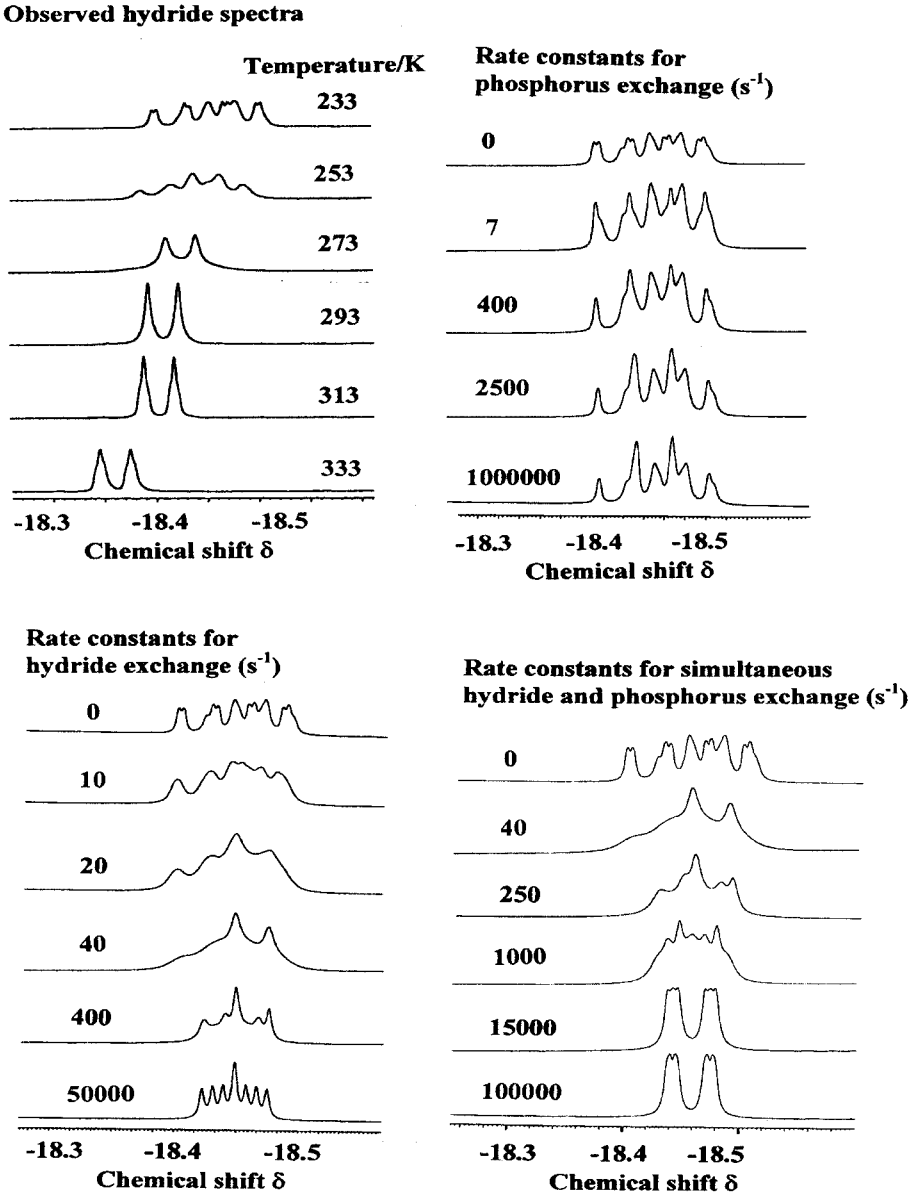

Figure 4. Top left: observed 500 MHz ^{1}H NMR spectra of $[Ru_3(\mu\text{-}H)_2(\mu_3\text{-}PPh)(CO)_7(\mu\text{-}dppm)]$ (**3**) in $CDCl_3$ in the hydride region recorded at various temperatures. Top right: Corresponding spectra of **3** simulated on the basis of exchange of the phosphorus nuclei of the dppm ligand without simultaneous exchange of the hydride ligands. Bottom left: corresponding spectra of **3** simulated on the basis of hydride exchange alone. Bottom right: corresponding spectra of **3** simulated on the basis of exchange of the hydride nuclei and exchange of the phosphorus nuclei both with the rate constants given.

Table 4. Chemical shifts (δ) and coupling constants (Hz) used for the 500-MHz NMR simulations for the compound $[Ru_3(\mu\text{-}H)_2(\mu\text{-}PPh)(CO)_7(\mu\text{-}dppm)]$ (**3**) at the lowest temperatures.

Nucleus		δ	Coupling constants with nucleus [Hz]			
			1	2	3	4
1	^{1}H	–18.450				
2	^{1}H	–18.466	1.00			
3	^{31}P	25.200	2.50	–13.00		
4	^{31}P	27.700	34.00	–13.50	59.7	
5	^{31}P	277.750	16.50	15.80	17.2	7.10

 © 2005 Wiley-VCH Verlag GmbH & Co. KGaA, Weinheim

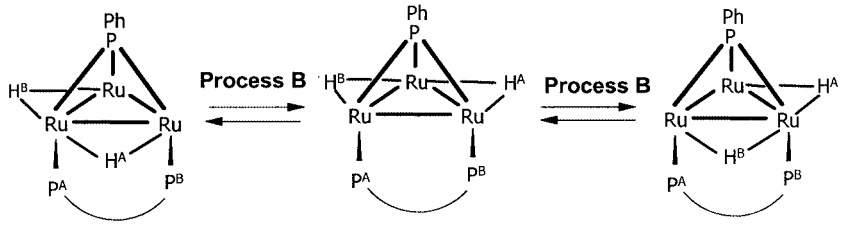

Scheme 3.

nous motion of both hydrides without the intermediate shown in Scheme 3. In this case there would be a transition state with a mirror plane.

In process B (or the modified single-step process described above) there is simultaneous exchange of H^A with H^B and of P^A with P^B, and Figure 4 shows the predicted outcome, again different to observed spectra. Process B does not lead to total exchange because, for example, H^A does not become equally correlated to P^A and to P^B. We have found that it is necessary to apply both processes A and B with different rates to obtain satisfactory correspondence of observed with calculated spectra. Figure 5 shows an excellent match, except that there is some observed drift of chemical shift with temperature which is not accounted for by exchange processes. It is surprising that there is such good correspondence, and we believe that this is because the H^A and H^B signals change chemical shifts in a similar way with changing temperature. A graphical presentation of these rate data is given in Figure 6. Note that the rates of process A obtained from a deconvolution of the two processes observed in the hydride spectra are closely similar to those obtained from the $^{31}P\{^1H\}$ spectra. Process B is about 5 times slower than process A and activation data for process **A** are $\Delta G^{\ddagger}$ = (52.2 ± 3.7) kJ·mol^{-1}, $\Delta H^{\ddagger}$ = (57.1 ± 3.7) kJ·mol^{-1}, $\Delta S^{\ddagger}$ = (16.7 ± 13.7) J·K^{-1}·mol^{-1} while those for process B are $\Delta G^{\ddagger}$ = (56.1 ± 3.0) kJ·mol^{-1}, $\Delta H^{\ddagger}$ = (60.0 ± 3.0) kJ·mol^{-1}, $\Delta S^{\ddagger}$ = (12.9 ± 9.6) J·K^{-1}·mol^{-1} The rate of migration of H^A from the most electron-rich site between the dppm-substituted Ru atoms is slower than migration of H^B which is in a less electron-rich site. However, the difference is very small, largely enthalpic and only represents a difference in $\Delta H^{\ddagger}$ of 2.9 kJ·mol^{-1}. A combination

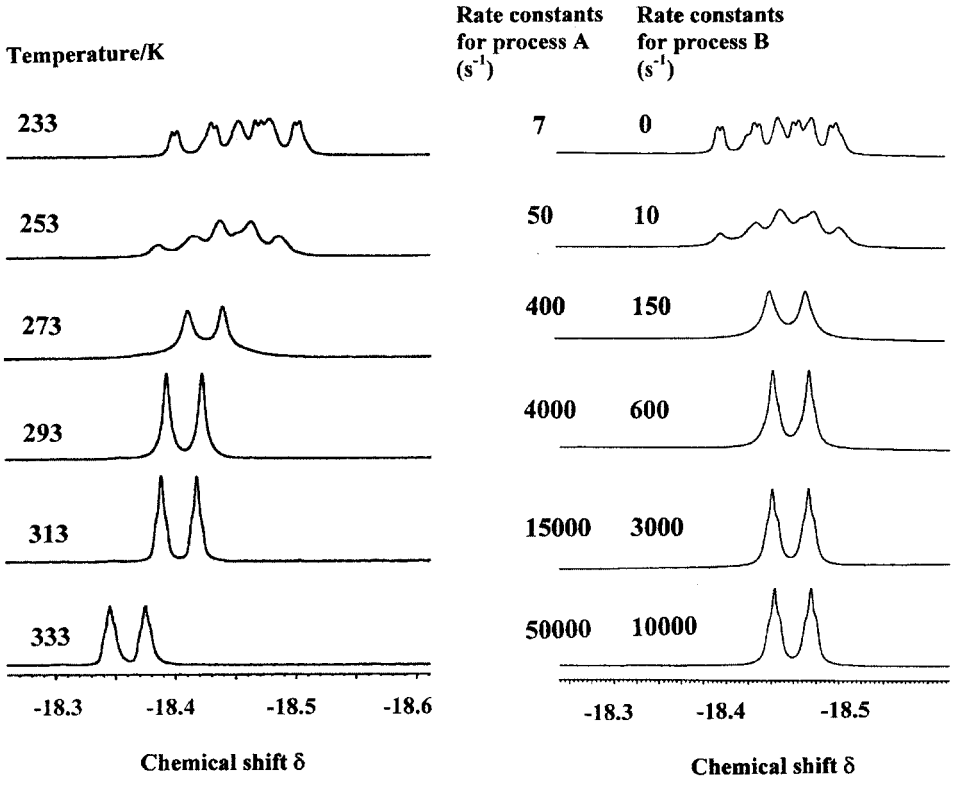

Figure 5. Left: observed 500 MHz ^1H NMR spectra of $[Ru_3(\mu\text{-}H)_2(\mu_3\text{-}PPh)(CO)_7(\mu\text{-}dppm)]$ (**3**) in $CDCl_3$ solution in the hydride region recorded at various temperatures. Right: corresponding spectra of **3** simulated on the basis of exchange by processes A and B with the rate constants given.

 © 2005 Wiley-VCH Verlag GmbH & Co. KGaA, Weinheim

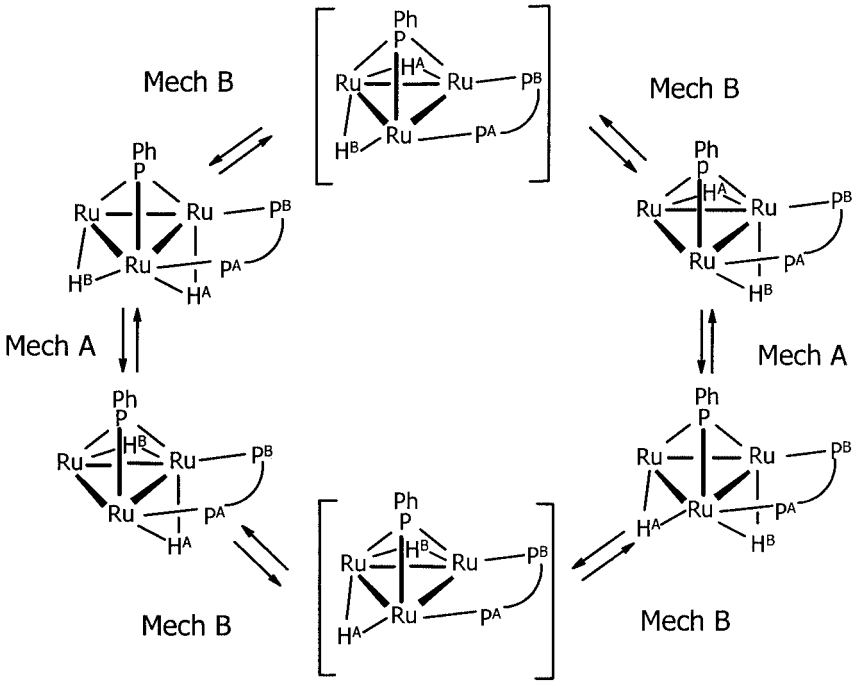

Scheme 4.

of processes A and B can be represented by Scheme 4. In the cycle each hydride jumps in turn and progresses through the three edges of the metal triangle.

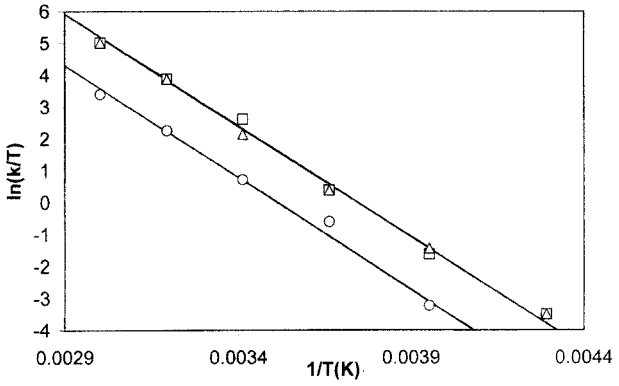

Figure 6. Graph of ln(k/T) for the processes **A** and **B** against (1/T)/K^{-1} for cluster [Ru_3(μ-H)$_2$(μ$_3$-PPh)(CO)$_7$(μ-dppm)] (**3**) in $CDCl_3$ solution. The rate of process **A** were obtained from the exchange of P nuclei observed in the $^{31}P\{^1H\}$ NMR spectrum (points Δ) and from ^1H NMR spectroscopic data (points □). Rates of process **B** were also obtained from ^1H NMR spectroscopic data (points ○).

Experimental Section

The compound [$Ru_3(CO)_{10}$(μ-dppm)] (**1**) was prepared according to the known method.[6] Infrared spectra were recorded with a Shimadzu FTIR 8101 spectrophotometer. ^1H and $^{31}P\{^1H\}$ NMR spectra were recorded with a Bruker DPX400 or DRX500 spectrometer.

Reaction of [$Ru_3(CO)_{10}$(μ-dppm)] (1) with $PPhH_2$: A 10% hexane solution of PH_2Ph (0.70 cm^3, 0.636 mmol) was added to a THF solution (35 cm^3) of **1** (0.205 g, 0.212 mmol) in a three-necked round-bottom flask. The reaction mixture was then refluxed for 6 h. The solvent was removed under reduced pressure and the residue was chromatographed by TLC on silica gel. Elution with cyclohexane/CH_2Cl_2 (7:3, v/v) developed two major and several very minor bands. The fastest moving band afforded unreacted **1** (0.005 g) and [Ru_3(μ-H)(μ-PHPh)(CO)$_8$(μ-dppm)] **2** (0.015 g, 7%) after fractional crystallization from hexane/CH_2Cl_2 at –15 °C.

Characterization of 2: $C_{39}H_{29}O_8P_3Ru_3$: calcd. C 45.84, H 2.87; found C 45.79, H 2.95. IR (νCO, CH_2Cl_2): $\tilde{\nu}$ = 2062 s, 2016 m, 1995 vs, 1950 m cm^{-1}. ^1H NMR ($CDCl_3$, 25 °C): δ = 4.26 (t, J = 10.8 Hz, 2 H), 7.35 (m, 26 H), –16.30 (t, J = 28.4 Hz, 1 H). FAB MS showed the parent molcular ion: m/z 1022. The second band yielded [Ru_3(μ-H)$_2$(μ$_3$-PPh)(CO)$_7$(μ-dppm)] (**3**) (0.042 g, 20%) as yellow crystals from hexane/CH_2Cl_2 at room temperature. $C_{38}H_{29}O_7P_3Ru_3$ calcd. C 45.92, H 2.95; found C 45.99, H 2.72. IR (νCO, CH_2Cl_2): $\tilde{\nu}$ = 2054 s, 2031 s, 1994 vs, 1985 sh, 1940 w cm^{-1}. FAB MS showed the parent molecular ion: m/z 994. The minor bands were too small for complete characterization.

Reaction of 1 with $PPhH_2$ in Presence of Me_3NO: To a dichloromethane solution (35 cm^3) of **1** (0.105 g, 0.109 mmol) was added a 10% hexane solution of $PPhH_2$ (0.24 cm^3, 0.218 mmol) followed by a dichloromethane solution (25 cm^3) of Me_3NO (0.017 g, 0.226 mmol). The reaction mixture was stirred at room temperature for 30 min. The solution was filtered through a short silica column, and the volatiles were removed under reduced pressure. Chromatographic separation as above developed one major and several minor bands. The major band gave unreacted **1** (0.010 g) and **2** (0.012 g, 11%) after fractional crystallization from hexane/CH_2Cl_2 at –4 °C. The minor bands were not completely characterized.

Conversion of 2 into 3: A THF solution of **2** (0.012 g, 0.012 mmol) was heated to reflux for 3 h. Removal of solvent under reduced pressure and chromatographic separation of the residue as above afforded **3** (0.007 g, 51%) as yellow crystals.

Synthesis of [Ru_3(μ-H)$_2$(μ$_3$-PPh)(CO)$_9$]: This cluster was prepared by a method modified from that in the literature. The cluster

 © 2005 Wiley-VCH Verlag GmbH & Co. KGaA, Weinheim

$[Ru_3(CO)_{12}]$ (0.252 g) was treated with equimolar PH_2Ph in cyclohexane at 60 °C for 45 min and then at 80 °C for 60 min. The product was separated by TLC on silica to give the product as yellow crystals (0.134 g, 51%) which were characterised by IR, MS, ^1H and ^{31}P NMR and by elemental analysis.

Synthesis of $[Ru_3(\mu\text{-}H)_2(\mu_3\text{-}PPh)(CO)_7(\mu\text{-}dppm)]$ from $[Ru_3(\mu\text{-}H)_2(\mu_3\text{-}PPh)(CO)_9]$: A standard procedure of preparing an acetonitrile derivative prior to substitution by phosphane was unsuccessful. Thus treatment of $[Ru_3(\mu\text{-}H)_2(\mu_3\text{-}PPh)(CO)_9]$ with $Me_3NO{\cdot}2H_2O$ in dichloromethane and acetonitrile did not form significant amounts of $[Ru_3(\mu\text{-}H)_2(\mu_3\text{-}PPh)(CO)_{9-x}(MeCN)_x]$, where $x = 1$ or 2. Treatment of the solution formed in this way with tertiary phosphanes did not give simple substitution products. Likewise visible photolysis of dichloromethane solutions of $[Ru_3(\mu\text{-}H)_2(\mu_3\text{-}PPh)(CO)_9]$ in the presence of dppm at room temperature did not lead to any significant reaction. However, direct thermal reaction of $[Ru_3(\mu\text{-}H)_2(\mu_3\text{-}PPh)(CO)_9]$ (0.0419 g) with dppm (0.0391 g) in refluxing cyclohexane (50 cm^3) under dinitrogen lead to the yellow solution becoming deep orange after 50 min. IR spectrsocopy indicated that most of the starting material had been consumed. Removal of the solvent under reduced pressure and separation of the residue by TLC [silica; eluent, petroleum ether (b. p. 40–60 °C)/dichloromethane, 3:1 by volume)] gave several bands. The major yellow band yielded $[Ru_3(\mu\text{-}H)_2(\mu_3\text{-}PPh)(CO)_7(\mu\text{-}dppm)]$ (**3**) as yellow crystals (0.020 g, 32%), whereas a minor yellow band gave $[Ru_3(\mu\text{-}H)_2(\mu_3\text{-}PPh)(CO)_8(\mu\text{-}dppm)]$ as a yellow solid (0.010 g, 16%). The latter compound has a similar IR spectrum [2072 w, 2047 m, 2038 vs, 2000 s, 1992 m cm^{-1} in cyclohexane] to monophosphane derivatives such as $[Ru_3(\mu\text{-}H)_2(\mu_3\text{-}PPh)(CO)_8(PMe_2Ph)]$[8] [2072 m, 2038 vs, 2003 m, 1989 m, 1973 cm^{-1} in cyclohexane], $[Ru_3(\mu\text{-}H)_2(\mu_3\text{-}PPh)(CO)_8(PH_2Ph)]$[2] [2077 m, 2048 s, 2041 s, 2009 s, 2001 m, 1993 m, 1978 w cm^{-1} in cyclohexane] and $[Ru_3(\mu\text{-}H)_2(\mu_3\text{-}PPh)(CO)_8(PMePh_2)]$.[9] Therefore, we believe the dppm is monodentate but we have not characterised the compound further.

X-Ray Crystal Structure Determinations for Compounds 2 and 3: Single crystals of compounds **2** and **3** were mounted on glass fibers and all geometric and intensity data were obtained with a Bruker SMART APEX CCD diffractometer using graphite-monochromated Mo-K_α radiation ($\lambda = 0.71073$ Å) at 150(2) K (compound **2**) and 293(2) K (compound **3**). Data reduction and integration was carried out with SAINT+ and absorption corrections were applied using the programme SADABS.[11,12] Structures were solved by Patterson synthesis for compound **2** or direct methods for compound **3** and developed using alternating cycles of least-squares refinement and difference-Fourier synthesis. All non-hydrogen atoms were refined anisotropically. Hydrogen atoms, except those bonded to ruthenium, were placed in calculated positions and their thermal parameters linked to those of the atoms to which they were attached (riding model). Hydrogen atoms bridging the ruthenium atoms were located and their positions refined using fixed isotropic thermal parameters. The SHELXTL PLUS V6.10 program package was used for structure solution and refinement.[13] General details: data collection method, ω rotation with narrow frames; absorption correction, semi-empirical from equivalents; refinement method, full-matrix least-squares on F^2.

CCDC-243253 (for **2**) and -243253 (for **3**) contain the supplementary crystallographic data for this paper. These data can be obtained free of charge from The Cambridge Crystallographic Data Centre via www.ccdc.cam.ac.uk/data_request/cif.

Acknowledgments

A. J. D. thanks the Wenner-Gren Foundation (Stockholm) for a fellowship to work with Dr. Nordlander at Lund University. Funds were also provided by the Royal Society (London) and the Swedish Academy of Sciences to support this collaboration. C. S. F. thanks the Chemistry Department, University College London for a teaching assistantship to carry out Ph. D. work. S. E. K. acknowledges the Royal Society for funds to work at UCL and the Swedish International Development Agency and the Swedish Science Research Council for support.

[1] a) Some recent examples: S. P. Tunik, T. S. Pilyugina, I. O. Koskevoy, S. I. Selivanov, M. Haukka, T. A. Pakkanen, *Organometallics* **2004**, *23*, 568; b) M. G. Ballinas-López, E. V. García-Báez, M. J. Rosales-Hoz, *Polyhedron* **2003**, *22*, 3403; c) T. Beringhelli, E. Cariati, C. Dragonetti, S. Galli, E. Lucenti, D. Roberto, A. Sironi, R. Ugo, *Inorg. Chim. Acta* **2003**, *354*, 79; d) G. Süss-Fink, L. Plasseraud, A. Maisse-François, H. Stoeckli-Evans, H. Berken, T. Fox, R. Gautier, J.-Y. Saillard, *J. Organomet. Chem.* **2000**, *609*, 196; e) M. P. Cifuentes, M. G. Humphrey, B. W. Skelton, A. H. White, *J. Organomet. Chem.* **1996**, *507*, 163; f) J. B. Keister, U. Frey, D. Zbinden, A. E. Merbach, *Organometallics* **1991**, *10*, 1497; g) L. R. Nevinger, J. B. Keister, *Organometallics* **1990**, *9*, 2313; h) P. Ewing, L. J. Farrugia, D. S. Rycroft, *Organometallics* **1988**, *7*, 859.

[2] F. Iwasaki, M. J. Mays, P. R. Raithby, P. L. Taylor, P. J. Wheatley, *J. Organomet. Chem.* **1981**, *213*, 185.

[3] S. P. Rowley, P. S. White, C. K. Schaver, *Inorg. Chem.* **1992**, *31*, 3158.

[4] E. Ngai-Man Ho, W.-T. Wong, *J. Chem. Soc., Dalton Trans.* **1998**, 51.

[5] a) A. Forster, B. F. G. Johnson, J. Lewis, T. W. Matheson, *J. Organomet. Chem.* **1976**, *104*, 225; b) J. Bracker-Novak, S. Hajela, M. Lord, M. Zhang, E. Rosenberg, R. Gobetto, L. Milone, D. Osella, *Organometallics* **1990**, *9*, 1379.

[6] M. I. Bruce, B. K. Nicholson, M. L. Williams, *Inorg. Synth.* **1989**, *26*, 276; M. I. Bruce, B. K. Nicholson, M. L. Williams, *Inorg. Synth.* **1990**, *28*, 225.

[7] A. J. Deeming, C. S. Forth, F. Rodgers, unpublished results.

[8] M. I. Bruce, O. Bin Shawkataly, M. L. Williams, *J. Organomet. Chem.* **1985**, *287*, 127.

[9] a) J. A. Clucas, M. M. Harding, A. K. Smith, *J. Chem. Soc., Chem. Commun.* **1985**, 1280; b) M. I. Bruce, E. Horn, O. Bin Shawkataly, M. R. Snow, E. Tiekink, M. L. Williams, *J. Organomet. Chem.* **1986**, *316*, 187; c) M. J. Stchedroff, S. Aime, R. Gobetto, L. Salassa, E. Nordlander, *Magnet. Reson. Chem.* **2002**, *40*, 107.

[10] gNMR, Ver. 4.1, Cherwell Scientific Ltd., Oxford, U. K., **1995**.

[11] SMART and SAINT software for CCD diffractometers, version 6.1, Bruker AXS, Madison, WI, **2000**.

[12] G. M. Sheldrick, SADABS software for empirical absorption correction, University of Göttingen, Germany, **2000**.

[13] G. M. Sheldrick, SHELXTL PLUS, version 6.1, Bruker AXS Inc., Madison, WI, **2000**.

Received: October 23, 2004
Published Online: September 13, 2005

 © 2005 Wiley-VCH Verlag GmbH & Co. KGaA, Weinheim

Synthesis and Electrochemical and Spectroscopic Properties of Molybdenum Complexes Bearing 5-Alkoxythiophene or -bithiophene Groups

António M. Fonseca,*[a] Maria Manuela M. Raposo,[a] Ana M. R. C. Sousa,[a] Gilbert Kirsch,[b] and Marc Beley[c]

Keywords: Sulfur heterocycles / Molybdenum / N ligands / Conjugated systems

trans-[MoF{NN=CH(5′-R-thienyl)}(dppe)$_2$][BF_4] (R = OMe and OEt) and *trans*-[MoF{NN=CH(5′-R-2,2′-bithienyl)}-(dppe)$_2$][BF_4] (R = OMe, OEt and O*i*Pr) were synthesised in good yields by treating 5-alkoxy-2-formylthiophenes and 5′-alkoxy-5-formyl-2,2′-bithiophenes, respectively, with the hydrazido(2–) complex *trans*-[MoF(NNH_2)(dppe)$_2$][BF_4]. The electrochemical, spectroscopic and solvatochromic properties of these compounds were studied. These results suggest that efficient π-conjugated systems are obtained due to the low-energy charge-transfer between the metal atom and the heterocyclic moieties.

(© Wiley-VCH Verlag GmbH & Co. KGaA, 69451 Weinheim, Germany, 2005)

Introduction

There is considerable interest in the synthesis of new organic and organometallic materials with large second-order optical nonlinearities because of their potential applications in telecommunications, optical computing, optical storage and optical information processing.[1–3]

Structural, redox and photophysical properties can easily be tuned in organometallic compounds. Consequently, they have been explored in the design of materials for nonlinear optical (NLO) applications.[4,5] In this case, for a molecule to be of interest it must present an excited state of similar energy to the ground state, as well as a dipolar moment that is quite different in the ground and excited states.[6,7] These requirements are satisfied in asymmetric conjugated complexes containing electron-acceptor and electron-donor groups connected by a conjugated π system.[8,9] For example, metal complexes based on nitrosylmolybdenum and -tungsten moieties stabilised by tris(3,5-dimethylpyrazolyl)-borate and attached to phenolato or anilido groups are strongly polarised and may therefore be able to act as electron termini of dipolar complexes having second-order NLO properties.[7] Thiophene and bithiophene chromophores exhibit greater β second-order polarisabilities compared to those of biphenyls or stilbenes.[10] Transition metal complexes of the general type *trans*-[MX(NNR)(dppe)$_2$]$^+$ [M = Mo or W; X = halide; dppe = 1,2-bis(diphenylphosphanyl)ethane; R = heterocyclic group] are particularly attractive because the conjugated structure, including the central metal atom and the square-planar {M(dppe)$_2$} assembly, is robust.[11,12]

In this paper we wish to report the synthesis and the electrochemical, spectroscopic and solvatochromic properties of the new electron-donor–π-acceptor systems *trans*-[MoF{NN=CH(thienyl-5′-alkoxy)}(dppe)$_2$][BF_4] **6** and **8** (alkoxy = OMe and OEt, respectively) and *trans*-[MoF{NN=CH(bithienyl-5′-alkoxy)}(dppe)$_2$][BF_4] **7**, **9** and **10** (alkoxy = OMe, OEt and O*i*Pr, respectively). As far as we know, the synthesis and the characterisation of molybdenum complexes bearing 2-alkoxythienyl groups and 2-alkoxybithienyl groups has not been reported previously.

Results and Discussion

Synthesis

As part of our ongoing effort to develop chromophores for nonlinear optical applications,[13–16] we synthesised several donor–acceptor 5,5′-disubstituted 2,2′-bithiophenes[13] by functionalisation of the corresponding 5-alkoxybithiophenes.[17] We have recently reported the synthesis of the 5′-alkoxy-5-formyl-2,2′-bithiophene derivatives **2**, **4** and **5** (alkoxy = OMe, OEt and O*i*Pr, respectively), which made these compounds available in reasonable amounts.[13] Indeed, we were able to use these compounds successfully as substrates for the synthesis of the molybdenum complexes. The versatile method to form carbon–nitrogen bonds involves the initial conversion of *trans*-[Mo(N_2)$_2$-

[a] Centro de Química, Universidade do Minho,
Campus de Gualtar, 4710-057 Braga, Portugal
Fax: +351-253-678-983
E-mail: amcf@quimica.uminho.pt
[b] Laboratoire d'Ingénierie Moléculaire et Biochimie Pharmacologique, UFR SciFA/Université de Metz,
1, Boulevard Arago, Metz Technopôle, CP 87811, 57078 Metz Cedex 3, France
[c] Laboratoire de Chimie et Applications, UFR SciFA/Université de Metz, Metz Technopôle, IPEM,
1, Boulevard Arago, 57078 Metz Cedex 3, France

$(dppe)_2$] into the hydrazido(2–) complex *trans*-$[MoF(NNH_2)(dppe)_2][BF_4]$, which then undergoes an electrophilic attack at the terminal nitrogen atom. It can therefore be used as a key intermediate in the preparation of organonitrogen complexes by subsequent reactions with organic carbonyl compounds.[18] Condensation with 5-alkoxy-2-formylthiophene [alkoxy = OMe (**1**) or OEt (**3**)] or 5′-alkoxy-5-formyl-2,2′-bithiophene [alkoxy = OMe (**2**), OEt (**4**) or O*i*Pr (**5**)] gave the molybdenum complexes **6**–**10** bearing the alkoxythiophenic or alkoxybithiophenic group, respectively, in good yields (65–78%; Scheme 1).

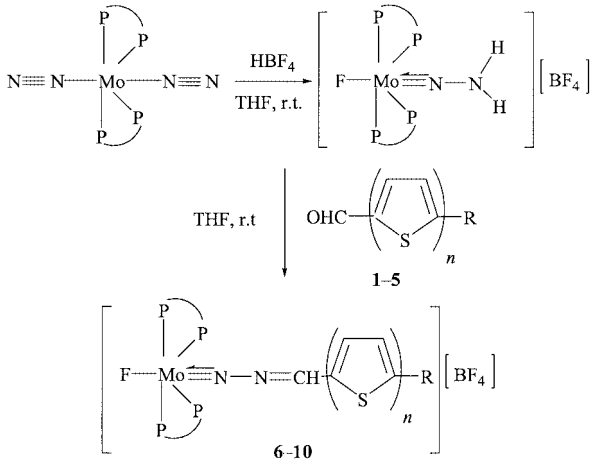

R	*n*	Thiophenic or bithiophenic group	Complex	Yield [%]
OMe	1	**1**	**6**	73
OMe	2	**2**	**7**	77
OEt	1	**3**	**8**	67
OEt	2	**4**	**9**	78
O*i*Pr	2	**5**	**10**	65

Scheme 1.

The structures of these complexes were confirmed by the usual spectroscopic methods. Each diazenido [hydrazido-(–2)] complex shows a characteristic band in the 1515–1550 cm^{-1} region of its FTIR spectrum that can be assigned to ν(C=N).[19] Their *trans* stereochemistry was confirmed by the $^{31}P\{^1H\}$NMR spectra, which show a single resonance.

Electrochemistry

Electrochemical data for compounds **1**–**5** are summarised in Table 1. Cyclic voltammetry shows an irreversible single-electron oxidation process (E_{pa}) which can be attributed to the formation of the radical cation of the heterocyclic part. As the HOMO levels in the heterocyclic part increase with the donor effect of the alkoxy groups along the series OMe < OEt < O*i*Pr, the ease of oxidation increases gradually. The oxidation processes of the bithienyl groups are systematically shifted to less positive potentials than those of the thienyl groups. This fact can be explained by the stabilisation of the cation radical due to its higher delocalisation on the bithienyl moiety. At low potentials (< –2 V vs. fc/fc^+) these compounds exhibit one irreversible single-electron process ($-E_{pr}$), which generates a radical anion. The electron goes into a π*-antibonding orbital of the heterocycle. This electron injection occurs at more negative potentials as the alkoxy group is an electron donor and its delocalisation on the heterocyclic part is difficult.

Electrochemical data for complexes **6**–**10** are collected in Table 2. A typical cyclic voltammogram of *trans*-$[MoF\{NN{=}CH(5'\text{-OEt-}2,2'\text{-bithienyl})\}(dppe)_2][BF_4]$ (**9**) in DMF/0.1 M $[Bu_4N][BF_4]$ at a vitreous carbon electrode is shown in Figure 1. The molybdenum complexes show three single-electron oxidation processes. The first ($E_{a1/2}$) and second processes (E_{pa1}) are reversible and irreversible, respectively, and correspond to the Mo^{IV}/Mo^{V} and Mo^{V}/Mo^{VI} waves. Controlled potential coulometry of the first oxidation step confirms a single-electron process. The resulting solution displays a cyclic voltammetric profile that resembles the original one. The parent complex *trans*-$[MoF(NNH_2)(dppe)_2][BF_4]$ has only one irreversible wave at 0.34 V vs. fc^+/fc. A comparison of the values obtained for **6**–**10** with that of the parent complex shows that the donor effect of the alkoxy substituent stabilises Mo^{V} completely and Mo^{VI} partially. However, the oxidation potentials of compounds **7** and **9**, which have a bithiophenic link, are slightly higher (40 mV) than those of **6** and **8,** which bear a thiophenic link. This fact can be explained by metal-to-heterocycle π*-orbital back-donation via the hydrazido ligand. This back-donation increases in the case of a bithiophenic link, which contributes to the stabilisation of the metal-centred HOMO orbital. In both cases this suggests a

Table 1. Electrochemical and electronic spectroscopic data for the thiophenic and bithiophenic groups **1**–**5**.

Compound	R	*n*	Electrochemical data[a] Reductions $-E_{pr}$ [V]	Oxidations E_{pa} [V]	Electronic spectroscopic data[b] λ_{max} [nm]	$10^{-3}\,\varepsilon$ [$M^{-1}\,cm^{-1}$]
1	OMe	1	2.30	0.86	310	24.7
2	OMe	2	2.00	0.76	362	16.3
3	OEt	1	2.34	0.82	316	21.2
4	OEt	2	2.08	0.74	391	24.5
5	O*i*Pr	2	2.14	0.73	393	23.8

[a] All measurements were recorded at 298 K in degassed acetonitrile solutions with $[Bu_4N][BF_4]$ (0.2 M) as supporting electrolyte at a carbon working electrode with a scan rate of 0.1 $V\,s^{-1}$. Ferrocene was added as an internal standard at the end of each measurement, potentials were converted into V vs. the ferrocene/ferrocenium couple [$E_{1/2}(fc^+/fc)$ = 0.38 V/SCE]. [b] Measured in acetonitrile.

 © 2005 Wiley-VCH Verlag GmbH & Co. KGaA, Weinheim

Table 2. Electrochemical and electronic spectroscopic data for complexes **6**–**10**.

Complex	R	*n*	Electrochemical data[a]				Electronic spectroscopic data[b]	
			Reduction		Oxidations			
			$-E_{c1/2}$ [V]	$E_{a1/2}$ [V]	E_{pa1} [V]	E_{pa2} [V]	λ_{max} [nm]	$10^{-3}\,\varepsilon$ [M^{-1} cm^{-1}]
6	OMe	1	1.45	0.24	0.47	0.87	469	17.2
7	OMe	2	1.36	0.28	0.53	0.76	482	17.4
8	OEt	1	1.50	0.20	0.42	0.83	474	18.1
9	OEt	2	1.40	0.24	0.50	0.74	497	16.7
10	O*i*Pr	2	1.43	0.20	0.47	0.74	496	19.3

[a] All measurements were recorded at 298 K in degassed acetonitrile solutions with $[Bu_4N][BF_4]$ (0.2 M) as supporting electrolyte at a carbon working electrode with a scan rate of 0.1 V s^{-1}. Ferrocene was added as an internal standard at the end of each measurement, potentials were converted into V vs. the ferrocenium/ferrocene couple [$E_{1/2}(fc^+/fc)$ = 0.38 V/SCE]. [b] Measured in acetonitrile.

π-conjugated system between the metal acceptor group and the alkoxythiophene and -bithiophene moieties. In complexes **6**–**10** the oxidation potentials (E_{pa2}) of the heterocyclic parts are not significantly modified in comparison with those of the corresponding compounds **1**–**5**. The reduction of the complexes occurs in a quasi-reversible one-electron process ($-E_{c1/2}$, ΔE_p = 200 mV). For **7**, **9** and **10**, with a bithiophenic linker, the reduction potentials are shifted to higher values than for **6** and **8**. The corresponding stabilisation of the LUMO (π*) ligand orbital does not correspond to an electron-donor effect of this link, but to a better delocalisation of the injected electron into the ligand on the bithiophene moiety via the imino bridge.

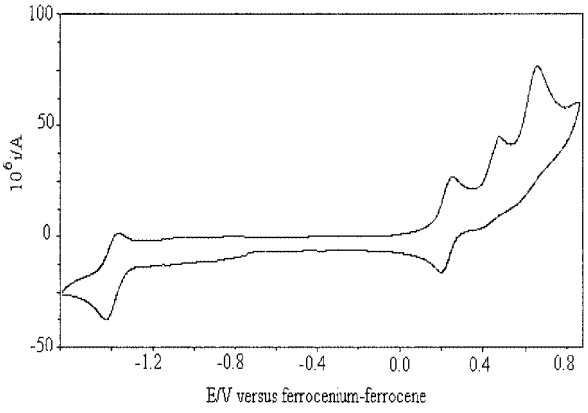

Figure 1. Cyclic voltammogram of *trans*-[MoF{NN=CH(5′-OEt-2,2′-bithienyl)}(dppe)$_2$][BF_4] (**9**) in DMF/0.1 M $[Bu_4N][BF_4]$ at a vitreous carbon electrode (area = 0.049 cm^2). Scan rate: 100 mV s^{-1}; concentration of complex: 2.3 mM.

UV/Vis and Solvatochromic Studies

The UV/Vis spectroscopic data for heterocycles **1**–**5** are presented in Table 1. The electronic absorption spectra show an absorption band in the near-UV region due to the π–π* transitions in the heterocyclic parts. The bithienyl groups show red-shifted absorption maxima relative to the thienyl groups. This is due to better delocalisation of the excited electron in the π*-orbital, which causes its stabilisation. Moreover, the position of these bands is influenced by the donor effect of the alkoxy group, which lowers the energy gap.

The UV/Vis spectroscopic data for complexes **6**–**10** are summarised in Table 2. The parent complex *trans*-[MoF(NNH_2)(dppe)$_2$][BF_4] shows a broad band at around 275 nm corresponding to a transition in the dppe ligand. Complexes **6**–**10**, which bear heterocyclic groups, show an absorption band in the visible region because the molybdenum part lowers the energies of the transition in the heterocycle. For example, the absorption maximum of **1**, which appears at 310 nm, is red-shifted to 469 nm for complex **6**. The intramolecular charge-transfer process, which originates in the Mo part and is propagated through the π-conjugated spacer ligand [hydrazido(2–)], gives rise to a considerable bathochromic shift of the alkoxythiophenic and -bithiophenic transitions (Figure 2). For these complexes, the alkoxy group effect and the better delocalisation in the bithienyl groups induce modifications of their electronic spectra similar to those described for compounds **1**–**5**. The influence of the incorporation of thiophene moieties in push-pull compounds on the charge-transfer properties has been described previously.[20]

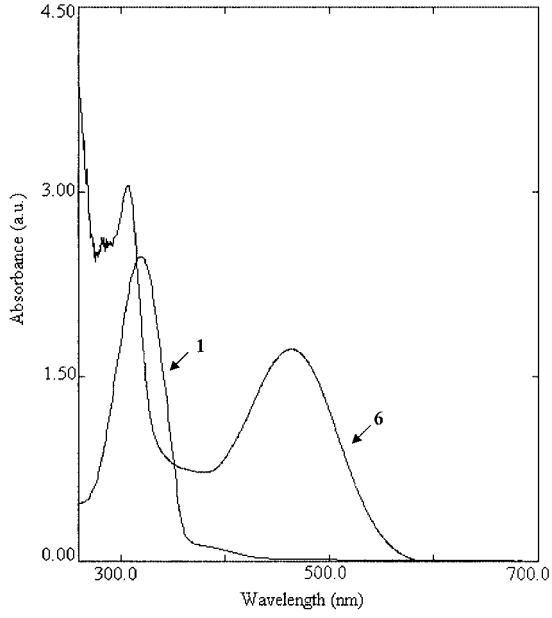

Figure 2. UV/Vis spectra of 2-formyl-5-methoxythiophene (**1**) and *trans*-[MoF{NN=CH(5′-methoxythienyl)}(dppe)$_2$][BF_4] (**6**) in acetonitrile, demonstrating the effect of the Mo part on the absorption maxima between 300 and 700 nm.

 © 2005 Wiley-VCH Verlag GmbH & Co. KGaA, Weinheim

Table 3. Solvatochromic data (λ_{max} [nm] and $\tilde{\nu}_0$ [cm^{-1}] of the charge-transfer band) for complexes **6**–**10** in selected solvents in comparison with the π* values of Kamlet and Taft.[24]

Complex	Solvent (π*) THF (0.58) λ_{max}, $\tilde{\nu}_0$	Acetone (0.71) λ_{max}, $\tilde{\nu}_0$	Acetonitrile (0.75) λ_{max}, $\tilde{\nu}_0$	CH_2Cl_2 (0.82) λ_{max}, $\tilde{\nu}_0$	DMSO (0.88) λ_{max}, $\tilde{\nu}_0$
6	466, 21459	468, 21413	469, 21322	471, 21231	474, 21097
7	479, 20877	481, 20790	482, 20747	485, 20619	488, 20492
8	479, 20877	482, 20747	484, 20661	487, 20534	490, 20408
9	493, 20284	495, 20202	497, 20121	501, 19960	505, 19802
10	491, 20366	494, 20243	496, 20161	499, 20040	502, 19920

In general, the stronger the donor and/or acceptor group, the smaller the energy difference between the ground and excited states and the longer the wavelength of the absorption. According to Zyss,[21] the increase in the β-values characteristic of the NLO effects is accompanied by an increase of λ_{max} in the UV/Vis spectra.

Solvatochromism is easily quantified by UV/Vis spectroscopy and is particularly suitable for the empirical determination of the polarity of a solvent[22,23] on a molecular-microscopic level. To evaluate the intermolecular forces between the solvents and the solute molecules we recorded absorption spectra of all complexes in five polar solvents of different solvation character (Table 3). Due to the insolubility of complexes **6**–**10** in apolar solvents the solvatochromic study of these compounds was only performed in polar solvents such as tetrahydrofuran, acetone, acetonitrile, dichloromethane and dimethyl sulfoxide. The electronic excitations are governed by a positive solvatochromism with increasing solvent polarity, indicating dipole changes within the ground excited state.

Good correlation with the π* parameters defined by Kamlet and Taft[24] was obtained. Table 4 summarises the results of the linear regression analyses of absorption maxima for complexes **6**–**10**. The most important values of the linear relationship between absorption maxima and π* are the correlation coefficient, *r*, and the slope, *s*, which describes the extent of solvatochromism from π* = 0.58 (tetrahydrofuran) to π* = 1.00 (DMSO). As shown in Table 4, the greatest value for *s* is found for complex **9**. The change in dipole moment on electronic excitation is shown to be oriented parallel to the transition dipole and is, moreover, constant over the whole charge-transfer band.

Table 4. Correlation of the UV/Vis absorption maxima of complexes **6**–**10** and the solvent parameter π*.[a]

Complexes	Regression analysis[b] $\tilde{\nu}_0$ [cm^{-1}]	*s*	*r*
6	22013	–917.62	0.9760
7	21448	–962.61	0.9843
8	21590	–1158.20	0.9814
9	20989	–1196.40	0.9863
10	20997	–1101.80	0.9760

[a] Applied solvents (π* value): THF (0.58), acetone (0.71), acetonitrile (0.75), dichloromethane (0.82) and dimethyl sulfoxide (1.0). [b] Intercept, slope, and correlation *r* of the linear solvation energy relationship, according to the equation $\nu_{max} = \nu_0 + s\pi^*$.

Conclusions

We have described the synthesis and characterisation of molybdenum complexes connected via a hydrazido(2–) bridge to alkoxythiophenic or alkoxybithiophenic groups. Their electrochemical, spectroscopic and solvatochromic behaviours exhibit an intramolecular charge-transfer effect. These new complexes are promising candidates for developing novel NLO materials.

Experimental Section

General: All reactions were carried out under nitrogen or argon using standard Schlenk techniques. Solvents were freshly distilled from appropriate drying agents under dinitrogen. The syntheses of 5′-alkoxy-5-formyl-2,2′-bithiophenes[13] and complexes *trans*-$[Mo(N_2)(dppe)_2]$ and *trans*-$[MoF(NNH_2)(dppe)_2]$[17] have already been described. The NMR spectra were obtained with a Varian Unity Plus Spectrometer at 300 MHz using the solvent peak as internal reference. Infrared spectra were recorded with a Perkin–Elmer 1600 FTIR spectrophotometer. UV/Vis absorption spectra were obtained with a Shimadzu UV/2501PC spectrophotometer. High-resolution mass spectra (HRMS) were obtained with a GV AutoSpec spectrometer with *m*-nitrobenzyl alcohol (NBA) as matrix. Elemental analyses were performed with a Leco CHNS-932 analyser. Voltammetric measurements were performed with a potentiostat/galvanostat (AUTOLAB /PSTAT 12 with low current module ECD from ECO-CHEMIE) and the data processed with the General Purpose Electrochemical System software package (ECO-CHEMIE). Three-electrode two-compartment cells equipped with vitreous carbon-disc working electrodes, a platinum-wire secondary electrode and a silver-wire pseudo-reference electrode were employed for cyclic voltammetric measurements. The ferrocenium-ferrocene redox couple was used as a secondary internal reference. The concentrations of the compounds were typically 1–2 mM, and 0.2 M $[Bu_4N][BF_4]$ was used as the supporting electrolyte in *N*,*N*-dimethylformamide solvent. The potential was measured with respect to ferrocinium/ferrocene as an internal standard. Controlled-potential electrolyses were carried out in an H-type cell with a vitreous carbon working electrode as described previously.[12]

General Procedure for the Preparation of Complexes 6–10: The complex *trans*-$[MoF(NNH_2)(dppe)_2][BF_4]$ (0.2 g, 0.19 mmol) was dis-

 © 2005 Wiley-VCH Verlag GmbH & Co. KGaA, Weinheim

solved in THF (20 mL) at room temperature. Formyl ligands **1**–**5** (0.40 mmol) were added in excess to the solution, which was stirred for 28 h. The volume of the solution was then reduced to about 5 mL and the precipitates were filtered off. These solids were dissolved in CH_2Cl_2 and filtered through a pad of Celite. The solutions were concentrated to dryness and the solids obtained washed with cold THF (3×5 mL), then Et_2O (2×3 mL), and dried in vacuo to give complexes **6**–**10** as coloured solids. In all cases, the solids thus obtained were crystallised from CH_2Cl_2/Et_2O.

6: Pink solid. Yield: 0.16 g (73%). ^{1}H NMR (300 MHz, $CDCl_3$): δ = 2.4–2.8 (m, 8 H, 2×PCH_2CH_2P), 3.4 (s, 3 H, OCH_3), 4.6 (s, 1 H, N=C*H*), 6.8–7.4 (m, 42 H, 40 H and 2 H of thienyl) ppm. ^{31}P{^{1}H}NMR (121.7 MHz, $CDCl_3$): δ = –100.3 (s, MoP) ppm. IR (KBr): $\tilde{\nu}$ = 1550 (N=C) cm^{-1}. HRMS (NBA): calcd. for $C_{58}H_{54}FMoN_2OP_4S$ $[M]^+$ 1067.1945; found 1067.1968. $C_{58}H_{54}BF_5MoN_2OP_4S$ (1152.8): calcd. C 60.43, H 4.72, N 2.43, S 2.78; found C 60.78, H 4.83, N 2.51, S 2.83.

7: Orange solid. Yield: 0.18 g (77%). ^{1}H NMR (300 MHz, $CDCl_3$): δ = 2.4–2.7 (m, 8 H, 2×PCH_2CH_2P), 3.6 (s, 3 H, OCH_3), 4.5 (s, 1 H, N=C*H*), 6.8–7.4 (m, 44 H, 40 H of phenyl and 4 H of bithienyl) ppm. ^{31}P{^{1}H}NMR (121.7 MHz, $CDCl_3$): δ = –100.1 (s, MoP) ppm. IR (KBr): $\tilde{\nu}$ = 1534 cm^{-1} (N=C). HRMS (NBA): calcd. for $C_{62}H_{56}FMoN_2OP_4S_2$ $[M]^+$ 1149.1823; found 1149.1816. $C_{62}H_{56}BF_5MoN_2OP_4S_2$ (1234.9): calcd. C 60.30, H 4.57, N 2.27, S 5.19; found C 60.47, H 4.72, N 2.41, S 5.25.

8: Pink solid. Yield: 0.15 g (67%). ^{1}H NMR (300 MHz, $CDCl_3$): δ = 1.6 (t, J = 6.4 Hz, 3 H, OCH_2CH_3), 2.4–2.7 (m, 8 H, 2×PCH_2CH_2P), 3.5 (q, J = 6.4 Hz, 2 H, OCH_2CH_3), 4.5 (s, 1 H, N=C*H*), 6.9–7.5 (m, 42 H, 40 H of phenyl and 2 H of thienyl) ppm. ^{31}P{^{1}H}NMR (121.7 MHz, $CDCl_3$): δ = –100.2 (s, MoP) ppm. IR (KBr): $\tilde{\nu}$ = 1546 cm^{-1} (N=C). HRMS (NBA): calcd. for $C_{59}H_{56}FMoN_2OP_4S$ $[M]^+$ 1081.2102; found 1081.2118. $C_{59}H_{56}BF_5MoN_2OP_4S$ (1166.81): calcd. C 60.73, H 4.84, N 2.40, S 2.75; found C 60.48, H 4.87, N 2.59, S 5.71.

9: Orange solid. Yield: 0.18 g (78%). ^{1}H NMR (300 MHz, $CDCl_3$): δ = 1.8 (t, J = 6.3 Hz, 3 H, OCH_2CH_3), 2.4–2.7 (m, 8 H, 2×PCH_2CH_2P), 3.8 (q, J = 6.3 Hz, 2 H, OCH_2CH_3), 4.3 (s, 1 H, N=C*H*), 7.0–7.6 (m, 44 H, 40 H of phenyl and 4 H of bithienyl) ppm. ^{31}P{^{1}H}NMR (121.7 MHz, $CDCl_3$): δ = –99.7 (s, MoP) ppm. IR (KBr): $\tilde{\nu}$ = 1515 cm^{-1} (N=C). HRMS (NBA): calcd. for $C_{63}H_{58}FMoN_2OP_4S_2$ $[M]^+$ 1163.1979; found 1163.1929. $C_{63}H_{58}BF_5MoN_2OP_4S_2$ (1248.9): calcd. C 60.59, H 4.68, N 2.24, S 5,14; found C 60.82, H 4.77, N 2.44, S 5.19.

10: Orange solid. Yield: 0.16 g (65%). ^{1}H NMR (300 MHz, $CDCl_3$): δ = 1.5 [d, J = 6.1 Hz, 6 H, $OCH(CH_3)_2$], 2.3–2.7 (m, 8 H, 2×PCH_2CH_2P), 3.4 [m, 1 H, $OCH(CH_3)_2$], 4.2 (s, 1 H, N=C*H*), and 6.9–7.6 (m, 44 H, 40 H of phenyl and 4 H of bithienyl) ppm. ^{31}P{^{1}H}NMR (121.7 MHz, $CDCl_3$): δ = –99.8 (s, MoP) ppm. IR (KBr): $\tilde{\nu}$ = 1519 cm^{-1} (N=C). HRMS (NBA): calcd. for $C_{64}H_{60}FMoN_2OP_4S_2$ $[M]^+$ 1177.2136; found 1177.2101. $C_{64}H_{60}BF_5MoN_2OP_4S_2$ (1263.0): calcd. C 60.87, H 4.79, N 2.22, S 5.08; found C 61.12, H 4.88, N 2.15, S 5.17.

Acknowledgments

We thank the Foundation for Science and Technology (Portugal) for financial support from IBQF (UM) and from FEDER, POCTI (ref. POCTI/QUI/37816/2001).

[1] *Nonlinear Optics of Organic Molecules and Polymers* (Eds.: H. S. Nalwa, S. S. Miyata), CRC Press, Boca Raton **1997**, p. 885.
[2] *Molecular Nonlinear Optics* (Ed.: J. Zyss), Academic Press, New York, **1994**.
[3] *Optical Materials for Non-linear Optics III* (Eds.: G. J. Ashwell, D. Bloor), Royal Society of Chemistry, Cambridge, **1993**.
[4] J. Heck, S. Dabek, T. Meyer-Friedrichsen, H. Wong, *Coord. Chem. Rev.* **1999**, *190–192*, 1217.
[5] D. Roberto, R. Ugo, S. Bruni, E. Cariati, F. Cariati, P. Fantucci, I. Invernizzi, S. Quici, I. Ledoux, J. Zyss, *Organometallics* **2000**, *19*, 1775.
[6] L. T. Cheng, W. Tam, S. H. Stevenson, G. R. Meredith, G. Rikken, S. R. Marder, *J. Phys. Chem.* **1991**, *95*, 10631.
[7] M. Malaun, R. Kowallick, A. M. McDonagh, M. Marcaccio, R. L. Paul, I. Asselberghs, K. Clays, A. Persoons, B. Bildstein, C. Fiorini, J.-M. Nunzi, M. D. Ward, J. A. McCleverty, *J. Chem. Soc., Dalton Trans.* **2001**, 3025.
[8] T. Meyer-Friedrichsen, H. Wong, M. H. Prosenc, J. Heck, *Eur. J. Inorg. Chem.* **2003**, 936.
[9] H. Wong, T. Meyer-Friedrichsen, T. Farrell, C. Mecker, J. Heck, *Eur. J. Inorg. Chem.* **2000**, 631.
[10] F. Steybe, F. Effenberger, V. Gubler, C. Bosshard, P. Gunter, *Tetrahedron* **1998**, *54*, 8469.
[11] Y. Ishii, H. Miyagi, S. Jitsukuni, H. Seino, B. S. Harkness, M. Hidai, *J. Am. Chem. Soc.* **1992**, *114*, 9890.
[12] S. A. Fairhurst, D. L. Hughes, S. K. Ibrahim, M.-L. Abasq, J. Talarmin, M. A. Queiros, A. Fonseca, C. J. Pickett, *J. Chem. Soc., Dalton Trans.* **1995**, 1973.
[13] M. M. M. Raposo, G. Kirsch, *Tetrahedron* **2003**, *59*, 4891.
[14] M. M. M. Raposo, A. M. C. Fonseca, G. Kirsch, *Tetrahedron* **2004**, *60*, 4071.
[15] M. M. M. Raposo, A. M. Fonseca, G. Kirsch, *Mater. Sci. Forum* **2004**, *455–456*, 157.
[16] R. M. Batista, S. P. G. Costa, M. M. M. Raposo, *Tetrahedron Lett.* **2004**, *45*, 2825.
[17] M. M. M. Raposo, G. Kirsch, *Heterocycles* **2001**, *55*, 1487.
[18] M. Hidai, Y. Mizobe, M. Sato, T. Kodama, Y. Uchida, *J. Am. Chem. Soc.* **1978**, *100*, 5740.
[19] J. Chatt, W. Hussain, G. J. Leigh, F. P. Terreros, *J. Chem. Soc., Dalton Trans.* **1980**, 1408.
[20] G. Mignani, F. Leising, R. Meyrueix, M. Samson, *Tetrahedron Lett.* **1990**, *31*, 4743.
[21] D. S. Zyss, in *Non-Linear Optical Properties of Organic Molecules and Crystals*, Academic Press, Orlando, **1987**, vols. 1 and 2.
[22] C. Reichardt, in *Solvents and Solvents Effects in Organic Chemistry*, 2nd ed., VCH, Weinheim, **1988**.
[23] Y. S. Sohn, D. N. Hendrickson, H. B. Grey, *J. Am. Chem. Soc.* **1971**, *93*, 3603.
[24] M. J. Kamlet, J.-L. M. Abboud, M. H. Abraham, R. W. Taft, *J. Org. Chem.* **1983**, *48*, 2877.

Received: December 9, 2004
Published Online: September 19, 2005

 © 2005 Wiley-VCH Verlag GmbH & Co. KGaA, Weinheim

A Facile and Controllable Synthesis of γ-Al_2O_3 Nanostructures without a Surfactant

Bo Tang*[a] Jiechao Ge,[a] Linhai Zhuo,[a] Guangli Wang,[a] Jinye Niu,[a] Zhiqiang Shi,[a] and Yubin Dong[a]

Keywords: γ-Alumina / Materials science / Nanostructures / Solvothermal synthesis

Boehmite [AlOOH] nanoneedles, nanorods, and nanotubes were successfully synthesized by a facile sol-hydrothermal method without using any surfactant. Calcination of the corresponding boehmite nanostructures at 700 °C gave the corresponding γ-Al_2O_3 nanoneedles, nanorods, and nanotubes. The resulting products were characterized by XRD, TEM, HRTEM, and FT-IR spectroscopy. We found that the conditions used to produce the sol and the pH value of the hydrothermal process have important effects on the nucleation and growth of nanostructured materials.
(© Wiley-VCH Verlag GmbH & Co. KGaA, 69451 Weinheim, Germany, 2005)

Introduction

Developing a controllable synthesis process is always one of the most important goals of materials scientists. Because of their application in adsorbents, catalysts, and catalyst supports, the synthesis of alumina nanostructured materials, especially one-dimensional (1D) nanostructures, has received considerable interest due to their novel properties, such as high elastic modulus, thermal and chemical stability, and optical characteristics.[1] However, the synthesis of these nanostructures is still a challenge owing to their extremely small size and their anisotropy. The control of nucleation and growth of nanostructured materials is therefore becoming crucial.

So far, materials scientists have succeeded in preparing various morphologies of boehmite [AlOOH] and Al_2O_3, such as nanowires,[2] nanotubes,[3] nanobelts,[2a] nanofibers,[4] nanorods,[5] and whiskers[6] by different methods. The hydrothermal synthesis of fibrillar boehmite was originally studied by Bugosh[7] and further developed by a number of researchers.[8] In particular, a surfactant-assisted hydrothermal method has been developed to synthesize 1D boehmite and γ-Al_2O_3 nanostructures in recent years.[9] However, the preparation of semiconducting oxide nanobelts,[10] MnO_2 nanowires,[11] TiO_2 nanotubes,[12] $La(OH)_3$ nanorods,[13] $Cd(OH)_2$ nanowires,[14] and CeO_2 nanowires[15] has shown that a 1D nanostructure can be prepared under properly controlled conditions, even without the presence of surfactants. This means that the formation of a 1D nanostructure is thermodynamically preferable for many substances under certain conditions. Herein, we report a facile and controllable sol-hydrothermal method for direct growth of three kinds of nanostructures of as-prepared boehmite and γ-Al_2O_3. The salient feature of this procedure is the convenient control of the morphologies, as the nucleation process of boehmite is easily tuned by the manner of adding the starting materials while the growth of the formed nucleus is adjusted by the pH value of the hydrothermal system. The subsequent calcinations do not change the shape of the synthesized boehmite, and therefore γ-Al_2O_3 with different morphologies of nanoneedles, nanorods, and nanotubes were obtained. This route is simple and controllable.

[a] College of Chemistry, Chemical Engineering and Materials Science, Shandong Normal University,
Jinan 250014, P. R. China

Results and Discussion

The crystalline phases were identified by X-ray diffraction (XRD). Representative XRD patterns of as-prepared and calcined samples are shown in Figure 1, parts A and B, respectively. All the diffraction peaks in Figure 1 (A) can be perfectly indexed to the data available in the JCPDS21-1307 powder diffraction file, thus indicating that all the samples contain only a boehmite crystalline phase. However, the samples prepared under different conditions exhibit XRD traces that differ from each other in relative peak intensities. We assumed that the relative intensities of the peaks are related to the changes in boehmite crystallization, which affects the degree of preferred orientation and, as a result, a change in the crystalline order of a sample could result in the change of the corresponding peak intensity if the crystal is perfect. The as-prepared samples were calcined at 700 °C, as previously reported.[16] The XRD patterns of the products are shown in Figure 1 (B), in which all the diffraction peaks can be indexed to the γ-Al_2O_3 phase (JCPDS29-63). The XRD patterns indicate that the nanostructures obtained by our methods consist of pure phases. Similarly, the relative intensities of the peaks corresponding to different

 © 2005 Wiley-VCH Verlag GmbH & Co. KGaA, Weinheim DOI: 10.1002/ejic.200500159

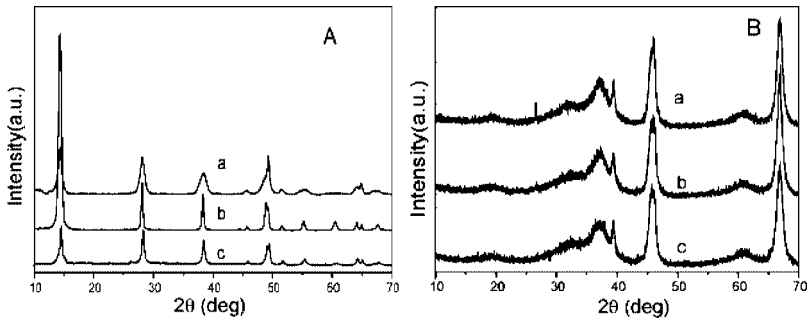

Figure 1. X-ray diffraction patterns for (A) as-prepared samples and (B) calcined samples: (a) nanoneedles, (b) nanorods, (c) nanotubes.

crystallizations of γ-Al_2O_3 are quite different, indicating that the degrees of crystallinity are different for the different nanostructures.

The morphologies and structures of the products were examined by transmission electron microscopy (TEM). As shown in Figure 2, three as-prepared products obtained by different synthetic routes display quite different morphologies, although the calcined samples exhibit almost the same morphologies as their precursors. Figure 2 (A, B) shows a needlelike shape and similar sizes, with a width of about 6 nm and a length of around 50 nm. It should be noted that when ammonia was added at room temperature during step (2), the morphology of the boehmite precursor of sample 2 changed from a needlelike shape to rodlike (Figure 2, C). These nanorods are straight, with uniform diameters of about 40 nm and lengths up to 800 nm. The cross-sectional dimensions of the calcined nanorods (sample 2) are slightly wider than the precursor (Figure 2, D). A representative HRTEM image of a nanorod (Figure 2, G) shows clear fringes, indicating that these nanorods are perfectly crystalline. Figure 2 (E) shows TEM images of the as-prepared boehmite nanotubes (precursor of sample 3). The nanotubes are typically about 40–60 nm in length with an outer diameter of around 5 nm. For the γ-Al_2O_3 nanotubes (sample 3) obtained by calcination of an as-prepared boehmite precursor (Figure 2, F), the outer diameter of the nanotubes is about 5–6 nm and the inner diameter is around 3–4 nm. The obtained nanotubes are thus characterized by their small inner diameter and thin inorganic wall, in contrast to other metal oxide nanotubes reported to date. An HRTEM image and the selected-area electron diffraction (SAED) pattern of the as-prepared nanotube are shown in Figure 2 (H), which reveals that the product is highly crystalline. According to the above XRD results, the boehmite nanostructures are converted into γ-Al_2O_3 nanostructures after calcination. It is well known that γ-Al_2O_3 is most commonly used as a high-temperature catalyst support and as a membrane due to its high surface area and mesoporous properties.[17] Therefore, the obtained γ-alumina nanostructures are expected to exhibit excellent catalytic properties.

In our synthetic system, there are three main reactions:

$$Al^{3+} + 3\,NH_3{\cdot}H_2O \rightarrow Al(OH)_3 + 3\,NH_4^+ \quad (1)$$

$$Al(OH)_3 \rightarrow AlOOH + H_2O \quad (2)$$

$$2\,AlOOH \rightarrow Al_2O_3 + H_2O \quad (3)$$

The formation of boehmite nanostructures indicates that nucleation and growth are well controlled. The manner of adding the precipitator and the pH value of the hydrothermal system play important roles in controlling the nucleation and growth of the boehmite nanostructures. In the first reaction, different conditions can lead to different morphologies of the crystal nucleus. At low temperatures, the particles form a smaller crystal nucleus faster, whereas at

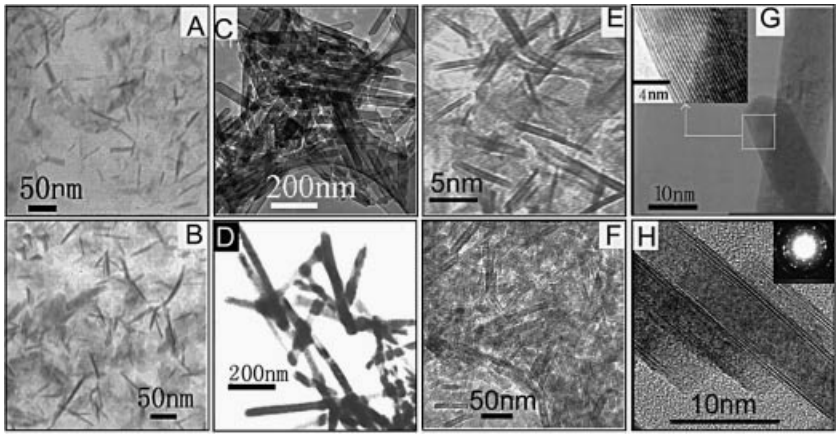

Figure 2. TEM images of the boehmite [AlOOH] samples (A, C, and E) and the corresponding γ-Al_2O_3 samples (B, D, and F): (A, B) nanoneedles, (C, D) nanorods, (E, F) nanotubes; (G) HRTEM images of γ-Al_2O_3 nanorods; (H) HRTEM images of AlOOH nanotubes.

 © 2005 Wiley-VCH Verlag GmbH & Co. KGaA, Weinheim

high temperatures the reverse is the case. We suppose that more homogeneous boehmite nanostructures are formed finally in the hydrothermal process by reaction (2). In the hydrothermal system with a pH value of around 6–7, boehmite possesses a cubic crystal structure exhibiting anisotropic growth, which makes it have the tendency to grow along a certain direction quickly. Finally, the bigger crystal nucleus forms rod-like structures whereas the smaller crystal nucleus forms needle-like structures. For the formation of nanotubes, the pH values in reactions (1) and (2) are thought to be crucial. These crystal nuclei obtained in a basic environment have different morphologies for samples 1 and 2. In reaction (2), it is reasonable to suggest that *n*-butylamine acts as a structure-directing-template in the formation of nanotubes owing to its amphiphilic nature. As reported previously,[9d] these different nuclei may grow into platelet-like ones, then curve into tubes. In reaction (3), the γ-alumina is formed upon dehydration of the boehmite after calcination at 700 °C. The internal water is lost in this process (from AlOOH to Al_2O_3), while the morphologies are maintained.

Figure 3 show the characteristic IR absorption spectra for three kinds of samples in the wavenumber range from 400 to 1000 cm^{-1}, which is the characteristic region for nano-Al_2O_3 powders.[18] Although the IR spectra of all samples exhibit double peaks, they have distinct differences. Comparing the spectra of samples 1–3, for instance, it can be seen that the characteristic infrared absorption peaks of the nanoneedles, nanotubes, and nanorods are at 750.32, 608.62, and 744.87 cm^{-1}, respectively, and are blue-shifted with a decrease in sample size. In accordance with the literature,[19] however, the changes in the infrared absorption spectra of nanomaterials may actually be due to different vibrations.

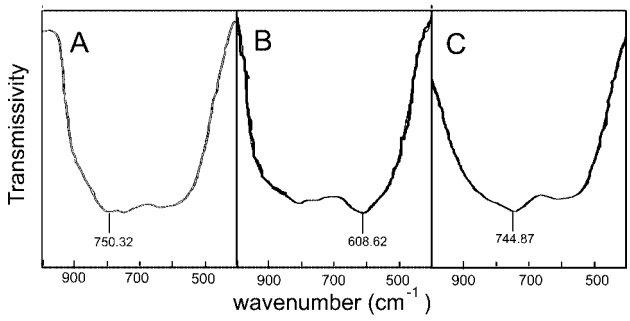

Figure 3. IR absorption spectra for three kinds of samples (A: nanoneedles; B: nanorods; C: nanotubes).

Conclusions

In summary, a facile and controllable hydrothermal synthesis method has been developed to synthesize three kinds of γ-Al_2O_3 nanomaterials without using any surfactant. These samples of nanoneedles, nanorods, and nanotubes exhibit relatively homogeneous sizes and regular morphologies, are were characterized by XRD, TEM, HRTEM, and FT IR spectroscopy.

Experimental Section

Synthesis: In a typical synthesis process there are four main steps: (1) 0.002 mol of $Al(NO_3)_3 \cdot 9H_2O$ was dissolved in 20 mL of distilled water; (2) 60 mL of 0.3 M $NH_3 \cdot H_2O$ was added to the above solution at 0 °C with vigorous stirring until the pH was around 8. This produced a transparent sol of $Al(OH)_3$. The mixture was centrifuged and washed until the pH was 6–7; (3) the obtained precipitate was redispersed in 16 mL of distilled water and then transferred into a 20-mL, Teflon-lined, stainless steel autoclave, which was sealed and maintained at 250 °C for 8 h. The resultant gels were vacuum-filtered in a Buchner funnel and washed with distilled water. The white product was dried at 60 °C for 4 h; (4) part of the product was heated at a heating rate of 3 °C min^{-1} up to 700 °C for 1 h to get sample 1 (nanoneedles). For the preparation of sample 2 (nanorods), the procedure was similar to that of sample 1 except that the ammonia was added quickly to the aqueous $Al(NO_3)_3$ solution at room temperature in step (2). To obtain sample 3 (nanotubes), the pH values of the neutral hydrothermal system and the transparent sol of $Al(OH)_3$ were adjusted to 14, with *n*-butylamine, and 10, with ammonia, respectively. The other steps were the same as for sample 1. This controllable synthetic route is shown in Scheme 1.

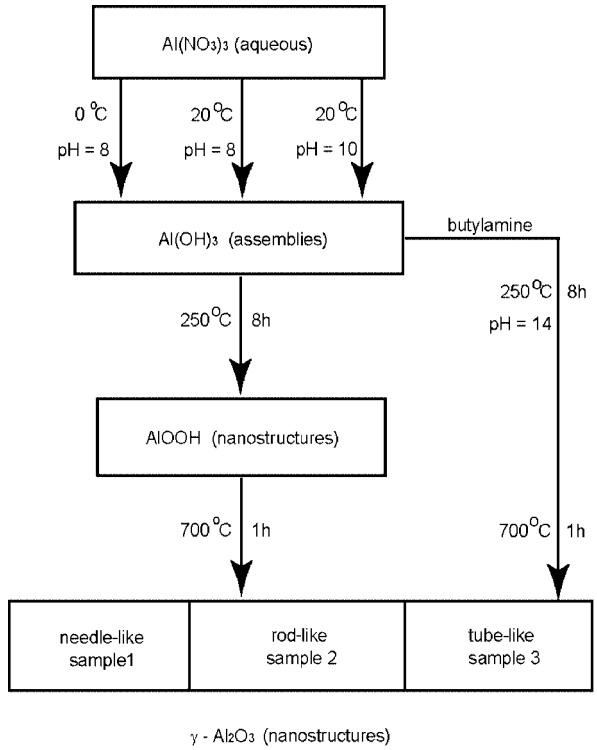

Scheme 1. Synthesis route of the γ-Al_2O_3 nanostructures.

Sample Characterization: The XRD patterns were recorded on a rigaku Dmax-rB X-ray diffractometer using Cu-K_α radiation (λ = 1.54178 Å) at a scanning rate of 0.02° s^{-1} in the 2θ range 10–70°. Transmission electron microscopy (TEM) analysis was conducted on a model Hitachi H-800 TEM with an accelerating voltage of 200 kV. The electron diffraction (ED) patterns and high-resolution transmission electron microscopy (HRTEM) images were recorded on a JEOL-2010 TEM at an acceleration voltage of 200 kV. FT IR spectra of the samples were recorded with a Tensor 27 (Bruker) FTIR spectrometer. Specimens for the measurements were prepared by mixing 2 mg of the sample with 100 mg of KBr and press-

 © 2005 Wiley-VCH Verlag GmbH & Co. KGaA, Weinheim

ing the mixture into pellets. The spectra were acquired in a wavenumber range between 400 and 1000 at 2 cm^{-1} resolution and averaged over 30 scans.

Acknowledgments

We would like to acknowledge an Important Project of the National Nature Science Foundation of China (grant no. 90401019), the Chinese National Foundation of Natural Science Research (grant no. 20335030), and the Excellent Young and Middle-aged Scientist Foundation of Shandong China (grant no. 2004BS04002) for financial support of this research.

[1] G. Das, *Ceram. Eng. Sci. Proc.* **1995**, *16*, 977–981.
[2] a) X. S. Peng, L. D. Zhang, G. W. Mong, X. F. Wang, Y. W. Wang, C. Z. Wang, G. S. Wu, *J. Phys. Chem. B.* **2002**, *106*, 11163–11167; b) Z. L. Xiao, Y. H. Catherine, U. Welp, H. H. Wang, W. K. Kwok, G. A. Willing, J. M. Hiller, R. E. Cook, D. J. Miller, G. W. Crabtree, *Nano Lett.* **2002**, *11*, 1293–1297.
[3] a) B. C. Satishkumar, A. Govindaraj, E. M. Vogl, L. Basumallick, C. N. R. Rao, *J. Mater. Res.* **1997**, *12*, 604–606; b) L. Pu, X. M. Bao, J. P. Zou, D. Feng, *Angew. Chem.* **2001**, *113*, 1538–1541; *Angew. Chem. Int. Ed.* **2001**, *40*, 1490–1493; c) J. Hwang, B. Min, J. S. Lee, K. Keem, K. Cho, M. Y. Sung, M. S. Lee, S. Kim, *Adv. Mater.* **2004**, *16*, 422–4257.
[4] a) V. Valcarcel, A. Perez, M. Cyrklaff, F. Guitian, *Adv. Mater.* **1998**, *10*, 1370–1373; b) S. C. Kuiry, E. Megen, S. D. Patail, S. A. Deshpande, S. Seal, *J. Phys. Chem. B* **2005**, *109*, 3868–3869.
[5] C. Kaya, J. Y. He, X. Gu, E. G. Butler, *Microporous Mesoporous Mater.* **2002**, *54*, 37–48.
[6] Z. Yu, Y. Du, *J. Mater. Res.* **1998**, *13*, 3017–3018.
[7] J. Bugosh, *J. Chem. Phys.* **1961**, *65*, 1789–1792.
[8] a) Z. S. Ying, B. Gevert, J. E. Otterstedt, J. Sterte, *Appl. Catal., A* **1997**, *153*, 69–82; b) P. A. Buining, A. P. Philipse, H. N. W. Lekkerkerker, *Langmuir* **1994**, *10*, 2106–2114; c) P. A. Buining, C. Pathmamanoharan, J. B. H. Jansen, H. N. W. Lekkerkerker, *J. Am. Ceram. Soc.* **1991**, *74*, 1303–1307; d) J. C. P. Gabriel1, P. Davidson, *Top. Curr. Chem.* **2003**, *226*, 119–172; e) B. S. Gevert, Z. S. Ying, *J. Porous. Mater.* **1999**, *6*, 63–67.
[9] a) H. Y. Zhu, J. D. Riches, J. C. Barry, *Chem. Mater.* **2002**, *14*, 2086–2093; b) Z. R. Zhang, T. J. Pinnavaia, *J. Am. Chem. Soc.* **2002**, *124*, 12294–12301; c) Z. R. Zhang, R. W. Hicks, T. R. Pauly, T. J. Pinnavaia, *J. Am. Chem. Soc.* **2002**, *124*, 1592–1593; d) D. B. Kuang, Y. P. Fang, H. Q. Liu, C. Frommen, D. Fonske, *J. Mater. Chem.* **2003**, *13*, 660–663; e) H. C. Lee, H. J. Kim, S. H. Chung, K. H. Lee, H. C. Lee, J. S. Lee, *J. Am. Chem. Soc.* **2003**, *125*, 2882–2883.
[10] A. M. Morales, C. M. Lieber, *Science* **1998**, *279*, 208–210.
[11] X. Wang, Y. D. Li, *J. Am. Chem. Soc.* **2002**, *124*, 2880–2881.
[12] a) Y. Zhu, H. Li, Y. Koltypin, Y. R. Hacohen, A. Gedanken, *Chem. Commun.* **2001**, *24*, 2616–2617; b) T. Kasuga, M. Hiramatsu, A. Hoson, T. Sekino, K. Niihara, *Langmuir* **1998**, *14*, 3160–3163.
[13] B. Tang, J. C. Ge, C. J. Wu, L. H. Zhuo, J. Y. Niu, Z. Q. Shi, Y. B. Dong, *Nanotechnology* **2004**, *15*, 1273–1275.
[14] B. Tang, L. H. Zhuo, J. C. Ge, J. Y. Niu, Z. Q. Shi, *Inorg. Chem.* **2005**, *44*, 2568–2569.
[15] B. Tang, L. H. Zhuo, J. C. Ge, G. L. Wang, Z. Q. Shi, J. Y. Niu, *Chem. Commun.* **2005**, 3565.
[16] C. Misra, *Industrial Alumina Chemical*, ACS Monogr. 184, American Chemical Society, Washington DC, **1986**.
[17] K. Okada, N. Otsuks, *J. Am. Ceram. Soc.* **1986**, *69*, 652–656.
[18] C. H. Shek, J. K. L. Lai, T. S. Gu, G. M. Lin, *Nanostruct. Mater.* **1997**, *8*, 605–610.
[19] C. J. Doss, R. Zallen, *Phys. Rev. B* **1993**, *48*, 15626–15637.

Received: February 22, 2005
Published Online: September 15, 2005

 © 2005 Wiley-VCH Verlag GmbH & Co. KGaA, Weinheim

Cationic Silver Coordination Compounds of Polydentate Ligands: Supramolecular Structures of $[Ag(Pz^{bp2}Py)_2(OSO_2CF_3)]$ and $[Ag_2(Pz^{bp2}Py)_2(OSO_2CF_3)_2]$ {$Pz^{bp2}Py$ = 2-[3,5-Bis(4-butoxyphenyl)pyrazol-1-yl]pyridine}

M. Luz Gallego,[a] Mercedes Cano,*[a] José A. Campo,[a] José V. Heras,[a] Elena Pinilla,[a,b] M. Rosario Torres,[b] Pilar Cornago,[c] and Rosa M. Claramunt*[c]

Keywords: N ligands / NMR spectroscopy / Silver / Supramolecular chemistry

The new silver complexes $[Ag(Pz^{bp2}Py)_2(OSO_2CF_3)]$, $[Ag_2(Pz^{bp2}Py)_2(OSO_2CF_3)_2]$, $[Ag(Pz^{bp}Py)_2(OSO_2CF_3)]$, $[Ag_3(TPz^{bp2}Tz)(OSO_2CF_3)_3]$ and $[Ag_3(TPz^{bp}Tz)(OSO_2CF_3)_3]$ (**5**–**9**) have been obtained by reaction of $Ag(OSO_2CF_3)$ with the corresponding polydentate ligand 2-[3,5-bis(4-butoxyphenyl)pyrazol-1-yl]pyridine ($Pz^{bp2}Py$, **1**), 2-[3-(4-butoxyphenyl)pyrazol-1-yl]pyridine ($Pz^{bp}Py$, **2**), 2,4,6-tris[3,5-bis(4-butoxyphenyl)pyrazol-1-yl]-1,3,5-triazine ($TPz^{bp2}Tz$, **3**) and 2,4,6-tris[3-(4-butoxyphenyl)pyrazol-1-yl]-1,3,5-triazine ($TPz^{bp}Tz$, **4**), respectively. The coordination effects induced on the ^1H, ^{13}C and ^{15}N NMR chemical shifts of the complexes in solution and in the solid state have been quantified, with the ^{15}N NMR spectra being used as a tool to establish the coordination site. All complexes are consistent with an *N*,*N*′-chelating coordination at each silver centre involving nitrogen atoms from pyrazole and pyridine groups for **5** and **7** or from pyrazole and triazine groups for **8** and **9**. An additional Ag···OSO_2CF_3 interaction completes the environment around the silver atom, giving rise to a five-coordination or a three-coordination for complexes **5** and **7** and **8** and **9**, respectively. The X-ray structures of **5** and **6** confirm the presence of the *N*,*N*′-chelating coordination of the $Pz^{bp2}Py$ ligands and the coordinative participation of the CF_3SO_3 counterion in the metal environment. The Ag···η^2-arene bonds between neighbouring units in **6** are responsible for the dimers containing four-coordinate silver atoms. At a supramolecular level, Ag···O, C–H···O or C–H···F interactions generate a 2D network in both compounds.

(© Wiley-VCH Verlag GmbH & Co. KGaA, 69451 Weinheim, Germany, 2005)

Introduction

Cationic silver(I) coordination compounds containing N-donor ligands have extensively been described as producing supramolecular arrays of different dimensionality in the solid, this fact being related with the coordinative versatility of the silver atom to adopt several coordination numbers and with the variety of N-donor ligands and counterions.[1,2]

In previous papers we began to study the molecular assemblies produced by silver or gold coordination to substituted pyrazole ligands (HPz^{R2}). The cationic coordination compounds containing monodentate HPz^{R2} ligands [HPz^{R2} = 3,5-bis(butoxyphenyl)pyrazole (HPz^{bp2}), 3,5-dimethyl-4-nitropyrazole (HPz^{NO_2})] were bonded to their respective counterions, NO_3^-, BF_4^- or $CF_3SO_3^-$, giving rise to 1D, 2D and 3D networks through hydrogen-bonding interactions between the counterion and the cationic fragment. Hydrogen bonds involving the H-atom of the pyrazole ligand and some other non-classical hydrogen-bonding interactions were responsible for the networks of different dimensionality.[3–5]

On this basis, we thought that related polydentate ligands based on the pyridine or triazine cores and pyrazole groups as substituents (in which the NH is absent) should be candidates for supramolecular arrays of metallic complexes centred on coordinative bonds or coordinative interactions. There are several examples described in the literature of supramolecular networks based on a silver centre and different types of N-donor ligands.[1,6]

We present here our studies of new silver complexes containing the polydentate ligands 2-[3,5-bis(4-butoxyphenyl)-pyrazol-1-yl]pyridine ($Pz^{bp2}Py$, **1**), 2-[3-(4-butoxyphenyl)pyrazol-1-yl]pyridine ($Pz^{bp}Py$, **2**), 2,4,6-tris[3,5-bis(4-butoxyphenyl)pyrazol-1-yl]-1,3,5-triazine ($TPz^{bp2}Tz$, **3**) and 2,4,6-tris[3-(4-butoxyphenyl)pyrazol-1-yl]-1,3,5-triazine ($TPz^{bp}Tz$, **4**; Scheme 1). The silver compounds **5**–**9** were obtained by treatment of $Ag(OSO_2CF_3)$ with the respective polydentate ligand. These new complexes exhibit variable environments around the metal centre in which the nitrogen atoms of the

[a] Departamento de Química Inorgánica I, Facultad de Ciencias Químicas, Universidad Complutense,
28040 Madrid, Spain
Fax: +34-91-394-4352
E-mail: mmcano@quim.ucm.es
[b] Laboratorio de Difracción de Rayos-X, Facultad de Ciencias Químicas, Universidad Complutense,
28040 Madrid, Spain
[c] Departamento de Química Orgánica y Bio-Orgánica, Facultad de Ciencias, UNED,
28040 Madrid, Spain

Supporting information for this article is available on the WWW under http://www.eurjic.org or from the author.

© 2005 Wiley-VCH Verlag GmbH & Co. KGaA, Weinheim

polydentate PzPy and PzTz units and the oxygen atoms from the counterion $CF_3SO_3^-$ are involved. In particular, an additional Ag···η^2-arene interaction is also established for **6** (Scheme 2). The structures of the complexes are supported by multinuclear magnetic resonance studies and, in the cases of **5** and **6**, by X-ray crystallography. Formation of one- and multidimensional networks through the interconnection of metallic centres by the inorganic $CF_3SO_3^-$ anion, as well as coordinative Ag···O and Ag···η^2-arene and other non-coordinative C–H···F, C–H···O, or π···π interactions, will be discussed.

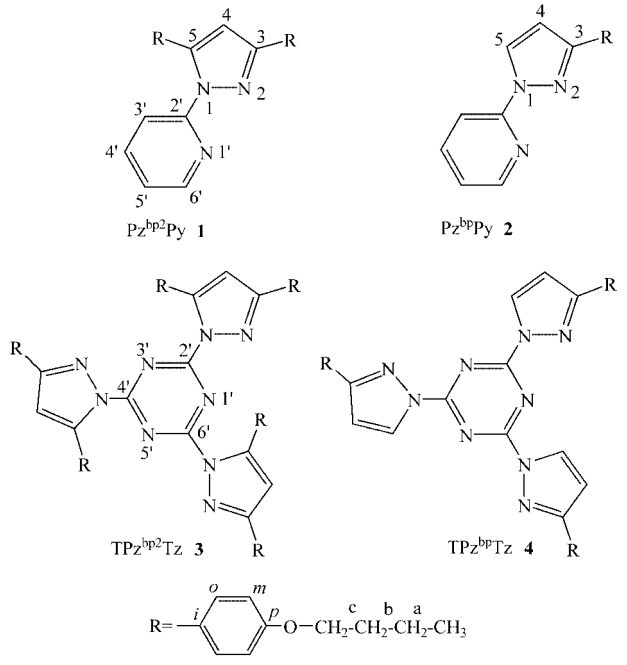

Scheme 1. Polydentate ligands used in this work, with the atomic numbering used for the NMR discussion.

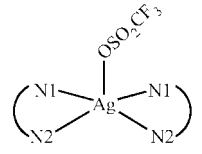

$[Ag(Pz^{bp2}Py)_2(OSO_2CF_3)]$ **5**
$[Ag(Pz^{bpPy})_2(OSO_2CF_3)]$ **7**

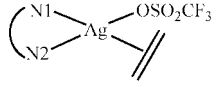

$[Ag_2(Pz^{bp2}Py)_2(OSO_2CF_3)_2]$ **6**

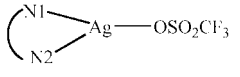

$[Ag_3(TPz^{bp2}Tz)(OSO_2CF_3)_3]$ **8**
$[Ag_3(TPz^{bpTz})(OSO_2CF_3)_3]$ **9**

N1 = nitrogen of the pyrazole group
N2 = nitrogen of the pyridyl or triazine group

Scheme 2. The complexes and their corresponding coordination environments described in this work.

Results and Discussion

Syntheses of Ligands and Silver(I) Complexes

The synthesis of 2-[3-(4-butoxyphenyl)pyrazol-1-yl]pyridine ($Pz^{bp}Py$, **2**) and 2,4,6-tris[3-(4-butoxyphenyl)pyrazol-1-yl]-1,3,5-triazine ($TPz^{bp}Tz$, **4**) was achieved by reaction of the sodium salt of 3-(4-butoxyphenyl)propane-1,3-dione with hydrazinopyridine and the sodium salt of 3-(4-butoxyphenyl)pyrazole with 2,4,6-trichlorotriazine, respectively, by similar procedures to those of the related compounds 2-[3,5-bis(4-butoxyphenyl)pyrazol-1-yl]pyridine ($Pz^{bp2}Py$, **1**) and 2,4,6-tris[3,5-bis(4-butoxyphenyl)pyrazol-1-yl]-1,3,5-triazine ($TPz^{bp2}Tz$, **3**) previously described by us.[4,7]

Silver complexes **5**–**9** were obtained by combining the inorganic salt $Ag(OSO_2CF_3)$ with ligands **1**–**4** in different stoichiometries, giving rise to monometallic $[Ag(Pz^{bp2}Py)_2(OSO_2CF_3)]$ (**5**) and $[Ag(Pz^{bp}Py)_2(OSO_2CF_3)]$ (**7**) (from 1:2), dimetallic $[Ag_2(Pz^{bp2}Py)_2(OSO_2CF_3)_2]$ (**6**) (from 1:1) or trimetallic $[Ag_3(TPz^{bp2}Tz)(OSO_2CF_3)_3]$ (**8**) and $[Ag_3(TPz^{bp}Tz)(OSO_2CF_3)_3]$ (**9**) (from 3:1) complexes. Scheme 2 shows the molecular characteristics of the three types of compounds. A more detailed description of trimetallic complexes **8** and **9** is given in Scheme 3.

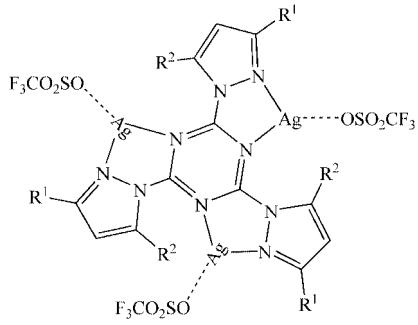

$[Ag_3(TPz^{bp2}Tz)(OSO_2CF_3)_3]$ **8** $R^1 = R^2 = C_6H_4OC_4H_9$

$[Ag_3(TPz^{bp}Tz)(OSO_2CF_3)_3]$ **9** $R^1 = C_6H_4OC_4H_9$; $R^2 = H$

Scheme 3. Schematic representation of trimetallic compounds **8** and **9**.

The IR spectra of the new complexes **5**–**9** were recorded in KBr in the 4000–400 cm^{-1} range. For comparative purposes, the IR spectra of the free ligands were also obtained. The new complexes exhibit the characteristic bands of the ligands, slightly modified by coordination. Compounds **5** and **6** were also characterised by X-ray diffraction and show Ag–O distances of 2.704(8) and 2.325(6) Å, respectively, as will be described below. The former one could be considered to be a coordinative Ag···O interaction[1c,1f,1g,1i,1l,1m,6a,8] or even an Ag–O bond, as has been reported by some authors,[1h,1m,9] whereas the latter is clearly characteristic of an Ag–O bond.[1i,1k,10] The IR spectra of **5** and **6** show absorption frequencies at 1273 and

 © 2005 Wiley-VCH Verlag GmbH & Co. KGaA, Weinheim

1288 cm^{-1}, respectively, assigned to $\nu_{as}(SO_3)$.[11] Thus, the $\nu_{as}(SO_3)$ values for related compounds are tentatively used to differentiate between interactions and/or covalent bonds. Following these results, the $\nu_{as}(SO_3)$ absorption at 1290 cm^{-1} in **8** suggests a strong Ag···O interaction. The related complex **9** exhibits a broad band centred at 1253 cm^{-1}, characteristic of the ligand, which could mask the $\nu_{as}(SO_3)$ absorption.

Multinuclear Magnetic Resonance Spectroscopy

The ^1H NMR spectroscopic data of the ligands and their complexes are gathered in Tables 1 and 2.

The ^1H NMR spectra of $[Ag(Pz^{bp2}Py)_2(OSO_2CF_3)]$ (**5**) and $[Ag_2(Pz^{bp2}Py)_2(OSO_2CF_3)_2]$ (**6**) show all the expected resonances of the $Pz^{bp2}Py$ units. In both cases, as expected, an inequivalence of the substituents at the 3- and 5-positions of the pyrazole ring is observed, in agreement with the lack of symmetry. This fact is reflected by the presence of two sets of signals for the OCH_2 groups and the aromatic H_o and H_m protons of the substituents. In solution, the two $Pz^{bp2}Py$ ligands appear to be equivalent in both complexes, as deduced from the unique signals observed for the H4 proton and the pyridine protons. The signals of the latter ones are shifted downfield in relation to the free ligand (specially noted in **6**), except the H3′ signal, which is shifted upfield by about 0.5 ppm. In contrast, the environment of the aromatic C_6H_4 protons is not significantly modified, thus indicating that metal–arene interactions do not exist in solution.[2e,2f,12]

When comparing the ^1H NMR spectra of $[Ag(Pz^{bp}Py)_2(OSO_2CF_3)]$ (**7**) with that of **5**, very close chemical shifts are observed for the signals of the pyridine protons H5′ and H6′, whereas for the signals of H3′ and H4′ the shift upon complexation is larger in complex **5**.

Complexes $[Ag_3(TPz^{bp2}Tz)(OSO_2CF_3)_3]$ (**8**) and $[Ag_3(TPz^{bp}Tz)(OSO_2CF_3)_3]$ (**9**) present analogous ^1H NMR spectra, the only differences coming from the pyrazole moieties. This fact suggests similar three-coordinate silver environments by considering the chelating complexation through the nitrogen atoms of the pyrazole and triazine rings (N-Pz and N-Tz) and the Ag···OSO_2CF_3 interaction proposed above from their IR spectra. Complex **8** exhibits two different types of signals for the aromatic protons H_o and H_m, the first set is broad and the second one shows sharp multiplets. An analogous behaviour is found for the 4-butoxyphenyl substituent in complex **9**. The broadness of the signals in both complexes can be explained on the basis

Table 1. ^1H NMR chemical shifts (δ in ppm) and coupling constants (J in Hz) of the pyrazole moiety in compounds **1**–**9**.[a]

Compound Solvent (pyrazole moiety)	$^aCH_3$	$^bCH_2$	$^cCH_2$	OCH_2	H_m	H_o	H4	H5
1	0.98 (t)	1.51 (m)	1.78 (m)	3.97 (t)	6.84 (m)	7.21 (m)	6.71 (s)	
$CDCl_3$	^3J = 7.4			^3J = 6.5				
(Pz^{bp2})	0.99(t)			4.01 (t)	6.95 (m)	7.86 (m)		
	^3J = 7.4			^3J = 6.5				
2	0.99 (t)	1.51 (m)	1.80 (m)	4.01 (t)	6.84 (m)	7.85 (m)	6.71 (d)	8.57 (d)
$CDCl_3$	^3J = 7.4			^3J = 6.5			^3J = 2.6	^3J = 2.6
(Pz^{bp})								
3	0.94 (t)	1.43 (m)	1.72 (m)	3.87 (t)	6.85 (m)	7.24 (m)	6.63 (s)	
$CDCl_3$	^3J = 7.4			^3J = 6.6				
(Pz^{bp2})	1.01 (t)	1.51 (m)	1.82 (m)	4.04 (t)	6.98 (m)	7.76 (m)		
	^3J = 7.4			^3J = 6.5				
4	1.00 (t)	1.51 (m)	1.79 (m)	4.00 (t)	6.97 (m)	7.91 (m)	6.77 (d)	8.71 (d)
$CDCl_3$	^3J = 7.4			^3J = 6.5			^3J = 2.9	^3J = 2.9
(Pz^{bp})								
5	0.93 (t)	1.40 (m)	1.66 (m)	3.77 (t)	6.67 (m)	7.64 (m)	6.76 (s)	
CD_2Cl_2	^3J = 7.4			^3J = 6.5				
(Pz^{bp2})	1.00 (t)	1.53 (m)	1.81 (m)	4.04 (t)	6.98 (m)	7.28 (m)		
	^3J = 7.4			^3J = 6.5				
6	0.92 (t)	1.29–1.88 (m)	1.29–1.88 (m)	3.79 (t)	6.76 (d)	7.35 (d)	6.98 (s)	
CD_3COCD_3	^3J = 7.3			^3J = 6.3	^3J = 8.8	^3J = 8.8		
(Pz^{bp2})	1.00 (t)			4.09 (t)	7.06 (d)	7.76 (d)		
	^3J = 7.3			^3J = 6.3	^3J = 8.8	^3J = 8.8		
7	0.96 (t)	1.46 (m)	1.72 (m)	3.88 (t)	6.67 (m)	7.72 (m)	6.94 (d)	8.51 (d)
CD_2Cl_2	^3J = 7.4	^3J = 7.5	^3J = 7.0	^3J = 6.5			^3J = 2.8	^3J = 2.8
(Pz^{bp})								
8	0.93 (t)	1.41 (br)	1.67 (br)	3.85 (br)	7.01 (m)	7.46 (m)	6.67(s)	
$CDCl_3$	^3J = 6.9							
(Pz^{bp2})	1.03 (t)	1.55 (br)	1.83 (br)	4.04 (br)	7.14 (br)	7.71 (br)		
	^3J = 6.6							
9	0.90 (t)	1.38 (br)	1.62 (br)	3.88 (br)	6.88 (br)	7.88 (br)	7.05 (br)	9.10 (br)
CD_3COCD_3	^3J = 7.2							
(Pz^{bp})								

[a] See Scheme 1 for numbering.

 © 2005 Wiley-VCH Verlag GmbH & Co. KGaA, Weinheim

Table 2. ^{1}H NMR chemical shifts (δ in ppm) and coupling constants (J in Hz) of the pyridine nucleus in compounds **1**, **2** and **5**–**7**.[a]

Compound Solvent	H3′	H4′	H5′	H6′
1	7.50 (d)	7.70 (ddd)	7.19 (m)	8.41 (m)
$CDCl_3$	^3J = 8.1	^3J = 8.1		
		^3J = 7.5		
		^4J = 1.8		
2	8.08 (ddd)	7.80 (ddd)	7.19 (ddd)	8.41 (ddd)
$CDCl_3$	^3J = 8.3	^3J = 8.3	^3J = 7.4	^3J = 4.9
	^4J = ^5J = 0.9	^3J = 7.4	^3J = 4.9	^4J = 1.8
		^4J = 1.8	^4J = 1.0	^5J = 0.8
5	6.95 (br)	7.72 (ddd)	7.35 (dd)	8.41 (dd)
CD_2Cl_2		^3J = ^3J = 7.9	^3J = 7.4	^3J = 5.1
		^4J = 1.6	^3J = 5.1	^4J = 1.6
6	7.14 (d)	7.99 (ddd)	7.60 (m)	8.81 (m)
CD_3COCD_3	^3J = 8.3	^3J = ^3J = 8.3		
		^4J = 1.7		
7	7.89 (d)	8.08 (ddd)	7.35 (ddd)	8.28 (ddd)
CD_2Cl_2	^3J = 8.5	^3J = 8.5	^3J = 7.4	^3J = 5.1
		^3J = 7.4	^3J = 5.1	^4J = 1.7
		^4J = 1.7	^4J = 0.7	^5J = 0.9

[a] See Scheme 1 for numbering.

of a hypothetical equilibrium between two forms (**a** and **b**), as represented in Scheme 4. These forms should present an asymmetric metal environment produced by a closer approach to one of the two different coordinated nitrogen atoms (N-Tz or N-Pz). In this way, the environment of the R^2 substituent at the 5-position should not be appreciably modified when moving from **a** to **b**, therefore it gives rise to well-defined signals. In contrast, the R^1 substituent at the 3-position will be strongly affected by this equilibrium; this causes a broadening of its signals. Dynamic experiments were undertaken, but unfortunately they proved to be inconclusive. A similar explanation was provided for a related case in a previous paper.[4]

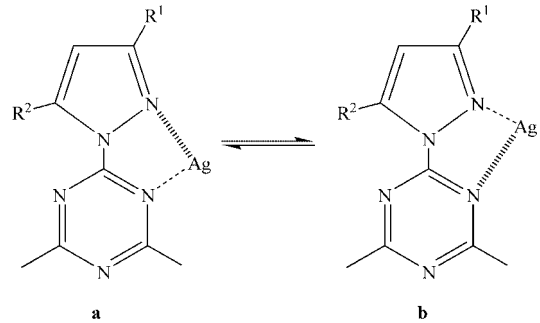

$R^1 = R^2 = C_6H_4OC_4H_9$ **8**
$R^1 = C_6H_4OC_4H_9$; R^2 = H **9**

Scheme 4. Hypothetical equilibrium in solution for **8** and **9**.

Table 3 shows the ^{15}N NMR chemical shifts of ligands **1**–**4** in $CDCl_3$ solution. Those corresponding to complexes **5**–**9** were recorded in solution and/or the solid state, where no fluxional processes would occur. We have already demonstrated that ^{15}N NMR spectroscopy is the most useful tool for establishing the coordination site, as the increase in the nitrogen shielding on metal complexation reflects the changes in the paramagnetic shielding term.[4,13]

In complexes **5** and **7**, it is clear that both the pyridine N1′ and the pyrazole N2 bind to the metal atom as the

Table 3. ^{15}N NMR chemical shifts (δ in ppm).[a] The silver coordination effects on the chemical shifts [$\Delta\delta(^{15}N) = \delta(^{15}N)$complex – $\delta(^{15}N)$ ligand] are given in brackets.

Compound Solvent	*N*-pyrazole (N-Pz) N1	 N2	*N*-pyridine (N-Py) N1′	*N*-triazine (N-Tz) N1′,N3′,N5′
1	–166.0	–85.0	–84.0	
$CDCl_3$				
2	–160.0[b]	–93.0[b]	–105.0[b]	
$CDCl_3$				
3	–169.0[b,c]	–86.0[b]		–156.8[b,c]
$CDCl_3$				
4	–163.0[b,c]	–93.4[b]		–177.0[c]
$CDCl_3$				
5[b]	–172.0	–108.0 (–23)	–118.0 (–34)	
CD_2Cl_2				
5	–167.0	–97.0 (–12)	–112.0 (–28)	
CPMAS	–171.0	–105.0 (–20)	–119.0 (–35)	
7[b]	–168.0	–105.0 (–12)	–129.0 (–24)	
CD_2Cl_2				
7	–163.0	–114.0 (–21)	–128.0 (–23)	
CPMAS	–168.0	–120.0 (–27)	–130.0 (–25)	
8[c]	–161.0	–130.0 (–44)		–192.0 (–35.2)
$CDCl_3$				
8	–173.0	–125.3 (–39.3)		–195.0 (–38.2)
CPMAS				
9	–165.0	–123.0 (–29.6)		–191.0 (–14)
CPMAS				

[a] See Scheme 1 for numbering. [b] (^{1}H-^{15}N) gs-HMBC and gs-HMQC spectra. [c] Inverse gated spectra.

 © 2005 Wiley-VCH Verlag GmbH & Co. KGaA, Weinheim

chemical shifts of their signals move upfield with respect to the free ligands **1** and **2** [$\Delta\delta(^{15}N) = \delta(^{15}N)$complex – $\delta(^{15}N)$ ligand]. In the solid state, the asymmetry of the PzPy units binding the silver cation in the crystal accounts for the two signals observed for each nitrogen. The X-ray structure of **5**, which will described below, supports the above suggestion.

When dealing with the data for **8** and **9** in comparison with those for **3** and **4**, the coordination effects [$\Delta\delta(^{15}N)$] on the triazine N atoms and the pyrazole N2 atom are also negative (Table 3). However, for **5** and **7** the $\Delta\delta$ value for N-Py is higher than that for N-Pz, while the opposite is observed for **8** and **9**. These results agree with a higher crowding of the N-Tz than that of the N-Py.

The ^{15}N NMR spectra of **8** in solution show a higher coordination shift for the N2 of the pyrazole than that for the nitrogen atoms of the triazine, which could be related to the greater strength of the Ag–N bond with the pyrazole. This result is in agreement with the proposed asymmetric silver environment for the complexes.

On the other hand, the chemical shift value of N1 of the pyrazole in all complexes is not significantly affected by the metal coordination, as expected due to the absence of its participation in coordination to the metal atom.

The ^{13}C NMR spectroscopic data for all complexes in solution and the solid state (Table 4 and Table S1 in the Supporting Information) are also in agreement with the proposed structures. The chemical shifts have been analysed relative to those of the corresponding ligands and the main conclusions are: (a) the chemical shifts of the carbon signals of the 4-butoxyphenyl chains are not shifted upon coordination, (b) a downfield coordination shift of the C4 signal of around +3.5 ppm occurs, (c) the downfield shift of the pyridine carbon signals follows the order C4′ (+2.5 ppm) > C6′ ≈ C5′ (+2.0 ppm) > C3′ (+0.6 ppm), with the C2′ signal showing an upfield shift of 2.5 ppm, (d) an upfield coor-

Table 4. ^{13}C NMR chemical shifts (δ in ppm) and coupling constants (J in Hz) of the pyrazole, pyridine and triazine moieties of compounds **1**–**9**.[a]

Compound Solvent	C3	C4	C5	C2′	C3′	C4′	C5′	C6′
1	152.4	105.5	144.9	152.7	118.9	138.0	122.1	148.5
$CDCl_3$	^2J = 4.1	^1J = 174.6	^2J = 7.6	^3J = 11.9	^1J = 166.3	^1J = 162.6	^1J = 164.9	^1J = 180.7
	^3J = 4.1		^3J = 3.8	^3J = 9.3				^2J = 3.7
	^3J = 4.1		^3J = 3.8					^3J = 7.4
2	154.0	105.3	128.5	151.9	112.7	138.9	121.3	148.2
$CDCl_3$	^2J = 4.1	^1J = 175.6	^1J = 191.7	^3J = 10.4	^1J = 169.4	^1J = 162.5	^1J = 165.2	^1J = 180.7
	^3J = 8.3	^2J = 8.7	^2J = 9.2	^3J = 10.4	^3J = 6.8	^3J = 6.6	^2J = 7.3	^2J = 4.1
	^3J = 4.1						^3J = 7.3	^3J = 7.3
	^3J = 4.1							
3	154.3	109.4	147.8	164.5		164.5		164.5
$CDCl_3$	^2J = 3.7	^1J = 175.5	^2J = 8.1					
	^3J = 3.7		^3J = 4.0					
	^3J = 3.7		^3J = 4.0					
4	157.0	107.7	131.8	162.9		162.9		162.9
$CDCl_3$	^2J = 4.1	^1J = 177.6	^1J = 194.9					
	^3J = 4.1		^2J = 9.0					
	^3J = 4.1							
5	154.0	108.6	146.8	150.1	119.2	140.1	124.0	150.5
CD_2Cl_2	^2J = 4.0	^1J = 178.2	^2J = 7.8	^2J = 10.2	^1J = 170.4	^1J = 166.3	^1J = 168.7	^1J = 184.5
	^3J = 4.0		^3J = 4.0	^3J = 10.2	^2J = 7.1	^2J = 6.5	^2J = 6.8	^2J = 3.3
	^3J = 4.0					^3J = 6.5	^3J = 6.8	^3J = 7.6
5	152.6	107.8	145.1	150.1	119.5	143.5	124.5	152.0
CPMAS	153.6	109.6						
7	154.8	108.6	131.0	149.4	113.6	141.7	123.4	149.7
CD_2Cl_2	^2J = 4.0	^1J = 180.4	^1J = 191.8	^3J = 10.1	^1J = 169.7	^1J = 166.1	^1J = 168.7	^1J = 184.0
	^3J = 8.2	^2J = 7.4	^2J = 8.8	^3J = 10.1	^3J = 7.0		^2J = 6.7	^3J = 7.2
	^3J = 4.0						^3J = 6.7	^2J = 4.3
	^3J = 4.0							
7	152.4	107.3	132.1	146.8	112.1	137.2	123.4	149.5
CPMAS		109.9		148.9	114.5	138.6		151.0
8	156.2	112.6	148.0	161.7		161.7		161.7
$CDCl_3$		^1J = 182.7						
8	154.3	115.3	148.2	161.5		161.5		161.5
CPMAS	155.8							
9	158.7 (br)	111.1	134.4 (br)	162.1		162.1		162.1
CD_3COCD_3		^1J = 181.5						
		^2J = 7.2						
9	156.0	110.0	135.3	161.5		161.5		161.5
CPMAS	156.6	112.7	138.8					

[a] See Scheme 1 for numbering.

 © 2005 Wiley-VCH Verlag GmbH & Co. KGaA, Weinheim

dination shift of the signals of the three equivalent triazine carbon atoms takes place.

The ^{13}C NMR spectra in solution show the equivalence of the pyrazole groups, as well as the inequivalence of their substituents, as already deduced by ^{1}H NMR spectroscopy. In the case of $[Ag(Pz^{bp2}Py)_2(OSO_2CF_3)]$ (**5**), the ^{13}C CPMAS NMR spectroscopic data indicate that both $Pz^{bp2}Py$ ligands are inequivalent as well as the two 4-butoxyphenyl groups of each ligand, as has also been established by X-ray crystallography. The splitting of the signals observed in all compounds in the solid state can also be attributed to packing effects.

The above results establish a bidentate coordination involving the N-Pz/N-Py in complexes **5** and **7** or N-Pz/N-Tz in **8** and **9**. A new coordinative position around the silver should be occupied by the oxygen atom from the triflate CF_3SO_3 groups, giving rise to five-coordinate species containing two PyPz ligands for **5** and **7**, while three-coordination is proposed for **8** and **9**.

In the search for additional structural information, the X-ray structures of **5** and **6** were solved, and the results are described in the following section.

Crystal and Molecular Structures of 5 and 6

Compounds **5** and **6** crystallised from dichloromethane solutions. Table 5 provides a selected list of bond lengths and angles.

As depicted in Figure 1, the silver centre in **5** is four-coordinate with the nitrogen atoms of two $Pz^{bp2}Py$ ligands in a distorted tetrahedral environment. This is reflected in the dihedral angle formed by the AgN1N3 and AgN4N5 planes of 124.8(2)°. The Ag–N bond lengths fall in the range of 2.28–2.50 Å found for related compounds.[1b,1h,1k,6e,6f,14] The mean Ag–N distance involving the N-Py atoms [2.318(8) Å] is shorter than that of the N-Pz atoms [2.467(8) Å]. The largest distortion from tetrahedral geometry is given by the N–Ag–N bite angle [N1–Ag–N3: 70.9(3)°; N6–Ag–N4: 69.7(3)°] associated with the chelating ligands.

Table 5. Selected bond lengths [Å] and angles [°] for **5** and **6**.

	5		
Ag–N1	2.359(8)	N6–Ag–N1	152.5(3)
Ag–N3	2.385(9)	N6–Ag–N3	136.6(3)
Ag–N4	2.574(8)	N1–Ag–N3	70.9(3)
Ag–N6	2.251(8)	N6–Ag–N4	69.7(3)
Ag···O5	2.704(8)	N1–Ag–N4	93.3(3)
		N3–Ag–N4	128.2(3)
		N1–Ag···O5	94.3(3)
		N3–Ag···O5	77.5(3)
		N4–Ag···O5	154.3(3)
		N6–Ag···O5	93.1(3)
	6		
Ag–N1	2.584(6)	N3–Ag–O3	142.4(2)
Ag–N3	2.307(6)	N3–Ag–N1	69.4(2)
Ag–O3	2.325(6)	O3–Ag–N1	103.4(2)
Ag–C25[a]	2.670(7)	N3–Ag–C25C26[b]	116.3(2)
Ag–C26[a]	2.706(7)	O3–Ag–C25C26[b]	101.5(3)
Ag–C25C26[b]	2.598(1)	N1–Ag–C25C26[b]	104.9(2)

[a] $-x + 1, -y + 1, -z + 1$. [b] C25C26 means the centroid of the C25–C26 bond.

The C_6H_4 group at the 3-position in one molecule of **5** is almost parallel to the C_6H_4 group at the 5-position of the other molecule [dihedral angle of 4.2(3)°], and the remaining aryl rings are orthogonal between them [86.7(2)°] with the butoxy chains in an opposite and almost symmetrical disposition. The four chains produce a crowding in one corner of the metal environment. As a consequence, the silver centre has a deprotected position that allows the approach of an oxygen atom of the triflate group. The Ag···O5 distance of 2.704(8) Å is smaller than the sum of the van der Waals radii of 2.84 Å.[14b] Similar values have been attributed to metal–oxygen bonds.[1h,1m,9] Therefore, the distance observed for **5** can be considered a "strong" coordinative interaction, giving rise to a distorted trigonal bipyramidal geometry around the metal atom.

Because of the usually found three-coordination around the silver centre, we thought that the coordination of the triflate group could be assessed by using a ratio of $Pz^{bp2}Py$ ligand/$Ag(OSO_2CF_3)$ = 1.

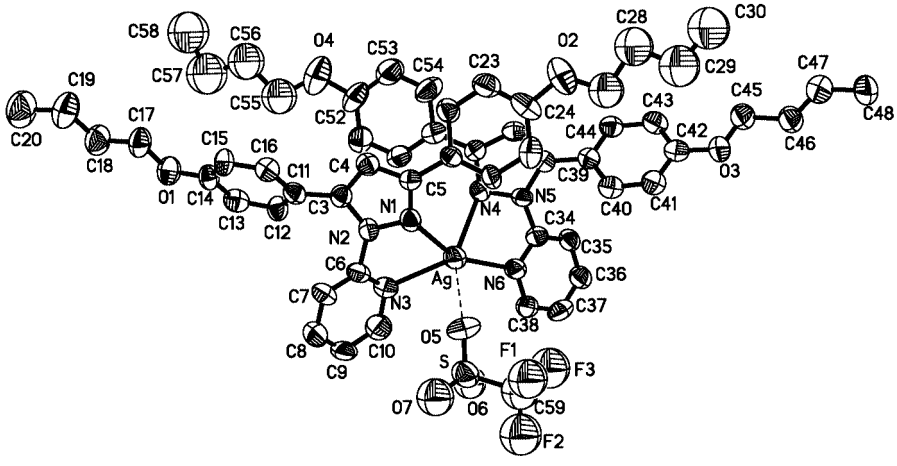

Figure 1. ORTEP plot of **5** with ellipsoids at 40% probability, showing the $Pz^{bp2}Py$ coordination and the Ag···O intermolecular bonds. Hydrogen atoms and the labelling of some atoms have been omitted for clarity.

 © 2005 Wiley-VCH Verlag GmbH & Co. KGaA, Weinheim

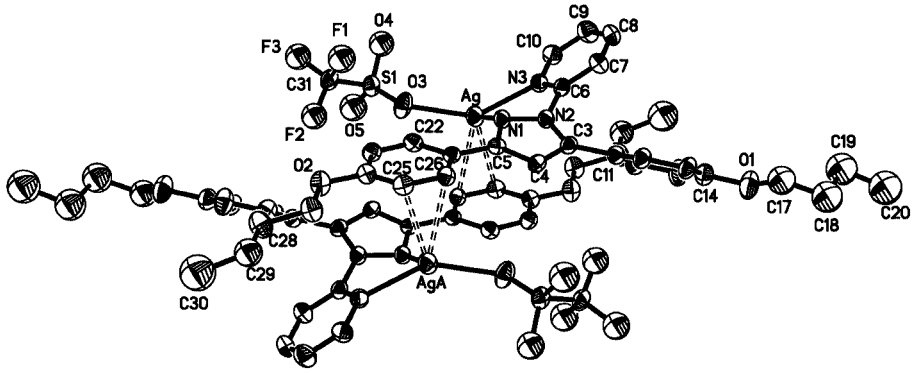

Figure 2. ORTEP plot of **6** with ellipsoids at 35% probability level, showing the dimeric unit formed by Ag···arene interactions. Hydrogen atoms and the labelling of some atoms have been omitted for clarity.

The molecular structure of **6** is shown in Figure 2 and corresponds to a dimeric entity produced by Ag···π(aryl ring) interactions between two molecules that are symmetrically related by an inversion centre. The coordination geometry around each silver atom in **6** is quite different from that in **5**. Thus, the metal atom in **6** adopts the usual three-coordination with the silver cation being trigonally coordinated by the two nitrogen atoms of the bidentate $Pz^{bp2}Py$ ligand and an oxygen atom from the triflate anion. The Ag–N1 and Ag–N5 distances of 2.584(6) and 2.307(6) Å, respectively, are almost equivalent to those found in **5**. The metal atom deviates 0.741(1) Å from the plane defined by the three coordinated atoms (N1, N3, O), this deviation being produced by the proximity of an aryl group from the second molecule, to which the silver atom is also coordinated by an Ag···π bond,[15] thus generating a distorted tetrahedral environment. The short Ag–C distances [mean value of 2.668(7) Å] are in the range found in other compounds containing η^2-Ag···π arene interactions (2.40–2.75 Å).[9,16] The contacts of the silver atom with the other aromatic carbon atom are greater than 3 Å [the shortest is Ag–C24 ($-x + 1$, $-y + 1$, $-z + 1$) with 3.22(3) Å], consisting of an asymmetric coordination of the silver atom with the two carbon atoms of the benzene ring. The separation of each silver atom from the mean plane of its coordinated aryl group of 2.567(5) Å lies in the range inherent to the bonding of an arene ligand.[16a] In addition, the positional parameters β and Δ (where Δ and β measure the deviation from the centroid axis;[16a] see Scheme 5) of the silver centre of 30.9° and 1.54 Å, respectively, are in agreement with the range of other structures showing an η^2-coordination of the arene.[16a] All the above arguments allow us unequivocally to establish the presence of a dimerisation through an η^2-Ag···π arene bond.

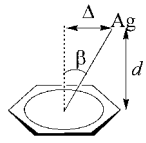

Scheme 5. Δ and β parameters for Ag···arene interactions.[16a]

In the crystal structures of **5** and **6** shown in Figures 3–6, the triflate anion intervenes in the organisation around the $[Ag(Pz^{bp2}Py)_2O]$ and $[Ag(Pz^{bp2}Py)O]$ units, either coordinating or forming a covalent bond with the metal atom in **5** and **6**, respectively. Such an anion is also employed to expand the supramolecular environment with one of the remaining oxygen atoms interacting with the silver centre or carbon atoms of neighbouring units. Thus, the coordination of the anion in **6**, or strong interaction in **5**, can be considered as the first stage of the supramolecular organi-

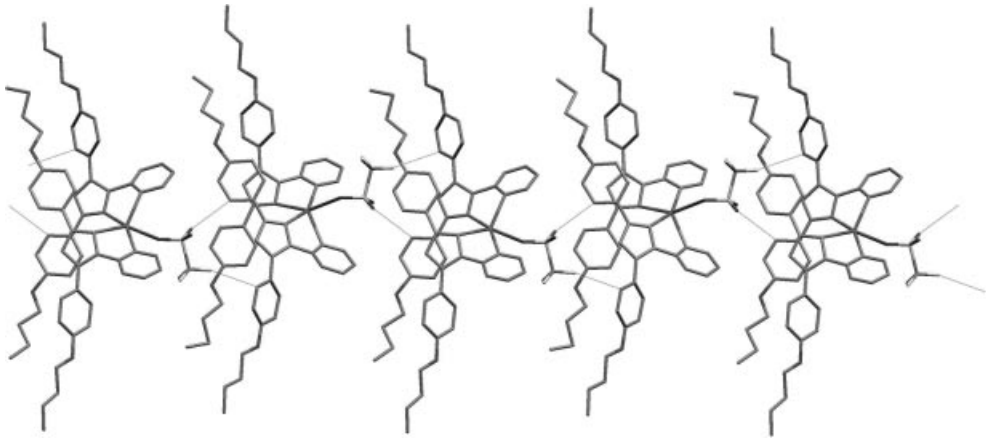

Figure 3. View of the strand along the *b* axis in **5**, showing the Ag···O, C–H···O and C–H···F contacts.

 © 2005 Wiley-VCH Verlag GmbH & Co. KGaA, Weinheim

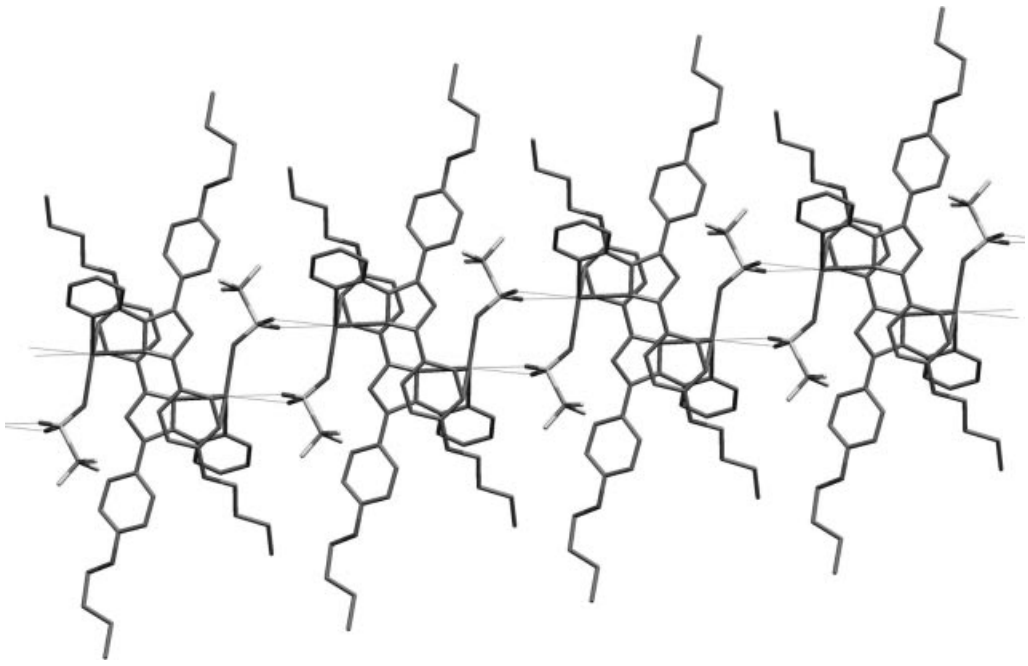

Figure 4. View of the double strand along the *b* axis in **6**, showing the Ag···O contacts between dimers.

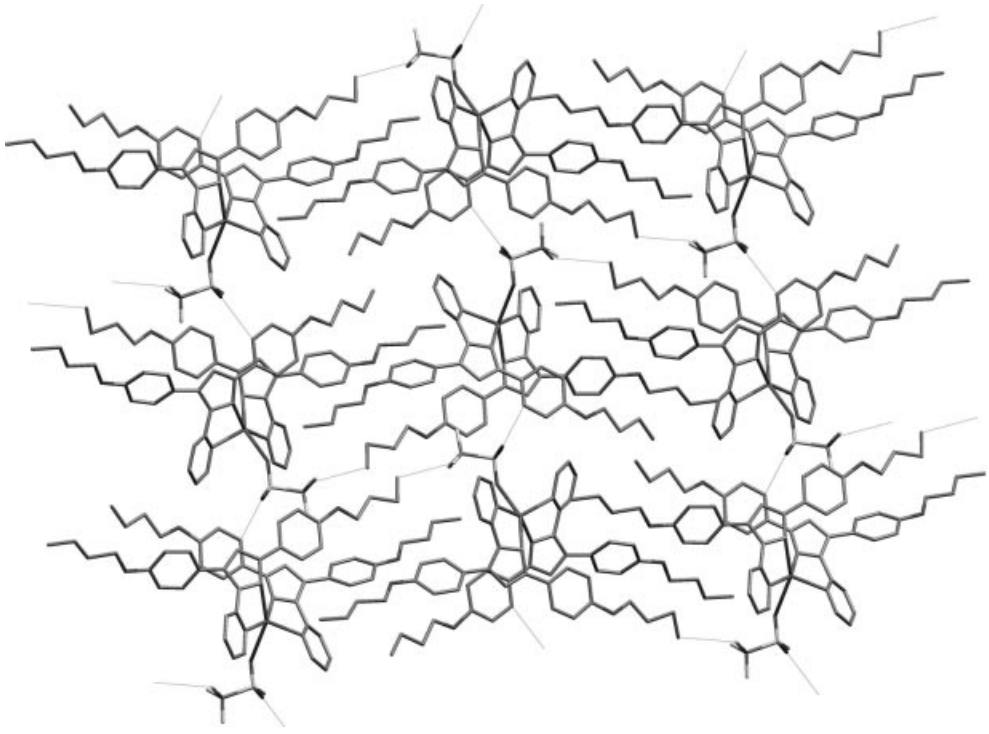

Figure 5. View of a layer parallel to the (101) plane of the 2D network of **5**.

sation, while the next one is consistent with the assembly of $[Ag(Pz^{bp2}Py)_2O]$ and $[Ag(Pz^{bp2}Py)O]$ units, which can be described as follows:

i) The oxygen atoms of the triflate, which are not involved in a direct bond or interaction with the silver atom, are bonded to a pair of adjacent molecules by Ag···O or C–H···O/F interactions, thus generating strands. In **5**, the strands are defined along the *b* axis by the C22···O7 [$-x$ + ½ + 1, y – ½, $-z$ + ½: 3.24(2) Å] and C16···F2 [$-x$ + ½ + 1, y – ½, $-z$ + ½: 3.04(2) Å] interactions (Figure 3). In **6**, the overall arrangement consists of a double strand along the *b* axis in which two triflate anions act as bridging groups of each neighbouring dimer [Ag1···O5 ($-x$ + 1, $-y$ + 2, $-z$ + 1): 2.84(1) Å; Ag1···O4 ($-x$ + 1, $-y$ + 2, $-z$ + 1): 3.32(1) Å; see Figure 4). In addition to related C–H···O interactions [C10···O5 ($-x$ + 1, $-y$ + 2, $-z$ + 1): 3.24(2) Å;

 © 2005 Wiley-VCH Verlag GmbH & Co. KGaA, Weinheim

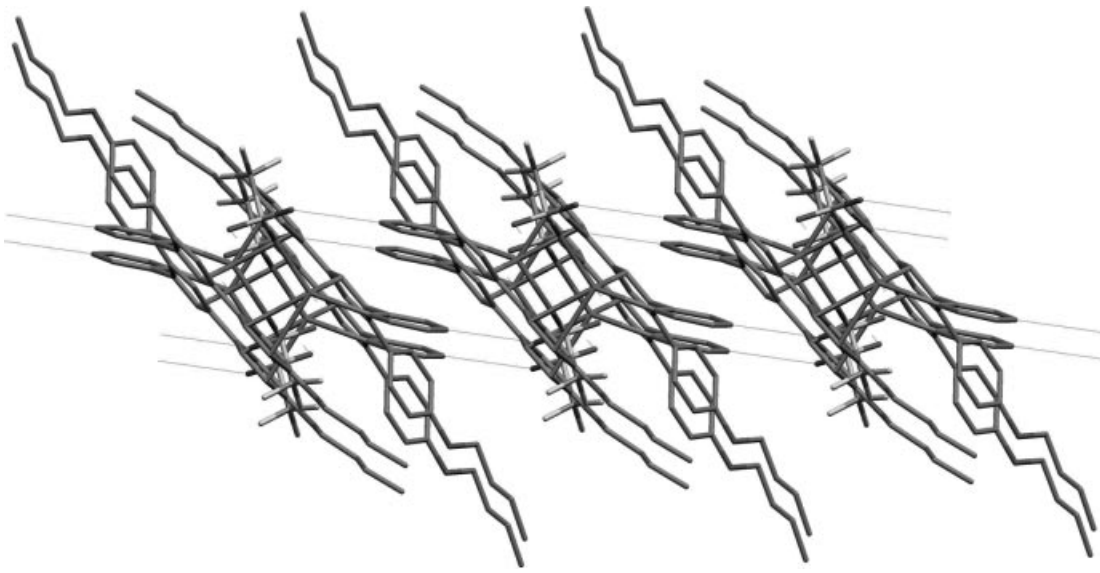

Figure 6. View of a layer parallel to the (001) plane of the 2D network of **6**.

C25···O4 (x, y – 1, z): 3.18(2) Å], the strands are mainly determined by a direct Ag···O bond. The triflate tecton in both **5** and **6** is responsible for the 1D arrangement.
ii) New non-conventional hydrogen-bonding interactions involving the CF_3 groups of the triflate group in **5** or bifurcated C–H···O interactions in **6** extend the supramolecular arrangements into a 2D network. Thus, the C–H···F interactions between the chains in **5** [C58···F3 (x + ½, $-y$ + ½ + 1, z – ½): 3.25(3) Å], where the F atoms proceed from alternating and symmetrically disposed bridging triflate groups along the c axis of the chain, give rise to layers which lie parallel to the (101) plane (Figure 5). In **6**, the same oxygen atom implicated in the strand interacts with the pyridine group of an adjacent strand [C8···O4 ($-x$, y + 2, $-z$ + 1): 3.31(1) Å], thereby extending these interactions through the (001) plane (Figure 6).

Concluding Remarks

Silver(I) coordination complexes containing $Pz^{bp2}Py$ (**1**), $Pz^{bp}Py$ (**2**), $TPz^{bp2}Tz$ (**3**) and $TPz^{bp}Tz$ (**4**) polydentate ligands have been obtained. An *N*,*N*′-bidentate coordination has been established in $[Ag(Pz^{bp2}Py)_2(OSO_2CF_3)]$ (**5**) and $[Ag(Pz^{bp}Py)_2(OSO_2CF_3)]$ (**7**), which involves the N-Pz/N-Py sites, and implicates the N-Pz/N-Tz ones in $[Ag_3(TPz^{bp2}Tz)(OSO_2CF_3)_3]$ (**8**) and $[Ag_3(TPz^{bp}Tz)(OSO_2CF_3)_3]$ (**9**). A new coordinative position is occupied by the oxygen atom from the triflate groups, giving rise to five-coordinate species containing two PzPy ligands for **5** and **7**, while three-coordination is proposed for **8** and **9**.

The compound $[Ag_2(Pz^{bp2}Py)_2(OSO_2CF_3)_2]$ (**6**), which contains Ag/$Pz^{bp2}Py$ in a 1:1 stoichiometric ratio, exhibits the expected metal environment determined by the *N*,*N*′-bidentate $Pz^{bp2}Py$ ligand and the oxygen atom of the triflate group. However, in this case, this environment is expanded through an M–π olefinic bond to give rise to dimeric units.

From the comparative study of the structures of **5** and **6**, several features can be established as determining factors of the supramolecular arrays: i) The structural role of the triflate anion takes place by coordination or strong interaction of the silver centre to an oxygen atom (Ag···O); ii) the coordination of the anion to the $[Ag(Pz^{bp2}Py)_2]^+$ units in **5** is less favoured than in **6** due to the crowding around the metal centre, which prevents the additional Ag···π interaction that is responsible for the dimer in **6**; iii) double or single strands are built on the basis of hydrogen-bonding interactions.

Experimental Section

Materials and Instrumentation: All commercial reagents were used as supplied. 3-(4-Butoxyphenyl)pyrazole (HPz^{bp}), 2-[3,5-bis(4-butoxyphenyl)pyrazol-1-yl]pyridine ($Pz^{bp2}Py$, **1**) and 2,4,6-tris[3,5-bis(4-butoxyphenyl)pyrazol-1-yl]-1,3,5-triazine ($TPz^{bp2}Tz$, **3**) were prepared according to the literature.[4,7,17] Commercial solvents were dried prior to use. Elemental analyses for C, H, N, S were carried out by the Microanalytical Service of the Complutense University. IR spectra were recorded with an FTIR Nicolet Magna-550 spectrophotometer with samples as KBr pellets in the 4000–400 cm^{-1} region. The exact mass of **4** was determined by high resolution mass spectrometry at 70 eV using the electron impact mode with a VG AutoSpec spectrometer.

NMR Parameters: Spectra were recorded at 298 K with a Bruker DRX 400 spectrometer (400.13 MHz for ^1H; 100.62 MHz for ^{13}C; 40.56 MHz for ^{15}N NMR), except for compound **6**, where only the ^1H NMR spectrum was registered with a Bruker AC 200 spectrometer. Chemical shifts (δ in ppm) are given relative to internal solvents [$CDCl_3$ (δ = 7.26 ppm), CD_2Cl_2 (δ = 5.32 ppm) and $(CD_3)_2CO$ (δ = 2.05 ppm) for ^1H NMR; $^{13}CDCl_3$ (δ = 77.0 ppm), CD_2Cl_2 (δ = 54.0 ppm) and $(CD_3)_2CO$ (δ = 29.9 and 206.7 ppm) for ^{13}C NMR; external nitromethane (δ = 0.0 ppm) for ^{15}N NMR]. Coupling constants (J in Hz) are accurate to ±0.2 Hz for ^1H and ^{13}C. ^2D inverse proton detected heteronuclear shift correlation spectra, ^1H-^{13}C gs-HMQC, ^1H-^{13}C gs-HMBC, ^1H-^{15}N gs-HMBC and ^1H-

 © 2005 Wiley-VCH Verlag GmbH & Co. KGaA, Weinheim

^{15}N gs-HMQC were recorded with the standard pulse sequences.[18] Solid-state ^{13}C (100.73 MHz) and ^{15}N (40.60 MHz) CPMAS NMR spectra were recorded with a Bruker WB-400 spectrometer at 300 K using a 4-mm DVT probehead. Samples were carefully packed in 4-mm diameter cylindrical zirconia rotors with Kel-F end-caps. Operating conditions involved 3.2-μs, 90° ^{1}H pulses and a decoupling field strength of 78.1 kHz with the TPPM sequence. ^{13}C NMR spectra were originally referenced to a glycine sample and then the chemical shifts were recalculated relative to $SiMe_4$ [for the carbonyl atom: δ(glycine) = 176.1 ppm], and ^{15}N spectra to $^{15}NH_4Cl$ and then converted to the nitromethane scale using the relationship $\delta(^{15}N)MeNO_2 = \delta(^{15}N)NH_4Cl - 338.1$ ppm. The typical acquisition parameters for ^{13}C CPMAS were: spectral width: 40 kHz; recycle delay: 5 s; acquisition time: 30 ms; contact time: 2 ms; accumulation number: 900–2200; spin rate: 12 kHz. In order to distinguish protonated and unprotonated carbon atoms, the NQS (non-quaternary suppression) experiment by conventional cross-polarisation was recorded; before the acquisition, the decoupler was switched off for a very short time of 25 μs.[18] Those for ^{15}N CPMAS were: spectral width: 40 kHz; recycle delay: 5 s; acquisition time: 35 ms; contact time: 6 ms; accumulation number: 80000–115000; and spin rate: 6 kHz.

Synthesis of 2-[3-(4-Butoxyphenyl)pyrazol-1-yl]pyridine ($Pz^{bp}Py$, 2): A solution of 4-butoxyacetophenone (1.81 g, 9.42 mmol) in ethyl formate (1.16 mL, 14.13 mmol) and toluene (15 mL) was added to a slurry of anhydrous sodium methoxide (0.51 g, 9.42 mmol) in toluene (50 mL). A clear solution was obtained, which became a slurry after 5 min. The solid was isolated by filtration after 2 h at room temperature and washed with hexane. The solid obtained (0.36 g, 1.48 mmol) was dissolved in 96% ethanol (10 mL), and then treated with hydrochloric acid (ca. 2.5 mL, spec. grav. 1.18). 2-Hydrazinopyridine (0.65 g, 5.92 mmol) dissolved in the minimum amount of 96% ethanol was added to this solution. The mixture was refluxed for 3 h, and then the solvent was evaporated to about half the original volume and the resulting solution kept in a refrigerator at 4 °C. Pale-yellow needles were obtained after 2 d, which were filtered off and washed with hexane. Yield: 0.30 g (69%). M.p. 79 °C. $C_{18}H_{19}N_3O$ (293.37): calcd. C 73.70, H 6.53, N 14.32; found C 73.61, H 6.45, N 14.25. IR (KBr): $\tilde{\nu}$ = 1616 and 1580 cm^{-1} ν(C=N).

Synthesis of 2,4,6-Tris[3-(4-butoxyphenyl)pyrazol-1-yl]-1,3,5-triazine ($TPz^{bp}Tz$, 4): NaH (95%, 63.9 mg, 2.53 mmol) was added to a solution of HPz^{bp} (438.5 mg, 2.03 mmol) in freshly distilled dry THF (30 mL) under argon. After 1.5 h at 90 °C, the solution was allowed to cool, and 2,4,6-trichlorotriazine (cyanuric chloride, 126.1 mg, 0.677 mmol) was added. The solution was heated at 90 °C for 11.5 h and at 60 °C for 15 h. The solvent was evaporated and the residue chromatographed on 60-F_{254} silica gel with chloroform/acetonitrile (92:8) as eluent. R_f = 0.35. Yield: 122 mg (25%). M.p. 197–199 °C. Exact mass calcd. for $C_{42}H_{45}N_9O_3$: 723.3645; found 723.5. IR (KBr): $\tilde{\nu}$ = 1612 cm^{-1} ν(C=N).

Synthesis of $[Ag(Pz^{bp2}Py)_2(OSO_2CF_3)]$ (5): $Ag(OSO_2CF_3)$ (45 mg, 0.17 mmol) was added under nitrogen to a solution of $Pz^{bp2}Py$ (**1**; 153 mg, 0.34 mmol) in dry THF (40 mL). After 24 h of stirring, the solution was filtered through a plug of Celite. Then, the solvent was removed in vacuo and 10 mL of dichloromethane was added. The solution was again filtered through a plug of Celite and concentrated. A colourless solid was isolated after addition of hexane at 4 °C. The product was crystallised from a solution of dichloromethane and hexane at 4 °C. Yield: 111 mg (38%). $C_{57}H_{62}AgF_3N_6O_7S$ (1140.1): calcd. C 60.05, H 5.48, N 7.37, S 2.81; found C 59.65, H 5.34, N 7.34, S 2.78. IR (KBr): $\tilde{\nu}$ = 1612 and 1573 cm^{-1} ν(C=N), 1273 $\nu_{as}(SO_3)$, 1028 $\nu_s(SO_3)$.

Synthesis of $[Ag_2(Pz^{bp2}Py)_2(OSO_2CF_3)_2]$ (6): This compound was prepared in a similar way to **5**, from $Ag(OSO_2CF_3)$ (35 mg, 0.14 mmol) and $Pz^{bp2}Py$ (**1**; 60 mg, 0.14 mmol). The product was crystallised from a solution of dichloromethane at 4 °C. Yield: 38 mg (40%). $C_{58}H_{62}Ag_2F_6N_6O_{10}S_2$ (1397.0): calcd. C 49.87, H 4.47, N 6.02, S 4.59; found C 49.82, H 4.57, N 5.93, S 4.56. IR (KBr): $\tilde{\nu}$ = 1605 and 1572 cm^{-1} ν(C=N), 1288 $\nu_{as}(SO_3)$, 1027 $\nu_s(SO_3)$.

Synthesis of $[Ag(Pz^{bp}Py)_2(OSO_2CF_3)]$ (7): The compound was prepared in a similar way to **5**, from $Ag(OSO_2CF_3)$ (87 mg, 0.34 mmol) and $Pz^{bp}Py$ (**2**; 200 mg, 0.68 mmol). The product was recrystallised from dichloromethane/hexane at 4 °C. Yield: 109 mg (38%). $C_{37}H_{38}AgF_3N_6O_5S$ (843.7): calcd. C 52.68, H 4.54, N 9.96, S 3.80; found C 52.49, H 4.47, N 9.95, S 3.81. IR (KBr): $\tilde{\nu}$ = 1608 and 1578 cm^{-1} ν(C=N), 1249 $\nu_{as}(SO_3)$, 1031 $\nu_s(SO_3)$.

Synthesis of $[Ag_3(TPz^{bp2}Tz)(OSO_2CF_3)_3]$ (8): $Ag(OSO_2CF_3)$ (33.7 mg, 0.13 mmol) was added to a solution of $TPz^{bp2}Tz$ (50.6 mg, 0.04 mmol) in 30 mL of dry THF. After 24 h of stirring, the solution was filtered through a plug of Celite. The solvent was then evaporated to about 5 mL, and pentane (10 mL) was added. The yellow solid formed was filtered off, washed with small portions of pentane and dried in vacuo. Yield: 40 mg (48%). $C_{75}H_{81}Ag_3F_9N_9O_{15}S_3$ (1939.3): calcd. C 46.45, H 4.21, N 6.50; found C 46.49, H 4.36, N 6.49. IR (KBr): $\tilde{\nu}$ = 1610 cm^{-1} ν(C=N), 1253 $\nu_{as}(SO_3)$, 1027 $\nu_s(SO_3)$.

Synthesis of $[Ag_3(TPz^{bp}Tz)(OSO_2CF_3)_3]$ (9): The compound was prepared as described for **8**, from $TPz^{bp}Tz$ (31.4 mg, 0.04 mmol) and $Ag(OSO_2CF_3)$ (33.3 mg, 0.13 mmol). Yield: 41.2 mg (63%). $C_{45}H_{45}Ag_3F_9N_9O_{12}S_3$ (1494.7): calcd. C 36.16, H 3.03, N 8.43; found C 36.34, H 3.41, N 8.38. IR (KBr): $\tilde{\nu}$ = 1610 cm^{-1} ν(C=N), 1253 $\nu_{as}(SO_3)$, 1027 $\nu_s(SO_3)$.

X-ray Structure Determinations: Colourless thin plate or prismatic single crystals of $[Ag(Pz^{bp2}Py)_2(OSO_2CF_3)]$ (**5**) and $[Ag_2(Pz^{bp2}Py)_2(OSO_2CF_3)_2]$ (**6**), respectively, were grown from dichloromethane solutions. Data collection was carried out at room temperature with a Bruker Smart CCD diffractometer using graphite-monochromated Mo-K_α radiation (λ = 0.71073 Å) operating at 50 kV and 20 mA. In all cases, data were collected over a hemisphere of the reciprocal space by combination of three exposure sets. Each exposure covered 0.3° in ω. The cell parameters were determined and refined by a least-squares fit of all reflections collected. The first 50 frames were recollected at the end of the data collection to monitor crystal decay; no appreciable decay was observed. A summary of the fundamental crystal and refinement data is given in Table 6. The structures were solved by direct methods and refined by full-matrix least squares on F^2.[19] Anisotropic parameters were used in the last cycles of refinement for all non-hydrogen atoms, with some exceptions. Thus, some carbon atoms of the butoxy chains, the fluorine and only two oxygen atoms of the triflate group were refined isotropically. The third oxygen atom of the triflate group, which interacts with the silver atom, was refined anisotropically. Some of these atoms were refined with geometrical restraints and variable common carbon–carbon and carbon–oxygen distances. Hydrogen atoms were included in calculated positions, and refined as riding on their respective carbon atoms with thermal parameters related to the bonded atoms. Hydrogen atoms were analysed with SHELXS-97 and PARST97.[20] The largest residual peaks in the final difference map were 1.173 and 1.266 e Å^{-3} for **5** and **6**, respectively, in the vicinity of the fluorine atoms. CCDC-266326 (**5**) and -266327 (**6**) contain the supplementary crystallographic data for this paper. These data can be obtained free of

 © 2005 Wiley-VCH Verlag GmbH & Co. KGaA, Weinheim

Table 6. Crystal and refinement data for **5** and **6**.

	5	**6**
Empirical formula	$C_{57}H_{62}AgF_3N_6O_7S$	$C_{58}H_{62}Ag_2F_6N_6O_{10}S_2$
Formula mass	1140.06	1397.03
Crystal system	monoclinic	triclinic
Space group	$P2_1/n$	$P\bar{1}$
a [Å]	9.4058(6)	10.602(1)
b [Å]	22.149(1)	10.912(1)
c [Å]	26.704(2)	14.735(1)
α [°]	90	72.466(2)
β [°]	98.577(1)	73.340(2)
γ [°]	90	72.473(2)
V [Å^3]	5508.4(6)	1513.6(4)
Z	4	1
F(000)	2368	1456
$D_{calcd.}$ [g cm^{-3}]	1.375	1.537
T [K]	296(2)	296(2)
μ(Mo-K_α) [mm^{-1}]	0.471	0.796
Crystal size [mm]	0.45 × 0.25 × 0.05	0.28 × 0.17 × 0.05
Scan technique	φ and ω	φ and ω
Data collected	–11,–24,–27 to 11,26,31	–12,–12,–17 to 6,10,17
θ [°]	1.20–25.00	1.48–25.00
Refls. collected	28738	7954
Refls. indep.	9664 (R_{int} = 0.120)	5269 (R_{int} = 0.038)
Data/restraints/parameters	9664/13/592	5269/10/305
Refls. observed [$I > 2\sigma(I)$]	3211	2965
GOF (F^2)	0.899	0.973
$R(F)$[a]	0.089	0.069
$wR(F^2)$ (all data)[b]	0.328	0.222
Largest residual peak [e Å^{-3}]	1.173	1.266

[a] $\Sigma(|F_o| - |F_c|)/\Sigma|F_o|$. [b] $\{\Sigma[w(F_o^2 - F_c^2)^2]/\Sigma[w(F_o^2)^2]\}^{1/2}$.

charge from The Cambridge Crystallographic Data Centre via www.ccdc.cam.ac.uk/data_request/cif.

Acknowledgments

Financial support from the Dirección General de Investigación/ Ministerio de Ciencia y Tecnología is gratefully acknowledged (projects BQU2003-07343 and BQU2003-00976).

[1] a) P. M. Hagrman, D. Hagrman, J. Zubieta, *Angew. Chem.* **1999**, *111*, 2798–2848; *Angew. Chem. Int. Ed.* **1999**, *38*, 2638–2684; b) L. Carlucci, G. Ciani, D. M. Prosperio, A. Sironi, *J. Am. Chem. Soc.* **1995**, *117*, 4562–4569; c) A. J. Blake, N. R. Champness, P. Hubberstey, W.-S. Li, M. A. Withersby, M. Schröder, *Coord. Chem. Rev.* **1999**, *183*, 117–138; d) O. M. Yaghi, H. Li, *J. Am. Chem. Soc.* **1996**, *118*, 295–296; e) A. J. Blake, N. R. Champness, M. Crew, S. Parsons, *New J. Chem.* **1999**, *23*, 13–15; f) F. Robinson, M. J. Zaworotko, *J. Chem. Soc., Chem. Commun.* **1995**, 2413–2414; g) C. V. K. Sharma, S. T. Griffin, R. D. Rogers, *Chem. Commun.* **1998**, 215–216; h) D. Venkataraman, S. Lee, J. S. Moore, P. Zhang, K. A. Hirsch, G. B. Gardner, A. C. Covey, C. L. Prentice, *Chem. Mater.* **1996**, *8*, 2030–2040; i) R. G. Vranka, E. L. Amma, *Inorg. Chem.* **1966**, *5*, 1020–1025; j) L. Carlucci, G. Ciani, D. M. Proserpio, A. Sironi, *J. Chem. Soc., Chem. Commun.* **1994**, 2755–2756; k) M. Munakata, M. Wen, Y. Suenaga, T. Kuroda-Sowa, M. Maekawa, M. Anahata, *Polyhedron* **2001**, *20*, 2037–2043; l) W.-H. Bi, D.-F. Sun, R. Cao, M.-C. Hong, *Acta Crystallogr., Sect. E* **2002**, *58*, m324–m325; m) M.-L. Tong, X.-M. Chen, S. W. Ng, *Inorg. Chem. Commun.* **2000**, *3*, 436–441; n) A. Jouaiti, M. W. Hosseini, N. Kyritsakas, *Eur. J. Inorg. Chem.* **2003**, 57–61.

[2] a) T. C. W. Mak, *Inorg. Chim. Acta* **1984**, *84*, 19–23; b) B.-L. Fei, W.-Y. Sun, T. Okamura, W.-X. Tang, N. Ueyama, *New J. Chem.* **2001**, *25*, 210–212; c) A. Bacchi, E. Bossetti, M. Carcelli, P. Pelagatti, D. Rogolino, *Eur. J. Inorg. Chem.* **2004**, 1985–1991; d) Q.-Y. Zhu, J. Dai, D.-X. Jia, L.-H. Cao, H.-H. Lin, *Polyhedron* **2004**, *23*, 2259–2264; e) D. L. Reger, J. R. Gardinier, R. F. Semeniuc, M. D. Smith, *Dalton Trans.* **2003**, 1712–1718; f) D. L. Reger, J. R. Gardinier, M. D. Smith, *Inorg. Chem.* **2004**, *43*, 3825–3832; g) D. Venkataraman, G. B. Gardner, S. Lee, J. S. Moore, *J. Am. Chem. Soc.* **1995**, *117*, 11600–11601; h) K. A. Hirsch, D. Venkataraman, S. R. Wilson, J. S. Moore, S. Lee, *J. Chem. Soc., Chem. Commun.* **1995**, 2199–2200; i) C. L. Schauer, E. Matwey, F. W. Fowler, J. W. Lauher, *J. Am. Chem. Soc.* **1997**, *119*, 10245–10246; j) M. Bertelli, L. Carlucci, G. Ciani, D. M. Proserpio, A. Sironi, *J. Mater. Chem.* **1997**, *7*, 1271–1276; k) S. R. Batten, R. Robson, *Angew. Chem.* **1998**, *110*, 1558–1595; *Angew. Chem. Int. Ed.* **1998**, *37*, 1460–1494; l) R. Wang, M.-C. Hong, J. Luo, F. Jiang, L. Han, Z. Lin, R. Cao, *Inorg. Chim. Acta* **2004**, *357*, 103–114.

[3] M. Cano, J. V. Heras, M. L. Gallego, J. Perles, C. Ruiz-Valero, E. Pinilla, M. R. Torres, *Helv. Chim. Acta* **2003**, *86*, 3194–3203.

[4] R. M. Claramunt, P. Cornago, M. Cano, J. V. Heras, M. L. Gallego, E. Pinilla, M. R. Torres, *Eur. J. Inorg. Chem.* **2003**, 2693–2704.

[5] M. L. Gallego, P. Ovejero, M. Cano, J. V. Heras, J. A. Campo, E. Pinilla, M. R. Torres, *Eur. J. Inorg. Chem.* **2004**, 3089–3098.

[6] a) M. A. Withersby, A. J. Blake, N. R. Champness, P. Hubberstey, W.-S. Li, M. Schröder, *Angew. Chem.* **1997**, *109*, 2421–2423; *Angew. Chem. Int. Ed. Engl.* **1997**, *36*, 2327–2329; b) M. J. Hannon, C. L. Painting, W. Errington, *Chem. Commun.* **1997**, 1805–1806; c) A. J. Blake, N. R. Champness, S. S. M. Chung, W.-S. Li, M. Schröder, *Chem. Commun.* **1997**, 1675–1676; d) B. F. Hoskins, R. Robson, D. A. Slizys, *J. Am. Chem. Soc.* **1997**, *119*, 2952–2953; e) L. Carlucci, G. Ciani, D. M. Proserpio, A. Sironi, *Inorg. Chem.* **1995**, *34*, 5698–5700; f) L. Carlucci, G. Ciani, D. M. Proserpio, A. Sironi, *Angew. Chem.* **1995**, *107*, 2037–2040; *Angew. Chem. Int. Ed. Engl.* **1995**, *34*, 1895–1898; g) L. Carlucci, G. Ciani, D. W. v. Gudenberg, D. M. Proserpio, *Inorg. Chem.* **1997**, *36*, 3812–3813.

 © 2005 Wiley-VCH Verlag GmbH & Co. KGaA, Weinheim

[7] J. A. Campo, M. Cano, J. V. Heras, M. C. Lagunas, J. Perles, E. Pinilla, M. R. Torres, *Helv. Chim. Acta* **2002**, *85*, 1079–1095.
[8] a) M. Burgos, O. Crespo, M. C. Gimeno, P. G. Jones, A. Laguna, *Eur. J. Inorg. Chem.* **2003**, 2170–2174; b) I. Boldog, E. B. Rusanov, A. N. Chernega, J. Sieler, K. V. Domasevith, *Polyhedron* **2001**, *20*, 887–897.
[9] M. Munakata, L. P. Wu, T. Kuroda-Sowa, M. Maekawa, Y. Suenaga, G. L. Ning, T. Kojima, *J. Am. Chem. Soc.* **1998**, *120*, 8610–8618.
[10] M. Munakata, M. Wen, Y. Suenaga, T. Kuroda-Sowa, M. Maekawa, M. Anahata, *Polyhedron* **2001**, *20*, 2321–2327.
[11] G. A. Lawrance, *Chem. Rev.* **1986**, *86*, 17–33.
[12] D. L. Reger, J. R. Gardinier, T. C. Grattan, M. R. Smith, M. D. Smith, *New J. Chem.* **2003**, *27*, 1670–1677.
[13] P. Cornago, R. M. Claramunt, M. Cano, J. V. Heras, M. L. Gallego, *ARKIVOC* **2005**, (ix), 21–29.
[14] a) D. L. Reger, R. F. Semeniuc, M. D. Smith, *Inorg. Chem. Commun.* **2002**, *5*, 278–282; b) C.-J. Lin, W.-S. Hwang, M. Y. Chiang, *Polyhedron* **2001**, *20*, 3275–3280.
[15] a) M. Munakata, L. P. Wu, T. Kuroda-Sowa, *Adv. Inorg. Chem.* **1999**, *46*, 173–303; b) M. Munakata, L. P. Wu, G. L. Ning, *Coord. Chem. Rev.* **2000**, *198*, 171–203.
[16] a) S. V. Lindeman, R. Rathore, J. K. Kochi, *Inorg. Chem.* **2000**, *39*, 5707–5716; b) H. C. Kang, A. W. Hanson, B. Eaton, V. Boekelheide, *J. Am. Chem. Soc.* **1985**, *107*, 1979–1985; c) C. Cohen-Addad, P. Baret, P. Chautemps, J.-L. Pierre, *Acta Crystallogr., Sect. C* **1983**, *39*, 1346–1349; d) F. R. Heirtzler, H. Hopf, P. G. Jones, P. Bubenitschek, V. Lehne, *J. Org. Chem.* **1993**, *58*, 2781–2784; e) S. Kammermeier, P. G. Jones, I. Dix, R. Herges, *Acta Crystallogr., Sect. C* **1998**, *54*, 1078–1081; f) J. Powell, A. Lough, T. Saeed, *J. Chem. Soc., Dalton Trans.* **1997**, 4137–4138; g) M. Munakata, L. P. Wu, G. L. Ning, T. Kuroda-Sowa, M. Maekawa, Y. Suenaga, N. Maeno, *J. Am. Chem. Soc.* **1999**, *121*, 4968–4976.
[17] M. Cano, J. V. Heras, M. Maeso, M. Álvaro, R. Fernández, E. Pinilla, J. A. Campo, A. Monge, *J. Organomet. Chem.* **1997**, *534*, 159–172.
[18] S. Braun, H.-O. Kalinowski, S. Berger, *150 and More Basic NMR Experiments*, Wiley-VCH, Weinheim, **1998**.
[19] G. M. Sheldrick, *SHELXTL, Program for refinement of Crystal Structure*, University of Göttingen, Göttingen, Germany, **1997**.
[20] M. Nardelli, *J. Appl. Crystallogr.* **1995**, *28*, 659–659.

Received: March 17, 2005
Published Online: September 12, 2005

 © 2005 Wiley-VCH Verlag GmbH & Co. KGaA, Weinheim

Early and Late Transition Metal Complexes Stabilised by Imidazopyridazine-Substituted Bisamido Ligands

Torsten Irrgang*[a] and Rhett Kempe*[a,b]

Keywords: Amido ligands / Imidazo[1,5-*b*]pyridazines / N ligands / Chromium / Iridium / Rhodium / Titanium / Zirconium

The preparation of a series of new imidazo[1,5-*b*]pyridazine-substituted diamines (**5**) is reported. They can be synthesised by the nucleophilic ring transformation of 2-amino-5-methyl-1,3,4-oxadiazolium halogenides (**1**) with diaminoalkanes followed by condensation reactions with 1,3-diketones. After deprotonation they were then used as bisamido ligands. These ligands stabilise early and late transition metal complexes as five-membered chelates. The reaction with selected group 4 metals (titanium and zirconium) leads via amine elimination to unusual dark blue and purple mononuclear amido complexes. Deprotonation of the bisamido ligands using BuLi and further reaction with group 6 metals like chromium results in a dinuclear octahedral Cr^{III} complex, where the different coordinated metal centres are bridged by two of the amido N atoms. The double deprotonation of **5** followed by reaction with the group 9 metals rhodium and iridium led to dinuclear complexes in a *trans* binding mode. The X-ray structures of one of the novel bisamido ligands (protonated) and all complexes are reported and discussed.

(© Wiley-VCH Verlag GmbH & Co. KGaA, 69451 Weinheim, Germany, 2005)

Introduction

Amido metal chemistry[1] has attracted much attention recently.[2] The amido ligands used to accomplish this chemistry are obtained mainly from the smooth and selective formation of Si–N bonds via salt elimination or from palladium catalysed aryl amination, which is highly efficient for forming C–N bonds.[3] Both systems have certain limitations e.g. the instability of the Si–N bond and the catalyst cost of the amination reactions. Thus we became interested in an amine synthesis protocol, which allows the synthesis of stable amido ligand precursors and the introduction of a large variety of substitution patterns. A further advantage is the classical bench top chemistry used to carry out the amine syntheses. In this paper synthesis of imidazo[1,5-*b*]-pyridazine-substituted diamines (Scheme 1) and the application of these amines as amido ligands to stabilise early and late transition metals, is reported.

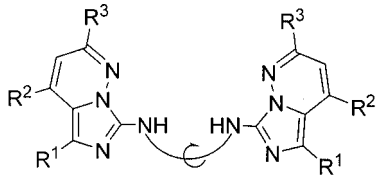

Scheme 1. Imidazo[1,5-*b*]pyridazine-substituted diamines ($R^{1–3}$ aryl or alkyl substituents).

[a] Lehrstuhl für Anorganische Chemie II, Universität Bayreuth, 95440 Bayreuth, Germany
E-mail: kempe@uni-bayreuth.de; torsten.irrgang@uni-bayreuth.de
[b] Leibniz-Institut für Organische Katalyse, Buchbinderstrasse 5–6, 18055 Rostock, Germany

Results and Discussion

Synthesis of the Ligand Precursors – Synthesis of the Diamines

2-Amino-5-methyl-1,3,4-oxadiazolium halogenides[4] **1** (Scheme 2) react with a large variety of primary and secondary amines to afford 2-amino-substituted 1-acetylamino-imidazoles via ring transformation.[5] Thus, the reaction with diaminoalkanes should give rise to *N*,*N*′-bis(1-acetylamino-4-alkyl/aryl-imidazol-2-yl)-1,ω-diaminoalkanes **2a**–**c** (Scheme 2).

In the course of the ring transformation one equiv. of the amine acts as a nucleophile, attacking the amine-substituted carbon atom of the oxadiazolium halide with HBr being eliminated. An excess of the amines is used to trap the HBr. Furthermore, water is eliminated and a new bond between the exocyclic N atom and the exocyclic C atom of the carbonyl group is formed. These ring transformations are extremely exothermic. Variation of the diamines and the oxadiazolium halogenides (substituent R^1) allows the formation of, for instance, **2a**–**c** (Scheme 2). Reaction of **2** with HCl in ethanol produces **3a**–**d** (deacetylation) and neutralisation with aqueous NaOH leads to **4a**–**c**.

The reactions of 1-amino-4-arylimidazoles[6] with diketones afford imidazo[1,5-*b*]pyridazines,[7] a class of substances with a very interesting potential as a suitable non-nucleoside inhibitor of HIV-1 (RT).[8] Analogously, **4** reacts

 © 2005 Wiley-VCH Verlag GmbH & Co. KGaA, Weinheim DOI: 10.1002/ejic.200500297

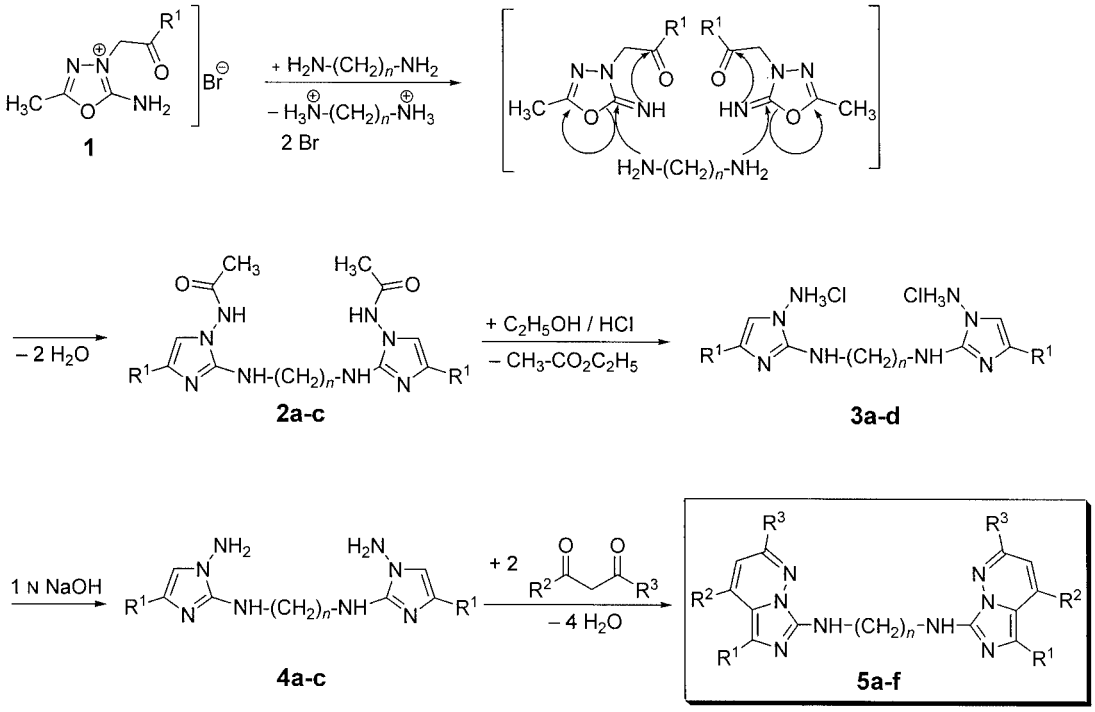

Scheme 2. Ring transformation with diaminoalkanes [n = 2: R^1 = –$C(CH_3)_3$ (**2a/3a/4a**), R^1 = C_6H_5 (**2b/3b/4b**); n = 3: R^1 = C_6H_5 (**2c/3c/4c**), R^1 = C_6H_4-$p$$CH_3$ (**3d**)] and synthesis of **5a**–**f** [n = 2: $R^1/R^2/R^3$ = –$C(CH_3)_3/CH_3/CH_3$ (**5a**), $R^1/R^2/R^3$ = -$C(CH_3)_3/C_6H_5/CH_3$ (**5b**), $R^1/R^2/R^3$ = $C_6H_5/CH_3/CH_3$ (**5c**); n = 3: $R^1/R^2/R^3$ = $C_6H_5/CH_3/CH_3$ (**5d**), $R^1/R^2/R^3$ = $C_6H_5/C_6H_5/CH_3$ (**5e**), $R^1/R^2/R^3$ = C_6H_4-$p$$CH_3/CH_3/CH_3$ (**5f**)].

with acetylacetone and/or benzoylacetone and diaminoalkyl-bridged imidazo[1,5-*b*]pyridazines **5a**–**f** (Scheme 2) are formed. The reactions with benzoylacetone lead to 2-methyl-4-phenyl-imidazopyridazines selectively, which means the methyl group is found in the 2- and the phenyl group in the 4-position. The reason for this might be the higher reactivity of the acetyl group towards the amine function of **4**. A methyl group in the 4-position is characterised by a doublet (^{1}H NMR signal) as well as the H atom in the 3-position. The splitting is about 3 Hz (both signals) and is caused by ^4J coupling due to the short C–C distances of the C–C double bond of the six-membered ring.

Substituents in the 2-(R^3), 4-(R^2) and 5-(R^1)-positions are easily modified with the synthetic protocol described above. Thus, the electronic properties, the steric demand and the solubility behaviour of the corresponding amido ligands can easily be fine-tuned. Compounds **5a**–**f** are obtained as orange to red crystalline materials in good yields after recrystallisation from ethanol water mixtures. X-ray crystal structure analysis was performed to determine the molecular structure (Figure 1) of **5a**. Experimental details are summarised in Table 1. The significantly shorter N1–C2 (1.30 Å) and C3–C4 (1.35 Å) bonds indicate the localisation of the double bonds of the six-membered pyridazine rings in **5a**. The ^{1}H NMR spectroscopic data of **5a**–**f** confirms this observation. The dihedral angles between the two-imidazopyridazine planes are 93.5° in **5a**. The deviations from planes are 0.0078 Å and 0.0071 Å. Both 7-substituted amido N atoms are in the plane with the imidazopyridazines. The deviations of the N1 and N5 atoms, out of the imidazopyridazine planes, are 0.0135 Å and 0.0097 Å, respectively. Complex **5a** is predicted to form inter- or intramolecular H bonds because it contains potential proton donor and acceptor functionalities. An intramolecular hydrogen bond[9] N5–HN5···N2 (with a HN5···N2 distance of 2.40 Å) forces **5a** into a transoid arrangement.

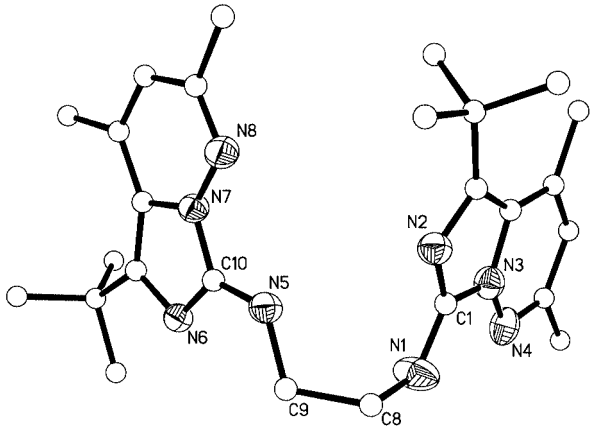

Figure 1. Molecular structure of **5a**; selected bond lengths [Å] and angles [°]: C1–N1 1.360(3), C1–N3 1.343(2), C1–N2 1.313(2), C8–N1 1.441(2), C9–N5 1.451(2), C10–N6 1.319(2), C10–N5 1.368(2), C10–N7 1.346(2), N3–N4 1.369(2), N7–N8 1.369(2), C8–C9 1.509(3); N1–C1–N3 120.95(17), N1–C1–N2 127.37(17), N3–C1–N2 111.68(16), C1–N3–N4 122.50(16), N5–C10–N7 122.06(15), N5–C10–N6 126.82(15), N7–C10–N6 111.11(14).

 © 2005 Wiley-VCH Verlag GmbH & Co. KGaA, Weinheim

Table 1. Details of the X-ray crystal structure analyses of **5a**, **6** and **7**.

	5a	**6**	**7**
Formula	$C_{26}H_{38}N_8$	$C_{26}H_{36}Cl_2N_8Ti$	$C_{34}H_{56}N_{10}Zr$
M [g mol^{-1}]	462.62	579.38	696.08
Crystal system	monoclinic	monoclinic	monoclinic
Space group	*P*21/*c*	*P*21/*n*	*P*2/*c*
a [Å]	9.5144(4)	10.347(1)	11.740(1)
b [Å]	12.8021(8)	9.506(1)	9.315(1)
c [Å]	21.3187(9)	30.407(3)	17.418(2)
β [°]	97.306(3)	97.65(1)	109.16(1)
V [Å^3]	2575.6(2)	2964(1)	1799(1)
Z	4	4	4
Crystal size [mm]	0.60 × 0.50 × 0.40	0.38 × 0.08 × 0.03	0.30 × 0.30 × 0.20
$\rho_{calcd.}$ [g cm^{-3}]	1.193	1.298	1.285
$\mu_{calcd.}$ [mm^{-1}] (Mo-K_α)	0.074	0.499	0.344
T [K]	193(2)	193(2)	200(2)
θ range [°]	1.86–25.71	2.18–25.83	1.84–24.26
Reflections collected	4865	5445	2862
Independent reflections	3834	2727	2240
F(000)	1000	1216	740
R value [$I > 2\sigma(I)$]	0.0497	0.0521	0.0474
wR_2 (all data)	0.1456	0.1238	0.1240

Complex Syntheses and Structures

Compounds **5** as well as the deprotonated versions have six different donor functions to coordinate transition metals. Thus, a range of binding modes depending on the nature of the transition metal as well its oxidation state, are expected. Possible binding modes of double deprotonated **5** are shown in Scheme 3.

A cisoid/transoid orientation concerning the diamido unit can be considered as well as the formation of four- or five-membered chelates. Thus, the binding modes A (*cis*55), B (*cis*44), C (*cis*45), D (*trans*45), E (*trans*55) and F (*trans*44) are expected (*cis* = cisoid, *trans* = transoid, 4 = four-membered and 5 = five-membered chelates). Coordination chemical studies were performed with **5a**. Group 4 metal complexes are efficiently accessible via amine elimination reactions,[2,10] especially since the availability of a variety of amido and mixed amido chloro starting material complexes.[11] The reaction of **5a** with one equiv. of bis(dimethylamido)titanium dichloride gave rise to **6** as a dark blue-purple crystalline material (Scheme 4). Due to the good solubility of **5a** in nonpolar solvents the reaction was accomplished in ether. We wondered about the dark blue to purple colour since titanium amides are usually red coloured and thus put the colour change down to the deprotonation of the ligand. The reaction of **5a** with tetrakis(di-

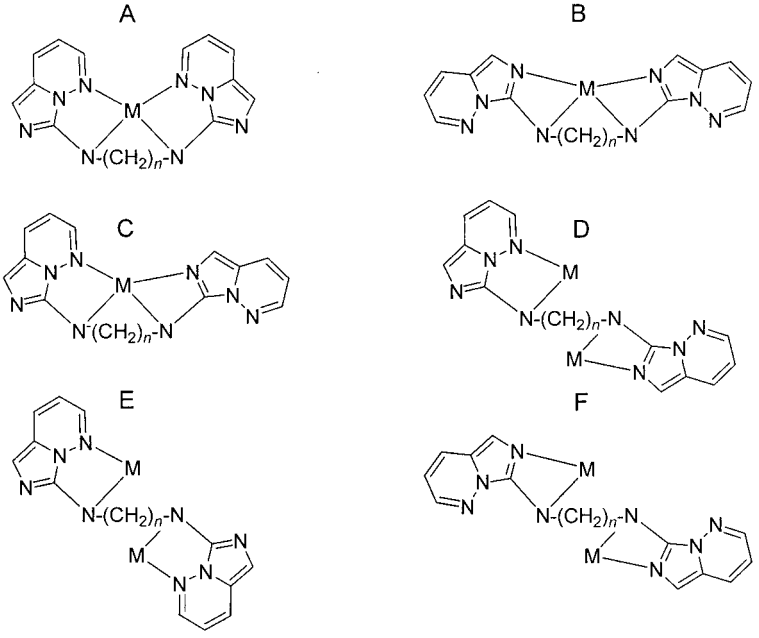

Scheme 3. Binding modes A (*cis*55), B (*cis*44), C (*cis*54), D (*trans*45), E (*trans*55) and F (*trans*44) of double deprotonated **5**.

 © 2005 Wiley-VCH Verlag GmbH & Co. KGaA, Weinheim

ethylamido)zirconium, during which **7** is formed as a crystalline purple material in high yield (Scheme 4) goes along with such a colour change, and supports this hypothesis since zirconium amides are usually colourless. The UV/Vis spectra of **5a**, **6** and **7** are shown in Figure 2. The optical spectra were recorded in C_6H_6 using the same concentrations for all compounds. The ligand shows a significant lower absorption (abs < 0.2) over a plateau with a major peak at 511.0 nm. The longer UV absorption wavelengths of the complexes **6** (626.0 nm) and **7** (572.3 nm, 553.9 nm) were consistent with the observed colour of **6** and **7** in the solid states and in solutions with different solvents. These absorption wavelengths indicate transitions between d levels of the metal ions. The shorter UV absorption wavelengths of **6** (422.0 nm) and **7** (520.0 nm, 347.6 nm) are attributed to electron transitions between the metal ion and ligand or within the ligand.[12] The NMR spectra of **6** and **7** show a single signal set of deprotonated **5a** and thus were indicative of the formation of mononuclear complexes.

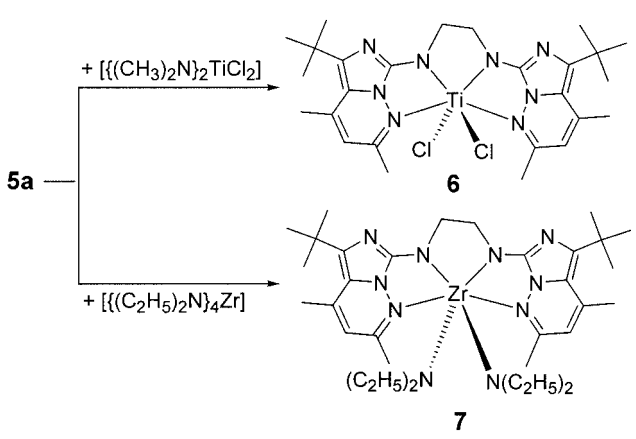

Scheme 4. Synthesis of **6** and **7** via amine elimination.

An X-ray crystal structure analysis of **6** and **7** was performed. Experimental details are summarised in Table 1. The molecular structures of **6** and **7** are shown in Figure 3 and Figure 4, respectively. Both compounds are best described as octahedrally coordinated and adopt the *cis*55 binding mode. The $M–N_{pyridazine}$ bond lengths in **6** (2.313 Å, 2.307 Å) and **7** (2.562 Å) are significantly longer than the $M–N_{amido}$ bond lengths (**6** = 1.973 Å, 1.991 Å; **7** = 2.184 Å), which indicates localised bonding modes for the five-membered chelates of both complexes . The $N_{amido}–Ti–N_{pyridazine}$ angle of the five-membered chelate (mean = 74.8°) is 6.3° larger and the $N_{amido}–Ti–N_{amido}$ (75.57°) is 4.8° larger than the corresponding angle in **7**. The Cl–Ti–Cl angle of the two chloro ligands and the N–Zr–N angles of the two diethylamido ligands are 138° and 123°, respectively. Considering the ideal angles in an octahedral scenario, 90° or 180° for these additional ligands, the smaller titanium seems closer to a *trans* arrangement and the larger zirconium closer to a *cis* arrangement. The dihedral angles

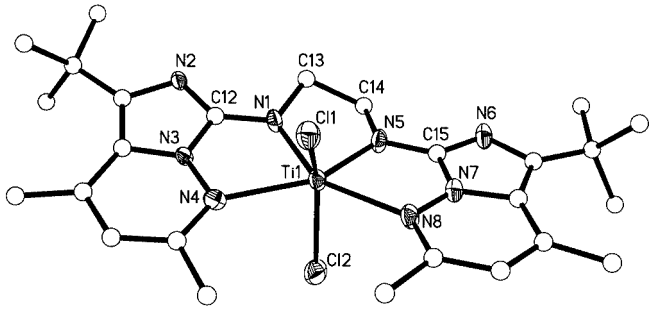

Figure 3. Molecular structure of **6**; selected bond lengths [Å] and angles [°]: Ti1–N1 1.973(4), Ti1–N5 1.991(4), Ti1–N4 2.313(4), Ti1–N8 2.307(4), Ti1–Cl1 2.328(15), Ti1–Cl2 2.329(14); N1–Ti1–N5 75.57(15), N1–Ti1–N8 149.34(14), N5–Ti1–N8 74.78(14), N1–Ti1–N4 74.85(14), N5–Ti1–N4 149.14(14), Cl1–Ti1–Cl2 138.37(6), N7–C15–N5 116.7(4), N7–N8–Ti1 107.8(2), C15–N5–Ti1 120.7(3).

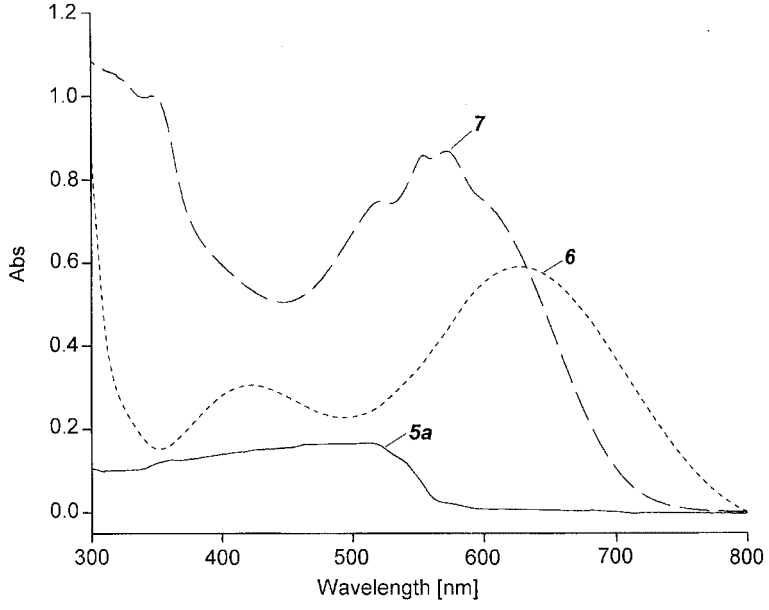

Figure 2. UV/Vis spectra of **5a**, **6** and **7** in C_6H_6.

 © 2005 Wiley-VCH Verlag GmbH & Co. KGaA, Weinheim

between the two imidazopyridazine planes are 15° in **6** and 27.2° in **7**. The deviations from planes are 0.0115 Å and 0.0140 Å in **6** and 0.035 Å for both imidazopyridazines in **7**.

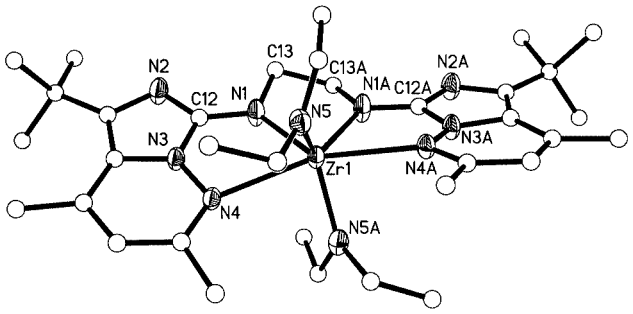

Figure 4. Molecular structure of **7**; selected bond lengths [Å] and angles [°]: Zr1–N1 2.184(3), Zr1–N5 2.007(3), Zr1–N4 2.562(3); N1–Zr1–N5 104.98(13), N1–Zr1–N4 68.54(10), N1–Zr1–N1A 70.77(16), N4–Zr1–N5 83.82(11), N5–Zr1–N5A 123.88(17), C12–N3–N4 120.4(3), N1–C12–N3 118.4(3), C13–N1–Zr1 121.4(2).

Group 6 metal amides do not eliminate as efficiently as group 4 metals and the variety of possible starting materials is much smaller. Thus the opportunities of salt metathesis reactions to synthesise chromium complexes were explored. The double lithiation of **5a** at –70 °C and the reaction of this mixture with $[CrCl_3(THF)_3]$ (THF = tetrahydrofuran) led to the crystalline material of the paramagnetic chromium complex **8** (Scheme 5). Due to the paramagnetic nature of this compound, structural characterisation by NMR spectroscopic methods was not of much help.

The molecular structure was explored by X-ray analysis. Experimental details are summarised in Table 2. The molecular structure of **8** is shown in Figure 5, and includes selected bond lengths and angles. Compound **8** is a dinuclear dichloro chromium(III) complex. Both chromium atoms adopt an octahedral coordination, as preferred by Cr^{III}

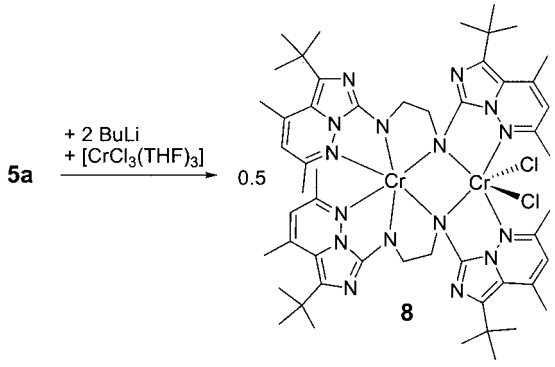

Scheme 5. Synthesis of **8**.

complexes,[13] bridged by two of the amido N atoms (Scheme 6). Cr^{III}, d^3, is the most stable and important state and octahedral complexes must have three unpaired electrons irrespective of the strength of the ligand field, giving a sort of half-filled shell stability. The magnetic moment of **8** is μ_{eff} = 4.28 μ_B. The chromium–chromium distance of 3.110 Å does not indicate a direct metal–metal interaction.

The Cl–Cr–Cl angle is 94° and fits well the octahedral coordination. Both chloro ligands are in the plane with the almost square-planar four-membered ring of Cr2, N13, Cr1 and N4 (deviation from plane 0.0072 Å) (Scheme 6). The bond lengths observed between N13–Cr1(Cr2) and N4–Cr1(Cr2) reflect a delocalised bonding mode. The lengths of the $Cr–N_{pyridazine}$ bonds are almost 0.20 Å longer than the $Cr–N_{amido}$ bonds. This difference indicates a localised bonding mode. The flexible coordination mode of the bis(imidazopyridazine) ligands allows a coordinative saturation of the metal centres, leaving two amido N atoms for bridging of two chromium(III) atoms.

Group 9 metal amides such as the late metal amido complexes are rarely described in general.[14] The mismatch of

Table 2. Details of the X-ray crystal structure analyses of **8**, **9** and **10**.

	8	**9**	**10**
Formula	$C_{52}H_{72}Cl_2Cr_2N_{16}$	$C_{42}H_{60}Ir_2N_8$	$C_{42}H_{60}N_8Rh_2$
M [g mol^{-1}]	1096.10	1061.38	882.78
Crystal system	triclinic	triclinic	monoclinic
Space group	$P\bar{1}$	$P\bar{1}$	$P21/a$
a [Å]	16.211(2)	13.359(3)	10.002(1)
b [Å]	18.948(2)	13.660(3)	25.587(2)
c [Å]	21.293(2)	19.280(4)	10.810(1)
α [°]	95.010(10)	92.26(3)	
β [°]	104.150(10)	104.63(3)	115.390(1)
γ [°]	94.010(10)	114.48(3)	
V [Å^3]	6289.5(12)	3056.7(11)	2499.3(18)
Z	4	3	4
Crystal size [mm]	0.30 × 0.30 × 0.10	0.24 × 0.18 × 0.16	0.40 × 0.26 × 0.21
$\rho_{calcd.}$ [g cm^{-3}]	1.265	1.730	1.418
$\mu_{calcd.}$ [mm^{-1}] (Mo-K_α)	0.483	6.564	0.706
T [K]	293(2)	293(2)	193(2)
θ range [°]	1.30–21.09	1.78–26.06	2.23–25.85
Reflections collected	12665	20282	4513
Independent reflections	4492	10906	3908
F(000)	2543	1566	1116
R value [$I > 2\sigma(I)$]	0.0772	0.0460	0.0283
wR_2 (all data)	0.2073	0.1282	0.0812

 © 2005 Wiley-VCH Verlag GmbH & Co. KGaA, Weinheim

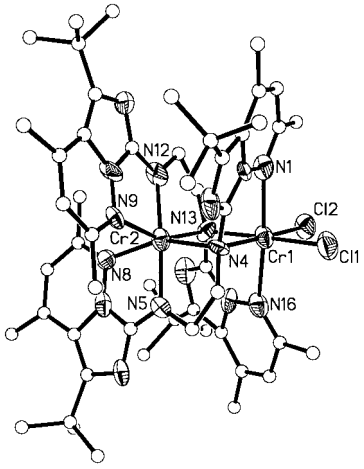

Figure 5. Molecular structure of **8**; selected bond lengths [Å] and angles [°]: N4–Cr1 2.088(8), N4–Cr2 2.065(10), N13–Cr1 2.082(10), N13–Cr2 2.071(8), Cr1–Cl1 2.309(4), Cr1–Cl2 2.319(3), N1–Cr1 2.212(10), N16–Cr1 2.218(11), N12–Cr2 1.987(10), N5–Cr2 2.023(10), N9–Cr2 2.224(9), N8–Cr2 2.198(11); N4–Cr2–N13 84.6(4), N4–Cr1–N13 83.7(3), Cr1–N13/N4–Cr2 95.8(4), Cl1–Cr1–Cl2 93.88(13), N1–Cr1–N16 175.2(3), N12–Cr2–N5 176.5(4), N8–Cr2–N9 94.5(3), N9–Cr2–N12 78.4(4), N8–Cr2–N5 77.8(4).

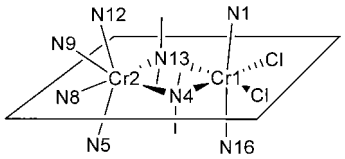

Scheme 6. Coordination sphere of **8**.

the rather hard amido ligands and the soft nature of the late transition metals might be one of the reasons for this shortage.[15] The most studied amido compounds of iridium and rhodium are dinuclear complexes containing the chelating and bridging ligands[16] and mononuclear complexes with chelating bifunctional ligands.[17] Dinuclear amido iridium[18] and rhodium[19] complexes with simple amides ($RR'N^-$ and RHN^-), as well as the very reactive mononuclear compounds[20] with these amides, have been scarcely studied. The double deprotonation of **5a** (using BuLi) followed by the reaction with $[IrCl(COD)]_2$ or $[RhCl(COD)]_2$ (COD = 1,5-cyclooctadiene) led to the group 9 metal amides **9** and **10** (Scheme 7). The ^1H and ^{13}C NMR spectroscopic data of **9** and **10** are similar, taking into consideration the fact that characteristic ligand signals are slightly

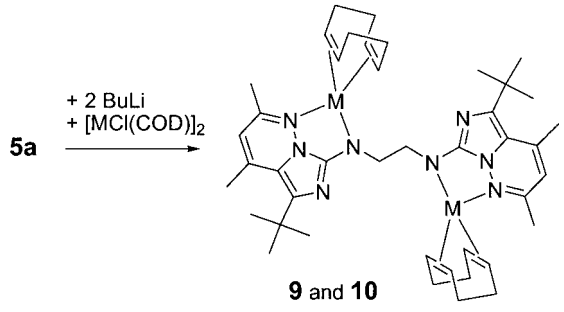

Scheme 7. Synthesis of **9** (M = Ir) and **10** (M = Rh).

different. Thus, only the spectra of **9** are discussed. Its ^1H NMR spectra exhibit a single signal and a doublet for the methyl groups and single signals at 1.5 ppm for the *tert*-butyl group and 3.8 ppm for the bridging CH_2. Furthermore, the H atom in the 3-position is characterised by a doublet as well as the methyl group in the 4-position. The splitting is about 1 Hz (both signals) and is caused by ^4J coupling. The coordinated COD ligand on the metal centre gives two broad signals for the CH and two broad multiplies for the CH_2 group. Thus, **9** and **10** possess symmetry

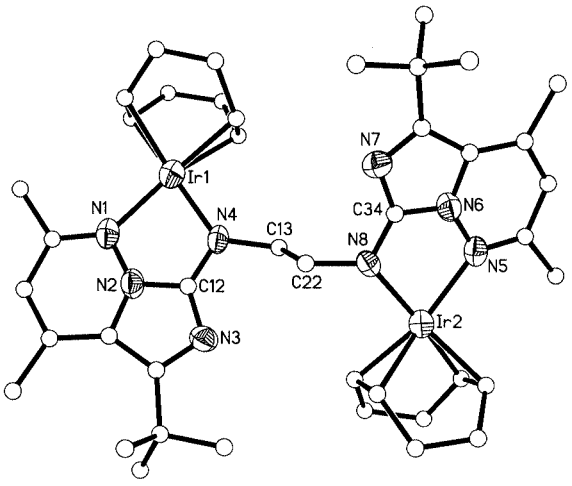

Figure 6. Molecular structure of **9**; selected bond lengths [Å] and angles [°]: Ir1–N4 2.005(7), Ir1–N1 2.141(7), Ir2–N8 2.033(7), Ir2–N5 2.166(7), N1–N2 1.390(10), N2–C12 1.340(10), N3–C12 1.345(11), N4–C12 1.357(11), N4–C13 1.475(10), C13–C22 1.542(12), N8–C22 1.474(10), N8–C34 1.343(11), N7–C34 1.354(12), N6–C34 1.339(10), N5–N6 1.388(10); N1–Ir1–N4 80.3(3), C12–N2–N1 119.6(7), C12–N4–C13 114.4(7), C12–N4–Ir1 113.9(5), N2–N1–Ir1 107.7(5), N8–Ir2–N5 79.3(3), C34–N8–Ir2 113.5(5), N6–N5–Ir2 107.1(4), C34–N6–N5 120.0(7), C34–N8–C22 114.9(7).

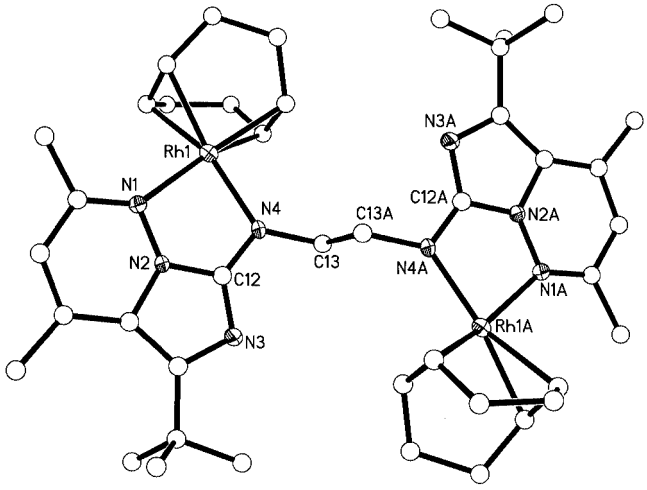

Figure 7. Molecular structure of **10**; selected bond lengths [Å] and angles [°]: Rh1–N4 2.055(2), Rh1–N1 2.164(2), N1–N2 1.389(3), N2–C12 1.345(4), N3–C12 1.348(3), N4–C12 1.348(3), N4–C13 1.456(3), C13–C13A 1.531(5); N1–Rh1–N4 80.41(8), C12–N2–N1 121.3(2), C12–N4–C13 116.0(2), C12–N4–Rh1 111.41(17), N2–N1–Rh1 105.43(15).

 © 2005 Wiley-VCH Verlag GmbH & Co. KGaA, Weinheim

in solution and only signals for half of the complexes are observed. The molecular structures (solid state) of **9** and **10** are shown in Figure 6 and Figure 7, respectively. Experimental details are summarised in Table 2.

In **9** and **10** deprotonated **5a** binds two metal centres accomplishing the *trans*55 binding mode. These dinuclear complexes are better described as mononuclear complexes with chelating bifunctional ligands in which only the ligands over an alkyl bridge are connected. Compounds **9** and **10** are not isostructural in the solid state.

Conclusions

The results of the present work allow several conclusions to be drawn. The alkyl-bridged imidazopyridazine-substituted bisamines can be synthesised by nucleophilic ring transformation followed by condensation reactions from nonexpensive starting materials in good yields, in large variety and in high purity. The deprotonated diamines can act as bisamido ligands. These ligands bind early and late transition metals as a five-membered chelate. Group 4 metal complexes are accessible via amine elimination and group 6 and 9 metal complexes via salt elimination reactions. In summary, we introduced a novel amido ligand system.

Experimental Section

General Procedures: All reactions and manipulations with air-sensitive compounds were performed under dry argon, using standard Schlenk and glove box techniques. Non-halogenated solvents were distilled from sodium benzophenone ketyl and halogenated solvents from P_2O_5. Deuterated solvents were obtained from Cambridge Isotope Laboratories and were degassed, dried and distilled prior to use. $[Ti(NMe_2)_2Cl_2]$ was prepared according a literature method.[11] All chemicals were purchased from commercial vendors and used without further purification. NMR spectra were obtained using either a Bruker ARX 250 or Bruker ARX 400 spectrometer. Chemical shifts are reported in ppm relative to the deuterated solvent. X-ray crystal structure analyses were performed by using a STOE-IPDS I or II equipped with an Oxford Cryostream low-temperature unit. Structure solution and refinement were accomplished using SIR97,[21] SHELXL-97[22] and WinGX.[23] Crystallographic details are summarised in Table 1 and Table 2. CCDC-267047 (for **5a**), -267042 (for **6**), -267044 (for **7**), -267043 (for **8**), -267046 (for **9**) and -267045 (for **10**) contain the supplementary crystallographic data for this paper. These data can be obtained free of charge from The Cambridge Crystallographic Data Centre via www.ccdc.cam.ac.uk/data_request/cif. Elemental analyses were carried out by the Vario elementar EL *III* or Leco CHNS-932 elemental analyser. Melting points were carried out in sealed capillaries, with a Büchi 535 apparatus or Stuart SMP3 apparatus. UV spectroscopic studies were carried out with a Varian CARY 3. The magnetic moment was determined with a magnetic susceptibility balance Sherwood Mark 1 MSB at room temperature.

Synthesis of Ligands and Ligand Precursors

***N*,*N*′-Bis(1-acetylamino-4-*tert*-butylimidazol-2-yl)ethylenediamine Hydrate (2a):** Ethylenediamine (0.48 mL, 0.43 g, 7.19 mmol) was added to 2-amino-5-methyl-3-(2-oxo-3,3-dimethylbutyl)-1,3,4-oxadiazolium bromide (2.00 g, 7.19 mmol) whilst stirring. The mixture was stirred for 1 min on a hot plate (250 °C) and was then allowed to reach room temperature. Water (20 mL) was added to the reaction mixture and colourless crystals formed after some hours. The product was recrystallised from ethanol/water (1:1 ratio). Yield 0.74 g (44%), m.p.146 °C. $C_{20}H_{34}N_8O_2{\cdot}2.5H_2O$ (463.53): calcd. C 51.82, H 8.84, N 24.17; found C 51.96, H 7.84, N 24.46. ^{1}H NMR ([D$_6$]DMSO): δ = 10.73 (sbs, 1 H, NH, acetylamino), 6.46 (s, 1 H, H-5, imidazole), 6.19 (br. s, 1 H, *NH*–CH_2), 3.57 (s, 2 H, CH_2), 2.18 (s, 3 H, CH_3), 1.38 [s, 9 H, –C*(CH$_3$)$_3$*] ppm. ^{13}C NMR ([D$_6$]-DMSO): δ = 169.21 (C=O), 148.35 (C-2, imidazole), 143.14 (C-4, imidazole), 108.67 (C-5, imidazole), 42.61 (CH_2), 31.52 [–*C*(CH_3)$_3$], 29.91 [–C*(CH$_3$)$_3$*], 21.15 (CH_3) ppm.

***N*,*N*′-Bis(1-acetylamino-4-phenylimidazol-2-yl)ethylenediamine (2b):** 2-Amino-5-methyl-3-phenacyl-1,3,4-oxadiazolium bromide (2.00 g, 6.72 mmol) and ethylenediamine (0.44 mL, 0.40 g, 6.72 mmol) were stirred for 1 min on a hot plate (250 °C) and then allowed to reach room temperature. After cooling to room temperature water was added. The resulting solid was recrystallised from ethanol. Yield 0.65 g (42%), m.p. 160 °C. $C_{24}H_{26}N_8O_2$ (458.48). ^{1}H NMR ([D$_6$]-DMSO): δ = 10.71 (s, 1 H, NH, acetylamino); 7.69–7.67 (d, 2 H, H$_o$, C_6H_5); 7.32–7.27 (t, 2 H, H$_m$, C_6H_5); 7.15–7.10 (t, 1 H, H$_p$, C_6H_5); 7.12 (s, 1 H, H-5, imidazole); 6.11 (br. s, 1 H, *NH*–CH_2); 3.49 (br. s, 2 H, *CH_2*–NH); 1.95 (s, 3 H, CH_3) ppm. ^{13}C NMR ([D$_6$]DMSO): δ = 168.78 (C=O); 149.25 (C-2, imidazole); 134.81 (C-1′, C_6H_5); 133.38 (C-4, imidazole); 128.11, 123.65 (C$_{o,m}$, C_6H_5); 125.48 (C$_p$, C_6H_5); 111.93 (C-5, imidazole); 42.34 (*CH_2*–NH); 20.64 (CH_3) ppm.

***N*,*N*′-Bis(1-acetylamino-4-phenylimidazol-2-yl)-1,3-diaminopropane Monohydrate (2c):** 1,3-Diaminopropane (0.56 mL, 0.50 g, 6.71 mmol) was added dropwise to 2-amino-5-methyl-3-phenacyl-1,3,4-oxadiazolium bromide (2.00 g, 6.71 mmol) and the reaction mixture was stirred for 1 min on a hot plate (250 °C). After cooling to room temperature water was added. The resulting solid was recrystallised from ethanol and a colourless product was obtained. Yield 0.57 g (34%), m.p. 179 °C. $C_{25}H_{28}N_8O_2{\cdot}H_2O$ (490.50): calcd. C 61.21, H 6.17, N 22.85; found C 61.55, H 5.85, N 22.85. ^{1}H NMR ([D$_6$]DMSO): δ = 10.98 (br. s, 1 H, NH, acetylamino), 7.93–7.92 (d, 2 H, H$_o$, C_6H_5), 7.57–7.53 (q, 2 H, H$_m$, C_6H_5), 7.40–7.38 (d, 1 H, H$_p$, C_6H_5), 7.36 (s, 1 H, H-5, imidazole), 6.32–6.29 (t, 1 H, *NH*–CH_2), 3.59–3.55 (q, 2 H, *CH_2*–NH), 2.20 (s, 3 H, CH_3), 2.15–2.09 (m, 1 H, *0,5CH_2*–CH_2–NH) ppm. ^{13}C NMR ([D$_6$]-DMSO): δ = 169.25 (C=O), 149.84 (C-2, imidazole), 135.29 (C-1′, C_6H_5), 133.86 (C-4, imidazole), 128.60, 124.08 (C$_{o,m}$, C_6H_5), 125.90 (C$_p$, C_6H_5), 112.27 (C-5, imidazole), 40.27 (CH_2–NH), 29.86 (*CH_2*–CH_2–NH), 21.15 (CH_3) ppm.

***N*,*N*′-Bis(1-amino-4-*tert*-butylimidazol-2-yl)ethylenediamine Dihydrochloride Dihydrate (3a):** Concentrated aqueous HCl (1.5 mL) was slowly added to a stirred suspension of *N*,*N*′-bis(1-acetylamino-4-*tert*-butylimidazol-2-yl)ethylenediamine hydrate (1.50 g, 3.24 mmol) in ethanol (20 mL). The mixture was heated for 1.5 h under reflux. The solvent was removed and colourless crystals were obtained and recrystallised from ethanol. Yield 1.40 g (98%), m.p. 230 °C. $C_{16}H_{30}N_8{\cdot}2HCl{\cdot}2H_2O$ (443.37): calcd. C 43.34, H 8.18, N 25.27; found C 42.98, H 7.81, N 25.02. ^{1}H NMR ([D$_6$]-DMSO): δ = 12.82 (s, 1 H, HCl), 8.01 (s, 1 H, NH), 6.76 (s, 1 H, H-5, imidazole), 6.15 (br. s, 2 H, NH_2), 3.89–3.88 (t, 2 H, CH_2), 1.44 [s, 9 H, –C*(CH$_3$)$_3$*] ppm. ^{13}C NMR ([D$_6$]DMSO): δ = 146.76 (C-2, imidazole), 133.62 (C-4, imidazole), 112.66 (C-5, imidazole), 42.44 (CH_2), 30.72 [–*C*(CH_3)$_3$], 29.04 [–C*(CH$_3$)$_3$*] ppm.

***N*,*N*′-Bis(1-amino-4-phenylimidazol-2-yl)ethylenediamine Dihydrochloride Trihydrate (3b):** Concentrated aqueous HCl (3 mL) was slowly added to a suspension of *N*,*N*′-bis(1-acetylamino-4-phenyl-

 © 2005 Wiley-VCH Verlag GmbH & Co. KGaA, Weinheim

imidazol-2-yl)ethylenediamine (1.85 g, 4.04 mmol) in ethanol (15 mL). The stirred reaction mixture was refluxed for 3 h. The solvent was removed and the resulting crystalline product was recrystallised from ethanol/water (ratio 2:1). Yield 1.62 g (80%), m.p. 262 °C. $C_{20}H_{22}N_8{\cdot}2HCl{\cdot}3H_2O$ (501.36): calcd. C 47.90, H 6.03, N 22.35; found C 47.75, H 5.62, N 22.49. ^{1}H NMR ([D$_6$]-DMSO): δ = 13.01 (br. s, 1 H, HCl), 8.16 (br. s, 1 H, NH), 7.89–7.87 (d, 2 H, H$_o$, C$_6$H$_5$), 7.55 (s, 1 H, H-5, imidazole), 7.45–7.40 (t, 2 H, H$_m$, C$_6$H$_5$), 7.36–7.31 (t, 1 H, H$_p$, C$_6$H$_5$), 6.16 (br. s, 2 H, NH$_2$), 3.87 (br. s, 2 H, *CH$_2$*–NH) ppm. ^{13}C NMR ([D$_6$]DMSO): δ = 147.07 (C-2, imidazole), 128.64, 124.73 (C$_{o,m}$, C$_6$H$_5$), 127.88 (C$_p$, C$_6$H$_5$), 127.54 (C-1′, C$_6$H$_5$), 123.65 (C-4, imidazole), 115.29 (C-5, imidazole), 41.96 (*CH$_2$*–NH) ppm.

***N*,*N*′-Bis(1-amino-4-phenylimidazol-2-yl)-1,3-diaminopropane Dihydrochloride Hydrate (3c):** Concentrated aqueous HCl (1 mL) was added to a stirred solution of *N*,*N*′-bis(1-acetylamino-4-phenylimidazol-2-yl)-1,3-diaminopropane monohydrate (1.90 g, 3.87 mmol) in ethanol (20 mL). The reaction mixture was refluxed for 30 min. The solvent was removed and the resulting crystalline product was recrystallised from ethanol/water (ratio 1:1). Yield 0.60 g (32%), m.p. 263 °C. $C_{21}H_{24}N_8{\cdot}2HCl{\cdot}1.5H_2O$ (488.37): calcd. C 51.64, H 5.9, N 22.94; found C 51.82, H 5.85, N 22.55. ^{1}H NMR ([D$_6$]DMSO): δ = 13.04 (br. s, 1 H, HCl), 8.34–8.31 (t, 1 H, NH), 8.11–8.09 (d, 2 H, H$_o$, C$_6$H$_5$), 7.73 (s, 1 H, H-5, imidazole), 7.62–7.59 (t, 2 H, H$_m$, C$_6$H$_5$), 7.54–7.51 (t, 1 H, H$_p$, C$_6$H$_5$), 6.39 (s, 2 H, NH$_2$), 3.93–3.91 (bd, 2 H, *CH$_2$*–NH), 2.16–2.13 (br. t, 1 H, ½ CH$_2$–CH$_2$–NH) ppm. ^{13}C NMR ([D$_6$]DMSO): δ = 147.53 (C-2, imidazole), 128.99, 125.17 (C$_{o,m}$, C$_6$H$_5$), 128.24 (C$_p$, C$_6$H$_5$), 127.89 (C-1′, C$_6$H$_5$), 123.93 (C-4, imidazole), 115.73 (C-5, imidazole), 40.05 (CH$_2$–NH), 29.31 (*CH$_2$*–CH$_2$–NH) ppm.

***N*,*N*′-Bis[1-amino-4-(4-methylphenyl)-imidazol-2-yl]-1,3-diaminopropane Dihydrochloride (3d):** 1,3-Diaminopropane (0.54 mL, 0.48 g, 6.41 mmol) was added to 2-amino-5-methyl-3-(4-methylphenacyl)-1,3,4-oxadiazolium bromide (2.00 g, 6.41 mmol) whilst stirring. The mixture was stirred for 1 min on a hot plate (250 °C) and then allowed to reach room temperature. The resulting product was suspended in 20 mL of ethanol and 2 mL of concd. aqueous HCl was slowly added. The reaction mixture was refluxed whilst stirring for 2 h. The solvent was removed and a colourless crystalline crude product was recrystallised from ethanol. Yield 1.52 g (97%), m.p. 263 °C. $C_{23}H_{28}N_8{\cdot}2HCl$ (489.41): calcd. C 56.44, H 6.18, N 22.90; found C 56.26, H 6.18, N 22.51. ^{1}H NMR ([D$_6$]-DMSO): δ = 12.88 (br. s, 1 H, HCl), 8.22 (s, 1 H, NH), 7.94 (d, 2 H, H$_o$, C$_6$H$_4$), 7.62 (s, 1 H, H-5, imidazole), 7.39–7.37 (d, 2 H, H$_m$, C$_6$H$_4$), 6.30 (s, 2 H, NH$_2$), 3.87–3.82 (q, 2 H, *CH$_2$*–NH), 2.50 (s, 3 H, CH$_3$), 2.11–2.08 (m, 1 H, *0,5CH$_2$*–CH$_2$–NH) ppm. ^{13}CNMR ([D$_6$]DMSO): δ = 147.39 (C-2, imidazole), 137.73 (*C*–CH$_3$, C$_6$H$_4$), 129.58, 125.14 (C$_{o,m}$, C$_6$H$_4$), 121.44 (C-1′, C$_6$H$_4$), 115.10 (C-5, imidazole), 115.07 (C-4, imidazole), 40.01 (*CH$_2$*–NH), 29.27 (*CH$_2$*–CH$_2$–NH), 21.13 (CH$_3$) ppm.

***N*,*N*′-Bis(1-amino-4-*tert*-butylimidazol-2-yl)ethylenediamine Monohydrate (4a):** Aqueous NaOH (1 N) was added dropwise to a solution of *N*,*N*′-bis(1-amino-4-*tert*-butylimidazol-2-yl)ethylenediamine dihydrochloride dihydrate (1.20 g, 2.71 mmol) in water (10 mL) to attain a basic pH. The resulting colourless solid was recrystallised from ethanol. Yield 0.79 g (83%), m.p. 187 °C. $C_{16}H_{30}N_8{\cdot}H_2O$ (352.47): calcd. C 54.52, H 9.15, N 31.79; found C 54.59, H 9.10, N 31.98. ^{1}H NMR ([D$_6$]DMSO): δ = 6.30 (s, 1 H, H-5, imidazole), 5.52 (br. s, 1 H, NH), 5.37 (s, 2 H, NH$_2$), 3.45 (s, 2 H, CH$_2$), 1.24 [s, 9 H, –C(CH$_3$)$_3$] ppm. ^{13}C NMR ([D$_6$]DMSO): δ = 149.13 (C-2, imidazole), 143.10 (C-4, imidazole), 109.52 (C-5, imidazole), 43.42 (CH$_2$), 31.54 [–*C*(CH$_3$)$_3$], 30.24 [–C*(CH$_3$)$_3$*] ppm.

***N*,*N*′-Bis(1-amino-4-phenylimidazol-2-yl)ethylenediamine (4b):** *N*,*N*′-Bis(1-amino-4-phenylimidazol-2-yl)ethylenediamine dihydrochloride (1.10 g, 2.46 mmol) was dissolved in water (10 mL). Aqueous NaOH (1 N) was added dropwise to this solution in order to obtain a basic pH and a colourless product was recovered. The product was recrystallised from ethanol. Yield 0.83 g (90%), m.p. 225 °C. $C_{20}H_{22}N_8$ (374.43): calcd. C 64.15, H 5.92, N 29.93; found C 63.98, H 5.74 N 29.48. ^{1}H NMR ([D$_6$]DMSO): δ = 7.69–7.66 (d, 2 H, H$_o$, C$_6$H$_5$), 7.29–7.23 (t, 2 H, H$_m$, C$_6$H$_5$), 7.10–7.05 (t, 1 H, H$_p$, C$_6$H$_5$), 7.09 (s, 1 H, H-5, imidazole), 5.81 (br. s, 1 H, NH), 5.50 (s, 2 H, NH$_2$), 3.52–3.50 (t, 2 H, CH$_2$) ppm. ^{13}C NMR ([D$_6$]-DMSO): δ = 150.05(C-2, imidazole), 135.43 (C-1′, C$_6$H$_5$), 132.38 (C-4, imidazole), 128.14, 123.55 (C$_{o,m}$, C$_6$H$_5$), 125.07 (C$_p$, C$_6$H$_5$), 113.19 (C-5, imidazole), 43.10 (CH$_2$) ppm.

***N*,*N*′-Bis(1-amino-4-phenylimidazol-2-yl)-1,3-diaminopropane Hemihydrate (4c):** *N*,*N*′-Bis(1-amino-4-phenylimidazol-2-yl)-1,3-diaminopropane dihydrochloride hydrate (1.13 g, 2.31 mmol) was dissolved in 10 mL of water/ethanol (ratio 2:1). Aqueous NaOH (1 N) was added dropwise to this solution in order to obtain a basic pH. The resulting solid was recrystallised from ethanol and a beige product was obtained. Yield 0.78 g (85%), m.p. 161 °C. $C_{21}H_{24}N_8{\cdot}½H_2O$ (397.46): calcd. C 63.46, H 6.34, N 28.19; found C 63.89, H 6.15, N 28.15. ^{1}H NMR ([D$_6$]DMSO): δ = 7.83–7.82 (d, 2 H, H$_o$, C$_6$H$_5$), 7.42–7.38 (t, 2 H, H$_m$, C$_6$H$_5$), 7.23–7.19 (m, 1 H, H$_p$, C$_6$H$_5$), 7.22 (s, 1 H, H-5, imidazole), 5.88–5.85 (t, 1 H, NH), 5.68 (s, 2 H, NH$_2$), 3.52–3.48 (q, 2 H, *CH$_2$*–NH), 2.00–1.95 (q, 1 H, ½ *CH$_2$*–CH$_2$–NH) ppm. ^{13}C NMR ([D$_6$]DMSO): δ = 150.54 (C-2, imidazole), 135.83 (C-1′, C$_6$H$_5$), 132.79 (C-4, imidazole), 128.51, 123.93 (C$_{o,m}$, C$_6$H$_5$), 125.38 (C$_p$, C$_6$H$_5$), 113.42 (C-5, imidazole), 40.01 (CH$_2$–NH), 30.34 (*CH$_2$*–CH$_2$–NH) ppm.

***N*,*N*′-Bis(2,4-dimethyl-5-*tert*-butylimidazo[1,5-*b*]pyridazin-7-yl)-ethylenediamine (5a):** Acetylacetone (0.43 mL, 0.42 g, 4.20 mmol) was slowly added to a suspension of *N*,*N*′-bis(1-amino-4-*tert*-butylimidazol-2-yl)ethylenediamine monohydrate (0.74 g, 2.10 mmol) in acetic acid (6 mL). The reaction mixture was refluxed for 4 h, and turned into a red colour. After removal of the solvent, water was added to the viscous product. The resulting orange solid was recrystallised from ethanol and orange crystals were obtained. Yield 0.44 g (52%), m.p. 153 °C. $C_{26}H_{38}N_8$ (462.62): calcd. C 67.50, H 8.28, N 24.22; found C 67.52, H 8.53, N 24.44. ^{1}H NMR (CDCl$_3$): δ = 6.06 (s, 1 H, H-3, imidazopyridazine), 5.36 (br. s, 1 H, NH), 4.16 (s, 2 H, CH$_2$), 2.81 (s, 3 H, CH$_3$–C-4), 2.51(s, 3 H, CH$_3$–C-2), 1.76 [s, 9 H, –C(CH$_3$)$_3$] ppm. ^{13}C NMR (CDCl$_3$): δ = 150.84 (C-7, imidazopyridazine), 141.64 (C-2, imidazopyridazine), 138.71 (C-4, imidazopyridazine), 138.55 (C-4a, imidazopyridazine), 116.76 (C-5, imidazopyridazine), 110.63 (C-3, imidazopyridazine), 44.35 (CH$_2$), 33.57 [–*C*(CH$_3$)$_3$], 32.85 [–C*(CH$_3$)$_3$*], 23.64 (*CH$_3$*–C-4), 21.47 (*CH$_3$*–C-2) ppm.

***N*,*N*′-Bis(2-methyl-4-phenyl-5-*tert*-butylimidazo[1,5-*b*]pyridazin-7-yl)ethylenediamine (5b):** A stirred suspension of *N*,*N*′-bis(1-amino-4-*tert*-butylimidazol-2-yl)ethylenediamine monohydrate (0.50 g, 1.42 mmol) and benzoylacetone (0.46 g, 2.84 mmol) in acetic acid (5 mL) was refluxed for 1.5 h. The solvent was removed from the red reaction mixture and water was added to the resulting viscous syrup. After recrystallisation from ethanol/chloroform (ratio 2:1) an orange crystalline solid was obtained. Yield 0.54 g (65%), m.p. 260 °C. $C_{36}H_{42}N_8$ (586.75): calcd. C 73.69, H 7.22, N 19.10; found C 73.61, H 7.15, N 19.08. ^{1}H NMR (CDCl$_3$): δ = 7.32–7.25 (m, 5 H, C$_6$H$_5$), 5.65 (s, 1 H, H-3, imidazopyridazine), 5.09 (br. s, 1 H, NH), 3.83 (s, 2 H, CH$_2$), 2.19 (s, 3 H, *CH$_3$*–C-2), 0.93 [s, 9 H, –C*(CH$_3$)$_3$*] ppm. ^{13}C NMR (CDCl$_3$): δ = 150.72 (C-7, imidazopyridazine), 143.46 (C-2, imidazopyridazine), 142.35 (C-4, imidazopyr-

 © 2005 Wiley-VCH Verlag GmbH & Co. KGaA, Weinheim

idazine), 140.90 (C-1′, C_6H_5), 139.48 (C-4a, imidazopyridazine), 129.07, 128.56 ($C_{o,m}$, C_6H_5), 128.80 (C_p, C_6H_5), 115.43 (C-5, imidazopyridazine), 111.43 (C-3, imidazopyridazine), 44.31 (CH_2), 33.99 [–*C*$(CH_3)_3$], 31.85 [–C*(CH₃)₃*], 21.61 (*CH₃*–C-2) ppm.

***N*,*N*′-Bis(2,4-dimethyl-5-phenylimidazo[1,5-*b*]pyridazin-7-yl)ethylenediamine (5c):** Acetylacetone (0.28 mL, 0.27 g, 2.68 mmol) was added to a suspension of *N*,*N*′-bis(1-amino-4-phenylimidazol-2-yl)-ethylenediamine (0.50 g, 1.34 mmol) in acetic acid (20 mL). The reaction mixture was stirred and refluxed for 2 h and then turned into a red colour. After removal of the solvent and addition of water an orange solid was obtained and recrystallised from ethanol. Yield 0.35 g (52%), m.p. 231 °C. $C_{30}H_{30}N_8$ (502.60): calcd. C 71.69,H 6.02, N 22.30; found C 71.45, H 6.23, N 22.19. ^{1}H NMR ($CDCl_3$): δ = 7.58–7.26 (m, 5 H, C_6H_5), 5.87–5.86 [d, 1 H, ^4J(H,H) = 3 Hz, H-3, imidazopyridazine], 5.25 (br. s, 1 H, NH), 3.96–3.94 (d, 2 H, *CH₂*–NH), 2.23 (s, 3 H, *CH₃*–C-2), 2.15–2.14 (d, 3 H, $^4J_{H,H}$ = 3 Hz, *CH₃*–C-4) ppm. ^{13}C NMR ($CDCl_3$): δ = 151.39 (C-7, imidazopyridazine), 143.61 (C-2, imidazopyridazine), 138.86 (C-4, imidazopyridazine), 136.08 (C-1′, C_6H_5), 130.32, 127.78 ($C_{o,m}$, C_6H_5), 128.55 (C-4a, imidazopyridazine), 126.88 (C_p, C_6H_5), 117.56 (C-5, imidazopyridazine), 111.33 (C-3, imidazopyridazine), 43.74 (CH_2), 21.35 (*CH₃*–C-2), 19.44 (*CH₃*–C-4) ppm.

***N*,*N*′-Bis(2,4-dimethyl-5-phenylimidazo[1,5-*b*]pyridazin-7-yl)-1,3-diaminopropane Hemihydrate (5d):** Acetylacetone (0.09 mL, 0.09 g, 0.84 mmol) was added to a stirred suspension of *N*,*N*′-bis(1-amino-4-phenylimidazol-2-yl)-1,3-diaminopropane hemihydrate (0.17 g, 0.43 mmol) in acetic acid (5 mL). The reaction mixture was refluxed for 2 h and turned into a red colour. After removal of the solvent and addition of water an orange solid was obtained and recrystallised from ethanol. Yield 0.14 g (62%), m.p. 163 °C. $C_{31}H_{32}N_8 \cdot ½H_2O$ (525.62): calcd. C 70.83, H 6.33, N 21.32; found C 70.62, H 6.15, N 21.39. ^{1}H NMR ($CDCl_3$): δ = 7.48–7.46 (d, 2 H, H_o, C_6H_5), 7.29–7.25 (t, 2 H, H_m, C_6H_5), 7.22–7.18 (t, 1 H, H_p, C_6H_5), 5.79 (s, 1 H, H-3, imidazopyridazine), 5.19 (br. s, 1 H, NH), 3.68 (br. s, 2 H, *CH₂*–NH), 2.14 (s, 3 H, CH_3–C-2), 2.06 (s, 3 H, CH_3–C-4), 2.05–1.98 (m, 1 H, *0,5CH₂*–CH_2–NH) ppm. ^{13}C NMR ($CDCl_3$): δ = 151.84 (C-7, imidazopyridazine), 144.16 (C-2, imidazopyridazine), 139.31 (C-4, imidazopyridazine), 136.44 (C-1′, C_6H_5), 130.79, 128.17 ($C_{o,m}$, C_6H_5), 128.84 (C-4a, imidazopyridazine), 127.30 (C_p, C_6H_5), 117.92 (C-5, imidazopyridazine), 111.78 (C-3, imidazopyridazine), 40.69 (CH_2–NH), 31.46 (*CH₂*–CH_2–NH), 21.78 (*CH₃*–C-2), 19.85 (*CH₃*–C-4) ppm.

***N*,*N*′-Bis(2-methyl-4,5-diphenylimidazo[1,5-*b*]pyridazin-7-yl)-1,3-diaminopropane Ethanol (5e):** *N*,*N*′-Bis(1-amino-4-phenylimidazol-2-yl)-1,3-diaminopropane hemihydrate (0.40 g, 1.01 mmol) and benzoylacetone (0.33 g, 2.02 mmol) in acetic acid (3 mL) were refluxed whilst stirring. After 1.5 h the solvent was removed from the red reaction solution. Water was added to the resulting highly viscous syrup, which yielded a red solid that was recrystallised from ethanol and red crystals were obtained. Yield 0.56 g (81%), m.p. 180 °C. $C_{41}H_{36}N_8 \cdot C_2H_5OH$ (686.81): calcd. C 75.19, H 6.16, N 16.32; found C 75.09, H 5.97, N 16.46. ^{1}H NMR ($CDCl_3$): δ = 7.17–6.85 (m, 10 H, 2×C_6H_5), 5.97–5.96 (d, 1 H, $^4J_{H,H}$ = 1 Hz, H-3, imidazopyridazine), 5.35 (br. s, 1 H, NH), 3.77–3.76 (d, 2 H, *CH₂*–NH), 3.60–3.55 (m, 1 H, CH_2, ½ C_2H_5OH), 2.25–2.24 (d, 3 H, $^4J_{H,H}$ = 1 Hz, CH_3–C-2), 2.12–2.06 (m, 1 H, *CH₂*–CH_2–NH), 1.13–1.09 (m, 1.5 H, CH_3, ½ C_2H_5OH) ppm. ^{13}C NMR ($CDCl_3$): δ = 151.87 (C-7, imidazopyridazine), 144.67 (C-2, imidazopyridazine), 142.81 (C-4, imidazopyridazine), 136.39 (C-1′, C_6H_5–C-5), 135.47 (C-1′, C_6H_5–C-3), 129.93, 128.78, 128.39, 127.49 ($C_{o,m}$, 2×C_6H_5), 129.40 (C-4a, imidazopyridazine), 129.11, 126.37(C_p, 2×C_6H_5), 115.51 (C-5, imidazopyridazine), 111.76 (C-3, imidazopyridazine), 58.69 (CH_2, C_2H_5OH), 40.76 (CH_2–NH), 31.49 (*CH₂*–CH_2–NH), 21.98 (*CH₃*–C-2), 18.84 (CH_3, C_2H_5OH) ppm.

***N*,*N*′-Bis{2,4-dimethyl-5-(4-methylphenyl)imidazo[1,5-*b*]pyridazin-7-yl}-1,3-diaminopropane Hemihydrate (5f):** Acetylacetone (0.47 mL, 0.46 g, 4.56 mmol) was added to a stirred solution of *N*,*N*′-bis[1-amino-4-(4-methylphenyl)imidazol-2-yl]-1,3-diaminopropane (0.95 g, 2.28 mmol) in acetic acid (15 mL). The reaction mixture was refluxed for 2 h and turned into a red colour. The solvent was removed under reduced pressure. Water was added to the resulting red highly viscous syrup and gave an orange solid, which was recrystallised from ethanol/water (ratio 2:1). Yield 1.07 g (85%), m.p. 180 °C. $C_{33}H_{36}N_8 \cdot ½H_2O$ (553.67): calcd. C 71.58, H 6.74, N 20.24; found C 71.63, H 6.88, N 20.15. ^{1}H NMR ($CDCl_3$): δ = 7.36–7.34 (d, 2 H, H_o, C_6H_4), 7.08–7.06 (d, 2 H, H_m, C_6H_4), 5.75 (s, 1 H, H-3, imidazopyridazine), 5.18 (br. s, 1 H, NH), 3.66–3.65 (bd, 2 H, *CH₂*–NH), 2.27 (s, 3 H, *CH₃*–C_6H_4), 2.12 (s, 3 H, *CH₃*–C-2), 2.05 (s, 3 H, *CH₃*–C-4), 2.02–1.96 (m, 1 H, ½ *CH₂*–CH_2–NH) ppm. ^{13}C NMR ($CDCl_3$): δ = 151.80 (C-7, imidazopyridazine), 144.06 (C-2, imidazopyridazine), 139.40 (C-4, imidazopyridazine), 136.91 (*C*–CH_3, C_6H_4), 133.53 (C-1′, C_6H_4), 130.67, 128.88 ($C_{o,m}$, C_6H_4), 128.94 (C-4a, imidazopyridazine), 117.76 (C-5, imidazopyridazine), 111.50 (C-3, imidazopyridazine), 40.69 (*CH₂*–NH), 31.48 (*CH₂*–CH_2–NH), 21.73 (*CH₃*–C-2), 21.68 (*CH₃*–C_6H_4), 19.83 (*CH₃*–C-4) ppm.

Complex Synthesis

Preparation of 6: A solution of bis(dimethylamino)titanium dichloride (0.22 g, 1.08 mmol) in diethyl ether (20 mL) was slowly added to a stirred orange solution of *N*,*N*′-bis(2,4-dimethyl-5-*tert*-butylimidazo[1,5-*b*]pyridazin-7-yl)ethylenediamine (0.50 g, 1.08 mmol) in diethyl ether (30 mL) and the reaction mixture turned into a dark violet colour. After stirring for 16 h the solvent was removed under vacuum. The residue was washed with 5 mL of hexane. The violet product was dried in vacuo. A concentrated solution of diethyl ether at –30 °C gave X-ray diffraction quality crystals. Yield 0.58 g (92%). $C_{26}H_{36}Cl_2N_8Ti$ (579.38): calcd. C 53.90, H 6.26, N 19.34; found C 54.43, H 6.48, N 19.66. ^{1}H NMR ([D_8]THF): δ = 6.25–6.24 (d, 1 H, $^4J_{H,H}$ = 1 Hz, H-3, imidazopyridazine); 4.99 (s, 2 H, *CH₂*–CH_2); 2.77 (s, 6 H, 2×CH_3); 1.56[s, 9 H, -C*(CH₃)₃*] ppm. ^{13}C NMR ([D_8]THF): δ = 153.46 (C-7, imidazopyridazine); 147.75(C-2, imidazopyridazine); 142.57, 142.03 (C-4, C-4a, imidazopyridazine); 124.46(C-5, imidazopyridazine); 109.86 (C-3, imidazopyridazine); 57.23 (*CH₂*–CH_2); 34.08 [–*C*$(CH_3)_3$]; 31.70 [–C*(CH₃)₃*]; 22.41 (*CH₃*–C-2); 20.63 (*CH₃*–C-4) ppm.

Preparation of 7: Tetrakis(diethylamino)zirconium (0.20 mL, 0.21 g, 0.54 mmol) was slowly added, via a syringe, to a stirred orange solution of *N*,*N*′-bis(2,4-dimethyl-5-*tert*-butylimidazo[1,5-*b*]-pyridazin-7-yl)ethylenediamine (0.25 g, 0.54 mmol) in diethyl ether (25 mL). The resulting dark violet reaction mixture was stirred for 3.5 h at room temperature. The solution was concentrated to 10 mL. After cooling to –78 °C dark violet crystals were obtained. The solution was decanted, concentrated and at –30 °C more crystalline product was obtained. The crystals were collected and dried under vacuum. Yield 0.27 g (73%), m.p. 236 °C. $C_{34}H_{56}N_{10}Zr$ (696.08): calcd. C 58.66, H 8.11, N 20.12; found C 57.41, H 8.01, N 19.74. ^{1}H NMR ([D_8]THF): δ = 5.77–5.76 (d, 1 H, $^4J_{H,H}$ = 1 Hz, H-3, imidazopyridazine), 4.14 (s, 2 H, *CH₂*–CH_2), 3.07–2.99 [q, 4 H, –*N*–(*CH₂*–CH_3)$_2$], 2.57–2.56 (d, 3 H, $^4J_{H,H}$ = 1 Hz, CH_3–C-4), 2.48(s, 3 H, CH_3–C-2), 1.47 [s, 9 H, –C*(CH₃)₃*], 0.57–0.51 [t, 6 H, (*CH₃*–CH_2)$_2$–*N*–] ppm. ^{13}C NMR ([D_8]THF): δ = 153.23 (C-7, imidazopyridazine), 149.02(C-2, imidazopyridazine), 143.70 (C-4, imidazopyridazine), 141.50 (C-4a, imidazopyridazine), 117.12 (C-5, imidazopyridazine), 107.60 (C-3, imidazopyridazine), 52.47

 © 2005 Wiley-VCH Verlag GmbH & Co. KGaA, Weinheim

(CH_2–CH_2), 43.24 [–N–(CH_2–CH_3)$_2$], 33.82 [–C(CH_3)$_3$], 31.97 [–C$(CH_3)_3$], 22.45 (CH_3–C-4), 20.83 (CH_3–C-2), 14.29 (CH_3–CH_2)$_2$–N–) ppm.

Preparation of 8: *n*BuLi (1.21 mL, 3.02 mmol, 2.5 M in hexane) was slowly added to a stirred solution of *N*,*N*′-bis(2,4-dimethyl-5-*tert*-butylimidazo[1,5-*b*]pyridazin-7-yl)ethylenediamine (0.70 g, 1.51 mmol) in THF (10 mL) at –60 °C. After complete addition, the dark blue mixture was stirred for 1.5 h at –60 °C and warmed to –40 °C. At this temperature a suspension of [$CrCl_3$(THF)$_3$] (0.57 g, 1.51 mmol) in THF (10 mL) was added. The resulting dark green reaction mixture was stirred for 30 min at –40 °C and warmed to room temperature and stirred for a further 24 h. The solution was concentrated to ¼ of its volume and 30 mL of diethyl ether was added. The mixture was filtered, the residue washed with 10 mL of diethyl ether and 10 mL of hexane. The combined filtrates were concentrated to 15 mL. By cooling to –30 °C a dark green/blue crystalline product was obtained. Yield 0.57 g (69%), m.p. 307 °C. $C_{52}H_{72}Cl_2Cr_2N_{16}$ (1096.10): calcd.C 56.98, H 6.62, N 20.45; found C 57.42, H 7.11, N 20.02. μ_{eff} = 4.28 μ_B.

Preparation of 9: A solution of *N*,*N*′-bis(2,4-dimethyl-5-*tert*-butylimidazo[1,5-*b*]pyridazin-7-yl)ethylenediamine (0.70 g, 1.51 mmol) in THF (20 mL) was cooled to –78 °C. *n*BuLi (1.88 mL, 3.02 mmol, 1.6 M in hexane) was slowly added to this stirred solution via a syringe. The resulting dark blue reaction mixture was stirred for 30 min at –78 °C and then warmed to room temperature. After stirring for 30 min a solution of chloro-1,5-cyclooctadieneiridium(I) dimer (1.01 g, 1.51 mmol) in THF (30 mL) was added at 0 °C. The resulting dark green reaction mixture was stirred for 18 h at room temperature. The solution was concentrated to ¼ of its volume and 30 mL of dichloromethane was added. The mixture was filtered and the filtrate concentrated to dryness under vacuum. The resulting residue was recrystallised from toluene and dark green crystals were collected at –30 °C. Yield 1.34 g (84%), $C_{42}H_{60}Ir_2N_8$ (1061.38): calcd. C 47.52, H 5.70, N 10.56; found C 48.02, H 5.82, N10.83. ^{1}H NMR (CD_2Cl_2): δ = 5.62–5.61 (d, 1 H, $^4J_{H,H}$ = 1 Hz, H-3, imidazopyridazine), 4.51 (br. s, 2 H, 2×CH, COD), 4.32 (br. s, 2 H, 2×CH, COD), 3.80 (s, 2 H, CH_2–N), 2.58–2.57 (d, 3 H, $^4J_{H,H}$ = 1 Hz, CH_3–C-4), 2.36 (s, 3 H, CH_3–C-2), 2.24–2.11 (m, 4 H, 2×CH_2, COD), 1.77–1.66 (m, 4 H, 2×CH_2, COD), 1.48 [s, 9 H, C(CH_3)$_3$] ppm. ^{13}C NMR (CD_2Cl_2): δ = 159.88 (C-7, imidazopyridazine), 155.07 (C-2, imidazopyridazine), 149.71 (C-4, imidazopyridazine), 139.98 (C-4a, imidazopyridazine), 119.34 (C-5, imidazopyridazine), 108.56 (C-3, imidazopyridazine), 62.09 (2×CH, COD), 51.21 (2×CH, COD), 47.55 (CH_2–N), 34.98 [C(CH_3)$_3$], 31.71 [C$(CH_3)_3$], 31.64 (2×CH_2, COD), 30.64 (2×CH_2, COD), 23.10 (CH_3–C-2), 20.35 (CH_3–C-4) ppm.

Preparation of 10: A solution of *N*,*N*′-bis(2,4-dimethyl-5-*tert*-butylimidazo[1,5-*b*]pyridazin-7-yl)ethylenediamine (0.50 g, 1.08 mmol) in THF (10 mL) was cooled to –78 °C. *n*BuLi (0.86 mL, 2.16 mmol, 2.5 M in hexane) was slowly added to this stirred solution via a syringe. The resulting dark blue reaction mixture was stirred for 30 min at –78 °C and then warmed to room temperature. After stirring for 30 min a suspension of chloro-1,5-cyclooctadienerhodium(I) dimer (0.54 g, 1.08 mmol) in THF (20 mL) was added. The resulting dark green reaction mixture was stirred for 18 h at room temperature. The solution was concentrated to ⅓ of its volume and 30 mL of diethyl ether was added. The mixture was filtered and the precipitate was washed twice with 10 mL of diethyl ether. The combined filtrates were concentrated to dryness under vacuum. Crystals of **10** were grown from toluene at –30 °C. Yield 0.51 g (54%), m.p. 275 °C. $C_{42}H_{60}N_8Rh_2$ (882.78): calcd. C 57.14, H 6.85, N 12.69; found C 57.62, H 7.21, N 12.27. ^{1}H NMR (CD_2Cl_2): δ = 5.46 (s, 1 H, H-3, imidazopyridazine); 4.60 (br. s, 4 H, 4×CH, COD); 3.30 (s, 2 H, CH_2–N); 2.50 (s, 3 H, CH_3–C-4); 2.39–2.35 (m, 4 H, 2×CH_2, COD); 2.15 (s, 3 H, CH_3–C-2); 1.89–1.83 (m, 4 H, 2×CH_2, COD); 1.43 [s, 9 H, C(CH_3)$_3$] ppm. ^{13}C NMR (CD_2Cl_2): δ = 156.50 (C-7, imidazopyridazine); 152.47 (C-2, imidazopyridazine); 146.50 (C-4, imidazopyridazine); 138.74 (C-4a, imidazopyridazine); 116.98 (C-5, imidazopyridazine); 106.55 (C-3, imidazopyridazine); 77.24, 77.13, 69.62, 69.53 (4×CH, COD); 46.58 (CH_2–N); 33.46 [C(CH_3)$_3$]; 31.35 [C$(CH_3)_3$]; 30.21 (2×CH_2, COD); 29.74 (2×CH_2, COD); 22.01 (CH_3–C-2); 19.00 (CH_3–C-4) ppm.

Acknowledgments

We thank Anke Spannenberg, Wolfgang Saak and Wolfgang Milius for their support in the X-ray laboratories and Dominikus Huttner for his assistance in obtaining the UV/Vis data. Financial support from the Fonds der Chemischen Industrie is gratefully acknowledged.

[1] M. F. Lappert, P. P. Power, A. R. Sanger, R. C. Srivastava, *Metal and Metalloid Amides*, Ellis Horwood Ltd., Chichester, England, **1980**, 567.
[2] R. Kempe, *Angew. Chem.* **2000**, *112*, 478–504; *Angew. Chem. Int. Ed.* **2000**, *39*, 468–493.
[3] a) S. Wagaw, S. L. Buchwald, *J. Org. Chem.* **1996**, *61*, 7240–7241; b) J. F. Hartwig, *Synlett* **1996**, 329–340; c) J. Silberg, T. Schareina, R. Kempe, K. Wurst, M. R. Buchmeiser, *J. Organomet. Chem.* **2001**, *622*, 6–18; d) T. Schareina, G. Hillebrand, R. Kempe, *Eur. J. Inorg. Chem.* **2001**, 2421–2426; e) M. R. Buchmeiser, T. Schareina, R. Kempe, K. Wurst, *J. Organomet. Chem.* **2001**, *634*, 39–46.
[4] a) H. Beyer, A. Hetzheim, *Chem. Ber.* **1964**, *97*, 1031–1036; b) A. Hetzheim, G. Müller, *DD. P. 200023*, **1983/1981**; *Chem. Abstr.* **1983**, *99*, 88205; c) K. Peters, E.-M. Peters, A. Hetzheim, T. Irrgang, *Z. Kristallogr. NCS* **2000**, *215*, 381–382.
[5] a) A. Hetzheim, O. Peters, H. Beyer, *Chem. Ber.* **1967**, *100*, 3418–3426; b) A. Hetzheim, G. Manthey, *Chem. Ber.* **1970**, *103*, 2845–2852.
[6] H. Beyer, A. Hetzheim, H. Honek, D. Ling, T. Pyl, *Chem. Ber.* **1968**, *101*, 3151–3162.
[7] a) G. M. Golubushina, G. N. Poshtaruk, V. A. Chuiguk, *Chem. Heterocycl. Compd.* **1974**, *10*, 735–739; b) G. M. Golubushina, G. N. Poshtaruk, V. A. Chuiguk, *Khim. Geterosikl. Soedin.* **1974**, *6*, 846–850; c) R. Brückner, J. P. Lavergne, P. Viallefont, *Liebigs Ann. Chem.* **1979**, 639–649; d) V. P. Kruglenko, A. A. Timoshin, V. A. Idzikovskii, N. A. Klyuev, M. V. Povstyanoi, *Ukr. Khim. Zh.* **1988**, *54*, 612–615.
[8] a) D. G. H. Livermore, R. C. Bethell, N. Cammack, A. P. Hancock, M. M. Hann, D. V. S. Green, R. B. Lamont, S. A. Noble, D. C. Orr, J. J. Payne, M. V. J. Ramsay, A. H. Shingler, C. Smith, R. Storer, C. Williamson, T. Willson, *J. Med. Chem.* **1993**, *36*, 3784–3794; b) M. Renoud-Grappin, C. Fossey, G. Fontaine, D. Laduree, A. M. Aubertin, A. Kirn, *Antivir. Chem. Chemoth.* **1998**, *9*, 221–237.
[9] G. A. Jeffrey, W. Saenger, *Hydrogen Bonding in Biological Structures*; Springer Verlag, Berlin, Heidelberg, **1991**.
[10] a) W. A. Herrmann, M. J. A. Morawietz, *J. Organomet. Chem.* **1994**, *482*, 169–181; b) D. G. Black, D. C. Swenson, R. F. Jordan, *Organometallics* **1995**, *14*, 3539–3550; c) H. Fuhrmann, S. Brenner, P. Arndt, R. Kempe, *Inorg. Chem.* **1996**, *35*, 6742–6745; d) R. M. Porter, S. Winston, A. A. Danopoulos, M. B. Hursthouse, *J. Chem. Soc. Daltron Trans.* **2002**, 3290–3299; e) R. Kempe, *Eur. J. Inorg. Chem.* **2003**, 791–803.
[11] a) E. Benzing, W. Kornicker, *Chem. Ber.* **1961**, *94*, 2263–2267; b) S. Brenner, R. Kempe, P. Arndt, *Z. Anorg. Allg. Chem.* **1995**, *621*, 2021–2024.

 © 2005 Wiley-VCH Verlag GmbH & Co. KGaA, Weinheim

[12] K. Doerffel, R. Geyer, *Analytikum*, Leipzig, **1990**, 265.
[13] F. A. Cotton, G. Wilkinson, C. A. Murillo, M. Bochmann, *Advanced, Inorg. Chem.* John Wiley & Sons, Inc., N. Y., Chichester, Weinheim, Brisbane, Singapore, Toronto, **1999**, 737–747.
[14] R. Kempe, H. Noss, H. Fuhrmann, *Chem. Eur. J.* **2001**, *7*, 1630–1636.
[15] a) R. G. Pearson, *J. Am. Chem. Soc.* **1963**, *85*, 3533–3539; b) R. G. Pearson, *J. Chem. Educ.* **1968**, *45*, 581–586; c) R. G. Pearson, *J. Chem. Educ.* **1968**, *45*, 643–654.
[16] a) L. A. Oro, M. J. Fernández, J. Modrego, C. Foces-Foces, F. H. Cano, *Angew. Chem.* **1984**, *96*, 897–898; *Angew. Chem. Int. Ed. Engl.* **1984**, *23*, 913; b) L. A. Oro, M. J. Fernández, J. M. López, *J. Organomet. Chem.* **1985**, *287*, 409–417; c) M. V. Jiménez, E. Sola, J. A. López, F. J. Lahoz, L. A. Oro, *Chem. Eur. J.* **1998**, *4*, 1398–1410; d) M. V. Jiménez, E. Sola, A. P. Martínez, F. J. Lahoz, L. A. Oro, *Organometallics* **1999**, *18*, 1125–1136; e) H. Matsuzaka, T. Kamura, K. Ariga, Y. Watanabe, T. Okubo, T. Ishii, M. Yamashita, M. Kondo, S. Kitagawa, *Organometallics* **2000**, *19*, 216–218; f) M. V. Jiménez, E. Sola, M. A. Egea, A. Huet, A. C. Francisco, F. J. Lahoz, L. A. Oro, *Inorg. Chem.* **2000**, *39*, 4868–4878; g) B. de Bruin, T. P. J. Peters, N. N. F. A. Suos, R. de Gelder, J. M. M. Smits, A. W. Gal, *Inorg. Chim. Acta* **2002**, *337*, 154–162; M. V. Jiménez, E. Sola, A. C. Francisco, L. A. Oro, F. J. Lahoz, A. P. Martínez, *Inorg. Chim. Acta* **2003**, *350*, 266–276.
[17] a) B. Cetinkaya, M. F. Lappert, S. Torroni, *J. Chem. Soc. Chem. Commun.* **1979**, 843–844; b) M. K. Cooper, G. J. Organ, P. A. Duckworth, K. Henrick, M. McPartlin, *J. Chem. Soc. Dalton Trans.* **1988**, 2287–2292; c) M. D. Fryzuk, X. Gao, K. Joshi, P. A. MacNeil, R. L. Massey, *J. Am. Chem. Soc.* **1993**, *115*, 10581–10590; d) K. Mashima, T. Abe, K. Tani, *Chem. Lett.* **1998**, 1201–1202; e) R. Fandos, M. Martínez-Ripoll, A. Otero, M. J. Ruiz, A. Rodríguez, P. Terreros, *Organometallics* **1998**, *17*, 1465–1470; f) L. Dahlenburg, K. Herbst, *J. Chem. Soc. Dalton Trans.* **1999**, 3935–3939; g) B. de Bruin, R. J. N. A. M. Kicken, N. F. A. Suos, M. P. J. Donners, C. J. den Reijer, A. J. Sandee, R. de Gelder, J. M. M. Smits, A. W. Gal, A. L. Spek, *Eur., J. Inorg. Chem.* **1999**, 1581–1592; h) T. Koike, T. Ikariya, *Organometallics* **2005**, *24*, 724–730, and references therein.
[18] a) M. K. Kolel-Veetil, A. L. Rheingold, K. J. Ahmed, *Organometallics* **1993**, *12*, 3439–3446; b) R. Dorta, A. Togni, *Helv. Chim. Acta* **2000**, *83*, 119–127; c) C. Tejel, M. A. Ciriano, M. Bordonaba, J. A. López, F. J. Lahoz, L. A. Oro, *Chem. Eur. J.* **2002**, *8*, 3128–3138.
[19] a) M. K. Kolel-Veetil, M. Rahim, A. J. Edwards, A. L. Rheingold, K. J. Ahmed, *Inorg. Chem.* **1992**, *31*, 3877–3878; b) J.-J. Brunet, J.-C. Daran, D. Neibecker, L. Rosenberg, *J. Organomet. Chem.* **1997**, *538*, 251–256.
[20] a) D. S. Glueck, R. G. Bergman, *Organometallics* **1991**, *10*, 1479–1486; b) D. S. Glueck, L. J. N. Winslow, R. G. Bergman, *Organometallics* **1991**, *10*, 1462–1479; c) M. Rahim, C. White, A. L. Rheingold, K. J. Ahmed, *Organometallics* **1993**, *12*, 2402–2403; d) M. Rahim, K. J. Ahmed, *Organometallics* **1994**, *13*, 1751–1756; e) M. Rahim, C. H. Bushweller, K. J. Ahmed, *Organometallics* **1994**, *13*, 4952–4958; f) J.-J. Brunet, G. Commenges, D. Neibecker, L. Rosenberg, *J. Organomet. Chem.* **1996**, *522*, 117–122.
[21] A. Altomare, M. C. Burla, M. Camalli, G. L. Cascarano, C. Giacovazzo, A. Guagliardi, A. G. G. Moliterni, G. Polidori, R. Spagna, *J. Appl. Cryst.* **1999**, *32*, 115–119.
[22] G. M. Sheldrick, *SHELX-97*, *Program for Crystal Structure Analysis* (Release 97–2). Institut für Anorganische Chemie der Universität, Göttingen, Germany, **1998**.
[23] L. J. Farrugia, *J. Appl. Crystallogr.* **1999**, *32*, 837–838.

Received: April 8, 2005
Published Online: September 15, 2005

 © 2005 Wiley-VCH Verlag GmbH & Co. KGaA, Weinheim

Mössbauer Investigation of Peroxo Species in the Iron(III)–EDTA–H_2O_2 System

Virender K. Sharma,[a] Petra Á. Szilágyi,[b] Zoltán Homonnay,*[b] Ernő Kuzmann,[c] and Attila Vértes[b,c]

Keywords: Chelates / EDTA / Iron / Mössbauer spectroscopy / Peroxo ligands

The reaction of a diiron(III)–EDTA complex with H_2O_2 in alkaline medium is studied by Mössbauer spectroscopy in conjunction with the rapid-freeze/quench technique in order to identify possible intermediate species during the formation and decomposition of the purple $(EDTA)Fe^{III}(\eta^2\text{-}O_2)^{3-}$ complex ion. Starting from the six-coordinate $[Fe^{III}EDTA]^-$ species at acidic pH, it is demonstrated that mononuclear complexes formed at a pH of about 1 are convert into the diiron(III)–EDTA complex $[(EDTA)Fe^{III}\text{-}O\text{-}Fe^{III}(EDTA)]^{4-}$ upon raising the pH to around 10.4. H_2O_2 reacts with the diiron(III) complex to give peroxide/hydroperoxide related adducts. Initially, the reaction tears apart the dimers to form a peroxo adduct, namely the seven-coordinate mononuclear $[(EDTA)Fe^{III}(\eta^2\text{-}O_2)]^{3-}$, which is stable only at very high pH. The decomposition of this peroxo adduct gives two new species, which are reported for the first time. The Mössbauer parameters of these species suggest a six-coordinate μ-peroxodiiron(III) complex $[(EDTA)Fe^{III}\text{-}(OO)\text{-}Fe^{III}(EDTA)]^{4-}$ and a seven-coordinate μ-hydroxo-μ-peroxodiiron(III) complex $[(EDTA)Fe^{III}\text{-}(OO)(OH)\text{-}Fe^{III}(EDTA)]^{5-}$. A badly resolved, extremely broad component is observed in the Mössbauer spectra during the conversion of the monomer to dimeric peroxo species, which may be attributed to the short-lived $[(EDTA)Fe^{III}\text{-}OO]^{3-}$ or $[(EDTA)Fe^{III}\text{-}OOH]^{2-}$ intermediate species.

(© Wiley-VCH Verlag GmbH & Co. KGaA, 69451 Weinheim, Germany, 2005)

Introduction

There has been increasing interest in the reactivity of the iron(III)–ethylenediaminetetraacetate (Fe^{III}-EDTA) system because of its importance in inorganic chemistry, biochemistry, and industrial chemistry.[1] One of the most important reactions is the formation of the purple peroxoiron complex $[Fe^{III}(EDTA)(\eta^2\text{-}O_2)]^{3-}$ in the reaction between $[Fe^{III}\text{-}(EDTA)]^-$ and hydrogen peroxide (H_2O_2)[1,2] as peroxoiron species play an important role in the oxygen activation and transfer reactions mediated by heme and nonheme iron proteins.[3,4] The characterization of a peroxoiron intermediate has been performed spectroscopically in methane monooxygenase and ribonucleotide reductase.[4,5] Peroxoiron complexes have also been shown to catalyze the polymerization of styrene and organic substrates.[6,7] The formation of a peroxoiron complex in the decomposition of hydrogen peroxide by Fe^{III} in aqueous solution is relevant in the chemistry of natural waters and atmospheric water droplets,[8–10] and the presence of a peroxo complex in Fenton-like ($Fe^{II} + H_2O_2$) and photo-Fenton ($Fe^{II} + H_2O_2 + UV$) reactions has been suggested.[11]

[a] Chemistry Department, Florida Institute of Technology, 150 West University Boulevard, Melbourne, FL 32901, USA
[b] Department of Nuclear Chemistry, Eötvös Loránd University, 1117 Budapest, Pázmány P. s. 1/A, Hungary
[c] MTA-ELTE Research Group for Nuclear Methods in Structural Chemistry, 1117 Budapest, Pázmány P. s. 1/A, Hungary

Recently, we have studied the kinetics of the formation of the purple complex, $[Fe^{III}(EDTA)(\eta^2\text{-}O_2)]^{3-}$ by the reaction of $[Fe^{III}(EDTA)H_2O]^-$ with hydrogen peroxide by using a stopped-flow technique.[2] The rate law for the formation of the complex was found to be $d[\{Fe^{III}(EDTA)(\eta^2\text{-}O_2)\}^{3-}]/dt = k[\{Fe^{III}(EDTA)H_2O\}^-][H_2O_2]$, where the observed second-order rate constant, k, decreases with an increase in pH and appears to be related to the deprotonation of $[Fe^{III}(EDTA)H_2O]^-$ [Equation (1)].

$$[Fe^{III}(EDTA)H_2O]^- \overset{K_1}{\leftrightarrows} [Fe^{III}(EDTA)OH]^{2-} + H^+ \qquad pK_1 = 7.58^{[12]} \qquad (1)$$

Brausam and van Eldik[1] have performed a detailed study on the reaction between $[Fe^{III}(EDTA)(H_2O)]^-$ and hydrogen peroxide. The reaction consists of two steps, in which the second step is independent of the hydrogen peroxide concentration. The first involves the reversible end-on coordination of H_2O_2 to give an intermediate, $[Fe^{III}(EDTA)\text{-}OOH]^{2-}$, which undergoes an intramolecular rearrangement to give the high-spin Fe^{III} side-on bound peroxo complex $[Fe^{III}(EDTA)(\eta^2\text{-}O_2)]^{3-}$.

The kinetic measurements in the work of Brausam and van Eldik[1] and in our study were conducted using a total Fe^{III} concentration of $\leq 1 \times 10^{-3}$. Under these conditions,

the Fe^{III}–EDTA complex exists predominantly in the monomeric form (>90%). However, at concentrations higher than 1×10^{-3} M of the complex, the formation of a dimer occurs[12–15] [Equations (2) and (3)].

$$2\,[Fe^{III}(EDTA)OH]^{2-} \overset{K_2}{\leftrightarrows} [(EDTA)Fe^{III}\text{–}O\text{–}Fe^{III}(EDTA)]^{4-} + H_2O \qquad (2)$$

$$pK_2 = -2.95$$

$$2\,[Fe^{III}(EDTA)H_2O]^{-} \overset{K_3}{\leftrightarrows} [(EDTA)Fe^{III}\text{–}O\text{–}Fe^{III}(EDTA)]^{4-} + 2\,H^+ + H_2O \qquad (3)$$

$$pK_3 = 12.21$$

The overall equilibrium (3) represents the combination of Equations (1) and (2).

The spectral studies of the Fe^{III}–EDTA system at various pH's indicated that the concentration of the dimer species depends on the pH and the concentration of the complex.[12–17] The maximum concentration of the dimer is obtained at pH $\geq$ pK_1.

In recent years, there has been tremendous interest in diiron complexes due to their role in biological systems.[3,4,18] For example, several metalloproteins contain a carboxylate-bridged diiron center, which performs a variety of functions.[19,20] This has prompted many workers to develop small molecule synthetic model compounds for nonheme, dinuclear iron-based metalloproteins.[19–22] Studies of such compounds with hydrogen peroxide help us to understand the function of an enzyme that catalyzes an important chemical transformation. Moreover, characterizing the peroxodiiron(III) intermediates in the reactions will eventually enhance our understanding in the biological environment.[19,23]

In the present work, we have selected diiron(III)–EDTA {i.e., $[(EDTA)Fe^{III}\text{-}O\text{-}Fe^{III}(EDTA)]^{4-}$} as a simple compound to study the formation of peroxo-bridged complexes in the reaction with hydrogen peroxide at a pH of around 10.4. Mössbauer spectroscopy in conjunction with the rapid-freeze/quench technique was used to characterize the formation of the Fe^{III}–peroxo species formed during the reaction. The results demonstrate the conversion of the diiron(III)–EDTA complex into a purple Fe^{III}–peroxo species. In addition to the formation of the already characterized monomeric species $[Fe^{III}(EDTA)(\eta^2\text{-}O_2)]^{3-}$, another two peroxodiiron(III) species are reported for the first time.

Results and Discussion

Initially, the Mössbauer spectrum of 0.05 M $Fe(NO_3)_3$ at a pH of around 1.0 was measured as a simple reproduction of literature data[24] (Figure 1, a). The spectrum shows a slightly broadened, relaxational line shape, which is in agreement with the expected slow paramagnetic relaxation of monomeric Fe^{3+} ($3d^5$) species at this concentration. Addition of a stoichiometric excess of EDTA to the 0.05 M $Fe(NO_3)_3$ stock solution resulted in the formation of iron–EDTA species, as shown in Figure 1 (b). A well-developed sextet shows up, with some broadening, with a typical relaxation spectrum in the middle. Our spectrum is similar to those published by other authors who have studied the aqueous Fe^{III}–EDTA system in frozen solutions by Mössbauer spectroscopy.[25–27] The spectrum obviously indicates two different species, so it was evaluated as a superposition of a relaxational component for the central part (Species **A1**) using the Blume–Tjon two-state relaxation model implemented in MossWinn 3.0,[28] and a Lorentzian sextet (Species **A2**). The parameters are given in Table 1. Both components indicate that the relaxation rate of the Fe^{3+} spins decreases as an effect of the complexing agent. More importantly, it also shows that association of the Fe species does not take place, the significance of which at high pH will be seen later. Our observation, and the spectrum of the Fe–EDTA system (Figure 1, b) itself, are very similar to the spectrum found by Morup and Knudsen[29] for frozen aqueous solution of $FeCl_3$ containing $[Fe(H_2O)_6]^{3+}$ and $[Fe(H_2O)_5Cl]^{2+}$ species in about a 1:1 proportion.

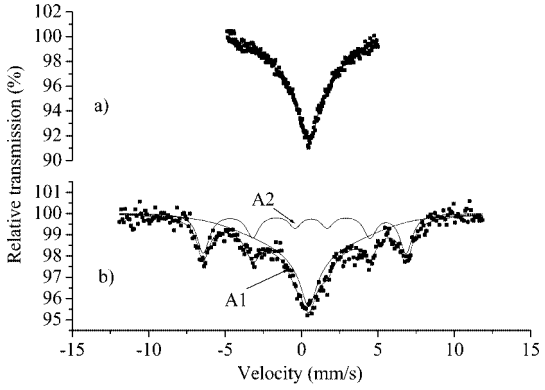

Figure 1. Mössbauer spectra of a frozen solution of 0.05 M $[Fe^{III}(EDTA)]^-$ at a pH of about 1 prepared with nitric acid (a) and after addition of EDTA in stoichiometric excess (b).

The structure of these monomeric species may be considered to be very close to that of $[Fe^{III}(EDTA)(H_2O)]^-$, which is present in solid $Na[Fe^{III}(EDTA)(H_2O)]\cdot 2H_2O$ (**S**). In this solid, the first water molecule is directly coordinated to the Fe^{3+} center, while the other two are crystal water molecules. We have measured the Mössbauer spectrum of solid $Na[Fe^{III}(EDTA)(H_2O)]\cdot 2H_2O$ at 80 K under the same conditions as the frozen solution samples so that direct comparison becomes possible. The well-known amplitude asymmetry of the doublet was observed, which is the result of the differing Larmor precession time of the m_I = 1/2 to 1/2 and m_I = 1/2 to 3/2 nuclear transitions (m_I is the magnetic quantum number) of the ^{57}Fe nucleus. Thus, the slight relaxational broadening of the doublet lines representing these two transitions is not the same under the same conditions. This phenomenon is often called the Blume effect.[30,31] The observed Mössbauer parameters (i.e., the

 © 2005 Wiley-VCH Verlag GmbH & Co. KGaA, Weinheim

Table 1. Mössbauer parameters of various Fe^{III}–EDTA species observed at 80 K. δ: isomer shift; Δ: quadrupole splitting; 2ε: quadrupole shift (in case of magnetic splitting); B: internal magnetic field. The uncertainties of the parameters are estimated on the basis of the errors of individual fits of those spectra in which the abundance of that particular species was larger than 10%.

Species	Description	pH	Coord. number	δ [mm s^{-1}]	Δ or 2ε* [mm s^{-1}]	B [T]
S	$[Fe(EDTA)(H_2O)]^-$ in solid $Na[Fe(EDTA)(H_2O)]\cdot 2H_2O$		7	0.57(1)	0.66(1)	≈0
A1	$[Fe(EDTA–H)(H_2O)]$	≈1.0	6	0.48(11)	+0.16(45)*	30(6)
A2	$[Fe(EDTA)]^-$	≈1.0	6	0.43(2)	–0.44(5)*	41.2(2)
B	$[(EDTA)Fe\text{-}O\text{-}Fe(EDTA)]^{4-}$	≈10.4	6	0.455(5)	1.60(5)	0
F	$[(EDTA)Fe(\eta^2\text{-}O_2)]^{3-}$	≈10.4	7	0.62(4)	+0.53(5)*	51.1(5)
D	$[(EDTA)Fe\text{-}(OO)(OH)\text{-}Fe(EDTA)]^{5-}$	≈10.4	7	0.57(1)	0.40(3)	0
E	$[(EDTA)Fe\text{-}(OO)\text{-}Fe(EDTA)]^{4-}$	≈10.4	6	0.47(3)	0.85(4)	0

high isomer shift) given in Table 1 are consistent with sevenfold coordination of Fe^{3+} in the solid species **S**.[32] Note that the solubility limit of $Na[Fe^{III}(EDTA)(H_2O)]\cdot 2H_2O$ did not allow us to perform experiments in aqueous solution, in which magnetic relaxation would be absent, because, even in the solid, the average distance between Fe^{3+} ions is not small enough to speed up spin relaxation, so no magnetic field is observed.

There is an apparent contradiction between the isomer shifts observed for solid $Na[Fe^{III}(EDTA)(H_2O)]\cdot 2H_2O$ (**S**) and the aqueous Fe^{III}–EDTA complexes (**A1** and **A2**) at a pH of around 1.0 (Table 1). This is not surprising because one of the carboxylic groups is very likely to become protonated in highly acidic solution, which results in dechelation of this carboxylic group from the coordinative bond and results in sixfold coordination of the central Fe^{3+}. Such species have been observed by Spijkerman et al.[33] in the solid $Fe^{III}(EDTA\text{-}H)(H_2O)$ with Mössbauer parameters δ = 0.45(5) mm s^{-1} and Δ = 0.42(5) mm s^{-1} at 78 K. It is reasonable to assume that due to a protolytic equilibrium (which means acid-catalyzed exchange of a water molecule and a carboxylate group at one of the six coordination sites of the central Fe^{3+} ion), one of the two subspectra in our Mössbauer spectrum represents $[Fe^{III}(EDTA\text{-}H)(H_2O)]$, while the other can be assigned to $[Fe^{III}(EDTA)]^-$, both of which contain sixfold coordinated Fe^{3+}, in agreement with the observed isomer shifts. Since both the magnetic field and the relaxation time are expected to increase with increasing electron donation to the Fe 3*d* orbitals, we can tentatively assign the structure $[Fe^{III}(EDTA\text{-}H)(H_2O)]$ to species **A1** and $[Fe^{III}(EDTA)]^-$ to species **A2**, although the quadrupole splitting for species **A1** observed by us is smaller than that in ref.[33] Note that the quadrupole shift of **A2** may not be directly related to quadrupole splitting data obtained from Lorentzian fits of nonmagnetic species because the relative orientation of the electric field gradient and the magnetic field is not known. We note here that Kanamori et al.[34] have found hexacoordinate Fe^{III}–EDTA species in solution only at even lower pH (in 1–2 M HCl) using Raman spectroscopy, while at pH 1.2 they identified heptacoordinate species. The presence of chloride vs. nitrate anions (the latter in our case) may have some significance in this discrepancy.

As a next step, measurements on the Fe^{III}–EDTA system were conducted in alkaline medium. The pH of the 0.05 M Fe^{III}–EDTA solution was raised to about 10.4, which resulted in precipitation of some hydrous iron(III) oxide, as checked by a Mössbauer run. (This precipitation is most probably due to kinetic effects, and has also been observed by other authors.[35]) The solution was filtered and the filtrate was frozen to record the Mössbauer spectrum (Figure 2, a). The expected species present in alkaline solution is $[Fe^{III}(EDTA)OH]^{2-}$ [Equation (1)]. However, the Mössbauer spectrum of the frozen solution showed no sign of any magnetic splitting (in agreement with the observation of Kachanova et al.[26]) due to very fast spin-spin relaxation. The doublet of Figure 2 (a) can therefore be assigned to a dimer species. The Mössbauer parameters of the doublet were found to be δ = 0.44(2) mm s^{-1} and Δ = 1.6(1) mm s^{-1} (Table 1). Marton et al.[16] have assigned this doublet to an oxo-bridged species $[(EDTA)Fe^{III}\text{-}O\text{-}Fe^{III}\text{-}(EDTA)]^{4-}$ (**B**), which implies a coordination number of 7 for both Fe^{3+} centers. If this assignment is correct, the simple rule that an increasing coordination number results in increasing isomer shift, which seems to work for momoneric species,[32] would not work when going from monomer to dimer [Equation (2)]. This isomer shift implies sixfold coordination, which would be in agreement with the suggestion of Kanamori et al.,[34] who claim that one carboxylate on each Fe center is dechelated. On the other hand, the driving force for dechelation could be a tendency to gain a more symmetrical (closer to octahedral) and therefore energetically favorable structure for the ligand sphere of iron, which would certainly result in a low quadrupole splitting. In contrast, a large quadrupole splitting is observed, which is not characteristic for Fe^{3+} (although not uncommon for μ-oxo dimers[36]), and shows a highly distorted electronic structure. It has been proposed that the [Fe-O-Fe] moiety has a closely linear structure,[14,15] and now it is logical to assume that this linearity is, at least partially, enforced by the bulky and spatially highly restricted EDTA ligand, and that even after the dechelation of one carboxylate arm, it still remains severely distorted, causing a high quadrupole splitting in the Mössbauer spectrum. The stability of the Fe–O–Fe bridge seems to overcompensate the destabilization of the ligand sphere of iron caused by distortion. Thus, there seem to be more arguments in favor of the sixfold coordination of iron in the dimeric species **B**. Our reasoning is strongly supported by the single crystal XRD study of Ozarowski et al.[37] on $Na_4[(EDTA)Fe^{III}\text{-}O\text{-}Fe^{III}(EDTA)]\cdot 3H_2O$, who

 © 2005 Wiley-VCH Verlag GmbH & Co. KGaA, Weinheim

found sixfold coordination with one dechelated carboxylate group for each EDTA ligand. Our results thus show that this coordination number is preserved in high pH aqueous solutions. On the other hand, it is interesting to note that Schugar et al.[35] have reported Mössbauer data on solid $Na_4[(EDTA)Fe^{III}\text{-}O\text{-}Fe^{III}(EDTA)]\cdot 12H_2O$, for which the isomer shift (0.44 mm s^{-1} at 77 K) matches our observation for dissolved $[(EDTA)Fe^{III}\text{-}O\text{-}Fe^{III}(EDTA)]^{4-}$ perfectly, although the quadrupole splitting is somewhat larger at 1.94 mm s^{-1}. This is an indication of different distortions of the ligand sphere of Fe^{3+} in the solid crystal and in the alkaline aqueous solution.

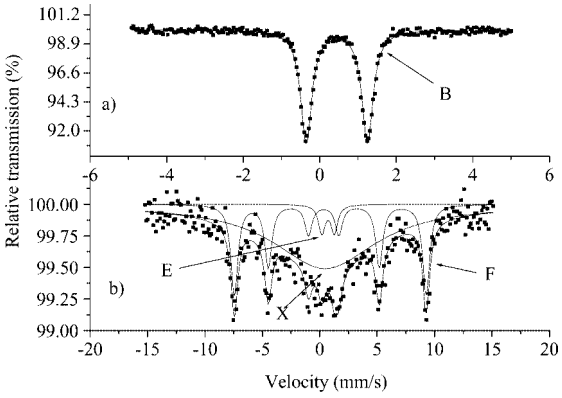

Figure 2. The Mössbauer spectrum of a frozen solution of the Fe^{III}–EDTA system at a pH of about 10.4 (a) and the spectrum after addition of excess H_2O_2 (b).

A very interesting example of the structure of the $[(EDTA)Fe^{III}\text{-}O\text{-}Fe^{III}(EDTA)]^{4-}$ moiety in solids has been presented by Gomez-Romero et al.,[38] who reported results on the heterobimetallic complex $[Cu^{II}(en)_2]_2[(EDTA)Fe^{III}\text{-}O\text{-}Fe^{III}(EDTA)]\cdot 2H_2O$ and also found six-coordinate iron, although the dechelated fourth carboxylate arm of EDTA is coordinated in this complex to the neighboring Cu center according to XRD analysis.

It should be pointed out that the Mössbauer parameters of monomeric $[Fe^{III}(EDTA)(OH)]^{2-}$ are not known because dissociation of the dimers at high pH would become significant in a low concentration range where recording a Mössbauer spectrum is not feasible even with ^{57}Fe-enriched material.

Finally, the Mössbauer study of the reaction of iron(III)–EDTA with H_2O_2 was conducted in alkaline medium. Addition of H_2O_2 to the Fe^{III}–EDTA system at a pH of around 10.4 gave a purple coloration of the solution, which has been attributed to the formation of an $[Fe^{III}(EDTA)(\eta^2\text{-}O_2)]^{3-}$ species (**F**) by several spectroscopic techniques.[39–41] The Mössbauer spectrum of the purple species shows a sextet (Figure 2, b), thus indicating that the dimer species (**B**) is converted into a monomer (**F**) by hydrogen peroxide. This is due to the side-on coordination of the peroxide ion, which saturates the coordination environment of the Fe center and steric hindrance does not allow the coordination of another Fe. The observed large isomer shift (Table 1) is consistent with an increased coordination number of the iron centers. Brausam and van Eldik[1] have suggested that iron is seven-coordinate in this complex, which means dechelation of one carboxylate arm (pentadentate EDTA), although they cited theoretical calculations in the literature that were in favor of sixfold coordination.[40] XAS measurements on peroxoiron(III) complexes with pentadentate N-donor ligands by Koehntop et al.[42] were not always conclusive either regarding the exact coordination number of iron (side-on or end-on bonding of O_2^{2-}). Our Mössbauer data support minimum sevenfold coordination on the basis of the large isomer shift. Horner et al.,[41] who prepared $[Fe^{III}(EDTA)(\eta^2\text{-}O_2)]^{3-}$ in a very pure form in solution, also found a large isomer shift but these authors did not discuss possible implications for the coordination number. A comparison with the six-coordinate $[Fe^{III}(EDTA\text{-}H)(H_2O)]$ (**A1**) and $[Fe^{III}(EDTA)]^-$ (**A2**) shows that the increase in the Fe 3*d* (spin-)density as a result of the "7th ligand" in the coordination sphere of Fe^{3+} appears to be enough to further raise the magnetic field to 50.4 T. It is also remarkable that the quadrupole shifts for the monomeric $[Fe^{III}(EDTA)]^-$ (**A2**) and monomeric $[Fe^{III}(EDTA)(\eta^2\text{-}O_2)]^{3-}$ (**F**) have opposite signs (Table 1). The exact interpretation of this observation would be difficult but the substantial difference in the symmetry of the two systems makes it quite reasonable.

In addition to species **F**, two other species, **E** and **X**, were also observed (Figure 2, b). A small doublet for species **E** co-exists with the sextet (species **F**), with an isomer shift of $\delta = 0.46$ mm s^{-1} (see Figure 2, b). This component was found to be formed from the sextet component. Doublet **E** has no magnetic splitting, therefore it was assigned to a dimer species (Table 1). It is worth mentioning that peroxodiiron(III) coordination compounds with other ligands have very similar Mössbauer parameters.[36] Species **X** shows-up with extreme line broadening, which is most probably due to relaxation.

The fate of the purple solution was studied in a separate experiment. In this experimental set-up, Fe^{III}–EDTA and H_2O_2 solutions were mixed in the dark and the Mössbauer spectrum of the frozen purple solution was recorded (Figure 3, a). We have observed many times in our experiments that light influences the rate of the reactions in the Fe–EDTA–H_2O_2 system. This effect is not unknown, but is rather unexplored in detail. We deliberately used this phenomenon to slow down or speed up reactions but we do not attempt in this work to give an explanation for this photochemical effect. The formation of species **F**, **E**, and **X** occurred similar to the observations made in the previous experiment (Figure 2, b). The frozen solution was then allowed to melt for 5 min at room temperature in the dark and a Mössbauer spectrum was recorded again after freezing of the solution (Figure 3, b). The fraction of doublet **E** increased slightly at the expense of **X**. Species **X** is thus an intermediate in the conversion of species **F** to **E**. After further aging at room temperature for 10 min under daylight conditions, an abrupt change in the Mössbauer spectra was observed. Species **F**, **E**, and **X** all disappeared, and a new species having a doublet with an isomer shift, δ, of 0.57 (**D**) formed in addition to the already known oxo-bridged species $[(EDTA)Fe^{III}\text{-}O\text{-}Fe^{III}(EDTA)]^{4-}$ (**B**; Figure 3, c).

 © 2005 Wiley-VCH Verlag GmbH & Co. KGaA, Weinheim

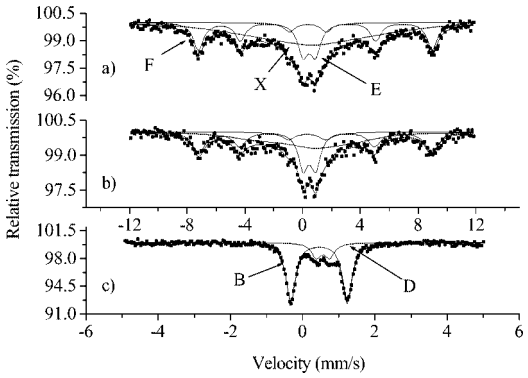

Figure 3.Mössbauer spectra of the Fe^{III}–EDTA–H_2O_2 system at a pH of about 10.4: a) initial state, b) after 5 min aging at room temperature (room temp.) in the dark, and c) after a further 10 min aging at room temp. in daylight.

The formation of species **B** from species **D** was confirmed by conducting the reaction between Fe^{III}–EDTA and H_2O_2 at room temperature in daylight, where formation and decay of the purple species is fast. The Mössbauer spectra of the reaction are given in Figure 4. Species **X** and **E** were not observed. This further suggests the intermediate nature of these species. The initial spectra show traces of the sextet of species **F** together with doublets of species **B** and **D** (Figure 4, a). Species **D** decays quickly to the original Fe^{III}–EDTA species **B** (Figure 4, b and c). It is noteworthy that the color of the solution belonging to the Mössbauer spectrum of Figure 4 (b) is still purple. Since **B** has a yellow color, species **D** should be responsible for the characteristic purple color of this solution. It is tentatively assumed (since it has been observed only together with the purple species **F**) that species **E** also has a purple color as a consequence of the presence of the peroxo moiety.

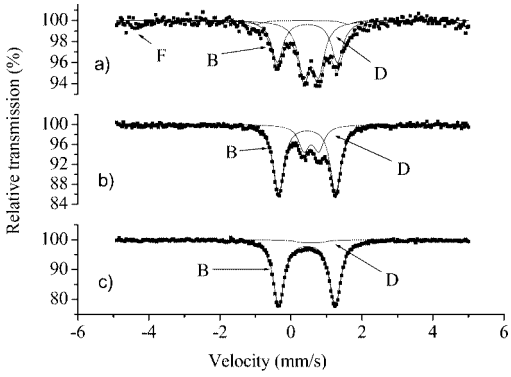

Figure 4. Evolution of Fe-bearing species in the Fe^{III}–EDTA–H_2O_2 system at a pH of about 10.4 in daylight: initial state (a), after 4 min aging at room temp. (b), and after 10 min aging at room temp. (c).

To further understand the conversions of species in the purple solution, another study was conducted at low temperature in darkness in order to slow down the reactions. The Fe^{III}–EDTA and H_2O_2 were mixed in an ice bath (ca. 0 °C) and the spectra were recorded after aging the mixture in consecutive three-minute steps (Figure 5). All agings were carried out at around 0 °C. A slow evolution of the various species from **B** to **F** (and **X**) to **E** at low temperature was observed. The formation and decomposition of species **X** is pronounced (Figure 5, c and d). Since species **X** shows up together with **F** and/or **E**, it is reconfirmed now that it should represent a very short-lived (to account for the extremely large line broadening) transitional state between **F** and **E**. We should note here that in the spectra c and d of Figure 5 and b of Figure 2, the assignment of the very small doublets (3–4%) to species E is rather tentative due to statistical insignificance; this doublet is fully developed only in the spectra in Figure 5 (e) and Figure 3 (a and b).

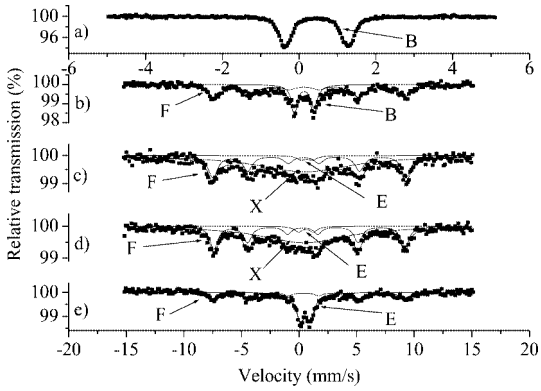

Figure 5. Evolution of Fe-bearing species in the Fe^{III}–EDTA–H_2O_2 system at a pH of about 10.4 (initial value before adding H_2O_2) at around 0 °C: a) before addition of H_2O_2, b) immediately after addition of H_2O_2, c) after 3 min aging at 0 °C, d) after an additional 3 min of aging at 0 °C, and e) after a second additional 3 min of aging at 0 °C.

The formation and the decomposition of species **F** may be summarized as shown in Schemes 1 and 2, respectively. In Scheme 1, the dimer species **B** is converted into the monomeric species **F** upon the addition of hydrogen peroxide. The decay of the monomer **F** to dimer **E** (Scheme 2) takes place through intermediate **X** (structure not shown).

The observation of species **X** is probably the consequence of an equilibrium giving a short-lived monomeric [(EDTA)-Fe^{III}-OO]$^{3-}$ species or its protonated form [(EDTA)Fe^{III}-OOH]$^{2-}$ (with end-on coordination of O_2^{2-} to iron). Only the much more stable dimer (**E**) clearly shows up in the Mössbauer spectra. The isomer shift of species **E** is practically the same as that of species **B** and formally corresponds to a sixfold coordinated monomeric species. This indicates that the dechelation of one carboxylate arm at each iron center occurs here, similar to the species **B**. At the same time, since the peroxo bridge allows larger separation of the Fe^{III}–EDTA moieties as compared to the case of a regular oxo bridge, the repulsion between the two pentadentate EDTAs and, inherently, their spatial distortion is smaller, which results in only half of the quadrupole splitting found for species **B**. It is noteworthy that in this picture, the isomer shift does not differ for a μ-oxo and a μ-peroxo species as the difference in the donicity of the oxo and peroxo oxygens (as a sixth ligand around the Fe^{3+} center) is probably not substantial.

 © 2005 Wiley-VCH Verlag GmbH & Co. KGaA, Weinheim

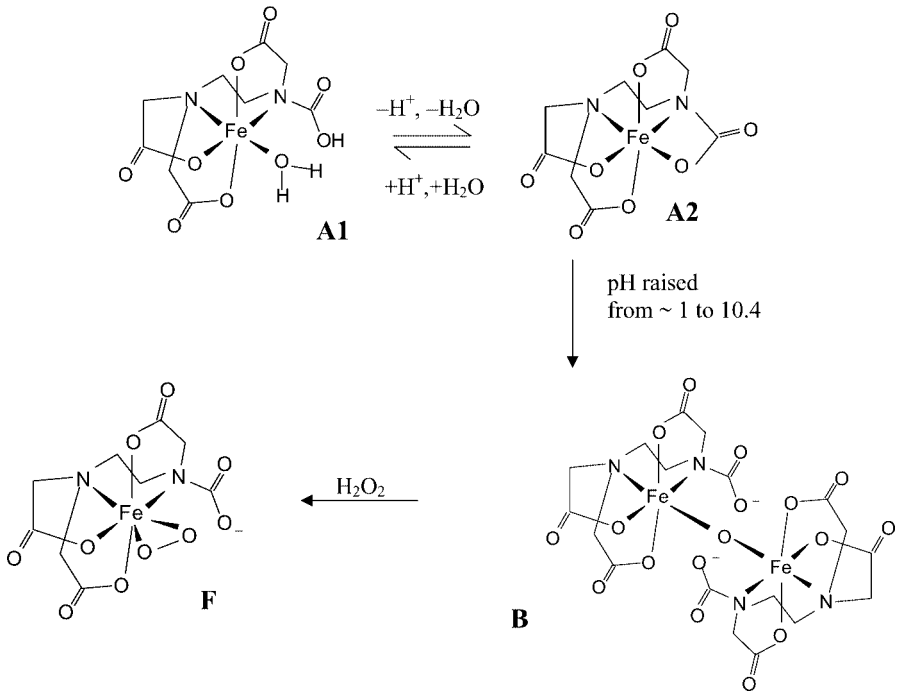

Scheme 1.

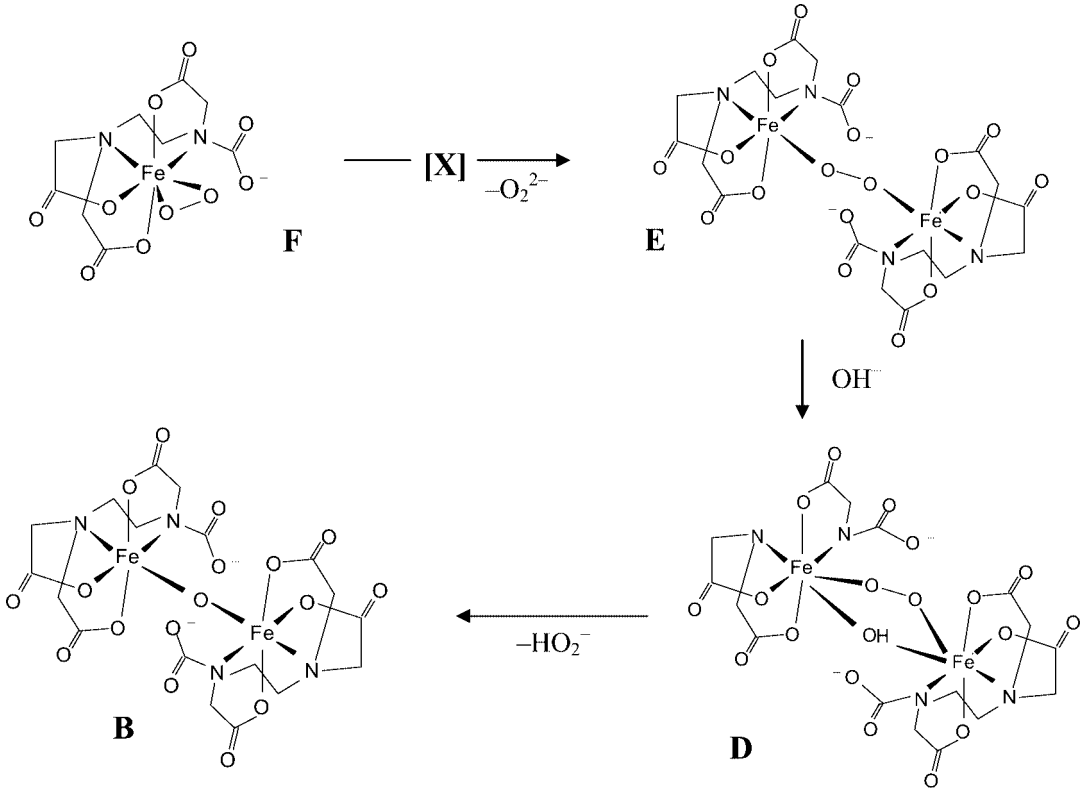

Scheme 2.

The driving force for the transformation of monomeric species **F** to dimeric species **E** could be the loss of H_2O_2 due to its decomposition. The decomposition of H_2O_2 results in an increase in the pH since H_2O_2 is more acidic then H_2O. Therefore, further decomposition of species **E** may occur through the addition an OH^- ion to form a doubly bridged species **D**. Doubly and triply bridged binuclear complexes of Fe^{III} with nonequivalent bridging ligands are known, for example (μ-carboxylato)(μ-oxo)diiron(III)-type compounds.[43] We are not aware of any reports of (μ-hy-

 © 2005 Wiley-VCH Verlag GmbH & Co. KGaA, Weinheim

droxo)(μ-peroxo)diiron(III) complexes, which may be due to their low stability, as found here. The isomer shift of species **D** is significantly higher than that of species **E**, which is in agreement with the increased coordination number (7). The decrease of the quadrupole splitting cannot be fully understood in this simple picture.

At this stage, decomposition (further loss) of H_2O_2 and the concomitant rise in pH logically drives us back to species **B**.

We have to mention here that the proposed structures for species **E** and **D**, which should be very logical, may not be the ultimate choice. For example, partial protonation of the peroxo bridge may occur, which would result in the species $[(EDTA)Fe^{III}\text{-}HOO\text{-}Fe^{III}(EDTA)]^{2-}$. However, such a species contains nonequivalent iron centers, and thus two doublets are always expected to be a pair in the Mössbauer spectrum. This is not observed. It is assumed that the position of the proton is not averaged out between the two oxygens on the Mössbauer timescale, and that the Mössbauer parameters of the two nonequivalent irons would be significantly different. Thus, since species **D** is a peroxo-type dimeric species, the increase of the isomer shift upon going from species **E** to **D** can be considered as a strong argument to support the formation of the double bridge.

Experimental Section

A stock solution of $Fe(NO_3)_3$ (0.05 M) was prepared by dissolving metallic iron (enriched in ^{57}Fe to ca. 90%) in nitric acid. The final pH of this stock solution was about 1.0. The Mössbauer measurements were performed by mixing the iron(III) solution (500 μL, 0.05 M) with solid EDTA. The amount of EDTA in the mixture was in excess and the final molar ratio of EDTA to Fe^{III} was 1.3:1. The pH of the solution, measured with a digital pH meter (Radelkis), was adjusted by adding KOH (0.5 M). At alkaline pH, some precipitate was observed in the Fe^{III}–EDTA solution. This precipitate were filtered off through a 5-μm filter. The filtrate was diluted with distilled water to achieve 1.0 mL total volume. No further precipitation of the solution was observed.

The reaction of Fe^{III}–EDTA with hydrogen peroxide was studied by adding H_2O_2 (50 μL, 30%) to the solution. The concentration of H_2O_2 in the final solution was in large excess. The resultant deep-purple solution was quenched immediately drop-by-drop on a pre-cooled metal slab almost completely immersed in liquid nitrogen. The freezing of the total volume (15–20 droplets) lasted for about half a minute. Vértes[24] has shown previously that this quenching technique (cooling speed ca. 30 °C s^{-1}) preserves the structure of the solution, and therefore the species existing in the liquid state can be studied. The frozen droplets were collected in a sample holder and placed into a bath-type cryostat filled with liquid nitrogen.

The frozen samples were measured by a conventional constant acceleration type Mössbauer spectrometer (Ranger). The spectrum evaluations were carried out with the assumption of a Lorentzian line-shape, unless otherwise stated, using MossWinn 3.0.[28] All isomer shifts are given relative to α-Fe at room temperature.

Acknowledgments

We acknowledge the support of the US−Hungary Partnership Program supported by the National Science Foundation, the Hungarian Academy of Science, and the National Scientific Research Fund of Hungary (MTA85-OTKA46138).

[1] A. Brausam, R. van Eldik, *Inorg. Chem.* **2004**, *43*, 5351–5359.
[2] V. K. Sharma, F. J. Millero, Z. Homonnay, *Inorg. Chim. Acta* **2004**, *357*, 3583–3587.
[3] M. Costas, M. P. Mehn, M. P. Jehnsen, L. Que Jr., *Chem. Rev.* **2004**, *104*, 939–986.
[4] E. I. Solomon, T. C. Brunold, M. I. Davis, J. N. Kemsley, S.-K. Lee, N. Lehnert, F. Neese, A. J. Skulan, Y.-S. Yang, J. Zhou, *Chem. Rev.* **2000**, *100*, 235–350.
[5] C. Bukk, J. A. Fee, *J. Am. Chem. Soc.* **1985**, *107*, 3295–3304.
[6] C. Walling, *Acc. Chem. Res.* **1975**, *8*, 125–131.
[7] J. Bond, C. W. Brown, G. S. Rushton, *J. Polym. Sci.* **1964**, *2*, 1015–1017.
[8] T. E. Graedel, M. L. Mandich, C. J. Weschler, *J. Geophys. Res.* **1986**, *91*, 5205–5221.
[9] D. L. Sedlak, J. Hoigné, *Environ. Sci. Technol.* **1994**, *28*, 1898–1906.
[10] J. D. de Laat, H. Gallard, S. Ancelin, B. Legube, *Environ. Sci. Technol.* **1999**, *33*, 2726–2732.
[11] J. J. Pignatello, D. Liu, P. Huston, *Environ. Sci. Technol.* **1999**, *33*, 1832–1839.
[12] R. L. Gustafson, A. E. Martell, *J. Phys. Chem.* **1963**, *67*, 576–582.
[13] R. G. Wilkins, R. E. Yelin, *Inorg. Chem.* **1969**, *8*, 1470–1473.
[14] H. J. Schugar, A. T. Hubbard, F. C. Anson, H. B. Gray, *J. Am. Chem. Soc.* **1969**, *91*, 71–77.
[15] G. McLendon, R. J. Motekaitis, A. E. Martell, *Inorg. Chem.* **1976**, *15*, 2306–2308.
[16] A. Marton, N. Sükösd-Roslosnik, A. Vértes, I. Nagy-Czakó, K. Burger, *Inorg. Chim. Acta* **1987**, *137*, 173–176.
[17] G. E. Stein, J. A. Marinsky, *J. Inorg. Nucl. Chem.* **1975**, *37*, 2421–2428.
[18] E. Y. Tshuva, S. J. Lippard, *Chem. Rev.* **2004**, *104*, 987–1012.
[19] D. M. Kurtz Jr., *J. Biol. Inorg. Chem.* **1997**, *2*, 159–167.
[20] D. Lee, S. J. Lippard, in *Comprehensive Coordination Chemistry II: From Biology to Nanotechnology*, Elsevier Ltd., Oxford, **2004**, vol. 8, p. 309.
[21] M. Fontecave, S. Menage, C. Duboc-Toia, *Coord. Chem. Rev.* **1998**, *178–180*, 1555–1572.
[22] R. H. Holm, P. Kennepohl, E. I. Solomon, *Chem. Rev.* **1996**, *96*, 2239–2314.
[23] J. B. Vincent, G. L. Oliver-Lilley, B. A. Averill, *Chem. Rev.* **1990**, *90*, 1447–1467.
[24] A. Vértes, D. L. Nagy, *Mössbauer Spectroscopy of Frozen Solution*, Akadémiai Kiadó, Budapest, **1990**.
[25] F. T. De Araújo, A. Dufresne, C. G. De Lima, J. M. Knudsen, *Chem. Phys. Lett.* **1970**, *7*, 333–336.
[26] Z. T. Kachanova, R. A. Stukan, A. P. Purmaly, *Teor. Eksp. Khim. (Kiew)* **1970**, *6*, 280–284.
[27] K. Garbett, G. Lang, R. J. P. Williams, *J. Chem. Soc. A* **1971**, 3433–3436.
[28] Z. Klencsár, E. Kuzmann, A. Vértes, *J. Radioanal. Nucl. Chem.* **1996**, *210*, 105–118.
[29] S. Mørup, J. E. Knudsen, *Chem. Phys. Lett.* **1976**, *40*, 292–293.
[30] M. Blume, *Phys. Rev. Lett.* **1965**, *14*, 96–98.
[31] S. Dattagupta, M. Blume, *Phys. Rev. A* **1976**, *14*, 480–494.
[32] M. Takeda, *Hyperfine Interact.* **1986**, *28*, 737–740.
[33] J. J. Spijkerman, L. H. Hall, J. L. Lambert, *J. Am. Chem. Soc.* **1968**, *90*, 2039–2048.
[34] K. Kanamori, H. Dohniwa, N. Ukita, I. Kanesaka, K. Kawai, *Bull. Chem. Soc. Jpn.* **1990**, *63*, 1447–1454.
[35] H. J. Schugar, G. R. Rossman, C. G. Barraclough, H. B. Gray, *J. Am. Chem. Soc.* **1972**, *94*, 2683–2690.

 © 2005 Wiley-VCH Verlag GmbH & Co. KGaA, Weinheim

[36] E. Y. Tshuva, S. J. Lippard, *Chem. Rev.* **2004**, *104*, 987–1012.
[37] A. Ozarowski, B. R. McGarvey, J. E. Drake, *Inorg. Chem.* **1995**, *34*, 5558–5566.
[38] P. Gomez-Romero, G. B. Jameson, J. J. Borras-Almenar, E. Escriva, E. Coronado, D. Beltran, *J. Chem. Soc., Dalton Trans.* **1988**, 2747–2751.
[39] S. Ahmad, J. D. McCallum, A. K. Shiemke, E. H. Appelman, T. M. Loehr, J. Sanders-Loehr, *Inorg. Chem.* **1988**, *27*, 2230–2233.
[40] F. Neese, E. I. Solomon, *J. Am. Chem. Soc.* **1998**, *120*, 12829–12848.
[41] O. Horner, C. Jeandey, J.-L. Oddou, P. Bonville, J.-M. Latour, *Eur. J. Inorg. Chem.* **2002**, *5*, 1186–1189.
[42] K. D. Koehntop, J.-U. Rohde, M. Costas, L. Que Jr., *Dalton Trans.* **2004**, 3191–3198.
[43] D. M. Kurtz Jr., *Chem. Rev.* **1990**, *90*, 585–606.

Received: April 11, 2005
Published Online: September 23, 2005

 © 2005 Wiley-VCH Verlag GmbH & Co. KGaA, Weinheim

Structural Trends in Divalent Benzil Bis(thiosemicarbazone) Complexes

David G. Calatayud,[a] Elena López-Torres,[a] M. Antonia Mendiola,*[a] César J. Pastor,[b] and Jesús R. Procopio[c]

Keywords: Copper / N ligands / S ligands / Thiosemicarbazone complexes / Zinc

Redox-related changes in the biological properties of copper bis(thiosemicarbazones) are induced by the backbone of the ligand. To get information about how these changes depend on the structural parameters, three X-ray structures of complexes with different behaviour of the benzil bis(thiosemicarbazone) ligand have been determined. These include two almost planar copper(II) complexes with different grades of deprotonation in the ligand and a Zn^{II} complex in which the ligand acts as a monoanion and a nitrate group is bonded to the metal ion in a square-based pyramid. The changes in the backbone bond lengths agree with the variation in the ionic radius and with the grade of electronic charge delocalisation in the chelate rings; these have consequences for the coordination sphere, allowing the metal to fit slightly better into the ligand cavity, which in turn may affect the complex stability and the redox potential.
(© Wiley-VCH Verlag GmbH & Co. KGaA, 69451 Weinheim, Germany, 2005)

Introduction

The increasing interest in thiosemicarbazones (TSCs) that has arisen in the last decades is related to their wide range of biological properties, for example as antiviral, antibacterial and anticancer agents.[1–4] These biological activities are often attributed to their chelating ability with metal ions. Copper complexes of bis(thiosemicarbazones) have been investigated for use as anti-cancer chemotherapeutic agents[5,6] and as superoxide dismutase-like radical scavengers.[7] It is, however, their use as delivery agents for radioactive copper in new copper-based radiopharmaceuticals and the hypoxic selectivity of certain copper bis(thiosemicarbazonate) complexes that has created much recent interest.[8–20] The biological characteristics of copper bis(thiosemicarbazonate) complexes derived from 1,2-diones are dependent on the nature of the "backbone" substituents in the ligand. The most detailed studies of these structure–activity relationship have been carried out in connection with hypoxia imaging.[14,15,21] These studies correlated hypoxic cell selectivity with the reduction potential, electronic structure and chemical behaviour and found that all of these properties are extraordinarily sensitive to the alkyl groups attached to the diimine backbone of the ligand. The trapping in a hypoxic cell is believed to occur by reduction of the copper(II) complex by intracellular reducing agents to give stable protonated Cu^{I} species, which are trapped inside the cell.[22] The structure–activity relationships of copper bis(thiosemicarbazone) radiopharmaceuticals derived from 1,2-diones show a correlation between the reduction potential for the Cu^{II}/Cu^{I} couple and the hypoxic cell selectivity.[14,23] The hypoxia-selective radiopharmaceutical [Cu(ATSM)] [ATSM = biacetyl bis(4-methylthiosemicarbazone)], for example, undergoes a reversible reduction at $E_{1/2}$ = –0.620 V in DMF at a glassy carbon working electrode. On the other hand, some zinc thiosemicarbazone complexes that have been shown to be active as anti-tumour agents are as cytotoxic as cisplatin and are also effective against cisplatin-resistant cell lines.[24] Recently, fluorescence studies and the cellular distribution of zinc bis(thiosemicarbazone) complexes have been reported.[25]

Since relatively superficial modifications induce remarkable changes in redox and biological properties, it is natural to enquire whether they might also significantly affect the core structural parameters of the complexes and, if so, whether this might be related to their biological behaviour. The aim of this work is to get information about the importance of the changes induced by the modification of the backbone of benzil bis(thiosemicarbazone) (LH_6) in some complexes. In particular, for copper(II) complexes these changes affect the redox properties and therefore their potential activity as hypoxia-selective radiopharmaceuticals. We report the X-ray structures of two copper complexes derived from LH_6 (Figure 1) whose reduction potential values are –0.550 and –0.520 V,[26] close to those of [Cu(ATSM)], a related zinc complex, as well as the structure of a nickel complex for comparison.[27] We also discuss structural variations as a function of the ligand behaviour and/or the metal ion.

[a] Departamento de Química Inorgánica, Universidad Autónoma, 28049 Madrid, Spain
E-mail: antonia.mendiola@uam.es
[b] Servicio Interdepartamental de Investigación, Universidad Autónoma, 28049 Madrid, Spain
[c] Departamento de Química Analítica y Análisis Instrumental, Universidad Autónoma, 28049 Madrid, Spain

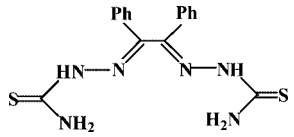

Figure 1. Drawing of benzil bis(thiosemicarbazone) (LH_6).

Results

All complexes were synthesised as described previously, except complex **2**, which was isolated from the mother liquor of the synthesis of a previously published complex.[26] Their analytical and spectroscopic properties are consistent with those reported previously.[26,28] Complex **2** presents a 1:1 ligand:copper molar ratio and has a nitrate group as a counterion.

In complex **1**, which was prepared from copper(II) chloride, benzil bis(thiosemicarbazone) acts as a dianion, while in complexes **2** and **3**, which were synthesised from copper and zinc nitrate, respectively, it has lost only a hydrazinic hydrogen atom and therefore acts as a monoanion. However, the nitrate ion contained in **2** and **3** shows a different behaviour: it is outside of the coordination sphere in the first complex but is bonded to the zinc atom in complex **3**.

The crystal structures of all complexes consist of discrete molecules where the ligand is tetradentate through the imine nitrogen and the sulfur atoms by changing the *trans* disposition of the thiosemicarbazone moieties in the free ligand to *cis* to form an N_2S_2 chelate, as has been observed in other complexes.[27]

The crystal structure of **1** consists of discrete molecules of [$CuLH_4$]. A perspective view of the complex, together with the atom-labelling scheme, is given in Figure 2 (the thermal ellipsoids are shown at 50% probability) and selected bond lengths and angles are given in Tables 1 and 2, respectively. The crystallographic data of the complex confirm the geometry proposed from spectroscopic data[26] and the cell parameters are close to those reported previously.[29] The copper(II) ion is tetracoordinate in a planar disposition. The coordination sphere of the copper atom is formed by two sulfurs and two imine nitrogens, as expected for this ligand.[30,31] The environment of the copper ion is planar, with a distance from the copper ion to the basal plane of 0.1219 Å. The phenyl rings C(5)–C(10) and C(11)–C(16) form dihedral angles of 81.9° and 81.0°, respectively, with respect to the basal plane. The molecules are held together in the crystal packing through an extended network of intermolecular hydrogen bonds involving the amino groups and the hydrazinic nitrogen atoms (see Figure 3 and Table 3).

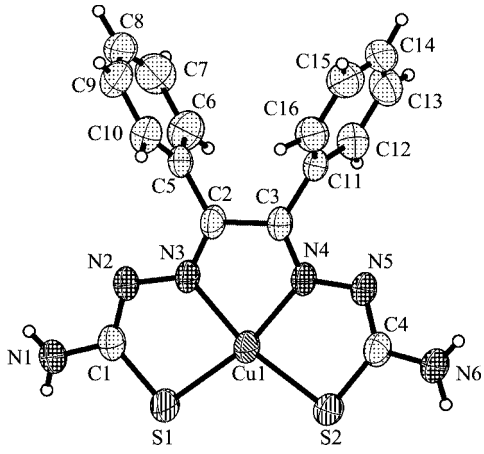

Figure 2. XSHELL view of [$CuLH_4$] (**1**).

The structure determination of [$CuLH_5$]NO_3 (**2**; Figure 4 with the thermal ellipsoids shown at 50% probability. See also Tables 1 and 2) shows a similar disposition for the copper ion as in complex **1**, but with a nitrate group acting as a counterion, although a weak interaction with the copper ion is also observed [*d*(Cu–O) = 2.46 Å]. The bis(thiosemicarbazone) acts as an N_2S_2 chelate ligand around the metal ion, giving a quasi-planar geometry for the copper with a deviation of 0.2084 Å from the basal plane. The main difference is the unusual asymmetric behaviour of the thiosemi-

Table 1. Selected bond lengths [Å] for the complexes and ligand LH_6.

	1	**2**	**3**	**4**[27]	LH_6[27]
C(2)–C(3)	1.485(3)	1.481(3)	1.491(3)	1.475(3)	1.478(3)
C(2)–C(5)	1.484(3)	1.480(3)	1.483(3)	1.474(3)	1.490(3)
C(3)–C(11)	1.482(3)	1.478(3)	1.490(3)	1.474(3)	1.490(3)
C(2)–N(3)	1.293(3)	1.305(3)	1.300(3)	1.308(3)	1.298(3)
C(3)–N(4)	1.296(3)	1.295(3)	1.285(3)	1.307(3)	1.294(3)
N(3)–N(2)	1.357(3)	1.351(2)	1.357(2)	1.372(3)	1.361(3)
N(4)–N(5)	1.363(3)	1.361(2)	1.357(3)	1.371(3)	1.362(3)
N(2)–C(1)	1.324(3)	1.333(3)	1.341(3)	1.329(3)	1.369(3)
N(5)–C(4)	1.327(3)	1.356(3)	1.352(3)	1.320(3)	1.367(3)
C(1)–S(1)	1.754(3)	1.751(2)	1.739(2)	1.745(3)	1.667(3)
C(4)–S(2)	1.744(3)	1.712(2)	1.707(2)	1.744(3)	1.668(3)
N(3)–M	1.976(2)	1.9873(17)	2.1407(19)	1.861(2)	
N(4)–M	1.968(2)	1.9682(17)	2.1290(18)	1.862(2)	
S(1)–M	2.2356(8)	2.2458(5)	2.3143(6)	2.1572(7)	
S(2)–M	2.2332(8)	2.2844(6)	2.3695(7)	2.1461(7)	
C(1)–N(1)	1.322(4)	1.329(3)	1.338(3)	1.330(3)	1.305(3)
C(4)–N(6)	1.334(4)	1.314(3)	1.319(3)	1.342(3)	1.306(4)
O(1)–M			2.1142(17)		

 © 2005 Wiley-VCH Verlag GmbH & Co. KGaA, Weinheim

Table 2. Bond angles [°] for the complexes and ligand LH_6.

	1	**2**	**3**	**4**[27]	LH_6[27]
N(3)–C(2)–C(3)	114.4(2)	114.13(18)	114.1(2)	111.8(2)	114.0(2)
N(4)–C(3)–C(2)	114.7(2)	113.90(18)	114.35(19)	113.1(2)	114.2(2)
C(2)–N(3)–M	114.50(16)	115.40(14)	117.66(15)	116.09(16)	
C(3)–N(4)–M	114.54(16)	116.64(14)	118.88(14)	115.41(17)	
N(2)–N(3)–M	123.05(16)	122.74(13)	121.04(14)	123.43(15)	
N(5)–N(4)–M	123.22(17)	119.56(13)	118.16(14)	123.89(16)	
N(3)–N(2)–C(1)	111.6(2)	111.75(16)	111.65(18)	110.1(2)	119.0(2)
N(4)–N(5)–C(4)	110.8(2)	116.89(17)	118.26(19)	109.5(2)	119.1(2)
N(2)–C(1)–S(1)	125.6(2)	125.80(16)	128.33(17)	124.41(19)	118.68(19)
N(5)–C(4)–S(2)	126.4(2)	122.09(16)	123.20(17)	124.81(19)	118.3(2)
C(1)–S(1)–M	94.71(9)	94.55(7)	95.68(8)	94.11(8)	
C(4)–S(2)–M	94.49(9)	95.76(7)	97.24(8)	94.26(8)	
N(3)–M–N(4)	81.06(8)	79.87(7)	73.46(7)	83.32(8)	
N(3)–M–S(1)	84.96(6)	84.89(5)	81.93(5)	87.62(6)	
N(4)–M–S(2)	85.09(6)	85.33(5)	81.37(5)	87.38(7)	
S(1)–M–S(2)	108.80(3)	108.52(2)	115.57(2)	101.69(3)	
N(3)–M–S(2)	165.73(6)	161.90(5)	147.35(5)	170.68(6)	
N(4)–M–S(1)	165.98(7)	163.79(5)	152.24(6)	170.87(7)	
C(2)–N(3)–N(2)	122.2(2)	121.83(17)	120.48(19)	120.5(2)	118.7(2)
C(3)–N(4)–N(5)	122.2(2)	123.65(17)	122.96(18)	120.7(2)	118.9(2)
C(5)–C(2)–C(3)	120.6(2)	121.15(18)	120.24(19)	123.2(2)	121.0(2)
C(11)–C(3)–C(2)	121.3(2)	121.91(18)	121.45(19)	122.7(2)	120.2(2)
C(5)–C(2)–N(3)	125.0(2)	124.72(18)	125.64(19)	125.0(2)	125.0(2)
C(11)–C(3)–N(4)	124.0(2)	124.13(18)	124.2(2)	124.1(2)	125.6(2)
N(2)–C(1)–N(1)	117.9(3)	116.93(19)	115.7(2)	117.3(2)	115.8(2)
N(5)–C(4)–N(6)	116.8(3)	115.9(2)	115.9(2)	117.9(2)	115.7(3)
N(1)–C(1)–S(1)	116.5(2)	117.26(16)	115.99(18)	118.3(2)	125.6(2)
N(6)–C(4)–S(2)	116.9(2)	122.00(17)	120.92(19)	117.3(2)	126.0(2)

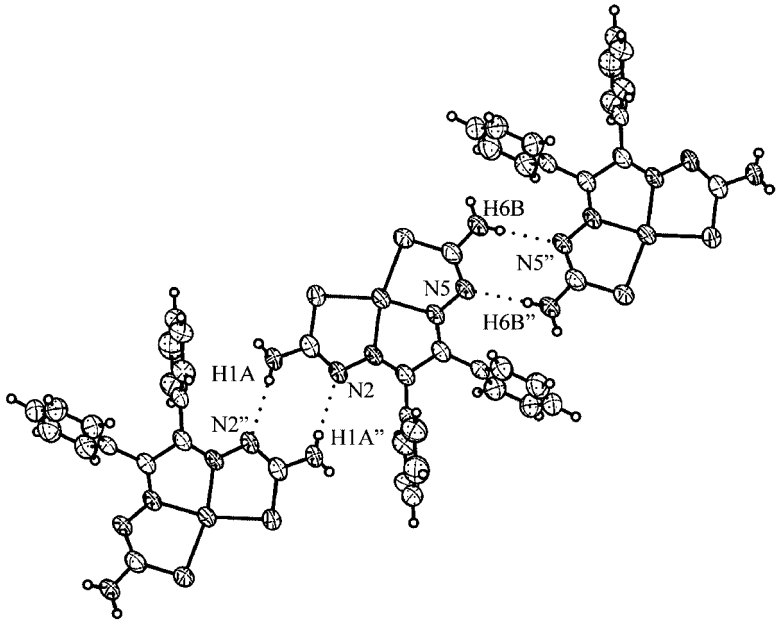

Figure 3. Plot of complex $[CuLH_4]$ (**1**) showing the hydrogen bonds.

carbazone branches of the ligand, due to the presence of the hydrogen atom in a secondary amine for only one thiosemicarbazone moiety. The phenyl rings C(5)–C(10) and C(11)–C(16) form dihedral angles of 65.0° and 58.3°, respectively, with respect to the basal plane. The presence of an additional hydrogen together with the nitrate group allows this complex to form additional hydrogen bonds, as shown in Figure 5 and Table 3.

Yellow crystals of complex **3** were obtained by recrystallisation from methanol. Discrete $[ZnLH_5NO_3]$ entities form

 © 2005 Wiley-VCH Verlag GmbH & Co. KGaA, Weinheim

Table 3. Hydrogen bonds for complexes [Å and °].

	Interaction	*d*(D–H)	*d*(H···A)	*d*(D···A)	<(DHA)
1[a]	N(6)–H(6B)···N(5)#1	0.79(3)	2.28(3)	3.066(4)	176(3)
	N(1)–H(1A)···N(2)#2	0.76(4)	2.28(4)	3.030(4)	174(3)
2[b]	N(6)–H(6A)···O(3)#2	0.87(3)	2.03(3)	2.901(3)	179(3)
	N(5)–H(5···O(2)#2	0.82(3)	2.20(3)	2.932(2)	150(3)
	N(1)–H(1B)···N(2)#3	0.83(3)	2.18(3)	2.999(3)	176(3)
3[c]	N(1)–H(1B)···N(2)#1	0.74(3)	2.29(3)	3.023(3)	172(3)
	N(6)–H(6A)···O(2)#2	0.86(3)	2.10(3)	2.944(3)	169(3)
	N(6)–H(6B)···O(1)#3	0.84(39)	2.47(3)	3.153(3)	139(2)
	N(5)–H(5)···O(3)#2	0.82(39)	2.42(3)	3.062(3)	136(2)

[a] Symmetry transformations used to generate equivalent atoms: #1 $-x$, $-y$, $-z$; #2 $-x+2$, $-y$, $-z+1$. [b] Symmetry transformations used to generate equivalent atoms: #2 $-x+1$, $-y+1$, $-z$; #3 $-x+2$, $-y+2$, $-z+1$. [c] Symmetry transformations used to generate equivalent atoms: #1 $-x+2$, $-y+1$, $-z+1$; #2 $-x+1$, $-y+1$, $-z$; #3 $x-1$, y, z.

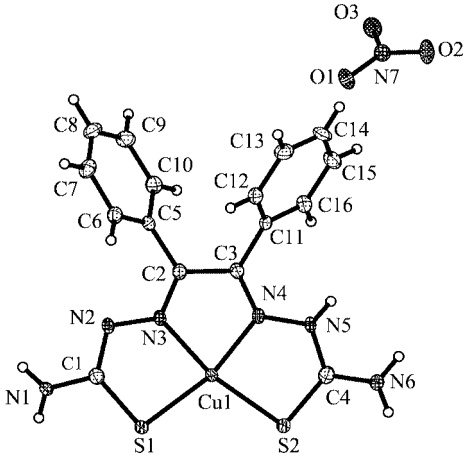

Figure 4. XSHELL view of $[CuLH_5]NO_3$ (**2**).

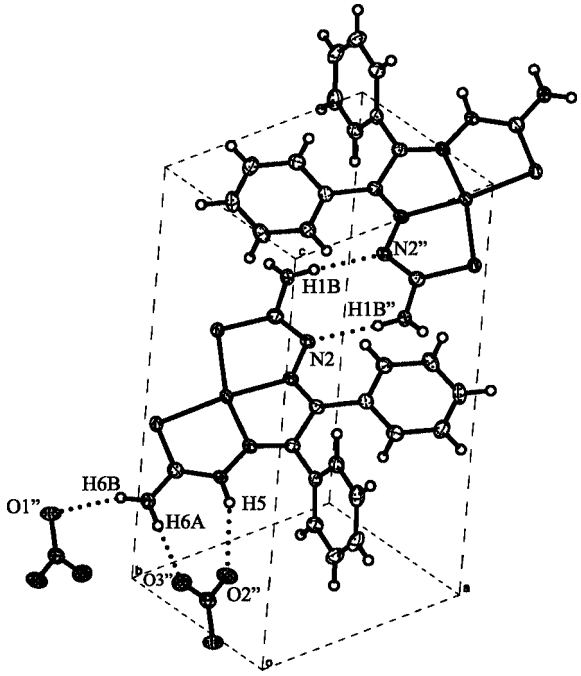

Figure 5. Plot of complex $[CuLH_5]NO_3$ (**2**) showing the hydrogen bonds.

the crystal structure of the complex (Figure 6 with the thermal ellipsoids shown at 50% probability. See also Tables 1 and 2). The benzil bis(thiosemicarbazone) acts as a monodeprotonated N_2S_2 ligand in a pseudo-planar disposition. The coordination sphere of the zinc atom is completed by an oxygen atom provided by the nitrate group to give a distorted square-based pyramidal geometry for the metal ion, as proposed from the spectroscopic data.[28] The value of the parameter, τ, defined by Addison et al.,[30] is 0.08 (τ = 0.0 for a regular square-based pyramid). The zinc atom is displaced by 0.439 Å out of the basal plane toward the oxygen atom at the apex of the pyramid. The phenyl rings C(5)–C(10) and C(11)–C(16) form dihedral angles of 63.6° and 57.0°, respectively, with respect to the basal plane. The molecules are bonded through hydrogen bonds between the amine and the nitrate groups (Figure 7, Table 3).

Discussion

The overall impression from the bonds and angles around the copper atoms (Tables 1 and 2) is that the ligand cavity is too small to accommodate the copper(II) ideally. The N–Cu–N bond angles are only 81.06° and 79.87° and the sulfur ends of the ligand arms are pushed outward well beyond the natural position that would be adopted by the planar ligand with 120° bond angles. For comparison, the Ni^{II} complex with the same ligand shows a much better fit[27] as a result of the smaller ionic radius of nickel, with Ni–N and Ni–S distances of 1.86 and 2.157 Å, respectively, compared to 1.976 Å (N) and 2.235 Å (S) and 1.987 Å (N) and 2.24 Å (S) for complexes **1** and **2**, respectively. All the angles at the nickel centre are significantly closer to the 90° preferred at the square-planar metal centre. Thus, the average N–Cu–N angle in our complexes is 80.45°, whereas for the nickel complex it is 83.32°. Similarly, the S–M–S angles are 108.7° for copper but only 101.68° for nickel, while the N–M–S angles are 85.21° for the copper complexes and 87.62° for the nickel complex.

Although the ligand appears somewhat strained in the copper complexes, it has been shown that the ligand can open up even further to accommodate Cd^{II} in its neutral form, while still maintaining an essentially planar structure.[28] As a result of the larger ionic radius of the zinc (giving two Zn–N distances of 2.1407 and 2.1290 Å and two Zn–S distances of 2.3143 and 2.3695 Å), all the angles are significantly far from 90°. Thus, the N–Zn–N angle is 73.46°, the S–Zn–S angle is 115.57° and the N–Zn–S angles are 81.93° and 81.37°. For comparison with the copper and nickel complexes, these data agree with the variation in the ionic radius for these ions even though the grade of deprotonation of the benzil bis(thiosemicarbazone) changes.

The backbone C(2)–C(3) distances in the complexes, except for the nickel complex, are larger than in the free ligand, ranging from 1.475 to 1.491 Å, in accordance with the metal ratio variations. The C(2)–N(3) distances range from 1.285 to 1.308 Å, and are consistent with a bond order greater than 1.5 but less than 2. The C(3)–N(4) bonds in

 © 2005 Wiley-VCH Verlag GmbH & Co. KGaA, Weinheim

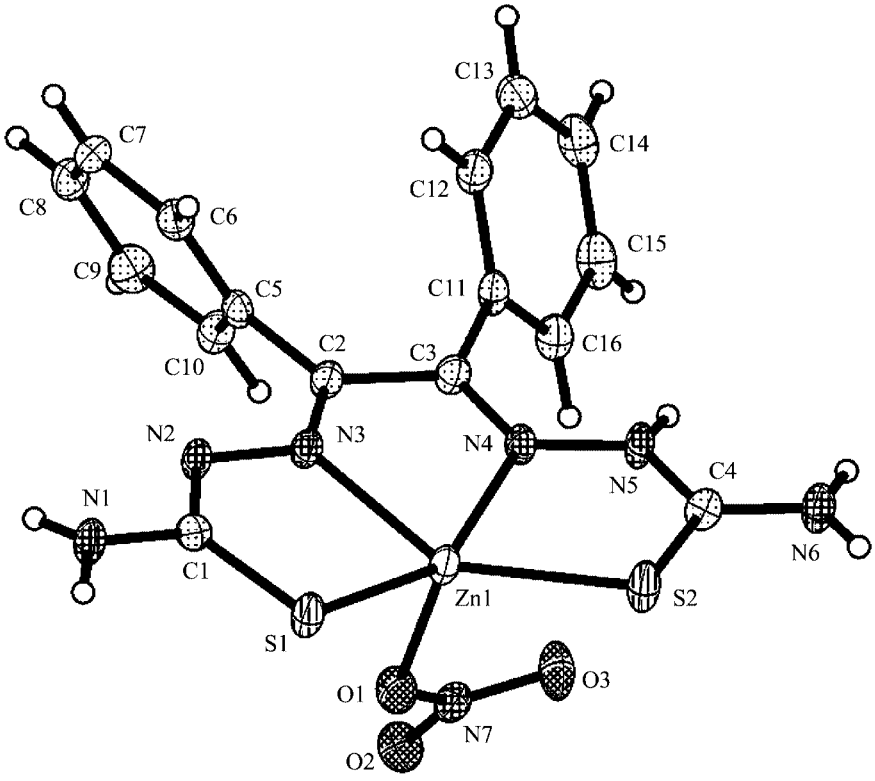

Figure 6. XSHELL view of $[ZnLH_5NO_3]$ (**3**).

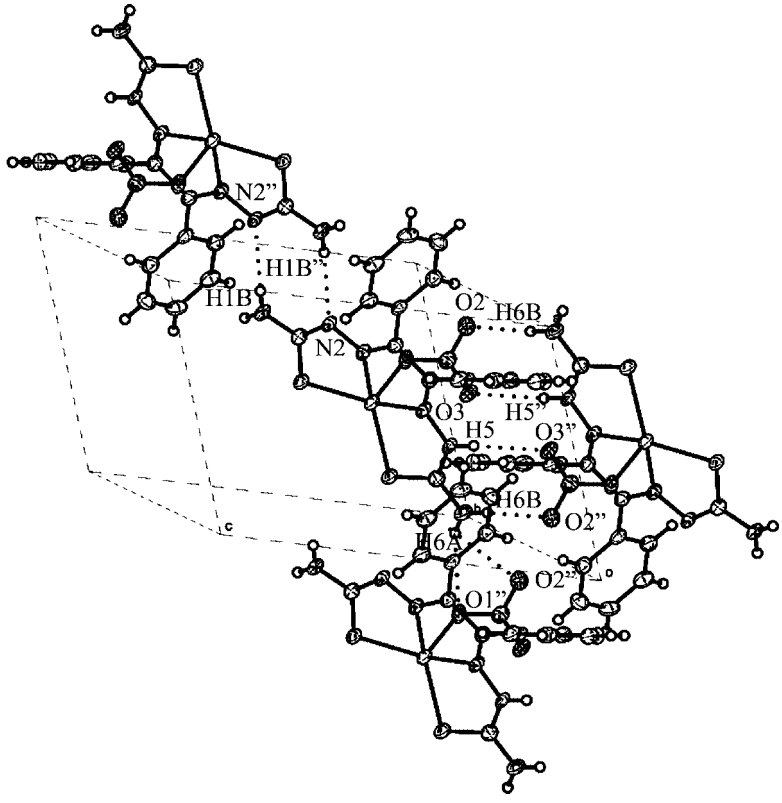

Figure 7. Plot of complex $[ZnLH_5NO_3]$ (**3**) showing the hydrogen bonds.

 © 2005 Wiley-VCH Verlag GmbH & Co. KGaA, Weinheim

the non-deprotonated thiosemicarbazone branch are closer to a full double bond than in the deprotonated one. The N(2)–N(3) distances, which range from 1.351 to 1.371 Å, are consistent with a bond order less than 1.5 but greater than 1. The N(2)–C(1) distances are larger than the C(2)–N(3) distances, but are still greater than 1, and the N(5)–C(4) distances are larger than before, but shorter than in the free ligand. The C(1)–S(1) distances in the deprotonated thiosemicarbazone branch are much larger than in the non-deprotonated one [C(4)–S(2)] and are consistent with a bond order close to 1. The largest difference (0.084 Å) appears between the free ligand (1.667 Å) and complex **2** (1.751 Å). The C(1)–N(1) distances range from 1.328 to 1.338 Å and the C(4)–N(6) distances from 1.314 to 1.319 Å; they are intermediate between the C–N and N–CS distances. These data confirm there is extensive conjugation within the ligand that is greater in the deprotonated thiosemicarbazone branch.

The study of the electrochemical behaviour of the copper complexes was carried out in the range from +1 to –1.5 V.[26] In the positive range (+1 to 0 V), a quasi-reversible Cu^{III}/Cu^{II} oxidation process can be observed. Cyclic scanning between 0 and –1.5 V permits the study of the copper-centred reduction processes and the ligand reductions; the values of the potential for the Cu^{II}/Cu^{I} reduction processes are related to the biological activity. The cyclic voltammogram of complex **1** in the latter range shows a peak at –0.520 V in the cathodic scan, which can be attributed to the Cu^{II}/Cu^{I} reduction. Under the same conditions, the cyclic voltammogram of complex **2** shows waves at –0.600 V and –0.500 V associated with a quasi-reversible Cu^{II}/Cu^{I} process.

It appears that a relationship exists between the backbone C(2)–C(3) bond length and the categorisation according to reduction potential, and, in turn, with the biological behaviour, although any relationship between these structural parameters and biological function remains speculative. Thus, complex **1**, with a longer C(2)–C(3) bond than complex **2**, has a lower reduction potential (harder to reduce). As was mentioned in the introduction, the hypoxia selectivity (HSI) is related to the electrochemical behaviour, and those complexes with an HIS greater than 0.4 have a low redox reduction potential (<0.58 V).[14] Therefore, some hypoxic selectivity of complex **1**, which has a reduction potential of –0.550 V vs. Ag/AgCl, could be expected.

The ease of deformation away from planarity could be connected to the redox potential and other aspects of the redox behaviour because distorting ions towards tetrahedral favours the copper reduction and decreases the stability of the copper(II) complex. Complex **2** shows a slightly larger distance to the plane formed by the ligand than complex **1**, which agrees with the values of the reduction potential.[26] The grade of the deviation from planarity can be determined from the least-squares displacement of the ligand atoms from the mean plane of the complex. Figure 8 shows the displacement of the ligand atoms from the least-squares plane for the complexes. Both copper and nickel complexes are closer to planarity than the zinc complex. Complexes **1** and **4**, which show the same behaviour of the ligand, show a similar pattern, although in the nickel complex both sulfur atoms show identical deviation with respect to the least-squares plane, which agrees with the minimum degree of deviation from planarity in this complex, probably due to the better fit of the nickel atom. Moreover, the deviation from planarity of complexes **2** and **3** shows the same pattern, namely two distances for the sulfur and the imine nitrogen atoms, which agrees with the asymmetry in the ligand and the tetragonal deformation in the metal environment. Additional information can be gained from the torsion angles: the value of the N(3)–C(2)–C(3)–N(4) torsion angle is less than 2° for the complexes, except for the zinc complex, where it is 4.1°.

The presence of terminal nitrogen atoms gives rise to intermolecular N–H–N hydrogen bonds, which lead to extended architectures in all complexes. The intermolecular contact distances are listed in Table 3. Complex **1** shows intermolecular interactions between the terminal amine group and the deprotonated secondary amine, as was shown in complex **4**, although N–H–S hydrogen bonds do

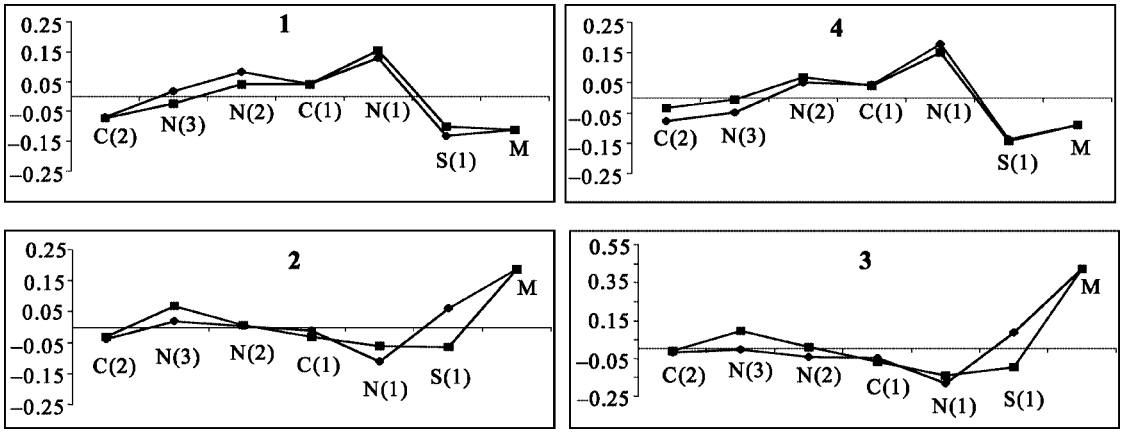

Figure 8. Displacement of atoms [Å] from least-squares plane defined by C(1), C(2), C(3), C(4), N(1), N(2), N(3), N(4), N(5), N(6), S(1), S(2) and M.

 © 2005 Wiley-VCH Verlag GmbH & Co. KGaA, Weinheim

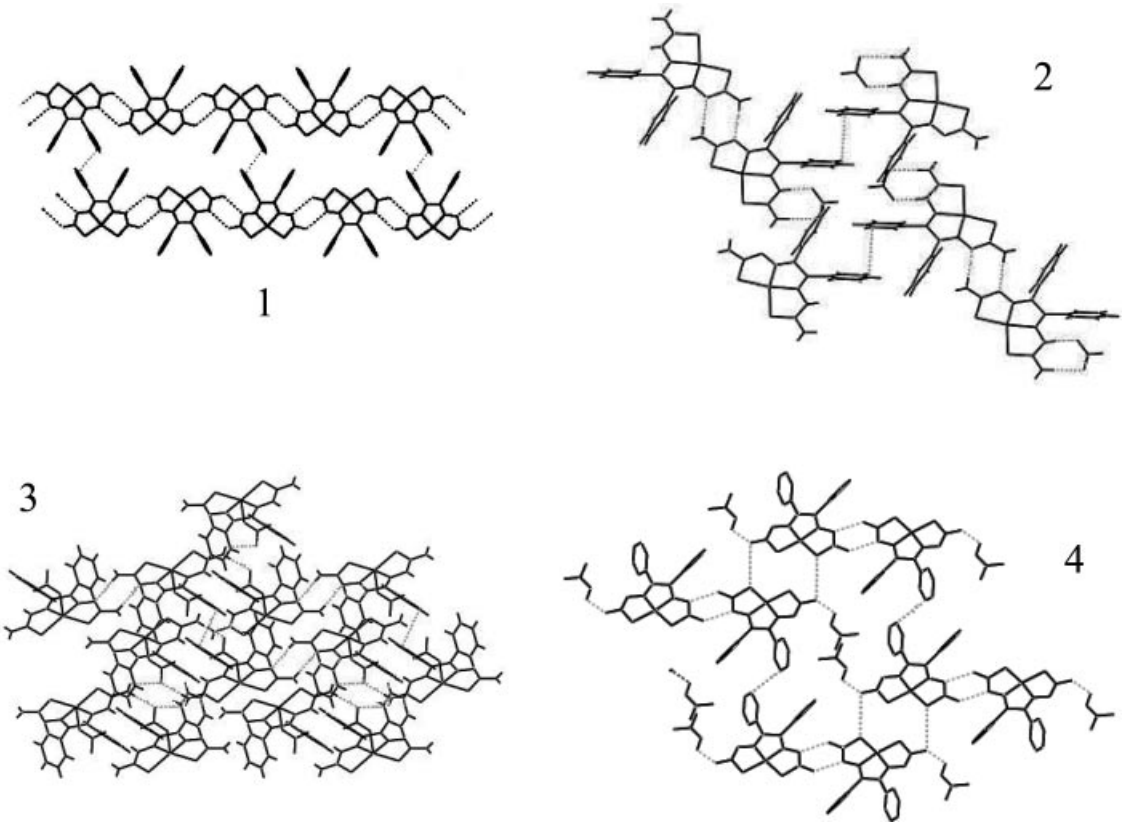

Figure 9. N–H–N hydrogen bonds and π–π interactions in the complexes.

not appear in the free ligand or in complex **4**.[27] Complex **1** is formed by flat ribbons that are linked through π–π interactions between the phenyl rings, which are at 3.644 Å (Figure 9). In complexes **2** and **3**, the molecules are linked to form couples by paired N(1)–H(1B)–N(2) hydrogen bonds, and these couples are linked by π–π interactions between the phenyl rings at 3.459 and 3.401 Å, respectively. They also contain hydrogen bonds to the nitrate ions, although in a different way: Complex **2** contains interactions between two oxygen atoms and both primary and secondary amine groups from the neutral thiosemicarbazone branch, whereas in complex **3** the nitrate group interacts also with NH and NH_2 groups, but belonging to two different chains, instead of to the same thiosemicarbazone arm (Figure 9). Complex **4** shows an intermolecular structure similar to those of complex **2**, but with hydrogen bonds with the DMF molecule. Couples are linked by π–π interactions with a distance of 3.376 Å.

Conclusions

The copper complexes are inherently planar and the zinc complex shows a distorted square-based pyramidal geometry with the nitrate group in the apical position, as proposed from the spectroscopic data. The bond length and angles for the complexes agree with the variable grade of deprotonation in the ligand and the requirements of the metal ion. The complexes present a variable grade of distortion from planarity although they all present intermolecular interactions, especially pairs of N(1)–H(1B)–N(2) hydrogen bonds and π–π interactions between the phenyl rings. Complex **1** shows the smallest deviation with respect to the planar nickel complex **4**. The presence of a hydrazinic hydrogen and a nitrate group in complexes **2** and **3** changes the intermolecular interactions, which increases the deviation from planarity, as reflected in the reduction potential of complex **2**. We have established the relationship between the distorted geometry and the reduction potential of copper complexes. In complex **1**, this parameter is close to those of copper bis(thiosemicarbazones) with hypoxic selectivity, therefore some activity could be expected.

Experimental Section

Physical Measurements: Microanalyses were carried out with a Perkin–Elmer 2400 II CHNS/O Elemental Analyser. IR spectra in the 4000–400 cm^{-1} range were recorded as KBr pellets on a Jasco FT/IR-410 spectrophotometer. FAB mass spectra were recorded on a VG Auto Spec instrument using Cs as the fast atom and *m*-nitrobenzyl alcohol (*m*-NBA) as the matrix. Conductivity data were measured for freshly prepared DMF solutions (ca. 10^{-3} M) at 25 °C with a Metrohm Herisau model E-518 instrument.

Synthesis: Thiosemicarbazide (Fluka), benzil (Aldrich), copper(II) nitrate trihydrate (Merck), copper(II) chloride dihydrate (Aldrich) and zinc(II) nitrate hexahydrate (Fluka) were used as received.

Benzil Bis(thiosemicarbazone) (LH_6): This compound was prepared following the procedure reported previously.[37] FAB-MS (*m*-NBA):

 © 2005 Wiley-VCH Verlag GmbH & Co. KGaA, Weinheim

m/z (%) = 357 (25) $[M + 1]^+$. IR (KBr): $\tilde{\nu}$ = 3420, 3386, 3342, 3330, 3210, 3151 (NH); 1608 (NH_2); 1581 (C=N); 848 (CS) cm^{-1}.

[$CuLH_4$] (1):[26] A solution of copper(II) chloride dihydrate (120 mg, 0.70 mmol) in methanol (20 mL) was added to a suspension of LH_6 (500 mg, 1.40 mmol) in methanol (20 mL). The mixture was stirred for 48 h at room temperature. The reddish solid formed was filtered off, washed with methanol and dried in vacuo (yield: 65 mg, 22%). FAB-MS (*m*-NBA): *m/z* (%) = 418 (30) $[M + 1]^+$. IR (KBr): $\tilde{\nu}$ = 3343, 3271, 3102 (NH) + (NH_2); 1626, 1600, 1569 (C=N) + (NH_2); 1467, 1427 thioamide II; 836 thioamide IV; 449 (Cu–N); 428 (Cu–S) cm^{-1}. Recrystallisation from DMSO gave reddish crystals suitable for X-ray analysis.

[$CuLH_5$]NO_3 (2): A solution of copper(II) nitrate trihydrate (360 mg, 1.49 mmol) in methanol (20 mL) was added to a suspension of LH_6 (500 mg, 1.40 mmol) in methanol (20 mL). The mixture was stirred for 19 h at room temperature. The brown solid formed was filtered off, washed with methanol and dried in vacuo.[26] A black solid (**2**) was isolated from the mother liquor. $C_{16}H_{15}CuN_7S_2O_3$ (480.55): calcd. C 39.95, H 3.12, N 20.39, S 13.31; found C 39.63, H 2.98, N 20.77, S 13.02. FAB-MS (*m*-NBA): *m/z* (%) = 418 (50) $[M - NO_3]^+$. IR (KBr): $\tilde{\nu}$ = 3443, 3408, 3274, 3097 (NH) + (NH_2); 1663, 1628, 1604 (C=N) + (NH_2); 1554, 1534, 1490, 1444 thioamide II; 778 thioamide IV; 475 (Cu–N); 428 (Cu–S) cm^{-1}. Λ_M = 86 $\Omega^{-1}cm^2mol^{-1}$. Black crystals suitable for X-ray analysis were obtained from the mother liquor after a week in the freezer.

[$ZnLH_5NO_3$] (3):[28] A solution of zinc(II) nitrate hexahydrate (520 mg, 1.75 mmol) in ethanol (10 mL) was added to a suspension of LH_6 (500 mg, 1.40 mmol) in ethanol (40 mL). The mixture was stirred under reflux for 4 h. The yellow-orange solid was filtered off, washed with ethanol and dried in vacuo (yield: 305 mg, 45%). FAB-MS (*m*-NBA): *m/z* (%) = 419 (100) $[M - NO_3]^+$. IR (KBr): $\tilde{\nu}$ = 3440, 3268, 3111 (NH); 3421, 3169 $\nu(NH_2)$; 1629, 1576 (C=N); 1615 (NH_2); 1439 thioamide II; 816 thioamide IV; 447 (Zn–N); 341 (Zn–S) cm^{-1}. Λ_M = 51 $\Omega^{-1}cm^2mol^{-1}$. Yellow crystals suitable for X-ray analysis were obtained by recrystallisation from methanol.

[$NiLH_4$] (4): This compound was prepared following the procedure previously described.[27]

Crystallography: Single crystals of complexes **1** and **3** were obtained by recrystallisation from DMSO and methanol, respectively, and crystals of **2** were isolated from the mother liquor of the reaction. Crystals of the compounds were mounted on a glass fibre and transferred to a Bruker SMART 6 K CCD area-detector three-circle diffractometer with a MAC Science Co., Ltd. Rotating Anode generator (Cu-K_α radiation, λ = 1.54178 Å) equipped with Goebel mirrors at settings of 50 kV and 110 mA. X-ray data were collected with a combination of six runs at different φ and 2θ angles for 3600 frames. The substantial redundancy in data allows empirical absorption corrections (SADABS)[32] to be applied using multiple measurements of symmetry-equivalent reflections (ratio of minimum to maximum apparent transmission: 0.578995 for complex **1**, 0.514195 for complex **2** and 0.722376 for complex **3**). The unit cell parameters were obtained by full-matrix least-squares refinements of 4562 reflections for complex **1**, 4593 reflections for complex **2** and 4356 reflections for complex **3**. Crystallographic details are reported in Table 4. The raw intensity data frames were integrated with the SAINT[33] program, which was also used to apply corrections for Lorentz and polarisation effects.

The software package SHELXTL[34] version 6.10 was used for space group determination, structure solution and refinement. The structures were solved by direct methods (SHELXS-97),[35] completed with difference Fourier syntheses, and refined with full-matrix least-squares using SHELXL-97[36] by minimizing $\omega(F_o^2 - F_c^2)^2$. Weighted *R* factors (R_w) and all goodness-of-fit (*S*) values are based on F^2; conventional *R* factors (*R*) are based on *F*. All non-hydrogen atoms were refined with anisotropic displacement parameters. All scattering factors and anomalous dispersions factors are contained in the SHELXTL 6.10 program library. The high quality of the data set allowed all hydrogen atoms to be located by difference maps and refined isotropically in all complexes.
CCDC-258838 (for **1**), -258839 (for **2**) and -258840 (for **3**) contain the supplementary crystallographic data for this paper. These data

Table 4. Crystal data and structure refinement for complexes **1**, **2** and **3**.

	1	**2**	**3**
Formula	$C_{16}H_{14}CuN_6S_2$	$C_{16}H_{15}CuN_7O_3S_2$	$C_{16}H_{15}N_7O_3S_2Zn$
Formula mass	417.99	481.01	482.84
Temperature [K]	296	100	293
Crystal system	triclinic	triclinic	triclinic
Space group	$P\bar{1}$	$P\bar{1}$	$P\bar{1}$
a [Å]	8.9504(10)	7.9999(10)	7.9889(10)
b [Å]	9.5991(10)	10.6314(10)	10.7110(13)
c [Å]	10.8885(10)	12.3778(2)	12.4027(17)
α [°]	99.456(10)	86.162(10)	85.859(8)
β [°]	106.114(10)	77.177(10)	75.065(9)
γ [°]	92.456(10)	68.452(10)	68.518(8)
Volume [Å^3]	882.66(16)	954.69(2)	953.9(2)
Z	2	2	2
Density (calcd.) [Mg m^{-3}]	1.573	1.673	1.681
Absorption coefficient	4.055 mm^{-1}	3.976 mm^{-1}	4.152 mm^{-1}
F(000)	426	490	492
Goodness of fit on F^2	1.076	1.038	1.029
Reflection collected	7179	7352	7141
Independent reflections	2613	3277	3261
Final *R* indices	R_1 = 0.0345	R_1 = 0.0294	R_1 = 0.0339
[$I > 2\sigma(I)$]	wR_2 = 0.0967	wR_2 = 0.0797	wR_2 = 0.0899
R indices (all data)	R_1 = 0.0385, wR_2 = 0.0999	R_1 = 0.312, wR_2 = 0.0809	R_1 = 0.0369, wR_2 = 0.0926

 © 2005 Wiley-VCH Verlag GmbH & Co. KGaA, Weinheim

can be obtained free of charge from The Cambridge Crystallographic Data Centre via www.ccdc.cam.ac.uk/data_request/cif.

Acknowledgments

We thank the DGICYT for financial support (project BQU2001-0151).

[1] D. X. West, S. B. Padhye, P. B. Sonawane, *Struct. Bond. (Berlin)* **1991**, *76*, 1–50.
[2] A. E. Liberta, D. X. West, *Biometals* **1992**, *5*, 121–126.
[3] *International Encyclopaedia of Pharmacology and Therapeutics* (Eds.: J. G. Cory, A. H. Cory), Pergamon Press, New York, **1989**.
[4] J. Easmon, G. Purstinger, G. Heinish, T. Roth, H. H. Fiebig, W. Holzer, W. Jager, M. Jenny, J. Hofman, *J. Med. Chem.* **2001**, *44*, 2164–2171.
[5] D. H. Petering, *Bioinorg. Chem.* **1972**, *1*, 255–271.
[6] D. X. West, A. E. Liberta, S. B. Padhye, R. C. Chikate, P. B. Sonawane, A. S. Kumbhar, R. G. Yeranda, *Coord. Chem. Rev.* **1993**, *123*, 49–71 and references cited therein.
[7] C. M. Liu, G. Xiong, X. Z. You, Y. J. Liu, *Polyhedron* **1996**, *15*, 4565–4571.
[8] P. J. Blower, T. C. Castle, A. R. Cowley, J. R. Dilworth, P. S. Donnelly, E. Labisbal, F. E. Sowrey, S. J. Teat, M. J. Went, *Dalton Trans.* **2003**, 4416–4425.
[9] Y. Fujibayashi, H. Taniuchi, Y. Yonekura, H. Ohtani, J. Konishi, A. Yokoyama, *J. Nucl. Med.* **1997**, *38*, 1155–1160.
[10] H. Okazawa, Y. Yonekura, Y. Fujibayashi, S. Nishizawa, Y. Magata, K. Ishizu, F. Tanaka, T. Tsuchida, N. Tamaki, J. Konishi, *J. Nucl. Med.* **1994**, *35*, 1910–1915.
[11] J. S. Lewis, J. M. Connett, J. R. Garbow, T. L. Buettner, Y. Fujibayashi, J. W. Fleshman, M. J. Welch, *Cancer Res.* **2002**, *62*, 442–449.
[12] A. Obata, S. Kasamatsu, J. S. Lewis, T. Furucawa, S. Takamatsu, J. Toyohara, T. Asai, M. J. Welch, S. G. Adams, H. Saji, Y. Yonekura, Y. Fujibayashi, *Nucl. Med. Biol.* **2005**, *32*, 21–28.
[13] J. L. J. Dearling, J. S. Lewis, D. W. McCarthy, M. J. Welch, P. J. Blower, *Chem. Commun.* **1998**, 2531–2532.
[14] J. L. J. Dearling, J. S. Lewis, G. D. Mullen, M. J. Welch, P. J. Blower, *J. Biol. Inorg. Chem.* **2002**, *7*, 249–259.
[15] A. R. Cowley, J. R. Dilworth, P. S. Donnelly, E. Labisbal, A. Sousa, *J. Am. Chem. Soc.* **2002**, *124*, 5270–5271.
[16] G. J. Mathias, M. J. Welch, D. J. Perry, A. H. McGuire, X. Zhu, J. M. Connett, M. A. Green, *Nucl. Med. Biol.* **1991**, *18*, 807–811.
[17] P. Herrero, J. J. Hartman, M. A. Green, C. J. Anderson, M. J. Welch, J. Markham, S. R. Bergmann, *J. Nucl. Med.* **1996**, *37*, 1294–1300.
[18] E. K. John, M. A. Green, *J. Med. Chem.* **1990**, *33*, 1764–1770.
[19] M. A. Green, *Transition Met. Chem.* **1997**, *22*, 427–429.
[20] L. J. Ackerman, P. E. Fanwick, M. A. Green, E. John, W. E. Running, J. K. Swearingen, J. W. Webb, D. X. West, *Polyhedron* **1999**, *18*, 2759–2767.
[21] J. L. J. Dearling, J. S. Lewis, G. D. Mullen, M. T. Rae, J. Zweit, P. J. Blower, *Eur. J. Nucl. Med.* **1998**, *25*, 788–792.
[22] C. J. Anderson, M. J. Welch, *Chem. Rev.* **1999**, *99*, 2219–2234.
[23] R. I. Maurer, J. P. Blower, J. R. Dilworth, C. D. Reynolds, Y. Zheng, G. D. Mullen, *J. Med. Chem.* **2002**, *45*, 1420–1431.
[24] H. Beraldo, D. Gambino, *Mini-Rev. Med. Chem.* **2004**, *4*, 31–39.
[25] A. R. Cowley, J. Davis, J. R. Dilworth, P. S. Donnelly, R. Dobson, A. Nightingale, J. M. Peach, D. Kerr, L. Seymur, *Chem. Commun.* **2005**, 845–847.
[26] E. Franco, E. López-Torres, M. A. Mendiola, M. T. Sevilla, *Polyhedron* **2000**, *19*, 441–451.
[27] E. López-Torres, M. A. Mendiola, C. J. Pastor, B. Souto Pérez, *Inorg. Chem.* **2004**, *43*, 5222–5230.
[28] E. López-Torres, M. A. Mendiola, J. Rodríguez-Procopio, M. T. Sevilla, E. Colacio, J. M. Moreno, I. Sobrados, *Inorg. Chim. Acta* **2001**, *323*, 130–138.
[29] a) G. W. Bushnell, A. Y. M. Tsang, *Can. J. Chem.* **1979**, *57*, 603–607; b) Y. Xinkan, W. Honggen, W. Ruji, H. Ling, W. Genglin, *Gaodeng Xuexiao Huaxue Xuebao* **1988**, *9*, 484–487.
[30] A. W. Addison, T. N. Rao, J. Reedijk, J. van Rijnand, G. C. Verschoor, *J. Chem. Soc., Dalton Trans.* **1984**, 1349–1356.
[31] H. Yokoi, A. W. Addison, *Inorg. Chem.* **1977**, *16*, 1341–1349.
[32] G. M. Sheldrick, SADABS version 2.03, *Program for Empirical Absorption Correction*, University of Göttingen, **1997**–**2001**.
[33] G. M. Sheldrick, *SAINT+NT* (version 6.04) *SAX Area-Detector Integration Program*, Bruker AXS, Madison, WI, **1997**–**2001**.
[34] Bruker AXS SHELXTL (version 6.10,) Structure Determination Package, Bruker AXS, Madison, WI, **2000**.
[35] SHELXS-97, *Program for Structure Solution*: G. M. Sheldrick, *Acta Crystallogr., Sect. A* **1990**, *46*, 467–473.
[36] G. M. Sheldrick, SHELXL-97, *Program for Crystal Structure Refinement*, University of Göttingen, **1997**.
[37] P. Souza, M. A. Mendiola, A. Arquero, V. Fernández, E. Gutiérrez-Puebla, C. Ruíz-Valero, *Z. Naturforsch. Teil B* **1994**, *49*, 263–271.

Received: April 25, 2005
Published Online: September 19, 2005

 © 2005 Wiley-VCH Verlag GmbH & Co. KGaA, Weinheim

Influence of Na Content on the Chemical Stability of Nanometric Layered Na_xRhO_2 ($0.7 \leq x \leq 1.0$)

Aúrea Varela,[a] Marina Parras,[a] and José M. González-Calbet*[a]

Keywords: Na_xRhO_2 nanoparticles / Layered oxides / High resolution electron microscopy

A new Na_xRhO_2 solid solution composed of nanometric particles of the α-$NaFeO_2$ structural type has been stabilised in the $0.7 \leq x \leq 1$ range. Its rhombohedral structure is built from close packed layers of edge-sharing [RhO_6] octahedra separated by intercalant layers consisting of octahedrally coordinated Na. Electron microscopy shows that compositional variations are indeed accommodated by means of stacking faults leading to a local change in the Na oxygen environment. Samples are air-sensitive, and the aged materials partially decompose, segregating sodium carbonate.
(© Wiley-VCH Verlag GmbH & Co. KGaA, 69451 Weinheim, Germany, 2005)

Introduction

AMO_2 layered oxides (A: alkaline, M: transition metal) have been widely studied because of their interesting physical properties.[1–5] Among them, Na_xCoO_2 has attracted particular interest due to the large thermoelectric power of the metallic conductor $NaCo_2O_4$[6–7] and the recent discovery of superconductivity near 4 K in hydrated $Na_{0.3}CoO_2{\cdot}1.3H_2O$.[8,9]

The structures of various Na_xCoO_2 phases have been reported. All of them are based on the stacking of CoO_2 layers, consisting of edge-sharing CoO_6 octahedra. The Na atoms form layers between the CoO_2 layers. $NaCoO_2$ (x = 1) crystallises in the α-$NaFeO_2$ structure.[10] This rock-salt type structure is built from a cubic stacking of oxygen layers (*ABCABC*) with Co and Na occupying the octahedral sites of alternating layers.[11] A decrease in the Na content changes the Na coordination from octahedral to trigonal prism, leading to the stabilisation of different structures.[10] Moreover, a recent electron diffraction study of various Na_xCoO_2 ($0.15 < x < 0.75$) compositions has shown the existence of several ordered distributions of the Na vacancies that lead to a wide range of superstructures of the basic hexagonal cell depending on the x value.[12]

The discovery of superconductivity in the cobalt oxyhydrate $Na_{0.3}CoO_2{\cdot}1.3H_2O$[8,9] spread the interest in this system. From a structural point of view, the oxyhydrate phases are formed by CoO_2 layers stacked together with one layer of Na^+ ions and two layers of water molecules. The insulating layers, which alternate with the CoO_2 layers, play the dual role of spacing provider and redox controller. In addition to this superconducting phase, a series of hydrated phases have been stabilised for the same Na/Co ratio, the H_2O content ranging from $Na_{0.3}CoO_2{\cdot}1.4H_2O$ to $Na_{0.3}CoO_2$.[13] In this work, Foo et al. studied the influence of Na and H_2O contents on the structural and physical properties of these compounds.

Much less attention has been devoted to 4d or 5d metal oxides. Among them, the ruthenium oxides have probably been the most studied because they exhibit a rich variety of magnetic and electrical properties.[14,15] Recently the structural characterisation of the new layered oxide $NaRuO_2$ and and oxyhydrate $Na_{0.22}RuO_2{\cdot}0.45H_2O$ have been reported but no superconducting behaviour has been observed in the hydrated phase.[16]

Rhodium oxides have also been studied recently, and a new sodium rhodate, $NaRh_2O_4$, has been stabilised under high pressure.[17] This compound crystallises in the $CaFe_2O_4$ structure, which is a 3-D structure comprising a network of edge-sharing RhO_6 octahedra. In addition to this 3-D material, layered $NaRhO_2$ has been reported by K. Hobbie et al.[18] The structural refinement carried out on a single crystal shows this compound to be isostructural to α-$NaFeO_2$. However, unlike the aforementioned Na_xCoO_2 system, where compositional variations have been extensively studied, only $NaRhO_2$ is known in the Na_xRhO_2 series. The present work is devoted to the systematic investigation of the compositional variations of the Na_xRhO_2 system and its structural and microstructural characterisation.

Results and Discussion

Chemical and Structural Characterisation

The Na:Rh cationic ratio, determined as described in the experimental section, is shown in Table 1. The Na content depends on both the time of the thermal treatment and the

[a] Departamento de Química Inorgánica, Facultad de Químicas, Universidad Complutense,
28040 Madrid, Spain
Fax: +34-91-394-43-52
E-mail: jgcalbet@quim.ucm.es

container used. Our results indicate that Na loss is favoured by long thermal times and by the use of Al_2O_3 crucibles.

Table 1. Preparation conditions of the Na_xRhO_2 samples.

Label	Crucible	Annealing time [h]	Chemical composition[a]
PT-24	Pt	24	$NaRhO_2$
PT-48	Pt	48	$Na_{0.85}RhO_2$
AL-24	Al_2O_3	24	$Na_{0.7}RhO_2$
AL-48	Al_2O_3	48	phase mixture[b]

[a] The estimated error in cationic composition is around 2%. [b] Hydrated and non-hydrated $NaRhO_2$ phases.

Na_xRhO_2 ($1 \geq x \geq 0.7$) samples were characterised by means of XRD. The pattern corresponding to $NaRhO_2$ (PT-24) is shown in Figure 1a. All maxima can be indexed on the basis of a rhombohedral unit cell (R-3m) of parameters a = 3.0903(1) and c = 15.5400(6) Å. The pattern has been refined by the Rietveld method by taking as the starting model the structural data of the isostructural α-$NaFeO_2$. The graphic result of this refinement can be seen in Figure 1a. Table 2 lists the refined structural parameters and selected interatomic distances are shown in Table 3. The crystallographic data obtained are in agreement with those previously reported for a $NaRhO_2$ single crystal.[18]

The XRD pattern corresponding to $Na_{0.85}RhO_2$ (PT-48), Figure 1b, is very similar to that of stoichiometric $NaRhO_2$. The only visible difference is that (00l) reflections are shifted toward lower 2θ values, indicating a slight increase in the c-axis length. Actually, the obtained cell parameters correspond to a = 3.0867(6), c = 15.5785(5) Å. The structure was refined in the R-3m space group, by using the $NaRhO_2$ structure model with a reduced Na content of 0.85 per unit formula, according to cationic analysis. The graphic result of this refinement is shown in Figure 1b, while Figure 2 depicts the crystal-structure view of $Na_{0.85}RhO_2$. As it can be observed, the structural features of stoichiometric $NaRhO_2$ are maintained. The rhombohedral structure is formed by close-packed layers of edge-sharing [RhO_6] octahedra perpendicular to the c-axis separated by intercalant Na layers, Na also being octahedrally

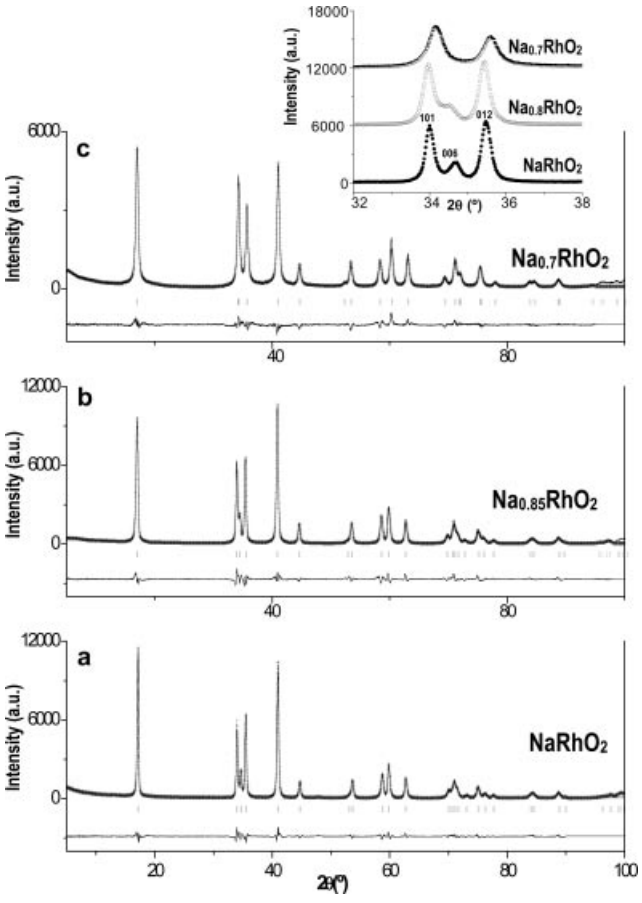

Figure 1. Experimental, calculated and difference powder XRD patterns corresponding to Na_xRhO_2 samples. (a) x = 1 (PT-24); (b) x = 0.85 (PT-48) and (c) x = 0.70 (AL-24). An enlargement of a portion of the XRD patterns is shown in the inset.

Table 2. Structural parameters of Na_xRhO_2 ($0 \leq x \leq 0.7$).

$NaRhO_2$ (PT-24)						
Atom	Site	x	y	z	Occ.	B [Å^2]
Rh	3b	0	0	0.5	1.0	0.28(1)
Na	3a	0	0	0	1.0	0.59(1)
O	6c	0	0	0.232(3)	1.0	0.31
a = 3.0903(1) Å, c = 15.5400(6) Å; R_B = 2.34, R_{exp} = 4.37, R_{wp} = 10.6, χ^2 = 5.84						
$Na_{0.85}RhO_2$ (PT-48)						
Atom	Site	x	y	z	Occ.	B [Å^2]
Rh	3b	0	0	0.5	1.0	0.11(8)
Na	3a	0	0	0	0.86(1)	0.08(2)
O	6c	0	0	0.234(2)	1.0	0.1(9)
a = 3.0867(6) Å, c = 15.5781(1) Å; R_B = 3.52, R_{exp} = 5.08, R_{wp} = 12.8, χ^2 = 6.3						
$Na_{0.7}RhO_2$ (AL-24)						
Atom	Site	x	y	z	Occ.	B [Å^2]
Rh	3b	0	0	0.5	1.0	0.17(1)
Na	3a	0	0	0	0.71(1)	0.94(2)
O	6c	0	0	0.230(3)	1.0	0.721(9)
a = 3.0750(3) Å, c = 15.766(1) Å; R_B = 6.34, R_{exp} = 4.97, R_{wp} = 10.34, χ^2 = 4.39						

 © 2005 Wiley-VCH Verlag GmbH & Co. KGaA, Weinheim

Table 3. Selected interatomic distances [Å] in Na_xRhO_2 ($0.7 \leq x \leq 1$).

	$NaRhO_2$	$Na_{0.85}RhO_2$	$Na_{0.7}RhO_2$
Rh–O	2.058(2)	2.069(2)	2.027(2)
Na–O	2.372(3)	2.358(3)	2.422(3)
Rh–Rh	3.090	3.090	3.075
Na–Na	3.090	3.090	3.075
Rh–Na	3.145	3.145	3.171

coordinated to the oxygen atoms. The refined structural parameters and some selected interatomic distances are listed in Table 2 and Table 3, respectively.

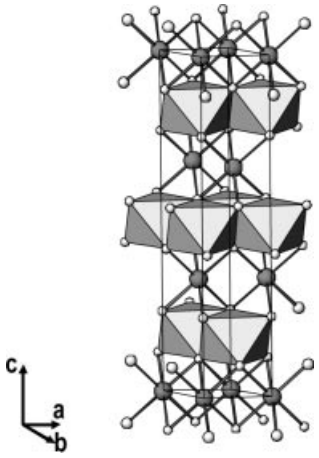

Figure 2. Crystal structure of $Na_{0.85}RhO_2$. Grey dots correspond to sodium and small dots to oxygen atoms.

It is well known that XRD is not the most powerful technique to study structural effects of light atoms such as oxygen or sodium. However, the refinement was stable, and it was possible to refine the Na fractional occupancy. The obtained value, corresponding to a Na content of 0.86 atoms per unit formula, nicely agrees with the cationic analysis. Moreover, the lack of extra maxima in the XRD patterns indicates a random distribution of the Na vacancies through the intercalant layers. The metal-oxygen distances correspond to 2.069(2) and 2.358(3) Å for Rh–O and Na–O, respectively, both comparable with their typical values.[17,18]

According to these results, the decrease in the Na concentration from $NaRhO_2$ occurs only with minor structural changes. The *c* parameter increases, indicating a slight increase in the thickness of the intercalant Na layers. Furthermore, a small shrinkage of the *a*-axis is also observed. The shrinking of the RhO_2 layers is probably due to the partial oxidation of Rh(III) to Rh(IV), which occurs in order to ensure charge neutralisation when Na ions are removed.

The above features are more pronounced in $Na_{0.7}RhO_2$ (AL-24), which also presents the structural characteristics of stoichiometric $NaRhO_2$. The corresponding structure has also been refined by the Rietveld method (Figure 1c), and the refined lattice parameters, a = 3.0750(2), c = 15.766(1) Å (see Table 2), show again the expansion of the *c*-axis as well as the contraction of the *a*-axis when Na content decreases. As a consequence, (101) and (006) reflections overlap, and only one diffraction maximum is observed (see inset of Figure 1). These structural features are also reflected in the corresponding interionic distances. Actually, as it can be seen in Table 3, the Na–Rh distance increases from 3.14 for $NaRhO_2$ to 3.17 Å for $Na_{0.7}RhO_2$. In addition, the Rh–O distance decreases from 2.058(2) to 2.0269(5) Å, because of the smaller size of Rh^{IV} ($r_{Rh^{IV}}$ = 0.60; $r_{Rh^{III}}$ = 0.65 Å in an octahedral environment[19]).

Similar behaviour has been previously observed in the Na_xCoO_2 system.[13] The *c*-axis is increased from 10.82 Å, for the stoichiometric $NaCoO_2$ (x = 0), to 11.23 Å for x = 0.3. A series of hydrated phases has recently been reported for this Na content.[8,20,21] The lower hydrate, $Na_{0.3}CoO_2{\cdot}0.6H_2O$, has a *c*-parameter of 13.8 Å that corresponds to an expansion of 1.3 Å per intercalant layer as compared to $Na_{0.3}CoO_2$. The H_2O molecules are found in the same plane as the Na atoms, unlike the model proposed for superconducting $Na_{0.3}CoO_2{\cdot}1.4H_2O$[8] in which the *c*-parameter is increased to 19.6 Å. This value corresponds to an expansion of 2.8 Å per intercalant layer, and, in this case, Na ions and H_2O molecules are not located in the same plane.

In Na_xRhO_2, the *c*-axis value increases from 15.540 for x = 1 to 15.766 Å for x = 0.7. This small expansion seems to indicate that, up to x = 0.7, the Na^+ ions lost into the intercalant layers are not replaced by H_2O molecules. However, to fully discard this possibility a thermogravimetric analysis of the above samples has been performed.

The weight change of PT-24, PT-48 and AL-24 samples, when heated at 0.2 °C/min in flowing O_2 in a thermogravimetric analyser (TGA), is presented in Figure 3. No substantial weight loss occurs over the temperature range of 30 to 300 °C. Actually, if we consider that the observed weight loss (close to 0.2%) corresponds to H_2O molecules, a content of only 0.02 water molecules per unit formula should be obtained. These results seem to indicate that down to 0.7-mol Na content, H_2O molecules are not introduced into the layer space, at least not in a significant amount.

A different result is obtained when the sample is treated at 800 °C for 48 h in alumina crucibles (AL-48). The corresponding XRD pattern is shown in Figure 4a. The main peaks of this pattern can be also indexed on the basis of the above-described rhombohedral unit cell with lattice parameters close to a = 3.09, c = 15.7 Å; however, extra maxima of very low intensity are also visible (marked in the figure with asterisks). This sample is air-sensitive, and, after 24 h in air, the intensities of the extra maxima increase (Figure 4b). This fact has also been reported for the isostructural $NaRuO_2$.[12] Actually, this compound is also air-sensitive, and, after one night in air, an oxyhydrate is formed with the stoichiometry $Na_{0.22}RuO_2{\cdot}0.45H_2O$. Therefore, the extra peaks of Figure 4 could correspond to a new $Na_xRhO_2{\cdot}yH_2O$ hydrate. In fact, all these maxima can be indexed on the basis of a rhombohedral unit cell of parameters a = 3.02, c = 20.46 Å. The high value of the *c*-axis should be a consequence of the intercalation of some H_2O molecules. Unfortunately, this oxyhydrate phase has

 © 2005 Wiley-VCH Verlag GmbH & Co. KGaA, Weinheim

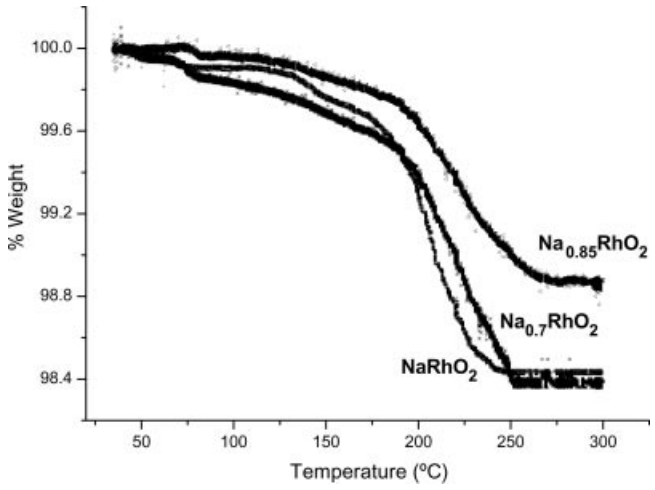

Figure 3. Thermogravimetric curves of Na_xRhO_2 samples ($1 \leq x \leq 0.7$). Experiments were carried out in O_2 for a ~100 mg specimen with a heating rate of 0.2 °C/min.

not been isolated up to now. Finally, it is worth recalling that this hydration process is highly reversible, and, after 1 hour at 800 °C in air, the non-hydrated phase is already stabilised (see Figure 4c).

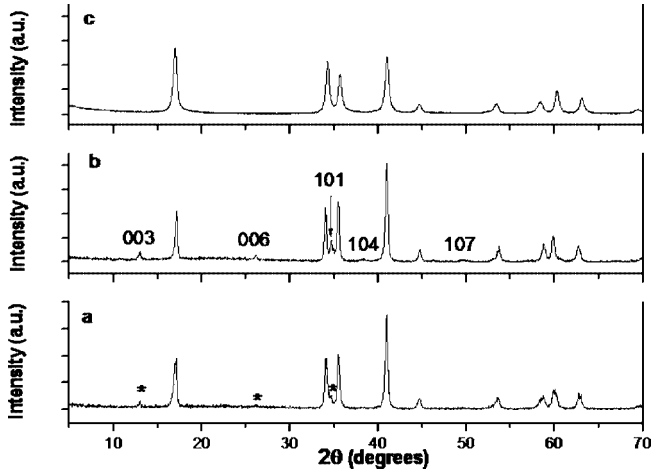

Figure 4. Experimental powder XRD patterns corresponding to (a) sample AL-48; (b) sample AL-48 after being aged 24 h in air and (c) the previous sample heated for 1 h at 800 °C in air.

As described above, the Na content of the samples varies, depending on the preparation conditions, from 1.0 to 0.7 mol per unit formula. Recently, Zandbergen et al.[12] have studied the Na_xCoO_2 system by electron diffraction. They have shown the existence of an extensive series of superstructures of the basic $NaCoO_2$ structure originating from different ordered distributions of the Na vacancies. In order to study the influence of the Na content in the microstructure of the Na–Rh–O system, a study by selected area electron diffraction (SAED) and high resolution electron microscopy (HREM) has been carried out.

Figure 5a corresponds to the SAED pattern of stoichiometric $NaRhO_2$ (PT-24) along the [010] zone axis. All the observed crystals show the same pattern. The local composition, analysed by energy-dispersive X-ray spectroscopy (EDS), nicely agrees with the experimental composition. All the spots appearing in the pattern can be indexed on the basis of the rhombohedral unit cell with parameters $a \approx 3.8$, $c \approx 15.6$ Å, which are in agreement with the XRD results. Moreover, the lack of streaking along the c^* axis is evidence of an ordered situation as confirmed by HREM. The HREM image along [010] (Figure 5b) shows a fully ordered material with interplanar distances of 2.7 and 15.6 Å, corresponding to d_{100} and d_{001}, respectively. The optical Fourier transform (inset in the figure) shows features similar to the experimental SAED pattern in Figure 5a. An enlargement of the image is depicted in Figure 5c. The observed differences can be associated to the atomic configuration shown in the structural model projection depicted in Figure 5c. The brightest dots are attributed to Rh atoms forming the ABCABC stacking sequence, which corresponds to the 3R structure. The dots of intermediate intensity correspond to the lighter Na and O atoms. The calculated image for $\Delta t = 7$ nm, $\Delta f = -60$ nm, shown in the inset, nicely fits the experimental data. All observed crystals have the same features, and no stacking faults are observed.

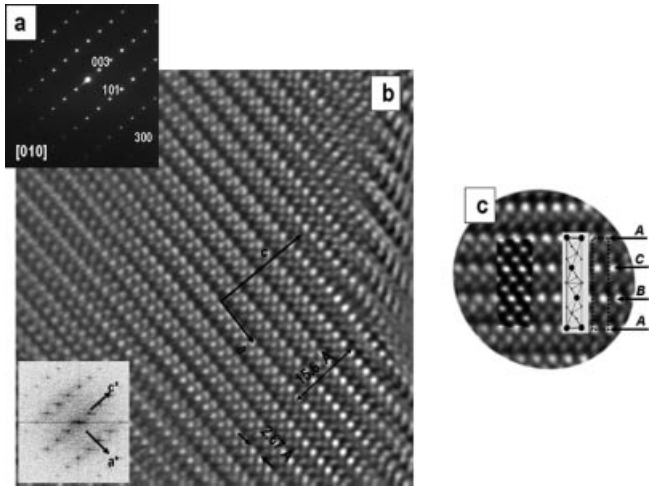

Figure 5. (a) SAED pattern corresponding to $NaRhO_2$ along [010]. (b) Corresponding HREM image. The Optical Fourier Transform and the calculated image are shown in the insets. (c) Enlargement of the above image. The unit cell shows the ...*ACB*... stacking sequence characteristic of the $NaRhO_2$ structure. The calculated image is shown in the inset. Big dots correspond to Rh, grey dots to Na and small black dots to oxygen atoms.

It is worth recalling that, under electron beam irradiation, crystals are unstable. Actually, Figure 6a and b shows the SAED pattern and the corresponding HREM, along [010], of a $NaRhO_2$ crystal after an extended period of electron beam illumination. Radical changes were observed and the microstructure was altered in such a way that some kind of disorder appeared, as evidenced by the presence of streaking along the c^*-axis (see Figure 6a). The corresponding HREM shows the presence of stacking faults along the crystal. These faults locally change the stacking of the 3R-$NaRhO_2$ phase by the incorporation of one A-layer in the ABC cubic sequence, giving rise to a local change in the

 © 2005 Wiley-VCH Verlag GmbH & Co. KGaA, Weinheim

Na sites from octahedral to trigonal prismatic. The electron damage is more important for thinner crystals. For this reason, in order to obtain images such as the ones in Figure 5, low exposure times should be used and crystals that are not too thin must be chosen.

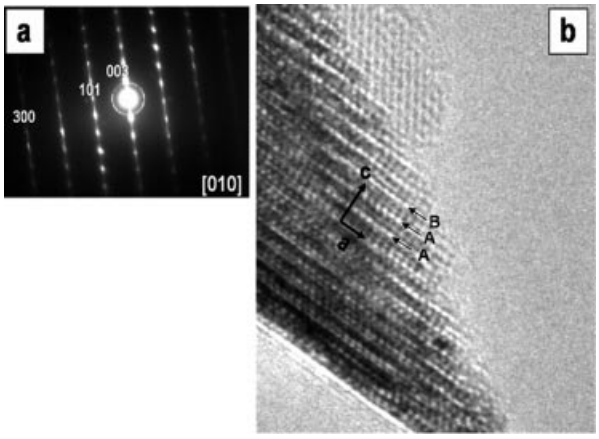

Figure 6. (a) SAED pattern corresponding to $NaRhO_2$ along [010] after electron beam irradiation. Streaking along the *c*-axis is apparent. (b) Corresponding HREM image showing stacking faults.

TEM characterisation of Na_xRhO_2 samples reveals a disordered stacking sequence apparent in the SAED pattern (Figure 7a) as diffuse streaking along the *c** axis, as well as in the corresponding image (Figure 7b) as planar defects. Note that the same disordered microstructure of Na-deficient materials is observed for stoichiometric $NaRhO_2$ under long beam time exposure. It seems that the electron beam favours the diffusion of Na out of the irradiated area, generating local Na-deficient areas with a disordered microstructure.

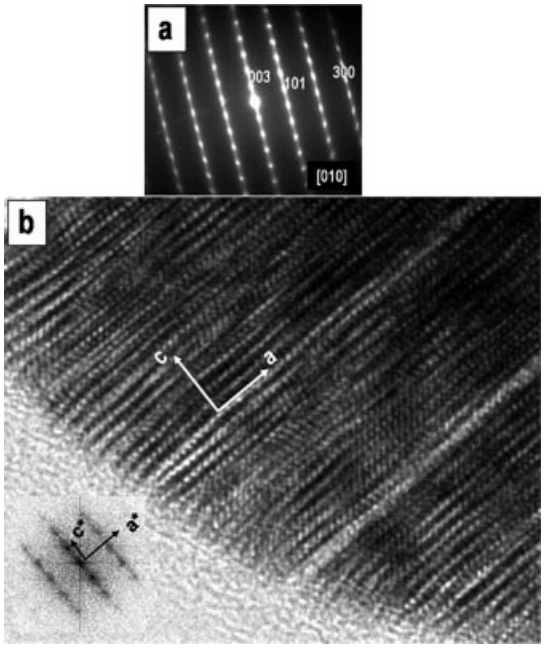

Figure 7. (a) SAED pattern corresponding to Na_xRhO_2 along [010]. (b) Corresponding HREM image.

Morphological Characterisation

In order to study the dependence of the morphology of the Na_xRhO_2 samples ($0.7 \leq x \leq 1$) on the duration of the thermal treatment and the crucibles used, a SEM characterisation was performed. Figure 8a–d shows SEM micrographs of the Na_xRhO_2 samples heated for 24 (24-PT) and 48 h (48-PT) in Pt (a, b), and for 24 (24-AL) and 48 h (48-AL) in Al_2O_3 (c,d) containers. All samples exhibit a similar platelike morphology with a quite homogeneous size distribution (100–200 nm). These small particles form agglomerates of around 1–2 μm. The powders obtained exhibit a partially sintered microstructure due to a certain degree of particle coarsening and sintering. All of the studied samples show analogous features. This fact seems to indicate that neither the thermal treatment nor the container used plays an important role in the morphology and crystallinity of the samples.

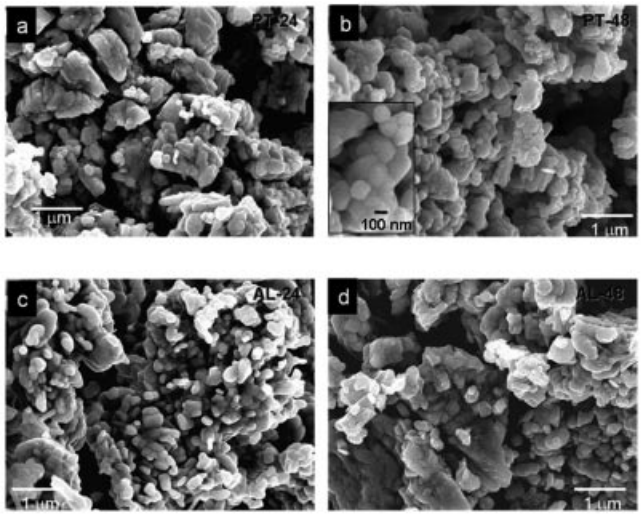

Figure 8. SEM micrographs of the Na_xRhO_2 samples heated at 800 °C, 24 and 48 h in Pt (a, b) and 24 and 48 h in Al_2O_3 (c,d) containers. Sintered microstructure of the nanoparticles can be observed in the enlargement of (b).

In addition to the morphology, SEM characterisation has evidenced an important common feature of these samples. Although the samples are carefully stored in a dry box, their morphology markedly changes with the aging time. Figure 9 corresponds to the $NaRhO_2$ sample (PT-24) 15 (a) and 30 (b) days after being prepared. It is clearly visible that, besides the platelike particles characteristic of $NaRhO_2$, needlelike particles (2–3 μm) appear to some extent. Both the amount as well as the particle size of these needles gradually increases with the aging time. In fact, these particles grow up to around 6 μm after 30 days, whereas the size of the platelike particles remains constant. The EDS analysis carried out on the needles indicates the presence of C and Na, but no Rh is detected. It follows that these particles should correspond to a minor phase of sodium carbonate segregated when the material is aged. At this stage, we have studied these samples by XRD. The XRD patterns of the aged samples are not different from a

 © 2005 Wiley-VCH Verlag GmbH & Co. KGaA, Weinheim

freshly prepared sample. Neither extra maxima nor intensity changes of the maxima are detected. This result, corroborated by electron diffraction, suggests that the segregated sodium carbonate is a noncrystalline phase. The decomposition process progresses over time and, after several months, it is visible in the XRD patterns by the appearance of broadened diffraction maxima corresponding to a hydrated and poorly crystalline sample. The other Na_xRhO_2 (x = 0.85, 0.7) samples undergo the same aging process.

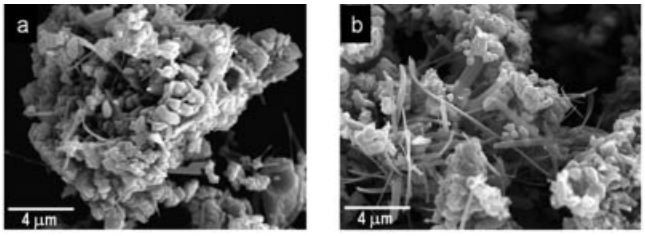

Figure 9. SEM micrographs of $NaRhO_2$ (PT-24): (a) 15 and (b) 30 days after preparation.

Concluding Remarks

On the basis of the XRD results, it can be concluded that a Na_xRhO_2 solid solution with the α-$NaFeO_2$ structure is stable in the $0.7 \leq x \leq 1$ compositional range. The relative disposition of the CoO_6 sheets is kept, and therefore no significant modifications in the Na environment are observed. In fact, in this compositional range, the main structural features of stoichiometric $NaRhO_2$ are maintained, and only a variation of the lattice parameters is observed. Finally, whereas no water is incorporated in the $0.7 \leq x \leq 1$ range, a hydrated phase appears for $x < 0.7$, which has not been isolated to date.

According to SAED and HREM results, variations in the amount of Na in Na_xRhO_2 are not totally randomly distributed throughout the crystal as indicated by XRD. In fact, the decrease in Na content gives rise to a local change in the stacking sequence of the RhO_2 sheets, leading to Na in a trigonal prism environment. However, no long-range order was attained, and no new ordered phases were stabilised in the compositional range studied. In this respect, the situation is different from the Na_xCoO_2 system,[12] where several structures have been stabilised as a function of the Na content. In this way, we would like to emphasize that, in spite of the presence of a significant Na vacancy concentration, none of the prepared samples show Na ion conductivity.

Finally, the morphological characterisation shows that all freshly prepared samples are composed of nanometric particles (100–200 nm) with the same platelike shape. In addition, all Na_xRhO_2 ($0.7 \leq x \leq 1$) samples are air-sensitive: the aging process leads to a final stage in which deliquescence takes place, and the sample decomposes, segregating sodium carbonate.

Experimental Section

Samples were prepared as polycrystalline powders by the solid state reaction of Na_2CO_3 and Rh_2O_3 in a 1:1 ratio with heating at 800 °C in flowing oxygen. It is well known that, during the synthesis process, Na can be lost because of the high volatility of Na_2O. Therefore, in order to obtain materials with various Na:Rh ratios, different annealing times as well as different crucibles were used.

The Na:Rh cationic ratio was determined on pellet samples by microprobe analysis with a JSEM-8600 scanning electron microscope working at an acceleration voltage of 10 KV. In addition, the local composition was analysed by EDS with an INCA analyser system attached to a JEOL 3000 FEG electron microscope.

To determine the precise water content of the samples, a thermal study was carried out with a high-sensitivity thermobalance (CAHN D-200) by heating in oxygen a specimen of around 80 mg up to 300 °C at a rate of 0.2 °C/min. This electrobalance allows the detection of weight variations within $\pm 5 \times 10^{-3}$ mg in a sample of about 100 mg.

Powder X-ray diffraction (XRD) patterns were collected using Cu-K_α radiation (λ = 1.5418 Å) at room temperature with a PHILIPS X′PERT diffractometer equipped with a graphite monochromator. Diffraction data were analysed by the Rietveld method,[22] using the Fullprof program.[23]

The samples were characterised by SAED and HREM with a JEOL 3000 FEG electron microscope fitted with a double-tilting goniometer stage (±22°, ±22°). Simulated HREM images were calculated by the multislice method using the MacTempas software package. The morphological study was carried out with a JSM-6330F FEG scanning electron microscope working at 10 kV.

Acknowledgments

Financial support through research projects MAT2004–01248 and MAT/0627/2004 are acknowledged

[1] J. R. Dahn, U. V. Sacken, C. A. Michel, *Solid State Ionics* **1990**, *44*, 87–97.
[2] K. Mizushima, P. C. Jones, P.-J. Wiseman, J. Goodenough, *Mater. Res. Bull.* **1980**, *15*, 783–789.
[3] M. M. Thackeray, *Prog. Solid State Chem.* **1997**, *25*, 1–71.
[4] J. M. Tarascon, M. Armand, *Nature* **2001**, *414*, 359–367.
[5] C. Delmas, *Mater. Sci. Eng.* **1989**, *B3*, 97–101.
[6] I. Terasaki, Y. Sasago, K. Uchinokura, *Phys. Rev. B* **1997**, *56*, R12685–12687.
[7] I. Terasaki, Y. Ishii, D. Tanaka, Y. Iguchi, *Jpn. J. Appl. Phys.* **2001**, *40*, L65–67.
[8] K. Takada, H. Sakurai, E. Takayama-Muromachi, F. Izumi, R. A. Dilanian, T. Sasald, *Nature* **2003**, *422*, 53–55.
[9] R. E. Schaak, T. Klimczuk, M. L. Foo, R. J. Cava, *Nature* **2003**, *424*, 527–529.
[10] C. Delmas, C. Fouassier, P. Hagenmuller, *Physica* **1980**, *B99*, 81–85.
[11] C. Fouassier, G. Matejka, J. M. Reau, P. Hagenmuller, *J. Solid State Chem.* **1973**, *6*, 532–537.
[12] H. W. Zandbergen, M. Foo, Q. Xu, V. Kumar, R. J. Cava, *Phys. Rev. B.* **2004**, *70*, 024101–024108.
[13] M. Foo, R. E. Schaak, V. L. Miller, T. Klimczuk, N. S. Rogado, Y. Wang, G. C. Lau, C. Craley, H. W. Zandbergen, N. P. Ong, R. J. Cava, *Solid State Commun.* **2003**, *127*, 33–37.
[14] Y. Maeno, H. Hashimoto, K. Yoshida, S. Nishizaki, T. Fujita, J. G. Berdnorz, F. Lichtenberg, *Nature* **1994**, *372*, 532–534.
[15] G. Cao, S. McCall, F. Freibert, M. Shepard, P. Henning, J. E. Crow, *Phys. Rev. B* **1996**, *53*, 12215–12219.

 © 2005 Wiley-VCH Verlag GmbH & Co. KGaA, Weinheim

[16] M. Shikano, C. Delmas, J. Darriet, *Inorg. Chem.* **2004**, *43*, 1214–1216.
[17] K. Yamaura, Q. Huang, M. Moldovan, D. Young, A. Satro, Y. Baba, T. Nagai, Y. Matsui, E. Takayama-Muromachi, *Chem. Mater.* **2005**, *17*, 359–365.
[18] K. Hobbie, R. Hoppe, *Z. Anorg. Allg. Chem.* **1988**, *505*, 106–110.
[19] R. D. Shanon, *Acta Crystallogr.* **1976**, *32*, 751–767.
[20] D. P. Chen, H. C. Chen, A. Maljuk, A. Kulakov, H. Zhang, P. Lemmens, C. T. Lin, *Phys. Rev. B* **2004**, *70*, 0245061–0245068.
[21] M. Karppinen, I. Asako, T. Mohashi, H. Yamuchi, *Chem. Mater.* **2004**, *16*, 1693–1696.
[22] H. V. J. Rietveld, *J. Appl. Crystallogr.* **1969**, *2*, 65–71.
[23] J. Rodríguez-Carvajal, *Physica B* **1993**, *192*, 55–69.

Received: May 19, 2005
Published Online: September 15, 2005

 © 2005 Wiley-VCH Verlag GmbH & Co. KGaA, Weinheim

Tuning pGa with Chelating Agents Related to (*o*-Hydroxybenzyl)iminodiacetic Acid

Olivier Jarjayes*[a] Florent Mortini,[a] Amaury du Moulinet d'Hardemare,[a] Christian Philouze,[a] and Guy Serratrice[a]

Keywords: Carboxylate ligands / Gallium / N ligands / Potentiometry / Stability constants

Gallium complexes with R-(*o*-hydroxybenzyl)iminodiacetate ligands (**Lx**) have been synthesized and their thermodynamic constants determined in aqueous solution by potentiometric titration. These quantitative results were also confirmed by ^{1}H and ^{19}F NMR spectroscopy. An X-ray study of Ga**L3** (R = NO_2) showed that the gallium(III) ion is hexacoordinate with two H_2O molecules in *cis* positions. The ability of the ligands to chelate Ga^{III} was evaluated at physiological pH and ionic strength from the pGa values. Among the different ligands studied, **L6** (R = OMe) has a pGa value two orders of magnitude higher than that of the complex between Ga and the blood serum protein transferrin.
(© Wiley-VCH Verlag GmbH & Co. KGaA, 69451 Weinheim, Germany, 2005)

Introduction

The design and synthesis of new chelating agents for effective coordination of Ga^{III} has received an important and increasing interest in the past decade. This is in part because of promising potential applications of ^{67}Ga and ^{68}Ga complexes as diagnostic radiopharmaceuticals.[1–4] In order to be considered as radiopharmaceuticals, these metal complexes must be stable with respect to demetalation by the blood serum protein transferrin and they must have a conditional stability constant greater than that of Ga–transferrin.[5] Moreover, the presence on the ligand of a second functional group that is not involved in the metal chelating process leads to a bifunctional chelator[6] and allows covalent linkage to targeting biomolecules such as antibodies, small proteins, or synthetic macromolecules. These conjugates are considered as in vivo metal carriers. Concerning the metal bonding unit, a large number of chelators have been synthesized and studied,[6] including groups such as catechols, hydroxamates, hydroxypyridinones, or aminophosphonates. Among them, aminocarboxylate groups presenting a high affinity towards Ga^{III} have been widely used to build polydentate ligands based on EDTA and DTPA backbones. However, ligands possessing both aminocarboxylate and phenolic sub-units have been studied to a lesser extent, even though they present the highest stability constants towards Ga^{III} [for HBED, i.e. *N*,*N*′-bis(2-hydroxybenzyl)ethylenediamine-*N*,*N*′-diacetic acid, $\log \beta_{110} = 37.7$].[7] The introduction of a conjugation group for the attachment to a biomolecule is rather difficult when several phenolic rings are present.[8,9] For this reason, we have reported the synthesis of bifunctional chelating agents based on phenol. This synthesis compares favorably in terms of simplicity and step saving with other bifunctional structures based on DTPA or DOTA. Moreover, a wide number of chemical functions can be made available in the *para* position of the phenol.

In this present work, we report the stability constants of the gallium complexes in aqueous solution with R-(*o*-hydroxybenzyl)iminodiacetate ligands (**Lx**; Figure 1) to determine if these systems are good candidates for radiopharmaceutical applications. These studies were performed by combining potentiometry and NMR (^{1}H and ^{19}F) spectroscopy. Solid-state characterizations were also performed for **L6** (R = OMe) and the complex Ga**L3** (R = NO_2).

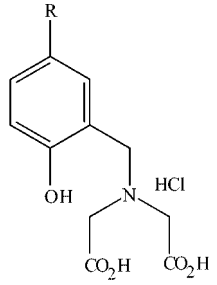

R	Me	CHO	NO_2	CH_2OH	F	OMe	H
Lx	L1	L2	L3	L4	L5	L6	HBIDA

Figure 1. Structure of the ligands **Lx**.

[a] Laboratoire d'Etudes Dynamiques et Structurales de la Sélectivité, Université Joseph Fourier, Grenoble 1, UMR 5616, ICMG FR CNRS 2607,
BP 53, 38041 Grenoble Cedex 09, France
Fax: +33-4-7651-4927
E-mail: Olivier.Jarjayes@ujf-grenoble.fr

Results and Discussion

Synthesis of the Ligands and Complexes

The **Lx** ligands are easily accessible from the appropriate *para*-substituted phenols and diethyl iminodiacetate in a solvent-less Mannich reaction, followed by the hydrolysis of the diethyl ester functions with hydrochloric acid. More details concerning the ligands' synthetic procedure have been described elsewhere.[10]

Solid-State Structure of the Ligand L6 and Complex GaL3

Crystals of **L6** (R = OMe) suitable for X-ray structure determination were obtained from an aqueous solution (10^{-2} M, pH 2.8) stored at room temperature. Details of the data collections are summarized in Table 4. The unit cell of **L6** is depicted in Figure 2 and the structural representation of **L6** is given in Figure 3.

The unit cell is shown down the *a* axis and displays two molecules, one of which is linked to three molecules of neighboring cells through hydrogen bonds (O5–H4···O5* = 1.22 Å, O3–H3···O3* = 1.21 Å, O1–H1···O2* = 1.95 Å). This representation explains the zwitterionic state of **L6**, since two hydrogens atoms (H3 and H4) of the molecule are shared with two molecules from adjacent unit cells. There is also a hydrogen bond between the hydrogen H1 of the phenol and the oxygen O2* of the carboxylic function. All of these intermolecular hydrogen bonds provide the stability of the crystal. In addition, three intramolecular hydrogen bonds are observed (N1–H2···O2 = 2.18 Å, N1–H2···O4 = 2.23 Å, N1–H2···O1 = 2.56 Å; see Figure 2). They realise the cohesion of the internal structure of the molecule, and might propitiously orientate the donor atoms for complexation.

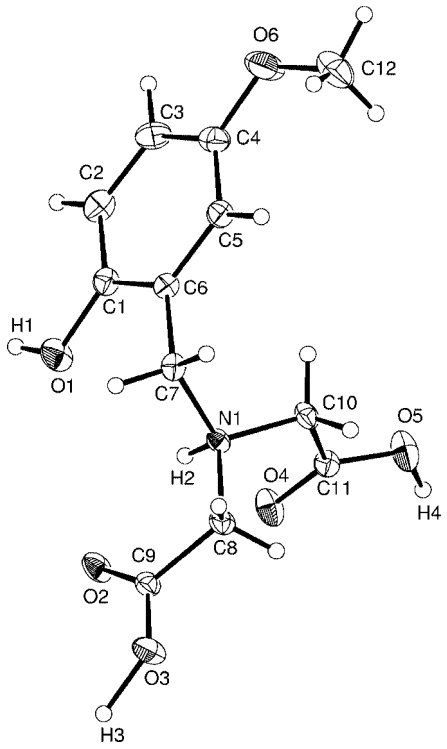

Figure 3. Structural representation of **L6**.

Among the different Ga**Lx** complexes, only Ga**L3** gave suitable crystals for an X-ray structural study. The ORTEP diagram of Ga**L3** (R = NO_2) is depicted in Figure 4, with selected bond lengths and angles listed in Table 1.

The gallium ion is located in a slightly distorted octahedral coordination environment formed by the deprotonated phenolic oxygen, two carboxylate oxygen atoms, the tertiary nitrogen atom, and two H_2O molecules coordinated in *cis* positions. The bond lengths of Ga to the tertiary amino

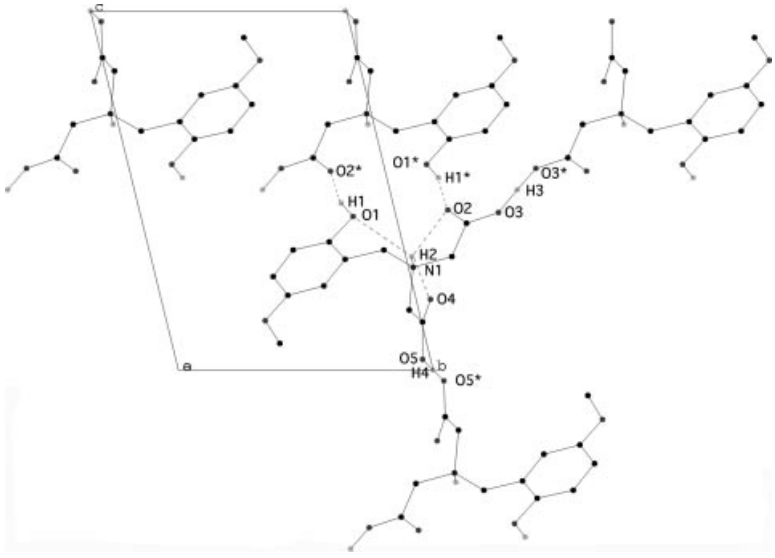

Figure 2. Unit cell representation down the *a* axis. This representation explains the zwitterionic state of **L6** as it can be seen that two protons of the molecule are shared with two molecules from adjacent unit cells (most of the hydrogen atoms have been omitted for clarity).

 © 2005 Wiley-VCH Verlag GmbH & Co. KGaA, Weinheim

Table 1. Selected bond lengths [Å] and angles [°] for Ga**L3**.

Ga–O(1)	1.884(2)	Ga–O(3)	2.077(2)	Ga–O(5)	1.938(1)
Ga–O(8)	1.964(2)	Ga–O(9)	1.956(2)	Ga–N(1)	2.097(2)
O(1)–Ga–O(3)	170.88(7)	O(1)–Ga–O(5)	95.87(7)	O(1)–Ga–O(8)	88.94(7)
O(1)–Ga–O(9)	97.78(7)	O(1)–Ga–N(1)	94.86(7)	O(3)–Ga–O(5)	88.91(7)
O(3)–Ga–O(8)	87.04(7)	O(3)–Ga–O(9)	90.23(7)	O(3)–Ga–N(1)	77.76(7)
O(5)–Ga–O(8)	172.97(7)	O(5)–Ga–O(9)	86.75(6)	O(5)–Ga–N(1)	85.24(6)
O(8)–Ga–O(9)	87.53(7)	O(8)–Ga–N(1)	99.49(7)	O(9)–Ga–N(1)	165.66(7)

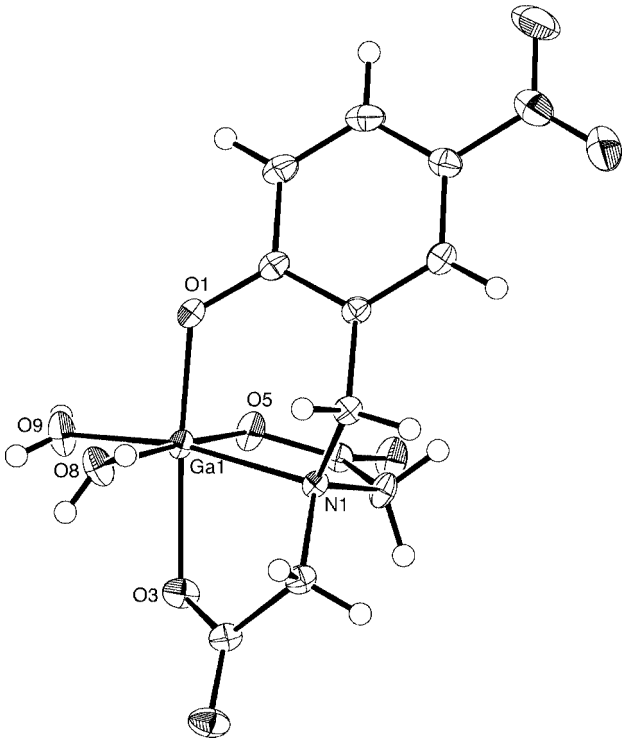

Figure 4. Structural representation of Ga**L3**.

nitrogen atom and to the carboxlate oxygen atoms presented in Table 1 are consistent with those observed in complexes obtained with other carboxylate ligands.[11,12] The gallium–phenolate bond length (1.884 Å) compares well with such bonds in other similar complexes,[13] but is significantly shorter than that found for the bridging phenolate in [Ga_2(HXTA)] [1.999 Å and 2.078 Å;[14] HXTA = *N*,*N*′-(2-hydroxy-5-methyl-1,3-xylene)bis(*N*-methoxycarbonylglycine].[15] The N(1)–Ga–OOC angles have the largest deviation from 90°, probably caused by the steric constraints of the five-membered chelate rings.

Ligand Deprotonation Constants

The deprotonation constants, K_{an}, of the ligands (as hydrochloride salts) investigated in this work were studied by potentiometric titrations. Analysis of the titration curve (part a of Figure 5, as an example) by the program SUPERQUAD[16] yielded the pK_{an} values defined by Equations (1) and (2) and reported in Table 2.

$$LH_n \rightleftharpoons LH_{n-1} + H^+ \quad (1)$$

$$K_{an} = [LH_{n-1}][H^+]/[LH_n] \quad (2)$$

For each ligand, three pK_a values out of the four possible ones were determined, corresponding to one carboxylic acid group, the ammonium group, and the phenolic hydroxyl group. The pK_a value of the other carboxylic acid was inferred to be significantly lower than 2, since if we tried to include this pK_a in the fit, this constant was discarded by the program. The pK_a values for the different **Lx** ligands are close to those given (see Table 2) for the ligand HBIDA [*N*-(2-hydroxybenzyl)iminodiacetic acid],[17,18] which has a similar structure.

From a general point of view, it should be noted that the substituent in the *para* position of the phenol plays an important part in its acidity. For example, the presence of an electron-withdrawing group for **L2** (R = CHO) and **L3** (R = NO_2) increases the phenol acidity (pK_{a1} = 10.35 and 10.05, respectively, instead of 11.7 for HBIDA). In the same way, the phenolate basicity of **L1** (R = Me) is slightly higher

Table 2. Deprotonation constants of the ligands **Lx**.

pK_{an}[a]	L1	L2	L3	L4	L5	L6	HBIDA[b]
pK_{a1}	12.1(1)[c]	10.35(2)	10.05(5) 10.22[e]	12.2(1)[c]	12.3[d]	12.5[g]	11.7
pK_{a2}	8.30(1) 8.0[f]	6.65(6)	6.20(4) 6.18[e]	8.05(9)	7.60(7) 7.5[d]	7.92(5)	8.07
pK_{a3}	2.3(1)[c]	2.1(1)[c]	2.4[c]	1.9[f]	1.8[d]	1.9[f]	2.34

[a] All values were determined at 25 °C and I = 0.1 M. Values in parentheses are standard deviations in the last significant digit. [b] *N*-(2-Hydroxybenzyl)iminodiacetic acid.[17] [c] Estimated value since the true uncertainty in these pK_a values is greater than the standard deviation obtained from the least-squares fitting of the potentiometric data. [d] Determined by ^{19}F NMR spectroscopy. [e] Ref.[18] [f] Determined by ^{1}H NMR spectroscopy. [g] Determined by UV/Vis spectroscopy.

 © 2005 Wiley-VCH Verlag GmbH & Co. KGaA, Weinheim

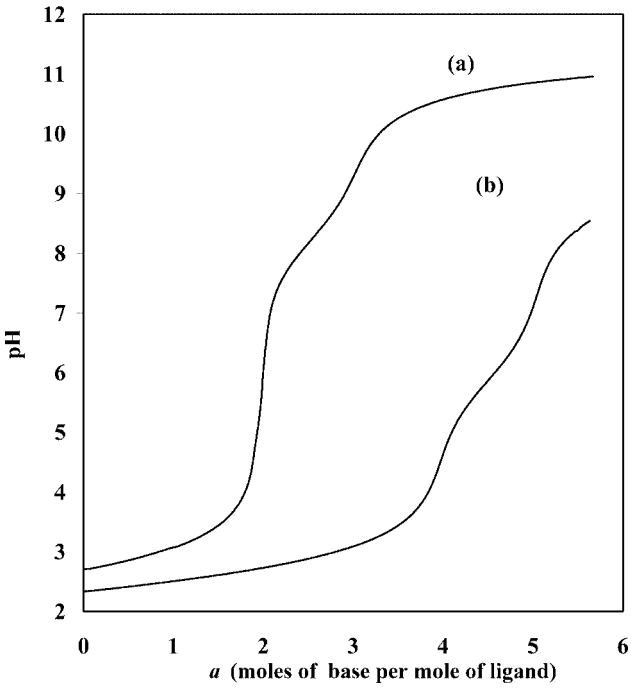

Figure 5. Potentiometric titration curves for (a) 1 mM ligand **L1** and (b) **L1** + Ga^{3+} (1:1, 1 mM). a = mols of base added per mol of ligand. All solutions were at 25 °C and I = 0.1 M ($NaNO_3$). The data were refined with the program SUPERQUAD (σ_{fit} = 3.5–4.5).

than that of HBIDA; this effect is due to the presence of the methyl group, which increases the electronic density on the phenolic ring. The effect of these groups also has an influence on the ammonium acidity, which is more acidic for ligands **L2** and **L3** (pK_{a2} values of 6.65 and 6.21, respectively). On the other hand, for ligands **L1** and **L4**, which bear low inductive groups (R = Me and CH_2OH, respectively), or with an electron-donating group (R = OMe, **L6**), the ammonium always has a pK_a value larger than 8.

Since low pK_a values are difficult to determine by potentiometric titration, some of the deprotonation constants of **L4** and **L6** were also calculated by ^1H NMR spectroscopy from the titration curves of δ vs. pH under the same conditions of ionic strength as used for the potentiometric study (Table 3). The K_{an} values were obtained from the chemical shift.[19] The resonances of the methylene protons of the benzylic and acetic (CH_2COO) positions (singlets) become more shielded upon addition of base ($\Delta\delta$ = 0.8 ppm in all the cases for pH ranging from 0.5 to 12) while the deprotonations only produce a small chemical shift (around 0.1 ppm) of the three aromatic protons. These observations make it clear that these protons are sensitive to the protonation state of the amine and one of the two carboxylic functions. In the same way, ^{19}F NMR spectroscopy can be considered as an excellent tool for the pK_a determination for **L5** because three constants out of the four can be determined. The fourth deprotonation produces a marked change in the ^{19}F chemical shift ($\Delta\delta$ = 6 ppm). This increased shielding of the fluorine ring substituent indicates a net increase of negative charge on the aromatic ring in this process. This observation is consistent with the loss of the phenolic proton, which cannot be determined by ^1H NMR spectroscopy. It is also very interesting to notice that the fluorine atom is a much more sensitive probe than ^1H, since a carboxylic function located in a ^9J position can affect the fluorine chemical shift. The agreement between the values from various experimental techniques is reasonable, and the dissociation constants correlate well with the data reported for HBIDA (see Table 2).

Table 3. Stability constants and pGa values.

Constants[a]	L1	L2	L3	L4	L5	L6	HBIDA[b]
$\log \beta_{110}^{FeLx}$	23.5	20.5	20.1	22.5	22.4	25.3	21.40
$\log \beta_{110}^{GaLx}$	22.1	19.4	19.1	21.1	21.4	25.2	21.55
pK_{OH}^{1}[c]	5.70(4) 5.3[d]	5.77(2)	5.54(2)	5.72(6)	6.21(3) 6.0[e]	6.42(1)	5.75
pK_{OH}^{2}[f]	8.2(1)				8.8(1) 8.8[f]		8.53
pGa [g]	19.1	19.0	19.2	18.2	18.3	21.5	19.1

[a] All values were determined at 25 °C and I = 0.1 M ($NaNO_3$). [b] Ref.[17] [c] K_{OH}^{1} = [Ga**Lx**(OH)][H^+]/[Ga**Lx**]for the equilibrium Ga**Lx** + H_2O ⇌ Ga**Lx**(OH) + H^+. [d] Determined by ^1H NMR titration. [e] Determined by ^{19}F NMR titration. [f] K_{OH}^{2} = [Ga**Lx**$(OH)_2$][H^+]/[Ga**Lx**(OH)] for the equilibrium Ga**Lx**(OH) + H_2O ⇌ Ga**Lx**$(OH)_2$ + H^+. [g] Calculated for [**Lx**]$_{tot}$ = 10^{-5} M and [Ga]$_{tot}$ = 10^{-6} M at pH 7.4.

Stability Constants of the Gallium Complexes

It was not possible to determine the stability constants β_{110}^{GaLx} of the complexes by potentiometric titration since the formation of the complexes is complete at low pH values (Figure 5b). The titration curves for a 1:1 ratio of Ga^{III} and ligand (Figure 5b as an example) exhibit two breaks at a = 4 and a = 5, where a is equal to the number of mols of base added per mol of ligand. This indicates the formation of the hydroxo complexes [Ga**Lx**(OH)] and [Ga**Lx**$(OH)_2$] at relatively low pH values. Analysis of the titration curves with the program SUPERQUAD[16] yielded the K_{OH}^{n} (n = 1 or 2) constants expressed by Equation (3).

$$K_{OH}^{n} = [Ga\mathbf{Lx}(OH)_n][H^+]/[Ga\mathbf{Lx}(OH)_{n-1}] \quad (3)$$

The K_{OH}^{n} values are given in Table 3, and can also be determined by ^1H NMR spectroscopy for Ga**L1**. In the case of Ga**L5**, ^{19}F NMR spectroscopy was used to determine the two hydrolysis constants, as shown in Figure 6, revealing two important chemical shift jumps ($\Delta\delta$ = 0.75 and 1.2 ppm) as a function of pH.

The obtained values are in good agreement with the potentiometric titrations. It should be noted that higher pK_{OH}^{1} values have been obtained for Ga**L5** and Ga**L6** in relation with the higher basicity of the phenolate group as it increases the electronic density on the metal ion. The stability constants β_{110}^{GaLx} were determined in acidic medium[19] (pH 2.01) by metal–metal competition, using the absorbance of Fe**Lx** as a spectral probe. In these experiments, exchange of Ga^{III} with Fe^{III} was allowed to occur [Equations (4) and (5)].

 © 2005 Wiley-VCH Verlag GmbH & Co. KGaA, Weinheim

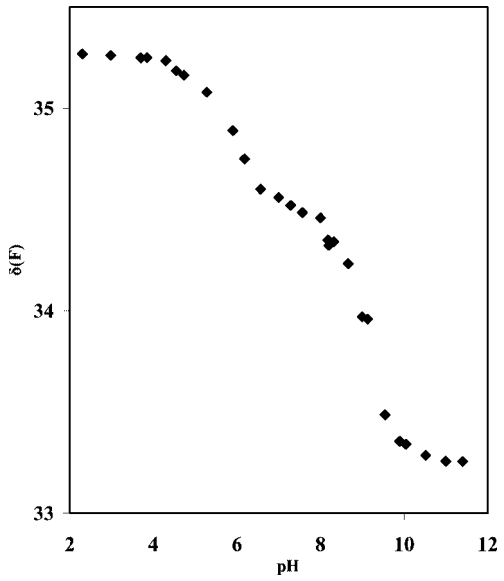

Figure 6. Dependence of the ^{19}F chemical shift (vs. C_6F_6) of Ga**L5** on the addition of NaOH [measured in an H_2O/D_2O (80:20) medium at 25 °C and I = 0.1 M $NaNO_3$].

$$Fe\mathbf{Lx} + Ga^{III} \rightleftharpoons Ga\mathbf{Lx} + Fe^{III} \quad (4)$$

$$K = \frac{[Ga\mathbf{Lx}][Fe^{III}]}{[Fe\mathbf{Lx}][Ga^{III}]} = \frac{\beta_{110}^{Ga\mathbf{Lx}}}{\beta_{110}^{Fe\mathbf{Lx}}} \quad (5)$$

The amount of uncomplexed **Lx** was assumed to be negligible.

Knowledge of the formation constants of Fe**Lx** complexes, along with mass balance, absorbance, and pH measurements, is necessary to calculate the formation constants of Ga**Lx**. Beforehand, the stability constants of Fe**Lx** ($\beta_{110}^{Fe\mathbf{Lx}}$) were determined by competition experiments against HEDTA[17] over the pH range 2–2.5. The following equation corresponds to the equilibrium [charges omitted for clarity, Equation (6)].

$$Fe\mathbf{Lx} + HEDTA \rightleftharpoons FeHEDTA + \mathbf{Lx} \quad (6)$$

where HEDTA is (hydroxyethyl)ethylenediaminetriacetic acid [Equation (7)].

$$K' = \frac{[\mathbf{Lx}][FeHEDTA]}{[Fe\mathbf{Lx}][HEDTA]} = \frac{\beta_{110}^{FeHEDTA}}{\beta_{110}^{Fe\mathbf{Lx}}} \quad (7)$$

The concentrations of Fe**Lx** complexes were calculated from the absorbances between 486 and 578 nm (depending on the ligand **Lx**), where Fe**Lx** is the only absorbing species. The concentration of the other species was calculated from mass balance equations and pH, using the usual α Ringbom coefficient.[21] With the known formation constant of Fe^{III}-HEDTA ($\log \beta_{110}^{FeHEDTA}$ = 19.8), and the deprotonation constants of HEDTA (pK_{a1} = 9.81, pK_{a2} = 5.37, and pK_{a3} = 2.6),[18] the values of $\beta_{110}^{Fe\mathbf{Lx}}$ and $\beta_{110}^{Ga\mathbf{Lx}}$ were calculated from Equations (6) and (7), respectively, and are reported in Table 3. They span over the range 19.1–25.3 and are consistent with the one obtained for the HBIDA ligand taken as the reference (no electronic effect).[17]

As we can observe, the stability of the complexes (Fe^{III} or Ga^{III}) increases with the basicity of the phenolate, i.e. with its greater electron donor ability. Ligands with an electron-withdrawing substituent (the more acidic) lead to complexes with a gallium stability constant lower than that of Ga-transferrin ($\log K$ = 19.8),[22] whereas ligands with electron-donating substituents (R = OMe, Me) give $\beta_{110}^{Ga\mathbf{Lx}}$ values up to five times higher than the complex Ga-transferrin. The distribution curves shown in Figure 7 for the 1:1 Ga^{III}:**L1** system provide a typical picture of the successive complexes formed as a function of pH. Ga**L1** is dominant in the pH range 2–4.5, while the first hydroxo complex [Ga-**L1**(OH)] is the major species at physiological pH. pK^1_{OH} values can also be related to the basicity of the phenolate group: this increases the electronic density on the metal ion and decreases its affinity towards coordinated water molecules, so the highest pK^1_{OH} values are obtained for Ga**L5** and Ga**L6**.

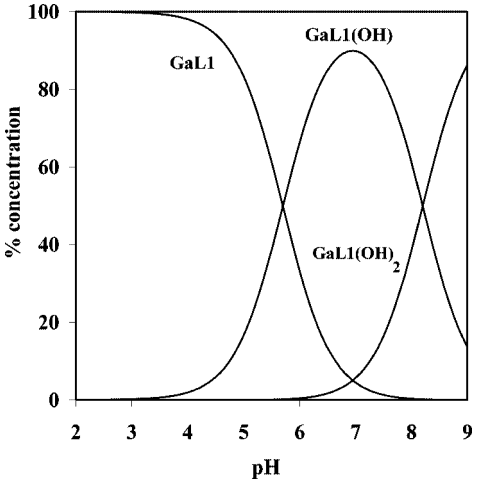

Figure 7. Distribution curves for the system Ga^{III}–**L1** as a function of pH. [Ga^{3+}] = 1 mM and [**L1**] = 10 mM.

Since the ligands are weak acids, proton competition occurs depending on their pK_a and the pH. The pGa (–log [Ga^{3+}]) is thus a better measure of the relative complexation efficiency of the ligands under given conditions of pH, Ga, and **Lx** concentrations: the larger the pGa values, the more effective the ligand. The pGa values for pH 7.4 ([Ga^{3+}] = 10^{-6} M, [**Lx**] = 10^{-5} M) are collected in Table 3. They have also been calculated for pH values over the range 2–8 and reported as the plot pGa = f(pH) presented in Figure 8. In this pH range, the uncertainty in the high pK_a values does not affect the calculations of the pGa values.

Except for **L6**, it is important to note a similar efficiency in the complexation of Ga^{III} by the various aminophenolate ligands. pGa values have small variations whenever **Lx** bears electron-withdrawing substituents (R = CHO, R = NO_2) or an electron-donating group (R = Me). These ligands' complexing abilities are thus similar to Ga-EDTA (pGa = 20.0)[22] and Ga-DTPA (pGa = 20.2)[22] but with a lower denticity. pGa vs. pH curves indicate that **L6** is the best complexing agent of this family over the whole pH range

 © 2005 Wiley-VCH Verlag GmbH & Co. KGaA, Weinheim

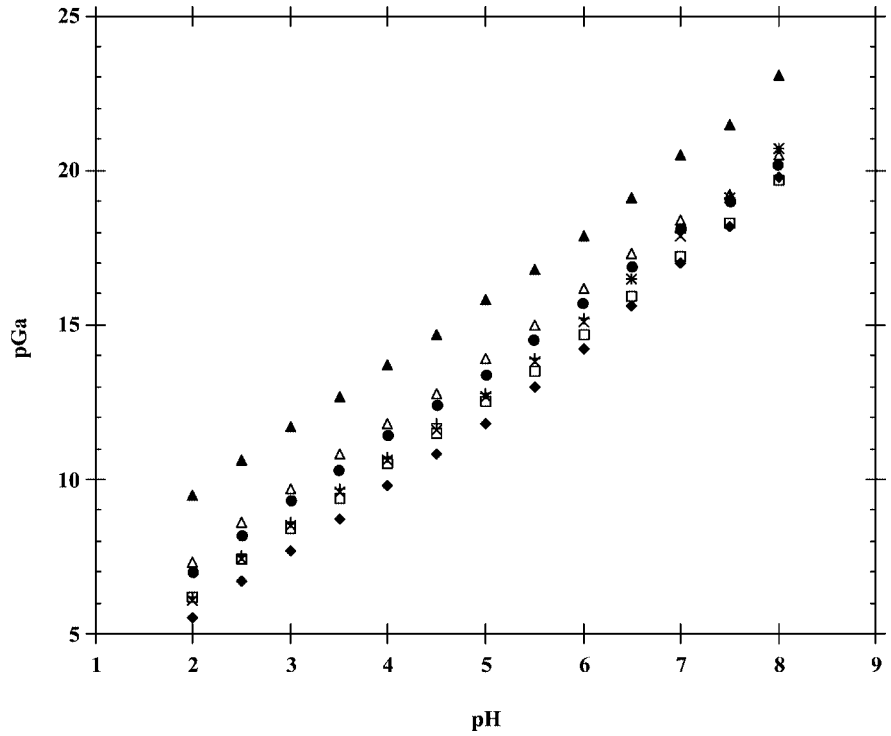

Figure 8. Plot of pGa (–log [Ga^{3+}]) vs. pH. pGa was calculated for [**Lx**] = 10^{-5} M and [Ga^{3+}] = 10^{-6} M. For HBIDA, the deprotonation constants and the complexation constants β_{110} were taken from ref.[20] (× **L1**, ● **L2**, Δ **L3**, ♦ **L4**, □ **L5**, ▲ **L6**, + HBIDA).

(pGa = 21.5 at pH 7.4). This good affinity is due to an increased basicity of the phenolate with a methoxy group in the *para* position. Indeed, according to Pearson's principle of hard and soft acids and bases (HSAB),[23] a very basic negative oxygen donor has a high affinity for a hard metal ion such as Ga^{III}. Except for **L6**, and as could be expected from theory, acidic ligands (those bearing electron-withdrawing substituents) have the best complexing ability at low pH. So, **L6** is a good Ga^{III} chelator compared to the Ga-transferrin (pGa = 19.7)[22] system (around two orders of magnitude difference). Ga**L6** may thus be resistant to demetalation in vivo, and radiopharmaceutical applications are possible in this context.

Conclusions

This work has shown that the R-(*o*-hydroxybenzyl)iminodiacetate ligands (obtained in only two steps) with a potential conjugating group in the *para* position to the phenol and a rather low denticity are strong chelators for Ga^{III}. For the Ga**L3** (R = NO_2) complex in the solid state, the Ga^{III} ion is hexacoordinate with two water molecules in *cis* positions. The protonation constants of the ligands and the hydoxo complexes' formation constants were measured by different techniques and gave consistent data. Considering the pGa values, Ga**L6** (R = OMe) appears to be a promising candidate for use in radioimaging since the stability constant of Ga-transferrin is two orders of magnitude lower. Studies with $^{67/68}$Ga radiolabeling are now in progress in order to confirm the kinetic inertness of these bifunctional chelating systems against common decomplexation pathways.

Experimental Section

General Remarks: ^{1}H NMR spectra were recorded on a Bruker AC 200 spectrometer. Chemical shifts are reported in ppm from internal sodium 3-(trimethylsilyl)propane-1-sulfonate. ^{19}F NMR spectra were recorded on a Varian U400 with chemical shifts in ppm relative to an external C_6F_6 reference in $CDCl_3$ (δ = –163 ppm relative to $CFCl_3$). The pH was adjusted with small additions of concentrated HCl or NaOH solutions (prepared in D_2O). The pK_a values were measured in pure D_2O and the pD was obtained from the pH meter readings by adding 0.4 units.[24] For the dissociation constants in D_2O and H_2O, the relationship pK_D = 1.018 pK_H + 0.43 was used.[25] Measurements were made in a H_2O/D_2O medium (80:20 v/v) and in this case no correction for isotopic or solvents effects was needed. Analyses were performed by the Service Central d'Analyse (CNRS Solaize). All chemicals were obtained from Acros or Aldrich and were used without further purification.

Synthesis of GaL3: 10 mL of an aqueous solution of NaOH (2 mmol) was added to a solution of **L3** (165 mg, 0.5 mmol) in water (10 mL). The gallium nitrate salt in H_2O (0.5 mmol in 10 mL) was then added to this homogeneous solution and the pH adjusted to 3–4. After stirring for 30 min, half of the solvent was slowly removed under reduced pressure. Slow concentration of the filtrate over a period of one week yielded suitable crystals for X-ray diffraction studies. Yield: 164 mg (81%). $C_{11}H_{15}GaN_2O_{10}$: calcd. C 32.62, H 3.73, Ga 17.22, N 6.92; found C 32.82, H 3.59, Ga 16.95, N 6.85. ^{1}H NMR (DMSO): δ = 3.16–3.38 (dd, J = 21 Hz, 4 H, H_{ac}), 3.95 (s, 2 H, H_{benz}), 6.65–6.67 (d, J = 6 Hz, 1 H, H_{ar}), 7.95–8.05 (m, 2 H, H_{ar}) ppm.

 © 2005 Wiley-VCH Verlag GmbH & Co. KGaA, Weinheim

Table 4. Summary of crystallographic data for **L6** and Ga**L3**.

	L6	Ga**L3**
Formula	$C_{12}H_{15}NO_6$	$C_{11}H_{13}GaN_2O_9$
M	269.25	386.95
Symmetry	triclinic	monoclinic
Morphology	pale yellow prism	pale yellow prism
Crystal dimensions [mm]	32 × 21 × 14	35 × 22 × 20
a [Å]	5.459(5)	6.9456(3)
b [Å]	9.268(4)	32.120(1)
c [Å]	12.902(3)	6.9606(2)
α [°]	103.97(3)	90
β [°]	93.58(4)	117.7(1)
γ [°]	78.52(5)	90
Unit-cell volume [Å^3]	620.7(6)	1374.9(7)
T [K]	293.0	293.0
Space group	$P\bar{1}$	$P2_1/a$
Z	2	4
Diffractometer	Enraf–Nonius CAD-4	Enraf–Nonius Kappa CCD
Monochromator	graphite	graphite
Radiation (wavelength)	Mo-K_α (0.71073 Å)	Mo-K_α (0.71073 Å)
μ [mm^{-1}]	0.116	2.055
No. of reflections (measured)	3756	20881
No. of reflections (unique)	3609	6097
No. of reflections	1981 [$I > 2.6\sigma(I)$]	2955 [$I > 3.0(I)$]
R_{int}	0.028	0.062
R	0.053	0.038
$R(w)$	0.056	0.038

Potentiometric Titrations: All the measurements were made at 25 °C and the solutions were prepared with deionized water that had been distilled twice. The ionic strength was fixed at I = 0.1 M with $NaNO_3$ (PROLABO puriss). The potentiometric titrations were performed using an automatic titrator system, DMS 716 Titrino (Metrohm), equipped with a combined glass electrode (Metrohm, filled with saturated NaCl solution) and connected to an IBM Aptiva microcomputer. The electrodes were calibrated to read pH according to the classical method[26] (from titration of 0.01 M $HClO_4$ with 0.025 M NaOH). The ligands and their gallium(III) complexes (ca. 0.001 M) were titrated with standardized 0.025 M sodium hydroxide. Argon was bubbled through the solutions to exclude CO_2 and O_2. Aqueous sodium hydroxide (0.1 M NaOH) was prepared from 1 M commercial NaOH solution (Prolabo) and was standardized against hydrogen phthalate solution. The titration data (120 points collected over the pH range 2.5–10.5 for the ligand solutions and 100 points collected over the pH range 2.5–10 for the Ga^{III}–ligand solution) were refined with the nonlinear least-squares refinement program SUPERQUAD[16] to determine the deprotonation constants (σ_{fit} in the range 3.5–4.5). The pK_{an} values were calculated from the cumulative constants determined with the above program. The uncertainties in the pK_{an} values correspond to the standard deviations (1σ) in the cumulative constants.

Spectrophotometric Experiments: UV/Vis absorption spectra were recorded with a Perkin–Elmer Lambda 2 spectrometer using 1-cm path-length quartz cells and connected to a microcomputer; the acquisition was made with the UV Winlab software (Perkin–Elmer). The temperature was maintained at 25 °C with a Perkin–Elmer PTP.1 variable temperature unit. The pH measurements were made with a 713 Metrohm digital pH meter equipped with a microelectrode. The ionic strength was fixed at I = 0.1 M with $NaNO_3$.

X-ray Crystallographic Data Collection and Refinement of the Structures: The main crystallographic features, the strategy used for the crystal structure determination, and its results are gathered in Table 4. Data collection was performed at room temperature. The U_{iso} of the H atoms was fixed to 1.2 U_{eq} of the C atom to which they are bound. All the structures were solved by direct methods (SIR92).[27]

CCDC-201447 (for **L6**) and -201562 (for Ga**L3**) contain the supplementary crystallographic data for this paper. These data can be obtained free of charge from The Cambridge Crystallographic Data Centre via www.ccdc.cam.ac.uk/data_request/cif.

[1] S. Jurisson, D. Berning, W. Jia, D. Ma, *Chem. Rev.* **1993**, *93*, 1137–1156.
[2] J. Burgess, *Chem. Soc. Rev.* **1996**, *25*, 85–92.
[3] C. J. Anderson, M. J. Welch, *Chem. Rev.* **1999**, *99*, 2219–2234.
[4] E. Arslantas, P. M. Smith-Jones, G. Ritter, R. R. Schmidt, *Eur. J. Org. Chem.* **2004**, *19*, 3979–3984.
[5] W. R. Harris, L. Messori, *Coord. Chem. Rev.* **2002**, *228*, 237–362.
[6] S. Liu, D. S. Edwards, *Bioconjugate Chem.* **2001**, *12*, 7–34.
[7] R. J. Motekaitis, Y. Sun, A. E. Martell, M. J. Welch, *Inorg. Chem.* **1991**, *30*, 2737–2740.
[8] C. J. Mathias, Y. Sun, J. M. Connett, G. W. Philpott, M. J. Welch, A. E. Martell, *Inorg. Chem.* **1990**, *29*, 1475–1480.
[9] C. J. Mathias, Y. Sun, M. J. Welch, J. M. Connett, G. W. Philpott, A. E. Martell, *Bioconjugate Chem.* **1990**, *1*, 204–211.
[10] A. du Moulinet d'Hardemare, O. Jarjayes, F. Mortini, *Synth. Commun.* **2004**, *34*, 3975–3988.
[11] B. Achour, J. Costa, R. Delgado, E. Garrigues, C. F. G. C. Geraldes, N. Korber, F. Nepveu, M. I. Prata, *Inorg. Chem.* **1998**, *37*, 2729–2740.
[12] W. Niu, E. H. Wong, G. R. Weisman, Y. Peng, C. J. Anderson, L. N. Zakharov, J. A. Golen, A. L. Rheingold, *Eur. J. Inorg. Chem.* **2004**, *16*, 3310–3315.
[13] S. Liu, S. J. Rettig, C. Orvig, *Inorg. Chem.* **1992**, *31*, 5400–5407.
[14] O. Jarjayes, A. du Moulinet d'Hardemare, A. Durif, M. T. Averbuch-Pouchot, *Acta Crystallogr., Sect. C* **1998**, *54*, 931–933.
[15] B. P. Murch, F. C. Bradley, P. D. Boyle, V. Papaefthymiou, L. Que Jr., *J. Am. Chem. Soc.* **1987**, *109*, 7993–8003.
[16] P. Gans, A. Sabatini, A. Vacca, *J. Chem. Soc., Dalton Trans.* **1985**, *6*, 1195–2000.

 © 2005 Wiley-VCH Verlag GmbH & Co. KGaA, Weinheim

[17] W. R. Harris, R. J. Motekaitis, A. E. Martell, *Inorg. Chem.* **1975**, *14*, 974–978.
[18] A. E. Martell, R. M. Smith, *Critical Stability Constants*, Plenum Press, New York, **1974**.
[19] G. Serratrice, A. Zeghli, C. G. Béguin, G. Gellon, P. Baret, J. L. Pierre, *J. Chim. Phys.* **1992**, *89*, 549–557.
[20] W. R. Harris, A. E. Martell, *Inorg. Chem.* **1976**, *15*, 713–720.
[21] A. Ringbom, *Complexation*, in *Analytical Chemistry*, Interscience, New York, **1963**.
[22] Y. Sun, C. J. Anderson, T. S. Pajeau, D. E. Reichert, R. D. Hancock, R. J. Motekaitis, A. E. Martell, M. J. Welch, *J. Med. Chem.* **1996**, *39*, 458–470.
[23] R. G. Pearson, *Surv. Prog. Chem.* **1967**, *5*, 1–52.
[24] P. K. Glasoe, F. A. Long, *J. Phys. Chem.* **1960**, *64*, 188–190.
[25] H. J. C. Yeh, K. L. Kirk, L. A. Cohen, J. S. Cohen, *J. Chem. Soc., Perkin Trans. 2* **1975**, 928–932.
[26] A. E. Martell, R. J. Motekaitis, *Determination and Use of Stability Constants*, 2nd ed., VCH Publishers, New York, **1992**.
[27] A. Altomare, A. Cascarano, G. Giacovazzo, A. Guagliardi, *J. Appl. Crystallogr.* **1993**, *26*, 343–350.

Received: December 17, 2004
Published Online: September 15, 2005

 © 2005 Wiley-VCH Verlag GmbH & Co. KGaA, Weinheim

Formation of 3-Sulfanylcoumarins by $SnPh_3OH$-Promoted Cyclization of 3-Aryl-2-Sulfanylpropenoic Acids

Pedro Álvarez-Boo,[a] José S. Casas,[b] María D. Couce,[a] Vanesa Fernández-Moreira,[a] Eduardo Freijanes,[a] Emilia García-Martínez,[a] José Sordo,*[b] and Ezequiel Vázquez-López[a]

Keywords: Tin / Triphenyltin complexes / 3-(2-hydroxyphenyl)-2-sulfanylpropenoic acids / 3-sulfanylcoumarin / X-ray diffraction

Reaction of $SnPh_3OH$ with 3-(2-hydroxyphenyl)sulfanylpropenoic acid [H_2(*o*-hpspa)] yielded [$SnPh_3$(SC)], where SC is deprotonated 3-sulfanylcoumarin (3-sulfanyl-2H-1-benzopyran-2-one, HSC), by a cyclization process. Similarly, when 3-(2-hydroxy-5-bromophenyl)- and 3-(2-hydroxy-3,5-dibromophenyl)-2-sulfanylpropenoic acids were treated with the same tin hydroxide, the cyclization resulted in [$SnPh_3$(BrSC)] and [$SnPh_3$(Br_2SC)], where BrSC and Br_2SC are the new ligands formed from the deprotonation of 3-sulfanyl-6-bromocoumarin and 3-sulfanyl-6,8-dibromocoumarin, respectively. The new compounds were characterized by elemental analysis, multinuclear NMR (^{1}H, ^{13}C and ^{119}Sn) and vibrational spectroscopy, and mass spectrometry. Single-crystal X-ray structures of these complexes all showed that the tin atom is surrounded by three phenyl C atoms and the S and O atoms of the bidentate ligand in a distorted trigonal-bipyramidal environment.

(© Wiley-VCH Verlag GmbH & Co. KGaA, 69451 Weinheim, Germany, 2005)

Introduction

In previous work,[1] treatment of 3-(phenyl)-2-sulfanylpropenoic acid (H_2pspa) with $SnPh_3OH$ in the presence of diisopropylamine afforded the compound [Q][$SnPh_3$(pspa)] (Q = diisopropylammonium), which showed antibacterial activity against *Staphylococcus aureus* and, although minor, against *Escherichia coli*. In an effort to synthesize a more soluble product with similar activity we have now prepared the 3-(2-hydroxyphenyl)-2-sulfanylpropenoic acid [H_2(*o*-hpspa)]. However, reaction of this compound with $SnPh_3OH$ yielded the unexpected complex [$SnPh_3$(SC)], where SC is deprotonated 3-sulfanylcoumarin. Formation of the same product in the absence of diisopropylamine showed that the amine played no role in the reaction.

Coumarin (1,2-benzopyrone, Scheme 1) is a natural product present in plants with widespread use in foodstuffs and cosmetic products. Furthermore, this substance is used in medicine as an anticoagulant. Coumarin derivatives (in particular those substituted at positions 3 or 4 of the pyrone cycle), have bacteriostatic and rodenticide applications.[2–4]

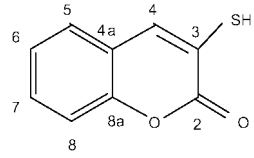

Scheme 1.

The synthesis of 3-sulfanylcoumarin had been previously carried out by Shi et al.[5] by reacting 5-(*o*-hydroxybenzylidene)rhodanine with hydrazine hydrate in EtOH at 80 °C. In this paper, we describe the formation of tin(IV) complexes containing this deprotonated species as well as its 6-

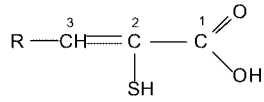

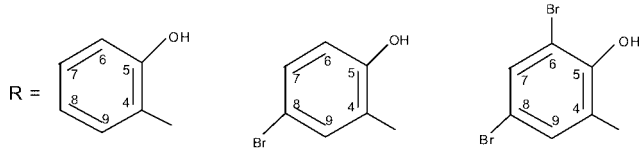

Scheme 2.

[a] Departamento de Química Inorgánica, Universidade de Vigo, 36200 Vigo, Spain
[b] Departamento de Química Inorgánica, Universidade de Santiago de Compostela, 15782 Santiago de Compostela, Spain
E-mail: qijsordo@usc.es
Supporting information for this article is available on the WWW under http://www.eurjic.org or from the author.

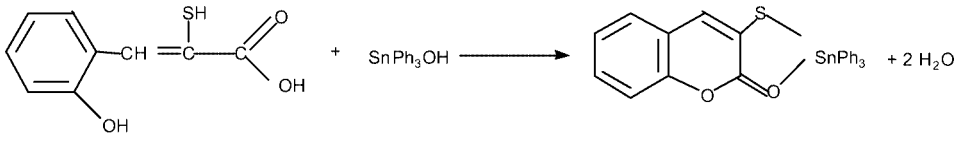

Scheme 3.

bromo- and 6,8-dibromo derivatives which resulted from the cyclization of 2-sulfanylpropenoic acids (Scheme 2), together with their structural study by means of X-ray diffraction and characterisation by vibrational and NMR spectroscopy. We chose Br-substituted derivatives in an effort to examine the influence of relatively bulky and electronegative atoms in the aromatic moiety of the acids on the cyclization process.

Results and Discussion

Synthesis of [$SnPh_3$(L)] (L = SC, BrSC, Br_2SC)

The reaction of the complex formation is shown in Scheme 3.

In the Experimental Section we describe the reactions carried out with excess $SnPh_3OH$. Besides these conditions, the reaction was also explored in a 1:1 mol ratio of reactants in the presence and absence of diisopropylamine in EtOH solution. In all cases, the solid isolated was determined to be the same sulfanylcoumarin derivative.

The reactions of $H_2(Br_2$-*o*-hpspa) with $Zn(OAc)_2$, $Cd(OAc)_2$, $Pb(OAc)_2$ and SnR_2O (R = Me, Et, Bu, Ph) were also explored. In all cases, the solids isolated have stoichiometries corresponding to the 3-aryl-2-sulfanylpropenoic acid derivatives. For example, the reaction of $H_2(Br_2$-*o*-hpspa) with $SnMe_2O$ afforded a solid with the analytical data C 26.4, H 1.9, S 6.3%; [$SnMe_2(Br_2$-*o*-hpspa)] requires C 26.4, H 2.0, S 6.4%, while [$SnMe_2(SC)_2$] requires C 29.3, H 1.5, S 7.8%. Further work to elucidate the role of the metal in the cyclization process is in progress. In order to explore the behaviour of [$SnPh_3$(SC)] in acidic medium, $HOOCCF_{3(aq.)}$ was used as a proton source; no formation of free sulfanylcoumarin was detected.

Crystal Structures

[$SnPh_3$(SC)]

Tin Coordination Sphere

Figure 1 shows the structure of the compound and the numbering scheme, and Table 1 lists the significant bond lengths and angles. The tin atom is coordinated to three phenyl C atoms and to the S and O donor atoms of the SC ligand, which results a distorted trigonal-bipyramidal environment in which O(1) and C(11) are apical. The equatorial C atoms are closer to Sn than the apical carbon, as expected in this type of polyhedron; i.e. for the apical C atom: Sn–C(11) = 2.154(3) Å, for the equatorial C atoms: Sn–C(21) = 2.137(3), Sn–C(31) = 2.131(3) Å – all three are within the range of 2.12–2.18 Å reported for other triphenyltin compounds.[6] On the other hand, the Sn–S bond length [2.4691(10) Å] is slightly greater than the sum of the covalent radii of tin and sulphur atoms (2.42 Å),[7] but within the range reported for triphenyltin thiolates (2.405–2.481 Å).[6,8–10] The most remarkable bond length around the tin atom is the long (even for an apical position) Sn–O distance [2.589(2) Å], which is greater than the sum of their covalent radii (2.13 Å),[7] though smaller than the sum of their van der Waals radii (3.70 Å)[7] and in the range that has confidently been reported to indicate Sn–O bonding.[11] This long bond length denotes a weak interaction between these atoms and is in line with the short C–O distance of 1.215(4) Å, indicating that the C=O bond is only slightly altered upon coordination [*d*(C=O) = 1.20 Å].[7]

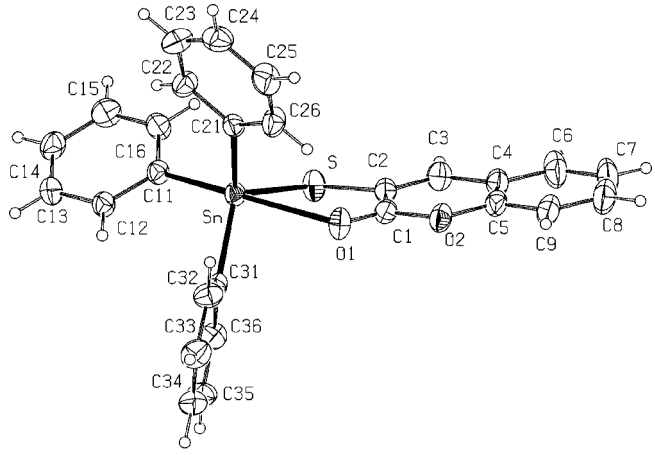

Figure 1. Displacement ellipsoid plot for [$SnPh_3$(SC)] with the atom numbering scheme. Ellipsoids at 30% probability.

The bond angles around the metal atom are indicative of the distortion from the regular trigonal-bipyramidal geometry. Thus, for instance, C(11)–Sn–S = 95.36(9)°, C(31)–Sn–C(11) = 105.09(12)° and C(21)–Sn–C(11) = 105.23(12)° (instead of 90°); C(31)–Sn–C(21) = 113.77(13)°, C(31)–Sn–S = 115.41(9)° and C(21)–Sn–S = 118.47(9)° (instead of 120°). The bond angles involving the two donor atoms of the sulfanylcoumarin ligand have values quite different from that expected for a regular polyhedron, namely: C(31)–Sn–O(11) = 78.01(10)°, C(21)–Sn–O(11) = 83.50(11)° and, specially, S–Sn–O(1) = 73.08(6)°, which are considerably narrower than the theoretical 90° angle because of the bite of the SC ligand. Nevertheless, according to Addison's τ-criterion,[12] (τ = 0.83) we can state that the coordination polyhedron is much closer to a trigonal bipyramid (τ = 1) than to a square pyramid (τ = 0).

The general features of the tin kernel are similar to those found in triphenyltin sulfanylcarboxylates,[1] in which an

 © 2005 Wiley-VCH Verlag GmbH & Co. KGaA, Weinheim

Table 1. Selected bond lengths [Å] and angles [°] for the prepared complexes with estimated standard deviations in parentheses.

	[$SnPh_3$(SC)]	[$SnPh_3$(BrSC)]·EtOH	[$SnPh_3(Br_2SC)$]
Sn–C(31)	2.131(3)	2.124(4)	2.143(7)
Sn–C(21)	2.137(3)	2.123(4)	2.129(7)
Sn–C(11)	2.154(3)	2.146(4)	2.170(7)
Sn–S	2.4691(10)	2.4540(10)	2.470(2)
Sn–O(1)	2.589(2)	2.784(3)	2.666(5)
S–C(2)	1.758(3)	1.751(4)	1.750(7)
O(1)–C(1)	1.215(4)	1.205(4)	1.200(8)
C(31)–Sn–C(21)	113.77(13)	118.56(14)	119.7(3)
C(31)–Sn–C(11)	105.09(12)	106.26(14)	103.9(3)
C(21)–Sn–C(11)	105.23(12)	108.64(14)	105.9(3)
C(31)–Sn–S	115.41(9)	112.17(11)	115.8(2)
C(21)–Sn–S	118.47(9)	115.47(10)	112.78(18)
C(11)–Sn–S	95.36(9)	91.76(10)	94.25(19)
C(31)–Sn–O(1)	78.01(10)	77.56(12)	81.9(2)
C(21)–Sn–O(1)	83.50(11)	83.74(12)	80.5(2)
C(11)–Sn–O(1)	168.04(11)	161.95(11)	167.0(2)
S–Sn–O(1)	73.08(6)	70.73(6)	72.77(12)
C(2)–S–Sn	105.87(13)	108.49(12)	107.4(2)
C(1)–O(1)–Sn	116.7(2)	113.3(2)	115.7(5)

SCCO donor fragment is also present; the main difference lies in the Sn–O bond length, which is longer in this case.

The SC Ligand

The C–C (1.44–1.46 Å) and C–O [1.354(4), 1.382(4) Å] bond lengths are as expected for a single bond between sp^2 carbon atoms, except for the C(12)–C(13) [1.345(5) Å] and C(1)–O(1) [1.215(4) Å] lengths which indicate some double bond character.

[SnPh$_3$(BrSC)]·EtOH and [SnPh$_3$(Br$_2$SC)]

The type of coordination and the bond lengths involving the tin atom are similar to those discussed above for [$SnPh_3$(SC)]. As seen in Table 1, the bond lengths around the metal atom are almost identical in all three compounds. The only noticeable difference in the metrical data of these complexes is the Sn–O bond length. Even though the Sn–O bond lengths are quite different [2.589(2), 2.784(3) and 2.666(5) Å], we can conclude that the presence of one or two Br atoms on the phenyl ring of the SC ligand does not induce any significant change in the molecular structure of the complex.

Spectroscopic Studies

The vibrational patterns of the complexes have been analysed in light of their structural study by X-ray diffraction. Thus, the position of ν(C=O) is consistent with the weak Sn–O bond, which is close to that found in inclusion complexes[13] in which a coumarin ligand is hydrogen-bonded via this group. The band at 360 cm^{-1}, present in both IR and Raman spectra and attributable to ν(Sn–S), is consistent with the coordination via the S atom, and ν_{asym}(Sn–C) and ν_{sym}(Sn–C) vibrations are located at positions typical of a non-planar SnC_3 framework.[1,14]

The ^{1}H NMR spectra agree with the evolution associated with the cyclization and deprotonation processes. For instance, carboxylic acid signal found in the spectra of the parent sulfanylpropenoic acids (between 13 and 11 ppm) is absent in the spectra of the tin derivatives due to cyclization. In addition, no signal attributable to the SH proton is observed in the spectra of any of these complexes. The ^{13}C NMR spectra for these complexes are consistent with those for other 3-substituted, 6-bromo-3-substituted or 6,8-dibromo-3-substituted coumarins.[15]

The ^{119}Sn NMR spectra show a singlet at about –101 ppm. This value for the chemical shift falls in the range proposed for a tetra-coordinated tin centre,[16,17] which seems to indicate the loss of the five-coordinate nature upon dissolution. This signal slightly shifts upfield as the temperature increases from 230 to 330 K, but no splitting occurs.

Experimental Section

Methods and Materials: Triphenyltin(IV) hydroxide, rhodanine and diisopropylamine (Aldrich-Chemie) were used as supplied. Elemental analyses were performed with a Carlo Erba 1108 apparatus. Melting points were determined using a GallenKamp MFB-595 apparatus. The IR spectra were recorded on a Bruker IFS 66v FT-IR spectrometer, and the Raman spectra were recorded with the same spectrometer using an FRA-106 accessory. NMR spectra were recorded at room temperature in $CDCl_3$. ^{1}H and ^{13}C NMR spectra were obtained with a Bruker AMX300 spectrometer operating at 300.14 and 75.48 MHz, respectively (referenced to $SiMe_4$). ^{119}Sn NMR spectra were recorded with a Bruker AMX500 apparatus operating at 186.50 MHz (referenced to $SnMe_4$). Downfield shifts were taken to be positive. Mass spectra were recorded with a Kratos MS50TC spectrometer connected to a DS90 data system and operating under EI (70 eV, 250 °C) and FAB conditions (Xe, 8 eV) using as liquid matrix 3-nitrobenzyl alcohol. Crystallographic data were recorded at room temperature on a Bruker CCD Smart apparatus using Mo-K_α radiation (λ = 0.71073 Å). An absorption correction was made by means of the SADABS program,[18] and the structure solution was carried out using the SHELXS-97 program.[19a] Least-squares full-matrix refinements on F^2 were performed using the program SHELXL97.[19a] Reflection data for [$SnPh_3$(BrSC)] were corrected for the diffuse scattering as a result of disordered ethanol molecules by means of the program SQUEEZE,[19b] and the illustrations were obtained with the PLATON package.[19c] Crystal data, details of data collections and refinements are given in Table 2. The molecular structures of the complexes are depicted in Figure 1 and Figures S1 and S2 (Supporting Information) and show ellipsoids at 30% probability level. CCDC reference numbers 265333–265335 contain the supplementary crystallographic data for this paper. These data can be obtained free of charge from The Cambridge Crystallographic Data Centre via www.ccdc.cam.ac.uk/data_request/cif.

Synthesis of the Compounds: 3-Aryl-2-sulfanylpropenoic acids were prepared[20] by condensation of the appropriate benzaldehyde with rhodanine, subsequent hydrolysis in NaOH (1 M) and subsequent acidification with aqueous HCl (1 M).

H_2(*o*-hpspa): From 2-hydroxybenzaldehyde (2.50 g, 10 mmol) as starting material. Colour: yellow. Yield: 1.14 g, 58%. Mp: 140 °C. IR and (Raman): 1682 vs ν(C=O), 1452 s δ(OH), 1264 s ν(C–O), 2568 m (2568 m) ν(S–H) cm^{-1}. EI (main signals): *m*/*z* (%) = 196 (16) [M^+], 178 (40) [$M^+ - H_2O$], 150 (100) [$M^+ - H_2O - CO$], 133

 © 2005 Wiley-VCH Verlag GmbH & Co. KGaA, Weinheim

Table 2. Crystal data and structure refinement for [$SnPh_3$(SC)], [$SnPh_3$(BrSC)]·EtOH and [$SnPh_3$(Br_2SC)].

Compound	[$SnPh_3$(SC)]	[$SnPh_3$(BrSC)]·EtOH	[$SnPh_3$(Br_2SC)]
Empirical formula	$C_{27}H_{20}O_2SSn$	$C_{29}H_{25}BrO_3SSn$	$C_{27}H_{18}Br_2O_2SSn$
Molecular weight	527.18	652.15	684.98
Crystal system	monoclinic	triclinic	monoclinic
Space group	$P2_1/n$	$P\bar{1}$	$C2/c$
a [Å]	9.5474(3)	9.4458(10)	16.3047(16)
b [Å]	24.5775(8)	9.8333(11)	10.0204(10)
c [Å]	10.2597(3)	15.8031(17)	31.026(3)
β [°]	108.6187(10)	99.854(2)	91.607(2)
Volume [Å^3]	2281.45(12)	1397.2(3)	5067.1(9)
Z	4	2	8
Density calcd. [g cm^{-3}]	1.535	1.550	1.796
Absorption coefficient [mm^{-1}]	1.233	2.446	4.267
F(000)	1056	648	2656
Crystal size [mm]	0.20 × 0.25 × 0.25	0.43 × 0.32 × 0.14	0.28 × 0.21 × 0.15
θ range for data collection	1.66–28.27	2.14–28.03	2.39–27.99
Limiting indices	$-12 \le h \le 12$, $-30 \le k \le 32$, $-13 \le 1 \le 7$	$-12 \le h \le 12$, $-12 \le k \le 10$, $-20 \le l \le 20$	$-21 \le h \le 20$, $-13 \le k \le 13$, $-24 \le l \le 40$
Reflections collected	15526	8621	14715
Reflections unique, R	5592 [R(int) = 0.0512]	6006 [R(int) = 0.0253]	5803 [R(int) = 0.0448]
Absorption correction	semi-empirical	semi-empirical	semi-empirical
Data/restrictions/parameters	5592/0/280	6006/0/283	5803/0/293
Goodness-of-fit on F^2	1.013	0.849	1.116
Final R indices [$I > 2\sigma(I)$]	R_1 = 0.0435 wR_2 = 0.0671	R_1 = 0.0359 wR_2 = 0.0696	R_1 = 0.0581 wR_2 = 0.1211
R indices (all data)	R_1 = 0.0892 wR_2 = 0.0788	R_1 = 0.0573 wR_2 = 0.0743	R_1 = 0.1101 wR_2 = 0.1307
Largest diff. peak and hole [e Å^{-3}]	0.476 and – 0.447	0.577 and –0.730	2.850 and –3.077

(5) [M^+ – COOH], 121 (67) [M^+ – H_2O–CO–CHO], 90 (41) [M^+ – H_2O – 2CO – S] 77 (28) [M^+ – H_2O – 2CO – S– CH]. The MS (FAB) spectrum shows the same signals. ^{1}H NMR: δ = 12.84 [br. s, 1 H, C(1)OH], 7.71 [s, 1 H, C(3)H], 10.07 [s, 1 H, C(5)OH], 6.86 [d, 1 H, C(6)H], 7.27 [1 H, C(7)H], 6.88 [d, 1 H, C(8)H], 7.67 [d, 1 H, C(9)H] ppm. ^{13}C NMR: δ = 168.7 C(1), 139.0 C(2), 132.2 C(3), 120.9 C(4), 153.7 C(5), 116.1 C(6), 131.0 C(7), 123.2 C(8), 129.6 C(9) ppm. $C_9H_8O_3S$: calcd. C 55.1, H 4.1, S 16.3%; found C 55.6, H 3.9, S 16.1%.

H_2(Br-*o*-hpspa): From 5-bromo-2-hydroxybenzaldehyde (3.16 g, 10 mmol) as starting material. Colour: yellow. Yield: 2.56 g, 93%. Mp. 133 °C. IR and (Raman): 1677 vs ν(C=O), 1414 m δ(OH), 1278 vs ν(C–O), 2566 w (2575 m) ν(S–H) cm^{-1}. EI (main signals): m/z (%) = 275 (36) [M^+ – H], 256 (100) [M^+ – H – H_2O], 228 (97) [M^+ – H_2O – CO], 230 (95) [M^+ – COOH], 168 (26) [M^+ – H_2O – 2CO – SH], 150 (44) [M^+ – COOH – Br], 120 (54) [M^+ – H_2O–CO–CHO – Br], 149 (98) [M^+ – H_2O–CO–Br]. The FAB spectrum shows the same signals. ^{1}H NMR: δ = 9.84 [s, 1 H, C(3)H], 10.88 [s, 1 H, C(5)OH], 6.90 [d, 1 H, C(6)H], 7.94 [dd, 1 H, C(7)H], 7.66 [d, 1 H, C(9)H] ppm. ^{13}C NMR: δ = 166.6 C(1)OH, 118.2 C(2)SH, 119.8 C(4), 160.1 C(5), 111.3 C(6), 139.6 C(7), 113.0 C(8), 135.5 C(9) ppm. $C_9H_7BrO_3S$: calcd. C 39.3, H 2.5, S 11.6%; found C 39.9, H 2.3, S 11.2%.

H_2(Br$_2$-*o*-hpspa): From 3,5-dibromo-2-hydroxybenzaldehyde (3.79 g, 10 mmol) as starting material. Colour: beige. Yield: 3.36 g, 95%. Mp: 120 °C. IR and (Raman): 1682 vs ν(C=O), 1448 s δ(OH), 1276 vs ν(C–O), 2565 m (2565 w) ν(S–H) cm^{-1}. EI (main signals): m/z (%) = 354 (25) [M^+], 336 (80) [M^+ – H_2O], 308 (100) [M^+ – H_2O – CO], 279 (24) [M^+ – H_2O–CO–CHO], 227 (46) [M^+ – H_2O–CO–BrH], 167 (24) [M^+ – H_2O – 2CO–SH–Br], 148 (21) [M^+ – H_2O – CO – 2Br], 119 (52) [M^+ – H – H_2O – 2CO – 2Br]. The FAB spectrum shows the same signals. ^{1}H NMR: δ = 9.81 [s, 1 H, C(3)H], 11.50 [s, 1 H, C(5)H], 7.94 [s, 1 H, C(7)H], 7.67 [d, 1 H, C(9)OH] ppm. ^{13}C NMR: δ = 157.6 C(1)OH, 118.3 C(2)SH, 122.0 C(4), 160.1 C(5), 111.3 C(6), 142.4 C(7), 111.8 C(8), 135.3 C(9) ppm. $C_9H_6Br_2O_3S$: calcd. C 30.5, H 1.7, S 9.0%; found C 30.7, H 1.6, S 8.8%.

[$SnPh_3$(SC)]: A solution of $SnPh_3OH$ (0.40 g, 1.0 mmol) in 10 mL of an ethanol/acetone mixture (1:1 v/v) was treated with a solution of H_2(*o*-hpspa) (0.10 g, 0.5 mmol) in 10 mL of the same solvent. After stirring and refluxing for 5 h, a beige solid was formed. Yield: 0.32 g, 60%. Mp: 135 °C.. IR and (Raman): 1676 s ν(C=O), 269 s ν_{asym}(Sn–C), 232 s ν_{sym}(Sn–C) 361 sh (360 w) ν(Sn–S) cm^{-1}. EI (main signals): m/z (%) = 528 (3) [M^+], 351 (35) [$SnPh_3$], 197 (8) [SnPh], 120 (6) [Sn]. Besides these signals, the EI spectrum shows signals for H_2(*o*-hpspa) and its fragments, and the FAB spectrum shows the same metallated signals. ^{1}H NMR: δ = 7.91 [s, C(4)H], 7.37–7.22 [m, C(5)H–C(8)H], 7.74–7.72 (m, Ph_o), 7.41–7.38 (m, $Ph_{m,p}$) ppm. ^{13}C NMR: δ = 162.8 C(2), 139.3 C(3), 126.5 C(4), 130.1 C(4a), 151.8 C(8a), 116.4 C(8), 126.5 C(7), 120.0 C(6), 124.9 C(5), 140.6 C_i, 136.7 C_o, 128.7 C_m, 129.3 C_p ppm. ^{119}Sn NMR: δ = –100.9 (s) ppm. $C_{27}H_{20}O_2SSn$: calcd. C 61.5, H 3.8, S 6.1%; found C 61.4, H 3.9, S 6.0%. From the mother liquor of the reaction flask, suitable crystals for X-ray diffraction were isolated.

[$SnPh_3$(BrSC)]: A solution of $SnPh_3OH$ (0.29 g, 0.8 mmol) in 10 mL of an ethanol/acetone mixture (1:1 v/v) was treated with a solution of H_2(Br-*o*-hpspa) (0.10 g, 0.4 mmol) in 10 mL of the same solvent. After refluxing for 5 h, a brown solid was formed. Yield: 0.19 g, 40%. Mp: 145 °C. IR (Raman): 1686 s ν(C=O), 261 s ν_{asym}(Sn–C), 233 s (235 w) ν_{sym}(Sn–C), 359 w (354 w) ν(Sn–S) cm^{-1}.EI (main signals): m/z (%) = 607 (2) [M^+ + H], 351 (65) [$SnPh_3$], 307 (7) [$HSSnPh_2$], 197 (80) [SnPh], 121 (9) [SnH], 120 (34) [Sn]. Besides these signals, the EI spectrum shows signals for H_2(Br-*o*-hpspa) and its fragments, and the FAB spectrum shows the same metallated signals. ^{1}H NMR: δ = 7.81 [s, 1 H, C(4)H], 7.71 [d, 1 H, C(5)H], 7.46 [dd, 1 H, C(7)H], 7.41 [d, 1 H, C(8)H], 7.70 (d, 6 H, Ph_o), 7.40 (q, 9 H, $Ph_{m,p}$) ppm. ^{13}C NMR: δ = 162.1 C(2), 119.8 C(3), 121.5 C(4a), 150.6 C(8a), 118.1 C(8), 128.3 C(7), 117.5 C(6), 132.7 C(5), 140.2 C_i, 136.6 C_o, 128.7 C_m, 129.5 C_p ppm. ^{119}Sn NMR: δ = –98.1 (s) ppm. $C_{27}H_{19}BrO_2SSn$: calcd. C 53.5, H

 © 2005 Wiley-VCH Verlag GmbH & Co. KGaA, Weinheim

3.1, S 5.3%; found C 52.6, H 3.3, S 4.6%. From the mother liquor, crystals of the ethanol solvate suitable for X-ray diffraction were isolated.

[$SnPh_3(Br_2SC)$]: A solution of $SnPh_3OH$ (0.20 g, 0.6 mmol) in 10 mL of an ethanol/acetone mixture (1:1 v/v) was treated with a solution of $H_2(Br_2$-*o*-hpspa) (0.10 g, 0.3 mmol) in 10 mL of the same solvent. After refluxing for 5 h, a white solid was formed. Yield: 0.22 g, 54%. Mp: 162 °C. IR (Raman): 1699 s ν(C=O), 273 w ν_{asym}(Sn–C), 258 s (255 w) ν_{sym}(Sn–C), 361 w ν(Sn–S) cm^{-1}. EI (main signals): *m*/*z* (%) = 609 (31) [$M^+ + H - Ph$], 351 (72) [$SnPh_3$], 308 (17) [$SnPh_2S + 2H$], 197 (93) [SnPh], 120 (43) [Sn]. Besides these signals, the EI spectrum shows signals for $H_2(Br_2$-*o*-hpspa) and its fragments, whilst the FAB spectrum shows the signals for the same metallated fragments as well as another signal at 685 (3) [M^+]. ^{1}H NMR: δ = 7.74 [s, 1 H, C(4)H], 7.42 [d, 1 H, C(7)H], 7.41 [d, 1 H, C(5)H], 7.69 (d, 6 H, Ph_o), 7.40 (q, 9 H, $Ph_{m,p}$) ppm. ^{13}C NMR: δ = 161.3 C(2), 122.2 C(3), 127.5 C(4a), 147.6 C(8a), 117.4 C(8), 137.3 C(7), 110.77 C(6), 135.4 C(5), 139.8 C_i, 136.6 C_o, 128.7 C_m, 129.6 C_p ppm. ^{119}Sn NMR: δ = –94.0 (s) ppm. $C_{27}H_{18}Br_2O_2SSn$: calcd. C 47.3, H 2.6, S 4.7%; found C 46.7, H 2.3, S 4.8%. From the mother liquor, suitable crystals for X-ray diffraction were isolated.

Supporting Information (see footnote on the first page of this article): Figures S1 and S2 showing the molecular structures and numbering schemes of the two complexes are provided.

Acknowledgments

We thank the EU Directorate General for Regional Policies and the Directorate General for Research of the Spanish Ministry of Science and Technology for financial support under ERDF programs (Project BQU2002–04524-C02–02), and the Xunta de Galicia, Galicia (Spain) (Project PGIDIT03PXIC30103PN).

[1] J. S. Casas, A. Castiñeiras, M. D. Couce, M. L. Jorge, U. Russo, A. Sánchez, R. Seoane, J. Sordo, J. M. Varela, *Appl. Organomet. Chem.* **2000**, *14*, 421 and references cited therein.
[2] A. N. Samokhvalov, G. M. Vishnyakova, T. V. Smirnova, *Izvestiya Akademii Nauk SSSR, Seriya Biologicheskaya* **1989**, *1*, 144.
[3] N. J. van Sittert, C. P. Tuinman, *Toxicology* **1994**, *91*, 71.
[4] U. Merkel, H. Sigusch, A. Hoffmann, *Eur. J. Clin. Pharmacol.* **1994**, *46*, 175.
[5] H. Shi, Z. Wang, H. Shi, *Huaxue Shiji* **1999**, *21*, 30.
[6] B. D. James, R. J. Magee, W. C. Patalinghug, B. W. Skelton, A. H. White, *J. Organomet. Chem.* **1994**, *467*, 51.
[7] E. J. Huheey, E. A. Keiter, R. L. Keiter, *Inorganic Chemistry. Principles of Structure and Reactivity*, Harper Collins College Publishers, New York, 4th ed., **1993**, p. 292.
[8] S. W. Ng, V. G. Kumar Das, G. Yap, A. L. Rheingold, *Acta Crystallogr., Sect. C* **1996**, *52*, 1369.
[9] D. N. Rau, Ph. D. Thesis, University of Massachusetts, USA, **1988**, University Microfilm International, Ann Arbor MI, **1990**.
[10] A. Kalsoom, M. Mazhar, S. Ali, M. F. Mahon, K. C. Molloy, M. I. Chaudry, *Appl. Organomet. Chem.* **1997**, *11*, 47 and references cited therein.
[11] A. R. Forrester, S. J. Garden, R. A. Howie, J. L. Wardell, *J. Chem. Soc., Dalton Trans.* **1992**, 2625 and references cited therein.
[12] A. W. Addison, T. N. Rao, J. Reedijk, J. van Rijn, G. C. Verschoor, *J. Chem. Soc., Dalton Trans.* **1984**, 1349.
[13] K. Tanaka, E. Mochizuki, N. Yasui, Y. Kai, I. Migahara, K. Hirotsu, F. Toda, *Tetrahedron* **2000**, *56*, 6853.
[14] G. Eng, D. Whalen, P. Masangatinimi, J. Tierney, M. de Rosa, *Appl. Organomet. Chem.* **1998**, *12*, 25.
[15] P. T. Kaye, M. A. Musa, *Synthesis* **2002**, *18*, 2701.
[16] J. S. Casas, A. Castiñeiras, E. García-Martínez, A. Sánchez-González, A. Sánchez, J. Sordo, *Polyhedron* **1997**, *16*, 795.
[17] J. Holeček, M. Nádvorník, K. Handlíř, A. Lyčka, *J. Organomet. Chem.* **1983**, *241*, 177.
[18] G. M. Sheldrick, *SADABS, "An Empirical Absorption Correction Program for Area Detector Data"*, University of Göttingen, Germany, **1996**.
[19] a) G. M. Sheldrick, *SHELX-97, "Program for Crystal Structure Solution and Refinement"*, University of Göttingen, Germany, **1997**; b) A. L. Spek, *Acta Crystallogr., Sect. A* **1990**, *34*, 46; c) A. L. Spek, *PLATON v. 3.04.02*, University of Utrecht, The Netherlands, **2002**, http://www.cryst.chem.uu.nl/platon/.
[20] E. Campaigne, R. E. Cline, *J. Org. Chem.* **1956**, *21*, 32.

Received: March 18, 2005
Published Online: September 21, 2005

 © 2005 Wiley-VCH Verlag GmbH & Co. KGaA, Weinheim

Pyrazolylamidino- and Bis(pyrazole)manganese(I) Complexes

Marta Arroyo,[a] Álvaro López-Sanvicente,[a] Daniel Miguel,[a] and Fernando Villafañe*[a]

Keywords: Manganese / N ligands / Pyrazole / Pyrazolylamidino ligands

The pyrazolylamidino complexes *fac*-[MnBr(CO)$_3${NH=C(R)-pz-κ^2*N*,*N*}] or *fac*-[MnBr(CO)$_3${NH=C(R)dmpz-κ^2*N*,*N*}] (R = CH_3, C_6H_5) are obtained by reaction of *fac*-[MnBr(CO)$_3$-(NCR)$_2$] and equimolar amounts of pzH or dmpzH (dmpz = 3,5-Me_2pz), although these reactions also afford the bis(pyrazole) complexes as by-products. The bispyrazole complexes *fac*-[MnBr(CO)$_3$(pzH)$_2$] or *fac*-[MnBr(CO)$_3$(dmpzH)$_2$] are selectively obtained from [MnBr(CO)$_5$] and two equivalents of pzH or dmpzH. Their solid-state structures, determined by X-ray diffraction methods, show the N-bound hydrogens of the pyrazoles pointing towards the bromine atom. The pyrazolylamidino complexes can also be prepared by reactions of equimolar amounts of the bispyrazole and the bisnitrile complexes. The solid-state structures of the pyrazolylamidino complexes containing the dmpz fragment were determined by X-ray diffraction methods.
(© Wiley-VCH Verlag GmbH & Co. KGaA, 69451 Weinheim, Germany, 2005)

Introduction

An increasing interest is being dedicated to pyrazole-containing chelating ligands.[1] Among them, those containing pyridyl and pyrazolyl fragments are receiving the highest attention, probably because they are involved in different and interdisciplinary aspects, such as the synthesis of supramolecular assemblies or the design of molecules displaying physical properties of interest.[2,3] At the opposite side concerning the attention received are pyrazolylamidines, since only molybdenum, iridium, ruthenium, and platinum complexes containing these ligands have been described so far.[4] However, amidino has been found to be a promising ligand,[5] which may be attributed to several special features of pyrazolylamidino complexes: (a) the different properties of the two donor atoms and the electron delocalization within the ligand makes them potentially interesting for electron-transfer processes and related physical properties, as occurs for the related pyridyl- and pyrazolyl-containing polydentate ligands; (b) the pyrazolylamidino ligands are synthesized in situ (Scheme 1), thus using different nitriles and pyrazoles allows the opportunity of controlling both the electronic and steric properties of the metal complexes, in contrast with most of the ligands, which must be previously synthesized; (c) the NH group may be deprotonated, giving rise to further reactivity by attack of different electrophiles including metal fragments, which would afford heterometallic complexes.

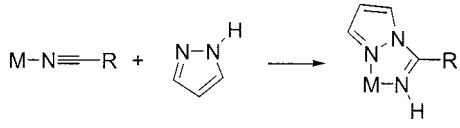

Scheme 1. General method for the synthesis of pyrazolylamidino complexes.

As part of our studies on the chemistry of group 6 and 7 complexes with N-donor chelating ligands,[6] we decided to study the coordination of the pyrazolylamidino ligand to these metals, which has not been explored so far. The first pyrazolylamidinomanganese complexes are reported here.[7] During the course of this work we unexpectedly obtained bis(pyrazole) manganese complexes, which had not been previously reported, therefore their selective syntheses are also described.

The chemistry of bis(pyrazole) complexes is also attracting our attention,[8] since both their structures and reactivity are promising aspects. Concerning their structures, the N-bound hydrogen of pyrazole complexes is commonly involved in hydrogen bonds that give rise to supramolecular arrangements.[9,10] Concerning their reactivity, terminal pyrazole ligands are very useful precursors for bridging pyrazolate homo- or heterobimetallic complexes, which may be obtained by deprotonating the N-bound hydrogen of the coordinated pyrazole when a second metallic substrate is present. This strategy has been successively used by different groups, mainly with middle and late transition elements.[11]

[a] Química Inorgánica, Facultad de Ciencias, Universidad de Valladolid,
47005 Valladolid, Spain
Fax: +34-983-423-013
E-mail: fervilla@qi.uva.es

 © 2005 Wiley-VCH Verlag GmbH & Co. KGaA, Weinheim **DOI: 10.1002/ejic.200500419**

Results and Discussion

Synthesis and Characterization of Bis(pyrazole)manganese Complexes

The bis(pyrazole)manganese(I) complexes *fac*-[$MnBr(CO)_3(pzH)_2$] (**1a**) and *fac*-[$MnBr(CO)_3(dmpzH)_2$] (**1b**) were obtained when [$MnBr(CO)_5$] was treated with a twofold excess of pzH or dmpzH in warm CH_2Cl_2. A white insoluble solid was detected in the reactions with pzH, although the yield of **1a** is still high.[12]

The *fac* geometry of both complexes is evident from their IR spectra in the C–O stretching region, which show three absorptions. The C–O frequencies are slightly higher for **1a** than for **1b**, as is to be expected considering that Hdmpz is a better donor than Hpz. This geometry is supported by the NMR spectroscopic data, as both pyrazole ligands are equivalent. The broadness of the HN signal must be due to a protolysis process involving this proton, which is common in pyrazole complexes. Homodecoupling experiments at low temperature carried out on previously reported complexes have allowed the unequivocal assignment of the signals of the pyrazolic hydrogens.[8a] However, this assignment cannot be unequivocally extended to the complexes described herein, since the chemical shifts of the hydrogens or methyl groups in positions 3 and 5 seem to be affected by different factors that are difficult to evaluate: whether the hydrogen (or methyl) group at position 3 resonates at higher field than that at position 5, or vice versa, may vary in the same family of complexes,[11g] or even depending on the solvent used.[13] Therefore, the assignment proposed for the rest of complexes in the Experimental Section shoud be considered as tentative.

Structure reports of pyrazolemanganese(II) complexes are quite common, but we have only been able to find one report of a crystal structure of a pyrazolemanganese(I) complex,[14] therefore the geometries of complexes **1** were determined by X-ray diffractometric studies. The structures are shown in Figure 1 and relevant distances and angles are collected in Table 1.[15] The distances and angles are very similar in both complexes, and the latter are also similar to those found in previously reported structures of halotricarbonylmanganese(I) complexes containing two monodentate N-donor ligands, which show a slightly distorted octahedral geometry.[16] These distortions are evidenced by the slight deviation from linearity shown by the ligands coordinated *trans* [174.84(17)–176.7(2)°], as well as by the angles formed by the ligands coordinated *cis* [85.71(13)–96.3(2)°]. In both structures the smaller angles are those formed by the two pyrazoles, as occurs in the related manganese(I) complexes containing two monodentate N-donor ligands indicated above.[16]

The N-bound hydrogens of the pyrazoles point to the bromine atom, which may be attributed both to steric and electronic reasons. Steric factors are obviously more important in **1b**, where this orientation brings the methyl groups bound to the 5-carbon close to a carbonyl group, which is smaller than the bromine atom. Therefore, this orientation

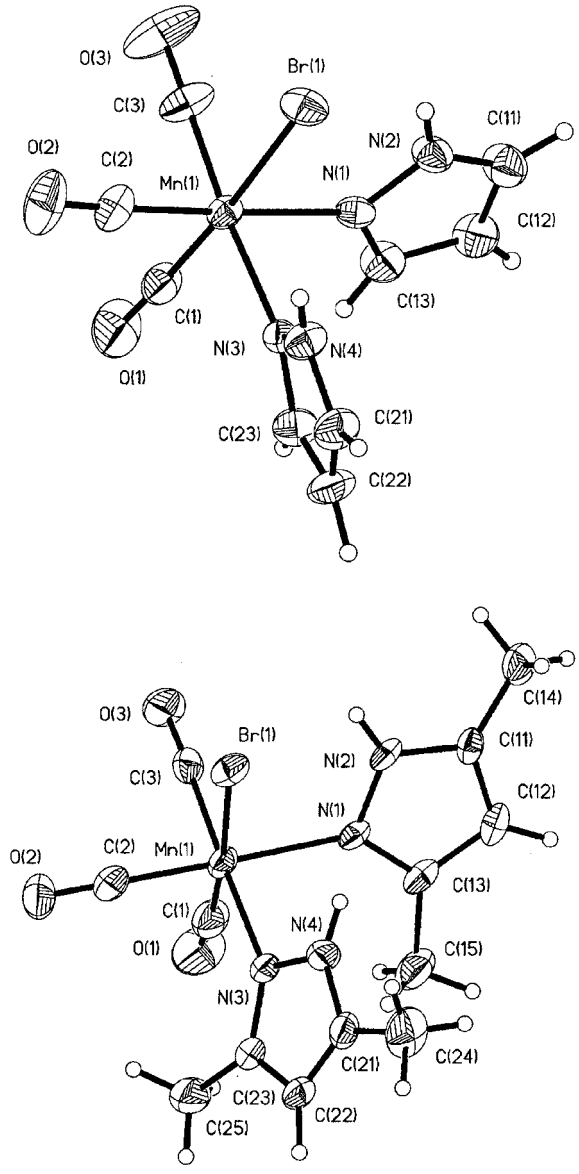

Figure 1. Perspective views of *fac*-[$MnBr(CO)_3(pzH)_2$] (**1a**, top), and *fac*-[$MnBr(CO)_3(dmpzH)_2$] (**1b**, bottom), showing the atom numbering.

reduces the steric hindrance, since the methyl groups bound to the 5-carbon and the bulky bromine atom are at opposite sides of the molecule. Steric hindrance is also responsible for the tilting of the Hdmpz ligands, which are bent in the same sense around the Mo–N bonds, as has been found in other bis(Hdmpz) complexes.[8b] The average dihedral angles are 37(1)° and 34(1)°, so they are close to the planes that bisect the angles between the *cis* substituents. This tilting is not observed in **1a**, where the deviation of the Hpz ligands from the plane perpendicular to that containing the metal and the nitrogen donor atoms is much lower [23(1)° and –10(1)°]. The second difference between the pyrazole ligands in **1a** and **1b** concerns their relative orientation: in **1b** they are tilted in the same direction in order to reduce their steric hindrance, whereas in **1a** the Hpz ligands are

 © 2005 Wiley-VCH Verlag GmbH & Co. KGaA, Weinheim

Table 1. Selected distances [Å] and angles [°] for *fac*-[MnBr(CO)$_3$(pzH)$_2$] (**1a**) and *fac*-[MnBr(CO)$_3$(dmpzH)$_2$] (**1b**).

	1a	1b
Mn(1)–C(1)	1.776(5)	1.760(6)
Mn(1)–C(3)	1.790(5)	1.799(6)
Mn(1)–C(2)	1.817(6)	1.780(6)
Mn(1)–N(3)	2.070(3)	2.080(4)
Mn(1)–N(1)	2.078(3)	2.085(4)
Mn(1)–Br(1)	2.5448(9)	2.5420(10)
C(1)–O(1)	1.135(6)	1.159(6)
C(2)–O(2)	1.127(6)	1.152(6)
C(3)–O(3)	1.144(6)	1.147(5)
C(1)–Mn(1)–C(3)	90.2(3)	86.9(2)
C(1)–Mn(1)–C(2)	90.0(3)	90.7(3)
C(3)–Mn(1)–C(2)	89.9(2)	89.2(2)
C(1)–Mn(1)–N(3)	91.93(19)	96.3(2)
C(3)–Mn(1)–N(3)	175.6(2)	176.7(2)
C(2)–Mn(1)–N(3)	93.9(2)	91.5(2)
C(1)–Mn(1)–N(1)	93.6(2)	94.1(2)
C(3)–Mn(1)–N(1)	90.3(2)	92.7(2)
C(2)–Mn(1)–N(1)	176.4(2)	174.9(2)
N(3)–Mn(1)–N(1)	85.71(13)	86.39(16)
C(1)–Mn(1)–Br(1)	176.06(16)	174.84(17)
C(3)–Mn(1)–Br(1)	88.98(18)	88.31(16)
C(2)–Mn(1)–Br(1)	86.19(19)	87.37(19)
N(3)–Mn(1)–Br(1)	89.17(10)	88.48(12)
N(1)–Mn(1)–Br(1)	90.26(10)	88.01(11)

tilted slightly such that the C5-bound hydrogens are closer than the N-bound hydrogens.

Electronic factors also explain why these hydrogens point to the bromine atom, since they are involved in weak intermolecular hydrogen bonds. In **1a**, only intramolecular hydrogen bonds are detected: 2.66 Å for H(2)···Br and 2.57 Å for H(4)···Br. These and the corresponding N···Br distances [3.206(1) and 3.212(1) Å] confirm the presence of a hydrogen bond, which may be considered as "weak".[17] The bromine atom in **1b** is also involved in two weak intramolecular hydrogen bonds with the N-bound hydrogens [2.62 Å for H(2)···Br and 2.57 Å for H(4)···Br], the corresponding N···Br distances being 3.218(1) and 3.191(1) Å, and by a weak intermolecular hydrogen bond to one of the N-bound hydrogen atoms of an adjacent molecule [2.68 Å for H(2)···Br, with N···Br = 3.519(1)]. Similar hydrogen bond lengths have been found for other bromo complexes containing pyrazoles.[8a,18]

The structure of the related rhenium complex *fac*-[ReBr(CO)$_3$(pzH)$_2$][18a] shows some analogies and differences with those reported here: the relative orientation of the pzH ligands is similar to that of Hdmpz in **1b**, but only one of the N-bound hydrogens in the rhenium complex is involved in a intermolecular hydrogen bond.

Synthesis and Characterization of Pyrazolylamidinomanganese Complexes

The synthesis of pyrazolylamidinomanganese(I) complexes was carried out by reacting equimolar amounts of the corresponding bis(nitrile) complexes and pyrazole (Scheme 1). Nucleophilic addition to metal-activated nitriles is a well-known reaction that has been extensively used to obtain a wide variety of ligands.[19]

The acetonitrile complex *fac*-[MnBr(CO)$_3$(NCMe)$_2$], which was first described more than thirty years ago,[20] was synthesized by heating [MnBr(CO)$_5$] in acetonitrile under controlled conditions in order to avoid bromide displacement to yield the cationic product. It is well known that the carbonyls are ejected before the substitution of the bromide when a thermal process is carried out.[21] A similar method was used to obtain *fac*-[MnBr(CO)$_3$(NCPh)$_2$] (see Exp. Sect.), for which we have not been able to find any previous report.[22]

The reactions of the bis(nitrile) complexes and pyrazole (Scheme 2, route *i*) afford the desired pyrazolylamidino complexes *fac*-[MnBr(CO)$_3${*N*H=C(R)pz-κ^2*N*,*N*}] (R = CH$_3$, **2a**; Ph, **3a**) or *fac*-[MnBr(CO)$_3${*N*H=C(R)dmpz-κ^2*N*,*N*}] (R = CH$_3$, **2b**; Ph, **3b**). However, variable amounts of the bis(pyrazole) complexes **1** are also obtained as by-products. The presence of the bispyrazole complexes could be due to the instability of the bisnitrile complexes under these reaction conditions, which would decrease the amount of available manganese and therefore would increase the manganese/pyrazole ratio. Thus, we decided to attempt the syntheses of the pyrazolylamidino complexes by reacting equimolar amounts of the bis(nitrile) and bis(pyrazole) complexes (Scheme 2, route *ii*) as we believed this would increase the amount of manganese present in the mixture and would not increase the manganese/pyrazole ratio. However, this method did not improve the selectivity of the

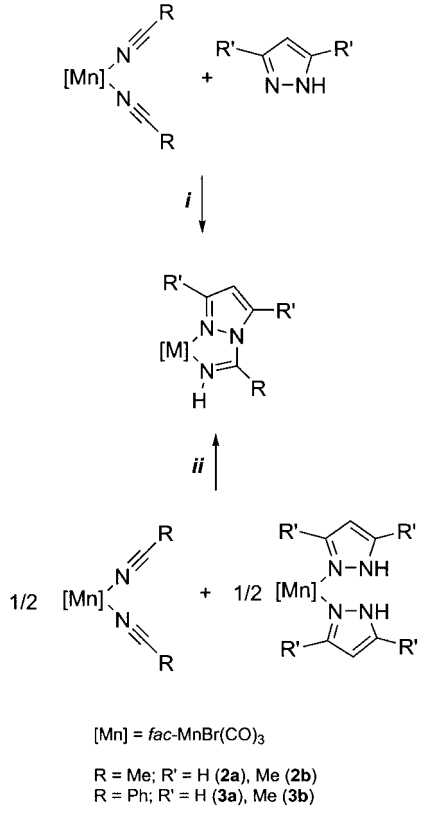

Scheme 2. Synthesis of pyrazolylamidino complexes.

 © 2005 Wiley-VCH Verlag GmbH & Co. KGaA, Weinheim

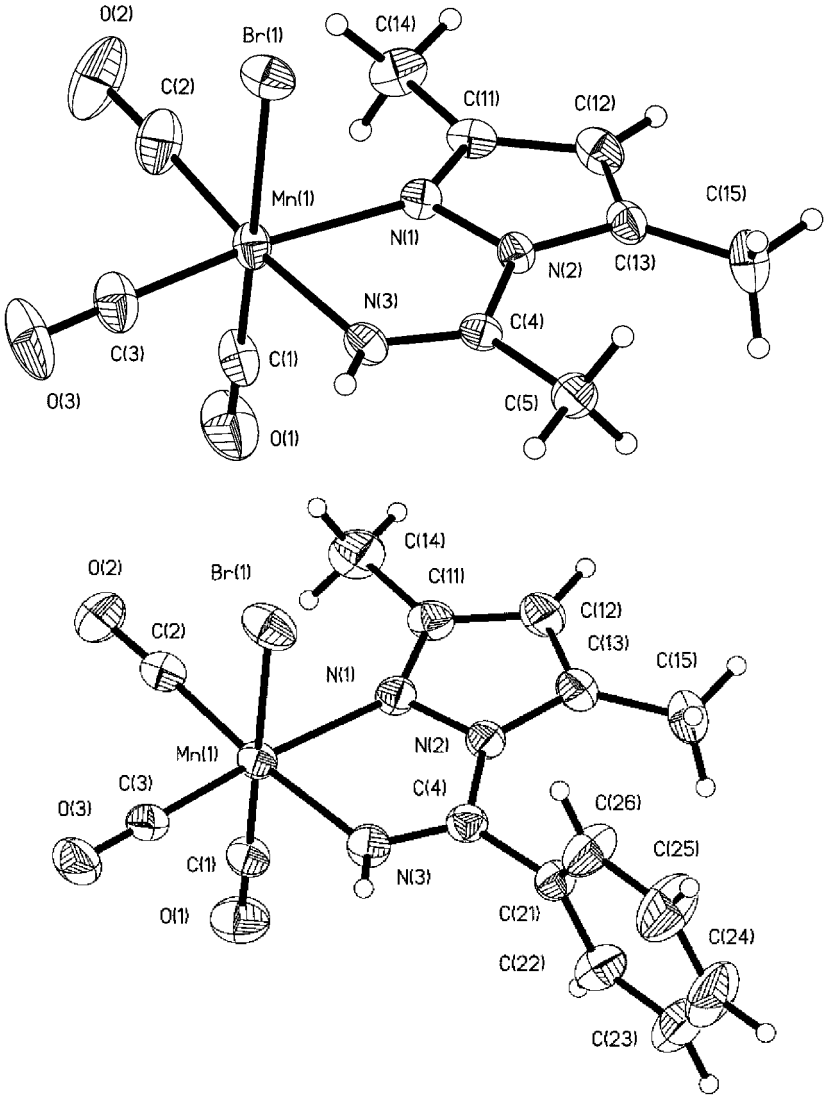

Figure 2. Perspective views of *fac*-[MnBr(CO)$_3${*N*H=C(Me)dmpz-κ^2*N*,*N*}] (**2b**, top) and *fac*-[MnBr(CO)$_3${*N*H=C(Ph)dmpz-κ^2*N*,*N*}] (**3b**, bottom) showing the atom numbering.

process since it afforded similar mixtures of **1** and **2** (see Exp. Sect.).

The C–O stretching region of **2** in the IR spectra also shows three absorptions, as expected for a *fac* geometry. The C–O frequencies follow the expected trends considering the better donor properties of (a) Hdmpz compared to Hpz, and (b) amidino ligands derived from acetonitrile compared to those derived from benzonitrile. The C–N stretching absorption of the amidine ligand is also evident in the IR spectra. The C–N frequencies are slightly higher for complexes **2** than for complexes **3**, which could point to a higher delocalization in the latter due to the presence of a phenyl group instead of a methyl.

The NMR spectroscopic data do not provide structural information, therefore one of each type of complex was subjected to a crystallographic study. The structures are shown in Figure 2 and relevant distances and angles are collected in Table 2. The structural data are essentially the same in both complexes, and very similar to those found in previously reported structures of halotricarbonylmanganese(I) complexes containing a bidentate N-donor ligand.[23] The distances and angles found in the pyrazolylamidino ligands are also similar to those found in other pyrazolylamidino complexes.[4]

The N-bound hydrogen atoms of both structures are involved in intermolecular hydrogen bonds, with the bromine atom in **2b** [H(3)···Br = 2.66 Å; N(3)···Br = 3.483(1) Å], which may be considered as "weak",[17] whereas in **3b** they are linked to a molecule of tetrahydrofuran present in the lattice [H(3)···O(90) = 1.90 Å; N(3)···O(90) = 2.873(7) Å] by a hydrogen bond which may be considered as "moderate".[17]

Experimental Section

General Remarks: All manipulations were performed under N_2 by conventional Schlenk techniques. Filtrations were carried out with dry Celite under N_2. Solvents were purified according to standard

 © 2005 Wiley-VCH Verlag GmbH & Co. KGaA, Weinheim

Table 2. Selected distances [Å] and angles [°] for *fac*-[MnBr(CO)$_3$-{*N*H=C(Me)dmpz-κ^2*N*,*N*}] (**2b**) and *fac*-[MnBr(CO)$_3${*N*H=C(Ph)-dmpz-κ^2*N*,*N*}] (**3b**).

	2b	**3b**
Mn(1)–C(1)	1.793(4)	1.790(5)
Mn(1)–C(2)	1.807(4)	1.802(5)
Mn(1)–C(3)	1.807(4)	1.786(5)
Mn(1)–N(1)	2.041(2)	2.039(3)
Mn(1)–N(3)	2.007(3)	1.995(4)
Mn(1)–Br(1)	2.5840(13)	2.5337(9)
N(1)–N(2)	1.391(3)	1.379(4)
N(2)–C(4)	1.391(3)	1.391(5)
N(3)–C(4)	1.275(3)	1.267(5)
C(1)–O(1)	1.148(4)	1.131(5)
C(2)–O(2)	1.147(4)	1.145(5)
C(3)–O(3)	1.140(3)	1.144(5)
C(1)–Mn(1)–C(3)	91.31(13)	90.37(19)
C(1)–Mn(1)–C(2)	89.78(15)	92.6(2)
C(3)–Mn(1)–C(2)	89.58(16)	88.81(19)
C(1)–Mn(1)–N(3)	95.65(13)	91.52(18)
C(3)–Mn(1)–N(3)	94.07(13)	94.88(18)
C(2)–Mn(1)–N(3)	173.38(13)	174.42(17)
C(1)–Mn(1)–N(1)	89.78(11)	93.97(17)
C(3)–Mn(1)–N(1)	170.62(12)	170.69(17)
C(2)–Mn(1)–N(1)	99.74(13)	93.97(17)
N(3)–Mn(1)–N(1)	76.56(10)	76.79(15)
C(1)–Mn(1)–Br(1)	177.55(10)	178.73(15)
C(3)–Mn(1)–Br(1)	89.26(9)	88.76(13)
C(2)–Mn(1)–Br(1)	87.84(12)	88.26(14)
N(3)–Mn(1)–Br(1)	86.68(8)	87.63(12)
N(1)–Mn(1)–Br(1)	90.04(7)	86.75(9)
N(2)–N(1)–Mn(1)	113.81(15)	113.1(2)
N(1)–N(2)–C(4)	115.0(2)	115.7(3)
C(4)–N(3)–Mn(1)	120.1(2)	120.3(3)
N(3)–C(4)–N(2)	114.4(2)	114.0(4)

procedures.[24] *fac*-[MnBr(CO)$_3$(NCMe)$_2$] was obtained as described below and its CO stretching bands were compared with those described previously.[20] *fac*-[MnBr(CO)$_3$(NCPh)$_2$] was obtained as described below and its CO stretching bands were compared with those displayed by a sample of *fac*-[MnBr(CO)$_3$-(NCPh)$_2$] obtained by the method previously described for the MeCN complex.[20] All other reagents were obtained from the usual commercial suppliers and used as received. IR spectra were recorded with a Perkin–Elmer RX I FT-IR apparatus as KBr pellets from 4000 to 400 cm^{-1}. NMR spectra were recorded with Bruker AC-300 or ARX-300 instruments in $(CD_3)_2CO$, at room temperature unless otherwise stated. NMR spectra are referenced to the internal residual solvent peak for ^{1}H and ^{13}C{^{1}H} NMR. Assignment of the ^{13}C{^{1}H} NMR spectroscopic data was supported by DEPT experiments and relative intensities of the resonance signals. Elemental analyses were performed on a Perkin–Elmer 2400B microanalyzer.

***fac*-[MnBr(CO)$_3$(Hpz)$_2$] (1a):** Hpz (0.041 g, 0.6 mmol) was added to a solution of [MnBr(CO)$_5$] (0.082 g, 0.3 mmol) in CH_2Cl_2 (20 mL). The solution was stirred at 40 °C for 2 h, during which time a white solid precipitated. The solvent was removed in vacuo and the yellow residue was extracted with THF (ca. 20 mL) and filtered. Hexane was added (ca. 20 mL) and the solution was concentrated and cooled to –20 °C to give a yellow-orange microcrystalline solid, which was decanted, washed with hexane (3 × 3 mL approximately), and dried in vacuo to yield 0.094 g (88%) of **1a**. IR (THF): $\tilde{\nu}$ = 2030 cm^{-1} vs, 1940 vs, 1910 vs. IR (KBr): $\tilde{\nu}$ = 3341 cm^{-1} m, 3302 m, 3144 w, 2921 w, 2035 vs, 1940 vs, 1918 vs, 1468 w, 1352 w, 1139 w, 1127 m, 1056 m, 763 m, 676 w, 634 w, 602 w, 583 w, 512 w. ^{1}H NMR (300 MHz): δ = 6.47 (s, 2 H, *H*^{4} Hpz), 7.81 (s, 2 H, *H*^{3} Hpz), 7.89 (s, 2 H, *H*^{5} Hpz), 12.16 (br., 2 H, *H*N) ppm. ^{13}C{^{1}H} NMR (75.78 MHz): δ = 107.9 (s, *C*^{4} Hpz), 132.6 (s, *C*^{3,5} Hpz), 144.2 (s, *C*^{5,3} Hpz), 222.8 (br., *C*O) ppm. $C_9H_8BrMnN_4O_3$ (355.03): calcd. C 30.45, H 2.27, N 15.78; found C 30.60, H 2.32, N 15.98.

***fac*-[MnBr(CO)$_3$(Hdmpz)$_2$] (1b):** Hdmpz (0.058 g, 0.6 mmol) was added to a solution of [MnBr(CO)$_5$] (0.082 g, 0.3 mmol) in CH_2Cl_2 (20 mL). The solution was stirred at 40 °C for 2 h. Hexane was added (ca. 20 mL) and the solution was concentrated and cooled to –20 °C to give a yellow-orange microcrystalline solid, which was decanted, washed with hexane (3 × 3 mL approximately), and dried in vacuo to yield 0.113 g (92%) of **1b**. IR (THF): $\tilde{\nu}$ = 2026 cm^{-1} vs, 1935 vs, 1904 vs. IR (KBr): $\tilde{\nu}$ = 3299 cm^{-1} m, 2930 w, 2022 vs, 1940 vs, 1898 vs, 1574 s, 1470 m, 1422 w, 1377 m, 1284 m, 1178 w, 1156 w, 1040 w, 1026 w, 817 w, 789 m, 686 w, 658 w, 637 m, 560 w, 519 w, 469 w. ^{1}H NMR (300 MHz): δ = 2.15 (s, 6 H, C*H*$_3$ Hdmpz), 2.25 (s, 6 H, C*H*$_3$ Hdmpz), 6.01 (s, 2 H, *H*^{4} Hdmpz), 11.02 (br., 2 H, *H*N) ppm. ^{13}C{^{1}H} NMR (75.78 MHz): δ = 10.8 (s, *C*H$_3$ Hdmpz), 14.2 (s, *C*H$_3$ Hdmpz), 107.8 (s, *C*^{4} Hdmpz), 143.1 (s, *C*^{3,5} Hdmpz), 154.2 (s, *C*^{5,3} Hdmpz), 222.8 (br., *C*O) ppm. $C_{13}H_{16}BrMnN_4O_3$ (411.13): calcd. C 37.98, H 3.92, N 13.63; found C 38.02, H 3.59, N 13.44.

***fac*-[MnBr(CO)$_3${*N*H=C(CH$_3$)pz-κ^2*N*,*N*}] (2a). Method A:** A solution of [MnBr(CO)$_5$] (0.137 g, 0.5 mmol) in CH_3CN (20 mL) was maintained at 60 °C for 30 min. Then, Hpz (0.034 g, 0.5 mmol) was added and the solution was heated for 30 min. The solvent was removed in vacuo and the yellow residue was extracted with THF (ca. 20 mL) and filtered. Hexane was added (ca. 10 mL) and the solution was concentrated and cooled to –20 °C to give a yellow-orange microcrystalline solid, which was decanted, washed with hexane (3 × 3 mL approximately), and dried in vacuo to yield 0.098 g (60%) of **2a**. Concentration of the mother liquor and further cooling to –20 °C, yielded 0.015 g (8% referred to manganese) of **1a** after decanting, washing with hexane (3 × 3 mL approximately), and drying in vacuo.

Method B: A solution of [MnBr(CO)$_5$] (0.082 g, 0.3 mmol) in CH_3CN (20 mL) was maintained at 60 °C for 30 min. Then, **1a** (0.106 g, 0.3 mmol) was added and the solution was heated for 30 min. The solvent was removed in vacuo and the yellow residue was extracted with THF (ca. 20 mL) and filtered. Hexane was added (ca. 10 mL) and the solution was concentrated and cooled to –20 °C to give a yellow-orange microcrystalline solid, which was decanted, washed with hexane (3 × 3 mL approximately), and dried in vacuo to yield 0.123 g (62%) of **2a**. Concentration of the mother liquor and further cooling to –20 °C gave 0.018 g (8%) of **1a**, after decanting, washing with hexane (3 × 3 mL approximately), and drying in vacuo. IR (THF): $\tilde{\nu}$ = 2027 cm^{-1} vs, 1939 vs, 1912 vs. IR (KBr): $\tilde{\nu}$ = 3191 cm^{-1} m, 3143 w, 2034 vs, 1938 vs, 1918 vs, 1655 m, 1520 w, 1458 w, 1434 w, 1408 m, 1397 w, 1373 w, 1330 w, 1241 m, 1221 w, 1128 w, 1070 w, 1050 w, 1042 w, 1000 w, 962 w, 766 m, 686 w, 688 m, 632 m, 600 w, 517 m. ^{1}H NMR (300 MHz): δ = 2.87 [s, 3 H, N=C(C*H*$_3$)], 6.83 (s, 1 H, *H*^{4} pz), 8.38 (d, *J* = 1.5 Hz, 1 H, *H*^{3} pz), 8.61 (d, *J* = 3.0 Hz, 1 H, *H*^{5} pz), 11.06 (br., 1 H, *H*N) ppm. ^{13}C{^{1}H} NMR (75.78 MHz): δ = 19.0 [s, HN=C(*C*H$_3$)], 112.4 (s, *C*^{4} pz), 133.4 (s, *C*^{3,5} pz), 147.7 (s, *C*^{5,3} pz), 161.8 [s, HN=*C*(CH$_3$)] ppm; *C*O not observed. $C_8H_7BrMnN_3O_3$ (328.00): calcd. C 29.29, H 2.15, N 12.81; found C 28.97, H 2.31, N 13.07.

***fac*-[MnBr(CO)$_3${*N*H=C(CH$_3$)dmpz-κ^2*N*,*N*}] (2b). Method A:** A solution of [MnBr(CO)$_5$] (0.137 g, 0.5 mmol) in CH_3CN (20 mL) was maintained at 60 °C for 30 min. Then, Hdmpz (0.048 g, 0.5 mmol) was added and the solution was heated for 30 min.

 © 2005 Wiley-VCH Verlag GmbH & Co. KGaA, Weinheim

Work-up as for **2a** yielded 0.090 g (50%) of **2b** and 0.005 g (2% referred to manganese) of **1b**.

Method B: A solution of $[MnBr(CO)_5]$ (0.082 g, 0.3 mmol) in CH_3CN (20 mL) was maintained at 60 °C for 30 min. Then, **1b** (0.106 g, 0.3 mmol) was added and the solution was heated for 30 min. Work-up as for **2a** yielded 0.135 g (57%) of **2b** and 0.007 g (2%) of **1b**. IR (THF): $\tilde{\nu}$ = 2023 cm^{-1} vs, 1934 vs, 1909 vs. IR (KBr): $\tilde{\nu}$ = 3444 cm^{-1} w, 3194 m, 2032 s, 1942 s, 1921 vs, 1909 vs, 1651 m, 1574 w, 1453 w, 1410 m, 1357 w, 1246 w, 1097 w, 1044 w, 843 w, 802 w, 684 w, 634 w, 520 w. ^1H NMR (300 MHz): δ = 2.58 (s, 3 H, CH_3 dmpz), 2.69 (s, 3 H, CH_3 dmpz), 2.89 [s, 3 H, N=C(CH_3)], 6.39 (s, 1 H, H^4 dmpz), 10.67 (br., 1 H, *H*N) ppm. $^{13}C\{^1H\}$ NMR (75.78 MHz): δ = 14.0 (s, *C*H_3 dmpz), 15.3 (s, *C*H_3 dmpz), 21.4 [s, HN=C(*C*H_3)], 114.3 (s, C^4 dmpz), 145.5 (s, $C^{5,3}$ dmpz), 157.0 (s, $C^{3,5}$ dmpz), 163.6 [s, HN=*C*(CH_3)] ppm; *C*O not observed. $C_{10}H_{11}BrMnN_3O_3$ (356.05): calcd. C 33.73, H 3.11, N 11.80; found C 33.63, H 3.00, N 11.51.

***fac*-[MnBr(CO)$_3${*N*H=C(C_6H_5)pz-κ^2*N*,*N*}] (3a). Method A:** C_6H_5CN (500 μL) was added to a solution of $[MnBr(CO)_5]$ (0.137 g, 0.5 mmol) in THF (20 mL) and the mixture was stirred at 70 °C for 1 h. Then, Hpz (0.034 g, 0.5 mmol) was added and the solution was heated at 70 °C for an additional hour. The solvent was removed in vacuo and the yellow residue was washed with hexane (5×3 mL approximately), extracted with THF (ca. 20 mL), and filtered. Hexane was added (ca. 10 mL) and the solution was concentrated and cooled to –20 °C to give a yellow-orange microcrystalline solid, which was decanted, washed with hexane (3×3 mL approximately), and dried in vacuo to yield 0.027 g (14%) of **3a**. Concentration of the mother liquor and further cooling to –20 °C, yielded 0.014 g (8% referred to manganese) of **1a**, after decanting, washing with hexane (3×3 mL approximately), and drying in vacuo.

Method B: C_6H_5CN (300 μL) was added to a solution of $[MnBr(CO)_5]$ (0.082 g, 0.3 mmol) in THF (20 mL) and the mixture was stirred at 70 °C for 1 h. Then, **1a** (0.106 g, 0.3 mmol) was added and the solution was heated at 70 °C for 45 min. Work-up as for **3a** yielded 0.039 g (17%) of **3a** and 0.013 g (5%) of **1a**. IR (THF): $\tilde{\nu}$ = 2027 cm^{-1} vs, 1941 s, 1914 s. IR (KBr): $\tilde{\nu}$ = 3401 cm^{-1} s, 2030 vs, 1936 vs, 1916 vs, 1628 m, 1560 w, 1452 w, 1429 w, 1406 w, 1383 w, 1262 w, 1218 w, 1088 w, 1054 w, 867 w, 776 m, 699 w, 684 w, 639 w, 625 w, 521 w. ^1H NMR (300 MHz): δ = 6.85 (s, 1 H, H^4 pz), 7.68 (d, *J* = 7.1 Hz, 2 H, C_6H_5), 7.72 (d, *J* = 7.1 Hz, 1 H, C_6H_5), 7.80 (d, *J* = 7.1 Hz, 2 H, C_6H_5), 8.34 (s, 1 H, H^3 pz), 8.51 (s, 1 H, H^5 pz), 11.53 (br., 1 H, *H*N) ppm. $^{13}C\{^1H\}$ NMR (75.78 MHz): δ = 112.4 (s, C^4 pz), 128.5 (s, C_6H_5), 128.7 (s, C_6H_5), 129.6 (s, C_6H_5), 132.9 (s, C_6H_5), 134.2 (s, $C^{3,5}$ pz), 143.3 (s, C_{ipso} C_6H_5), 147.9 (s, $C^{5,3}$ pz), 161.8 [s, HN=*C*(C_6H_5)] ppm; *C*O not observed. $C_{13}H_9BrMnN_3O_3$ (390.07): calcd. C 40.03, H 2.32, N 10.77; found C 40.31, H, 2.30, N 10.43.

***fac*-[MnBr(CO)$_3${*N*H=C(C_6H_5)dmpz-κ^2*N*,*N*}] (3b): Method A:** C_6H_5CN (300 μL) was added to a solution of $[MnBr(CO)_5]$ (0.082 g, 0.3 mmol) in THF (20 mL) and the mixture was stirred at 70 °C for 1 h. Then, Hdmpz (0.029 g, 0.3 mmol) was added and the solution was heated at 70 °C for 30 min. Work-up as for **3a** yielded 0.031 g (24%) of **3b** and 0.038 g (32%) of **1b**.

Method B: C_6H_5CN (300 μL) was added to a solution of $[MnBr(CO)_5]$ (0.082 g, 0.3 mmol) in THF (20 mL) and the mixture was stirred at 70 °C for 1 h. Then, **1b** (0.123 g, 0.3 mmol) was added and the solution was heated at 70 °C for 45 min. Work-up as for **3a** yielded 0.064 g (25%) of **3b** and 0.013 g (22%) of **1b**. IR (THF): $\tilde{\nu}$ = 2024 cm^{-1} vs, 1936 vs, 1912 vs. IR (KBr): $\tilde{\nu}$ = 3164 cm^{-1} w, 2026 s, 1918 vs, 1637 w, 1508 w, 1420 m, 1356 m, 1259 w, 1122 w, 1055 w, 887 w, 822 w, 706 w, 683 w, 669 w, 646 w, 634 w, 520 w. ^1H NMR (300 MHz): δ = 1.80 (s, 3 H, CH_3 dmpz), 2.65 (s, 3 H,

Table 3. Crystal data and refinement details for **1a**, **1b**, **2b**, and **3b**.

	1a	**1b**	**2b**	**3b**·THF
Formula	$C_9H_8BrMnN_4O_3$	$C_{13}H_{16}BrMnN_4O_3$	$C_{10}H_{11}BrMnN_3O_3$	$C_{19}H_{21}BrMnN_3O_4$
Mol. mass	355.04	411.15	356.07	490.24
Crystal system	triclinic	monoclinic	monoclinic	monoclinic
Space group	$P\bar{1}$	$P2_1/c$	$P2_1/c$	$P2_1/n$
a [Å]	8.194(2)	13.562(3)	8.721(6)	8.150(2)
b [Å]	8.447(2)	18.551(4)	11.356(7)	13.754(4)
c [Å]	10.857(3)	13.973(3)	14.363(9)	19.635(6)
α [°]	84.365(5)	90	90	90
β [°]	83.156(5)	96.008(4)	101.665(12)	98.714(6)
γ [°]	65.663(4)	90	90	90
V [Å^3]	678.8(3)	3496.2(12)	1393.1(15)	2175.5(11)
Z	2	8	4	4
T [K]	296	296	296	296
$D_{calcd.}$ [g cm^{-3}]	1.737	1.562	1.698	1.497
F(000)	348	1648	704	992
λ (Mo-$K_α$) [Å]	0.71073	0.71073	0.71073	0.71073
Crystal size [mm]	0.18×0.19×0.30	0.07×0.14×0.29	0.12×0.15×0.22	0.10×0.11×0.35
Color	orange	orange	orange	orange
μ [mm^{-1}]	3.920	3.056	3.818	2.471
Scan range [°]	1.89 ≤ *θ* ≤ 23.30	1.51 ≤ *θ* ≤ 23.29	2.30 ≤ *θ* ≤ 23.30	1.81 ≤ *θ* ≤ 23.30
Absorption correction	SADABS	SADABS	SADABS	SADABS
Corr. factors (max., min.)	1.000000, 0.249439	1.000, 0.658220	1.00000, 0.694409	1.00000, 0.605570
No. of refl. measured	2979	15633	6110	9576
No. of refl. independent [*R*(int.)]	1924 [0.0184]	5029 [0.0616]	2002 [0.0223]	3118 [0.0391]
No. of refl. observed [$I \geq 2\sigma(I)$]	1677	3141	1606	2155
GOF on F^2	1.051	1.006	1.014	1.005
No. of parameters	172	421	170	259
Residuals *R*, wR_2	0.0429, 0.1274	0.0412, 0.0721	0.0240, 0.0564	0.0383, 0.0922

 © 2005 Wiley-VCH Verlag GmbH & Co. KGaA, Weinheim

CH_3 dmpz), 6.40 (s, 1 H, H^4 dmpz), 7.45 (m, 1 H, C_6H_5), 7.64 (m, 3 H, C_6H_5), 7.77 (m, 1 H, C_6H_5), 11.11 (br.,, 1 H *H*N) ppm. $^{13}C\{^1H\}$ NMR (75.78 MHz): δ = 14.0 (s, *C*H_3 dmpz), 15.3 (s, *C*H_3 dmpz), 114.6 (s, C^4 dmpz), 128.9 (s, C_6H_5), 129.9 (s, C_6H_5), 131.3 (s, C_{ipso} C_6H_5), 132.6 (s, C_6H_5), 146.0 (s, $C^{3,5}$ dmpz), 157.9 (s, $C^{3,5}$ dmpz), 164.3 [s, HN=*C*(C_6H_5)], 221.1 (s, *C*O), 223.9 (s, *C*O), 224.0 (s, *C*O) ppm. $C_{15}H_{13}BrMnN_3O_3$ (418.12): calcd. C 43.09, H 3.13, N 10.05; found C 42.84, H, 3.03, N 9.99.

X-ray Crystallographic Study of 1a, 1b, 2b, and 3b: Crystals were grown by slow diffusion of hexane into concentrated solutions of the complexes in CH_2Cl_2 (for **1a** and **1b**) or THF (for **2b** and **3b**) at –20 °C. Relevant crystallographic details are given in Table 3. A crystal was attached to a glass fiber and transferred to a Bruker AXS SMART 1000 diffractometer with graphite-monochromated Mo-K_α radiation and a CCD area detector. A hemisphere of the reciprocal space was collected up to 2θ = 48.6°. Raw frame data were integrated with the SAINT program.[25] The structure was solved by direct methods with SHELXTL.[26] A semi-empirical absorption correction was applied with the program SADABS.[27] All non-hydrogen atoms were refined anisotropically. Hydrogen atoms were set in calculated positions and refined as riding atoms, with a common thermal parameter. All calculations and graphics were made with SHELXTL.

CCDC-266383 (for **1a**), -266384 (for **1b**), -266385 (for **2b**), and -266386 (for **3b**) contain the supplementary crystallographic data for this paper. These data can be obtained free of charge from The Cambridge Crystallographic Data Centre via www.ccdc.cam.ac.uk/data_request/cif.

Acknowledgments

The authors thank the Spanish DGICYT (BQU2002-03414) and the Junta de Castilla y León (VA052/03) for financial support, and the MEC (Program FPI) for a grant to M. A.

[1] R. Mukherjee, *Coord. Chem. Rev.* **2000**, *203*, 151–218.
[2] Review: E. C. Constable, P. J. Steel, *Coord. Chem. Rev.* **1989**, *93*, 205–223.
[3] For some recent references, see: a) S. A. Willison, H. Jude, R. M. Antonelli, J. M. Rennekamp, N. A. Eckert, J. A. K. Bauer, W. B. Connick, *Inorg. Chem.* **2004**, *43*, 2548–2555; b) B. A. Leita, B. Moubaraki, K. S. Murray, J. P. Smith, J. D. Cashion, *Chem. Commun.* **2004**, 156–157; c) V. A. Money, I. R. Evans, M. A. Halcrow, A. E. Goeta, J. A. K. Howard, *Chem. Commun.* **2003**, 158–159; d) P.-C. Wu, J.-K. Yu, Y.-H. Song, Y. Chi, P.-T. Chou, S.-M. Peng, G.-H. Lee, *Organometallics* **2003**, *22*, 4938–4946; e) D. B. Grothjahn, S. Van, D. Combs, D. A. Lev, C. Schneider, C. D. Incarvito, K.-C. Lam, G. Rossi, A. L. Rheingold, M. Rideout, C. Meyer, G. Hernandez, L. Mejorado, *Inorg. Chem.* **2003**, *42*, 3347–3355; f) K. Singh, J. R. Long, P. Stavropoulos, *Inorg. Chem.* **1998**, *37*, 1073; g) M. H. W. Lam, S. T. C. Cheung, K.-M. Fung, W.-T. Wong, *Inorg. Chem.* **1997**, *36*, 4618–4619; h) J. C. Jeffery, P. L. Jones, K. L. V. Mann, E. Psillakis, J. A. McCleverty, M. D. Ward, C. M. White, *Chem. Commun.* **1997**, 175–176.
[4] a) M. R. Kollipara, P. Sarkhel, S. Chakraborty, R. Lalrempuia, *J. Coord. Chem.* **2003**, *56*, 1085–1091; b) D. Carmona, J. Ferrer, F. J. Lahoz, L. A. Oro, M. P. Lamata, *Organometallics* **1996**, *15*, 5175–5178; c) J. López, A. Santos, A. Romero, A. M. Echavarren, *J. Organomet. Chem.* **1993**, *443*, 221–228; d) M. A. Cinellu, S. Stoccoro, G. Minghetti, A. L. Bandini, G. Banditelli, B. Bovio, *J. Organomet. Chem.* **1989**, *372*, 311–325; e) G. D. Gracey, S. T. Rettig, A. Storr, J. Trotter, *Can. J. Chem.* **1987**, *65*, 2469–2477; f) A. Romero, A. Vegas, A. Santos, *J. Organomet. Chem.* **1986**, *310*, C8–C10; g) C. J. Jones, J. A. McCleverty, A. S. Rothin, *J. Chem. Soc., Dalton Trans.* **1986**, 109–111.
[5] J. Baker, M. Kilner, *Coord. Chem. Rev.* **1994**, *133*, 219–300.
[6] For some recent references concerning group 6 complexes, see: a) J. Pérez, D. Morales, S. Nieto, L. Riera, V. Riera, D. Miguel, *Dalton Trans.* **2005**, 884–888; b) L. Coue, L. Cuesta, D. Morales, J. A. Halfen, J. Pérez, L. Riera, V. Riera, D. Miguel, N. G. Connelly, S. Boonyuen, *Chem. Eur. J.* **2004**, *10*, 1906–1912; c) D. Morales, M. E. Navarro Clemente, J. Pérez, L. Riera, V. Riera, D. Miguel, *Organometallics* **2003**, *22*, 4124–4128; d) D. Morales, J. Pérez, L. Riera, V. Riera, D. Miguel, M. E. G. Mosquera, S. García-Granda, *Chem. Eur. J.* **2003**, *9*, 4132–4143; e) J. Pérez, E. Hevia, L. Riera, V. Riera, S. García-Granda, E. García-Rodríguez, D. Miguel, *Eur. J. Inorg. Chem.* **2003**, 1113–1120; f) D. Morales, M. E. Navarro Clemente, J. Pérez, L. Riera, V. Riera, D. Miguel, *Organometallics* **2002**, *21*, 4934–4938; g) E. Hevia, J. Pérez, L. Riera, V. Riera, I. del Río, S. García-Granda, D. Miguel, *Chem. Eur. J.* **2002**, *8*, 4510–4521; h) D. Morales, J. Pérez, L. Riera, V. Riera, D. Miguel, *Inorg. Chem.* **2002**, *41*, 4111–4113; i) E. Hevia, J. Pérez, L. Riera, V. Riera, D. Miguel, *Organometallics* **2002**, *21*, 1750–1752; j) D. Morales, J. Pérez, L. Riera, V. Riera, R. Corzo-Suárez, S. García-Granda, D. Miguel, *Organometallics* **2002**, *21*, 1540–1545; k) J. Pérez, L. Riera, V. Riera, S. García-Granda, E. García-Rodríguez, D. Miguel, *Organometallics* **2002**, *21*, 1622–1626; l) J. Pérez, L. Riera, V. Riera, S. García-Granda, E. García-Rodríguez, D. Miguel, *Chem. Commun.* **2002**, 384–385. For some recent references concerning group 7 complexes, see: m) L. Cuesta, E. Hevia, D. Morales, J. Pérez, V. Riera, M. Seitz, D. Miguel, *Organometallics* **2005**, *24*, 1772–1775; n) S. Nieto, J. Pérez, V. Riera, D. Miguel, C. Alvarez, *Chem. Commun.* **2005**, 546–548; o) L. Cuesta, E. Hevia, D. Morales, J. Pérez, V. Riera, E. Rodríguez, D. Miguel, *Chem. Commun.* **2005**, 116–116; p) L. Cuesta, D. C. Gerbino, E. Hevia, D. Morales, M. E. N. Clemente, J. Pérez, L. Riera, V. Riera, D. Miguel, I. del Río, S. García-Granda, *Chem. Eur. J.* **2004**, *10*, 1765–1777; q) E. Hevia, J. Pérez, V. Riera, D. Miguel, P. Campomanes, M. I. Menéndez, T. L. Sordo, S. García-Granda, *J. Am. Chem. Soc.* **2003**, *125*, 3706–3707; r) D. C. Gerbino, E. Hevia, D. Morales, M. E. N. Clemente, J. Pérez, L. Riera, V. Riera, D. Miguel, *Chem. Commun.* **2003**, 328–329; s) E. Hevia, J. Pérez, V. Riera, D. Miguel, *Organometallics* **2003**, *22*, 257–263; t) E. Hevia, J. Pérez, V. Riera, D. Miguel, *Angew. Chem. Int. Ed.* **2002**, *41*, 3858–3860; u) E. Hevia, J. Pérez, V. Riera, D. Miguel, *Chem. Commun.* **2002**, 1814–1815.
[7] We have also obtained pyrazolylamidino Mo, W, and Re complexes, which will be published separately elsewhere.
[8] a) P. Paredes, D. Miguel, F. Villafañe, *Eur. J. Inorg. Chem.* **2003**, 995–1004; b) P. Paredes, M. Arroyo, D. Miguel, F. Villafañe, *J. Organomet. Chem.* **2003**, *667*, 120–125.
[9] For some examples of chains, see: a) R. Graziani, U. Castellato, R. Ettore, G. Plazzogna, *J. Chem. Soc., Dalton Trans.* **1982**, 805–808; b) J. D. Crane, O. D. Fox, E. Sinn, *J. Chem. Soc., Dalton Trans.* **1999**, 1461–1465; c) K. Sakai, Y. Tomita, T. Ue, K. Goshima, M. Ohminato, T. Tsubomura, K. Matsumoto, K. Ohmura, K. Kawakami, *Inorg. Chim. Acta* **2000**, *297*, 64–71; d) A. Chadghan, J. Pons, A. Caubet, J. Casabó, J. Ros, A. Alvarez-Larena, J. F. Piniella, *Polyhedron* **2000**, *19*, 855–862.
[10] For some examples of dimers, see: a) M. A. Cinellu, S. Stoccoro, G. Minghetti, A. L. Bandini, G. Banditelli, B. Bovio, *J. Organomet. Chem.* **1989**, *372*, 311–325; b) M. Munakata, L. P. Wu, M. Yamamoto, T. Kuroda-Sowa, M. Maekawa, S. Kawata, S. Kitagawa, *J. Chem. Soc., Dalton Trans.* **1995**, 4099–4106; c) G. A. Ardizzoia, G. La Monica, S. Cenini, M. Moret, N. Maschioni, *J. Chem. Soc., Dalton Trans.* **1996**, 1351–1357; d) I. A. Guzei, C. H. Winter, *Inorg. Chem.* **1997**, *36*, 4415–4420; e) S. M. Couchman, J. C. Jeffery, M. D. Ward, *Polyhedron* **1999**, *18*, 2633–2640.
[11] See, for example: a) L. A. Oro, D. Carmona, J. Reyes, C. Foces-Foces, F. H. Cano, *J. Chem. Soc., Dalton Trans.* **1986**, 31–37;

 © 2005 Wiley-VCH Verlag GmbH & Co. KGaA, Weinheim

b) D. Carmona, J. Ferrer, F. J. Lahoz, L. A. Oro, J. Reyes, M. Esteban, *J. Chem. Soc., Dalton Trans.* **1991**, 2811–2820; c) G. López, J. Ruiz, C. Vicente, J. M. Martí, G. García, P. A. Chaloner, P. B. Hitchcock, R. M. Harrison, *Organometallics* **1992**, *11*, 4090–4096; d) D. Carmona, J. Ferrer, R. Atencio, F. J. Lahoz, L. A. Oro, M. P. Lamata, *Organometallics* **1995**, *14*, 2057–2065; e) G. A. Ardizzoia, G. La Monica, A. Maspero, N. Masciocchi, M. Moret, *Eur. J. Inorg. Chem.* **1999**, 1301–1307; f) G. A. Ardizzoia, G. La Monica, A. Maspero, M. Moret, N. Masciocchi, *Eur. J. Inorg. Chem.* **2000**, 181–187; g) R. Contreras, M. Valderrama, E. M. Orellana, D. Boys, D. Carmona, L. A. Oro, M. P. Lamata, J. Ferrer, *J. Organomet. Chem.* **2000**, *606*, 197–202.

[12] All attempts to determine the nature of this white solid were unsuccessful. Its IR spectra show bands which may be assigned to pzH but do not show CO stretching bands; no reliable ^{1}H NMR spectra could be obtained, which points to a paramagnetic material.

[13] T. Beringhelli, G. D'Alonso, M. Panigati, F. Porta, P. Mercandelli, M. Moret, A. Sironi, *Organometallics* **1998**, *17*, 3282–3292.

[14] S. E. Anslow, K. S. Chong, S. J. Rettig, A. Storr, J. Trotter, *Can. J. Chem.* **1981**, *59*, 3123–3135.

[15] For **1b**, two crystallographically independent but chemically equivalent molecules were found in the asymmetric unit, with their distances and angles being very similar. Figure 1 and Table 1 collect one of them.

[16] a) N. I. Pyshnograeva, V. N. Setkina, V. G. Andrianov, Y. T. Struchkov, D. N. Kursanov, *J. Organomet. Chem.* **1980**, *186*, 331–338; b) S. U. Son, K. H. Park, Y. K. Chung, *Organometallics* **2000**, *19*, 5241–5243; c) W.-Y. Wong, W.-K. Wong, C. Sun, W.-T. Wong, *J. Organomet. Chem.* **2000**, *612*, 160–171.

[17] a) G. A. Jeffrey, *An Introduction to Hydrogen Bonding*, Oxford University Press, New York, **1997**. Chapter 2; b) T. Steiner, *Angew. Chem. Int. Ed.* **2002**, *41*, 48–76.

[18] a) G. A. Ardizzoia, G. La Monica, A. Maspero, M. Moret, N. Maschiocchi, *Eur. J. Inorg. Chem.* **1998**, 1503–1511; b) J. Cámpora, J. A. López, C. M. Maya, P. Palma, E. Carmona, C. Ruiz, *Organometallics* **2000**, *19*, 2707–2715.

[19] a) V. Y. Kukushkin, A. J. L. Pombeiro, *Chem. Rev.* **2002**, *102*, 1771–1802; b) R. A. Michelin, M. Mozzon, R. Bertani, *Coord. Chem. Rev.* **1996**, *147*, 299–338.

[20] M. F. Farona, K. F. Kraus, *Inorg. Chem.* **1970**, *9*, 1700–1704.

[21] R. H. Reimann, E. Singleton, *J. Chem. Soc., Dalton Trans.* **1974**, 808–813.

[22] In a separate experiment, *fac*-[$MnBr(CO)_3(NCPh)_2$] was synthesized as described previously for the MeCN complex (ref. [20]). Its molecular structure was determined by X-ray diffraction. Although the quality of the data are insufficient to be reported, they confirm the expected *fac*-tricarbonyl-*cis*-bis(benzonitrile)geometry.

[23] a) E. Horn, M. R. Snow, E. R. T. Tiekink, *Acta Crystallogr., Sect. C* **1987**, *43*, 792–794; b) G. Schmidt, H. Paulus, R. van Eldik, H. Elias, *Inorg. Chem.* **1988**, *27*, 3211–3214; c) G. J. Stor, D. J. Stufkens, P. Vernooijs, E. J. Baerends, J. Fraanje, K. Goubitz, *Inorg. Chem.* **1995**, *34*, 1588–1594.

[24] D. D. Perrin, W. L. F. Armarego, *Purification of Laboratory Chemicals*, 3rd ed., Pergamon Press, Oxford, **1988**.

[25] *SAINT+*. SAX area detector integration program. Version 6.02. Bruker AXS, Inc. Madison, WI, **1999**.

[26] G. M. Sheldrick; *SHELXTL*, An integrated system for solving, refining, and displaying crystal structures from diffraction data. Version 5.1. Bruker AXS, Inc. Madison, WI, **1998**.

[27] G. M. Sheldrick; *SADABS*, Empirical Absorption Correction Program. University of Göttingen, Germany, **1997**.

Received: May 9, 2005
Published Online: September 15, 2005

 © 2005 Wiley-VCH Verlag GmbH & Co. KGaA, Weinheim

Guanidinate Complexes of Heavier Alkaline-Earth Metals (Ca, Sr): Syntheses, Structures, Styrene Polymerization and Unexpected Reaction Behaviour

Florian Feil[b] and Sjoerd Harder*[a]

Keywords: Alkaline earth metals / Amides / Amidinates / Guanidinates / Polystyrene

The guanidinate complex [Ca{(Cy)N–C{N(SiMe$_3$)$_2$}–N(Cy)}$_2$] can be prepared in good yields and in crystalline purity by two different routes: 1) addition of [Ca{N(SiMe$_3$)$_2$}$_2$] to (Cy)-N=C=N(Cy) or 2) addition of KN(SiMe$_3$)$_2$ to (Cy)N=C=N(Cy) followed by a metathesis reaction of the obtained potassium guanidinate complex with CaI$_2$. Crystallization from Et$_2$O yielded [Ca{(Cy)N–C[N(SiMe$_3$)$_2$]–N(Cy)}$_2$·(Et$_2$O)] (**1**), which shows a C_2-symmetric structure in the crystal. A Sr analogue could be prepared likewise and also crystallizes as the mono-etherate [Sr{(Cy)N–C{N(SiMe$_3$)$_2$}–N(Cy)}$_2$·(Et$_2$O)] (**2**) with a very similar crystal structure. The Schlenk equilibrium between (**1**) and [Ca{α-(Me$_3$Si)-*o*-(Me$_2$N)-benzyl}$_2$·(THF)$_2$] (**3**) in benzene is not completely on the heteroleptic side; however, an excess of (**1**) yields predominantly the heteroleptic benzylcalcium complex [Ca{(Cy)N–C{N(SiMe$_3$)$_2$}–N(Cy)}{α-(Me$_3$Si)-*o*-(Me$_2$N)-benzyl}] (**4**). Styrene polymerization with this mixture results largely in atactic polystyrene of which the molecular weight distribution shows a tailing in the lower range. This could be due to decomposition of the guanidinate ligand under the given polymerization conditions. It is shown that heating a mixture of **1** and **3** gives the crystalline decomposition product [Ca{(Cy)N–C{N(SiMe$_3$)$_2$}–N(Cy)}{(Cy)-(TMS)N}] (**5**), which crystallizes as a dimer with bridging amide ligands.
(© Wiley-VCH Verlag GmbH & Co. KGaA, 69451 Weinheim, Germany, 2005)

Introduction

The coordination chemistry of amidinates and the related guanidinates has been well-explored for main-group metals as well as for transition metals.[1–9] These powerful electron-donating ligands not only coordinate to a remarkably wide range of metal ions from all parts of the periodic table, but also show a rich variety of coordination modes.[1–3] Other advantages of this class of ligands are their easy accessibility and the possibility of substituent variation, which allows for tuning of their steric and electronic properties. The latter advantage makes these ligands well-suitable as spectator ligands in catalysis and this opportunity has been well-exploited in the design of polymerization catalysts.[10–22]

In the course of our studies on polymerization catalysts based on alkaline-earth metals,[23–27] we have now prepared guanidinate complexes of the heavier alkaline-earth metals Ca and Sr and explored their structures, reactivity and their behaviour in styrene polymerization.

Results and Discussion

The homoleptic calcium bis(guanidinate) complex (**1**) was prepared by two alternative routes (Scheme 1): i) direct addition of [Ca{N(SiMe$_3$)$_2$}$_2$] to 1,3-dicyclohexylcarbodiimide or ii) addition of KN(SiMe$_3$)$_2$ to 1,3-dicyclohexylcarbodiimide and subsequent reaction of the potassium guanidinate with CaI$_2$. The analogous strontium bis(guanidinate)

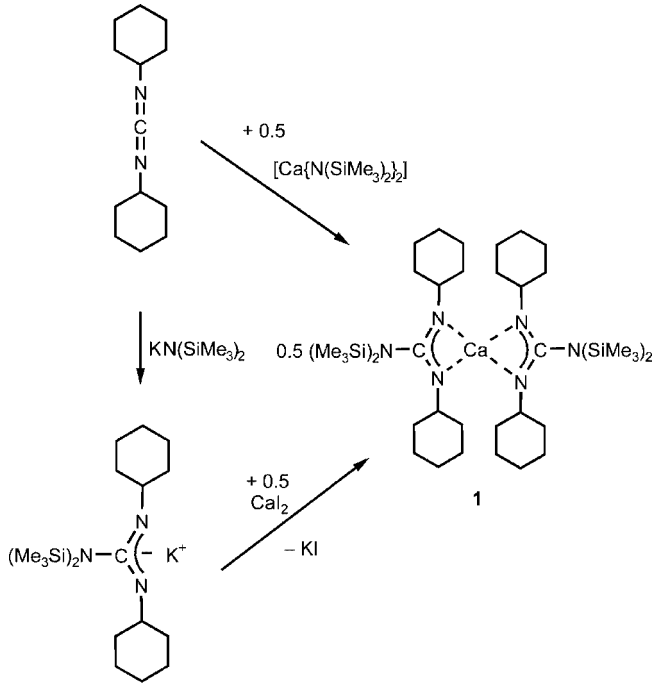

Scheme 1.

[a] Anorganische Chemie, Universität Duisburg-Essen, Universitätsstraße 5, 45117 Essen, Germany
Fax: +49-201-183-2621
E-mail: sjoerd.harder@uni-essen.de
[b] Universität Konstanz, Postfach 5560-M738, 78457 Konstanz, Germany

 © 2005 Wiley-VCH Verlag GmbH & Co. KGaA, Weinheim **DOI: 10.1002/ejic.200500514**

complex **2** was synthesized by reaction of the potassium guanidinate with SrI_2.

The calcium bis(guanidinate) complex **1** crystallizes as a mono-etherate. The crystal structure has two independent molecules in the asymmetric unit, which are geometrically similar within their standard deviations (Figure 1). Both molecules show crystallographic C_2-symmetry with the C_2-axis going through Ca and O.

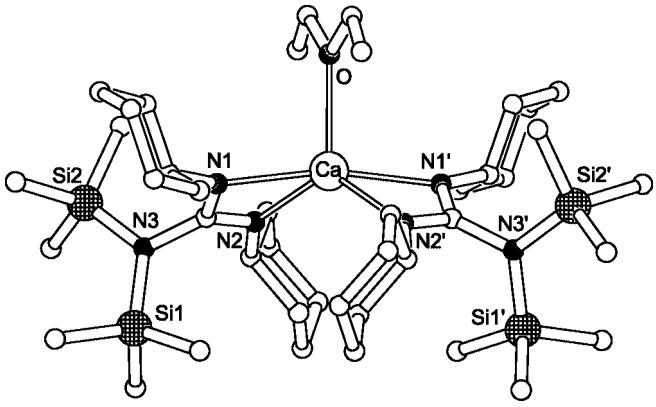

Figure 1. (a) Crystal structure of **1**. Hydrogen atoms have been omitted for clarity and only one of the two crystallographic independent, but very similar, molecules is shown. Selected bond lengths [Å] and angles [°] (values for the other independent molecule are given in square brackets): Ca–N1 2.387(2) [2.369(3)], Ca–N2 2.380(3) [2.388(3)], Ca–O 2.424(3) [2.421(3)]; N1–Ca–N2 56.12(8) [56.47(8)]. The strontium complex **2** is isostructural with **1**; selected bond lengths [Å] and angles [°]: Sr–N1 2.534(3) [2.526(3)], Sr–N2 2.514(3) [2.520(3)], Sr–O 2.559(3) [2.559(3)]; N1–Sr–N2 53.01(9) [53.13(9)].

The N_3C units of the guanidinate ligands are planar (maximum deviations from their least-squares planes are 0.004 and 0.008 Å). The $N(SiMe_3)_2$ substituents oriented themselves perpendicular to the NCN plane with dihedral Si_2N/NCN angles of 96.1(1)° and 91.7(1)°, thus preventing N(*p*)–$CN_2(\pi)$ interactions. A similar conformation has been observed in the alkali-metal salts of the (Cy)N–C{N-$(SiMe_3)_2$}–N(Cy) anion.[9]

The guanidinate ligands act as bidentate ligands with an average bite angle of 56.3(8)° and are twisted with respect to each other, which gives rise to C_2-chirality of the molecule. The two independent molecules in the asymmetric cell are nearly mirror images. The coordination geometry of the Ca metal is not clear-cut due to the small bite angle of the guanidinate ligands.

The Ca^{2+} ion is located slightly out of the N_3C planes by 0.301 and 0.358 Å. The Ca–N bond lengths [average 2.381(3) Å] are shorter than those in the structure of the calcium amidinate complex [Ca{Me_3SiN–C(Ph)–$NSiMe_3$}$_2$·$(THF)_2$] for which an average Ca–N bond of 2.431(2) Å has been reported.[28] The longer amide–metal coordination in the latter can be explained by the presence of two neutral ether donor ligands instead of one. The steric bulk of the two guanidinate ligands in **1** allows only one ether molecule in the coordination sphere of Ca and is therefore comparable to the steric bulk of 1,3-$(SiMe_3)_2Cp^-$ or *i*$Pr(Me)_4Cp^-$. Both these Cp ligands form calcocenes also with only one Et_2O molecule in the coordination sphere of Ca.[29]

The strontium bis(guanidinate) complex **2** likewise crystallizes as a mono-etherate complex which is isostructural to **1** (Figure 1). The Sr–N and Sr–O bond lengths are, on average, 0.143 Å and 0.137 Å longer than those in the Ca analogue, which nicely represents the difference of 0.13 Å in the ionic radii of the two alkaline-earth metals. The Sr–N bond lengths in **2** [average 2.524(3) Å] are somewhat shorter than those in the strontium amidinate complex [Sr{Me_3SiN–C(Ph)–$NSiMe_3$}$_2$·$(THF)_2$] for which the average Sr–N bond measures 2.583(9) Å.[30] The longer metal–ligand bond length in the latter complex can again be explained by the presence of one extra donor molecule. The N–Sr–N′ bite-angle in **2** [53.1(1)°] is, however, very similar to that in the amidinate complex [Sr{Me_3SiN–C(Ph)–$NSiMe_3$}$_2$·$(THF)_2$] [53.3(3)°].

Our continuing interest in the use of benzylcalcium complexes for the living and syndiotactic polymerization of styrene spurred us to prepare heteroleptic benzylcalcium complexes containing the chelating guanidinate ligand. Such heteroleptic initiators were prepared by ligand exchange between homoleptic **1** and the dibenzylcalcium complex **3** (Scheme 2). Mixing benzene solutions of **1** and **3** does not result in complete ligand exchange, but a Schlenk equilibrium between homoleptic (**1** and **3**) and heteroleptic (**4**) species is observed. NMR studies in [D_6]benzene show that the equilibrium constant at 20 °C amounts to about 6. For this reason, further polymerization studies were performed with

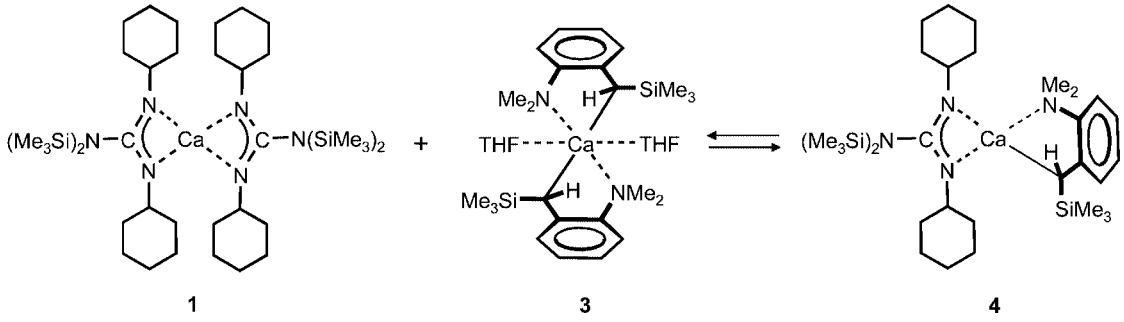

1 **3** **4**

Scheme 2.

 © 2005 Wiley-VCH Verlag GmbH & Co. KGaA, Weinheim

mixtures of **1** and **3** in which homoleptic **1** is in excess. This largely results in the formation of heteroleptic **4** mixed with homoleptic **1**. Since the latter is not an active initiator in styrene polymerization, the polymerization is mainly initiated by the heteroleptic benzylcalcium species **4**.

Styrene polymerizations (see Exp. Sect. for details) with 2:1 or 4:1 mixtures of **1** and **3** both yield predominantly atactic polystyrene (also in the absence of solvent). Although the guanidinate ligand has no effect on the stereoselectivity of the polymerization, it has a distinct accelerating influence on the polymerization rate. Styrene polymerization with a 2:1 mixture of **1** and **3** (k = $5.7 \pm 0.3\ L\,mol^{-1}\,s^{-1}$) is more than twice as fast as styrene polymerization with **3** ($k = 2.48 \pm 0.11\ L\,mol^{-1}\,s^{-1}$). This increased polymerization rate could be the consequence of the excellent donor properties of the chelating bidentate guanidinate ligand: this would weaken the benzylcalcium bond and increase the nucleophilicity of the propagating chain-end. Although fast propagation is advantageous for a stereoselective polymerization (the competing inversion of the chiral chain-end results in racemization and therefore loss in stereocontrol)[24] we find essentially atactic polymer. Apparently the guanidinate ligand also increases the rate of inversion of the chiral chain-end.

The molecular-weight distributions of the obtained polymers all show relatively large dispersion indices (>1.5) and a very pronounced tailing in the low molecular weight range. This could be an indication of decomposition of the propagating species during the polymerization experiment. Since it is known from our earlier work that the benzylic group in heteroleptic benzylcalcium compounds can react with the spectator ligand,[27,31] we investigated a benzene solution of **1** and **3** at higher temperatures, i.e. the conditions of the polymerization experiment. Keeping the initiator solution overnight at 80 °C yielded, after subsequent concentration and cooling, a colourless crystalline product (**5**), which dissolves badly in benzene. Analysis of these crystals by X-ray diffraction revealed that one of the guanidinate ligands had decomposed into the amide (Cy)-$(Me_3Si)N^-$, which forms a heteroleptic complex with the original guanidinate ligand (Figure 2). In the solid state, this complex forms a centrosymmetric dimer in which the amide ligands bridge the Ca^{2+} ions and the guanidinate anions act as bidentate ligands located in terminal positions.

The geometry of the guanidinate ligand in **5** is very similar to that observed in **1** and **2**: the N_3C unit is planar (maximum deviation from the least-squares plane is 0.005 Å) and the $(Me_3Si)_2N$ substituent is oriented perpendicular to this plane [the dihedral Si_2N/NCN angle is 87.1(1)°]. The Ca^{2+} ion is located only 0.023 Å out of the N_3C plane. The bite angle of the chelating bidentate guanidinate ligand amounts to 57.6(1)° and is similar to that in **1**. As can be seen from the somewhat shorter Ca–N bond lengths [average 2.337(3) Å], the guanidinate ligand in **5** binds slightly more strongly to the metal than that in **1**. The Ca–N bond lengths to the bridging amides are longer [average 2.435(3) Å].

The formation of $(Cy)(Me_3Si)N^-$ can only be explained by assuming a 1,3-shift of the Me_3Si substituent as the first step (a precedent for a similar shift in an amidinate ligand[22] is known). A possible mechanism for the formation of the amide is proposed in Scheme 3. Ring-flip of the cyclohexane substituents brings the attached N into the axial position and creates more space for the $(Me_3Si)_2N$ substituent in the backbone of the ligand. This allows for rotation of the $(Me_3Si)_2N$ group and delocalization of the N lone-pair into the π-system. Such a resonance structure with enhanced ligand basicity is known for guanidinate ligands with smaller substituents in the backbone.[5,8] A 1,3-shift of the Me_3Si substituent gives a new guanidinate ligand, which could be in equilibrium with $(Cy)(Me_3Si)N^-$ and (Cy)-N=C=N–$SiMe_3$. Such an equilibrium would be strongly on the side of the guanidinate ligand. However, trapping of the

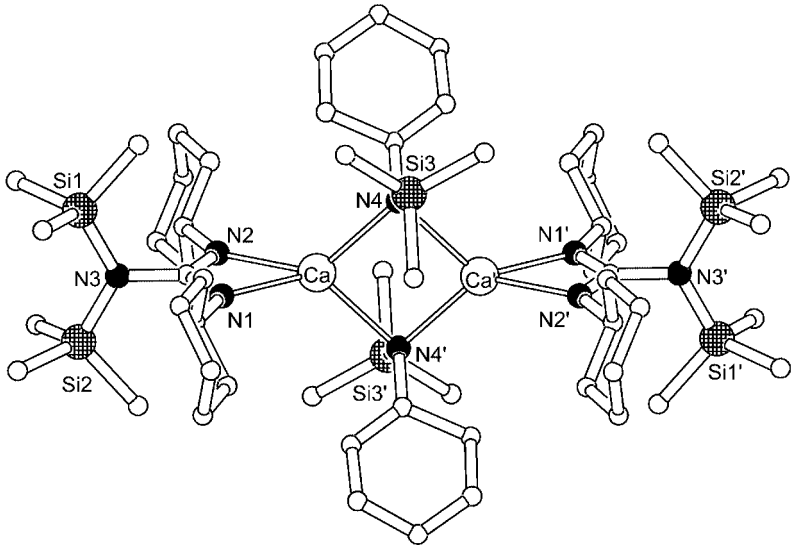

Figure 2. (a) Crystal structure of centrosymmetric **5**. Hydrogen atoms have been omitted for clarity. Selected bond lengths [Å] and angles [°]: Ca–N1 2.316(4), Ca–N2 2.357(3), Ca–N4 2.422(3), Ca–N4′ 2.447(3); N1–Ca–N2 57.6(1), N4–Ca–N4′ 90.1(1).

 © 2005 Wiley-VCH Verlag GmbH & Co. KGaA, Weinheim

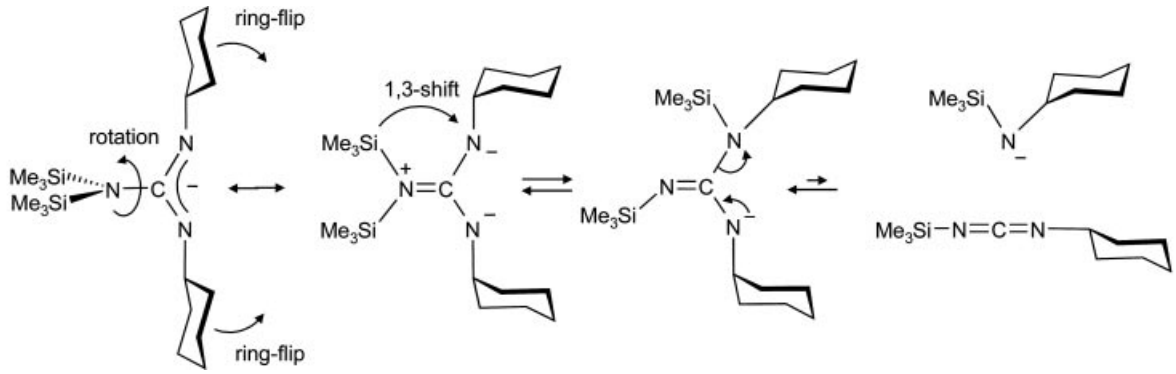

Scheme 3.

carbodiimide by-product by addition of the α-(Me_3Si)-*o*-(Me_2N)-benzyl anion to the C=N bond would result in formation of (Cy)(Me_3Si)N^-.[38] A similar mechanism during the polymerization of styrene would result in partial degradation of the guanidinate ligand and partial quenching of the polystyryl chain-end due to reaction with the carbodiimide.

Conclusions

The homoleptic calcium bis(guanidinate) complex **1** can be prepared in high yields and crystalline purity by two routes, both based on addition of an organometallic compound to a carbodiimide. The analogous strontium complex **2** was obtained likewise. Both the Ca and the Sr complex crystallize as C_2-symmetric mono-etherates. This indicates that the steric bulk of the anionic (Cy)N–C{N-($SiMe_3$)$_2$}–N(Cy) ligand is similar to that of 1,3-($SiMe_3$)$_2$-Cp^- or *i*Pr(Me)$_4$$Cp^-$.

The Schlenk equilibrium between homoleptic calcium bis(guanidinate) **1** and [Ca{α-(Me_3Si)-*o*-(Me_2N)-benzyl}$_2$·(THF)$_2$] is mainly, but not completely, on the heteroleptic side. An excess of **1**, however, results in nearly exclusive formation of the heteroleptic benzylcalcium complex. Polymerization of styrene with such mixtures yields atactic polystyrene. Since the molecular-weight distribution of these polymers shows a strong tailing in the low molecular weight range, it is expected that these polymerizations are not completely living. It has been shown that heating mixtures of **1** and **3** results in decomposition of the guanidinate ligand. A similar reaction could be responsible for quenching of the polymer chains during styrene polymerization.

Experimental Section

General Comments: All experiments were carried out under argon using predried solvents and Schlenk techniques. [Ca{N-($SiMe_3$)$_2$}$_2$][32] and [Ca{(2-Me_2N-α-Me_3Si-benzyl)}$_2$·(THF)$_2$][23] were prepared according to literature procedures. NMR spectra were recorded on Bruker AC250 and AMX600 machines. Polymerizations of styrene were performed in a thermostatted 100-mL, stainless-steel reactor at normal pressure. Polymerizations were carried out either in cyclohexane (0.1 M styrene solution, 0.1 mM catalyst, 50 °C) or in pure styrene (0.1 mM catalyst, 20 °C). In a typical polymerization experiment, the reactor was loaded with 90 mL of dry cyclohexane and 11.5 mL (ca. 100 mmol) of freshly distilled (from alox-perls) styrene. A solution of the initiator (0.05 mmol **3** and 0.1 or 0.2 mmol of **1**) in 1.0 mL of benzene/cyclohexane was added through a port. The usual appearance of a red colour indicated that the polymerization started immediately. After a polymerization time of 30 min, the mixture was quenched with oxygen-free methanol. Evaporation of all solvents yielded the polymer in quantitative yields. The polymers were analyzed by GPC and high temperature ^{1}H and ^{13}C NMR spectroscopy (solvent: [D_2]tetrachloroethane). The tacticity of the polymer was checked by analyzing the ^{13}C NMR signal for the C_{ipso} in the phenyl ring.[33]

Synthesis of [K{(Cy)NC{N($SiMe_3$)$_2$}N(Cy)}]: A solution of dicyclohexylcarbodiimide (1.00 g, 4.85 mmol) and KN($SiMe_3$)$_2$ (0.97 g, 4.85 mmol) in 30 mL of Et_2O was stirred overnight at room temperature. The solvents were removed under vacuum and the precipitate was washed twice with 10 mL portions of hexane. The residue was dried under vacuum (0.01 Torr, 50 °C, 30 min). The remaining white powder was identified by NMR analysis as [K{(Cy)-NC{N($SiMe_3$)$_2$}N(Cy)}] (1.92 g, 98%). ^{1}H NMR ([D_6]benzene/[D_8]THF (9:1), 600 MHz, 20 °C): δ = 0.31 (s, 18 H, Me_3Si), 1.30 (m, 4 H, Cy), 1.38 (m, 2 H, Cy), 1.51 (m, 4 H, Cy), 1.64 (m, 4 H, Cy), 1.79 (m, 2 H, Cy), 1.90 (m, 4 H, Cy), 3.26 (m, 2 H, Cy) ppm. ^{13}C NMR ([D_6]benzene/[D_8]THF (9:1), 62.86 MHz, 20 °C): δ = 2.9 (Me_3Si), 26.8 (Cy), 27.1 (Cy), 39.1 (Cy), 56.1 (Cy), 157.5 (NCN) ppm.

Synthesis of [Ca{(Cy)NC{N($SiMe_3$)$_2$}N(Cy)}$_2$·(Et_2O)] (1): This complex was prepared by two different methods. **Method A:** A suspension of [K{(Cy)NC{N($SiMe_3$)$_2$}N(Cy)}] (1.46 g, 3.60 mmol) and CaI_2 (0.53 g, 1.80 mmol) in 30 mL of Et_2O was stirred for three days at room temperature. The solvent was removed under vacuum and the product was extracted with two 20-mL portions of hexane. The hexane layers were concentrated to 15 mL and 2 mL of Et_2O was added. Slow cooling of the remaining solution to –30 °C yielded large colourless crystals of **1** (yield: 0.98 g, 65%). **Method B:** A solution of dicyclohexylcarbodiimide (1.98 g, 9.60 mmol) and [Ca{N($SiMe_3$)$_2$}$_2$] (1.73 g, 4.80 mmol) in 30 mL of Et_2O was stirred overnight at room temperature. After removing the solvent under vacuum a white residue remained, which was recrystallized from 20 mL of hexane and 2 mL of Et_2O at –30 °C (yield: 3.10 g, 76%). Decomposition temperature: approx. 185 °C. $C_{42}H_{90}CaN_6OSi_4$ (847.65): calcd. C 59.51, H 10.70; found C 59.23, H 10.61. ^{1}H NMR ([D_6]benzene, 600 MHz, 20 °C): δ = 0.37 (s, 36 H, Me_3Si), 1.20 (t, J = 7.1 Hz, 6 H, Et_2O), 1.27 (m, 4 H, Cy), 1.36 (m, 8 H, Cy), 1.45 (m, 8 H, Cy), 1.70 (m, 4 H, Cy), 1.86 (m, 8 H, Cy), 1.92

 © 2005 Wiley-VCH Verlag GmbH & Co. KGaA, Weinheim

Table 1. Crystal data for compounds **1**, **2** and **5**.

	1	**2**	**5**
Formula	$C_{42}H_{90}CaN_6OSi_4$	$C_{42}H_{90}N_6OSi_4Sr$	$C_{56}H_{120}Ca_2N_8Si_6$
Mol. mass	847.65	895.18	1154.31
Size [mm^3]	0.5×0.5×0.5	0.5×0.5×0.4	0.5×0.5×0.4
Crystal system	monoclinic	monoclinic	monoclinic
Space group	*P*2/c	*P*2/c	*C*2/*c*
a [Å]	26.118(8)	26.104(2)	25.763(4)
b [Å]	9.806(2)	9.9874(8)	11.950(3)
c [Å]	22.799(4)	22.549(4)	24.218(4)
α [°]	90	90	90
β [°]	114.260(10)	113.632(8)	91.501(12)
γ [°]	90	90	90
V [Å^3]	5324(2)	5386(1)	7453(3)
Z	4	4	4
ρ [g cm^{-3}]	1.058	1.104	1.134
μ (Mo-$K_α$) [mm^{-1}]	0.242	1.124	0.285
T [°C]	–90	–90	–90
θ (max.)	25.4	24.2	25.4
Unique reflections	9448	8482	6867
R_{int}	0.030	0.031	0.033
Obsd. reflections [$I > 2σ(I)$]	6213	6540	3208
Parameters	560	489	375
R_1	0.047	0.043	0.063
wR_2	0.164	0.111	0.154
GOF	1.04	1.02	0.93
Max./min. residual electron density [e Å^{-3}]	–0.39/0.46	–0.60/0.83	–0.38/0.46

(m, 8 H, Cy), 3.34 (m, 4 H, Cy), 3.35 (q, J = 7.0 Hz, 4 H, Et_2O) ppm. ^{13}C NMR ([D$_6$]benzene, 62.86 MHz, 20 °C): $δ$ = 2.8 (Me_3Si), 14.6 (Et_2O), 26.6 (Cy), 26.8 (Cy), 39.1 (Cy), 55.0 (Cy), 66.3 (Et_2O), 159.2 (NCN) ppm.

Synthesis of [Sr{(Cy)NC{N(SiMe$_3$)$_2$}N(Cy)}$_2$·(Et$_2$O)] (2): A mixture of [K{(Cy)NC{N(SiMe$_3$)$_2$}N(Cy)}] (1.41 g, 3.48 mmol) and SrI_2 (0.59 g, 1.74 mmol) in 50 mL of Et_2O was stirred for five days at room temperature. The resulting suspension was centrifuged and the mother liquor was isolated. The solid residue was extracted with 20 mL of Et_2O and the solvent of the combined ether fractions was removed under vacuum. The solid product was dissolved in 10 mL of hexane and 10 mL of Et_2O and the solution was concentrated at 30 °C to a volume of about 8 mL. Slow cooling to room temperature yielded large colourless crystalline cubes of **2** (yield: 0.98 g, 68%). Decomposition temperature: approx 168 °C. $C_{42}H_{90}N_6OSi_4Sr$ (895.19): calcd. C 56.35, H 10.13; found C 55.98, H 9.98. ^{1}H NMR ([D$_6$]benzene/[D$_8$]THF (9:1), 600 MHz, 20 °C): $δ$ = 0.33 (s, 36 H, Me_3Si), 1.06 (t, J = 7.0 Hz, 6 H, Et_2O), 1.25 (m, 12 H, Cy), 1.40 (m, 8 H, Cy), 1.68 (m, 4 H, Cy), 1.81 (m, 8 H, Cy), 1.84 (m, 8 H, Cy), 3.27 (q, J = 7.0 Hz, 4 H, Et_2O), 3.33 (m, 4 H, Cy) ppm. ^{13}C NMR ([D$_6$]benzene/[D$_8$]THF (9:1), 62.86 MHz, 20 °C): $δ$ = 3.0 (Me_3Si), 14.6 (Et_2O), 26.8 (Cy), 27.0 (Cy), 39.3 (Cy), 55.5 (Cy), 66.3 (Et_2O), 162.4 (NCN) ppm.

Reaction of 1 with 3: A solution of **1** (0.30 g, 0.36 mmol) and [Ca{α-(Me_3Si)-*o*-(Me_2N)-benzyl}$_2$·(THF)$_2$] (**3**; 0.22 g, 0.37 mmol) in 10 mL of benzene was heated overnight at 80 °C. Concentration of the solution to 50% of its original volume yielded, after cooling to 5 °C, a batch of nicely formed colourless crystals of **5** (54 mg, 0.047 mmol, 26% yield). Decomposition temperature: approx. 160 °C. $C_{56}H_{120}Ca_2N_8Si_6$ (1154.3): calcd. C 58.27, H 10.48; found C 58.04, H 10.21. The crystals are only sparingly soluble in benzene or THF and NMR spectra in both solvents give broad signals also at higher temperatures. ^{1}H NMR ([D$_6$]benzene, 250 MHz, 50 °C): $δ$ = 0.25 (s, 18 H, Me_3Si), 0.33 (s, 36 H, Me_3Si), 1.03–2.15 (broad m's, 60 H, Cy), 3.31 (broad m's, 6 H, Cy) ppm. ^{13}C NMR spectroscopic data could not be recorded due to the low solubility of the complex and broad signals as a consequence of dynamic processes.

Crystal Structures: Crystal diffraction data were measured on an Enraf–Nonius CAD4 diffractometer (crystal data are given in Table 1). All crystal structures were solved with DIRDIF[34] and refined with SHELXL-97.[35] Absorption correction was applied for **2** using the psi-scans method incorporated in PLATON,[36] which was also used for geometry calculations and graphics for all structures described here. For all structures, hydrogen atoms were placed at calculated positions and were refined isotropically. The bridging amide in **5** shows disorder in the cyclohexane substituent but no appropriate disorder model could be found and the disordered molecule is described by large anisotropy in the ring atoms. Crystals of **5** also contain one equivalent of disordered benzene which was treated with the SQUEEZE procedure[37] incorporated in PLATON.

CCDC-272452–272454 (for **1**, **2** and **5**, respectively) contain the supplementary crystallographic data for this paper. These data can be obtained free of charge from The Cambridge Crystallographic Data Centre via www.ccdc.cam.ac.uk/data_request/cif.

Acknowledgments

We thank the DFG for financing this project and are grateful to the BASF AG (Ludwigshafen, Germany) for their interest and for GPC analyses of the polymers. Mrs. Anke Friemel is thanked for measuring 600-MHz spectra.

[1] J. Barker, M. Kilner, *Coord. Chem. Rev.* **1994**, *133*, 219.
[2] F. T. Edelmann, *Coord. Chem. Rev.* **1994**, *137*, 403.
[3] P. J. Bailey, S. Pace, *Coord. Chem. Rev.* **2001**, *214*, 91.
[4] P. J. Bailey, L. A. Mitchell, S. Parsons, *J. Chem. Soc., Dalton Trans.* **1996**, 2839.
[5] P. J. Bailey, S. F. Bone, L. A. Mitchell, S. Parsons, S. J. Taylor, L. J. Yellowlees, *Inorg. Chem.* **1997**, *36*, 867.

 © 2005 Wiley-VCH Verlag GmbH & Co. KGaA, Weinheim

[6] P. J. Bailey, R. O. Gould, C. N. Harmer, S. Pace, A. Steiner, D. S. Wright, *Chem. Commun.* **1997**, 1161.
[7] S. J. Aeilts, M. P. Coles, D. C. Swenson, R. F. Jordan, V. G. Young, *Organometallics* **1998**, *17*, 3265.
[8] A. P. Kenney, G. P. A. Yap, D. S. Richeson, S. T. Barry, *Inorg. Chem.* **2005**, *44*, 2926.
[9] G. R. Giesbrecht, A. Shafir, J. Arnold, *J. Chem. Soc., Dalton Trans.* **1999**, 3601.
[10] D. Herskovics-Korine, M. S. Eisen, *J. Organomet. Chem.* **1995**, *503*, 307.
[11] J. R. Hagadorn, J. Arnold, *J. Chem. Soc., Dalton Trans.* **1997**, 3087.
[12] J. C. Flores, J. C. W. Chien, M. D. Rausch, *Organometallics* **1995**, *14*, 1827.
[13] R. Gómez, R. Duchateau, A. N. Chernega, J. H. Teuben, F. T. Edelmann, M. L. H. Green, *J. Organomet. Chem.* **1995**, *491*, 153.
[14] H. Fuhrmann, S. Brenner, P. Arndt, R. Kempe, *Inorg. Chem.* **1996**, *35*, 6742.
[15] A. Martin, R. Uhrhammer, T. G. Gardner, R. F. Jordan, *Organometallics* **1998**, *17*, 382.
[16] M. P. Coles, R. F. Jordan, *J. Am. Chem. Soc.* **1997**, *119*, 8125.
[17] G. R. Giesbrecht, G. D. Whitener, J. Arnold, *J. Chem. Soc., Dalton Trans.* **2001**, *6*, 923.
[18] A. P. Duncan, S. M. Mullins, J. Arnold, R. G. Bergman, *Organometallics* **2001**, *20*, 1808.
[19] M. P. Coles, P. B. Hitchcock, *Eur. J. Inorg. Chem.* **2004**, 2662.
[20] L. Zhou, Y. Yao, Y. Zhang, M. Xue, J. Chen, Q. Shen, *Eur. J. Inorg. Chem.* **2004**, 2167.
[21] M. O. Kristen, H. H. Görtz, B.-J. Deelman, M. F. Lappert, W.-P. Leung and H.-K. Lee, European Patent EP 0803520 B1, **1998**.
[22] M. P. Coles, D. C. Swenson, R. F. Jordan, V. G. Young Jr., *Organometallics* **1997**, *16*, 5183.
[23] S. Harder, F. Feil, A. Weeber, *Organometallics* **2001**, *20*, 1044–1046.
[24] F. Feil, S. Harder, *Angew. Chem.* **2001**, *113*, 4391; *Angew. Chem. Int. Ed. Engl.* **2001**, *40*, 4261.
[25] S. Harder, F. Feil, *Organometallics* **2002**, *21*, 2268.
[26] F. Feil, C. Müller, S. Harder, *J. Organomet. Chem.* **2003**, *683*, 56.
[27] F. Feil, S. Harder, *Eur. J. Inorg. Chem.* **2003**, 3401.
[28] M. Westerhausen, W. Schwarz, *Z. Naturforsch., Teil B* **1992**, *47*, 453.
[29] L. M. Engelhardt, P. C. Junk, C. L. Raston, A. H. White, *J. Chem. Soc., Chem. Commun.* **1988**, *22*, 1500; H. Schumann, J. Gottfriedsen, M. Glanz, S. Dechert, J. Demtschuk, *J. Organomet. Chem.* **2001**, *617/618*, 588–600.
[30] M. Westerhausen, H. D. Hausen, W. Schwarz, *Z. Anorg. Allg. Chem.* **1992**, *618*, 121.
[31] S. Harder, *Angew. Chem.* **2003**, *115*, 3553–3556; *Angew. Chem. Int. Ed.* **2003**, *42*, 3430.
[32] M. Westerhausen, *Inorg. Chem.* **1991**, *30*, 96.
[33] F. Feil, S. Harder, *Macromolecules* **2003**, *36*, 3446.
[34] P. T. Beurskens, G. Admiraal, G. Beurskens, W. P. Bosman, R. de Gelder, R. Israel, *The DIRDIF Program System* **1994**, Crystallography Laboratory, University of Nijmegen, The Netherlands.
[35] G. M. Sheldrick, SHELXL-97, Programs for the Determination of Crystal Structures **1997**, University of Göttingen, Germany.
[36] A. L. Spek, *PLATON, A Multipurpose Crystallographic Tool*, Utrecht University, Utrecht, The Netherlands, **2000**.
[37] P. A. van der Sluis, A. L. Spek, *Acta Crystallogr., Sect. A* **1990**, *46*, 194.
[38] Reaction of **3** with dicyclohexylcarbodiimide indeed gives a fast addition to yield diastereomers of the calcium complex: [Ca{[α-(Me_3Si)-*o*-(Me_2N)-benzyl]-CN_2}$_2$] unpublished results, S. Harder.

Received: May 20, 2005
Published Online: September 13, 2005

 © 2005 Wiley-VCH Verlag GmbH & Co. KGaA, Weinheim

A Structural and Magnetic Investigation of Ferromagnetically Coupled Copper(II) Isophthalates

Wei-Zheng Shen,[a] Xiao-Yan Chen,[a] Peng Cheng,*[a] Shi-Ping Yan,[a] Bin Zhai,[a] Dai-Zheng Liao,[a] and Zong-Hui Jiang [a]

Keywords: Copper / Magnetic properties / N ligands / Organic-inorganic hybrid composites

Page 2304 of ref.[1]: In Table 2. Data collection and processing parameters, the c cell value for complex ***2*** *should be 15.190(10) and* ***not*** *16.2328(6) Å. The authors apologise for this mistake and thank Ms Lorna Rouse of the CCDC centre for bringing this to their attention.*

[1] W.-Z. Shen, X.-Y. Chen, P. Cheng, S.-P. Yan, B. Zhai, D.-Z. Liao, Z.-H. Jiang, *Eur. J. Inorg. Chem.* **2005**, 2297–2305.

Received: August 9, 2005

The Authors

[a] Department of Chemistry, Nankai University,
Tianjin 300071, P. R. China
Fax: +86-22-23502458
E-mail: pcheng@nankai.edu.cn

 DOI: 10.1002/ejic.200500728 © 2005 Wiley-VCH Verlag GmbH & Co. KGaA, Weinheim

EurJIC
European Journal of Inorganic Chemistry

Issue 22/2005

Pages 4449–4668

Papers available ahead of print in Early View at www.interscience.wiley.com

Earliest available Table of Contents:
Automatically, free of charge by e-mail through
www.interscience.wiley.com/alerts

COVER PICTURE

The cover picture shows the postulated catalytic cycle for the pH-dependent, enantioselective transfer hydrogenation of acetophenone to give phenylethanol in water, using formate as hydrogen donor and (arene)ruthenium(*trans*-diaminocyclohexane) as chiral catalyst. This work illustrates the increasing interest for water-soluble enantioselective catalysts operating in aqueous solution. Details are discussed in the article by G. Süss-Fink et al. on p. 4493ff.

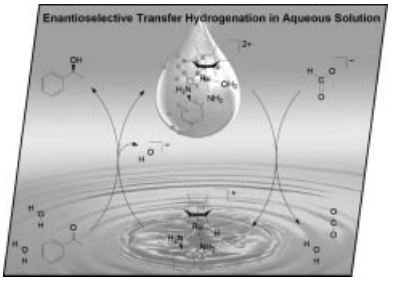

MICROREVIEW

Contents

4465 **E. A. Turner, Y. Huang,* J. F. Corrigan***

Synthetic Routes to the Encapsulation of II–VI Semiconductors in Mesoporous Hosts

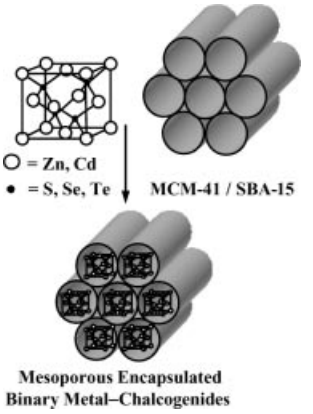

Keywords: Mesoporous materials / Semiconductors / Host–guest systems / Nanostructures

 © 2005 Wiley-VCH Verlag GmbH & Co. KGaA, Weinheim

SHORT COMMUNICATIONS

4479 **A. Ghosh,* I. H. Wasbotten, W. Davis, J. C. Swarts**

Norcorrole and Dihydronorcorrole: A Predictive Quantum Chemical Study

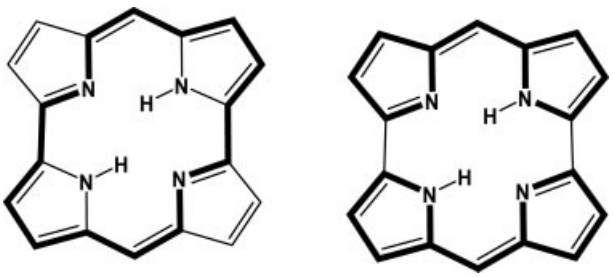

Keywords: Norcorrole / Quantum chemical calculations

4486 **D. John, W. Urland***

Crystal Structure and Magnetic Behaviour of the New Gadolinium Complex Compound $Gd_2(ClH_2CCOO)_6(bipy)_2$

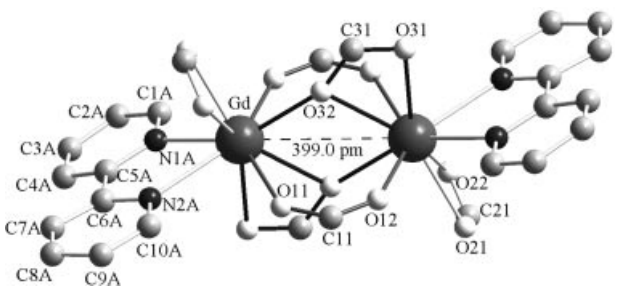

Keywords: Gadolinium / Carboxylate ligands / N ligands / X-ray diffraction / Crystal structure / Magnetic properties

4490 **J. Lewiński,* W. Bury, I. Justyniak**

Significance of Intermolecular S···C(π) Interaction Involving M−S and −C=O Centers in Crystal Structures of Metal Thiolate Complexes

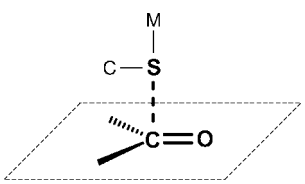

Keywords: Database analysis / Noncovalent interactions / Thiolates / Metal complexes

FULL PAPERS

4493 **J. Canivet, G. Labat, H. Stoeckli-Evans, G. Süss-Fink***

Water-Soluble Arene Ruthenium Complexes Containing a *trans*-1,2-Diaminocyclohexane Ligand as Enantioselective Transfer Hydrogenation Catalysts in Aqueous Solution

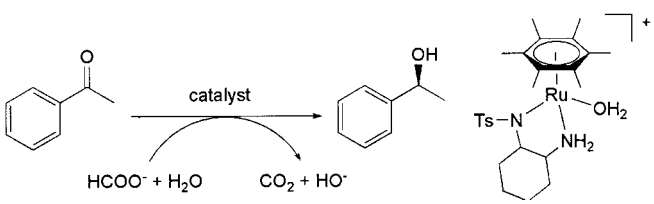

Keywords: Ruthenium complexes / Transfer hydrogenation / Enantioselective catalysis

 © 2005 Wiley-VCH Verlag GmbH & Co. KGaA, Weinheim

4501 **H. Stephan,* G. Geipel, G. Bernhard, P. Comba, G. Rajaraman, U. Hahn, F. Vögtle***

Synthesis and Binding Properties of Dendritic Oxybathophenanthroline Ligands towards Copper(II)

Keywords: Dendrimers / Phenanthroline / Copper(II) / Solvent extraction / Laser fluorescence spectroscopy

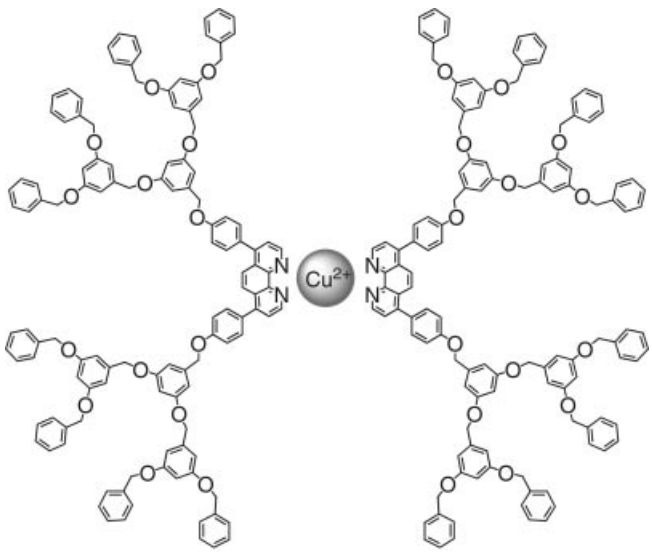

4509 **V. Kriegisch, C. Lambert***

Synthesis and Linear Optical Properties of Tris-(catecholato)metal(III,IV) Complexes with Acceptor-Substituted Ligands

Keywords: Nonlinear optics / Octupolar complexes / Chromophores / Donors / Acceptors / Catecholate

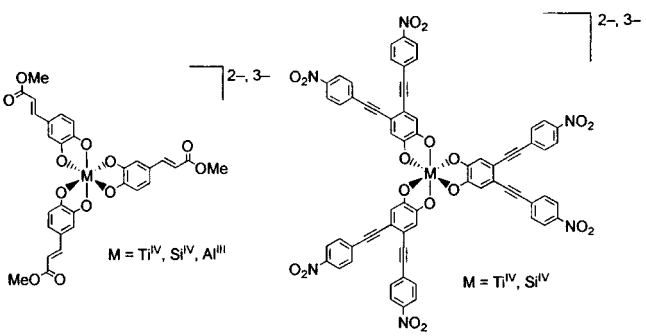

4516 **I. O. Koshevoy, O. V. Sizova, S. P. Tunik,* A. Lough, A. J. Poë**

A Novel Five-Coordinate Rhodium(I) Complex

Keywords: Solid-state structures / Rhodium / Electronic structure / Phosphane ligands / Carbonyl ligands

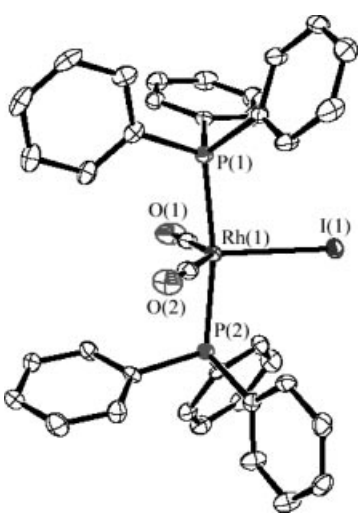

 © 2005 Wiley-VCH Verlag GmbH & Co. KGaA, Weinheim

4521 **L. Huang, Q. Xiao, H. Ma, G. Li, F. Liao, C. Qi, X. Zhao***

Phase Behaviors of the $ZrMo_{2-x}W_xO_8$ (x = 0.2−2.0) System and the Preparation of an Mo-Rich Cubic Phase

Keywords: Calorimetry / Materials science / Phase diagrams / Phase transitions / Zirconium

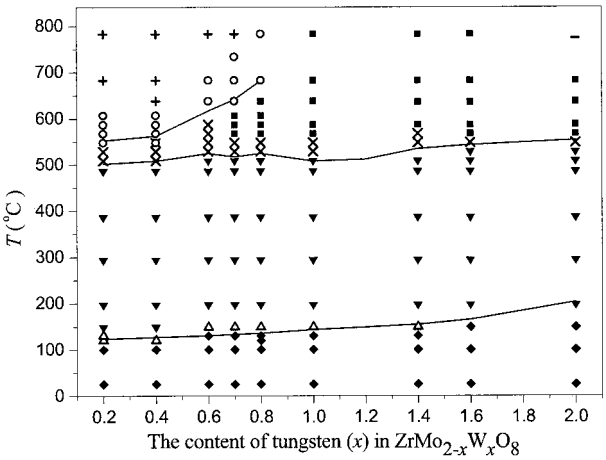

4527 **S. E. Duff, J. E. Barclay, S. C. Davies, P. B. Hitchcock, D. J. Evans***

Synthesis and Structural Characterisation of Group 10 Homo- and Hetero-Dimetallic Sulfur-Bridged Complexes of the [Ni(ema)(μ-*S*,*S*′)-M(diphos)] (M = Ni, Pd, Pt) Type

Keywords: Nickel / Palladium / Platinum / Heterometallic complexes

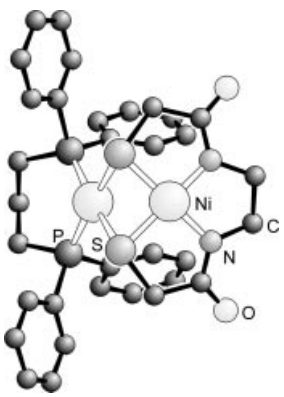

4533 **T. K. Ronson, H. Adams, M. D. Ward***

Mononuclear and Polynuclear Chain Complexes of a Series of Multinucleating N/S Donor Ligands

Keywords: Chelates / Coordination chemistry / Copper / Silver / Helical structures

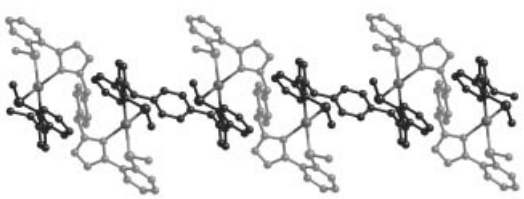

4550 **F. Li, R. Delgado,* V. Félix**

Hexaazamacrocycle Containing Pyridine and Its Dicopper Complex as Receptors for Dicarboxylate Anions

Keywords: Hexaazamacrocycle / Dicarboxylate anion recognition / Cascade dicopper complexes / Molecular dynamics / Receptors

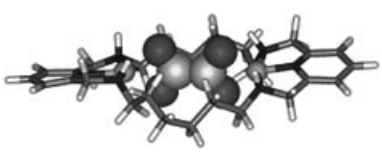

 © 2005 Wiley-VCH Verlag GmbH & Co. KGaA, Weinheim

4562 **M. Sinha Ray, S. Chattopadhyay, M. G. B. Drew, A. Figuerola, J. Ribas, C. Diaz,* A. Ghosh***

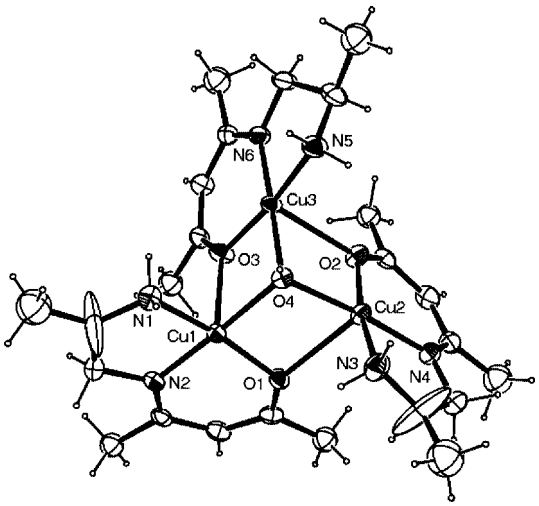

Trinuclear Cu^{II} Complexes Containing Peripheral Ketonic Oxygen Bridges and a μ_3-OH Core: Syntheses, Crystal Structures, Spectroscopic and Magnetic Properties

Keywords: Copper trimers / Schiff bases / X-ray structures / Magnetic properties

4572 **H.-D. Yin,* M. Hong, H.-L. Xu, Z.-J. Gao, G. Li, D.-Q. Wang**

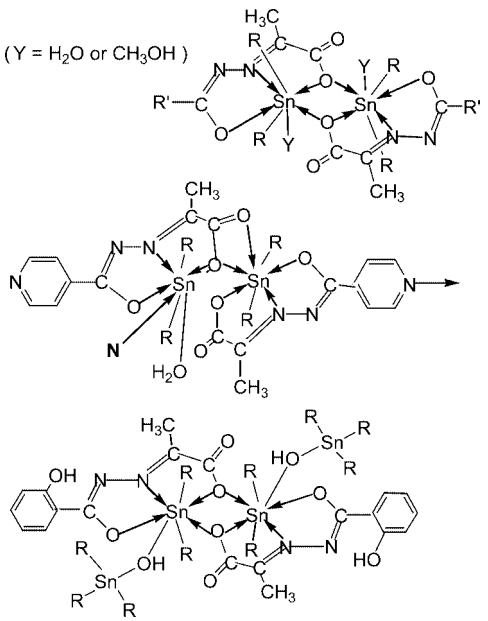

Self-Assembly of Organotin(IV) Moieties with the Schiff-Base Ligands Pyruvic Acid Isonicotinyl Hydrazone and Pyruvic Acid Salicylhydrazone: Synthesis, Characterization, and Crystal Structures of Monomeric or Polymeric Complexes

Keywords: N,O ligands / Self-assembly / Schiff bases / Tin

4582 **B. Jarrais, A. R. Silva, C. Freire***

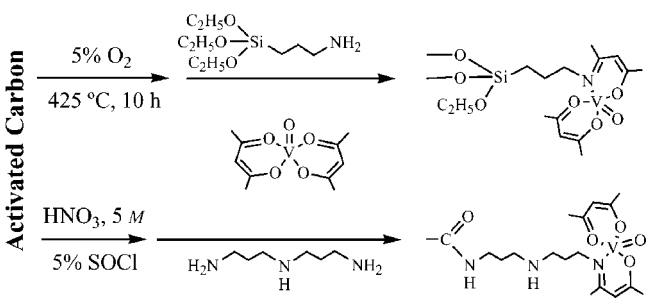

Anchoring of Vanadyl Acetylacetonate onto Amine-Functionalised Activated Carbons: Catalytic Activity in the Epoxidation of an Allylic Alcohol

Keywords: Activated carbon / Anchoring / Epoxidation / EPR spectroscopy / Vanadium

 © 2005 Wiley-VCH Verlag GmbH & Co. KGaA, Weinheim

4590 **L. Weber,* U. Lassahn, H.-G. Stammler, B. Neumann**

Inversely Polarized Phosphaalkenes as Phosphinidene- and Carbene-Transfer Reagents

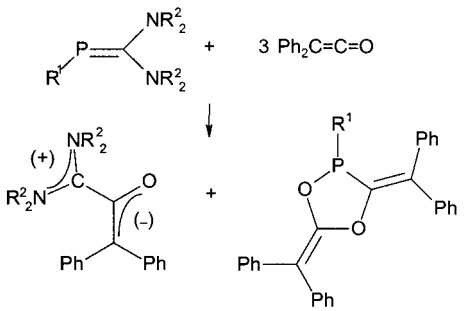

Keywords: Carbenes / Ketenes / Phosphaalkenes / Phosphinidenes

4598 **X. He, C.-Z. Lu,* D.-Q. Yuan, L.-J. Chen, Q.-Z. Zhang, C.-D. Wu**

Hydrothermal Synthesis, Crystal Structures, and Properties of a Class of 2D Coordination Polymers

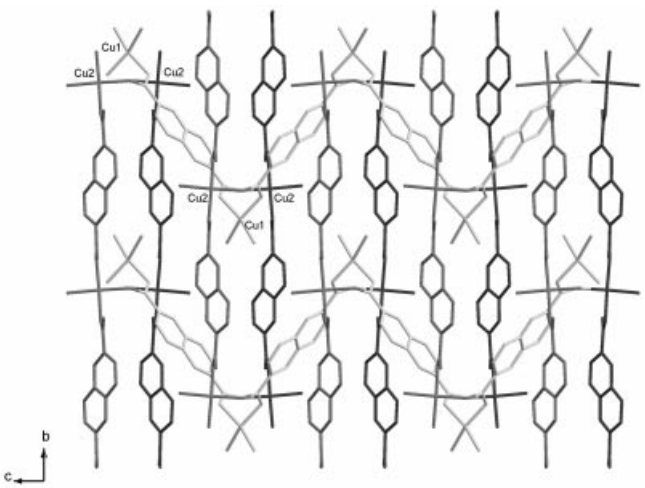

Keywords: Coordination polymers / Copper / Magnetic properties / Photoluminescence / Zinc

4607 **V. Gallo, M. Latronico, P. Mastrorilli,* C. F. Nobile, G. P. Suranna, G. Ciccarella, U. Englert**

Synthesis of Phosphido-Bridged Phosphinito Platinum(I) Complexes by Reaction of *cis*-$PtCl_2(PHCy_2)_2$ with Oxygenated Bases − Crystal Structure of $[(PCy_2OMe)Pt(\mu\text{-}PCy_2)]_2$(*Pt*−*Pt*)

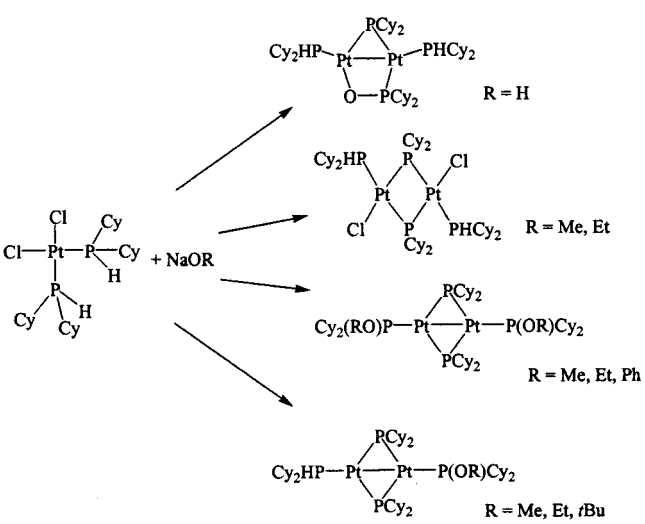

Keywords: Platinum / Bridging ligands / Phosphinites / Oxygenated bases

 © 2005 Wiley-VCH Verlag GmbH & Co. KGaA, Weinheim

4617 **V. Pashchenko,* B. Brendel, B. Wolf, M. Lang, K. Lyssenko, O. Shchegolikhina, Y. Molodtsova, L. Zherlitsyna, N. Auner,* F. Schütz, M. Kollar, P. Kopietz, N. Harrison**

Synthesis, Structure and Magnetic Properties of a Novel Linear Cu^{II}-Trimer Complex

Keywords: Copper / Cluster compounds / Sandwich complexes / Magnetic properties

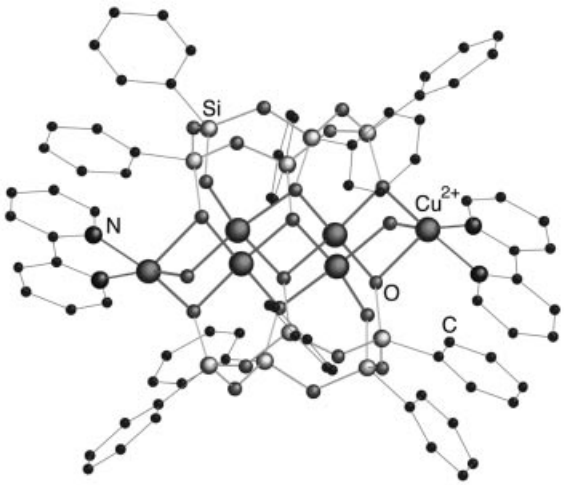

4626 **A. W. Kleij,* D. M. Tooke, A. L. Spek, J. N. H. Reek***

A Convenient Synthetic Route for the Preparation of Nonsymmetric Metallo-salphen Complexes

Keywords: N,O ligands / Nonsymmetric / Salen / Templated synthesis / Zinc

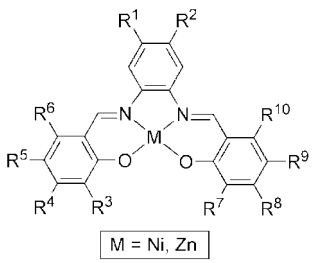

4635 **B. Sreenivasulu, M. Vetrichelvan, F. Zhao, S. Gao,* J. J. Vittal***

Copper(II) Complexes of Schiff-Base and Reduced Schiff-Base Ligands: Influence of Weakly Coordinating Sulfonate Groups on the Structure and Oxidation of 3,5-DTBC

Keywords: Biomimetic studies / Copper / Schiff-base complexes / Organosulfonate ligands / Catecholase activity / Magnetic properties

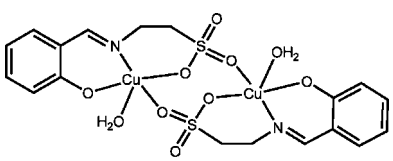

$[Cu_2(Saes)_2(H_2O)_2]$

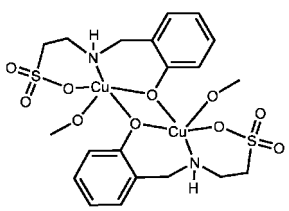

$[Cu_2(Sac)_2]$

4646 **S. C. Manna, S. Konar, E. Zangrando, K. Okamoto, J. Ribas,* N. Ray Chaudhuri***

Mn^{II}/Co^{II}-Terephthalate Frameworks Containing Dipyridine Coligands: Syntheses, Crystal Structures, Magnetic Behaviors, and Thermal Studies

Keywords: Manganese(II) / Cobalt(II) / Crystal structure / Magnetic behavior / Supramolecular chemistry

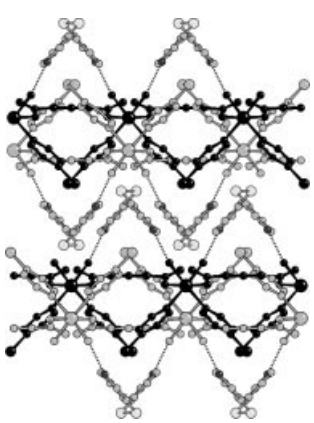

 © 2005 Wiley-VCH Verlag GmbH & Co. KGaA, Weinheim

4655 **Y. Chen,* Y. Araki, M. Hanack, M. Fujitsuka, O. Ito***

Steady-State and Time-Resolved Photophysical Studies on a Series of Gallium Phthalocyanine Monomers and Dimers

Keywords: Optical properties / Photophysics / Gallium / Phthalocyanines

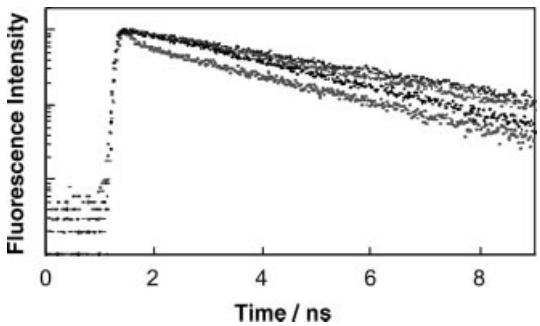

4659 **M. A. M. Abu-Youssef,* A. Escuer, V. Langer**

New Polymeric Manganese Azide Derivatives with Quinazoline

Keywords: Azides / Coordination polymers / Magnetic properties / Manganese

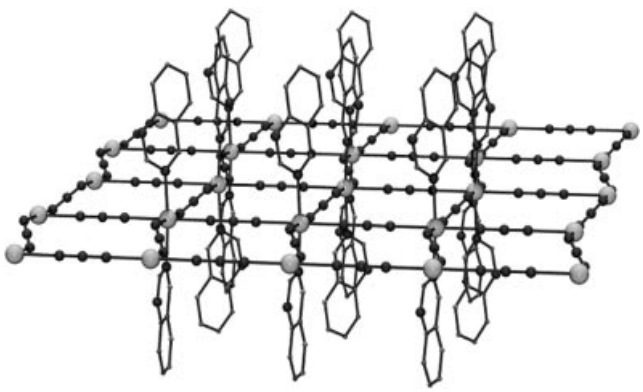

CORRECTION

4665 **A. W. Addison,* R. J. Butcher, Z. Homonnay, V. V. Pavlishchuk,* M. J. Prushan, L. K. Thompson**

The Hexakis(thiocyanato)ferrate(III) Ion: a Coordination Chemistry Classic Reveals an Interesting Geometry Pattern for the Thiocyanate Ligands

Keywords: Iron / Thiocyanate / X-ray diffraction / Magnetic properties / IR spectroscopy / Moessbauer spectroscopy / Coordination modes / Isomers

 © 2005 Wiley-VCH Verlag GmbH & Co. KGaA, Weinheim

Synthetic Routes to the Encapsulation of II–VI Semiconductors in Mesoporous Hosts

Elizabeth A. Turner,[a] Yining Huang,*[a] and John F. Corrigan*[a]

Keywords: Mesoporous materials / Semiconductors / Host–guest systems / Nanostructures

Ordered mesoporous silicate materials, such as MCM-41 and SBA-15, offer a nanometre-sized environment for the inclusion of quantum-confined materials. The channel walls of the framework hinder cluster-cluster interactions thereby restricting particle growth and thus limiting the size of the enclosed particles to the nanometre-size regime. In particular, the past decade has seen substantial progress in the synthesis and encapsulation of II–VI nanoparticles within MCM-41 and SBA-15. This microreview highlights the recent developments in this area, with notable emphasis on the synthetic routes used in the growth and anchoring of CdS, CdSe and ZnS nanoparticles within a mesoporous host. Of relevance are the methods of ion-exchange, interior pore wall modification, quantum-dot doping, incorporation of preformed nanoparticles and clusters and external surface passivation through organic functionalization. In addition to synthetic methods employed, the interesting photochemical properties of the composite materials are discussed.
(© Wiley-VCH Verlag GmbH & Co. KGaA, 69451 Weinheim, Germany, 2005)

Introduction

Ordered porous silicate materials have been the subject of intense investigation over the past several decades.[1] These materials are generally categorized according to pore size, corresponding to the spherical diameter of the aperture. IUPAC has defined three classifications of porous materials which include microporous (< 2 nm in diameter), mesoporous (2–50 nm) and macroporous (> 50 nm).[2] Although microporous materials have been successfully used in the formation of inorganic–organic hybrid materials, the advent of the first ordered mesoporous materials[3] marked a pivotal moment in the advancement of host–guest chemistry.

Since the development of MCM-41 (**M**obil's **c**omposition of **m**atter) in the early nineties[3] and the subsequent discovery of SBA-15 (**S**anta **B**arbar**a**) in 1998,[4] a considerable amount of work has focused on understanding both the mechanistic formation[5] and characterization[6] of these intriguing silicate/aluminosilicate materials. Recognizing that

[a] Department of Chemistry, The University of Western Ontario, London, Ontario, N6A 5B7, Canada
Fax: +1-519-661-3022
E-mail: yhuang@uwo.ca
jfcorrig@uwo.ca

Elizabeth A. Turner (centre) was born in Halifax, Nova Scotia, Canada in 1980. She obtained her B. Sc. (Honours) from Saint Mary's University in Halifax, Nova Scotia in 2002. She is currently pursuing her Ph. D. at The University of Western Ontario in London, Ontario under the supervision of Dr. John F. Corrigan and Dr. Yining Huang. Her research interests are in the synthesis and characterization of ternary metal–metal chalcogenides in mesoporous materials and the development of new binary chalcogenide reagents. Yining Huang (right) was born in Beijing, P. R. China. He earned his B.Sc., M.Sc. from Peking University and his Ph. D. from McGill University with Ian S. Butler and Denis F. R. Gilson. He was a NSERC post-doctoral fellow with Colin A. Fyfe at the University of British Colombia. He started his academic career at Laurentian University as an Assistant Professor in 1995 and then moved to The University of Western Ontario in 1997 where he is currently Professor of Chemistry. His major research interests include characterization of nanoporous materials and the host–guest interactions in these systems. John F. Corrigan (left) was born in Oshawa, Ontario, Canada. He obtained his B.Sc. (Chemistry Specialist) from the University of Toronto in 1990 and his Ph. D. degree from the University of Waterloo in 1995 with Arthur J. Carty. After a NSERC post-doctoral fellowship at the University of Karlsruhe with Dieter Fenske, he joined the faculty at The University of Western Ontario in 1997 where he is currently an Associate Professor. His current research interests focus on metal chalcogenolate and chalcogenide complexes, from coordination complexes to nanomaterials.

MICROREVIEWS: This feature introduces the readers to the authors' research through a concise overview of the selected topic. Reference to important work from others in the field is included.

the distinctive hexagonal array of uniform mesoporous channels can be used in inclusion chemistry,[7] the past decade has seen an explosion of growth in the use of mesoporous materials as a host environment for catalysis,[8] adsorption/separation,[9] polymerization,[10] and in particular, the subject of this microreview, quantum-confined materials.

The original synthesis for purely siliceous MCM-41 is done under acidic conditions with the use of alkyltrimethylammonium halide as an organic structure directing agent and sodium silicate as a silica source.[3] A liquid-crystal templating method (Figure 1) has been proposed for the formation of MCM-41, where surfactant species form micellar rods in aqueous solution which can align in a hexagonal array.[3,5] The addition of an anionic inorganic species into the aqueous domain initiates the formation of inorganic walls between the surfactant micelles in an effort to balance the cationic charge of the hydrophilic micelle. Increasing the alkyl chain length of the surfactant and the use of an organic auxiliary swelling agent (e.g. 1,3,5-trimethylbenzene) have been found to result in pore-size expansion, further supporting the proposed liquid-crystal templating mechanism. The porous silica skeleton is obtained through calcination of the surfactant-silica material at 540 °C, thus removing all organic components from the interior pore.

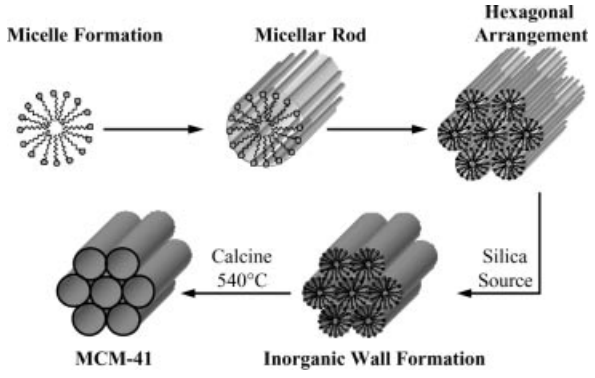

Figure 1. Proposed liquid-crystal templating method for the formation of mesoporous MCM-41.

Although the pore size of MCM-41 can range from 1.6–10 nm, the larger pore systems generally show decreased regularity of the hexagonal array as observed by transmission electron microscopy (TEM), Figure 2, a–b. In addition, the thin walls of MCM-41 (1–1.5 nm) are not strong enough to retain the framework structure upon hydrothermal treatment. The pore walls can be strengthened using a secondary crystallization technique,[11] modified reaction conditions[12] and post-synthesis restructuring.[13] These approaches, however, result in a pore-wall thickness having an upper limit of ca. 3 nm. On the other hand, SBA-15[4] is a thicker-walled mesoporous material (3.1–6.4 nm) with pore sizes spanning 4.7–30 nm. Although SBA-15 has a similar hexagonal arrangement of mesoporous channels to MCM-41, the material is formed from a nonionic triblock copolymer of poly(ethylene oxide)–poly(propylene oxide)–poly(ethylene oxide). Pore-size engineering can be accomplished by adjusting the reaction temperature (35–140 °C) and time (11–74 h), as well as by altering copolymer composition or through the addition of an organic swelling agent. The increased pore thickness enables SBA-15 to exhibit greater hydrothermal stability as compared to its MCM-41 counterpart. Furthermore, SBA-15 displays increased regularity in pore size uniformity as is shown in Figure 2c–d.

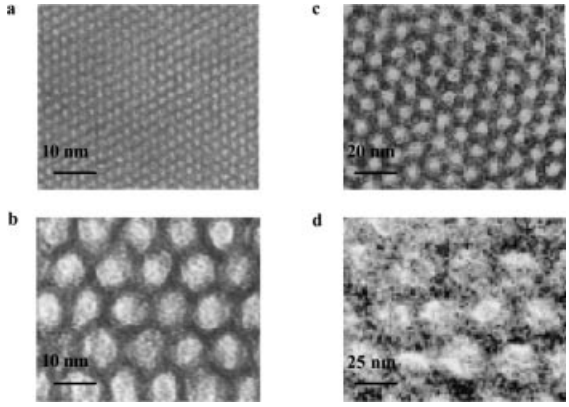

Figure 2. Transmission electron microscope images of MCM-41: Pore size a) 2 nm, b) 10 nm and SBA-15: Pore size c) 6 nm, d) 26 nm. (Figure 1, a–b, adapted with permission from ref.[3b]. Copyright 1992, American Chemical Society. Figure 1, c–d, reprinted and modified with permission from ref.[4a]; D. Zhao, J. Feng, Q. Huo, N. Melosh, G. H. Fredrickson, B. F. Chmelka, G. D. Stucky, Science 1998, 279, 548–552. Copyright 1998, AAAS).

One of the many attractive features of MCM-41 and SBA-15 is the relatively high surface area offered by the mesoporous framework, typically ranging between 700 and 1000 $m^2 g^{-1}$, thus rendering these surfaces available for guest molecule inclusion. Upon occupying the host with a guest species a notable decrease in surface area is observed. Nitrogen adsorption is the most commonly used technique to monitor changes in pore size, surface area and pore volume.[14] Type-IV isotherms[2] are observed for both MCM-41 and SBA-15 and are marked with a sharp inflection point at a value P/P_0, corresponding to capillary condensation within the primary mesopores (Figure 3). The surface area is calculated based on the Brunauer–Emmett–Teller (BET) method,[15] where a decrease in BET surface area is characterized by a decrease in the P/P_0 position for capillary condensation. The results from nitrogen adsorption can also be used in the calculation of pore size distribution based on the Barrett–Joyner–Halenda (BJH) method.[16] It is important to note, however, that the BJH calculation tends to underestimate the pore size by approximately 1 nm for pore dimensions less than 4 nm.[17] Nonetheless, the trend in decreasing pore size as a result of pore filling can be monitored using this calculation.

Upon enclosing guest molecules within the host material it is essential that the siliceous framework remains intact both during and after inclusion of the desired species. The hexagonal array is unambiguously monitored by TEM, however, powder X-ray diffraction (PXRD) is another useful tool in surveying the framework structure. MCM-41 displays a very strong d_{100} spacing at low angle with slightly weaker reflections corresponding to lattice planes (110) and

 © 2005 Wiley-VCH Verlag GmbH & Co. KGaA, Weinheim

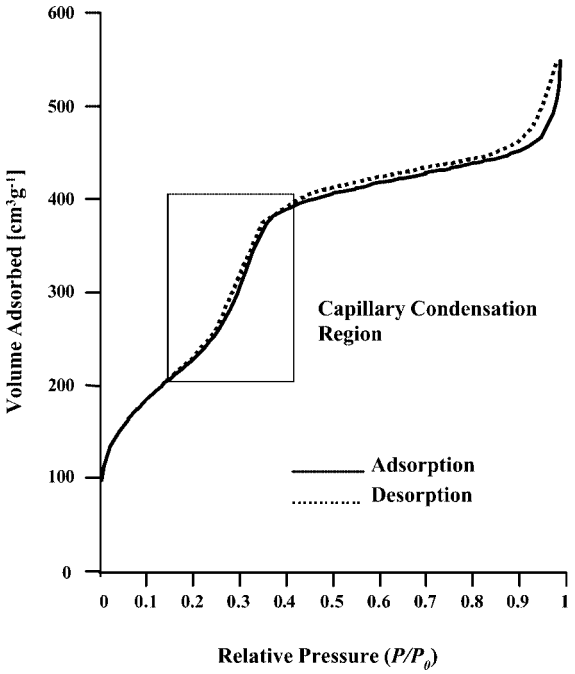

Figure 3. Typical type-IV isotherm observed for mesoporous materials. Depicted is the adsorption–desorption isotherm for calcined MCM-41.

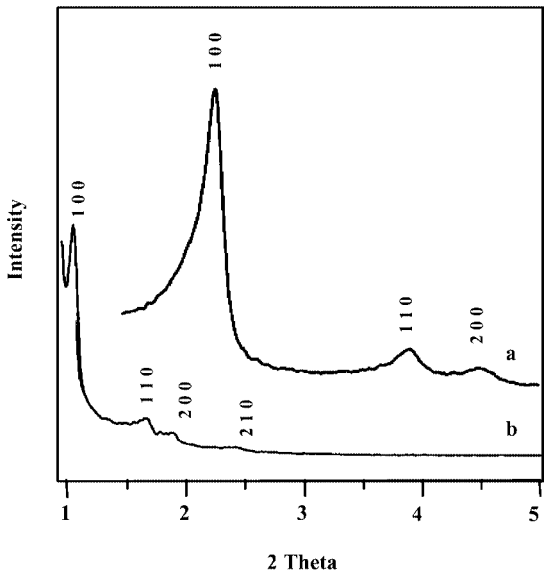

Figure 4. Powder X-ray diffraction patterns for a) MCM-41 and b) SBA-15. (Figure adapted with permission from ref.[42]. Copyright 2002, American Chemical Society).

(200) at higher angle, as seen in Figure 4 (a).[3] Similarly, SBA-15 displays a predominant d_{100} spacing with three additional well-resolved peaks related to the (110), (200) and (210) lattice planes at higher angles (Figure 4, b).[4] Retention of these peaks upon guest-molecule inclusion is indicative of framework stability. Typical pore filling is accompanied by a reduction in peak intensity of the composite material in the corresponding PXRD pattern. This results from a decrease in scattering contrast between the pores and the walls of the mesoporous material upon pore filling. In addition, the position of the d_{100} peak is often shifted to lower angles as pore size decreases.

The field of quantum-confined nanocrystals has grown tremendously with the discovery of the size-dependent chemical, electronic and physical properties of semiconductor materials.[18] Conventional semiconductors are characterized by a filled valence band and empty conduction band separated by a discrete bandgap energy. The progression to smaller-sized particles (smaller than the Bohr radius[19]) having the same chemical composition as that of the bulk material results in an increase in bandgap energy, coupled with the quantization of both the valence and conduction bands (Figure 5). Upon entering this nanometre size regime, the Bohr radius of the exciton exceeds the size of the particle itself and thus, the exciton "fits" into the given particle by adopting a higher kinetic energy. As such, an increase in bandgap energy is observed as a result of quantum-confinement effects. These effects are readily monitored using UV/Vis absorption spectroscopy where shifts to higher energy with decreasing size vs. the bulk material are observed. Thus UV/Visible spectroscopy can be used to demonstrate the effects of quantum confinement in II–VI particles of various sizes, highlighted by the systematic shift of the excitonic transition to higher energy with decreasing particle size. These materials are composed of metal atoms from group 12 (Zn, Cd, Hg) and chalcogen atoms from group 16 (S, Se, Te). Hence, a blue shift in absorbance onset from that of the bulk material is observed.[18c] The photoluminescence (PL) of II–VI nanoparticles occurs as two types; band-edge PL and deep-trap PL. Band-edge emission occurs due to the recombination of trapped charge carriers from shallow trap states within the particle, and this results in a slight red shift with respect to the absorption due to the relaxation of the trapped charge carrier into lower lying energy states prior to recombination. Deep-trap emission occurs through recombination of trapped localized carriers from deep mid-gap trap states, which are usually hole traps at the surface of the particle. Trapped emission is characterized by a broad line width which is shifted significantly to the red of the excitonic absorption.[18,19]

One of the challenges in obtaining monodisperse nanoparticles is in controlling their growth and thus preventing their aggregation to the bulk state. In particular, there has been substantial interest in developing suitable chemical capping agents for these nanometre-sized particles. Recent efforts have focused on the use of polymers,[20] organic ligands[21] and inorganic functionalization in core/shell materials[22] to passivate the nanoparticle surface, although particle size distribution is inevitable within these systems. An alternative method potentially leading to monodisperse or nearly monodisperse particles is through the use of an ordered mesoporous host such as MCM-41 and SBA-15. The pore-size structure of these materials is ideal for the growth of nanoparticle semiconductor materials, where the confining nanosized environment hinders particle–particle interactions thus preventing cluster aggregation.

Perhaps the most extensively studied class of semiconductor materials is that referred to as the II–VI semi-

 © 2005 Wiley-VCH Verlag GmbH & Co. KGaA, Weinheim

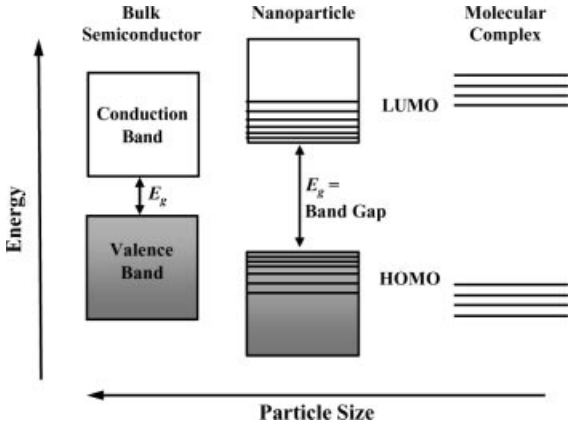

Figure 5. Energy diagram depicting the relationship between particle size and bandgap for a bulk semiconductor, nanoparticle and molecular species.

conductors. Two polymorphs of these metal chalcogenide materials are known, referred to as zinc blende (or sphalerite) and wurtzite, where both M^{2+} (M = Zn, Cd, Hg) and E^{2-} (E = S, Se, Te) are tetrahedrally coordinated.[23] Zinc blende can be represented as two interpenetrating face-centred cubic lattices, where the anion occupies one cubic lattice in which a quarter of the tetrahedral holes are populated by the cation of a second cubic lattice. In contrast, the wurtzite structure has hexagonal symmetry where anions form a hexagonal closest-packed arrangement in which half of the tetrahedral holes are occupied by metal atoms of a second hexagonal closest-packed array. For some metal chalcogenides both polymorphs are observed where one form is thermodynamically favoured over the other.[24] For metal sulfides, both forms occur naturally, however, zinc blende is more stable for ZnS, whereas the thermodynamically favoured wurtzite structure is observed for CdS. In comparison, both structures are observed in the case of CdSe (preferentially wurtzite), while ZnSe is only found in the zinc blende form. The reverse is true for metal tellurides, where CdTe is found only as a zinc blende structure, while for ZnTe the zinc blende form is preferred but it also displays the wurtzite structure.

It is the intention of this microreview to discuss the various synthetic strategies employed in the formation of II–VI materials within a mesoporous host with emphasis on the quantum-confinement effects observed within these composite materials.

Ion-Exchange Method for the Synthesis of II–VI Mesoporous Materials

Prior to the discoveries of mesoporous MCM-41[3] and SBA-15,[4] the importance of confining the dimensions of II–VI semiconductor materials in a suitable size-restricting host had been recognized. The microporous nature of zeolites provides an ideal environment for the inclusion of nanosized semiconducting materials. The ionic character of these zeolites offers the opportunity to exchange host cations for desired metal cations in the pursuit of enclosing binary metal chalcogenides within the framework cages. As such the ion-exchange method for the synthesis of II–VI materials in zeolites was developed for the synthesis of CdS in zeolites-X, Y and A.[25] Since that time there have been numerous studies investigating the synthesis of CdS,[26] CdTe[27] and ZnS[28] in various zeolite hosts using this general approach.

The typical procedure uses the sodium form of the respective zeolite. Sodium cations within the framework can be exchanged for preferred metal cations through mechanical mixing of the zeolite with a given metal salt. Generally nitrate salts are used,[25,26a–26c,27,28c] although chloride[26d,26e,28a,28b] and sulfate[28b] salts and even Me_2M (M = Zn, Cd)[28d] have also found utility. The ion-exchanged materials are often calcined at 400 °C and, in the case of the sulfides, are treated with a flow of H_2S at 100 °C. Sulfidization has also been achieved using thiourea[26e] and Na_2S.[28c] An alternative approach has been employed in the formation of CdTe, where tellurium metal is incorporated into the framework of zeolite-A at high temperature prior to cation exchange.[27] A wide variety of zeolites have been investigated in this manner and include zeolite-A,[25b,25c,26c,27] zeolite-X,[25b,25c,26e] zeolite-Y,[25,26d] mordenite[26a,26b,28] and SAPO-5.[26c]

The microporous environment of zeolites used for the encapsulation of semiconducting materials often leads to composite materials which show broad particle size distributions. This generally results from poor channel filling from ion-exchange, ultimately leading to a high density of defect sites. There are reports that clusters, superclusters and aggregates can co-exist within the same host,[26e] and in some instances larger particles are found to passivate the external surface.[28a] Although in most cases quantum-confinement effects are noted by the blue shift in the absorption edge,[26–28] identifying metal chalcogenide material within the host through PXRD is hindered by the overlapping of diffraction peaks of the II–VI material with those of the zeolite framework.[26–28]

Mesoporous materials offer a larger pore diameter for the inclusion of semiconductor materials and may thus offer better control over particle size. The improvement over microporous zeolites is illustrated by a similar ion-exchange method with a commercially available mesoporous zeolite.[29] Using the sodium form of the zeolite, Na^+ is exchanged for Cd^{2+}, and the material is sulfidized with Na_2S at room temperature. Size and loading of CdS can be controlled by varying the amount of Cd^{2+} introduced during the exchange process. From the wide-angle XRD pattern (Figure 6) the observed diffraction peaks are indexed to cubic crystalline zinc blende CdS, where the peaks become sharper as the Cd^{2+} concentration is increased in the material, thus leading to an increase in particle size as determined by the Scherrer formula.[30]

Quantum-confinement effects are readily observed in the photoluminescence (PL) and photoluminescence excitation (PLE) spectra, where two bands are observed in the PL spectra and three bands are present in the PLE spectra. In both, the bands are found to blue shift as particle size de-

 © 2005 Wiley-VCH Verlag GmbH & Co. KGaA, Weinheim

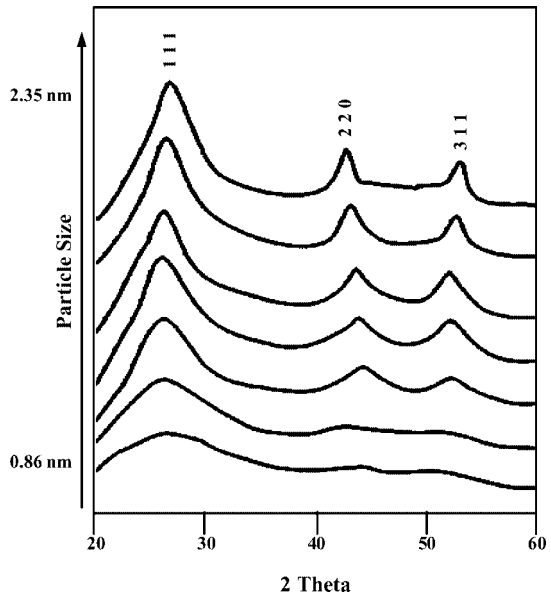

Figure 6. Wide-angle XRD patterns for zinc blende CdS formed in a mesoporous zeolite. Diffraction peaks become sharper as the amount of Cd^{2+} incorporated is increased, thus leading to larger-sized particles. (Figure reprinted and modified from ref.[29], Formation, Structure and Fluorescence of CdS Clusters in a Mesoporous Zeolite, Copyright 1998, with permission from Elsevier).

creases. In the PL spectra the strong Stokes-shifted band at 550 nm arises from trapped luminescence at the surface while a shoulder at 420 nm is assigned to band-edge emission (Figure 7).

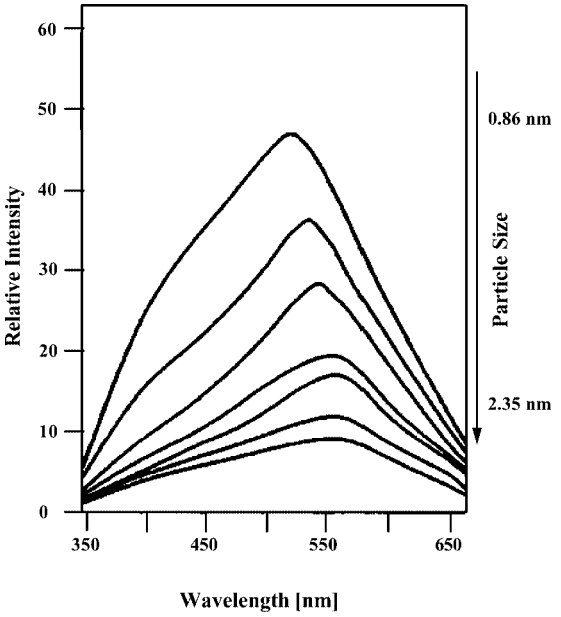

Figure 7. Photoluminescence spectra for zinc blende CdS formed in a mesoporous zeolite. As particle size decreases the emission peaks become blue-shifted. (Figure reprinted and modified from ref.[29], Formation, Structure and Fluorescence of CdS clusters in a Mesoporous Zeolite, Copyright 1998, with permission from Elsevier).

With the advent of MCM-41 and SBA-15 new methods for the incorporation of II–VI materials within a mesoporous framework have been pursued. Typically MCM-41 and SBA-15 are used in their purely siliceous forms, and thus there are no counter-cations that can be exchanged for desired metal ions, hence a modified route to developing metal chalcogenides within the mesopores through ion-loading was designed. Of recent interest has been the synthesis of manganese-doped II–VI semiconductors within a mesoporous host through the use of this method.[31–33] In particular $Zn_{1-x}Mn_xS$,[31] $Cd_{1-x}Mn_xS$[32] and $Cd_{1-x}Mn_xSe$[33] have been synthesized in MCM-41 and SBA-15 to investigate their unique optical and magnetic properties. In this approach metal acetate salts of Zn or Cd are mixed with $Mn(OAc)_2$ and solution loaded into both MCM-41 and SBA-15. Treatment with either H_2S or H_2Se at 100 °C leads to the formation of sulfides and selenides, respectively.

As determined from electron paramagnetic resonance (EPR) spectroscopy, when $x = 0.01$ the resulting encapsulated nanowires are of the zinc blende structure, while in cases where $x > 0.01$ the materials are characteristically found to display the wurtzite structure. This is true in the case of both Zn- and Cd-based materials. The X-ray absorption near-edge structure (XANES) region of the X-ray absorption spectra suggest that Mn^{2+} is present within the composite materials but not in the form of MnS. The results from XANES analyses suggest rather that Mn^{2+} is found to substitute for M^{2+} (M = Zn, Cd) sites within the ME (E = S, Se) structure, thus becoming intimately incorporated within the material. XANES spectra also indicate that only a small percentage of Mn^{2+} is found on the surface of the ME structure. All of the composite materials show quantum-confinement effects that increase with decreasing wire diameter (where the diameter is controlled by the chosen mesoporous host). These quantum-confinement effects ultimately lead to an increase in the direct bandgap energy.

Typically II–VI composite materials prepared using ion-exchange/loading as well as surface functionalization of the mesoporous material (vide infra) are in microcrystalline (powder) form. Although it is important to develop the chemistry using powder-based composites, these powders are generally unfavourable for their application in non-linear optics and optical characterization, where diffuse reflectance techniques are often employed. Thus there has been an emergence in the development of mesoporous thin films,[34–36] monoliths[34] and membranes[37] incorporating II–VI materials. Specifically, CdS[34,35,37] CdSe[35] and CdTe[36] have been prepared in these forms using a similar ion-loading technique, where a cadmium salt is introduced to the mesopores typically during the synthesis of the framework. The general procedure involves the use of alkyl-(ethylene oxide) as the structure-directing agent of which a sol is formed under acidic conditions in the presence of tetraethoxysilane. Cadmium nitrate[34] (or acetate[35]) salts are added to the sol from which thin films are formed by dip-coating, and monoliths are prepared by spreading the sol over a glass slide. Metal chalcogenides are thus formed through exposure to H_2E. An alternative approach used in the synthesis of mesoporous CdTe thin films utilizes the electrochemical codeposition of cadmium sulfate and tel-

 © 2005 Wiley-VCH Verlag GmbH & Co. KGaA, Weinheim

lurium dioxide.[36] Prior to electrodeposition, the salts are incorporated into a lytropic liquid crystalline domain composed of octaethyleneglycol monohexadecyl ether as the templating agent. Using a similar synthetic approach as detailed above, porous alumina membranes are used as a template in the formation of CdS mesoporous structures.[37] Using this route, surfactant, silica and cadmium salts are incorporated into the channels of the alumina membrane, followed by H_2S treatment. Much like their powder counterparts, these materials have particle sizes on the order of 2.5 nm when formed in thin films and monoliths and ca. 6 nm when synthesized as a membrane structure. In addition, all enclosed materials display similar quantum-confinement effects to those observed in MCM-41 and SBA-15.

Surface Modification of Mesoporous Hosts for the Synthesis of II–VI Materials

Organic functionalization of the interior pore structure of a mesoporous material has been studied extensively, resulting in the formation of inorganic–organic hybrid materials.[38] Pore modification can be achieved through either a direct co-condensation method[38d–38f] or post-synthesis grafting.[38g–38j] The method of post-synthesis grafting is most often utilized in the inclusion of II–VI semiconductor species within a mesoporous host. This modification procedure exploits the presence of multiple reactive silanol moieties populating the surface of the pore walls. Through condensation reaction with a designated alkoxysilane, the organic functional group is effectively anchored to the pore surface by the formation of silicon–oxygen bonds (Figure 8). Thiol[39] and ethylenediamine[40] moieties can be incorporated into the pore structures of MCM-41 and SBA-15 and have been used as a method of developing and/or confining metal sulfide nanoparticles within the host framework.[41–46] In this vein, these organic groups can meet several objectives which include acting as an anchor for the prepared metal sulfide, enhancing the hydrophobicity of the interior pore structure and, in the case of the anchored thiol moiety, pre-positioning the sulfide source.

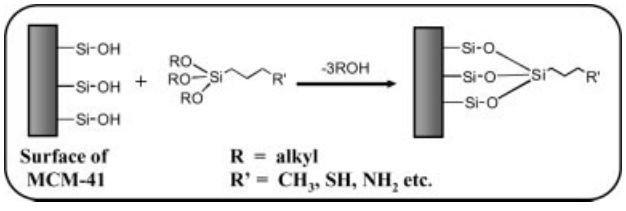

Figure 8. General reaction scheme used in the surface modification of siliceous mesoporous materials, utilizing an alkoxysilane. The rectangular area represents the pore wall of MCM-41 (or SBA-15) populated by surface silanol groups.

Cadmium sulfide is the most comprehensively studied II–VI material that has been encapsulated in a mesoporous host. In particular, the method of organic functionalization has found utility in both the synthesis and constriction of the resulting CdS particles. In studies pertaining to both MCM-41 and SBA-15, the interior pore surface is initially functionalized with 3-(mercaptopropyl)trimethoxysilane in either refluxing or room temperature solvent.[41–43] The degree of functionalization has been shown to be dependant on reaction temperature, where the higher the temperature the greater the extent of modification (as monitored by nitrogen adsorption and IR spectroscopy).[41] Cd^{2+} is adsorbed into the pores through stirring a methanolic solution of $Cd(OAc)_2{\cdot}2H_2O$ with the organo–mesoporous material. The resulting material is treated either with a stream of 5 vol-% H_2S in nitrogen[41,42] or calcined at 300 °C in nitrogen[43] resulting in the formation of CdS nanorods, as depicted in Figure 9.

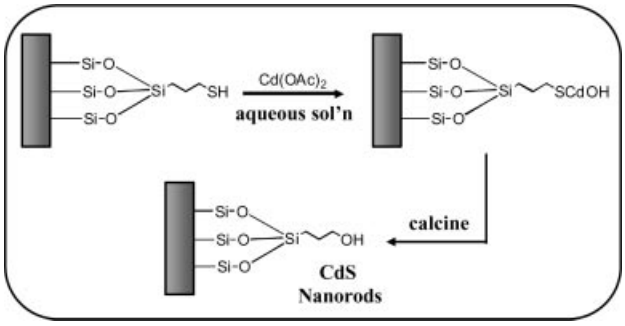

Figure 9. Formation of CdS nanorods in thiol-modified SBA-15 through the addition of $Cd(OAc)_2$ followed by calcination under nitrogen.

The incorporation of CdS nanoparticles within the porous structure is confirmed by wide-angle PXRD and diffuse reflectance UV/Vis spectroscopy. From PXRD analysis, the wide-angle peaks are indexed to the hexagonal cell (wurtzite structure) of CdS, shown in Figure 10, as opposed to the cubic form of CdS generated from the ion-exchange method. The UV/Vis spectra indicate a blue shift in the absorption edge (305–485 nm) of the resulting CdS–mesoporous materials compared to bulk CdS (515 nm), and this blue shift is consistent with the enclosed particles exhibiting quantum-confinement effects. CdS–SBA-15 composite materials are found to show a smaller blue shift of the exciton peak given the larger diameter of the pore, consistent with larger-sized particles confined within the framework.[42] The size, however, of the CdS particles grown in SBA-15 is strictly dependent on the synthetic method employed: H_2S treatment produces smaller-sized particles (3.4 nm),[42] while post-synthesis calcination is found to produce larger-sized particles (6 nm).[43] The sizes for both particles are calculated from the PXRD data using the Scherrer formula.

It has also been demonstrated that the size of the CdS particles grown inside MCM-41 is dependent on both the degree of organic functionalization and the temperature of H_2S treatment.[41] CdS particles grown in MCM-41 with the greatest coverage of thiol moieties are found to grow from 1.2 to 2.2 nm upon changing the temperature of formation from 30 °C to 230 °C. At the highest temperature of formation the particles are found to grow to the available

 © 2005 Wiley-VCH Verlag GmbH & Co. KGaA, Weinheim

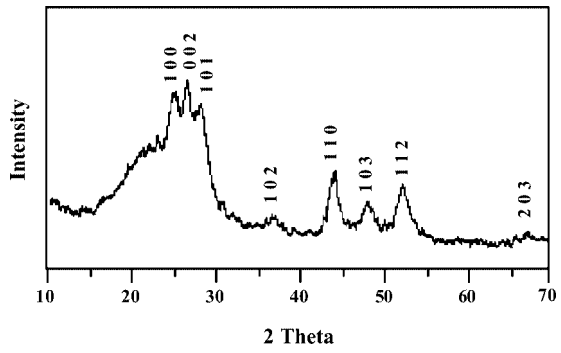

Figure 10. Wide-angle XRD pattern of wurtzite CdS nanorods synthesized within SBA-15. (Figure reprinted and modified from ref.[43], in situ Adsorption Method for Synthesis of Binary Semiconductor CdS Nanocrystals Inside Mesoporous SBA-15, Copyright 2002, with permission from Elsevier).

pore diameter, while at lower temperature there is stronger interaction of Cd^{2+} with the thiol groups, consequently leading to impeded mobility of the metal ions. Conversely, the size of the nanoparticles is found to decrease with increasing surface functionalization, as confirmed by the blue-shifted exciton peak (430 to 320 nm). This result can be correlated with the decreased pore diameter of the functionalized materials with increasing the temperature of modification, thereby reducing the available pore space for nanoparticle growth.

Although the majority of published reports study the incorporation of cadmium chalocogenides in a mesoporous host, there have been fewer cited examples of encapsulated nanosized zinc sulfide. Of these, there are several that utilize organic functionalization of MCM-41 with ethylenediamine as a means of forming ZnS nanoparticles within the framework.[44,45] Surface modification is achieved through refluxing calcined MCM-41 with *N*-[3-(trimethoxysilyl)propyl]ethylenediamine in dry toluene. The anchored chelating group provides the ability to adsorb Zn^{2+} from an ethanolic solution of $Zn(OAc)_2{\cdot}2H_2O$ while stirring at room temperature.

The desired ZnS nanoparticles can then be generated through several approaches. One method involves calcining the resulting Zn–MCM-41 material at 600 °C in air, thus removing all organic constituents from the pore while retaining the adsorbed Zn^{2+}, present in the host as ZnO as a result of calcination.[44] Similar to the formation of CdS materials within MCM-41, both Zn–MCM-41 modified with ethylenediamine and ZnO–MCM-41 are treated with H_2S for up to 6 hours leading to the synthesis of ZnS nanoparticles.[44] Six hours of exposure to H_2S is required to ensure the ratio between Zn and S reaches ca. 1:1, as confirmed by energy dispersion X-ray (EDX) analysis. An alternative method involves mixing the organically modified Zn–MCM-41 with an ethanolic solution of carbon disulfide at room temperature, thus producing ZnS within the pores of MCM-41.[45] In this method, however, no diffraction peaks in the wide-angle XRD are observed for ZnS thus suggesting the incomplete formation of ZnS crystallites at room temperature, however, the ratio of Zn to S is still found to be close to 1:1. This is quite different to the ZnS nanoparticles formed from H_2S treatment,[44] where the diffraction peaks in the wide-angle XRD are indexed to zinc blende ZnS. From this XRD study the ZnS nanoparticles are found to be less than 2.5 nm in size, as determined from the Scherrer formula.

Confirmation that the synthesized particles were located in the interior of the framework vs. the exterior surface was attained from TEM analysis and from thermal treatment of the ZnS–MCM-41 materials.[44] The TEM images show no indication of the formation of ZnS on the exterior pore surface whether the electron beam is parallel or perpendicular to the channel direction. ZnS particles in the pores of MCM-41, however, are not observed directly using TEM, likely due to the weak contrast between ZnS and the silica framework. In the event ZnS particles formed on the external surface of MCM-41, thermal treatment of the composite material should result in the generation of larger-sized particles, given that the exterior pore surface provides no restriction to particle growth. Treating the materials at 150 °C while under vacuum results in no obvious change in the wide-angle XRD, therefore suggesting that all ZnS nanoparticles are confined to the pores of MCM-41 and as such their growth is impeded.

As observed for CdS formed in organically modified mesoporous materials,[41–43] the absorption edge of ZnS confined in MCM-41 (ca. 350 nm) is found to be blue-shifted from that of bulk ZnS (410 nm). Variation in the synthetic method does not result in any appreciable change in the absorption edge whereby the exciton peak of calcined ZnS–MCM-41 is found to be red-shifted by 10–20 nm from that of Zn–MCM-41-containing anchored ethylenediamine. This blue shift from the bulk material is indicative of the resulting materials exhibiting quantum-confinement effects. In both studies[44,45] the photoluminescence properties of the composite materials were investigated. From the PL spectra, the ZnS-MCM-41 materials are found to emit in the blue between 430 and 475 nm, and this has been assigned to defects associated with sulfur vacancies.[44]

Despite the ethylenediamine moiety within the framework, the resulting ZnS nanoparticles are found to leach out of the pores (as observed with TEM analysis) upon stirring for more than 4 hours in aqueous solution, consequently growing into larger-sized particles (Figure 11).[44] This problem is even more pronounced in the case where the ethylenediamine moiety is removed through calcination. To circumvent this problem with leaching, bifunctional mesoporous materials have been designed and offer advantages over monofunctionalized mesoporous materials, especially in the formation of II–VI nanoparticles within the host.[46] This synthesis uses two methods of grafting, where initially ethylenediamine-modified MCM-41 is formed through direct co-condensation[47] followed by post-synthesis grafting of a thiol moiety. The post-synthesis grafting is carried out in supercritical fluid to ensure uniform distribution of the organic groups. CdS nanoparticles are then prepared in the same manner as already described using thioacetamide as the source of S^{2-}. It is believed that the ethyl-

 © 2005 Wiley-VCH Verlag GmbH & Co. KGaA, Weinheim

enediamine group strongly chelates Cd^{2+}, while the thiol moiety anchors the formed CdS particles. By releasing Cd^{2+} from ethylenediamine more Cd^{2+} can be adsorbed, ultimately until the pores of MCM-41 are filled entirely with CdS. It is thought that these bifunctional MCM-41 materials can offer a stronger host–guest interaction over conventional monofunctionalized materials[44] while allowing a greater density of binary semiconductor material to fill the pore structure.

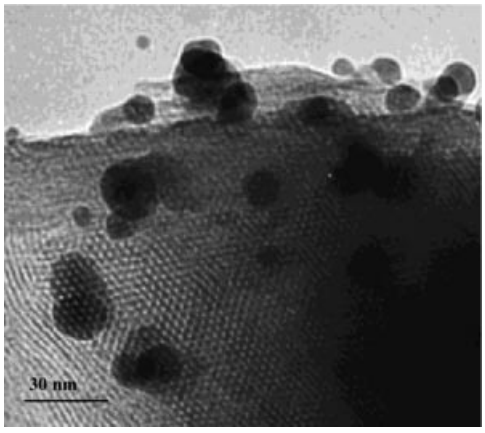

Figure 11. Transmission electron microscope image of ZnS particles leaching out of ethylenediamine-modified MCM-41 after ethanolic treatment. It is apparent from the image that particles aggregate to larger species upon leaching from the channel structure. (Figure reprinted with permission from ref.[44]. Copyright 2001, American Chemical Society).

Surface Functionalization Used to Incorporate Preformed Nanoparticles

In addition to the synthesis of II–VI nanoparticles within a mesoporous host, surface functionalization has also found utility in directing the incorporation of preformed nanoparticles within the modified framework.[48–51] In particular, post-synthesis grafting of an organic thiol is often used to develop a hydrophobic interior to the pore structure, thus promoting the delivery of II–VI nanoparticles into the host. Recent efforts have focused on the synthesis of semiconducting nanoparticles within the hydrophilic core of reverse micelles.[52] The columnar structure of the reverse micelles makes these ideal candidates for their inclusion within MCM-41 and SBA-15. The passivation of the mesoporous surface with a hydrophobic moiety ultimately facilitates the inclusion of the reverse micelles and consequently semiconducting nanoparticles within the siliceous framework.

Cadmium[48–50] and zinc sulfide,[51] formed from reverse micellar solutions, have been encapsulated within MCM-41. The typical procedure uses a reverse micellar solution containing bis(2-ethylhexyl)sulfosuccinate (AOT), water and isooctane. A reverse micellar solution of a specified water content (W_o = [H_2O]/[AOT]) containing either $Cd(NO_3)_2$ or $ZnSO_4$ is added rapidly to a second micellar solution, of equal water content, containing Na_2S. Within minutes the MS (M = Zn, Cd) nanoparticles form and the mesoporous material, modified through post-synthesis grafting of a propyl thiol group, is added to solution. The percent incorporation of MS into the mesoporous host is determined by subtracting the absorbance of MS in the supernatant of the reaction from that of the original reverse micellar solution. The use of large-pore MCM-41 leads to the inclusion of all preformed nanoparticles, as observed by the lack of absorbance for MS in the supernatant.

Nanoparticles of cadmium sulfide are only found to insert into the mesoporous channel if the pore wall has been functionalized with a propyl thiol moiety. The presence of the organic thiol promotes bonding between itself and the encapsulated CdS nanoparticles.[48,49] Although incorporation of CdS is easily achieved in larger-pore systems (ca. 4 nm), the percent incorporation is found to be strongly dependant on the micellar water content (W_o) in medium-pore systems (ca. 3.5 nm) and not at all dependant on W_o in smaller-pore systems (2 nm).[48,49] It is suggested that in large- and medium-pore MCM-41 a particle-sieving effect is observed where percent incorporation decreases with increasing W_o. This can be directly correlated with observed particle size, where smaller-sized particles are formed in micellar solutions with low water content. Consequently, the pore diameter dictates the size of CdS nanoparticles that can enter the framework, where particles exceeding the diameter of the pore will not be encapsulated. Conversely, for smaller-pore MCM-41, all values of W_o lead to more than 90% inclusion of CdS within the framework despite the size of the preformed nanoparticles exceeding the pore diameter. It is believed that these nanoparticles are immobilized in the macropores of MCM-41 (20–40 nm) and on the surface of the framework.

A mechanism for the incorporation of II–VI nanoparticles from reverse micellar solutions into mesoporous frameworks has been proposed.[49] It is believed that water droplets from the reverse micellar solution are absorbed into the pores of the given framework. As such, these droplets contain preformed MS nanoparticles which are transfixed to the pore through anchored thiol groups. Increased loading amounts of MS in the pore structure can be achieved through additional treatment with a second MS micellar solution.[49,51] Exchange of MS-free water droplets for MS-containing water droplets facilitates this process. Although sequential treatment with a MS micellar solution leads to an increased cumulative amount of MS within the framework, the successive increase in MS loading decreases with each treatment.

Diffuse reflectance UV/Vis spectroscopy of the composite MCM-41 materials reveals a blue shift in the absorption onset for CdS (450 nm) and ZnS (272 nm) from the parent bulk materials.[50,51] Although the absorption is very broad, possibly resulting from a distribution of exciton states due to varying particle sizes, these observed blue shifts in absorption onset are consistent with the enclosed particles demonstrating quantum-confinement effects. ZnS particles are found to be ca. 2 nm,[50] while CdS particles are found

 © 2005 Wiley-VCH Verlag GmbH & Co. KGaA, Weinheim

to range between 3–3.4 nm[48,50] In all cases, the size of the enclosed particles does not exceed the diameter of the MCM-41 pore.

The PL spectrum (Figure 12) of encapsulated CdS shows two broad emission bands at 430 nm (sub-band I) and 530 nm (sub-band II).[50] The authors attribute the emission at 430 nm to band-edge emission, caused by excitonic recombination, while the largely Stokes-shifted emission at 530 nm is the result of surface-defect states. The emission of sub-band I is blue-shifted (420 nm) upon calcination of the composite material (to remove all organic constituents), as observed in Figure 12b, while the emission of sub-band II is red-shifted (560 nm). These changes in the PL spectrum are associated with the slight reduction of particle size upon calcination. On the other hand, ZnS emits in the spectral region associated with the emission resulting from the modified MCM-41 framework (390 nm), however, the emission due to confined ZnS (373 nm) can be distinguished from that of MCM-41 due to its increased intensity.[51] The emission of ZnS is also found to be enhanced with sequential treatment of ZnS–micellar solutions (Figure 13). Unlike the broad blue emission associated with ZnS formed within modified MCM-41,[44] these enclosed ZnS particles show emission in the UV. Luminescence does thus not result from surface sulfur vacancies but rather from recombination processes at core lattice sulfur vacancies. This is further confirmed by the PLE spectrum that is centred at 308 nm, and hence the observed emission is Stokes-shifted from the corresponding PLE spectrum. Confined CdS is found to have both fast (ca. 0.1 ns) and slow (5–13 ns) lifetime components associated with band-edge and Stokes-shifted emission, respectively, while encapsulated ZnS was found to have a single recombination lifetime of 1.3 ns resulting from a highly selective emission state.[50,51]

Surface modification of the silicate framework is not necessary to encapsulate II–VI nanoparticles prepared in reverse micelles into the mesoporous host if a gas antisolvent technique (supercritical CO_2) is used, rather than solution loading of the reverse micelles.[53] It has been found that by adding compressed CO_2 to a MS–micellar solution leads to the removal of MS nanoparticles from the hydrophilic core of the micelle.[54] ZnS has been loaded into MCM-41 using this technique, where CO_2 is added to a dispersion of ZnS–reverse micelles and calcined MCM-41.[53] Upon removing ZnS from the reverse micelles, the nanoparticles can diffuse into the pores of MCM-41 and are thus absorbed by the pore wall. In the absence of CO_2, ZnS is not found to be enclosed within the pores of MCM-41 and therefore the antisolvent behaviour of CO_2 is necessary for their inclusion.

In addition to modifying the framework with propyl thiol groups, to be used to attach preformed CdS to the mesoporous host, other organic modifiers have been used. Zn-doped SBA-15 has been modified with an alkane dithiol moiety, where Zn–S bond formation anchors the organic to the pore wall.[55] The pendant thiol provides a hydrophobic interior to the pore structure thus allowing the movement of CdS–reverse micelles into the framework. The incorporation of Zn is required to enhance the photocatalytic activity for H_2 generation of the resulting composite materials.

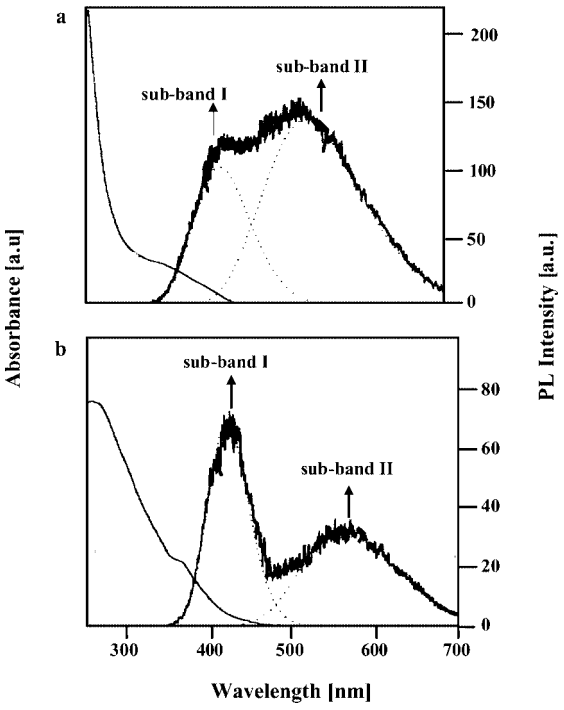

Figure 12. Diffuse reflectance UV/Vis spectra (solid line) and PL spectra of CdS encapsulated into thiol–modified MCM-41: a) as-synthesized composite material and b) after calcination of CdS–MCM-41 material. (Figure reprinted and modified from ref.[50], Emission Characteristics of CdS Nanoparticles Induced by Confinement within MCM-41 Nanotubes, Copyright 2002, with permission from Elsevier).

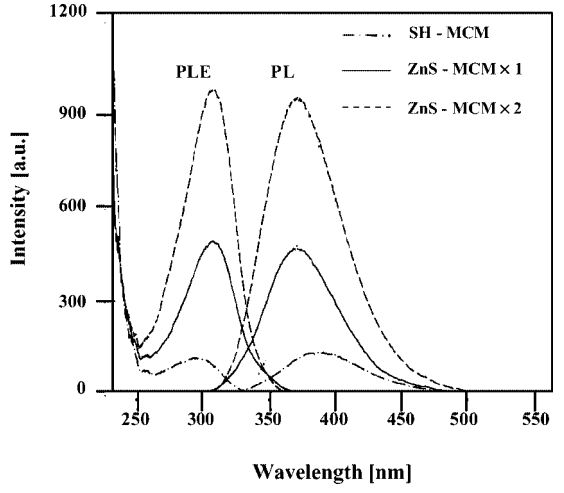

Figure 13. PL and PLE spectra of thiol-modified MCM-41, ZnS–MCM-41 after first exposure to ZnS–reverse micellar solution and ZnS–MCM-41 after two treatments with ZnS–reverse micellar solutions. (Figure adapted with permission from ref.[51]. Copyright 2004, American Chemical Society).

The utility of functionalizing the pore wall to promote nanoparticle attachment has shown promise in the field of stimuli-responsive controlled-release drug-delivery systems.[56] A mesoporous silica nanosphere (having MCM-41

 © 2005 Wiley-VCH Verlag GmbH & Co. KGaA, Weinheim

type hexagonally packed mesopores) can be modified with (2-propyldisulfanyl)ethylamine, following which drug molecules such as vancomycin can be absorbed by the material. The openings of the nanosphere are then capped by mercaptoacetic acid-derived CdS through the formation of amide bonds to the organic anchor. The lability of the disulfide bond existing between the nanosphere and CdS allows for facile bond cleavage with various disulfide reducing agents (e.g. mercaptoethanol, dithiothreitol) thereby allowing controlled release of the absorbed drug molecules to the targeted area.

Preformed Clusters Used for the Formation of II–VI Materials in Mesoporous Hosts

Incorporating clusters within mesoporous frameworks has been studied extensively,[57] and the development of condensed nanoparticle structures within the framework from these cluster precursors is also of interest.[57a–57d] Recently, it was demonstrated that $[Cu_6(TePh)_6(PPh_2Et)_5]$ can be loaded into the pores of MCM-41 at 110 °C.[58] As a discrete molecule, the cluster is known to undergo a series of condensation reactions through photochemical elimination of Ph_2Te to yield $[Cu_{50}(TePh)_{20}Te_{17}(PPh_2Et)_8]^{4-}$.[59] This same photochemical behaviour was observed for the Cu_6 cluster enclosed in MCM-41 as marked by the red shift (440 nm) in the UV/Vis absorption spectrum upon irradiation, from that of the original Cu_6 cluster (249 nm). Thermal condensation of the cluster is found to lead to the formation of Cu_2Te nanoparticles within the host.[58b]

The hexagonally arranged channel structure of MCM-41 and SBA-15 makes these materials ideal candidates for the formation of nanowire arrays.[60] The siliceous framework acts as a hard-surface template that can be removed after formation of the desired nanowire assemblies. This template technique has been employed in the formation of CdS nanowires within SBA-15.[61,62] The method initially requires impregnation of a precursor cluster, containing both Cd and S within a single source. The resulting materials are treated thermally to promote cluster decomposition to CdS, upon which the siliceous framework is etched away from the surface of the CdS nanowires through treatment with aqueous NaOH.

In one method, $Cd(NO_3)_2{\cdot}4H_2O$ is combined with thiourea in an ethanolic solution to which a suspension of SBA-15 is added.[61] The mixture of $Cd(NO_3)_2$ with thiourea leads to the formation of complex cadmium–thiourea precursors. Upon evaporating ethanol from the suspended materials, the cadmium–thiourea precursors are incorporated into the channels of SBA-15 by capillary condensation. In heating the materials to 150 °C, (cubic) zinc blende CdS nanowires are formed, as confirmed by wide-angle XRD and high-resolution TEM analysis. Alternatively, cadmium thioglycolate $[Cd_{10}S_{16}C_{32}H_{80}N_4O_{28}]$ has been used as a Cd–S single source precursor in SBA-15, followed by thermal treatment thus leading to the formation of (hexagonal) wurtzite CdS as observed by wide-angle XRD and selected area electron diffraction (SAED).[62] From TEM analysis, the CdS assembly appears as a hexagonal array of nanowires having a diameter of ca. 6 nm and a particle spacing of ca. 3 nm. TEM analysis also indicates that the nanowire array is exactly an inverse replica of SBA-15. EDX confirmed the 1:1 ratio between Cd and S with negligible contribution from Si.

A similar single-source-precursor approach has also been utilized in the formation of CdS within Al–MCM-41 and zeolitic mordenite.[63] Initially $CdCl_2$ and thiourea are added to the silica materials and then treated thermally to promote the formation of CdS. EDX results, however, suggest lower sulfur content than the expected (1:1, Cd:S), which could potentially lead to vacancies and defects within the materials. In these materials the siliceous framework is maintained, and as a result a broad size distribution of nanoparticles is observed. Smaller-sized particles are found to be enclosed within the Al–MCM-41 host, while larger particles are immobilized on the external surface. Conversely, the zeolite is only found to contain CdS on the exterior surface.

In the revision stage of this microreview a new synthetic methodology exploiting a molecular single-source-precursor approach in the formation of cadmium chalcogenides was reported.[64] Using melt permeation, the molecular precursors TMEDA-$Cd(EPh)_2$ (where TMEDA = tetramethylethylenediamine and E = S, Se, Te) are incorporated into the mesopores of SBA-15. Through subsequent pyrolysis of the encapsulated precursors, CdS, CdSe and CdTe nanoparticles are formed within the pores of SBA-15, having a particle size of roughly 7 nm. The given cadmium chalcogenide forms in the most thermodynamically favoured polymorph; CdS as wurtzite, CdTe as zinc blende and CdSe as a mixture of both the wurtzite and zinc blende forms.

Quantum-Dot Doping in Mesoporous Materials

The recent use of quantum dot (QD) and quantum wire (QW) cadmium chalcogenides in device fabrication has led to the development of LEDs, biological probes and field-effect thin-film transistors with tunable properties.[65] One of the major obstacles in fostering new devices of one-, two-, and three-dimensional QD arrays is being able to manipulate and control their spatial orientation. As such, mesoporous hosts offer an ideal environment for controlling the organization of QDs.[66,67]

A recent example has been detailed, where CdSe nanoparticles are synthesized in the pores of MCM-41, combining the methods of solution loading and hot injection into a coordinating medium.[66] There have been many examples on the growth of nanoparticles in a highly coordinating solvent (e.g. trioctylphosphane oxide – TOPO)[18b,68] but none that has extended this technique to the inclusion of such nanoparticles within MCM-41. In this approach, Me_2Cd and Se (dissolved in tributylphosphane) are encapsulated into the pores of MCM-41. The wet suspension is rapidly injected into hot TOPO (325 °C), thereby initiating the

 © 2005 Wiley-VCH Verlag GmbH & Co. KGaA, Weinheim

growth of CdSe. Upon completion the materials are washed repeatedly with toluene to remove excess TOPO and larger CdSe nanoparticles that may have grown on the exterior surface. UV/Vis spectroscopy of the resulting composite material indicates a blue shift in absorption maxima from that of bulk CdSe suggesting the encapsulated nanoparticles exhibit characteristic quantum-confinement effects. X-ray photoelectron spectroscopy (XPS) of Cd and Se show broad asymmetric peaks indicating there could possibly be multiple bonding domains. Either Cd or Se could react with surface silanols of MCM-41, hence Si–O–Cd or Si–O–Se bonding interactions have been proposed.

Preformed core–shell QDs of ZnS-capped CdSe have been loaded into the pores of mesoporous beads whose surface is covered with hydrocarbons.[67] The QDs are confined into the pores through interdigitation of the hydrocarbon and surface TOPO on the nanoparticle. These materials were found to exhibit higher luminescence than latex and nonporous polystyrene beads doped with similar QDs.

Preventing Particle Aggregation with Exterior Surface Functionalization

One limitation to the approaches used to incorporate II–VI materials within a mesoporous host is the potential to form large aggregated nanoparticles on the exterior surface. Recent efforts have focused on the selective functionalization of mesoporous materials, where exterior functionalization can be performed prior to removal of the structure-directing agent (surfactant).[69] Upon removing the surfactant, internal grafting can be achieved in a similar manner as has been described earlier (vide supra).

The success of external grafting has led to its use in the inclusion of II–VI materials within MCM-41 and SBA-15.[70–73] External grafting has demonstrated utility in both the ion-exchange approach[70,71] as well as in the internal pore functionalization method.[72,73]

Cadmium sulfide has been synthesized in a mesoporous host using an ion-exchange approach that incorporates exterior surface modification with phenyltrimethoxysilane.[70,71] Removal of the protonated surfactant renders cationic vacancies within the framework that can be filled by Cd^{2+} in the form of $Cd(OAc)_2$. Similar to the conventional ion-exchange method, this Cd^{2+}–mesoporous material is subsequently sulfidized with H_2S forming CdS exclusively within the pores of both MCM-41[70] and SBA-15.[71] The motivation of this method is that the surface phenyl groups create a hydrophobic coverage of the outer pore surface, and thus the pore interior is the only environment to which Cd^{2+} absorbs. The UV/Vis spectra for CdS, formed in both MCM-41 and SBA-15, show a blue shift in the absorption onset (450 nm and 470 nm, respectively) suggesting that the confined materials exhibit quantum-confinement effects. In addition, the wide-angle XRD of both composite materials indicate the formation of cubic crystalline CdS having a size of < 2.5 nm and 3 nm in MCM-41 and SBA-15, respectively, as determined by the Scherrer formula.

External passivation of SBA-15 with chlorotrimethylsilane, followed by internal functionalization with (3-aminopropyl)triethoxysilane (Figure 14) has led to the successful incorporation of quantum-confined CdSe[72] and CdS.[73] In the case of CdSe, $Cd(NO_3)_2$ is solution-loaded into amino-functionalized SBA-15 that has previously undergone surface functionalization, thus promoting the complexation of Cd^{2+} with the NH_2 groups. After incorporation of Cd^{2+}, the composite material is exposed to sodium selenosulfate (Na_2SeSO_3) under basic conditions (pH, 8). In the presence of a basic medium, Cd^{2+} is converted to $Cd(OH)_2$, while $SeSO_3^{2-}$ gradually releases Se^{2-} within the pores. Se^{2-} readily replaces the hydroxy groups bound to Cd^{2+} due to the lower solubility of CdSe vs. $Cd(OH)_2$. Alkaline conditions are required to promote the formation of CdSe, as similar attempts using a pH < 8 resulted in no reaction.

In a slightly modified procedure, CdS[73] was incorporated into SBA-15 with exterior modification and interior amino functionalization. In this example the chalcogen is added to the framework prior to the metal: Mercaptoacetic

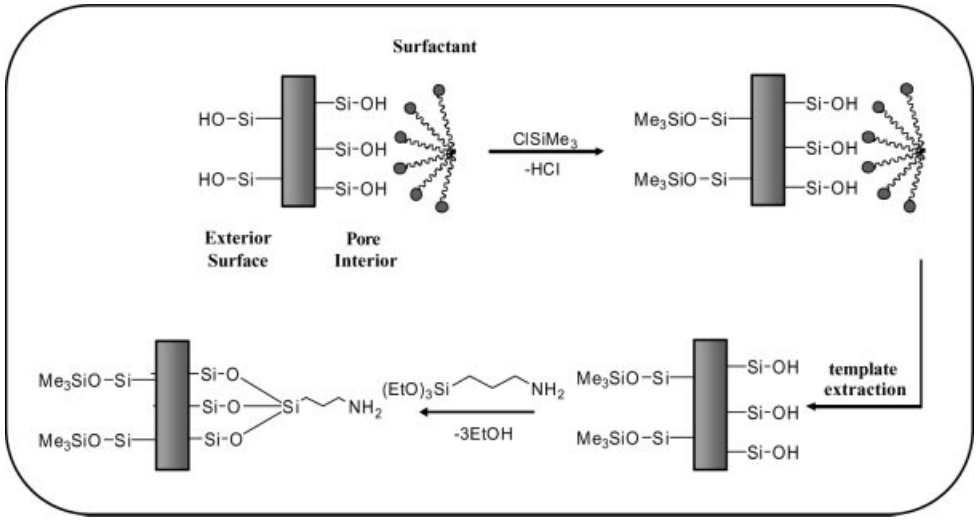

Figure 14. Synthetic pathway used for exterior functionalization followed by interior pore modification with a second organic molecule.

 © 2005 Wiley-VCH Verlag GmbH & Co. KGaA, Weinheim

acid in KOH is added to surfactant-free SBA-15. The FTIR spectrum of thiol-SBA-15 indicates the appearance of two stretching vibrations associated with $–COO^–$ that are slightly blue-shifted (1380 and 694 $cm^{–1}$) accompanied by an additional red-shifted peak (1630 $cm^{–1}$) related to $–NH_3^+$ distortion. The shift in these three IR peaks suggests binding of $COO^–$ and NH_3^+. The authors report that mercaptoacetic acid ionizes H^+, which combines with amine to form $–NH_3^+$. This observed coordination between $–COO^–$ and $–NH_3^+$ is what effectively anchors the sulfur source to the framework. Solution loading of $Cd(NO_3)_2$ followed by calcination at 300 °C leads to the formation of CdS.

The UV/Vis spectra for both CdS (519 nm) and CdSe–SBA-15 (622 nm) materials thus prepared show a blue shift in the absorption onset from that of the parent bulk materials; 550 nm and 698 nm, respectively. If no surface modification is employed in the case of CdSe, the absorption onset is only slightly shifted (660 nm) from that of the bulk material, indicating the formation of larger particles. Thus, the overall effect of exterior functionalization leads to smaller particles (5 and 7 nm for CdS and CdSe, respectively) that are found solely within the pores of the host framework.

Conclusions

Mesoporous environments, such as MCM-41 and SBA-15, have been readily used in the quantum confinement of II–VI materials. The unique nanosized siliceous channels are ideal for the inclusion of nanoparticle species. As such, there are several routes that can be employed in the synthesis of II–VI composites, in particular those accessing CdS, CdSe and ZnS particles. The ionic nature of these mesoporous hosts enables ion-exchange of framework ions for desired metal cations that can be successively used to form sulfide and selenide binary materials within the channel structure. An alternative route exploits the multiple silanol moieties populating the interior pore surface, whereby the choice of an appropriate alkoxysilane leads to the formation of new Si–O–Si bonding interactions, thus effectively anchoring an organic functional group to the pore walls. Anchored organic moieties have shown to be valuable in synthesizing, securing and directing II–VI nanoparticles into the interior pore structure. Perhaps a limitation of both these methods is the potential to form aggregated species on the exterior pore surface. In an effort to circumvent this issue and possibly access monodisperse or nearly monodisperse particles within the framework, exterior surface modification has been combined with the methods of ion-exchange and interior pore functionalization. Thus the exterior surface is protected by a hydrophobic layer thereby preventing M^{2+} from adsorbing to the exterior pore walls.

All of the described synthetic routes lead to quantum-confined materials which can be monitored by the blue shifts in the absorption onset from that of the bulk II–VI material. In addition, depending on the synthetic method employed, different polymorphs of the same binary material can be obtained. Although the above methods have been met with a significant amount of success, there is still a tremendous need to develop and explore this field fully. In particular, future studies should be geared towards rationally developing nanoparticle vs. nanowire assemblies within the mesoporous host. As such, researchers need to devise specific synthetic routes that will ultimately generate either nanowire or nanoparticle materials.

The developments presented in this microreview have pioneered the field of quantum-confined materials within mesoporous hosts. With the rapidly and vastly growing interest in nanoparticle construction, the next few years will see an evolution in the area of mesoporous encapsulated II–VI materials.

[1] a) F.-S. Xiao, S. Qiu, W. Pang, R. Xu, *Adv. Mater.* **1999**, *11*, 1091–1099; b) A. Corma, *Chem. Rev.* **1997**, *97*, 2373–2419; c) U. Ciesla, F. Schüth, *Microporous Mesoporous Mater.* **1999**, *27*, 131–149; d) R. C. Schroden, A. Stein, *Colloids and Colloid Assemblies* (Ed.: F. Caruso), Wiley-VCH, Weinheim (Germany), **2004**, 465–493.

[2] K. S. W. Sing, D. H. Everett, R. A. W. Haul, L. Moscou, R. A. Pierotti, J. Rouquérol, T. Siemieniewska, *Pure Appl. Chem.* **1985**, *57*, 603–619.

[3] a) C. T. Kresge, M. E. Leonowicz, W. J. Roth, J. C. Vartuli, J. S. Beck, *Nature* **1992**, *359*, 710–712; b) J. S. Beck, J. C. Vartuli, W. J. Roth, M. E. Leonowicz, C. T. Kresge, K. D. Schmitt, C. T.-W. Chu, D. H. Olson, E. W. Sheppard, S. B. McCullen, J. B. Higgins, J. L. Schlenker, *J. Am. Chem. Soc.* **1992**, *114*, 10834–10843.

[4] a) D. Zhao, J. Feng, Q. Huo, N. Melosh, G. H. Fredrickson, B. F. Chmelka, G. D. Stucky, *Science* **1998**, *279*, 548–552; b) D. Zhao, Q. Huo, J. Feng, B. F. Chmelka, G. D. Stucky, *J. Am. Chem. Soc.* **1998**, *120*, 6024–6036.

[5] a) C.-Y. Chen, S. L. Burkett, H.-X. Li, M. E. Davis, *Microporous Mater.* **1993**, *2*, 27–34; b) J. C. Vartuli, C. T. Kresge, M. E. Leonowicz, A. S. Chu, S. B. McCullen, I. D. Johnson, E. W. Sheppard, *Chem. Mater.* **1994**, *6*, 2070–2077; c) C.-F. Cheng, Z. Luan, J. Klinowski, *Langmuir* **1995**, *11*, 2815–2819.

[6] a) C.-Y. Chen, J.-X. Li, M. E. Davis, *Microporous Mater.* **1993**, *2*, 17–26; b) J. S. Beck, J. C. Vartuli, *Curr. Opin. Solid State Mater. Sci.* **1996**, *1*, 76–87; c) V. Y. Gusev, X. Feng, Z. Bu, G. L. Haller, J. A. O'Brien, *J. Phys. Chem.* **1996**, *100*, 1985–1988; d) M. Kruk, M. Jaroniec, A. Sayari, *J. Phys. Chem. B* **1997**, *101*, 583–589; e) M. Kruk, M. Jaroniec, A. Sayari, *Chem. Mater.* **1999**, *11*, 492–500; f) M. Kruk, M. Jaroniec, C. H. Ko, R. Ryoo, *Chem. Mater.* **2000**, *12*, 1961–1968; K. Morishige, M. Ito, *J. Chem. Phys.* **2002**, *117*, 8036–8041.

[7] K. Moller, T. Bein, *Chem. Mater.* **1998**, *10*, 2950–2963.

[8] a) A. Sayari, *Chem. Mater.* **1996**, *8*, 1840–1852; b) A. Corma, *Top. Catal.* **1997**, *4*, 249–260; c) F. Schüth, A. Wingen, J. Sauer, *Microporous Mesoporous Mater.* **2001**, *44–45*, 465–476.

[9] a) J. M. Kisler, A. Dähler, G. W. Stevens, A. J. O'Connor, *Microporous Mesoporous Mater.* **2001**, *44–45*, 769–774; b) Y. Shiraishi, G. Nishimura, T. Hirai, I. Komasawa, *Ind. Eng. Chem. Res.* **2002**, *41*, 5065–5070; c) B. L. Newalkar, N. V. Choudary, P. Kumar, S. Komarneni, T. S. G. Bhat, *Chem. Mater.* **2002**, *14*, 304–309.

[10] a) K. Tajima, T. Aida, *Chem. Commun.* **2000**, 2399–2412; b) A. M. Showkat, K.-P. Lee, A. I. Gopalan, M.-S. Kim, S.-H. Choi, H.-D. Kang, *Polymer* **2005**, *46*, 1804–1812; c) M. Choi, F. Kleitz, D. Liu, H. Y. Lee, W.-S. Ahn, R. Ryoo, *J. Am. Chem. Soc.* **2005**, *127*, 1924–1932.

[11] R. Mokaya, *J. Phys. Chem. B* **1999**, *103*, 10204–10208.

[12] a) N. Coustel, F. Di Renzo, F. Fajula, *J. Chem. Soc., Chem. Commun.* **1994**, 967–968; b) C.-F. Cheng, W. Zhou, J. Klinowski, *Chem. Phys. Lett.* **1996**, *263*, 247–252.

 © 2005 Wiley-VCH Verlag GmbH & Co. KGaA, Weinheim

[13] A. Sayari, P. Liu, M. Kruk, M. Jaroniec, *Chem. Mater.* **1997**, *9*, 2499–2506.

[14] H. Lao, C. Detellier, *Comprehensive Supramolecular Chemistry* (Eds.: J. E. D. Davies, J. A. Ripmeester), Pergamon, **1996,** vol. 8, 277–306.

[15] S. Brunauer, P. H. Emmett, E. Teller, *J. Am. Chem. Soc.* **1938**, *60*, 309–319.

[16] E. P. Barrett, L. G. Joyner, P. P. Halenda, *J. Am. Chem. Soc.* **1951**, *73*, 373–380.

[17] a) C. Lastoskie, K. E. Gubbins, N. Quirke, *J. Phys. Chem.* **1993**, *97*, 4786–4796; b) P. I. Ravikovitch, S. C. Ó Domhnaill, A. V. Neimark, F. Schüth, K. K. Unger, *Langmuir* **1995**, *11*, 4765–4772.

[18] a) L. E. Brus, *J. Chem. Phys.* **1984**, *80*, 4403–4409; b) C. B. Murray, D. J. Norris, M. G. Bawendi, *J. Am. Chem. Soc.* **1993**, *115*, 8706–8715; c) A. P. Alivisatos, *J. Phys. Chem.* **1996**, *100*, 13226–13239; d) L. Brus, *J. Phys. Chem. Solids* **1998**, *59*, 459–465; e) M. Nirmal, L. Brus, *Acc. Chem. Res.* **1999**, *32*, 407–414; f) T. Trindade, P. O'Brien, N. L. Pickett, *Chem. Mater.* **2001**, *13*, 3843–3858; g) N. L. Pickett, P. O'Brien, *Chem. Rec.* **2001**, *1*, 467–479; h) S. Sapra, D. D. Sarma, *The Chemistry of Nanomaterials Synthesis, Properties and Applications* (Eds.: C. N. R. Rao, A. Müller, A. K. Cheetham), Wiley-VCH, Weinheim (Germany), **2004**, vol 2, 371–404.

[19] J. H. Adair, T. Li, T. Kido, K. Havey, J. Moon, J. Mecholsky, A. Morrone, D. R. Talham, M. H. Ludwig, L. Wang, *Mater. Sci. Eng. R. Rep.* **1998**, *23*, 139–242.

[20] a) R. Premachandran, S. Banerjee, V. T. John, G. L. McPherson, J. A. Akkara, D. L. Kaplan, *Chem. Mater.* **1997**, *9*, 1342–1347; b) S. H. Liu, X. F. Qian, J. Yin, X. D. Ma, J. Y. Yuan, Z. K. Zhu, *J. Phys. Chem. Solids* **2003**, *64*, 455–458.

[21] a) A. A. Guzelian, U. Banin, A. V. Kadavanich, X. Peng, A. P. Alivisatos, *Appl. Phys. Lett.* **1996**, *69*, 1432–1434; b) M. Green, P. O'Brien, *Chem. Commun.* **1999**, 2235–2241; c) M. Green, P. O'Brien, *Chem. Commun.* **2000**, 183–184.

[22] a) H. S. Zhou, H. Sasahara, I. Honma, H. Komiyama, J. W. Haus, *Chem. Mater.* **1994**, *6*, 1534–1541; b) M. A. Malik, P. O'Brien, N. Revaprasadu, *Chem. Mater.* **2002**, *14*, 2004–2010; c) T. Mokari, U. Banin, *Chem. Mater.* **2003**, *15*, 3955–3960.

[23] C. E. Housecroft, A. G. Sharpe, *Inorganic Chemistry*, Pearson Education Limited, **2001**, 129–132.

[24] F. A. Cotton, G. Wilkinson, *Advanced Inorganic Chemistry A Comprehensive Text* 3rd ed., Interscience Publishers, **1972**, 511.

[25] a) Y. Wang, N. Herron, *J. Phys. Chem.* **1987**, *91*, 257–260; b) Y. Wang, N. Herron, *J. Phys. Chem.* **1988**, *92*, 4988–4994; c) N. Herron, Y. Wang, M. M. Eddy, G. D. Stucky, D. E. Cox, K. Moller, T. Bein, *J. Am. Chem. Soc.* **1989**, *111*, 530–540.

[26] a) H. Villavicencio-García, M. Hernández-Vélez, O. Sánchez-Garrido, J. M. Martínez-Duart, J. Jiménez, *Solid-State Electron.* **1999**, *43*, 1171–1175; b) R. J. Martín-Palma, M. Hernández-Vélez, I. Díaz, H. Villavicencio-García, M. M. García-Poza, J. M. Martínez-Duart, J. Pérez-Pariente, *Mater. Sci. Eng. C* **2001**, *15*, 163–166; c) A. Aparisi, V. Fornés, F. Márquez, R. Moreno, C. López, F. Meseguer, *Solid-State Electron.* **1996**, *40*, 641–645; d) H. Yahiro, T. Kyakuno, G. Okada, *Top. Catal.* **2002**, *19*, 193–195; e) M. Sotelo-Lerma, M. A. Quevedo-López, R. A. Orozco-Terán, R. Ramírez-Bon, F. J. Espinoza-Beltrán, *J. Phys. Chem. Solids* **1998**, *59*, 145–149.

[27] E. S. Brigham, C. S. Weisbecker, W. E. Rudzinski, T. E. Mallouk, *Chem. Mater.* **1996**, *8*, 2121–2127.

[28] a) M. M. García, H. Villavicencio, M. Hernández-Vélez, O. Sánchez, J. M. Martínez-Duart, *Mater. Sci. Eng. C* **2001**, *15*, 101–104; b) O. Raymond, H. Villavicencio, V. Petranovskii, J. M. Siqueiros, *Mater. Sci. Eng. A* **2003**, *360*, 202–206; c) F. Iacomi, *Surf. Sci.* **2003**, *532–535*, 816–821; d) G. A. Ozin, M. R. Steele, A. J. Holmes, *Chem. Mater.* **1994**, *6*, 999–1010.

[29] W. Chen, Y. Xu, Z. Lin, Z. Wang, L. Lin, *Solid State Commun.* **1998**, *105*, 129–134.

[30] a) P. Scherrer, *Nachr. Ges. Wiss. Göttingen* **1918**, 96–100; b) A. L. Patterson, *Phys. Rev.* **1939**, *54*, 978–982.

[31] a) L. Chen, P. J. Klar, W. Heimbrodt, F. J. Brieler, M. Fröba, H.-A. Krug von Nidda, T. Kurz, A. Loidl, *J. Appl. Phys.* **2003**, *93*, 1326–1328; b) L. Chen, P. J. Klar, W. Heimbrodt, F. J. Brieler, M. Fröba, *J. Supercond.* **2003**, *16*, 99–102; c) F. J. Brieler, P. Grundmann, M. Fröba, L. Chen, P. J. Klar, W. Heimbrodt, H.-A. Krug von Nidda, T. Kurz, A. Loidl, *J. Am. Chem. Soc.* **2004**, *126*, 797–807.

[32] a) L. Chen, P. J. Klar, W. Heimbrodt, F. Brieler, M. Fröba, *Appl. Phys. Lett.* **2000**, *76*, 3531–3533; b) L. Chen, P. J. Klar, W. Heimbrodt, F. Brieler, M. Fröba, H.-A. Krug von Nidda, A. Loidl, *Physica E* **2001**, *10*, 368–372; c) F. J. Brieler, M. Fröba, L. Chen, P. J. Klar, W. Heimbrodt, H.-A. Krug von Nidda, A. Loidl, *Chem. Eur. J.* **2002**, *8*, 185–194; d) F. J. Brieler, P. Grundmann, M. Fröba, L. Chen, P. J. Klar, W. Heimbrodt, H.-A. Krug von Nidda, T. Kurz, A. Loidl, *Chem. Mater.* **2005**, *17*, 795–803.

[33] L. Chen, H. Falk, P. J. Klar, W. Heimbrodt, F. Brieler, M. Fröba, H.-A. Krug von Nidda, A. Loidl, Z. Chen, Y. Oka, *Phys. Status Solidi B* **2002**, *229*, 31–34.

[34] C. Tura, N. Coombs, Ö. Dag, *Chem. Mater.* **2005**, *17*, 573–579.

[35] M. Wark, H. Wellmann, J. Rathousky, *Thin Solid Films* **2004**, *458*, 20–25.

[36] I. S. Nandhakumar, T. Gabriel, X. Li, G. S. Attard, M. Markham, D. C. Smith, J. J. Baumberg, *Chem. Commun.* **2004**, 1374–1375.

[37] W.-S. Chae, S.-W. Lee, S.-J. Im, S.-W. Moon, W.-C. Zin, J.-K. Lee, Y.-R. Kim, *Chem. Commun.* **2004**, 2554–2555.

[38] a) A. Stein, B. J. Melde, R. C. Schroden, *Adv. Mater.* **2000**, *12*, 1403–1419; b) A. Sayari, S. Hamoudi, *Chem. Mater.* **2001**, *13*, 3151–3168; c) M. H. Lim, A. Stein, *Chem. Mater.* **1999**, *11*, 3285–3295; d) T. Asefa, M. J. MacLachlan, N. Coombs, G. A. Ozin, *Nature* **1999**, *402*, 867–871; e) N. Igarashi, K. Hashimoto, T. Tatsumi, *J. Mater. Chem.* **2002**, *12*, 3631–3636; f) M. Jia, A. Seifert, M. Berger, H. Giegengack, S. Schulze, W. R. Thiel, *Chem. Mater.* **2004**, *16*, 877–882; g) A. Cauvel, G. Renard, D. Brunel, *J. Org. Chem.* **1997**, *62*, 749–751; h) B. M. Choudary, M. Lakshmi Kantam, P. Sreekanth, T. Bandopadhyay, F. Figueras, A. Tuel, *J. Mol. Catal. A: Chem.* **1999**, *142*, 361–365; i) C. D. Nunes, A. A. Valente, M. Pillinger, A. C. Fernandes, C. C. Romão, J. Rocha, I. S. Gonçalves, *J. Mater. Chem.* **2002**, *12*, 1735–1742; j) M. Alvaro, A. Corma, D. Das, V. Fornés, H. García, *J. Catal.* **2005**, *231*, 48–55.

[39] a) X. Feng, G. E. Fryxell, L.-Q. Wang, A. Y. Kim, J. Liu, K. M. Kemner, *Science* **1997**, *276*, 923 –926; b) L. Mercier, T. J. Pinnavaia, *Adv. Mater.* **1997**, *9*, 500–503; c) A. M. Liu, K. Hidajat, S. Kawi, D. Y. Zhao, *Chem. Commun.* **2000**, 1145–1146; d) M. H. Lim, C. F. Blanford, A. Stein, *Chem. Mater.* **1998**, *10*, 467–470.

[40] a) J. F. Díaz, K. J. Balkus, F. Bedioui, V. Kurshev, L. Kevan, *Chem. Mater.* **1997**, *9*, 61–67; b) W.-H. Zhang, J.-L. Shi, L.-Z. Wang, D.-S. Yan, *Chem. Mater.* **2000**, *12*, 1408–1413; c) Y. S. Cho, J. C. Park, B. Lee, Y. Kim, J. Yi, *Catal. Lett.* **2002**, *81*, 89–96.

[41] H. Wellmann, J. Rathousky, M. Wark, A. Zukal, G. Schulz-Ekloff, *Microporous Mesoporous Mater.* **2001**, *44–45*, 419–425.

[42] W. Xu, Y. Liao, D. L. Akins, *J. Phys. Chem. B* **2002**, *106*, 11127–11131.

[43] F. Gao, Q. Lu, D. Zhao, *Chem. Phys. Lett.* **2002**, *360*, 585–591.

[44] W.-H. Zhang, J.-L. Shi, H.-R. Chen, Z.-L. Hua, D.-S. Yan, *Chem. Mater.* **2001**, *13*, 648–654.

[45] H. Xi, X. Qian, J. Yin, L. Bian, R. He, Z. Zhu, *Mater. Lett.* **2003**, *57*, 2657–2661.

[46] W.-H. Zhang, X.-B. Lu, J.-H. Xiu, Z.-L. Hua, L.-X. Zhang, M. Robertson, J.-L. Shi, D.-S. Yan, J. D. Holmes, *Adv. Funct. Mater.* **2004**, *14*, 544–552.

[47] a) M. A. Markowitz, J. Klaehn, R. A. Hendel, S. B. Qadriq, S. L. Golledge, D. G. Castner, B. P. Gaber, *J. Phys. Chem. B.* **2000**, *104*, 10820–10826; b) T. Yokoi, H. Yoshitake, T. Tatsumi, *J. Mater. Chem.* **2004**, *14*, 951–957.

 © 2005 Wiley-VCH Verlag GmbH & Co. KGaA, Weinheim

[48] T. Hirai, H. Okubo, I. Komasawa, *J. Phys. Chem. B* **1999**, *103*, 4228–4230.
[49] T. Hirai, H. Okubo, I. Komasawa, *J. Colloid Interface Sci.* **2001**, *235*, 358–364.
[50] W.-S. Chae, J.-H. Ko, I.-W. Hwang, Y.-R. Kim, *Chem. Phys. Lett.* **2002**, *365*, 49–56.
[51] W.-S. Chae, J.-H. Yoon, H. Yu, D.-J. Jang, Y.-R. Kim, *J. Phys. Chem. B* **2004**, *108*, 11509–11513.
[52] a) P. Lianos, J. K. Thomas, *Chem. Phys. Lett.* **1986**, *125*, 299–302; b) C. Petit, M. P. Pileni, *J. Phys. Chem.* **1988**, *92*, 2282–2286; c) M. P. Pileni, L. Motte, C. Petit, *Chem. Mater.* **1992**, *4*, 338–345; d) P. Calandra, M. Goffredi, V. Turco Liveri, *Colloids Surf., A* **1999**, *160*, 9–13; e) F. T. Quinlan, J. Kuther, W. Tremel, W. Knoll, S. Risbud, P. Stroeve, *Langmuir* **2000**, *16*, 4049–4051.
[53] J. Zhang, B. Han, Z. Hou, Z. Liu, J. He, T. Jiang, *Langmuir* **2003**, *19*, 7616–7620.
[54] J. Zhang, M. Xiao, Z. Liu, B. Han, T. Jiang, J. He, G. Yang, *J. Colloid Interface Sci.* **2004**, *273*, 160–164.
[55] T. Hirai, M. Nanba, I. Komasawa, *J. Colloid Interface Sci.* **2003**, *268*, 394–399.
[56] C.-Y. Lai, B. G. Trewyn, D. M. Jeftinija, K. Jeftinija, S. Xu, S. Jeftinija, V. S.-Y. Lin, *J. Am. Chem. Soc.* **2003**, *125*, 4451–4459.
[57] a) W. Zhou, J. M. Thomas, D. S. Shephard, B. F. G. Johnson, D. Ozkaya, T. Maschmeyer, R. G. Bell, Q. Ge, *Science* **1998**, *280*, 705–708; b) F. Schweyer, P. Braunstein, C. Estournès, J. Guille, H. Kessler, J.-L. Paillaud, J. Rosé, *Chem. Commun.* **2000**, 1271–1272; c) B. Folch, J. Larionova, Y. Guari, C. Guérin, A. Mehdi, C. Reyé, *J. Mater. Chem.* **2004**, *14*, 2703–2711; d) S. Behrens, G. Spittel, *Dalton Trans.* **2005**, 868–873; e) M. D. Jones, M. J. Duer, S. Hermans, Y. Z. Khimyak, B. F. G. Johnson, J. M. Thomas, *Angew. Chem. Int. Ed.* **2002**, *41*, 4726–4729; f) S. Hermans, S. Sadasivan, C. M. G. Judkins, B. F. G. Johnson, S. Mann, D. Khushalani, *Adv. Mater.* **2003**, *15*, 1853–1857; g) M. D. Jones, M. J. Duer, *Inorg. Chim. Acta* **2003**, *354*, 75–78; h) M. Clemente-León, E. Coronado, A. Forment-Aliaga, P. Amorós, J. Ramírez-Castellanos, J. M. González-Calbet, *J. Mater. Chem.* **2003**, *13*, 3089–3095.
[58] a) C. Kowalchuk, J. F. Corrigan, Y. Huang, *Chem. Commun.* **2000**, 1811–1812; b) C. M. Kowalchuk, G. Schmid, W. Meyer-Zaika, Y. Huang, J. F. Corrigan, *Inorg. Chem.* **2004**, *43*, 173–180.
[59] J. F. Corrigan, D. Fenske, *Angew. Chem. Int. Ed. Engl.* **1997**, *36*, 1981–1983.
[60] a) C.-M. Yang, H.-S. Sheu, K.-J. Chao, *Adv. Funct. Mater.* **2002**, *12*, 143–148; b) P. V. Adhyapak, P. Karandikar, K. Vijayamohanan, A. A. Athawale, A. J. Chandwadkar, *Mater. Lett.* **2004**, *58*, 1168–1171; c) A. A. Eliseev, K. S. Napolskii, A. V. Lukashin, Y. D. Tretyakov, *J. Magn. Magn. Mater.* **2004**, *272–276*, 1609–1611.
[61] X. Liu, B. Tian, C. Yu, B. Tu, Z. Liu, O. Terasaki, D. Zhao, *Chem. Lett.* **2003**, *32*, 824–825.
[62] F. Gao, Q. Lu, D. Zhao, *Adv. Mater.* **2003**, *15*, 739–742.
[63] I. Díaz, M. Hernández-Vélez, R. J. Martín Palma, H. Villavicencio García, J. Pérez Pariente, J. M. Martínez-Duart, *Appl. Phys. A: Mater.* **2004**, *79*, 565–572.
[64] M. Yosef, A. K. Schaper, M. Fröba, S. Schlecht, *Inorg. Chem.* **2005**, *44*, 5890–5896.
[65] a) V. L. Colvin, M. C. Schlamp, A. P. Alivisatos, *Nature* **1994**, *370*, 354–357; b) D. E. Fogg, L. H. Radzilowski, B. O. Dabbousi, R. R. Schrock, E. L. Thomas, M. G. Bawendi, *Macromolecules* **1997**, *30*, 8433–8439; c) B. A. Ridley, B. Nivi, J. M. Jacobson, *Science* **1999**, *286*, 746–749; d) X. Duan, C. Niu, V. Sahi, J. Chen, J. W. Parce, S. Empedocles, J. L. Goldman, *Nature* **2003**, *425*, 274–278; e) J. A. Kloepfer, S. E. Bradforth, J. L. Nadeau, *J. Phys. Chem. B* **2005**, *109*, 9996–10003.
[66] H. Parala, H. Winkler, M. Kolbe, A. Wohlfart, R. A. Fischer, R. Schmechel, H. von Seggern, *Adv. Mater.* **2000**, *12*, 1050–1055.
[67] X. Gao, S. Nie, *J. Phys. Chem. B* **2003**, *107*, 11575–11578.
[68] a) T. Trindade, P. O'Brien, X.-M. Zhang, *Chem. Mater.* **1997**, *9*, 523–530; b) N. Revaprasadu, M. A. Malik, P. O'Brien, M. M. Zulu, G. Wakefield, *J. Mater. Chem.* **1998**, *8*, 1885–1888; c) N. Revaprasadu, M. A. Malik, P. O'Brien, G. Wakefield, *Chem. Commun.* **1999**, 1573–1574; d) P. S. Nair, T. Radhakrishnan, N. Revaprasadu, G. A. Kolawole, P. O'Brien, *Chem. Commun.* **2002**, 564–565.
[69] a) D. S. Shephard, W. Zhou, T. Maschmeyer, J. M. Matters, C. L. Roper, S. Parsons, B. F. G. Johnson, M. J. Duer, *Angew. Chem. Int. Ed.* **1998**, *37*, 2719–2723; b) V. Antochshuk, M. Jaroniec, *Chem. Commun.* **1999**, 2373–2374; c) F. de Juan, E. Ruiz-Hitzky, *Adv. Mater.* **2000**, *12*, 430–432.
[70] Z. Zhang, S. Dai, X. Fan, D. A. Blom, S. J. Pennycook, Y. Wei, *J. Phys. Chem. B* **2001**, *105*, 6755–6758.
[71] S. Wang, D.-G. Choi, S.-M. Yang, *Adv. Mater.* **2002**, *14*, 1311–1314.
[72] Y. Shan, L. Gao, S. Zheng, *Mater. Chem. Phys.* **2004**, *88*, 192–196.
[73] Y. Shan, L. Gao, *Mater. Chem. Phys.* **2005**, *89*, 412–416

Received: June 8, 2005
Published Online: September 23, 2005

 © 2005 Wiley-VCH Verlag GmbH & Co. KGaA, Weinheim

Norcorrole and Dihydronorcorrole: A Predictive Quantum Chemical Study

Abhik Ghosh,*[a] Ingar H. Wasbotten,[a] Wade Davis,[b] and Jannie C. Swarts[b]

Dedicated to Professor Emeritus Dr. Dr. h. c. Emanuel Vogel

Keywords: Norcorrole / Quantum chemical calculations

DFT calculations indicate norcorrole (NCH_2), a 16π-electron doubly contracted porphyrin, to be a promising synthetic target, especially when complexed to a small cation such as Ni^{II}. The relative stability of norcorrole derivatives appears to reflect the fact that they are not antiaromatic, but should rather be viewed as bis(dipyrrins). However, norcorrole (NC) complexes are expected to be prone to reduction and we predict that high-valent transition metal dihydronorcorrole (DHNC) derivatives should exist as reasonably stable substances. Our calculations further predict that both NC and DHNC complexes should exhibit short metal–nitrogen distances and moderate to strong doming of the macrocycle. Overall, a number of calculated results suggest that NC and DHNC derivatives should be of unique electronic-structural interest, as conceptual links between aromatic tetrapyrroles such as porphyrin and corrole on the one hand and open-chain pyrrole-based ligands such as dipyrrins and biliverdines on the other.

(© Wiley-VCH Verlag GmbH & Co. KGaA, 69451 Weinheim, Germany, 2005)

The study of porphyrin analogues such as expanded and contracted porphyrins and heteroatom-substituted porphyrins (e. g. porphyrazines and corrolazines) has been a major new direction of porphyrin-related research.[1] In many cases, the new macrocycles have resulted in new metal spin states and novel chemical behavior, relative to the analogous porphyrin complexes. In 2002, Professor Emanuel Vogel encouraged one of us (AG) to investigate by theoretical means the question of stability of the doubly contracted porphyrin shown in Figure 1, for which we have used the trivial name norcorrole (NCH_2; "nor" signifying one fewer carbon than in corrole), as well as its potential as a ligand in coordination chemistry. Given the 16π-electron, possibly antiaromatic, nature of the ring system and the extremely contracted nature of the central N_4 core, we were not optimistic about the prospects. Nonetheless, we undertook a DFT[2] investigation of the problem and have been pleasantly surprised by the results, which seem quite promising, as described below.[3–5]

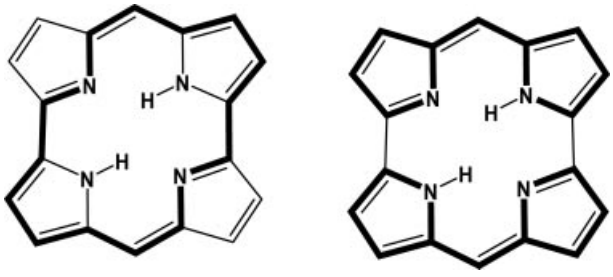

Figure 1. Two views of norcorrole. Left: antiaromatic; right: a bis(dipyrrin) structure.

Despite the small N_4 core size, a geometry optimization indicated an essentially planar, near-C_{2h} geometry for NCH_2, some highlights of which are depicted in Figure 2. Note the compact N_4 core and the short N–H···N hydrogen bonds.[6] Remarkably, the optimized NCH_2 structure does not exhibit the strong bond length alternation for the various skeletal CC and CN bonds that one might expect for

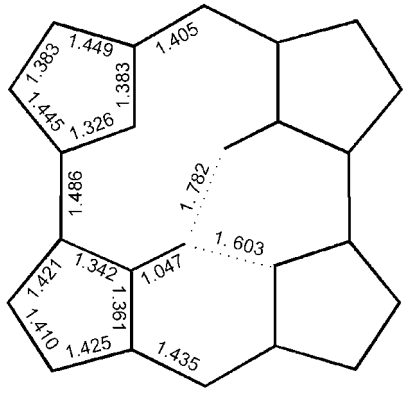

Figure 2. Selected symmetry-unique bond lengths [Å] in free-base norcorrole. Note the crowded core and the short N–H···N hydrogen bond.

[a] Department of Chemistry, University of Tromsø, 9037 Tromsø, Norway
E-mail: abhik@chem.uit.no
[b] Department of Chemistry, University of The Free State, Bloemfontein 9300, Republic of South Africa

Supporting information for this article is available on the WWW under http://www.eurjic.org or from the author.

an antiaromatic system. Thus, adjacent C_α–C_{meso} distances differ by only 0.03 Å. The long, nearly single bond-like, C_α–C_α distance of 1.486 Å provided the key insight into this structure, namely that NCH_2 should not be viewed as antiaromatic but rather as a cyclic bis(dipyrrin),[7,8] and indeed as a unique conceptual link between aromatic tetrapyrroles on the one hand and dipyrrins and other open-chain oligopyrroles on the other.[9]

Might NCH_2 serve as a macrocyclic ligand and exhibit interesting coordination behavior? Given the small size of the low-spin Ni^{II} cation, Ni(NC) (S = 0) seemed like an ideal candidate for a DFT study. A C_2 symmetry-constrained geometry-optimization yielded a near-C_{2v} geometry, the essential symmetry-equivalence of the four pyrrole units once again signifying that the structure is best viewed as a bis(dipyrrin) complex. The optimized geometry, depicted in Figure 3, exhibits a significant doming, but is otherwise quite strain-free. The Ni–N distances of 1.85 Å are short (but not exceptionally so), and the direct C_α-C_α linkages are once again nearly single bond-like in length

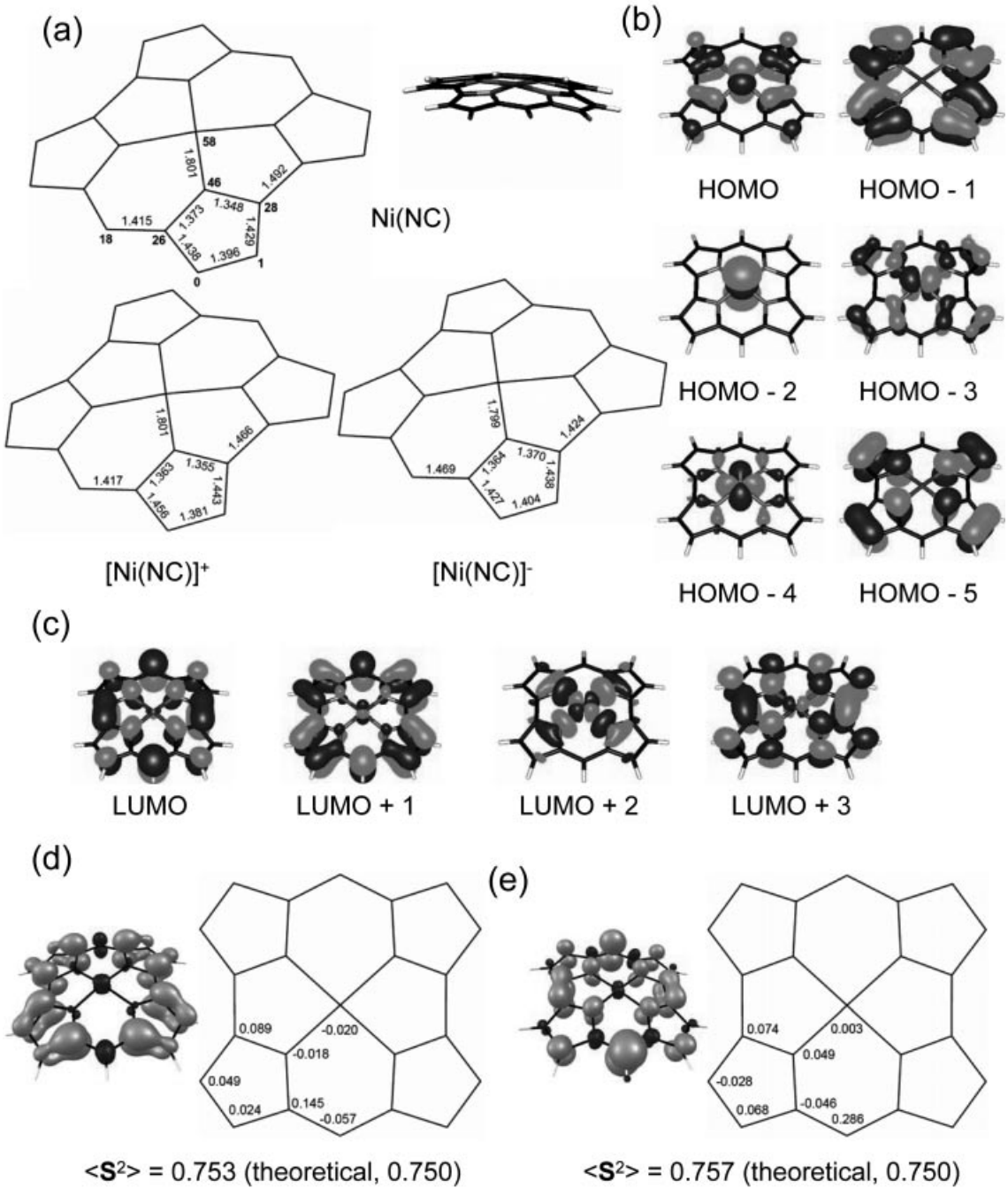

Figure 3. Selected computed results on Ni(NC): (a) Optimized structures [Å], (b) HOMOs, (c) LUMOs, (d) spin density for $[Ni(NC)]^+$, (e) and spin density for $[Ni(NC)]^-$. In part (a), the numbers in bold indicate the "elevation" of the atoms in question in pm "above" the "lowest" β-carbons, to give an estimate of the amount of doming.

 © 2005 Wiley-VCH Verlag GmbH & Co. KGaA, Weinheim

(1.493 Å). Overall, the geometry parameters of Ni(NC) are similar to those of a typical Ni(dipyrrin)$_2$ complex.[7]

Figure 3 also depicts several frontier MOs of Ni(NC), including the HOMO and LUMO, which are both macrocycle-based π MOs, as well as geometrical highlights and spin density profiles for the cationic and anionic states of Ni(NC), for which we also carried out geometry optimizations. Note the strong C_α–C_α bonding interaction in the Ni(NC) LUMO and the shortening of these bonds ($d_{C\alpha-C\alpha}$ = 1.469 Å) in the Ni(NC)$^-$ anion. The calculations on the ionized states yielded an adiabatic ionization potential of 6.91 eV and an adiabatic electron affinity of 2.47 eV for Ni(NC). The ionization potential is roughly comparable to that of a typical metalloporphyrin (e. g. zinc porphyrin[4a,10]), indicating that Ni(NC) should not be particularly sensitive to oxidative degradation. However, the electron affinity is extremely high (compared to about 1.2–1.5 eV for typical porphyrins[4a,11]), suggesting that norcorrole derivatives should be very prone to reduction. The high amplitude of the LUMO at the *meso* positions suggests that either of these positions is a plausible site of nucleophilic attack. We therefore carried out some exploratory DFT studies on dihydronorcorrole (DHNC) complexes, featuring one *meso* CH_2 unit.

By analogy with the corroles and biliverdines,[12,13] we suspected that the trianionic DHNC^{3-} ligand might form highly oxidized transition-metal complexes and our calculations suggest that it indeed should do so. Figure 4 depicts the optimized geometry Cu(DHNC), which exhibits a clear singlet "Cu^{III}" ground state, the lowest S = 1 Cu^{II} π-cation radical state being at least several tenths of an eV higher in energy. Clearly, the highly contracted N_4 core favors the smaller Cu^{III} ion ($d_{CuN} \approx 1.82$ Å, Figure 4) over the significantly larger Cu^{II} ion. The optimized structure of Cu(DHNC) exhibits the same kind of strain-free doming as Ni(NC), but note that the C_α-C_α linkages are significantly shorter (1.44 Å) than in Ni(NC), indicating reasonably effective conjugation across the entire π-system.

The extreme stabilization of the Cu^{III} state in Cu(DHNC) is probably most reminiscent of Cu^{III} corrolazines, where Goldberg[14] and co-workers have experimentally shown that a Cu^{III} ground state is also clearly favored over a Cu^{II} ligand π-cation radical state.[15] In contrast, using temperature-dependent NMR measurements (as well as DFT calculations[4]), we[16,17] and others[18,19] have shown that the Cu^{III} and the Cu^{II} ligand π-cation radical states are essentially isoenergetic for corroles, whereas Cu biliverdines clearly exhibit Cu^{II} ligand π-cation radical ground states. As in the DHNC case, the stability of the Cu^{III} state for corrolazines seems readily ascribable to their significantly tighter N_4 cores, compared with corroles. Interestingly, DFT calculations predict that Cu isocorroles, whose central cavities are expected to be only slightly smaller relative to Cu corroles, should also exhibit clear Cu^{III} ground states.[20]

We have carried out DFT calculations for a number of additional high-valent DHNC complexes, namely Fe(DHNC)Cl (Figure 5), Mn(DHNC)Cl (Figure 6),

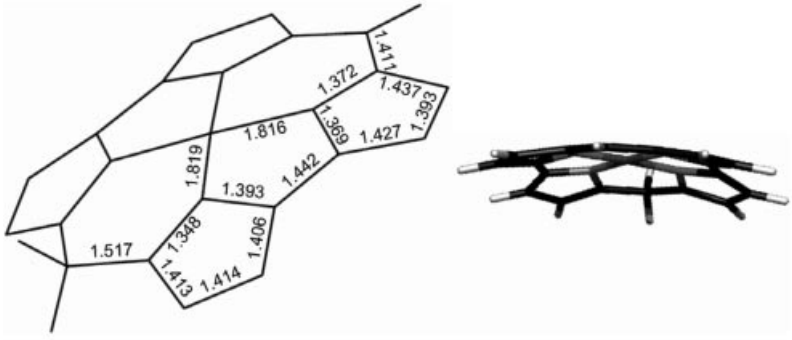

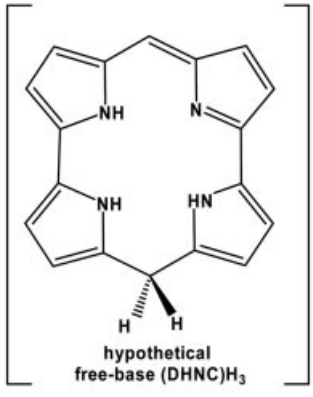

Figure 4. Highlights [Å] of the optimized structure of Cu(DHNC). For clarity, only the *meso* C–H bonds are explicitly shown in the diagram to the left. Note the structure of the hypothetical free-base dihydronorcorrole.

 © 2005 Wiley-VCH Verlag GmbH & Co. KGaA, Weinheim

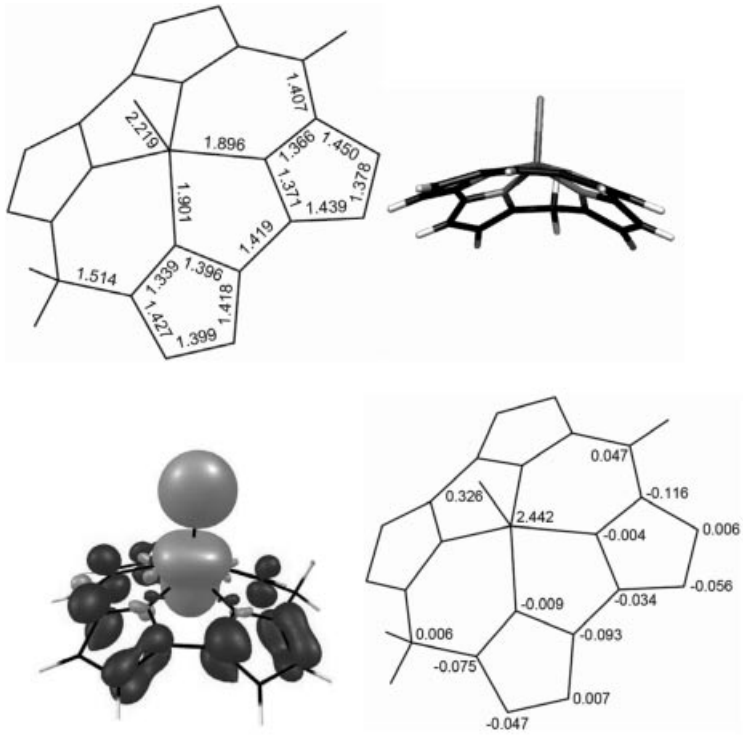

Figure 5. Selected computed results on Fe(DHNC)Cl; top: optimized geometry [Å], bottom: spin density and populations.

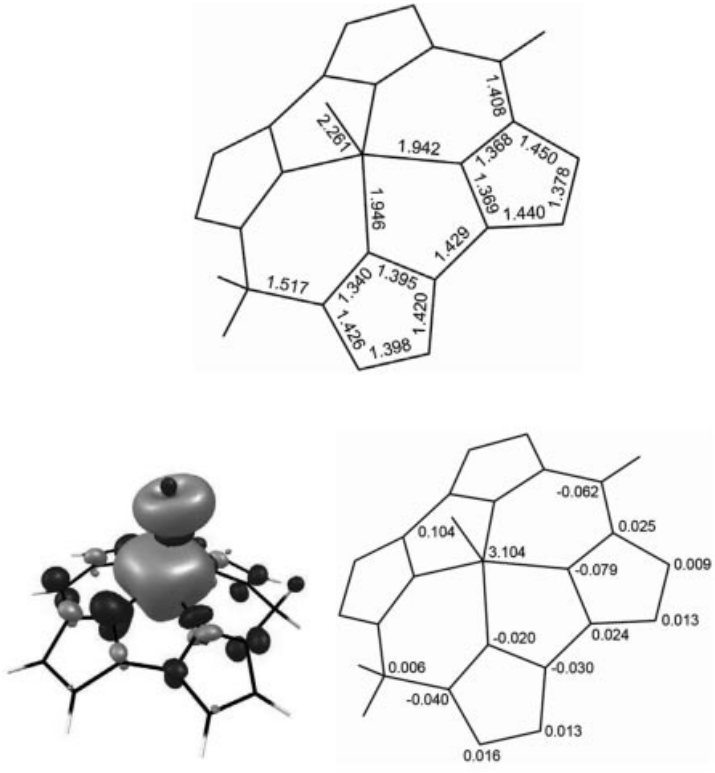

Figure 6. Selected computed results on Mn(DHNC)Cl; top: optimized geometry [Å], bottom: spin density and populations.

Fe(DHNC)Ph (Figure 7), Mn(DHNC)Ph (Figure 8), and Co(DHNC)Ph (Figure 9). The corrole analogues of these complexes have also been studied by DFT and, in some cases, also experimentally, which allows us to make some interesting comparisons.[4–6] Our main findings on these molecules are as follows.

All the five-coordinate DHNC complexes exhibit short metal–nitrogen distances, which are shorter than those in

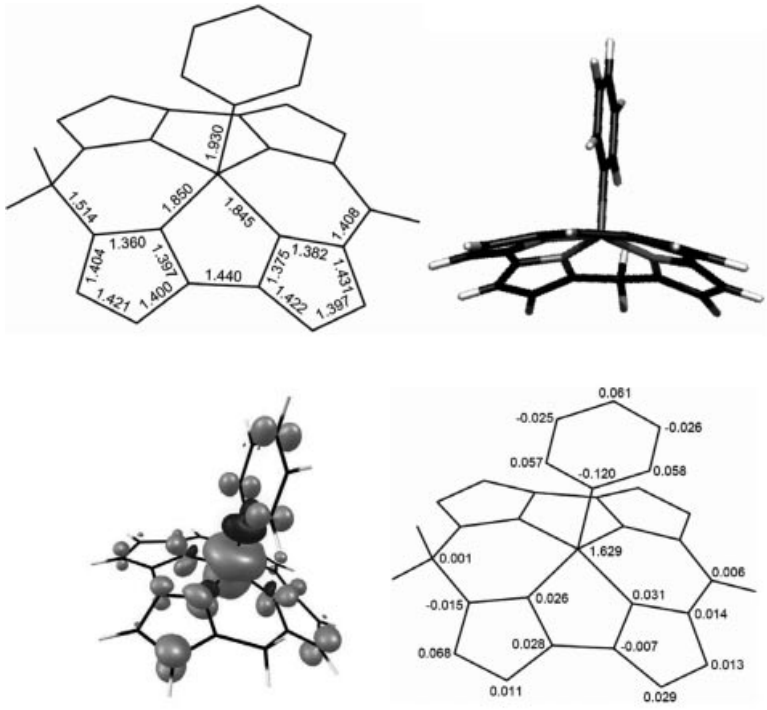

Figure 7. Selected computed results on Fe(DHNC)Ph; top: optimized geometry [Å], bottom: spin density and populations.

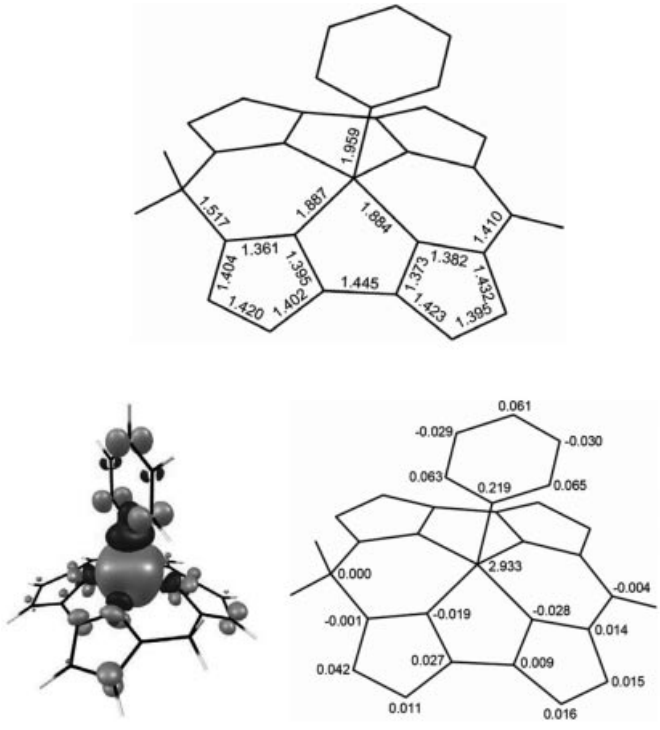

Figure 8. Selected computed results on Mn(DHNC)Ph; top: optimized geometry [Å], bottom: spin density and populations.

corroles, and considerable doming, which is more pronounced than in Ni(NC) and Cu(DHNC). Thus, the metal atom in Fe(DHNC)Cl, Mn(DHNC)Cl, Fe(DHNC)Ph, and Mn(DHNC)Ph is above the DHNC N_4 plane by 0.590, 0.650, 0.400, and 0.444 Å, respectively.

As shown in Figure 5, the Fe(DHNC)Cl results show considerable spatial separation of the majority and minority spin densities. In other words, the calculations suggest that electronic structure might best be described as involving an $S = 3/2$ Fe^{III} center antiferromagnetically coupled to a

 © 2005 Wiley-VCH Verlag GmbH & Co. KGaA, Weinheim

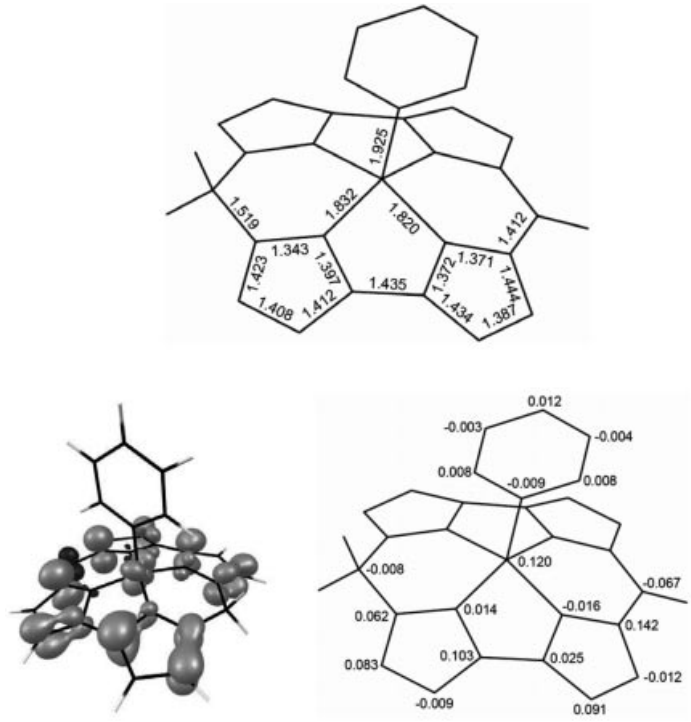

Figure 9. Selected computed results on Co(DHNC)Ph; top: optimized geometry [Å], bottom: the spin density.

$DHNC^{2-\cdot}$ radical. A similar electronic-structural description has also been found for FeCl corrole derivatives on the basis of ^1H NMR spectroscopy and DFT calculations.[5,6,21,22]

Compared to Fe(DHNC)Cl, we found only small amounts of minority spin on the DHNC ligand in Mn(DHNC)Cl (Figure 6). According to our calculations, Mn(DHNC)Cl therefore seems best viewed as a "true" Mn^{IV} complex. In contrast, we found approximately the same amount of ligand radical character (noninnocence) for MnCl corrole as we did for FeCl corrole.[4] In other words, there are both qualitative similarities and intriguing differences between the ways ligand noninnocence plays out in corroles vs. DHNC derivatives.

The spin density profiles of Fe(DHNC)Ph (Figure 7) and Mn(DHNC)Ph (Figure 8) are similar to those of Fe(Cor)Ph and Mn(Cor)Ph, respectively, in the following way.[23] Unlike Fe(DHNC)Cl and Fe(Cor)Cl, Fe(DHNC)Ph and Fe(Cor)Ph do not exhibit significant spatial separation of majority and minority spin densities; in both cases, 80–90% of the majority spin is localized on the Fe, the remainder being distributed over selected sites on both the macrocycle and the phenyl group. In contrast, Co(DHNC)Ph exhibits only a small spin population on the metal but almost pure majority-spin radical character for the DHNC ligand. In other words, the Co compound is best viewed as made up of a $Co^{III}Ph$ center and a $DHN^{2-\cdot}$ ligand.[20] Overall, all the phenyl complexes exhibit very close to the theoretically expected values of $<\mathbf{S}^2>$.

In conclusion, our calculations clearly point to norcorrole as a promising synthetic target, especially when complexed to a small cation such as Ni^{II}. However, NC complexes should be prone to reduction and we predict that high-valent metal-DHNC complexes should exist as reasonably stable substances. However, the successful preparation of NC and DHNC derivatives is likely to be much more than a synthetic exercise: These molecules may be viewed as conceptual links between aromatic tetrapyrroles such as porphyrin and corrole on the one hand and open-chain pyrrole-based ligands such as dipyrrins and biliverdines on the other and detailed studies of their electronic structure is likely to be of unusual interest.

Acknowledgments

As mentioned, one of us (AG) is indebted to Prof. Emanuel Vogel for prompting us to undertake this research. This work was supported by a grant of computer time from the Norwegian Research Council as well as by travel support from the National Research Fund of the Republic of South Africa.

[1] For overviews of porphyrin isomer and analogue chemistry, see: a) E. Vogel, *J. Heterocycl. Chem.* **1996**, *33*, 1461–1487; b) D. Seidel, J. L. Sessler, *Angew. Chem. Int. Ed.* **2003**, *42*, 5134–5175; c) R. Paolesse, in *The Porphyrin Handbook* (Eds.: K. M. Kadish, K. M. Smith, R. Guilard), Academic: **2000**, vol. 2, chapter 11, 201–232; d) C. Erben, S. Will, K. M. Kadish, in *The Porphyrin Handbook* (Eds.: K. M. Kadish, K. M. Smith, R. Guilard), Academic: **2000**, vol. 2, chapter 12, 233–300.

[2] All calculations were carried out using the ADF 2004 program system, the PW91 generalized gradient approximation (GGA) for both exchange and correlation, Slater-type TZP basis sets, tight criteria for SCF convergence and geometry optimization,

 © 2005 Wiley-VCH Verlag GmbH & Co. KGaA, Weinheim

and a spin-unrestricted formalism. For a description of the methods used, see: G. T. Velde, F. M. Bickelhaupt, E. J. Baerends, C. F. Guerra, S. J. A. Van Gisbergen, J. G. Snijders, T. Ziegler, *J. Comp. Chem.* **2001**, *22*, 2001.

[3] Reviews on high-valent metalloporphyrins: a) A. Ghosh, E. Steene, *J. Biol. Inorg. Chem.* **2001**, *6*, 739–752; b) A. Ghosh, in *The Porphyrin Handbook* (Eds.: K. M. Kadish, K. M. Smith, R. Guilard), Academic: **2000**, vol. 7, chapter 47, 1–38.

[4] a) A. Ghosh, T. Wondimagegn, A. B. J. Parusel, *J. Am. Chem. Soc.* **2000**, *122*, 5100–5104; b) E. Steene, T. Wondimagegn, A. Ghosh, *J. Phys. Chem. B* **2001**, *105*, 11406–11413; addition/CorrectionE. Steene, T. Wondimagegn, A. Ghosh, *J. Phys. Chem. B* **2002**, *106*, 5312–5312.

[5] O. Zakharieva, V. Schunemann, M. Gerdan, S. Licoccia, S. Cai, F. A. Walker, A. X. Trautwein, *J. Am. Chem. Soc.* **2002**, *124*, 6636–6648.

[6] A. Ghosh, J. Moulder, M. Bröring, E. Vogel, *Angew. Chem. Int. Ed.* **2001**, *40*, 431–434.

[7] C. Brückner, V. Karunaratne, S. J. Rettig, D. Dolphin, *Can. J. Chem.* **1996**, *74*, 2182–2193.

[8] X-ray crystal structure of an Fe^{III} tris(dipyrrin): S. M. Cohen, S. R. Halper, *Inorg. Chim. Acta* **2002**, *341*, 12–16. For the ^1H NMR spectrum of this compound, see: E. Steene, A. Ghosh, S. Cohen, *J. Porphyrins Phthalocyanines* **2004**, *8*, 840–840. A full paper based on this study is under preparation: E. Steene, E. Tangen, S. Halper, S. Cohen, A. Ghosh, manuscript in preparation.

[9] Of particular relevance to this analogy may be Scott and coworkers' recent report of an intramolecular oxidative coupling of a $Ni(dipyrrin)_2$ complex to generate a Ni[bis(dipyrrin)] derivative: H. S. Gill, I. Finger, I. Bozidarevic, F. Szydlo, M. J. Scott, *New J. Chem.* **2005**, *29*, 68–71. It is intriguing to speculate that a second, similar oxidative coupling would directly lead to a norcorrole derivative.

[10] A. Ghosh, T. Vangberg, *Theor. Chem. Acc.* **1997**, *97*, 143–149; T. Vangberg, R. Lie, A. Ghosh, *J. Am. Chem. Soc.* **2002**, *124*, 8122–8130.

[11] H. I. Chen, P. E. Ellis, T. Wijesekera, T. E. Hagan, S. E. Groh, J. E. Lyons, D. P. Ridge, *J. Am. Chem. Soc.* **1994**, *116*, 1086–1089.

[12] K. T. Nguyen, S. P. Rath, L. Latos-Grazynski, M. M. Olmstead, A. L. Balch, *J. Am. Chem. Soc.* **2004**, *126*, 6210–6211.

[13] A. L. Balch, M. Mazzanti, B. C. Noll, M. M. Olmstead, *J. Am. Chem. Soc.* **1993**, *115*, 12206–12207.

[14] J. P. Fox, B. Ramdhanie, A. A. Zareba, R. S. Czernuszewicz, D. P. Goldberg, *Inorg. Chem.* **2004**, *43*, 6600–6608.

[15] E. Tangen, A. Ghosh, *J. Am. Chem. Soc.* **2002**, *124*, 8117–8121.

[16] a) I. Halvorsen, T. Wondimagegn, A. Ghosh, *J. Am. Chem. Soc.* **2002**, *124*, 8104–8116; b) Z. Ou, J. Shao, H. Zhao, K. Ohkubo, I. H. Wasbotten, S. Fukuzumi, A. Ghosh, K. M. Kadish, *J. Porphyrins Phthalocyanines* **2004**, *8*, 1236–1247.

[17] C. E. Steene, A. Dey, A. Ghosh, *J. Am. Chem. Soc.* **2003**, *125*, 16300–16309.

[18] C. Brückner, R. P. Brinas, J. A. K. Bauer, *Inorg. Chem.* **2003**, *42*, 4495–4497.

[19] I. Luobeznova, L. Simkhovich, I. Goldberg, Z. Gross, *Eur. J. Inorg. Chem.* **2004**, *8*, 1724–1732.

[20] B. van Oort, E. Tangen, A. Ghosh, *Eur. J. Inorg. Chem.* **2004**, 2442–2445.

[21] For a debate on the electronic structure of FeCl corroles, see:L. Simkhovich, Z. Gross, *Inorg. Chem.* **2004**, *43*, 6136–6138 and references cited therein.

[22] This kind of metal-ligand antiferromagnetic coupling is difficult to describe via single-determinant quantum chemical methods. For relevant ab initio multiconfigurational perturbation theory calculations, see: a) A. Ghosh, P. R. Taylor, *Curr. Opin. Chem. Biol.* **2003**, *7*, 113–124; b) A. Ghosh, B. J. Persson, P. R. Taylor, *J. Biol. Inorg. Chem.* **2003**, *8*, 507–511.

[23] R. Guilard, A. Tabard, E. Van Caemelbecke, K. M. Kadish, in *The Porphyrin Handbook* (Eds.: K. M. Kadish, K. M. Smith, R. Guilard), Academic: **2000**, vol. 3, chapter 21, 295–345.

Received: April 5, 2005
Published Online: October 11, 2005

 © 2005 Wiley-VCH Verlag GmbH & Co. KGaA, Weinheim

Crystal Structure and Magnetic Behaviour of the New Gadolinium Complex Compound $Gd_2(ClH_2CCOO)_6(bipy)_2$

Daniela John[a] and Werner Urland*[a]

Keywords: Gadolinium / Carboxylate ligands / N ligands / X-ray diffraction / Crystal structure / Magnetic properties

Single crystals of the title compound have been obtained by reaction of $Gd_3(ClH_2CCOO)_9(H_2O)_5$ with 2,2′-bipyridyl (bipy) in a solution of ethanol and water. $Gd_2(ClH_2CCOO)_6(bipy)_2$ crystallises in the triclinic space group $P\bar{1}$ ($Z = 2$) with a = 959.5(3) pm, b = 980.9(3) pm, c = 1163.9(4) pm, α = 68.67(3) °, β = 84.82(4)° and γ = 82.47(4)°. The crystal structure is built up of discrete molecules of dinuclear Gd^{3+}–Gd^{3+} units. The corresponding residual (all data) for the refined structure is 4.46 %. The magnetic behaviour of the compound was investigated in the temperature range of 1.76–300 K. The magnetic data were interpreted considering exchange interactions within the dimeric unit (J_{ex} = –0.020 cm^{-1}).
(© Wiley-VCH Verlag GmbH & Co. KGaA, 69451 Weinheim, Germany, 2005)

Introduction

The research on molecular magnetic materials with lanthanides (Ln) is up to now mostly focused on the interaction of transition metal with lanthanide ions. There are several publications[1–5] concerning magnetic interactions in Ln–Cu, Ln–Ni and Ln–Fe units but only few Ln-Ln interactions in molecular magnetic materials have been studied yet.[6–10] There are no simple rules, such as the ones of Goodenough and Kanamori for compounds of d elements, to predict the occurrence of ferro- or antiferromagnetic coupling.[11] In order to fill this lack of knowledge we synthesised the title compound and determined the magnetic behaviour. The magnetic data were interpreted considering magnetic exchange coupling in the dinuclear Gd^{3+}–Gd^{3+} unit.[11,12]

Results and Discussion

The crystal data and details of the refinements for $Gd_2(ClH_2CCOO)_6(bipy)_2$ are summarised in Table 1, selected bond lengths can be found in Table 2.

The title compound crystallises in the triclinic space group $P\bar{1}$ ($Z = 2$) with a = 959.5(3) pm, b = 980.9(3) pm, c = 1163.9(4) pm, α = 68.67(3)°, β = 84.82(4)° and γ = 82.47(4)°. The crystal structure is shown in Figure 1 (H atoms are not displayed). The structure is built up by discrete dimers (Gd^{3+}–Gd^{3+}-distance: 399.0 pm) with two kinds of bridging carboxylate groups (μ_2-carboxylato-κ^1O:κ^1O' and μ_2O';κ^2O,O') and besides a chelating monochloroacetate ion (Figure 2).[13] The Gd^{3+} ion is ninefold coordinated by seven oxygen atoms originating from the carboxylate groups (Gd^{3+}–O distances: 236.3 pm to 260.3 pm) and two nitrogen atoms stemming from a 2,2′-bipyridyl molecule (Gd^{3+}–N distances: 255.1 pm and 258.5 pm).

Table 1. Crystallographic data for $Gd_2(ClH_2CCOO)_6(bipy)_2$.

Compound	$Gd_2(ClH_2CCOO)_6(bipy)_2$
Crystal system	triclinic
Space group	$P\bar{1}$
Lattice constants [pm, °]	a = 959.5(3), α = 68.67(3) b = 980.9(3), β = 84.82(4) c = 1163.9(4), γ = 82.47(4)
V [pm^3]	$1010.5(5)\cdot10^6$
Z	2
ρ (X-ray) [g/cm^3]	1.952
Absorption coefficient μ [mm^{-1}]	3.713
$F(000)$	574
Crystal dimensions [mm^3]	$0.481\times0.1184\times0.592$
Temperature [K]	293(2)
Wavelength	Mo-K_α (λ = 71.073 pm)
θ range [°]	$2.14 \le 2\theta \le 26.17$
Index range (h, k, l)	$-11 \le h \le 11$ $-12 \le k \le 12$ $-14 \le l \le 14$
No. of collected reflections	14707
No. of independent reflections	3771
Observed reflections with $F > 2\sigma$	3253
R_{int}	0.1161
Programs used	SHELXS-97[23] and SHELXL-97[24]
Structure refinement	Full-matrix least squares
No. of refined parameters	248
Goodness-of-fit[a]	1.117
Residuals [$I > 2\sigma(I)$][a]	R_1 = 0.0357, wR_2 = 0.0835
Residuals (all data)[a]	R_1 = 0.0446, wR_2 = 0.0933
Largest differential hole and peak [$e\cdot pm^{-3}$]	$-1.198\cdot10^{-6}/1.050\cdot10^{-6}$
CCDC deposition number[26]	280805

[a] Definition given in the literature.[24]

[a] Institut für Anorganische Chemie der Universität Hannover, Callinstr. 9, 30167 Hannover, Germany
Fax: +49-511-762-19032
E-mail: urland@acc.uni-hannover.de

 © 2005 Wiley-VCH Verlag GmbH & Co. KGaA, Weinheim **DOI: 10.1002/ejic.200500734**

Table 2. Selected interatomic distances [pm] for $Gd_2(ClH_2CCOO)_6(bipy)_2$.

Gd–Gd[a]	399.0(2)
Gd–O12	236.3(4)
Gd–O32	237.2(4)
Gd–O11	237.7(4)
Gd–O21	243.5(5)
Gd–O22	250.0(4)
Gd–O31	250.2(4)
Gd–O32[a]	260.3(4)
Gd–N(2A)	255.1(5)
Gd–N(1A)	258.5(5)

[a] Symmetry transformation used to generate atoms: $-x + 1, -y + 1, -z + 2$.

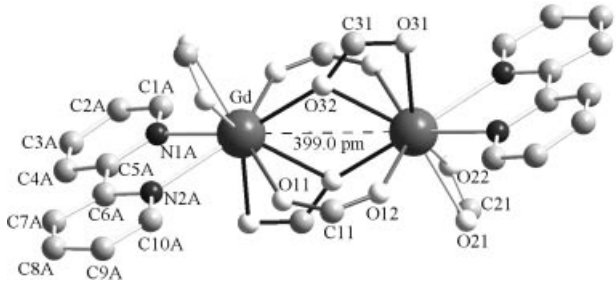

Figure 2. Dimeric unit in $Gd_2(ClH_2CCOO)_6(bipy)_2$; Gd atoms, carboxylate groups and 2,2′-bipyridyl molecules are given. The dashed line shows the Gd^{3+}–Gd^{3+}-distance, dark-grey lines indicate the μ_2-carboxylato-κ^1O:κ^1O'- and the black ones the μ_2O';κ^2O,O'-bridging mode.

The extended structure is formed by π–π stacking of the ligating 2,2′-bipyridyl molecules (Figure 3).[14,15] The shortest orthogonal distance between two aromatic fragments is 345.0 pm.

Former results have shown, that the μ_2O';κ^2O,O'- is responsible for a ferromagnetic interaction whereas the μ_2-carboxylato-κ^1O:κ^1O'-bridging mode leads to an antiferromagnetic interaction.[13,16–20] The title compound with the obtained crystal structure is interesting for magnetic investigations in order to study the influence of the coexistence of both bridging modi.

The presentation of the magnetic data follows the recommendation of S. Hatscher et al.[21] Figure 4 displays the measured effective Bohr magneton number (μ_{eff}) of the $Gd_2(ClH_2CCOO)_6(bipy)_2$ in the temperature range between 1.76 and 300 K ($H^{(ir)}$ = 500 Oe). The curve progression shows an antiferromagnetic behaviour. The measured magnetic susceptibility ($\chi_m^{(ir)}$) is interpreted by Equation (1) given below, where the intramolecular interaction within the dimeric unit is described by the Heisenberg model with a spin Hamiltonian $\hat{H}_{ex} = -2J_{ex}\hat{\boldsymbol{S}}_{Gd1}\cdot\hat{\boldsymbol{S}}_{Gd2}$ ($S_{Gd1} = S_{Gd2} = 7/2$), where N_A is the Avogadro constant, μ_B the Bohr magneton, g the Landé factor, k_B the Boltzmann constant, T the absolute temperature and J_{ex} the magnetic exchange parameter.[12]

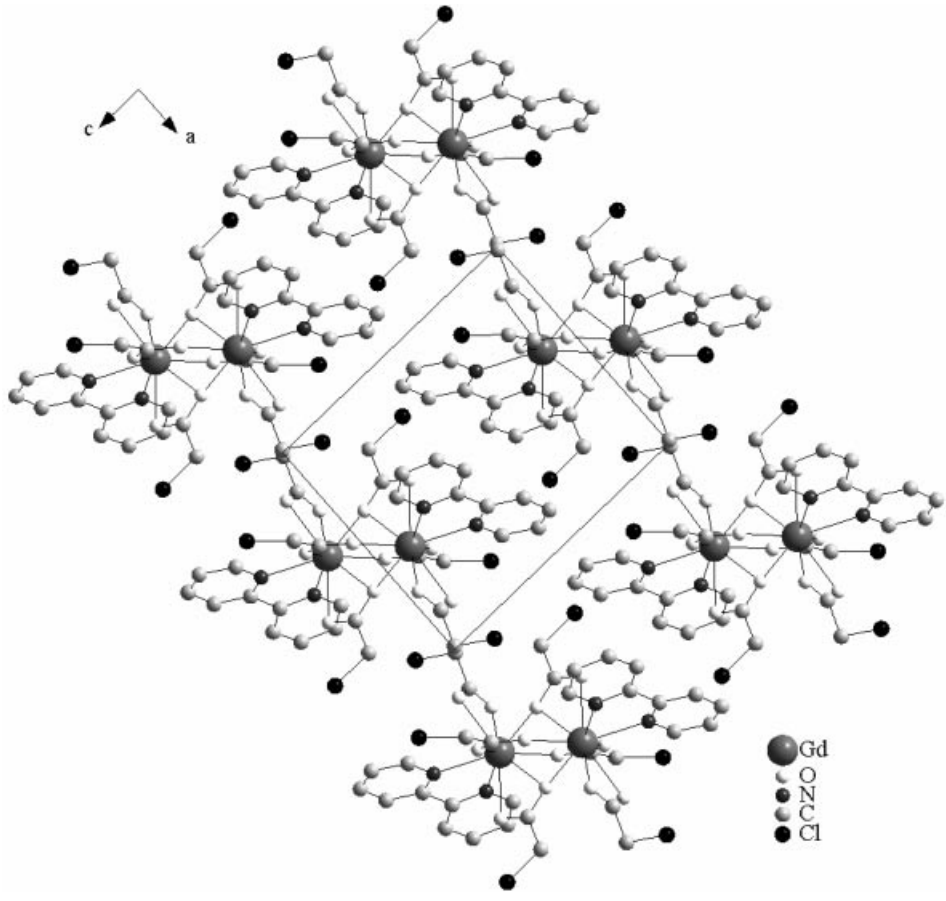

Figure 1. Crystal structure of $Gd_2(ClH_2CCOO)_6(bipy)_2$. The triclinic unit cell is given; H atoms are not displayed.

 © 2005 Wiley-VCH Verlag GmbH & Co. KGaA, Weinheim

$$\chi_m^{(ir)} = \frac{N_A \mu_B^2 g^2}{k_B T} \cdot \frac{e^{2x} + 5e^{6x} + 14e^{12x} + 30e^{20x} + 55e^{30x} + 91e^{42x} + 140e^{56x}}{1 + 3e^{2x} + 5e^{6x} + 7e^{12x} + 9e^{20x} + 11e^{30x} + 13e^{42x} + 15e^{56x}}$$

with $x = J_{ex} / k_B T$ (1)

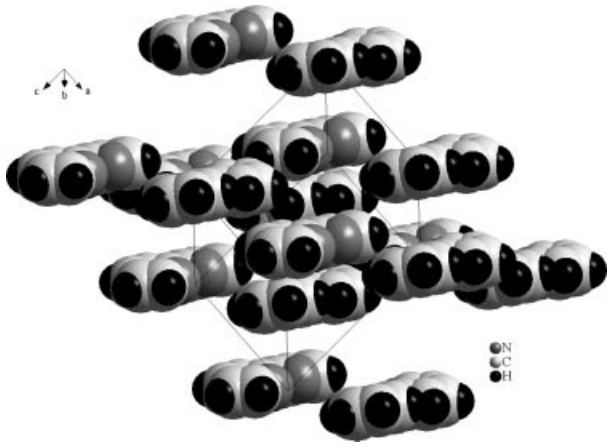

Figure 3. π–π Stacking of the 2,2′-bipyridyl molecules in $Gd_2(ClH_2CCOO)_6(bipy)_2$. The unit cell is given.

The fitting procedure leads to J_{ex} = –0.020 cm^{-1}, with g = 2.00. The accordance of the measured and calculated μ_{eff} values is shown in Figure 4.

The value of J_{ex} for the title compound is comparable with the ones of other carboxylates containing Gd^{3+} (cf. Table 3). The coexistence of the $\mu_2O';\kappa^2O,O'$- and the μ_2-carboxylato-$\kappa^1O:\kappa^1O$-bridging mode in $Gd_2(ClH_2CCOO)_6(bipy)_2$ leads to a negative exchange parameter, meaning a dominating antiferromagnetic interaction, as found in (**2**).[20]

Experimental Section

Transparent, colourless, air-stable, single crystals of $Gd_2(ClH_2CCOO)_6(bipy)_2$ have been obtained by reaction of $Gd_3(ClH_2CCOO)_9(H_2O)_5$ with 2,2′-bipyridyl (Fluka, ≥ 98.0%%) (molar ratio 2:1) in a solution of ethanol and water (1:1). The starting compound $Gd_3(H_2ClCCOO)_9(H_2O)_5$ was prepared as given in the literature.[22]

Well grown single crystals were mounted on a STOE imaging plate diffractometer. The data collection was carried out at room temperature. The structure was solved by Patterson methods and were refined with anisotropic displacement parameters based on F^2 using SHELXS-97[23] and SHELXL-97[24] programs. Data analysis indicate the space group $P\bar{1}$. The final refinement yielded R_1 (all data) = 4.46%. Hydrogen atoms were included using a riding model. The crystal data and details of the refinement are summarised in Table 1 and selected bond lengths can be found in Table 2. Elemental analysis (Vario EL, Elementar Analysesysteme GmbH, Hanau, Germany) for $C_{16}H_{20}Cl_3GdN_2O_6$ (593.91): calcd. C 32.36, H 2.38, N 4.72; found C 32.29, H 2.47, N 4.69.

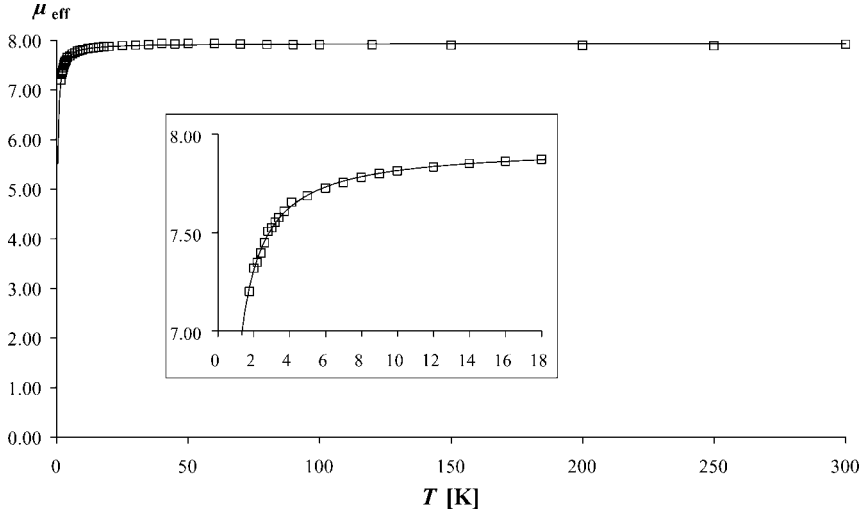

Figure 4. Comparison of measured (□, $H^{(ir)}$ = 0.5 kOe) and calculated (−) effective Bohr magneton numbers for $Gd_2(ClH_2CCOO)_6(bipy)_2$.

Table 3. Comparison of J_{ex} [cm^{-1}], bridging mode and Gd^{3+}–Gd^{3+}-distance (pm) for $Gd_2(ClH_2CCOO)_6(bipy)_2$ (**1**) $Gd(CF_2HCOO)_3(phen)$ (**2**), $[NH_3C_2H_5][Gd(Cl_2HCCOO)_4]$ (**3**), $[NH_3CH_3][Gd(Cl_2HCCOO)_4]$ (**4**), $Gd(H_3CCOO)_3(H_2O)_2{\cdot}2H_2O$ (**5**) and $Gd(F_2HCCOO)_3(H_2O)_2{\cdot}H_2O$ (**6**).

Compound	J_{ex}	Bridging mode	Gd^{3+}–Gd^{3+} distance	Ref.
1	–0.020	$\mu_2O';\kappa^2O,O'$ and μ_2-carboxylato-$\kappa^1O:\kappa^1O'$	399.0	this work
2	–0.016	$\mu_2O';\kappa^2O,O'$ and μ_2-carboxylato-$\kappa^1O:\kappa^1O'$	403.4	[20]
3	+0.029	$\mu_2O';\kappa^2O,O'$	418.1	[19]
4	+0.023	$\mu_2O';\kappa^2O,O'$	418.4	[18]
5	+0.025	$\mu_2O';\kappa^2O,O'$	420.6	[16]
6	–0.012	μ_2-carboxylato-$\kappa^1O:\kappa^1O'$	445.6	[13]
4	–0.007	μ_2-carboxylato-$\kappa^1O:\kappa^1O'$	451.6	[18]

 © 2005 Wiley-VCH Verlag GmbH & Co. KGaA, Weinheim

Pulverised single crystals of the title compound were measured with a SQUID magnetometer (MPMS5, Quantum Design) in a temperature range of 1.76 to 300 K at magnetic fields ($H^{(ir)}$) of 500 and 1000 Oe. No field dependence of the magnetic data was observed. The sample was weighed into the lid of a gelantine capsule. To avoid orientation effects during the measurement, another gelantine capsule was pressed on the sample to fix it. Subsequently the container was sewn in a plastic straw. Using the increments of Haberditzl, the raw magnetic data were corrected for diamagnetism of the sample carrier and the sample.[25]

[1] G. Oczko, J. Legendziewicz, J. Mrozinski, G. Meyer, *J. Alloys Compd.* **1998**, *275–277*, 219.
[2] T. Kido, Y. Ikuta, Y. Sunatsuki, Y. Ogawa, N. Matsumoto, *Inorg. Chem.* **2003**, *42*, 398.
[3] C. Benelli, D. Gatteschi, *Chem. Rev.* **2002**, *102*, 2369, and there cited.
[4] A. Figuerola, C. Diaz, J. Ribas, V. Tangoulis, J. Granell, F. Lloret, J. Mahia, M. Maestro, *Inorg. Chem.* **2003**, *42*, 641.
[5] J.-P. Costes, F. Dahan, A. Dupuis, J.-P. Laurent, *Chem. Eur. J.* **1998**, *4*, 1616.
[6] J.-P. Costes, F. Nicodeme, *Chem. Eur. J.* **2002**, *8*, 3442.
[7] J. Legendziewicz, M. Borzechowska, G. Oczko, G. Meyer, *New J. Chem.* **2000**, *24*, 53.
[8] J. Legendziewicz, M. Borzechowska, G. Oczko, J. Mronzinski, *Spectrochim. Acta, Part A* **1998**, *54*, 2197.
[9] G. Oczko, J. Legendziewicz, M. Wickleder, G. Meyer, *J. Alloys Compd.* **2002**, *341*, 255.
[10] J. Legendziewicz, M. Borzechowska, G. Oczko, G. Meyer, *New J. Chem.* **2000**, *24*, 53.
[11] O. Kahn, *Molecular Magnetism*, first ed., VCH, Weinheim, **1993**.
[12] H. Lueken, *Magnetochemie*, first ed., Teubner, Stuttgart, **1999**.
[13] A. Rohde, S. T. Hatscher, W. Urland, *J. Alloys Compd.* **2004**, *374*, 137.
[14] C. Janiak, *Dalton Trans.* **2000**, 3885.
[15] M. D. Curtis, J. Cao, J. W. Kampf, *J. Am. Chem. Soc.* **2004**, *126*, 4318.
[16] S. T. Hatscher, W. Urland, *Angew. Chem.* **2003**, *115*, 2969; *Angew. Chem. Int. Ed.* **2003**, *42*, 2862.
[17] A. Rohde, W. Urland, *Z. Anorg. Allg. Chem.* **2004**, *630*, 2434.
[18] A. Rohde, W. Urland, *Z. Anorg. Allg. Chem.* **2005**, *631*, 417.
[19] A. Rohde, W. Urland, *J. Alloys Compds.* **2005**, in press.
[20] D. John, W. Urland, *Z. Anorg. Allg. Chem.* **2005**, *631*, in press.
[21] S. Hatscher, H. Schilder, H. Lueken, W. Urland, *Pure Appl. Chem.* **2005**, *77*, 497.
[22] A. Rohde, W. Urland, *Z. Anorg. Allg. Chem.* **2003**, *629*, 2069.
[23] G. M. Sheldrick, SHELXS-97. Program for crystal structure solution, University of Göttingen: Göttingen, Germany, **1990**.
[24] G. M. Sheldrick, SHELXL-97. Program for the refinement of crystal structures from diffraction data, University of Göttingen: Göttingen, Germany, **1997**.
[25] W. Haberditzl, *Angew. Chem.* **1966**, *78*, 277; *Angew. Chem. Int. Ed. Engl.* **1966**, *5*, 288.
[26] CCDC-280805 contains the supplementary crystallographic data for this paper. These data can be obtained free of charge from The Cambridge Crystallographic Data Centre via www.ccdc.cam.ac.uk/data_request/cif.

Received: August 19, 2005
Published Online: October 11, 2005

 © 2005 Wiley-VCH Verlag GmbH & Co. KGaA, Weinheim

Significance of Intermolecular S···C(π) Interaction Involving M–S and –C=O Centers in Crystal Structures of Metal Thiolate Complexes

Janusz Lewiński,*[a] Wojciech Bury,[a] and Iwona Justyniak[b]

Keywords: Database analysis / Noncovalent interactions / Thiolates / Metal complexes

The database analysis of intermolecular S···C(π) distances involving a metal-bonded thiolate sulfur atom and various C(π)-centered Lewis acid domains provided evidences for M–S···C(π) contacts as resulting from specific noncovalent interactions.

(© Wiley-VCH Verlag GmbH & Co. KGaA, 69451 Weinheim, Germany, 2005)

Introduction

A plethora of noncovalent interactions account for a number of known binding and structural motifs in biological systems, synthetic catalysis and supramolecular chemistry.[1] In this regard hydrogen bonding plays a dominant role,[2] but many other less conventional noncovalent forces like the C–H···π,[3] cation···π,[4] and anion···π interactions,[5] π–π aromatic stacking,[6] halogen bonding,[7] or chalcogen–chalcogen[8] interactions have been identified and extensively explored recently. Nevertheless, some structural and functional aspects of biomolecular or catalytic functions remain an active problem which partly results from the fact that less obvious specific forces involving different chemical entities are only rarely encountered. In this regard, studies on identifying and characterizing noncovalent interactions are essential for a more complete understanding of biochemical processes and could provide useful tools in the field of molecular recognition. One of such emerging areas of research are interactions between divalent sulfur centers and electron-deficient π-systems. It is over 30 years since the seminal work of Dunitz et al. revealed that a large number of the close contacts between an electrophilic carbonyl group and a nucleophilic group exist in the crystal structures of small organic molecules, and based on the correlation analysis the authors mapped out reaction pathways of the nucleophilic addition to a carbonyl group.[9] More recently, it has been found that the nucleophilic attack by an amino acid S-terminal side chain on a peptide carbonyl atom is the crucial step in the mechanism of self-catalyzed peptide bond rearrangement.[10] An attractive intramolecular interaction between the thiolate group of a metal-bound cysteine and a carbonyl carbon atom of a peptide group is also essential in the determination of metalloprotein structures.[11–13] Nevertheless, the chemistry of specific weak interactions involving a thiolate center in metal complexes and metalloproteins has been so far explored only fleetingly.[14] Very recently, we have revealed that the intermolecular S···C(π) interaction between an M–S thiolate unit and the π-surface of an ester functionality can compete with the potential sulfur–metal dative bond of group 13 metal–alkyl compounds derived from methyl thiosalicylate, $Me_2M(SC_6H_4\text{-}2\text{-}CO_2Me)$ (cf. structures **I** and **II**; Figure 1).[15] In order to verify the significance of the M–S···C(π) interaction between the M–S–C thiolate sulfur atom and the carbonyl carbon atom as an intermolecular force, we have performed detailed structural analysis of intermolecular contacts for various types of metal thiolate complexes retrieved from the Cambridge Structural Database (CSD).

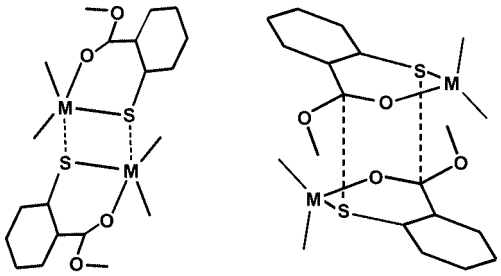

I **II**

Figure 1. Coordination mode variation of the group 13 organometallic derivatives of methyl thiosalicylate: five-coordinate dimer $[Me_2In(\mu\text{-}SC_6H_4\text{-}2\text{-}CO_2Me)]_2$ (**I**) and four-coordinate non-covalently bonded dimer $Me_2Al(SC_6H_4\text{-}2\text{-}CO_2Me)$ (**II**).

[a] Department of Chemistry, Warsaw University of Technology, Noakowskiego 3, 00-664 Warsaw, Poland,
E-mail: lewin@ch.pw.edu.pl
[b] Institute of Physical Chemistry, Polish Academy of Sciences, Kasprzaka 44, 01-224 Warsaw, Poland

Supporting information for this article is available on the WWW under http://www.eurjic.org or from the author.

 © 2005 Wiley-VCH Verlag GmbH & Co. KGaA, Weinheim **DOI: 10.1002/ejic.200500668**

Results and Discussion

The collection of structural data was obtained through the systematic search of the CSD using CCDC software (version 5.25).[16] The searches were performed for structures containing a sulfur atom bonded to any metal atom and carbonyl group moieties of the type X–C=O (where X = C, N, O, S). Only the intermolecular contacts between the sulfur atom and the carbonyl carbon atom were examined (the S···C=O intermolecular contact). The coordinate system, the atom labeling scheme and the resulting geometric parameters used in our analysis are sketched in Figure 2.

The position of the sulfur atom relative to the carbonyl group plane is specified in spherical polar coordinates by two angles, φ and θ and the distance r. The carbonyl group lies in the xy plane and the vector C=O defines the direction of the X axis. The search was subjected to the following criteria: S···C intermolecular contacts up to 4.0 Å, R-factor less than 0.075 and error free, the position of the sulfur atom was specified relative to the π-phase of C=O moieties in spherical polar coordinates. The restricted searches revealed 101 compounds and the total data set used for the correlation analysis was 141 data points. In our analysis were excluded all intermolecular contacts between the sulfur atom and a carbonyl group corresponding to the S···O=C interaction between a C–S–C unit and a carbonyl oxygen atom.[8b] A survey of available crystal structures shows several types of functional groups acting as the C(π)-centered Lewis acid domains. In total 27 contacts were found in which the sulfur lone pair is directed to the carbon atom of the carboxylate group bonded to a metal center, 48 contacts involve metal-bonded thiocarboxylates, 23 amides, 21 esters, and 22 ketones. The corresponding histogram plots of the S···C=O distances for various type of X–C=O carbonyl moieties are offset essentially regularly (Figure 2). This observation is consistent with the expectation taking into account that the functional groups in question are both bound (or not bound at all) to various metal centers and with various coordination modes, and thus the metal–ligand interactions have a different character which affects the Lewis acidity of the X–C=O carbon center. Not surprisingly, the effect is most pronounced for the carboxylate groups which exhibit the greatest metal–ligand bonding diversity.[17] Interestingly, it appears from the considered data set that in the short range of contacts (i.e., below 3.5 Å) there are interactions involving essentially all types of functional groups except the ester group. Thus, this fact suggests that the ester group Lewis acid domain is one of the weakest acidity. On the other hand, the S···C(π) distance recently found by us for $Me_2Al(SC_6H_4\text{-}2\text{-}CO_2Me)$ is one of the shortest intermolecular contacts observed to date between the M–S center and the carbon atom of the ester group. Furthermore, the analysis of angular attributes of the S···C(π) interactions clearly show the directional nature of this novel noncovalent force, Figure 3 (see also Figures S3 and S4 of the Supporting Information).

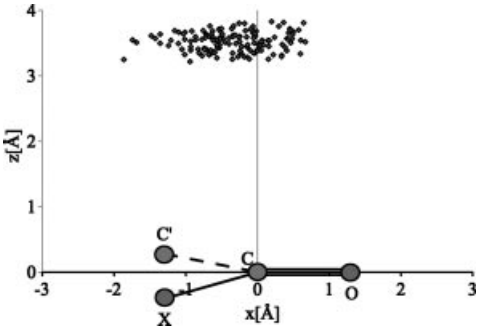

Figure 3. Distribution of the axial positions for the sulfur atom of a metal thiolate unit position relative to the X–C=O π-face projected on the xz plane.

In conclusion, detailed structural analysis was performed for crystal structures of metal thiolate complexes retrieved from the CSD which demonstrates that the intermolecular S···C(π) interactions involving a metal-bonded thiolate sulfur atom and various C(π)-centered Lewis acid domains appear very frequently and play a crucial role in the molecular assembly of these compounds in the solid state {cf. the crystal structures of $[Co(SC_6H_4\text{-}2\text{-}CO_2)N(C_2H_4NH_2)_3]ClO_4$ (**III**)[18] and $Zn(SC_6F_5)_2(C_5H_4N\text{-}2\text{-}COCH_3)$ (**IV**)[19] see Figure 4}.

There are already more than 100 crystal structures deposited in the CSD and surprisingly the S···C(π) interaction as well its role on the supramolecular structure of various

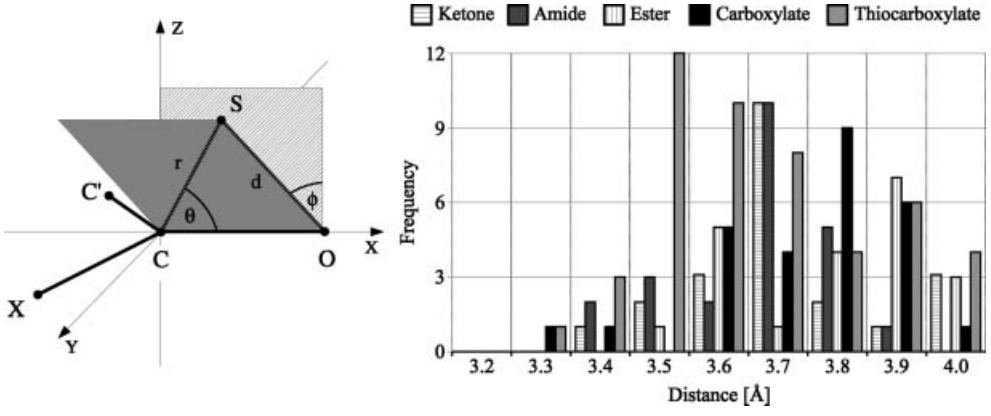

Figure 2. Geometrical parameters and histogram of S···C=O distances involving metal thiolates and various types of X–C=O carbonyl moieties (where X = C, N, O, S).

 © 2005 Wiley-VCH Verlag GmbH & Co. KGaA, Weinheim

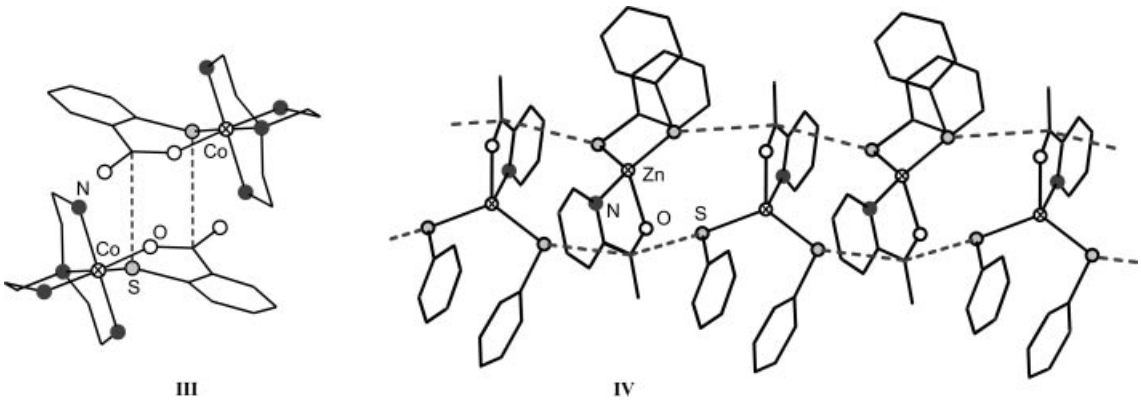

Figure 4. Structures of non-covalently bonded dimer $[Co(SC_6H_4\text{-}2\text{-}CO_2)N(C_2H_4NH_2)_3]ClO_4$ (**III**) and polymer chain of $Zn(SC_6F_5)_2(C_5H_4N\text{-}2\text{-}COCH_3)$ (**IV**).

complexes has not been recognized in any case by the original authors. Furthermore, it is reasonable that the M–S···C=O interactions may be expected to be responsible for the high bioactivity of sulfur, because such an interaction may occur at an early stage along the reaction coordinate or stabilize the folded protein structure as well as it might be a controlling factor in regulating the reactivity and specificity of metal–thiolate bonds.[20] The fact that the chemistry of specific weak interactions involving a thiolate center in metalloenzymes has been often underestimated in model studies is well expressed by the investigation involving the above-mentioned complex **IV**.[19] Further studies on both the relationship between dative bonds in metal complexes and secondary interactions, and the significance of the intermolecular S···C(π) interaction between M–S thiolate units and the π-surface of a carbonyl functionality in various systems are in progress.

Supporting Information (see footnote on the first page of this article) is available online for this manuscript, including parameterization data, histograms, scatter plots based on analyzed datasets and CCDC reference codes used in the database analysis can be found there.

Acknowledgments

The work was supported by the State Committee for Scientific Research (grant no. 4T09A16523).

[1] S. Scheiner (Ed.), *Molecular Interactions, From van der Waals to Strongly Bound Complexes*, Wiley, New York, **1997**.
[2] T. Steiner, *Angew. Chem. Int. Ed.* **2002**, *41*, 48; G. R. Desiraju, T. Steiner, in: *The Weak Hydrogen Bond in Structural Chemistry and Biology*, Oxford University Press, Oxford, **1999**.
[3] M. Nishio, M. Hirota, Y. Umezawa, in: *The CH/π interaction*, Wiley-VCH, New York, **1998**.
[4] J. C. Ma, D. A. Dougherty, *Chem. Rev.* **1997**, *97*, 1303.
[5] D. Quiñonero, C. Garau, C. Rotger, A. Frontera, P. Ballester, A. Costa, P. M. Deya, *Angew. Chem. Int. Ed.* **2002**, *41*, 3389; M. Mascal, A. Armstrong, M. D. Bartberger, *J. Am. Chem. Soc.* **2002**, *124*, 6274.
[6] C. A. Hunter, J. K. M. Sanders, *J. Am. Chem. Soc.* **1990**, *112*, 5525.
[7] A. Legon, *Angew. Chem. Int. Ed.* **1999**, *38*, 2687. P. Metrangolo, G. Resnati, *Chem. Eur. J.* **2001**, *7*, 2511.
[8] See for example: a) R. Gleiter, D. B. Werz, B. J. Rausch, *Chem. Eur. J.* **2003**, *9*, 2676; b) M. Iwaoka, S. Takemoto, S. Tomoda, *J. Am. Chem. Soc.* **2002**, *124*, 10613.
[9] H. B. Burgi, J. D. Dunitz, E. Shefter, *J. Am. Chem. Soc.* **1973**, *95*, 5065; R. E. Rosenfield, Jr., R. Parthasarathy, J. D. Dunitz, *J. Am. Chem. Soc.* **1977**, *99*, 4860.
[10] H. Paulus, *Chem. Soc. Rev.* **1998**, *27*, 375.
[11] P. Chakrabatrti, P. Debnathpal, *Protein Sci.* **1997**, *6*, 6851.
[12] For the role of the acyl–enzyme complexes in biochemical systems, see for example: M. Topf, W. G. Richards, *J. Am. Chem. Soc.* **2004**, *126*, 14631 and references cited therein.
[13] We also note that interactions between the sulfur atom of C–S–C or C–S–S–C units and aromatic rings have also been increasingly observed in biological systems: E. A. Meyer, R. K. Castellano, F. Diederich, *Angew. Chem. Int. Ed.* **2003**, *42*, 1210.
[14] For the role of the M–S···H hydrogen bonding on the reactivity of zinc thiolate species in Zn–S proteins or the redox potential of Fe–S proteins, see: J. N. Smith, Z. Shirin, C. J. Carrano, *J. Am. Chem. Soc.* **2003**, *125*, 868; X. Yang, S. Niu, T. Ichiye, L. S. Wang, *J. Am. Chem. Soc.* **2004**, *126*, 15790.
[15] J. Lewiński, W. Bury, T. Kopeć, E. Tratkiewicz, I. Justyniak, J. Lipkowski, *Eur. J. Inorg. Chem.* **2005**, 3414.
[16] The CSD 3D Graphics Search System: F. H. Allen, *Acta Crystallogr., Sect. B* **2002**, *58*, 380.
[17] See for example: R. K. Hocking, T. W. Hambley, *Inorg. Chem.* **2003**, *42*, 2833; T. Dudev, C. Lim, *J. Phys. Chem.* **2004**, *108*, 4546, and references therein.
[18] Adapted from: K. M. A. Malik, S. Mitra, R. K. B. Singh, *J. Chem. Crystallogr.* **1999**, *29*, 877.
[19] A. Schneider, H. Vahrenkamp, *Z. Anorg. Allg. Chem.* **2003**, *629*, 2122.
[20] Metal thiolate species are of seminal importance in biological systems, G. Berton (Ed.), *Handbook of Metal-Ligand Interactions in Biological Fluids*, Marcel Dekker, New York, **1995**.

Received: July 26, 2005
Published Online: October 13, 2005

 © 2005 Wiley-VCH Verlag GmbH & Co. KGaA, Weinheim

Water-Soluble Arene Ruthenium Complexes Containing a *trans*-1,2-Diaminocyclohexane Ligand as Enantioselective Transfer Hydrogenation Catalysts in Aqueous Solution

Jérôme Canivet,[a] Gael Labat,[a][‡] Helen Stoeckli-Evans,[a][‡] and Georg Süss-Fink*[a]

Keywords: Ruthenium complexes / Transfer hydrogenation / Enantioselective catalysis

The cationic chloro complexes $[(arene)Ru(H_2N\cap NH_2)Cl]^+$ (**1**: arene = C_6H_6; **2**: arene = *p*-MeC_6H_4iPr; **3**: arene = C_6Me_6) have been synthesised from the corresponding arene ruthenium dichloride dimers and enantiopure (*R*,*R* or *S*,*S*) *trans*-1,2-diaminocyclohexane ($H_2N\cap NH_2$) and isolated as the chloride salts. The compounds are all water-soluble and, in the case of the hexamethylbenzene derivative **3**, the aqua complex formed upon hydrolysis $[(C_6Me_6)Ru(H_2N\cap NH_2)OH_2]^{2+}$ (**4**) could be isolated as the tetrafluoroborate salt. The molecular structures of **3** and **4** have been determined by single-crystal X-ray diffraction analyses of $[(C_6Me_6)Ru(H_2N\cap NH_2)Cl]Cl$ and $[(C_6Me_6)Ru(H_2N\cap NH_2)OH_2][BF_4]_2$. Treatment of $[Ru_2(arene)_2Cl_4]$ with the monotosylated *trans*-1,2-diaminocyclohexane derivative ($TsHN\cap NH_2$) does not yield the expected cationic complexes, analogous to **1**–**3** but the neutral deprotonated complexes $[(arene)Ru(TsN\cap NH_2)Cl]$ (**5**: arene = C_6H_6; **6**: arene = *p*-MeC_6H_4iPr; **7**: arene = C_6Me_6; **8**: arene = C_6H_5COOMe). Hydrolysis of the chloro complex **7** in aqueous solution gave, upon precipitation of silver chloride, the corresponding monocationic aqua complex $[(C_6Me_6)Ru(TsHN\cap NH_2)(OH_2)]^+$ (**9**) which was isolated and characterised as its tetrafluoroborate salt. The enantiopure complexes **1**–**9** have been employed as catalysts for the transfer hydrogenation of acetophenone in aqueous solution using sodium formate and water as a hydrogen source. The best results were obtained (60 °C) with **7**, giving a catalytic turnover frequency of 43 h^{-1} and an enantiomeric excess of 93 %.

(© Wiley-VCH Verlag GmbH & Co. KGaA, 69451 Weinheim, Germany, 2005)

Introduction

Water-soluble organometallic complexes continue to attract growing interest for applications in catalysis because of environmentally friendly processing, simple product separation and pH dependent selectivity in aqueous media.

The first arene ruthenium aqua complexes were observed by NMR spectroscopy in 1972 when Zelonka and Baird dissolved $[(C_6H_6)Ru_2Cl_4]$ in D_2O.[1] The osmium complex $[(C_6H_6)Os(H_2O)_3]^{2+}$ was synthesised in an analogous manner and characterised spectroscopically by Hung et al.[2] Stebler-Röthlisberger et al. finally succeeded in isolating the first cationic benzene aqua complexes $[(C_6H_6)Ru(H_2O)_3]^{2+}$ and $[(C_6H_6)Os(H_2O)_3]^{2+}$ as the tosylate salts. The structure of the triaqua(benzene)ruthenium(II) cation was confirmed by a single-crystal X-ray structure analysis of the sulfate.[3]

Since these early reports, the chemistry of organometallic aqua ions of the transition metals has steadily grown during the 1980s and this topic was comprehensively reviewed by Koelle.[4] Related reviews deal with water-soluble organometallics complexed by hydrophilic ligands,[5] metal-mediated organic synthesis in water[6] and catalysis by water-soluble organometallic complexes in biphasic systems.[7] Recently, Ogo reported the transfer hydrogenation of ketones with HCO_2Na as a hydrogen donor, catalysed by achiral water-soluble Ru(II) complexes.[8] The intermediary formato and hydrido complexes $[(C_6Me_6)Ru(bipy)(OCHO)]^+$ and $[(C_6Me_6)Ru(bipy)H]^+$ could be isolated and structurally characterised.[8,9] We have also described the synthesis and catalytic activity of cationic arene ruthenium complexes containing 1,10-phenanthroline and its derivatives as chelating *N*,*N*-donor ligands.[10]

Several recent reports deal with asymmetric transfer hydrogenation of ketones with formate in aqueous media using active catalytic systems based on $[(p\text{-}MeC_6H_4iPr)RuCl_2]_2$ and *N*-(*p*-toluenesulfonyl)-1,2-diphenyl-ethylenediamine and its derivatives[11–14] 2-(*N*-anilinocarboxy)-pyrrolidine[15] or aminoethanol attached to cyclodextrin.[16] These catalytic systems show good activities and enantioselectivities but the catalysts are formed in situ from precursors and are not isolated. 1,2-dephenylethylendiamine ("Noyori's ligand")[17,18] and also *trans*-1,2-diaminocyclohexane form, in combination with $[(p\text{-}MeC_6H_4iPr)RuCl_2]_2$, an active catalytic system for the transfer hydrogenation of ketones in 2-propanol or in an Et_3N/HCOOH azeotropic mixture.[19]

In this paper we report a series of water-soluble arene ruthenium complexes containing enantiopure *trans*-1,2-di-

[a] Institut de Chimie, Université de Neuchâtel, Case postale 2, 2007 Neuchâtel, Switzerland
E-mail: georg.suess-fink@unine.ch
[‡] Crystal structure analysis.

 DOI: 10.1002/ejic.200500498 © 2005 Wiley-VCH Verlag GmbH & Co. KGaA, Weinheim

aminocyclohexane and derivatives thereof as chelating *N*,*N*-donor ligands. We also describe the catalytic activity of these complexes in the transfer hydrogenation of aromatic ketones to give the corresponding chiral secondary alcohol with sodium formate as a hydrogen donor in aqueous solution.

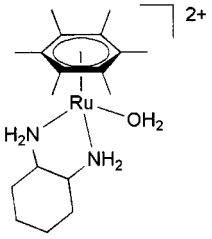

4

Results and Discussion

Synthesis of Enantiopure Arene Ruthenium Complexes Containing the *trans*-1,2-Diaminocyclohexane Ligand (1–4)

The monocationic chloro complexes $[(arene)Ru(H_2N\cap NH_2)Cl]^+$ (**1**–**3**) containing the *N*,*N* donor as a chelating ligand are accessible by treatment of the dimeric arene ruthenium complexes $[(arene)RuCl_2]_2$ with enantiopure (*R*,*R* or *S*,*S*) *trans*-1,2-diaminocyclohexane ($H_2N\cap NH_2$) at room temperature in dichloromethane solution [Equation (1)].

$$0.5\ [(arene)RuCl_2]_2 + H_2N\cap NH_2 \rightarrow [(arene)Ru(H_2N\cap NH_2)Cl]^+ + Cl^- \quad (1)$$

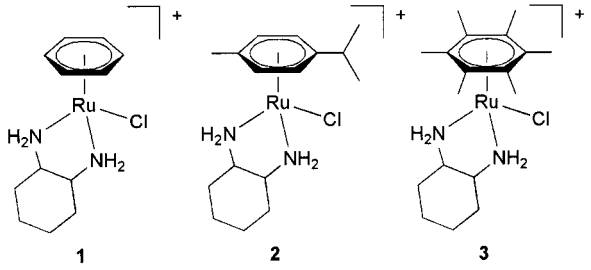

1 **2** **3**

The chloride salts of **1**–**3** are orange solids that dissolve well in water, a property which can be used to remove unreacted materials. Since there is a risk of hydrolysis in water, the aqueous solutions were filtered immediately and then evaporated to dryness to give the analytically pure salts [**1**–**3**]Cl. All compounds were obtained for both *trans*-1,2-diaminocyclohexane enantiomers (*R*,*R* or *S*,*S*) and were subsequently characterised by ^1H and ^{13}C spectroscopy, mass spectroscopy and elemental analysis. The molecular structure of **3** has been confirmed by a single-crystal X-ray structure analysis.

The chloro complex $[(C_6Me_6)Ru(H_2N\cap NH_2)Cl]^+$ (**3**) undergoes hydrolysis in aqueous solution and gives, upon precipitation of silver chloride, the enantiopure dicationic aqua complex $[(C_6Me_6)Ru(H_2N\cap NH_2)(OH_2)]^+$ (**4**). Both enantiomers (*R*,*R* or *S*,*S*) have been isolated as tetrafluoroborate salts and characterised by ^1H and ^{13}C spectroscopy, mass spectroscopy, elemental analysis and single-crystal X-ray structure analysis.

Synthesis of Enantiopure Arene Ruthenium Complexes Containing the *N*-Tosyl-*trans*-1,2-diaminocyclohexane Ligand (5–9)

The reaction of $[Ru_2(arene)_2Cl_4]$ with the monotosylated *trans*-1,2-diaminocyclohexane[20] ($TsHN\cap NH_2$) at room temperature in dichloromethane solution does not give the expected cationic complexes, analogous to **1**–**3**, but the deprotonated neutral complexes $[(arene)Ru(TsN\cap NH_2)Cl]$ (**5**–**8**) [Equation (2)].

$$0.5\ [(arene)RuCl_2]_2 + TsHN\cap NH_2 \rightarrow [(arene)Ru(TsN\cap NH_2)Cl] \quad (2)$$

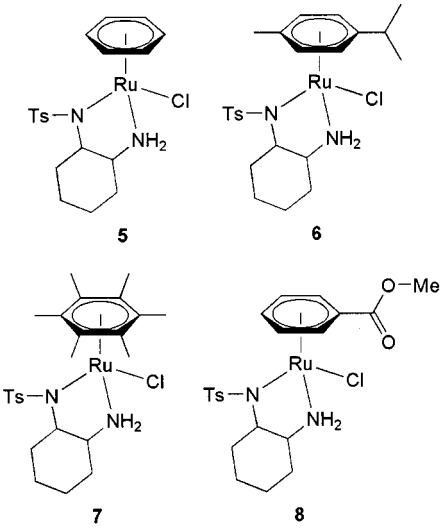

5 **6** **7** **8**

Similar to the known complex **6**,[21] complexes **5**, **7** and **8** are orange solids. The products obtained are quite soluble in water but in order to avoid hydrolysis they were purified by column chromatography on aluminium oxide using methanol as eluent. All compounds were obtained for both the *N*-Tosyl-*trans*-1,2-diaminocyclohexane enantiomers (*R*,*R* or *S*,*S*) and were subsequently characterised by ^1H and ^{13}C spectroscopy, mass spectroscopy and elemental analysis.

The chloro complex $[(C_6Me_6)Ru(TsN\cap NH_2)Cl]$ (**7**) undergoes hydrolysis in aqueous solution and gives, upon precipitation of silver chloride, the enantiopure monocationic aqua complex $[(C_6Me_6)Ru(TsN\cap NH_2)(OH_2)]^+$ (**9**). Both enantiomers (*R*,*R* or *S*,*S*) were isolated as the tetrafluoroborate salts and characterised by ^1H and ^{13}C spectroscopy, mass spectroscopy and elemental analysis.

 © 2005 Wiley-VCH Verlag GmbH & Co. KGaA, Weinheim

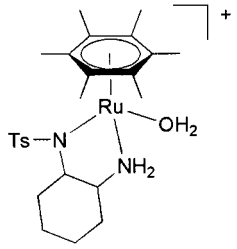

9

Molecular Structures of $[(C_6Me_6)Ru(R,R\text{-}H_2N\cap NH_2)Cl]^+$ (*R*,*R*-3) and $[(C_6Me_6)Ru(S,S\text{-}H_2N\cap NH_2)(OH_2)]^{2+}$ (*S*,*S*-4)

The compound $[R,R\text{-}3][Cl]\cdot 2CHCl_3$ crystallises in the orthorhombic non-centrosymmetric space group $P2_12_12_1$. The molecular structure of $[R,R\text{-}3][Cl]\cdot 2CHCl_3$ is depicted in Figure 1. The structure of the cation consists of a pseudo-tetrahedral arrangement of a ruthenium atom coordinated to the η^6-hexamethylbenzene ligand, the two nitrogen atoms of the (*R*,*R*) *trans*-1,2-diaminocyclohexane ligand and a chlorine atom. Ru–C distances fall within the range 2.183(2)–2.218(2) Å. As expected, the two amino groups of the (*R*,*R*) *trans*-1,2-diaminocyclohexane ligand are in equatorial positions which is the more stable conformation.

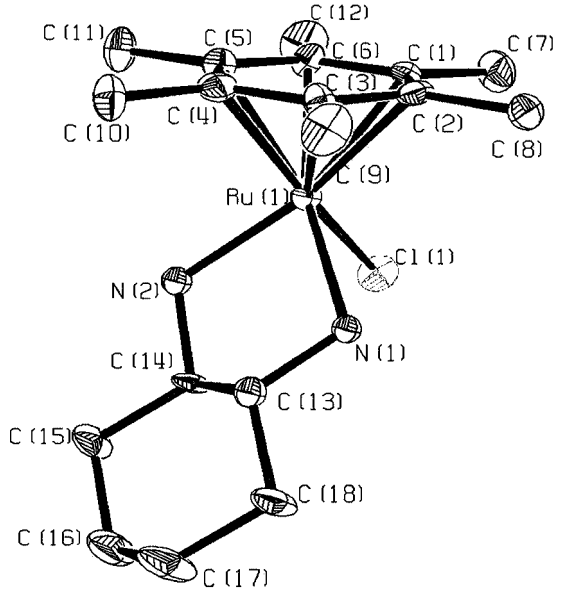

Figure 1. Molecular structure of *R*,*R*-**3**; displacement ellipsoids are shown at the 50% probability level; hydrogen atoms, the chloride counter anion and chloroform molecule are omitted for clarity; selected bond lengths [Å] and angles [°]: Ru(1)–N(1) 2.129(4), Ru(1)–N(2) 2.130(4), Ru(1)–Cl(1) 2.4052(16); N(1)–Ru(1)–N(2) 79.26(16), N(1)–Ru(1)–Cl(1) 83.06(15), N(2)–Ru(1)–Cl(1) 84.89(14).

The compound $[S,S\text{-}4][BF_4]_2\cdot H_2O$ crystallises in the orthorhombic noncentrosymmetric space group $P2_12_12_1$. The molecular structure of $[S,S\text{-}4][BF_4]_2\cdot H_2O$ is depicted in Figure 2. The structure of the cation consists of a pseudo-tetrahedral arrangement of a ruthenium atom coordinated to the η^6-hexamethylbenzene ligand, the two nitrogen atoms of the (*S*,*S*) *trans*-1,2-diaminocyclohexane ligand and a water molecule. Ru–C distances fall within the range 2.183(2)–2.218(2) Å. As expected, the two amino groups of the (*S*,*S*) *trans*-1,2-diaminocyclohexane ligand are in equatorial positions which is the more stable conformation.

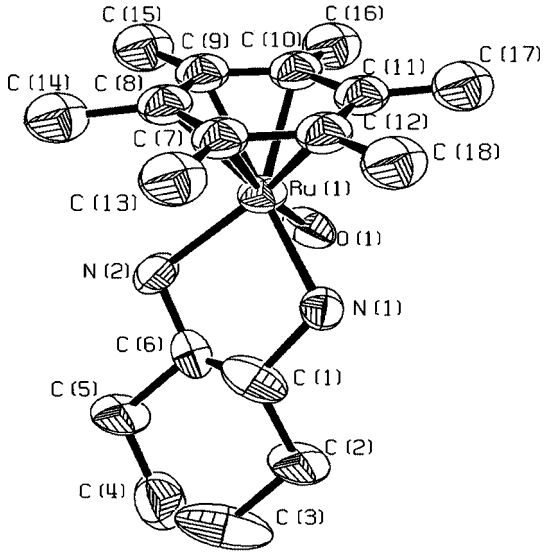

Figure 2. Molecular structure of *S*,*S*-**4**; displacement ellipsoids are shown at the 50% probability level; hydrogen atoms, tetrafluoroborate counter anions and water molecule are omitted for clarity; selected bond lengths [Å] and angles [°]: Ru(1)–N(1) 2.127(10), Ru(1)–N(2) 2.125(11), Ru(1)–O(1) 2.188(7); N(1)–Ru(1)–N(2) 78.8(3), N(1)–Ru(1)–O(1) 81.9(4), N(2)–Ru(1)–O(1) 82.6(4).

Catalytic Application of 1–9 for the Transfer Hydrogenation of Acetophenone and Derivatives with Sodium Formate in Aqueous Solution

Based on the studies using a catalytic system composed of the tosylated diphenylethanediamine (TsDPEN) with $[(p\text{-}MeC_6H_4iPr)RuCl_2]_2$ for the asymmetric transfer hydrogenation of ketones with sodium formate as hydrogen donor in water,[11–14] we evaluated the catalytic potential of the *trans*-diaminocyclohexane complexes **1**–**9** for this reaction using acetophenone as a test substrate. The solubility of the catalysts in water varies from 10 $\mu mol\,mL^{-1}$ for the neutral complexes **5**–**8** to 40 $\mu mol\,mL^{-1}$ for the ionic compounds **1**–**4** and **9** at 60 °C.

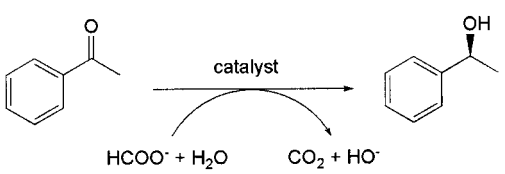

All *trans*-diaminocyclohexane complexes **1**–**9** (both *R*,*R* *and* *S*,*S* enantiomers) were found to catalyse the transfer hydrogenation reaction of acetophenone to give phenylethanol in aqueous solution with sodium formate as a hy-

 © 2005 Wiley-VCH Verlag GmbH & Co. KGaA, Weinheim

drogen source (Table 1). However, the tosylated derivatives **5**–**7** and **9** shown higher activities and selectivities than the non-tosylated complexes. The contribution of the donor effect of the substituents on the arene ligand is also obvious as the enantiomeric excess (*ee*) increases from 54% for the benzene complex **5** to 93% for the hexamethylbenzene complex **7**. This result is also consistent with the CH/π attraction model reported by Noyori.[22] The beneficial effect of the donor substituents at the arene ligand was confirmed by the use of complex **8** which gave a lower activity and selectivity than those observed for the benzene complex **5**.

Table 1. Catalytic enantioselective transfer hydrogenation of acetophenone using the (1*R*,2*R*)-diaminocyclohexane ruthenium complexes as catalysts and HCOONa as a hydrogen donor in water.[a]

Catalyst	Conversion % (h)[b]	*ee* %[b]	TOF [h^{-1}][c]
1	74 (16)	29	4.6
2	89 (16)	17	5.6
3	82 (16)	47	5.1
4	86 (16)	38	5.4
5	94 (2)	54	47
6	93 (2)	81	46.5
7	86 (2)	93	43
8	7 (2)	44	3.5
9	85 (2)	91	42.5

[a] Conditions: Reactions were carried out at 60 °C, pH = 9, in 5 mL of water and with acetophenone (1 mmol); the ratio catalyst/substrate/formate was 1:100:500. [b] The conversion and the enantiomeric excesses were determined by chiral HPLC analysis. [c] TOF: turnover frequencies (mol of acetophenone converted to phenylethanol per mol of catalyst per hour) were taken after 60% conversion.

It may be assumed that the chloro complexes **1**–**3** and **5**–**8** undergo hydrolysis to the corresponding aqua complexes under catalytic conditions. Thus, the isolated aqua complex **9** shows the same activity and selectivity as the corresponding chloro complex **7**. We believe that the aqua complexes react with the formate anion to give the corresponding formato complexes as the catalytically active species. A proposed catalytic cycle for derivative **9**, based on the pioneering work of Noyori[17c] and Ogo[8] is shown in Figure 3.

The hypothesis of an η^4 transition state (Figure 3) postulated by Ogo, in the case of the $[(C_6Me_6)Ru(bipy)(OH_2)]^{2+}$ complex[8] (bipy = 2,2' bipyrimidine) is substantiated by the arene substituent dependence of the catalytic activity described above. Indeed, complex **7** containing donor substituents on the arene ligand (arene = C_6Me_6, TOF = 43 h^{-1}), which would stabilise the transition species, shows activity more than ten times greater than that of the analogue **8** with an electron-withdrawing substituent at the arene ligand (arene = $C_6H_4CO_2Me$, TOF = 3.5 h^{-1}).

The pH dependence of the catalytic activity[8,10] of **7** was studied for the transfer hydrogenation of acetophenone to give phenylethanol in aqueous solution. As Figure 4 reveals, the best pH conditions were found to be around 9 which corresponds to the pH obtained by addition of sodium formate in water under catalytic conditions.

The temperature dependence of the catalytic activity of **7** was also studied for the same reaction. The curve obtained (Figure 5) clearly shows that the catalytic conditions for the activity of this reaction were found to be the best at 60 °C without significant modification to the selectivity.

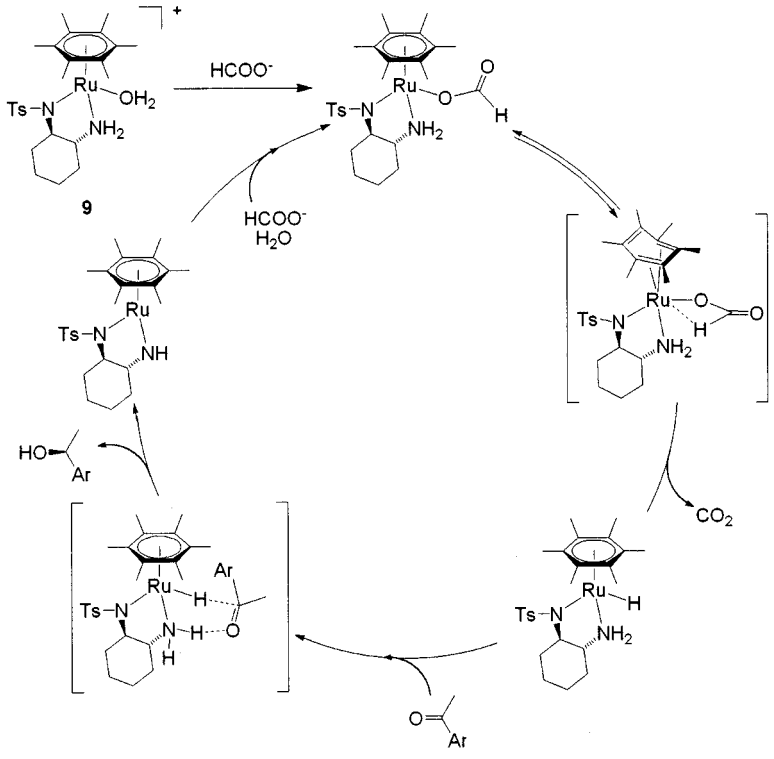

Figure 3. Postulated catalytic cycle for transfer hydrogenation catalysed by **9**.

 © 2005 Wiley-VCH Verlag GmbH & Co. KGaA, Weinheim

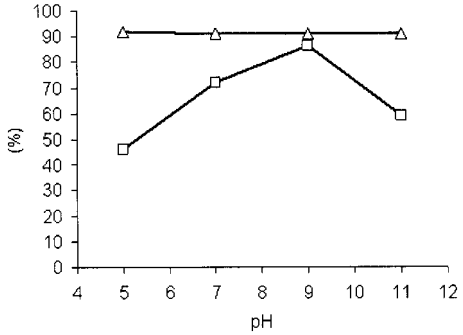

Figure 4. pH-dependent profile of conversion (□) and enantiomeric excess (ρ) for transfer hydrogenation of acetophenone (1 mmol) using complex **7** as the catalyst and HCOONa as a hydrogen donor in water (5 mL), at 60 °C, for 2 h, the catalyst/substrate/formate ratio being 1:100:500.

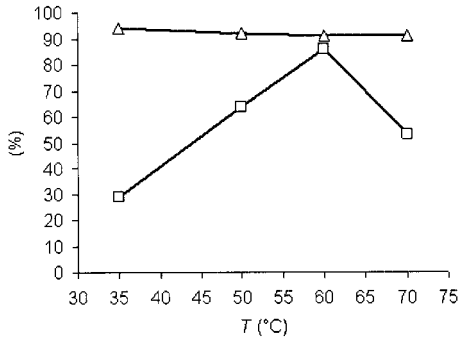

Figure 5. Temperature-dependent profile of conversion (□) and enantiomeric excess (Δ) for transfer hydrogenation of acetophenone (1 mmol) using complex **7** as catalyst and HCOONa as hydrogen donor in water (5 mL), at pH = 9, for 2 h, the catalyst/substrate/formate ratio being 1:100:500.

The kinetic plot (Figure 6) shows that under these conditions the reaction is almost complete after 3 h. The turnover frequency calculated in this case, using the best catalyst precursor **7**, is 43 h^{-1}, comparable to those found for the TsDPEN catalysts.[11–14]

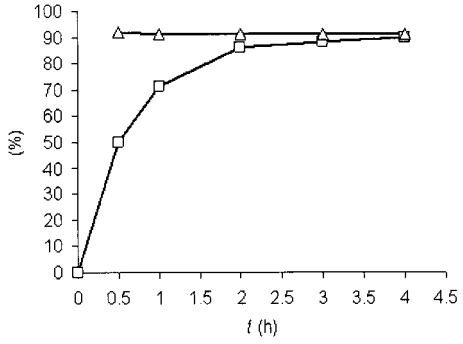

Figure 6. Time dependence of conversion (□) and enantiomeric excess (Δ) for transfer hydrogenation of acetophenone (1 mmol) using complex **7** as catalyst and HCOONa as hydrogen donor in water (5 mL), at 60 °C, pH = 9, the catalyst/substrate/formate ratio being 1:100:500.

The catalytic activity and selectivity of complex **7** have also been determined for the transfer hydrogenation reaction of *para*-substituted acetophenone under the same catalytic conditions (Table 2).

Table 2. Enantioselective catalytic transfer hydrogenation of *para*-substituted acetophenone using complex **7** as catalyst and HCOONa as a hydrogen donor in water.[a]

Substituent	Conversion % (h)	*ee* %	TOF [h^{-1}][d]
CF_3	70 (2)[c]	90[c]	35
NO_2	57 (2)[c]	79[c]	28.5
Br	88 (2)[b]	90[b]	44
Me	84 (2)[b]	92[b]	42
OMe	65 (2)[c]	93[c]	32.5

[a] Conditions: reactions were carried out at 60 °C, at pH = 9, in 5 mL of water, acetophenone (1 mmol), the ratio catalyst/substrate/formate being 1:100:500. [b] The conversion and the enantiomeric excess were determined by chiral HPLC analysis. [c] The conversion and the enantiomeric excess were determined by chiral GC analysis. [d] TOF: turnover frequencies (mol of acetophenone converted to phenylethanol per mol of catalyst per hour) were taken at 50% conversion.

The catalytic system is rather tolerant with respect to the substrate. There is no substantial limitation by electronic effects of the substituents at the substrate molecule. Thus, the enantioselectivity varies only slightly from 79% (*para*-nitroacetophenone) to 93% (*para*-methoxyacetophenone) with dramatically varying electronic densities in the aromatic rings of the substrates. The variation of the catalytic activity from 28.5 h^{-1} (*para*-nitroacetophenone) to 44 h^{-1} (*para*-bromoacetophenone) is also not very pronounced.

Conclusions

In conclusion, we report here nine water-soluble chiral arene ruthenium complexes containing *trans*-1,2-diaminocyclohexane or derivatives thereof as chelating ligands. All these complexes were found to catalyse the enantioselective transfer hydrogenation of acetophenone to give 1-phenylethanol using sodium formate as a hydrogen source in aqueous solution. The best results were obtained for **7** at 60 °C, giving a turnover frequency of 43 h^{-1} and an enantiomeric excess of 93%. The corresponding aqua complex **9**, presumed to be the catalytic species, has been isolated and characterised as its tetrafluoroborate salt.

Experimental Section

General: All manipulations were carried out in an inert atmosphere using standard Schlenk techniques and freshly distilled solvents saturated with nitrogen prior to use. The starting dimer [(arene)Ru-$Cl_2]_2$[23,24] and the monotosylated diaminocyclohexane ($TsHN\cap NH_2$)[20] were prepared according to the published methods. All other reagents were commercially available and were used without further purification. NMR spectra were recorded on a Bruker 400 MHz spectrometer using sodium 2,2-dimethyl-2-silapentane-5-sulfonate in D_2O as a ^{13}C locking agent. Electrospray mass spectra were obtained in the positive-ion mode with an LCQ Finnigan mass spectrometer. Microanalyses were carried out by the Laboratoire de Chimie Pharmaceutique, Université de Genève

 © 2005 Wiley-VCH Verlag GmbH & Co. KGaA, Weinheim

(Switzerland). All chemical characterisations given below were found for both *R,R* and *S,S* enantiomers.

Preparation of the Enantiopure Chloro Complexes [(arene)-Ru($H_2N\cap NH_2$)Cl]$^+$ (arene = C_6H_6, *p*-MeC_6H_4iPr or C_6Me_6; $H_2N\cap NH_2$ = *trans*-1,2-diaminocyclohexane): Two equiv. (0.30 mmol) of the appropriate enantiomer of *trans*-1,2-diaminocyclohexane ($H_2N\cap NH_2$) were added to a suspension of [(arene)-$RuCl_2]_2$ (0.15 mmol) in dichloromethane (30 mL). The mixture was stirred for 4 h at room temperature, during this time the orange colour became darker. After evaporation to dryness, the residue was dissolved in water (20 mL). The solution was filtered, washed with diethyl ether (2× 10 mL), and the aqueous solution was evaporated to dryness giving the product in 75–85% yield.

[(C_6H_6)Ru($H_2N\cap NH_2$)Cl]Cl ([1]Cl): Yield 74%, 80.8 mg. ^{1}H NMR (400 MHz, D_2O, 21 °C): δ = 1.03 (m, CH_2), 1.18 (m, $^3J_{cis}$ = 3.96, $^3J_{trans}$ = 11.36 Hz, CH), 1.57 (m, CH_2), 1.83 (m, $^3J_{cis}$ = 3.72, $^3J_{trans}$ = 12.28 Hz, CH), 1.94 (m, CH_2), 5.78 (s, C_6H_6) ppm. ^{13}C NMR (200 MHz, D_2O, 21 °C): δ = 24.1 (CH_2), 24.3 (CH_2), 32.9 (CH_2), 34.4 (CH_2), 56.7 (CH), 61.0 (CH), 84.4 (C_6H_6) ppm. MS (ESI) *m*/*z* = 329 [M]$^+$. $C_{12}H_{20}Cl_2N_2Ru$ (364.28): calcd. C 39.57, H 5.53, N 7.69; found N 39.63, H 5.48, N 7.58.

[(*p*-$MeC_6H_4Pr^i$)Ru($H_2N\cap NH_2$)Cl]Cl ([2]Cl): Yield 85%, 107.1 mg. ^{1}H NMR (400 MHz, D_2O, 21 °C): δ = 1.07 (m, CH_2), 1.21 (m, CH), 1.28 (d, $^3J_{H,H}$ = 7 Hz, $(CH_3)_2CH$), 1.55 (m, CH_2), 1.78 (m, CH), 1.92 (m, CH_2), 2.84 (m, $^3J_{H,H}$ = 7 Hz, $CH(CH_3)_2$), 5.61 (d, $^3J_{H,H}$ = 6 Hz, C_6H_4), 5.75 (d, $^3J_{H,H}$ = 6 Hz, C_6H_4) ppm. ^{13}C NMR (200 MHz, D_2O, 21 °C): δ = 18.4 (CH_3), 21.4 ($CH(CH_3)_2$), 24.1 (CH_2), 24.3 (CH_2), 31.0 ($CH(CH_3)_2$), 32.9 (CH_2), 34.4 (CH_2), 57.2 (CH), 61.1 (CH), 86.7 (C_6H_4), 103.9 (C_6H_4), 105.6 (C_6H_4) ppm. MS (ESI): *m*/*z* = 385 [M$^+$]. $C_{16}H_{28}Cl_2N_2Ru$ (420.38): calcd. C 45.71, H 6.71, N 6.66; found N 45.58, H 6.69, N 6.58.

[(C_6Me_6)Ru($H_2N\cap NH_2$)Cl]Cl ([3]Cl): Yield 81%, 108.9 mg. ^{1}H NMR (400 MHz, D_2O, 21 °C): δ = 1.11 (m, CH_2), 1.21 (m, CH), 1.53 (m, CH_2), 1.85 (m, CH), 1.98 (m, CH_2), 2.08 (s, $C_6(CH_3)_6$) ppm. ^{13}C NMR (200 MHz, D_2O, 21 °C): δ = 15.2 ($C_6(CH_3)_6$), 24.0 (CH_2), 24.2 (CH_2), 33.5 (CH_2), 34.3 (CH_2), 57.0 (CH), 60.9 (CH), 92.1 ($C_6(CH_3)_6$) ppm. MS (ESI): *m*/*z* = 413 [M$^+$]. $C_{18}H_{32}N_2Cl_2Ru$ (448.44): calcd. C 48.21, H 7.19, N 6.25; found N 48.07, H 7.22, N 6.23.

Preparation of the Enantiopure Chloro [(arene)Ru(TsN∩NH_2)Cl] (arene = C_6H_6, *p*-MeC_6H_4iPr, C_6Me_6 or C_6H_4COOMe; TsHN∩NH_2 = *N*-tosyl-*trans*-1,2-diaminocyclohexane): Two equiv. (0.30 mmol) of the appropriate enantiomer of *N*-tosyl-*trans*-1,2-diaminocyclohexane (TsHN∩NH_2) were added to a suspension of [(arene)$RuCl_2]_2$ (0.15 mmol) in dichloromethane (30 mL). The mixture was stirred for 4 h at room temperature, during this time the orange colour became darker. After evaporation to dryness the residue was dissolved in a minimum of dichloromethane and then submitted to column chromatography on aluminium oxide using methanol as eluent. The orange-yellow fraction was collected and the solvent was evaporated to dryness giving the product in 70–75% yield.

[(C_6H_6)Ru(TsN∩NH_2)Cl] (5): Yield 70%, 93.9 mg. ^{1}H NMR (400 MHz, $CDCl_3$, 21 °C): δ = 0.95 (m, CH_2), 1.22 (m, 2 CH_2), 1.43 (m, CH), 1.60 (m, CH_2), 1.88 (m, CH), 2.28 (s, *p*-$(CH_3)C_6H_4SO_2$), 5.78 (s, C_6H_6), 7.17 (d, *J* = 7.3 Hz, *p*-$(CH_3)C_6H_4SO_2$), 7.71 (d, *J* = 7.3 Hz, *p*-$(CH_3)C_6H_4SO_2$) ppm. ^{13}C NMR (200 MHz, $CDCl_3$, 21 °C): δ = 21.5 (*p*-$(CH_3)C_6H_4SO_2$), 24.4 (CH_2), 25.0 (CH_2), 31.8 (CH_2), 32.5 (CH_2), 59.3 (CH), 60.0 (CH), 83.4 (C_6H_6), 127.2 (2 CH), 128.3 (2 CH), 137.9 (*p*-$(CH_3)C_6H_4SO_2$), 143.3 (*p*-$(CH_3)C_6H_4SO_2$) ppm. MS (ESI): *m*/*z* = 447 [M – Cl]$^+$. $C_{19}H_{25}ClN_2O_2RuS$ (482): calcd. C 47.34, H 5.23, N 5.81; found N 47.13, H 5.32, N 5.69.

[(*p*-MeC_6H_4iPr)Ru(TsN∩NH_2)Cl] (6): Yield 73%, 110.2 mg. ^{1}H NMR (400 MHz, $CDCl_3$, 21 °C): δ = 1.05 (m, CH_2), 1.25 (m, 2 CH_2), 1.32 (d, $^3J_{H,H}$ = 7 Hz, $(CH_3)_2CH$), 1.53 (m, CH), 1.71 (m, CH_2), 1.99 (m, CH), 2.36 (s, *p*-$(CH_3)C_6H_4SO_2$), 2.86 (m, $^3J_{H,H}$ = 7 Hz, $(CH_3)_2CH$), 5.57 (d, $^3J_{H,H}$ = 6 Hz, C_6H_4), 5.77 (d, $^3J_{H,H}$ = 6 Hz, C_6H_4), 7.17 (d, $^3J_{H,H}$ = 8 Hz, *p*-$(CH_3)C_6H_4SO_2$), 7.71 (d, $^3J_{H,H}$ = 8 Hz, *p*-$(CH_3)C_6H_4SO_2$) ppm. ^{13}C NMR (200 MHz, $CDCl_3$, 21 °C): δ = 18.4 (CH_3), 21.4 ($CH(CH_3)_2$), 21.5 (*p*-$(CH_3)C_6H_4SO_2$), 24.1 (CH_2), 24.3 (CH_2), 31.0 ($CH(CH_3)_2$), 33.5 (CH_2), 34.2 (CH_2), 57.2 (CH), 60.6 (CH), 86.8 (C_6H_4), 104.0 (C_6H_4), 105.5 (C_6H_4), 127.1 (*p*-$(CH_3)C_6H_4SO_2$), 128.3 (*p*-$(CH_3)C_6H_4SO_2$), 138.0 (*p*-$(CH_3)C_6H_4SO_2$), 142.7 (*p*-$(CH_3)C_6H_4SO_2$) ppm. MS (ESI): *m*/*z* = 503 [M – Cl]$^+$. $C_{23}H_{33}ClN_2O_2RuS$ (538): calcd. C 51.34, H 6.18, N 5.21; found N 51,28, H 6.06, N 5.16.

[(C_6Me_6)Ru(TsN∩NH_2)Cl] (7): Yield 76%, 121.1 mg. ^{1}H NMR (400 MHz, $CDCl_3$, 21 °C): δ = 1.05 (m, CH_2), 1.23 (m, CH), 1.33 (m, CH_2), 1.44 (m, $CH–CH_2$), 1.80 (m, CH), 2.09 (s, $C_6(CH_3)_6$), 2.39 (s, *p*-$(CH_3)C_6H_4SO_2$), 7.28 (d, $^3J_{H,H}$ = 8 Hz, *p*-$(CH_3)C_6H_4SO_2$), 7.77 (d, $^3J_{H,H}$ = 8 Hz, *p*-$(CH_3)C_6H_4SO_2$) ppm. ^{13}C NMR (200 MHz, $CDCl_3$, 21 °C): δ = 15.1 ($C_6(CH_3)_6$), 21.4 (*p*-$(CH_3)C_6H_4SO_2$), 24.1 (CH_2), 24.1 (CH_2), 33.4 (CH_2), 34.2 (CH_2), 57.1 (CH), 61.1 (CH), 92.1 ($C_6(CH_3)_6$), 127.1 (*p*-$(CH_3)C_6H_4SO_2$), 128.1 (*p*-$(CH_3)C_6H_4SO_2$), 137.8 (*p*-$(CH_3)C_6H_4SO_2$), 143.0 (*p*-$(CH_3)C_6H_4SO_2$) ppm. MS (ESI): *m*/*z* = 531 [M – Cl]$^+$. $C_{25}H_{37}ClN_2O_2RuS$ (566.16): calcd. C 53.04, H 6.59, N 4.95; found N 52.96, H 6.48, N 5.12.

[(C_6H_4COOMe)Ru(TsN∩NH_2)Cl] (8): Yield 71%, 110.8 mg. ^{1}H NMR (400 MHz, $CDCl_3$, 25 °C): δ = 0.95 (m, CH_2), 1.18 (m, CH_2), 1.37 (m, CH), 1.65 (m, CH_2), 1.92 (m, CH), 2.26 (s, *p*-$(CH_3)C_6H_4SO_2$), 3.81 (s, $C_6H_5COOCH_3$), 5.26 (dd, $^3J_{H,H}$ = 7.5, *J* = 8 Hz, $C_6H_5COOCH_3$), 5.86 (t, $^3J_{H,H}$ = 8 Hz, $C_6H_5COOCH_3$), 6.32 (d, $^3J_{H,H}$ = 7.5 Hz, $C_6H_5COOCH_3$), 7.21 (d, $^3J_{H,H}$ = 7.3 Hz, *p*-$(CH_3)C_6H_4SO_2$), 7.68 (d, $^3J_{H,H}$ = 7.3 Hz, *p*-$(CH_3)C_6H_4SO_2$), ppm. ^{13}C NMR (200 MHz, $CDCl_3$, 25 °C): δ = 21.5 (*p*-$(CH_3)C_6H_4SO_2$), 24.4 (CH_2), 25.0 (CH_2), 31.7 (CH_2), 32.48 (CH_2), 52.9 ($C_6H_5COOCH_3$), 59.3 (CH), 60.01 (CH), 80.5 ($C_6H_5COOCH_3$), 82.1 ($C_6H_5COOCH_3$), 88.6 ($C_6H_5COOCH_3$), 90.0 ($C_6H_5COOCH_3$), 127.2 (2 CH), 128.3 (2 CH), 138.0 (*p*-$(CH_3)C_6H_4SO_2$), 142.8 (*p*-$(CH_3)C_6H_4SO_2$), 165.4 ($C_6H_5COOCH_3$) ppm. MS (ESI): *m*/*z* = 520 [M – Cl]$^+$. $C_{22}H_{30}ClN_2O_4RuS$ (555): calcd. C 47.60, H 5.45, N 5.05; found N 47.48, H 5.28, N 4.96.

Preparation of the Enantiopure Aqua Complex [(C_6Me_6)-Ru($H_2N\cap NH_2$)(OH_2)]$^{2+}$ (4) and [(C_6Me_6)Ru(TsN∩NH_2)(OH_2)]$^+$ (9) ($H_2N\cap NH_2$ = *trans*-1,2-diaminocyclohexane; TsHN∩NH_2 = *N*-tosyl-*trans*-1,2-diaminocyclohexane): To an aqueous solution of the appropriate chloro complex, [(arene)Ru($H_2N\cap NH_2$)Cl]$^+$ or [(arene)Ru(TsN∩NH_2)Cl], was added one equiv. of silver sulfate (0.30 mmol, 93.6 mg) in water (30 mL). After stirring for 1 h in the dark at room temperature the white precipitate (AgCl) was removed by filtration from the yellow solution. Solid $NaBF_4$ was added until saturation and a yellow precipitate appeared. The suspension was then centrifuged, the solid dissolved in dry acetonitrile (10 mL) and the resultant solution filtered through celite to eliminate the excess $NaBF_4$. After evaporation of the solvent, the tetrafluoroborate salt was obtained as a yellow-orange powder in quantitative yield.

[(C_6Me_6)Ru($H_2N\cap NH_2$)(OH_2)](BF_4)$_2$ ([4](BF_4)$_2$): Yield 98%, 167.6 mg. ^{1}H NMR (400 MHz, D_2O, 21 °C): δ = 1.09 (m, CH_2), 1.22 (m, CH), 1.63 (m, CH_2), 1.85 (m, CH), 1.89 (m, CH_2), 2.12 (s, $C_6(CH_3)_6$). ^{13}C NMR (200 MHz, D_2O, 21 °C): δ = 15.2 ($C_6(CH_3)_6$),

 © 2005 Wiley-VCH Verlag GmbH & Co. KGaA, Weinheim

24.0 (CH_2), 24.2 (CH_2), 33.5 (CH_2), 34.2 (CH_2), 57.0 (CH), 60.9 (CH), 92.1 ($C_6(CH_3)_6$). MS (ESI): m/z = 396 $[M]^+$. $C_{18}H_{34}B_2F_8N_2ORu$ (569.15): calcd. C 37.98, H 6.02, N 4.92; found N 38.06, H 6.08, N 4.95.

$[(C_6Me_6)Ru(TsN\cap NH_2)(OH_2)](BF_4)$ ([9]BF_4): Yield 97%, 185.4 mg. ^{1}H NMR (400 MHz, D_2O, 21 °C): δ = 1.03 (m, 2 CH_2), 1.21 (m, CH_2), 1.29 (m, CH), 1.39 (m, CH_2), 1.78 (m, CH), 2.11 (s, $C_6(CH_3)_6$), 2.42 (s, CH_3), 7.26 (d, $^3J_{H,H}$ = 7 Hz, C_6H_4), 7.74 (d, $^3J_{H,H}$ = 7 Hz, C_6H_4). ^{13}C NMR (200 MHz, D_2O, 21 °C): δ = 15.1 ($C_6(CH_3)_6$), 21.3 (p-$(CH_3)C_6H_4SO_2$), 24.1 (CH_2), 24.1 (CH_2), 33.3 (CH_2), 34.1 (CH_2), 57.2 (CH), 61.0 (CH), 92.0 (C_6Me_6), 127.0 (p-$(CH_3)C_6H_4SO_2$), 128.0 (p-$(CH_3)C_6H_4SO_2$), 137.8 (p-$(CH_3)C_6H_4SO_2$), 143.0 (p-$(CH_3)C_6H_4SO_2$). MS (ESI): m/z = 550 $[M]^+$. $C_{25}H_{39}BF_4N_2O_3RuS$ (635.53): calcd. C 47.25, H 6.19, N 4.41; found N 47.41, H 6.31, N 4.32.

Single Crystal X-ray Structure Analyses: A yellow crystal of compound [*R*,*R*-**3**][Cl]·2$CHCl_3$, obtained from recrystallisation of [*R*,*R*-**3**][Cl] with chloroform by slow evaporation, was mounted on a Stoe Imaging Plate Diffractometer System (Stoe & Cie, 1995) equipped with a one-circle φ goniometer and a graphite-monochromator. Data collection was performed at –100 °C using Mo-K_α radiation (λ = 0.71073 Å). 133 exposures (6 min per exposure) were obtained at an image plate distance of 70 mm with $0 < \varphi < 198°$ and with the crystal oscillating through 1.5° in φ. The resolution was D_{min}–D_{max} 12.45–0.81 Å. This compound crystallised in a noncentrosymmetric orthorhombic cell [$P2_12_12_1$, Flack parameter x = 0.00(5)]. The molecular formula of this compound is {[RuCl($C_{12}H_{18}$)($C_6H_{14}N_2$)]Cl($CHCl_3$)$_2$}. The structure was solved by direct methods using the program SHELXS-97[25] and refined by full-matrix least-squares on F^2 with SHELXL-97.[26] The positions of the protons N2H3 and N2H4 were derived from difference Fourier maps and refined with the N–H distance constrained to the theoretical value, the remaining hydrogen atoms were included in calculated positions and treated as riding atoms using SHELXL-97 default parameters. All non-hydrogen atoms, were refined anisotropically. A semi-empirical absorption correction was applied using MULABS (PLATON03, $T_{min.}$ = 0.804, $T_{max.}$ = 0.839). Selected crystallographic data for the complex are summarised in Table 3.

A yellow crystal of compound [*S*,*S*-**4**][BF_4]$_2$·H_2O, obtained by recrystallisation of [*S*,*S*-**4**][BF_4]$_2$ from water, was mounted on a Stoe Mark II-Imaging Plate Diffractometer System (Stoe & Cie, 2002) equipped with a graphite monochromator. Data collection was performed at –100 °C using Mo-K_α radiation (λ = 0.71073 Å). 171 exposures (6 min per exposure) were obtained at an image plate distance of 135 mm, 171 frames with φ = 0° and $0 < \omega < 171°$, with the crystal oscillating through 1° in ω. The resolution was $D_{min.} - D_{max.}$ 17.78–0.72 Å. This compound crystallises in a noncentrosymmetric space group with an orthorhombic cell ($P2_12_12_1$). The absolute structure could not be defined [Flack parameter = 0.16(12)]. The molecular formula of this compound is {[Ru($C_{12}H_{18}$)($C_6H_{14}N_2$)(H_2O)](BF_4)$_2$.(H_2O)}. As a result of the high disorder found in the anions and solvent molecules, the SQUEEZE instruction in PLATON03[27] was used to calculate the remaining potential solvent accessible area in the unit cell; 602.1 Å^3 was calculated containing about 173 electrons. Therefore, one BF_4 (4×41 electrons) per asymmetric unit was included in all further calculations. The structure was solved by direct methods using the program SHELXS-97[25] and refined by full-matrix least-squares on F^2 with SHELXL-97.[26] The hydrogen atoms were included in calculated positions and treated as riding atoms using SHELXL-97 default parameters. All non-hydrogen atoms were refined anisotropically.

Table 3. Crystallographic data for the structure of [*R*,*R*-**3**]-[Cl]·2$CHCl_3$.

Chemical formula	$C_{20}H_{34}Cl_8N_2Ru$
Formula mass	687.16
Crystal colour and shape	yellow block
Crystal size	0.30×0.20×0.10
Crystal system	orthorhombic
Space group	$P2_12_12_1$
a [Å]	9.04557(8)
b [Å]	15.5966(9)
c [Å]	20.1964(12)
α [°]	90
β [°]	90
γ [°]	90
V [Å^3]	2849.4(3)
Z	4
$D_{calcd.}$ [g·cm^{-3}]	1.602
μ (Mo-K_α) [mm^{-1}]	1.313
Temperature [K]	173(2)
F(000)	1392
Scan range [°]	$2< \theta < 25.75$
Cell refinement parameters reflections	8000
Reflections measured	22511
Independent reflections	5556
Reflections observed [$I > 2\sigma(I)$]	3385
R_{int}	0.1068
Final R indices [$I > 2\sigma(I)$]	0.0369
R indices (all data)	0.0820
Goodness-of-fit	0.747
Residual density: max., min. $\Delta\rho$ [e·Å^{-3}]	0.524, –1.200
The structure was refined on F_o^2: wR_2 = $\{\Sigma[w(F_o^2 - F_c^2)^2]/\Sigma w(F_o^2)^2\}^{1/2}$, where w^{-1} = $[\Sigma(F_o^2) + (aP)^2 + bP]$ and P = $[\max(F_o^2,0) + 2F_c^2]/3$	

Table 4. Crystallographic data for the structure of [*S*,*S*-**4**][BF_4]$_2$·H_2O.

Chemical formula	$C_{18}H_{36}B_2F_8N_2O_2Ru$
Formula mass	587.18
Crystal colour and shape	yellow block
Crystal size [mm]	0.25×0.18×0.10
Crystal system	orthorhombic
Space group	$P2_12_12_1$
a [Å]	10.4410(8)
b [Å]	15.2988(16)
c [Å]	15.9586(13)
α [°]	90
β [°]	90
γ [°]	90
V [Å^3]	2549.1(4)
Z	4
$D_{calcd.}$ [g cm^{-3}]	1.530
μ (Mo-K_α) [mm^{-1}]	0.690
Temperature [K]	173(2)
F(000)	1200
Scan range [°]	$1.84 < \theta < 25.18$
Cell refinement parameters reflections	8869
Reflections measured	15808
Independent reflections	4528
Reflections observed [$I > 2\sigma(I)$]	2748
R_{int}	0.1083
Final R indices [$I > 2\sigma(I)$]	0.0743
R indices (all data)	0.1122
Goodness-of-fit	0.968
Residual density: max., min. $\Delta\rho$ [e Å^{-3}]	0.774, –1.471
The structure was refined on F_o^2: wR_2 = $\{\Sigma[w(F_o^2 - F_c^2)^2]/\Sigma w(F_o^2)^2\}^{1/2}$, where w^{-1} = $[\Sigma(F_o^2) + (aP)^2 + bP]$ and P = $[\max(F_o^2,0) + 2F_c^2]/3$	

 © 2005 Wiley-VCH Verlag GmbH & Co. KGaA, Weinheim

tropically. Selected crystallographic data for the complex are summarised in Table 4.

CCDC-273653 (for [**3**]Cl·2CHCl$_3$) and -273652 (for [**4**](BF$_4$)$_2$·H$_2$O) contain supplementary crystallographic data for this paper. These data can be obtained free of charge via www.ccdc.cam.ac.uk/data_request/cif, by emailing data_request@ccdc.cam.ac.uk, or by contacting The Cambridge Crystallographic Data Centre, 12, Union Road, Cambridge CB2 1EZ, UK; Fax: +44-1223-336033.

Transfer Hydrogenation Catalysis: The transfer hydrogenation reactions of acetophenone (1 mmol), using **1–9** as their chloride (**1–3** and **5–8**) or sulfate (**4** and **9**) salts (10 μmol) with HCOONa (5 mmol), were carried out in water (5 mL) in an inert atmosphere. The reactions were quenched by cooling the mixtures to 0 °C. The products were extracted with Et$_2$O, filtered through silica and identified (and conversion and enantiomeric excesses were determined) by HPLC on a Chiracel OB-H capillary column for acetophenone and its Br and Me *para*-substituted derivatives or by gas chromatography on a 6-*tert*-butyl-2,3-diethyl-β-cyclodextrin (30% in 5% phenyl polymer) capillary column for the CF_3, NO_2 and MeO *para*-substituted substrates. The pH was monitored using a pH meter (Mettler Toledo InLab® 413) and adjusted using HNO_3 (for pH = 4 to 9) or NaOH (for pH = 10).

Acknowledgments

Financial support of this work from the Swiss National Science Foundation and a generous loan of ruthenium(III) chloride hydrate from the Johnson Matthey Research Centre are gratefully acknowledged.

[1] R. A. Zelonka, M. C. Baird, *Can. J. Chem.* **1972**, *50*, 3063–3072.
[2] Y. Hung, W.-J. Kung, H. Taube, *Inorg. Chem.* **1981**, *20*, 457–463.
[3] M. Stebler-Röthlisberger, W. Hummel, P.-A. Pittet, H.-B. Bürgi, A. Ludi, A. E. Merbach, *Inorg. Chem.* **1988**, *27*, 1358–1363.
[4] U. Koelle, *Coord. Chem. Rev.* **1994**, *135l136*, 623–650.
[5] M. Barton, J. D. Atwood, *J. Coord. Chem.* **1991**, *24*, 43–51.
[6] A. G. Samuelson, *Curr. Sci.* **1992**, *63*, 547–550.
[7] W. A. Herrmann, C. W. Kohlpaintner, *Angew. Chem., Int. Ed. Engl.* **1993**, *32*, 1524–1544.
[8] S. Ogo, T. Abura, Y. Watanabe, *Organometallics* **2002**, *21*, 2964–2969.
[9] S. Ogo, K. Uehara, T. abura, Y. Watanabe, S. Fukuzumi, *Organometallics* **2004**, *23*, 3047–3052.
[10] J. Canivet, L. Karmazin-Brelot, G. Süss-Fink, *J. Organomet. Chem.* **2005**, *690*, 3202–3211.
[11] X. Wu, X. Li, W. Hems, F. King, J. Xiao, *Org. Biomol. Chem.* **2004**, *2*, 1818–1821.
[12] Y. Ma, H. Liu, L. Chen, X. Cui, J. Zhu, J. Deng, *Org. Lett.* **2003**, *5*, 2103–2106.
[13] a) X. Li, X. Wu, W. Chen, F. E. Hancock, F. King, J. Xiao, *Org. Lett.* **2004**, *6*, 3321–3324; b) X. Wu, X. F. King, J. Xiao, *Angew. Chem. Int. Ed.* **2005**, *44*, 3407–3411.
[14] P. N. Liu, J. G. Deng, Y. Q. Tu, S. H. Wang, *Chem. Commun.* **2004**, 2070–2071.
[15] a) H. Y. Rhyoo, H.-J. Park, W. H. Suh, Y. K. Chung, *Tetrahedron Lett.* **2002**, *43*, 269–272; b) H. Y. Rhyoo, H.-J. Park, Y. K. Chung, *Chem. Commun.* **2001**, 2064–2065.
[16] A. Schlatter, M. K. Kundu, W.-D. Woggon, *Angew. Chem. Int. Ed.* **2004**, *43*, 6731–6734.
[17] a) M. Watanabe, K. Murata, T. Ikariya, *J. Org. Chem.* **2002**, *67*, 1712–1715; b) K. Okano, K. Murata, T. Ikariya, *Tetrahedron Lett.* **2000**, *41*, 9277–9280; c) R. Noyori, M. Yamakawa, S. Hashiguchi, *J. Org. Chem.* **2001**, *66*, 7931–7944; d) M. Yamakawa, H. Ito, R. Noyori, *J. Am. Chem. Soc.* **2000**, *122*, 1466–1478; e) K. Murata, K. Okano, M. Miyagi, H. Iwane, R. Noyori, T. Ikariya, *Org. Lett.* **1999**, *1*, 1119–1121; f) K. Matsumura, S. Hashiguchi, T. Ikariya, R. Noyori, *J. Am. Chem. Soc.* **1997**, *119*, 8738–8739; g) S. Hashiguchi, A. Fujii, K.-J. Haack, K. Matsumura, T. Ikariya, R. Noyori, *Angew. Chem., Int. Ed. Engl.* **1997**, *36*, 285–288; h) N. Uematsu, A. Fujii, S. Hashiguchi, T. Ikariya, R. Noyori, *J. Am. Chem. Soc.* **1996**, *118*, 4916–4917; i) A. Fujii, S. Hashiguchi, N. Uematsu, T. Ikariya, R. Noyori, *J. Am. Chem. Soc.* **1996**, *118*, 2521–2522.
[18] a) J. Hannedouche, G. J. Clarkson, M. Wills, *J. Am. Chem. Soc.* **2004**, *126*, 986–987; b) N. Debono, M. Besson, C. Pinel, L. Djakovitch, *Tetrahedron Lett.* **2004**, *45*, 2235–2238; c) Y. C. Chen, D. Xue, J. G. Deng, X. Cui, J. Zhu, Y. Z. Jiang, *Tetrahedron Lett.* **2004**, *45*, 1555–1558; d) D. J. Cross, I. Houson, A. M. Kawamoto, M. Wills, *Tetrahedron Lett.* **2004**, *45*, 843–846; e) D. Sterk, M. S. Stephan, B. Mohar, *Tetrahedron Lett.* **2004**, *45*, 535–537; f) P. N. Liu, P. M. Gu, F. Wang, Y. Q. Tu, *Org. Lett.* **2004**, *6*, 169–172; g) B. Basu, M. M. H. Bhuiyan, P. Das, I. Hossain, *Tetrahedron Lett.* **2003**, *44*, 8931–8934; h) M. Pasto, A. Riera, M. A. Pericas, *Eur. J. Org. Chem.* **2002**, 2337–2341; i) K. Everaere, A. Mortreux, M. Bulliard, J. Brussee, A. van der Gen, G. Nowogrocki, J.-F. Carpentier, *Eur. J. Org. Chem.* **2001**, 275–291; j) A. M. Maj, K. M. Pietrusiewicz, I. Suisse, F. Agbossou, A. Mortreux, *J. Organomet. Chem.* **2001**, *626*, 157–160; k) K. Everaere, A. Mortreux, J.-F. Carpentier, *Adv. Synth. Catal.* **2003**, *345*, 67–77; l) H. Y. Rhyoo, Y. A. Yoon, H. J. Park, Y. K. Chung, *Tetrahedron Lett.* **2001**, *42*, 5045–5048; m) D. G. I. Petra, P. C. J. Kamer, A. L. Spek, H. E. Schoemaker, P. W. N. M. van Leeuwen, *J. Org. Chem.* **2000**, *65*, 3010–3017; n) T. Mizugaki, Y. Kanayama, K. Ebitani, K. Kaneda, *J. Org. Chem.* **1998**, *63*, 2378–2381.
[19] a) J. Cossy, F. Eustache, P. I. Dalko, *Tetrahedron Lett.* **2001**, *42*, 5005–5007; b) C. Bubert, J. Blacker, S. M. Brown, J. Crosby, S. Fitzjohn, J. P. Muxworthy, T. Thorpe, J. M. J. Williams, *Tetrahedron Lett.* **2001**, *42*, 4037–4039; c) K. Püntener, L. Schwink, P. Knochel, *Tetrahedron Lett.* **1996**, *37*, 8165–8168; d) D. Sterk, M. S. Stephan, B. Mohar, *Tetrahedron: Asymmetry* **2002**, *13*, 2605–2608; e) B. Mohar, A. Valleix, J.-R. Desmurs, M. Felemez, A. Wagner, C. Miokowski, *Chem. Commun.* **2001**, 2572–2573; f) C. Z. Flores-Lòpez, L. Z. Flores-Lòpez, G. Aguirre, L. H. Hellberg, M. Parra-Hake, R. Somanathan, *J. Mol. Cat. A: Chemical* **2004**, *215*, 73–79.
[20] a) J. Balsells, L. Mejorado, M. Phillips, F. Ortega, G. Aguirre, R. Somanathan, P. J. Walsh, *Tetrahedron: Asymmetry* **1998**, *9*, 4135–4142b) K. Ng, R. Somanathan, P. J. Walsh, *Tetrahedron: Asymmetry* **2001**, *12*, 1719–1722.
[21] K. Murata, H. Konishi, M. Ito, T. Ikariya, *Organometallics* **2002**, *21*, 253–255.
[22] M. Yamakawa, I. Yamada, R. Noyori, *Angew. Chem. Int. Ed.* **2001**, *40*, 2818–2821.
[23] P. Pinto, G. Marconi, F. W. Heinemann, U. Zenneck, *Organometallics* **2004**, *23*, 374–380.
[24] A. Bennett, T.-N. Huang, T. W. Matheson, A. K. Smith, *Inorg. Synth.* **1982**, *21*, 74–78.
[25] G. M. Sheldrick, *Acta Crystallogr., Sect. A* **1990**, *46*, 467–473.
[26] G. M. Sheldrick, *SHELXL-97, Program for crystal structure refinement*, University of Göttingen, Germany, **1997**.
[27] A. L. Spek, *J. Appl. Crystallogr.* **2003**, *36*, 7–13.

Received: June 2, 2005
Published Online: September 26, 2005

Synthesis and Binding Properties of Dendritic Oxybathophenanthroline Ligands towards Copper(II)

Holger Stephan,*[a] Gerhard Geipel,[b] Gert Bernhard,[b] Peter Comba,[c] Gopalan Rajaraman,[c] Uwe Hahn,[d] and Fritz Vögtle*[d]

Keywords: Dendrimers / Phenanthroline / Copper(II) / Solvent extraction / Laser fluorescence spectroscopy

Dendritic oxybathophenanthroline ligands (generation 0 to 3) have been synthesized by treatment of 4,7-bis(4′-hydroxyphenyl)-1,10-phenanthroline with the corresponding Fréchet-type dendrons carrying a benzylic bromide function at the focal point. The complexation of copper(II) has been studied by liquid–liquid extraction using the radioisotope ^{64}Cu and time-resolved laser-induced fluorescence spectroscopy (TRLFS) in organic media indicating the formation of 1:3 complexes (Cu:dendritic ligand). Electronic and EPR spectroscopy were used to characterize the copper(II) chromophore, which is shown to have the expected distorted square-planar geometry with two phenanthroline donors coordinated to the copper(II) center. The third dendritic ligand therefore is proposed to be bound by secondary interactions. The stability constants of the 1:3 complexes were found to be in the order of log $K \approx 16$ in $CHCl_3$. On the other hand, increasing generation of the dendritic Fréchet-type branches leads to enhanced shielding of the copper ion from the environment. Additional information about this behaviour was obtained by the fluorescence lifetimes, which are much less influenced upon addition of copper(II) salt to solutions of the higher generation ligands.
(© Wiley-VCH Verlag GmbH & Co. KGaA, 69451 Weinheim, Germany, 2005)

Introduction

Derivatives of 1,10-phenanthroline and their metal complexes are of considerable interest in bioinorganic chemistry, biology and medicine.[1] Oxidative substitutions of 1,10-phenanthroline give versatile 5,6-disubstituted intermediates for the introduction of less bulky groups into the chelating unit. Such 5,6-substituted phenanthrolines play an important role as hydrophobic DNA intercalators (dipyridophenazine[2]), and most representatives of chromophore-containing derivatives base on this substitution pattern.[3] Also, metallodendrimers consisting of ruthenium(II) complexes with bisphenanthroline ligands bridged in the 5,6-positions have been described as robust, structurally rigid and well-defined nanoscopic complexes.[4] Dendritic modifications gain in importance as they open the way for tailoring nano dimension, solubility or complexation behaviour (complex stability, kinetics of formation) in manifold directions.[5] Due to steric reasons, the attachment of highly branched units particularly in the 4,7- and 3,8-positions of the 1,10-phenanthroline core seems to be suited in this respect (Scheme 1). In addition Fréchet-type dendrons being attached adjacent to the metal coordination centre (2,9-positions) have also been presented.[6]

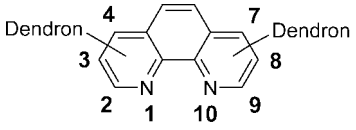

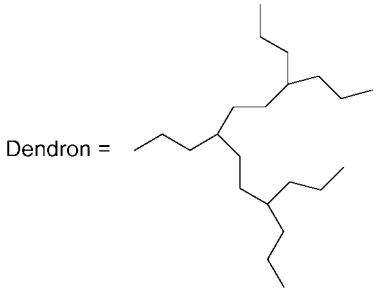

Scheme 1. Suitable positions for dendritic modification of 1,10-phenanthroline.

Ruthenium(II) complexes containing 4,7-bis(benzyloxy)-1,10-phenanthroline units[7] and also dendritic rutheni-

[a] Institut für Bioanorganische und Radiopharmazeutische Chemie, Forschungszentrum Rossendorf,
Postfach 510119, 01314 Dresden, Germany
Fax: +49-351-260-3232
E-mail: h.Stephan@fz-rossendorf.de
[b] Institut für Radiochemie, Forschungszentrum Rossendorf,
Postfach 510119, 01314 Dresden, Germany
[c] Anorganisch-Chemisches Institut, Universität Heidelberg,
Im Neuenheimer Feld 270, 69120 Heidelberg
[d] Kekulé-Institut für Organische Chemie und Biochemie, Universität Bonn,
Gerhard-Domagk-Str. 1, 53121 Bonn, Germany
Fax: +49-228-73-3495
E-mail: voegtle@uni-bonn.de
Supporting information for this article is available on the WWW under http://www.eurjic.org or from the author.

um(II) complexes bearing bis-substituted 2,2′-bipyridine moieties have been reported to exhibit interesting luminescence and redox properties.[8] Ruthenium(II) dendrimers containing carbazole-based chromophores as branches in the 4,7-positions of phenanthroline exhibit significant absorption and luminescence characteristics.[9] Complexation of appropriate metals with phenanthroline ligands carrying branched units in the 3,8-positions induces the formation of supramolecular self-assemblies with tuneable coordination geometry.[10] In this respect, we are interested to characterize the self-assembly system involving novel dendritic compounds and copper(II). Here, we report the synthesis of 1,10-phenanthroline ligands $\mathbf{L^{G0}}$–$\mathbf{L^{G3}}$ with attached Fréchet-type dendrons (generation 0 to 3) in the 4,7-positions (Scheme 2). The complexation behaviour of these hydrophobic dendritic oxybathophenanthroline derivatives towards Cu^{II} has been studied by liquid-liquid extraction experiments, time-resolved laser-induced fluorescence spectroscopy and electronic as well as EPR spectroscopy.

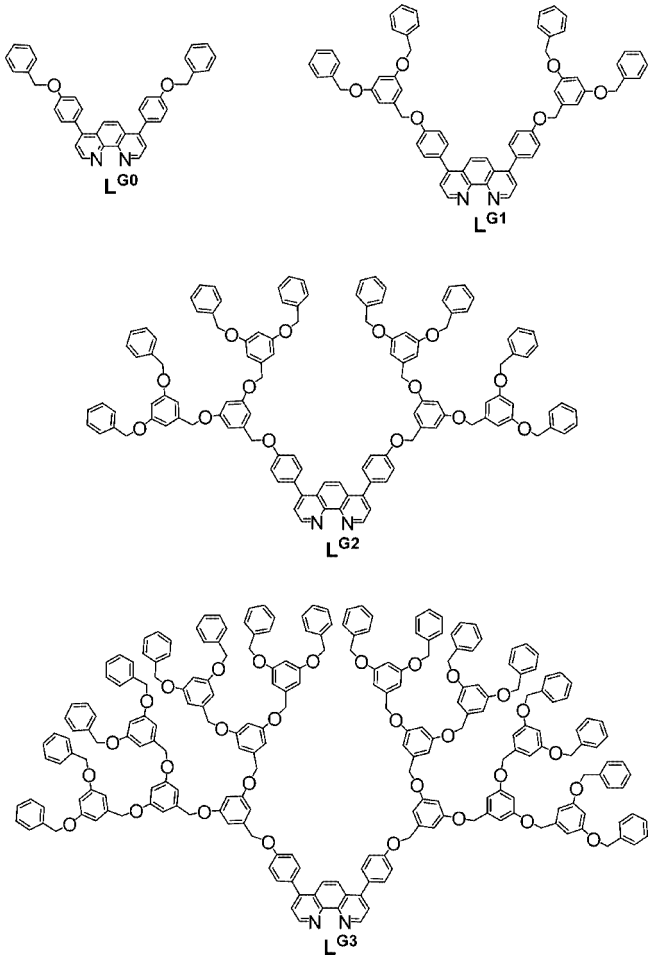

Scheme 2. Constitutions of the investigated dendritic OBP ligands $\mathbf{L^{G0}}$–$\mathbf{L^{G3}}$.

Results and Discussion

Syntheses

The parent phenanthroline ligand **8** with two *p*-hydroxyphenyl groups in the positions 4 and 7 was synthesized in a multi-step sequence (Scheme 3).[11] The β-chloro ketone **3** was prepared by a Friedel–Crafts acylation of 3-chloropropionyl chloride (**2**) and anisole (**1**) in dry 1,2-dichloroethane at 0 °C in the presence of anhydrous aluminum chloride to yield a colourless solid. The reaction of the β-chloro ketone **3** with *o*-nitroaniline (**4**) under the conditions of the Yale modification of the Skraup quinoline synthesis, gave the 4-substituted 8-nitroquinoline **5** as a yellow solid. The nitro group was subsequently reduced with tin(II) chloride dihydrate in dry ethanol under reflux conditions to form the 4-(4′-methoxyphenyl)-8-aminoquinoline **6** as a yellow solid. The 4,7-disubstituted 1,10-phenanthroline **7** was obtained by a second Skraup reaction of aminoquinoline **6** and β-chloro ketone **3** using again the conditions of the Yale modification. Demethylation of the bisanisyl-1,10-phenanthroline (**7**) was performed in dry dichloromethane at –20 °C by treatment with boron tribromide to yield the phenanthroline building block **8** carrying two hydroxy functions to which the various dendritic wedges could be attached.[12]

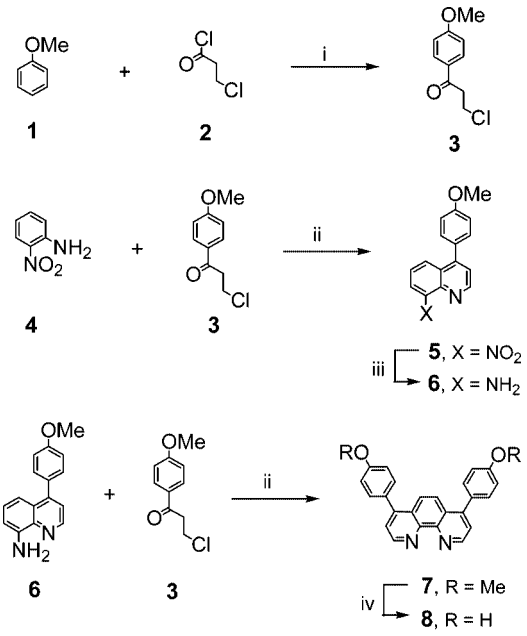

Scheme 3. Preparation of the 4,7-bis(*p*-hydroxyphenyl)-1,10-phenanthroline (**8**); (i) 0 °C, 3 h, 1,2-dichloroethane; (ii) addition of **3** at 100–120 °C, aq. As_2O_5 (80%), concd. H_3PO_4, 140 °C, 1 h, (iii) $SnCl_2{\cdot}2H_2O$, reflux, 4 h, EtOH, (iv) addition of BBr_3 at –20 °C, 2 h, room temp., CH_2Cl_2.

The dendritic oxybathophenanthroline (OBP) ligands $\mathbf{L^{G0}}$–$\mathbf{L^{G3}}$ were synthesized according to Scheme 4. Thus, 1 equiv. of 4,7-bis(4′-hydroxyphenyl)-1,10-phenanthroline (**8**) was dissolved in DMF and deprotonated by treatment with sodium hydride. Addition of 2 equiv. of benzyl bromide (**9**) or the corresponding dendritic benzyl bromides[13] **10**–**12** followed by purification on silica gel gave the products in medium to high yields as colourless solids in the case of the benzyl derivative, or as viscous oils for the higher generations. The medium yield for the benzyl-substituted derivative $\mathbf{L^{G0}}$ may be explained by the formation of a *N*,*O*-

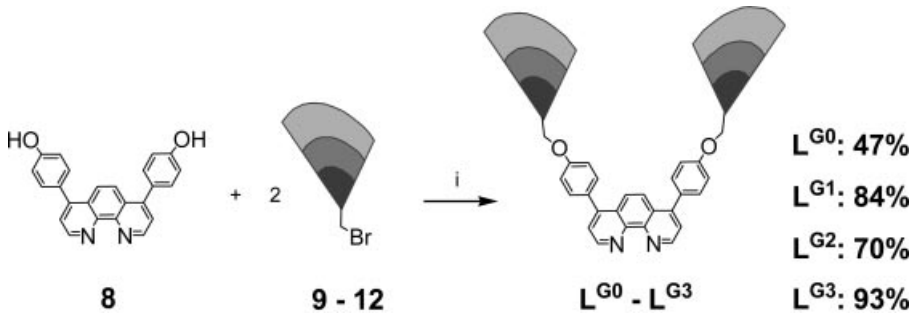

Scheme 4. Schematic representation for the preparation of the dendritic oxybathophenanthroline (OBP) ligands; (i) NaH (60% in paraffin), room temp., 1 d, DMF.

dibenzyl derivative, in which one nitrogen of the phenanthroline unit is substituted by a benzylic moiety.[14] Due to the small size of benzyl bromide such a cyclohexa-2,5-dienone derivative can be formed in higher quantities. But for the dendritic generations with an increased steric demand this side reaction seems to be less favoured and leads therefore to higher yields. Additionally, the purification of $\mathbf{L^{G0}}$ on silica gel was more difficult as a result of the higher polarity of the phenanthroline unit. Substitution of the phenanthroline building block **8** with dendritic units of a various size leads to an increased lipophilicity of the ligands and thus to easier purification by column chromatography. The structures of all new oxybathophenanthroline ligands could be readily deduced from ^1H and ^{13}C NMR spectra as well as from mass spectrometric analysis.

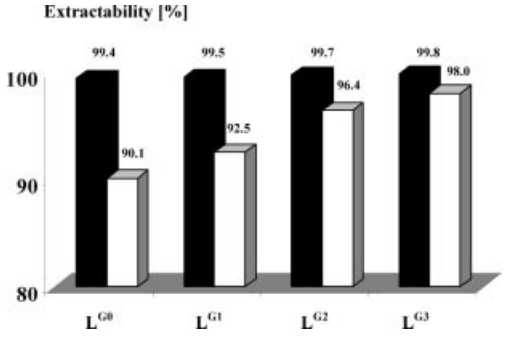

Figure 1. Extractability of copper(II) by dendritic OBP ligands $\mathbf{L^{G0}}$–$\mathbf{L^{G3}}$; black bars $c_{Cu(NO_3)_2} = 1\times10^{-4}$ M, $c_{HPic} = 5\times10^{-3}$ M, pH = 5.3 (MES/NaOH); white bars $c_{Cu(NO_3)_2} = 1\times10^{-4}$ M, pH = 5.3 (MES/NaOH); $c_{\text{dendritic ligand}} = 1\times10^{-3}$ M in $CHCl_3$, time = 30 minutes.

Liquid–Liquid Extraction

1,10-Phenanthroline is known to form strong complexes with copper(II). Depending on the experimental conditions, the resulting complexes may have 1:1, 1:2 or 1:3 stoichiometry (metal/ligand), and show different coordination geometries.[15] Due to the Jahn–Teller lability 1:3 stoichiometry (pseudo-octahedral coordination geometry) is unlikely with the rigid phenanthroline-type chelates. By virtue of the high lipophilicity of the dendritic oxybathophenanthrolines, liquid–liquid extraction experiments have been chosen to characterise the binding properties of the OBP ligands $\mathbf{L^{G0}}$–$\mathbf{L^{G3}}$ towards Cu^{II} in the aqueous-organic system $Cu(NO_3)_2$/buffer/H_2O/dendritic ligand/$CHCl_3$. Precise data of the efficiency of complex formation and the stoichiometry of the copper(II) complexes with the ligands investigated were obtained using the radiotracer technique with ^{64}Cu as radioisotope.[16] First extraction experiments have been performed in the presence of the lipophilic picrate anion (Figure 1). In this case the extractability of Cu^{II} is almost quantitative for all ligands. But also in the absence of the picrate anion, Cu^{II} is very efficiently extracted into the organic phase. Here, a dendritic effect is clearly visible caused most likely by the increasing lipophilicity of the complexes formed.

Interestingly, a rapid attainment of extraction equilibrium (within few minutes) was observed. Even in the case of the most bulky ligand $\mathbf{L^{G3}}$ the equilibrium was attained after 10 minutes.[17] As expected, the Cu^{II} extraction is enhanced with increasing pH accompanied by decreasing protonation of the chelating moiety.[18] Information about the overall stoichiometry of the complexation was obtained by measuring the distribution ratio D_{Cu}[19] as a function of the ligand concentration in the organic solvent (Figure 2).

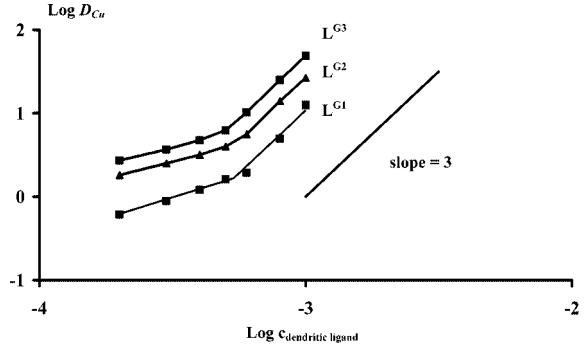

Figure 2. Variation of log D_{Cu} with ligand concentration for the extraction of copper(II) with dendritic OBP ligands $\mathbf{L^{G1}}$–$\mathbf{L^{G3}}$; $c_{Cu(NO_3)_2} = 1\times10^{-4}$ M, pH = 5.3 (MES/NaOH), time = 30 minutes, $c_{\text{dendritic ligand}} = 2\times10^{-4}$ M to 1×10^{-3} M in $CHCl_3$.

 © 2005 Wiley-VCH Verlag GmbH & Co. KGaA, Weinheim

Surprisingly, in all cases, the slopes of the lines in the log D_{Cu}/logc_{ligand} plots were 3 if the ligand excess is high enough compared to the copper concentration. This finding indicates the formation of 1:3 complexes (Cu^{II}: dendritic ligand).[20] However, this is not an indication for three phenanthroline donors, coordinated to the copper(II) centers (see below).[21]

Luminescence Characteristics

The fluorescence properties of the ligands $\mathbf{L^{G0}}$–$\mathbf{L^{G3}}$ are summarized in Table 1. The time-resolved fluorescence spectrum of $\mathbf{L^{G0}}$ is shown in Figure 3 as an example.

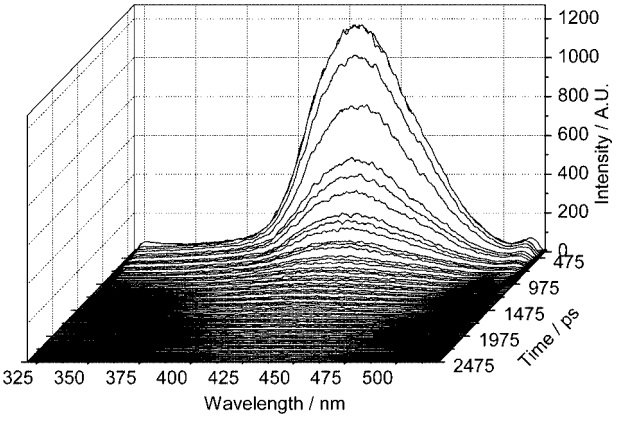

Figure 3. Time-resolved fluorescence spectrum of the dendritic OBP ligand $\mathbf{L^{G0}}$, $c_{dendritic\ ligand} = 1 \times 10^{-5}$ M in $CHCl_3$.

For all four ligands a two-exponential fluorescence decay behaviour was observed in the absence of Cu^{II}. The component with the shorter fluorescence decay time shows the higher fluorescence intensity. The maximum of this fluorescence emission is located at ca. 430 nm. The fluorescence maximum for the second emitting component was found at ca. 420 nm. Additionally the fluorescence decay time of this component depends on the size of the dendritic wedges. Going to higher generations the fluorescence decay times decrease. This may be due to an increasing number of deactivation channels.

Addition of copper(II) to the solution of the ligands leads to a decrease in fluorescence intensity (static fluorescence quenching). As expected, the complexes formed do not show any fluorescence. The fluorescence with the shorter fluorescence lifetime was mainly influenced by the formation of the complexes (see Table 1 in the Supporting Information; for details see the footnote on the first page of this article). At Cu^{II}/ligand ratios of 1:3 the fluorescence of the 430 nm component disappears. This behaviour is in agreement with the results of the liquid–liquid extraction (1:3 complexes). The ligand $\mathbf{L^{G2}}$ shows a somewhat different behaviour. Here, the fluorescence disappears at a 1:2 ratio of Cu^{II} to ligand. In a separate measurement with a metal to ligand ratio of 1:3 only a monoexponential fluorescence decay with the longer fluorescence lifetime was observed. This is strong evidence that also a 1:3 adduct is formed.

In addition the fluorescence intensities were used to confirm complex formation. Due to the observation that mainly the fluorescence intensity of the component with the shorter fluorescence lifetime is influenced by the complex formation these data were evaluated for the stability of the complexes. The species concentration can be calculated from the fluorescence intensities of the free ligand. The resulting stability constants are summarized in Table 2.

Table 2. Stability constants of the formed Cu^{II} complexes.

Ligand	Metal	Stoichiometry	log K	Solvent
$\mathbf{L^{G0}}$	Cu^{II}	3:1	16.4 ± 0.8	$CHCl_3$
$\mathbf{L^{G1}}$	Cu^{II}	3:1	17.5 ± 0.9	$CHCl_3$
$\mathbf{L^{G2}}$	Cu^{II}	3:1	15.6 ± 0.7	$CHCl_3$
$\mathbf{L^{G3}}$	Cu^{II}	3:1	16.6 ± 0.7	$CHCl_3$

It was found that the fluorescence decay times of the longer decay component decrease with increasing size of the dendritic branches if no copper(II) is added. The addition of copper(II) influences the fluorescence lifetime (Supporting Information, Table 2). However, this effect decreases with increasing size of the dendritic wedge. The longer fluorescence lifetime as function of the cooper(II) concentration shows no clear behaviour. For the ligand $\mathbf{L^{G0}}$ a clear dynamic quench effect was observed, which is much less remarkable for the ligand $\mathbf{L^{G1}}$. The ligand $\mathbf{L^{G2}}$ shows an increase of the fluorescence lifetime. For the ligand $\mathbf{L^{G3}}$ addition of copper(II) resulted in much less influence. However, also intermediate deviations from this trend were observed. A profound explanation of this behaviour is not possible at this time. The fluorescence lifetime of the second component with the shorter lifetime is also influenced by the addition of Cu^{II}. This behaviour can be explained by a less pronounced dynamic quenching effect of the Cu^{II} or in reverse, that the increasing generation of the dendritic structure leads to an increased shielding effect on the deexcitation channels of the copper(II).

Geometry of the Copper(II) Chromophores

Due to the Jahn–Teller lability of the d^9 copper(II) ions the formation of stable $[Cu(L)_3]^{2+}$ complexes, where L is a

Table 1. Fluorescence properties of the dendritic OBP ligands.

Ligand	Center of gravity (1) nm	Fluorescence decay time (1) ps	Center of gravity (2) nm	Fluorescence decay time (2) s	Intensity ratio (1)/(2)	Intensity relative to L^0
$\mathbf{L^{G0}}$	430.1	160 ± 2	423.7	1860 ± 10	22.6	1
$\mathbf{L^{G1}}$	430.3	270 ± 2	417.0	1080 ± 10	3.3	1.45
$\mathbf{L^{G2}}$	431.8	240 ± 2	419.9	990 ± 10	3.6	1.57
$\mathbf{L^{G3}}$	430.1	260 ± 2	417.2	890 ± 10	3.3	1.05

 © 2005 Wiley-VCH Verlag GmbH & Co. KGaA, Weinheim

bidentate ligand, is not likely, specifically with L = 1,10-phenanthroline derivatives. One would rather expect the stabilization of a distorted square planar (tetragonally distorted octahedral or square pyramidal) chromophore derived from $[Cu(L)_2(X)_n]^{2+}$, where X may be OH_2 and n = 0, 1, 2. The third dendritic phenanthroline ligand found in the extraction and luminescence experiments may then be bound by secondary interactions (outer sphere coordination) to the distorted square-planar complex. The type of chromophore was analyzed by electronic and EPR spectroscopy and supported by molecular mechanics modeling.

Solutions for the UV/Vis-NIR and EPR spectra ($\mathbf{L^{G0}}$ and $\mathbf{L^{G3}}$) were prepared as those for the liquid–liquid extractions ($[Cu(trif)_2]^{2+}$, H_2O/L, $CHCl_3$; $[Cu^{2+}] \approx 1.0$ mM, $[Cu^{2+}]$:[L] = 1:3). The electronic spectra (Supporting Information) show two broad transitions centered at approx. 708 nm and 925 nm for $\mathbf{L^{G0}}$, and 734 nm and 925 nm for $\mathbf{L^{G3}}$, respectively. The lower energy band is due to the $d_{z^2} \rightarrow d_{x^2-y^2}$ transition and was not well resolved in our spectra (relatively low concentration), the feature at higher energy is due to transitions from d_{xy}, d_{xz}, d_{yz} and therefore is, as expected, very broad. While $[Cu(phen)_3]^{2+}$ (phen = 1,10-phenanthroline) was reported to have transitions at 680 nm and 1250 nm,[22] $[Cu(phen)_2(OH_2)_n]^{2+}$ (n = 0, 1, 2) has transitions at 750–800 nm and ca. 980 nm.[22,23] Addition of up to 3 equiv. of phen did not change the spectroscopic parameters. The assignment of these transitions to CuN_4O_n (n = 0, 1, 2) chromophores is supported by EPR spectra (identical solutions, T = 100 K). The analysis of the spin Hamiltonian parameters (g_x = 2.06, g_y = 2.08, g_z = 2.22, $A_x = A_y$ = 45 G, A_z = 128 G) supports this conclusion (experimental and simulated spectra are given in the Supporting Information): the major features are similar to those reported for the EPR spectra of distorted square planar $[Cu(phen)_2]^{2+}$-type chromophores,[24] the minor features are similar to those of $[Cu(phen)_2(OH_2)](NO_3)_2$ (g_x = 2.02, g_y = 2.13, g_z = 2.23).[25]

The conclusion that the extracted copper(II) species are $[Cu(L)_2(OH_2)_n]^{2+}\cdot L$ is supported by strain energy minimized structures, using the MOMEC program[26] and force field[27] (for structural data and plots of the optimized structures see Supporting Information). The optimized structures ($[Cu(L)_2(OH_2)_2]^{2+}$) have Cu–N distances (ca. 1.97 Å) and tetrahedral distortions of the CuN_4 chromophores (ca. 42°) which are very similar to those of reported $[Cu(phen)_2(OH_2)_n]^{2+}$-type structures.[28]

Conclusions

An efficient synthetic strategy has been developed for the preparation of new dendritic ligands consisting of a 1,10-phenanthroline core unit to which hydrophobic polybenzyl ether dendrons are attached in the 4,7-positions. These oxybathophenanthroline ligands rapidly form very stable 1:3 adducts in organic media with Cu^{II}. Electronic and EPR spectroscopy suggest that two of the ligands are coordinated to copper(II) by the phenanthroline donors, the third ligand probably is bound by secondary interactions. The dendritic ligands are capable to extract Cu^{II} with high efficiency. For extraction experiments a dendritic effect was found most likely caused by the increasing lipophilicity when going to higher generations. As obtained by titration experiments using TRLFS, the dendritic ligands $\mathbf{L^{G0}}$–$\mathbf{L^{G3}}$ form strong 1:3 adducts with copper(II) in $CHCl_3$ ($\log K \approx$ 16). Studies of the fluorescence lifetimes show an increased shielding effect with increasing generation of the dendritic wedge attached to the phenanthroline unit. The results obtained for the copper(II) complexation with hydrophobic dendritic phenanthroline ligands have encouraged us to develop water-soluble analogues having targeting units at the periphery in view of binding and selective transport of the diagnostically and therapeutically relevant radioisotopes ^{64}Cu and ^{67}Cu.

Experimental Section

General Remarks: All starting materials were purchased from commercial sources and used without further purification. The dendritic bromides[13] **9**–**12** and the 4,7-(bisanisyl)phenanthroline[11] (**7**) have been prepared according to literature. The solvents were dried using standard techniques. Reactions were monitored by thin-layer chromatography using TLC plates pre-coated with silica gel $60F_{254}$ (Merck) and compounds detected by UV light (254 nm). Column chromatography was carried out using silica gel (Merck 15101). Melting points were determined with a Reichert Thermovar microscope and were not corrected. ^1H and ^{13}C NMR spectra were recorded using Avance 300 and AM 400 MHz Bruker instruments; the solvent signal was used for internal calibration. Mass spectra were recorded using a MS-50 from A.E.I., Manchester, GB (EI), a Concept 1H from Kratos Analytical Ltd., Manchester, GB (FAB), or a MALDI-TofSpec-E from MICROMASS, GB (MALDI). Electronic spectra were recorded with a JASCOV-570 UV/Vis-NIR spectrophotometer and EPR spectra were obtained from a Bruker ELEXSYS-E-500 instrument (X-band); spin-Hamiltonian parameters were obtained by simulation of the spectra with XSophe (version 1.1.4).[29]

3-Chloro-1-(4′-methoxyphenyl)propan-1-one (3): To a suspension of powdered aluminum chloride (7.23 g, 54.2 mmol) in dry 1,2-dichloroethane (40 mL) were added slowly 3-chloropropionyl chloride (**2**) (4.55 mL, 47.4 mmol) at 0 °C and anisole (**1**) (4.91 mL, 45.2 mmol) under cooling with water. The orange solution was stirred at room temp. for 3 h and left standing for about 12 h. The dark orange solution was poured onto ice (50 g), the organic phase separated and the aqueous phase extracted two times with CH_2Cl_2. The collected organic phases were washed with water, several times with aqueous NaOH (2%, 50 mL) until the organic phase did not turn back to yellow, and then twice with water. The organic phase was dried with $MgSO_4$ and the solvent removed under reduced pressure. Purification by gradient column chromatography [SiO_2, CH_2Cl_2/petroleum ether (40/60), 20:1 to CH_2Cl_2] gave 9.23 g (97% yield) of a colourless solid. R_f = 0.68 (CH_2Cl_2); m.p. 63–64 °C. ^1H NMR (300 MHz, $CDCl_3$, 25 °C): δ = 3.29 (t, J = 7 Hz, 2 H, CH_2Cl), 3.75 (s, 3 H, OCH_3), 3.80 (t, J = 7 Hz, 2 H, $COCH_2$), 6.82 (AA′ part of the AA′BB′ system, 2 H, H_{ar}), 7.82 (BB′ part of the AA′BB′ system, 2 H, H_{ar}) ppm. ^{13}C NMR (75 MHz, $CDCl_3$, 25 °C): δ = 39.0, 40.9, 55.5, 113.9, 129.6, 130.4, 163.9, 195.2 ppm. MS (EI, 70 eV): m/z (%) = 198 (12) [$M^{+\cdot}$].

 © 2005 Wiley-VCH Verlag GmbH & Co. KGaA, Weinheim

4-(4′-Methoxyphenyl)-8-nitroquinoline (5): To a solution of *o*-nitroaniline (**4**) (1.38 g, 10.0 mmol), aq. As_2O_5 (3.37 g, 80%) and concd. H_3PO_4 (9 mL) was added portionwise β-chloro ketone **3** (2.48 g, 12.5 mmol) at 100 °C in 10 min so that the temperature is not rising above 120 °C. The solution was stirred at 120 °C for 5 min and then heated to 140 °C for 1 h. The deep red solution was cooled to room temp., poured onto CH_2Cl_2 (150 mL) and water (100 mL), and neutralized with aq. KOH (30%). The aqueous phase was extracted several times with CH_2Cl_2, the collected organic phase dried with $MgSO_4$, and the solvent removed under reduced pressure. Column chromatography (SiO_2, CH_2Cl_2) gave 1.56 g (56%) of a yellow coloured solid. R_f = 0.40 (CH_2Cl_2); m.p. 134–135 °C. ^{1}H NMR (400 MHz, $CDCl_3$, 25 °C): δ = 3.95 (s, 3 H, CH_3), 7.09 (AA′ part of the AA′BB′ system, 2 H, H_{ar}), 7.41 (BB′ part of the AA′BB′ system, 2 H, H_{ar}), 7.43 (d, J = 4 Hz, 1 H, H_{ar}), 7.55 (dd, J = 9, J = 8 Hz, 1 H, H_{ar}), 7.98 (dd, J = 8, J = 1 Hz, 1 H, H_{ar}), 8.17 (dd, J = 9, J = 1 Hz, 1 H, H_{ar}), 9.02 (d, J = 4 Hz, 1 H, H) ppm. ^{13}C NMR (75 MHz, $CDCl_3$, 25 °C): δ = 55.6, 114.5, 122.9, 123.4, 125.1, 128.1, 129.2, 130.2, 131.0, 140.2, 148.7, 149.0, 152.1, 160.5 ppm. MS (EI, 70 eV): *m*/*z* (%) = 280 (100) [$M^{+\cdot}$].

8-Amino-4-(4′-methoxyphenyl)quinoline (6): A solution of nitrochinoline **5** (1.15 g, 4.1 mmol) and tin(II) chloride dihydrate (2.78 g, 12.3 mmol) in dry ethanol (30 mL) was refluxed for 4 h. The solution was cooled to room temp. and made alkaline with concd. ethanolic NaOH. The precipitate was filtered off, and the solvent removed under reduced pressure. Purification by gradient column chromatography (SiO_2, CH_2Cl_2 to CH_2Cl_2/methanol, 30:1) gave 0.91 g (89%) of a yellow solid. R_f = 0.18 (CH_2Cl_2); m.p. 148–149 °C. ^{1}H NMR (400 MHz, $CDCl_3$, 25 °C): δ = 3.78 (s, 3 H, CH_3), 4.95 (br. s, 2 H, NH_2), 6.81 (dd, J = 6, J = 3 Hz, 1 H, H_{ar}), 6.93 (AA′ part of the AA′BB′ system, 2 H, H_{ar}), 7.16 (m, 3 H, H_{ar}), 7.24 (BB′ part of the AA′BB′ system, 2 H, H_{ar}), 8.62 (d, J = 4 Hz, 1 H, H_{ar}) ppm. ^{13}C NMR (100 MHz, $CDCl_3$, 25 °C): δ = 55.4, 109.9, 114.0, 114.2, 121.7, 127.2, 127.6, 130.8, 131.0, 138.9, 144.3, 147.0, 148.1, 159.8 ppm. MS (EI, 70 eV): *m*/*z* (%) = 250 (100) [$M^{+\cdot}$].

4,7-Bis(4′-methoxyphenyl)-1,10-phenanthroline (7): To a solution of the aminoquinoline **6** (1.43 g, 5.7 mmol), aq. As_2O_5 (1.61, 80%) and concd. H_3PO_4 (9 mL) was added portionwise the β-chloro ketone **3** (1.58 g, 7.1 mmol) at 100 °C in 10 min so that the temperature is not rising above 120 °C. The solution was stirred at 120 °C for 5 min and then heated to 140 °C for 1 h. The deep red reaction mixture was cooled to room temp., poured onto CH_2Cl_2 (150 mL) and water (100 mL) and neutralized with aqueous NaOH (20%). The aqueous phase was extracted several times with CH_2Cl_2, the collected organic phase dried with $MgSO_4$ and the solvent removed under reduced pressure. Column chromatography (SiO_2, CH_2Cl_2) yielded a brownish solid (1.50 g, 67%). R_f = 0.35 (CH_2Cl_2/MeOH, 5:1); m.p. 208–209 °C. ^{1}H NMR (400 MHz, 1:1 $CDCl_3$/CD_3OD, 25 °C): δ = 2.41 (s, 6 H, CH_3), 5.58 (AA′ part of the AA′BB′ system, 4 H, H_{ar}), 5.95 (BB′ part of the AA′BB′ system, 4 H, H_{ar}), 6.10 (d, J = 5 Hz, 2 H, H_{ar}), 6.40 (s, 2 H, H_{ar}), 7.62 (d, J = 5 Hz, 2 H, H_{ar}) ppm. ^{13}C NMR (100 MHz, $CDCl_3$, 25 °C): δ = 54.9, 114.0 123.6, 123.9, 126.5, 129.7, 130.8, 146.2, 148.6, 149.1, 160.1 ppm. MS (EI, 70 eV): *m*/*z* (%) = 392 (100) [$M^{+\cdot}$].

4,7-Bis(4′-hydroxyphenyl)-1,10-phenanthroline (8): To a solution of 4,7-bis(4′-methoxyphenyl)-1,10-phenanthroline (**7**) (6.77 g, 17.3 mmol) in dry dichloromethane (90 mL) was added dropwise boron tribromide (4.91 mL, 51.8 mmol) at –20 °C. The red suspension was stirred at room temp. for 2 h, poured onto ice and let stand still for 30 min. The solution was neutralized with aq. KOH (5%), the organic phase separated and the aqueous phase extracted several times with 10:1 CH_2Cl_2/MeOH. The collected organic phase was dried with $MgSO_4$ and the solvent removed under reduced pressure. The remaining solid was three times suspended in CH_2Cl_2 and filtered. The solid was dried to yield a yellow solid (3.20 g, 47%). M.p. 285–288 °C. ^{1}H NMR (400 MHz, [D_6]DMSO, 25 °C): δ = 6.98 (AA′ part of the AA′BB′ system, 4 H, H_{ar}), 7.41 (BB′ part of the AA′BB′ system, 4 H, H_{ar}), 7.65 (d, J = 5 Hz, 2 H, H_{ar}), 7.92 (s, 2 H, H_{ar}), 9.08 (d, J = 5 Hz, 2 H, H_{ar}) ppm. ^{13}C NMR (100 MHz, [D_6]DMSO, 25 °C): δ = 116.1, 124.0, 124.3, 126.3, 128.0, 131.5, 145.9, 148.7, 149.5, 158.6 ppm. MS (EI, 70eV): *m*/*z* (%) = 392 (100) [$M^{+\cdot}$].

General Procedure for the Preparation of Dendritic OBP Ligands (L^{G0}–L^{G3}): To a suspension of 4,7-bis(4′-hydroxyphenyl)-1,10-phenanthroline (**8**) (0.1 mmol) in dry DMF (10 mL) was added NaH (0.22 mmol, 60% in paraffin). The reaction mixture turned to red. After 5 min a solution of the corresponding bromides[13] **9**–**12** (0.21 mmol) in dry DMF (5 mL) was added, and the suspension stirred for 1 d at room temp. The residual NaH was deactivated by slow addition of water at 0 °C. CH_2Cl_2 (30 mL) was added, the suspension neutralized with aq. HCl (2 N), and the aqueous phase extracted several times with CH_2Cl_2. The collected organic phase was washed with concd. aq. $NaHCO_3$, water, dried with $MgSO_4$ and the solvent removed under reduced pressure. The crude product was purified by column chromatography on silica gel.

4,7-Bis(4′-benzyloxyphenyl)-1,10-phenanthroline (L^{G0}): 4,7-Bis(4′-hydroxyphenyl)-1,10-phenanthroline (**8**) (100.0 mg, 0.27 mmol), benzyl bromide **9** (98.6 mg, 0.58 mmol), NaH (24.2 mg, 0.60 mmol, 60% in paraffin) in dry DMF (15 mL). Column chromatography (SiO_2, CH_2Cl_2/MeOH, 50:1 to 20:1) gave a colourless solid (69.8 mg, 47%). R_f = 0.42 (CH_2Cl_2/MeOH, 5:1); m.p. 230–231 °C. ^{1}H NMR (400 MHz, $CDCl_3$): δ = 5.12 (s, 4 H, OCH_2), 7.10 (AA′ part of the AA′BB′ system, 4 H, H_{ar}), 7.30–7.47 (m, 14 H, H_{ar}), 7.52 (d, J = 5 Hz, 2 H, H_{ar}), 7.85 (s, 2 H, H_{ar}), 9.16 (d, J = 5 Hz, 2 H, H_{ar}) ppm. ^{13}C NMR (100 MHz, $CDCl_3$): δ = 70.2, 115.1, 123.5, 124.0, 126.5, 127.5, 128.1, 128.7, 130.6, 131.0, 136.7, 147.0, 148.1, 149.7, 159.2 ppm. MS (FAB, NBA): *m*/*z* (%) = 545.2 ([M + H]$^+$, 100), 454.1 (12), 307.0 (18).

4,7-Bis{4′-[3′′,5′′-bis(benzyloxy)benzyloxy]phenyl}-1,10-phenanthroline (L^{G1}): 4,7-Bis(4′-hydroxyphenyl)-1,10-phenanthroline (**8**) (120.0 mg, 0.33 mmol), dendritic Fréchet-type G1 bromide **10** (256.1 mg, 0.69 mmol), NaH (29.0 mg, 0.73 mmol, 60% in paraffin) in dry DMF (15 mL). Column chromatography (SiO_2, CH_2Cl_2/MeOH, 50:1 to 20:1) gave a brownish viscous oil (269.5 mg, 84%). R_f = 0.55 (CH_2Cl_2/MeOH, 10:1). ^{1}H NMR (400 MHz, $CDCl_3$): δ = 5.05 (s, 8 H, OCH_2), 5.08 (s, 4 H, OCH_2), 6.58 (t, J = 2 Hz, 2 H, H_{ar}), 6.72 (d, J = 2 Hz, 4 H, H_{ar}), 7.10 (AA′-part of the AA′BB′-system, 4 H, H_{ar}), 7.26–7.47 (m, 24 H, H_{ar}), 7.51 (d, J = 5 Hz, 2 H, H_{ar}), 7.90 (s, 2 H, H_{ar}), 9.18 (d, J = 5 Hz, 2 H, H_{ar}) ppm. ^{13}C NMR (100 MHz, $CDCl_3$): δ = 70.1, 70.2, 101.7, 106.5, 115.1, 123.5, 124.0, 126.5, 127.6, 128.6, 130.6, 131.0, 136.8, 139.3, 147.0, 148.1, 149.7, 159.1, 160.3 ppm. MS (FAB, NBA): *m*/*z* (%) = 969.5 ([M + H]$^+$, 60), 307.1 (100).

4,7-Bis(4′-{3′′,5′′-bis[3′′′,5′′′-bis(benzyloxy)benzyloxy]benzyl}-phenyl)-1,10-phenanthroline (L^{G2}): 4,7-Bis(4′-hydroxyphenyl)-1,10-phenanthroline (**8**) (70.0 mg, 0.19 mmol), dendritic Fréchet-type G2 bromide **11** (325.9 mg, 0.40 mmol), NaH (16.9 mg, 0.42 mmol, 60% in paraffin) in dry DMF (15 mL). Column chromatography (SiO_2, CH_2Cl_2/MeOH, 50:1 to 20:1) gave a brownish viscous oil (246.0 mg, 70%). R_f = 0.51 (CH_2Cl_2/MeOH, 10:1). ^{1}H NMR (400 MHz, $CDCl_3$): δ = 4.86 (s, 8 H, OCH_2), 4.89 (s, 16 H, OCH_2), 4.96 (s, 4 H, OCH_2), 6.58 (t, J = 2 Hz, 6 H, H_{ar}), 6.57 (d, J = 2 Hz, 8 H, H_{ar}), 6.59 (d, J = 2 Hz, 4 H, H_{ar}), 7.00 (AA′ part of the AA′BB′ system, 4 H, H_{ar}), 7.17–7.28 (m, 40 H, H_{ar}), 7.12 (BB′

 © 2005 Wiley-VCH Verlag GmbH & Co. KGaA, Weinheim

part of the AA′BB′ system, 4 H, H_{ar}), 7.40 (d, J = 5 Hz, 2 H, H_{ar}), 7.88 (s, 2 H, H_{ar}), 9.08 (d, J = 5 Hz, 2 H, H_{ar}) ppm. ^{13}C NMR (100 MHz, $CDCl_3$): δ = 70.0, 70.1, 70.2, 101.7, 101.7, 106.5, 106.6, 115.2, 123.6, 124.0, 126.5, 127.6, 128.1, 128.3, 128.6, 130.6, 131.1, 136.8, 136.9, 139.3, 139.4, 147.0, 148.1, 149.8, 159.1, 160.1, 160.2 ppm. MS (FAB, NBA): m/z (%) = 1818.6 ([M + H]$^+$, 17), 303.1 (100).

4,7-Bis[4′-(3′′,5′′-bis{3′′′,5′′′-bis[3′′′′,5′′′′-bis(benzyloxy)benzyloxy]benzyloxy}benzyl)phenyl]-1,10-phenanthroline (L^{3G}): 4,7-Bis(4′-hydroxyphenyl)-1,10-phenanthroline (**8**) (40.0 mg, 0.11 mmol), dendritic Fréchet-type G3 bromide **12** (381.9 mg, 0.23 mmol), NaH (9.7 mg, 0.24 mmol, 60% in paraffin) in dry DMF (15 mL). Column chromatography (SiO_2, CH_2Cl_2/MeOH, 50:1 to 20:1) gave a brownish viscous oil (360.0 mg, 93%). R_f = 0.55 (CH_2Cl_2/MeOH, 10:1). ^1H NMR (400 MHz, $CDCl_3$): δ = 4.86 (s, 16 H, OCH_2), 4.89 (s, 8 H, OCH_2), 4.92 (s, 32 H, OCH_2), 4.95 (s, 4 H, OCH_2), 6.49 (m, 12 H, H_{ar}), 6.61 (m, 26 H, H_{ar}), 6.65 (d, J = 2 Hz, 4 H, H_{ar}), 7.03 (AA′ part of the AA′BB′ system, 4 H, H_{ar}), 7.18–7.34 (m, 80 H, H_{ar}), 7.36 (BB′ part of the AA′BB′ system, 4 H, H_{ar}), 7.42 (d, J = 5 Hz, 2 H, H_{ar}), 7.84 (s, 2 H, H_{ar}), 9.11 (d, J = 5 Hz, 2 H, H_{ar}) ppm. ^{13}C NMR (100 MHz, $CDCl_3$): δ = 70.0, 70.1, 70.2, 70.3, 101.6, 101.7, 101.8 106.5, 106.6, 106.8, 115.2, 123.6, 124.0, 126.5, 127.6, 128.0, 128.6, 130.6, 131.1, 136.9, 139.3, 139.4, 139.5, 147.0, 148.1, 149.8, 159.1, 160.1, 160.2, 160.3 ppm. MS (MALDI-TOF, DHB): m/z = 3515.9 (34) [M + H]$^+$, 1940.7 (24), 1621.5 (100).

Liquid–Liquid Extraction Procedure: Extraction studies were performed at 25 ± 1 °C in 2 cm^3 microcentrifuge tubes by mechanical shaking. The phase ratio $V_{(org)}$:$V_{(w)}$ was 1:1 (0.5 cm^3 each); the shaking period was 30 min. The extraction equilibrium was achieved during this period. All samples were centrifuged after extraction. The copper concentration in both phases was determined radiometrically using γ-radiation [^{64}Cu, NaI(Tl) scintillation counter Cobra II/Canberra Packard]. The aqueous solution was adjusted using 0.05 mol·dm^{-3} 2-[*N*-morpholino]ethanesulfonic acid (MES)/ NaOH (pH = 5.3–5.9).

Time-Resolved Laser-Induced Fluorescence Spectroscopy (TRLFS): Fluorescence measurements were carried out by use of a spectrometer system described elsewhere.[30] The ligands (L^{0G}–L^{3G}) were dissolved in $CHCl_3$. The total concentration of the ligand was $1 \cdot 10^{-5}$ mol·dm^{-3}. The fluorescence of solutions with increasing concentration of added Cu^{II} trifluoromethanesulfonate were measured. The ligand to Cu^{II} ratio was varied from 10:1 to 1:1. The fluorescence of the non-complexed ligand was excited by 130 fs laserpulses at 266 nm. The repetition rate of the laser system was 1 kHz. The emitted fluorescence was focussed into a 270 mm spectrograph (Acton Research) and the spectrum was measured by an intensified CCD (charged coupled device) camera (LaVision). The gate of the camera system was set to be 120 ps and the observed wavelength range was set from 350 nm to 510 nm. The range for time-resolved measurements was limited from 0 to 4000 ps with steps of 25 ps.

Acknowledgments

Financial support by the Saxon State Ministry of Science and Art (project 4–7531.50–03–0370–01/4) is acknowledged with thanks. We are grateful for advice by Dr. H.-J. Josel (Roche Diagnostics) during earlier studies on luminescent complexes.

[1] a) C. R. Luman, F. N. Castellano, in: *Comprehensive Coordination Chemistry II: From Biology to Nanotechnology* (Eds: J. A. McCleverty, T. J. Meyer), Elsevier-Pergamon, Amsterdam, Boston, Heidelberg, London, New York, Oxford, Paris, San Diego, San Francisco, Singapore, Sydney, Tokyo, **2004**, vol. 1, 25–39; b) A. von Zelewsky, *Stereochemistry of Coordination Compounds*, Wiley, Chichester, New York, **1996**.

[2] a) M. Yamada, Y. Tanaka, Y. Yoshimoto, S. Kuroda, I. Shimao, *Bull. Chem. Soc.* **1992**, *65*, 1006–1011; b) J.-C. Chambron, J.-P. Sauvage, E. Amouyal, P. Koffi, *New J. Chem.* **1985**, *9*, 527–529; c) E. Amouyal, A. Homsi, J.-C. Chambron, J.-P. Sauvage, *J. Chem. Soc., Dalton Trans.* **1990**, 1841–1845; d) Y. Jenkins, J. K. Barton, *J. Am. Chem. Soc.* **1992**, *114*, 8736–8738; e) V. W.-W. Yam, K. K.-W. Lo, K.-K. Cheung, R. Y.-C. Kong, *J. Chem. Soc., Chem. Commun.* **1995**, 1191–1193.

[3] a) T. Mizuno, W.-H. Wie, L. R. Eller, J. L. Sessler, *J. Am. Chem. Soc.* **2002**, *124*, 1134–1135; b) P. Anzenbacher Jr., D. S. Tyson, K. Jurisková, F. N. Castellano, *J. Am. Chem. Soc.* **2002**, *124*, 6232–6233; c) D. S. Tyson, C. R. Luman, X. Zhou, F. N. Castellano, *Inorg. Chem.* **2001**, *40*, 4046–4071; d) D. S. Tyson, F. N. Castellano, *Inorg. Chem.* **1999**, *38*, 4382–4383; e) D. S. Tyson, I. Gryczynski, F. N. Castellano, *J. Phys. Chem. A* **2000**, *104*, 2919–2924; f) W. E. Ford, M. A. J. Rodgers, *J. Phys. Chem.* **1992**, *96*, 2917–2920; g) N. Armaroli, *Chem. Soc. Rev.* **2001**, *30*, 113–124.

[4] a) F. M. MacDonnel, S. Bodige, *Inorg. Chem.* **1996**, *35*, 5758–5759; b) S. Bodige, A. S. Torres, D. J. Maloney, D. Tate, G. R. Kinsel, A. K. Walker, F. M. MacDonnel, *J. Am. Chem. Soc.* **1997**, *119*, 10364–10369; c) F. M. MacDonnel, M.-J. Kim, S. Bodige, *Coord. Chem. Rev.* **1999**, *185/186*, 535–549; d) M.-J. Kim, F.-M. MacDonnel, M. E. Gimon-Kinsel, T. Du Bois, N. Asgharian, J. C. Griener, *Angew. Chem. Int. Ed.* **2000**, *39*, 615–619; e) F. M. MacDonnel, M. D. Meser Ali, M.-J. Kim, *Inorg. Chem.* **2000**, *39*, 203–225.

[5] a) G. R. Newkome, C. N. Moorefield, F. Vögtle, *Dendrimers and Dendrons*, Wiley-VCH, Weinheim **2001**; b) J. M. J. Fréchet, D. A. Tomalia, *Dendrimers and Other Dendritic Polymers*, Wiley, Chichester **2001**; c) Dendrimers, V: C. A. Schalley, F. Vögtle, *Top. Curr. Chem.* **2003**, *228*, and previous volumes I–IV.

[6] a) J.-F. Nierengarten, D. Felder, J.-F. Nicoud, *Tetrahedron Lett.* **1999**, *40*, 273–276; b) J.-F. Nierengarten, *C. R. Chim.* **2003**, *6*, 725–733; c) E. Gumienna-Kontecka, Y. Rio, C. Bourgogne, M. Elhabiri, R. Louis, A.-M. Albrecht-Gary, J.-F. Nierengarten, *Inorg. Chem.* **2004**, *43*, 3200–3209.

[7] S. Serroni, S. Campagna, A. Juris, M. Venturi, V. Balzani, D. Denti, *Gazz. Chim. Ital.* **1994**, *124*, 423–427.

[8] a) F. Vögtle, M. Plevoets, M. Nieger, G. C. Azzellini, A. Credi, L. De Cola, V. De Marchis, M. Venturi, V. Balzani, *J. Am. Chem. Soc.* **1999**, *121*, 6290–6298; b) M. Plevoets, F. Vögtle, L. De Cola, V. Balzani, *New J. Chem.* **1999**, *23*, 63–69; c) D. S. Tyson, C. R. Luman, F. N. Castellano, *Inorg. Chem.* **2002**, *41*, 3578–3586; d) T. H. Ghaddar, J. F. Wishart, J. P. Kirby, J. K. Whitesell, M. A. Fox, *J. Am. Chem. Soc.* **2001**, *123*, 12832–12836; e) J. Issberner, F. Vögtle, L. De Cola, V. Balzani, *Chem. Eur. J.* **1997**, *3*, 706–712.

[9] N. D. McClenaghan, R. Passalacqua, F. Loiseau, S. Campagna, B. Verheyde, A. Hameurlaine, W. Dehaen, *J. Am. Chem. Soc.* **2003**, *125*, 5356–5365.

[10] a) D. Tzalis, Y. Tor, *Tetrahedron Lett.* **1996**, *37*, 8293–8296; b) Y. Tor, *C. R. Chim.* **2003**, *6*, 755–766.

[11] a) P. C. Alford, M. J. Cook, A. P. Lewis, G. S. G. McAuliffe, V. Skarda, A. J. Thomson, J. L. Glasper, D. J. Robbins, *J. Chem. Soc., Perkin Trans. 2* **1985**, 705–709; b) F. H. Case, P. F. Strohm, *J. Org. Chem.* **1962**, *27*, 1641–1643; c) F. H. Case, *J. Org. Chem.* **1951**, *16*, 1541–1545.

[12] E. H. Vickery, L. F. Pahler, E. J. Eisenbraun, *J. Org. Chem.* **1979**, *44*, 4444–4446.

[13] a) C. J. Hawker, J. M. J. Fréchet, *J. Am. Chem. Soc.* **1990**, *112*, 7638–7647; b) C. J. Hawker, J. M. J. Fréchet, *J. Chem. Soc. Chem. Commun.* **1990**, 1010–1013.

[14] a) P. Ballesteros, R. M. Claramunt, J. Elguero, *Tetrahedron* **1987**, *43*, 2557–2564; b) S. Strömberg, M. Oksman, L. Zhang, K. Zetterberg, *Acta Chem. Scan.* **1995**, *49*, 689–695; c) S. Ser-

 © 2005 Wiley-VCH Verlag GmbH & Co. KGaA, Weinheim

roni, S. Campagna, A. Juris, M. Venturi, V. Balzani, G. Denti, *Gazz. Chim. Ital.* **1994**, *124*, 423–427; d) P. Maslak, R. D. Guthrie, *J. Am. Chem. Soc.* **1986**, *108*, 2628–2636.
[15] a) B. J. Hathaway, in: *Comprehensive Coordination Chemistry* (Eds.: G. Wilkinson, R. D. Gillard, J. A. McCleverty), Pergamon, Oxford, **1987**, vol. 5, 533–594; b) R. Mukherjee, in: *Comprehensive Coordination Chemistry II: From Biology to Nanotechnology* (Eds: J. A. McCleverty, T. J. Meyer), Elsevier-Pergamon, Amsterdam, Boston, Heidelberg, London, New York, Oxford, Paris, San Diego, San Francisco, Singapore, Sydney, Tokyo, **2004**, vol. 5, 747–910.
[16] K. Gloe, P. Mühl, *Isotopenpraxis* **1983**, *19*, 257–260.
[17] Graphs about influence of time and pH on the Cu^{II} extraction with dendritic ligands are available as Supporting Information.
[18] pK_a of 1,10-phenanthroline = 4.93; D. A. Brisbin, W. A. E. McBryde, *Can. J. Chem.* **1963**, *41*, 1135–1141.
[19] D_{Cu} is defined as the quotient of the relative amounts of the Cu^{II} species present in the organic and aqueous phase.
[20] K. Gloe, P. Mühl, *Isotopenpraxis* **1979**, *15*, 236–239.
[21] Optimized structures of copper(II) complexes with dendritic oxybathophenanthroline ligands $\mathbf{L^{G0}}$–$\mathbf{L^{G3}}$ as obtained by mechanics calculations are available as Supporting Information.
[22] C. K. Jørgensen, *Acta Chem. Scand.* **1955**, *9*, 1362–1377.
[23] S. Tyagi, B. J. Hathaway, *J. Chem. Soc. Dalton Trans.* **1983**, 199–203.
[24] M. F. Ottaviani, S. Bossmann, N. J. Turro, D. A. Tomalia, *J. Am. Chem. Soc.* **1994**, *116*, 661–671.
[25] G. Murphy, C. Murphy, B. Murphy, B. Hathaway, *J. Chem. Soc. Dalton Trans.* **1997**, 2653–2660.
[26] P. Comba, T. W. Hambley, N. Okon, "MOMEC, a molecular modeling package for inorganic compounds", University of Heidelberg, www.comba-group.uni-hd.de, **1997**.
[27] P. V. Bernhardt, P. Comba, *Inorg. Chem.* **1992**, *31*, 2638–2644.
[28] a) K. Amournjarusiri, B. J. Hathaway, *Acta Crystallogr. Sect. C* **1991**, *47*, 1383–1385; b) M. T. Miller, P. K. Gantzel, T. B. Karpishin, *Inorg. Chem.* **1998**, *37*, 2285–2290; c) K. J. Catalan, S. Jackson, J. D. Zubkowski, D. L. Perry, E. J. Valente, L. A. Felin, A. Polanco, *Polyhedron* **1995**, *14*, 2165–2171.
[29] a) D. Wang, G. R. Hanson, *J. Magn. Reson. A.* **1995**, *117*, 1–8; b) D. Wang, G. R. Hanson, *Appl. Magn. Reson.* **1996**, *11*, 401–415.
[30] G. Geipel, M. Acker, D. Vulpius, G. Bernhard, H. Nitsche, T. Fanghänel, *Spectrochim. Part A* **2004**, *60/1–2*, 417–424.

Received: February 28, 2005
Published Online: October 5, 2005

 © 2005 Wiley-VCH Verlag GmbH & Co. KGaA, Weinheim

Synthesis and Linear Optical Properties of Tris(catecholato)metal(III,IV) Complexes with Acceptor-Substituted Ligands

Volker Kriegisch[a] and Christoph Lambert*[a]

Dedicated to the memory of Prof. Dr. Rüdiger Wortmann (1959–2005)

Keywords: Nonlinear optics / Octupolar complexes / Chromophores / Donors / Acceptors / Catecholate

The synthesis of C_3-symmetric chromophores (**2**–**4**, **9**, **10**, **14**) with acceptor-substituted catecholato ligands and different central metal atoms (Si, Al, Ti) is described. These complexes might serve as octupolar chromophores with first-order nonlinear optical properties. UV/Vis spectroscopic investigations show a red-shift of the lowest-energy charge-transfer band on going from Si^{IV}, Al^{III} to Ti^{IV} complexes, dependent on the increasing ionic character of the M–O bond.
(© Wiley-VCH Verlag GmbH & Co. KGaA, 69451 Weinheim, Germany, 2005)

Introduction

Over the past two decades, there has been considerable interest in the nonlinear optical (NLO) properties of organic and organometallic materials because of their potential application in various fields such as telecommunications, optical data storage and optical information processing. Many organic chromophores possess very high NLO efficiencies which derive from the high polarisability of electrons in unsaturated systems.[1–6] In one-dimensional NLO chromophores, in which a π-system is terminated by an electron acceptor and a donor, the electronic structure can be described by a mixture of a neutral valence-bond structure and a polar charge-separated mesomeric structure. The dipole moments of the ground and the first excited charge-transfer (CT) state depend on the degree of mixing. Those species, in which the neutral mesomeric structure constitutes the major part of the ground-state wave function, have a small ground-state dipole moment but a high dipole moment in the excited state. The prototype is 4-(dimethylamino)-4′-nitrostilbene (DANS).[3,4] Those systems, in which the dipolar mesomeric structure is the one which dominates the ground state, display zwitterionic character in the ground state but have a small dipole moment in the excited state. Brooker's dye is the prototype.[7,8]

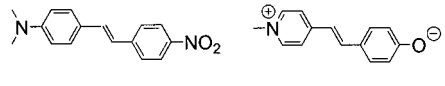

DANS Brooker´s dye

[a] Universität Würzburg, Institut für Organische Chemie, Am Hubland 1, 97074 Würzburg, Germany
Fax: +49-931-888-4606
E-mail: lambert@chemie.uni-wuerzburg.de

While most NLO chromophores are one-dimensional and show, owing to the difference of the ground- and excited-state dipole moments, a strong solvatochromism, there are also D_3-symmetrical two-dimensional "octupolar" NLO chromophores which have the advantage that they do not show solvatochromism and, therefore, no loss of transparency in a polar environment. This is a consequence of the vanishing dipole moments in a D_3-symmetric chromophore.[9–11] Therefore, in recent years many investigations were devoted to this type of NLO chromophore.[2,12–16]

Although Brooker's dye shows exceptionally high quadratic NLO properties, its accurate investigation is hampered because of the sensitivity of the electronic structure to protonation or even because of hydrogen bonding of the phenolate oxygen atom.[17–23] Therefore, the goal of this investigation is to synthesise octupolar chromophores in which the phenolate part of a chromophore ligand is complexed by a metal ion in order to reduce its sensitivity to protic impurities. On the other hand, the metal ion serves as a template to organise three chromophores in a threefold symmetric arrangement. In order to gain thermodynamic stability, we used ligands based on catecholate rather than on phenolate as in Brooker's dye. The metal ions are Al^{III},[24] Ti^{IV},[25–27] and Si^{IV}[28,29] because these ions are known to form stable complexes with catecholate. The ions also form highly polar bonds to oxygen atoms, which will allow the catecholate to retain most of its anionic electronic structure, which is important in order to serve as a good electron donor in the ligand chromophores. The ligands used are given below. While **1** is derived from caffeic acid that has a carboxylic ester function as the electron acceptor, the ligands **8** and **13** have a nitro and a trimethylammonio group, respectively, as the acceptor functionalities. In the

 DOI: 10.1002/ejic.200500401 © 2005 Wiley-VCH Verlag GmbH & Co. KGaA, Weinheim

forthcoming sections we describe the syntheses and the linear optical properties of some metal complexes derived from the above-mentioned ligands.

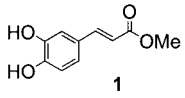

1

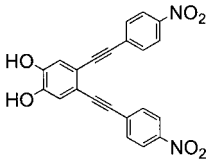

8

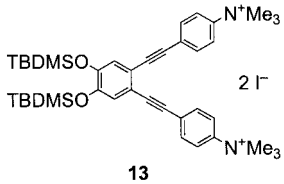

13

Results and Discussion

Synthesis and Characterisation

The synthesis of the (catecholato)M (M = metal) complexes **2**–**4** is illustrated in Scheme 1. The tris(catecholato)-Ti^{IV} complex **2** has been prepared in high yield using a procedure by Albrecht et al.[25,30]

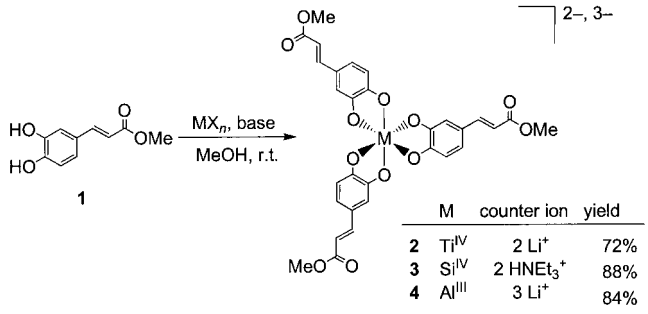

Scheme 1. Synthesis of octupolar (catecholato)M^{IV,III} complexes **2**–**4**.

To explore the preparation of tris(catecholato) complexes with different central atoms, **1** was used as an easily accessible ligand. In case of the Ti^{IV} and Al^{III} complexes Li_2CO_3 was used as the base. For the Si^{IV} complex **3** triethylamine was used as the base for the preparation. NMR and IR spectroscopic investigations confirm the formation of the complexes. An intense band occurs in the IR spectra at about 1200–1300 cm^{-1} which is typical of C–O stretching modes in catecholato–metal structures.[24,31] In the case of the unsymmetrical ligand **1** diastereomeric complexes form which we were unable to separate. These diastereomers are likely to show slightly different optical properties, which are not considered in the following text.

In order to avoid problems with diastomeric mixtures, 4,5-substituted catecholate systems were used to synthesise D_3-symmetrical complexes that will only consist of enantiomers.

The ligands **8** and **13** were prepared starting from the *tert*-butyldimethylsilyl-(TBDMS-)protected diiodo compound **5** which was synthesised according to Lulinski et al. and Kinder et al.[31,32] Using Hagihara coupling reaction conditions, compound **5** and 2 equiv. of **6** gave the 4,5-disubstituted ligand **7** in 75% yield. The reaction time has to be limited to 2 h because of the increasing formation of by-products with a prolonged reaction time. Deprotection of the TBDMS group led to the catechol ligand **8** in high yields (Scheme 2). The Ti^{IV} (**9**) and Si^{IV} complexes (**10**) were prepared in the same way as the caffeic acid complexes. Although the corresponding Al^{III} complex could be synthesised in an analogous manner, we were unable to purify this complex.

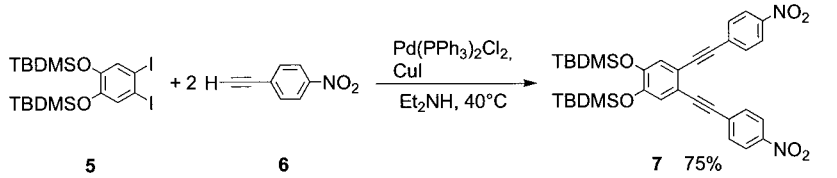

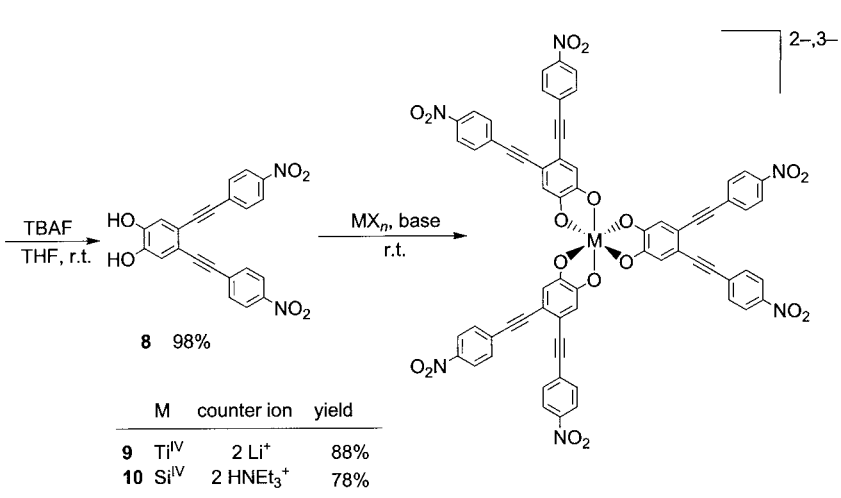

Scheme 2. Syntheses of the acceptor-substituted catechol ligand **8** and the corresponding octupolar Ti^{IV} (**9**) and Si^{IV} complexes (**10**).

 © 2005 Wiley-VCH Verlag GmbH & Co. KGaA, Weinheim

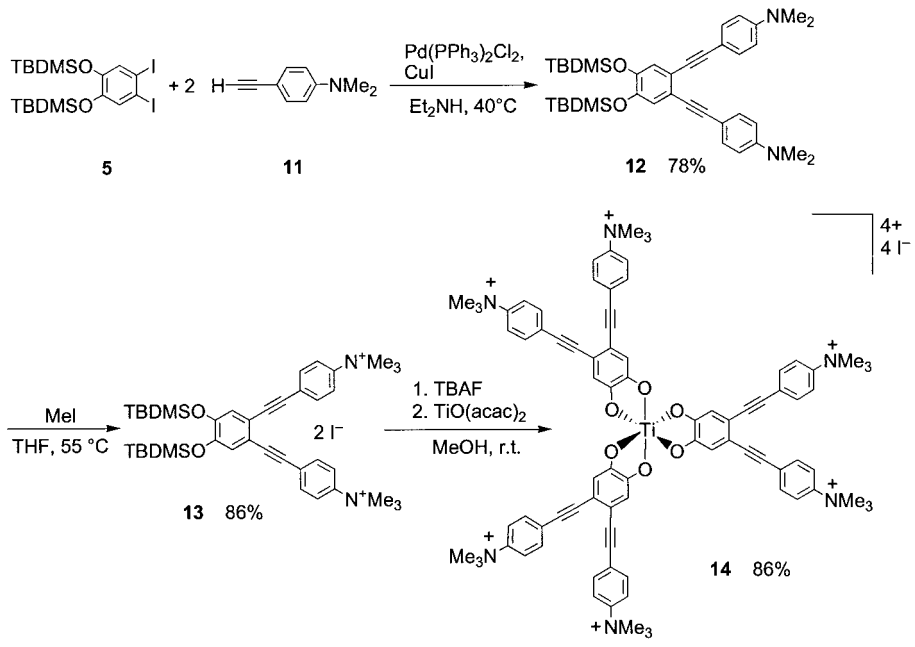

Scheme 3. Syntheses of the TBDMS-protected acceptor-substituted catechol ligand **13** and the corresponding octupolar Ti^{IV} complex **14**.

Ligand **13** was built up in the same way as alkyne **8**: the alkyne **11** was coupled with **5** in a palladium-catalysed reaction to give compound **12**. Subsequently, the amino groups of **12** were quaternised with methyl iodide. The Ti^{IV} complex **14** was prepared by in situ deprotection of **13** and reaction with $TiO(acac)_2$ (Scheme 3).

UV/Vis Absorption Spectra

Owing to the ionic character of all complexes, absorption spectra could only be recorded in relatively polar solvents. The UV/Vis spectra of the free ligand **1** show a concentration-dependent behaviour in DMSO. At high concentrations **1** has an absorption maximum at λ_{max} = 335 nm. Dilution leads to the formation of a new band at 425 nm, associated with an increase of this band (Figure 1).

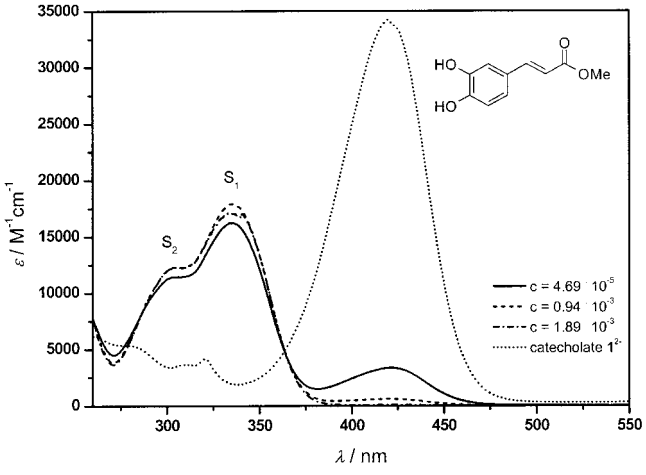

Figure 1. Concentration-dependent UV/Vis spectra of **1** and the catecholate $\mathbf{1}^{2-}$ in DMSO.

The reason for this behaviour is, as for ligand **8**, the concentration-dependent shift of the acid/base equilibrium to the deprotonated species and finally to the catecholate dianion $\mathbf{1}^{2-}$. Quantitative preparation of the catecholate dianion $\mathbf{1}^{2-}$ by adding sodium *tert*-butoxide to a solution of **1** results in a bathochromic shift and in the formation of an intense band at λ_{max} = 420 nm which corresponds to the one observed for **1** at high dilution. In contrast to **1** the UV/Vis spectra of the metal complexes **2**–**4** in DMSO, DMF and MeCN are concentration-independent. Comparison of the UV/Vis spectra of the tris(catecholato)M complexes of **1** in DMSO with that of $\mathbf{1}^{2-}$ shows a hypsochromic shift of the absorption maximum for M = Si^{IV} (**3**) (λ_{max} = 394 nm) over Al^{III} (**4**) (λ_{max} = 404 nm) to Ti^{IV} (**2**) (λ_{max} = 423 nm). The latter shows a maximum at about the same wavelength as the free ligand $\mathbf{1}^{2-}$ (Figure 2). This behaviour reflects the different degree of ionicity in the M–O bond increasing from Si^{IV}–O over Al^{III}–O to Ti^{IV}–O. The high ionicity of the M–O bond concentrates charge on the catecholate oxygen atoms, which become stronger donors the more ionic the bond is. This results in an intraligand CT absorption as observed in, for example, other tris(catecholato)Ti^{IV} complexes.[26] Interestingly, the band width of this CT band is much broader for **2** than for **3** and **4**. Whether this effect has to do with diastereomeric mixtures or is due to electronic effects is presently unclear.

While the spectra of **2**–**4** do not vary much in DMSO, DMF and MeCN, further studies of their possible solvatochromism were hampered by the insolubility in less polar solvents. In MeOH decomposition of **3** was observed and free ligand **1** was formed.

The complexes **9** and **10** show a similar behaviour of the absorption spectra as the complexes **2**–**4** (Figure 3). The spectra of both compounds **9** and **10** are shifted batho-

 © 2005 Wiley-VCH Verlag GmbH & Co. KGaA, Weinheim

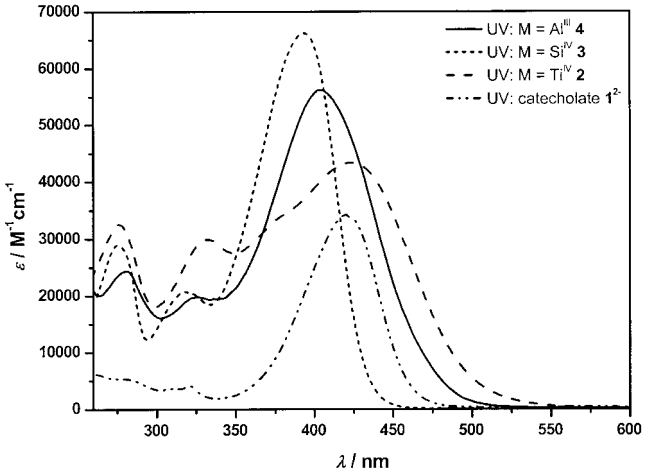

Figure 2. Absorption spectra of tris(catecholato)M complexes **2**–**4** and of catecholate $\mathbf{1}^{2-}$ in DMSO.

chromically vs. the free ligand **8**. Even here the increasing ionic character of the M^{IV}–O bonding is responsible for the red shift of the absorption maximum of the Si^{IV} compound **10** vs. the Ti^{IV} compound **9**. In DMSO the band maximum for **9** is at λ_{max} = 460 nm and for **10** at λ_{max} = 442 nm. Surprisingly, even the absorption maximum of the Ti^{IV} complex **9** does not reach that of the free deprotonated ligand $\mathbf{8}^{2-}$. This contrasts the behaviour of **2**. Neither the free ligand **8** nor the complexes themselves show fluorescence in DMSO, but their absorption is slightly solvatochromic (see Table 1). Ligand **8** shows, as for ligand **1**, a concentration-dependent deprotonation of the hydroxy groups to form the catecholate $\mathbf{8}^{2-}$. Although the Ti^{IV} complex **9** has a higher stability compared to the Si^{IV} species **10**, we observe ligand exchange in methanol.

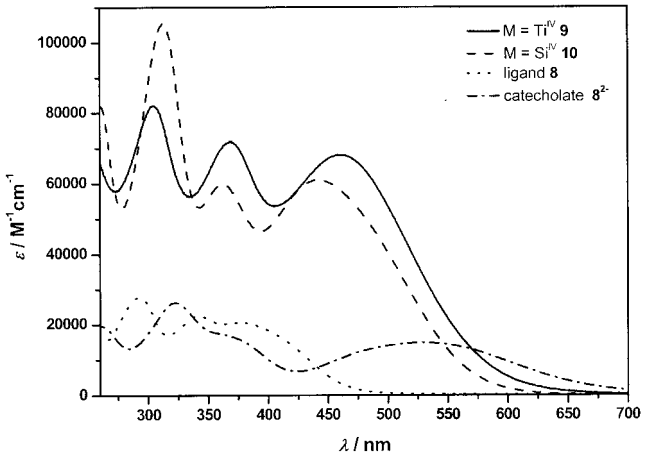

Figure 3. Absorption spectra of the tris(catecholato)M complexes **9**, **10** and the corresponding ligand **8** and catecholate $\mathbf{8}^{2-}$ in DMSO.

The UV/Vis spectrum of **14** in DMSO is similar to the spectrum of **9** but has a maximum at λ_{max} = 391 nm which is blue-shifted vs. **9** due to the R_3N^+ electron acceptor that is weaker than the NO_2 group in **9** (Figure 4).

Table 1. UV/Vis data {λ_{max} [nm] (ε [$M^{-1}cm^{-1}$])} of ligands **1**, **8**, **13**, the corresponding catecholates $\mathbf{1}^{2-}$, $\mathbf{8}^{2-}$ and tris(catecholato)$M^{III,IV}$ complexes **2**–**4**, **9**, **10**, **14**.

	DMSO	DMF	MeCN
1	340 (17100)		
$\mathbf{1}^{2-}$	420 (34261)		
2	423 (43300)	426 (46400)	409 (41000)
3	394 (65200)	394 (69800)	378 (67000)
4	404 (56100)	408 (61800)	
8	377 (20500)		
$\mathbf{8}^{2-}$	531 (14813)		
9	460 (68100)	463 (70900)	446 (71200)
10	442 (60900)	447 (62200)	429 (69100)
13	292 (21400)		
14	391 (63600)	397 (64800)	389 (65500)

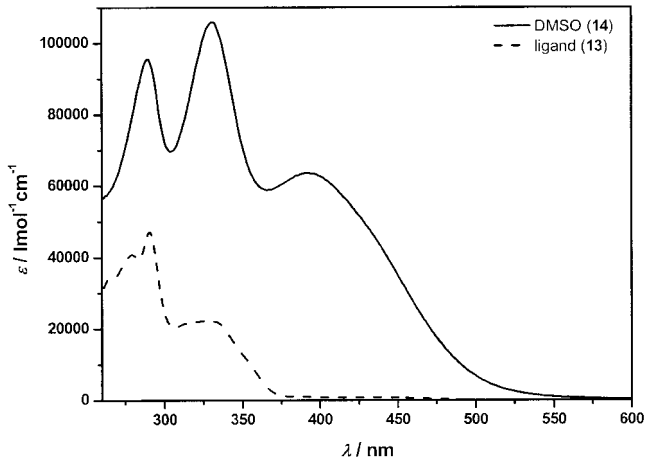

Figure 4. Absorption spectra of tris(catecholato)M complex **14** and ligand **13** in DMSO.

Conclusions

Although we could not measure the absorption spectra of the metal catecholates in solvents with strongly different polarity due to solubility/instability problems, the bathochromic shift of the lowest-energy transition for the ligands **1** and **8** on going from Si^{IV} via Al^{III} to Ti^{IV} complexes **2**–**4**, **9**, and **10** supports the assignment to an intraligand charge-transfer transition. The bathochromic shift of this transition reflects the increasing ionic character of the M–O bonding which in turn causes the catecholate oxygen atom to become a stronger donor in the Ti^{IV} complexes than in the Si^{IV} compounds. For this reason the spectroscopic properties of the Ti^{IV} complexes **2** and **9** approach those of the deprotonated free ligands $\mathbf{1}^{2-}$ and $\mathbf{8}^{2-}$. The higher energy transition of Ti^{IV} complex **14** compared to **9** reflects the much weaker electron acceptor strength of the trimethylammonio substituent compared to the nitro group.[33] The former substituent acts by a purely inductive (field) effect while in the latter mesomeric effects also play a role.

In conclusion, we were able to synthesise a series of octupolar chromophores and to characterise their linear optical properties. The metal complexes described in this paper can serve as reasonably stable substitutes for the much more sensitive free-ligand chromophores. Owing to their intense

 © 2005 Wiley-VCH Verlag GmbH & Co. KGaA, Weinheim

intraligand CT transitions these complexes might be good candidates as chromophores for first-order nonlinear applications.[34]

Experimental Section

General Remarks: All operations were performed under nitrogen or argon using standard Schlenk-line techniques. All reagents were purchased from commercial sources and used as received. Methyl 3-(3,4-dihydroxy)phenyl-2-propenoate (**1**),[35] 1,2-bis(*tert*-butyldimethylsilyloxy)-4,5-diiodobenzene (**5**),[31] 1-ethynyl-4-nitrobenzene (**6**),[36] and (4-ethynylphenyl)dimethylamine (**11**)[36] were prepared according to literature procedures.

Instrumental: ^{1}H and ^{13}C NMR spectra were recorded with a Bruker Avance 400 FT NMR spectrometer. Elemental analyses were obtained from the Institut für Anorganische Chemie of the Universität Würzburg using an apparatus from Leco (CHNS-932). Infrared spectra were recorded in the range 4000–200 cm^{-1} as KBr pellets with a Jasco 410 FT-IR spectrometer. UV/Vis spectra were recorded with a Jasco V-570 UV/Vis/NIR spectrometer using Uvasol® solvents from Merck.

Dilithium Tris{4-[2-(methoxycarbonyl)ethenyl]-1,2-benzenediolato}-titanate(IV) (2): To a mixture of methyl 3-(3,4-dihydroxy)phenyl-2-propenoate (**1**; 250 mg, 1.28 mmol) and Li_2CO_3 (32.0 mg, 433 μmol) in dry MeOH (15 mL) $TiO(acac)_2$ (112 mg, 430 mmol) was added. The solution turned deep red and was stirred at room temperature for 24 h. The solvent was removed in vacuo, the red solid was dissolved in ethyl acetate and carefully covered with a layer of petroleum ether. The crystalline precipitate was filtered off, washed with petroleum ether and dried in vacuo to yield a red solid. Yield 72% (225 mg). ^{1}H NMR (250 MHz, [D$_6$]acetone, 25 °C): δ = 7.49 (d, $^3J_{HH}$ = 15.9 Hz, 1 H, CH=C*H*), 6.72 (dd, $^3J_{HH}$ = 8.2, $^4J_{HH}$ = 2.2 Hz, 1 H, 5-H), 6.56 (d, $^4J_{HH}$ = 2.1 Hz, 1 H, 3-H), 6.23 (d, $^3J_{HH}$ = 7.9 Hz, 1 H, 6-H), 6.06 (d, $^3J_{HH}$ = 15.9 Hz, 1 H, C*H*=CH), 3.67 (s, 3 H, MeO) ppm. ^{13}C NMR (62.9 MHz, [D$_6$]-acetone, 295 K): δ = 168.3, 160.6, 147.9, 125.0, 122.7, 112.2, 111.6, 109.9, 106.1, 51.2 ppm. $C_{30}H_{24}Li_2O_{12}Ti{\cdot}5H_2O$ (728.35): calcd. C 49.47, H 4.71; found C 49.69, H 5.13. IR (KBr): $\tilde{\nu}$ = 3052 (aryl-C–H), 3016 (w, aryl-C–H), 2975 (w, C–H), 1686 (m, C=O), 1624 (m), 1579 (w), 1486 (s), 1436 (m), 1261 (s, C–O), 1197 (w), 1118 (w), 1042 (vw), 977 (vw), 824 (w), 641 (m), 613 (w), 505 (w) cm^{-1}.

Bis(triethylammonium) Tris{4-[2-(methoxycarbonyl)ethenyl]-1,2-benzenediolato}silicate(IV) (3): To a mixture of methyl 3-(3,4-dihydroxy)phenyl-2-propenoate (**1**; 250 mg, 1.28 mmol) and Et_3N (119 mg, 908 μmol) in dry MeOH (5 mL) $Si(MeO)_4$ (63.9 mg, 409 μmol) was added. The solution turned yellow and was stirred at room temperature for 24 h. The solvent was removed in vacuo. The yellow solid was dissolved in dichloromethane and the solution added dropwise to petroleum ether. The precipitate was filtered off, washed with petroleum ether and dried in vacuo. Yield 88% (300 mg) of a yellow solid. ^{1}H NMR (250 MHz, [D$_4$]methanol, 25 °C): δ = 7.53 (d, $^3J_{HH}$ = 15.5 Hz, 1 H, CH=C*H*), 6.86 (s, 1 H, 3-H), 6.72 (d, $^3J_{HH}$ = 7.9 Hz, 1 H, 6-H), 6.53 (dd, $^3J_{HH}$ = 8.0, $^4J_{HH}$ = 1.2 Hz, 1 H, 5-H), 6.13 (d, $^3J_{HH}$ = 15.5 Hz, 1 H, C*H*=CH), 3.72 (s, 3 H, MeO), 3.08 (q, 12 H, CH_3CH_2N), 1.21 (t, 18 H, CH_3CH_2N) ppm. ^{13}C NMR (62.9 MHz, [D$_4$]methanol, 295 K): δ = 170.9, 156.5, 152.6, 149.5, 125.5, 123.6, 111.8, 111.2, 109.2, 50.8, 48.0 (CH_3CH_2N), 9.62 (CH_3CH_2N) ppm. $C_{42}H_{58}N_3O_{12}Si$ (811.00): calcd. C 62.20, H 7.21, N: 3.45; found C 61.32, H 7.15, N 3.46. IR (KBr): $\tilde{\nu}$ = 3057 (aryl-C–H), 3019 (w, aryl-C–H), 2986 (w, C–H), 2949 (w, C–H), 1697 (m, C=O), 1623 (m), 1590 (m), 1497 (s), 1447 (m), 1354 (w), 1259 (s, C–O), 1157 (s), 1117 (m), 1035 (vw), 985 (vw), 926 (vw), 835 (m), 790 (w), 694 (m), 578 (vw), 523 (w) cm^{-1}.

Trilithium Tris{4-[2-(methoxycarbonyl)ethenyl]-1,2-benzenediolato}-aluminate(III) (4): To a mixture of methyl 3-(3,4-dihydroxy)phenyl-2-propenoate (**1**; 300 mg, 1.54 mmol) and Li_2CO_3 (56.2 mg, 758 μmol) in dry MeOH (15 mL) $Al(acac)_3$ (165 mg, 509 μmol) was added. The solution turned yellow and was stirred at room temperature for 24 h. The solvent was removed in vacuo, the remaining yellow solid was suspended in hot ethyl acetate and filtered off. The precipitate was washed twice with hot ethyl acetate and dried in vacuo. Yield 84% (268 mg) of a yellow solid. ^{1}H NMR (250 MHz, [D$_4$]methanol, 25 °C): δ = 7.49 (d, $^3J_{HH}$ = 15.4 Hz, 1 H, CH=C*H*), 6.78 (d, $^4J_{HH}$ = 1.8 Hz, 1 H, 3-H), 6.57 (dd, $^3J_{HH}$ = 7.9, $^4J_{HH}$ = 1.8 Hz, 1 H, 5-H), 6.42 (d, $^3J_{HH}$ = 7.9 Hz, 1 H, 6-H), 6.00 (d, $^3J_{HH}$ = 15.5 Hz, 1 H, C*H*=CH), 3.70 (s, 3 H, MeO) ppm. ^{13}C NMR (62.9 MHz, [D$_4$]methanol, 295 K): δ = 171.3, 162.0, 156.4, 150.3, 123.3, 123.0, 112.9, 110.0, 108.5, 51.6 ppm. $C_{30}H_{24}AlLi_3O_{12}{\cdot}5H_2O$ (714.34): calcd. C 50.44, H 4.80; found C 50.79, H 4.84. IR (KBr): $\tilde{\nu}$ = 3054 (vw, aryl-C–H), 2984 (w, C–H), 1685 (m, C=O), 1622 (m), 1582 (m), 1497 (s), 1437 (m), 1346 (vw), 1269 (s, C–O), 1199 (m), 1166 (m), 1120 (w), 1042 (vw), 980 (w), 929 (vw), 827 (w), 784 (vw), 655 (w), 616 (w) cm^{-1}.

1,2-Bis(*tert*-butyldimethylsilyloxy)-4,5-bis[2-(4-nitrophenyl)ethynyl]-benzene (7): To a mixture of 4,5-bis(*tert*-butyldimethylsilyloxy)-1,2-diiodobenzene (**5**; 189 mg, 320 μmol), $(PPh_3)_2PdCl_2$ (24.0 mg, 34.2 μmol) and $Cu^{I}I$ (4.00 mg, 21.0 μmol) in dry Et_2NH (5 mL) was added 1-ethynyl-4-nitrobenzene (**6**; 100 mg, 680 μmol). The red solution was heated to 60 °C for 1 h, cooled to room temperature and the solvent was evaporated in vacuo. The remaining black solid was purified by flash chromatography on silica gel (dichloromethane/petroleum ether, 2:3) to yield a yellow solid. The solid was dissolved in dichloromethane and the solution added dropwise to petroleum ether. The dichloromethane was removed in a rotary evaporator, the precipitate was filtered and dried in vacuo. Yield 75% (163 mg) of a yellow solid. ^{1}H NMR (250 MHz, $CDCl_3$, 25 °C): δ = 8.22 (AA′, 4 H), 7.65 (BB′, 4 H), 7.03 (s, 2 H, 3-H, 6-H), 1.01 [s, 18 H, $(CH_3)_3CSi$], 0.26 [s, 12 H, $(CH_3)_2Si$] ppm. ^{13}C NMR (62.9 MHz, $CDCl_3$, 295 K): δ = 149.5, 148.2, 133.2, 130.7, 125.3, 124.8, 119.6, 93.3, 91.7, 26.2, 19.2, –3.85 ppm. $C_{34}H_{40}N_2O_6Si_2$ (677.24): calcd. C 64.94, H 6.41, N 4.45; found C 64.69, H 6.24, N 4.52. IR (KBr): $\tilde{\nu}$ = 3041 (vw, aryl-C–H), 2951 (w, C–H), 2930 (w, C–H), 2857 (w, C–H), 2204 (vw, C≡C), 1592 (m), 1536 (w), 1510 (s, NO_2), 1410 (w), 1345 (w), 1336 (s, NO_2), 1256 (m), 1213 (vw), 1105 (w), 1083 (w), 939 (m), 886 (vw), 871 (w), 848 (m), 843 (m), 783 (w), 748 (vw), 684 (vw) cm^{-1}.

1,2-Dihydroxy-4,5-bis[2-(4-nitrophenyl)ethynyl]benzene (8): To a solution of 1,2-bis(*tert*-butyldimethylsilyloxy)-4,5-bis[2-(4-nitrophenyl)ethynyl]benzene (**7**; 95.0 mg, 140 μmol) in dry THF (10 mL) tetrabutylammonium fluoride (101 mg, 386 μmol, 1 M solution in THF) was added. The deep purple solution was stirred at room temperature for 30 min and a cold H_3PO_4 solution (30 mL, 1 M) was added. The mixture was extracted with Et_2O (3 × 30 mL). The organic phases were combined, dried with Na_2SO_4 and the solvent was removed in vacuo. The remaining brown solid was purified by flash chromatography on silica gel (ethyl acetate/*n*-hexane/CH_3COOH, 10:25:1) to yield an orange solid. The solid was dissolved in ethyl acetate and the solution added dropwise to *n*-hexane. The precipitate was filtered off and dried in vacuo. Yield 98% (55.0 mg) of an orange solid. ^{1}H NMR (250 MHz, [D$_6$]acetone, 25 °C): δ = 8.31 (AA′, 4 H), 7.84 (BB′, 4 H), 7.44 (br., 2 H, HO), 7.17 (s, 2 H, 3-H, 6-H) ppm. ^{13}C NMR (62.9 MHz, [D$_6$]acetone, 295 K): δ = 148.0, 147.9, 133.1, 131.0, 124.8, 119.7, 118.0,

 © 2005 Wiley-VCH Verlag GmbH & Co. KGaA, Weinheim

94.2, 90.8 ppm. $C_{22}H_{12}N_2O_6{\cdot}H_2O$ (418.35): calcd. C 63.16, H 3.37, N 6.70; found C 63.51, H 3.49, N 6.41. IR (KBr): $\tilde{\nu}$ = 3480 (br., O–H), 3046 (vw, aryl-C–H), 2204 (m, C≡C), 1590 (s), 1508 (s, NO_2), 1441 (vw), 1349 (s, NO_2), 1308 (m), 1261 (w), 1182 (w), 1145 (w), 1074 (vw), 848 (m), 749 (w), 686 (vw) cm^{-1}.

Dilithium Tris{4,5-bis[2-(4-nitrophenyl)ethynyl]-1,2-benzenediolato}-titanate(IV) (9): To a mixture of 1,2-dihydroxy-4,5-bis[2-(4-nitrophenyl)ethynyl]benzene (**8**; 50.0 mg, 125 μmol) and Li_2CO_3 (3.10 mg, 41.9 μmol) in dry MeOH (10 mL) $TiO(acac)_2$ (10.9 mg, 41.5 μmol) was added. The solution turned deep red and was stirred at room temperature for 24 h. The solvent was removed in vacuo, the red solid was dissolved in THF and Et_2O and carefully covered with a layer of petroleum ether. Overnight a red solid crystallised which was filtered off and recrystallised from MeCN. Yield 88% (49.0 mg) of a red solid. ^{1}H NMR (250 MHz, [D$_4$]methanol, 25 °C): δ = 8.25 (AA′, 12 H), 7.68 (BB′, 12 H), 6.62 (s, 6 H, 3-H, 6-H) ppm. ^{13}C NMR (62.9 MHz, [D$_4$]methanol, 295 K): δ = 161.6, 147.6, 132.5, 132.2, 124.5, 116.4, 115.4, 96.7, 89.9 ppm. $C_{66}H_{36}Li_2N_6O_{18}Ti{\cdot}4H_2O$ (1328.86): calcd. C 59.66, H 2.88, N 6.32; found C 59.41, H 2.58, N 6.16. IR (KBr): $\tilde{\nu}$ = 3056 (vw, aryl-C–H), 2196 (m, C≡C), 1592 (m, NO_2), 1509 (m), 1498 (m), 1477 (m), 1341 (s, NO_2), 1241 (s, C–O), 1106 (w), 887 (w), 850 (w), 792 (w), 748 (w), 705 (vw), 687 (vw), 613 (w) cm^{-1}.

Bis(triethylammonium) Tris{4,5-bis[2-(4-nitrophenyl)ethynyl]-1,2-benzenediolato}silicate(IV) (10): To a mixture of 1,2-dihydroxy-4,5-bis[2-(4-nitrophenyl)ethynyl]benzene (**8**; 100 mg, 249 μmol) and Et_3N (16.2 mg, 124 μmol) in dry MeCN (10 mL) a 1 M solution of $Si(MeO)_4$ (12.1 mg, 77.4 μmol) in dry MeCN was added. The solution turned orange and was stirred at room temperature for 24 h. Overnight a solid precipitated which was filtered off, washed with MeCN and dried in vacuo. Yield 78% (76.0 mg) of an orange solid. ^{1}H NMR (250 MHz, [D$_6$]DMSO, 25 °C): δ = 8.26 (AA′, 12 H), 7.73 (BB′, 12 H), 6.55 (s, 6 H, 3-H, 6-H), 3.06 (q, 12 H, CH_3CH_2N), 1.16 (t, 18 H, CH_3CH_2N) ppm. ^{13}C NMR (62.9 MHz, [D$_6$]DMSO, 295 K): δ = 154.6, 146.0, 131.7, 130.5, 124.1, 112.8, 111.9, 97.1, 88.9, 45.8, 8.8 ppm. $C_{78}H_{64}N_8O_{18}Si$ (1429.5): calcd. C 65.54, H 4.51, N 7.84; found C 64.13, H 4.38, N 7.56. IR (KBr): $\tilde{\nu}$ = 3071 (w, C–H-aryl), 2197 (m, C≡C), 1591 (s, NO_2), 1498 (s), 1384 (w), 1340 (s, NO_2), 1244 (s, C–O), 1173 (vw), 1105 (w), 1073 (vw), 891 (w), 852 (w), 795 (w), 748 (w), 711 (vw), 687 (vw), 655 (w), 596 (vw), 565 (vw) cm^{-1}.

1,2-Bis(*tert*-butyldimethylsilyloxy)-4,5-bis{2-[4-(dimethylamino)-phenyl]ethynyl}benzene (12): To a mixture of 4,5-bis(*tert*-butyldimethylsilyloxy)-1,2-diiodobenzene (**5**; 189 mg, 320 μmol), $(PPh_3)_2$-$PdCl_2$ (24.0 mg, 34.2 μmol) and Cu^{I}I (4.00 mg, 21.0 μmol) in dry Et_2NH (5 mL) (4-ethynylphenyl)dimethylamine (**11**; 100 mg, 680 μmol) was added. The red solution was heated to 50 °C for 24 h, cooled to room temperature and the solvent was evaporated in vacuo. The remaining brown solid was purified by chromatography on Al_2O_3 (neutral, act. V; dichloromethane/petroleum ether, 1:9) to yield a colourless solid. Yield 78% (156 mg) of a colourless solid. ^{1}H NMR (250 MHz, [D$_6$]acetone, 25 °C): δ = 7.38 (AA′, 4 H), 6.99 (s, 2 H, 3-H, 6-H), 6.72 (BB′, 4 H), 2.99 (s, 12 H, Me_2N), 1.02 [s, 18 H, $(CH_3)_3CSi$], 0.28 [s, 12 H, $(CH_3)_2Si$] ppm. ^{13}C NMR (62.9 MHz, [D$_6$]acetone, 25 °C): δ = 151.6, 148.0, 133.6, 124.7, 121.2, 113.1, 111.2, 94.5, 87.3, 40.5, 26.6, 19.4, –3.50 ppm. $C_{38}H_{52}N_2O_2Si_2$ (625.02): calcd. C 73.03, H 8.39, N 4.48; found C 72.88, H 8.19, N 4.58. IR (KBr): $\tilde{\nu}$ = 3045 (vw, aryl-C–H), 2953 (w, C–H), 2929 (m, C–H), 2885 (w, C–H), 2857 (m, N–Me), 2199 (vw, C≡C), 1608 (s), 1523 (s), 1496 (w), 1362 (s), 1254 (m), 1187 (w), 1136 (w), 929 (m), 887 (vw), 861 (w), 840 (m), 816 (w), 782 (w) cm^{-1}.

1,2-Bis(*tert*-butyldimethylsilyloxy)-4,5-bis{2-[4-(trimethylammonio)-phenyl]ethynyl}benzene Diiodide (13): To a solution of 1,2-bis(*tert*-butyldimethylsilyloxy)-4,5-bis{2-[4-(dimethylamino)phenyl]-ethynyl}benzene (**12**; 1.45 g, 2.31 mmol) in THF (20 mL) methyl iodide (5 mL) was added. The reaction mixture was sealed in a Schlenk tube and heated to 55 °C for 4 d. Excess methyl iodide and the solvent were removed in vacuo. The light yellow solid was dissolved in acetone by heating the mixture to 40 °C, *n*-hexane was added and the acetone was removed in a rotary evaporator. The precipitate was filtered off and washed twice with *n*-hexane to yield a colourless solid. Yield 86% (1.78 g). ^{1}H NMR (250 MHz, [D$_6$]-DMSO, 25 °C): δ = 8.06–8.03 (4 H), 7.79–7.74 (4 H), 7.11–7.00 (2 H, 3-H, 6-H), 3.64 (18 H, Me_3N), 0.98–0.83 [18 H, $(CH_3)_3CSi$], 0.25 to –0.04 [12 H, $(CH_3)_2Si$] ppm. ^{13}C NMR (62.9 MHz, [D$_6$]-DMSO, 25 °C): δ = 147.78, 146.78, 132.51, 132.42, 132.34, 132.24, 124.10, 123.91, 121.29, 121.24, 118.10, 90.26, 89.60, 56.41, 56.34, 25.50, 25.32, 25.26, 18.15, 18.13, 17.72, –3.24, –4.26, –4.54 ppm. $C_{40}H_{58}I_2N_2O_2Si_2$ (908.89): calcd. C 52.86, H 6.43, N 3.08; found C 52.59, H 6.18, N 3.11. IR (KBr): $\tilde{\nu}$ = 3013 (vw, C–H-aryl), 2955 (w, C–H), 2929 (w, C–H), 2885 (vw, C–H), 2857 (w, N–Me), 2210 (vw, C≡C), 1532 (m), 1513 (s), 1492 (m), 1471 (w), 1407 (w), 1357 (m), 1254 (s), 1117 (vw), 1082 (vw), 1013 (vw), 934 (s), 887 (w), 840 (s), 804 (w), 783 (m), 687 (vw), 564 (vw) cm^{-1}.

Tris(4,5-bis{2-[4-(trimethylammonio)phenyl]ethynyl}-1,2-benzenediolato)titanium(IV) Tetraiodide (14): To a solution of 1,2-bis(*tert*-butyldimethylsilyloxy)-4,5-bis{2-[4-(trimethylammonio)phenyl]-ethynyl}benzene diiodide (**13**; 200 mg, 220 μmol) in dry MeOH (13 mL) was added nBu_4NF (151 mg, 578 μmol, 1 M solution in THF) followed by $TiO(acac)_2$ (19.2 mg, 73.2 μmol). The solution turned red and was stirred at room temperature for 24 h. The orange precipitate was filtered off and washed carefully with MeOH. The solid was suspended in MeOH (15 mL) and the suspension added dropwise to a concd. solution of $NH_4(PF_6)$ in MeOH (10 mL). The precipitate was filtered off and the procedure was repeated twice to yield an orange solid. Yield 86% (114 mg). ^{1}H NMR (250 MHz, [D$_6$]DMSO, 25 °C): δ = 7.98 (AA′, 12 H), 7.70 (BB′, 12 H), 6.30 (s, 6 H, 3-H, 6-H), 3.62 (s, 18 H, Me_3N) ppm. ^{13}C NMR (62.9 MHz, [D$_6$]DMSO, 25 °C): δ = 162.1, 146.0, 132.0, 125.4, 121.1, 113.4, 93.4, 88.3, 56.4 ppm. $C_{84}H_{90}I_4N_6O_6Ti{\cdot}4H_2O$ (1901.19): calcd. C 53.07, H 4.87, N 4.42; found C 53.08, H 4.98, N 4.42. IR (KBr): $\tilde{\nu}$ = 3014 (vw, C–H-aryl), 2955 (w, C–H), 2929 (w, C–H), 2885 (w, C–H), 2857 (w, N–Me), 2198 (w, C≡C), 1508 (w), 1479 (s), 1413 (w), 1369 (m), 1278 (w), 1244 (s, C–O), 1200 (w), 1113 (w), 1011 (vw), 955 (vw), 936 (w), 884 (w), 844 (m), 798 (w), 635 (m), 565 (m), 502 (m) cm^{-1}.

Acknowledgments

We thank the Deutsche Forschungsgemeinschaft for financial support. We also thank Heraeus GmbH and Wacker AG for support with chemicals and Prof. Dr. J. Heck and Dr. C. Wittenburg (Institut für Anorganische Chemie, Universität Hamburg) for preliminary hyper-Rayleigh scattering measurements.

[1] J. Zyss, I. Ledoux, *Chem. Rev.* **1994**, *94*, 77–105.
[2] J. J. Wolff, D. Längle, D. Hillenbrand, R. Wortmann, R. Matschiner, C. Glania, P. Krämer, *Adv. Mater.* **1997**, *9*, 138–143.
[3] M. Blanchard-Desce, V. Alain, P. V. Bedworth, S. R. Marder, A. Fort, C. Runser, M. Barzoukas, S. Lebus, R. Wortmann, *Chem. Eur. J.* **1997**, *3*, 1091–1104.
[4] C. A. van Walree, O. Franssen, A. W. Marsman, M. C. Flipse, L. W. Jenneskens, *J. Chem. Soc. Perkin Trans. 2* **1997**, 799–807.

 © 2005 Wiley-VCH Verlag GmbH & Co. KGaA, Weinheim

[5] C. Lambert, G. Nöll, E. Schmälzlin, K. Meerholz, C. Bräuchle, *Chem. Eur. J.* **1998**, *4*, 2129–2135.
[6] C. Lambert, S. Stadler, G. Bourhill, C. Bräuchle, *Angew. Chem.* **1996**, *108*, 710–712.
[7] L. G. S. Brooker, G. H. Keyes, R. H. Sprague, R. H. Van Dyke, E. Va Zandt, F. L. White, H. W. J. Cressman, S. G. Dent, *J. Am. Chem. Soc.* **1951**, *73*, 5332–5350.
[8] L. G. S. Brooker, G. H. Keyes, D. W. Heseltine, *J. Am. Chem. Soc.* **1951**, *73*, 5350–5356.
[9] a) F. W. Vance, J. T. Hupp, *J. Am. Chem. Soc.* **1999**, *121*, 4047–4053. b) O. Maury, H. Le Bozec, *Acc. Chem. Res.* **2005**, *38*, 691–704.
[10] I. G. Voigt-Martin, G. Li, A. Yakimanski, G. Schulz, J. J. Wolff, *J. Am. Chem. Soc.* **1996**, *118*, 12830–12831.
[11] J. L. Bredas, F. Meyers, B. M. Pierce, J. Zyss, *J. Am. Chem. Soc.* **1992**, *114*, 4928–4929.
[12] J. J. Wolff, R. Wortmann, *J. Prakt. Chem./Chem.-Ztg.* **1998**, 1–18.
[13] J. Zyss, S. Brasselet, *J. Nonlinear Opt. Phys. Mater.* **1998**, *7*, 397–439.
[14] O. Riant, G. Bluet, S. Brasselet, N. Druze, I. Ledoux, F. Lefloch, A. Sxbniewski, J. Zyss, *Mol. Cryst. Liq. Cryst. Sci. Technol. Sect. A* **1998**, *322*, 35–42.
[15] C. Lambert, E. Schmälzlin, K. Meerholz, C. Bräuchle, *Chem. Eur. J.* **1998**, *4*, 512–521.
[16] R. Wortmann, C. Glania, P. Krämer, R. Matschiner, J. J. Wolff, S. Kraft, B. Treptow, E. Barbu, D. Längle, G. Görlitz, *Chem. Eur. J.* **1997**, *3*, 1765–1773.
[17] C. Bosshard, F. Pan, M. Shing Wong, S. Manetta, R. Spreiter, C. Cai, P. Günter, V. Gramlich, *Chem. Phys.* **1999**, *245*, 377–394.
[18] M. Shing Wong, C. Bosshard, P. Günter, *Adv. Mater.* **1997**, *9*, 837–842.
[19] F. Pan, M. S. Wong, V. Gramlich, C. Bosshard, P. Günter, *J. Am. Chem. Soc.* **1996**, *118*, 6315–6316.
[20] M. S. Wong, F. Pan, V. Gramlich, C. Bosshard, P. Günter, *Adv. Mater.* **1997**, *9*, 554–557.
[21] M. S. Wong, F. Pan, M. Bosch, R. Spreiter, C. Bosshard, P. Günter, V. Gramlich, *J. Opt. Soc. Am. B* **1998**, *15*, 426–431.
[22] F. Pan, M. S. Wong, V. Gramlich, C. Bosshard, P. Günter, *Chem. Commun.* **1996**, *13*, 1557–1558.
[23] F. Pan, M. S. Wong, C. Bosshard, P. Günter, V. Gramlich, *Adv. Mater. Opt. Electron.* **1996**, *6*, 261–266.
[24] T. B. Karpishin, T. D. P. Stack, K. N. Raymond, *J. Am. Chem. Soc.* **1993**, *115*, 182–192.
[25] M. A. Albrecht, *Chem. Eur. J.* **1997**, *3*, 1466–1471.
[26] B. A. Borgias, S. R. Cooper, Y. B. Koh, K. N. Raymond, *Inorg. Chem.* **1984**, *23*, 1009–1016.
[27] X. Sun, D. W. Johnson, D. L. Caulder, K. N. Raymond, E. H. Wong, *J. Am. Chem. Soc.* **2001**, *123*, 2752–2763.
[28] J. V. Kingston, M. N. Sudhendra Rao, *Tetrahedron Lett.* **1997**, *38*, 4841–4844.
[29] A. Boudin, G. Cerveau, C. Chuit, R. J. P. Corriu, C. Reye, *Organometallics* **1988**, *7*, 1165–1171.
[30] M. A. Albrecht, M. Schneider, *Chem. Commun.* **1998**, 137–138.
[31] J. D. Kinder, W. J. Youngs, *Organometallics* **1996**, *15*, 460–463.
[32] P. Lulinski, L. Skulski, *Bull. Chem. Soc. Jpn.* **1997**, *70*, 1665–1669.
[33] C. Lambert, W. Gaschler, G. Nöll, M. Weber, E. Schmälzlin, C. Bräuchle, K. Meerholz, *J. Chem. Soc. Perkin Trans. 2* **2001**, 964–974.
[34] Hyper Rayleigh scattering measurements were performed in cooperation with the working group of Prof. Heck (Institute of Inorganic Chemistry, University of Hamburg). Due to self-absorption of the complexes no reliable values for β could be obtained.
[35] H. Tanaka, I. Kato, K. Ito, *Chem. Pharm. Bull.* **1987**, *35*, 3603–3608.
[36] S. Takahashi, Y. Kuroyama, K. Sonogashira, N. Hagihara, *Synthesis* **1980**, 628–630.

Received: May 4, 2005
Published Online: October 5, 2005

 © 2005 Wiley-VCH Verlag GmbH & Co. KGaA, Weinheim

A Novel Five-Coordinate Rhodium(I) Complex

Igor O. Koshevoy,[a,b] Olga V. Sizova,[a] Sergey P. Tunik,*[a] Alan Lough,[b] and Anthony J. Poë[b]

Keywords: Solid-state structures / Rhodium / Electronic structure / Phosphane ligands / Carbonyl ligands

An unusual five-coordinate isomer of the mononuclear complex $[Rh(CO)_2(PPh_3)_2I]$ has been isolated, and its crystallographic structure determined. The molecule has a slightly distorted trigonal-bipyramidal structure, with both PPh_3 ligands being in axial positions. A combination of IR and NMR spectroscopy with the results of DFT calculations shows that the complex maintains the same structure in solution.

(© Wiley-VCH Verlag GmbH & Co. KGaA, 69451 Weinheim, Germany, 2005)

Introduction

The adventitious detection[1] of $[Rh(CO)_2(PPh_3)_2Br]$ as a probable product of the reaction of $[Rh_6(CO)_{15}(PPh_3)]$ with Br^- led us to attempt to confirm its structure indirectly by crystallography of its more stable iodo analogue $[Rh(CO)_2(PPh_3)_2I]$ (**1**). This has been prepared more conveniently by reaction of $[Rh_4(CO)_{12}]$ with PPh_3 and NBu_4I under CO, and has been fully characterized by crystallography, IR and NMR spectroscopy. Five-coordinate $[Rh(CO)_2(PR_3)_2(Hal)]$ rhodium complexes had previously been reported[2–5] but were characterized only by NMR and IR spectroscopy. The spectroscopic data obtained for these complexes were not in good agreement but they are all compatible with four symmetrical structures described below. Two structures are based on a trigonal-bipyramidal motif[2–5] with either two COs or two phosphane ligands in the axial positions. Two other possibilities are represented by tetragonal pyramids with *cis* and *trans* arrangement of the ligands in the basal plane.[5] The disagreements in the experimental NMR spectroscopic data can be partially explained by fast exchange between the isomeric species[5] or by dissociative equilibria with the parent square planar $[Rh(CO)(PPh_3)_2(Hal)]$ complexes.[4]

The importance of a clear assignment of the structures of this sort lies in the general significance of five-coordinate Rh^I complexes in terms of the boundary between four-coordinate planar and five-coordinate (usually trigonal bipyramidal, sometimes square pyramidal) d^8 complexes in general, and their occurrence as intermediates in associative substitution reactions of planar Rh^I complexes and in similar reactions proposed for catalytic systems.[6] In particular, it has been clearly shown[5] that occurrence of the $[Rh(CO)_2(PPh_3)_2(Hal)]$ species must be taken into account in catalytic systems that contain the starting square-planar $[Rh(CO)(PPh_3)_2Hal]$ complexes under CO, a typical situation for carbonylation catalysis.

This aspect of the complex's importance is that there are only *two* other five-coordinate Rh^I complexes, the structures of which have been reported quite recently in the Cambridge Structural Database. One is the not exactly analogous $[Rh(PR_3)_2(CO)_3]^+$ cation[7] (trigonal-bipyramid with *trans* P donors), and the other is a closely analogous dinuclear $[Rh(CO)_2X(PP)]_2$ neutral complex, where two Rh^I centers are bridged by two long-chain bidentate diphosphane (PP) ligands. This has a trigonal-bipyramidal structure, with *trans* P donors. In general five-coordinate complexes of Rh^I are rare and/or unstable towards loss of the 5th ligand. In this paper we describe the isolation and detailed characterization (X-ray crystallography, IR, NMR) of the $[Rh(CO)_2(PPh_3)_2I]$ complex. The DFT optimization of the structure, and calculation of the IR spectroscopic characteristics are presented.

Results

The five-coordinate $[Rh(CO)_2(PPh_3)_2I]$ (**1**) complex, can be obtained either by addition of CO to the square-planar $[Rh(CO)(PPh_3)_2I]$[3] or by disproportionation of $[Rh_6(CO)_{15}(PPh_3)]$ in the presence of I^-.[1] In this paper we suggest another high-yield synthesis of **1** by the reaction of $[Rh_4(CO)_{12}]$ with I^- and PPh_3 under CO, according to the proposed stoichiometry:

$$3\,[Rh_4(CO)_{12}] + 4\,PPh_3 + 4\,I^- = 2\,[Rh_5(CO)_{15}I]^{2-} + 2\,[Rh(CO)_2(PPh_3)_2I]$$

[a] Department of Chemistry, St. Petersburg University, Universitetskii pr., 26, St. Petersburg, 198504, Russian Federation
E-mail: stunik@chem.spbu.ru
[b] Lash Miller Chemical Laboratories, University of Toronto, 80 St. George Street, Toronto M5S 3H6, Ontario, Canada

Supporting information for this article is available on the WWW under http://www.eurjic.org or from the author.

 © 2005 Wiley-VCH Verlag GmbH & Co. KGaA, Weinheim **DOI: 10.1002/ejic.200500444**

The complex is relatively stable in the solid state but in solution it must be kept under CO to prevent decarbonylation and formation of the square-planar $[Rh(CO)(PPh_3)_2I]$ complex as was observed earlier.[3] The solid-state structure of **1** has been characterized by a single-crystal X-ray diffraction study. The IR, ^{31}P, ^{13}C and VT ^{1}H NMR spectroscopic characteristics of **1** in solution were also measured. A very good agreement of the NMR spectroscopic data obtained for **1** and those reported earlier[3] for $[Rh(CO)_2(PPh_3)_2I]$ [^{31}P NMR: δ = 34.0 ppm, ^{1}J(Rh–P) = 91 Hz, ^{13}C: δ = 191.1 ppm, ^{1}J(Rh–C) = 70 Hz, ^{2}J(P–C), CD_2Cl_2, –50 °C] clearly indicates identity of these complexes. An ORTEP view of the molecule is shown in Figure 1 together with its principal structural parameters. The IR and ^{31}P NMR spectroscopic data are presented in the Experimental Section, and the mid-IR spectrum is shown in Figure 2. Quantum Chemical (DFT) calculations have been performed using the GAUSSIAN98 program package.[11] The DFT-B3LYP method,[12] and the basis set LanL2DZ with effective core potentials (ECP) for the Rh, P and I atoms,[13,14] were applied. The geometry optimizations were carried out without any symmetry constraints. The trigonal-bipyramidal structures with axial disposition of either phosphane or CO ligands were used as the starting geometries, but "no symmetry constraints" were imposed. Other feasible structures with the mixed axial/equatorial disposition of CO (PPh_3) ligands were not analyzed because they contradict the NMR spectroscopic data for **1**. In both cases we found local minima on the potential energy surface related to the corresponding structures. Selected results of these calculations are given in Table 1.

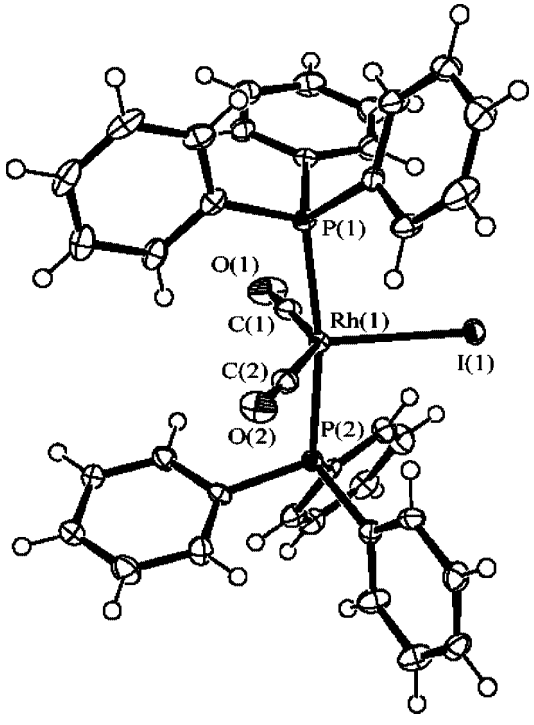

Figure 1. ORTEP plot of the molecular structure of $[Rh(CO)_2(PPh_3)_2I]$ (**1**). Thermal ellipsoids are drawn at the 50% level. Selected bond lengths [Å], Rh(1)–P(1) 2.3385(8), Rh(1)–P(2) 2.3298(7), Rh(1)–C(1) 1.915(3), Rh(1)–C(2) 1.903(3), Rh(1)–I(1) 2.8241(3), O(1)–C(1) 1.148(3), O(2)–C(2) 1.144(3) and angles [°], P(2)–Rh(1)–P(1) 170.34(3), C(2)–Rh(1)–C(1) 143.46(13), C(2)–Rh(1)–I(1) 111.11(9), C(1)–Rh(1)–I(1) 105.42(9).

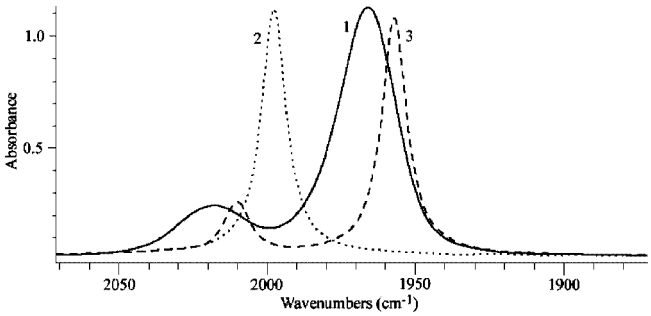

Figure 2. The IR spectroscopic patterns of the two trigonal-bipyramidal isomers of $[Rh(CO)_2(PPh_3)_2I]$. Experimental spectrum of **1** (−). Calculated spectra for the isomer with two axial (-----) and two equatorial (·····) PPh_3 ligands.

Discussion

In the solid state the molecule of **1** forms a trigonal pyramid with two phosphane ligands in the axial positions. The iodide and two carbonyl ligands occupy three equatorial sites. The molecule can be assigned to the C_{2v} idealized symmetry group. Two bonds connecting the phosphorus and rhodium atoms in **1** are slightly bent to form the angle of 170.34(3)°. This distortion from the idealized axial geometry of the phosphanes seems to be dictated by nonbonding interaction of the iodide with the phenyl substituents of the ligands. The angle between Rh–C(O) bonds in the equatorial plane [143.46(13)°] considerably exceeds the I–Rh–C(O) angles [111.11(9)° and 105.42(9)°] to accommodate the phenyl substituents tilted from the iodide to the carbonyl ligands because of the P–Rh–P angle distortion mentioned above. It is worth noting at this point that in the cobalt $[Co(CO)_2(PEt_3)_2I]$[15] and iridium $[Ir(CO)_2(PPh_3)_2I]$[16] congeners the angular distortions are minimal [e.g. P–Co–P and P–Ir–P angles equal to 179.0° and 179.1°, respectively] due to the smaller effective cone angle of the phosphane in the former complex, and to larger metal-to-ligands distances in the latter.

These distortions from an exact trigonal-bipyramidal conformation place **1** on the trajectory involved in a Berry rotation process of the sort usually invoked in scrambling reactions of trigonal-bipyramidal complexes. Because of this it is important to confirm that **1** exists in solution in the same isomeric form as that observed in the solid state. The ^{31}P NMR spectrum displays a doublet resonance (δ = 31.2 ppm [d, ^{1}J(Rh–P) 94.4 Hz]) that points to structurally equivalent phosphane ligands bound to rhodium. The $^{13}C\{^{1}H\}$ spectrum also displays one signal in the carbonyl region, split into doublet of triplets due to the couplings with rhodium [^{1}J(Rh–C) 70.0 Hz] and phosphorus [^{2}J(P–C) 14.5 Hz], the latter being typical of *cis* two-bond coupling. These data are compatible with two structural patterns,

 © 2005 Wiley-VCH Verlag GmbH & Co. KGaA, Weinheim

Table 1. Selected experimental and calculated parameters for the two trigonal-bipyramidal isomers of $[Rh(CO)_2(PPh_3)_2I]$.

	Experimental	Calculated Both PPh_3 ligands axial	Both PPh_3 ligands equatorial
E [a.u]		–1750.286712	–1750.284387
E + ZPE [a.u]		–1749.715615	–1749.713262
H_{298} [a.u]		–1749.672208	–1749.669831
G_{298} [a.u]		–1749.800687	–1749.798956
S [cal/(mol·K)]		270.408	271.766
ΔE [kcal/mol]		–1.46	
Bond lengths [Å]			
Rh–P	2.338; 2.330	2.450	2.526; 2.494
Rh–C	1.903; 1.916	1.906; 1.928	1.910; 1.916
Rh–I	2.824	2.962	2.888
C–O	1.147; 1.143	1.185; 1.181	1.175; 1.177
Bond angles [deg]			
(O)C–Rh–C(O)	143.4	142.4	168.5
P–Rh–P	170.3	177.6	124.4
IR carbonyl frequencies [cm^{-1}]			
$\nu_{antisym}$ (int., [km/mol])	1967 (1010)	1898 (1017)	1938 (1025)
$\nu_{antisym}$ corrected[a]		1956 (1017)	1997 (1025)
ν_{sym} (int.)	2022 (240)	1949 (225)	2001 (13)
ν_{sym} corrected[a]		2009 (225)	2062 (13)

[a] The values of band frequencies are multiplied by the scaling factor 1.03 (see text).

which contain either phosphane or carbonyl ligands in the axial positions of the trigonal bipyramid. Four signals of aromatic carbon atoms between δ = 133 and 128 ppm are indicative of free rotation of the phosphane ligands and their phenyl substituents about the P–C and Rh–P bonds. The proton spectra of **1** display two typical multiplets (2/3 relative intensities) of aromatic protons in the temperature range +25 °C to –40 °C (see Figure S1 in the supporting information; for details see also the footnote on the first page of this article) and this also points to the absence of steric hindrance to rotation in the molecule under these conditions. The latter observations make it more probable that the phosphane ligands are in the axial positions so that nonbonding interactions in the ligand sphere of **1** are minimized. Nevertheless, the NMR spectroscopic data do not allow an unambiguous decision on the stereochemistry of **1**. Analysis of the IR spectroscopic patterns corresponding to the alternative structural hypotheses (see below) showed that this type of spectroscopy provides more reliable background to make a choice in favor of one or another structure. The IR spectrum of **1** in the carbonyl region displays two bands of significant intensity (see Table 1) that is in contrast with the first report on the synthesis of $[Rh(CO)_2(PPh_3)_2I]$[3] where only one carbonyl absorption band was found. The NMR spectroscopic data for **1** are in a good agreement with the data obtained for the above compound[3] [$^{31}P\{^1H\}$ 34 ppm, $^{13}C\{^1H\}$ 191.1 ppm, ^1J(Rh–P) = 91 ppm, ^1J(Rh–C) = 70 Hz, ^2J(C–P) = 16 Hz], and it seems very probable that in the early study[3] the high-frequency band has been missed in the spectrum either because of low sensitivity of the instrument used or due to low concentration of the sample. It has to be also noted that structurally analogous complexes of cobalt[15] and iridium,[16] as well as the chloride and bromide rhodium derivatives[5] $\{[Rh(CO)_2(PPh_3)_2X]\}$ also display two absorption bands in the carbonyl region with essentially similar location and relative intensities. A very similar trigonal-bipyramidal environment of the Rh^I center has been recently found[17] in the dinuclear rhodium complex $[Rh(CO)_2I(PP)]_2$ where two rhodium atoms are bridged by a long-chain diphosphane (PP) ligand with the phosphorus functionalities in axial positions. The structure of this complex found in the solid state must be retained in solution because of the rigidity of the macrocyclic structure of this molecule and two carbonyl absorption bands observed in solution must be associated with the trigonal-bipyramidal structure bearing two phosphorus ligands in the axial positions. Thus the further analysis of geometry of **1** will be based on the presence of two carbonyl absorption bands in its IR spectrum, something that is evidently of crucial importance for a proper assignment of its solution structure.

The DFT calculations of the electronic structure of **1** have shown that the full energy of the isomer with *axial* PPh_3 ligands is slightly lower (1.5 kcal/mol) than that of the form with equatorial phosphanes. Although this small difference cannot be considered as a decisive argument in favor of one or another structure, it would allow for there being as little as ca. 10% of the equatorial isomer to be present in solution. Inclusion of thermochemical corrections does not change this ratio. The bond angles (Table 1), calculated for the isomer with two axial phosphane ligands, are in good agreement with the crystallographic data obtained for **1**. Higher values of the calculated Rh–C, Rh–I and C–O bonds are quite expected because polarizing functions were not included in the basis set of orbitals. Calculation of the IR spectra gave two carbonyl stretch bands (ν_{asymm} and ν_{symm}) for both isomeric forms with, however, essentially different relative intensities. Comparison of the calculated band frequencies with the experimental data shows considerable underestimation of the calculated values. However, this is quite typical for complexes of this sort, and an independent study[18] of another family of five-coor-

 © 2005 Wiley-VCH Verlag GmbH & Co. KGaA, Weinheim

dinate carbonyl rhodium compounds ([$Rh(RCOO)(PPh_3)_2(CO)$], R = H, CH_3, CF_3) showed that similar calculations gave consistent values of the band frequencies with the use of scaling factor equal to 1.03. When we applied this factor in the present study it led to much better agreement between experimental and calculated values of the band frequencies. However, in the present case these parameters alone do not allow distinguishing the two possible structures of **1**. Relative intensities of the bands are much stronger discriminative factor due to their well-documented dependence on the angle between carbonyl groups in dicarbonyl complexes.[6,16,19] The greater (O)C–Rh–C(O) bond angle when the CO ligands are both axial resulted in a decrease of the $I_{sym}/I_{antisym}$ value down to ca. 0.01, a value that would actually result in the disappearance of this band from the experimental spectrum. The agreement between experimental and calculated (O)C–Rh–C(O) bond angles when the phosphanes are both axial is completely in line with the excellent fit of the relative intensities of the calculated IR bands and those observed in the experimental spectrum, as shown in Figure 2. Thus, the combination of the spectroscopic data with the calculations described above allows an unambiguous assignment of the solution structure of **1**, which was arguable until the present time.

Experimental Section

General Comments: The complex [$Rh_4(CO)_{12}$] was prepared according to published procedure.[8] [NBu_4]I and PPh_3 (Aldrich) were used as received. Chloroform, hexanes and methanol (Aldrich) were used without additional purification. Tetrahydrofuran was distilled from over Na-benzophenone ketyl under nitrogen prior to use. Infrared spectra were recorded with a Nicolet Magna IR 550 FTIR spectrometer. ^{31}P, ^{1}H and ^{13}C NMR spectra were recorded with Varian Gemini 300 or Unity 500 instruments, and referenced to external 85% H_3PO_4 and residual solvent resonances, respectively.

Preparation of [$Rh(CO)_2(PPh_3)_2I$] (1): [$Rh_4(CO)_{12}$] (206 mg, 0.28 mmol) was dissolved in $CHCl_3$ (10 cm^3) and a slight excess of PPh_3 (97 mg, 0.37 mmol) was added to the solution under nitrogen. After the liberation of gaseous CO was complete, the reaction mixture was degassed (3 freeze-pump-thaw cycles) and saturated with CO. NBu_4I (184 mg, 0.5 mmol) was added to the solution under CO. The course of the reaction was monitored by ^{31}P NMR spectroscopy. After 6–7 hours the ^{31}P NMR spectrum displayed one doublet signal that indicated formation of a phosphorus-containing rhodium complex. The solvent was removed under a flow of gaseous CO. The resulting dark red oily material was first diluted with CO-saturated THF (1 cm^3) and then with CO-saturated methanol (10 cm^3) to give a yellow crystalline precipitate of [$Rh(CO)_2(PPh_3)_2I$] (**1**) and a dark red solution containing anionic cluster species. The suspension obtained was stirred under a flow of CO for 15 minutes to complete precipitation of the product. The mother liquor was then carefully decanted, and the residue was washed with CO-saturated methanol (2×3 cm^3) and dried under a flow of CO to afford 108 mg of **1**. Single crystals of **1** suitable for an X-ray diffraction study were obtained by slow gas-phase diffusion of heptane into a THF/2-propanol solution under CO. IR (CH_2Cl_2, cm^{-1}): ν(CO) = 2018 w br, 1967 s br. $^{13}C\{^1H\}$ NMR (CD_2Cl_2, –80 °C): δ = 191.4 [dt, ^1J(Rh–C) = 70.0, ^2J(P–C) = 14.5 Hz], 134.2 (2 C_{Ph}), 132.9 (multiplet, *ipso*-C_{Ph}), 131.2 (1 C_{Ph}), 128.7 (2 C_{Ph}) ppm. $^{31}P\{^1H\}$ NMR ($CDCl_3$, 20 °C): δ = 31.2 ppm [d, ^1J(Rh–P) = 94.4 Hz].

X-ray Structure Determinations: Data were collected with a Nonius Kappa-CCD diffractometer using monochromated Mo-K_α radiation and were measured using a combination of φ scans and ω scans with κ offsets, to fill the Ewald sphere. The data were processed by using the Denzo-SMN software package.[9] The structure was solved and refined using SHELXTL V6.1[10] for full-matrix least-squares refinement that was based on F^2. All H atoms were included in calculated positions and allowed to refine in riding-motion approximation with U_{iso} tied to the carrier atom. Crystallographic data for the compounds is given in Table 2. Selected structural parameters are given in Table 1.

Table 2. Crystal data and structure refinement for [$Rh(CO)_2(PPh_3)_2I$] (**1**).

Empirical formula	$C_{38}H_{30}IO_2P_2Rh$
Formula mass	810.37
Temperature	100.0(1) K
Wavelength	0.71073 Å
Crystal system	monoclinic
Space group	*P*21/*n*
Unit cell dimensions	a = 11.8571(2) Å, α = 90°
	b = 14.0879(2) Å, β = 97.8310(10)°
	c = 20.8420(3) Å, γ = 90°
Volume	3449.01(9) $Å^3$
Z	4
Density (calculated)	1.561 Mg/m^3
Absorption coefficient	1.515 mm^{-1}
F(000)	1608
Crystal size	0.20 × 0.17 × 0.07 mm
Theta range for data collection	4.14–30.03°
Index ranges	$0 \le h \le 16$, $0 \le k \le 19$, $-29 \le l \le 29$
Reflections collected	38993
Independent reflections	10020 [R(int.) = 0.068]
Completeness to θ = 30.03°	99.4%
Absorption correction	Multi-scan (Denzo-SMN)
Max. / min. transmission	0.9014 / 0.7515
Refinement method	Full-matrix least-squares on F^2
Data / restraints / parameters	10020 / 0 / 397
Goodness-of-fit on F^2	0.891
Final R indices [$I > 2\sigma(I)$]	R_1 = 0.0376, wR_2 = 0.0658
R indices (all data)	R_1 = 0.0795, wR_2 = 0.0717
Largest diff. peak and hole	1.033 and –0.721 e·$Å^{-3}$

CCDC-271952 contains the supplementary crystallographic data for this paper. These data can be obtained free of charge from The Cambridge Crystallographic Data Centre via www.ccdc.cam.ac.uk/data_request/cif.

Supporting Information: (see footnote on the first page of this article): 400-MHz ^1H NMR variable-temperature spectra of **1**.

Acknowledgments

We are grateful to the NATO, for support through a Collaborative Research Grant (OUTR.CRG 951482) and for the award of a postdoctoral fellowship to IOK, and to the Natural Science and Engineering Research Council, Ottawa, for additional support. We also thank the University of Joensuu (Finland) for the opportunity to use the computer facilities of the Department of Chemistry and Dr. Matti Haukka for running the DFT calculations.

[1] C. Babij, D. H. Farrar, I. O. Koshevoy, A. J. Poë, S. P. Tunik, *Dalton Trans.* **2005**, 116–122.

 © 2005 Wiley-VCH Verlag GmbH & Co. KGaA, Weinheim

[2] A. R. Sanger, *Can. J. Chem.* **1984**, *62*, 2168–2169.
[3] A. R. Sanger, *Can. J. Chem.* **1985**, *63*, 571–575.
[4] E. Rotondo, G. Battaglia, G. Giordano, F. P. Cusmano, *J. Organomet. Chem.* **1993**, *450*, 245–252.
[5] M. J. Payne, D. J. Cole-Hamilton, *J. Chem. Soc., Dalton Trans.* **1997**, 3167–3175.
[6] R. H. Crabtree, *The Organometallic Chemistry of Transition Metals*, 2nd ed., John Wiley &Sons: New York, **1994**.
[7] H.-S. Lee, J.-Y. Bae, J. Ko, Y. S. Kang, H. S. Kim, S.-J. Kim, J.-H. Chung, S. O. Kang, *J. Organomet. Chem.* **2000**, *614/615*, 83–91.
[8] S. Martinengo, P. Chini, G. Giordano, *J. Organomet. Chem.* **1971**, *27*, 389–391.
[9] Z. Otwinowski, W. Minor, *Methods in Enzymology, Macromolecular Crystallography*, part A (Eds.: C. W. Carter, Jr., R. M. Sweet), Academic Press, New York, **1997**, vol. 276, pp. 307–326.
[10] G. M. Sheldrick, Bruker Analytical X-ray Systems, Bruker AXS, Inc.Madison: Wisconsin, USA, **2001**.
[11] M. J. Frisch, G. W. Trucks, H. B. Schlegel, G. E. Scuseria, M. A. Robb, J. R. Cheeseman, V. G. Zakrzewski, J. A. J. Montgomery, R. E. Stratmann, J. C. Burant, S. Dapprich, J. M. Millam, A. D. Daniels, K. N. Kudin, M. C. Strain, O. Farkas, J. Tomasi, V. Barone, M. Cossi, R. Cammi, B. Mennucci, C. Pomelli, C. Adamo, S. Clifford, J. Ochterski, G. A. Petersson, P. Y. Ayala, Q. Cui, K. Morokuma, D. K. Malick, A. D. Rabuck, K. Raghavachari, J. B. Foresman, J. Cioslowski, J. V. Ortiz, B. B. Stefanov, G. Liu, A. Liashenko, P. Piskorz, I. Komaromi, R. Gomperts, R. L. Martin, D. J. Fox, T. Keith, M. A. Al-Laham, C. Y. Peng, A. Nanayakkara, C. Gonzalez, M. Challacombe, P. M. W. Gill, B. Johnson, W. Chen, M. W. Wong, J. L. Andres, C. Gonzalez, M. Head-Gordon, E. S. Replogle, J. A. Pople, in "GAUSSIAN-98", Pittsburgh, PA, Revision A.7 ed.; **1998**.
[12] A. D. Becke, *J. Chem. Phys.* **1993**, *98*, 5648–5651.
[13] W. R. Wadt, P. J. Hay, *J. Chem. Phys.* **1985**, *82*, 284–298.
[14] P. J. Hay, W. R. Wadt, *J. Chem. Phys.* **1985**, *82*, 299–310.
[15] A. C. Marr, E. J. Ditzel, A. C. Benyei, P. Lightfoot, D. J. Cole-Hamilton, *Chem. Commun.* **1999**, 1379–1380.
[16] F. Abu-Hasanayn, T. J. Emge, J. A. Maguire, K. Krogh-Jespersen, A. S. Goldman, *Organometallics* **1994**, *13*, 5177–5180.
[17] F. M. Dixon, A. H. Eisenberg, J. R. Farrell, C. A. Mirkin, L. M. Liable-Sands, A. L. Rheingold, *Inorg. Chem.* **2000**, *39*, 3432–3433.
[18] O. V. Sizova, Y. S. Varshavskii, T. G. Cherkasova, A. B. Nikol'skii, *Russian Coord. Chem.* **2005**, *in press.*
[19] F. A. Cotton, G. Wilkinson, *Advanced Inorganic Chemistry*; 5th ed., John Wiley & Sons: New York, **1988**.

Received: May 17, 2005
Published Online: October 5, 2005

 © 2005 Wiley-VCH Verlag GmbH & Co. KGaA, Weinheim

Phase Behaviors of the $ZrMo_{2-x}W_xO_8$ (x = 0.2–2.0) System and the Preparation of an Mo-Rich Cubic Phase

Ling Huang,[a] Qiu-guo Xiao,[a] Hui Ma,[b] Guo-bao Li,[c] Fu-hui Liao,[c] Chuan-min Qi,[a] and Xin-hua Zhao*[a]

Keywords: Calorimetry / Materials science / Phase diagrams / Phase transitions / Zirconium

The phase behaviors of $ZrMo_{2-x}W_xO_8$ (x = 0.2 to 2.0) solid solutions have been studied systematically by variable-temperature X-ray diffraction (XRD) and differential scanning calorimetric (DSC) techniques. A low-temperature (LT) orthorhombic $ZrMo_{2-x}W_xO_8$ (x = 0.2–2.0) phase is formed by dehydration of the precursors $ZrMo_{2-x}W_xO_7(OH)_2(H_2O)_2$ (x = 0.2–2.0) within a temperature range from 124 to 203 °C. Among them, the orthorhombic $ZrMo_{2-x}W_xO_8$ solid solutions are able to convert further into metastable cubic phases within an x-dependent temperature range from 502 to 552 °C; the trigonal phases become dominant at higher temperature for Mo-rich solid solutions. However, no trigonal phases are formed in the high-temperature region for W-rich solid solutions. The absence of decomposition of $ZrMo_{2-x}W_xO_8$ (x = 0.2 to 1.6) solid solutions up to 800 °C indicates that the molybdenum substitution leads to a remarkable improvement of the thermal stability in comparison with ZrW_2O_8. Based on the phase behaviors reported in this paper, an approach for the preparation of cubic Mo-rich solid solutions $ZrMo_{2-x}W_xO_8$ with attractive negative thermal expansion (NTE) properties is demonstrated.

(© Wiley-VCH Verlag GmbH & Co. KGaA, 69451 Weinheim, Germany, 2005)

Introduction

The considerable interest in the study of cubic AM_2O_8 (A = Zr, Hf; M = W, Mo) compounds,[1–4] as well as their solid solutions $ZrMo_{2-x}W_xO_8$,[5–8] has been fueled recently by their isotropic negative thermal expansion (NTE) over a very wide temperature range. These compounds are usually synthesized by dehydration of the corresponding hydrate precursors. Typically, $ZrMo_2O_8$ and ZrW_2O_8 are obtained by dehydration of the precursors $ZrMo_2O_7(OH)_2(H_2O)_2$[9] and $ZrW_2O_7(OH)_2(H_2O)_2$,[10] respectively. The similarity in chemical and crystallographic properties between W^{VI} and Mo^{VI} suggests that the compounds ZrW_2O_8 and $ZrMo_2O_8$ should be isomorphic and readily form solid solutions. Solid solutions of $ZrMo_{2-x}W_xO_8$ have indeed been synthesized and the properties of $ZrMoWO_8$, including thermal expansion and oxygen migration at low temperature, have also been reported.[11] However, conspicuous gaps are seen with respect to the temperature-dependent phase behaviors of solid solutions of different compositions.

In this paper, the synthesis and phase behaviors of $ZrMo_{2-x}W_xO_8$ (x = 0.2–2.0) solid solutions are studied using variable-temperature X-ray diffraction (XRD) and different scanning calorimetric (DSC) techniques. It has been found that different structural phases of Mo-rich and W-rich $ZrMo_{2-x}W_xO_8$ solid solutions can be formed under the same heating conditions due to the differences in the thermal stabilities of ZrW_2O_8 and $ZrMo_2O_8$ polymorphs. Cubic, Mo-rich solid solutions of $ZrMo_{2-x}W_xO_8$ (x = 0.2, 0.4, 0.6, 0.7, 0.8) can be synthesized successfully by controlling the temperature within the appropriate range.

[a] Department of Chemistry, Beijing Normal University, Beijing, 100875, P. R. China
[b] Analyzing and Testing Center, Beijing Normal University, Beijing, 100875, P. R. China
[c] College of Chemistry and Molecular Engineering, Peking University, Beijing, 100871, P. R. China

Results and Discussion

Thermal Analysis

DSC curves were recorded in the temperature range of 40–800 °C for molybdenum-rich (x = 0.2, 0.4, 0.6, 0.7, or 0.8) and tungsten-rich (x = 1.0, 1.2, 1.4, 1.6, or 2.0) $ZrMo_{2-x}W_xO_7(OH)_2(H_2O)_2$ precursors. Typical DSC curves of the Mo-rich precursors $ZrMo_{1.6}W_{0.4}O_7(OH)_2(H_2O)_2$ and W-rich precursors $ZrMo_{0.4}W_{1.6}O_7(OH)_2(H_2O)_2$ are presented in Figure 1 (parts a and b), respectively. The single endothermic peak appearing in each of these curves (at 127 and 165 °C, respectively) indicates the formation of anhydrous orthorhombic phases due to dehydration in both cases. However, the DSC curve of the Mo-rich solid solution $ZrMo_{1.6}W_{0.4}O_8$ shows two exothermic peaks located at 508 and 562 °C assigned to the formation of a cubic and trigonal phase, respectively, although only one exothermic peak due to the formation of a cubic phase is observed at 542 °C in the DSC curve of the W-rich $ZrMo_{0.4}W_{1.6}O_8$ solid solu-

tion. This difference indicates clearly that there are two distinct phase-transition mechanisms operating during heating of Mo- and W-rich $ZrMo_{2-x}W_xO_8$ solid solutions.

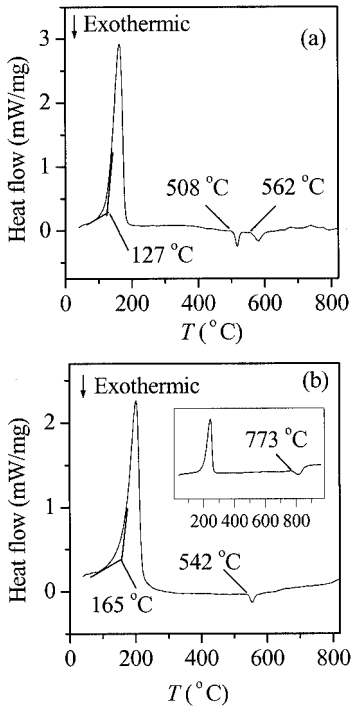

Figure 1. DSC curves of $ZrMo_{1.6}W_{0.4}O_7(OH)_2(H_2O)_2$ (a) and $ZrMo_{0.4}W_{1.6}O_7(OH)_2(H_2O)_2$ (b). The DSC of $ZrW_2O_7(OH)_2(H_2O)_2$, which indicates that ZrW_2O_8 decomposes at 773 °C, is given in the inset.

Increasing the tungsten fraction x leads to a gradual shift of the endothermic peak of the solid solutions $ZrMo_{2-x}W_xO_7(OH)_2(H_2O)_2$ (x = 0.2–2.0) from 124 up to 203 °C.

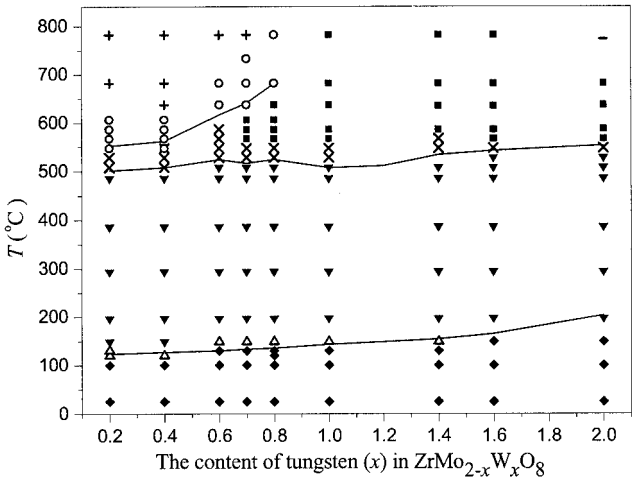

Figure 2. The overall process of phase transition for the $ZrMo_{2-x}W_xO_7(OH)_2(H_2O)_2$ system during the heating procedure. The solid lines link the onset peak values of the DSC curves. The crystal structures of precursor (black diamond) and dehydrates of specific composition x at different temperatures are indicated with different symbols: tetragonal: black diamond (♦); orthorhombic: black triangle (▼); tetragonal and orthorhombic: open triangle (Δ); orthorhombic and cubic: ×; cubic: black square (■); cubic and trigonal: open circle (○); trigonal: +; decomposition: –.

Similarly, the increase in x also causes an up-shift of the first exothermic peak from 502 to 552 °C. However, the second exothermic peak of $ZrMo_{2-x}W_xO_8$ ($1 \leq x < 2$) disappears at higher temperature, although it shows a more remarkable shift for solid solutions $ZrMo_{2-x}W_xO_8$ with x less than 1.0 (see Figure 2). The appearance of the exothermic peak in the DSC curve of ZrW_2O_8 suggests its decomposition temperature is located at 773 °C (see the inset in Figure 1, b). This observation indicates that these solid solutions have a higher decomposition temperature than ZrW_2O_8. A similar feature has been observed for the $ZrMo_{2-x}W_xO_8$ solid solution.[6] In addition, no enthalpy changes due to MoO_3 sublimation of $ZrMo_{2-x}W_xO_8$ compounds (x = 0.2–1.6) are detected at temperatures up to 800 °C even though MoO_3 sublimation has been reported to occur for $ZrMo_2O_8$ at 750 °C.[4]

Variable-Temperature XRD Analysis

The composition- and temperature-dependence of the phase behaviors of $ZrMo_{2-x}W_xO_7(OH)_2(H_2O)_2$ solid solutions were examined by variable-temperature XRD measurement in real time as they are expected to indicate the mechanism responsible for the phase transition detected by the DSC measurements. Figures 3 and 4 show the variable-temperature XRD patterns of $ZrMo_{1.6}W_{0.4}O_7(OH)_2(H_2O)_2$ and $ZrMo_{0.4}W_{1.6}O_7(OH)_2(H_2O)_2$, respectively. Based on refined XRD patterns of $ZrMo_{2-x}W_xO_7(OH)_2(H_2O)_2$, it is evident that precursors at the temperature below the endothermic peak exist in the form of a tetragonal phase. As demonstrated by the typical XRD patterns of $ZrMo_{1.6}W_{0.4}O_8$ in the temperature range 120–508 °C and $ZrMo_{0.4}W_{1.6}O_8$ in the temperature range 197–567 °C, all $ZrMo_{2-x}W_xO_8$ solid solutions (x = 0.2–2.0) formed by precursor dehydration show XRD patterns similar to that observed for o-$ZrMo_{0.4}W_{1.6}O_8$.[12] Hence, the XRD patterns of all $ZrMo_{2-x}W_xO_8$ solid solutions can be indexed using the orthorhombic structure of o-$ZrMo_{0.4}W_{1.6}O_8$ with the space group $Pmn2_1$ as reference; the indexed results are summarized in Table 1.

A close inspection of the XRD pattern of $ZrMo_{1.6}W_{0.4}O_7(OH)_2(H_2O)_2$ collected at 120 °C (Figure 3) reveals a shoulder diffraction peak located at 21° (2θ), which seems to be assignable to the 111 diffraction of o-$ZrMo_{1.6}W_{0.4}O_8$. The appearance of this shoulder indicates the beginning of the dehydration of the $ZrMo_{1.6}W_{0.4}O_7(OH)_2(H_2O)_2$ precursor; this dehydration process is complete at around 149 °C, as demonstrated by the disappearance of the XRD pattern of the hydrate precursor at this temperature. The accompanied enhancement and sharpening of the XRD peaks upon increasing the temperature from 149 to 486 °C illustrates that o-$ZrMo_{1.6}W_{0.4}O_8$ grows subsequently to the fine crystal. Combing the XRD patterns with the DSC curves displayed in Figure 2 shows that the o-$ZrMo_{1.6}W_{0.4}O_8$ phase converts into the cubic phase c-$ZrMo_{1.6}W_{0.4}O_8$ at 508 °C, which converts, in turn, into the thermodynamically stable trigo-

 © 2005 Wiley-VCH Verlag GmbH & Co. KGaA, Weinheim

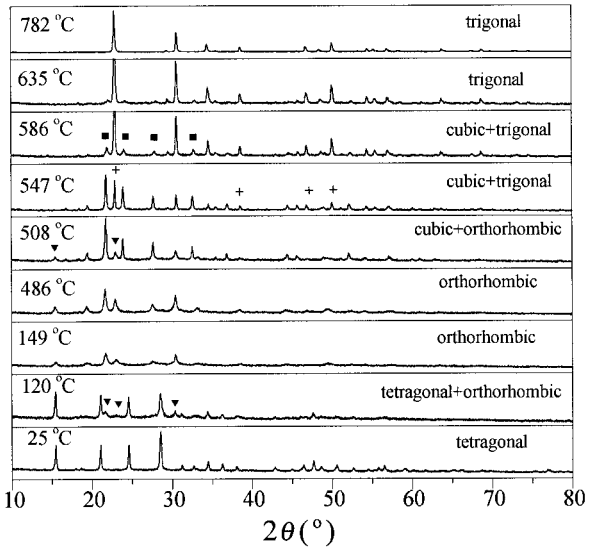

Figure 3. The variable-temperature XRD patterns of $ZrMo_{1.6}W_{0.4}O_7(OH)_2(H_2O)_2$ (25 °C) and $ZrMo_{1.6}W_{0.4}O_8$. The diffraction peaks characterizing the polymorphs are marked by a black triangle (▼) (orthorhombic), a black square (■) (cubic), or (+) (trigonal). The denoted temperatures were calibrated against KCl.

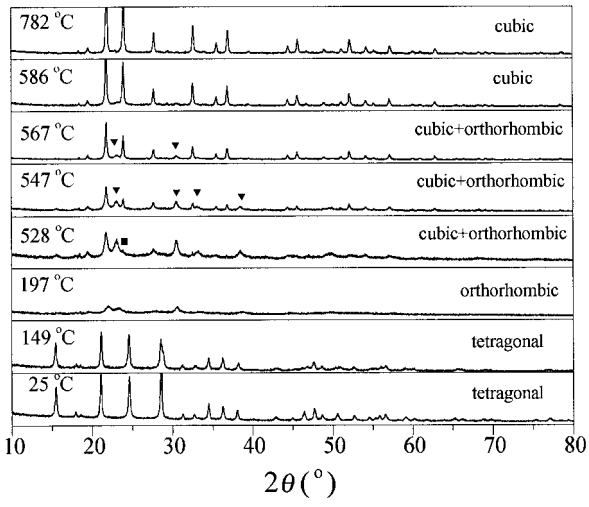

Figure 4. The variable-temperature XRD patterns of $ZrMo_{0.4}W_{1.6}O_7(OH)_2(H_2O)_2$ (≤149 °C) and $ZrMo_{0.4}W_{1.6}O_8$. The diffraction peaks characterizing the polymorphs are marked by a black triangle (▼) (orthorhombic) or a black square (■) (cubic). The denoted temperatures were calibrated against KCl.

nal phase within a narrower temperature "window" of about 54 °C (508–562 °C) at the expense of formation of a pure cubic phase. Therefore, the pure cubic phases of Mo-rich solid solutions can be formed only under carefully controlled temperature conditions.

The pure trigonal $ZrMo_{2-x}W_xO_8$ (x = 0.2–0.7) was prepared at 782 °C and was indexed by using the α′-$ZrMo_2O_8$ model of space group $P\bar{3}m1$[13] rather than α-$ZrMo_2O_8$ of space group $P\bar{3}1c$,[14] because of the absence of 201, 103, and 211 diffractions in the XRD pattern of trigonal $ZrMo_{1.6}W_{0.4}O_8$. The pure trigonal phases of $ZrMo_{2-x}W_xO_8$ (x = 0.2–0.7) are thermodynamically stable up to 800 °C; their lattice parameters are summarized in Table 2.

Table 1. Lattice parameters of o-$ZrMo_{2-x}W_xO_8$ solid solutions at 386 °C.

x	a [Å]	b [Å]	c [Å]	V [Å^3]
0.2	5.86	7.33	9.13	392
0.4	5.86	7.34	9.15	393
0.6	5.86	7.25	9.12	387
0.7	5.86	7.24	9.12	387
0.8	5.85	7.23	9.11	386
1.0	5.85	7.24	9.10	386
1.2	5.85	7.23	9.10	385
1.4	5.85	7.22	9.10	384
1.6	5.85	7.21	9.11	384
2.0	5.85	7.21	9.10	384

Table 2. The lattice parameters of the trigonal phase of $ZrMo_{2-x}W_xO_8$ (x = 0.2–0.7) solid solutions at 782 °C.

x	a [Å]	c [Å]	V [Å^3]
0.2	5.824	6.051	177.7
0.4	5.833	6.075	178.9
0.6	5.825	6.040	177.4
0.7	5.823	6.036	177.3

The stability of cubic $ZrMo_{2-x}W_xO_8$ solid solutions (x = 0.2–0.8) increases rapidly with increasing W-fraction (x) from 0.2 to 0.8. As indicated in Figure 2, the metastable pure cubic phases of the solid solutions of x = 0.7 and 0.8 exist over a wide temperature range, and when x is greater than or equal to 1.0 the metastable cubic phase can be found even at temperature up to 800 °C.

Figure 4 indicates that the W-rich solid solution $ZrMo_{0.4}W_{1.6}O_7(OH)_2(H_2O)_2$ converts completely into orthorhombic o-$ZrMo_{0.4}W_{1.6}O_8$ at 197 °C, which is stable up to 528 °C. This observation suggests that the orthorhombic isomorphs of W-rich solid solutions appear to be more stable than those of Mo-rich solid solutions.

The appearance of the small peak located at about 23.8° (2θ) due to the 211 diffraction of the cubic phase in the XRD pattern collected at 528 °C indicates further that W-rich o-$ZrMo_{2-x}W_xO_8$ solid solutions, including o-$ZrMo_{0.4}W_{1.6}O_8$, convert into a cubic phase at 528 °C and that these cubic phases, except x = 2.0, are stable at temperatures up to 782 °C. Since the 310 diffraction of 31° (2θ) disappears at this temperature, the cubic phase can be assigned to the structure type β-ZrW_2O_8. This feature is true for all W-rich solid solutions.

Phase Behaviors of Solid Solutions

Figure 2 displays the phase-transition processes of $ZrMo_{2-x}W_xO_7(OH)_2(H_2O)_2$ solid solutions deduced on the basis of the XRD and DSC experiments outlined above. It can be seen that decomposition of the precursors proceeds through a sequential phase-transition process, namely tetragonal → orthorhombic → cubic → trigonal polymorphs. The phase-transition temperatures increase with increasing

 © 2005 Wiley-VCH Verlag GmbH & Co. KGaA, Weinheim

W-fractions. This dependence is understandable in terms of the bond strength of W–O, which is stronger than that of Mo–O (the bond-dissociation energies for these bonds are 672.0 ± 41.8 and 560.2 ± 20.9 kJ mol^{-1}, respectively).[15]

The difference in phase-transition mechanism of W-rich and Mo-rich solid solutions can be interpreted in terms of trigonal phase formation. Cubic ZrW_2O_8 is metastable over a wide temperature range below 777 °C, whereas the cubic phase of $ZrMo_2O_8$ is dynamically stable only over a narrower window ranging from 480 to 520 °C, above which trigonal $ZrMo_2O_8$ crystallizes.[4] So, it would be expected that the stability of cubic phases of $ZrMo_{2-x}W_xO_8$ solid solutions at high temperature would be greater for W-rich $ZrMo_{2-x}W_xO_8$ solid solutions due to prevention of trigonal phase formation. A close inspection of the phase-composition dependence of behaviors for the $ZrMo_{2-x}W_xO_8$ solid solution reveals indeed that a dynamic equilibrium between these two processes can be established at $x = 1.0$, above which, i.e. $1 \leq x < 2$, the cubic phase is stable at temperatures up to 800 °C; however, the stable cubic phase is difficult to form in solid solutions of $x \leq 0.8$ in the same temperature range.

It is of interest to note that the stability of $ZrMo_{2-x}W_xO_8$ solid solutions can be improved by increasing the Mo fraction. In this way, the decomposition of this solid solution to the corresponding oxides can be prevented even at 800 °C. Therefore, as compared to both ZrW_2O_8 and $ZrMo_2O_8$, $ZrMo_{2-x}W_xO_8$ solid solutions appear to be more stable due to the entropy effect induced by W or Mo doping. Moreover, $ZrMo_{2-x}W_xO_8$ ($1 \leq x \leq 1.6$) solid solutions show a lower phase-transition temperature and have negative expansion coefficients; they are also stable over a wider temperature range. All these factors make solid solutions of this kind more attractive for use in optical and electronic devices.

Preparation of an Mo-Rich $ZrMo_{2-x}W_xO_8$ Solid Solution of a Pure Cubic Phase

Variable-temperature XRD measurements of $ZrMo_{2-x}W_xO_8$ in real time demonstrate that the yield for the orthorhombic → cubic as well as the cubic → trigonal phase-transition depends not only on the system composition and temperature, but also on the temperature-holding time. Hence, strict control of both the temperature and temperature-holding time are crucial for preparation of an Mo-rich cubic phase. The pure cubic phase of $ZrMo_2O_8$ has been synthesized by Lind[4] under rigorously controlled experimental conditions. Following the thermal phase-transition process formulated on the basis of our DSC and XRD data outlined above, we have successfully prepared a pure cubic phase of Mo-rich solid solutions $ZrMo_{2-x}W_xO_8$ with $x = 0.4$, 0.6 and 0.7, 0.8 by holding the temperature at 520 and 530 °C, respectively, for 2 h, followed by rapid cooling to room temperature. It should be noted that a higher temperature is able to accelerate the trigonal phase formation. In addition, a pure cubic phase of $x = 0.2$ cannot be formed in this way, although it can be prepared by two-step heating, i.e. by heating at 365 °C for 12 h and then 5 h at 450 °C. The cubic phases prepared under such conditions do not show a 310 (30.9°) diffraction, and hence are assignable to crystalline β-ZrW_2O_8 type structure, for which the indexed pattern is displayed in Figure 5; lattice parameters of c-$ZrMo_{2-x}W_xO_8$ ($x = 0.2$, 0.4, 0.6, 0.7, and 0.8) are listed in Table 3.

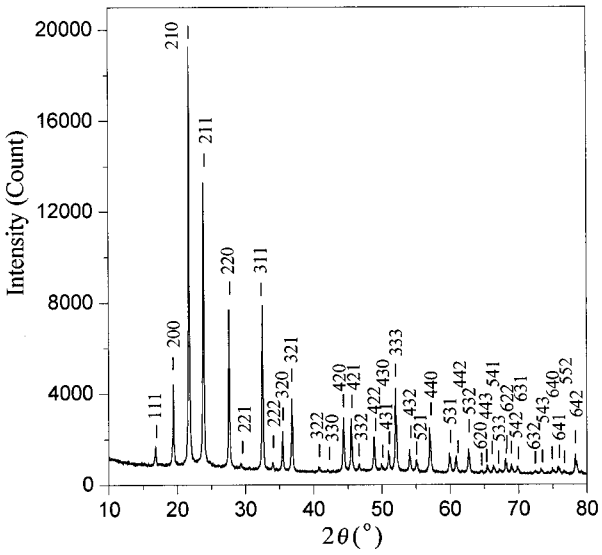

Figure 5. The indexed X-ray diffraction pattern for c-$ZrMo_{1.6}W_{0.4}O_8$.

Table 3. Lattice parameters of c-$ZrMo_{2-x}W_xO_8$ ($x = 0.2$, 0.4, 0.6, 0.7, and 0.8).

x	a [Å]
0.2	9.1311(1)
0.4	9.1312(1)
0.6	9.1311(2)
0.7	9.1318(9)
0.8	9.1317(1)

Conclusions

The precursors $ZrMo_{2-x}W_xO_7(OH)_2(H_2O)_2$ ($x = 0.2$–2.0) are converted into a $ZrMo_{2-x}W_xO_8$ orthorhombic phase within an x-dependent temperature range from 124 to 203 °C by removal of three water molecules. The temperature dependence of $ZrMo_{2-x}W_xO_8$ shows two types of phase behavior: the orthorhombic phases of Mo-rich $ZrMo_{2-x}W_xO_8$ ($x = 0.2$–0.8) are able to convert into trigonal phases, with cubic phase formation as the intermediate step, and the metastable pure cubic phases can be prepared by carefully controlling the temperature and temperature-holding time in the appropriate temperature range. However, no trigonal phases can be formed in the W-rich solid solutions $ZrMo_{2-x}W_xO_8$ ($x = 1.0$–1.6). In addition, the solid solutions of this type do not decompose even at temperatures up to 800 °C, even though the decomposition

 © 2005 Wiley-VCH Verlag GmbH & Co. KGaA, Weinheim

temperature of ZrW_2O_8 is 773 °C. Therefore, doping of tungsten into cubic $ZrMo_2O_8$ increases its stability towards decomposition.

Experimental Section

Preparation and Characterization of $ZrMo_{2-x}W_xO_7(OH)_2(H_2O)_2$ Precursors: Precursors $ZrMo_{2-x}W_xO_7(OH)_2(H_2O)_2$ were prepared following procedures described previously.[5,7] Briefly, the reactants $Na_2WO_4{\cdot}2H_2O$, $Na_2MoO_4{\cdot}2H_2O$, and $ZrOCl_2{\cdot}8H_2O$ (A.R. grade) were first heated at 800 °C for 6 h and the exact hydration number was re-determined based on the water loss. Dropwise addition of 50 mL of an aqueous solution of 0.5 M Zr^{4+}, together with 50 mL of an aqueous solution of 1 M mixed ionic solution [W^{6+} + Mo^{6+}] with different x (x = 0.2, 0.4, 0.6, 0.7, 0.8, 1.0, 1.2, 1.4, 1.6, or 2.0), into 30 mL of distilled water led to immediate formation of a white precipitate. The white turbid solution formed was then mixed with 182 mL of 6 M aqueous HCl solution with continuous stirring for 4 h and then refluxed for 48 h. The white precipitate was finally separated by centrifugation and washed sequentially with 1.5 M aqueous HCl and distilled water. The obtained products were confirmed to have the desired Zr to W/Mo ratios as indicated by the negligible amounts (<1%) of these ions in the decanted liquid determined by ICP-AES (JY, ULTIMA, France).

The hydration number of the precursors $ZrMo_{2-x}W_xO_7(OH)_2(H_2O)_2$ was estimated from the weight-loss percentage of the dried white precipitate measured by TG (Netzsch Sta 409C).

The refined XRD pattern of $ZrMo_{1.6}W_{0.4}O_7(OH)_2(H_2O)_2$, as a typical example, is shown in Figure 6; it indicates that all white or slightly pale $ZrMo_{2-x}W_xO_7(OH)_2(H_2O)_2$ powders are isomorphs of tetragonal $ZrMo_2O_7(OH)_2(H_2O)_2$. The final refinement results are listed in Table 4.

DSC Measurements: DSC curves in the temperature range 40–800 °C were recorded with a DTA-404 PC (Netzsch), under argon, at a heating rate of 10 °C min^{-1}; an empty crucible was used as the reference. The DSC curve of the samples was calibrated using those recorded for a pair of blank platinum crucibles under the same conditions. The peak temperatures were calibrated using the metals In, Sn, Bi, Zn, Al, Ag, Au, and Ni as standard substances and the precision was estimated to be ±1 °C.

X-ray Crystallographic Equipment and Temperature Calibration: The XRD patterns were collected on a Philips X′-Pert MPD diffractometer with X′Celerator detector using Cu-K_α radiation (40 kV, 40 mA). Each ground sample was mounted on a platinum strip, which served as sample holder as well as heater attached with Anton Parr high-temperature units used for variable temperature XRD measurements. The routine XRD patterns were collected within the 2θ range 10–120° with a step width of 0.0167° (2θ) and

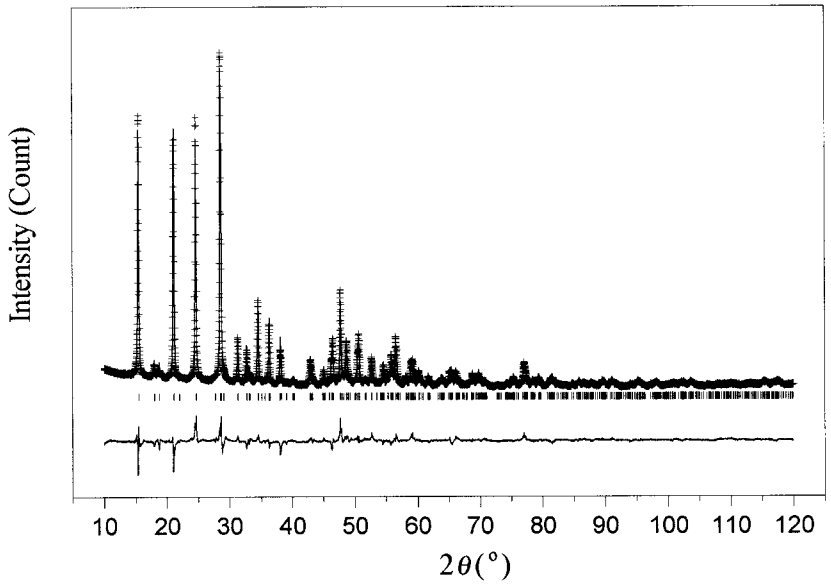

Figure 6. Experimental, calculated, and difference X-ray diffraction patterns for $ZrMo_{1.6}W_{0.4}O_7(OH)_2(H_2O)_2$.

Table 4. The crystal structural parameters of $ZrMo_{2-x}W_xO_7(OH)_2(H_2O)_2$ refined using Rietveld method.

x	a [Å]	c [Å]	v [Å^3]	Zr (8a: 0,0,z)	W/Mo (16b: x,y,z)	Rp [%]	Rwp [%]
0.2	11.443(9)	12.492(1)	1635.9	–0.0071(1)	0.0173(2), 0.1626(2), 0.2255(1)	7.75	10.78
0.4	11.4460(3)	12.4861(4)	1635.8	–0.0037(3)	0.0176(2), 0.1644(2), 0.2291(3)	5.95	7.81
0.6	11.441 (2)	12.482(2)	1633.8	–0.0079(6)	0.0177(2), 0.1642(1), 0.2283(6)	5.98	7.80
0.7	11.436(2)	12.474(2)	1631.4	–0.0086(7)	0.0174(2), 0.1641(2), 0.2289(7)	6.29	7.95
0.8	11.435(2)	12.474(2)	1631.1	–0.0060(7)	0.0180(2), 0.1664(2), 0.2282(7)	5.93	7.98
1.0	11.431(2)	12.468 (4)	1629.4	–0.0106(8)	0.0165(2), 0.1637(1), 0.2275(7)	5.95	7.80
1.2	11.429(2)	12.470(3)	1628.9	–0.0103(9)	0.0147(2), 0.1625(2), 0.2298(8)	7.16	9.47
1.4	11.436(2)	12.473(2)	1631.4	–0.0104(9)	0.0152(2), 0.1635(1), 0.2267(8)	6.39	8.39
1.6	11.432(2)	12.475(2)	1630.4	–0.0128(9)	0.0146(2), 0.1638(1), 0.2268(9)	7.10	9.21
1.6[12]	11.4245(5)	12.4619(7)	1625.5	–0.0140(2)	0.0167(2), 0.1638(2), 0.2223(3)	7.12	8.79
2.0	11.4432(4)	12.4865(5)	1635.1	–0.0053(9)	0.0186(1), 0.1646(1), 0.2297(8)	9.76	12.62

 © 2005 Wiley-VCH Verlag GmbH & Co. KGaA, Weinheim

step time of 20 s, whereas the variable temperature XRD patterns were recorded within the 2θ range 10–80° with the same step width and a step time of 30 s. The measurements were carried out under argon at temperatures at which the possible phase transition was suggested to occur according to the DSC data. The heating rate between two neighboring temperature was about 2 °C min^{-1} and at each point the temperature was held for 20 min. The temperatures during the measurement were controlled with a TCU 2000 unit and were calibrated using an interpolation technique based on the Pathak equation[16] with KCl as the external standard.

The observed profiles of the XRD patterns for the precursors were refined using the Rietveld method contained in the GSAS program[17] by fitting to tetragonal $ZrMo_2O_7(OH)_2(H_2O)_2$[8] as the model. The refinement was started with lattice parameters and atomic coordinates assigned from the model. The site fraction of Mo/W atom was fixed as the intended ratio according to the precursor formula. The fitting was carried out for the lattice parameters, the scale parameters, background coefficients, and profile coefficients. Finally, the atomic coordinates and the isotropic thermal factors of metals (Zr, Mo, W) were refined.

Analysis and indexing of the XRD patterns for $ZrMo_{2-x}W_xO_8$ were performed using the PowderX program.[18] The zero-point shifts was corrected using the line-pair method. SiO_2 was used as an internal standard to correct the XRD peak positions used to calculate the precise lattice parameters of cubic $ZrMo_{2-x}W_xO_8$.

Acknowledgments

Support for this research from the National Science Foundation of China under grants NSFC 20471010 and 20371009 and the Foundation of Beijing Key Discipline of Inorganic Chemistry of Beijing Education Committee are gratefully acknowledged.

[1] T. A. Mary, J. S. O. Evans, T. Vogt, A. W. Sleight, *Science* **1996**, *272*, 90–92.
[2] J. S. O. Evans, T. A. Mary, T. Vogt, M. A. Subramanian, A. W. Sleight, *Chem. Mater.* **1996**, *8*, 2809–2823.
[3] C. Lind, A. P. Wilkinson, Z. Hu, S. Short, J. D. Jorgensen, *Chem. Mater.* **1998**, *10*, 2335–2337.
[4] C. Lind, A. P. Wilkinson, C. J. Rawn, E. A. Payzant, *J. Mater. Chem.* **2001**, *11*, 3354–3359.
[5] C. Closmann, A. W. Sleight, J. C. Haygarth, *J. Solid State Chem.* **1998**, *139*, 424–426.
[6] U. Kameswari, A. W. Sleight, J. S. O. Evans, *Int. J. Inorg. Mater.* **2000**, *2*, 333–337.
[7] S. Zhang, X. Zhao, H. Ma, X. Wu, *Chin. J. Chem.* **2000**, *18*, 571–575.
[8] J. S. O. Evans, P. A. Hanson, R. M. Ibberson, N. Duan, U. Kameswari, A. W. Sleight, *J. Am. Chem. Soc.* **2000**, *122*, 8694–8699.
[9] A. Clearfield, R. H. Blessing, *J. Inorg. Nucl. Chem.* **1972**, *34*, 2643–2663.
[10] A. Clearfield, R. H. Blessing, *J. Inorg. Nucl. Chem.* **1974**, *36*, 1174–1176.
[11] S. Allen, J. S. O. Evans, *J. Mater. Chem.* **2004**, *14*, 151–156.
[12] X. Zhao, L. Huang, P. Liu, H. Ma, *Chin. J. Chem.* **2003**, *21*, 1529–1531.
[13] S. Allen, R. J. Ward, M. R. Hampson, R. K. B. Gover, J. S. O. Evans, *Acta Crystallogr., Sect. B* **2004**, *60*, 32–40.
[14] M. Auray, M. Quarton, P. Tarte, *Acta Crystallogr., Sect. C* **1986**, *42*, 257–259.
[15] D. R. Lide, *CRC Handbook of Chemistry and Physics*, CRC Press Ltd., Boca Raton, Florida, **2001**.
[16] P. D. Pathak, N. G. Vasavada, *Acta Crystallogr., Sect. A* **1970**, *26*, 655–658.
[17] A. C. Larson, V. Dreele, R. B. Lansce, Los Alamos National Lab, Los Alamos, NM, **1994**.
[18] C. Dong, *J. Appl. Crystallogr.* **1999**, *32*, 838.

Received: May 30, 2005
Published Online: October 11, 2005

 © 2005 Wiley-VCH Verlag GmbH & Co. KGaA, Weinheim

Synthesis and Structural Characterisation of Group 10 Homo- and Hetero-Dimetallic Sulfur-Bridged Complexes of the [Ni(ema)(μ-*S*,*S*′)M(diphos)] (M = Ni, Pd, Pt) Type

Samantha E. Duff,[a] J. Elaine Barclay,[a] Sian C. Davies,[a] Peter B. Hitchcock,[b] and David J. Evans*[a]

Keywords: Nickel / Palladium / Platinum / Heterometallic complexes

The series of group 10 homo- and hetero-dimetallic sulfur-bridged complexes [Ni(ema)(μ-*S*,*S*′)M(diphos)], [M = nickel, palladium or platinum; diphos = 1,3-bis(diphenylphosphanyl)-propane or 1,2-bis(diphenylphosphanyl)ethane], have been synthesised. Their properties and the crystal structures of five of the series are described. The dinickel complexes are good structural analogues of the dinickel subunit of the nickel-containing enzyme acetyl-CoA synthase.
(© Wiley-VCH Verlag GmbH & Co. KGaA, 69451 Weinheim, Germany, 2005)

Introduction

The nickel enzyme acetyl-CoA synthase catalyses the synthesis of acetyl-CoA. The reaction parallels the industrially important Reppe process for the synthesis of acetic acid, both apparently involving metal–carbonyl, methyl–metal and acyl–metal intermediates.[1] Protein crystallography[2–4] shows at the active site, the A cluster, an Fe_4S_4 cluster bridged through cysteinylthiolate sulfur to a proximal nickel that is then linked to a distal nickel(II) atom in an N_2S_2 coordination environment, Figure 1. The *cis*-planar N_2S_2 coordination is from a deprotonated Cys–Gly–Cys sequence of the protein. Following publication of the crystal structures there has been a renewed vigour in the preparation of dinuclear group 10 complexes as mimics for the dinickel sub-site of the A cluster.[5–10] Herein we report the synthesis and properties of the series of complexes [Ni(ema)(μ-*S*,*S*′)M(diphos)], where M is nickel, palladium or platinum, H_4ema is *N*,*N*′-ethylenebis(2-mercaptoacetamide) and where diphos is 1,3-bis(diphenylphosphanyl)propane (dppp) or 1,2-bis(diphenylphosphanyl)ethane (dppe).

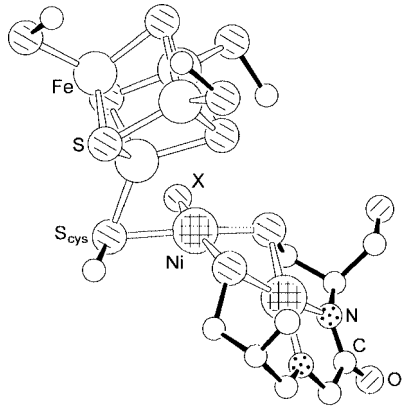

Figure 1. The active site, A cluster, of acetyl-CoA synthase.

[a] Department of Biological Chemistry, John Innes Centre, Norwich Research Park, Colney, Norwich, NR4 7UH, UK
E-mail: dave.evans@bbsrc.ac.uk
[b] Department of Chemistry, University of Sussex, Falmer, Brighton, BN1 9QJ, UK

Results and Discussion

Synthesis and Spectroscopy

Previously, we have demonstrated that the homonuclear complexes [Ni(ema)(μ-*S*,*S*′)Ni(dppp)] (**1**) and [Ni(ema)(μ-*S*,*S*′)Ni(dppe)] (**2**) can be readily prepared from the reaction of equimolar amounts of $[NEt_4]_2$[Ni(ema)] and [$NiCl_2$(diphos)] in acetonitrile solution.[5] Here, a similar methodology has been applied to isolate, from the appropriate [MCl_2(diphos)], the heteronuclear dimetallic complexes [Ni(ema)(μ-*S*,*S*′)M(diphos)], M = Pd, diphos = dppp (**3**) or dppe (**4**); M = Pt, diphos = dppp (**5**) or dppe (**6**), in good yield, Equation (1).

$$[NEt_4]_2[Ni(ema)] + [MCl_2(diphos)] \rightarrow [Ni(ema)(\mu\text{-}S,S')M(diphos)] + 2[NEt_4]Cl \quad (1)$$

All complexes have been characterised by EI-MS and the structures of **1**[5] and **3**–**6** have been confirmed by X-ray crystallography. Satisfactory elemental analyses (C, H, N) are obtained for all compounds except **3**, which, for reasons unknown, gave consistently poor results. However, spectroscopic parameters and the mass spectrum of this compound are fully consistent with the crystal structure.

In the solid, complexes **1**–**6** exhibit an infra-red amidocarbonyl stretch in the range 1566–1578 cm^{-1}. The $^{31}P\{H\}$ NMR chemical shifts for solutions in methanol and in dimethyl sulfoxide are consistent with diphosphane chelate ligation and, as expected, depend on the chelate ring size; the chemical shifts observed for five-membered (dppe) chelate rings (ca. 49 to 62 ppm) are larger than those for six-membered (dppp) rings (ca. –5 to 1 ppm).[11] The single resonance observed in each case confirms the equivalence of the phosphorus atoms in solution at ambient temperature. The values for **2** are comparable to those of the related complexes [Ni(L)(μ-*S*,*S*′)Ni(dppe)]$(PF_6)_2$ {L = *N*,*N*′-diethyl-3,7-diazanonane-1,9-dithiolate(2–)} (CD_2Cl_2, 61.1 ppm)[6] and [Ni(CGC)(μ-*S*,*S*′)Ni(dppe)] (CGC = cys–gly–cys) (CD_3CN, 56.7 and 57.5 ppm).[8]

In the solid state the nickel complexes are coloured green, palladium blue-black and platinum red. The electronic absorption spectra of solutions of **1**–**6** exhibit several absorbance peaks as expected, and their parameters are collected in Table 1. The colour in solution is dependent on solvent, Table 2. The nickel and palladium complexes show a dramatic colour difference on changing solvent from acetonitrile to methanol. This is a consequence of the ability of such square-planar complexes to coordinate extra (solvent) ligands in solution to establish an equilibrium between four-, five- and six-coordinate species.[12] However, the NMR in methanol does not support the presence of a six-coordinate, paramagnetic species.

Table 2. Colour of solutions of complexes **1**–**6** in acetonitrile and methanol.

Complex		MeCN	MeOH
[Ni(ema)Ni(dppp)]	(**1**)	emerald green	midnight blue
[Ni(ema)Ni(dppe)]	(**2**)	emerald green	indigo
[Ni(ema)Pd(dppp)]	(**3**)	royal blue	deep red
[Ni(ema)Pd(dppe)]	(**4**)	violet	burgundy
[Ni(ema)Pt(dppp)]	(**5**)	cerise	pink
[Ni(ema)Pt(dppe)]	(**6**)	peach	orange

The cyclic voltammogram of **1** in dichloromethane shows a reversible one electron process at $E_{1/2}$ = –0.42 V (vs. SCE) assigned to a Ni^{II}/Ni^{I} couple of the NiP_2S_2 moiety, a similar process at $E_{1/2}$ = –0.47 V (vs. SCE) has been reported for [Ni(L)(μ-*S*,*S*′)Ni(dppe)]$(PF_6)_2$.[6] A second feature at E_{pc} = –1.39 V (vs. SCE) may be assigned to an irreversible reduction Ni^{I}/Ni^{0} at NiP_2S_2 or an irreversible Ni^{II}/Ni^{I} couple at the other nickel site. The cyclic voltammetry of the complexes **2**–**6** has not been investigated.

It has been observed that 1,10-phenanthroline will chelate and extract the proximal nickel from the acetyl-CoA synthase A cluster.[13] The effect has been observed also in a synthetic analogue, [Ni(PhPepS)(μ-*S*,*S*′)Ni(dppe)] {$PhPepSH_4$ = *N*,*N*′-phenyl(*o*-mercaptobenzamide)}, of the dinickel subsite of the A cluster where it is proposed that the nickel is removed from the NiP_2S_2 unit.[9] The same reaction occurs with complexes **1** and **2**, in dichloromethane solvent, using a ten-fold excess of 1,10-phenanthroline.

Table 1. Electronic absorption spectrum parameters for complexes **1**–**6** in acetonitrile and methanol solution.

Complex	MeCN		MeOH	
	λ [nm]	ε [dm^3mol^{-1} cm^{-1}]	λ [nm]	ε [dm^3mol^{-1} cm^{-1}]
[Ni(ema)Ni(dppp)] (**1**)	630	1230	586	2550
	468	250	447	1500
	280	22590	320	12710
	–	–	256	28930
	–	–	222	52760
[Ni(ema)Ni(dppe)] (**2**)	623	1040	575	1170
	472	860	459	890
	282	14480	308	8490
			287	9510
			242	13420
[Ni(ema)Pd(dppp)] (**3**)	581	1540	545	1710
	449	2570	438	1760
	319 sh	3860	325 sh	7960
	278 sh	20220	263 sh	21140
	225 sh	44260	221 sh	40470
[Ni(ema)Pd(dppe)] (**4**)	581	1130	546	820
	443	750	445	980
	274	11480	–	–
	224	27770	229	14510
[Ni(ema)Pt(dppp)] (**5**)	535	2910	522	590
	411	5780	395	1890
	365	6740	351	2830
	319	3057	–	–
	227	97080	225	43550
[Ni(ema)Pt(dppe)] (**6**)	533	430	518	340
	414	2290	405	1380
	382	2080	361	2150
	323	2850	–	–
	244	60760	226	24540

 © 2005 Wiley-VCH Verlag GmbH & Co. KGaA, Weinheim

There is, however, under similar conditions, no reaction of 1,10-phenanthroline with the heterometallic complexes **3**–**6**, with $[NEt_4]_2$[Ni(ema)] or with the trinickel complex $[NEt_4]_2$-[Ni{Ni(ema)(μ-*S*,*S*′)}$_2$],[5] which provides further confirmation that the phosphine-ligated nickel is lost and that the nickel atom associated with the Ni(ema) moiety is not chelated by 1,10-phenanthroline.

Structures

The crystal structure of **1**·Et_2O[5] (Figure 2) shows that each nickel ligand sphere is slightly distorted square planar, with nickel(1) ligated by the two phosphorus atoms from the dppp ligand and the two sulfur atoms of the ema ligand and the other nickel, (2), ligated by the two nitrogen and two sulfur atoms of the ema ligand. The dppp-ligated nickel atom may be considered to lie within the S_2P_2 mean plane [displaced 0.0035(5) Å from the plane towards the ema-ligated Ni], which is essentially flat [deviations from the mean planes lie in the range –0.0238(9) to 0.0241(9) Å, where the negative sign indicates opposite side of the mean plane]; the most distorted angle about this nickel is 80.93(3)°. This is similar in the other two dppp-ligated metal complexes, with the metal atoms lying within 0.020(2) Å of the S_2P_2 mean planes, which in turn have atoms lying in the ranges –0.017(3) to 0.017(4) and –0.010(2) to 0.010(2) Å from the mean planes in **3** and **5**, respectively. This is, however, different to the arrangement in the dppe-ligated complexes. In these, the S_2P_2 planes are twisted with atoms lying in the ranges –0.2134(13) to 0.2109(13) Å and –0.2556(13) to 0.2590(13) Å in the two independent molecules in **4** and –0.1925(3) to 0.1949(13) in **6**. The metal atoms lie 0.1075(6) and 0.0712(6) Å from the mean planes in **4** and 0.0591(6) in **6**. The ema-chelated nickel atom lies 0.1534(6) Å from the N_2S_2 plane [displaced in the direction away from Ni(1)] with an angle of 169.52(8)° for a N–Ni–S angle being the most distorted. This distortion is similar in all the complexes. The dihedral (hinge) angle at the bridging sulfur atoms in **1** is 111.22°. The Ni–S bond lengths within the chelate ring (2.12 Å) are slightly shorter and the bridge distances (2.28 Å) slightly longer than those observed (2.14–2.19 Å and 2.19–2.24 Å, respectively) for other synthetic sulfur-bridged dinickel complexes such as [Ni(L)(μ-*S*,*S*′)-Ni(dppe)]$(PF_6)_2$.[6] Other angles and bond lengths about the nickel atoms and the Ni···Ni distance [2.6897(5) Å] are similar to those reported for related "Ni(μ-S)$_2$NiN_2" structures.[7]

The Ni(ema) group of the complex forms a curved "wall" around two of the phenyl groups of the dppp ligand, which are orientated "edge-on" to the Ni(ema) group. Within each PPh group, the normals to the second phenyl rings are orientated at 111.3 and 102.6°, respectively, to those of the first two. The complex molecules are arranged with the Ni(ema) groups forming approximate (due to the curved nature of the ema ligands) planes parallel to the crystallographic *bc* plane; viewed along the crystallographic *b* direction, the molecules are arranged in pairs with the Ni(dppp) groups in

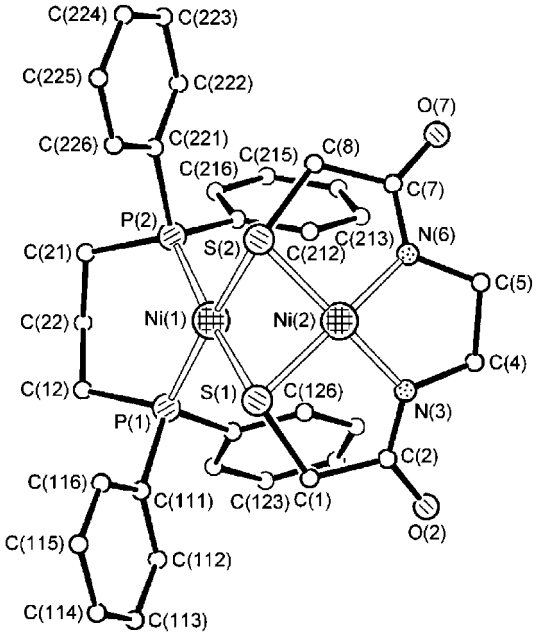

Figure 2. A view of [Ni(ema)(μ-*S*,*S*′)Ni(dppp)] (**1**) showing atom numbering scheme, hydrogen atoms omitted for clarity.

alternating *ab* planes lying on opposite sides of the Ni(ema) planes (Figure 3). This packing arrangement is identical to that in **3** and **5**, while the Ni–ema planes are also found in **4** and **6**. There is a difference in the packing in **6**, however, as the Pt–dppe groups are not "staggered" along the crystallographic *a* vector as they are in the other four arrangements.

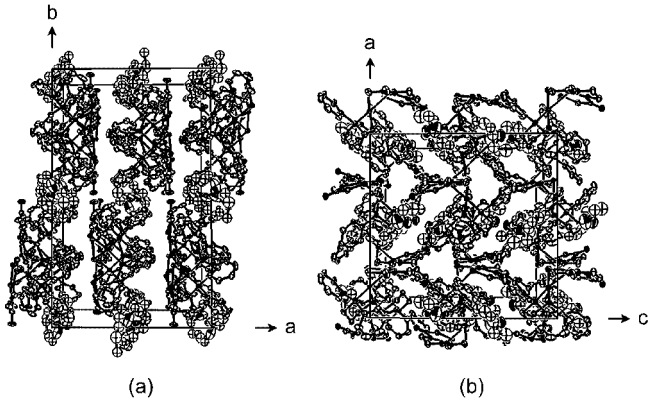

Figure 3. Packing arrangements of [Ni(ema)(μ-*S*,*S*′)Ni(dppp)] (**1**) as viewed along (a) the crystallographic *c* axis and (b) the *b* axis.

The [Ni(ema)(μ-*S*,*S*′)M(diphos)] molecules in complexes **3**, **4**, **5** and **6** have structures similar to complex **1**. In **4** there are two independent molecules within the asymmetric unit. Representative structures of the heterometallic complexes **3** and **4** are shown in Figure 4 and Figure 5, respectively. A comparison of selected bond lengths and angles are given in Table 3. On substitution of nickel(1) by palladium, there is no significant change in the average Ni–N bond length and only a very slight lengthening of the average Ni–S bond length within the Ni(ema); replacement of palladium by

 © 2005 Wiley-VCH Verlag GmbH & Co. KGaA, Weinheim

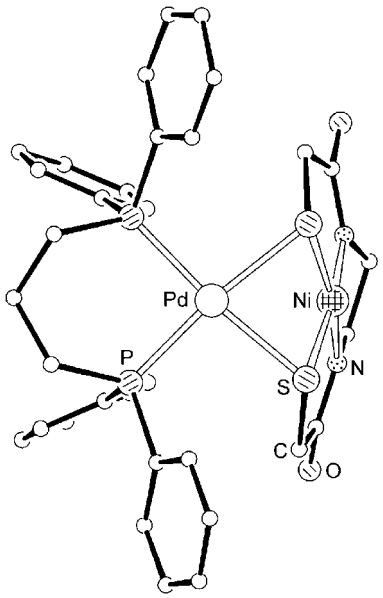

Figure 4. A molecule of [Ni(ema)(μ-*S*,*S*′)Pd(dppp)] (**3**), hydrogen atoms omitted for clarity.

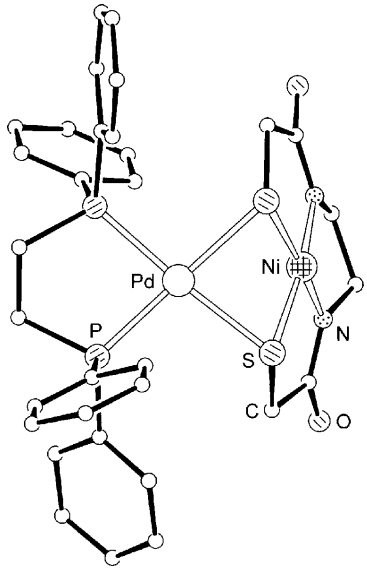

Figure 5. Molecular structure of [Ni(ema)(μ-*S*,*S*′)Pd(dppe)] (**4**), hydrogen atoms omitted for clarity.

platinum leads to no further increase in bond length. Within the NiP_2S_2 fragment there is again an elongation of the M–P and M–S bond lengths on substitution of nickel(1) by palladium (0.08 and 0.13 Å, respectively) but no further change when palladium is replaced by platinum. On changing from dppp to dppe chelation, independent of metal, there is a decrease in the M–P–C(alkane) angle from ca. 116° to ca. 108° that helps maintain the square-planar environment. The dihedral (hinge) angle at the bridging sulfur atoms is similar in all complexes, ranging from 111–117°. The nickel to metal distance increases from 2.6897(8) Å in **1** to 2.780(2) Å in **3**, which is similar to the distance in the heterometallic complexes **4** and **5** and slightly shorter than that in **6** [2.8653(5) Å]. The longer platinum–nickel distance is consistent with the larger hinge angle in the latter complex.

Conclusions

The series of six group 10 homo- and hetero-dimetallic sulfur-bridged complexes of the [Ni(ema)(μ-*S*,*S*′)-M(diphos)] (M = Ni, Pd, Pt; diphos = dppp, dppe) type have been prepared and characterised; five by X-ray crystallography. The geometric parameters about the metal atoms for complex **1** and **3**–**6** resemble those reported for the dinickel subunit of the A-cluster of acetyl-CoA synthase: in complex **1** the nickel(1) and nickel(2) atoms mimic the A cluster distal nickel and proximal nickel, respectively.

Experimental Section

General: All manipulations were performed under dinitrogen, unless otherwise stated, using either Schlenk or vacuum-line techniques. Solvents were dried with appropriate drying agents and distilled under dinitrogen prior to use. [$NiCl_2$(dppp)] was purchased from Aldrich and [Pd(1,5-cylcooctadiene)Cl_2], [Pt(1,5-cylcooctadiene)Cl_2] and [$PdCl_2$(dppe)] were purchased from Alfa Aeser. [NEt_4]$_2$-[Ni(ema)],[14] [$PtCl_2$(dppp)], [$PtCl_2$(dppe)] and [$PdCl_2$(dppp)] were obtained by adaptation of published procedures.[15] [Ni(ema)(μ-*S*,*S*′)Ni(dppp)] (**1**) and [Ni(ema)(μ-*S*,*S*′)Ni(dppe)] (**2**) were prepared as we recently reported.[5] IR spectra were recorded with a Shimadzu FTIR-8000 spectrophotometer and UV/Vis spectra with a Perkin–Elmer Lambda 25. ^{31}P NMR were obtained with a Jeol Lambda 400 spectrometer. Electrospray ionisation mass spectra, in methanol solution, were measured with a Deca XP_{plus} ion trap mass spectrometer from Thermo Finnigan. Elemental analyses were by Medac Ltd, Egham, Surrey, UK.

Table 3. Comparison of selected bond lengths [Å], metal–metal separation [Å] and hinge angle [°] in complexes **1** and **3**–**6**.

Complex		Ni(2)–S	Ni(2)–N	M–P	M–S	M–Ni	Hinge angle
[Ni(ema)Ni(dppp)]	(**1**)	2.1224(5)	1.8298(76)	2.1892(2)	2.2812(2)	2.6897(5)	111.22
[Ni(ema)Pd(dppp)]	(**3**)	2.1465(20)	1.8338(64)	2.2712(3)	2.4092(18)	2.7803(14)	110.37
[Ni(ema)Pd(dppe)]	(**4**)[a]	2.1556(35)	1.8400(19)	2.2651(44)	2.4064(48)	2.7927(129)	112.16
[Ni(ema)Pt(dppp)]	(**5**)	2.1560(24)	1.8377(21)	2.2624(20)	2.4098(8)	2.7950(7)	110.78
[Ni(ema)Pt(dppe)]	(**6**)	2.1597(92)	1.8398(41)	2.2578(65)	2.4084(93)	2.8653(5)	117.22

[a] Average values from the two independent molecules within the asymmetric unit.

 © 2005 Wiley-VCH Verlag GmbH & Co. KGaA, Weinheim

Preparations

[Ni(ema)(μ-*S*,*S*′)Pd(dppp)] (3): A slurry of [$PdCl_2$(dppp)] (0.146 g, 2.49×10^{-4} mol) in MeCN (20 mL) was added to a stirred solution of [NEt_4]$_2$[Ni(ema)] (0.130 g, 2.49×10^{-4} mol) in MeCN (10 mL). The resultant black solution was stirred at room temp. for 12 h, then diethyl ether (10 mL) was added dropwise. Within 4 h blue-black crystals were formed and collected by filtration (0.12 g, 62%). IR (KBr): $\tilde{\nu}_{max}$ = (CO) 1578 cm^{-1}. ^{31}P NMR (162 MHz. CD_3OD; ref. H_3PO_4): δ = –5.11 (s) ppm, ([D_6]DMSO): δ = 5.22 (s) ppm. MS: *m*/*z* = 783 (100) [$M^+ + H^+$].

[Ni(ema)(μ-*S*,*S*′)Pd(dppe)] (4): To a slurry of [$PdCl_2$(dppe)] (0.300 g, 5.22×10^{-4} mol) in MeCN (10 mL) was added solid [NEt_4]$_2$-[Ni(ema)] (0.273 g, 5.22×10^{-4} mol) and additional MeCN (5 mL). The resultant black solution was stirred at room temp. for 30 min, then diethyl ether (5 mL) was added dropwise. A brown solid (0.25 g, 63%) was collected by filtration. $C_{32}H_{32}N_2NiO_2P_2PdS_2$ (767.80): calcd. C 50.1, H 4.2, N 3.7; found C 50.0, H 4.2, N 3.7. IR (KBr): $\tilde{\nu}_{max}$ = (CO) 1567 . ^{31}P NMR (162 MHz. CD_3OD; ref. H_3PO_4): δ = 62.64 (s) ppm, ([D_6]DMSO): δ = 61.96 (s) ppm. MS: *m*/*z* = 769 (100) [$M^+ + H^+$]. Recrystallisation from a methanol/diethyl ether mixture gave blue-black crystals of **4**·1½MeOH (0.22 g, 52%).

[Ni(ema)(μ-*S*,*S*′)Pt(dppp)] (5): To a white slurry of [$PtCl_2$(dppp)] (0.330 g, 4.87×10^{-4} mol) in MeCN (20 mL) was added a solution of [NEt_4]$_2$[Ni(ema)] (0.255 g, 4.87×10^{-4} mol) in MeCN (10 mL). The solution was stirred for a further 10 min before the volume was decreased in vacuo to 15 mL. Diethyl ether was layered onto the solution and a red product precipitated overnight which was collected by filtration (0.29 g, 68%). $C_{33}H_{34}N_2NiO_2P_2PtS_2$ (870.48): calcd. C 45.5, H 3.9, N 3.2; found C 46.0, H 4.4, N 3.2. IR (KBr): $\tilde{\nu}_{max}$ = (CO) 1578 cm^{-1}. ^{31}P NMR (162 MHz. CD_3OD; ref. H_3PO_4): δ = –3.70 (s) ppm; ([D_6]DMSO): δ = –2.87 (s) ppm. MS: *m*/*z* =871 (100) [$M^+ + H^+$]. Recrystallisation from dichloromethane gave crystals of **5**·2CH_2Cl_2.

[Ni(ema)(μ-*S*,*S*′)Pt(dppe)] (6): Compound **6** was prepared similarly to **5** in 69% yield from [$PtCl_2$(dppe)]. $C_{32}H_{32}N_2NiO_2P_2PtS_2$ (856.46): calcd. C 44.9, H 3.8, N 3.3; found C 43.9, H 4.0, N 3.3. IR (KBr): $\tilde{\nu}_{max}$ = (CO) 1566 cm^{-1}. ^{31}P NMR (162 MHz. CD_3OD; ref. H_3PO_4): δ = 49.01 (s) ppm; ([D_6]DMSO): δ = 48.92 (s) ppm. MS: *m*/*z* =857 (100) [$M^+ + H^+$].

Crystal Data

[Ni(ema)(μ-*S*,*S*′)Ni(dppp)]·Et_2O (1·Et_2O): $C_{33}H_{34}N_2Ni_2O_2P_2S_2$, $C_4H_{10}O$, *M* = 808.2; orthorhombic, space group *Pcab* (equiv. to *Pbca*, no. 61), *a* = 16.557(3), *b* = 16.799(8), *c* = 26.931(5) Å, *V* = 7491(4) $Å^3$, *Z* = 8, $D_{calcd.}$ = 1.433 mg/m^3; data collection method: CAD4 scintillation counter, ω scans at *T* = 150(2) K, λ = 0.71073 Å, θ_{max} = 28.0°; 9000 unique reflections used, 5793 with $I > 2\sigma_I$, *F*(000) = 3376, μ = 1.240 mm^{-1}, R_1/wR_2 [$I > 2\sigma(I)$] = 0.039/0.078, R_1/wR_2 (all data) = 0.073/0.094, goodness-of-fit on F^2 = 1.040.

[Ni(ema)(μ-*S*,*S*′)Pd(dppp)]·Et_2O (3·Et_2O): $C_{33}H_{34}N_2NiO_2P_2PdS_2$, $C_4H_{10}O$, *M* = 855.9; orthorhombic, space group *Pbca*, *a* = 16.7601(8), *b* = 27.0435(14), *c* = 16.9278(5) Å, *V* = 7672.6(6) $Å^3$, *Z* = 8, $D_{calcd.}$ = 1.482 mg/m^3; data collection method: 95 mm CCD camera on κ-goniostat, CCD rotation images, thick slices, scans at *T* = 173(2) K, λ = 0.71073 Å, θ_{max} = 24.12°; 6067 unique reflections used, 3610 with $I > 2\sigma(I)$, *F*(000) = 3520, μ = 1.189 mm^{-1}, R_1/wR_2 [$I > 2\sigma(I)$] = 0.084/0.128, R_1/wR_2 (all data) = 0.158/0.149, goodness-of-fit on F^2 = 1.128.

[Ni(ema)(μ-*S*,*S*′)Pd(dppe)]·1.5MeOH (4·1.5MeOH): $C_{32}H_{32}N_2$-$NiO_2P_2PdS_2$·1.5(CH_4O) *M* = 815.8; triclinic, space group $P\bar{1}$, *a* = 11.8017(3), *b* = 16.9502(4), *c* = 19.2990(4) Å, *α* = 65.591(1), *β* = 72.565(1), *γ* = 81.065(1), *V* = 3351.81(14) $Å^3$, *Z* = 4, D_c = 1.617 mg/m^3; data collection method: 95 mm CCD camera on κ-goniostat, CCD rotation images, thick slices, scans at *T* = 173(2) K, λ = 0.71073 Å, θ_{max} = 25.02°; 11766 unique reflections used, 9510 with $I > 2\sigma_I$, *F*(000) = 1668, μ = 1.358 mm^{-1}, R_1/wR_2 ($I > 2\sigma_I$) = 0.036/0.077, R_1/wR_2 (all data) = 0.052/0.084, goodness-of-fit on F^2 = 1.016.

[Ni(ema)(μ-*S*,*S*′)Pt(dppp)]·2CH_2Cl_2 (5·2CH_2Cl_2): $C_{33}H_{34}N_2Ni$-$O_2P_2PtS_2$, CH_2Cl_2, *M* = 1040.33; orthorhombic, space group *Pbca*, *a* = 16.6045(3), *b* = 27.3310(5), *c* = 17.1881(2) Å, *V* = 7800.3(2) $Å^3$, *Z* = 8, D_c = 1.772 mg/m^3; data collection method: 95 mm CCD camera on κ-goniostat, CCD rotation images, thick slices, scans at *T* = 173(2) K, λ = 0.71073 Å, θ_{max} = 26.01°; 7652 unique reflections used, 5827 with [$I > 2\sigma(I)$], *F*(000) = 4112, μ = 4.564 mm^{-1}, R_1/wR_2 ($I > 2\sigma_I$) = 0.038/0.083, R_1/wR_2 (all data) = 0.061/0.092, goodness-of-fit on F^2 = 1.045

[Ni(ema)(μ-*S*,*S*′)Pt(dppe)] (6): $C_{32}H_{32}N_2NiO_2P_2PtS_2$, *M* = 856.46; monoclinic, space group $P2_1/c$, *a* = 11.0225(4), *b* = 16.4895(5), *c* = 17.3899(4) Å, *β* = 100.920(2), *V* = 3103.5(2) $Å^3$, *Z* = 4, $D_{calcd.}$ = 1.833 mg/m^3; data collection method: 95 mm CCD camera on κ-goniostat, CCD rotation images, thick slices, scans at *T* = 173(2) K, λ = 0.71073 Å, θ_{max} = 26.02°; 6094 unique reflections used, 5193 with [$I > 2\sigma(I)$], *F*(000) = 1688, μ = 5.381 mm^{-1}, R_1/wR_2 [$I > 2\sigma(I)$] = 0.027/0.051, R_1/wR_2 (all data) = 0.038/0.054, goodness-of-fit on F^2 = 1.041.

CCDC-258104 (for **1**), -279513 (for **3**), -279514 (for **4**), -279515 (for **5**) and -279516 (for **6**) contain the supplementary crystallographic data for this paper. These data can be obtained free of charge from The Cambridge Crystallographic Data Centre via www.ccdc.cam.ac.uk/data_request/cif.

Acknowledgments

The Biotechnology and Biological Sciences Research Council are thanked for funding and the John Innes Foundation for a postgraduate studentship (S. E. D). Dr Lionel Hill, JIC Metabolite Service is thanked for mass spectrometry.

[1] D. J. Evans, *Coord. Chem. Rev.* **2005**, *249*, 1582–1595.
[2] T. I. Doukov, T. M. Iverson, J. Seravalli, S. W. Ragsdale, C. L. Drennan, *Science* **2002**, *298*, 567–572.
[3] C. Darnault, A. Volbeda, E. J. Kim, P. Legrand, X. Vernède, P. A. Lindahl, J. C. Fontecilla-Camps, *Nat. Struct. Mol. Biol.* **2003**, *10*, 271–279.
[4] V. Svetlitchnyi, H. Dobbek, W. Meyer-Klaucke, T. Meins, B. Thiele, P. Römer, R. Huber, O. Meyer, *Proc. Natl. Acad. Sci. U. S. A.* **2004**, *101*, 446–451.
[5] S. E. Duff, J. E. Barclay, S. C. Davies, D. J. Evans, *Inorg. Chem. Commun.* **2005**, *8*, 170–173.
[6] Q. Wang, A. J. Blake, E. S. Davies, E. J. L. McInnes, C. Wilson, M. Schröder, *Chem. Commun.* **2003**, 3012–3013.
[7] P. V. Rao, S. Bhaduri, J. Jiang, R. H. Holm, *Inorg. Chem.* **2004**, *43*, 5833–5849.
[8] R. Krishnan, C. G. Riordan, *J. Am. Chem. Soc.* **2004**, *126*, 4484–4485.
[9] T. C. Harrop, M. M. Olmstead, P. K. Mascharak, *J. Am. Chem. Soc.* **2004**, *126*, 14714–14715.
[10] P. V. Rao, S. Bhaduri, J. Jiang, D. Hong, R. H. Holm, *J. Am. Chem. Soc.* **2005**, *127*, 1933–1945.
[11] P. E. Garrou, *Chem. Rev.* **1981**, *81*, 229–266.
[12] M. Schröder, in: *Encyclopedia of Inorganic Chemistry* (Ed.: R. B. King), John Wiley & Sons, Chichester, England, **1994**, *5*, pp. 2392–2412.

 © 2005 Wiley-VCH Verlag GmbH & Co. KGaA, Weinheim

[13] W. Shin, P. A. Lindahl, *J. Am. Chem. Soc.* **1992**, *114*, 9718–9719.
[14] H.-J. Krüger, G. Peng, R. H. Holm, *Inorg. Chem.* **1991**, *30*, 734–742.
[15] J. DePriest, G. Y. Zheng, C. Woods, D. R. Rillema, N. A. Mikirova, M. E. Zandler, *Inorg. Chim. Acta* **1997**, *264*, 287–296.
Received: July 28, 2005
Published Online: October 11, 2005

 © 2005 Wiley-VCH Verlag GmbH & Co. KGaA, Weinheim

Mononuclear and Polynuclear Chain Complexes of a Series of Multinucleating N/S Donor Ligands

Tanya K. Ronson,[a] Harry Adams,[a] and Michael D. Ward*[a]

Keywords: Chelates / Coordination chemistry / Copper / Silver / Helical structures

We have prepared a series of five ligands with potentially N,S-bidentate chelating arms derived from 3-[2-(methylsulfanyl)phenyl]pyrazole linked to central aromatic spacers by methylene units. Complexes with a variety of architectures have been obtained, including simple mononuclear complexes and polynuclear chain complexes. The *p*-xylyl-spaced ligand L^1 forms one-dimensional helical coordination polymers with copper(I) and silver(I) ions. These polymers display interligand aromatic stacking interactions within each helical chain. The *m*-xylyl-spaced ligand L^2 forms a coordination polymer with copper(I) but a mononuclear complex with the larger silver(I) ion in which the central phenyl ring is involved in an η^1 π-type Ag···C interaction with the Ag^I. The 3,3′-biphenyl-spaced ligand L^3 also forms one-dimensional polymers with silver(I) and copper(I) ions, but in this case the sequence of bridging ligands between one metal centre and the next follows a zig-zag path rather than being helical. The 1,8-naphthyl-spaced ligand L^4 only forms mononuclear complexes with copper(I) and silver(I) ions showing that this spacer is not large enough to enforce a bridging coordination mode. The three-armed ligand L^5, prepared from 2,4,6-tris-(bromomethyl)mesitylene, also forms a mononuclear complex with silver(I) ions, where one of the three arms is pendant. However, when excess silver(I) ions are present two of these mononuclear complexes can be assembled into the trinuclear complex $[Ag_3(L^5)_2](ClO_4)_3$.
(© Wiley-VCH Verlag GmbH & Co. KGaA, 69451 Weinheim, Germany, 2005)

Introduction

Metal-directed self assembly of elaborate polynuclear complexes relies in part on a good match between the stereoelectronic properties of the metal ion and the arrangement and type of donor sites on the bridging ligand.[1] With respect to the ligands, a minimum condition is that the binding sites must be arranged so that they bridge two or more metal centres, otherwise simple mononuclear complexes will result. If a bridging ligand is conformationally flexible, the competition between bridging and chelating coordination modes is an important factor in determining the course of a self-assembly reaction. To this end we have been investigating the coordination chemistry of ligands in which two N,N-bidentate, chelating pyrazolylpyridine groups are connected by a range of different spacer groups, which results in different separations between the two metal-ion binding sites. Depending on the nature of the spacer (a phenyl group, a biphenyl group, 1,8-naphthyl, and so on) and the coordination preferences of the metal ion, complexes have been isolated ranging in complexity from simple mononuclear species to dodecanuclear truncated-tetrahedral cages.[2]

In this paper we describe the synthesis and coordination behaviour of a related series of ligands based on N,S-donor chelating (pyrazolyl/thioether) fragments, the structures of whose complexes depend on the nature of the spacer separating the two chelating components. Potentially bridging N,S-donor ligands of this general type have been of some interest recently with respect to coordination with soft metal ions such as Cu^I and Ag^I; the combination of flexible bridging ligands with metal ions, which are tolerant of a wide range of coordination geometries has led to a remarkable collection of oligomeric and polymeric structures.[3] The complexes described in this paper illustrate in particular the propensity of the N,S-donor bridging ligands to afford one-dimensional helical coordination polymers, in contrast to the discrete M_2L_2 dinuclear double helicates which tend to form with the analogous N,O-donor ligands containing pyrazolylphenolate donor sites that we described recently.[4]

[a] Department of Chemistry, University of Sheffield, Sheffield S3 7HF, UK
E-mail: m.d.ward@sheffield.ac.uk

Results and Discussion

Syntheses and Structures of the Ligands

The ligands are shown in Scheme 1. 3-[2(Methylsulfanyl)-phenyl]pyrazole was prepared as described earlier,[5] and was treated with an appropriate bromomethylated aromatic compound under phase-transfer conditions[2] to give the new ligands L^1–L^5. The ligands L^1, L^2, L^3 and L^4 contain two potentially bidentate N,S-chelating units, with pyrazolyl and thioether donors, but differ in length due to variation in the length of the spacer unit. In contrast ligand L^5 is a

 DOI: 10.1002/ejic.200500704 © 2005 Wiley-VCH Verlag GmbH & Co. KGaA, Weinheim

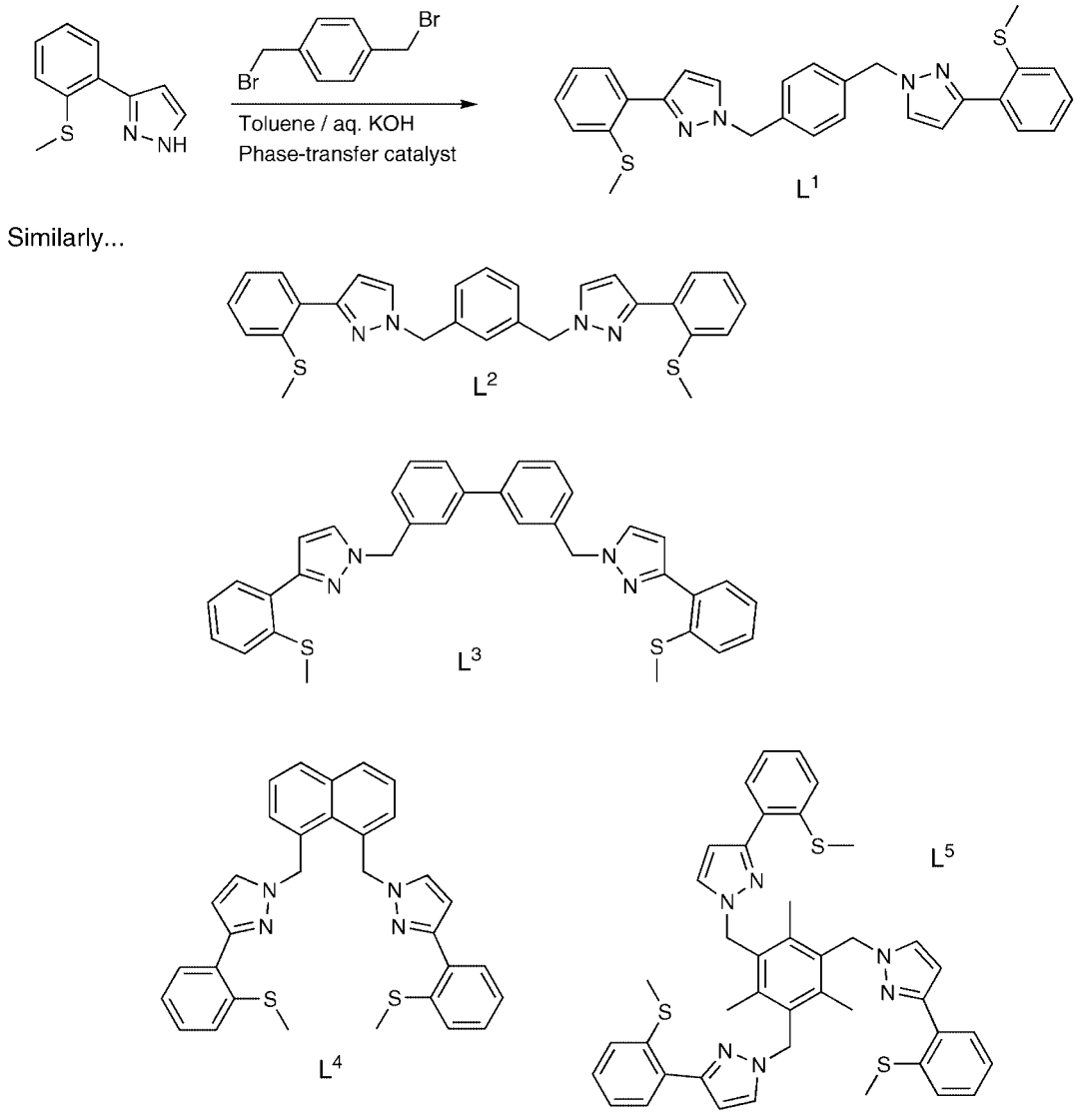

Scheme 1.

potentially hexadentate tripodal ligand with three bidentate arms linked to a central aromatic unit though methylene groups. The ligands were characterised by ^{1}H NMR and ^{13}C NMR spectroscopy, mass spectrometry and elemental analyses. Ligands L^1, L^4 and L^5 were also characterised by X-ray crystallography and their structures are shown in Figure 1, Figure 2, and Figure 3.

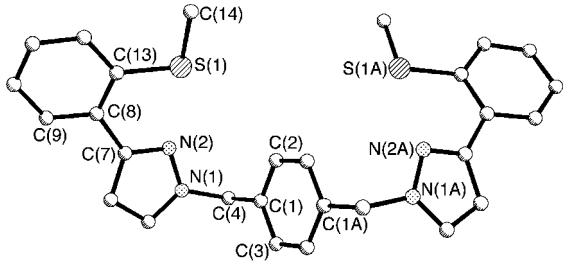

Figure 1. Molecular structure of L^1. Symmetry operation to generate equivalent atoms: ($-x$, y, $3/2 - z$).

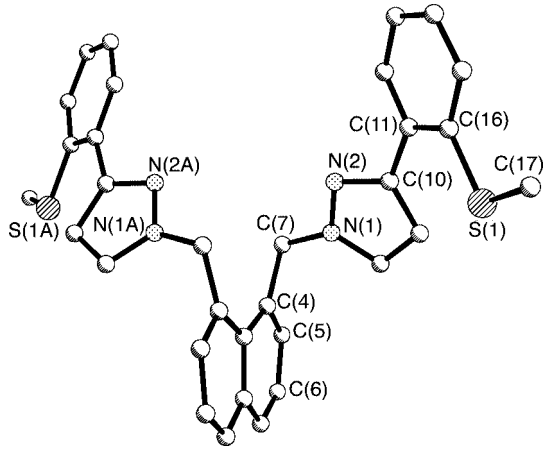

Figure 2. Molecular structure of L^4. Symmetry operation to generate equivalent atoms: ($1-x$, y, $1/2 - z$).

 © 2005 Wiley-VCH Verlag GmbH & Co. KGaA, Weinheim

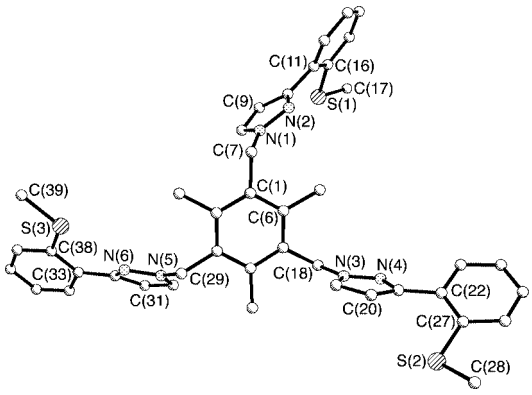

Figure 3. Molecular structure of L^5.

For L^1 the molecule lies astride a twofold axis of symmetry through the centre of the phenyl spacer, such that the two halves are crystallographically equivalent. The (methylsulfanylphenyl)pyrazole units adopt a *cisoid* configuration with the methyl group pointing away from the lone pairs of the pyrazole nitrogen atoms. The chelating units show a significant deviation from planarity with an angle of 26.6° between the methylsulfanylphenyl and pyrazole rings. The *cisoid* arrangement of the rings is, on the face of it, surprising because it brings the lone pairs of electrons on N(2) and S(1) into proximity; in polypyridyl ligands such as 2,2′-bipyridine, and the higher oligomers by contrast, adjacent pyridyl rings are always *transoid* so that the nitrogen lone pairs can avoid each other.[6] In fact the non-bonded N(2)···S(1) distance of 2.863(2) Å is in agreement with the known propensity of divalent S (and Se) atoms to become involved in relatively short contacts with nucleophilic atoms.[7] The nucleophile [here, pyrazolyl N(2)] tends to approach the S atom of an S–X bond in a direction corresponding to elongation of that bond, because of the involvement of the S–X σ* orbital in the interaction; in consequence the N···S–C angle should be nearly linear, consistent with other steric constraints, and in fact the angle N(2)–S(1)–C(14) is almost perfectly linear at 177.9(1)°.

L^4 also lies astride a twofold axis of symmetry which lies through the centre of the naphthyl spacer. The (methylsulfanylphenyl)pyrazole units this time adopt a *transoid* configuration, unlike the *cisoid* configuration observed in L^1; the chelating units show a significant deviation from planarity with an angle of 34.7° between the methylsulfanylphenyl and pyrazole rings. The two chelating arms are arranged on opposite sides of the plane of the central naphthyl spacer, and rotation of the methylsulfanylphenyl rings would be required in order for both arms to chelate to a single metal ion. It is clear from these structures that in L^1 the bidentate units are too far apart from one another to coordinate to a single metal ion, and L^1 must necessarily act as a bridging ligand. However, this is not the case for L^4 where a tetradentate chelating mode is also possible. There is no evidence for any inter- or intramolecular N···S interactions of the type seen for L^1.

Molecules of L^5 have no internal symmetry in the crystal. The chelating units show a significant deviation from planarity with angles of 39.5, 38.5 and 23.9° between the methylsulfanylphenyl and pyrazole rings. One of the (methylsulfanylphenyl)pyrazole units [involving atoms S(3) and N(6)] adopts a *cisoid* conformation, resulting again (as in L^1, above) in a relatively short N(6)···S(3) separation of 2.832 Å, and a near-linear N(6)···S(3)–C(39) angle of 175.7°, both consistent with an intermolecular donor-acceptor interaction involving the lone pair of N(3) and the S–C σ* orbital.[7] The torsion angle between these pyrazolyl and sulfanylphenyl rings is 23.9°. The other two methylsulfanylphenyl-pyrazole units, which have approximately *transoid* conformations, have a greater degree of twist between the aromatic rings (39.5 and 38.5°) because there is no N···S interaction which tends to keep the rings concerned more coplanar. Sulfur atoms S(1) and S(2) are not involved in any intermolecular N···S contacts comparable to that seen for S(3).

Complexes with L^1

The reaction of L^1 with one equivalent of $[Cu(CH_3CN)_4]PF_6$ in dry acetonitrile under nitrogen resulted in a pale yellow solution. Diethyl ether diffusion into the reaction mixture gave pale yellow crystals whose elemental analysis indicates the stochiometry $[CuL^1][PF_6]$, i.e. a 1:1 metal/ligand ratio as expected for a complex between a tetradentate ligand and a metal ion with preference for tetrahedral geometry. The presence of the PF_6^- anion was confirmed by the presence of peaks at 839 and 558 cm^{-1} in the IR spectrum,[8] and the electrospray mass spectrum showed a molecular ion peak at m/z = 545 for $\{CuL^1\}^+$.

The X-ray crystal structure (Figure 4) shows that the crystalline material is an infinite one-dimensional helical coordination polymer $\{[CuL^1](PF_6)\}_\infty$; helical chains have become well known recently with examples based on N,S-chelating[4] and other[9] bridging ligands. The Cu^I ion and the phosphorus atom of the PF_6^- are at special positions such that the asymmetric unit contains half a Cu^I ion, half a ligand and half a PF_6^- ion. Each Cu^I ion is in a four-coordinate environment, coordinated by an N,S-chelating arm from each of two separate ligands. Each ligand therefore bridges two metal ions. The Cu···Cu separation between metals linked by the same bridging ligand is 9.85 Å. The geometry around the Cu^I ion is distorted tetrahedral with an angle of 75.5° between the two Cu(NS) planes (Figure 4, a); the twist angle within each bidentate (methylsulfanylphenyl)pyrazole unit is 28.7°. The ligands are arranged around the Cu^I ions such that each polymeric chain is helical with equal amounts of each enantiomer in the crystal. There are interligand aromatic stacking interactions within each helical strand, which is a common feature of helical complexes.[10] Each central phenyl spacer is stacked to a (methylsulfanyl)phenyl ring from a ligand on each side of it, with the stacked rings inclined at 6.7° to each other. The distance between these stacked rings (distance of atoms in one from the mean plane of the other) is in the range 3.2–3.7 Å. The angle between the planes of alternating central

 © 2005 Wiley-VCH Verlag GmbH & Co. KGaA, Weinheim

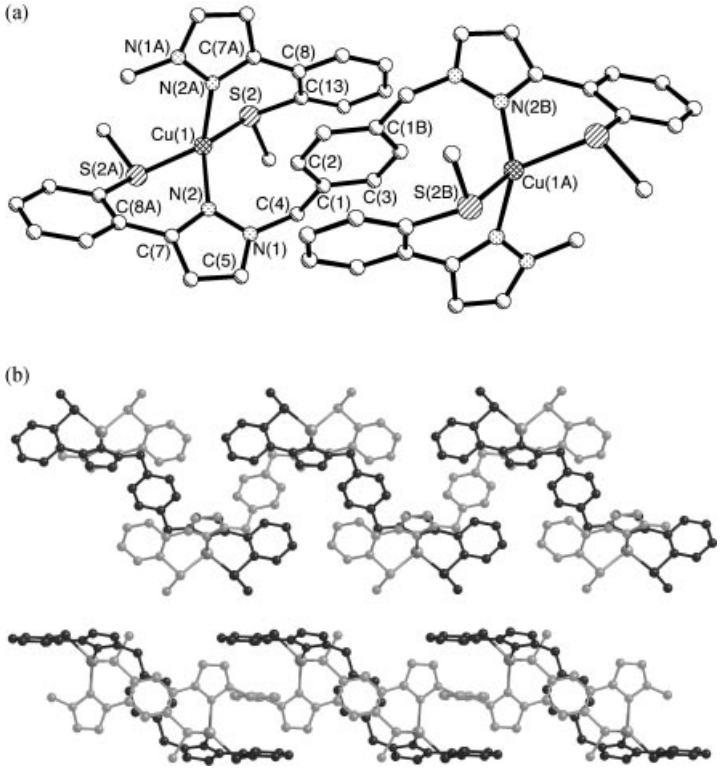

Figure 4. (a) Structure of the metal complex unit of $\{[CuL^1](PF_6)\}_\infty$ showing the coordination geometry around the Cu^I centres. (b) Two views of the one-dimensional helical chain of $\{[CuL^1](PF_6)\}_\infty$, with alternate ligands shaded differently for clarity. The bottom view shows the interligand aromatic stacking interactions within each chain.

phenyl rings is 73.6°, hence stacking can be seen in two almost perpendicular directions (Figure 4, b) (Table 1).

Table 1. Selected bond lengths [Å] and angles [°] for $\{[CuL^1](PF_6)\}_\infty$.

Cu(1)–N(2A)	2.014(2)
Cu(1)–N(2)	2.014(2)
Cu(1)–S(2A)	2.2933(8)
Cu(1)–S(2)	2.2933(8)
N(2A)–Cu(1)–N(2)	118.65(12)
N(2A)–Cu(1)–S(2A)	129.48(7)
N(2)–Cu(1)–S(2A)	87.61(6)
N(2A)–Cu(1)–S(2)	87.61(6)
N(2)–Cu(1)–S(2)	129.48(7)
S(2A)–Cu(1)–S(2)	108.80(4)

Symmetry transformations used to generate equivalent atoms: $-x$, y, $-z + 1/2$.

Reaction of L^1 in methanol with a solution of one equivalent of $AgNO_3$ in H_2O gave a white powder after filtration, whose elemental analysis indicated the composition $\{[AgL^1](NO_3)\}_\infty$. The IR spectrum confirmed the presence of the NO_3^- counterion with a broad band centred around 1339 cm^{-1}, and the FAB mass spectrum (see Experimental Section) showed peaks arising from 1:1, 2:1 and 2:1 Ag/L^1 fragments.

X-ray quality crystals were grown from slow evaporation of the filtrate; the structure of the complex (Figure 5) shows it to be an infinite helical polymer $\{[AgL^1](NO_3)\cdot MeOH\}_\infty$, with a similar structure to $\{[CuL^1](PF_6)\}_\infty$. Each Ag^I ion is in a four-coordinate N_2S_2 environment, coordinated by a N,S-chelating arm from two separate ligands. The nitrate counterions are non-coordinating. The Ag···Ag separation is 7.62 Å, significantly shorter than the inter-metal separation in $\{[CuL^1](PF_6)\}_\infty$. The geometry around the Ag^I ion is almost tetrahedral with an angle of 80.2° between the two Ag(NS) planes. The bidentate (methylsulfanylphenyl)-pyrazole unit show large deviations from planarity with twist angles between the two rings of 43.5 and 47.8°. The central phenyl spacers of successive ligands in the chain are oriented at 72.5° to each other. Unlike in $\{[CuL^1](PF_6)\}_\infty$, only every second phenyl spacer is involved in interligand stacking interactions, being sandwiched between pyrazolyl rings on either side of it to which it is near-parallel (6.9° between planes); the distance between the stacked rings is 3.1–3.5 Å (Table 2).

Table 2. Selected bond lengths [Å] and angles [°] for $\{[AgL^1](NO_3)\}_\infty$.

Ag(1)–N(4)	2.231(5)
Ag(1)–N(2)	2.410(5)
Ag(1)–S(1)	2.4782(18)
Ag(1)–S(2)	2.6950(18)
N(4)–Ag(1)–N(2)	120.82(17)
N(4)–Ag(1)–S(1)	150.59(13)
N(2)–Ag(1)–S(1)	77.71(13)
N(4)–Ag(1)–S(2)	75.52(13)
N(2)–Ag(1)–S(2)	99.66(13)
S(1)–Ag(1)–S(2)	126.93(6)

 © 2005 Wiley-VCH Verlag GmbH & Co. KGaA, Weinheim

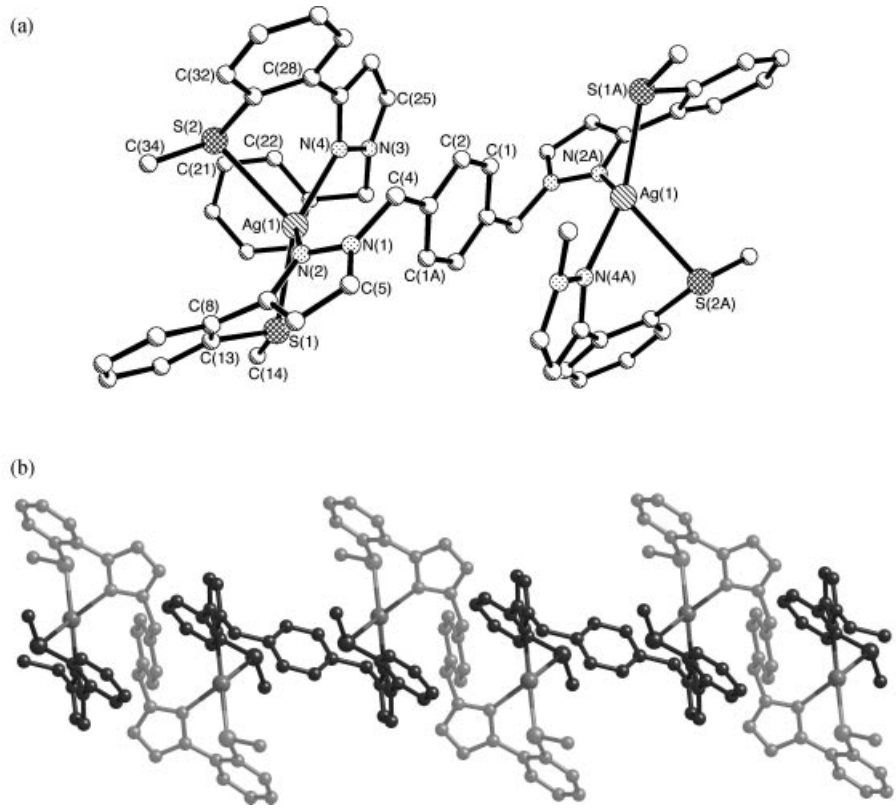

Figure 5. (a) Structure of the metal complex unit of $\{[AgL^1](NO_3)\}_\infty$ showing the coordination geometry around the Ag^I centres. (b) Structure of the one-dimensional helical chain of $\{[AgL^1](NO_3)\}_\infty$ with alternate ligands shaded differently for clarity.

Complexes with L^2

The reaction of L^2 with one equivalent of $[Cu(CH_3CN)_4]BF_4$ in dry acetonitrile under nitrogen resulted in a colourless solution. Diethyl ether diffusion into the reaction mixture gave almost colourless crystals whose elemental analysis indicates a 1:1 metal/ligand ratio. The IR spectrum confirms the presence of the BF_4^- counterion at 1056 cm^{-1}. The electrospray mass spectrum shows a peak at m/z = 545 for the mononuclear species $\{CuL^2\}^+$. The X-ray crystal structure (Figure 6) shows that the crystalline material is an infinite one-dimensional coordination polymer $\{[CuL^2](BF_4)\}_\infty$. However, unlike the structure of $\{[CuL^1](PF_6)\}_\infty$ the chains are not helical. Each ligand is folded back on itself with the two coordinating arms almost overlapping but pointing in opposite directions, coordinating to separate Cu^I ions.

The Cu^I ion and the boron atom of the BF_4^- are at special positions such that the asymmetric unit contains half a Cu^I ion, half a ligand and half of an anion, as well as fractions of two acetonitrile and a diethyl ether molecule which are also at special positions. Each Cu^I ion is in a four-coordinate environment, coordinated by an N,S-chelating arm from each of two separate ligands. The Cu···Cu separation between metals linked by the same bridging ligand is 6.17 Å, significantly shorter than that found in $\{[CuL^1](PF_6)\}_\infty$ (9.85 Å). The geometry around the Cu^I ion is distorted tetrahedral with an angle of 77.2° between the two Cu(NS) planes (Figure 6, a); the twist angle within each bidentate (methylsulfanylphenyl)pyrazole unit is 28.6°. There are no close π-π stacking interactions within each chain (Table 3).

The reaction of L^2 with one equivalent of $[Ag(CH_3CN)_4]BF_4$ in dry acetonitrile under nitrogen resulted in a colourless solution. Diethyl ether diffusion into the reaction mixture gave almost colourless crystals whose elemental analysis was consistent with the formulation $[Ag(L^2)](BF_4)$. The IR spectrum showed the presence of the BF_4^- counterion with a broad band at 1050 cm^{-1}. The electrospray mass spectrum showed a molecular ion peak at m/z = 589 for $\{AgL^2\}^+$ with no peaks for higher oligomers. The X-ray structure of the complex shows it to be the mononuclear complex $[Ag(L^2)](BF_4)$, in contrast to the infinite chain that was observed with Cu^I. There are two unique molecules in the asymmetric unit, which are associated into a dimer by face-to-face π-stacking between the phenyl rings of the aromatic spacers with an average distance of 3.60 Å between the overlapping rings.

The two complex molecules in the asymmetric unit display similar geometries. If only the N,S-donors are considered, both Ag^I ions are in a flattened tetrahedral environment [angles of 80.8° and 80.6° between the Ag(NS) planes], coordinated by an L^2 ligand acting as a tetradentate chelate. One of the bidentate arms shows a larger dihedral twist [44.9° and 49.3° for the molecules containing Ag(1) and Ag(2), respectively] between the two rings than the

 © 2005 Wiley-VCH Verlag GmbH & Co. KGaA, Weinheim

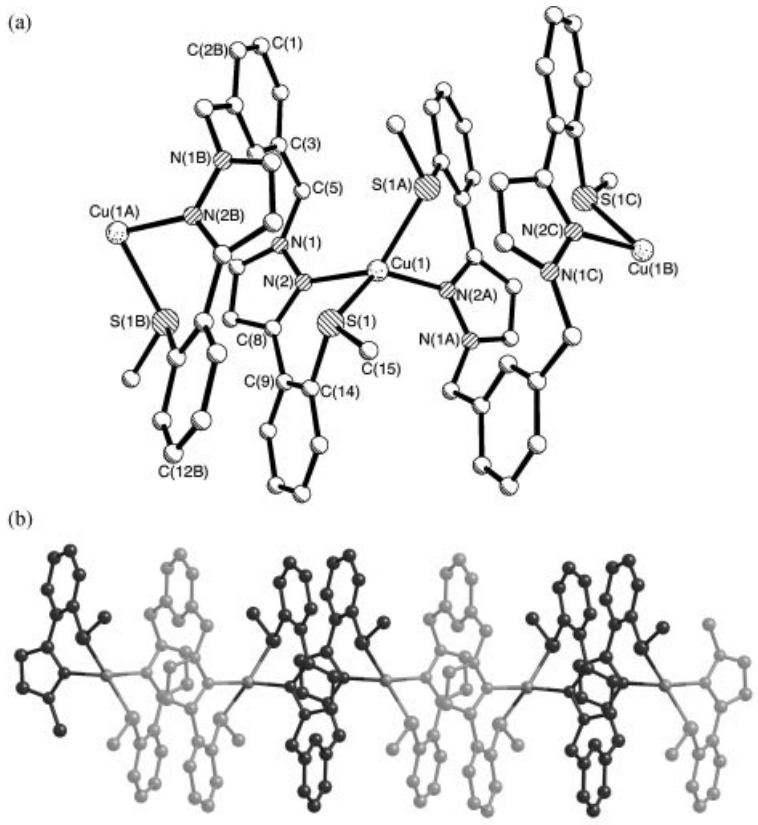

Figure 6. (a) Structure of the metal complex unit of $\{[CuL^2](BF_4)\}_\infty$ showing the coordination geometry around the Cu^I centres. (b) Structure of the one-dimensional chain of $\{[CuL^2](BF_4)\}_\infty$, with alternate ligands shaded differently for clarity.

Table 3. Selected bond lengths [Å] and angles [°] for $\{[CuL^2](BF_4)\}_\infty$.

Cu(1)–N(2A)	2.057(2)
Cu(1)–N(2)	2.057(2)
Cu(1)–S(1A)	2.2992(7)
Cu(1)–S(1)	2.2992(7)
N(2A)–Cu(1)–N(2)	113.93(12)
N(2A)–Cu(1)–S(1A)	84.10(6)
N(2)–Cu(1)–S(1A)	130.48(6)
N(2A)–Cu(1)–S(1)	130.48(6)
N(2)–Cu(1)–S(1)	84.10(6)
S(1A)–Cu(1)–S(1)	119.85(4)

Symmetry transformations used to generate equivalent atoms: $x, -y + 2, -z$.

other [17.7° and 22.7° for the molecules containing Ag(1) and Ag(2), respectively]. The average Ag–N bond length is 2.39 Å and the average Ag–S bond length is 2.64 Å (Table 4). However, the near-linearity of the N–Ag–N angles [169° at each metal centre] results in a large gap in the Ag^I coordination sphere, which is filled by an interaction of each Ag^I ion with the "capping" phenyl ring. The Ag^I ions do not sit centrally above the phenyl rings but are slightly offset, such that they interact with just one C atom (dotted line in Figure 7). The Ag(1)···C(1) separation is 2.76 Å, and the corresponding Ag(2)···C(101) separation in the independent molecule is 2.74 Å. This type of η^1 interaction of an Ag^I ion with a phenyl ring, although less common than the η^2 π-type interaction in which the metal ion interacts with one edge of a phenyl ring,[11] is still well known[12] with many dozens of examples in the Cambridge Structural Database. It is characterised by a contact in the range 2.4–2.8 Å between the Ag^I ion and one C atom such that the Ag–C vector is near-perpendicular to the aromatic ring, as we see for $[Ag(L^2)](BF_4)$, where these angles are 77°

Table 4. Selected bond lengths [Å] and angles [°] for $[AgL^2](BF_4)$.

Ag(1)–N(1)	2.331(3)
Ag(1)–N(4)	2.408(3)
Ag(1)–S(2)	2.6311(10)
Ag(1)–S(1)	2.6602(11)
Ag(1)–C(1)	2.763(3)
Ag(2)–N(101)	2.367(3)
Ag(2)–N(104)	2.446(3)
Ag(2)–S(102)	2.6100(10)
Ag(2)–S(101)	2.6686(11)
Ag(2)–C(101)	2.737(3)
N(1)–Ag(1)–N(4)	169.09(10)
N(1)–Ag(1)–S(2)	116.08(7)
N(4)–Ag(1)–S(2)	70.66(7)
N(1)–Ag(1)–S(1)	76.45(8)
N(4)–Ag(1)–S(1)	110.44(8)
S(2)–Ag(1)–S(1)	107.77(3)
N(101)–Ag(2)–N(104)	168.91(10)
N(101)–Ag(2)–S(102)	114.65(7)
N(104)–Ag(2)–S(102)	72.36(7)
N(101)–Ag(2)–S(101)	74.70(8)
N(104)–Ag(2)–S(101)	112.09(8)
S(102)–Ag(2)–S(101)	108.22(3)

 © 2005 Wiley-VCH Verlag GmbH & Co. KGaA, Weinheim

for Ag(1) and 83° for Ag(2). In this case, this results in a coordination geometry about the metal ions that is best described as trigonal bipyramidal, with the C and two S donors forming the trigonal plane and the two N donors being axial. The τ parameter for this complex is 0.67 [0.64 for the independent complex molecular containing Ag(2)],

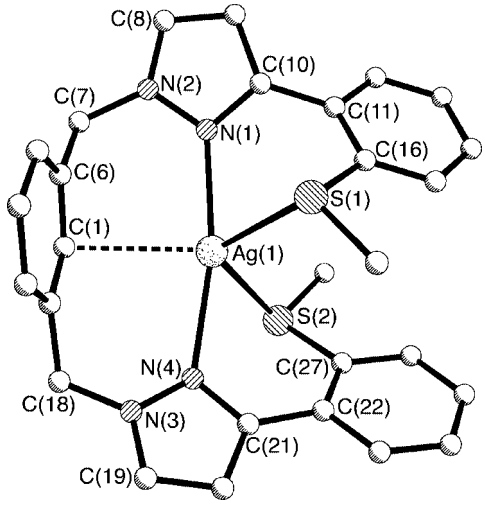

Figure 7. Structure of the metal complex unit of $[AgL^2](BF_4)$. The Ag···C interaction to the phenyl ring is shown with a dashed line.

where 1.0 denotes a perfect trigonal bipyramid and 0.0 denotes a perfect square pyramid.[13]

The presence of this metal–carbon interaction with Ag^I, but not Cu^I, is likely to be an important factor in explaining why $\{[CuL^2](BF_4)\}_\infty$ forms an infinite chain whereas $[Ag(L^2)](BF_4)$ is mononuclear; the binding mode in $[Ag(L^2)](BF_4)$ in which both bidentate arms of L^2 coordinate to the same metal ion necessarily brings the phenyl spacer into close contact with the metal ion. In addition, this mononucleating, tetradentate coordination mode would be harder to achieve with the smaller Cu^I ions in any case.

Complexes with L^3

The reaction of L^3 with one equivalent of $[Cu(CH_3CN)_4]$-BF_4 in ethanol resulted in a suspension from which an off-white solid was isolated after filtration. The infrared spectrum showed a broad band centred around 1083 cm^{-1} for the BF_4^- counterions and the FAB mass spectrum showed peaks consistent with 1:1, 1:2 and 2:2 Cu/L^3 fragments; the elemental analysis was consistent with a 1:1 metal/ligand ratio.

X-ray quality crystals were grown by diffusion of diethyl ether vapour into a solution of the complex in MeCN. The

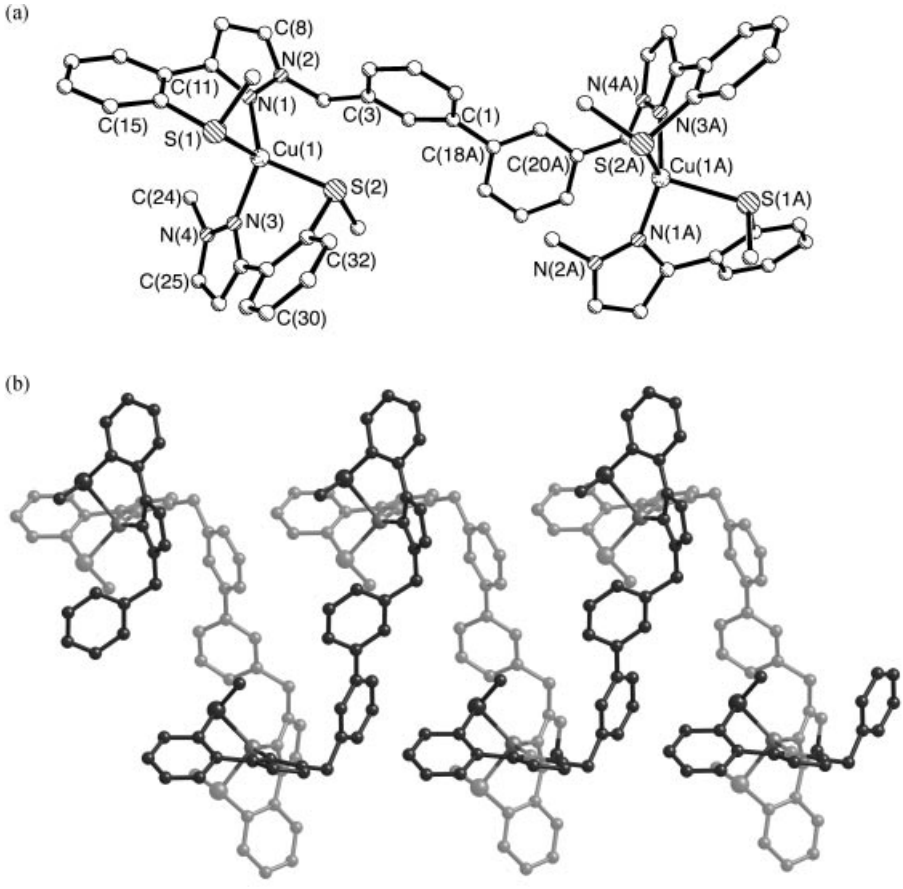

Figure 8. (a) Structure of the metal complex unit of $\{[CuL^3](BF_4)\}_\infty \cdot 1.53CH_3CN \cdot 0.47Et_2O$ showing the coordination geometry around the Cu^I centres. (b) Structure of the one-dimensional polymeric chain of $\{[CuL^3](BF_4)\}_\infty \cdot 1.53CH_3CN \cdot 0.47Et_2O$, with alternate ligands shaded differently for clarity.

 © 2005 Wiley-VCH Verlag GmbH & Co. KGaA, Weinheim

structure of the complex (Figure 8) shows it to be the one-dimensional coordination polymer $\{[CuL^3](BF_4)\}_\infty$ with one Cu^I ion and one complete ligand in the asymmetric unit. Unlike the complexes of L^1, the structure of $\{[CuL^3](BF_4)\}_\infty$ is not helical. Rather, the sequence of bridging ligands between one ligand and the next follows a zig-zag path. The Cu^I ions are in a four-coordinate N_2S_2 environment with an almost tetrahedral geometry [angle of 87.2° between the Cu(NS) planes]. The Cu···Cu separation between metal atoms which are linked by the same bridging ligand is 10.645 Å, and the separation between alternate Cu^I centres is almost identical at 10.649 Å. The twist angle within the biphenyl spacer is 40.6° and the twist angles within each bidentate (methylsulfanylphenyl)pyrazole units are 34.7 and 36.7°. Unlike the structure of L^1 there is no face-to-face π-stacking within the polymer chains (Table 5).

Table 5. Selected bond lengths [Å] and angles [°] for $\{[CuL^3](BF_4)\}_\infty \cdot 1.53CH_3CN \cdot 0.47Et_2O$.

Cu(1)–N(1)	1.961(5)
Cu(1)–N(3)	1.996(5)
Cu(1)–S(2)	2.3045(17)
Cu(1)–S(1)	2.3567(18)
N(1)–Cu(1)–N(3)	127.27(18)
N(1)–Cu(1)–S(2)	128.63(14)
N(3)–Cu(1)–S(2)	92.35(14)
N(1)–Cu(1)–S(1)	94.48(15)
N(3)–Cu(1)–S(1)	107.71(14)
S(2)–Cu(1)–S(1)	103.55(6)

The reaction of L^3 with one equivalent of $[Ag(CH_3CN)_4]BF_4$ in dry acetonitrile under nitrogen resulted in a colourless solution. Diethyl ether diffusion into the reaction mixture gave almost colourless crystals whose elemental analysis indicates a 1:1 metal/ligand ratio. The IR spectrum confirms the presence of the BF_4^- counterion at 1061 cm^{-1}. The FAB mass spectrum shows peaks arising from 1:1, 1:2 and 2:2 Ag/L^3 fragments. The X-ray crystal structure (Figure 9) shows that the crystalline material is another infinite one-dimensional coordination polymer $\{[AgL^3](BF_4)\}_\infty$. One of the coordinating arms [containing S(4) and N(7)] is disordered and has been modelled over two sites; unless otherwise stated only the major component of this disorder will be discussed. Each metal/ligand chain shows a clear zig-zag (non-helical) structure, similar to that of $\{[CuL^3](BF_4)\}_\infty$. The Ag···Ag separations between metal atoms which are linked by the same bridging ligand are 8.95 and 9.05 Å, less than the equivalent distances in $\{[CuL^3](BF_4)\}_\infty$. The separations between alternate Ag^I centres are however greater at 11.97 Å.

The Ag^I ions in each chain alternate between being four-coordinate [Ag(1)] and three-coordinate [Ag(2)]. Ag(1) is in an almost tetrahedral N_2S_2 environment [angle of 87.2° between the Ag(NS) planes], coordinated by two bidentate arms from separate ligands. Ag(2) is in an N_2S environment approximating a T-shape, with the silver atom sitting ca. 0.1 Å above the plane of the donor atoms [N(4), N(5) and S(2)]. The remaining donor atom [S(3)] is too far from the

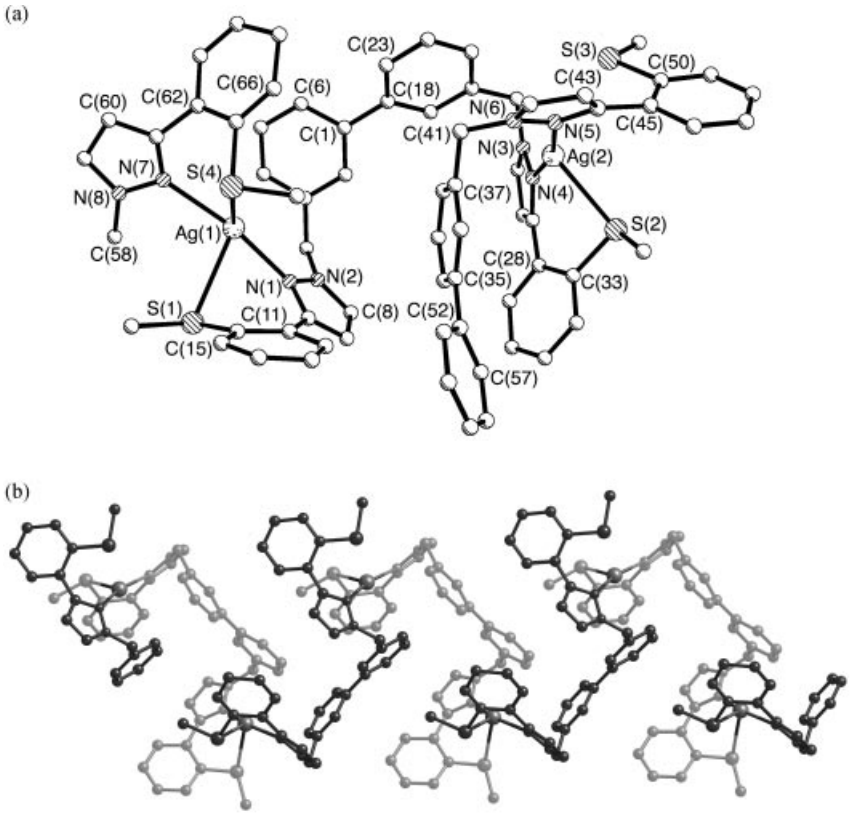

Figure 9. (a) Structure of the metal complex unit of $\{[AgL^3](BF_4)\}_\infty$ showing the asymmetric unit and the coordination geometry around the Ag^I centres. (b) Structure of the one-dimensional polymeric chain of $\{[AgL^3](BF_4)\}_\infty$, with alternate ligands shaded differently for clarity.

 © 2005 Wiley-VCH Verlag GmbH & Co. KGaA, Weinheim

metal to be considered as forming a normal coordinate bond [Ag(2)···S(3), 3.02 Å compared to 2.6934(12) Å for Ag(2)–S(2), Table 6] but may interact weakly with Ag(2). The bonds to the N-donors are slightly shorter than those to Ag(1) [Ag(2)–N(4) 2.213(3) Å, Ag(2)–N(5) 2.191(3) Å] as a consequence of the lower coordination number. Despite the low coordination numer there is no evidence for additional Ag···C contacts of the type described above for $[Ag(L^2)](BF_4)$. The twist angles within the biphenyl spacers are 35.4 and 34.2° and the twist angles within each bidentate (methylsulfanyl)phenyl-pyrazole units are in the range 37.7–47.4°. There is no face-to-face π-stacking within the polymer chains. However there is a CH-π interaction between one of the rings of the biphenyl spacer and the CH in the 4-position of the next biphenyl spacer (separation of 2.78 Å between the H^4 of the biphenyl unit and the centroid of the relevant phenyl ring).

Table 6. Selected bond lengths [Å] and angles [°] for $\{[AgL^3](BF_4)\}_\infty$.

Ag(1)–N(7′)	2.133(8)
Ag(1)–N(1)	2.215(3)
Ag(1)–N(7)	2.328(9)
Ag(1)–S(4)	2.632(3)
Ag(1)–S(4′)	2.810(3)
Ag(1)–S(1)	2.8543(13)
Ag(2)–N(5)	2.191(3)
Ag(2)–N(4)	2.213(3)
Ag(2)–S(2)	2.6934(12)
N(7′)–Ag(1)–N(1)	173.3(2)
N(1)–Ag(1)–N(7)	161.2(2)
N(1)–Ag(1)–S(4)	119.95(13)
N(7)–Ag(1)–S(4)	78.4(2)
N(7′)–Ag(1)–S(4′)	75.6(3)
N(1)–Ag(1)–S(4′)	110.28(12)
N(7′)–Ag(1)–S(1)	109.4(2)
N(1)–Ag(1)–S(1)	73.54(9)
N(7)–Ag(1)–S(1)	101.4(2)
S(4)–Ag(1)–S(1)	98.75(7)
S(4′)–Ag(1)–S(1)	97.49(7)
N(5)–Ag(2)–N(4)	164.86(12)
N(5)–Ag(2)–S(2)	115.06(9)
N(4)–Ag(2)–S(2)	79.00(9)

typical for this series (average Cu–N 2.03 Å, average Cu–S 2.30 Å, Table 7). The bidentate arms are not individually coplanar with substantial dihedral twists of 38.7° and 36.5° between the pyrazolyl and methylsulfanylphenyl rings.

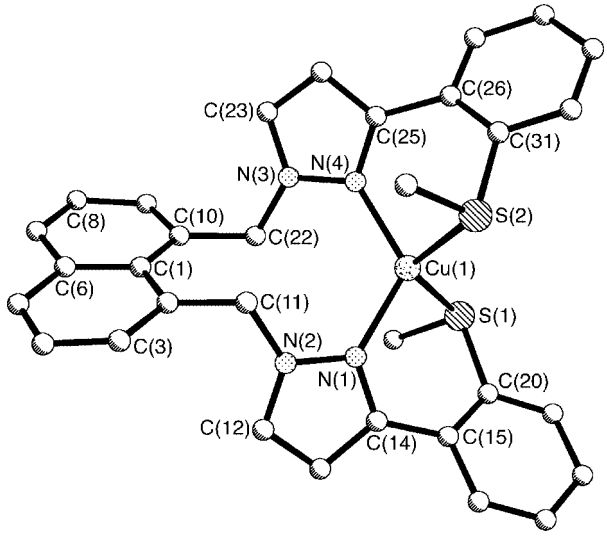

Figure 10. Molecular structure of the metal complex unit of $[CuL^4](PF_6)$.

Table 7. Selected bond lengths [Å] and angles [°] for $[CuL^4](PF_6)\cdot 2MeCN\cdot 2H_2O$.

Cu(1)–N(4)	2.020(4)
Cu(1)–N(1)	2.032(4)
Cu(1)–S(1)	2.2973(14)
Cu(1)–S(2)	2.2998(14)
N(4)–Cu(1)–N(1)	121.28(9)
N(4)–Cu(1)–S(1)	115.85(11)
N(1)–Cu(1)–S(1)	92.81(12)
N(4)–Cu(1)–S(2)	93.24(11)
N(1)–Cu(1)–S(2)	115.43(11)

Complexes with L^4

Reaction of L^4 with one equivalent of $[Cu(CH_3CN)_4]PF_6$ in dry acetonitrile under nitrogen resulted in a colourless solution. Diethyl ether diffusion into the reaction mixture gave colourless crystals whose elemental analysis was consistent with a 1:1 metal/ligand ratio. The IR spectrum showed peaks at 841 and 557 cm^{-1} for the PF_6^- counterions. The FAB mass spectrum showed a molecular ion peak at *m/z* = 595 for $\{CuL^4\}^+$ but no peaks for higher oligomers. A subsequent X-ray crystal structure determination (Figure 10) showed that the crystalline material is the mononuclear complex $[Cu(L^4)](PF_6)$, in obvious contrast to the polymeric structures obtained with L^1, L^2 and L^3. The Cu^I ion is in a distorted tetrahedral N_2S_2 environment [angle of 85.6° between the Cu(NS) planes] with L^4 acting as a tetradentate chelate. The bond lengths to the Cu^I ion are

The reaction of L^4 with one equivalent of $[Ag(CH_3CN)_4]BF_4$ in ethanol resulted in a suspension from which an off-white solid was isolated after filtration. The elemental analysis of the powder is consistent with the formulation $[AgL^4](BF_4)$. The IR spectrum showed the presence of the BF_4^- counterion with a broad band at 1071 cm^{-1}. The FAB mass spectrum showed a molecular ion peak at *m/z* = 641 for $\{AgL^4\}^+$ with no peaks for higher oligomers. The crystal structure of the complex shows it to be the mononuclear complex $[Ag(L^4)](BF_4)$ (Figure 11). There are two unique complex molecules in the unit cell which are associated into a dimer by weak, long-range Ag···N interactions (> 3 Å) between the Ag^I ion of one complex and the pyrazolyl N atoms of another. The two silver ions are 4.20 Å apart, which precludes any Ag···Ag interaction between them, and the two naphthalene spacers are at opposite sides of the dimer.

 © 2005 Wiley-VCH Verlag GmbH & Co. KGaA, Weinheim

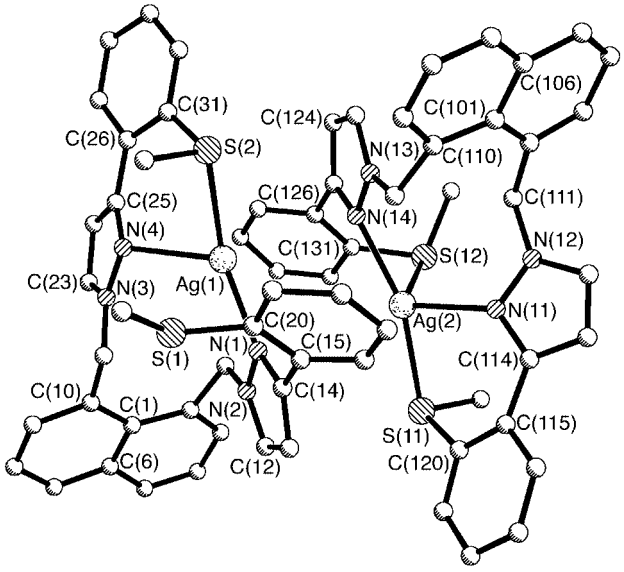

Figure 11. Molecular structure of the metal complex unit of $[AgL^4](BF_4)$ showing the stacking of two independent molecules in the unit cell.

One Ag^I ion [Ag(2)] is in a flattened tetrahedral environment [angle of 75.6° between the Ag(NS) planes] coordinated by an L^4 ligand acting as a tetradentate chelate. The Ag–N bonds are 2.246(10) and 2.367(9) Å and the Ag–S bonds are longer at 2.468(3) and 2.785(4) Å and are typical of the silver complexes in this series. One of the bidentate arms shows a larger dihedral twist between the two rings than the other [59.0° for the arm containing N(11) and S(11), and 22.8° for the arm containing N(14) and S(12)]. The other Ag^I ion is in a three-coordinate N_2S environment with all donor atoms coming from a single L^4 molecule. Here the remaining sulfur atom is too far from the metal to be considered as forming a normal coordinate bond [Ag(1)–S(1) = 3.02 Å compared to 2.445(3) Å for Ag(1)–S(2), Table 8]. The coordination environment is almost planar with the Ag(1) sitting ca. 0.1 Å above the plane of the donor atoms. The bond to one of the N-donors is significantly longer than that to the other N-donor [Ag(1)–N(1), 2.146(9) Å; Ag(1)–N(4), 2.446(9) Å]. The bidentate arm where the sulfur atom is not coordinated to the metal shows a greater dihedral angle between the pyrazole and methylsulfanylphenyl rings (58.0°) than the arm where both donor atoms are coordinated (21.5°).

Table 8. Selected bond lengths [Å] and angles [°] for $[AgL^4](BF_4)$.

Ag(1)–N(1)	2.146(9)
Ag(1)–S(2)	2.445(3)
Ag(1)–N(4)	2.446(9)
Ag(2)–N(14)	2.246(10)
Ag(2)–N(11)	2.367(9)
Ag(2)–S(11)	2.468(3)
Ag(2)–S(12)	2.785(4)
N(1)–Ag(1)–S(2)	161.3(3)
N(1)–Ag(1)–N(4)	114.0(3)
S(2)–Ag(1)–N(4)	83.6(2)
N(14)–Ag(2)–N(11)	110.5(3)
N(14)–Ag(2)–S(11)	162.7(3)
N(11)–Ag(2)–S(11)	85.3(2)
N(14)–Ag(2)–S(12)	81.5(3)
N(11)–Ag(2)–S(12)	108.8(2)
S(11)–Ag(2)–S(12)	100.35(13)

The NMR spectra of $[CuL^4](PF_6)$ and $[AgL^4](BF_4)$ show that the complexes have twofold symmetry in solution.

Complexes with L^5

The reaction of L^5 with 1.5 equivalents of $Ag(ClO_4)_4 \cdot H_2O$ in dry acetonitrile under nitrogen resulted in a colourless solution. Diethyl ether diffusion into the reaction mixture gave colourless crystals whose elemental analysis indicates the stochiometry $[AgL^5](ClO_4)$, i.e. a 1:1 metal/ligand ratio rather than the 3:2 ratio expected for a complex between a hexadentate ligand and a metal ion with preference for tetrahedral geometry. The IR spectrum showed the presence of the ClO_4^- counterions at 1091 and 623 cm^{-1}, and the FAB mass spectrum showed a molecular ion peak at m/z = 835 for the fragment $\{AgL^5\}^+$ all indicating formation of a 1:1 complex.

X-ray crystallography confirmed (Figure 12) that the complex is mononuclear, with some obvious structural similarities to $[AgL^2](BF_4)$ as a consequence of the *meta* substitution pattern of the central phenyl spacer. The Ag^I ion is bound by two of the bidentate N,S-donor arms of L^5 with the third arm pendant. As we saw with $[AgL^2](BF_4)$, the orientation of the two chelating bidentate arms to the same face of the phenyl spacer necessarily results in a close contact between the metal ion and the phenyl ring, resulting in an η^1 π-type interaction with C(2) of the phenyl ring [Ag(1)···C(2), 2.70 Å (dotted line in Figure 12; Table 9), with the angle between the Ag–C vector and the phenyl plane being 89°]. The Ag^I centre is therefore five coordinate; the τ parameter of 0.12 indicates that the geometry is best described as square-based pyramidal, with S(2) being the "axial" donor. Although the third pendant arm is directed

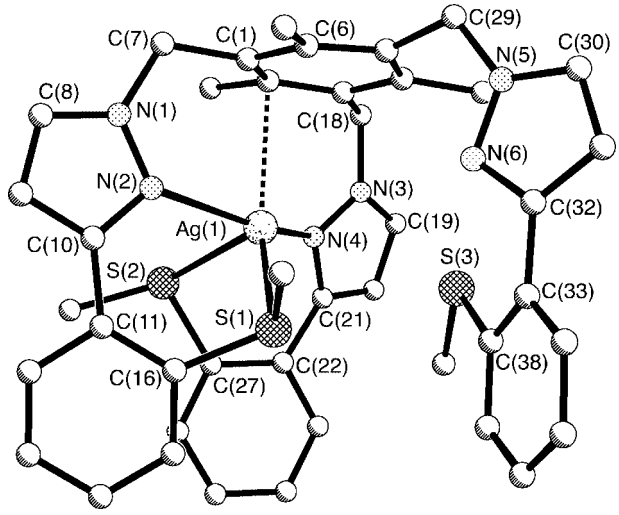

Figure 12. Molecular structure of the metal complex unit of $[AgL^5](ClO_4)$. The Ag···C interaction to the phenyl ring is shown with a dashed line.

 © 2005 Wiley-VCH Verlag GmbH & Co. KGaA, Weinheim

towards the same face of the aromatic spacer as the two other arms, the remaining donor atoms are not interacting with the Ag^{I} centre [Ag(1)–N(6), 4.69 Å; Ag(1)–S(3), 3.71 Å]. All three bidentate arms show substantial deviations from planarity (twist angles of 17.7 and 33.5° between the pyrazolyl and methylsulfanylphenyl rings for the coordinated arms and 34.6° for the non-coordinated arm).

Table 9. Selected bond lengths [Å] and angles [°] for $[AgL^5](ClO_4)$.

Ag(1)–N(4)	2.3172(19)
Ag(1)–N(2)	2.436(2)
Ag(1)–S(1)	2.5201(7)
Ag(1)–S(2)	2.8347(7)
Ag(1)–C(2)	2.701(2)
N(4)–Ag(1)–N(2)	151.66(7)
N(4)–Ag(1)–S(1)	124.95(5)
N(2)–Ag(1)–S(1)	79.22(5)
N(4)–Ag(1)–S(2)	69.23(5)
N(2)–Ag(1)–S(2)	90.61(5)
S(1)–Ag(1)–S(2)	107.53(2)

Despite the asymmetry of the complex in the solid state, the ^{1}H NMR spectrum of $[AgL^5](ClO_4)$ showed that all three arms of the ligand are equivalent in solution, indicating that the silver(I) ion is coordinated by all three arms or, more likely, that the structure is fluxional in solution.

The structure of $[Ag(L^5)](ClO_4)$ suggested that the pendant arm would be able to coordinate a second metal ion, but only after the conformation of L^5 alters such that the pendant arm is rotated away from the metal ion. Reaction of L^5 with a 10 fold excess of $AgClO_4{\cdot}H_2O$ in dry acetonitrile under nitrogen resulted in a colourless solution. Diethyl ether vapour diffusion into this solution gave crystals of unreacted $[Ag(CH_3CN)_4]ClO_4$ in addition to crystals of the trinuclear complex $[Ag_3(L^5)_2](ClO_4)_3$. The FAB mass spectrum of these latter crystals shows a peak at m/z = 835 for $\{Ag(L^5)\}^+$ and additional peaks at m/z = 1041 for $\{Ag_2(L^5)(ClO_4)\}^+$ and 1768 for $\{Ag_2(L^5)_2(ClO_4)\}^+$. No peaks were observed for intact trinuclear $\{Ag_3(L^5)_2(ClO_4)_x\}$ species. The ^{1}H NMR spectrum showed a symmetrical structure in solution with identical chemical shifts to that of $[AgL^5](ClO_4)$, suggesting that $[Ag_3(L^5)_2]^{3+}$ only exists in the solid state. Attempts to isolate pure $[Ag_3(L^5)_2](ClO_4)_3$ by using a smaller excess of $Ag(ClO_4)_4{\cdot}H_2O$ were unsuccessful resulting in a mixture of $[Ag_3(L^5)_2](ClO_4)_3$ and $[Ag(L^5)_2](ClO_4)$.

In the crystal structure of $[Ag_3(L^5)_2](ClO_4)_3$ (Figure 13), the pendant arms of two mononuclear $\{Ag(L^5)\}^+$ units are coordinated to another Ag^{I} ion, linking two such units together via a third Ag^{I} centre. The two terminal Ag^{I} ions [Ag(1), Ag(3)] are in the familiar five-coordinate environments from two bidentate N,S-chelating ligand arms and an η^1 π-type interaction with the capping phenyl ring [Ag(1)···C(2), 2.79 Å; Ag(3)···C(102), 2.83 Å, Table 10; angles between Ag–C vectors and phenyl mean planes, 82° and 83° respectively; τ parameters 0.72 and 0.61 at Ag(1) and Ag(3) respectively]. The central Ag^{I} ion [Ag(2)] is in a five coordinate N_2SO_2 environment arising from an N,S bidentate arm from one ligand, just the pyrazolyl N-donor from the other ligand, and two oxygen atoms from one of the perchlorate anions [Ag–O distances, 2.85 and 2.87 Å]. The remaining non-coordinated S atom, S(103), is 3.82 Å away from Ag(2).

The two ligands are arranged such that the silver ions form a rough triangle. The inter-metallic distances between silver ions linked by the same ligand are 8.72 Å [Ag(1)···Ag(2)] and 7.47 Å [Ag(2)···Ag(3)]; the Ag(1)···Ag(3) separation is 9.58 Å. The bidentate arms show twist angles of 11.2–49.3° between pyrazolyl and methylsulfanylphenyl rings, whereas the arm where only the pyrazolyl donor is coordinated shows a larger twist angle of 78.2° in order to avoid unfavourable steric interactions between the thioether group and the nearby bidentate arm from the other ligand.

The reaction of L^5 with $[Cu(CH_3CN)_4]BF_4$ in a 2:3 ratio in dry ethanol resulted in an off-white precipitate which was isolated by filtration. The elemental analysis of the powder

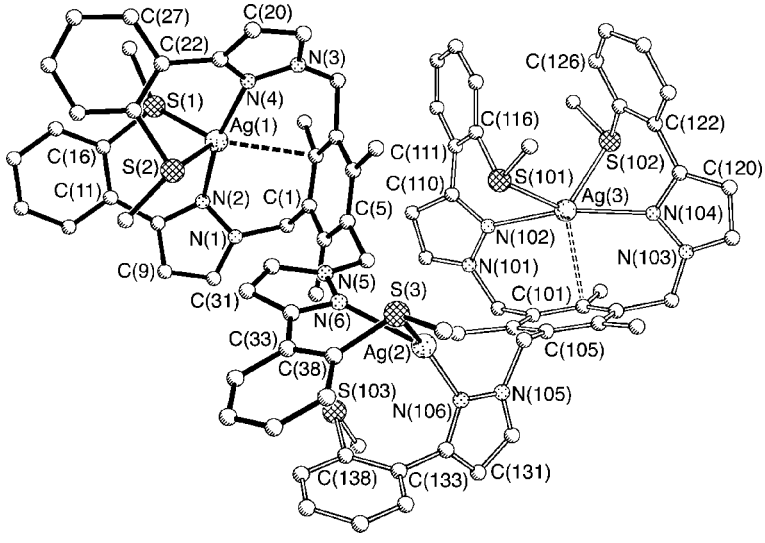

Figure 13. Molecular structure of the metal complex unit of $[Ag_3(L^5)_2](ClO_4)_3$; one ligand is shown with hollow bonds for clarity. The Ag···C interactions to the phenyl rings are shown with dashed lines.

 © 2005 Wiley-VCH Verlag GmbH & Co. KGaA, Weinheim

Table 10. Selected bond lengths [Å] and angles [°] for $[Ag_2(L^5)_3](ClO_4)_3$.

Ag(1)–N(4)	2.308(6)
Ag(1)–N(2)	2.439(6)
Ag(1)–S(1)	2.586(2)
Ag(1)–S(2)	2.626(2)
Ag(1)–C(2)	2.785(6)
Ag(2)–N(106)	2.154(6)
Ag(2)–N(6)	2.336(6)
Ag(2)–S(3)	2.539(2)
Ag(2)–O(11)	2.848(7)
Ag(2)–O(12)	2.871(7)
Ag(3)–N(104)	2.375(6)
Ag(3)–N(102)	2.385(6)
Ag(3)–S(101)	2.603(2)
Ag(3)–S(102)	2.667(2)
Ag(3)–C(102)	2.823(6)
N(4)–Ag(1)–N(2)	168.2(2)
N(4)–Ag(1)–S(1)	114.18(16)
N(2)–Ag(1)–S(1)	71.62(15)
N(4)–Ag(1)–S(2)	78.16(16)
N(2)–Ag(1)–S(2)	109.53(14)
S(1)–Ag(1)–S(2)	113.54(7)
N(106)–Ag(2)–N(6)	129.7(2)
N(106)–Ag(2)–S(3)	152.01(16)
N(6)–Ag(2)–S(3)	72.58(15)
N(104)–Ag(3)–N(102)	162.7(2)
N(104)–Ag(3)–S(101)	120.34(15)
N(102)–Ag(3)–S(101)	75.28(14)
N(104)–Ag(3)–S(102)	72.05(15)
N(102)–Ag(3)–S(102)	109.47(15)
S(101)–Ag(3)–S(102)	115.13(6)

was consistent with a 1:1 metal/ligand ratio suggesting that the product is a mononuclear complex similar in structure to $[AgL^5](ClO_4)$. The IR spectrum is consistent with the presence of the BF_4^- anion with a broad band centred around 1064 cm^{-1}. The FAB mass spectrum shows a main peak at 789 for $\{CuL^5\}^+$ but also very weak peaks for 1006 ($\{Cu_2(L^5) + NOBA\}^+$), 1515 ($\{Cu(L^5)_2\}^+$) and 1669 ($\{Cu(L^5)_2 + NOBA\}^+$) suggesting that a complex of higher nuclearity could have formed. The poor solubility of this complex did not permit study by NMR spectroscopy. All attempts to crystallise this complex have been unsuccessful.

Conclusions

Reaction of the bidentate N,S-donor fragment 3-[2-(methylsulfanyl)phenyl]pyrazole with a range of aromatic groups having two or three bromomethyl substituents allows two or three N,S-donor units to be linked to a central aromatic spacer. Depending on the separation between the N,S-donor units they can either each bind to a separate metal ion, giving one-dimensional (helical or zig-zag) chains with Ag^I and Cu^I, or can chelate to a single metal centre giving smaller mononuclear (metal/ligand, 1:1) or trinuclear (metal/ligand, 3:2) complexes. Whereas the Cu^I centres in these complexes are all four coordinate from two N,S-donor units, the Ag^I centres are sometimes three-coordinate due to incomplete coordination of the N,S-donor units. An additional factor responsible for the differences between Cu^I and Ag^I complexes with the same ligand is the presence of η^1 π-type Ag···C(phenyl) interactions which do not occur with Cu^I.

Experimental Section

General Details: 2′-(Methylthio)acetophenone,[14] 3,3′-bis(bromomethyl)biphenyl[15] and $[Cu(CH_3CN)_4]X$ (X = PF_6, BF_4)[16] were prepared according to literature methods. All other organic reagents and metal salts were purchased from Aldrich or Avocado and used as received. ^1H NMR spectra were recorded with a Bruker AC 250 or Bruker AMX2 400 spectrometer, and all mass spectra (FAB and EI) with a VG AutoSpec magnetic sector instrument. IR spectra were recorded with a Perkin–Elmer Spectrum One instrument. Samples for elemental analysis were vacuum-dried.

Preparation of 1,8-Bis(bromomethyl)naphthalene: This is a slight variant of a literature method.[17] PBr_3 (6.0 cm^3, 0.064 mol) was added to a suspension of 1,8-bis(hydroxymethyl)naphthalene (3.93 g, 0.0209 mol) in dry dichloromethane (50 cm^3) under nitrogen. The resulting clear solution was stirred at room temperature for 5 h. After this period water was carefully added dropwise until the evolution of gas ceased. The organic layer was separated, washed with water and dried ($MgSO_4$). Removal of the solvent afforded the crude product as an off-white solid. Recrystallisation from dichloromethane/hexane gave 5.29 g of off-white crystals (81%). All analytical data match those previously published.[17]

Preparation of 3-[(2-Methylthio)phenyl]pyrazole: This is a slight variant of the method published earlier.[5] A solution of 2′-(methylthio)acetophenone (4.28 g, 0.0257 mol) in dimethylformamide–dimethylacetal (10 cm^3, a large molar excess) was refluxed for 3 days under nitrogen to yield a dark brown solution. Removal of excess dimethylformamide-dimethylacetal in vacuo gave crude 3-(dimethylamino)-1-[2-(methylthio)phenyl]-2-propen-1-one as an orange/brown oil. To this was added ethanol (60 cm^3) and hydrazine hydrate (10 cm^3, a large molar excess), and the mixture refluxed in air for 2 h. The pale yellow solution was cooled and added to ice/water (300 cm^3) resulting in a pale yellow precipitate. The mixture was refrigerated overnight to complete the precipitation of the product. The solid was filtered off, washed with cold water (50 cm^3) and hexane (50 cm^3) and dried in vacuo. Subsequent recrystallisation from dichloromethane/hexane afforded 3-[(2-methylthio)phenyl]pyrazole as pale yellow needle crystals (4.35 g, 89%). EI MS: m/z = 190 [M^+]. ^1H NMR (250 MHz): $CDCl_3$: δ (ppm) = 7.63 (d, 1 H, pyrazolyl H^5), 7.50 (m, 1 H, phenyl H^3), 7.31–7.36 (m, 2 H, phenyl H^5, phenyl H^6), 7.21 (m, 1 H, phenyl H^4), 6.62 (d, 1 H, pyrazolyl H^4), 2.41 (s, 3 H, SCH_3). $C_{10}H_{10}N_2S$ (190.27): calcd. C 63.1, H 5.3, N, 14.7; found C 62.7, H 5.2, N 14.7.

Preparation of L^1: A two-phase mixture of 3-[(2-methylthio)phenyl]-pyrazole (1.26 g, 6.60 mmol), α,α′-dibromo-*p*-xylene (0.711 g, 2.70 mmol), toluene (90 cm^3), nBu_4NOH (0.10 cm^3) and aqueous 10 M NaOH (15 cm^3) was heated to 75 °C and stirred vigorously at this temperature for 24 h. After cooling the mixture was diluted with water (100 cm^3) and the aqueous layer extracted with toluene (2 × 100 cm^3). The combined organic layers were washed with water and dried ($MgSO_4$). The solvent was removed in vacuo and the crude product was purified by column chromatography (alumina, dichloromethane) to give 0.767 g of pale yellow solid (59%). FAB MS: m/z = 483 [MH^+]. ^1H NMR (250 MHz, $CDCl_3$): δ (ppm) = 7.55 (dd, 2 H, methylthiophenyl H^3), 7.38 (d, 2 H, pyrazolyl H^5), 7.23–7.35 (m, 8 H, phenyl, methylthiophenyl H^5, H^6), 7.17 (dd, 2 H, methylthiophenyl H^4), 6.63 (d, 2 H, pyrazolyl H^4), 5.36 (s, 4 H, CH_2), 2.42 (s, 6 H, SCH_3) ppm. ^{13}C NMR (100 MHz, $CDCl_3$): δ =

 © 2005 Wiley-VCH Verlag GmbH & Co. KGaA, Weinheim

150.6, 137.3, 136.5, 132.4, 129.7 (two closely spaced signals), 128.2, 128.1, 125.2, 124.6, 106.9, 55.7, 16.1 ppm. IR (KBr disk): $\tilde{\nu}$ = 2916 (w), 2854 (w), 1588 (w), 1514 (m), 1489 (m), 1426 (m), 1355 (m), 1322 (w), 1304 (w), 1261 (m), 1217 (w), 1065 (m), 1051 (s), 1000 (w), 952 (w), 861 (w), 777 (w), 754 (s), 722 (m), 705 (m), 946 (w), 629 (w), 521 (w) cm^{-1}. $C_{28}H_{26}N_4S_2$ (482.67): calcd. C 69.7, H 5.4, N 11.6; found C 69.6, H 5.4, N 11.2. X-ray quality crystals of L^1 were grown from slow evaporation of an acetonitrile solution.

Preparation of L^2: A two-phase mixture of 3-[(2-methylthio)phenyl]-pyrazole (1.00 g, 5.26 mmol), α,α′-dibromo-*m*-xylene (0.630 g, 2.39 mmol), toluene (100 cm^3), *n*Bu_4NOH (0.10 cm^3) and aqueous 10 M NaOH (15 cm^3) was heated to 65 °C and stirred vigorously at this temperature for 24 h. After cooling the mixture was diluted with water (100 cm^3) and the aqueous layer extracted with toluene (2 × 100 cm^3). The combined organic layers were washed with water and dried ($MgSO_4$). The solvent was removed in vacuo and the crude product was purified by column chromatography (alumina, dichloromethane) to give 0.691 g of colourless oil (60%). EI MS: *m*/*z* = 483 [MH^+]. ^{1}H NMR (500 MHz, $CDCl_3$): δ = 7.54 (dd, 2 H, methylthiophenyl H^3), 7.39 (d, 2 H, pyrazolyl H^5), 7.25–7.34 (m, 5 H, phenyl H^5, methylthiophenyl H^5, H^6), 7.15–7.22 (m, 5 H, phenyl H^2, H^4, methylthiophenyl H^4), 6.62 (d, 2 H, pyrazolyl H^4), 5.36 (s, 4 H, CH_2), 2.42 (s, 6 H, SCH_3) ppm. ^{13}C NMR (125 MHz, $CDCl_3$): δ = 150.5, 137.4, 137.2, 132.3, 129.8 (two closely spaced signals), 129.2, 128.2, 127.3, 126.9, 125.2, 124.6, 106.9, 55.8, 16.0 ppm. IR (neat): $\tilde{\nu}$ = 3111 cm^{-1} (w), 3052 (w), 2979 (w), 2920 (m), 2854 (w), 1610 (w), 1591 (w), 1563 (w), 1516 (m), 1490 (s), 1453 (s), 1436 (s), 1400 (s), 1335 (s), 1259 (s), 1221 (s), 1164 (w), 1106 (w), 1064 (m), 1052 (s), 1002 (w), 967 (w), 947 (w), 753 (s), 710 (m), 654 (w) cm^{-1}. $C_{28}H_{26}N_4S_2$ (482.67): calcd. C 69.7, H 5.4, N 11.6; found C 69.4, H 5.8, N 11.4.

Preparation of L^3: A two-phase mixture of 3-[(2-methylthio)phenyl]-pyrazole (1.23 g, 6.46 mmol), 3,3′-bis(bromomethyl)biphenyl (1.00 g, 2.94 mmol), toluene (55 cm^3), *n*Bu_4NOH (0.03 cm^3) and aqueous 10 M NaOH (12 cm^3) was heated to 70 °C and stirred vigorously at this temperature for 24 h. After cooling the mixture was diluted with water (100 cm^3) and the aqueous layer extracted with toluene (2 × 100 cm^3). The combined organic layers were washed with water and dried ($MgSO_4$). The solvent was removed in vacuo and the crude product was purified by column chromatography (alumina, 20% hexane in dichloromethane) to give 0.701 g of white foam (43%). EI MS: *m*/*z* = 558 [M^+]. ^{1}H NMR (250 MHz, $CDCl_3$): δ (ppm) 7.50–7.59 (m, 6 H), 7.43 (d, 2 H, pyrazolyl H^5), 7.23–7.42 (m, 8 H), 7.17 (ddd, 2 H, methylthiophenyl H^4), 6.62 (d, 2 H, pyrazolyl H^4), 5.43 (s, 4 H, CH_2), 2.39 (s, 6 H, SCH_3) ppm. ^{13}C NMR (100 MHz, $CDCl_3$): δ = 150.6, 141.2, 137.4, 137.2, 132.4, 129.8 (two closely spaced signals), 129.2, 128.2, 126.8 (two closely spaced signals), 126.6, 125.2, 124.6, 106.9, 56.0, 16.0 ppm. IR (KBr disk): $\tilde{\nu}$ 3050 (w), 2917 (m), 2853 (w), 1603 (w), 1588 (w), 1515 (w), 1488 (m), 1453 (m), 1434 (s), 1399 (m), 1334 (m), 1257 (m), 1220 (m), 1105 (w), 1063 (m), 1050 (m), 1000 (w), 946 (w), 751 (s), 732 (m), 695 (m), 654 (w) cm^{-1}. $C_{34}H_{30}N_4S_2$ (558.77): calcd. C 73.1, H 5.4, N 10.0; found C 72.8, H 5.6, N 9.6.

Preparation of L^4: A two-phase mixture of 3-[(2-methylthio)phenyl]-pyrazole (2.50 g, 13.1 mmol), 1,8-bis(bromomethyl)naphthalene (1.99 g, 6.34 mmol), toluene (120 cm^3), *n*Bu_4NOH (0.20 cm^3) and aqueous 10 M NaOH (26 cm^3) was heated to 65 °C and stirred vigorously at this temperature for 24 h. After cooling the mixture was diluted with water (100 cm^3) and the aqueous layer extracted with toluene (2 × 100 cm^3). The combined organic layers were washed with water and dried ($MgSO_4$). The solvent was removed in vacuo and the crude product was recrystallised twice from dichloromethane/hexane to give 0.86 g of off-white needle crystals. A second crop of 1.17 g of off-white powder was obtained from the recrystallisation filtrates by column chromatography (alumina, 20% hexane in dichloromethane). Total yield: 2.03 g (60%). FAB MS: *m*/*z* = 533 [MH^+]. ^{1}H NMR (500 MHz, $CDCl_3$): δ (ppm) = 7.89 (dd, 2 H, napthyl H^4), 7.57 (ddd, 2 H, methylthiophenyl H^3), 7.45 (dd, 2 H, napthyl H^3), 7.24–7.32 (m, 4 H, methylthiophenyl H^5, H^6), 7.23 (dd, 2 H, naphthyl H^2), 7.20 (d, 2 H, pyrazolyl H^5), 7.16 (ddd, 2 H, methylthiophenyl H^4), 6.59 (d, 2 H, pyrazolyl H^4), 5.93 (s, 4 H, CH_2), 2.39 (s, 6 H, SCH_3) ppm. ^{13}C NMR (100 MHz, $CDCl_4$): δ (ppm) = 150.9, 137.4, 135.8, 132.4, 131.8, 130.8, 130.5, 130.4, 130.1, 129.7, 128.2, 125.5, 125.3, 124.5, 106.7, 56.7, 16.1. IR (KBr disk): $\tilde{\nu}$ 3117 (w), 2918 (w), 1586 (w), 1562 (w), 1509 (m), 1489 (m), 1454 (s), 1440 (m), 1399 (w), 1331 (m), 1258 (m), 1213 (m), 1170 (w), 1107 (w), 1052 (s), 976 (w), 960 (w), 944 (w), 844 (w), 782 (s), 769 (m), 753 (s), 737 (m), 676 (m), 622 (w) cm^{-1}. $C_{32}H_{28}N_4S_2$ (532.73): calcd. C 72.1, H 5.3, N 10.5; found C 72.0, H 5.3, N 10.5. X-ray quality crystals were grown from diethyl ether diffusion into an NMR sample of L^4 in $CDCl_3$.

Preparation of L^5: A two-phase mixture of 3-[(2-methylthio)phenyl]-pyrazole (1.54 g, 8.09 mmol), 2,4,6-tris(bromomethyl)mesitylene (0.981 g, 2.46 mmol), toluene (70 cm^3), *n*Bu_4NOH (0.10 cm^3) and aqueous 10 M NaOH (25 cm^3) was heated to 70 °C and stirred vigorously at this temperature for 24 h. After cooling the mixture was diluted with water (100 cm^3) and the aqueous layer extracted with toluene (2 × 100 cm^3). The combined organic layers were washed with water and dried ($MgSO_4$). The solvent was removed in vacuo and the crude product was purified by column chromatography (alumina, 1% methanol in dichloromethane) to give 0.551 g of off-white foam (31%). EI MS: *m*/*z* = 726 [M^+], 536 {M^+-[3-(2-methylthiophenyl)pyrazole]}, 347 {M^+ – 2[3-(2-methylthiophenyl)pyrazole]}. ^{1}H NMR (250 MHz, $CDCl_3$): δ (ppm) = 7.56 (dd, 3 H, methylthiophenyl H^3), 7.23–7.35 (m, 6 H, methylthiophenyl H^5, H^6), 7.17 (ddd, 3 H, methylthiophenyl H^4), 7.09 (d, 3 H, pyrazolyl H^5), 6.56 (d, 3 H, pyrazolyl H^4), 5.54 (s, 6 H, CH_2), 2.47 (s, 9 H, CH_3), 2.42 (s, 9 H, SCH_3) ppm. ^{13}C NMR (100 MHz, $CDCl_3$): δ (ppm) = 150.4, 139.7, 137.3, 132.2, 131.3, 129.6, 128.4, 128.2, 125.2, 124.6, 106.2, 50.9, 16.5, 16.1. IR (KBr disk): $\tilde{\nu}$ 3050 (w), 2977 (w), 2916 (m), 1589 (w), 1562 (w), 1514 (w), 1488 (m), 1453 (s), 1436 (s), 1398 (m), 1323 (m), 1256 (m), 1215 (s), 1106 (w), 1063 (m), 1051 (s), 998 (w), 944 (m), 752 (s), 732 (s), 654 (w), 618 (w) cm^{-1}. $C_{42}H_{42}N_6S_3$ (727.03): calcd. C 69.4, H 5.8, N 11.6; found C 69.2, H 5.9, N 11.5. X-ray quality crystals were grown from the diffusion of pentane vapour into an acetonitrile solution of L^5.

Preparation of $\{[CuL^1](PF_6)\}_\infty$: A solution of $[Cu(CH_3CN)_4]PF_6$ (62 mg, 0.17 mmol) in MeCN (5 cm^3) was added to a solution of L^1 (80 mg, 0.17 mmol) in MeCN (20 cm^3). The colourless solution was stirred for 4 h and the volume reduced to ca. 10 cm^3. Diethyl ether diffusion into the solution gave off-white crystals of $\{[CuL^1](PF_6)\}_\infty$ which were suitable for X-ray crystallography. Yield: 86 mg, 75%. ES MS: *m*/*z* = 545 [$CuL^1]^+$. ^{1}H NMR (250 MHz, $CDCl_3$): δ (ppm) = 7.69 (d, 2 H, pyrazolyl H^5), 7.48 (m, 2 H, methylthiophenyl H^3), 7.30-7.75 (m, 4 H, methylthiophenyl H^5, H^6), 7.18–7.25 (m, 2 H, methylthiophenyl H^4), 7.12 (s, 4 H, phenyl), 6.62 (d, 2 H, pyrazolyl H^4), 5.27 (s, 4 H, CH_2), 2.32 (s, 6 H, SMe). ^{13}C NMR (100 MHz, CD_3CN): δ (ppm) = 151.4, 137.8, 136.2, 132.8, 132.5, 131.1 129.7, 128.6, 127.8, 126.7, 107.6, 55.9, 17.3 ppm. IR (KBr disk): $\tilde{\nu}$ 3156 (w), 3138 (w), 3052 (w), 2997 (w), 2925 (w), 1631 (w), 1589 (w), 1564 (w), 1518 (s), 1501 (s), 1462 (w), 1425 (s), 1401 (w), 1357 (s), 1325 (s), 1277 (w), 1225 (m), 1075 (s), 1020 (w), 971 (m), 954 (m), 879 (m), 839 (s), 786 (s), 760 (s), 729 (m), 649 (w), 619 (w), 558 (s) cm^{-1}. $C_{28}H_{26}CuF_6N_4PS_2$ (691.18): calcd. C 48.7, H 3.8, N 8.1; found C 48.8, H 3.7, N 8.0.

 © 2005 Wiley-VCH Verlag GmbH & Co. KGaA, Weinheim

Preparation of $\{[AgL^1](NO_3)\}_\infty$: A solution of $AgNO_3$ (29 mg, 0.17 mmol) in H_2O (3 cm^3) was added to a solution of L^1 (81 mg, 0.17 mmol) in hot MeOH (10 cm^3). The colourless solution was stirred for 4 h and the volume reduced to ca. 5 cm^3. The mixture was filtered to give $\{[AgL^1](NO_3)\}_\infty$ as a white powder. Yield: 71 mg, 65%. X-ray quality crystals were obtained from slow evaporation of the filtrate. FAB MS: *m*/*z* = 591 $[AgL^1]$, 651 $[Ag(L^1)(NO_3)]$, 697 $[Ag_2(L^1)]$, 760 $[Ag_2(L^1)(NO_3)]$, 850 $[Ag_2(L^1)$ + NOBA], 1179 $[Ag_2(L^1)_2]$, 1242 $[Ag_2(L^1)_2(NO_3)]$, 1333 $[Ag_2(L^1)_2$ + NOBA]. ^1H NMR (250 MHz, CD_3CN): δ (ppm) = 7.69 (d, 2 H, pyrazolyl H^5), 7.42 (dd, 2 H, methylthiophenyl H^3), 7.33 (ddd, 2 H, methylthiophenyl H^5), 7.25 (dd, 2 H, methylthiophenyl H^6), 7.19 (td, 2 H, methylthiophenyl H^4), 7.10 (s, 4 H, phenyl), 6.56 (d, 2 H, pyrazolyl H^4), 5.22 (s, 4 H, CH_2), 2.28 (s, 6 H, SMe); (500 MHz, CD_3NO_2): δ (ppm) = 7.80 (d, 2 H, pyrazolyl H^5), 7.37–7.42 (m, 4 H, methylthiophenyl H^3, H^5), 7.29 (td, 2 H, methylthiophenyl H^4), 7.28 (d, 2 H, methylthiophenyl H^6), 6.86 (s, 4 H, phenyl), 6.61 (d, 2 H, pyrazolyl H^4), 5.17 (s, 4 H, CH_2), 2.24 (s, 6 H, SMe). IR (KBr disk): $\tilde{\nu}$ 3108 (w), 2920 (w), 1624 (w), 1590 (w), 1519 (m), 1495 (m), 1430 (s), 1384 (s), 1339 (s), 1321 (s), 1259 (m), 1226 (m), 1065 (m), 1038 (w), 963 (m), 948 (m), 758 (s), 734 (m), 705 (w) cm^{-1}. $C_{28}H_{26}AgN_5O_3S_2$ (652.54): calcd. C 51.5, H 4.2, N 10.7; found C 51.4, H 4.1, N 10.6.

Preparation of $\{[CuL^2](BF_4)\}_\infty$: $[Cu(CH_3CN)_4]BF_4$ (61 mg, 0.19 mmol) was added to a solution of L^2 (94 mg, 0.19 mmol) in dry MeCN (20 cm^3). The colourless solution was stirred overnight under nitrogen and the volume reduced to ca. 10 cm^3. Diethyl ether diffusion into the solution gave off-white crystals of $[CuL^2](BF_4)$ which were suitable for X-ray crystallography. Yield: 70 mg, 56%. ES MS: *m*/*z* = 545 $[CuL^2]^+$. ^1H NMR (500 MHz, CD_3CN): δ = 7.68 (br. s, 2 H, pyrazolyl H^5), 7.47 (d, 2 H), 7.29–7.36 (m, 5 H), 7.11–7.23 (m, 4 H), 7.07 (s, 1 H), 6.61 (br. s, 2 H, pyrazolyl H^4), 5.32 (s, 4 H, CH_2), 2.34 (br. s, 6 H, SMe) ppm. IR (KBr disk): $\tilde{\nu}$ = 3135 (w), 3057 (w), 2975 (w), 2924 (w), 1610 (w), 1590 (w), 1567 (w), 1518 (m), 1500 (m), 1433 (s), 1406 (m), 1385 (w), 1356 (m), 1327 (w), 1280 (w), 1223 (w), 1169 (w), 1056 (s), 951 (w), 877 (w), 757 (s), 729 (m), 709 (w), 651 (w), 631 (w), 520 (w) cm^{-1}. $C_{28}H_{26}BCuF_4N_4S_2$ (633.02): calcd. C 53.1, H 4.1, N 8.9; found C 52.7, H 4.3, N 8.7.

Preparation of $[AgL^2](BF_4)$: $[Ag(CH_3CN)_4]BF_4$ (71 mg, 0.20 mmol) was added to a solution of L^2 (96 mg, 0.20 mmol) in dry MeCN (20 cm^3). The colourless solution was stirred overnight protected from light and the volume reduced to ca. 10 cm^3. Diethyl ether diffusion into the solution gave off-white crystals of $[AgL^2](BF_4)$ which were suitable for X-ray crystallography. Yield: 98 mg, 73%. ES MS: *m*/*z* = 589 $[AgL^2]^+$. ^1H NMR (500 MHz, CD_3CN): δ = 7.88 (d, 2 H, pyrazolyl H^5), 7.70 (s, 1 H, phenyl H^2), 7.45–7.49 (m, 4 H), 7.34–7.39 (m, 4 H), 7.28 (td, 2 H), 6.95 (dd, 2 H), 6.53 (d, 2 H, pyrazolyl H^4), 5.38 (s, 4 H, CH_2), 1.89 (s, 6 H, SMe) ppm. IR (KBr disk): $\tilde{\nu}$ = 3140 (w), 3127 (w), 3054 (w), 3007 (w), 2926 (w), 1590 (w), 1566 (w), 1516 (m), 1497 (s), 1456 (m), 1431 (s), 1410 (m), 1366 (w), 1351 (m), 1296 (w), 1273 (w), 1260 (w), 1217 (s), 1050 (s), 949 (m), 896 (m), 777 (m), 760 (s), 740 (s), 707 (m), 650 (w), 620 (w), 521 (s) cm^{-1}. $C_{28}H_{26}AgBF_4N_4S_2$ (677.34): calcd. C 49.7, H 3.9, N 8.3; found C 49.6, H 3.6, N 8.2.

Preparation of $\{[CuL^3](BF_4)\}_\infty$: $[Cu(CH_3CN)_4]BF_4$ (50 mg, 0.16 mmol) was added to a suspension of L^3 (89 mg, 0.16 mmol) in dry MeOH (20 cm^3). The resulting suspension was sonicated for 10 min then stirred overnight under nitrogen. Filtration gave $\{[CuL^3](BF_4)\}_\infty$ as an off-white solid which was dried in vacuo. Yield: 86 mg, 76%. FAB MS: *m*/*z* = 621 $[CuL^3]$, 1179 $[Cu(L^3)_2]$, 1331 $[Cu_2(L^3)_2(BF_4)$ and/or $Cu(L^3)_2$ + NOBA]. ^1H NMR (500 MHz, CD_3CN): δ (ppm) = 7.71 (br. s, 2 H, pyrazolyl H^5), 7.46–7.55 (m, 6 H), 7.41 (t, 2 H), 7.27–7.35 (m, 4 H), 7.25 (d, 2 H), 7.21 (m, 1 H), 6.58 (d, 2 H, pyrazolyl H^4), 5.40 (s, 4 H, CH_2), 2.28 (s, 6 H, SCH_3) ppm. IR (KBr disk): $\tilde{\nu}$ = 3143 (w), 2925 (w), 1602 (w), 1519 (w), 1502 (m), 1435 (m), 1412 (m), 1360 (w), 1329 (w), 1232 (m), 1083 (s, br), 1060 (s), 785 (m), 771 (m), 756 (s), 732 (w), 699 (m), 623 (w), 520 (w) cm^{-1}. $C_{34}H_{30}BCuF_4N_4S_2$ (709.12): calcd. C 57.6, H 4.3, N 7.9; found C 57.3, H 4.2, N 7.9. X-ray quality crystals were grown from diethyl ether diffusion into an acetonitrile solution of the complex.

Preparation of $\{[AgL^3](BF_4)\}_\infty$: $[Ag(CH_3CN)_4]BF_4$ (61 mg, 0.17 mmol) was added to a suspension of L^3 (95 mg, 0.17 mmol) in dry MeCN (20 cm^3). The colourless solution was protected from light and stirred overnight. The volume was then reduced to ca. 10 cm^3 in vacuo. Diethyl ether diffusion into the resulting solution gave off-white crystals of $\{[AgL^3](BF_4)\}_\infty$ which were suitable for X-ray crystallography. Yield: 114 mg, 89%. FAB MS: *m*/*z* = 667 $[Ag(L^3)]$, 1225 $[Ag(L^3)_2]$, 1332 $[Ag_2(L^3)_2]$, 1378 $[Ag(L^3)_2$ + NOBA], 1419 $[Ag_2(L^3)_2(BF_4)]$, 1485 $[Ag_2(L^3)_2$ + NOBA]. ^1H NMR (500 MHz, CD_3CN): δ (ppm) = 7.78 (d, 2 H, pyrazolyl H^5), 7.43–7.47 (m, 4 H), 7.40 (ddd, 2 H), 7.37 (td, 2 H), 7.30 (ddd, 2 H), 7.22 (td, 2 H), 7.18 (ddd, 2 H), 7.09 (dd, 2 H), 6.51 (d, 2 H, pyrazolyl H^4), 5.30 (s, 4 H, CH_2), 2.04 (s, 6 H, SMe). IR (KBr disk): $\tilde{\nu}$ = 3139 (w), 2924(w), 1604 (w), 1589 (w), 1519 (w), 1497 (m), 1432 (m), 1410 (m), 1356 (m), 1324 (w), 1262 (w), 1220 (m), 1061 (s, br), 786 (m), 757 (s), 728 (m), 703 (w), 520 (w) cm^{-1}. $C_{34}H_{30}AgBF_4N_4S_2$ (753.43): calcd. C 54.2, H 4.0, N 7.4; found C 54.1, H 3.9, N 7.4.

Preparation of $[CuL^4](PF_6)$: $[Cu(CH_3CN)_4]PF_6$ (57 mg, 0.15 mmol) was added to a suspension of L^4 (82 mg, 0.15 mmol) in dry MeCN (20 cm^3) and the colourless solution was stirred overnight. The volume was then reduced to ca. 10 cm^3 in vacuo and the solution filtered to remove a small amount of solid. Diethyl ether diffusion into the resulting solution gave off-white crystals of $[CuL^4](PF_6)$ which were suitable for X-ray crystallography. Yield: 57 mg, 50%. FAB MS: *m*/*z* = 595 $[Cu(L^4)]$. ^1H NMR (500 MHz, CD_3CN): δ (ppm) = 8.17 (dd, 2 H), 7.75 (dd, 2 H), 7.60–7.70 (m, 6 H), 7.42–7.49 (m, 6 H), 6.72 (d, 2 H, pyrazolyl H^4), 5.64 (s, 4 H, CH_2), 2.42 (s, 6 H, SMe). IR (KBr disk): $\tilde{\nu}$ = 2923 (w), 1624 (w), 1515 (w), 1499 (w), 1487 (w), 1431 (m), 1371 (m), 1325 (m), 1211 (m), 1065 (m), 841 (s), 781 (m), 760 (s), 685 (w), 557 (s) cm^{-1}. $C_{32}H_{28}CuF_6N_4PS_2$ (741.24): calcd. C 51.9, H 3.8, N, 7.6; found C 51.5, H 3.8, N, 7.7.

Preparation of $[AgL^4](BF_4)$: $[Ag(CH_3CN)_4]BF_4$ (137 mg, 0.38 mmol) was added to a suspension of L^4 (204 mg, 0.38 mmol) in EtOH (20 cm^3) protected from light and the mixture was stirred overnight. The off-white solid was collected by filtration and dried in vacuo. Yield: 247 mg, 89%. FAB MS: *m*/*z* = 641 $[Ag(L^4)]$. ^1H NMR (400 MHz, CD_3CN): δ (ppm) = 8.15 (dd, 2 H), 7.69 (dd, 2 H), 7.63 (dd, 2 H), 7.49 (m, 2 H), 7.41–7.45 (m, 4 H), 7.31 (m, 2 H), 7.16 (d, 2 H, pyrazolyl H^5), 6.47 (d, 2 H, pyrazolyl H^4), 5.78 (s, 4 H, CH_2), 2.50 (s, 6 H, SMe). ^{13}C NMR (100 MHz, CD_3CN): δ (ppm) = 152.6, 137.6, 135.7, 135.4, 133.3, 132.1, 131.7 (2 closely spaced signals), 131.1, 130.3, 129.8, 127.0 (2 closely spaced signals), 126.7, 107.9, 57.7, 16.9. IR (KBr disk): $\tilde{\nu}$ = 3144 (w), 2924 (w), 1590 (w), 1515 (w), 1496 (w), 1485 (w), 1429 (m), 1362 (w), 1324 (m), 1212 (m), 1103 (m), 1070 (s, br), 1048 (s), 849 (w), 825 (w), 779 (m), 765 (s), 684 (w), 520 (w) cm^{-1}. $C_{32}H_{28}AgBF_4N_4S_2$ (727.40): calcd. C 52.8, H 3.9, N 7.7; found C 52.3, H 3.8, N 7.6. X-ray quality crystals were obtained from slow evaporation of the filtrate when the reaction was carried out in methanol.

Preparation of $[CuL^5](BF_4)$: $[Cu(CH_3CN)_4]BF_4$ (54 mg, 0.17 mmol) was added to a suspension of L^5 (84 mg, 0.12 mmol) in dry and

 © 2005 Wiley-VCH Verlag GmbH & Co. KGaA, Weinheim

degassed EtOH (20 cm^3) and the suspension was stirred overnight under nitrogen. The volume was then reduced to ca. 10 cm^3 in vacuo and the off-white powder filtered off. Yield: 90 mg, 89%. FAB MS: *m*/*z* = 789 [Cu(L^5)], 1006 [$Cu_2(L^5)$ + NOBA], 1515 [$Cu(L^5)_2$], 1669 [$Cu(L^5)_2$ + NOBA]. IR (KBr disk): $\tilde{\nu}$ =3134 (w), 2978 (w), 2918 (w), 1630 (w), 1588 (w), 1563 (w), 1486 (m), 1454 (m), 1433 (s), 1399 (m), 1326 (m), 1256 (w), 1216 (m), 1083 (s), 1064 (s), 1048 (s), 945 (w), 753 (s), 733 (m), 652 (w), 617 (w) cm^{-1}. $C_{42}H_{42}BCuF_4N_6S_3$ (877.38): calcd. C 57.5, H 4.8, N 9.6; found C 57.2, H 5.0, N 9.4.

Preparation of [AgL^5](ClO_4): ***Caution: Perchlorate salts are potentially explosive and should only be prepared in small quantities and handled with care!*** $AgClO_4 \cdot H_2O$ (38 mg, 0.18 mmol) was added to a suspension of L^5 (90 mg, 0.12 mmol) in dry MeCN (20 cm^3) and the colourless solution was stirred overnight while protected from light. The volume was then reduced to ca. 10 cm^3 in vacuo. Diethyl ether diffusion into the resulting solution gave colourless crystals of [AgL^5](ClO_4) which were suitable for X-ray crystallography. Yield: 93 mg, 80%. FAB MS: *m*/*z* = 835 {Ag(L^5)}. ^{1}H NMR (250 MHz, CD_3CN): δ (ppm) 7.79 (d, 3 H, pyrazolyl H^5), 7.44 (dd, 3 H, meth-

Table 11. Crystallographic data for the ligands L^1, L^4 and L^5.

Ligand	L^1	L^4	L^5
Formula	$C_{28}H_{26}N_4S_2$	$C_{32}H_{28}N_4S_2$	$C_{42}H_{42}N_6S_3$
Formula weight	482.65	532.70	727.00
T [K]	150(2)	150(2)	150(2)
Crystal system, space group	orthorhombic, *Pbcn*	monoclinic, *P*2/*c*	triclinic, $P\bar{1}$
a [Å]	30.251(5)	12.548(4)	8.5155(11)
b [Å]	8.8015(14)	8.423(2)	15.452(2)
c [Å]	9.2578(15)	12.579(4)	16.190(2)
α [°]	90	90	62.058(2)
β [°]	90	94.604(5)	82.603(2)
γ [°]	90	90	84.463(2)
V [$Å^3$]	2464.9(7)	1325.3(6)	1864.7(4)
Z	4	2	2
$D_{calcd.}$ [mg/m^3]	1.301	1.335	1.295
μ [mm^{-1}]	0.240	0.231	0.238
Crystal size [mm]	0.50×0.48×0.39	0.50×0.41×0.07	0.41×0.20×0.10
Reflections collected	25818	14511	21704
Independent reflections	2821 [*R*(int) = 0.0283]	3018 [*R*(int) = 0.0521]	8385 [*R*(int) = 0.0434]
Data/restraints/parameters	2821/0/155	3018/0/174	8385/2/467
Final *R* indices[a]	R_1 = 0.0377 wR_2 = 0.1138	R_1 = 0.0413 wR_2 = 0.1009	R_1 = 0.0590 wR_2 = 0.1677
Largest diff. peak and hole [e·$Å^{-3}$]	0.228 and –0.233	0.273 and –0.282	1.857 and –0.585

[a] The value of R_1 is based on selected data with $I > 2\sigma(I)$; the value of wR_2 is based on all data.

Table 12. Crystallographic data for Cu^+ and Ag^+ complexes with L^1 and L^2.

Ligand	{[Cu(L^1)](PF_6)}$_\infty$	{[AgL^1](NO_3)·MeOH}$_\infty$	{[CuL^2](BF_4)}$_\infty$·1.5MeCN·0.5Et_2O	[AgL^2](BF_4)
Formula	$C_{28}H_{26}CuF_6N_4PS_2$	$C_{29}H_{30}AgN_5O_4S_2$	$C_{33}H_{37}BCuF_4N_{5.5}O_{0.5}S_2$	$C_{28}H_{26}AgBF_4N_4S_2$
Formula weight	691.16	684.57	733.15	677.33
T [K]	150(2)	150(2)	150(2)	150(2)
Crystal system, space group	monoclinic, *C*2/*c*	monoclinic, *P*21/*c*	orthorhombic, *Pmna*	orthorhombic, *P*2(1)2(1)2(1)
a [Å]	14.310(3)	12.963(3)	21.129(2)	12.794(3)
b [Å]	21.062(5)	12.529(3)	13.7026(15)	18.763(4)
c [Å]	11.250(3)	17.935(4)	11.7024(13)	23.184(5)
α [°]	90	90	90	90
β [°]	121.070(4)	93.948(4)	90	90
γ [°]	90	90	90	90
V [$Å^3$]	2904.2(12)	2906.0(11)	3388.1(6)	5566(2)
Z	4	4	4	8
$D_{calcd.}$ [mg/m^3]	1.581	1.565	1.437	1.617
μ [mm^{-1}]	1.016	0.882	0.824	0.928
Crystal size [mm]	0.48×0.38×0.30	0.36×0.24×0.10	0.41×0.20×0.20	0.23×0.22×0.10
Reflections collected	16217	17458	36991	62930
Independent reflections	3322 [*R*(int) = 0.0649]	4043 [*R*(int) = 0.1387]	4034 [*R*(int) = 0.0725]	12643 [*R*(int) = 0.0544]
Data/restraints/parameters	3322/0/192	4043/0/375	4034/7/242	12643/26/722
Final *R* indices[a]	R_1 = 0.0403 wR_2 = 0.1025	R_1 = 0.0555 wR_2 = 0.1489	R_1 = 0.0456 wR_2 = 0.1340	R_1 = 0.0360 wR_2 = 0.0777
Largest diff. peak and hole [e·$Å^{-3}$]	0.519 and –0.408	1.926 and –1.375	0.597 and –0.315	0.942 and –0.490

[a] The value of R_1 is based on selected data with $I > 2\sigma(I)$; the value of wR_2 is based on all data.

 © 2005 Wiley-VCH Verlag GmbH & Co. KGaA, Weinheim

ylthiophenyl H[3]), 7.32 (td, 3 H, methylthiophenyl H[5]), 7.23 (td, 3 H, methylthiophenyl H[4]), 6.83 (dd, 3 H, methylthiophenyl H[6]), 6.55 (d, 3 H, pyrazolyl H[4]), 5.58 (s, 6 H, CH_2), 2.47 (s, 9 H, CH_3), 1.77 (s, 9 H, SCH_3) ppm. IR (KBr disk): $\tilde{\nu}$ = 3127 (w), 3112 (w), 2970 (w), 2911 (w), 1625 (w), 1589 (w), 1563 (w), 1515 (w), 1492 (m), 1440 (m), 1429 (s), 1409 (m), 1348 (m), 1270 (w), 1258 (w), 1210 (s), 1091 (s, br), 980 (w), 961 (w), 946 (w), 802 (m), 754 (s), 733 (m), 623 (s), 613 (m) cm^{-1}. $C_{42}H_{42}AgClN_6O_4S_3$ (934.35): calcd. C 54.0, H 4.5, N 9.0; found C 53.9, H 4.3, N 8.9.

X-ray Crystallography: X-ray crystallographic data are summarised in Table 11, Table 12, Table 13 and Table 14. For each compound a suitable crystal was coated with hydrocarbon oil and attached to the tip of a glass fibre and transferred to Bruker-SMART diffractometer under a stream of cold N_2. Data were collected using a Siemens SMART CCD area diffractometer (graphite-monochromated Mo-K_α radiation, λ = 0.71073 Å) with an Oxford Cryosystems low temperature system. The data were corrected for Lorentz and polarisation effects and for absorption by semi-empirical methods (SADABS)[18] based on symmetry-equivalent and repeated reflections. The structures were solved by direct methods or heavy atom Patterson methods and refined by full-matrix least-squares methods on F^2. Hydrogen atoms were placed geometrically and refined with a riding model and with U_{iso} constrained to be 1.2 (1.5 for methyl groups) times U_{eq} of the carrier atom. Structures were solved and refined using the SHELX suite of programs.[19] Selected

Table 13. Crystallographic data for Cu^+ and Ag^+ complexes with L^3 and a Cu^+ complex with L^4.

Complex	$\{[CuL^3](BF_4)\}_\infty \cdot 1.53CH_3CN \cdot 0.47Et_2O$	$\{[AgL^3](BF_4)\}_\infty$	$[CuL^4](PF_6) \cdot 2MeCN \cdot 2H_2O$
Formula	$C_{38.95}H_{39.33}BCuF_4N_{5.53}O_{0.47}S_2$	$C_{34}H_{30}AgBF_4N_4S_2$	$C_{36}H_{38}CuF_6N_6O_2PS_2$
Formula weight	806.90	753.42	859.35
T [K]	150(2)	150(2)	150(2)
Crystal system	monoclinic, $P21/n$	triclinic, $P\bar{1}$	monoclinic, Cc
a [Å]	11.607(3)	11.666(2)	17.757(3)
b [Å]	10.649(2)	11.973(2)	22.728(4)
c [Å]	31.565(6)	24.485(5)	13.059(2)
α [°]	90	89.231(4)	90
β [°]	97.547(5)	81.743(4)	132.495(2)
γ [°]	90	71.756(3)	90
V [Å^3]	3867.6(14)	3212.6(11)	3886.0(12)
Z	4	4	4
$D_{calcd.}$ [mg/m^3]	1.386	1.558	1.469
μ [mm^{-1}]	0.729	0.812	0.781
Crystal size [mm]	0.38 × 0.21 × 0.06	0.45 × 0.38 × 0.23	0.38 × 0.32 × 0.21
Reflections collected	18589	36999	21450
Independent reflections	6456 [R(int) = 0.1053]	14378 [R(int) = 0.0543]	4408 [R(int) = 0.0321]
Data/restraints/parameters	6456/4/477	14378/78/817	4408/74/549
Final R indices[a]	R_1 = 0.0647, wR_2 = 0.1790	R_1 = 0.0516, wR_2 = 0.1298	R_1 = 0.0337, wR_2 = 0.0894
Largest diff. peak and hole [e·Å^{-3}]	0.630 and –0.896	1.076 and –0.661	0.575 and –0.328

[a] The value of R_1 is based on selected data with $I > 2\sigma(I)$; the value of wR_2 is based on all data.

Table 14. Crystallographic data for Ag^+ complexes with L^4 and L^5.

Ligand	$[Ag(L^4)](BF_4)$	$[AgL^5](ClO_4)$	$[Ag_3(L^5)_2](ClO_4)_3$
Formula	$C_{32}H_{28}AgBF_4N_4S_2$	$C_{42}H_{42}AgClN_6O_4S_3$	$C_{84}H_{85}Ag_3Cl_3N_{12}O_{12}S_6$
Formula weight	727.38	934.32	2076.96
T [K]	150(2)	150(2)	120(2)
Crystal system, space group	orthorhombic, $P2(1)2(1)2(1)$	orthorhombic, $Pbca$	triclinic, $P\bar{1}$
a [Å]	11.430(4)	12.3282(14)	11.666(4)
b [Å]	21.880(8)	21.611(3)	15.388(5)
c [Å]	23.840(8)	30.241(3)	25.033(9)
α [°]	90	90	72.435(8)
β [°]	90	90	89.156(7)
γ [°]	90	90	85.591(7)
V [Å^3]	5962(4)	8056.7(16)	4272(3)
Z	8	8	2
$D_{calcd.}$ [mg/m^3]	1.621	1.541	1.615
μ [mm^{-1}]	0.872	0.774	0.990
Crystal size [mm]	0.20 × 0.17 × 0.08	0.41 × 0.32 × 0.21	0.32 × 0.21 × 0.12
Reflections collected	58451	87723	41978
Independent reflections	10523 [R(int) = 0.2292]	9248 [R(int) = 0.0479]	15010 [R(int) = 0.1254]
Data/restraints/parameters	10523/0/799	9248/0/520	15010/0/1093
Final R indices[a]	R_1 = 0.0816, wR_2 = 0.2343	R_1 = 0.0345, wR_2 = 0.0943	R_1 = 0.0569, wR_2 = 0.1193
Largest diff. peak and hole [e·Å^{-3}]	1.506 and –1.323	1.016 and –0.705	0.860 and –1.212

[a] The value of R_1 is based on selected data with $I > 2\sigma(I)$; the value of wR_2 is based on all data.

 © 2005 Wiley-VCH Verlag GmbH & Co. KGaA, Weinheim

bond lengths and angles for the structures of the metal complexes are in Tables 1–10.

Acknowledgments

We thank the New Zealand Tertiary Education Commission for a Top Achiever Doctoral scholarship to T. K. R.

[1] a) D. L. Caulder, K. N. Raymond, *Acc. Chem. Res.* **1999**, *32*, 975; b) G. F. Swiegers, T. J. Malefetse, *Chem. Eur. J.* **2001**, *7*, 3637; c) B. J. Holliday, C. A. Mirkin, *Angew. Chem. Int. Ed.* **2001**, *40*, 2022; d) D. Philp, J. F. Stoddart, *Angew. Chem. Int. Ed. Engl.* **1996**, *35*, 1155; e) S. Leininger, B. Olenyuk, P. J. Stang, *Chem. Rev.* **2000**, *100*, 853; f) S. R. Seidel, P. J. Stang, *Acc. Chem. Res.* **2002**, *35*, 972; g) L. K. Thompson, *Coord. Chem. Rev.* **2002**, *233*, 193.

[2] a) M. D. Ward, J. A. McCleverty, J. C. Jeffery, *Coord. Chem. Rev.* **2001**, *222*, 251; b) R. L. Paul, S. P. Argent, J. C. Jeffery, L. P. Harding, J. M. Lynam, M. D. Ward, *Dalton Trans.* **2004**, 3453; c) Z. R. Bell, L. P. Harding, M. D. Ward, *Chem. Commun.* **2003**, 2432; d) Z. R. Bell, J. C. Jeffery, J. A. McCleverty, M. D. Ward, *Angew. Chem. Int. Ed.* **2002**, *41*, 2515; e) R. L. Paul, Z. R. Bell, J. C. Jeffery, J. A. McCleverty, M. D. Ward, *Proc. Natl. Acad. Sci. USA* **2002**, *99*, 4883.

[3] a) M. C. Hong, W. P. Su, R. Cao, M. Fujita, J. X. Lu, *Chem. Eur. J.* **2000**, *6*, 427; b) C. Y. Su, S. Liao, H. L. Zhu, B. S. Kang, X. M. Chen, H. Q. Liu, *J. Chem. Soc., Dalton Trans.* **2000**, 1985; c) S. Liao, C. Y. Su, H. X. Zhang, J. L. Shi, Z. Y. Zhou, H. Q. Liu, A. S. C. Chan, B. S. Kang, *Inorg. Chim. Acta* **2002**, *336*, 151; d) S. Tavacoli, T. A. Miller, R. L. Paul, J. C. Jeffery, M. D. Ward, *Polyhedron* **2003**, *22*, 507; e) Y. Zheng, M. Du, J.-R. Li, R.-H. Zhang, X.-H. Bu, *Dalton Trans.* **2003**, 1509; f) M. Oh, C. L. Stern, C. A. Mirkin, *Chem. Commun.* **2004**, 2684; g) Y.-B. Xie, C. Zhang, J.-R. Li, X.-H. Bu, *Dalton Trans.* **2004**, 562; h) D. A. McMorran, C. M. Hartshorn, P. J. Steel, *Polyhedron* **2004**, *23*, 1055.

[4] T. K. Ronson, H. Adams, M. D. Ward, *Inorg. Chim. Acta* **2005**, *358*, 1943.

[5] E. R. Humphrey, K. L. V. Mann, Z. R. Reeves, A. Behrendt, J. C. Jeffery, J. P. Maher, J. A. McCleverty, M. D. Ward, *New J. Chem.* **1999**, *23*, 417.

[6] a) E. C. Constable, S. M. Elder, J. V. Walker, P. D. Wood, D. A. Tocher, *J. Chem. Soc., Chem. Commun.* **1992**, 229; b) K. T. Potts, K. A. G. Rayford, M. Keshavarz-K, *J. Am. Chem. Soc.* **1993**, *115*, 2793; c) R. L. Cleary, D. A. Bardwell, M. Murray, J. C. Jeffery, M. D. Ward, *J. Chem. Soc., Perkin Trans. 2* **1997**, 2179.

[7] a) A. M. W. Cargill Thompson, D. A. Bardwell, J. C. Jeffery, L. H. Rees, M. D. Ward, *J. Chem. Soc., Dalton Trans.* **1997**, 721; b) R. E. Rosenfeld, Jr., R. Parthasarathy, J. D. Dunitz, *J. Am. Chem. Soc.* **1977**, *99*, 4860; c) F. T. Burling, B. M. Goldstein, *J. Am. Chem. Soc.* **1992**, *114*, 2313; d) F. T. Burling, B. M. Goldstein, *Acta Crystallogr., Sect. B* **1993**, *49*, 738; e) G. R. Desiraju, V. Nalini, *J. Mater. Chem.* **1991**, *1*, 201; f) D. Britton, J. D. Dunitz, *Helv. Chim. Acta* **1980**, *63*, 1068; g) M. Iwaoka, S. Tomoda, *J. Am. Chem. Soc.* **1996**, *118*, 8077; h) M. Iwaoka, S. Takemoto, M. Okada, S. Tomoda, *Bull. Chem. Soc. Japan* **2002**, *75*, 1611; i) I. Vargas-Baca, T. Chivers, *Phosphorus, Sulfur, Silicon and the Related Elements* **2000**, *164*, 207; j) R. M. Minyaev, V. I. Minkin, *Can. J. Chem.* **1998**, *76*, 776.

[8] K. Nakamoto, *Infrared and Raman Spectra of Inorganic and Coordination Compounds*, 4th ed., Wiley, New York, **1986**.

[9] a) Y.-P. Cai, H.-X. Zhang, A.-W. Xu, C.-Y. Su, C.-L. Chen, H.-Q. Liu, L. Zhang, B.-S. Kang, *J. Chem. Soc., Dalton Trans.* **2001**, 2429; b) E. Psillakis, J. C. Jeffery, J. A. McCleverty, M. D. Ward, *J. Chem. Soc., Dalton Trans.* **1997**, 1645; c) X. Meng, B. Xiao, Y. Fan, H. Hou, G. Li, *Inorg. Chim. Acta* **2004**, *357*, 1471; d) L. Carlucci, G. Ciani, D. W. von Gudenberg, D. M. Proserpio, *Inorg. Chem.* **1997**, *36*, 3812; e) R. Horikoshi, T. Mochida, H. Moriyama, *Inorg. Chem.* **2002**, *41*, 3017; f) P. L. Caradoc-Davies, L. R. Hanton, *Chem. Commun.* **2001**, 1098; g) Y. Kang, S. S. Lee, K.-M. Park, S. J. Lee, S. O. Kang, J. Ko, *Inorg. Chem.* **2001**, *40*, 7027.

[10] a) C. Piguet, G. Bernardinelli, G. Hopfgartner, *Chem. Rev.* **1997**, *97*, 2005; b) E. C. Constable, *Prog. Inorg. Chem.* **1994**, *42*, 67; c) M. Albrecht, *Chem. Rev.* **2001**, *101*, 3457.

[11] a) J. M. Baumeister, R. Alberto, K. Ortner, B. Spingler, P. A. Schubiger, T. A. Kaden, *J. Chem. Soc., Dalton Trans.* **2002**, 4143; b) H. C. Kang, A. W. Hanson, B. Eaton, V. Boekelheide, *J. Am. Chem. Soc.* **1985**, *107*, 1979; c) Y.-B. Dong, G.-X. Jin, M. D. Smith, R.-Q. Huang, B. Tang, H.-C. zur Loye, *Inorg. Chem.* **2002**, *41*, 4909; d) D. Song, S. Wang, *Eur. J. Inorg. Chem.* **2003**, 3774; e) Y.-B. Dong, Z. Zhao, G.-X. Jin, R.-Q. Huang, M. D. Smith, *Eur. J. Inorg. Chem.* **2003**, 4017; f) J. Budka, P. Lhotak, I. Stibor, J. Sykora, I. Cisarova, *Supramol. Chem.* **2003**, *15*, 353; g) C.-W. Tsang, Q. Yang, E. T.-P. Sze, T. C. W. Mak, D. T. W. Chan, Z. Xie, *Inorg. Chem.* **2000**, *39*, 5851.

[12] a) D. Eisler, R. J. Puddephatt, *Inorg. Chem.* **2005**, *44*, 4666; b) W. Xu, R. J. Puddephatt, K. W. Muir, A. A. Torabi, *Organometallics* **1994**, *13*, 3054; c) M. Munakata, L. P. Wu, T. Kuroda-Sowa, M. Maekawa, Y. Suenaga, G. L. Ning, T. Kojima, *J. Am. Chem. Soc.* **1998**, *120*, 8610.

[13] A. W. Addison, T. N. Rao, J. Reedijk, J. van Rijn, G. C. Verschoor, *J. Chem. Soc., Dalton Trans.* **1984**, 1349.

[14] a) S. H. Pines, *J. Org. Chem.* **1976**, *41*, 884; b) D. V. Griffiths, P. A. Griffiths, K. Karim, B. J. Whitehead, *J. Chem. Res.* **1996**, *176*, 901.

[15] M. Asakawa, P. R. Ashton, S. E. Boyd, C. L. Brown, S. Menzer, D. Pasini, J. F. Stoddart, M. S. Tolley, A. J. P. White, D. J. Williams, P. G. Wyatt, *Chem. Eur. J.* **1997**, *3*, 463.

[16] G. J. Kubas, *Inorg. Synth.* **1976**, *19*, 90.

[17] U. Azzena, S. Demartis, L. Pilo, E. Piras, *Tetrahedron* **2000**, *56*, 8375.

[18] G. M. Sheldrick, SADABS, A program for absorption correction with the Siemens SMART area-detector system; University of Göttingen, **1996**.

[19] a) Siemens SHELXTL, An integrated system for solving and refining crystal structures from diffraction data, revision 5.1; Siemens Analytical X-ray Instruments Ltd, Madison, WI, **1996**; b) G. M. Sheldrick, SHELXS-97, a Program for Automatic Solution of Crystal Structures; University of Göttingen, Göttingen, Germany, **1997**; c) G. M. Sheldrick, SHELXL-97, a Program for Crystal Structure Refinement; University of Göttingen, Göttingen, Germany, **1997**.

Received: August 4, 2005
Published Online: October 4, 2005

 © 2005 Wiley-VCH Verlag GmbH & Co. KGaA, Weinheim

Hexaazamacrocycle Containing Pyridine and Its Dicopper Complex as Receptors for Dicarboxylate Anions

Feng Li,[a] Rita Delgado,*[a,b] and Vítor Félix[c]

Keywords: Hexaazamacrocycle / Dicarboxylate anion recognition / Cascade dicopper complexes / Molecular dynamics / Receptors

The host–guest binding interactions of the hexaazamacrocycle [26]py_2N_4, in its tetraprotonated form H_4[26]$py_2N_4^{4+}$ as well as in its dicopper(II) complex $[Cu_2([26]py_2N_4)(H_2O)_4]^{4+}$, with dicarboxylate anions of different stereoelectronic requirements, such as oxalate (ox^{2-}), malonate (mal^{2-}), succinate (suc^{2-}), fumarate (fu^{2-}) and maleate (ma^{2-}), were evaluated. The association constants were determined using potentiometric methods in aqueous solution, at 298.0 K and 0.10 mol·dm^{-3} KCl. These values for the tetraprotonated ditopic receptor with the dicarboxylate anions revealed that the main species in solution corresponds to the formation of $\{H_4[26]py_2N_4(A)\}^{2+}$ (pH ≈ 4–9), A being the substrate anion. The values determined are not especially high, but the receptor exhibits selectivity for the malonate anion. The study of the cascade complexes revealed several species in solution, involving mononuclear and dinuclear complexes, mainly protonated and hydrolysed species, as well as the expected complexes $[Cu_2([26]py_2N_4)(A)(H_2O)_x]^{2+}$ or $[Cu_2([26]py_2N_4)(A)_2(H_2O)_y]$. Ox^{2-} and mal^{2-} form cascade complexes with only one anion, which will necessarily bridge the two copper atoms because of the symmetrical arrangement of the dinuclear complex. The two other studied anions, suc^{2-} and ma^{2-}, form species involving two substrate anions, although species with only one suc^{2-} anion were also found. UV/Vis and EPR spectroscopy have shown that the dicopper complex can operate as a sensor to detect and quantitatively determine oxalate spectrophotometrically because of the red shift of the maximum of the visible band observed by addition of ox^{2-} to an aqueous solution of the dinuclear copper complex. However the selectivity of $[Cu_2([26]py_2N_4)(H_2O)_4]^{4+}$ as a receptor for ox^{2-} in the studied series is not sufficiently high to detect ox^{2-} spectrophotometrically in the presence of the other anions. Molecular dynamics simulations indicated that the $H_4[26]py_2N_4^{4+}$ receptor provides a large and flexible cavity to accommodate the studied anions. Molecular recognition is based in electrostatic interactions rather than in multiple hydrogen-bonding interactions acting cooperatively. By contrast, the $[Cu_2([26]py_2N_4)]^{4+}$ receptor has a well-shaped cavity with adequate size to uptake these anions as bridging ligands with formation of four Cu–O bonds. The ox^{2-} anion is encapsulated within the cascade complex while the remaining anions are located above the N_6 macrocyclic plane, suggesting a selective coordination behaviour of this receptor. In spite of our molecular simulation being carried out in gas phase, the modelling results are consistent with the solution studies.

(© Wiley-VCH Verlag GmbH & Co. KGaA, 69451 Weinheim, Germany, 2005)

Introduction

Anion recognition is an active area of supramolecular chemistry, stimulated by the chemical and biological importance of anions.[1–4] The design and synthesis of unusual receptors are also a challenge for researchers. Up to now various types of synthetic receptors for the binding of anions have been developed, although receptors for the selective binding of nonspherical anions are scarce.[1–6] Therefore there is a great need for novel anion receptors in order to better characterise anion association patterns and to obtain novel binding features.

Carboxylate anions play an important role in organic, environmental and biological processes. The carboxylate functions of enzymes and antibodies contribute to their specific biochemical behaviour and they are critical components of numerous metabolic processes.[5]

The binding of anionic substrates by a specific receptor results essentially from electrostatic interactions and hydrogen-bonding formation. Additional π–π stacking, van der Waals interactions or hydrophobic effects strongly contribute to the selective recognition process. Protonated polyazamacrocycles and cryptands can bind anions by electrostatic interactions, and simultaneously by hydrogen-bonding interactions between protonated nitrogen of the receptor and an acceptor atom from the substrate. These receptors are particularly interesting in the recognition of anions when they are completely charged in neutral or slightly acidic

[a] Instituto de Tecnologia Química e Biológica, UNL, Apartado 127, 2781-901 Oeiras, Portugal
Fax: +351-214-41-12-77
E-mail: delgado@itqb.unl.pt
[b] Instituto Superior Técnico, Departamento de Química, Av. Rovisco Pais, 1049-001 Lisboa, Portugal
[c] Departamento Química, CICECO, Universidade de Aveiro, 3810-193 Aveiro, Portugal

Supporting information for this article is available on the WWW under http://www.eurjic.org or from the author.

aqueous solutions. Therefore, among the various types of synthetic receptors for the recognition of anions, polyamines have an important place, especially in aqueous environments.[1–6] The binding of anions by one or more metal centres forming cascade complexes is also a rich field of research. Metal complexes as receptors covalently bind anions, and then the interactions are in general stronger than those observed when only electrostatic or hydrogen-bonding interactions exist.[7,8]

In the present work the hexaazamacrocycle, 3,10,18,25,31,32-hexaazatricyclo[25.3.1.1^{12,16}]dotriaconta-1(31),12,14,16(32),27,29-hexaene ([26]py$_2$N$_4$),[9] was used directly as a ditopic receptor in the form of tetraammonium hydrochloride salt (H$_4$[26]py$_2$N$_4$·4Cl) for the study of anion-binding properties (see Scheme 1). The dicopper(II) complex of [26]py$_2$N$_4$ was also used as a receptor in cascade associations with the same anions. These receptors allowed a systematic evaluation of the main features involved in host–guest binding interactions with dicarboxylate anions with different sizes and flexibilities, such as ox^{2-}, mal^{2-}, suc^{2-}, fu^{2-} and ma^{2-} (see Scheme 2). The association constants were determined using potentiometric methods. Additional UV/Vis and EPR spectroscopic techniques were performed for the study of the cascade dicopper complexes. In order to give further insight into the solution results, molecular modelling studies comprising molecular mechanics and dynamics simulations were undertaken in gas phase.

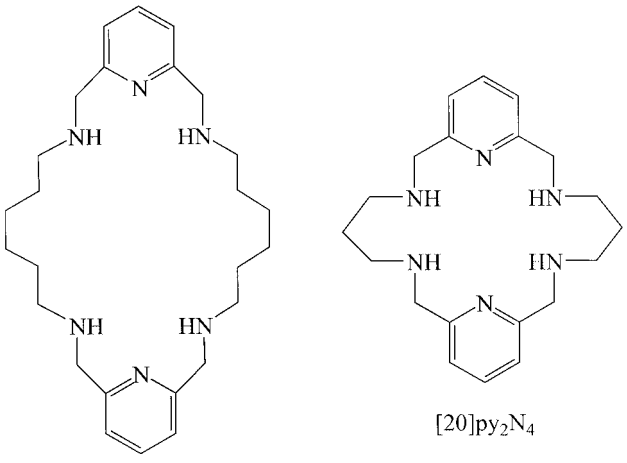

Scheme 1.

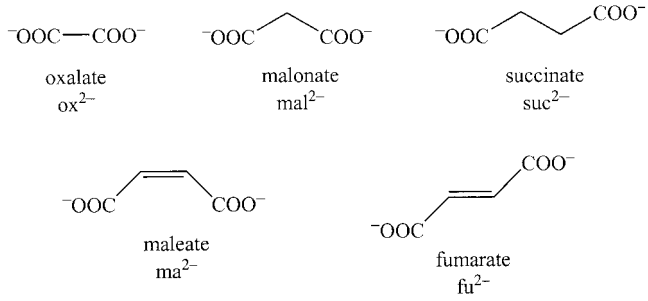

Scheme 2.

Results and Discussion

Anionic Associations with the Receptor H$_4$[26]py$_2$N$_4^{4+}$

The association constants of H$_4$[26]py$_2$N$_4^{4+}$ with ox^{2-}, mal^{2-}, suc^{2-}, fu^{2-} and ma^{2-} were determined in aqueous solutions at 298.0 K and 0.10 mol·dm^{-3} KCl, using the HYPERQUAD programme.[10] The guests are dicarboxylate anions that differ in shape, size and rigidity. The values obtained were collected in Table 1.

As the final results strongly depend on the protonation constants of the guest anions and the reported values are spread out,[11] we redetermined them in our experimental conditions and the values obtained are compiled in Table 2. The protonation constants of [26]py$_2$N$_4$ were also determined in the same experimental conditions. The values found were within the usual standard deviations for those determined before in KNO$_3$, therefore the values already published have been adopted[9] (see Table 3).

Only three constants, corresponding to the following equilibria, were found:

$$H_4[26]py_2N_4^{4+} + HA^- \rightleftharpoons \{H_5[26]py_2N_4(A)\}^{3+} \text{ (species 511)} \qquad K_1$$

$$H_4[26]py_2N_4^{4+} + A^{2-} \rightleftharpoons \{H_4[26]py_2N_4(A)\}^{2+} \text{ (species 411)} \qquad K_2$$

$$H_3[26]py_2N_4^{3+} + A^{2-} \rightleftharpoons \{H_3[26]py_2N_4(A)\}^{+} \text{ (species 311)} \qquad K_3$$

The main species corresponds to the formation of $\{H_4[26]py_2N_4(A)\}^{2+}$, which exists in solution from about 4 to 9 pH. The $\{H_5[26]py_2N_4(A)\}^{3+}$ and $\{H_3[26]py_2N_4(A)\}^{+}$ species exist in smaller percentages, the former at lower pH and the latter at higher pH values. A typical species distribution diagram is represented in Figure 1 for the case of malonate anion, using the HYSS programme.[12]

Table 1. Overall stability constants (log $\beta_{H_hL_lA_a}$)[a,b] and stepwise formation constants ($K_{H_hL_lA_a}$)[a] for the interaction of H$_4$[26]py$_2$N$_4^{4+}$ with ox^{2-}, mal^{2-}, suc^{2-}, fu^{2-} and ma^{2-}, where L denotes the [26]py$_2$N$_4$ ligand and A the anion. I = 0.10 mol·dm^{-3} in KCl at 298.0 K.

Species	ox^{2-}		mal^{2-}		suc^{2-}		fu^{2-}		ma^{2-}	
hla	log $\beta_{H_hL_lA_a}$	$K_{H_hL_lA_a}$	log $\beta_{H_hL_lA_a}$	$K_{H_hL_lA_a}$	log $\beta_{H_hL_lA_a}$	$K_{H_hL_lA_a}$	log $\beta_{H_hL_lA_a}$	$K_{H_hL_lA_a}$	log $\beta_{H_hL_lA_a}$	$K_{H_hL_lA_a}$
511	39.97(7)	91.2	41.54(5)	93.3	40.95(8)	24.0	39.91(5)	44.7	41.75(9)	50.1
411	36.53(3)	204.2	36.80(2)	380.2	36.65(1)	269.2	36.60(1)	239.9	36.55(3)	213.8
311	28.11(8)	52.5	28.57(5)	151.3	–	–	28.47(3)	120.2	28.34(5)	89.1

[a] See text for definition of the association constants. [b] Values in parentheses are standard deviations in the last significant figures.

 © 2005 Wiley-VCH Verlag GmbH & Co. KGaA, Weinheim

Table 2. Protonation constants (log $\beta_{H_hA_a}$) of oxalate (ox^{2-}), malonate (mal^{2-}), succinate (suc^{2-}), maleate (ma^{2-}) and fumarate (fu^{2-}), their stability constants (log $\beta_{Cu_mH_hA_a}$) with Cu^{2+}, and the corresponding stepwise constants, log K. T = 298.0 ± 0.1 K; I = 0.10 mol·dm^{-3} in KCl.[a]

Ion	Species	ox^{2-}		mal^{2-}		suc^{2-}		ma^{2-}		fu^{2-}	
	mha	log β	log K	log β	log K	log β	log K	log β	log K	log β	log K
H^+	011	3.792(3)	3.792	5.35(1)	5.35	5.350(7)	5.350	5.826(4)	5.826	4.043(4)	4.043
	021	5.04(9)	1.25	8.04(1)	2.69	9.376(8)	4.026	7.61(2)	1.78	6.833(6)	2.790
Cu^{2+}	101	5.23(8)	5.23	4.76(2)	4.76	2.94(4)	2.93	3.45(3)	3.45	–	–
	102	8.82(5)	3.59	7.45(9)	2.69	–	–	6.02(9)	2.57	–	–

[a] Values in parenteses are standard deviations in the last significant figures. A denotes the anion.

Table 3. Protonation constants (log β_{H_hL}) of [26]py_2N_4 and its stability constants with Cu^{2+} (log $\beta_{Cu_mH_hL_l}$) and the corresponding stepwise constants, log K. T = 298.0 ± 0.1 K; I = 0.10 mol·dm^{-3} in KCl.[a]

Ion	Species *mhl*	log β	log K
H^+	011	9.18	9.18
	021	17.87	8.69
	031	26.39	8.52
	041	34.22	7.83
	051	35.73	1.51
Cu^{2+}	101	14.09	14.09
	111	22.27	8.18
	121	29.49	7.22
	131	33.02	3.53
	201	25.20	11.11
	211	29.38	4.18
	2–11	17.45	–7.75
	2–21	8.63	–8.82
	2–31	–2.64	–11.27
	2–41	–14.18	–11.54

[a] See also ref.[9]

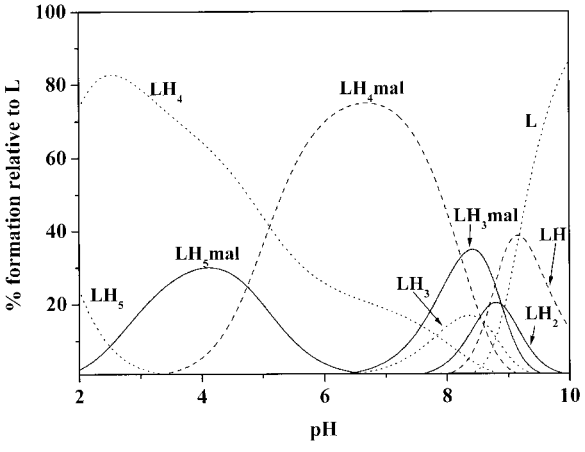

Figure 1. Species distribution curves calculated for the H_4[26]-$py_2N_4^{4+}$/mal^{2-} association in 1:1 ratio, C_L = C_{mal} = 2.00×10^{-3} mol·dm^{-3}, L being the macrocyclic ligand.

The values determined are not especially high, but the receptor is selective for malonate anion (see Figure 2). As can be observed, the K_2 values increase from oxalate to malonate and then successively decrease for the other anions, indicating that the size of the anion is the most important feature for the best association to the receptor. The overall basicity and the rigidity of the anions seem not to be very important factors for the interaction.

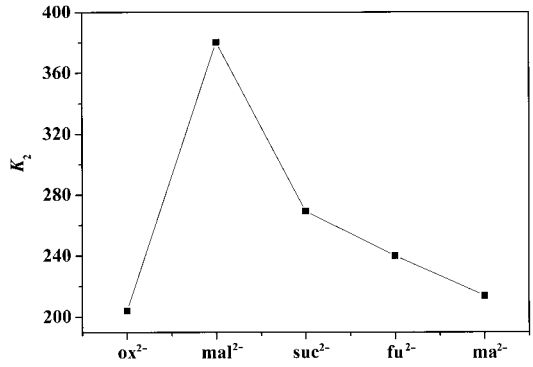

Figure 2. Plot of K_2 in function of the studied anions with different sizes and rigidities.

Cascade Dicopper Complexes

Potentiometric Measurements

The stability constants of [26]py_2N_4 with Cu^{2+} ion determined in aqueous solution at 298.0 K and 0.10 mol·dm^{-3} in KCl are also collected in Table 3.[9] For the Cu^{2+}/[26]py_2N_4 2:1 stoichiometry only dinuclear species are formed, {$[Cu_2L(H_2O)_4]^{4+}$, $[Cu_2(HL)(H_2O)_4]^{5+}$ and $[Cu_2L(H_2O)_{4-i}(OH)_i]^{4-i}$ (i = 1–4 and L = [26]py_2N_4 after pH = 4).[9] Free Cu^{2+} ions almost disappear from the solution at pH values of about 5 to yield $[Cu_2L(H_2O)_4]^{4+}$, which is the main species from pH 5 to about 8, followed by the successive hydrolysis of the four H_2O molecules directly bound to the two copper centres, $[Cu_2L(OH)_i]^{4-i}$ (i = 1–4) (see also Table 3). The X-ray single-crystal structure of the dicopper complex with a related ligand [20]py_2N_4, having propyl spacers between the pyridine heads (see Scheme 1), showed that two water molecules are directly coordinated to each copper centre,[9] and the same species was confirmed in aqueous solution.[13] Each copper centre is located at each head of the macrocycle, displaying a distorted square-pyramidal coordination environment with the basal plane defined by three consecutive nitrogen donors and one water molecule and the apical position fulfilled with the other water molecule at a longer distance than the equatorial one.[9] Therefore the presence of $[Cu_2L(H_2O)_4]^{4+}$ confirmed in our solution results led us to assume that an iden-

tical structure is adopted by the complex studied in the present work.

The predisposition of $[26]py_2N_4$ to form dinuclear complexes with copper centres, also confirmed by EPR studies,[9] led us to take advantage of this specific feature for the study of cascade complexes with dicarboxylate anions to investigate whether these guests bridge the two metal centres or, in contrast, two guests coordinate to each copper centre.

The association constants of the cascade complexes formed by addition of the anions to aqueous solutions of $[Cu_2([26]py_2N_4)(H_2O)_4]^{4+}$ at 298.0 K were determined using potentiometric measurements. The studied anions are ox^{2-}, mal^{2-}, suc^{2-} and ma^{2-} (see Scheme 2). The results are summarised in Table 4, and were obtained using the protonation constants of $[26]py_2N_4$ and of the anions and their stability constants with copper determined in our experimental conditions compiled in Table 2 and Table 3.

Several species were found in solution involving mononuclear and dinuclear complexes, mainly protonated and hydrolysed species as well as the expected complexes $[Cu_2([26]py_2N_4)(A)(H_2O)_x]^{2+}$ or $[Cu_2([26]py_2N_4)(A)_2(H_2O)_y]$, A being the guest anion, as can be seen in Table 4.

The first conclusion derived from the data of Table 4 is the distinct behaviour exhibited by oxalate and malonate substrates when compared with maleate, the succinate displaying intermediate features. Oxalate and malonate form cascade complexes with $[Cu_2([26]py_2N_4)(H_2O)_4]^{4+}$ involving only one anion, which necessarily will bridge the two copper atoms because of the symmetrical arrangement of the dinuclear complex. The two other studied anions, succinate and maleate, form species containing two anionic substrates, although species with only one suc^{2-} anion were also found. When two substrates are involved, each one can be directly coordinated to each copper, forming a dinuclear complex of independent centres, or both anions bridge the two metal centres. The adopted structure will be the result of a delicate balance of strain energies. Indeed the folded structure adopted by the dinuclear complex will rearrange for the encapsulation of the bridging anion(s), and the expended energy for the rearrangement should only be compensated by stronger interactions of the anion to the copper centres; this means anions can be better accommodated into the topology offered by the cavity formed between both copper centres.

The main species formed in the 5–9 pH range is $[Cu_2([26]py_2N_4)(A)(H_2O)_x]^{2+}$ for A = ox^{2-} or mal^{2-}, while for A = suc^{2-} this species and $[Cu_2([26]py_2N_4)(A)_2(H_2O)_x]$ overlap (and also with $[Cu_2([26]py_2N_4)(H_2O)_4]^{4+}$ when the amount of substrate is increased, such as for 2:1:2 Cu/$[26]py_2N_4$/suc^{2-} stoichiometries). For A = ma^{2-}, $[Cu_2([26]py_2N_4)(A)_2(H_2O)_y]$ is the major species, at least for the 2:1:2 ratio, although for lower substrate proportions the significance of $[Cu_2([26]py_2N_4)(H_2O)_4]^{4+}$ increases for slightly lower pH values. By potentiometric measurements, the number of water molecules in the complexes, *x* and *y*, was not possible to be determined, because in all cases the best models with coordination chemistry sense, accepted by the HYPERQUAD programme,[10] only contain species with one water molecule for which the corresponding hydrolysis constant was determined (see Table 4). For pH values lower than 5, mononuclear and dinuclear protonated complexes, involving the anion or not, are formed, and for pH values higher than 8 the water molecule of the cascade complexes starts to be hydrolysed.

However, in all cases the hydrolysed complexes $[Cu_2([26]py_2N_4)(H_2O)_{4-x}(OH)_x]^{4-x}$ replace the cascade dinuclear species containing the dicarboxylate, at high pH (>8), al-

Table 4. Overall stability constants ($\log \beta_{Cu_mH_hL_lA_a}$)[a,b] for the equilibria of $[Cu_2([26]py_2N_4)(H_2O)_4]^{4+}$ with ox^{2-}, mal^{2-}, suc^{2-} and ma^{2-}, where L is the macrocyclic ligand $[26]py_2N_4$ and A the anion. I = 0.10 mol·dm^{-3} in KCl at 298.0 K.

Species *mhla*	ox^{2-} $\log \beta_{Cu_mH_hL_lA_a}$	mal^{2-} $\log \beta_{Cu_mH_hL_lA_a}$	suc^{2-} $\log \beta_{Cu_mH_hL_lA_a}$	ma^{2-} $\log \beta_{Cu_mH_hL_lA_a}$
1411	43.94(2)	42.29(1)	41.82(4)	–
1311	39.87(7)	38.92(1)	–	–
1211	[35.0][c]	[33.5][c]	–	–
1111	31.04(9)	29.70(1)	30.52(9)	–
1011	–	23.29(4)	–	–
1–111	–	–	13.29(5)	
2011	30.17(1)	29.13(1)	28.78(7)	–
2111	35.49(6)	34.34(2)	33.41(9)	–
2211	39.78(5)	–	–	–
2–111	21.07(2)	20.44(2)	–	–
1412	–	–	–	47.52(2)
1312	–	–	–	43.47(4)
1212	–	–	–	39.35(4)
1112	–	–	–	34.56(3)
1012	–	–	–	26.64(7)
2012	–	–	32.07(5)	32.59(3)
2112	–	–	36.98(9)	–
2–112	–	–	23.23(6)	23.39(8)

[a] See Experimental, Calculation of Stability Constants, for definitions. [b] Values in parenthesis are standard deviations in the last significant figures. [c] Values in brackets are determined with large standard deviations; because the species exist in solution in small amounts (<10%), the final model was refined without these species.

 © 2005 Wiley-VCH Verlag GmbH & Co. KGaA, Weinheim

though, depending on A, small amounts of mononuclear species, $\{Cu([26]py_2N_4)A\}$ or $\{Cu([26]py_2N_4)A_2\}^{2-}$, were also found. This indicates that the dicarboxylate anions, whether bridging the two copper centres or not, are replaced by OH^- groups at high pH values, or in other words, the cascade complexes dissociate, yielding successively the species $[Cu_2([26]py_2N_4)(H_2O)_{4-x}(OH)_x]^{4-x}$ with an increase of pH.

These and other features of the behaviour of these complexes in aqueous solutions as a function of the pH can be observed in Figure 3 and Figure 4 for mal^{2-} and suc^{2-} anions, respectively. The comparison of the species distribution diagrams for suc^{2-} and ma^{2-} anions (see the diagram for ma^{2-} in the Supporting Information) emphasises the intermediate behaviour of the succinate anions, as already mentioned. Indeed between pH 5 and 9 both species, $[Cu_2([26]py_2N_4)(suc)(H_2O)_x]^{2+}$ and $[Cu_2([26]py_2N_4)(suc)_2(H_2O)_x]$, exist in solution in percentages depending on the suc^{2-} ratio, while only the $[Cu_2([26]py_2N_4)(ma)_2(H_2O)_x]$ complex is formed in the same pH range (for lower anion ratios the percentage of $[Cu_2([26]py_2N_4)(H_2O)_4]^{4+}$ increases in both cases).

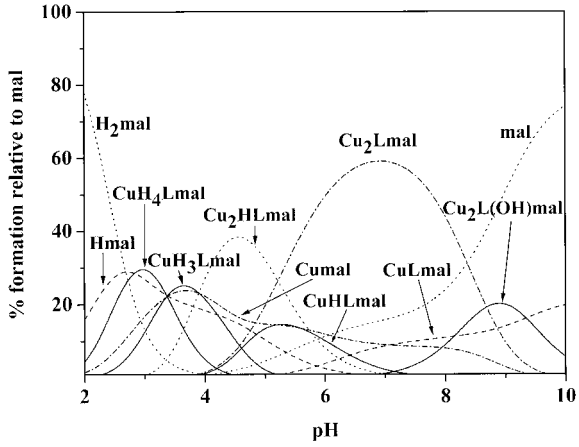

Figure 3. Species distribution curves calculated for the system $[Cu_2([26]py_2N_4)(H_2O)_x]^{4+}/mal^{2-}$ for 1:1 ratio, $C_{complex} = C_{mal} = 2.00 \times 10^{-3}$ mol·dm^{-3}, "complex" being the dicopper complex, L the $[26]py_2N_4$ and mal^{2-} the malonate anion guest.

The copper–substrate interaction, measured by the magnitude of the association constant corresponding to the equilibrium $[Cu_2([26]py_2N_4)(H_2O)_4]^{4+} + A^{2-} \rightleftharpoons [Cu_2([26]py_2N_4)(A)(H_2O)_x]^{2+}$ (Table 4 and Table 5) is stronger for A = ox^{2-}, followed by mal^{2-} and then suc^{2-}, the values being 4.97, 3.93 and 3.58 log units, respectively (see Table 5, where the stepwise constants and the corresponding equilibrium reactions are summarised). On the other hand, the corresponding constant for the equilibrium $[Cu_2([26]py_2N_4)(H_2O)_4]^{4+} + 2\ A^{2-} \rightleftharpoons [Cu_2([26]py_2N_4)(A)_2(H_2O)_x]$ is higher for ma^{2-} anions, being 7.39 for this anion and 6.87 for suc^{2-}, in log units. Then the strength of the Cu···A···Cu interaction decreases with the increase of the length of the spacer between the two carboxylate sites, being stronger for oxalate and weaker for succinate anions. This trend is opposite to the overall basicity of the anions, which follows the order succinate > malonate >> oxalate (see Table 2). The same happens with the species involving two carboxylate anions, suggesting that the size of the anion and its rigidity are the most important factors for the verified order of association constants.

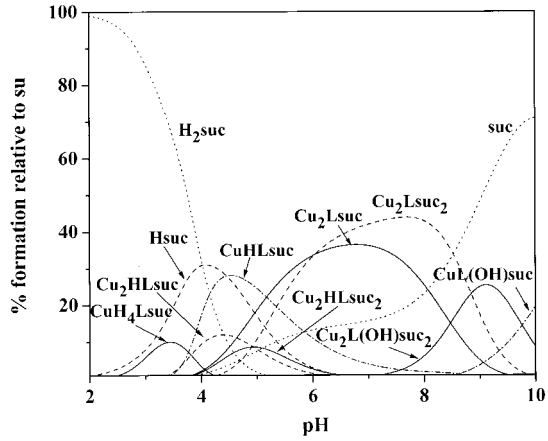

Figure 4. Species distribution curves calculated for the system $[Cu_2([26]py_2N_4)(H_2O)_x]^{4+}/suc^{2-}$ for 1:1 ratio, $C_{complex} = C_{suc} = 2.00 \times 10^{-3}$ mol·dm^{-3}, "complex" being the dicopper complex and suc^{2-} the guest succinate anion.

Table 5. Stepwise association constants (log *K*) corresponding to the indicated equilibrium calculated from the values of Table 4.

Equilibrium	ox^{2-}	mal^{2-}	suc^{2-}	ma^{2-}
$CuH_4L + A \rightleftharpoons CuH_4LA$	7.13	3.92	3.45	–
$CuH_3L + A \rightleftharpoons CuH_2LA$	6.85	5.90	–	–
$CuHL + A \rightleftharpoons CuHLA$	8.77	7.43	8.25	–
$CuL + A \rightleftharpoons CuLA$	–	9.2	–	–
$Cu_2H_2L + A \rightleftharpoons Cu_2H_2LA$	6.61	–	–	–
$Cu_2HL + A \rightleftharpoons Cu_2HLA$	6.11	4.96	4.63	–
$Cu_2L + A \rightleftharpoons Cu_2LA$	4.97	3.93	3.58	–
$Cu_2(H_{-1}L) + A \rightleftharpoons Cu_2(H_{-1}L)A$	3.62	2.99	–	–
$CuH_4L + 2\ A \rightleftharpoons CuH_4LA_2$	–	–	–	7.67
$CuH_3L + 2\ A \rightleftharpoons CuH_3LA_2$	–	–	–	10.45
$CuH_2L + 2\ A \rightleftharpoons CuH_2LA_2$	–	–	–	9.86
$CuHL + 2\ A \rightleftharpoons CuHLA_2$	–	–	7.60	12.29
$CuL + 2\ A \rightleftharpoons CuLA_2$	–	–	–	12.55
$Cu_2L + 2\ A \rightleftharpoons Cu_2LA_2$	–	–	6.87	7.39
$Cu_2(H_{-1}L) + 2\ A \rightleftharpoons Cu_2(H_{-1}L)A_2$	–	–	5.78	5.94

Spectroscopic Measurements

The UV/Vis spectrum of aqueous $[Cu_2([26]py_2N_4)(H_2O)_4]^{4+}$ solution was recorded at pH ≈ 6. The complex exhibits a broad d-d band at 660 nm and three main bands in the UV region at 288, 262 and 206 nm (see Table 6). The intense band at 262 nm was attributed to ligand-to-metal charge transfer absorption (LMCT). The addition of increasing amounts of the studied anion guests led to a hypochromism (a decrease in the molar absorptivity) and to a shift in wavelength of the visible band in all cases, the shifts being smaller in the UV region (see Table 6). However, while the shift of the visible band is to the red in the presence of ox^{2-}, a blue shift is observed for the other three anions, although very small for mal^{2-}.

 © 2005 Wiley-VCH Verlag GmbH & Co. KGaA, Weinheim

Table 6. Spectroscopic UV/Vis data for $[Cu_2([26]py_2N_4)(H_2O)_4]^{4+}$ and upon addition of dicarboxylate anions.

Complex	pH	UV/Vis λ_{max}/nm (ε_{molar}/dm^3·mol^{-1}·cm^{-1})
$[Cu_2([26]py_2N_4)(H_2O)_4]^{4+}$	5.76	206 (sh., 19744.1); 246 (sh., 9707.5); 262 (16352.8); 266 (sh., 14140.8); 288 (5978.1); 660 (351.0)
$[Cu_2([26]py_2N_4)(H_2O)_4]^{4+}$ + ox^{2-}	7.54	200 (sh., 33290.7); 206 (sh., 30466.2); 248 (sh., 12285.2); 260 (17404.0); 266 (sh., 15128.0); 282 (sh., 6517.4); 674 (341.3); 820 (sh., 138.9)
$[Cu_2([26]py_2N_4)(H_2O)_4]^{4+}$ + mal^{2-}	7.10	204 (sh., 19323.6); 244 (sh., 10804.4); 260 (15493.6); 266 (sh., 13025.6); 280 (5402.2); 658 (338.2); 820 (sh., 55)
$[Cu_2([26]py_2N_4)(H_2O)_4]^{4+}$ + suc^{2-}	7.16	204 (sh., 19890.3); 246 (sh., 12669.1); 260 (16855.6); 266 (sh., 14012.8); 280 (5968.9); 650 (296.2)
$[Cu_2([26]py_2N_4)(H_2O)_4]^{4+}$ + ma^{2-}	7.72	202 (38592.3); 208 (sh., 33418.6); 250 (sh., 16517.4); 258 (18446.1); 266 (sh., 15511.9); 282 (6663.6); 650 (336.4)

The red shift of the visible band observed when the substrate is ox^{2-} assigns the presence of this anion, but also reveals a change of the structure adopted by the copper centres in this complex because of the bridging anion,[14–17] while the blue shifts resulting from the presence of the other dicarboxylates should be a consequence of the stronger equatorial field derived from the replacement of a water molecule by the oxygen atom of the carboxylate group of the anion.

The X-band EPR spectrum of a frozen water/DMSO (1:1 v/v) solution of $[Cu_2([26]py_2N_4)(H_2O)_4]^{4+}$ is typical of a coupled dinuclear copper triplet-state centre with a $S = 1$ state and zero-field splitting, having two types of signals in the $\Delta M_s = 1$ and $\Delta M_s = 2$ regions[9,18,19] (see Figure 5). The $\Delta M_s = 2$ transition signal reveals a spin-exchange interaction between the two copper atoms, but the signal is very small and the seven hyperfine lines resulting from the coupling of each unpaired electron with the two copper nuclei cannot be observed.

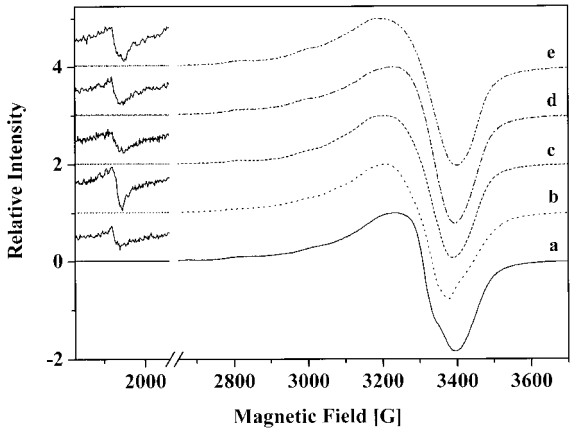

Figure 5. EPR X-band spectra of $[Cu_2([26]py_2N_4)(H_2O)_4]^{4+}$ (bottom) at 6.4 K and of $[Cu_2([26]py_2N_4)(A)(H_2O)_x]^{2+}$, A being successively ox^{2-} (at 11.4 K), mal^{2-} (at 11.4 K), suc^{2-} (at 6.4 K) and ma^{2-} (at 6.4 K). The signal at low field for each complex was amplified and placed above the axis. All the complexes were prepared at 2.0×10^{-3} mol·dm^{-3} in DMSO/H_2O (1:1). The spectra were recorded at the microwave power of 2.4 mW, modulation amplitude of 1.0 mT and at the frequency (ν) 9.646 GHz.

When oxalate anion is added to the solution of the dinuclear copper complex, a new signal at ≈3500 G appears, and in the $\Delta M_s = 2$ region the hyperfine structure is now perceptible, revealing a shorter distance between both copper centres because of the presence of the bridging anion. Indeed for $\Delta M_s = 1$ transitions, two groups of peaks spaced on either side of $g \approx 2$ emerge, showing an overall width as a function of r (the distance between the two copper centres).[20] Considering D, the zero-field splitting within the triplet state, built up from a dipolar contribution D_{dip}, and an exchange contribution, D_{ex}: $D = D_{ex} + D_{dip}$, and if we consider $D_{ex} \approx 0$ (valid for $-J \leq 30$ cm^{-1}), the r distance can be evaluated directly from D.[21] It was possible to estimate the D value from the spectrum only for the case of $[Cu_2([26]py_2N_4)ox]^{2+}$. The spectra of the cascade complexes for the other anions are too broad to allow the determination of the D value (see Figure 5). However for $[Cu_2([26]py_2N_4)ox]^{2+}$ the $2D$ value was calculated by the difference between the Hz_2 and Hz_1 transitions, yielding to 0.0128 cm^{-1}. Even in this case it was difficult to observe all the lines of the two expected septets, however from the more intense lines (third to fifth) it was possible to obtain a satisfactorily accurate value of the zero-field splitting constant. Taking $g_{\|} = 2.237$ and $g_{\perp} = 2.10$, obtained directly from the spectrum, the value of 6.3 ± 0.2 Å was determined for the copper–copper distance in the $[Cu_2([26]py_2N_4)ox]^{2+}$ complex.

Molecular Modelling

In order to give a further insight in our solution studies, the binding ability of $[26]py_2N_4$ to accommodate ox^{2-}, mal^{2-}, suc^{2-} and ma^{2-} anions in its tetraprotonated form or, alternatively, as bridging ligands in its copper dinuclear complex was evaluated in gas phase through molecular mechanics (MM) and molecular dynamics (MD) simulations using the Universal Force Field[22] within the Cerius2 software package.[23]

The molecular modelling studies started with the conformational analysis of the $H_4[26]py_2N_4^{4+}$ following quenching dynamics methods over 2 ns. 10000 conformations were generated and subsequently minimised by MM as described in the experimental section. The final structures have energies in a wide range of 667.43–716.94 kcal·mol^{-1}. In spite of the presence of the two pyridine heads in the macrocyclic framework, between these two limits, the energy changes almost continuously. This result is expected due to the large

 © 2005 Wiley-VCH Verlag GmbH & Co. KGaA, Weinheim

number of single bonds with corresponding endocyclic torsion angles determining a geometric arrangement between a *gauche* and a *trans* configuration. The two pyridine rings oscillate continuously, with the dihedral angle between them ranging from 0.1° to 134.3°. Furthermore, the intermolecular distance between the pyridine nitrogen donors, ranging from 7.591 to 11.261 Å, indicates that the receptor can adopt conformational shapes with different cavity sizes. The interactions between this receptor and ox^{2-}, mal^{2-}, suc^{2-} and ma^{2-} were further investigated, docking each one of these four anions to the lowest energy conformation of $H_4[26]py_2N_4^{4+}$, also using a MD quenching methodology. The lowest energy structures found, presented in Figure 6, show that the $H_4[26]py_2N_4^{4+}$ receptor adopts different conformational shapes providing a suitable cavity to encapsulate all four of these dicarboxylate anions. The electrostatic bonding interactions dictate the molecular recognition between the receptor and each anion in gas phase. Indeed the binding energy determined from the difference between the energy of the inclusion compound and the sum of the individual energies of the $H_4[26]py_2N_4^{4+}$ receptor (lowest energy conformation) and the anion, listed in Table 7, indicates that in all cases the inclusion process is highly favourable, the electrostatic term being the largest contributor. Further, the dynamic behaviour of each inclusion compound was evaluated by MD at 300 K over 1 ns. In Table 8 the most significant short N–H···O hydrogen contacts found during the simulations using a cut-off of 2.5 Å for H···O distances are listed. The number of hydrogen-bonding interactions increases with the size of the anion following the order ox^{2-}, ma^{2-}, mal^{2-} and suc^{2-}. The ox^{2-} anion establishes with the $H_4[26]py_2N_4^{4+}$ receptor only one N–H···O hydrogen bond during about 170 ps of simulation with a Φ frequency of only 3.2 s^{-1}, while the oxygen atoms of the two carboxylate groups of ma^{2-} are involved in two hydrogen bonds with two N–H binding sites for almost the entire duration of the simulation. However, these contacts have low frequencies of 2.7 and 3.1 ps^{-1}, occurring separately for almost the whole time. The mal^{2-} and suc^{2-} form through two oxygen atoms, respectively, four and five N–H···O hydrogen bonds with the $H_4[26]py_2N_4^{4+}$ receptor. Again in both cases all these intermolecular contacts show low frequencies and only occasionally (without statistical significance) act cooperatively for the molecular recognition phenomena. These results show that the $H_4[26]py_2N_4^{4+}$ receptor has high flexibility and a too large cavity that is inappropriate for molecular recognition of the anions.

Table 7. Binding energy for $\{(H_4[26]py_2N_4)(A)\}^{2+}$ supramolecular compounds in gas phase.

	Energy/kcal·mol^{-1}			
	Total energy	Electrostatic energy	ΔE_{total}[a]	$\Delta E_{electrostatic}$[b]
$\{(H_4[26]py_2N_4)(ox)\}^{2+}$	424.05	351.75	–495.56	–490.37
$\{(H_4[26]py_2N_4)(mal)\}^{2+}$	285.48	223.16	–492.94	–479.71
$\{(H_4[26]py_2N_4)(suc)\}^{2+}$	272.98	212.06	–474.35	–460.96
$\{(H_4[26]py_2N_4)(ma)\}^{2+}$	334.81	261.78	–481.24	–468.86
ox^{2-}	240.63	234.22	–	–
mal^{2-}	99.43	94.96	–	–
suc^{2-}	68.35	65.12	–	–
ma^{2-}	137.07	122.73	–	–
$H_4[26]py_2N_4^{4+}$	678.98	607.90	–	–

[a] $\Delta E_{total} = E_{t(supramolecule)} - E_{t(anion)} - E_{t(receptor)}$. [b] $\Delta E_{electrostatic} = E_{e(supramolecule)} - E_{e(anion)} - E_{e(receptor)}$.

The length of the bridge between the two copper centres supported by the $[Cu_2([26]py_2N_4)]^{4+}$ complex can be established ascertaining the Cu···Cu distances allowed by the macrocycle without any additional steric strain from the presence of other ligands in the metal co-ordination spheres. On the other hand, when two copper centres are

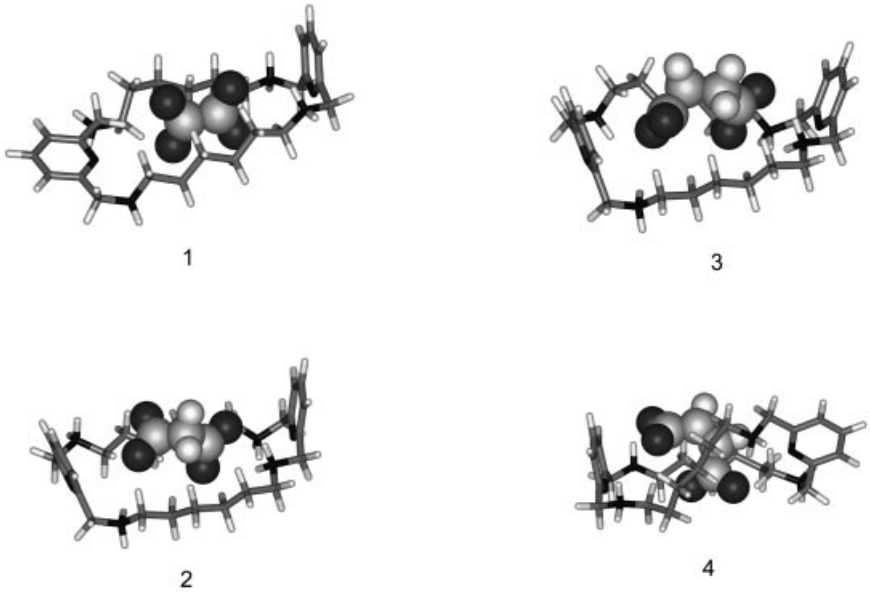

Figure 6. Lowest energy structures found for $\{(H_4[26]py_2N_4)(A)\}^{2+}$ supramolecular compounds, with A equal to ox^{2-} (1), mal^{2-} (2), suc^{2-} (3) and ma^{2-} (4).

 © 2005 Wiley-VCH Verlag GmbH & Co. KGaA, Weinheim

Table 8. Hydrogen-bonding interactions found for $\{(H_4[26]py_2N_4)(ox)\}^{2+}$ supramolecular compounds during the molecular dynamics simulations.

Anion	Period of simulation/ps	Φ/s^{-1}[a]	Hydrogen-bonding interactions[b]
ox^{2-}	828.3–999.8	3.2	N_1–H_a···O_1
mal^{2-}	0.8–704.1	0.71	N_1–H_b···O_1
	0.3–779.4	1.14	N_1–H_a···O_1
	1.5–905.7	0.96	N_1–H_a···O_2
	20.3–706.5	0.55	N_2–H_a···O_2
suc^{2-}	8.4–996.0	0.28	N_1–H_a···O_1
	421.4–650.7	1.33	N_1–H_b···O_1
	0.1–408.3	0.52	N_2–H_a···O_1
	5.9–642.5	0.48	N_3–H_a···O_3
	364.1–792.9	1.06	N_4–H_a···O_3
ma^{2-}	0.1–999.8	2.72	N_1–H_a···O_1
	0.3–999.6	1.20	N_3–H_a···O_3

[a] Φ is given by the ratio between the number of times and the period of simulation in which a short contact is observed. For each anion, the N–H-binding groups are labelled in a clockwise manner. [b] The oxygen donor atoms of the anions are labelled using the following atomic notation scheme: O_1 and O_2 for the first carboxylate group and O_3 and O_4 for the second one.

coordinated to $[26]py_2N_4$, the relative positions of the N–H groups, below (–) and above (+) the N_6 macrocyclic plane determine five independent conformations: + + + +, + + – –, + + + –, – + – + and + – – +. All these arrangements have to be considered in a complete analysis of the structural preferences of the coordinated macrocycle, which was undertaken following an identical MD methodology to that described for the $H_4[26]py_2N_4^{4+}$ receptor. For each $[Cu_2([26]py_2N_4)]^{4+}$ conformation a short MD simulation of 100 ps was carried out. The lowest energy conformations found are shown in Figure 7, while their corresponding energies are given in Table 9 together with the Cu···Cu distance and the dihedral angle between the two pyridine rings (called the α angle here). The energies range only between 452.0 and 464.7 kcal·mol^{-1} for + + + + and – + – + conformations, respectively. The + + – – conformation has an energy only 0.9 kcal·mol^{-1} higher than the lowest one. The electrostatic energy term is again the largest contributor for the total energy. The + + + + conformation adopts a cleft topology with an α angle of 59.5° while in the + + – – conformation the two pyridine rings are in antiperiplanar arrangement with an α angle of 164.4°. The remaining three conformations adopt an almost planar shape with the α angle ranging from 151.9° for + – – + to 173.2° for + + + –. The Cu···Cu distance is in a wide range of values between 7.790 and 8.768 Å, so it is not possible to establish any straight relationship between the separation of the two copper centres and the shape or conformation adopted. The first + + + + conformation having an almost planar shape appears at 464.3 kcal·mol^{-1} with an α angle of 160.2° and a Cu···Cu distance of 7.857 Å.

Table 9. Lowest energy conformations for the $[Cu_2([26]py_2N_4)]^{4+}$ receptor.

Conformation	Energy/kcal·mol^{-1}	Cu···Cu/Å	α/°[a]
+ + + +	452.0	8.768	59.5
+ + – –	452.9	8.814	164.4
+ + + –	457.6	8.225	173.2
+ – – +	462.1	7.750	151.9
– + – +	464.7	7.790	163.7

[a] α angle definition is given in the text.

The 3D scatter plot of the α dihedral angle versus steric energy and the Cu···Cu distance found for the conformational analysis of $[Cu_2([26]py_2N_4)]^{4+}$ in the + + + + conformation is presented in Figure 8. This plot shows that most of the conformations have a cleft shape, with the Cu···Cu distance in a narrow range from 8.9 to 9.0 Å. By contrast, the few conformations with almost planar or antiparallel arrangements accommodate a wide range of distances between 8.1 and 9.0 Å.

Alternatively, the distance between the two copper centres tolerated by the macrocyclic cavity can be ascertained from the energy profile for $[Cu_2([26]py_2N_4)]^{4+}$, calculated using our published method.[24] Here, the Cu···Cu dis-

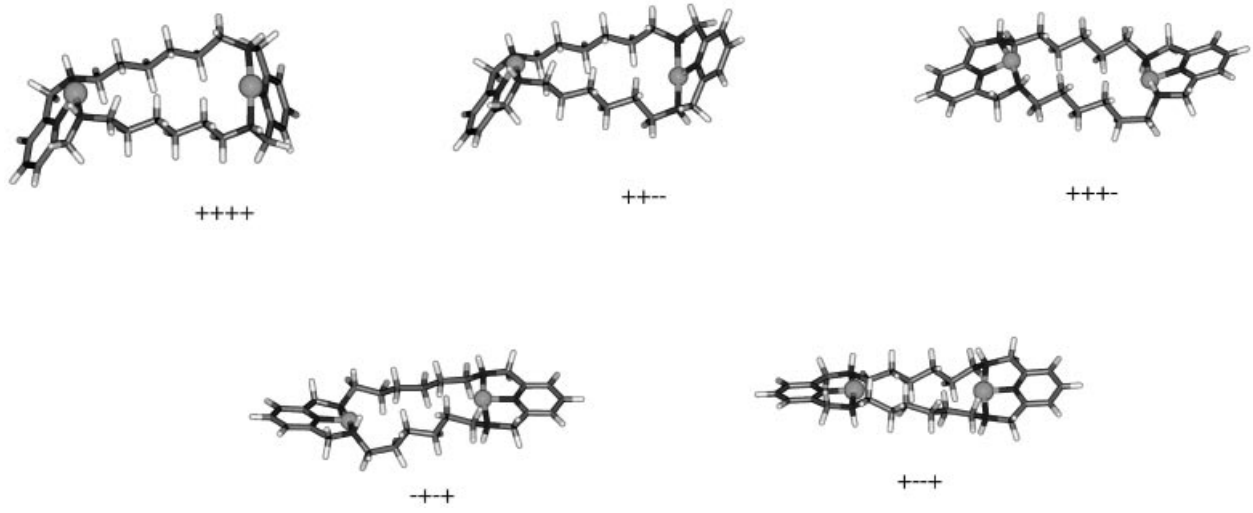

Figure 7. Lowest energy conformations for $[Cu_2([26]py_2N_4)]^{4+}$ receptor.

 © 2005 Wiley-VCH Verlag GmbH & Co. KGaA, Weinheim

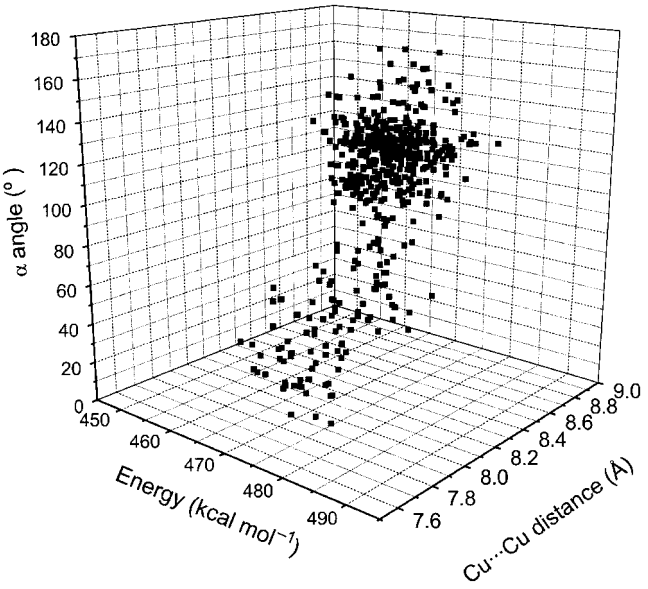

Figure 8. 3D scatter plot of the α angle against steric energy and Cu···Cu distance for $[Cu_2([26]py_2N_4)]^{4+}$ receptor.

tance was varied at 0.1 Å intervals between the limits 7.2–10.0 Å. At each distance the macrocyclic energy is minimised by MM and the resulting energies found for the + + + + cleft conformation (see Table 9), shown in Figure 9, represent the steric strain in the macrocycle caused by a specific Cu···Cu distance. The plot of Figure 9 (bottom) shows an almost deep energy profile with a minimum at 8.75 Å. When this calculation was repeated without charges (Figure 9, top), the energy profile is broad, with the macrocyclic cavity having a better tolerance for short Cu···Cu distances. This result is expected, given that the main repulsive electrostatic interaction derived from the presence of the two Cu^{2+} centres was eliminated. However, the centre of the broad minimum was only shifted 0.25 Å for shorter distances. This result suggests that the macrocycle must adopt a different conformational shape in order to accommodate bridging anions requiring shorter Cu···Cu distances, typically below 8.0 Å.

Having evaluated the steric requirements of the $[Cu_2([26]py_2N_4)]^{4+}$ complex, the interaction between this receptor (+ + + + conformation) and the ox^{2-}, mal^{2-}, suc^{2-} and ma^{2-} anions was investigated through the MD quenching technique for 100 ps. No bonds between the oxygen donors and the two copper centres were included and consequently the host–guest interactions are purely electrostatic. In Figure 10 the lowest energy arrangements found for the four cascade complexes are shown. The sum of MM energies found for isolated anions and $[Cu_2([26]py_2N_4)]^{4+}$ (lowest energy conformation) largely exceed the energy of the corresponding cascade complex, which indicates that in gas phase its formation is highly favourable in all four cases. This binding energy takes the values of –784.4, –755.6, –747.1 and –732.4 kcal·mol^{-1} for ox^{2-}, mal^{2-}, suc^{2-} and ma^{2-}, respectively. The dicarboxylate anions bridge the two copper centres through all four oxygen donors, with Cu–O

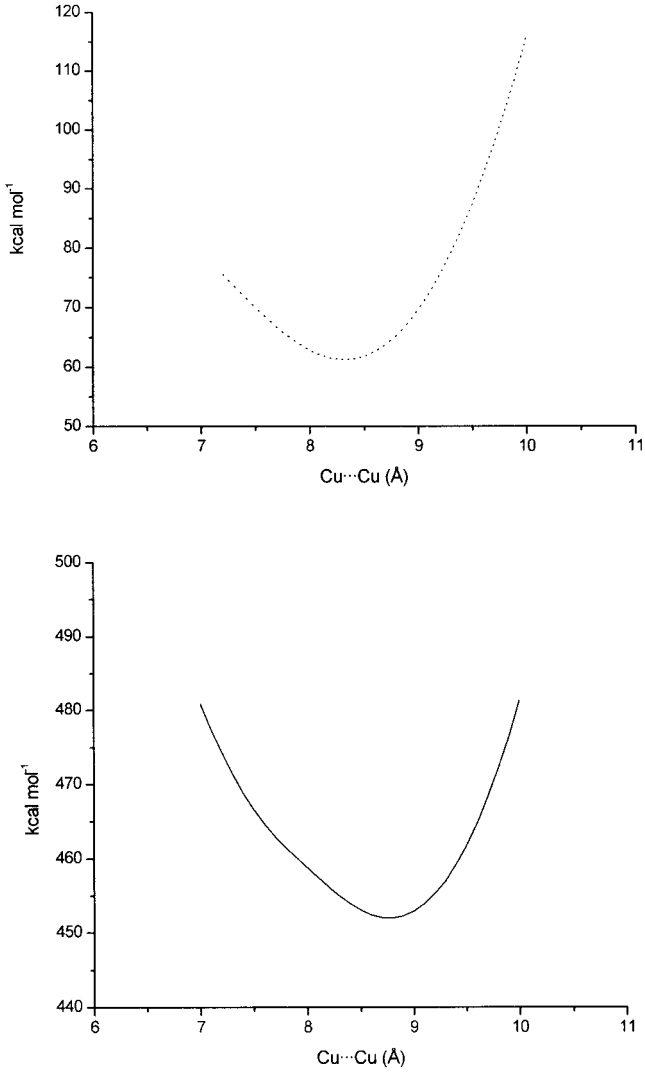

Figure 9. Plot of steric energy profile against Cu···Cu distance for $[Cu_2([26]py_2N_4)]^{4+}$ receptor with charges (solid line) and without charges (dotted line).

distances taking normal values for this type of bond, typically about 2.0 Å. However, the smaller anion ox^{2-} is inside the macrocyclic cavity, while the remaining three anions are located above the plane determined by the six nitrogen donors of the receptor. The pyridine rings are almost in a planar arrangement, making a dihedral angle of 16.3, 33.2 and 9.7° for ox^{2-}, mal^{2-} and suc^{2-}, respectively; while for ma^{2-} these rings are twisted, giving an angle of 128.1°.

Subsequently the cascade complexes were submitted to MD runs of 1 ns at room temperature. The average distances from the copper to oxygen atoms of the anions together with their small standard deviations, listed in Table 10, clearly indicate that each bridged anion remains coordinated by all four Cu–O bonds for the entire period of the simulation. In addition, the Cu···Cu distances are largely dependent on the size and the steric requirements of the bridge. Indeed the Cu···Cu distance of the lowest energy conformation of 8.768 Å was substantially shortened to 6.44(6) Å when the smallest ox^{2-} anion was included, while

 © 2005 Wiley-VCH Verlag GmbH & Co. KGaA, Weinheim

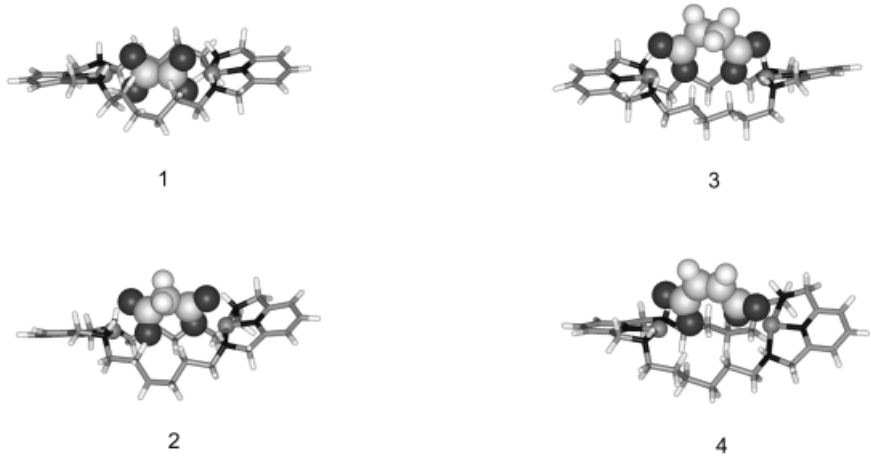

Figure 10. Lowest energy structures found for $[Cu_2([26]py_2N_4)(A)]^{2+}$ cascade complexes, with A equal to ox^{2-} (1), mal^{2-} (2), suc^{2-} (3) and ma^{2-} (4).

the ma^{2-} anion having a *cis* double bond between the two carboxylate groups kept the two metal centres at a longer distance of 6.88(15) Å. The distances between the copper centres supported by mal^{2-} and suc^{2-} bridges are 6.58(10) and 6.62(14) Å, respectively. These values are shorter than the average Cu···Cu distances for $[Cu_2([26]py_2N_4)]^{4+}$ in + + + + cleft [8.73(14) Å] and roughly planar [8.64(18) Å] topologies found from two MD simulations carried out at 300 K over 1 ns.

Table 10. Cu–O and Cu···Cu distances [Å] found for $[Cu_2([26]py_2N_4)(A)]^{2+}$ cascade complexes from MD at 300 K (A = ox^{2-}, mal^{2-}, suc^{2-} and ma^{2-}).

	ox^{2-}	mal^{2-}	suc^{2-}	ma^{2-}
Cu–O	2.045(43)	2.094(51)	2.106(54)	2.067(47)
	2.061(46)	2.082(50)	2.046(44)	2.074(48)
	2.045(43)	2.084(50)	2.058(45)	2.073(48)
	2.062(46)	2.096(51)	2.083(50)	2.067(47)
Cu···Cu	6.44(6)	6.58(10)	6.62(14)	6.88(15)

Certainly other binding scenarios between the receptor and the substrates are possible, for instance the docking of the anions from the opposite side of the N–H groups of the macrocycle. However the evaluation of all of them would be a huge task. On the other hand, the presence of other ligands leading to five- or six-coordination geometries to the copper centres were not taken into account in our calculations. In spite of these modelling studies being carried out in the gas phase, neglecting important solution effects, they show that the selective binding of ox^{2-}, mal^{2-}, suc^{2-} and ma^{2-} to the $[Cu_2([26]py_2N_4)]^{4+}$ receptor occurs. In other words, in contrast to the $H_4([26]py_2N_4)^{4+}$ receptor, in the dinuclear copper complex the macrocycle has a preorganised cavity with the two copper centres located at apparent flexible positions able to promote the uptake of these anions.

Conclusions

The macrocycle $[26]py_2N_4$ has been used as a receptor, in its tetraprotonated form or as a dicopper complex, for the recognition of dicarboxylate anions. Our solution studies revealed that the tetraprotonated form, $H_4[26]py_2N_4^{4+}$, is a weak receptor for the studied anions when compared with others,[25–30] although it is more selective for malonate. On the other hand, the dicopper complex of $[26]py_2N_4$ forms cascade complexes with oxalate and malonate with strong association constants,[31–34] the association with the bridging anion being stronger for oxalate. Additionally, the $[Cu_2([26]py_2N_4)(H_2O)_4]^{4+}$ complex can act as an optical sensor to detect and quantitatively measure oxalate spectrophotometrically by the red shift of the maximum of the visible band observed by addition of oxalate to an aqueous solution of the dinuclear copper complex. However the selectivity for oxalate is not sufficiently high for the selective detection of this anion in the presence of malonate.

Molecular mechanics and dynamics simulations were carried out in gas phase, ignoring the solvent effects. However, in spite of this limitation, our modelling studies support entirely the experimental results, showing that the cavity of $H_4[26]py_2N_4^{4+}$ is too large and too flexible for the selective binding of the studied anions. By contrast, in the $[Cu_2([26]py_2N_4)]^{4+}$ receptor the two copper centres define a well-shaped cavity suitable for the selective encapsulation of the small dicarboxylate anion, ox^{2-}. Larger dicarboxylate anions such as mal^{2-}, suc^{2-} and ma^{2-} also bridge the two copper centres, but they are located above the N_6 macrocyclic plane. Of course the receptor can interact with the oxygen donor atoms from the anions in a different way, leading to cascade complexes with R/S ratios other than 1:1. Other possible binding modes are: two bridging anions between the copper centres of the receptor or two anions axially coordinated to each copper centre. Alternatively, two $[Cu_2([26]py_2N_4)]^{4+}$ complexes are eventually linked by two anion bridges leading to the formation of dimeric or

 © 2005 Wiley-VCH Verlag GmbH & Co. KGaA, Weinheim

polymeric species. However the evaluation of all binding modes even by molecular mechanics calculations is a huge task and is beyond the aims of these preliminary modelling studies.

Experimental Section

Potentiometric Measurements

Reagents and Solutions: All the chemicals were of reagent grade and used as supplied without further purification. The receptor $[26]py_2N_4$ and its tetraprotonated salt, $H_4[26]py_2N_4{\cdot}4Cl$, were prepared and characterised as reported.[9] Dicarboxylate anion solutions were prepared at about 5.00×10^{-2} mol·dm^{-3} to 2.00×10^{-3} mol·dm^{-3} from the corresponding dicarboxylic acids (analytical grade purchased to Merck) and the concentrations were checked by titration with standard 0.100 mol·dm^{-3} KOH solutions, except for fumarate, for which the disodium salt from Aldrich was used. Solutions of $Cu(NO_3)_2$ were prepared at about 0.025 mol·dm^{-3} (analytical grade) and the exact concentration checked by titration with K_2H_2edta following standard methods.[35] All the solutions were prepared using demineralised water (obtained by a Millipore/Milli-Q system). Carbonate-free solutions of the KOH titrant were obtained and maintained as described,[9] and they were discarded when the percentage of carbonate was about 0.5% of the total amount of base.

Equipment and Work Conditions: The equipment used has been described previously.[9] The temperature was kept at 298.0 ± 0.1 K; atmospheric CO_2 was excluded from the cell during the titration by passing purified nitrogen across the top of the solution in the reaction cell. The ionic strength was kept at 0.10 mol·dm^{-3} with KCl.

Measurements: The $[H^+]$ of the solutions was determined by the measurement of the electromotive force of the cell, $E = E'° + Q{\cdot}\log[H^+] + E_j$. $E'°$, Q, E_j and $K_w = ([H^+][OH])$ were obtained as described previously.[9] The term pH is defined as $-\log[H^+]$. The value of K_w was found to be equal to $10^{-13.80}$ mol^2·dm^{-6}.

The potentiometric equilibrium measurements were carried out using 25.00 cm^3 of about 2.00×10^{-3} mol·dm^{-3} $[26]py_2N_4$ solutions diluted to a final volume of 30.00 cm^3, in the absence of dicarboxylate anions and of copper(II) salt, then in the presence of each anion at 1:1 and 2:1 C_L/C_A ratios, and finally in the simultaneous presence of copper(II) and each anion at 2:1:1 and 2:1:2 $C_{Cu}/C_L/C_A$ stoichiometries. A minimum of two replicate measurements were performed. All the anions were also independently titrated alone and in the presence of copper(II) ion in the conditions described above, at 1:1 and 1:2 C_{Cu}/C_A ratios.

Calculation of Equilibrium Constants: Overall protonation constants, β_i^H, were calculated by fitting the potentiometric data obtained for all the performed titrations with the HYPERQUAD programme.[10] The protonation constants of $[26]py_2N_4$ and its stability constants with the Cu^{2+} ion had been determined before in 0.10 mol·dm^{-3} KNO_3[9] and redetermined in the present work in 0.10 mol·dm^{-3} KCl. The protonation constants of the dicarboxylic acids (oxalic, malonic, succinic, fumaric and maleic acids) and their stability constants with Cu^{2+} ion were also determined from the experimental data in the same experimental conditions, also using the HYPERQUAD programme. All these constants were taken as fixed values to obtain the equilibrium constants of the new species from the experimental data corresponding to all the titrations in different Cu/L/A or L/A stoichiometries, also using the HYPERQUAD programme. The initial computations were obtained in the form of overall stability constants, $\beta_{Cu_mH_hL_lA_a}$ or $\beta_{H_hL_lA_a}$ values, $\beta_{Cu_mH_hL_lA_a} = [Cu_mH_hL_lA_a]/([Cu]^m\times[H]^h\times[L]^l\times[A]^a)$ or $\beta_{H_hL_lA_a} = [H_hL_lA_a]/([H]^h\times[L]^l\times[A]^a)$. Cascade mononuclear species CuLA, CuH_iLA (i = 1–4), $CuLH_{-1}A$, $CuLA_2$, CuH_iLA_2 (i = 1–4), and also dinuclear species Cu_2LA, Cu_2H_iLA (i = 1–2), $Cu_2LH_{-1}A$, Cu_2LA_2, Cu_2HLA_2 and $Cu_2LH_{-1}A_2$ were found [$\beta_{CuLH_{-1}A} = \beta_{CuL(OH)A}\times K_w$, $\beta_{Cu_2LH_{-1}A} = \beta_{Cu_2L(OH)A}\times K_w$ and $\beta_{Cu_2LH_{-1}A_2} = \beta_{Cu_2L(OH)A_2}\times K_w$]. The species considered in a particular model were those that could be justified by the principles of coordination and supramolecular chemistry. The errors quoted are the standard deviations of the overall stability constants given directly by the programme for the input data, which include all the experimental points of all titration curves.

The stability constants for the cascade species between Cu^{2+}, $[26]py_2N_4$ and the different anions were determined from a minimum of 192 (for ox^{2-}) to 253 (for suc^{2-}) experimental points, while the association constants for the equilibrium between each anion and protonated $[26]py_2N_4$ were determined from a minimum of 135 (for fu^{2-}) to 175 (for suc^{2-}) experimental points and a minimum of two titration curves.

UV/Vis and EPR Spectrophotometric Measurements

Electronic spectra were recorded with a UNICAM model UV-4 spectrophotometer for UV/Vis, using aqueous solutions of the complexes prepared by the addition of different dicarboxylate anions (in the form of sodium or potassium salts) to the dicopper complex of $[26]py_2N_4$ at the appropriate pH value. All the solutions were prepared in the range 1.0×10^{-4} to 5×10^{-4} mol·dm^{-3}. EPR spectroscopic measurements of the $[Cu_2([26]py_2N_4)(H_2O)_4]^{4+}$ and of its cascade complexes with the different anions were recorded with a Bruker ESP 380 spectrometer equipped with continuous-flow cryostat for liquid helium, operating at X-band. The solutions were prepared at 2.0×10^{-3} mol·dm^{-3} in water/DMSO (1:1), at 6.4–11.4 K.

Molecular Modelling

The MM and MD calculations were carried out using the Universal Force Field[22] within the Cerius2[23] package software. The atomic charges were calculated with the Qeq equilibration method implemented within Cerius2. The conformational analyses of $H_4[26]py_2N_4^{4+}$ and $[Cu_2([26]py_2N_4)]^{4+}$ complexes, as well as the docking of these receptors to the anions, were undertaken thorough the quenched dynamics at 3000 K. The dynamic behaviour of the host–guest complexes was investigated by MD simulations at 300 K.

The molecular modelling studies started with conformational analysis on the $H_4[26]py_2N_4^{4+}$ receptor. The starting model was obtained from the manipulation of the X-ray atomic coordinates of a related compound. The structure was subsequently minimised and the charges recalculated, then this process was repeated successively until the steric energy remained constant. Finally, the minimised structure was heated at 3000 K over 2 ns and the snapshots were saved every 0.2 ps leading to a total of 10000 conformations, which were concomitantly minimised by MM. Subsequently the lowest energy conformation found for $H_4[26]py_2N_4^{4+}$ was docked with the anions ox^{2-}, mal^{2-}, suc^{2-} and ma^{2-} by a quench dynamics run of 500 ps. The structures of the anions were also previously minimised by MM and their charges were calculated by the Qeq equilibration method with the total charge adjusted to –2. The dynamic behaviour of each of the lowest energy arrangements found for the inclusion compounds was subsequently evaluated by MD at room temperature over 1 ns.

The starting models of $[Cu_2([26]py_2N_4)]^{4+}$ in five different conformations were obtained from manipulation of the atomic coordi-

 © 2005 Wiley-VCH Verlag GmbH & Co. KGaA, Weinheim

nates retrieved from the X-ray structure of a related compound. Charges of +2 were given to the two Cu^{2+} ions and the charges on the atoms of the macrocycle were calculated independently of the metal centres by the Qeq equilibration method assuming a neutral ligand. The structures were subsequently minimised and the charges recalculated, then this process was repeated successively until the steric energy remained constant. The Cu–N bonds were retained in the calculation, being described through a theta harmonic function with ideal distances of 2.00 and 1.93 Å for Cu–Nsp^3 and Cu–Nsp^2 bonds respectively. The bending N–Cu–N angles were restrained to the ideal angles of 90 and 180° using a cosine harmonic function. Then all minimised structures were subjected to a quenching dynamics runs of 100 ps.

The study of host–guest interactions with $[Cu_2([26]py_2N_4)]^{4+}$ receptor also started with docking of its lowest + + + + conformation found on conformational analyses and the bridging anions (ox^{2-}, mal^{2-}, suc^{2-} and ma^{2-}) positioned above the macrocyclic cavity and on the same side of the N–H groups. No bonds between the donor atoms of the bridging ligands and the copper centres were considered and therefore the host–guest bonding interactions were purely electrostatic. Each starting model was subject to a MD quenching simulation of 100 ps. The dynamic behaviour of the lowest energy structures found for each cascade complex was subsequently investigated by MD simulations over 1 ns. All simulations were carried out using a constant NVE thermostat with default parameters and a time step of 1.0 fs. The events were saved at intervals of 0.1 ps, except on the conformational analysis of $[Cu_2([26]py_2N_4)]^{4+}$ where the frames were saved every 0.2 ps as stated above.

Acknowledgments

The authors acknowledge the financial support from Fundação para a Ciência e a Tecnologia (FCT) and POCTI, with co-participation of the European Community fund FEDER (Projects n. POCTI/1999/QUI/35396 and POCTI/QUI/49114/2002). The authors also acknowledge R. Mortágua and M. Pereira for assistance in the computer modelling studies and EPR experiments, respectively. F.L. also acknowledges FCT for a grant (SFRH/BD/9113/2002).

[1] C. A. Ilioudis, J. W. Steed, *J. Supramol. Chem.* **2001**, *1*, 165–187.
[2] R. J. Fitzmaurice, G. M. Kyne, D. Douheret, J. D. Kilburn, *J. Chem. Soc., Perkin Trans. 1* **2002**, 841–864.
[3] R. Martínez-Máñez, F. Sancenón, *Chem. Rev.* **2003**, *103*, 4419–4476.
[4] J. M. Llinares, D. Powell, K. Bowman-James, *Coord. Chem. Rev.* **2003**, *240*, 57–75.
[5] P. A. Gale, *Coord. Chem. Rev.* **2003**, *240*, 191–221.
[6] J. L. Sessler, P. I. Sansom, A. Andrievsky, V. Kral in *Supramolecular Chemistry of Anions* (Eds.: A. Bianchi, K. Bowman-James, E. García-España), Wiley-VCH, **1997**, pp. 355–419.
[7] V. Amendola, L. Fabbrizzi, C. Mangano, P. Pallavicini, A. Poggi, A. Taglietti, *Coord. Chem. Rev.* **2001**, *219–221*, 821–837.
[8] L. Fabbrizzi, M. Licchelli, G. Rabaioli, A. Taglietti, *Coord. Chem. Rev.* **2000**, *205*, 85–108.
[9] F. Li, R. Delgado, J. Costa, M. G. B. Drew, V. Félix, *Dalton Trans.* **2005**, 82–91.
[10] P. Gans, A. Sabatini, A. Vacca, *Talanta* **1996**, *43*, 1739–1753.
[11] L. D. Pettit, H. K. J. Powell, *IUPAC Stability Constants Database*, Academic Software, Timble, **2003**.
[12] L. Alderighi, P. Gans, A. Ienco, D. Peters, A. Sabatini, A. Vacca, *Coord. Chem. Rev.* **1999**, *184*, 311–318.
[13] L. Branco, J. Costa, R. Delgado, M. G. B. Drew, V. Félix, B. J. Goodfellow, *J. Chem. Soc., Dalton Trans.* **2002**, 3539–3550.
[14] T. G. Fawcett, E. E. Bernarducci, K. Krogh-Jespersen, H. J. Schugar, *J. Am. Chem. Soc.* **1980**, *102*, 2598–2604.
[15] K. A. Meadows, F. Liu, J. Sou, B. P. Hudson, D. R. McMillin, *Inorg. Chem.* **1993**, *32*, 2919–2923.
[16] J. Liu, T.-B. Lu, H. Li, Q.-L. Zhang, L.-N. Ji, T.-X. Zhang, L.-H. Qu, H. Zhou, *Transition Met. Chem.* **2002**, *27*, 686–690.
[17] T. Lu, X. Zhuang, Y. Li, S. Chen, *J. Am. Chem. Soc.* **2004**, *126*, 4760–4761.
[18] T. D. Smith, J. R. Pilbrow, *Coord. Chem. Rev.* **1974**, *13*, 173–278.
[19] D. M. Duggan, D. N. Hendrickson, *Inorg. Chem.* **1974**, *13*, 2929–2940.
[20] C.-L. O'Young, J. C. Dewan, H. R. Lilienthal, S. J. Lippard, *J. Am. Chem. Soc.* **1978**, *100*, 7291–7300.
[21] S. Carvalho, C. Cruz, R. Delgado, M. G. B. Drew, V. Félix, *Dalton Trans.* **2003**, 4261–4270.
[22] A. K. Rappe, C. J. Casewit, K. S. Colwell, W. A. Goddard III, W. M. Skiff, *J. Am. Chem. Soc.* **1992**, *114*, 10024–10035.
[23] *CERIUS2*, version 4.2, Molecular Simulations Inc, San Diego, **2000**.
[24] S. E. Matthews, P. Schmitt, V. Félix, M. G. B. Drew, P. D. Beer, *J. Am. Chem. Soc.* **2002**, *124*, 1341–1355.
[25] B. Dietrich, M. W. Hosseini, J. M. Lehn, R. B. Sessions, *J. Am. Chem. Soc.* **1981**, *103*, 1282–1283.
[26] M. W. Hosseini, J. M. Lehn, *J. Am. Chem. Soc.* **1982**, *104*, 3525–3527.
[27] M. W. Hosseini, J. M. Lehn, *Helv. Chim. Acta* **1986**, *69*, 587–603.
[28] R. J. Motekaitis, A. Martell, *Inorg. Chem.* **1992**, *31*, 5534–5542.
[29] Q. Lu, R. J. Motekaitis, J. Reibenspies, A. Martell, *Inorg. Chem.* **1995**, *34*, 4958–4968.
[30] C. Anda, A. Llobet, A. Martell, J. Reibenspies, E. Berni, X. Solans, *Inorg. Chem.* **2004**, *43*, 2793–2802.
[31] J. B. English, A. E. Martell, R. J. Motekaitis, I. Murase, *Inorg. Chim. Acta* **1997**, *258*, 183–192.
[32] T. F. Pauwels, W. Lippens, G. G. Herman, A. M. Goeminne, *Polyhedron* **1998**, *17*, 1715–1723.
[33] T. F. Pauwels, W. Lippens, P. W. Smet, G. G. Herman, A. M. Goeminne, *Polyhedron* **1999**, *18*, 1029–1037.
[34] G. T. S. Martins, B. Szpoganicz, V. Tomisic, N. Humbert, M. Elhabiri, A.-M. Albrecht-Gary, L. F. Sala, *Inorg. Chim. Acta* **2004**, *357*, 2261–2268.
[35] G. Shwardzenbach, W. Flaschka, *Complexometric Titrations*, Methuen & Co, London, **1969**.

Received: December 29, 2004
Published Online: October 5, 2005

 © 2005 Wiley-VCH Verlag GmbH & Co. KGaA, Weinheim

Trinuclear Cu^{II} Complexes Containing Peripheral Ketonic Oxygen Bridges and a μ_3-OH Core: Syntheses, Crystal Structures, Spectroscopic and Magnetic Properties

Mau Sinha Ray,[a] Shouvik Chattopadhyay,[a] Michael G. B. Drew,[b] Albert Figuerola,[c] Joan Ribas,[c] Carmen Diaz,*[c] and Ashutosh Ghosh*[a]

Keywords: Copper trimers / Schiff bases / X-ray structures / Magnetic properties

Four new trinuclear copper(II) complexes, $[(CuL^1)_3(\mu_3\text{-}OH)](ClO_4)_2\cdot H_2O$ (**1**), $[(CuL^2)_3(\mu_3\text{-}OH)](ClO_4)_2$ (**2**), $[(CuL^3)_3(\mu_3\text{-}OH)](ClO_4)_2\cdot H_2O$ (**3**), and $[(CuL^4)_3(\mu_3\text{-}OH)](ClO_4)_2\cdot H_2O$ (**4**), where HL^1 = 8-amino-4,7,7-trimethyl-5-azaoct-3-en-2-one, HL^2 = 7-amino-4-methyl-5-azaoct-3-en-2-one, HL^3 = 7-(ethylamino)-4-methyl-5-azahept-3-en-2-one, and HL^4 = 4-methyl-7-(methylamino)-5-azahept-3-en-2-one, have been derived from the four tridentate Schiff bases (HL^1, HL^2, HL^3, and HL^4) and structurally characterized by X-ray crystallography. For all compounds, the cationic part is trinuclear with a Cu_3OH core held by three carbonyl oxygen bridges between each pair of copper(II) atoms. The copper atoms are five-coordinate with a distorted square-pyramidal geometry; the equatorial plane consists of the bridging oxygen atom of the central OH group together with three atoms (N, N, O) from one ligand whereas an oxygen atom of a second ligand occupies the axial position. Magnetic measurements have been performed in the 2–300 K temperature range. The experimental data could be satisfactorily reproduced by using an isotropic exchange model, $H = -J(S_1S_2+S_2S_3+S_1S_3)$ yielding as best-fit parameters: J = –66.7 and g = 2.19 for **1**, J = –36.6 and g = 2.20 for **2**, J = –24.5 and g = 2.20 for **3**, and J = –14.9 and g = 2.05 for **4**. EPR spectra at low temperature show the existence of spin frustration in complexes **3** and **4**, but it has not been possible to carry out calculations of the antisymmetric exchange parameter, G, from magnetic data. In frozen methanolic solution, at 4 K, hyperfine splitting in all complexes and spin frustration in complex **4** seem to be confirmed.

(© Wiley-VCH Verlag GmbH & Co. KGaA, 69451 Weinheim, Germany, 2005)

Introduction

Cyclic trinuclear metal complexes[1] are of interest because these systems can be regarded as geometrically spin-frustrated and offer the opportunity to test magnetic exchange models.[2] In fact, geometrically frustrated antiferromagnetic compounds have attracted much attention over the past few years because of their propensity to adopt unusual, even exotic magnetic ground states, which remain poorly understood.[3]

μ-Hydroxo or μ-oxo ions have generally been observed as central bridging ligands in cyclic trinuclear compounds. The existence of the M_3O core held by the peripheral bridging ligands is well documented in the chemistry of iron(II/III) and chromium(III).[4] There are only a few reports with a $Cu_3O(H)$ core of which the majority contain oxime-oximate-,[5] *N*,*N*-pyrazole-[6], or *N*,*N*-triazole[7]-type peripheral ligands. Examples of cyclic trinuclear complexes with ketonic oxygen bridges are, however, very rare. To the best of our knowledge, in the literature only three such complexes containing Schiff-base ligands, for example, 7-amino-4-methyl-5-azahept-3-en-2-one (AMAH),[8] 8-amino-4-methyl-5-azaoct-3-en-2-one (AMAO),[9] and 7-(dimethylamino)-4-methyl-5-azahept-3-en-2-one (AE)[10] are known. The first complex having an AMAH ligand was isolated accidentally during the preparation of the ternary complex, having pyridine as the other ligand. All three complexes were synthesized conveniently by adding triethylamine to the respective reaction mixtures. In order to investigate if the existence of these complexes is an exception or the formation of such trinuclear Cu^{II} complexes is a general phenomenon for this type of ligand, we synthesized four very similar tridentate N,N,O donor Schiff-base ligands derived from C- or N-substituted diamines and 2,4-pentanedione (Scheme 1, HL^1–HL^4) to obtain the desired complexes. Another objective of the synthesis of these compounds is to study their magnetic properties, especially the existence of spin frustration, which has not been detected in the other three reported complexes.[8–10] This paper re-

[a] Department of Chemistry, University College of Science, University of Calcutta,
92 A. P. C. Road, Kolkata 700009, India
E-mail: ghosh_59@yahoo.com
[b] School of Chemistry, The University of Reading,
P. O. Box 224, Whiteknights, Reading RG6 6AD, UK
[c] Departament de Química Inorgànica, Universitat de Barcelona,
Marti i Franques 1–11, 08028 Barcelona, Spain
E-mail: carme.diaz@qi.ub.es

Supporting information for this article is available on the WWW under http://www.eurjic.org or from the author.

ports the synthesis, crystal structure, and magnetic properties of the four cyclic trinuclear compounds. The structural and magnetic properties of the complexes will be compared with the data of the other three similar compounds reported in the literature.

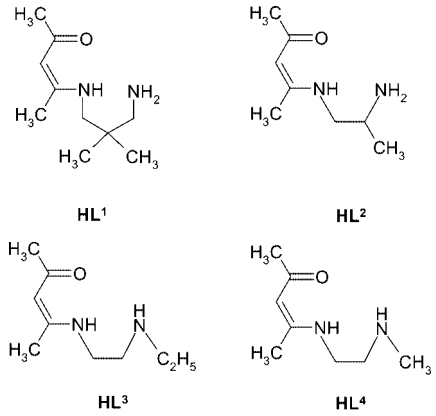

Scheme 1.

Results and Discussion

The four tridentate ligands HL^1, HL^2, HL^3, and HL^4, on treatment with a methanol solution of copper perchlorate hexahydrate and triethylamine in a 2:2:3 ratio, yielded the trinuclear complexes **1**–**4**, respectively (Scheme 2). Complexes **2** and **3** were obtained readily on mixing the constituents; no hydrolysis of the product occurred during synthesis. On the other hand, ligands HL^1 and HL^4 are rather susceptible to hydrolysis and for higher yields of **1** and **4** dry methanol was used as the reaction medium. All the complexes, however, can easily be purified by recrystallization from methanol. The formation and stability of these self-assembled cyclic trinuclear complexes may be visualized in the following way:

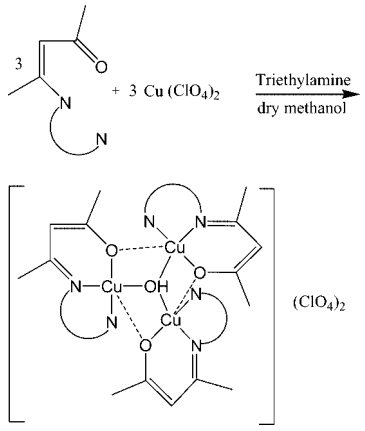

Scheme 2.

The chelating tridentate ligand coordinates to the Cu^{II} centers as usual to occupy the three coordination sites. In a slightly alkaline medium, the hydroxy ion, which is well known for its bridging ability, can be coordinated to the fourth coordination site to bridge two metal centers. However, coordination of the hydroxy ion to the three metal centers is not very common, as steric crowding may destabilize the resulting tetrahedral arrangement until and unless it gains some additional stability by other means. In the present systems, the three mononuclear units are assembled around the hydroxy ion in such a way that the ketonic oxygen atom of one unit is coordinated to the apical position of the Cu^{II} ion of the neighboring unit to result in a cyclic peripheral bridging that provides the required stability for the trinuclear structure (Scheme 2). As a requirement of the basal–apical bridging, the mononuclear units need to be perpendicular to each other which, fortuitously, seems to be the preferred arrangement to minimize steric contacts.

Description of the Structure of Complexes 1–4

The crystal structures of all four compounds (**1**–**4**) are built up from discrete trinuclear cations $[Cu_3L_3(\mu_3\text{-}OH)]^{2+}$ and noncoordinated perchlorate anions in a ratio of two anions per cation. In each of the complexes **1**, **3**, and **4** there is, in addition, one lattice water molecule. The trinuclear structure of **2** is shown in Figure 1 together with the common numbering scheme [complexes **1**, **3**, and **4** have very similar molecular structures, see Figures S1, S2, and S3, respectively in the Supporting Information (see also the footnote on the first page of this article)]. Selected bond lengths and bond angles are summarized in Tables 1 and 2, respectively.

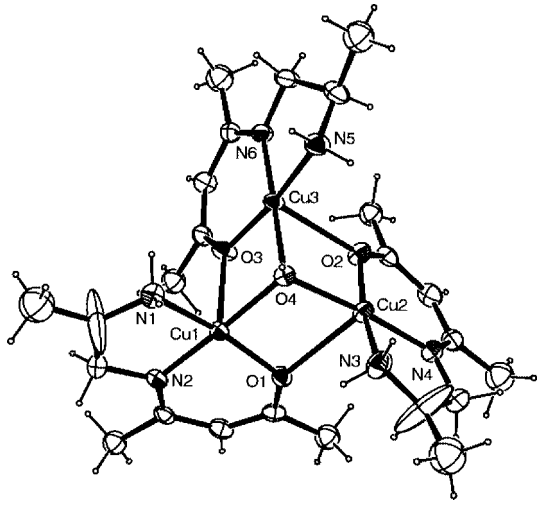

Figure 1. ORTEP-3 view of the $[(CuL^2)_3(OH)]^{2+}$ cation of complex **2** (30% thermal ellipsoids) including the atom numbering scheme.

The trinuclear cationic part is comprised of three CuL subunits in which each copper(II) ion is coordinated to a deprotonated tridentate monoanionic ligand L. The subunits are held together by two distinct bridging systems: (i) the oxygen atom (O4) of a single, triply bridging hydroxo group, which is coordinated to each of the three copper centers, and (ii) the three bridging carbonyl oxygen atoms, each of them from a different ligand molecule. The resulting trinuclear species do not contain any threefold symmetry

 © 2005 Wiley-VCH Verlag GmbH & Co. KGaA, Weinheim

Table 1. Selected bond lengths [Å] of complexes **1**–**4**.

	1	2	3	4
Cu1–O1	1.918(6)	1.914(5)	1.911(6)	1.912(8)
Cu1–O3	2.475(6)	2.375(6)	2.370(7)	2.318(9)
Cu1–O4	2.058(5)	2.020(5)	2.032(7)	2.016(6)
Cu1–N1	1.999(8)	1.996(6)	2.029(8)	2.054(14)
Cu1–N2	1.947(8)	1.932(6)	1.939(10)	1.970(10)
Cu2–O1	2.508(8)	2.496(5)	2.306(7)	2.359(7)
Cu2–O2	1.916(5)	1.902(6)	1.916(6)	1.915(8)
Cu2–O4	2.033(5)	2.001(5)	2.018(6)	2.024(7)
Cu2–N3	2.029(7)	1.985(8)	2.025(8)	1.985(11)
Cu2–N4	1.984(6)	1.931(6)	1.917(8)	1.921(11)
Cu3–O2	2.418(7)	2.406(5)	2.326(6)	2.290(8)
Cu3–O3	1.953(6)	1.912(5)	1.907(8)	1.909(9)
Cu3–O4	2.014(5)	2.025(5)	2.003(5)	2.033(7)
Cu3–N5	2.023(8)	1.993(6)	2.026(9)	2.038(10)
Cu3–N6	1.980(7)	1.944(7)	1.936(8)	1.932(11)
Cu1–Cu2	3.329(3)	3.238(2)	3.172(4)	3.182(3)
Cu2–Cu3	3.241(4)	3.211(4)	3.165(3)	3.164(4)
Cu1–Cu3	3.303(3)	3.165(3)	3.205(3)	3.173(3)

Table 2. Selected bond angles [°] for complexes **1**–**4**.

	1	2	3	4
O1–Cu1–O3	95.1(2)	97.2(2)	94.9(2)	95.6(3)
O1–Cu1–O4	82.9(2)	86.4(2)	83.6(3)	85.6(3)
O1–Cu1–N1	165.6(3)	166.1(2)	168.6(3)	168.6(5)
O1–Cu1–N2	94.3(3)	94.5(2)	93.4(3)	91.8(4)
O3–Cu1–O4	71.1(2)	74.6(2)	73.4(2)	74.8(3)
O3–Cu1–N1	91.5(3)	96.4(2)	96.4(3)	95.5(5)
O3–Cu1–N2	107.5(3)	102.7(2)	108.7(3)	111.2(4)
O4–Cu1–N1	87.1(2)	94.3(2)	98.6(3)	94.9(4)
O4–Cu1–N2	176.7(3)	177.2(2)	176.6(3)	173.8(4)
N1–Cu1–N2	95.9(3)	85.5(2)	84.0(4)	86.5(5)
O1–Cu2–O2	92.9(2)	97.7(2)	90.9(3)	97.3(3)
O1–Cu2–O4	70.0(2)	72.7(2)	74.6(2)	74.6(2)
O1–Cu2–N3	85.4(2)	93.3(2)	96.3(3)	94.4(3)
O1–Cu2–N4	112.4(2)	101.3(2)	110.4(3)	108.0(4)
O2–Cu2–O4	83.4(2)	85.1(2)	84.4(2)	84.4(2)
O2–Cu2–N3	172.1(3)	168.8(3)	172.6(3)	168.1(4)
O2–Cu2–N4	94.7(2)	94.7(2)	93.6(3)	93.1(4)
O4–Cu2–N3	88.8(2)	96.6(2)	96.0(2)	96.8(4)
O4–Cu2–N4	177.1(2)	173.9(2)	174.7(3)	176.7(4)
N3–Cu2–N4	93.0(3)	84.7(3)	85.4(3)	85.2(4)
O2–Cu3–O3	96.9(2)	91.1(2)	98.2(2)	91.8(3)
O2–Cu3–O4	72.1(2)	72.6(2)	74.9(2)	75.3(3)
O2–Cu3–N5	108.6(2)	96.9(2)	93.8(3)	94.2(3)
O2–Cu3–N6	100.2(3)	109.5(2)	104.9(3)	113.0(3)
O3–Cu3–O4	84.1(2)	85.6(2)	85.0(3)	84.1(3)
O3–Cu3–N5	149.3(3)	171.7(2)	167.8(3)	173.4(4)
O3–Cu3–N6	94.9(3)	94.8(2)	93.2(4)	94.3(4)
O4–Cu3–N5	87.6(3)	94.8(3)	96.0(3)	94.8(4)
O4–Cu3–N6	172.0(3)	177.9(2)	178.1(4)	171.6(3)
N5–Cu3–N6	97.1(3)	84.5(3)	85.9(4)	85.8(5)
Cu1–O4–Cu2	108.9(2)	107.3(2)	103.1(3)	103.9(3)
Cu1–O4–Cu3	108.4(2)	102.9(2)	105.2(3)	103.2(3)
Cu2–O4–Cu3	106.4(2)	105.8(2)	103.8(2)	102.5(3)

axis. In all four compounds no specific chirality for the propeller arrangements around the hydroxide ion is found. The three copper(II) ions and the bridging hydroxo group form a flattened trigonal pyramid, with the copper atoms falling at the corners of approximately equilateral sides and angles: 3.329(4), 3.241(4), 3.303(3) Å and 60.3(1), 61.2(1), 58.5(1)° for complex **1**; 3.238(2), 3.211(4), 3.165(3) Å and 58.8(1), 61.0(1), 60.2(1)° for complex **2**; 3.172(4), 3.165(3), 3.205(3) Å and 60.8(4), 59.7(4), 59.5(4)° for complex **3**; and 3.182(3), 3.164(4), 3.173(3) Å and 60.0(5), 60.3(5), 59.7(5)° for complex **4**. The face-capping oxygen atom (O4) is located at 0.728(5), 0.797(4), 0.836(6), and 0.861(6) Å above the plane defined by the Cu_3 triangle for complexes **1**–**4**, respectively. The presence of Cu_3OH is confirmed by (a) the location of the hydrogen atom at the expected position in the final difference Fourier map, (b) the electroneutrality of the crystal, and (c) the refined Cu–O(H) distances and Cu–O(H)–Cu′ angles, which, on the basis of the trends observed in similar structures,[6c,7b,8–10] agree well with a roughly tetrahedral or pseudotetrahedral sphere of Cu, Cu, Cu, H ligands around the oxygen atom.

As for the copper environment, in all four structures the three copper atoms of the trinuclear entity are five-coordinate, with a (4+1) square-pyramidal (NNOO and O) geometry. The four coordinating atoms making up the basal plane are the carbonyl oxygen atom, one imine nitrogen atom, and one amino nitrogen atom from the tridentate Schiff-base ligand (L), and the hydroxo group OH^-, while the apical site is occupied by one oxygen atom of another tridentate Schiff-base ligand, which, in turn, is basal to a second copper atom. As expected, the axial Cu–O bond is much longer than the equatorial one. It may be emphasized that the oxygen atom involved in this basal–apical bridge pertains to a carbonyl function, which is generally considered as a nonbridging group. Within each mononuclear unit the copper atom does not lie in the basal plane. As usual, each copper ion is displaced from the least-squares plane through the basal atoms towards the apical oxygen atom by 0.071(1), 0.085(1), 0.112(1), and 0.137(2) Å for Cu(1); 0.031(1), 0.023(1), 0.105(2), and 0.118(2) Å for Cu(2); and 0.159(1), 0.079(1), 0.099(1), and 0.130(2) Å for Cu(3) in complexes **1**–**4** respectively. The lengths of the bonds between the copper atoms and the donor sites (O, N, N) of the tridentate ligand are within the range of values normally found for such bonds.[8–11] They show only small variations in going from one unit to the other. The six-membered chelate ring formed by the acetylacetone moiety is essentially planar and the interatomic distances and angles of the ring are roughly identical in the three mononuclear units of **2** and **3**. However, in **1** and **4** the same rings deviate considerably from planarity and the deviation is different in the three subunits. The highest deviation is observed in the subunit with Cu1 for both **1** and **4** in which the six-membered ring assumes almost a boat and twist-boat conformation, respectively, with puckering parameters φ = 195(2) and 199(4)°, θ = 124.0(17) and 120.7(33)° and Q = 0.269(6) and 0.206(9) Å.[12] The trimethylene fragment in complex **1** and dimethylene fragments in the other three complexes from the starting diamines constitute the other chelate ring in the complexes. In all three subunits these six-membered chelate rings of complex **1** and five-membered chelate rings of complex **2** assume half-boat and envelope conformations, respectively. However, considerable differences have been found in the bond angles of the chelate rings among the subunits in both the complexes (7.0° for **1** and 11.7° for **2**).

 © 2005 Wiley-VCH Verlag GmbH & Co. KGaA, Weinheim

Table 3. Selected structural parameters for complexes **1**–**4** and three reported complexes **A**, **B**, and **C** related to their magnetic properties.

	1	**2**	**3**	**4**	**A**	**B**	**C**
Cu(1)–O(H)–Cu(2) [°]	108.9(3)	107.3(2)	103.1(3)	103.9(3)	104.8(1)	105.4(2)	102.9(1)
Cu(1)–O(H)–Cu(3) [°]	108.4(2)	102.9(2)	105.2(3)	103.2(3)	104.9(1)	106.5(2)	102.9(1)
Cu(2)–O(H)–Cu(3) [°]	106.4(2)	105.8(2)	103.8(2)	102.5(3)	105.5(1)	108.3(2)	102.9(1)
Cu–O(H)–Cu′ [°] (av)	107.9	105.3	104.0	103.2	105.1(1)	106.7(2)	102.9
O(H)···Cu3 plane [Å][a]	0.728(5)	0.797(4)	0.836(6)	0.861(6)	0.804(2)	0.796(5)	0.881(6)
Cu/Cu′ [°] (av)[b]	89.7	85.8	94.6	92.5	82.9(1)	83.7(3)	92.3
τ	0.19, 0.08, 0.39	0.19, 0.08, 0.10	0.13, 0.04, 0.17	0.09, 0.14, 0.03	0.01, 0.11, 0.09	0.26, 0.09, 0.20	0.04, 0.05, 0.03
$-J$ [cm^{-1}][c]	–66	–36	–24	–15	–24	–30	–2.4
Ref.	this work	this work	this work	this work	[8]	[9]	[10]

[a] Deviation of the oxygen atom of the triply bridging hydroxy group above the plane of the three copper atoms. [b] Coplanarity between the least-squares planes defined by [O(H), N, N, O]; average value calculated from the Cu1/Cu2, Cu1/Cu3, Cu2/Cu3 dihedral angles. [c] The J values from the literature have been modified according to the Hamiltonian used in this paper.

Conformational analysis shows different conformations for the five-membered chelate rings in complexes **3** and **4**. In complex **3**, the ring with Cu2 is in envelope conformation on C12, whereas the rings with Cu1 and Cu3 have half-chair conformation twisted on N1···C3 and N5···C21, respectively. But for complex **4**, both the five-membered chelate rings with Cu1 and Cu2 assume half-chair conformation twisted on N1···C3 and N3···C12, respectively, whereas the ring with Cu3 is in envelope conformation on C21. However, among the subunits in each complex a considerable difference in the bond angles of the chelate rings has been found in complex **4** only (14.1°), whereas in complex **3** the difference is negligible (2.5°).

The distortions of the coordination polyhedron from the square pyramid to the trigonal bipyramid have been calculated by the Addison parameter (τ)[13] as an index of the degree of trigonality. The value of τ is defined as the difference between the two largest donor–metal–donor angles divided by 60, a value that is 0 for the ideal square pyramid and 1 for the trigonal bipyramid. The τ values are 0.19, 0.19, 0.13, and 0.09 for Cu(1); 0.08, 0.08, 0.04, and 0.14 for Cu(2); and 0.39, 0.10, 0.17, and 0.03 for Cu(3) in complexes **1**–**4**, respectively. The values clearly indicate that in **1** the distortion towards a trigonal bipyramid is significantly different in the three mononuclear units and that in Cu(3) it is considerably high. The τ values of the other three reported complexes[8–10] are also shown in Table 3 for comparison.

The perchlorate anions in the complexes show some disorder. In **1**, one of the perchlorate ions is disordered such that the oxygen atoms are distributed over two sets of tetrahedral sites around the same chlorine atom, while the other shows the complete anion distributed over two separate sites. By contrast, the perchlorate ions in **2** and **3** are ordered. In **4** the oxygen atoms show very high thermal motion but no discernible disorder pattern could be refined successfully. In complex **3**, one perchlorate oxygen atom,

Table 4. Hydrogen bonding distances [Å] and angles [°] for complexes **1**–**4**.

Compound	D–H···A[a]	D–H	D···A	H···A	D–H···A
1	N1−H1a···Ow	0.90	3.223(13)	2.36	161
	N5–H5b···O5	0.90	3.132(11)	2.29	156
	N3–H3a···O8	0.90	3.331(15)	2.47	160
	N3–H3b···O10	0.90	2.92(2)	2.06	160
	O4–H4···Ow	0.98	2.848(10)	1.87	175
2	N1–H1a···O7	0.90	3.201(13)	2.31	168
	N1–H1b···O9	0.90	3.389(15)	2.59	148
	N1–H1b···O12	0.90	3.07(2)	2.22	158
	N5–H5a···O9	0.90	2.991(15)	2.30	133
	N3–H3b···O8	0.90	3.018(14)	2.34	132
	O4–H4···O5	0.90	2.972(11)	2.03	161
	N5–H5b···O6^{i}	0.90	3.354(12)	2.47	167
	N3–H3a···O5^{i}	0.90	3.302(11)	2.43	162
3	N1–H1···O5	0.90	3.319(13)	2.51	148
	N1–H1···O8	0.90	3.475(14)	2.70	143
	N3–H3···O12	0.90	3.43(3)	2.54	165
	N5–H5···O10	0.90	3.144(15)	2.24	170
	O4–H4···Ow	0.98	2.820(11)	1.86	166
4	N3–H3···O9	0.90	3.415(17)	2.61	147
	N3–H3···O10	0.90	3.263(16)	2.43	151
	N5–H5···O5	0.90	3.124(17)	2.38	139
	N5–H5···O6^{j}	0.90	3.683(30)	2.90	145
	O4–H4···Ow	0.98	2.762(13)	1.80	164

[a] Symmetry equivalent: i) $1-x, -y, 1-z$; j) $1-x, 1-y, 2-z$.

 © 2005 Wiley-VCH Verlag GmbH & Co. KGaA, Weinheim

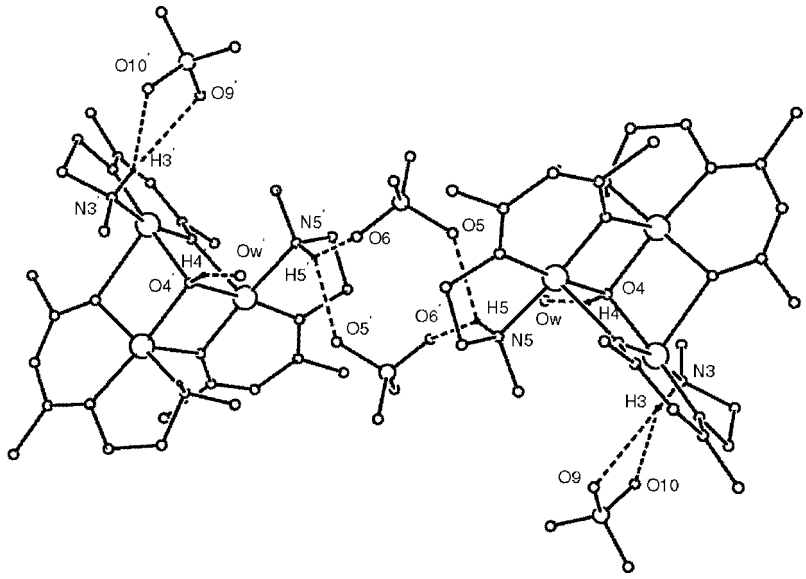

Figure 2. Illustration of the aggregation of the isolated trimeric unit by hydrogen-bonding interactions between the $[(CuL^4)_3(OH)]^{2+}$ cation and perchlorate anions in the solid state of complex **4**. Atoms marked with a prime are transformed by symmetry element $1 - x$, $1 - y$, $2 - z$.

O10, forms a weak association with the Cu2 ion at a distance of 2.961(13) Å, whereas all other Cu–O(perchlorate) distances are about 4 Å. The perchlorate ions play a significant role in the H-bonding network in all complexes.

In all four complexes hydrogen-bonding interactions are observed among the isolated trimeric units, the perchlorate anions, and the water of crystallization (Table 4). A detailed discussion of these interactions for complexes **1**–**3** along with diagrams is presented in the Supporting Information. H bonding of complex **4** is only discussed here as an example. In complex **4** two centrosymmetrically related trinuclear units are linked by an N–H···O hydrogen bond involving hydrogen atom H5(N5) and oxygen atom O6 of the two centrosymmetrically related perchlorate ions (Figure 2, Table 4). The hydrogen atom H5(N5), through which two trimers are linked, is also involved in another N–H···O contact with O5 of one of two perchlorate anions showing bifurcated hydrogen-bond formation. H3(N3) also forms strong bifurcated hydrogen bonds with two oxygen atoms, O9 and O10, of another perchlorate ion. One of the three hydrogen atoms, H1(N1), does not participate in hydrogen bonding. The water of crystallization (Ow) is stabilized, contributing to the hydrogen-bonding network, with H4 of the triply bridging hydroxo group by an O–H···O contact.

IR and Electronic Spectra

Compounds **1**, **3**, and **4** contain a noncoordinating water molecule, which makes the assignment of O–H stretching somewhat ambiguous. However, the well-defined bands at 3520, 3505, 3556, and 3550 cm^{-1} for complexes **1**–**4**, respectively, appear within the typical range for O–H stretching vibrations in monohydroxo-bridged copper complexes.[14] Therefore these bands can be attributed to ν(O–H) of the triply bridging hydroxo group. The additional broad but well-defined bands with the maximum at 3430 cm^{-1} for complex **1**, 3425, 3390 cm^{-1} for complex **3** and 3420, 3377 cm^{-1} for complex **4** are attributable to the presence of a noncoordinating water molecule with a strong hydrogen-bonding network (vide crystal structure). The remaining bands for the complexes above 3000 cm^{-1} may be assigned to ν(N–H) stretching vibrations. Concerning the ClO_4^- anions, the ν_3 mode at 1091, 1100, 1102, and 1097 cm^{-1} for **1**–**4**, respectively, is somewhat broadened, but the ν_4 band at 623, 620, 623, and 622 cm^{-1}, respectively, is devoid of any splitting and consistent with the IR-active normal modes for T_d symmetry, suggesting that these anions are not coordinated to the copper atoms as substantiated by the crystal structures.

The electronic spectra in the solid state and in methanol solution have been recorded for the four complexes. The observed ligand-field band is in agreement with the fact that the trinuclear structure is retained in methanol, as similar visible absorption bands are observed in the solid state and in methanol solution for all complexes. The reflectance electronic spectra of all four complexes display a single absorption band at 595, 593, 601, and 586 nm in the solid state and 612, 615, 587, and 595 nm in methanol. The positions of these bands are consistent with the observed square-based geometry around the copper centers.[15]

Magnetic Properties

Magnetic susceptibilities were determined for complexes **1**–**4** over the temperature range 2–300 K in an applied field of 0.1 T. The temperature dependence of $\chi_M T$ (χ_M being the magnetic susceptibility per Cu_3 entity) for complex **1** is shown in Figure 3 (complexes **2**, **3**, and **4** have very similar temperature dependences of $\chi_M T$: see Figures S7, S8, and S9, respectively, in the Supporting Information). At room

 © 2005 Wiley-VCH Verlag GmbH & Co. KGaA, Weinheim

temperature the $\chi_M T$ values for all four complexes are close to 1.2 $cm^3 mol^{-1} K$, as expected for the three independent Cu^{II} ions. As T is lowered, $\chi_M T$ decreases, reaching values close to 0.40 $cm^3 mol^{-1} K$ at 2 K. Complexes **1**–**3** show a plateau before reaching the final value, while **4** does not show this plateau. This value (0.4 $cm^3 mol^{-1} K$) is close to the spin-only value for a system with one unpaired electron with $g > 2.00$. This behavior indicates an antiferromagnetic interaction between the Cu^{II} ions, with an unpaired electron per Cu_3 unit in the ground state. The formation of this plateau ($S = 1/2$) is dependent upon the corresponding existence of noticeable intermolecular (intertrimer) exchange interactions. This situation has also been observed in other similar compounds.[8–10]

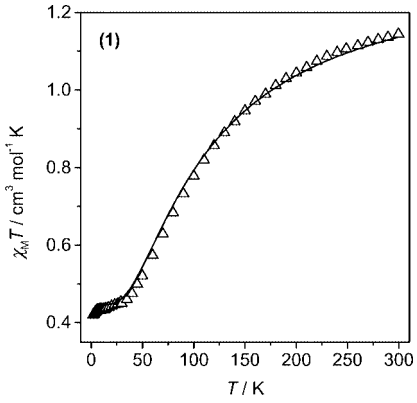

Figure 3. Plot of the $\chi_M T$ [$cm^3 mol^{-1} K$] vs T [K] in the range 2–300 K for **1**. The solid line is generated from the best-fit magnetic parameters.

The magnetic-exchange interaction in a triangular arrangement of three $S = 1/2$ ions results in three electronic states, that is, a quartet state ($S = 3/2$; $^4A_2$) and two doublet states ($S = 1/2$; ^2E) (Scheme 3). Within the simple model of an isotropic exchange interaction for an equilateral triangle, both of the doublet states have the same energy, which differs 3J from the energy of the quartet state. From the known structures of **1**–**4**, and considering that the three copper atoms of the $Cu_3O(H)$ unit are structurally almost equivalent, and so that $J_{12} = J_{13} = J_{23} = J$, the isotropic Heisenberg–Dirac–van Vleck (HDVV) Hamiltonian formalism [Equation (1)] was used to describe the interactions of the spins.

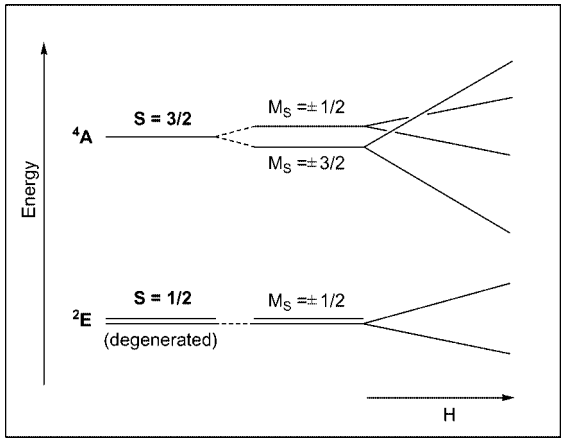

Scheme 3.

$$H_{HDVV} = -J_{12}S_1S_2 - J_{13}S_1S_3 - J_{23}S_2S_3 \quad (1)$$

From this Hamiltonian, a solution of the magnetic susceptibility may be derived as follows [Equation (2)]:[7a,7b,16]

$$\chi_M = (N\beta^2 g^2/4kT)[1 + 5\exp(3J/2kT)]/[1 + \exp(3J/2kT)] \quad (2)$$

where N, g, β, k, and T have their usual meanings. Because of the above-mentioned experimental variation of $\chi_M T$ at low temperatures, the inclusion of an additional Weiss-like parameter θ [so that T is replaced by $T - \theta$ in Equation (2)], which would account for possible, low-temperature, intertrimer magnetic interaction mainly due to the hydrogen bonds among trinuclear entities, was deemed appropriate.

Experimental data for **1**–**4**, corrected for diamagnetic contributions and TIP (0.3×10^{-3} $cm^3 mol^{-1}$), were analyzed with the theoretical expression, which results from the modified Equation (2). Fitting was performed on $\chi_M T$. The best-fitted curves are plotted in Figure 3 and Figures S7, S8, and S9, along with the experimental data. The best-fit parameters obtained are $J = -66.7$ cm^{-1}, $g = 2.19$, and $\theta = -0.13$ with $R = 2 \times 10^{-4}$ for **1**; $J = -36.6$ cm^{-1}, $g = 2.2$, and $\theta = -0.22$ with $R = 1.9 \times 10^{-4}$ for **2**; $J = -24.5$ cm^{-1}, $g = 2.2$, and $\theta = -0.24$ with $R = 2.1 \times 10^{-4}$ for **3** and $J = -14.9$ cm^{-1}, $g = 2.05$, and $\theta = -0.13$ with $R = 2.2 \times 10^{-4}$ for **4** (where R is the agreement factor defined as $\Sigma_i[(\chi_M T)_i^{exp} - (\chi_M T)_i^{calc}]^2/\Sigma_i[(\chi_M T)_i^{exp}]^2$. The θ values are consistent with the intertrimer interactions, mainly the hydrogen bonds that link the trinuclear entities. All J values are gathered in Table 3 together with the most important structural parameters: Cu–O–Cu angles, Cu–O distances, distance from the O(H) atom to the mean Cu3 plane and the τ distortion parameter of each copper(II) ion. Considering that we have used only one J value, angles and distances given in Table 3 correspond to the average values of the triangles. However, it is clear that these values agree with those reported in the literature for similar triangular complexes.[8–10]

The most interesting feature concerning these triangular complexes is the possibility to show the spin frustration when the geometry is almost equilateral. Indeed, as indicated by Haasnoot et al.,[7a] the canonical example of spin frustration in any lattice is based on an equilateral triangular plaquette. With the typical isotropic spin Hamiltonian $-\Sigma_{ij} J_{ij} S_i S_j$, if J_{ij} is negative, which favors the antiparallel correlation, and J_{ij} is equal for all nearest neighbor pairs, then only two of the three spin constraints can be satisfied simultaneously, that is the system is geometrically frustrated. In order to interpret the magnetic properties of these frustrated systems it is necessary to go beyond the framework of the above isotropic exchange model and to introduce *antisymmetric exchange interactions*.[7a]

The spin frustration requires a highly symmetrical (equilateral) triangle. Complexes **1**–**4** are not fully equilateral,

 © 2005 Wiley-VCH Verlag GmbH & Co. KGaA, Weinheim

thus spin-frustration behavior might not be expected. From magnetic data it is very difficult − mostly impossible − to calculate the antisymmetric exchange term G_{AB}. In most cases, the possibilities of intertrimeric exchange − such as in **1**–**4** because of the hydrogen bonds − preclude any exact calculation of this parameter. However, some very interesting calculations have been recently reported on singular cases:[7a] for example, Solomon et al. have reported an exhaustive study on a symmetric hydroxo-bridged trinuclear Cu^{II} complex (such as **1**–**4**) by means of nonconventional techniques, such as variable-temperature variable-field magnetic circular dichroism combined with powder/single-crystal EPR.[17] From all literature data it seems more appropriate to utilize EPR measurements for the study of the spin frustration. Obviously, in this study it is important to investigate EPR behavior at a very low temperature, when only the degenerate $S = 1/2$ states are populated. In this case, one of the signatures of spin frustration is the appearance of some g values lower than 2.00.[18]

EPR Spectra

The X-band EPR spectra of complexes **1**–**4** were recorded on powder samples varying the temperature between 4 and 295 K (Figure 4). The EPR spectra of trinuclear $S = 1/2$ compounds have been analyzed in terms of three active states (one quartet and two doublets), with temperature-dependent population.[18–22] In the light of the superexchange parameter from the magnetic measurements, at low temperatures only the doublets should be populated, whereas at room temperature signals due to the transitions inside the quartet may also be observed. This transition may show noticeable zero-field splitting (ZFS) ($S = 3/2$). Complexes **1**–**3** show a broad band (mainly complex **2**) at low fields, due undoubtedly to the presence of ZFS of the $S = 3/2$ state. Complex **4** does not show any mark of the ZFS (D parameter). Only one quasi-isotropic band is observed at this temperature. The possible spin frustration can only be observed at low temperatures. From Figure 4 it can be seen that complexes **1** and **2** do not have any signal that could be attributed to spin frustration. However, complexes **3** and **4** show unequivocally a band at high field that corresponds to $g = 1.98$, which cannot be explained as g_x, g_y, g_z for an $S = 1/2$ state without the introduction of spin frustration.[18] The antisymmetric exchange in spin-frustrated systems can give $g_\perp$ values close to 1.5.[18]

We have also carried out the EPR measurements in frozen methanol solution (Figures 5 and S10). The X-band spectra at low temperatures (60 K to 4 K) clearly show the hyperfine splitting in the $g_\parallel$ approximately of 190 Gauss for all four triangles. In $g_\perp$ there is also a significant partial splitting, mainly in complex **4** (Figure 5). In this case the splitting can be masked by the band at $g \approx 1.98$, as already shown in the solid state. Thus, the EPR data in solution seem to confirm, at least in complex **4**, the existence of the spin frustration together with the hyperfine splitting.

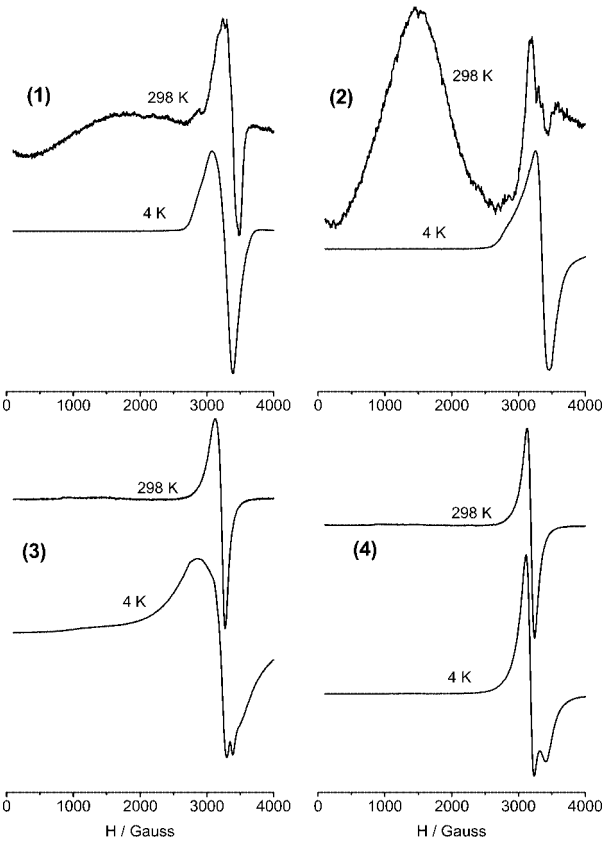

Figure 4. Polycrystalline X-band EPR spectra for complexes **1**–**4** at room temperature and 4 K.

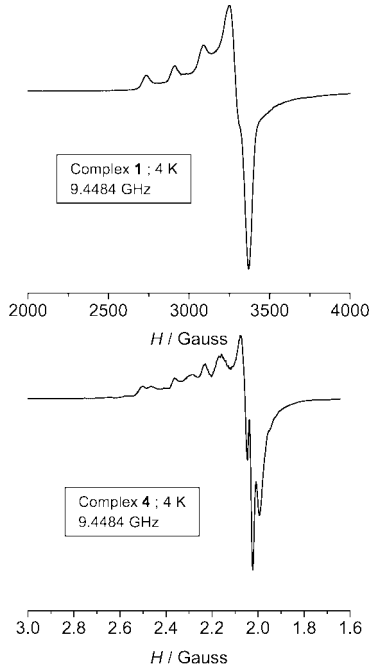

Figure 5. X-band EPR spectra for **1** and **4** in frozen methanolic solution at 4 K. For **1** the abscissa is given in Gauss to see the hyperfine splitting; for **4** the abscissa is given in g values to see the low values of $g_\perp$ attributed to the spin frustration already shown in solid state.

 © 2005 Wiley-VCH Verlag GmbH & Co. KGaA, Weinheim

Discussion

Previous work has established relationships between magnetic coupling and certain structural features.[5c,6c,7a] Most of the trinuclear compounds containing a pyramidal $Cu_3O(H)$ core described in the literature can be systematized in four groups depending on the type of peripheral bridge: those with an N,O (mainly from an oxime-oximate ligand bridge),[5] those with an *N*,*N*-pyrazole bridge,[6] those with an *N*,*N*-triazole bridge,[7] and those with Schiff bases that act as tridentate N_2O ligands with only three compounds reported,[8–10] which have arisen from the condensation of the carbonyl function with only one end of the diamine. Because the electronic factors related to the nature of the ligands that afford the bridge are decisive,[7a] we were prevented from correlating the magnitude of the magnetic coupling within the above four classes of Cu_3O clusters.[8,9] From Table 3 it can be seen that the main structural differences for complexes **1**–**4** lie in the difference in the distance of the oxygen atom above the plane of the copper atoms (the maximum difference is 0.13 Å) and in the average of the Cu–O(H)–Cu′ angles (the maximum difference is 4.7°). The maximum variation in the $-J$ values is 51 cm^{-1}. These features indicate that the shortest distance of the O(H) group above the plane formed by the three copper ions in the trinuclear Cu^{II} complexes and the greatest Cu–O–Cu′ angle provide the strongest antiferromagnetic coupling.

In triangular arrangements of symmetric antiferromagnetically coupled metal ions, the magnetic properties at low temperatures can become complicated by the possible presence of spin-frustration effects, because of the presence of the antisymmetric exchange interaction (ASE) term.[7a,7b] The experimental EPR data for **3** and **4** indicate that this term is non-zero and the phenomenon of spin frustration occurs. For **1** and **2** all data seem to indicate that there is no spin frustration.

Concluding Remarks

The carbonyl functional group is generally considered as a nonbridging group but the facile synthesis of the four new trinuclear complexes **1**–**4** and the other three reported complexes suggests that the monocondensation products of various diamines and acetylacetone are a group of tridentate ligands that can readily be involved in *basal–apical*-type peripheral oxo bridging to result in the formation of trinuclear Cu^{II} complexes with a Cu_3OH core by self-assembly. All four complexes show antiferromagnetic coupling, as was also found in the three similar peripheral bridging complexes.[8–10] The magnetostructural correlation suggests that the greatest coplanarity of the three principal ligand planes, the shortest distance of the O(H) group above the Cu_3 plane, and the greatest Cu–O–Cu′ angles provide the strongest antiferromagnetic coupling.

Experimental Section

Materials: All the chemicals were of reagent grade and used without further purification. The four monocondensed ligands, HL^1, HL^2, HL^3, and HL^4, were synthesized in our laboratory by the methods described below. The ligand HL^1 was prepared for the first time. ***Caution!*** *Although no problems were encountered in this work, perchlorate salts containing organic ligands are potentially explosive. They should be prepared in small quantities and handled with care.*

Physical Measurements: Elemental analyses (C, H, N) were performed using a Perkin–Elmer 240C elemental analyzer and the Cu contents in all the complexes were estimated spectrophotometrically.[23] IR spectra in KBr (4500–500 cm^{-1}) were recorded using a Perkin–Elmer RXI FTIR spectrophotometer. Electronic spectra in methanol (1200–350 nm) were recorded with a Hitachi U-3501 spectrophotometer. The magnetic measurements were carried out in the "Servei de Magnetoquimica (Universitat de Barcelona)" on polycrystalline samples (20 mg) with a Quantum Design SQUID MPMSXL magnetometer in the temperature range of 2–300 K and the magnetic field was 1 T. The diamagnetic corrections were evaluated from Pascal's constants. EPR spectra were recorded on powder samples at X-band frequency with a Bruker 300E automatic spectrometer, varying the temperature between 4 and 300 K.

Preparation of 8-Amino-4,7,7-trimethyl-5-azaoct-3-en-2-one (HL^1) and 7-Amino-4-methyl-5-azaoct-3-en-2-one (HL^2): These two ligands are the single-condensation products of 2,2-dimethyl-1,3-propanediamine and 1,2-propanediamine, respectively, with 2,4-pentanedione. They were prepared by applying a method similar to that adopted for the half condensation of 1,2-ethanediamine or 1,3-propanediamine with 2,4-pentanedione as reported earlier, that is by allowing the constituents to react in chloroform under high dilution.[8,9,24–27] A solution of 2,4-pentanedione (1.1 mL, 10 mmol) in chloroform (50 mL) was added dropwise to a solution of 2,2-dimethyl-1,3-propanediamine (1.03 mL, 10 mmol) or 1,2-propanediamine (0.80 mL, 10 mmol) in chloroform (50 mL) at room temperature. After addition, the solution was stirred for an additional 3 h and the chloroform was evaporated under reduced pressure. The resultant viscous oil was collected as the ligand and dissolved in methanol (30 mL).

Preparation of 7-(Ethylamino)-4-methyl-5-azahept-3-en-2-one (HL^3) and 4-Methyl-7-(methylamino)-5-azahept-3-en-2-one (HL^4): HL^3 and HL^4 were prepared by condensation of the NH_2 group of *N*-ethyl-1,2-ethanediamine (0.90 mL, 10 mmol) and *N*-methyl-1,2-ethanediamine (0.74 mL, 10 mmol) with 2,4-pentanedione (1.1 mL, 10 mmol), respectively, in methanol (30 mL) under reflux for 3 h. The Schiff-base ligands were not isolated and the yellow methanolic solutions were used directly for complex formation.

Synthesis of $[(CuL^1)_3(\mu_3\text{-}OH)](ClO_4)_2\cdot H_2O$ (1), $[(CuL^2)_3(\mu_3\text{-}OH)](ClO_4)_2$ (2), $[(CuL^3)_3(\mu_3\text{-}OH)](ClO_4)_2\cdot H_2O$ (3), and $[(CuL^4)_3(\mu_3OH)](ClO_4)_2\cdot H_2O$ (4): A solution of $Cu(ClO_4)_2\cdot 6H_2O$ (3.7 g, 10 mmol) in methanol (20 mL) was added to a stirred solution of each of the ligands, HL^1, HL^2, HL^3, and HL^4 (10 mmol), in methanol (10 mL). Triethylamine (2.1 mL, 15 mmol) was then added dropwise to this solution with constant stirring. In the case of **1** and **4**, an immediate separation of a small amount of green hydrolyzed product occurred during the addition of triethylamine, which was filtered off. If the methanol contained water, the amount of the hydrolyzed products for these two compounds increased. Therefore, the methanol was dried before using as solvent for the synthesis of **1** and **4**. The resulting green and blue filtrates of **1** and **4**, respectively, were set aside at room temperature. Overnight, single crystals appeared, as green prisms for **1** and blue hexagons for **4**. The resulting blue and green solutions for HL^2 and HL^3, respectively, upon stirring at room temperature slowly yield the desired compounds, complex **2** as a precipitate and complex **3** as a microcrys-

 © 2005 Wiley-VCH Verlag GmbH & Co. KGaA, Weinheim

Table 5. Crystal data and refinement details of complexes **1**–**4**.

	1	**2**	**3**	**4**
Empirical formula	$C_{30}H_{60}Cl_2Cu_3N_6O_{13}$	$C_{24}H_{46}Cl_2Cu_3N_6O_{12}$	$C_{27}H_{52}Cl_2Cu_3N_6O_{13}$	$C_{24}H_{46}Cl_2Cu_3N_6O_{13}$
Formula mass	972.37	872.22	930.30	888.22
Space group	*Pbca*	$P\bar{1}$	$P\bar{1}$	$P\bar{1}$
Crystal system	orthorhombic	triclinic	triclinic	triclinic
a [Å]	17.450(19)	11.818(14)	12.342(15)	12.500(14)
b [Å]	14.586(19)	12.161(14)	12.352(15)	12.499(14)
c [Å]	34.30(4)	15.190(16)	15.136(18)	13.790(14)
α [°]	90	71.05(1)	79.55(1)	84.01(1)
β [°]	90	78.44(1)	81.97(1)	79.66(1)
γ [°]	90	62.72(1)	64.11(11)	63.64(1)
V [Å^3]	8730(18)	1832(4)	2037(4)	1898(4)
Z	8	2	2	2
$D_{calcd.}$ [g cm^{-3}]	1.480	1.581	1.517	1.554
μ [mm^{-1}]	1.63	1.9	1.746	1.869
R indices	$R_1 = 0.080$	$R_1 = 0.0697$	$R_1 = 0.0800$	$R_1 = 0.0840$
$[I > 2\sigma(I)]$	$wR_2 = 0.1257$	$wR_2 = 0.1465$	$wR_2 = 0.2251$	$wR_2 = 0.2579$

talline precipitate. Stirring was continued for 1 h for both complexes. The products were collected by filtration and were recrystallized from methanol. The filtrates were left to stand overnight in a refrigerator. Single crystals suitable for X-ray diffraction analysis were obtained as blue plates for complex **2** and as hexagonally shaped green single crystals for complex **3**.

Complex 1: Yield: 2.0 g (60%). $C_{30}H_{60}Cl_2Cu_3N_6O_{13}$ (972.37): calcd. C 36.94, H 6.16, Cu 19.55, N 8.62; found C 37.02, H 6.37, Cu 19.98, N 8.49. UV/Vis (methanol): λ_{max} (ε_{max}) = 593 (249 dm^3 mol^{-1} cm^{-1}) nm. IR: $\tilde{\nu}$ = 3325, 3279, 3170 [ν(N–H)]; 1516 cm^{-1} [ν(C=N)]; 3520 [ν(O–H)] cm^{-1}.

Complex 2: Yield: 2.3 g (80%). $C_{24}H_{46}Cl_2Cu_3N_6O_{12}$ (872.22): calcd. C 33.02, H 5.27, Cu 21.84, N 9.63; found C 33.52, H 5.49, Cu 22.09, N 9.48. UV/Vis (methanol): λ_{max} (ε_{max}) = 615 (298 dm^3 mol^{-1} cm^{-1}) nm. IR: $\tilde{\nu}$ = 3330, 3266, 3158 [ν(N–H)]; 1515 [ν(C=N)]; 3505 [ν(O–H)] cm^{-1}.

Complex 3: Yield: 2.0 g (65%). $C_{27}H_{52}Cl_2Cu_3N_6O_{13}$ (930.30): calcd. C 34.83, H 5.59, Cu 20.47, N 9.03; found C 35.03, H 5.92, Cu 20.01, N 9.37. UV/Vis (methanol): λ_{max} (ε_{max}) = 587 (282 dm^3 mol^{-1} cm^{-1}) nm. IR: $\tilde{\nu}$ = 3390 3243 [ν(N–H)]; 1518 [ν(C=N)]; 3556 [ν(O–H)] cm^{-1}.

Complex 4: Yield: 1.3 g (45%). $C_{24}H_{46}Cl_2Cu_3N_6O_{13}$ (888.22): calcd. C 32.42, H 5.18, Cu 21.45, N 9.46; found C 32.83, H 5.03, Cu 20.97, N 9.98. UV/Vis (methanol): λ_{max} (ε_{max}) = 595 (249 dm^3 mol^{-1} cm^{-1}) nm. IR: $\tilde{\nu}$ = 3377, 3247 [ν(N–H)]; 1515 [ν(C=N)]; 3550 [ν(O–H)] cm^{-1}.

Crystallographic Studies: Suitable single crystals of all four complexes were positioned at 70 mm from the image plate. A total of 100 frames were measured at 2° intervals with a counting time of 2 min. 5786, 6505, 6526 and 6690 independent reflections for complexes **1**–**4**, respectively, were measured with Mo-K_α radiation using the MARresearch Image Plate System at 293 K. Data analyses were carried out with the XDS program.[28] The structures were solved by direct methods with the SHELX86 program.[29] The non-hydrogen atoms were refined with anisotropic thermal parameters. The hydrogen atoms bonded to carbon and nitrogen atoms were included in geometric positions and given thermal parameters equivalent to 1.2 times those of the atom to which they are attached. Empirical absorption corrections were carried out using the DIFABS program.[30] The structures were refined on F^2 using SHELXL[31] for 3318, 5056, 3482, and 2303 reflections respectively, with $I > 2\sigma(I)$. The crystal structure illustrations were generated using ORTEP-3.[32] Selected crystallographic data are summarized in Table 5. CCDC-236467 (**1**), -236468 (**2**), -259938 (**3**), and -259939 (**4**) contain the supplementary crystallographic data for this paper. These data can be obtained free of charge from The Cambridge Crystallographic Data Centre via www.ccdc.cam.ac.uk/data_request/cif.

Supporting Information: Discussion of H bonds of complexes **1**–**3**.

Acknowledgments

M. S. R. and S. C. are thankful to UGC, India, and CSIR, India, respectively, for research fellowships [Sanction No. UGC/750/Jr. Fellow Sc. 2000/2001 and 9/28(614)/2003-EMR-I]. We also thank EPSRC and the University of Reading for funds for the Image Plate System. A. F., J. R., and C. D. also acknowledge financial support from the Spanish Government (Grant BQU2003-00539).

[1] a) P. Chowdhury, I. Karpenstein, M. Winter, C. Butzlaff, E. Bill, A. X. Trautwein, U. Florke, H.-J. Haupt, *J. Chem. Soc., Chem. Commun.* **1992**, 321; b) A. P. Cole, D. E. Root, P. Mukherjee, E. I. Solomon, T. D. P. Stack, *Science* **1996**, *273*, 1848; c) S. T. Frey, H. H. J. Sun, N. N. Murthy, K. D. Karlin, *Inorg. Chim. Acta* **1996**, *242*, 329; d) L. Spiccia, B. Graham, M. T. W. Hearn, G. Lazarev, B. Moubaraki, K. S. Murray, E. R. T. Tiekink, *J. Chem. Soc., Dalton Trans.* **1997**, 4089.

[2] a) D. Gatteschi, O. Kahn, J. S. Miller, F. Palacio (Eds.), *Magnetic Molecular Materials*, Kluwer Academic, Dordrecht, The Netherlands, **1991**; b) O. Kahn, Y. Pei, Y. Yournaux, in *Inorganic Materials* (Eds.: D. W. Bruce, O. O. Hare), John Wiley & Sons, Chichester, UK, **1992**; c) O. Kahn, *Molecular Magnetism*, VCH Publishers, New York, **1993**; d) M. M.Turnbull, T. Sugimoto, L. K. Thompson (Eds.), *Molecular-Based Magnetic Materials: Theory, Techniques and Applications*, ACS Symposium, Series 644, American Chemical Society, Washington, DC, **1996**.

[3] J. E. Greedan, *J. Mater. Chem.* **2001**, *11*, 37.

[4] a) G. J. Wilkinson, *J. Chem. Soc., Dalton Trans.* **1973**, 2565; b) S. Uemura, A. Spencer, G. Wilkinson, *J. Chem. Soc., Dalton Trans.* **1973**, 3565; c) R. D. Cannon, R. P. White, *Prog. Inorg. Chem.* **1998**, *36*, 195; d) C. E. Anson, J. P. Bourke, R. D. Cannon, U. A. Jayasooriya, M. Molinier, A. K. Powell, *Inorg. Chem.* **1997**, *36*, 1265; e) T. Nakamoto, M. Hanaya, M. Katada, K. Endo, S. Kitagawa, H. Sano, *Inorg. Chem.* **1997**, *36*, 4347; f) R. Wu, M. Poyraz, F. E. Sowrey, C. E. Anson, S. Wocadlo, A. K. Powell, Y. A. Jayasooriya, R. D. Cannon, T. Nakamoto, M. Katada, H. Sano, *Inorg. Chem.* **1998**, *37*, 1913.

[5] a) R. Beckett, B. F. Hoskins, *J. Chem. Soc., Dalton Trans.* **1972**, 291; b) P. F. Ross, R. K. Murmann, E. O. Schelempers, *Acta Crystallogr., Sect. B* **1974**, *30*, 1120; c) R. J. Butcher, C. J. O.

Connor, E. Sinn, *Inorg. Chem.* **1981**, *20*, 537; d) S. Baral, A. Chakravorty, *Inorg. Chim. Acta* **1980**, *39*, 1; e) Y. Agnus, R. Louis, B. Metz, C. Boudon, J. P. Gisselbrecht, M. Gross, *Inorg. Chem.* **1991**, *30*, 3155; f) F. Akagi, Y. Michihiro, Y. Nakao, K. Matsumoto, T. Sato, W. Mori, *Inorg. Chim. Acta* **2004**, *357*, 684.

[6] a) F. B. Hulsbergen, R. W. M. ten Hoedt, J. Verschoor, J. Reedijk, A. L. Spek, *J. Chem. Soc., Dalton Trans.* **1983**, 539; b) K. Sakai, Y. Yamada, T. Tsubomura, M. Yabuki, M. Yamaguchi, *Inorg. Chem.* **1996**, *35*, 542; c) M. Angaroni, G. A. Ardizzoia, T. Beringhelli, G. La Monica, D. Gatteschi, N. Masciocchi, M. Moret, *J. Chem. Soc., Dalton Trans.* **1990**, 3305.

[7] a) S. Ferrer, F. Lloret, I. Bertomeu, G. Alzuet, J. Borrás, S. García-Granada, M. Liu-González, J. G. Haasnoot, *Inorg. Chem.* **2002**, *41*, 5821 and references cited therein; b) S. Ferrer, J. G. Haasnoot, J. Reedijk, E. Müller, M. B. Cingi, M. Lanfranchi, A. M. Lanfredi, J. Ribas, *Inorg. Chem.* **2000**, *39*, 1859; c) A. V. Virovets, N. V. Podberezskaya, L. G. Lavrenova, *J. Struct. Chem.* **1997**, *38*, 441.

[8] J. P. Costes, F. Dahan, J. P. Laurent, *Inorg. Chem.* **1986**, *25*, 413.

[9] M. Kwiatkowski, E. Kwiatkowski, A. Olechnowicz, D. M. Ho, E. Deutsch, *Inorg. Chim. Acta* **1988**, *150*, 65.

[10] H.-D. Bian, J.-Y. Xu, W. Gu, S.-P. Yan, P. Cheng, D.-Z. Liao, Z.-H. Jiang, *Polyhedron* **2003**, *22*, 2927.

[11] a) J.-P. Costes, F. Dahan, J. P. Laurent, *J. Coord. Chem.* **1984**, *13*, 355; b) J. P. Costes, F. Dahan, J. P. Laurent, *Inorg. Chem.* **1985**, *24*, 1018.

[12] a) D. Cremer, J. A. Pople, *J. Am. Chem. Soc.* **1975**, *97*, 1354; b) J. C. A. Boyens, *J. Cryst. Mol. Struct.* **1978**, *8*, 31.

[13] A. W. Addison, T. N. Rao, J. Reedijk, J. van Rijn, G. C. Verschoor, *J. Chem. Soc., Dalton Trans.* **1984**, 1349.

[14] J. R. Ferraro, W. R. Walker, *Inorg. Chem.* **1965**, *4*, 1382.

[15] B. J. Hathaway, A. A. G. Tomlinson, *Coord. Chem. Rev.* **1970**, *5*, 1.

[16] B. S. Tsukerblat, M. I. Belinskii, V. E. Fainzil'berg, *Sov. Sci. Rev. B (Engl. Trans.)* **1987**, *9*, 339.

[17] J. Ion, L. M. Mirica, D. P. Stack, E. I. Solomon, *J. Am. Chem. Soc.* **2004**, *126*, 12586.

[18] X. Liu, M. P. de Miranda, E. J. L. McInnes, C. A. Kilner, M. A. Halcrow, *Dalton Trans.* **2004**, 59.

[19] J. Padilla, D. Gatteschi, P. Chaudhuri, *Inorg. Chim. Acta* **1997**, *260*, 217.

[20] H. López-Sandoval, R. Contreras, A. Escuer, R. Vicente, S. Bernès, H. Nöth, G. J. Leigh, N. Barba-Behrens, *J. Chem. Soc., Dalton Trans.* **2002**, 2648.

[21] B. Cage, F. A. Cotton, N. S. Dalal, E. A. Hillard, B. Rakvin, C. M. Ramsey, *J. Am. Chem. Soc.* **2003**, *125*, 5270.

[22] L. Spiccia, B. Graham, M. T. W. Hearn, G. Lazarev, B. Moubaraki, K. S. Murray, E. R. T. Tiekink, *J. Chem. Soc., Dalton Trans.* **1997**, 4089.

[23] *Vogel's Text Book of Quantitative Analysis*, 5th ed., Longman Scientific and Technical, New York, **1989**, p. 689.

[24] a) J.-P. Costes, G. Cros, M.-H. Darbieu, J.-P. Laurent, *Inorg. Chim. Acta* **1982**, *60*, 111; b) G. Cros, J.-P. Costes, *C. R. Acad. Sci. II* **1982**, *294*, 173.

[25] a) M. Sinha Ray, R. Bhattacharya, S. Chaudhuri, L. Righi, G. Bocelli, G. Mukhopadhyay, A. Ghosh, *Polyhedron* **2003**, *22*, 617; b) M. Sinha Ray, A. Ghosh, G. Mukhopadhyay, M. G. B. Drew, *J. Coord. Chem.* **2003**, *56*, 1141; c) M. Sinha Ray, A. Ghosh, R. Bhattacharya, G. Mukhopadhyay, M. G. B. Drew, J. Ribas, *Dalton Trans.* **2004**, 252.

[26] a) J.-P. Costes, *Inorg. Chim. Acta* **1987**, *130*, 17; b) E. Kwiatkowski, M. Kwiatkowski, A. Olechnowiez, *Inorg. Chim. Acta* **1984**, *90*, 145; c) H. Adams, N. A. Bailey, I. S. Bard, D. E. Fenton, J.-P. Costes, G. Cros, J.-P. Laurent, *Inorg. Chim. Acta* **1985**, *101*, 7; d) E. Kwiatkowski, M. Kwiatkowski, *Inorg. Chim. Acta* **1986**, *117*, 145; e) M. Kwiatkowski, G. Bandoli, *J. Chem. Soc., Dalton Trans.* **1992**, 379; f) M. Kwiatkowski, E. Kwiatkowski, A. Olechnowiez, D. M. Ho, E. Deutsch, *J. Chem. Soc., Dalton Trans.* **1990**, 2497; g) M. Kwiatkowski, E. Kwiatkowski, A. Olechnowiez, D. M. Ho, E. Deutsch, *J. Chem. Soc., Dalton Trans.* **1990**, 3063; h) N. Matsumoto, S. Yamashita, A. Ohyoshi, S. Kohata, H. Okawa, *J. Chem. Soc., Dalton Trans.* **1988**, 1943; i) N. Matsumoto, H. Murakami, T. Akui, J. Honto, H. Okawa, A. Ohyoshi, *Bull. Chem. Soc. Jpn.* **1986**, *59*, 1609; j) T. Nagahara, M. Suzuki, K. Kasuga, *Inorg. Chim. Acta* **1988**, *149*, 279; k) C. T. Brewer, G. Brewer, *J. Chem. Soc., Chem. Commun.* **1988**, 85; l) E. Kwiatkowski, M. Kwiatkowski, *Inorg. Chim. Acta* **1984**, *82*, 101.

[27] a) N. Matsumoto, T. Akui, H. Murakami, J. Kanesaka, A. Ohyoshi, H. Okawa, *J. Chem. Soc., Dalton Trans.* **1988**, 1021; b) J. P. Costes, F. Dahan, A. Dupuis, J. P. Laurent, *J. Chem. Soc., Dalton Trans.* **1998**, 1307.

[28] W. Kabsch, *J. Appl. Crystallogr.* **1988**, *21*, 916.

[29] SHELX-86: G. M. Sheldrick, *Acta Crystallogr. Sect. A* **1990**, *A46*, 467.

[30] N. Walker, D. Stuart, *Acta Crystallogr., Sect. A* **1983**, *A39*, 158.

[31] G. M. Sheldrick, *SHELXL, Program for crystal structure refinement*, University of Göttingen, **1993**.

[32] M. N. Burnett, C. K. Johnson, *ORTEP-3: Oak Ridge thermal ellipsoid plot program for crystal structure illustrations*, Report ORNL-6895, Oak Ridge National Laboratory, Oak Ridge, TN, USA, **1996**.

Received: April 5, 2005
Published Online: October 5, 2005

 © 2005 Wiley-VCH Verlag GmbH & Co. KGaA, Weinheim

Self-Assembly of Organotin(IV) Moieties with the Schiff-Base Ligands Pyruvic Acid Isonicotinyl Hydrazone and Pyruvic Acid Salicylhydrazone: Synthesis, Characterization, and Crystal Structures of Monomeric or Polymeric Complexes

Handong Yin,*[a] Min Hong,[a] Haolong Xu,[a] Zhongjun Gao,[a] Gang Li,[a] and Daqi Wang[a]

Keywords: N,O ligands / Self-assembly / Schiff bases / Tin

A series of organotin(IV) complexes of the type $[R_2SnLY]_2$ or $[R_2SnL(R_3SnOH)]_2$ [L = 4-$NC_5H_4CON_2C(CH_3)CO_2$ or 2-$HOC_6H_4CON_2C(CH_3)CO_2$, and Y = H_2O or CH_3OH] have been synthesized by the condensation reaction of R_2SnO (R = Ph **1**, nC_8H_{17} **2**) or R_3SnCl (R = *o*-ClBz **3**, *o*-FBz **4**, *p*-FBz **5**, *p*-CNBz **6**) with the Schiff-base ligand pyruvic acid isonicotinyl hydrazone in a 1:1 molar ratio or $(R_3Sn)_2O$ (R = *n*Bu **7**, Bz **8**, *p*-CNBz **9**) or R_3SnCl (R = *o*-ClBz **10**, *p*-ClBz **11**, *p*-CNBz **12**) with the Schiff-base ligand pyruvic acid salicylhydrazone in a 1:1 molar ratio. All complexes were characterized by elemental analysis and IR, ^1H, and ^{119}Sn NMR spectroscopy. The crystal structures of complexes **1**, **2**, **3**, **7**, and **10** have been determined by X-ray single crystal diffraction analyses, which show that the tin atoms of **1**, **2**, **3**, and **10** are all seven-coordinate in distorted pentagonal bipyramid geometries, of which only complex **1** exhibits an asymmetric structure containing two different types of tin atoms. The crystal structure of **7** exhibits a dimeric structure containing distannoxane units with two types of tin atoms, in which one tin atom appears to be seven-coordinate with a distorted pentagonal bipyramid geometry and the other is four-coordinate with a distorted tetrahedral geometry. A comparison of the IR spectra of the ligands with those of the corresponding complexes reveals that the ligands coordinate to tin in the enol form due to the disappearance of the bands assigned to the carbonyl group.

(© Wiley-VCH Verlag GmbH and Co. KGaA, 69451 Weinheim, Germany, 2005)

Introduction

Schiff bases still play an important role as ligands in metal coordination chemistry even after almost a century since their discovery.[1–4] Organotin(IV) complexes with Schiff bases have received increasing attention owing to their antitumor activities and potential applications in biotechnology.[5–11] In addition, Schiff base organotin(IV) complexes are of interest for structural reasons. The coordination chemistry of some tridentate ONO- and ONS-donor Schiff bases has been described,[12,13] and we have recently reported some organotin(IV) complexes with the potentially ONO tridentate Schiff-base ligands salicylideneamino acids and pyruvic acid isonicotinyl hydrazone.[14,15] As part of our ongoing project dealing with the study of the interaction of tin(IV) and organotin(IV) species with *O*-donor and *N*-donor ligands, we have now synthesized twelve new organotin(IV) complexes of pyruvic acid isonicotinyl hydrazone and salicylhydrazone by self-assembly of metal ions, utilizing their preference for different coordination geometry, choice of suitable ligands, and intermolecular interactions such as hydrogen bonding. The details of the structural and spectroscopic characterization of complexes **1**–**12** are reported herein. Five of the complexes have been studied by X-ray diffraction, and reveal that there exist five different types of coordinated tin atoms (shown in Scheme 1).

Complexes **2**, **3**, and **10** are coordinated in mode A, and each reveals a highly centrosymmetric dimeric structure containings a distannoxane unit. This is the more usual structure adopted by this class of complexes.[15,16] It is worthwhile to note that crystals containing an *n*-octyl group were obtained by the reaction of pyruvic acid isonicotinyl hydrazone with di-*n*-octyltin oxide and recrystallized from acetone, as structural information for complexes containing *n*-octyl groups was lacking until now. Meanwhile, to our surprise, we obtained an unusual asymmetric linear chain polymer complex **1** containing two different types of tin atom from the reaction of Schiff-base ligand pyruvic acid isonicotinyl hydrazone with diphenyltin oxide. These two types of tin atom contain ligands in mode B. One of the two types is coordinated by tridentate formation of the Schiff base, while the other is not in the same way due to

[a] Department of Chemistry, Liaocheng University, Liaocheng 252059, China
E-mail: handongyin@lctu.edu.cn

Supporting information for this article is available on the WWW under http://www.eurjic.org or from the author.

 © 2005 Wiley-VCH Verlag GmbH & Co. KGaA, Weinheim **DOI: 10.1002/ejic.200500412**

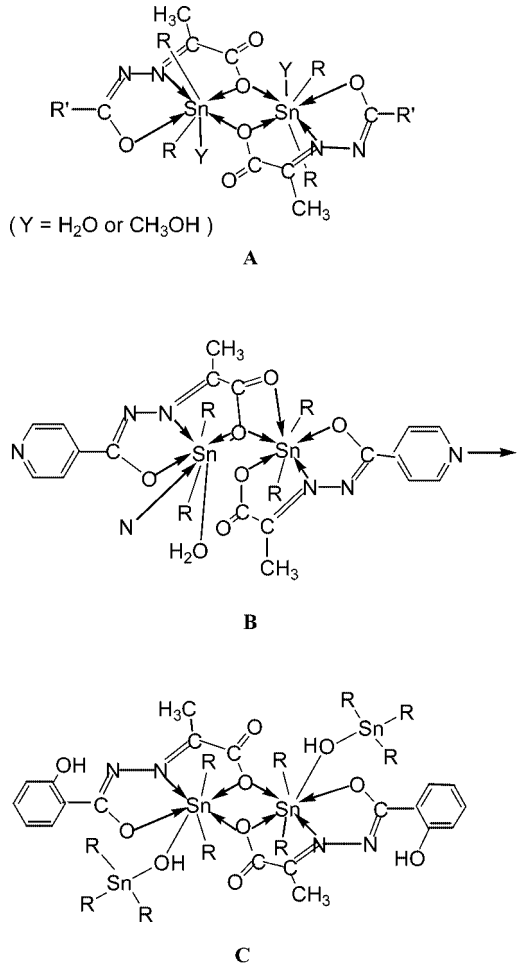

Scheme 1.

coordination between tin and two oxygen atoms derived from the carboxyl group of the adjacent ligand.

Interestingly, we also succeeded in preparing a novel tetranuclear organotin(IV) complex $[(n\text{Bu})_2\text{Sn}\{2\text{-HOC}_6\text{H}_4\text{-CON}_2\text{C(CH}_3)\text{CO}_2\}\{(n\text{Bu})_3\text{SnOH}\}]_2$ (**7**) by treatment of $[(n\text{Bu})_3\text{Sn}]_2\text{O}$ with the Schiff-base ligand pyruvic acid salicylhydrazone in a 1:1 molar ratio, which exhibits a dimeric structure containing distannoxane units with two types of tin atoms, of which one tin atom appears to be seven-coordinate with a distorted pentagonal bipyramid geometry and the other is four-coordinate with a distorted tetrahedral geometry (mode C).

Results

IR Spectra

A remarkable difference between the IR spectra of the ligands and those of the corresponding complexes is that the stretching vibration bands of the carbonyl group disappear from the spectra of all the complexes. The absence of the bands assigned to the carbonyls unambiguously confirms that the ligands coordinated to the tin are in their enol form. The characteristic absorptions at 1622–1640 and 1595–1608 cm^{-1} in the spectra of these complexes indicate the presence of C=N and C=N–N=C groups.[17] The stretching frequencies of interest are those associated with the acid COO and the Sn–O and Sn–N groups. The spectra of all complexes have some common features. The explicit feature in the infrared spectra of all complexes is the strong absorption at about 700 cm^{-1} in the spectra of the complexes, which is absent in the free ligands, which is assigned to the Sn–O stretching mode of vibration. The weak- or medium-intensity band in the region 476–486 cm^{-1} can be assigned to the Sn–N stretching vibration. All these values are consistent with those detected in a number of organotin(IV) derivatives.[18,19]

The IR spectra of organotin carboxylate complexes can provide useful information concerning the coordination behavior of the carboxyl groups. The IR spectrum of complex **1** shows that the ν_{as} and ν_{as} bands are assigned to the regions 1603, 1505 cm^{-1} and 1366, 1312 cm^{-1}, respectively. The magnitude of $\Delta\nu$ [ν_{as}(COO) – ν_s(COO)] is 237 and 193 cm^{-1}, and therefore indicates the presence of mono- and didentate carboxyl groups.[20] Moreover, the magnitude of $\Delta\nu$ (231–285 cm^{-1}) for complexes **2**–**12** indicates that the carboxylate ligand functions as a monodentate ligand in these complexes.[20] These conclusions are supported by the results of X-ray diffraction studies.

NMR Spectra

In ^{1}H NMR spectra of the free ligands, the single resonance for the proton of the -NHN= group is observed at either δ = 3.75 or 3.89 ppm, and is absent in the spectra of the complexes, thus indicating deprotonation of the -NHN= group and confirming that the ligand coordinate to the tin in the enol form. For complexes **1**–**6**, the spectra show that the chemical shifts of the protons on the pyridine ring exhibit two sets of signal in the ranges δ = 7.57–8.89 ppm, as a doublet, and δ = 7.22–8.13 ppm, also as a doublet. The coupling constant is equal to 4.80–8.40 Hz. The Ar-OH resonance appears in the region δ = 10.87–11.43 ppm, as a singlet, for the complexes **7**–**12**, which strongly suggests that the phenolic oxygen atoms do not participate in coordination to the tin atoms; this is quite different to the four complexes we have reported previously.[14]

The ^{119}Sn NMR resonance at around δ = –450 ppm is characteristic[21] of the seven-coordinate tin atom observed in the crystalline state for all the complexes. As reported in the literature,[22–24] values of $\delta_{^{119}\text{Sn}}$ in the ranges δ = –210 to –400, –90 to –190, and 200 to –60 ppm have been associated with six-, five-, and four-coordinate tin centers, respectively. On this basis we can conclude that the $\delta_{^{119}\text{Sn}}$ value for the other type of tin atom in **1** is δ = –226.9 ppm in solution, which suggests that the intermolecular Sn–N interaction probably does not survive in solution and that a six-coordinate species is formed. Therefore, it can reasonably be assumed that the structure of complex **1** in solution is different from that observed in the solid state. For com-

 © 2005 Wiley-VCH Verlag GmbH & Co. KGaA, Weinheim

plexes **7**–**9**, the ^{119}Sn chemical shifts (δ = 102.3–111.7 ppm) in $CDCl_3$ indicate that there is also a type of four-coordinate tetrahedral tin atom in these complexes.

Description of the Structures

Crystal Structure of {$Ph_2Sn[4\text{-}NC_5H_4CON_2C(CH_3)CO_2](H_2O)\}_2$ (1)

The molecular structure of complex **1** is shown in Figure 1. Figure 2 shows a particular one-dimensional linear chain polymeric structure. Selected bond lengths and angles are listed in Table 1. The crystal structure of complex **1** reveals a dinuclear complex containing two types of tin atom (mode B), where a one-dimensional chain polymeric structure forms through an interaction between the N atoms of the pyridine ring and the tin atoms of an adjacent molecule. Both of the tin atoms Sn1 and Sn2 have a seven-coordinate geometry in a distorted pentagonal bipyramidal arrangement.

The Sn1 atom is rendered seven-coordinate by coordination of the nitrogen atom N6#1 of the 4-pyridinecarbonyl group from an adjacent molecule. The tin atom is surrounded by one water molecule, one tridentate pyruvic acid isonicotinyl hydrazone ligand, two *trans* phenyl groups, and nitrogen atom N6#1 (x – 1/2, $-y$ + 3/2, z). Thus, the atoms O1, N1, O3, N6#1, and O7 are coplanar within ±0.0263 Å,

Table 1. Selected bond lengths [Å] and bond angles [°] for complex **1**.

Sn1–C19	2.089(15)	Sn2–C31	2.116(18)
Sn1–C25	2.135(13)	Sn2–C37	2.136(14)
Sn1–O3	2.221(11)	Sn2–O4	2.207(9)
Sn1–N1	2.327(11)	Sn2–O6	2.210(7)
Sn1–O7	2.370(10)	Sn2–N4	2.249(12)
Sn1–O1	2.387(7)	Sn2–O2	2.388(10)
Sn1–N6#1	2.394(9)	Sn2–O1	2.594(8)
C19–Sn1–C25	176.8(6)	C31–Sn2–C37	169.9(6)
C19–Sn1–O3	91.5(4)	C31–Sn2–O4	93.1(5)
C25–Sn1–N1	90.5(5)	C37–Sn2–O6	90.1(5)
C25–Sn1–O7	87.0(5)	C37–Sn2–N4	94.3(5)
C19–Sn1–O1	89.5(4)	C31–Sn2–O2	83.8(6)
C25–Sn1–O1	90.3(5)	C37–Sn2–O2	86.2(5)
N1–Sn1–O1	66.2(3)	O6–Sn2–O2	87.8(3)
C19–Sn1–N6#1	87.8(4)	C31–Sn2–O1	86.5(5)
O3–Sn1–N6#1	72.7(4)	O4–Sn2–O1	77.6(3)
O1–Sn1–N6#1	151.2(3)	O2–Sn2–O1	52.2(2)

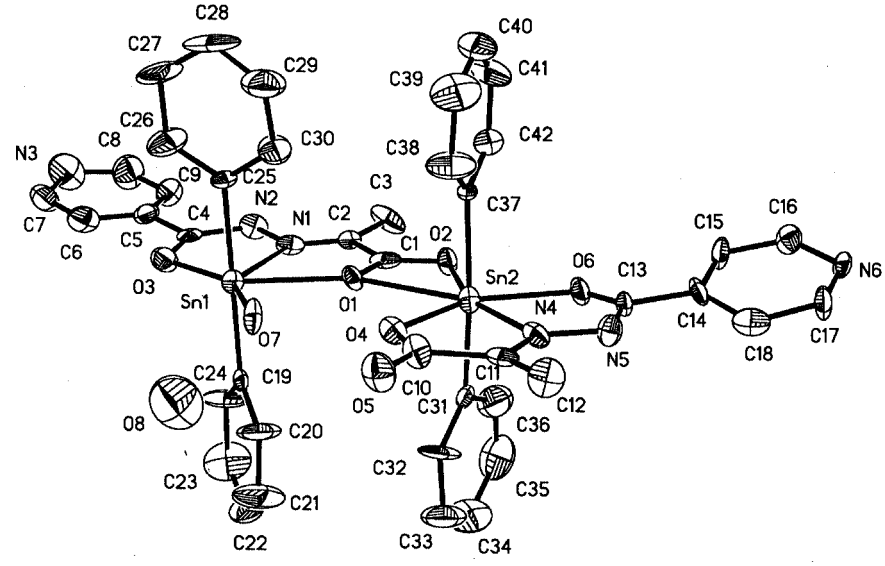

Figure 1. Molecular structure of complex **1**; ellipsoids shown at the 30% probability level.

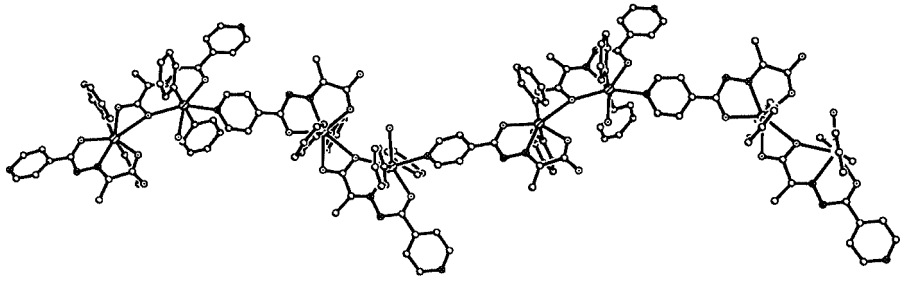

Figure 2. Perspective view of the one-dimensional chain of complex **1**.

 © 2005 Wiley-VCH Verlag GmbH & Co. KGaA, Weinheim

and form the equatorial plane. While two *trans* phenyl carbon atoms occupy the axial sites, the angle of the axial C25–Sn1–C19 is 176.8(6)°, which deviates from the linear angle of 180°. These data indicate that the Sn1 atom is in a distorted pentagonal bipyramid geometry. The intermolecular Sn1–N6#1 distance of 2.394(9) Å is longer than the sum of the covalent radii of Sn and N (2.15 Å), but considerably less than the sum of the van der Waals radii (3.75 Å),[25] therefore it should be considered as a bonding interaction. In this connection it is relevant to note the Sn–N bond lengths found in other crystal structures of organotin complexes containing a pyridinecarboxylate ligand.[20,26] For instance, in the dicarboxylate tetraorganostannoxane $\{[(n\text{Bu})_2\text{Sn}(2\text{-pic})]_2\text{O}\}_2$ the two Sn–N bond lengths are 2.550(5) Å and 3.150(5) Å,[26] and in the linear polymer $[(\text{PhCH}_2)_3\text{Sn}(\text{OO}_2\text{CC}_5\text{H}_4\text{N-4})]$ the Sn–N distance is 2.563 Å.[20]

The Sn2 atom is bonded to the carboxyl oxygens O1 and O2, with Sn2–O1 and Sn2–O2 bond lengths of 2.594(8) and 2.388(10) Å, respectively. Thus, the Sn2 atom is surrounded by C31 and C37 of the two *trans* phenyl groups along the axial direction while O1, O2, O6, N4, and O4 form the equatorial plane. The pentagonal bipyramid geometry of Sn2 is distorted, as indicated by the bonding angles of 169.9(6)°, 93.1(5)°, 90.1(5)°, 142.5(4)°, 95.4(5)°, 83.8(6)°, 157.4(3)° and 86.4(4)° for C31–Sn2–C37, C31–Sn2–O4, C37–Sn2–O6, O4–Sn2–O6, C31–Sn2–N4, C31–Sn2–O2, N4–Sn2–O2, and C37–Sn2–O1, respectively.

Crystal Structure of $[(nC_8H_{17})_2Sn\{4\text{-}NC_5H_4CON_2C(CH_3)CO_2\}(H_2O)]_2$ *(2)*

The molecular structure of compolex **2** is shown in Figure 3. Figure S2 shows the packing of the molecule in the unit cell as seen in projection on the plane. Selected bond lengths and angles are listed in Table 2. In this complex, the Sn atom exists in a seven-coordinate environment in which one water molecule, two tridentate pyruvic acid isonicotinyl hydrazone ligands, and two *trans n*-octyl groups coordinate to each Sn center (mode A). The atoms O1, O5, O4, O3, and N1 are coplanar within ±0.0244 Å, and form the equatorial plane. Furthermore, the angle of the axial C18–Sn1–C10 is 164.4(10)°, which deviates from the linear angle of 180°. These data indicate that the tin atom of this complex is in a distorted pentagonal bipyramid geometry. The O1 atom of the carboxylate residue also binds the other tin atom, Sn2, generating an Sn_2O_2 four-membered ring. The Sn2–O1#2 (x, y + 1, z) distance [2.745(10) Å] is longer than that of Sn1–O1 [2.340(10) Å], but is comparable with those found in related seven-coordinate diorganotin systems.[20,23] The structure of this complex can therefore be described as a *trans*-C_2SnO_4N pentagonal bipyramid with the two *n*-octyl groups occupying *trans* positions [C18–Sn1–C10 = 164.4(10)° and C35–Sn2–C43 = 165.1(8)°]. It also has intradimer hydrogen bonds [O4···O6 = 2.642 Å and O8···O2 = 2.661 Å] and interdimer hydrogen bonds [O4···N6#3 (x – 1/2, –y + 1/2, z) = 2.718 Å and O8···N3#4 (x – 1/2, –y + 3/2, z) = 2.756 Å]. Neighboring molecules are held together by hydrogen bonds (O4···N6#3 and O8···N3#4). These hydrogen bonds contribute to the crystal stability and compactness and result in a one-dimensional chain arrangement. It is worthwhile to note that, for organotin(IV) complexes containing straight-chain alkyl groups, there are plenty of *n*-butyl group complexes, while complexes with *n*-octyl groups are lacking until now. This

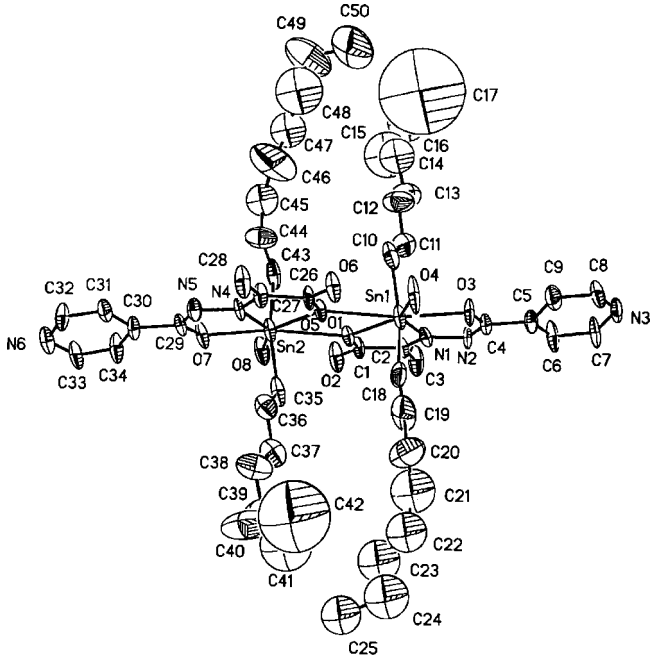

Figure 3. Molecular structure of complex **2**; ellipsoids shown at the 30% probability level.

Table 2. Selected bond lengths [Å] and bond angles [°] for complexes **2** and **3**.

$[(n\text{C}_8\text{H}_{17})_2\text{Sn}\{4\text{-NC}_5\text{H}_4\text{CON}_2\text{C}(\text{CH}_3)\text{CO}_2\}(\text{H}_2\text{O})]_2$ (**2**)			
Sn1–C18	2.06(3)	Sn1–O1	2.340(10)
Sn1–C10	2.09(3)	Sn1–O4	2.354(13)
Sn1–O3	2.219(9)	Sn1–O5#1	2.715(10)
Sn1–N1	2.283(16)		
C18–Sn1–C10	164.4(10)	O3–Sn1–O4	77.4(4)
C10–Sn1–O3	94.2(7)	N1–Sn1–O4	147.4(4)
C18–Sn1–N1	98.5(8)	O1–Sn1–O4	143.9(4)
O3–Sn1–N1	70.0(5)	C10–Sn1–O5#1	83.9(7)
C10–Sn1–O1	90.1(7)	O3–Sn1–O5#1	154.8(4)
O3–Sn1–O1	138.6(4)	N1–Sn1–O5#1	135.1(4)
N1–Sn1–O1	68.6(4)	O1–Sn1–O5#1	66.6(3)
C18–Sn1–O4	80.8(9)	O4–Sn1–O5#1	77.4(3)
$[(o\text{ClBz})_2\text{Sn}\{4\text{-NC}_5\text{H}_4\text{CON}_2\text{C}(\text{CH}_3)\text{CO}_2\}(\text{H}_2\text{O})]_2$ (**3**)			
Sn1–C17	2.145(9)	Sn1–N1	2.275(6)
Sn1–C10	2.166(8)	Sn1–O4	2.323(6)
Sn1–O3	2.180(5)	Sn1–O1	2.400(5)
Sn1–O1#1	2.614(5)		
C17–Sn1–C10	165.0(3)	C10–Sn1–O1	88.1(3)
C17–Sn1–O3	96.2(3)	O3–Sn1–O1	139.10(18)
C10–Sn1–N1	94.8(3)	N1–Sn1–O1	68.53(18)
O3–Sn1–N1	70.6(2)	C17–Sn1–O1#1	83.0(3)
C17–Sn1–O4	87.3(3)	O3–Sn1–O1#1	155.71(15)
O3–Sn1–O4	76.9(2)	N1–Sn1–O1#1	133.69(17)
N1–Sn1–O4	147.43(19)	O1–Sn1–O1#1	65.19(19)

 © 2005 Wiley-VCH Verlag GmbH & Co. KGaA, Weinheim

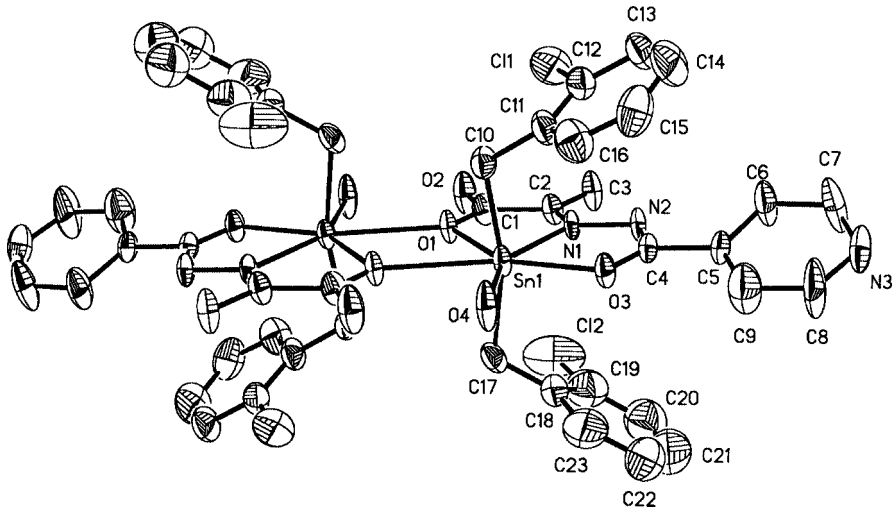

Figure 4. Molecular structure of complex **3**; ellipsoids shown at the 30% probability level.

is possibly because the *n*-octyl group chain is so long that crystals with it are not easy to form.

Although we abtained complex $[(o\text{ClBz})_2\text{Sn}\{4\text{-NC}_5\text{H}_4\text{CON}_2\text{C(CH}_3)\text{CO}_2\}(\text{H}_2\text{O})]_2$ (**3**) by a different method, the structure of **3** (Figure 4) is very similar to complex **2** (mode A), and complex **3** also contains a one-dimensional chain polymer (Figure S2) due to intermolecular hydrogen bonds (O–H···N).

Crystal Structure of $[(n\text{Bu})_2\text{Sn}\{2\text{-HOC}_6\text{H}_4\text{CON}_2\text{C(CH}_3)\text{CO}_2\}\{(n\text{Bu})_3\text{SnOH}\}]_2$ (7)

The molecular structure is illustrated in Figure 5 and selected bond lengths and angles are listed in Table 3. The molecular possesses a dimeric structure containing distannoxane units with two types of tin atoms (mode C).

The Sn1 atom lies in a distorted pentagonal bipyramidal coordination environment [Sn1–C11 = 2.087(12) Å, Sn1–C15 = 2.095(12) Å, Sn1–O3 = 2.188(8) Å, Sn1–O5 = 2.259(9) Å, Sn1–N1 = 2.324(11) Å, Sn1–O1 = 2.419(8) Å, Sn1–O1#1 = 2.585(7) Å] in which one tridentate pyruvic acid isonicotinyl hydrazone ligand, two *trans* *n*-butyl groups, and the O5 atom coordinate to each Sn center. The sum of the angles subtended at the tin atom in the pentagonal plane is 378.16°, so O3, O5, N(1), O1, and O1#1 ($-x + 2, -y + 2, -z$) lie almost in the same plane, with the Sn atom only 0.0062 Å away from the equatorial plane, while the two

Table 3. Selected bond lengths [Å] and bond angles [°] for complex **7**.

Sn1–C11	2.087(12)	Sn2–O5	2.024(9)
Sn1–C15	2.095(12)	Sn2–C19	2.073(17)
Sn1–O3	2.188(8)	Sn2–C23	2.088(14)
Sn1–O5	2.259(9)	Sn2–C27	2.116(17)
Sn1–O1	2.419(8)	N1–C2	1.247(14)
Sn1–N1	2.324(11)	N1–N2	1.345(12)
Sn1–O1#1	2.585(7)	N2–C4	1.315(17)
O3–C4	1.274(15)	O2–O5#1	2.545
C11–Sn1–C15	167.5(5)	O5–Sn2–C19	101.6(6)
C11–Sn1–O3	95.5(4)	O5–Sn2–C23	107.8(5)
C11–Sn1–O5	87.9(5)	C19–Sn2–C23	113.9(7)
O3–Sn1–O5	79.7(3)	O5–Sn2–C27	98.9(6)
C11–Sn1–N1	95.3(4)	C19–Sn2–C27	116.7(8)
O5–Sn1–O1#1	77.6(3)	C23–Sn2–C27	115.2(8)
C11–Sn1–O1	87.1(4)	N1–Sn1–O1	67.0(3)
C11–Sn1–O1#1	83.3(4)	O1–Sn1–O1#1	66.6(3)

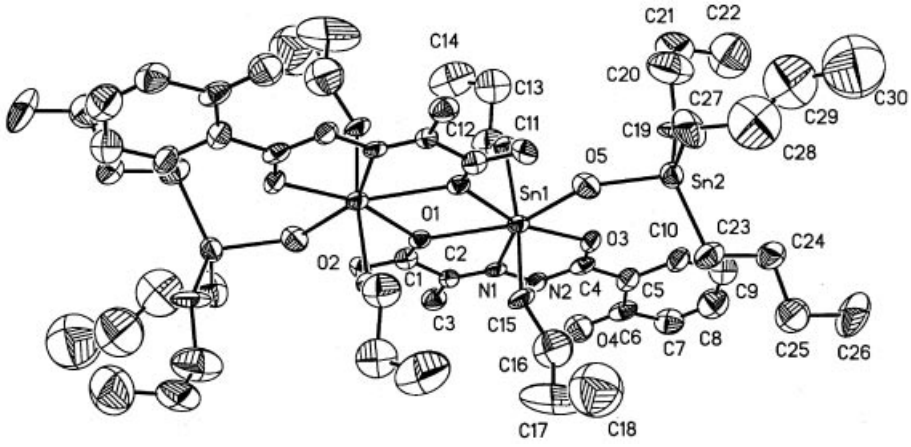

Figure 5. Molecular structure of complex **7**; ellipsoids shown at the 30% probability level.

 © 2005 Wiley-VCH Verlag GmbH & Co. KGaA, Weinheim

trans n-butyl carbon atoms take up the axial sites around the Sn1 atom; the angle of the axial C11–Sn1–C15 is 167.5(5)°. The O1 atom of the carboxylate residue also binds the other tin atom, Sn1#1, generating an Sn_2O_2 four-membered ring, therefore the structure of this complex can be described as a dimer.

The coordination at the tin atom Sn2 is distorted tetrahedral, as indicated by bonding angles of 101.6(6)°, 107.8(5)°, 113.9(7)°, 98.9(6)°, 116.7(8)°, and 115.2(8)° for O5–Sn2–C19, O5–Sn2–C23, C19–Sn2–C23, O5–Sn2–C27, C19–Sn2–C27, and C23–Sn2–C27, respectively. In this complex, two different types of tin atom are connected through the bridging O atom, and intramolecular hydrogen bonds O5–H5···O2#1 [2.565(11) Å] and O4–H4···N2 [2.535(15) Å] are also found. The phenolate oxygen atoms do not participate in coordination to the tin atom.

Crystal Structure of [(oClBz)$_2$Sn{2-HOC$_6$H$_4$CON$_2$C(CH$_3$)CO$_2$}(CH$_3$OH)]$_2$ (10)

The crystal structure of complex **10** is shown in Figure 6. All hydrogen atoms have been omitted for the purpose of clarity. Table 4 lists selected bond lengths and angles.

Table 4. Selected bond lengths [Å] and bond angles [°] for complex **10**.

Sn1–O3	2.138(7)	N1–C2	1.266(15)
Sn1–N1	2.270(9)	N1–N2	1.377(12)
Sn1–O1	2.331(7)	N2–C4	1.304(13)
Sn1–O5	2.394(7)	O1–C1	1.297(12)
Sn1–O1#1	2.647(7)	O3–C4	1.252(12)
C11–Sn1–C18	163.8(4)	C11–Sn1–O5	82.6(4)
C11–Sn1–O3	92.9(4)	N1–Sn1–O5	148.0(3)
O3–Sn1–N1	70.7(3)	O1–Sn1–O5	142.1(3)
C11–Sn1–N1	95.5(4)	O3–Sn1–O1#1	153.8(2)
O3–Sn1–O1	140.4(3)	C11–Sn1–O1#1	85.3(3)
C18–Sn1–O1	90.2(4)	N1–Sn1–O1#1	135.5(3)
N1–Sn1–O1	69.8(3)	O1–Sn1–O1#1	65.7(3)
O3–Sn1–O5	77.5(3)	O5–Sn1–O1#1	76.4(2)

The crystal structure of **10** is also very similar to that of complex **2**. In this complex, the Sn atom exists in a distorted pentagonal bipyramidal coordination environment in which one methanol molecule, two tridentate pyruvic acid salicylhydrazone ligands, and two *trans o*-chlorobenzyl groups coordinate to each Sn center. The atoms O1, O1#1, O5, O3, and N1 are coplanar within ±0.0334 Å, and form the equatorial plane. Furthermore, the angles of the axial C18–Sn1–C11 is 163.8(4)°, which deviates from the linear angle of 180°. The O1 atom of the carboxylate residue also binds the other tin atom Sn1#1 (–x + 2, –y + 1, z), generating an Sn_2O_2 four-membered ring. Thereby the molecular structure of this compound can be described as a dimer, and the coordination geometry of tin can be also described as a *trans*-C_2SnO_4N pentagonal bipyramid, with the two *o*-chlorobenzyl groups occupying *trans* positions. From these data we can see that the crystal structure of complex **10** is very similar to those of **2** and **3**. Obviously, the nature of the alkyl group bonding to the Sn center does not exert a great influence on the overall structural motif. The Sn1–O5 bond length is 2.394(7) Å, which is longer than those in analogous complexes[20,27] due to the formation of intradimeric hydrogen bonds (O2···O5#1 = 2.583 Å). There are also strong intramolecular O–H···N hydrogen bonds (O4···N2 = 2.537 Å) involving atom N2 and the phenolic hydroxyl oxygen atom O4, which does not coordinate to the Sn center. Undoubtedly, these hydrogen bonds contribute to the compactness of the dimer.

Discussion

The complexes $[R_2SnLY]_2$ and $[R_2SnL(R_3SnOH)]_2$ (mode A, B, or C) are produced by the reaction between pyruvic acid isonicotinyl hydrazone and dialkyltin oxide or triaryltin chloride and pyruvic acid salicylhydrazone and triaryltin chloride or bis(trialkyltin) oxide, in a 1:1 molar ratio. It is clear that the presence of the enolic proton of the ligands leads to the dealkylation of the trialkyltin carboxylates $[R_3Sn\{4\text{-}NC_5H_4C(O)NHN{=}C(CH_3)CO_2\}]$ and $[R_3Sn\{2\text{-}HOC_6H_4C(O)NHN{=}C(CH_3)CO_2\}]$, which are the

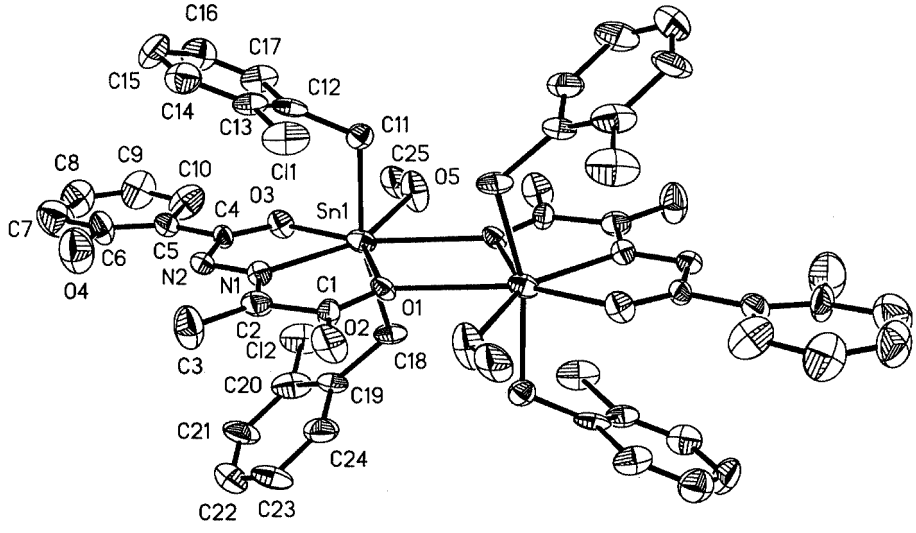

Figure 6. Molecular structure of complex **10**; ellipsoids shown at the 30% probability level.

 © 2005 Wiley-VCH Verlag GmbH & Co. KGaA, Weinheim

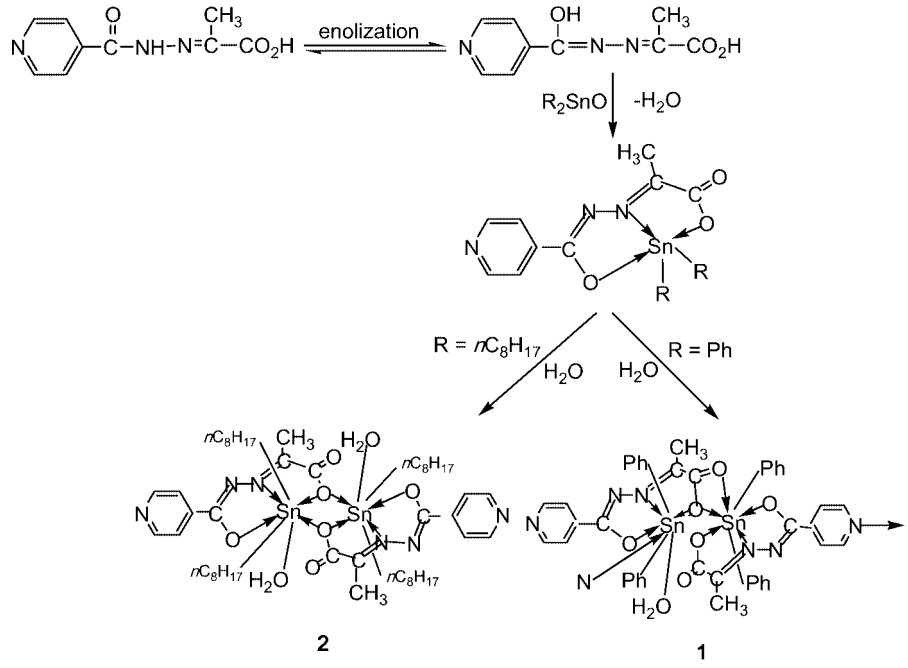

Scheme 2.

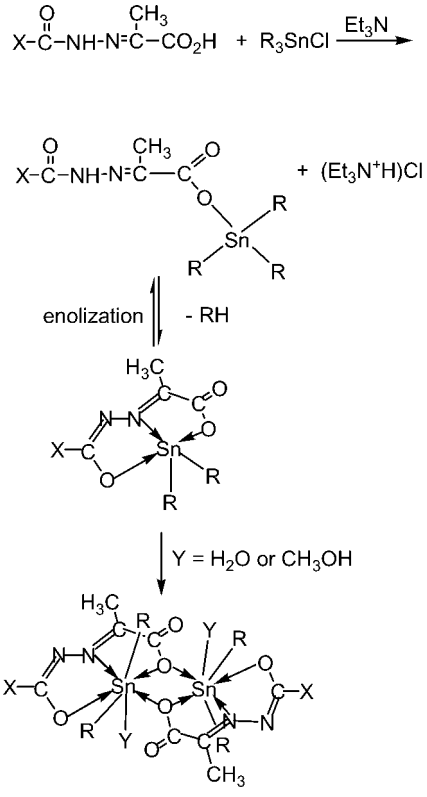

Scheme 3.

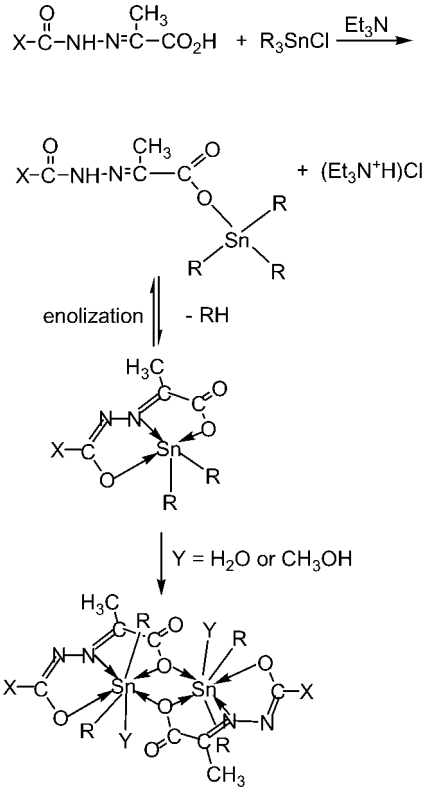

Scheme 4.

 © 2005 Wiley-VCH Verlag GmbH & Co. KGaA, Weinheim

major products of the reaction of R_3SnCl or $(R_3Sn)_2O$ with Schiff-base ligands. Seven-coordinate dimers are formed as a result of steric or solvent effects in the recrystallization. The crystal-structure determinations show that the structures of complexes **1**–**3** are one-dimensional infinite chain polymers due to intermolecular hydrogen-bond interactions between the coordinated water molecule and the pyridine nitrogen atom of the adjacent unit. Complexes **7** and **10**, which contain pyruvic acid salicylhydrazone, are monomers. Their possible reaction mechanisms are shown in Schemes 2, 3, and 4.

Conclusions

The pyruvic acid hydrazone ligands have been shown to be able to form monomeric or polymeric complexes. The nuclearity and stereochemistry are found to be dependent on the nature of the starting acceptor and the reaction conditions. The ligand chelates to tin atoms, bonding through the oxygen of the carboxyl or enolic hydroxy group and the nitrogen atoms. In the polymeric complex, the dimers are connected through intermolecular hydrogen bonds or interactions between the nitrogen atoms of the pyridine ring and the tin atoms of an adjacent molecule. The monomeric complexes possess a highly centrosymmetric dimeric structure containing a distannoxane unit. The reaction of $[(n\mathrm{Bu})_3Sn]_2O$ with pyruvic acid salicylhydrazone gives a novel tetranuclear organotin complex, which exhibits a dimeric structure containing a distannoxane unit with two types of tin atoms that are seven- or four-coordinate.

Experimental Section

Diphenyltin oxide, di-*n*-octyltin oxide and bis(tri-*n*-butyltin) oxide are commercially available, and were used without further purification. The ligands, bis(triaryltin) oxide and triaryltin chloride were prepared by the methods reported in the literature.[28–30] The melting points were obtained with a Kolfer micro melting point apparatus and are uncorrected. IR spectra were recorded with a Nicolet-460 spectrophotometer, as KBr discs. ^1H and ^{119}Sn NMR spectra were recorded with a Mercury Plus-400 NMR spectrometer in $CDCl_3$. The spectra were acquired at room temperature (298 K) unless otherwise specified. The chemical shifts are reported in ppm with respect to the references and are stated relative to external tetramethylsilane (TMS) for ^1H, and to neat tetramethyltin for ^{119}Sn NMR spectroscopy. Elemental analyses were performed with a PE-2400II elemental analyzer.

Pyruvic Acid Isonicotinyl Hydrazone: This Schiff base was prepared from isonicotinic acid hydrazide and pyruvic acid in ethanol according to the literature.[28] A white powder was obtained. Yield: 95% (864.2 mg). M.p. 222–223 °C. $C_9H_9N_3O_3$ (207.19): calcd. C 48.14, H 5.00, N 18.38; found C 48.00, H 4.89, N 18.67.

Pyruvic Acid Salicylhydrazone: This Schiff base was prepared from salicylhydrazide and pyruvic acid in ethanol according to the literature.[29] White, needle-shaped crystals were obtained. Yield: 80% (931.6 mg). M.p. 216 °C. $C_{10}H_{10}N_2O_4$ (222.19): calcd. C 54.92, H 4.54, N 12.61; found C 54.72, H 4.68, N 12.85.

$[Ph_2Sn\{4\text{-}NC_5H_4CON_2C(CH_3)CO_2\}(H_2O)]_2$ (1): Pyruvic acid isonicotinyl hydrazone (2.0 mmol) was added to a benzene/ethanol (3:1, v/v) solution (50 mL) of Ph_2SnO (2.0 mmol). The mixture was heated under reflux with stirring for 6 h. The clear solution thus obtained was evaporated under vacuum to form a brown solid and recrystallized from dichloromethane/hexane to give red crystals. Yield: 78% (113.2 mg). M.p. 165–167 °C. $C_{42}H_{38}N_6O_8Sn_2$ (992.16): calcd. C 50.81, H 3.73, N 8.47; found C 50.73, H 3.69, N 8.52. ^1H NMR ($CDCl_3$, 400 MHz): δ = 2.66 (s, 6 H, CH_3), 5.31 (s, 4 H, H_2O), 7.44–7.79 (m, 20 H, Ph-H), 8.13 (d, J = 6.00 Hz, 4 H, 3,5-pyridine-H), 8.84 (d, J = 5.20 Hz, 4 H, 2,6-pyridine-H) ppm. ^{119}Sn NMR ($CDCl_3$): δ = –226.9, –451.0 ppm.

$[(n\mathrm{C_8H_{17}})_2Sn\{4\text{-}NC_5H_4CON_2C(CH_3)CO_2\}(H_2O)]_2$ (2): Complex **2** was prepared in the same way as complex **1** by adding di-*n*-octyltin oxide (2.0 mmol) to pyruvic acid isonicotinyl hydrazone (2.0 mmol). Unlike the analogous reaction mixtures with di-*n*-butyl-[15] or diphenyltin(IV) oxide, crystallization from dichloromethane/hexane failed to generate the desired crystals of **2**, which is the di-*n*-octyltin analog of the di-*n*-butyltin complex.[15] However, when acetone was used as crystallization solvent colorless crystals of **3** were obtained. Yield: 88% (121.0 mg). M.p. 77 °C. $C_{25}H_{43}N_3O_4Sn$ (568.31): calcd. C 52.73, H 7.57, N, 7.39; found C 52.81, H 7.42, N 7.35. IR (KBr): $\tilde{\nu}$ = 2924 cm^{-1}, 2854 (s, C–H), 1640 (s, C=N), 1606 (s, C=N–N=C), 1619, 1334 (s, CO_2), 1207 (s, C–O), 694 (s, Sn–O), 541 (w, Sn–C), 476 (w, Sn–N). ^1H NMR ($CDCl_3$, 400 MHz): δ = 0.85 (t, J = 10.0 Hz, 6 H, CH_3), 1.22–1.31 [m, 8 H, $Sn(CH_2)_2$ (α,β)], 1.64–1.75 [m, 20 H, CH_2 (ω)], 2.65 (s, 3 H, CH_3), 7.99 (d, J = 5.60 Hz, 2 H, 3,5-pyridine-H), 8.77 (d, J = 5.20 Hz, 2 H, 2,6-pyridine-H) ppm. ^{119}Sn NMR ($CDCl_3$): δ = –460.6 ppm.

$[(o\mathrm{ClBz})_2Sn\{4\text{-}NC_5H_4CON_2C(CH_3)CO_2\}(H_2O)]_2$ (3): Pyruvic acid isonicotinyl hydrazone (2.0 mmol) and tri-*o*-chlorobenzyltin chloride (2.0 mmol) were added to a solution of absolute toluene (30 mL) and heated under reflux with stirring for 1 h. After the addition of triethylamine (2.0 mmol) to the reactor, the reaction mixture was refluxed for 1 h more. The clear solution thus obtained was evaporated under vacuum to form a white solid and recrystallized from methanol to give colorless crystals. Yield: 81% (104.8 mg). M.p. 151 °C. $C_{46}H_{42}Cl_4N_6O_8Sn_2$ (1186.0): calcd. C 46.54, H 3.54, N, 7.08; found C 46.66, H 3.51, N 7.05. ^1H NMR ($CDCl_3$, 400 MHz): δ = 2.46 (s, 6 H, CH_3), 3.19 (s, 8 H, $ArCH_2Sn$), 7.05–7.54 (m, 16 H, Ar-H), 7.72 (d, J = 6.60 Hz, 4 H, 3,5-pyridine-H), 8.70 (d, J = 4.80 Hz, 4 H, 2,6-pyridine-H) ppm. ^{119}Sn NMR ($CDCl_3$): δ = –457.2 ppm.

$[(o\mathrm{FBz})_2Sn\{4\text{-}NC_5H_4CON_2C(CH_3)CO_2\}]_2$ (4): Complex **4** was prepared in the same way as **3** by adding tri-*o*-fluorobenzyltin chloride (2.0 mmol) to pyruvic acid isonicotinyl hydrazone (2.0 mmol). The solid was then obtained from methanol. Yield: 80% (90.6 mg). M.p. 145 °C. $C_{46}H_{38}F_4N_6O_6Sn_2$ (1084.24): calcd. C 50.96, H 3.53, N 7.75; found C 50.84, H 3.48, N 7.88. IR (KBr): $\tilde{\nu}$ = 3007 cm^{-1} (m, Ar–H), 2937, 2738 (s, C–H), 1622 (s, C=N), 1608 (s, C=N–N=C), 1618, 1334 (s, CO_2), 1229 (s, C–O), 694 (s, Sn–O), 480 (w, Sn–N). ^1H NMR ($CDCl_3$, 400 MHz): δ = 2.20 (s, 6 H, CH_3), 3.15 (s, 8 H, $ArCH_2Sn$), 6.60–7.27 (m, 16 H, Ph-H), 7.78 (d, J = 5.60 Hz, 4 H, 3,5-pyridine-H), 8.74 (d, J = 5.80 Hz, 4 H, 2,6-pyridine-H) ppm. ^{119}Sn NMR ($CDCl_3$): δ = –456.3 ppm.

$[(p\mathrm{FBz})_2Sn\{4\text{-}NC_5H_4CON_2C(CH_3)CO_2\}]_2$ (5): Complex **5** was prepared in the same way as **3** by adding tri-*p*-fluorobenzyltin chloride (2.0 mmol) to pyruvic acid isonicotinyl hydrazone (2.0 mmol). The solid was then obtained from methanol. Yield: 86% (98.4 mg). M.p. 138 °C. $C_{46}H_{38}F_4N_6O_6Sn_2$ (1084.24): calcd. C 50.96, H 3.53, N 7.75; found C 50.91, H 3.61, N 7.61. IR (KBr): $\tilde{\nu}$ = 3021 cm^{-1} (s, Ar–H), 2944 (s, C–H), 1620 (s, C=N), 1605 (m, C=N–N=C), 1617, 1341 (s, CO_2), 1233 (s, C–O), 688 (m, Sn–O), 491 (w, Sn–N). ^1H NMR ($CDCl_3$, 400 MHz): δ = 2.25 (s, 6 H, CH_3), 3.23 (s, 8 H,

 © 2005 Wiley-VCH Verlag GmbH & Co. KGaA, Weinheim

$ArCH_2Sn$), 6.63–7.39 (m, 16 H, Ph-H), 7.78 (d, J = 4.80 Hz, 4 H, 3,5-pyridine-H), 8.89 (d, J = 6.40 Hz, 4 H, 2,6-pyridine-H) ppm. ^{119}Sn NMR ($CDCl_3$): δ = –449.8 ppm.

[(*p*CNBz)$_2$Sn{4-NC$_5$H$_4$CON$_2$C(CH$_3$)CO$_2$}]$_2$ (6): Complex **6** was prepared in the same way as **3** by adding tri-*p*-cyanobenzyltin chloride (2.0 mmol) to pyruvic acid isonicotinyl hydrazone (2.0 mmol). The solid was then obtained from methanol. Yield: 91% (115.8 mg). M.p. 210 °C. $C_{50}H_{38}N_{10}O_6Sn_2$ (1112.3): calcd. C 53.98, H 3.42, N 12.60; found C 53.62, H 3.41, N 12.77. IR (KBr): $\tilde{\nu}$ = 3007 cm^{-1} (m, Ar–H), 2922, 2852 (s, C–H), 1630 (m, C=N), 1619, 1385 (m, CO_2), 1602 (m, C=N–N=C), 1200 (m, C–O), 692 (m, Sn–O), 540 (w, Sn–C), 478 (w, Sn–N). ^1H NMR ($CDCl_3$, 400 MHz): δ = 2.42 (s, 6 H, CH_3), 3.08 (s, $ArCH_2Sn$), 7.21–7.35 (m, 16 H, Ph-H), 7.22 (d, J = 8.00 Hz, 4 H, 3,5-pyridine-H), 7.57 (d, J = 8.40 Hz, 4 H, 2,6-pyridine-H) ppm. ^{119}Sn NMR ($CDCl_3$): δ = –453.9 ppm.

[(*n*Bu)$_2$Sn{2-HOC$_6$H$_4$CON$_2$C(CH$_3$)CO$_2$}{(*n*Bu)$_3$SnOH}]$_2$ (7): Pyruvic acid salicylhydrazone (1.0 mmol) was added to a benzene suspension (30 mL) of bis(tri-*n*-butyltin) oxide (1.0 mmol), then the mixture was stirred and heated at reflux for 6 h. The clear solution obtained after fliteration was evaporated in vacuo to give a solid, which was then recrystallized from dichloromethane/hexane to give colorless crystals. Yield: 83% (71.5 mg). M.p. 101 °C. $C_{30}H_{54}N_2O_5Sn_2$ (759.12): calcd. C 47.40, H 7.16, N 3.68; found C 47.32, H 7.15, N 3.77. IR (KBr): $\tilde{\nu}$ = 3423 cm^{-1} (m, OH), 2955 (s, Ar–H), 2922, 2853 (s, C–H), 1627 (m, C=N), 1608, 1334 (s, CO_2), 1583 (m, C=N–N=C), 1205 (s, C–O), 672 (m, Sn–O), 560 (w, Sn–C), 502 (w, Sn–N). ^1H NMR ($CDCl_3$, 400 MHz): δ = 0.83 (t, J = 6.40 Hz, 15 H, CH_3), 1.19–1.61 (m, 30 H, $SnCH_2CH_2CH_2$), 2.38 (s, 3 H, CH_3), 6.88–7.35 (m, 4 H, Ph-H), 11.22 (s, 1 H, Ar-OH) ppm. ^{119}Sn NMR ($CDCl_3$): δ = 102.3, –453.9 ppm.

[Bz$_2$Sn{2-HOC$_6$H$_4$CON$_2$C(CH$_3$)CO$_2$}{Bz$_3$SnOH}]$_2$ (8): Complex **8** was prepared in the same way as **7** by adding bis(tribenzyltin) oxide (1.0 mmol) to pyruvic acid salicylhydrazone (1.0 mmol). The solid was then obtained from dichloromethane/hexane. Yield: 91% (82.2 mg). M.p. 215 °C. $C_{45}H_{43}N_2O_5Sn_2$ (929.25): calcd. C 58.10, H 4.77, N 3.01; found C 58.25, H 4.53, N 3.11. IR (KBr): $\tilde{\nu}$ = 3411 cm^{-1} (m, OH), 3035 (s, Ph–H), 2952, 2859 (s, C–H), 1630 (s, C=N), 1596, 1347 (s, CO_2), 1579 (m, C=N–N=C), 1202 (s, C–O), 679 (m, Sn–O), 555 (m, Sn–C), 477 (w, Sn–N). ^1H NMR ($CDCl_3$, 400 MHz): δ = 2.65 (d, J = 5.60 Hz, 3 H, CH_3), 2.81 (t, $J_{Sn,H}$ = 68.88 Hz, 6 H, $ArCH_2Sn$), 3.16 (s, 4 H, $ArCH_2Sn$), 6.93–7.28 (m, 29 H, Ar-H and Ph-H), 11.43 (s, 1 H, Ar-OH) ppm. ^{119}Sn NMR ($CDCl_3$): δ = 111.7, –449.5 ppm.

[(*p*CNBz)$_2$Sn{2-HOC$_6$H$_4$CON$_2$C(CH$_3$)CO$_2$}{(*p*CNBz)$_3$SnOH}]$_2$ (9): Complex **9** was prepared in the same way as **7** by adding bis(tri-*p*-cyanobenzyltin) oxide (1.0 mmol) to pyruvic acid salicylhydrazone (1.0 mmol). The solid was then obtained from dichloromethane/hexane. Yield: 93% (99.7 mg). M.p. 218 °C. $C_{50}H_{38}N_7O_5Sn_2$ (1054.30): calcd. C 56.91, H 3.72, N 9.29; found C 57.15, H 3.55, N 9.21. IR (KBr): $\tilde{\nu}$ = 3423 cm^{-1} (s, OH), 3017 (s, Ph–H), 2988, 2889 (m, C–H), 1621 (m, C=N), 1606, 1367 (s, CO_2), 1542 (s, C=N–N=C), 1211 (s, C–O), 674 (m, Sn–O), 547 (w, Sn–C), 485 (w, Sn–N). ^1H NMR ($CDCl_3$, 400 MHz): δ = 2.44 (d, J = 5.40 Hz, 3 H, CH_3), 2.79 (t, $J_{Sn,H}$ = 65.48 Hz, 6 H, $ArCH_2Sn$), 3.22 (s, 4 H, $ArCH_2Sn$), 6.81–7.42 (m, 24 H, Ar-H and Ph-H), 10.91 (s, 1 H, Ar-OH) ppm. ^{119}Sn NMR ($CDCl_3$): δ = 109.5, –452.3 ppm.

[(*o*ClBz)$_2$Sn{2-HOC$_6$H$_4$CON$_2$C(CH$_3$)CO$_2$}(CH$_3$OH)]$_2$ (10): Pyruvic acid salicylhydrazone (2.0 mmol) and tri-*o*-chlorobenzyltin chloride (2.0 mmol) were added to a solution of absolute toluene (30 mL) and heated under reflux, with stirring, for 1 h. After the addition of triethylamine (2.0 mmol) to the reactor, the reaction mixture was refluxed for 1 h more. The clear solution thus obtained was evaporated under vacuum to form a white solid and recrystallized from methanol to give colorless crystals. Yield: 85% (111.8 mg). M.p. 131 °C. $C_{50}H_{48}Cl_4N_4O_{10}Sn_2$ (1244.1): calcd. C 48.27, H 3.89, N, 4.49; found C 48.36, H 3.71, N 4.55. IR (KBr): $\tilde{\nu}$ = 3417 cm^{-1} (m, OH), 3021 (m, Ar–H), 2916 (m, C–H), 1618 (m, C=N), 1603 (s, C=N–N=C), 1586, 1321 (s, CO_2), 1209 (m, C–O), 677 (m, Sn–O), 525 (w, Sn–C), 465 (w, Sn–N). ^1H NMR ($CDCl_3$, 400 MHz): δ = 1.66 (s, 12 H, CH_3), 3.39 (s, 8 H, $ArCH_2Sn$), 6.84–7.59 (m, 24 H, Ar-H and Ph-H), 8.09 (s, 2 H, R-OH), 11.16 (s, 2 H, Ar-OH) ppm. ^{119}Sn NMR ($CDCl_3$): δ = –445.8 ppm.

[(*p*ClBz)$_2$Sn{2-HOC$_6$H$_4$CON$_2$C(CH$_3$)CO$_2$}]$_2$ (11): Complex **11** was prepared in the same way as **10** by adding tri-*p*-chlorobenzyltin chloride (2.0 mmol) to pyruvic acid salicylhydrazone (2.0 mmol). The solid was then obtained from methanol. Yield: 87% (115.3 mg). M.p. 144 °C. $C_{48}H_{40}Cl_4N_4O_8Sn_2$ (1179.6): calcd. C 48.84, H 3.39, N 4.75; found C 48.91, H 3.47, N 4.62. IR (KBr): $\tilde{\nu}$ = 3379 cm^{-1} (s, OH), 3023 (m, Ar–H), 2916 (m, C–H), 1633 (m, C=N), 1602 (s, C=N–N=C), 1594, 1367 (s, CO_2), 1202 (m, C–O), 685 (m, Sn–O), 525 (w, Sn–C), 474 (w, Sn–N). ^1H NMR ($CDCl_3$, 400 MHz): δ = 1.66 (s, 6 H, CH_3), 3.26 (s, 8 H, $ArCH_2Sn$), 6.26–7.63 (m, 24 H, Ar-H and Ph-H), 11.18 (s, 2 H, Ar-OH) ppm. ^{119}Sn NMR ($CDCl_3$): δ = –443.5 ppm.

[(*p*CNBz)$_2$Sn{2-HOC$_6$H$_4$CON$_2$C(CH$_3$)CO$_2$}]$_2$ (12): Complex **12** was prepared in the same way as **10** by adding tri-*p*-cyanobenzyltin chloride (2.0 mmol) to pyruvic acid salicylhydrazone (2.0 mmol). The solid was then obtained from methanol. Yield: 72% (92.1 mg). M.p. 215 °C. $C_{52}H_{40}N_8O_8Sn_2$ (1142.3): calcd. C 54.67, H 3.53, N 9.81; found C 54.81, H 3.44, N 9.72. IR (KBr): $\tilde{\nu}$ = 3411 cm^{-1} (m, OH), 3102 (m, Ar–H), 2922 (m, C–H), 1612 (m, C=N), 1600 (m, C=N–N=C), 1588, 1352 (s, CO_2), 1206 (m, C–O), 677 (w, Sn–O), 523 (m, Sn–C), 459 (w, Sn–N). ^1H NMR ($CDCl_3$, 400 MHz): δ = 1.52 (s, 6 H, CH_3), 3.35 (s, 8 H, $ArCH_2Sn$), 6.35–7.61 (m, 24 H, Ar-H and Ph-H), 10.87 (s, 2 H, Ar-OH) ppm. ^{119}Sn NMR ($CDCl_3$): δ = –452.8 ppm.

X-ray Crystallographic Study: All measurements were made on a Bruker Smart 1000 CCD diffractometer at 298(2) K with graphite-monochromated Mo-K_α (λ = 0.71073 Å). Semi-empirical absorption corrections were applied using the SADABS program. The structures were solved by direct methods and difference Fourier maps using SHELXL-97,[31] and refined by full-matrix least-squares on F^2. All non-hydrogen atoms were included in the model at their calculated positions.

CCDC-250084 (**1**), -255498 (**2**), -255497 (**3**), -269987 (**7**), and -269988 (**10**) contain the supplementary crystallographic data for this paper. These data can be obtained free of charge from The Cambridge Crystallographic Data Center via www.ccdc.cam.ac.uk/data_request/cif.

Supporting Information (see footnote on the first page of this article): Figures S1, S2, S3, and S4 show the unit cell of complexes **2**, **3**, **7**, and **10**, respectively Crystal data and details of the structure determinations are listed in Tables S1 and S2.

Acknowledgments

We acknowledge the financial support of the Natural Science Foundation of China (no. 20271025), the Shandong Province Science Foundation (no. L2003B01), and the State Key Laboratory of Crystal Materials, Shandong University, P. R. China.

[1] L. Sacconi, *Coord. Chem. Rev.* **1966**, *1*, 126–142.
[2] S. Yamada, *Coord. Chem. Rev.* **1966**, *1*, 415–441.

[3] C. Mehrotra, G. Srivastava, B. S. Saraswat, *Rev. Silicon, Germanium, Tin Lead Compd.* **1982**, *6*, 171–194.
[4] M. Nath, S. Goyal, *Main Group Met. Chem.* **1996**, *19*, 75–89.
[5] R. S. Collinson, D. E. Ferton, *Coord. Chem. Rev.* **1996**, *148*, 19–40.
[6] P. Yang, M. Guo, *Coord. Chem. Rev.* **1999**, *185*, 189–211.
[7] M. Gielen, *Metal-Based Drugs* **1994**, *1*, 213–220.
[8] M. Nath, S. Pokharia, R. Yadav, *Coord. Chem. Rev.* **2001**, *215*, 99–149.
[9] A. J. Crowe, P. J. Smith, C. J. Cardin, H. E. Parge, F. E. Smith, *Cancer Lett.* **1984**, *24*, 45–48.
[10] V. I. Bregadze, S. A. Glazun, P. V. Petrovakii, Z. A. Starikova, V. Y. Rochev, H. Dalil, M. Biesemans, R. Willem, M. Gielen, D. D. Vos, *Appl. Organomet. Chem.* **2003**, *17*, 453–459.
[11] K. C. Joshi, V. N. Pathak, P. Panwar, *Agric. Biol. Chem.* **1977**, *41*, 543–548.
[12] A. Saxena, J. P. Tandon, A. J. Crowe, *Polyhedron* **1985**, *4*, 1085–1089.
[13] G. Y. Yeap, H. K. Fun, S. B. Teo, S. G. Teoh, *Acta Crystallogr., Sect. C* **1992**, *48*, 1109–1110.
[14] H. D. Yin, Q. B. Wang, S. C. Xue, *J. Organomet. Chem.* **2004**, *689*, 2480–2485.
[15] H. D. Yin, M. Hong, Q. B. Wang, *Indian J. Chem.* **2004**, *43A*, 2301–2306.
[16] M. Hong, H. D. Yin, D. Q. Wang, *Acta Crystallogr., Sect. E* **2005**, *61*, 801–803.
[17] D. K. Rastogi, S. K. Dua, V. B. Rana, S. K. Shni, *J. India Chem. Soc.* **1978**, 1323–1331.
[18] J. T. Wang, F. Q. Liu, Y. W. Zhang, R. J. Wang, H. G. Wang, X. K. Yao, *J. Organomet. Chem.* **1989**, *375*, 173–181.
[19] F. Q. Liu, J. T. Wang, R. J. Wang, H. G. Wang, X. K. Yao, *J. Organomet. Chem.* **1989**, *371*, 35–41.
[20] M. Gielen, H. Dalil, L. Ghys, B. Boduszek, E. R. T. Tiekink, J. C. Martins, M. Biesemans, R. Willem, *Organometallics* **1998**, *17*, 4259–4263.
[21] F. Kayser, M. Biesemans, M. Boualam, E. R. T. Tiekink, A. El Khloufi, J. Meunier-Piret, A. Bouhdid, K. Jurkschat, M. Gielen, R. Willem, *Organometallics* **1994**, *13*, 1098–1104.
[22] J. Holecek, M. Nadvornik, K. Handlir, A. Lycka, *J. Organomet. Chem.* **1986**, *315*, 299–305.
[23] D. Dakternieks, A. Duthie, D. R. Smyth, C. P. D. Stapleton, E. R. T. Tiekink, *Organometallics* **2003**, *22*, 4599–4603.
[24] F. P. Pruchnik, M. Banbula, Z. Ciunik, M. Latocha, B. Skop, T. Wilczok, *Inorg. Chim. Acta* **2003**, *356*, 62–68.
[25] A. Bondi, *J. Phys. Chem.* **1964**, *68*, 441–445.
[26] a) C. S. Parulekar, V. K. Jain, T. K. Das, A. R. Gupta, B. F. Hoskins, E. R. T. Tiekink, *J. Organomet. Chem.* **1989**, *372*, 193–199; b) T. P. Lockhart, F. Davidson, *Organometallics* **1987**, *6*. 2471–2477.
[27] H. D. Yin, C. H. Wang, Y. Wang, C. L. Ma, J. X. Shao, *Chem. J. Chin. Univ.* **2003**, *24*, 68–72.
[28] Z. Y. Yang, L. F. Wang, J. G. Wu, X. Y. Li, *Chin. J. Appl. Chem.* **1992**, *9*, 31–36.
[29] S. Y. He, W. K. Cao, J. L. Chen, J. S. Zhao, Q. Z. Shi, R. X. Wang, J. Sun, *Chem. J. Chin. Univ.* **2002**, *23*, 991–995.
[30] Q. L. Xie, X. H. Xu, D. K. Zhang, *Acta Chim. Sin. (Chin. Ed.)* **1992**, *50*, 508–514.
[31] G. M. Sheldrick, *SHELXL-97 and SHELXS-97*, University of Göttingen, Germany, **1997**.

Received: May 8, 2005
Published Online: October 13, 2005

 © 2005 Wiley-VCH Verlag GmbH & Co. KGaA, Weinheim

Anchoring of Vanadyl Acetylacetonate onto Amine-Functionalised Activated Carbons: Catalytic Activity in the Epoxidation of an Allylic Alcohol

Bruno Jarrais,[a] Ana Rosa Silva,[a] and Cristina Freire*[a]

Keywords: Activated carbon / Anchoring / Epoxidation / EPR spectroscopy / Vanadium

Vanadyl(IV) acetylacetonate was anchored onto two different amine-functionalised activated carbons. The starting activated carbon supports were air (A2) and nitric acid oxidised (B1) carbons; the phenol surface groups of carbon A2 were subsequently treated with (3-aminopropyl)triethoxysilane (A3) and afterwards the free amine groups were used for Schiff condensation with $[VO(acac)_2]$ (A4). Carbon B1, which possesses carboxylic surface groups, was treated with thionyl chloride to give surface acyl chloride groups (B2), which were then reacted with the amine groups of bis(3-aminopropyl)amine (B3); subsequent attachment of $[VO(acac)_2]$ was also achieved by Schiff condensation between the free amine groups of the functionalised carbon and the ligand oxygen atoms (B4). All the materials were characterised by XPS, and the $[VO(acac)_2]$-based materials were also characterised by vanadium elemental analysis and EPR spectroscopy. A combination of all the data provides evidence for the covalent attachment of the vanadium complex onto the modified activated carbons. The catalytic activity of the $[VO(acac)_2]$-based materials in the epoxidation of 3-buten-2-ol using *tert*-butyl hydroperoxide as oxygen source was assessed and compared to that of the homogeneous phase reaction. The alkene conversion in the heterogeneous phase is similar to that observed in the homogeneous phase, although the rate of oxidation is less than half that of the homogeneous system. Material A4 exhibits higher catalytic efficiency than B4; upon reuse, both materials show no significant decrease in their catalytic properties.
(© Wiley-VCH Verlag GmbH & Co. KGaA, 69451 Weinheim, Germany, 2005)

Introduction

Vanadyl(IV) acetylacetonate has been found to be a useful homogeneous catalyst in several oxidation reactions, such as the oxidation of alcohols,[1] oxidation of sulfides to sufoxides,[1,2] oxidation of thiols to disulfides[3] and in the epoxidation of allylic alcohols.[1,2] Moreover, the catalytic activity of vanadyl(IV) acetylacetonate is not only restricted to oxidation reactions; it has also been employed in ring-cleavage reactions[4] and in oxidative polymerisation reactions[5] and polymerisation of diphenyl disulfides,[6] thus making it a versatile and readily available catalyst.

Epoxides are extremely useful building blocks in the synthesis of organic compounds as they act as excellent intermediates that can yield a great variety of products.[7] The homogeneous epoxidation of allylic alcohols by vanadyl(IV) acetylacetonate under mild conditions and using *tert*-butyl hydroperoxide as the oxygen source has been widely studied and exhibits high activity, selectivity and regioselectivity.[1,2,8,9] The catalytically active oxo-peroxo intermediate is formed in situ by oxidation of V^{IV} to V^{V} with an excess of *tert*-butyl hydroperoxide, yielding a *tert*-butyl hydroperoxovanadium(V) complex. A good example of the high regioselectivity of this complex is the epoxidation of geraniol, an allylic alcohol containing an isolated double bond, which is catalysed by a $[VO(acac)_2]$–*tert*-butyl hydroperoxide system, where the allylic double bond is selectively oxidised, whereas peracids preferentially epoxidise the isolated double bond.[1]

The heterogenisation of these transition metal complexes on solid supports allows the combination of their homogeneous catalytic properties with those of heterogeneous catalysts, such as the ease of separation from reaction media, shape selectivity and reuseability.[10–13] Early approaches to heterogenisation consisted of ion exchanging or simple adsorption of the metal complexes onto the supports, but these procedures did not prevent active-phase leaching.[12,13] This problem was recently overcome by the development of several grafting and tethering methodologies, which allow the covalent attachment of transition metal complexes to organic polymers, silica, zeolites and other micro- and mesoporous inorganic materials.[10–13]

Activated carbons and other carbon-based materials are widely used as catalysts and as supports for metals in their reduced state,[14,15] and a few reports have appeared on the heterogenisation of metal complexes, mainly of noble metals with simple ligands, to be used in hydrogenation and hydroformylation reactions.[16–18] We have been developing several anchoring procedures to immobilise Schiff-base transition metal complexes onto activated carbons and

[a] REQUIMTE, Departamento de Química, Faculdade de Ciências, Universidade do Porto,
4169-007 Porto, Portugal
Fax: +351-22-608-2959
E-mail: acfreire@fc.up.pt

 © 2005 Wiley-VCH Verlag GmbH & Co. KGaA, Weinheim **DOI: 10.1002/ejic.200500435**

other supports.[19–23] In one of these works, copper(II) acetylacetonate was irreversibly anchored onto a chemically oxidised activated carbon functionalised with bis(3-aminopropyl)amine (trien) by Schiff-base condensation between the free amine groups of trien covalently attached to the activated carbon surface and the oxygen atoms of acetylacetonate coordinated to copper(II).[23] In the present work, we report an extension of this latter procedure to vanadyl(IV) acetylacetonate and a new route for complex immobilisation, in which an oxygen-oxidised activated carbon, previously functionalised with (3-aminopropyl)triethoxysilane (APTES), is used to anchor vanadyl(IV) acetylacetonate by Schiff-base condensation between the free amine groups of APTES and the ligand oxygen atoms. The functionalisation steps were followed by X-ray photoelectron spectroscopy (XPS), and the $[VO(acac)_2]$-based materials were characterised by vanadium ICP-AES analysis and by EPR spectroscopy. The catalytic activity of these two novel carbon-based vanadyl(IV) acetylacetonate heterogeneous catalysts was tested at 0 °C in the epoxidation of an allylic alcohol (3-buten-2-ol) in dichloromethane using *tert*-butyl hydroperoxide (*t*BuOOH) as the oxygen source. Their reusability was also tested.

Results and Discussion

Vanadyl(IV) acetylacetonate was anchored onto two different amine-functionalised activated carbons using the methods summarised in Scheme 1. In method A, an air-oxidised activated carbon (A2) with a high amount of surface phenol groups was treated with (3-aminopropyl)triethoxysilane (APTES), resulting in a surface with free amine groups (A3). In method B, the starting material was a nitric acid oxidised activated carbon (B1), which possesses a high concentration of carboxylic acid groups. These were converted into more reactive acyl chloride functionalities by treatment with thionyl chloride (B2), and then reacted with the amine groups of bis(3-aminopropyl)amine (trien, B3). The free amine groups in both carbons A3 and B3 were used for Schiff-base condensation with $[VO(acac)_2]$ to give A4 and B4, respectively. All the materials were characterised by XPS, and the $[VO(acac)_2]$-based materials were also characterised by vanadium ICP-AES analysis and EPR spectroscopy. The XPS data of materials A1, A2, B1, B2 and B3 have already been described in previous papers[22,23] and thus here we will focus on the characterisation of the new materials, only recalling relevant aspects of the previous ones.

Characterisation of the Heterogeneous Catalysts

X-ray Photoelectron Spectroscopy and Elemental Analysis

Table 1 contains the XPS atomic percentages of all the carbon-based materials and Figure 1 shows the XPS high-resolution spectra in the O 1s region (for the series of carbons A) and in the V 2p region (for carbons with anchored vanadyl complexes, A4 and B4).

Table 1. XPS atomic percentages for carbon-based materials.

Sample	Atom %						Ref.
	O	N	Cl	C	Si	V	
A1	7.66	0.58	0.86	90.41	–	–	this work
A2	12.58	0.70	0.30	86.15	–	–	this work
A3	17.08	2.83	–	73.44	6.66	–	this work
A4	17.71	2.55	0.23	73.24	5.28	0.98	this work
B1	20.27	0.58	0.13	78.61	[a]	–	[23]
B2	10.98	0.60	3.03	84.84	[a]	–	[23]
B3	9.01	3.64	1.81	85.06	[a]	–	[23]
B4	8.56	2.07	1.05	87.10	0.49[b]	0.72	this work

[a] Not analysed. [b] Silica impurity on carbon matrix.

There is a significant increase in the oxygen content when the parent carbon A1 is submitted to the two different oxidation procedures (Table 1), thus indicating the formation of new oxygen functionalities at the surface of the activated carbon.[19–24]

In the O 1s region (Figure 1, a), sample A1 exhibits a symmetrical broad peak centred at 532.3 eV, whereas sample A2 shows a more-intense and asymmetric peak centred at 533.6 eV with a shoulder at 532.0 eV. The air oxidation of A1 increases the number of phenol and carbonyl groups,[24] which exhibit O 1s peaks in the region 532–533 eV,[25–27] therefore the shoulder in A2 is assigned to these basic groups. After reaction with APTES (A3), there is an increase in the area under the bands in the N 1s, O 1s and Si 2p regions, as can be seen in Table 1, thus confirming

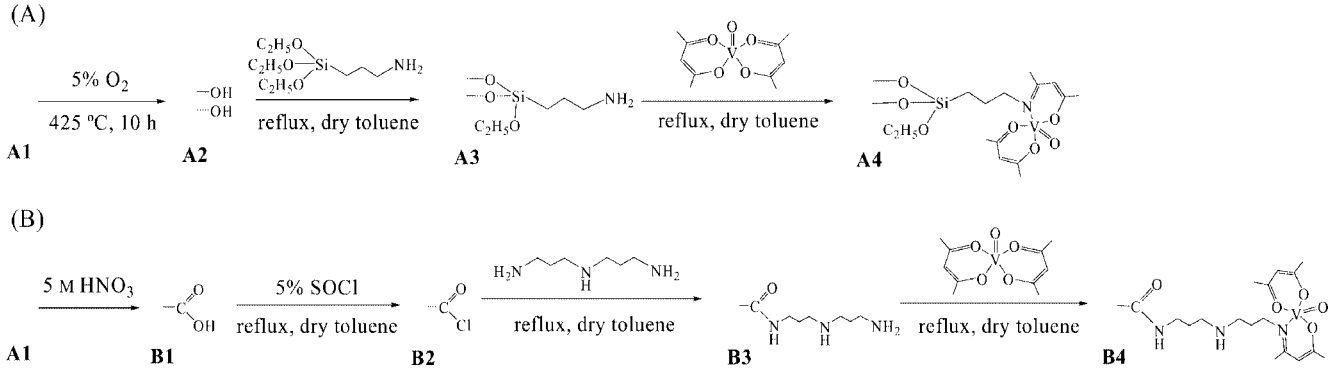

Scheme 1. Proposed structures for the anchored $[VO(acac)_2]$ on functionalised activated carbons prepared by methods A and B.

 © 2005 Wiley-VCH Verlag GmbH & Co. KGaA, Weinheim

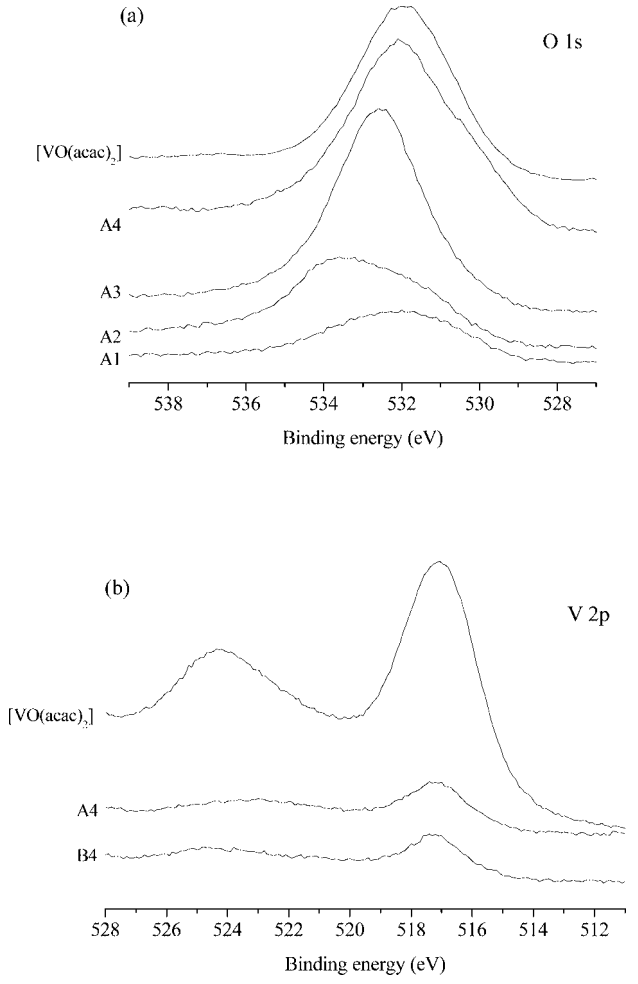

Figure 1. High-resolution XPS spectra of carbon-based materials in the O 1s (a) and V 2p (b) regions.

that APTES has been successfully anchored onto the air-oxidised carbon. The spectra of A3 in the O 1s region (Figure 1, a) is quite different from carbon A2 and shows a very intense and symmetric peak at 532.6 eV; this peak may be assigned not only to ether-type oxygen atoms, which result from the reaction between the APTES ethoxy functionalities and carbon surface phenol groups, but also to unreacted ethoxy groups from the aminoalkylsilane.[25,28] Upon complex anchoring on carbon A3, a new peak at 531.6 eV is observed in the O 1s region, which may be assigned to oxygen atoms from $[VO(acac)_2]$ (BE = 531.7 eV; Figure 1, a);[19–23] an increase in intensity in the high binding energies of the N 1s peak is also detected, suggesting the presence of nitrogen atoms in a new and different chemical environment.

Upon reaction of carbon B1 with thionyl chloride there is an increase in the chlorine content accompanied by a decrease in the oxygen content, thus indicating the formation of acyl chloride groups.[21,23] With the introduction of trien in B2, there is a significant increase in the nitrogen content, accompanied by a decrease in the chlorine surface quantity. This indicates that reaction between the amine groups of trien and the carbon acyl chloride functionalities has occurred, with formation of new amide groups and loss of hydrogen chloride. A loss of the surface oxygen is also observed, which can be explained by the parallel reaction of trien with other carbon surface groups, such as carbonyl groups, thus increasing the effectiveness of the trien anchoring.[23] Similarly, after reaction of B3 with $[VO(acac)_2]$, an increase in the peak at 532.0 eV in the O 1s region is observed (assigned to the oxygen atoms of the complex) and an increase in the broadness of the N 1s peak is also detected as a consequence of the presence of new nitrogen atoms in different chemical environments.

The observation of peaks in the V $2p_{3/2}$ region of the high-resolution spectra of A4 and B4 (Figure 1, b) confirms the presence of the metal complexes in both modified activated carbons. The areas under these bands allow the calculation of the surface amount of vanadium per weight of material, which are 697 and 554 $\mu mol\,g^{-1}$, respectively (Table 2). The similarity between the V 2p band profiles of the free and the anchored complexes (A4 and B4) suggests that the complex has kept its integrity upon immobilisation on the activated carbons. Furthermore, a comparison of the V $2p_{3/2}$ peak of free $[VO(acac)_2]$ (BE = 516.8 eV) with those of anchored complexes in A4 and B4 (BE = 517.0 and 517.2 eV, respectively; Figure 1, b) gives additional information on the V metal centre: the observed shift to higher binding energies suggests the presence of a more deshielded V centre. This observation, combined with the results referred to above, suggest complex anchoring through Schiff-base condensation between the carbon amine groups and ligand oxygen atoms, with the formation of a V–N in-plane bond, which induces a higher degree of in-plane covalence. Nonetheless, on the basis of the XPS data alone, we cannot exclude some direct axial coordination of the complex (available sixth position) onto the carbon oxygen surface

Table 2. Vanadium and silicon bulk contents obtained by ICP-AES.

Sample	Si [wt.-%]	n_i[a] [mmol g^{-1}]	n_f[b] [mmol g^{-1}]	η[c] [%]	V [wt.-%]	n_i[d] [μmol g^{-1}]	n_f[e] [μmol g^{-1}]	η[c] [%]
A4	3.00	1.42	1.10 (3.76)[f]	77	0.65	198	128 (697)[f]	65
B4	–	–	–	–	0.85	198	170 (554)[g]	86

[a] n_i = initial APTES mol (solution)/weight activated carbon. [b] n_f = adsorbed APTES mol/weight activated carbon. [c] $\eta = n_f \times 100/n_i$. [d] n_i = initial $[VO(acac)_2]$ mol (solution)/weight activated carbon. [e] n_f = adsorbed $[VO(acac)_2]$ mol/weight activated carbon. [f] Silicon surface content per weight of sample calculated from XPS data in Table 1: mmol Si/weight of sample = atom % Si/[atom % C × Ar(C) + atom % N × Ar(N) + atom % O × Ar(O) + atom % Si × Ar(Si) + atom % Cl × Ar(Cl) + atom % V × Ar(V)]. [g] Vanadium surface content per weight of sample calculated from XPS data in Table 1: μmol V/weight of sample = atom % V/[atom % C × Ar(C) + atom % N × Ar(N) + atom % O × Ar(O) + atom % Si × Ar(Si) + atom % Cl × Ar(Cl) + atom % V × Ar(V)].

 © 2005 Wiley-VCH Verlag GmbH & Co. KGaA, Weinheim

groups, as a similar effect on the vanadium binding energy would be expected. The other hypothesis for complex anchoring via vanadium axial coordination through the free NH_2 groups of trien or APTES can be excluded, as it would induce an increase in V electronic density (NH_2 groups behave as electron donors), thus leading to a more shielded V atom, which would give rise to a decrease in the binding energy.

The vanadium bulk content of carbons A4 and B4 was determined by ICP-AES and from this it was possible to calculate the complex loading (mass of vanadium/mass of carbon × 100) and the immobilisation efficiency (amount of adsorbed complex/amount in original solution × 100), which are summarised in Table 2. In the case of material A4, the silicon bulk content was also obtained, allowing the calculation of APTES loading and its anchoring efficiency on carbon A4 (1.10 μmol g^{-1} and 77%, respectively). The complex is anchored more efficiently onto the trien-functionalised carbon (86%) than onto the APTES-functionalised carbon (65%).

The vanadium bulk contents for A4 and B4 are 128 and 170 μmol g^{-1}, respectively, and are therefore lower than the surface content obtained by XPS (697 and 554 μmol g^{-1}, respectively). This suggests that both vanadyl(IV) acetylacetonate complexes are mainly anchored at the outer pores of the carbon matrix (although this is more evident for material A4), probably as a consequence of size constraints imposed by the size of the innermost pores of the activated carbon. Similarly, the Si surface content in A3 is higher than that obtained by bulk analysis (3.76 and 1.10 mmol g^{-1}, respectively); this constitutes indirect evidence that the complex has been anchored preferentially onto the APTES sites within the activated carbon.

Electron Paramagnetic Resonance

The EPR spectra of A4 and B4 (Figure 2) are very similar and show a typical signal of V^{IV} $3d^1$ centres with eight-line hyperfine patterns due to the interaction of the unpaired electron with the ^{51}V nucleus (I = 7/2); the spectra are typical of magnetically diluted monomeric vanadyl ($V{=}O^{2+}$) species with g values and vanadium hyperfine coupling constants characteristic of a square-pyramidal structure with approximate axial geometry;[29–31] this indicates that there is no significant magnetic interactions between vicinal V centres and that the carbon matrix acts as a diamagnetic host.

The similarity between the EPR spectra of A4 and B4 with those observed for the free VO complexes[29–31] allows the same orientation scheme to be used for the tensor axes: $g_1 = g_2 = g_\perp$, $g_3 = g_\parallel$ (or $g_1 = g_x$, $g_2 = g_y$, $g_3 = g_z$), where g_1 and g_3 refer to the lowest and highest magnetic-field g values (obviously, $A_1 = A_2 = A_\perp$, $A_3 = A_\parallel$ or $A_1 = A_x$, $A_2 = A_y$, and $A_3 = A_z$); in this context, as $g_x = g_y > g_z$ the ground state is d^1_{xy}. The EPR spectra of A4 and B4 are presented in Figure 2, and the spin-Hamiltonian parameters for free $[VO(acac)_2]$ magnetically diluted in KBr and the carbon-anchored complexes are summarised in Table 3.

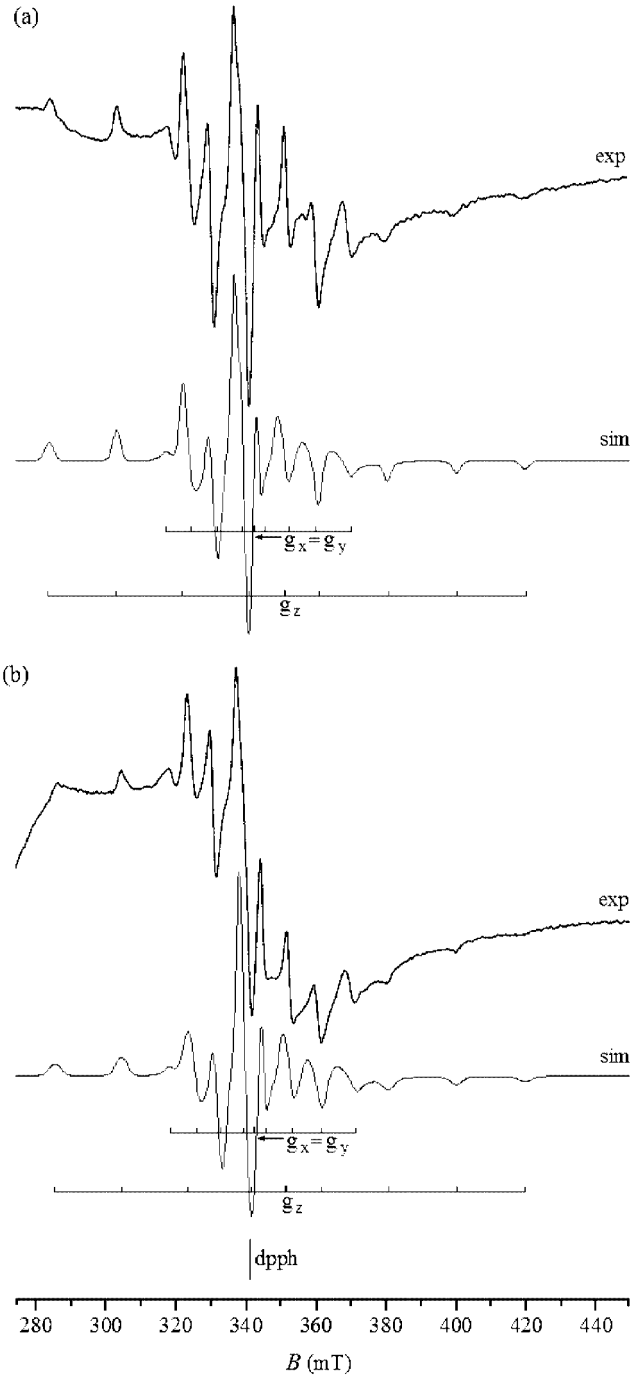

Figure 2. EPR spectra (ν = 9.57 GHz) for carbon B4 at 125 K (a) and carbon A4 at 165 K (b) (exp = measured, sim = simulated).

Table 3. Spin-Hamiltonian parameters for the free and supported $[VO(acac)_2]$ complex.

Sample	$g_\perp$	$g_\parallel$	$A_\perp$[a]	$A_\parallel$[a]	g_{av}[b]	A_{av}[a,c]
$[VO(acac)_2]$[d]	1.986	1.944	71	177	1.972	106
A4	1.984	1.937	71	173	1.968	105
B4	1.987	1.944	70	176	1.973	105

[a] Units of hyperfine coupling constants: $\times 10^{-4}$ cm^{-1}. [b] $g_{av} = 1/3(2\times g_\perp + g_\parallel)$. [c] $A_{av} = 1/3(2\times A_\perp + A_\parallel)$. [d] Powered sample magnetically diluted in KBr: 0.085 mmol $[VO(acac)_2]$ in 0.5 g KBr.

 © 2005 Wiley-VCH Verlag GmbH & Co. KGaA, Weinheim

The EPR band profile of both materials indicates that there is only one major VO EPR active species within the carbon matrix (small bandwidth and no additional peaks besides those that are predicted for one species) and corroborates the V 2p XPS data. Both materials, when compared to the free complex, show a decrease in $A_{\parallel}$, although this is quite small for B4, suggesting a decrease in the unpaired spin density at the V centre upon carbon anchoring. This excludes the axial coordination of APTES or trien through the NH_2 functionalities, as this would increase the $A_{\parallel}$ values. In the light of the model developed by Wuthrich and refined later by Chasteen,[29,30,32] this result can be interpreted as an increase in the in-plane covalency: in our context, complex anchoring through the Schiff-base condensation between amine functionalities from trien or APTES and the acetylacetone ligand would lead to a new in-plane V–N bond, which would increase the delocalisation of the electron density towards the equatorial ligand, thus inducing a decrease in $A_{\parallel}$. Although new equatorial V–N bonds would give rise to the appearance of superhyperfine splittings due to the interaction of the vanadium unpaired spin with the equatorial nitrogen atom ($I = 1$; d_{xy} ground state), no splitting due to the presence of N atoms could be detected in the EPR spectra, probably due to the relatively big bandwidth that is associated with solid-state spectra.

Parallel with the decrease in $A_{\parallel}$, an increase in $g_{\parallel}$ (towards the g_e value) is usually observed as a consequence of the increase in the equatorial bonding covalence.[30–32] However, our data do not follow this trend, since no variation in the g values is observed for B4 and a decrease in g values is detected for A4 when compared to free $[VO(acac)_2]$. Nonetheless, these results do not contradict the above explanations as strong distortions of the anchored complexes within the matrix are expected to occur and, under this circumstances, the g values can show dissimilar changes upon complex distortion:[30] the g_z values are usually insensitive to the degree of the distortion of complex structure, whereas g_x and g_y exhibit a greater variation, although in an unpredicted random manner.

No characterisation of the material is possible by FTIR and UV/Vis spectroscopy in order to get further information on complex distortion induced by the anchoring procedure, as the strongly absorbing carbon matrix prevents the observation of the typical complex responses. Although EPR spectra could not give straightforward evidence for the molecular structure of the anchored complexes, a combination of all the data allowed us to propose the anchoring of $[VO(acac)_2]$ onto the amine-functionalised carbons via Schiff-base condensation with the acetylacteonate ligand, as summarised in Scheme 1.

Further indirect information on the complex anchoring can be gained by the assessment of the heterogeneous catalytic activity of the new materials in a typical reaction where the homogeneous $[VO(acac)_2]$ complex shows high catalytic performance. In fact, the catalytic activity of a homogeneous catalyst (reaction conversion and products yields) is only kept upon its heterogenisation when no significant changes occur in the coordination sphere of the active centre, namely coordination atoms and available coordination sites for the substrate. In this context, we studied the catalytic activity of $[VO(acac)_2]$ towards the epoxidation of an allylic alcohol after immobilisation on the functionalised activated carbon.

Epoxidation of 3-Buten-2-ol Catalysed by Heterogeneous [VO(Acac)$_2$] Catalysts

The results obtained in the epoxidation of 3-buten-2-ol at 0 °C using vanadyl(IV) acetylacetonate based materials as heterogeneous catalysts and *tert*-butyl hydroperoxide as the oxygen source, in dichloromethane, are summarised in Table 4 and in Figure 3; data from the homogeneous phase and a blank experiment run under identical conditions are also included.

Table 4. Epoxidation of 3-buten-2-ol at 0 °C catalysed by $[VO(acac)_2]$ in homogeneous and heterogeneous phase.[a]

Catalyst	Time [h]	Cycle	Conversion[b] [%]	TON[c]	TOF[d] [h^{-1}]
$[VO(acac)_2]$	1	1st	2	1	1.0
	2	1st	5	3	1.5
	24	1st	56	29	1.2
	27	1st	59	31	1.2
	51	1st	90	47	0.9
	76	1st	93	49	0.6
A1 (blank)	24	1st	9	–	–
	48	1st	18	–	–
	72	1st	24	–	–
	144	1st	46	–	–
A4	24	1st	18	9	0.4
	48	1st	49	25	0.5
	72	1st	76	38	0.5
	144	1st	100	50	0.4
	144	2nd	94	48	0.3
B4	24	1st	3	2	0.08
	48	1st	9	5	0.1
	72	1st	20	11	0.2
	192	1st	100	53	0.3
	192	2nd	94	48	0.2

[a] Typical reaction conditions used: 0.850 mmol of 3-buten-2-ol, 0.425 mmol of chlorobenzene (internal standard), 0.017 mmol of $[VO(acac)_2]$ or 0.100 g of heterogeneous catalyst (2% of catalyst relative to 3-buten-2-ol), 1.70 mmol of *t*BuOOH. [b] Based on 3-buten-2-ol consumption. [c] TON = mmol of converted 3-buten-2-ol/mmol of vanadium. [d] TOF = TON/reaction time.

The 3-buten-2-ol conversion was approximately 100% in both heterogeneous-phase reactions, with total TONs slightly higher than the homogeneous-phase reaction, thus indicating that the catalyst conversion performances did not decrease upon heterogenisation of $[VO(acac)_2]$. The high catalytic activity of the new vanadium-based materials clearly supports the proposed structure for complexes being anchored by the ligand and not through axial coordination (spacers or carbon surface oxygen groups), which would result in a six-coordinate species without an available coordination site for the oxidant. Therefore, the axial coordination would hinder the formation of the active intermediate V species (peroxovanadium intermediate),[8] leading to inactive anchored V complexes.

 © 2005 Wiley-VCH Verlag GmbH & Co. KGaA, Weinheim

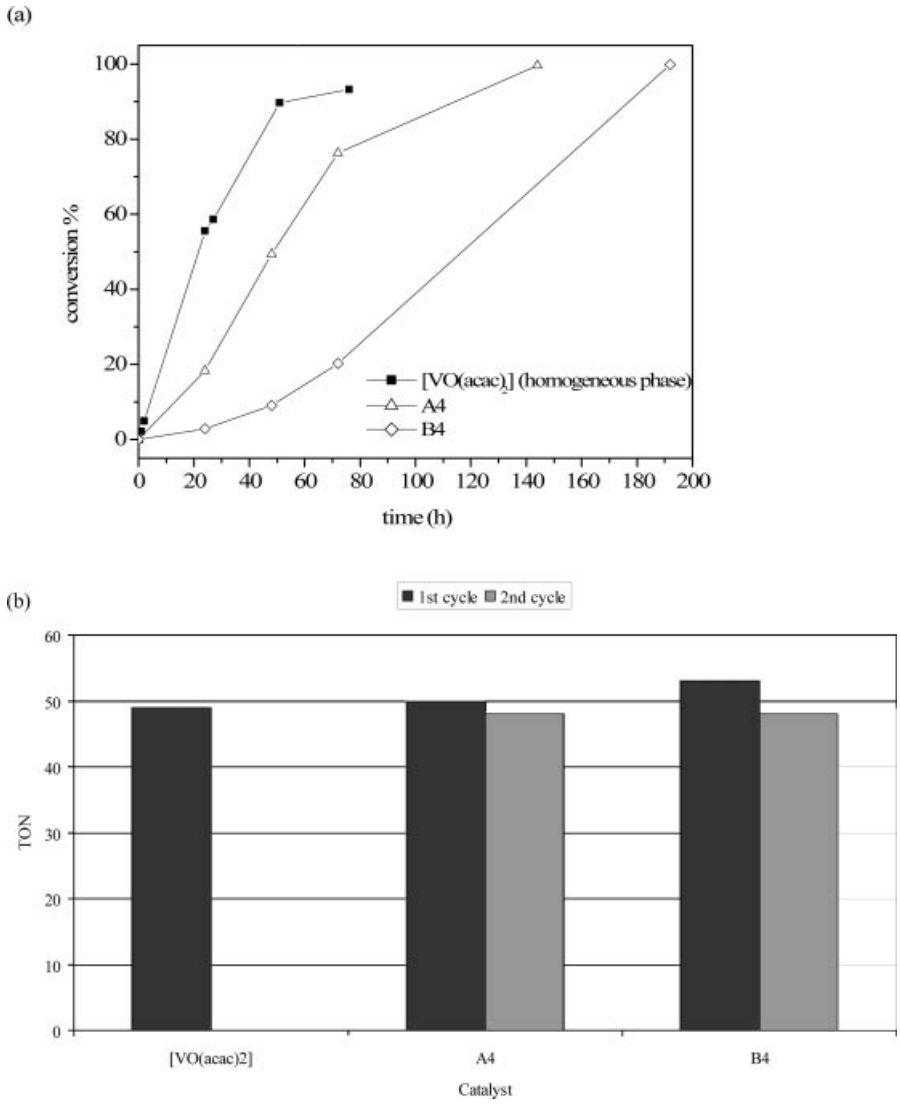

Figure 3. Epoxidation of 3-buten-2-ol catalysed by the $[VO(acac)_2]$ complex in the homogeneous phase and heterogenised onto two different functionalised activated carbons (A4 and B4): (a) conversion vs. time and (b) TON vs. catalyst.

However, on going from the homogeneous to the heterogeneous phase, an increase in the reaction time is observed in both heterogeneous catalyst runs under identical reaction conditions. This is a general effect that arises upon immobilisation of metal complexes in porous matrices, and has been attributed to diffusion constraints imposed on substrates and reactants by the porous network of the matrices.[20] As the catalytic conversions of the immobilised complexes are similar to that of free $[VO(acac)_2]$, we propose the same justification for the observed increase in the reaction time.

Comparing the two epoxidation reactions using A4 and B4 as heterogeneous catalysts, it can be observed that the former proceeds more rapidly in the initial 72 hours, a result that can be directly associated with the more external location of the metal complex in material A4, which lessens diffusion constraint effects.

Reutilisation is one of the greatest advantages of heterogeneous catalysts, and can also provide useful information about the anchoring process and catalyst stability along the catalytic cycle. As can be seen in Table 4 and in Figure 3, it is clear that neither A4 nor B4 lose their catalytic efficiency significantly after two catalytic cycles. This is an important result for heterogeneous vanadium-based catalysis and indicates that the two anchoring procedures are very effective at preventing complex deactivation and leaching, at least up to two cycles.

Concluding Remarks

New heterogeneous catalysts were prepared by heterogenisation of $[VO(acac)_2]$ onto amine-functionalised activated carbons prepared by two different methodologies: (a) using an air-oxidised carbon functionalised with APTES and (b) using an acid-oxidised carbon functionalised with trien. The combination of XPS and EPR data showed that complex anchoring was achieved by Schiff-base condensa-

 © 2005 Wiley-VCH Verlag GmbH & Co. KGaA, Weinheim

tion between the free amine groups of the functionalised carbon and the oxygen ligand atoms. These new vanadium-based materials show high catalytic activity in the epoxidation of 3-buten-2-ol and are not very different from $[VO(acac)_2]$ (conversion and TON), which corroborates the proposed anchoring methodologies. Material A4 proved to be a more efficient catalyst, as can be seen by its greater values of TON in the first 72 hours. Both materials were used two times with no significant loss in the alkene conversion and TON, thus indicating that the complexes have been anchored irreversibly to the carbon surface, which prevents leaching of the active phase and its deactivation.

Experimental Section

Materials and Solvents: The starting carbon material was a NORIT ROX 0.8 activated carbon (rodlike pellets with 0.8 mm diameter and 5 mm length). This material has a pore volume of 0.695 $cm^3 g^{-1}$, as determined by porosimetry (corresponding to meso- and macropores), a micropore volume of 0.359 $cm^3 g^{-1}$ and a mesopore area of 122 $m^2 g^{-1}$, as determined by N_2 adsorption at 77 K (*t*-method),[19–23] an ash content of 2.6% (w/w), an iodine number of 1000 and mercury and helium densities of 0.666 and 2.11 $g cm^{-3}$, respectively. The activated carbon was purified by Soxhlet extraction with 2 M HCl for 6 h, washed with deionised water until pH 6–7 and then dried in an oven at 150 °C for 13 h under vacuum (A1).

(3-Aminopropyl)triethoxysilane, bis(3-aminopropyl)amine, vanadyl(IV) acetylacetonate, a *tert*-butyl hydroperoxide solution in decane (5 M), chlorobenzene and 3-buten-2-ol were obtained from Aldrich and were used as received. All the reagents and solvents used in the modification of the activated carbon and in the anchoring procedure were also obtained from Aldrich, except for ethanol, toluene and thionyl chloride, which were purchased from Merck (pro analysi). The reagents and solvents used in the catalytic experiments were obtained from Aldrich, except for dichloromethane, which was purchased from Romil (HPLC grade).

$[VO(acac)_2]$: XPS (eV): C 1s 285.0 and 287.1; O 1s 531.7; V $2p_{3/2}$ 516.8.

Preparation of the Heterogeneous Catalysts: The immobilisation of the vanadium complex was performed by two different methods, A and B, that are described below and summarised in Scheme 1.

Support Oxidation: The activated carbon (A1) was oxidised by two methods:[22,23] (a) with a mixture of N_2 and air (5% O_2) at 698 K for 10 h (A2; burn-off = 11%), (b) refluxed with a 5 M nitric acid solution for 6 h (1 g/30 mL), washed with deionised water until pH 6–7 and then dried in an oven at 110 °C for 13 h under vacuum (B1). Carbon A2 was used as the support for the complex anchoring by method A whereas carbon B1 was used as support for method B.

Method A. Functionalisation of A2 with (3-Aminopropyl)triethoxysilane (APTES): Carbon A2 (3.0 g) was refluxed with a solution containing 4.3 mmol of (3-aminopropyl)triethoxysilane in 100 mL of dry toluene for 24 h, then filtered and washed extensively with dry toluene. The material was Soxhlet extracted for 8 h with toluene and 8 h with ethanol and was then dried in an oven at 120 °C for 13 h under vacuum (carbon A3).

Anchoring of $[VO(Acac)_2]$ onto the A3 Carbon: The activated carbon functionalised with (3-aminopropyl)triethoxysilane (A3, 0.60 g) was added to 100 mL of a solution of $[VO(acac)_2]$ in dry toluene (118 μmol), and the mixture was refluxed for 9 h; during the reflux a progressive disappearance of the green colour of the solution was observed. The resulting material was extensively washed with toluene and then purified by Soxhlet extraction with toluene for 8 h, and dried in an oven at 120 °C for 13 h under vacuum (carbon A4).

Method B. Reaction of B1 with Thionyl Chloride ($SOCl_2$): Carbon B1 (12.0 g) was refluxed with 40 mL of a 5% (v/v) solution of thionyl chloride in toluene for 5 h, extensively washed with toluene, and then purified by Soxhlet extraction with toluene for 2 h, and finally dried in an oven at 150 °C for 13 h under vacuum (carbon B2).[23]

Functionalisation of B2 with Bis(3-aminopropyl)amine (Trien): Carbon B2 (3.0 g) was refluxed with a solution containing 390 μmol of bis(3-aminopropyl)amine (trien) in 40 mL of dry toluene for 4 h, then filtered and extensively washed with toluene. The material was also Soxhlet extracted for 2 h with toluene and dried in an oven at 150 °C for 13 h under vacuum (carbon B3).[23]

Anchoring of $[VO(Acac)_2]$ onto the B3 Carbon: The activated carbon functionalised with trien (B3, 0.60 g) was added to 100 mL of a solution of $[VO(acac)_2]$ in dry toluene (119 μmol), and the mixture was refluxed for 9 h; during the reflux a progressive disappearance of the green colour of the solution was observed. The resulting material was extensively washed with toluene and then purified by Soxhlet extraction with toluene for 7 h, and dried in an oven at 150 °C for 13 h under vacuum (carbon B4).

Physical Measurements: Vanadium and silicon bulk contents were obtained by inductively coupled plasma emission spectrometry (ICP-AES) at "Laboratório de Análises", IST, Lisboa (Portugal). X-ray photoelectron spectroscopy (XPS) was performed at "Centro de Materiais da Universidade do Porto" (Portugal), with a VG Scientific ESCALAB 200A spectrometer using non-monochromated Mg-K_α radiation (1253.6 eV). In order to correct for possible deviations caused by the electric charge of the samples, the graphitic C 1s band at 284.6 eV was taken as internal standard.[33,34] EPR spectra were obtained with an X-band Bruker ESP 300E spectrometer. The powdered samples were diluted in KBr (5%), the microwave frequency was calibrated with diphenylpicrylhydrazyl (dpph; g = 2.0037) and the magnetic field was calibrated against Mn^{II} in MgO. Experimental conditions: modulation frequency: 100 kHz; modulation amplitude: 9 G; microwave power: 1 mV. The EPR parameters were obtained by simulation using the program WINEPR SimFonia (Bruker) by assuming axial spin-Hamiltonians. The line widths used in the simulations were 15–30 G. Gas chromatography experiments (GC) were performed with a Varian CP-3380 chromatograph equipped with an FID detector and using helium as carrier gas and a fused silica Varian Chrompack capillary column CP-Sil 8 CB Low Bleed/MS (30 m × 0.25 mm i.d.; 0.25 μm film thickness). The chromatographic conditions were: 40 °C (3 min), 5 °C min^{-1} to 170 °C (2 min), 20 °C min^{-1} to 200 °C (10 min); injector temperature: 200 °C; detector temperature: 300 °C. Aliquots of 0.1 mL were withdrawn from the reaction mixture with a hypodermic syringe, filtered through PTFE 0.22-μm syringe filters and injected directly into the injector using a 1-μL Hamilton syringe.

Catalysis Experiments: The reactions were carried out in CH_2Cl_2, at 0 °C, with constant stirring. The composition of the reaction medium was 0.85 mmol of 3-buten-2-ol, 0.425 mmol of chlorobenzene (internal standard), 0.10 g of heterogeneous catalyst (A4 or B4) in 5.00 mL of solvent. The oxidant, *tert*-butyl hydroperoxide (1.70 mmol), was progressively added to the reaction medium using a Bioblock Scientific Syringe Pump at a rate of 0.5 mL h^{-1}. For

 © 2005 Wiley-VCH Verlag GmbH & Co. KGaA, Weinheim

each complex the reaction time for maximum conversion percentage was determined by withdrawing 0.1-mL aliquots periodically from the reaction mixture, and this time was used to monitor the efficiency of the catalyst. The composition of the reaction media was determined by GC with 3-buten-2-ol, *tert*-butyl hydroperoxide, *tert*-butanol and decane being quantified by the internal standard method (chlorobenzene). The catalysts were then washed sequentially by Soxhlet extraction with 100 mL of toluene and 100 mL of ethanol for 1–2 hours, and dried at an oven at 120 °C for 13 h, under vacuum. The catalysts were then reused using the same experimental conditions. Control experiments using the initial carbon A1 and the homogeneous reaction with vanadyl(IV) acetylacetonate in identical reaction conditions were also performed.

Acknowledgments

The authors are indebted to Dr. Carlos Sá (CEMUP) for assistance with XPS analysis and to NORIT N.V., Amersfoort, Netherlands, for providing the activated carbon. This work was partially funded by the Fundação para a Ciência e a Tecnologia (FCT, Portugal) and FEDER through project ref. POCTI/EQU/57369/2004. ARS thanks FCT and the European Social Fund for a postdoctoral fellowship.

[1] V. Conte, F. Di Furia, G. Licini, *Appl. Catal., A* **1997**, *157*, 335–361.
[2] C. Bolm, *Coord. Chem. Rev.* **2003**, *237*, 245–256.
[3] S. Raghavan, A. Rajander, S. C. Joseph, *Synth. Commun.* **2001**, *31*, 1477–1480.
[4] M. Kirihara, M. Ichinose, S. Takisawa, *Chem. Commun.* **1998**, 1691–1692.
[5] T. Okada, M. Ueda, *React. Funct. Polym.* **1996**, *30*, 157–163.
[6] K. Yamamoto, E. Tsuchida, H. Nishide, *Macromolecules* **1993**, *26*, 3432–3437.
[7] T. Katsuki, *Coord. Chem. Rev.* **1995**, *140*, 189–214.
[8] B. E. Rossiter, T. R. Verhoeven, K. B. Sharpless, *Tetrahedron Lett.* **1979**, *20*, 4733–4736.
[9] A. G. J. Ligtenbarg, R. Hage, B. L. Feringa, *Coord. Chem. Rev.* **2003**, *237*, 89–101.
[10] L. Canali, D. C. Sherrington, *Chem. Soc. Rev.* **1999**, *28*, 85–93.
[11] Q.-H. Fan, Y.-M. Li, A. S. C. Chan, *Chem. Rev.* **2002**, *102*, 3385–3466.
[12] N. E. Leadbeater, M. Marco, *Chem. Rev.* **2002**, *102*, 3217–3274.
[13] D. Brunel, N. Belloq, P. Sutra, A. Cauvel, M. Laspéras, P. Moreau, F. Di Renzo, A. Galarneau, F. Fajula, *Coord. Chem. Rev.* **1998**, *178–180*, 1085–1108.
[14] F. Rodríguez-Reinoso, *Carbon* **1998**, *36*, 159–175.
[15] A. J. Bird, in *Catalyst Supports and Supported Catalysts* (Ed.: A. B. Stiles), Butterworths, Boston, **1987**, chapter 5.
[16] P. C. L'Argentière, E. A. Cagnola, D. A. Liprandi, M. C. Román-Martínez, C. Salinas-Martínez de Lecea, *Appl. Catal., A* **1998**, *172*, 41–48.
[17] J. A. Díaz-Auñón, M. C. Román-Martínez, C. Salinas-Martínez de Lecea, P. C. L'Argentière, E. A. Cagnola, D. A. Liprandi, M. E. Quiroga, *J. Mol. Catal. A: Chem.* **2000**, *153*, 243–256.
[18] J. A. Díaz-Auñón, M. C. Román-Martínez, C. Salinas-Martínez de Lecea, *J. Mol. Catal. A: Chem.* **2001**, *170*, 81–93.
[19] A. R. Silva, M. M. A. Freitas, C. Freire, B. de Castro, J. L. Figueiredo, *Langmuir* **2002**, *18*, 8017–8024.
[20] A. R. Silva, J. L. Figueiredo, C. Freire, B. de Castro, *Microporous Mesoporous Mater.* **2004**, *68*, 83–89.
[21] A. R. Silva, M. Martins, M. M. A. Freitas, A. Valente, C. Freire, B. de Castro, J. L. Figueiredo, *Microporous Mesoporous Mater.* **2002**, *55*, 275–284.
[22] A. R. Silva, C. Freire, B. de Castro, M. M. A. Freitas, J. L. Figueiredo, *Microporous Mesoporous Mater.* **2001**, *46*, 211–221.
[23] A. R. Silva, M. Martins, M. M. A. Freitas, J. L. Figueiredo, C. Freire, B. de Castro, *Eur. J. Inorg. Chem.* **2004**, 2027–2035.
[24] J. L. Figueiredo, M. F. R. Pereira, M. M. A. Freitas, J. J. M. Órfão, *Carbon* **1999**, *37*, 1379–1389.
[25] A. M. Yacynych, T. Kuwana, *Anal. Chem.* **1978**, *50*, 640–645.
[26] Z. R. Yue, W. Jiang, L. Wang, S. Gardner, C. U. Pittman Jr., *Carbon* **1999**, *37*, 1785–1796.
[27] E. Desimoni, G. I. Casella, A. M. Salvi, *Carbon* **1992**, *30*, 521–526.
[28] M. F. Dautartas, J. F. Evans, T. Kuwana, *Anal. Chem.* **1979**, *51*, 104–110.
[29] A. J. Tasiopoulos, A. N. Troganis, A. Evangelou, C. P. Raptopoulou, A. Terzis, Y. Deligiannakis, T. A. Kabanos, *Chem. Eur. J.* **1999**, *5*, 910–921.
[30] E. Garribba, G. Micera, A. Panzanelli, D. Sanna, *Inorg. Chem.* **2003**, *42*, 3981–3987.
[31] E. J. Tolis, V. I. Teberekidis, C. P. Raptopoulou, A. Terzis, M. P. Sigalas, Y. Deligiannakis, T. A. Kabanos, *Chem. Eur. J.* **2001**, *7*, 2698–2710.
[32] T. S. Smith II, R. LoBrutto, V. L. Pecoraro, *Coord. Chem. Rev.* **2002**, *228*, 1–18.
[33] J. F. Moulder, W. F. Stickle, P. E. Sobol, K. D. Bomben, in *Handbook of X-ray Photoelectron Spectroscopy* (Ed.: J. Chastain), Perkin–Elmer, **1992**.
[34] Y. M. Xie, P. M. A. Sherwood, *Chem. Mater.* **1990**, *2*, 293–299.

Received: May 12, 2005
Published Online: October 10, 2005

 © 2005 Wiley-VCH Verlag GmbH & Co. KGaA, Weinheim

Inversely Polarized Phosphaalkenes as Phosphinidene- and Carbene-Transfer Reagents

Lothar Weber,*[a] Ulrich Lassahn,[a] Hans-Georg Stammler,[a] and Beate Neumann[a]

Keywords: Carbenes / Ketenes / Phosphaalkenes / Phosphinidenes

The reaction of the inversely polarized phosphaalkenes $RP=C(NMe_2)_2$ [R = *t*Bu (**1a**), Cy (**1b**), 1-Ad (**1c**), Ph (**1d**), Mes (**1e**)] with an excess of diphenyl ketene in *n*-pentane affords the zwitterionic adduct $(Me_2N)_2C–C(O)=CPh_2$ (**2**) and the 3,5-dibenzhydrylidene-1,4,2-dioxaphospholanes **4a**–**e**. The reaction of **1a** with $Ph_2C=C=O$ in concentrated acetonitrile solution gives **4a** and 5-benzhydrylidene-2-*tert*-butyl-4,4-diphenyl-1,2-oxaphospholan-3-one (**6a**) as a by-product. In contrast, treatment of $Me_3SiP=C(NMe_2)_2$ (**1i**) with the ketene leads to the formation of 2-phospha-1,3-butadiene (**5**). The thermolabile phosphaalkene **8** decomposes into an imidazolylidene and (*t*BuP), the latter species spontaneously oligomerizes to $(tBuP)_n$ (n = 3, 4). Obviously, compounds **1a**–**e** serve as a convenient source of phosphinidenes and the carbene $C(NMe_2)_2$. A Wanzlick-type equilibrium between these species, however, must be excluded according to exchange and cross-coupling experiments. The molecular structures of **2**, **4e** and **6a** were determined by X-ray structure analyses.

(© Wiley-VCH Verlag GmbH & Co. KGaA, 69451 Weinheim, Germany, 2005)

Introduction

The phosphorus atom of inversely polarized phosphaalkenes such as $R–P=C(NR'_2)_2$ (R = H, alkyl, aryl, $SiMe_3$, R′ = Me, Et) is highly nucleophilic, which is rationalized by an effective π-electron delocalization of the lone pairs at the trigonal-planar amino substituents into the P–C multiple bond (Scheme 1).[1]

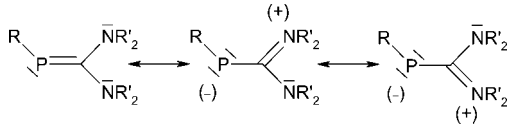

Scheme 1. Limiting formulae of amino-substituted phosphaalkenes.

Protonation,[2] alkylation,[2,3] silylation,[3] and coordination to metal centers occur at the P atom with increase of the coordination number.[2,4,5] Treatment of $tBuP=C(NMe_2)_2$ with [$(Ph_3P)AuCl$], for example, leads to the cleavage of the P–C bond of some of the phosphaalkene units to yield phosphanediide units [$tBuP^{2-}$], which are incorporated as ligands in the decanuclear cluster cation $[Au_8(AuCl)_2(\mu^3\text{-}PtBu)_2\{tBuP=C(NMe_2)_2\}_6]^{4+}$. The carbodiimmonium dication $[Me_2N=C=NMe_2]^{2+}$ formed as a by-product has been trapped by chloride to afford the spectroscopically detected chloroformamidinium ion $[(Me_2N)_2CCl]^+$.[6] This transformation is formally related to the synthetic pathway to carbene complexes of transition metals via the C=C bond cleavage of bis(imidazol-2-ylidenes) in the coordination sphere of a metal atom.[7]

The conceivable dissociation of tetraamino-substituted alkenes into carbenes was already postulated by Wanzlick in the 1960s.[8] However, the ^1H NMR spectroscopic proof of Wanzlick's ideas was only provided by Hahn some 40 years later.[9]

In line with the diagonal relationship in the periodic table between the elements carbon and phosphorus, the quest for a Wanzlick-type reaction of the electron-abundant bis(amino)phosphaalkenes seems intriguing as, in addition to a relatively stable bis(amino)carbene,[10] the homolytic cleavage of the phosphaalkene would furnish reactive phosphin-

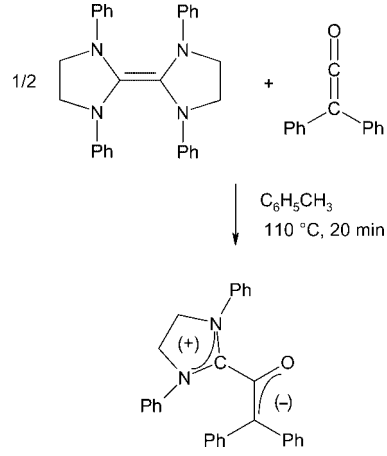

Scheme 2. Formation of a carbene/ketene adduct.

[a] Fakultät für Chemie der Universität Bielefeld,
Universitätsstraße 25, 33615 Bielefeld, Germany
Fax: +49-521-106-6146
E-mail: lothar.weber@uni-bielefeld.de

 © 2005 Wiley-VCH Verlag GmbH & Co. KGaA, Weinheim **DOI: 10.1002/ejic.200500454**

idene fragments under relatively mild conditions. For our work, the reaction of 1,1′,3,3′-tetraphenyl-2,2′-bis(imidazolidinylidene) with diphenyl ketene by Regitz et al. serves as a model reaction for the trapping of a carbene produced in agreement with Wanzlick's postulate[11] (Scheme 2).

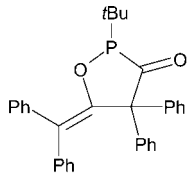

6a

Results and Discussion

Reaction of the phosphaalkenes R–P=C(NMe_2)$_2$ [**1a**–**e**; R = *t*Bu (**1a**),Cy = *c*C_6H_{11} (**1b**), 1-Ad (**1c**), Ph (**1d**), Mes (**1e**)] with an excess of diphenyl ketene in pentane at 0–20 °C for 16 h led to the precipitation of the light-yellow zwitterionic compound **2** in about 85% yield. The product was purified by chromatography on a silica column. After removal of **2**, the mother liquor was treated with an excess of powdered NaOH to destroy the excess of ketene. Filtration and concentration of the filtrate to dryness gave 3,5-dibenzhydrylidene-1,4,2-dioxaphospholanes **4a**–**e** as colorless waxy solids in 45–53% yield. Purification of these products was accompanied by decomposition (Scheme 3).

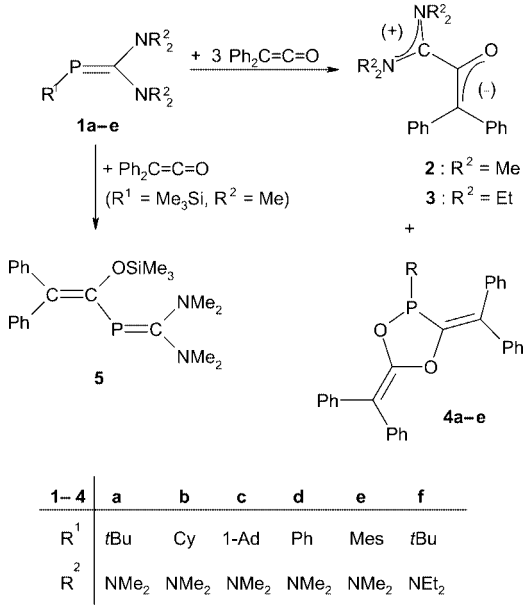

1–4	a	b	c	d	e	f
R^1	*t*Bu	Cy	1-Ad	Ph	Mes	*t*Bu
R^2	NMe_2	NMe_2	NMe_2	NMe_2	NMe_2	NEt_2

Scheme 3. Formation of compounds **2**, **3**, **4a**–**e**, and **5**.

The reactions between **1a**–**e** and diphenyl ketene were also performed in acetonitrile. Treatment of concentrated solutions of the phosphaalkene in acetonitrile (ca. 20% v/v) with neat Ph_2C=C=O gave rise to the instantaneous formation of dark-violet emulsions and generation of heat. From NMR evidence it was clear that the same products **2** and **4a**–**e** were generated as previously in pentane solution. Workup, however, did not afford pure compounds. In the case of *t*BuP=C(NMe_2)$_2$ a few crystals of 5-benzhydrylidene-2-*tert*-butyl-4,4-diphenyl-1,2-oxaphospholan-3-one (**6a**) were isolated as a by-product. This species is isomeric to **4a** and has also to be considered as the formal result of the cyclization of 2 equiv. of ketene with *tert*-butyl-phosphinidene.

Analogously to the behavior of **1a**, *t*BuP=C(NEt_2)$_2$ (**1f**) and an excess of diphenyl ketene in pentane underwent reaction to yield yellow solid **3** (73%) in addition to **4a** (Scheme 3).

The reactions under discussion are the first examples where phosphaalkenes serve as convenient sources of carbenes as well as phosphinidenes. The use of this synthetic principle, however, is limited. Thus, treatment of phosphaalkene HP=C(NMe_2)$_2$ (**1g**) with diphenyl ketene under comparable conditions led to complete decomposition of the reagents, and no reaction occurred between the ketene and the sterically encumbered compound Mes*P=C(NMe_2)$_2$ (**1h**). The behavior of Me_3SiP=C(NMe_2)$_2$ (**1i**) towards diphenyl ketene is different from that of **1a**–**f**. Here, the carbonyl group of the ketene is inserted into the P–Si bond of **1h** with the formation of the 2-phospha-1,3-butadiene **5**. This thermolabile product was identified by spectroscopy without prior purification (Scheme 3).

This process parallels the reaction of **1i** with Me_3SiCH=C=O, where 1,1-bis(dimethylamino)-3-trimethylsiloxy-4-trimethylsilyl-2-phosphabutadiene ($\delta_{^{31}P}$ = 30.0 ppm) was obtained. Obviously, the reactivity of the P–Si bond in **1i** precludes the cleavage of the P=C bond of the phosphaalkene.[12]

The ^{1}H NMR spectrum of **2** shows two singlets at δ = 2.74 and 3.21 ppm of equal intensity, which are assigned to the protons of chemically and magnetically different dimethylamino groups. Resonances in the $^{13}C\{^1H\}$ NMR spectra at δ = 42.3 and 42.6 ppm also correspond to these groups. The singlets at δ = 141.6 and 175.4 ppm are caused by the carbon atom of the carbenium unit and by that of the carbonyl group. Two intense bands at $\tilde{\nu}$ = 1713 and 1613 cm^{-1} in the IR spectrum of the adduct can be assigned to the coupled CO and C=C stretching modes.

The $^{31}P\{^1H\}$ NMR spectra of the 1,4,2-dioxaphospholanes **4a**–**e** show singlets at δ = 90.6–122.3 ppm, in the region typical for (alkyl/aryl)(alkoxy)phosphanes. The resonances in the precursors **1a**–**e** are encountered at considerably higher field (δ = 9–91 ppm). The phosphorus atom in 2-phosphabutadiene (**5**) gives rise to a singlet at δ = 17.3 ppm in the $^{31}P\{^1H\}$ NMR spectrum.

X-ray Structural Analysis of 2

To confirm the spectroscopic evidence for the adduct formation between carbene [$(Me_2N)_2$C] and diphenyl ketene, an X-ray structural analysis of **2** was performed (Figure 1, Table 1).

 © 2005 Wiley-VCH Verlag GmbH & Co. KGaA, Weinheim

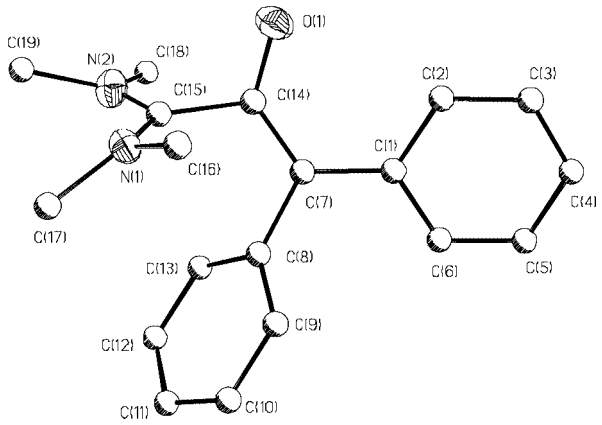

Figure 1. Molecular structure of **2** in the crystal. Selected bond lengths [Å] and angles [°]: N(1)–C(15) 1.336(10), N(1)–C(16) 1.480(10), N(1)–C(17) 1.463(10), N(2)–C(15) 1.325(10), N(2)–C(18) 1.471(10), N(2)–C(19) 1.480(10), C(14)–C(15) 1.516(11), O(1)–C(14) 1.295(9), C(7)–C(14) 1.372(11), C(7)–C(8) 1.502(11), C(1)–C(7) 1.461(11); C(16)–N(1)–C(17) 113.5(6), C(15)–N(1)–C(16) 121.3(6), C(15)–N(1)–C(17) 123.5(7), C(15)–N(2)–C(18) 121.3(7), C(15)–N(2)–C(19) 123.9(7), C(18)–N(2)–C(19) 114.6(7), N(1)–C(15)–C(14) 118.1(8), N(2)–C(15)–C(14) 119.5(7), N(1)–C(15)–N(2) 122.1(7), C(7)–C(14)–C(15) 117.6(8), O(1)–C(14)–C(15) 113.0(7), O(1)–C(14)–C(7) 129.3(7), C(14)–C(7)–C(8) 116.6(7), C(1)–C(7)–C(8) 118.9(7), C(1)–C(7)–C(14) 124.5(8).

Single crystals of **2** were grown from a CH_2Cl_2 solution at +4 °C. The analysis confirms the presence of a planar carbenium center, the positive charge of which is stabilized by π-conjugation with the two planar amino group [sum of angles at N(1) = 358.3°; N(2) = 359.8°]. In keeping with this, relatively short N(1)–C(15) [1.336(10) Å] and N(2)–C(15) [1.325(10) Å] bonds are also observed. The single bonds between the N atom and the methyl groups − N(1)–C(16) and N(1)–C(19) − are markedly longer [1.463(10)–1.480(10) Å]. The trigonal-planar configured atom C(15) (sum of angles 359.7°) is connected to the ketene part of the adduct by a C–C single bond of 1.516(11) Å. The C(14)–O(1) bond length of 1.295(9) Å clearly exceeds that of a localized carbonyl group (ca. 1.23 Å). This points to π-delocalization within the enolate part of the molecule, which means that the atoms C(14) (sum of angles 359.9°) and C(7) (sum of angles 360.0°) are trigonal-planar. The aryl ring C(1) to C(6) and the plane defined by the atoms O(1), C(14), C815), and C(7) form a dihedral angle of 22.2°. This plane forms an angle of 65.2° with the plane of the carbenium part defined by the atoms N(1), N(2), and C(15). The second aryl ring at C(7) is also twisted by 57.7° out of the plane of the atoms O(1), C(14), and C(7).

X-ray Structural Analysis of 4e

The constitution and configuration of the 3,5-dibenzhydrylidene-1,4,2-dioxaphospholanes **4a**–**c** and **4e** were also confirmed by X-ray structural analyses. Single crystals of **4a**–**c** and **4e** were grown from CH_2Cl_2 at +4 °C. As no significant differences were observed between the five-membered heterocycle of these compounds, only the structure of **4e** (R = Mes) is discussed here (Figure 2, Table 1).

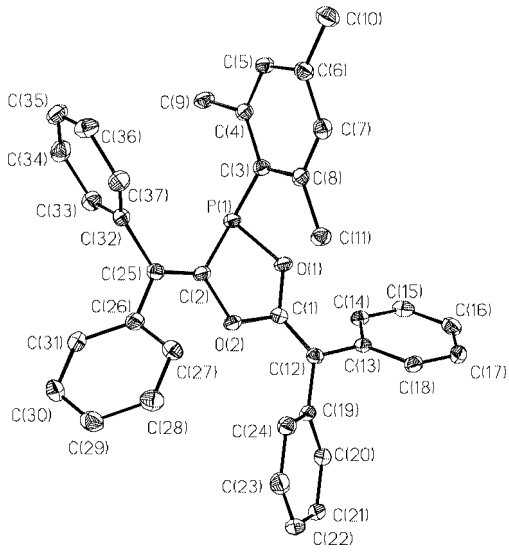

Figure 2. Molecular structure of **4e** in the crystal. Selected bond lengths [Å] and angles [°]: P(1)–C(2) 1.833(1), P(1)–C(3) 1.835(1), P(1)–O(1) 1.696(1), O(1)–C(1) 1.370(2), O(2)–C(1) 1.370(2), O(2)–C(2) 1.394(2), C(2)–C(25) 1.333(2), C(25)–C(26) 1.490(2), C(25)–C(32) 1.495(2), C(1)–C(12) 1.343(2), C(12)–C(13) 1.492(2), C(12)–C(19) 1.495(2); C(2)–P(1)–C(3) 104.22(6), O(1)–P(1)–C(3) 105.22(5), O(1)–P(1)–C(2) 88.08(5), P(1)–O(1)–C(1) 115.73(8), O(1)–C(1)–O(2) 112.59(1), C(1)–O(2)–C(2) 113.55(19), P(1)–C(2)–O(2) 109.40(10), P(1)–C(2)–C(25) 120.69(11), P(1)–C(2)–C(25) 129.86(10), O(1)–C(1)–C(12) 124.67(11), O(2)–C(1)–C(12) 122.73(11).

The key structural feature is the almost planar five-membered heterocycle (the largest deviation from the best plane is 0.0423 Å). The sum of the endocyclic angles is 539.35°, which is close to the theoretical value of 540°. The P(1)–O(1) bond [1.696(1) Å] is slightly shorter than the sum of the covalent radii of P (1.10 Å) and O (O.66 Å).[13] The endocyclic P(1)–C(2) bond [1.833(1) Å] is equally long as the exocyclic distance P(1)–C(3) [1.835(1) Å] to the mesityl substituent. The same is true for the endocyclic bond lengths C(1)–O(2) [1.370(2) Å] and C(2)–O(2) [1.394(2) Å]. All of them have a bond order of one. The exocyclic bonds C(1)–C(12) [1.343(2) Å] and C(2)–C(25) [1.333(2) Å] are double bonds. The phosphorus atom has a trigonal-pyramidal configuration (sum of angles = 297.52°). The P(1)–C(3) vector and the best plane of the heterocycle enclose an angle of 114.2°.

X-ray Structural Analysis of 6a

Yellow single crystals of **6a**, which is an isomer of **4a**, were grown from a saturated acetonitrile solution at ambient temperature (Figure 3, Table 1). The X-ray analysis revealed the molecule as a puckered 1,2-oxaphospholan-3-one (sum of angles = 530.53°). The trigonal-pyramidal phosphorus atom P(1) (sum of angles = 294.29°) forms P(1)–C(1) [1.869(2) Å], P(1)–O(1) [1.664(1) Å], and P(1)–C(5) [1.861(1) Å] single bonds to the neighboring atoms. The trigonal-planar C(5) atom is part of a carbonyl group [C(5)–O(2) = 1.206(2) Å]. The endocyclic bond O(1)–C(19)

 © 2005 Wiley-VCH Verlag GmbH & Co. KGaA, Weinheim

of 1.406(2) Å is comparable to the C–O bonds in **4e** [1.394(2) and 1.370(2) Å]. The endocyclic C–C bond of the quaternary carbon atom C(6) to the carbonyl atom C(5) of 1.568(2) Å is markedly longer than the C(6)–C(19) distance of 1.522(2) Å, which is presumably due to steric interactions between the phenyl rings and the CO function. The exocyclic C(19)–C(20) bond of 1.340(2) Å matches well with the C=C double bonds of **4e**.

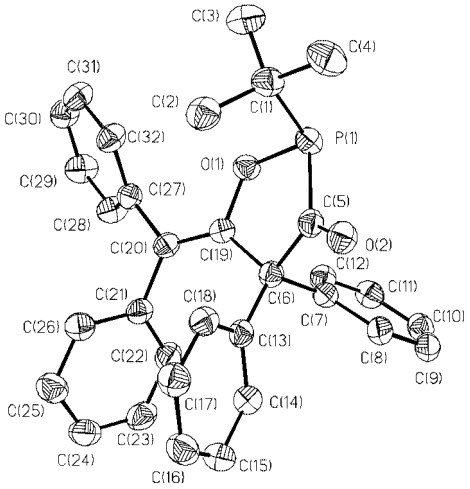

Figure 3. Molecular structure of **6a** in the crystal. Selected bond lengths [Å] and angles [°]: P(1)–C(1) 1.869(2), P(1)–O(1) 1.664(1), O(1)–C(19) 1.406(2), C(6)–C(19) 1.522(2), C(5)–C(6) 1.568(2), P(1)–C(5) 1.861(1), O(2)–C(5) 1.206(2), C(19)–C(20) 1.340(2); O(1)–P(1)–C(1) 103.45(6), C(1)–P(1)–C(5) 100.18(7), O(1)–P(1)–C(5) 90.66(5), P(1)–C(5)–C(6) 107.54(9), C(5)–C(6)–C(19) 103.42(10), O(1)–C(19)–C(6) 110.94(11), P(1)–O(1)–C(19) 117.97(8), P(1)–C(5)–O(2) 127.12(11), O(2)–C(5)–C(6) 125.24(12), O(1)–C(19)–C(20) 118.07(2), C(6)–C(19)–C(20) 130.81(12), C(19)–C(20)–C(21) 123.47(12), C(19)–C(20)–C(27) 121.50(12), C(21)–C(20)–C(27) 114.97(11).

Cross-Coupling and Exchange Experiments

From a formal point of view, the phosphaalkenes employed here display a reactivity similar to tetraaminoalkenes as concerns the homolytic cleavage of the P=C double bond, as the carbene and phosphinidene fragments are efficiently trapped by $Ph_2C{=}C{=}O$. Similar to Wanzlick's observations, however, the question remained open as to whether a genuine equilibrium exists between phosphaalkenes and the electron-sextet species or whether a more complex mechanism is responsible. In order to obtain more information, a number of cross-coupling and exchange experiments were carried out (Scheme 4).

It is known that tri-*tert*-butylcyclotriphosphane serves as a source of the phosphinidene [*t*BuP]. In keeping with this, heating of a mixture of $(t\text{BuP})_3$ and $Ph_2C{=}C{=}O$ in toluene furnished heterocycle **4a** in about 6% yield.

Reaction of $(t\text{BuP})_3$ with $(Me_2N)_2C{=}C(NMe_2)_2$ did not, however, yield the expected phosphaalkene *t*BuP=$C(NMe_2)_2$ (**1a**). Similarly, the treatment of $(t\text{BuP})_3$ with CyP=$C(NMe_2)_2$ (**1b**) to give **1a** failed. Reaction of $(Me_2N)_2C{=}C(NMe_2)_2$ with $Ph_2C{=}C{=}O$ did not afford tractable products as, for example, the adduct **2**. Reaction of $(Me_2N)_2C{=}C(NMe_2)_2$ with *t*BuP=$C(NEt_2)_2$ (**6**) did not give the expected exchange product **1a**. Thus, all these experiments exclude the notable formation of free electron-sextet species. Also, the cross-coupling experiment between *t*BuP=$C(NEt_2)_2$ and CyP=$C(NMe_2)_2$ did not lead to the conceivable metathesis products *t*BuP=$C(NMe_2)_2$ and CyP=$C(NEt_2)_2$.

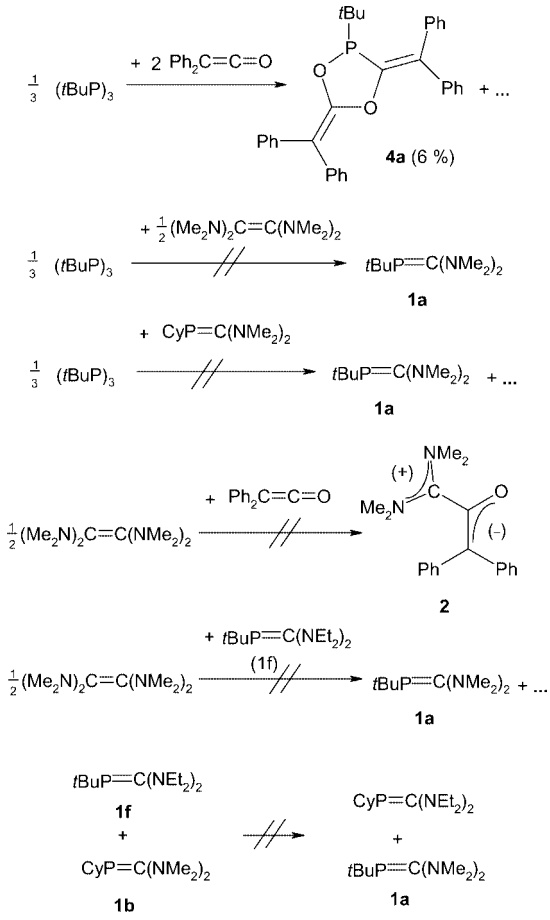

Scheme 4. Attempted exchange experiment.

Synthesis of Labile Phosphaalkenes

According to our results, it is obvious that the phosphaalkenes studied here do show the reactivity of carbenes and phosphinidenes, although transient free electron-sextet species have to be excluded as intermediates. This is in accordance with our knowledge of Wanzlick's equilibrium of tetraaminoalkenes, where spectroscopic evidence of carbenes is restricted to only the most reactive alkenes. Quantum chemical calculations indicate that phosphaalkenes with a cyclic diaminomethylene unit should exhibit a decreased stability towards dissociation,[14] therefore it was obvious to synthesize such a thermolabile phosphaalkene and to study its decomposition.

Condensation of [LiP(*t*Bu)($SiMe_3$)] with thiouronium iodide (**7**) in THF led to a red solution, the $^{31}P\{^1H\}$ NMR spectrum of which shows a prominent singlet at $\delta = -5$ ppm

 © 2005 Wiley-VCH Verlag GmbH & Co. KGaA, Weinheim

in the region known for inversely polarized phosphaalkenes and which therefore we assigned to compound **8** (Scheme 5).

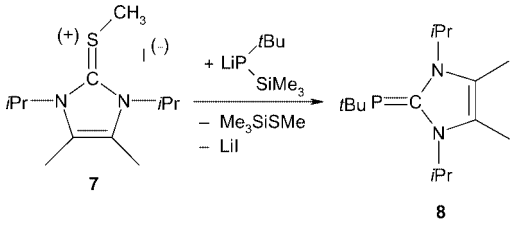

Scheme 5. Synthesis of **8**.

After distillation, this resonance nearly disappeared, and new intense signals appeared in the NMR spectrum of the distillate. An AB_2 spin system at δ = –108.9 and –70.3 ppm ($J_{A,B}$ = 201 Hz) and a singlet at δ = –57.6 ppm are due to $(t\text{BuP})_3$ and $(t\text{BuP})_4$, respectively, which cover 78% of all the resonances observed. These rings presumably result from the oligomerization of *tert*-butylphosphinidene. The imidazolium cation **9** was identified in the residue of the distillation by ^{1}H and ^{13}C{^{1}H} NMR spectroscopy. This ion is most likely formed by protonation of the strong Brønsted base **10**.

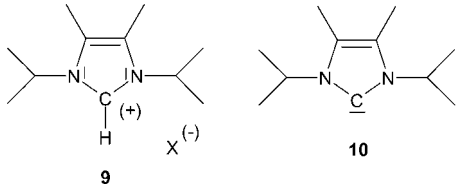

The P=C bonds have been homolytically cleaved and this process is most certainly not part of a genuine equilibrium.

Phosphaalkenes of type **8** have been synthesized previously from equivalent amounts of 1,3,4,5-tetramethylimidazol-2-ylidene and pentaphenylcyclopentaphosphane in 79% yield.[15] Similar results were obtained with 1,3-dimesitylimidazol-2-ylidene and the cyclophosphanes $(PhP)_5$ and $(CF_3P)_4$.[16]

For a mechanism that rationalizes the formation of adduct **2** as well as of the heterocycles **4** and **6a**, we propose the initial cleavage of one molecule of phosphaalkene **1** by reaction with 2 equiv. of $Ph_2C{=}C{=}O$. In addition to **2**, a zwitterion **11** is formed (Scheme 6). Intermediate **11** then undergoes a 1,3-dipolar addition to the C=O bond of another ketene molecule to yield main product **4** (path A). Alternatively, the 1,3-cycloaddition to the C=C double bond of the ketene affords **6a**.

Molecules with the structural feature of a 3,5-dibenzhydrylidene-1,4,2-dioxaphospholane are rare and there are only a few examples documented with pentavalent phosphorus. For example, the reaction of triethyl phosphite with $Ph_2C{=}C{=}O$ furnishes heterocycle **12**.[17]

Similarly, cyclic trialkyl phosphites and 2 equiv. of dimethyl ketene or its dimer give rise to the formation of 2,2,2-trialkoxy-3,5-diisopropylidenephospholanes.[18] Treatment of 3,4-dimethyl-1-phenylphosphole with diphenyl ketene under high pressure (ca. 10 kbar) afforded compound

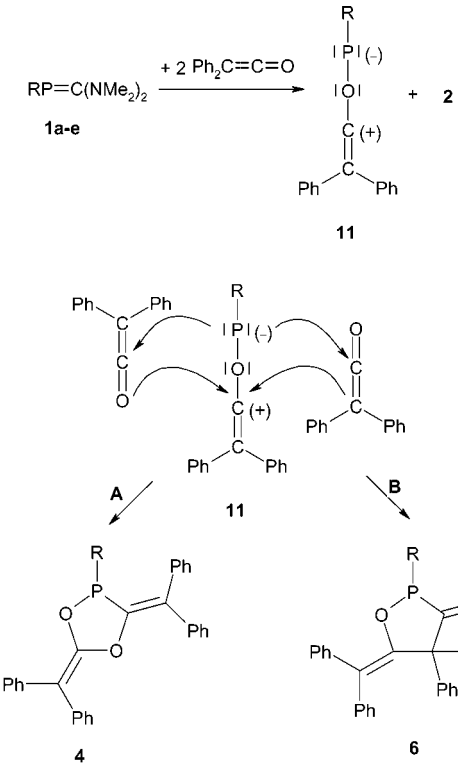

Scheme 6. Proposed mechanism for the formation of compounds **2**, **4**, and **6**.

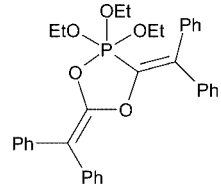

13. A cycloreversion of the phosphole to yield a transient phenylphosphinidene has been invoked to rationalize this result.[19]

Conclusions

We have demonstrated that inversely polarized phosphaalkenes $RP{=}C(NMe_2)_2$ (**1a**–**e**) and $t\text{BuP}{=}C(NEt_2)_2$ (**1f**) serve as convenient sources for the generation of phosphinidenes [RP] and carbenes $[(Me_2N)_2C]$ and $[(Et_2N)_2C]$ under mild conditions. These carbenes are trapped by diphenyl ketene, which leads to the formation of the zwitterionic carbene/ketene adducts **2** and **3**. On the other hand, the phosphinidene fragment can also combine with 2 equiv. of ketene in a 1,3-dipolar cycloaddition between the intermediate $RP{-}O{-}C{=}CPh_2$ and $Ph_2C{=}C{=}O$ to give heterocycles **4a**–**e** and **6a**. From cross-coupling and exchange reaction it is obvious that free carbenes and/or phosphinidenes are not involved in these processes.

 © 2005 Wiley-VCH Verlag GmbH & Co. KGaA, Weinheim

Experimental Section

General: All reactions were performed under dry, oxygen-free nitrogen using standard Schlenk techniques. The phosphaalkenes *t*BuP=C(NMe$_2$)$_2$ (**1a**),[20] CyP=C(NMe$_2$)$_2$ (**1b**),[21] PhP=C(NMe$_2$)$_2$ (**1d**),[22] MesP=C(NMe$_2$)$_2$ (**1e**),[20] and Me$_3$SiP=C(NMe$_2$)$_2$ (**1i**),[23] as well as Ph$_2$C=C=O,[24] AdPH$_2$,[25] *t*BuP(H)SiMe$_3$,[26] thiouronium salt **7**,[27] and (*t*BuP)$_3$[28] were prepared as described in the literature. Infrared spectra were recorded with a Bruker FT-IR IFS 66 spectrometer. NMR spectra: Bruker AM Avance DRX 500; standards: SiMe$_4$ (^{1}H, ^{13}C), external 85% H$_3$PO$_4$ (^{31}P).

1-AdP(H)SiMe$_3$: A 1.6 M *n*-hexane solution of *n*-butyllithium (59.4 mL, 95.0 mmol) was added dropwise to a solution of 1-AdPH$_2$ (16.8 g, 100.0 mmol) in THF (100 mL) at 0 °C. This slurry was added at 20 °C to a solution of Me$_3$SiCl (11.9 g, 110.0 mmol) in 30 mL of THF, and the mixture was stirred for 16 h. The volatile components were then removed in vacuo and the residue was triturated with *n*-pentane (50 mL). It was then filtered and the filter cake was washed with *n*-pentane (3 × 20 mL). The filtrate was liberated from solvents and the residue was distilled to furnish 15.0 g (69% yield) of 1-AdP(H)SiMe$_3$ as a colorless oil. ^{1}H NMR (CDCl$_3$): δ = 0.25 (d, $^3J_{P,H}$ = 5 Hz, 9 H, SiMe$_3$), 2.16 (d, $^1J_{P,H}$ = 204 Hz, 1 H, PH), 1.6–2.0 (m, 15 H, Ad) ppm. ^{31}P{^{1}H} NMR (CDCl$_3$): δ = –85.7 ppm.

1-AdP=C(NMe$_2$)$_2$ (1c): An *n*-hexane solution of *n*-butyllithium (1.6 M, 28.1 mL, 45.0 mmol) was added dropwise, at 0 °C, to a solution of 1-Ad-P(H)SiMe$_3$ (12.2 g, 50 mmol) in THF (50 mL). The resulting slurry was added dropwise to a suspension of pentamethylthiouronium iodide (13.7 g, 50 mmol) in 50 mL of THF. After 16 h of stirring at room temp., the solvent and volatile components were removed in vacuo. The residue was triturated with *n*-pentane (50 mL) and filtered. The filter cake was washed with diethyl ether (3 × 20 mL) and the filtrate was liberated from solvent in vacuo. The residue was distilled in vacuo to give 10.0 g (75%) of **1c** as an orange oil, which slowly solidified to a wax. ^{1}H NMR (C$_6$D$_6$): δ = 1.6–2.0 (m, 15 H, Ad), 2.56 (m, 12 H, NMe$_2$) ppm. ^{31}P{^{1}H} NMR (C$_6$D$_6$): δ = 89.7 ppm.

Reaction of 1a–e with Ph$_2$C=C=O (General Procedure): A sample of neat Ph$_2$C=C=O (0.27 g, 1.39 mmol) was transferred dropwise, via a cannula, into a chilled solution (0 °C) of phosphaalkene **1** (0.40 mmol) in 30 mL of *n*-pentane. The resulting slurry was stirred at ambient temp. for 18 h and then filtered. The bright-yellow filter cake was washed with *n*-pentane (3 × 10 mL) and then dried in vacuo. Purification of crude **2** was effected by column chromatography on silica. Impurities were eluted with CH$_2$Cl$_2$ before product **2** was eluted with CH$_3$OH. Removal of solvent in vacuo afforded 0.10 g (85% yield) of bright-yellow, microcrystalline **2**. ^{1}H NMR (CDCl$_3$): δ = 2.74 (s, 6 H, NMe$_2$), 3.21 (s, 6 H, NMe$_2$), 7.00–7.56 (m, 10 H, Ph) ppm. ^{13}C{^{1}H} NMR (CDCl$_3$): δ = 42.3 [s, N(CH$_3$)$_2$], 42.6 [s, N(CH$_3$)$_2$], 123–130 (s, Ph), 141.6 [s, *C*(NMe$_2$)], 143.0 (s, *C*Ph$_2$), 175.4 (s, CO) ppm. IR (KBr): $\tilde{\nu}$ = 1713 cm^{-1} (CO), 1613 (C=C). MS/ESI: *m*/*z* = 295.0 [**2** + H$^+$]. Peak matching: C$_{19}$H$_{22}$N$_2$O: calcd. 295.18049; found 295.18032. After removal of **2**, the obtained filtrate was treated with powdered NaOH (0.50 g, 12.5 mmol) and stirred at 20 °C for 18 h to destroy the excess of Ph$_2$C=C=O. It was then filtered and the colorless filtrate was concentrated to dryness to afford the heterocycles **4a–e**.

4a (R = *t*Bu): Yield: 0.10 g (53%) of an oily wax. ^{1}H NMR (CDCl$_3$): δ = 0.89 (d, $^3J_{P,H}$ = 12.6 Hz, 9 H, *t*Bu), 7.17–7.37 (m, 20 H, Ph) ppm. ^{13}C{^{1}H} NMR (CDCl$_3$): δ = 24.7 [d, $^2J_{P,C}$ = 14.9 Hz, C(*C*H$_3$)$_3$], 38.5 [d, $^1J_{P,C}$ = 33.2 Hz, *C*(CH$_3$)$_3$], 93.1 (s, Ph$_2$*C*=CO$_2$), 125.5 (d, $^2J_{P,C}$ = 6.9 Hz, Ph$_2$*C*=COP), 127–131 (20s, Ph), 150.4 (d, $^1J_{P,C}$ = 41.1 Hz, PCO), 157.4 (d, $^2J_{P,C}$ = 11.4 Hz, OCO) ppm. ^{31}P{^{1}H} NMR (CDCl$_3$): δ = 122.3 ppm (s). IR (KBr): $\tilde{\nu}$ = 1761 cm^{-1} s, 1663 m, 1599 m. MS/EI: *m*/*z* (%) = 476 (27) [**4a**]$^+$, 194 (100) [Ph$_2$C=C=O]$^+$. High resolution MS: calcd. 479.19052; found 479.1902. C$_{32}$H$_{29}$O$_2$P (476.19): calcd. C 80.65, H 6.13; found C 80.40, H 6.12.

4b (R = Cy): Yield: 0.10 g (50%) of a colorless oily wax. ^{1}H NMR (CDCl$_3$): δ = 0.90–1.77 (m, 11 H, Cy), 7.17–7.36 (m, 20 H, Ph) ppm. ^{13}C{^{1}H} NMR (CDCl$_3$): δ = 26.2 (d, $J_{P,C}$ = 5.7 Hz, Cy), 26.3 (d, $J_{P,C}$ = 6.9 Hz, Cy), 26.7 (d, $J_{P,C}$ = 11.4 Hz, Cy), 27.1 (d, $J_{P,C}$ = 12.6 Hz, Cy), 43.4 (d, $J_{P,C}$ = 34.3 Hz, Cy), 93.7 (s, Ph$_2$*C*=CO$_2$), 125.6 (d, $^2J_{P,C}$ = 28.5 Hz, Ph$_2$*C*=COP), 127–131 (20s, Ph), 137.1 (s, *i*-*C*Ph), 138.4 (s, *i*-*C*Ph), 138.6 (s, *i*-*C*Ph), 138.8 (s, *i*-*C*Ph) 150.3 (d, $^1J_{P,C}$ = 34.3 Hz, PCO), 157.5 (d, $^2J_{P,C}$ = 11.4 Hz, OCO) ppm. ^{31}P{^{1}H} NMR (CDCl$_3$): δ = 117.8 ppm (s). IR (KBr): $\tilde{\nu}$ = 1727 cm^{-1} s, 1657 m, 1597 m. MS/EI: *m*/*z* (%) = 502 (57) [**4b**]$^+$, 194.1 (100) [Ph$_2$C=C=O]$^+$. High resolution MS: calcd. for C$_{34}$H$_{31}$O$_2$P 502.20617; found 502.20571.

4c (R = Ad): Yield: 0.10 g (45%) of a colorless oily wax. ^{1}H NMR (CDCl$_3$): δ = 1.57–1.91 (m, 15 H, Ad), 7.20–7.38 (m, 20 H, Ph) ppm. ^{13}C{^{1}H} NMR (CDCl$_3$): δ = 27.8 (d, $J_{P,C}$ = 8.0 Hz, Ad), 36.0 (d, $J_{P,C}$ = 12.6 Hz, Ad), 36.5 (s, Ad), 41.9 (d, $J_{P,C}$ = 33.2 Hz, Ad), 92.5 (s, Ph$_2$*C*=CO$_2$), 125.5 (d, $^2J_{P,C}$ = 9.1 Hz, Ph$_2$*C*=COP), 127–131 (20s, Ph), 137.9 (s, *i*-*C*Ph), 138.5 (s, *i*-*C*Ph), 138.6 (s, *i*-*C*Ph), 139.6 (s, *i*-*C*Ph), 149.5 (d, $^1J_{P,C}$ = 40.0 Hz, P*C*O), 157.7 (d, $^2J_{P,C}$ = 11.4 Hz, O*C*O) ppm. ^{31}P{^{1}H} NMR (CDCl$_3$): δ = 117.1 ppm (s). IR (KBr): $\tilde{\nu}$ = 1654 cm^{-1} m, 1596 m. MS/EI: *m*/*z* (%) = 554 (53) [**4c**]$^+$, 194 (47) [Ph$_2$C=C=O]$^+$, 165 (58) [CPh$_2$]$^+$, 135 (100) [Ad]$^+$. High resolution MS: calcd. for C$_{38}$H$_{35}$O$_2$P 554.23747; found 554.23790.

4d (R = Ph): Yield 0.10 g (50%) of a colorless oily wax. ^{1}H NMR (CDCl$_3$): δ = 7.02–7.35 (m, 25 H, Ph) ppm. ^{13}C{^{1}H} NMR (CDCl$_3$): δ = 95.5 (s, Ph$_2$*C*=CO$_2$), 125.9 (d, $^2J_{P,C}$ = 40.0 Hz, Ph$_2$*C*=COP), 127–135 (25s, Ph), 136.8 (d, $J_{P,C}$ = 2.0 Hz, *i*-*C*Ph), 138.1 (s, *i*-*C*Ph), 138.3 (s, *i*-*C*Ph), 138.4 (s, *i*-*C*Ph), 138.6 (s, *i*-*C*Ph), 150.7(d, $^1J_{P,C}$ = 26.3 Hz, PCO), 156.4 (d, $^2J_{P,C}$ = 11.4 Hz, OCO) ppm. ^{31}P{^{1}H} NMR (CDCl$_3$): δ = 90.6 ppm (s). IR (KBr): $\tilde{\nu}$ = 1764 cm^{-1} s, 1656 m, 1597 m. MS/EI: *m*/*z* (%) = 496 (52) [**4d**]$^+$, 194 (51) [Ph$_2$C=C=O]$^+$. High resolution MS: calcd. for C$_{34}$H$_{25}$O$_2$P 496.15922; found 496.15834.

4e (R = Mes): Yield: 0.10 g (48%) of a colorless oily wax. ^{1}H NMR (CDCl$_3$): δ = 2.28 (s, 3 H, *p*-Me), 3.76 (s, 6 H, *o*-Me), 7.20–7.38 (m, 22 H, Ph + Mes) ppm. ^{13}C{^{1}H} NMR: δ = 52.3 (s, *p*-CH$_3$), 57.0 (s, *o*-CH$_3$), 94.0 (s, Ph$_2$*C*=CO$_2$), 127–131 (26s, Ph + Mes + Ph$_2$*C*=COP), 133.7 (d, $^1J_{P,C}$ = 19.4 Hz, *i*-*C*Mes), 136.8 (s, *i*-*C*Ph), 138.0 (s, *i*-*C*Ph), 138.2 (s, *i*-*C*Ph), 138.7 (s, *i*-*C*Ph), 142.3 (d, $^1J_{P,C}$ < 1 Hz, PCO), 144.8 (d, $^2J_{P,C}$ = 20.6 Hz, OCO) ppm. ^{31}P{^{1}H} NMR (CDCl$_3$): δ = 103.1 ppm (s). IR (KBr): $\tilde{\nu}$ = 1731 cm^{-1} s, 1649 m, 1601 m. MS/EI: *m*/*z* (%) = 538 (43) [**4e**]$^+$, 194 (51) [Ph$_2$C=C=O]$^+$, 165 (58) [CPh$_2$]$^+$. High resolution MS: calcd. for C$_{37}$H$_{31}$O$_2$P 538.20617; found 538.20634.

3: A sample of diphenyl ketene (0.27 g, 1.39 mmol) was slowly added to a solution of phosphaalkene *t*BuP=C(NEt$_2$)$_2$ (**1f**; 0.10 g, 0.40 mmol) in 30 mL of chilled *n*-pentane (0 °C). The resulting slurry was stirred at room temp. for 18 h and was then filtered. The bright-yellow filter cake was washed with *n*-pentane (3 × 10 mL) and dried in vacuo to give 0.10 g (73%) of **3** as a bright-yellow powder. ^{1}H NMR (CDCl$_3$): δ = 1.0 (br. s, 12 H, CH$_3$), 3.3 (br. s, 8 H, NCH$_2$), 6.96–7.38 (m, 10 H, Ph) ppm. ^{13}C{^{1}H} NMR (CDCl$_3$): δ = 24.6 (br. s, NCH$_3$), 45.7 (s, NCH$_2$), 126–140 [14 s, Ph + *C*(NEt$_2$)$_2$ + *C*Ph$_2$], 174.4 (s, CO) ppm. MS/EI: *m*/*z* = 351 [**3** +

 © 2005 Wiley-VCH Verlag GmbH & Co. KGaA, Weinheim

Table 1. Crystallographic data for **2**, **4e**, and **6**.

	2	**4e**	**6a**
Formula	$C_{19}H_{22}N_2O$	$C_{37}H_{31}O_2P$	$C_{32}H_{29}O_2P$
Color	yellow	colorless	yellow
Size [mm^3]	0.15 × 0.03 × 0.03	0.16 × 0.11 × 0.10	0.30 × 0.30 × 0.18
M_r	294.39	538.59	476.52
Crystal system	orthorhombic	monoclinic	monoclinic
Space group	$P2_12_12_1$	$P2_1/n$	$P2_1/n$
a [Å]	8.400(2)	19.4460(2)	16.5600(2)
b [Å]	10.766(1)	6.0100(1)	9.3890(1)
c [Å]	17.539(4)	25.4100(3)	17.2190(3)
β [°]	90	110.2910(6)	109.8970(7)
V [Å^3]	1586.1(5)	2785.39(6)	2517.43(6)
$\rho_{calcd.}$ [g cm^{-3}]	1.233	1.284	1.257
Z	4	4	4
F(000)	632	1136	1008
μ [mm^{-1}]	0.077	0.132	0.137
Θ [°]	3.08 to 20.00	3.13 to 27.48	2.95 to 27.48
T [K]	100	100	150
Refl. measured	2435	55718	31518
Unique refl.	1406	6378	5737
R(int)	0.112	0.046	0.031
No. refl. (I) > 2σ(I)	927	5240	4694
Refined parameters	109	364	319
R_F [$I > 2\sigma(I)$]	0.0733	0.0372	0.0406
wR_F^2 [$I > 2\sigma(I)$]	0.1480	0.0896	0.1037
$\Delta\rho$ max/min [e Å^{-3}]	0.230/–0.213	0.446/–0.314	0.255/–0.356

H^+]. High resolution MS: calcd. for $C_{23}H_{30}N_2O$ 351.24309; found 351.24295.

5: A sample of $Ph_2C{=}C{=}O$ (0.27 g, 1.39 mmol) was combined with an *n*-pentane solution (30 mL) of phosphaalkene Me_3Si-$P{=}C(NMe_2)_2$ (**1i**; 0.05 g, 0.40 mmol) at 0 °C. The resulting solution was stirred at 20 °C for 18 h and then freed from solvent. The residue, consisting of crude **5**, was not purified further. ^{1}H NMR (C_6D_6): δ = 0.11 (s, 9 H, $SiMe_3$), 2.36 (s, 6 H, NMe_2), 2.71 (s, 6 H, NMe_2), 7.00–7.57 (m, 10 H, Ph) ppm. $^{31}P\{^1H\}$ NMR (C_6D_6): δ = 17.3 ppm (s). MS/EI: *m*/*z* (%) = 398 (47) [**5**]$^+$.

Reaction of $Ph_2C{=}C{=}O$ with (tBuP)$_3$: A mixture of (tBuP)$_3$ (0.10 g, 0.38 mmol) and $Ph_2C{=}C{=}O$ (0.20 g, 1.03 mmol) in 1 mL of toluene was stirred at room temp. for 18 h and then heated to 100 °C for 5 h. The $^{31}P\{^1H\}$ NMR spectrum of the resulting solution showed the resonance of **4a** at δ = 121.9 ppm (ca. 6 mol-% P), a singlet at δ = –57.8 for (tBuP)$_4$ (ca. 14 mol-% P) and the AB pattern of (tBuP)$_3$ at δ = –70.1 and –108.6 ppm.

2-*tert*-Butylphosphanylidene-1,3-diisopropyl-4,5-dimethyl-2,3-dihydro-1*H*-imidazole (8): A 1.6 M *n*-hexane solution of *n*-butyllithium (25 mL, 40.0 mmol) was added dropwise at 0 °C to a solution of tBuP(H)$SiMe_3$ (6.57 g, 40.4 mmol) in THF (35 mL). The mixture was combined with a slurry of 1,3-diisopropyl-4,5-dimethyl-2,3-dihydroimidazol-2-ylidenemethylsulfonium iodide (**7**; 14.5 g, 40.9 mmol) in THF (80 mL) at 0 °C. Stirring was continued at room temp. in the dark for 3 d to give a suspension of a colorless solid and a red solution. A $^{31}P\{^1H\}$ NMR taken from this mixture showed a singlet at δ = 5.0 ppm. The slurry was filtered, and the filtrate was concentrated to dryness. The oily red-brown residue was dissolved in *n*-pentane and filtered. The obtained filter cake was washed with 10 mL of diethyl ether and dried. An ^{1}H NMR spectrum in $CDCl_3$ showed signals at δ = 1.69 [d, $^3J_{H,H}$ = 7.0 Hz, 12 H, $NCH(CH_3)_2$], 2.28 (s, 6 H, CH_3-C=C-CH_3), 4.57 [sept, $^3J_{H,H}$ = 7.0 Hz, 2 H, $NCH(CH_3)_2$], 9.77 ppm (s, 1 H, CH), which agree with the presence of the imidazolium ion **10**. The solvent was then removed from the filtrate and the residual orange oil was distilled. The $^{31}P\{^1H\}$ NMR spectrum of the distillate shows prominent signals at $\delta_{^{31}P}$ = –108.7, –70.5 ppm (AB-spin system) due to (tBuP)$_3$ (ca. 68 mol-% P), –57.6 (tBuP)$_4$ (ca. 10 mol-% P) and 4.3 ppm (**8** ca. 5 mol-% P).

X-ray Crystallography: Details are listed in Table 1. CCDC-273086 (**2**), -273087 (**4e**), and -273088 (**6a**) contain the supplementary crystallographic data for this paper. These data can be obtained free of charge from The Cambridge Crystallographic Data Centre via www.ccdc.cam.ac.uk/data_request/cif.

[1] Review: L. Weber, *Eur. J. Inorg. Chem.* **2000**, 2425–2441.
[2] L. Weber, S. Uthmann, H.-G. Stammler, B. Neumann, W. W. Schoeller, R. Boese, D. Bläser, *Eur. J. Inorg. Chem.* **1999**, 2369–2381.
[3] L. Weber, M. H. Scheffer, H.-G. Stammler, B. Neumann, W. W. Schoeller, A. Sundermann, K. K. Laali, *Organometallics* **1999**, *18*, 4216–4221.
[4] L. Weber, O. Kaminski, B. Quasdorff, H.-G. Stammler, B. Neumann, *J. Organomet. Chem.* **1997**, *529*, 329–341.
[5] L. Weber, M. H. Scheffer, H.-G. Stammler, A. Stammler, *Eur. J. Inorg. Chem.* **1999**, 1607–1611.
[6] L. Weber, U. Lassahn, H.-G. Stammler, B. Neumann, K. Karaghiosoff, *Eur. J. Inorg. Chem.* **2002**, 3272–3277.
[7] a) Reviews:M. F. Lappert, *J. Organomet. Chem.* **1975**, *100*, 139–159; b) H. Fischer, in *Transition Metal Carbene Complexes*, VCH, Weinheim **1983**, p. 34–35 and references cited therein.
[8] a) H. W. Wanzlick, E. Schikora, *Angew. Chem.* **1960**, *72*, 494; b) H. W. Wanzlick, E. Schikora, *Chem. Ber.* **1961**, *94*, 2389–2393; c) H. W. Wanzlick, *Angew. Chem.* **1962**, *74*, 129–134.
[9] F. E. Hahn, L. Wittenbecher, D. Le van, R. Fröhlich, *Angew. Chem.* **2000**, *112*, 551–554; *Angew. Chem. Int. Ed.* **2000**, *39*, 541–544.
[10] R. W. Alder, L. Chaker, F. P. V. Paolini, *Chem. Commun.* **2004**, 2172–2173.
[11] M. Regitz, J. Hocker, B. Weber, *Angew. Chem.* **1970**, *82*, 394–395; *Angew. Chem. Int. Ed. Engl.* **1970**, *9*, 375–376.

 © 2005 Wiley-VCH Verlag GmbH & Co. KGaA, Weinheim

[12] L. N. Markovskii, V. D. Romanenko, T. V. Pidvarko, *Zh. Obshch. Khim.* **1983**, *53*, 1672–1673; *Chem. Abstr.* **1983**, *99*, 195100g.
[13] Holleman-Wiberg, *Lehrbuch der Anorganischen Chemie*, 91st–100th ed., de Gruyter, Berlin, **1985**, p. 133.
[14] G. Frison, A. Sevin, *J. Organomet. Chem.* **2002**, *643*, 105–111.
[15] A. J. Arduengo III, H. V. Rasika Dias, J. C. Calabrese, *Chem. Lett.* **1997**, 143–144.
[16] a) A. J. Arduengo III, C. J. Carmalt, J. A. C. Clyburne, A. H. Cowley, R. Pyati, *Chem. Commun.* **1997**, 981–982; b) A. J. Arduengo III, J. C. Calabrese, A. H. Cowley, H. V. Rasika Dias, J. R. Goerlich, W. J. Marshall, B. Riegel, *Inorg. Chem.* **1997**, *36*, 2151–2158.
[17] J. E. Baldwin, J. C. Swallow, *J. Org. Chem.* **1970**, *35*, 3583–3584.
[18] a) W. G. Bentrude, W. D. Johnson, W. A. Kahn, *J. Am. Chem. Soc.* **1972**, *94*, 3058–3067; b) W. G. Bentrude, W. D. Johnson, W. A. Kahn, *J. Am. Chem. Soc.* **1972**, *94*, 923.
[19] N. S. Isaac, G. N. El-Din, G. B. Drew, *Recl. Trav. Chim. Pays-Bas* **1989**, *108*, 120–121.
[20] L. Weber, M. Meyer, H.-G. Stammler, B. Neumann, *Chem. Eur. J.* **2001**, *7*, 5401–5408.
[21] L. Weber, G. Noveski, U. Lassahn, H.-G. Stammler, B. Neumann, *Eur. J. Inorg. Chem.* **2005**, 1940–1946.
[22] H. Oehme, E. Leißring, H. Meyer, *Z. Chem.* **1981**, 407–408.
[23] L. Weber, O. Kaminski, *Synthesis* **1995**, 158.
[24] H. Staudinger, *Ber. Dtsch. Chem. Ges.* **1911**, *44*, 1619–1623.
[25] H. Stetter, W. Last, *Chem. Ber.* **1969**, *102*, 3364–3366.
[26] G. Becker, O. Mundt, M. Rössler, E. Schneider, *Z. Anorg. Allg. Chem.* **1978**, *443*, 42–52.
[27] H. Lecher, C. Heuck, *Justus Liebigs Ann. Chem.* **1924**, *438*, 169–184.
[28] M. Baudler, *Inorg. Synth.* **1989**, *25*, 2–4.

Received: May 18, 2005
Published Online: September 27, 2005

 © 2005 Wiley-VCH Verlag GmbH & Co. KGaA, Weinheim

Hydrothermal Synthesis, Crystal Structures, and Properties of a Class of 2D Coordination Polymers

Xiang He,[a] Can-Zhong Lu*[a] Da-Qiang Yuan,[a] Li-Juan Chen,[a] Quan-Zheng Zhang,[a] and Chuan-De Wu[a]

Keywords: Coordination polymers / Copper / Magnetic properties / Photoluminescence / Zinc

Hydrothermal reactions between 2,6-naphthalenedicarboxylic acid (H_2NDC), 1,10-phenanthroline (1,10-phen) or 2,2′-bipyridine (2,2′-bpy), and transition metal acetates give rise to four coordination polymers, namely $[Cu_3(NDC)_3(2,2'\text{-bpy})(H_2O)_2]_n{\cdot}nH_2O$ (**1**), $[Cu(NDC)(1,10\text{-phen})]_n$ (**2**), $[Zn(NDC)(1,10\text{-phen})]_n$ (**3**), and $[Zn_4(OH)_2(NDC)_3(2,2'\text{-bpy})_2]_n$ (**4**), which show different two-dimensional layered architectures. Compound **1** consists of three kinds of polymeric chains that are interconnected to form an unusual two-dimensional layered motif, while compound **4** features a two-dimensional honeycomb network structure with a noninterpenetrating ABCDABCD packing pattern. Compounds **2** and **3** show a two-dimensional grid-type framework but have different space-filling styles. The magnetic properties for **1** and **2** and the solid-state emission spectra of **3** and **4** have also been studied.
(© Wiley-VCH Verlag GmbH & Co. KGaA, 69451 Weinheim, Germany, 2005)

Introduction

The construction of extended porous metal–organic frameworks (MOFs) is of current interest in the fields of supramolecular chemistry and crystal engineering, not only because of their intriguing architectures but also because of their unexpected properties for potential practical applications in a wide number of fields, such as gas storage, exploitable magnetics, photoluminescence, and molecular recognition.[1–4] The self-assembly of MOFs using suitable ligands and metal centers has been proved to be an efficient route for the formation of one- to three-dimensional networks with fascinating structural topologies. The selection of organic ligands with appropriate coordination sites is the key to the formation of MOFs with desirable physical and chemical properties. Recently, the strategy using metal ions and organic carboxylates as starting building blocks to generate extended networks has been of great interest.[5–14] For example, 1,4-benzenedicarboxylate-(BDC-)bridged metal-organic frameworks have been studied extensively.[15] Polycyclic aromatic bidentate ligands such as 2,2′-bipyridine and 1,10-phenanthroline are frequently used together with polycarboxylates, leading to many novel architectures. Most of the coordination polymers with BDC and 2,2′-bipyridine or 1,10-phenanthroline ligands are often one-dimensional structures.[16] We are currently interested in employing 2,6-naphthalenedicarboxylate (NDC) as a bridging ligand since this molecule is more rigid than BDC and might not only establish bridges between several metal centers and exhibit rich coordination modes but also be expected to form a porous framework because of its rigidity and stability. On the other hand, because the presence of conjugated aromatic rings causes its low solubility in aqueous media, quite a few examples of polymeric structures containing both NDC and other multipyridine ligands have been reported.[17]

In the present work, we have selected Cu^{II} and Zn^{II} cations as metal nodes and NDC as a rigid bridging ligand and obtained four interesting 2D polymeric compounds, namely $[Cu_3(NDC)_3(2,2'\text{-bpy})(H_2O)_2]_n{\cdot}nH_2O$ (**1**), $[Cu(NDC)(1,10\text{-phen})]_n$ (**2**), $[Zn(NDC)(1,10\text{-phen})]_n$ (**3**), and $[Zn_4(OH)_2(NDC)_3(2,2'\text{-bpy})_2]_n$ (**4**). Compound **1** consists of three different chains that are interconnected to form an unusual two-dimensional layered motif, while compound **4** features a two-dimensional honeycomb network structure with a noninterpenetrating ABCDABCD packing pattern. Compounds **2** and **3** show a two-dimensional grid-type framework but have different space-filling styles.

Results and Discussion

Synthesis

Although it is difficult to control and predict the crystal structures under hydrothermal conditions, the hydrothermal reaction is still an optimum method for the synthesis of some novel MOFs. We used Cu^{II} and Zn^{II} salts and mixed bridging ligands to obtain four 2D compounds with distinct structures under hydrothermal conditions. Subtle adjust-

[a] State Key Laboratory of Structural Chemistry, Fujian Institute of Research on the Structure of Matter, The Chinese Academy of Sciences,
Fuzhou, Fujian, 350002, China
Fax: +86-591-8371-4946
E-mail: czlu@ms.fjirsm.ac.cn

 © 2005 Wiley-VCH Verlag GmbH & Co. KGaA, Weinheim DOI: 10.1002/ejic.200500490

ments of the conditions result in the formation of very different structures.

Crystal Structures

[Cu$_3$(NDC)$_3$(2,2′-bpy)(H$_2$O)$_2$]$_n$·nH$_2$O (1)

Compound **1** consists of three different chains that are interconnected to form an unusual two-dimensional layered motif − one is a zigzag chain and the other two are linear chains. The NDC ligands in the zigzag chain act as the junctions to link the two linear chains into a layered structure. As shown in Figure 1, the asymmetric unit contains two crystallographically unique Cu centers. Each Cu^{II} center has a quite different coordination environment: the first one has a $\{CuO_2N_2\}$ coordination sphere and is coordinated by two nitrogen atoms from one 2,2′-bpy [Cu–N = 1.984(6) Å] and two oxygen atoms from two NDC ligands [Cu–O = 1.966(5) Å] with O(N)–Cu–O(N) angles involving the neighboring atoms ranging from 82.5(2) to 97.7(2)°, showing a disordered square-planar structure, and the second one has a $\{CuO_4\}$ square-planar coordination sphere and is defined by three oxygen donors from three individual NDC ligands [Cu–O = 1.932(5)–1.996(5) Å] and one from a water molecule [Cu–O = 1.969(6) Å]. The trinuclear copper unit formed can be taken as an isosceles triangular array linked by the NDC ligands. The NDC ligands in compound **1** exhibit two different coordination modes (Scheme 1): one (NDC with O5) acts as a tetradentate ligand to link four copper(II) centers (mode I), while another (NDC with O1) acts as a bidentate ligand connecting two copper(II) centers in an *anti* fashion (mode II). As shown in Figure 2, the bidentate carboxyl groups bridge the Cu(2) atom to form linear chains running alone the *b*-axis, which are parallel to each other. The tetradentate carboxyl groups bridge the Cu(1) atom to form zigzag chains running along the *c*-axis, which also link the neighboring copper atoms in

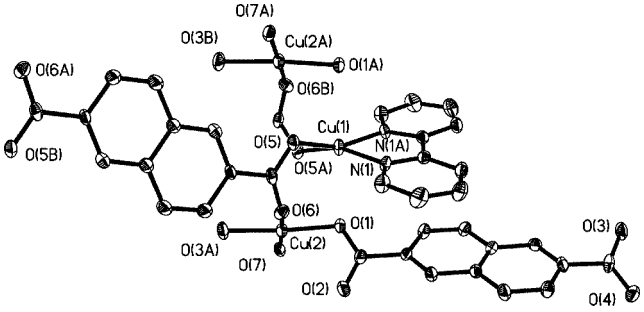

Figure 1. ORTEP representation of the symmetry-expanded structure of **1**, showing the coordination environments of the Cu^{II} atoms (30% probability thermal ellipsoids; hydrogen atoms and solvent molecules have been omitted for clarity).

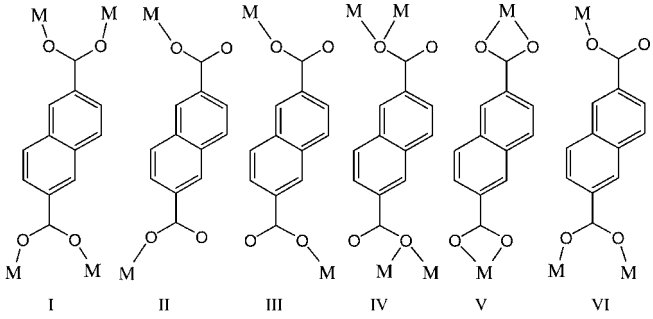

Scheme 1. Different kinds of coordination modes of the NDC ligand.

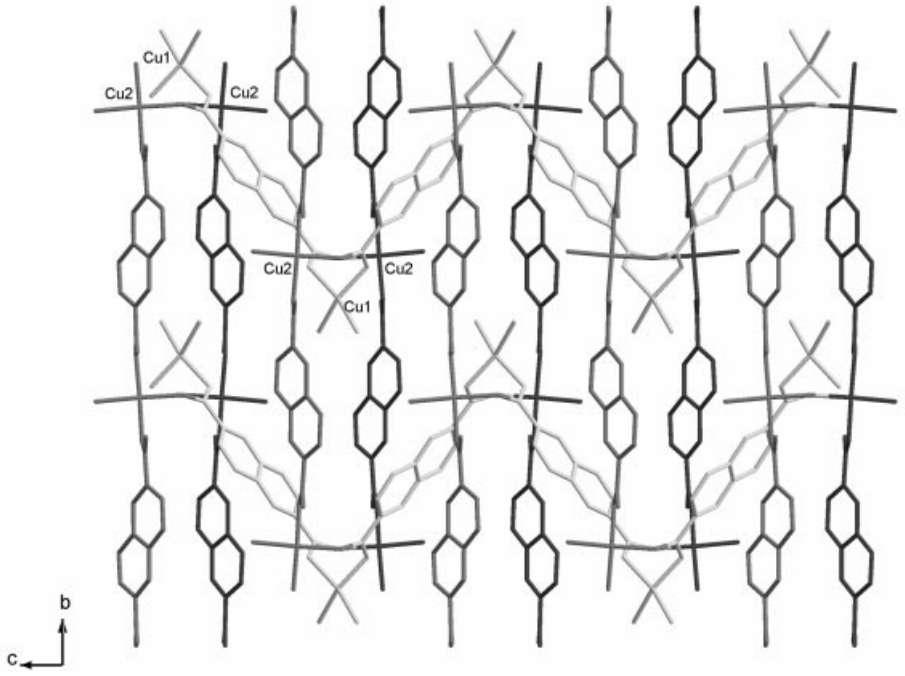

Figure 2. Perspective view of the 2D layer structure of **1**.

 © 2005 Wiley-VCH Verlag GmbH & Co. KGaA, Weinheim

linear chains to form a thick, trilayer network. Each zigzag chain is parallel to the others, while the linear chains located behind and ahead of the zigzag chain are parallel to each other too.

The Cu···Cu distance within the zigzag chain bridged by the NDC ligand is 13.022(1) Å, while the Cu···Cu distance is 13.006(1) Å in the linear chain. The Cu···Cu distance between two neighboring linear chains is 5.638(8) Å, and the Cu···Cu distance between zigzag and linear chains is 3.395(3) Å. It is notable that the lamellar framework is made up by zigzag chains sandwiched between two adjacent linear chains. To the best of our knowledge, no documented example of such a layered structure has been reported.

[Cu(NDC)(1,10-phen)]$_n$ (2)

Compound **2** is a two-dimensional, square-grid network structure. As shown in Figure 3, the copper(II) atom exhibits a square-pyramidal configuration, coordinated by two nitrogen atoms of one 1,10-phen ligand [Cu–N = 2.029(2)–2.050(2) Å] and three oxygen atoms of the carboxyl groups from different NDC ligands [Cu–O = 1.9139(18)–2.2421(17) Å]. The O–Cu–O bond angles range from 95.89(8) to 102.41(7)° and the O–Cu–N bond angles range from 90.52(8) to 170.58(8)°. The NDC ligands in compound **2** exhibit two different coordination modes (Scheme 1): one (NDC with O3) acts as a tetradentate ligand to link four copper(II) centers (mode I), while another (NDC with O1) acts as a bidentate ligand that connects two copper(II) centers in a *trans* fashion (mode III). As shown in Figure 4a, the carboxylate groups at both ends of the NDC ligands doubly bridge the Cu dimers with a Cu···Cu separation of 4.319(3) Å to yield an infinite chain running along the *a*-axis, in which the four carboxylate oxygen atoms and two Cu atoms form an O_4Cu_2 six-membered ring. The 1D chains are stitched by the bis(monodentate) bridges along the *b*-axis to form a 2D square-grid coordination polymer with dimensions of 13.801(1) × 12.082(1) Å^2, of which the effective pore-size is partly diminished by the phen ligands. Calculations with PLATON show that the pores occupy about 47.0% of the crystal volume. Intramolecular nonclassical weak hydrogen-bonding interactions between the carbon atoms of the 1,10-phen ligand and the oxygen atoms of the carboxylate groups C(10)–H(10A)···O(4) (*–x*, *–y*, *–z*) [3.063(3) Å] exist in compound **2**. In addition, there are π–π stacking interactions between adjacent aromatic rings of phen ligands, with a plane-to-plane separation of about 3.528 Å in **2**.

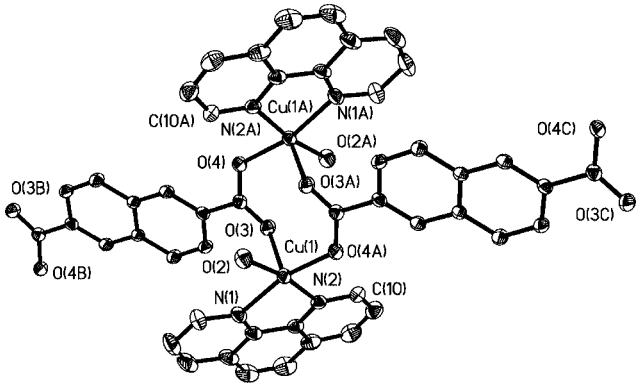

Figure 3. ORTEP representation of the symmetry-expanded structure of **2**, showing the coordination environments of the Cu^{II} atoms (30% probability thermal ellipsoids; hydrogen atoms have been omitted for clarity).

[Zn(NDC)(1,10-phen)]$_n$ (3)

The structure of **3** is also a two-dimensional square-grid network. As shown in Figure 5, the zinc(II) atom exhibits a distorted octahedral configuration, coordinated by two nitrogen atoms of a 1,10-phen ligand [Zn–N = 2.109(6)–2.173(7) Å] and four oxygen atoms of the carboxyl groups from different NDC ligands. The Zn–O distances range from 2.074(5) to 2.177(5) Å, the O–Zn–O bond angles range from 60.8(2) to 155.1(2)°, and the O–Zn–N bond angles range from 90.8(2) to 169.5(2)°. The NDC ligands in compound **3** also exhibit two different coordination modes (Scheme 1): one (NDC with O4) acts as a tetradentate ligand to link four zinc(II) atoms by two carboxylate oxygen atoms on two side (mode IV), while another (NDC with O1) bidentate NDC ligand chelates two zinc(II) centers

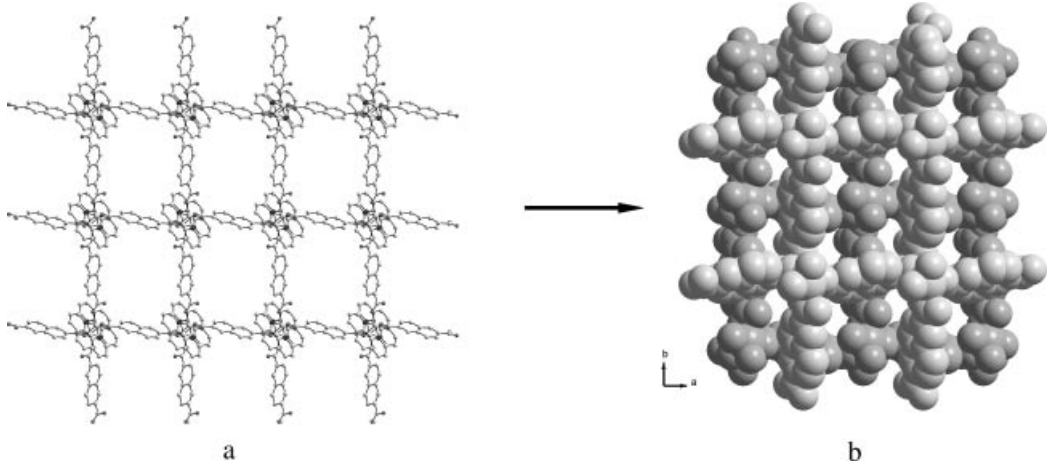

Figure 4. a) Structure of **2**, showing the 2D square grid. b) Space-filling representation of the stacking of 2D layers in **2**.

 © 2005 Wiley-VCH Verlag GmbH & Co. KGaA, Weinheim

(mode V). As shown in Figure 6a, the carboxylate groups at both ends of the NDC ligands doubly bridge Zn dimers with a Zn···Zn separation of 3.207(2) Å to yield an infinite chain in which the two carboxylate oxygen atoms and two Zn atoms form O_2Zn_2 four-membered rings. These chains are stitched by the bis(bidentate) bridges to give a 2D layer architecture. It is interesting to note that the adjacent layers possess large channels with approximate dimensions of $12.899(7) \times 11.147(10)$ Å^2, with the phen ligands inserted inside such grids. Calculations with PLATON show that the pores occupy about 39.2% of the crystal volume. Intramolecular nonclassical weak hydrogen-bonding interactions between the carbon atoms of the 1,10-phen ligand and the oxygen atoms of the carboxylate groups C(1)–H(1A)···O(3) ($-x + 1, -y + 1, -z + 2$) [3.281(12) Å] also exist in compound **3**. In addition, there are π–π stacking interactions between adjacent aromatic rings of the phen ligands, with a plane-to-plane separation of about 3.568 Å in **3**.

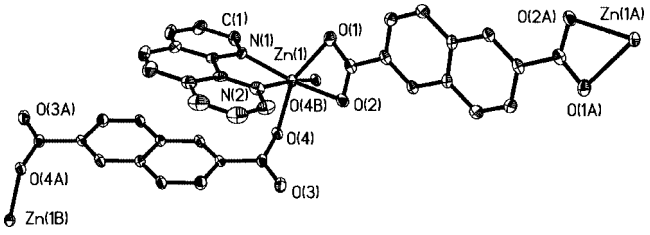

Figure 5. ORTEP representation of the symmetry-expanded structure in **3**, showing the coordination environments of the Zn^{II} atoms (30% probability thermal ellipsoids; hydrogen atoms have been omitted for clarity).

Comparing the different space-filling styles between compounds **2** and **3**, we find that the phen ligands fill the grids, resulting in the different space-filling frameworks. In compound **2**, the phen ligands align above and below one sheet and protrude into the cavities of neighboring networks. Two adjacent square grids are stacked parallel but in a staggered manner to each other along the *c*-direction. This arrangement ultimately leads to an ABAB repeat pattern of layers (Figure 4b). The phen ligands are inserted into the square grids like guest molecules in compound **3**, leading to an AA stacking pattern in the *bc* plane (Figure 6b).

[Zn$_4$(OH)$_2$(NDC)$_3$(2,2′-bpy)$_2$]$_n$ (4)

Compound **4** is a two-dimensional honeycomb network structure with a Zn_2O core as building block that is bridged by a hydroxy group. As shown in Figure 7, the Zn^{II} atoms comprise two different coordination environments: Zn(1) is coordinated by four oxygen atoms in a disordered tetrahedral geometry, with three oxygen donors from individual NDC ligands [Zn(1)–O = 1.932(2)–2.005(2) Å] and one from a hydroxy group [Zn(1)–O = 1.918(2) Å], while Zn(2) is five-coordinated by two 2,2′-bpy nitrogen atoms [Zn(2)–N = 2.078(5)–2.203(6) Å], two oxygen atoms of NDC ligands [Zn(2)–O = 2.028(2)–2.065(3) Å], and one hydroxy group [Zn(2)–O(5) = 1.918(2) Å] to furnish a square-pyramidally coordinated environment. The carboxylate groups exhibit two different coordinating modes (Scheme 1): one (NDC with O1) acts as a tridentate ligand to link three zinc(II) centers (mode VI), while another (NDC with O3)

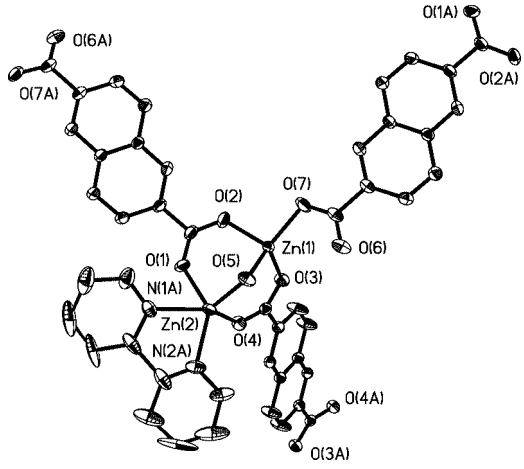

Figure 7. ORTEP representation of the symmetry-expanded structure of compound **4**, showing the coordination environments of the Zn^{II} atoms (30% probability thermal ellipsoids; hydrogen atoms and one disordered bipy have been omitted for clarity).

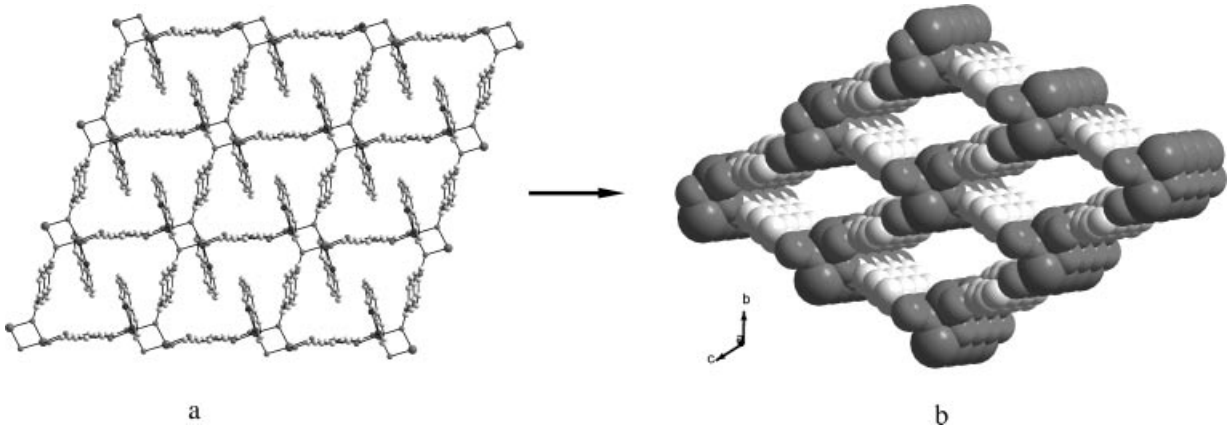

Figure 6. a) Structure of **3**, showing the 2D square grid. b) Space-filling representation of the 2D nanosized channels (2,2′-bpy ligands omitted) in **3**.

 © 2005 Wiley-VCH Verlag GmbH & Co. KGaA, Weinheim

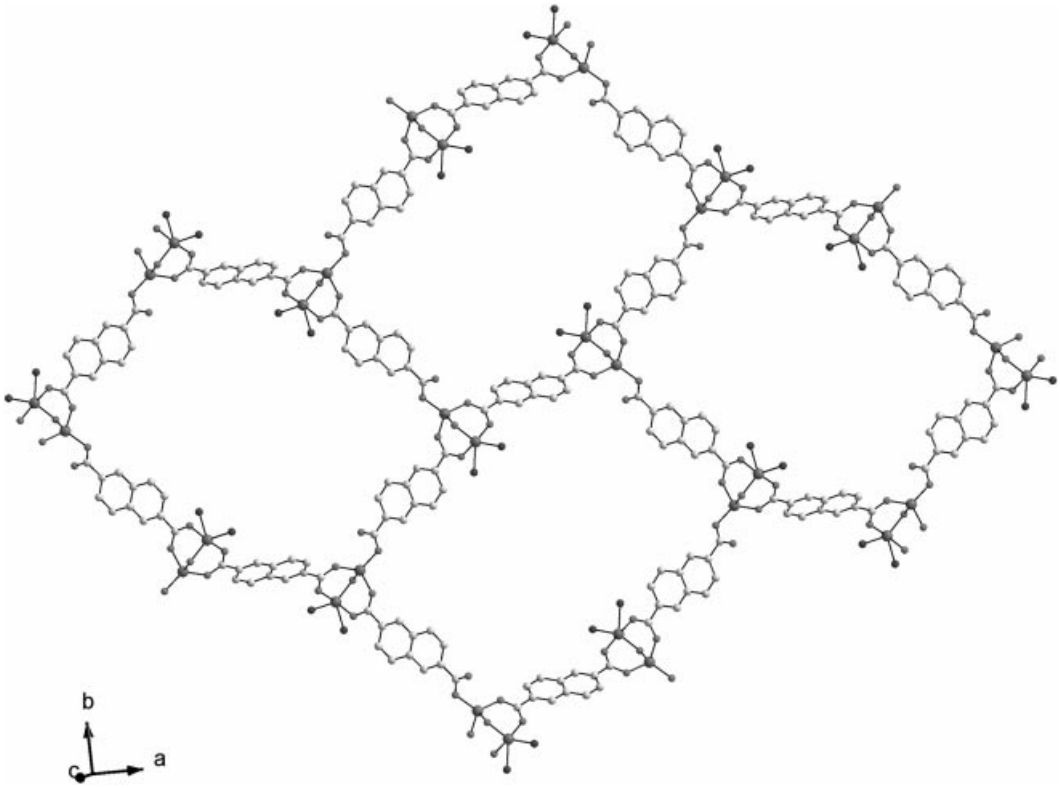

Figure 8. View of the 2D hexagonal grid (2,2′-bpy ligands omitted) of compound **4**.

acts as a tetradentate ligand to link four zinc(II) centers (mode I).

The Zn_2O building units are bridged by four tridentate and two tetradentate NDC ligands to form a hexagon with dimensions of 18.9×26.1 Å^2 (Figure 8). To the best of our knowledge, the simultaneous presence of two coordination modes of NDC ligands to form a hexagon has not been reported until now. Each hexagon shares six edges with six adjacent hexagons to form a 2D framework. It is noteworthy that the topology of compound **4** can be simplified as a (6,3) network.

Other examples of honeycomb compounds often form interpenetrated networks − one 3D fourfold interpenetrated[18] and one 2D twofold interpenetrated[19] supramolecular architectures have been reported. In contrast, compound **4** is an unusual example of a 2D noninterpenetrated honeycomb structure in which these 2D honeycomb networks are stacked together in an ABCDABCD packing mode along the *c*-axis (Figure 9), which is different to that of the other reported noninterpenetrated networks.[20,21] To the best our knowledge, compound **4** is the first example of a 2D noninterpenetrated honeycomb structure with an ABCDABCD packing pattern.

The NDC ligands possess rich coordination modes in the above four 2D structures, which results in the formation of four interesting compounds. The aromatic and rigid part of naphthalene may help the growth of high-quality crystals. Polycyclic N-heterocyclic ligands such as 2,2′-bipyridine or 1,10-phenanthroline might affect the structures due to steric factors. Finally, the different metal cations may also play important roles in the synthesis of novel multidimensional open-framework materials due to their intrinsic ability to form diverse geometric structures.

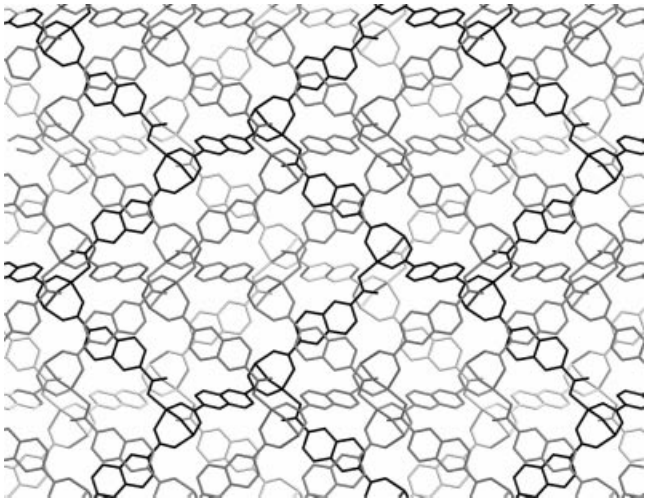

Figure 9. View of the stacking of sheets along the *c*-axis of compound **4** (different shades of gray represent distinct sheets).

Thermogravimetric Analysis

To study the thermal stabilities of these polymers, the thermogravimetric analyses (TGA) of compounds **2**–**4** were

 © 2005 Wiley-VCH Verlag GmbH & Co. KGaA, Weinheim

performed. The TGA diagram of **2** shows two main weight-loss steps. From 30 to 260 °C compound **2** is stable. In the temperature range of 260–327 °C, the observed weight loss of 39.11% is attributed to the elimination of the phen ligands (calcd. 39.35%). The second step is attributed to the further decomposition of NDC ligands. The TGA diagram of **3** is similar to that of **2**, as compound **3** is stable up to 385 °C. In the temperature range of 385–444 °C, the weight loss of 39.21% is attributed to the elimination of phen ligands (calcd. 39.20%). The next step is attributed to the further decomposition of the NDC ligands. The TGA diagram of **4** also indicates two main weight-loss steps. The observed weight loss of 25.54% (322–412 °C) is attributed to the elimination of bpy ligands (calcd. 24.98%), while the second step is attributed to the further decomposition of NDC ligands and the hydroxy group. The stabilities of **3** and **4** make them potential candidates for practical applications.

Magnetic Properties

The magnetic susceptibilities, χ_M, of compound **1** were measured between 5 and 300 K in a 5 kOe applied magnetic field and all data were corrected for diamagnetism of the ligands estimated from Pascal's constants.[22] The plots of μ_{eff} and χ_M vs. T of compound **1** are shown in Figure 10. The μ_{eff} value is 3.28 μ_B at room temperature, which slightly exceeds the value expected for three independent copper(II) ions (3.00 μ_B). The value of μ_{eff} decreases upon cooling, reaching a value of 2.07 μ_B at 5 K. A number of trinuclear copper compounds have been reported and classified from a structural point of view as linear,[23] isosceles triangle,[24] equilateral triangle,[25] and angular trinuclear.[26] The trinuclear copper center in compound **1** can be taken as an isosceles triangle array, therefore an equation that uses two different J values was tried. In this case, the exchange Hamiltonian takes on the form $H = -2J_1(S_1S_2 + S_1S_3) - 2J_2S_2S_3$. As can be seen from the crystal structure of **1**, there is no magnetic exchange interaction between atoms Cu2 and Cu2A, and therefore we can ignore this interaction ($J_2 = 0$) (Scheme 2). The corresponding molar magnetic susceptibility is expressed by Equation (1), in which a Weiss-like parameter was considered. The symbols in that equation have their usual meaning. It is assumed that the g values for all three copper atoms are equal.

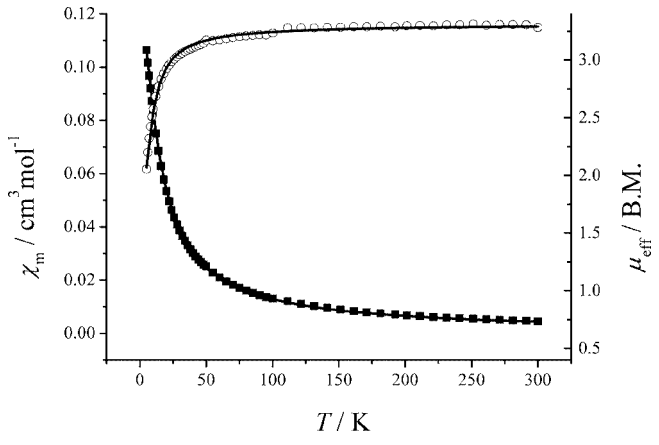

Figure 10. Temperature-dependent experimental molar susceptibility (χ_M) and effective magnetic moment (μ_{eff}) of compound **1**. The solid lines represent the calculated values.

$$\chi_M = \frac{Ng^2\beta^2[15\exp(J_1/KT) + 3/2\exp(-2J_1/KT) + 3/2]}{3k(T-\theta)[4\exp(J_1/kT) + 2\exp(-2J_1/KT) + 2]} \quad (1)$$

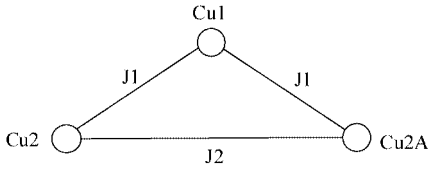

Scheme 2. Different J values for compound **1**.

A satisfactory least-squares fitting of the observed data at 5–300 K leads to $g = 2.20$, $J_1 = -4.36$ cm^{-1}, $J_2 = 0$, and $\theta = 0.04$ K with the agreement factor $R = \Sigma(\chi_{M_{obs}} - \chi_{M_{calcd.}})^2/\Sigma(\chi_{M_{obs}})^2 = 8.37 \times 10^{-7}$. The value of J_1 indicates that an antiferromagnetic Cu1···Cu2 exchange interaction occurs through the bridging carboxylate groups of the NDC ligand, while the θ value indicates very weak ferromagnetic interactions between the trinuclear units through the tetradentate bridging carboxylate groups of the NDC ligand.

From the plots of μ_{eff} and χ_M vs. T of **2** (Figure 11), it can be seen that the μ_{eff} value at room temperature is 1.64 μ_B, which is close to the spin-only value of 1.73 μ_B for the Cu^{II} center ($S = 1/2$). To quantitatively interpret the magnetic behavior of the compound, its magnetic data were analyzed by the theoretical expression by using the HDDV model ($H = -2J_1S_1S_2$). The corresponding molar magnetic susceptibility is expressed by Equation (2), in which a Weiss-like parameter was considered. The symbols in this equation have their usual meaning.

$$\chi_M = \frac{Ng^2\beta^2}{k(T-\theta)[3 + \exp(-2J/kT)]} \quad (2)$$

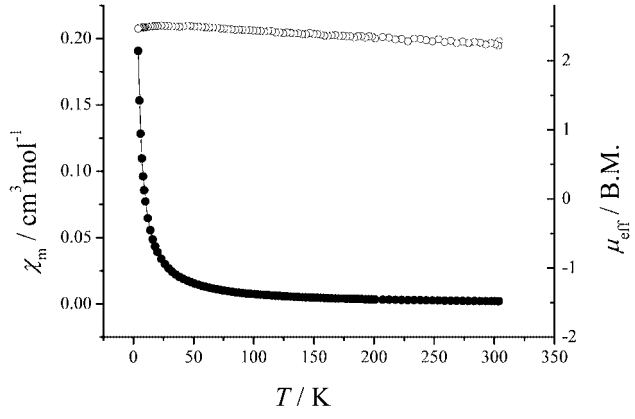

Figure 11. Temperature-dependent experimental molar susceptibility (χ_M) and effective magnetic moment (μ_{eff}) of compound **2**. The solid lines represent the calculated values.

A satisfactory least-squares fitting of the observed data at 5–300 K leads to $g = 2.02$, $J = -2.04$, and $\theta = 1.21$ with

 © 2005 Wiley-VCH Verlag GmbH & Co. KGaA, Weinheim

the agreement factor $R = \Sigma(\chi_{M_{obs}} - \chi_{M_{calcd.}})^2/\Sigma(\chi_{M_{obs}})^2 = 3.50\times10^{-7}$. The J value indicates that an antiferromagnetic Cu···Cu exchange interaction occurs through the bidentate bridging carboxylate groups of the NDC ligand, while the θ value indicates that the dinuclear unit presents ferromagnetic interactions through the bis(monodentate) bridging carboxylate groups of the NDC ligand.

Photoluminescent Properties

We also investigated the photoluminescent properties of compounds **3** and **4**. The emission spectra of compounds **3** and **4** in the solid state at room temperature are shown in Figure 12. It can be seen that compound **3** exhibits an intense blue photoluminescence upon photoexcitation at 386 nm. The emission peak is located at 488 nm for **3**, which means that it is bathochromically shifted by about 20 nm relative to that of the free NDC ligand, probably due to ligand-to-metal charge transfer (LMCT). The blue fluorescent emission of **3** suggests that it might be used as a new blue-light-emitting material. Compound **4** exhibits intense green photoluminescence upon photoexcitation at 380 nm. The emission peak is located at 549 nm for **4**, and compared with the NDC ligand a clearly bathochromic shift occurs in **4**, which might also be attributed to LMCT.[27–29]

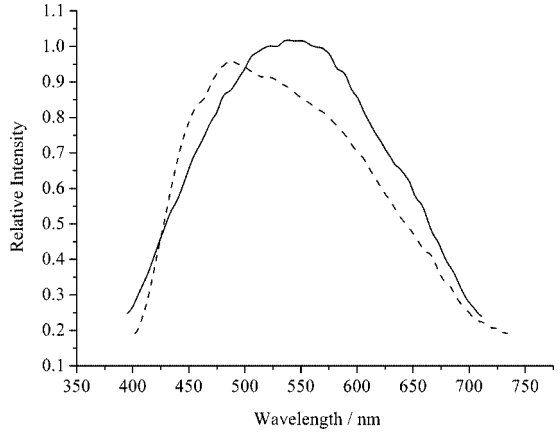

Figure 12. Emission spectra of **3** (broken line) and **4** measured in the solid state at room temperature.

Conclusions

Despite the extensive use of organic carboxylate ligands in the construction of new MOFs, combining both 2,6-naphthalenedicarboxylic acid and some other N-heteroaromatic ligands is a fairly small subset of MOFs. Four two-dimensional layer coordination compounds bridged by 2,6-naphthalenedicarboxylate and N-heteroaromatic ligands have been prepared and characterized. Substitution of metal cations or N-heteroaromatic ligands results in significant different frameworks. Compound **1** consists of three different chains that are interconnected to form an unusual two-dimensional layered motif, while compound **4** features a two-dimensional honeycomb network structure with a noninterpenetrated ABCDABCD packing pattern. Compounds **2** and **3** show a two-dimensional grid-type framework but with different space-filling styles. The magnetic studies indicate antiferromagnetic interactions transferred by the carboxylate groups of the NDC ligand in compounds **1** and **2**. Compounds **3** and **4** display strong fluorescence emission at different wavelengths.

Experimental Section

General Remarks: The syntheses were performed in Teflon-lined stainless steel autoclaves under autogenous pressure. Reagents were purchased commercially and were used without further purification. Elemental analyses of C and H were performed with an EA1110 CHNS-0 CE elemental analyzer. The IR (KBr pellet) spectra were recorded with a Nicolet Magna 750FT-IR spectrometer. TGA analyses were carried out under nitrogen at a heating rate of 10 °C min^{-1} with an STA449C integration thermal analyzer. Variable-temperature (5–300 K) magnetic susceptibility measurements were carried out with a Quantum Design MPMS-7 SQUID magnetometer at a magnetic field of 5 T using the SQUID method. The fluorescent data were collected with an Edinburgh FL-FS920 TCSPC system.

$[Cu_3(NDC)_3(2,2'\text{-bpy})(H_2O)_2]_n\cdot nH_2O$ (1): A mixture of $Cu(CH_3COO)_2\cdot H_2O$ (0.20 g, 1 mmol), NDC (0.26 g, 1 mmol), 2,2′-bpy (0.16 g, 1 mmol), and triethylamine (0.28 mL, 2 mmol) in H_2O (18 mL) was heated at 170 °C for 5 d in a sealed 30-mL Teflon-lined stainless steel vessel under autogenous pressure. Slow cooling of the reaction mixture to room temperature gave green crystals (yield: 0.19 g, 56% based on Cu). $C_{46}H_{32}Cu_3N_2O_{15}$ (1043.4): calcd. C 52.95, H 3.09, N 2.68; found C 53.13, H 2.95, N 2.54. IR (solid KBr pellet): $\tilde{\nu}$ = 3649 m, 3076 m, 1606 s, 1545 s, 1498 m, 1477 m, 1404 s, 1350 s, 1194 m, 931 w, 910 w, 843 w, 791 s, 775 s, 727 m, 650 w, 582 w, 513 w, 480 m, 447 w cm^{-1}.

$[Cu(NDC)(1,10\text{-phen})]_n$ (2): A mixture of $Cu(CH_3COO)_2\cdot H_2O$ (0.30 g, 1.5 mmol), NDC (0.13 g, 0.5 mmol), 1,10-phen (0.20 g, 1 mmol), and triethylamine (0.28 mL, 2 mmol) in H_2O (18 mL) was heated at 160 °C for 3 d in a sealed 30-mL Teflon-lined stainless steel vessel under autogenous pressure. Slow cooling of the reaction mixture to room temperature gave blue crystals (yield: 0.28 g, 62% based on Cu). $C_{24}H_{14}CuN_2O_4$ (457.93): calcd. C 62.95, H 3.08, N 6.12; found C 62.73, H 3.14, N 6.26. IR (solid KBr pellet): $\tilde{\nu}$ = 1633 s, 1616 s, 1587 s, 1518 m, 1493 m, 1425 m, 1390 s, 1350 sh, 1298 m, 1196 m, 1178 m, 1136 w, 1105 w, 937 w, 872 w, 852 s, 791 sh, 739 m, 723 s, 648 m, 577 m, 494 w, 430 w cm^{-1}.

$[Zn(NDC)(1,10\text{-phen})]_n$ (3): Compound **3** was synthesized in an analogous manner to **2** except that $Zn(CH_3COO)_2\cdot 2H_2O$ (0.22 g, 1 mmol) was used instead of $Cu(CH_3COO)_2\cdot H_2O$. The reaction mixture was cooled, which led to the formation of yellow crystals of **3** (yield: 0.24 g, 52% based on Zn). $C_{24}H_{14}N_2O_4Zn$ (459.77): calcd. C 62.70, H 3.07, N 6.09; found C 62.65, H 3.02, N 6.46. IR (solid KBr pellet): $\tilde{\nu}$ = 1628 s, 1603 m, 1556 s, 1520 m, 1495 m, 1435 s, 1421 s, 1331 s, 1296 s, 1178 m, 1132 m, 1105 w, 1047 w, 924 w, 843 m, 795 s, 768 m, 725 s, 642 w, 557 m, 540 w, 488 w, 424 w cm^{-1}.

$[Zn_4(OH)_2(NDC)_3(2,2'\text{-bpy})_2]_n$ (4): Compound **4** was synthesized in a similar manner to **3** except that 2,2′-bpy (0.16 g, 1 mmol) was used instead of 1,10-phen. The reaction mixture was cooled, which led to the formation of light yellow crystals of **4** (yield: 0.12 g, 40%

 © 2005 Wiley-VCH Verlag GmbH & Co. KGaA, Weinheim

based on Zn). $C_{56}H_{36}N_4O_{14}Zn_4$ (1250.4): calcd. C 53.79, H 2.90, N 4.48; found C 53.36, H 2.68, N 4.23. IR (solid KBr pellet): $\tilde{\nu}$ = 3521 m, 3088 w, 1616 s, 1581 s, 1493 m, 1471 m, 1444 m, 1400 s, 1360 s, 1192 m, 1155 m, 1097 w, 1024 w, 924 w, 839 w, 785 s, 735 w, 667 m, 652 w, 580 w, 486 w cm^{-1}.

X-ray Crystallographic Study: Suitable single crystals with dimensions of 0.56×0.24×0.14 mm (**1**), 0.50×0.35×0.20 mm (**2**), 0.36×0.32×0.16 mm (**3**), and 0.35×0.25×0.20 mm (**4**) were glued to thin glass fibers with epoxy resin. Crystal structure measurements for compounds **1**–**4** were performed with a Rigaku Mercury CCD diffractometer with graphite-monochromated Mo-K_α radiation (λ = 0.71073 Å) at room temperature. A total of 3394, 4479, 3271, and 5639 unique reflections were collected by the $\omega/2\theta$ scan mode for **1**–**4**, respectively. The structures were solved by direct methods and refined on F^2 with the SHELXL-97 program.[30] All non-hydrogen atoms were refined with anisotropic displacement parameters, and the hydrogen atoms were treated as riding atoms

Table 1. Crystal data and structures refinement for compounds **1**–**4**.

	1	**2**	**3**	**4**
Empirical formula	$C_{46}H_{32}Cu_3N_2O_{15}$	$C_{24}H_{14}CuN_2O_4$	$C_{24}H_{14}N_2O_4Zn$	$C_{56}H_{36}N_4O_{14}Zn_4$
Formula mass	1043.36	457.91	459.74	1250.37
Crystal system	monoclinic	monoclinic	triclinic	monoclinic
Space group	*C*2/*c*	$P2_1/n$	$P\bar{1}$	$P2_1/c$
a [Å]	21.3745(6)	12.0819(11)	9.22740(10)	8.5939(5)
b [Å]	13.0065(2)	13.8007(11)	11.0681(2)	20.5943(13)
c [Å]	15.5522(2)	12.1050(10)	11.06780(10)	14.0052(11)
α [°]	90	90	119.5250(10)	90
β [°]	115.452(2)	103.563(4)	91.5900(10)	96.317(3)
γ(°)	90	90	104.6890(10)	90
V [Å^3]	3904.00(13)	1962.1(3)	935.63(2)	2463.7(3)
Z	4	4	2	2
$D_{calcd.}$ [gcm^{-3}]	1.765	1.550	1.632	1.686
F(000)	2116	932	468	1264
μ [mm^{-1}]	1.702	1.149	1.350	2.000
GOF	1.062	1.003	1.048	1.071
R_1, wR_2 [$I > 2\sigma(I)$][a]	0.0820, 0.1975	0.0420, 0.1251	0.0847, 0.1778	0.0427, 0.0925
R_1, wR_2 (all data)	0.1159, 0.2278	0.0504, 0.1334	0.0917, 0.1827	0.0503, 0.0968

[a] $R_1 = \sum(|F_o| - |F_c|)/\sum|F_o|$; $wR_2 = [\sum w(F_o^2 - F_c^2)^2/\sum w(F_o^2)^2]^{0.5}$.

Table 2. Selected bond lengths [Å] and angles [°] for compounds **1**–**4**.

Compound 1					
Cu(1)-O(5)	1.966(5)	O(5)^{I}-Cu(1)-O(5)	89.2(3)	O(3)^{I}-Cu(2)-O(7)	87.9(2)
Cu(1)-N(1)^{I}	1.984(6)	O(5)^{I}-Cu(1)-N(1)	159.6(2)	O(1)-Cu(2)-O(7)	90.2(2)
Cu(2)-O(3)^{II}	1.932(5)	O(5)-Cu(1)-N(1)	97.7(2)	O(3)^{I}-Cu(2)-O(6)	89.9(2)
Cu(2)-O(1)	1.934(5)	O(5)-Cu(1)-N(1)^{I}	159.6(2)	O(1)-Cu(2)-O(6)	92.2(2)
Cu(2)-O(7)	1.969(6)	N(1)-Cu(1)-N(1)^{I}	82.5(4)	O(7)-Cu(2)-O(6)	176.6(2)
Cu(2)-O(6)	1.996(5)	O(3)^{II}-Cu(2)-O(1)	174.6(2)		
Compound 2					
Cu(1)-O(2)	1.9139(18)	O(2)-Cu(1)-O(4)^{III}	95.89(8)	O(4)^{III}-Cu(1)-N(1)	166.19(8)
Cu(1)-O(4)^{III}	1.9437(16)	O(2)-Cu(1)-N(2)	170.58(8)	N(2)-Cu(1)-N(1)	80.94(8)
Cu(1)-N(2)	2.029(2)	O(4)^{III}-Cu(1)-N(2)	91.63(7)	O(2)-Cu(1)-O(3)	98.80(8)
Cu(1)-N(1)	2.050(2)	O(2)-Cu(1)-N(1)	90.52(8)	O(4)^{III}-Cu(1)-O(3)	102.41(7)
Cu(1)-O(3)	2.2421(17)				
Compound 3					
Zn(1)-O(4)^{IV}	2.074(5)	O(4)^{IV}-Zn(1)-O(4)	79.2(2)	O(2)-Zn(1)-N(2)	90.8(2)
Zn(1)-O(4)	2.087(5)	O(4)^{IV}-Zn(1)-N(1)	97.9(2)	O(4)^{IV}-Zn(1)-O(1)	96.1(2)
Zn(1)-N(1)	2.109(6)	O(4)-Zn(1)-N(1)	97.1(2)	O(4)-Zn(1)-O(1)	155.1(2)
Zn(1)-O(2)	2.158(5)	O(4)^{IV}-Zn(1)-O(2)	95.6(2)	N(1)-Zn(1)-O(1)	107.8(2)
Zn(1)-N(2)	2.173(7)	O(4)-Zn(1)-O(2)	95.1(2)	O(2)-Zn(1)-O(1)	60.8(2)
Zn(1)-O(1)	2.177(5)	N(1)-Zn(1)-O(2)	163.3(2)	N(2)-Zn(1)-O(1)	94.3(2)
		O(4)^{IV}-Zn(1)-N(2)	169.5(2)	O(4)-Zn(1)-N(2)	92.0(2)
				N(1)-Zn(1)-N(2)	77.4(2)
Compound 4					
Zn(1)-O(5)	1.918(2)	O(5)-Zn(1)-O(7)	132.88(11)	O(4)-Zn(2)-O(1)	93.58(13)
Zn(1)-O(7)	1.932(2)	O(5)-Zn(1)-O(3)	106.47(9)	O(5)-Zn(2)-N(2A)	127.44(19)
Zn(1)-O(3)	1.981(2)	O(7)-Zn(1)-O(3)	108.69(11)	O(4)-Zn(2)-N(2A)	89.53(18)
Zn(1)-O(2)	2.005(2)	O(5)-Zn(1)-O(2)	102.66(10)	O(1)-Zn(2)-N(2A)	133.3(2)
Zn(2)-O(5)	1.918(2)	O(7)-Zn(1)-O(2)	98.76(11)	O(5)-Zn(2)-N(1A)	116.73(17)
Zn(2)-O(4)	2.028(2)	O(3)-Zn(1)-O(2)	103.23(10)	O(4)-Zn(2)-N(1A)	141.13(17)
Zn(2)-O(1)	2.065(3)	O(5)-Zn(2)-O(4)	100.97(9)	O(1)-Zn(2)-N(1A)	73.28(18)
Zn(2)-N(2A)	2.078(5)	O(5)-Zn(2)-O(1)	97.66(10)	N(2A)-Zn(2)-N(1A)	75.5(2)
Zn(2)-N(1A)	2.203(6)				

Symmetry transformations used to generate equivalent atoms: I: $-x$, y, $-z + 1/2$; II: x, $y + 1$, z for compound **1**; III: $-x$, $-y$, $-z$ for compound **2;** IV: $-x + 1$, $-y + 1$, $-z + 2$ for compound **3.**

 © 2005 Wiley-VCH Verlag GmbH & Co. KGaA, Weinheim

using the SHELX-97 default parameters. For **1**, the hydrogen atoms of the water molecules were neither found nor calculated. For **4**, the 2,2′-bpy ring was found to be disordered and was modeled in two positions with occupancies of 51.2 and 48.8%. The crystal data and details of refinements for the compounds are summarized in Table 1, while their selected bond lengths and angles are listed in Table 2. CCDC-271318 (**1**), -255855 (**2**), -271317 (**3**), and -271319 (**4**) contain the supplementary crystallographic data for this paper. These data can be obtained free of charge from The Cambridge Crystallographic Data Centre via www.ccdc.cam.ac.uk/data_request/cif.

Acknowledgments

This work was supported by the 973 program of the MOST (001CB108906), the National Science Foundation of China (20425313, 90206040, 20333070, and 20303021), the NSF of Fujian, and the Chinese Academy of Sciences.

[1] J. S. Seo, D. H. L. Whang, S. I. Jun, J. Oh, Y. J. Jeon, K. Kim, *Nature* **2000**, *404*, 982–986.
[2] S. Noro, S. Kitagawa, M. Kondo, K. Seki, *Angew. Chem. Int. Ed.* **2000**, *39*, 2081–2084.
[3] J. Zhang, W. B. Lin, Z. F. Chen, R. G. Xiong, B. F. Abrahams, H. K. Fun, *J. Chem. Soc., Dalton Trans.* **2001**, 1806–1808.
[4] B. H. Ye, M. L. Tong, X. M. Chen, *Coord. Chem. Rev.* **2005**, *249*, 545–565.
[5] a) N. L. Rosi, J. Eckert, M. Eddaoudi, D. T. Vodak, J. Kim, M. O'Keeffe, O. M. Yaghi, *Science* **2003**, *300*, 1127–1129; b) J. Kim, B. L. Chen, T. M. Reineke, H. Li, M. Eddaoudi, D. B. Moler, M. O'Keeffe, O. M. Yaghi, *J. Am. Chem. Soc.* **2001**, *123*, 8239–8247; c) B. L. Chen, M. Eddaoudi, S. T. Hyde, M. O'Keeffe, O. M. Yaghi, *Science* **2001**, *291*, 1021–1023; d) M. Eddaoudi, J. Kim, N. Rosi, D. Vodak, J. Wachter, M. O'Keeffe, O. M. Yaghi, *Science* **2002**, *295*, 469–472; e) N. L. Rosi, M. Eddaoudi, J. Kim, M. O'Keeffe, O. M. Yaghi, *Angew. Chem. Int. Ed.* **2002**, *41*, 284–287; f) H. Li, M. Eddaoudi, M. O'Keeffe, O. M. Yaghi, *Nature* **1999**, *402*, 276–279; g) M. Eddaoudi, D. B. Moler, H. Li, B. L. Chen, T. M. Reineke, M. O'Keette, O. M. Yaghi, *Acc. Chem. Res.* **2001**, *34*, 319–330; h) N. L. Rosi, J. Kim, M. Eddaoudi, B. Chen, M. O'Keeffe, O. M. Yaghi, *J. Am. Chem. Soc.* **2005**, *127*, 1504–1518; i) D. T. Vodak, M. E. Braun, J. Kim, M. Eddaoudi, O. M. Yaghi, *Chem. Commun.* **2001**, 2534–2535.
[6] A. Filipe, P. Almeida, K. Jacek, *Chem. Commun.* **2003**, 1484–1485.
[7] S. Dalai, P. S. Mukherjee, E. Zangrando, F. Lloret, N. R. Chaudhuri, *J. Chem. Soc., Dalton Trans.* **2002**, 822–823.
[8] Z. He, E. Q. Gao, Z. M. Wang, C. H. Yan, M. Kurmoo, *Inorg. Chem.* **2005**, *44*, 862–874.
[9] B. H. Ye, B. B. Ding, Y. Q. Weng, X. M. Chen, *Cryst. Growth Des.* **2005**, *5*, 801–806.
[10] X. J. Li, R. Cao, Y. Q. Sun, W. H. Bi, X. Li, Y. Q. Wang, *Eur. J. Inorg. Chem.* **2005**, 321–329.
[11] C. Y. Su, A. M. Goforth, M. D. Smith, P. J. Pellechia, H. C. zur Loye, *J. Am. Chem. Soc.* **2004**, *126*, 3576–3586.
[12] a) T. K. Maji, G. Mostafa, H. C. Chang, S. Kitagawa, *Chem. Commun.* **2005**, 2436–2438; b) S. Furukawa, M. Ohba, S. Kitagawa, *Chem. Commun.* **2005**, 865–867; c) T. K. Maji, K. Uemura, H. C. Chang, R. Matsuda, S. Kitagawa, *Angew. Chem. Int. Ed.* **2004**, *43*, 3269–3272.
[13] B. L. Wu, D. Q. Yuan, F. L. Jiang, R. H. Wang, L. Han, Y. F. Zhou, M. C. Hong, *Eur. J. Inorg. Chem.* **2004**, 2695–2700.
[14] E. Y. Choi, Y. U. Kwon, *Inorg. Chem.* **2005**, *44*, 538–545.
[15] a) Y. B. Go, X. Q. Wang, E. V. Anokhina, A. J. Jacobson, *Inorg. Chem.* **2004**, *43*, 5360–5367; b) R. H. Groenman, L. R. MacGillivaray, J. L. Atwood, *Chem. Commun.* **1998**, 2735–2736; c) C. S. Hong, Y. Do, *Inorg. Chem.* **1998**, *37*, 4470–4472.
[16] a) X. Shi, G. Zhu, Q. Fang, G. Wu, G. Tian, R. Wang, D. Zhang, M. Xue, S. Qiu, *Eur. J. Inorg. Chem.* **2004**, 185–191; b) X. M. Zhang, M. L. Tong, M. L. Gong, X. M. Chen, *Eur. J. Inorg. Chem.* **2003**, 138–142; c) D. F. Sun, R. Cao, Y. Liang, Q. Shi, W. P. Su, M. C. Hong, *J. Chem. Soc., Dalton Trans.* **2001**, 2335–2340.
[17] a) K. O. Kongshaug, H. Fjellvag, *Solid State Sci.* **2003**, *5*, 303–310; b) K. O. Kongshaug, H. Fjellvag, *Solid State Sci.* **2002**, *4*, 443–447; c) S. W. Lee, H. J. Kim, Y. K. Lee, K. Park, J. H. Son, Y. U. Kwon, *Inorg. Chim. Acta* **2003**, *353*, 151–158.
[18] J. C. Dai, X. T. Wu, S. M. Hu, Z. Y. Fu, J. J. Zhang, W. X. Du, H. H. Zhang, R. Q. Sun, *Eur. J. Inorg. Chem.* **2004**, 2096–2106.
[19] L. Carlucci, G. Ciani, D. M. Proserpio, A. Sironi, *Angew. Chem. Int. Ed. Engl.* **1996**, *35*, 1088–1090.
[20] E. Colacio, J. M. Dominguez-Vera, F. Lloret, J. M. M. Sanchez, R. Kivekas, A. Rodriguez, R. Sillanpaa, *Inorg. Chem.* **2003**, *42*, 4209–4214.
[21] B. L. Chen, F. R. Fronczek, A. W. Maverick, *Inorg. Chem.* **2004**, *43*, 8209–8211.
[22] P. Pascal, *Ann. Chim. Phys.* **1910**, *19*, 5–7.
[23] Y. F. Song, P. Gamez, O. Roubeau, M. Lutz, A. L. Spek, J. Reeijk, *Eur. J. Inorg. Chem.* **2003**, 2924–2928.
[24] J. C. Liu, G. C. Guo, J. S. Huang, X. Z. You, *Inorg. Chem.* **2003**, *42*, 235–243.
[25] Y. Agnus, R. Louis, B. Metz, C. Boudon, J. P. Gisselbrecht, M. Gross, *Inorg. Chem.* **1991**, *30*, 3155–3161.
[26] S. Gupta, A. Mukherjee, M. Nethaji, A. R. Chakravarty, *Polyhedron* **2004**, *23*, 643–647.
[27] a) J. Tao, X. Yin, Y.-B. Jiang, L. F. Yang, R. B. Huang, L. S. Zheng, *Eur. J. Inorg. Chem.* **2003**, 2678–2682; b) J. Tao, Y. Zhang, M. L. Tong, X. M. Chen, T. Yuan, C. L. Lin, X. Y. Huang, J. Li, *Chem. Commun.* **2002**, 1342–1343.
[28] X. L. Wang, C. Qin, E. B. Wang, Y. G. Li, N. Hao, C. W. Hu, L. Xu, *Inorg. Chem.* **2004**, *43*, 1850–1856.
[29] S. L. Zheng, J. H. Yang, X. L. Yu, X. M. Chen, W. T. Wong, *Inorg. Chem.* **2004**, *43*, 830–838.
[30] G. M. Sheldrick, *SHELXS97, Program for Solution of Crystal Structures*; University of Göttingen, Göttingen, Germany, **1997**.

Received: May 31, 2005
Published Online: October 10, 2005

 © 2005 Wiley-VCH Verlag GmbH & Co. KGaA, Weinheim

Synthesis of Phosphido-Bridged Phosphinito Platinum(I) Complexes by Reaction of *cis*-$PtCl_2(PHCy_2)_2$ with Oxygenated Bases – Crystal Structure of $[(PCy_2OMe)Pt(\mu\text{-}PCy_2)]_2$(*Pt–Pt*)

Vito Gallo,[a] Mario Latronico,[a,d] Piero Mastrorilli,*[a] Cosimo F. Nobile,[a] Gian P. Suranna,[a] Giuseppe Ciccarella,[b] and Ulli Englert[c]

Keywords: Platinum / Bridging ligands / Phosphinites / Oxygenated bases

Reaction of *cis*-$PtCl_2(PHCy_2)_2$ (**1**) with oxygenated bases leads to phosphido-bridged dinuclear complexes. The product obtained using sodium hydroxide is the asymmetric Pt^I complex $[(Cy_2PH)Pt(\mu\text{-}PCy_2)(\kappa^2P,O\text{-}\mu\text{-}Cy_2PO)Pt(Cy_2PH)]$(*Pt–Pt*) (**2**), which represents a rare example of a complex containing a Pt–Pt–P–O cycle. The reaction products between **1** and NaOR (R = Me, Et) depend on experimental conditions: lack of base results in the formation of *trans*-$[Pt(PHCy_2)Cl(\mu\text{-}PCy_2)]_2$ (**3**) as the main product. Using an excess of base at 50 °C allowed the isolation of the symmetric Pt^I dimers $[(PCy_2OR)Pt(\mu\text{-}PCy_2)]_2$(*Pt–Pt*) (**5**, R = Me; **7**, R = Et) containing two alkyl dicyclohexylphosphinito ligands. The asymmetric compounds $[(PCy_2H)Pt(\mu\text{-}PCy_2)_2Pt(PCy_2OR)]$(*Pt–Pt*) (**4**, R = Me; **8**, R = Et) form after work-up of the reaction of **1** with excess NaOR (8 equiv.) in toluene/methanol at room temperature. Investigations on the mechanism of formation of phosphinito Pt^I complexes (carried out also employing Na-O*t*Bu and NaOPh as oxygenated bases) show that the first two steps of the overall reaction are the metathesis leading to *cis*-$Pt(OR)_2(PHCy_2)_2$ and the subsequent formation of terminal phosphido complexes through ROH elimination. Single crystal X-ray diffraction showed that molecules of **5** are located on crystallographic inversion centres; hence their necessarily planar Pt_2P_2 core contains a Pt–Pt bond.
(© Wiley-VCH Verlag GmbH & Co. KGaA, 69451 Weinheim, Germany, 2005)

Introduction

Secondary phosphanes are attractive as ligands for transition metals because they add some peculiar characteristics to the typical σ basicity and π acidity of the trivalent phosphorus compounds because of the presence of the reactive P–H bond: (i) the capability to form polynuclear complexes in which the metal atoms are linked by phosphido bridges; (ii) the possibility to give rise to a metal–hydrogen bond by intramolecular oxidative addition.

Pursuing our studies on platinum complexes with bulky secondary phosphanes such as di-*tert*-butylphosphane[1,2] and dicyclohexylphosphane,[3] we recently became interested in the reactivity of *cis*-$PtCl_2(PHCy_2)_2$ (**1**) with NaOR (R = H, Me, Et, Ph, *t*Bu). The latter compounds, in fact, can act either as nucleophiles and/or as bases, triggering different reaction pathways depending on both the nature of R and the experimental conditions.

The reaction of alkaline alkoxides with phosphanyl Pt^{II} complexes has been used for the preparation of alkoxo complexes, starting from the corresponding chloro species.[4–8] In some cases the alkoxo complexes are not stable and give rise to redox processes leading to decomposition products,[9] to hydride complexes of platinum(II)[10] or to zerovalent platinum compounds.[11] The reducing ability of alkaline alkoxides towards halide metal complexes has been demonstrated also for Ni[12] and Pd[13] compounds.

Herein we describe the reactivity of *cis*-$PtCl_2(PHCy_2)_2$ (**1**) with sodium hydroxide, alkoxides and phenoxide, which led to phosphido-bridged binuclear platinum compounds, the nature of which depended on both the base and the reaction conditions (Scheme 1).

Results and Discussion

Contrary to *trans*-$PtCl_2(PHtBu_2)_2$, whose reaction with oxygenated bases such as NaOMe,[2] NaOEt[14] or NaOH[15] was ineffective, the reaction of **1** with NaOH in a biphasic CH_2Cl_2/H_2O system proceeded smoothly to form a new dinuclear Pt^I complex whose spectroscopic features and ESI-MS analysis indicate as $[(Cy_2PH)Pt(\mu\text{-}PCy_2)(\kappa^2P,O\text{-}\mu\text{-}$

[a] Dipartimento di Ingegneria delle Acque e di Chimica del Politecnico di Bari,
via Orabona 4, 70125 Bari, Italy
Fax: +39-080-5963611
E-mail: p.mastrorilli@poliba.it
[b] Dipartimento di Ingegneria dell'Innovazione, University of Lecce,
Via Monteroni, 73100 Lecce, Italy
[c] Institut für Anorganische Chemie der RWTH,
Landoltweg 1, 52074 Aachen, Germany
[d] On leave of absence from Dipartimento di Ingegneria e Fisica dell'Ambiente, Università della Basilicata,
viale dell'Ateneo Lucano 10, 85100 Potenza, Italy
Supporting information for this article is available on the WWW under http://www.eurjic.org or from the author.

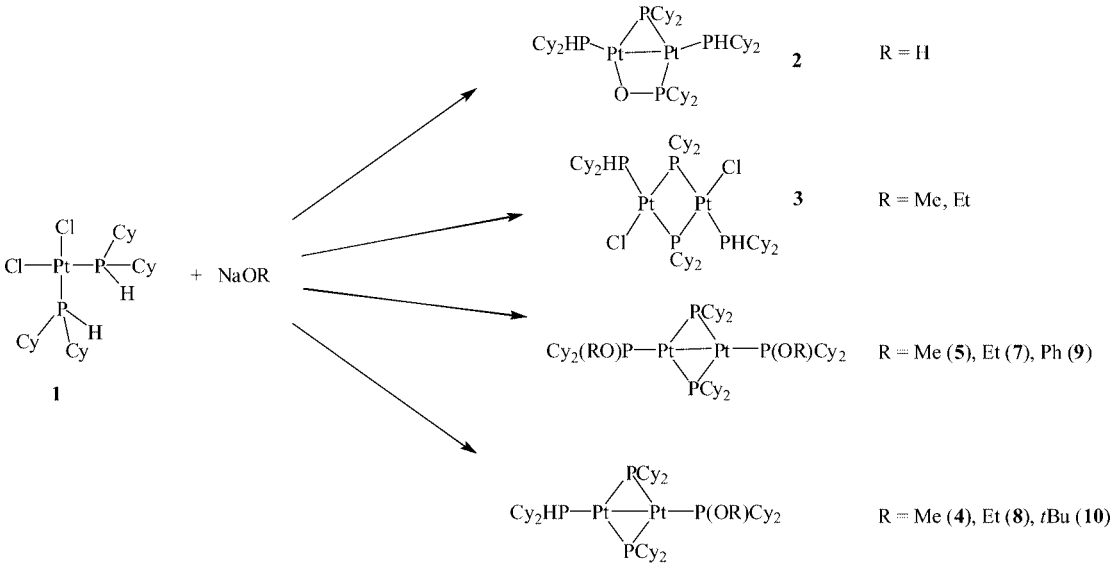

Scheme 1.

$Cy_2PO)Pt(Cy_2PH)](Pt–Pt)$ (**2**). The $^{31}P\{^1H\}$ NMR spectrum of **2** (Figure 1) showed 4 mutually coupled doublets of doublets of doublets flanked by ^{195}Pt satellites centred at δ = 134.4, δ = 94.6, δ = 18.5 and δ = 15.9 ppm.

Of these, the latter two can be ascribed to coordinated PCy_2H (comparison with proton-coupled spectrum gave $^1J_{P,H}$ of 310 Hz and 323 Hz respectively) while that at δ = 94.6 is ascribable to a deshielded P–O ligand. The remaining low field signal at δ = 134.4 is flanked by three different sets of satellites and can be attributed to a phosphide involved in a three-membered Pt_2P ring[16,17] bridging two inequivalent Pt atoms. The ^1H NMR spectrum showed, beside cyclohexyl protons, two signals attributable to the hydrogens directly bound to P in coordinated PCy_2H, which were attributed to the proper PCy_2H ligand on the basis of $^1H–^{31}P$ HMQC experiments (Supporting Information, ESI 1). The $^{195}Pt\{^1H\}$ NMR spectrum consisted of two dddd centred at δ = –4798 (Pt^1) and δ = –5205 (Pt^2) (Figure 2).

The characterisation of **2** was completed by IR, elemental and ESI-MS analysis. In particular, the IR spectrum showed two weak bands in the region of P–H stretching (2279 and 2252 cm^{-1}) and bands at 816 and 1024 cm^{-1} ascribable to the P–O stretchings. Eventually, the ESI-MS spectrum showed the signals corresponding to $[M + H]^+$ with an isotope pattern identical to that calculated on the basis of the natural abundances (Figure 3).

Complex **2** is a rare example of an asymmetric monophosphido-bridged Pt^I complex. The spectroscopic data summarised above are consistent either with structure **A**, in which the $P(O)Cy_2$ ligand acts as monodentate (κ-*P* bound to Pt^2), or with structure **B**, in which the $P(O)Cy_2$ acts as bidentate (κ^2-*P,O*) bridging the two Pt atoms (Figure 4).

An equilibrium between the two structures might also be conceived. NMR features can help in discriminating between the two structures. We have previously noticed that binuclear monobridged dicyclohexylphosphane complexes of Pd and Pt such as $[(Cy_2PH)(Cl)Pt(\mu\text{-}PCy_2)Pt(Cy_2PH)_2]$-

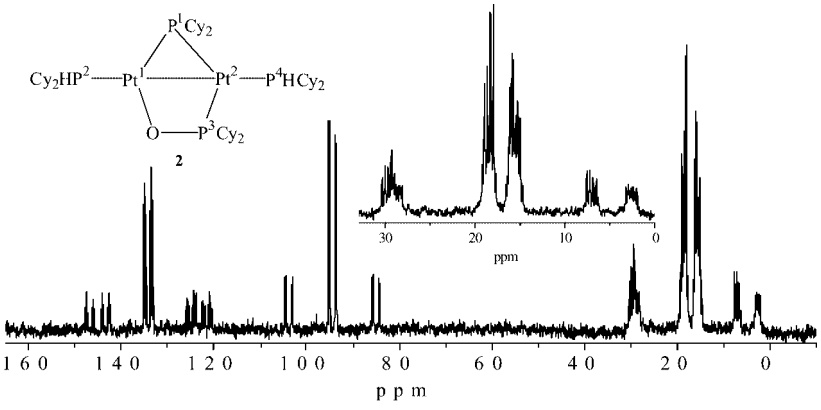

Figure 1. $^{31}P\{^1H\}$ NMR spectrum of **2** (161 MHz, 295 K, C_6D_6).

 © 2005 Wiley-VCH Verlag GmbH & Co. KGaA, Weinheim

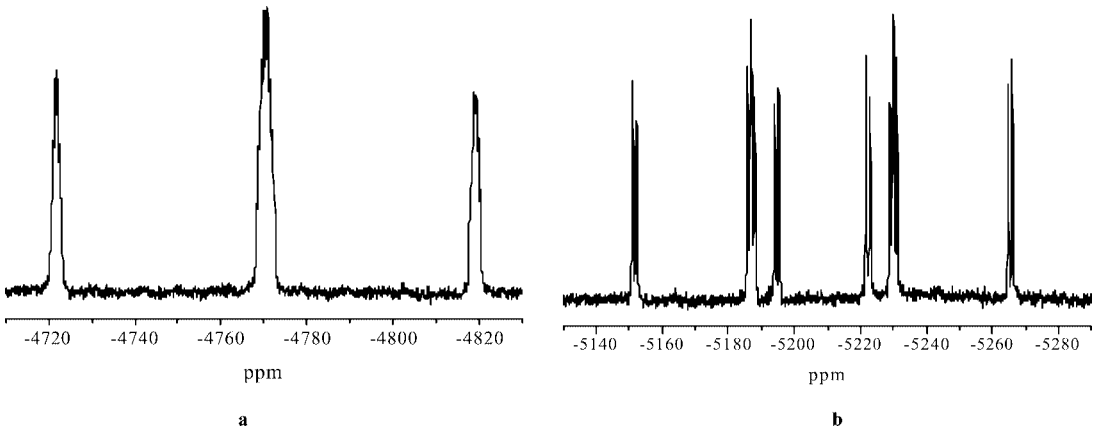

Figure 2. $^{195}Pt\{^1H\}$ NMR spectrum of **2** (295 K, C_6D_6). a: Pt^1; b: Pt^2.

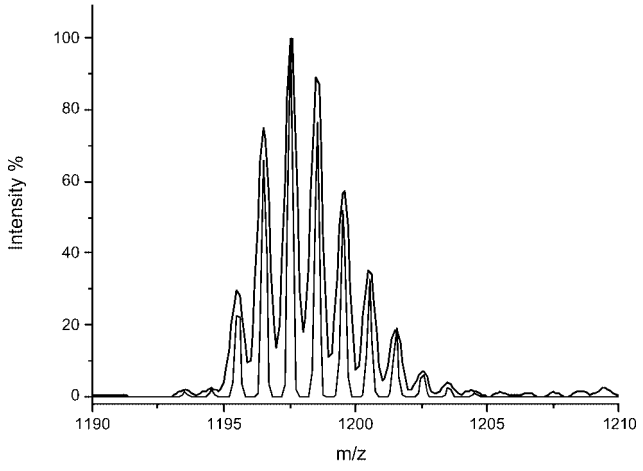

Figure 3. ESI-MS spectrum of **2** (bottom trace: calculated).

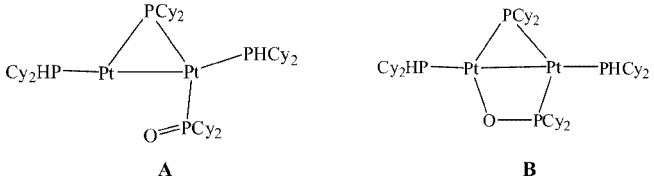

Figure 4. Possible structures of **2**.

(*Pt–Pt*)[3] or $[(Cy_2PH)(Cl)Pd(\mu\text{-}PCy_2)Pd(Cy_2PH)_2]$-(*Pd–Pd*)[18] (Supporting Information, ESI 2) are characterised by broad $^{31}P\{^1H\}$ NMR signals for all ligands except the bridging PCy_2, a feature that was ascribed to hindered rotation of the $PHCy_2$ ligands about the metal–P bond. The sharp signals found in the $^{31}P\{^1H\}$ NMR of **2** (Figure 1) favour structure **B**, in which both $PHCy_2$ (in particular that bound to Pt^2) have more room to freely rotate around the Pt–P bonds.

The presence of a Pt–P–O–Pt ring in **2** is corroborated by the literature. In fact, XRD analysis of the related Pt^I complex $[Pt(\kappa^2P,O\text{-}\mu\text{-}OPPh_2)(PMePh_2)]_2$ showed that each platinum atom is involved in a four-membered Pt–P–O–Pt ring.[19]

Finally, equilibrium between structures **A** and **B** seems unlikely because the signals found in the $^{195}Pt\{^1H\}$ NMR spectrum recorded at 195 K did not differ significantly from those found at 295 K.

The reaction of **1** with solid sodium methoxide (2 equiv.) in toluene at room temperature gave the symmetric dimer *trans*-$[Pt(PHCy_2)Cl(\mu\text{-}PCy_2)]_2$ (**3**) as the main product (82% yield).[20] Complex **3** was characterised by multinuclear NMR, IR, ESI-MS and elemental analysis. The appearance of an AA′XX′ spin system in the $^{31}P\{^1H\}$ NMR spectrum for the isotopomer not containing ^{195}Pt substantiates the *trans* geometry of the complex. Computer simulation of the spectrum, using as starting chemical shifts and coupling constants those extractable directly from the experimental spectrum,[21] gave the spectroscopic features reported in Table 1 (Supporting Information, ESI 3–4). The values found for $^3J_{P^{A'},Pt^1} = {}^3J_{P^A,Pt^2}$, for $^2J_{P^X,P^{X'}}$ and for $^3J_{P^A,P^X} = {}^3J_{P^{A'},P^{X'}}$ are consistent with a planar geometry of the Pt_2P_2 core.[22]

Table 1. Spectroscopic features for **3** ($CDCl_3$, 295 K).

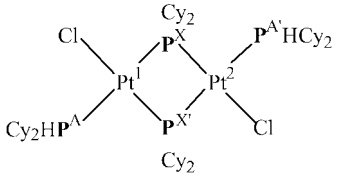

	P^A	$P^{A'}$	P^X	$P^{X'}$	Pt^1	Pt^2
P^A	15.1	4.2	357.3	9.2	1948	79
$P^{A'}$	4.2	15.1	9.2	357.3	79	1948
P^X	357.3	9.2	–137.9	–150.8	2048	2399
$P^{X'}$	9.2	357.3	–150.8	–137.9	2399	2048
Pt^1	1948	79	2048	2399	–4014	
Pt^2	79	1948	2399	2048		–4014

The analogous palladium(II) complex *trans*-$[Pd(PHCy_2)$-$Cl(\mu\text{-}PCy_2)]_2$ is the reaction product between *cis*-$PdCl_2(PHCy_2)_2$ and 1 equiv. NaOPh and reacts at 50 °C with 1 more equiv. NaOPh to afford the bis(dicyclohexyl)-phenylphosphinito palladium(I) complex $[(PhOPCy_2)Pd(\mu\text{-}PCy_2)]_2$.[23] This reaction is not transferable to our system because **3** was recovered unaltered after 24 h stirring with 2 equiv. NaOMe in toluene at 50 °C (Scheme 2). A possible

 © 2005 Wiley-VCH Verlag GmbH & Co. KGaA, Weinheim

explanation for the different reactivity of *trans*-[Pd(PHCy$_2$)Cl(μ-PCy$_2$)]$_2$ and **3** might reside in a different strength of the metal–Cl bond. IR stretching of the Pd–Cl bond (275 cm^{-1}) is in fact 14 cm^{-1} red-shifted with respect to that of the Pt–Cl in **3** (289 cm^{-1}).

The reaction of **1** with excess NaOMe (5 equiv.) in toluene/methanol at room temperature for 1 day afforded, after work-up, a mixture of products made up of the asymmetric Pt^{I} complex [(PCy$_2$H)Pt(μ-PCy$_2$)$_2$Pt(PCy$_2$OMe)](*Pt–Pt*) (**4**, 60%), the symmetric Pt^{I} dimer [(PCy$_2$OMe)Pt(μ-PCy$_2$)]$_2$-(*Pt–Pt*) (**5**, 35%) and traces of **3** (Scheme 3).

Complex **4** showed in the ^{31}P{^{1}H} NMR spectrum two low field signals and one signal in the region of coordinated PHCy$_2$ (each flanked by ^{195}Pt satellites due to isotopomers containing one or two NMR active Pt atoms). The low field signals are a doublet of doublets centred at δ = 245.7 and a doublet of triplets centred at δ = 173.6. Both signals are due to phosphorus atoms not directly bound to hydrogens (comparison with proton coupled spectra) and are easily assigned, the first to a dicyclohexylphosphido group involved in three-membered rings, and the second, according to ^{1}H NMR and ESI-MS data, to a coordinated PCy$_2$OMe. The remaining signal is a doublet of triplets (further split in the proton-coupled spectrum due to the 318 Hz $^{1}J_{P,H}$) centred at δ = 19.1 ascribed to a coordinated PHCy$_2$. The ^{1}H NMR spectrum showed, beside resonances due to cyclohexyl protons, a doublet at δ = 3.94 [3 H, $^{3}J_{P,H}$ = 13 Hz] ascribable to the methyl group of the coordinated PCy$_2$-OMe and a doublet of multiplets due to the hydrogen directly bound to the phosphorus of the coordinated PCy$_2$H [δ = 6.36, $^{1}J_{P,H}$ = 318 Hz]. The two ^{195}Pt{^{1}H} NMR signals of the atoms directly bound to PHCy$_2$ and PCy$_2$OMe were mutually coupled [$^{1}J_{Pt,Pt}$ = 337 Hz)] and were centred at δ = –5530 and δ = –5570 respectively.

The symmetric dimer **5** showed in the ^{31}P{^{1}H} NMR spectrum the signal of the bridging phosphide at δ = 245.3 and that of the terminal methyl dicyclohexylphosphinite at δ = 171.2. The ^{195}Pt{^{1}H} NMR spectrum consisted of a doublet of triplets centred at δ = –5570 ppm.

Prolonging to 7 days the stirring time of the reaction between **1** and excess NaOMe described above resulted in the synthesis of the dimer **5** as the main product, devoid of the asymmetric complex **4**. This result prompted us to monitor the reaction by ^{31}P{^{1}H} NMR in order to ascertain whether **4** is the precursor of **5**, so as to shed some light on the reaction mechanism. The spectrum recorded after 30 min reaction showed the transformation of **1** into *cis*-Pt(PHCy$_2$)$_2$(OMe)$_2$ (**6**) and traces of **3**. Prolonging the reaction time resulted in the progressive decrease of signals due to **6** with contemporary appearance of signals due to **5**, which became predominant after 2 days.

Complex **6** gave a singlet with ^{195}Pt satellites in the ^{31}P{^{1}H} NMR spectrum [δ = 7.2, $^{1}J_{P,Pt}$ = 3267 Hz], which split into a doublet in the proton-coupled spectrum [$^{1}J_{P,H}$ = 341 Hz)]. The corresponding ^{195}Pt{^{1}H} NMR spectrum consisted in a triplet centred at δ = –4233 [$^{1}J_{P,Pt}$ = 3267 Hz]. Experiments carried out in deuterated solvent allowed assignation of the ^{1}H NMR resonance of the coordinated Cy$_2$P*H* [δ = 3.6, $^{1}J_{H,P}$ = 341 Hz] and OC*H*$_3$ [δ = 3.5, $^{4}J_{H,P}$ = 3.9 Hz; $^{3}J_{H,Pt}$ = 25 Hz]. Complex **6**, which is very soluble in the reaction mixture so as to prevent its precipitation at low temperature, could not be isolated in a pure state because of its fast and irreversible transformation into **4** during solvent removal either by reduced pressure or by bub-

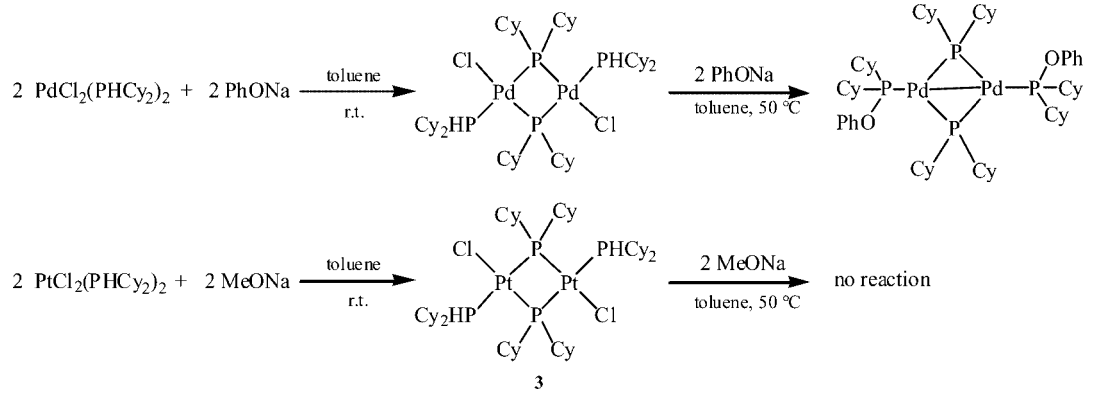

Scheme 2.

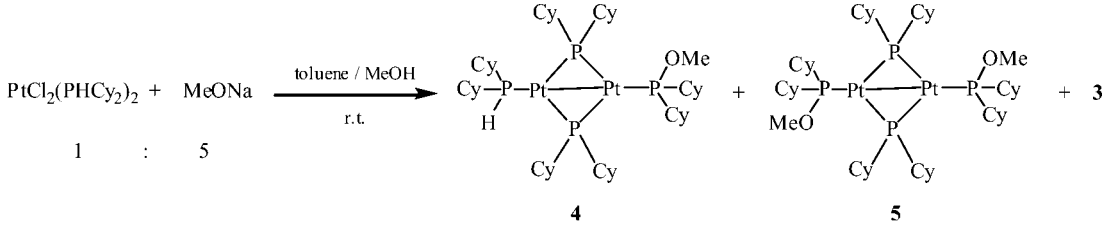

Scheme 3.

bling of inert gas. This explains our experimental results: the starting complex **1** reacts with excess methoxide to give **6** (and traces of **3**, which does not further react), which slowly transforms into **5**. If the reaction is stopped when **6** is still present (e.g. 1 day), work-up of the crude results in the formation of a mixture containing **4** (formed mainly during solvent removal) and **5**. Complex **4** could be obtained in a pure state after work-up of the reaction of **1** with excess NaOMe (8 equiv.) in toluene/methanol at room temperature, and **5** could be obtained in 67% yield after 6 h by reacting **1** with excess NaOMe (8 equiv.) in toluene/methanol at 50 °C. Longer reaction times resulted in lower isolated yields because of decomposition of **5** into unidentified products.

Slow evaporation of a toluene solution of **5** deposited yellow-orange crystals suitable for single-crystal X-ray diffraction. The structure of a molecule in the crystal is shown in Figure 5. Significant bond lengths and angles are given in Table 2. The complex crystallises in the monoclinic space group $P2_1/c$. The molecule contains an inversion centre, and therefore the Pt_2P_2 quadrilater with angles of 110.30(4)° and 69.70(4)° is planar for reasons of symmetry; the OCH_3 oxygen atoms also lie in this plane within experimental error. The presence of a Pt–Pt bond is evidenced by an intermetal distance of 2.6307(5) Å, which is comparable with the 2.6127(6) Å and 2.604(1) Å Pt–Pt distances of $[(Pt^tBu_2H)Pt(\mu\text{-}P^tBu_2)_2Pt(CO)]$(*Pt–Pt*)[24] and $[(PPh_3)Pt(\mu\text{-}PPh_2)_2Pt(PPh_3)]$(*Pt–Pt*)[25] respectively. The average Pt–Pt bond length for 66 error-free observations in the CSD[26] amounts to 2.633 Å.

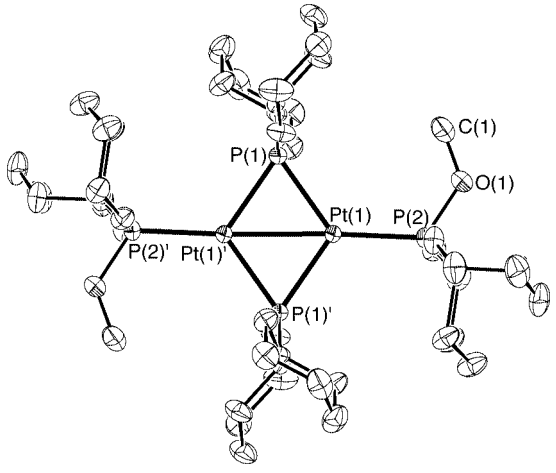

Figure 5. Displacement ellipsoid plot of **5**;[27] ellipsoids are scaled to 30% probability, H atoms have been omitted for clarity.

The Pt–P_μ distances (2.30 Å) are longer than Pt–P_t [2.2150(14) Å]. The external angle P(1)′–Pt(1)–P(2) [122.17(5)°] is smaller than P(1)–Pt(1)–P(2) [127.53(5)°] because of a rather short (2.01 Å) and repulsive H···H contact between a methoxy hydrogen and a H atom of a cyclohexyl substituent bonded to P(1).

The reactivity shown by **1** towards NaOEt parallels that found for NaOMe: the reaction of **1** with 8 equiv. EtONa at 50 °C in a toluene/ethanol mixture afforded $[(PCy_2OEt)Pt(\mu\text{-}PCy_2)]_2$(*Pt–Pt*) (**7**) in 55% yield after only 2 h. However, because of the higher reactivity shown by EtONa, in this case it was not possible to isolate the asymmetric complex $[(PCy_2H)Pt(\mu\text{-}PCy_2)_2Pt(PCy_2OEt)]$(*Pt–Pt*) (**8**) in a pure state. It was observed in mixture with **7** and characterised in solution by multinuclear NMR spectroscopy.

Table 2. Selected bond lengths [Å] and angles [°] for **5**.

Pt(1)–P(2)	2.2150(14)
Pt(1)–P(1)′	2.2982(15)
Pt(1)–P(1)	2.3058(14)
Pt(1)–Pt(1)′	2.6307(5)
P(2)–O(1)	1.626(4)
C(1)–O(1)	1.365(7)
P(1)–Pt(1)–P(2)	127.53(5)
P(1)′–Pt(1)–P(2)	122.17(5)
Pt(1)′–Pt(1)–P(1)	55.01(4)
Pt(1)′–Pt(1)–P(1)′	55.29(4)
Pt(1)′–Pt(1)–P(2)	177.45(4)

The experimental data presented so far allow some mechanistic considerations to be put forward.

A possible explanation for the selectivity towards **3** of the reaction between **1** and NaOMe (2 equiv.) in toluene could be the accumulation, in these conditions, of the monosubstituted methoxo complex *cis*-$PtCl(OMe)(PHCy_2)_2$, which can dimerise to **3** by loss of methanol (Scheme 4). Such accumulation could derive from the constant lack of methoxide present in the reaction medium, because of its scarce solubility in toluene. Complex *cis*-$PtCl(OMe)(PHCy_2)_2$ could be detected by recording $^{31}P\{^1H\}$ NMR spectra of CD_2Cl_2 solutions of **1**, to which an equimolar amount of NaOMe was added. The solution showed, along with the singlets of residual **1** and **6**, two mutually coupled [$^2J_{P,P}$ = 15 Hz] doublets centred at δ = 17.3 [$^1J_{P,Pt}$ = 3814 Hz] and δ = 8.7 [$^1J_{P,Pt}$ = 2942 Hz] attributable to the P *trans* to Cl and P *trans* to OMe respectively. Analogous results were obtained by using NaOEt instead of NaOMe as limiting reagent. In this case the spectroscopic features of *cis*-$PtCl(OEt)(PHCy_2)_2$ are δ = 16.6 [$^1J_{P,Pt}$ = 3734 Hz, P *trans* to Cl] and δ = 7.4 [$^1J_{P,Pt}$ = 2966 Hz, P *trans* to OEt] [$^2J_{P,P}$ = 18 Hz].

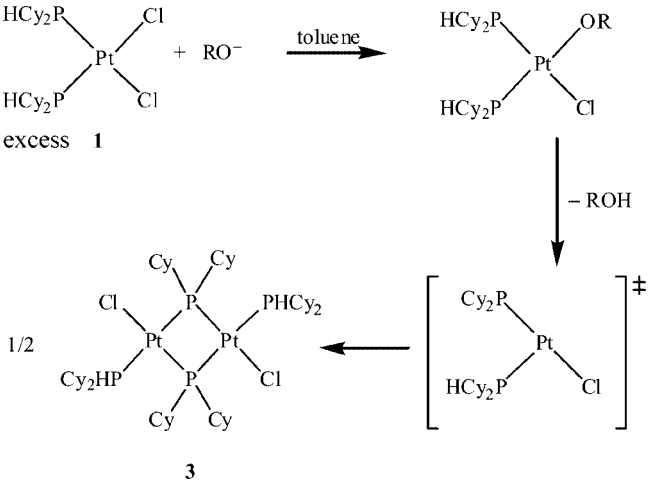

Scheme 4. Proposed mechanism for the formation of **3**.

 © 2005 Wiley-VCH Verlag GmbH & Co. KGaA, Weinheim

As to the formation of the alkylphosphinito Pt^{I} dimers observed when the reaction was carried out in the presence of excess NaOR (R = H, Me, Et), a possible mechanism is depicted in Scheme 5.

The initially formed metathesis product *cis*-$Pt(PHCy_2)_2(OR)_2$ can formally lose ROH, giving the terminal phosphido species **a**. The latter can give rise to an intramolecular process involving the metal, the coordinated RO group and the coordinated terminal phosphide, resulting in the phosphinito intermediates **b**. When R is an alkyl group, intramolecular oxidative addition of the P–H bond to Pt followed by hydrogen elimination and dimerisation (path 1) would account for the observed formation of the symmetric dimers $[(PCy_2OR)Pt(\mu\text{-}PCy_2)]_2$(*Pt–Pt*). The sequence of reactions leading from **b** to $[(PCy_2OR)Pt(\mu\text{-}PCy_2)]_2$(*Pt–Pt*) has already been proposed for the synthesis of several analogous systems.[3,18,28]

When R is H, the intramolecular oxidative addition of the P–H bond to Pt is disfavoured by the co-presence in the hypothetically formed $Pt(PCy_2)(H)(PCy_2OH)$ of a strongly basic centre (the terminal phosphide) and an acidic proton ($Cy_2PO\mathit{H}$). Reaction of **a** with **b** (R = H, path 2) can give intermediate **c**, which evolves into the final product **2** after loss of water and ring closure.

The central point of the suggested mechanism is the metal assisted formation of the P–O bond that leads to the dicyclohexylphosphinito ligands. In the literature, few examples can be found of such a transformation. In particular, the following have been reported: (*i*) $PhOPCy_2$ from $PHCy_2$ and phenoxide ion coordinated to palladium;[23] (*ii*) $MeOPPh_2$ from PPh_2Im (Im = 1-methylimidazole) and methoxide coordinated to ruthenium;[29] (*iii*) 1-phenyl-3*H*-2,1-benzoxaphosphole from *o*-(diphenylphosphanyl)benzyl alkoxide coordinated to platinum;[30] (*iv*) (4-methylphenyl)-dimethylphosphinite from PMe_3 and 4-methylphenoxide coordinated to ruthenium;[31] (*v*) MeOP(Ph)R (R = H, Ph, OMe) from $PPhR^-$ coordinated to osmium and methoxide.[32] In all cases the formation of the P–O bond is explained in terms of intramolecular [intermolecular in case *v*] attack of RO^- on a coordinated phosphide (or phosphane), substantially identical to our proposal for the transformation of **a** into **b**.

Path 2 of Scheme 5 could also explain the formation of the asymmetric complexes $[(PCy_2H)Pt(\mu\text{-}PCy_2)_2Pt(PCy_2OR)]$(*Pt–Pt*), which could be derived from intermediate **c** (R = Me, Et) after loss of alcohol and ring closure. The circumstance that the asymmetric compounds formed only when reaction mixtures containing significant amounts of complexes *cis*-$Pt(PHCy_2)_2(OR)_2$ were evaporated can be explained by the fact that, under reaction conditions, the transformation from **a** to **b** is fast, so that **a** never accumulates in the reaction medium. Putting mixtures containing *cis*-$Pt(PHCy_2)_2(OR)_2$ under vacuum would progressively enhance the amount of **a** in solution, rendering the formation of **c** competitive with Path 1.

The transformation of *cis*-$Pt(PHCy_2)_2(OR)_2$ into **a** when R is Me or Et deserves comment. It is known that mononuclear dimethoxo Pt^{II} complexes are unstable and give aldehyde, alcohol and traces of CO.[9] In our case, intermediate **a** could form either by alcohol elimination or a dehydrogenative pathway consisting in the formation of Pt hydride with loss of aldehyde and subsequent loss of H_2 (Scheme 6).

In order to ascertain which of the above-mentioned pathways is operative in our system, we have carried out reactions between **1** and phenoxide or *tert*-butoxide, two bases incapable of forming the aldehyde contemplated by path *ii*.

The reaction of **1** with NaOPh (8 equiv.) in toluene at 50 °C for 1 day afforded the symmetrical Pt^{I} dimer $[(PCy_2OPh)Pt(\mu\text{-}PCy_2)]_2$(*Pt–Pt*) (**9**), whereas the asymmetric Pt^{I} complex $[(PCy_2H)Pt(\mu\text{-}PCy_2)_2Pt(PCy_2O\mathit{t}Bu)]$(*Pt–Pt*) (**10**)

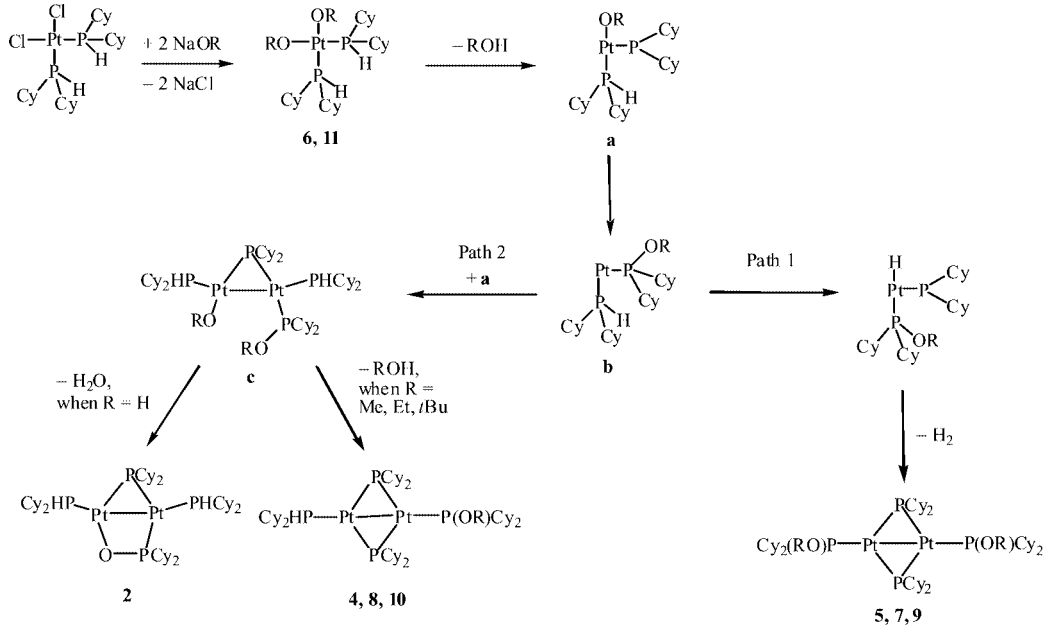

Scheme 5. Proposed mechanism for reactions carried out with excess NaOR.

 © 2005 Wiley-VCH Verlag GmbH & Co. KGaA, Weinheim

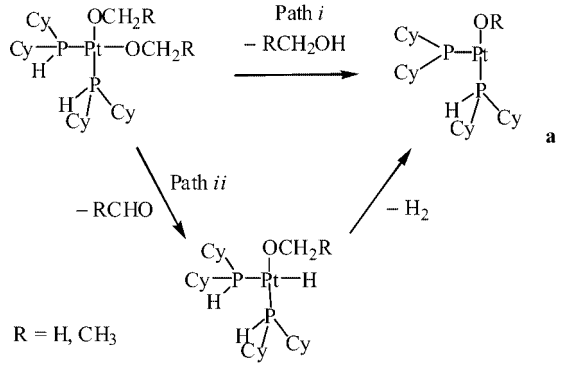

Scheme 6.

was the main product of the reaction of **1** with NaO*t*Bu (8 equiv.) in toluene at 50 °C.

Although the dehydrogenative pathway *ii* of Scheme 6 cannot be conclusively ruled out when NaOMe or NaOEt were the bases, these findings indicate that the loss of alcohol (path *i*) can be responsible (as in the cases of NaOPh or NaO*t*Bu) for the transformation of *cis*-Pt($PHCy_2$)$_2$-$(OR)_2$ into the intermediate Pt($PHCy_2$)(PCy_2)(OR) (**a**).

The diverse behaviour observed passing from NaOPh to NaO*t*Bu can be explained on the basis of the high difference in basicity exhibited by the two oxygenated bases and further supports the mechanism proposed. In fact, according to Scheme 5, the formation of asymmetric monophosphinito dimers is related to the contemporary presence in solution of significant amounts of intermediates **a** and **b**. In the case of NaOPh the formation of **a** is disfavoured because of the low basicity of phenoxide[33] and it is presumable that as soon as it forms it gives **b**, which evolves into **9**. On the contrary, with the very strong base NaO*t*Bu, the loss of *t*BuOH leading to **a** is very fast, so that path 2 of Scheme 5 becomes predominant.

In conclusion, the presence of the relatively weak P–H bonds determines a rich reactivity of **1** with oxygenated bases. Depending on the base and on the experimental conditions it is possible to address the reaction towards the phosphido-bridged Pt^{II} complex **3**, the asymmetric alkyl dicyclohexylphosphinito complexes **4**, **8**, **10** or the bis dicyclohexylphosphinito complexes **5**, **7**, **9**. Using NaOH resulted in the smooth formation of a Pt^{I} complex, showing a rare example of a Pt–P–O–Pt ring.

Experimental Section

General Remarks: All manipulations were carried out under pure dinitrogen, using freshly distilled, thoroughly dehydrated and oxygen-free solvents. All aromatic deuterated solvents were carefully dehydrated (molecular sieves) and deoxygenated (freeze and pump). *cis*-Dichlorobis(dicyclohexylphosphane)platinum(II) (**1**) was prepared as described in ref.[3].

C, H elemental analyses were carried out on a Eurovector CHNS-O Elemental Analyser. Cl elemental analysis was performed by potentiometric titration using a Metrohm DMS Titrino. Melting points were measured with a Gallenkamp apparatus and are uncorrected. Infrared spectra were recorded with a Bruker Vector 22 spectrometer. THF (CH_2Cl_2 in the case of **3**) solutions of the complexes were infused with a Cole-Parmer syringe pump. All the ESI-MS spectra were recorded with an Agilent LC/MS SL series instrument adopting the following general conditions: electrospray, positive ions, flow rate 0.200 mL min^{-1}, drying gas flow 4.0 l min^{-1}, nebuliser pressure 25 psi, drying gas temperature 300 °C, capillary voltage 4000 V, mass range 400–1400 *m*/*z*. The isotopic pattern was calculated by the Isotope Pattern Viewer software, downloadable free of charge from the www.surfacespectra.com website. NMR spectra were recorded with a BRUKER Avance 400 spectrometer; frequencies are referenced to Me_4Si (^1H and ^{13}C), 85% H_3PO_4 (^{31}P) and H_2PtCl_6 (^{195}Pt). NMR simulation was performed using the program WINDAISY.

[(Cy_2PH)Pt(μ-PCy_2)(κ^2*P*,*O*-μ-Cy_2PO)Pt(Cy_2PH)](*Pt*–*Pt*) (2): An aqueous solution of NaOH (0.7 mL, 0.90 M) was added to a vigorously stirred colourless CH_2Cl_2 solution (10 mL) of *cis*-[Pt($PHCy_2$)$_2$-Cl_2] (0.203 g, 0.306 mmol) at room temperature. After 3 days the yellow organic phase was separated, washed twice with water and dried on Na_2SO_4. After filtration the solvent was evaporated to dryness under reduced pressure, affording 152 mg of pure **2** as a yellow powder (83%). The complex was air sensitive in solution, very soluble in dichloromethane, toluene and *n*-hexane and scarcely soluble in acetone. $C_{48}H_{90}OP_4Pt_2$ (1197.28): calcd. C 48.15, H 7.58; found C 48.25, H 7.60. LC-MS: exact mass calcd. for $C_{48}H_{90}OP_4Pt_2$: 1196.52 amu; found: 1197.5 [M + H]$^+$. M.p. 135 °C (dec.). IR (KBr): $\tilde{\nu}_{max}$ = 2279 (w, P–H), 2252 (w, P–H), 1024 (s, P=O) cm^{-1}. ^1H NMR (400 MHz, C_6D_6, 295 K): δ = 5.68 [m, $^1J_{H(2),P(4)}$ = 310, $^2J_{H(2),Pt(2)}$ = 53 Hz, H(2)], 4.85 [m, $^1J_{H(1),P(2)}$ = 323, $^2J_{H(1),Pt(1)}$ = 112 Hz, H(1)] ppm. $^{31}P\{^1H\}$ NMR (161 MHz, C_6D_6, 295 K): δ = 134.4 [sharp ddd, $^2J_{P(1),P(2)}$ = 48, $^2J_{P(1),P(3)}$ = 229, $^2J_{P(1),P(4)}$ = 54, $^1J_{P(1),Pt(1)}$ = 4091, $^1J_{P(1),Pt(2)}$ = 2985 Hz, P(1)], 94.6 [sharp ddd, $^2J_{P(3),P(1)}$ = 229, $^3J_{P(3),P(2)}$ = 29, $^2J_{P(3),P(4)}$ = 5, $^1J_{P(3),Pt(2)}$ = 3061, $^2J_{P(3),Pt(1)}$ = 42 Hz, P(3)], 18.5 [broad ddd, $^2J_{P(4),P(1)}$ = 54, $^3J_{P(4),P(2)}$ = 112, $^2J_{P(4),P(3)}$ = 5, $^1J_{P(4),Pt(2)}$ = 3682, $^2J_{P(4),Pt(1)}$ = 83 Hz, P(4)], 15.9 [broad ddd, $^2J_{P(2),P(1)}$ = 48, $^3J_{P(2),P(3)}$ = 29, $^3J_{P(2),P(4)}$ = 112, $^1J_{P(2),Pt(1)}$ = 4230, $^2J_{P(2),Pt(2)}$ = 107 Hz, P(2)] ppm. $^{195}Pt\{^1H\}$ NMR (86 MHz, C_6D_6, 295 K): δ = –4798 [dddd, $^1J_{Pt(1),P(1)}$ = 4091, $^1J_{Pt(1),P(2)}$ = 4230, $^2J_{Pt(1),P(3)}$ = 42, $^2J_{Pt(1),P(4)}$ = 83 Hz, Pt(1)], –5205 [dddd, $^1J_{Pt(2),P(1)}$ = 2985, $^2J_{Pt(2),P(2)}$ = 107, $^1J_{Pt(2),P(3)}$ = 3061, $^1J_{Pt(2),P(4)}$ = 3682 Hz, Pt(2)] ppm.

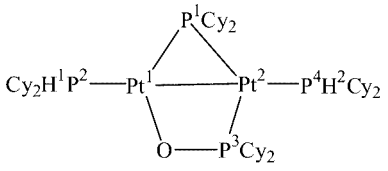

***trans*-Dichlorodi-μ-cyclohexylphosphidobis(dicyclohexylphosphane)-platinum(II) (3):** A suspension of *cis*-[Pt($PHCy_2$)$_2$$Cl_2$] (0.564 g, 0.85 mmol), CH_3ONa (0.092 g, 1.70 mmol) in toluene (20 mL) was vigorously stirred at room temperature (21 °C) for 3 days. The resulting pale yellow suspension was evaporated under reduced pressure. The residue was washed twice with *n*-hexane and the product was extracted with 10 mL CH_2Cl_2. Evaporation of the solvent afforded *trans*-[Pt($PHCy_2$)(PCy_2)Cl]$_2$ as a white powder (0.439 g, 82%). The complex was air stable, very soluble in dichloromethane and chloroform, scarcely soluble in toluene and insoluble in *n*-hexane. $C_{48}H_{90}Cl_2P_4Pt_2$ (1252.18): calcd. C 46.04, H 7.24, Cl 5.66; found C 46.15, H 7.25, Cl 5.68. LC-MS: exact mass calcd. for $C_{48}H_{90}Cl_2P_4Pt_2$: 1250.5 amu; found: 1251.5 [M + H]$^+$. M.p. >300 °C. IR (nujol mull): $\tilde{\nu}_{max}$ = 2337 (m, P–H), 289 (m, Pt–Cl) cm^{-1}. ^1H NMR (400 MHz, $CDCl_3$, 295 K): δ = 3.9 (m, $^1J_{H,P}$ = 322,

 © 2005 Wiley-VCH Verlag GmbH & Co. KGaA, Weinheim

$^2J_{H,Pt}$ = 72 Hz, P*H*) ppm. $^{31}P\{^1H\}$ NMR and $^{195}Pt\{^1H\}$ NMR spectroscopic data are reported in Table 1.

{(Cy$_2$PH)Pt(μ-PCy$_2$)$_2$Pt[Cy$_2$(MeO)P]}(*Pt–Pt*) (4): A solution of CH_3ONa in methanol (1.0 M, 3.2 mL) was added to a vigorously stirred suspension of *cis*-[Pt(PHCy$_2$)$_2$Cl$_2$] (0.262 g, 0.395 mmol) in toluene (10 mL) at room temperature. After 2 h the resulting orange suspension was evaporated under reduced pressure. The product was extracted with 3 × 5 mL hexane and precipitated, as a yellow powder, with acetone (hot/cold). Isolated yield: 0.129 g, 54%. The complex was air sensitive in solution, very soluble in dichloromethane, chloroform, hexane and toluene, scarcely soluble in acetone and methanol. $C_{49}H_{92}OP_4Pt_2$ (1211.31): calcd. C 48.59, H 7.66; found C 48.45, H 7.56. LC-MS: exact mass calcd. for $C_{49}H_{92}OP_4Pt_2$: 1210.54 amu; found: 1211.5 $[M + H]^+$. M.p. 150 °C (dec.). IR (KBr): $\tilde{\nu}_{max}$ = 2234 (w, P–H), 1095 (s), 1020 (s, P–O), 809 (s, P–O) cm^{-1}. ^1H NMR (400 MHz, C_6D_6, 295 K): δ = 6.36 [m, $^1J_{H,P}$ = 318 Hz, H(1)], 3.94 (d, $^3J_{H,P}$ = 13 Hz, POC*H*$_3$) ppm. $^{31}P\{^1H\}$ NMR (161 MHz, C_6D_6, 295 K): δ = 245.7 [dd, $^2J_{P(1),P(3)}$ = 67, $^2J_{P(1),P(2)}$ = 55, $^1J_{P(1),Pt(1)}$ = 2625, $^1J_{P(1),Pt(2)}$ = 2450 Hz, P(1)], 173.6 [dt, $^3J_{P(3),P(2)}$ = 76, $^2J_{P(3),P(1)}$ = 67, $^1J_{P(3),Pt(2)}$ = 5477 Hz, P(3)], 19.1 [dt, $^3J_{P(2),P(3)}$ = 76, $^2J_{P(2),P(1)}$ = 55, $^1J_{P(2),Pt(1)}$ = 4800, $^2J_{P(2),Pt(2)}$ = 47 Hz, P(2)] ppm. $^{195}Pt\{^1H\}$ NMR (86 MHz, C_6D_6, 295 K): δ = –5530 [dt, $^1J_{Pt(1),P(1)}$ = 2625, $^1J_{Pt(1),P(2)}$ = 4800, $^1J_{Pt(1),Pt(2)}$ = 337 Hz, Pt(1)], –5570 [dtd, $^1J_{Pt(2),P(1)}$ = 2450, $^2J_{Pt(2),P(2)}$ = 47, $^1J_{Pt(2),P(3)}$ = 5477, $^1J_{Pt(2),Pt(1)}$ = 337 Hz, Pt(2)] ppm.

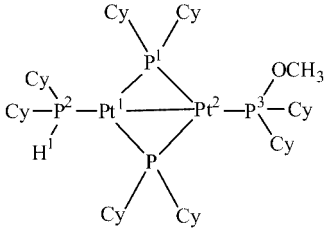

{[Cy$_2$(MeO)P]Pt(μ-PCy$_2$)}$_2$(*Pt–Pt*) (5): A solution of CH_3ONa in methanol (1.0 M, 2.9 mL) was added to a vigorously stirred suspension of *cis*-[Pt(PHCy$_2$)$_2$Cl$_2$] (0.240 g, 0.362 mmol) in toluene (10 mL) at 50 °C. After 6 h the resulting orange suspension was evaporated under reduced pressure. The product was extracted with 3 × 5 mL hexane and precipitated, as a yellow powder, with acetone (hot/cold). Isolated yield: 0.150 g, 67%. The complex was air sensitive in solution, very soluble in dichloromethane, chloroform, hexane and toluene, scarcely soluble in acetone and methanol. $C_{50}H_{94}O_2P_4Pt_2$ (1241.33): calcd. C 48.38, H 7.63; found C 48.48, H 7.65. LC-MS: exact mass calcd. for $C_{50}H_{94}O_2P_4Pt_2$: 1240.55 amu; found: 1241.5 $[M + H]^+$. M.p. 188 °C (dec.). IR (nujol mull): $\tilde{\nu}_{max}$ = 1259 (m, C–O), 1175 (w), 1103 (m), 1054 (m, P–O) cm^{-1}. ^1H NMR (400 MHz, C_6D_6, 295 K): δ = 3.92 (d, $^3J_{H,P}$ = 13 Hz, C*H*$_3$O). $^{31}P\{^1H\}$ NMR (161 MHz, C_6D_6, 295 K): δ = 245.3 [dd, $^2J_{P(1),P(2)}$ = 68, $^1J_{P(1),Pt(1)}$ = 2475 Hz, P(1)], 171.2 [dd, $^2J_{P(2),P(1)}$ = 68, $^3J_{P(2),P(3)}$ = 81, $^1J_{P(2),Pt(1)}$ = 5468, $^2J_{P(2),Pt(2)}$ = 126 Hz, P(2)] ppm. $^{195}Pt\{^1H\}$ NMR (86 MHz, C_6D_6, 295 K): δ = –5570 [dtd, $^1J_{Pt(1),P(1)}$ = 2475, $^1J_{Pt(1),P(2)}$ = 5468, $^2J_{Pt(1),P(3)}$ = 64 Hz, Pt(1)] ppm.

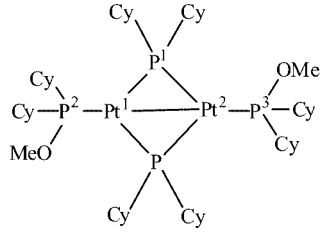

{[Cy$_2$(EtO)P]Pt(μ-PCy$_2$)}$_2$(*Pt–Pt*) (7): A solution of EtONa in dry ethanol (1.0 M, 2.5 mL) was added to a vigorously stirred suspension of *cis*-[Pt(PHCy$_2$)$_2$Cl$_2$] (0.206 g, 0.311 mmol) in toluene (10 mL) at 50 °C. After 2 h the resulting orange suspension was evaporated under reduced pressure. The product was extracted with 3 × 5 mL hexane and precipitated, as a yellow powder, with acetone (hot/cold). Isolated yield: 0.109 g, 55%. The complex was air sensitive in solution, very soluble in dichloromethane, chloroform, hexane and toluene, scarcely soluble in acetone and methanol. $C_{52}H_{98}O_2P_4Pt_2$ (1269.38): calcd. C 49.20, H 7.78; found C 49.12, H 7.75. LC-MS: exact mass calcd. for $C_{52}H_{98}O_2P_4Pt_2$: 1268.58 amu; found: 1269.6 $[M + H]^+$. IR (nujol mull): $\tilde{\nu}_{max}$ = 1263 (m, C–O), 1177 (w), 1102 (m), 1059 (m, P–O), 1001 (m), 849 (m), 818 (w), 749 (m), 525 (m), 462 (m) cm^{-1}. ^1H NMR (400 MHz, C_6D_6, 295 K): δ = 4.39 (m, $^3J_{H,H}$ = 7.1 Hz, CH_3CH_2O) ppm. $^{31}P\{^1H\}$ NMR (161 MHz, C_6D_6, 295 K): δ = 244.0 [t, $^2J_{P(1),P(2)}$ = 68, $^1J_{P(1),Pt(1)}$ = 2481 Hz, P(1)], 167.3 [t, $^2J_{P(2),P(1)}$ = 68, $^3J_{P(2),P(3)}$ = 77, $^1J_{P(2),Pt(1)}$ = 5451, $^2J_{P(2),Pt(2)}$ = 132 Hz, P(2)] ppm. $^{195}Pt\{^1H\}$ NMR (86 MHz, C_6D_6, 295 K): δ = –5567 [dtd, $^1J_{Pt(1),P(1)}$ = 2481 Hz, $^1J_{Pt(1),P(2)}$ = 5451, $^2J_{Pt(1),P(3)}$ = 132 Hz, Pt(1)] ppm.

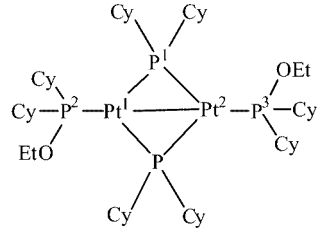

NMR Spectroscopic Features for 8: ^1H NMR (400 MHz, C_6D_6, 295 K): δ = 6.23 [dm, $^1J_{H(1),P(2)}$ = 318 Hz, P(1)], 4.40 (pseudoquintet, $^3J_{H,P}$ = 7, $^3J_{H,H}$ = 7 Hz, POC*H*$_2$CH$_3$), 1.56 (t, $^3J_{H,H}$ = 7 Hz, POCH$_2$C*H*$_3$) ppm. $^{31}P\{^1H\}$ NMR (161 MHz, C_6D_6, 295 K): δ = 245.4 [dd, $^2J_{P(1),P(3)}$ = 64, $^2J_{P(1),P(2)}$ = 54, $^1J_{P(1),Pt(1)}$ = 2710, $^1J_{P(1),Pt(2)}$ = 2461 Hz, P(1)], 169.5 [dt, $^3J_{P(3),P(2)}$ = 77, $^2J_{P(3),P(1)}$ = 64, $^1J_{P(3),Pt(2)}$ = 5458 Hz, P(3)], 19.5 [dt, $^3J_{P(2),P(3)}$ = 77, $^2J_{P(2),P(1)}$ = 54, $^1J_{P(2),Pt(1)}$ = 4894, $^2J_{P(2),Pt(2)}$ = 54 Hz, P(2)] ppm. $^{195}Pt\{^1H\}$ NMR (86 MHz, C_6D_6, 295 K): δ = –5524 [dt, $^1J_{Pt(1),P(1)}$ = 2710, $^1J_{Pt(1),P(2)}$ = 4894, $^1J_{Pt(1),Pt(2)}$ = 333 Hz, Pt(1)], –5567 [dtd, $^1J_{Pt(2),P(1)}$ = 2461, $^2J_{Pt(2),P(2)}$ = 54, $^1J_{Pt(2),P(3)}$ = 5458, $^1J_{Pt(2),Pt(1)}$ = 337 Hz, Pt(2)] ppm.

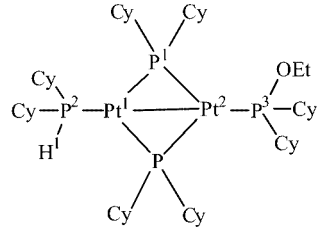

{[Cy$_2$(PhO)P]Pt(μ-PCy$_2$)}$_2$(*Pt–Pt*) (9): Sodium phenoxide (0.285 g, 2.46 mmol) was added to a stirred suspension of *cis*-[Pt(PHCy$_2$)$_2$-Cl$_2$] (0.204 g, 0.308 mmol) in toluene (5 mL). After 24 h stirring at 50 °C the suspension was filtered and the filtrate was concentrated to 3 mL under reduced pressure. The product was obtained, as a yellow solid, by precipitation with acetone (50 mg, 24%). The complex was air sensitive in solution, very soluble in dichloromethane, chloroform, hexane and toluene, scarcely soluble in acetone and methanol. $C_{60}H_{98}O_2P_4Pt_2$ (1365.47): calcd. C 52.78, H 7.23; found C 52.59, H 7.20. LC-MS: exact mass calcd. for $C_{60}H_{98}O_2P_4Pt_2$: 1364.58 amu; found: 1365.6 $[M + H]^+$. IR (KBr): $\tilde{\nu}_{max}$ = 2925 (m), 2848 (m), 1262 (s), 1229 (m), 1100 (vs, P–O), 1021 (vs, P–O), 873

 © 2005 Wiley-VCH Verlag GmbH & Co. KGaA, Weinheim

(m), 801 (vs), 678 (w), 518 (w), 501 (w) cm^{-1}. ^1H NMR (400 MHz, CD_2Cl_2, 295 K): δ = 7.25–7.02 (10 H, Ph), 2.4–0.7 (88 H, Cy) ppm. $^{31}P\{^1H\}$ NMR (161 MHz, C_6D_6, 295 K) (Supporting Information, ESI 5): δ = 242.7 [t, $^2J_{P(1),P(2)}$ = 71, $^1J_{P(1),Pt(1)}$ = 2469 Hz, P(1)], 163.6 [t, $^2J_{P(2),P(1)}$ = 71, $^3J_{P(2),P(3)}$ = 82, $^1J_{P(2),Pt(1)}$ = 5489, $^2J_{P(2),Pt(2)}$ = 49 Hz, P(2)] ppm. $^{195}Pt\{^1H\}$ NMR (86 MHz, CD_2Cl_2, 295 K): δ = –5524 [dtd, $^1J_{Pt(1),P(1)}$ = 2469, $^1J_{Pt(1),P(2)}$ = 5489, $^2J_{Pt(1),P(3)}$ = 49 Hz, Pt(1)] ppm.

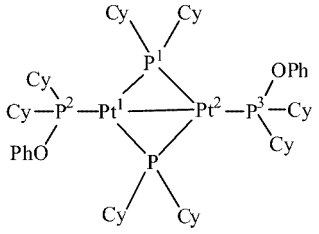

NMR Spectroscopic Features for {(Cy_2PH)Pt(μ-PCy_2)$_2$Pt-[Cy_2(*t*BuO)P]}(*Pt–Pt*) (10): Compound **10** was the main product of reaction of **1** with NaO*t*Bu (8 equiv.) in toluene at 50 °C. ^1H NMR (400 MHz, C_6D_6, 295 K): δ = 6.38 [m, $^1J_{H(1),P(2)}$ = 317 Hz, 2 H, H(1)]; 1.66 (s, 9 H, *t*Bu) ppm. $^{31}P\{^1H\}$ NMR (161 MHz, C_6D_6, 295 K): δ = 235.8 [dd, $^2J_{P(1),P(3)}$ = 57, $^2J_{P(1),P(2)}$ = 53, $^1J_{P(1),Pt(1)}$ = 2594, $^1J_{P(1),Pt(2)}$ = 2528 Hz, P(1)], 128.7 [dt, $^3J_{P(3),P(2)}$ = 78, $^2J_{P(3),P(1)}$ = 57, $^1J_{P(3),Pt(2)}$ = 5378 Hz, P(3)], 18.4 [dt, $^3J_{P(2),P(3)}$ = 78, $^2J_{P(2),P(1)}$ = 54, $^1J_{P(2),Pt(1)}$ = 4794 Hz, P(2)] ppm. $^{195}Pt\{^1H\}$ NMR (86 MHz, C_6D_6, 295 K): δ = –5492 [dt, $^1J_{Pt(1),P(1)}$ = 2594, $^1J_{Pt(1),P(2)}$ = 4794 Hz, (1)]; –5445 [dt, $^1J_{Pt(2),P(1)}$ = 2528, $^1J_{Pt(2),P(3)}$ = 5378 Hz, Pt(2)] ppm.

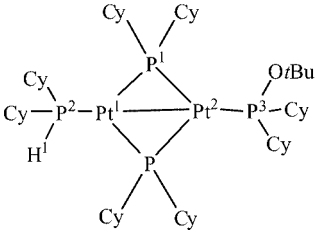

***cis*-[Pt($PHCy_2$)$_2$(OPh)$_2$] (11):** Sodium phenoxide (0.116 g, 0.999 mmol) was added to a toluene suspension of *cis*-[Pt($PHCy_2$)$_2$-Cl_2] (0.224 g, 0.338 mmol in 10 mL) and the mixture was stirred at room temperature for 2 h. The resulting suspension was filtered, giving a white solid and a yellow solution. The white solid was washed with water, extracted with CH_2Cl_2 and precipitated with toluene, affording 98 mg (41%) of pure *cis*-[Pt($PHCy_2$)$_2$(Cl)(OPh)] (**12**). The yellow filtrate was evaporated under reduced pressure. The residue was redissolved in 4 mL of dichloromethane and *n*-hexane added , which caused the precipitation of *cis*-[Pt($PHCy_2$)$_2$-(OPh)$_2$] (**11**) as a white solid (0.155 g, 59%). Complex **11** was air stable, very soluble in dichloromethane, toluene, scarcely soluble in hexane. $C_{36}H_{56}O_2P_2Pt$ (777.85): calcd. C 55.59, H 7.26; found C 55.45, H 7.38. M.p. 129–131 °C (dec.). IR (nujol mull): $\tilde{\nu}_{max}$ = 2333 (m, P–H) cm^{-1}. ^1H NMR (400 MHz, $CDCl_3$, 295 K): δ = 3.8 (m, $^1J_{H,P}$ = 367 Hz, P*H*) ppm. $^{31}P\{^1H\}$ NMR (161 MHz, $CDCl_3$, 295 K): δ = 5.6 (s, $^1J_{P,Pt}$ = 3389 Hz) ppm. $^{195}Pt\{^1H\}$ NMR (86 MHz, $CDCl_3$, 295 K): δ = –4155 (t, $^1J_{P,Pt}$ = 3389 Hz) ppm.

***cis*-[Pt($PHCy_2$)$_2$(Cl)(OPh)] (12):** $C_{30}H_{51}ClOP_2Pt$ (720.20): calcd. C 50.03, H 7.14, Cl 4.92; found C 50.11, H 7.18, Cl 4.88. M.p. >300 °C (dec.). IR (nujol mull): $\tilde{\nu}_{max}$ = 2330, 2345 (m, P–H), 306 (m, Pt–Cl) cm^{-1}. ^1H NMR (400 MHz, $CDCl_3$, 295 K): δ = 3.83 (m, $^1J_{H,P}$ = 359, $^2J_{H,Pt}$ = 102 Hz, P*H* trans Cl), 3.67 (m, $^1J_{H,P}$ = 352, $^2J_{H,Pt}$ = 91 Hz, P*H* trans OPh) ppm. $^{31}P\{^1H\}$ NMR (161 MHz, $CDCl_3$, 295 K): δ = 8.7 (d, $^1J_{P,Pt}$ = 3174, $^2J_{P,P}$ = 14 Hz, P *trans* OPh), 15.2 (d, $^1J_{P,Pt}$ = 3653, $^2J_{P,P}$ = 14 Hz, P *trans* Cl) ppm. $^{195}Pt\{^1H\}$ NMR (86 MHz, $CDCl_3$, 295 K): δ = –4323 (dd, $^1J_{P,Pt}$ = 3174, $^1J_{P,Pt}$ = 3653 Hz) ppm.

X-ray Data Collection, Structure Solution and Refinement of 5:[34] Crystal data, parameters for intensity data collection and convergence results are compiled in Table 3. A yellow platelet of approximate dimensions 0.20 × 0.11 × 0.04 mm was studied at room temperature with a BRUKER-AXS SMART APEX diffractometer. An empirical absorption correction[35] was applied before averaging symmetry-related reflections. The structure was solved by direct methods[36] and refined on F^2.[37]

Table 3. Crystal data and structure refinement for **5**.

Empirical formula	$C_{50}H_{94}O_2P_4Pt_2$
Molecular mass	1241.31
Temperature [K]	293(2)
Wavelength [Å]	0.71073
Crystal system	monoclinic
Space group	$P2_1/c$ (no. 14)
Unit cell dimensions	
a [Å]	11.1753(13)
b [Å]	21.220(2)
c [Å]	12.2712(14)
β [°]	113.052(2)
V [Å^3]	2677.6(5)
Z	2
$D_{calcd.}$ [Mg m^{-3}]	1.540
Absorption coeff. [mm^{-1}]	5.4
θ Range for data coll. [°]	1.9–28.4
Independent reflections	6689
Observed reflections	4198
Data/parameters	6689/262
Goodness-of-fit on F^2	0.997
R[a] [$I > 2\sigma(I)$]	0.0453
wR_2[b] (all data)	0.0615
Largest diff. peak/hole [e Å^{-3}]	2.55, –1.08 (close to Pt)

[a] $R = \Sigma||F_o| - |F_c||/\Sigma|F_o|$. [b] $wR_2 = [\Sigma w(F_o^2 - F_c^2)^2/\Sigma w(F_o^2)^2]^{1/2}$.

Supporting Information: The ^1H-^{31}P HMQC NMR spectrum of **2**, the $^{31}P\{^1H\}$ NMR spectrum of [(Cy_2PH)(Cl)Pt(μ-PCy_2)Pt-(Cy_2PH)$_2$](*Pt–Pt*), the comparison of the experimental $^{31}P\{^1H\}$ NMR spectrum of **3** with that calculated, and the $^{31}P\{^1H\}$ NMR spectrum of **9** are given as supporting information.

Acknowledgments

Italian MIUR (PRIN 2004, project 2004030719_005) is gratefully acknowledged for financial support. We thank Dr. A. Fiore for experimental assistance, Dr. C. Hu for help with the X-ray experiment and Prof. F. P. Fanizzi for helpful discussions.

[1] R. Giannandrea, P. Mastrorilli, C. F. Nobile, M. Palma, F. P. Fanizzi, U. Englert, *Eur. J. Inorg. Chem.* **2000**, 2573–2576.
[2] P. Mastrorilli, M. Palma, C. F. Nobile, F. P. Fanizzi, *J. Chem. Soc., Dalton Trans.* **2000**, 4272–4276.
[3] P. Mastrorilli, C. F. Nobile, F. P. Fanizzi, M. Latronico, C. Hu, U. Englert, *Eur. J. Inorg. Chem.* **2002**, 1210–1218.
[4] R. A. Michelin, M. Napoli, R. Ros, *J. Organomet. Chem.* **1979**, *175*, 239–255.
[5] D. R. Coulson, *J. Am. Chem. Soc.* **1976**, *98*, 3111–3119.
[6] F. Giordano, A. Vitagliano, *Inorg. Chem.* **1981**, *20*, 633–635.
[7] H. E. Bryndza, S. A. Kretchmar, T. H. Tulip, *J. Chem. Soc., Chem. Commun.* **1985**, 977–978.

 © 2005 Wiley-VCH Verlag GmbH & Co. KGaA, Weinheim

[8] R. T. Boere, C. J. Willis, *Inorg. Chem.* **1985**, *24*, 1059–1065.
[9] H. E. Bryndza, J. C. Calabrese, M. Marsi, D. C. Roe, W. Tam, J. E. Bercaw, *J. Am. Chem. Soc.* **1986**, *108*, 4805–4813.
[10] D. P. Arnold, M. A. Bennett, *J. Organomet. Chem.* **1980**, *199*, C17–C20.
[11] P. Roffia, G. Gregorio, F. Conti, G. F. Pregaglia, R. Ugo, *J. Mol. Catal.* **1977**, *2*, 191–201.
[12] A. Sacco, P. Mastrorilli, *J. Chem. Soc., Dalton Trans.* **1994**, 2761–2764.
[13] J. Sieler, M. Helms, W. Gaube, A. Svensson, O. Lindqvist, *J. Organomet. Chem.* **1987**, *320*, 129–136.
[14] The reaction was carried out in toluene for 3 h at 50 °C with a NaEtO/Pt molar ratio of 2.
[15] The reaction was carried out in dichloromethane at reflux and the starting material was recovered unaltered after 12 h.
[16] P. E. Garrou, *Chem. Rev.* **1981**, *81*, 229–266.
[17] A. J. Carty, S. A. Maclaughlin, D. Nucciarone, in *Phosphorus-31 NMR Spectroscopy in Stereochemical Analysis* (Eds.: J. G. Verkade, L. D. Quin), VCH Publishers, New York, **1987**, p. 559.
[18] R. Giannandrea, P. Mastrorilli, C. F. Nobile, U. Englert, *J. Chem. Soc., Dalton Trans.* **1997**, 1355–1358.
[19] N. W. Alcock, P. Bergamini, T. M. Gomes-Carniero, R. D. Jackson, J. Nicholls, A. G. Orpen, P. G. Pringle, S. Sostero, O. Traverso, *J. Chem. Soc., Chem. Commun.* **1990**, 980–982.
[20] Complex **4** was obtained in variable amounts also when NaOH, NaOEt or NaOPh were reacted with **1** in toluene with a **1**/base molar ratio of 1/2.
[21] J. B. Brandon, K. R. Dixon, *Can. J. Chem.* **1981**, *59*, 1188–1200.
[22] R. Glaser, D. J. Kountz, R. D. Waid, J. C. Gallucci, D. W. Meek, *J. Am. Chem. Soc.* **1984**, *106*, 6324–6333.
[23] M. Sommovigo, M. Pasquali, P. Leoni, U. Englert, *Inorg. Chem.* **1994**, *33*, 2686–2688.
[24] P. Leoni, G. Chiaradonna, M. Pasquali, F. Marchetti, *Inorg. Chem.* **1999**, *38*, 253–259.
[25] N. J. Taylor, P. C. Chieh, A. J. Carty, *J. Chem. Soc., Chem. Commun.* **1975**, 448–449.
[26] F. H. Allen, *Acta Crystallogr., Sect. B* **2002**, *B58*, 380–388.
[27] A. L. Spek, *PLATON, A Multipurpose Crystallographic Tool*, Utrecht University, Utrecht, The Netherlands, **2001**.
[28] P. Leoni, M. Sommovigo, M. Pasquali, P. Sabatino, D. Braga, *J. Organomet. Chem.* **1992**, *423*, 263–270.
[29] A. Caballero, F. A. Jalón, B. R. Manzano, G. Espino, M. Pérez-Manrique, A. Mucientes, F. J. Poblete, M. Maestro, *Organometallics* **2004**, *23*, 5694–5706.
[30] P. W. N. M. Van Leeuwen, C. F. Roobeek, A. G. Orpen, *Organometallics* **1990**, *9*, 2179–2181.
[31] J. F. Hartwig, R. G. Bergman, R. A. Andersen, *J. Organomet. Chem.* **1990**, *394*, 417–432.
[32] D. S. Bohle, T. C. Jones, C. E. F. Rickard, W. R. Roper, *Organometallics* **1986**, *5*, 1612–1619.
[33] The scarce basicity of NaOPh can be held responsible for the successful isolation in the state of purity of the phenoxo Pt^{II} complexes *cis*-[$Pt(PHCy_2)_2(OPh)_2$] (**11**) and *cis*-[$Pt(PHCy_2)_2$-(Cl)(OPh)] (**12**), as described in the Exp. Sect.
[34] CCDC-269199 contains the supplementary crystallographic data for this paper. These data can be obtained free of charge from The Cambridge Crystallographic Data Centre via www.ccdc.cam.ac.uk/data_request/cif.
[35] G. M. Sheldrick, SADABS, program for empirical absorption correction of area detector data, University of Göttingen, **1996**.
[36] G. M. Sheldrick *SHELXS97*, program for crystal structure solution, University of Göttingen, **1997**.
[37] G. M. Sheldrick *SHELXL97*, program for crystal structure refinement, University of Göttingen, **1997**.

Received: June 7, 2005
Published Online: September 26, 2005

 © 2005 Wiley-VCH Verlag GmbH & Co. KGaA, Weinheim

Synthesis, Structure and Magnetic Properties of a Novel Linear Cu^{II}-Trimer Complex

Vladimir Pashchenko,*[a] Bernhard Brendel,[a] Bernd Wolf,[a] Michael Lang,[a] Konstantin Lyssenko,[b] Olga Shchegolikhina,[b] Yulia Molodtsova,[b] Larisa Zherlitsyna,[c] Norbert Auner,*[c] Florian Schütz,[d] Marcus Kollar,[d][‡] Peter Kopietz,[d] and Neil Harrison[e]

Keywords: Copper / Cluster compounds / Sandwich complexes / Magnetic properties

A new hexanuclear copper(II) sandwich complex based on two 10-membered macrocyclic phenylsiloxanolate ligands, $\{Cu_6[(C_6H_5SiO_2)_5]_2(OH)_2(C_{10}H_8N_2)_2\}\cdot 4(DMF)\cdot 3(H_2O)$ (**1**), was synthesized and characterized by single-crystal X-ray diffraction and measurements of the magnetic susceptibility and isothermal magnetization. The cluster compound crystallizes in the triclinic system, space group $P\bar{1}$ (No. 2), with a = 14.925(3) Å, b = 16.745(2) Å, c = 23.053(3) Å, α = 83.079(9)°, β = 84.836(13)°, γ = 65.019(17)°, and Z = 2. The unit cell contains two identical molecules, each consisting of six interacting Cu^{2+} (S = 1/2) ions. Within the molecule, the six Cu^{2+} ions are arranged in two almost linear, parallel trimers. While pairs of oxygen atoms link the Cu^{2+} ions within the trimers, single oxygen atoms residing at the ends of the trimers provide the strongest intertrimer bonds. Magnetic measurements reveal an antiferromagnetic *intra*trimer exchange interaction, J/k_B = 85 K, as the dominant magnetic coupling of the complex. By introducing a weak antiferromagnetic *inter*trimer coupling, J'/k_B = 3.5 K, a satisfactory description of the magnetic behavior over a wide range of temperature and magnetic field is obtained. The departure of the model curves from the data at the lowest available temperature indicates the presence of additional, weak *intra*- and/or *inter*molecular interactions.
(© Wiley-VCH Verlag GmbH & Co. KGaA, 69451 Weinheim, Germany, 2005)

Introduction

The synthesis of new magnetic clusters with unprecedented spin topologies is a central topic in the field of molecular magnetism. Among different strategies that have been developed, serendipitous assembly[1] and rational design[2] represent opposite limiting approaches. Following on from the latter route, the rational construction of heptanuclear clusters with high-spin ground states has been reported very recently, starting from hexacyanometalates $[M(CN)_6]^{3-}$ (M = Cr, Fe) and mononuclear complexes bearing a capping ligand.[2]

Moreover, a decanuclear copper(II) cluster, $\{[Cu_6\{(PhSiO_2)_6\}_2]\cdot[Cu(tmpa)CN]_4\}\cdot(PF_6)_4$ (**2**) [tmpa = tris(2-pyridilmethyl)amine], was designed and synthesized by a self-assembly between a hexacopper(II) siloxanolate cage and the monomeric complex $[Cu(tmpa)CN]\cdot(PF_6)$.[3] This cluster compound exhibits interesting magnetic properties with a low-lying S = 5 state arising from a unique spin arrangement.

In the past decade, a widespread series of copper-containing siloxanolate complexes was synthesized and structurally characterized,[4] basically showing two different types of structural features: a sandwich-like molecular structure was found for $\{K_4[\{(RSiO_2)_6\}_2Cu_4]\}\cdot 4(n\text{BuOH})$ [R = Et (**3**),[4a] Ph[4b]] and $\{Cu_6[(PhSiO_2)_6]_2\}\cdot 6(L)$ [L = EtOH (**4**),[4c] L = DMF (**5**)[4d]]. These clusters are composed of two 12-membered (6 Si + 6 O) stereoregular organosiloxanolate fragments, *cis*-$[RSi(O)O^-]_6$, linked together through four or six copper atoms. In contrast, compounds such as $\{Na_4[(PhSiO_2)_{12}Cu_4]\}\cdot 8(n\text{BuOH})$ (**6**),[4e,4f] $\{M_4[(ViSiO_2)_{12}Cu_4]\}\cdot m(n\text{BuOH})$ [M = K, Vi = vinyl, m = 6 (**7**);[4e] M = Na, m = 4 (**8**)[4f]] and $\{Na_4[(EtSiO_2)_{12}Cu_4]\}\cdot 4(n\text{BuOH})$[4g] are based on a 24-membered stereoregular organosiloxanolate fragment $[RSi(O)O^-]_{12}$ (R = Et, Vi, Ph) of tris-*cis*-tris-*trans* configuration and fixed in the "horse saddle" conformation

[a] Physikalisches Institut, J. W. Goethe-Universität Frankfurt, FOR 412,
60438 Frankfurt (M), Germany
Fax: +49-069-798-47250
E-mail: pashchenko@physik.uni-frankfurt.de
[b] A. N. Nesmeyanov Institute of Organoelement Compounds, Russian Academy of Sciences,
117813 Moscow, Russian Federation
[c] Institut für Anorganische Chemie, J. W. Goethe-Universität Frankfurt, FOR 412,
60439 Frankfurt (M), Germany
Fax: +49-069-798-29188
E-mail: auner@chemie.uni-frankfurt.de
[d] Institut für Theoretische Physik, J. W. Goethe-Universität Frankfurt, FOR 412,
60438 Frankfurt (M), Germany
[e] Los Alamos National Laboratory, MS E536,
Los Alamos, NM 87545, USA
[‡] New permanent address: Theoretische Physik III, Universität Augsburg,
86135 Augsburg, Germany
Supporting information for this article is available on the WWW under http://www.eurjic.org or from the author.

by four Cu and four alkaline metal atoms. Investigations of the magnetic properties of the globular tetranuclear complex $\{Na_4[(PhSiO_2)_{12}Cu_4]\}\cdot 8(n\text{BuOH})$ (**6**) and the sandwich-like tetranuclear complex $\{K_4[\{(EtSiO_2)_6\}_2Cu_4]\}\cdot 4(n\text{BuOH})$ (**3**), as well as the hexanuclear sandwich complex $\{Cu_6[(PhSiO_2)_6]_2\}\cdot 6(\text{EtOH})$ (**4**), revealed that the six copper ions in **4** are ferromagnetically coupled with a total spin $S = 3$, whereas strong antiferromagnetic Cu–Cu interactions with an $S = 0$ ground state were detected in the tetranuclear complexes **3** and **6**. These experimental findings prompted us to recrystallize complex **6** with additional ligands that would assemble the molecular unit into a supramolecular structure with new physical properties. Thus, recrystallization of **6**, which contains four sodium ions along with four copper ions, in DMF as solvent and in the presence of 2,2′-bipyridine (bipy), was performed. Unexpectedly, a completely new hexanuclear Cu complex with a sandwich-like structure not containing any alkaline metal ions was obtained.

Here we report the synthesis, structural and magnetic properties of a novel hexacopper(II) siloxanolate cluster compound $\{Cu_6[(PhSiO_2)_5]_2(OH)_2(C_{10}H_8N_2)_2\}\cdot 4(\text{DMF})\cdot 3(H_2O)$, which is unique in that the six Cu^{2+} ions are arranged in two parallel 3-site strings, that is, coupled $S = 1/2$ trimers. A preliminary account of the work has been published in ref.[5]

Results and Discussion

According to Scheme 1, the hexanuclear Cu sandwich complex **1**, which is based on 10-membered *cis*-pentaphenylcyclopentasiloxanolate ligands, was obtained by recrystallization of a tetranuclear Cu complex **6**, which is based on a 24-membered dodecaphenylcyclododecasiloxanolate ligand of tris-*cis*-tris-*trans* configuration possessing the globule-like structure $\{Na_4[(PhSiO_2)_{12}Cu_4]\}\cdot 8(n\text{BuOH})$,[4e,4f] in DMF and in the presence of 2,2′-bipyridine (bipy) at about 30 °C.

Under these experimental conditions, the initial complex **6** underwent a dramatic rebuilding with a formation of complex **1**, no longer containing alkaline ions in yields up to 92%. Crystals of sodium phenylsiloxanolate and of polyhedral phenylsilsesquioxane can easily be separated from the blue crystals of **1** (crystal size ca. 1 mm) and were detected as by-products of the complex formation.

The surprising transformation of complex **6** into **1** is reproducible, but strongly depends on the reaction conditions. The amount of 2,2′-bipyridine is of great importance on product formation. While from the stoichiometric ratio of 1 × complex **6**/4 × bipy in DMF, $\{Cu_6[(PhSiO_2)_5]_2(OH)_2(C_{10}H_8N_2)_2\}\cdot 4(\text{DMF})\cdot 3(H_2O)$ (**1**) is obtained, mixtures of 1 × **6**/2 × bipy in DMF and toluene gave $\{Cu_6[(PhSiO_2)_6]_2\}\cdot 6(\text{DMF})$, and without toluene the complex $\{Cu_6[(PhSiO_2)_5]_2(OH)_2(C_{10}H_8N_2)_2\}\cdot 3(\text{DMF})$ was isolated. Reaction of **6** with bipy in DMF in a molar ration of 1:1 gave $\{Cu_6[(PhSiO_2)_6]_2\}\cdot 6(\text{DMF})$. DMF was not especially dried prior to use. Performing the two months' recrystallization in an open system, even the moisture from air might influence the product formation, resulting in the introduction of different amounts of hydroxy ligands and water into the crystals. All the compounds formed have been fully characterized by single-crystal X-ray analysis and will be published elsewhere.[6] These very complex reaction pathways are currently being investigated in detail in our laboratories.

Crystal Structure of $\{Cu_6[(PhSiO_2)_5]_2(OH)_2(C_{10}H_8N_2)_2\}\cdot 4(\text{DMF})\cdot 3(H_2O)$ (1)

Complex **1** exhibits a sandwich-like structure (Figure 1) and consists of two pentaphenylcyclopentasiloxanolate ligands connected by six Cu^{II} atoms arranged in a $Cu_6O_{10}(OH)_2$ moiety (Figure 2). Notably, this is the first example of a metallasiloxane with an odd number of Si–O units in the siloxanolate rings, which seem to predominantly determine the structural and physical features of the complex.

The two 10-membered siloxanolate $(Si–O)_5$ rings are coaxial and shifted in respect to each other and to the central $Cu_6O_{10}(OH)_2$ segment (Figure 1). The siloxanolate cycles are characterized by an envelope conformation with the deviation of Si(2) or Si(9) atoms from the plane of the remaining silicon atoms by 0.52 and 0.60 Å, respectively. The Ph groups exhibit an all-*cis* arrangement. The Si–O bond lengths vary in the range of 1.591(2)–1.652(2) Å, which is usual for this class of compounds.[7] The $Cu_6O_{10}(OH)_2$ segment is built up of two almost parallel Cu–O_2–Cu–O_2–Cu–

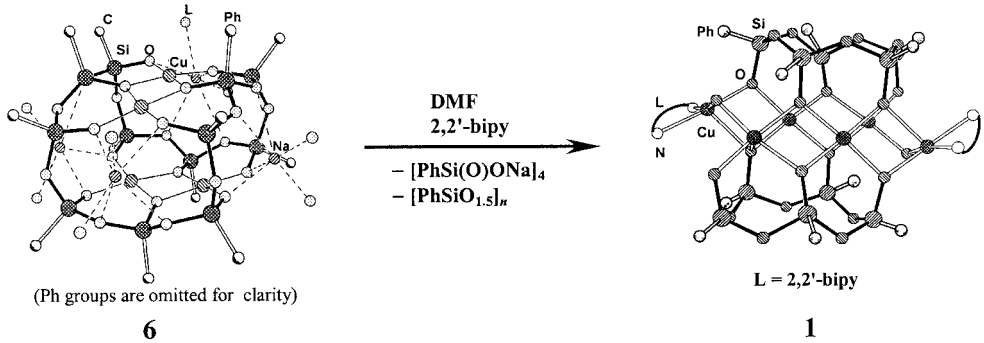

Scheme 1.

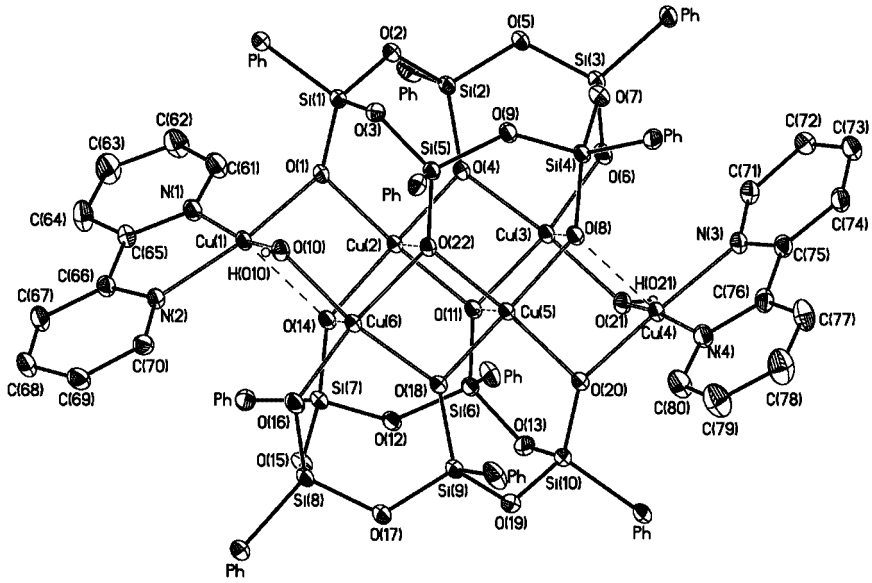

Figure 1. General view of complex **1** (50% probability ellipsoids). Ph groups are omitted for clarity. The dashed lines indicate the apical coordination of copper atoms.

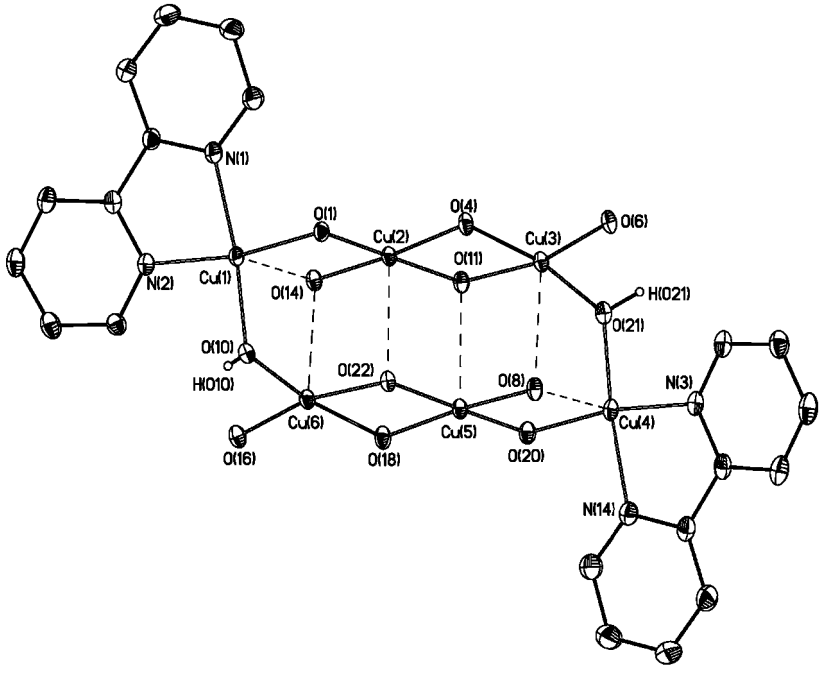

Figure 2. The $Cu_6O_{10}(OH)_2 \cdot bipy_2$ moiety in **1**.

(O,OH) layers. The three copper atoms within the layer form a nearly linear trimer with a Cu–Cu–Cu angle of 173.5(1)° (Figure 2). The nonbonded Cu···Cu distances in the trimer are within the range of 2.9931(6)–3.0310(6) Å, which is significantly longer than corresponding distances described earlier in the sandwich-like copperphenylsiloxanes $\{Cu_6[(PhSiO_2)_6]_2\} \cdot 6(EtOH)$ (**4**),[4c] $\{Cu_6[(PhSiO_2)_6]_2\} \cdot 6(DMF)$ (**5**),[4d] and $\{[Cu_6\{(PhSiO_2)_6\}_2] \cdot [Cu(tmpa)CN]_4\} \cdot (PF_6)_4$ (**2**),[3a] yielding an average value of about 2.82 ± 0.03 Å.

The coordination surrounding of the copper atoms in the layers is different and consists of solely siloxanolate oxygen atoms [for Cu(2), Cu(5)], siloxanolate and hydroxyl oxygen atoms [Cu(3), Cu(6)], or, finally, siloxanolate as well as hydroxyl oxygen atoms and bipyridyl nitrogen atoms [Cu(1), Cu(4)].

Despite the differences in the coordination environment of the copper atoms, all of them exhibit a slightly distorted square-pyramidal (SP) configuration. An analogous configuration of Cu^{II} atoms was found earlier for sandwich-

 © 2005 Wiley-VCH Verlag GmbH & Co. KGaA, Weinheim

like (phenylsiloxane)copper compounds **2**, **4**, and **5**. For globular-type copper-containing organosiloxanolates $\{Na_4[(PhSiO_2)_{12}Cu_4]\}\cdot 8(n\text{BuOH})$ (**6**), $\{K_4[(ViSiO_2)_{12}Cu_4]\}\cdot 6(n\text{BuOH})$ (**7**), and $\{Na_4[(ViSiO_2)_{12}Cu_4]\}\cdot 4(n\text{BuOH})$ (**8**), a square-planar configuration was determined.[4e,4f] It should be noted that in compounds **2**, **4**, or **5** the copper–oxygen moieties are organized in cyclic forms and the SP configuration arises from the apical bonding with solvent (**4**, **5**) or organometallic cluster (**2**) molecules. In contrast, for complex **1** the apical positions are occupied by oxygen atoms of the $Cu_6O_{10}(OH)_2$ segment.

The equatorial Cu–O bonds in **1** vary in the range of 1.907(2)–2.013(2) Å (average value 1.95 Å) (Table 1), which is close to the expected values for copper atoms with an SP coordination environment. In the recently reported sandwich-type complex **2**, it was demonstrated that the Cu–O bond lengths in the basal plane for SP [1.909(5)–2.005(4), av. 1.96 Å] and square-planar coordination [1.876(5)–1.922(5), av. 1.90 Å] are different.[3a] The Cu–N bonds in **1** are 1.999(2)–2.015(2) Å long.

Table 1. Selected bond lengths and angles in the $Cu_6O_{10}(OH)_2$ segment of **1**.

Bond lengths [Å]			
Cu(1)–O(1)	1.973(2)	Cu(4)–O(8)	2.182(2)
Cu(1)–O(10)	1.917(2)	Cu(4)–O(20)	1.980(2)
Cu(1)–O(14)	2.242(2)	Cu(4)–O(21)	1.921(2)
Cu(1)–N(1)	2.014(2)	Cu(4)–N(3)	2.016(2)
Cu(1)–N(2)	2.002(2)	Cu(4)–N(4)	2.010(2)
Cu(2)–O(1)	1.961(2)	Cu(5)–O(8)	1.924(2)
Cu(2)–O(4)	1.928(2)	Cu(5)–O(11)	2.572(2)
Cu(2)–O(11)	1.963(2)	Cu(5)–O(18)	1.924(2)
Cu(2)–O(14)	1.923(2)	Cu(5)–O(20)	1.956(2)
Cu(2)–O(22)	2.532(2)	Cu(5)–O(22)	1.952(2)
Cu(3)–O(4)	2.001(2)	Cu(6)–O(10)	1.925(2)
Cu(3)–O(6)	1.907(2)	Cu(6)–O(14)	2.413(2)
Cu(3)–O(8)	2.593(2)	Cu(6)–O(16)	1.916(2)
Cu(3)–O(11)	1.985(2)	Cu(6)–O(18)	1.987(2)
Cu(3)–O(21)	1.925(2)	Cu(6)–O(22)	2.013(2)
Bond angles [°]			
Cu(2)–O(1)–Cu(1)	100.78(7)	Cu(2)–O(14)–Cu(1)	93.09(6)
Cu(2)–O(4)–Cu(3)	99.30(7)	Cu(2)–O(14)–Cu(6)	92.79(6)
Cu(5)–O(8)–Cu(4)	93.37(6)	Cu(1)–O(14)–Cu(6)	84.09(5)
Cu(5)–O(8)–Cu(3)	89.37(6)	Cu(5)–O(18)–Cu(6)	100.61(7)
Cu(4)–O(8)–Cu(3)	82.64(5)	Cu(5)–O(20)–Cu(4)	98.99(7)
Cu(1)–O(10)–Cu(6)	108.60(9)	Cu(4)–O(21)–Cu(3)	110.92(9)
Cu(2)–O(11)–Cu(3)	98.63(7)	Cu(5)–O(22)–Cu(6)	98.72(7)
Cu(2)–O(11)–Cu(5)	89.42(6)	Cu(5)–O(22)–Cu(2)	90.82(6)
Cu(3)–O(11)–Cu(5)	88.66(6)	Cu(6)–O(22)–Cu(2)	87.21(6)

The apical positions of all copper polyhedra in **1** are occupied by siloxanolate oxygen atoms and the bonds are always significantly longer than the equatorial ones. Regarding the Cu(1) and Cu(4) atoms, the apical positions [O(14) and O(8), respectively] are occupied by siloxanolate oxygen atoms of the same layer with the Cu–O bonds being 2.242(2) and 2.182(2) Å long, while for all other copper atoms the apical oxygen atom belongs to the adjacent layer. The apical Cu–O bonds between layers vary in the range of 2.413(2)–2.593(2) Å, the shortest one being the Cu(6)–O(14) bond.

Interestingly, such an architecture of a copper–oxide moiety with Cu–O interlayer interactions is rather rare. Thus, in the series of globular-like copper-containing organosiloxanes **6**, **7**, and **8**, the corresponding interlayer Cu···O distances are in the range of 3.371(5)–3.899(3) Å, which fully excludes any interlayer bonding.

The Cu–O–Cu angles, which mainly determine the magnetochemical behavior of polynuclear clusters, differ within a Cu–O_2–Cu–O_2–Cu–(O,OH) layer and between the layers significantly. For a single layer, these angles are close to 100°, with the exception of one angle, the Cu(1)–O(14)–Cu(2) angle, for example, for the top layer, which is equal to 93.13(6)° (Table 1). In contrast, the Cu–O–Cu angles formed by copper atoms of different layers are closer to 90°, with the exception of two angles at the hydroxy oxygen atoms O(10) and O(21) [108.59(8)° and 110.94(9)°, respectively]. It is interesting that the range of Cu–O–Cu angles of **1** contains all of the corresponding angles typical for other copper-containing organosiloxanes. Thus, Cu–O–Cu angles for sandwich-like (phenylsiloxane)copper compounds **4** and **5** are close to 100°, while in globular-type **6**, **7**, and **8** they are approximately equal to 90°.

The analysis of the crystal packing in **1** revealed that the stacking of the bipyridyl cycles is the only direct intercomplex interaction. Because of the overlap of the π-systems, neighboring complexes are arranged into stacking-bonded chains parallel to the [011] direction (Figure 3). It should be noted that the interplanar distances (3.43 and 3.22 Å) between the bipyridyl ligands are rather short[8] and a significant π-orbital overlap between adjacent complexes can be expected.

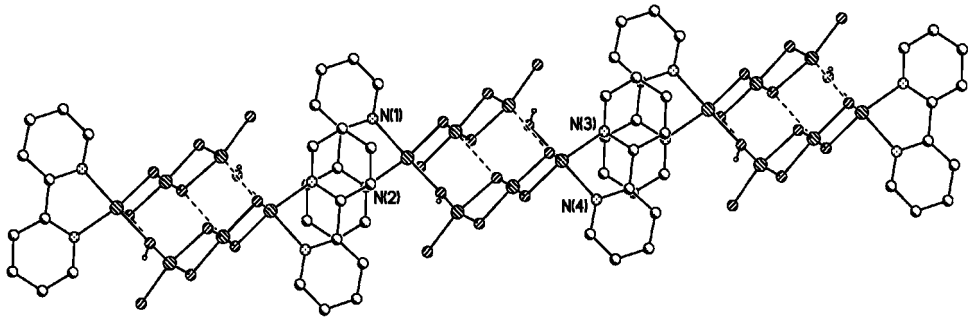

Figure 3. Illustration of the stacking-bonded chains in **1**.

 © 2005 Wiley-VCH Verlag GmbH & Co. KGaA, Weinheim

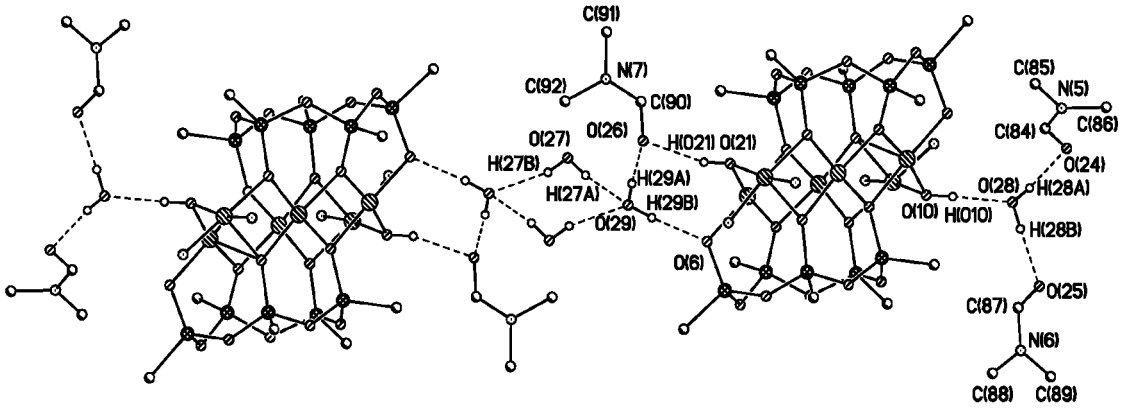

Figure 4. The O–H···O mediated bridging of adjacent complexes in crystals of **1**.

Additionally, the complexes in **1** are connected by intermolecular O–H···O bonds [O···O 2.717(3)–2.894(3) Å] of solvate water molecules (Figure 4). The combination of H-bonding and stacking interactions results in a layered supramolecular arrangement in the crystal.

Magnetic Properties

Magnetic susceptibility and magnetization measurements were performed on polycrystalline samples of $\{Cu_6[(PhSiO_2)_5]_2(OH)_2(C_{10}H_8N_2)_2\}\cdot 4(DMF)\cdot 3(H_2O)$ (**1**). The data were corrected for the contribution of the sample holder and for the diamagnetic core contribution. Notably, the temperature-independent diamagnetic contribution of $\chi_{dia} = -2\times10^{-3}$ cm^3/mol, determined by analyzing the high-temperature magnetic behavior, is in reasonable agreement with the core contribution of $\chi_{core} = -1.7\times10^{-3}$ cm^3/mol calculated by using tabulated values for Pascal's constants.[9]

Figure 5 shows the susceptibility $\chi(T) = M(T)/B$ of complex **1** in a representation $\chi^{-1}(T)$ versus T, where M denotes the magnetic moment of the sample (see also ref.[5]). The data were found to be reversible upon cooling and heating, with no indications of hysteretic behavior. Moreover, no sign of long-range magnetic ordering was observed in the temperature range under investigation.

Figure 5 discloses, to a good approximation, two linear regimes of $\chi^{-1}(T)$ that are separated by a broad crossover range. In an attempt to set up a simple model, capable of describing the main feature of the magnetic susceptibility, these linear sections can be assigned to Curie–Weiss-like temperature dependencies $\chi(T) = C_i\times(T + \theta_i)^{-1}$, with different Curie constants C_i and Weiss temperatures θ_i for the low- (i = LT) and high- (i = HT) -temperature range. At high temperatures of 100–300 K, the best fit reveals C_{HT} = 5.25 cm^3 K/mol and θ_{HT} = 47 K. This Curie constant is consistent with the presence of six Cu^{2+} ions per molecule (two molecules per unit cell) yielding a spin-only value of C_{HT} = 4.96 cm^3 K/mol. The latter number is based on an average spectroscopic g value of 2.09 ± 0.05, as determined by our ESR measurements operated at X- and Q-band frequencies. The positive Weiss constant indicates a dominant antiferromagnetic spin–spin interaction in the high-temperature regime.

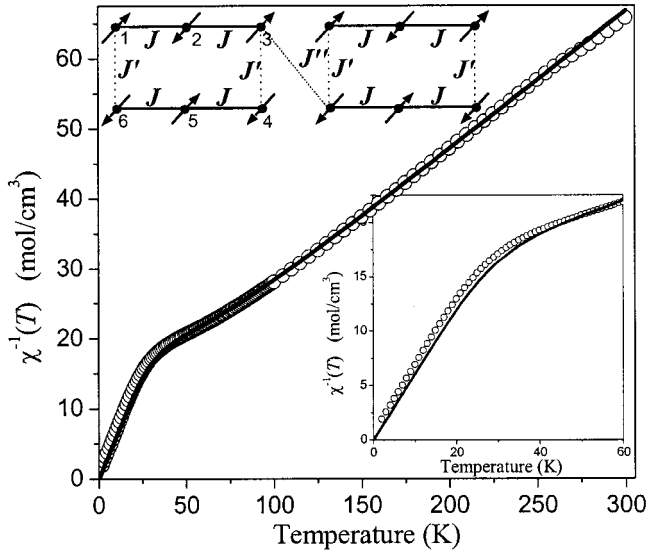

Figure 5. Temperature dependence of the inverse magnetic susceptibility of complex **1** for temperatures 2–300 K. The data have been taken at a magnetic field of 0.05 T. The solid line corresponds to the best fit for the model of isolated, linear S = 1/2 trimers with an antiferromagnetic intratrimer exchange coupling constant J/k_B = 85 K, i.e. $J' = J'' = 0$ in the scheme for the exchange coupling interactions of two adjacent molecules indicated in the upper left of the figure. The inset shows the low-temperature part on expanded scales.

From the linear behavior of $\chi^{-1}(T)$ versus T at low temperatures, that is, in the range 2–15 K, a Curie constant of C_{LT} = 1.61 cm^3 K/mol and an antiferromagnetic Weiss temperature as small as θ_{LT} = 1.05 K were found. A reduction of the Curie constant by a factor close to 3 indicates that the low-temperature magnetic system behaves essentially like an effective "2-spin" S = 1/2 configuration per molecule. In fact, in this case, a Curie constant of 1.65 cm^3 K/mol (for g = 2.09) is expected, which is very close to the C_{LT} value derived from the experiment.

Thus, the magnetic susceptibility of the present hexanuclear complex **1** is reminiscent of that observed in a variety

 © 2005 Wiley-VCH Verlag GmbH & Co. KGaA, Weinheim

of systems containing largely isolated trimers.[10,11] This suggests that the dominant magnetic coupling is provided by an *intra*trimer Cu–Cu exchange interaction J within the 3-site Cu strings (cf. the coupling scheme given in the inset of Figure 5).

In a first approach, which has been discussed also in ref.[5], we therefore consider isolated trimers with a uniform isotropic Heisenberg *intra*trimer exchange coupling constant J and an isotropic g factor described by the spin Hamiltonian given in Equation (1).

$$\hat{H}_3 = J(\hat{\boldsymbol{S}}_1\cdot\hat{\boldsymbol{S}}_2 + \hat{\boldsymbol{S}}_2\cdot\hat{\boldsymbol{S}}_3) - g\mu_B\boldsymbol{B}\cdot(\hat{\boldsymbol{S}}_1 + \hat{\boldsymbol{S}}_2 + \hat{\boldsymbol{S}}_3) \quad (1)$$

The energy spectrum of Equation (1) consists of a doublet ground state separated from an excited doublet and quartet by an energy gap $\Delta = J$ and $3J/2$, respectively (see Figure 6). In Figure 6 the spin states of the isolated trimer are labeled according to the eigenvalues of the square of the total spin operator $\hat{\boldsymbol{S}}_{123} = \hat{\boldsymbol{S}}_1 + \hat{\boldsymbol{S}}_2 + \hat{\boldsymbol{S}}_3$, $\hat{\boldsymbol{S}}_{456} = \hat{\boldsymbol{S}}_4 + \hat{\boldsymbol{S}}_5 + \hat{\boldsymbol{S}}_6$ (the coupling scheme of Figure 5) and an intermediate coupling quantum number, S_{13} and S_{46}, defined through the relations $\hat{\boldsymbol{S}}_{13} = \hat{\boldsymbol{S}}_1 + \hat{\boldsymbol{S}}_3$ and $\hat{\boldsymbol{S}}_{46} = \hat{\boldsymbol{S}}_4 + \hat{\boldsymbol{S}}_6$, respectively.

From the partition function the magnetic susceptibility can be derived in a straightforward way yielding Equation (2), where $x = \exp(-J/2k_BT)$.

$$\chi(T) = \frac{N\mu_B^2g^2}{k_B}\cdot\frac{1}{4T}\cdot\frac{1 + x^2 + 10x^3}{1 + x^2 + 2x^3} \quad (2)$$

The result for the magnetization of the isolated linear trimer can be written as Equation (3), where $h = g(\mu_B/k_B)B$.

$$M(T,h) = N\mu_Bg\cdot\frac{1}{2}\cdot\frac{(1 + x^2 + x^3)s_1 + 3x^3s_3}{(1 + x^2 + x^3)c_1 + x^3c_3} \quad (3)$$

We have used the following shorthand notations: $c_1 = \cosh(h/2T)$, $c_3 = \cosh(3h/2T)$, $s_1 = \sinh(h/2T)$, and $s_3 = \sinh(3h/2T)$. In the limit $J\rightarrow\infty$ or $T << J/k_B$, that is, $x\rightarrow 0$, the trimer is locked into a spin-1/2 state and $M(T,h)$ reduces to the spin-1/2 Brillouin function $B_{1/2}(T,h) = (1/2)\tanh(h/2T)$. On the contrary, for vanishing exchange coupling J or $T >> J/k_B$, that is, for $x\rightarrow 1$, the spins of the trimer are independent and $M(T,h)$ can easily be shown to be equivalent to $3B_{1/2}(T,h)$.

Fitting Equation (2) to the susceptibility data in Figure 5 for temperatures between 300 and 25 K, we find a good overall agreement (solid line in Figure 5) for an antiferromagnetic *intra*trimer exchange coupling constant of $J/k_B = 85\pm1$ K (see also ref.[5]). Figure 5 demonstrates that the simple trimer model according to Equation (1) covers the main features of the susceptibility, in particular the increase of the slope of $\chi^{-1}(T)$ by a factor of 3, that is, a reduction of the Curie constant by 2/3, upon cooling. However, a closer look at the low-temperature behavior in Figure 5 (cf. inset) discloses deviations of the model curve from the data, indicating the presence of additional, weaker interactions such as the intertrimer (J') and/or intermolecular couplings (J'') indicated in Figure 5.

A finite trimer–trimer interaction can, indeed, be expected because of the presence of the hydroxy oxygen atoms O(10) and O(21), which may provide an exchange path between the terminal Cu^{II} atoms of adjacent trimers (see Figure 2). Likewise, weak trimer–trimer interactions can arise through the apical oxygen atoms O(14), O(22), O(11), and O(8). Because the latter exchange paths involve rather long Cu–O bonds ranging from 2.413 to 2.593 Å, we expect their coupling strength to be much weaker than those of the above Cu(1)–O(10)–Cu(6) and Cu(3)–O(21)–Cu(4) bonds (cf. Table 1). In a second step we thus model the trimer–trimer interactions by introducing the coupling constant J' that links the ends of the linear trimers within the molecule (cf. the coupling scheme indicated in the upper left of Figure 5).

The resulting Hamiltonian of such an isolated 6-spin $S = 1/2$ assembly, that is, two coupled trimers, then reads as Equation (4).

$$\hat{H}_6 = J(\hat{\boldsymbol{S}}_1\cdot\hat{\boldsymbol{S}}_2 + \hat{\boldsymbol{S}}_2\cdot\hat{\boldsymbol{S}}_3 + \hat{\boldsymbol{S}}_4\cdot\hat{\boldsymbol{S}}_5 + \hat{\boldsymbol{S}}_5\cdot\hat{\boldsymbol{S}}_6) + J'(\hat{\boldsymbol{S}}_1\cdot\hat{\boldsymbol{S}}_6 + \hat{\boldsymbol{S}}_3\cdot\hat{\boldsymbol{S}}_4) - g\mu_B\boldsymbol{B}\cdot(\hat{\boldsymbol{S}}_1 + \hat{\boldsymbol{S}}_2 + \hat{\boldsymbol{S}}_3 + \hat{\boldsymbol{S}}_4 + \hat{\boldsymbol{S}}_5 + \hat{\boldsymbol{S}}_6) \quad (4)$$

As a consequence of the finite trimer–trimer coupling, the degeneracy of the $S = 1/2$ ground state doublets for the isolated trimers within the molecule is lifted and a singlet ($S = 0$) ground state (for an antiferromagnetic coupling $J' > 0$) is formed, which is separated from the first excited triplet ($S = 1$; $M = 1, 0, -1$) state by a zero-field gap of $(8/9)|J'|$, up to higher order corrections in J'/J (see Figure 6). In case of a ferromagnetic coupling $J' < 0$, the order of the low-lying singlet and triplet states is reversed.

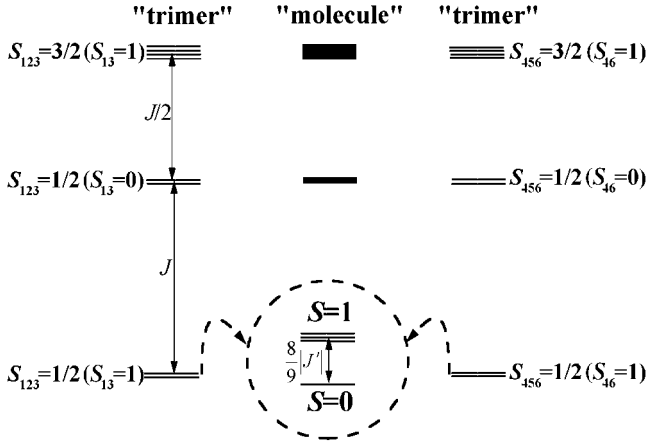

Figure 6. Ground-state splitting of two trimers within the molecule because of antiferromagnetic intertrimer coupling. The spin states of the isolated trimers are labeled as $S(S^*)$. S is the total spin and $S^* = S_1 + S_3$ or $S_4 + S_6$, respectively.

For the magnetic susceptibility, a perturbative approach for $|J'| << |J|$ yields Equation (5), where $x = \exp(-J/2k_BT)$ and $y = \exp(-2J'/9k_BT)$.

$$\chi(T) = \frac{N\mu_B^2g^2}{k_B}\cdot\frac{1}{2T}\cdot\frac{(1 + x^2 + 2x^3)(1 + x^2 + 10x^3) + y - 1}{(1 + x^2 + 2x^3)^2 + (y^{-3} + 3y)/4 - 1} \quad (5)$$

The magnetization is given by Equation (6), where the same shorthands as in Equation (3) are used.

 © 2005 Wiley-VCH Verlag GmbH & Co. KGaA, Weinheim

$$M(T,h) = N\mu_B g \cdot \frac{[(1 + x^2 + x^3)c_1 + x^3c_3][(1 + x^2 + x^3)s_1 + 3x^3s_3] + (y - 1)c_1s_1}{[(1 + x^2 + x^3)c_1 + x^3c_3]^2 + c_1^2(y - 1) + (y^{-3} - y)/4} \quad (6)$$

Equations (5) and (6) can be checked by comparison with numerical diagonalization for the full model. At least up to $|J'/J| \leq 0.1$, we obtain excellent agreement with the exact result. For $J' = 0$, Equations (5) and (6) result in twice the susceptibility and the magnetization of an isolated trimer given in Equations (2) and (3), respectively, as expected. Note that the influence of J' on susceptibility is rather small and deviations from the pure trimer model become visible only at low temperatures. To visualize the effect of a weak intertrimer coupling on the susceptibility more clearly, the data together with the model curves for the isolated and coupled trimers are plotted in Figure 7 in a representation χT versus T.

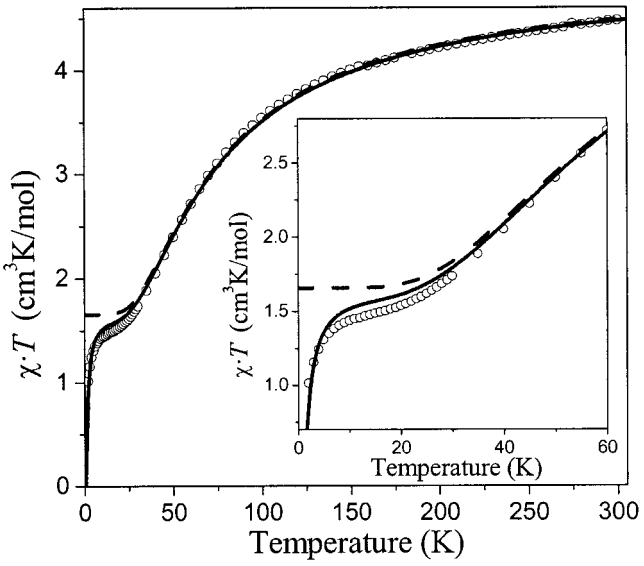

Figure 7. Magnetic susceptibility data of complex **1** taken at a field of 0.05 T plotted as χT versus T. The inset shows the low-temperature behavior on expanded scales. The dashed lines correspond to the best fit for the isolated linear trimer model with $J/k_B = 85$ K; the solid lines are the result of the model for antiferromagnetically coupled trimers with $J/k_B = 85$ K and $J'/k_B = 3.5$ K.

Figure 7 shows the best fit for weakly coupled trimers with an *intra*trimer coupling $J/k_B = 85$ K and a weak antiferromagnetic *inter*trimer coupling $J'/k_B = 3.5$ K, while the dashed line indicates the results for the isolated trimer model with $J/k_B = 85$ K. Figure 7 clearly demonstrates that the incorporation of a finite intertrimer coupling J' improves the fit considerably at low temperatures, although small deviations of the model curve from the data are still visible below 30 K. This is most likely due to the presence of additional, weaker interaction pathways between the copper atoms of adjacent trimers such as the coupling through the apical oxygen atoms mentioned above. As has been discussed by Zaspel et al.,[12] who carried out a high-temperature series expansion for the Heisenberg model with the intertrimer coupling constants as expansion parameters, the low-temperature behavior of such a generalized coupled-trimer model depends on the sign combinations and magnitudes of the intertrimer coupling constants. As the above coupled-trimer model covers the main properties of the susceptibility of complex **1** in the temperature range under investigation, we refrain from introducing additional coupling constants at the present stage. This also includes the introduction of a finite intermolecular coupling J'', which does not significantly improve the quality of the fit. Thus, we conclude that the temperature dependence of the magnetic susceptibility of complex **1** can be satisfactorily described by coupled trimers with an average antiferromagnetic trimer–trimer interaction $J'/k_B = 3.5$ K.[13]

Further support for this assignment can be gained from the results of isothermal magnetization measurements (see Figure 8). The figure also shows the calculated magnetization curves for the above-discussed models of isolated [dashed lines, Equation (3)] and antiferromagnetically coupled [solid lines, Equation (6)] trimers. Figure 8 clearly demonstrates that, for temperatures below 20 K, the isolated-trimer model progressively departs from the experimental data. On the other hand, a very good description of the magnetization curves, except the data taken at the lowest temperature of 2 K, is achieved by the model of antiferromagnetically coupled trimers, with the best fit obtained for the parameters $J/k_B = 85$ K and $J'/k_B = 3.4 \pm 0.5$ K. This model also explains the high-field data taken at $T = 4.2$ K, showing a saturation of the magnetization at a value close to $2\mu_B$ per molecule, as expected for two weakly coupled $S = 1/2$ (trimer) states. However, deviations of the above model from the experimental data become visible at the lowest temperature of 2 K for fields $B \geq 2$ T. This indicates the presence of additional weak *intra*- and/or *inter*molecular interactions giving rise to a more complicated low-energy spectrum of this cluster compound. We note that for

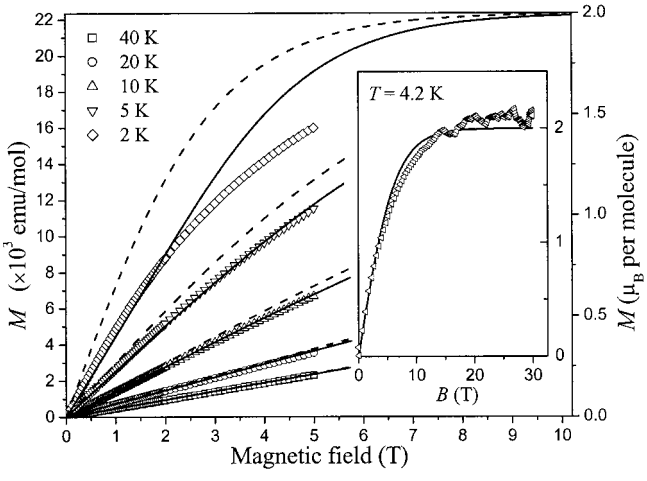

Figure 8. Isothermal magnetization measurements in dc fields from 0 to 5 T (main panel) and pulsed fields from 0 to 30 T (inset) at varying temperatures as indicated in the figure. The right scales of the main panel and inset are given in units of μ_B per molecule. The dashed and solid lines correspond to the model curves for isolated and antiferromagnetically coupled trimers, respectively, with the coupling parameters given in the text.

 © 2005 Wiley-VCH Verlag GmbH & Co. KGaA, Weinheim

a ferromagnetic coupling $J' < 0$, as suggested in ref.[5], the initial slope of the corresponding magnetization curves even exceeds that for the isolated trimers (broken lines), which would make the fit worse.

Conclusions

This paper reports on the synthesis, X-ray crystal structure, and magnetic properties of a new hexanuclear copper(II) siloxanolate cluster compound **1**, $\{Cu_6[(C_6H_5SiO_2)_5]_2(OH)_2(C_{10}H_8N_2)_2\}\cdot 4(DMF)\cdot 3(H_2O)$. This molecular complex differs from the known hexacopper(II) cluster compounds in its unique $S = 1/2$ trimer arrangement: each molecule contains two linear oxygen-bridged three-site Cu^{II} strings that are parallel to each other.

According to magnetic measurements, an antiferromagnetic *intra*trimer coupling constant marks the dominant magnetic coupling in this complex. Indeed, an $S = 1/2$ Heisenberg trimer model with an isotropic antiferromagnetic exchange coupling $J/k_B = 85$ K covers the main features of the magnetic susceptibility, namely the formation of an effective $S = 1/2$ low-temperature trimer state. This model, however, fails to describe adequately the magnetic behavior at low temperatures. The model can be improved significantly by introducing a weak antiferromagnetic *inter*trimer interaction $J'/k_B = 3.5$ K, giving rise to a singlet ($S = 0$) ground state and a nearby [with energy gap $\Delta = (8/9)|J'|$] excited triplet ($S = 1$) state for the molecules. The small deviations of the model curves from the experimental data at low temperatures indicate the action of additional, weaker magnetic interaction pathways such as additional couplings between the copper atoms of adjacent trimers within a single molecule or a finite *inter*molecular coupling. The latter might originate in the overlap of π-orbitals from the bipyridine groups of adjacent molecules.

Experimental Section

Synthesis of the Hexanuclear Copper Complex $\{Cu_6[(PhSiO_2)_5]_2(OH)_2(C_{10}H_8N_2)_2\}\cdot 4(DMF)\cdot 3(H_2O)$ (1): A solution of complex **6** (0.5 g, 0.25 mmol), which was prepared as described in ref.[4f], was made up of DMF (25 mL) and 2,2′-bipyridine (0.156 g, 1 mmol) in DMF (25 mL). Within two months, blue crystals precipitated. They were isolated and dried under vacuum (1 Torr, 50 °C). Yield: 0.33 g (91.7%). Anal.: Calcd. for $\{Cu_6[(PhSiO_2)_5]_2(OH)_2(C_{10}H_8N_2)_2\}\cdot(DMF)$, $[C_{83}H_{75}Si_{10}Cu_6N_5O_{23}]$, %: C 45.88, H 3.49, Si 12.93, Cu 17.55, N 3.22; found, %: C 46.14, H 4.28, Si 12.38, Cu 17.34, N 2.39. Notably, metallasiloxane compounds always contained some amount of solvate molecules. During the separation of the crystals from the mother liquor and during the drying process in vacuo, some of the solvate molecules evaporated. Consequently, the molecular formula determined by X-ray analysis of a single crystal differed from the molecular formula obtained by an elemental analysis including solvate ligands. The composition of the hexanuclear complex **1** was determined by single-crystal X-ray analysis as $\{Cu_6[(PhSiO_2)_5]_2(OH)_2(C_{10}H_8N_2)_2\}\cdot 4(DMF)\cdot 3(H_2O)$ and by elemental analysis as $\{Cu_6[(PhSiO_2)_5]_2(OH)_2(C_{10}H_8N_2)_2\}\cdot(DMF)$. Magnetic measurements were performed with crystals directly isolated from the mother liquor and thus corresponding to the formula determined by X-ray analysis.

X-ray Crystallography: The crystallographic data for complex **1**, $\{Cu_6[(PhSiO_2)_5]_2(OH)_2(C_{10}H_8N_2)_2\}\cdot 4(DMF)\cdot 3(H_2O)$, are listed in Table 2. The X-ray diffraction measurements were performed employing a Smart CCD diffractometer (Mo-K_α radiation, graphite-monochromator, ω-scan technique). A numerical absorption correction was carried out based on six indexed crystal faces. The transmission factor ranges from 0.609 to 0.784. The structure was solved by direct methods and refined by full-matrix least squares against F^2 in the anisotropic (H-atoms isotropic) approximation, using the SHELXTL-97 package.[14] The H positions of the Ph groups were calculated from a geometrical point of view, while the methyl and hydroxyl groups and the hydrogen atoms of water molecules were located in the Fourier electron-density synthesis. CCDC-269903 contains the supplementary crystallographic data for this paper. These data can be obtained free of charge from The Cambridge Crystallographic Data Centre via www.ccdc.cam.ac.uk/data_request/cif.

Table 2. Crystallographic data for **1**.

	1
Empirical formula	$C_{92}H_{102}Cu_6N_8O_{29}Si_{10}$
Crystal dimensions [mm]	$0.23 \times 0.26 \times 0.32$
M	2445.96
T [K]	146(2)
Crystal system, space group	triclinic, $P\bar{1}$
a [Å]	14.925(3)
b [Å]	16.745(2)
c [Å]	23.053(3)
α [°]	83.079(9)
β [°]	84.836(13)
γ [°]	65.019(17)
V [Å^3], Z	5179.6(14), 2
μ [cm^{-1}]	14.06
$F(000)$	2512
$\rho_{calcd.}$ [g/cm^{-3}]	1.568
$2\theta_{max}$ [°]	60
No. of reflections measured (R_{int})	101967 (0.0466)
No. of independent reflections	29492
No. of reflections with $I > 2\sigma(I)$	20220
No. of parameters	1330
R_1	0.0390
wR_2	0.0901
GOF	1.061
Max./min. peak [e/Å^{-3}]	0.545/–0.563

Magnetic Susceptibility and Magnetization Measurements: Variable-temperature magnetic susceptibility measurements in the temperature range 2–300 K and magnetic fields up to 5 T were carried out using a Quantum Design SQUID magnetometer MPMS-XL. These measurements were complemented by isothermal magnetization runs at temperatures between 2 and 40 K for fields up to 5 T. In addition, pulsed-field magnetization measurements up to 35 T were performed at the NHMFL, Los Alamos, using a wire-wound extraction magnetometer.

Supporting Information (see also footnote on the first page of this article): Figures of the crystal packing (Figures S1–S4) and ESR spectrum of polycrystalline sample (Figure S5) for complex **1**.

Acknowledgments

The work was supported by the DFG (Forschergruppenprogramm "Spin- und Ladungskorrelationen in niedrigdimensionalen metall-

organischen Festkörpern", FOR412). We thank J. Bats (Institut für Anorganische Chemie, J. W. Goethe-Universität Frankfurt) for collection of the X-ray data.

[1] R. E. P. Winpenny, *J. Chem. Soc., Dalton Trans.* **2002**, 1.
[2] a) T. Mallah, C. Auberger, M. Verdaguer, P. Veillet, *J. Chem. Soc., Chem. Commun.* **1995**, 61; b) A. Scuiller, T. Mallah, M. Verdaguer, A. Nivorozkhin, J.-L. Tholence, P. Veillet, *New J. Chem.* **1996**, *20*, 1; c) G. Rogez, A. Marvilliers, E. Rivière, J.-P. Audière, F. Lloret, F. Varret, A. Goujon, N. Mendenez, J.-J. Girerd, T. Mallah, *Angew. Chem.* **2000**, *112*, 3007–3009; *Angew. Chem. Int. Ed.* **2000**, *39*, 2885.
[3] a) G. L. Abbati, A. Caneschi, A. Cornia, A. C. Fabretti, Yu. A. Pozdniakova, O. I. Shchegolikhina, *Angew. Chem. Int. Ed.* **2002**, *41*, 4517–4520; b) G. L. Abbati, A.-L. Barra, A. Caneschi, A. Cornia, A. Fabretti, D. Gatteschi, Yu. A. Pozdniakova, O. I. Shchegolikhina, *C. R. Chim.* **2003**, *6*, 645–656.
[4] a) V. A. Igonin, S. V. Lindeman, Yu. T. Struchkov, Yu. A. Molodtsova, O. I. Shchegolikhina, A. A. Zhdanov, *Izv. Akad. Nauk, Ser. Khim.* **1993**, *4*, 752; [English translation: *Russ. Chem. Bull.* **1993**, *42*, 718]; b) O. Shchegolikhina, Yu. Pozdniakova, Yu. Molodtsova, I. Blagodatskhih, D. Katsoulis, *Abstracts of XII International Symposium on Organosilicon Chemistry*, **1999**, May 23–27, Sendai, Japan, P180, p. 234; c) E. Rentschler, D. Gatteschi, A. Cornia, A. C. Fabretti, A.-L. Barra, O. I. Shchegolikhina, A. A. Zhdanov, *Inorg. Chem.* **1996**, *35*, 4427–4431; d) S. V. Lindeman, O. I. Shchegolikhina, Yu. A. Molodtsova, A. A. Zhdanov, *Acta Crystallogr., Sect. C* **1997**, *53*, 305–309; e) V. A. Igonin, S. V. Lindeman, Yu. T. Struchkov, O. I. Shchegolikhina, A. A. Zhdanov, Yu. A. Molodtsova, I. V. Razumovskaya, *Organomet. Chem. USSR* **1991**, *4*, 672; f) Yu. A. Molodtsova, Yu. A. Pozdniakova, K. A. Lyssenko, I. V. Blagodatskikh, D. E. Katsoulis, O. I. Shchegolikhina, *J. Organomet. Chem.* **1998**, *571*, 31; g) C. Zucchi, M. Mattioli, G. Gavioli, M. Moret, A. Sironi, R. Ugo, M. Pizzotti, O. I. Shchegolikhina, G. Pályi, *Eur. J. Inorg. Chem.* **2000**, 1327–1331.
[5] V. A. Pashchenko, B. Brendel, B. Wolf, M. Lang, M. Kollar, F. Schütz, P. Kopietz, Y. Molodtsova, O. Shchegolikhina, N. Auner, *J. Magn. Magn. Mater.* **2004**, *272–276*, e755.
[6] Yu. Molodtsova, L. Zherlitsyna, J. Bats, M. Bolte, V. Pashchenko, N. Auner, O. Shchegolikhina, manuscript in preparation.
[7] Yu. T. Struchkov, S. V. Lindeman, *J. Organomet. Chem.* **1995**, *488*, 9.
[8] E. A. Meyer, R. K. Castellano, F. Diederich, *Angew. Chem. Int. Ed.* **2003**, *42*, 1210.
[9] a) E. König, "Magnetic Properties of Coordination and Organo-Metallic Transition Metal Compounds", in *Landolt-Börnstein, Neue Serie*, Springer, Berlin, **1966**, vol. II/2, pp. 1–16; b) R. Boča, *Theoretical Foundations of Molecular Magnetism*, vol. 1 ("Current Methods in Inorganic Chemistry"), Elsevier, Amsterdam, **1999**, appendix 4.
[10] K.-F. Hsu, S.-L. Wang, *Inorg. Chem.* **2000**, *39*, 1773–1778.
[11] a) P. King, R. Clérac, C. E. Anson, C. Coulon, A. K. Powell, *Inorg. Chem.* **2003**, *42*, 3492–3500; b) J. L. Manson, J. Gu, J. A. Schlueter, H. H. Wang, *Inorg. Chem.* **2003**, *42*, 3950–3955.
[12] a) C. E. Zaspel, G. V. Rubenacker, S. L. Hutton, J. E. Drumheller, R. S. Rubins, R. D. Willet, M. R. Bond, *J. Appl. Phys.* **1988**, *63*, 3028; b) M. R. Bond, R. D. Willet, R. S. Rubins, P. Zhou, C. E. Zaspel, S. L. Hutton, J. E. Drumheller, *Phys. Rev. B* **1990**, *42*, 10280.
[13] In ref.[5], a weak ferromagnetic trimer–trimer coupling $J'/k_B = -7$ K has been claimed from the temperature evolution of the absorption signal in a preliminary ESR study. For such a ferromagnetic coupling $J' < 0$, the order of the low-lying singlet–triplet states in the energy spectrum in Figure 6 is just reversed, resulting in an $S = 1$ ground state. In the presence of additional weak anisotropies in the exchange couplings, which can be expected for the present system, the selection rule is no longer valid, enabling transitions between the singlet and triplet states to be observed by ESR measurements. As a result, the ESR studies are not very sensitive to the difference between a ferromagnetic and an antiferromagnetic coupling, unless the data are available for covering the low-temperature range of the order of $(1/2)J'/k_B$.
[14] G. M. Sheldrick, *SHELXS-97 and SHELXL-97, Programs for the determination and refinement of crystal structures*, University of Göttingen, Germany, **1997**.

Received: June 19, 2005
Published Online: September 27, 2005

 © 2005 Wiley-VCH Verlag GmbH & Co. KGaA, Weinheim

A Convenient Synthetic Route for the Preparation of Nonsymmetric Metallo-salphen Complexes

Arjan W. Kleij,*[a] Duncan M. Tooke,[b] Anthony L. Spek,[b] and Joost N. H. Reek*[a]

Keywords: N,O ligands / Nonsymmetric / Salen / Templated synthesis / Zinc

New nonsymmetric metallo(II)-salphen complexes **1**–**6** [salphen = *N*,*N*′-bis(salicylidene)-1,2-diaminobenzene, M = Zn, Ni] have been prepared in high yield by a templated, one-pot two-step procedure starting from substituted *ortho*-phenylenediamines, salicylaldehydes and metal acetates in MeOH under mild conditions. The procedure allows the introduction of functional groups in the bridging phenyl fragment, whereas the use of the substituted monoimine intermediates **7**–**10** results in complexes with two structurally different phenyl side groups with various functionalities (complexes **11**–**21**) upon reaction with a second, different, salicylaldehyde reagent. A range of analytical tools confirmed the structures of these nonsymmetric salphen derivatives and the X-ray molecular structure of one of these nonsymmetric Zn^{II}-salphen complexes (i.e., **4**) is also reported.

(© Wiley-VCH Verlag GmbH & Co. KGaA, 69451 Weinheim, Germany, 2005)

Introduction

Salen ligands[1] are interesting tetradentate ligands with a rich coordination chemistry. Since the discovery of the effective use of salen-type ligands in the epoxidation of olefins,[2] asymmetric homogeneous catalysis with these systems has been subject of widespread investigations.[3] In order to achieve a constructive transformation of chiral information to a substrate molecule, an effective use of the steric and electronic information of the applied ligand is needed. However, such a desired variation of an asymmetrical ligand is often troublesome and synthetic methods in most cases give rise to a limited number of ligands. Our interest in the salen ligand was recently aroused as the salphen structure [salphen = *N*,*N*′-(phenylene)salicylidene] proved to be a highly useful building block for the construction of supramolecular architectures such as molecular boxes.[4] In these Zn^{II}-salphen complexes the metal ion is located in a nearly planar, rigid N_2O_2 coordination geometry with a vacant axial coordination site. We, and others, have used these planar structures in supramolecular synthesis, where the axial coordination site provides a binding site for suitable N donor systems that allows the construction of multicomponent tailored materials.[5] Beside their use in supramolecular technology, Zn^{II}-salen complexes have also recently gained renewed interest as a result of their scope in a number of catalytic conversions.[6] The blend of these two complementing aspects could launch new opportunities for the construction of catalytically active, functional assemblies.[7] Here, we disclose new, attractive templated methods for nonsymmetrical M^{II}-salphen building blocks, that circumvent the isolation of the salphen ligand prior to metalation.[8] The variation of the steric and electronic features using these flexible procedures will be demonstrated by the introduction of different (functional) groups that ultimately can be used to fine-tune the (donor) properties of the nonsymmetric ligand backbone.

Results and Discussion

The synthetic approach towards nonsymmetric Zn^{II}-salphen complexes **1**–**6** is outlined in Scheme 1. Commercially available, mono-substituted *ortho*-phenylene diamines or diamino-pyridines were used as starting materials.[4] Generally, the aldehyde and phenylene diamine precursors combined with a metal precursor $M(OAc)_2 \cdot nH_2O$ (M = Zn: $n = 2$; M = Ni: $n = 4$) were mixed in the appropriate stoichiometry to afford in a one-pot two step protocol complexes **1**–**6**. In most cases, the product could be simply isolated by one filtration step and isolation of the ligands prior to metalation is thus not necessary. This procedure therefore allows the introduction of functional groups in the phenyl bridge of the salphen structure and also different metal ions can be incorporated concomitantly (cf. complex **6**).

The molecular structure for Zn^{II}-salphen complex **4** was determined by X-ray crystallography (Figure 1). Interestingly, complex **4** is, unlike **1**–**3**, only moderately soluble in

[a] Van 't Hoff Institute for Molecular Sciences, University of Amsterdam,
Nieuwe Achtergracht 166, 1018 WV, Amsterdam, The Netherlands
Fax: +31-20-5256422
E-mail: reek@science.uva.nl
kleij@science.uva.nl
[b] Crystal and Structural Chemistry, Bijvoet Center for Biomolecular Research, Utrecht University,
Padualaan 8, 3584 CH, Utrecht, The Netherlands
Fax: +31-30-2533940

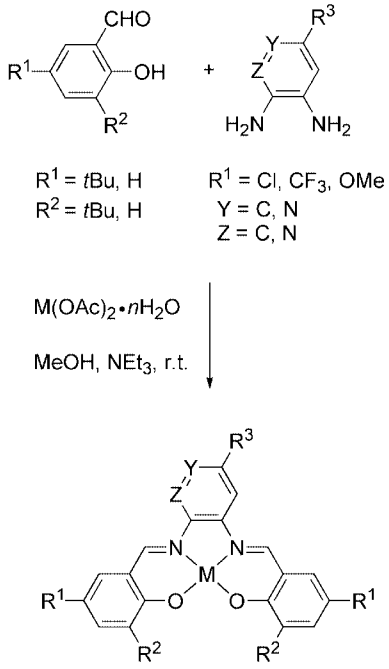

1 $R^1 = R^2 = t$Bu; R^3 = Cl; Y = Z = C; M = Zn
2 $R^1 = R^2 = t$Bu; $R^3 = CF_3$; Y = Z = C; M = Zn
3 $R^1 = R^2 = t$Bu; R^3 = OMe; Y = Z = C; M = Zn
4 $R^1 = R^2 = t$Bu; R^3 = H; Y = C; Z = N; M = Zn
5 $R^1 = R^2$ = H; R^3 = H; Y = N; Z = C; M = Zn
6 $R^1 = R^2$ = H; $R^3 = CF_3$; Y = Z = C; M = Ni

Scheme 1. Synthesis of nonsymmetric M^{II}-salphen complexes **1**–**6** starting from nonsymmetric *ortho*-phenylenediamine precursors.

toluene and CH_2Cl_2 and re-crystallization was achieved from hot toluene. X-ray quality crystals were, however, only obtained from a mixture of hot acetone/pyridine.[9] As expected from our previous studies using the Zn^{II}-salphen structure as a supramolecular building block through axial pyridine ligation,[4,5] complex **4** was analysed as its pyridine adduct under these conditions. Obviously, the presence of an internal pyridine donor in both **4** and **5** could provoke intermolecular association through supramolecular Zn–N_{pyr} interactions, which could account for their low solubility in the common organic solvents. In the presence of an excess of an external pyridine donor the intermolecular association is broken and monomeric **4**·pyridine was obtained exclusively this way. The LC-MS analysis for **5** also revealed the presence of an intensive peak for the dimeric species $[2M^+ + H]$, whereas for other Zn^{II}-salphen species in this work with small 3- and/or 3′-substituents present in the salphen backbone these species were not observed or with very low intensity. These dimeric species observed under the mass spectrometric conditions are generally associated to a dimerization process involving the O atoms of the individual monomers.[10] Obviously, this dimerization process is not only dependent on the size of the salphen substituents, but will also be influenced by the presence of nitrogen donor atoms such as in pyridines (vide supra, Figure 1) and the presence of donor solvents such as acetonitrile (cf. LC-MS studies, Exp. Sect.). The lower solubility features found for **4** and **5** are thus accountable for the presence of larger, associated species. It should be noted that their respective NMR spectra were recorded in the presence of solvent(s) combinations able to compete with this association behav-

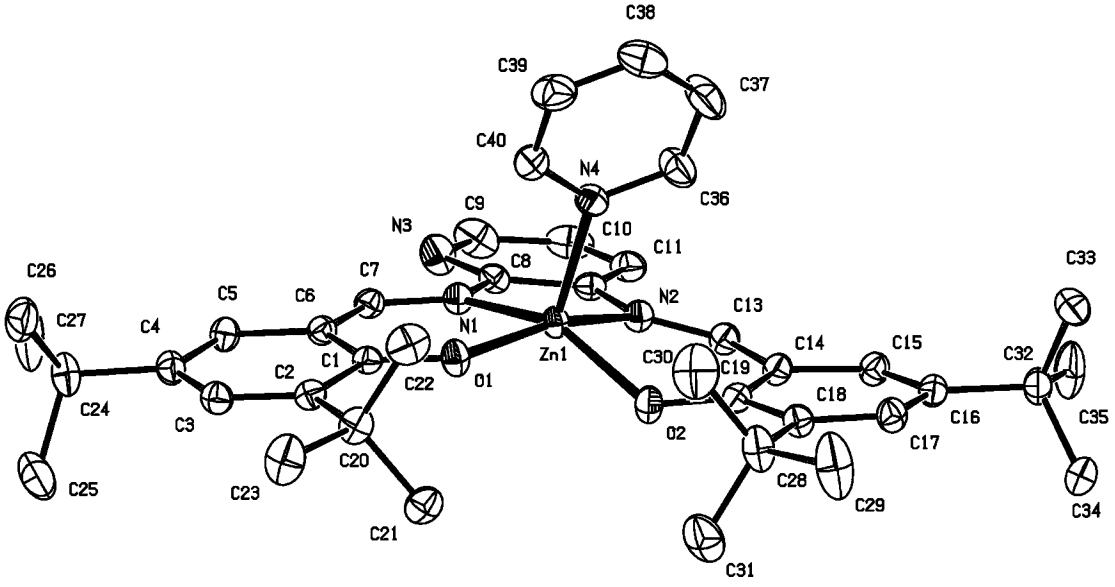

Figure 1. Displacement ellipsoid plot at the 50% probability level of the molecular structure for **4** in the crystal. H atoms have been omitted for clarity. Selected bond lengths [Å] and angles [°] with esd's in parentheses: Zn(1)–N(1) = 2.0620(11), Zn(1)–N(2) = 2.1168(11), Zn(1)–O(1) = 1.9755(9), Zn(1)–O(2) = 1.9617(10), Zn(1)–N(4) = 2.1164(12), O(1)–Zn(1)–N(2) = 160.49(4), O(2)–Zn(1)–N(2) = 87.00(4), O(1)–Zn(1)–N(1) = 88.72(4), O(2)–Zn(1)–N(1) = 148.27(4), O(1)–Zn(1)–O(2) = 96.30(4), N(1)–Zn(1)–N(2) = 78.77(4), O(1)–Zn(1)–N(4) = 95.66(4), O(2)–Zn(1)–N(4) = 98.54(4), N(1)–Zn(1)–N(4) = 112.16(5), N(2)–Zn(1)–N(4) = 102.88(4).

 © 2005 Wiley-VCH Verlag GmbH & Co. KGaA, Weinheim

iour (for, **4**: [D_5]pyridine and for **5**: [D_6]dmso) leading to the predominant observation of monomeric Zn^{II}-salphen complexes.[11]

The coordination geometry around the central zinc atom (Figure 1) is best described as distorted square pyramidal. Interestingly, the distances Zn(1)–N(2) and Zn(1)–N(4) are identical within experimental limits [2.1168(11) Å vs. 2.1164(12) Å], while the remaining Zn(1)–N(1) bond length is significantly shorter [2.0620(11) Å]. This leads to a non-symmetrical positioning of the Zn^{II} center above the N_2O_2 plane since both the Zn–O distances are rather similar [1.9755(9) and 1.9617(10) Å]. The bond length of the axial Zn–N interaction corresponds well with earlier reports on similar Zn^{II}salphen–pyridine interactions in the solid state (Zn–N distance in the range 2.10–2.14 Å),[4,12a] but is somewhat longer than communicated for Zn–pyridine interactions based on cyclohexyl-bridging salen ligands [Zn–N = 2.089(3) Å].[12b]

The introduction of functional entities in the aromatic bridge of the salphen structure was achieved by using a step-wise approach starting with the pre-isolation of the monoimine reagents **7**–**10**.[13] The monoimines **8**–**10** were isolated as mixture of regioisomers.[14] Particularly important in the selective isolation of monoimine products is the choice for an excess of the phenylene diamine reagent, and mono Schiff bases **7**–**10** were isolated as yellow to orange crystalline materials in moderate to good yield (26–84%, Scheme 2).[15]

Synthesis of complexes **11**–**15** was carried out with monoimine precursors **7**–**10** and a second aldehyde reagent in the presence of $Zn(OAc)_2{\cdot}2H_2O$ and NEt_3 (see Scheme 3). Complexes **11**–**14** were isolated in high yield (60–94%) while the yield of **15** was low (25%). Interestingly,

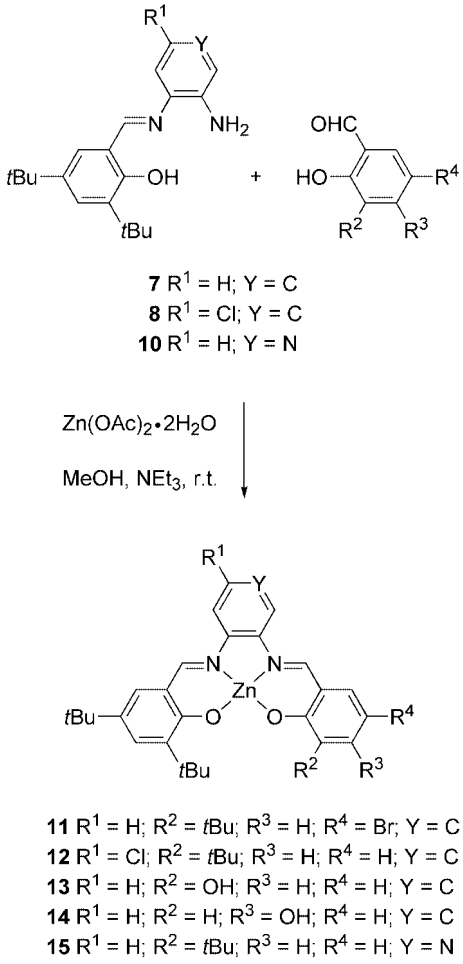

7 R^1 = H; Y = C
8 R^1 = Cl; Y = C
10 R^1 = H; Y = N

11 R^1 = H; R^2 = *t*Bu; R^3 = H; R^4 = Br; Y = C
12 R^1 = Cl; R^2 = *t*Bu; R^3 = H; R^4 = H; Y = C
13 R^1 = H; R^2 = OH; R^3 = H; R^4 = H; Y = C
14 R^1 = H; R^2 = H; R^3 = OH; R^4 = H; Y = C
15 R^1 = H; R^2 = *t*Bu; R^3 = H; R^4 = H; Y = N

Scheme 3. Synthesis of Zn^{II}-salphen complexes **11**–**15** via monoimine precursors **7**–**9**.

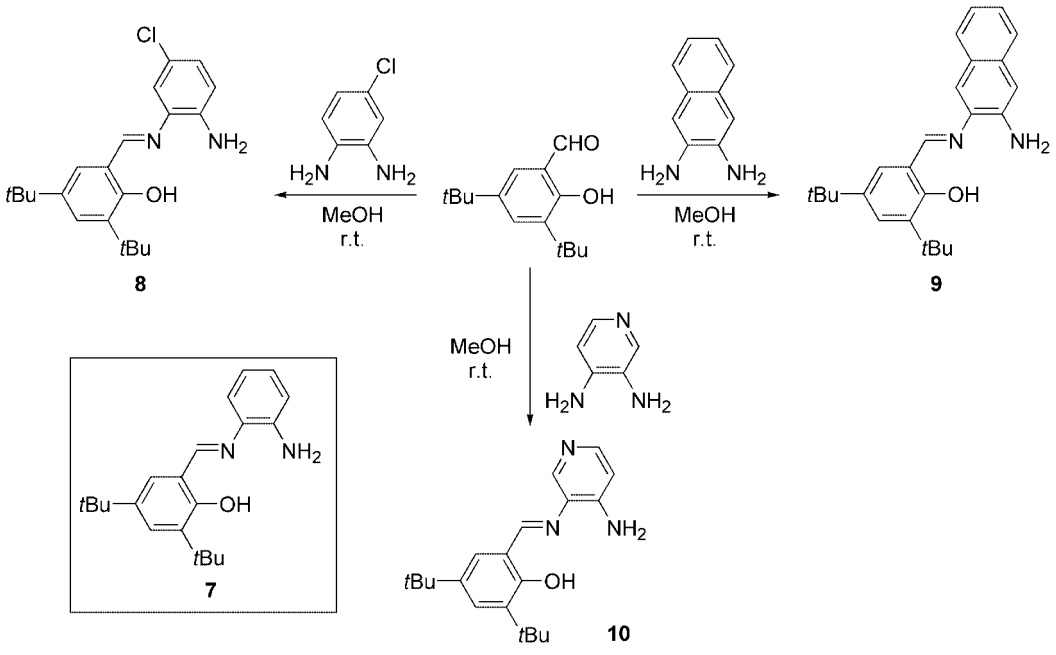

Scheme 2. Synthesis of monoimine precursors **8**–**10**.

 © 2005 Wiley-VCH Verlag GmbH & Co. KGaA, Weinheim

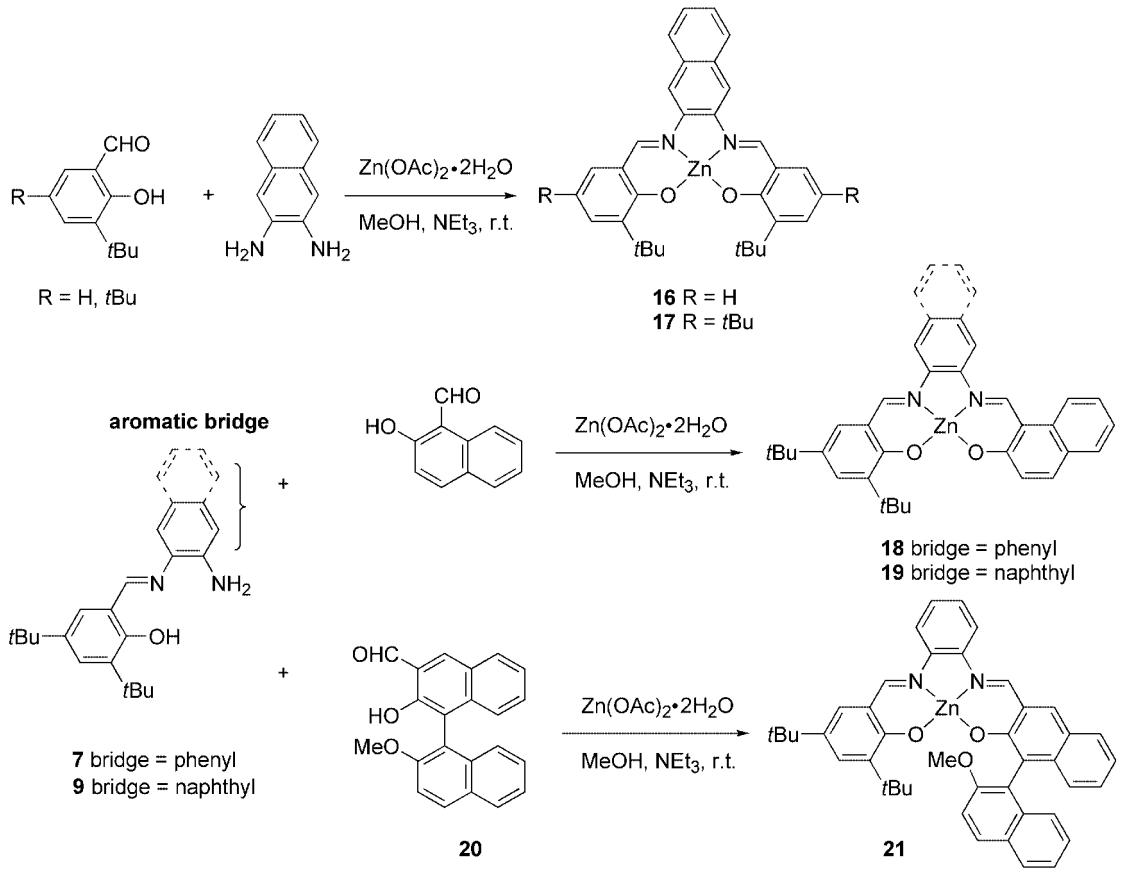

Scheme 4. Synthesis of (bi)naphthyl-based Zn^{II}-salphen complexes **16**–**19** and **21**.

the use of dihydroxybenzaldehydes allows the easy introduction of synthetically powerful phenol groups (cf. complexes **13**–**14**). We have previously shown that *meso*-phenol-substituted Zn^{II}porphyrins can be readily converted into their respective tri-phosphite derivatives by treatment with PCl_3 and applied in homogeneously catalysed hydroformylation.[16] One important drawback in these cases, however, is the synthetic accessibility of these Zn^{II}porphyrin complexes and the labour-intensive purification procedures. Thus, Zn^{II}-salphen complexes **13**–**14** represent excellent alternatives and their phenol positions could be used for the preparation of new phosphite/phosphinite ligands and their subsequent application in homogeneous catalysis.

We were also interested in the introduction of larger aromatic groups than phenyl in the salphen structure. Obviously, like in conjugated systems such as porphyrin rings, this could lead to interesting photophysical phenomena.[17] Therefore, we first prepared symmetrical Zn^{II}-salphen complex **16** and **17** as model derivatives and these were isolated in high yield (84% and 96%, respectively) (Scheme 4. The use of monoimine reagents **7** and **9** allows the presence of both phenyl as well as naphthyl groups in the final product (cf. complexes **18**, **19** and **21**) and therefore the photochemical properties can be fine-tuned by simple variation of the polyaromatic reagents and/or monoimine precursor.

Please note that complex **21** represents an interesting chiral Zn^{II}-salphen building block with the chiral information located in (only) one of the aromatic side groups. In principle, this procedure can be extended using different chiral aldehyde/ketone reagents and enables simple variation in the salphen structure. This could open up possibilities for the construction of a new combinatorial libraries of chiral (Zn^{II})salphen-based catalysts, a field which has attracted much recent interest.[6] Additionally, such chiral building blocks could also be used for the construction of optically active, multi-component supramolecular assemblies.[4,5]

In summary, this contribution shows that the salphen structure is a versatile building unit that can be functionalised both at the bridging phenyl unit as well as the aromatic side groups with relative ease. Such new complexes will find their way in further synthesis (e. g. cross-coupling procedures and preparation of phosphite ligands) or can be simply used to fine-tune the electronic/steric properties of the salphen building block. This makes the salphen structure extremely useful for the creation of supramolecular materials and salphen-based homogeneous catalysts.[18] Studies along these lines are currently in progress in our laboratory.

Experimental Section

General: All reactions were carried out in air using commercial solvents, and reagent grade starting materials were purchased and used without purification. Compounds **20**,[19] 5-bromo-3-(*tert*-bu-

 © 2005 Wiley-VCH Verlag GmbH & Co. KGaA, Weinheim

tyl)salicylaldehyde[20] and complexes **1** and **2**[4] were prepared according to literature procedures. All NMR spectra were recorded at ambient temperature with a Mercury/Inova (Varian) 300 or 500 MHz spectrometer; chemical shift values (δ) are given in ppm. Elemental analyses were carried out by Dornis und Kolbe, Mikroanalytisches Laboratorium, Mülheim a. d. Ruhr, Germany. MS measurements were carried out in CH_3CN with a Shimadzu LCMS 2010-A spectrometer using atmospheric pressure chemical ionization.

Zn^{II}-salphen Complex 3: A mixture of 4-methoxy-*o*-phenylenediamine (0.51 g, 2.42 mmol), 3,5-bis(*tert*-butyl)salicylaldehyde (1.22 g, 5.21 mmol), $Zn(OAc)_2{\cdot}2H_2O$ (0.56 g, 2.55 mmol) and neat NEt_3 (2 mL) in MeOH (40 mL) was stirred at room temp. for 24 h. Then the product was isolated as reported for complexes **1** and **2** to furnish, after trituration with pentane, a yellow-orange solid (1.17 g, 76%). ^{1}H NMR (300 MHz, [D$_6$]acetone): δ = 1.31 [s, 18 H, $C(CH_3)_3$], 1.53 [s, 18 H, $C(CH_3)_3$], 3.90 (s, 3 H, OCH_3), 6.93 [d, ^3J(H,H) = 8.9, $^3J_{H,H}$ = 2.7 Hz, 1 H, ArH], 7.21 (d, $^4J_{H,H}$ = 2.1 Hz, 1 H, ArH), 7.23 (d, $^4J_{H,H}$ = 2.7 Hz, 1 H, ArH), 7.40 (d, $^4J_{H,H}$ = 2.7 Hz, 1 H, ArH), 7.43 (d, $^4J_{H,H}$ = 2.7 Hz, 1 H, ArH), 7.47 (d, $^4J_{H,H}$ = 2.7 Hz, 1 H, ArH), 7.86 (d, $^3J_{H,H}$ = 9.0 Hz, 1 H, ArH), 9.01 [s, 1 H, C(H)=N], 9.10 [s, 1 H, C(H)=N] ppm. ^{13}C{^{1}H} NMR (75 MHz, [D$_6$]acetone): δ = 31.86, 31.93, 34.42, 36.29, 55.96, 101.43, 113.97, 117.59, 119.29, 119.41, 124.03, 124.37, 124.71, 129.32, 130.16, 130.44, 134.37, 134.56, 136.97, 137.26, 142.13, 142.39, 149.44, 149.82, 150.19, 159.91, 162.11, 171.56, 172.35 ppm. UV/Vis (toluene, c = 0.844 mg/50 mL): λ_{max} (ε) = 428 nm (22400 $mol^{-1}\,dm^3\,cm^{-1}$). MS (LC-MS, direct inlet, CH_3CN, APCI): m/z = 632 [M^+ + H], 674 [M^+ + H + CH_3CN]. $C_{37}H_{48}N_2O_3Zn$ (632.30): calcd. C 70.07, H 7.63, N 4.42; found C 69.92, H 7.74, N 4.32.

Zn^{II}-salphen Complex 4: A mixture of 2,3-diaminopyridine (0.47 g, 4.31 mmol), 3,5-bis(*tert*-butyl)salicylaldehyde (2.09 g, 8.92 mmol) and $Zn(OAc)_2{\cdot}2H_2O$ (1.13 g, 5.15 mmol) in MeOH (40 mL) was stirred at room temp. for 18 h. Then the product was collected by filtration to furnish a deep orange solid (2.19 g, 84%). ^{1}H NMR (300 MHz, [D$_6$]acetone/5% [D$_5$]pyridine): δ = 1.31 [s, 9 H, $C(CH_3)_3$], 1.33 [s, 9 H, $C(CH_3)_3$], 1.55 [s, 9 H, $C(CH_3)_3$], 1.56 [s, 9 H, $C(CH_3)_3$], 7.24 (d, $^4J_{H,H}$ = 2.7 Hz, 1 H, ArH), 7.26 (d, $^4J_{H,H}$ = 2.7 Hz, 1 H, ArH), 7.31 (dd, $^3J_{H,H}$ = 4.8 Hz, 1 H, pyr-H), 7.49 (d, $^4J_{H,H}$ = 2.7 Hz, 1 H, ArH), 7.51 (d, $^4J_{H,H}$ = 2.7 Hz, 1 H, ArH), 8.27 (d, $^3J_{H,H}$ = 8.3, $^4J_{H,H}$ = 1.4 Hz, 1 H, pyr-H), 8.33 (d, $^3J_{H,H}$ = 4.7, $^4J_{H,H}$ = 1.4 Hz, 1 H, pyr-H), 9.15 [s, 1 H, C(H)=N], 9.61 [s, 1 H, C(H)=N] ppm. ^{13}C{^{1}H} NMR (75 MHz, [D$_2$]dichloromethane/5% [D$_5$]pyridine): δ = 29.90, 31.63, 31.66, 34.30, 36.16, 118.72, 118.64, 122.23, 123.23, 129.57, 130.43, 130.71, 131.00, 135.01, 135.09, 135.51, 142.81, 142.85, 146.03, 151.54, 163.71, 164.56, 172.20, 173.33 ppm. UV/Vis (DMF, c = 0.928 mg/50 mL): λ_{max} (ε) = 433 nm (25900 $mol^{-1}\,dm^3\,cm^{-1}$). MS (LC-MS, direct inlet, CH_3CN, APCI): m/z = 603 [M^+ + H], 644 [M^+ + H + CH_3CN], 683 [M^+ + H + 2CH_3CN]. $C_{35}H_{45}N_3O_2Zn$ (603.28): calcd. C 69.47, H 7.50, N 6.94; found C 69.27, H 7.40, N 7.06.

Zn^{II}-salphen Complex 5: A yellow solution of 3,4-diaminopyridine (0.42 g, 3.85 mmol), salicylaldehyde (0.98 g, 8.02 mmol), $Zn(OAc)_2{\cdot}2H_2O$ (0.84 g, 3.83 mmol) and NEt_3 (1 mL) in MeOH (40 mL) was stirred at room temp. for 18 h. In due course, an orange suspension was obtained, which was filtered to furnish the product as an orange solid. Yield: 1.32 g (90%). ^{1}H NMR (500 MHz, [D$_6$]DMSO): δ = 6.52–6.56 (m, 2 H, ArH), 6.73 (d, $^3J_{H,H}$ = 8.5 Hz, 2 H, ArH), 7.25–7.32 (m, 2 H, ArH), 7.42 (dd, $^3J_{H,H}$ = 8.5 Hz, 2 H, ArH), 7.86 (d, $^3J_{H,H}$ = 5.0 Hz, 1 H, pyr-H$_{meta}$), 8.49 (d, $^3J_{H,H}$ = 5.3, $^4J_{H,H}$ = 1.5 Hz, 1 H, pyr-H$_{ortho}$), 9.12, 9.14, 9.16 [3×s, 3 H, 2×C(H)=N and other pyr-H$_{ortho}$] ppm. ^{13}C{^{1}H} NMR (75 MHz, [D$_6$]DMSO): δ = 110.88, 113.43, 113.68, 119.34, 119.56, 123.43, 123.74, 135.00, 135.34, 135.87, 136.50, 137.00, 139.19, 145.74, 147.48, 163.89, 165.91, 172.69, 173.79 ppm. UV/Vis (DMF, c = 1.648 mg/50 mL): λ_{max} (ε) = 410 nm (21600 $mol^{-1}\,dm^3\,cm^{-1}$). MS (LC-MS, direct inlet, CH_3CN, APCI): m/z = 377 [M^+ + H], 418 [M^+ + H + CH_3CN], 457 [M^+ + H + 2CH_3CN], 763 [2M^+ + H]. $C_{28}H_{30}N_2O_3Zn$ (379.03): calcd. C 59.94, H 3.44, N 11.04; found C 60.08, H 3.51, N 10.84.

Ni^{II}-salphen Complex 6: To a solution of salicylaldehyde (1.22 g, 10.0 mmol) and 4-trifluoromethyl-*o*-phenylenediamine (0.76 g, 4.31 mmol) in MeOH (50 mL) was added a solution of $Ni(OAc)_2{\cdot}4H_2O$ (1.07 g, 4.30 mmol) in MeOH (15 mL). Slowly a red solid started to precipitate that was collected after 3 h in different fractions. All fractions were combined and dried in vacuo to yield 1.62 g (85%) of **6**. ^{1}H NMR (300 MHz, [D$_6$]acetone): δ = 6.67 (dt, $^3J_{H,H}$ = 7.4, $^4J_{H,H}$ = 1.0 Hz, 2 H, ArH), 6.95 (d, $^3J_{H,H}$ = 8.7 Hz, 2 H, ArH), 7.32–7.39 (m, 2 H, ArH), 7.58 (dt, $^3J_{H,H}$ = 8.1, $^4J_{H,H}$ = 1.8 Hz, 2 H, ArH), 7.65 (d, $^3J_{H,H}$ = 8.7 Hz, 1 H, ArH), 8.31 (d, $^3J_{H,H}$ = 8.7 Hz, 1 H, ArH), 8.46 (s, 1 H, ArH), 8.90 [s, 1 H, C(H)=N], 8.99 [s, 1 H, C(H)=N] ppm. ^{19}F NMR (282 MHz, [D$_6$]-acetone): δ = –57.1 ppm. The product was too insoluble for a proper ^{13}C{^{1}H} NMR analysis. UV/Vis (DMF, c = 1.193 mg/50 mL): λ_{max} (ε) = 382 nm (26300 $mol^{-1}\,dm^3\,cm^{-1}$), 485 nm (8750 $mol^{-1}\,dm^3\,cm^{-1}$). MS (LC-MS, direct inlet, CH_3CN, APCI): m/z = 441 [M^+ + H]. $C_{21}H_{13}F_3N_2NiO_2$ (440.03): calcd. C 57.19, H 2.97, N 6.35; found C 56.93, H 3.08, N 6.22.

Monoimine 8: A mixture of 4-chloro-*o*-phenylenediamine (4.31 g, 30.23 mmol) and 3,5-di(*tert*-butyl)salicylaldehyde (2.02 g, 8.62 mmol) in MeOH (100 mL) was stirred at room temp. for 16 h. Then the solution was slowly concentrated upon which the title compound separated as a yellow solid. The product was collected by filtration and dried. Yield: 0.79 g (26%). ^{1}H NMR (300 MHz, [D$_6$]acetone, major isomer): δ = 1.33 [s, 9 H, $C(CH_3)_3$], 1.45 [s, 9 H, $C(CH_3)_3$], 5.05 (br. s, 2 H, NH_2), 6.67 (d, $^3J_{H,H}$ = 8.3, $^4J_{H,H}$ = 2.1 Hz, 1 H, ArH), 6.90 (d, $^4J_{H,H}$ = 2.4 Hz, 1 H, ArH), 7.17 (d, $^3J_{H,H}$ = 8.7 Hz, 1 H, ArH), 7.47–7.50 (m, 2 H, ArH), 8.84 [s, 1 H, C(H)=N], 13.44 (s, 1 H, OH) ppm. ^{13}C{^{1}H} NMR (75 MHz, [D$_6$] acetone, major isomer): δ = 31.70, 34.79, 35.64, 115.42, 117.75, 119.83, 120.57, 128.32, 128.51, 133.29, 134.60, 137.11, 141.53, 144.47, 158.67, 164.87 ppm. UV/Vis (toluene, c = 1.163 mg/50 mL): λ_{max} (ε) = 382 nm (11200 $mol^{-1}\,dm^3\,cm^{-1}$). MS (LC-MS, direct inlet, CH_3CN, APCI): m/z = 359 [M^+ + H]. $C_{21}H_{27}ClN_2O$ (358.18): calcd. C 70.28, H 7.58, N 7.81; found C 70.21, H 7.64, N 7.73.

Monoimine 9: A mixture of 2,3-diaminonaphthalene (0.78 g, 4.93 mmol) and 3,5-di(*tert*-butyl)salicylaldehyde (1.10 g, 4.69 mmol) in MeOH (40 mL) was stirred at room temp. for 3 d. Then the mixture was filtered and the product collected by filtration and dried. Yield: 0.78 g (44%). ^{1}H NMR (300 MHz, [D$_6$]-acetone): δ = 1.36 [s, 9 H, $C(CH_3)_3$], 1.48 [s, 9 H, $C(CH_3)_3$], 5.00 (br. s, 2 H, NH_2), 7.14–7.20 (m, 2 H, ArH), 7.30 (t, $^3J_{H,H}$ = 7.7, $^4J_{H,H}$ = 1.5 Hz, 1 H, ArH), 7.53–7.60 (m, 4 H, ArH), 7.73 (d, $^3J_{H,H}$ = 8.1 Hz, 1 H, ArH), 8.97 [s, 1 H, C(H)=N], 13.52 (s, 1 H, OH) ppm. ^{13}C{^{1}H} NMR (75 MHz, [D$_6$]acetone): δ = 29.87, 31.85, 34.92, 35.76, 109.21, 116.93, 119.99, 123.08, 126.12, 126.62, 128.61, 128.67, 128.80, 128.85, 135.26, 137.22, 139.80, 141.81, 142.10, 158.60, 166.35 ppm. UV/Vis (toluene, c = 0.945 mg/50 mL): λ_{max} (ε) = 366 nm (12500 $mol^{-1}\,dm^3\,cm^{-1}$). MS (LC-MS, direct inlet, CH_3CN, APCI): m/z = 375 [M^+ + H]. $C_{25}H_{30}N_2O$ (374.24): calcd. C 80.17, H 8.07, N 7.48; found C 79.97, H 8.10, N 7.36.

 © 2005 Wiley-VCH Verlag GmbH & Co. KGaA, Weinheim

Monoimine 10: A mixture of 3,4-diaminopyridine (2.48 g, 22.73 mmol) and 3,5-di(*tert*-butyl)salicylaldehyde (1.84 g, 7.85 mmol) in MeOH (40 mL) was stirred at room temp. for 24 h. Then the mixture was filtered and the product collected by filtration and dried. Concentration of the mother liquor yielded a second fraction of a yellow solid. Total yield: 1.73 g (68%). ^{1}H NMR (300 MHz, [D$_6$]acetone): δ = 1.34 [s, 9 H, C(CH$_3$)$_3$], 1.46 [s, 9 H, C(CH$_3$)$_3$], 5.60 (br. s, 2 H, NH$_2$), 6.75 (d, $^3J_{H,H}$ = 5.7 Hz, 1 H, pyr-H), 7.51 (pseudo s, 2 H, ArH), 8.01 (d, $^3J_{H,H}$ = 5.4 Hz, 1 H, pyr-H), 8.11 (s, 1 H, pyr-H), 8.86 [s, 1 H, C(H)=N], 13.30 (s, 1 H, OH) ppm. ^{13}C{^{1}H} NMR (75 MHz, [D$_6$]acetone): δ = 29.84, 31.81, 34.84, 35.68, 110.12, 119.83, 128.50, 128.71, 132.99, 137.15, 140.24, 141.60, 148.76, 148.94, 158.73, 165.85 ppm. UV/Vis (toluene, *c* = 1.753 mg/50 mL): λ_{max} (ε) = 365 nm (9400 mol^{-1} dm^3 cm^{-1}). MS (LC-MS, direct inlet, CH$_3$CN, APCI): *m*/*z* = 322 [M$^+$ + H]. C$_{20}$H$_{27}$N$_3$O (325.22): calcd. C 73.65, H 8.42, N 12.78; found C 73.81, H 8.36, N 12.91.

Zn^{II}-salphen Complex 11: A mixture of monoimine **1** (0.44 g, 1.36 mmol), 5-bromo-3-(*tert*-butyl)salicylaldehyde[20] (0.35 g, 1.36 mmol), Zn(OAc)$_2$·2H$_2$O (0.33 g, 1.50 mmol) and neat NEt$_3$ (2 mL) in MeOH (40 mL) was stirred at room temp. for 68 h. Then two volumes of H$_2$O were added and the product collected by filtration, dried and triturated with pentane to furnish an orange-yellow solid. Yield: 0.50 g (60%). ^{1}H NMR (300 MHz, [D$_6$]acetone): δ = 1.31 [s, 9 H, C(CH$_3$)$_3$], 1.51 [s, 9 H, C(CH$_3$)$_3$], 1.53 [s, 9 H, C(CH$_3$)$_3$], 7.26 (d, $^4J_{H,H}$ = 2.7 Hz, 1 H, ArH), 7.29 (d, $^4J_{H,H}$ = 2.7 Hz, 1 H, ArH), 7.37–7.40 (m, 2 H, ArH), 7.45 (d, $^4J_{H,H}$ = 2.7 Hz, 1 H, ArH), 7.93–7.96 (m, 2 H, ArH), 9.05 [s, 1 H, C(H)=N], 9.12 [s, 1 H, C(H)=N] ppm. ^{13}C{^{1}H} NMR (75 MHz, [D$_6$]acetone): δ = 30.00, 30.15, 34.40, 36.23, 103.74, 116.53, 116.70, 119.25, 121.89, 127.38, 128.11, 129.94, 130.35, 133.67, 134.79, 136.09, 140.23, 141.04, 142.25, 145.86, 162.13, 163.65, 171.92, 172.08 ppm. UV/Vis (toluene, *c* = 0.814 mg/50 mL): λ_{max} (ε) = 427 nm (17000 mol^{-1} dm^3 cm^{-1}). MS (LC-MS, direct inlet, CH$_3$CN, APCI): *m*/*z* = 627 [M$^+$ + H], 668 [M$^+$ + H + CH$_3$CN], 707 [M$^+$ + H + 2CH$_3$CN]. C$_{32}$H$_{37}$BrN$_2$O$_2$Zn (624.13): calcd. C 61.30, H 5.95, N 4.47; found C 61.39, H 6.05, N 4.55.

Zn^{II}-salphen Complex 12: A mixture of monoimine **2** (0.65 g, 1.81 mmol), 3-(*tert*-butyl)salicylaldehyde (0.33 g, 1.85 mmol), Zn(OAc)$_2$·2H$_2$O (0.42 g, 1.91 mmol) and neat NEt$_3$ (1 mL) in MeOH (40 mL) was stirred at room temp. for 41 h. Then the product was collected by filtration and dried to furnish a yellow solid. Yield: 0.99 g (94%). ^{1}H NMR (300 MHz, [D$_6$]acetone): δ = 1.31 [s, 9 H, C(CH$_3$)$_3$], 1.51 [s, 9 H, C(CH$_3$)$_3$], 1.53 [s, 9 H, C(CH$_3$)$_3$], 6.49 (t, $^3J_{H,H}$ = 7.2 Hz, 1 H, ArH), 7.24 (d, $^4J_{H,H}$ = 2.7 Hz, 1 H, ArH), 7.29–7.33 (m, 2 H, ArH), 7.36 (d, $^4J_{H,H}$ = 2.1 Hz, 1 H, ArH), 7.45 (d, $^4J_{H,H}$ = 2.7 Hz, 1 H, ArH), 7.93 (d, $^3J_{H,H}$ = 5.7 Hz, 1 H, ArH), 7.95 (s, 1 H, ArH), 9.10 [s, 1 H, C(H)=N], 9.11 [s, 1 H, C(H)=N] ppm. ^{13}C{^{1}H} NMR (75 MHz, [D$_2$]dichloromethane/5% [D$_5$]pyridine): δ = 29.80, 29.90, 31.65, 34.30, 35.87, 36.11, 113.41, 116.50, 117.35, 118.56, 119.80, 127.02, 129.72, 130.42, 131.90, 132.47, 134.80, 135.04, 139.57, 141.58, 142.64, 143.42, 163.24, 163.38, 172.02, 173.90 ppm. UV/Vis (toluene, *c* = 0.728 mg/50 mL): λ_{max} (ε) = 429 nm (20700 mol^{-1} dm^3 cm^{-1}). MS (LC-MS, direct inlet, CH$_3$CN, APCI): *m*/*z* = 583 [M$^+$ + H], 622 [M$^+$ + H + CH$_3$CN], 661 [M$^+$ + H + 2CH$_3$CN]. C$_{32}$H$_{37}$ClN$_2$O$_2$Zn·H$_2$O (580.18 for complex without H$_2$O): calcd. C 64.00, H 6.55, N 4.66; found C 63.85, H 6.78, N 4.51.

Zn^{II}-salphen Complex 13: A green suspension of 2,3-dihydroxybenzaldehyde (0.30 g, 2.17 mmol), monoimine **1** (0.71 g, 2.19 mmol) and Zn(OAc)$_2$·2H$_2$O (0.48 g, 2.19 mmol) in MeOH (40 mL) was stirred at room temp. for 24 h. In due course, a yellow-ish suspension was obtained, which was filtered to furnish the product as a yellow-orange solid. Yield: 0.89 g (81%). ^{1}H NMR (300 MHz, [D$_6$]acetone/5% [D$_5$]pyridine): δ = 1.30 [s, 9 H, C(CH$_3$)$_3$], 1.53 [s, 9 H, C(CH$_3$)$_3$], 6.45 (t, $^3J_{H,H}$ = 7.8 Hz, 1 H, ArH), 6.82 (d, $^3J_{H,H}$ = 8.4 Hz, 1 H, ArH), 6.94 (d, $^3J_{H,H}$ = 7.8 Hz, 1 H, Ar-H), 7.23 (d, $^4J_{H,H}$ = 2.7 Hz, 1 H, ArH), 7.36 (t, $^3J_{H,H}$ = 6.3, $^4J_{H,H}$ = 2.1 Hz, 2 H, ArH), 7.44 (d, $^4J_{H,H}$ = 2.7 Hz, 1 H, pyr-H), 7.46 (d, $^4J_{H,H}$ = 2.7 Hz, 1 H, ArH), 7.84 (t, $^3J_{H,H}$ = 8.7 Hz, 1 H, pyr-H), 9.00 [s, 1 H, C(H)=N], 9.05 [s, 1 H, C(H)=N] ppm. The OH proton was in exchange with residual water in the solvent. ^{13}C{^{1}H} NMR (75 MHz, [D$_6$]DMSO/5% [D$_5$]pyridine): δ = 29.40, 31.29, 33.53, 35.18, 113.16, 113.47, 116.75, 117.28, 118.21, 125.27, 126.81, 127.73, 128.80, 129.74, 133.61, 139.19, 140.16, 140.71, 148.88, 159.24, 163.13, 164.11, 170.53 ppm. UV/Vis (DMF, *c* = 1.746 mg/50 mL): λ_{max} (ε) = 414 nm (15500 mol^{-1} dm^3 cm^{-1}). MS (LC-MS, direct inlet, CH$_3$CN, APCI): *m*/*z* = 507 [M$^+$ + H], 548 [M$^+$ + H + CH$_3$CN], 1017 [2M$^+$ + H]. C$_{28}$H$_{30}$N$_2$O$_3$Zn (506.15): calcd. C 66.21, H 5.95, N 5.52; found C 66.07, H 6.10, N 5.38.

Zn^{II}-salphen Complex 14: A yellow suspension of 2,4-dihydroxybenzaldehyde (0.22 g, 1.59 mmol), monoimine **1** (0.47 g, 1.45 mmol) and Zn(OAc)$_2$·2H$_2$O (0.35 g, 1.59 mmol) in MeOH (40 mL) was stirred at room temp. for 18 h. Hereafter, water was added to precipitate the product, which was washed with pentane and isolated by filtration. Drying in vacuo afforded a yellow solid. Yield: 0.51 g (69%). ^{1}H NMR (300 MHz, [D$_6$]acetone/5% [D$_5$]pyridine): δ = 1.30 [s, 9 H, C(CH$_3$)$_3$], 1.49 [s, 9 H, C(CH$_3$)$_3$], 6.13 (d, $^3J_{H,H}$ = 8.7, $^4J_{H,H}$ = 8.7 Hz, 1 H, ArH), 6.26 (d, $^4J_{H,H}$ = 2.4 Hz, 1 H, ArH), 7.21–7.30 (m, 4 H, Ar-H), 7.42 (d, $^4J_{H,H}$ = 2.7 Hz, 1 H, ArH), 7.72–7.76 (m, 2 H, ArH), 8.85 [s, 1 H, C(H)=N], 8.96 [s, 1 H, C(H)=N] ppm. The OH proton was in exchange with residual water in the solvent which appeared as a broad signal at δ = 3.01 ppm. ^{13}C{^{1}H} NMR (75 MHz, [D$_6$]DMSO/10% [D$_5$]pyridine): δ = 29.63, 30.69, 31.41, 33.61, 35.29, 105.12, 107.06, 113.89, 115.92, 116.39, 118.37, 123.48, 123.80, 124.13, 126.25, 126.80, 128.49, 129.66, 133.34, 136.58, 138.20, 139.74, 140.01, 140.76, 148.44, 148.81, 149.15, 161.15, 164.11, 170.50, 174.77 ppm. UV/Vis (toluene, *c* = 1.888 mg/50 mL): λ_{max} (ε) = 398 nm (15800 mol^{-1} dm^3 cm^{-1}). MS (LC-MS, direct inlet, CH$_3$CN, APCI): *m*/*z* = 505 [M$^+$ + H], 546 [M$^+$ + H + CH$_3$CN], 1017 [2M$^+$ + H]. C$_{28}$H$_{30}$N$_2$O$_3$Zn·3.5H$_2$O (506.15 for complex without H$_2$O): calcd. C 58.90, H 6.53, N 4.91; found C 58.73, H 6.51, N 4.83.

Zn^{II}-salphen Complex 15: A mixture of monoimine **4** (0.42 g, 1.29 mmol), 3-(*tert*-butyl)salicylaldehyde (0.24 g, 1.35 mmol) and Zn(OAc)$_2$·2H$_2$O (0.33 g, 1.50 mmol) in MeOH (40 mL) was stirred at room temp. for 3 d. Then the product was collected by filtration to furnish an orange-red solid (178.6 mg, 25%). ^{1}H NMR (300 MHz, [D$_6$]acetone): δ = 1.33 [s, 9 H, C(CH$_3$)$_3$], 1.53 [s, 9 H, C(CH$_3$)$_3$], 1.58 [s, 9 H, C(CH$_3$)$_3$], 6.53 (t, $^3J_{H,H}$ = 7.2 Hz, 1 H, ArH), 7.31–7.37 (m, 3 H, ArH), 7.52 (d, $^4J_{H,H}$ = 2.7 Hz, 1 H, ArH), 7.75 (d, $^3J_{H,H}$ = 6.0 Hz, 1 H, pyr-H$_{meta}$), 8.46 (d, $^3J_{H,H}$ = 5.7 Hz, 1 H, pyr-H$_{ortho}$), 8.61 (s, 1 H, pyr-H$_{ortho}$), 9.16 [s, 1 H, C(H)=N], 9.28 [s, 1 H, C(H)=N] ppm. ^{13}C{^{1}H} NMR (75 MHz, [D$_2$]dichloromethane/30% [D$_5$]pyridine): δ = 29.72, 29.85, 31.52, 34.12, 35.74, 36.01, 109.84, 113.67, 118.69, 119.66, 129.74, 130.40, 132.52, 135.06, 139.10, 142.55, 143.52, 146.19, 147.69, 163.71, 164.89, 172.08, 174.90 ppm. UV/Vis (DMF, *c* = 1.294 mg/50 mL): λ_{max} (ε) = 426 nm (20900 mol^{-1} dm^3 cm^{-1}). MS (LC-MS, direct inlet, CH$_3$CN, APCI): *m*/*z* = 547 [M$^+$ + H], 588 [M$^+$ + H + CH$_3$CN], 626 [M$^+$ + H + 2CH$_3$CN]. C$_{31}$H$_{37}$N$_3$O$_2$Zn (547.22): calcd. C 67.82, H 6.79, N 7.65; found C 68.64, H 6.66, N 7.72.

Zn^{II}-salphen Complex 16: A mixture of 2,3-diaminonaphthalene (0.42 g, 2.65 mmol), 3-(*tert*-butyl)salicylaldehyde (1.10 g,

 © 2005 Wiley-VCH Verlag GmbH & Co. KGaA, Weinheim

6.17 mmol), $Zn(OAc)_2{\cdot}2H_2O$ (0.66 g, 3.01 mmol) and neat NEt_3 (2 mL) in MeOH (65 mL) was stirred at room temp. for 17 h. Then the product was collected by filtration and dried to furnish an orange solid (1.21 g, 84%). ^{1}H NMR (300 MHz, [D$_6$]acetone): δ = 1.55 [s, 18 H, C(CH$_3$)$_3$], 6.50 (t, $^3J_{H,H}$ = 7.5 Hz, 2 H, ArH), 7.31 (d, $^3J_{H,H}$ = 7.8 Hz, 4 H, ArH), 7.47–7.50 (m, 2 H, ArH), 7.92–7.95 (m, 2 H, ArH), 8.32 (s, 2 H, ArH), 9.22 [s, 2 H, C(H)=N] ppm. ^{13}C{^{1}H} NMR (75 MHz, [D$_6$]acetone/5% [D$_5$]pyridine): δ = 30.18, 36.03, 113.57, 114.27, 120.72, 126.89, 128.69, 131.89, 133.25, 135.47, 140.56, 143.02, 165.18, 174.13 ppm. UV/Vis (toluene, c = 0.751 mg/50 mL): λ_{max} (ε) = 431 nm (25400 mol^{-1} dm^3 cm^{-1}). MS (LC-MS, direct inlet, CH$_3$CN, APCI): m/z = 539 [M$^+$ + H], 581 [M$^+$ + H + CH$_3$CN]. $C_{32}H_{32}N_2O_2Zn{\cdot}H_2O$ (540.18 for complex without H_2O): calcd. C 68.63, H 6.12, N 5.00; found C 68.24, H 6.65, N 4.59.

Zn^{II}-salphen Complex 17: A mixture of 2,3-diaminonaphthalene (0.37 g, 2.34 mmol), 3,5-di(*tert*-butyl)salicylaldehyde (1.24 g, 5.29 mmol), $Zn(OAc)_2{\cdot}2H_2O$ (0.54 g, 2.46 mmol) and neat NEt_3 (2 mL) in MeOH (40 mL) was stirred at room temp. for 17 h. Then the product was collected by filtration and dried to furnish an orange solid (1.47 g, 96%). ^{1}H NMR (300 MHz, [D$_6$]acetone): δ = 1.34 [s, 18 H, C(CH$_3$)$_3$], 1.55 [s, 18 H, C(CH$_3$)$_3$], 7.25 (d, $^4J_{H,H}$ = 3.0 Hz, 2 H, ArH), 7.44 (d, $^4J_{H,H}$ = 2.7 Hz, 2 H, ArH), 7.45–7.48 (m, 2 H, ArH), 7.92–7.95 (m, 2 H, ArH), 8.30 (s, 2 H, ArH), 9.21 [s, 2 H, C(H)=N] ppm. ^{13}C{^{1}H} NMR (75 MHz, [D$_6$]acetone/5% [D$_5$]pyridine): δ = 30.30, 31.86, 34.48, 36.33, 113.63, 114.01, 114.35, 119.55, 126.76, 128.64, 130.47, 133.30, 134.76, 140.95, 142.47, 165.47, 172.61 ppm. UV/Vis (toluene, c = 1.013 mg/50 mL): λ_{max} (ε) = 443 nm (25800 mol^{-1} dm^3 cm^{-1}). MS (LC-MS, direct inlet, CH$_3$CN, APCI): m/z = 652 [M$^+$ + H], 694 [M$^+$ + H + CH$_3$CN]. $C_{40}H_{48}N_2O_2Zn$ (652.30): calcd. C 73.44, H 7.40, N 4.28; found C 73.24, H 7.29, N 4.18.

Zn^{II}-salphen Complex 18: A mixture of monoimine **1** (0.66 g, 2.03 mmol), 2-hydroxy-1-naphthalenecarbaldehyde (0.35 g, 2.03 mmol), $Zn(OAc)_2{\cdot}2H_2O$ (0.52 g, 2.37 mmol) and neat NEt_3 (2 mL) in MeOH (40 mL) was stirred at room temp. for 16 h. Then the product was collected by filtration and dried to furnish an orange/brown solid (0.60 g, 55%). Analytically pure **18** was obtained by crystallization from hot CH$_3$CN. ^{1}H NMR (300 MHz, [D$_6$]acetone/10% [D$_5$]pyridine): δ = 1.32 [s, 9 H, C(CH$_3$)$_3$], 1.56 [s, 9 H, C(CH$_3$)$_3$], 7.00 (d, $^3J_{H,H}$ = 9.0 Hz, 1 H, ArH), 7.17–7.47 (m, 6 H, ArH), 7.66–7.82 (m, 3 H, ArH), 8.01 (d, $^3J_{H,H}$ = 7.8, $^4J_{H,H}$ = 1.8 Hz, 1 H ArH), 8.38 (d, $^3J_{H,H}$ = 8.7 Hz, 1 H, ArH), 9.02 [s, 1 H, C(H)=N], 9.91 [s, 1 H, C(H)=N] ppm. ^{13}C{^{1}H} NMR (75 MHz, [D$_6$]acetone/10% [D$_5$]pyridine): δ = 31.85, 34.44, 36.26, 110.17, 116.96, 117.55, 119.44, 120.04, 122.41, 127.04, 127.36, 127.77, 128.24, 128.61, 129.74, 129.95, 130.49, 134.74, 136.57, 141.06, 142.23, 142.44, 157.66, 164.34, 172.15, 175.50 ppm. UV/Vis (toluene, c = 0.734 mg/50 mL): λ_{max} (ε) = 423 nm (23000 mol^{-1} dm^3 cm^{-1}). MS (LC-MS, direct inlet, CH$_3$CN, APCI): m/z = 539 [M$^+$ + H], 581 [M$^+$ + H + CH$_3$CN], 1088 [2M$^+$ + H]. $C_{32}H_{32}N_2O_2Zn$ (540.18): calcd. C 70.91, H 5.95, N 5.17; found C 70.81, H 6.04, N 5.35.

Zn^{II}-salphen Complex 19: A mixture of monoimine **3** (0.50 g, 1.34 mmol), 2-hydroxy-1-naphthalenecarbaldehyde (0.26 g, 1.51 mmol), $Zn(OAc)_2{\cdot}2H_2O$ (0.37 g, 1.69 mmol) and neat NEt_3 (2 mL) in MeOH/acetone (40:20 mL) was stirred at room temp. for 18 h. Then, extra MeOH (40 mL) was added and the precipitated product was collected by filtration and dried to furnish an orange solid (0.52 g, 66%). Analytically pure **19** was obtained by crystallization from hot CH_3CN/CH_2Cl_2. ^{1}H NMR (300 MHz, [D$_6$]acetone/10% [D$_5$]pyridine): δ = 1.36 [s, 9 H, C(CH$_3$)$_3$], 1.62 [s, 9 H, C(CH$_3$)$_3$], 7.07 (d, $^3J_{H,H}$ = 9.0 Hz, 1 H, ArH), 7.24 (t, $^3J_{H,H}$ = 7.8 Hz, 1 H, ArH), 7.33 (s, 1 H, ArH), 7.44–7.55 (m, 4 H, ArH), 7.69–7.79 (m, 2 H, ArH), 7.93 (m, 1 H, ArH), 8.00 (m, 1 H, ArH), 8.47 (m, 2 H, ArH), 9.18 [s, 1 H, C(H)=N], 10.09 [s, 1 H, C(H)=N] ppm. ^{13}C{^{1}H} NMR (75 MHz, [D$_2$]dichloromethane/10% [D$_5$]pyridine): δ = 29.90, 31.68, 34.27, 36.06, 109.94, 113.62, 113.87, 119.01, 119.29, 122.26, 126.42, 126.70, 127.90, 128.20, 129.51, 129.88, 130.25, 132.63, 132.91, 135.04, 136.55, 140.62, 142.00, 142.24, 158.19, 164.55, 171.99, 175.38 ppm. UV/Vis (toluene, c = 1.188 mg/50 mL): λ_{max} (ε) = 434 nm (28200 mol^{-1} dm^3 cm^{-1}). MS (LC-MS, direct inlet, CH$_3$CN, APCI): m/z = 590 [M$^+$ + H], 631 [M$^+$ + H + CH$_3$CN]. $C_{36}H_{34}N_2O_2Zn{\cdot}1/3CH_2Cl_2{\cdot}1/3CH_3CN$. (590.19 for complex without solvent): calcd. C 70.09, H 5.67, N 5.15; found C 70.29, H 5.24, N 5.30.

Zn^{II}-salphen Complex 21: A mixture of **1** (166.0 mg, 0.512 mmol), (*S*)-2-hydroxy-2′-methoxy-1,1′-binaphthalene-3-carboxaldehyde (168.1 mg, 0.512 mmol), $Zn(OAc)_2{\cdot}2H_2O$ (115.3 mg, 0.525 mmol) and neat NEt_3 (0.5 mL) in hot MeOH (50 mL). The initial dark-red colored solution gradually turned into a suspension, which was filtered after 17 h to give, after drying, an orange to red solid (180.4 mg, 0.258 mmol, 50%). Analytically pure **21** was obtained by crystallization from CH_3CN/CH_2Cl_2. ^{1}H NMR ([D$_6$]acetone): δ = 1.06 [s, 9 H, C(CH$_3$)$_3$], 1.24 [s, 9 H, C(CH$_3$)$_3$], 3.74 (s, 3 H, OCH$_3$), 6.83 (d, $^3J_{H,H}$ = 8.7 Hz, 1 H, ArH), 7.29–6.97 (m, 7 H, ArH), 7.48–7.41 (m, 2 H, ArH), 7.53 (d, $^3J_{H,H}$ = 8.7 Hz, 1 H, ArH), 7.77 (d, $^3J_{H,H}$ = 7.2 Hz, 1 H, ArH), 7.87 (t, $^3J_{H,H}$ = 8.7 Hz, 2 H, ArH), 7.98 (t, $^3J_{H,H}$ = 7.2 Hz, 2 H, ArH), 8.20 (s, 1 H, ArH), 8.94 [s, 1 H, C(H)=N], 9.36 [s, 1 H, C(H)=N] ppm. ^{13}C{^{1}H} NMR (CD_2Cl_2/d$_5$-pyridine, 95:5): δ = 29.41, 31.55, 34.17, 35.51, 114.90, 116.42, 116.49, 118.20, 120.65, 121.15, 122.99, 123.25, 123.36, 124.17, 124.90, 125.87, 126.06, 126.94, 128.41, 128.46, 128.72, 128.86, 129.36, 129.62, 130.08, 130.21, 134.51, 135.01, 138.03, 138.24, 139.68, 142.00, 142.52, 155.73, 162.91, 163.75, 165.82, 172.00 ppm. UV/Vis (toluene, c = 1.087 mg/50 mL): λ_{max} (ε) = 357, 453 nm (27200, 12800 mol^{-1} dm^3 cm^{-1}). MS (LC-MS, direct inlet, CH$_3$CN, APCI): m/z = 697 [M$^+$ + H]. $C_{44}H_{42}N_2O_3Zn$ (696.23): calcd. C 74.20, H 5.71, N 3.93; found: C 74.05, H 5.94, N 4.01.

Crystal Structure Determination of Zn^{II}-salphen Complex 4: $C_{40}H_{50}N_4O_2Zn$, Fw = 684.21, orange block, 0.34×0.26×0.23 mm. Monoclinic crystal system, space group $P2_1/c$. Cell parameters: a = 12.8185(14) Å, b = 15.3860(12) Å, c = 18.6414(15) Å, β = 91.442(9)°, V = 3675.4(6) Å^3, Z = 4, $D_{calcd.}$ = 1.237 gcm^{-3}. 110831 reflections were measured on a Nonius KappaCCD diffractometer with rotating anode and Mo-K_α radiation (graphite monochromator, λ = 0.71073 Å) at a temperature of 150(2) K, using Collect,[21] DIRAX[22] and EvalCCD.[23] A multi-scan absorption correction was applied using SADABS[24] (μ = 0.707 mm^{-1}, 0.74–0.85 transmission). 8401 unique reflections (R_{int} = 0.0306), of which 7376 were observed [$I > 2\sigma(I)$]. The structure was solved with the program DIRDIF,[25] and refined using the program SHELXL-97[26] against F^2 of all reflections up to a resolution of sinθ/λ = 0.65. Non-hydrogen atoms were freely refined with anisotropic displacement parameters. H atoms were placed in geometrically idealized positions [d(C–H) = 0.98 for methyl H atoms and 0.95 for other H atoms] and constrained to ride on their parent atoms, with U_{iso}(H) = 1.5U_{eq}(C) for methyl H atoms and U_{iso}(H) = 1.2U_{eq}(C) for all other H atoms. 436 refined parameters, 0 restraints. R(obsd. refl.): R_1 = 0.0269, wR_2 = 0.0681. R (all data): R_1 = 0.0342, wR_2 = 0.0722. Weighting Scheme $w = 1/[\sigma^2(F_o^2) + (0.0367P)^2 + 1.1877P]$, where $P = (F_o^2 + 2F_c^2)/3$. GoF = 1.056. Residual electron density between –0.307 and 0.384 e/Å^3. The drawings, structure calculations, and checking for additional symmetry were performed with the program PLATON.[27]

 © 2005 Wiley-VCH Verlag GmbH & Co. KGaA, Weinheim

Acknowledgments

We gratefully acknowledge the Netherlands Organisation for Scientific Research (NWO, ViCi program of JNHR) and the Universities of Amsterdam (UvA) and Utrecht for financial contributions.

[1] For reviews see: a) L. Canali, D. C. Sherrington, *Chem. Soc. Rev.* **1999**, *28*, 85–93; b) E. N. Jacobsen, *Acc. Chem. Res.* **2000**, *33*, 421–431; c) T. Katsuku, *Coord. Chem. Rev.* **1995**, *140*, 189–214; d) D. A. Atwood, M. J. Harvey, *Chem. Rev.* **2001**, *101*, 37–52.

[2] For some examples seea) W. Zhang, J. L. Loebach, S. R. Wilson, E. N. Jacobsen, *J. Am. Chem. Soc.* **1990**, *112*, 2801–2803; b) E. N. Jacobsen, W. Zhang, A. R. Muci, J. R. Ecker, L. Deng, *J. Am. Chem. Soc.* **1991**, *113*, 7063–7064; c) L. Deng, E. N. Jacobsen, *J. Org. Chem.* **1992**, *57*, 4320–4323.

[3] For a selection see: a) Z. Li, K. R. Conser, E. N. Jacobsen, *J. Am. Chem. Soc.* **1993**, *115*, 5326–5327; b) Z. Li, R. W. Quan, E. N. Jacobsen, *J. Am. Chem. Soc.* **1995**, *117*, 5889–5890; c) T. Uchida, B. Saha, T. Katsuki, *Tetrahedron Lett.* **2001**, *42*, 2521–2524; d) W. Zhang, E. N. Jacobsen, *J. Org. Chem.* **1991**, *56*, 2296–2298; e) C.-W. Ho, W.-C. Cheng, M.-C. Cheng, S.-M. Peng, K. F. Cheng, C.-M. Che, *J. Chem. Soc. Dalton Trans.* **1996**, 405–414; f) X.-G. Zhou, X.-Q. Yu, J.-S. Huang, C.-M. Che, S.-G. Li, L.-S. Li, *Chem. Commun.* **1999**, 1789–1790; g) C.-M. Che, H.-L. Kwong, W.-C. Chu, K.-F. Cheng, W.-S. Lee, H.-S. Yu, C.-T. Yeung, K.-K. Cheung, *Eur. J. Inorg. Chem.* **2002**, 1456–1463; h) M. Bandini, P. G. Cozzi, A. Umani-Ronchi, *Angew. Chem. Int. Ed.* **2000**, *39*, 2327–2330; i) R. Fiammengo, C. M. Bruinink, M. Crego-Calama, D. N. Reinhoudt, *J. Org. Chem.* **2002**, *67*, 8552–8557; j) J. A. Miller, W. Jin, S. T. Nguyen, *Angew. Chem. Int. Ed.* **2004**, *41*, 2953–2956; k) G. M. Semmis, H. Danjo, E. N. Jacobsen, *J. Am. Chem. Soc.* **2004**, *126*, 9928–9929.

[4] A. W. Kleij, M. Kuil, D. M. Tooke, M. Lutz, A. L. Spek, J. N. H. Reek, *Chem. Eur. J.* **2005**, *11*, 4743–4750. Note that the synthesis of compounds **1** and **2** are also described herein.

[5] A. W. Kleij, M. Lutz, A. L. Spek, P. W. N. M. van Leeuwen, J. N. H. Reek, *Chem. Commun.* **2005**, 3361–3363.

[6] a) P. G. Cozzi, *Angew. Chem. Int. Ed.* **2003**, *42*, 2895–2898; b) E. F. DiMauro, M. C. Kozlowski, *Org. Lett.* **2001**, *3*, 3053–3056; c) E. F. DiMauro, M. C. Kozlowski, *J. Am. Chem. Soc.* **2002**, *124*, 12668–12669; d) E. F. DiMauro, M. C. Kozlowski, *Org. Lett.* **2002**, *4*, 3781–3784.

[7] a) G. A. Morris, S. T. Nguyen, J. T. Hupp, *J. Mol. Cat. A* **2001**, *174*, 15–20; b) V. F. Slagt, J. N. H. Reek, P. C. J. Kamer, P. W. N. M. van Leeuwen, *Angew. Chem. Int. Ed.* **2001**, *40*, 4271–4274; c) V. F. Slagt, P. W. N. M. van Leeuwen, J. N. H. Reek, *Angew. Chem. Int. Ed.* **2003**, *42*, 5619–5623; d) V. F. Slagt, P. J. C. Kamer, P. W. N. M. van Leeuwen, J. N. H. Reek, *J. Am. Chem. Soc.* **2004**, *126*, 1526–1536; e) B. Breit, W. Seiche, *Angew. Chem. Int. Ed.* **2005**, *44*, 1640–1643; f) J. M. Takacs, D. S. Reddy, S. A. Moteki, D. Wu, H. Palencia, *J. Am. Chem. Soc.* **2004**, *126*, 4494–4495; <lit_ g>V. F. Slagt, P. W. N. M. van Leeuwen, J. N. H. Reek, *Chem. Commun.* **2003**, 2474–2475; h) M. L. Merlau, M. P. Mejia, S. T. Nguyen, J. T. Hupp, *Angew. Chem. Int. Ed.* **2001**, *40*, 4239–4242; i) D. H. Leung, D. Fiedler, R. G. Bergman, K. N. Raymond, *Angew. Chem. Int. Ed.* **2004**, *43*, 963–966; j) M. Yoshizawa, Y. Takeyama, T. Kusukawa, M. Fujita, *Angew. Chem. Int. Ed.* **2002**, *41*, 1347–1349; k) M. Ziegler, J. L. Brumaghim, K. N. Raymond, *Angew. Chem. Int. Ed.* **2000**, *39*, 4119–4121; l) D. Fiedler, D. H. Leung, R. G. Bergman, K. N. Raymond, *Acc. Chem. Res.* **2005**, *38*, 349–358.

[8] a) R. G. Konsler, J. Karl, E. N. Jacobsen, *J. Am. Chem. Soc.* **1998**, *120*, 10780–10781; b) E. J. Campbell, S. T. Nguyen, *Tetrahedron Lett.* **2001**, *42*, 1221–1225; c) A. M. Daly, C. T. Dalton, M. F. Renehan, D. G. Gilheany, *Tetrahedron Lett.* **1999**, *40*, 3617–3620; d) D. M. Boghaei, S. Mohebi, *Tetrahedron* **2002**, *58*, 5357–5366; e) D. A. Annis, E. N. Jacobsen, *J. Am. Chem. Soc.* **1999**, *121*, 4147–4154. Please note that the majority of these reported methods make use of a step-wise synthetic protocol involving trapping of the monoimine intermediate using protection/deprotection sequences. Ref. 8d describes an interesting templated approach using Co^{II}-acetate but here only two examples were reported. In order to use the nonsymmetric ligands for further synthesis, the authors had to demetalate the Co^{II}-salen complexes with dimethyl glyoxime and reengage in new metalation procedures. In strong contrast, our approach directly affords the desired metallated salphen complexes and any desired suitable metal precursor can be chosen in advance to afford different metallo-salphen systems.

[9] CCDC-278364 contains the supplementary crystallographic data for this paper. These data can be obtained free of charge from The Cambridge Crystallographic Data Centre via www.ccdc.cam.ac.uk/data_request/cif.

[10] A. W. Kleij, M. Kuil, D. M. Tooke, M. Lutz, A. L. Spek, P. C. J. Kamer, P. W. N. M. Van Leeuwen, J. N. Reek, *Inorg. Chim. Acta* **2005**, in press, available online at http://www.elsevier.com/wps/find/journaldescription.cws_home/504086/description#description.

[11] Please note that the presence of [D_5]pyridine as co-solvent for those species lacking a large 3- and/or 3′-substituent or comprising internal pyridine-N atoms in the salphen backbone (i.e., compounds **5**, **13**–**15** and **18**–**19**) greatly increased their solubility as a result of the formation of [D_5]pyridine adducts; see also references 4 and 5.

[12] a) A. L. Singer, D. A. Atwood, *Inorg. Chim. Acta* **1998**, *277*, 157–162; b) G. A. Morris, H. Zhou, C. L. Stern, S. T. Nguyen, *Inorg. Chem.* **2001**, *40*, 3222–3227.

[13] The synthesis of monoimine **7** was reported previously: M.-A. Muñoz-Hernández, T. S. Keizer, S. Parkin, B. Patrick, D. A. Atwood, *Organometallics* **2000**, *19*, 4416–4421.

[14] Please note that for compounds **8**–**10** two regio–isomers can be formed. For mono–imine **10** one of these isomers was isolated exclusively, while for **8** and **9** mixtures of both species were obtained. The isomer ratios were determined by signal integration (93:7 for **8** and ca. 60:40 for **9**). For simplicity, for **8**–**10** only the major species are presented in the main text and their structures were corroborated by NMR spectroscopy.

[15] Note that the nonsymmetric monoimine products **8**–**10** were rather soluble in MeOH and significant concentration of the mixture was needed to isolate pure materials.

[16] V. F. Slagt, M. Roeder, P. C. J. Kamer, P. W. N. M. van Leeuwen, J. N. H. Reek, *J. Am. Chem. Soc.* **2004**, *126*, 4056–4057.

[17] For an investigation towards the fluorescence properties of Zn^{II}-salphen based structures see: a) K. E. Splan, A. M. Massari, G. A. Morris, S.-S. Sun, E. Reina, S. T. Nguyen, J. T. Hupp, *Eur. J. Inorg. Chem.* **2003**, 2348–2351; b) S. Di Bella, N. Leonardi, G. Consiglio, S. Sortino, I. Fragala, *Eur. J. Inorg. Chem.* **2004**, 4561–4565; c) K.-H. Chang, C.-C. Huang, Y.-H. Liu, Y.-H. Hu, P.-T. Chou, Y.-C. Lin, *Dalton Trans.* **2004**, 1731–1738; d) P. G. Cozzi, L. S. Dolci, A. Garelli, M. Montalti, L. Prodi, N. Zaccheroni, *New J. Chem.* **2003**, *27*, 692–697.

[18] a) P. G. Cozzi, *Chem. Soc. Rev.* **2004**, *33*, 410–421; b) P. G. Cozzi, R. Hilgraf, N. Zimmermann, *Eur. J. Org. Chem.* **2004**, 4095–4105.

[19] a) A. Raffaelli, F. Minutolo, B. L. Feringa, P. Salvadori, *Inorg. Chim. Acta* **1998**, *275–276*, 462–469; b) A. R. van Doorn, D. J. Rushton, M. Bos, W. Verboom, D. N. Reinhoudt, *Recl. Trav. Chim. Pays-Bas* **1992**, *111*, 415–420.

[20] J. F. Larrow, E. N. Jacobsen, Y. Gao, Y. Hong, X. Nie, C. M. Zepp, *J. Org. Chem.* **1994**, *59*, 1939–1942.

[21] R. W. W. Hooft, *Nonius Collect Software*, Nonius B.V., Delft, **1998**, The Netherlands.

[22] A. J. M. Duisenberg, *J. Appl. Crystallogr.* **1992**, *25*, 92–96.

[23] A. J. M. Duisenberg, L. M. J. Kroon-Batenburg, A. M. M. Schreurs, *J. Appl. Crystallogr.* **2003**, *36*, 220–229.

 © 2005 Wiley-VCH Verlag GmbH & Co. KGaA, Weinheim

[24] G. M. Sheldrick, *SADABS*, program for absorption correction, Bruker AXS, Karlsruhe, **2004**, Germany.
[25] P. T. Beurskens, G. Beurskens, R. de Gelder, S. Garcia-Granda, R. O. Gould, R. Israel, J. M. M. Smits, *The DIRDIF-99 program system*, Crystallography Laboratory, University of Nijmegen, **1999**, The Netherlands.
[26] G. M. Sheldrick, *SHELXL97*, program for crystal structure refinement, University of Göttingen, **1997**, Germany.
[27] A. L. Spek, *J. Appl. Crystallogr.* **2003**, *36*, 7–13.
Received: July 15, 2005
Published Online: October 5, 2005

 © 2005 Wiley-VCH Verlag GmbH & Co. KGaA, Weinheim

Copper(II) Complexes of Schiff-Base and Reduced Schiff-Base Ligands: Influence of Weakly Coordinating Sulfonate Groups on the Structure and Oxidation of 3,5-DTBC

Bellam Sreenivasulu,[a] Muthalagu Vetrichelvan,[a] Fei Zhao,[b] Song Gao,*[b] and Jagadese J. Vittal*[a]

Keywords: Biomimetic studies / Copper / Schiff-base complexes / Organosulfonate ligands / Catecholase activity / Magnetic properties

The copper(II) complexes of the Schiff-base ligands H_2Sams and H_2Saes and the reduced Schiff-base ligands H_2Sam and H_2Sae formed between salicylaldehyde and aminomethanesulfonic acid or 2-aminoethanesulfonic acid (taurine) have been synthesized in moderate yields. The solid-state structures of the five dinuclear complexes, $[Cu_2(Sams)_2(H_2O)_2]$ (**1**), $[Cu_2(Sam)_2(H_2O)_2]\cdot H_2O$ (**2**), $[Cu_2(Saes)_2(H_2O)_2]\cdot 2H_2O$ (**3**), $[Cu_2(Sae)_2]\cdot 2H_2O$ (**4**), and $[Cu_2(Sae)_2(DMF)_2]\cdot 2DMF$ (**5**), have been determined by X-ray crystallography, showing that the Cu^{II} centers have distorted square-pyramidal geometry. The Schiff-base copper complexes **1** and **3** have hydrogen-bonded 2D sheet structures while the reduced Schiff-base complexes **4** and **5** display a 2D coordination network and a hydrogen-bonded 2D structure respectively. All these complexes have been investigated for their catecholase activity and activity measurements have been compared with those of dinuclear copper(II) complexes of similar ligands obtained with carboxylate analogues of the corresponding sulfonic acids; these studies show that **4** has significantly higher activity. Further, a strong antiferromagnetic interaction between Cu^{II} ions in dimeric complexes **1** [$J = -9.04(2)$ cm^{-1}], **3** [$J = -272(4)$ cm^{-1}), and **4** [$J = -237(4)$ cm^{-1}] has been observed.

(© Wiley-VCH Verlag GmbH & Co. KGaA, 69451 Weinheim, Germany, 2005)

Introduction

In the past decades, significant progress has been made in understanding the coordination chemistry of copper(II) complexes of various Schiff-base ligands.[1] Most of the model studies of the metal complexes of Schiff-base ligands containing salicylaldehyde and amino acids have focused upon the binding mode of these ligands.[2] X-ray crystal structures of complexes thus obtained demonstrated that the Schiff-base ligand acts as a tridentate moiety, coordinating through the phenolato oxygen, imine nitrogen, and carboxylate oxygen.

Our research group is interested in tridentate reduced Schiff-base ligands, specifically *N*-(2-hydroxybenzyl)amino acids, as they are more flexible because of the reduction of the C=N bond of the Schiff base, and help to overcome the ligand instability. Further, in addition to their potential hydrogen-bond donor–acceptor functionalities, these ligands can form conformationally flexible five- and six-membered rings upon complexation. Several copper complexes of reduced Schiff-base ligands formed between salicylaldehyde and amino acids were explored to serve as models for the intermediate species in biological racemization and transamination reactions.[3] Making use of these advantages, we employed such reduced Schiff-base ligands to synthesize dinuclear Cu^{II} and Zn^{II} complexes that exhibit interesting structural transformations in the solid state.[4] Further, in our recent report, we showed that incorporation of an additional carboxylate group in the side arm of the ligand *N*-(2-hydroxybenzyl)-L-glutamic acid formed between salicylaldehyde and L-glutamic acid resulted in a novel structural display of a spiral staircase conformation.[5] Copper(II) complexes of the reduced Schiff-base ligand derived from salicylaldehyde and histidine have been found to self-assemble to form a capsule incorporating four pyridine molecules.[6]

Various dicopper active sites found in copper-containing metalloenzymes have similar structural aspects with three histidine donors for each of the two Cu centers, which are separated by a distance of about 3.5 Å, and catechol oxidase as one of the prominent members of the type III copper proteins that catalyze the two-electron oxidation of *ortho*-diphenols to the corresponding quinones.[7] Conse-

[a] Department of Chemistry, National University of Singapore, 3 Science Drive 3, Singapore 117543, Singapore
Fax: +65-6779-1691
E-mail: chmjjv@nus.edu.sg
[b] College of Chemistry and Molecular Engineering, Peking University,
Beijing 100871, P.R. China
Fax: +86-10-6275-1708
E-mail: gaosong@pku.edu.cn
Supporting information for this article is available on the WWW under http://www.eurjic.org or from the author.

quently, quite a number of dinuclear copper complexes have been investigated as biomimetic catalysts for catechol oxidation by employing the most common and convenient model substrate, 3,5-di-*tert*-butylcatechol (3,5-DTBC), which can be oxidized to 3,5-di-*tert*-butylquinone (3,5-DTBQ).[8] With regard to this, we have recently reported a series of dinuclear copper(II) complexes of the tridentate and binucleating reduced Schiff-base ligands and their functional relationship with catecholase activity.[9] Apart from the reduced Schiff-base ligands with carboxylate donor group, their sulfonic acid analogues are expected not only to improve solubility in aqueous media but also form interesting supramolecular architectures by modifying the connectivity at the metal centers as well as the hydrogen-bonding pattern.[10] However, the coordination chemistry of transition metals with a similar ligand system containing organosulfonate species is not well documented.[11] Despite the available literature showing the organosulfonate anions as good hydrogen-bonding acceptors to form strongly hydrogen-bonded networks,[12] there are few metal-based supramolecular arrays in the literature.[13]

Encouraged by our previous results, we were prompted to synthesize such tridentate *N*-(2-hydroxybenzyl)aminomethane/ethanesulfonic acids (Scheme 1), and their corresponding dinuclear copper(II) complexes of both Schiff-base and reduced Schiff-base ligands. In order to evaluate these complexes for the effect of the sulfonate donor group, compared to the corresponding carboxylate analogues, on the crystal structures and the consequent influence on the catecholase activity, herein we report and highlight different structural features between Schiff-base and reduced Schiff-base dicopper(II) complexes, and their catecholase activity. Variable temperature magnetic studies have also been discussed for the Cu^{II} complexes containing *syn-syn* O–S–O-bridged **1** and **3** and phenoxo-bridged **4**, which can mediate magnetic interaction effectively within the dimeric Cu unit.

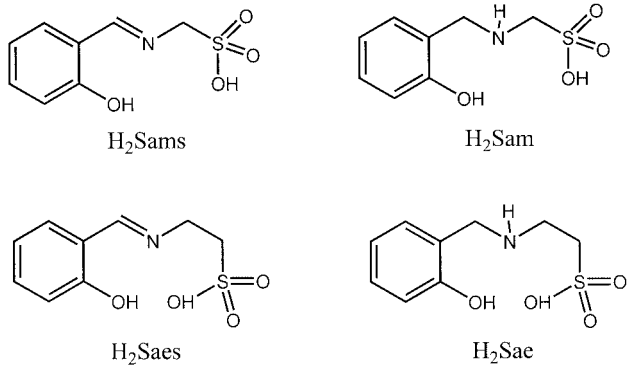

Scheme 1. Ligands employed for complexation.

Results and Discussion

Copper complexes **1** and **3** were prepared by treating copper(II) nitrate trihydrate solution with the Schiff bases formed in situ between salicylaldehyde and aminomethanesulfonic acid and/or aminoethanesulfonic acid. The reduced Schiff-base complex $[Cu_2(Sam)_2(H_2O)_2]\cdot H_2O$ (**2**) was obtained by treating a copper(II) nitrate trihydrate solution with H_2Sam generated in situ. On the other hand, reduced Schiff-base H_2Sae was synthesized first and then complexed with copper(II) acetate monohydrate to obtain $[Cu_2(Sae)_2]\cdot 2H_2O$ (**4**). The complex $[Cu_2(Sae)_2(DMF)_2]\cdot 2DMF$ (**5**) resulted when **4** was recrystallized from the DMF/acetone solvent mixture. We were unable to isolate *N*-(2-hydroxybenzyl)aminopropanesulfonic acid or prepare its Cu^{II} complex in situ as in the case of the H_2Sam ligand. Complexes **1**–**4** show absorption bands at 3400, 3443, and 3410 cm^{-1} corresponding to the presence of water molecules. The C=N stretching frequencies are observed at 1629 cm^{-1} in **1** and 1617 cm^{-1} in **3**. As the C=N bond is reduced in **2**, **4**, and **5**, the N–H stretching frequencies appeared in the range of 2920–2935 cm^{-1}. The frequencies characteristic of the S–O stretching modes are observed in the range 1000–1380 cm^{-1}.[14]

The electronic spectra of **1** and **3** in water display weak bands at 678 and 688 nm followed by intense bands at 367 and 322 nm respectively. The high intensity can be attributed to the delocalization of charge in the conjugated Schiff base. Copper(II) complexes of Schiff bases and related ligands exhibit weak bands in the range 620–680 nm which are due to d-d transitions.[15] For an octahedral geometry, the expected ^2E_g to $^2T_{2g}$ transition takes place at around 800 nm. This band will undergo a significant blue shift when octahedral geometry distorts to square pyramidal and square planar structure.[16] For the reduced Schiff-base copper(II) complexes with square pyramidal geometry, the d-d transitions and charge transfer transitions generally occur in the ranges 650–720 and 360–450 nm respectively.[9,17] In the case of **2**, **4**, and **5** the absorption bands at 717–736 nm correspond to d-d transitions and a strong band at 405–420 nm is due to ligand-to-metal charge transfer.

TG analysis of **1** showed a weight loss of 6.8% (calculated 6.1%) for the loss of two aqua ligands in the temperature range 159–192 °C. In **2**, the loss of three water molecules, including two aqua ligands and a lattice water, was indicated by a weight loss of 8.1% (calculated 8.4%) in the temperature range 148–183 °C. Similarly, a weight loss of 11.7% (calculated 11.0%) corresponding to two aqua ligands and two lattice water molecules has been found to occur at 30–155 °C in **3**. TG weight loss of 5.7% (calculated 5.8%) agrees well with the loss of two lattice water molecules in **4**.

Description of X-ray Crystal Structures

Selected crystallographic data and refinement details are displayed in Table 1.

Crystal Structure of $[Cu_2(Sams)_2(H_2O)_2]$ (1)

Dark green prismatic single crystals of **1** suitable for single-crystal X-ray crystallographic studies were obtained from the filtrate of the reaction mixture on slow evaporation. Compound **1** is a centrosymmetric dimer with copper centers assuming square pyramidal geometry ($\tau = 0.16$).[18]

 © 2005 Wiley-VCH Verlag GmbH & Co. KGaA, Weinheim

Table 1. Crystallographic data and structure refinement details for **1**, **3**, **4**, and **5**.

Complex	**1**	**3**	**4**	**5**
Formula	$C_{16}H_{18}Cu_2N_2O_{10}S_2$	$C_9H_{13}CuNO_6S$	$C_{18}H_{23}Cu_2N_2O_9S_2$	$C_{30}H_{46}Cu_2N_6O_{12}S_2$
Formula mass	589.52	326.8	602.6	873.93
T [K]	223(2)	223(2)	223(2)	223(2)
Wavelength, λ [Å]	0.71073	0.71073	0.71073	0.71073
Crystal system	triclinic	triclinic	monoclinic	monoclinic
Space group	$P\bar{1}$	$P\bar{1}$	$P2_1/n$	$P2_1/n$
a [Å]	7.0092(7)	6.9079(7)	10.8222(7)	13.2137(9)
b [Å]	9.0004(8)	9.226(1)	8.7872(6)	9.7141(7)
c [Å]	9.0516(8)	10.439(1)	11.9314(8)	14.944(1)
α [°]	97.012(2)	109.042(2)	90	90
β [°]	109.829(2)	101.162(2)	108.024(1)	99.130(1)
γ [°]	107.720(2)	104.906(2)	90	90
V [Å^3]	495.24(8)	579.0(1)	1079.0(1)	1893.9(2)
Z	1	1	2	2
D_{calcd} [g cm^{-3}]	1.977	1.875	1.855	1.532
μ [mm^{-1}]	2.420	2.086	2.220	1.299
Reflections collected	2880	4727	6007	14925
Independent reflections	1754	3168	1902	5330
R_{int}	0.0233	0.0174	0.0195	0.0238
Gof	1.024	1.034	0.741	1.013
Final $R[I > 2\sigma]$, R_1[a]	0.0346	0.0380	0.0226	0.0399
wR_2[b]	0.0822	0.0848	0.0612	0.1023

[a] $R_1 = \Sigma||F_o| - |F_c||/\Sigma|F_o|$. [b] $wR_2 = [\Sigma w(F_o^2 - F_c^2)^2/\Sigma w(F_o^2)^2]^{1/2}$.

At each copper center, the basal plane of the square pyramid is occupied by three oxygen atoms, one each from the phenolate group [Cu1–O1, 1.898(2) Å], the sulfonate group [Cu1–O2, 2.019(2) Å], and the aqua ligand [Cu1–O5, 1.932(2) Å]; and nitrogen [Cu1–N1, 1.936(3) Å] from the imine group. The apical sites of the Cu^{II} centers have *anti* configuration and are occupied by the oxygen atoms [Cu1–O3A, 2.393(3) Å; Cu1A–O3, 2.393(3) Å] of the sulfonate group from the neighboring molecule as shown in Figure 1. Selected bond lengths and bond angles are given in Table 2.

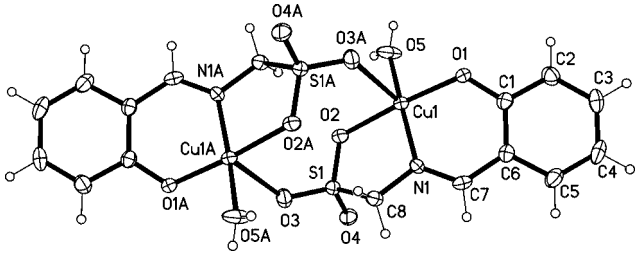

Figure 1. An ORTEP diagram of **1**.

Unlike the complexes obtained with reduced Schiff bases displaying the phenoxo-bridged dinuclear Cu^{II} centers with the usual Cu···Cu distance of about 3 Å, H_2Sams gave rise to the dinuclear copper core with Cu···Cu separation of 5.12 Å without bridging phenolate moiety. Instead, the centrosymmetric dinuclear core forms an interesting eight-membered ring consisting of Cu1, O2, S1, O3, Cu1A, O2A, S1A, and O3A (Figure 1). Further, compared with the phenolato-bridged structures formed by the reduced Schiff-base Cu^{II} compounds, formation of an entirely different structure of **1** may be attributed to kinetic factors, as several phenolato-bridged dinuclear complexes have been reported in the literature.[19–21]

The dimers are packed in the solid state to give a hydrogen-bonded 2D structure in the *ac* plane (Figure 2). Two types of complementary hydrogen bonds are present: the first one is between the phenoxo oxygen and one of the hydrogen atoms of the aqua ligand from the adjacent dimer along the *c*-direction; the next one is between the free oxygen atom of the sulfonate group with another hydrogen atom of the aqua ligand, normal to (100) plane. In addition, these 2D sheets are also supported by C–H···O hydrogen-bonding interactions, C(3)–H(3)···O(4), 2.53 Å; C(7)–H(7)···O(4), 2.52 Å, which are considered medium strong when compared with the shorter and stronger C–H···O interac-

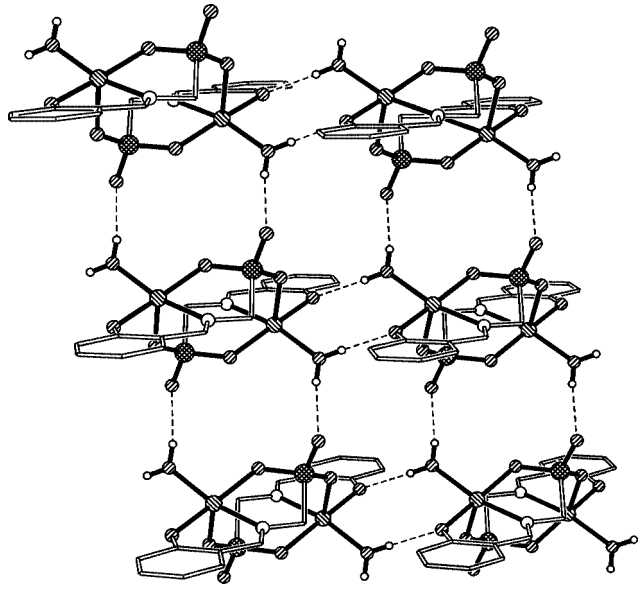

Figure 2. Hydrogen-bonded 2D sheet structure of **1** in *ac* plane.

 © 2005 Wiley-VCH Verlag GmbH & Co. KGaA, Weinheim

Table 2. Selected bond lengths [Å] and angles [°] in **1**, **3**, **4**, and **5**.

Compound **1**			
Cu(1)–O(1)	1.898(2)	S(1)–O(2)–Cu(1)	117.7(1)
Cu(1)–O(5)	1.932(2)	S(1)–O(3)–Cu(1)[a]	131.6(1)
Cu(1)–N(1)	1.936(3)	O(1)–Cu(1)–O(5)	91.3(1)
Cu(1)–O(2)	2.019(2)	O(1)–Cu(1)–N(1)	92.2(1)
Cu(1)–O(3)[a]	2.393(3)	O(5)–Cu(1)–N(1)	165.8(1)
O(3)–Cu(1)[a]	2.393(3)	O(1)–Cu(1)–O(2)	175.2(1)
N(I)–C(7)	1.291(4)	O(1)–Cu(1)–O(3)[a]	96.82(1)
N(1)–C(8)	1.452(4)	O(5)–Cu(1)–O(3)[a]	89.1(1)
Cu(1)···Cu(1)[a]	5.12	N(1)–Cu(1)–O(3)[a]	104.2(1)
Compound **3**			
Cu(1)–O(1)	1.886(2)	S(1)–O(2)–Cu(1)	131.3(1)
Cu(1)–O(2)	1.967(2)	S(1)–O(3)–Cu(1)[a]	134.76(1)
Cu(1)–N(1)	1.968(2)	O(1)–Cu(1)–O(2)	168.87(8)
Cu(1)–O(5)	1.989(2)	N(1)–Cu(1)–O(5)	166.92(9)
Cu(1)–O(3)[a]	2.410(2)	O(1)–Cu(1)–N(1)	94.08(9)
C(7)–N(1)	1.282(3)	O(2)–Cu(1)–N(1)	97.04(8)
N(1)–C(8)	1.479(3)	O(1)–Cu(1)–O(5)	85.74(9)
O(3)–Cu(1)[a]	2.410(2)	O(2)–Cu(1)–O(5)	83.56(8)
Cu(1)···Cu(1)[a]	5.33	O(1)–Cu(1)–O(3)[a]	87.32(8)
		O(2)–Cu(1)–O(3)[a]	89.54(7)
		N(1)–Cu(1)–O(3)[a]	103.30(8)
		O(5)–Cu(1)–O(3)[a]	89.76(8)
Compound **4**			
Cu(1)–O(1)[a]	1.931(1)	S(1)–O(2)–Cu(1)	120.58(8)
Cu(1)–O(1)	1.972(1)	S(1)–O(4)–Cu(1)[c]	132.93(9)
Cu(1)–N(1)	1.986(1)	O(1)[a]–Cu(1)–O(1)	78.09(6)
Cu(1)–O(2)	2.002(1)	O(1)[a]–Cu(1)–N(1)	172.15(7)
Cu(1)–O(4)[b]	2.330(1)	O(1)–Cu(1)–N(1)	94.31(6)
O(1)–Cu(1)[a]	1.931(1)	O(1)[a]–Cu(1)–O(2)	95.32(6)
O(4)–Cu(1)[c]	2.330(1)	O(1)–Cu(1)–O(2)	152.72(7)
Cu(1)–O(1)[a]	1.931(1)	O(1)[a]–Cu(1)–O(4)[b]	94.63(6)
C(7)–N(1)	1.494(3)	O(1)–Cu(1)–O(4)[b]	99.55(6)
N(1)–C(8)	1.476(3)	N(1)–Cu(1)–O(4)[b]	84.60(6)
O(4)–Cu(1)[c]	2.330(1)	O(2)–Cu(1)–O(4)[b]	107.40(6)
Cu(1)···Cu(1)[a]	3.031(5)	O(2)–Cu(1)–Cu(1)[a]	129.59(5)
		O(4)[b]–Cu(1)–Cu(1)[a]	99.17(4)
Compound **5**			
Cu(1)–O(1)[a]	1.958(1)	O(1)[a]–Cu(1)–O(1)	77.96(7)
Cu(1)–O(1)	1.981(1)	O(1)[a]–Cu(1)–O(2)	95.31(7)
Cu(1)–N(1)	1.991(1)	O(1)[a]–Cu(1)–N(1)	172.38(7)
C(7)–N(1)	1.496(3)	O(1)–Cu(1)–O(2)	156.95(8)
Cu(1)···Cu(1)[a]	3.06		

[a] Symmetry transformations used to generate equivalent atoms $-x + 1, -y, -z$ in **1** and **3**; $-x + 1, -y + 1, -z + 1$ in **4** and **5**. [b] $-x + 3/2, y - 1/2, -z + 3/2$. [c] $-x + 3/2, y + 1/2, -z + 3/2$.

tions of about 2.0 Å available in the literature.[22] Hydrogen bond parameters in **1** are tabulated in Table 3.

Crystal Structure of [Cu$_2$(Saes)$_2$(H$_2$O)$_2$]·2H$_2$O (3)

Compound **3** is also a binuclear complex of formula [Cu$_2$(Saes)$_2$(H$_2$O)$_2$]·2H$_2$O with a crystallographic center of inversion as in **1**. An ORTEP diagram of **3** with numbering scheme is shown in Figure 3. Selected bond lengths and bond angles are given in Table 2. Each Cu^{II} center has square pyramidal geometry.

The ligand connectivity in **3** is very similar to that found in **1** except that this Saes dianion forms two six-membered rings. The ring expansion is due to an additional methylene group in the H$_2$Saes ligand, which reduces the ring strain

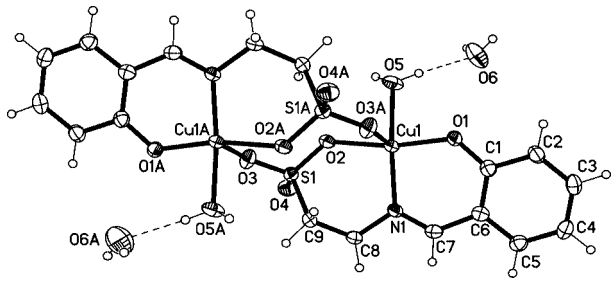

Figure 3. An ORTEP diagram of **3**.

and thus lowers the τ-value to 0.03. As observed in **1**, the dinuclear core in **3** also shows the axial coordination mode by sulfonato oxygen atoms in the centrosymmetric dimer. The introduction of a –CH$_2$ group in the H$_2$Saes ligand changed a five-membered ring to a six-membered ring and hence increased the Cu···S distances (3.01 Å in **1** vs 3.15 Å in **3**). This is also reflected in the widening of the Cu(1)–O(2)–S(1) angle from 117.7° in **1** to 131.3° in **3** and an increase in the Cu···Cu separation to 5.33 Å.

Compound **3** also forms hydrogen-bonded sheets similar to **1** (Figure 4). However, a water molecule is strongly hydrogen bonded between the phenoxo oxygen atom and the aqua ligand. The second hydrogen atom of the lattice water is disordered and found to be hydrogen bonded to another lattice water molecule as well as to other oxygen atoms of the sulfonate group. Table 3 shows the hydrogen bond parameters.

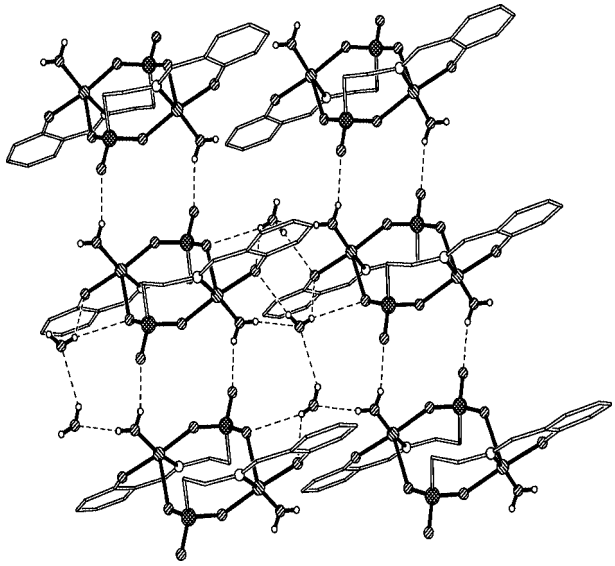

Figure 4. Hydrogen-bonded 2D sheets in **3**.

Crystal Structure of [Cu$_2$(Sae)$_2$]·2H$_2$O (4)

When the C=N double bond is reduced, the complexation behavior of the Sae dianion is completely different from that of the Saes dianion. The Sae ligand with flexible backbone behaves like other reduced Schiff-base ligands in terms of forming a phenolato-bridged Cu^{II} dimer having the expected connectivity of the donor atoms.[4,9] A perspective view of **4** exhibiting the coordination environments

 © 2005 Wiley-VCH Verlag GmbH & Co. KGaA, Weinheim

Table 3. Hydrogen bond lengths [Å] and angles [°] in **1**, **3**, **4**, and **5**.

Complex	D–H	*d*(D–H)	*d*(H–A)	∠DHA	*d*(D–A)	A	Symmetry
1	O5–H5A	0.80(4)	1.98(4)	171(4)	2.775(5)	O4	$-x, -y, -z$
	O5–H5B	0.78(4)	1.85(3)	178(6)	2.626(4)	O1	$1-x, -y, 1-z$
3	C3–H3[a]	0.94	2.53	147	3.358(5)	O4	$1-x, 1-y, 1-z$
4	C7–H7[a]	0.94	2.52	172	3.453(4)	O4	$1-x, 1-y, -z$
5	O5–H5A	0.81(3)	2.00(3)	156(3)	2.761(3)	O4	$-x, -y, -z$
	O5–H5B	0.81(2)	1.87(2)	166(4)	2.666(4)	O6	$-x, -y, -z$
	O6–H6A	0.81(3)	2.17(3)	157(5)	2.927(7)	O6	$-x, -y, 1-z$
	O6–H6B	0.81(4)	2.45(4)	140(4)	3.108(4)	O3	$x, y, 1+z$
	O6–H6B	0.81(4)	2.31(5)	142(4)	2.987(5)	O1	$1-x, -y, 1-z$
	N1–H1[a]	0.92	2.32	144	3.144(2)	O2	$3/2-x, -1/2+y, 3/2-z$
	N1–H1	0.92	2.20	145	3.007(3)	O3	$3/2-x, 1/2+y, 3/2-z$
	C9–H9B[a]	0.98	2.20	165	3.438(3)	O4	$3/2-x, 1/2+y, 3/2-z$
	C10–H10[a]	0.94	2.54	153	3.406(3)	O4	$1-x, 1-y, 1-z$
	C12–H12A[a]	0.97	2.57	156	3.482(4)	O4	$1-x, 1-y, 1-z$

[a] The hydrogen atoms were placed in calculated positions.

around the Cu^{II} atoms is shown in Figure 5. Selected bond lengths and bond angles in **4** are shown in Table 2. The phenolato oxygen atoms, a nitrogen atom from the imine group, and an oxygen atom of the sulfonate group form the basal square. The apical site in each Cu^{II} center is occupied by another oxygen atom of the sulfonate group from the neighboring dimer. This interdimer connectivity leads to the formation of a 2D (4, 4) network structure as shown in Figure 6. The two axial oxygen atoms have *trans* geometry due to the crystallographic center of inversion present at the center of the Cu_2O_2 ring. Such geometry has also been observed in several Cu^{II} dimers having nonchiral reduced Schiff-base ligands.[9] Interestingly the infinite 2D network structure with (4, 4) net formed in **4** is the first of its kind observed in the Cu^{II} and Zn^{II} complexes containing reduced Schiff-base ligands although these nets are ubiquitous in the literature.[23]

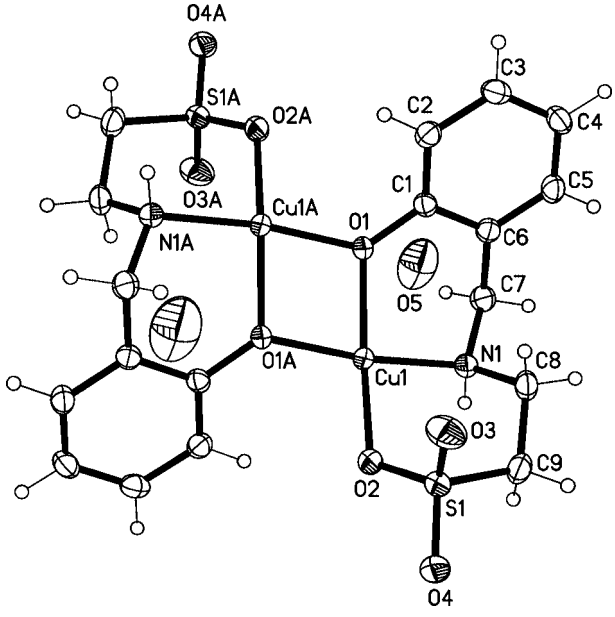

Figure 5. An ORTEP diagram of **4**.

The N–H proton is weakly hydrogen bonded to one of the sulfonate oxygen atoms (N1–H1···O2, 2.324 Å). The

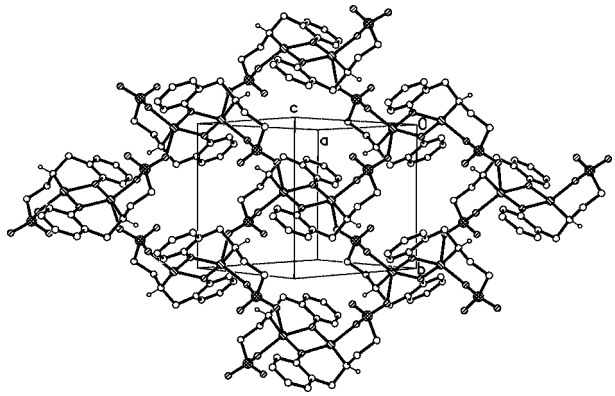

Figure 6. A portion of the 2D structure in **4**.

intermolecular N–H···O hydrogen bond between the NH_2 and sulfonate groups in the solid state and in solution has been utilized as a crystal engineering tool.[12] The properties and the functions of the N–H···O hydrogen bonds involving coordinated $-SO_3^-$ groups in a dinuclear calcium complex have been reported.[24] As in **1**, medium strong C–H···O hydrogen bonds have also been observed in the solid state.

Crystal Structure of [Cu₂(Sae)₂(DMF)₂]·2DMF (5)

Complex **5** is formed upon recrystallization of **4** from strongly coordinating solvent DMF. The axial sulfonate groups in **4** are replaced by DMF molecules in **5** and hence discrete dinuclear compounds are formed. Two more DMF molecules were found in the crystal lattice. The crystal packing of **5** generated 2D hydrogen-bonded polymeric structures parallel to the $(10\bar{1})$ planes. The solid-state structure exhibits N–H···O hydrogen bonding between one of the sulfonate oxygen and NH hydrogen atoms (Table 3).

Magnetic Properties of 1, 3, and 4

The temperature dependences of χ_m and $\chi_m T$ for crystalline samples of **1**, **3**, and **4** are presented in Figure 7. For compound **1**, χ_m increases upon cooling and reaches a maximum at 16 K; the data above 30 K can be well fitted with the Curie–Weiss law [$\chi_m = C/(T-\theta)$], giving C =

 © 2005 Wiley-VCH Verlag GmbH & Co. KGaA, Weinheim

0.802 $cm^3 mol^{-1} K$, and θ = –12.7(5) K. The maximum and negative Weiss constant suggests an antiferromagnetic coupling between Cu^{II} ions. The susceptibility data in the 2–330 K range were fitted with a Cu_2 dimer model ($H = -2JS_1S_2$), giving the intradimer coupling J = –9.04(2) cm^{-1}, and g = 2.002(3) with $R = 2.3\times10^{-4}$ ($R = \Sigma[(\chi_m)_{obs} - (\chi_m)_{calc}]^2/\Sigma[(\chi_m)_{obs}]^2$).

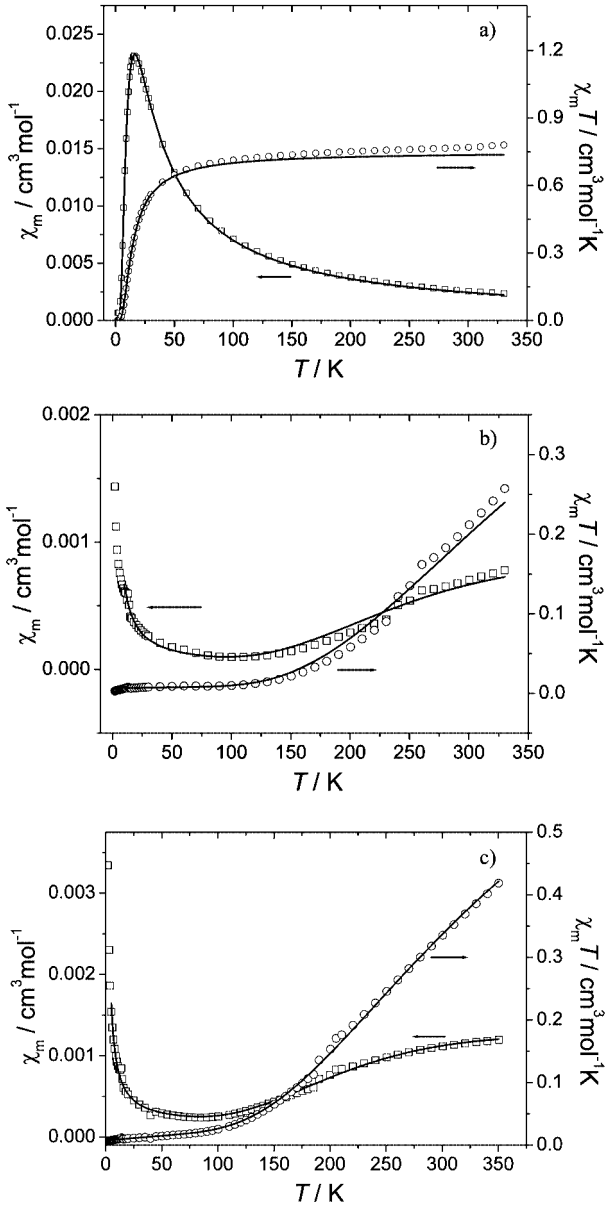

Figure 7. The temperature dependences of χ_m and $\chi_m T$ in the range of 2–350 K for a) **1**, b) **3**, and c) **4**. The solid lines are fits using a Cu_2 dimer model.

Compounds **3** and **4** show similar behavior; on lowering the temperature, χ_m decreases gradually, and there is an increase below about 100 K while the $\chi_m T$ value even at 330 or 350 K is quite small compared with the expected value of 0.75 $cm^3 mol^{-1} K$ for two noninteracting Cu^{II} ions. Upon cooling it decreases rapidly to a value close to zero at 2 K. The increase of χ_m at low temperature is probably due to trace paramagnetic impurity (ρ). Overall, the data suggest a strong antiferromagnetic coupling between the adjacent Cu^{II} ions in **3** and **4**. Based on the structure of **3**, two Cu^{II} ions are bridged by two sulfonate O–S–O bridges in *syn-syn* mode with Cu···Cu separation at 5.32 Å. Although the distance is quite large compared to the phenoxo-bridged Cu_2 in **4** with a distance of 3.03 Å, the basal planes of the two Cu^{II} ions are almost parallel, which might favor the overlap of $d_{x^2-y^2}$ orbitals of Cu^{II} ions within the dimer. On the other hand, the coupling between the dinuclear moiety in the 2D layer of **4** is negligible, as expected, because of both the *anti–syn* sulfonate bridging mode and the orthogonal relationship of the planes of the neighboring Cu_2O_2.[4d] Therefore, the magnetic data of **3** and **4** can be analyzed by fitting the susceptibilities to an equation calculated using an $H = -2JS_1S_2$ Hamiltonian for a dimer plus impurity of monomer model. The parameters have their usual meanings. As shown in Figure 7b and 7c, quite good fits were obtained for **3**: J = –272(4) cm^{-1}, g = 2.05(5), ρ = 0.0164; Na = 22×10^{-6} with $R = 7.4\times10^{-3}$; and for **4**: J = –237(4) cm^{-1}, g = 2.21(3), ρ = 0.0163; Na = 149×10^{-6} with $R = 2.4\times10^{-3}$.

Catecholase Activity

Many copper-containing metalloenzymes, characterized by the dinuclear active site with two copper atoms operating within their convenient intermetallic distance, are involved in distinct processes in living systems among which the type III copper protein catechol oxidase catalyzes the oxidation of a wide range of *ortho*-di-phenols to *ortho*-di-quinones.[7,8] Hence, dinuclear copper complexes with two metal atoms in close proximity have received a great deal of attention, particularly in relation to their potential uses as bimetallic catalysts, mimicking the activity of enzymes.[8,25–27] Such di-copper(II) complexes exhibiting the catecholase activity are probably crucial for a better understanding of the oxygenation reactions mediated by catechol oxidase.[28–32] The Cu^{II} complexes of Schiff-base and reduced Schiff-base ligands studied here have structurally distinct features. Hence we have evaluated their ability to oxidize catechols to quinones by employing 3,5-DTBC, a common and convenient model substrate. Figure 8 shows the course of oxidation of 3,5-DTBC with time in the presence of **4**. The results are shown in Table 4.

A linear relationship between the initial rates and the concentration of the complexes has been obtained for **2**–**4**, which shows a first-order dependence on the catalyst concentration for these systems. An example of the Lineweaver–Burk plot[29f] is given in Figure 9 for **4**. The data obtained from the Lineweaver–Burk plot model is employed for a comparison of catalytic activity.

It is obvious that catalytic ability towards the oxidation of 3,5-DTBC has been found to follow the order: **4** > **2** > **3**. The least activity observed in the case of Schiff-base complex **3** can be attributed to the inefficient binding of the substrate to the catalyst caused by the formation of the

 © 2005 Wiley-VCH Verlag GmbH & Co. KGaA, Weinheim

Table 4. Kinetic parameters for the activity of complexes **2**–**4**.

Complex	k_{cat} [h^{-1}]	K_m [mM]	V_{max} [10^{-6} Ms^{1}]
$[Cu_2(Sam)_2(H_2O)_2]\cdot H_2O$, **2** in MeOH	1140 (±14)	5.4 (±0.2)	41 (±1)
$[Cu_2(Saes)_2(H_2O)_2]\cdot 2H_2O$, **3** in MeOH	133 (±15)	14.3 (±0.1)	5 (±1)
$[Cu_2(Sae)_2]\cdot 2H_2O$, **4** in MeOH	4612 (±28)	4.3 (±0.1)	163 (±2)
$[Cu_2(Sae)_2]\cdot 2H_2O$, **4** in MeOH/H_2O (95:5)	5048 (±42)	3.2 (±0.1)	178 (±3)

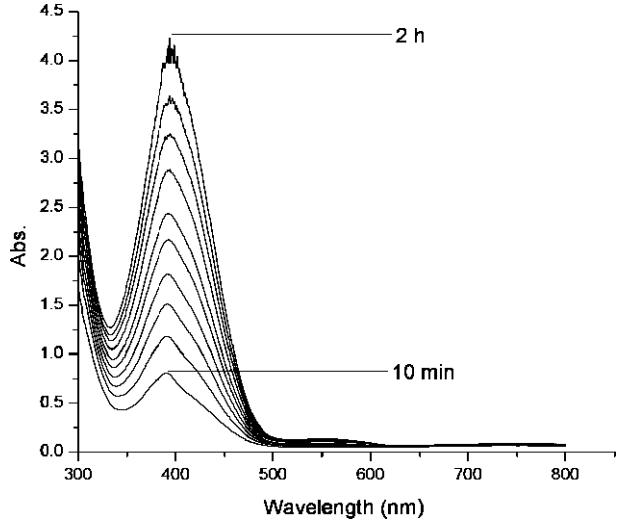

Figure 8. Oxidation of 3,5-DTBC by **4** monitored by UV/Vis spectroscopy.

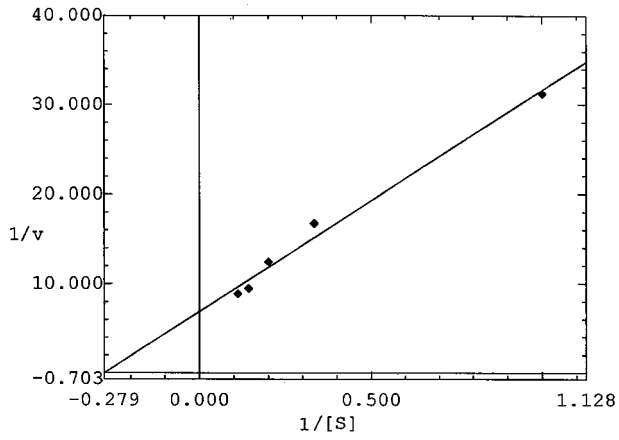

Figure 9. Lineweaver–Burk plot for catalysis by **4**.

eight-membered ring with largely separated Cu^{II} ions. Thus, the larger Cu···Cu distance of 5.33 Å in **3** is highly unfavorable for the efficient binding of the substrate. Furthermore, very distinct structural differences between **3** and **4** account for the difference in their activity.

The catecholase activity of copper(II) compounds with different structural parameters has been investigated and compared to some extent by varying the properties of chelating ligands with respect to their conformation, and the number as well as the nature of the donor atoms.[8] In our earlier report,[9] the reduced Schiff-base complexes $[Cu_2(Sab4)_2(H_2O)_2]$ and $[Cu_2(Sbal)_2(H_2O)_2]$, containing 4-aminobutanoic acid and 3-aminopropanoic acid (β-alanine) respectively, were found to exhibit higher activity, which has been attributed to the larger ring size due to a longer alkyl chain in the side arm of the corresponding ligands. It has been proposed that the formation of seven-membered rings in $[Cu_2(Sab4)_2(H_2O)_2]$ and six-membered rings in $[Cu_2(Sbal)_2(H_2O)_2]$ resulted in higher activity, with K_{cat} values of 3800 and 1280 h^{-1} respectively. The lower activity (K_{cat} = 563 h^{-1}) in $[Cu_2(Sgly)_2(H_2O)]$ due to the shorter glycine side-chain forming five-membered rings appears to support this view. In the present set of complexes, **2** contains aminomethanesulfonate, which is the sulfonic acid analogue of glycine, and **4** has aminoethanesulfonate, which is the sulfonic acid analogue of β-alanine. Based on the connectivity observed in the structures of Cu^{II} complexes containing Schiff bases, as well as chemical, spectroscopic, and catalytic data, the structure of **2** is expected to be similar to that of $[Cu_2(Sgly)_2(H_2O)]$. As a consequence, these five-membered rings formed by the side arm of the ligand in **2** would account for the lower catalytic activity as compared to **4**.

It is important to emphasize here that the K_{cat} value of 4612 h^{-1} observed in **4**, under similar experimental conditions, is much higher than that observed for **2** and **3** and is significantly greater than even the highest activity (K_{cat} = 3800 h^{-1}) reported for $[Cu_2(Sab4)_2(H_2O)_2]$.[9] Quite remarkably, complex **4** has also considerably superior catalytic activity compared to its carboxylate analogue $[Cu_2(Sbal)_2(H_2O)_2]$ (K_{cat} = 1287 h^{-1}).[9] It should be noted that for the five-coordinate dicopper(II) complexes to act as active catalysts, dissociation of the axial bonds should easily occur so that a free coordination site will be readily available for the binding of the substrate in a bridging mode.[31,32] A conformationally flexible ligand backbone can easily assist the conformational changes in the dinuclear core and hence the effective binding of the substrate. Compared to the strongly coordinating carboxylate oxygen atoms as in $[Cu_2(Sab4)_2(H_2O)_2]$ or $[Cu_2(Sbal)_2(H_2O)_2]$, the sulfonate groups are weakly coordinating and can be readily dissociated in solution to accommodate the substrate.[11,13] The combined effect of the sufficiently longer alkyl side arm and the weakly coordinating sulfonate donor group facilitate easy binding of the substrate, especially in **4**, and hence enhance its catalytic activity. Further, the presence of a weakly coordinating sulfonate donor group in **2** makes it a more efficient catalyst (K_{cat} = 1140 h^{-1}) than its carboxylate analogue $[Cu_2(Sgly)_2(H_2O)]$ (K_{cat} = 563 h^{-1}).

Our attempts to evaluate the catecholase activity of **2**, **3**, and **4** in pure water have been unsuccessful because of the insolubility of the product 3,5-DTBQ in water. Hence we tried to employ various ratios of MeOH/H_2O in order to investigate the solvent influence on the activity. Nonethe-

 © 2005 Wiley-VCH Verlag GmbH & Co. KGaA, Weinheim

less, reliable data could only be collected in 95:5 of MeOH/H_2O for **4**. From this result, it has been found that the activity of **4** increased by about 10% in the presence of water.

Summary

Several Cu^{II} complexes of the Schiff-base and reduced Schiff-base ligands formed between salicylaldehyde and aminomethane/ethanesulfonic acid have been synthesized and characterized by spectroscopic methods, and the solid-state structures have been determined by X-ray crystallography.

The salient structural features displayed by the Schiff-base copper complexes **1** and **3** provided an opportunity to perform comparative studies with those of the reduced Schiff-base complexes **2** and **4**. Copper centers in **1** and **3** assumed square pyramidal geometry with the apical position preferably occupied by the sulfonate oxygen atoms. While the reduced Schiff-base complexes **4** and **5** form a phenoxo-bridged dinuclear Cu_2O_2 core with intermetallic distances of 3.03 and 3.06 Å, the Schiff-base complexes **1** and **3** resulted in the formation of eight-membered rings with Cu···Cu distances of 5.12 and 5.33 Å, respectively. Apart from the expected dinuclear copper complexes with a Cu_2O_2 core, there are also reports of mononuclear copper complexes formed preferentially from Schiff bases containing amino acid residues.[33] But strikingly, because of the rigid C=N double bonds, H_2Sams and H_2Saes with sulfonic group offered the formation of eight-membered sulfonato-bridged dinuclear copper centers. Furthermore, **1** and **3** generated a hydrogen-bonded 2D structure unlike the 2D (4, 4) coordination polymeric network containing channels in **4**. Recrystallization of **4** in DMF/acetone mixture gave rise to **5** with the solvent DMF coordinated Cu^{II} centers. DMF, being a strong coordinating solvent, is able to displace the axial oxygen atoms of sulfonate groups in **4** and convert a (4, 4) net to a 2D hydrogen-bonded structure in **5**.

The crystal structures of **4** and **5** exhibit N–H···O hydrogen bonds from the metal-coordinated imine N–H and the sulfonate O while **1** and **3** illustrate a 2D hydrogen-bonding pattern involving the O(w)–H and sulfonate O atoms. These results will further enhance the structural insight into the transition-metal coordination chemistry of organosulfonates and their derivatives.[11–13,24] Variable temperature magnetic studies show that the *syn–syn* sulfonate O–S–O bridges in **3** can mediate antiferromagnetic interaction between Cu^{II} ions quite effectively, as well as the expected strong antiferromagnetic coupling through phenoxo bridges in **4**.

While investigating complexes **2**–**4** as synthetic functional models for the catechol oxidase, **4** has been found to show significantly higher activity than **2** and **3**. Comparative structural studies made between the Schiff-base complexes and the corresponding reduced Schiff-base complexes have provided more insight into the understanding of their catalytic activity. The trend observed in this study using different types of functional groups in the side arm of the ligand complements our earlier observation that the ring size of the side arm in these Cu^{II} complexes has profound influence on the kinetics of the oxidation of 3,5-DTBC. Further, the complexes described here with a weakly coordinating sulfonate group in the ligands have exhibited higher catecholase activity than that of the corresponding carboxylate analogues with strongly coordinating carboxylate groups. These findings are in agreement with the available data in the literature.[28–32]

Experimental Section

Materials: All reagents were purchased from commercial sources and used as received without any further purification.

Physical Measurements: The ^{1}H NMR spectra were recorded with a Bruker ACF300 FT-NMR instrument using TMS as an internal reference by using appropriate deuterated solvents and the IR spectra were recorded using an FTS165 Bio-Rad FTIR spectrometer in the range 4000–450 cm^{-1}. The absorption spectra were recorded with a Shimadzu UV-2501/PC UV/Vis spectrophotometer in aqueous solution. ESI-MS spectra were recorded with a Finnigan MAT LCQ mass spectrometer. The elemental analyses were performed in the Microanalytical Laboratory, Department of Chemistry National University of Singapore. Water present in the compounds was determined by an SDT 2960 TGA thermal analyzer with a heating rate of 10 °C min^{-1} under nitrogen using a sample size of about 10 mg per run. Variable temperature magnetic studies were made using a Quantum Design MPMS-XL5 SQUID magnetometer operating in an applied field of 5 kOe. The experimental susceptibilities were corrected for the diamagnetism (Pascal's tables).

Ligand

***N*-(2-Hydroxybenzyl)aminoethanesulfonic Acid (H_2Sae):** Salicylaldehyde (0.29 g, 2.50 mmol) in MeOH (5 mL) was added to a solution of aminoethanesulfonic acid (0.31 g, 2.50 mmol) in MeOH (10 mL) containing NaOH (0.11 g, 2.50 mmol). The yellow solution was stirred for about 45 min at room temperature prior to cooling in an ice bath. The intermediate Schiff base that formed was reduced with an excess of $NaBH_4$ (0.10 g, 2.65 mmol). The yellow color slowly discharged, and after half an hour the solution was acidified with acetic acid to pH 3–5. Then the solvent was reduced to half and Et_2O was added to get the product, which was filtered off, washed with Et_2O, dried, and stored in a desiccator, as H_2Sae is very hygroscopic. Because of its highly hygroscopic nature, elemental analysis results of H_2Sae were not consistent and hence are not provided. Yield: 0.35 g (60%). MS (EI): *m*/*z* (%) = 257.0 [(L^{2-} + Na)]. ^{1}H NMR ([D_6]DMSO): δ = 7.31 and 6.92 ppm (m, 4 H, aromatic), 4.21 (s, 2 H, benzylic –CH_2), 3.32 (t, 2 H, –CH_2), 3.21 (t, 2 H, –CH_2), 2.01 (s, –SO_3H). ^{13}C NMR: δ = 157.1 (=C_{ar}–O), 115.5 ($C2_{ar}$), 128.2 ($C3_{ar}$), 120.8 ($C4_{ar}$), 129.5 ($C5_{ar}$), 124.4 ($C6_{ar}$), 49.4 (–CH_2SO_3H), 48.9 (benzylic –CH_2), 44.0 (–CH_2CH_2). IR (KBr): $\tilde{\nu}$ = 3365 (OH), 2942 (NH), 1401 and 1115 (SOO^-), 1030 (SO), 1267 (phenolic CO) cm^{-1}.

Complexes

[Cu_2(Sams)$_2$(H_2O)$_2$] (1): Salicylaldehyde (0.1 mL, 0.94 mmol) was added to the clear solution containing aminomethanesulfonic acid (0.10 g, 0.94 mmol) and NaOH (0.04 g, 0.94 mmol) in aqueous MeOH (20 mL, 1:1, v/v) to obtain the yellow Schiff base. After stirring for 30 min, copper nitrate trihydrate in MeOH (0.23 g, 0.94 mmol) was directly added in portions and the resulting green product was further stirred for 30 min and filtered, washed with

 © 2005 Wiley-VCH Verlag GmbH & Co. KGaA, Weinheim

water, MeOH, Et_2O and dried under vacuum. Dark green prismatic single crystals suitable for X-ray diffraction were obtained from the filtrate after one day. Yield: 0.2 g (67%). IR (KBr): $\tilde{\nu}$ = 3400 (OH), 1629 (C=N), 1305 and 1128 (SOO^-), 1247 (phenolic CO) cm^{-1}. UV/Vis (H_2O): λ_{max} (ε, $M^{-1}cm^{-1}$): 678 nm (200), 367 nm (13135). MS (ESI): *m/z* (%) = 276.7 $[CuL]^+$, 553.5 $[Cu_2L_2]$. $C_{16}H_{14}Cu_2N_2S_2O_8(H_2O)_2$ (589.5): calcd. C 32.6, H 3.1, N 4.7, S 10.9, H_2O 6.1; found C 32.5, H 3.0, N 4.4, S 10.8, H_2O 6.8 (from TG weight loss).

$[Cu_2(Sam)_2(H_2O)_2]\cdot H_2O$ (2): Salicylaldehyde (0.1 mL, 0.94 mmol) in MeCN (10 mL) was added to a clear solution of aminomethanesulfonic acid (0.10 g, 0.94 mmol) and NaOH (0.08 g, 1.88 mmol) in MeOH (10 mL) and the resulting yellow Schiff base solution was stirred for 30 min. The mixture was then cooled in an ice bath followed by the addition of $NaBH_4$ (0.02 g, 0.47 mmol). The yellow color of the Schiff base slowly discharged after 20 min and the clear solution was maintained at a pH of 4–6 by adding a few drops of CH_3COOH. Copper nitrate trihydrate (0.23 g, 0.94 mmol) was added to this acidic solution to facilitate in situ complexation. The dark green product obtained after stirring for 1 h was filtered off, washed with MeOH (2 mL), Et_2O (5 mL), and then dried under vacuum. Yield: 0.22 g (66%). IR (KBr): $\tilde{\nu}$ = 3450 (OH), 2920 (NH), 1380 and 1147 (SOO^-), 1037 (SO), 1279 (phenolic CO) cm^{-1}. MS (ESI): *m/z* (%) = 278.7 $[CuL]^+$, 557.8 $[Cu_2L_2]$, 580.7 $[Cu_2L_2Na]^+$. UV/Vis (MeOH) λ_{max} (ε, $M^{-1}cm^{-1}$): 717 nm (190), 405 nm (870). $C_{16}H_{18}Cu_2N_2S_2O_8(H_2O)_3$ (611.6): calcd. C 31.4, H 4.0, N 4.7, S 10.5, H_2O 8.4; found C 31.7, H 4.1, N 4.6, S 10.8, H_2O 8.0 (from TG weight loss).

$[Cu_2(Saes)_2(H_2O)_2]\cdot 2H_2O$ (3): Compound **3** was prepared by a method similar to that described for **1** by using 2-aminoethanesulfonic acid. Yield: 0.2 g (71%). IR (KBr): $\tilde{\nu}$ = 3443 (OH), 1617 (C=N), 1287 and 1173 (SOO^-), 1244 (phenolic CO) cm^{-1}. UV/Vis (H_2O): λ_{max} (ε, $M^{-1}cm^{-1}$): 688 nm (160), 322 nm (5000). $C_{18}H_{18}Cu_2N_2S_2O_8(H_2O)_4$ (653.6): calcd. C 33.1, H 4.0, N 4.3, S 10.0, H_2O, 11.1; found C 33.3, H 4.1, N 4.4, S 10.1, H_2O 11.9 (from TG weight loss).

$[Cu_2(Sae)_2]\cdot 2H_2O$ (4): Copper acetate (0.08 g, 0.40 mmol) in MeOH (10 mL) was added to a solution of the ligand H_2Sae (0.09 g, 0.40 mmol) in MeOH (20 mL) and the resultant solution stirred for about 6 h. The green precipitate formed was filtered, washed with MeOH and Et_2O, and dried under vacuum. Slow evaporation of the dark green clear aqueous solution of **4** furnished dark green single crystals after 4–5 d. Yield: 0.06 g (55%). IR (KBr): $\tilde{\nu}$ = 3410 (OH), 2935 (NH), 1312 and 1181 (SOO^-), 1020 (SO), 1255 (phenolic CO) cm^{-1}. UV/Vis (H_2O): λ_{max} (ε, $M^{-1}cm^{-1}$): 736 nm (190), 420 nm (855). MS (ESI): *m/z* (%) = 291.0 $[(CuL)^-]$, 522.0 $[(CuL_2)^-]$, 584.2 $[(Cu_2L_2)^-]$, 875.0 $[(Cu_3L_3)^-]$, 1106.0 $[(Cu_3L_4)^-]$, 1397.7 $[(Cu_4L_5)^-]$, 1689.6 $[(Cu_5L_6)^-]$. $C_{18}H_{22}Cu_2N_2S_2O_8$ (H_2O) (602.18): calcd. C 34.7, H 4.2, N 4.5, S 10.3, H_2O 5.8; found C 34.3, H 4.2, N 4.6, S 10.3, H_2O 5.9 (from TG weight loss).

$[Cu_2(Sae)_2(DMF)_2]\cdot 2DMF$ (5): The filtered and clear dark green solution of **4** (0.04 g) in DMF (4 mL) was slowly diffused into acetone (10 mL) in a small beaker. Dark green crystals suitable for the single-crystal X-ray diffraction studies were obtained after a week. Yield: 0.02 g (50%). IR (KBr): $\tilde{\nu}$ = 2928 (NH), 1387 and 1150 (SOO^-), 1023 (SO), 1260 (phenolic CO) cm^{-1}. UV/Vis (MeOH) λ_{max} (ε, $M^{-1}cm^{-1}$): 731 nm (195), 412 nm (660). MS (ESI): *m/z* (%) = 292.2 $[(CuL)^-]$, 522.3 $[(CuL_2)^-]$, 584.2 $[(Cu_2L_2)^-]$, 875.0 $[(Cu_3L_3)^-]$. $C_{30}H_{46}Cu_2N_6S_2O_{12}$ (873.9): calcd. C 41.2, H 5.3, N 9.6, S 7.0; found C 41.8, H 5.1, N 9.2, S 7.2.

Catalytic Activity for the Oxidation of 3,5-DTBC and Kinetic Measurements: Catecholase activity of complexes for the oxidation of 3,5-DTBC by complexes **2**–**4** was measured by recording their electronic spectra at 25 °C by time-dependent UV/Vis spectroscopy. For this purpose, 10^{-4} M solutions of complexes **1**–**4** were treated with 50 equiv. of 3,5-DTBC under aerobic conditions. The UV/Vis spectra of the original solution directly after the addition and after 10, 20, and 30 min were recorded and corrected for volume changes up to 2 h.

The kinetics of oxidation of 3,5-DTBC were measured at 25 °C by the method of initial rates by monitoring the growth of the absorption band at 390 nm of the product 3,5-DTBQ. The complex (2 mg) was added to the 3,5-DTBC solution (25 mL) of concentrations 1.0×10^{-3}–1.5×10^{-2} M so that the concentration of the complex was maintained at 10^{-4} M. During the first 10 min of the reaction, the development of the absorption band at 390 nm was monitored. In order to determine the kinetic parameters, the Michaelis–Menten approach was applied.[8,34]

The reactivity studies were performed in methanol solution because of the good solubility of the substrate, 3,5-DTBC, and of its product 3,5-DTBQ. Also, because of the considerable solubility of **4** in water, investigations have also been attempted in a MeOH/H_2O mixture for comparison. Attempts to record the activity of **2** and **3** in MeOH/H_2O were unsuccessful because of the solubility problem producing unreliable data. Preliminary qualitative studies on the activity of **1** have also been unsuccessful owing to its insolubility in common solvents.

X-ray Crystallography: The diffraction experiments were carried out on a Bruker AXS SMART CCD diffractometer. The program SMART[35a] was used for collecting frames of data, indexing reflection and determination of lattice parameter, SAINT[35a] for integration of the intensity of reflections and scaling, SADABS[35b] for absorption correction, and SHELXTL[35c] for space group and structure determination, least-squares refinements on F_2. Positional and thermal parameters of the non-hydrogen atoms were refined in the least-squares cycles. The hydrogen atom positions and individual *U*'s were refined for the water molecules in **1**. One of the hydrogen atoms of the lattice water in **3** was found to be disordered. The option DFIX was used in the model to idealize the geometry. No hydrogen atoms could be located for the lattice water in **4**. The methyl carbon atom of the lattice DMF was found to be disordered (0.65/0.35) in **5**. Only isotropic thermal parameters were refined for the minor component of the disorder.

CCDC-266070 (for **1**), CCDC-266071 (for **3**), CCDC-266072 (for **4**), and CCDC-266073 (for **5**) contain the supplementary crystallographic data for this paper. These data can be obtained free of charge from The Cambridge Crystallographic Data Centre via www.ccdc.cam.ac.uk/data_request/cif.

Supporting Information (see also the footnote on the first page of this article): Molecular and packing diagrams of **5**, thermogravimetry of **1**–**5**, UV/Vis plots and Lineweaver–Burk plots for **2**–**4** (total number of pages: 7).

Acknowledgments

We gratefully acknowledge the financial support from NUS (R143-000-252-112) and from NSFC (20125104, 20490210).

[1] See for example: a) Y. Nakao, K. Sakurai, A. Nakahara, *Bull. Chem. Soc. Jpn.* **1967**, *40*, 1536; b) K. S. Bai, D. L. Leussing, *J. Am. Chem. Soc.* **1967**, *89*, 6126; c) M. J. O'Connor, R. E. Ernst, J. E. Schoenborn, R. H. Holm, *J. Am. Chem. Soc.* **1968**, *90*, 1744; d) L. Casella, M. Gullotti, *J. Am. Chem. Soc.* **1981**, *103*, 6338; e) L. Casella, M. Gullotti, G. Pacchionic, *J. Am.*

 © 2005 Wiley-VCH Verlag GmbH & Co. KGaA, Weinheim

Chem. Soc. **1982**, *104*, 2386; f) M. R. Wagner, F. Ann Walker, *Inorg. Chem.* **1983**, *22*, 3021; g) R. D. Gillard, R. Wootton, *J. Chem. Soc. B* **1970**, 364.

[2] a) K. Tatsumoto, A. E. Martell, *J. Am. Chem. Soc.* **1981**, *103*, 6203; b) K. Tatsumoto, A. E. Martell, R. J. Motekaitis, *J. Am. Chem. Soc.* **1981**, *103*, 6197; c) H. M. Dawes, J. M. Waters, T. N. Waters, *Inorg. Chim. Acta* **1982**, *66*, 29; d) I. Bkouche-Waksman, J. M. Barbe, A. Kvick, *Acta Crystallogr. Sect. B* **1988**, *44*, 595; e) R. Hamalainen, U. Turpeinen, *Acta Crystallogr. Sect. C* **1985**, *41*, 1726; f) K. Korhonen, R. Hamalainen, U. Turpeinen, *Acta Crystallogr. Sect. C* **1984**, *40*, 1175; g) K. Nakagima, M. Kojima, K. Foriumi, K. Saito, J. Fujita, *Bull. Chem. Soc. Jpn.* **1989**, *62*, 760; h) V. Kettmann, E. Fresova, *Acta Crystallogr. Sect. C* **1993**, *49*, 1932.

[3] L. L. Koh, J. D. Ranford, W. T. Robinson, J. O. Stevenson, A. L. C. Tan, D. Wu, *Inorg. Chem.* **1996**, *35*, 6466.

[4] a) J. D. Ranford, J. J. Vittal, D. Wu, *Angew. Chem. Int. Ed. Engl.* **1998**, *37*, 1114; b) J. D. Ranford, J. J. Vittal, D. Wu, X. Yang, *Angew. Chem. Int. Ed.*. **1999**, *38*, 3498; c) B. Sreenivasulu, J. J. Vittal, *Cryst. Growth Des.* **2003**, *3*, 635; d) C. T. Yang, B. Moubaraki, K. S. Murray, J. D. Ranford, J. J. Vittal, *Inorg. Chem.* **2001**, *40*, 5934.

[5] B. Sreenivasulu, J. J. Vittal, *Angew. Chem. Int. Ed.* **2004**, *43*, 5769.

[6] M. A. Alan, M. Nethaji, M. Ray, *Angew. Chem. Int. Ed.* **2003**, *42*, 1940.

[7] K. D. Karlin, Z. Tyeklar (Eds.), *Bioinorganic Chemistry of Copper*, Chapman & Hill, New York, **1993**.

[8] a) R. Than, A. A. Feldman, B. Krebs, *Coord. Chem. Rev.* **1999**, *182*, 211; b) C.-J. Lee, C.-H. Kao, H.-H. Wei, Y.-H. Liu, G.-H. Lee, Y. Wang, *J. Inorg. Biochem.* **2001**, *84*, 171; c) J. Reim, B. Krebs, *J. Chem. Soc., Dalton Trans.* **1997**, 3793.

[9] C.-T. Yang, M. Vetrichelvan, X. D. Yang, M. Moubaraki, K. S. Murray, J. J. Vittal, *Dalton Trans.* **2004**, *1*, 113.

[10] a) Y. Wang, L. Feng, Y. Li, C. Hu, E. Wang, N. Hu, H. Jia, *Inorg. Chem.* **2002**, *41*, 6351, and references cited therein; b) V. A. Russell, M. C. Etter, M. D. Ward, *Chem. Mater.* **1994**, *6*, 1206.

[11] a) J. Cai, C.-H. Chen, X.-L. Feng, C.-Z. Liao, X.-M. Chen, *J. Chem. Soc., Dalton Trans.* **2001**, 2370; b) M. E. Thompson, *Chem. Mater.* **1994**, *6*, 1168; c) D. Grohol, F. Ging, A. Clearfield, *Inorg. Chem.* **1999**, *38*, 751, and references therein.

[12] a) V. A. Russell, M. C. Etter, M. D. Ward, *J. Am. Chem. Soc.* **1994**, *116*, 1941; b) V. A. Russell, C. C. Evans, W. Li, M. D. Ward, *Science* **1997**, *276*, 575.

[13] a) G. K. H. Shimizu, G. D. Enright, J. A. Ripmeester, *Can. J. Chem.* **1999**, *77*, 313; b) G. K. H. Shimiju, G. D. Enright, C. I. Ratcliffe, K. F. Pretson, J. L. L. Reid, J. A. Ripmeester, *Chem. Commun.* **1999**, 1485; c) A. P. Cote, G. K. H. Shimizu, *Inorg. Chem.* **2004**, *43*, 6663; d) A. P. Cote, G. K. H. Shimizu, *Chem. Eur. J.* **2003**, *9*, 5361; e) J. Cai, *Coord. Chem. Rev.* **2004**, *248*, 1061.

[14] J. Cai, C.-H. Chen, C.-Z. Liao, J.-H. Yao, X.-P. Hu, X.-M. Chen, *J. Chem. Soc., Dalton Trans.* **2001**, 1137.

[15] a) H. S. Maslen, T. N. Waters, *Coord. Chem. Rev.* **1975**, *17*, 137; b) S. Karunakaran, J. Kandaswamy, *J. Chem. Soc., Dalton Trans.* **1995**, 1851.

[16] a) L. Sacconi, M. Ciampolini, *J. Chem. Soc.* **1964**, 276; b) A. B. P. Lever, *Inorganic Electronic Spectroscopy*, Elsevier, New York, **1968**.

[17] a) A. B. P. Lever, *Inorganic Electronic Spectroscopy*, Elsevier, Amsterdam, **1984**; b) C. T. Yang, B. Moubaraki, K. S. Murray, J. D. Ranford, J. J. Vittal, *Inorg. Chem.* **2001**, *40*, 5934.

[18] a) A. W. Addison, T. N. Rao, J. Reedijk, J. V. Rijn, G. C. Verschoor, *J. Chem. Soc., Dalton Trans.* **1984**, 1349; b) G. Murphy, C. O. Sullivan, B. Murphy, B. Hathaway, *Inorg. Chem.* **1998**, *37*, 240; c) D. S. Marlin, M. M. Olmstead, P. K. Mascharak, *Inorg. Chem.* **2001**, *40*, 7003; d) C. T. Yang, J. J. Vittal, *Inorg. Chim. Acta* **2003**, *344*, 65, and references therein.

[19] C. S. Chan, L. L. Koh, P.-H. Leung, J. D. Ranford, K. Y. Sim, *Inorg. Chim. Acta* **1995**, *236*, 101.

[20] P. Li, N. K. Solanki, H. Ehrenberg, N. Feeder, J. E. Davies, J. M. Rawson, M. A. Halcrow, *J. Chem. Soc., Dalton Trans.* **2000**, 1559.

[21] N. R. Sangeetha, B. Kavitha, G. Rajeev, P. Chandane Kumar, M. Vadivelu, S. Pal, *Polyhedron* **1999**, *18*, 1425.

[22] a) P. D. J. Grootenhuis, J. van Eerden, P. J. Dijkstra, S. Harkema, D. N. Reinhoudt, *J. Am. Chem. Soc.* **1987**, *109*, 8044; b) T. Steiner, *Chem. Commun.* **1997**, 727; c) T. Steiner, G. R. Desiraju, *Chem. Commun.* **1998**, 891; d) G. R. Desiraju, *Acc. Chem. Res.* **2002**, *35*, 565.

[23] a) B. F. Hoskins, R. Robson, *J. Am. Chem. Soc.* **1990**, *112*, 1546; b) R. W. Gable, B. F. Hoskins, R. Robson, *J. Chem. Soc., Chem. Commun.* **1990**, 1677; c) M. J. Zaworotko, *Chem. Commun.* **2001**, 1; d) B. Moulton, M. J. Zaworotko, *Chem. Rev.* **2001**, *101*, 1629; e) A. N. Khlobystov, A. J. Blake, N. R. Champness, D. A. Lemenovskii, A. G. Majouga, N. V. Zyk, M. Schröder, *Coord. Chem. Rev.* **2001**, *222*, 155; f) B. Kumar, M. Fujita, *J. Chem. Soc., Dalton Trans.* **2000**, 3805; g) L. Carlucci, G. Ciani, D. M. Proserpio, *New J. Chem.* **1998**, *22*, 1319; h) S. R. Batten, R. Robson, *Angew. Chem. Int. Ed. Engl.* **1998**, *37*, 1460; i) S. R. Batten, B. F. Hoskins, R. Robson, *Chem. Eur. J.* **2000**, *6*, 156; j) S. R. Batten, *Cryst. Eng. Comm.* **2001**, *3*, 67.

[24] A. Onoda, Y. Yamada, M. Doi, T.-A. Okamura, N. Ueyama, *Inorg. Chem.* **2001**, *40*, 516.

[25] a) T. N. Sorrell, *Tetrahedron* **1989**, *45*, 3; b) P. A. Vigato, S. Tamburini, D. Fenton, *Coord. Chem. Rev.* **1990**, *106*, 25.

[26] a) C. Gerdermann, C. Eicken, B. Krebs, *Acc. Chem. Res.* **2002**, *35*, 183; b) T. Klabunde, C. Eicken, J. C. Sacchettini, B. Krebs, *Nat. Struct. Mol. Biol.* **1998**, *5*, 1084; c) C. Eicken, F. Zippel, K. Buldt-Karentzopoulos, B. Krebs, *FEBS Lett.* **1998**, *436*, 293.

[27] a) E. I. Solomon, U. M. Sundaram, T. E. Machonkin, *Chem. Rev.* **1996**, *96*, 2563; b) A. Sanchez-Ferrer, J. N. Rodriguez-Lopez, F. Garcia-Canovas, F. Carcia-Carmona, *Biochim. Biophys. Acta* **1995**, *1247*, 1; c) C. Eicken, B. Krebs, J. C. Sacchettini, *Curr. Opin. Struct. Biol.* **1999**, *9*, 677.

[28] a) P. L. Holland, W. B. Tolman, *Coord. Chem. Rev.* **1999**, *190–192*, 855, and references cited therein; b) T. Plenge, R. Dillinger, L. Santagostini, L. Casella, F. Z. Tuczek, *Z. Anorg. Allg. Chem.* **2003**, *629*, 2258; c) T. M. Simandi, Z. May, I. C. Szigyarto, L. I. Simandi, *Dalton Trans.* **2005**, 365.

[29] a) N. Oishi, Y. Nishida, K. Ida, S. Kida, *Bull. Chem. Soc. Jpn.* **1980**, *53*, 2847; b) P. Gentschev, N. Möller, B. Krebs, *Inorg. Chim. Acta* **2000**, *300*, 442; c) S. Parimala, K. N. Gita, M. Kandaswamy, *Polyhedron* **1998**, *17*, 3445; d) M. R. Malachowski, B. T. Dorsey, M. J. Parker, M. E. Adams, R. S. Kelly, *Polyhedron* **1998**, *17*, 1289; e) M. R. Malachowski, H. B. Huynh, L. J. Tomlinson, R. S. Kelly, J. W. Furbee, *J. Chem. Soc., Dalton Trans.* **1995**, 31; f) R. Wegner, M. Gottschaldt, H. Gorl, E.-G. Jager, D. Klemm, *Chem. Eur. J.* **2001**, *7*, 2143; g) M. Thirumavalavan, P. Akilan, M. Kandaswamy, *Supramol. Chem.* **2004**, *16*, 137.

[30] a) F. Zippel, F. Ahlers, R. Werner, W. Haase, H.-F. Nolting, B. Krebs, *Inorg. Chem.* **1996**, *35*, 3409; b) J. Reim, B. Krebs, *J. Chem. Soc., Dalton Trans.* **1997**, 3793; c) L. M. Berreau, S. Mahapatra, J. A. Halfen, R. P. Houser, V. G. Young, W. B. Tolman, *Angew. Chem. Int. Ed.* **1999**, *38*, 207; d) E. Monzani, G. Battaini, A. Perotti, L. Casella, M. Gullitti, L. Santogostini, G. Nardin, L. Randaccio, S. Geramia, P. Zanello, G. Opromolla, *Inorg. Chem.* **1999**, *38*, 5359; e) E. Monzani, L. Quinti, A. Perotti, L. Casella, M. Gullitti, L. Randaccio, S. Geramia, G. Nardin, P. Faleschini, G. Tabbi, *Inorg. Chem.* **1998**, *37*, 553; f) S. Torelli, C. Belle, S. Hamman, J. L. Pierre, *Inorg. Chem.* **2002**, *41*, 3983; g) A. A. Mukherjee, I. Rudra, S. G. Naik, S. Ramasesha, M. Nethaji, A. R. Chakravarty, *Inorg. Chem.* **2003**, *42*, 5660.

[31] a) J. Mukherjee, R. Mukherjee, *Inorg. Chim. Acta* **2002**, *337*, 429; b) K. D. Karlin, M. S. Nasin, B. I. Cohen, R. W. Cruse, S. Kaderli, A. D. Zuberbuhler, *J. Am. Chem. Soc.* **1994**, *116*, 1324;

c) G. Battaini, E. Monzani, L. Casella, L. Santagostini, R. J. Pagliarin, *J. Biol. Inorg. Chem.* **2000**, *5*, 262.
[32] a) M. Merkel, N. Moller, M. Piacenza, S. Grimme, A. Rompel, B. Krebs, *Chem. Eur. J.* **2005**, *11*, 1201; b) I. A. Koval, D. Pursche, A. F. Stassen, P. Gamez, B. Krebs, J. Reedijk, *Eur. J. Inorg. Chem.* **2003**, 1669; c) I. A. Koval, M. Huisman, A. F. Stassen, P. Gamez, M. Lutz, A. L. Spek, *Eur. J. Inorg. Chem.* **2004**, 591; d) N. Moller, M. Luken, M. B. Krebs, *J. Inorg. Biochem.* **2001**, *86*, 344; e) J. Ackermann, F. Meyer, E. Kaifer, H. Pritzkow, *Chem. Eur. J.* **2002**, *8*, 247.
[33] See for example: a) R. J. Butcher, G. M. Mockler, O. McKern, *Acta Crystallogr.* **2003**, *E59*, m61; b) R. J. Butcher, G. M. Mockler, O. McKern, *Acta Crystallogr.* **2003**, *E59*, m20.
[34] K. D. Karlin, A. D. Zuberbuhler in *Bioinorganic Catalysis* (Eds.: J. Reedjik, E. Bouwman), M. Dekker, New York, **1999**, pp. 469–534.
[35] a) *SMART & SAINT Software Reference Manuals*, Version 6.22, Bruker AXS Analytic X-ray Systems, Inc., Madison, WI, **2000**; b) G. M. Sheldrick, *SADABS*, Software for Empirical Absorption Correction, University of Göttingen, Germany, **2000**; c) *SHELXTL Reference Manual*, Version 5.1, Bruker AXS, Analytic X-ray Systems, Inc., Madison, WI, **1997**.

Received: July 19, 2005
Published Online: October 17, 2005

 © 2005 Wiley-VCH Verlag GmbH & Co. KGaA, Weinheim

Mn^{II}/Co^{II}-Terephthalate Frameworks Containing Dipyridine Coligands: Syntheses, Crystal Structures, Magnetic Behaviors, and Thermal Studies

Subal Chandra Manna,[a] Sanjit Konar,[a] Ennio Zangrando,[b] Ken-ichi Okamoto,[c] Joan Ribas,*[d] and Nirmalendu Ray Chaudhuri*[a]

Keywords: Manganese(II) / Cobalt(II) / Crystal structure / Magnetic behavior / Supramolecular chemistry

Three new metal–organic hybrid polymeric networks of Co^{II} and Mn^{II} with the molecular formulae $[Co(bpp)(tp)(H_2O)_2]$ (**1**), $[Mn(bpds)(tp)(H_2O)_2]\cdot(bpds)$ (**2**), and $[Mn(4,4'\text{-bipy})(H_2O)_4]\cdot(tp)$ (**3**) (bpp = 4,4′-trimethylenedipyridine; bpds = 4,4′-bipyridyl disulfide; 4,4′-bipy = 4,4′-dipyridyl; tp = terephthalate) have been synthesized and characterized by single-crystal X-ray diffraction studies, low temperature (300–2 K) magnetic measurements, and thermal behaviors. The structure determination of complexes **1** and **2** reveals a parallel interpenetrated structure of 2D layers with (4,4) topology, with metal ions at the nodes connected through tp and *N*,*N*-donor coligands. The octahedral N_2O_4 chromophore surrounding the metal ion results from *trans* located tp oxygens, two water molecules, and two nitrogen donors of the co-ligands in the *cis* position. The presence of uncoordinated bpds between the interpenetrated layers leads to the formation of a wafer-like structure for **2**. In complex **3**, however, manganese(II) ions bridged by 4,4′-bipy and coordinated by four water molecules give rise to a 1D polymeric chain. The adjoining chains encapsulate terephthalate anions (tp) to give a 3D structure through H-bonding. Low-temperature magnetic data indicate weak antiferromagnetic coupling in complexes **1** and **2**.

(© Wiley-VCH Verlag GmbH & Co. KGaA, 69451 Weinheim, Germany, 2005)

Introduction

The construction of one- to three-dimensional functional metal-organic hybrid materials of paramagnetic metal ions is of great interest as their intriguing network topologies lead to potential applications,[1] for example in electrical, conductivity, magnetism, host–guest chemistry, ion exchange, catalysis, nanotechnology, fluorescence, nonlinear optics, etc. Research in this field has been carried out by a number of eminent groups, in particular those of Rao,[2] Yaghi,[3] Fujita,[4] Zaworotko,[5] etc. The availability of new polyfunctional ligands, as well as the discovery of alternative synthetic procedures, has led to the syntheses of unique and novel metal–organic frameworks (MOFs) that suggest routes for chemists and physicists to pursue in search of such materials. A literature survey shows that the most commonly used strategies for the synthesis of MOFs are the use of (a) anionic bridging ligands, which, in addition, can partially or fully counterbalance the charge of the metal centers, (b) anionic as well as neutral spacers to increase the possibility of enhancing the dimension of molecular materials, and (c) only neutral spacers, where charges of the metal centers are counterbalanced by noncoordinating anions.

Recently, we have reported the synthesis of some structurally and magnetically interesting MOFs using strategy (a), such as $[Ni_3(fum)_2(\mu_3\text{-}OH)_2(H_2O)_4]_n\cdot 2nH_2O$,[6] $[Cu(\mu\text{-}fum)(NH_3)_2]_n\cdot 2nH_2O$,[7] $[Mn(mal)(H_2O)_2]_n$,[8] and $[Co(H_2O)_4(fum)]_n\cdot nH_2O$,[9] where fumarate (fum) and malonate (mal) dicarboxylates act as anionic bridging ligands only. We have also reported MOFs obtained through strategies (b), where dicarboxylates are used in combination with neutral spacers, such as $[\{Cu_3(mal)_2(bpe)_3(H_2O)_2\}(NO_3)_2(H_2O)_2]_n$,[10] $[Cu_2(fum)_2(4,4'\text{-bipy})]_n\cdot 0.5nH_2O$,[11] $[Mn_2(mal)_2(4,4'\text{-bipy})(H_2O)_2]_n$,[8] $[Cu_4(mal)_4(urotropin)]\cdot 7H_2O$ and $[Co_2(mal)_2(urotropin)]\cdot 2H_2O$,[12] and $[Ni_3(maleate)_2(bpe)_4(H_2O)_4](NO_3)_2\cdot H_2O$, [Mn(adipate)(bpe)],[13] [Ni(fum)(bpe)], and [Ni(fum)(bpp)(H_2O)][14] [bpe = 1,2-(bispyridine)ethane, bpp = 1,3-bis(4-pyridyl)propane], and (c), where noncoordinated dicarboxylates counterbalance the charge of the metal ions, as in $[Co(H_2O)_4(4,4'\text{-bipy})]_n(fum)_n\cdot 4nH_2O$[9] and $[\{Mn(bpe)(H_2O)_4\}(C_4O_4)\cdot 4.5H_2O]$ ($C_4O_4^{2-}$ = acetylene dicarboxylate).[15] Thus, depending on the metal ion and dicarboxylate or dicarboxylate/neutral bipyridine spacer, several MOFs with novel structural diversity and interesting

[a] Department of Inorganic Chemistry, Indian Association for the Cultivation of Science,
Kolkata-700032, India
Fax: +91-33-2473-2805
E-mail: icnrc@iacs.res.in
[b] Dipartimento di Scienze Chimiche, University of Trieste,
34127 Trieste, Italy
[c] Department of Chemistry, University of Tsukuba,
Tsukuba, Ibaraki 305, Japan
[d] Departament de Química Inorgánica, Universitat de Barcelona,
Diagonal 647, 08028 Barcelona, Spain
E-mail: joan.ribas@qi.ub.es

Supporting information for this article is available on the WWW under http://www.eurjic.org or from the author.

 © 2005 Wiley-VCH Verlag GmbH & Co. KGaA, Weinheim **DOI: 10.1002/ejic.200500258**

magnetic properties have been reported. This has prompted us to synthesize new MOFs using a well-known but less-documented dicarboxylate anion − terephthalate − in combination with other neutral bipyridines. The choice of terephthalate arises as it possesses versatile coordination modes (Scheme 1) and has the ability to form large and tightly bound metal cluster aggregates with specific and directional hydrogen bonds in building the molecular architecture,[16] as well as to undergo π–π stacking due to the presence of aryl rings (Scheme 2).

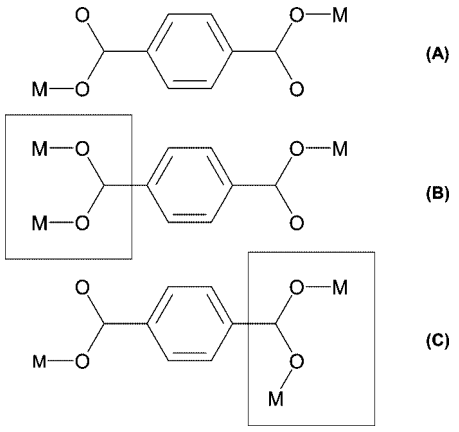

Scheme 1.

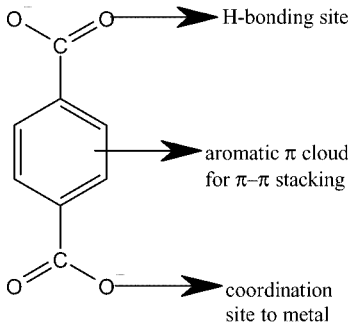

Scheme 2.

Herein we report the syntheses, crystal structures, low-temperature magnetic studies, and thermal behaviors of three novel Mn^{II}/Co^{II}-terephthalate frameworks containing dipyridyl coligands, namely $[Co(bpp)(tp)(H_2O)_2]$ (**1**), $[Mn(bpds)(tp)(H_2O)_2]\cdot(bpds)$ (**2**), and $[Mn(4,4'\text{-bipy})(H_2O)_4]\cdot(tp)$ (**3**) (tp = terephthalate; bpp = 4,4′-trimethylenedipyridine; bpds = 4,4′-bipyridyl disulfide; 4,4′-bipy = 4,4′-dipyridyl). Complexes **1** and **2** show unexpected 2D parallel interpenetrated structural motifs, whereas in complex **3** the use of linear 4,4′-bipy spacers gives rise to 1D coordination polymers with encapsulated tp anions. The low-temperature magnetic data of complexes **1** and **2** show weak antiferromagnetic coupling. Complex **1** exhibits thermally induced reversible octahedral (pink) ⇌ tetrahedral (blue) thermochromism upon dehydration/rehydration.

Results and Discussion

Description of the Structures

Complex 1

The crystal structure of complex **1** consists of 2D corrugated layers of square meshes of composition $[Co(tp)(bpp)(H_2O)_2]_n$, as depicted in Figure 1. The cobalt ions, with octahedral coordination geometry, occupy the 4-connecting nodes while bridging tp and bpp ligands give rise to a square grid of equal sides (11.486 × 11.486 Å). Intranet hydrogen bonds reinforce the overall structure [O(1w)–O(4) = 2.66; O(2w)–O(6) = 2.64 Å]. The N_2O_4 chromophore about the cobalt(II) center involves *trans* located tp oxygens and two water molecules, with two bpp nitrogen donors in the *cis* positions. The coordination bond lengths cover the range 2.106(2) Å [Co–O(1w)] to 2.140(2) Å [Co–N(2)] (Table 1). The bpp ligand exhibits a *TG* conformation[17] with torsion angles of –174.5(3)° and 73.4(4)° about the propyl chain. A careful analysis of the crystal structure shows parallel interpenetrated layers,[18,19] as illustrated in Figure 2, where weak π–π tp ring interactions are evident (distance between centroids = 3.807 Å). The spacing between the mean planes through the cobalt atoms of each sheet is 2.381 Å. Both the layers involved in interpenetration (A and B are structurally equal) are linked to the adjacent sheet to form a concatenated -AB-BA-AB- structure, where hyphens indicate H-bonds involving the water molecule O(1w) and the tp oxygen O(6) (O···O = 2.76 Å). As shown in Figure 3, these interactions contribute to the enhancement of molecular dimensionality. It is worthwhile to note that the aqua ligand O(1w) forms intra- and interlayer H-bonds and presents a shorter coordination distance in comparison to Co–O(2w) [2.106(2) vs. 2.132(2) Å]. The tp carboxylates are rather tilted from a coplanar conformation and form dihedral angles of 26.0(2)° and 37.6(2)° with the aromatic ring as a subtle balance to favor the intranet

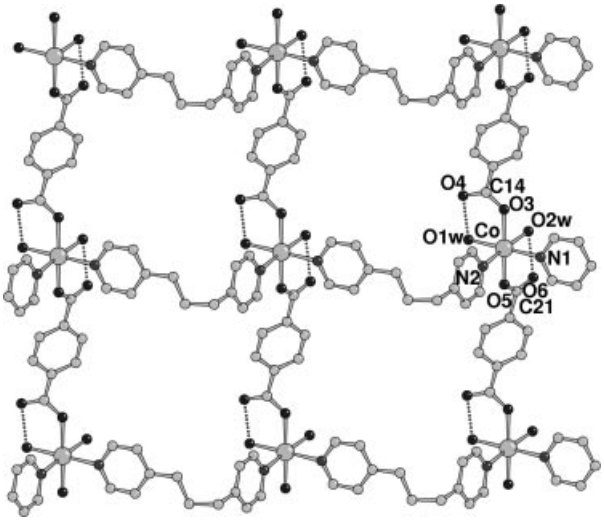

Figure 1. View down axis *c* of the 2D sheet of complex **1** with relevant atom labeling scheme about the Co atom.

 © 2005 Wiley-VCH Verlag GmbH & Co. KGaA, Weinheim

H-bonding (Figure 1) and, at the same time, the stacking between phenyl rings of the interpenetrated nets (Figure 2).

Table 1. Selected bond lengths [Å] and angles [°] for complexes **1**–**3**.

1			
Co–O(1w)	2.106(2)	Co–O(5)	2.127(2)
Co–O(2w)	2.132(2)	Co–N(1)	2.136(2)
Co–O(3)	2.127(2)	Co–N(2)	2.140(2)
O(1w)–Co–O(2w)	95.02(7)	O(2w)–Co–N(2)	175.45(7)
O(1w)–Co–O(3)	88.89(6)	O(3)–Co–O(5)	172.19(6)
O(1w)–Co–O(5)	86.93(6)	O(3)–Co–N(1)	91.36(7)
O(1w)–Co–N(1)	179.68(6)	O(3)–Co–N(2)	96.43(7)
O(1w)–Co–N(2)	89.48(7)	O(5)–Co–N(1)	92.84(7)
O(2w)–Co–O(3)	84.33(7)	O(5)–Co–N(2)	90.13(7)
O(2w)–Co–O(5)	89.47(7)	N(1)–Co–N(2)	90.30(8)
O(2w)–Co–N(1)	85.20(7)	O(4)–C(14)–O(3)	125.03(19)
		O(6)–C(21)–O(5)	125.12(19)
2[a]			
Mn–O(2)	2.131(2)	Mn–N(1)	2.309(3)
Mn–O(1w)	2.204(3)		
O(2)–Mn–O(2′)	176.02(14)	O(1w)-Mn–O(1w′)	90.68(16)
O(2)–Mn–O(1w)	88.29(10)	O(1w)–Mn–N(1′)	176.41(11)
O(2)–Mn–O(1w′)	88.91(10)	O(1w)–Mn–N(1)	86.64(11)
O(2)–Mn–N(1)	88.63(10)	N(1)–Mn–N(1′)	96.14(15)
O(2)–Mn–N(1′)	94.03(10)	O(3)–C(1)–O(2)	124.8(3)
3[b]			
Mn–O(1w)	2.208(2)	Mn–N(1)	2.210(2)
Mn–O(2w)	2.188(2)	Mn–N(2)	2.269(3)
O(1w)–Mn–O(1w′)	169.87(9)	O(2w)-Mn–O(2w′)	171.29(9)
O(1w)–Mn–O(2w)	94.25(7)	O(2w)–Mn–N(1)	85.65(4)
O(1w′)–Mn–O(2w)	86.52(7)	O(2w)–Mn–N(2)	94.35(4)
O(1w)–Mn–N(1)	95.06(4)	N(1)–Mn–N(2)	180.0
O(1w)–Mn–N(2)	84.94(4)	O(3)–C(7)–O(3′′)	124.5(3)
		O(4)–C(12)–O(4′′)	124.8(3)

[a] Symmetry code: (′) $-x + 1/4, -y + 1/4, z$. [b] Symmetry code: (′) $-x + 1/2, y, -z + 3/2$; (′′) $-x + 1/2, y, -z + 1/2$.

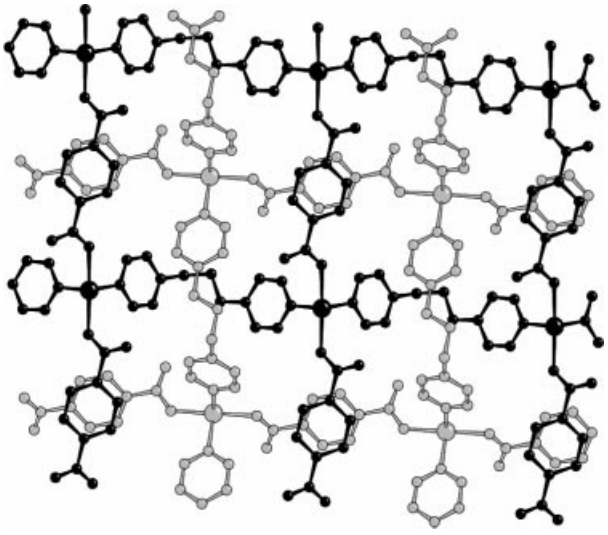

Figure 2. Parallel interpenetration of 2D sheets in complex **1** (coordinated water oxygens not shown for sake of clarity).

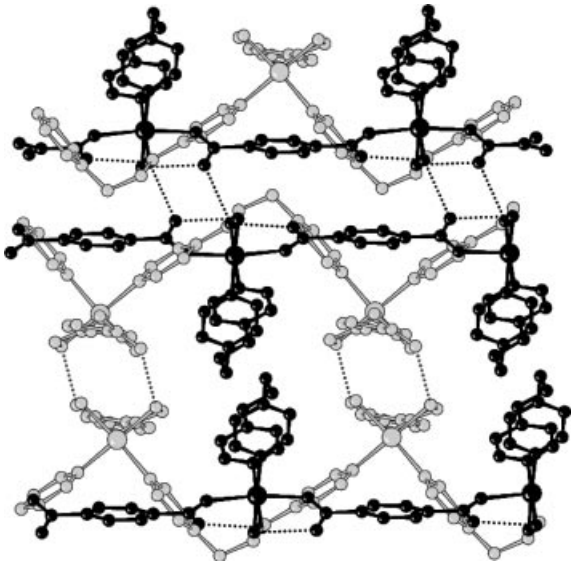

Figure 3. Interpenetrated sheets (each pair indicated in black and gray) concatenated by H-bonds (dotted lines) in complex **1**.

Complex 2

Complex **2** contains a 2D undulating $[Mn(tp)(bpds)(H_2O)_2]_n$ sheet (Figure 4), extending in the *ab* plane, where octahedral manganese ions occupy the 4-connecting nodes of the square grid, which has equal sides of 11.425 Å. The square grid is strengthened by hydrogen bonds involving the aqua ligand and the adjacent carboxylate oxygen [O(1w)–O(3′) = 2.71 Å]. The manganese(II) ion is positioned on a twofold axis with *trans* located tp oxygens, with the coordination geometry being completed by two water molecules and two bpds N donors in the *cis* position. The Mn–O(2), Mn–O(1w), and Mn–N(1) bond lengths are 2.131(2), 2.204(3), and 2.309(3) Å, respectively (Table 1). The 2D layers reveal a parallel interpenetration with a topology closely comparable to that observed in complex **1** (Figure 5). The entangled layers in the present arrangement seem more tightly connected, with the mean planes through the metals being separated by 2.228 Å and the π-stacking of tp rings being more efficient (centroid-to-centroid distance = 3.568 Å). The conformation assumed by the tp is also very similar to that found in the cobalt complex, with angles between the carboxylate groups and aromatic ring of 26.3(3)°. However, compared with complex **1**, the main difference emerges from the presence of uncoordinated bpds between the interpenetrated layers. This peculiar feature leads to the formation of a wafer-like structure, where the bidentate bpds ligands are linked to water molecules through hydrogen bonds (N···O = 2.840 Å;L N···HO = 158.9°). A view of the crystal packing is given in Figure 6.

An estimation of the torsion angles around the disulfide bonds in a series of coordination polymers indicates rigidity in the bpds ligands [C–S–S–C angles between 83.8(6)° and 95.5(8)°],[20] regardless of the different coordination environment. The present value for the coordinated bpds ligand falls in the range reported (92.5°), while it is 102.7° in free bpds. Correspondingly, the N···N distance is longer in the

 © 2005 Wiley-VCH Verlag GmbH & Co. KGaA, Weinheim

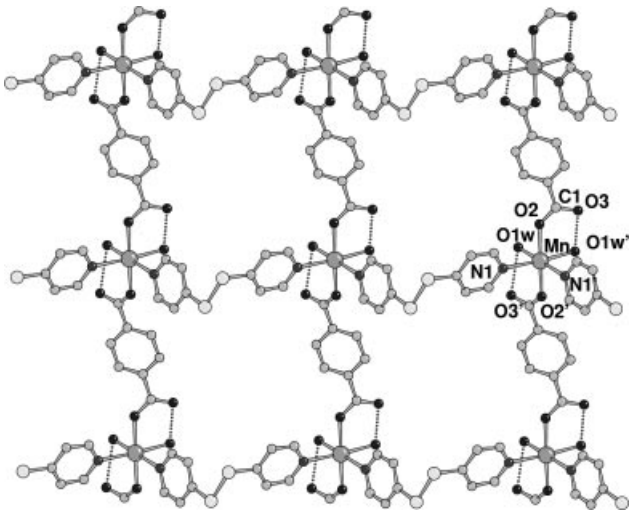

Figure 4. 2D sheet of complex **2** with relevant atom labeling scheme about the Mn ion located on a twofold axes (primed atoms at $-x + 1/4, -y + 1/4, z$).

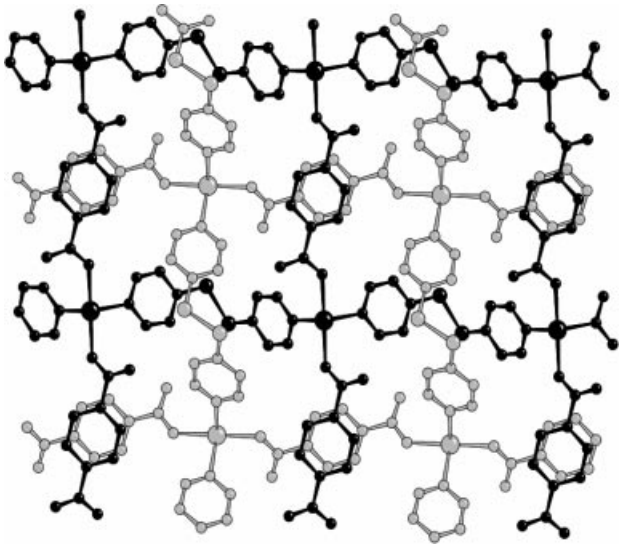

Figure 5. View of parallel interpenetration of 2D sheets (*ab* plane) in complex **2**. The larger circles represent Mn ions (coordinated water oxygens not shown for sake of clarity).

latter (8.494 vs. 8.029 Å), a conformation that appears to assist the N–OH_2 hydrogen bond.

As a comparison, in the 1D polymer [Mn(bpds)(F_6-acac)$_2$],[21] (F_6-acac = hexafluoroacetylacetonate), which represents the only known example of manganese(II) ions bridged by a bpds ligand, longer Mn–N distances of 2.282 Å are found, with the metals separated by 11.785 Å.

Complex 3

The $Mn(H_2O)_4$ units in complex **3** are bridged by 4,4′-bipy ligands to give a 1D coordination polymeric array along the crystallographic *b* direction, with metals located on twofold axes. A drawing of the packing with the atom labeling scheme is shown in Figure 7; a selection of bond

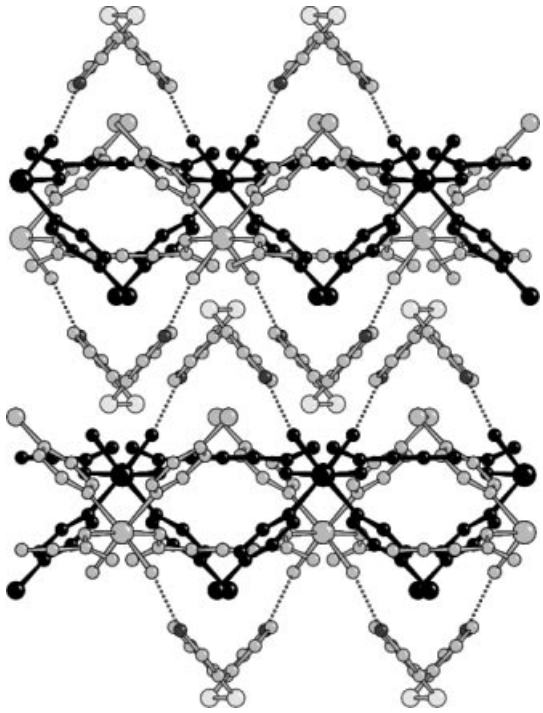

Figure 6. Crystal packing (view along axis *b*) of complex **2** with uncoordinated bpds ligands sandwitched between the parallel interpenetrated layers and connected through H-bonds (dotted lines) to coordinated water molecules. The larger circles indicate Mn ions.

lengths and bond angles is given in Table 1. The MnN_2O_4 chromophore presents a slightly distorted octahedral coordination geometry, with the equatorial oxygens showing a tetrahedral distortion (±0.18 Å). The Mn–O(1w) and Mn–O(2w) distances are 2.208(2) and 2.188(2) Å, respectively; the nitrogen bipy donors N(1) and N(2) occupy the *trans* axial positions with Mn–N(1) and Mn–N(2) distances of 2.210(2), 2.269(3) Å, respectively. The rings of the 4,4′-bipy ligand are not coplanar, but are tilted by about 20°. The terephthalate dianions are also located on twofold axes and are sandwiched by 4,4′-bipy ligands of contiguous polymeric chains to give rise to a three-dimensional structure through a H-bonding scheme with the water molecules. In fact, O2w is involved in H-bonding with the sandwiched tp anions (O3 and O4 at 2.74 Å, mean value), while O1w is connected to O4 at a longer distance (2.90 Å) and also a symmetry-related O3 of a side-located tp at 2.71 Å (not shown in Figure 7).

The 4,4′-bipy ligand spans the metal ions at a distance correspondening to the length of the crystallographic *b* axis, namely 11.565 Å (Figure 7), while the shortest interchain Mn···Mn separation in the 3D architecture is 6.562 Å. The orientations (dihedral angles) taken up by carboxylate groups with respect to the phenyl ring are 4.86(5)° and 22.03(6)°, which is assumed to favor the H-bonding.

The overall structure presents structural features comparable to those observed in the analogous Mn polymeric derivative with croconate $(C_5O_5)^{2-}$ dianions.[22] However, accounting for the smaller dimensions of $(C_5O_5)^{2-}$ (with re-

 © 2005 Wiley-VCH Verlag GmbH & Co. KGaA, Weinheim

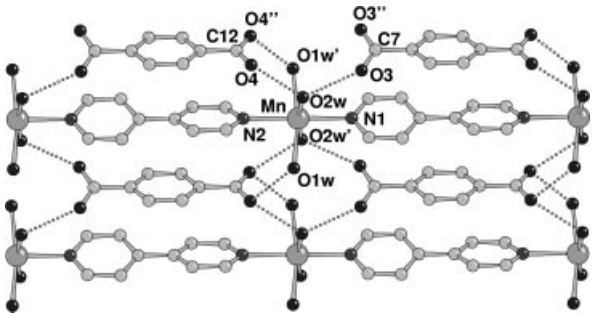

Figure 7. Crystal packing of complex **3** viewed down the *c* axis showing the terephthalate anions encapsulated between the -$Mn(H_2O)_4$-(4,4′-bipy)- polymers [dotted lines indicate H-bonds, symmetry operation: (′) $-x + 1/2$, y, $-z + 3/2$; (″) $-x + 1/2$, y, $-z + 1/2$].

spect to tp) in the latter, an additional water molecule was detected in the lattice in order to favor the H-bonding interactions.

Magnetic Properties

Although the crystal nets consist of a two-dimensional structure with terephthalate and bpp or bpds as bridging ligands in complexes **1** and **2**, respectively, we assumed the possible couplings between the long amines bpp and bpds to be zero. With this hypothesis, the magnetic data can be interpreted as being derived from a pseudo-one-dimensional structure formed by cobalt(II) and manganese(II) ions (for **1** and **2**, respectively) linked by terephthalate at a long distance. For complex **3**, the terephthalate dianion remains encapsulated and the manganese ions are bridged by long 4,4′-bipy ligands (Mn···Mn = 11.565 Å). Such a type of bridging ligand usually gives negligible antiferromagnetic interactions,[23] therefore we did not study the magnetic behavior.

Complex 1

Considering the spin-orbit coupling due to the $^4T_{1g}$ ground state for octahedral Co^{II} complexes,[24] precise calculations to derive the *J* parameter from experimental data in all the temperature range are not possible except for dinuclear[25] or small polynuclear complexes.[26] One-dimensional systems of Co^{II} are frequently associated with anisotropic Ising systems, and they can be fitted in the low-temperature zone by assuming again an effective spin, *S*′, of ½.[27] More recently, Rueff et al.[28] have proposed a phenomenological approach for some low-dimensional Co^{II} systems that allows an estimation of the strength of the antiferromagnetic exchange interactions. They postulated the phenomenological equation:

$$A\chi_M T = A \exp(-E_1/kT) + B \exp(-E_2/kT)$$

where $A + B$ is the Curie constant [approx. 2.8–3.4 $cm^3 mol^{-1} K$ for octahedral cobalt(II) ions], and E_1 and E_2 represent the "activation energies" corresponding to the spin-orbit coupling and the antiferromagnetic exchange interaction, respectively. E_1/k, the effect of spin-orbit coupling and site distortion, is of the order of +100 K.[28,29] Excellent results have been reported in one- and two-dimensional cobalt(II) complexes.[28]

The $\chi_M T$ vs. *T* plot for **1** (χ_M is the molar magnetic susceptibility for one Co^{II} ion) is shown in Figure 8. A $\chi_M T$ value of 3.27 $cm^3 mol^{-1} K$ at 300 K is a typical value for the Co^{II} system.[30,31] Upon decreasing the temperature, the $\chi_M T$ values decrease continuously to 1.91 $cm^3 mol^{-1} K$ at 2 K. To calculate an estimated *J* value we used the Rueff expression, which suitable for any temperature greater than the possible T_c.[28] The fit values obtained with this procedure are: A + B = 3.5 $cm^3 mol^{-1} K$, in agreement with those given in the literature.[28] The E_1/k value of 69.09 K is of the same magnitude as those reported by Rueff et al. for several one- and two-dimensional cobalt(II) complexes.[30b] As for the value found for the antiferromagnetic exchange interaction, it is very weak (E_2/k = 0.21 K), corresponding to $J = -0.42$ K (ca. -0.3 cm^{-1}), according to the Ising chain approximation, $\chi_M T = \exp(J/2kT)$ (Figure 8). The reduced magnetization curve, $M/N\beta$, at 2 K tends to 2.35 $N\beta$ at 5 T, a typical value for isolated or quasi-isolated cobalt(II) ions (Figure 8 inset).

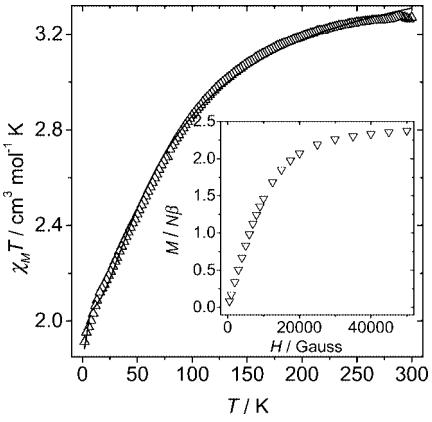

Figure 8. Plot of $\chi_M T$ vs. *T* for complex **1** (solid line represents the best fit using the Rueff formula). Inset: plot of the reduced magnetization ($M/N\beta$) vs. *H* at 2 K for complex **1**.

Complex 2

The $\chi_M T$ vs. *T* plot is given in Figure 9 for one manganese(II) ion. The $\chi_M T$ values start at 4.35 $cm^3 mol^{-1} K$, corresponding to the value for one isolated manganese(II) ion (with $g \approx 2.00$). This value decreases smoothly to close to 4.0 $cm^3 mol^{-1} K$ at 2 K. Such behavior is typical for a very weak antiferromagnetic coupling between manganese(II) ions in the chain. The magnetism of this kind of one-dimensional Mn^{II} system has been studied theoretically mainly by Fisher by assuming an infinite number of classical spins (S = 5/2).[32] The best-fit parameters were: $J = -0.045 \pm 0.01$, $g = 2.00 \pm 0.004$, and $R = 4.1 \times 10^{-3}$ (R is the agreement factor defined as $\Sigma_i[(\chi_M T)_{obs} - (\chi_M T)_{calc}]^2/\Sigma_i[(\chi_M T)_{obs}]$).[33] The g value agrees perfectly with that expected for a manganese(II) ion (S = 5/2, g = 2.00). The reduced magnetization (Figure 9, inset) is also indicative of a very weak antiferromag-

 © 2005 Wiley-VCH Verlag GmbH & Co. KGaA, Weinheim

netic coupling. The experimental values tend to 4.8 $N\beta$ and practically follow the Brillouin formula at 2 K for $S = 5/2$ and $g = 2.0$.

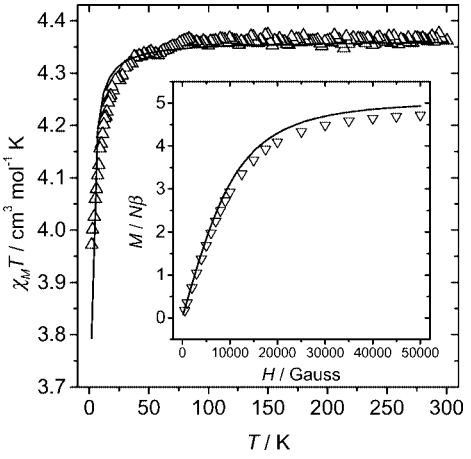

Figure 9. Plot of $\chi_M T$ vs. T for complex **2** (solid line represents the best fit). Inset: plot of the reduced magnetization, $M/N\beta$ (solid line indicates the Brillouin formula for $S = 5/2$ and $g = 2.0$).

The small antiferromagnetic J values for **1** and **2** may be interpreted as being due to the terephthalate bridging ligand. When the coordination mode is that shown in Scheme 1A (complexes **1** and **2**), the terephthalate bridging ligand shows a very small antiferromagnetic coupling for M = Mn^{II}, Co^{II}, Ni^{II}, and Cu^{II}.[33] To the best of our knowledge, only two Mn complexes with this kind of coordination have been reported to date – $[\{Mn(dca)(terpy)(MeOH)\}_2(\mu\text{-ta})]$[34] and $[Mn_2(phen)_4(H_2O)_2(\mu\text{-ta})](ClO_4)_2$.[35] The calculated J values of –0.06 cm^{-1} and –0.065 cm^{-1}, respectively, are in good agreement with that found in complex **2**. All these very weak J values are in accordance with the MO calculations made by Cano et al.,[35] which show that a terephthalate bridge is not a suitable bridging unit to mediate significant exchange coupling.

Thermal Studies

The pink complex **1** starts to lose its coordinated water molecules, upon heating, at around 125 °C and becomes dehydrated at 190 °C, yielding the species [Co(bpp)(tp)] (**1a**, blue), which reverts to **1** in a humid atmosphere (relative humidity of ca. 60%) at ambient temperature. This dehydration-rehydration process involves an octahedral ⇌ tetrahedral transformation of Co^{II} that shows thermochromism, as evidenced from the solid state electronic spectra [(19455, ca. 16666, and 8510 cm^{-1} for **1**) and (19300, 17985, 14000–15500, and 8802 cm^{-1} for **1a**; Figure S1)] and room temperature magnetic measurements [μ_{eff} for **1** (see magnetic properties) and for **1a** 4.82 μ_B (at 300 K)].

Complex **2** starts to lose water molecules, upon heating, at 110 °C and shows continuous decomposition with concomitant formation of an intermediate species. The initial temperature of dehydration suggests the presence of coordinated water molecules as well as their involvement in H-bonding. It should be noted that after dehydration the network in **2** collapses as the terephthalate carboxylate fails to function here as a chelate to attain octahedral geometry, which is a requirement for the existence of Mn^{II} in the polymeric networks according to the crystal structure (Figure 4).

Complex **3** is thermally stable up to 100 °C, a lower temperature than that of **2**. It undergoes dehydration in two steps that overlap each other and is fully dehydrated at 150 °C. The dehydrated species collapses immediately upon further heating as the manganese centers fail to attain the required geometry after removal of their water molecules.

Conclusions

We have reported the syntheses, crystal structures, low-temperature magnetic studies, and thermal behaviors of three metal–organic hybrid polymeric networks. The tp and bipyridine ligands in complexes **1** and **2**, respectively, take part in formation of a covalently bonded 2D parallel interpenetrated polymeric architecture, whereas in complex **3** the tp anions are encapsulated by 1D Mn(4,4′-bipy) chains. The presence of uncoordinated bpds ligands in **2** between the interpenetrated layers leads to formation of a wafer-like structure where bpds is anchored to coordinated water molecules through H-bonds. All these crystal structures contain extensive H-bonding between the water molecules and the tp oxygens, which increases the dimensionality of the architectures to 3D. As a consequence, in order to favor H-bonding connections the tp carboxylate groups show different conformations, as indicated by the dihedral angles of the carboxylates with respect to the phenyl ring. These are about 30° in complexes **1** and **2**, and quite different in **3** (about 5° and 22°). The variable-temperature magnetic data reveal weak antiferromagnetic coupling for **1** and **2**.

Experimental Section

Materials: High purity 4,4′-trimethylenedipyridine (98%), 4,4′-bipyridyl disulfide (Aldrithiol-4; 98%), 4,4′-dipyridyl (98%), disodium terephthalate (96%), and manganese(II) chloride tetrahydrate (98%) were purchased from the Aldrich Chemical Co. Inc. and were used. All other chemicals were of AR grade.

Physical Measurements: Elemental analyses (carbon, hydrogen, and nitrogen) were performed with a Perkin–Elmer 240C elemental analyzer. IR spectra were measured as KBr pellets on a Nicolet 520 FTIR spectrometer. Magnetic measurements were carried out with polycrystalline samples (20–30 mg) by the Servei de Magnetoquímica, Universitat de Barcelona, with a Quantum Design MPMS SQUID magnetometer operating at a magnetic field of 0.1 T, in the temperature range 2–300 K. The diamagnetic corrections were evaluated from Pascal's constants. Thermogravimetric analyses were carried out with a Mettler Toledo Star system. The UV/Vis reflectance spectra were recorded between 300–1400 nm with a Hitachi U-3501 spectrophotometer at room temperature in the solid state.

Crystallographic Data Collection and Refinement: Crystal data and details of data collections and refinements for the structures re-

 © 2005 Wiley-VCH Verlag GmbH & Co. KGaA, Weinheim

ported are summarized in Table 2. Diffraction data for all complexes were carried out on a Rigaku Mercury CCD area detector using graphite-monochromated Mo-K_α radiation. Cell refinement, indexing, and scaling of the data sets were carried out using the Crystal package.[36] All the structures were solved with SIR97[37] and subsequent Fourier analyses[38] and refined by the full-matrix least-squares method based on F^2 with all observed reflections.[38] Most of the water hydrogens detected in the difference Fourier map were restrained with a fixed O–H bond length (0.85 Å). All the calculations were performed using the WinGX System, Ver 1.64.05.[39]

CCDC-262151 to -262153 (for **1**–**3**, respectively) contain the supplementary crystallographic data for this paper. These data can be obtained free of charge from The Cambridge Crystallographic Data Centre via www.ccdc.cam.ac.uk/data_request/cif.

Table 2. Crystallographic data and details of structure refinements for complexes **1**–**3**.

	1	**2**	**3**
Empirical formula	$C_{21}H_{22}CoN_2O_6$	$C_{28}H_{24}MnN_4O_6S_4$	$C_{18}H_{20}MnN_2O_8$
M_r [g mol^{-1}]	457.35	695.70	447.30
Crystal system	monoclinic	orthorhombic	monoclinic
Space group	*C*2/*c*	*Fddd*	*P*2/*n*
a [Å]	16.883(7)	15.635(7)	6.995(4)
b [Å]	15.579(6)	16.663(8)	11.565(6)
c [Å]	18.317(8)	45.74(2)	11.420(6)
β [°]	123.778(3)	90.00	101.824(6)
Volume [Å^3]	4004.3(29)	11916.2(95)	904.2(8)
Z	8	16	2
$D_{calcd.}$ [g cm^{-3}]	1.517	1.551	1.643
μ (Mo-K_α) [mm^{-1}]	0.899	0.773	0.782
F(000)	1896	5712	462
θ_{max} [°]	27.48	27.48	27.48
Reflection collected	32844	49378	14916
Unique reflections	4735	3696	2165
R_{int}	0.035	0.079	0.038
Observed reflections $I > 2\sigma(I)$	3643	2125	1625
Parameters refined	287	201	152
Goodness of fit (F^2)	1.087	1.058	1.019
R_1 [$I > 2\sigma(I)$] [a]	0.0397	0.0517	0.0350
wR_2 [a]	0.0798	0.0983	0.0684
$\Delta\rho$ [e Å^{-3}]	0.264, –0.232	0.381, –0.337	0.282, –0.295

[a] $R_1 = \Sigma||F_o| - |F_c||/\Sigma|F_o|$; $wR_2 = [\Sigma w(F_o^2 - F_c^2)^2/\Sigma w(F_o^2)^2]^{1/2}$.

[Co(bpp)(tp)(H$_2$O)$_2$] (1): A methanolic solution (5 mL) of bpp (1 mmol, 0.198 g) was added dropwise to a methanolic solution (5 mL) of $Co(NO_3)_2{\cdot}6H_2O$ (1 mmol, 0.291 g) with constant stirring. An aqueous solution (10 mL) of disodium terephthalate (1 mmol, 0.210 g) was added to the resulting light-pink reaction mixture and stirred for 1 h. A deep-pink complex separated out. Single crystals suitable for X-ray analysis were obtained by diffusing a methanolic solution (10 mL) of bpp into an aqueous (10 mL) layer containing $Co(NO_3)_2{\cdot}6H_2O$ and disodium terephthalate (1:1) in a tube. The deep-pink crystals deposited at the junction of the two layers after a few days. Yield: 0.320 g (70%). $C_{21}H_{22}CoN_2O_6$ (457.35): calcd. C 55.10, H 4.81, N 6.12; found C 55.18, H 4.80, N 6.16. IR: $\tilde{\nu}$ = 3604 (vs), 3256 (s), 3071 (w), 2943 (s), 2872 (vw), 1615 (vs), 1546 (vs), 1501 (w), 1380 (s) 1018 (w), 795 (s), 757 (s), 510 (w) cm^{-1}.

[Mn(bpds)(tp)(H$_2$O)$_2$]·(bpds) (2): A methanolic solution (10 mL) of manganese(II) chloride tetrahydrate (1 mmol, 0.197 g) was allowed to react with an aqueous solution (10 mL) of disodium terephthalate (1 mmol, 0.210 g) and stirred for 20 min. Then, a methanolic solution (5 mL) of bpds (1 mmol, 0.220 g) was poured slowly into it and the resulting mixture was refluxed for 4 h. It was then allowed to cool and filtered. The filtrate was kept in a $CaCl_2$ desiccator and shiny, yellowish single crystals suitable for X-ray determination were obtained after a few days. Yield: 0.500 g (72%). $C_{28}H_{24}MnN_4O_6S_4$ (695.70): calcd. C 48.30, H 3.45, N 8.05; found C 48.29, H 3.45, N 8.04. IR: $\tilde{\nu}$ = 3500–3090 (s), 3008 (w), 2904 (w), 1579 (vs), 1566 (vs), 1379 (s), 1319 (w), 1222 (vw), 815 (w), 758 (w), 704 (w) cm^{-1}.

[Mn(4,4′-bipy)(H$_2$O)$_4$]·(tp) (3): This complex was synthesized following the procedure adopted for complex **2** using 4,4′-bipy (1 mmol, 0.156 g) instead of bpds. Colorless crystals of **3** suitable for X-ray diffraction were obtained from the $CaCl_2$ desiccator after a few days. Yield: 0.313 g (70%). $C_{18}H_{20}MnN_2O_8$ (447.30): calcd. C 48.29, H 4.47, N 6.26; found C 48.28, H 4.48, N 6.27. IR: $\tilde{\nu}$ = 3500–3020 (s, v br.), 1656 (vw), 1610 (s), 1559 (vs), 1419 (vw), 1368 (vs), 1067 (vw), 807 (w), 752 (w), 632 (vw) cm^{-1}.

Supporting Information: A table containing H-bonding parameters, the thermogravimetric curves of complexes **1**, **2**, and **3**, and the solid-state electronic spectra for complexes **1** and **1a**, see also footnote on the first page of this article.

Acknowledgments

N. R. C. thanks Council of Scientific and Industrial Research, New Delhi, and J. R. thanks the Spanish Goverment (BQU2003/00539) for financial support.

[1] a) D. W. Bruce, D. O'Hare. *Inorganic Materials*, John Wiley & Sons, New York, **1992**; b) R. D. Willet, D. Gatteschi, O. Kahn, *Magneto Structural Correlations in Exchange Coupled System*, NATO ATI Series C140, Reidal, Dordrecht, The Netherlands **1985**; c) B. Multon, M. J. Zaworotko, *Chem. Rev.* **2001**, *101*, 1629; d) P. J. Hagrman, D. Hagrman, J. Zubieta, *Angew. Chem. Int. Ed.* **1999**, *38*, 2638; e) R. Robson, *J. Chem. Soc., Dalton Trans.* **2000**, 3735; f) W. Su, M. Hong, J. Weng, R. Cao, S. Lu, *Angew. Chem. Int. Ed.* **2000**, *39*, 2911; g) D. Gatteschi, O. Kahn, J. Miller, *Molecular Magnetic Materials*, Nato ASI Series EI98, Kluwer, Dordrecht, The Netherlands, **1991**; h) O. M. Yaghi, G. Li, H. Li, *Nature* **1995**, *378*, 703; i) K. Marouka, N. Murase, H. Yamamoto, *J. Org. Chem.* **1993**, *58*, 2938; j) C. Chen, K. S. Suslick, *Coord. Chem. Rev.* **1993**, *128*, 293 and references cited therein; k) O. C. Montelro, H. I. S. Noguelra, T. Trindade, *Chem. Mater.* **2001**, *13*, 2103; l) A. J. Waddon, E. B. Coughlin, *Chem. Mater.* **2003**, *15*, 4555; m) M. Kondo, Y. Irie, Y. Shimizu, M. Miyazawa, H. Kawaguchi, A. Nakamura, T. Naito, K. Maeda, H. Uchida, *Inorg. Chem.* **2004**, *43*, 6139; n) S. C. Johannessen, R. G. Brisbois, *J. Am. Chem. Soc.* **2001**, *123*, 3818; o) J.-W. Park, E. L. Thomas, *J. Am. Chem. Soc.* **2002**, *124*, 515.

[2] a) C. N. R. Rao, S. Natarajan, A. Chaudhury, S. Neeraj, A. A. Ayi, *Acc. Chem. Res.* **2001**, *34*, 80; b) R. Vaidhyanathan, S. Natarajan, C. N. R. Rao, *Chem. Mater.* **2001**, *13*, 185; c) C. N. R. Rao, E. V. Sampathkumaran, R. Natarajan, G. Paul, J. N. Behera, A. Chaudhury, *Chem. Mater.* **2004**, *16*, 1441; d) A. Chaudhury, S. Natarajan, C. N. R. Rao, *Inorg. Chem.* **2000**, *39*, 4295; e) R. Vaidhyanathan, S. Natarajan, C. N. R. Rao, *Inorg. Chem.* **2002**, *41*, 4496; R. Vaidhyanathan, S. Natarajan, C. N. R. Rao, *Inorg. Chem.* **2002**, *41*, 5226; f) J. N. Behera, K. V. Gopalkrishnan, C. N. R. Rao, *Inorg. Chem.* **2004**, *43*, 2636; g) S. Natarajan, S. Neeraj, A. Chaudhury, C. N. R. Rao, *Inorg. Chem.* **2000**, *39*, 1426; h) C. N. R. Rao, S. Natarajan, S. Neeraj, *J. Am. Chem. Soc.* **2000**, *122*, 2810.

[3] a) M. Eddaoudi, D. B. Moler, H. Li, B. Chen, T. M. Reineke, M. O'Keeffe, O. M. Yaghi, *Acc. Chem. Res.* **2001**, *34*, 319; b)

 © 2005 Wiley-VCH Verlag GmbH & Co. KGaA, Weinheim

T. M. Reineke, M. Eddaoudi, D. Moler, M. O'Keeffe, O. M. Yaghi, *J. Am. Chem. Soc.* **2000**, *122*, 4843; c) B. Chen, M. Eddaoudi, T. M. Reineke, J. W. Kampf, M. O'Keeffe, O. M. Yaghi, *J. Am. Chem. Soc.* **2000**, *122*, 11559; d) H. Li, J. Kim, T. L. Groy, M. O'Keeffe, O. M. Yaghi, *J. Am. Chem. Soc.* **2001**, *123*, 4867; e) M. Eddaoudi, J. Kim, J. B. Wachter, H. K. Chae, M. O'Keeffe, O. M. Yaghi, *J. Am. Chem. Soc.* **2001**, *123*, 4368; f) J. Kim, B. Chen, T. M. Keineke, H. Li, M. Eddaoudi, D. B. Moler, M. O'Keeffe, O. M. Yaghi, *J. Am. Chem. Soc.* **2001**, *123*, 8239; g) H. K. Chae, M. Eddaoudi, J. Kim, S. I. Hauck, J. F. Hartwig, M. O'Keeffe, O. M. Yaghi, *J. Am. Chem. Soc.* **2001**, *123*, 11482; h) M. Eddaoudi, J. Kim, M. O'Keeffe, O. M. Yaghi, *J. Am. Chem. Soc.* **2002**, *124*, 377; i) J. L. C. Rowsell, A. R. Millward, K. S. Park, O. M. Yaghi, *J. Am. Chem. Soc.* **2004**, *126*, 5667; j) M. Eddaoudi, H. Li, O. M. Yaghi, *J. Am. Chem. Soc.* **2000**, *122*, 1391.

[4] a) K. Kumazawa, K. Biradha, T. Kusukawa, T. Okano, M. Fujita, *Angew. Chem. Int. Ed.* **2003**, *42*, 3909; b) S. Tashiro, M. Tominaga, T. Kusukawa, M. Kawano, S. Sakamoto, K. Yamaguchi, M. Fujita, *Angew. Chem. Int. Ed.* **2003**, *42*, 3267; c) S.-Y. Yu, H. Huang, H.-B. Liu, Z.-N. Chen, R. Zhang, M. Fujita, *Angew. Chem. Int. Ed.* **2003**, *42*, 686; d) K. Biradha, Y. Hongo, M. Fujita, *Angew. Chem. Int. Ed.* **2002**, *41*, 3395; e) K. Biradha, M. Fujita, *Angew. Chem. Int. Ed.* **2002**, *41*, 3392; f) A. Hori, A. Akasaka, K. Biradha, S. Sakamoto, K. Yamaguchi, M. Fujita, *Angew. Chem. Int. Ed.* **2002**, *41*, 3269; g) M. Tominaga, K. Suzuki, M. Kawano, T. Kusukawa, T. Ozeki, S. Sakamoto, K. Yamaguchi, M. Fujita, *Angew. Chem. Int. Ed.* **2004**, *43*, 5621; h) M. Fujita, S.-Y. Yu, T. Kusukawa, H. Funaki, K. Ogura, K. Yamaguchi, *Angew. Chem. Int. Ed.* **1998**, *37*, 2082.

[5] a) K. Biradha, A. Mondal, B. Moulton, M. J. Zaworotko, *J. Chem. Soc., Dalton Trans.* **2000**, 3837; b) M. J. Zaworotko, *Chem. Commun.* **2001**, 1; c) S. A. Bourne, J. Lu, B. Moulton, M. J. Zaworotko, *Chem. Commun.* **2001**, 861; d) H. Abourahma, A. W. Coleman, B. Moulton, B. Rather, P. Shahgaldian, M. J. Zaworotko, *Chem. Commun.* **2001**, 2380; e) B. Rather, B. Moulton, R. D. B. Walsh, M. J. Zaworotko, *Chem. Commun.* **2002**, 694; f) B. D. Wagner, G. J. McManus, B. Moulton, M. J. Zaworotko, *Chem. Commun.* **2002**, 2176; g) B. Rather, M. J. Zaworotko, *Chem. Commun.* **2003**, 830; h) J. J. Perry, G. J. McManus, M. J. Zaworotko, *Chem. Commun.* **2004**, 2534; i) B. Moulton, J. Lu, A. Mondal, M. J. Zaworotko, *Chem. Commun.* **2001**, 863; j) K. Biradha, C. Corey Seward, M. J. Zaworotko, *Angew. Chem. Int. Ed.* **1999**, *38*, 492; k) S. A. Bourne, J. Lu, A. Mondal, B. Moulton, M. J. Zaworotko, *Angew. Chem. Int. Ed.* **2001**, *40*, 2111; l) J. Lu, A. Mondal, B. Moulton, M. J. Zaworotko, *Angew. Chem. Int. Ed.* **2001**, *40*, 2113.

[6] S. Konar, P. S. Mukherjee, E. Zangrando, F. Lloret, N. Ray Chaudhuri, *Angew. Chem. Int. Ed.* **2002**, *41*, 1561.

[7] P. S. Mukherjee, T. K. Maji, G. Mostafa, J. Ribas, M. S. E. Fallah, N. Ray Chaudhuri, *Inorg. Chem.* **2001**, *40*, 928.

[8] T. K. Maji, S. Sain, G. Mostafa, T.-H. Lu, J. Ribas, M. Monfort, N. Ray Chaudhuri, *Inorg. Chem.* **2003**, *42*, 709.

[9] S. Konar, E. Zangrando, N. Ray Chaudhuri, *Inorg. Chim. Acta* **2003**, *355*, 264.

[10] S. Sain, T. K. Maji, G. Mostafa, T.-H. Lu, N. Ray Chaudhuri, *New J. Chem.* **2003**, *27*, 185.

[11] S. Dalai, P. S. Mukherjee, E. Zangrando, F. Lloret, N. Ray Chaudhuri, *J. Chem. Soc., Dalton Trans.* **2002**, 822.

[12] S. Konar, P. S. Mukherjee, M. G. B. Drew, J. Ribas, N. Ray Chaudhuri, *Inorg. Chem.* **2003**, *42*, 2545.

[13] P. S. Mukherjee, S. Konar, E. Zangrando, T. Mallah, J. Ribas, N. Ray Chaudhuri, *Inorg. Chem.* **2003**, *42*, 2695.

[14] S. Konar, E. Zangrando, M. G. B. Drew, J. Ribas, N. Ray Chaudhuri, *Dalton Trans.* **2004**, 260.

[15] D. Ghoshal, T. K. Maji, G. Mostafa, T.-H. Lu, N. Ray Chaudhuri, *Cryst. Growth Des.* **2003**, *3*, 9.

[16] a) K. S. Burger, P. Chaudhuri, K. Wieghardt, B. Nuber, *Chem. Eur. J.* **1995**, *1*, 583; b) C. S. Hong, Y. Do, *Inorg. Chem.* **1997**, *36*, 5684; c) C. MacDonald, G. M. Whitesides, *Chem. Rev.* **1994**, *94*, 2383; d) S. Kawata, S. R. Breeze, S. Whang, J. E. Greedan, N. P. Raju, *Chem. Commun.* **1997**, 717; e) A. J. Blake, S. J. Hill, P. Hubberstey, W.-S. Li, *J. Chem. Soc., Dalton Trans.* **1997**, 913; f) S. J. Gieb, C. Vicent, E. Fan, A. D. Hamilton, *Angew. Chem. Int. Ed. Engl.* **1993**, *32*, 119; g) Z.-Y. Fu, X.-T. Wu, J.-C. Dai, S.-M. Hu, W.-X. Du, H.-H. Zhang, R.-Q. Sun, *Eur. J. Inorg. Chem.* **2002**, 2730.

[17] L. Carlucci, G. Ciani, D. M. Proserpio, S. Rizzato, *CrystEngComm* **2002**, *4*, 121.

[18] S. R. Batten, R. Robson, *Angew. Chem. Int. Ed.* **1998**, *37*, 1460.

[19] S. R. Batten, *CrystEngComm* **2001**, *3*, 67.

[20] R. Horikoshi, T. Mochida, N. Maki, S. Yamada, H. Motiyama, *J. Chem. Soc., Dalton Trans.* **2002**, 28 and references cited therein.

[21] R. Horikoshi, T. Mochida, H. Moriyama, *Inorg. Chem.* **2001**, *40*, 2430.

[22] S. Sain, T. K. Maji, N. Ray Chaudhuri, E. Zangrando, *Transition Met. Chem.* **2002**, *27*, 716.

[23] a) M.-X. Li, G.-Y. Xie, Y.-D. Gu, J. Chen, P.-J. Zheng, *Polyhedron* **1995**, *14*, 1235; b) Y. Rodríguez-Martín, C. Ruiz-Pérez, J. Sanchiz, F. Lloret, M. Julve, *Inorg. Chim. Acta* **2001**, *318*, 159; c) H.-Y. Shen, D.-Z. Liao, Z.-H. Jiang, S.-P. Yan, B.-W. Sun, G.-L. Wang, X.-K. Yao, H.-G. Wang, *Polyhedron* **1998**, *17*, 1953.

[24] a) F. E. Mabbs, D. J. Machin, *Magnetism and Transition Metal Complexes*, Chapman and Hall, London, **1973**; b) J. W. Raebiger, J. L. Manson, R. D. Sommer, U. Geiser, A. L. Rheingold, J. S. Miller, *Inorg. Chem.* **2001**, *40*, 2578; c) E. W. Lee, Y. J. Kim, D. Y. Junag, *Inorg. Chem.* **2002**, *41*, 501; d) B. N. Figgis, M. A. Hitchman, *Ligand Field Theory and its Applications*, Wiley-VCH, New York, **2000**; e) D. Armentano, G. de Munno, F. Lloret, M. Julve, *Inorg. Chem.* **1999**, *38*, 3744; f) S. J. Retting, R. C. Thompson, J. Trotter, S. Xia, *Inorg. Chem.* **1999**, *38*, 1360.

[25] a) G. de Munno, M. Julve, F. Lloret, J. Faus, A. Canneschi, *J. Chem. Soc., Dalton Trans.* **1994**, 1175; b) M. E. Lines, *J. Chem. Phys.* **1971**, *55*, 2977.

[26] MAGPACK Program: a) J. J. Borrás-Almenar, J. M. Clemente-Juan, E. Coronado, B. S. Tsukerblat, *Inorg. Chem.* **1999**, *38*, 6081; b) J. J. Borrás-Almenar, J. M. Clemente-Juan, E. Coronado, B. S. Tsukerblat, *J. Comput. Chem.* **2001**, *22*, 985.

[27] a) M. E. Fisher, *J. Math. Phys.* **1963**, *4*, 124; b) S. Angelow, M. Drillon, E. Zhecheva, R. Stoyanova, M. Belaiche, A. Derory, A. Herr, *Inorg. Chem.* **1992**, *31*, 1514.

[28] a) J.-M. Rueff, N. Masciocchi, P. Rabu, A. Sironi, A. Skoulios, *Eur. J. Inorg. Chem.* **2001**, 2843; b) J.-M. Rueff, N. Masciocchi, P. Rabu, A. Sironi, A. Skoulios, *Chem. Eur. J.* **2002**, *8*, 1813 and references cited therein.

[29] R. L. Carlin, *Magnetochemistry*, Springer, Berlin, **1986**.

[30] a) E. A. Boudreaux, L. N. Mulay, Eds. *Theory and Applications of Molecular Paramagnetism*, John-Wiley, New York, **1976**; chapter 3, p. 135; b) L. L. Lohr, J. C. Miller, R. R. Sharp, *J. Chem. Phys.* **1999**, *111*, 10148; c) S. G. Telfer, T. Sato, R. Kuroda, J. Lefebvre, D. B. Leznoff, *Inorg. Chem.* **2004**, *43*, 421.

[31] I. R. Little, B. P. Straughan, P. J. Thornton, *J. Chem. Soc., Dalton Trans.* **1986**, 2211.

[32] M. E. Fisher, *Am. J. Phys.* **1964**, *32*, 343.

[33] L. Li, D. Liao, Z. Jiang, S. Yan, *Inorg. Chem.* **2002**, *41*, 421.

[34] A. Escuer, F. A. Mautner, N. Sanz, R. Vicente, *Inorg. Chim. Acta* **2002**, *340*, 163.

[35] J. Cano, G. de Munno, J. L. Sanz, R. Ruiz, J. Faus, F. Lloret, M. Julve, A. Caneschi, *J. Chem. Soc., Dalton Trans.* **1997**, 1915.

[36] a) D. J. Watkin, C. K. Prout, J. R. Carruthers, P. W. Betteridge, (**1996**) CRYSTALS Issue 10, Chemical Crystallography Laboratory, Oxford, UK; b) Single Crystal Structure Analysis Software. Version 3.5.1. Rigaku/MSC, 9009 New Trails Drive, The Woodlands, TX, USA 77381-5209. Rigaku, 3-9-12 Akishima, Tokyo 196-8666, Japan.

 © 2005 Wiley-VCH Verlag GmbH & Co. KGaA, Weinheim

[37] *SIR97*, A. Altomare, M. C. Burla, M. Camalli, G. L. Cascarano, C. Giacovazzo, A. Guagliardi, A. G. G. Moliterni, G. Polidori, R. Spagna, *J. Appl. Crystallogr.* **1999**, *32*, 115.
[38] Programs for Crystal Structure Analysis (Release 97-2). G. M. Sheldrick, University of Göttingen, Germany, **1998**.
[39] L. J. Farrugia, *J. Appl. Crystallogr.* **1999**, *32*, 837.
Received: March 24, 2005
Published Online: October 5, 2005

 © 2005 Wiley-VCH Verlag GmbH & Co. KGaA, Weinheim

Steady-State and Time-Resolved Photophysical Studies on a Series of Gallium Phthalocyanine Monomers and Dimers

Yu Chen,*[a,b] Yasuyuki Araki,[b] Michael Hanack,[c] Mamoru Fujitsuka,[b] and Osamu Ito*[b]

Keywords: Optical properties / Photophysics / Gallium / Phthalocyanines

Intramolecular interaction between coplanar-stacked phthalocyanine (Pc) and porphyrin molecules plays an important role in the energy- and electron-transfer process. A series of results from different photophysical experiments on gallium phthalocyanine compounds are initially described. The PcGa dimer with a direct gallium–gallium bond, i.e. [tBu$_4$PcGa]$_2$·2dioxane, may exist in two different conformations: one in which the two phthalocyanines are poorly interacting and the other in which they are very close and strongly interacting. In the former, the emission lifetime is quite close to that of the monomer model compounds; in the latter, it is much shorter probably due to different radiative and nonradiative deactivation constants from those of the monomers. Because no significant difference between the absorption spectra of the monomer and dimer was observed in the photophysical experiments, implying that no ground-state interaction can be assessed, the results regarding triplet excited state lifetimes of [tBu$_4$PcGa]$_2$·2dioxane can be attributed to strong intramolecular interactions existing only in the excited state.
(© Wiley-VCH Verlag GmbH & Co. KGaA, 69451 Weinheim, Germany, 2005)

Introduction

Phthalocyanines (Pcs) offer a high structural flexibility, which facilitates the tailoring of their physical, optoelectronic and chemical parameters over a very broad range. The exploitation of the chemical reactivity of the M–Cl (M = Ga, In) bond allows the preparation of a series of highly soluble, axially substituted and bridged phthalocyanine complexes.[1] Very recently, we have prepared a new dimeric gallium phthalocyanine complex with a direct gallium–gallium bond, i.e. [tBu$_4$PcGa]$_2$·2dioxane.[2] The Extended X-ray Absorption Fine Structure (EXAFS)-determined gallium–gallium bond length of this compound was found to be 2.46 Å, which is in good agreement with the reported values in the literature.[3–6] The gallium center is located 0.45 Å out of the plane, which is quite close to the reported out-of-plane value of 0.439 Å in crystalline PcGaCl.[7] Z-scan experiments show that dimerization of tBu$_4$PcGaCl is clearly a viable method of tuning saturation energy density (F_{Sat}) of the material. As a result, [tBu$_4$PcGa]$_2$·2dioxane exhibits a significantly lower F_{Sat} than that of tBu$_4$PcGaCl,[8] by approximately a factor of 3. This reduction in F_{Sat} is coupled with a slight increase in the non-linear absorption coefficient (β_I) at low incident intensity and with approximately equivalent β_Is at higher intensities. The ratio of the excited- and ground-state absorption cross sections (κ) is reduced by approximately 22% after dimerization of tBu$_4$PcGaCl to [tBu$_4$PcGa]$_2$·2dioxane. However, this can probably be mostly attributed to the increase in the linear absorption coefficient (α_0) by approximately 18% over the same molecular modification.[2]

It has long been recognized that the intramolecular interaction between coplanar-stacked phthalocyanine and porphyrin molecules plays an important role in the energy- and electron-transfer process.[9] Studies on the facial interaction between the phthalocyanine macrocycles are thus very interesting. In the case of the μ-oxo-bridged silicon phthalocyanine dimer (PcSi–O–SiPc), strong intramolecular interaction between PcSi macrocycles was observed by us previously.[10] In contrast to this complex, μ-oxo-bridged gallium and indium phthalocyanine dimers ([tBu$_4$PcGa]$_2$O and [tBu$_4$PcIn]$_2$O)[11] exhibit no apparent intramolecular interaction. The inter-Pc distances in [tBu$_4$PcGa]$_2$O and [tBu$_4$PcIn]$_2$O are 3.72 and 4.32 Å, respectively.[1d] In this contribution, we report on the steady-state and time-resolved photophysical properties of [tBu$_4$PcGa]$_2$·2dioxane (**5**). The photophysical data of the other four gallium phthalocyanine compounds, tBu$_4$PcGaCl (**1**);[8] tBu$_4$PcGa(p-CPO) (**2**, p-CPO = p-chlorophenoxy);[12] {[tBu$_4$Pc Ga]$_2$·SDPO}(**3**, SDPO = 4,4′-sulfonyl-diphenoxy)[12] and [tBu$_4$PcGa]$_2$O (**4**),[11] are also given in this paper for comparison. Figure 1

[a] Department of Chemistry, Laboratory for Advanced Materials, East China University of Science and Technology, 130 Meilong Road, Shanghai 200237, P. R. China
Fax: + 86-21-64252485
E-mail: chentangyu@yahoo.com
[b] Institute of Multidisciplinary Research for Advanced Materials, Tohoku University, CREST(JST), Katahira 2-1-1, Sendai 980-8577, Japan
E-mail: ito@tagen.tohoku.ac.jp
[c] Institut für Organische Chemie, Universität Tübingen, Auf der Morgenstelle 18, 72076 Tübingen, Germany

shows the molecular structures of these five phthalocyanine compounds.

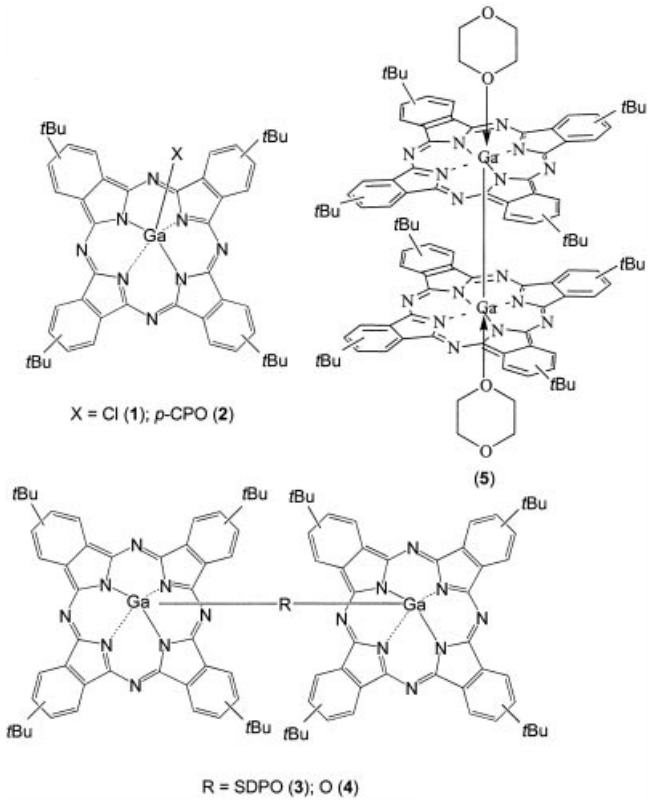

Figure 1. Molecular structures of **1**–**5**.

Results and Discussion

Axial substitution in Pc complexes favorably influences non-linear optical absorption towards the presence of a dipole moment perpendicular to the macrocycle in the axially substituted phthalocyanines, but does not generally affect the linear optical properties of phthalocyanines; the Q- and B-bands in the UV/Vis absorption spectra are shifted only slightly by a few nanometers on exchanging the axial ligands on the metal.[1] Likewise, dimerization of tBu$_4$PcGaCl does not considerably affect the spectral profile, as shown in Figure 2. The Q-band maxima of **1** and **5** are located at 695 and 693 nm, respectively. The extent of electronic conjugation in both compounds **1** and **5** is virtually identical, since compound **5** has a gallium–gallium single bond of σ-type lacking delocalized electrons. As expected, the main differences between the spectral features of these two complexes are related to the change in the extinction coefficient value because of the different number of absorbing Pc rings per molecular unit in the monomer relative to the gallium–gallium bridged dimer. Upon excitation with a laser light of 355 nm, both compounds display a Stokes shift of the emission peak with respect to the location of the Q-band absorption. Although dimerization affects both the UV/Visible and emission spectra differently, it influences the emission energy more strongly, since the extent of the Stokes shift is larger for the monomer than for the [tBu$_4$PcGa]$_2$·2dioxane dimer. Maximum emission peaks for **1** and **5** are found at 713 and 700 nm, respectively. Such a difference could be assigned to the more rigid structure of the dimer than of the monomer. This means that the dimer relaxes radiatively from the electronic excited state π* in a higher vibrational level.[13–15] Similarly, the photoluminescence spectra of **2**–**4** also show the mirror images of the corresponding UV/Vis absorption spectra with small Stokes shift, suggesting that the structural change between the ground state and excited singlet state is small.

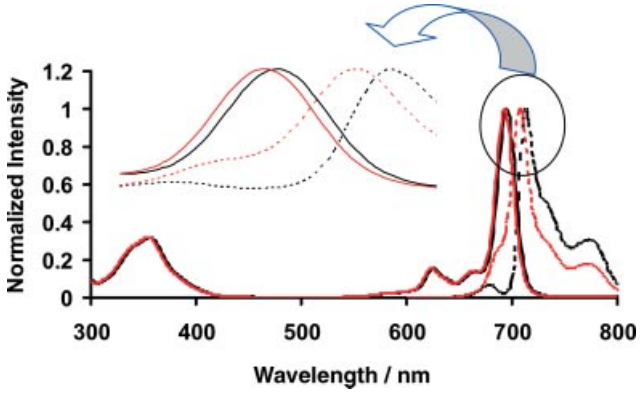

Figure 2. UV/Vis absorption spectra (solid line) and photoluminescence spectra (dashed line, λ_{ex} = 355 nm) of **1** (black line) and **5** (red line) in dilute chloroform solutions.

The fluorescence-decay time profiles of **1**–**4** display a single exponential decay yielding long fluorescence lifetimes (τ_{fluo}) in the range of 2570–3570 ps (see Table 1). On the contrary, the fluorescence-decay time profile of **5** was curve-fitted with two exponential functions, as shown in Figure 3, giving two fluorescence lifetimes [τ_{f1} = 180 ps (42%) and τ_{f2} = 2480 ps (58%)]. The τ_{f1} value is much shorter than those of **1**–**4**, while the τ_{f2} value is slightly smaller than those of the gallium phthalocyanine compounds mentioned above. This experimental finding suggests that the dimer may exist in two different conformations: one in which the two phthalocyanines are poorly interacting and the other in which they are very close and strongly interacting. In the former, the emission lifetime is quite close to that of the monomer model compounds; in the latter, it is much shorter probably due to different radiative and nonradiative deactivation constants from those of the monomer compounds.

Figure 4 shows that the nanosecond transient absorption spectra (λ_{ex} = 355 nm) obtained in argon-saturated anhydrous toluene for all gallium phthalocyanine compounds studied here are very similar. After the laser pulse irradiation, the transient absorption band appeared at 520 nm, accompanying the depletion at about 700 nm due to the transient consumption of ground state of **5**. On addition of O_2, the decay of the 520 nm band, which is attributed to the triplet-triplet (T-T) absorption of the Pc compounds[11,12] was accelerated, indicating that quenching by O_2 takes place from the triplet excited state of **5** to O_2, probably yielding $^1O_2$. The decay of the 520 nm band in the presence

 © 2005 Wiley-VCH Verlag GmbH & Co. KGaA, Weinheim

Table 1. The photophysical data of the gallium phthalocyanine complexes **1**–**5**. a_0: linear absorption coefficient; τ_{fluo}: fluorescence lifetime at emission peak wavelength, λ_{ex} = 410 nm; τ_T: triplet excited state lifetime, λ_{ex} = 355 nm; k_{O2}: second-order rate constant.

Samples	a_0 [cm^{-1}]	Stokes shift [cm^{-1}]	$\lambda_{max}{}^T$ [nm]	τ_{fluo} [ps]	τ_T [μs]	k_{O2} [$M^{-1}s^{-1}$]
1	1.10	185	520	2570	257	2.2×10^9
2	1.37	185	520	3110	324	2.0×10^9
3	3.13	406	520	3460	667	2.1×10^9
4	1.60	186	520	3570	357	2.0×10^9
5	1.30	144	520	180 (42%) 2480 (58%)	2.1 (39%) 71 (61%)	2.3×10^9

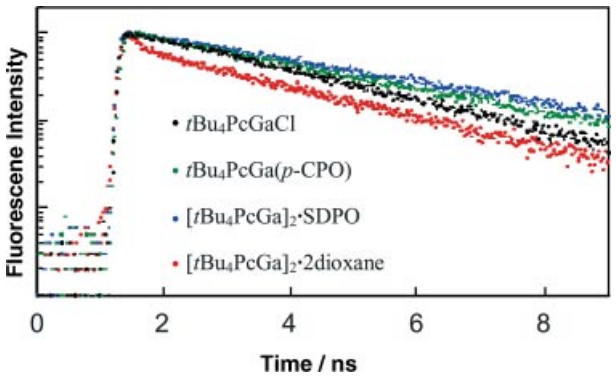

Figure 3. Time profiles of fluorescence intensities at 700–705 nm of **1**, **2**, **3** and **5** in deoxygenated anhydrous toluene by the excitation at 410 nm.

of O_2 obeys first-order kinetics, giving $k_{first\text{-}order}$, which increases with the concentration of added O_2; from the pseudo-first-order relation, the second-order rate constants for the reaction with O_2 (k_{O2}) were evaluated as listed in Table 1. Dimers and monomers have almost the same k_{O2} values, but they are all less than the diffusion controlled limit ($k_{diff} = 1.1\times10^{10}$ $mol^{-1}dm^3s^{-1}$ in toluene).

In the absence of O_2, the decay rates depend on the laser power. Fast decay observed at high laser power is attributed to the T-T annihilation because of the collision between the highly concentrated triplet excited states. The time profile at 520 nm observed for ^{3}(*t*Bu$_4$PcGa–X)* (X = Cl; *p*-CPO; O–*t*Bu$_4$PcGa; SDPO–*t*Bu$_4$PcGa) under the irradiation of low laser power reveals a single exponential decay giving the triplet excited state lifetimes (τ_T) in the range of 257–667 μs. In contrast, two exponential-decay processes were observed for ^{3}([*t*Bu$_4$PcGa]$_2$·2dioxane)* as shown in Figure 5. From the initial fast decay process, the triplet excited state lifetime (τ_{T1}) of ^{3}([*t*Bu$_4$PcGa]$_2$·2dioxane)* was evaluated to be 2.1 μs (39%), much shorter than the τ_T values of **1**–**4**. From the slow decay process of **5**, the second lifetime (τ_{T2}) was found to be 71 μs (61%), which is still shorter than those of the other four gallium phthalocyanine compounds. It should be noted that in the photophysical characterization, no significant difference between the absorption spectra of the monomer and dimer was observed, suggesting that no ground-state interaction can be assessed. The results regarding triplet excited state lifetimes can thus be attributed to strong intramolecular interactions existing only in the excited state.

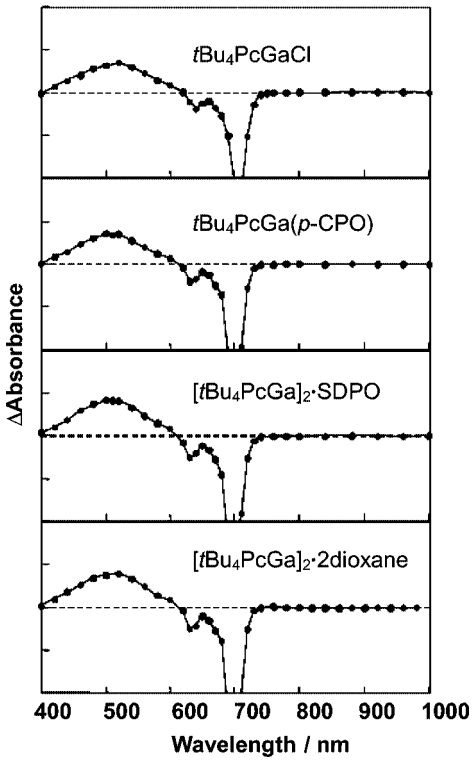

Figure 4. Nanosecond transient absorption spectra of **1**, **2**, **3** and **5** in deoxygenated anhydrous toluene by the excitation at 355 nm.

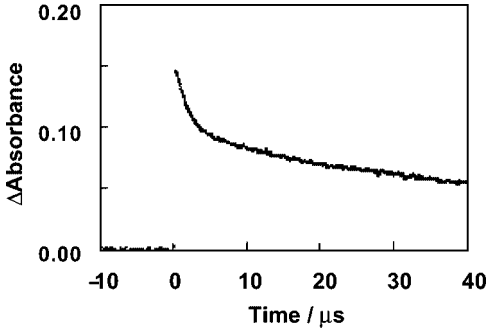

Figure 5. Absorption-time profile of 520 nm band of **5** in deoxygenated anhydrous toluene.

Experimental Section

Materials: *t*Bu$_4$PcGaCl was obtained by the reaction of 4-*tert*-butylphthalonitrile with anhydrous $GaCl_3$ in doubly distilled, deoxygenated quinoline at 180 °C in the presence of catalytic amounts

 © 2005 Wiley-VCH Verlag GmbH & Co. KGaA, Weinheim

of the non-nucleophilic base 1,8-diazabicyclo-[5.4.0]-undec-7-ene (DBU).[8] tBu$_4$PcGa(p-CPO) was prepared by the reaction of tBu$_4$PcGaCl with p-chlorophenol in anhydrous DMSO at 110 °C in the presence of K_2CO_3.[12] The [tBu$_4$PcGa]$_2$O dimer was synthesized by the reaction of tBu$_4$PcGaCl with excess concentrated H_2SO_4 at –20 °C.[11] The 4,4′-sulfonyldiphenoxy (SDPO)-axially bridged gallium phthalocyanine dimer {[tBu$_4$PcGa]$_2$.SDPO} was synthesized by the reaction of tBu$_4$PcGaCl with bis(4-hydroxyphenyl)sulfone in anhydrous DMSO at 110 °C in the presence of K_2CO_3.[12] [tBu$_4$PcGa]$_2$.2dioxane was obtained in 83% yield by the reaction of soluble tBu$_4$PcGaCl with activated magnesium in freshly dried THF, in the presence of 1,4-dioxane.[2]

Photophysical Measurements: UV/Vis absorption spectra were recorded on a JASCO V-530 spectrophotometer. Fluorescence spectra and lifetimes were measured by a single-photon counting method using an argon ion laser, a pumped Ti:sapphire laser (Spectra-Physics, Tsunami 3960, fwhm 150 fs) with a pulse selector (Spectra-Physics, 3980), a second harmonic generator (Spectra-Physics, GWU-23PS), and a streakscope (Hamamatsu Photonics, C4334–01). Each sample was excited in deoxygenated anhydrous toluene with 410 nm laser light. Nanosecond-transient absorption measurements were carried out using third harmonic generation (THG, 355 nm) of an Nd:YAG laser (Spectra-Physics, Quanta-Ray GCR-130, 6 ns FWHM) as an excitation source. For transient absorption spectra in the near-IR region (600–1400 nm), monitoring light from a pulsed Xe-lamp was detected with a Ge-avalanche photodiode (Hamamatsu Photonics, B2834). For the visible region (400–1000 nm), a Si–PIN photodiode (Hamamatsu Phonics, S1722–02) was employed as a detector.

Acknowledgments

This work was kindly supported by China/Ireland Science and Technology Collaboration Research Foundation (No. CI-2004-06), National Natural Science Foundation of China (No. 20546002), East China University of Science and Technology, SRF for ROCS, and STCSM (No. 05XD14004). Y.C. also thanks the Japan Science and Technology Agency and the Alexander von Humboldt Foundation of Germany for a fellowship.

[1] a) Y. Chen, M. Hanack, Y. Araki, O. Ito, *Chem. Soc. Rev.* **2005**, *34*, 517–529; b) M. Barthel, S. Vagin, D. Dini, M. Hanack, *Eur. J. Org. Chem.* **2002**, 3756–3762; c) Y. Chen, D. Dini, M. Hanack, M. Fujitsuka, O. Ito, *Chem. Commun.* **2004**, 340–341; d) V. Krishnan, M. P. Feth, E. Wendel, Y. Chen, M. Hanack, H. Bertagnolli, *Z. Phys. Chem.* **2004**, *218*, 1–15; e) Y. Chen, M. Barthel, M. Seiler, L. R. Subramanian, H. Bertagnolli, M. Hanack, *Angew. Chem. Int. Ed. Eng.* **2002**, *41*, 3239–3242; f) Y. Chen, S. O'Flaherty, M. Fujitsuka, M. Hanack, L. R. Subramanian, O. Ito, W. J. Blau, *Chem. Mater.* **2002**, *14*, 5163–5168; g) Y. Chen, M. Hanack, S. O'Flaherty, G. Bernd, A. Zeug, B. Roeder, W. J. Blau, *Macromolecules* **2003**, *36*, 3786–3788.

[2] H. Bertagnolli, W. J. Blau, Y. Chen, D. Dini, M. P. Feth, S. M. O'Flaherty, M. Hanack, V. Krishnan, *J. Mater. Chem.* **2005**, *15*, 683–689.

[3] W. Uhl, T. Spies, R. Koch, *J. Chem. Soc., Dalton Trans.* **1999**, 2385–2392.

[4] P. Wei, X. W. Li, G. H. Robinson, *Chem. Commun.* **1999**, 1287–1288.

[5] K. S. Klimek, C. Cui, H. W. Roesky, M. Noltemeyer, H. G. Schmidt, *Organometallics* **2000**, *19*, 3085–3090.

[6] W. Uhl, T. Spies, *Z. Anorg. Allg. Chem.* **2000**, *626*, 1059–1064.

[7] K. J. Wynne, *Inorg. Chem.* **1984**, *23*, 4658–4663.

[8] Y. Chen, L. R. Subramanian, M. Barthel, M. Hanack, *Eur. J. Inorg. Chem.* **2002**, 1032–1034.

[9] S. Takagi, H. Inoue, *Molecular and Supramolecular Photochemistry* (Eds.: V. Ramamurthy, K. S. Schanze), vol. 4, Marcel Dekker, New York, **1999**.

[10] M. Fujitsuka, O. Ito, H. Konami, *Bull. Chem. Soc. Jpn.* **2001**, *74*, 1823–1829.

[11] Y. Chen, L. R. Subramanian, M. Fujitsuka, O. Ito, S. M. O'Flaherty, W. J. Blau, T. Schneider, D. Dini, M. Hanack, *Chem. Eur. J.* **2002**, *8*, 4248–4254.

[12] Y. Chen, S. M. O'Flaherty, M. Hanack, W. J. Blau, *J. Mater. Chem.* **2003**, *13*, 2405–2408.

[13] S. Dhami, A. J. De Mello, G. Rumbles, S. M. Bishop, D. Phillips, A. Beeby, *Photochem. Photobiol.* **1995**, *61*, 341–346.

[14] M. L. Spaeth, W. R. Sooy, *J. Chem. Phys.* **1998**, *48*, 2315–2323.

[15] T. H. Huang, J. H. Sharp, *Chem. Phys.* **1982**, *65*, 205–216.

Received: April 21, 2005
Published Online: October 10, 2005

 © 2005 Wiley-VCH Verlag GmbH & Co. KGaA, Weinheim

New Polymeric Manganese Azide Derivatives with Quinazoline

Morsy A. M. Abu-Youssef,*[a] Albert Escuer,[b] and Vratislav Langer[c]

Keywords: Azides / Coordination polymers / Magnetic properties / Manganese

Two new polymeric derivatives of the (azido)Mn^{II} system with formula $[Mn(H_2O)(\mu\text{-}N_3)(N_3)(quinaz)_2]_n$ (**1**) and $[Mn(\mu\text{-}N_3)_2(quinaz)_2]_n$ (**2**) (quinaz = quinazoline) have been structurally and magnetically characterised. Compound **1** crystallises in the triclinic system, space group $P\bar{1}$, and consists of 1D chains with single end-to-end azido bridges. These chains give a two-dimensional supramolecular arrangement by means of H-bond interactions. Compound **2** crystallises in the monoclinic system, space group $C2/c$, and contains a square alternating 2D network bridged by azido ligands in the end-to-end coordination mode. Compound **2** exhibits some unusual features, such as the unprecedented linear coordination of the azido bridge. Magnetic analysis reveals moderate antiferromagnetic coupling, with J values in good agreement with the expected range, as a function of the Mn–N–N bond angles.
(© Wiley-VCH Verlag GmbH & Co. KGaA, 69451 Weinheim, Germany, 2005)

Introduction

The azido ligand is currently one of the most interesting bridging ligands in the attempt to build polynuclear or *n*-dimensional architectures, which combine its interest as a ligand in coordination chemistry with a large variety of magnetic responses.[1] The versatility of this ligand is a direct consequence of its ability to act as a bridge in a large variety of coordination modes. For example, it is able to link two cations [in either end-to-end (EE)[2–4] or end-on (EO)[3,5] modes], three cations in the more exotic $\mu_{1,1,1}$ or $\mu_{1,1,3}$ modes,[4] or act as a bridge between four metallic centres in the rare examples of $\mu_{1,1,1,1}$ and $\mu_{1,1,3,3}$ modes.[5] The simultaneous presence of more than one of these coordination modes in the same compound is not rare, and this increases the number of possible topologies.[6,7] The interest of magnetochemists in this ligand lies in the well-established relationship between its coordination mode and the resulting magnetic properties, which cover a wide range of ferro-, ferri- and antiferromagnetic responses,[1] although it should be pointed out that the topology of the resulting systems is far from being controllable. The large structural variations of azide derivatives reported in the last few years provides experimental proof of the effects of minor changes in the synthetic conditions or in the co-ligands bridged to the metallic centre. One of the most complete series of compounds, with general formula $[Mn(N_3)_2(R\text{-}py)_2]_n$, (R-py = substituted pyridyl ligands) is a paradigmatic example of how minor differences in R can change the dimensionality or the coordination mode of the azido bridges, which are generally related to weak supramolecular π–π stacking interactions or to the packing forces in the solid, drastically.

In this paper, we present the synthesis and X-ray and magnetic characterisation of two new polymeric manganese azide derivatives with formula $[Mn(H_2O)(\mu\text{-}N_3)(N_3)(quinaz)_2]_n$ (**1**) and $[Mn(\mu\text{-}N_3)_2(quinaz)_2]_n$ (**2**). The co-ligand quinazoline (quinaz) was chosen in order to combine the versatility of the azido ligand with the possibility of a second bridging ligand closely related to previously reported systems such as pyrimidine,[8] but introducing structural differences in the ligand in order to generate new topologies. The resulting compounds show that quinaz, in contrast to pyrimidine, coordinates through only one of its donor N-atoms in a similar way to classical pyridine ligands. Compound **1** is a 1D alternating system with single EE bridges in a *cis* arrangement, giving an uncommon 1D zigzag topology. Extended H-bonds between terminal azide and water molecules coordinated to the manganese atom generate a supramolecular 2D network. Compound **2** is an alternating square 2D layer of manganese EE azido bridges with *trans*-quinaz coordinated ligands. The magnetic behaviour agrees with the antiferromagnetic coupling expected for this kind of bridge.

[a] Chemistry Department, Faculty of Science, Alexandria University,
P. O. Box 426, Ibrahimia, 21321 Alexandria, Egypt
Fax: +20-3-391-1794
E-mail: morsy5@link.net
[b] Departament de Química Inorgànica, Universitat de Barcelona, Martí I Franqués 1-11, 08028-Barcelona, Spain
Fax: +34-93-490-7725
E-mail: albert.escuer@qi.ub.es
[c] Department of Chemical and Biological Engineering, Division of Materials and Surface Chemistry, Subdivision of Environmental Inorganic Chemistry, Chalmers University of Technology,
41296 Göteborg, Sweden
Fax: +46-31-772-2853
E-mail: langer@chalmers.se

Results and Discussion

Synthesis

Slow concentration of water/methanol solutions of manganese nitrate tetrahydrate, the quinazoline ligand and sodium azide gave single crystals of **1** (cold solutions) and **2** (room temperature crystallization).

Structure of $[Mn(H_2O)(\mu\text{-}N_3)(N_3)(quinaz)_2]_n$ (1)

A labelled ORTEP plot of the structure is shown in Figure 1. Selected distances and angles are listed in Table 1. The structure of this compound can be described as zigzag chains of manganese atoms linked by single azido bridges coordinated in the EE mode.

The manganese atoms are placed in an octahedral environment and are linked to two quinazoline ligands in a *trans* position, two azide N atoms corresponding to the bridging end-to-end ligands, one terminal azido and one water molecule. Larger bond lengths are found to the N(quinazoline) atoms (2.318 Å), intermediate distances (around 2.2 Å) to the N(azide) atoms and a shorter distance (2.179 Å) to the O atom. The azido bridges along the chain are not equivalent and show similar, but not identical, Mn–N–N bond angles [142.6° for Mn(1)–N(11)–N(12) and 137.3° for Mn(1)–N(31)–N(32)]. The terminal azido ligand shows a larger Mn(1)–N(21)–N(22) bond angle of 150.4°. The torsion angle for the two non-equivalent Mn–N–N–N–Mn units is 180°. The water molecule and the N(23) atom

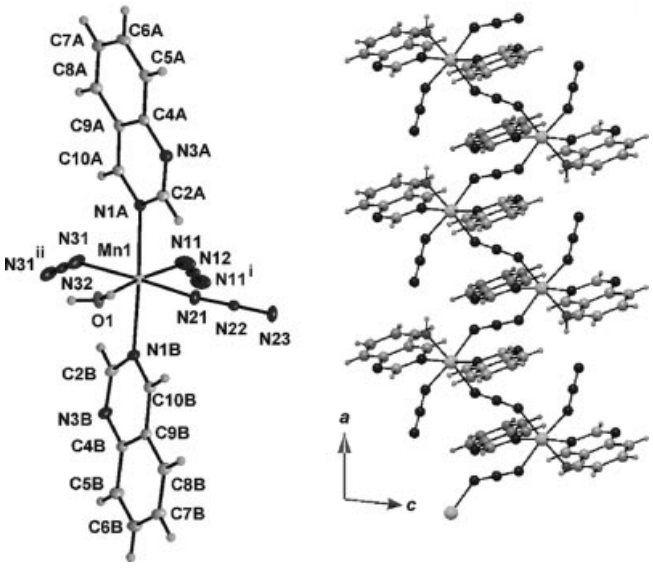

Figure 1. Left: labelled ORTEP plot of the basic unit of $[Mn(H_2O)(\mu\text{-}N_3)(N_3)(quinaz)_2]_n$ (**1**) with thermal ellipsoids at 30% probability. Right: 1D structure shown in projection along the *b*-axis.

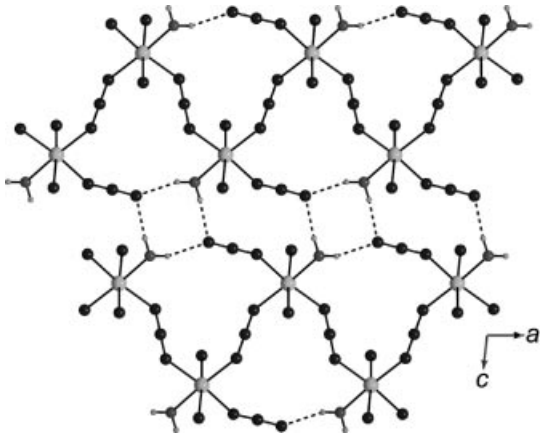

Figure 2. View of the zigzag arrangement of the individual chains of $[Mn(H_2O)(\mu\text{-}N_3)(N_3)(quinaz)_2]_n$ (**1**) and the 2D arrangement generated from the interaction of H(11) and H(12) with the terminal N(23) atoms.

Table 1. Selected bond lengths [Å] and angles [°] for $[Mn(H_2O)(\mu\text{-}N_3)(N_3)(quinaz)_2]_n$ (**1**).[a]

Mn(1)–N(1A)	2.318(1)	N(11)–N(12)	1.169(1)	
Mn(1)–N(1B)	2.318(1)	N(12)–N(11)i	1.169(1)	
Mn(1)–N(11)	2.205(1)	N(21)–N(22)	1.171(1)	
Mn(1)–N(21)	2.188(1)	N(22)–N(23)	1.174(1)	
Mn(1)–N(31)	2.215(1)	N(31)–N(32)	1.175(1)	
Mn(1)–O(1)	2.179(1)	N(32)–N(31)ii	1.175 (1)	
N(1A)–Mn(1)–N(1B)	173.64(4)	Mn(1)–N(11)–N(12)	142.6(1)	
N(1A)–Mn(1)–N(11)	94.24(5)	Mn(1)–N(21)–N(22)	150.4(1)	
N(1A)–Mn(1)–N(21)	89.56(4)	Mn(1)–N(31)–N(32)	137.3(1)	
N(1A)–Mn(1)–N(31)	89.71(4)			
N(1A)-Mn(1)- O(1)	88.60(4)	N(11)–N(12)–N(11)i	180.00	
N(1B)–Mn(1)–N(11)	92.01(5)	N(21)–N(22)–N(23)	178.1(1)	
N(1B)–Mn(1)–N(21)	88.89(4)	N(31)–N(32)–N(31)ii	180.00	
N(1B)–Mn(1)–N(31)	91.09(4)			
N(1B)–Mn(1)–O(1)	85.07(4)			
N(11)–Mn(1)–N(21)	93.46(6)	H-bonds	O···N	O–H···N
N(11)–Mn(1)–N(31)	93.48(6)	O(1)–H(11)···N(23)iii	2.775(2)	159(2)
N(11)–Mn(1)–O(1)	174.02(5)	O(1)–H(12)···N(23)iv	2.829(2)	175(2)
N(21)–Mn(1)–N(31)	173.06(5)			
N(21)–Mn(1)–O(1)	81.28(4)			
N(31)–Mn(1)–O(1)	91.80(5)			

[a] Symmetry transformations used to generate equivalent atoms: (i): $-x + 2, -y + 1, -z + 1$; (ii): $-x + 1, -y + 1, -z + 1$; (iii): $x - 1, y, z$; (iv): $-x + 2, -y + 1, -z + 2$; (v): $x, y - 1, z$.

 © 2005 Wiley-VCH Verlag GmbH & Co. KGaA, Weinheim

from the terminal azido ligand are related by means of H-bonds through H(11) and H(12) giving a 2D supramolecular arrangement (Figure 2). The Mn···Mn intrachain distances are 6.426(1) Å [bridge N(11)–N(12)–N(11)′] and 6.360(1) Å [bridge N(31)–N(32)–N(33)]. The minimum interchain Mn···Mn distance is 7.214(1) Å.

Structure of $[Mn(\mu\text{-}N_3)_2(quinaz)_2]_n$ (2)

A labelled ORTEP plot of the structure is shown in Figure 3. Selected distances and angles are listed in Table 2. The structure consists of a 2D square network of Mn^{II} cations bridged by EE azido bridges (Figure 4).

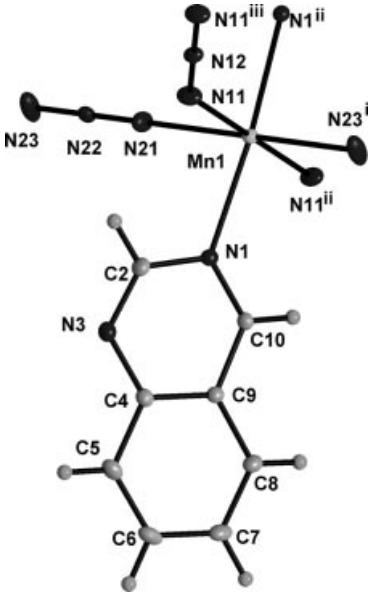

Figure 3. Labelled ORTEP plot of the basic unit of $[Mn(\mu\text{-}N_3)_2(quinaz)_2]_n$ (**2**) with thermal ellipsoids at 50% probability.

Each manganese atom is surrounded by two quinazoline ligands in a *trans* position and four N(azide) atoms, which act as a bridge to the four neighbouring manganese atoms. As observed in **1**, the Mn–N(quinazoline) bonds (ca. 2.285 Å) are longer than those found for the Mn–N(azide) bonds (2.217–2.254 Å). The Mn–N–N bond angles show large differences: Mn(1)–N(11)–N(12) is 144.3(1)°, which lies in the normal range for this ligand, whereas the two bond angles Mn(1)–N(21)–N(22) and Mn(1)iv–N(23)–N(22) have a value of 180°, which means that this Mn–NNN–Mn subunit is fully linear. The torsion angle for the Mn–N(11)–N(12)–N(13)–Mn units is 180°. The Mn···Mn intraplane distances are 6.8045(1) Å [bridge N(21)–N(22)–N(23)] and 6.4921(1) Å [bridge N(11)–N(12)–N(11)′], and the minimum interplane Mn···Mn distance is 9.845(1) Å.

The most singular detail of this structure is the linear coordination of one of the azide bridges. Some unusually large Mn–N–N bond angles have previously been found in the 2D system $[Mn(DENA)_2(N_3)_2]$ (DENA = diethylnicotinamide),[9] for which one of the bridges exhibits a pair of Mn–N–N bond angles of 148.4° and 171.7°. Large bond angles have also been found in one dinuclear (cryptand)

Table 2. Selected bond lengths [Å] and angles [°] for $[Mn(\mu\text{-}N_3)_2(quinaz)_2]_n$ (**2**).[a]

Mn(1)–N(1)	2.285(1)	N(11)–N(12)	1.171(1)
Mn(1)–N(1)ii	2.285(1)	N(12)–N(11)iii	1.171(1)
Mn(1)–N(11)	2.222(1)	N(21)–N(22)	1.158(3)
Mn(1)–N(11)ii	2.222(1)	N(22)–N(23)	1.175(3)
Mn(1)–N(21)	2.254(2)		
Mn(1)–N(23)i	2.217(2)		
N(1)–Mn(1)–N(1)ii	174.68(6)	Mn(1)–N(11)–N(12)	144.3(1)
N(1)–Mn(1)–N(11)	88.41(5)	Mn(1)–N(21)–N(22)	180.0
N(1)–Mn(1)–N(11)ii	91.60(5)	Mn(1)iv–N(23)–N(22)	180.0
N(1)–Mn(1)–N(21)	87.34(3)		
N(1)–Mn(1)–N(23)i	92.66(3)		
N(1)ii–Mn(1)–N(11)	91.60(5)	N(11)–N(12)–N(11)iii	180.0
N(1)ii–Mn(1)–N(11)ii	88.41(5)	N(21)–N(22)–N(23)	180.00(1)
N(1)ii–Mn(1)–N(21)	87.34(3)		
N(1)ii–Mn(1)–N(23)i	92.66(3)		
N(11)–Mn(1)–N(11)ii	179.79(8)		
N(11)–Mn(1)–N(21)	90.10(4)		
N(11)–Mn(1)–N(23)i	89.90(4)		
N(11)ii–Mn(1)–N(21)	90.10(4)		
N(11)ii–Mn(1)–N(23)i	89.90(4)		
N(21)–Mn(1)–N(23)i	180.0		

[a] Symmetry transformations used to generate equivalent atoms: (i): $x, y-1, z$; (ii): $-x, y, -z+1/2$; (iii): $-x, -y, -z$; (iv): $x, y+1, z$; (v): $x, -y, z+1/2$.

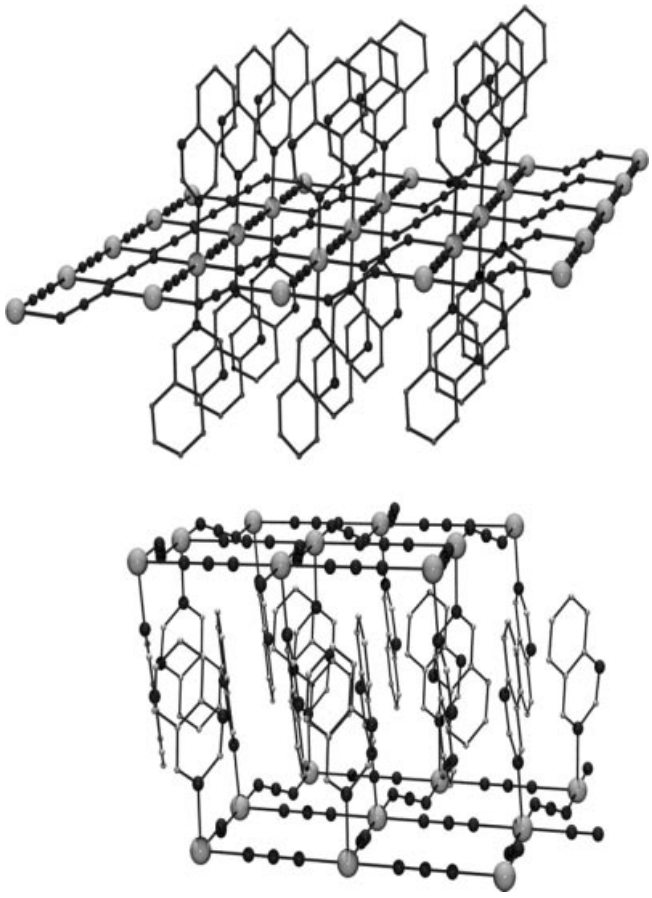

Figure 4. Top: view of one layer of $[Mn(\mu\text{-}N_3)_2(quinaz)_2]_n$ (**2**). In this figure the linear manganese–azido bonds along the *b*-axis can be clearly differentiated. Bottom: view of the interlayer π–π stacking between adjacent sheets.

 © 2005 Wiley-VCH Verlag GmbH & Co. KGaA, Weinheim

Mn^{II} compound,[10] but in all cases the coordination of the bridge is far from linear.

Magnetic Measurements and Coupling Constant Calculations

The magnetic measurements were performed on powdered crystalline samples in the 2–300 K temperature range. The overall interaction is moderately antiferromagnetic for the two compounds.

The plot of the susceptibility vs. temperature for compound **1** shows a regular increase on cooling up to a maximum value at 20 K (Figure 5). The $\chi_M T$ value at room temperature is 3.93 $cm^3 K mol^{-1}$ for the manganese atom, which is lower than the expected value for an isolated Mn^{II} ion (4.375 $cm^3 K mol^{-1}$), and decreases continuously, tending to zero at low temperature. Based on the structural data, compound **1** is strictly an alternating one-dimensional system which shows similar bond lengths, identical torsion angles and quite similar Mn–N–N bond angles in the bridging region. Two alternative and complementary fits were performed on the χ_M data in order to determine coherent values for the coupling constants. The first fit was made assuming that the differences in the bond parameters are a minor effect, and the fit of the experimental data was performed as a system with only one average J coupling constant by applying the analytical expression for a regular chain derived from the Hamiltonian $H = -JS_i \cdot S_{i+1}$ for local $S = 5/2$.[11] The best-fit parameters were $J = -4.4(1)$ cm^{-1} and $g = 2.00(1)$ (paramagnetic impurities: 1.3%). As would be expected from the similar bond parameters, attempts to differentiate two J coupling constants in a second fit on the basis of the Hamiltonian $H = J_1 \Sigma S_{2i} \cdot S_{2i+1} - J_2 \Sigma S_{2i+1} \cdot S_{2i+2}$, as proposed by Drillon et al.,[12] did not improve the results obtained in the fit as a homogeneous chain, giving similar J_1 and J_2 values around the –4.35 cm^{-1} average value.

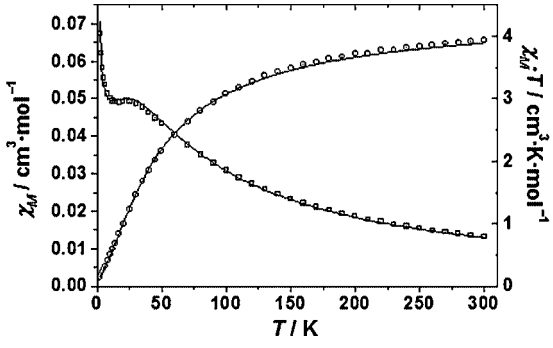

Figure 5. Plot of χ_M (open squares) and $\chi_M T$ product (open circles) for compound **1**. Solid lines correspond to the best fit (see text).

Compound **2** shows a similar shape for the susceptibility plot, with a maximum at 32 K and a $\chi_M T$ value of 4.04 at room temperature (Figure 6). In this case, the structural data indicate a 2D system with two clearly different J coupling constants, as would be expected from the very different Mn–N–N bond angles found in the network. Analytical expressions for the calculation of the coupling constants for systems of this kind are not available, so only an approximation can be made for **2**. The fit as a simplified 2D quadratic layer by means of the high-temperature expansion series derived from the Hamiltonian $H = \Sigma_{nn} - JS_iS_j$, (where Σ_{nn} runs over all pairs of nearest spins i and j),[13] gives a relatively poor fit [dotted line in Figure 6, $J = -2.5$ cm^{-1}, $g = 2.00(1)$], thus indicating that the magnetic behaviour of this system is far from a homogeneous 2D response. Not surprisingly, a better fit of the experimental data was obtained by treating the system as a homogeneous 1D system [solid line in Figure 6, $J = -4.9(1)$ cm^{-1}, $g = 2.03(1)$].

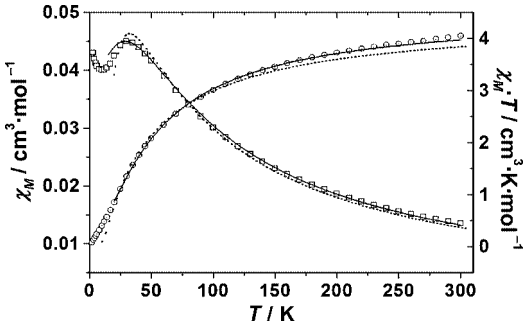

Figure 6. Plot of χ_M (open squares) and $\chi_M T$ product (open circles) for compound **2**. The dotted line shows the best fit as a homogeneous 2D system. The solid line shows the best fit as a one-dimensional system (see text).

Magnetostructural Correlations

As was calculated previously,[14] the superexchange interaction for a d^5 ion should be antiferromagnetic in nature and mediated by two kind of pathways. The main interaction goes via σ-interactions involving one of the non-bonding π-MOs of the azide and the atomic e_g-orbitals of the metallic ions. As shown in Figure 7,[14] this interaction pathway is very effective at small Mn–N–N bond angles and is practically negligible for large bond angles. The contribution of this pathway to the antiferromagnetic component of the interaction is therefore very sensitive to the experimental Mn–N–N bond angle. This fact has been checked experimentally for Cu^{II} and Ni^{II} cryptand systems with M–N–N bond angles close to 165°,[10] for which the antiferromagnetic component is close to zero and the global coupling is ferromagnetic. The second interaction pathway, which is active in our case, corresponds to pπ–dπ interactions between the non-bonding π-MOs of the azido and two of the atomic t_{2g}-orbitals of the metallic ion (Scheme 1). This second interaction mechanism is much less effective than the σ-pathway due to the worse overlap at any Mn–N–N angle value.[10]

Compound **1** is an alternating system with similar Mn–N–N bond angles. From Figure 7, is easy to justify the reason for the failure of the fit as an alternating system: the antiferromagnetic components for the two kinds of bridges should be very similar and therefore the two J values cannot be differentiated. The calculated J value as a homogeneous chain can be assumed as a good mean value with poor

 © 2005 Wiley-VCH Verlag GmbH & Co. KGaA, Weinheim

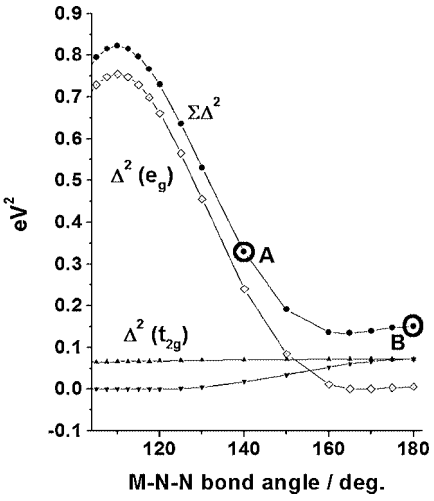

Figure 7. Walsh diagram of the Δ^2 gaps. Filled triangles correspond to the t_{2g}-components, open diamonds show the e_g-component and the filled circles show the global contribution to the antiferromagnetic interaction for a d^5-ion like Mn^{II}. Points A and B correspond to the antiferromagnetic contribution for 145° and 180° Mn–N–N bond angles, respectively.

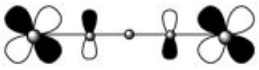

Scheme 1. One of the pπ–dπ superexchange pathways that are active for d^5-ions bridged by a linear azido bridge.

deviation for these bond parameters. Comparison with other 1D azido systems with similar bond parameters is reasonable.[1]

Compound **2** shows two very different bond angles, one of which (144.1°) is slightly larger than the mean values of compound **1**, and 180° for the second Mn–N–N bond angle. Therefore a moderate antiferromagnetic coupling should be expected for the bridge with normal bond angles for compound **2** (A in Figure 7), in contrast to the much lower antiferromagnetic coupling for the linear bridge (B in Figure 7) and agreeing with the poor fit as a 2D system with only one mean *J* value. It is obviously erroneous to assume that the interaction mediated by the linear Mn^{II}–azido units is negligible, and it is not surprising that the susceptibility plot shows better fit as a 1D system and with a calculated *J* value close to compound **1**. It is not possible to evaluate the correct *J* values from analytical fits, but the above result is indicative of the low antiferromagnetic contribution of the 180° azido bridge, as expected from theoretical predictions.[14]

Conclusions

The reported results are new examples of the importance of synthetic conditions and weak supramolecular interactions in the resulting topologies of high-dimensional manganese azide systems. Compound **2** shows an unprecedented linear coordination between two metallic centres, which has not been obtained even with previously studied cryptand systems. This kind of coordination can be assumed to be a special case of the EE coordination mode. Magnetic measurements afford the first experimental confirmation of the low antiferromagnetic coupling for such large Mn–N–N bond angles, as was predicted previously.

Experimental Section

General Remarks: Magnetic susceptibility measurements were carried out on polycrystalline samples with a Quantum Design susceptometer working in the 2–300 K range in a magnetic field of 0.3 T and remeasured in a field of 0.03 T in the 20–2 K range. Diamagnetic corrections were estimated from Pascal's tables. Infrared spectra (4000–200 cm^{-1}) were recorded from KBr pellets with a Bruker IFS-125 FT-IR spectrophotometer.

$[Mn(N_3)_2(H_2O)(quinaz)_2]_n$ (1): A solution of quinazoline (0.52 g, 4 mmol) in methanol (15 mL) was added to a methanolic solution (15 mL) of manganese nitrate tetrahydrate (0.5 g, 2 mmol). Then, a concentrated aqueous solution of sodium azide (0.65 g, 10 mmol) was added dropwise with continuous stirring. The resulting clear solution was allowed to stand for several days in a refrigerator. Yellow crystals suitable for X-ray measurements were collected and dried in air. Yield: 0.58 g (70%). $C_{16}H_{14}MnN_{10}O$ (417.31): calcd. C 46.04, H 3.35, Mn 13.16, N 33.57; found C 45.98, H 3.11, Mn 12.89, N 34.14. IR (KBr): $\tilde{\nu}$ = 3347 vs, 3233 vs, 3043 ms, 2122 vs, 2089 vs, 1619 vs, 1573 vs, 1554 w, 1519 w, 1489 vs, 1465 m, 1428 m, 1408 m, 1381 vs, 1306 s, 1277 m, 1257 m, 1239 m, 1212 vs, 1154 w, 1139 s, 1065 s, 1013 m, 987 m, 955 vs, 930 vs, 874 s, 832 s, 794 vs, 762 vs, 633 vs, 593 vs, 521 s, 473 vs, 409 wm, 387 m, 368 m, 343 m, 316 m, 293 m, 269 vs cm^{-1}.

$[Mn(N_3)_2(quinaz)_2]_n$ (2): An aqueous solution (10.0 mL) of manganese nitrate tetrahydrate (0.25 g, 1.0 mmol) was mixed with a methanolic solution (10 mL) of quinazoline (0.26 g, 2.0 mmol) and the mixture was stirred for about 5 min. A solution of sodium azide (0.32 g, 5 mmol) in water (5 mL) was then added dropwise with vigorous stirring. The resulting clear solution was allowed to stand at room temperature for several weeks. Brown-yellowish crystals suitable for X-ray measurements were collected and dried in air. Yield: 0.26 g (65%). $C_{16}H_{12}MnN_{10}$ (399.30): calcd. C 48.12, H 3.00, Mn 13.76, N 35.08; found C 47.98, H 3.11, Mn 13.89, N 35.24. IR (KBr): $\tilde{\nu}$ = 3439 w, 3046 w, 2096 vs, 1618 s, 1573 s, 1489 s, 1458 m, 1409 m, 1379 s, 1308 m, 1269 m, 1239 m, 1210 ms, 1139 ms, 1103 wm, 1066 ms, 1012 wm, 983 wm, 955 ms, 926 m, 881 m, 832 m, 795 s, 762 s, 636 s, 617 m, 598 m, 588 m, 524 wm, 479 m, 451 vw, 409 vw, 387 vw, 367 vw, 343 vw, 317 vw, 294 vw, 269 m, 235 s cm^{-1}.

It should be pointed out that the two compounds were obtained with the same stoichiometric ratio of reagents. The factors that control the final compound are difficult to evaluate and the solubility of the products, the temperature and the reaction time play an important role. In this case, the coordination of a second azido ligand in **2** in comparison with **1** is probably related to the higher temperature of the reaction mixture that favours the replacement of the coordinated water molecule.

X-ray Crystallographic Study: All diffraction data were collected with a Siemens SMART CCD diffractometer with Mo-K_α radiation (λ = 0.71073 Å, graphite monochromator). The crystals were cooled to 173(2) K by a flow of nitrogen gas using an LT-2A device. Full spheres of reciprocal lattices were scanned by 0.3° steps in ω with a crystal-to-detector distance of 3.97 cm. Preliminary orientation matrices were obtained from the first frames using SMART.

 © 2005 Wiley-VCH Verlag GmbH & Co. KGaA, Weinheim

The collected frames were integrated using the preliminary orientation matrices, which were updated every 100 frames. Final cell parameters were obtained by refinement on the positions of reflections with $I > 10\sigma(I)$ after integration of all the frames with SAINT.[15] The data were empirically corrected for absorption and other effects with SADABS.[16] The structures were solved by direct methods and refined by full-matrix least squares on all F^2 data with SHELXTL.[17] The non-H atoms were refined anisotropically, while hydrogen atoms were refined isotropically with the use of geometrical restraints. Selected crystallographic and refinement data are summarised in Table 3. Molecular graphics were prepared with Diamond.[18] CCDC-264957 (**1**) and -264958 (**2**) contain the supplementary crystallographic data for this paper. These data can be obtained free of charge from The Cambridge Crystallographic Data Centre via www.ccdc.cam.ac.uk/data_request/cif.

Table 3. Crystal data and structure refinement for $[Mn(H_2O)(\mu\text{-}N_3)(N_3)(quinaz)_2]_n$ (**1**) and $[Mn(\mu\text{-}N_3)_2(quinaz)_2]_n$ (**2**).

Empirical formula	$C_{16}H_{14}MnN_{10}O$	$C_{16}H_{12}MnN_{10}$
Formula mass	417.31	399.30
Crystal system	triclinic	monoclinic
Space group	$P\bar{1}$	$C2/c$
a [Å]	7.6986(1)	18.4779(2)
b [Å]	10.9472(2)	6.8045(1)
c [Å]	11.7535(2)	12.8417(1)
α [°]	116.357(1)	90
β [°]	94.948(1)	99.920(1)
γ [°]	90.752(1)	90
V [Å^3]	882.81(2)	1590.48(3)
Z	2	4
T [K]	173(2)	173(2)
λ (Mo-K_α) [Å]	0.71073	0.71073
μ(Mo-K_α) [mm^{-1}]	0.780	0.857
$d_{calcd.}$ [g cm^{-3}]	1.570	1.668
Crystal size [mm]	$0.38 \times 0.20 \times 0.04$	$0.42 \times 0.36 \times 0.24$
Max./min. transmission	0.9695/0.7560	0.8207/0.7148
$\theta_{min./max.}$ [°]	1.94/32.87	2.24/32.95
Reflections collected	15595	13739
Independent refl./R_{int}	6160/0.0295	2876/0.0512
Parameters/observations	276/6160	132/2876
R [$I > 2\sigma(I)$][a]	0.0331	0.0373
R_w [all][b]	0.0861	0.0939

[a] $R(F_o) = \Sigma||F_o| - |F_c||/\Sigma|F_o|$. [b] $R_w(F_o)^2 = \{\Sigma w[(F_o)^2 - (F_c)^2]^2/[\Sigma w(F_o)^4]\}^{1/2}$.

Acknowledgments

This work was supported by the SIDA–Swedish Research Links program (grants 348-2002-6879 and 348-2004-5473) and the CICYT project PB03/0538.

[1] J. Ribas, A. Escuer, M. Monfort, R. Vicente, R. Cortés, L. Lezama, T. Rojo, *Coord. Chem. Rev.* **1999**, *193–195*, 1027.
[2] M. L. Hernández, M. G. Barandika, M. K. Urtiaga, R. Cortés, L. Lezama, M. I. Arriortua, *J. Chem. Soc., Dalton Trans.* **2000**, 79.
[3] M. A. M. Abu-Youssef, A. Escuer, D. Gatteschi, M. A. S. Goher, F. A. Mautner, R. Vicente, *Inorg. Chem.* **1999**, *38*, 5716.
[4] A. Escuer, R. Vicente, M. A. S. Goher, F. A. Mautner, *Inorg. Chem.* **1998**, *37*, 782.
[5] J. L. Manson, A. M. Arif, J. S. Miller, *Chem. Commun.* **1999**, 1479.
[6] J. Cano, Y. Journaux, M. A. S. Goher, M. A. M. Abu-Youssef, F. A. Mautner, G. J. Reib, A. Escuer, R. Vicente, *New J. Chem.* **2005**, *29*, 306.
[7] A. Escuer, F. A. Mautner, M. A. S. Goher, M. A. M. Abu-Youssef, R. Vicente, *Chem. Commun.* **2005**, 605.
[8] A. Escuer, R. Vicente, F. A. Mautner, M. A. S. Goher, M. A. M. Abu-Youssef, *Chem. Commun.* **2002**, 64.
[9] M. A. S. Goher, M. A. M. Abu-Youssef, F. A. Mautner, A. Escuer, R. Vicente, *Eur. J. Inorg. Chem.* **2000**, 1819.
[10] A. Escuer, C. J. Harding, Y. Dussart, J. Nelson, V. McKee, R. Vicente, *J. Chem. Soc., Dalton Trans.* **1999**, 223.
[11] M. E. Fisher, *Am. J. Phys.* **1964**, *32*, 343.
[12] R. Cortés, M. Drillon, X. Solans, L. Lezama, T. Rojo, *Inorg. Chem.* **1997**, *36*, 677.
[13] M. E. Lines, *J. Phys. Chem. Solids* **1970**, *31*, 101.
[14] A. Escuer, R. Vicente, M. A. S. Goher, F. A. Mautner, *Inorg. Chem.* **1998**, *37*, 782.
[15] *SMART & SAINT, Area Detector Control and Integration Software*, Siemens AXS, Madison, WI, USA, **1995**.
[16] G. M. Sheldrick, *SADABS, Program for Empirical Absorption Correction of Area Detectors*, version 2.03, University of Göttingen, Germany, **2002**.
[17] *SHELXTL, Structure Determination Programs*, version 6.10, Bruker AXS Inc., Madison, Wisconsin, USA, **2001**.
[18] K. Brandenburg, *Diamond, Visual Crystal Structure Information System*, version 2.1e, Crystal Impact GbR, Bonn, Germany, **2001**.

Received: April 22, 2005
Published Online: October 5, 2005

 © 2005 Wiley-VCH Verlag GmbH & Co. KGaA, Weinheim

The Hexakis(thiocyanato)ferrate(III) Ion: a Coordination Chemistry Classic Reveals an Interesting Geometry Pattern for the Thiocyanate Ligands

Anthony W. Addison,*[a] Raymond J. Butcher,[b] Zoltán Homonnay,[c] Vitaly V. Pavlishchuk,*[d] Michael J. Prushan,[e] and Laurence K. Thompson[f]

Keywords: Iron / Thiocyanate / X-ray diffraction / Magnetic properties / IR spectroscopy / Moessbauer spectroscopy / Coordination modes / Isomers

We are grateful to Professor Ulrich Müller, of Philipps-Universität Marburg, for drawing the attention of ourselves and the referees to a prior structure report for $(NMe_4)_3[Fe(NCS)_6]$.[1] The 1977 and 2005[2] reports differ only in the choice of unit cell origin. The conclusions from the structure–spectra relationships discussed in the 2005 paper remain the same.

[1] U. Müller, *Acta Crystallogr.* **1977**, *B33*, 2197–2201.
[2] A. W. Addison, R. J. Butcher, Z. Homonnay, V. V. Pavlishchuk, M. J. Prushan, L. K. Thompson, *Eur. J. Inorg. Chem.* **2005**, 2404–2408.

Received: September 26, 2005
The Authors

[a] Chemistry Department, Drexel University, Philadelphia, PA 19104-2875, USA
[b] Chemistry Department, Howard University, Washington, DC 20059, USA
[c] Department of Nuclear Chemistry, Eötvös Loránd University, Pázmány P. s 1/A, 1117 Budapest, Hungary
[d] L.V. Pisarzhevskii Institute of Physical Chemistry, Ukrainian Academy of Sciences, Prospekt Nauki 31, Kiev, 03028 Ukraine
[e] Department of Chemistry & Biochemistry, LaSalle University, Philadelphia, PA 19141, USA
[f] Chemistry Department, Memorial University, St. John's NFD, A1B 3X7 Canada

 DOI: 10.1002/ejic.200500864 © 2005 Wiley-VCH Verlag GmbH & Co. KGaA, Weinheim

EurJIC
European Journal of Inorganic Chemistry

Issue 23/2005

Pages 4669–4848

Papers available ahead of print in Early View at www.interscience.wiley.com

Earliest available Table of Contents: Automatically, free of charge by e-mail through www.interscience.wiley.com/alerts

COVER PICTURE

The cover picture shows the properties of the antiferromagnetic molecular spin-ladder built by combining the $5NAP^+$ diamagnetic cations and the $CuBr_4^{2-}$ radical anions. The upper left box shows the structure of the two ions, the middle box its magnetic topology (the weakly interacting two-leg ladders are clearly marked), while the lower box shows the experimental and computed magnetic susceptibility curves. Details are discussed in the article by M. Deumal, J. J. Novoa et al. on p. 4697ff.

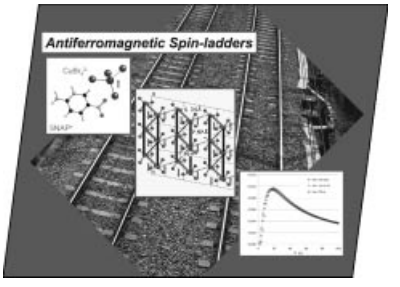

MICROREVIEW

Contents

4683 **R. Choukroun,* C. Lorber**

Adventures in Vanadocene Chemistry

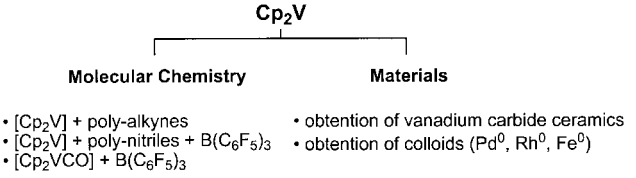

Keywords: Alkynes / Ceramics / Colloids / Metallocenes / Nitriles / Vanadium

 © 2005 Wiley-VCH Verlag GmbH & Co. KGaA, Weinheim

SHORT COMMUNICATION

4693 **M.-R. Li, W. Liu, H.-H. Chen, X.-X. Yang, Z.-B. Wei, D.-H. Cao, M. Gu, J.-T. Zhao***

Low-Temperature Flux Synthesis, Crystal Structure and Ce-Doped Luminescence of the First Lutetium Diphosphate $NH_4LuP_2O_7$

Keywords: Low-temperature self-flux synthesis / Structure / Diphosphate / Luminescence

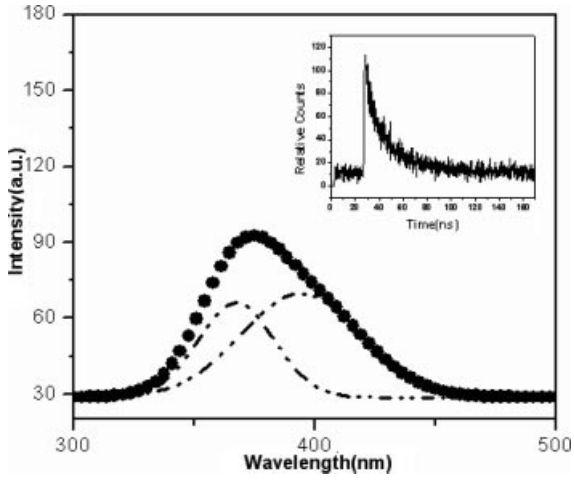

FULL PAPERS

4697 **M. Deumal,* G. Giorgi, M. A. Robb, M. M. Turnbull, C. P. Landee, J. J. Novoa***

The Mechanism of Magnetic Interaction in Spin-Ladder Molecular Magnets: A First-Principles, Bottom-Up, Theoretical Study of the Magnetism in the Two-Legged Spin-Ladder Bis(2-amino-5-nitropyridinium) Tetrabromocuprate Monohydrate

Keywords: Copper / Density functional calculations / Magnetic properties / Spin-ladders / Structure-activity relationships

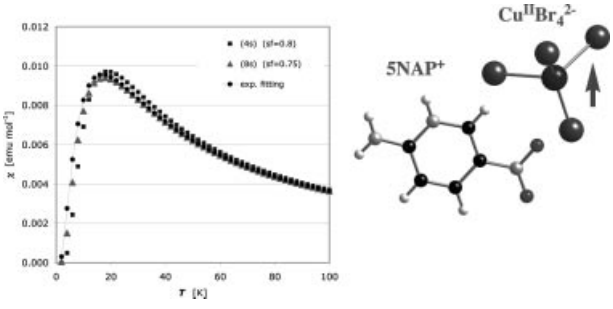

4707 **A. Del Zotto,* E. Zangrando, W. Baratta, A. Felluga, P. Martinuzzi, P. Rigo**

[MCl(ligand)]$^+$ Complexes (M = Ni, Pd, Pt) with a P,N,N Terdentate Ligand − Solid State and Solution Structures and Catalytic Activity of the Pd^{II} Derivative in the Heck Reaction

Keywords: Nickel / Palladium / Platinum / Terdentate hybrid ligands / Heck reaction

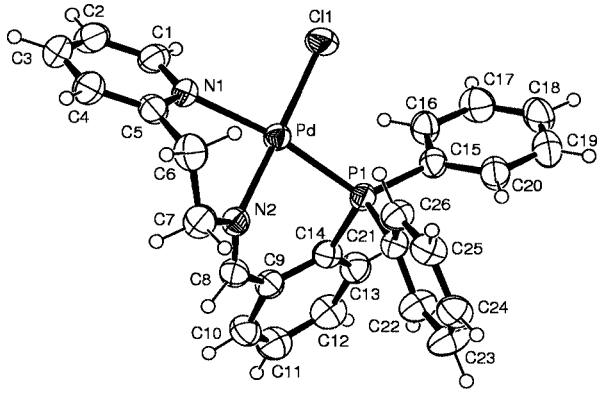

4715 **L. Weber,* I. Domke, H.-G. Stammler, B. Neumann**

Synthetic, Structural, and Electrochemical Studies of 2-Ferrocenyl- and 2-Cymantrenyl-Functionalized 2,3-Dihydro-1*H*-1,3,2-diazaboroles and 1,3,2-Diazaborolidenes

Keywords: Boron / Cyclic voltammetry / Ferrocene / Methylcymantrene

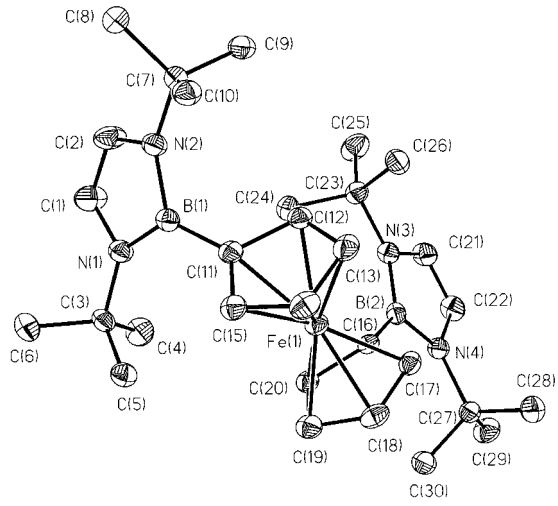

4723 **W.-C. Yeo, G.-K. Tan, L. L. Koh, P.-H. Leung***

Asymmetric [2+2] Cycloaddition of (*E*)-2-(Diphenylphosphanyl)styrene Promoted by a Chiral Metal Template

Keywords: Asymmetric synthesis / Cycloaddition / Platinum / Phosphane ligands / Template synthesis

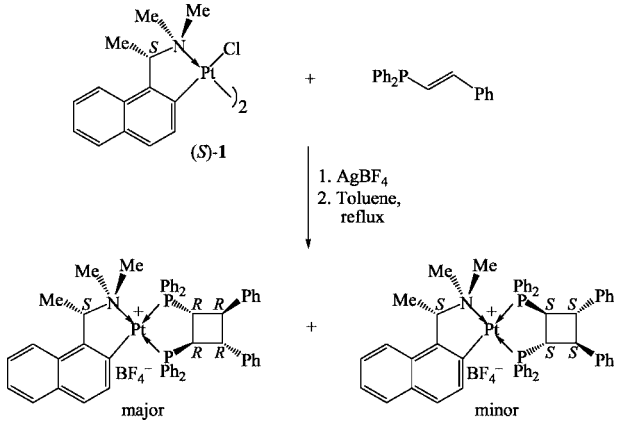

4729 **J. A. Fernandes, S. Lima, S. S. Braga, M. Pillinger, J. E. Rodríguez-Borges, P. Ribeiro-Claro,* J. J. C. Teixeira-Dias, I. S. Gonçalves***

Experimental and Theoretical Study of the Encapsulation of a Linear Oligo(ferrocenylsilane) Trimer with β-Cyclodextrin

Keywords: Cyclodextrins / Ferrocene / Inclusion compounds / Oligo(ferrocenes) / Ab initio calculations

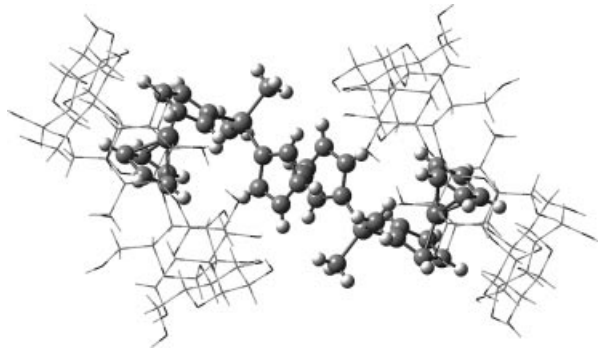

4735 **S. Ye, B. Sarkar, M. Niemeyer, W. Kaim***

Mixed-Ligand Copper Complexes with 8-Methylthioquinoline and Triphenylphosphane or the *o*-Semiquinone/Catecholate Redox System

Keywords: Copper / Crystal structure / EPR spectroscopy / Heterocycles / Thioether ligands

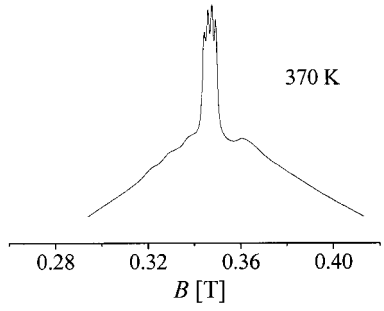

 © 2005 Wiley-VCH Verlag GmbH & Co. KGaA, Weinheim

4739 **L. N. Puntus, K. J. Schenk, J.-C. G. Bünzli***

Intense Near-Infrared Luminescence of a Mesomorphic Ionic Liquid Doped with Lanthanide β-Diketonate Ternary Complexes

Keywords: Ionic liquids / Liquid crystals / Lanthanides / Near infrared luminescence / Quantum yield / Small-angle X-ray diffraction

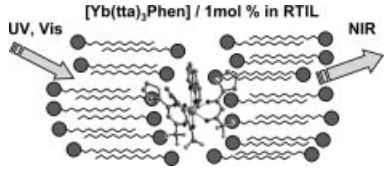

4745 **S. Gischig, A. Togni***

Pd^{II} Complexes of Tridentate PCP N-Heterocyclic Carbene Ligands: Structural Aspects and Application in Asymmetric Hydroamination of Cyano Olefins

Keywords: N-heterocyclic carbene ligands / Ferrocenes / Palladium complexes / Asymmetric catalysis / Hydroamination / Aminonitriles

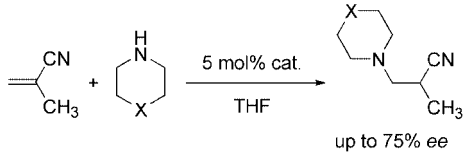

4755 **C. F. Weber, R. van Eldik***

Influence of Solvent on Ligand-Substitution Reactions of Pt^{II} Complexes as Function of the π-Acceptor Properties of the Spectator Chelate

Keywords: Solvent effects / Kinetics / Platinum(II) chemistry / Ligand effects / UV/Vis spectroscopy

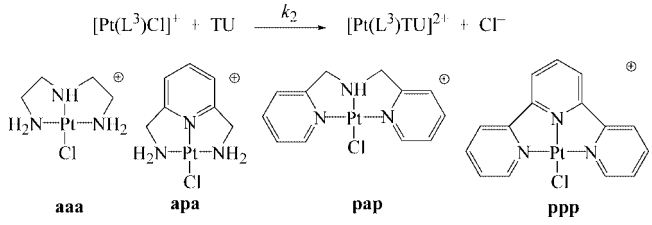

4762 **A. B. Chaplin, R. Scopelliti, P. J. Dyson***

The Synthesis and Characterisation of Bis(phosphane)-Linked (η^6-*p*-Cymene)Ruthenium(II)–Borane Compounds

Keywords: Ruthenium / P ligands / Bridging ligands / Coordination modes / Boranes

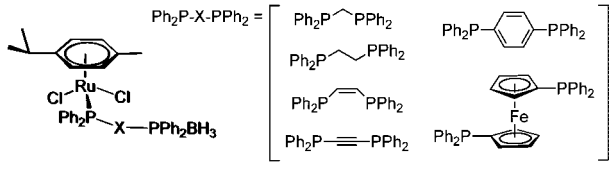

4775 **X. Wu, G. Shi,* S. Wang, P. Wu**

Formation of 3D Dandelions and 2D Nanowalls of Copper Phosphate Dihydrate on a Copper Surface and Their Conversion into a Nanoporous CuO Film

Keywords: Copper / Materials science / Nanostructures / Oxides / Phosphates

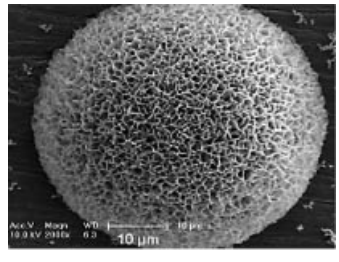

 © 2005 Wiley-VCH Verlag GmbH & Co. KGaA, Weinheim

4780 **Q.-F. Zhang, K.-M. Cheung, I. D. Williams, W.-H. Leung***

Cyclometalated Ruthenium Compounds Containing 2-(2′-Pyridyl)-4-methylphenyl and Benzo-[*h*]quinolyl Ligands

Keywords: Ruthenium / Cyclometalated ligands / Organometallic compounds / Transition metals

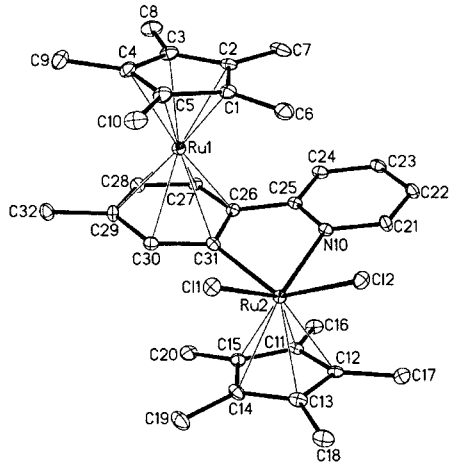

4788 **X. Ni, Q. Zhao, H. Zheng,* B. Li, J. Song, D. Zhang, X. Zhang**

A Novel Chemical Reduction Route towards the Synthesis of Crystalline Nickel Nanoflowers from a Mixed Source

Keywords: Nickel / Nanostructures / Chemical reduction / Crystal growth

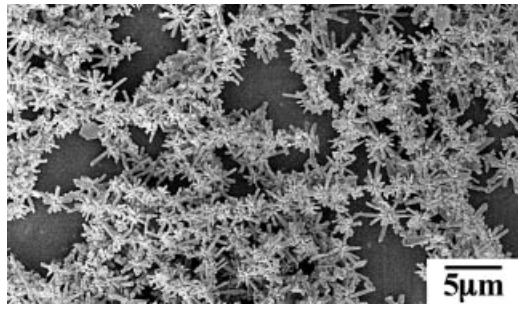

4794 **C. Bianchini, G. Lenoble, W. Oberhauser,* S. Parisel, F. Zanobini**

Synthesis, Characterization, and Reactivity of Neutral and Cationic Pd−C,N,N Pincer Complexes

Keywords: Pd pincer / NMR spectroscopy / IR spectroscopy / Secondary phosphanes / Suzuki reaction

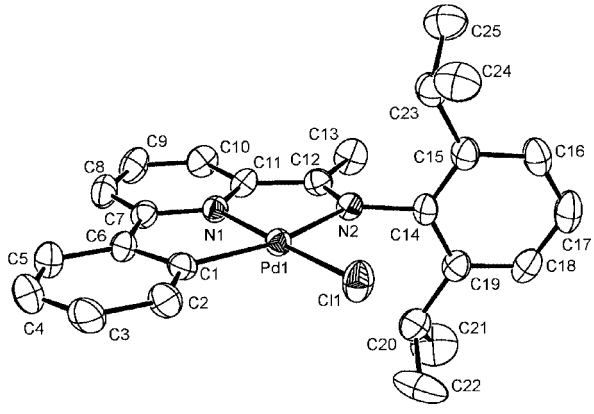

4801 **C. Shi, R. Wang, G. Zhu, S. Qiu,* J. Long***

Synthesis, Characterization, and Catalytic Properties of SiPW-X Mesoporous Silica with Heteropolyacid Encapsulated into Their Framework

Keywords: Heteropolyacids / Mesoporous materials / Encapsulation / Cracking / Esterification / Bulky molecule reactions

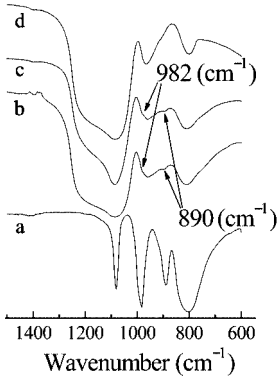

 © 2005 Wiley-VCH Verlag GmbH & Co. KGaA, Weinheim

4808 **C. Hureau,* E. Anxolabéhère-Mallart,* G. Blondin, E. Rivière, M. Nierlich**

Synthesis, Structure and Characterisation of a New Trinuclear Di-μ-phenolato-μ-carboxylato $Mn^{III}Mn^{II}Mn^{III}$ Complex with a Bulky Pentadentate Ligand: Chemical Access to Mononuclear Mn^{IV}−OH Entities

Keywords: EPR spectroscopy / Manganese / Mass spectrometry / N,O ligands / Oxidation

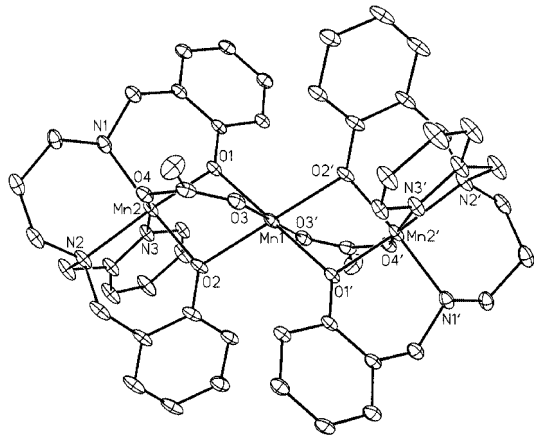

4818 **C. S. Hong,* J. H. Yoon, J. H. Lim, H. H. Ko**

A Terephthalato-Bridged Ni^{II} Complex Capped with a Nonchelating Ligand Displays a Three-Dimensional Supramolecular Network Constructed by Coordination and Multi-Intermolecular Forces

Keywords: Magnetic properties / Nickel / Noncovalent interactions / O ligands / Supramolecular chemistry

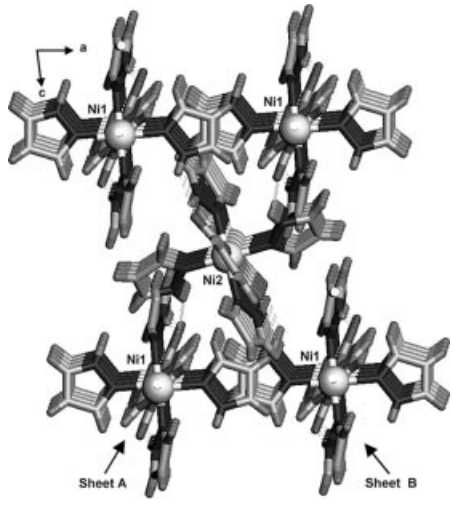

4822 **D. V. Konarev,* A. Yu. Kovalevsky, S. S. Khasanov, G. Saito,* A. Otsuka, R. N. Lyubovskaya**

Crystal Structures, EPR Spectra, and Magnetic Properties of a Series of Ionic Multi-Component Complexes $[(TBPDA)_2 \cdot (C_{60}^{\bullet -}) \cdot (D^+)]$ (D = Cp^*_2Cr, Cp^*_2Co, TDAE)

Keywords: Crystal engineering / EPR spectroscopy / Fullerenes / IR spectroscopy / Magnetic properties / Metallocenes

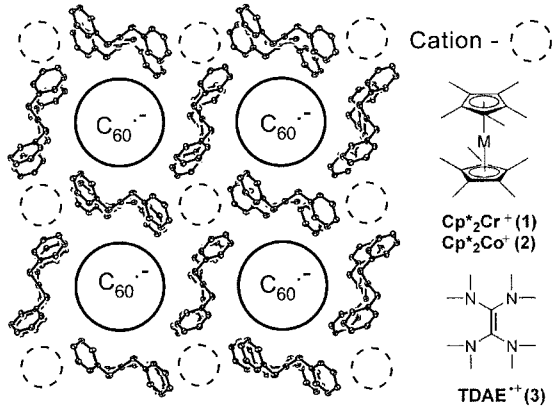

4829 **K. S. Woodin, K. J. Heroux, C. A. Boswell, E. H. Wong,* G. R. Weisman,* W. Niu, S. A. Tomellini, C. J. Anderson, L. N. Zakharov, A. L. Rheingold**

Kinetic Inertness and Electrochemical Behavior of Copper(II) Tetraazamacrocyclic Complexes: Possible Implications for in Vivo Stability

Keywords: Macrocyclic ligands / N ligands / Copper

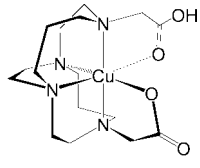

 © 2005 Wiley-VCH Verlag GmbH & Co. KGaA, Weinheim

4834 **M. G. B. Drew, J. P. Naskar, S. Chowdhury, D. Datta***

A Fluxional $Cu^{I}N_2O_2$ Core: Binding of a Keto Oxygen Atom to Cu^{I} and Ag^{I}

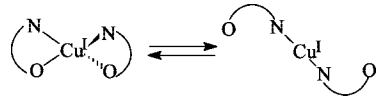

Keywords: Copper / Fluxional compounds / N ligands / O ligands / Silver

4840 **M. Gorol, H. W. Roesky,* M. Noltemeyer, H.-G. Schmidt**

(η^5-Pentamethylcyclopentadienyl)iridium(III) Complexes with η^2-N,O and η^2-P,S Ligands

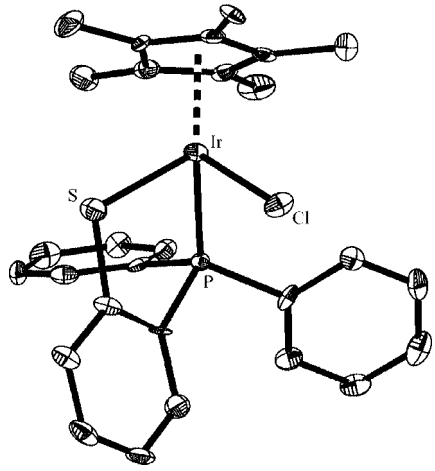

Keywords: Cyclopentadienyl ligands / Iridium / N,O ligands / P,S ligands

DOI: 10.1002/ejic.200500371

Adventures in Vanadocene Chemistry

Robert Choukroun,*[a] and Christian Lorber[a]

Keywords: Alkynes / Ceramics / Colloids / Metallocenes / Nitriles / Vanadium

This review surveys some aspects of the chemistry of $[VCp_2]$. The high potential of vanadocene $[VCp_2]$ (and $[V(CO)Cp_2]$) in organometallic chemistry is illustrated by new organometallic architectures. The rich redox chemistry of $[VCp_2]$ is shown by incorporation of this fragment into various C≡C and C≡N bonds. This molecular approach allows the connection of two (or more) paramagnetic centers through an organic linker in order to build magnetic nanoscopic organometallic wires. $[VCp_2]$ has also been studied in the field of materials such as vanadium carbide (VC) ceramics and in its role as a reducing agent toward elements of groups 8–10 to prepare Fe, Rh, and Pd colloids.
(© Wiley-VCH Verlag GmbH & Co. KGaA, 69451 Weinheim, Germany, 2005)

Introduction

Vanadocene, which is the only stable and easily accessible metallocene of the early transition metals, is an electronically and coordinatively unsaturated molecule. Other metallocenes of the early transition metals, such as titanocene and zirconocene, do not exist in their original sandwich structure and need another ligand (alkyne, butadiene) to stabilize the metallocene fragment.[1] The reactivity of vanadocene $[VCp_2]$, in spite of its accessibility,[2] has scarcely been studied, probably due to the formation of various paramagnetic V^{III} and V^{IV} compounds that prevent further spectroscopic analysis. This paramagnetism excludes classical NMR techniques, and the literature on the reactivity of vanadocene is often dominated by EPR and IR spectroscopic characterization, chemical derivatization, or by analogy with its diamagnetic titanium analogue.[3,4]

[a] Laboratoire de Chimie de Coordination du CNRS, UPR 8241, 205 route de Narbonne, 31077 Toulouse Cedex 04, France
Fax: +33-5-6155-3003
E-mail: choukrou@lcc-toulouse.fr
lorber@lcc-toulouse.fr

Robert Choukroun was born in Alger (in the former French department of Algeria) on June 24, 1944, and arrived in France in 1962. He received all of his degrees from the Université Paul Sabatier, in Toulouse, where he joined the CNRS in 1968 (Doctorat d'Etat, in 1975, under the Supervision of Professor Danièle Gervais). After a postdoctoral stay in 1975–1976 at the Unit of Nitrogen Fixation, University of Sussex (Brighton, U.K.) under the direction of Professor Chatt, he joined the Laboratoire de Chimie de Coordination de Toulouse, where he has remained to this day, becoming Directeur de Recherche in 1996. His current research interests are concerned with organometallic chemistry of the early transition metals of groups 4 and 5 and their development and use as catalysts for homogeneous catalysis and molecular precursors to ceramic materials and colloids.

Christian Lorber did his undergraduate studies at Louis Pasteur University in Strasbourg (France; 1985–1989). In 1989 he joined the group of Professor John A. Osborn at the Chemistry Department of Louis Pasteur University, where he studied homogeneous catalysis with oxo complexes of transition metals (oxidation and isomerization reactions). He obtained his PhD in 1995 and spent three years as a Postdoctoral Fellow, first at the Inorganic Chemistry Department of Lund University (Sweden) with Dr. Ebbe Nordlander (1996), and then in the group of Professor Richard H. Holm at the Chemistry and Chemical Biology Department of Harvard University (Cambridge, USA; 1997–1998) where he participated in the synthesis and studies of new models of Mo- and W-oxotransferase enzymes. In fall 1998 he obtained a research position at the Centre National de la Recherche Scientifique (CNRS) and moved to the Laboratoire de Chimie de Coordination in Toulouse (France). His interests include the inorganic and organometallic chemistry of high-oxidation-state early transition metal complexes, especially those that contain an amido, imido, diamido, alkyl, or alkoxy group, and related cationic species, catalytic reactions and mechanisms of reactions involving these complexes, especially in olefin-polymerization reactions, the controlled synthesis of polymers prepared using well-defined organometallic initiators, and hydroamination of alkynes. He is also involved in the synthesis of nanoparticles and their use in various catalytic transformations.

MICROREVIEWS: This feature introduces the readers to the authors' research through a concise overview of the selected topic. Reference to important work from others in the field is included.

 © 2005 Wiley-VCH Verlag GmbH & Co. KgaA, Weinheim

Ideally, X-ray structure analysis is a highly recommended tool to determine the real chemical environment around the metal center.

The starting point of our research was, in part, the recent development of the so-called "carbon-rich chemistry", which allows access to different kinds of polyalkynes,[5] and also the pioneering work of Floriani and others[6] on the addition of an activated alkyne to $[VCp_2]$ (**1**). The synthesis of olefin and acetylene derivatives of vanadocene is readily achieved by treating **1** with the appropriate substrates. The reaction can be formally described as the addition of the metal carbene to the C–C multiple bond to afford a metallacyclopropane $[Cp_2V(\eta^2\text{-}EtO_2CCHCHCO_2Et)]$ (**2**) and metallacyclopropene $[Cp_2V(\eta^2\text{-}C_2R_2)]$ (**3**; Scheme 1). It behaves as a carbene-like unit and adds to many organic functional groups (ketene, thioketene, ketene imine, ...; Scheme 1).[7–9] The interest in this η^2-C,X (X = C, O, S, N) bonding was originally as model compounds for studying molecular activation promoted by transition metals and associated to the problem of CO_2 activation. All these complexes can be related both structurally and chemically to some intermediates believed to be formed in the reaction between a metal center and carbon dioxide. As an example, carbonylsulfide (COS), when it reacts with vanadocene, undergoes a disproportionation reaction to form COS_2^- and CO, resulting in the formation of divalent $[Cp_2V(CO)]$ and $[(Cp_2V)_2(COS_2)]$ (**7**) in which the COS_2^- ligand is chelated to one metal center through both sulfur atoms and to the second metal center through the O atom.[10]

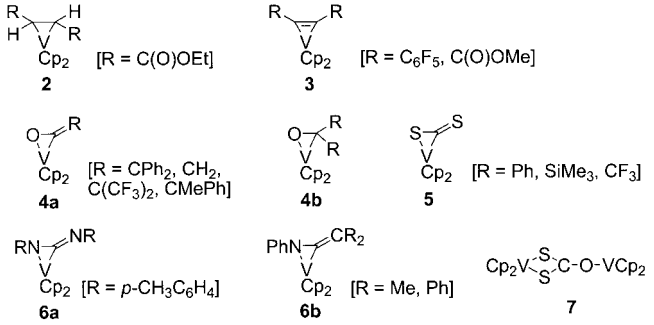

Scheme 1.

This review covers mostly our work aimed at the reactivity of vanadocene (or the carbonyl vanadium complex $[Cp_2VCO]$, another form of the d^2 vanadocene) with polyalkynes, polynitriles, and tris(perfluorophenyl)borane. Materials are also emerging from the chemistry of $[VCp_2]$ that illustrate the diversity of its potential applications (Scheme 2). Only the literature dealing with $[VCp_2]$ is reviewed.

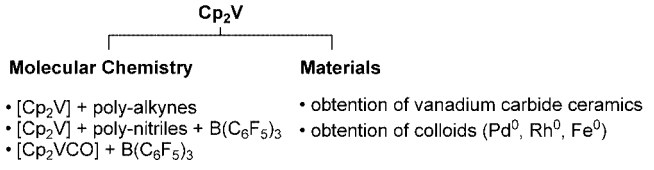

Scheme 2.

Reactivity of $[VCp_2]$ with Polyalkynes

From the reactivity of vanadocene toward C=C and C≡C described above, it appeared to us that we could use the same strategy to prepare new vanadocene systems using polyalkynes $R–(C{\equiv}C)_n–R'$ (n = 2–4; R, R′ = Me, *t*Bu, PPh_2, $SiMe_3$). One might expect that two identical species possessing one unpaired electron connected by an acetylenic carbon chain could produce different structural and magnetic situations. Synthetic work is facilitated by the solubility of $[VCp_2]$ (**1**) and many yne ligands in pentane, a solvent in which crystalline compounds are usually formed.

Treatment of **1** with the diyne R–C≡C–C≡C–R (R = $SiMe_3$, PPh_2) resulted in the oxidative addition of **1** to both alkyne bonds and the formation of homobimetallic vanadium complexes $[(Cp_2V)_2(1,2\text{-}\eta\text{:}3,4\text{-}\eta\text{-}R–C{=}C–C{=}C–R)]$ (**8a**: R = $SiMe_3$; **8b**: R = PPh_2) whatever the stoichiometry of the reaction.[11]

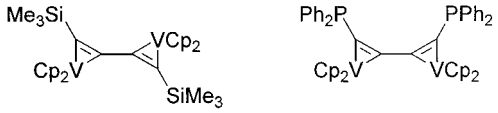

8a **8b**

This result encouraged us to pursue the reactivity of **1** with tri- and tetraynes. The reaction of the octatetrayne ligand RC≡C–C≡C–C≡C–C≡CR (**L¹**: R = *t*Bu; **L²**: R = Ph) is dependent on the substituent R attached to the tetrayne and on the stoichiometry of the reaction (Scheme 3).[12] First, the reaction performed with one equivalent of **1** and **L¹** in pentane gives the organometallic complex $[Cp_2V(3,4\text{-}\eta\text{-}t\text{BuC}{\equiv}C–C_2–C{\equiv}C–C{\equiv}Ct\text{Bu})]$ (**9a**) in which the $[VCp_2]$ unit is located at the internal position of the C8 carbon chain, whereas the reaction of two equivalents of **1** with one equivalent of **L¹** in pentane leads to the homodimetallic complex $[(Cp_2V)_2(1,2\text{-}\eta\text{:}7,8\text{-}\eta\text{-}t\text{BuC}_2–C{\equiv}C–C{\equiv}C–C_2t\text{Bu})]$ (**10a**). The Cp_2V units are nearly *trans* and are located at both extremities of the C8 carbon chain.

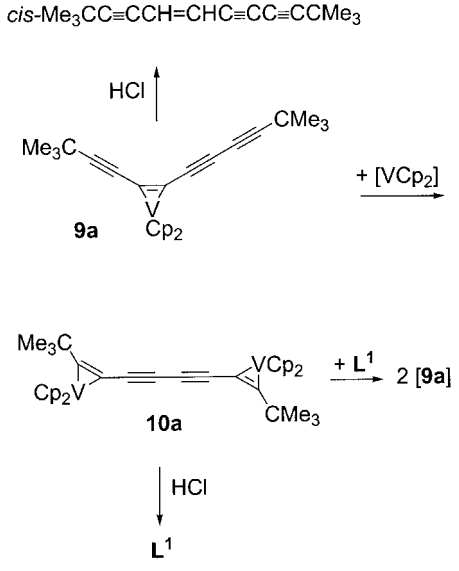

Scheme 3.

 © 2005 Wiley-VCH Verlag GmbH & Co. KGaA, Weinheim

On the other hand, the reaction of one or two equivalents of **1** with $\mathbf{L^2}$ in toluene gives exclusively the homodimetallic complex $[(Cp_2V)_2(1,2\text{-}\eta\text{:}7,8\text{-}\eta\text{-}PhC_2\text{–}C{\equiv}C\text{–}C{\equiv}C\text{–}C_2Ph)]$ (**10b**).

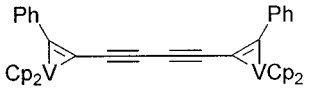

10b

These results offer synthetically attractive but puzzling features as the $[VCp_2]$ unit could migrate reversibly by sliding from an internal 3,4-η position to an external 1,2-η position on the carbon chain of the tetrayne ligand. The shift of the vanadocene unit could be dependent on a dissociation process between $[VCp_2]$ and the ligand in solution or on the existence of an η^4 complex $[Cp_2V(\eta^4\text{-}t\text{Bu}C_4\text{–}C{\equiv}C\text{–}C{\equiv}Ct\text{Bu})]$.[13]

The bond lengths and angles associated with the vanadium–acetylene interaction in **8**–**10** indicate that the acetylene molecule is symmetrically attached to the vanadium atom by two σ-type V–C bonds. This produces a metallacyclopropene structure for the central VC_2 moiety. The different orientation of the Cp_2VC_2 unit could be due to the steric effects of the substituent R ($SiMe_3$, PPh_2, *t*Bu, Ph) on the polyynes. Another difference in the structural aspects is the carbon skeleton of the ligand, which is distorted for **8a** and **10b** whereas all the carbon atoms are nearly coplanar in **8b** and **10a**.

As a result of such a situation, paramagnetic vanadium centers of d^1 electronic configuration could produce different magnetic behavior.[14] The antiferromagnetic interaction was calculated and found to be J = –10.5 and –59.8 cm^{-1} for **8a** and **8b** respectively, and J = –12.5 and –4.1 cm^{-1} for **10a** and **10b**, respectively. The antiferromagnetic interaction for **8b** and **10a** is greater than that for **8a** and **10b**, whereas the vanadium–vanadium distances show an opposite relation. In fact, the interaction is propagated by the carbon chain, and a consideration of the bonding situation in the complex seems necessary. The orientation of the Cp_2VC_2 unit in the molecule suggests a favorable "in-plane π-type" interaction for the complexes **8b** and **10a**. This can be described as a linear combination of mainly p-orbital character of the carbon of the diyne with the main contribution of the d_{z^2} orbital of the HOMO in a d^1-type system.[6b,6c] This is disfavored in **8a** and **10b**, where the Cp_2VC_2 unit and its magnetic orbital contributions can be considered to be orthogonal.

Particular attention was given to the reactivity of **1** with the triyne $Me_3SiC{\equiv}C\text{–}C{\equiv}C\text{–}C{\equiv}CSiMe_3$ ($\mathbf{L^3}$), which gives a crystalline black solid of a homodimetallic d^2-d^2 complex $[(Cp_2V)_2(3,4\text{-}\eta\text{-}Me_3SiC{\equiv}C\text{–}C{=}C\text{–}C{\equiv}CSiMe_3)]$ (**11**; Scheme 4). The main feature of **11** is the bonding mode of the two vanadocene moieties, which are attached to both the internal carbon atoms of the triyne by a single σ-type V–C bond of 2.165 Å. This brings the vanadium oxidation state from +2 to +3 instead of the expected classical V^{IV} that has been observed in all other cases. This unexpected reactivity seems to be due to the odd number of C≡C bonds in $\mathbf{L^3}$. The central C≡C bond of $\mathbf{L^3}$, which is more electron-rich than the other C≡C bonds, may favor the reaction at the central core of the ligand.[15] Variable-temperature magnetic susceptibility measurements have been carried out to confirm the V^{III} homobimetallic d^2-d^2 nature of **11**. The effective moment (μ_{eff} = 4.01 μ_B at 300 K) is consistent with two noninteracting vanadium(III) units, and a weak antiferromagnetism (J = –3.7 cm^{-1}) is observed.

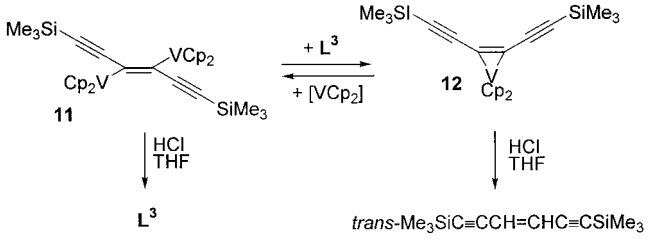

Scheme 4.

When one equivalent of **1** was treated with only one equivalent of $\mathbf{L^3}$, in pentane, small, brown needles of the vanadium(IV) complex $[Cp_2V(3,4\text{-}\eta^2\text{-}Me_3SiC{\equiv}C\text{–}C{=}C\text{–}C{\equiv}CSiMe_3)]$ (**12**) were obtained (μ_{eff} = 1.9 μ_B). A vanadocene cyclopropene structure could be suggested on the basis of its hydrolysis with HCl (*trans*-$Me_3SiC{\equiv}C\text{–}CH{=}CH\text{–}C{\equiv}CSiMe_3$ was obtained; $\mathbf{L^3}$ is liberated upon hydrolysis of **11** with HCl). Treatment of **12** in C_6D_6 with another equivalent of **1** leads to **11**. A comproportionation reaction between V^{IV} (**12**) and V^{II} (**1**) to give two V^{III} centers (**11**) is probably operative, but a full mechanistic description must await further experimental evidence.

The reaction of the phosphane $ArP(C{\equiv}CPh)_2$ (Ar = 2,4,6-$t\text{Bu}_3C_6H_2$) with one equivalent of **1** in pentane, at room temperature, leads to the formation of the V^{IV} complex $[Cp_2V(\eta^2\text{-}PhC{=}C)P(C{\equiv}CPh)Ar]$ (**13**) as a crystalline product.[16] The reactivity of **13** towards HCl was examined (Scheme 5). Reaction of **13** in THF with HCl gives, selectively, the starting phosphane as the main product, along with a green precipitate of $[Cp_2VCl_2]$. The same reaction performed in toluene leads to the alkenyl-alkynylphosphane (1:1 ratio of *cis* and *trans* isomers), isolated as its sulfur derivative, and $[Cp_2VCl_2]$. The solvents (THF, toluene) could account for the reactivity of **13**. However, the IR and EPR spectra of **13** in these solvents do not show any detectable difference; similar data are observed for both solvents. This observation supports the view that the facile protonation of **13** could occur equally in toluene or in THF, in contrast to the release of the phosphane observed in THF.

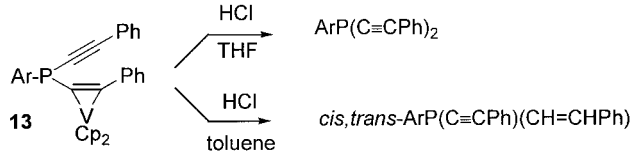

Scheme 5.

Another interesting reactivity is the reaction of $[VCp_2]$ with carbyne complexes. A typical example for the forma-

 © 2005 Wiley-VCH Verlag GmbH & Co. KGaA, Weinheim

tion of a dimetallic compound containing **1** has been realized with [W(≡CR)(CO)$_2$Cp] (R = 4 Me-C$_6$H$_4$), since this complex and alkynes have similar reactivity patterns.[17] The reaction of **1** with the tungsten complex afforded black crystals of [Cp$_2$V(μ-CR)W(CO)$_2$Cp] (**14**). A weak attachment between **1** and the tungsten complex is observed from the structure, as exemplified by the dissociation of the heterodimetallic complex in solution.

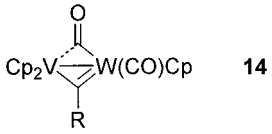

14

Oxidative addition of a diyne of a ligand-stabilized metallocene of a group 4 element, or reaction of an alkyne compound of a group 4 element with a Lewis metal complex, have been reported to give dimetallic complexes.[18] These results showed the way towards heterodimetallic [Ti,V] or [Zr,V] complexes involving the reaction of acetylenic titanium or zirconium compounds with **1**. Reaction of [(C$_5$H$_4$R)$_2$M(C≡CPh)$_2$] (M = Ti, R = H; M = Zr, R = H, Me, *t*Bu, SiMe$_3$) with **1** yields the heterobimetallic complex [Cp$_2$V(μ-η^2:η^4-butadiyne)M(C$_5$H$_4$R)$_2$] (Scheme 6).[19,20] The measured magnetic moments show that the formal oxidation state of vanadium has increased from II to IV.

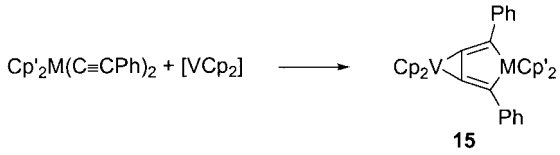

15

15a: M = Ti, Cp' = C$_5$H$_5$
15b: M = Zr, Cp' = C$_5$H$_5$
15c: M = Zr, Cp' = C$_5$H$_4$Me
15d: M = Zr, Cp' = C$_5$H$_4$CMe$_3$
15e: M = Zr, Cp' = C$_5$H$_4$SiMe$_3$

Scheme 6.

The ease of solving the crystal structure of the series of compounds **15** seems to be very much dependent on the nature and size of the different substituents on the cyclopentadienyl groups of the metal–alkyne compound. Nevertheless, an overall arrangement similar to that observed in the fully resolved structures of **15d** and **15e**, in which the two metal centers are strongly differentiated by the substituents on their respective cyclopentadienyl groups, was found. The vanadium atom adopts a metallacyclopropane environment. The interatomic distances between C^2 and C^3 and their four neighboring atoms (Zr, V, C^1, and C^3 and Zr, V, C^2, and C^4, respectively), and the 360° value for the sum of the angles around C^2 and C^3, indicate that these carbon atoms are planar tetracoordinate carbons (ptC). Most of the ptC-containing transition metal complexes reported to date, mainly by Erker et al., are group 4 homo- and groups 4 and 10 or 13 heterodimetallic complexes.[21]

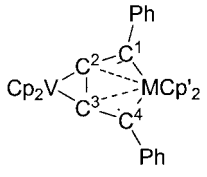

15d,e

ELF analysis[22] reveals the existence of three multicenter bonds involving the Zr atom and the four carbon atoms of the butadiyne fragment. The existence of electron-sharing interactions between each of the two central carbon atoms of the butadiyne fragment and four neighbors (for example, C^2 interacts with Zr, V, C^1, and C^3) has been established.[20] Both these central carbon atoms are involved in three bonds, two of which are three-center bonds. Therefore, these central carbon atoms may be considered as planar tetracoordinate.

The mechanism of formation of these complexes has been elucidated. Analogous complexes obtained by reaction of [Ni(PPh$_3$)(η^2-PhC≡C–C≡CPh)] and "Cp$_2$Ti" or "Cp$_2$Zr" to give heterodimetallic [Cp$_2$M(μ-η^2:η^4-PhC≡C–C≡CPh)Ni(PPh$_3$)$_2$][23] show the same skeletal (μ-η^2:η^4-PhC≡C–C≡CPh) arrangement as that observed in compounds **15**, and the formation of an intermediate zirconacyclocumulene species [Cp$_2$Zr(η^4:1,2,3,4-PhC=C=C=CPh)] was therefore suggested.[23] Some partial dissociation of **15** in solution (estimated by EPR spectroscopy to be ca. 10–20%; Scheme 7) shows the presence of the zirconacyclocumulene species **16**.

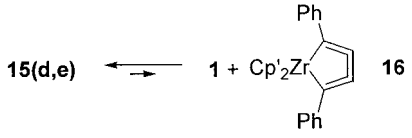

16

Scheme 7.

Interestingly, the formation and the reactivity of **16** is governed by the nature of the substituents attached to the alkyne.[18e,24,25] In contrast, attempts to prepare a similar heterodimetallic complex from **1** and [Cp$_2$Zr(C≡CSiMe$_3$)$_2$] failed.[26] On the other hand, the use of different electron-donating R groups on the Cp ring of the dialkyne zirconocene (H in **15b**, Me in **15c**, *t*Bu in **15d**, and SiMe$_3$ in **15e**) does not change the nature of the resulting heterodimetallic [Zr,V] complex.

The transformation of the dialkynylzirconocene precursors [(C$_5$H$_4$R)$_2$Zr(C≡CPh)$_2$] (R = H, Me, *t*Bu, SiMe$_3$) into the corresponding zirconacyclocumulene species **16** in daylight is complete in around four days. Zirconacyclocumulene complexes **16** can also be generated by treating the corresponding dialkynylzirconocene with a catalytic amount of **1** (ratio 10:1) for about two days (this is a shorter time than the same reaction in daylight), which implies the involvement of **1** in forming the zirconacyclocumulene (Scheme 8). Finally, complexes **15d** and **15e** can be generated from the corresponding zirconacumulene by treatment with a stoichiometric amount of **1**.

 © 2005 Wiley-VCH Verlag GmbH & Co. KGaA, Weinheim

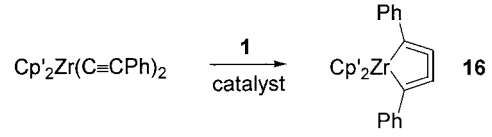

Scheme 8.

The observed reaction between the bis(phenylethynyl-metallocene and -vanadocene and the formation of the heterodimetallic [M,V] compounds can be understood as resulting from the partial transfer of the phenylethynyl group from M to vanadium. Thus, both pathways, i.e. irradiation and/or Cp_2V catalysis, lead to the same zirconacyclocumulene species, and their relative importance in our reactions is difficult to assess. Nevertheless, our results clearly show that, the two C≡CPh alkynyl moieties of [Cp′$_2$Zr-(C≡CPh)$_2$] undergo a C–C coupling, vanadocene being actually involved in the mechanism of formation of compounds **8** through a transfer of the C≡CPh moiety from Zr to V, and that a zirconacyclocumulene species is a key intermediate in this mechanism. The formation of the zirconacyclocumulene species may proceed through the catalytic cycle proposed in Scheme 9.

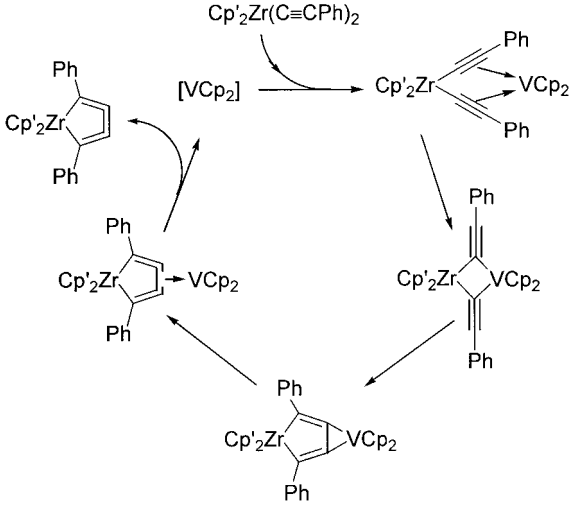

Scheme 9.

Other dimetallic complexes containing a vanadium atom have been prepared from **1**. Reduction of **1** with naphthalenylpotassium leads to a suitable source of the CpV fragment from isolated [CpV($C_{10}H_8$)].[27] Reduction of **1** to vanadium(0) by naphthalenylytterbium [($C_{10}H_8$)Yb(THF)$_2$] in THF generates the polymeric, two-dimensional, multidecker complex [CpV(μ-η^6:η^2-$C_{10}H_8$)Yb(THF)Cp]$_n$ (**17**),[28] the molecular structure of which consists of infinite zig-zag chains formed by CpYb moieties with one CpV(η^6-$C_{10}H_8$) unit η^2-coordinated through the naphthalene to each Yb atom.

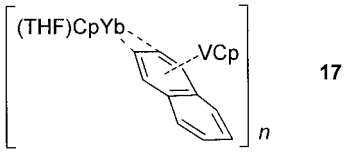

The reactivity of **1** towards the cobalt complex [Co_2-($CO)_8$] was also re-examined and the salt [$Cp_2V(CO)_2$]-[$Co(CO)_4$] was isolated.[29]

Reactivity of [Cp_2VCO] − Another Source of Vanadocene

Turning now to another source of vanadocene, carbonylbis(cyclopentadienyl)vanadium(II) [Cp_2VCO] is easily obtained by treatment of **1** with CO.[30] A few reactivity studies have been conducted with olefins[31] and dinitrogen oxides[32] in which, in the absence of X-ray analysis, IR spectroscopy plays an important role in the characterization of the resulting compounds.

In light of the tremendous amount of work on the reactivity of tris(perfluorophenyl)borane [$B(C_6F_5)_3$] with organometallic complexes and as an activator in olefin polymerization,[1a,33] we explored the reactivity of $B(C_6F_5)_3$ towards our vanadium compounds.[34] In this context, the reactivity of [Cp_2VCO] and $B(C_6F_5)_3$ was studied as an extension of our previous report showing that a related dicarbonyltitanocene gives the acylborane complex [$Cp_2Ti(CO)$-{η^2-$OCB(C_6F_5)_3$}] by attack of the Lewis acid at the carbonyl carbon atom.[35] Although the reaction with [Cp_2VCO] resulted in the formation of four complexes, all of them were fully characterized by X-ray structure elucidation after careful separation by hand.[36] Particularly interesting and intriguing is the formation of the zwitterionic, ring-borylated vanadium(III) complex [(Cp){C_5H_4B-($C_6F_5)_3$}V] (**18**) and [(Cp){$C_5H_4B(C_6F_5)_3$}$V(CO)_2$] (**19**), and of the salt [$Cp_2V(CO)_2$][$HB(C_6F_5)_3$] (**20**) and the hydride [Cp_2V(μ-H)$B(C_6F_5)_3$] (**21**).[37] In **18**, the borane is linked to one of the cyclopentadienyl rings, and an *ortho*-fluorine atom of one perfluorophenyl group of the borane is coordinated to the vanadium center. Complex **21** can be described as a vanadocene hydride stabilized by the borane. Formation of the vanadium(IV) hydride [(Cp){C_5H_4B-(C_6F_5)}$_3$VH(CO)] by the electrophilic addition of the borane at the Cp ring, followed by redox and disproportiona-

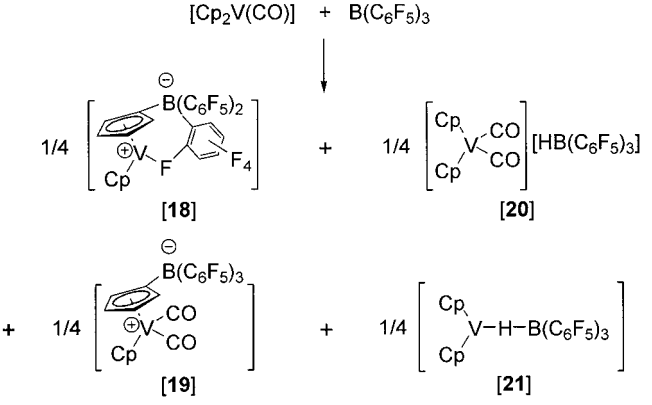

Scheme 10.

 © 2005 Wiley-VCH Verlag GmbH & Co. KGaA, Weinheim

tion reactions, is thought to account for these results (Scheme 10).

Reactivity of [VCp_2] with Nitrile Ligands

The literature reveals that the reaction between vanadocene and the nitrilium salt [RC≡NMe][BF_4] (R = Me, Ph) produces iminoacyl vanadocene; the ionic complex [$Cp_2V\{\eta^2$-(Ph)C=$NCH_3\}$][BF_4] (**22**) was characterized by an X-ray structure determination.[38] On the other hand, adducts of nitriles RC≡N with a Lewis acid have been known for a long time and have been widely studied.[39] From the large increase in the ν(C≡N) stretching frequency induced by complexation with a strong Lewis acid, it was found that the polarity of the nitrile group is increased in the complex.[40] Considering that the Lewis acid could modify the reactivity of the C≡N bond, the RCN·Lewis acid adduct can be considered as a ligand containing an "activated" C≡N bond.

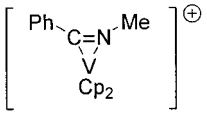

22

Addition of various BR_3 Lewis acids to acetonitrile and trifluoro-*p*-tolunitrile (R′C≡N) in toluene to form the expected RC≡N·BR_3 adduct in situ, followed by the addition of **1** in toluene, gives, after two to three days, the crystalline borane adduct of the vanadaazirine complexes [$Cp_2V\{\eta^2$-(R′C=N·BR_3)}] (**23** and **24**; Scheme 11).

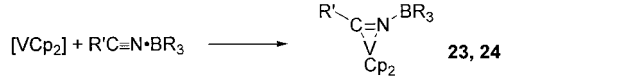

	23	24a	24b	24c	24d	24e
R'	CH_3	$F_3C(C_6H_4)$	$F_3C(C_6H_4)$	$F_3C(C_6H_4)$	$F_3C(C_6H_4)$	$F_3C(C_6H_4)$
R	C_6F_5	C_6F_5	2,6-$F_2C_6H_3$	3,4,5-$F_3C_6H_2$	Ph	Cl

Scheme 11.

These complexes are paramagnetic due to the presence of one unpaired electron, in agreement with the spin value for a formally vanadium(IV) (d^1) system. The main feature of the X-ray structures is that the nitrile group attached to the vanadium atom by two σ-type V–C and V–N bonds of 2.04 Å (av.) and 2.08 Å (av.). This produces a metallacycloimine structure. Changing $B(C_6F_5)_3$ to $B(C_6H_5)_3$ or BCl_3 in the vanadaazirine(IV) complex adduct produces slight differences in the VNC cycle, in which a C=N double bond is now formed. In contrast, the B–N distances are modified according to the expected Lewis acidity of the boranes [$BCl_3 > B(C_6F_5)_3 > BPh_3$] and in agreement with the $\nu_{C=N}$ frequencies observed for these complexes.

X- and Q-band EPR studies were carried out in THF solution. An expected eight-line pattern was observed for **24c**–**e** [average: g = 1.998; $A(^{51}V)$ = 41 G]. For **23** and **24a**,**b**, the formation of a doublet of octets was observed. An additional hyperfine coupling of the unpaired electron of the vanadium atom with a fluorine atom of the borane $B(C_6F_5)_3$ is responsible for the second coupling constant [average: g = 1.997, $A(^{51}V)$ = 42 G; $a(^{19}F)$ = 15 G]. This fact can be explained by the absence of any fluorine atom in the *ortho* position of the boranes in **24c**,**d**. The presence of two fluorine atoms in the *ortho* position of the phenyl rings in **23** and **24a**,**b** contributes to the C–F···V interaction and a subsequent $a(^{19}F)$ hyperfine coupling is observed. A careful investigation of the X-ray structures of **23** and **24a**,**b** does not indicate such an interaction in the solid state. However, a dynamic process involving the rotation of B–C and N–B allows the fluorine atom to approach the vanadium center in solution. A model can be drawn to take into account this flexibility, and the best situation for a C–F···V interaction is a plane containing the V–C(1)–N–B–$C_{ipso}(C_6F_5)$ atoms where one *ortho* fluorine atom of the fluorophenyl ligand could approach the vanadium center by the formation of a six-membered ring (Scheme 12). Moreover, the presence of a doublet signal indicates the retention of only one V···F coordinative bond in solution. These results support the view that the *ortho* fluorine atom of the phenylborane interacts with the vanadium.

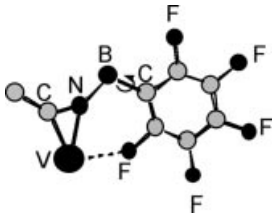

Scheme 12.

It is remarkable that the nitrile RC≡N can react with the borane BPh_3 in the presence of **1**. In the absence of **1**, the IR spectra of a mixture of the nitrile $F_3CC_6H_4C$≡N and BPh_3 (1:1 or 1:5 ratio) in toluene do not show any change in the position of the ν_{CN} absorption due to an eventual formation of the borane–Lewis acid adduct. Nevertheless, it is clear that an undetectably small amount of the adduct is formed, which allows the formation of **24d**.

In attempts to synthesize a bimetallic vanadium d^1-d^1 complex with a potential magnetic interaction between the two metal centers,[41] the first ligands of choice were 1,4-benzene dicarbonitrile N≡C–(C_6H_4)–C≡N, malononitrile N≡CCH_2C≡N, and adiponitrile N≡$C(CH_2)_4$C≡N. Microcrystalline, blue-violet solids of [$(VCp_2)_2\{\eta^2$:*C*,*N*-($C_6F_5)_3$B·N=$C(C_6H_4)$C=N·$B(C_6F_5)_3\}$] (**25**), [$VCp_2\{\eta^2$:*C*,*N*-($C_6F_5)_3$B·N=C–CH_2C≡N·$B(C_6F_5)_3\}$] (**26**), and [$(VCp_2)_2\{\eta^2$:*C*,*N*-($C_6F_5)_3$B·N=$C(CH_2)_4$C=N·$B(C_6F_5)_3\}$] (**27**), respectively, were isolated (Scheme 13).

The X-band EPR spectra of **25**–**27** in THF were recorded and the formation of a doublet of octets was observed. Coupling of the unpaired electron of the vanadium atom with the ^{51}V (I = 7/2) nucleus and the *ortho*-fluorine atoms of the borane $B(C_6F_5)_3$, via a C–F···V interaction, give rise to these spectra [average: g = 1.996, $a(^{51}V)$ = 43 G, $a(^{19}F)$

 © 2005 Wiley-VCH Verlag GmbH & Co. KGaA, Weinheim

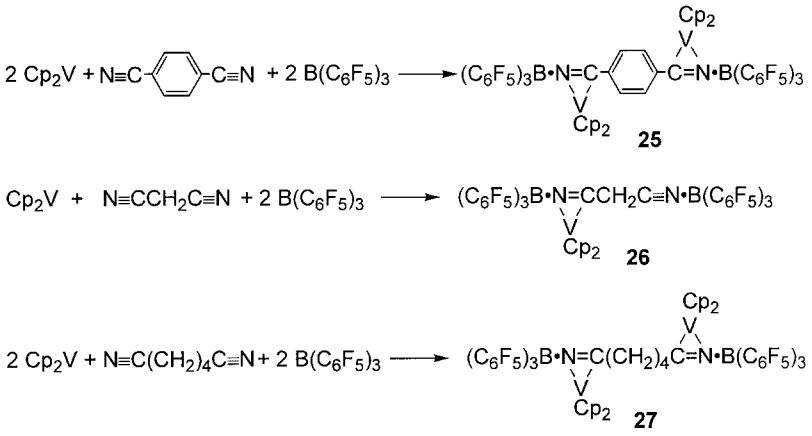

Scheme 13.

= 17 G]. Complexes **25** and **27** were also studied by variable-temperature magnetic susceptibility measurements resulting from homobimetallic d^1-d^1 situations. Unfortunately, these paramagnetic d^1-d^1 systems do not present any antiferromagnetic interaction due to the presence of a long sp^3 alkyl chain when adiponitrile is used (in **27**) and to a suggested disfavored orientation of the VCp_2CN units within the $NC(C_6H_4)CN$ ligand (in **25**). This latter situation has already been observed in the case of **8b** and **10b**, where the dihedral angle between both Cp_2VC_2 units is nearly 110–120° and thus prevents a favorable "in-plane π-type" geometry in the molecule.[11]

[VCp_2] as a Source for VC-Containing Ceramics

Transition metal nitrides or carbides, like other ceramic materials, show outstanding physical and chemical properties. They are usually prepared by reaction of the corresponding metal halides with nitrogen and ammonia, and sometimes in the presence of hydrogen. These reactions have to be carried out at high temperature, usually above 1000 °C. Such drastic conditions restrict applications such as the protective coating of materials whose mechanical properties are sensitive to high temperature, i. e. steel or materials for electronics. The use of coordination compounds as organometallic precursors allows the preparation of thin-film ceramic materials by the so-called organometallic chemical vapor deposition (OMCVD), which is a process that involves much lower temperatures.[42] Compound **1** is a suitable precursor for CVD of vanadium carbide (VC). The precursor sublimes at 60 °C/20 Pa and has a sufficient vapor pressure under these conditions. Films containing crystalline vanadium carbide (VC) have also been deposited from **1** by plasma-assisted CVD (PACVD).[43]

Compound **1** was also selected for the preparation of the quaternary ceramic system vanadium-titanium carbonitride,[44] which is a solid solution though to exhibit better mechanical properties than those of the binary ones TiN, TiC, VN, and VC, by OMCVD.[45] To reach this goal, appropriate molecular organometallic precursors are needed. The most elegant approach, but maybe not the most efficient, could be the use of a single precursor containing all the desired elements. However, to date, such molecules are not known.

An introduction to this type of molecule was provided by the dimetallic [Ti,V], complex described above by reaction of $[Cp_2Ti(C{\equiv}CPh)_2]$ with **1**. However, this molecule is not suitable for OMCVD due to its poor volatility.[46] Therefore, the use of pairs of independent precursors was investigated, each precursor being the source of the desired elements, for example TiN and VC or TiC and VN. Moreover, as the pairs of precursors are introduced simultaneously into the CVD reactor, they should exhibit compatible thermal behaviors. Given the applied aspects of this work, the selection of the precursors should rest on criteria based on industrial and economic grounds. Among the several VC precursors studied for this purpose, **1** (under H_2, at 700 °C in a cold wall reactor) yields 13-μm-thick, crystallized, vanadium carbide films which were characterized by XRD (X-ray diffraction) and EPMA/WDS (electron probe microanalysis with wavelength-dispersive spectroscopy).[47] The influence of deposition rate and grain size on the composition of the deposits was investigated by varying three factors: the substrate temperature, the hydrogen carrier flow rate, and the distance between the substrate and the precursor handling crucible. The residence time of the gaseous species in the reactor was found to be an important factor, leading to a maximum of the deposition rate. Even when drastic conditions are applied (high purity hydrogen carrier gas) the use of a low temperature is not thermodynamically in favor of the formation of carbides over that of oxides, and the high C-to-metal ratio in the precursor molecule often leads to contamination of the films by graphitic carbon. Therefore, it is worth noting that *tert*-butyl-substituted vanadocene $[V(C_5H_4\text{-}t\text{Bu})_2]$ was shown to be an excellent precursor for the preparation of crystalline VC thin films not contaminated by graphitic carbon or oxygen.[48] These films were fully characterized by XRD, scanning electron microscopy, X-ray photoelectron spectroscopy, and EPMA/WDS. Within the "pairs of precursors" approach it

 © 2005 Wiley-VCH Verlag GmbH & Co. KGaA, Weinheim

should be noted that another vanadium derivative, namely $[Cp_2VMe_2]$, and $[CpTiCl_2(NSiMe_3)_2]$ afford (Ti, V, C, N)-containing films.[49]

$[VCp_2]$: A Reducing Agent for Chloride Organometallic Precursors to Colloids

The use of **1** as a reducing agent in the fabulous area of nanoparticles must be cited. The past decade has demonstrated the importance of the role of colloids in various catalytic reactions, primarily for hydrogenation of arenes. Different synthetic pathways are presently studied to obtain various types of colloids displaying a controlled size and chemical environment.[50] The most popular method for the preparation of noble metal particles involves reduction of chloride precursors by various reducing agents, for example refluxing alcoholic solutions in the presence of a polymer. The role of vanadocene $[VCp_2]$ as an organometallic reducing agent to prepare metal colloids embedded in a PVP polymer matrix [PVP: poly(vinylpyrrolidone)] has been successfully demonstrated in the case of $FeCl_2$, $[Rh(C_2H_4)_2Cl]_2$, and $[Pd(\eta^3\text{-allyl})_2Cl]_2$ to give Fe, Rh, and Pd nanoparticles, respectively.[51–53] This unusual synthetic organometallic route allows the preparation of colloids from organometallic complexes containing chloride group(s) (Scheme 14).

$$2\,[VCp_2] + FeCl_2 \xrightarrow{PVP} [Fe^0(PVP)] + 2\,(Cp_2VCl)$$

$$[VCp_2] + MCl(L)_x \xrightarrow{PVP} [M^0(PVP)] + (Cp_2VCl) + L_x$$

$$MCl(L)_x = [Rh(\mu\text{-}Cl)(C_2H_4)_2]_2,\ [Pd(\mu\text{-}Cl)(\eta^3\text{-}C_3H_5)_2]_2$$

Scheme 14.

The reaction of a THF solution of $[Rh(C_2H_4)_2Cl]_2$, $[Pd(\eta^3\text{-allyl})_2Cl]_2$, or a solid suspension of $FeCl_2$ with a stoichiometric amount of $[VCp_2]$ per chloride atom in the presence of poly(vinylpyrrolidone) (K30-PVP; average molecular weight: 40000) as protecting polymer, at room temperature, leads to metal colloids dispersed in PVP and isolated as the black solid [M-PVP]. A low-magnification TEM micrograph registered for each solid shows that the particles are well dispersed. The HREM micrograph evidences fringes in the particles. The regular periodicity of the fringes allows the determination of the fcc structure of the particles. From $FeCl_2$, big agglomerates of Fe particles with diameters ranging from 50 to 200 nm are present in which individual nearly 8-nm-diameter nanoparticles are observed. All these individual grains have a common orientation inside one large Fe grain, as observed by HRTEM experiments.[51] A relatively narrow size distribution is observed for Rh particles, with a mean diameter of about 1.3 nm. Structural characterization of the metal colloids by wide-angle X-ray scattering (WAXS) was performed in the solid state on the same batch that was used for the TEM experiments, using procedures previously validated for colloids in PVP. This technique, in which the radial distribution function (RDF) gives the M–M distances, confirms the fcc structure of the particles. Structural characterization of the rhodium colloids by WAXS was consistent in size and structure with a proposed model, a small 55-atom cuboctahedron.[52] The size of the Pd particles shows a mean diameter of about 1.8 nm with a relatively large size distribution. The coherence length can be evaluated to be 2 nm, in agreement with TEM measurements.[53] The same RDF was observed when solids [Rh-PVP] and [Pd-PVP] were treated with O_2 or CO (20 bar, 4 d). With O_2, the RDF gives direct evidence of the absence of significant oxidation of the solid sample, at least in the core of the nanoparticles. The concentration of metal embedded in the polymer can be modulated as a function of the different amounts of PVP added (2% to 13% in M weight).

The catalytic potential of the [Rh-PVP] and [Pd-PVP] nanoparticles, which are soluble in alcoholic solvents as well as in water, has been explored in heterogeneous and biphasic conditions, as well as ionic liquids, for the hydrogenation of different types of substrates (benzene, quinoline, adiponitrile, aromatic nitro compounds, ...).[54]

The main advantage of this $[VCp_2]$ method for reducing chloride-containing organometallic precursors to nanoparticles is the availability of the organometallic complexes $M^I(L)_x$ of groups 8–10. Large-scale synthesis of nanoparticles embedded with PVP can be performed and their use in different catalytic processes from the same batch is possible, thus allowing kinetic measurements under various experimental conditions.

Concluding Remarks

Throughout this review we have mainly reported the isolation and characterization of various vanadocene complexes. Importantly, all pathways have been confirmed by a structural elucidation of the molecules present in the reaction. We have to point, again, this necessity to ensure the chemical nature of the different species when paramagnetism, disproportionation, and redox reactions are possible due to the nature of the vanadium center. Indeed, starting from divalent vanadocene different redox reactions are observed with formation of V^{III} and V^{IV} species. Vanadocene has been shown to react with various poly-ynes, and some similarities were observed with related titanocene or zirconocene chemistry. Their intrinsic reactivity towards small organic molecules has not yet been explored but we can predict a high chemical potential for all these compounds. On the other hand, the incorporation of two paramagnetic centers along a chain constitutes a challenge in the realization of new homodimetallic systems that are able to convey magnetic coupling. The reactivity with nitriles and polynitriles could constitute a new approach to the fascinating area of molecular magnets developed by Miller from TCNE and TCNQ with $[V(CO)_6]$ or $[V(C_6H_6)_2]$.[55] Indeed, some

 © 2005 Wiley-VCH Verlag GmbH & Co. KGaA, Weinheim

research on TCNE with **1** in the presence of a borane is in progress in our group.

The role of vanadocene as a source of vanadium carbide (VC) or as a reducing agent for the formation of metal nanoparticles seems an efficient starting point for expending the number of new applications in the ever-growing field of advanced materials chemistry.

Acknowledgments

We are indebted to all the people in our research group and collaborators cited in references for their partnership. Particularly, we are very grateful to B. Donnadieu and L. Vendier for their kind and helpful technical contributions to the X-ray analysis of the vanadium compounds described in this review. This work was supported by the CNRS, and the Direction des Recherches, Etudes et Techniques (DGA-DRET) under a contract of Research Program "Dépôt Chimique en Phase Vapeur pour l'Obtention de Couches Dures" (SDI, 5578)

[1] a) *Metallocenes: Synthesis, Reactivity, Applications*, vol. 1 (Eds.: A. Togni, R. L. Haltermann), **1998**, Wiley-VCH Weinheim (Germany); b) For recent references on the accessibility and the chemistry of the metallocenes dedicated to group 4 and poly-ynes, see: U. Rosenthal, V. V. Burlakov, P. Arndt, W. Baumann, A. Spannenberg, V. B. Shur, *Eur. J. Inorg. Chem.* **2004**, 4739–4749 and references cited therein; c) G. Erker, G. Kehr, R. Froehlich, *Adv. Organomet. Chem.* **2004**, *51*, 109–162; d) M. Horacek, P. Stepnicka, J. Kubista, R. Gyepes, K. Mach, *Organometallics* **2004**, *23*, 3388–3397 and references cited therein.

[2] a) J. J Eisch, R. B. King, *Organometallic Syntheses*, vol. 1 ("Transition Metal Compounds"), Academic Press, New York, **1965**, pp. 64–66; b) C. Floriani, V. Mange, *Inorg. Synth.* **1990**, *28*, 263–267.

[3] a) G. Fochi, C. Floriani, J. C. Bart, G. Giunchi, *J. Chem. Soc., Dalton Trans.* **1983**, 1515–1521; b) A. S. Gordetsov, S. V. Zimina, N. V. Kulagina, E. M. Moseeva, Yu. A. Kurskii, L. A. Lopatin, *J. General Chem.* **2003**, *73*, 1557–1560, translated from *Zhurn. Obsch. Khiim.* **2003**, *73*, 1650–1653, and references cited therein; c) F. Calderazzo, F. Marchetti, G. Pampaloni, V. Passarelli, *J. Chem. Soc., Dalton Trans.* **1999**, 4389–4396.

[4] R. Choukroun, C. Lorber, B. Donnadieu, B. Henner, R. Frantz, C. Guerin, *Chem. Commun.* **1999**, 1099–1100.

[5] a) P. Siemsen, R. C. Livingston, F. Diederich, *Angew. Chem. Int. Ed.* **2000**, *39*, 2632–2657; b) A. de Meijere, *Carbon-Rich Compounds, I and II*, in *Top. Curr. Chem.* **1999**, vol. 196 and 197; c) Special Issue devoted to carbon-rich organometallics, *J. Organomet. Chem.* **1999**, *578*, 1–264; d) *Modern Acetylene Chemistry* (Eds.: P. J. Stang, F. Diederich), **1995**, VCH, Weinheim, Germany.

[6] a) D. F. Foust, M. D. Rausch, W. E. Hunter, J. L. Atwood, E. Samuel, *J. Organomet. Chem.* **1980**, *197*, 217–224; b) J. L. Petersen, L. Griffith, *Inorg. Chem.* **1980**, *19*, 1852–1858; c) G. Fachinetti, C. Floriani, A. Chiesi-Villa, C. Guastini, *Inorg. Chem.* **1979**, *18*, 2282–2287; d) S. Gambarotta, M. Pasquali, C. Floriani, A. Chiesi-Villa, C. Guastini, *Inorg. Chem.* **1981**, *20*, 1173–1178.

[7] a) S. Gambarotta, M. Pasquali, C. Floriani, A. Chiesi-Villa, C. Guastini, *Inorg. Chem.* **1981**, *20*, 1173–1178; b) S. Gambarotta, C. Floriani, A. Chiesi-Villa, C. Guastini, *Organometallics* **1986**, *5*, 2525–2533; c) M. Wiederhold, U. Behrens, *J. Organomet. Chem.* **1994**, *476*, 101–109; d) J. M. Galante, J. W. Bruno, P. N. Hazin, K. Folting, J. C. Huffman, *Organometallics* **1998**, *17*, 1066–1073.

[8] a) M. Pasquali, P. Leoni, C. Floriani, A. Chiesi-Villa, C. Guastini, *Inorg. Chem.* **1983**, *22*, 841–844; b) G. Fachinetti, C. Floriani, A. Chiesi-Villa, C. Guastini, *J. Chem. Soc., Dalton Trans.* **1979**, 1612–1617; c) J. Benecke, R. Drews, U. Behrens, F. Edelmann, K. Keller, H. W. Roesky, *J. Organomet. Chem.* **1987**, *320*, C31–C34.

[9] a) R. Drews, D. Wormsbächer, U. Behrens, *J. Organomet. Chem.* **1984**, C40–C44; b) T. Sielisch, U. Behrens, *J. Organomet. Chem.* **1986**, *310*, 179–187; c) M. Pasquali, S. Gambarotta, C. Floriani, A. Chiesi-Villa, C. Guastini, *Inorg. Chem.* **1981**, *20*, 165–171.

[10] M. Pasquali, C. Floriani, A. Chiesi-Villa, C. Guastini, *Inorg. Chem.* **1980**, *19*, 3847–3850.

[11] R. Choukroun, B. Donnadieu, I. Malfant, S. Haubrich, R. Frantz, C. Guerin, B. Henner, *Chem. Commun.* **1997**, 2315–2316.

[12] R. Choukroun, B. Donnadieu, C. Lorber, P.-M. Pellny, W. Baumann, U. Rosenthal, *Chem. Eur. J.* **2000**, *6*, 4505–4509.

[13] There is a precedent in zirconium chemistry: observation of the sliding of a permethylzirconocene complex along a polyyne chain (hexatriyne) has been demonstrated by NMR spectroscopy to occur via a zirconacumulene species, see: P.-M. Pellny, V. V. Burlakov, P. Arndt, W. Baumann, A. Spannenberg, U. Rosenthal, *J. Am. Chem. Soc.* **2000**, *122*, 6317–6318.

[14] a) L. C. Francesconi, D. R. Corbine, A. W. Clauss, D. N. Hendrickson, G. D. Stucky, *Inorg. Chem.* **1981**, *20*, 2059–2069; b) L. S. Kramer, A. W. Clauss, L. C. Francesconi, D. R. Corbin, D. N. Hendrickson, G. D. Stucky, *Inorg. Chem.* **1981**, *20*, 2070–2077; c) E. Samuel, J. F. Harrod, D. Gourier, Y. Dromzee, F. Robert, Y. Jeannin, *Inorg. Chem.* **1992**, *31*, 3252–3259.

[15] a) G. N. Patel, *J. Polym. Sci., Polym Phys. Ed.* **1979**, *17*, 1591–1600; b) Y. Rubin, S. S. Lin, C. B. Knobler, J. Anthony, A. M. Boldi, F. Diederich, *J. Am. Chem. Soc.* **1991**, *113*, 6943–6949; c) F. Diederich, Y. Rubin, O. L. Chapman, N. S. Goroff, *Helv. Chim. Acta* **1994**, *77*, 1441–1457; d) H. D. Kalinowski, S. Berger, S. Braun, *Carbon-13 NMR Spectroscopy*, John Wiley & Sons, New York, **1988**.

[16] R. Choukroun, Y. Miquel, B. Donnadieu, A. Igau, C. Blandy, J.-P. Majoral, *Organometallics* **1999**, *18*, 1795–1797.

[17] U. Behrens, F. G. A. Stone, *J. Chem. Soc., Dalton Trans.* **1984**, 1605–1607.

[18] a) M. H. Chisholm, *Angew. Chem. Int. Ed. Engl.* **1991**, *30*, 673–674; b) R. Nast, *Coord. Chem. Rev.* **1982**, *47*, 89–124; c) S. Lotz, P. H. Van Rooyen, R. Meyer, *Adv. Organomet. Chem.* **1995**, *37*, 219–313; d) H. Lang, K. Köhler, S. Blau, *Coord. Chem. Rev.* **1995**, *143*, 113–168; e) U. Rosenthal, P.-M. Pellny, F. G. Kirchbauer, V. V. Burlakov, *Acc. Chem. Res.* **2000**, *33*, 119–129.

[19] C. Danjoy, J. Zhao, B. Donnadieu, J.-P. Legros, L. Valade, R. Choukroun, A. Zwick, P. Cassoux, *Chem. Eur. J.* **1998**, *4*, 1100–1105.

[20] R. Choukroun, B. Donnadieu, J.-S. Zhao, P. Cassoux, C. Lepetit, B. Silvi, *Organometallics* **2000**, *19*, 1901–1911.

[21] Some selected references on ptC: a) G. Erker, R. Zwettler, C. Krüger, R. Noe, S. Werner, *J. Am. Chem. Soc.* **1990**, *112*, 9620–9621; b) G. Erker, *Comments Inorg. Chem.* **1992**, *31*, 111–131; c) A. D. Hornton, A. G. Orpen, *Angew. Chem. Int. Ed. Engl.* **1992**, *31*, 876–878; d) M. Albrecht, G. Erker, C. Krüger, *Synlett* **1993**, 441–448; e) D. Röttger, G. Erker, R. Fröhlich, M. Grehl, S. J. Silverio, I. Hyla-Kryspin, R. Gleiter, *J. Am. Chem. Soc.* **1995**, *117*, 10503–10512; f) W. Alhers, B. Temme, G. Erker, R. Fröhlich, F. Zippel, *Organometallics* **1997**, *16*, 1440–1444; g) D. Rottger, G. Erker, *Angew. Chem. Int. Ed. Engl.* **1997**, *36*, 812–827; h) W. M. Jones, J. Klosin, *Adv. Organomet. Chem.* **1998**, *42*, 147–221; i) ; R. Choukroun, P. Cassoux, *Acc. Chem. Res.* **1999**, *32*, 494–502; j) G. Erker, S. Venne-Dunker, G. Kehr, N. Kleigrewe, R. Froehlich, C. Mueck-Lichtenfeld, S. Grimme, *Organometallics* **2004**, *23*, 4391–4395.

 © 2005 Wiley-VCH Verlag GmbH & Co. KGaA, Weinheim

[22] a) A. D. Becke, K. E. Edgecombe, *J. Chem. Phys.* **1990**, *92*, 5397–5403; b) B. Silvi, A. Savin, *Nature* **1994**, *371*, 683–686; c) M. E. Alikhani, Y. Bouteiller, B. Silvi, *J. Phys. Chem.* **1996**, *100*, 16092–16097; d) A. Savin, R. Nesper, S. Wengert, T. F. Fässler, *Angew. Chem. Int. Ed. Engl.* **1997**, *36*, 1808–1832.
[23] a) S. Pulst, P. Arndt, B. Heller, W. Baumann, R. Kempe, U. Rosenthal, *Angew. Chem. Int. Ed. Engl.* **1996**, *35*, 1112–1114; b) P.-M. Pellny, N. Peulecke, V. V. Burlakov, A. Tillack, W. Baumann, A. Spannenberg, R. Kempe, U. Rosenthal, *Angew. Chem. Int. Ed. Engl.* **1997**, *36*, 2615–2617.
[24] For some selected references on cyclocumulene species, see: a) U. Rosenthal, V. V. Burlakov, P. Arndt, W. Baumann, A. Spannenberg, *Organometallics* **2005**, *24*, 456–471; b) U. Rosenthal, *Angew. Chem. Int. Ed.* **2004**, *43*, 3882–3887.
[25] R. Choukroun, J. Zhao, C. Lorber, P. Cassoux, B. Donnadieu, *Chem. Commun.* **2000**, 1511–1512.
[26] C. Danjoy, PhD Thesis, Institut National Polytechnique de Toulouse, France, **1996**, no. 1197.
[27] a) K. Jonas, W. Rüsseler, C. Krüger, E. Raabe, *Angew. Chem. Int. Ed. Engl.* **1986**, *25*, 925–927; b) K. Jonas, W. Rüsseler, C. Krüger, E. Raabe, *Angew. Chem. Int. Ed. Engl.* **1986**, *25*, 928–929; c) I. L. Fedushkin, V. I. Nevodchikov, V. K. Cherkasov, M. N. Bochkarev, H. Schumann, F. Girgsdies, F. H. Görlitz, G. Kociok-Köhn, J. Pickardt, *J. Organomet. Chem.* **1996**, *511*, 157–162.
[28] M. N. Bochkarev, I. L. Fedushkin, V. K. Cherkasov, V. I. Nevodchikov, H. Schumann, F. H. Görlitz, *Inorg. Chim. Acta* **1992**, *201*, 69–74.
[29] a) J. Martin, M. Fauconet, C. Moïse, *J. Organomet. Chem.* **1989**, *371*, 87–89; b) F. Calderazzo, I. Ferry, G. Pampaloni, U. Englert, *Organometallics* **1999**, *18*, 2452–2458.
[30] F. Calderazzo, G. Fachinetti, C. Floriani, *J. Am. Chem. Soc.* **1974**, *96*, 3695–3696.
[31] F. Calderazzo, M. Guelfi, G. Pampaloni, *Organometallics* **2004**, *23*, 1519–1524.
[32] F. Bottomley, J. Darkwa, *Inorg. Chem.* **1983**, *22*, 399–400.
[33] a) *Metallocenes: Synthesis, Reactivity, Applications*, vol. 2 (Eds.: A. Togni, R. L. Haltermann), **1998**, Wiley-VCH, Weinheim, Germany; b) W. E. Piers, *Adv. Organomet. Chem.* **2005**, *52*, 1–76; c) W. E. Piers, T. Chivers, *Chem. Soc. Rev.* **1997**, *26*, 345–354; d) J. M. Stoddard, K. J. Shea, *Organometallics* **2003**, *22*, 1124–1131; e) D. J. Parks, W. E. Piers, M. Parvez, R. Atencion, M. J. Zaworotko, *Organometallics* **1998**, *17*, 1369–1377; f) D. J. Parks, J. M. Blackwell, W. E. Piers, *J. Org. Chem.* **2000**, *65*, 3090–3098; g) A. J. Mountford, D. L. Hughes, S. Lancaster, *Chem. Commun.* **2003**, 2148–2149; h) I. D. Watson, A. Yudinn, *J. Org. Chem.* **2003**, *68*, 5160–5167; i) E. Y.-X. Chen, J. T. Marks, *Chem. Rev.* **2000**, *100*, 1391–1434; j) G. J. P. Britovsek, V. C. Gibson, D. F. Wass, *Angew. Chem. Int. Ed.* **1999**, *38*, 429–447.
[34] a) R. Choukroun, P. Moumboko, S. Chevalier, M. Etienne, B. Donnadieu, *Angew. Chem. Int. Ed.* **1998**, *37*, 3169–3172; b) C. Lorber, B. Donnadieu, R. Choukroun, *Organometallics* **2000**, *19*, 1963–1966; c) R. Choukroun, C. Lorber, B. Donnadieu, *Organometallics* **2002**, *21*, 1124–1126; d) F. Wolff, R. Choukroun, C. Lorber, B. Donnadieu, *Eur. J. Inorg. Chem.* **2003**, 628–632.
[35] R. Choukroun, C. Lorber, C. Lepetit, B. Donnadieu, *Organometallics* **2003**, *22*, 1995–1997.
[36] R. Choukroun, C. Lorber, B. Donnadieu, *Organometallics* **2004**, *23*, 1434–1437.
[37] This structure was recently established; R. Choukroun, C. Lorber, L. Vendier, unpublished results.
[38] A. M. Carrier, J. G. Davidson, E. K. Barefield, D. G. Van Derveer, *Organometallics* **1987**, *6*, 454–458.
[39] a) D. F. Shriver, B. Swanson, *Inorg. Chem.* **1971**, *10*, 1354–1365; b) B. Swanson, D. F. Shriver, *Inorg. Chem.* **1969**, *8*, 1406–1416; c) J. L. Hoard, T. B. Owen, A. Buzzell, O. N. Salmon, *Acta Crystallogr.* **1950**, *3*, 130–137; d) J. L. Hoard, S. Geller, T. B. Owen, *Acta Crystallogr.* **1951**, *4*, 405–407; e) L. Li, T. J. Marks, *Organometallics* **1998**, *17*, 3996–4003; f) I. C. Tornieporth-Oetting, T. M. Klapötke, T. S. Cameron, J. Vallonen, P. Rademacher, K. Kowski, *J. Chem. Soc., Dalton Trans.* **1992**, 537–541.
[40] a) R. Hoti, Z. Mihalic, H. Vancik, *Croat. Chem. Acta* **1995**, *2*, 359–371; b) H. Jacobsen, H. Berke, S. Döring, G. Kehr, G. Erker, R. Fröhlich, O. Meyer, *Organometallics* **1999**, *18*, 1724–1735.
[41] F. Paul, C. Lapinte, *Coord. Chem. Rev.* **1998**, *178–180*, 431–509.
[42] M. J. Hampden-Smith, W. G. Klemperer, C. J. Brinker, *Better Ceramics through Chemistry V*, *MRS Symp. Proc.* **1992**, 271.
[43] L. Deutschmann, J. Messelhäuser, H. Suhr, W. A. Herrmann, P. Härter, *Adv. Mater.* **1994**, *6*, 392–395.
[44] a) L. Valade, R. Choukroun, P. Cassoux, F. Teyssandier, L. Poirier, M. Ducarroir, R. Feurer, P. Bonnefond, F. Maury, in *The Chemistry of Transition Metal Carbides and Nitrides* (Ed.: S. T. Oyama), Blackie Academic & Professional, **1996**, 290–310; b) F. Maury, F. Teyssandier, L. Valade, *Ann. Chim. Sci. Mater.* **1998**, *23*, 637–653.
[45] J. H. Holleck, *J. Vac. Sci. Technol. A* **1986**, *4*, 2661–2669.
[46] L. Valade, R. Choukroun, C. Danjoy, B. Chansou, D. de Caro, P. Cassoux, *Ann. Chim. Sci. Mater.* **1998**, *23*, 721–732.
[47] L. Poirier, O. Richard, M. Ducarroir, M. Nadal, F. Teyssandier, F. Laurent, O. Cyr-Athis, R. Choukroun, L. Valade, P. Cassoux, *Thin Solid Films* **1994**, *249*, 62–69.
[48] Y. Derraz, O. Cyr-Athis, R. Choukroun, L. Valade, P. Cassoux, F. Dahan, F. Teyssandier, *J. Mater. Chem.* **1995**, *5*, 1775–1778.
[49] L. Valade, C. Danjoy, B. Chansou, E. Riviere, J.-L. Pellegatta, R. Choukroun, P. Cassoux, *Appl. Organomet. Chem.* **1998**, *12*, 173–187.
[50] Leading recent references: a) *Clusters and Colloids. From Theory to Applications* (Ed.: G. Schmid), **1994**, VCH, Weinheim, Germany; b) *Nanoparticles*, (Ed.: G. Schmid), **2004**, VCH, Weinheim, Germany; c) J. A. Widegreen, R. G. Finke, *J. Mol. Catal.* **2003**, *191*, 187–207; d) K. Philippot, B. Chaudret, *C. R. Chimie* **2003**, *6*, 1019–1034; e) A. Roucoux, J. Schulz, H. Patin, *Chem. Rev.* **2002**, *102*, 3757–3778.
[51] R. Choukroun, D. de Caro, S. Mateo, C. Amiens, B. Chaudret, E. Snoeck, M. Respaud, *New J. Chem.* **1998**, *22*, 1295–1299.
[52] R. Choukroun, D. de Caro, B. Chaudret, P. Lecante, E. Snoeck, *New J. Chem.* **2001**, *25*, 525–527.
[53] J.-L. Pellegatta, C. Blandy, R. Choukroun, C. Lorber, B. Chaudret, P. Lecante, E. Snoeck, *New J. Chem.* **2003**, *27*, 1528–1532.
[54] a) J. L. Pellegatta, C. Blandy, V. Collière, R. Choukroun, B. Chaudret, P. Cheng, K. Philipot, *J. Mol. Catal.* **2002**, *178*, 55–61; b) W. Wojtkow, A. M. Trzeciak, R. Choukroun, J. L. Pellegatta, *J. Mol. Catal. A* **2004**, *224*, 81–86.
[55] a) J. S. Miller, *Inorg. Chem.* **2000**, *39*, 4392–4408; b) J. S. Miller, A. J. Epstein, *Chem. Commun.* **1998**, 1319–1325; c) J. S. Miller, J. L. Manson, *Acc. Chem. Res.* **2001**, *34*, 563–570.

Received: April 27, 2005
Published Online: October 25, 2005

 © 2005 Wiley-VCH Verlag GmbH & Co. KGaA, Weinheim

DOI: 10.1002/ejic.200500477

Low-Temperature Flux Synthesis, Crystal Structure and Ce-Doped Luminescence of the First Lutetium Diphosphate $NH_4LuP_2O_7$

Man-Rong Li,[a,b] Wei Liu,[a] Hao-Hong Chen,[a] Xin-Xin Yang,[a] Zan-Bin Wei,[c] Dun-Hua Cao,[d] Mu Gu,[d] and Jing-Tai Zhao*[a]

Keywords: Low-temperature self-flux synthesis / Structure / Diphosphate / Luminescence

The first lutetium diphosphate $NH_4LuP_2O_7$ has been prepared by a two-step, low-temperature self-flux synthesis in the presence of the F^- anion, functioning as a mineralizer, which played a significant role in the synthetic process. The crystal structure has been characterized by single-crystal X-ray diffraction. The title compound crystallizes in a monoclinic system of the space group $P2_1/c$ (No. 14), a = 7.651(2) Å, b = 10.789(2) Å, c = 8.577(2) Å, β = 105.75(3)°, V = 681.4(2) Å^3, Z = 4. The three-dimensional framework of $NH_4LuP_2O_7$, composed of $Lu_2P_4O_{14}$ building units formed by vertex-linking LuO_6 and P_2O_7 goups, is isostructural with compounds of the type $KAlP_2O_7$ in the ternary diphosphate($A^IM^{III}P_2O_7$) system. X-ray-excited luminescence measurements of Ce-activated samples show insteresting scintillation properties with a short decay time of 16 ns at room temperature.
(© Wiley-VCH Verlag GmbH & Co. KGaA, 69451 Weinheim, Germany, 2005)

Introduction

Recently, investigation of the synthesis and characterization of wide-bandgap rare-earth (RE) phosphate materials has gained much more attention, for their potential applications in diverse areas such as X- and gamma-radiation detectors, lighting, display phosphors, light-emitting diodes, scintillators, and solid state lasers, and because they are highly transparent, easily shaped, and cost-effective.[1–4] In contrast to the well-known ternary rare-earth phosphates, the diphosphates, which should have had potentially attractive applications on the basis of their analogous structure with the phosphates, are still to be explored, except for the compounds already reported, partly because it is difficult to synthesize them in the crystalline and pure phase requested for considerable applications. $MLaP_2O_7$ (M = Li, Na, K),[5] $NaCeP_2O_7{\cdot}4.5H_2O$,[6] and $NaGdP_2O_7{\cdot}4.5H_2O$,[7] obtained from reaction in solution, have been reported, but only some complex X-ray powder diffraction patterns have been given without further indexing for the lattice parameters, and no single-crystal X-ray structural determinations have been reported to support the lattice parameters until now. In addition, the function of the pH value is rather subtle in the solution method. Jansen et al.[8] prepared $CsYbP_2O_7$ by rigorous solid-state reaction (under argon at 1173 K) and characterized the crystal structure without further investigation. Most often it is not so easy to obtain the pure phase and carry out further purification by high-temperature solid reactions, as reported in the preparations of $NaGdP_2O_7$,[7] AYP_2O_7 (A = Na,[9] K,[10] Cs[11]), and $NaEuP_2O_7$[12] in the presence of an auxiliary solvent.

The above compounds have been mostly prepared by reaction in solution and by the high-temperature flux method. In addition, other relevant characterization data and optical properties of this type of compounds have been seldom reported. Along this line of research, we present here the novel two-step, low-temperature self-flux synthesis, crystal structure, and Ce-activated luminescence of $NH_4LuP_2O_7$.

Results and Discussion

F^--Optimized Procedure

The preparation procedure is outlined in reaction (1) and reaction (2). As shown in reaction (1), sodium lutetium tetrafluoride, $NaLuF_4$, was obtained under mild water-free flux of abundant H_3BO_3, with a low melting point of 458 K, instead of the traditional synthetic method for this type of compounds.[13] Excess H_3BO_3 and a stoichiometric quantity of NaF were essential in the first reaction.

[a] State Key Laboratory of High Performance Ceramics and Superfine Microstructure, Shanghai Institute of Ceramics, The Chinese Academy of Sciences,
Shanghai, 200050, China
Fax: + 86-021-52413122
E-mail: jtzhao@mail.sic.ac.cn
[b] Graduate School of The Chinese Academy of Sciences, Beijing, China
[c] Department of Chemistry, Xiamen University, Xiamen, 361005, China
[d] Department of Physics, Tongji University, Shanghai, 200020, China

 © 2005 Wiley-VCH Verlag GmbH & Co. KgaA, Weinheim

$$Lu_2O_3 + 8\ NaF + 2\ H_3BO_3 \xrightarrow{523\ K} 2\ NaLuF_4 + 2\ Na_3BO_3 + 3\ H_2O\uparrow \quad (1)$$

$$NaLuF_4 + 3\ NH_4H_2PO_4 + 2\ NaF \xrightarrow{553\ K} NH_4LuP_2O_7 + Na_3PO_4 + 2\ NH_3\uparrow + HF\uparrow + H_2O\uparrow \quad (2)$$

In reaction (2), the mixture of prepared $NaLuF_4$, excess $NH_4H_2PO_4$, and the correct quantity of NaF was heated in a Teflon-lined stainless steel autoclave at 553 K. Here the excess $NH_4H_2PO_4$ (melting point: 453 K) was used as the self-flux, and the quantity of NaF played a very important role. Lots of $LuPO_4$ powder and a few crystals of $NH_4LuP_2O_7$ were produced in the absence of NaF. The yield of $NH_4LuP_2O_7$ increased by adding NaF, and the pure phase of the target compound could only be obtained when the molar ratio of F/Lu was larger than two. This observation indicates that reaction (2) tends to yield $NH_4LuP_2O_7$ instead of $LuPO_4$ in the presence of a large quantity of F^-.

Related investigations were carried out for systems with RE (RE = Y, La, Nd, Gd, Er, Yb) instead of Lu. $NH_4YP_2O_7$ and $NH_4YbP_2O_7$ were obtained with the same structure type, while $REPO_4$ was produced in systems containing La, Nd, and Gd. The Er system yielded a mixture of $ErPO_4$ and $NaErF_4$. Obviously, the size of the ion plays a very important role in the synthetic procedure.

Crystal Structures of $NH_4LuP_2O_7$

The many structural investigations devoted to the $A^IM^{III}P_2O_7$-type diphosphates in the past two decades have shown the existence of eight structural types.

The compounds of type I exhibit the $KAlP_2O_7$[14] structure, whereas those of type II are isotypic with $NaFeP_2O_7$.[15] The lithium-containing compounds constitute the third family and adopt the $LiFeP_2O_7$ structure.[16] The fourth type is only represented by α-$NaTiP_2O_7$.[17] A fifth type occurs for the $NaYP_2O_7$ structure,[9] and KYP_2O_7 belongs to structural type VI.[10] The structural investigation of $NaEuP_2O_7$[12] and $NaGaP_2O_7$[7] reveals new structural arrangements of type VII and type VIII, respectively.

The crystal structure of the title compound $NH_4LuP_2O_7$ was determined by single-crystal X-ray diffraction. It is isotypic with type I compounds and possesses a three-dimensional framework consisting of $Lu_2P_4O_{14}$ building units as shown in Figure 1. The NH_4^+ cations occupy the one-dimensional six-membered ring tunnels (about 3.83 × 3.83 Å, evaluated from the O···O distances) and participate in moderate hydrogen bonding with the framework oxygen atoms (N–H···O hydrogen bonds with distances of 2.884–3.344 Å). The tunnels running along [001] result from the stacking of rings formed by the edges of three LuO_6 octahedra and four PO_4 tetrahedra. Adjacent layers are generated by the *c*-glide plane, and these layers form a three-dimensional network with tunnels running along the *c*-axis.

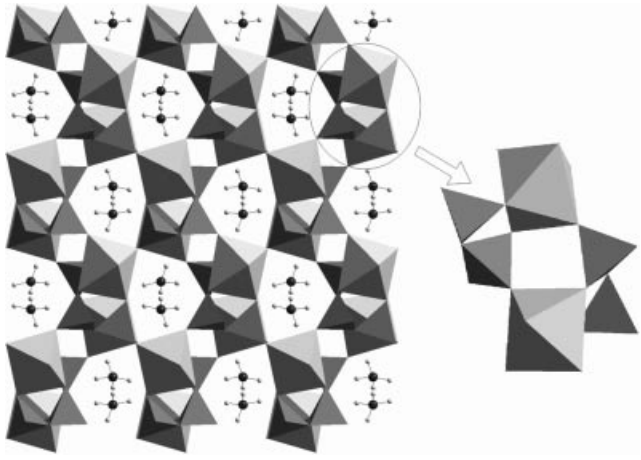

Figure 1. (a) 3D polyview structure along the [001] direction (b) $Lu_2P_4O_{14}$ structural building unit in the crystal structure of $NH_4LuP_2O_7$ (LuO_6, light-gray octahedra; PO_4, dark-gray tetrahedra; N atoms black spheres; H atoms, light gray spheres).

Lu atoms have a hexagonal close-packed arrangement. Each LuO_6 group is connected, through Lu–O–P bonds, to five P_2O_7 groups: two corners of the LuO_6 octahedron are linked to one P_2O_7 group, and the other four corners are connected with four distinct P_2O_7 groups. The LuO_6 octahedra are also distorted [the bond valence sum (BVS) of Lu is 3.19], as shown by the Lu–O distances ranging from 2.143(12) to 2.223(11) Å and O–Lu–O bond angles ranging from 82.8(4) to 178.9(5)°. The P_2O_7 group presents a staggered configuration with one long P–O bond and three much shorter P–O bonds (Figure 2), which is very common in the $A^IM^{III}P_2O_7$ family except for the semi-staggered configuration in several compounds ($NaInP_2O_7$,[18] $NH_4VP_2O_7$,[19] and $NaYP_2O_7$[9]) and the eclipsed configuration in type II, III, VI, VII, and VIII compounds. The P–$O_{terminal}$ bonds (average: 1.511 Å) are shorter than the P–$O_{bridging}$ bonds (average: 1.597 Å), and the P–O–P bond angle is 128.9(8)°, which falls into the generally observed range of 122–141° for ternary diphosphate compounds. The O–P–O angles show distortion from the ideal tetrahedral geometry [105.1(6) to 113.9(8)°], and the BVSs of the two P atoms are 4.93 and 4.90. The calculated BVSs are very close to the chemical valences; this confirms the reliability of the determined structure.[20,21]

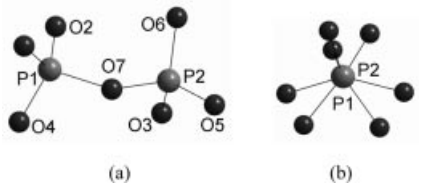

Figure 2. Configuration of P_2O_7 in $NH_4LuP_2O_7$ viewed (a) in plane (b) along the P–P direction.

Luminescence Properties

The Ce-doped crystals were grown under the same conditions by adding CeF_3 in reaction (1). X-ray-excited lumines-

 © 2005 Wiley-VCH Verlag GmbH & Co. KGaA, Weinheim

cence (XEL) measurements showed that $NH_4LuP_2O_7$ activated with 0.5 at.-% Ce^{3+} exhibited the strongest band emission when the concentration of Ce^{3+} was in the range 0.1–3 at.-% (stoichiometric amounts of lutetium oxide). The XEL spectrum of $NH_4LuP_2O_7$:Ce^{3+} (0.5 at.-%) shows a band emission with a maximum at 375 nm (Figure 3), which can be explained by transitions occurring between the lowest level of the excited 5d (2D) sate and the ground $^2F_{5/2}$ and $^2F_{7/2}$ levels of 4f(^{2}F) in the Ce^{3+} ion. Compared with the reported Ce^{3+}-activated spectrum of lutetium phosphate,[22] the emission band in Figure 3 is less well-resolved because of increased overlap. A Gaussian fit reveals that the emission band consists of two sub-bands centered at about 364 and 395 nm. An energy discrepancy of about 2156 cm^{-1}, which is a typical value for the spin-orbit-split ground level of the Ce^{3+} ion ($^2F_{5/2}$ and $^2F_{7/2}$), confirms the Ce^{3+} d-f origin of this emission.

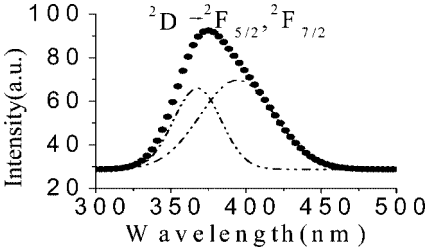

Figure 3. The X-ray-excited luminescence spectra of 0.5 at.-% Ce-activated $NH_4LuP_2O_7$ measured at room temperature.

The scintillation pulse shape for the 0.5 at.-% Ce-activated sample is shown in Figure 4, which exhibits a decay time of about 16 ns. The large contribution and very short decay time of this compound produces an excellent zero-time (initial) scintillation amplitude. This is very advantageous, since for the majority of (and especially for timing) applications, it is the zero-time scintillation amplitude that is the most important factor.[23]

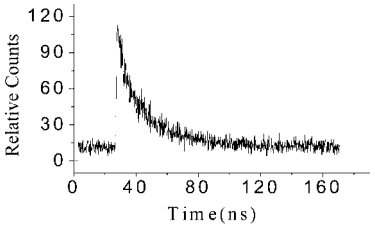

Figure 4. Scintillation decay curve of 0.5 at.-% Ce-activated $NH_4LuP_2O_7$ measured after pulsed X-ray excitation.

The luminescence properties of Ce^{3+} in different phosphate hosts are interesting because of their influence on the crystal field.[24] $LuPO_4$:Ce^{3+} (0.1 at.-%)[25] has the strongest band emission (360 nm) with a decay time of 24 ns, while $K_3Lu(PO_4)_2$:Ce^{3+} (0.5 at.-%)[22,26] and $Rb_3Lu(PO_4)_2$:Ce^{3+} (1 at.-%)[26] show strong band emissions (410 nm) with decay times of 37 and 34 ns respectively.

Conclusions

The first lutetium diphosphate $NH_4LuP_2O_7$ was synthesized under novel two-step, mild reaction conditions. The F^- optimized synthetic procedure is very significant. The open-framework crystal structure is isotypic with $KAlP_2O_7$ type compounds. The P_2O_7 group is staggered. The Ce-doped sample shows interesting luminescence and scintillation properties with a very fast decay time of 16 ns. Ternary diphosphates of other representative rare-earth systems are being investigated by this new method of synthesis for their analogous properties, and further researche will be carried out on the relation between activator concentration and activator type and luminescence and scintillation properties.

Experimental Section

Materials and Measurements: All chemicals were obtained from commercial sources and used as received. The products were examined by powder X-ray diffraction (Rigaku D/max 2550 V diffractometer, Cu-K_α) in order to confirm their phase identity and purity. Single-crystal X-ray diffraction data were collected with a Nonius Kappa CCD with graphite monochromatized Mo-K_α radiation (λ = 0.71073 Å). The XEL and decay time measurements were carried out at room temperature with a FluoMain X-ray-excited luminescence spectrometer and a pulsed X-ray-excited decay measuring equipment designed at Tongji University. IR spectra were recorded with a Nicolet-NEXUS spectrophotometer using KBr discs. Elemental analysis was performed with an EPMA-8705H_2 (Lu, P) and a PE-2004II (N) apparatus.

Reaction (1): Lu_2O_3 (1.592 g), H_3BO_3 (1.855 g), and NaF (0.67 g) were mixed in the molar ratio 2:15:8. The mixture was sealed in a 40-mL Teflon-lined stainless steel autoclave after grinding fully and heated under autogenous pressure at 523 K for 120 h. It was cooled to 443 K at a rate of 1 K h^{-1} and then left to cool to room temperature. The product was washed with hot deionized water for purification (2.081 g, 95% based on Lu_2O_3). X-ray powder diffraction indicated that $NaLuF_4$ was obtained (J.C.P.D.S No. 27–726).

Reaction (2): $NaLuF_4$ (2.08 g), $NH_4H_2PO_4$ (3.68 g), and NaF (0.67 g) were mixed in the molar ratio 1:4:2 and heated in a Teflon-lined stainless steel autoclave at 553 K for 120 h. It was cooled to 453 K at a rate of 1 K h^{-1} and then left to cool to room temperature. The product was washed with hot deionized water for purification, and colorless, octahedral bipyramidal crystals of $NH_4LuP_2O_7$ were obtained (2.120 g, 76% based on $NaLuF_4$). $NH_4LuP_2O_7$(366.949): calcd. N 3.81, P 16.88, Lu 47.68; found N 3.48, P 17.46, Lu 48.26. IR(KBr): υ_3(N–H) (3286 cm^{-1}), υ_1(N–H) (3035 cm^{-1}), $2\upsilon_4$(N–H) (2850 cm^{-1}), υ_4(N–H) (1434 cm^{-1}), $\upsilon_s(PO_3)$ (1203 cm^{-1}, 1110 cm^{-1}), υ_{as}(POP) (941 cm^{-1}), υ_s(POP) (748 cm^{-1}), $\delta(PO_2$ terminal bending) (624, 574, 470, 420 cm^{-1}).

X-ray Crystallographic Study: Monoclinic, space group $P2_1/c$ (No. 14), a = 7.6507(15) Å, b = 10.789(2) Å, c = 8.577(2) Å, β = 105.75(3)°, V = 681.4(2) $Å^3$, Z = 4, D = 3.577 g cm^{-3}, crystal dimensions [mm], 0.07 × 0.03 × 0.02; μ = 14.951 cm^{-1}, F(000) = 672, T = 293(2) K; 1588 unique reflections (R_{int} = 0.0874) and 101 parameters were used for the full-matrix, least-squares refinement of F^2 using the direct method in the program package SHELXL-97/2,[27] R_1 = 0.0690 [$I > 2\sigma(I)$], R_1 = 0.0842 (all data); wR_2 = 0.1211 [$I > 2\sigma(I)$], wR_2 = 0.1271 (all data). Further details of the crystal-struc-

 © 2005 Wiley-VCH Verlag GmbH & Co. KGaA, Weinheim

ture investigation(s) may be obtained from the Fachinformationszentrum Karlsruhe, 76344 Eggenstein-Leopoldshafen, Germany, on quoting the CSD-391320 (crysdata@FIZ-Karlsruhe.de).

Acknowledgments

This work was supported by the Fund for Distinguished Young Scholars and Key Project from the NNSF of China, State "863" project and funds from the Committee for Science and Technology of the Shanghai municipal government. The authors would like to thank Ms. Juan Hu for IR analysis, Ms. Jian-Hua Gao for elemental analysis, and Ms. Linhong Wong and Zhenxia Chen for their help in single-crystal X-ray analysis.

[1] A. A. Kaminskii, *Laser Crystals*, Springer, Berlin, **1994**.
[2] T. Jüstel, H. Nikolb, C. Ronda, *Angew. Chem. Int. Ed.* **1998**, *37*, 3084–3103.
[3] S. Heer, O. Lehmann, M. Haase, H. Güdel, *Angew. Chem. Int. Ed.* **2003**, *42*, 3179–3182.
[4] D. G. Shchukin, D. G. Sukhorukov, H. Möhwald, *J. Phys. Chem. B* **2004**, *108*, 19109–19113.
[5] V. G. Kuznetsov, V. P. Vasil′eva, *Inorg. Mater.* **1967**, *3*, 316–321.
[6] E. Giesbrecht, M. Perrier, *Anais Ass. Brasil de Quim.* **1960–1961**,*121*, 19.
[7] M. Kizilyalli, M. Darras, *J. Solid State Chem.* **1993**, *107*, 373–380.
[8] M. Jansen, G. Q. Wu, K. Königstein, *Z. Kristallogr.* **1991**, *197*, 245–246.
[9] A. Hamady, T. Jouini, *Acta Crystallogr. Sect. C* **1996**, *52*, 2949–2951.
[10] A. Hamady, M. Faouzi Zid, T. Jouini, *J. Solid State Chem.* **1994**, *113*, 120–124.
[11] M. Daoud, D. Zambon, R. Mahiou, A. Ammar, B. Tanouti, *Mater. Res. Bull.* **1998**, *33*, 597–603.
[12] M. Ferid, K. Horchani, J. Amami, *Mater. Res. Bull.* **2004**,*39*, 1949–1955.
[13] P. Rambaldi, R. Moncorgé, J. P. Wolf, C. Pedrini, J. Y. Gesland, *Opt. Commun.* **1998**, *146*, 163–166.
[14] H. N. Ng, C. Calvo, *Can. J. Chem.* **1973**, *51*, 2613–2620.
[15] M. Gabelica-Robert, M. Goreaud, P. Labbe, B. Raveau, *J. Solid State Chem.* **1982**, *45*, 389–395.
[16] D. Riou, N. Nguyen, R. Benloucif, B. Raveau, *Mater. Res. Bull.* **1990**, *25*, 1363–1369.
[17] A. Leclaire, A. Benmoussa, M. M. Borel, A. Grandin, B. Raveau, *J. Solid State Chem.* **1988**, *77*, 299–305.
[18] Y. C. Zhang, W. D. Cheng, D. S. Wu, H. Zhang, D. G. Chen, Y. J. Gong, Z. G. Kan, *Chem. Mater.* **2004**, *16*, 4150–4159.
[19] L. Benhamada, A. Grandin, M. M. Borel, A. Leclaire, B. Raveau, *Acta Crystallogr. Sect. C* **1991**, *47*, 424–425.
[20] I. D. Brown, D. Altermatt, *Acta Crystallogr. Sect. B* **1985**, *41*, 244–247.
[21] N. E. Brese, M. O'Keeffe, *Acta Crystallogr. Sect. B* **1991**, *47*, 192–197.
[22] D. Wisniewski, A. J. Wojtowicz, W. Drozdowski, J. M. Farmer, L. A. Boatner, *J. Alloys Compd.* **2004**, *380*, 191–195.
[23] P. A. Rodnyi, *Radiat. Meas.* **2001**, *33*, 605–614.
[24] P. Dorenbos, *Phys. Rev. B* **2001**, *64*, 125117–125129.
[25] Y. S. Lu, C. S. Mao, X. W. Tang, *Proc. SCINT97*, 18–23.
[26] W. W. Moses, M. J. Weber, S. E. Derenzo, D. Perry, P. Berdahl, *Proc. SCINT97*, 358–361.
[27] G. M. Sheldrick, *SHELXS-97/2, Program for the Solution of Crystal Structure* and *SHELXL-97/2, Program for Crystal Structure Refinement*, University of Göttingen, Germany, **1997**.

Received: May 26, 2005
Published Online: October 25, 2005

 © 2005 Wiley-VCH Verlag GmbH & Co. KGaA, Weinheim

DOI: 10.1002/ejic.200500614

The Mechanism of Magnetic Interaction in Spin-Ladder Molecular Magnets: A First-Principles, Bottom-Up, Theoretical Study of the Magnetism in the Two-Legged Spin-Ladder Bis(2-amino-5-nitropyridinium) Tetrabromocuprate Monohydrate

Mercè Deumal,*[a] Giacomo Giorgi,[b] Michael A. Robb,[c] Mark M. Turnbull,[d] Christopher P. Landee,[e] and Juan J. Novoa*[a][‡]

Keywords: Copper / Density functional calculations / Magnetic properties / Spin-ladders / Structure-activity relationships

The magnetic properties of the isotropic ($J_{rail} \approx J_{rung}$), two-legged spin-ladder bis(2-amino-5-nitropyridinium) tetrabromocuprate monohydrate, $[(5NAP)_2CuBr_4 \cdot H_2O]$, have been studied using a first-principles, bottom-up approach, which allows computation of macroscopic magnetic properties (for instance, the magnetic susceptibility) of a crystal from only a knowledge of its crystal packing. Evaluation of the J_{AB} parameters, using the 163 K X-ray structure of $[(5NAP)_2CuBr_4 \cdot H_2O]$, indicates that the magnetic topology of this crystal is a two-legged antiferromagnetic spin-ladder, with values of J_{rail} and J_{rung} of $-22.2\ cm^{-1}$ and $-19.7\ cm^{-1}$, respectively. These values are very close to those that best fit the experimental magnetic susceptibility curve, which are $-13.59\ cm^{-1}$ and $-14.16\ cm^{-1}$, respectively. Very weak diagonal interactions within each ladder [$J(d3) = -0.9\ cm^{-1}$] and between nearby ladders [$J(d4) = -0.3\ cm^{-1}$] are also found. The computed magnetic susceptibility curve obtained using the two-legged spin-ladder properly reproduces the experimental magnetic curve (a quantitative agreement is obtained by applying a linear scaling factor of about 0.75 to the energies). The singlet–triplet spin-gap of this spin-ladder was computed to be 17 K, in close agreement with the experimental result (11 K). The change of the spin-gap/J_{rail} with the size (2xL) of the magnetic spin-ladder model space was found to converge towards 0.5, while that for a single-legged (1xL) spin-ladder converges towards zero, both in good agreement with the known trends for these systems.

(© Wiley-VCH Verlag GmbH & Co. KGaA, 69451 Weinheim, Germany, 2005)

Introduction

Current research in molecular magnetism (understood here as all forms of molecule-based magnetism) aims to rationally design and synthesize molecular materials with tailor-made magnetic properties that, in some cases, will coexist with other technological properties of interest, such as conductivity or superconductivity. As a result of the combined work of many experimental and theoretical groups, progress in the field during recent years has been spectacular.[1] A rational design of molecular magnets requires the existence of: (i) properly based magneto-structural correlations, which would allow us to correlate the nature of the magnetic interaction with the relative orientations of the radical units, (ii) a rigorous form for correlating the microscopic magnetic interactions with the macroscopic magnetic properties, (iii) a reliable methodology to predict the most likely polymorphs of a crystal, and (iv) methodologies to control the growth of the desired polymorph of a crystal. Progress along these lines has been achieved, however more is required before a rational design of molecular magnets can be achieved.

One form of improving our knowledge on magneto-structural correlations is by having a better (and properly based) knowledge of the mechanism of the magnetic interaction for materials that present properties of special interest. Such studies should be performed using a rigorous first-principles methodology that avoids approximations or over-simplifications and, thus, does not reach averaged results or misleading conclusions. These studies should allow us to generate a database of first-principles information regard-

[a] Departament de Química Física, Universitat de Barcelona and Centre de Recerca en Química Teòrica (CeRQT), Parc Científic de Barcelona,
Martí i Franquès 1, 08028 Barcelona, Spain
Fax: +34-93-402-1231
E-mail: m.deumal@qf.ub.es
juan.novoa@ub.edu
[b] Dipartimento di Chimica, Universita' degli Studi di Perugia, Via Elce di Sotto 8, 06123 Perugia, Italy
[c] Chemistry Department, Imperial College London, South Kensington Campus, London SW7 2AZ, UK
[d] Chemistry Department, Clark University, 950 Main St., Worcester, MA 01610, USA
[e] Physics Department, Clark University, 950 Main St., Worcester, MA 01610, USA
[‡] Associate Member of the CEPBA-IBM Research Institute
Supporting information for this article is available on the WWW under http://www.eurjic.org or from the author.

 © 2005 Wiley-VCH Verlag GmbH & Co. KgaA, Weinheim

ing the keys governing the magnetic interaction in molecular materials.

Spin-ladders[2] are one of these materials of special interest. They result from assembling a given number (n) of chains (L) and connecting them magnetically (nxL). In the literature, the connected chains are referred to as either the legs or rails of the spin-ladder. The connections between the chains are referred to as rungs. Within this field, antiferromagnetic spin-ladders have attracted much interest for two main reasons: (i) their connection with high-temperature superconductors, which are lightly-doped 2D antiferromagnets, and (ii) the special properties that are present depending on the number of legs (ladders with an even number of legs present a finite spin-gap between singlet ground state, E_0, and lowest energy triplet state, E_1, energies, while ladders with an odd number of legs behave as single chains and show no spin-gap; such results have been verified both theoretically and experimentally[2]).

Up to now, the study of the magnetic properties of spin-ladders has been based on finding a good empirical model to fit the experimental magnetic susceptibility, and then rationalizing the experimental properties using the available solutions for that model, usually found in the literature as a function of the J_{rung}/J_{rail} ratio.[2] In this work we will carry out for the first time, to the best of our knowledge, a first-principles, bottom-up, theoretical analysis of the mechanism of magnetic interactions in a two-legged antiferromagnetic spin-ladder. We have selected for study the bis(2-amino-5-nitropyridinium) tetrabromocuprate monohydrate spin-ladder [see Figure 1 (a)], herein identified as [$(5NAP)_2CuBr_4{\cdot}H_2O$], whose crystal structure has been determined by X-ray diffraction at 163 K. This is an antiferromagnetic, two-legged spin-ladder[3] with the added interest of having similar values for the experimental J_{rail} and J_{rung} values (–13.59 and –14.16 cm^{-1}, respectively, obtained from fitting the magnetic susceptibility as a function of temperature). The isotropic exchange ($J_{rail} \approx J_{rung}$) case is where the effect of the quantum fluctuations is most pronounced; the physics is the most complex and cannot be properly treated by perturbation theory. We will apply to [$(5NAP)_2CuBr_4{\cdot}H_2O$] our recently proposed, first-principles, bottom-up, theoretical procedure[4] to find the mechanism of the magnetic interaction within this system and properly justify the available experimental magnetic data.

Our first-principles, bottom-up, theoretical analysis of molecular magnetic materials[4] is a tool that connects the microscopic and macroscopic magnetic properties using a rigorous numerical procedure. It could thus become a practical tool for the rational design of molecular magnets, once good magneto-structural correlations are found[5] and a better control of the crystal packing prediction and growth is also achieved. The first-principles, bottom-up, theoretical analysis starts by computing the strength of all unique radical–radical magnetic interactions (the J_{AB} constants of the Heisenberg Hamiltonian). There are no prior assumptions of the relative importance of J_{AB}, so the procedure is fully nonbiased. The values of the J_{AB} magnetic interactions are then used to define the magnetic topology of the crystal,[6]

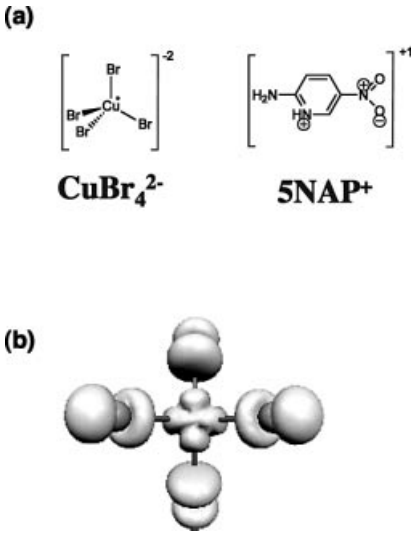

Figure 1. (a) Structure of the ions present in [$(5NAP)_2CuBr_4{\cdot}H_2O$]. (b) Spin distribution in the $CuBr_4^{2-}$ anion (isodensity surface of 0.002 au).

a property that allows the selection of a finite model space representative of the magnetic interactions in the full-sized crystal. The matrix representation of the Heisenberg Hamiltonian is then computed in the space of all the spin functions of the finite model space, and the energy of all possible magnetic states is calculated by diagonalization of that matrix. This allows the connection of the microscopic and macroscopic [e.g. magnetic susceptibility $\chi(T)$ and heat capacity $C_p(T)$] magnetic properties using the appropriate expressions from statistical mechanics.[4] The magnetic topology also allows identification of the magnetic pathways along which the magnetic interactions propagate over the whole crystal. We should mention that this first-principles, bottom-up, theoretical approach has already been successfully applied to the study of the magnetic properties of a variety of prototype systems.[4,7]

Results and Discussion

Here we will briefly describe the main steps and underlying physics behind the first principles, bottom-up procedure that we will then apply to the study of [$(5NAP)_2CuBr_4{\cdot}H_2O$]. For the interested reader, a detailed mathematical and physical account of the procedure and its basis is available in the literature.[4]

We have found that the following four steps allow us to carry out the proposed first principles, bottom-up procedure in a nonbiased form:

1) The first step consists of performing a detailed analysis of the crystal packing to identify all unique A-B radical–radical pairs whose interpair distance is smaller than a given threshold value (above which the magnetic interaction between radicals is expected to be negligible). This threshold is deliberately chosen to select more pairs than the first nearest neighbors (the usual candidates in the literature).

 © 2005 Wiley-VCH Verlag GmbH & Co. KGaA, Weinheim

Such a selection procedure of radical–radical pairs is completely nonbiased.

2) Secondly, for all A-B radical–radical pairs selected in the previous step, we evaluate the value of the corresponding J_{AB} magnetic interactions using quantum chemical methods.

3) Using the computed J_{AB} parameter values, we then determine the magnetic topology of the crystal in terms of how non-negligible J_{AB} interactions propagate along the crystal axes. Two neighboring A-B radical sites are connected whenever its magnetic interaction presents a $|J_{AB}|$ value larger than a given threshold, which in previous calculations was estimated to be $|0.05|$ cm^{-1}. Then, we search for the smallest (finite-sized) minimal magnetic model space that describes the magnetic interactions of the whole crystal in a balanced way. The repetition of such a minimal model along the (*a*,*b*,*c*) crystallographic directions should regenerate the magnetic topology of the whole crystal. The radical centers constituting the minimal magnetic model define a spin-space that is used to compute the matrix representation of the corresponding Heisenberg Hamiltonian (see Computational Data section). Note that the only parameters required to compute that matrix representation of the Heisenberg Hamiltonian are the J_{AB} parameters computed in step 2.

4) In the fourth and final step, the Heisenberg Hamiltonian matrix is diagonalized to obtain the energy for all possible spin-states. These energies are then used to compute the magnetic susceptibility $\chi(T)$ and/or heat capacity $C_p(T)$ using the appropriate expressions obtained from a statistical mechanical treatment.[4]

The magnetic properties of $[X_2CuBr_4]$ compounds have been reported for a large variety of systems.[8] The packing of these crystals can be modified by changing the size and shape of the X^+ organic cation, which, in turn, induces modifications in the observed magnetic properties. Some of these $[X_2CuBr_4]$ crystals are low-dimensional 1D and 2D magnetic systems.

The structure of the $[(5NAP)_2CuBr_4{\cdot}H_2O]$ ionic crystal was determined by X-ray diffraction at 163 K.[3] It crystallizes in the $P\bar{1}$ space group, with cell parameters a = 7.566, b = 9.359, c = 14.909 Å, α = 77.073°, β = 75.912°, γ = 76.393°, and Z = 2. The packing can be rationalized as a stack of double-decked planes [see Figure 2 (a) for a general view and Figure 2 (b) for a view of a single double-decked plane]. Each individual plane constituting the double-decked planes [Figure 2 (c)] presents a structure where the $5NAP^+$ cations surround the $CuBr_4^{2-}$ anions in a T-shaped disposition (this allows the formation of short C–H···O contacts between the cations, with distances within the 2.46–2.56 Å range, in addition to the C–H···Br contacts between anions and cations, in the 3.0–3.2 Å range). The disposition of the spin-containing units (the $CuBr_4^{2-}$ anions) in the crystal is shown in Figure 3. The topology of a two-legged ladder along the crystal *a*-axis, previously proposed to explain the magnetism of this crystal,[3] is clearly observed when looking at the shortest intermolecular Cu···Cu distances [6.34 and 7.57 Å; Figure 3 (b)].

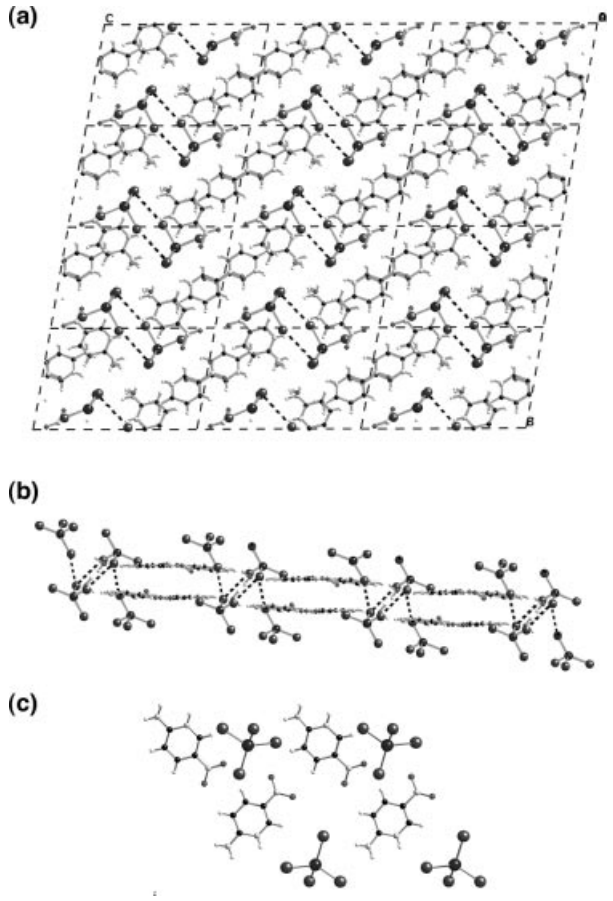

Figure 2. (a) *bc*-view of the $[(5NAP)_2CuBr_4{\cdot}H_2O]$ ionic crystal, where double-decked planes run along the *a*-axis (Br···Br contacts in the 3.9–4.1 Å range are indicated). (b) View along the *a*-axis of a double-decked plane. (c) *bc*-view of one of the two planes forming the double-decked planes, where the $5NAP^+$ cations surround the $CuBr_4^{2-}$ anions in a T-shaped disposition.

The only available experimental data on the magnetic properties of this crystal are magnetic susceptibility measurements.[3] The experimental $\chi(T)$ data were fitted to a two-legged spin-ladder model based on two facts: (i) the magnetic pathways between $CuBr_4^{2-}$ radicals were expected to be through-space (by means of short Br···Br contacts), and (ii) the shortest Cu···Cu (and Br···Br) contacts showed the topology of a two-legged spin-ladder [see Figure 3 (b)]. The expression used for fitting the experimental $\chi(T)$ data for the spin-ladder was derived by extensive Monte Carlo calculations using a Heisenberg Hamiltonian that included both J_{rung} and J_{rail} at an arbitrary ratio of the two interactions.[3c] Johnston et al.[3c] have obtained two different expressions for the spin-ladder susceptibility, depending on the ratio J_{rung}/J_{rail}. Both expressions were applied to fit the experimental data without knowing in advance the ratio of the exchange parameters. The dominant rung expression ($|J_{rung}| > |J_{rail}|$) gave an excellent description of our data with the reported J_{rung} = –14.16 cm^{-1} and J_{rail} = –13.59 cm^{-1};[3a] the dominant rail expression ($|J_{rung}| < |J_{rail}|$) would not converge, yielding a susceptibility curve of entirely the wrong shape, for any combination of parameters.

 © 2005 Wiley-VCH Verlag GmbH & Co. KGaA, Weinheim

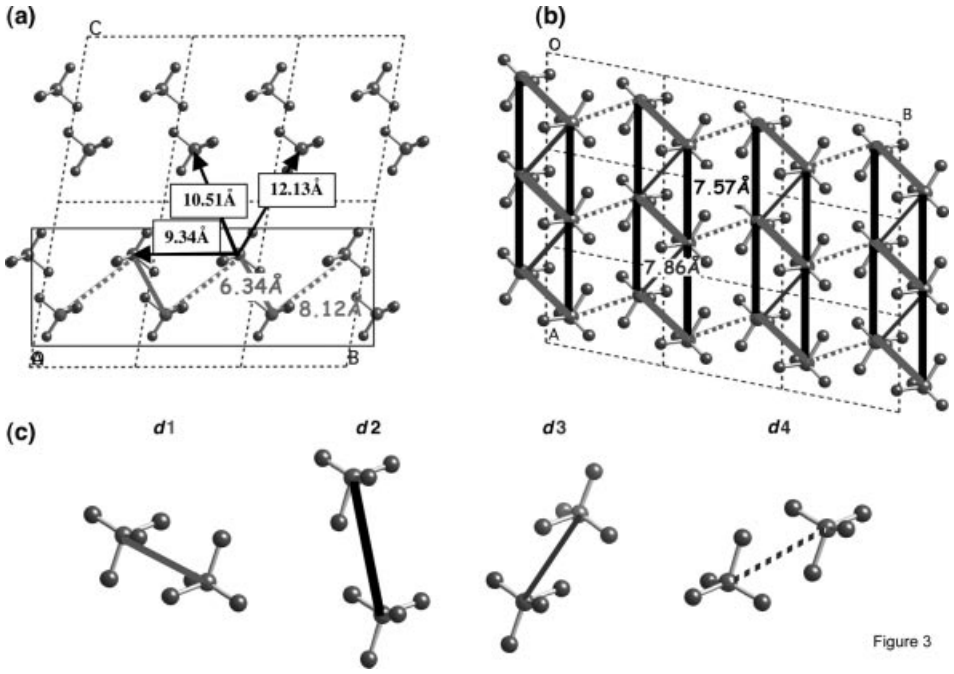

Figure 3. Views of the $CuBr_4^{2-}$ anion within the structure of the $[(5NAP)_2CuBr_4{\cdot}H_2O]$ crystal along (a) the *bc* and (b) the *ab* crystallographic axes. Note that the Cu···Cu distances for all *di* radical pairs are given. The topology of a two-legged ladder is clearly envisaged. (c) Selected *di* radical pairs verifying a spin-carrier interradical distance cutoff of 8.5 Å (see Table 1 for details on main distances).

At this point, it is essential to stress that, although a ladder model was explicitly used to fit the experimental available $\chi(T)$ data by means of J_{rung} and J_{rail}, it could not get the origin of these *J*'s. As we will show shortly, we can contribute to explicitly get the origin of J_{rung} and J_{rail} by identifying the radical pairs that are responsible for such microscopic magnetic interactions.

Keeping in mind the packing described above for the $[(5NAP)_2CuBr_4{\cdot}H_2O]$ crystal, we can now start the first-principles, bottom-up study of the magnetism of this crystal. On the basis of calculations that show that the $CuBr_4^{2-}{\cdots}CuBr_4^{2-}$ magnetic interaction becomes negligible at Cu···Cu distances above 8.5 Å, in step (1) we selected all $CuBr_4^{2-}{\cdots}CuBr_4^{2-}$ pairs with Cu···Cu distances shorter than 8.5 Å [see Figure 3 (a) and (b)]. This resulted in the four $CuBr_4^{2-}{\cdots}CuBr_4^{2-}$ pairs depicted in Figure 3 (c) whose Cu···Cu distances are 6.34, 7.57, 7.86, and 8.12 Å [the next three pairs of radicals have Cu···Cu pair distances of 9.34, 10.51, and 12.13 Å, see Figure 3 (a)]. Each radical–radical pair is identified as *d*1–*d*4, according to an increasing ordering of the Cu···Cu distance (Table 1 contains the values of the main intermolecular parameters).

We can now proceed to step (2) and compute the value of J_{AB} for all *di* radical–radical pairs selected in step (1). As mentioned above, these parameters are obtained by subtracting the total energy of the singlet and triplet states for each *di* radical–radical pair at its crystal geometry. One could think of doing such a calculation using an $(anion)_2$ cluster, but numerical tests (see Table 1 and discussion below) indicated that the $(anion)_2$ cluster does not properly reproduce the electronic structure of the radical anions within the crystal and that one has to include in the calculation at least the first-neighboring cations of the radical-anion pairs of interest. Therefore, the calculation must be done on an $(anion)_2(cation)_x$ cluster. As the crystal is neutral, we selected four cations to build a neutral $(anion)_2(cation)_4$ cluster (note that, in this case, the anions have a –2 charge and the cations have +1 charge). The inclusion of the cations also has an extra advantage as it automatically takes into account the possible participation of the diamagnetic cations in the through-space radical–radical magnetic interaction.

Table 1. Values of the Cu···Cu and shortest Br···Br distances for the four $CuBr_4^{2-}{\cdots}CuBr_4^{2-}$ radical–radical pairs of the $[(5NAP)_2CuBr_4{\cdot}H_2O]$ crystal having a Cu···Cu distance smaller than 8.5 Å [see Supporting Information Figure S1 for the actual geometry of the *d*1–*d*4 $(anion)_2(cation)_4$ clusters used to compute *J*(*di*)]. Also included are the values of the *J*(*di*) parameters for each pair.

di	Cu···Cu [Å]	Br···Br [Å]	Model	*J*(*di*) [cm^{-1}]
*d*1	6.34	4.07(2) – 4.25 – 5.98(2)	$(anion)_2$	–43.54
			$(anion)_2(cation)_4$	–19.73
*d*2	7.57	3.93 – 6.00 – 6.32	$(anion)_2$	–28.38
			$(anion)_2(cation)_4$	–22.17
*d*3	7.86	4.68 – 4.94(2) – 7.26	$(anion)_2$	+0.18
			$(anion)_2(cation)_4$	–0.85
*d*4	8.12	5.24(2) – 6.13 – 6.62	$(anion)_2$	–0.79
			$(anion)_2(cation)_4$	–0.31

There is more than one form of selecting four cations for each di radical–radical pair [see Figure 3 (c) for *d*1–*d*4]. Therefore, we have to evaluate the effect that such selection has on the computed J_{AB} values [hereafter *J*(*di*)]. We did this evaluation for all four pairs, but we only report the results for *d*1, as the trends are similar in all cases. The test was done using the three $(anion)_2(cation)_4$ clusters shown in

 © 2005 Wiley-VCH Verlag GmbH & Co. KGaA, Weinheim

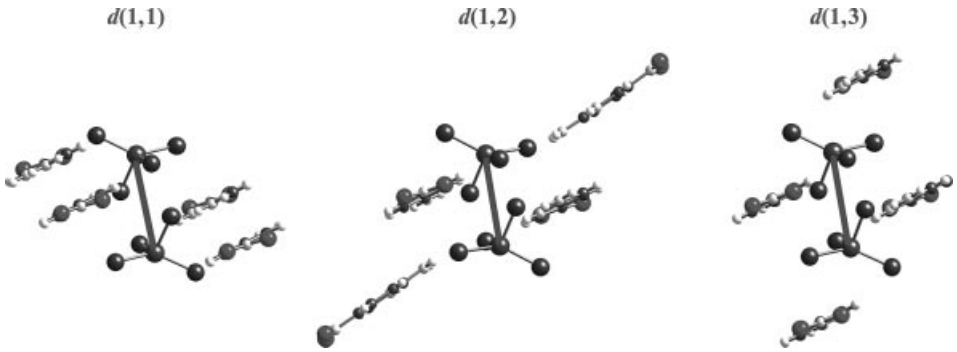

Figure 4. Geometry of the various $(anion)_2(cation)_4$ clusters used to evaluate the effect of the selected cations on the computed $J(d1)$ value.

Figure 4, identified as $d(1,1)$, $d(1,2)$, and $d(1,3)$. The results collected in Table 2 show a change smaller than 3 cm^{-1} in the computed $J(d1)$ value. We also tested the effect that the Madelung field[9] generated by the rest of the crystal has on the computed $J(d1)$ value. For the specific case of the $d(1,2)$ cluster (see Figure 4), the computed $J(d1)$ value accounting for the Madelung field is –19.84 cm^{-1}, while without this field it is –19.73 cm^{-1}. Due to the small impact of the inclusion of the Madelung field, we did not evaluate its effect on the other di radical–radical pairs. Finally, we can discuss the origin of the difference between the $J(d1)$ results obtained using either an $(anion)_2(cation)_4$ model [e.g. the $d(1,2)$ cluster] or an only an $(anion)_2$ cluster (J_{AB} values of –19.73 and –43.54 cm^{-1}, respectively). To test if this difference is due to the lack of electrostatic confinement induced by the cations in the anion wavefunction, we did further calculations to mimic such electrostatic effects by using point atomic charges (fitted to reproduce the electrostatic potential of the nuclei of the isolated cations) instead of the atoms themselves. The computed J_{AB} value was –26.60 cm^{-1}, which differs by 6.87 cm^{-1}, in absolute terms, from the computed J_{AB} using the $d(1,2)$ $(anion)_2(cation)_4$ cluster. Such small difference can be attributed to two factors: (a) the use of point charges does not reproduce the Pauli repulsion (due to the Pauli Exclusion Principle) induced by the electrons of the cations on the electrons of the anions, and (b) the presence of a cation-mediated through-space interaction, where the cation orbitals are used to magnetically connect the anions (a sort of superexchange through-space mechanism). It is difficult to evaluate the relative importance of each factor accurately, but in any case our results indicate that it is safer to use $(anion)_2(cation)_4$ clusters to include both a proper description of the anions' environment and any possible cation-mediated exchange.

Table 2. Dependence of the computed $J(d1)$ value on the selected cations included in the $(anion)_2(cation)_4$ cluster. The values are for the $d(1,1)$, $d(1,2)$, and $d(1,3)$ $(anion)_2(cation)_4$ clusters shown in Figure 4.

d(1,*j*)	$J(d1,j)$ [cm^{-1}]	Model
$d(1,1)$	–19.05	$(anion)_2(cation)_4$
$d(1,2)$	–19.73	$(anion)_2(cation)_4$
	–19.84	$(anion)_2cation_4$ + Madelung (ref.[16])
$d(1,3)$	–16.18	$(anion)_2(cation)_4$

Table 1 shows the all computed $J(di)$ values using appropriate $(anion)_2(cation)_4$ clusters. All four $J(di)$ magnetic interactions are antiferromagnetic, with $J(d1)$ and $J(d2)$ almost identical and much larger than the values of $J(d3)$ and $J(d4)$. These results show that there is no direct correspondence between the Cu···Cu and Br···Br distances and the size of the $J(di)$ parameter. The value and connectivity of the $J(di)$ magnetic interactions define the magnetic topology of the $[(5NAP)_2CuBr_4{\cdot}H_2O]$ crystal (see Figure 5). The main magnetic motif consists of two-legged spin-ladders along the crystallographic *a*-axis, where $J_{rail} = J(d2) =$ –22.17 cm^{-1} and $J_{rung} = J(d1) =$ –19.73 cm^{-1}. Within any individual two-legged spin-ladder there is a small diagonal magnetic interaction, $J(d3) =$ –0.85 cm^{-1}, and adjacent two-legged spin-ladders interact very weakly along the *b*-axis through $J(d4) =$ –0.31 cm^{-1}. Therefore, the magnetic topology of $[(5NAP)_2CuBr_4{\cdot}H_2O]$ seems to be better described as consisting of isolated two-legged spin-ladders (a 1D topology), but could also be described as a set of noninteracting *ab*-planes, each formed by weakly interacting, two-legged spin-ladder motifs (a 2D topology). Below, we will show the results of numerical simulations that indicate that the 1D topology gives a proper description of the magnetism for $[(5NAP)_2CuBr_4{\cdot}H_2O]$.

To perform steps (3) and (4) of the bottom-up procedure, we have to select a minimal magnetic model space. For an isolated two-legged spin-ladder, based on previous work,[7] we expect that a four-sites (4s) model [Figure 6 (a)] should be an appropriate minimal magnetic model space. For $[(5NAP)_2CuBr_4{\cdot}H_2O]$, we will validate this model by studying the convergence of the macroscopic magnetic susceptibility $\chi(T)$ values when the minimal 4s model is replicated along the three crystallographic axes. Thus, the 4s model is propagated along (i) the *a*-axis, obtaining the 6s, 8s, ..., up to 14s models [Figure 6 (a)], and (ii) the *b*-axis by selecting the 4s4s and 4s4s4s models [Figure 6 (b)]. No replication is required along the *c*-axis, as there are no J_{AB} magnetic interactions along this direction, therefore the propagated model gives exactly the same results as the 4s model. As a further test, we also propagated the 4s4s model along the *a*-axis to generate the 6s6s and 8s8s models. The matrix

 © 2005 Wiley-VCH Verlag GmbH & Co. KGaA, Weinheim

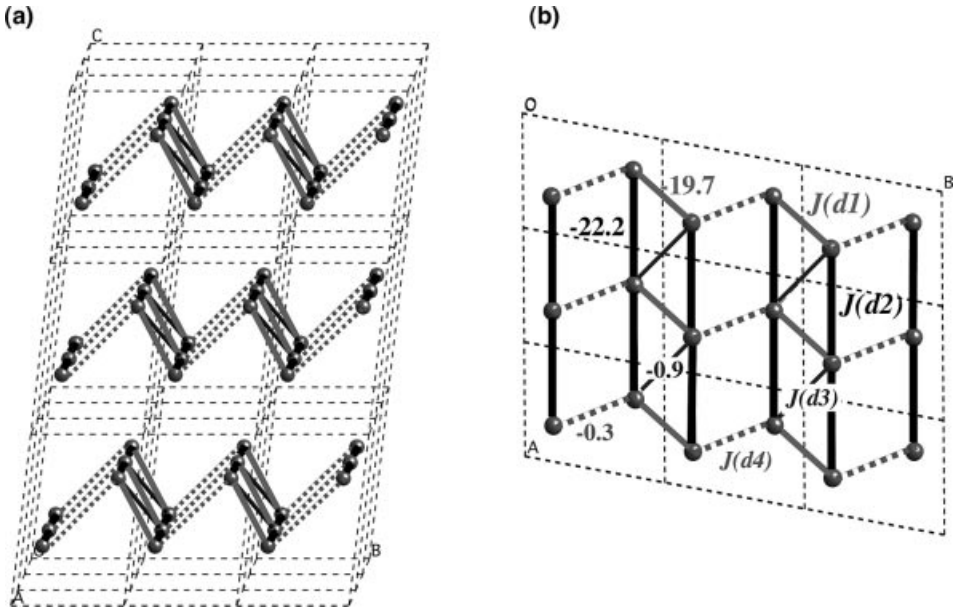

Figure 5. Magnetic topology of the $[(5NAP)_2CuBr_4{\cdot}H_2O]$ crystal: (a) magnetically noninteracting *ab*-layers; (b) magnification of any given *ab*-layer, which consists of two-legged spin-ladder motifs with $J(d2) = -22.2\ cm^{-1}$ as rail and $J(d1) = -19.7\ cm^{-1}$ as rung magnetic interactions. Within any individual two-legged spin-ladder there is a small diagonal magnetic interaction, $J(d3) = -0.9\ cm^{-1}$, and adjacent two-legged spin-ladders interact very weakly along the *b*-axis through $J(d4) = -0.3\ cm^{-1}$.

representation of the Heisenberg Hamiltonian was built[11] and diagonalized for all these model spaces. The resulting energy levels and corresponding spin quantum numbers were then used to calculate the magnetic susceptibility $\chi(T)$ (see Figure 6).

The simulated $\chi(T)$ data shown in Figure 6 allow us to conclude: (i) all the $\chi(T)$ curves show a shape similar to the experimental curve; (ii) there is a good convergence on $\chi(T)$ as the size of the model increases by propagating the minimal 4s model along both the *a*-axis [Figure 6 (a)], and the

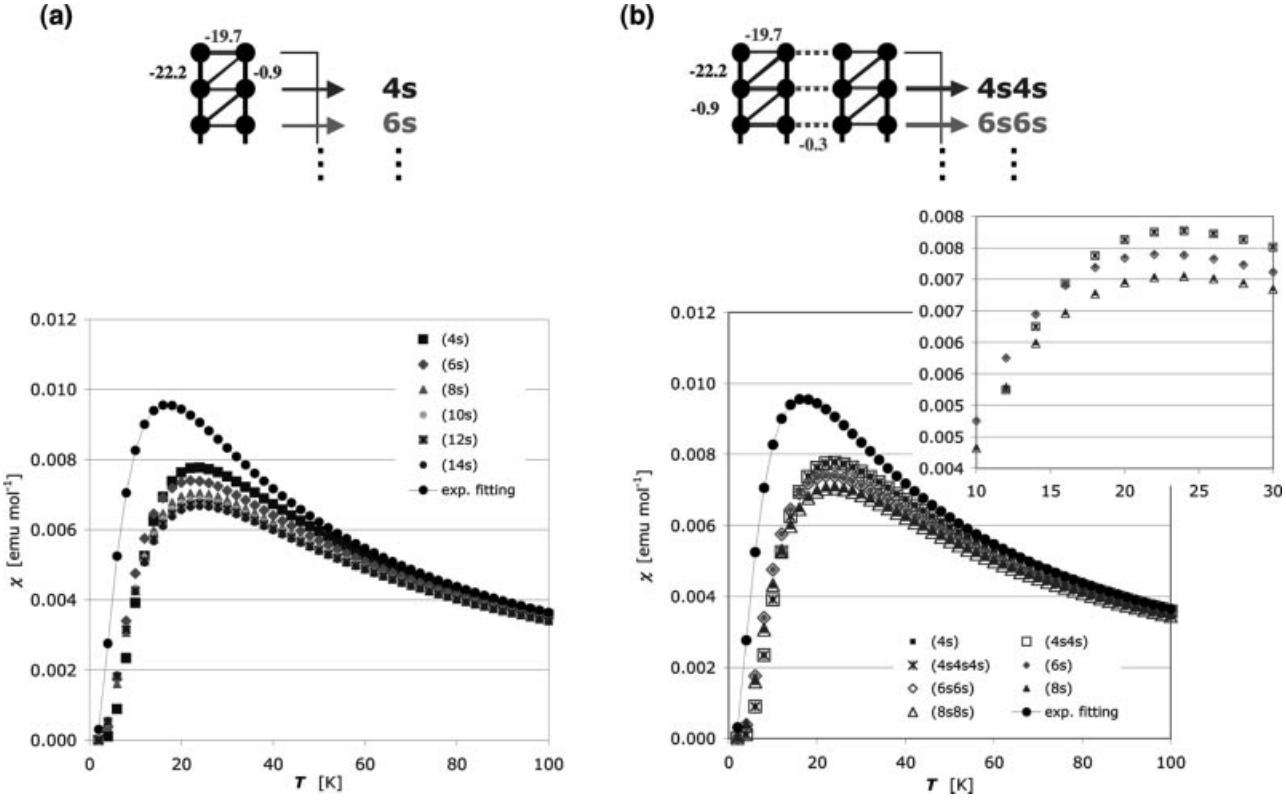

Figure 6. Magnetic susceptibility $\chi(T)$ numerically calculated values extending the minimal 4s magnetic model along the (a) *a*-axis (intra spin-ladder 6s–14s models) and (b) *b*-axis (inter spin-ladder 4s4s, 4s4s4s, 6s6s and 8s8s models).

 © 2005 Wiley-VCH Verlag GmbH & Co. KGaA, Weinheim

b-axis [Figure 6 (b)]; and (iii) the $\chi(T)$ values obtained with the inter-ladder *nsn*s models reproduce the $\chi(T)$ values obtained using the intra-ladder *ns* models perfectly [Figure 6 (b)], thus suggesting that there is no need to account for $J(d4)$ in the minimal magnetic model space. The latter conclusion is the final indication that our magnetic topology consists of basically noninteracting spin-ladders, i.e. it is a 1D topology.

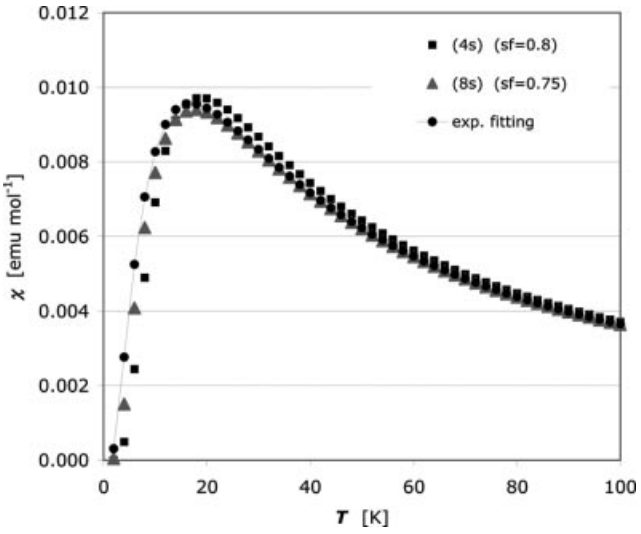

Figure 7. Required scaling factor (sf) to quantitatively reproduce the experimental magnetic susceptibility $\chi(T)$ data using both a 4s and an 8s model.

Although in all cases the shape of the computed magnetic susceptibility curves closely resembles the experimental curve, the agreement is not perfect. Previous studies[7] have suggested that such a difference can be attributed to various factors: (i) the use of high-temperature crystal structures, (ii) errors due to the use of a nonexact DFT functional and the broken-symmetry approach, and (iii) the use of a cluster approximation to compute the values of the $J(di)$ parameters, which neglects possible collective effects. In the case of $[(5NAP)_2CuBr_4{\cdot}H_2O]$, the crystal structure used throughout this study was determined at 163 K, which is a low enough temperature as to expect only small distortions due to temperature factors. We have also found[7] that it is possible to account for the difference between computed and experimental magnetic susceptibility curves by applying a constant linear scaling factor to all energy levels. For $[(5NAP)_2CuBr_4{\cdot}H_2O]$, when we apply a factor of 0.8 to all energy levels of the 4s minimal model we can quantitatively reproduce the experimental $\chi(T)$ curve (Figure 7). However, an even better agreement is found by applying a linear scaling factor of 0.75 to the 8s model (Figure 7).

A final test of the quality of the first-principles, bottom-up procedure in describing the properties of two-legged spin-ladder systems consists of computing the value of the singlet–triplet spin-gap (experimental data[3,12] indicate that

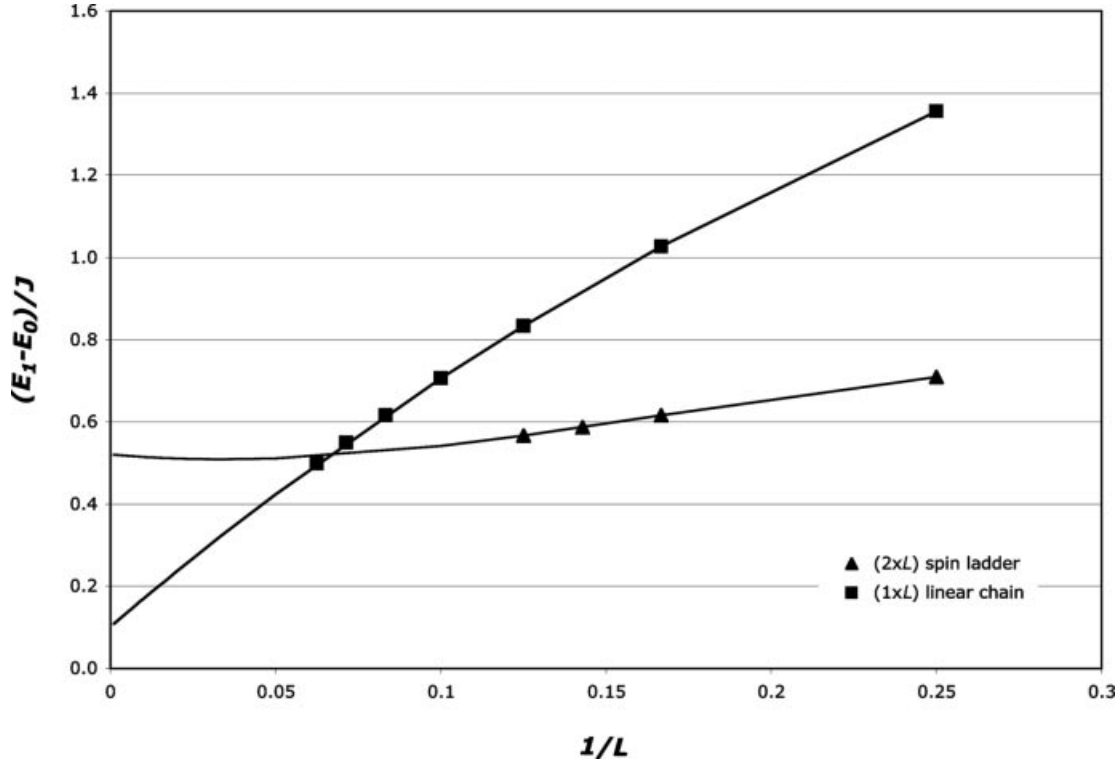

Figure 8. Values of $\Delta = (E_1 - E_0)/J$ as a function of the length of both a two-legged (2xL, with L = 4–8) and a single-legged (1xL, with L = 4–16) spin-ladder. In both cases the Δ values vary as $1/L$. In the limiting case of an infinite, two-legged spin-ladder the extrapolated Δ value is 0.5211. For an antiferromagnetic single-legged spin-ladder (i.e. a linear chain), the extrapolated result of Δ for the infinite chain (i.e. $1/L = 0$) is 0.1015, which is slightly larger than the expected zero value.

 © 2005 Wiley-VCH Verlag GmbH & Co. KGaA, Weinheim

it should be 11 K) and its changes with the size of the model space. For a two-legged spin-ladder, previous studies indicate that there is a finite spin-gap[2] whose value decreases as the size of the model space increases.[2] Using the 4s magnetic model space with a linear scaling factor of 0.8, the computed value of the singlet–triplet spin gap ($E_1 - E_0$) is 24.24 K, about twice the experimental value. However, it decreases to 17.0 K when using the 8s model with a linear scaling factor of 0.75. Furthermore, as shown in Figure 8, the value of the expression $\Delta = (E_1 - E_0)/J$ decreases with the ladder length (2xL, with L = 4–8) as 1/L, as reported in the literature.[2] Extrapolating our fitted results to an infinite two-legged spin-ladder we found a Δ value of 0.5211 (see Figure 8), which agrees well with the best estimates (0.504) of this property.[2] As a further test, we also computed the value of $\Delta = (E_1 - E_0)/J$ for an antiferromagnetic single-legged spin-ladder (that is, a linear chain) for lengths L = 4–16. For an infinite linear chain, Δ is expected to be zero.[2] The results, also shown in Figure 8, follow a similar trend with respect to 1/L to those reported in the literature:[2] as L increases, the value of Δ approaches zero. However, our extrapolated result of Δ for the infinite chain (i.e., 1/L = 0) is 0.1015, which is slightly larger than zero. This small deviation is due to the fact that it may be necessary to look at a chain as long as 100 spins to actually see the gap vanish,[2] and this is obviously out of the reach of our current code. However, we have successfully described the main trends known for the spin-gap of the two main classes of spin-ladders. Consequently, we can conclude that our first-principles, bottom-up procedure properly describes the experimentally known properties of spin-ladder magnets.

Conclusions

Using the X-ray crystal structure determined at 163 K, we have computed the magnetic interactions in the [$(5NAP)_2CuBr_4 \cdot H_2O$] crystal. There are two dominant antiferromagnetic interactions, whose magnetic topology is found to consist of noninteracting, two-legged spin-ladders, with similar values for the rail $J(d2)$ (–22.2 cm^{-1}) and rung $J(d1)$ (–19.7 cm^{-1}) magnetic interactions. It is essential to stress that our contribution has been to explicitly get the origin of J_{rung} and J_{rail} by identifying the $(anion)_2(cation)_4$ clusters that are responsible for such microscopic magnetic interactions. The magnetic topology is in agreement with the experimentally proposed magnetic pathways, which were based only on the crystal packing of the $CuBr_4^{2-}$ radical-anions within the [$(5NAP)_2CuBr_4 \cdot H_2O$] crystal. However, we believe that the exchange interaction between Cu^{2+} ions does not only result from Br···Br direct contacts, but also from $5NAP^+ \cdots CuBr_4^{2-}$ contacts, since the organic ligands play the role of spin couplers.

The simulated $\chi(T)$ data reproduce the shape of the experimental $\chi(T)$ curve, although a linear scaling factor of about 0.75 is required to quantitatively reproduce the experimental values. Such a factor compensates for the use of a high-temperature (163 K) X-ray crystal structure and errors associated with the quantum chemical methods employed to compute the $J(di)$ parameters.

We have computed the singlet–triplet spin-gap ($E_1 - E_0$) for [$(5NAP)_2CuBr_4 \cdot H_2O$] two-legged spin-ladder and found it to be in the range of the experimental results (11 K). Furthermore, the values of $\Delta = (E_1 - E_0)/J$ show the same dependence on 1/L (L being the length of the spin-ladder) as reported in the literature: for a two-legged spin-ladder Δ decreases towards 0.5211 as 1/L tends to zero, while for a single-legged spin-ladder Δ approaches a value near zero (we believe that the small differences with the tabulated results[2] are due to the fact that it may be necessary to look at a chain as long as 100 spins to actually see the gap vanish, which is out of the reach of our current code).

Computational Data

The basic idea behind our first principles, bottom-up procedure[4] is to find a finite model space that properly describes the properties of the magnetic topology of the crystal. Within this space we then compute the matrix representation of the Heisenberg Hamiltonian (1)

$$\hat{H} = -\sum_{A,B}^{N} J_{AB}(2\hat{S}_A \cdot \hat{S}_B + \tfrac{1}{2}\hat{I}_{AB}) \quad (1)$$

where $\hat{S}_A$ is the spin operator associated with radical A, and $\hat{I}_{AB}$ the identity operator. Note that the only variables in this Hamiltonian are the microscopic J_{AB} parameters, which define the nature and size of the radical–radical magnetic interactions present in our model space. These microscopic J_{AB} parameters depend on the relative orientation of the radicals A and B, and can be computed using the appropriate quantum chemical methods. Once the matrix representation of the Heisenberg Hamiltonian is known, we can compute the energy spectrum of all spin states, and then apply the corresponding statistical mechanics expressions to compute the macroscopic magnetic properties of interest [$\chi(T)$, $C_p(T)$, ...]. Note that the individual energy values obtained by diagonalizing expression (1) are equivalent to those obtained using the more familiar $\hat{H} = -2\Sigma J_{AB}\hat{S}_A \cdot \hat{S}_B$ Heisenberg Hamiltonian, except for a shift in all energy values. Therefore, the corresponding energy differences will be the same. As the statistical mechanics expressions used to compute $\chi(T)$ and $C_p(T)$ use energy differences, both Hamiltonians give the same macroscopic results.

The entire procedure depends only on the microscopic radical–radical magnetic interactions (J_{AB}). The values of the J_{AB} parameters are also used to define the magnetic topology in terms of the connectivity that the J_{AB} parameters establish between the radicals that form the crystal. The magnetic topology provides a very useful pictorial representation of the magnetism within the crystal.

The minimal magnetic model space must be small enough to keep the Heisenberg Hamiltonian matrix at a reasonable size (in our current implementation $N \leq 16$ spin radical sites), but it must also be large enough to contain all significant magnetic pathways detected within the crystal. From our experience, the most important step in the above procedure is the selection of a proper minimal magnetic model space. In order to legitimate the selected minimal magnetic model space, we check the convergence of macroscopic properties [e.g. $\chi(T)$] as the model space is replicated along the three crystallographic directions by applying a regionally reduced density matrix approach: if the minimal magnetic model space is properly

 © 2005 Wiley-VCH Verlag GmbH & Co. KGaA, Weinheim

chosen, the computed $\chi(T)$ values using such extended models should rapidly converge to the values obtained with the non-replicated minimal model space. All sets of results should also numerically reproduce the experimental $\chi(T)$ data.

As indicated above, the values of the microscopic J_{AB} pair interactions are computed using quantum chemical methods. In the $[(5NAP)_2CuBr_4{\cdot}H_2O]$ crystal, the $CuBr_4^{2-}$ anions are the only spin-carrier units; the $5NAP^+$ cations are closed-shell molecules with no spin whose primary function in the crystal is to act as spacers of the $CuBr_4^{2-}$ spin-carrier units. The ground electronic state of $CuBr_4^{2-}$ anions is a doublet, with the spin partially distributed over the bromine and Cu^{II} atoms (Figure 1, b). As the radicals are doublets, the value of J_{AB} is obtained by subtracting the energy of the most stable open-shell singlet (E^S_{BS}) and triplet (E^T) states, both computed at the geometry of the radical–radical pair found in the crystal, according to Equation (2).

$$J_{AB} = E^S_{BS} - E^T \quad (2)$$

The broken-symmetry approximation[13,14] is used to compute the energy of the open-shell singlet state. The E^S_{BS} and E^T energy values have been computed using the UB3LYP functional[15] (a 10^{-8} convergence criterion on the total energy and 10^{-10} on the integrals was used to ensure enough accuracy in the computation of the J_{AB} parameters). All DFT calculations performed in this study were carried out using the Gaussian-03 package.[16] We used in our calculations an Ahlrichs all-electron basis set[17] for Cu, and a 6-31+G basis set[18] for C, H, N, and O. For Br^-, we used the 6-31+G(d) basis set.[19]

Supporting Information: Table S1 shows the charges computed according to a Merz–Singht–Kollman scheme and employed to account for the Madelung field created by the nearest-neighboring $CuBr_4^{2-}$ anions and $5NAP^+$ cations to the *d*(1,*2*) $(anion)_2(cation)_4$ cluster. Figure S1 shows the final geometry of *d*1–*d4* of the $(anion)_2(cation)_4$ clusters used to compute *J*(*di*).

Acknowledgments

M. D. and J. J. N. acknowledge the Spanish "Ministerio de Ciencia y Tecnología" (BQU2002-04587-C02-02), and the Catalan "CIRIT" (2001SGR-0044) for funding. The authors also thank the CEPBA-IBM Research Institute, CEPBA and CESCA for allocation of CPU time on their computers. M. D. acknowledges the financial support of the "Ramón y Cajal" Program of the Spanish "Ministerio de Educación y Ciencia". G. G. acknowledges the European Union for funding within the "Transnational Access of HPC-Europe" Program (RII3-CT-2003-506079). M. M. T. and C. P. L. acknowledge financial support from the NSF (USA) grant DMR-9803813.

[1] a) *Magnetic Molecular Materials* (Eds.: D. Gatteschi, O. Kahn, J. S. Miller, F. Palacio), NATO ASI Series, Kluwer, Dordrecht, **1991**; b) J. S. Miller, A. J. Epstein, *Angew. Chem.* **1994**, *106*, 399; *Angew. Chem. Int. Ed. Engl.* **1994**, *33*, 385; c) O. Kahn, *Molecular Magnetism*, VCH, New York, **1993**; d) *Molecular Magnetism: from Molecular Assemblies to the Devices* (Eds.: E. Coronado, P. Delhaès, D. Gatteschi, J. S. Miller), NATO ASI Series, Kluwer, Dordrecht, **1996**; e) *Magnetic Properties of Organic Materials* (Ed.: P. M. Lahti), Marcel Dekker, New York, **1999**; f) *Molecular Magnetism: New Magnetic Materials* (Eds.: K. Itoh, M. Kinoshita), Gordon and Breach, Amsterdam, **2000**; g) *π-Electron Magnetism: From Molecules to Magnetic Materials* (Ed.: J. Veciana), Structure and Bonding, vol. 100, Springer, **2001**; h) *Magnetism: Molecules to Materials (I–IV)* (Eds.: J. S. Miller, M. Drillon), Wiley-VCH, Weinheim, **2003**.

[2] a) E. D. Dagotto, T. M. Rice, *Science* **1996**, *271*, 618; b) B. Frischmuth, B. Ammon, M. Troyer, *Phys. Rev. B* **1996**, *54*, R3714; c) M. Greven, R. J. Birgeneau, U.-J. Wiese, *Phys. Rev. Lett.* **1996**, *77*, 1865; d) T. Barnes, E. Dagotto, J. Riera, E. S. Swanson, *Phys. Rev. B* **1993**, *47*, 3196; e) E. Dagotto, J. Riera, D. Scalapino, *Phys. Rev. B* **1992**, *45*, 5744; f) S. R. White, R. M. Noack, D. J. Scalapino, *Phys. Rev. Lett.* **1994**, *73*, 886; g) M. Troyer, H. Tsunetsugu, D. Würtz, *Phys. Rev. B* **1994**, *50*, 13515; h) T. Barnes, J. Riera, *Phys. Rev. B* **1994**, *50*, 6817.

[3] a) C. Galeriu, M. A. Thesis, Dept. of Physics, Clark University, **2002**. Originally, a Heisenberg Hamiltonian such as $H = +\Sigma(J_{AB}{\cdot}S_A{\cdot}S_B)$ was used, and so positive *J* parameters correspond to antiferromagnetic interactions. Thus, in order to be consistent with Heisenberg Hamiltonian (1) we have translated J_{rung} and J_{rail} into –14.16 and –13.59 cm^{-1}, respectively; b) M. M. Turnbull, C. Galeriu, J. Giantsidis, C. P. Landee, *Mol. Cryst. Liq. Cryst.* **2002**, *376*, 469; c) Johnston et al.; the Monte Carlo expression used for fitting $\chi(T)$ data is available online at the archive website arXiv:cond-mat/0001147.

[4] M. Deumal, M. J. Bearpark, J. J. Novoa, M. A. Robb, *J. Phys. Chem. A* **2002**, *106*, 1299.

[5] The currently available magneto-structural correlations for through-space magnetic interactions, the so-called McConnell-I and McConnell-II mechanisms, lack a solid theoretical foundation and fail to properly describe the nature of the magnetic interactions in many crystals. For studies of these failures, see: a) M. Deumal, J. Cirujeda, J. Veciana, J. J. Novoa, *Adv. Mater.* **1998**, *10*, 1461; b) M. Deumal, J. Cirujeda, J. Veciana, J. J. Novoa, *Chem. Eur. J.* **1999**, *5*, 1631; c) M. Deumal, J. J. Novoa, M. J. Bearpark, P. Celani, M. Olivucci, M. A. Robb, *J. Phys. Chem. A* **1998**, *102*, 8404; d) C. Kollmar, O. Kahn, *Acc. Chem. Res.* **1993**, *26*, 259.

[6] In our first papers[4,7a–7c] we used the term "magnetic structure" for this property. In this paper we have re-named it as "magnetic topology" in order to avoid misunderstandings with experimental information related to polarized neutron diffraction measurements.

[7] a) M. Deumal, M. A. Robb, J. J. Novoa, *Polyhedron* **2003**, *22*, 1935; b) M. Deumal, C. P. Landee, J. J. Novoa, M. A. Robb, M. M. Turnbull, *Polyhedron* **2003**, *22*, 2235; c) M. Deumal, J. Ribas-Ariño, M. A. Robb, J. Ribas, J. J. Novoa, *Molecules* **2004**, *9*, 757; d) M. Deumal, M. J. Bearpark, M. A. Robb, Y. Pontillon, J. J. Novoa, *Chem. Eur. J.* **2004**, *10*, 6422.

[8] M. M. Turnbull, C. P. Landee, B. W. Wells, *Coord. Chem. Rev.* **2005**, in press.

[9] The Madelung field was taken into account by selecting all first nearest neighbors surrounding the two $CuBr_4^{2-}$ and four $5NAP^+$ clusters, i.e. 34 radical $CuBr_4^{2-}$ anions and 68 closed shell $5NAP^+$ cations, and attributing to the atoms of such molecules a Merz–Singht–Kollman charge (ref.[10]). The charges used are shown in Table S1.

[10] Electrostatic potential-derived charges according to the Merz–Singht–Kollman scheme: a) B. H. Besler, K. M. Merz Jr., P. A. Kollman, *J. Comput. Chem.* **1990**, *11*, 431; b) U. C. Singh, P. A. Kollman, *J. Comput. Chem.* **1984**, *5*, 129.

[11] The Heisenberg Hamiltonian (1) is used for diagonalization purposes in order to obtain all the energy eigenvalues required in the statistical mechanics expression of $\chi(T)$. For a numerical calculation of the energy eigenvalues, we use *J*(*di*)/2 values (–11.085, –9.865, –0.425, and –0.155 cm^{-1}) rather than *J*(*di*) values (–22.17, –19.73, –0.85, and –0.31 cm^{-1}) in Hamiltonian (1) in order to be consistent with the definition of *J*(*di*).

[12] The 11 K value for the singlet–triplet gap was determined experimentally using the equation: $(E_1 - E_0) = g{\cdot}\mu_B{\cdot}H_{C1}$, where *g* is the gyromagnetic factor ($g = 2.15$, for a polycrystalline sample), μ_B is the Bohr magneton, and H_{C1} is the critical field. The lower critical field was determined to be 7.6 T from the magnetization data collected at 0.65 K.

 © 2005 Wiley-VCH Verlag GmbH & Co. KGaA, Weinheim

[13] a) L. Noodlemann, *J. Chem. Phys.* **1981**, *74*, 5737; b) L. Noodlemann, E. R. Davidson, *Chem. Phys.* **1986**, *109*, 131.
[14] a) E. Ruiz, P. Alemany, S. Alvarez, J. Cano, *J. Am. Chem. Soc.* **1997**, *119*, 1297; b) R. Caballol, O. Castell, F. Illas, I. D. R. Moreira, J. P. Malrieu, *J. Chem. Phys. A* **1997**, *101*, 7860; c) M. Nishino, Y. Shigeta, T. Soda, Y. Kitagawa, T. Onishi, Y. Yoshioka, K. Yamaguchi, *Coord. Chem. Rev.* **2000**, *198*, 265; d) J.-M. Mouesca, *J. Chem. Phys.* **2000**, *113*, 10505; e) F. Illas, I. D. R. Moreira, C. de Graaf, V. Barone, *Theor. Chem. Acc.* **2000**, *104*, 265.
[15] a) A. D. Becke, *Phys. Rev. A* **1988**, *38*, 3098; b) C. Lee, W. Yang, R. G. Parr, *Phys. Rev. B* **1988**, *37*, 785; c) A. D. Becke, *J. Chem. Phys.* **1993**, *98*, 5648.
[16] M. J. Frisch, G. W. Trucks, H. B. Schlegel, G. E. Scuseria, M. A. Robb, J. R. Cheeseman, J. A. Montgomery Jr., T. Vreven, K. N. Kudin, J. C. Burant, J. M. Millam, S. S. Iyengar, J. Tomasi, V. Barone, B. Mennucci, M. Cossi, G. Scalmani, N. Rega, G. A. Petersson, H. Nakatsuji, M. Hada, M. Ehara, K. Toyota, R. Fukuda, J. Hasegawa, M. Ishida, T. Nakajima, Y. Honda, O. Kitao, H. Nakai, M. Klene, X. Li, J. E. Knox, H. P. Hratchian, J. B. Cross, C. Adamo, J. Jaramillo, R. Gomperts, R. E. Stratmann, O. Yazyev, A. J. Austin, R. Cammi, C. Pomelli, J. W. Ochterski, P. Y. Ayala, K. Morokuma, G. A. Voth, P. Salvador, J. J. Dannenberg, V. G. Zakrzewski, S. Dapprich, A. D. Daniels, M. C. Strain, O. Farkas, D. K. Malick, A. D. Rabuck, K. Raghavachari, J. B. Foresman, J. V. Ortiz, Q. Cui, A. G. Baboul, S. Clifford, J. Cioslowski, B. B. Stefanov, G. Liu, A. Liashenko, P. Piskorz, I. Komaromi, R. L. Martin, D. J. Fox, T. Keith, M. A. Al-Laham, C. Y. Peng, A. Nanayakkara, M. Challacombe, P. M. W. Gill, B. Johnson, W. Chen, M. W. Wong, C. Gonzalez, J. A. Pople, *Gaussian 03*, Revision B.04, Gaussian, Inc., Pittsburgh, PA, **2003**.
[17] Ahlrichs' pVDZ basis set: A. Schafer, H. Horn, R. Ahlrichs, *J. Chem. Phys.* **1992**, *97*, 2571.
[18] 6-31+G split-valence basis set: a) P. C. Hariharan, J. A. Pople, *Theor. Chim. Acta* **1973**, *28*, 213; b) M. M. Francl, W. J. Petro, W. J. Hehre, J. S. Binkley, M. S. Gordon, D. J. DeFrees, J. A. Pople, *J. Chem. Phys.* **1982**, *77*, 3654.
[19] 6-31+G(d) basis set: a) R. C. Binning Jr., L. A. Curtiss, *J. Comput. Chem.* **1990**, *11*, 1206; b) Primitive Exponents: T. H. Dunning Jr., *J. Chem. Phys.* **1977**, *66*, 1382.

Received: May 31, 2005
Published Online: October 25, 2005

 © 2005 Wiley-VCH Verlag GmbH & Co. KGaA, Weinheim

DOI: 10.1002/ejic.200500491

[MCl(ligand)]$^+$ Complexes (M = Ni, Pd, Pt) with a P,N,N Terdentate Ligand – Solid State and Solution Structures and Catalytic Activity of the Pd^{II} Derivative in the Heck Reaction

Alessandro Del Zotto,*[a] Ennio Zangrando,[b] Walter Baratta,[a] Alessandro Felluga,[a] Paolo Martinuzzi,[a] and Pierluigi Rigo[a]

Keywords: Nickel / Palladium / Platinum / Terdentate hybrid ligands / Heck reaction

Ni^{II}, Pd^{II} and Pt^{II} cationic complexes of the general formula [MCl(PNN)]PF_6, where PNN is the terdentate ligand *N*-[2-(diphenylphosphanyl)benzylidene][2-(2-pyridyl)ethyl]amine, have been synthesised and fully characterised in solution by NMR spectroscopy. The diamagnetic Ni^{II} complex **1** shows fluxionality, which can be attributed to a conformational rearrangement of the two six-membered chelate rings. On the contrary, the Pd^{II} **2** and Pt^{II} **3** derivatives are stereochemically rigid on the NMR timescale. The crystal structures of **1** and **2** are reported, which show a planar geometry for both complexes. Complex **2** has been investigated as a precatalyst in the Heck coupling between styrene and bromobenzene. Interestingly, the nature of the solvent has a critical role in determining the yield of the reaction product.
(© Wiley-VCH Verlag GmbH & Co. KGaA, 69451 Weinheim, Germany, 2005)

Introduction

In recent years, transition-metal complexes bearing multidentate ligands that contain significantly different types of hard (N- or O-) and soft (P-) donor functions have been extensively studied because of their potential application in homogeneous catalysis.[1] These ligands possess weakly coordinating groups that can be reversibly released during the catalytic cycle providing unsaturation at the metal centre. Thus, the less strongly bound moiety of this type of ligand, called hemilabile, can be seen as an intramolecular solvent molecule that is capable of temporarily holding a coordination site on the metal. There are several hemilabile ligands containing a substitutionally inert phosphorus function and a labile oxygen or nitrogen donor. Among the various kinds of P,N hybrid ligands, those showing pyridyl or imine arms have been widely used to prepare complexes of different transition metals,[1b,1c,1e,1f] some of which have been successfully employed in catalytic reactions. Thus, for example, Ni^{II} complexes have been tested in olefin polymerisation, while Pd^{II} complexes have been found to be very active in asymmetric allylic alkylation and cross-coupling reactions. Also, our group has worked in this field with particular interest in complexes with phosphane–pyridyl bidentate ligands.[2]

By contrast, few terdentate P,N,N-type ligands showing mixed functionalities such as phosphane-, imine- and pyridyl-donating groups have been reported so far.[3] The presence of two different sp^2 N-donors affects the way the ligand binds to the metal, with effects on both reactivity and catalytic activity of the resulting complexes. Effectively, some of these complexes have shown valuable efficiency in different catalysed reactions, such as enantioselective conjugate addition of diethylzinc to enones,[3e] olefin hydrogenation,[3f] asymmetric allylic alkylation[3h] and asymmetric olefin cyclopropanation.[3j]

Vrieze and co-workers have described the potentially terdentate P,N,N ligand *N*-[2-(diphenylphosphanyl)benzylidene][2-(2-pyridyl)ethyl]amine[4] (PNN) (Figure 1), which shows the P-sp^3, N-sp^2 (imine), N-sp^2 (pyridyl) donors sequence. Several different transition-metal complexes bearing PNN have been reported, in particular with group 10 metals,[4] the ligand acting as both terdentate[4–6] or bidentate with a dangling pyridyl arm.[4–6] Among these species, the Pd^{II} η^1-allyl cationic complex has shown good catalytic activity in allylic alkylation[4b] and 1,3-butadiene telomerisation with methanol.[7]

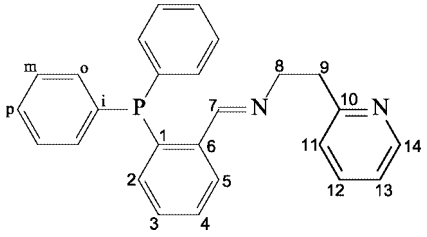

Figure 1. The ligand PNN along with the numbering scheme.

For our part, we decided to investigate the coordination chemistry of PNN towards group 10 metal halides, as the

[a] Dipartimento di Scienze e Tecnologie Chimiche, Universitá di Udine,
33100 Udine, Italy
E-mail: alessandro.delzotto@dstc.uniud.it
[b] Dipartimento di Scienze Chimiche, Università di Trieste,
34127 Trieste, Italy

 © 2005 Wiley-VCH Verlag GmbH & Co. KgaA, Weinheim

first step of a more detailed study on the catalytic properties of PNN-containing late transition-metal complexes. In this paper we present the preparation and characterisation of the cationic complexes [MCl(PNN)]PF_6 [M = Ni (**1**), Pd (**2**), Pt (**3**)], also describing preliminary results on the catalytic activity of **2** in the Heck C–C coupling[8] using aryl bromides as starting material (Scheme 1). The choice for this reaction was stimulated by the fact that PNN is able to stabilise Pd^0 species without the need of additional stabilising ligands[4b] and that the couple Pd^0/Pd^{II} is thought to be involved in the Pd-catalysed Heck reaction.[8]

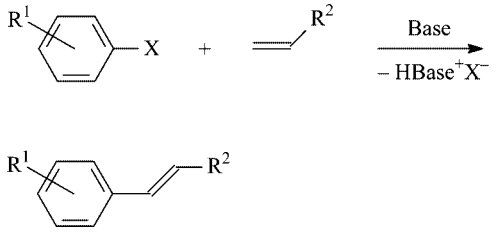

Scheme 1.

Complexes **1**–**3** have been fully characterised by spectroscopic and analytical methods. In addition, as the NMR investigation has evidenced that, unlike complexes **2** and **3**, the Ni^{II} derivative **1** is fluxional in the whole temperature range 293–183 K, the crystal structure determination of **1** and **2** has been performed to establish whether the different behaviour in solution of the two species could be related to structural modifications due to the nature of the metal ion.

Results and Discussion

The compound PNN was prepared as described in the literature[4b] and obtained as a cream-coloured powder after double recrystallisation from *n*-hexane. In the original publication,[4b] besides ^{31}P and ^{15}N NMR spectroscopic data, only selected ^1H and ^{13}C values were reported for PNN. Also two later papers dealt with selected ^1H NMR values only.[5,6] Therefore, we decided by means of $^1H\{^{31}P\}$, ^1H–^1H COSY, ^1H–^{13}C HETCOR, ^{13}C DEPT and ^{13}C PENDANT experiments to assess all ^1H (confirmed by computer simulation) and ^{13}C parameters. The ^1H and ^{13}C NMR spectroscopic data have been collected in Table 1 and Table 2, respectively, to allow a direct comparison with the data of complexes **1**–**3**. The numbering scheme of carbon and hydrogen atoms of PNN is reported in Figure 1.

Solution Structure of Complexes 1–3

Complexes [PdCl(PNN)]PF_6 (**2**) and [PtCl(PNN)]PF_6 (**3**) have been prepared by the room-temperature reaction between the appropriate [$MCl_2(RCN)_2$] precursor (M = Pd, R = CH_3; M = Pt, R = C_6H_5) and the ligand PNN in a 1:1 molar ratio in CH_2Cl_2 solution, followed by addition of an excess of NH_4PF_6 in propan-2-ol and vacuum elimination of CH_2Cl_2. The complexes were obtained pure as pale yellow crystals by recrystallisation from CH_2Cl_2/propan-2-ol. For both **2** and **3**, the best fit of the elemental analysis data is obtained for the formula [MCl(PNN)]$PF_6 \cdot 0.5CH_2Cl_2$. The presence of dichloromethane within the crystals has

Table 1. ^1H NMR values of the ligand PNN (in $CDCl_3$) and complexes **1**–**3** (in CD_2Cl_2) at 293 K.[a,b]

	H^2	H^3	H^4	H^5	H^7	H^8	H^9	H^{11}	H^{12}	H^{13}	H^{14}	H^{Ph}[c]
PNN[d]	7.93 m	7.37 m	7.24 m	6.87 m[e]	8.85 dt	3.88 dt	2.98 t	7.03 m	7.48 m	7.02 m	8.48 m	7.15–7.45 m
1				7.12 br. d	8.04 br. s	3.61 br. t	4.03 br. m		7.85 dt		8.72 br. d	7.30–7.85 m
2[f]	7.81 m			7.16 m	8.51 dt	3.93 m	3.47 m		7.93 m		8.83 m	7.36–7.74 m
3[g]	7.89 m			7.21 m	8.75 dt	4.07 m	3.50 m		8.00 m		8.81 m	7.42–7.72 m

[a] The numbering of the H atoms is shown in Figure 1. [b] The resonances not reported overlap with those of aromatic protons. [c] $H^{Ph} = H^o + H^m + H^p$. [d] Coupling constants in Hz: $J(H^2–H^3) = 7.7$; $J(H^2–H^4) = 1.6$; $J(H^3–H^4) = 7.5$; $J(H^3–H^5) = 1.3$; $J(H^4–H^5) = 7.6$; $J(H^5–H^7) = 4.7$; $J(H^7–H^8) = 1.3$; $J(H^{11}–H^{12}) = 7.7$; $J(H^{11}–H^{13}) = 1.5$; $J(H^{11}–H^{14}) = 0.8$; $J(H^{12}–H^{13}) = 7.5$; $J(H^{12}–H^{14}) = 1.9$; $J(H^{13}–H^{14}) = 4.8$; $J(H^{2_31}P) = 3.9$; $J(H^{3_31}P) = 0.5$; $J(H^{5_31}P) = 4.6$; $J(H^{7_31}P) = 4.7$; no splitting due to ^1H–^{31}P coupling is observed on the signal of H^4, as previously reported.[4b] [e] An uncorrected value (7.03) has been previously reported.[4b] [f] Coupling constants in Hz: $J(H^{2_31}P) = 2.1$; $J(H^{5_31}P) = 10.7$; $J(H^{7_31}P) = 1.7$; $J(H^{14_31}P) = 3.3$. [g] Coupling constants in Hz: $J(H^{2_31}P) = 2.2$; $J(H^{5_31}P) = 11.0$; $J(H^{7_31}P) = 0.5$; $J(H^{14_31}P) = 3.4$; $J(H^{7_195}Pt) = 115$; $J(H^{8_195}Pt) = 26$; $J(H^{14_195}Pt) = 25$.

Table 2. $^{13}C\{^1H\}$ NMR values of the ligand PNN (in $CDCl_3$) and complexes **1**–**3** (in CD_2Cl_2).[a,b]

	C^1	C^2	C^3	C^4	C^5	C^6	C^7	C^8	C^9	C^{10}	C^{11}	C^{12}	C^{13}	C^{14}	C^i	C^o	C^m	C^p
PNN[c]	139.5 [17.6]	127.6 [4.4]	128.8	130.1 [1.1]	133.3	137.3 [19.7]	160.3 [21.1]	60.8	39.4	159.8	123.4	136.0	121.1	149.2	136.2 [10.0]	133.9 [20.0]	128.5 [7.3]	128.7
1[d]	119.4 [44.0]	135.9 [8.2]	134.0 [7.0]	132.6	133.6	134.7 [13.5]	171.0 [7.6]	52.4	35.0	155.8	123.6	140.0	123.5	150.4	122.7 [56.9]	133.4 [11.6]	128.7 [11.7]	132.3
2[c]	120.0 [50.5]	138.1 [8.8]	135.3 [8.2]	134.1 [2.9]	134.6 [2.9]	136.2 [15.3]	168.0 [8.5]	57.1	37.6	158.2	125.1 [3.5]	141.0	124.2 [2.9]	151.7 [1.2]	125.2 [62.8]	134.3 [11.2]	129.6 [12.3]	133.1 [2.9]
3[c]	120.4 [59.9]	137.7 [8.8]	135.2 [8.2]	133.9 [2.3]	134.0 [3.5]	136.2 [13.5]	166.6 [7.6]	57.5	37.8	158.3	125.1 [3.5]	141.5	124.6 [3.5]	151.5 [1.2]	125.2 [70.4]	134.3 [11.1]	129.3 [12.3]	132.8 [2.9]

[a] The numbering of the C atoms is shown in Figure 1. [b] $J(^{13}C–^{31}P)$ in Hz are reported in brackets. [c] At 293 K. [d] At 183 K.

 © 2005 Wiley-VCH Verlag GmbH & Co. KGaA, Weinheim

been confirmed by ^{1}H NMR analysis and crystal structure determination of complex **2** (see below).

The ^{1}H NMR spectra of **2** and **3**, which are very similar, indicate that the structures of the cations are static on the NMR timescale. Meaningful shifts of some resonances can be observed upon coordination of the ligand to the metal centre (Table 1). For example, the signal of the H^9 proton, which is at δ = 2.98 in the free ligand, is shifted to lower fields in complexes **2** (δ = 3.47) and **3** (δ = 3.50), while that of the H^8 proton does not show an appreciable shift. Furthermore, both methylene signals of the –CH_2CH_2– chain appear as unsymmetric multiplets whose lines have about the same intensity. This spectral feature is diagnostic of the presence of diastereotopic pairs of protons within each methylene group, arising from the rigidity of the chelate N,N ring. The H^7 resonance, which is at δ = 8.85 in the free ligand, is shifted to higher fields in complexes **2** (δ = 8.51) and **3** (δ = 8.75). On the contrary, the H^{14} resonance, which is at δ = 8.48 in the free ligand, is markedly shifted to lower fields (**1**, δ = 8.83; **2**, δ = 8.81 ppm).

In the free ligand, H^2, H^3, H^5 and H^7 protons are coupled to the ^{31}P nucleus. In complexes **2** and **3** the ^{1}H–^{31}P coupling constants are not lost but considerably modified. In particular, the $^4J(^1H–^{31}P)$ value on H^7, which is 4.7 Hz in free PNN, is reduced to 1.7 Hz in **2** and 0.5 Hz in **3**. This observation contrasts with the lack of coupling between H^7 and ^{31}P nuclei found in previously reported Pd^{II} and Pt^{II} complexes bearing PNN.[4b] It is worth noting that also H^{14} shows a coupling with phosphorus both in **2** [$^4J(^1H–^{31}P)$ = 3.3 Hz] and **3** [$^4J(^1H–^{31}P)$ = 2.9 Hz]. This feature again confirms that the pyridyne nitrogen of the ligand is coordinated to the metal centre.

Interestingly, the H^7, H^8 and H^{14} resonances in the spectrum of **3** show the presence of satellites due to ^{1}H–^{195}Pt coupling. While H^8 and H^{14} show similar low ^3J values (28 and 26 Hz, respectively), the coupling constant on H^7 is 115 Hz. As can be seen in Figure 2, these hydrogen atoms are the closest to the metal centre, all others being separated from it by four or more bonds. The ^{1}H–^{195}Pt coupling value found for H^7 is much higher than that reported by Puddephatt and co-workers for the imine proton in other Pt^{II} four-coordinate complexes.[9]

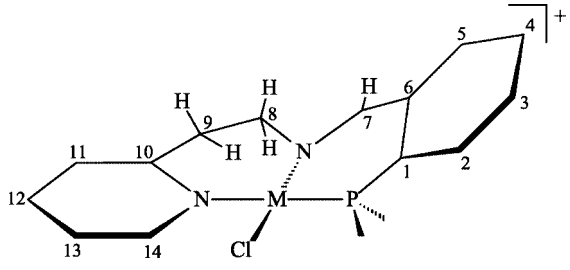

Figure 2. Structure of the cationic complexes (the two phenyl rings bound to phosphorus have been omitted for clarity).

The orange cationic diamagnetic complex [NiCl(PNN)]-PF_6 (**1**) was prepared by reacting equimolar amounts of $NiCl_2·6H_2O$ and PNN in methanol, followed by addition of an excess of NH_4PF_6 dissolved in propan-2-ol and concentration of the solution. The ^{31}P{^{1}H} NMR spectrum of **1** recorded at 293 K in CD_2Cl_2 solution shows a broad singlet at δ = 22.4 ($\Delta\nu_{1/2} \approx$ 340 Hz) along with the regular sharp septet at δ = –143.9 [$^1J(^{19}F–^{31}P)$ = 711 Hz], which is typical of the PF_6^- ion. On lowering the temperature, the width of the broad signal progressively sharpens and at 183 K, the lowest available temperature, $\Delta\nu_{1/2}$ is reduced to 4 Hz (δ = 24.7). The process is completely reversible and also the room-temperature ^{1}H and ^{13}C{^{1}H} spectra of complex **1** exhibit broad signals and no ^{31}P–^{13}C coupling constant is shown.

We have examined the possibility that the broadening of the signals may arise from the presence of a paramagnetic Ni^{II} species. In this regard, it should be noted that complexes [NiX_2(P-N)], where P-N is a phosphane-pyridyl[10] or a phosphane-imine[10d,11] ligand, are tetrahedral, with magnetic moments in the range 1.82–2.62 μ_B. Furthermore, for a Ni^{II} derivative with a PNNX donor set the possibility for a temperature-dependent equilibrium between diamagnetic square-planar and high-spin tetrahedral structures should be considered.[12] However, determinations of the magnetic moment in dichloromethane (183–293 K) and 1,2-dichloroethane (293–343 K) solutions show that complex **1** is diamagnetic in agreement with a square-planar structure. This finding fits well with the observation that there is no colour change of the solutions in the whole temperature range 183–343 K. Another Ni^{II} complex with a X(P–N–N) donor set has been found to be diamagnetic.[13]

In the ^{13}C{^{1}H} spectrum of **1** recorded at 183 K almost all signals are rather sharp and ^{31}P–^{13}C couplings are shown by C^7 and several carbon atoms of both phenyl and phenylene rings. Unfortunately, the slow-exchange limit spectrum is not reached and the resonances of C^8 and C^9 appear as still broad signals. However, the comparison between the ^{13}C{^{1}H} spectra of **1** (at 183 K) and **2** (at 293 K) allows us to conclude that, as chemical shifts and coupling constants do not exhibit remarkable differences (see Table 2), the "frozen" structure of **1** is analogous to that of **2**. Most probably, the dynamic process observed for complex **1** in solution is due to a conformational flexibility of the chelate ring, which allows both chair and boat conformations. In this regard, several different transition-metal complexes bearing bidentate ligands that form a six-membered chelate ring,[14] including square-planar species of the type [Ni(P-P)X_2],[14b] exhibit a fluxional behaviour due to δ-twist-boat−λ-twist-boat rearrangement through a higher-energy chair conformation. It is likely that the dynamic process shown by complex **1** involves a rearrangement of both rings; that formed by the nitrogen donors being more flexible, as suggested by the observation that the most significant modifications of the spectral pattern mainly involve the resonances of the –CH_2CH_2– bridge of the PNN ligand. It should be noted that the other chelate ring exhibits a chain of four sp^2-hybridised atoms (–C–C–C–N–), which reduces the conformational flexibility of the cycle. At very low temperatures, the rate of the rearrangement processes is strongly slowed down and the two rings most probably adopt the conformation characteristic of the solid-state

 © 2005 Wiley-VCH Verlag GmbH & Co. KGaA, Weinheim

structure of the complex (see below). Another interpretation of the fluxional behaviour of **1** invoking the rupture of the metal–nitrogen bond *trans* to the P atom is less precedented.

Crystal Structure Determination of Complexes 1 and 2

Structural analysis of complexes **1** and **2** in the solid state was undertaken in order to understand the different dynamic behaviour of the two species observed in solution. Orange-red needles of **1**, as well as pale yellow needles of **2**, suitable for X-ray analysis were obtained by slow diffusion of propan-2-ol into a dichloromethane solution of the complex. The molecular structures of **1** and **2** are presented in Figure 3 and Figure 4, respectively. The metal in both the complexes exhibits the expected square-planar geometry with coordination distances that are slightly shorter in **1** because of the smaller radius of the Ni^{II} ion. The bond lengths and angles are reported in Table 3, and data of the Pd derivative have values similar to those measured in similar complexes.[4] In both complexes, the ring formed by the N,N donor set shows a nearly ideal boat conformation, while the other one can be seen as a slightly twisted half-chair (Figure 3). It should be noted that the former is considered to be an unconventional form.[14c] These conformations cause a twist of the ligand around the metal centre. However, the overall configuration of **1** and **2** is closely comparable and there are no significant geometrical differences. The slight differences in the orientation of pyridine and of the imine moiety C(7)–N(2)–C(8)–C(9) with respect to the coordination plane likely originate in the crystal packing. On the other hand, a detailed examination of the coordination environment shows a slight tetrahedral distor-

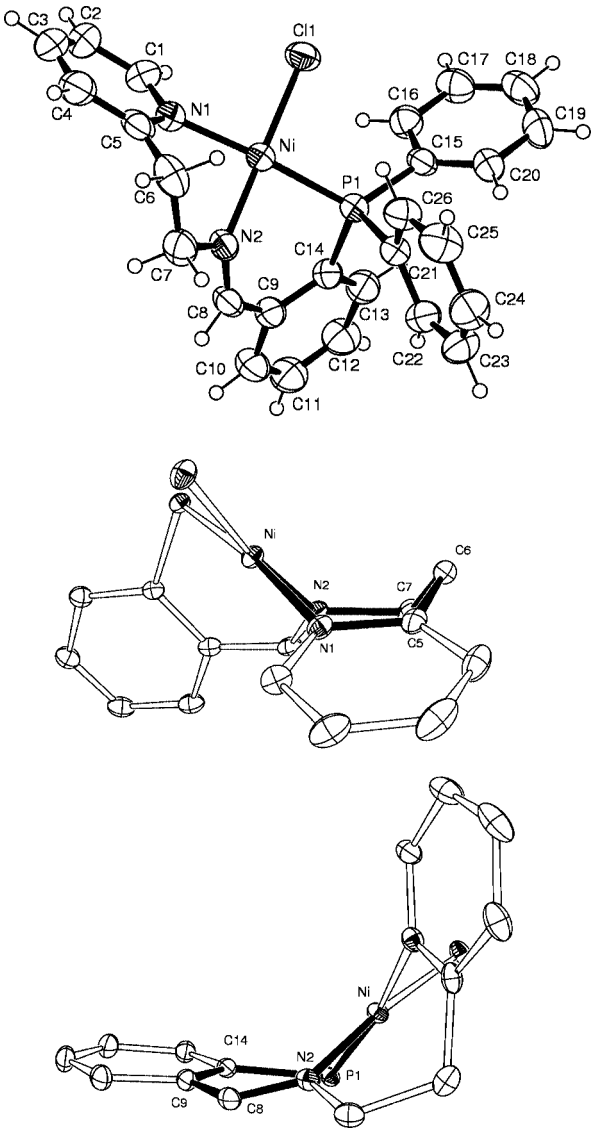

Figure 3. X-ray structure of the cation of complex **1** (ORTEP drawing, thermal ellipsoids at 40% probability level) and a view of the conformations of the two chelate rings.

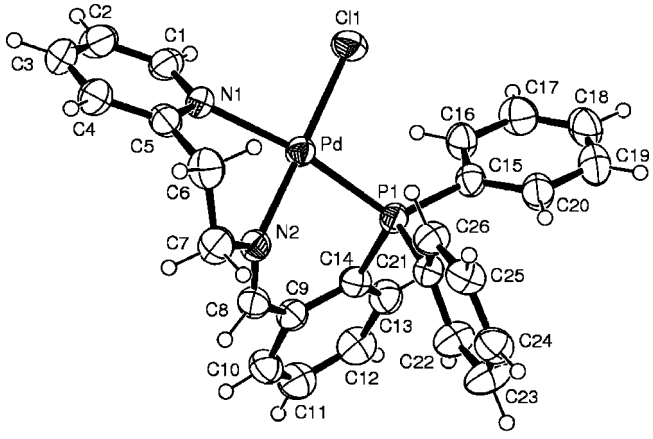

Figure 4. X-ray structure of the cation of complex **2** (ORTEP drawing, thermal ellipsoids at 40% probability level).

Table 3. Coordination bond lengths [Å] and angles [°] and selected geometrical data for **1** and **2**.

	1	**2**	Δ
M–N(1)	1.944(3)	2.125(4)	0.181
M–N(2)	1.904(3)	2.037(4)	0.133
M–P(1)	2.155(1)	2.226(1)	0.071
M–Cl(1)	2.143(1)	2.282(1)	0.139
N(1)–M–N(2)	89.38(12)	87.12(16)	
N(1)–M–P(1)	172.97(9)	170.28(11)	
N(1)–M–Cl(1)	89.87(9)	91.73(12)	
N(2)–M–P(1)	88.41(9)	85.05(12)	
N(2)–M–Cl(1)	173.05(10)	178.09(11)	
P(1)–M–Cl(1)	93.12(4)	96.25(5)	
N(2)–C(8)	1.283(5)	1.269(7)	
N(2)–C(7)	1.499(5)	1.490(6)	
C(8)–N(2)–C(7)	115.9(3)	117.7(4)	
C(8)–N(2)–Ni	128.5(3)	125.8(3)	
C(7)–N(2)–Ni	115.5(2)	116.4(3)	
C(5)–C(6)–C(7)–N(2)	60.1(4)	59.0(6)	
Py/coord. plane	56.9(1)	50.8(1)	
Imino group/ coord plane	44.7(3)	47.7(2)	
Dev [Å][a]	±0.112(1)	±0.066(2)	

[a] Dev = mean deviation of donors in the square-planar geometry.

 © 2005 Wiley-VCH Verlag GmbH & Co. KGaA, Weinheim

tion in the square-planar geometry of the Ni derivative [±0.112(1) Å] in contrast to the more coplanar donors, ±0.066(2) Å in the case of Pd. The packing in compound **1** shows a PF_6^- anion located close to the nickel ion with a Ni–F distance of 3.335 Å. This is a feature often encountered in square-planar complexes containing this anion.[15]

Catalytic Properties of Complexes 1 and 2 in the Heck Reaction

To evaluate the catalytic activity of complex **2** in the Heck reaction, the process of formation of *trans*-stilbene from bromobenzene and styrene has been chosen as a model (Scheme 2). The results of the investigation are collected in Table 4. For all trials, samples of the reaction mixture have been extracted and then analysed by GC after 4, 8 and 20 h. First, we have examined how the nature of the solvent influences yield and selectivity. Thus, the reaction between C_6H_5Br and styrene was performed under argon at 120 °C, using Cs_2CO_3 as the base, in the following solvents: *N*-methylpyrrolidinone (NMP), dimethyl sulfoxide (DMSO), dimethylformamide (DMF), ethylene glycol monomethyl ether (EGME) and 2,2′-thiodiethanol (TDE). NMP, DMF and DMSO are commonly used solvents for the Heck reaction, while the same is not true for the protic solvents EGME and TDE, which have been chosen mainly to ensure a complete dissolution of both the cationic complex and the base. The high final yield (89%) of *trans*-stilbene obtained using EGME (entry 5) with respect to the other solvents (entries 1–4) is rather surprising. Conversely, both regio- and stereoselectivity are rather low, as 9% of a mixture of 1,1-diphenylethene (main byproduct) and *cis*-stilbene is formed. The use of DMF resulted in the immediate formation of an insoluble brown material and only very small amounts of products were detected. The almost negligible activity of complex **2** in DMSO is most probably due to the strong coordinating ability of this solvent, which does not allow substrate activation on the metal centre. Notably, using EGME the yield is very high within a short time (83% after 4 h), despite the formation of palladium black after only a few minutes. We have found that the catalytic activity of complex **2** drastically decreases after the addition of a second batch of reagents. Thus, the *trans*-stilbene yield drops from 83 to 49% after 4 h in the second run. Such a finding agrees with the observed increasing formation of palladium black in the reaction vessel. In this regard, several authors have reported that palladium black is not an active Heck catalyst.[16] Apparently, the effective catalyst is longer lived, but slightly less active, in TDE, the final yield being good nevertheless (85%). The best base to use in combination with EGME is Cs_2CO_3, as with dimethylcyclohexylamine, K_2CO_3 and $CsOH·H_2O$ lower yields have been obtained (entries 6–8). In the case of cesium hydroxide the conversion of C_6H_5Br into products is almost complete, but a dramatic lowering of the selectivity is observed. To reduce palladium black formation, the reaction has been performed at lower temperature (80 °C), but in this case the reaction rate is too low to obtain an acceptable yield (entry 9). Surprisingly, the use of C_6H_5I instead of C_6H_5Br does not correspond to the expected neat increase of the reaction rate[8g] (entry 10). The mechanism of the reaction is currently under investigation, but some preliminary results can be briefly discussed. ^{31}P NMR measurements indicate that complex **2** is stable at 120 °C in EGME alone and even in the presence of both C_6H_5Br and styrene, but immediately after the introduction of Cs_2CO_3 the pale yellow colour of the solution turns dark orange. The $^{31}P\{^1H\}$ NMR spectrum of this solution shows that a singlet at δ = 33.0 has completely replaced the signal at δ = 31.1 because of complex **2**, while no other resonance is detectable. Thus, the starting complex is no longer present in solution under catalytic conditions but is transformed into a new species, most probably the effective catalyst. Attempts to isolate this derivative were unsuccessful. A prolonged warming of the dark orange solution at 120 °C results in the formation of increasing amounts of palladium black.

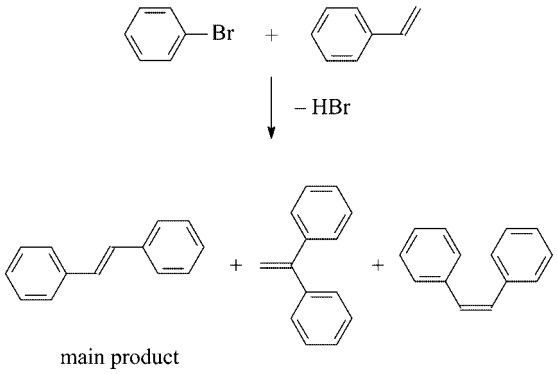

Scheme 2.

Finally, the Ni^{II} derivative **1** does not show any catalytic property in the reaction between C_6H_5Br and styrene, or in the presence of an excess of zinc dust (entry 11). It is well known that Ni^{II} compounds are less active than Pd^{II} compounds, but the beneficial role of a reductant such as zinc has been demonstrated in several cases.[17] The complete lack of catalytic activity of **1** is most probably due to the more difficult β-elimination and HBr removal steps for Ni^{II} with respect to Pd^{II}.[18]

It should be noted that α,β-unsaturated esters, used as starting material in combination with bromobenzene in EGME, undergo a transesterification process, promoted by Cs_2CO_3, giving the corresponding 2-methoxyethyl ester, which then undergoes the Heck reaction. Thus, for example, a mixture of *cis*- and *trans*-2-methoxyethyl-2-methyl-3-phenylpropenoate (major product) has been obtained from ethyl methacrylate.

In conclusion, complex **2** shows a good catalytic performance in the Heck reaction starting from aryl bromides, and the use of EGME as solvent is crucial to achieve good yields.

 © 2005 Wiley-VCH Verlag GmbH & Co. KGaA, Weinheim

Table 4. Catalytic activity of complexes **1** and **2** (1 mol-%) in the Heck reaction.[a]

Entry	Complex	Aryl halide	Alkene	Solvent[b]	Base[c]	Temp. (°C)	*trans*-Stilbene yield (%)[d]		
							4 h	8 h	20 h
1	**2**	C_6H_5Br	styrene	NMP	Cs_2CO_3	120	42	45	46 (53)
2	**2**	C_6H_5Br	styrene	TDE	Cs_2CO_3	120	58	71	83 (89)
3	**2**	C_6H_5Br	styrene	DMSO	Cs_2CO_3	120	–	1	2 (5)
4	**2**	C_6H_5Br	styrene	DMF	Cs_2CO_3	120	1	2	3 (7)
5	**2**	C_6H_5Br	styrene	EGME	Cs_2CO_3	120	83	86	89 (98)
6	**2**	C_6H_5Br	styrene	EGME	DMCA	120	13	28	41 (45)
7	**2**	C_6H_5Br	styrene	EGME	K_2CO_3	120	64	67	68 (74)
8	**2**	C_6H_5Br	styrene	EGME	$CsOH·H_2O$	120	69	74	75 (98)
9	**2**	C_6H_5Br	styrene	EGME	Cs_2CO_3	80	11	14	18 (24)
10	**2**	C_6H_5I	styrene	EGME	Cs_2CO_3	120	87	88	90 (100)
11	**1**[e]	C_6H_5Br	styrene	EGME	Cs_2CO_3	120	–	–	–

[a] Experimental conditions: aryl halide (1.0 equiv.), alkene (1.2 equiv.), base (1.2 equiv.). [b] NMP = 1-methyl-2-pyrrolidinone, DMSO = dimethyl sulfoxide, TDE = 2,2′-thiodiethanol, EGME = ethylene glycol monomethyl ether. [c] DMCA = dimethylcyclohexylamine. [d] GC yield. Aryl halide conversion after 20 h is reported in parenthesis. [e] With 10% Zn (dust) added.

Experimental Section

General Remarks: All reagents were purchased from Aldrich and used without further purification. Commercial solvents were dried according to standard methods[19] and freshly distilled under argon before use. All syntheses and manipulations were carried out under argon using standard Schlenk techniques. The ligand *N*-[2-(diphenylphosphanyl)benzylidene][2-(2-pyridyl)ethyl]amine (PNN) was prepared as described in the literature[4b] and was obtained very pure as a cream-coloured powder after double recrystallisation from *n*-hexane.

Instrumentation and Analyses: The ^1H, ^{13}C and ^{31}P NMR spectra (at 200.13, 50.32 and 81.02 MHz, respectively) were recorded with a Bruker AC 200 F QNP spectrometer equipped with a variable-temperature probe. The ^1H and ^{13}C chemical shifts were referenced to $SiMe_4$, while positive ^{31}P chemical shifts were downfield from 85% H_3PO_4 as external standard. The temperature in the range 273–183 K was calibrated with methanol. The simulation of the 293 K ^1H spectrum of PNN was performed with an Aspect 2000 computer using the programme PANIC (Bruker Spectrospin AG). The GC-MS analyses, run to control the identity of the compounds obtained in the catalytic trials, were carried out with a Fisons TRIO 2000 gas chromatograph-mass spectrometer working in the positive ion 70 eV electron impact mode. Injector temperature was kept at 250 °C and the column (Supelco® SE-54, 30 m long, 0.25 mm i.d., coated with a 0.5 μm phenyl methyl silicone film) temperature was programmed from 50 °C to 310 °C with a gradient of 10 °C/min. The GC analyses were run on a Fisons GC 8000 Series gas chromatograph equipped with a Supelco® PTA-5 column [30 m long, 0.53 mm i.d., coated with a 3.0 μm poly(5% diphenyl/95% dimethylsiloxane) film]. Injector and column temperatures were as indicated above. The elemental analyses (C, H, N) were carried out in the Microanalytical Laboratory of our department.

Synthesis of [NiCl(PNN)]PF_6 (1): A methanol solution (10 mL) of PNN (158 mg, 0.40 mmol) was added to 15 mL of a methanol solution of $NiCl_2·6H_2O$ (90 mg, 0.38 mmol). The red solution was stirred for 10 min and then NH_4PF_6 (196 mg, 1.2 mmol) dissolved in propan-2-ol (20 mL) was added. An orange powder immediately formed, which was filtered off, washed with methanol and dried. The product was then recrystallised from dichloromethane/propan-2-ol. Needle-shaped red crystals were obtained by slow diffusion of propan-2-ol into a dichloromethane solution of the complex. Yield: 195 mg, 81%. $C_{26}H_{23}ClF_6N_2NiP_2$ (633.57): calcd. C 49.29, H 3.66, N 4.42; found C 48.93, H 3.62, N 4.37. ^{31}P NMR (CD_2Cl_2, 183 K): δ = 24.7 ppm. ^1H and ^{13}C NMR spectroscopic data are reported in Table 1 and Table 2, respectively.

Synthesis of [PdCl(PNN)]PF_6 (2): A mixture of [$PdCl_2(CH_3CN)_2$] (156 mg, 0.60 mmol) and PNN (245 mg, 0.62 mmol) in dichloromethane (20 mL) was stirred for 30 min. NH_4PF_6 (294 mg, 1.8 mmol) dissolved in propan-2-ol (25 mL) was then added to the yellow solution and the dichloromethane was pumped off. The pale yellow precipitate, which was filtered off, washed with propan-2-ol and vacuum dried, was then recrystallised from dichloromethane/propan-2-ol. Needle-shaped pale yellow crystals were obtained by slow diffusion of propan-2-ol into a dichloromethane solution of the complex. The crystals contain half mol of CH_2Cl_2 per mol of complex. Yield: 379 mg, 87%. $C_{26}H_{23}ClF_6N_2P_2Pd·0.5CH_2Cl_2$ (723.76): calcd. C 43.98, H 3.34, N 3.87; found C 43.72, H 3.37, N 3.81. ^{31}P NMR (CD_2Cl_2, 293 K): δ = 31.0 ppm. ^1H and ^{13}C NMR spectroscopic data are reported in Table 1 and Table 2, respectively.

Synthesis of [PtCl(PNN)]PF_6 (3): A mixture of [$PtCl_2(C_6H_5CN)_2$] (118 mg, 0.25 mmol) and PNN (103 mg, 0.26 mmol) in dichloromethane (20 mL) was stirred for 30 min. After the addition of NH_4PF_6 (130 mg, 0.8 mmol) dissolved in propan-2-ol (20 mL), the dichloromethane was eliminated in vacuo affording a pale yellow product, which was filtered off, washed with propan-2-ol and vacuum dried. The crude product was recrystallised from dichloromethane/propan-2-ol. Needle-shaped pale yellow crystals were obtained by slow diffusion of propan-2-ol into a dichloromethane solution of the complex. The crystals contain half mol of CH_2Cl_2

 © 2005 Wiley-VCH Verlag GmbH & Co. KGaA, Weinheim

per mol of complex. Yield: 186 mg, 91%. $C_{26}H_{23}ClF_6N_2P_2Pt\cdot 0.5CH_2Cl_2$ (812.42): calcd. C 39.18, H 2.98, N 3.45; found C 38.94, H 3.03, N 3.40. ^{31}P NMR (CD_2Cl_2, 293 K): δ = 1.4; $^1J(^{31}P–^{195}Pt)$ = 3459 Hz. ^1H and ^{13}C NMR spectroscopic data are reported in Table 1 and Table 2, respectively.

Magnetic Moment Measurements on Complex 1 in Solution: Measurements were run on CH_2Cl_2 and $ClCH_2–CH_2Cl$ solutions of the complex, at temperatures below and above 293 K, respectively. The method described by Evans[20] was adopted using a 5-mm NMR tube with a 2-mm coaxial capillary inside containing the pure solvent. The solutions (5×10^{-2} M) were prepared by dissolving 15.8 mg (25 μmol) of **1** into 0.5 mL of the appropriate solvent. Spectra were recorded at 183, 193, 213, 233, 253, 273, 293, 313, 333 and 343 K.

General Procedure for the Heck Reaction: Under argon, a 10-mL Schlenk flask containing a magnetic stir bar was charged with the catalyst (2.0 mg for each single experiment, 1 mol-%) and appropriate amounts of aryl halide (1.0 equiv.), alkene (1.2 equiv.) and base (1.2 equiv.). After addition of the solvent (2 mL), the flask was capped with a silicon stopper and heated at 120 °C in an oil bath. The reaction mixture was extracted from the flask by syringe after 4, 8 and 20 h. The samples were treated with water, extracted with ethyl ether, dried with Na_2SO_4 and then analysed by GC.

Crystallographic Structure Determination: Diffraction data of the structures reported were carried out on a rotating anode Nonius FR591 (Cu-K_α radiation λ = 1.54178 Å) equipped with a Kappa CCD imaging plate. Cell refinement, indexing and scaling of the data sets were carried out using Denzo[21] and Scalepack.[21] Both the structures were solved by Patterson and Fourier analyses[22] and refined by the full-matrix least-squares method based on F^2 with all observed reflections.[22] A ΔF map of **2** revealed, besides the PF_6^- anion, a disordered molecule of CH_2Cl_2 (occupancy factor 0.5, based on the electron density peaks). The hydrogen atoms were located at geometrically calculated positions. All the calculations were performed using the WinGX System, version 1.70.00.[23] Crystallographic data and details of structure refinements are reported in Table 5.

Table 5. Crystallographic data and details of structure refinements for **1** and **2**.

	1	**2**·0.5CH_2Cl_2
Formula	$C_{26}H_{23}ClF_6N_2NiP_2$	$C_{26.5}H_{24}Cl_2F_6N_2P_2Pd$
M_r	633.56	723.72
Crystal system	triclinic	triclinic
Space group	$P\bar{1}$	$P\bar{1}$
a [Å]	10.125(3)	8.544(2)
b [Å]	12.214(3)	13.097(4)
c [Å]	13.101(4)	13.643(4)
α [°]	103.51(2)	102.97(2)
β [°]	111.03(3)	103.63(2)
γ [°]	106.81(2)	97.57(2)
Volume [Å^3]	1340.5(7)	1418.1(7)
Z	2	2
$D_{calcd.}$ [g cm^{-3}]	1.570	1.695
μ (Mo-K_α) [mm^{-1}]	3.647	8.627
F(000)	644	722
θ_{max} [°]	64.56	64.70
Reflections collected	15767	20902
Unique reflections	3954	4352
R_{int}	0.0751	0.0438
Observed $I > 2\sigma(I)$	3404	4024
Parameters	343	355
Goodness of fit (F^2)	1.078	1.073
R_1 [$I > 2\sigma(I)$][a]	0.0631	0.0564
wR_2[b]	0.1808	0.1521
$\Delta\rho$ [e/Å^3]	0.364, –0.429	0.885, –0.984

[a] $R_1 = \Sigma||F_o| - |F_c||/\Sigma|F_o|$. [b] $wR_2 = [\Sigma w(F_o^2 - F_c^2)^2/\Sigma w(F_o^2)^2]^{0.5}$.

CCDC-282001 (for **2**) and -282002 (for **1**) contain the supplementary crystallographic data for this paper. These data can be obtained free of charge from The Cambridge Crystallographic Data Centre via www.ccdc.cam.ac.uk/data_request/cif.

Acknowledgments

This research has been financially supported by the Italian Ministero dell'Istruzione, dell'Università e della Ricerca (MIUR), Rome. We wish to thank Mr. P. Polese for carrying out elemental analyses.

[1] a) A. Bader, E. Lindner, *Coord. Chem. Rev.* **1991**, *108*, 27–110; b) G. R. Newkome, *Chem. Rev.* **1993**, *93*, 2067–2089; c) Z.-Z. Zhang, H. Cheng, *Coord. Chem. Rev.* **1996**, *147*, 1–39; d) E. Lindner, S. Pautz, M. Haustein, *Coord. Chem. Rev.* **1996**, *155*, 145–162; e) P. Espinet, K. Soulantica, *Coord. Chem. Rev.* **1999**, *193–195*, 499–556; f) C. S. Slone, D. A. Weinberger, C. A. Mirkin, *Progr. Inorg. Chem.* **1999**, *48*, 233–350; g) P. Braunstein, F. Naud, *Angew. Chem. Int. Ed.* **2001**, *40*, 680–699.

[2] a) L. Costella, A. Del Zotto, A. Mezzetti, E. Zangrando, P. Rigo, *J. Chem. Soc., Dalton Trans.* **1993**, 3001–3008; b) A. Del Zotto, A. Mezzetti, P. Rigo, *J. Chem. Soc., Dalton Trans.* **1994**, 2257–2264; c) A. Del Zotto, G. Nardin, P. Rigo, *J. Chem. Soc., Dalton Trans.* **1995**, 3343–3351; d) A. Del Zotto, P. Rigo, G. Nardin, *Inorg. Chim. Acta* **1996**, *247*, 183–188; e) A. Del Zotto, E. Zangrando, *Inorg. Chim. Acta* **1998**, *277*, 111–117; f) A. Del Zotto, P. Di Bernardo, M. Tolazzi, P. L. Zanonato, *J. Chem. Soc., Dalton Trans.* **1999**, 979–986; g) R. Romeo, L. Monsù Scolaro, M. R. Plutino, A. Romeo, F. Nicolò, A. Del Zotto, *Eur. J. Inorg. Chem.* **2002**, 629–638.

[3] a) K. K. Hii, S. D. Perera, B. L. Shaw, *J. Chem. Soc., Dalton Trans.* **1995**, 625–631; b) A. Bacchi, M. Carcelli, M. Costa, A. Leporati, E. Leporati, P. Pelagatti, C. Pelizzi, G. Pelizzi, *J. Organomet. Chem.* **1997**, *535*, 107–120; c) C. Lee, Y. Kang, S. O. Kang, J. Ko, J. W. Yoo, M. H. Cho, *J. Organomet. Chem.* **1999**, *587*, 165–175; d) A. Bacchi, M. Carcelli, M. Costa, A. Fochi, C. Monici, P. Pelagatti, C. Pelizzi, G. Pelizzi, L. M. Sanjuan Roca, *J. Organomet. Chem.* **2000**, *593–594*, 180–191; e) T. Morimoto, Y. Yamaguchi, M. Suzuki, A. Saitoh, *Tetrahedron Lett.* **2000**, *41*, 10025–10029; f) J.-P. Masson, A. A. Bahsoun, M.-T. Youinou, J. A. Osborne, *C. R. Chim.* **2002**, *5*, 303–308; g) S. Doherty, J. G. Knight, T. H. Scanlan, M. R. J. Elsegood, W. Clegg, *J. Organomet. Chem.* **2002**, *650*, 231–248; h) X. Hu, H. Dai, C. Bai, H. Chen, Z. Zheng, *Tetrahedron: Asymmetry* **2004**, *15*, 1065–1068; i) M. A. Garralda, R. Hernández, L. Ibarlucea, E. Pinilla, M. Rosario Torres, M. Zarandona, *Inorg. Chim. Acta* **2004**, *357*, 2818–2826; j) H. Dai, X. Hu, H. Chen, C. Bai, Z. Zheng, *J. Mol. Catal. A: Chem.* **2004**, *211*, 17–21.

[4] a) P. Wehman, R. E. Rülke, V. E. Kaasjager, P. C. J. Kamer, H. Kooijman, A. L. Spek, C. J. Elsevier, K. Vrieze, P. W. N. M. van Leeuwen, *J. Chem. Soc., Chem. Commun.* **1995**, 331–332; b) R. E. Rülke, V. E. Kaasjager, P. Wehman, C. J. Elsevier, P. W. N. M. van Leeuwen, K. Vrieze, J. Faanje, K. Goubitz, A. L. Spek, *Organometallics* **1996**, *15*, 3022–3031.

[5] C.-C. Yang, W.-Y. Yeh, G.-H. Lee, S.-M. Peng, *J. Organomet. Chem.* **2000**, *598*, 353–358.

[6] W.-Y. Yeh, C.-C. Yang, S.-M. Peng, G.-H. Lee, *J. Chem. Soc., Dalton Trans.* **2000**, 1649–1654.

[7] F. Benvenuti, C. Carlini, M. Marchionna, R. Patrini, A. M. Raspolli Galletti, G. Sbrana, *J. Mol. Catal. A: Chem.* **1999**, *140*, 139–155.

[8] a) R. F. Heck, *Org. React.* **1982**, *27*, 345–390; b) A. de Mejiere, F. E. Meyer, *Angew. Chem. Int. Ed. Engl.* **1994**, *33*, 2379–2411;

 © 2005 Wiley-VCH Verlag GmbH & Co. KGaA, Weinheim

c) W. Cabri, I. Candiani, *Acc. Chem. Res.* **1995**, *28*, 2–7; d) W. A. Herrmann in *Applied Homogeneous Catalysis with Organometallic Compounds* (Eds.: B. Cornils, W. A. Herrmann), Wiley VCH, Weinheim, **1996**, pp. 712–732; e) G. T. Crisp, *Chem. Soc. Rev.* **1998**, *27*, 427–436; f) I. P. Beletskaya, A. V. Cheprakov, *Chem. Rev.* **2000**, *100*, 3009–3066; g) N. J. Whitcombe, K. K. Hii, S. E. Gibson, *Tetrahedron* **2001**, *57*, 7449–7476.

[9] a) M. C. Anderson, M. Crespo, M. C. Jennings, A. J. Lough, G. Ferguson, R. J. Puddephatt, *Organometallics* **1991**, *10*, 2672–2679; b) M. C. Anderson, M. Crespo, G. Ferguson, A. J. Lough, R. J. Puddephatt, *Organometallics* **1992**, *11*, 1177–1181; c) C. R. Baar, L. P. Carbray, M. C. Jennings, R. J. Puddephatt, J. J. Vittal, *Organometallics* **2001**, *20*, 408–417.

[10] a) H. P. Chen, Y. H. Liu, S. M. Peng, S. T. Liu, *Organometallics* **2003**, *22*, 4893–4899; b) F. Speiser, P. Braunstein, L. Saussine, *Organometallics* **2004**, *23*, 2633–2640; c) F. Speiser, P. Braunstein, L. Saussine, *Dalton Trans.* **2004**, 1539–1545; d) F. Speiser, P. Braunstein, L. Saussine, R. Welter, *Inorg. Chem.* **2004**, *43*, 1649–1658.

[11] a) Z. Guan, W. J. Marshall, *Organometallics* **2002**, *21*, 3580–3586; b) F. Speiser, P. Braunstein, L. Saussine, R. Welter, *Organometallics* **2004**, *23*, 2613–2624.

[12] F. A. Cotton, G. Wilkinson, C. A. Murillo, M. Bochmann (Eds.), *Advanced Inorganic Chemistry*, 6th ed., Wiley, New York, **1999**, pp. 840–846.

[13] I. Bertini, P. Dapporto, G. Fallani, L. Sacconi, *Inorg. Chem.* **1971**, *10*, 1703–1707.

[14] a) A. Frick, V. Schulz, G. Huttner, *Eur. J. Inorg. Chem.* **2002**, 3129–3147; b) R. Faissner, G. Huttner, E. Kaifer, P. Kircher, P. Rutsch, L. Zsolnai, *Eur. J. Inorg. Chem.* **2003**, 2219–2238; c) R. Faissner, G. Huttner, E. Kaifer, P. Rutsch, *Eur. J. Inorg. Chem.* **2003**, 1681–1693.

[15] A. Scarel, B. Milani, E. Zangrando, M. Stener, S. Furlan, G. Fronzoni, G. Mestroni, S. Gladiali, C. Carfagna, L. Mosca, *Organometallics* **2004**, *23*, 5593–5605.

[16] See for example: a) W. A. Herrmann, C. Bossmer, K. Öfele, C.-P. Reisinger, T. Priermeier, M. Beller, H. Fischer, *Angew. Chem. Int. Ed. Engl.* **1995**, *34*, 1844–1848; b) L. F. Tietze, K. Kahle, T. Raschke, *Chem. Eur. J.* **2002**, *8*, 401–407; c) M. T. Reetz, J. G. de Vries, *Chem. Commun.* **2004**, 1559–1563; d) J. R. Dilworth, C. A. Maresca von Beckh, W. S. I. Pascu, *Dalton Trans.* **2005**, 2151–2161.

[17] a) G. P. Boldrini, D. Savoia, E. Tagliavini, C. Trombini, A. Umani Ronchi, *J. Organomet. Chem.* **1986**, *301*, C62–C64; b) S. A. Lebedev, V. S. Lopatina, E. S. Petrov, I. P. Beletskaya, *J. Organomet. Chem.* **1988**, *344*, 253–259; c) R. Sustmann, P. Hopp, P. Holl, *Tetrahedron Lett.* **1989**, *30*, 689–692; d) K.-C. Kong, C.-H. Cheng, *Organometallics* **1992**, *11*, 1972–1975; e) A. A. Kelkar, T. Hanaoka, Y. Kubota, Y. Sugi, *Catal. Lett.* **1994**, *29*, 69–75.

[18] B.-L. Lin, L. Liu, Y. Fu, S.-W. Luo, Q. Chen, Q.-X. Guo, *Organometallics* **2004**, *23*, 2114–2123.

[19] D. D. Perrin, W. L. F. Armarego, D. R. Perrin (Eds.), *Purification of Laboratory Chemicals*, 2nd ed., Pergamon Press, Oxford, **1980**.

[20] a) D. F. Evans, *J. Chem. Soc.* **1959**, 2003–2005; b) S. K. Sur, *J. Magn. Reson.* **1989**, *82*, 169–173.

[21] Z. Otwinowski, W. Minor, *Methods Enzymol.* **1997**, *276*, 307–326.

[22] G. M. Sheldrick, *SHELX97* Programs for Crystal Structure Analysis (Release 97-2), University of Göttingen, Germany, **1998**.

[23] L. J. Farrugia, *J. Appl. Crystallogr.* **1999**, *32*, 837–838.

Received: June 1, 2005
Published Online: October 25, 2005

 © 2005 Wiley-VCH Verlag GmbH & Co. KGaA, Weinheim

DOI: 10.1002/ejic.200500495

Synthetic, Structural, and Electrochemical Studies of 2-Ferrocenyl- and 2-Cymantrenyl-Functionalized 2,3-Dihydro-1*H*-1,3,2-diazaboroles and 1,3,2-Diazaborolidenes

Lothar Weber,*[a] Imme Domke,[a] Hans-Georg Stammler,[a] and Beate Neumann[a]

Keywords: Boron / Cyclic voltammetry / Ferrocene / Methylcymantrene

Reaction of (dibromoboryl)ferrocene (**1**) with 1 equiv. of the diazabutadiene *t*BuN=CH–CH=N*t*Bu, and subsequent reduction of the obtained borolium salt **2** with sodium amalgam, affords the first ferrocenyl-functionalized 1,3,2-diazaborole (**3**). Similarly, 1,1′-bis(dibromoboryl)ferrocene (**4**) can be transformed into compound **6**, which contains two diazaborolyl substituents at the ferrocene core. Treatment of precursors **1** and **4** with 1,2-bis(*tert*-butylamino)ethane in the presence of Et_3N gives rise to the formation of the diazaborolidine derivatives **13** and **14**. 1-Dibromoboryl-3-methylcymantrene (**7**) was also treated with *t*BuN=CH–CH=N*t*Bu to give the borolium salt **8**, which was subsequently reduced to the 2-cymantrenyl-diazaborole **9**. Treatment of **7** with *t*BuN(H)-CH_2CH_2N(H)*t*Bu in the presence of Et_3N furnished the corresponding 2-cymantrenyl-diazaborolidine **15**. The novel compounds were characterized by elemental analyses and various spectroscopic techniques (IR; ^{1}H, ^{13}C, and ^{11}B NMR; MS). The molecular structures of **3**, **6**, and **15** were elucidated by X-ray diffraction analyses. Cyclovoltammetric studies of the ferrocene derivatives at high scan rates show features of a quasireversible oxidation at the iron center. The heterocyclic groups serve as electron donors, considerably lowering the oxidation potential of the central iron atoms when compared to the parent compound ferrocene.
(© Wiley-VCH Verlag GmbH & Co. KGaA, 69451 Weinheim, Germany, 2005)

Introduction

Boryl- and borate-functionalized metallocenes are of great current interest. Two recent reviews have described their applications in homogeneous catalysis, anion sensing, and organometallic polymer chemistry.[1,2] Another point of interest is related to the influence of the boryl substituent on the electronic and structural properties of the metallocene moiety. The boron systems that concern us are 2,3-dihydro-1*H*-1,3,2-diazaboroles **A**, for which we have recently developed high-yield syntheses.[3] With this, the door was opened to an exceedingly rich chemistry of these heterocycles, including reactions where the structural integrity of the ring system is retained (e.g. nucleophilic displacements at the boron atom)[4] as well as processes where the ring is reorganized (e.g. in the reaction with diphenylketene to afford 1,3,2-oxazaborolidenes **B**;[5] Scheme 1).

At this point, it was of particular interest to combine such inorganic heterocycles with metallocene fragments. It is conceivable that the 6π-electron-containing heterocycle communicates electronically with the metallocene by (pp)π-interactions and/or σ-bonding, thus altering the electronic properties of the organometallic moiety.

In this paper we report on the synthesis and molecular structures of ferrocenyl- and cymantrenyl-functionalized 1,3,2-diazaboroles as well as their saturated counterparts, the respective 1,3,2-diazaborolidines. Moreover, electrochemical studies should provide information on the influence of the boron heterocycles on the redox-active center of the organometallic fragment.

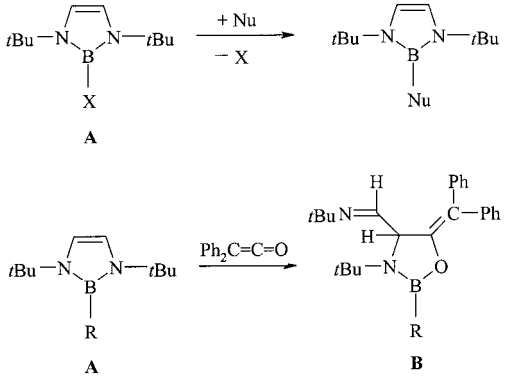

Scheme 1. Reactivity of 1,3,2-diazaboroles **A**.

Results and Discussion

Several synthetic pathways for the construction of the 2,3-dihydro-1*H*-1,3,2-diazaborole system are currently available:

a) the catalytic dehydrogenation of the corresponding saturated 1,3,2-diazaborolidines;[6]

[a] Fakultät für Chemie der Universität Bielefeld,
Universitätsstraße 25, 33615 Bielefeld, Germany
Fax: +49-521-106-6146
E-mail: lothar.weber@uni-bielefeld.de

 © 2005 Wiley-VCH Verlag GmbH & Co. KgaA, Weinheim

b) the reaction of di- or trihaloboranes with 1,4-diazabutadienes to afford borolium salts and the reduction of the latter species with sodium amalgam;[4,7]
c) the cyclocondensation of di- and trihaloboranes with dilithiated diazabutadienes;[4] and
d) nucleophilic substitution processes at the boron atom of preformed 2-halo-1,3,2-diazaboroles[4] (Scheme 2).

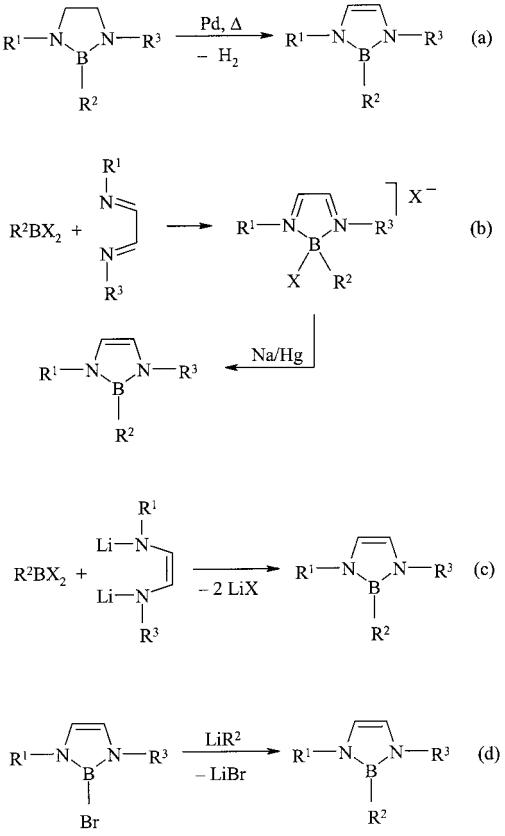

Scheme 2. Synthethic pathways to 1,3,2-diazaboroles.

Path (b) seems promising for the synthesis of 2-ferrocenyl- and 2-(methylcymantrenyl)-functionalized diazaboroles as the required precursors (dibromoboryl)ferrocene (**1**), 1,1′-bis(dibromoboryl)ferrocene (**4**), and 1-dibromoboryl-3-methylcymantrene (**7**) are readily available from ferrocene and methylcymantrene by Friedel–Crafts-type reactions with BBr_3 (Scheme 3).[8]

Reaction of **1** with the diazabutadiene (tBuN=CH)$_2$[9] in n-hexane gave an olive-green precipitate of borolium salt **2**, which shows resonances in the $^{11}B\{^1H\}$ NMR spectrum in the region of tetracoordinate boron [δ = 3.8, 7.1 ppm (CD_3CN)]. The two different signals are presumably due to different counterions in the salts. This phenomenon has frequently been encountered during the synthesis of borolium salts from diazabutadienes and boron halides.[4c,10] The obtained slurry was reduced in situ with an excess of sodium amalgam for2 d in the absence of light. Red crystals of product **3** were isolated in 74% yield from the resulting dark-red n-hexane phase. Similarly, the treatment of 1,1′-bis(dibromoboryl)ferrocene with2 equiv. of diazabutadiene gave borolium salt **5** [$\delta_{^{11}B}$ = 3.8, 7.1 ppm (CD_3CN)], which

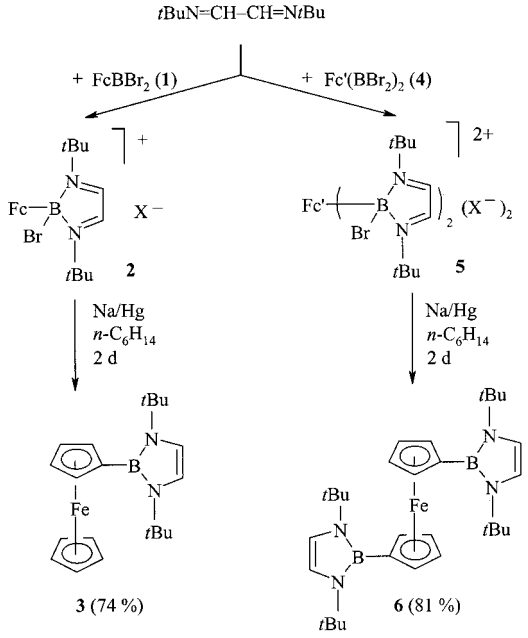

Scheme 3. Syntheses of **3** and **6** {Fc = [(C_5H_5)(C_5H_4)Fe]; Fc′ = [(C_5H_4)$_2$Fe]; X = Br}.

was subsequently reduced to bis(borolyl)ferrocene **6**. The product was isolated as cherry-red crystals in 81% yield (Scheme 3).

Yellow, crystalline methylcymantrenyl-1,3,2-diazaborole (**9**) was synthesized in 63% yield by the reaction of complex **7** with the diazabutadiene in n-hexane and the usual reduction of the borolium salt [$\delta_{^{11}B}$ = 5.0 ppm (CD_3CN)] with sodium amalgam (Scheme 4).

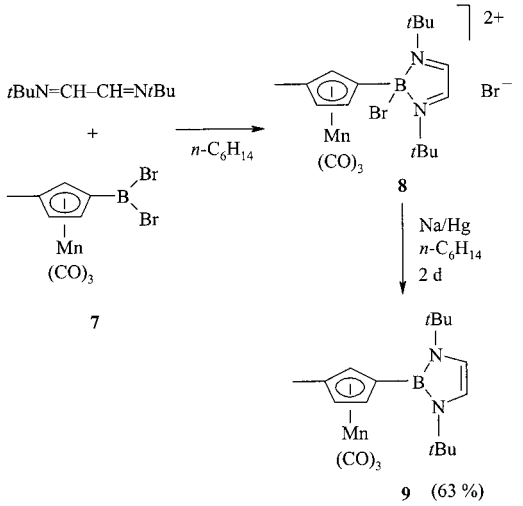

Scheme 4. Synthesis of **9**.

Thermolabile 2-ferrocenyl[1,3,2]diazaborolo[1,5-*a*]pyridine (**11**) was accessible by treatment of **1** with *N*-(2-pyridylmethylene)-*tert*-butylamine[11] and the subsequent reduction of borolium salt **10** ($\delta_{^{11}B}$ = 6.3, 7.8 ppm) to produce the orange solid product (Scheme 5).

 © 2005 Wiley-VCH Verlag GmbH & Co. KGaA, Weinheim

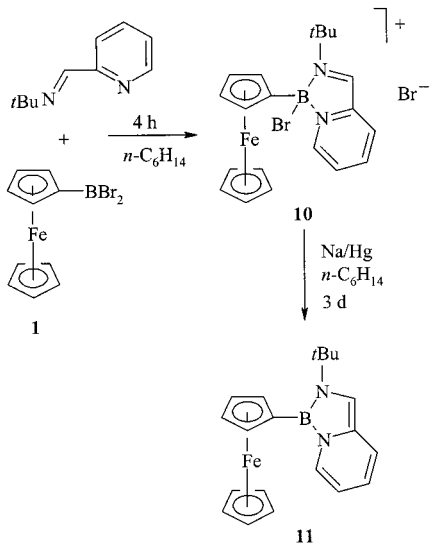

Scheme 5. Synthesis of **11**.

For comparison, the saturated analogs of the organometallic diazaboroles **3**, **6**, and **9** − the respective 1,3,2-diazaborolidenes − were also studied. One complex of this type, compound **12**, has previously been synthesized by the reaction of 1,1′-dilithioferrocene with 2-chloro-1,3-dimethyl-1,3,2-diazaborolidine.[12]

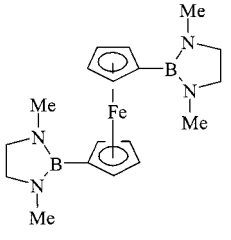

In this study, the aminolysis of the B–Br bonds in **1**, **4**, and **7** by *N*,*N*′-di-*tert*-butylethane-1,2-diamine in the presence of triethylamine was preferred as a synthetic approach (Scheme 6).

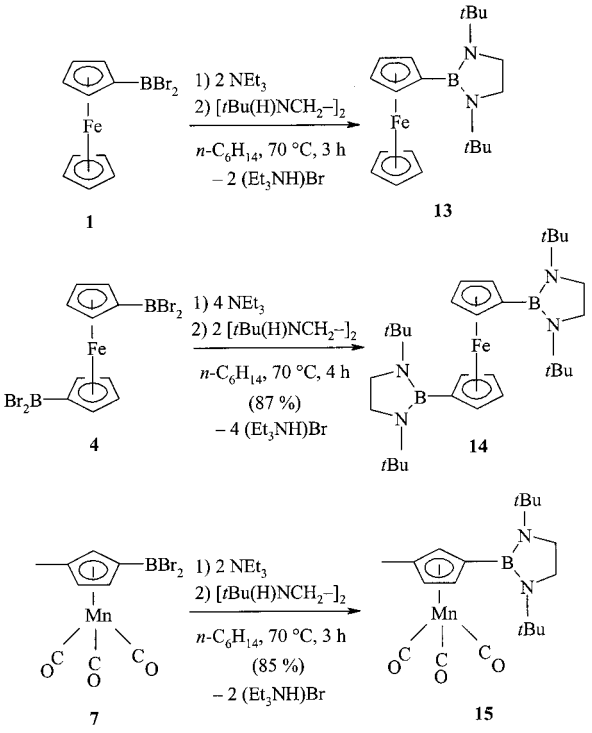

Scheme 6. Synthesis of diazaborolidines **13**–**15**.

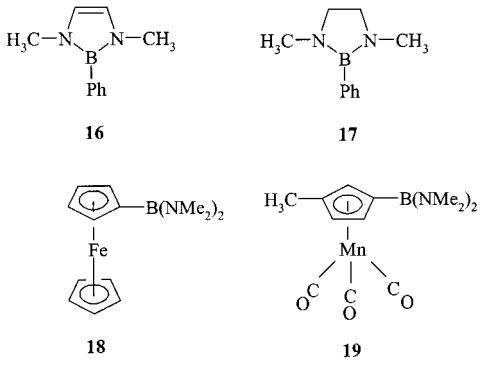

The reactions were performed in boiling *n*-hexane for 3–4 h to afford red, oily **13**, dark-red, crystalline **14**, and colorless, crystalline **15** in good yields (85–87%). All the novel organometallic diazaboroles and diazaborolidines are sensitive to air and moisture. Moreover, the thermolability of compound **11** precluded reliable elemental analyses.

The $^{11}B\{^1H\}$ NMR spectra of the ferrocenyl-diazaboroles **3** and **6** display resonances at δ = 25.3 ppm, which are comparable with the ^{11}B NMR signal of 2-phenyl-1,3,2-diazaborole (**16**; δ = 25.6 ppm).[6] Generally, the shielding of the ^{11}B nuclei in 1,3-dialkyl-1,3,2-diazaboroles is mainly governed by the substituents at the boron atom.

This resonance is shifted by 6.5 ppm to δ = 31.8 ppm on going to the saturated systems **13** and **14**. Again, these resonances compare well with the ^{11}B NMR signal of 1,3-dimethyl-2-phenyl-1,3,2-diazaborolidine (**17**; δ = 32.2 ppm).[6] The ^{11}B NMR signal in the acyclic (diaminoboryl)ferrocene **18** appears at δ = 33.3 ppm,[8b] thus indicating that the ferrocenyl and the phenyl group at the boron atom contribute similarly to the shielding of the boron center. The situation is similar in the ^{11}B NMR spectra of the methylcymantrenyl derivatives. In the methylcymantrenyl-substituted diazaborole **9**, for example, the ^{11}B NMR resonance is observed at δ = 23.2 ppm. The ^{11}B atom of diazaborolidine **15** is more deshielded (δ = 29.6 ppm) as in the corresponding 6π-electron heterocycle. The ^{11}B NMR signal of the acyclic bis(aminoboryl) derivative **19** appears at δ = 30.1 ppm.[8b]

The chemical shifts of the ^1H and ^{13}C nuclei of the C_5H_5 ring in monoborylated ferrocenes in comparison to the parent compound is thought to reflect the donor/acceptor properties of the boryl substituent. Thus, on going from $[FeCp_2]$ ($\delta_{^{13}C}$ = 68.2 ppm) to the dibromoboryl derivative **1** ($\delta_{^{13}C}$ = 71.7 ppm) this resonance is shifted by 3.5 ppm. In comparison, the 1,3,2-diazaborolyl- and 1,3,2-diazaborolidinyl substituents in **3** and **13** (δ = 69.6 ppm) give rise to

 © 2005 Wiley-VCH Verlag GmbH & Co. KGaA, Weinheim

the considerably smaller low-field shift of only 1.4 ppm. In ferrocene **18**, which contains the $B(NMe_2)_2$ group as a substituent, a singlet is observed at $\delta_{^{13}C}$ = 68.6 ppm. The signals of the α- and the β-C atoms of the C_5H_4B unit in **1** are found at $\delta_{^{13}C}$ = 77.4 and 78.4 ppm, respectively, whereas the corresponding signals in the bis(dibromoboryl)ferrocene **4** appear at δ = 79.0 and 80.3 ppm. In the monoborolyl- and monoborolidinyl ferrocenes **3** and **13** the nuclei $^{13}C_\alpha$ and $^{13}C_\beta$ resonate at δ = 76.2, 68.6 (**3**) and 76.2, 68.3 (**13**) ppm. For comparison, the corresponding signals in **18** appear at $\delta_{^{13}C}$ = 76.0 and 70.1 ppm.[12] The resonances for the $^{13}C_\alpha$- and $^{13}C_\beta$ atoms of the diborylated species **6** and **14** are found at $\delta_{^{13}C}$ = 79.3 (**6**) and 79.0 (**14**), and 68.6 (**6**) and 68.3 (**14**) ppm. The pronounced difference in the resonances of C_α and C_β in **3**, **6**, **13**, **14**, and **18** agrees with a significant transfer of negative charge from the heterocycles to the organometallic unit via the B–C σ-bond. Singlets at δ = 112.7 or 112.9 ppm in the ^{13}C NMR spectra of **3** and **6**, respectively, were assigned to the C=C groups of the diazaborole.

The ^1H NMR spectra of complexes **1**, **3**, **13**, and **18** show singlets in the narrow range of δ = 4.06–4.12 ppm for the C_5H_5 groups. The electron-withdrawing effect of one or two Br_2B units in **1** and **4** is reflected by the separation of the multiplets for H_α and H_β of the substituted rings by $\Delta\delta$ = 0.35 and 0.20 ppm, respectively, with δ_{H_β} at lower field. No such separation is observable in the monoborylated complexes **3**, **14**, and **18**, and in the diborylated ferrocenes **6** and **14** a separation of signals of only $\Delta\delta$ = 0.11–0.14 ppm is found. Singlets in the ^1H NMR spectrum of **9** at δ = 1.34 (18 H), 1.56 (3 H), 4.04 (1 H), 4.57 (1 H), 4.65 (1 H), and 6.34 (2 H) ppm are attributed to the protons of the *tert*-butyl groups, the ring methyl group, the protons H(4), H(2), and H(5) of the methylcyclopentadienyl ligand, and to the CH=CH unit, respectively. The corresponding resonances in the borolidinyl derivative **15** are found at δ = 1.30 (18 H), 1.68 (3 H), 4.14 (1 H), 4.64 (1 H), and 4.68 (1 H) ppm, whereas the protons of the CH_2–CH_2 fragment are observed as a singlet at δ = 3.11 ppm (4 H). The ^{13}C NMR spectra of **9** and **15** show singlets for the CO ligands at δ = 226.2 and 226.0 ppm, respectively, which are close to the resonance in methylcymantrene [δ(CO) = 225.7 ppm]. The ^{13}C NMR signals of the η^5-ligand in **9** and **15** are similar to those of **7**, where the Br_2B group is clearly electron-withdrawing. Here, singlets for C(3), C(5), C(2), and C(4) are found at δ = 107.2, 96.6, 95.8, and 90.0 ppm. In **9**, the respective resonances appear at δ = 99.8, 95.2, 94.8, and 90.0 ppm, which points to a higher electron density in the ring than in **7**. This tendency is even more pronounced in **15**, where singlets are observed at δ = 98.8, 94.1, 93.5, and 81.7 ppm. This is also mirrored in the ν(CO) region of the IR spectra of **7**, **9**, **15**, and $[(CH_3C_5H_4)Mn(CO)_3]$ (Table 1).

Two strong ν(CO) bands are observed at $\tilde{\nu}$ = 2025 and 1944 cm^{-1} due to the local C_{3v} symmetry of the $Mn(CO)_3$ group in the starting material. Strong absorptions at $\tilde{\nu}$ = 2020 and 1938 cm^{-1} in the spectra of **9** and **15**, respectively, show the transfer of electron density from the heterocyclic substituents to the carbonyl groups. In comparison to that, ν(CO) bands are found at higher wavenumbers for the dibromoboryl precursor **7** ($\tilde{\nu}$ = 2033, 1949 cm^{-1}) than for methylcymantrene.

Table 1. IR data of the methylcymantrene derivatives in *n*-hexane solutions.

Compound	$[(CH_3C_5H_4)Mn(CO)_3]$	**7**	**9**	**15**
$\tilde{\nu}$ [cm^{-1}]	2025, 1944	2033, 1949	2020, 1938	2020, 1938

X-ray Structural Analysis of 3, 6, and 15

X-ray analyses of compounds **3**, **6**, and **15** were carried out to determine the mutual orientation of the 1,3,2-diazaborolyl substituent and the η^5-C_5H_4 ring ligand, and for an evaluation of a possible π-conjugation between these cycles in the solid state (Table 3).

X-ray Structural Analysis of 3

An ORTEP drawing of **3** is shown in Figure 1; selected bond lengths and angles are given in the caption.

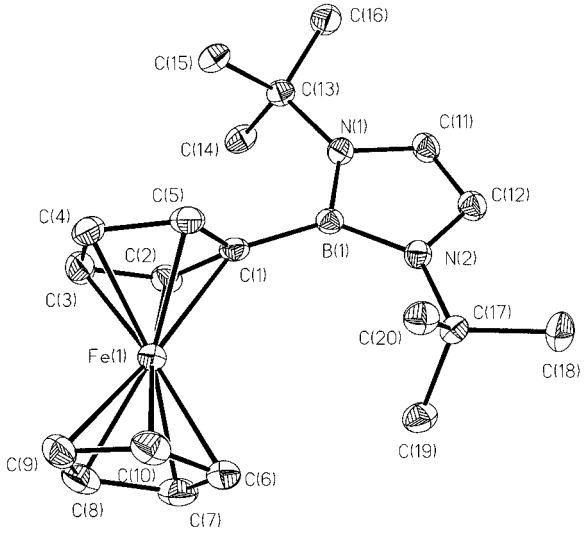

Figure 1. Molecular structure of **3** in the crystal. Selected bond lengths [Å] and angles [°]: B(1)–C(1) 1.588(2), B(1)–N(1) 1.455(2), B(1)–N(2) 1.444(2), N(1)–C(11) 1.400(2), N(2)–C(12) 1.396(2), N(1)–C(13) 1.497(2), N(2)–C(17) 1.488(2), C(11)–C(12) 1.342(2), Fe(1)–C(1) 2.132(2), Fe(1)–C(2) 2.053(2), Fe(1)–C(3) 2.031(2), Fe(1)–C(4) 2.038(2), Fe(1)–C(5) 2.066(2), Fe(1)–C(6,-10) 2.048(2)–2.070(2), C(1)–C(2) 1.434(2), C(2)–C(3) 1.421(2), C(3)–C(4) 1.424(3), C(4)–C(5) 1.426(2), C(1)–C(5) 1.437(2); N(1)–B(1)–N(2) 104.84(13), B(1)–N(1)–C(11) 107.21(13), N(1)–C(11)–C(12) 110.16(14), C(11)–C(12)–N(2) 109.75(14), B(1)–N(2)–C(12) 107.99(13), C(1)–B(1)–N(2) 133.04(15), C(1)–B(1)–N(1) 122.12(13), B(1)–N(2)–C(17) 130.51(13), B(1)–N(1)–C(13) 132.59(13), C(13)–N(1)–C(11) 120.19(13), C(12)–N(2)–C(17) 121.49(12), B(1)–C(1)–C(2) 124.81(14), B(1)–C(1)–C(5) 126.58(14), C(2)–C(1)–C(5) 105.24(14).

The molecular structure of **3** features a planar 1,3,2-diazaborole ring with a ferrocenyl substituent that is linked to the boron atom by a B–C single bond of 1.588(2) Å. This

 © 2005 Wiley-VCH Verlag GmbH & Co. KGaA, Weinheim

value compares well with the B–C bond in the borolylimidazolium ion **20** [1.580(11) Å].[4d]

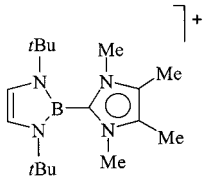

20

The atomic distances and valence angles are in good agreement with the equivalent data for cation **20**. The B–N bond lengths in **3** [1.444(2), 1.455(2) Å] indicate multiple-bond character. The B–N bond lengths in a series of diazaboroles range from 1.407(3) to 1.450(2) Å. The atomic distance C(11)–C(12) [1.342(2) Å] and the N–C(sp^2) bond lengths [1.396(2) and 1.400(2) Å] also indicate multiple bonding. Bond lengths of 1.497(2) and 1.488(2) Å are found for the N(sp^2)–C(sp^3) single bonds N(1)–C(13) and N(2)–C(17), respectively. The endocyclic angles in **3** [N(1)–B(1)–N(2) = 104.84(13)°, B(1)–N(1)–C(11) = 107.21(13)°, B(1)–N(2)–C(12) = 107.99(13)°, N(1)–C(11)–C(12) = 110.16(14)°, and N(2)–C(12)–C(11) = 109.75(14)°] resemble those in **20** [107.1(6), 105.9(4), and 110.5(3)°]. The exocyclic angle C(1)–B(1)–N(2) is much wider [133.04(15)°] than the C(1)–B(1)–N(1) angle of only 122.12(13)°, presumably due to severe steric interaction between the *tert*-butyl group at N(2) and the ferrocenyl unit. In the ferrocenyl part of the molecule it is obvious that the Fe(1)–C(1) bond of 2.132(2) Å significantly exceeds the distances between the metal atom and the remaining ring carbon atoms [2.031(2)–2.066(2) Å]. The Fe–C distances to the C_5H_5 ligand range from 2.048(2) to 2.070(2) Å, and the planes of the two Cp rings form an angle of 9.8°. The boron atom is not coplanar with ring C(1) to C(5), but is located 0.49 Å above this plane. The vector B(1)–C(1) and the ring plane enclose an angle of 17.6°. The diazaborole ring and the ring C(1) to C(5) form an angle of 73.1°, thus excluding significant π-communication between the two units.

X-ray Structural Analysis of 6

The molecular structure of **6** (Figure 2, Table 3) features a ferrocene scaffold, with each ring substituted by a planar 1,3,2-diazaborolyl group by single bonds [B(1)–C(11) = 1.596(3) Å; B(2)–C(16) = 1.584(4) Å].

The two cyclopentadienyl rings are not parallel but are bent by an angle of 12.9°. The heterocycle defined by the atoms B(1), N(1), N(2), C(1), and C(2) and the ring C(11)–C(15) show an interplanar angle of 46.6°. The plane of the second diazaborolyl substituent and the plane defined by the atoms C(16) to C(20) feature an interplanar angle of 103.1°. The boron atoms B(1) and B(2) are located 0.31 and 0.51 Å above their respective cyclopentadienyl ligands, which means that the vectors B(1)–C(11) and B(2)–C(16) form angles of 10.7° and 18.1° with the respective C_5H_4 planes. The vectors B(1)–C(11) and B(2)–C(16) form an angle of 75.7°, which mirrors a *gauche* conformation of both substituents. As already observed with complex **3**, the

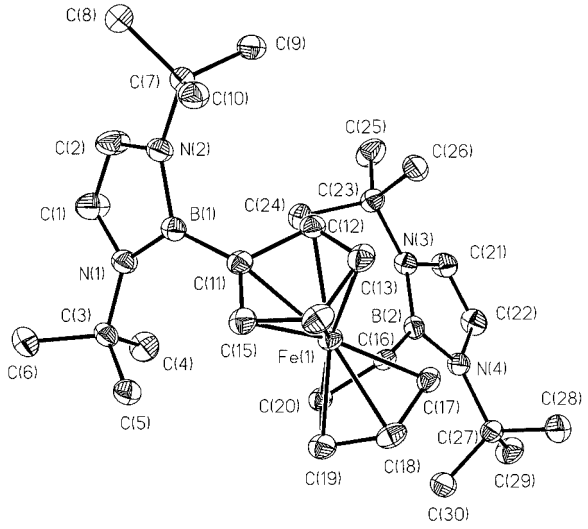

Figure 2. Molecular structure of **6** in the crystal. Selected bond lengths [Å] and angles [°]: B(1)–C(11) 1.596(3), B(1)–N(1) 1.450(3), B(1)–N(2) 1.464(3), N(1)–C(1) 1.396(3), N(1)–C(3) 1.485(3), N(2)–C(2) 1.379(3), N(2)–C(7) 1.499(3), C(1)–C(2) 1.343(3), B(2)–C(16) 1.584(4), B(2)–N(3) 1.447(3), B(2)–N(4) 1.462(3), N(3)–C(21) 1.404(3), N(3)–C(23) 1.483(3), N(4)–C(22) 1.397(3), N(4)–C(27) 1.497(3), Fe(1)–C(11) 2.136(2), Fe(1)–C(12) 2.051(2), Fe(1)–C(13) 2.044(2), Fe(1)–C(14) 2.042(2), Fe(1)–C(15) 2.072(2), Fe(1)–C(16) 2.155(2), Fe(1)–C(17) 2.059(2), Fe(1)–C(18) 2.026(2), Fe(1)–C(19) 2.035(2), Fe(1)–C(20) 2.079(2), C–C(Cp) 1.407(3)–1.436(3); B(1)–N(1)–C(1) 106.9(2), N(1)–C(1)–C(2) 110.4(2), N(2)–C(2)–C(1) 110.3(2), B(1)–N(2)–C(2) 107.3(2), N(1)–B(1)–N(2) 104.8(2), N(1)–B(1)–C(11) 132.8(2), N(2)–B(1)–C(11) 122.2(2), B(1)–N(1)–C(3) 135.7(2), C(1)–N(1)–C(3) 117.3(2), C(2)–N(2)–C(7) 118.0(2), B(1)–N(2)–C(7) 134.6(2), B(1)–C(11)–C(15) 132.5(2), B(1)–C(11)–C(12) 121.7(2), C(12)–C(11)–C(15) 104.7(2), B(2)–N(3)–C(21) 107.6(2), N(3)–C(21)–C(22) 110.2(2), N(4)–C(22)–C(21) 110.1(2), B(2)–N(4)–C(22) 107.5(2), N(3)–B(2)–N(4) 104.6(2), C(16)–B(2)–N(3) 132.6(2), B(2)–N(3)–C(23) 130.4(2), C(21)–N(3)–C(23) 121.2(2), C(16)–B(2)–N(4) 122.7(2), B(2)–C(16)–C(17) 124.4(2), B(2)–C(16)–C(20) 127.2(2), C(17)–C(16)–C(20) 104.8(2).

Fe(1)–C(11) [2.136(2) Å] and Fe(1)–C(16) [2.155(2) Å] contacts are much longer than the remaining Fe–[C(12)–C(15)] [2.042(2)–2.072(2) Å] or Fe–[C(17)–C(20)] [2.026(2)–2.079(2) Å] bonds, although the bond lengths and angles within the heterocycles are similar to those in **3**. As is also the case in **3**, the exocyclic angles N(1)–B(1)–C(11) [132.8(2)°] and N(3)–B(2)–C(16) [132.6(2)°] are more obtuse than the angles N(2)–B(1)–C(11) [122.2(2)°] and N(4)–B(2)–C(16) [122.7(2)°], which reflects the steric requirements of the ferrocene unit.

X-ray Structural Analysis of 15

The molecule of **15** (Figure 3, Table 3) adopts the structure of a three-legged piano-stool with three essentially linear carbonyl ligands. The C–Mn–C angles range from 89.9(2) to 93.6(2)°. The most interesting feature of **15** is the methylcyclopentadienyl ligand, which is linked to a 1,3,2-diazaborolidinyl substituent by a B–C single bond of 1.594(5) Å. The heterocycle is slightly puckered (sum of angles: 532.8°; mean deviation from the best plane: 0.1037 Å), and features a dihedral angle with the cyclopentadienyl ring of 39.6°. The boron atom is located 0.20 Å

 © 2005 Wiley-VCH Verlag GmbH & Co. KGaA, Weinheim

above the carbocycle and C(11) is situated 0.44 Å underneath the plane of the heterocycle. The vector B(1)–C(11) forms angles of 7.1° and 13.3° with the carbocycle and the borolidine, respectively.

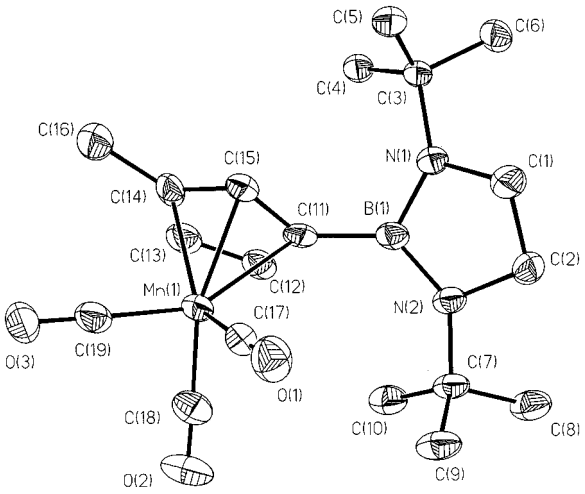

Figure 3. Molecular structure of **15** in the crystal. Selected bond lengths [Å] and angles [°]: B(1)–N(1) 1.445(5), B(1)–N(2) 1.431(5), N(1)–C(1) 1.470(4), N(2)–C(2) 1.469(4), C(1)–C(2) 1.502(5), N(1)–C(3) 1.481(4), N(2)–C(7) 1.489(4), B(1)–C(11) 1.594(5), Mn(1)–C(11) 2.187(3), Mn(1)–C(12) 2.172(4), Mn(1)–C(13) 2.163(4), Mn(1)–C(14) 2.138(4), Mn(1)–C(15) 2.109(3), Mn(1)–C(17) 1.787(4), Mn(1)–C(18) 1.794(4), Mn(1)–C(19) 1.793(4), C–O 1.152(5)–1.156(5); B(1)–N(1)–C(1) 106.8(3), B(1)–N(1)–C(3) 135.4(3), N(1)–C(1)–C(2) 104.1(3), C(1)–N(1)–C(3) 117.8(3), N(2)–C(2)–C(1) 105.5(3), B(1)–N(2)–C(2) 108.2(3), N(1)–B(1)–N(2) 108.2(3), N(1)–B(1)–C(11) 119.7(3), N(2)–B(1)–C(11) 131.7(3), B(1)–C(11)–C(15) 121.4(3), B(1)–C(11)–C(12) 133.9(3), C(12)–C(11)–C(15) 104.1(3), C(17)–Mn(1)–C(18) 93.6(2), C(17)–Mn(1)–C(19) 90.8(2), C(18)–Mn(1)–C(19) 89.9(2), Mn(1)–C–O 177.5(3)–178.9(3).

The manganese atom is unsymmetrically attached to the carbocycle with Mn–C bond lengths ranging from 2.109(3) Å [Mn(1)–C(15)] to 2.187(3) Å [Mn(1)–C(11)]. The B–N distances 1.431(5) and 1.445(5) Å indicate multiple bonding. The remaining endocyclic distances N(1)–C(1) [1.470(4) Å], N(2)–C(2) [1.469(4) Å], and C(1)–C(2) [1.502(5) Å] are single bonds and differ markedly from those in **3** and **6**. The exocyclic angle N(2)–B(1)–C(11) [131.7(3)°] is similar to those of the previously discussed molecules **3** and **6**, and it is wider than the angle N(1)–B(1)–C(11) [119.7(3) Å]. As a consequence of steric hindrance, the exocyclic angles B(1)–N(1)–C(3) [135.4(3)°] and B(1)–N(2)–C(7) [136.7(3)°] clearly exceed the angles C(1)–N(1)–C(3) [117.8(3)°] and C(2)–N(2)–C(7) [115.1(3)°].

Electrochemistry

All the ferrocenyl- and methylcymantrenyl-functionalized diazaboroles and diazaborolidines described here were also investigated by cyclic voltammetry. With the ferrocene derivatives **3**, **6**, **11**, **13**, and **14** a quasi-reversible Fe^{2+}/Fe^{3+} oxidation was observed (Table 2). At low scan rates ($5\ mV\ s^{-1}$) the cyclovoltammograms feature an irreversible wave, which changes to a quasi-reversible one on going to higher rates. The oxidation potentials, $E^{0\prime}$, have been taken from square-wave voltammograms with reference to the redox pair Fc/Fc^+. From these data it is obvious that the diazaborole and the diazaborolidine group transfer electron density onto the redox-active center of the ferrocene unit. The diborolylated ferrocene **6** is more easily oxidized ($E^{0\prime}$ = –0.34 V) than the monoborolylated analog **3** ($E^{0\prime}$ = –0.18 V), and the same trend is observed with compounds **13** ($E^{0\prime}$ = –0.11 V) and **14** ($E^{0\prime}$ = –0.20 V), where one or two diazaborolidinyl substituents are present. Moreover, it is evident that the oxidation of the ferrocenyl-diazaboroles **3** and **6** is easier than the saturated congeners **13** and **14**; no decomposition of the ferrocene derivatives was observed during these experiments. This is not the case with the methylcymantrenyl systems **9** ($E^{0\prime}$ = +0.21 V) and **15** ($E^{0\prime}$ = +0.49 V), where an irreversible oxidation process with the formation of free methylcymantrene ($E^{0\prime}$ = +0.84 V) was observed. Wagner et al. have previously reported that boryl-substituted ferrocenes also suffer from degradation to ferrocene during their cyclovoltammetric studies.[13]

Table 2. Voltammetric data ($E^{0\prime}$) of ferrocenyl- and methylcymantrenyl-functionalized diazaboroles and diazaborolidines vs. Fc/Fc^+ standard.

Compound	**3**	**6**	**9**	**11**	**13**	**14**	**15**
$E^{0\prime}$ [V]	–0.18	–0.34	+0.21	–0.32	–0.11	–0.20	+0.49

Conclusions

We have extended methodologies for the synthesis of 1,3,2-diazaboroles to the construction of ferrocenyl- and cymantrenyl-functionalized diazaboroles. X-ray structure analyses show that the heterocycle is twisted out of the plane of the adjacent cyclopentadienyl ligand in the crystal, thus preventing significant electronic communication by π-electron delocalization. According to the cyclic voltammetric studies, borole and borolidine substituents serve as electron donors and cause cathodic shifts of the oxidation potentials of the iron center relative to the parent system Fc/Fc^+.

Experimental Section

General: All reactions were performed under dry, oxygen-free nitrogen using standard Schlenk techniques. The dibromoboryl derivatives $[(\eta^5\text{-Cp})(\eta^5\text{-}C_5H_4BBr_2)Fe]$ (**1**), $[(\eta^5\text{-}C_5H_4BBr_2)_2Fe]$ (**4**), and $[\{\eta^5\text{-}(3\text{-}CH_3)(1\text{-}Br_2B)C_5H_3\}Mn(CO)_3]$ (**9**), as well as the imines *t*BuN=CH–CH=N*t*Bu[9] and *N*-(2-pyridylmethylene)-*tert*-butylamine,[11] were synthesized as described in the literature. *N*,*N*′-Di-*tert*-butylethane-1,2-diamine and triethylamine were purchased commercially. Infrared spectra were recorded with a Bruker FT-IR IFS 66 spectrometer. NMR spectra: Bruker AM Avance DRX 500. Standards: $SiMe_4$ (^1H, ^{13}C), $BF_3{\cdot}OEt_2$ (^{11}B). Mass spectra were recorded with a VG Autospec sector field mass spectrometer (Micromass). The electrochemical experiments were performed

 © 2005 Wiley-VCH Verlag GmbH & Co. KGaA, Weinheim

with a PAR Model 270 A and the relevant software (Model 270). A system of microelectrodes with a three-electrode array was used, with a platinum wire as working electrode (1.5 cm length, 0.5 mm diameter), which was wound as a helix around the counter electrode and a silver wire (1.5 cm length, 1 mm diameter) as pseudo-reference electrode. All experiments were conducted in a glass device, which was flame-dried prior to use and filled with dry nitrogen. The determinations were performed in a 0.1 M solution of tetrabutylammonium hexafluorophosphate (TBAPF) in dichloromethane with concentrations of the analyte of ca. 1×10^{-4} M. The cyclovoltammograms were recorded with scan rates of 5–700 mV s^{-1}. All published potentials were determined by means of square-wave voltammetry (frequency: 5 Hz). Ferrocene and octamethylferrocene were used for calibration. All the potentials with octamethylferrocene were converted into the ferrocene standard.

[(η^5-C_5H_5){η^5-$C_5H_4BN^a$(*t*Bu)CH=CHN^b(*t*Bu)}Fe](*B*–*N*^{b}) (3): Solutions of (dibromoboryl)ferrocene (**1**; 3.10 g, 8.7 mmol) and *N*,*N*′-di-*tert*-butyl-1,4-diazabutadiene (1.46 g, 8.7 mmol), each in *n*-hexane (70 mL), were simultaneously added dropwise to *n*-hexane (50 mL). An olive-green precipitate of borolium salt **2** [^{11}B NMR (CD_3CN): δ = 3.8 and 7.1 ppm] separated. A sample of freshly prepared sodium amalgam (obtained from 1.30 g of Na and 120 g of Hg) was added to the slurry, which was subsequently vigorously stirred in the dark for 2 d. A dark-red solution was decanted and concentrated in vacuo until the solution became cloudy. Storing at –80 °C for 10 d furnished 2.35 g of **3** as red crystals (yield 74%). ^{1}H NMR (C_6D_6): δ = 1.40 (s, 18 H, *t*Bu), 4.10 (s, 5 H, C_5H_5), 4.23 (s, 4 H, C_5H_4B), 6.42 (s, 2 H, NCH) ppm. ^{13}C{^{1}H} NMR (C_6D_6): δ = 32.7 [s, C(*C*H$_3$)$_3$], 53.2 [s, *C*(CH$_3$)$_3$], 68.6 (s, BC$_2{}^a$*C*$_2{}^b$H$_4$), 69.6 (s, C_5H_5), 76.2 (s, BC$_2{}^a$C$_2{}^b$H$_4$), 112.7 (s, NCH) ppm. ^{11}B{^{1}H} NMR (C_6D_6): δ = 25.3 ppm. MS-EI: *m*/*z* (%) = 364 (100) [M$^+$]. $C_{20}H_{29}BFeN_2$ (364.12): calcd. C 65.97, H 8.03, N 7.69; found C 64.78, H. 7.67, N 7.22. Repeated attempts to obtain better analyses were unsuccessful. $E^{0\prime}$ = –0.18 V (vs. Fc/Fc$^+$).

[{η^5-$C_5H_4BN^a$(*t*Bu)CH=CHN^b(*t*Bu)}]Fe(*B*–*N*^{b}) (6): Solutions of 1,1′-Bis(dibromoboryl)ferrocene (**4**; 2.20 g, 6.2 mmol) and *N*,*N*′-di-*tert*-butyl-1,4-diazabutadiene (2.09 g, 12.4 mmol), each in *n*-hexane (70 mL), were simultaneously added dropwise to *n*-hexane (25 mL), whereby the olive-green borolium salt **5** (^{11}B{^{1}H} NMR: δ = 3.8, 7.1 ppm) separated. Freshly prepared sodium amalgam (obtained from 1.30 g of Na and 120 g of Hg) was added, and the slurry was vigorously stirred in the dark for 2 d. A dark-red solution was decanted from the mercury phase and concentrated in vacuo until the solution turned cloudy. Storing of the solution at –80 °C for 12 d and then at –10 °C for 2 d gave 2.72 g (81% yield) of compound **6** as cherry-red crystals. ^{1}H NMR (C_6D_6): δ = 1.42 (s, 36 H, *t*Bu), 4.23 (s, 4 H, Cp), 4.36 (s, 4 H, Cp), 6.39 (s, 4 H, NCH) ppm. ^{13}C{^{1}H} NMR (C_6D_6): δ = 32.8 [s, C(*C*H$_3$)$_3$], 53.2 [s, *C*(CH$_3$)$_3$], 69.2 (s, CH-Cp), 79.3 (s, CH-Cp), 112.9 (s, NCH) ppm. ^{11}B{^{1}H} NMR (C_6D_6): δ = 25.3 ppm. MS-EI: *m*/*z* (%) = 542 (100) [M$^+$]. $C_{30}H_{48}BFeN_2$ (542.21): calcd. C 66.46, H 8.92, N 10.33; found C 66.53, H 9.12, N 9.90. $E^{0\prime}$ = –0.34 V (vs. Fc/Fc$^+$).

[{(3-Me)[1-BN^a(*t*Bu)CH=CHN^b(*t*Bu)]C_5H_3}Mn(CO)$_3$](*B*–*N*^{b}) (9): Solutions of 1-dibromoboryl-3-methylcymantrene (**7**; 4.00 g, 10.3 mmol) and *N*,*N*′-di-*tert*-butyl-1,4-diazabutadiene (1.74 g, 10.3 mmol), each in *n*-hexane (100 mL), were slowly added (one drop per second!) to *n*-hexane (50 mL). The dark-yellow borolium salt **8** [^{11}B{^{1}H} NMR (CD_3CN): δ = 5.0 ppm] separated. It was filtered and washed with *n*-hexane (3 × 40 mL). The salt was suspended in *n*-hexane (100 mL), sodium amalgam (from 1.60 g of Na and 165 g of Hg) was added, and the resulting slurry was vigorously stirred in the dark for 2 d. Storing at –30 °C for 4 d gave yellow crystals of thermolabile **9** (2.58 g, 63%). Decomposition at room temp. was complete after 24 h. ^{1}H NMR (C_6D_6): δ = 1.34 (s, 18 H, *t*Bu), 1.56 (s, 3 H, CH_3), 4.04 (s, 1 H, C_5H_3), 4.57 (s, 1 H, C_5H_3), 4.65 (s, 1 H, C_5H_3), 6.34 (s, 2 H, NCH) ppm. ^{13}C{^{1}H} NMR (C_6D_6): δ = 12.8 (s, CH_3), 32.9 [s, C(*C*H$_3$)$_3$], 53.6 [s, *C*(CH$_3$)$_3$], 82.1 (s, C4), 94.4; 95.2 (2s, C2, C5), 99.8 (s, C3), 113.7 (s, NCH), 226.2 (s, CO) ppm. ^{11}B{^{1}H} NMR (C_6D_6): δ = 23.2 (s) ppm. MS-EI: *m*/*z* (%) = 396 (21) [M$^+$], 312 (63) [M$^+$ – 3CO], 296 (100) [M$^+$ – 3CO – CH_4]. $C_{19}H_{26}BMnN_2O_3$ (396.18): calcd. C 57.60, H 6.61, N 7.07; found C 57.09, H 6.87, N 7.08. $E^{0\prime}$ = +0.21 V (vs. Fc/Fc$^+$).

[*t*BuN^aC^{b}H=C^{c}C^{d}H=C^{e}HC^{f}H=C^{g}HN^hBC_5H_4](C_5H_5)Fe(*N*^{a}–*B*,*N*^{h}–*C*^{e}) (11): Solutions of (dibromoboryl)ferrocene (**1**; 1.70 g, 4.78 mmol) and *N*-(2-pyridylmethylene)-*tert*-butylamine (0.70 g, 4.78 mmol), each in *n*-hexane (20 mL), were simultaneously added dropwise to *n*-hexane (50 mL). Stirring for 4 h led to the precipitation of borolium salt **10** as an olive-green solid [^{11}B{^{1}H} NMR (CD_3CN): δ = 6.3, 7.8 ppm]. Sodium amalgam (obtained from 0.23 g of Na and 213 g of Hg) was added and the suspension was stirred in the dark for 3 d. The *n*-hexane phase was decanted and concentrated until the beginning of cloudiness. Storing at –80 °C for 2 d gave 1.16 g (68% yield) of **11** as an orange solid. ^{1}H NMR (C_6D_6): δ = 1.35 (s, 9 H, *t*Bu), 4.00 (s, 5 H, C_5H_5), 4.21 (s, 2 H, C_5H_4), 4.31 (s, 2 H, C_5H_4), 5.78 (m, 1 H, CH), 6.16 (m, 1 H, CH), 6.47 (s, 1 H, *t*BuNC*H*), 6.78 (m, 1 H, CH), 8.33 (s, 1 H, CH) ppm. ^{13}C{^{1}H} NMR (C_6D_6): δ = 32.6 [s, C(*C*H$_3$)$_3$], 53.7 [s, *C*(CH$_3$)$_3$], 68.0 (s, C_5H_4), 68.7 (s, C_5H_5), 69.7 (s, C_5H_4), 74.4(s, C_5H_4), 105.1 (s, *t*BuN*C*H), 105.7 (s, CH), 117.7 (s, CH), 119.0 (s, CH), 126.6 (s, *t*BuNCH=*C*), 130.9 (s, CH) ppm. ^{11}B{^{1}H} NMR (C_6D_6): δ = 23.9 ppm. MS-EI: *m*/*z* (%)= 318 (9) [M$^+$ – 2 CH_3]. $C_{20}H_{23}BFeN_2$ (358.09): calcd. C 67.08, H 6.47, N 7.82; because of the thermolability of **11** no reliable elemental analyses could be obtained. $E^{0\prime}$ = –0.32 V (vs. Fc/Fc$^+$).

[{η^5-$C_5H_4BN^a$(*t*Bu)$CH_2CH_2N^b$(*t*Bu)}(η^5-C_5H_5)Fe](*B*–*N*^{b}) (13): A solution of **1** (2.80 g, 7.8 mmol) in *n*-hexane (10 mL) was added to a chilled (0 °C) solution of NEt_3 (1.60 g, 15.6 mmol) in *n*-hexane (50 mL). It was warmed to room temp., 1.40 g (8.00 mmol) of neat *N*,*N*′-di-*tert*-butylethane-1,2-diamine was added dropwise, and the mixture was heated under reflux for 3 h. It was then filtered and the filtrate was concentrated to dryness. Distillation of the residue at 250 °C and 10^{-6} bar afforded 2.46 g (86%) of product **13** as a red oil (b.p. 210 °C, 10^{-6} bar). ^{1}H NMR (C_6D_6): δ = 1.26 (s, 18 H, *t*Bu), 3.11 (s, 4 H, NCH_2), 4.08 (s, 5 H, C_5H_5), 4.18 (s, 2 H) and 4.19 (s, 2 H, C_5H_4B) ppm. ^{13}C{^{1}H} NMR (C_6D_6): δ = 31.3 [s, C(*C*H$_3$)$_3$], 45.5 (s, NCH_2), 51.7 [s, *C*(CH$_3$)$_3$], 68.3 (s) and 76.2 (s, C_5H_4B), 69.6 (s, C_5H_5) ppm. ^{11}B{^{1}H} NMR (C_6D_6): δ = 31.8 ppm. MS-EI: *m*/*z* (%) = 366 (63) [M$^+$], 351 (20) [M$^+$ – CH_3], 294 (31) [M$^+$ – *t*Bu – H$^+$]. $C_{20}H_{31}BFeN_2$ (366.64): calcd. C 65.46, H 8.51, N 7.63; found C 64.82, H 8.69, N 7.40. $E^{0\prime}$ = –0.11 V (vs. Fc/Fc$^+$).

[{$C_5H_4BN^a$(*t*Bu)$CH_2CH_2N^b$(*t*Bu)}$_2$Fe](*B*–*N*$_b$) (14): A solution of **4** (4.00 g, 7.6 mmol) in *n*-hexane (40 mL) was added dropwise to a chilled (0 °C) solution of Et_3N (3.08 g, 30.4 mmol) in *n*-hexane (100 mL). The mixture was then warmed to room temp., combined with neat *N*,*N*′-di-*tert*-butylethane-1,2-diamine (2.63 g, 15.2 mmol), and heated under reflux for 4 h. It was then filtered and the filtrate concentrated to dryness. The deep-red solid residue was dissolved in *n*-hexane (20 mL), and the solution was stored at –80 °C for 7 d to give 3.62 g (87% yield) of red solid **14**. ^{1}H NMR (C_6D_6): δ = 1.43 (s, 18 H, *t*Bu), 3.23 (s, 8 H, NCH_2), 4.30 and 4.44 (m, 8 H, C_5H_4B) ppm. ^{13}C{^{1}H} NMR (C_6D_6): δ = 31.4 [C(*C*H$_3$)$_3$], 45.5 (s, NCH_2), 51.8 [s, *C*(CH$_3$)$_3$], 68.9 [s, C(3),(4)], 79.0 [s, C(2),(5)] ppm. ^{11}B{^{1}H} NMR (C_6D_6): δ = 31.8 ppm. MS-EI: *m*/*z* (%) = 546

 © 2005 Wiley-VCH Verlag GmbH & Co. KGaA, Weinheim

Table 3. Crystallographic data for **3**, **6**, and **15**.

	3	**6**	**15**
Empirical formula	$C_{20}H_{29}BFeN_2$	$C_{30}H_{48}B_2FeN_4$	$C_{19}H_{28}BMnN_2O_3$
Color	red	orange	colorless
Size [mm]	0.24 × 0.20 × 0.17	0.21 × 0.14 × 0.06	0.15 × 0.07 × 0.06
M_r	364.11	542.19	398.18
Crystal system	orthorhombic	triclinic	triclinic
Space group	$P2_12_12_1$	$P\bar{1}$	$P\bar{1}$
a [Å]	9.3010(2)	10.6860(2)	9.0730(9)
b [Å]	10.7800(2)	11.8430(3)	10.5250(7)
c [Å]	18.4140(3)	13.2840(4)	11.5870(12)
α [°]	90	108.3010(15)	82.936(6)
β [°]	90	93.1290(17)	88.844(6)
γ [°]	90	112.0801(15)	65.658(5)
V [Å^3]	1846.28(6)	1450.30(6)	999.89(16)
$\rho_{calcd.}$ [g cm^{-3}]	1.310	1.242	1.323
Z	4	2	2
F(000)	776	584	420
μ [mm^{-1}]	0.820	0.546	0.680
Θ [°]	3.10–27.5	2.91–27.45	2.95–25.00
T [K]	100	100	100
Refl. measured	24538	37733	9676
Unique refl.	4206	6599	3509
R(int)	0.049	0.086	0.061
No refl. [$I > 2\sigma(I)$]	3949	4865	2689
Refined parameters	223	346	242
R_F [$I > 2\sigma(I)$]	0.0244	0.0474	0.0540
wR_F^2 [$I > 2\sigma(I)$]	0.0584	0.1014	0.1373
$\Delta\rho_{max./min.}$ [e Å^{-3}]	0.259/–0.278	0.394/–0.274	0.935/–0.661
CCDC-	273089	273090	273091

(100) [M$^+$], 490 (10) [M$^+$ – $Me_2C{=}CH_2$]. $C_{30}H_{52}BFeN_4$ (546.26): calcd. C 65.97, H 9.59, N 10.26; found C 65.97, H 9.64, N 9.98. $E^{0\prime}$ = –0.20 V (vs. Fc/Fc$^+$).

[{(3-Me)[1-BN^a(*t*Bu)CH$_2$CH$_2$N^b(*t*Bu)][C$_5$H$_3$}Mn(CO)$_3$](*B*–*N*^{b}) (15): A sample of neat **7** (5.30 g, 13.6 mmol) was combined with a chilled (0 °C) solution of Et_3N (2.80 g, 27.1 mmol) in *n*-hexane (100 mL), whereby a colorless precipitate separated. It was warmed to room temp. and 2.30 g (27.1 mmol) of neat *N*,*N*′-di-*tert*-butylethane-1,2-diamine was added dropwise. This mixture was heated under reflux for 3 h. After filtration, the filtrate was freed from solvent and the yellow oily residue was distilled at 10^{-6} bar and 150 °C bath temperature. The distillate was dissolved in *n*-pentane (40 mL) and stored at –30 °C for 7 d to afford crystalline **15** (yield: 4.60 g, 85%). ^{1}H NMR (C_6D_6): δ = 1.30 (s, 18 H, *t*Bu), 1.68 (s, 3 H, CH_3), 3.11 (s, 4 H, CH_2), 4.14 [s, 1 H, H(4)], 4.63 and 4.68 [s, 2 H, H(2),(5)] ppm. ^{13}C{^{1}H} NMR (C_6D_6): δ = 12.8 (s, CH_3), 31.2 [s, C(CH_3)$_3$], 45.3 (s, NCH_2), 51.9 [s, $C(CH_3)_3$], 81.7 [s, C(4)], 93.5 and 94.1 [2 s, C(2),(5)], 99.8 [s, C(3)], 226.0 (s, CO) ppm. ^{11}B{^{1}H} NMR (C_6D_6): δ = 29.6 ppm. IR (KBr): $\tilde{\nu}$ = 2009 cm^{-1} (s, CO), 1908 (br. s, CO). MS-EI: *m*/*z* (%) = 398 (10) [M$^+$], 314 (85) [M$^+$ – 3 CO], 298 (100) [M$^+$ – 3 CO – CH_4]. $C_{19}H_{28}BN_2MnO_3$ (398.19): calcd. C 57.31, H 7.09, N 7.04; found C 56.94, H 6.88, N 6.71. $E^{0\prime}$ = +0.49 V (vs. Fc/Fc$^+$). CCDC-273089 to -273091 contain the supplementary crystallographic data for this paper. These data can be obtained free of charge via www.ccdc.cam.ac.uk/data_request/cif (see also Table 3).

[1] S. Aldridge, C. Bresner, *Coord. Chem. Rev.* **2003**, *244*, 71–92.
[2] K. Ma, M. Scheibitz, S. Scholz, M. Wagner, *J. Organomet. Chem.* **2002**, *652*, 11–19.
[3] Review: L. Weber, *Coord. Chem. Rev.* **2001**, *215*, 39–77.
[4] a) L. Weber, E. Dobbert, A. Rausch, H.-G. Stammler, B. Neumann, *Z. Naturforsch., Teil B* **1999**, *54*, 363–371; b) L. Weber, E. Dobbert, H.-G. Stammler, R. Boese, D. Bläser, *Eur. J. Inorg. Chem.* **1999**, 491–497; c) L. Weber, E. Dobbert, R. Boese, M. T. Kirchner, D. Bläser, *Eur. J. Inorg. Chem.* **1998**, 1145–1152; d) L. Weber, E. Dobbert, H.-G. Stammler, B. Neumann, R. Boese, D. Bläser, *Chem. Ber./Recueil* **1997**, *130*, 705–710.
[5] a) L. Weber, M. Schnieder, T. C. Maciel, H. Wartig, M. Schimmel, R. Boese, D. Bläser, *Organometallics* **2000**, *19*, 5791–5794; b) L. Weber, A. Rausch, H.-G. Stammler, B. Neumann, *Z. Anorg. Allg. Chem.* **2005**, *631*, 1633–1639.
[6] a) J. S. Merriam, K. Niedenzu, *J. Organomet. Chem.* **1973**, *51*, C1–C2; b) K. Niedenzu, J. S. Merriam, *Z. Anorg. Allg. Chem.* **1974**, *406*, 251–259; c) G. Schmid, M. Polk, R. Boese, *Inorg. Chem.* **1990**, *29*, 4421–4429.
[7] a) L. Weber, G. Schmid, *Angew. Chem.* **1974**, *86*, 519; *Angew. Chem. Int. Ed. Engl.* **1974**, *13*, 467; b) G. Schmid, J. Schulze, *Chem. Ber.* **1977**, *110*, 2744–2750.
[8] a) N. Ruf, T. Renk, W. Siebert, *Z. Naturforsch., Teil B* **1976**, *31*, 1028–1034; b) T. Renk, W. Ruf, W. Siebert, *J. Organomet. Chem.* **1976**, *120*, 1–25.
[9] J. M. Klugman, R. K. Barnes, *Tetrahedron* **1970**, *26*, 2555–2560.
[10] I. Domke, L. Weber, unpublished results.
[11] A. J. Clark, D. J. Duncalf, R. P. Filik, D. W. Haddleton, G. H. Thomas, H. Wongtap, *Tetrahedron Lett.* **1999**, *40*, 3807.
[12] M. Herberhold, U. Dörfler, B. Wrackmeyer, *Polyhedron* **1995**, *14*, 2683–2689.
[13] a) M. Fontani, F. Peters, W. Scherer, W. Wachter, M. Wagner, P. Zanello, *Eur. J. Inorg. Chem.* **1998**, 1453–1465; b) K. Ma, H.-W. Lerner, S. Scholz, J. W. Bats, M. Bolte, M. Wagner, *J. Organomet. Chem.* **2002**, *664*, 94–105.

Received: June 2, 2005
Published Online: October 13, 2005

 © 2005 Wiley-VCH Verlag GmbH & Co. KGaA, Weinheim

DOI: 10.1002/ejic.200500549

Asymmetric [2+2] Cycloaddition of (*E*)-2-(Diphenylphosphanyl)styrene Promoted by a Chiral Metal Template

Wee-Chuan Yeo,[a] Geok-Kheng Tan,[a] Lip Lin Koh,[a] and Pak-Hing Leung*[b]

Keywords: Asymmetric synthesis / Cycloaddition / Platinum / Phosphane ligands / Template synthesis

An organoplatinum complex containing the (*S*)-form of orthometalated [1-(dimethylamino)ethyl]naphthalene as the chiral auxiliary promotes the asymmetric [2+2] dimerization of (*E*)-2-(diphenylphosphanyl)styrene to generate two isomeric chelating diphosphanyl-substituted cyclobutane platinum template complexes in the ratio of 6:1. The four substituents on the cyclobutane rings adopt the pseudo-equatorial positions with an *all-trans* arrangement. The naphthylamine auxiliary can be removed chemoselectively from the template products by treatment with concentrated hydrochloric acid to form the corresponding dichloroplatinum(II) complexes, which, upon subsequent ligand displacement with aqueous cyanide, liberate the enantiomerically enriched free diphosphane ligand in high yields. Recomplexation of the liberated diphosphane to the (*R*)-form of the platinum template, followed by fractional crystallization, allows separation of the optically pure platinum template complex containing the diphosphane ligand (1*R*,2*R*,3*R*,4*R*)-1,2-bis(diphenylphosphanyl)-3,4-diphenylcyclobutane, from which the free diphosphane can be subsequently liberated efficiently.
(© Wiley-VCH Verlag GmbH & Co. KGaA, 69451 Weinheim, Germany, 2005)

Introduction

The [2+2] cycloaddition reaction is an important method for the synthesis of cyclobutane derivatives.[1] According to the Woodward–Hoffmann rules, concerted thermal $[_{\pi}2_{s}+_{\pi}2_{s}]$ cycloadditions are symmetry-forbidden, but reactions involving $[_{\pi}2_{s}+_{\pi}2_{a}]$ cycloaddition, stepwise addition involving biradical or zwitterionic intermediates, and photocycloaddition are possible.[2] Lewis acids[3] and transition metal complexes[4] have been shown to be useful for the activation of the [2+2] cycloaddition reaction. Recently, it has been reported that the intramolecular [2+2] photochemical dimerization of *trans*-1,2-bis(diphenylphosphanyl)-ethene can be promoted efficiently by platinum and palladium ions.[5] The resultant tetradentate phosphane and other phosphane ligands with the cyclobutane backbone have been successfully applied to many metal-catalyzed reactions.[6]

Over the years, chiral cyclometalated-amine complexes have contributed significantly in many aspects of synthetic chemistry. These organometallic compounds have been used as resolving agents for chiral ligands,[7] clear and reliable references for the NMR assignment of unknown absolute configurations,[7g,8] chiral derivatizing agents (CDAs) for enantiomeric purity determination of chiral compounds,[9] efficient chiral catalysts for asymmetric Claisen rearrangements,[10] reaction promoters for the oxidative coupling between vinylphosphanes and imines,[11] chiral templates for asymmetric Diels–Alder reactions,[12] asymmetric hydroamination,[13] and hydrophosphanylation[14] reactions. In pursing our interest in the application of chiral cyclometalated-amine complexes in asymmetric transformations, we present here the organoplatinum-promoted asymmetric [2+2] dimerization of (*E*)-2-(diphenylphosphanyl)styrene.

Results and Discussion

In the absence of a metal ion, no dimerization of (*E*)-2-(diphenylphosphanyl)styrene is observed upon heating. In principle, the use of the chiral metal promoter (*S*)-**1** for this reaction could be beneficial in several aspects as it could: (a) provide electronic activation, (b) enable the *cis* coordinated vinylphosphane ligands to approach each other closely for the intramolecular cycloaddition reaction, and (c) provide stereochemical induction. Indeed, upon removal of the chloro ligands with silver tetrafluoroborate,[12b,12c,15] the chiral metal template (*S*)-**1** promotes the targeted asymmetric [2+2] cycloaddition reaction of (*E*)-2-(diphenylphosphanyl)styrene (Scheme 1). The reaction is complete after refluxing the mixture in toluene for four days. Prior to purification, the ^{31}P NMR spectrum of the crude reaction mixture in $CDCl_3$ indicated that two major products, together with (*E*)-diphenylstyrylphosphane oxide and trace amounts of other, as-yet unidentified compounds, had formed. The two desired major products − the diastereomeric cycloadducts (*S*)-**2** and (*S*)-**3** − exhibit two pairs of doublet phos-

[a] Department of Chemistry, National University of Singapore, Kent Ridge, Singapore 119260, Singapore
[b] Division of Chemistry and Biological Chemistry, Nanyang Technological University, Singapore 637616, Singapore
E-mail: pakhing@ntu.edu.sg

 © 2005 Wiley-VCH Verlag GmbH & Co. KgaA, Weinheim

phorus resonance signals at δ = 30.3 ($J_{P,P}$ = 15.3, $J_{Pt,P}$ = 3719 Hz) and 35.2 ppm ($J_{P,P}$ = 15.3, $J_{Pt,P}$ = 1793 Hz) and δ = 29.4 ($J_{P,P}$ = 15.3, $J_{Pt,P}$ = 3780 Hz) and 35.9 ppm ($J_{P,P}$ = 15.3, $J_{Pt,P}$ = 1789 Hz)], respectively, with an intensity ratio of 6:1. It is important to note that this reaction is sensitive to the counterion present. With the tetrafluoroborate or hexafluorophosphate anion, the two desired products, (*S*)-**2** and (*S*)-**3** were formed predominantly. Between the tetrafluoroborate and hexafluorophosphate anions, the use of the former is somewhat more efficient as slightly fewer side-products are formed. However, when perchlorate was used as the counterion, the amount of (*E*)-diphenylstyrylphosphane oxide formed increased significantly, and only trace amounts of the desired cycloadducts were formed (<10%), under identical conditions. The use of a lower reaction temperature also resulted in lower yields of cycloaddition products.

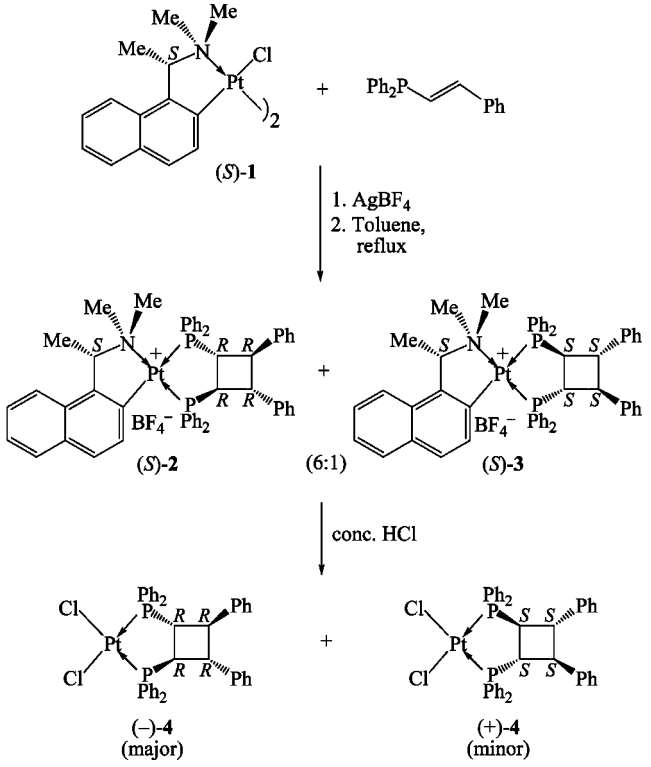

Scheme 1.

The two cycloadducts generated could not, however, be purified by fractional crystallization or column chromatography, hence the naphthylamine auxiliary was removed by treatment with concentrated hydrochloric acid to generate the corresponding dichloro complexes (Scheme 1). After purification by column chromatography and fractional crystallization, an enantiomerically enriched mixture of dichloro complexes **4** [enriched in (–)-**4**] was obtained as colorless crystals. Despite repeated recrystallization, dichloro complex (–)-**4** could not be isolated in its enantiomerically pure state [the optical purity was checked by liberation of the free diphosphane ligand and recoordination to the chiral dimeric complexes (*S*)-**1** and (*R*)-**1** separately, see below]. The X-ray crystallographic analysis of a single crystal from the enantiomeric mixture of dichloro complexes **4** indeed showed that both enantiomers were present in the unit cell. The structure of one of the enantiomers is shown in Figure 1, and selected bond lengths and angles are given in Table 1. The structural analysis confirmed that the tetrasubstituted cyclobutane adducts were formed as depicted in Scheme 1. The cyclobutane ring in **4** is folded with an angle of 142.4° between the C(9)–C(1)–C(2) and C(9)–C(10)–C(2) planes. All the diphenylphosphanyl and phenyl substituents on the cyclobutane ring adopt the pseudo-equatorial positions with an *all-trans* arrangement. The two phosphorus atoms are equivalent as the molecule is C_2-symmetrical, and indeed the ^{31}P NMR spectrum of **4** in $CDCl_3$ exhibits only a singlet at δ = 26.8 ppm ($J_{Pt,P}$ = 3727 Hz).

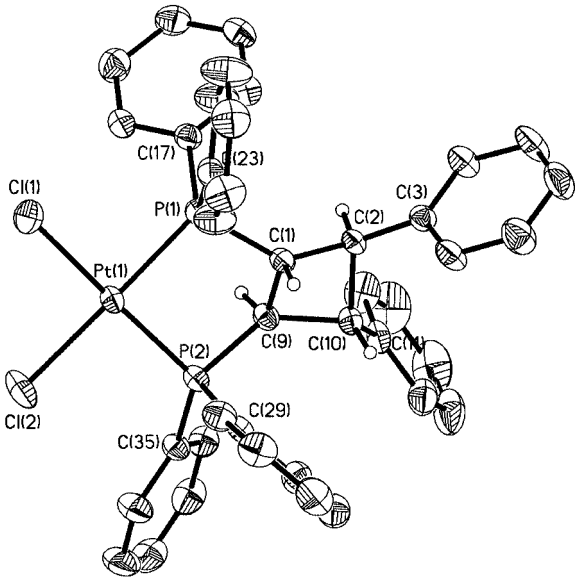

Figure 1. Molecular structure of one of the enantiomers of the dichloro complex **4**.

Table 1. Selected bond lengths [Å] and angles [°] for dichloro complex **4**.

Pt(1)–P(1)	2.2487(8)	P(1)–Pt(1)–P(2)	90.15(3)
Pt(1)–P(2)	2.2431(9)	P(2)–Pt(1)–Cl(1)	176.52(3)
Pt(1)–Cl(1)	2.3426(9)	P(2)–Pt(1)–Cl(2)	91.12(3)
Pt(1)–Cl(2)	2.3446(9)	Pt(1)–P(1)–C(1)	103.1(1)
P(1)–C(1)	1.828(3)	Pt(1)–P(2)–C(9)	101.3(1)
P(2)–C(9)	1.819(3)	P(1)–C(1)–C(9)	108.9(2)
C(1)–C(2)	1.559(4)	P(1)–C(1)–C(2)	135.2(2)
C(2)–C(3)	1.498(4)	P(2)–C(9)–C(1)	107.3(2)
C(2)–C(10)	1.564(5)	P(2)–C(9)–C(10)	135.3(3)
C(10)–C(11)	1.501(5)	C(1)–C(2)–C(3)	122.7(3)
C(9)–C(10)	1.557(4)	C(1)–C(2)–C(10)	86.6(2)
C(1)–C(9)	1.545(4)	C(2)–C(10)–C(11)	119.6(3)
P(1)–Pt(1)–Cl(1)	88.09(3)	C(2)–C(10)–C(9)	86.4(2)
P(1)–Pt(1)–Cl(2)	178.72(3)	C(1)–C(9)–C(10)	87.4(2)

Further treatment of the enantiomerically enriched dichloro complexes **4** with aqueous cyanide liberated an enantiomeric mixture of free diphosphane ligands **5** [enriched

 © 2005 Wiley-VCH Verlag GmbH & Co. KGaA, Weinheim

in (–)-**5**] in quantitative yield (Scheme 2). The ^{31}P NMR spectrum of **5** in $CDCl_3$ shows a singlet resonance signal at $\delta = -0.5$ ppm. Recomplexation of the liberated C_2-symmetrical diphosphane ligands **5** to the optically pure dimeric complex (*R*)-**1**, followed by replacement of the chloride counterion with a tetrafluoroborate ion, gave two diastereomeric products, (*R*)-**3** and (*R*)-**2**, in a ratio of 5:1 (Scheme 2), which indicated the presence of both enantiomeric forms of **5** in the liberated diphosphane mixture. Importantly, these two recomplexation products exhibit identical ^{31}P NMR spectra to those recorded for the two cycloadducts generated directly from the asymmetric [2+2] cycloaddition reaction. Eventually, the major recomplexation product, with phosphorus resonance signals at $\delta = 29.4$ ($J_{P,P} = 15.3$, $J_{Pt,P} = 3780$ Hz) and 35.9 ppm ($J_{P,P} = 15.3$, $J_{Pt,P} = 1789$ Hz), could be isolated in a diastereomerically pure form by fractional crystallization from dichloromethane/diethyl ether as colorless crystals in 66% yield {$[\alpha]_D = +148$ (CH_2Cl_2)}. Due to the unique *trans*-electronic influences which originate from the organoplatinum unit, the larger platinum–phosphorus coupling constant observed for the doublet signal at $\delta = 29.4$ ppm is diagnostic of the PPh_2 group coordinated *trans* to the σ-donating nitrogen atom.[12b,12c,15] On the other hand, the doublet at $\delta = 35.9$ ppm, which shows the smaller platinum–phosphorus coupling constant, is unambiguously assigned to the PPh_2 group that is coordinated *trans* to the strong π-accepting orthometalated carbon atom. This crystalline product was confirmed by X-ray crystallography to be complex (*R*)-**3**, as shown in Scheme 2 and Figure 2. Selected bond lengths and angles are given in Table 2. The cyclobutane ring in complex (*R*)-**3** is folded with an angle of 141.9° between the C(16)–C(15)–C(18) and C(16)–C(17)–C(18) planes. The absolute configurations at C(11), C(15), C(16), C(17), and C(18) are established to be *R*, *R*, *R*, *R*, and *R*, respectively, with the diphenylphosphanyl and phenyl substituents on the cyclobutane ring adopting the pseudo-equatorial positions in an *all-trans* arrangement. The minor recomplexation product was assigned to complex (*R*)-**2**, which differs from (*R*)-**3** only in the absolute configurations of the C_2-symmetrical diphosphane chelate. It is noteworthy that complexes (*R*)-**3** and (*R*)-**2** are the enantiomeric forms of (*S*)-**3** and (*S*)-**2**, respectively. In the absence of any chiral NMR solvent, the NMR spectra of (*R*)-**3** and (*R*)-**2** would show identical resonance signals to those recorded for their enantiomeric counterparts. Hence from the ^{31}P NMR spectroscopic data it could be established that complex (*S*)-**3** is

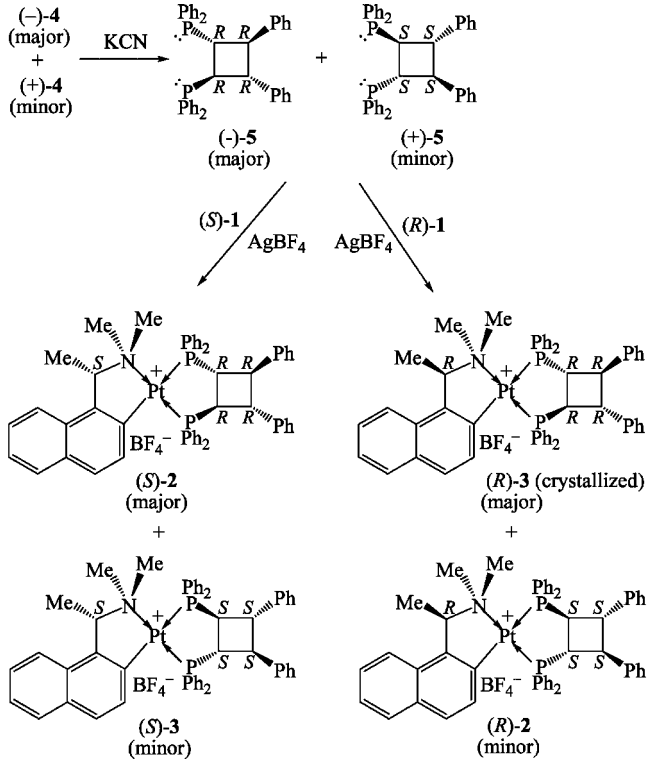

Scheme 2.

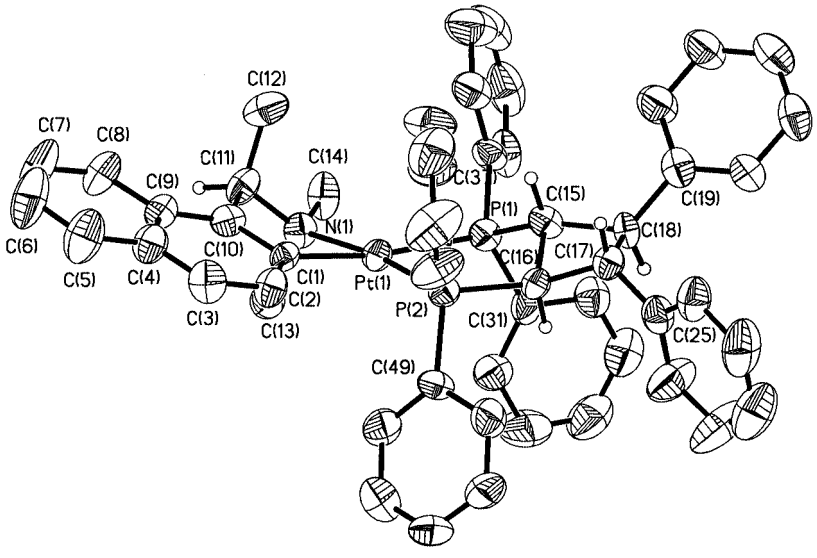

Figure 2. Molecular structure of the cationic complex (*R*)-**3**.

 © 2005 Wiley-VCH Verlag GmbH & Co. KGaA, Weinheim

the minor component of the diastereomeric mixture generated directly from the asymmetric dimerization reaction, while complex (*S*)-**2** is the major cycloaddition product formed.

Table 2. Selected bond lengths [Å] and angles [°] for (*R*)-**3**.

Pt(1)–C(1)	2.043(7)	N(1)–Pt(1)–P(1)	100.3(2)
Pt(1)–N(1)	2.127(6)	N(1)–Pt(1)–P(2)	171.1(2)
Pt(1)–P(1)	2.373(2)	P(1)–Pt(1)–P(2)	87.88(7)
Pt(1)–P(2)	2.250(2)	Pt(1)–P(1)–C(15)	99.5(3)
P(1)–C(15)	1.823(6)	Pt(1)–P(2)–C(16)	105.0(2)
P(2)–C(16)	1.816(6)	P(1)–C(15)–C(16)	107.9(4)
C(15)–C(16)	1.51(1)	P(1)–C(15)–C(18)	134.2(6)
C(16)–C(17)	1.567(9)	P(2)–C(16)–C(15)	112.0(5)
C(17)–C(25)	1.48(1)	P(2)–C(16)–C(17)	135.6(5)
C(17)–C(18)	1.58(1)	C(15)–C(16)–C(17)	87.8(5)
C(18)–C(19)	1.52(1)	C(16)–C(17)–C(18)	84.8(5)
C(15)–C(18)	1.541(9)	C(16)–C(17)–C(25)	123.1(7)
C(1)–Pt(1)–P(1)	171.2(2)	C(17)–C(18)–C(15)	86.4(5)
C(1)–Pt(1)–P(2)	93.1(2)	C(17)–C(18)–C(19)	119.6(6)
C(1)–Pt(1)–N(1)	79.4(2)	C(18)–C(15)–C(16)	88.0(5)

Recomplexation of the liberated enantiomerically enriched diphosphane ligands **5** to (*S*)-**1**, followed by treatment with silver tetrafluoroborate, gave the two diastereomeric complexes (*S*)-**2** and (*S*)-**3** in a ratio of 5:1 (Scheme 2). This is in agreement with the earlier assignments of the respective complexes and the presence of both enantiomers of **5** in the liberated diphosphane mixture.

Enantiomerically pure diphosphane ligand (–)-**5** {$[\alpha]_D$ = –108 ($CHCl_3$)}, was obtained in 87% yield by similar treatment of the diastereomerically pure complex (*R*)-**3** with concentrated hydrochloric acid, followed by ligand displacement with aqueous cyanide. Recomplexation of (–)-**5** to (*S*)-**1**, followed by replacement of the chloride counterion with a tetrafluoroborate ion, gave complex (*S*)-**2** as the sole product. This confirmed the optical purity of the diphosphane ligand (–)-**5** and reaffirmed the earlier assignments of the cycloadducts and recomplexation products.

From these recoordination experiments and spectroscopic and crystallographic studies, the two cycloadducts generated by [2+2] cycloaddition reaction of (*E*)-2-(diphenylphosphanyl)styrene promoted by the chiral metal complex [(*S*)-**1**] were established to be complexes (*S*)-**2** and (*S*)-**3** in the ratio of 6:1, respectively. This dimerization reaction proceeds with high stereoselectivity and the substituents on the cyclobutane ring of the cycloadducts generated adopt the pseudo-equatorial positions with an *all-trans* arrangement, while the diastereoselectivity of the reaction is moderately high [(*S*)-**2**:(*S*)-**3** = 6:1]. Similarly, the enantiomeric products (*R*)-**2** and (*R*)-**3** can be obtained in the same ratio of 6:1 when the equally accessible complex (*R*)-**1** is used as the chiral metal promoter for the cycloaddition reaction. As related transition-metal-assisted thermal or photodimerizations of vinylphosphanes and phospholes have been reported to proceed via a stepwise biradical mechanism,[5,16] it is possible that the present chiral organoplatinum-template-promoted dimerization of (*E*)-2-(diphenylphosphanyl)styrene also follows such a biradical pathway. However, a stepwise addition involving zwitterionic intermediates and a concerted pathway cannot be ruled out.

Experimental Section

Reactions involving air-sensitive compounds were performed under a positive pressure of purified nitrogen. NMR spectra were recorded at 25 °C on Bruker ACF 300 and AMX500 spectrometers. The spectral assignments in the ^{1}H NMR spectra are based on selective decoupling of the two types of ^{31}P nucleus, and NOE data from the 2D-ROESY spectrum.[8b] The phase-sensitive ROESY NMR experiments were acquired into a 1024 × 512 matrix with a 250-ms spin-locking time and a spin-lock field strength such that $\gamma B_1/2\pi$ = 5000 Hz and then transformed into 1024 × 1024 points using a sine bell weighting function in both dimensions. Optical rotations were measured on the specified solution in a 0.1-dm cell at 25 °C with a Perkin–Elmer Model 341 polarimeter. Melting points were determined on a Büchi melting point B-540. Elemental analyses were performed by the Elemental Analysis Laboratory of the Department of Chemistry at the National University of Singapore.

(*E*)-2-(diphenylphosphanyl)styrene[17] and dimeric platinum complexes (*S*)- and (*R*)-**1**[12b] were prepared according to literature methods.

Asymmetric Dimerization of (*E*)-2-(Diphenylphosphanyl)styrene and Removal of the Chiral Naphthylamine Auxiliary: An aqueous solution of silver tetrafluoroborate (0.35 g, 1.80 mmol) was added to a solution of (*S*)-**1** (0.546 g, 0.579 mmol) and (*E*)-2-(diphenylphosphanyl)styrene (0.770 g, 2.40 mmol, 90% pure) in dichloromethane (80 mL). The mixture was stirred vigorously at room temperature for 2 h, then filtered through Celite, washed with water (3 × 80 mL), and dried ($MgSO_4$). After removal of dichloromethane from the mixture, it was redissolved in toluene (350 mL) and refluxed for 4 d. After that the toluene was removed under reduced pressure and the reaction mixture was redissolved in dichloromethane (90 mL). The naphthylamine auxiliary was removed by vigorous stirring of the crude reaction mixture with concentrated hydrochloric acid (25 mL) for 14 h. The mixture was washed with water (4 × 100 mL) and dried ($MgSO_4$). The crude product was chromatographed on a silica column with dichloromethane/acetone (20:1) as eluent. Subsequent fractional crystallization from dichloromethane/petroleum ether gave an enantiomerically enriched mixture of dichloro complexes (–)-**4** and (+)-**4** as colorless crystals: 0.273 g (28% yield). $C_{40}H_{34}Cl_2P_2Pt$ (842.7): calcd. C 57.0, H 4.1; found C 57.0, H 4.1. ^{1}H NMR ($CDCl_3$): δ = 2.69–2.79 (m, 2 H, PC*H*), 3.26–3.34 (m, 2 H, PhC*H*), 6.79–8.19 (m, 30 H, aromatics) ppm. ^{31}P NMR ($CDCl_3$): δ = 26.8 (s, $J_{Pt,P}$ = 3727 Hz, 2 P, P^1, P^2) ppm.

Synthesis and Isolation of [{(*R*)-1-[1-(Dimethylamino)ethyl]naphthyl-*C*^{2},*N*}{(1*R*,2*R*,3*R*,4*R*)-1,2-bis(diphenylphosphanyl)-3,4-diphenylcyclobutane-*P*^{1},*P*^{2}}]platinum(II) Tetrafluoroborate [(*R*)-3]: Enantiomerically enriched dichloro complexes **4** (0.129 g, 0.153 mmol) dissolved in dichloromethane (30 mL) were stirred vigorously with a saturated aqueous solution of potassium cyanide (2 g) for 2 h. The organic portion was separated, washed with water (3 × 25 mL), and dried ($MgSO_4$). After that it was added to a solution of (*R*)-**1** (0.068 g, 0.072 mmol) in dichloromethane (10 mL), followed by the addition of aqueous $AgBF_4$ (0.050 g, 0.26 mmol). The mixture was stirred vigorously for 2 h, then filtered through Celite, washed with water (3 × 40 mL), and dried ($MgSO_4$). Recrystallization of the crude product from dichloromethane/diethyl ether gave complex (*R*)-**3** as colorless crystals: m.p. 278–279 °C (decomp.). $[\alpha]_D$ = +148 (*c* = 0.7, CH_2Cl_2); 0.106 g (66% yield). $C_{54}H_{50}BF_4NP_2Pt$ (1056.8): calcd. C 61.4, H 4.8, N 1.3; found C 61.0, H 4.8, N 1.4. ^{1}H NMR ($CDCl_3$): δ = 1.67 (d, $^3J_{H,H}$ = 6.0 Hz, 3 H, CH*Me*), 2.37–2.52 (m, 1 H, H_1), 2.58–2.73 (m, 1 H, H_2), 2.82 (dd, $^4J_{P,H}$ = 4.3, $^4J_{P,H}$ = 2.7 Hz, 3 H, NMe_{eq}), 3.05–3.17 (m, 1 H, H_3), 3.17 (d, $^4J_{P,H}$ =

 © 2005 Wiley-VCH Verlag GmbH & Co. KGaA, Weinheim

1.9 Hz, 3 H, NMe_{ax}), 3.26–3.38 (m, 1 H, H_4), 4.92 (quin, $^3J_{H,H}$ = $^4J_{P,H}$ = 6.0 Hz, 1 H, C*H*Me), 6.57–8.14 (m, 36 H, aromatics), ppm. ^{31}P NMR ($CDCl_3$): δ = 29.4 (d, $J_{P,P}$ = 15.3, $J_{Pt,P}$ = 3780 Hz, 1 P, P^1), 35.9 (d, $J_{P,P}$ = 15.3, $J_{Pt,P}$ = 1789 Hz, 1 P, P^2) ppm.

Liberation of (1*R*,2*R*,3*R*,4*R*)-1,2-Bis(diphenylphosphanyl)-3,4-diphenylcyclobutane [(–)-5]: The naphthylamine auxiliary in complex (*R*)-**3** was first removed chemoselectively by stirring a solution of the complex (0.036 g, 0.034 mmol) vigorously in dichloromethane (12 mL) with concentrated hydrochloric acid (4 mL) at room temperature for 7 h. After that more dichloromethane (15 mL) was added and the mixture was washed with water (4 × 20 mL) and dried ($MgSO_4$). The resultant dichloro complex (–)-**4** solution was stirred vigorously with a saturated aqueous solution of KCN (2 g) for 2 h. The organic portion was separated, washed with water (3 × 30 mL), and dried ($MgSO_4$). A white solid was obtained after removal of the solvent: $[\alpha]_D$ = –108 (*c* = 0.6, $CHCl_3$); 0.017 g (87% yield). $C_{40}H_{34}P_2$ (576.7): calcd. C 83.3, H 5.9; found C 82.9, H 6.1. ^{1}H NMR ($CDCl_3$): δ = 3.20–3.37 (m, 4 H, PC*H*, PhC*H*), 6.65–7.44 (m, 30 H, aromatics) ppm. ^{31}P NMR ($CDCl_3$): δ = –0.5 (s, 2 P, P^1, P^2), ppm.

Crystal Structure Determination of Complexes 4 and (*R*)-3: X-ray crystallographic data for complexes **4** and (*R*)-**3** are given in Table 3. The structures were analyzed at the National University of Singapore using a Siemens SMART CCD diffractometer with graphic monochromated Mo-K_α radiation. SADABS absorption corrections were applied for both complexes. All non-hydrogen atoms were refined anisotropically. Hydrogen atoms were introduced at a fixed distance from carbon atoms and were assigned fixed thermal parameters. The absolute configurations of complex (*R*)-**3** was determined unambiguously using the Flack parameter.[18]

Table 3. Crystallographic data for complexes **4** and (*R*)-**3**.

	4	(*R*)-**3**
Formula	$C_{40}H_{34}Cl_2P_2Pt$	$C_{54}H_{50}BF_4NP_2Pt$
Mol. mass	842.60	1056.79
Space group	$P\bar{1}$	$P2_12_12_1$
Crystal system	triclinic	orthorhombic
a [Å]	9.6147(4)	9.981(2)
b [Å]	11.2803(4)	21.649(5)
c [Å]	16.8636(7)	22.601(5)
α [°]	83.660(1)	90
β [°]	77.750(1)	90
γ [°]	73.856(1)	90
V [Å^3]	1714.3(1)	4883(2)
Z	2	4
T [K]	223(2)	223(2)
$\rho_{calcd.}$ [g cm^{-3}]	1.632	1.437
λ [Å]	0.71073 (Mo)	0.71073 (Mo)
μ [cm^{-1}]	43.70	29.90
Flack parameter	–	0.015(7)
*R*1 (obsd. data)[a]	0.0363	0.0575
*wR*2 (obsd. data)[b]	0.0739	0.0912

[a] $R_1 = \Sigma||F_o| - |F_c||/\Sigma|F_o|$. [b] $wR_2 = \{\Sigma[w(F_o^2 - F_c^2)^2]/\Sigma[w(F_o^2)^2]\}$, $w^{-1} = \sigma^2(F_o^2) + (aP)^2 + bP$.

CCDC-265224 [for (*R*)-**3**] and -265225 (for **4**) contain the supplementary crystallographic data for this paper. These data can be obtained free of charge from The Cambridge Crystallographic Data Centre via www.cdcc.cam.ac.uk/data_request/cif.

Acknowledgments

We are grateful to the National University of Singapore for support of this research, and a research scholarship to W. C. Y.

[1] E. Lee-Ruff, G. Mladenova, *Chem. Rev.* **2003**, *103*, 1449–1483 and references cited therein.

[2] a) R. B. Woodward, R. Hoffmann, *Angew. Chem. Int. Ed. Engl.* **1969**, *8*, 781–932; b) R. B. Woodward, *The Conservation of Orbital Symmetry*, Verlag Chemie, Germany, **1970**; c) T. L. Gilchrist, R. C. Storr, *Organic Reactions and Orbital Symmetry*, Cambridge University Press, London, 2nd ed., **1979**.

[3] a) H. M. R. Hoffmann, Z. M. Ismail, A. Weber, *Tetrahedron Lett.* **1981**, *22*, 1953–1956; b) B. B. Snider, E. Ron, *J. Org. Chem.* **1986**, *51*, 3643–3652; c) Y. Hayashi, S. Niihata, K. Narasaka, *Chem. Lett.* **1990**, 2091–2094; d) S. Ahmad, *Tetrahedron Lett.* **1991**, *32*, 6997–7000; e) K. Narasaka, Y. Hayashi, H. Shimadzu, S. Niihata, *J. Am. Chem. Soc.* **1992**, *114*, 8869–8885; f) T. A. Engler, K. Agrios, J. P. Reddy, R. Iyengar, *Tetrahedron Lett.* **1996**, *37*, 327–330.

[4] a) M. Lautens, W. Klute, W. Tam, *Chem. Rev.* **1996**, *96*, 49–92 and references cited therein; b) H. W. Frühauf, *Chem. Rev.* **1997**, *97*, 523–596 and references cited therein; c) K. H. Dötz, A. W. Koch, B. Weyershausen, H. Hupfer, M. Nieger, *Tetrahedron* **2000**, *56*, 4925–4934; d) T. G. Baik, A. L. Luis, L. C. Wang, M. J. Krische, *J. Am. Chem. Soc.* **2001**, *123*, 6716–6717.

[5] W. Oberhauser, C. Bachmann, T. Stampfl, R. Haid, C. Langes, H. Kopacka, A. Rieder, P. Brüggeller, *Inorg. Chim. Acta* **1999**, *290*, 167–179.

[6] a) R. Glaser, J. Blumenfeld, M. Twaik, *Tetrahedron Lett.* **1977**, *18*, 4639–4642; b) T. Hayashi, M. Tanaka, Y. Ikeda, I. Ogata, *Bull. Chem. Soc. Jpn.* **1979**, *52*, 2605–2608; c) T. Hayashi, Y. Kawabata, T. Isoyama, I. Ogata, *Bull. Chem. Soc. Jpn.* **1981**, *54*, 3438–3446; d) T. Hayashi, M. Tanaka, I. Ogata, *J. Mol. Catal.* **1984**, *26*, 17–30; e) C. Bianchini, H. M. Lee, A. Meli, W. Oberhauser, F. Vizza, P. Brüggeller, R. Haid, C. Langes, *Chem. Commun.* **2000**, 777–778; f) C. Bianchini, G. Mantovani, A. Meli, W. Oberhauser, P. Brüggeller, T. Stampfl, *J. Chem. Soc., Dalton Trans.* **2001**, 690–698; g) C. Bianchini, L. Gonsalvi, W. Oberhauser, D. Sémeril, P. Brüggeller, R. Gutmann, *Dalton Trans.* **2003**, 3869–3875; h) D. Zhao, K. Ding, *Org. Lett.* **2003**, *5*, 1349–1351; i) D. Zhao, J. Sun, K. Ding, *Chem. Eur. J.* **2004**, *10*, 5952–5963.

[7] a) S. B. Wild, *Coord. Chem. Rev.* **1997**, *166*, 291–311 and references cited therein; b) A. Miyashita, A. Yasuda, H. Takaya, K. Toriumi, T. Ito, T. Souchi, R. Noyori, *J. Am. Chem. Soc.* **1980**, *102*, 7932–7934; c) R. Schmid, M. Cereghetti, B. Heiser, P. Schönholzer, H. J. Hansen, *Helv. Chim. Acta* **1988**, *71*, 897–929; d) N. W. Alcock, J. M. Brown, D. I. Hulmes, *Tetrahedron: Asymmetry* **1993**, *4*, 743–756; e) V. V. Dunina, E. B. Golovan, *Tetrahedron: Asymmetry* **1995**, *6*, 2747–2754; f) H. Doucet, J. M. Brown, *Tetrahedron: Asymmetry* **1997**, *8*, 3775–3784; g) V. V. Dunina, L. G. Kuz'mina, M. Y. Rubina, Y. K. Grishin, Y. A. Veits, E. I. Kazakova, *Tetrahedron: Asymmetry* **1999**, *10*, 1483–1497; h) F. Bienewald, L. Ricard, F. Mercier, F. Mathey, *Tetrahedron: Asymmetry* **1999**, *10*, 4701–4707; i) J. Albert, M. Cadena, J. Granell, G. Muller, J. I. Ordinas, D. Panyella, C. Puerta, C. Sañudo, P. Velerga, *Organometallics* **1999**, *18*, 3511–3518.

[8] a) J. L. Bookham, W. McFarlane, *J. Chem. Soc., Chem. Commun.* **1993**, 1352–1354; b) B. H. Aw, S. Selvaratnam, P. H. Leung, N. H. Rees, W. McFarlane, *Tetrahedron: Asymmetry* **1996**, *7*, 1753–1762; c) B. H. Aw, T. S. A. Hor, S. Selvaratnam, K. F. Mok, A. J. P. White, D. J. Williams, N. H. Rees, W. McFarlane, P. H. Leung, *Inorg. Chem.* **1997**, *36*, 2138–2146.

[9] a) E. P. Kyba, S. P. Rines, *J. Org. Chem.* **1982**, *47*, 4800–4801; b) A. Miyashita, H. Karino, J. Shimamura, T. Chiba, K. Nagano, H. Nohira, H. Takaya, *Chem. Lett.* **1989**, 1849–1852; c) S. Y. M. Chooi, P. H. Leung, C. C. Lim, K. F. Mok, G. H.

 © 2005 Wiley-VCH Verlag GmbH & Co. KGaA, Weinheim

Quek, K. Y. Sim, M. K. Tan, *Tetrahedron: Asymmetry* **1992**, *3*, 529–532; d) C. López, R. Bosque, D. Sainz, X. Solans, M. Font-Bardía, *Organometallics* **1997**, *16*, 3261–3266; e) V. V. Dunina, L. G. Kuz'mina, M. Y. Kazakova, Y. K. Grishin, Y. A. Veits, E. I. Kazakova, *Tetrahedron: Asymmetry* **1997**, *8*, 2537–2545; f) A. Böhm, T. Hauck, W. Z. Beck, *Z. Naturforsch., Teil B* **1999**, *54*, 1360–1362; g) A. Böhm, D. Seebach, *Helv. Chim. Acta* **2000**, *83*, 3262–3278.

[10] a) T. K. Hollis, L. E. Overman, *J. Organomet. Chem.* **1999**, *576*, 290–299 and references cited therein; b) P. H. Leung, K. H. Ng, Y. Li, A. J. P. White, D. J. Williams, *Chem. Commun.* **1999**, 2435–2436.

[11] X. M. Liu, K. F. Mok, J. J. Vittal, P. H. Leung, *Organometallics* **2000**, *19*, 3722–3729.

[12] a) P. H. Leung, *Acc. Chem. Res.* **2004**, *37*, 169–177 and references cited therein; b) W. C. Yeo, J. J. Vittal, A. J. P. White, D. J. Williams, P. H. Leung, *Organometallics* **2001**, *20*, 2167–2174; c) W. C. Yeo, J. J. Vittal, L. L. Koh, G. K. Tan, P. H. Leung, *Organometallics* **2004**, *23*, 3474–3482.

[13] X. M. Liu, K. F. Mok, P. H. Leung, *Organometallics* **2001**, *20*, 3918–3926.

[14] W. C. Yeo, S. Y. Tee, H. B. Tan, G. K. Tan, L. L. Koh, P. H. Leung, *Inorg. Chem.* **2004**, *43*, 8102–8109.

[15] G. He, Y. Qin, K. F. Mok, P. H. Leung, *Chem. Commun.* **2000**, 167–168.

[16] a) W. L. Wilson, J. A. Rahn, N. W. Alcock, J. Fischer, J. H. Frederick, J. H. Nelson, *Inorg. Chem.* **1994**, *33*, 109–117; b) W. L. Wilson, J. Fischer, R. E. Wasylishen, K. Eichele, V. J. Catalano, J. H. Frederick, J. H. Nelson, *Inorg. Chem.* **1996**, *35*, 1486–1496; c) H. L. Ji, J. H. Nelson, A. DeCian, J. Fischer, B. Li, C. Wang, B. McCarty, Y. Aoki, J. W. Kenny III, L. Solujic, E. B. Milosavljevic, *J. Organomet. Chem.* **1997**, *529*, 395–408.

[17] A. M. Aguiar, T. G. Archibald, *Tetrahedron Lett.* **1966**, *7*, 5471–5475.

[18] H. D. Flack, *Acta Crystallogr., Sect. A* **1983**, *39*, 876–881.

Received: June 23, 2005
Published Online: October 25, 2005

 © 2005 Wiley-VCH Verlag GmbH & Co. KGaA, Weinheim

DOI: 10.1002/ejic.200500551

Experimental and Theoretical Study of the Encapsulation of a Linear Oligo(ferrocenylsilane) Trimer with β-Cyclodextrin

José A. Fernandes,[a] Sérgio Lima,[a] Susana S. Braga,[a] Martyn Pillinger,[a] José E. Rodríguez-Borges,[b] Paulo Ribeiro-Claro,*[a] José J. C. Teixeira-Dias,[a] and Isabel S. Gonçalves*[a]

Keywords: Cyclodextrins / Ferrocene / Inclusion compounds / Oligo(ferrocenes) / Ab initio calculations

An inclusion compound comprising β-cyclodextrin (β-CD) and the trimetallic oligo(ferrocenylsilane) $FcSiMe_2[(\eta^5\text{-}C_5H_4)Fe(\eta^5\text{-}C_5H_4SiMe_2)]Fc$ [Fc = $(\eta^5\text{-}C_5H_5)Fe(\eta^5\text{-}C_5H_4)$] has been prepared and characterised in the solid state by elemental analysis, powder X-ray diffraction, thermogravimetric analysis and magic angle spinning NMR spectroscopy (^{13}C, ^{29}Si). The results are consistent with the formation of a 2:1 (host-to-guest) inclusion complex. Ab initio calculations were carried out in order to investigate the possible inclusion geometries. The best host–guest fit was obtained for a tilted geometry of the ferrocene fragment relative to the β-CD axis (φ = 29°) with a 140-pm inclusion of the corresponding Fe centre below the plane of the rim. The structure of the organometallic trimer allows its inclusion interaction with a second β-CD host, leading to the 2:1 stoichiometry.

(© Wiley-VCH Verlag GmbH & Co. KGaA, 69451 Weinheim, Germany, 2005)

Introduction

Ferrocene has captured the interest of chemists, leading to the formation of countless derivatives with applications in areas as diverse as catalysis,[1] nonlinear optics,[2] electrochemistry,[3] medicine and biology.[4] Recently, macromolecular derivatives with luminescent properties have been created, with promising applications in biosciences.[5] Polymers containing ferrocene units either in the side chain or in the main chain have also attracted increasing attention as they may feature new electrical, optical or even magnetic properties.[6] Research into main chain polymers began to really expand with the development of new polymerisation techniques, in particular the discovery of the ring-opening polymerisation (ROP) of strained [1]ferrocenophanes.[7] ROP of silicon-bridged [1]ferrocenophanes gives poly(ferrocenylsilanes), which have been shown to yield magnetic composite ceramics at 500–1000 °C.[8] Poly(ferrocenylsilanes) are thermoplastic materials that become liquid above 150 °C and can be shaped into films, tablets or nanometric fibres.[9] Their thermoplastic properties are a result of the molecular flexibility and of the helix-shaped molecular packing. In order to gain insight into the conformation and packing of these polymers in the solid state, linear oligo(ferrocenes) have been prepared and studied by single-crystal X-ray diffraction and computer modelling.[10,11] The structure observed for the pentamer, $FcSiMe_2[(\eta^5\text{-}C_5H_4)Fe(\eta^5\text{-}C_5H_4SiMe_2)]_nFc$ [Fc = $(\eta^5\text{-}C_5H_5)Fe(\eta^5\text{-}C_5H_4)$, n = 3], appears to be a good model for the corresponding prototypical high polymer, poly(ferrocenyldimethylsilane).[10a,10b]

The oligo(ferrocenyldimethylsilanes) with n = 0–7 can be prepared by the anionic ring-opening oligomerisation of (1,1′-ferrocenediyl)dimethylsilane (**1**). The [1]ferrocenophane **1** is also the precursor used to prepare the corresponding high polymers (by ROP). We recently reported on the modification of β-cyclodextrin (β-CD) with ferrocenyl groups by ring-opening of encapsulated molecules of **1**.[12] This work has led us to study the interaction of cyclodextrins with oligo(ferrocenyldimethylsilanes).[13] CDs are cyclic oligosaccharides capable of binding hydrophobic molecules, called guests, noncovalently in the ring cavity. Inclusion of ferrocene in α-, β- and γ-CDs was first described in 1984.[14] Since then, the binding of a broad variety of ferrocene derivatives with CDs has been reported.[15] However, to the best of our knowledge, the only ferrocene–cyclodextrin adduct to be successfully characterised by single-crystal X-ray diffraction is the 2:1 (host-to-guest) α-CD–ferrocene complex.[16] This makes theoretical calculations a very important tool to evaluate the structures of CD–organometallic inclusion compounds. Two possible inclusion geometries of ferrocene derivatives in cyclodextrins were proposed by Harada and Takahashi,[14] namely axial and equatorial inclusion. Molecular mechanics studies in 1988 confirmed Harada's conclusions.[17] In the present work, we describe an experimental and theoretical study of the interaction of the trimer $FcSiMe_2[(\eta^5\text{-}C_5H_4)Fe(\eta^5\text{-}C_5H_4SiMe_2)]Fc$ (**2**) with β-CD. We anticipated that these

[a] Department of Chemistry, CICECO, University of Aveiro, 3810-193 Aveiro, Portugal
Fax: +351-234-370084
E-mail: igoncalves@dq.ua.pt
[b] CIQ, Department of Chemistry, University of Porto, Rua do Campo Alegre, 4169-007 Porto, Portugal

 © 2005 Wiley-VCH Verlag GmbH & Co. KgaA, Weinheim

studies would yield information about the flexibility and conformation of the oligo(ferrocenes), as well as providing a new family of potentially interesting organometallic-cyclodextrin inclusion compounds.

Results and Discussion

Synthesis and Characterisation

A solution of the trimer $FcSiMe_2[(\eta^5\text{-}C_5H_4)Fe(\eta^5\text{-}C_5H_4SiMe_2)]Fc$ (**2**) in CH_2Cl_2 was added to an aqueous solution of β-CD at 50 °C, in a 2:1 (β-CD:**2**) stoichiometry. A pale orange solid precipitated slowly at the interface between the two solutions. After stirring the mixture for 4 days, the product was isolated by decantation and rinsed with water. Elemental analysis indicated the formation of a 2:1 (host-to-guest) inclusion compound, designated as $(\beta\text{-CD})_2\cdot\mathbf{2}$. The yield was 36%. Figure 1 shows the powder XRD patterns for pristine β-CD hydrate, the trimer **2** and the product $(\beta\text{-CD})_2\cdot\mathbf{2}$. The pattern for $(\beta\text{-CD})_2\cdot\mathbf{2}$ indicates that the solid is microcrystalline and does not contain measurable amounts of either pure β-CD or compound **2**. The formation of a new phase is a good indication for the presence of a true inclusion compound.[18] Elemental analysis and thermogravimetry (TG, not shown) showed that the encapsulation of the trimetallic guest was accompanied by a slight decrease in the overall crystal water contents, from 14.4% for β-CD (10–11 water molecules per β-CD molecule) to 8.5% for $(\beta\text{-CD})_2\cdot\mathbf{2}$ (about 8 water molecules per β-CD molecule). This is usual for CD inclusion complexes, as a certain fraction of the water molecules initially present in the cyclodextrin cavity must be expelled upon encapsulation of the guest molecule. TG of $(\beta\text{-CD})_2\cdot\mathbf{2}$ showed a second mass loss of about 60% between 250 and 315 °C, because of simultaneous decomposition of the guest and the host. The fact that the two components decompose in the same range is another indication for the formation of an inclusion complex.

Figure 2 shows the solid-state ^{13}C CP MAS NMR spectra of β-CD hydrate, the trimer **2** and the inclusion compound $(\beta\text{-CD})_2\cdot\mathbf{2}$. The spectrum of β-CD hydrate is similar to that reported previously and exhibits multiple resonances for each type of carbon atom.[19,20] This has been mainly correlated with different torsion angles about the (1→4) linkages for C-1 and C-4,[19] and with torsion angles describing the orientation of the hydroxy groups.[20] The different carbon resonances are assigned to C-1 (101–104 ppm), C-4 (78–84 ppm), C-2,3,5 (71–76 ppm) and C-6 (57–65 ppm). The spectrum of the trimer **2** shows single sharp peaks for the Cp ($\eta^5\text{-}C_5H_5$) and methyl groups at 68.5 and 0 ppm, respectively. Several overlapping signals in the range 71–73 ppm are assigned to the carbon atoms of substituted cyclopentadienyl rings. In the spectrum of $(\beta\text{-CD})_2\cdot\mathbf{2}$, a single sharp peak is observed at δ = 68.6 ppm for the guest Cp group, and the methyl groups give rise to one main peak at 0.5 ppm. The multiplicities in the resonances for the β-CD carbon atoms are reduced in the spectrum of the inclusion compound, giving broad signals with very little structure. This is a common result for CD inclusion compounds containing either organic or organometallic guests, and can be attributed to an increase in the symmetry of the

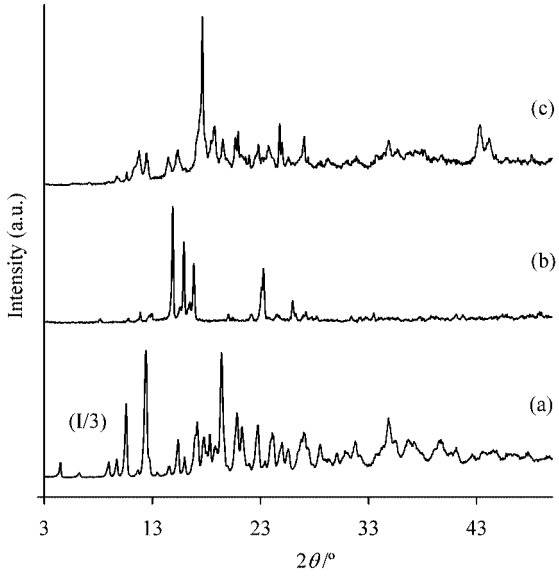

Figure 1. Powder XRD patterns of β-CD hydrate (a), the trimer **2** (b) and the inclusion compound $(\beta\text{-CD})_2\cdot\mathbf{2}$ (c).

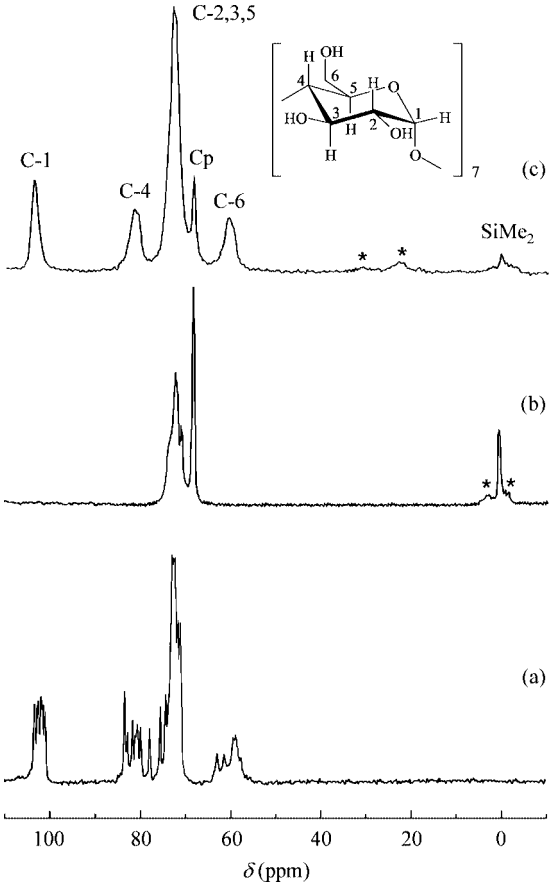

Figure 2. Solid-state ^{13}C CP MAS NMR spectra of β-CD hydrate (a), the trimer **2** (b) and the inclusion compound $(\beta\text{-CD})_2\cdot\mathbf{2}$ (c). Spinning sidebands are denoted by asterisks.

 © 2005 Wiley-VCH Verlag GmbH & Co. KGaA, Weinheim

β-CD macrocycle upon inclusion complexation.[21] In other words, encapsulation of the guest molecule induces the ring to adopt a more symmetrical conformation, with each glucose unit in a similar environment. ^{29}Si CP MAS NMR spectra were also recorded for the trimer **2** and (β-CD)$_2$·**2** (Figure 3). Crystalline **2** exhibits one fairly broad peak for the bridging dimethylsilyl group at δ = –8.0 ppm. After inclusion in β-CD, four resolved signals are found at –6.7, –6.9, –7.6 and –8.0 ppm. At the time of writing, attempts to prepare single crystals of the inclusion compound suitable for X-ray diffraction have been unsuccessful. Therefore, we cannot be certain about the reasons for having nonequivalent silicon nuclei in the complex. It may simply be due to crystal packing effects, subtle conformational changes of the guest molecule, variations in the host–guest interaction (even within a single β-CD/trimer complex) and/or the effect of inclusion complexation, which results in "isolation" of the trimetallic guest. It is interesting to note that the ^{29}Si NMR resonances for solutions of oligo(ferrocenyldimethylsilanes), FcSiMe$_2$[(η^5-C$_5$H$_4$)Fe(η^5-C$_5$H$_4$SiMe$_2$)]$_n$Fc (n = 0–7), are all found at –6.6 ± 0.1 ppm.[10a,10b]

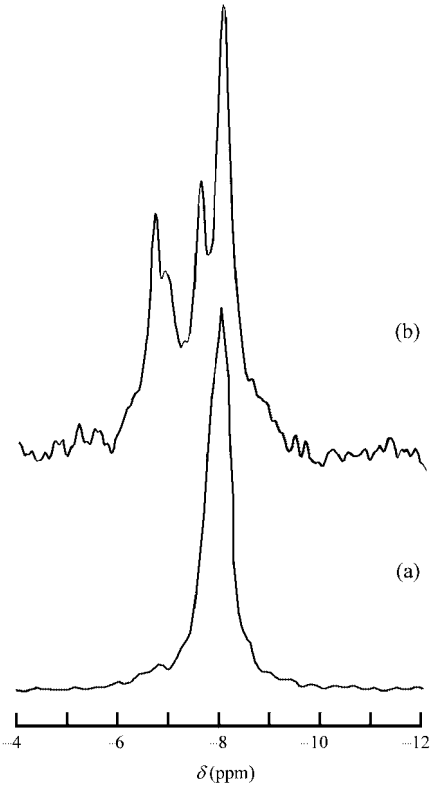

Figure 3. Solid-state ^{29}Si CP MAS NMR spectra of the trimer **2** (a) and the inclusion compound (β-CD)$_2$·**2** (b).

Ab Initio Calculations

Ab initio calculations were used in order to obtain information concerning the possible inclusion geometries, with particular attention being given to the plausibility of the host–guest fit. Figure 4 presents three conformers found for 1,1′-bis(ferrocenyldimethylsilyl)ferrocene (**2**). These conformers were obtained from a set of different starting geometries (generated by the combination of *trans* and *gauche* Fe–C$_{(ring)}$–Si–C$_{(ring)}$ dihedral angles) and are thought to be representative of the minimum energy configurations for the trimer. The most stable form, **2a**, has a helical-type structure, with Fe–C$_{(ring)}$–Si–C$_{(ring)}$ dihedral angles of about 103°, 156° and 66°, 69°. Conformers **2b** and **2c** lie above **2a** by about 4.7 and 5.9 kJ·mol^{-1}, respectively. Conformer **2b** mimics the extended structure found in the crystal and conformer **2c** has a ladder-type structure. The relative orientations of the cyclopentadienyl rings in the ferrocene units of **2b** are staggered for the central ferrocene and eclipsed for the terminal ones, as found in the crystal.[10d] The preference for the staggered configuration in the central ferrocene fragment in **2b** is probably due to repulsion between the substituent groups. In fact, for ferrocene itself, calculations at the same level predict the eclipsed D_{5h} form to be about 3.1 kJ·mol^{-1} more stable than the staggered D_{5d} form.

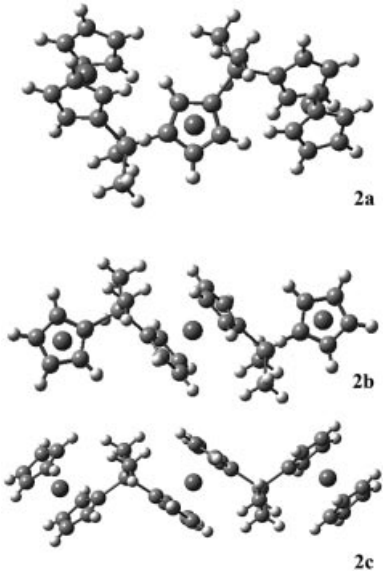

Figure 4. The three conformers found for the trimer **2**.

Figure 5 shows the definition of the coordinates used in the geometry scanning procedure to locate the best inclusion geometry of ferrocene units in β-CD. In a first step, the inclusion geometry of the complex containing ferrocene itself was determined in order to assess the reliability of the method used and to provide a starting point for the search of optimum β-CD·**2** inclusion geometries. Three different structures were found for the β-CD·ferrocene adduct (Figure 6). The lowest energy structure is achieved with axial orientation of the ferrocene guest, with ΔE = –102 kJ·mol^{-1} and z_{Fe} = –380 pm (Figure 6, b). This is a less-common structure, with the ferrocene guest protruding from the lower rim of the β-CD. The equatorial orientation shown in Figure 6 (a) has an inclusion energy of –28 kJ·mol^{-1} and z_{Fe} = –30 pm. The possible occurrence of a tilted inclusion geometry, as found for the (α-CD)$_2$·ferrocene complex,[16] was tested. A stable geometry was found at (r_{Fe}, z_{Fe}) = (100, –40) pm and φ = 18°, with an inclusion energy of –70 kJ·mol^{-1}. As expected, a and θ values present sevenfold

 © 2005 Wiley-VCH Verlag GmbH & Co. KGaA, Weinheim

and fivefold periodicity, with barriers between minima of about 8 and 23 kJ·mol^{-1}, respectively. This structure, represented in part c of Figure 6, was considered to be the most reasonable starting point for the calculations of the β-CD·**2** inclusion geometry.

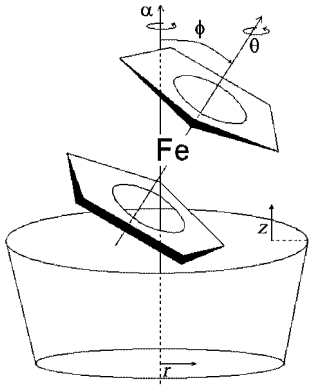

Figure 5. Definition of the variables used in the single-point scanning calculations.

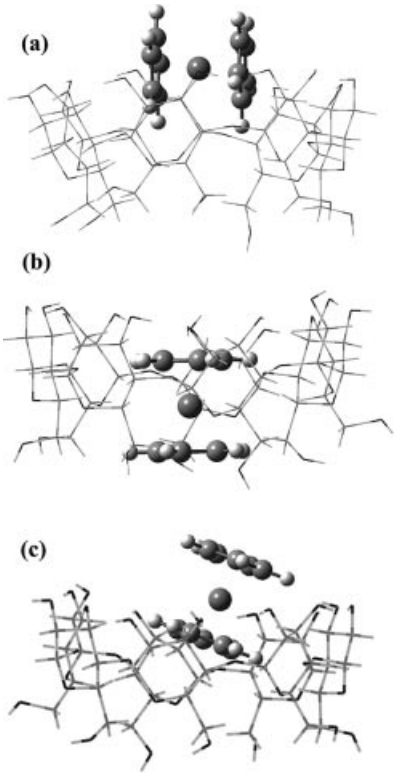

Figure 6. Inclusion geometries found for the β-CD·ferrocene adduct: (a) equatorial, (b) axial and (c) tilted.

Figure 7 shows the minimum energy structure found for the complex β-CD·**2b**. Structure **2b** was selected for the guest because it provides a better host–guest fit than either **2a** or **2c**. The corresponding optimised values are (r_{Fe}, z_{Fe}) = (110, –140) pm and φ = 29°. This structure presents some short contact interactions between the oxygen atoms of β-CD and the cyclopentadienyl hydrogen atoms of terminal and central ferrocenes. These C–H···O interactions, which lie within the 208–244 pm range, are likely to contribute to the stability of the complex.[22]

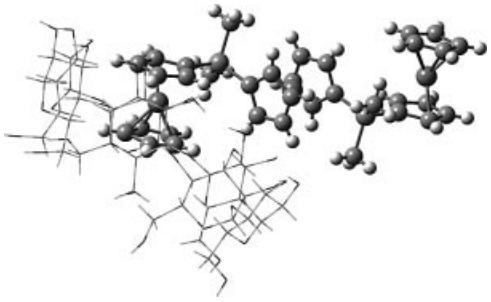

Figure 7. Best geometry obtained for a 1:1 inclusion compound comprising β-CD and **2b**.

The reliability of the inclusion geometries obtained at different computational levels has recently been assessed by Casadesús et al.,[23] based on the occurrence of unrealistic H···H host–guest contacts. In the present structure, there are only three H···H contacts which fall below the 220-pm limit (at 184, 209 and 212 pm). As noted in ref.[23], a small number of short contacts is acceptable and even values below 200 pm are not necessarily unphysical. Thus we may assume that the calculated structure is plausible, despite the well-known limitations of the present approach.

The 2:1 inclusion complex (β-CD)$_2$·**2b** was built from the previous 1:1 structure using the symmetry properties of the inversion centre located at the central iron atom of the guest molecule (Figure 8). This operation assumes that the two CD host molecules do not interact with one another, which is a reasonable approximation for the structure shown, because the distance between the two CDs is about 7 Å. The inclusion energy found for the 2:1 adduct (–302 kJ·mol^{-1}) is roughly double that for the 1:1 adduct (–157 kJ·mol^{-1}), as would be expected. Both values are quite large compared with the corresponding value of –70 kJ·mol^{-1} for the β-CD·ferrocene complex. This increase can be explained by the additional interaction provided by the central ferrocenyl moiety with the CD hosts. Nevertheless, a word of caution is required concerning the magnitude of these values, as they are not corrected for basis set superposition error (BSSE), expected to be important when small basis sets are used, or for zero point vibrational energy (the BSSE correc-

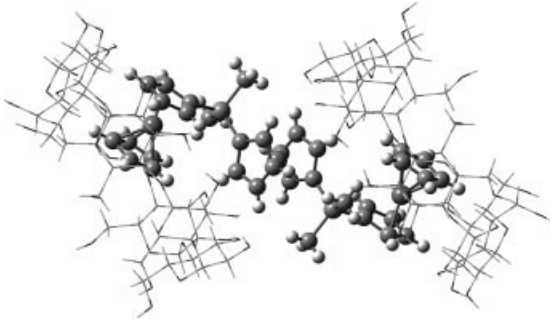

Figure 8. Possible geometry for a 2:1 inclusion compound comprising β-CD and **2b**.

 © 2005 Wiley-VCH Verlag GmbH & Co. KGaA, Weinheim

tion is not available for ONIOM calculations and frequency calculations only apply to fully-optimised structures).

Conclusions

The encapsulation of a trimetallic oligo(ferrocenyldimethylsilane) by β-cyclodextrin has been achieved and supported by a combination of experimental and theoretical methods. This compound and the corresponding adduct containing diferrocenyldimethylsilane are a potentially interesting family of organic–organometallic inclusion compounds. Future work in our laboratories will be directed towards investigating the effect of CD inclusion on certain properties of the guest molecules, for example, their electrochemical behaviour. We are also studying the interaction of the oligo(ferrocenes) with other CDs, such as α- and γ-CD.

Experimental Section

General Methods and Procedures: All air-sensitive reactions and manipulations were performed using standard Schlenk techniques under oxygen-free and water-free argon. Solvents were dried by standard procedures (*n*-hexane, THF and Et_2O over Na/benzophenone ketyl; CH_2Cl_2 and NCMe over CaH_2), distilled under argon and kept over 4-Å molecular sieves. β-CD (Fluka) and ferrocene (Aldrich) were obtained from commercial sources and used as received. Monolithioferrocene[24] and (1,1′-ferrocenediyl)dimethylsilane (**1**)[13] were prepared using published procedures.

Microanalyses for CHN were performed at the ITQB, Oeiras, Portugal (by C. Almeida), and Fe was determined by ICP-AES at the Central Laboratory for Analysis, University of Aveiro (by E. Soares). Powder XRD data were collected with a Philips X′pert diffractometer using Cu-K_α radiation filtered by Ni (λ = 1.5418 Å). TGA studies were performed using a Mettler TA3000 system at a heating rate of 5 K·min^{-1} under static air. Infrared spectra were recorded with a Unican Mattson Mod 7000 FTIR spectrophotometer using KBr pellets. Solid state ^{13}C and ^{29}Si CP MAS NMR spectra were recorded at 100.62 and 79.49 MHz respectively, on a (9.4-T) Bruker Avance MSL 400P spectrometer. ^{13}C CP MAS NMR spectra were recorded with 4.5 μs ^1H 90° pulses, 1.0 ms contact time, a spinning rate of 5.0 kHz and 4-s recycle delays. ^{29}Si CP MAS NMR spectra were recorded with 5 μs ^1H 40° pulses, 5.0 ms contact time, a spinning rate of 5.0 kHz and 5-s recycle delays. Chemical shifts are quoted in parts per million from TMS.

1,1′-Bis(ferrocenyldimethylsilyl)ferrocene (2): Following the literature method,[10a,10b] a mixture of ferrocenylsilane oligomers was obtained from the reaction of (1,1′-ferrocenediyl)dimethylsilane (**1**) (15.4 g, 64 mmol) with monolithioferrocene (29.6 mg, 108 mmol). The mixture was fractionated using an alumina chromatographic column (90 active, acidic [Activity I] Merck 0.063–0.200 mm, 70–230 mesh ASTM) and a 9:1 hexane/dichloromethane mixture as the mobile phase. Fractions of 250 mL were collected, of which the first six contained pure ferrocene. Fractions 7–39, containing a mixture of ferrocene, diferrocenyldimethylsilane and 1,1′-bis(ferrocenyldimethylsilyl)ferrocene (**2**), were submitted to a second chromatography using neutral alumina (Typ. 507C Brockmann I, STD grade, Approx. 150 Mesh, 58 Å) and the same mobile phase to yield 0.9 g of pure **2**. Fractions 40–65, containing a mixture of **2**, traces of diferrocenyldimethylsilane and larger oligomers, were also submitted to another chromatography using neutral alumina and 0.15 g of **2** was isolated. The total amount of compound **2** obtained was therefore 1.05 g. ^1H and ^{13}C solution NMR spectroscopic data for **2** were in agreement with those reported.[10a,10b] IR (KBr): $\tilde{\nu}$ = 3096 (m), 3089 (m), 3072 (m), 2958 (m), 2924 (m), 2904 (m), 1419 (m), 1409 (m), 1383 (m), 1367 (m), 1245 (vs), 1164 (vs), 1104 (s), 1036 (vs), 1027 (s), 1000 (m), 895 (m), 886 (m), 863 (m), 820 (vs), 798 (vs), 775 (vs), 666 (m), 486 (s), 434 (s) cm^{-1}. ^{13}C CP MAS NMR: δ = 72.5, 72.1, 71.2 (η^5-C_5H_4), 68.5 (η^5-C_5H_5), 0.0 ($SiMe_2$). ^{29}Si CP MAS NMR: δ = –8.0 ppm ($SiMe_2$).

Reaction of β-CD with 1,1′-Bis(ferrocenyldimethylsilyl)ferrocene [(β-CD)$_2$·2]: β-CD (157 mg, 0.12 mmol) was dissolved in water (10 mL) at 50 °C. This solution was treated with **2** (40 mg, 0.06 mmol) dissolved in CH_2Cl_2 (8 mL). The mixture was stirred for 4 days at room temperature, during which time a homogeneous solid product formed at the water–dichloromethane interface. The mixture was left to settle and the product isolated by centrifugation, washed twice with 2 mL-aliquots of water, and dried under air in a desiccator. Yield: 70 mg (36%). $(C_{42}H_{70}O_{35})_2$·$(C_{34}H_{38}Fe_3Si_2)$·$15H_2O$ (3210.6): calcd. C 44.14, H 6.53, Fe 5.22; found C 43.77, H 6.06, Fe 5.28. IR (KBr): $\tilde{\nu}$ = 3373 (vs), 2925 (m), 1638 (m), 1419 (m), 1383 (m), 1368 (m), 1333 (m), 1299 (m), 1245 (m), 1158 (s), 1105 (s), 1081 (s), 1053 (sh), 1029 (vs), 1002 (s), 938 (m), 861 (m), 819 (m), 797 (m), 775 (m), 756 (m), 703 (m), 665 (m), 606 (m), 576 (m), 530 (m), 502 (m), 482 (m), 444 (m) cm^{-1}. ^{13}C CP MAS NMR: δ = 103.9 (β-CD, C-1), 81.8 (β-CD, C-4), 73.1 (β-CD, C-2,3,5), 68.6 (guest, Cp), 60.8 (β-CD, C-6), 0.5 (guest, $SiMe_2$). ^{29}Si CP MAS NMR: δ = –6.7, –6.9, –7.6, –8.0 ppm (guest, $SiMe_2$).

Computational Details: Ab initio calculations were carried out using the Gaussian 03W programme package, running on a personal computer.[25] Compound **2** and ferrocene were fully optimised at the B3LYP/LanL2DZ level. The internal rotation of Cp rings about the C_5 axis in ferrocene allows the existence of eclipsed (D_{5h}) and staggered (D_{5d}) conformations. For compound **2**, the additional degrees of freedom due to the rotation about the $C_{(ring)}$–Si bonds lead to the existence of several conformers. Some attempts to characterise these conformers using computational methods have been reported in the literature.[10d,11,26] In ferrocene, the eclipsed form was found to be more stable than the staggered form by 2.78 kJ·mol^{-1}.[26] Molecular mechanics studies of **2** yield somewhat conflicting results. While Pannell et al. point to large energy differences between conformers,[10d] Barlow et al. found at least 10 noncentrosymmetrical conformers within an interval of 8.8 kJ·mol^{-1}, with the centrosymmetrical conformers lying 12 kJ·mol^{-1} above the absolute minimum.[11]

The models of the inclusion compound were performed by single-point calculations scanning, using the two-layer approximation of Morokuma et al.,[27] with the organometallic guests treated at high layer (B3LYP/LanL2DZ), and cyclodextrins set as low layer (HF/CEP-4G). The crystal structures of β-cyclodextrin hydrate[28] and the trimer **2**[10c,10d] were used to generate the model for the host and the initial model (structure **2b**) for the guest. The optimisation through single-point calculations was used because of the failure of the built-in optimisation procedures to converge to a stable geometry under the ONIOM conditions. The scanning was performed on a 20 pm/4° grid for the r, z, φ, θ and α coordinates (see Figure 5 for the definition of these coordinates). The minimum energy structure was determined from quadratic interpolation, using the lowest energy points in the grid.

Acknowledgments

This work was partly funded by the FCT, POCTI and FEDER (Project POCTI/CTM/46780/2002). S. S. B. and J. A. F. thank the

 © 2005 Wiley-VCH Verlag GmbH & Co. KGaA, Weinheim

FCT for grants. S. L. acknowledges grants from the University of Aveiro. We also wish to thank Prof. João Rocha for access to research facilities, and Paula Esculcas and Paula Brandão for assistance in the NMR experiments.

[1] a) R. C. J. Atkinson, V. C. Gibson, N. J. Long, *Chem. Soc. Rev.* **2004**, *33*, 313–328; b) T. J. Colacot, *Chem. Rev.* **2003**, *103*, 3101–3108; c) R. L. Halterman, *Chem. Rev.* **1992**, *92*, 965–994.
[2] a) I. R. Whittall, A. M. McDonagh, M. G. Humphrey, M. Samoc, *Adv. Organomet. Chem.* **1998**, *42*, 291–362; b) I. R. Whittall, A. M. McDonagh, M. G. Humphrey, M. Samoc, *Adv. Organomet. Chem.* **1999**, *43*, 349–405.
[3] D. Astruc, *Electron Transfer and Radical Processes in Transition-Metal Chemistry*, VCH, New York, **1995**.
[4] D. R. van Staveren, N. Metzler-Nolte, *Chem. Rev.* **2004**, *104*, 5931–5985.
[5] S. Fery-Forgues, B. Delavaux-Nicot, *J. Photochem. Photobiol. A* **2000**, *132*, 137–159.
[6] a) R. D. A. Hudson, *J. Organomet. Chem.* **2001**, *637–639*, 47–69; b) A. S. Abd-El-Aziz, *Macromol. Rapid Commun.* **2002**, *23*, 995–1031.
[7] I. Manners, *Adv. Organomet. Chem.* **1995**, *37*, 131–168.
[8] K. Kulbaba, I. Manners, *Macromol. Rapid Commun.* **2001**, *22*, 711–724.
[9] I. Manners, *Chem. Commun.* **1999**, 857–865.
[10] a) R. Rulkens, A. J. Lough, I. Manners, *J. Am. Chem. Soc.* **1994**, *116*, 797–798; b) R. Rulkens, A. J. Lough, I. Manners, S. R. Lovelace, C. Grant, W. E. Geiger, *J. Am. Chem. Soc.* **1996**, *118*, 12683–12695; c) A. J. Lough, I. Manners, R. Rulkens, *Acta Crystallogr. C* **1994**, *50*, 1667–1669; d) K. H. Pannell, V. V. Dementiev, H. Li, F. Cervantes-Lee, M. T. Nguyen, A. F. Diaz, *Organometallics* **1994**, *13*, 3644–3650.
[11] S. Barlow, A. L. Rohl, S. Shi, C. M. Freeman, D. O'Hare, *J. Am. Chem. Soc.* **1996**, *118*, 7578–7592.
[12] P. Ferreira, I. S. Gonçalves, M. Pillinger, J. Rocha, P. Santos, J. J. C. Teixeira-Dias, *Organometallics* **2000**, *19*, 1455–1457.
[13] J. A. Fernandes, S. Lima, S. S. Braga, P. Ribeiro-Claro, J. E. Rodriguez-Borges, C. Teixeira, M. Pillinger, J. J. C. Teixeira-Dias, I. S. Gonçalves, *J. Organomet. Chem.*, in press.
[14] A. Harada, S. Takahashi, *J. Chem. Soc., Chem. Commun.* **1984**, 645–646.
[15] a) A. Harada, Y. Hu, S. Yamamoto, S. Takahashi, *J. Chem. Soc., Dalton Trans.* **1988**, 729–732; b) A. E. Kaifer, *Acc. Chem. Res.* **1999**, *32*, 62–71; c) L. Cunha-Silva, I. S. Gonçalves, M. Pillinger, W.-M. Xue, J. Rocha, J. J. C. Teixeira-Dias, F. E. Kühn, *J. Organomet. Chem.* **2002**, *656*, 281–287; d) Ž. Petrovski, S. S. Braga, S. S. Rodrigues, C. C. L. Pereira, I. S. Gonçalves, M. Pillinger, C. Freire, C. C. Romão, *New J. Chem.* **2005**, *29*, 347–354.
[16] Y. Odagaki, K. Hirotsu, T. Higuchi, A. Harada, S. Takahashi, *J. Chem. Soc., Perkin Trans. 1* **1990**, 1230–1231.
[17] a) F. M. Menger, M. J. Sherrod, *J. Am. Chem. Soc.* **1988**, *110*, 8606–8611; b) H. J. Thiem, M. Brandl, R. Breslow, *J. Am. Chem. Soc.* **1988**, *110*, 8612–8616.
[18] W. Saenger, *Angew. Chem. Int. Ed. Engl.* **1980**, *19*, 344–362.
[19] a) M. J. Gidley, S. M. Bociek, *J. Am. Chem. Soc.* **1988**, *110*, 3820–3829; b) S. J. Heyes, N. J. Clayden, C. M. Dobson, *Carbohydr. Res.* **1992**, *233*, 1–14.
[20] R. P. Veregin, C. A. Fyfe, R. H. Marchessault, M. G. Tayler, *Carbohydr. Res.* **1987**, *160*, 41–56.
[21] S. S. Braga, I. S. Gonçalves, P. Ribeiro-Claro, A. D. Lopes, M. Pillinger, J. J. C. Teixeira-Dias, J. Rocha, C. C. Romão, *Supramol. Chem.* **2002**, *14*, 359–366, and references therein.
[22] a) G. A. Jeffrey, W. Saenger, *Hydrogen Bonding in Biological Structures*, Springer-Verlag, Berlin, **1991**; b) G. R. Desiraju, T. Steiner, *The Weak Hydrogen Bond: In Structural Chemistry and Biology*, Oxford University Press, New York, **1999**; c) A. M. Amado, P. J. A. Ribeiro-Claro, *J. Raman Spectrosc.* **2000**, *31*, 971–978.
[23] R. Casadesús, M. Moreno, À. González-Lafont, J. M. Lluch, M. P. J. Repasky, *J. Comput. Chem.* **2004**, *25*, 99–105.
[24] F. Rebiere, O. Samuel, H. B. Hagan, *Tetrahedron Lett.* **1990**, *31*, 3121–3124.
[25] M. J. Frisch, G. W. Trucks, H. B. Schlegel, G. E. Scuseria, M. A. Robb, J. R. Cheeseman, J. A. Montgomery, Jr., T. Vreven, K. N. Kudin, J. C. Burant, J. M. Millam, S. S. Iyengar, J. Tomasi, V. Barone, B. Mennucci, M. Cossi, G. Scalmani, N. Rega, G. A. Petersson, H. Nakatsuji, M. Hada, M. Ehara, K. Toyota, R. Fukuda, J. Hasegawa, M. Ishida, T. Nakajima, Y. Honda, O. Kitao, H. Nakai, M. Klene, X. Li, J. E. Knox, H. P. Hratchian, J. B. Cross, V. Bakken, C. Adamo, J. Jaramillo, R. Gomperts, R. E. Stratmann, O. Yazyev, A. J. Austin, R. Cammi, C. Pomelli, J. W. Ochterski, P. Y. Ayala, K. Morokuma, G. A. Voth, P. Salvador, J. J. Dannenberg, V. G. Zakrzewski, S. Dapprich, A. D. Daniels, M. C. Strain, O. Farkas, D. K. Malick, A. D. Rabuck, K. Raghavachari, J. B. Foresman, J. V. Ortiz, Q. Cui, A. G. Baboul, S. Clifford, J. Cioslowski, B. B. Stefanov, G. Liu, A. Liashenko, P. Piskorz, I. Komaromi, R. L. Martin, D. J. Fox, T. Keith, M. A. Al-Laham, C. Y. Peng, A. Nanayakkara, M. Challacombe, P. M. W. Gill, B. Johnson, W. Chen, M. W. Wong, C. Gonzalez, J. A. Pople, *Gaussian 03*, Revision B.04, Gaussian, Inc., Wallingford, CT, **2003**.
[26] S. Carter, J. N. Murrell, *J. Organomet. Chem.* **1980**, *192*, 399–408.
[27] a) S. Humbel, S. Sieber, K. Morokuma, *J. Chem. Phys.* **1996**, *105*, 1959–1967; b) T. Matsubara, S. Sieber, K. Morokuma, *Int. J. Quantum Chem.* **1996**, *60*, 1101–1109; c) M. Svensson, S. Humbel, R. D. J. Froese, T. Matsubara, S. Sieber, K. Morokuma, *J. Phys. Chem.* **1996**, *100*, 19357–19363.
[28] T. Steiner, G. Koellner, *J. Am. Chem. Soc.* **1994**, *116*, 5122–5128.

Received: June 23, 2005
Published Online: October 25, 2005

 © 2005 Wiley-VCH Verlag GmbH & Co. KGaA, Weinheim

DOI: 10.1002/ejic.200500567

Mixed-Ligand Copper Complexes with 8-Methylthioquinoline and Triphenylphosphane or the *o*-Semiquinone/Catecholate Redox System

Shengfa Ye,[a] Biprajit Sarkar,[a] Mark Niemeyer,[a] and Wolfgang Kaim*[a]

Keywords: Copper / Crystal structure / EPR spectroscopy / Heterocycles / Thioether ligands

The complex $[Cu(MTQ)(PPh_3)_2](BF_4)$, MTQ = 8-methylthioquinoline, exhibits distorted tetrahedral coordination at the copper(I) center. One of two crystallographically independent molecules found in the unit cell exhibits a more pronounced inclination towards a (3+1) coordination arrangement. In comparison to the analogous complex with the related imine/thioether chelate ligand 1-methyl-2-(methylthiomethyl)-*1H*-benzimidazole, the cation $[Cu(MTQ)(PPh_3)_2]^+$ shows stronger bonding of Cu^I to S and weaker interaction with N. With 3,5-di-*tert*-butyl-*o*-semiquinone as co-ligand instead of two PPh_3 ligands a valence-tautomer equilibrium situation involving the copper(II)-catecholate state can be observed by EPR spectroscopy, showing an unusually large isotropic $^{63,65}Cu$ hyperfine coupling of 2.1 mT and an untypically small isotropic *g* value of 1.975.

(© Wiley-VCH Verlag GmbH & Co. KGaA, 69451 Weinheim, Germany, 2005)

Introduction

Imino and thioether donor atoms have different characteristics for metal ions, especially for copper in its two biorelevant oxidation states +1 and +2.[1,2] While a "soft" thioether S (such as in methionine) prefers copper(I), the imino function (as in the imidazole ring of histidine) tolerates both the Cu^I and Cu^{II} states.[1,2] In an attempt to mimic the biochemically relevant[3] valence tautomerism [Equation (1)] between the copper(I)-*o*-semiquinone and copper(II)-catecholate combinations, we have used a corresponding mixed-donor ligand system in the form of 1-methyl-2-(methylthiomethyl)-*1H*-benzimidazole (mmb) to observe such a temperature-dependent valence-tautomer equilibrium outside biological material.[4]

$$(L)Cu^{I}(Q^{\bullet-}) \rightleftharpoons (L)Cu^{II}(Q^{2-})$$

Q = *o*-quinone (1)

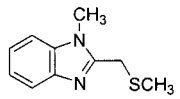

mmb

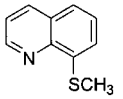

MTQ

[a] Institut für Anorganische Chemie, Universität Stuttgart, Pfaffenwaldring 55, 70550 Stuttgart, Germany
E-mail: kaim@iac.uni-stuttgart.de

Valence-tautomer (or redox isomer) equilibria are not only of interest for the enzymatic mechanism of copper-dependent amine oxidases;[3] (1) has also been implicated in catechol-enhanced Fenton processes for wood decay.[5] In general, valence-tautomer equilibria[6] involving cobalt,[7] manganese, copper,[4,8] nickel,[9] and iron[10] have been discussed with respect to potential applications in molecular electronics ("switching").[6–11]

While thioether (methionine) coordination to biological copper(I/II) is observed for electron transfer proteins[1,2a] and enzymes,[12] there has also been a recent report describing N–S five-membered ring chelate binding of copper in methanobactin.[13]

Extending our previous approach[4] to other N–S chelate ligands we have focused on 8-methylthioquinoline (MTQ),[14–16] which contains an azine (pyridyl) nitrogen donor instead of the more basic but less π-accepting azole (imidazole) N in mmb. Also, mmb contains a flexible dialkylthioether substituent, whereas MTQ offers an arylalkythioether sulfur in a more rigid chelate setting. Accordingly, a comparison between mmb and MTQ compounds with d^6-configured metal complex fragments has revealed considerable differences in the metal–donor bond lengths within the five-membered chelate ring.[15] A homoleptic complex of MTQ with copper(I), $[Cu(MTQ)_2](ClO_4)$, was also reported recently,[16] showing relatively short bonds from the metal to N (2.0165 Å) and S (2.3242 Å).

Results and Discussion

The chelate ligand MTQ forms a stable complex with $[Cu(PPh_3)_2]^+$ [Equation (2)]. The results of the structural analysis as shown in Figure 1 and summarized in Table 1

 © 2005 Wiley-VCH Verlag GmbH & Co. KgaA, Weinheim

Table 1. Selected bond lengths [Å] and angles [°] for $[Cu(MTQ)(PPh_3)_2](BF_4)$ and calculated values for $[Cu(MTQ)(PH_3)_2]^+$.

	Exp.				Calcd.[a]
	Molecule 1		Molecule 2		
Cu–N	2.101(7)	(Cu–N1)	2.077(8)	(Cu2–N2)	2.051
Cu–S	2.363(3)	(Cu1–S1)	2.376(2)	(Cu2–S2)	2.387
Cu–P	2.256(3)	(Cu1–P2)	2.255(3)	(Cu2–P3)	2.281
Cu–P	2.289(3)	(Cu1–P1)	2.287(2)	(Cu2–P4)	2.304
N–Cu–S	84.2(2)	(N1–Cu1–S1)	84.9(2)	(N2–Cu2–S2)	87.1
N–Cu–P	111.0(2)	(N1–Cu1–P2)	108.3(2)	(N2–Cu2–P3)	115.9
N–Cu–P	103.0(2)	(N1–Cu1–P1)	107.2(2)	(N2–Cu2–P4)	112.4
S–Cu–P	119.88(9)	(P2–Cu1–S1)	117.08(10)	(P3–Cu2–S2)	116.7
S–Cu–P	104.84(10)	(P1–Cu1–S1)	107.51(9)	(P4–Cu2–S2)	107.8
P–Cu–P	125.19(9)	(P2–Cu1–P1)	124.34(9)	(P3–Cu2–P4)	114.0

[a] Calculation for $[Cu(MTQ)(PH_3)_2]^+$.

for the two crystallographically independent molecules reveal a slight asymmetry in the binding of the two triphenylphosphane ligands as is typical for many such copper(I) compounds.[17]

$$MTQ + [Cu(CH_3CN)_2(PPh_3)_2](BF_4) \longrightarrow [Cu(MTQ)(PPh_3)_2](BF_4) + 2\ CH_3CN \quad (2)$$

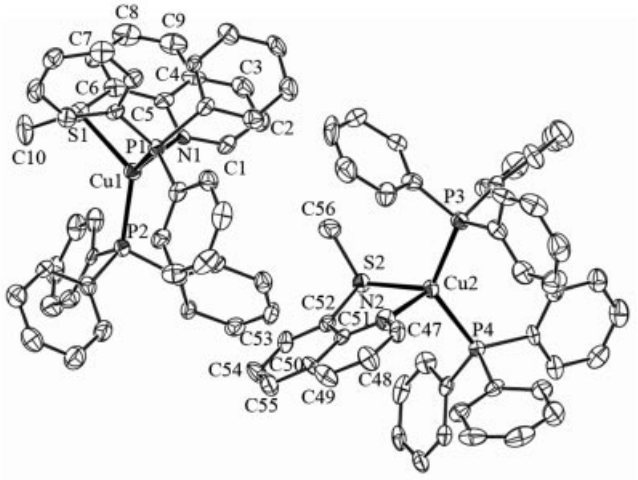

Figure 1. Molecular structures of two independent complex ions in the crystal of $[Cu(MTQ)(PPh_3)_2](BF_4)$.

The tendency of the $3d^{10}$ system for (3+1) instead of 4 coordination may be further enhanced by π–π interactions between different coordinated ligands.[17]

In comparison to the homoleptic $[Cu(MTQ)_2]^+$ ion[16] the Cu–N and Cu–S distances in $[Cu(MTQ)(PPh_3)_2]^+$ are significantly lengthened from about 2.02 to 2.09 Å and from about 2.32 to 2.37 Å, respectively. The Cu–N and Cu–S bond length data represent the average bond lengths of the two crystallographically independent molecules. Relative to several reported d^6 metal complexes[15] of MTQ, the copper(I) compound described here exhibits a balanced binding of the metal to N and S. In contrast, Ru^{II} prefers to bind to N and Pt^{IV} exhibits strong bonding to S.[15] In comparison with $[Cu(mmb)(PPh_3)_2]^+$,[18] the $[Cu(MTQ)(PPh_3)_2]^+$ ion is distinguished by longer Cu–N and shorter Cu–S bonds; the difference Δ_{NS} [d(Cu–S) – d(Cu–N)] is 0.394 Å for $[Cu(mmb)(PPh_3)_2]^+$[18] but only about 0.28 Å for the two molecules of $[Cu(MTQ)(PPh_3)_2]^+$. Apparently, the higher degree of rigidity conferred by the aromatic chelate ligand MTQ enforces a more balanced coordination by the two donor atoms, whereas mmb, which has a higher flexibility due to the CH_2 group in the chelate ring, allows for a more disparate binding of N and S to the metal.

The optimized geometry of $[Cu(MTQ)(PH_3)_2]^+$ is in reasonable agreement with the experimental results. Some deviations (Table 1) result from the approximation of PPh_3 by PH_3. The highest occupied molecular orbital (HOMO) of this complex is mainly formed by a combination between d orbitals of Cu (42%) and p orbitals of S (18%). The next lower lying orbital consists of 45% d orbitals from the Cu center and 12% p orbitals on the two P atoms. The lowest unoccupied molecular orbital (LUMO) comprises π* orbitals of the ligand with about 2% contribution from Cu orbitals. The contribution of d orbitals of Cu to the LUMO can be viewed as metal-to-ligand π-back-bonding. HOMO and LUMO diagrams of $[Cu(MTQ)(PH_3)_2]^+$ are depicted in Figure 2.

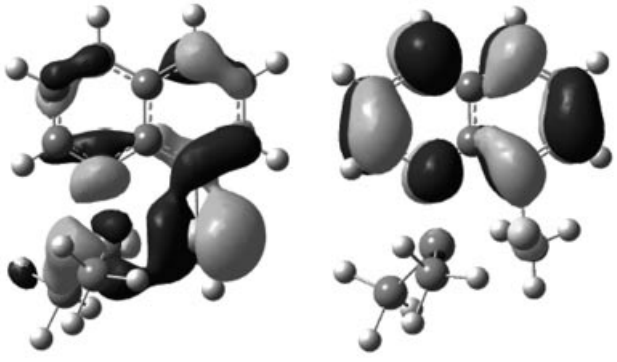

Figure 2. Composition of the HOMO (left) and LUMO (right) of $[Cu(MTQ)(PH_3)_2]^+$.

The successful use[4] of the mmb ligand in combination with the Cu^{n+}/Q_x^{n-} valence-tautomer system (n = 1 or 2; Q_x = 3,5-di-*tert*-butyl-*o*-benzoquinone) has prompted us to employ MTQ in a similar set of EPR experiments. The EPR results from mixing equimolar amounts of MTQ and

 © 2005 Wiley-VCH Verlag GmbH & Co. KGaA, Weinheim

Q_x with excess activated copper[4] [Equation (3)] are shown in Figure 3.

$$MTQ + Q_x + Cu \longrightarrow [Cu^{n+}(MTQ)(Q_x)^{n-}] \quad n = 1 \text{ or } 2 \qquad (3)$$

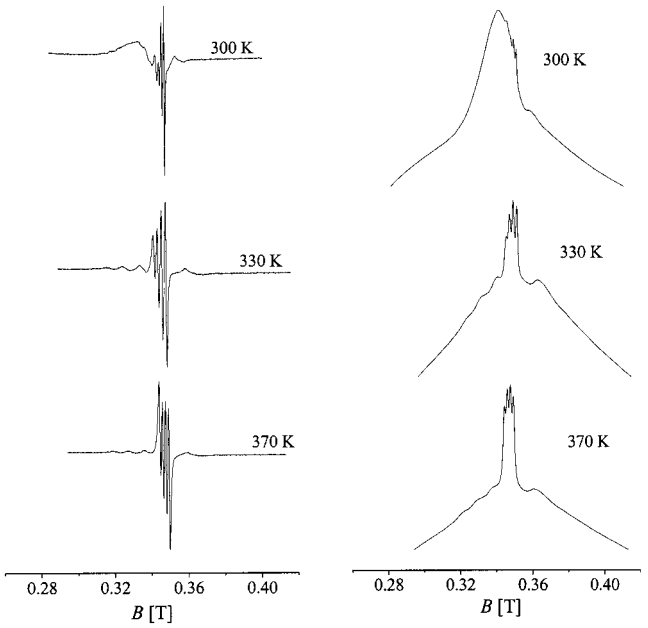

Figure 3. Temperature-dependent EPR spectra of the solution obtained by treating MTQ and 3,5-di-*tert*-butyl-*o*-semiquinone (1:1) with excess copper in toluene: derivative spectra (left) and integrated (nonderivative) spectra (right).

Although a uniform product could not be isolated from this reaction, an EPR pattern corresponding to a temperature-dependent solution equilibrium [Equation (1)] was observed with a major catecholato-copper(II) component characterized by broad signals with the typical Cu^{II} features of $a_{iso}(^{63,65}Cu) = 8.5$ mT and $g_{iso} = 2.077$ ($A_{\parallel} = 19.0$ mT, $g_{\parallel} = 2.16$, $A_{\perp} = 3.0$ mT, $g_{\perp} = 2.036$ at 110 K; ^{63}Cu: 69.2%, $I = 3/2$; ^{65}Cu: 30.8%, $I = 3/2$). The minor component, emerging to an appreciable extent at $T > 270$ K, can be expected to exhibit semiquinone/copper(I) features [$a_{iso}(^{63,65}Cu) < 1.2$ mT, $g_{iso} \approx 2.005$],[19] as for [Cu^{I}(mmb)($Q_x^{\cdot-}$)],[4] however, the parameters observed here are very unusual: The resolved quartet from the $^{63,65}Cu$ hyperfine coupling shows a large spacing of 2.1 mT which lies between typical values of 0.5–1.2 mT for semiquinone/copper(I) species[19] and 8 mT for copper(II) systems.[20] A semiquinone–H (H^4) hyperfine coupling is not observed here because of the relatively broad lines (peak-to-peak distance ca. 2.0 mT). Even more unusual is the isotropic *g* factor at 1.975 for this quartet signal which has no precedent in either copper(II) or semiquinone/copper(I) EPR spectroscopy.[19,20] The unusually low value indicates[21] the presence of a low-energy excited state, possibly involving the π* orbital of MTQ, lying close to the doublet ground state. At this point we can only speculate that the rigidity of the unsaturated MTQ chelate ligand enforces a strictly four-coordinate copper(I) arrangement with significant contribution from the thioether S center of MTQ, whereas more flexible chelate ligands such as mmb [see Equation (2)] with partially saturated chelate ring centers allow for a 3+1 coordination. This interpretation is supported by the shorter Cu–S bond observed in [Cu(MTQ)(PPh_3)$_2$](BF_4) relative to the mmb analogue. The electronic effect alone would favor the Cu^{I}-semiquinone alternative because MTQ is a better π acceptor than mmb.[15,16]

Experimental Section

Instrumentation: EPR spectra were recorded in the X band with a Bruker System ESP 300 equipped with a Bruker ER035M gaussmeter and a HP 5350B microwave counter. ^1H NMR spectra were recorded with a Bruker AC 250 spectrometer.

Synthesis: A solution containing 130 mg (0.172 mmol) [Cu(CH_3CN)$_2$(PPh_3)$_2$]BF_4 and 30.5 mg (0.172 mmol) MTQ[15,16] was heated to reflux in 20 mL of dry CH_2Cl_2 for 4 h. After evaporating half of the solvent volume, the precipitate was collected by filtration and washed with cold diethyl ether to yield 117 mg (80%) of light yellow microcrystals. Single crystals were obtained from a CH_2Cl_2 solution layered with diethyl ether at –10 °C. $C_{46}H_{39}BCuF_4NP_2S$: calcd. C 64.99, H 4.62, N 1.65; found C 64.65, H 4.65, N 1.63. ^1H NMR (250 MHz, 300 K, $CDCl_3$): $\delta = 8.70$ (dd, $^3J = 4.6$ Hz, $^4J = 1.6$ Hz, 1 H, H2), 8.62(dd, $^3J = 8.4$ Hz, $^4J = 1.6$ Hz, 1 H, H4), 8.11 (d, $^3J = 8.0$ Hz, 1 H, H7), 8.06 (d, $^3J = 8.0$ Hz, 1 H, H5), 7.77 (t, $^3J = 8.0$ Hz, 8.0 Hz, 1 H, H6), 7.65 (dd, $^3J = 8.4$ Hz, 4.6 Hz, 1 H, H3), 7.38–7.04 (m, 15 H, aromatic), 2.15 (s, 3 H, SCH_3) ppm.

Crystallography: Data for [Cu(MTQ)(PPh_3)$_2$](BF_4) were collected at 173 K with a Siemens P3 four-circle diffractometer using graphite-monochromated Mo-K_α radiation ($\lambda = 0.71073$ Å). Formula $C_{46}H_{39}BCuF_4NP_2S$; formula weight = 850.13 g·mol^{-1}; monoclinic space group *Pc*; $a = 21.520(4)$, $b = 10.607(2)$, $c = 19.993(4)$ Å; $\beta = 116.61(3)°$; $V = 4080.3(14)$ Å^3; $Z = 4$ (2 independent molecules); $F(000) = 1752$; $\rho_{calcd.} = 1.384$ g·cm^{-3}; $\mu = 0.717$ mm^{-1}, $T = 173(2)$ K; θ range 1.92 – 25.02°; number of unique reflections 7376 ($R_{int} = 0.064$), number of parameters 1011; Flack parameter = –0.009(18); $R_1 = 0.0566$, $wR2 = 0.0988$ [for, 5436 reflections with $I > 2\sigma(I)$]; $R_1 = 0.0955$, $wR_2 = 0.1145$ (all data); $GOF = 1.073$. The structure was solved by direct methods and refined by full-matrix least-squares against F_2 of all data using the SHELXTL software package.[22] Anisotropic thermal factors were assigned to the non-hydrogen atoms. The hydrogen atoms were included in calculated positions (riding model) and refined with fixed $U_{iso} = 1.2\ U_{iso}$ of the carbon atoms to which they are bonded.

CCDC-275097 contains the supplementary crystallographic data for this paper. These data can be obtained free of charge from The Cambridge Crystallographic Data Centre via www.ccdc.cam.ac.uk/data_request/cif.

Computational Details: Ground-state electronic structure calculations on [Cu(MTQ)(PH_3)$_2$]$^+$ have been done by density functional theory (DFT) methods, using the Gaussian 03 program package.[23] Within the Gaussian program, the quasirelativistic effect core potential basis sets[24] were employed for the Cu atom; for other atoms Dunning's DZP basis sets[25] were used. The geometry optimization was performed by using the pure density BP86 functional[26] at the spin-restricted level; the single point energy was calculated using the hybrid density B3LYP functional[27] with optimized geometry.

 © 2005 Wiley-VCH Verlag GmbH & Co. KGaA, Weinheim

[1] a) J. J. R. Fraústo da Silva, R. J. P Williams, *The Biological Chemistry of the Elements*, Clarendon Press, Oxford, **1991**; b) R. J. P Williams, J. J. R. Fraústo da Silva, *Bringing Chemistry to Life*, Oxford University Press, Oxford, **1999**.
[2] a) W. Kaim, J. Rall, *Angew. Chem.* **1996**, *108*, 47; *Angew. Chem. Int. Ed. Engl.* **1996**, *35*, 43; b) M. Albrecht, K. Hübler, S. Zalis, W. Kaim, *Inorg. Chem.* **2000**, *39*, 4731.
[3] a) D. M. Dooley, M. A. McGuirl, D. E. Brown, P. N. Turowski, W. S. McIntire, *Nature* **1991**, *349*, 262; b) M. Mure, *Acc. Chem. Res.* **2004**, *37*, 131.
[4] a) J. Rall, E. Waldhör, B. Schwederski, M. Schwach, S. Kohlmann, W. Kaim, in: *Bioinorganic Chemistry: Transition Metals in Biology and their Coordination Chemistry*, (Ed.: A. X. Trautwein), Wiley-VCH, Weinheim, **1997**, p. 476; b) J. Rall, M. Wanner, M. Albrecht, F. M. Hornung, W. Kaim, *Chem. Eur. J.* **1999**, *5*, 2802; c) W. Kaim, M. Wanner, A. Knödler, S. Zalis, *Inorg. Chim. Acta* **2002**, *337*, 163.
[5] R. Liu, B. Goodell, J. Jellison, A. Amirbahman, *Environ. Sci. Technol.* **2005**, *39*, 175.
[6] a) C. G. Pierpont, *Coord. Chem. Rev.* **2001**, *216–217*, 99; b) C. G. Pierpont, *Coord. Chem. Rev.* **2001**, *219–221*, 415.
[7] a) P. Gütlich, A. Dei, *Angew. Chem.* **1997**, *109*, 2852; *Angew. Chem. Int Ed.* **1997**, *36*, 2734; b) D. M. Adams, A. Dei, A. L. Rheingold, D. N. Hendrickson, *J. Am. Chem. Soc.* **1993**, *115*, 8221; c) D. Ruiz-Molina, J. Veciana, K. Wurst, D. N. Hendrickson, C. Rovira, *Inorg. Chem.* **2000**, *39*, 617; d) C. Carbonera, A. Dei, J.-F. Létard, C. Sangregorio, L. Sorace, *Angew. Chem.* **2004**, *116*, 3198; *Angew. Chem. Int. Ed.* **2004**, *43*, 3136; e) C. Sporer, I. Ratera, D. Ruiz-Molina, Y. Zhao, J. Vidal-Gancedo, K. Wurst, P. Jaitner, K. Clays, A. Persoons, C. Rovira, J. Veciana, *Angew. Chem.* **2004**, *116*, 5378; *Angew. Chem. Int. Ed.* **2004**, *43*, 5266.
[8] a) J. Manzur, A. M. Garcia, V. Rivas, A. M. Atria, J. Valenzuela, E. Spodine, *Polyhedron* **1997**, *16*, 2299; b) G. Speier, Z. Tyeklár, P. Töth, E. Speier, S. Tisza, A. Rockenbauer, A. M. Whalen, N. Alkire, C. G. Pierpont, *Inorg. Chem.* **2001**, *40*, 5653; c) See also G. A. Abakumov, V. A. Garnov, V. I. Nevodchikov, V. K. Cherkasov, *Dokl. Akad. Nauk SSSR* **1989**, *304*, 109.
[9] H. Ohtsu, K. Tanaka, *Angew. Chem.* **2004**, *116*, 6461; *Angew. Chem. Int. Ed.* **2004**, *43*, 6301.
[10] N. Shaikh, S. Goswami, A. Panja, X.-Y. Wang, S. Gao, R. J. Butcher, P. Banerjee, *Inorg. Chem.* **2004**, *43*, 5908.
[11] a) A. Dei, D. Gatteschi, C. Sangregorio, L. Sorace, *Acc. Chem. Res.* **2004**, *37*, 827; b) O. Kahn, J. P. Launay, *Chemtronics* **1998**, *3*, 140.
[12] a) S. T. Prigge, A. S. Kolhekar, B. A. Eipper, R. E. Mains, L. M. Amzel, *Nat. Struct. Mol. Biol.* **1999**, *6*, 976; b) S. T. Prigge, R. E. Mains, B. A. Eipper, L. M. Amzel, *Cell. Mol. Life Sci.* **2000**, *57*, 1236.
[13] H. J. Kim, D. W. Graham, A. A. DiSpirito, M. A. Alterman, N. Galeva, C. K. Larive, D. Asunskis, P. M. A. Sherwood, *Science* **2004**, *305*, 1612.
[14] L. F. Lindoy, S. E. Livingstone, T. N. Lockyer, *Aust. J. Chem.* **1966**, *19*, 1391.
[15] S. Ye, W. Kaim, M. Albrecht, F. Lissner, T. Schleid, *Inorg. Chim. Acta* **2004**, *357*, 3325.
[16] C.-Y. Su, S. Liao, M. Wanner, J. Fiedler, C. Zhang, B.-S. Kang, W. Kaim, *Dalton Trans.* **2003**, 189.
[17] a) M. Schwach, H.-D. Hausen, W. Kaim, *Chem. Eur. J.* **1996**, *2*, 446; b) S. Ye, W. Kaim, B. Sarkar, B. Schwederski, F. Lissner, T. Schleid, C. Duboc-Toia, J. Fiedler, *Inorg. Chem. Commun.* **2003**, *6*, 1196.
[18] M. Albrecht, K. Hübler, T. Scheiring, W. Kaim, *Inorg. Chim. Acta* **1999**, *287*, 204.
[19] a) J. Rall, W. Kaim, *J. Chem. Soc. Faraday Trans.* **1994**, *90*, 2905; b) S. Ye, B. Sarkar, F. Lissner, Th. Schleid, J. van Slageren, J. Fiedler, W. Kaim, *Angew. Chem.* **2005**, *117*, 2140; *Angew. Chem. Int. Ed.* **2005**, *44*, 2103.
[20] B. A. Goodman, J. B. Raynor, *Adv. Inorg. Chem. Radiochem.* **1970**, *13*, 135.
[21] W. Kaim, *Coord. Chem. Rev.* **1987**, *76*, 187.
[22] SHELXTL, Version 5.10, Bruker Analytical X-ray System, Madison, WI, 1998.
[23] M. J. Frisch, G. W. Trucks, H. B. Schlegel, G. E. Scuseria, M. A. Robb, J. R. Cheeseman, J. A. Montgomery, Jr., T. Vreven, K. N. Kudin, J. C. Burant, J. M. Millam, S. S. Iyengar, J. Tomasi, V. Barone, B. Mennucci, M. Cossi, G. Scalmani, N. Rega, G. A. Petersson, H. Nakatsuji, M. Hada, M. Ehara, K. Toyota, R. Fukuda, J. Hasegawa, M. Ishida, T. Nakajima, Y. Honda, O. Kitao, H. Nakai, M. Klene, X. Li, J. E. Knox, H. P. Hratchian, J. B. Cross, V. Bakken, C. Adamo, J. Jaramillo, R. Gomperts, R. E. Stratmann, O. Yazyev, A. J. Austin, R. Cammi, C. Pomelli, J. W. Ochterski, P. Y. Ayala, K. Morokuma, G. A. Voth, P. Salvador, J. J. Dannenberg, V. G. Zakrzewski, S. Dapprich, A. D. Daniels, M. C. Strain, O. Farkas, D. K. Malick, A. D. Rabuck, K. Raghavachari, J. B. Foresman, J. V. Ortiz, Q. Cui, A. G. Baboul, S. Clifford, J. Cioslowski, B. B. Stefanov, G. Liu, A. Liashenko, P. Piskorz, I. Komaromi, R. L. Martin, D. J. Fox, T. Keith, M. A. Al-Laham, C. Y. Peng, A. Nanayakkara, M. Challacombe, P. M. W. Gill, B. G. Johnson, W. Chen, M. W. Wong, J. L. Andres, M. Head-Gordon, E. S. Replogle, J. A. Pople, *Gaussian 03*, Revision B.02, Gaussian, Inc., Wallingford, CT, **2004**.
[24] P. Fuentealba, H. Preuss, H. Stoll, L. v. Szentpaly, *Chem. Phys. Lett.* **1982**, *89*, 418.
[25] T. H. Dunning Jr., P. J. Hay, in: *Modern Theoretical Chemistry*, vol. 3, (Ed.: H. F. Schaefer, III), Plenum, New York, **1976**.
[26] a) A. D. Becke, *Phys. Rev. A* **1988**, *38*, 3098; b) J. P. Perdew, *Phys. Rev. B* **1986**, *33*, 8822.
[27] a) C. Lee, W. Yang, R. G. Parr, *Phys Rev. B* **1988**, *37*, 785; b) A. D. Becke, *J. Chem. Phys.* **1993**, *98*, 5648.

Received: June 27, 2005
Published Online: October 25, 2005

 © 2005 Wiley-VCH Verlag GmbH & Co. KGaA, Weinheim

DOI: 10.1002/ejic.200500593

Intense Near-Infrared Luminescence of a Mesomorphic Ionic Liquid Doped with Lanthanide β-Diketonate Ternary Complexes

Lada N. Puntus,[a,c] Kurt J. Schenk,[b] and Jean-Claude G. Bünzli*[c]

Keywords: Ionic liquids / Liquid crystals / Lanthanides / Near infrared luminescence / Quantum yield / Small-angle X-ray diffraction

The ionic liquid 1-dodecyl-3-methylimidazole chloride ([C_{12}-mim]Cl) is doped with 1 mol-% of the lanthanide ternary complexes [Ln(tta)$_3$(phen)] (tta = thenoyltrifluoroacetonate, phen = 1,10-phenanthroline, Ln = Nd, Eu, Er, Yb), resulting in luminescent mesogenic phases at room temperature. According to DSC and SAXS measurements, the temperature of the crystal → liquid crystal transition is below 10 °C. Analysis of vibrational and luminescence data points to the inner co-ordination sphere of the Eu^{III} ion being very similar in both the mesomorphic sample and the parent β-diketonate complex. The mesomorphic samples containing Nd^{III}, Er^{III}, or Yb^{III} display relatively intense near-infrared luminescence. This emission is enhanced in the liquid crystalline phases with respect to the initial compounds, as demonstrated for instance by the quantum yield of the [Yb(tta)$_3$(phen)]-containing mesogenic sample which amounts to 2.1 %, as compared to 1.6 and 1.1 % for the powdered ternary complex and its solution in toluene, respectively.
(© Wiley-VCH Verlag GmbH & Co. KGaA, 69451 Weinheim, Germany, 2005)

Introduction

The development of smaller, more penetrable probes for biological imaging using near-infrared (NIR) light,[1,2] as well as of luminescent polymers for optical amplifiers[3] and light-emitting diodes working in the telecommunication window (1–1.6 μm)[4] have attracted a lot of attention recently. In this context, near-infrared lanthanide-based emitters are presenting considerable interest in view of their peculiar spectroscopic properties, namely narrow and easily recognizable emission lines and relatively long lifetimes of their excited states, compared with organic chromophores, which allows the use of time-resolved spectroscopy in analytical procedures, thus enhancing considerably the signal-to-noise ratio. In recent papers, we have demonstrated how Yb($^2F_{5/2}$) can be populated through energy transfer from Cr^{III} in a heterobimetallic d-f helicate, leading to an apparent lengthening of the Yb^{III} lifetime in the ms range,[5,6] and we have proposed an octadentate podand yielding highly stable and luminescent complexes in water.[7]

Liquid crystalline phases provide anisotropic media which are used in displays (LCD) and succeeding in producing emissive LCD by rendering the liquid crystalline phase luminescent would be a definitive advantage.[8] In addition, NIR-emitting mesomorphic materials could be useful in optical telecommunications since they would act as switchable light-converting devices. One strategy for producing lanthanide-containing mesophases is the doping of existing liquid crystalline phases with luminescent lanthanide salts and complexes.[9–16] For instance, we have recently shown how the emission color of a room temperature ionic liquid (RTIL) presenting a liquid crystalline phase at room temperature, 1-dodecyl-3-methylimidazolium chloride ([C_{12}-mim]Cl) can be tuned by the introduction of various Eu^{III} salts and by varying the excitation wavelength.[10] Ionic liquids present definitive advantages over classical solvents,[17–19] and some of them have been used for generating lanthanide-containing solutions emitting in the NIR range.[20,21] In this paper, we report the thermal, structural, and photophysical properties of solutions of lanthanide tris(thenoyltrifluoroacetylacetonate)[22] with *o*-phenanthroline in [C_{12}-mim]Cl and demonstrate an exaltation of their NIR-emitting properties with respect to solutions of these complexes in toluene and in the solid state.

Results and Discussion

Characterization of the Mesophases

Imidazolium chlorides with long alkyl chains form lamellar arrays in the crystalline phase and an enantiomeric

[a] Russian Academy of Sciences, Institute of Radio-Engineering and Electronics,
125009 Moscow, Russia
E-mail: lada_puntus@mail.ru
[b] Laboratory of Crystallography, École Polytechnique Fédérale de Lausanne, BSP,
1015 Lausanne, Switzerland
E-mail: kurt.schenk@epfl.ch
[c] Laboratory of Lanthanide Supramolecular Chemistry, École Polytechnique Fédérale de Lausanne, BCH 1405,
1015 Lausanne, Switzerland
E-mail: jean-claude.bunzli@epfl.ch
Supporting information for this article is available on the WWW under http://www.eurjic.org or from the author.

 © 2005 Wiley-VCH Verlag GmbH & Co. KgaA, Weinheim

smectic liquid crystalline phase (SmA_2) at higher temperature.[23] The temperature of the crystal→smectic A_2 transition of [C_{12}-mim]Cl heavily depends on hydration (44.5 °C for the monohydrate and –2.8 °C for an anhydrous salt) owing to the significant structural stabilization induced by hydrogen bonds with water molecules. The H-bond array is destroyed at elevated temperature and under vacuum, which allowed Guillet et al.[10] to obtain 10 mol-% solutions of Eu salts (chloride, nitrate, perchlorate, and triflate) in [C_{12}-mim]Cl without disturbing the mesomorphic properties of this RTIL. In our case, the [Ln(tta)$_3$(phen)] complexes are too sensitive to thermal decomposition and since they have low solubility in anhydrous [C_{12}-mim]Cl, we have settled for a partially dehydrated ionic liquid (<1 water molecule per molecule of ionic liquid, probably around 0.25), in which 1 mol-% solutions of ternary complexes could be prepared. In the following description, we use **Ln1** to designate the samples prepared in this way. DSC data indicate the formation of a SmA_2 phase starting between 6 and 10 °C and ending by isotropization between 99 and 102 °C for all the Ln-containing materials obtained (Figure 1).

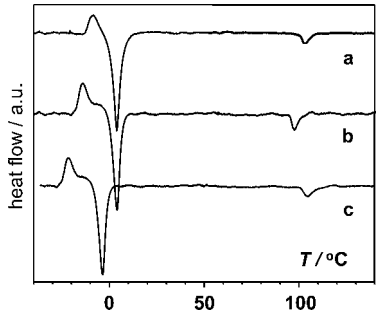

Figure 1. DSC traces (first heating-cooling cycle) of (a) **Nd1**, (b) partially dehydrated [C_{12}-mim]Cl and (c) anhydrous [C_{12}-mim]Cl.

We have resorted to small-angle X-ray scattering (SAXS) experiments to get more insight into a correlation between the structural and liquid crystalline properties of the doped mesophases. Data were collected both for the monohydrated imidazolium salt and the **Eu1** sample as a function of temperature and typical SAXS patterns are shown on Figure 2. At room temperature the most intense peak in the low-angle region (2θ = 1.89°) is assigned to the (001) layer repeat unit in the [C_{12}-mim]Cl·H_2O structure with d spacing of 46.6 Å (Figure 2c, Table 1). This d value corresponds to the double/extended bilayer spacing and is reported for the first time for [C_{12}-mim]Cl·H_2O. Similar values of layer spacing have been determined for [C_n-mim]Cl·H_2O with longer alkyl chains (n = 14, 16, 18).[23] Another, less intense peak at 2θ = 3.80° corresponds to a layer spacing of 23.3 Å and is assigned to the (002) regular repeat unit. In addition, a very weak peak at 2θ = 2.79° reveals the presence of a small amount of anhydrous [C_{12}-mim]Cl under its liquid crystalline SmA_2 phase (d = 31.8 Å). At 90 °C only one intense peak is observed at 2θ = 3.08°, corresponding to a layer spacing of 28.7 Å, and is characteristic of the SmA_2 phase. The latter value of the d spacing, as well as the one found for the crystalline phase (d = 23.3 Å) are slightly different from the ones reported by Bradley et al. for fully anhydrous [C_{12}-mim]Cl (22.5 Å in the crystalline phase and 31.7 Å in the SmA_2 phase determined on cooling the isotropic phase[23]). On the other hand, Guillet et al. have extracted a d value of 22.8 Å from the crystal structure of [C_{12}-mim]-Cl·H_2O.[10] These small differences may originate from the hydration state and thermal history of the sample (whether partial or full dehydration was performed) and from the SAXS experimental conditions (during heating or cooling cycles and from which phase SAXS data were collected).[23,24] Depending on these factors different phases such as the extended bilayer and/or double bilayer structures can form both in the initial crystalline phase and in the subsequent re-crystallization process after isotropization. The SAXS pattern for **Eu1** prepared from the previously partially dehydrated imidazolium salt, which feature a single peak at 2θ = 2.79° (Figure 2, a), is totally consistent with the presence of the SmA_2 phase at 26 °C (d = 31.8 Å) similar to that found for pure [C_{12}-mim]Cl (Figure 2, b). Thus, both DSC and SAXS data point to **Ln1** having a structural behavior close to the one of anhydrous [C_{12}-mim]-Cl and therefore, the experimental procedure proposed for preparing the **Ln1** samples successfully produces Ln-containing phases with mesomorphic SmA_2 properties at room temperature.

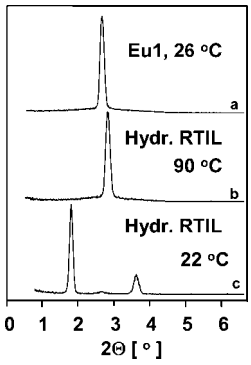

Figure 2. SAXS patterns for **Eu1** at 26 °C (a) and for [C_{12}-mim]-Cl·H_2O at 90 °C (b) and 22 °C (c) obtained during the heating.

Table 1. Layer spacing determined for the crystalline and SmA_2 phases from the position of the lowest-angle diffraction peak.

Sample	T [°C]	Layer spacing (d) [Å]	Phase[a]
[C_{12}-mim]Cl·H_2O	22	23.3 (46.6[b])	Cr
	90	28.7	LC
Eu1	26	31.8	SmA_2

[a] Cr = crystalline, LC = liquid crystalline. [b] Peak due to double/extended bilayer spacing.

Photophysical Properties

The Eu-containing samples have been used to probe changes in the local structure of the lanthanide ions upon the transition from both the crystalline to the liquid crystalline phase and from the solid state to the solution. The crys-

 © 2005 Wiley-VCH Verlag GmbH & Co. KGaA, Weinheim

tal-field splitting of the $^5D_0$–^7F_J transitions (J = 1–4), which is very sensitive to differences in the nearest environment of Eu^{III} are alike for all samples, except for some broadening which masks finer details in the luminescence spectra of **Eu1** and of [Eu(tta)$_3$(phen)] in toluene (Figure 3). In the luminescence spectra of powdered [Eu(tta)$_3$(phen)] and **Eu1**, emission from the $^5D_1$ level is also detected, pointing to a not so fast nonradiative relaxation from $^5D_1$ to $^5D_0$ (Figure 4). The luminescence spectra of all the Eu^{III}-containing compounds reveal maximum (2J +1) splitting of the ^7F_J electronic levels, consistent with a low symmetry (at most C_{2v}) of the immediate Eu^{III} surroundings. Judging from the qualitative criterion of the integrated intensity of the $^5D_0 \rightarrow {}^7F_0$ transition relative to the magnetic dipole $^5D_0 \rightarrow {}^7F_1$ transition, the symmetry around the metal ion seems to be lower in the mesophase compared to the powdered sample (0.14 and 0.17, respectively).

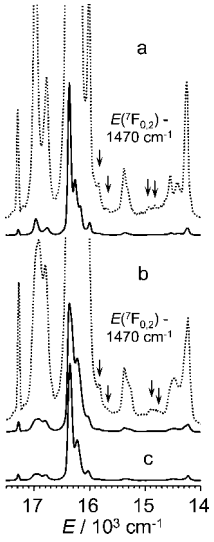

Figure 3. Luminescence spectra at 295 K of (a) [Eu(tta)$_3$(phen)] (solid state), (b) **Eu1**, and (c) [Eu(tta)$_3$(phen)] 10^{-3} M in toluene with inserts showing the vibronic satellites associated to $^5D_0 \rightarrow {}^7F_0$ and $^5D_0 \rightarrow {}^7F_2$ transitions; the excitation wavelength is 385 nm.

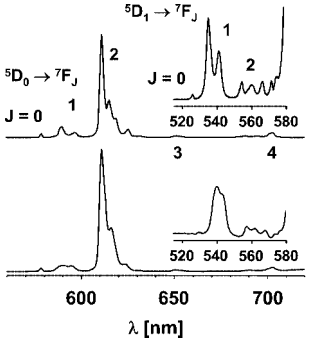

Figure 4. Luminescence spectra of [Eu(tta)$_3$(phen)] (top) and **Eu1** (bottom) at 295 K obtained under ligand excitation at 385 nm.

Both broad structured bands of the ligands and narrow lines of f-f transitions are observed in all the excitation spectra of **Ln1** (Figure 5). These spectra are similar and their coincidence with the absorption spectra indicates a sizeable energy transfer from the ligands onto the lanthanide ion. A broad shoulder with a low-frequency edge at 19665 cm^{-1} and a maximum around 22200 cm^{-1} is most remarkable in the spectrum of [Eu(tta)$_3$(phen)]. Its absence in the excitation spectrum of **Nd1** allows one to assign it to a ligand→metal charge transfer (LMCT) transition. The mean optical electronegativity[25] is equal to χ_{opt} = 2.73, a value obtained by using the optical electronegativity of Eu^{III} reported by Demirbilek et al.[26] This value can then be used to estimate the energy of the LMCT states in the complexes with the other lanthanide ions (Table 2). According to these calculated energies, influence of the LMCT state on the energy migration within the ternary complex should be much smaller in the cases of NIR-emitting ions compared to Eu^{III}.

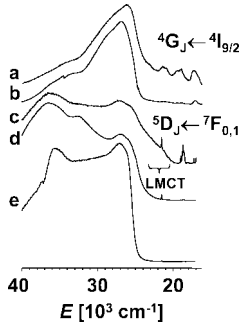

Figure 5. Luminescence excitation spectra of (a) [Nd(tta)$_3$(phen)] (solid state), (b) **Nd1**, (c) [Eu(tta)$_3$(phen)] (solid state), (d) **Eu1**, and (e) [Eu(tta)$_3$(phen)] 10^{-3} M in toluene; λ_{an} are 614 (Eu) and 1060 nm (Nd).

Table 2. Lifetimes of the Ln excited state at room temperature and energy of $^1\pi\pi^*$, $^3\pi\pi^*$, and LMCT states for powdered [Ln(tta)$_3$(phen)] and **Ln1** samples.

Compound	τ_{obs} [μs]	$E(^1\pi\pi^*)$ [cm^{-1}][a]	$E(^3\pi\pi^*)$ [cm^{-1}][b]	E(LMCT) [cm^{-1}][c]
[Nd(tta)$_3$(phen)]	1.29 ± 0.03	24690	20400	40200
Nd1	1.52 ± 0.01	24845		–
[Er(tta)$_3$(phen)]	1.86 ± 0.02	24855	20480	44400
Er1	1.95 ± 0.04	24940		–
[Yb(tta)$_3$(phen)]	12.01 ± 0.02	23920	20340	27900
Yb1	12.4 ± 0.03	24235		–

[a] From fluorescence spectra at 295 K. [b] From phosphorescence spectra at 77 K. [c] Calculated values, see text.

To help characterize the liquid crystalline phases, we have resorted to vibronic satellites appearing in the emission spectra of the Eu-containing samples. They are similar for powdered and mesomorphic samples and the most intense ones are assigned to the symmetric vibration of the β-diketonate chelating ring with a large contribution of the C···O bond stretching with a frequency of 1470 cm^{-1} (Figure 3, cf. the bands marked by arrows in the 15900–15600 and 15110–14800 cm^{-1} spectral ranges). A comparison with the IR spectra of [C_{12}-mim]Cl·H_2O, [Yb(tta)$_3$(phen)], and **Yb1** reveals a homogeneous mixture of both components in the doped liquid crystalline sample (Figure S1, Supporting Information): vibrations of both the ionic liquid and the β-

 © 2005 Wiley-VCH Verlag GmbH & Co. KGaA, Weinheim

diketonate complex (although very weak) are indeed seen in the IR spectrum.

On the other hand, the lifetime of the Eu($^5D_0$) state hints at some differences between **Eu1** and the powdered sample. Both luminescence decays are single exponential, but lifetimes amount to 0.64 ± 0.02 and 0.97 ± 0.03 ms for **Eu1** and [Eu(tta)$_3$(phen)], respectively. The shorter lifetime in the former could be explained as follows. In a fluent system, energy transfer quenching involves collisions between complexes during diffusion.[27] The critical distance for nonradiative energy transfer, as calculated from known theory for energy transfer via electric dipole-dipole interaction[28,29] is larger than the collision distance, which leads to energy transfer via cross-relaxation and excitation migration. Moreover, collisional deactivation with [C_{12}-mim]$^+$ cations should also be taken into account. In summary, the luminescence analysis of **Eu1** confirms that dissolution of [Eu(tta)$_3$(phen)] in the RTIL does not modify substantially the inner co-ordination sphere of the europium ion, although it reveals an influence of the ionic liquid on the deactivation processes.

NIR Luminescence

The luminescence excitation spectra of NIR-emitting lanthanide complexes as well as the corresponding **Ln1** (Ln = Nd, Er, Yb) samples are similar (Figure S2, Supporting Information). Comparison of the normalized excitation spectra of powdered and mesophase samples reveals a much lower excitation efficiency of the lanthanide ions through ligand levels in the powdered samples. This reduced luminescence efficiency at high concentration is known as concentration quenching. In spite of the low concentration of the doped ternary complex (1 mol-%), relatively intense luminescence is obtained for all the **Ln1** samples, as ascertained by the intensity ratios found between the total integrated emission intensity of the pure complexes and that of the **Ln1** samples: 6, 3, and 5 for Nd, Er, and Yb, respectively. The near-infrared luminescence spectra of mesomorphic **Ln1** samples at room temperature are presented in Figure 6 and relevant photophysical data are given in Table 2. The observed f-f emission bands correspond to the typical electronic transitions of the NIR-emitting lanthanide ions: $^4F_{3/2}\rightarrow{}^4I_J$ (J = 9/2, 11/2, 13/2) for Nd, $^4I_{13/2}\rightarrow{}^4I_{15/2}$ for Er, and $^2F_{5/2}\rightarrow{}^2F_{7/2}$ for Yb. We have determined the quantum yields of the Yb-centered luminescence taking [Yb(tta)$_3$(H$_2$O)$_2$] as standard. Upon excitation at 390 nm, the quantum yield of **Yb1** amounts to 2.1 ± 0.3%, compared with 1.1 ± 0.1% for a solution of [Yb(tta)$_3$(phen)] in toluene and 1.6 ± 0.2% for a solid-state sample of [Yb(tta)$_3$(phen)] (Figure 6). Thus, the quantum efficiency increases in the order **Yb1** > [Yb(tta)$_3$(phen)] powdered > [Yb(tta)$_3$(phen)] solution, which agrees well with the corresponding lengthening of the emission lifetime. This correlation means that nonradiative relaxation processes are minimized in the ionic liquid used. The improvement in the photophysical properties of the **Ln1** samples is further substantiated by the lifetimes of the metal-centered excited states, which are slightly longer compared with those of the pure ternary complexes (Table 2).

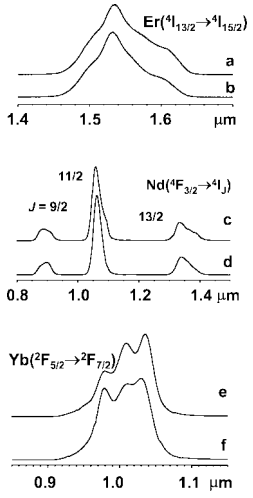

Figure 6. Near-infrared photoluminescence of (a) [Er(tta)$_3$(phen)], (b) **Er1**, (c) [Nd(tta)$_3$(phen)], (d) **Nd1**, (e) [Yb(tta)$_3$(phen)], and (f) **Yb1** at 295 K. The excitation wavelength is 385 nm.

At room temperature, [C_{12}-mim]Cl displays a bright-blue fluorescence with a maximum at 410 nm upon excitation between 225 and 280 nm.[10] Therefore, both a sensitization of the lanthanide-centered NIR luminescence and fluorescence from the RTIL are obtained upon UV excitation. Moreover, owing to the energy transfer from the ionic liquid, lanthanide-centered luminescence can be observed with excitation wavelengths as large as 410 nm (cf. Figures 5, 7, and S2), which is interesting because getting near-infrared emission upon excitation by visible light is an attractive aim for various industrial and analytical applications.

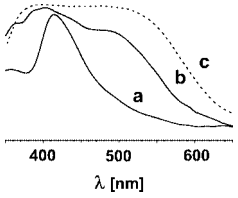

Figure 7. Luminescence spectra of (a) [Nd(tta)$_3$Phen] (solid state), (b) **Nd1** and (c) [C_{12}-mim]Cl at 295 K. The excitation wavelength is 385 nm.

Conclusions

In summary, a method for obtaining [C_{12}-mim]Cl mesophases doped by 1 mol-% [Ln(tta)$_3$(phen)] complexes at room temperature has been developed. The layer spacing in the liquid crystalline phases is independent of the presence of 1 mol-% of [Ln(tta)$_3$(phen)] complexes and identical with the one measured for the anhydrous ionic liquid.[23] The prepared **Ln1** samples have an enantiomeric smectic liquid crystalline phase in the temperature range 10–102 °C. The inner co-ordination sphere of the lanthanide ion remains

 © 2005 Wiley-VCH Verlag GmbH & Co. KGaA, Weinheim

essentially unchanged, while the photoluminescence properties are enhanced. The studied liquid crystalline phases display relatively intense near-infrared photoluminescence, thus opening up interesting perspectives for the design of NIR-emitting materials since emission lines from 0.9 to 1.6 μm are easily obtained at the expense of a small amount of β-diketonate complexes (1 mol-%) and since sensitization of this luminescence can be obtained with visible light.

Experimental Section

All reagents and solvents were used as received (Acros); monohydrate of 1-dodecyl-3-methylimidazolium chloride ([C_{12}-mim]Cl·H_2O, Scheme 1)[23] as well as the lanthanide ternary complexes [Ln(tta)$_3$(phen)][30] where Ln = Nd, Eu, Er, Yb were synthesized according to literature procedures and characterized by elemental analyses, IR, and NMR spectroscopy. Thermogravimetric analyses (TGA) under normal atmospheric pressure showed the monohydrated imidazolium salt losing one water molecule per formula weight between 120 and 150 °C and no degradation occurring until 320 °C but decomposition started at 330 °C. In order to obtain a mesophase material at room temperature and to avoid thermal decomposition, the ionic liquid was dehydrated before the introduction of the lanthanide compounds, although complete dehydration was avoided because [Ln(tta)$_3$(phen)] complexes have very low solubility in anhydrous [C_{12}-mim]Cl. All preparations were performed under N_2 using Schlenk techniques and further handling of the samples was performed in a glove-box. Monohydrated [C_{12}-mim]Cl·H_2O was heated from room temperature to 230 °C at a speed of 10 °C/min and under reduced pressure (6.5×10^{-1} Torr), left 5 min at this temperature and then cooled to room temp. The resulting partially dehydrated RTIL showed a crystal → liquid crystal (Cr-LC) transition at 6 °C and isotropization (LC-I transition) at 99 °C. Determination of the transition temperature was performed by means of differential scanning calorimetry (DSC) experiments during the first heating from –90 to 160 °C (Table 3). A DSC experiment was carried out every time before addition of the lanthanide ternary complex for confirmation of the partial dehydration of ionic liquid. Then the lanthanide complexes (1 mol-%) were added to the molten ionic liquid and the mixtures were stirred for 30 min at 130 °C under vacuum. The thermal properties of the Ln-containing samples were tested by DSC again and temperatures of the phase transitions for prepared samples are reported in Table 1. The following notation is used for the samples: **Nd1**, **Eu1**, **Er1**, **Yb1**. Heating the mixtures at higher temperature and during a longer span of time allows the doping of larger quantities of ternary complexes in [C_{12}-mim]Cl but we observed some thermal decomposition. The mesomorphic samples were transferred into 0.1-cm quartz Suprasil® cells under controlled atmosphere and the cells were sealed with paraffin.

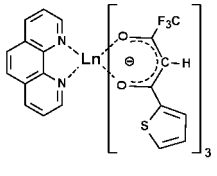

[Ln(tta)$_3$(phen)]

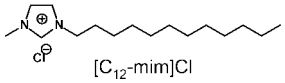

[C_{12}-mim]Cl

Scheme 1.

Table 3. Transition temperatures (in °C, ± 0.5 °C) of the studied samples prepared from partially de-hydrated [C_{12}-mim]Cl (see text), as determined from DSC curves during the first heating-cooling cycle.

Sample	Cr-LC	LC-I	I-LC	LC-Cr
[C_{12}-mim]Cl[a]	6	99	89	3
Nd1	6	102	90	3
Eu1	10	102	93	5
Er1	6	102	89	4
Yb1	9	99	89	2

[a] Partially dehydrated.

Elemental analyses were performed by the Ilse Beetz Laboratory (96301 Kronach, Germany). IR spectra were obtained with a Perkin–Elmer Spectrum One FT-IR spectrometer equipped with a Universal ATR sampling accessory. DSC thermograms were recorded with a Setaram DSC 131 instrument equipped with a liquid nitrogen cooler under nitrogen with cooling-heating cycles between –90 and 160 °C at a rate of 10 °C/min. Thermogravimetric traces were obtained with a Pyris 6 thermogravimetric analyzer from Perkin–Elmer. UV/Visible spectra were measured at 295 K with a Perkin–Elmer Lambda 900 spectrometer. Luminescence measurements (spectra and lifetimes) were recorded with a Fluorolog FL3-22 spectrometer from Jobin–Yvon at 295 and 77 K. Lifetimes for NIR-emitting lanthanides were determined with a high resolution instrumental set-up equipped with a Hamamatsu H9170-75 photomultiplier as described previously.[5] The quantum yields of **Yb1** and of the solution of [Yb(tta)$_3$(phen)] in toluene were determined upon ligand excitation and taking [Yb(tta)$_3$-(H_2O)$_2$] as standard (0.35% in toluene at room temp.).[31] Refractive indices were 1.4964 for the toluene solutions and 1.5059 for **Yb1**.[10] The quantum yield of a powdered sample of [Yb(tta)$_3$-(phen)] was measured by means of an integration sphere from Spex-Jobin Yvon-Horiba 99FL-PLQY, using a described procedure.[32] SAXS patterns were recorded, on samples in 1-mm borosilicate capillaries from Hilgenberg sealed with Araldite®, with a SAXS system from Molecular Metrology equipped with a Cu-K_α Bede micro source configured with confocal Max-Flux™ optics, a variable-temperature universal sample chamber, and a two-dimensional multi-wire gas detector; analysis was performed with the open-source analysis software from Molecular Metrology. The diffraction patterns of pure [C_{12}-mim]Cl were isotropic, whereas those for **Eu1** were somewhat anisotropic. The traces reported in Figure 2 are azimuthally averaged. The Electronic Supporting Information contains IR spectra and excitation luminescence spectra of pure and doped ionic liquids.

Acknowledgments

This work is supported by the Swiss National Science Foundation (National Research Program 47). We thank F. Gumy and D. Baumann for their help in measuring the luminescence lifetimes and obtaining thermal data as well as Frédéric Thomas for the synthesis of [C_{12}-mim]Cl·H_2O.

[1] R. Weissleder, V. Ntziachristos, *Nature Med.* **2003**, *9*, 123–128.
[2] S. Faulkner, S. J. A. Pope, B. P. Burton-Pye, *Appl. Spectrosc. Rev.* **2005**, *40*, 1–31.
[3] G. A. Hebbink, J. W. Stouwdam, D. N. Reinhoudt, F. C. J. M. Van Veggel, *Adv. Mater.* **2002**, *14*, 1147–1150.

 © 2005 Wiley-VCH Verlag GmbH & Co. KGaA, Weinheim

[4] T. S. Kang, B. S. Harrison, M. Bouguettaya, T. J. Foley, J. M. Boncella, K. S. Schanze, J. R. Reynolds, *Adv. Funct. Mater.* **2003**, *13*, 205–210.
[5] S. Torelli, D. Imbert, M. Cantuel, G. Bernardinelli, S. Delahaye, A. Hauser, J.-C. G. Bünzli, C. Piguet, *Chem. Eur. J.* **2005**, *11*, 3228–3242.
[6] D. Imbert, M. Cantuel, J.-C. G. Bünzli, G. Bernardinelli, C. Piguet, *J. Am. Chem. Soc.* **2003**, *125*, 15698–15699.
[7] D. Imbert, S. Comby, A.-S. Chauvin, J.-C. G. Bünzli, *Chem. Commun.* **2005**, 1432–1434.
[8] K. Binnemans, C. Görller-Walrand, *Chem. Rev.* **2002**, *102*, 2303–2345.
[9] K. Driesen, K. Binnemans, *Liq. Cryst.* **2004**, *31*, 601–605.
[10] E. Guillet, D. Imbert, R. Scopelliti, J.-C. G. Bünzli, *Chem. Mater.* **2004**, *16*, 4063–4070.
[11] R. Van Deun, D. Moors, B. De Fre, K. Binnemans, *J. Mater. Chem.* **2003**, *13*, 1520–1522.
[12] K. Binnemans, D. Moors, *J. Mater. Chem.* **2002**, *12*, 3374–3376.
[13] J. Boyaval, C. Li, F. Hapiot, M. Warenghem, N. Isaert, Y. Guyot, G. Boulon, P. Carette, *Mol. Cryst. Liq. Cryst.* **2001**, *359*, 337–350.
[14] K. Binnemans, C. Bex, R. Van Deun, *J. Incl. Phenom. Mol. Recogn. Chem.* **1999**, *35*, 63–73.
[15] J. Boyaval, F. Hapiot, C. Li, N. Isaert, M. Warenghem, P. Carette, *Mol. Cryst. Liq. Cryst.* **1999**, *330*, 1387–1394.
[16] L. J. Yu, M. M. Labes, *Appl. Phys. Lett.* **1977**, *31*, 719–720.
[17] P. Wasserscheid, T. Welton, *Ionic Liquids in Synthesis*, Wiley-VCH, Weinheim, **2005**.
[18] G. Moutiers, I. Billard, *Techniques de l'Ingénieur* **2004**, Report AF 6 712.
[19] T. Welton, *Chem. Rev.* **1999**, *99*, 2071–2083.
[20] S. Arenz, A. Babai, K. Binnemans, K. Driesen, R. Giernoth, A.-V. Mudring, P. Nockemann, *Chem. Phys. Lett.* **2005**, *402*, 75–79.
[21] K. Driesen, P. Nockemann, K. Binnemans, *Chem. Phys. Lett.* **2004**, *395*, 306–310.
[22] K. Binnemans in *Handbook on the Physics and Chemistry of Rare Earths* (Eds.: K. A. Gschneidner Jr., J.-C. G. Bünzli, V. K. Pecharsky), Elsevier, Amsterdam, **2005**, vol. 35, ch. 225.
[23] A. E. Bradley, C. Hardacre, J. D. Holbrey, S. Johnston, S. E. J. McMath, M. S. Nieuwenhuizen, *Chem. Mater.* **2002**, *14*, 629–635.
[24] A. Downard, M. J. Earle, C. Hardacre, S. E. J. McMath, M. Nieuwenhuyzen, S. J. Teat, *Chem. Mater.* **2004**, *16*, 43–48.
[25] C. K. Jörgensen, *Mol. Phys.* **1962**, *5*, 271–277.
[26] R. Demirbilek, J. Heber, S. I. Nikitin, *Proceedings of SPIE* **2002**, *4766*, 47–50.
[27] Y. Hasegawa, Y. Wada, S. Yanagida, *J. Photochem. Photobiol. C: Photochem. Rev.* **2004**, *5*, 183–202.
[28] T. Förster, *Ann. Phys.* **1948**, *2*, 55–75.
[29] D. L. Dexter, *J. Chem. Phys.* **1953**, *21*, 836–850.
[30] L. R. Melby, N. J. Rose, E. Abramson, J. C. Caris, *J. Am. Chem. Soc.* **1964**, *86*, 5117–5117.
[31] S. B. Meshkova, Z. M. Topilova, D. V. Bolshoy, S. V. Beltyukova, M. P. Tsvirko, V. Y. Venchikov, *Acta Phys. Pol. A* **1999**, *95*, 983–990.
[32] S. Wrighton, D. S. Ginley, D. L. Morse, *J. Phys. Chem.* **1974**, *78*, 2229–2233.

Received: July 5, 2005
Published Online: October 25, 2005

 © 2005 Wiley-VCH Verlag GmbH & Co. KGaA, Weinheim

DOI: 10.1002/ejic.200500612

Pd^{II} Complexes of Tridentate PCP N-Heterocyclic Carbene Ligands: Structural Aspects and Application in Asymmetric Hydroamination of Cyano Olefins

Sebastian Gischig[a] and Antonio Togni*[a]

Keywords: N-heterocyclic carbene ligands / Ferrocenes / Palladium complexes / Asymmetric catalysis / Hydroamination / Aminonitriles

The synthesis of the ligand precursor 1,3-bis{(*R*)-1-[(*S*)-2-(diphenylphosphanyl)ferrocenyl]ethyl}imidazolium iodide ([PCPH]I, **1**) was extended to the electronically and sterically modified ligand precursors 1,3-bis{(*R*)-1-[(*S*)-2-{[3,5-bis(trifluoromethyl)phenyl]phosphanyl}ferrocenyl]ethyl}imidazolium iodide ([3,5-CF_3-PCPH]I, **6**), and 1,3-bis[(*R*)-1-{(*S*)-2-[bis(3,5-dimethylphenyl)phosphanyl]ferrocenyl}ethyl]imidazolium iodide ([3,5-Me-PCPH]I, **7**). Palladium complexes were prepared starting from $[Pd(OAc)_2]_3$ in THF to afford [PdI(PCP)]OAc (**8**), [Pd(OAc)(3,5-CF_3-PCP)]I (**9**), and [PdI(3,5-Me-PCP)]OAc (**10**), in excellent yields. The crystal structures of the ligand precursor [3,5-CF_3-PCPH]I (**6**), the complex [PdI(3,5-CF_3-PCP)]PF_6 (**14**), as well as the dicationic complex [Pd($NCCH_3$)(PCP)]$(PF_6)_2$ (**11**), were determined by X-ray diffraction. Complex **11** and its derivative [Pd($NCCH_3$)-(3,5-Me-PCP)]$(PF_6)_2$ (**13**) have been tested as catalysts in the asymmetric addition of, for example, thiomorpholine to methacrylonitrile giving selectivities up to 63 and 75% *ee*, respectively, at –80 °C.

(© Wiley-VCH Verlag GmbH & Co. KGaA, 69451 Weinheim, Germany, 2005)

Introduction

N-Heterocyclic carbenes (NHCs), their corresponding metal complexes, and their applications in catalysis have become a well-established area of research in organometallic chemistry.[1–5] An important step in the development of carbene ligands is their chiral modification and many chiral NHCs acting as monodentate[6–10] as well as bidentate ligands[11–15] in asymmetric reactions have been reported.[5]

Our interest in tridentate ligands based on the ferrocene scaffold derives from the successful application of the triphosphane Pigiphos (see Scheme 1)[16] in, for instance, Ni-catalyzed hydroamination and hydrophosphanation of cyano olefins.[17,18] The replacement of the central PCy unit of Pigiphos by an NHC fragment generates a C_2-symmetric ligand. We speculated that this should lead, in the case of square-planar complexes, to a chiral environment that is better defined than in Pigiphos. We previously reported the synthesis of the PCP ligand precursor **1** as well as its complexation with ruthenium and palladium.[19] In this work we address the modification of the ligand, the complexation with palladium, and the formation of dicationic complexes. The X-ray crystal structures of the activated palladium complex **11**, the CF_3-modified ligand precursor **6** and the palladium complex of this ligand (**14**) are presented, along with the application of these NHC complexes in the catalytic hydroamination reaction of cyano olefins.

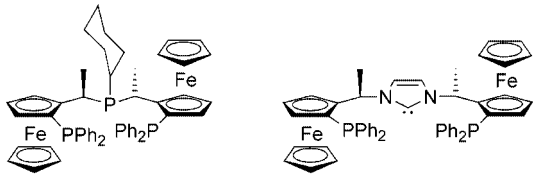

(*R*)-(*S*)-Pigiphos (*R*)-(*S*)-PCP

Scheme 1. The C_1-symmetric triphosphane Pigiphos and a structurally related C_2-symmetric PCP ligand.

Results and Discussion

Ligand Synthesis

The introduction of substituents at the 3- and 5-positions of the phenyl groups in diphenylphosphanyl derivatives is a common approach in view of modifying both the steric and electronic properties of such ligands. Modifications of this kind, as applied to carbene precursor **1** ([PCPH]I), should lead to altered catalytic properties of the corresponding Pd complexes. The synthesis of the ligand precursors—via the amines **2** and **3**, as well as the acetates **4** and **5**, i.e. the (diarylphosphanyl)ferrocene derivatives bearing either a dimethylamino group or an acetate at the stereogenic center—containing methyl and trifluoromethyl substituents,

[a] Department of Chemistry and Applied Biosciences, Swiss Federal Institute of Technology,
ETH Hönggerberg, 8093 Zürich, Switzerland
E-mail: togni@inorg.chem.ethz.ch

 © 2005 Wiley-VCH Verlag GmbH & Co. KgaA, Weinheim

respectively, has been accomplished analogously to the one of the unsubstituted derivative **1**. The preparation of [3,5-CF_3-PCPH]I (**6**) and [3,5-Me-PCPH]I (**7**) from the corresponding acetate derivatives **4** and **5**, respectively, and imidazole was carried out in a mixture of acetonitrile and water in a ratio of 4:1 for **6** and 2:1 for **7**. However, for reactions at room temperature as described for **1**, no substitution of the acetate by imidazole was observed. Heating of the reaction mixture at 60 °C followed by ion exchange with NaI in ethanol yielded **6** in 50% yield after 24 h and **7** in 51% yield after 32 h, respectively (Scheme 2). The yields are lower than the one obtained for **1** and could not be improved by longer reaction times or by using different reaction conditions (temperature, acetonitrile/water mixture).

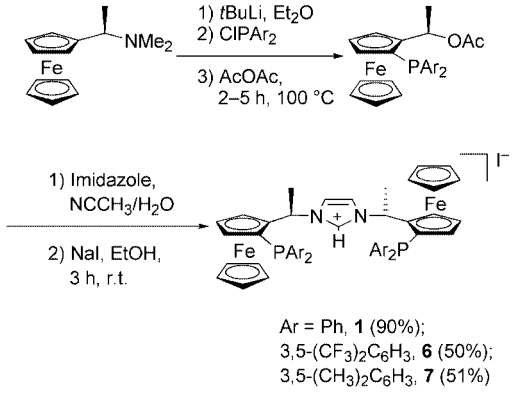

Scheme 2. Synthesis of the ligand precursors **1**, **6**, and **7**.

Treatment of **1**, **6**, and **7** with NaO*t*Bu in THF resulted in the deprotonation of the imidazolium salts. However, the attempted isolation of the free carbenes was not successful. For ^{13}C NMR spectroscopic reasons, these imidazolium salts were also prepared in the form containing a ^{13}C label at position 2 of the imidazole.[20] The deprotonation of the labeled **1**, **6**, and **7** using an excess of NaO*t*Bu in THF allowed us to observe broad ^{13}C NMR signals of the free carbenes at room temperature (Table 1). While the NMR spectroscopic data of the free carbenes confirm the clean generation of these reactive species, the significant line widths account for the difficulties in observing the same signals for the nonlabeled compounds. Furthermore, solutions of these species in C_6D_6 showed the formation of the imidazolium ion within minutes, indicating that the acidic sites of the NMR tube glass are sufficient to protonate the carbenes. The C(2)–H coupling constants (J_{CH}) of the imidazolium salts of 218.7, 222.6, and 218.8 Hz for **1**, **6**, and **7**, respectively, could be estimated with the help of 2D one-bond HMQC experiments. Interestingly, the coupling constant for the more electron-deficient compound **6**, containing the CF_3 substituents, is larger than for **1** and **7**.

Table 1. ^{13}C NMR chemical shifts of the free carbenes derived from **1**, **6**, and **7**.

Free carbene of	δ [ppm]	Line width [Hz]	J_{CP} [Hz]
1	209.0	36	–
6	209.8	–	13.3 (t)
7	209.5	25	–

Synthesis of Palladium Complexes

As already shown for the ligand precursor **1**, the method of choice for the complexation of these carbene ligands to Pd^{II} is to start from $[Pd(OAc)_2]_3$ {see the synthesis of [PdI(PCP)]OAc (**8**), giving 98% yield}.[19] Analogously, the reaction of (3,5-CF_3-PCPH)I (**6**) and (3,5-Me-PCPH)I (**7**) with $[Pd(OAc)_2]_3$ generates the complexes [Pd(OAc)(3,5-CF_3-PCP)]I (**9**) and [PdI(3,5-Me-PCP)]OAc (**10**) in 91% and 95% yield, respectively (Scheme 3).

In order to isolate the complexes containing iodide as a ligand and acetate as the counterion, an ionic ligand exchange reaction is necessary. This ion exchange was studied by NMR on samples of the ^{13}C-labeled complexes (Table 2). It is reasonable to expect that iodide and acetate will exert a different influence on the chemical shift of the carbene carbon atom in the *trans* position. Addition of NaI to a dichloromethane solution of the palladium complexes **8**, **9**, and **10** shifts the ion exchange equilibrium towards the iodo complex (Table 2, Entries 1, 3, and 5). Abstraction of the counterion and the fourth ligand with Et_3OPF_6 (vide infra), followed by the addition of Bu_4NOAc leads to the formation of the complexes having acetate as a ligand (Table 2, Entries 2, 4, and 6). These experiments show a slight downfield shift of the ^{13}C carbene signal in going from coordinated acetate to coordinated iodide, this effect being more pronounced for [Pd(OAc)(3,5-CF_3-PCP)]I (**9**). We also observed a larger coupling constant J_{CP} between the carbene carbon atom and the P atoms for the iodo complexes. Comparing the chemical shifts and the coupling constants observed for compounds **8**, **9**, and **10** we concluded that there is an ion exchange for [PdI(PCP)]OAc (**8**)

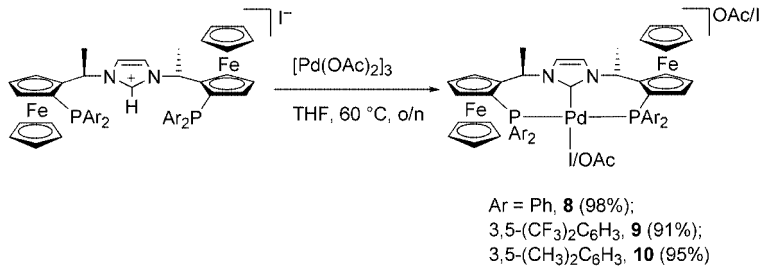

Scheme 3. Synthesis of the palladium complexes **8**, **9**, and **10**.

 © 2005 Wiley-VCH Verlag GmbH & Co. KGaA, Weinheim

Table 2. ^{13}C NMR spectroscopic data for labeled carbene derivatives.

Entry	Complex	Ligand	δ [ppm] (by ion exchange)	J_{CP} [Hz]	δ [ppm] (by synthesis)	J_{CP} [Hz]
1	[PdI(PCP)]OAc (**8**)	I^-	152.3 (t)	12.0	151.4 (t)	13.2
2	[Pd(OAc)(PCP)]PF_6	^-OAc	149.8 (t)	14.6		
3	[PdI(3,5-CF_3-PCP)]OAc	I^-	151.5 (br)	–		
4	[Pd(OAc)(3,5-CF_3-PCP)]I (**9**)	^-OAc	145.7 (t)	13.5	146.8 (t)	13.3
5	[PdI(3,5-Me-PCP)]OAc (**10**)	I^-	152.5 (t)	12.4	151.8 (t)	12.4
6	[Pd(OAc)(3,5-Me-PCP)]PF_6	^-OAc	149.9 (t)	13.6		

and [PdI(3,5-Me-PCP)]OAc (**10**), resulting in products with iodide as the ligand, instead of acetate. This exchange is quite slow and takes approximately 1 d to reach completeness in dichloromethane. Therefore, for further synthesis the equilibrium mixture was used. However, the clean product [PdI(3,5-Me-PCP)]OAc (**10**) could only be obtained by flash chromatography (silica, dichloromethane + 4% methanol). For the electron-poorer complex [Pd(OAc)(3,5-CF_3-PCP)]I (**9**), ion exchange seems to be absent, resulting in a complex with acetate as the fourth ligand. Only the addition of an excess of NaI to **9** allowed us to observe the iodo complex characterized by a rather broad ^{13}C NMR signal (Table 2, Entry 3).

In order to obtain catalytically active species acting as chiral Lewis acids, complexes **8** and **10** were converted into the dicationic derivatives [Pd($NCCH_3$)(PCP)]$(PF_6)_2$ (**11**) and [Pd($NCCH_3$)(3,5-Me-PCP)]$(PF_6)_2$ (**13**) in 79% and 94% yield, respectively, using Et_3OPF_6 in acetonitrile (Scheme 4). The acetonitrile complexes **11** and **13** are characterized by higher ^{31}P chemical shifts and significantly lower ^{13}C carbene chemical shifts with respect to their corresponding precursors, as summarized in Table 3. Somewhat surprisingly, the activation of **9** with Et_3OPF_6 was not selective and led to product mixtures from which the dicationic species could not be identified. It is important to note that all complexes described in this section give NMR spectra consistent with C_2-symmetric structures in solution.

Crystal Structures

Crystals of imidazolium salt **6** suitable for X-ray analysis could be obtained from a dichloromethane solution overlayered with hexane. An ORTEP representation of the structure is shown in Figure 1 and selected bond lengths and angles are listed in Table 4. The overall structure is only approximately C_2-symmetric, i.e., the two ferrocenyl units are not symmetry-related. Three CF_3 groups with the atoms C(6), C(12), and C(15) are disordered over two positions, a phenomenon which can be observed very often for crystal structures containing CF_3 substituents. Iodide was also found to be disordered over two positions with an occupational ratio of 93:7. One of the most specific structural features of this compound is that the molecule backbone, i.e., the chain joining the two phosphorus atoms, displays helical chirality with (*P*) configuration. This chain approximately describes a full screw turn in going from one P atom to the other. The distance between the two P atoms is 7.353 Å and can be viewed as the screw pitch, the backbone being the screw thread. The three donor atoms are already positioned in such a way that the coordination to a metal center only requires a relatively minor conformational change that can be best viewed as a compression of the screw pitch of the ligand backbone (vide infra). Two of the aryl groups, one of each of the phosphane units, are placed on each side of the imidazole plane indicating a possible

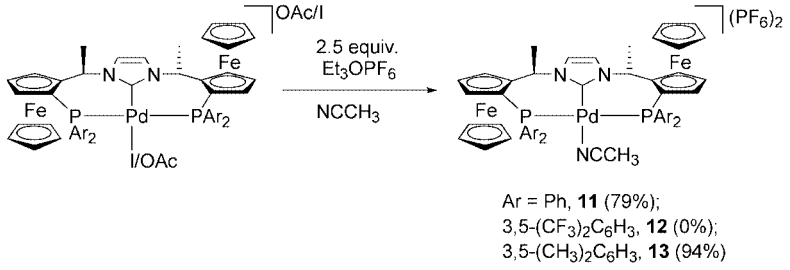

Scheme 4. Synthesis of the dicationic complexes **11** and **13**.

Table 3. ^{31}P and ^{13}C NMR chemical shifts of **8**, **10**, and the dicationic complexes **11** and **13**.

Complex	^{31}P δ [ppm] (J_{CP} [Hz])	^{13}C δ [ppm] (J_{CP} [Hz])
[PdI(PCP)]OAc (**8**)	–1.46 (d, J_{CP} = 12.0)	152.7 (t, J_{CP} = 12.0)
[Pd($NCCH_3$)(PCP)]$(PF_6)_2$ (**11**)	1.81 (d, J_{CP} = 11.7)	144.8 (t, J_{CP} = 11.7)
[PdI(3,5-Me-PCP)]OAc (**10**)	–2.11 (d, J_{CP} = 12.4)	152.5 (t, J_{CP} = 12.4)
[Pd($NCCH_3$)(3,5-Me-PCP)]$(PF_6)_2$ (**13**)	0.93 (d, J_{CP} = 11.6)	144.5 (t, J_{CP} = 11.6)

 © 2005 Wiley-VCH Verlag GmbH & Co. KGaA, Weinheim

weak π-stacking interaction of the aryl groups and the imidazole ring (the average distance between the aromatic rings is 4.02 Å and the interplanar angles are 23.7 and 31.4°). The orientation of the ferrocenyl moieties can be described as pseudo-equatorial with respect to the imidazole plane.

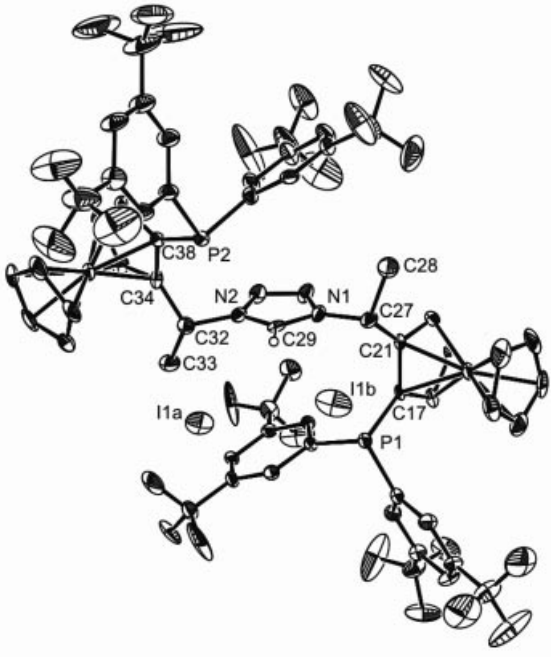

Figure 1. ORTEP representation of (3,5-CF_3-PCPH)I (**6**). Hydrogen atoms and the CF_3 disorder are omitted for clarity. Thermal ellipsoids are set to 30% probability.

The N(1)–C(29)–N(2) angle is with 109.3(5)° at the upper limit of the range found for derivatives of this kind (usually 107.6–109.7°[21–24]). It is also larger than the values measured in the complexes [PdCl(PCP)]PF_6 [106.2(7)°], [Pd($NCCH_3$)(PCP)]$(PF_6)_2$ [106.2(7)]°, [PdI(3,5-CF_3-PCP)]-PF_6 [108.4(10)°], and [RuClI(PCP)] [103.7(19), 104(2)°].

Although it was not possible to isolate the complex [PdI(3,5-CF_3-PCP)]PF_6 (**14**) on a preparative scale, we obtained crystals suitable for X-ray analysis from a chloroform solution of the mixture obtained from the activation of [Pd(OAc)(3,5-CF_3-PCP)]I (**9**) with Et_3OPF_6. The structure is represented in Figure 2 and selected bond lengths and angles are listed in Table 4.

The geometry around the Pd atom is almost square-planar with a slight tetrahedral distortion, as indicated for instance by the C(29)–Pd(1)–I(1) angle of 165.7(4)°. The Pd(1)–C(29) bond of 2.040(12) Å is longer than the reported Pd^{II}–carbene distances with iodide *trans* to a carbene C atom [1.984(4),[25] 1.990(3),[26] 1.990(9),[27] 2.004(3),[27] 1.991(5) Å,[28] 1.994(5),[28] 1.962(8) Å[19] are examples of previously reported distances]. The P(1)–Pd(1)–C(29) and P(2)–Pd(1)–C(29) bite angles are 83.0(4) and 86.3(4)°, which is less than the ideal value of 90°. Contrary to what is found for many (carbene)Pd^{II} complexes, the imidazole plane is not orthogonal to the coordination plane, as illustrated by the torsion angle P(2)–Pd(1)–C(29)–N(2) of –68.2(12)° and the angle between the least-squares planes

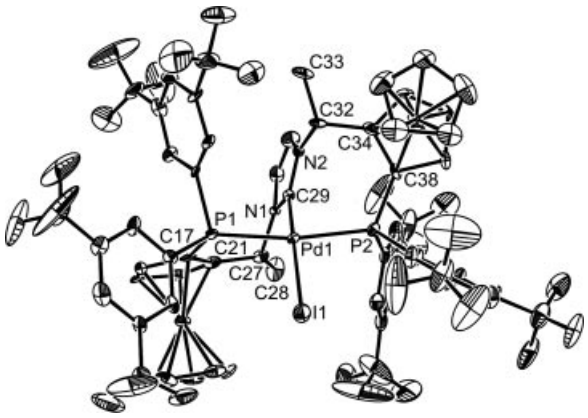

Figure 2. ORTEP representation of the cation in [PdI(3,5-CF_3-PCP)]PF_6 (**14**). Hydrogen atoms are omitted for clarity. Thermal ellipsoids are set to 30% probability.

containing C(29), N(1), C(30), C(31), N(2) and Pd(1), I(1), P(1), P(2), C(29), respectively, which is 70.8°. This deviation from the perpendicular situation of the two planes is inherently due to the helical conformation of the ligand backbone. It has also been found in the previously reported structure of the complex [PdCl(PCP)]PF_6 (**15**), with the corresponding torsion angle of –75.6(7)° and the angle between the coordination plane and the imidazole plane of 72.9°. As opposed to the case of [PdCl(PCP)]PF_6 (**15**), the solid-state structure of **14** is almost, but not perfectly C_2-symmetric. Therefore, the aryl groups on each side of the ligand have very similar orientations. One aryl group at each phosphorus atom is lying roughly in the coordination plane defined by Pd(1), P(1), P(2) and C(29) pushing the iodo ligand out of this plane by 0.7468 Å. The other two aryl groups assume a pseudo-axial orientation.

As was the case for the precursor **6**, the ligand backbone of **14** displays helical chirality with (*P*) configuration. From a topological point of view, the essential difference between the two compounds is the compression of the screw pitch on going from **6** to **14**. In fact, the distance between the two P atoms decreases from 7.353 Å to 4.601 Å, as a consequence of a conformational change. There are only two pairs of equivalent single bonds potentially susceptible to significant conformational changes, i.e., the linkages joining the stereogenic centers to the respective Cp and N atom. An inspection of the torsion angles provided in Table 4 reveals that a counterclockwise rotation around the two N–C bonds by ca. 35 and 47°, respectively, mainly accounts for the observed change of conformation. Indeed, rotation around the crucial pair of single C–C bonds occurs in a clockwise manner, but only to an extent of ca. 19 and 3°, respectively, in going from **6** to **14**.

It was also possible to obtain X-ray quality crystals of the moisture-sensitive complex [Pd($NCCH_3$)(PCP)]$(PF_6)_2$ (**11**) by slow diffusion of diethyl ether into an acetonitrile solution at –20 °C. The structure is represented in Figure 3 and selected bond lengths and angles are collected in Table 4. This complex shows in the solid state an almost square-planar geometry. The overall structure is approxi-

 © 2005 Wiley-VCH Verlag GmbH & Co. KGaA, Weinheim

Table 4. Selected bond lengths [Å] angles [°], and torsion angles [°] of the ligand precursor (3,5-CF_3-PCPH)I (**6**) and the complexes [PdI(3,5-CF_3-PCP)]PF_6 (**14**) and [Pd($NCCH_3$)(PCP)]$(PF_6)_2$ (**11**).

(3,5-CF_3-PCPH)I (**6**)			
C(29)–N(1)	1.336(8)	C(29)–N(1)–C(27)	125.1(5)
C(29)–N(2)	1.325(7)	C(29)–N(1)–C(30)	107.4(5)
N(1)–C(30)	1.394(8)	C(30)–N(1)–C(27)	127.5(5)
N(2)–C(31)	1.391(7)	C(29)–N(2)–C(32)	125.4(5)
C(30)–C(31)	1.330(9)	C(29)–N(2)–C(31)	108.2(5)
N(1)–C(27)	1.481(8)	C(31)–N(2)–C(32)	126.3(5)
N(2)–C(32)	1.486(8)		
C(29)–N(1)–C(27)–C(21)	133.9(6)	C(29)–N(2)–C(32)–C(34)	120.7(6)
C(17)–C(21)–C(27)–N(1)	–78.7(7)	N(2)–C(32)–C(34)–C(38)	–69.9(7)
C(17)–C(21)–C(27)–C(28)	161.2(6)	C(33)–C(32)–C(34)–C(38)	167.8(6)
[PdI(3,5-CF_3-PCP)]PF_6 (**14**)			
Pd(1)–C(29)	2.040(12)	Pd(1)–P(2)	2.299(4)
Pd(1)–P(1)	2.324(4)	Pd(1)–I(1)	2.6142(15)
P(1)–Pd(1)–C(29)	83.0(4)	P(2)–Pd(1)–C(29)	86.3(4)
I(1)–Pd(1)–C(29)	165.7(4)	P(1)–Pd(1)–P(2)	168.76(13)
I(1)–Pd(1)–P(1)	98.62(10)	I(1)–Pd(1)–P(2)	92.59(10)
P(1)–Pd(1)–C(29)–N(1)	–72.8(11)	P(1)–Pd(1)–C(29)–N(2)	108.2(13)
I(1)–Pd(1)–C(29)–N(1)	25(2)	I(1)–Pd(1)–C(29)–N(2)	–154.3(9)
P(2)–Pd(1)–C(29)–N(1)	110.9(11)	P(2)–Pd(1)–C(29)–N(2)	–68.2(12)
C(29)–N(1)–C(27)–C(21)	87.1(16)	C(29)–N(2)–C(32)–C(34)	85.7(15)
C(17)–C(21)–C(27)–N(1)	-60.0(17)	N(2)–C(32)–C(34)–C(38)	–67.2(18)
C(17)–C(21)–C(27)–C(28)	173.2(14)	C(33)–C(32)–C(34)–C(38)	172.0(14)
[Pd($NCCH_3$)(PCP)]$(PF_6)_2$ (**11**)			
Pd(1)–C(25)	1.993(9)	Pd(1)–P(2)	2.334(3)
Pd(1)–P(1)	2.351(3)	Pd(1)–N(3)	2.037(8)
N(3)–C(52)	1.126(10)		
P(1)–Pd(1)–C(25)	87.3(2)	P(2)–Pd(1)–C(25)	83.7(2)
N(3)–Pd(1)–C(25)	177.9(4)	P(1)–Pd(1)–P(2)	170.56(8)
N(3)–Pd(1)–P(1)	92.7(2)	N(3)–Pd(1)–P(2)	96.5(2)
P(1)–Pd(1)–C(25)–N(1)	–71.7(7)	P(1)–Pd(1)–C(25)–N(2)	107.0(7)
N(3)–Pd(1)–C(25)–N(1)	16(11)	N(3)–Pd(1)–C(25)–N(2)	–165(10)
P(2)–Pd(1)–C(25)–N(1)	111.0(7)	P(2)–Pd(1)–C(25)–N(2)	–70.3(7)
C(25)–N(1)–C(23)–C(14)	84.8(8)	C(25)–N(2)–C(28)–C(30)	86.1(9)
C(13)–C(14)–C(23)–N(1)	–71.1(9)	N(2)–C(28)–C(30)–C(31)	–63.8(9)
C(13)–C(14)–C(23)–C(24)	165.9(7)	C(29)–C(28)–C(30)–C(31)	170.7(7)

mately C_2-symmetric with one pair of phenyl rings located very close to the coordination plane and the second pair, together with the ferrocenyl units, in a pseudo-axial position. The C(25)–Pd(1)–N(3) angle of 177.9(4)° is much closer to the ideal value of 180° than the corresponding angles of the previously discussed complexes [PdI(3,5-CF_3-PCP)]PF_6 (**14**), with 165.7(4)°, and [PdCl(PCP)]PF_6 (**15**), containing the unsubstituted PCP ligand, with 164.3(3)°.[19] The Pd(1)–C(25) bond length for **11** is 1.993(9) Å which is longer than that observed in [PdCl(PCP)]PF_6 (**15**), with a value of 1.962(8) Å. Lee recently reported crystal structures of a cationic $[PdCl(PCP)]^+$ complex, as well as of the corresponding dicationic counterpart $[Pd(NCCH_3)(PCP)]^{2+}$, containing the tridentate NHC ligand PCP = PPh_2–$(CH_2)_2$–NHC–$(CH_2)_2$–PPh_2, i.e., compounds structurally related to ours.[29] However, in contrast to our results, Lee found that the Pd–C distance is longer in the chloro complex than in the dicationic acetonitrile derivative [1.983(7) vs. 1.961(4) Å]. The bite angles P(1)–Pd(1)–C(25) of 87.3(2)° and P(2)–Pd(1)–C(25) of 83.7(2)° are slightly larger than the corresponding values for [PdCl(PCP)]PF_6 (**15**) [86.6(3)

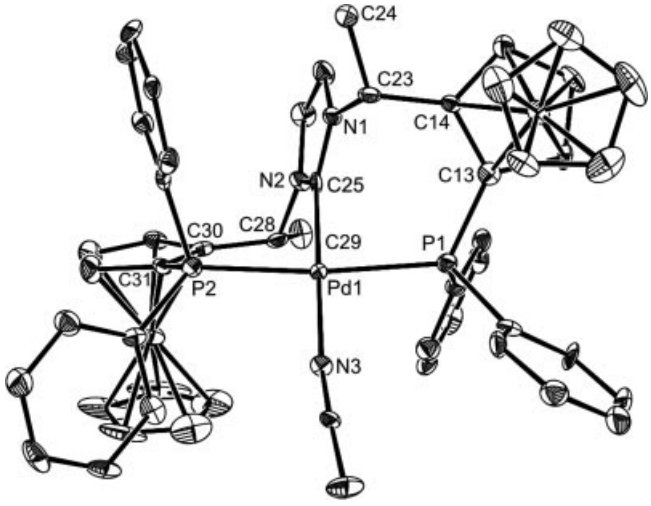

Figure 3. ORTEP representation of the dication in [Pd($NCCH_3$)(PCP)]$(PF_6)_2$ (**11**). Hydrogen atoms are omitted for clarity. Thermal ellipsoids are set to 30% probability.

 © 2005 Wiley-VCH Verlag GmbH & Co. KGaA, Weinheim

and 82.2(3)°]. The imidazole plane is again tilted away from the orientation perpendicular to the coordination plane. The torsion angle P(1)–Pd(1)–C(25)–N(1) has a value of –71.7(7)° and the angle between the least-squares planes containing C(25), N(1), C(26), C(27), N(2) and Pd(1), P(1), P(2), N(3), C(25), respectively, is 70.9°. The N(3)–C(52) bond length in the acetonitrile ligand is 1.126(10) Å which lies within the range of N–C distances found for palladium complexes containing phosphanes (1.114–1.144 Å),[30–34] or pincer-type carbene ligands (1.124–1.135 Å)[35–38] *trans* to the acetonitrile.

Catalysis

The acetonitrile ligand in the complexes $[Pd(NCCH_3)(PCP)](PF_6)_2$ (**11**) and $[Pd(NCCH_3)(3,5\text{-Me-PCP})](PF_6)_2$ (**13**) can be readily replaced by a substrate containing a functional group. This allows an activation of such substrates with the complex acting as a Lewis acid. Encouraged by the results achieved in our group[17,18] with $[Ni(PPP)(THF)](ClO_4)_2$ (PPP = Pigiphos, Scheme 1) as a Lewis acidic catalyst, we also tested our complexes in the asymmetric hydroamination of cyano olefins (Scheme 5).

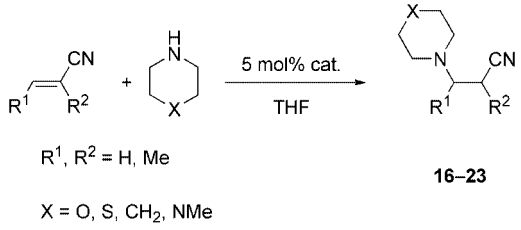

Scheme 5. Hydroamination of cyano olefines.

In most experiments we used 5 mol-% of catalyst and the typical reaction time was 24 h at room temperature. The amines tested for this reaction were morpholine, thiomorpholine, piperidine, *N*-methylpiperazine, and aniline affording always the isolated product of the *anti*-Markovnikoff addition. The first experiments were carried out with the complex $[Pd(NCCH_3)(PCP)](PF_6)_2$ (**11**) using methyl methacrylate as the activated olefin; however, no activity was found. The test runs with crotonitrile as the amine acceptor afforded good to excellent yields (76–98%) but low enantioselectivities (up to 6% *ee*) in the case of aliphatic amines, whereas aniline showed no activity at all. We reasoned that aniline is poisoning the catalyst by coordination to the active site, but we never succeeded in isolating an aniline complex. The first promising results could be obtained with methacrylonitrile, having the methyl group in the α-position with respect to the electron-withdrawing group. The results involving methacrylonitrile as the substrate are summarized in Table 5. While aniline still showed no activity, the products derived from the aliphatic olefins were isolated in good to excellent yields, but the enantioselectivities were still low (up to 36% *ee* for *N*-methylpiperazine). No improvement was found by using acetone (no activity), or 1,2-dichloroethane as solvents. In this latter solvent, thiomorpholine could be added to methacrylonitrile affording 78% yield and 27% *ee*. Lowering of the reaction temperature from room temperature to –20 °C resulted, as expected, in lower isolated yields after a reaction time of 24 h (Table 5, Entries 5–8). The enantioselectivity could be somewhat improved for morpholine (38% *ee*) and thiomorpholine (44% *ee*). Surprisingly, for piperidine (23% *ee*) and *N*-methylpiperazine (33% *ee*) the enantioselectivity was reproducibly lower at –20 °C than at room temperature. Lowering of the temperature to –80 °C while using longer reaction times (3 d) in order to reach complete conversion, resulted in an improvement of the selectivity (except for piperidine) up to 63% *ee* (Table 5, Entries 9–12).

In view of a possible improvement of the enantioselectivity, the ligands bearing 3,5-disubstituted phenyl rings were tested. As mentioned earlier, the activation of the complex [Pd(OAc)(3,5-CF_3-PCP)]I (**9**) with Et_3OPF_6 re-

Table 5. Asymmetric addition of aliphatic amines to methacrylonitrile (see Scheme 5).

Entry	X	Catalyst [Ar]	*T* [°C]	*t*	Yield [%]	*ee* [%]
1	O	**11** [Ph]	20	24 h	96	32
2	S	**11** [Ph]	20	24 h	99	33
3	CH_2	**11** [Ph]	20	24 h	60	26
4	NMe	**11** [Ph]	20	24 h	84	36
5	O	**11** [Ph]	–20	24 h	82	38
6	S	**11** [Ph]	–20	24 h	83	44
7	CH_2	**11** [Ph]	–20	24 h	67	23
8	NMe	**11** [Ph]	–20	24 h	73	33
9	O	**11** [Ph]	–80	3 d	94	47
10	S	**11** [Ph]	–80	3 d	91	63
11	CH_2	**11** [Ph]	–80	3 d	94	22
12	NMe	**11** [Ph]	–80	3 d	98	46
13	O	**13** [3,5-$(CH_3)_2C_6H_3$]	20	24 h	99	54
14	S	**13** [3,5-$(CH_3)_2C_6H_3$]	20	24 h	96	61
15	CH_2	**13** [3,5-$(CH_3)_2C_6H_3$]	20	24 h	99	54
16	NMe	**13** [3,5-$(CH_3)_2C_6H_3$]	20	24 h	99	51
17	O	**13** [3,5-$(CH_3)_2C_6H_3$]	–80	3 d	91	71
18	S	**13** [3,5-$(CH_3)_2C_6H_3$]	–80	3 d	83	75
19	CH_2	**13** [3,5-$(CH_3)_2C_6H_3$]	–80	3 d	93	56
20	NMe	**13** [3,5-$(CH_3)_2C_6H_3$]	–80	3 d	92	73

 © 2005 Wiley-VCH Verlag GmbH & Co. KGaA, Weinheim

sulted in a mixture from which the active species could not be identified. Using this mixture as the catalyst did not result in any activity even after heating the reaction mixture at 60 °C. Therefore, the less electron-deficient complex $[Pd(NCCH_3)(3,5\text{-Me-PCP})](PF_6)_2$ (**13**) was tested for the methacrylonitrile system. The activity at room temperature (Table 5, Entries 13–16) as well as at –80 °C (Table 5, Entries 17–20) was found to be in the same range as when using the unsubstituted ligand. The enantioselectivities, however, were improved up to 61% *ee* (thiomorpholine) at room temperature and finally up to 75% *ee* (thiomorpholine) at –80 °C. Interestingly, the lowering of the reaction temperature again had no significant influence on the selectivity for piperidine. This indicates that in this system the additional heteroatom (O, S, NMe) has an influence on the stereodifferentiating step during the catalysis.

Conclusions

The three-step synthesis of the ligand precursor [PCPH]-I (**1**) was extended to the synthesis of the electronically and sterically modified ligand precursors (3,5-CF_3-PCPH)I (**6**) and (3,5-Me-PCPH)I (**7**), bearing substituents at the 3- and 5-positions of the aryl groups. The reaction of the imidazolium salts **1**, **6**, and **7** with $[Pd(OAc)_2]_3$ in THF is the most efficient route to Pd^{II} complexes of the corresponding carbene ligands affording [PdI(PCP)]OAc (**8**), [Pd(OAc)(3,5-CF_3-PCP)]I (**9**), and [PdI(3,5-Me-PCP)]OAc (**10**) in excellent yields. These complexes displayed a different behavior concerning the exchange of the anions acetate and iodide as addressed by NMR studies. Reaction of these complexes with Et_3OPF_6 in acetonitrile afforded the dicationic species $[Pd(NCCH_3)(PCP)](PF_6)_2$ (**11**) and $[Pd(NCCH_3)(3,5\text{-Me-PCP})](PF_6)_2$ (**13**) in good to excellent yields. However, a similar activation of [Pd(OAc)(3,5-CF_3-PCP)]I (**9**) failed and resulted in a product mixture that was catalytically not active.

The solid-state structures of the ligand precursor (3,5-CF_3-PCPH)I (**6**) and its corresponding complex [PdI(3,5-CF_3-PCP)]PF_6 (**14**) show that their common molecule backbone assumes a helical conformation and that the most relevant conformational difference between the two compounds is accounted for mainly by a different torsion around the two N–C single bonds.

The dicationic complexes $[Pd(NCCH_3)(PCP)](PF_6)_2$ (**11**) and $[Pd(NCCH_3)(3,5\text{-Me-PCP})](PF_6)_2$ (**13**) are active catalysts for the addition of cyclic aliphatic secondary amines to cyano olefins. The additions to methacrylonitrile catalyzed by $[Pd(NCCH_3)(PCP)](PF_6)_2$ (**11**) showed moderate enantioselectivities which increased at low temperatures. The sterically modified complex $[Pd(NCCH_3)(3,5\text{-Me-PCP})](PF_6)_2$ (**13**) showed higher enantioselectivities at room temperature (up to 61% *ee*) as well as at –80 °C (up to 75% *ee*). Comparing Pd(PCP) and Ni(Pigiphos) catalysts having the same absolute configuration of the ferrocenyl units, it is interesting to note that products of opposite absolute configuration are obtained. Somewhat surprisingly and disappointingly, it appears that the C_2-symmetric PCP ligands described here do not offer any significant advantage when compared to the asymmetric ligand Pigiphos in the Ni/Pd-catalyzed addition of amines to methacrylonitrile.

Experimental Section

General Methods: (*R*)-*N*,*N*-Dimethyl-1-ferrocenylethylamine was generously provided by Solvias AG (Basel) and was recrystallized as tartrate salt according to the reported procedure.[39] The chlorophosphanes $[3,5\text{-}(CF_3)_2C_6H_3]_2PCl$ and $[3,5\text{-}(CH_3)_2C_6H_3]_2PCl$ were prepared as described.[40] Derivatives **2**–**5** have been prepared before in our laboratory.[41] All reactions were performed under an inert gas and air-sensitive substances were handled in a glove box. NMR: The routine ^1H, ^{13}C, and ^{31}P NMR spectra were measured in the given solvent with either a Bruker DPX250 or Bruker DPX300 instrument. The 2D experiments were generally carried out with a Bruker DPX500 instrument. EI-MS, FAB-MS, MALDI-MS: Measurements were performed by the MS service of the "Laboratorium für Organische Chemie der ETHZ". The signals are given as *m*/*z*. Elemental analyses were performed by the micro elemental analysis service of the "Laboratorium für Organische Chemie der ETHZ". Crystallography: X-ray structural measurements were carried out with a Bruker CCD diffractometer (Bruker SMART PLATFORM, with a CCD detector, graphite monochromator, and Mo-K_α radiation). The program SMART served for data collection. Integration was performed with SAINT. The structure solution (direct methods) and refinement on F^2 were accomplished with SHELXTL-97. Model plots were made with ORTEP32. For the structures of **6**, **14** (with exceptions), and **11** all non-hydrogen atoms were refined freely with anisotropic refinement parameters. For **6** a CH_2Cl_2 molecule was found to be disordered over two sites. The C–Cl bond lengths were restrained to standard values. Iodide and some of the CF_3 groups are disordered over two sites. The C–F distances were restrained by the use of a variable and the F···F distances were equalized with the SADI instruction. In the structure of **14** there are three $CHCl_3$ molecules present. The carbon atom in one of the $CHCl_3$ molecules is disordered over two positions. The C–Cl bond lengths were restrained to standard values. For the disordered CF_3 groups of C(6) and C(45) the same procedure was adopted as for **6**. Due to the low data-to-parameter ratio, the atoms C(1), C(10), C(62), C(29), and N(2) were refined anisotropically in combination with the ISOR instruction. In the structure of **11** one ethanol and one diethyl ether molecule are present. C(55) of the ether molecule and C(58) of ethanol is disordered over two positions. Hydrogen atoms were refined at calculated positions riding on their carrier atoms. Weights were optimized in the final refinement cycles. Crystallographic data are given in Table 6. CCDC-240665 (**6**), -240662 (**14**), and -240664 (**11**) contain the supplementary crystallographic data for this paper. These data can be obtained free of charge from The Cambridge Crystallographic Data Centre via www.ccdc.cam.ac.uk/data_request/cif.

1,3-Bis{(*R*)-1-[(*S*)-2-{[3,5-bis(trifluoromethyl)phenyl]phosphanyl}-ferrocenyl]ethyl}imidazolium Iodide (6): A suspension of **4** (1.51 g, 2.07 mmol) and imidazole (77.5 mg, 1.14 mmol, 0.55 equiv.) in a mixture of acetonitrile (14 mL) and water (3.5 mL) was heated at 60 °C for 24 h. After addition of benzene (9 mL), the organic phase was separated and concentrated in vacuo. The residue was dissolved together with NaI (683 mg, 4.55 mmol, 2 equiv.) in ethanol (15 mL) and stirred for 3 h. After evaporation of the solvent in vacuo, the crude product was filtered through silica (CH_2Cl_2, then

 © 2005 Wiley-VCH Verlag GmbH & Co. KGaA, Weinheim

Table 6. Crystallographic data for (3,5-CF_3-PCPH)I (**6**), [PdI(3,5-CF_3-PCP)]PF_6 (**14**), and [Pd($NCCH_3$)(PCP)]$(PF_6)_2$ (**11**).

	(3,5-CF_3-PCPH)I (**6**)	[PdI(3,5-CF_3-PCP)]PF_6 (**14**)	[Pd($NCCH_3$)(PCP)]$(PF_6)_2$ (**11**)
Color, shape	yellow cube	red cube	yellow needle
Empirical formula	$C_{59}H_{39}F_{24}Fe_2N_2P_2$, I, CH_2Cl_2	$C_{59}H_{38}F_{24}Fe_2IN_2P_2Pd$, PF_6, 3($CHCl_3$)	$C_{53}H_{49}Fe_2N_3P_2Pd$, 2(PF_6), C_2H_6O, $C_4H_{10}O$
Formula mass	1615.37	2053.28	1401.99
Temperature [K]	200	200	150
Wavelength [Å]	0.71073	0.71073	0.71073
Crystal system	monoclinic	monoclinic	triclinic
Space group	$P2_1$	$P2_1$	$P\bar{1}$
Unit cell dimensions [Å; °]	a = 8.3762(4); α = 90 b = 33.4516(16); β = 109.0080(10) c = 12.4853(6); γ = 90	a = 10.781(3); α = 90 b = 28.236(8); β = 114.11 c = 13.194(4); γ = 90	a = 10.645(9); α = 94.368(17) b = 11.133(9); β = 107.592(19) c = 13.707(11); γ = 109.542(18)
Volume [Å^3]	3307.6(3)	3665.9(17)	1431(2)
Z	2	2	1
Calcd. density [g cm^{-3}]	1.622	1.860	1.627
Absorption coeff. [mm^{-1}]	1.141	1.486	1.009
Crystal size [mm]	0.94 × 0.42 × 0.36	0.32 × 0.23 × 0.16	0.24 × 0.07 × 0.04
Reflns. collected, unique	18999, 10593	21112, 9648	9837, 7953
R_{int}	0.0352	0.1028	0.0287
Refinement method	Full-matrix least-squares on F^2	Full-matrix least-squares on F^2	Full-matrix least-squares on F^2
Data, restraints, params.	10593, 29, 958	9648, 48, 1008	7953, 3, 766
Goodness of fit	1.094	1.021	1.000
R, R_w	0.0581, 0.1304	0.0811, 0.1655	0.0525, 0.0892
Abs. structure parameter	0.006(16)	0.06(4)	0.02(2)
Min./max. resd. [e·Å^{-3}]	1.108/–0.369	1.211/–0.941	1.028/–0.753

CH_2Cl_2 + 4% MeOH) and chromatographed (silica, hexane/ethyl acetate, 1:1 + 2% acetic acid). Yield: 793 mg (0.52 mmol, 50%), orange crystals. TLC (hexane/ethyl acetate, 1:1): R_f = 0.64. $C_{59}H_{39}F_{24}Fe_2IN_2P_2$ (1532.46): calcd. C 46.24, H 2.57, N 1.83; found C 45.95, H 2.83, N 1.97. MS-MALDI: m/z = 669 [Ar_2PFcEt^+]. ^{1}H NMR (300 MHz, CD_2Cl_2): δ = 1.21 (d, J_{CHMe} = 6.9 Hz, 6 H, CH*Me*), 3.91 (t, J_{CHCH} = 1.2 Hz, 2 H, Cp), 4.08 (s, 10 H, Cp′), 4.69 (t, J_{CHCH} = 2.6 Hz, 2 H, Cp), 4.79 (m, 2 H, Cp), 6.44 (dq, J_{CHMe} = 6.9 Hz, J_{PH} = 3.0 Hz, 2 H, C*H*Me), 6.50 (d, J_{CHCH} = 1.2 Hz, 2 H, HC=CH Im), 7.24 (s, 2 H, P*Ar*$_2$), 7.26 (s, 2 H, P*Ar*$_2$), 7.79 (s, 2 H, P*Ar*$_2$), 8.06 (s, 4 H, P*Ar*$_2$), 8.09 (s, 2 H, P*Ar*$_2$), 10.65 (s, 1 H, $^+$CH, Im) ppm. ^{13}C NMR (300 MHz, CD_2Cl_2): δ = 20.6 (CH_3, CH*Me*), 55.1 (d, J_{CP} = 9.8 Hz, CH, *C*HMe), 70.4 (d, J_{CP} = 4.5 Hz, CH, Cp), 70.7 (CH, Cp′), 72.3 (d, J_{CP} = 4.7 Hz, CH, Cp), 72.5 (CH, Cp), 90.3 (d, J_{CP} = 29.7 Hz, C, Cp), 118.1 (CH, HC=CH Im), 122.5 (CH, P*Ar*$_2$), 123.0, (dq, J_{CP} = 7.8 Hz, J_{CF} = 273.2 Hz, C, CF_3), 124.2 (CH, P*Ar*$_2$), 131.1 (d, J_{CP} = 16.5 Hz, CH, P*Ar*$_2$), 131.3 (dq, J_{CP} = 4.2 Hz, C, *C*CF_3), 131.8 (dq, J_{CP} = 8.2 Hz, J_{CF} = 33.5 Hz, C, *C*CF_3), 134.3 ($^+$CH, Im), 135.1 (d, J_{CP} = 4.2 Hz, C, P*Ar*$_2$), (d, J_{CP} = 22.9 Hz, CH, P*Ar*$_2$), 138.8 (d, J_{CP} = 14.3 Hz, C, P*Ar*$_2$), 142.4 (d, J_{CP} = 17.2 Hz, C, P*Ar*$_2$) ppm. ^{31}P NMR (300 MHz, CD_2Cl_2): δ = –25.32 (*P*Ar$_2$) ppm.

1,3-Bis[(*R*)-1-{(*S*)-2-[(3,5-Dimethylphenyl)phosphanyl]ferrocenyl}-ethyl]imidazolium Iodide (7): A suspension of **5** (300 mg, 0.59 mmol) and imidazole (20.3 mg, 0.30 mmol, 0.51 equiv.) in a mixture of acetonitrile (8 mL) and water (4 mL) was heated at 60 °C for 32 h. After addition of benzene (5 mL), the organic phase was separated and concentrated in vacuo. The residue was dissolved together with NaI (193 mg, 1.29 mmol, 2 equiv.) in ethanol (10 mL) and stirred for 3 h. After evaporation of the solvent in vacuo, the crude product was filtered through silica (CH_2Cl_2, then CH_2Cl_2 + 4% MeOH) and chromatographed (silica, ethyl acetate, then ethyl acetate + 2% MeOH). Yield: 163.3 mg (0.15 mmol, 51%), orange crystals. $C_{59}H_{63}Fe_2IN_2P_2$ (1100.69): calcd. C 64.38, H 5.77, N 2.55; found C 64.45, H 5.87, N 2.41. MS-MALDI: m/z = 973 [3,5-Me-PCPH$^+$], 453 [Ar_2PFcEt^+]. ^{1}H NMR (300 MHz, CD_2Cl_2): δ = 1.58 (d, J_{CHMe} = 6.9 Hz, 6 H, CH*Me*), 2.37 (s, 6 H, Ar-*Me*), 2.42 (s, 6 H, Ar-*Me*), 4.10 (s, 10 H, Cp′), 4.14 (s, 2 H, Cp), 4.58 (t, J_{CHCH} = 2.4 Hz, 2 H, Cp), 4.89 (m, 2 H, Cp), 5.38 (q, J_{CHMe} = 6.9 Hz, 2 H, C*H*Me), 6.66 (s, 2 H, P*Ar*$_2$), 6.68 (s, 2 H, P*Ar*$_2$), 7.04 (s, 2 H, P*Ar*$_2$), 7.17 (s, 2 H, P*Ar*$_2$), 7.18 (s, J_{CHCH} = 1.5 Hz, 2 H, HC=CH Im), 7.26 (s, 2 H, P*Ar*$_2$), 7.29 (s, 2 H, P*Ar*$_2$), 8.08 (t, J_{CHCH} = 1.6 Hz, 1 H, $^+$CH, Im) ppm. ^{13}C NMR (300 MHz, CD_2Cl_2): δ = 20.4 (CH_3, CH*Me*), 21.2 (CH, Ar*Me*), 21.4 (CH, Ar*Me*), 55.4 (d, J_{CP} = 9.8 Hz, CH, *C*HMe), 69.7 (CH, Cp), 70.3 (CH, Cp′), 71.0 (CH, Cp), 73.1 (CH, Cp), 75.8 (d, J_{CP} = 9.1 Hz, C, Cp), 90.6 (d, J_{CP} = 25.4 Hz, C, Cp), 119.4 (CH, HC=CH Im), 129.7 (d, J_{CP} = 17.8 Hz, CH, P*Ar*$_2$), 130.3 (CH, P*Ar*$_2$), 131.5 (CH, P*Ar*$_2$), 132.5 ($^+$CH, Im), 132.8 (d, J_{CP} = 20.8 Hz, CH, P*Ar*$_2$), 135.4 (C, P*Ar*$_2$), 137.9 (C, P*Ar*$_2$), 138.0 (C, P*Ar*$_2$), 138.9 (d, J_{CP} = 4.5 Hz, C, P*Ar*$_2$) ppm. ^{31}P NMR (300 MHz, CD_2Cl_2): δ = –28.36 (*P*Ar$_2$) ppm.

(SP-4)-(1,3-Bis{(*R*)-1-[(*S*)-2-{[3,5-bis(trifluoromethyl)phenyl]phosphanyl-κ*P*}ferrocenyl]ethyl}imidazol-2-ylidene)(iodo)palladium(II) Acetate, [Pd(OAc)(3,5-CF_3-PCP)]I (9): [$Pd(OAc)_2$]$_3$ (44 mg, 0.065 mmol) and **6** (300 mg, 0.196 mmol) were dissolved in THF (6 mL) and heated at 60 °C for 12 h. After evaporation of the solvent in vacuo, the residue was dissolved in CH_2Cl_2 and the product precipitated with hexane, filtered off, washed three times with hexane and dried in vacuo. Yield: 313.6 mg (0.272 mmol, 91%), deep red crystals. ^{1}H NMR (250 MHz, [D$_6$]acetone): δ = 1.16 (d, 6 H, J_{CHMe} = 7.0 Hz, CH*Me*), 2.85 (br., 3 H, OAc), 4.08 (m, 2 H, Cp), 4.35 (s, 10 H, Cp′), 4.66 (t, J_{CHCH} = 2.5 Hz, 2 H, Cp), 4.98 (m, 2 H, Cp), 6.30 (q, J_{CHMe} = 7.0 Hz, 2 H, C*H*Me), 7.53 (s, 2 H, HC=CH Im), 7.83 (t, J_{CHCH} = 4.5 Hz, 4 H, P*Ar*$_2$), 8.19 (br., 2 H, P*Ar*$_2$), 8.35 (br., 2 H, P*Ar*$_2$), 9.41 (t, J_{CHCH} = 5.3 Hz, 4 H, P*Ar*$_2$) ppm. ^{13}C NMR (250 MHz, [D$_6$]acetone): δ = 14.0 (CH_3, CH*Me*), 52.8 (CH, *C*HMe), 53.7, 54.14 (CH_3, O*Ac*), 70.0 (CH, Cp), 71.0 (CH, Cp), 71.3 (CH, Cp), 71.7 (CH, Cp′), 73.7 (C, Cp), 93.1 (C, Cp), 121.3 (CH, HC=CH Im), 120.9, 124.3, 125.2, 125.6, 130.3, 130.7, 131.3, 131.9, 136.2, 136.9 (CH, C, P*Ar*$_2$), 146.8 (br., CPd, Im) ppm. ^{31}P NMR (250 MHz, [D$_6$]acetone): δ = 1.79 (*P*Ar$_2$) ppm.

(SP-4)-(1,3-Bis{(*R*)-1-{(*S*)-2-[(3,5-dimethylphenyl)phosphanyl-κ*P*]-ferrocenyl}ethyl}imidazol-2-ylidene)(iodo)palladium(II) Acetate, [PdI(3,5-Me-PCP)]OAc (10): [$Pd(OAc)_2$]$_3$ (165.4 mg, 0.25 mmol)

 © 2005 Wiley-VCH Verlag GmbH & Co. KGaA, Weinheim

and **7** (811 mg, 0.74 mmol) were dissolved in THF (20 mL) and heated at 60 °C for 12 h. After evaporation of the solvent in vacuo, the residue was dissolved in CH_2Cl_2 and the product precipitated with hexane, filtered off, washed three times with hexane, and dried in vacuo. Yield: 883.6 mg (0.70 mmol; 95%), brown solid. $C_{61}H_{65}Fe_2IN_2O_2P_2Pd$ (1265.14): calcd. C 53.16, H 4.69; found: C 52.00, H 5.30. MS-MALDI: *m*/*z* = 1205 [PdI(3,5-Me-PCP)$^+$], 1077 [Pd(3,5-Me-PCP)$^+$]. ^{1}H NMR (250 MHz, CD_2Cl_2): δ = 1.27 (d, J_{CHMe} = 7.0 Hz, 6 H, CH*Me*), 2.04 (s, 3 H, OAc), 2.30 (s, 6 H, Ar*Me*), 2.40 (s, 6 H, Ar*Me*), 3.65 (m, J_{CHCH} = 1.3 Hz, 2 H, Cp), 4.28 (s, 10 H, Cp′), 4.51 (t, J_{CHCH} = 2.6 Hz, 2 H, Cp), 4.87 (m, 2 H, Cp), 5.56 (q, J_{CHCH} = 7.2 Hz, 2 H, C*H*Me), 6.54 (t, J_{CHCH} = 5.5 Hz, 4 H, P*Ar*$_2$), 6.90 (s, 2 H, HC=CH Im), 7.16 (br., 2 H, P*Ar*$_2$), 7.22 (br., 2 H, P*Ar*$_2$), 7.50 (t, J_{CHCH} = 5.8 Hz, 4 H, P*Ar*$_2$) ppm. ^{13}C NMR (250 MHz, CD_2Cl_2): δ = 15.6 (CH_3, CH*Me*), 21.2 (CH, Ar*Me*), 53.9 (CH, *C*HMe), 70.5 (t, J_{CP} = 3.5 Hz, CH, Cp), 71.8 (t, J_{CP} = 2.8 Hz, CH, Cp), 71.2 (CH, Cp′), 71.7 (t, C, Cp), 76.0 (t, J_{CP} = 2.8 Hz, CH, Cp), 90.2 (t, J_{CP} = 6.6 Hz, C, Cp), 118.7 (CH, HC=CH Im), 128.2 (t, J_{CP} = 27.9 Hz, C, P*Ar*$_2$), 128.4 (t, J_{CP} = 6.0 Hz, CH, P*Ar*$_2$), 132.5 (CH, P*Ar*$_2$), 133.0 (CH, P*Ar*$_2$), 133.6 (t, J_{CP} = 24.7 Hz, C, P*Ar*$_2$), 134.1 (t, J_{CP} = 5.5 Hz, CH, P*Ar*$_2$), 136.8 (t, J_{CP} = 5.9 Hz, C–Me, P*Ar*$_2$), 138.8 (t, J_{CP} = 5.3 Hz, CMe, P*Ar*$_2$), 152.7 (t, J_{CP} = 12.4 Hz, CPd, Im) ppm. ^{31}P NMR (250 MHz, CD_2Cl_2): δ = –2.11 (P*Ar*$_2$) ppm.

(SP-4)-(Acetonitrilo)(1,3-bis{(*R*)-1-[(*S*)-2-(Diphenylphosphanyl-κ*P*)-ferrocenyl]ethyl}imidazol-2-ylidene)palladium(II) Bis(hexafluorophosphate), [PdPCP(NCCH$_3$)](PF$_6$)$_2$ (11): A solution of **8** (253 mg, 0.22 mmol) and Et_3OPF_6 (136 mg, 0.55 mmol, 2.5 equiv.) in acetonitrile (10 mL) was stirred at room temperature for 10 h. The mixture was concentrated to an amount of 2 mL and the product was precipitated with diethyl ether, filtered off, washed two times with diethyl ether and dried in vacuo. Yield: 225 mg (0.17 mmol, 79%), brown solid. ^{1}H NMR (300 MHz, $NCCD_3$): δ = 1.27 (d, J_{CHMe} = 7.2 Hz, 6 H, CH*Me*), 2.25 (br., 3 H, $NCCH_3$), 3.93 (m, J_{CHCH} = 1.2 Hz, 2 H, Cp), 4.25 (s, 10 H, Cp′), 4.65 (t, J_{CHCH} = 2.6 Hz, 2 H, Cp), 4.89 (d, J_{CHCH} = 1.2 Hz, 2 H, Cp), 5.47 (q, J_{CHCH} = 6.9 Hz, 2 H, C*H*Me), 6.90 (s, 2 H, HC=CH Im), 7.10 (q, J_{CHCH} = 6.9 Hz, 4 H, P*Ph*$_2$), 7.53 (t, J_{CHCH} = 7.5 Hz, 4 H, P*Ph*$_2$), 7.61–7.84 (m, 12 H, P*Ph*$_2$) ppm. ^{13}C NMR (300 MHz, $NCCD_3$): δ = 0.4 (NC*C*H$_3$), 15.1 (CH_3, CH*Me*), 55.0 (CH, *C*HMe), 68.6 (t, J_{CP} = 29.4 Hz, C, Cp), 70.9 (t, J_{CP} = 3.4 Hz, CH, Cp), 71.5 (t, J_{CP} = 4.2 Hz, CH, Cp), 71.6 (CH, Cp′), 75.1 (t, J_{CP} = 3.1 Hz, CH, Cp), 90.6 (t, J_{CP} = 6.9 Hz, C, Cp), 117.7 (N*C*CH$_3$), 120.1 (CH, HC=CH Im), 126.9 (t, J_{CP} = 27.7 Hz, CH, P*Ph*$_2$), 128.9 (t, J_{CP} = 5.6 Hz, CH, P*Ph*$_2$), 129.7 (t, J_{CP} = 5.3 Hz, CH, P*Ph*$_2$), 130.8 (t, J_{CP} = 27.2 Hz, CH, P*Ph*$_2$), 131.3 (t, J_{CP} = 6.3 Hz, CH, P*Ph*$_2$), 131.8 (CH, P*Ph*$_2$), 132.5 (CH, P*Ph*$_2$), 134.2 (t, J_{CP} = 6.5 Hz, CH, P*Ph*$_2$), 144.5 (t, J_{CP} = 11.6 Hz, CPd, Im) ppm. ^{31}P NMR (300 MHz, $NCCD_3$): δ = –144.45 (sept, J_{PF} = 706.8, PF_6), 1.57 (*P*Ph$_2$) ppm.

(SP-4)-(Acetonitrilo)(1,3-bis[(*R*)-1-{(*S*)-2-[(3,5-dimethylphenyl)phosphanyl-κ*P*]ferrocenyl}ethyl]imidazol-2-ylidene)palladium(II) Bis(hexafluorophosphate), [Pd(3,5-Me-PCP)(NCCH$_3$)](PF$_6$)$_2$ (13): A solution of **10** (81.9 mg, 0.065 mmol) and Et_3OPF_6 (40.3 mg, 0.16 mmol, 2.5 equiv.) in acetonitrile (4 mL) was stirred at room temperature for 10 h. The mixture was concentrated to an amount of 2 mL and the product was precipitated with diethyl ether, filtered off, washed two times with diethyl ether and dried in vacuo. Yield: 86.2 mg (0.06 mmol, 94%), brown solid. ^{1}H NMR (300 MHz, $NCCD_3$): δ = 1.26 (d, J_{CHMe} = 7.2 Hz, 6 H, CH*Me*), 1.99 (s, 3 H, $NCCH_3$), 2.31 (s, 6 H, Ar*Me*), 2.45 (s, 6 H, Ar*Me*), 3.92 (m, J_{CHCH} = 1.8 Hz, 2 H, Cp), 4.23 (s, 10 H, Cp′), 4.63 (t, J_{CHCH} = 2.4 Hz, 2 H, Cp), 4.86 (m, 2 H, Cp), 5.39 (q, J_{CHCH} = 6.9 Hz, 2 H, C*H*Me), 6.62 (t, J_{CHCH} = 6.3 Hz, 4 H, P*Ar*$_2$), 6.93 (s, 2 H, HC=CH Im), 7.27 (br., J_{CHCH} = 7.5 Hz, 2 H, P*Ar*$_2$), 7.40 (m, 6 H, P*Ar*$_2$) ppm. ^{13}C NMR (300 MHz, $NCCD_3$): δ = 0.3 (NC*C*H$_3$), 14.7 (CH_3, CH*Me*), 20.4 (CH, Ar*Me*), 20.5 (CH, Ar*Me*), 54.8 (CH, *C*HMe), 69.3 (t, J_{CP} = 29.1 Hz, C, Cp), 70.6 (t, J_{CP} = 3.0 Hz, CH, Cp), 71.3 (m, CH, Cp), 71.4 (CH, Cp′), 75.3 (t, J_{CP} = 2.8 Hz, CH, Cp), 90.4 (t, J_{CP} = 6.8 Hz, C, Cp), 118.1 (N*C*CH$_3$), 119.9 (CH, HC=CH Im), 126.7 (t, J_{CP} = 27.2 Hz, C, P*Ar*$_2$), 128.6 (t, J_{CP} = 6.2 Hz, CH, P*Ar*$_2$), 130.8 (t, J_{CP} = 27.0 Hz, C, P*Ar*$_2$), 131.8 (t, J_{CP} = 6.4 Hz, CH, P*Ar*$_2$), 133.2 (CH, P*Ar*$_2$), 134.0 (CH, P*Ar*$_2$), 138.7 (t, J_{CP} = 5.8 Hz, CMe, P*Ar*$_2$), 139.5 (t, J_{CP} = 5.5 Hz, CMe, P*Ar*$_2$), 144.5 (t, J_{CP} = 11.6 Hz, CPd, Im) ppm. ^{31}P NMR (300 MHz, $NCCD_3$): δ = –144.47 (sept, J_{PF} = 706.6, PF_6), 1.01 (*P*Ph$_2$) ppm.

General Procedure for the Pd-Catalyzed Hydroamination of Cyano Olefins: A solution of palladium complex (0.025 mmol; 5 mol-%) and olefin (1 mmol; 2 equiv.) in THF (3 mL) was stirred at room temperature for 5 min. The amine (0.5 mmol) was then added and the reaction mixture was stirred at the required temperature for the corresponding time. The reaction was stopped by the addition of hexane. Filtration and evaporation of the solvent yielded the hydroamination product. If necessary, the product was purified by chromatography (silica, hexane/ethyl acetate, 1:1 + 5% NEt_3). Enantioselectivities were determined by GC or HPLC analysis.

3-(Morpholino)butanenitrile (16): TLC (hexane/ethyl acetate, 1:1 + 5% NEt_3): R_f = 0.47. ^{1}H NMR (250 MHz, $CDCl_3$): δ = 1.20 (d, J = 6.8 Hz, 3 H, CHC*H*$_3$), 2.38 (dd, J = 7.3 Hz, J = 16.8 Hz, 1 H, C*H*H′CN), 2.52 (t, J = 4.8 Hz, 4 H, C*H*$_2$N), 2.52 (dd, J = 6.5 Hz, J = 16.8 Hz, 1 H, CH*H*′CN), 2.94 (m, J = 6.0 Hz, 1 H, NC*H*CH$_3$), 3.70 (t, J = 4.6 Hz, 4 H, C*H*$_2$O) ppm. ^{13}C(DEPT) NMR (250 MHz, $CDCl_3$): δ = 15.2 (CH*C*H$_3$), 21.3 (*C*HH′CN), 48.8 (*C*H$_2$N), 56.3 (N*C*HCH$_3$), 67.1 (*C*H$_2$O) ppm. GC (β-dex, 90 °C iso): t_r = 267.50, 267.64 min.

3-(Thiomorpholino)butanenitrile (17): TLC (hexane/ethyl acetate, 1:1 + 5% NEt_3): R_f = 0.60. ^{1}H NMR (250 MHz, $CDCl_3$): δ = 1.14 (d, J = 6.8 Hz, 3 H, CHC*H*$_3$), 2.32 (dd, J = 7.3 Hz, J = 16.8 Hz, 1 H, C*H*H′CN), 2.48 (dd, J = 6.5 Hz, J = 16.8 Hz, 1 H, CH*H*′CN), 2.63 (m, 4 H, C*H*$_2$N), 2.77 (m, 4 H, C*H*$_2$S), 2.99 (m, J = 7.0 Hz, 1 H, NC*H*CH$_3$) ppm. ^{13}C(DEPT) NMR (250 MHz, $CDCl_3$): δ = 15.1 (CH*C*H$_3$), 21.1 (*C*HH′CN), 28.3 (*C*H$_2$N), 50.8 (*C*H$_2$S), 57.7 (N*C*HCH$_3$) ppm. HPLC (OJ, hexane/*i*PrOH, 95:5, 0.5 mL/ min, 25 °C, DAD 210 nm): t_r = 38.12, 41.18 min.

3-(Piperidin-1-yl)butanenitrile (18): ^{1}H NMR (250 MHz, $CDCl_3$): δ = 1.19 (d, J = 6.8 Hz, 3 H, CHC*H*$_3$), 1.42 (m, 2 H, CH$_2$), 1.56 (m, J = 5.4 Hz, 4 H, CH$_2$), 2.32 (dd, J = 8.0 Hz, J = 16.8 Hz, 1 H, C*H*H′CN), 2.47 (m, 4 H, C*H*$_2$N), 2.51 (dd, J = 5.5 Hz, J = 16.8 Hz, 1 H, CH*H*′CN), 2.99 (m, 1 H, NC*H*CH$_3$) ppm. ^{13}C(DEPT) NMR (250 MHz, $CDCl_3$): δ = 15.5 (CH*C*H$_3$), 20.6 (*C*HH′CN), 24.6 (CH$_2$), 26.2 [(CH$_2$)$_2$], 49.4 (*C*H$_2$N), 56.8 (N*C*HCH$_3$) ppm. GC (β-dex, 80 °C iso): t_r = 324.7, 325.2 min.

3-(4-Methylpiperazin-1-yl)butanenitrile (19): ^{1}H NMR ($CDCl_3$): δ = 1.16 (d, J = 6.8 Hz, 3 H, CHC*H*$_3$), 2.24 (s, 3 H, NCH$_3$), 2.32 (dd, J = 7.5 Hz, J = 16.8 Hz, 1 H, C*H*H′CN), 2.40 (br. s, 4 H, C*H*$_2$N), 2.49 (dd, J = 5.5 Hz, J = 16.8 Hz, 1 H, CH*H*′CN), 2.52 (br. m, 4 H, C*H*$_2$NCH$_3$), 2.96 (m, 1 H, NC*H*CH$_3$) ppm. ^{13}C(DEPT) NMR ($CDCl_3$): δ = 15.4 (CH*C*H$_3$), 21.1 (*C*HH′CN), 45.9 (NCH$_3$), 48.1 (*C*H$_2$N), 55.2 (*C*H$_2$NCH$_3$), 56.8 (N*C*HCH$_3$) ppm. GC (β-dex, 90 °C iso): t_r = 352.4, 360.1 min.

2-Methyl-3-(morpholino)propionitrile (20): TLC (hexane/ethyl acetate, 1:1 + 5% NEt_3): R_f = 0.55. ^{1}H NMR (250 MHz, $CDCl_3$): δ = 1.28 (d, J = 7.0 Hz, 3 H, CHC*H*$_3$), 2.37 (dd, J = 6.3 Hz, J = 12.5 Hz, 1 H, C*H*H′), 2.47 (t, J = 4.6 Hz, 4 H, C*H*$_2$N), 2.57 (dd, J = 8.3 Hz, J = 12.5 Hz, 1 H, CH*H*′), 2.75 (m, 1 H, C*H*CH$_3$), 3.67

 © 2005 Wiley-VCH Verlag GmbH & Co. KGaA, Weinheim

(t, J = 4.6 Hz, 4 H, CH_2O) ppm. ^{13}C(DEPT) NMR (250 MHz, $CDCl_3$): δ = 15.9 (CHCH$_3$), 24.1 (CHCH$_3$), 53.6 (CH$_2$N), 61.3 (CHH′), 66.8 (CH$_2$O) ppm. GC (β-dex, 92 °C iso): t_r = 128.1 (R), 130.3 (S) min.

2-Methyl-3-(thiomorpholino)propionitrile (21): TLC (hexane/ethyl acetate, 1:1 + 5% NEt_3): R_f = 0.58. ^{1}H NMR (250 MHz, $CDCl_3$): δ = 1.26 (d, J = 7.0 Hz, 3 H, CHCH_3), 2.42 (dd, J = 6.3 Hz, J = 12.8 Hz, 1 H, CHH′), 2.59 (dd, J = 8.3 Hz, J = 12.8 Hz, 1 H, CHH′), 2.65 (m, 4 H, CH_2N), 2.75 (m, 1 H, CHCH$_3$, 4 H, CH_2S) ppm. ^{13}C(DEPT) NMR (250 MHz, $CDCl_3$): δ = 15.9 (CHCH$_3$), 24.5 (CHCH$_3$), 27.9 (CH$_2$N), 55.2 (CH$_2$S), 61.7 (CHH′) ppm. HPLC (OJ, hexane/*i*PrOH, 95:5, 0.5 mL/ min, 25 °C, DAD 230 nm): t_r = 25.52, 28.06 min.

2-Methyl-3-(piperidin-1-yl)propionitrile (22): TLC (hexane/ethyl acetate, 1:1 + 5% NEt_3): R_f = 0.8. ^{1}H NMR (250 MHz, $CDCl_3$): δ = 1.31 (d, J = 7.0 Hz, 3 H, CHCH_3), 1.43 (m, 2 H, CH_2), 1.58 (m, J = 5.3 Hz, 4 H, CH_2), 2.37 (dd, J = 6.5 Hz, J = 12.5 Hz, 1 H, CHH′), 2.44 (t, J = 5.5 Hz, 4 H, CH_2N), 2.59 (dd, J = 8.0 Hz, J = 12.5 Hz, 1 H, CHH′), 2.76 (m, 1 H, CHCH$_3$) ppm. ^{13}C(DEPT) NMR (250 MHz, $CDCl_3$): δ = 16.2 (CHCH$_3$), 24.2 (CH_2), 24.3 (CHCH$_3$), 25.9 [$(CH_2)_2$], 54.7 (CH$_2$N), 61.8 (CHH′) ppm. GC (α-dex, 50 °C iso): t_r = 566, 578 min.

2-Methyl-3-(4-methylpiperazin-1-yl)propionitrile (23): TLC (hexane/ethyl acetate, 1:1 + 5% NEt_3): R_f = 0.1. ^{1}H NMR (250 MHz, $CDCl_3$): δ = 1.25 (d, J = 7.0 Hz, 3 H, CHCH_3), 2.22 (s, 3 H, NCH_3), 2.36 (dd, J = 6.3 Hz, J = 2.5 Hz, 1 H, CHH′), 2.37 (s br, 4 H, CH_2N), 2.49 (s br, 4 H, CH_2NCH$_3$), 2.57 (dd, J = 8.5 Hz, J = 12.5 Hz, 1 H, CHH′), 2.72 (m, 1 H, CHCH$_3$) ppm. ^{13}C(DEPT) NMR (250 MHz, $CDCl_3$): δ = 16.0 (CHCH$_3$), 24.3 (CHCH$_3$), 45.9 (NCH_3), 53.2 (CH$_2$N), 54.9 (CH$_2$NCH$_3$), 60.9 (CHH′) ppm. GC (α-dex, 80 °C iso): t_r = 223, 228 min.

Acknowledgments

Support from the Swiss National Science Foundation is gratefully acknowledged.

[1] D. J. Cardin, B. Cetinkaya, M. F. Lappert, *Chem. Rev.* **1972**, *72*, 545.
[2] D. Bourissou, O. Guerret, F. P. Gabbaï, G. Bertrand, *Chem. Rev.* **2000**, *100*, 39.
[3] W. A. Herrmann, T. Weskamp, V. P. W. Böhm, *Adv. Organomet. Chem.* **2001**, *48*, 1.
[4] W. A. Herrmann, *Angew. Chem. Int. Ed.* **2002**, *41*, 1290.
[5] M. C. Perry, K. Burgess, *Tetrahedron: Asymmetry* **2003**, *14*, 951.
[6] F. Guillen, C. L. Winn, A. Alexakis, *Tetrahedron: Asymmetry* **2001**, *12*, 2083.
[7] T. J. Seiders, D. W. Ward, R. H. Grubbs, *Org. Lett.* **2001**, *3*, 3225.
[8] J. Huang, L. Jafarpour, A. C. Hillier, E. D. Stevens, S. P. Nolan, *Organometallics* **2001**, *20*, 2878.
[9] D. Broggini, A. Togni, *Helv. Chim. Acta* **2002**, *85*, 2518.
[10] C. Bolm, M. Kesselgruber, G. Raabe, *Organometallics* **2002**, *21*, 707.
[11] M. C. Perry, X. Cui, M. T. Powell, D.-R. Hou, J. H. Reibenspies, K. Burgess, *J. Am. Chem. Soc.* **2003**, *125*, 113.
[12] C. Bolm, T. Focken, G. Raabe, *Tetrahedron: Asymmetry* **2003**, *14*, 1733.
[13] L. G. Bonnet, R. E. Douthwaite, R. Hodgson, *Organometallics* **2003**, *22*, 4384.
[14] H. Seo, H.-J. Park, B. Y. Kim, J. H. Lee, S. U. Son, Y. K. Chung, *Organometallics* **2003**, *22*, 618.
[15] C. Marshall, M. F. Ward, W. T. A. Harrison, *Tetrahedron Lett.* **2004**, *45*, 5703.
[16] P. Barbaro, A. Togni, *Organometallics* **1995**, *14*, 3570.
[17] L. Fadini, A. Togni, *Chem. Commun.* **2003**, 30.
[18] A. D. Sadow, I. Haller, A. Togni, *J. Am. Chem. Soc.* **2004**, *126*, 14704.
[19] S. Gischig, A. Togni, *Organometallics* **2004**, *23*, 2479.
[20] A. A. Gridnev, I. M. Mihaltseva, *Synth. Commun.* **1994**, *24*, 1547.
[21] A. J. I. Arduengo, L. R. Harlow, M. Kline, *J. Am. Chem. Soc.* **1991**, *113*, 361.
[22] A. J. I. Arduengo, S. F. Gamper, M. Tamm, J. C. Calabrese, F. Davidson, H. A. Craig, *J. Am. Chem. Soc.* **1995**, *117*, 572.
[23] A. J. Arduengo, R. Krafczyk, R. Schmutzler, H. A. Craig, J. R. Goerlich, W. J. Marshall, M. Unverzagt, *Tetrahedron* **1999**, *55*, 14523.
[24] B. Bildstein, M. Malaun, H. Kopacka, K. Wurst, M. Mitterböck, K.-H. Ongania, G. Opromolla, P. Zanello, *Organometallics* **1999**, *18*, 4325.
[25] M. V. Baker, B. W. Skelton, A. H. White, C. C. Williams, *J. Chem. Soc., Dalton Trans.* **2001**, 111.
[26] R. A. Batey, M. Shen, A. J. Lough, *Org. Lett.* **2002**, *4*, 1411.
[27] W. A. Herrmann, J. Schwarz, *Organometallics* **1999**, *18*, 4082.
[28] J. Schwarz, V. P. W. Böhm, M. G. Gardiner, M. Grosche, W. A. Herrmann, W. Hieringer, G. Raudaschl-Sieber, *Chem. Eur. J.* **2000**, *6*, 1773.
[29] H.-M. Lee, J. Y. Zeng, C.-H. Hu, M.-T. Lee, *Inorg. Chem.* **2004**, *43*, 6822.
[30] M. A. Zuideveld, B. H. G. Swennenhuis, M. D. K. Boele, Y. Guari, G. P. F. van Strijdonck, J. N. H. Reek, P. C. J. Kamer, K. Goubitz, J. Fraanje, M. Lutz, A. L. Spek, P. W. N. M. van Leeuwen, *J. Chem. Soc., Dalton Trans.* **2002**, 2308.
[31] S. A. Wander, A. Miedaner, B. C. Noll, R. M. Barkley, D. L. DuBois, *Organometallics* **1996**, *15*, 3360.
[32] K. R. Reddy, K. Surekha, G.-H. Lee, S.-M. Peng, J.-T. Chen, S.-T. Liu, *Organometallics* **2001**, *20*, 1292.
[33] A. Miedaner, B. C. Noll, D. L. DuBois, *Organometallics* **1997**, *16*, 5779.
[34] R. R. Guimerans, M. M. Olmstead, A. L. Balch, *Inorg. Chem.* **1983**, *22*, 2224.
[35] P. Steenwinkel, H. Kooijman, W. J. J. Smeets, A. L. Spek, D. M. Grove, G. van Koten, *Organometallics* **1998**, *17*, 5411.
[36] J. E. Kickham, S. J. Loeb, *Inorg. Chem.* **1994**, *33*, 4351.
[37] A. M. Kelly, S. A. Macgregor, A. C. Willis, J. H. Nelson, E. Wenger, *Inorg. Chim. Acta* **2003**, *351*, 79.
[38] L. R. Falvello, S. Fernández, R. Navarro, A. Rueda, E. P. Urriolabeitia, *Organometallics* **1998**, *17*, 5887.
[39] G. W. Gokel, I. K. Ugi, *J. Chem. Educ.* **1972**, *49*, 294.
[40] A. L. Casalnuovo, T. V. RajanBabu, T. A. Ayers, T. H. Warren, *J. Am. Chem. Soc.* **1994**, *116*, 9869.
[41] a) C. Gambs, G. Consiglio, A. Togni, *Helv. Chim. Acta* **2001**, *84*, 3105. See also: b) C. Gambs, ETH Ph. D. thesis no. 14156, Zürich, **2001**; c) L. Fadini, ETH Ph. D. thesis no. 15593, Zürich, **2004**.

Received: July 11, 2005
Published Online: October 25, 2005

 © 2005 Wiley-VCH Verlag GmbH & Co. KGaA, Weinheim

DOI: 10.1002/ejic.200500663

Influence of Solvent on Ligand-Substitution Reactions of Pt^{II} Complexes as Function of the π-Acceptor Properties of the Spectator Chelate

Christian F. Weber[a] and Rudi van Eldik*[a]

Keywords: Solvent effects / Kinetics / Platinum(II) chemistry / Ligand effects / UV/Vis spectroscopy

A detailed kinetic study of the substitution reactions of $[Pt^{II}(L^3)Cl]^+$ complexes, where L^3 represents a tridentate N-donor chelate which contains different numbers of π-acceptor pyridine units, with thiourea as a function of nucleophile concentration, temperature and pressure was undertaken in a series of solvents of different polarity, viz. 1-pentanol, 1-propanol, ethanol, methanol and water. The substitution behaviour of [Pt(diethylenetriamine)Cl]$^+$ (**aaa**), [Pt{2,6-bis(aminomethyl)pyridine}Cl]$^+$ (**apa**), [Pt{bis(2-pyridylmethyl)amine}Cl]$^+$ (**pap**) and [Pt(terpy)Cl]$^+$ (**ppp**) was studied in the selected solvents. In the case of alcoholic solutions, an increase in the substitution rate with increasing length of the carbon chain was observed, which is ascribed to the possible role of van der Waals forces in stabilizing the transition state. In the case of methanol and water as solvent, the second-order rate constants correlate with the polarity of the solvent. The activation parameters for the substitution of the **aaa**, **apa**, **pap**, and **ppp** complexes in methanol and water were determined, from which evidence for an associative mechanism was obtained. The introduction of π-acceptor ligands leads to a higher electrophilicity of the platinum(II) centre and consequently a higher lability of the complex. The reactivity of the complexes is controlled by a combination of solvent and π-acceptor effects.
(© Wiley-VCH Verlag GmbH & Co. KGaA, 69451 Weinheim, Germany, 2005)

Introduction

We are interested in the effect of solvent on ligand-substitution reactions of Pt^{II} complexes because of the high activity of some Pt complexes against certain tumour cells.[1] For this reason ligand-substitution reactions of square-planar (low-spin d^8) Pt^{II} complexes are among the best investigated dynamic processes in chemistry.[2] Up to now the kinetic and thermodynamic data show that in nearly all cases the substitution mechanism has an associative character,[2,3] according to which the entering ligand forms a bond with the metal centre prior to bond cleavage with the leaving group, which involves an increase in the coordination number of the Pt centre from four (square-planar) to five (trigonal-bipyramidal) in the transition state. In some rare cases ligand-substitution reactions on Pt^{II} complexes follow a dissociative reaction mechanism.[4–6]

The rate constants for such ligand-substitution reactions vary considerably and depend on the nature of the solvent, entering nucleophile, spectator ligand, leaving group, charge on the complex and pH. For a series of (aqua)Pt^{II} complexes with a varying number of π-acceptor ligands (viz. pyridine ligands), it was shown that the π-acceptor effect controls the substitution rate since it causes a decrease in the electron density and an increase in electrophilicity of the Pt^{II} centre.[7] Kotowski et al. determined rate and activation parameters for the reaction of *trans*-$[Pt(py)_2(NO_2)Cl]$ with pyridine in nitromethane, methanol, ethanol and dichloromethane.[8,9] The solvent dependence of the activation volume, $\Delta V^{\neq}$, could be used to separate intrinsic and solvational volume contributions which result from changes in bond lengths and angles, and changes in polarity, dipole interactions and electrostriction during formation of the transition state of the reaction, respectively. Such information is crucial for a full understanding of the intimate nature of the substitution mechanism.[8,9]

In this paper we report the effect of solvent on ligand-substitution reactions of Pt^{II} complexes as a function of the π-acceptor properties of the spectator chelate. The investigated reaction is given in Equation (1).

$$[Pt(L^3)Cl]^+ + TU \xrightarrow{k_2} [Pt(L^3)TU]^{2+} + Cl^- \quad (1)$$

Thiourea (TU) was used as a neutral entering ligand such that the overall reaction is accompanied by charge creation on which basis a characteristic solvent dependence is to be expected. In addition, formation of the five-coordinate transition state may involve changes in dipole moment which will affect the activation parameters, especially the entropy and volume of activation. The selected Pt^{II} complexes are [Pt(diethylenetriamine)Cl]$^+$ (**aaa**), [Pt{2,6-bis(aminomethyl)pyridine}Cl]$^+$ (**apa**), [Pt{bis(2-pyridylmethyl)amine}Cl]$^+$ (**pap**) and [Pt(2,2′:6′,2′′-terpyridine)Cl]$^+$ (**ppp**), where **a** and **p** represent amine and pyridine, respectively. The structures of the complexes[7] and adopted abbrevi-

[a] Institute for Inorganic Chemistry, University of Erlangen-Nürnberg,
Egerlandstr. 1, 91058 Erlangen, Germany
Supporting information for this article is available on the WWW under http://www.eurjic.org or from the author.

 © 2005 Wiley-VCH Verlag GmbH & Co. KgaA, Weinheim

Table 1. The employed solvents and the corresponding dielectric constant ε (25 °C) and boiling points (101.3 kPa).

Solvent	1-Pentanol	1-Propanol	Ethanol	Methanol	Water	Formamide
Dielectric constant	13.9	20.45	24.55	32.66	78.36	109.5
Boiling point [°C]	138	97	78.3	64.5	100	210

ations are summarized in Scheme 1. A series of solvents of different polarity were selected and are summarized in Table 1.[10] We report the effect of the solvent on the π-acceptor properties, activation parameters and polar nature of the transition state for the studied reaction.

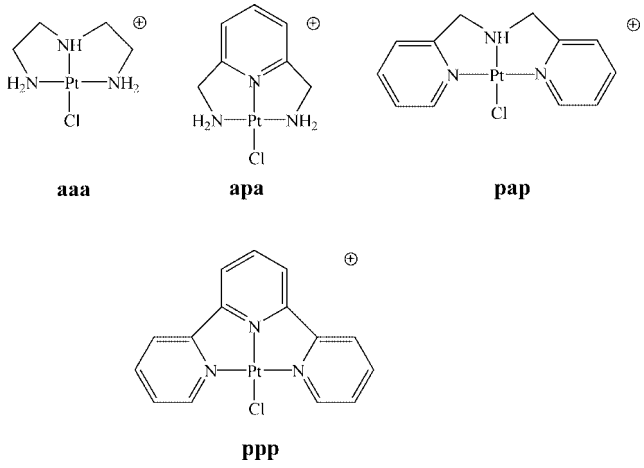

Scheme 1.

Results and Discussion

In order to investigate the solvent dependence of ligand-substitution reactions on Pt^{II} complexes as a function of the π-acceptor property of the spectator chelate, a total of four (chloro)Pt^{II} complexes were synthesized and characterized. More information on the crystal structure of the complexes is available from the literature.[7] Solutions of the complexes were prepared by dissolving known amounts of the chloro complexes in the selected solvents in the presence of 0.002 M LiCl in order to prevent spontaneous solvolysis reactions. The solubility of the complexes differed significantly and UV/Vis spectra were recorded to monitor the solvolysis reactions.

The ligand-substitution reactions were studied as a function of the thiourea (TU) concentration, temperature and pressure for the series of solvents. An example of the UV/Vis spectral changes and a representative kinetic trace are shown in Figures 1 and 2, respectively. The wavelengths used to monitor the reactions are listed in Table 2. All kinetic traces showed excellent fits to a single exponential function. We studied the effect of the concentration of trifluoromethanesulfonic acid on the observed rate constants for the substitution reactions of the **apa** complex in water and methanol. In water as solvent, following $k_{obsd.}$ values were obtained at 25 °C (concentration of trifluoromethanesulfonic acid is given in parentheses): 0.0497 s^{-1} (0.001 M), 0.0439 s^{-1} (0.01 M), and 0.0466 s^{-1} (0.02 M) for [TU] = 0.0274 M. From these results it is clear that no significant protonation of thiourea occurs in water in the acidity range employed in this study. For the same reaction in methanol the following values were found: 0.0151 s^{-1} (0.001 M), 0.0141 s^{-1} (0.01 M), and 0.0125 s^{-1} (0.02 M) for [TU] = 0.0367 M. The observed trend is ascribed to partial protonation of thiourea at higher acid concentrations. Apparently, there is quite some confusion in the literature concerning the protonation constant of thiourea. We have therefore performed a reinvestigation (experimental and theoretical) of the protonation constant of thiourea in different solvents and will report the results separately.[11] Furthermore, the influence of low concentrations of water on the rate constants for the reactions in methanol and propanol was also studied. In methanol as solvent the following $k_{obsd.}$ values were obtained at 25 °C (vol.% of water is given in parentheses): 0.0141 s^{-1} (as received), 0.01503 s^{-1} (1 vol.%), 0.01514 s^{-1} (2 vol.%), 0.01403 s^{-1} (3 vol.%), 0.01438 s^{-1} (4 vol.%) and 0.01460 s^{-1} (5 vol.%) for [TU] = 0.0367 M. In propanol as solvent the following values were obtained: 0.0212 s^{-1} (as received), 0.0215 s^{-1} (1 vol.%), 0.0205 s^{-1} (2 vol.%), 0.0199 s^{-1} (3 vol.%), 0.0197 s^{-1} (4 vol.%) and 0.0194 s^{-1} (5 vol.%) for [TU] = 0.0265 M. It follows that low concentrations of water have no significant effect on the observed rate constant.

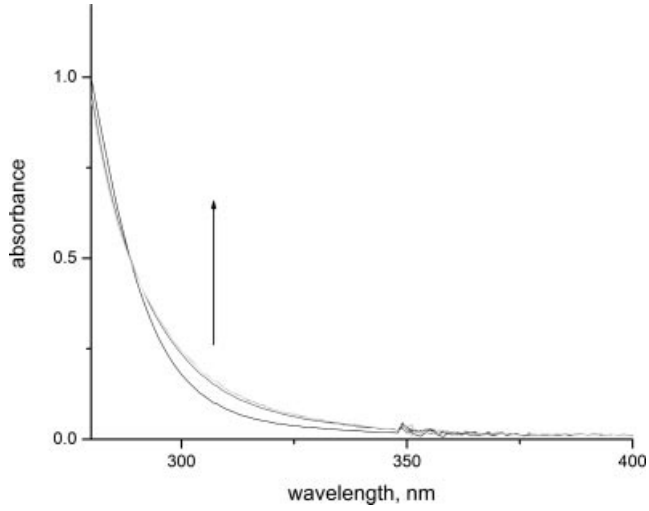

Figure 1. UV/Vis spectral changes recorded for the reaction between the **apa** complex and thiourea in water at 25 °C. The concentrations of **apa** and thiourea are 1.9×10^{-4} M and 0.0106 M, respectively.

The observed pseudo-first-order rate constants, $k_{obsd.}$, were plotted against the thiourea concentration, and for all studied reactions a linear dependence with a negligible in-

 © 2005 Wiley-VCH Verlag GmbH & Co. KGaA, Weinheim

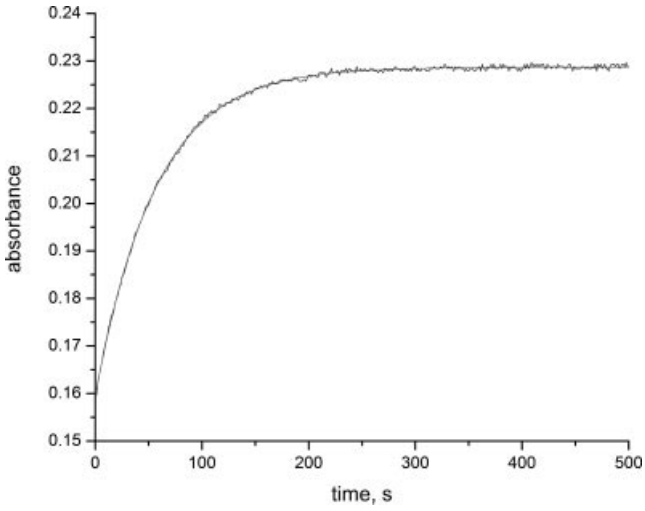

Figure 2. Typical kinetic trace for the reaction between the **apa** complex and thiourea in water at 25 °C. Experimental conditions: [**apa**] = 0.95×10^{-4} M, [TU] = 0.0106 M, 0.002 M LiCl, pH = 2 (0.01 M trifluoromethanesulfonic acid).

Table 2. Summary of the wavelengths [nm] used in the kinetic experiments.

Solvent	Complex			
	aaa	**apa**	**pap**	**ppp**
1-Pentanol	–	300	–	336
1–Propanol	–	300	300	336
Ethanol	–	300	300	333
Methanol	–	300	300	333
Water	300	305	285	336

tercept was observed. Two typical plots are shown in Figures 3 and 4, respectively, from which it follows that $k_{obsd.}$ can be expressed by Equation (2), where k_2 is the second-order rate constant for the overall reaction in Equation (1). The corresponding plots for all other studied reactions are reported as Supporting Information (see also the footnote on the first page of this article).

$$k_{obsd.} = k_2 [TU] \quad (2)$$

The values of k_2 for the substitution of chloride by thiourea on complexes of the type $[Pt^{II}(L^3)Cl]^+$ are summarized in Table 3 for the selected solvents. Formamide (FMA) was in general unsuitable as solvent due to the rapid displacement of chloride by the solvent and formation of $[Pt(L^3)\text{-}FMA]^{2+}$. Also the substitution reactions of **aaa** in methanol and **pap** in 1-pentanol could not be studied due to the formation of insoluble products. The higher charge on the product led to a decrease in solubility in relative nonpolar solvents. The k_2 values show that the substitution reactions in water and methanol depend on polarity, viz. the k_2 values decrease with decreasing polarity. Changing the solvent from water to methanol causes a fourfold deceleration in the case of **apa**, a sixfold deceleration in the case of **pap** and a twofold deceleration in the case of **ppp**. This can be related to the creation of charge during the overall displacement of the chloride anion by neutral thiourea, viz. leading to a partial increase in polarity in the transition state of the process. According to the Hughes–Ingold rules a decrease in solvent polarity results in a decrease in the rates of those reactions in which the charge density is larger in the activated complex than in the initial reactants. The change to a less polar solvent will decrease the reaction rate when the activated complex is more polar than the initial reactants.[12] In the case of water as solvent the polar transition state is even more stabilized.

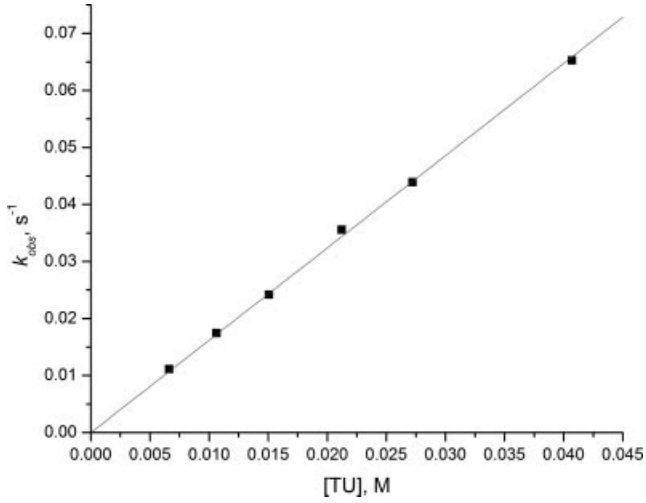

Figure 3. Plot of $k_{obsd.}$ vs. thiourea concentration for the **apa** complex in water. Experimental conditions: [**apa**] = 1.9×10^{-4} M. 25 °C, 0.002 M LiCl, pH = 2 (0.01 M trifluoromethanesulfonic acid).

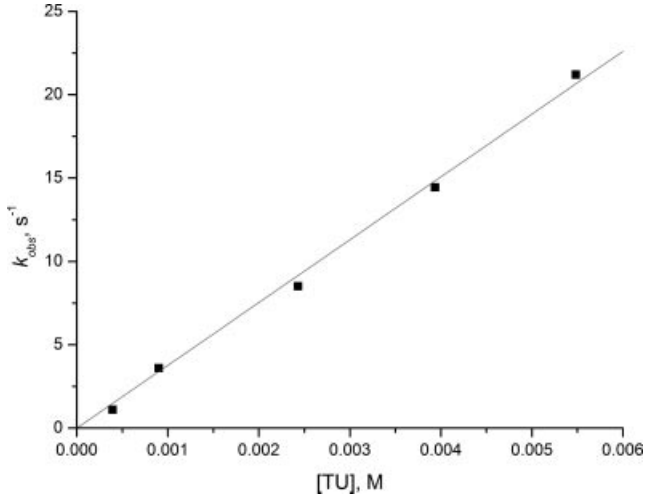

Figure 4. Plot of $k_{obsd.}$ vs. thiourea concentration for the **ppp** complex in 1-propanol. Experimental conditions: [**ppp**] = 1.16×10^{-4} M. 25 °C, 0.002 M LiCl, 0.01 M trifluoromethanesulfonic acid.

On changing the solvent to methanol, ethanol, 1-propanol and 1-pentanol, an acceleration of all substitution reactions for the complexes **apa**, **pap** and **ppp** was observed. This tendency was also observed by Kotowski et al.[9] for substitution reactions on related Pt^{II} complexes. Various attempts were undertaken to correlate the reported second-order rate constants with physical parameters that describe

 © 2005 Wiley-VCH Verlag GmbH & Co. KGaA, Weinheim

Table 3. Summary of the second-order rate constants for the displacement of chloride by thiourea in complexes of the type $[Pt^{II}(L^3)Cl]^+$ in a range of solvents. Experimental conditions: 25 °C, 0.002 M LiCl, pH = 2 (0.01 M trifluoromethanesulfonic acid).

Solvent	k_2 [M^{-1} s^{-1}]			
	aaa	**apa**	**pap**	**ppp**
1-Pentanol	–	0.90 ± 0.03	–[a]	2570 ± 58
				2640 ± 80
1-Propanol	–	0.793 ± 0.006	0.878 ± 0.012	3768 ± 71
Ethanol	–	0.410 ± 0.003	0.784 ± 0.010	3323 ± 63
Methanol	–[a]	0.385 ± 0.002	0.588 ± 0.003	1344 ± 21
Water	0.538 ± 0.007	1.62 ± 0.01	3.67 ± 0.02	2797 ± 42

[a] Formation of colloid particles.

the solvent properties. No direct correlation could be found for solvent polarity or the possible influence of hydrogen bonding. Furthermore, no correlation was found between the second-order rate constant and the Kamlet and Taft solvatochromic parameters that measure the solvent hydrogen-bond donor acidity (α), solvent hydrogen-bond acceptor basicity (β) and solvent dipolarity/polarizability (π^*).[13] The only apparently meaningful correlation that could be found is based on the observation that an increase in the van der Waals forces with increasing carbon-chain length of the alcohols seemed to play an important role. With increasing carbon-chain length the van der Waals forces, as indicated by the boiling points of the solvents, increase to the point that they become stronger than the hydrogen bonding network.[14] The boiling points of the employed alcohols are listed in Table 1. A similar trend is observed in the second-order rate constants. A comparison of both trends is shown in Figure 5, from which it is concluded that van der Waals forces apparently contribute significantly to the stabilization of the transition state. A referee suggested that the longer-chain alcohols could behave as nano-micelles with the alcohol portions directed toward the evolving charge centre. In this way the reaction in the higher alcohols could occur inside a polar sphere, not in contact with the non-polar alcohol tails.

It is well known that the rate of associative substitution reactions strongly depend on the nucleophilicity of the entering nucleophile, viz. the stronger the nucleophile, the faster the rate of the substitution reaction. The four complexes **aaa**, **apa**, **pap** and **ppp** show different k_2 values in the same solvent. In water as solvent we obtained a second-order rate constant of 0.54 M^{-1} s^{-1} for the reaction between **aaa** and TU at 25 °C, 1.62 M^{-1} s^{-1} for **apa**, 3.67 M^{-1} s^{-1} for **pap** and 2797 M^{-1} s^{-1} for **ppp** as reactant. In methanol as solvent we found 0.39 M^{-1} s^{-1} for **apa**, 0.59 M^{-1} s^{-1} for **pap** and 1344 M^{-1} s^{-1} for **ppp** as reactant. This shows that the second-order rate constants increase with increasing number of π-acceptor ligands on the spectator chelate. π-Acceptor ligands have the ability to withdraw electron density from the Pt^{II} centre, thus making it more electrophilic for a nucleophilic attack and enabling stabilization of the electron-rich, five-coordinate transition state. This results in a reduction of the activation barrier and an acceleration of the reaction. The π-acceptor effect is also used to account for the unusually high lability of the **ppp** complex. This effect was investigated in more detail for Pt^{II} complexes in which the number of pyridine ligands was varied systematically.[7] The **ppp** complex shows the highest reactivity relative to the corresponding **aaa** complex due to π-back-bonding from the Pt^{II} centre to the empty π*-orbitals of the pyridine moieties of the terpy ligand.

The activation parameters ($\Delta H^{\neq}$, $\Delta S^{\neq}$ and $\Delta V^{\neq}$) were determined for the substitution reaction of the **aaa** complex in water and of the **apa**, **pap** and **ppp** complexes in methanol and water, respectively, and are listed in Table 4. Two representative plots showing typical temperature and pressure

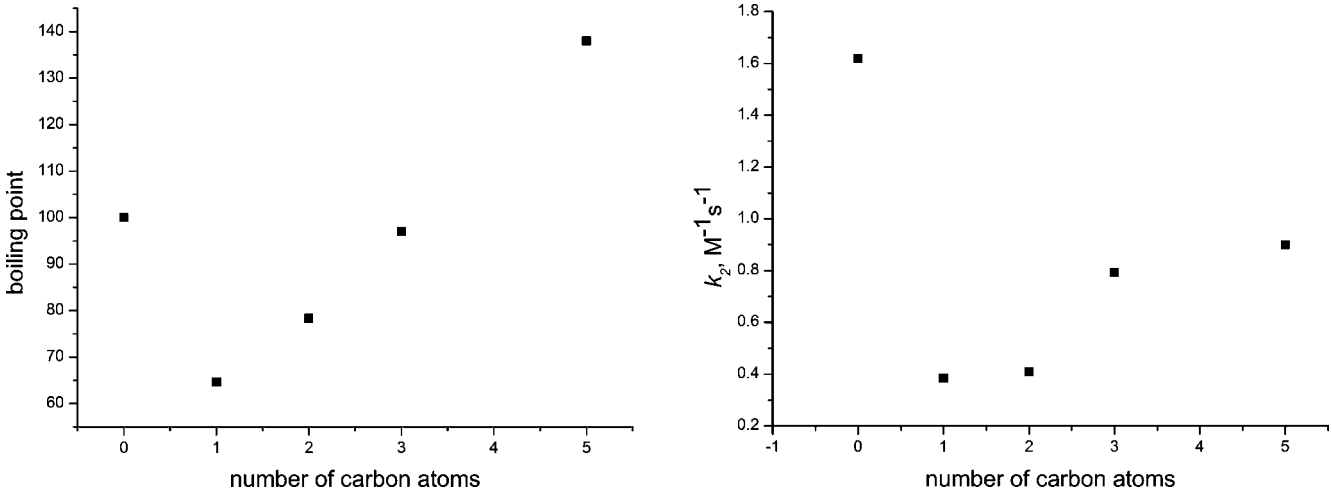

Figure 5. Plots of k_2 and boiling point vs. number of carbon atoms of the employed solvents.

 © 2005 Wiley-VCH Verlag GmbH & Co. KGaA, Weinheim

Table 4. Rate and activation parameters for the reaction of the **aaa**, **apa**, **pap**, and **ppp** complexes with thiourea (TU) in water and methanol as solvent at 25 °C.

Complex	Solvent	k_2 [M^{-1} s^{-1}]	$\Delta H^{\neq}$ [kJ mol^{-1}]	$\Delta S^{\neq}$ [J K^{-1} mol^{-1}]	$\Delta V^{\neq}$ [cm^3 mol^{-1}]
aaa	water	0.538 ± 0.007	40 ± 1	–116 ± 4	–5.9 ± 0.2
apa	methanol	0.385 ± 0.002	63 ± 1	–42 ± 4	–6.65 ± 0.06
apa	water	1.62 ± 0.01	49 ± 1	–77 ± 4	–10.4 ±0.5
pap	methanol	0.588 ± 0.003	55 ± 1	–65 ± 3	–[a]
pap	water	3.67 ± 0.02	46 ± 1	–81 ± 2	–7.0 ± 0.3
ppp	methanol	1344 ± 21	35 ± 1	–67 ± 3	–2.6 ± 0.1
ppp	water	2797 ± 42	29 ± 1	–82 ± 2	–[b]

[a] Not possible to measure. [b] Not possible due to low solubility of **ppp** in water.

dependences are reported in Figures 6 and 7, respectively. The corresponding plots for all other studied reactions are reported as Supporting Information. The acceleration of the substitution reactions by pressure is indicative of an associative substitution mechanism, which is supported by the negative $\Delta S^{\neq}$ values. The decrease in entropy is associated with a highly structured transition state which is accompanied by a decrease in volume due to the compact nature of the transition state as a result of bond formation and an increase in solvation due to an increase in polarity of the transition state.[15]

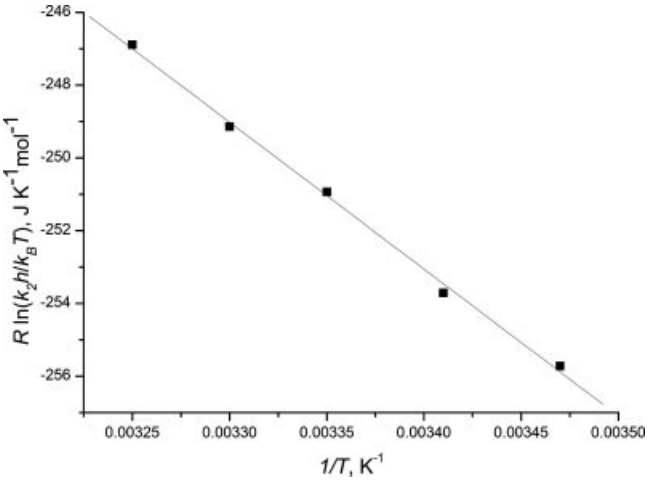

Figure 6. Temperature dependence of the reaction of the **aaa** complex with thiourea in water. Experimental conditions: [**aaa**] = 3.36×10^{-4} M, [TU] = 0.271 M, 0.002 M LiCl, pH = 2 (0.01 M trifluoromethanesulfonic acid).

For all investigated reactions, changing the solvent from methanol to water leads to more negative entropies of activation and in the case of **apa** the volume of activation changes from –6.6 to –10.4 cm^3 mol^{-1}, which corresponds to the tendency shown by the entropies of activation. $\Delta S^{\neq}$ decreases from –42 to –77 J K^{-1} mol^{-1} in the case of **apa**, from –65 to –81 J K^{-1} mol^{-1} for **pap** and from –67 to –82 J K^{-1} mol^{-1} **ppp** on changing the solvent from methanol to water. This can be ascribed to a larger number of highly structured water molecules as compared to the number of structured methanol molecules in the second coordination sphere of the transition state, in which hydrogen bonding plays a major role. Activation volumes were found to be –5.9 cm^3 mol^{-1} for the reaction of **aaa** with TU in water, –7.0 cm^3 mol^{-1} for **pap** in water and –2.6 cm^3 mol^{-1} for **ppp**

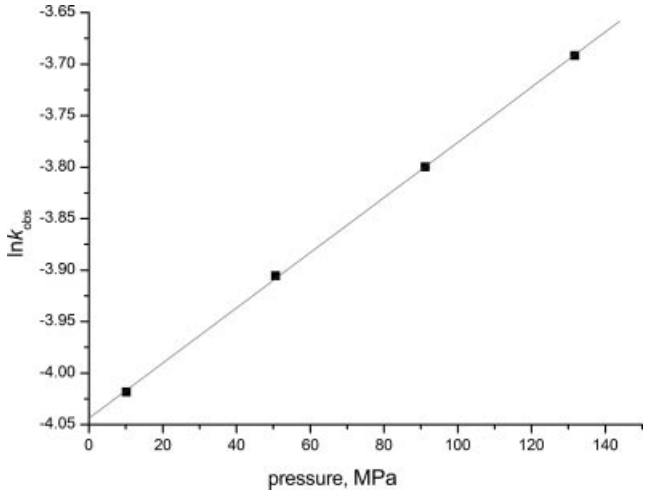

Figure 7. Pressure dependence of the reaction of the **apa** complex with thiourea in methanol. Experimental conditions: [**apa**] = 4.75×10^{-4} M, [TU] = 0.059 M, 25 °C, 0.002 M LiCl, 0.01 M trifluoromethanesulfonic acid.

in methanol. These values parallel the trends in the activation entropies and can be interpreted in a similar way.

As mentioned above, changing the solvent from methanol to water causes an acceleration of all studied reactions. Thus, in general an increase in solvent polarity leads to higher rate constants and lower $\Delta H^{\neq}$ values. We observed a change in $\Delta H^{\neq}$ from 63 to 49 kJ mol^{-1} for the reaction of **apa** with thiourea, from 55 to 46 kJ mol^{-1} for **pap** and from 35 to 29 kJ mol^{-1} for **ppp** on changing the solvent from methanol to water. In the case of **apa**, the decrease in $\Delta H^{\neq}$ is more significant than for **pap** and **ppp** for the two solvents. This must be related to the increase in the number of pyridine ligands which causes an increase in the electrophilicity of the Pt^{II} centre and apparently makes $\Delta H^{\neq}$ less sensitive to the polarity of the solvent.

Conclusions

The effect of solvent on ligand-substitution reactions of Pt^{II} complexes as a function of the π-acceptor property of the spectator chelate was studied systematically. Four mono(chloro)Pt^{II} complexes were synthesized and characterized. A series of solvents were selected as a function of polarity, viz. 1-pentanol, 1-propanol, ethanol, methanol, water, and formamide. The ligand-substitution reactions

 © 2005 Wiley-VCH Verlag GmbH & Co. KGaA, Weinheim

were studied as a function of the nucleophile (thiourea) concentration, temperature and pressure. Formamide as solvent was ruled out due to the formation of solvento complexes.

In the case of alcohols as solvent, we observed a systematic increase in the second-order rate constant with increasing length of the carbon chain of the alcohol and ascribed it to a possible role of van der Waals forces in stabilizing the transition state of the substitution process. An increase in rate constant was observed in going from methanol to water, which is in line with the expected trend in terms of the polarity of the solvent, viz. a more polar solvent will stabilize the polar transition state formed through the associative attack of the neutral nucleophile. The negative $\Delta S^{\neq}$ and $\Delta V^{\neq}$ values are indicative of an associative substitution mechanism. The magnitude of $\Delta V^{\neq}$ favours the operation of an associative interchange (I_a) mechanism and can be interpreted in terms of an intrinsic volume collapse due to bond formation with the entering nucleophile, accompanied by solvational changes resulting from changes in the polarity of the five-coordinate transition state. In all investigated reactions, a change in polarity from a relative nonpolar to a polar solvent resulted in more negative entropies and volumes of activation. Furthermore, the results suggest that in the case of water as solvent a larger number of structured water molecules are present in the second coordination sphere of the transition state, as compared to the number of structured methanol molecules in the case of methanol as solvent.

The four complexes **aaa**, **apa**, **pap**, and **ppp** showed in the same solvent a steady increase in rate constant with increasing electrophilicity of the platinum centre. The π-acceptor pyridine ligands have the ability to withdraw electron density from the Pt^{II} centre to make it more electrophilic which is accompanied by an increase in rate constant for nucleophilic attack. In the case of the **ppp** complex the rate constant is much less solvent dependent than in the case of the **apa** and **pap** complexes, indicating that a highly electrophilic metal centre will lead to a less polar transition state making the substitution reaction less solvent dependent.

Experimental Section

General: All chemicals used were of analytical reagent grade and of the highest purity commercially available. The ligands diethylenetriamine, bis(2-pyridylmethyl)amine and 2,2′:6′,2′′-terpyridine were purchased from Aldrich. K_2PtCl_4 was obtained from Strem. K_2PtCl_4 was separated from metallic Pt and K_2PtCl_6 by dissolution in water and filtering.[16] All chemicals were used without further purification. Ultra pure water was used for the spectroscopic as well as kinetic measurements. The organic solvents used were of analytical reagent grade (see Results and Discussion).

Synthesis of Complexes

[Pt(diethylenetriamine·HCl)Cl_2]: The complex was prepared in a similar way as described by Mahal and van Eldik.[17] K_2PtCl_4 (0.5 g, 1.2 mmol) was dissolved in water (8 mL), filtered and diethylenetriamine (0.240 mL, 0.23 g, 2.27 mmol) was added. The pH of the solution was adjusted to ca. 3 by the addition of HCl, followed by heating to reflux for 3 d. The yellow solution was filtered, concentrated to ca. 2.5 mL and cooled with ice. A yellow product precipitated, which was recrystallized from 1 M HCl (0.315 g, 65%). $C_4H_{14}Cl_3N_3Pt$ (405.6): calcd. C 11.9, H 3.5, N 10.4; found C 11.64, H 3.51, N 10.15.

[Pt(diethylenetriamine)Cl]Cl:[17] The above prepared compound was dissolved in water and the pH adjusted to 10 with LiOH. After that, the solution was heated at 80 °C for 30 min during which the pH was kept at 10 with LiOH. The colourless solution was cooled, the pH adjusted to 4 with HCl, concentrated and cooled. White crystals precipitated, which were washed with ethanol and ether (0.182 g, 63%). $C_4H_{13}Cl_2N_3Pt$ (369.2): calcd. C 13.0, H 3.5, N 11.4; found C 12.72, H 3.53, N 11.14.

[Pt(diethylenetriamine)Cl]CF_3SO_3 (aaa):[18] Concentrated solutions of [Pt(diethylenetriamine)Cl]Cl (0.161 g, 0.4 mmol) and $Ag(CF_3SO_3)$ (0.112 g, 0.4 mmol) were prepared in warm water. The $Ag(CF_3SO_3)$ solution was added dropwise and AgCl precipitated immediately. After repeated filtration, the solvent was removed and the product was dried (0.149 g, 77%). $C_5H_{13}ClF_3N_3O_3PtS$ (482.8): calcd. C 12.44, H 2.71, N 8.70, S 6.64; found C 12.62, H 2.66, N 8.46, S 6.52.

[Pt{2,6-bis(aminomethyl)pyridine}Cl]Cl·H_2O (apa): The ligand 2,6-bis(aminomethyl)pyridine was prepared according to a method used to synthesize 6-(aminomethyl)-2,2′-bipyridine[19] by using 2,6-bis(bromomethyl)pyridine[20] as starting material.[7] The corresponding platinum complex was prepared as described in the literature[7] and was obtained in the same quality (0.260 g, 38%). $C_7H_{13}Cl_2N_3OPt$ (421.2): calcd. C 19.95, H 3.09, N 9.98 ;found C 19.76, H 3.19, N 9.76. ^{1}H NMR (300 MHz, D_2O): δ = 7.7 (t, 1 H, 1 CH, *para*), 7.25 (d, 2 H, 2 CH, *meta*), 4.25 (s, 4 H, 2 CH_2) ppm.

[Pt{bis(2-pyridylmethyl)amine}Cl]CF_3SO_3 (pap): K_2PtCl_4 (0.2 g, 0.48 mmol) was dissolved in 0.005 M HCl (200 mL) and then 97% bis(2-pyridylmethyl)amine (0.1 mL) was added. The solution was stirred under reflux for 3 d and then cooled to room temperature. The colourless solution was filtered and concentrated to about 10 mL. Addition of saturated CF_3SO_3Na solution (2–3 mL) produced the precipitate of the desired complex. This was collected by filtration, washed with small amounts of water, ethanol and ether, and dried under vacuum. $C_{13}H_{13}ClF_3N_3O_3PtS$ (578.9): calcd. C 26.97, H 2.26, N 7.26, S 5.54; found C 26.49, H 2.16, N 7.05, S 5.57. ^{1}H NMR (400 MHz, D_2O): δ = 8.70 (d, 2 H, 2 CH, *ortho*), 8.05 (td, 2 H, 2 CH, *para*), 7.52 (d, 2 H, 2 CH, *meta*), 7.41 (dd, 2 H, 2 CH, *meta*) ppm.

[Pt(2,2′:6′,2′′-terpyridine)Cl]CF_3SO_3 (ppp): A mixture of K_2PtCl_4 (0.5 g, 1.2 mmol) and 2,2′:6′,2′′-terpyridine (terpy) (0.33 g, 1.4 mmol) in water (25 mL) was stirred under reflux until a clear red solution had formed, which took about 75 h. The solution was filtered and concentrated to about 3 mL. The red trihydrate salt of [Pt(2,2′:6′,2′′-terpyridine)Cl]Cl precipitated upon cooling. This was collected by vacuum filtration, washed with dilute 0.1 M HCl and acetone, and the product [Pt(2,2′:6′,2′′-terpyridine)Cl]Cl·$3H_2O$ was dried under vacuum (0.181 g, 28%).[21] Concentrated solutions of [Pt(2,2′:6′,2′′-terpyridine)Cl]Cl·$3H_2O$ (0.161 g, 0.3 mmol) and $Ag(CF_3SO_3)$ (0.075 g, 0.3 mmol) were prepared in warm water. The $Ag(CF_3SO_3)$ solution was added dropwise and AgCl precipitated immediately. An additional red precipitate was observed. The solution was stirred at room temperature for 1 h, diluted to 250 mL and stirred at 60 °C overnight. After repeated filtration, the solvent was removed and the product was dried (0.108 g, 61%). $C_{16}H_{11}ClF_3N_3O_3PtS$ (612.9): calcd. C 31.36, H 1.81, N 6.86, S 5.23; found C 30.81, H 1.83, N 6.65, S 5.18.

 © 2005 Wiley-VCH Verlag GmbH & Co. KGaA, Weinheim

Instrumentation and Measurements: A Carlo Erba Elemental Analyser 1106 and 1108, and NMR spectroscopy (Bruker Avance DPX 300 and DRX 400) were used for chemical analysis and compound characterization. UV/Vis spectra for the study of slow reactions were recorded with a Varian Cary 1G spectrophotometer, equipped with a thermostatted cell holder. The chloro complexes all show absorbance maxima between 280 and 340 nm. Addition of an excess of thiourea causes a large increase in absorbance below 350 nm. Appropriate wavelengths (see Table 2) were selected to monitor the substitution of chloride by thiourea. Kinetic measurements for fast reactions were studied with an Applied Photophysics SX 18MV stopped-flow instrument. For experiments at elevated pressure (1–130 MPa), a laboratory-made high-pressure stopped-flow instrument was used.[22] The temperature of the instruments was controlled with an accuracy of ±0.1 °C. Thiourea (TU) was selected as entering ligand since its high nucleophilicity prevents the back reaction. LiCl solutions (0.002 M) were used to avoid spontaneous solvolysis of the chloro complexes. In the case of alcohol as solvent, trifluoromethanesulfonic acid (0.01 M) was used to avoid formation of alcoholate species that can compete as nucleophiles (see Results and Discussion). The ligand-substitution reactions were studied under pseudo-first-order conditions by using at least a ten-fold excess of TU. All listed rate constants represent an average value of at least five kinetic runs under each experimental condition.

Supporting Information (see also footnote on the first page of this article): Plots showing the concentration, temperature, and pressure dependence of the reactions between the Pt^{II} complexes and thiourea.

Acknowledgments

The authors gratefully acknowledge financial support from the Deutsche Forschungsgemeinschaft, the Fonds der Chemischen Industrie, and the European Community Project No. MRTN-CT-2003-50386 (AQUACHEM).

[1] B. Lippert, *Cisplatin. Chemistry and Biochemistry of a Leading Anticancer Drug*, Wiley-VCH, Weinheim, **1999**.
[2] R. G. Wilkins, *Kinetics and Mechanisms of Reactions of Transition Metal Complexes*, VCH, Weinheim, **1991**.
[3] M. L. Tobe, J. Burgess, *Inorganic Reaction Mechanisms*, 1st ed., Addison Wesley Longman Limited, Essex, UK, **1999**.
[4] G. Alibrandi, D. Minniti, L. Monsù Scolaro, R. Romeo, *Inorg. Chem.* **1989**, *28*, 1939.
[5] R. Romeo, A. Grassi, L. Monsù Scolaro, *Inorg. Chem.* **1992**, *31*, 4383.
[6] M. R. Plutino, L. Monsù Scolaro, R. Romeo, A. Grassi, *Inorg. Chem.* **2000**, *39*, 2712.
[7] A. Hofmann, D. Jaganyi, O. Q. Munro, G. Liehr, R. van Eldik, *Inorg. Chem.* **2003**, *42*, 1688.
[8] M. Kotowski, R. van Eldik, in: *Inorganic High Pressure Chemistry, Kinetics and Mechanisms* (Ed.: R. van Eldik), Elsevier, Amsterdam, **1986**, chapter 4.
[9] M. Kotowski, D. A. Palmer, H. Kelm, *Inorg. Chem.* **1979**, *18*, 2555.
[10] C. Reichardt, *Solvents and Solvent Effects in Organic Chemistry*, Wiley-VCH, Weinheim, Germany, **2003**, p. 472.
[11] W. C. Schiessl, N. K. Summa, C. F. Weber, S. Gubo, C. Dücker-Benfer, R. Puchta, N. J. R. van Eikema Hommes, R. van Eldik, *Z. Anorg. Allg. Chem.*, in press.
[12] Ref.[10], p. 163ff.
[13] Ref.[10], p. 431ff.
[14] H. R. Christen, F. Vögtle, Organische Chemie, *Von den Grundlagen zur Forschung*, Otto Salle Verlag, Frankfurt am Main, **1988**, vol. 1, p. 191.
[15] M. L. Tobe, J. Burgess, *Inorganic Reaction Mechanisms*, Addison Wesley Longman Limited, Essex, UK, **1999**, p. 10.
[16] G. Arena, G. Calogero, S. Campagna, L. M. Scolaro, V. Ricevuto, R. Romeo, *Inorg. Chem.* **1998**, *37*, 2763.
[17] G. Mahal, R. van Eldik, *Inorg. Chim. Acta* **1987**, *127*, 203.
[18] Triflate as anion increases the solubility of the complex.
[19] R. Ziessel, J.-M. Lehn, *Helv. Chim. Acta* **1990**, *73*, 1149.
[20] W. Baker, K. M. Buggle, J. F. W. McOmie, D. A. M. Watkins, *J. Chem. Soc.* **1958**, 3594.
[21] M. Howe-Grant, S. J. Lippard, *Inorg. Synth.* **1980**, *20*, 101.
[22] R. van Eldik, W. Gaede, S. Wieland, J. Kraft, M. Spitzer, D. A. Palmer, *Rev. Sci. Instrum.* **1993**, *64*, 1355.

Received: July 25, 2005
Published Online: October 17, 2005

 © 2005 Wiley-VCH Verlag GmbH & Co. KGaA, Weinheim

DOI: 10.1002/ejic.200500706

The Synthesis and Characterisation of Bis(phosphane)-Linked (η^6-*p*-Cymene)-ruthenium(II)–Borane Compounds

Adrian B. Chaplin,[a] Rosario Scopelliti,[a] and Paul J. Dyson*[a]

Keywords: Ruthenium / P ligands / Bridging ligands / Coordination modes / Boranes

The reaction of $[(\eta^6\text{-}p\text{-cymene})RuCl_2]_2$ with some bis(phosphane) ligands (dppm, dppe, dppv, dppa, dpp14b, dppf) has been investigated. In general mixtures of products were obtained, although the pendant phosphane complexes $[(\eta^6\text{-}p\text{-cymene})RuCl_2(\eta^1\text{-dppv})]$ and $[(\eta^6\text{-}p\text{-cymene})RuCl_2(\eta^1\text{-dppa})]$ were isolated and characterized in the solid state by X-ray diffraction. The later complex was obtained in lower yield and undergoes an equilibration reaction resulting in the formation of a dimeric species, where the dppa bridges two ruthenium centres, and uncoordinated phosphane; the bridging species was also structurally characterised in the solid state. In contrast, the reaction of $[(\eta^6\text{-}p\text{-cymene})RuCl_2(PPh_3)]$ with dppa in the presence of $[NH_4]PF_6$ results in the formation of $[(\eta^6\text{-}p\text{-cymene})RuCl(PPh_3)(\eta^1\text{-dppa})]PF_6$, which is stable in solution. A series of linked ruthenium–borane complexes, viz. $[(\eta^6\text{-}p\text{-cymene})RuCl_2(\eta^1\text{-phosphane-}BH_3)]$ (phosphane = dppm, dppe, dppv, dppa, dpp14b, dppf) and $[(\eta^6\text{-}p\text{-cymene})RuCl(PPh_3)(\eta^1\text{-dppa-}BH_3)]PF_6$ have been prepared from isolated pendant phosphane complexes, those generated in situ, or from a preformed phosphane–borane adduct. The solid-state structures of $[(\eta^6\text{-}p\text{-cymene})RuCl_2(\eta^1\text{-dppm-}BH_3)]$, $[(\eta^6\text{-}p\text{-cymene})RuCl_2(\eta^1\text{-dppe-}BH_3)]$ and $[(\eta^6\text{-}p\text{-cymene})RuCl_2(\eta^1\text{-dppv-}BH_3)]$ have been determined by X-ray diffraction analysis.
(© Wiley-VCH Verlag GmbH & Co. KGaA, 69451 Weinheim, Germany, 2005)

Introduction

The use of chelating phosphane ligands is prevalent in the coordination chemistry of the transition metals,[1] with complexes incorporating chelating phosphane ligands finding many applications in catalysis, where the versatility of this ligand class has allowed the rational design of highly active and selective compounds.[2] Bis(phosphane) ligands can also be found to bridge metal centers and coordinate selectively through one phosphorus centre, leading the other end free.[3–5] Such pendant coordination provides a way to link a variety of fragments, including simple metal complexes, metal cluster compounds, and main group fragments.[3c–g,4,6]

Ruthenium(II) complexes have well documented catalytic utility in organic chemistry,[2d] among which half sandwich (η^6-arene)ruthenium(II) complexes constitute an important class. As part of our continuing investigation of these complexes for catalytic hydrogenation reactions,[7] we have embarked on developing methodologies for the preparation of compounds in which the catalytically active ruthenium fragment is linked to other metal and non-metal moieties. These include functionalisation of the coordinated arene with imidazolium groups or crown ether moieties,[8] and formation of a heterometallic carbene complex.[9] In this paper we describe the preparation of model-linked (η^6-*p*-cymene)-ruthenium(II) systems using bis(phosphane) ligands.

For these linked systems the borane moiety, BH_3, was selected as a model-linked species as phosphane–borane adducts are formed rapidly and tend to be thermally stable.[10] Furthermore, coordination of a phosphane to BH_3 is a common method for protecting valuable (usually chiral) phosphanes from oxidation, either during storage or during synthetic transformations.[10] Phosphane–borane adducts have also been used as bidentate ligands, coordinating through a P centre and agostic B–H interactions (**a**,[11] **b**,[12] **c**–**e**[13] in Figure 1). In addition, as models for metalloborane ruthenium clusters, Barton and co-workers have previously prepared $[(\eta^6\text{-}p\text{-cymene})RuCl_2PPh_2CH_2C_6H_4\text{-}CH_2PPh_2BH_3]$ (**f**) and $[(\eta^6\text{-}p\text{-cymene})RuCl_2PPh_2(CH_2)_6\text{-}PPh_2BH_3]$ (**g**) from the reaction of either isolated or in-situ generated (η^6-*p*-cymene)ruthenium pendant phosphane complexes with BH_3·THF.[4]

Results and Discussion

The direct reaction between $[(\eta^6\text{-}p\text{-cymene})RuCl_2]_2$ and bis(phosphane) ligands in a 1:2 ratio generally results in the formation of the desired pendant phosphane complexes, viz. $[(\eta^6\text{-}p\text{-cymene})RuCl_2(\eta^1\text{-phosphane})]$, together with other ruthenium-containing species. In the case of potentially chelating phosphane ligands, formation of the η^2-coordinated complex, presumably following initial η^1-coordination followed by intramolecular chloride substitution,

[a] Institut des Sciences et Ingénierie Chimiques, Ecole Polytechnique Fédérale de Lausanne (EPFL),
1015 Lausanne, Switzerland
E-mail: paul.dyson@epfl.ch

 © 2005 Wiley-VCH Verlag GmbH & Co. KGaA, Weinheim

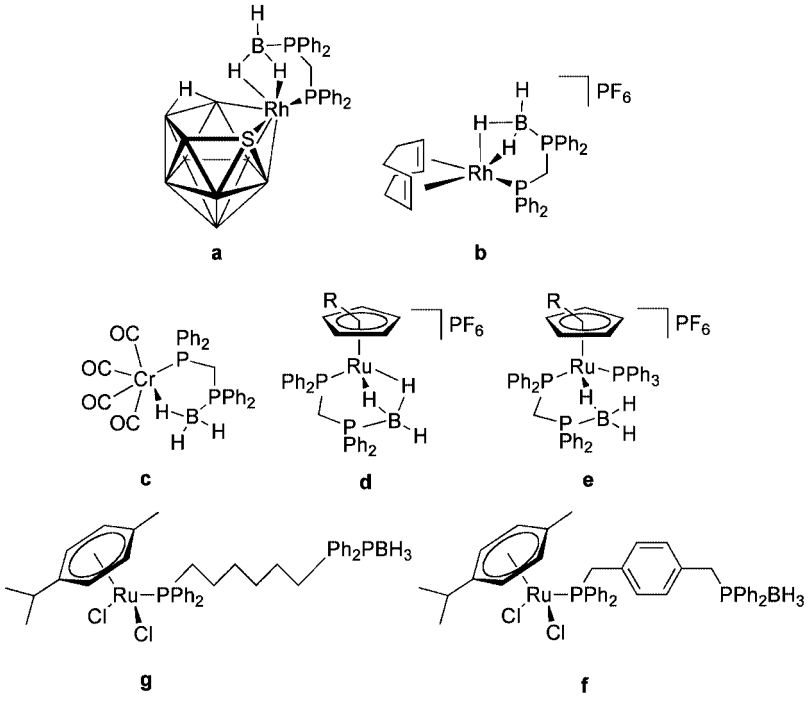

Figure 1. Examples of metal-containing phosphane–borane adducts.

can be suppressed by avoiding polar solvents, such as methanol and ethanol, which promote chloride loss. In such a way the previously reported complex [(η^6-*p*-cymene)-$RuCl_2$(η^1-dppm)] (**1**) has been prepared in high yield (76%) [7a] using benzene as a solvent.[5,7a] However, reaction of the phosphane ligands investigated in this report, see Figure 2, even in large excess, with [(η^6-*p*-cymene)$RuCl_2$]$_2$ in dichloromethane generally resulted in the formation of mixtures composed of the η^1-coordinated phosphane complex and a linked ruthenium–ruthenium complex where the phosphane ligand bridges the two metal centres. The *cis*-bis(1,2-diphenylphosphanyl)ethylene (dppv) ligand was, however, a notable exception to this generalisation, forming only the desired pendant phosphane complex [(η^6-*p*-cymene)-$RuCl_2$(η^1-dppv)] (**2**) in 89% yield using a stoichiometric phosphane to ruthenium ratio. The η^1-coordination mode is clearly evidenced by the presence of two doublets at δ = 15.1 and –30.6 ppm ($^3J_{PP}$ = 9.1 Hz) in the ^{31}P NMR spectrum, with the high-frequency resonance corresponding to the coordinated P centre. Selected NMR spectroscopic data for **2** and the other compounds described herein are listed in Table 1.

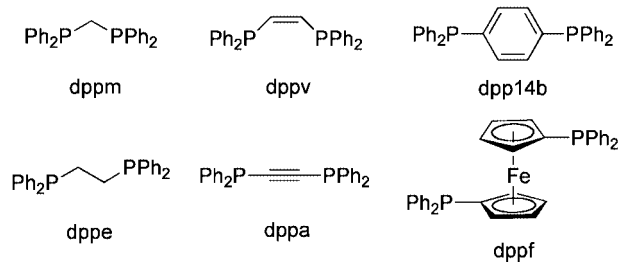

Figure 2. Bis(phosphane)s used in this study with their abbreviations.

To provide a possible explanation for the selective formation of these pendant phosphane complexes the solid-state structures of **2** and the oxide derivative of **1**, [(η^6-*p*-cymene)-$RuCl_2$(η^1-dppmO)] (**3**), obtained by slow oxidation of **1** in solution over a period of months,[16] were determined by X-

Table 1. Selected ^{31}P and ^{11}B NMR spectroscopic data.[a]

	Noncoordinated	Pendant phosphane complex			Bridged	Phosphane–borane complex			
		Ru–*P*	pend-*P*	J_{PP}	Ru–*P*	Ru–*P*	*P*BH_3	J_{PP}	P*B*H_3
dppm	–22.4	26.1[5c]	–27.6[5c]	31.8	21.1[14]	22.7	11.9	33.5	–38.4
dppe	–12.5	25.5	–12.6	34.8	22.5[7a]	23.6	18.2	42.8	–40.6
dppv	–23.1	15.1	–30.6	9.1	12.0	18.4[b]	9.2[b]	12.9[b]	–37.3[b]
dppa	–32.0	0.4[b]	–34.2[b]	3.6[b]	10.1[15]	3.2[b]	5.8[b]		–37.3[b]
PPh_3*dppa*	–32.0	1.0	–31.7	4.0	29.7,–2.8[c]	5.7	7.8		–37.7
dppf	–17.2	19.0	–17.6		18.3[14]	18.5	15.8		–38.5
dpp14b	–5.6	24.2	–5.2		24.6	24.9	20.5		–38.1

[a] $CDCl_3$, 298 K. Chemical shifts in ppm and coupling constants, *J*, in Hz. [b] 248 K. [c] $^2J_{PP}$ = 56.9 Hz.

 © 2005 Wiley-VCH Verlag GmbH & Co. KGaA, Weinheim

ray diffraction analysis (see Figure 3 and Figure 4). The solid-state structure of **3** is much the same as that of **1**,[5b,5c] and the related pendant oxide complex [(η^6-*p*-cymene)-$RuCl_2\{\eta^1$-$PPh_2PCH(CH_3)P(O)Ph_2\}$] (**4**).[17] Each adopt the expected "piano-stool" geometries, with the phosphane chelate angle directed away from the chloride ligands. The Ru–P bond length in **3** is similar to that in **1** [2.355(7) vs. 2.368(7)[5b] Å], and the P–O bond in **3** is comparable with that in **4** [1.49(1) vs. 1.484(3) Å]. The structure of **2** bears close resemblance to **1** and **3** in many respects including the conformation of phosphane with respect to the ruthenium arene moiety and the Ru–P bond length [2.362(2) Å]. Of particular relevance to the reactivity of the pendant phosphane is the close proximity of the P centres in both **2** and **3** (and **1**). In the case of **2**, with a P···P distance of 3.481(3) Å, the close approach originates from the *cis* conformation of the alkene backbone, whereas in **3** the close approach [3.173(6) Å – averaged over the asymmetric cell, cf. **1**, 3.138(2) Å][5b] is a consequence of the small chelate angle [120.6(7)°]. These constraints provide a satisfactory explanation for the selective formation of the pendant phosphane complexes for dppm and dppv, as the steric bulk from the coordinated phosphane moieties, notably from the phenyl groups, can act to hinder further coordination.

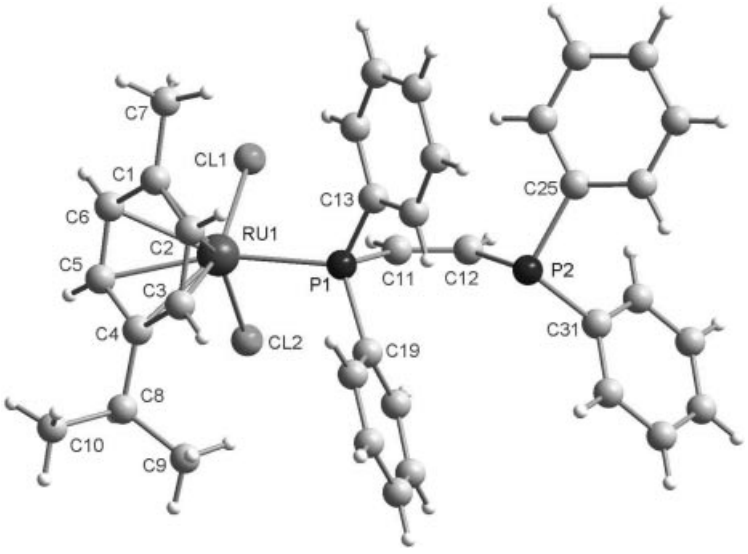

Figure 3. Ball-and-stick depiction of **2** in the solid state. Key bond lengths [Å] and angles [°]: Ru1–Cl1, 2.438(2); Ru1–Cl2, 2.418(1); Ru1–P1, 2.362(2): Cl1–Ru1–Cl2, 89.26(5); Cl1–Ru1–P1, 86.82(6); Cl2–Ru1–P1, 82.58(5); Ru1–C_{avg}, 2.21(3); Ru1–centroid, 1.7002(4); P1–C11, 1.833(5); P2–C12, 1.845(5); C11–C12, 1.336(7); P1–C11–C12, 126.9(4); P2–C12–C11, 124.4(4).

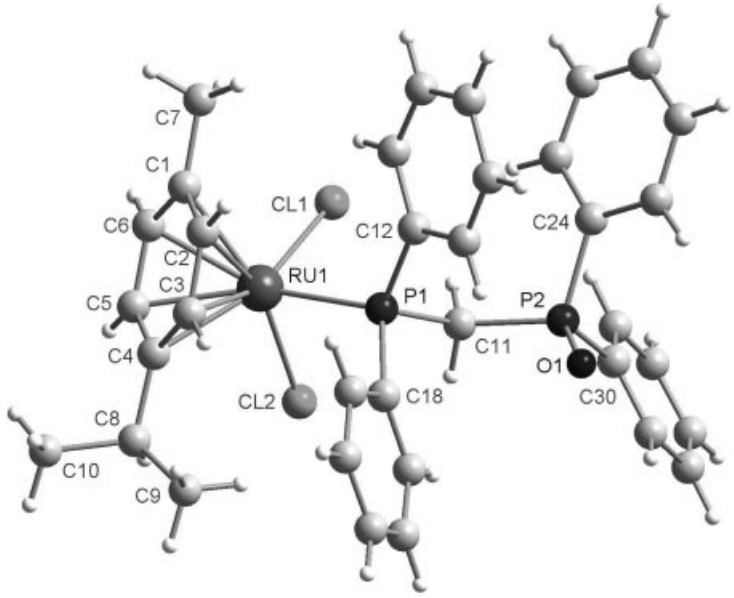

Figure 4. Ball-and-stick depiction of **3** in the solid state [selected molecule from the asymmetric cell]. Key bond lengths [Å] and angles [°] [averaged over asymmetric cell]: Ru–Cl, 2.432(7); Ru–Cl′, 2.420(3); Ru–P, 2.355(7): Cl–Ru–Cl′, 88.7(9); Cl–Ru–P, 87.2(9); Cl′–Ru–P, 83.4(8); Ru–C_{avg}, 2.21(2); Ru–centroid, 1.700(5); P–C, 1.84(2); P′–C, 1.82(1); P–C–P′, 120.6(7); P′–O, 1.49(1).

 © 2005 Wiley-VCH Verlag GmbH & Co. KGaA, Weinheim

The competing formation of the bridged diruthenium species, by coordination of the pendant P centre to another ruthenium unit, encumbers the isolation of the desired pendant phosphane complexes. For example, the pendant phosphane complex, [(η^6-*p*-cymene)$RuCl_2$(η^1-dppa)] (**5**) was separated from the corresponding bridged species [(η^6-*p*-cymene)$RuCl_2$(μ-dppa)$RuCl_2$(η^6-*p*-cymene)] (**6**), in ca. 17% yield, following successive recystallisations from dichloromethane/pentane at –20 °C. Compound **5** is, however, unstable at room temperature and undergoes an equilibration reaction, liberating free phosphane and generating the bridged species **6**, as depicted in Scheme 1. After ca. 1 day in $CDCl_3$ an equilibrium composition is reached, corresponding to an equilibrium constant of $K = 0.42$ (Figure 5). Likewise, this equilibration can also be effected starting from **6** and dppa (≈ 1:1) on a similar timescale (ca. 1 day at room temperature in $CDCl_3$). Both these reactions follow first-order reaction kinetics, consistent with a mechanism involving dissociation of dppa and formation of the coordinately unsaturated arene ruthenium species "[(η^6-*p*-cymene)-$RuCl_2$]", as depicted in Scheme 1. An alternative proposal in which chloride dissociation leads to the intermediate species [(η^6-*p*-cymene)$RuCl_2$(η^1-dppa){(μ-dppa)$RuCl_2$(η^6-*p*-cymene)}]$^+$, moderately stable in solution,[18] can be dismissed because it was not detected by NMR spectroscopy during the equilibration process.

Using toluene as the solvent instead of dichloromethane for the reaction between [(η^6-*p*-cymene)$RuCl_2$]$_2$ and dppa (1.1 equiv. per Ru, room temperature), **6** selectively precipitates on formation, driving the equilibrium to the right hand side, resulting in a **5**/**6** product distribution of ca. 2 compared to the equilibrium ratio of 0.63.[19] The reaction was also carried out in dichloromethane at –78 °C with an excess of phosphane (2.3 equiv. per Ru). The resultant ratio of **5**/**6** was ca. 0.2, as determined by ^{31}P NMR spectroscopy, much lower than that of the equilibrium composition. Below –50 °C the rate of formation of **6** is slow enough to allow NMR characterisation of **5**. The ^{31}P NMR spectrum (as for complex **2**) displays the characteristic pair of doublets, with the coordinated phosphane resonance at $\delta = 0.4$ and the pendant P centre at $\delta = -34.2$, although the coupling constant, $^3J_{PP}$, is reduced in comparison to **2** [9.1 vs. 3.6 Hz]. The solid-state structures of **5** and **6** have been determined by X-ray diffraction analysis, and are depicted in Figure 6 and Figure 7, respectively. Each have "pianostool" geometries about the Ru centres, although as sug-

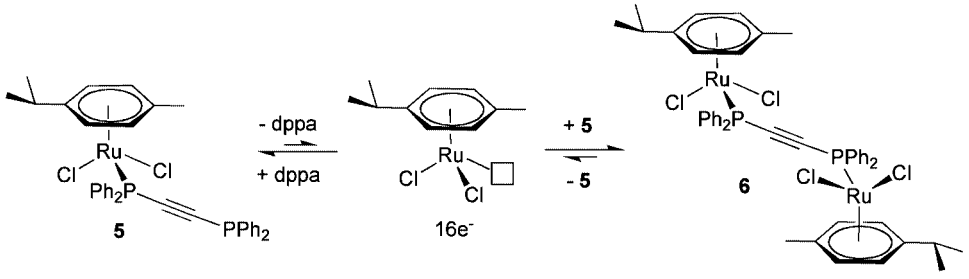

Scheme 1. Proposed mechanism for the equilibration of [(η^6-*p*-cymene)$RuCl_2$(η^1-dppa)] (**5**) with [(η^6-*p*-cymene)$RuCl_2$(μ-dppa)$RuCl_2$(η^6-*p*-cymene)] (**6**).

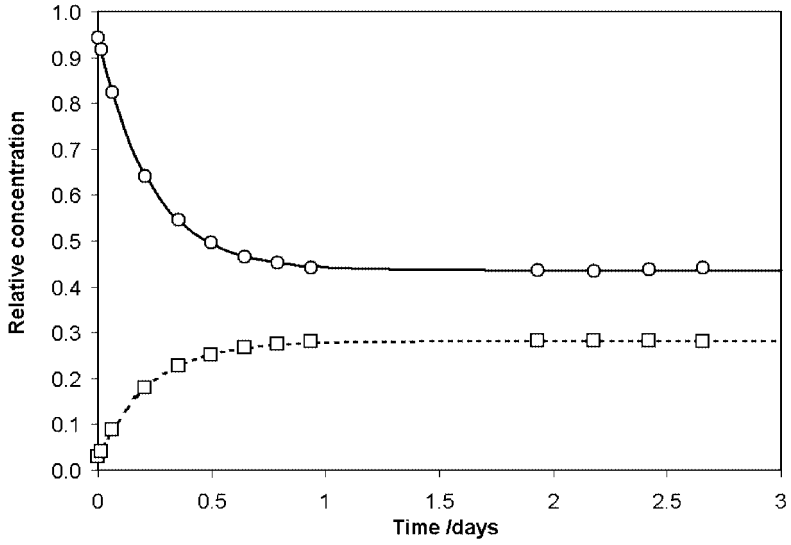

Figure 5. Equilibrium between complexes **5** and **6** at room temperature in $CDCl_3$. Relative concentrations of **5** (circles) and **6** (squares) were determined by integration of ^{1}H NMR spectroscopic data. Note, the concentration of dppa is not shown as it is identical to that of **6**.

 © 2005 Wiley-VCH Verlag GmbH & Co. KGaA, Weinheim

gested by the difference in the coordinated phosphane resonances [**5**, δ = 0.4; **6**,[15] δ = 10.1] there are slight differences in the coordination sphere geometries. In particular the Ru–P bond in **5**, is elongated in comparison to **6** [2.336(1) vs. 2.319(1) Å] together with increased Cl–Ru–P angles [87.18(8) vs. 85.1(7)°] and a reduced Cl–Ru–Cl angle [86.08(4) vs. 88.10(4)°]. These differences are likely to originate from the steric constraints present in **6** owing to the rigid backbone of the dppa ligand, which deviates from linearity slightly more in **6**.

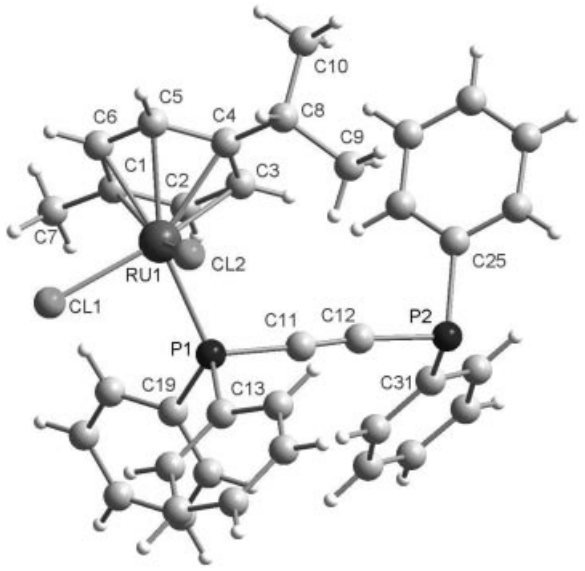

Figure 6. Ball-and-stick depiction of **5** in the solid state. Key bond lengths [Å] and angles [°]: Ru1–Cl1, 2.418(1); Ru1–Cl2, 2.402(1); Ru1–P1, 2.336(1): Cl1–Ru1–Cl2, 86.08(4); Cl1–Ru1–P1, 87.12(5); Cl2–Ru1–P1, 87.24(5); Ru1–C_{avg}, 2.21(2); Ru1–centroid, 1.7006(5); P1–C11, 1.782(5); P2–C12, 1.765(6); C11–C12, 1.202(7); P1–C11–C12, 175.1(5); P2–C12–C11, 174.0(5).

To further investigate the coordination chemistry of dppa it was reacted with the monosubstituted triphenylphosphane derivative [(η^6-*p*-cymene)$RuCl_2(PPh_3)$] together with one equivalent of $[NH_4]PF_6$ in methanol, resulting in the selective formation of the cationic pendant phosphane complex [(η^6-*p*-cymene)$RuCl(PPh_3)$(η^1-dppa)]PF_6 (**7**). The proposed structure was unambiguously identified by NMR spectroscopy, ES-MS and elemental analysis. The ^{31}P NMR spectrum shows three distinct phosphane resonances; a high-frequency doublet at δ = 24.2 ppm (Ru–*P*Ph_3, $^2J_{PP}$ = 55.1 Hz), a doublet of doublets at δ = 1.0 (Ru–*P*Ph_2CCPPh_2, $^2J_{PP}$ = 55.1, $^3J_{PP}$ = 3.2 Hz), and low frequency doublet at δ = –31.7 ppm corresponding to the pendant P centre ($^3J_{PP}$ = 4.9 Hz), in accordance with the proposed structure. In contrast to **5**, the cationic complex **7** is stable in solution over long periods of time, as evidenced by no discernible changes in its ^{31}P NMR spectrum after ca. 3.5 days in $CDCl_3$ solution. In **7** the signal of the quaternary carbon of the isopropyl group at the *p*-cymene ring (C^4 in Figure 8) is located at δ = 129.7 ppm by ^{1}H,^{13}C long-range correlation NMR spectroscopy, ca. 20 ppm to higher frequency than in **5** and **6** (and also to the other ruthenium complexes). This is indicative of weaker coordination to the metal centre, presumably from the increased steric bulk in the ruthenium coordination sphere. The ES-MS spectrum recorded in MeOH exhibits a strong molecular ion peak at *m*/*z* +927 with the expected isotope pattern. Structural information was obtained by selective fragmentation[20] of the parent peak resulting primary in loss of the PPh_3 ligand.

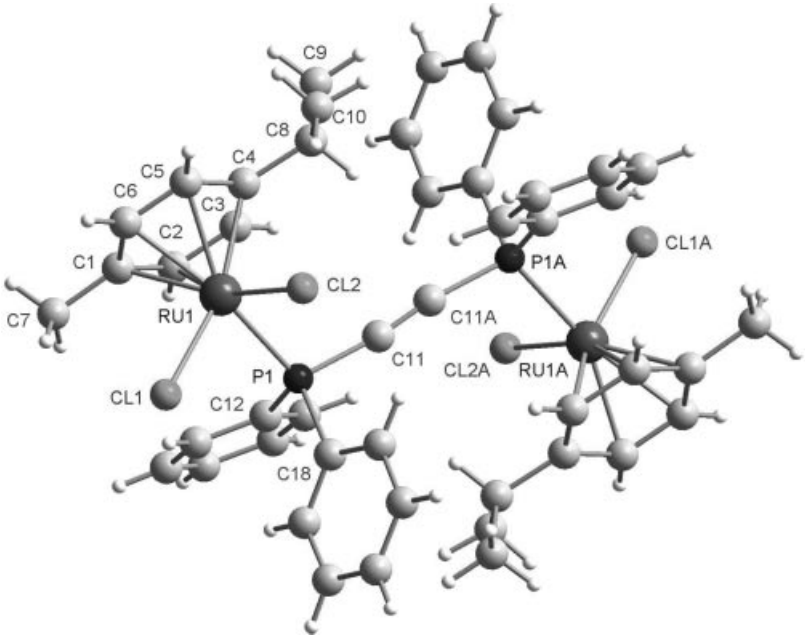

Figure 7. Ball-and-stick depiction of **6** in the solid state. Symmetry equivalent atoms, labeled with an A, are obtained by the symmetry operation –*x*, –*y*, 2 – *z*. Key bond lengths [Å] and angles [°]: Ru1–Cl1, 2.403(1); Ru1–Cl2, 2.204(1); Ru1–P1, 2.319(1): Cl1–Ru1–Cl2, 88.10(4); Cl1–Ru1–P1, 84.56(4); Cl2–Ru1–P1, 85.56(4); Ru1–C_{avg}, 2.22(3); Ru1–centroid, 1.7045(3); P1–C11, 1.762(4); C11–C11#, 1.207(8); P1–C11–C11#, 172.4(5).

 © 2005 Wiley-VCH Verlag GmbH & Co. KGaA, Weinheim

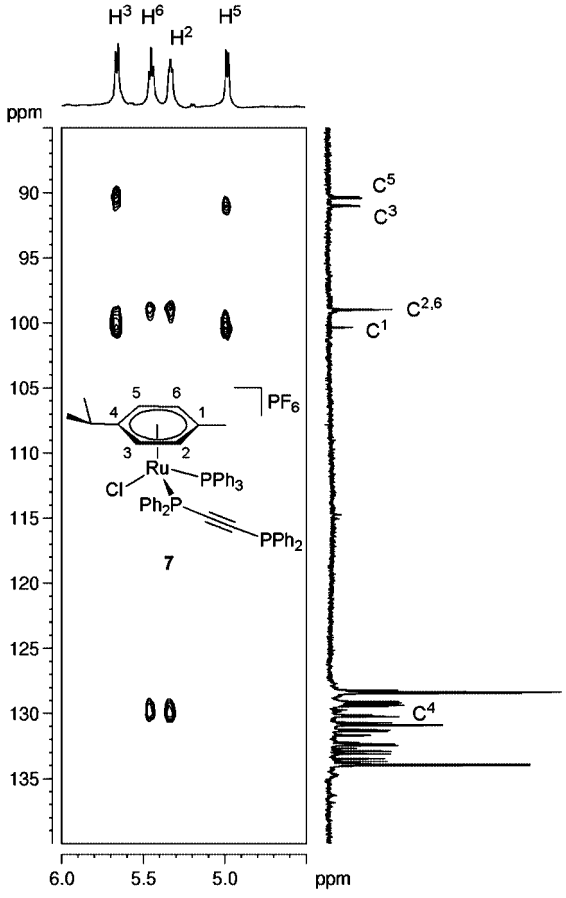

Figure 8. Section of the $^1H,^{13}C$ long-range correlation NMR spectrum of **7**. Cross peaks originate from $^3J_{CH}$ couplings ($CDCl_3$, room temperature).

Synthesis and Characterisation of Ruthenium–Borane Adducts

The isolated pendant phosphane complexes, **1**, **2**, **5** and **7**, react readily with BH_3·THF to give the corresponding ruthenium–borane adducts, **1B**, **2B**, **5B** and **7B**, in good yield as depicted in Scheme 2. For complexes **5** and **7**, it was necessary to carry out the reaction at –78 °C to prevent hydroboration of the alkyne moiety. Similarly, complexes **8B** (dppe) and **9B** (dppf) can be prepared by reaction of BH_3·THF with the corresponding pendant phosphane complexes formed, instead, in situ (Scheme 3). Partial separation from the corresponding bridging species, formed in parallel to the pendant phosphane complexes, can be achieved by extraction of the solid residue with toluene and recyrstallisation from dichloromethane/pentane, although chromatography is necessary for complete separation.

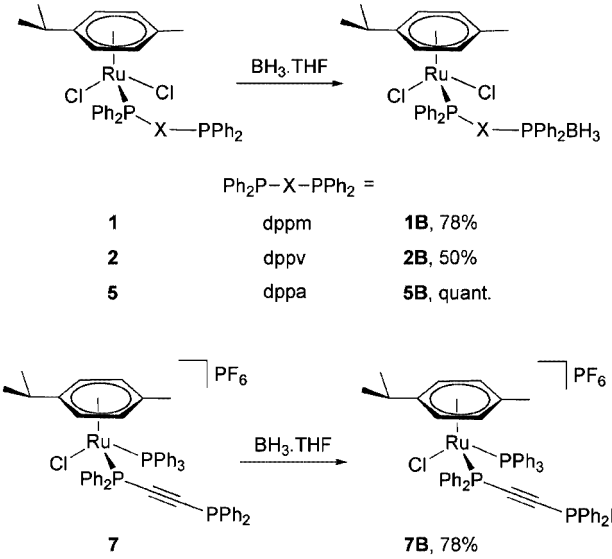

Scheme 2. Preparation of **1B**, **2B**, **5B** and **7B**.

A high-yielding method for the preparation of the ruthenium–borane species linked with the 1,4-bis(diphenylphosphanyl)benzene ligand (dpp14b) has been devised. The route, depicted in Scheme 4, involves the reaction of a preformed phosphane–borane, prepared in good yield (61%, 2 steps) from 1,4-bromo(diphenylphosphane)benzene, directly with $[(\eta^6$-*p*-cymene)$RuCl_2]_2$ (82% yield).

Large shifts of ca. δ = 35 ppm (see Table 1) and characteristic line broadening of the pendant P-centre resonances are observed in the ^{31}P NMR spectra for the ruthenium–borane complexes, although the frequencies of the coordinated P-centre resonances remain similar. Distinctive resonances at ca. δ = –38 ppm in the ^{11}B NMR spectra (see Table 1) are in agreement with related, previously reported, phosphane–borane adducts.[4] ^1H and ^{13}C NMR spectroscopic data for complexes **1B**, **2B**, **5B**, and **7B** are comparable with those of the isolated pendant phosphane complexes. In particular, the signal of the isopropyl quaternary carbon of the *p*-cymene ring in **7B** is similarly located at high frequency (δ = 131 ppm) as observed for **7**. The ES-MS spectrum of **7B** in MeOH exhibits a peak at *m*/*z* +927 resulting from loss of BH_3. If dichloromethane is used instead, the molecular ion peak at *m*/*z* +941 is observed to-

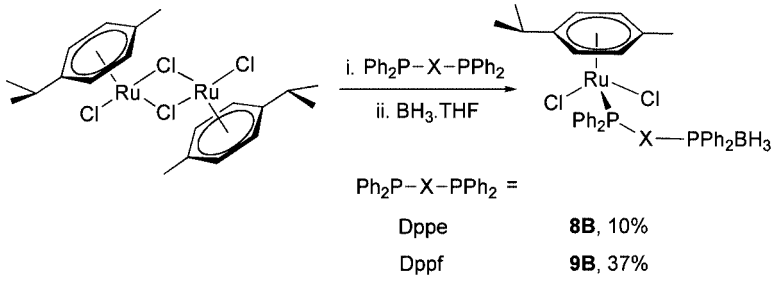

Scheme 3. Preparation of **8B** and **9B**.

 © 2005 Wiley-VCH Verlag GmbH & Co. KGaA, Weinheim

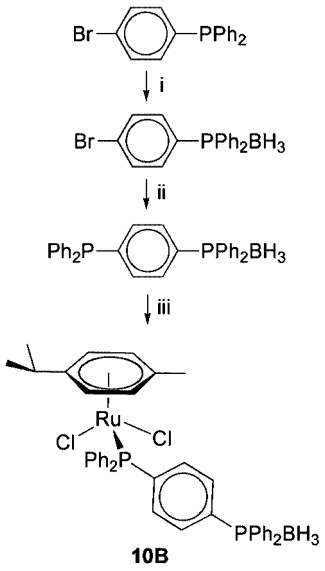

Scheme 4. Stepwise preparation of **10B**. Reagents and conditions: i. BH_3·THF, 0 °C; ii. BuLi, –78 °C, followed by $ClPPh_2$; iii. $[(\eta^6\text{-}p\text{-cymene})RuCl_2]_2$, room temp.; overall yield: 50%.

gether with a weaker peak at *m/z* +927. MS/MS of the parent peak correspondingly results in loss of BH_3, further selective fragmentation of this peak results resulting primary in loss of the PPh_3 ligand as for **7**.

Spectroscopic data for complexes **8B**, **9B** and **10B** corroborate the structure of the complexes well. Using NOESY it was possible to unambiguously determine the conformation of the dppf ligand in solution in **9B**, as depicted in Figure 9. In this conformation, the ferrocenyl rings adopt the expected antiperiplanar configuration, with both the borane moiety and ruthenium centre directed away from the ligand.

The solid-state structures of the complexes **1B**, **2B** and **8B** have been determined by X-ray diffraction analysis and are depicted in Figure 10, Figure 11 and Figure 12. Complexes **1B** and **2B** retain similar conformations as their parent pendant phosphane complexes **1**[5b] (also **3**, Figure 4) and **2** (Figure 3), although in both cases Ru–P bond lengths are slightly contracted in the borane adducts [2.351(2) vs. 2.368(7) Å for dppm; 2.3424(8) vs. 2.362(2) Å for dppv]. The structure of complex **8B** exhibits similar bonding parameters around the ruthenium centre to those observed in the related bridging species $[(\eta^6\text{-}p\text{-cymene})Ru(S_2C_2\{B_{10}H_{10}\})(\mu\text{-dppe})Ru(S_2C_2\{B_{10}H_{10}\})(\eta^6\text{-}p\text{-cymene})]$.[21] The P–B bond lengths range from 1.91–1.93 Å and are comparable to other phosphane–BH_3 adducts.[4,12,13]

In conclusion, a series of neutral bis(phosphane)-linked ruthenium–borane complexes have been prepared using a variety of phosphane ligands. While the use of isolated pendant phosphane complexes is more desirable and higher yielding, the formation of these complexes is usually accompanied by the formation of dimeric ruthenium–ruthenium species. In the case of the reaction between bis(diphenylphosphanyl)acetylene (dppa) and $[(\eta^6\text{-}p\text{-cymene})RuCl_2]_2$, equilibration between these two species occurs in

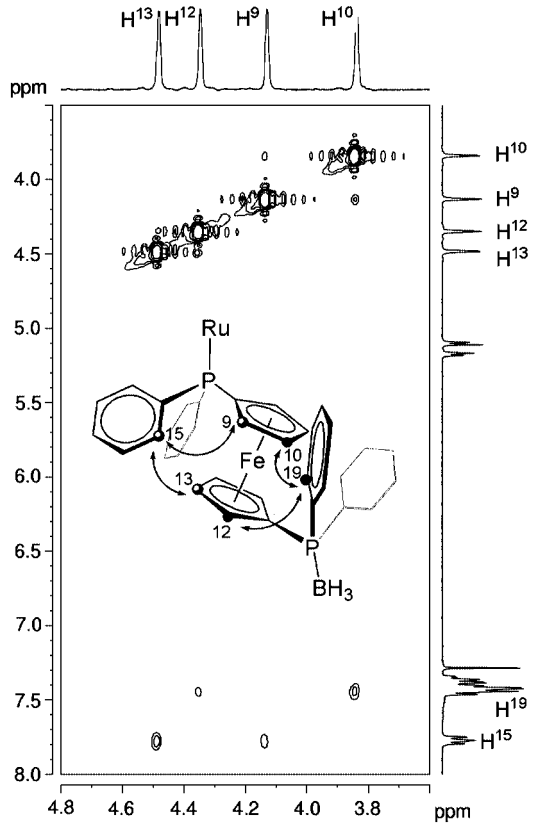

Figure 9. Section of the NOESY spectrum of **9B** ($CDCl_3$, room temperature).

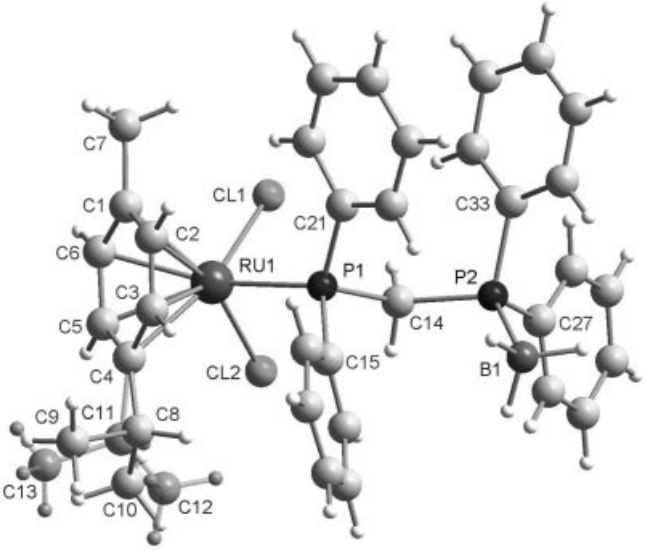

Figure 10. Ball-and-stick depiction of **1B** in the solid state. The minor disordered component of the *p*-cymene ring is composed of atoms C11–C13. Key bond lengths [Å] and angles [°]: Ru1–Cl1, 2.417(2); Ru1–Cl2, 2.393(2); Ru1–P1, 2.351(2): Cl1–Ru1–Cl2, 85.65(8); Cl1–Ru1–P1, 86.47(9); Cl2–Ru1–P1, 87.33(8); Ru1–C_{avg}, 2.19(3); Ru1–centroid, 1.7045(6); P1–C14, 1.831(8); P2–C14, 1.841(8); P1–C14–P2, 123.4(4); P2–B1, 1.91(1).

 © 2005 Wiley-VCH Verlag GmbH & Co. KGaA, Weinheim

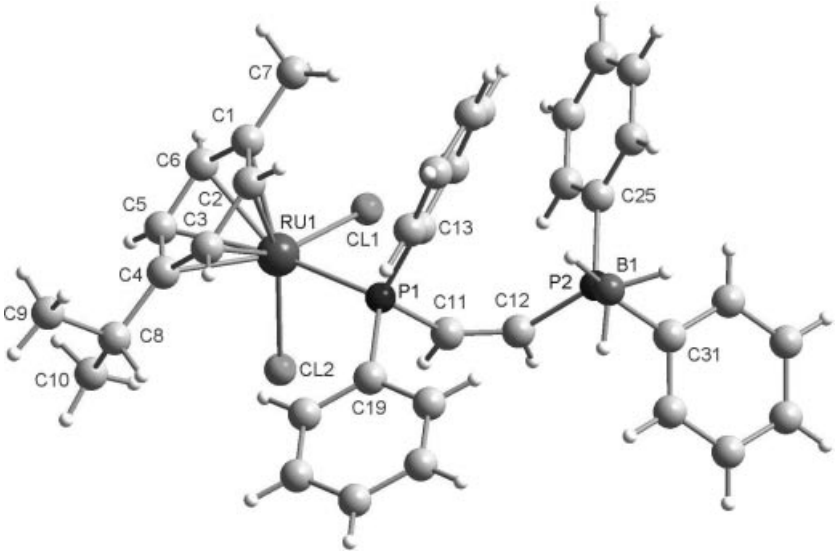

Figure 11. Ball-and-stick depiction of **2B** in the solid state. Key bond lengths [Å] and angles [°]: Ru1–Cl1, 2.4107(8); Ru1–Cl2, 2.4307(8); Ru1–P1, 2.3424(8): Cl1–Ru1–Cl2, 88.11(3); Cl1–Ru1–P1, 83.32(3); Cl2–Ru1–P1, 86.28(3); Ru1–C_{avg}, 2.22(4); Ru1–centroid, 1.7116(3); P1–C11, 1.823(3); P2–C12, 1.813(3); C11–C12, 1.327(4); P1–C11–C12, 139.3(3); P2–C12–C11, 135.3(3); P2–B1, 1.932(4).

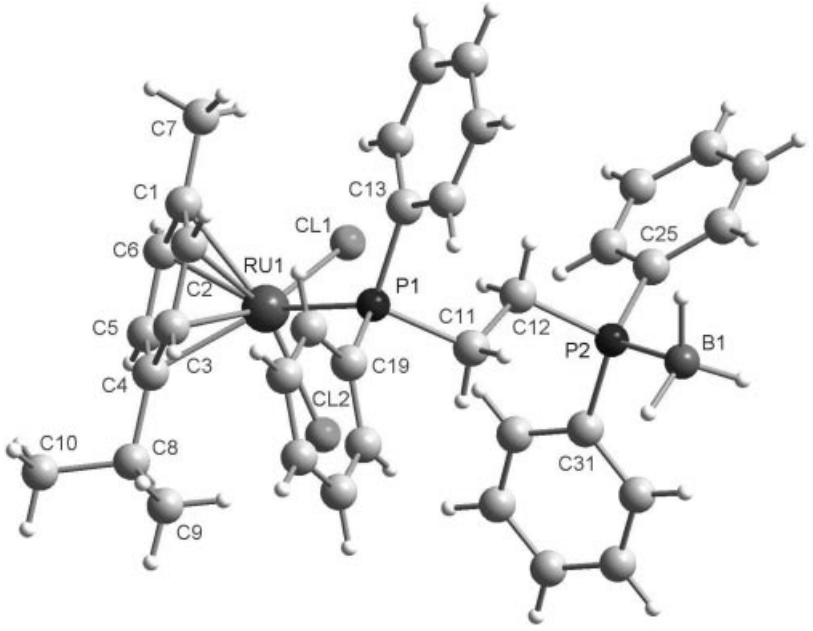

Figure 12. Ball-and-stick Depiction of **8B** in the solid state. Key bond lengths [Å] and angles [°]: Ru1–Cl1, 2.436(2); Ru1–Cl2, 2.413(2); Ru1–P1, 2.356(2): Cl1–Ru1–Cl2, 88.86(5); Cl1–Ru1–P1, 90.42(6); Cl2–Ru1–P1, 84.49(6); Ru–C_{avg}, 2.21(2); Ru1–centroid, 1.7005(5); P1–C11, 1.858(5); P2–C12, 1.817(6); C11–C12, 1.538(8); P1–C11–C12, 113.0(4); P2–C12–C11, 112.8(4); P2–B1, 1.933(8).

solution. In contrast, the reaction between *cis*-bis(1,2-diphenylphosphanyl)ethylene (dppv) and $[(\eta^6\text{-}p\text{-cymene})\text{-}RuCl_2]_2$ results in the selective formation of the pendant phosphane complex akin to dppm. These observations were rationalised by inspection of their solid-state structures (and related oxide and borane adducts), which show a close proximity between the P centres. In contrast for dppe and dppf the solid-state structure and solution conformation determined by NOESY, respectively, of the linked ruthenium–borane complexes are suggestive (vide infra) of little steric hindrance to further coordination. Correspondingly, the linked ruthenium–borane systems using these ligands are prepared in lower yield and require chromatographic purification. As an alternative methodology, a preformed phosphane–borane ligand was prepared preventing contamination from the corresponding bridging species.

Experimental Section

All organometallic manipulations were carried out under nitrogen using standard Schlenk techniques. CH_2Cl_2, diethyl ether, hexane, THF and toluene were dried using a solvent purification system,

 © 2005 Wiley-VCH Verlag GmbH & Co. KGaA, Weinheim

manufactured by innovative technology inc., in which nitrogen-saturated solvents are passed through a series of alumina columns or, for the hydrocarbons, through one column of alumina then another containing a copper catalyst under a positive pressure of nitrogen. All other solvents were p. a. quality and saturated with nitrogen prior to use. Chromatographic separations were carried out in air using 1.0×20×20 mm silica gel 60 F_{254} plates (Merck). [(η^6-*p*-cymene)$RuCl_2$]$_2$,[22] [(η^6-*p*-cymene)$_2Ru_2(\mu$-Cl)$_3$]PF_6,[23] [(η^6-*p*-cymene)-$RuCl_2(PPh_3)$],[23] [(η^6-*p*-cymene)$RuCl_2(\eta^1$-dppm)],[7a] dpp14b,[24] and 1,4-bromo(diphenylphosphane)benzene,[24] were prepared as described elsewhere. All other chemicals are commercial products and were used as received. Spectra were recorded with a Bruker Avance 400 spectrometer at room temperature, unless otherwise stated. Chemical shifts are given in ppm and coupling constants (*J*) in Hz. ES mass spectra were recorded with a Thermo Finnigan LCQ DECA XPPlus and microanalyses performed at the EPFL. Numerical analysis for the equilibration of **5** – (**6** + dppa) was carried out using Origin 7.5 (OriginLab).

Preparation of [(η^6-*p*-Cymene)$RuCl_2(\eta^1$-*cis*-$PPh_2CHCHPPh_2$)] (2): A solution of [(η^6-*p*-cymene)$RuCl_2$]$_2$ (0.160 g, 0.26 mmol) and dppv (0.207 g, 0.26 mmol) in CH_2Cl_2 (50 mL) was stirred at room temperature for 1 h. The product was obtained as an orange solid following concentration and precipitation with diethyl ether. Yield 0.32 g (89%). Crystals suitable for X-ray crystallography were obtained by recrystallisation from CH_2Cl_2/diethyl ether at 4 °C. ^{1}H NMR ($CDCl_3$): δ = 8.1–8.2 [m, 4 H, RuP(*o*-C_6H_5)$_2$ {^{31}P@δ = 15.1} δ = 8.15, d, $^3J_{HH}$ = 7.2], 7.54 (ddd, $^3J_{HH}$ = 13.5, $^2J_{PH}$ = 28.5, $^3J_{PH}$ = 31.0 Hz, 1 H, $RuPPh_2CHCH$), 7.38–7.44 [m, 2 H, RuP(*p*-C_6H_5)$_2$], 7.30–7.38 [m, 4 H, RuP(*m*-C_6H_5)$_2$], 7.18–7.24 [m, 2 H, pend-P(*p*-C_6H_5)$_2$], 7.12–7.18 [m, 4 H, pend-P(*m*-C_6H_5)$_2$], 7.06 (ddd, $^3J_{PH}$= 13.5, $^2J_{HH}$ = 4.0, $^3J_{PH}$ = 38.1 Hz, 1 H, $CHCHPPh_2$), 6.85–6.95 [m, 4 H, pend-P(*o*-C_6H_5)$_2$ {^{31}P@δ = –30.6} δ = 6.91 dd, $^4J_{HH}$ = 1.2, $^3J_{HH}$ = 8.2 Hz], 5.26 (d, $^3J_{HH}$ = 5.1, 2 H, *o*-$CH_3C_6H_4$), 5.15 (d, $^3J_{HH}$ = 6.0, 2 H, *m*-$CH_3C_6H_4$), 2.55 [sept, $^3J_{HH}$ = 6.9 Hz, 1 H, $CH(CH_3)_2$], 1.84 (s, 3 H, CH_3–C_6H_4), 0.85 [d, $^3J_{HH}$ = 6.9 Hz, 6 H, $CH(CH_3)_2$] ppm. ^{13}C{^{1}H} NMR ($CDCl_3$): δ = 145.2 (dd, $^1J_{PC}$ = 7.6, $^2J_{PC}$ = 17.4 Hz, $CHCHPPh_2$), 140.3 (dd, $^1J_{PC}$ = 21.5, $^2J_{PC}$ = 44.4 Hz, $RuPPh_2CHCH$), 137.6 [d, $^1J_{PC}$ = 10.6, pend-P(*i*-C_6H_5)$_2$], 134.2 [d, $^1J_{PC}$ = 45.6, RuP(*i*-C_6H_5)$_2$], 133.5 [dd, $^4J_{PC}$ = 4.5, $^2J_{PC}$ = 9.7, RuP(*o*-C_6H_5)$_2$], 132.5 [d, $^2J_{PC}$ = 18.4, pend-P(*o*-C_6H_5)$_2$], 130.4 [d, $^4J_{PC}$ = 2.4, RuP(*p*-C_6H_5)$_2$], 128.2–128.4 [obscured, pend-P(*p*-C_6H_5)$_2$], 128.3 [d, $^3J_{PC}$ = 10.9, P(*m*-C_6H_5)$_2$], 128.2 [d, $^3J_{PC}$ = 10.0, P(*m*-C_6H_5)$_2$], 108.6 [s, $CCH(CH_3)_2$], 93.7 (s, CH_3–*C*), 90.3 (d, $^2J_{PC}$ = 4.2, *o*-$CH_3C_6H_4$), 85.2 (d, $^2J_{PC}$ = 6.0, *m*-$CH_3C_6H_4$), 30.1 [s, $CH(CH_3)_2$], 21.4 [s, $CH(CH_3)_2$], 17.4 (s, CH_3–C_6H_4) ppm. ^{31}P{^{1}H} NMR ($CDCl_3$): δ = 15.1 (d, $^3J_{PP}$ = 9.1 Hz, 1 P, Ru–*P*), –30.6 (d, $^3J_{PP}$ = 9.1 Hz, 1 P, pend-*P*) ppm. $C_{36}H_{36}Cl_2P_2Ru$ (702.60): calcd. C 61.54, H 5.16; found C 60.98, H 5.25.

Preparation of [(η^6-*p*-Cymene)$RuCl_2(\eta^1$-*cis*-$PPh_2CHCHPPh_2BH_3$)] (2B): To a solution of **2** (0.100 g, 0.14 mmol) in CH_2Cl_2 (15 mL, 0 °C) a solution of BH_3·THF in THF (0.12 mL of ca. 1.2 M, 0.14 mmol) was added dropwise. The solution was then warmed to room temperature and stirred for 1 h. The solvent was then removed in vacuo, and the solid washed with diethyl ether (25 mL) and then recrystallised from CH_2Cl_2/pentane at –20 °C to give red crystals suitable for X-ray diffraction. Yield: 0.05 g (50%) ^{1}H NMR ($CDCl_3$, –50 °C): δ = 7.9–8.1 [m, 4 H, RuP(*o*-C_6H_5)$_2$ {^{31}P@δ = 18.4} δ = 7.97, d, $^3J_{HH}$ = 7.3], 7.69 (ddd, $^3J_{HH}$ = 16.2, J_{PH} = 21.2, J_{PH} = 39.7, 1 H, PPh_2CH), 7.2–7.5 [m, 16 H, P(*o*-C_6H_5)$_2BH_3$ and P(*m*,*p*-C_6H_5)$_2$], 6.86 (ddd, J_{PH} = 4.7, $^3J_{HH}$ = 16.2, J_{PH} = 36.9, 1 H, PPh_2CH), 5.17 (d, $^3J_{HH}$ = 5.8, 2 H, *m*-$CH_3C_6H_4$), 5.11 (d, $^3J_{HH}$ = 5.9, 2 H, *o*-$CH_3C_6H_4$), 2.62 [sept, $^3J_{HH}$ = 6.6, 1 H, $CH(CH_3)_2$], 1.75 (s, 3 H, CH_3–C_6H_4), 0.83 [d, $^3J_{HH}$ = 6.7, 6 H, $CH(CH_3)_2$], 0.1–0.7 [br., 3 H, BH_3; {^{11}B@δ = –37.3} δ = 0.42, d, $^2J_{PH}$ = 16.3]. ^{13}C{^{1}H} NMR ($CDCl_3$, –50 °C): δ = 145.6 (d, $^1J_{PC}$ = 39.0, PPh_2CH), 133.8 [d, $^2J_{PC}$ = 10.0, RuP(*o*-C_6H_5)$_2$], 133.3–133.9 (obscured, PPh_2CH), 132.1 [d, $^2J_{PC}$ = 9.5, P(*o*-C_6H_5)$_2BH_3$], 131.4 [br., RuP(*p*-C_6H_5)$_2$], 131.2 [br., P(*p*-C_6H_5)$_2BH_3$], 130.7 [d, $^1J_{PC}$ = 47.5, P(*i*-C_6H_5)$_2$], 130.4 [d, $^1J_{PC}$ = 60.3, P(*i*-C_6H_5)$_2$], 128.9 [d, $^3J_{PC}$ = 10.2, P(*m*-C_6H_5)$_2$], 128.5 [d, $^3J_{PC}$ = 10.6, P(*m*-C_6H_5)$_2$], 109.7 [d, $^2J_{PC}$ = 1.8, $CCH(CH_3)_2$], 94 (m, CH_3–*C*), 89.7 (d, $^2J_{PC}$ = 2.8, *o*-$CH_3C_6H_4$), 85.9 (d, $^2J_{PC}$ = 5.4 *m*-$CH_3C_6H_4$), 30.4 [s, $CH(CH_3)_2$], 21.4 [s, $CH(CH_3)_2$], 17.8 (s, CH_3–C_6H_4). ^{31}P{^{1}H} NMR ($CDCl_3$, –50 °C): δ = 18.4 (d, $^3J_{PP}$ = 12.9, 1 P, Ru–*P*), 9.3–10.1 (m, 1P, *P*–BH_3). ^{11}B{^{1}H} NMR ($CDCl_3$, –50 °C): δ = –37.3 (br). IR (nujol, cm^{-1}): $\tilde{\nu}_{v(BH)}$ = 2448 (br), 2380 (sh). $C_{36}H_{39}BCl_2P_2Ru{\cdot}CH_2Cl_2$ (801.37): calcd. C 55.46, H 5.16; found C 55.65, H 5.33.

Oxidation of [(η^6-*p*-Cymene)$RuCl_2(\eta^1$-$PPh_2CH_2PPh_2$)]: Orange crystals of [(η^6-*p*-cymene)$RuCl_2(\eta^1$-dppmO)] (**3**) suitable for X-ray diffraction were obtained by recrystallisation of a reaction mixture containing [(η^6-*p*-cymene)$RuCl_2(\eta^1$-dppm)] over several months from chloroform/pentane at 4 °C. Alternatively, [(η^6-*p*-cymene)-$RuCl_2(\eta^1$-dppm)] can be quantitatively converted to **2** by treatment with H_2O_2 in THF. ^{1}H and ^{31}P NMR spectroscopic data were in agreement with the literature data.[17]

Preparation of [(η^6-*p*-Cymene)$RuCl_2(\eta^1$-PPh_2CCPPh_2)] (5): To a vigorously stirred solution of dppa (0.17 g, 0.43 mmol) in CH_2Cl_2 (15 mL, –78 °C) a solution of [(η^6-*p*-cymene)$RuCl_2$]$_2$ (0.10 g, 0.16 mmol) in CH_2Cl_2 (15 mL) was added rapidly. Following an additional 5 min stirring, the solvent was removed in vacuo at room temperature. The resultant orange solid material was an ca. 0.4:1.0:0.7 mixture of **6**/**5**/dppa as determined by ^{31}P NMR spectroscopy. Successive recrystallisation from CH_2Cl_2/pentane at –20 °C gave orange crystals of **5** in ca. 0.04 g (17%) yield. Crystals of **6** suitable for X-ray analysis were obtained by slow diffusion of pentane into a CH_2Cl_2 solution of the reaction mixture at room temperature, whereas those of **5** were obtained after successive recrystallisation of the reaction mixture from CH_2Cl_2/pentane at –20 °C. ^{1}H NMR ($CDCl_3$, –50 °C): δ = 7.97 [dd, $^3J_{HH}$ = 7.2, $^3J_{PH}$ = 11.5, 4 H, RuP(*o*-C_6H_5)$_2$], 7.6–7.9 [m, 4 H, pend-P(*o*-C_6H_5)$_2$], 7.3–7.6 [m, 12 H, P(*m*,*p*-C_6H_5)$_2$], 5.31 (d, $^3J_{HH}$ = 5.9, 2 H, *m*-$CH_3C_6H_4$), 5.22 (d, $^3J_{HH}$ = 5.6, 2 H, *o*-$CH_3C_6H_4$), 2.80 [sept, $^3J_{HH}$ = 6.5, 1 H, $CH(CH_3)_2$], 1.85 (s, 3 H, CH_3–C_6H_4), 1.04 [d, $^3J_{HH}$ = 6.6, 6 H, $CH(CH_3)_2$]. ^{13}C{^{1}H} NMR ($CDCl_3$, –50 °C): δ = 133.7 [m, P(*i*-C_6H_5)$_2$], 133.0–133.5 [m, P(*o*-C_6H_5)$_2$], 131.0 [s, RuP(*p*-C_6H_5)$_2$], 130.2 [s, pend-P(*p*-C_6H_5)$_2$], 129.3 [d, $^3J_{PC}$ = 8.0, P(*m*-C_6H_5)$_2$], 128.4 [d, $^3J_{PC}$ = 10.9, P(*m*-C_6H_5)$_2$], 109.6 [s, $CCH(CH_3)_2$], 96.1 (s, CH_3–*C*), 89.9 (d, $^2J_{PC}$ = 3.5, *o*-$CH_3C_6H_4$), 87.3 (d, $^2J_{PC}$ = 5.2, *m*-$CH_3C_6H_4$), 30.5 [s, $CH(CH_3)_2$], 22.0 [s, $CH(CH_3)_2$], 17.9 (s, CH_3–C_6H_4), the signals of $RuPPh_2CCPPPh_2$ were not unambiguously located. ^{31}P{^{1}H} NMR ($CDCl_3$, –50 °C): δ = 0.4 (s, 1 P, Ru–*P*), –34.2 (d, $^3J_{PP}$ = 3.6, 1 P, pend-*P*). IR (nujol, cm^{-1}): $\tilde{\nu}_{v(CC)}$ = 2110 (w).

Preparation of [(η^6-*p*-Cymene)$RuCl_2(\eta^1$-$PPh_2CCPPh_2BH_3$)] (5B): To a solution of **5** (0.007 g, 0.01 mmol) in THF (2 mL, –78 °C) a solution of BH_3·THF in THF (0.01 mL of ca. 1.2 M, 0.012 mmol) was added dropwise. The solution was then stirred for 1 h, and the solvent was removed in vacuo as the solution warmed to room temperature. Yield: quantitative (by ^{1}H NMR). ^{1}H NMR ($CDCl_3$, –50 °C): δ = 7.8–7.95 [m, 8 H, {^{31}P@δ = 3.2} δ = 7.90, d, RuP(*o*-C_6H_5)$_2$, $^3J_{HH}$ = 7.2; {^{31}P@δ = 5.8} δ = 7.88, d, P(*o*-C_6H_5)$_2$-BH_3, $^3J_{HH}$ = 7.3], 7.3–7.65 [m, 12 H, P(*m*,*p*-C_6H_5)$_2$], 5.36 (d, $^3J_{HH}$ = 6.0, 2 H, *m*-$CH_3C_6H_4$), 5.28 (d, $^3J_{HH}$ = 5.7, 2 H, *o*-$CH_3C_6H_4$), 2.75 [sept, $^3J_{HH}$ = 6.7, 1 H, $CH(CH_3)_2$], 1.86 (s, 3 H, CH_3–C_6H_4), 1.02 [d, $^3J_{HH}$ = 6.8, 6 H, $CH(CH_3)_2$], 1.0–1.6 [br., 3 H, BH_3;

 © 2005 Wiley-VCH Verlag GmbH & Co. KGaA, Weinheim

{^{11}B@δ = –37.3} δ = 1.30, d, $^2J_{PH}$ = 17.0]. ^{13}C{^{1}H} NMR ($CDCl_3$, –50 °C): δ = 133.3 [d, $^2J_{PC}$ = 10.6, RuP(*p*-C_6H_5)$_2$], 132.7 [s, P(*p*-C_6H_5)$_2$$BH_3$], 132.4 [d, $^2J_{PC}$ = 11.6, P(*p*-C_6H_5)$_2$$BH_3$], 131.4 [s, RuP(*p*-$C_6H_5$)$_2$], 130 [d, $^1J_{PC}$ ca. 60, P(*i*-C_6H_5)$_2$], 129.6 [d, $^3J_{PC}$ = 11.3, P(*m*-C_6H_5)$_2$$BH_3$], 128.7 [d, $^3J_{PC}$ = 11.0, RuP(*m*-C_6H_5)$_2$], 126.7 [d, $^1J_{PC}$ = 64.6, P(*i*-C_6H_5)$_2$], 110.4 [s, *C*CH(CH_3)$_2$], 104.5 [dd, $^1J_{PC}$ = 65.7, $^2J_{PC}$ = 7.5, PC*C*P], 99.2 (dd, $^1J_{PC}$ = 89.4, $^2J_{PC}$ < 2, P*C*CP), 96.9 (s, CH_3–*C*), 90.0 (d, $^2J_{PC}$ = 3.5, *o*-$CH_3C_6H_4$), 87.4 (d, $^2J_{PC}$ = 5.6, *m*-$CH_3C_6H_4$), 30.5 [s, *C*H(CH_3)$_2$], 21.9 [s, CH(*C*H_3)$_2$], 17.9 (s, *C*H_3–C_6H_4). ^{31}P{^{1}H} NMR ($CDCl_3$, –50 °C): δ = 5.8 (br., 1 P, *P*BH_3), 3.2 (s, 1 P, Ru*P*). ^{11}B{^{1}H} NMR ($CDCl_3$): δ = –37.3 (br).

Preparation of [(η^6-*p*-Cymene)RuCl(PPh_3)(η^1-PPh_2CCPPh_2)]PF_6 (7): A suspension of [(η^6-*p*-cymene)$RuCl_2$(PPh_3)] (0.70 g, 1.23 mmol), $[NH_4]PF_6$ (0.20 g, 1.23) and dppa (0.49 g, 1.23 mmol) in MeOH (150 mL) was heated at 35 °C for 3 h. The solvent was removed in vacuo, and the residue taken up in a minimal amount of CH_2Cl_2. A small amount of (unidentified) solid material was removed by the addition of hexane and filtration. Removal of the solvent gave an orange oil that solidified under high vacuum. Yield: 0.74 g (56%). ^{1}H NMR ($CDCl_3$): δ = 7.97 [dd, $^3J_{HH}$ = 7.2, $^3J_{PH}$ = 12.3, 2 H, RuP(*o*-C_6H_5)$_2$CCPPh_2], 7.60–7.75 [m, 4 H, pend-P(*o*-C_6H_5)$_2$ and pend-P(*o*-C_6H_5')$_2$], 7.30–7.60 (m, 20 H, P*Ph*), 7.10–7.25 [m, 7 H, RuP(*m*-C_6H_5)$_3$ and RuP(*p*-C_6H_5')$_2$], 6.92 [td, $^4J_{PH}$ = 2.9, $^3J_{HH}$ = 7.7, 2 H, RuP(*m*-C_6H_5')$_2$CCPPh_2], 5.66 (d, $^3J_{HH}$ = 6.2, 1 H, *m*-$CH_3C_6H_4$), 5.42–5.48 [m, 1 H, *o*-$CH_3C_6H_4'$ {^{31}P@δ = 1.0} δ = 5.45, d, $^3J_{HH}$ = 6.3], 5.30–5.35 [m, 1 H, *o*-$CH_3C_6H_4$ {^{31}P@δ = 24.1} δ = 5.33, d, $^3J_{HH}$ = 6.4], 4.99 (d, $^3J_{HH}$ = 6.1, 1 H, *m*-$CH_3C_6H_4'$), 2.79 [sept, $^3J_{HH}$ = 6.9, 1 H, C*H*(CH_3)$_2$], 1.28 (s, 3 H, C*H*$_3$–C_6H_4), 1.23 [d, $^3J_{HH}$ = 6.4, 3 H, CH(C*H*$_3$)$_2$], 1.21 [d, $^3J_{HH}$ = 6.4, 3 H, CH(C*H*$_3'$)$_2$]. ^{13}C{^{1}H} NMR ($CDCl_3$): δ = 134.0 [d, $^2J_{PC}$ = 9.6, RuP(*o*-C_6H_5)$_3$], 133.6 [d, $^2J_{PC}$ = 21.8, pend-P(*o*-C_6H_5)$_2$ or pend-P(*o*-$C_6'H_5$)$_2$], 133.0 [d, $^2J_{PC}$ = 21.0, pend-P(*o*-$C_6'H_5$)$_2$ or pend-P(*o*-C_6H_5)$_2$], 132.5 [d, $^1J_{PC}$ = 47.9, P(*i*-C_6H_5)$_2$], 132.4 [d, $^2J_{PC}$ = 9.9, RuP(*o*-$C_6'H_5$)$_2$], 131.7 [d, $^4J_{PC}$ = 2.3, P(*p*-C_6H_5)$_2$], 131.3 [d, $^2J_{PC}$ = 10.8, RuP(*o*-C_6H_5)$_2$], 130.9 [d, $^4J_{PC}$ = 2.3, P(*p*-C_6H_5)$_3$], 130.5 [d, $^1J_{PC}$ = 47.4, P(*i*-C_6H_5)$_3$], 130.2 [d, $^4J_{PC}$ = 2.9, P(*p*-C_6H_5)$_2$], 129.7 [s, *C*CH(CH_3)$_2$], 129.4 [d, $^3J_{PC}$ = 11.3, pend-P(*m*-C_6H_5)$_2$ or pend-P(*m*-$C_6'H_5$)$_2$], 128.4 [d, $^3J_{PC}$ = 10.5, pend-P(*m*-$C_6'H_5$)$_2$ or pend-P(*m*-C_6H_5)$_2$], 129.1 [d, $^3J_{PC}$ = 11.2, RuP(*m*-C_6H_5)$_2$], 128.4 [d, $^3J_{PC}$ = 10.5, RuP(*m*-C_6H_5)$_3$], 128.3 [d, $^3J_{PC}$ = 11.9, RuP(*m*-$C_6'H_5$)$_2$], 114.8 (m, RuPPh_2*CC*PPh_2), 100.3 (s, CH_3–*C*), 99.0 (s, *o*-$CH_3C_6H_4$ and *o*-$CH_3C'_6H_4$), 91.0 (d, $^2J_{PC}$ = 9.6, *m*-$CH_3C_6H_4$), 90.4 (d, $^2J_{PC}$ = 9.4, *m*-$CH_3C_6'H_4$), 31.3 [s, *C*H(CH_3)$_2$], 21.6 [s, CH(*C*H_3)$_2$ or CH(*C*′H_3)$_2$], 21.1 [s, CH(*C*′H_3)$_2$ or CH(*C*H_3)$_2$], 15.5 (s, *C*H_3–C_6H_4). ^{31}P{^{1}H} NMR ($CDCl_3$): δ = 24.2 (d, $^2J_{PP}$ = 55.1, 1 P, Ru–*P*Ph_3), 1.0 (dd, $^3J_{PP}$ = 3.2, $^2J_{PP}$ = 55.1, 1 P, Ru–*P*Ph_2), –31.7 (d, $^3J_{PP}$ = 4.9, 1 P, pend-*P*Ph_2), –144.4 (sept, $^1J_{PF}$ = 712.7, 1 P, *P*F_6). IR (nujol, cm^{-1}): $\tilde{\nu}_{\nu(CC)}$ = 2105 (w). ESI-MS (MeOH) positive ion: *m*/*z* = 533 (15) [M – PPh_2CCPPh_2]$^+$, 665 (20) [M – PPh_3]$^+$, 927 (100) [M]$^+$. ESI-MS^2 (+927): *m*/*z* = 665 [M – PPh_3]$^+$. ESI-MS negative ion: *m*/*z* = 145 [PF_6]$^-$. $C_{54}H_{49}ClF_6P_4Ru$·0.75CH_2Cl_2 (1136.09): calcd. C 57.88, H 4.48; found C 57.54, H 4.53.

Preparation of [(η^6-*p*-Cymene)RuCl(PPh_3)(η^1-PPh_2CCPPh_2-BH_3)]PF_6 (7B): To a solution of **7** (0.150 g, 0.12 mmol) in THF (25 mL, –78 °C) a solution of BH_3·THF in THF (0.10 mL of ca. 1.2 M, 0.12 mmol) was added dropwise. The solution was then stirred for 1 h. The solvent was removed in vacuo as the solution warmed to room temperature, the residue washed with diethyl ether (2 × 20 mL) and then dried in vacuo. Yield: 0.095 g (78%). ^{1}H NMR ($CDCl_3$): δ = 8.03 [dd, $^3J_{HH}$ = 7.6, $^3J_{PH}$ = 12.4, 2 H, RuP(*o*-C_6H_5)$_2$CCPPh_2], 7.94 [dd, $^3J_{HH}$ = 7.4, $^3J_{PH}$ = 12.3, 2 H, pend-P(*o*-C_6H_5)$_2$], 7.88 [dd, $^3J_{HH}$ = 7.4, $^3J_{PH}$ = 12.1, 2 H, pend-P(*o*-C_6H_5')$_2$], 7.1–7.7 (m, 27 H, P*Ph*), 7.00 [td, $^4J_{PH}$ = 2.6, $^3J_{HH}$ = 7.6, 2 H, RuP(*m*-C_6H_5')$_2$CCPPh_2], 5.73–5.80 [m, 1 H, *o*-$CH_3C_6H_4'$ {^{31}P@δ = 5.7} δ = 5.77, d, $^3J_{HH}$ = 6.3], 5.70 (d, $^3J_{HH}$ = 6.1, 1 H, *m*-$CH_3C_6H_4$), 5.30–5.23 [m, 1 H, *o*-$CH_3C_6H_4$ {^{31}P@δ = 24.5} δ = 5.26, d, $^3J_{HH}$ = 6.5], 5.07 (d, $^3J_{HH}$ = 6.1, 1 H, *m*-$CH_3C_6H_4'$), 2.80 [sept, $^3J_{HH}$ = 6.9, 1 H, C*H*(CH_3)$_2$], 0.8–1.8 [br., 3 H, B*H*$_3$; {^{11}B@δ = –37.7} δ = 1.46, d, $^2J_{PH}$ = 16.2], 1.1–1.4 [m, $^3J_{HH}$ = 6.4, 9 H, CH(C*H*$_3$)$_2$, CH(C*H*$_3'$)$_2$ and C*H*$_3$–C_6H_4]. ^{13}C{^{1}H} NMR ($CDCl_3$, –50 °C): δ = 128–134 (poorly resolved, P*Ph*), 133 [pend-P(*o*-C_6H_5)$_2$ and pend-P(*o*-$C_6'H_5$)$_2$], 132 [RuP(*o*-C_6H_5)$_3$], 131 [*C*CH(CH_3)$_2$], 129 [RuP(*m*-$C_6'H_5$)$_2$CCPPh_2], 125.6 (m, RuPPh_2*CC*PPh_2), 99 (CH_3–*C*), 99 (*o*-$CH_3C_6H_4$), 97 (*o*-$CH_3C_6'H_4$), 91 (*m*-$CH_3C_6'H_4$), 90 (*m*-$CH_3C_6H_4$), 31.6 [s, *C*H(CH_3)$_2$], 21.8 [s, CH(*C*H_3)$_2$ or CH(*C*′H_3)$_2$], 21.5 [s, CH(*C*′H_3)$_2$ or CH(*C*H_3)$_2$], 15.1 (s, *C*H_3–C_6H_4). ^{31}P{^{1}H} NMR ($CDCl_3$): δ = 24.5 (d, $^2J_{PP}$ = 55.1, 1 P, Ru–*P*Ph_3), 7.8 (br., 1 P, *P*–BH_3), 5.7 (d, $^3J_{PP}$ = 55.1, 1 P, Ru–*P*Ph_2), –144.3 (sept, $^1J_{PF}$ = 712.7, 1 P, *P*F_6). ^{11}B{^{1}H} NMR ($CDCl_3$): δ = –37.7 (br). IR (nujol, cm^{-1}): $\tilde{\nu}$ = ν(CC) not observed; ν(BH) 2393 (br). ESI-MS (MeOH) positive ion: *m*/*z* = 927 (100) [M – BH_3]$^+$, 941 (10) [M]$^+$. ESI-MS (CH_2Cl_2) positive ion: *m*/*z* = 927 (14) [M – BH_3]$^+$, 941 (100) [M]$^+$. ESI-MS^2 (+941): *m*/*z* = 927 [M – BH_3]$^+$. ESI-MS^3 (+941; +927): *m*/*z* = 665 [M – PPh_3 – BH_3]$^+$. ESI-MS (CH_2Cl_2) negative ion: *m*/*z* = 145 (100) [PF_6]$^-$.

Preparation of [(η^6-*p*-Cymene)$RuCl_2$(η^1-$PPh_2CH_2PPh_2BH_3$)] (1B): To a solution of [(η^6-*p*-cymene)$RuCl_2$(η^1-dppm)] (0.08 g, 0.116 mmol) in CH_2Cl_2 (5 mL, 0 °C) a solution of BH_3·THF in THF (0.12 mL of ca. 1 M, 0.12 mmol) was added dropwise. The solution was then warmed to room temperature and stirred for 30 minutes. The product was isolated as an orange powder, following concentration of the solution in vacuo and the addition of excess hexane. Yield: 0.06 g (78%). Orange crystals suitable for X-ray diffraction were obtained by slow diffusion of pentane into a chloroform solution of **1B** at room temperature. ^{1}H NMR ($CDCl_3$): δ = 7.9–8.1 [m, 4 H, RuP(*o*-C_6H_5)$_2$; {^{31}P@δ = 22.7} δ = 8.02, d, $^3J_{HH}$ = 7.1], 7.35–7.44 [m, 4 H, P(*o*-C_6H_5)$_2$$BH_3$; {^{31}P@$\delta$ = 11.9} δ = 7.39, d, $^3J_{HH}$ = 7.2], 7.1–7.35 [m, 12 H, P(*m*,*p*-C_6H_5)$_2$], 5.23 (d, $^3J_{HH}$ = 5.6, 2 H, *o*-$CH_3C_6H_4$), 5.11 (d, $^3J_{HH}$ = 6.0, 2 H, *m*-$CH_3C_6H_4$), 3.92 (t, $^2J_{PH}$ = 10.4, 2 H, P–C*H*$_2$–P), 2.49 [sept, $^3J_{HH}$ = 6.9, 1 H, C*H*(CH_3)$_2$], 1.79 (s, 3 H, C*H*$_3$–C_6H_4), 0.87 [d, $^3J_{HH}$ = 6.9, 6 H, CH(C*H*$_3$)$_2$], 0.1–1.2 [br., 3 H, B*H*$_3$; {^{11}B@δ = –38.4} δ = 0.70, d, $^2J_{PH}$ = 15.6]. ^{13}C{^{1}H} NMR ($CDCl_3$): δ = 133.9 [d, $^2J_{PC}$ = 9.7, RuP(*o*-C_6H_5)$_2$], 131.4 [d, $^2J_{PC}$ = 9.6, P(*o*-C_6H_5)$_2$$BH_3$], 131.2 [d, $^4J_{PC}$ = 2.5, RuP(*p*-C_6H_5)$_2$], 130.5 [d, $^4J_{PC}$ = 2.3, P(*p*-C_6H_5)$_2$-BH_3], 129.5–130.5 [m, P(*i*-C_6H_5)$_2$], 128.5 [d, $^3J_{PC}$ = 10.2, P(*m*-C_6H_5)$_2$], 127.9 [d, $^3J_{PC}$ = 10.3, P(*m*-C_6H_5)$_2$], 108.7 [s, *C*CH(CH_3)$_2$], 94.3 (s, CH_3–*C*), 90.2 (d, $^2J_{PC}$ = 4.3, *o*-$CH_3C_6H_4$), 85.5 (d, $^2J_{PC}$ = 6.0, *m*-$CH_3C_6H_4$), 30.0 [s, *C*H(CH_3)$_2$], 21.4 [s, CH(*C*H_3)$_2$], 17.2 (s, *C*H_3–C_6H_4), 16.7 (dd, $^1J_{PC}$ = 19.4, $^1J_{PC}$ = 24.3, P–*C*H_2–P). ^{31}P{^{1}H} NMR ($CDCl_3$): δ = 22.7 (d, $^2J_{PP}$ = 29.2, 1 P, Ru–*P*), 11.9 (br., 1 P, *P*–BH_3). ^{11}B{^{1}H} NMR ($CDCl_3$): δ = –38.4 (br). IR (nujol, cm^{-1}): $\tilde{\nu}_{\nu(BH)}$ = 2419 (br), 2389 (br). $C_{35}H_{39}BCl_2P_2Ru$·CH_2Cl_2 (789.36): calcd. C 54.78, H 5.24; found C 55.24, H 5.26.

Preparation of [(η^6-*p*-Cymene)$RuCl_2$(η^1-$PPh_2CH_2CH_2PPh_2BH_3$)] (8B): To a solution of dppe (0.104 g, 0.26 mmol) in CH_2Cl_2 (10 mL, 0 °C) a solution of [(η^6-*p*-cymene)$RuCl_2$]$_2$ (0.100 g, 0.16 mmol) in CH_2Cl_2 (5 mL) followed, ca. 1 min later, by a solution of BH_3·THF in THF (0.16 mL of ca. 1.2 M, 0.19 mmol)] were added rapidly. The solution was then warmed to room temperature and stirred for 1 h. The solvent was then removed in vacuo, and the residue extracted with toluene (25 mL). Further [(η^6-*p*-cymene)$RuCl_2$(μ-dppe)-$RuCl_2$(η^6-*p*-cymene)] could be separated from the reaction mixture by recrystallisation from CH_2Cl_2/pentane, at –20 °C. Purification of the remaining material by preparative TLC (acetone/CH_2Cl_2, 1:11), extracting the first orange band with acetone, give the pure

 © 2005 Wiley-VCH Verlag GmbH & Co. KGaA, Weinheim

product. Yield: 0.02 g (19%/BH_3, 10%/Ru). Orange crystals suitable for X-ray diffraction were obtained by recrystallisation of **8B** from CH_2Cl_2/pentane at –20 °C. ^{1}H NMR ($CDCl_3$): δ = 7.68–7.78 [m, 4 H, RuP(*o*-C_6H_5)$_2$; {^{31}P@δ = 23.6} m′], 7.58–7.68 [m, 4 H, P(*o*-C_6H_5)$_2$$BH_3$; {^{31}P@$\delta$ = 18.2} m′], 7.58–7.8 [m, 12 H, P(*m*,*p*-C_6H_5)$_2$], 5.19 (d, $^3J_{HH}$ = 5.7, 2 H, *o*-$CH_3C_6H_4$), 5.12 (d, $^3J_{HH}$ = 6.0, 2 H, *m*-$CH_3C_6H_4$), 2.7–2.9 [m, 2 H, $CH_2PPh_2BH_3$; {^{31}P@δ = 23.6} δ = 2.77, $^3J_{HH}$ = 4.2, $^2J_{PC}$ = 12.9], 2.58 [sept, $^3J_{HH}$ = 6.9, 1 H, $CH(CH_3)_2$], 2.2–2.4 [m, 2 H, $RuPPh_2CH_2$; {^{31}P@δ = 18.2} δ = 2.29, $^3J_{HH}$ = 3.9, $^2J_{PC}$ = 13.2], 1.90 (s, 3 H, CH_3–C_6H_4), 1.01 [d, $^3J_{HH}$ = 6.9, 6 H, $CH(CH_3)_2$], 0.3–1.2 [br., 3 H, BH_3; {^{11}B@δ = –40.6} δ = 0.80, d, $^2J_{PH}$ = 16.0]. ^{13}C{^{1}H} NMR ($CDCl_3$): δ = 133.6 [d, $^1J_{PC}$ = 42.6, P(*i*-C_6H_5)$_2$], 133.2 [d, $^2J_{PC}$ = 9.0, RuP(*o*-C_6H_5)$_2$], 132.2 [d, $^1J_{PC}$ = 9.4, P(*o*-C_6H_5)$_2$$BH_3$], 131.1 [d, $^4J_{PC}$ = 2.2, P(*p*-C_6H_5)$_2$$BH_3$], 130.9 [d, $^4J_{PC}$ = 2.2, RuP(*p*-C_6H_5)$_2$], 128.5–129.1 [obscured, P(*i*-C_6H_5)$_2$], 128.7 [d, $^2J_{PC}$ = 10.0, P(*m*-C_6H_5)$_2$], 128.6 [d, $^1J_{PC}$ = 9.5, P(*m*-C_6H_5)$_2$], 109.5 [s, *C*$CH(CH_3)_2$], 95.7 (s, CH_3–*C*), 89.8 (d, $^2J_{PC}$ = 4.0, *o*-$CH_3C_6H_4$), 85.9 (d, $^2J_{PC}$ = 5.6, *m*-$CH_3C_6H_4$), 30.1 [s, *C*$H(CH_3)_2$], 21.8 [s, $CH(CH_3)_2$], 21.7 (d, $^1J_{PC}$ = 29.8, *C*$H_2PPh_2BH_3$), 20.0 (d,, $^1J_{PC}$ = 36.9), 17 $RuPPh_2CH_2$.6 (s, *C*H_3–C_6H_4). ^{31}P{^{1}H} NMR ($CDCl_3$): δ = 23.6 (d, $^3J_{PP}$ = 42.8, 1 P, Ru–*P*), 18.2 (br., 1 P, *P*–BH_3). ^{11}B{^{1}H} NMR ($CDCl_3$): δ = –40.6 (br). IR (nujol, cm^{-1}): $\tilde{\nu}_{v(BH)}$ = 2370 (br).

Preparation of [(η^6-*p*-Cymene)$RuCl_2$(η^1-$PPh_2C_5H_4FeC_5H_4PPh_2$-BH_3)] (9B): To a solution of dppf (0.145 g, 0.26 mmol) in CH_2Cl_2 (10 mL, 0 °C ice slurry) a solution of [(η^6-*p*-cymene)$RuCl_2$]$_2$ (0.100 g, 0.16 mmol) in CH_2Cl_2 (5 mL) followed, ca. 1 min later, by a solution of BH_3·THF in THF (0.16 mL of ca. 1.2 M, 0.19 mmol) were added. The solution was then warmed to room temperature and stirred for 1 h, and the solvent was removed in vacuo. Extraction of the solid with toluene (40 mL) followed by recrystallisation of this extract from CH_2Cl_2/pentane at –20 °C gave the product as a orange solid. Yield: 0.11 g (61% /BH_3, 37% /Ru). Further purification is achieved by preparative TLC (acetone/CH_2Cl_2, 1:10), extracting the first orange band with acetone. ^{1}H NMR ($CDCl_3$): δ = 7.7–7.8 [m, 4 H, RuP(*o*-C_6H_5)$_2$; {^{31}P@δ = 18.5} δ = 7.77, dd, $^4J_{HH}$ = 1.4, $^3J_{HH}$ = 7.7], 7.3–7.5 [m, 16 H, P(*o*-C_6H_5)$_2$$BH_3$ and P(*m*,*p*-C_6H_5)$_2$], 5.17 (d, $^3J_{HH}$ = 5.8, 2 H, *o*-$CH_3C_6H_4$), 5.10 (d, $^3J_{HH}$ = 6.1, 2 H, *m*-$CH_3C_6H_4$), 4.45–4.50 [m, 2 H, (*m*-C_5H_4)PPh_2BH_3], 4.32–4.37 [m, 2 H, (*o*-C_5H_4)PPh_2BH_3], 4.10–4.15 [m, 2 H, RuP-Ph_2(*o*-C_5H_4)], 4.80–4.86 [m, 2 H, $RuPPh_2$(*m*-C_5H_4)], 2.53 [sept, $^3J_{HH}$ = 6.9, 1 H, *C*$H(CH_3)_2$], 1.78 (s, 3 H, CH_3–C_6H_4), 0.94 [d, $^3J_{HH}$ = 7.0, 6 H, $CH(CH_3)_2$], 0.7–1.5 [br., 3 H, BH_3; {^{11}B@δ = –38.5} δ = 1.13, d, $^2J_{PH}$ = 16.4]. ^{13}C{^{1}H} NMR ($CDCl_3$): δ = 136.8 [d, $^1J_{PC}$ = 47.1, RuP(*i*-C_6H_5)$_2$], 133.8 [d, $^2J_{PC}$ = 9.5, RuP(*o*-C_6H_5)$_2$], 132.5 [d, $^2J_{PC}$ = 9.7, P(*o*-C_6H_5)$_2$$BH_3$], 131.0 [d, $^1J_{PC}$ = 59.2, P(*i*-C_6H_5)$_2$$BH_3$], 130.9 [d, $^4J_{PC}$ = 2.3, RuP(*p*-C_6H_5)$_2$], 130.2 [d, $^3J_{PC}$ = 2.1, P(*p*-C_6H_5)$_2$], 128.4 [d, $^3J_{PC}$ = 10.2, P(*m*-C_6H_5)$_2$], 127.7 [d, $^3J_{PC}$ = 9.7, P(*m*-C_6H_5)$_2$], 109.7 [s, *C*$CH(CH_3)_2$], 95.1 (s, CH_3–*C*), 90.4 (d, $^2J_{PC}$ = 4.2, *o*-$CH_3C_6H_4$), 85.9 (d, $^2J_{PC}$ = 6.0, *m*-$CH_3C_6H_4$), 76.53 [d, $^3J_{PC}$ = 7.4, (*m*-C_5H_4)PPh_2BH_3], 76.49 [d, $^2J_{PC}$ = 10.0, $RuPPh_2$(*o*-C_5H_4)], 73.3 [d, $^3J_{PC}$ = 9.8, $RuPPh_2$(*m*-C_5H_4)], 72.5 [d, $^2J_{PC}$ = 7.5, (*o*-C_5H_4)PPh_2BH_3], 69.0 [d, $^1J_{PC}$ = 67.4, $RuPPh_2$(*i*-C_5H_4)], 29.9 [s, *C*$H(CH_3)_2$], 21.7 [s, $CH(CH_3)_2$], 17.0 (s, *C*H_3–C_6H_4); the signal of (*i*-C_5H_4)PPh_2BH_3 was not unambiguously located. ^{31}P{^{1}H} NMR ($CDCl_3$): δ = 18.5 (s, 1 P, Ru–*P*), 15.8 (br., 1 P, *P*–BH_3). ^{11}B{^{1}H} NMR ($CDCl_3$): δ = –38.5 (br). IR (nujol, cm^{-1}): $\tilde{\nu}_{v(BH)}$ = 2373 (br).

Preparation of 1,4-$BrC_6H_4PPh_2BH_3$: To a solution of 1,4-$BrC_6H_4PPh_2$ (1.50 g, 4.40 mmol) in THF (50 mL, 0 °C) a solution of BH_3·THF in THF (3.7 mL, ca. 1.2 M, 4.40 mmol) was added dropwise. The solution was warmed to room temperature after 15 minutes and then concentrated to approximately 30 mL. The product was then precipitated by the addition of hexane, filtered, washed with hexane (ca. 20 mL) and dried in vacuo. Yield 1.30 g (83%). ^{1}H NMR ($CDCl_3$): δ = 7.4–7.7 [m, 14 H, BH_3PPh_2(C_6H_4Br)], 0.8–1.8 [br., 3 H, BH_3 {^{11}B@δ = –38.0} δ = 1.27, d, $^2J_{PH}$ = 16.3]. ^{31}P{^{1}H} NMR ($CDCl_3$): δ = 20.8 (d, $^1J_{PB} \approx$ 55). ^{11}B{^{1}H} NMR ($CDCl_3$): δ = –38.0 (d, $^1J_{PB} \approx$ 55). IR (nujol, cm^{-1}): $\tilde{\nu}_{v(BH)}$ = 2385 (br).

Preparation of 1,4-$PPh_2C_6H_4PPh_2BH_3$: To a solution of 1,4-$BrC_6H_4PPh_2BH_3$ (0.60 g, 1.69 mmol) in THF (30 mL, –78 °C) a solution of BuLi in hexane (1.1 mL, ≈ 1.6 M, 1.7 mmol) followed by $ClPPh_2$ (0.32 mL, 1.78 mmol) were added dropwise. The solution was stirred for a further 20 minutes and then warmed to room temperature. The product was precipitated as a white solid by concentration and then collected by filtration, washed with methanol (2 × 10 mL) and dried in vacuo. Yield 0.61 g (73%). ^{1}H NMR ($CDCl_3$): δ = 7.4–7.7 [m, 14 H, BH_3PPh_2(C_6H_4Br)], 0.8–1.8 [br., 3 H, BH_3 {^{11}B@δ = –38.0} δ = 1.27, d, $^2J_{PH}$ = 16.3]. ^{31}P{^{1}H} NMR ($CDCl_3$): δ = 20.8 (br., 1 P, PPh_2BH_3), –4.9 (s, 1 P, pend-PPh_2). ^{11}B{^{1}H} NMR ($CDCl_3$): δ = –38.0 (br). IR (nujol, cm^{-1}): $\tilde{\nu}_{v(BH)}$ = 2398 (br).

Preparation of [(η^6-*p*-Cymene)$RuCl_2$(η^1-1,4-$PPh_2C_6H_4PPh_2BH_3$)] (10): A solution of [(η^6-*p*-cymene)$RuCl_2$]$_2$ (0.20 g, 0.33 mmol) and 1,4-$PPh_2C_6H_4PPh_2BH_3$ (0.30 g, 0.65 mmol) in CH_2Cl_2 was stirred at room temperature for 1 h. After concentration to ca. 25 mL the product was precipitated with hexane. The orange solid was collected by filtration, washed with hexane (3 × 10 mL) and dried in vacuo. Yield: 0.41 g (82%). ^{1}H NMR ($CDCl_3$): δ = 7.79–7.93 [m, 6 H, $RuPPh_2$(*o*-$C_6H_4PPh_2BH_3$) and RuP(*o*-C_6H_5)$_2$; {^{31}P@δ = 24.9} δ = 7.89, dd, 2 H, $RuPPh_2$(*o*-$C_6H_4PPh_2BH_3$), $^3J_{PH}$ = 1.2, $^3J_{HH}$ = 8.3 Hz; δ = 7.85, dd, 4 H, RuP(*o*-C_6H_5)$_2$, $^4J_{HH}$ = 1.5, $^3J_{HH}$ = 7.9], 7.52–7.6 [m, 4 H, P(*o*-C_6H_5)$_2$$BH_3$; {^{31}P@$\delta$ = 20.5} δ = 7.56, dd, $^4J_{HH}$ = 1.4, $^3J_{HH}$ = 8.3], 7.3–7.52 [m, 14 H, $RuPPh_2$(*m*-$C_6H_4PPh_2BH_3$) and P(*m*,*p*-C_6H_5)$_2$], 5.22 (d, $^3J_{HH}$ = 6.1, 2 H, *m*-$CH_3C_6H_4$), 5.02 (d, $^3J_{HH}$ = 5.6, 2 H, *o*-$CH_3C_6H_4$), 2.85 [sept, $^3J_{HH}$ = 6.9, 1 H, *C*$H(CH_3)_2$], 1.88 (s, 3 H, CH_3–C_6H_4), 1.11 [d, $^3J_{HH}$ = 6.9, 6 H, $CH(CH_3)_2$], 0.6–1.76 [br., 3 H, BH_3; {^{11}B@δ = –38.1} δ = 1.23, d, $^2J_{PH}$ = 16.3]. ^{13}C{^{1}H} NMR ($CDCl_3$): δ = 137.1 [dd, $RuPPh_2$(*i*-$C_6H_4PPh_2BH_3$), $^4J_{PC}$ = 2.3, $^1J_{PC}$ = 44.1], 134.4 [m, RuP-Ph_2(*o*-$C_6H_4PPh_2BH_3$)], 134.3 [d, $^2J_{PC}$ = 9.7, RuP(*o*-C_6H_5)$_2$], 133.4 [d, $^1J_{PC}$ = 45.0, P(*i*-C_6H_5)$_2$], 132.1 [m, $RuPPh_2$(*m*-$C_6H_4PPh_2BH_3$)], 131.2 [dd, $^4J_{PC}$ = 2.2, $^1J_{PC}$ = 56.2, $RuPPh_2$(*p*-$C_6H_4PPh_2BH_3$)], 131.4 [d, $^4J_{PC}$ = 2.3, P(*p*-C_6H_5)$_2$$BH_3$], 130.7 [d, $^4J_{PC}$ = 2.2, RuP(*p*-C_6H_5)$_2$], 128.8 [d, $^3J_{PC}$ = 10.3, P(*m*-C_6H_5)$_2$], 128.4 [d, $^1J_{PC}$ = 58.2, P(*i*-C_6H_5)$_2$], 128.3 [d, $^3J_{PC}$ = 9.9, P(*m*-C_6H_5)$_2$], 111.4 [d, $^2J_{PC}$ = 3.4, *C*$CH(CH_3)_2$], 96.2 (s, CH_3–*C*), 89.0 (d, $^2J_{PC}$ = 3.0, *o*-$CH_3C_6H_4$), 87.3 (d, $^2J_{PC}$ = 5.5, *m*-$CH_3C_6H_4$), 30.3 [s, *C*$H(CH_3)_2$], 21.8 [s, $CH(CH_3)_2$], 17.8 (s, *C*H_3–C_6H_4). ^{31}P{^{1}H} NMR ($CDCl_3$): δ = 24.9 (s, 1 P, Ru–*P*), 20.5 (br., 1 P, *P*–BH_3). ^{11}B{^{1}H} NMR ($CDCl_3$): δ = –38.1 (br). IR (nujol, cm^{-1}): $\tilde{\nu}_{v(BH)}$ = 2372 (br). $C_{40}H_{41}BCl_2PRu \cdot {}^1/_3CH_2Cl_2$ (794.81): calcd. C 60.95, H 5.28; found C 60.78, H 5.19.

X-ray Crystallography: Relevant details about the structure refinements are given in Table 2 and Table 3. Selected geometrical parameters are included in the captions of Figure 3, Figure 4, Figure 6, Figure 7, Figure 10, Figure 11 and Figure 12. Data collection for the X-ray structure determinations for compounds **2**, **3**, **5**, **2B** and **8B** were performed with a four-circle Kappa goniometer equipped with an Oxford Diffraction KM4 Sapphire CCD at 140(2) K. For compounds **6** and **1B** diffraction data were collected with a mar345 IPDS instrument at 140(2) K. Data reduction was performed using CrysAlis RED.[25] Structure solutions were solved by direct methods using SIR92 (**8B**),[26] SIR97 (**2**, **6**, **1B**),[27] or

 © 2005 Wiley-VCH Verlag GmbH & Co. KGaA, Weinheim

SHELXTL[28] (**3**, **5**), or by Patterson interpretation using SHELXTL (**2B**).[28] Structure refinements were performed using the SHELXTL software package for all compounds. An empirical absorption correction (DELABS)[29] was applied to all data sets except for that of **3**. The structures of all compounds were refined using full-matrix least-squares on F^2 with the exception of **3**, which was refined using full-matrix-block least-squares on F^2. All non-hydrogen atoms were refined anisotropically, with hydrogen atoms placed in calculated positions using the riding model with the exception of the BH hydrogen atoms, which were located on the Fou-

Table 2. Crystal data and details of the structure determinations for **2**, **3**, **5** and **6**.

	2	**3**	**5**	**6**
CCDC	280165	280166	280167	280168
Chemical formula	$C_{36}H_{36}Cl_2P_2Ru$	$C_{35}H_{36}Cl_2OP_2Ru{\cdot}1.5CHCl_3$	$C_{36}H_{34}Cl_2P_2Ru{\cdot}3CHCl_3$	$C_{46}H_{50}Cl_2P_2Ru_2{\cdot}2CHCl_3$
Formula mass	702.56	885.60	1058.65	1176.58
Crystal system	triclinic	triclinic	monoclinic	monoclinic
Space group	$P\bar{1}$	$P\bar{1}$	$P2_1/n$	$P2_1/n$
a [Å]	10.5479(7)	15.4477(11)	15.9347(10)	12.710(4)
b [Å]	12.5815(13)	22.0211(12)	11.5059(10)	11.4016(18)
c [Å]	12.8323(14)	25.5063(12)	25.7256(15)	17.294(5)
α	81.579(9)°	72.314(5)°		
β	82.482(8)°	85.723(5)°	98.777(5)°	101.06(2)°
γ	85.270(7)°	88.496(5)°		
V [Å^3]	1666.6(3)	8243.4(8)	4661.4(6)	2459.6(11)
Z	2	8	4	2
$D_{calcd.}$ (g cm^{-3})	1.400	1.427	1.509	1.589
F(000)	720	3592	2128	1188
μ [mm^{-1}]	0.750	0.907	1.063	1.147
Temp. [K]	140(2)	140(2)	140(2)	140(2)
Wavelength [Å]	0.71073	0.71073	0.71073	0.71073
Measd. reflns.	9849	49686	26017	14479
Unique reflns.	5142	25535	7835	4336
Unique reflns. [$I > 2\sigma(I)$]	3659	12102	5586	3513
No. of data / restraints / parameters	5142 / 0 / 373	25535 / 90 / 1706	7835 / 12 / 518	4336 / 3 / 284
R[a] [$I > 2\sigma(I)$]	0.0463	0.0686	0.0593	0.0452
wR_2[a] (all data)	0.1066	0.1991	0.1708	0.1023
GoF[b]	0.923	0.912	1.060	1.065

[a] $R = \Sigma||F_o| - |F_c||/\Sigma|F_o|$, $wR_2 = \{\Sigma[w(F_o^2 - F_c^2)^2]/\Sigma[w(F_o^2)^2]\}^{1/2}$. [b] GoF = $\{\Sigma[w(F_o^2 - F_c^2)^2]/(n - p)\}^{1/2}$ where n is the number of data and p is the number of parameters refined.

Table 3. Crystal data and details of the structure determinations for **1B**, **2B** and **8B**.

	1B	**2B**	**8B**
CCDC	280169	280170	280171
Empirical formula	$C_{35}H_{39}BCl_2P_2Ru{\cdot}CHCl_3$	$C_{36}H_{39}BCl_2P_2Ru{\cdot}CH_2Cl_2$	$C_{36}H_{41}BCl_2P_2Ru{\cdot}2CH_2Cl_2$
Formula mass	823.75	801.32	888.26
Crystal system	monoclinic	monoclinic	triclinic
Space group	$C2/c$	$P2_1/c$	$P\bar{1}$
a [Å]	39.660(17)	14.5111(8)	8.7826(6)
b [Å]	11.024(3)	16.6311(10)	14.5506(15)
c [Å]	18.413(10)	17.1449(9)	16.754(2)
α			81.354(9)°
β	111.29(7)°	114.847(5)°	88.283(8)°
γ			80.581(7)°
V [Å^3]	7501(6)	3754.7(4)	2088.2(4)
Z	8	4	2
$D_{calcd.}$ (g cm^{-3})	1.459	1.418	1.413
F(000)	3360	1640	908
μ [mm^{-1}]	0.885	0.813	0.862
Temp. [K]	140(2)	140(2)	140(2)
Wavelength [Å]	0.71073	0.71073	0.71073
Measd. reflns.	23670	21520	12575
Unique reflns.	6594	6295	6465
Unique reflns. [$I > 2\sigma(I)$]	3801	5483	4171
No. of data / restraints / parameters	6594 / 74 / 450	6295 / 6 / 420	6465 / 12 / 447
R[a] [$I > 2\sigma(I)$]	0.0781	0.0390	0.0516
wR_2[a] (all data)	0.2331	0.1057	0.1326
GoF[b]	0.993	1.050	0.937

[a] $R = \Sigma||F_o| - |F_c||/\Sigma|F_o|$, $wR_2 = \{\Sigma[w(F_o^2 - F_c^2)^2]/\Sigma[w(F_o^2)^2]\}^{1/2}$. [b] GoF = $\{\Sigma[w(F_o^2 - F_c^2)^2]/(n - p)\}^{1/2}$ where n is the number of data and p is the number of parameters refined.

 © 2005 Wiley-VCH Verlag GmbH & Co. KGaA, Weinheim

rier difference map and then constrained to equal BH bond lengths and H–B–H angles. Disorder in the *p*-cymene ring in complex **1B** was satisfactorily modeled by splitting the isopropyl moiety (with constrained geometries) over two sites, constraining the ring and restraining the atomic displacement parameters of the ring using SIMU and ISOR commands. Some of the solvent molecules in **3**, **5** and **6** were constrained or split over multiple sites. It was also necessary to restrain the atomic displacement parameters of some atoms in the structures of **3**, **5**, and **8B**. Graphical representations of the structures were made with Diamond.[30] CCDC-280165–280171 contain the supplementary crystallographic data for this paper (see Table 2 and Table 3). These data can be obtained free of charge from The Cambridge Crystallographic Data Centre via www.ccdc.cam.ac.uk/data_request/cif.

Acknowledgments

We thank the New Zealand Foundation for Research, Science and Technology for a Top Achiever Doctoral Fellowship (A. B. C.), the EPFL and the Swiss National Science Foundation for financial support.

[1] F. A. Cotton, G. Wilkinson, C. A. Murillo, M. Bochman, *Advanced Inorganic Chemistry*, 6th ed., John Wiley & Sons, New York, **1999**.

[2] For examples see: a) L. H. Pignolet (Ed.), *Homogeneous Catalysis with Metal Phosphine Complexes*, Plenum Press, New York, **1983**; b) R. Noyori, *Asymmetric Catalysis in Organic Synthesis*, Wiley, New York, **1994**; c) P. A. Chaloner, M. A. Esteruelas, F. Joó, L. A. Oro, *Homogeneous Hydrogenation*, Kluwer Academic Press, Dordrecht, **1994**; d) T. Naota, H. Takaya, S.-I. Murahashi, *Chem. Rev.* **1998**, *98*, 2599–2660; e) O. W. N. M. van Leeuwen, P. C. J. Kamer, J. N. H. Reek, P. Dierkes, *Chem. Rev.* **2000**, *100*, 2741–2769.

[3] For examples see: a) A. Santos, J. López, J. Montoya, P. Noheda, A. Romero, A. M. Echavarren, *Organometallics* **1994**, *13*, 3605–3615; b) J. W. Benson, R. L. Keiter, E. A. Keiter, A. L. Rheingold, G. P. A. Yap, V. V. Mainz, *Organometallics* **1998**, *17*, 4275–4281 and references cited therein; c) J. E. Mague, M. S. Balakrishna, *Polyhedron* **1996**, *15*, 4259–4268; d) E. Louattani, J. Suades, K. Urtiaga, M. I. Arriortua, X. Solans, *Organometallics* **1996**, *15*, 468–471; e) N. E. Leadbeater, J. Lewis, P. R. Raithby, A. J. Edwards, *J. Organomet. Chem.* **1997**, *545–546*, 567–572; f) Y. Yang, K. A. Abboud, L. McElwee-White, *Dalton Trans.* **2003**, 4288–4296; g) W.-Y. Yeh, C.-I. Li, S.-M. Peng, G.-H. Lee, *J. Organomet. Chem.* **2004**, *689*, 105–110.

[4] a) P. McQuade, N. P. Rath, L. Barton, *Inorg. Chem.* **1999**, *38*, 5468–5470 and references cited therein; b) P. McQuade, R. E. K. Winter, N. P. Rath, L. Barton, *Inorg. Chim. Acta* **2005**, *358*, 1545.

[5] a) A. W. Coleman, D. F. Jones, P. H. Dixneuf, C. Brisson, J.-J. Bonnet, G. Lavigne, *Inorg. Chem.* **1984**, *23*, 952–956; b) A. W. Coleman, H. Zhang, S. G. Bott, J. L. Atwood, P. H. Dixneuf, *J. Coord. Chem.* **1987**, *16*, 9–17; c) D. K. Gupta, A. N. Sahay, D. S. Pandey, N. K. Jha, P. Sharma, G. Espinosa, A. Cabrera, M. C. Puerta, P. Valerga, *J. Organomet. Chem.* **1998**, *568*, 13–20.

[6] For examples see: a) C. J. Adams, M. I. Bruce, B. W. Skelton, A. H. White, *J. Organomet. Chem.* **1992**, *423*, 83–96; b) E. Stein, F. Y. Fujiwara, *J. Organomet. Chem.* **1996**, *525*, 31–37; c) P. M. van Calcar, M. M. Olmstead, A. L. Balch, *Inorg. Chim. Acta* **1998**, *270*, 28–33.

[7] For recent examples see: a) C. Daguenet, P. J. Dyson, *Catal. Commun.* **2003**, *4*, 153–157; b) P. J. Dyson, D. J. Ellis, W. Henderson, G. A. Laurenczy, *Adv. Synth. Catal.* **2003**, *345*, 216–221; c) C. Daguenet, R. Scopelliti, P. J. Dyson, *Organometallics* **2004**, *23*, 4849–4857; d) C. Daguenet, P. J. Dyson, *Organometallics* **2004**, *23*, 6080–6083.

[8] a) T. J. Geldbach, P. J. Dyson, *J. Am. Chem. Soc.* **2004**, *126*, 8114–8115; b) T. J. Geldbach, M. R. H. Brown, R. Scopelliti, P. J. Dyson, *J. Organomet. Chem.* **2005**, Online Advanced Article: April 29.

[9] M.-E. Moret, A. B. Chaplin, A. K. Lawrence, R. Scopelliti, P. J. Dyson, *Organometallics* **2005**, *24*, 4039–4048.

[10] a) J. M. Brunel, B. Faure, M. Maffei, *Coord. Chem. Rev.* **1998**, *178–180*, 665–698; b) B. Carboni, L. Monnier, *Tetrahedron* **1999**, *55*, 1197–1248.

[11] R. Macías, N. P. Rath, L. Barton, *Angew. Chem. Int. Ed.* **1999**, *38*, 162–164.

[12] M. Ingleson, N. J. Patmore, G. D. Ruggiero, C. G. Frost, M. F. Mahon, M. C. Wills, A. S. Weller, *Organometallics* **2001**, *20*, 4434–4436.

[13] N. Merle, G. Koicok-Köhn, M. F. Mahon, C. G. Frost, G. D. Ruggerio, A. S. Weller, M. C. Willis, *Dalton Trans.* **2004**, 3883–3892.

[14] F. Estevan, P. Lahuerta, J. Latorre, A. Sanchez, C. Sieiro, *Polyhedron* **1987**, *6*, 473–478.

[15] I. Moldes, E. de la Encarnación, J. Ros, Á. Alvanez-Larena, J. F. Piniella, *J. Organomet. Chem.* **1998**, *566*, 165–174.

[16] Alternatively, [(η^6-*p*-cymene)$RuCl_2$(η^1-dppm)] can be quantitatively converted to [(η^6-*p*-cymene)$RuCl_2$(η^1-dppmO)] by treatment with H_2O_2 in THF. ^{1}H and ^{31}P NMR spectroscopic data were in agreement with the literature data.[17]

[17] J. W. Faller, B. P. Patel, M. A. Albrizzio, M. Curtis, *Organometallics* **1999**, *18*, 3096–3104.

[18] Refluxing a solution of [(η^6-*p*-cymene)$_2Ru_2(\mu$-Cl)$_3$]PF_6 and dppa (1.5 equivalents) in CH_2Cl_2 for 2.5 h leads to a mixture containing [(η^6-*p*-cymene)$RuCl_2$(η^1-dppa){(μ-dppa)$RuCl_2$(η^6-*p*-cymene)}]$^+$ {^{31}P NMR ($CDCl_3$): δ = 29.0 (s, 1 P, $RuCl_2$*P*), 22.4 (d, $^2J_{PP}$ = 61, 1 P, Ru*P*Ph_2CCPPh_2), 2.4 (d, $^2J_{PP}$ = 62, 1 P, Ru*P*Ph_2CCPPh_2RuCl_2), –30.7 (d, $^3J_{PP}$ = 5, 1 P, pend-*P*). ESI-MS (CH_2Cl_2) positive ion: *m*/*z* = +1365 [M]$^+$}. Although small amounts can be purified by preparative TLC (acetone/CH_2Cl_2, 1:24), this complex undergoes an equilibration reaction leading to a mixture containing [(η^6-*p*-cymene)RuCl(η^1-dppa)$_2$]$^+$ {^{31}P NMR ($CDCl_3$): δ = 11.9 (s, 1 P, RuCl*P*), –31.3 (s, 1 P, pend-*P*). ESI-MS (CH_2Cl_2) positive ion: *m*/*z* = +1059 [M]$^+$} and [(η^6-*p*-cymene)RuCl{(μ-dppa)$RuCl_2$(η^6-*p*-cymene)}$_2$]$^+$ {^{31}P NMR ($CDCl_3$): δ = 24.4 (br., 1 P, Ru*P*), 8.3 (br., 1 P, Ru*P*). ESI-MS (CH_2Cl_2) positive ion: *m*/*z* = +1671 [M]$^+$}.

[19] Determined by ^{31}P NMR of an aliquot taken from the solution after 2 h, the solvent removed in vacuo and then the solid redissolved in $CDCl_3$.

[20] P. J. Dyson, J. S. McIndoe, *Inorg. Chima Acta* **2003**, *354*, 68.

[21] M. Herberhold, H. Yan, W. Milius, *J. Organomet. Chem.* **2000**, *598*, 142–149.

[22] M. A. Bennett, T. N. Huang, T. W. Matheson, A. K. Smith, *Inorg. Synth.* **1982**, *21*, 74.

[23] M. A. Bennett, A. K. Smith, *J. Chem. Soc., Dalton Trans.* **1974**, 233.

[24] R. A. Baldwin, M. T. Cheng, *J. Org. Chem.* **1967**, *32*, 1572–1577.

[25] Oxford Diffraction Ltd., Abingdon, Oxfordshire, U. K., **2003**.

[26] A. Altomare, M. C. Burla, G. Camalli, G. Cascarano, C. Giacovazzo, A. Guagliardi, G. Polidori, *J. Appl. Crystallogr.* **1994**, *27*, 435–436.

[27] A. Altomare, M. C. Burla, M. Camalli, G. L. Cascarano, C. Giacovazzo, A. Guagliardi, A. G. G. Moliterni, G. Polidori, R. Spagna, *J. Appl. Crystallogr.* **1999**, *32*, 115–119.

[28] G. M. Sheldrick, *SHELXTL*; University of Göttingen, Germany, **1997**; Bruker AXS, Inc., Madison, WI, **1997**.

[29] N. Walker, D. Stuart, *Acta Crystallogr., Sect. A* **1983**, *39*, 158.

[30] Diamond 3.0a; Crystal Impact GbR, Bonn, Germany, **2004**.

Received: August 5, 2005
Published Online: October 25, 2005

 © 2005 Wiley-VCH Verlag GmbH & Co. KGaA, Weinheim

DOI: 10.1002/ejic.200500413

Formation of 3D Dandelions and 2D Nanowalls of Copper Phosphate Dihydrate on a Copper Surface and Their Conversion into a Nanoporous CuO Film

Xufeng Wu,[a] Gaoquan Shi,*[a] Shibin Wang,[a] and Peiyi Wu[b]

Keywords: Copper / Materials science / Nanostructures / Oxides / Phosphates

3D dandelion-like porous nanostructures and 2D nanowalls of copper phosphate dihydrate built up of thin nanosheets have been synthesized simply by corrosion of a copper foil with aqueous phosphoric acid under mild conditions. The composition of the nanostructures has been confirmed by XRD, ICP-AES, and Raman spectroscopy. Controlling the initial concentration of the acid and the conditions of drop drying allows control of the morphology of the nanostructures. The phosphate nanostructures can be converted into nanoporous CuO films by pyrolysis.
(© Wiley-VCH Verlag GmbH & Co. KGaA, 69451 Weinheim, Germany, 2005)

Introduction

Over the past ten years, metal-based nanomaterials have attracted extensive interest due to their promising applications in catalysis, energy storage or conversion, and data storage and memory devices.[1,2] To date, many interesting zero-dimensional (0D) and one-dimensional (1D) nanomaterials have been synthesized.[3–5] However, the fabrication of well-controlled two-dimensional (2D) or three-dimensional (3D) nanostructures is usually difficult because control of the nucleation and growth of nanomaterials is still a challenge:[6–9] simply mixing two incompatible solutions of metal salts will lead to the formation of a polycrystalline deposit with an irregular structure. It is known that a double-jet technique can be used to provide supersaturation conditions by continuously replenishing nutrients. However, the impurity of the counterions often leads to an unpredictable change in the crystal morphology.[6] Thus, it is important to develop innovative and convenient techniques for fabricating metal-based nanomaterials with 2D or 3D structures under mild conditions and at low cost.

On the other hand, copper phosphates are catalysts for the oxidation of aromatic compounds.[10–12] Nanostructures of these salts provide high specific surface areas that enhance their catalytic activity and selectivity. Cupric oxide (CuO) and basic Cu^{II} salts with layered structures have also been studied extensively in the past few years.[13–18] CuO is a p-type semiconductor with a narrow bandgap and its nanostructures have potential applications in catalysis, superconductors, and the fabrication of sensors and solar cells.[19–22] Orthorhombic [$Cu_2(OH)_3Cl$] was the first copper-based biomineral found in living organisms. It exists as polycrystalline nanofibers arranged along the outer contour of the tooth tip, leading to an extraordinary resistance to abrasion.[23] Galvanic cell corrosion is a general phenomenon in everyday life and it may provide a continuous low concentration of metal ions for controlling the formation of characteristic micro- or nanostructures.[18] In this paper, we report a 3D dandelion-like nanostructure and a 2D nanowall of copper phosphate dihydrate by simple corrosion of a copper foil with aqueous phosphoric acid. Furthermore, a nanoporous CuO film is also produced by pyrolysis of these phosphate nanostructures.

Results and Discussion

Drying of a drop of aqueous phosphorus acid solution on a copper foil leads to the formation of many pale-blue particles on its surface. Figure 1 shows the typical SEM images of the particles. As shown in Figure 1 (A) nearly all the particles are round with a size in the range of 40 to 50 μm. When two or more particles merge together a peanut-like 3D architecture is formed. When a single particle as shown in part A of Figure 1 was further magnified, a crystalline dandelion-like structure was revealed. This dandelion-like structure is made up of uniform nanosheets and its surface is porous, with pore sizes ranging from several hundreds of nanometers to one micrometer (Figure 1, B). Figure 1 (C) indicates that the dandelion grows at almost the same rate from the core in all directions above the copper surface. A magnified view of the top of the dandelion reveals that the nanosheets are about 35 nm thick (Figure 1,

[a] Department of Chemistry and Key Lab of Organic Optical Electronics and Molecular Engineering of Chinese Education Commission, Tsinghua University,
Beijing 100084, People's Republic of China
[b] Department of Macromolecular Sciences and Key Lab of Molecular Engineering and Polymers of Chinese Education Commission, Fudan University,
Shanghai 200433, People's Republic of China

 © 2005 Wiley-VCH Verlag GmbH & Co. KgaA, Weinheim

D). Figure 1, part E, is the bottom view of a single dandelion. It reveals that there is an obvious core at the center of the dandelion and that the nanosheets grow with their thin face perpendicular to the bottom plane. Figure 1 (F) is a magnified view of the core, the formation mechanism of which is not very clear yet.

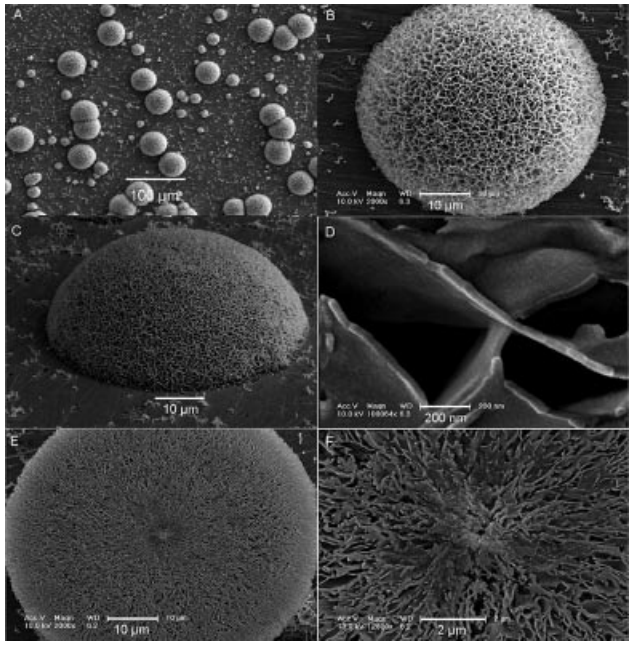

Figure 1. Typical SEM images of $Cu_3(PO_4)_2{\cdot}2H_2O$ dandelion-like nanostructures formed by drop-drying of 100 μL of 5 mM phosphorus acid on a copper foil surface. A) Overview SEM image of the copper surface. B) A dandelion-like 3D nanostructure. C) Side view of a dandelion. D) Magnified view of a dandelion. E) Bottom view of a dandelion. F) Magnified view of the dandelion bottom.

In order to study the composition of the dandelion-like nanostructures, the blue product was collected and washed repeatedly with deionized water, then dissolved in aqueous HNO_3 solution. The ion concentrations of copper and phosphorus in the solution were determined by ICP-AES and the results confirmed a strict stoichiometric Cu/P ratio of 1.5:1.0. Furthermore, the chemical weight of the blue product was calculated to be 416.60, thus indicating its chemical formula to be $[Cu_3(PO_4)_2{\cdot}2H_2O]$ (416.67). The formation of crystalline copper phosphate dihydrate $[Cu_3(PO_4)_2{\cdot}2H_2O]$ was further confirmed by the use of wide-angle X-ray diffraction. Figure 2 shows the XRD pattern of an as-prepared $[Cu_3(PO_4)_2{\cdot}2H_2O]$ powder sample. The diffraction lines are in agreement with those reported in the literature.[24] The X-ray photoelectron spectrum (XPS) of a dandelion exhibits peaks at 935.4, 531.5, and 133.4 eV, which are attributed to Cu $2p_{3/2}$, O 1s, and P $2p_{1/2}$ of $[Cu_3(PO_4)_2{\cdot}2H_2O]$,[25] respectively.

The chemical structure of the as-prepared $[Cu_3(PO_4)_2{\cdot}2H_2O]$ dandelion-like nanostructures was also confirmed by Raman spectroscopy. Figure 3 is the 633-nm-excited Raman spectrum of a dandelion and the inset is its optical microscope image. The band at 994 cm^{-1} is assigned to the PO_3 symmetric stretching vibration, the two bands at 646 and 553 cm^{-1} belong to the PO_3 out-of-plane bending vibrations, and the band at 450 cm^{-1} is attributed to the PO_3 symmetric bending vibration.[26,27]

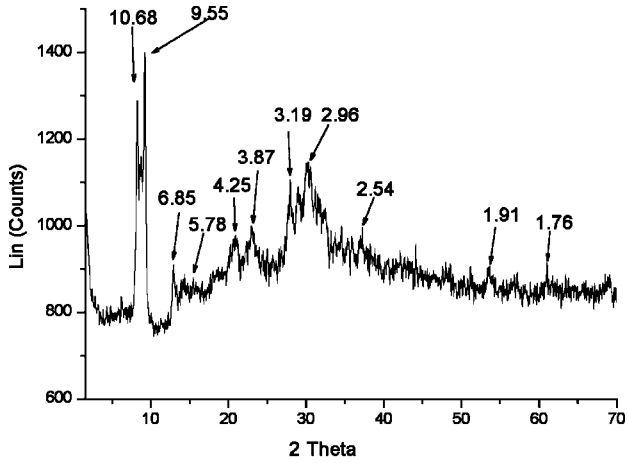

Figure 2. An XRD pattern of an as-prepared $[Cu_3(PO_4)_2{\cdot}2H_2O]$ powder sample formed by drop drying of a 50 mM H_3PO_4 solution on a copper foil at 15 °C and 49% humidity.

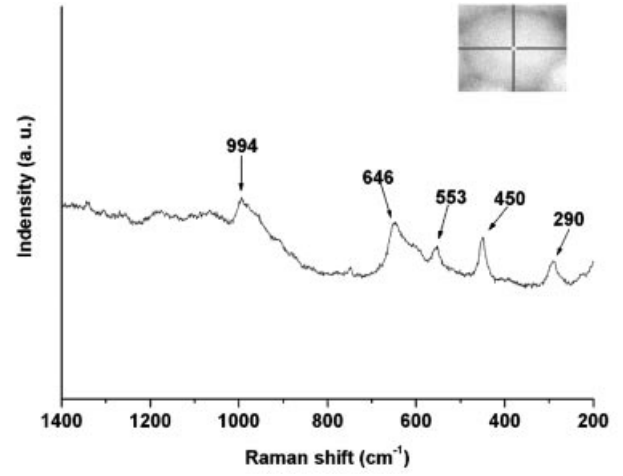

Figure 3. 633-nm-excited Raman spectra of as-prepared $[Cu_3(PO_4)_2{\cdot}2H_2O]$ dandelion (typically sample) recorded in the region of 200–1400 cm^{-1}; the inset image is the optical image of the dandelion.

The growth process of the dandelion has been carefully investigated. Figure 4 shows the SEM images of the copper surface recorded at different drying times after removing the residual solutions with a capillary tube. As shown in part A of Figure 4, the heterogeneous nucleation process is very slow, and sheet-like nuclei grow on the copper surface in the initial 60 minutes. When the drying time is increased from 60 to 120 minutes, the sheet-like nuclei form branches on the surface and gradually grow upward into small cores with a size of around 4 μm (Figure 4, B). This small core grows at nearly the same rate in all directions above the surface of the substrate to form a 3D dandelion (ca. 24 μm) as the drying time is increased further to 240 minutes (Figure 4, C). Finally, a dandelion with a diameter of about 45 μm is generated after 420 minutes (Figure 4, D).

 © 2005 Wiley-VCH Verlag GmbH & Co. KGaA, Weinheim

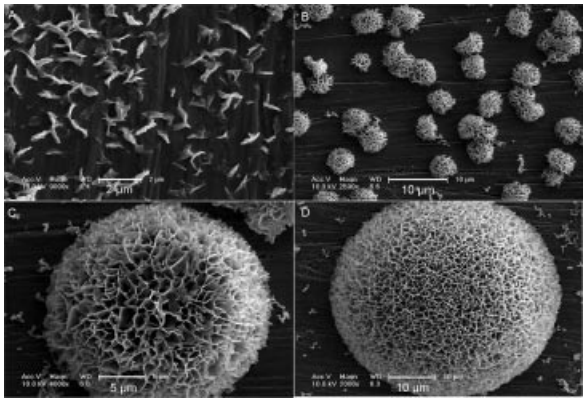

Figure 4. Typical SEM images of the copper surface recorded after drop drying 100 μL of 5 mM phosphorus acid for different times and removal of the residual solutions with a capillary tube: (A) 60 min; (B) 120 min; (C) 240 min; (D) 420 min.

It is known that copper can be corroded easily in a moist atmosphere. Under our experimental conditions, the corrosion mechanism can be simply illustrated by the two half electrochemical reactions

Anode: $Cu - 2\ e^- \rightarrow Cu^{2+}$

Cathode: $O_2 + 4\ H^+ + 4\ e^- \rightarrow 2\ H_2O$

There are a lot of microelectrodes on the corroding copper surface. During the process of corrosion, more and more copper atoms are changed into ions and enter into solution, which results in a high copper(I) ion concentration in anodic domains. Simultaneously, the pH of the solutions in the cathodic domains becomes higher than that of the host solution. The diffusion of copper ions causes the slow crystallization of $[Cu_3(PO_4)_2{\cdot}2H_2O]$ and leads to the formation of the dandelions. As can be seen from Figures 1 (F), 4 (A), and 5, a core is formed in the initial stage of generation of the dandelion-like nanostructure, and because the cathodic domain is uniformly distributed in the solution, the dandelion grows at almost the same rate in all directions from the core.

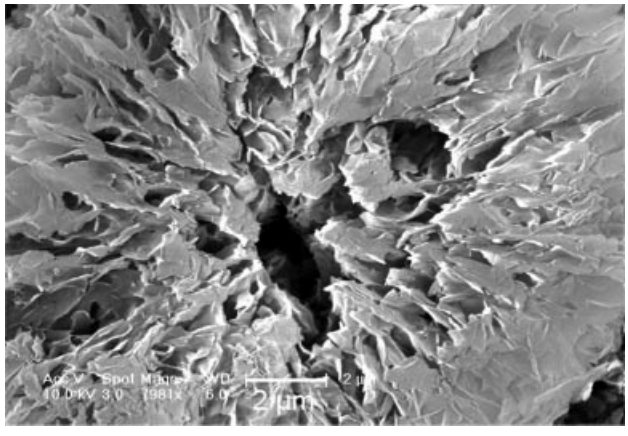

Figure 5. SEM image of a crushed dandelion bottom.

We found that the concentration of phosphorus acid ($C_{p.a.}$) can strongly affect the morphology of the dandelions. As is shown in Figure 6 (A), when $C_{p.a.}$ = 0.5 mM, small particles with sizes of 5–8 μm are formed that cover the copper surface sparsely. The shapes of the particles are irregular and an obvious number density gradient is observed. This is mainly due to the fact that the dioxygen concentration in the edge region is higher than that in the central region of the droplet. As $C_{p.a}$ was increased to 2 mM, the structures of dandelions became more regular and their sizes also increased to about 25 μm (Figure 6, B). As described above, the formation of the dandelions depends mainly on the concentration of the phosphate ions. Increasing the phosphorus acid concentration will therefore result in the formation of more and larger dandelions. When $C_{p.a}$ is higher than 10 mM, the sizes of the resulting dandelions no longer increase. In this case a large number of "nuclei" are generated and two neighboring dandelions expand and intermesh with each other to form an interconnected porous structure of nanosheets in their boundary region (Figure 6, C).[6,28,29] A further increase of $C_{p.a}$ makes the dandelions cover the whole copper surface compactly to form a lotus-like micro-nanostructure (Figure 6, D).

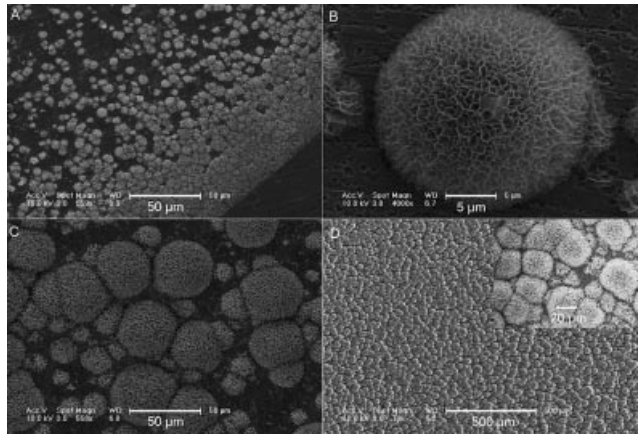

Figure 6. SEM images of the copper surface after drying of different phosphorus acid concentrations: A) 0.5 mM; B) 2 mM; C) 10 mM; D) 20 mM (droplet: 100 μL).

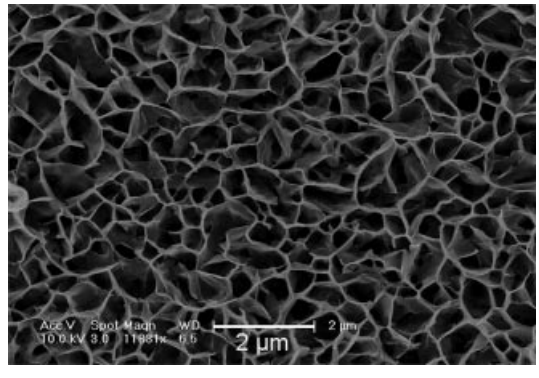

Figure 7. SEM images of the nanowalls. (100 μL of 2 mM aqueous phosphorus acid solution was dropped onto the surface of a piece of copper foil in a sealed box filled with oxygen gas at a temperature of 15–17 °C and humidity of 100% for 48 h. The foil was dried at 15 °C with a humidity of 30%).

 © 2005 Wiley-VCH Verlag GmbH & Co. KGaA, Weinheim

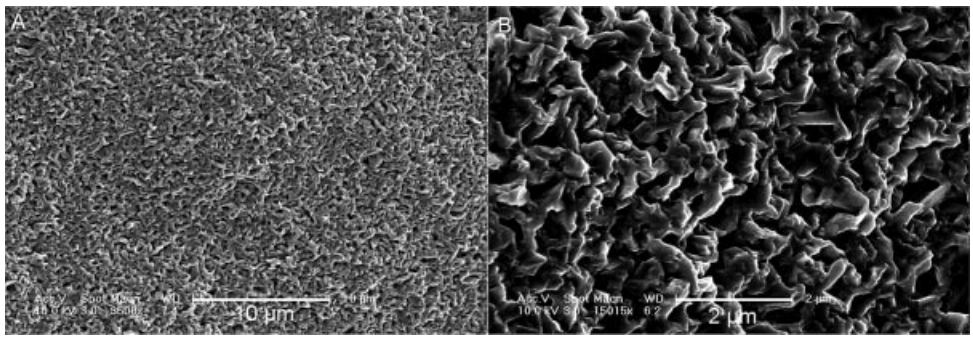

Figure 8. SEM images of the copper foil prepared from 50 mM H_3PO_4 heated at 650 °C for 6 h under nitrogen: A) overall view; B) magnified view.

It was interesting to find that control of the evaporation conditions can also change the morphology of the copper surface from 3D dandelions to 2D nanowalls. Figure 7 shows a typical image of copper phosphate dihydrates nanowalls formed by drop-drying 5 mM phosphoric acid on a copper foil surface in an environment with a humidity of 100% and at a temperature of15–17 °C. As can be seen from this figure, the nanosheets grow with their surfaces perpendicular to the copper surface and have a thickness of about 35 nm. The nanosheets intermesh with each other to form a porous film with a pore size ranging from 100 to 400 nm. In this case, the drying time is much longer than those described above and more nuclei are generated to form nanowalls.

When the film prepared from 50 mM H_3PO_4 was heated at 650 °C for 6 h under nitrogen and then cooled naturally to room temperature a nanoporous CuO film was produced. Figure 8 shows the SEM images of the as-prepared CuO film. Rod-like CuO particles intermesh with each other to form a porous film. It is clear from this figure that the original walls of the $[Cu_3(PO_4)_2{\cdot}2H_2O]$ nanostructures have collapsed. This is mainly due to the decomposition of copper phosphate dihydrate in the reaction that can be simply expressed as follow: $[Cu_3(PO_4)_2{\cdot}2H_2O] \rightarrow 3CuO + 2H_2O\uparrow + P_2O_5\uparrow$. The release of water and phosphorus pentoxide at temperatures higher than 400 °C destroys the framework of the copper phosphate dihydrate and results in the formation of a porous CuO film. The composition of the CuO film was confirmed by its EDS spectrum (Cu/O = 1:1; no phosphorus peak was observed). The composition of the film was also supported by its Raman spectrum (Figure 9): the bands at 301, 348, and 630 cm^{-1} correspond to the Ag, $Bg^{(1)}$, and $Bg^{(2)}$ modes of CuO crystals.[30]

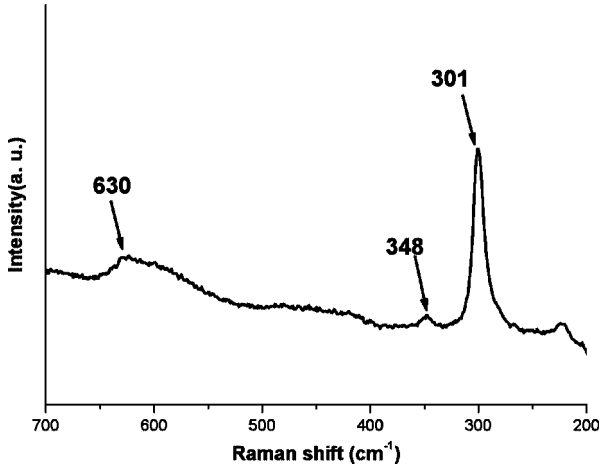

Figure 9. Raman spectrum of the as-prepared CuO film excited at 785 nm.

Conclusions

In summary, 3D dandelion-like porous nanostructures and 2D nanowalls of copper phosphate dihydrate built up of thin nanosheets can be fabricated by automatic drop-drying an aqueous solution of phosphoric acid on the surface of a copper foil under mild conditions. Controlling the initial concentration of the acid and the conditions of drop-drying can modulate the morphology of the nanostructures. The complex structure reported here brings new insights into understanding the mineralization mechanisms of nanostructured natural minerals. This work develops a simple, template-free method for fabricating high surface-to-volume ratio complex 3D nanostructures of metal-based materials. We believe this technique could be extended to fabricate 3D nanostructures of other materials by changing the solute or the substrate.

Experimental Section

Materials: Copper foil (99.9%, Shanghai Chemical Reagent Co. Ltd., Shanghai, China) with a thickness of 0.1 mm was polished with abrasive paper (1200 mesh), then cleaned with deionized water repeatedly and dried before each experiment. Phosphorous acid (analytical grade, Beijing Chemical Co. Ltd., Beijing, China) was used as received.

Preparation of $[Cu_3(PO_4)_2{\cdot}2H_2O]$ 3D Dandelions: Typically, in a sealed box (the bottom of the box was covered with allochroic silica gel) filled with dioxygen gas, 100 μL of aqueous phosphorus acid solution was dropped onto the surface of a piece of copper foil and dried automatically at a temperature of 15–17 °C. After the reaction, the copper foil was washed with deionized water and dried under vacuum at 40 °C overnight before characterization.

Preparation of $[Cu_3(PO_4)_2{\cdot}2H_2O]$ 2D Nanowall Films and CuO Nanoporous Films: Typically, a $[Cu_3(PO_4)_2{\cdot}2H_2O]$ 2D nanowall film

 © 2005 Wiley-VCH Verlag GmbH & Co. KGaA, Weinheim

was synthesized by putting a copper foil in an sealed box filled with dioxygen gas at a humidity of 100% and then dropping 100 μL of 2 mM aqueous phosphorus acid solution onto the foil surface and drying at a temperature of 15–17 °C for 48 h. Finally, the foil with the nanostructures was dried at 15 °C in an environment with a humidity of 30%. The CuO nanoporous film was produced by putting the copper foil covered with $[Cu_3(PO_4)_2{\cdot}2H_2O]$ nanostructures (fabricated from 50 mM H_3PO_4) into a furnace, heating to 650 °C for 6 h under nitrogen, and cooling naturally to room temperature.

Characterizations: Scanning electron micrographs (SEM) were taken with a FEI Sirion 200 or a S530 (Hitachi) scanning electron microscope. Ion concentrations were measured by using an inductively coupled plasma-atomic emission spectrometer (ICP-AES) model Vista-MP (Varian). X-ray diffraction (XRD) patterns were obtained with a D8 Advance (Bruker) X-ray diffractometer. X-ray photoelectron spectra (XPS) were recorded with an AEM PHI5300 (PE) photoelectron spectrometer. Raman spectra were recorded with a RM 2000 microscopic confocal Raman spectrometer (Renishaw PLC., England) employing a 633- or 785-nm laser beam and a CCD detector with 4 cm^{-1} resolution. The spectra were obtained by focusing a 10-μm laser spot on the sample using a 20 objective and accumulated three times for 30 s each. The powers were always kept very low (≈ 0.05 mW) to avoid destruction of the samples.

Acknowledgments

This research was supported by the National Natural Science Foundation of China (90401011, 20374034, 50225311, 50533030) and the 973 Project (2003CB615700).

[1] H. T. Ng, J. Li, M. K. Smith, P. Nguyen, A. Cassell, J. Han, M. Meyyappan, *Science* **2003**, *300*, 1249–1249.
[2] A. C. Chen, X. S. Peng, K. Koczkur, B. Miller, *Chem. Commun.* **2004**, *17*, 1964–1965.
[3] J. Goldberger, R. R. He, Y. F. Zhang, S. K. Lee, H. Q. Yang, H. J. Choi, P. D. Yang, *Nature* **2003**, *422*, 599–602.
[4] Y. L. Hou, S. Gao, T. Ohta, H. Kondoh, *Eur. J. Inorg. Chem.* **2004**, *6*, 1169–1173.
[5] J. Y. Lao, J. Y. Huang, D. Z. Wang, Z. F. Ren, *Nano Lett.* **2003**, *3*, 235–238.
[6] Z. P. Zhang, X. Q. Shao, H. D. Yu, Y. B. Wang, M. Y. Han, *Chem. Mater.* **2005**, *17*, 332–336.
[7] B. Y. Zong, Y. H. Wu, G. C. Han, B. J. Yang, P. Luo, L. Wang, J. J. Qiu, K. B. Li, *Chem. Mater.* **2005**, *17*, 1515–1520.
[8] B. Liu, H. C. Zeng, *J. Am. Chem. Soc.* **2004**, *126*, 8124–8125.
[9] B. Liu, H. C. Zeng, *J. Am. Chem. Soc.* **2004**, *126*, 16744–16746.
[10] F. S. Xiao, J. M. Sun, X. J. Meng, R. B. Yu, R. R. Xu, *J. Catal.* **2001**, *199*, 273–281.
[11] F. S. Xiao, J. M. Sun, X. J. Meng, R. B. Yu, H. M. Yuan, D. Z. Jiang, R. R. Xu, *Appl. Catal. A: General* **2001**, *207*, 267–271.
[12] X. J. Meng, F. S. Xiao, *Acta Phys.-Chim. Sin.* **2004**, *20*, 939–945.
[13] R. Rodríguez-Clemente, C. J. Serna, M. Ocaña, E. Matijević, *J. Cryst. Growth* **1994**, *143*, 277–286.
[14] G. H. Du, G. H. Van Tendeloo, *Chem. Phys. Lett.* **2004**, *393*, 64–69.
[15] C. H. Lu, L. M. Qi, J. H. Yang, D. Y. Zhang, N. Z. Wu, J. M. Ma, *J. Phys. Chem. B* **2004**, *108*, 17825–17831.
[16] X. Y. Song, S. X. Sun, W. M. Zhang, H. Y. Yu, W. L. Fan, *J. Phys. Chem. B* **2004**, *108*, 5200–5205.
[17] X. G. Wen, W. X. Zhang, S. H. Yang, *Nano Lett.* **2002**, *2*, 1397–1401.
[18] X. G. Wen, W. X. Zhang, S. H. Yang, *Langmuir* **2003**, *19*, 5898–5903.
[19] A. H. MacDonald, *Nature* **2001**, *414*, 409–410.
[20] C. Macilwain, *Nature* **2000**, *403*, 121–122.
[21] J. Z. Xu, J. J. Zhu, H. Wang, H. Y. Chen, *Anal. Lett.* **2003**, *36*, 2723–2733.
[22] K. Nakaoka, J. Ueyama, K. Ogura, *J. Electrochem. Soc.* **2004**, *151*, C661–C665.
[23] H. C. Lichtenegger, T. Schoberl, M. H. Bartl, H. Waite, G. D. Stucky, *Science* **2002**, *298*, 389–392.
[24] V. A. Kopilevich, L. N. Shchegrov, *Russ. J. Inorg. Chem. (Engl. Trans.)* **1987**, *32* 1264–1266.
[25] John F. Moulder, *Handbook of X-ray Photoelectron Spectroscopy*, Perkin–Elmer Physical Electronics Division, **1992**.
[26] R. L. Frost, T. Kloprogge, P. A. Williams, W. Martens, T. E. Johnson, P. Leverett, *Spectrochim. Acta, Part A* **2002**, *58*, 2861–2868.
[27] R. L. Frost, P. A. Williams, W. Martens, J. T. Kloprogge, P. Leverett, *J. Raman Spectrosc.* **2002**, *33*, 260–263.
[28] R. C. Jin, Y. C. Cao, C. A. Markin, K. L. Kelly, G. C. Schatz, J. G. Zheng, *Science* **2001**, *294*, 1901–1903.
[29] M. Gross, *Eur. J. Inorg. Chem.* **2003**, *39*, 33–35.
[30] T. Yu, X. Zhao, Z. X. Shen, Y. H. Wu, W. H. Su, *J. Cryst. Growth* **2004**, *268*, 590–595.

Received: May 8, 2005
Published Online: October 17, 2005

 © 2005 Wiley-VCH Verlag GmbH & Co. KGaA, Weinheim

DOI: 10.1002/ejic.200500420

Cyclometalated Ruthenium Compounds Containing 2-(2′-Pyridyl)-4-methylphenyl and Benzo[*h*]quinolyl Ligands

Qian-Feng Zhang,[a] Ka-Man Cheung,[a] Ian D. Williams,[a] and Wa-Hung Leung*[a]

Keywords: Ruthenium / Cyclometalated ligands / Organometallic compounds / Transition metals

Transmetalation of $Hg(ptpy)_2$ [Hptpy = 2-(4-tolylpyridine) with $Cp^*Ru(NO)Cl_2$ ($Cp^* = \eta^5$-C_5Me_5)] gave $[Cp^*Ru(NO)(ptpy)]_2[Hg_2Cl_6]$ ($[\mathbf{1}]_2{\cdot}Hg_2Cl_6$) whereas that with $[Cp^*RuCl_2]_x$ gave the dinuclear Ru^{II}–Ru^{IV} compound $[Cp^*Ru(\mu\text{-}\eta^6{:}\eta^2\text{-}ptpy)RuCl_2Cp^*][Hg_2Cl_6]$ (**2**). Treatment of Ru(3-phenylindenylid-1-ene)$Cl_2(PPh_3)_2$ with $Hg(ptpy)_2$ resulted in coupling of ptpy with the 3-phenylidenylid-1-ene ligand, and the formation of Ru(Ph-ind-ptpy)$(PPh_3)Cl$ {Ph-ind-tpy = 3-phenyl-1-[2-(4-toyl)pyridyl]indenyl} (**3**), in which the chelated [Ph-ind-tpy]$^-$ ligand binds to Ru through the η^5-indenyl ring and the pendant pyridyl group. Treatment of $[Ru(CO)_2Cl_2]_n$ with $[Hg(ptpy)Cl]_2$ afforded $[Ru(ptpy)(CO)_2]_2(\mu\text{-}Cl)_2$ (**8**). Irradiation of *cis*-$[Ru(bzq)_2(CO)_2]$ (Hbzq = benzo[*h*]quinoline) with UV light in MeCN afforded *cis*-$[Ru(bzq)_2(CO)(MeCN)]$ (**9**). Photolysis of *cis*-$[Ru(bzq)_2(CO)_2]$ in THF in the presence of PPh_3 and pyridine (py) afforded *cis*-$[Ru(bzq)_2(CO)(L)]$ [L = PPh_3 (**10**), py (**11**)]. The crystal structures of complexes **1**–**3**, **8**, and **10** have been determined.
(© Wiley-VCH Verlag GmbH & Co. KGaA, 69451 Weinheim, Germany, 2005)

Introduction

Transition-metal complexes containing cyclometalated N^C ligands, notably 2-phenylpyridine (ppy), have attracted much attention because of their interesting photoluminescent properties[1] and their potential applications in organic synthesis[2] and bioinorganic chemistry.[3,4] Of note are cyclometalated Ir^{III} complexes, which have been used as phosphorescent dopants for organic light-emitting diodes,[5] chemical sensors,[6] and luminescent labels for biomolecules.[7] While the coordination chemistry of cyclometalated Ir^{III} compounds of the types $[Ir(ppy)_3]$ and $[Ir(ppy)_2(L)(X)]$[1,8–10] is well developed, the isoelectronic Ru^{II} analogues have received less attention.[9,10] This is in sharp contrast with cationic Ru^{II} complexes with 2,2′-bipyridyl (bpy) and polypyridyl ligands that exhibit rich redox- and photochemistry.[11] Owing to the anionic nature of ppy$^-$, it is anticipated that high-valence Ru–ppy complexes are more easily accessible than the bpy analogues. Recently, electron-rich Ru^{II} cyclometalated complexes have been used as mediators for electron transfer with horseradish peroxidase and glucose oxidase.[3]

To date, the most extensively explored Ru–ppy complexes are those supported by polypyridyl ligands.[12] Cyclometalated Ru^{II} N^C complexes containing η^6-arene[13] and phosphane[14,15] co-ligands have also been synthesized. These complexes were generally prepared by either transmetalation with organomercurials or direct cycloruthenation of N^CH ligands. In contrast to $[M(ppy)_2]^+$ (M = Rh, Ir), Ru^{II} bis-cyclometalated complexes are rather rare, the only structurally characterized example being *cis*-$[Ru(bzq)_2(CO)_2]$ (Hbzq = benzo[*h*]quinoline).[16] As part of our continuing effort to explore the organometallic chemistry of high-valence Ru complexes, we set out to investigate the transmetalation between $Hg(ptpy)_2$ [Hptpy = 2-(4-tolyl)-pyridine] and a variety of organoruthenium chloride compounds. Herein, we report on the syntheses and crystal structures of some cyclometalated ruthenium compounds containing the ptpy ligand. Furthermore, in order to prepare new Ru bis-cyclometalated complexes, photosubstitution of *cis*-$[Ru(bzq)_2(CO)_2]$ with two-electron ligands has been studied.

Results and Discussion

Cyclometalated Ru Cp* Complexes

Treatment of $Cp^*Ru(NO)Cl_2$ with $Hg(ptpy)_2$ in refluxing THF gave $[Cp^*Ru(ptpy)(NO)]_2[Hg_2Cl_6]$ ($[\mathbf{1}]_2{\cdot}[Hg_2Cl_6]$). Anion metathesis of $[\mathbf{1}]_2{\cdot}[Hg_2Cl_6]$ with $NaPF_6$ in acetone afforded Hg-free $[Cp^*Ru(ptpy)(NO)][PF_6]$ ($\mathbf{1}[PF_6]$) (Scheme 1). The formation of the chloromercurate anion $[Hg_2Cl_6]^{2-}$ from $HgCl_2$ and chloride salts is well documented.[13c,17,18] It may be noted that Djukic et al. previously reported that treatment of $[(\eta^6\text{-}p\text{-cymene})RuCl_2]_2$ with Hg(ppy)Cl afforded $[(\eta^6\text{-}p\text{-cymene})Ru(ppy)Cl]{\cdot}HgCl_2$.[13c] The IR spectrum of $[\mathbf{1}]_2{\cdot}[Hg_2Cl_6]$ shows the N–O band at about 1780 cm^{-1}, which is higher than that for $[Cp^*Ru(NO)Ph_2]$ (1755 cm^{-1}).[19] The structure of $[\mathbf{1}]_2{\cdot}[Hg_2Cl_6]$ has been established by an X-ray diffraction study. The $[Hg_2Cl_6]^{2-}$

[a] Department of Chemistry, The Hong Kong University of Science and Technology,
Clear Water Bay, Kowloon, Hong Kong, P.R. China
Fax: +852-2358-1594
E-mail: chleung@ust.hk

 © 2005 Wiley-VCH Verlag GmbH & Co. KGaA, Weinheim

anion lies on a twofold rotation axis between two $[Cp^*Ru(ptpy)(NO)]^+$ cations. The molecular structure of the cation $[\mathbf{1}]^+$ is shown in Figure 1. The Ru–C(ptpy) [2.080(4) Å] and Ru–N [2.097(4) Å] distances and C(21)–Ru(1)–N(10) angle [77.95(17)°] in $\mathbf{1}^+$ are similar to those in $[(\eta^6\text{-}p\text{-cymene})Ru(ppy)Cl]\cdot HgCl_2$.[13c] The Ru–NO distance of 1.751(4) Å is shorter than that in $[Ru(ppy)(tpy)(NO)][PF_6]$ (tpy = 2,2′:6′,6′′-terpyridine) [1.826(4) Å],[12d] indicating the strong Ru–to-NO π-backbonding in $\mathbf{1}^+$. The N–O distance of 1.146(5) Å and the Ru–N–O angle of 174.4(4)° are normal by comparison with other linear nitrosyl compounds.[20]

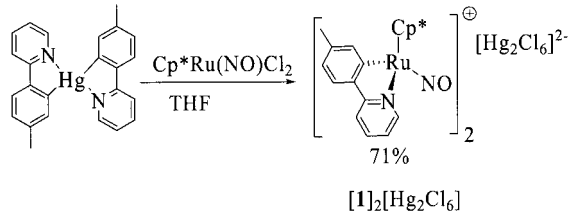

Scheme 1. Synthesis of $[\mathbf{1}]_2\cdot[Hg_2Cl_6]$.

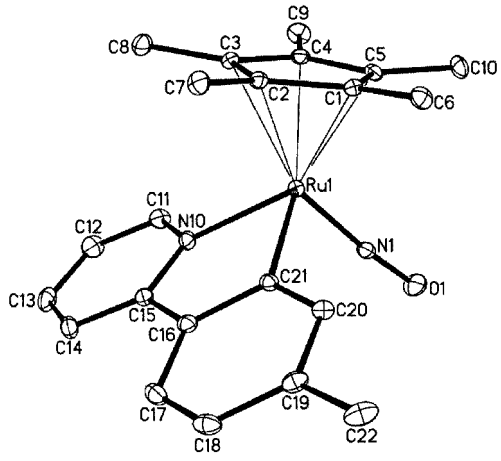

Figure 1. Perspective view of the cation $[Cp^*Ru(ptpy)(NO)]^+$ (displacement ellipsoids drawn at the 50% probability level). Selected bond lengths [Å] and angles [°]: Ru–Cp*(centroid) 1.898(3), Ru(1)–N(1) 1.751(4), Ru(1)–N(10) 2.097(4), Ru(1)–C(21) 2.080(4), N(1)–O(1) 1.146(5); N(10)–Ru(1)–C(21) 78.0(2), N(1)–Ru(1)–N(10) 99.9(2), N(1)–Ru(1)–C(21) 94.5(2), Ru(1)–N(1)–O(1) 174.4(4).

Treatment of $[Cp^*RuCl_2]_x$ with $[Hg(ptpy)_2]$ afforded a dark green material from which air-stable dark crystals characterized as $[Cp^*Ru(\mu\text{-}ptpy)RuCp^*Cl_2]_2[Hg_2Cl_6]$ (**2**) were isolated (Scheme 2). The ^1H NMR spectrum shows two Cp* signals at δ = 1.87 and 1.99 ppm, consistent with the solid-state structure. Upon binding to the Cp^*Ru^{II} fragment the resonant signals for the tolyl ring of the ptpy ligand are shifted to the upfield region (δ = 4.86–5.36 ppm; cf. δ = 7.40–7.72 ppm for $\mathbf{1}^+$). The identity of **2** has been established by a single-crystal X-ray diffraction study (Figure 2). The molecular structure of the cation $[Cp^*Ru(\mu\text{-}ptpy)RuCp^*Cl_2]^+$ in **2** consists of a $[Cp^*Cl_2Ru^{IV}(ptpy)]^+$ moiety, the 4-tolyl ring of which binds to the Cp^*Ru^{II} fragment in an η^6 fashion. It may be noted that a related bimetallic complex, $[(CO)_3Cr(\mu\text{-}ppy)Ru(\eta^6\text{-}p\text{-cymene})Cl]$, which contains a $\mu\text{-}\eta^2\text{:}\eta^6$-ppy ligand, has been synthesized recently.[13c] The geometry around Ru^{IV} in **2** is four-legged piano-stool whereas the Ru^{II}-containing moiety has a sandwich structure. The 4-tolyl and pyridine rings of the ptpy ligand are not coplanar, with a dihedral angle of about 12.3°. Cyclometalated Ru^{IV} complexes are rare. To the best of our knowledge, the only structurally characterized Ru^{IV} ppy complex is the mixed-valence Ru^{III}–Ru^{IV} compound $[\{Ru(ppy)(phen)Cl\}_2(\mu\text{-}O)][PF_6]$ (phen = 1,10-phenanthroline).[12e] The Ru^{IV}–Cp*(centroid) distance in **2** of 1.912(3) Å is comparable to reported Cp^*Ru^{IV} compounds (e.g. 1.916(4) Å for $[Cp^*Ru(\eta^2\text{-}Se_2P\mathit{i}Pr_2)(\eta^2\text{-}SeP\mathit{i}Pr_2)][PF_6]$),[21] but is obviously longer than the Ru^{II}–Cp*(centroid) distance [1.717(2) Å]. The Ru^{IV}–N and Ru^{IV}–C(ptpy) distances [2.132(7) and 2.081(8) Å, respectively] in **2** are similar to those in $\mathbf{1}^+$. The average Ru^{IV}–Cl distance of 2.417(2) Å is slightly longer than that of $[Cp^*Ru^{IV}Cl_2]_2[\mu\text{-}O]$ [2.356(8) Å].[22]

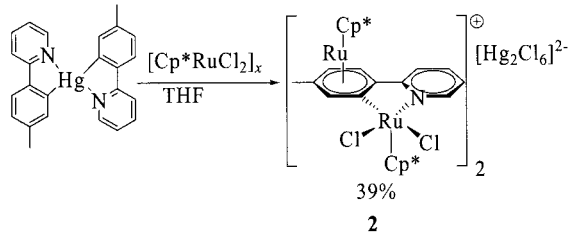

Scheme 2. Synthesis of **2**.

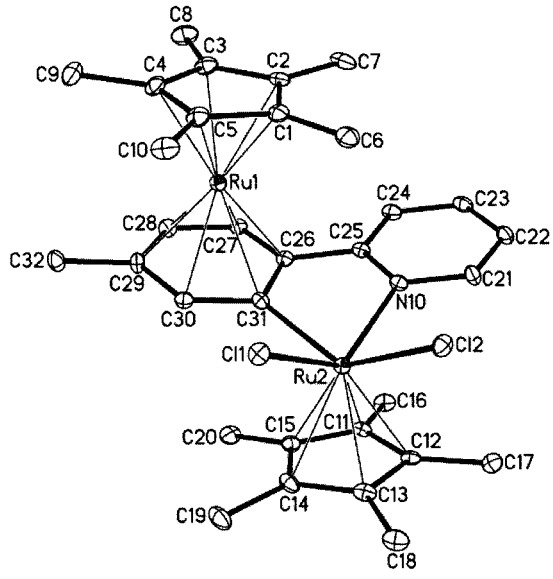

Figure 2. Perspective view of the cation $[Cp^*Ru(\mu\text{-}ptpy)RuCp^*Cl_2]^+$ (displacement ellipsoids drawn at the 50% probability level). Selected bond lengths [Å] and angles [°]: Ru(1)–Cp*(centroid) 1.717(2), Ru(1)–tolyl(centroid) 1.810(2), Ru(2)–N(10) 2.132(7), Ru(2)–C(31) 2.291(8), Ru(2)–Cl(1) 2.429(2), Ru(2)–Cl(2) 2.405(2), Ru(2)–Cp*(centroid) 1.912(3); N(10)–Ru(2)–C(31) 75.7(3), N(10)–Ru(2)–Cl(1) 129.1(2), N(10)–Ru(2)–Cl(2) 84.5(2), C(31)–Ru(2)–Cl(1) 82.1(2), C(31)–Ru(2)–Cl(2) 134.4(2), Cl(1)–Ru(2)–Cl(2) 79.40(7).

 © 2005 Wiley-VCH Verlag GmbH & Co. KGaA, Weinheim

Transmetalation of [Hg(ptpy)$_2$] with Ru Carbene

Attempts to synthesize cyclometalated Ru complexes containing metal–carbon multiple bonds starting from Ru carbene and vinylidene species such as Ru(=CHPh)(PCy_3)$_2$Cl$_2$ and Ru(=C=CHPh)(PCy_3)$_2$Cl$_2$ were unsuccessful. In most cases, dark intractable materials were obtained. However, treatment of Ru(3-phenylindenylid-1-ene)(PPh_3)$_2$Cl$_2$ with Hg(ptpy)$_2$ afforded an air-stable crystalline product that has been characterized as Ru(Ph-ptpy-ind)(PPh_3)Cl (**3**) (Ph-ptpy-ind = η^5:κ*N*-3-phenyl-1-[2-(2-pyridyl)-4-tolyl]indenyl). It seems likely that **3** was formed by insertion of the indenylid-1-ene group into the Ru–C(ptpy) σ-bond. The insertion of carbene group into the M–C(N^C) bonds in M(N^C)(CO)$_4$ (M = Mn, Re) has been studied in detail by Djukic, Dötz, and Pfeffer and their co-workers.[23,24] It was found that treatment of Mn(CO)$_4$(ppy) with PhLi followed by addition of MeOTf led to insertion of the carbene ligand C(Ph)(OMe) into the Mn–C(ppy) bond and the formation of a η^3-benzyltricarbonyl Mn^I complex **4** (Scheme 3).[23a] On the other hand, thermolysis of Mn(CO)$_4$(Me-ppy) in the presence of 7-diazofluorene resulted in the insertion of the *exo*-alkylidene group into the Mn–C(ppy) bond. Subsequent cleavage of the Mn–N bond coupled with a series of haptotropic ring slippages afforded the Mn^I η^5-fluorenyl complex **5** (Scheme 4).[23e] On the basis of these results, we propose that the transmetalation of Ru(3-phenylindenylid-1-ene)(PPh_3)$_2$Cl$_2$ with Hg(ppy)$_2$ initially afforded a Ru^{II} indenylid-1-ene intermediate **6** (Scheme 5). Insertion of the indenylid-1-ene ligand into the Ru–C bond in **6** followed by haptotropic ring shifts, possibly via an η^3-allyl intermediate **7**, afforded **3**. Unlike the Mn(CO)$_4$(N^C) system, in which arenes tethered with cymantranes were formed,[23e] insertion of indenylidene into the Ru–C(ppy) bond led to formation of a chelated η^5-indenyl-ppy ligand, presumably because the PPh_3 ligand in **3** can be dissociated more easily than the carbonyl in the Mn counterparts.

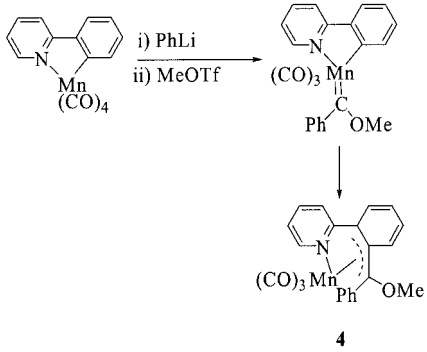

4

Scheme 3. Insertion of carbene into the Mn–C(ppy) bond.[23a]

The $^{31}P\{^1H\}$ NMR spectrum of **3** shows a singlet at δ = 33.1 ppm due to the PPh_3 ligand. The solid-state structure of **3** is shown in Figure 3. Similar to other Ru^{II} indenyl complexes, the Ru–C distances involving the bridging carbon atoms C(25) and C(29) [2.354(3) and 2.307(3) Å] are longer than those for C(26), C(27), and C(28) [2.105(3)–2.196(3) Å]. The Ru–P distance [2.2690(8) Å] is similar to

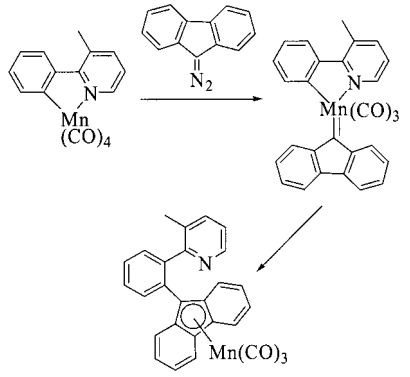

5

Scheme 4. Reaction of Mn(CO)$_4$(Me-ppy) with 7-diazofluorene.[23e]

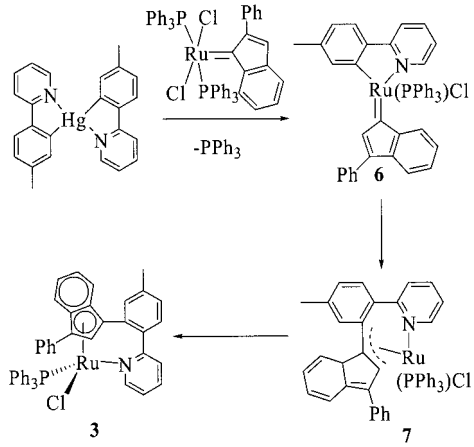

Scheme 5. Proposed mechanism for the formation of **3**.

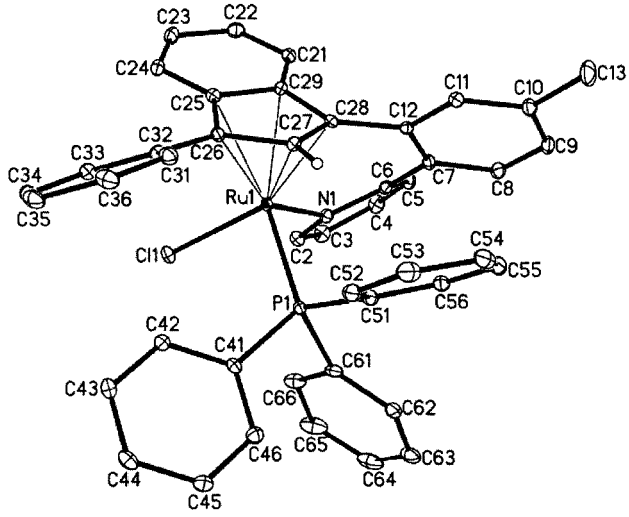

Figure 3. Perspective view of [Ru(Ph-ind-ptpy)(PPh_3)Cl] (**3**) (displacement ellipsoids drawn at the 50% probability level). Selected bond lengths [Å] and angles [°]: Ru–indenyl(centroid) 1.849(3), Ru(1)–C(25) 2.354(3), Ru(1)–C(26) 2.196(3), Ru(1)–C(27) 2.125(3), Ru(1)–C(28) 2.105(3), Ru(1)–C(29) 2.307(3), Ru(1)–N(1) 2.169(3), Ru(1)–P(1) 2.2690(8), Ru(1)–Cl(1) 2.4575(8); Cl(1)–Ru(1)–N(1) 93.56(7), Cl(1)–Ru(1)–P(1) 93.30(3), N(1)–Ru(1)–P(1) 95.88(7).

 © 2005 Wiley-VCH Verlag GmbH & Co. KGaA, Weinheim

that in $[Ru(CO)(PPh_3)_2(\eta^5\text{-}C_9H_7)][ClO_4]$ [2.273(3) Å].[25] The pendant ptpy substituent of the indenyl group is significantly twisted and nonplanar with a dihedral angle between the 4-tolyl and pyridyl rings of about 36.8°.

Cyclometalated Ru Carbonyl Complexes

Treatment of $[Ru(CO)_2Cl_2]_x$ with $Hg(ptpy)_2$ afforded a yellow compound characterized as *cis*-$[Ru(ptpy)(CO)_2]_2(\mu\text{-}Cl)_2$ (**8**) in 18% yield. A higher yield (62%) of **8** was obtained when $[Hg(ptpy)(\mu\text{-}Cl)]_2$ was employed as the transmetalating agent (Scheme 6). The cyclometalated azobenzene analogue, $[Ru(N\text{^}C)(CO)_2Cl]_2$ (N^CH = azobenzene), has been previously prepared by Bruce et al.[26] The IR spectrum of **6** shows $\nu(C{\equiv}O)$ at 2039 and 2104 cm^{-1}, indicative of the *cis* geometry of the carbonyl ligands. The molecular structure of **8** consisting of two symmetry-related $Ru(ptpy)(CO)_2Cl$ fragments is shown in Figure 4. The geometry around Ru is pseudo-octahedral, with the *cis*-disposed CO ligands opposite the pyridyl ring and chloride. The Ru–C(ptpy) distance [2.048(6) Å] in **8** is shorter than that in *cis*-$[Ru(bzq)_2(CO)_2]$ [2.161(5) Å],[16] in which both the Ru–C(bzq) bonds are *trans* to CO. The Ru–CO distances [1.888(7) and 1.830(7) Å] in **8** are comparable to those in *cis*-$[Ru(bzq)_2(CO)_2]$ [1.87(1) and 1.81(1) Å].[16b] The Ru–Cl(*trans* to 4-tolyl) [2.542(2) Å] is longer than Ru–Cl(*trans* to CO) [2.465(2) Å], suggesting that the σ 4-tolyl group has a stronger *trans* influence than carbonyl.

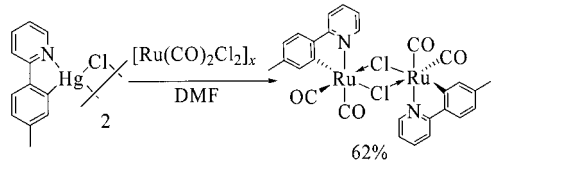

Scheme 6. Synthesis of **8**.

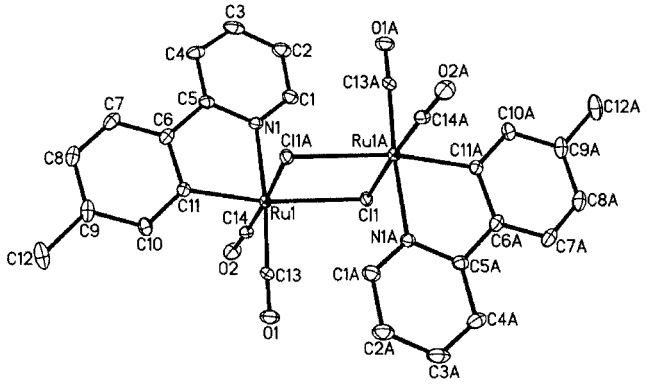

Figure 4. Perspective view of *cis*-$[Ru(ptpy)(CO)_2]_2(\mu\text{-}Cl)_2$ (**8**) (displacement ellipsoids drawn at the 50% probability level). Selected bond lengths [Å] and angles [°]: Ru(1)–C(11) 2.048(6), Ru(1)–N(1) 2.139(5), Ru(1)–C(13) 1.888(7), Ru(1)–C(14) 1.830(7), Ru(1)–Cl(1) 2.542(2), Ru(1)–Cl(1A) 2.465(2); C(14)–Ru(1)–C(13) 88.0(3), C(14)–Ru(1)–C(11) 87.7(3), C(13)–Ru(1)–C(11) 94.5(3), C(14)–Ru(1)–N(1) 92.7(2), C(13)–Ru(1)–N(1) 174.5(2), C(11)–Ru(1)–N(1) 80.1(2), C(14)–Ru(1)–Cl(1A) 175.8(2), C(13)–Ru(1)–Cl(1A) 91.1(2), C(11)–Ru(1)–Cl(1A) 88.3(2), N(1)–Ru(1)–Cl(1A) 88.0(1), C(14)–Ru(1)–Cl(1) 101.1(2), C(13)–Ru(1)–Cl(1) 92.3(2), C(11)–Ru(1)–Cl(1) 169.1(2), N(1)–Ru(1)–Cl(1) 93.0(2), Cl(1A)–Ru(1)–Cl(1) 83.00(5), Ru(1A)–Cl(1)–Ru(1) 97.00(5) (symmetry code: $-x + 1, -y, -z + 1$).

Photosubstitution of *cis*-$[Ru(bzq)_2(CO)_2]$

Attempts to prepare Ru^{II} bis-cyclometalated complexes by treatment of $[Ru(CO)_2Cl_2]_x$ with excess $[Hg(ptpy)(\mu\text{-}Cl)]_2$ were unsuccessful. We then turned our attention to substitution of the reported compound *cis*-$Ru(bzq)_2(CO)_2$ with Lewis bases. Prolonged reaction of *cis*-$[Ru(bzq)_2(CO)_2]$ with excess PPh_3 in refluxing DMF afforded the mono carbonyl compound *cis*-$[Ru(bzq)_2(CO)(PPh_3)]$ in low yield (about 7%). The substitution of *cis*-$[Ru(bzq)_2(CO)_2]$ was found to be accelerated by UV light. Photolysis of *cis*-$[Ru(bzq)_2(CO)_2]$ in THF at room temperature afforded a highly air-sensitive, yellow species, presumably $Ru(bzq)_2(CO)(THF)$, which exhibited a C–O band at 2000 cm^{-1} in the IR spectrum. The MeCN adduct *cis*-$[Ru(bzq)_2(CO)(MeCN)]$ (**9**) was prepared similarly by photolysis of *cis*-$[Ru(bzq)_2(CO)_2]$ in MeCN and isolated as an air-sensitive red solid. Photosubstitution of *cis*-$[Ru(bzq)_2(CO)_2]$ with PPh_3 in THF afforded *cis*-$[Ru(bzq)_2(CO)(PPh_3)]$ (**10**) (Scheme 7). Compound **10** could also be prepared in good yield from **9** and PPh_3. An X-ray diffraction study revealed that the photosubstitution of *cis*-$[Ru(bzq)_2(CO)_2]$ led to a change in the stereochemistry of the complex. The two Ru–C(bzq) σ-bonds that are *trans* to each other in *cis*-$[Ru(bzq)_2(CO)_2]$ become mutually *cis* in **10** (vide infra). Similarly, the pyridine (py) adduct $Ru(bzq)_2(CO)(py)$ (**11**) was prepared by photosubstitution of *cis*-$[Ru(bzq)_2(CO)_2]$ with pyridine in THF. An attempt to prepare the bis-pyridine complex $Ru(bzq)_2(py)_2$ by photolysis of *cis*-$[Ru(bzq)_2(CO)_2]$ in neat pyridine was unsuccessful. Unlike **9** and **11**, **10** is air stable in both solutions and the solid state. The solid-state structure of **10** is shown in Figure 5. In contrast to *cis*-$[Ru(bzq)_2(CO)_2]$, both the Ru–N and Ru–C bonds for the bzq ligands adopt the *cis* arrangement. The Ru–C(bzq) [2.088(9) and 2.033(8) Å], Ru–N [2.157(7) and 2.194(7) Å], and Ru–CO [1.84(1) Å] distances in **10** are similar to those in *cis*-$[Ru(bzq)_2(CO)_2]$ [Ru–C(bzq) 2.13(1) and 2.12(1) Å, Ru–N 2.148(8) and 2.161(9) Å, Ru–CO 1.81(1) and 1.87(1) Å].[16b]

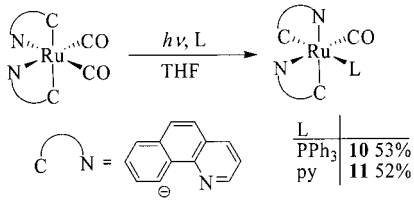

Scheme 7. Photosubstitution of *cis*-$[Ru(bzq)_2(CO)_2]$.

Attempts to prepare bis-cyclometalated Ru carbene species by reactions of **9** with alkynes and alkynols were unsuccessful. Treatment of **9** in THF with ethyl diazoacetate (EDA) resulted in a brown solution, which possibly contained a Ru carbene species given its ability in carbene

 © 2005 Wiley-VCH Verlag GmbH & Co. KGaA, Weinheim

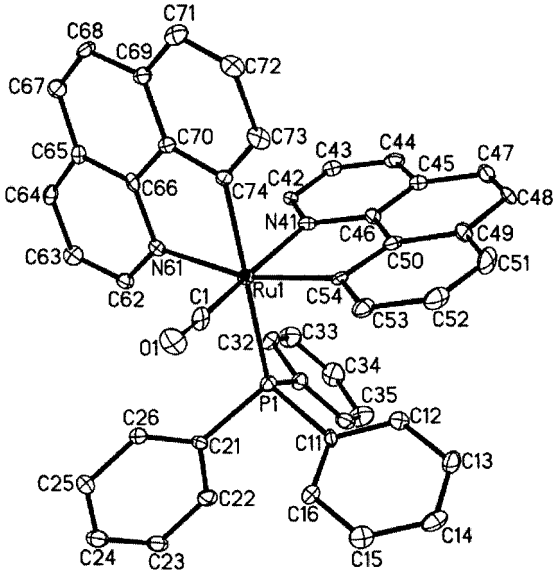

Figure 5. Perspective view of *cis*-[Ru(bzq)$_2$(CO)(PPh$_3$)] (**10**) (displacement ellipsoids drawn at the 50% probability level). Selected bond lengths [Å] and angles [°]: Ru(1)–C(1) 1.84(1), Ru(1)–C(54) 2.033(8), Ru(1)–C(74) 2.088(9), Ru(1)–N(41) 2.157(7), Ru(1)–N(61) 2.194(7), Ru(1)–P(1) 2.385(3), C(1)–O(1) 1.14(1); C(1)–Ru(1)–C(54) 90.3(4), C(1)–Ru(1)–C(74) 87.9(4), C(54)–Ru(1)–C(74) 89.0(3), C(1)–Ru(1)–N(41) 168.7(3), C(54)–Ru(1)–N(41) 80.0(3), C(74)–Ru(1)–N(41) 86.2(3), C(1)–Ru(1)–N(61) 98.7(3), C(54)–Ru(1)–N(61) 165.0(3), C(74)–Ru(1)–N(61) 79.4(3), N(41)–Ru(1)–N(61) 89.7(3), C(1)–Ru(1)–P(1) 92.2(3), C(54)–Ru(1)–P(1) 91.6(3), C(74)–Ru(1)–P(1) 179.4(3), N(41)–Ru(1)–P(1) 93.8(2), N(61)–Ru(1)–P(1) 100.1(2), O(1)–C(1)–Ru(1) 173.8(9).

transfer (vide infra). Unfortunately, no crystalline products were isolated from the brown reaction mixture. A preliminary result showed that **9** is an active catalyst for cyclopropanation of styrene. For example, treatment of styrene with EDA in the presence of 5 mol-% of **9** afforded 2-phenylcyclopropane carboxylate in 76% yield along with a small amount of the homo-coupling product $C_2H_2(CO_2Et)_2$ (<5%). At present, efforts are being made to isolate the reactive cyclometalated Ru carbene species.

Conclusions

In summary, we have studied the transmetalation of [Hg(ptpy)$_2$] with a variety of organoruthenium compounds. Treatment of [Hg(ptpy)$_2$] with [Cp*RuCl$_2$]$_x$ afforded a mixed-valence Ru^{II}–Ru^{IV} complex that contains a μ-η^6:η^2 ptpy ligand. Transmetalation of [Hg(ptpy)$_2$] with [Ru(3-phenylindenylid-1-ene)(PPh$_3$)$_2$Cl$_2$] resulted in coupling of the carbene and the ptpy ligand and the formation of a Ru^{II} complex with a η^5:κ*N*-Ph-ind-ptpy ligand. The bis-cyclometalated Ru monocarbonyl complexes *cis*-[Ru(bzq)$_2$(CO)L] were prepared by photosubstitution of *cis*-[Ru(bzq)$_2$(CO)$_2$] with L (MeCN, PPh$_3$, and py).

Experimental Section

General: All manipulations were carried out under nitrogen by standard Schlenk techniques. Solvents were purified, distilled, and degassed prior to use. NMR spectra were recorded with a Bruker ALX 300 spectrometer operating at 300 and 121.5 MHz for ^{1}H and ^{31}P, respectively. Chemical shifts (δ, ppm) were reported with reference to SiMe$_4$ (^{1}H) and H$_3$PO$_4$ (^{31}P). Infrared spectra were recorded with a Perkin–Elmer 16 PC FT-IR spectrophotometer, and mass spectra with a Finnigan TSQ 7000 spectrometer. Elemental analyses were performed by Medac Ltd., Surrey, UK.

The compounds [Cp*RuCl$_2$]$_x$,[27] [Cp*Ru(NO)Cl$_2$][28] (Cp* = η^5-C$_5$Me$_5$), [Ru(3-phenylindenylid-1-ene)(PPh$_3$)$_2$Cl$_2$],[29] *cis*-[Ru(bzq)$_2$(CO)$_2$],[16a] [Hg(ptpy)$_2$], and [Hg(ptpy)(μ-Cl)]$_2$[30] were synthesized according to literature methods. Hydrogen atom labeling schemes for cyclometalated ptpy$^-$ and bzq$^-$ ligands are shown below.

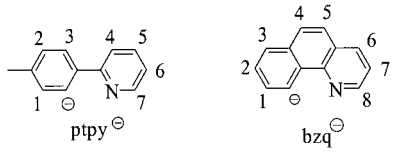

[Cp*Ru(ptpy)(NO)]$_2$[Hg$_2$Cl$_6$] ([1]$_2$·[Hg$_2$Cl$_6$]): A mixture of Cp*Ru(NO)Cl$_2$ (80 mg, 0.237 mmol) and Hg(ptpy)$_2$ (65 mg, 0.120 mmol) in THF (25 mL) was heated at reflux for 4 h, during which time the reaction color changed from green to orange. The solvent was pumped off, and the residue was washed with Et$_2$O and then extracted into CH$_2$Cl$_2$. Recrystallization from CH$_2$Cl$_2$/Et$_2$O gave orange crystals. Yield: 125 mg (71%). $C_{44}H_{50}Cl_6Hg_2N_4O_2Ru_2$·1/2THF (1520.0): calcd. C 36.5, H 3.65, N 3.69; found C 36.3, H 3.32, N 3.75. ^{1}H NMR ([D$_6$]acetone): δ = 2.04 (s, 30 H, Cp*), 2.61 (s, 6 H, CH$_3$), 7.40 (m, 4 H, H^1 and H^2), 7.72 (d, *J* = 6.7 Hz, 2 H, H^3), 8.13 (m, 4 H, H^5 and H^6), 8.45 (d, *J* = 7.2 Hz, 2 H, H^4), 8.94 (d, *J* = 6.2 Hz, 2 H, H^7) ppm. IR (KBr): $\tilde{\nu}$ = 1783 (s) [*ν*(NO)]. MS (FAB): *m*/*z* (%) = 435 ([Cp*Ru(ptpy)(NO)]$^+$), 406 ([Cp*Ru(ptpy)]$^+$ + 1).

[Cp*Ru(ptpy)(NO)][PF$_6$] (1[PF$_6$]): Na[PF$_6$] (1 equiv., 14 mg, 0.081 mmol) was added to a solution of [**1**]$_2$·[Hg$_2$Cl$_6$] (60 mg, 0.081 mmol) in acetone (20 mL) and the mixture was stirred at room temperature for 2 h and filtered through a Celite pad. The filtrate was evaporated to dryness and the residue recrystallized from acetone/Et$_2$O to give an orange crystalline solid. Yield: 48 mg (79%). $C_{22}H_{25}F_6N_2OPRu$ (579.48): calcd. C 45.5, H 4.3, N 4.83; found C 46.1, H 4.26, N 4.77. ^{1}H NMR ([D$_6$]acetone): δ = 2.01 (s, 15 H, Cp*), 2.64 (s, 3 H, CH$_3$), 7.42 (m, 2 H, H^1 and H^2), 7.70 (d, *J* = 6.7 Hz, 1 H, H^1), 8.12 (m, 2 H, H^5 and H^6), 8.47 (d, *J* = 7.2 Hz, 1 H, H^4), 8.98 (d, *J* = 6.2 Hz, 1 H, H^7) ppm. ^{31}P{^{1}H} NMR ([D$_6$]-acetone): δ = 76.8 ppm. IR (KBr): $\tilde{\nu}$ = 1779 cm^{-1} [*ν*(NO)]. MS (FAB): *m*/*z* (%) = 435 (M$^+$ – PF$_6$), 405 (M$^+$ – PF$_6$ – NO).

[Cp*Ru(μ-ptpy)RuCl$_2$Cp*]$_2$[Hg$_2$Cl$_6$] (2): A mixture of [Cp*RuCl$_2$]$_x$ (85 mg, 0.138 mmol) and [Hg(ptpy)$_2$] (94 mg, 0.135 mmol) in THF (30 mL) was stirred at room temperature overnight and filtered. The filtrate was evaporated to dryness and the residue was recrystallized from CH$_2$Cl$_2$/Et$_2$O to give dark red crystals, which were suitable for X-ray diffraction analysis. Yield: 54 mg (39%). [$C_{32}H_{40}Cl_5HgNRu_2$]$_2$·HgCl$_2$ (1136.65): calcd. C 33.8, H 3.52, N 1.23; found C 34.1, H 3.64, N 1.21. ^{1}H NMR ([D$_6$]acetone): δ = 1.87 (s, 30 H, Cp*), 1.99 (s, 30 H, Cp*), 2.46 (s, 6 H, CH$_3$), 4.86–5.03 (m, 4 H, H^1 and H^2), 5.36 (d, *J* = 6.2 Hz, 2 H, H^3), 7.86–7.94 (m, 4 H, H^5 and H^6), 8.63 (d, *J* = 7.1 Hz, 2 H, H^6), 9.08 (d, 2 H, *J* = 6.8 Hz, H^7) ppm. MS (FAB): *m*/*z* (%) 712 ([Cp*Ru(ptpy)RuCp*Cl$_2$]$^+$).

[Ru(Ph-ind-ptpy)(PPh$_3$)Cl] (3): Hg(ptpy)$_2$ (94 mg, 0.175 mmol) was added to a solution of Ru(3-phenylindenylid-1-ene)(PPh$_3$)$_2$Cl$_2$ (100 mg, 0.113 mmol) in THF (20 mL) and the mixture was stirred

 © 2005 Wiley-VCH Verlag GmbH & Co. KGaA, Weinheim

at room temperature overnight and filtered. The solvent was pumped off and the residue was washed with hexane/Et_2O and extracted with CH_2Cl_2. Recrystallization from CH_2Cl_2/hexane gave red crystals. Yield: 37 mg (43%). $C_{45}H_{35}ClNPRu\cdot 1/2H_2O$ (766.29): calcd. C 70.5, H 4.74, N 1.83; found C 70.0, H 4.55, N 1.84. ^1H NMR ($CDCl_3$): δ = 2.17 (s, 3 H, CH_3), 5.30 (s, 1 H, CH), 6.88–7.49 (m, 27 H, Ph), 7.68 (d, J = 5.8 Hz, 1 H, H^4), 7.81 (m, 2 H, H^5 and H^6), 8.61 (d, J = 7.2 Hz, 1 H, H^7) ppm. $^{31}P\{^1H\}$ NMR ($CDCl_3$): δ = 33.1 ppm. MS (FAB): m/z (%) = 758 ($M^+ + 1$), 722 ($M^+ - Cl$).

[Ru(ptpy)(CO)$_2$]$_2$(μ-Cl)$_2$ (8): A mixture of $[Ru(CO)_2Cl_2]_x$ (80 mg, 0.35 mmol) and [Hg(ptpy)(μ-Cl)]$_2$ (285 mg, 0.35 mmol) in DMF (15 mL) was heated at reflux overnight. The solvent was removed in vacuo and the residue was extracted with CH_2Cl_2. The extract was concentrated to about 10 mL and excess Et_2O was added until a yellow solid was formed. The product was purified by column chromatography (silica) using CH_2Cl_2/acetone (9:1) as eluent. Recrystallization from CH_2Cl_2/Et_2O afforded pale yellowish green crystals. Yield: 68 mg (62%). $C_{28}H_{20}Cl_2N_2O_4Ru_2$ (721.50): calcd. C 46.6, H 2.77, N 3.88; found C 47.3, H 2.71, N 3.79. ^1H NMR ($CDCl_3$): δ = 2.21 (s, 6 H, CH_3), 6.92–7.03 (m, 4 H, H^1 and H^2), 7.14 (d, J = 6.2 Hz, 2 H, H^3), 7.76–7.96 (m, 4 H, H^5 and H^6), 8.49 (d, J = 7.4 Hz, 2 H, H^6), 9.17 (d, J = 7.0 Hz, 2 H, H^7) ppm. IR (KBr): $\tilde{\nu}$ = 2039, 2104 cm^{-1} [ν(C≡O)]. MS (FAB): m/z = 360 ([1/2M]$^+$).

***cis*-[Ru(bzq)$_2$(CO)(MeCN)] (9):** A solution of *cis*-[Ru(bzq)$_2$(CO)$_2$] (30 mg, 0.058 mmol) in MeCN (25 mL) was irradiated with a mercury lamp under N_2 for 1 h, during which time the color changed from pale yellow to dark red. The solvent was pumped off, and the residue was washed with Et_2O and then extracted with MeCN. Recrystallization from MeCN–CH_2Cl_2–Et_2O gave an air-sensitive dark red crystalline solid. Yield: 23 mg (76%). $C_{29}H_{19}N_3ORu\cdot CH_2Cl_2\cdot 1/2CHCl_3$ (671.19): calcd. C 54.6, H 3.23, N 6.26; found C 54.7, H 3.27, N 6.21. ^1H NMR (CD_3CN): δ = 6.69 (d, J = 7.5 Hz, 1 H, H^1), 6.87 (t, J = 7.5 Hz, 1 H, H^2), 6.98–7.03 (m, 1 H, H^1), 7.10–7.25 (m, 2 H, H^2 and H^3), 7.48–7.58 (m, 2 H, H^3 and H^7), 7.55 (t, J = 7.5 Hz, 1 H, H^7), 7.75 (s, 2 H, H^4), 7.82–7.87 (m, 2 H, H^5), 8.09 (d, J = 8.0 Hz, 1 H, H^6), 8.45 (d, J = 7.0 Hz, 1 H, H^8), 8.55 (d, J = 7.8 Hz, 1 H, H^6), 9.40 (d, J = 4.8 Hz, 1 H, H^8) ppm. IR (KBr): $\tilde{\nu}$ = 1890 [ν(C≡O)], 2014 [ν(C≡N)] cm^{-1}.

***cis*-[Ru(bzq)$_2$(CO)(PPh$_3$)] (10):** A mixture of *cis*-[Ru(bzq)$_2$(CO)$_2$] (50 mg, 0.097 mmol) and PPh_3 (51 mg, 0.195 mmol) in THF (25 mL) was irradiated with UV light under N_2 for 1 h, during which time the reaction color changed from pale yellow to dark yellow. The solvent was pumped off, and the residue was washed with Et_2O and extracted with CH_2Cl_2. Recrystallization from CH_2Cl_2/Et_2O/hexane gave yellow crystals that were suitable for X-ray diffraction. Yield: 38 mg (53%). $C_{45}H_{31}N_2OPRu\cdot 1/2H_2O$ (756.81): calcd. C 71.4, H 4.26, N 3.70; found C 71.3, H 4.29, N 3.68. ^1H NMR ($CDCl_3$): δ = 6.47–6.52 (m, 1 H, H^1), 6.66 (d, J = 5.0 Hz, 1 H, H^2), 6.92–7.00 (m, 2 H, H^1 and H^2), 7.02–7.18 (m, 15 H, PPh_3), 7.27–7.35 (m, 4 H, H^4 and H^5), 7.55–7.58 (m, 1 H, H^6), 7.67–7.99 (m, 4 H, H^3 and H^7), 8.12–8.15 (m, 1 H, H^8), 8.27 (d, J = 7.8 Hz, 1 H, H^6), 8.88 (d, J = 4.8 Hz, 1 H, H^8) ppm. IR (KBr): $\tilde{\nu}$ = 1912 cm^{-1} [ν(C≡O)].

[Ru(bzq)$_2$(CO)(py)] (py = pyridine) (11): A mixture of *cis*-[Ru(bzq)$_2$(CO)$_2$] (30 mg, 0.058 mmol) and pyridine (10 μL, 0.116 mmol) in THF (25 mL) was irradiated with UV light under N_2 for 1 h, during which time the color changed from pale yellow to orange red. The solvent was filtered and pumped off, and the residue was washed with Et_2O and then extracted with THF. Recrystallization from THF/Et_2O gave an air-sensitive, orange crystalline solid. Yield: 17 mg (52%). Despite several attempts, we have not been able to obtain satisfactory analytical data for the compound. ^1H NMR ([D$_6$]benzene): δ = 6.02–6.08 (m, 2 H, H^1), 6.85–6.89 (m, 2 H, H^2), 7.00 (m, 4 H, H^3 and H^7), 7.27–7.36 (m, 2 H, py), 7.56 (t, J = 7.4 Hz, 2 H, py), 7.62–7.69 (m, 4 H, H^4 and H^5), 7.76 (t, J = 8.6 Hz, 1 H, py), 8.37 (d, J = 4.8 Hz, 2 H, H^6), 9.31 (d, J = 7.4 Hz, 2 H, H^8) ppm. IR (KBr): $\tilde{\nu}$ = 1898 cm^{-1} [ν(C≡O)].

Table 1. Crystallographic data and structure refinement parameters for complexes [**1**]$_2$·[Hg_2Cl_6], **2**·$HgCl_2$, **3**·C_4H_8O, **8**, and **10**·C_6H_{14}·Et_2O.

Complex	[**1**]$_2$·[Hg_2Cl_6]	**2**·$HgCl_2$	**3**·C_4H_8O	**8**	**10**·C_6H_{14}·Et_2O
Empirical formula	$C_{22}H_{25}Cl_3HgN_2ORu$	$C_{32}H_{40}Cl_{5.5}Hg_{1.5}NRu_2$	$C_{49}H_{43}ClNOPRu$	$C_{28}H_{20}Cl_2N_2O_4Ru_2$	$C_{52}H_{48}N_2O_2PRu$
Formula mass	741.45	1136.65	829.33	721.50	864.96
Crystal system	monoclinic	triclinic	monoclinic	orthorhombic	monoclinic
Space group	$P2_1/n$	$P\bar{1}$	$P2_1/n$	$Pbca$	$P2_1/n$
a [Å]	12.154(1)	10.1424(8)	11.6814(6)	11.850(1)	13.819(3)
b [Å]	10.854(1)	10.4592(8)	22.678(1)	13.583(1)	15.047(3)
c [Å]	19.439(2)	17.146(1)	14.7302(8)	16.832 (2)	20.414(4)
α [°]	90	96.572(1)	90	90	90
β [°]	107.583(1)	90.416(1)	92.447(1)	90	101.100(5)
γ [°]	90	102.348(1)	90	90	90
V [Å^3]	2444.5(3)	1764.2(2)	3898.7(4)	2709.0(5)	4165.0(2)
Z	4	2	4	4	4
D_{calcd} [g cm^{-3}]	2.015	2.140	1.413	1.769	1.379
T [K]	100(2)	100(2)	100(2)	298(2)	100(2)
μ [mm^{-1}]	7.235	7.791	0.551	1.350	0.459
F(000)	1416	1081	1712	1424	1796
Reflections collected	14064	14915	23888	14203	23644
Independent reflections	5719	7934	9230	3056	8456
R_{int}	0.0400	0.0303	0.0446	0.0966	0.0964
R_1[a], wR_2[b] [$I > 2\sigma(I)$]	0.0406, 0.0602	0.0519, 0.1384	0.0477, 0.1086	0.0536, 0.0904	0.0626, 0.1077
R_1, wR_2 (all data)	0.0732, 0.0686	0.0606, 0.1445	0.0686, 0.1184	0.0719, 0.1225	0.1112, 0.1800
Gof[c]	0.903	1.029	1.017	1.073	0.902

[a] $R_1 = \Sigma F_o - F_c|/\Sigma F_o$. [b] $wR_2 = [\Sigma w(F_o^2 - F_c^2)^2/\Sigma wF_o^{22}]^{1/2}$. [c] Gof = $[\Sigma w(F_o - F_c)^2/(N_{obs} - N_{param})]^{1/2}$.

 © 2005 Wiley-VCH Verlag GmbH & Co. KGaA, Weinheim

X-ray Crystallographic Study: A summary of crystallographic data and experimental details for complexes $[\mathbf{1}]_2 \cdot [Hg_2Cl_6]$, $\mathbf{2} \cdot HgCl_2$, $\mathbf{3} \cdot C_4H_8O$, **8**, and $\mathbf{10} \cdot C_6H_{14} \cdot Et_2O$ are listed in Table 1. All intensity data were collected with a Bruker SMART-APEX diffractometer using graphite-monochromated Mo-K_α radiation (λ = 0.70173 Å). The data were integrated and sorted using SAINT v6.26A software[31] and were corrected for absorption by empirical methods. The structures were solved by direct methods and refined by full-matrix least-squares analyses on F^2. Calculations were performed using the SHELXTL[32] crystallographic software package. All non-hydrogen atoms were refined anisotropically with suitable restraints. Hydrogen atoms were generated geometrically (C–H = 0.95 Å) and allowed to ride on their respective parent carbon or nitrogen atoms before the final cycle of least-squares refinement.

CCDC-269638 to -269642 contain the supplementary crystallographic data for this paper. These data can be obtained free of charge from The Cambridge Crystallographic Data Centre via www.ccdc.cam.ac.uk/data_request/cif.

Acknowledgments

The financial support from the Hong Kong University of Science and Technology and the Hong Kong Research Grants Council is gratefully acknowledged.

[1] a) K. A. King, S. Sprouse, R. J. Watts, *J. Am. Chem. Soc.* **1985**, *107*, 1431–1432; b) Y. Ohsawa, S. Sprouse, K. A. King, M. K. DeArmond, K. W. Hanck, R. J. Watts, *J. Phys. Chem.* **1987**, *91*, 1047–1057; c) A. P. Wilde, K. A. King, R. J. Watts, *J. Phys. Chem.* **1991**, *95*, 629–634.

[2] a) A. D. Ryabov, *Chem. Rev.* **1990**, *90*, 403–424; b) V. Ritleng, C. Sirlin, M. Pfeffer, *Chem. Rev.* **2002**, *102*, 1731–1770; c) J. Dupont, C. S. Consorti, J. Spencer, *Chem. Rev.* **2005**, *105*, 2527–2572.

[3] a) A. D. Ryabov, Y. N. Firsova, V. N. Goral, E. S. Ryabova, A. N. Shevelkova, L. L. Troitskaya, T. V. Demeschik, V. I. Sokolov, *Chem. Eur. J.* **1998**, *4*, 806–813; b) E. V. Krooglyak, G. M. Kazankov, S. A. Kurzeev, V. A. Polyakov, A. N. Semenov, A. D. Ryabov, *Inorg. Chem.* **1996**, *35*, 4804–4806; c) L. Alexandrova, O. G. D′yachenko, G. M. Kazankov, V. A. Polyakov, P. V. Samuleev, E. Sansores, A. D. Ryaobv, *J. Am. Chem. Soc.* **2000**, *122*, 5189–5200; d) A. D. Ryabov, *Adv. Inorg. Chem.* **2004**, *55*, 201–269.

[4] a) R. E. Holmlin, J. K. Barton, *Inorg. Chem.* **1995**, *34*, 7–8; b) J. L. Kisko, J. K. Barton, *Inorg. Chem.* **2000**, *39*, 4942–4949.

[5] a) M. A. Baldo, S. Lamansky, P. E. Burrows, M. E. Thompson, S. R. Forrest, *Appl. Phys. Lett.* **1999**, *75*, 4–6; b) M. Sudhakar, P. I. Djurovich, T. E. Hogen-Esch, M. E. Thompson, *J. Am. Chem. Soc.* **2003**, *125*, 7796–7797; c) A. B. Tamayo, B. D. Alleyne, P. I. Djurovich, S. Lamansky, I. Tsyba, N. N. Ho, R. Bau, M. E. Thompson, *J. Am. Chem. Soc.* **2003**, *125*, 7377–7387.

[6] a) G. DiMarco, M. Lanza, A. Mamo, I. Sterfio, C. Di Pietro, G. Romeo, S. Campagna, *Anal. Chem.* **1998**, *70*, 5019–5023; b) R. Gao, D. G. Ho, B. Hernandez, M. Selke, D. Murphy, P. I. Djurovich, M. E. Thompson, *J. Am. Chem. Soc.* **2002**, *124*, 14828–14829.

[7] K. K.-W. Lo, C.-K. Chung, N. Zhu, *Chem. Eur. J.* **2003**, *9*, 475–483.

[8] a) S. Sprouse, K. A. King, P. J. Spellane, R. J. Watts, *J. Am. Chem. Soc.* **1984**, *106*, 6647–6653; b) A. B. Tamayo, B. D. Alleyne, P. I. Djurovich, S. Lamansky, I. Tsyba, N. N. Ho, R. Bau, M. E. Thompson, *J. Am. Chem. Soc.* **2003**, *125*, 7377–7387.

[9] a) S. Lamansky, P. Djurovich, D. Murphy, F. Abdel-Razzaq, R. Kwong, I. Tsyba, M. Bortz, B. Mui, R. Bau, M. E. Thompson, *Inorg. Chem.* **2001**, *40*, 1704–1711; b) J. Li, P. I. Djurovich, B. D. Alleyne, M. Yousufuddin, N. N. Ho, J. C. Thomas, J. C. Peters, R. Bau, M. E. Thompson, *Inorg. Chem.* **2005**, *44*, 1713–1727.

[10] a) A. D. Ryabov, V. S. Sukharev, L. Alexandrova, R. Le Lagadec, M. Pfeffer, *Inorg. Chem.* **2001**, *40*, 6529–6532; b) I. S. Alpeeva, V. S. Soukharev, L. Alexandrova, N. V. Shilova, N. V. Bovin, E. Csöregi, A. D. Ryabov, I. Yu. Sakharov, *J. Biol. Inorg. Chem.* **2003**, *8*, 683–688.

[11] a) K. Kalyarasundaram, *Coord. Chem. Rev.* **1982**, *46*, 159–244; b) V. Balzani, F. Scandola, *Supramolecular Photochemistry*, Ellis Horwood, Chichester, UK, **1991**; c) V. Balzani, A. Juris, M. Venturi, S. Campagna, S. Serroni, *Chem. Rev.* **1996**, *96*, 759–834.

[12] a) E. C. Constable, J. M. Holmes, *J. Organomet. Chem.* **1986**, *301*, 203–208; b) P. Reveco, R. H. Schmehl, W. R. Cherry, F. R. Fronczek, J. Selbin, *Inorg. Chem.* **1985**, *24*, 4078–4082; c) A. D. Ryabov, V. S. Sukharev, L. Alexandrova, R. Le Lagadec, M. Pfeffer, *Inorg. Chem.* **2001**, *40*, 6529–6532; d) H. Hadazaheh, M. C. DeRosa, G. P. A. Yap, A. R. Rezvani, R. J. Crutchley, *Inorg. Chem.* **2002**, *41*, 6521–6526; e) A. D. Ryabov, R. Le Lagadec, H. Estevez, R. A. Toscano, S. Hernandez, L. Alexandrova, V. S. Kurova, A. Fischer, C. Sirlin, M. Pfeffer, *Inorg. Chem.* **2005**, *44*, 1626–1634.

[13] a) S. Fernandez, M. Pfeffer, V. Ritleng, C. Sirlin, *Organometallics* **1999**, *18*, 2390–2394; b) D. L. Davies, O. Al-Duaij, J. Fawcett, M. Giardiello, S. T. Hilton, D. R. Russell, *Dalton Trans.* **2003**, 4132–4138; c) J. P. Djukic, A. Berger, M. Duquenne, M. Pfeffer, A. De Cian, N. Kyritsakas-Gruber, J. Vachon, J. Lacour, *Organometallics* **2004**, *23*, 5757–5767.

[14] a) A. M. Clark, C. E. F. Rickard, W. R. Roper, L. J. Wright, *Organometallics* **1999**, *18*, 2813–2820; b) A. M. Clark, C. E. F. Rickard, W. R. Roper, L. J. Wright, *J. Organomet. Chem.* **2000**, *598*, 262–275.

[15] a) J. Matthes, S. Grundemann, A. Toner, Y. Guari, B. Donnadieu, J. Sapndl, S. Sao-Etienne, E. Clot, H.-H. Limbach, B. Chaudret, *Organometallics* **2004**, *23*, 1424–1433; b) K. Hiraki, M. Koizumi, S. Kira, H. Kawano, *Chem. Lett.* **1998**, *27*, 47–48.

[16] a) M. I. Bruce, B. L. Goodall, F. G. A. Stone, *J. Organomet. Chem.* **1973**, *60*, 343–349; b) J. M. Patrick, A. H. White, M. I. Bruce, M. J. Beatson, D. S. C. Black, G. B. Deacon, N. C. Thomas, *J. Chem. Soc., Dalton Trans.* **1983**, 2121–2123.

[17] A. Berger, J. P. Djukic, M. Pfeffer, J. Lacour, L. Vial, A. de Cian, N. Kyritsakas-Gruber, *Organometallics* **2003**, *22*, 5243–5260.

[18] T. J. Kistenmacher, M. Rossi, C. C. Chiang, R. P. Van Duyne, A. R. Siedle, *Inorg. Chem.* **1980**, *19*, 3604–3608.

[19] J. Chang, R. G. Bergman, *J. Am. Chem. Soc.* **1987**, *109*, 4298–4304.

[20] G. B. Richter-Addo, P. Legzdins, *Metal Nitrosyls*, Oxford University Press, New York, **1992**.

[21] Q.-F. Zhang, F. K. M. Cheung, W.-Y. Wong, I. D. Williams, W.-H. Leung, *Organometallics* **2001**, *20*, 3777–3781.

[22] K. M. Rao, C. L. Day, R. A. Jacobson, R. J. Angelici, *Organometallics* **1992**, *11*, 2303–2304.

[23] a) J.-P. Djukic, K. H. Dötz, M. Pfeffer, A. De Cian, J. Fischer, *Organometallics* **1997**, *16*, 5171–5182; b) J.-P. Djukic, A. Maisse, M. Pfeffer, K. H. Dötz, M. Nieger, *Eur. J. Inorg. Chem.* **1998**, 1781–1790; c) J.-P. Djukic, A. Maisse-François, M. Pfeffer, K. H. Dötz, A. De Cian, J. Fischer, *Organometallics* **2000**, *19*, 5484–5499; d) C. Michon, J.-P. Djukic, Z. Ratkovic, J.-P. Collin, M. Pfeffer, A. De Cian, J. Fischer, D. Heiser, K. H. Dötz, N. Nieger, *Organometallics* **2002**, *21*, 3519–3535; e) J.-P. Djukic, C. Machon, D. Heiser, N. Kyrisakas-Gruber, A. De Cian, K. H. Dötz, M. Pfeffer, *Eur. J. Inorg. Chem.* **2004**, 2107–2122.

[24] J.-P. Djukic, A. Maisse, M. Pfeffer, K. H. Dötz, M. Nieger, *Organometallics* **1999**, *18*, 2786–2790.

 © 2005 Wiley-VCH Verlag GmbH & Co. KGaA, Weinheim

[25] L. A. Oro, M. A. Ciriano, M. Campo, M. C. C. Foces-Foces, F. H. Cano, *J. Organomet. Chem.* **1985**, *289*, 117–131.
[26] M. I. Bruce, M. Z. Iqbal, F. G. A. Stone, *J. Chem. Soc. A* **1971**, 2820–2828.
[27] T. D. Tilley, R. H. Grubbs, J. E. Bercaw, *Organometallics* **1984**, *3*, 274–278.
[28] M. C. Seidler, R. G. Bergman, *J. Am. Chem. Soc.* **1984**, *106*, 6110–6111.
[29] H.-J. Schandz, L. Jafarpour, E. D. Stevens, S. P. Nolan, *Organometallics* **1999**, *18*, 5187–5190.
[30] D. St. C. Black, G. B. Deacon, G. L. Edwards, B. M. Gatehouse, *Aust. J. Chem.* **1993**, *46*, 1323–1336.
[31] *SMART and SAINT+ for Windows NT V6.02a*. Bruker Analytical X-ray Instruments Inc., Madison, WI, USA, **1998**.
[32] G. M. Sheldrick, *SHELXTL-Plus V5.1 Software Reference Manual*, Bruker AXS Inc., Madison, WI, USA, **1997**.

Received: May 10, 2005
Published Online: October 25, 2005

 © 2005 Wiley-VCH Verlag GmbH & Co. KGaA, Weinheim

DOI: 10.1002/ejic.200500453

A Novel Chemical Reduction Route towards the Synthesis of Crystalline Nickel Nanoflowers from a Mixed Source

Xiaomin Ni,[a] Qingbiao Zhao,[a] Huagui Zheng,*[a] Beibei Li,[a] Jimei Song,[a] Dongen Zhang,[a] and Xiaojun Zhang[a]

Keywords: Nickel / Nanostructures / Chemical reduction / Crystal growth

A novel chemical reduction route was designed for the synthesis of nickel nanocrystals with distinct flowery shapes by using a mixture of two complexes of $Ni(N_2H_4)_3^{2+}$ and $Ni(dmg)_2$ (nickel dimethylglyoximate) as the nickel source. Formation of these flowers, comprising spherical centers and swordlike petals, was related to the varying stability and structural properties of the two precursors as well as the reaction conditions. Investigations of the time-dependent shape-evolution process indicated that spherical particles were formed first as flower centers, and then swordlike petals grew radially from the particle surfaces. A rational mechanism of formation was proposed on the basis of a range of contrasting experiments. Compared with bulk nickel, these nanoflowers exhibited an enhanced coercivity (H_c) and a decreased saturation magnetization (M_s); this fact is attributed to their peculiar morphology.
(© Wiley-VCH Verlag GmbH & Co. KGaA, 69451 Weinheim, Germany, 2005)

Introduction

For many years, control of the morphology of nanomaterials has been of great interest for their shape-dependent properties and potential applications in nanoelectronics, photonics, magnetics, catalysis, and so forth.[1] Exploration of various shape-controlling synthetic methods and studies on their unusual properties will inevitably drive the progress in nanotechnology. Templates such as macroporous membranes, carbon nanotubes, aluminum anode oxides (AAO), block copolymers, microemulsions, polymers, and complexing agents are often utilized during synthesis to control the shape of nanomaterials.[2] Among these templates, utilizing coordination complexes as precursors has attracted particular attention for its simplicity and convenience. A range of novel-shaped nanocrystals have been fabricated by this method, for example Cu_2O nanowires, cubic FeS_2 crystallites, and several different shaped ZnO nanostructures including hollow spheres, ringlike nanosheets standing on spindlelike rods, nanoparticles nanoribbons, flowerlike cupped-end microrod bundles, branched spindles, and prismatic whiskers.[3] In this technique, the morphology of the target product was closely associated with the structure and shape of the complex precursors. Upon removal of the ligand molecules in a rational and controllable manner, inorganic nanomaterials with the desired size and shape could be synthesized.[3e]

In addition to the effect of templates, modification of the reaction steps also has great influence on the crystal configuration. Generally, the formation processes of crystals include nucleation and growth, which is practically a continuous process. However, in the two-step, seed-mediated synthesis technique, the nucleation and growth are purposely separated for adjusting the crystal morphology. In the first step, the seed nanocrystals, whose characteristic symmetry and structure are critical for directing the final crystal shape, are synthesized and added to the synthetic system. Then, precursors to the desired structures are chemically reduced in the presence of capping molecules and seed nanocrystals that serve as nucleation sites.[4] Following this methodology, a series of different shaped nanocrystals were fabricated. For example, uniform Au and Ag nanorods, dumbbell-shaped Au–Ag core-shell nanocrystals were all created from the seed-mediated growth in solution.[5a–5c] Oriented arrays of ZnO nanorods were produced from citrate solution in the presence of nanosized ZnO seeds.[5d] Likewise, using Ag nanoparticles as seeds, a peculiar netlike Ag skeleton could be synthesized by reduction of silver ions with Raney nickel.[5e] These results indicate this synthetic approach has great potential for the anisotropic growth of inorganic nanocrystals, but the interface issues between the seed and growing materials have not been well resolved, and further research is required for their general applicability and extension to the synthesis of complex nanostructures.[4b]

Nanosized particles of nickel have diverse applications in the fields of catalysis, magnet recording, medical diagnosis, and conduction.[6] In the past decade, nickel nanocrystals with the following shapes have been fabricated: nanotubes,

[a] Department of Chemistry, University of Science and Technology of China,
Hefei, Anhui, 230026, People's Republic of China
Fax: +86-551-3601600
E-mail: hgzheng@ustc.edu.cn

 InterScience © 2005 Wiley-VCH Verlag GmbH & Co. KGaA, Weinheim

hollow spheres, nanobelts, nanorods, nanoprisms, and hexagonal flakes. However, the creation of nickel nanoflowers has seldom been reported.[7] In this paper, we have designed a new reaction route which combines coordination control with the step modulation technique and yields nickel nanocrystals with a novel flower shape. This strategy involves the monitoring of crystal nucleation and growth through chemical reactions. In contrast to previous methods using a single-source precursor, two complexes, $Ni(N_2H_4)_3^{2+}$ and $Ni(dmg)_2$, comprise the nickel source. The reaction process involves two steps: firstly, $Ni(N_2H_4)_3^{2+}$ is reduced, and the resulting spherical nanocrystals serve as the flower centers. Then, $Ni(dmg)_2$ yields swordlike nanocrystals which grow radially on the existing spherical centers as petals. A series of experiments were conducted to investigate the possible formation process.

Results and Discussion

The phase and purity of the as-prepared product was determined by X-ray diffraction (XRD), as shown in Figure 1. All the diffraction peaks could be indexed as face-centered cubic (fcc) nickel (JCPDS 01–1260). No characteristic peaks due to the impurities of nickel oxides or hydroxides were detected, indicating that pure crystalline nickel was fabricated under such conditions.

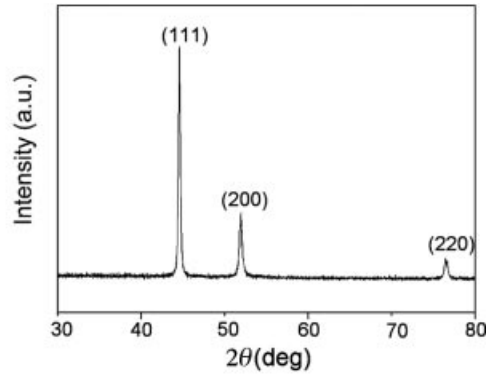

Figure 1. XRD pattern of as-prepared flowerlike nickel crystals.

The morphology of the sample was investigated by field emission scanning electron microscopy (FE-SEM) and transmission electron microscopy (TEM). A low-magnification image, shown in Figure 2a, demonstrates that the product exhibits novel flowerlike shapes. A magnified image of an individual crystallite indicated that the flower comprised dozens of swordlike petals radiating from the center, which can be seen in Figure 2b. The petals with sharp ends and protruding surface ridges have sizes in the range of 30–80 nm in diameter, 20–50 nm in thickness, and 0.5–2.0 μm in length. Sonication for 10 min did not break this nanostructure into discrete particles, indicating that the nanoflowers were actually integrated, and were not only aggregations of spherical and swordlike particles. TEM images of the nanoflowers with petals assembled at the center, agreeing well with the FE-SEM observations, can be seen in Figure 2c. Besides the flowerlike nanostructures, it was noted that a small fraction of hexagonal flakes (about 1%, as arrowed in Figure 2a) emerged in the final product. Shown in Figure 2d is a TEM image of two overlapping flakes with a side length of about 100 nm. The corresponding selected area electron diffraction (SAED) pattern indicated that they are also due to fcc nickel.

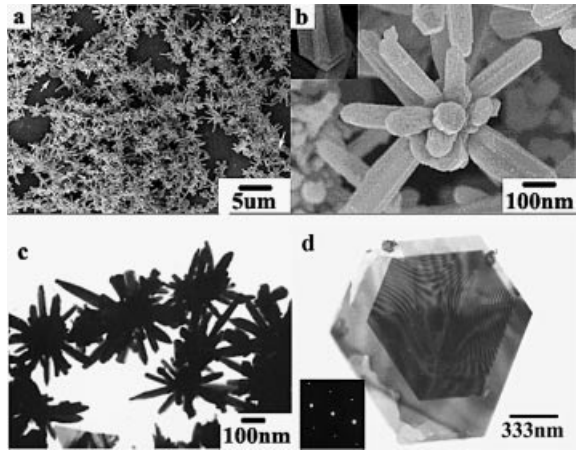

Figure 2. SEM images of as-prepared samples: (a) a low-magnification SEM image; (b) a high-magnification SEM image of an individual flower (the inset is a typical petal); TEM images of the sample: (c) several typical nickel flowers; (d) two overlapping hexagonal flakes of fcc Ni.

More details of the flowerlike structure were investigated by high resolution transmission electron microscopy (HRTEM) and SAED. A typical sharp-ended petal (Figure 3a) with a diameter of about 20 nm was chosen as the object of investigation. The HRTEM image in Figure 3b shows three sets of lattice spacings of ≈ 0.20, 0.18, and 0.12 nm that are in accordance with the separation between the (111), (200), and (220) planes of fcc Ni, respectively. From the HRTEM image, the growth direction of the petal could be indexed as along [01$\bar{1}$]. The corresponding ED pattern in Figure 3c was recorded with the electron beam along the [011] zone axis, revealing the single crystalline nature of the petal. It was noted that in the SAED pattern additional diffraction spots along the directions of [111] and [200] appeared, which implied the presence of five superlattices in both directions.

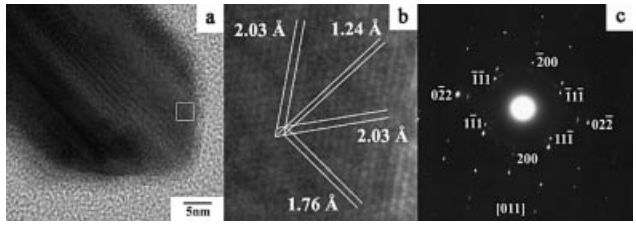

Figure 3. (a) TEM image of the tip of a typical petal. (b) HRTEM image taken from the petal. (c) The corresponding SAED pattern, taken from the [011] zone axis. The additional diffraction spots along [111] and [200] implied the presence of five superlattices of nickel in these two directions.

 © 2005 Wiley-VCH Verlag GmbH & Co. KGaA, Weinheim

To probe into the growth process of the nanoflowers, we studied the shape evolution of the product over time by FE-SEM. Figure 4 shows the images of three samples hydrothermally treated for 3 h, 7 h, and 11 h, respectively (Figure 4a, b, and c). It was shown that spherical nickel particles with diameters of about 100 nm emerged as the initial product after the mixture was heated at 120 °C for 3 h. With time, short rods grew out on these spherical particles, and some particles developed into flowery crystals. After 11 h, most of the product had evolved into flower-shaped crystallites with swordlike petals.

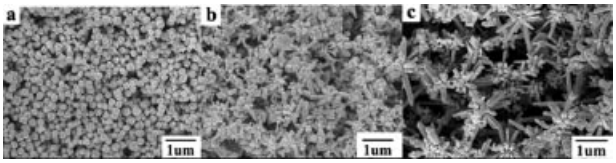

Figure 4. SEM images of the samples obtained at different reaction stages. (a) 3 h, (b) 7 h, (c) 11 h.

On the basis of previous studies of nickel nanocrystals from different complexes and the evolution of nickel flowers described above, the possible mechanism of formation of the nickel nanoflowers was detailed. It is known that Ni^{2+} ions can react with dimethylglyoxime (dmgH) and hydrazine (N_2H_4) in aqueous solution to form the complexes of $Ni(dmg)_2$ and $Ni(N_2H_4)_3^{2+}$, respectively. In basic solution, the $Ni(N_2H_4)_3^{2+}$ (with an instability constant of 4.5×10^{-8}) can react with OH^- in the following manner:

$$2\ Ni(N_2H_4)_3^{2+} + 4\ OH^- \rightarrow 2\ Ni + N_2 + 4\ H_2O + 5\ N_2H_4$$

When the pH of the solution was above 12 and the temperature was higher than 85 °C, the reaction proceeded very fast and produced spherical particles.[8] Because of its higher stability (with an instability constant of 4×10^{-24}) and special planar square structure, $Ni(dmg)_2$ reacted with hydrazine at a relatively slow rate and yielded nickel nanocrystals with a hexagonal flakelike shape.[9,7f] In our system, about 60 mol-% Ni^{2+} ions were coordinated by dmgH and the rest yielded $Ni(N_2H_4)_3^{2+}$. These two complexes coexisted in one system and comprised the nickel source. However, because of their different stability and structure, they were reduced at different reaction stages and resulted in differently shaped particles. $Ni(N_2H_4)_3^{2+}$ was reduced first and yielded spherical particles, which were dispersed in the system. As the reaction proceeded, $Ni(dmg)_2$ was attacked, and the newly formed nickel atoms tended to spontaneously transfer onto the surfaces of the existing particles which served as seed sites for further growth. Because of the higher stability of $Ni(dmg)_2$, the reaction rate at this stage slowed down, and the concentration of nickel atoms was not enough for the former spherical particles to grow from the circumference. This would lead to undersaturation around the existing particles, and the continuous addition of nickel atoms to the as-formed particle surface would preferentially occur at the active sites of the circumferential edges which had relatively higher free energies than other sites on the surface. As a result, a flowerlike structure was formed because of the lack of mass transport of nickel atoms to the seed particles for their further growth.[10] The reduced particles grew around each seed particle until all the $Ni(dmg)_2$ was reduced, eventually resulting in radially oriented petals on the surfaces. It is worth noting that the growth of nickel nanocrystals from $Ni(dmg)_2$ proceeded in a different manner relative to that from $Ni(N_2H_4)_3^{2+}$. As a special planar complex, $Ni(dmg)_2$ imposes obvious confinement on the growth of the resultant particles, orienting them along a certain direction.[7f] Therefore, anisotropic petals with swordlike shapes were produced. A schematic pattern of the formation process is shown in Scheme 1. However, it is interesting that the petals did not grow into hexagonal flakes as before, but mainly into swordlike rods, which may be attributed to the effect of the spherical nanocrystals formed at the initial stage. Since the seed particles greatly affected the shape of the crystals, the nickel nanocrystals grown in the presence of spherical particles may develop into a different shape.[11] In fact, if the spherical nanoparticles were prepared first and then dispersed into the system with $Ni(dmg)_2$ and hydrazine, a similar flowerlike nanostructure (as seen in Figure 5c) could also be pro-

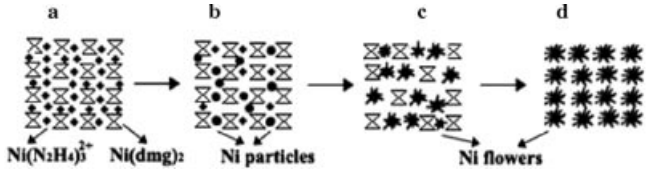

Scheme 1. Schematic illustration of the formation process of the nickel nanoflowers. (a) mixture of $Ni(dmg)_2$ and $Ni(N_2H_4)_3^{2+}$ complexes in the system. (b) spherical nickel nanoparticles were formed which came from the reduction of $Ni(N_2H_4)_3^{2+}$ (c) part of the spherical nickel particles had evolved into small flowers with the reduction of $Ni(dmg)_2$. (d) nickel nanoflowers emerged as the final product.

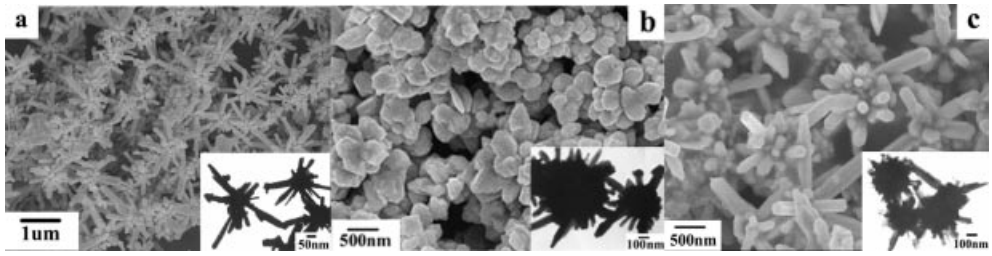

Figure 5. SEM and TEM images of the samples from the system with different molar ratios (ω) of $Ni(N_2H_4)_3^{2+}$ to $Ni(dmg)_2$ (a) ω = 20:80 (b) ω = 80:20, (c) TEM image of the sample in which the spherical particles were added externally to the system.

 © 2005 Wiley-VCH Verlag GmbH & Co. KGaA, Weinheim

duced, which supported the two-step formation process proposed above.

Following the formation of the nickel flowers, it was rationally proposed that the size of the flower centers and petals could be adjusted by changing the molar ratio (ω) of $Ni(N_2H_4)_3^{2+}$ to $Ni(dmg)_2$, considering their different contribution to the flowerlike structure. This supposition was validated by the FE-SEM images of two samples obtained at different ω values while the other reaction conditions were kept the same. Figure 5a and b shows the images of two samples from the systems with ω values of 20:80 and 80:20, respectively. It is clear that increasing the proportion of $Ni(dmg)_2$ obviously promoted the size of petals, while a higher proportion of $Ni(N_2H_4)_3^{2+}$ led to flowers with bigger centers.

In all the samples, a small quantity of hexagonal nickel flakes appeared regardless of the reaction time and the ratio of the two Ni sources, as shown in Figure 2, Figure 4, and Figure 5. It was believed that they originated solely from the precursor of $Ni(dmg)_2$, and not through the two-step process observed above for the flowers. When $Ni(dmg)_2$ is the only source of nickel, hexagonal flakelike nickel crystals can be produced exclusively. The current system, however, became inhomogeneous because of flocculent $Ni(dmg)_2$ suspended in the solution, which caused differences in the local concentrations of the reactants. In places where the concentration of hydrazine was relatively high, part of $Ni(dmg)_2$ would be reduced simultaneously with $Ni(N_2H_4)_3^{2+}$ and directly developed into flakes. Careful observations indicated that small hexagonal flakes appeared even when the mixture was only heated for 3 h (shown in Figure 4a), which well validated our supposition.

The present synthetic route monitored crystal nucleation and growth through two matching chemical reactions in one system. For the two complexes, their different stability resulted in reduction reactions at different stages, and the different structures resulted in particles with different shapes. Cooperation of the two precursors was responsible for the formation of the unique flowerlike nanostructure. Controlled experiments show that, keeping the rest of the conditions the same, substitution of the two complexes with other pairs of Ni sources such as $Ni(NH_3)_6^{2+}$-$Ni(dmg)_2$, $Ni(N_2H_4)_3^{2+}$-$Ni(C_4H_2O_6)^{2-}$ (tartrate), $Ni(N_2H_4)_3^{2+}$-$Ni(C_9NOH_7)_2$ (nickel 8-hydroxyquinoline), or $Ni(NH_3)_6^{2+}$-$Ni(en)_3^{2+}$ (ethylenediamine) did not all result in nanoflower formation (as seen in Figure 6). This lack of nanoflower formation is possibly due to a mismatch of the stability or structure of the two starting materials, which idd not meet the conditions required for the formation of the flowers. The role of the temperature was also studied, and it was found that the flowers could be reproducibly prepared over an optimized temperature range of 100–150 °C. Temperatures above 150 °C led to spherical particles due to a faster reducing rate, while at temperatures below 100 °C, $Ni(dmg)_2$ was not completely reduced.

It is known that the magnetic properties of nanomaterials are closely related to the sample size, shape, crystallinity etc. The M–H hysteresis loop of the flowers obtained was

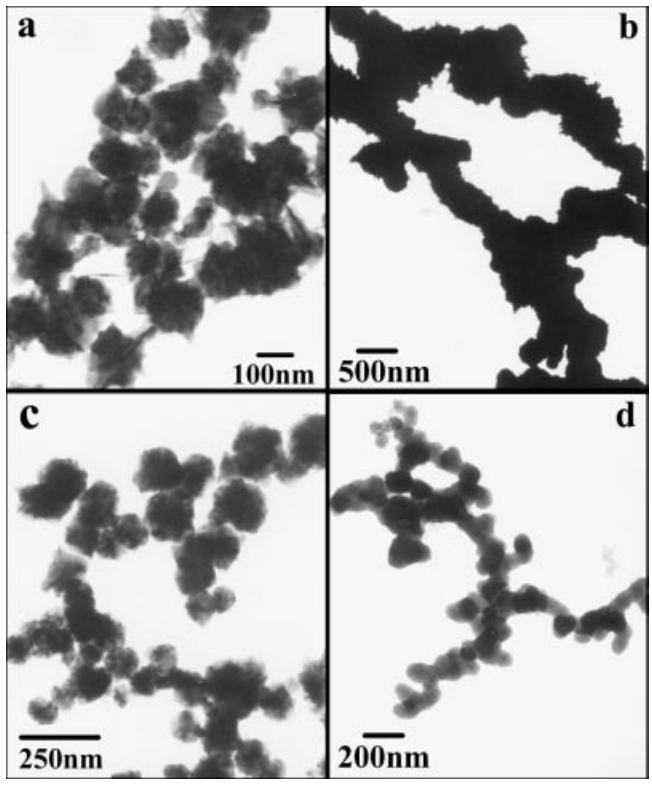

Figure 6. TEM images of the samples prepared from the other mixed nickel sources. (a) $Ni(NH_3)_6^{2+}$-$Ni(dmg)_2$; (b) $Ni(N_2H_4)_3^{2+}$-$Ni(C_4H_2O_6)^{2-}$ (tartrate); (c) $Ni(N_2H_4)_3^{2+}$- $Ni(C_9H_7NO)_2$ (nickel 8-hydroxyquinoline); (d) $Ni(NH_3)_6^{2+}$-$Ni(en)_3^{2+}$ (ethylenediamine).

measured at room temperature (Figure 7), showing coercivity (H_c), saturation magnetization (M_s), and remanent magnetization (M_r) values of approximately 173.2 Oe, 30.8 emu g^{-1}, and 9.9 emu g^{-1}, respectively. Compared with that of the bulk nickel (100 Oe, 55 emu g^{-1}, 2.7 emu g^{-1}), the H_c value was much enhanced. As ultrafine ferromagnetic particles often exhibit enhanced coercivity relative to the corresponding bulk material, the small size and shape anisotropy of the flowers may be responsible for the increased H_c value.[12] However, it was noted that this value was much lower than that of the 1D nanorods (332 Oe) or nanobelts (640 Oe), which was possibly attributed to the special 3D

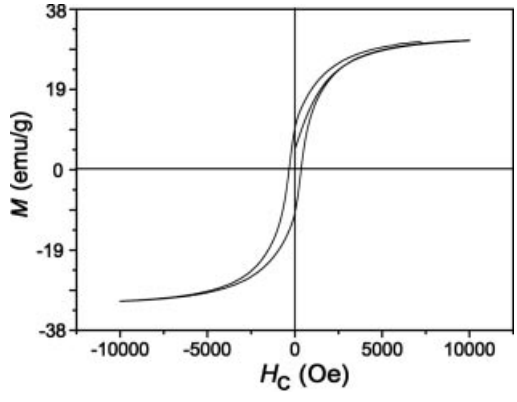

Figure 7. Magnetic hysteresis loop of as-prepared nickel nanoflowers measured at room temperature.

 © 2005 Wiley-VCH Verlag GmbH & Co. KGaA, Weinheim

flowerlike structure. Because of the radial orientation of the petals, it was difficult for all of them to be aligned simultaneously along the direction of the external magnetic field compared with the 1D nanomaterials. Therefore, a relatively low H_c value was observed.[13,7e] As for the decrease in M_s, it might likewise be due to the decrease in particle size accompanied by an increased surface area, together with the magnetic interaction between the petals, which reduced the total magnetic moment at a given field.[14]

Conclusions

Flower-shaped nickel nanocrystals were successfully prepared by reduction of the mixed complexes of $Ni(N_2H_4)_3^{2+}$ and $Ni(dmg)_2$ in alkaline solution with hydrazine hydrate. Spherical nickel nanocrystals formed first from $Ni(N_2H_4)_3^{2+}$ and served as the nucleation sites for the growth of the swordlike petals, which originated from the reduction of $Ni(dmg)_2$. The different stability and structure of the two complexes played an important role in the formation of the distinct nickel nanoflowers. The size of the flower centers and petals could be adjusted by changing the molar ratio of the two complexes. Due to their unique flowery shapes, these crystals exhibited an enhanced coercivity and a decreased M_s value as compared with that of bulk nickel. The present work realized the control of the crystal shape through rationally matching different chemical reactions to adjust the crystal nucleation and growth processes. Such a novel and facile strategy is being further explored for the preparation of other materials under controlled conditions.

Experimental Section

X-ray diffraction (XRD) patterns of the samples were recorded with a Philips X′pert diffractometer with Cu-K_α radiation (λ = 0.15418 nm). Field emission scanning electron microscopy (FE-SEM) images were recorded with a JEOL JSM-6300F SEM. Transmission electron microscopy (TEM) images were collected with a Hitachi, H-800 electron microscope with an accelerating voltage of 200 kV. High-resolution transmission electron microscopy (HRTEM) images and the selected area electron diffraction (SAED) patterns were recorded with a JEOL-2010 TEM at an acceleration voltage of 200 kV. M–H hysteresis loops were recorded with a vibrating sample magnetometer (BHV-55) at an applied field of 10^4 Oe and a magnetization scale of 2.5 emu on a 0.0352-g sample sealed in a 6.6×10^{-2} mL vessel.

Nickel chloride ($NiCl_2 \cdot 6H_2O$), dimethylglyoxime (dmgH), sodium hydroxide (NaOH) were all of analytical purity. In a typical experiment, $NiCl_2 \cdot 6H_2O$ (0.166 g) was dissolved in distilled water (25 mL) to give a green transparent solution. Then an ethanol solution (13 mL) containing 1 wt.-% dmgH was added dropwise into the solution. Red flocculates emerged, indicating the formation of $Ni(dmg)_2$. Subsequently, $N_2H_4 \cdot H_2O$ (2.0 mL, 80 wt.-%) was added under continuous stirring. The solution pH was adjusted to above 12 using sodium alkali. The mixture was stirred for 30 min and transferred into a Teflon-lined autoclave with a capacity of 50 mL. The autoclave was sealed, heated at 110 °C for 12 h, and then cooled naturally to room temperature. The resulting black powders were collected and washed, and finally dried in vacuum at 60 °C for 4 h.

[1] a) A. P. Alivisatos, *Science* **1996**, *271*, 933–937; b) C. B. Murray, D. J. Norris, M. G. Bawendi, *J. Am. Chem. Soc.* **1993**, *115*, 8706–8715; c) K. M. Krishnan, A. P. Alivisatos, *Science* **2001**, *291*, 2115–2117; d) R. Heitz, S. Rodt, A. Schliwa, D. Bimberg, *Phys. Status Solidi B* **2003**, *238*, 273–280; e) R. Narayanan, M. A. El-Sayed, *Nano Lett.* **2004**, *4*, 1343–1348.

[2] a) J. K. N. Mbindyo, T. E. Mallouk, J. B. Mattzela, I. Kratochvilova, B. Razavi, T. M. Jackson, T. S. Mayer, *J. Am. Chem. Soc.* **2002**, *124*, 4020–4026; b) Y. Zhang, H. Dai, *Appl. Phys. Lett.* **2000**, *77*, 3015–3017; c) D. S. Xue, L. Y. Zhang, A. B. Gui, X. F. Xu, *Appl. Phys. A: Mater. Sci. Process* **2005**, *80*, 439–442; d) D. Zhang, L. Qi, J. Ma, H. Cheng, *Chem. Mater.* **2001**, *13*, 2753–2755; e) X. Zhang, Y. Xie, F. Xu, X. B. Tian, *J. Colloid Interface Sci.* **2004**, *274*, 118–121; f) H. Q. Cao, Z. Xu, H. Sang, D. Sheng, C. Y. Tie, *Adv. Mater.* **2001**, *13*, 121–123; g) Y. Deng, G. Wei, C. Nan, *Chem. Phys. Lett.* **2003**, *368*, 639–643.

[3] a) Y. Xiong, Z. Li, R. Zhang, Y. Xie, J. Yang, C. Wu, *J. Phys. Chem. B* **2003**,*107*, 3697–3702; b) X. Chen, Z. Wang, J. Wan, J. Liu, Y. Qian, *Inorg. Chem.* **2005**, *44*, 951–954; c) Z. Li, Y. Xie, Y. Xiong, R. Zhang, *New J. Chem.* **2003**, *27*, 1518–1521; d) B. Liu, S. H. Yu, F. Zhang, L. Li, Q. Zhang, L. Ren, K. Jiang, *J. Phys. Chem. B* **2004**, *108*, 4338–4341; e) Z. Gui, J. Liu, Z. Wang, L. Song, Y. Hu, W. Fan, D. Chen, *J. Phys. Chem. B* **2005**, *109*, 1113–1117; f) C. Jiang, W. Zhang, G. Zou, W. Yu, Y. Qian, *J. Phys. Chem. B* **2005**, *109*, 1361–1363; g) H. S. Qian, S. H. Yu, J. Y. Gong, L. B. Luo, L. L. Wen, *Cryst. Growth Des.* **2005**, *5*, 935–939.

[4] a) Y. W. Jun, S. M. Lee, N. J. Kang, J. Cheon, *J. Am. Chem. Soc.* **2001**, *123*, 5150–5151; b) S. M. Lee, S. N. Cho, J. Cheon, *Adv. Mater.* **2003**, *15*, 441–444.

[5] a) C. J. Murphy, N. R. Jana, *Adv. Mater.* **2002**, *14*, 80–82; b) C. C. Huang, Z. Yang, H. T. Chang, *Langmuir* **2004**, *20*, 6089–6092; c) Z. R. Tian, J. A. Voigt, J. Liu, B. Mckenzie, M. J. McDermott, M. A. Rodriguez, H. Konishi, H. F. Xu, *Nat. Mater.* **2003**, *2*, 821–826; d) Z. R. Tian, J. A. Voigt, J. Liu, B. Mckenzie, M. J. McDermott, M. A. Rodriguez, H. Konishi, H. F. Xu, *Nat. Mater.* **2003**, *2*, 821–826; e) Y. C. Zhu, M. R. Ji, H. G. Zheng, Y. Li, Z. P. Yang, Y. T. Qian, *Mater. Lett.* **2004**, *58*, 1121–1126.

[6] a) W. X. Zhang, C. B. Wang, H. L. Lien, *Catal. Today* **1998**, *40*, 387–395; b) V. F. Puntes, K. M. Krishnan, A. P. Alivisatos, *Science* **2001**, *291*, 2115–2117; c) M. P. Pileni, *Adv. Funct. Mater.* **2001**, *11*, 323–336; d) R. Hernandez, S. Polizu, S. Turenne, L. Yahia, *Bio-Med. Mater. Eng* **2002**, *12*, 37–45; e) A. Smogunov, A. Dal Corso, E. Tosatti, *Surf. Sci.* **2002**, *507*, 609–614.

[7] a) J. Bao, C. Tie, Z. Xu, Q. Zhou, D. Shen, Q. Ma, *Adv. Mater.* **2001**, *13*, 1631–1633; b) J. Bao, Y. Liang, Z. Xu, L. Si, *Adv. Mater.* **2003**, *15*, 1832–1835; c) J. S. Bradley, B. Tesche, W. Buser, M. Maase, M. T. Reetz, *J. Am. Chem. Soc.* **2000**, *122*, 4631–4636; d) N. Cordente, R. M. Espaud, F. Secocq, M. J. Casanove, C. Amiens, B. Chaudret, *Nano Lett.* **2001**, *1*, 565–568; e) Z. Liu, S. Li, Y. Yang, S. Peng, Z. Hu, Y. Qian, *Adv. Mater.* **2003**, *15*, 1946–1948; f) X. Ni, L. Cheng, H. Zheng, D. Zhang, Q. Zhao, J. Song, *Chem. Lett.* **2004**, *33*, 1564–1565.

[8] a) Y. D. Li, C. W. Li, H. R. Wang, L. Q. Li, Y. T. Qian, *Mater. Chem. Phys.* **1999**, *59*, 88–90; b) G. Schwarzenbach, A. Zobrist, *Helv. Chim. Acta* **1952**, *35*, 129.

[9] W. Chang, K. Li, *Concise Handbook of Analytic Chemistry*, 1st ed., Science Press **1980**, p. 75.

[10] a) H. Zhang, D. Yang, X. Ma, Y. Ji, J. Xu, D. Que, *Nanotechnology* **2004**, *15*, 622–626; b) Z. P. Liu, S. Li, Y. Yang, Z. K. Hu, S. Peng, J. B. Liang, Y. T. Qian, *New J. Chem.* **2003**, *27*, 1748–1752.

[11] A. Gole, C. J. Murphy, *Chem. Mater.* **2004**, *16*, 3633–3640.

[12] a) J. H. Hwang, V. P. Dravid, M. H. Teng, J. J. Host, B. R. Elliott, D. L. Johnson, T. O. Mason, *J. Mater. Res.* **1997**, *12*,

 © 2005 Wiley-VCH Verlag GmbH & Co. KGaA, Weinheim

1076–1082; b) D. L. LesliePelecky, R. D. Rieke, *Chem. Mater.* **1996**, *8*, 1770–1783; c) H. O. Cao, Z. Xu, H. Sang, D. Sheng, C. Y. Tie, *Adv. Mater.* **2001**, *13*, 121–123; d) T. M. Whitney, J. S. Jiang, P. C. Searson, C. L. Chien, *Science* **1993**, *261*, 1316–1319.

[13] X. M. Ni, X. B. Su, Z. P. Yang, H. G. Zheng, *J. Cryst. Growth* **2003**, *252*, 612–617.

[14] a) D. H. Chen, S. H. Wu, *Chem. Mater.* **2000**, *12*, 1354–1360; b) N. Cordente, C. Amiens, B. Chaudret, M. Respaud, F. Senocq, M. J. Casanove, *J. Appl. Phys.* **2003**, *94*, 6358–6365; c) K. V. P. M. Shaf, A. Gedanken, R. Prozorov, J. Balogh, *Chem. Mater.* **1998**, *10*, 3445–3450.

Received: May 19, 2005
Published Online: October 25, 2005

 © 2005 Wiley-VCH Verlag GmbH & Co. KGaA, Weinheim

DOI: 10.1002/ejic.200500479

Synthesis, Characterization, and Reactivity of Neutral and Cationic Pd–C,N,N Pincer Complexes

Claudio Bianchini,[a] Géraldine Lenoble,[a] Werner Oberhauser,*[a] Sébastien Parisel,[a] and Fabrizio Zanobini[a]

Keywords: Pd pincer / NMR spectroscopy / IR spectroscopy / Secondary phosphanes / Suzuki reaction

The *ortho*-palladation of the iminophosphane ligand 6-phenyl-2-[(2,6-diisopropylphenyl)imino]pyridine (**HL**) with $Pd(OAc)_2$ and $PdCl_2(PhCN)_2$ in benzene yields the neutral Pd–C,N,N pincer complexes $Pd(OAc)(\kappa^3$-C,N,N-L) (**1**) and $PdCl(\kappa^3$-C,N,N-L) (**2**), respectively. In the presence of Na-BAr'_4 [Ar′ = 3,5-$(CF_3)_2C_6H_3$], **2** reacts in CH_2Cl_2 with MeCN, PPh_3, or PH[*o*-$MeO(C_6H_4)$]$_2$ to give the cationic palladium(II) pincer complexes $[Pd(CH_3CN)(\kappa^3$-C,N,N-L)]BAr'_4 (**3**), $[Pd(PPh_3)(\kappa^3$-C,N,N-L)]BAr'_4 (**4**) and {Pd[PH(*o*-$MeOC_6H_4)_2$]-(κ^3-C,N,N-L)}BAr'_4 (**5**), respectively. Complexes **1**–**5** have been characterized by multinuclear NMR and IR spectroscopy. The solid-state structures of **1** and **2** have been determined by single-crystal X-ray diffraction techniques. Both the neutral compounds **1** and **2** and the cationic derivatives **3**, **4**, and **5** were tested as catalyst precursors for the Suzuki cross-coupling of 4-bromo- and 4-chloroacetophenone with phenylboronic acid.

(© Wiley-VCH Verlag GmbH & Co. KGaA, 69451 Weinheim, Germany, 2005)

Introduction

Palladacycles constitute a numerous and thoroughly investigated class of organometallics commonly stabilized by four-electron (bidentate) or six-electron (tridentate) donor ligands.[1] The synthesis of palladacycles is relatively facile and the modulation of their electronic and steric properties can be achieved by varying (i) the size of the metallacyclic ring, (ii) the nature of the metallated carbon atom (aliphatic, aromatic, vinylic), (iii) the type of donor atoms (N, P, S, O) in the supporting ligand, and (iv) the nature of the co-ligands. Proper combinations of these factors determine whether dinuclear, mononuclear, neutral, or cationic compounds are formed.

Herrmann's discovery in 1995 that palladacycles can be effective catalysts for Heck coupling reactions of aryl halides has stimulated much research aimed at using these organometallics in C–C bond-forming processes.[2] The most important applications reported so far include Heck coupling, Suzuki and Stille cross-couplings, and Sonogashira reactions.[1a] Some of the most active palladacycle catalysts for Suzuki coupling reactions are reported in Scheme 1.

The C,N-palladacycles **g** and **h** reported by Milstein[3a] and Nájera,[3b] respectively, are the only really efficient phosphane-free catalysts for the Suzuki reaction of bromoarenes and chloroarenes, while the C,N- and C,O-palladacycles **b**–**f** in conjunction with either secondary bulky phosphanes[4] or N-heterocyclic carbenes[5] are very active catalytic systems for the Suzuki reaction of chloroarenes. The phosphinite P,C,P pincer complex **i** described by Bedford exhibits a good activity for bromoarenes and constitutes a successful example of the application of a terdentate palladium(II) pincer complex in a Suzuki reaction.[6] Terdentate Pd–C,N,N pincer complexes have also been used to catalyze Heck and Heck-type reactions.[7]

The ligands that have been employed so far for the synthesis of Pd–C,N,N pincer complexes are shown in Scheme 2.[8] A common structural motif to most ligands is a planar assembly of nitrogen donor atoms from either pyridine rings or imine groups, yet the combination of both moieties in the same molecule has never been tested in palladium *ortho*-metallation.

Aimed at filling this gap, we decided to study the coordination chemistry of the (imino)pyridine ligand 6-phenyl-2-[(2,6-diisopropylphenyl)imino]pyridine (**HL**) (Scheme 3) that has been successfully employed to oligomerize ethylene in conjunction with $CoCl_2$ and MAO.[9] As a result, both neutral and cationic Pd^{II}–C,N,N pincer complexes have been obtained and fully characterized. A preliminary study of the performance of these complexes in Suzuki cross-coupling reactions of 4-bromo- and 4-chloroacetophenone with phenylboronic acid has been carried out and is herein reported.

[a] ICCOM-CNR, Area della Ricerca di Firenze,
Via Madonna del Piano, 50019 Sesto Fiorentino (Firenze), Italy
Fax: +39-055-522-5203
E-mail: Werner.oberhauser@iccom.cnr.it

 © 2005 Wiley-VCH Verlag GmbH & Co. KGaA, Weinheim

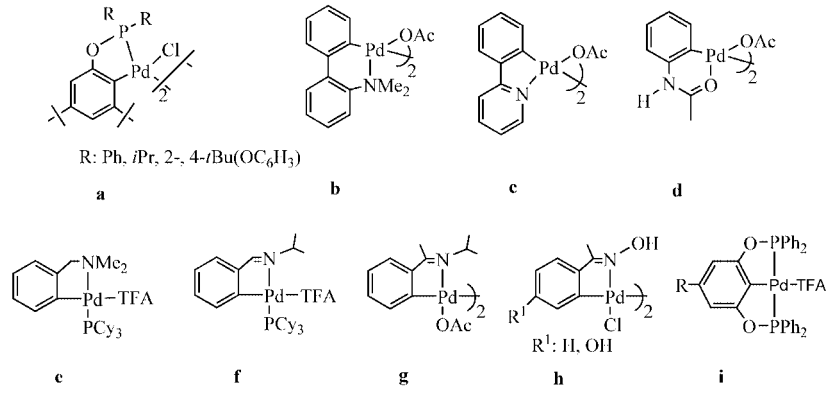

Scheme 1.

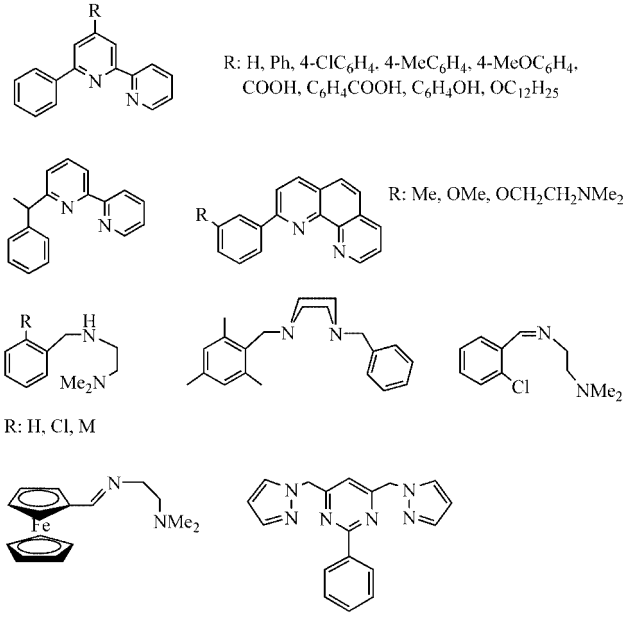

Scheme 2.

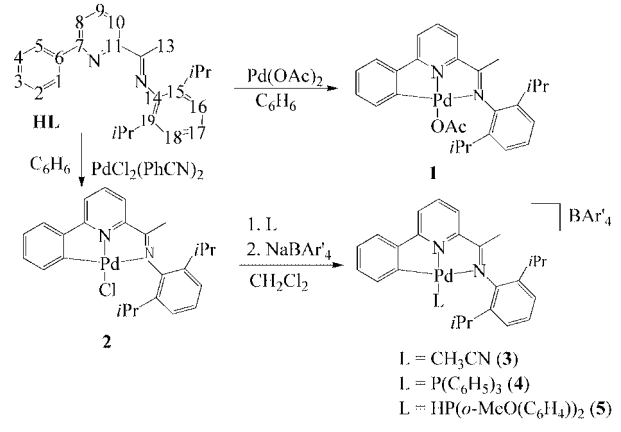

Scheme 3.

Results and Discussion

The reaction of **HL** with $Pd(OAc)_2$ and $PdCl_2(PhCN)_2$ in refluxing benzene yields the yellow, air-stable, neutral terdentate Pd–C,N,N pincer complexes Pd(OAc)L (**1**) and PdClL (**2**) in fairly good yields (57 and 81%), respectively. Complex **2** was transformed into the monocationic Pd–C,N,N pincer compounds **3**, **4**, and **5** by scavenging the chloride ion with $NaBAr'_4$ in the presence of MeCN, PPh_3, or $PH(o\text{-}MeOC_6H_4)_2$. The synthesis of the latter compounds was readily achieved by dissolving **2** in oxygen-free dichloromethane and adding acetonitrile, PPh_3, or the new secondary monophosphane $PH(o\text{-}MeOC_6H_4)_2$ (Scheme 3).

The cationic complexes were isolated in good yields, from 60–70%, as yellow, air- and moisture-stable solids. All our attempts to isolate **3**, **4**, and **5** with chloride as the counterion were unsuccessful.

The solid-state structures of **1** and **2** have been determined by a single-crystal X-ray diffraction analysis. Crystallographic data as well as selected bond lengths and angles of both compounds are reported in Tables 1 and 2, respectively, while ORTEP illustrations are presented in Figure 1.

The asymmetric unit of **1** contains one molecule of the neutral pincer complex, while that of **2** contains one molecule of **2** together with one molecule of CH_2Cl_2 and half a molecule of toluene located on an inversion center. Both complexes exhibit a distorted square-planar coordination geometry. The metal center in **1** deviates by 0.004(6) Å in the direction of C(20) from the plane defined by the atoms C(1), N(1), and N(2). From the analogous plane, **2** deviates by 0.016(6) Å in the direction of C(23). In both structures, the Pd atom is coordinated by nitrogen atoms from pyridine and imine groups and by one carbon atom, C(1), from the 6-phenyl ring. The square-planar geometry is completed by an oxygen atom, O(1) from an acetate ligand in **1**, and by a chloride atom in **2**. The slightly longer Pd(1)–N(2) bond in **1** as compared to **2** is probably due to a significant steric interaction between the acetate unit and an isopropyl group of the ligand [shortest O···H contact distance of 2.844 Å between O(2) and H(21B)]. A longer $Pd–N_{imine}$ distance in **1** was also inferred from the IR spectrum which shows a less pronounced red shift of the C=N band in **1** (21 cm^{-1})

 © 2005 Wiley-VCH Verlag GmbH & Co. KGaA, Weinheim

Table 1. Crystallographic data for **1** and **2**·CH_2Cl_2·0.5 C_7H_8.

	1	**2**·CH_2Cl_2·0.5 C_7H_8
Empirical formula	$C_{27}H_{30}N_2O_2Pd$	$C_{29.5}H_{33}Cl_3N_2Pd$
Formula mass	520.93	628.33
Temperature [K]	293(2)	293(2)
Wavelength [Å]	0.71073	0.71073
Crystal system	orthorhombic	monoclinic
Space group	$P2_12_12_1$	$P2_1/c$
a [Å]	12.050(3)	9.788(7)
b [Å]	13.909(15)	12.924(2)
c [Å]	14.530(9)	23.027(6)
β [°]	90.0	91.97(3)
V [Å^3]	2435(3)	2911(2)
Z [g m^{-3}]	4	4
$D_{calcd.}$ [g m^{-3}]	1.421	1.434
Absorption coefficient [mm^{-1}]	0.787	0.933
F(000)	1072	1284
Crystal size [mm]	0.70×0.28×0.25	0.4×0.2×0.2
θ range for data collection [°]	2.03–25.08	2.08–25.02
Limiting indices	$0 \le h \le 14$	$-11 \le h \le 11$
	$0 \le k \le 16$	$0 \le k \le 15$
	$0 \le l \le 17$	$0 \le l \le 27$
Measured reflections	2427	5087
Unique reflections	2427	5087
GOF on F^2	1.066	1.012
Data/restraints/parameters	2427/0/289	5087/8/302
Final R indices [$I > 2\sigma(I)$]	R_1 = 0.0470, wR_2 = 0.1226	R_1 = 0.0583, wR_2 = 0.1291
R indices (all data)	R_1 = 0.0555, wR_2 = 0.1281	R_1 = 0.1474, wR_2 = 0.1586
Largest diff. peak/hole [e·Å^{-3}]	1.076/–1.271	0.762/–0.892

Table 2. Selected bond lengths [Å] and angles [°] for compounds **1** and **2**·CH_2Cl_2·0.5 C_7H_8.

	1	**2**·CH_2Cl_2·0.5 C_7H_8
Pd(1)–N(1)	1.954(6)	1.955(5)
Pd(1)–N(2)	2.184(6)	2.156(6)
Pd(1)–C(1)	1.957(8)	1.970(7)
Pd(1)–O(1)	2.051(6)	
Pd(1)–Cl(1)		2.295(2)
N(2)–C(12)	1.262(10)	1.286(9)
N(1)–Pd(1)–N(2)	77.7(3)	77.4(2)
N(1)–Pd(1)–C(1)	81.8(3)	81.6(3)
C(1)–Pd(1)–O(1)	98.7(3)	
N(1)–Pd(1)–O(1)	171.5(3)	
C(1)–Pd(1)–Cl(1)		97.6(2)
N(1)–Pd(1)–Cl(1)		177.9(2)

as compared to **2** (30 cm^{-1}). The Pd(1)–C(1) bond lengths of either structure [1.957(8) Å in **1** and 1.970(7) Å in **2**] match well the values reported for other pincer Pd^{II} systems.[8a,8c,8d,8f,8h,8i] The two bite angles [N(1)–Pd(1)–C(1): 81.8(3)° in **1**; 81.6(3)° in **2**; N(1)–Pd(1)–N(2): 77.7(3)° in **1**; 77.4(2)° in **2**] are comparable in either structure, while the coordination angle N(1)–Pd(1)–O(1) of 171.5(3)° in **1** and the coordination angle N(1)–Pd(1)–Cl(1) of 177.9(2)° in **2** are significantly different. Indeed, **1** shows a deviation of the bonded oxygen atom O(1) by 0.292(17) Å from the plane defined by C(1), N(1), and N(2) in the direction of C(23), while **2** exhibits a deviation of Cl(1) by 0.111(16) Å from the analogous plane in the direction of C(23). In both crystal structures, the 2,6-(diisopropyl)phenyl moiety is, as

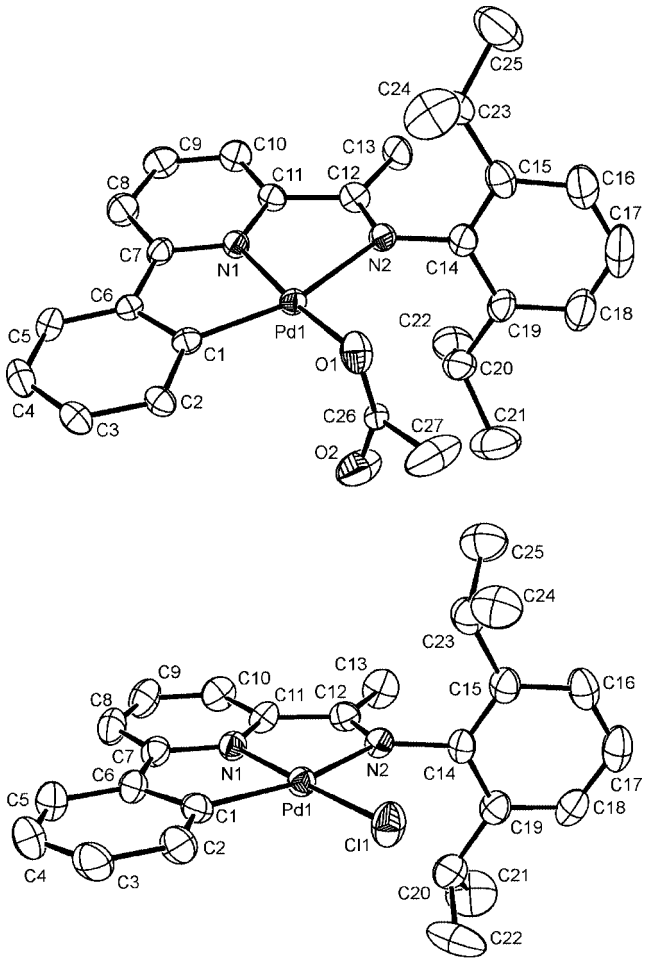

Figure 1. ORTEP representation (30% probability displacement ellipsoids) of compounds **1** (top) and **2** (bottom). Hydrogen atoms as well as solvent molecules are omitted for clarity.

expected, tilted with respect to the coordination plane, showing a dihedral angle of 76.1(5)° and 85.8(4)° in **1** and **2**, respectively, due to the pronounced steric repulsion between the coordinating acetate and an isopropyl group from the ligand.

Compounds **1**–**5** have been characterized in solution by multinuclear 1D and homo- and heteronuclear correlated 2D NMR spectroscopy.[10a] $^{13}C\{^1H\}$ NMR spectroscopy has proved to be a useful technique to elucidate the solution structure of all compounds, especially to assess the presence of a Pd–C bond involving the phenyl ring attached at the 6-position of the pyridine unit.[10b–10e] Significant ^{13}C NMR chemical shifts, namely those pertaining to the C-1, C-2,

Table 3. Selected $^{13}C\{^1H\}$ chemical shifts for HL and for compounds 1–5.

	C-1 ($^2J_{C,P}$ [Hz])	C-2 ($^3J_{C,P}$ [Hz])	C-4	C-12
HL	127.67	129.69	136.73	168.50
1	153.22	135.80	124.88	172.30
2	153.16	137.71	125.15	172.70
3	153.17	136.08	128.03	176.43
4	150.22 (4.9)	140.21 (10.5)	126.72	178.30
5	151.98 (5.4)	136.72 (10.5)	126.54	177.40

 © 2005 Wiley-VCH Verlag GmbH & Co. KGaA, Weinheim

Table 4. Selected ^{1}H chemical shifts for **HL** and for compounds **1**–**5**.

	2-H (multiplicity) ([$^3J_{H,H}$, $^4J_{H,H}$, $^4J_{P,H}$ [Hz])	3-H (multiplicity) ($^3J_{H,H}$, $^4J_{H,H}$ [Hz])	4-H (multiplicity) ($^3J_{H,H}$, $^4J_{H,H}$ [Hz])	5-H (multiplicity) ($^3J_{H,H}$, $^4J_{H,H}$ [Hz])	13-H (multiplicity)
HL	7.54 (t) (7.4)	7.48 (tt) (7.2, 1.2)	7.54 (t) (7.4)	8.18 (d) (7.2, 1.4)	2.38 (s)
1	7.19 (dd) (7.5, 1.2)	7.08 (td) (7.4, 1.6)	7.02 (td) (7.5, 1.4)	7.33 (dd) (6.6, 1.5)	2.19 (s)
2	7.41 (dd) (7.4, 1.7)	7.15 (td) (7.4, 1.7)	7.11 (td) (7.4, 1.5)	7.84 (dd) (7.4, 1.6)	2.21 (s)
3	6.99 (dd) (7.6, 1.1)	7.21 (td) (7.5, 1.2)	7.13 (td) (7.6, 1.6)	7.40 (dd) (7.6, 1.5)	2.24 (s)
4	6.32 (ddd) (8.1, 0.9, 5.3)	6.52 (td) (8.1, 1.6)	6.99 (td) (7.5, 0.8)	7.43 (dd) (7.7, 1.6)	2.10 (s)
5	6.24 (ddd) (7.8, 1.0, 5.3)	6.74 (td) (7.7, 1.5)	7.06 (td) (7.4, 1.0)	7.44 (dd) (7.8, 1.5)	2.27 (s)

and C-4 carbon atoms from the phenyl ring and to the imine carbon atom C-12 are reported in Table 3, which also provides ^{13}C NMR spectroscopic data for the free ligand. In line with the literature, the signals of C-1 and C-2 are shifted down-field as compared to the free ligand, while the signal of C-4 is shifted up-field.[10e] The ^2J(C,P) coupling constants of 4.9 Hz in **4** and 5.4 Hz in **5** provide further evidence for *ortho*-palladation involving the 6-phenyl ring. The coordination of the imine nitrogen atom to the Pd^{II} center can be safely assessed on the basis of the down-field shift of the imine carbon signal of C-12.

The ^{1}H NMR spectra of **1**–**5** are fully consistent with *ortho*-palladation of the 6-phenyl ring (Table 4).

Of particular relevance to confirm the occurrence of *ortho*-metallation are the multiplicities of the resonances of the 6-phenyl ring. Indeed, the signals of 2-H and 5-H appear as a doublet of doublet and 3-H and 4-H show a triplet of doublet, while the free ligand exhibits a doublet for the *ortho* protons 1-H and 5-H, triplets for 2-H and 4-H and a triplet of triplet for the *para* proton 3-H. The small $^4J_{P,H}$ coupling constant of 5.3 Hz observed for 2-H in the ^{1}H NMR spectra of compounds **4** and **5** is consistent with the coordination of PPh_3 and HP[*o*-MeO(C_6H_4)]$_2$. The coordination of the imine nitrogen atom to the palladium atom is confirmed by an up-field shift of the methylimine resonance (13-H), as compared to the free ligand.

Compounds **1**–**5** have been tested as catalyst precursors for the Suzuki cross-coupling reaction of 4-bromo- and 4-chloroacetophenone with phenylboronic acid in the presence of Cs_2CO_3 as the basic co-reagent in 1,4-dioxane at 100 °C (Scheme 4). This catalytic protocol is rather common for Suzuki reactions leading to selective production of the unsymmetrically substituted biaryl.[1a,1b] Selected results are given in Table 5.

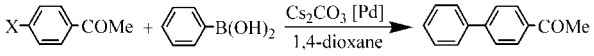

X: Br, Cl

Scheme 4.

All catalytic coupling reactions were carried out under an inert gas in freshly distilled 1,4-dioxane in order to avoid the risk of imine hydrolysis, which may be responsible for the low catalytic activity observed in a water/dioxane mixture (Entry 6). Examination of withdrawn samples showed the formation of the biaryl product after only 5 min. Unlike the reaction catalyzed by $Pd(OAc)_2$, no Pd metal precipitation was observed using **1**–**5** as the catalyst precursors. In situ NMR experiments showed the absence of free phosphane ligands during the reaction catalyzed by **4** and **5**.

In line with the results reported in the literature, 4-bromoacetophenone is much more reactive than the analogous chloro derivative, due to the lower bond strength of Ar–Br as compared to Ar–Cl.[11] The coupling of 4-bromoacetophenone with phenylboronic acid is catalyzed by both the phosphane-free precursors **1**, **2**, and **3** and the phosphane-modified precursors **4** and **5**. However, the latter form much

Table 5. Suzuki coupling of 4-bromo- and 4-chloroacetopheneone with phenylboronic acid in the presence of **1**, **2**, **3**, **4** and **5**.

Entry[a]	Complex	Substrate	[Pd] [%]	Time [h]	TON[b]
1	$Pd(OAc)_2$	Br	1.0	2	64
2	$Pd(OAc)_2$	Br	1.0	4	89
3	$Pd(OAc)_2$	Br	0.01	4	70
4	**1**	Br	1.0	2	25
5	**1**	Br	1.0	4	99
6[c]	**1**	Br	1.0	4	31
7	**2**	Br	1.0	2	83
8	**2**	Br	1.0	4	85
9	**3**	Br	1.0	2	13
10	**3**	Br	1.0	4	46
11	**4**	Br	1.0	2	100
12	**4**	Br	0.01	2	6200
13	**4**	Br	0.01	4	8900
14	**5**	Br	1.0	2	98
15	**5**	Br	0.01	2	3400
16	**5**	Br	0.01	4	9700
17	$Pd(OAc)_2$	Cl	1.0	8	0
18	**1**	Cl	1.0	8	17
19	**2**	Cl	1.0	8	2
20	**3**	Cl	1.0	8	14
21	**4**	Cl	1.0	4	17
22	**4**	Cl	1.0	8	57
23	**5**	Cl	1.0	4	61
24	**5**	Cl	1.0	8	86

[a] Catalytic conditions: 2×10^{-6} mol of Pd precatalyst, 2×10^{-4} mol of substrate, 3×10^{-4} mol of phenylboronic acid, 6×10^{-4} mol of Cs_2CO_3, *T*: 100 °C, solvent: 1,4-dioxane (15 mL). [b] TON determined by ^{1}H NMR in $CDCl_3$. [c] 1,4-Dioxane/water (14:1, v:v).

 © 2005 Wiley-VCH Verlag GmbH & Co. KGaA, Weinheim

more active catalysts, which has been previously observed and attributed to the formation of coordinatively unsaturated (phosphane)Pd^0 catalysts.[1b] As a general trend, the cationic precursors originate more efficient catalysts.

In the Suzuki cross-coupling of 4-chloroacetophenone only the monophosphane-modified precursors **4** and **5** have shown a significant activity.[12] Interestingly, the catalyst modified with the secondary phosphane $PH(o\text{-}MeOC_6H_4)_2$ is the most active with both 4-bromo- and 4-chloroacetophenone, which is consistent with Indolese's finding that bulky secondary monophosphanes in conjunction with Pd–C,N or Pd–C,O palladacycles provide powerful systems for Suzuki and Heck reactions.[4] Indeed, most of the really efficient catalytic systems for Suzuki cross-coupling contain bulky monophosphanes,[12] hemilable P–O[13] and P–N ligands,[14] and 1,3-disubstituted imidazol-2-ylidenes.[15]

In the case of **5**, an in situ NMR study under catalytic conditions has shown the occurrence of phosphane deprotonation to give various unidentified phosphido–palladium species, which might be responsible for the high catalytic activity.

Conclusions

New Pd^{II}–C,N,N pincer complexes have been synthesized and fully characterized in both the solid state and solution. As a probe reaction to test their potential in homogeneous catalysis, these complexes have been employed as catalyst precursors for cross-coupling reactions of 4-bromo- and 4-chloroacetophenone with phenylboronic acid to give 4-acetylbiphenyl. Only the phosphane-modified complexes have shown significant activity. This activity, however, is far lower than the most active catalysts reported in the literature.

Experimental Section

General: All manipulations were carried out under nitrogen using Schlenk-type techniques. All the solid compounds were collected on sintered-glass frits and washed with appropriate solvents before being dried in a stream of nitrogen. $PdCl_2(C_6H_5CN)_2$[16] and $NaB[C_6H_3(CF_3)_2]_4$ ($NaBAr'_4$)[17] were prepared according to literature methods. The ligands (2,6-diisopropylphenyl)[1-(6-phenylpyridin-2-yl)ethylidene]amine (**HL**) and 1-(6-phenylpyridin-2-yl)ethanone were prepared as reported in the literature.[9] The solvents were distilled under nitrogen from Na (*n*-pentane, diethyl ether, benzene) or CaH_2 (CH_2Cl_2). All the other reagents and solvents were used as purchased from commercial suppliers. Deuterated solvents for NMR measurements were dried with molecular sieves. Elemental analyses were performed with a Carlo Erba Model 1106 elemental analyzer. Infrared spectra were recorded with an FT-IR Spectrum GX instrument. ^1H, $^{13}C\{^1H\}$, and $^{31}P\{^1H\}$ NMR spectra were recorded at 200.13, 50.32, and 81.01 MHz, respectively, with a Bruker ACP-200 spectrometer or at 400.13, 100.62, and 161.98 MHz, respectively, with a Bruker Avance DRX-400 spectrometer. Chemical shifts are reported in ppm (δ) with reference to either TMS as an internal standard [^1H and $^{13}C\{^1H\}$ NMR spectra] or 85% H_3PO_4 as an external standard [$^{31}P\{^1H\}$ NMR spectra]. The assignment of ^1H and ^{13}C signals was based on 1D and 2D NMR experiments, such as ^1H COSY, ^1H NOESY, and ^1H-^{13}C correlations using degassed nonspinning samples. All the 2D NMR spectra were recorded with a Bruker Avance DRX-400 instrument using pulse sequences suitable for phase-sensitive representations using TPPI. The ^1H-^{13}C correlations were recorded using an HMQC sequence with decoupling during acquisition. GC analyses were performed with a Shimadzu GC-14A gas chromatograph equipped with a flame ionization detector and a 30 m (0.25 mm i.d., 0.25 μm film thickness) SPB-1 Supelco fused silica capillary column. GC-MS analyses were performed with a Shimadzu QP 5000 apparatus equipped with a column identical to that used for GC analysis.

Catalytic Reactions: 1,4-Dioxane (15 mL) was degassed in a round-bottomed flask by means of vacuum/nitrogen cycles. To this solvent were added 4-bromoacetophenone or 4-chloroacetophenone (2×10^{-4} mol), phenylboronic acid (36 mg, 3×10^{-4} mol), $CsCO_3$ (115 mg, 6×10^{-4} mol) and the appropriate precatalyst (2×10^{-6} mol) at room temperature under nitrogen. The resulting suspension was heated under nitrogen to 100 °C with stirring to give a clear solution. Heating was continued for the desired time. Then, the solution was cooled to room temperature and ethyl acetate (15 mL) was added. The solid products were removed from the solution by filtration and the organic layer was washed with water (three 30 mL portions) to remove $CsCO_3$. The aqueous layer was extracted three times with ethyl acetate. The combined organic layers were washed with brine, dried with $MgSO_4$ and concentrated to yield a pale yellow solid. The yield of the product was determined by ^1H NMR in $CDCl_3$.

Syntheses

$PH(o\text{-}CH_3OC_6H_4)_2$: The bis(*o*-methoxyphenyl)phosphane oxide $HPO(o\text{-}CH_3OC_6H_4)_2$ was synthesized as described in the literature.[18] The subsequent reduction of the phosphane oxide was performed applying a protocol similar to that published by Vineyard.[19] $HSiCl_3$ (12.1 mL, 120.0 mmol) was added to a solution of bis(*o*-methoxyphenyl)phosphane oxide (10.48 g, 40.0 mmol) and triethylamine (16.7 mL, 120.0 mmol) in acetonitrile (250 mL) at room temperature. The reaction mixture was refluxed for 8 h. Afterwards, the solution was cooled to 0 °C and a solution of KOH (40 g) in water (150 mL) was slowly added to the reaction mixture. An off-white solid precipitated that was, however, dissolved at the end of the addition to form a clear two-phase system. The organic phase was separated and the solvent was removed under reduced pressure. The crude product was washed with degassed ethanol (30 mL) and the product was filtered off and dried in a stream of nitrogen. Yield: 7.19 g (73%). $C_{14}H_{14}O_2P$ (245.1): calcd. C 68.60, H 5.71; found C 68.20; H 5.60. ^1H NMR (200.13 MHz, $CDCl_3$, 294 K): δ = 3.78 (s, 6 H, OCH_3), 5.23 (d, $^1J_{H,P}$ = 229 Hz, 1 H, PH), 6.80–7.40 (m, 8 H, C_6H_4) ppm. $^{31}P\{^1H\}$ NMR (81.01 MHz, $CDCl_3$, 294 K): δ = –71.70 (s) ppm.

[6-C_6H_4-py-2-C(Me)=N(2,6-iPr$_2C_6H_3$)]PdOAc (1): The ligand **HL** (300 mg, 0.84 mmol) and $Pd(OAc)_2$ (190 mg, 0.84 mmol) were dissolved in degassed benzene (30 mL). The resultant red solution was heated at 60 °C for 16 h. Afterwards, this solution was filtered through Celite and concentrated to 2 mL. To this solution diethyl ether (15 mL) was added to precipitate a yellow-green compound, which was filtered off and dried in a stream of nitrogen. Yield: 250 mg (57%). $C_{27}H_{30}N_2O_2Pd$ (520.69): calcd. C 62.28, H 5.76, N 5.38; found C 62.10, H 5.55, N 5.10. ^1H NMR (400.13 MHz, $CDCl_3$, 294 K): δ = 1.15 [d, $^3J_{H,H}$ = 6.8 Hz, 6 H, $CH(CH_3)_2$], 1.40 [d, $^3J_{H,H}$ = 6.8 Hz, 6 H, $CH(CH_3)_2$], 1.75 [s, 3 H, CH_3CO_2], 2.19 [s, 3 H, 13-H], 3.17 [sept, $^3J_{H,H}$ = 6.8 Hz, 2 H, $CH(CH_3)_2$], 7.02 (td, $^3J_{H,H}$ = 7.5, $^4J_{H,H}$ = 1.4 Hz, 1 H, 4-H), 7.08 (td, $^3J_{H,H}$ = 7.4,

 © 2005 Wiley-VCH Verlag GmbH & Co. KGaA, Weinheim

$^4J_{H,H}$ = 1.6 Hz, 1 H, 3-H), 7.19 (dd, $^3J_{H,H}$ = 7.5, $^4J_{H,H}$ = 1.2 Hz, 1 H, 2-H), 7.22–7.29 (m, 3 H, 16–18-H), 7.33 (dd, $^3J_{H,H}$ = 6.6, $^4J_{H,H}$ = 1.5 Hz, 1 H, 5-H), 7.35 (dd, $^3J_{H,H}$ = 6.1, $^4J_{H,H}$ = 0.9 Hz, 1 H, 10-H), 7.73 (dd, $^3J_{H,H}$ = 8.4, $^4J_{H,H}$ = 0.9 Hz, 1 H, 8-H), 7.94 (t, $^3J_{H,H}$ = 7.7 Hz, 1 H, 9-H) ppm. $^{13}C\{^1H\}$ NMR (100.62 MHz, $CDCl_3$, 294 K): δ = 17.59 (C-13), 23.25 (CH_3CO_2), 23.72 [$CH(CH_3)_2$], 23.87 [$CH(CH_3)_2$], 28.71 [$CH(CH_3)_2$], 121.05 (C-8), 121.07 (C-10), 123.48 (C-16, C-18), 124.01 (C-5), 124.88 (C-4), 126.92 (C-17), 130.85 (C-3), 135.80 (C-2), 138.72 (C-15, C-19), 139.47 (C-9), 141.02 (C-14), 146.83 (C-6), 153.20 (C-11), 153.22 (C-1), 165.34 (C-7), 172.30 (C-12), 176.81 (CH_3COO) ppm. IR (KBr): $\tilde{\nu}$ = 1617 (C=N), 1717 (C=O) cm^{-1}.

[6-C_6H_4-py-2-C(Me)=N(2,6-*i*$Pr_2C_6H_3$)]PdCl (2): The ligand **HL** (150 mg, 0.42 mmol) and $PdCl_2(C_6H_5CN)_2$ (160 mg, 0.42 mmol) were dissolved in benzene (20 mL) at room temperature. The orange suspension was refluxed for 12 h. During this time a yellow precipitate formed. The suspension was concentrated to dryness and the yellow powder was suspended in diethyl ether and filtered off, washed several times with diethyl ether and then dried in a stream of nitrogen. Yield: 180 mg (86.1%). $C_{25}H_{27}ClN_2Pd$ (497.14): calcd. C 60.40, H 5.43, N 5.63; found C 60.62, H 5.57, N 5.70. ^1H NMR (400.13 MHz, $CDCl_3$, 294 K): δ = 1.16 [d, $^3J_{H,H}$ = 6.9 Hz, 6 H, $CH(CH_3)_2$], 1.40 [d, $^3J_{H,H}$ = 6.8 Hz, 6 H, $CH(CH_3)_2$], 2.21 (s, 3 H, 13-H), 3.06 [sept, $^3J_{H,H}$ = 7.0 Hz, 2 H, $CH(CH_3)_2$], 7.11(td, $^3J_{H,H}$ = 7.4, $^4J_{H,H}$ = 1.5 Hz, 1 H, 4-H), 7.15 (td, $^3J_{H,H}$ = 7.4, $^4J_{H,H}$ = 1.7 Hz, 1 H, 3-H), 7.23–7.30 (m, 3 H, 16–18-H), 7.41 (dd, $^3J_{H,H}$ = 7.4, $^4J_{H,H}$ = 1.7 Hz, 1 H, 2-H), 7.53 (dd, $^3J_{H,H}$ = 7.8, $^4J_{H,H}$ = 0.9 Hz, 1 H, 10-H), 7.75 (dd, $^3J_{H,H}$ = 8.3, $^4J_{H,H}$ = 0.7 Hz, 1 H, 8-H), 7.84 (dd, $^3J_{H,H}$ = 7.4, $^4J_{H,H}$ = 1.6 Hz, 1 H, 5-H), 7.99 (t, $^3J_{H,H}$ = 7.8 Hz, 1 H, 9-H) ppm. $^{13}C\{^1H\}$ NMR (100.62 MHz, $CDCl_3$, 294 K): δ = 17.40 (C-13), 23.47 [$CH(CH_3)_2$], 24.02 [$CH(CH_3)_2$], 28.74 [$CH(CH_3)_2$], 120.71 (C-8), 121.0 (C-10), 123.50 (C-16, C-18), 124.31 (C-5), 125.15 (C-4), 127.20 (C-17), 131.0 (C-3), 137.71 (C-2), 138.2 (C-15, C-19), 138.91 (C-9), 141.0 (C-14), 147.0 (C-6), 152.98 (C-11), 153.15 (C-1), 165.20 (C-7), 172.70 (C-12) ppm. IR (KBr): $\tilde{\nu}$ = 1612 (C=N) cm^{-1}.

{[6-C_6H_4-py-2-C(Me)=N(2,6-*i*$Pr_2C_6H_3$)]Pd($NCCH_3$)}BAr'_4 (3): Compound **2** (60 mg, 0.12 mmol) was dissolved in a mixture of dichloromethane (15 mL) and acetonitrile (1 mL). To this yellow solution $NaBAr'_4$ (115 mg, 0.13 mmol) was added. The yellow solution was stirred for 30 min. During this time NaCl precipitated, which was removed by filtration through Celite. The clear yellow solution was then concentrated to dryness. No recrystallization was needed. Yield: 120 mg (73.0%). $C_{59}H_{39}BF_{24}N_3Pd$ (1362.61): calcd. C 52.00, H 2.86, N 3.08; found C 52.10, H 2.92, N 3.15. ^1H NMR (400.13 MHz, $CDCl_3$, 294 K): δ = 1.19 [d, $^3J_{H,H}$ = 6.9 Hz, 6 H, $CH(CH_3)_2$], 1.30 [d, $^3J_{H,H}$ = 6.8 Hz, 6 H, $CH(CH_3)_2$], 2.00 (s, 3 H, CH_3CN), 2.24 (s, 3 H, 13-H), 2.95 [sept, $^3J_{H,H}$ = 6.8 Hz, 2 H, $CH(CH_3)_2$], 6.99 (dd, $^3J_{H,H}$ = 7.6, $^4J_{H,H}$ = 1.1 Hz, 1 H, 2-H), 7.13 (td, $^3J_{H,H}$ = 7.6, $^4J_{H,H}$ = 1.6 Hz, 1 H, 4-H), 7.21 (td, $^3J_{H,H}$ = 7.5, $^4J_{H,H}$ = 1.2 Hz, 1 H, 3-H), 7.28–7.35 (m, 3 H, 16–18-H), 7.40 (dd, $^3J_{H,H}$ = 7.6, $^4J_{H,H}$ = 1.5 Hz, 1 H, 5-H), 7.41 (dd, $^3J_{H,H}$ = 7.8, $^4J_{H,H}$ = 0.9 Hz, 1 H, 10-H), 7.54 [br. s, 4 H, *p*- $B[C_6H_3(CF_3)_2]_4$], 7.66 (dd, $^3J_{H,H}$ = 8.4, $^4J_{H,H}$ = 0.8 Hz, 1 H, 8-H), 7.73 [m, 8 H, *o*-$B[C_6H_3(CF_3)_2]_4$], 7.83 (t, $^3J_{H,H}$ = 7.9 Hz, 1 H, 9-H) ppm. $^{13}C\{^1H\}$ NMR (100.12 MHz, $CDCl_3$, 294 K): δ = 3.07 (CH_3CN), 17.52 (C-13), 23.35 [$CH(CH_3)_2$], 23.94 [$CH(CH_3)_2$], 28.91 [$CH(CH_3)_2$], 118.21 [*p*-$C_6H_3(CF_3)_2$], 121.19 (CH_3CN), 122.77 (C-8), 123.31 (C-10), 124.96 (C-16, C-18), 125.28 (q, $^1J_{C,F}$ = 272.6 Hz, CF_3), 126.70 (C-5), 128.03 (C-4), 129.01 (C-17), 129.71 (q, $^2J_{C,P}$ = 32.5 Hz, CCF_3), 132.96 (C-3), 135.60 [*o*-$C_6H_3(CF_3)_2$], 136.08 (C-2), 138.87 (C-15, C-19), 140.76 (C-14), 142.32 (C-9), 147.87 (C-6), 153.17 (C-1), 154.39 (C-11), 162.68 (q, $^1J_{C,B}$ = 49.5 Hz, *ipso*-C–B), 167.36 (C-7), 176.43 (C-12) ppm. IR (KBr): $\tilde{\nu}$ = 1609 (C=N), 2327 (C–N), 2300 (C–N) cm^{-1}.

{[6-C_6H_4-py-2-C(Me)=N(2,6-*i*$Pr_2C_6H_3$)]Pd[$P(C_6H_5)_3$]}BAr'_4 (4): Compound **2** (80 mg, 0.16 mmol) and PPh_3 (40 mg, 0.16 mmol) were dissolved in degassed CH_2Cl_2 (20 mL). To this yellow solution $NaBAr'_4$ (170 mg, 0.19 mmol) was added. During a reaction time of 3 h, NaCl was formed, which was removed by filtration through Celite. The clear yellow solution was then concentrated to 2 mL and *n*-hexane was added to precipitate a yellow product, which was filtered off and dried in a stream of nitrogen. Yield: 160 mg (62.7%). $C_{75}H_{54}BF_{24}N_2PPd$ (1586.78): calcd. C 56.77, H 3.40, N 1.76; found C 56.62, H 3.55, N 1.84. ^1H NMR (400.13 MHz, $CDCl_3$, 294 K): δ = 0.79 [d, $^3J_{H,H}$ = 6.8 Hz, 6 H, $CH(CH_3)_2$], 1.01 [d, $^3J_{H,H}$ = 6.8 Hz, 6 H, $CH(CH_3)_2$], 2.10 (s, 3 H, 13-H), 2.86 [sept, $^3J_{H,H}$ = 6.8 Hz, 2 H, $CH(CH_3)_2$], 6.32 (ddd, $^3J_{H,H}$ = 8.1, $^3J_{H,P}$ = 5.3, $^4J_{H,H}$ = 0.8 Hz, 1 H, 2-H), 6.52 (td, $^3J_{H,H}$ = 8.1, $^4J_{H,H}$ = 1.6 Hz, 1 H, 3-H), 6.88 (d, $^3J_{H,H}$ = 7.8 Hz, 2 H, 16-H, 18-H), 6.99 (td, $^3J_{H,H}$ = 7,5, $^4J_{H,H}$ = 0.8 Hz, 1 H, 4-H), 7.15 (t, $^3J_{H,H}$ = 7.8 Hz, 1 H, 17-H), 7.23 (m, 12 H, *o*+*m*-PPh_3), 7.41 (m, 3 H, *p*-PPh_3), 7.43 (dd, $^3J_{H,H}$ = 7.7, $^4J_{H,H}$ = 1.6 Hz, 1 H, 5-H), 7.52 (d, 1 H, 10-H), 7.53 {br. s, 4 H, *p*-$B[C_6H_3(CF_3)_2]_4$}, 7.74 {m, 8 H, *o*-$B[C_6H_3(CF_3)_2]_4$}, 7.88 (t, $^3J_{H,H}$ = 8.2 Hz, 1 H, 9-H), 7.89 (d, $^3J_{H,H}$ = 8.2 Hz, 1 H, 8-H) ppm. $^{13}C\{^1H\}$ NMR (100.62 MHz, $CDCl_3$, 294 K): δ = 18.90 (C-13), 22.71 [$CH(CH_3)_2$], 23.50 [$CH(CH_3)_2$], 28.73 [$CH(CH_3)_2$], 117.50 [*p*-$C_6H_3(CF_3)_2$], 122.10 (C-8), 122.60 (C-10), 124.20 (C-16, C-18), 124.50 (q, $^1J_{CF}$ = 272.6 Hz, CF_3), 125.80 (C-5), 126.72 (C-4), 128.0 (*p*-PPh_3), 128.80 (d, $^3J_{C,P}$ = 10.8 Hz, *m*-PPh_3), 128.80 (q, $^2J_{C,P}$ = 32.5 Hz, CCF_3), 128.90 (C-17), 128.90 (d, $^1J_{C,P}$ = 49.8 Hz, *ipso*-PPh_3), 130.90 (d, $^4J_{C,P}$ = 4.5 Hz, C-3), 131.50 (*o*-PPh_3), 134.80 [*o*-$C_6H_3(CF_3)_2$], 137.80 (C-15, C-19), 140.21 (d, $^3J_{C,P}$ = 10.5 Hz, C-2), 141.80 (C-9), 142.80 (C-14), 148.10 (C-6), 150.22 (d, $^2J_{C,P}$ = 4.9 Hz, C-1), 151.98 (C-11), 161.80 (q, $^1J_{C,B}$ = 49.5 Hz, *ipso*-CB), 164.20 (C-7), 178.30 (C-12) ppm. $^{31}P\{^1H\}$(161.98 MHz, $CDCl_3$, 294 K): δ = 39.2 (s) ppm. IR (KBr): $\tilde{\nu}$ = 1608 (C=N) cm^{-1}.

{[6-C_6H_4-py-2-C(Me)=N(2,6-*i*$Pr_2C_6H_3$)]Pd[PH(*o*-$MeOC_6H_4$)]$_2$}-BAr'_4 (5): Compound **2** (100 mg, 0.22 mmol) and PH(*o*-MeO-C_6H_4)$_2$(53 mg, 0.22 mmol) were dissolved in degassed CH_2Cl_2 (20 mL). To this yellow solution $NaBAr'_4$ (190 mg, 0.21 mmol) was added. During a reaction time of 2 h NaCl was formed, which was removed by filtration through Celite. The clear yellow solution was then concentrated to 3 mL and *n*-hexane was added to precipitate a bright yellow product, which was filtered off and dried in a stream of nitrogen. Yield: 0.16 g, (60.0%). $C_{71}H_{54}BF_{24}N_2O_2PPd$ (1570.71): calcd. C 54.29, H 3.44, N 1.78; found C 54.15, H 3.33, N 1.67. ^1H NMR (400.13 MHz, $CDCl_3$, 294 K): δ = 0.85 [d, $^3J_{H,H}$ = 6.8 Hz, 6 H, $CH(CH_3)_2$], 1.06 [d, $^3J_{H,H}$ = 6.8 Hz, 6 H, $CH(CH_3)_2$], 2.27 (s, 3 H, 13-H), 2.86 [sept, $^3J_{H,H}$ = 6.8 Hz, 2 H, $CH(CH_3)_2$], 3.66 (s, 3 H, OCH_3), 5.39 (d, $^1J_{P,H}$ = 381.5 Hz, 1 H, PH), 6.24 (ddd, $^3J_{H,H}$ = 7.8, $^4J_{H,H}$ = 1.0, $^4J_{PH}$ = 5.3 Hz, 2-H), 6.74 (td, $^3J_{H,H}$ = 7.7, $^4J_{H,H}$ = 1.5 Hz, 3-H), 6.84–6.95 (m, 6 H, *m* + *o*-Anisyl), 7.06 (td, $^3J_{H,H}$ = 7.4, $^4J_{H,H}$ = 1.0 Hz, 1 H, 4-H), 7.22 (m, 2 H, 16-H, 18-H), 7.34 (m, 1 H, 17-H), 7.44 (dd, $^3J_{H,H}$ = 7.8, $^4J_{H,H}$ = 1.5 Hz, 1 H, 5-H), 7.46 (dt, $^3J_{H,H}$ = 8.7, $^4J_{H,H}$ = 1.0, $^5J_{H,P}$ = 1.0 Hz, 1 H, 10-H), 7.50 (m, 2 H, *p*-Anisyl), 7.53 {m, 4 H, *p*-$B[C_6H_3(CF_3)_2]_4$}, 7.71 (dt, $^3J_{H,H}$ = 7.7, $^4J_{H,H}$ = 1.0, $^5J_{H,P}$ = 1.0 Hz, 1 H, 8-H), 7.73 {m, 8 H, *o*-$B[C_6H_3(CF_3)_2]_4$}, 7.81 (dd, $^3J_{H,H}$ = 7.7, $^3J_{H,H}$ = 8.4 Hz, 1 H, 9-H) ppm. $^{13}C\{^1H\}$ NMR (100.62 MHz, $CDCl_3$, 294 K): δ = 18.92 (C-13), 22.40 [$CH(CH_3)_2$], 23.98 [$CH(CH_3)_2$], 28.73 [$CH(CH_3)_2$], 55.70 (OCH_3), 111.35 (d, $^2J_{C,P}$ = 4.7 Hz, *o*-Anisyl), 111.41 (d, $^1J_{C,P}$ = 54.5 Hz, *ipso*-Anisyl), 117.80 {*p*-$[C_6H_3(CF_3)_2]$}, 121.64 (d, $^3J_{C,P}$ = 4.7 Hz, *m*-Anisyl), 121.93 (C-8), 122.29 (C-10) 124.37 (C-17), 124.50 (d, $^1J_{C,F}$ = 272.6 Hz, CF_3),

 © 2005 Wiley-VCH Verlag GmbH & Co. KGaA, Weinheim

125.89 (C-5), 126.54 (C-4), 127.96 (C-16, C-18), 128.80 (d, $^2J_{C,F}$ = 32.5 Hz, *C*CF_3), 129.50 (q, $^2J_{C,F}$ = 32.5 Hz, *C*CF_3), 131.86 (d, $^4J_{C,P}$ = 4.0 Hz, C-3), 134.80 {*o*-[$C_6H_3(CF_3)_2$]}, 135.57 (d, $^3J_{C,P}$ = 8.0 Hz, *m*-Anisyl), 134.24 (*p*-Anisyl), 136.72 (d, $^3J_{C,P}$ = 10.5 Hz, C-2), 138.06 (C-15, C-19), 140.98 (C-14), 141.51 (C-9), 148.60 (C-6), 151.98 (d, $^2J_{C,P}$ = 5.4 Hz, C-1), 152.24 (C-11), 160.82 (d, $^2J_{C,P}$ = 3.3 Hz, *C*–OCH_3), 162.30 (q, $^1J_{C,B}$ = 49.5 Hz, *ipso*-*C*–B), 164.25 (C-7), 177.40 (C-12) ppm. $^{31}P\{^1H\}$(161.98 MHz, $CDCl_3$, 294 K): δ –23.34 (s) ppm. IR (KBr): $\tilde{\nu}$ = 1607 (C=N) cm^{-1}.

X-ray Crystallographic Analysis of 1 and 2: Single crystals of both compounds were obtained by slow diffusion of toluene at room temperature into a saturated CH_2Cl_2 solution of **1** and **2**, respectively. Diffraction data were collected at room temperature with an Enraf Nonius CAD4 automatic diffractometer with Mo-K_α radiation (graphite monochromator). Unit cell parameters of both structures were determined from a least-squares refinement of the setting angles of 25 carefully centered reflections. Crystal data and data collection details are given in Table 1. Lorentz polarization and absorption corrections were applied.[20a] Atomic scattering factors were taken from ref.[20b] and an anomalous dispersion correction, with a real and imaginary part, was applied.[20c] The structures were solved by direct methods and refined by full-matrix F^2 refinement. While in **1** anisotropic thermal parameters were assigned to all non-hydrogen atoms, in **2** only the disordered toluene molecule was treated isotropically. In both structures, the hydrogen atoms were introduced in their calculated positions, with thermal parameters 20% larger than those of the respective carbon atoms. All the calculations were performed with a PC using the WINGX package[20d] with SIR-97,[20e] SHELX-97,[20f] and ORTEP-3 programs.[20g] CCDC-271410 (**1**), and -271409 (**2**) contain the supplementary crystallographic data for this paper. These data can be obtained free of charge from The Cambridge Crystallographic Data Centre via www.ccdc.cam.ac.uk/data_request/cif.

Acknowledgments

Thanks are due to the European Commission (Contract HPRN-CT-2002-00196, PALLADIUM project) for financial support. Thanks are also due to the Ente Cassa di Risparmio di Firenze for a generous grant.

[1] a) J. Dupont, M. Pfeffer, J. Spencer, *Eur. J. Inorg. Chem.* **2001**, 1917; b) R. B. Bedford, *Chem. Commun.* **2003**, 1787; c) A. Zapf, M. Beller, *Chem. Commun.* **2005**, 431.

[2] a) W. A. Herrmann, C. Brossmer, K. Öfele, C. P. Reisinger, T. Priermeier, M. Beller, H. Fischer, *Angew. Chem. Int. Ed. Engl.* **1995**, *34*, 1844; b) M. Beller, H. Fischer, W. A. Herrmann, K. Öfele, C. Brossmer, *Angew. Chem. Int. Ed. Engl.* **1995**, *34*, 1848.

[3] a) H. Weissman, D. Milstein, *Chem. Commun.* **1999**, 1901; b) L. Botella, C. Nájera, *Angew. Chem. Int. Ed.* **2002**, *41*, 179.

[4] A. Schnyder, A. F. Indolese, M. Studer, H. U. Blaser, *Angew. Chem. Int. Ed.* **2002**, *41*, 3668.

[5] O. Navarro, R. A. Kelly, S. P. Nolan, *J. Am. Chem. Soc.* **2003**, *125*, 16194.

[6] a) R. B. Bedford, C. S. J. Cazin, S. J. Coles, T. Gelbrich, M. B. Hursthouse, V. J. M. Scordia, *Dalton Trans.* **2003**, 3350; b) R. B. Bedford, S. M. Draper, P. N. Scully, S. L. Welch, *New J. Chem.* **2000**, *24*, 745.

[7] a) C.-T. Chen, Y.-S. Chan, Y.-R. Tzeng, M.-T. Chen, *Dalton Trans.* **2004**, 2691; b) J. Bravo, C. Cativiela, R. Navarro, E. P. Urriolabeitia, *J. Organomet. Chem.* **2002**, *650*, 157.

[8] a) G. Minghetti, M. A. Cinellu, G. Chelucci, S. Gladiali, F. Demartin, M. Manassero, *J. Organomet. Chem.* **1986**, *307*, 107; b) G. Bombieri, L. Cagliati, L. Cattalini, E. Forsellini, F. Gasparrini, R. Graziani, P. A. Vigato, *Chem. Commun.* **1971**, 1415; c) J. W. Suggs, M. J. Dube, M. Nichols, *J. Chem. Soc., Chem. Commun.* **1993**, 307; d) A. J. Blake, C. O. Dietrich-Buchecker, T. I. Hyde, J. P. Sauvage, M. Schröder, *J. Chem. Soc., Chem. Commun.* **1989**, 1663; e) F. Neve, M. Ghedini, A. Crespini, *J. Chem. Soc., Chem. Commun.* **1996**, 2463; f) F. Neve, A. Crispini, C. Di Dietro, S. Campagna, *Organometallics* **2002**, *21*, 3511; g) E. C. Constable, R. P. G. Henney, T. A. Leese, D. A. Tocher, *J. Chem. Soc. Dalton Trans.* **1990**, 443; h) E. C. Constable, R. P. G. Henney, T. A. Leese, D. A. Tocher, *J. Chem. Soc. Chem. Commun.* **1990**, 513; i) S.-W. Lai, T.-C. Cheung, M. C. W. Chan, K.-K. Cheung, S.-M. Peng, C.-M. Che, *Inorg. Chem.* **2000**, *39*, 255; j) C. Lòpez, A. Pawelczyk, X. Solans, M. Font-Bardìa, *Inorg. Chem. Commun.* **2003**, *6*, 451; k) J. M. Vila, M. Gayoso, M. T. Pereira, M. L. Torres, J. J. Fernàndez, J. M. Ortigueira, *J. Organomet. Chem.* **1997**, *532*, 171; l) P. L. Alsters, P. F. Engel, M. P. Hogerheide, M. Copijn, A. L. Spek, G. van Koten, *Organometallics* **1993**, *12*, 1831.

[9] C. Bianchini, G. Mantovani, A. Meli, F. Migliacci, F. Laschi, *Organometallics* **2003**, *22*, 2545.

[10] a) R. Benn, H. Günther, *Angew. Chem. Int. Ed. Engl.* **1983**, *22*, 350; b) P. J. Steel, G. B. Caygill, *J. Organomet. Chem.* **1987**, *327*, 101; c) R. Bosque, C. Lòpez, J. Sales, D. Tramuns, X. Solans, *J. Chem. Soc. Dalton Trans.* **1995**, 2445; d) G. R. Newkome, W. E. Puckett, V. K. Gupta, G. E. Kiefer, *Chem. Rev.* **1986**, *86*, 451; e) A. R. Garber, P. E. Garrou, G. E. Hartwell, M. J. Smas, J. R. Wilkinson, L. J. Todd, *J. Organomet. Chem.* **1975**, *86*, 219.

[11] V. V. Grushin, H. Alper, *Chem. Rev.* **1994**, *94*, 1047.

[12] a) A. Zapf, A. Ehrentraut, M. Beller, *Angew. Chem. Int. Ed.* **2000**, *39*, 4153; b) J. P. Wolfe, S. L. Buchwald, *Angew. Chem. Int. Ed.* **1999**, *38*, 2413; c) J. P. Wolfe, R. A. Singer, B. H. Yang, S. L. Buchwald, *J. Am. Chem. Soc.* **1999**, *121*, 9550; d) A. F. Littke, G. C. Fu, *Angew. Chem. Int. Ed.* **2002**, *41*, 4176; e) A. F. Littke, G. C. Fu, *Angew. Chem. Int. Ed. Engl.* **1998**, *37*, 3387; f) S.-Y. Liu, M. J. Choi, G. C. Fu, *Chem. Commun.* **2001**, 2408.

[13] X. Bei, H. W. Turner, W. H. Weinberg, A. S. Guram, *J. Org. Chem.* **1999**, *64*, 6797.

[14] M. L. Clarke, D. J. Cole-Hamilton, J. D. Woollins, *J. Chem. Soc. Dalton Trans.* **2001**, 2721.

[15] a) C. Zhang, J. Huang, M. L. Trudell, S. P. Nolan, *J. Org. Chem.* **1999**, *64*, 3804; b) V. P. W. Böhm, C. W. K. Gstöttmayr, T. Weskamp, W. A. Herrmann, *J. Organomet. Chem.* **2000**, *595*, 186.

[16] G. K. Anderson, M. Lin, *Inorg. Synth.* **1989**, *28*, 61.

[17] M. Brookhart, B. Grant, A. F. Volpe, *Organometallics* **1992**, *11*, 3920.

[18] R. L. Wife, A. B. van Oort, J. A. van Doorn, P. W. N. M. van Leeuwen, *Synthesis* **1983**, *1*, 71.

[19] B. D. Vineyard, W. S. Knowles, M. J. Sabacky, G. L. Bachman, D. J. Weinkauff, *J. Am. Chem. Soc.* **1977**, *99*, 5946.

[20] a) S. Parkin, B. Moezzi, H. Hope, *J. Appl. Crystallogr.* **1995**, *28*, 53; b) J. C. Wilson, *International Tables for X-ray Crystallography*, Kluwer, Dordrecht, **1992**, p. 500; c) J. C. Wilson, *International Tables for X-ray Crystallography*, Kluwer, Dordrecht, **1992**, p. 219; d) L. J. Farrugia, *J. Appl. Crystallogr.* **1999**, *32*, 837; e) A. Altomare, M. C. Burla, M. Cavalli, G. L. Cascarano, C. Giacovazzo, A. Gagliardi, G. G. Moliterni, G. Polidori, R. Spagna, *J. Appl. Crystallogr.* **1999**, *32*, 115; f) G. M. Sheldrick, *SHELX-97*, University of Göttingen, **1997**; g) M. N. Burnett, C. K. Johnson, Report ORNL-6895, Oak Ridge National Laboratory, Oak Ridge, TN, **1996**.

Received: May 26, 2005
Published Online: October 11, 2005

 © 2005 Wiley-VCH Verlag GmbH & Co. KGaA, Weinheim

DOI: 10.1002/ejic.200500488

Synthesis, Characterization, and Catalytic Properties of SiPW-X Mesoporous Silica with Heteropolyacid Encapsulated into Their Framework

Chunfeng Shi,[a,b] Runwei Wang,[a] Guangshan Zhu,[a] Shilun Qiu,*[a] and Jun Long*[b]

Keywords: Heteropolyacids / Mesoporous materials / Encapsulation / Cracking / Esterification / Bulky molecule reactions

A series of SiPW-X mesoporous silica with Keggin-type heteropolyacids (HPAs) encapsulated into their framework have been synthesized under strong acidic conditions. During hydrolysis of tetraethyl orthosilicate (TEOS), Na_2HPO_4 (P source) and Na_2WO_4 (W Source) are added into the initial sol-gel system to form Keggin type HPAs. The final products have been intensively characterized by various techniques, such as XRD, TEM, N_2 adsorption isotherm analysis, and by IR, UV/Visible, and ^{31}P Magic Angle Spinning (MAS) NMR spectroscopy. Characterization results suggest that samples with an HPA weight percent of 13.3–20.7 % show very ordered hexagonal mesostructures. In addition, HPAs incorporated in the mesosilica are insoluble during catalysis. Results of catalytic tests show that SiPW-X materials have catalytic activities that are comparable to bulk HPA in catalytic tests implementing chemical reactions of both small (cumene cracking and esterification of ethanol with acetic acid) and bulky (1,3,5-triisopropylbenzene cracking and esterification of benzoic acid with *tert*-butanol) molecules. It can be readily separated from the reaction system for reuse, which suggests the potential industrial application.

(© Wiley-VCH Verlag GmbH & Co. KGaA, 69451 Weinheim, Germany, 2005)

Introduction

The discovery of mesoporous materials (such as M41S, MSU and the SBA series) in the last decade has attracted much attention because of their potential uses as catalysts or catalyst supports in industrial applications. .[1–5] Incorporation of heteroatoms into mesoporous silica frameworks to form active sites in catalysis has been widely reported. For example, Al species have been introduced into the mesostructure and used as acidic catalysts in many catalytic reactions.[6–13] In addition, mesoporous silica has often been used as a solid support in catalysis because of its high surface area and relatively large pore size. Some mesoporous materials with strong acidic sites on the surface have shown relatively high activities in many catalytic reactions.[14–49]

It is well known that heteropolyacids (HPAs) with Keggin structures, especially 12-tungstophosphoric acid (HPW), have been widely applied in catalysis due to its strong acidity, facile preparation, and acceptable stability.[32–49] However, the catalytic activities of HPAs are greatly limited because of their very low specific surface areas.[16] Therefore, some researchers have carried on the investigation of HPAs supported on mesoporous materials.[14–31] For example, Corma et al. and Xia et al. have used HPAs supported on MCM-41 carriers, and these materials show high activity in isobutene alkylation and in the synthesis of MTBE.[16,17] Nevertheless, their success and widespread use is limited for two reasons. First, HPA clusters block some pores causing the surface area of the modified mesoporous materials to be reduced significantly. Second, HPAs, from modified samples, leach into polar solvents leading to a decrease in catalytic activity and making it impossible to recycle in liquid-phase reactions.[36] Some new synthetic routes and techniques for supporting HPAs on the porous materials have been reported that avoid these two problems.[37–41] Hu et al. have prepared silica-supported Keggin-type HPAs by encapsulating HPAs into a silica matrix by a sol-gel technique involving the hydrolysis of tetraethoxysilane (TEOS).[40] Recently, Nowińska et al. have reported the incorporation of HPAs into mesoporous materials by introducing the HPA into the sol-gel during the hydrolysis of TEOS in the preparation of SBA-3.[41] However, after heating to reflux in methanol, HPA is extracted and the mesostructure collapsed. The relatively low stability of the materials can be attributed to their relatively thin wall thickness.

It has been widely reported that mesoporous silica of SBA-15 has been extensively used as support and host because of its larger pore size, thicker wall and higher hydrothermal stability than MCM-41 (SBA-3).[4,5] We have introduced Na_2HPO_4 (P source) and Na_2WO_4 (W Source) into the initial sol-gel during preparation of SBA-15 and suc-

[a] State Key Laboratory of Inorganic Synthesis and Preparative Chemistry, Department of Chemistry, Jilin University, Changchun 130012, P. R. China
Fax: + 86-431-5168589
E-mail: sqiu@mail.jlu.edu.cn
[b] Research Institute of Petroleum Processing, China Petroleum & Chemical Corporation (SINOPEC), Beijing 100083, P. R. China
Fax: + 86-10-62311290
E-mail: chfshi@yahoo.com.cn

 © 2005 Wiley-VCH Verlag GmbH & Co. KgaA, Weinheim

cessfully synthesized new mesoporous silica encapsulated with Keggin-type HPA. Here, we report the synthesis, characterization, and catalytic properties of SiPW-X mesosilica with Keggin-type 12-tungstophosphoric acid (HPW) encapsulated into their framework.

Results and Discussions

Spectroscopy

X-ray Diffraction

Figure 1 shows small-angle powder XRD patterns of SiPW-X samples with various HPW content. Obviously, the mesostructure ordering of the samples gradually decreases with increasing HPW content. The samples of SiPW-16 and SiPW-8 (Figure 1b and c, and Table 1) exhibit three well-resolved peaks indexed as (100), (110), and (200), which can be associated with *p6mm* hexagonal symmetry that is similar to that of pure silica SBA-15 (Figure 1a).[4,5] In fact, the ordering of the samples with high HPW content is very small. For example, sample SiPW-4 only gives one broad peak (Figure 1d) and sample SiPW-2 gives no obvious diffraction pattern (Figure 1e). These results indicate that the content of HPW in mesosilica with a highly ordered structure is 13.3–20.7 wt.-%. Additionally, the only difference in the XRD patterns of pure silica SBA-15, SiPW-8, and SiPW-16 is the intensity of the three observed diffraction peaks (Figure 1), and this suggests that the formation of HPW by the addition of Na_2HPO_4 and Na_2WO_4 into the sol-gel during the hydrolysis of TEOS does not disturb the formation of the mesoporous structure. Moreover, wide-angle powder XRD patterns recorded for modified samples (not given) do not show any obvious characteristic signals for HPW, indicating very high HPW dispersion in the mesosilica matrix.[30]

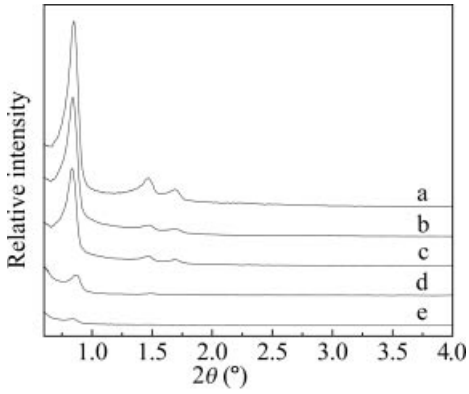

Figure 1. Small-angle XRD patterns of various samples: (a) SBA-15, (b) SiPW-16, (c) SiPW-8, (d) SiPW-4, and (e) SiPW-2.

Table 1. HPW content and parameters for the pore structure of SiPW-X, SBA-15, HPW, and HPW/SBA.

Samples	HPW content		*d* (nm)	*a* (nm)	Pore size (nm)	Wall thickness (nm)[a]	BET surface area (m^2/g)	Pore volume (cm^3/g)
	sol-gel (wt.%)	Product (wt.%)						
SiPW -4	50.0	23.2	10.2	11.8	6.8	5.0	570	0.77
SiPW -8	33.2	20.7	10.6	12.2	7.5	4.7	805	0.94
SiPW -16	20.0	13.3	10.5	12.1	7.6	4.5	828	1.03
SBA-15	0.0	0.0	10.3	11.9	7.9	4.0	860	1.15
HPW/SBA	20.0	20.0	10.2	11.8	7.8	4.0	366	0.65
HPW	100	100	-	-	-	-	7	-

[a] Pore size distributions were determined from N_2 adsorption isotherms, and the wall thickness was calculated as: thickness = *a* – pore size ($a = 2d_{(100)}/3^{1/2}$).

Transmission Electron Microscopy

TEM images of mesoporous samples with varied HPW content are shown in Figure 2. Obviously, the pores of all the samples are hexagonal analogous to those of pure silica SBA-15.[4,5] Compared with Figure 2c–f, the images shown in Figure 2a and b suggest that the ordering of the SiPW-4 sample is less than that of the SiPW-8 and SiPW-16 samples, which is in agreement with the results of XRD. Moreover, it can also be observed that there are many out-of-order components deposited in the mesoporous channels of

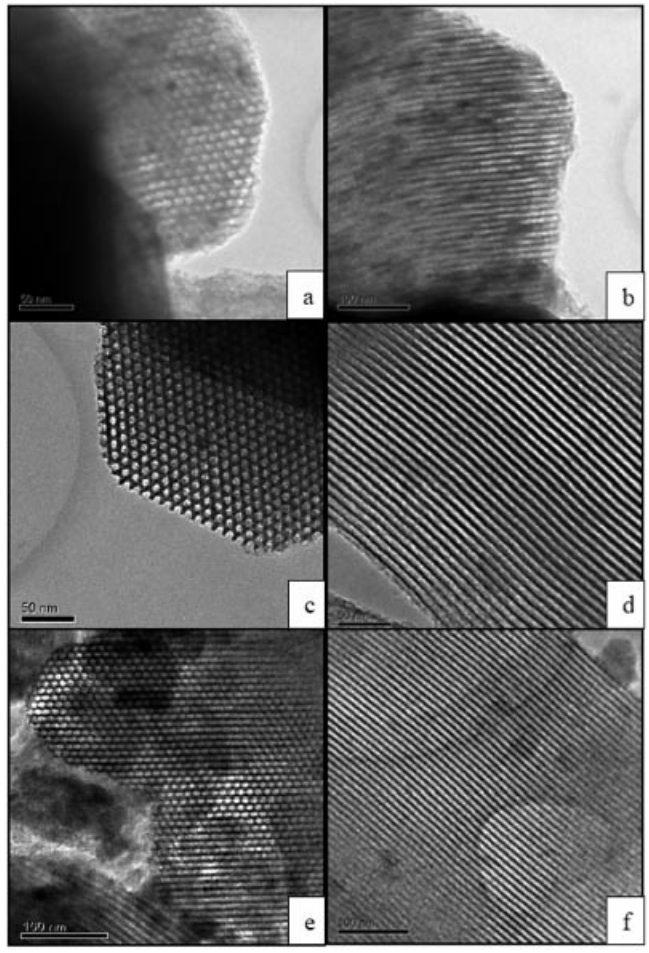

Figure 2. TEM images of various samples: (a) SiPW-4 in [100] direction, (b) SiPW-4 in [110] direction, (c) SiPW-8 in [100] direction, (d) SiPW-8 in [110] direction, (e) SiPW-16 in [100] direction, and (f) SiPW-16 in [110] direction.

 © 2005 Wiley-VCH Verlag GmbH & Co. KGaA, Weinheim

the SiPW-4 sample (Figure 2a and b). The weight content of HPW in the SiPW-4 sample is a little higher (23.2%) than those of the other samples. Therefore, some HPW species cannot be incorporated into the wall of the mesoporous silica but rather be deposited in the mesoporous channels as small, silica-HPW domains.

N_2 Adsorption Isotherms

Figure 3 shows the N_2 adsorption isotherms of the SiPW-X samples with varied HPW content. The porous parameters are listed in Table 1. Obviously, SiPW-8 and SiPW-16 show a typical adsorption curve of type IV with an obvious hysteresis loop at a relative pressure of $0.6<P/P_0<0.9$ (Figure 3c and d), which is very similar to that of pure silica SBA-15.[4,5] However, increasing the content of HPW leads to a decrease in surface area and pore volume. For example, the Brunauer, Emmett and Teller (BET) surface area and pore volume of SiPW-16 were found to be 828 m^2/g and 1.03 cm^3/g, the corresponding values of SiPW-8 and SiPW-4 were 805 m^2/g and 0.94 cm^3/g, and 570 m^2/g and 0.77 cm^3/g, respectively. Additionally, there is no obvious difference in the porous parameters of pure silica SBA-15 and of the SiPW-8 and SiPW-16 samples, indicating the formation and presence of HPW in the initial gel does not disturb the formation of the mesostructure, which is in agreement with the XRD results.

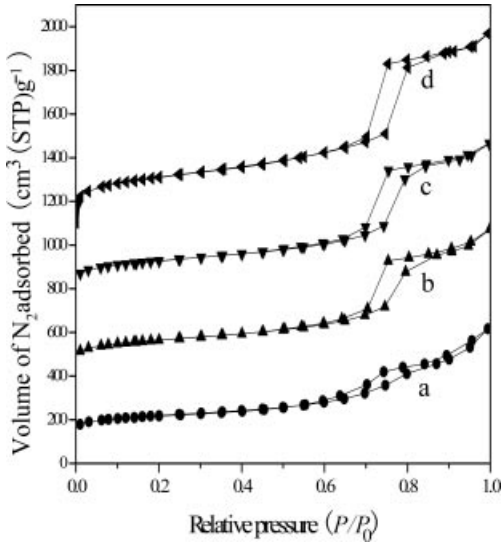

Figure 3. N_2 adsorption/desorption isotherms of various samples at STP: (a) SiPW-4, (b) SiPW-8, (c) SiPW-16, and (d) SBA-15.

IR Spectra

Infrared spectra of various samples are shown in Figure 4. It has been widely reported that HPWs with Keggin structures give several strong, typical IR bands at ca. 1080 cm^{-1} (stretching frequency of P–O in the central PO_4 tetrahedron), 983 cm^{-1} (terminal bands for W=O in the exterior WO_6 octahedron), 889 and 803 cm^{-1} (bands for the $W–O_b–W$ and $W–O_c–W$ bridge, respectively)[21,22,24] [Figure 4a]. It is well known that pure mesoporous SBA-15 silica shows framework bands at 805 cm^{-1} (symmetric stretching frequency of Si–O–Si), 960 cm^{-1} (stretching frequency of Si–O–H), 1060–1100 cm^{-1} (*anti*-symmetric stretching of Si–O–Si) [Figure 4d]. In our case, the SiPW-8 and SiPW-16 samples give bands at 1080, 963, 890, 803 cm^{-1} and one shoulder band at 982 cm^{-1} in the 600–1400 cm^{-1} region (Figure 4b and c). The band at 890 cm^{-1} and the weak shoulder band at 982 cm^{-1} can be attributed to the characteristic Keggin type HPW $W–O_b–W$ bridge and the terminal W=O, respectively,[21] the broadened bands at 1080 and 800 cm^{-1} are the characteristic bands of HPW, which overlap with the bands of mesoporous SBA-15.[22,43] These results confirm the presence of HPW encapsulated into the mesoporous silica framework.

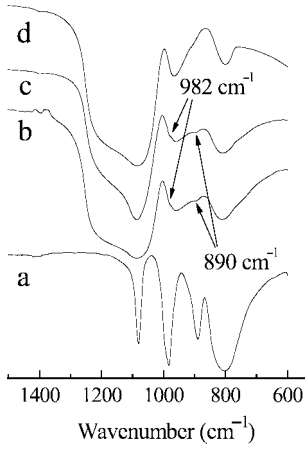

Figure 4. IR spectra of various samples: (a) HPW, (b) SiPW-8, (c) SiPW-16, and (d) SBA-15.

UV/Visible Diffuse Reflectance Spectra

Some evidence of the presence of HPW in the mesoporous silica framework is also provided by UV/Visible spectroscopy. The UV/Visible spectra of mesoporous samples with varied HPW content are shown in Figure 5. Bulk HPW shows a maximum UV absorption peak at 265 nm, which is attributed to the oxygen–tungsten charge-transfer absorption band for Keggin anions[40] (Figure 5a). Pure SBA-15 silica shows no UV absorption (Figure 5d). In our case, both SiPW-8 (Figure 5b) and SiPW-16 (Figure 5c) samples have a broad UV absorption in the range of 200–300 nm – a characteristic UV absorption peak is centered at 263–266 nm, which is similar to that of the $PW_{12}O_{40}^{3-}$ species. These results indicate that the primary Keggin structure has been introduced into the mesostructure framework and is very stable even after the surfactants are extracted and washed by deionized water; this is in agreement with the IR results.

^{31}P MAS NMR Spectra

Figure 6 shows the ^{31}P MAS NMR spectra of SiPW-8 and HPW. The spectrum for bulk HPW, consisting of a single peak at –15.3 ppm, agrees well with the literature data.[16,46] The spectrum for SiPW-8 is practically the same as that of bulk HPW with one signal at –15.3 ppm, which is attributed to homogeneously dispersed HPW clusters that

 © 2005 Wiley-VCH Verlag GmbH & Co. KGaA, Weinheim

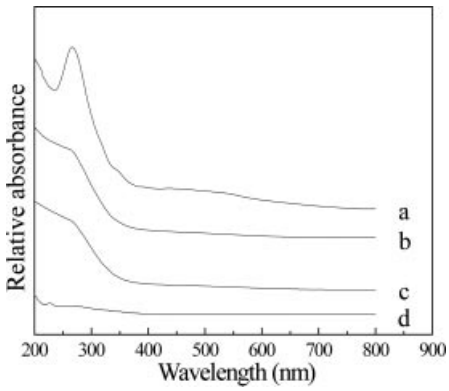

Figure 5. UV/Visible spectra of various samples: (a) HPW, (b) SiPW-8, (c) SiPW-16, and (d) SBA-15.

retain the Keggin structure; however, there is another resonance of lower intensity at –14.1 ppm. This new signal at –14.1 ppm may be induced by chemical interactions of HPW with the framework of the mesoporous material, which is constituted of a network of SiO_2.[46]

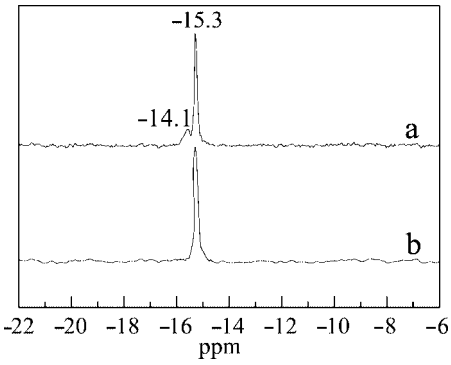

Figure 6. ^{31}P MAS NMR spectra of: (a) SiPW-8 and (b) HPW.

Catalytic Results

Cumene Cracking

The cumene cracking reaction is used to evaluate the acidity of the samples. As shown in Table 2, mesoporous pure silica (SBA-15) shows a very low catalytic activity (conversion at 1.2%) in this reaction. All SiPW-X samples show relatively high catalytic activities. The conversion of cumene is 13.7% for the reaction with the SiPW-16 sample, while a higher catalytic activity, with a conversion of 28.6%, is observed for the reaction with SiPW-8. It has been reported that HPW supported on the surface of SBA-15 by the impregnation method give cumene cracking conversions of 46.1 and 5.7%, with the weight content of HPW at 40 and 20%, respectively.[43] In our case, HPW supported on the surface of SBA-15 prepared by the same method gives 9.1% conversion with a weight content of HPW at 20%, and SiPW-8 shows much higher conversion (28.6%) with a similar HPW weight content. These results indicate that HPWs have been well encapsulated in the mesoporous framework and show good catalytic activities.

TIPB Cracking

In TIPB cracking, as shown in Table 2, pure SBA-15 silica shows low catalytic activity (3.8%) and, according to previous reports, HPW supported on the surface of MCM-41 by impregnation methods gives a conversion of 55%, with an HPW weight content of 23%.[30] In our case, SiPW-8 (20.7 wt.-%) and SiPW-16 (13.3 wt.-%) show high catalytic activities and give conversions of 70.2 and 58.5%, respectively, which are higher than those of previous reports.[30] The results suggest the potential use of these compounds as catalysts for bulky molecule catalysis.

Esterification of Acetic Acid with Ethanol and of Benzoic Acid with tert-Butanol

In the esterification of acetic acid with ethanol, the SiPW-16 and SiPW-8 samples give conversions of 17.2 and 31.5%, respectively. HPW/SBA prepared by the impregnation method shows a similar catalytic activity (32.3%). Moreover, after the catalysts were reused five times (Table 2), the SiPW-8 and SiPW-16 samples still showed catalytic activities similar to those of the fresh catalysts, while that of HPW/SBA prepared by the impregnation method decreases remarkably, which is attributed to the leaching of HPW supported on the surface of SBA-15.[36]

Table 2. Catalytic activity of SiPW-X, SBA-15, HPW, and HPW/SBA, and the element analysis of spent catalysts and liquid solution for P- and W content.

Samples	Conversion of cumene (wt. %)	Conversion of TIPB (wt. %)	Conversion 1[a] (wt. %)		Conversion 2[b] wt. %)		P content		W content	
			fresh	used[c]	fresh	used[c]	sc[d]	ls[e]	sc[d]	ls[e]
SiPW-8	28.6	70.2	31.5	30.9	10.3	10.1	0.223	≈ 0	15.9	≈ 0
SiPW-16	13.7	58.5	17.2	17.0	7.5	7.2	0.143	≈ 0	10.2	≈ 0
HPW/SBA	9.1	19.7	32.3	3.4	3.8	0.7	0.009	0.04	0.64	0.51
HPW	35.8	53.5	50.8	–	8.0	–	–	–	–	–
SBA-15	1.2	3.8	1.5	1.0	0	0	–	–	–	–

[a] Esterification reactions of acetic acid with ethanol. [b] Esterification reactions of benzoic acid with *tert*-butanol. [c] The catalysts were used five times. [d] Spent catalysts (sc) in esterification reactions of benzoic acid with *tert*-butanol after being used five times, the units for P- and W content are wt.-%. [e] Liquid solution (ls) in esterification reactions of benzoic acid with *tert*-butanol after separation of the catalysts after being used five times, the units for P- and W content are $\times 10^{-3}$ mmol/ml.

 © 2005 Wiley-VCH Verlag GmbH & Co. KGaA, Weinheim

Similar phenomena have also been observed in the esterification of benzoic acid with *tert*-butanol. The SiPW-16 and SiPW-8 samples give conversions of 7.2 and 10.1%, respectively, even after being reused five times, while the HPW/SBA samples only show a conversion of 0.7% after five uses. The above results suggest that the SiPW-X samples are very stable in liquid reactions even when reused many times, and leaching of HPW in these samples is hardly observed relative to that in the samples prepared by the impregnation method.

In order to help the reader better understand the difference between SiPW-X and HPW/SBA prepared by the impregnation method, we give a simple schematic model of SiPW-X (bottom part of Figure 7). We also give a schematic model of the interactions of silicon species with heteropolyanions under strong acidic conditions during preparation of SiPW-X (top part of Figure 7) and of terminal silicon hydroxyl groups of SBA-15 with heteropolyanions during preparation of conventional SBA-15 supported HPW (Figure 8). From Figure 7 and 8, we can see that the interaction of the silicon species with the heteropolyanions under strong acidic conditions is much stronger than that of the terminal silicon hydroxyl groups of SBA-15 with the heteropolyanions. Therefore, the stability of the composite materials (SiPW-X) comes from the fact that HPW is dispersed in the silica wall.

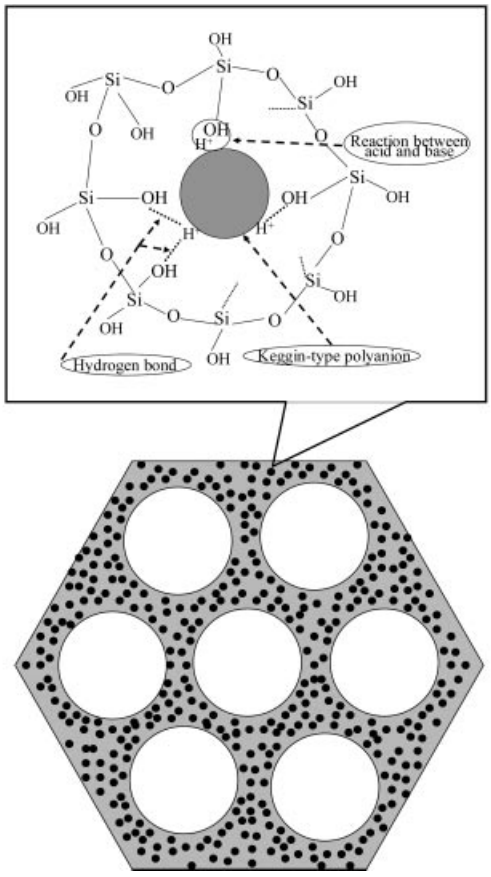

Figure 7. Simple schematic model of the interaction of the silicon species with heteropolyanions under strong acidic conditions during preparation of SiPW-X.

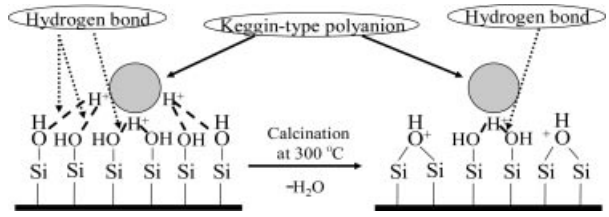

Figure 8. Simple schematic model of the interaction of terminal silicon hydroxyl groups of SBA-15 with heteropolyanions during preparation of conventional SBA-15 supported HPW.

In summary, the SiPW-X mesosilica materials with Keggin-type heteropolyacids encapsulated into their framework are excellent acidic catalysts for both small and bulky molecules. Additionally, other properties, such as easy separation, reusability etc., ensure the potential use in industrial applications.

Conclusion

Mesoporous silica with Keggin-type heteropolyacids encapsulated into their framework has been synthesized by addition of Na_2HPO_4 and Na_2WO_4 into the initial sol-gel system during hydrolysis of TEOS under strong acidic conditions. Characterization results suggest that samples with HPA contents of 13.3–20.7 wt.-% show very ordered hexagonal mesostructures. The HPA incorporated in the mesosilica is insoluble during catalysis. Catalytic cracking results suggest that these samples are very active in both small molecule (cumene) and bulky molecule (1,3,5-triisopropylbenzene) reactions. Additionally, esterification results in liquid reactions (polar solvent) after recycling indicate that these materials are can be easily separated and recycled.

Experimental Section

Materials: Tetraethyl orthosilicate (TEOS), hydrochloric acid (HCl), cumene, benzoic acid, tertiary butanol, ethanol, and acetic acid were of analytical grade and purchased from Tianjin Chemical Co. (China). Sodium tungstate (Na_2WO_4) and sodium monohydrogen phosphate (Na_2HPO_4) were of analytical grade and supplied by Beijing Chemical Co. (China). $EO_{20}PO_{70}EO_{20}$ (Pluronic P123) and 1,3,5-triisopropylbenzene (TIPB) were from Aldrich.

Synthesis: The typical synthesis process was as follows: (1) Pluronic P123 (4.0 g) was dissolved in a solution of deionized water (100 mL) containing hydrochloric acid (20 mL, 36 wt.-%), followed by addition of TEOS (10 mL). The mixture was stirred at 40 °C for 3 h. (2) A requisite amount of Na_2WO_4 and Na_2HPO_4 was added simultaneously to the above mixture to form a white precipitate. (3) The mixture was further stirred at 40 °C for 20 h and then transferred to a stainless steel autoclave for crystallization at 100 °C for 48 h.

The obtained products were collected and dried in vacuo ($<10^{-2}$ Pa) at 150 °C for 6 h and washed with an ethanol solution containing HCl and distilled water three times, and finally dried in vacuo ($< 10^{-2}$ Pa) at 300 °C for 5 h. The final products were desig-

 © 2005 Wiley-VCH Verlag GmbH & Co. KGaA, Weinheim

nated as SiPW-X, where X stands for the Si/W molar ratio in the initial gel.

For comparison, pure silica SBA-15 and HPW were synthesized according to the literature procedures;[5,42] conventional SBA-15 supported HPW was made by immersing SBA-15 powder into an HPW solution for 3 h followed by drying at 100 °C for 24 h, and then calcining at 300 °C for 5 h; this is denoted as HPW/SBA.

Characterization: Powder X-ray diffraction (XRD) data were recorded on a Siemens D5005 (30 kV, 30 mA) using nickel-filtered Cu-K_α radiation with a wavelength of $\lambda = 0.15418$ nm, diffraction patterns were collected under ambient conditions in the 2θ range of 0.6–4° at a scanning rate of 0.6°/min and in the 2θ range of 4–70° at a scanning rate of 6°/min. Transmission electron microscopy (TEM) experiments were performed on a JEM-3010F electron microscope (JEOL, Japan) with an acceleration voltage of 300 kV. The nitrogen isotherms at the temperature of liquid nitrogen were measured using a Micromeritics ASAP 2010M system. The samples were outgassed for 10 h at 300 °C before the measurements. Infrared (IR) spectroscopy was performed on a Bruker IFS 66v/S infrared spectrometer in the range 400–4000 cm^{-1} using KBr pellets in vacuo (<0.4 Pa) at ambient temperature. The diffuse reflectance UV/Visible spectra for powder samples were obtained on a Perkin–Elmer Lambda 20 UV/Visible spectrometer equipped with an integrating sphere, with $BaSO_4$ as an internal standard. Solid-state ^{31}P NMR experiments were performed with magic angle spinning (MAS) on an Infinity Plus-400 spectrometer operating at a frequency of 104.26 MHz, chemical shifts were referenced to 85% H_3PO_4 as an external standard. The HPW content in solid samples were determined by the results of inductively-coupled plasma analysis (ICP, Perkin–Elmer 3300DV).

Catalytic Test

Catalytic Cracking of Cumene and 1,3,5-Triisopropylbenzene (TIPB): Catalytic cracking of cumene and 1,3,5-triisopropylbenzene were carried out using the pulse technique in a micro-reactor, and the analyses of the catalytic products were performed by gas chromatography (GC-17A, Shimadzu Co.) equipped with a flame ionization detector (FID). The catalytic cracking was performed according to the following standard conditions: the reaction temperature was 300 °C (no thermal cracking); the reaction pressure was atmospheric pressure; the mass of the catalyst was 0.050 g; 0.2 μL of cumene or 1,3,5-triisopropylbenzene was injected for each test; nitrogen was used as the carrier gas at a flow rate of 45 mL/min.

Esterification of Acetic Acid with Ethanol and of Benzoic Acid with *tert*-Butanol: The esterification of acetic acid with ethanol was performed under nitrogen at 40 °C in a flask (50 mL) containing suspended catalyst powder (60 mesh pass), acetic acid (0.15 mol), and ethanol (0.15 mol), and with vigorous agitation for 4 h. The amount of catalyst used was 0.10 g. The product esters were analyzed by gas chromatography (6890N, Agilent Co.) equipped with a flame ionization detector (FID) with an HP-5 flexible quartz capillary column (30 m in length).

The esterification of benzoic acid with *tert*-butanol was performed under nitrogen at 80 °C in a flask (50 mL) containing suspended catalyst powder (60 mesh pass), benzoic acid (5 mmol), and *tert*-butanol (10 mmol), and with vigorous agitation for 5 h. The amount of catalyst used was 0.10 g. The product esters were analyzed by gas chromatography (6890N, Agilent Co.) equipped with a flame ionization detector (FID) with an HP-5 flexible quartz capillary column (30 m in length).

Acknowledgments

We are grateful for the financial support of the State Basic Research Project (G2000077507) and the National Natural Science Foundation of China (Grant No. 29873017 and 20101004).

[1] C. T. Kresge, M. E. Leonowicz, W. J. Roth, J. C. Vartuli, J. S. Beck, *Nature* **1992**, *359*, 710–712.
[2] J. Beck, J. Vartuli, W. Roth, M. Leonowica, C. Kresge, K. Schmitt, C. Chu, D. Olson, E. Sheppard, S. McCullen, J. Higgins, J. Schlenkler, *J. Am. Chem. Soc.* **1992**, *114*, 10834–10843.
[3] S. S. Kim, W. Zhang, T. J. Pinnavaia, *Science* **1998**, *282*, 1302–1305.
[4] D. Zhao, J. Feng, Q. Huo, N. Melosh, G. H. Fredrickson, B. F. Chmelka, G. D. Stucky, *Science* **1998**, *279*, 548–552.
[5] D. Zhao, Q. Huo, J. Feng, B. F. Chmelka, G. D. Stucky, *J. Am. Chem. Soc.* **1998**, *120*, 6024–6036.
[6] A. Corma, *Chem. Rev.* **1997**, *97*, 2373–2419.
[7] C. Y. Chen, S. L. Burkett, H. X. Li, M. E. Davis, *Micropor. Mater.* **1993**, *2*, 27.
[8] A. Corma, V. Fornés, M. T. Navarro, J. Pérez-Pariente, *J. Catal.* **1994**, *148*, 569.
[9] R. Schmidt, D. Akporiaye, M. Stöcker, O. H. Ellestad, *J. Chem. Soc., Chem. Commun.* **1994**, 1493.
[10] M. J. Climent, A. Corma, S. Iborra, M. C. Navarro, J. Primo, *J. Catal.* **1996**, *161*, 783–789.
[11] R. Mokaya, W. Jones, *Chem. Commun.* **1996**, 983.
[12] A. Corma, M. S. Grange, V. Gonzales-Alfaro, A. V. Orchilles, *J. Catal.* **1996**, *159*, 375–382.
[13] Y. Liu, Y. Cao, N. Yi, W. Feng, W. Dai, S. Yan, H. He, K. Fan, *J. Catal.* **2004**, *224*, 417–428.
[14] A. Corma, A. Martinez, V. Martinez-Soria, J. B. Monton, *J. Catal.* **1995**, *153*, 25–31.
[15] A. Corma, A. Martinez, V. Martinez-Soria, *J. Catal.* **1997**, *169*, 480–494.
[16] T. Blasco, A. Corma, A. Martinez, P. Martinez-Escolano, *J. Catal.* **1998**, *177*, 306–313.
[17] Q.-H. Xia, K. Hidajat, S. Kawi, *J. Catal.* **2002**, *209*, 433–444.
[18] Q.-H. Xia, K. Hidajat, S. Kawi, *J. Catal.* **2002**, *205*, 318–331.
[19] B. Bachiller-Baeza, J. A. Anderson, *J. Catal.* **2002**, *212*, 231–239.
[20] Q.-H. Xia, K. Hidajat, S. Kawi, *Catal. Today* **2001**, *68*, 255–262.
[21] P. A. Jalil, M. A. Al-Daous, A. A. Al-Arfaj, A. M. Al-Amer, J. Beltramini, S. A. I. Barri, *Appl. Catal. A* **2001**, *207*, 159–171.
[22] L. R. Pizzio, P. G. Vázquez, C. V. Cáceres, M. N. Blanco, *Appl. Catal. A* **2003**, *256*, 125–139.
[23] J. Haber, K. Pamin, L. Matachowski, D. Mucha, *Appl. Catal. A* **2003**, *256*, 141–151.
[24] I. V. Kozhevnikov, A. Sinnema, R. J. J. Jansen, K. Pamin, H. van Bekkum, *Catal. Lett.* **1995**, *30*, 241.
[25] S. Mukai, T. Sugiyama, H. Tamon, *Appl. Catal. A* **2003**, *256*, 99–105.
[26] K. Nowińska, W. Kaleta, *Appl. Catal. A* **2003**, *256*, 91–100.
[27] S. Damyanova, L. Dimitrov, R. Mariscal, J. Fierro, L. Petrov, I. Sobrados, *Appl. Catal. A* **2003**, *256*, 183–197.
[28] A. Bielánski, A. Lubanska, J. Pozniczek, A. Micek-Ilnicka, *Appl. Catal. A* **2003**, *256*, 153–171.
[29] H. Kosslick, G. Lischike, B. Parlitz, W. Storek, R. Fricke, *Appl. Catal. A* **1999**, *184*, 49–60.
[30] A. Ghanbari-Siahkali, A. Philippou, J. Dwyer, M. Anderson, *Appl. Catal. A* **2000**, *192*, 57–69.
[31] I. V. Kozhevnikov, *Appl. Catal. A* **2003**, *256*, 3–18.
[32] I. V. Kozhevnikov, *Catal. Rev. Sci. Eng.* **1995**, *29*, 311–352.
[33] M. N. Timofeeva, *Appl. Catal. A* **2003**, *256*, 19–35.
[34] T. Okuhara, *Appl. Catal. A* **2003**, *256*, 213–224.
[35] M. Misono, *Chem. Commun.* **2001**, 1141–1152.
[36] Y. Di, Y. Yu, Y. Sun, X. Yang, S. Lin, M. Zhang, S. Li, F. Xiao, *Microporous Mesoporous Mater.* **2003**, *62*, 221–228.

 © 2005 Wiley-VCH Verlag GmbH & Co. KGaA, Weinheim

[37] Y. Izumi, K. HIsano, T. Hida, *Appl. Catal. A* **1999**, *181*, 277–282.
[38] R. L. Augustine, S. K. Tanielyan, N. Mahata, Y. Gao, A. Zsigmond, H. Yang, *Appl. Catal. A* **2003**, *256*, 69–76.
[39] H. Li, N. Perkas, Q. Li, Y. Gofer, Y. Koltypin, A. Gedanken, *Langmuir* **2003**, *19*, 10409–10413.
[40] Y. Guo, Y. Wang, C. Hu, Y. Wang, E. Wang, *Chem. Mater.* **2000**, *12*, 3501–3508.
[41] K. Nowińska, R. Fórmaniak, W. Kaleta, A. Wacław, *Appl. Catal. A* **2003**, *256*, 115–123.
[42] R. Thouvenot, M. Fournier, R. Franck, C. Rocchiccioli-Deltcheff, *Inorg. Chem.* **1984**, *23*, 598–605.
[43] X. Zhang, Y. Yue, Z. Gao, *Chem. J. Chinese Universities* **2001**, *22*, 1169–1172.
[44] A. Taguchi, F. Schüth, *Microporous Mesoporous Mater.* **2005**, *77*, 1–45.
[45] L. Yang, Y. Qi, X. Yuan, J. Shen, J. Kim, *J. Mol. Catal. A: Chem.* **2005**, *229*, 199–205.
[46] H. Yun, M. Kuwabara, H. Zhou, I. Honma, *J. Mater. Sci.* **2004**, *39*, 2341–2347.
[47] P. M. Rao, A. Wolfson, S. Kababya, S. Vega, M. V. Landau, *J. Catal.* **2005**, *232*, 210–225.
[48] Q. Liu, W. Wu, J. Wang, X. Ren, Y. Wang, *Microporous Mesoporous Mater.* **2004**, *76*, 51–60.
[49] C. Shi, M. Xin, R. Wang Y. Xie, L. Hu, L. Xu, R. Zhang, G. Zhu, S. Qin, *Chem. J. Chin. Univ.* **2005**, *26*, 1198–1201.

Received: May 31, 2005
Published Online: October 25, 2005

 © 2005 Wiley-VCH Verlag GmbH & Co. KGaA, Weinheim

DOI: 10.1002/ejic.200500501

Synthesis, Structure and Characterisation of a New Trinuclear Di-μ-phenolato-μ-carboxylato $Mn^{III}Mn^{II}Mn^{III}$ Complex with a Bulky Pentadentate Ligand: Chemical Access to Mononuclear Mn^{IV}–OH Entities

Christelle Hureau,*[a,b] Elodie Anxolabéhère-Mallart,*[a] Geneviève Blondin,[a] Eric Rivière,[a] and Martine Nierlich[c]

Keywords: EPR spectroscopy / Manganese / Mass spectrometry / N,O ligands / Oxidation

A new trinuclear $Mn^{III}Mn^{II}Mn^{III}$ complex has been isolated and X-ray characterised, namely $[(py\text{-}salpn)Mn^{III}(\mu\text{-}OAc)Mn^{II}(\mu\text{-}OAc)Mn^{III}(py\text{-}salpn)]^{2+}$ (**1**), where H_2py-salpn is the new bulky $[N_3O_2]$ ligand derived from the H_2salpn Schiff base by the addition of one pyridine arm and the reduction of the imine function. The crystal structure reveals that the complex has a strictly 180° $Mn^{III}\cdots Mn^{II}\cdots Mn^{III}$ angle, the Mn^{II} ion being located at an inversion centre. The complex is valence-trapped, with the terminal Mn^{III} ions showing a Jahn–Teller elongation along the pyridine–Mn^{III}–acetate axis. The $Mn^{II}\cdots Mn^{III}$ separation is 3.1224(13) Å. The EPR spectra recorded on solid and frozen solutions are consistent with an $Mn^{III}Mn^{II}Mn^{III}$ species. The electrochemical response of complex **1** in acetonitrile solution exhibits two, one-electron reduction waves at $E_{1/2}$ = 0.140 and –0.075 V vs. SCE. Phenolato and acetato→Mn^{III} ligand-to-metal charge-transfer transitions are detected by UV/Visible spectroscopy at 359 and 587 nm, respectively. Chemical oxidation of an acetonitrile solution with *tert*-butyl hydroperoxide leads to mononuclear Mn^{IV}–hydroxo species, as evidenced by UV/Visible and EPR spectroscopy as well as ESI mass spectrometry.

(© Wiley-VCH Verlag GmbH & Co. KGaA, 69451 Weinheim, Germany, 2005)

Introduction

The development of bioinorganic manganese chemistry has been stimulated by the involvement of manganese ions in many biological systems,[1,2] such as superoxide dismutase,[3] catalase[4] and photosystem II of green plants.[5–8] In this last intricate machinery, an oxomanganese entity is the key element of the oxygen evolving complex (OEC), which performs the light-induced oxidation of water into dioxygen. This reaction requires the photogeneration of four oxidative equivalents and their storage by the OEC. These two processes are accomplished during the first four steps of the Kok cycle,[9,10] ($S_0\rightarrow S_1$, $S_1\rightarrow S_2$, $S_2\rightarrow S_3$ and $S_3\rightarrow S_4$) where S_i (i = 0–4) denote the five oxidation states of the OEC, dioxygen being released during the last step ($S_4\rightarrow S_0$). High-valent oxidation states are thus reached by the manganese ions in the S_4 state. Recently, two X-ray structures obtained for the photosystem II (PSII) of the cyanobacterium *Thermosynechococcus elongatus* have appeared in the literature, one at 3.5 Å[11] and the other at 3.2 Å resolution.[12] The structure of the Mn cluster, however, is still a matter of debate. Nevertheless, the resolution level allows the authors to propose two models of the OEC that agree in terms of having two moieties: a small one containing one cation and a larger one containing three or more cations. Zouni et al. describe the OEC cluster as containing only four metal ions, whereas Ferreira et al. describe the oxomanganese entity as a "3+1" tetranuclear manganese complex. More precisely, in the latter case three manganese ions together with one calcium ion are arranged in a tetrahedral geometry at four corners of a distorted cube, the other four corners being occupied by bridging oxo ions. The fourth manganese ion is linked to the Mn–Ca–oxo cube by a unique oxo bridge. Two amino acid residues are involved in the coordination of the fourth manganese ion, namely Asp170 and Glu333, and Asp61 is coordinated through a water molecule. Lastly, one exogenous labile hydrogencarbonate ligand is proposed to interact with the fourth manganese and the calcium ions. Due to its peculiar location and to the presence in its surroundings of labile positions along with the tightly bound Ca^{2+}, this fourth manganese ion is anticipated to ensure a special role in the water oxidation process. In particular, the present structure supports recent hypotheses in which one of the four manganese ions binds a water molecule, thus producing a highly reactive intermediate. This electrophilic species is then predisposed

[a] Laboratoire de Chimie Inorganique, UMR 8613, LCR-CEA no. 33V, Institut de Chimie Moléculaire et des Matériaux d'Orsay, Université Paris Sud,
91405 Orsay Cedex, France
E-mail: eanxolab@icmo.u-psud.fr
[b] Current address: Service de Bioénergétique, CNRS URA 2096, Département de Biologie Joliot Curie, CEA Saclay, Bât 532,
91191 Gif-sur-Yvette, France
E-mail: hureau@ozias.saclay.cea.fr
[c] CEA Saclay, DRECAM/SCM Bât 125,
91191 Gif-sur-Yvette, France

Supporting information for this article is available on the WWW under http://www.eurjic.org or from the author.

 © 2005 Wiley-VCH Verlag GmbH & Co. KGaA, Weinheim

to be attacked by the second water molecule bound to the calcium ion to form the O–O bond.[13]

The water oxidation mechanisms proposed by Siegbahn et al.[14–16] and Brudvig et al.[17] all rely on a tightly bound Ca^{2+} ion located close to a manganese ion. Indeed, it is proposed that during the Kok cycle only one of the Mn ions binds a water substrate molecule and, before dioxygen formation, produces either a highly reactive electrophilic intermediate or an Mn^{IV}–oxyl radical. A Mn^{V} centre has also been advocated by Pecoraro et al.[18] In these assumptions, the reactive manganese ion would be the fourth manganese ion of the "3+1" tetranuclear complex.

The large number of papers found in the literature attests that high-valent manganese compounds have been developed as selective organic oxidation catalysts,[19–25] and tested in bleaching processes.[26–28] Consequently, generating high-valent and/or Mn–oxo complexes is a relevant challenge for inorganic chemists, both for OEC modelling and for the development of oxidation catalysts.

Among the numerous manganese compounds synthesised, complexes containing Schiff-base ligands, like H_2salen or H_2salpn,[29] or their derivatives, have been intensively studied as much for their biological relevance[30–33] as for their catalytic activity.[25,28,34–38] Indeed, these complexes possess the ability to form high-valent Mn–oxo species,[39,40] the sixth position being occupied by various ligands.[41,42] In particular, the use of pyridine as the sixth ligand has been proposed to assist the formation of Mn^{V}–oxo species from the $[(salen)Mn^{III}]^+$ complex, using *tert*-butyl hydroperoxide as the oxidant.[25]

Taking into account these different elements, we designed a new bulky pentadentate ligand, derived from reduced H_2salpn by the addition of one pyridine arm and denoted H_2py-salpn (see Scheme 1). In the present work, we describe the synthesis and the crystal structure of the new trinuclear manganese complex $[(py\text{-}salpn)Mn^{III}(\mu\text{-}OAc)Mn^{II}(\mu\text{-}OAc)Mn^{III}(py\text{-}salpn)](BPh_4)_2$ [**1**$(BPh_4)_2$]. The magnetic and EPR properties of **1**$(BPh_4)_2$ have been investigated on crystalline product. Characterisations of complex **1**$(BPh_4)_2$ upon dissolution in acetonitrile have been performed by EPR and UV/Visible spectroscopy, as well as cyclic voltammetry and mass spectrometry. We also describe the reactivity of **1** upon addition of *tert*-butyl hydroperoxide, where EPR spectroscopy suggests the formation of mononuclear Mn^{IV} species that are identified as Mn^{IV}–OH complexes by mass spectrometry measurements.

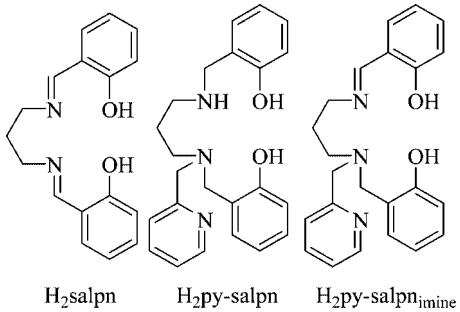

Scheme 1. H_2salpn, H_2py-salpn and H_2py-salpn$_{imine}$.

Results and Discussion

The reaction of H_2py-salpn with $Mn^{III}(OAc)_3{\cdot}2H_2O$ in ethanol solution leads to the formation of the cation $[(py\text{-}salpn)Mn^{III}(\mu\text{-}OAc)Mn^{II}(\mu\text{-}OAc)Mn^{III}(py\text{-}salpn)]^{2+}$ (**1**), which was precipitated by addition of two equivalents of sodium tetraphenylborate. It is worth noting that the presence of Mn^{II} in the complex is not unexpected considering that the $Mn^{III}(OAc)_3{\cdot}2H_2O$ starting material contains Mn^{II} species, even after recrystallisation.

Crystal Structure of $[(py\text{-}salpn)Mn^{III}(\mu\text{-}OAc)Mn^{II}(\mu\text{-}OAc)Mn^{III}(py\text{-}salpn)]^{2+}$ (1)

The structure of complex **1** is presented in Figure 1 and principal bond lengths and angles are listed in Table 1. The cation consists of three manganese ions, two $(py\text{-}salpn)^{2-}$

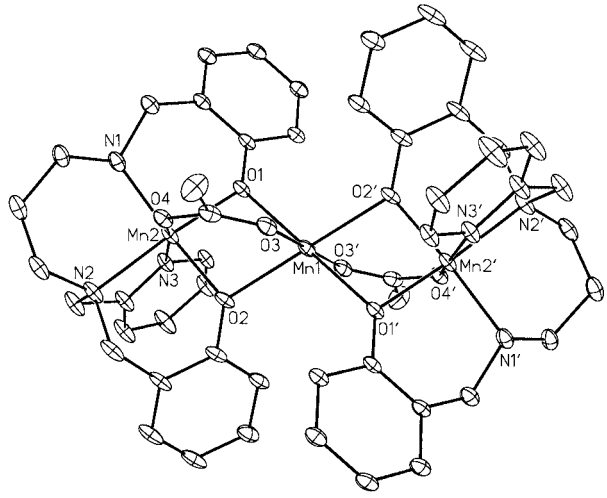

Figure 1. ORTEP view of the cation of **1**, with 10% thermal ellipsoids, showing the atom labelling scheme.

Table 1. Selected bond lengths [Å] and angles [°] for **1**.[a]

Mn1–O1	2.158(3)	Mn2–O4	2.099(3)
Mn1–O2	2.191(3)	Mn2–N1	2.059(5)
Mn1–O3	2.155(4)	Mn2–N2	2.141(4)
Mn2–O1	1.940(3)	Mn2–N3	2.234(4)
Mn2–O2	1.924(4)	Mn1···Mn2	3.1224(13)
O1–Mn1–O1′	180.0	O2–Mn2–N1	175.86(14)
O2–Mn1–O2′	180.0	O2–Mn2–O4	91.60(14)
O3–Mn1–O3′	180.0	O2–Mn2–N2	92.67(18)
O1–Mn1–O2	72.85(12)	O2–Mn2–N3	86.87(16)
O1–Mn1–O3	86.70(14)	O4–Mn2–N1	88.39(16)
O2–Mn1–O3	86.03(13)	O4–Mn2–N2	91.26(14)
O1–Mn2–N1	91.98(16)	O4–Mn2–N3	169.62(13)
O1–Mn2–O2	83.89(14)	N1–Mn2–N2	91.47(19)
O1–Mn2–O4	93.90(13)	N1–Mn2–N3	93.89(18)
O1–Mn2–N2	173.87(17)	N2–Mn2–N3′	78.57(15)
O1–Mn2–N3	96.14(14)	Mn2···Mn1···Mn2′	180.0

[a] Symmetry transformation used to generate equivalent atoms: $-x, -y, -z + 1$.

 © 2005 Wiley-VCH Verlag GmbH & Co. KGaA, Weinheim

ligands and two bridging acetate ions. The Mn1 ion is located at the inversion centre of the cation in a quasi-regular octahedral geometry. The Mn1 and Mn2 (or Mn2′) ions are held together by two bridging phenolato arms from one $(py\text{-}salpn)^{2-}$ ligand and by one bridging acetate ion. Mn1 is coordinated by the four phenolic bridging oxygen atoms from the two $(py\text{-}salpn)^{2-}$ ligands that indeed form a plane and, quasi-perpendicularly to it, by two oxygen atoms from the two acetate bridging ligands. Mn2 and Mn2′ are coordinated by the three nitrogen atoms and the two bridging phenolato arms of the $(py\text{-}salpn)^{2-}$ ligand and by one oxygen atom from the acetate bridging ligand. The phenolato arms are in a *cis* position, as are two amine nitrogen atoms, whereas the pyridine nitrogen atom and the oxygen atom of the acetate ion are in a *trans* position. The metal–ligand distances reported in Table 1 reveal that **1** is a valence-trapped $Mn^{III}Mn^{II}Mn^{III}$ complex, with the terminal Mn^{III} ions exhibiting a Jahn–Teller elongation along the acetate–Mn–pyridine (O4–Mn2–N3) direction. The bridging acetate ions are in the usual *syn-syn* coordination mode, as reported for analogous trinuclear manganese complexes.[43] The distance between the Mn^{II} and the Mn^{III} ions in **1** is 3.1224(13) Å, which is slightly shorter than that reported in similar core units (3.137–3.173 Å).[44] It is, however, significantly shorter than in μ-alkoxo-bis-μ-carboxylato-bridged $Mn^{III}Mn^{II}Mn^{III}$ trinuclear complexes (3.419–3.551 Å).[45–49] The presence of two phenolato bridges in **1** is the origin of this shortening of the distance. Crystal data also reveal that the secondary amine function is not oxidised during the metallation [N1–C7 = 1.501(7) Å], as could be anticipated from reported syntheses of similar complexes.[50]

IR, Magnetic and EPR Properties of $1(BPh_4)_2$

The IR spectrum of $\mathbf{1}(BPh_4)_2$ presents significant absorption bands at 1602, 1559, 1424, 760, 734 and 708 cm^{-1}. The three bands detected below 800 cm^{-1} are assigned to the tetraphenylborate counterions, whereas the two broad bands detected at 1559 and 1424 cm^{-1} are attributed to the bridging acetate ions.[51,52] The difference of 135 cm^{-1} calculated between the symmetrical and the unsymmetrical C=O vibration bands is in agreement with the *syn-syn* bridging coordination mode of the acetate ions.[51] The C=N vibration band of the pyridine function is detected at 1602 cm^{-1}. Lastly, the absence of a broad absorption band near 1630 cm^{-1} confirms the absence of the imine function in **1**.[53]

The product of the molar magnetic susceptibility, χ_M, and the temperature, T, recorded on a powder sample of $\mathbf{1}(BPh_4)_2{\cdot}3CH_3CN$ is approximately constant between 50 and 300 K. The $\chi_M T$ product lies between 10.31 and 10.37 $cm^3 mol^{-1} K$. This is close to the theoretical value of 10.375 $cm^3 mol^{-1} K$ expected for two $S_{Mn^{III}} = 2$ and one $S_{Mn^{II}} = 5/2$ uncoupled spins with g-factor values fixed to 2. The observed temperature dependence indicates that the manganese ions are very weakly coupled. This contrasts with the μ-alkoxo-bis-μ-carboxylato-$Mn^{II}Mn^{III}$ core complexes that are usually found to be weakly antiferromagnetically coupled, with $J_{Mn^{II}Mn^{III}}$ lying between –8 and –14.2 cm^{-1}, using the expression $-JS_{Mn^{II}}{\cdot}S_{Mn^{III}}$ for the exchange Hamiltonian within a pair.[47–49] A weak exchange interaction, either antiferromagnetic or ferromagnetic, has been observed in analogous $Mn^{III}Mn^{II}Mn^{III}$ trinuclear systems where the Mn^{III} and the Mn^{II} ions are connected by one phenolato, one alkoxo and one carboxylato bridge.[44] The magnitude of the exchange interaction is indeed controlled by the presence of two alkoxo or phenoxo bridges. Such doubly bridged $Mn^{II}Mn^{III}$ core units present J values ranging from –3.4 to 13.2 cm^{-1}.[31,54–56]

The X-band EPR spectrum was recorded at 10 K using the conventional perpendicular mode on a powder sample of complex $\mathbf{1}(BPh_4)_2{\cdot}3CH_3CN$ and is presented in Figure S1 (trace a). An intense and broad line is observed at 335 mT ($g_{eff} = 2$). Two weaker lines are also detected at 145 and 558 mT, which are strongly indicative of weak interactions between the Mn ions within complex **1**. In the absence of an interaction between the metal ions, the EPR signal would originate solely from the Mn^{II} site as the Jahn–Teller-elongated Mn^{III} centres exhibit a strong zero-field splitting effect that prevents the detection of any EPR signal at 9 GHz. In addition, the regular environment of the Mn^{II} ion should induce a small zero-field splitting effect. Consequently, a broad line at $g_{eff} = 2$ is expected. The dipolar and isotropic exchange interactions between the central Mn^{II} site and the two terminal Mn^{III} ions split this signal quasi-symmetrically and new lines appear at both lower and higher fields. This was checked by calculating powder X-band EPR spectra for a fictitious system containing two terminal $S = 1$ and one central $S = 1/2$ sites. The profile is, however, strongly dependent on the relative orientation of the terminal zero-field splitting tensors towards that of the dipolar tensors and on the nature − ferro- or antiferromagnetic − of the exchange interaction (see Figure S2 in the Supporting Information). Due to the important spin values of the manganese ions and to the number of parameters, no simulation was attempted on the real system.

Characterisation of $1(BPh_4)_2$ upon Dissolution in Acetonitrile

The X-band EPR spectra of millimolar dichloromethane and acetonitrile solutions of complex **1** at 10 K are presented in Figure S1 (see Supporting Information; traces b and c, respectively). The EPR signatures of complex **1** upon dissolution are close to that recorded for a powder sample. In acetonitrile solvent, however, an additional six-line signal is detected at $g_{eff} = 2$, which is attributed to solvated Mn^{II}. This contribution has been quantified (See Experimental Section for details) and accounts for less than 5% of the total Mn-based species. This experiment shows that the trinuclear structure of complex **1** is essentially maintained upon dissolution in acetonitrile.

The UV/Visible spectrum of complex **1** in acetonitrile is reproduced in Figure 2 (dashed line-left scale). Two major

 © 2005 Wiley-VCH Verlag GmbH & Co. KGaA, Weinheim

bands are detected at 587 and 359 nm, with extinction coefficient values (ε) of 3.1 and 8.9×10^3 $M^{-1}cm^{-1}$, respectively, with a shoulder at 450 nm ($\varepsilon = 4.0\times10^3$ $M^{-1}cm^{-1}$). The band at 587 nm is attributed to a phenolato→Mn^{III} ligand-to-metal charge transfer (LMCT) transition,[50,53,57,58] whereas the other two transitions may originate from either phenolato→Mn^{III} or acetato→Mn^{III} LMCT transitions.[59] The large ε values of the LMCT transitions prevent the observation of the Mn^{III} d–d transitions, which are theoretically expected with lower ε values.[60,61]

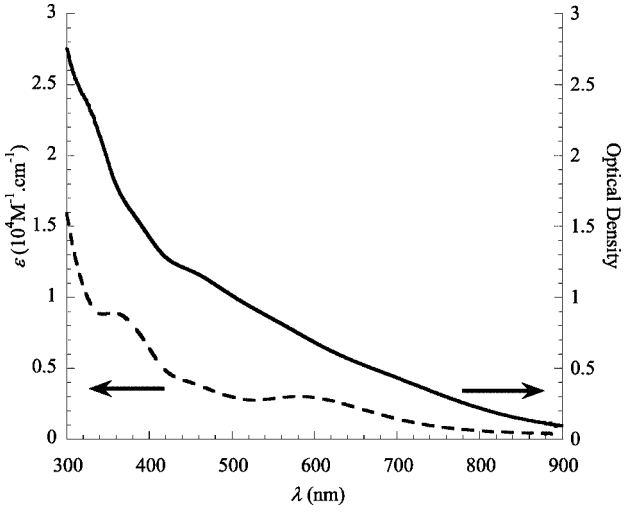

Figure 2. UV/Visible spectra of complex $\mathbf{1}(BPh_4)_2$ (10^{-3} M in acetonitrile, dashed line) and immediately after the addition of 20 equivalents of *t*BuOOH (solid line). T = 20 °C, l = 1 mm.

The cyclic voltammogram recorded under argon on a millimolar solution of complex **1** in acetonitrile in the presence of 0.1 M tetrabutylammonium perchlorate is presented in Figure 3. Two quasi-reversible waves of equal intensity are detected when scanning towards cathodic potentials at $E_{1/2}$ = 0.140 (ΔE^P = 80 mV) and –0.075 V vs. SCE (ΔE^P = 80 mV), respectively.[62] When scanning towards anodic potentials, an intense irreversible wave is observed at E^P = 0.88 V vs. SCE that remains irreversible when reversing the scan at 1.0 V vs. SCE. A second, weaker-intensity, irreversible wave is detected at E^P = 1.16 V vs. SCE. The two reduction waves are attributed to two successive one-electron reductions of complex **1**, leading firstly to [(py-salpn)-Mn^{III}(μ-OAc)Mn^{II}(μ-OAc)Mn^{II}(py-salpn)]$^+$ and then to [(py-salpn)Mn^{II}(μ-OAc)Mn^{II}(μ-OAc)Mn^{II}(py-salpn)]. The Mn^{III}/Mn^{II} reduction process presents low potential values, as it is to be expected considering the anionic environment of the Mn^{III} centre. These values are close to those reported for other diphenolato-coordinated Mn^{III} complexes.[63] The detection of two single-electron Mn^{III}/Mn^{II} processes presenting $E_{1/2}$ potentials that differs by 225 mV ($\Delta E_{1/2}$) is indicative of a weak electrostatic interaction between the two Mn^{III} ions. The low $\Delta E_{1/2}$ value is related to the long distance between the two Mn^{III} ions (6.24 Å).[64] The first anodic process detected is attributed to the oxidation of the tetraphenylborate counterion of complex **1**,[65] and the second irreversible anodic process may be attributed to the oxidation of complex **1**, leading to the formation of [(py-salpn)-Mn(μ-OAc)Mn(μ-OAc)Mn(py-salpn)]$^{3+}$, which further evolves chemically. Unfortunately, the interaction of the oxidised tetraphenylborate ion generated at the electrode surface with complex **1** and/or with the [(py-salpn)Mn(μ-OAc)Mn(μ-OAc)Mn(py-salpn)]$^{3+}$ species renders the process difficult to analyse.

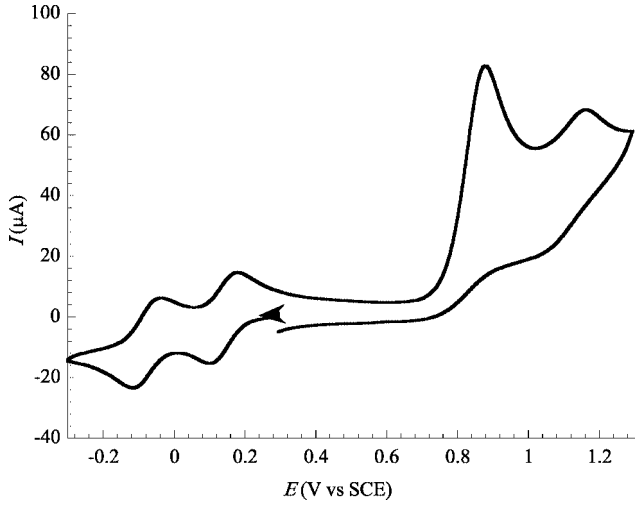

Figure 3. Cyclic voltammograms of $\mathbf{1}(BPh_4)_2$ (10^{-3} M in acetonitrile with 0.1 M of tetrabutylammonium perchlorate). T = 20 °C and scan rate = 100 $mV\,s^{-1}$.

Chemical Oxidation

The chemical oxidation of complex **1** was performed on a millimolar acetonitrile solution with *tert*-butyl hydroperoxide (*t*BuOOH) as the oxidant. The oxidant was added in large excess (20 equivalents). Upon addition, the solution turned from dark green to black. We will show in the next

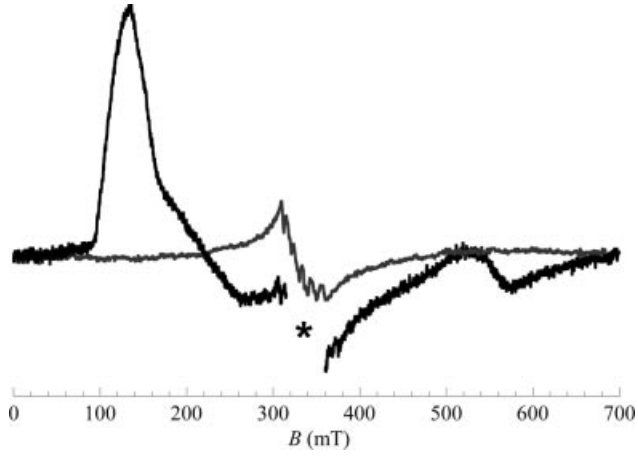

Figure 4. EPR spectra of complex $\mathbf{1}(BPh_4)_2$ (10^{-3} M in acetonitrile, grey line) and immediately after the addition of 20 equivalents of *t*BuOOH (black line). Recording conditions: 0.5 mT modulation amplitude, 100 kHz modulation frequency, T = 100 K, 2.0 mW microwave power, ν = 9.39 GHz. The $tBuO^{\cdot-}$ radical signal has been removed off the black trace.

 © 2005 Wiley-VCH Verlag GmbH & Co. KGaA, Weinheim

section that the chemical oxidation of complex **1** leads to the formation of high-valent Mn species (**1ox**). The **1ox** species were characterised by UV/Visible and EPR spectroscopy and ESI mass spectrometry.

The UV/Visible spectrum of **1ox**, shown in Figure 2 (solid line, right scale), is mainly featureless in the visible region and presents a strong absorbance in the UV domain. Shoulders are observed at 463 and 685 nm. These observations are reminiscent of previous observations for hydroxyl-rich[66] or for carboxylato[67] mononuclear Mn^{IV} Schiff-base complexes. The intense absorption band in the UV region may therefore be attributed to a phenolato→Mn^{IV} or to a

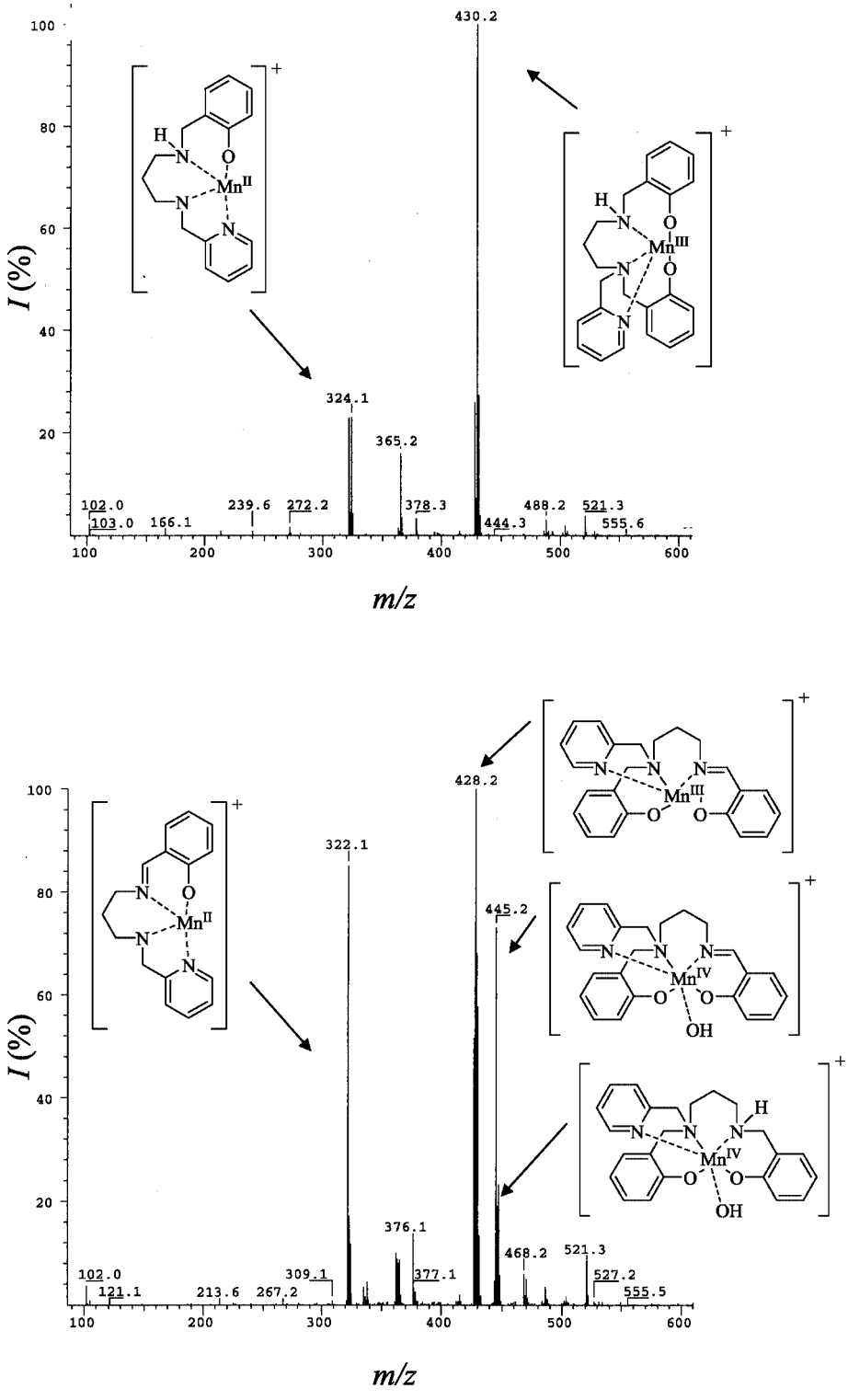

Figure 5. Electrospray mass spectrum of complex **1** (10^{-4} M in acetonitrile) recorded for the starting solution (top) and after addition of 20 equivalents of *t*BuOOH (bottom).

 © 2005 Wiley-VCH Verlag GmbH & Co. KGaA, Weinheim

hydroxo→Mn^{IV} LMCT transition. The shoulders observed in the visible region can be attributed to a poorly resolved phenolato→Mn^{IV} MLCT[50,53,57] or to Mn^{IV} d–d transitions, the strong intensity of which originates from the tail of the absorption in the UV region.

The X-band EPR spectrum of **1ox** at 100 K, recorded in the perpendicular detection mode, is presented in Figure 4 (black line). An intense $g = 2$ signal corresponding to an organic radical has been removed for clarity. The EPR signature of complex **1** recorded under the same conditions is also reproduced (grey line in Figure 4). The signal of complex **1** differs slightly from trace c of Figure S2, with the low-field transitions being undetectable at this recording temperature. Four new transitions appear at $g_{eff} = 4.9$, 3.0, 1.5 and 1.17 after the addition of the oxidant.[68] These resonances are broad and show no evidence for ^{55}Mn hyperfine coupling. The EPR signature of **1ox** is indicative of an $S = 3/2$ Mn^{IV} ion. The complexity of the EPR spectrum of a d^3 species depends on the magnitude of the zero-field splitting (ZFS) compared to the applied microwave frequency. In axial symmetry ($E/D = 0$), two limiting cases can be discussed depending on the relative magnitude of $|2D|$ vs. $h\nu$, where D is the axial ZFS parameter. At X-band ($h\nu = 0.3\ cm^{-1}$), and when $|2D| >> h\nu$, the ZFS effect dominates the Zeeman effect, and a strong transition is expected at low field ($g_{eff} \approx 4$) with a weak component at around $g_{eff} = 2$. This behaviour has been observed for numerous Mn^{IV} centres with anionic chelating ligands, such as hydroxo, phenolato, carboxylato or anilido.[57,66,67,69–74] When $|2D| << h\nu$, the Zeeman effect dominates the ZFS effect and the signal is centred at $g_{eff} \approx 2$, with weaker lines at both the low- and high-field edges. This behaviour has been reported for rare Mn^{IV}–tetraphenolato,[72] Mn^{IV}–thiohydroxamato,[75] and Mn^{IV}–thiocarbamato[76] complexes. The strong absorption detected at $g_{eff} = 4.9$ and the weaker one near $g_{eff} = 1.5$ suggest that the present Mn^{IV} species exhibits a strong ZFS effect. The divergence from a g_{eff} value of around 4 originates from the rhombicity of the ZFS. According to the diagram showing the evolution of the g_{eff} values for the two Kramer doublets as a function of E/D,[77] one can see that the line positions at $g_{eff} = 4.9$, 3.0, 1.5 and 1.17 can be well reproduced with $E/D = 0.17$. These first two characterisations suggest that **1ox** is a mononuclear Mn^{IV} species.

In order to identify the Mn^{IV} species formed, ESI/MS experiments were performed. The mass spectra of complexes **1** and **1ox** are presented in Figure 5. The mass spectrum of complex **1** exhibits a major molecular peak at m/z = 430 amu and three other peaks at m/z = 322, 324 and 365 amu.[78] The first peak is attributed to the mononuclear Mn^{III} entity $\{[(py\text{-}salpn)Mn]\}^+$, and the peaks at 322 and 324 amu correspond to Mn^{II} species, namely $\{[(L^1_{imine})\text{-}Mn]\}^+$ and $\{[(L^1)Mn]\}^+$, where L^1 stands for the $(py\text{-}salpn)^{2-}$ ligand after the loss of one phenolato arm and L^1_{imine} for L^1 with a reduced secondary amine function (see Figure 5). The peak at m/z = 365 amu can be attributed to the adduct $\{[(L^1)Mn]CH_3CN\}^+$, even though such solvated species are rarely detected under the present recording conditions. After addition of *t*BuOOH, the peak at m/z = 430 amu disappears and the peak at 322 amu increases in intensity together with the apparition of three new peaks at m/z = 428, 445 and 447 amu. The peak at 428 amu corresponds to the Mn^{III} species $\{[(py\text{-}salpn_{imine})Mn]\}^+$, where subscript imine means that the secondary amine function has been oxidised to an imine (Scheme 1). The peaks at 445 and 447 are attributed to the mononuclear hydroxo Mn^{IV} entities $\{[(py\text{-}salpn_{imine})Mn(OH)]\}^+$ and $\{[(py\text{-}salpn)\text{-}Mn(OH)]\}^+$, respectively. It is worth noting that the formation of the imine function may be due to the use of the oxidant *t*BuOOH. Species **1ox** is subsequently attributed to

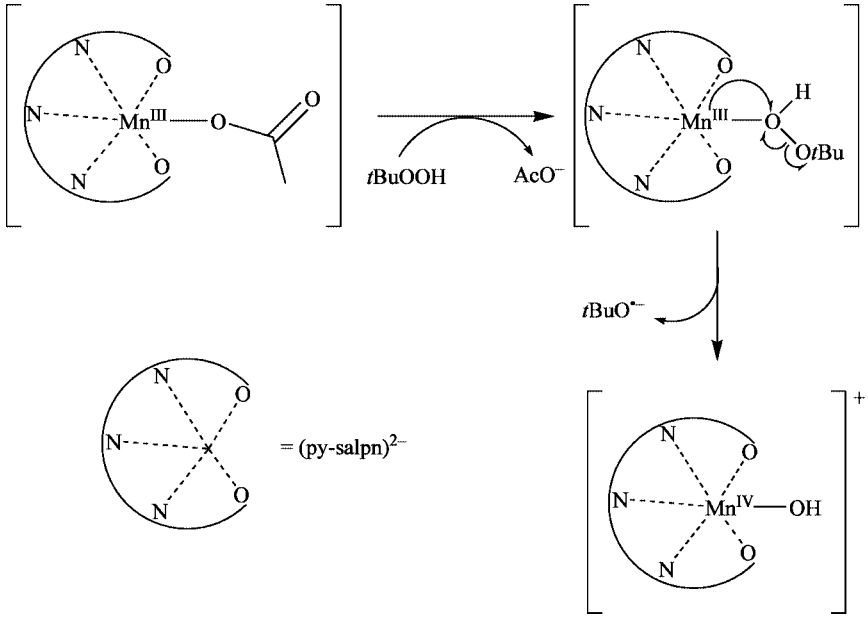

Scheme 2. Proposed mechanism for the formation of the Mn^{IV}–OH species.

 © 2005 Wiley-VCH Verlag GmbH & Co. KGaA, Weinheim

the mixture of the two Mn^{IV} monocations $\{[(py\text{-}salpn_{imine})Mn(OH)]\}^+$ and $\{[(py\text{-}salpn)Mn(OH)]\}^+$.

Lastly, according to the EPR spectra, we can propose that the central Mn^{II} ion is oxidised into an EPR-silent Mn^{III} species, the UV/Visible signature of which may be masked by the tail of the UV absorbance of complexes **1ox**.

Formation of the Mn^{IV}–hydroxo Entities

A mechanism for the formation of the Mn^{IV}–hydroxo species **1ox** is tentatively proposed in Scheme 2. For clarity, only the terminal Mn^{III} ions of complex **1** are considered. We propose that after the coordination of the *t*BuOOH oxidant to the Mn^{III} centre, the homolytic breakage of the O–O bond[79] would lead to the release of the radical *t*BuO$^{\cdot}$– and to the formation of the Mn^{IV}–OH complex.

We should mention that it is also plausible that the acetate ion, which is a particularly strong base in acetonitrile (pK_a = 22)[80] would be able to deprotonate the hydroxo ion coordinated to the Mn^{IV} ion, thus forming a Mn^{IV}–oxo species. The EPR and UV/Visible spectra do not allow us to discriminate an oxo from a hydroxo Mn^{IV} species. The detection in of peaks at 445 and 447 amu in the ESI mass spectrum may then be explained by the formation of a proton adduct of the neutral Mn^{IV}–oxo entities, leading to $\{[(py\text{-}salpn_{imine})Mn(O)]H\}^+$ and $\{[(py\text{-}salpn)Mn(O)]H\}^+$. It is also worth noting that the presence of the oxidised ligand may be due to the formation of Mn^{IV} species or to the *t*BuOOH itself.

Concluding Remarks

A new trinuclear $Mn^{III}Mn^{II}Mn^{III}$ complex **1** containing a bulky $[N_3O_2]$ ligand derived from the H_2salpn Schiff-base ligand by the addition of one pyridine arm has been isolated and X-ray characterised. This complex has been fully characterised by magnetic studies, UV/Visible, IR and EPR spectroscopy, cyclic voltammetry and ESI mass spectrometry. The chemical oxidation of the trinuclear complex **1** by *t*BuOOH leads to the formation of Mn^{IV} entities, which are UV/Visible and EPR characterised and identified by mass spectrometry as mononuclear Mn^{IV}–OH species.

From the recent crystallographic data obtained for the *Synechococcus elongatus* PSII, a "3+1" structure has been proposed for the OEC. Some water oxidation mechanisms consistent with this recent structure favour the role of a unique highly reactive Mn ion. In this context, the synthesis and the complete characterisation of trinuclear species as well as high-valence mononuclear Mn entities remains highly relevant for the spectroscopic OEC modelling. In the near future, it will be interesting to substitute the central Mn^{II} ion in complex **1** by a calcium ion as such a putative complex should present some OEC relevant Mn–Ca–carboxylate interactions.

Experimental Section

General Remarks: Reagents and solvents were purchased commercially and used as received. Elemental Analysis was performed by the Service de Microanalyse of the CNRS (Gif sur Yvette, France) for carbon, nitrogen and hydrogen and by the Service Central d'Analyse of CNRS (Vernaison, France) for manganese and chloride. Infrared spectra were recorded as KBr pellets in the range of 4000 to 200 cm^{-1} with a Perkin–Elmer Spectrum 1000 spectrophotometer. ^1H NMR spectra were recorded withg a Bruker AM-250 (250 MHz) spectrometer. Electrospray ionisation mass spectra were recorded with a Finnigan Mat95S in a BE configuration at low resolution on millimolar acetonitrile solutions.

Caution: *Perchlorate salts of metal complexes with organic ligands are potentially explosive. Only small quantities of these compounds should be prepared and they should be handled behind suitable protective shields.*

Synthesis of H_2py-salpn: The two-step synthesis of the ligand H_2py-salpn from the reduced H_2salpn is shown in Scheme 3. The reduced H_2salpn ligand 2.86 g, (10 mmol), prepared according to a previously reported synthesis,[57] was dissolved in 100 mL of methanol and 2-pyridinecarboxaldehyde (1 mL, 10 mmol) was added with stirring. The white precipitate that appeared was filtered and washed with methanol, and then redissolved in methanol by addition of two equivalents of trifluoroacetic acid. Two equivalents of sodium cyanoborohydride were added and the solution and was stirred for 12 h. Methanol was eliminated and 150 mL of water was added. The aqueous solution was extracted three times with 50 mL of dichloromethane. After removal of the solvent, H_2py-salpn was obtained as a yellow oil. Yield: 62% (2.3 g). ^1H NMR (250 MHz, $CDCl_3$): δ = 8.29 (d, J = 4.6 Hz, 1 H, *H*-Py), 7.62–7.55 (m, 2 H, *H*-Ar), 7.18–7.05 (m, 3 H, *H*-Ar), 7.00–6.93 (m, 2 H, *H*-Ar), 6.86 (d, 1 H, *H*-PhOH), 6.79 (d, 1 H, *H*-PhOH), 6.72–6.65 (m, 2 H, *H*-Ar), 3.91 (s, 2 H, RN-CH_2-PhOH), 3.77 (s, 2 H, RN-CH_2-Py), 3.54 (s, 2 H, HN-CH_2-PhOH), 2.65 (t, J = 5.8 Hz, 2 H, HN-CH_2-CH_2), 2.55 (t, J = 5.8 Hz, 2 H, RN-CH_2-CH_2), 1.78 (q, J = 5.8 Hz, 2 H, CH_2-CH_2-CH_2) ppm. ^{13}C NMR (62.9 MHz, $CDCl_3$) 157.5, 157.3, 156.6, 148.7, 137.3, 130.5, 129.8, 129.5, 129.3, 123.4, 122.9, 122.5, 120.0, 119.2, 119.1, 116.6, 58.2, 56.7, 52.2, 51.0, 47.6, 24.4 ppm. IR: $\tilde{\nu}$ = 1674 cm^{-1} (s), 1613 (m), 1595 (s), 1489 (m), 1460 (s), 1436 (m), 1383 (m), 1265 (s), 1201 (m), 1134 (m), 1104 (w), 737 (s). ESI-MS: *m*/*z* (%) = 378.2 (45) $[M + H]^+$, 272.2 (100) $[M - CH_2PhOH + H]^+$, 166.1 (60) $[M - 2CH_2PhOH + H]^+$.

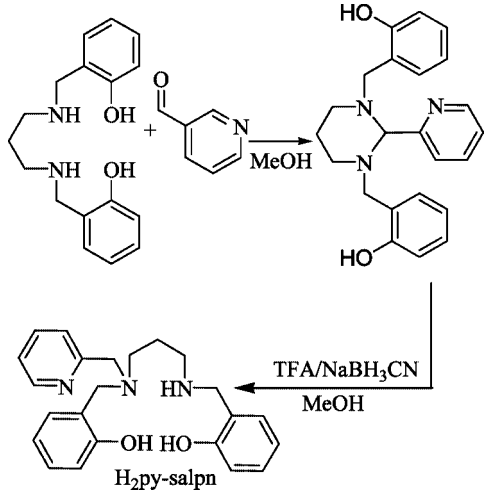

Scheme 3. Synthetic route from reduced H_2salpn to H_2py-salpn.

Synthesis of $[(py\text{-}salpn)Mn^{III}(\mu\text{-}OAc)Mn^{II}(\mu\text{-}OAc)Mn^{III}(py\text{-}salpn)](BPh_4)_2{\cdot}2CH_3CN{\cdot}0.5H_2O$ [$1(BPh_4)_2{\cdot}2CH_3CN{\cdot}0.5H_2O$]: $Mn(OAc)_3{\cdot}2H_2O$ (268 mg, 1.0 mmol) was added to a 5 mL ethanol solution

 © 2005 Wiley-VCH Verlag GmbH & Co. KGaA, Weinheim

of H_2py-salpn (377 mg, 1.0 mmol). The solution turned from purple to dark green. Addition of an excess (1.5 mmol) of sodium tetraphenylborate led to the precipitation of a dark green powder, which was collected by filtration and washed carefully with ethanol. Yield: 68% (239 mg). $C_{102}H_{103}B_2N_8O_{8.5}Mn_3$ [**1**$(BPh_4)_2$·$2CH_3CN$·$0.5H_2O$] (1761): calcd. C 69.5, H 5.9, N 6.3, B 1.2, Mn 9.3; found C 69.3, H 5.7, B 1.2, Mn 9.4, N 6.2. IR: $\tilde{\nu}$ = 3439 cm^{-1} (m), 3176 (m), 3054 (m), 1602 (m), 1558 (s), 1483 (s), 1458 (m), 1444 (m), 1425 (s), 1345 (w), 1249 (s), 1204 (w), 1113 (w), 1006 (w), 791 (w), 760 (m), 734 (m), 708 (m), 655 (w), 612 (m), 573 (w). The powder was then redissolved in acetonitrile and the solution was filtered and placed in an atmosphere of diethyl ether. Crystals of **1**$(BPh_4)_2$·$3CH_3CN$ suitable for X-ray crystallographic study were obtained, collected by filtration, washed with diethyl ether and dried in air.

Crystallographic Data Collection and Refinement of the Structure of 1$(BPh_4)_2$·$3CH_3CN$: The crystal data of **1**$(BPh_4)_2$·$3CH_3CN$ and the parameters of data collection are summarised in Table 2. Crystal data for **1**$(BPh_4)_2$·$3CH_3CN$ were collected on a Nonius Kappa-CCD area detector diffractometer using graphite-monochromated Mo-K_α radiation. The lattice parameters were determined from ten images recorded with 2° φ-scans and later refined on all data. The data were recorded at 123 K. A 180° φ-range was scanned with 2° steps with a crystal-to-detector distance fixed at 30 mm. Data were corrected for Lorentz polarisation. The structures were solved by direct methods with SHELXS-86[81] and refined by full-matrix least-squares on F^2 with anisotropic thermal parameters for all non-H atoms with SHELXTL-93.[82] H atoms (unless H of CH_3CN solvent molecule) were introduced at calculated positions as riding atoms with an isotropic displacement parameter equal to 1.2 (CH, and CH_2) or 1.5 (CH_3) times that of the parent atom. The CH_3CN solvent molecules were found disordered over two positions with 0.5 occupancy factors. The molecular plots were drawn with SHELXTL.[83] All calculations were performed on a Silicon Graphics R10000 workstation.

Table 2. Details of structure determination, refinement and experimental parameters for **1**$(BPh_4)_2$·$3CH_3CN$.

Empirical formula	$C_{104}H_{103}B_2Mn_3N_9O_8$
Formula mass [g mol^{-1}]	1793.39
Temperature [K]	123(2)
Wavelength [Å]	0.71073
Crystal system	triclinic
Space group	$P\bar{1}$
a [Å]	11.573(2)
b [Å]	14.073(3)
c [Å]	15.889(3)
α [°]	71.26(3)
β [°]	85.08(3)
γ [°]	72.05(3)
Volume [Å^3]	2331.0(9)
Z	1
Density (calculated) [g cm^{-3}]	1.278
Absorption coefficient [mm^{-1}]	0.462
Crystal size [mm]	0.15 × 0.10 × 0.10
θ range for data collection [°]	2.47 to 24.70
Index ranges	$0 \le h \le 13$, $-15 \le k \le 16$, $-18 \le l \le 18$
Reflections collected	14334
Independent reflections/R(int)	7285 [R(int) = 0.0530]
Data	4705
Parameters	601
Goodness-of-fit on F^2	0.913
Final R indices [$I > 2\sigma(I)$]	R_1 = 0.0704, wR_2 = 0.1893
R indices (all data)	R_1 = 0.1131, wR_2 = 0.2265
Largest diff. peak/hole [e Å^{-3}]	0.631/–0.433

CCDC-233590 contains the supplementary crystallographic data for this paper. These data can be obtained free of charge from The Cambridge Crystallographic Data Centre via www.ccdc.cam.ac.uk/data_request/cif.

Magnetic Susceptibility Measurements: Magnetic susceptibility data were recorded on a MPMS5 magnetometer (Quantum Design Inc.). The calibration was made at 298 K using a palladium reference sample furnished by Quantum Design Inc. The data were collected over a temperature range of 50–300 K at a magnetic field of 5000 Oe and were corrected for diamagnetism.

EPR Spectroscopy: EPR spectra were recorded with a Bruker ELEXSYS 500 spectrometer at X-band. For low-temperature studies, an Oxford Instruments continuous flow liquid helium cryostat and a temperature control system were used. The quantity of free Mn^{II} was estimated by comparison with spectra of $Mn(ClO_4)_2$·$6H_2O$ dissolved in acetonitrile to various concentrations.

Cyclic Voltammetry: Cyclic voltammetry measurements were recorded with an EGG PAR potentiostat (M273 model). The counter electrode was an Au wire, the working electrode a glassy carbon disk, which was carefully polished before each voltammogram with a 1-μm diamond paste, sonicated in an ethanol bath and then washed carefully with ethanol. The reference electrode was an Ag/$AgClO_4$ electrode (0.530 V vs. NHE electrode), isolated in a fritted bridge. The solvent used was distilled acetonitrile and tetrabutylammonium perchlorate was added to obtain a 0.1 M supporting electrolyte.

UV/Visible Spectroscopy: UV/Visible spectra were recorded with a Cary 300 Bio spectrophotometer at 20 °C with 0.1-cm quartz cuvettes.

Supporting Information (see footnote on the first page of this article): The X-band 10 K EPR spectra of millimolar dichloromethane and acetonitrile solutions of complex **1** are presented in Figure S1 (traces b and c, respectively). Theoretical powder X-band EPR spectra calculated for a trinuclear system with two terminal S_{t1} = S_{t2} = 1 and one central S_c = 1/2 spins (ν = 9.39 GHz, T = 10 K) is given in Figure S2.

Acknowledgments

We are grateful to Félix Perez for mass spectrometry measurements, to Guillaume Blain for EPR technical assistance, and to Dr. Alain Boussac (Service de Bioénergétique, URA CNRS 2096, CEA Saclay, Gif-sur-Yvette, France) for EPR facilities. Laurent Sabater is acknowledged for NMR technical assistance. We thank Prof. Jean-Jacques Girerd and Prof. Vincent L. Pecoraro for stimulating discussions. The Conseil Régional de l'Ile de France is acknowledged for its contribution to the acquisition of the Bruker ELEXSYS X-band EPR spectrometer. The COST D21 European action and the LRC-CEA project are acknowledged for their financial support.

[1] E. J. Larson, V. L. Pecoraro, in *Manganese Redox Enzymes* (Ed.: V. L. Pecoraro), VCH Publishers, Inc., New York, **1992**, pp. 1–28.
[2] J. D. Crowley, D. A. Traynor, D. C. Weatherburn, in *Metal Ions in Biological Processes* (Eds.: A. Sigel, H. Sigel), Marcel Dekker, Basel, Switzerland, **2000**, pp. 209–278.
[3] R. H. Holm, P. Kennepohl, E. I. Solomon, *Chem. Rev.* **1996**, *96*, 2239–2314.

 © 2005 Wiley-VCH Verlag GmbH & Co. KGaA, Weinheim

[4] V. V. Barynin, M. M. Whittaker, S. V. Antonyuk, V. S. Lamzin, P. M. Harrison, P. J. Artymiuk, J. W. Whittaker, *Structure* **2001**, *9*, 725–738.
[5] V. K. Yachandra, K. Sauer, M. P. Klein, *Chem. Rev.* **1996**, *96*, 2927–2950.
[6] A. W. Rutherford, P. Faller, *Trends Biochem. Sci.* **2001**, *26*, 341–344.
[7] V. K. Yachandra, *Philos. Trans. R. Soc. London, Ser. B* **2002**, *357*, 1347–1358.
[8] A. W. Rutherford, A. Boussac, *Science* **2004**, *303*, 1782–1784.
[9] P. Joliot, G. Barbieri, R. Chabaud, *Photochem. Photobiol.* **1969**, *10*, 309–329.
[10] B. Kok, B. Forbush, M. McGloin, *Photochem. Photobiol.* **1970**, *11*, 457–475.
[11] K. N. Ferreira, T. M. Iverson, K. Maghlaoui, J. Barber, S. Iwata, *Science* **2004**, *303*, 1831–1838.
[12] J. Biesiadka, B. Loll, J. Kern, K.-D. Irrgang, A. Zouni, *Phys. Chem. Chem. Phys.* **2004**, *6*, 4733–4736.
[13] J. P. McEvoy, G. W. Brudvig, *Phys. Chem. Chem. Phys.* **2004**, *6*, 4754–4763.
[14] P. E. M. Siegbahn, R. H. Crabtree, *J. Am. Chem. Soc.* **1999**, *121*, 117–127.
[15] P. E. M. Siegbahn, *Inorg. Chem.* **2000**, *39*, 2923–2935.
[16] P. E. M. Siegbahn, *Curr. Opin. Chem. Biol.* **2002**, *6*, 227–235.
[17] J. S. Vrettos, J. Limburg, G. W. Brudvig, *Biochim. Biophys. Acta* **2001**, *1503*, 229–245.
[18] V. L. Pecoraro, M. J. Baldwin, M. T. Caudle, W.-Y. Hsieh, N. A. Law, *Pure Appl. Chem.* **1998**, *70*, 925–929.
[19] E. M. McGarrigle, D. G. Gilheany, *Chem. Rev.* **2005**, *105*, 1563–1602.
[20] V. C. Quee-Smith, L. DelPizzo, S. H. Jureller, J. L. Kerschner, R. Hage, *Inorg. Chem.* **1996**, *35*, 6461–6465.
[21] D. De Vos, T. Bein, *Chem. Commun.* **1996**, 917–918.
[22] A. Berkessel, C. A. Sklorz, *Tetrahedron Lett.* **1999**, *40*, 7965–7968.
[23] J. Brinksma, L. Schmieder, G. Van Vliet, R. Boaron, R. Hage, D. E. De Vos, P. L. Alsters, B. L. Feringa, *Tetrahedron Lett.* **2002**, *43*, 2619–2622.
[24] C. Zondervan, R. Hage, B. L. Feringa, *Chem. Commun.* **1997**, 419–420.
[25] K. Srinivasan, P. Michaud, J. K. Kochi, *J. Am. Chem. Soc.* **1986**, *108*, 2309–2320.
[26] R. Hage, J. E. Iburg, J. Kerschner, J. H. Koek, E. L. M. Lempers, R. J. Martens, U. S. Racherla, S. W. Russell, T. Swarthoff, M. R. P. van Vliet, J. B. Warnaar, L. van der Wolf, B. Krijnen, *Nature* **1994**, *369*, 637–639.
[27] T. Tzedakis, Y. Benzada, M. Comtat, *Ind. Eng. Chem. Res.* **2001**, *40*, 3435–3444.
[28] W. Zhang, J. L. Loebach, S. R. Wilson, E. N. Jacobsen, *J. Am. Chem. Soc.* **1990**, *112*, 2801–2803.
[29] H_2salen = *N*,*N*′-bis(salicylidene)ethane-1,2-diamine, H_2salpn = *N*,*N*′-bis(salicylidene)propane-1,3-diamine, H_2py-salpn = *N*-(2-pyridylmethyl)-*N*,*N*′-bis(2-hydroxybenzyl)propane-1,3-diamine.
[30] A. J. Wu, J. E. Penner-Hahn, V. L. Pecoraro, *Chem. Rev.* **2004**, *104*, 903–938.
[31] A. Gelasco, M. L. Kirk, J. W. Kampf, V. L. Pecoraro, *Inorg. Chem.* **1997**, *36*, 1829–1837.
[32] M. J. Baldwin, V. L. Pecoraro, *J. Am. Chem. Soc.* **1996**, *118*, 11325–11326.
[33] N. Aurangzeb, C. E. Hulme, C. A. McAuliffe, R. G. Pritchard, M. Watkinson, M. R. Bermejo, A. Garcia-Deibe, M. Rey, J. Sanmartin, A. Sousa, *J. Chem. Soc., Chem. Commun.* **1994**, 1153–1155.
[34] A. Gelasco, S. Bensiek, V. L. Pecoraro, *Inorg. Chem.* **1998**, *28*, 3301–3309.
[35] F. M. MacDonnell, N. L. P. Flacker, C. Stern, T. V. O'Halloran, *J. Am. Chem. Soc.* **1994**, *116*, 7431–7432.
[36] E. J. Larson, V. L. Pecoraro, *J. Am. Chem. Soc.* **1991**, *113*, 7809–7810.
[37] T. J. Collins, R. D. Powell, C. Slebodnick, E. S. Uffelman, *J. Am. Chem. Soc.* **1990**, *112*, 899–901.
[38] T. J. Collins, S. W. Gordon-Wylie, *J. Am. Chem. Soc.* **1989**, *111*, 4511–4513.
[39] D. Feichtinger, D. A. Plattner, *Chem. Eur. J.* **2001**, *7*, 591–599.
[40] D. Feichtinger, D. A. Plattner, *Angew. Chem. Int. Ed. Engl.* **1997**, *36*, 1718–1719.
[41] J. El-Bahraoui, O. Wiest, D. Feichtinger, D. A. Plattner, *Angew. Chem. Int. Ed.* **2001**, *40*, 2073–2076.
[42] D. Feichtinger, D. A. Plattner, *J. Chem. Soc., Perkin Trans. 2* **2000**, 1023–1028.
[43] M. Hirotsu, M. Kojima, W. Mori, Y. Yoshikawa, *Bull. Chem. Soc. Jpn.* **1998**, *71*, 2873–2884.
[44] M. Hirotsu, M. Kojima, Y. Yoshikawa, *Bull. Chem. Soc. Jpn.* **1997**, *70*, 649–657.
[45] X. Li, D. P. Kessissoglou, M. L. Kirk, C. J. Bender, V. L. Pecoraro, *Inorg. Chem.* **1988**, *27*, 1–3.
[46] D. P. Kessissoglou, M. L. Kirk, C. A. Bender, M. S. Lah, V. L. Pecoraro, *J. Chem. Soc., Chem. Commun.* **1989**, 84–86.
[47] D. P. Kessissoglou, M. L. Kirk, M. S. Lah, X. Li, C. Raptopoulou, W. E. Hatfield, V. L. Pecoraro, *Inorg. Chem.* **1992**, *31*, 5424–5432.
[48] V. Tangoulis, D. A. Malamatari, K. Soulti, V. Stergiou, C. P. Raptopoulou, A. Terzis, T. A. Kabanos, D. P. Kessissoglou, *Inorg. Chem.* **1996**, *35*, 4974–4983.
[49] V. Tangoulis, D. A. Malamatari, G. A. Spyroulias, C. P. Raptopoulou, A. Terzis, D. P. Kessissoglou, *Inorg. Chem.* **2000**, *39*, 2621–2630.
[50] C. Hureau, L. Sabater, E. Anxolabéhère-Mallart, M. Nierlich, M.-F. Charlot, F. Gonnet, E. Rivière, G. Blondin, *Chem. Eur. J.* **2004**, *10*, 1998–2010.
[51] S. Pal, J. W. Gohdes, W. C. A. Wilisch, W. H. Armstrong, *Inorg. Chem.* **1992**, *31*, 713–716.
[52] K. Wieghardt, U. Bossek, L. Zsolnai, G. Huttner, G. Blondin, J.-J. Girerd, F. Babonneau, *J. Chem. Soc., Chem. Commun.* **1987**, 651–653.
[53] O. Horner, E. Anxolabéhère-Mallart, M.-F. Charlot, L. Tchertanov, J. Guilhem, T. A. Mattioli, A. Boussac, J.-J. Girerd, *Inorg. Chem.* **1999**, *38*, 1222–1232.
[54] J. Yoo, A. Yamaguchi, M. Nakano, J. Krzystek, W. E. Streib, L.-C. Brunel, H. Ishimoto, G. Christou, D. N. Hendrickson, *Inorg. Chem.* **2001**, *40*, 4604–4616.
[55] A. Yoshino, T. Miyagi, E. Asato, M. Mikuriya, Y. Sakata, K.-i. Sugiura, K. Iwasaki, S. Hino, *Chem. Commun.* **2000**, 1475–1476.
[56] H. Diril, H.-R. Chang, X. Zhang, S. K. Larsen, J. A. Potenza, C. G. Pierpont, H. J. Schugar, S. S. Isied, D. N. Hendrickson, *J. Am. Chem. Soc.* **1987**, *109*, 6207–6208.
[57] A. Neves, S. M. D. Erthal, I. Vencato, A. S. Ceccato, Y. P. Mascarenhas, O. R. Nascimento, M. Hörner, A. A. Batista, *Inorg. Chem.* **1992**, *31*, 4749–4755.
[58] J. A. Bonadies, M. J. Maroney, V. L. Pecoraro, *Inorg. Chem.* **1989**, *28*, 2044–2051.
[59] C. Hureau, E. Anxolabéhère-Mallart, M. Nierlich, F. Gonnet, E. Rivière, G. Blondin, *Eur. J. Inorg. Chem.* **2002**, 2710–2719.
[60] T. S. Davis, J. P. Fackler, M. J. Weeks, *Inorg. Chem.* **1968**, *7*, 1994–2002.
[61] R. Dingle, *Acta Chem. Scand.* **1966**, *20*, 33–44.
[62] $E_{1/2}$ is defined as $(E^{P}_{a} + E^{P}_{c})/2$ and $\Delta E^{P} = |E^{P}_{a} - E^{P}_{c}|$, where E^{P}_{a} (E^{P}_{c}) is defined as the potential of the maximum of current intensity when scanning toward anodic (cathodic) potentials.
[63] See ref.[57] and references cited therein.
[64] J.-J. Girerd, E. Anxolabéhère-Mallart, in *Spectroscopic Methods in Bioinorganic Chemistry, Vol. 14* (Eds.: E. I. Solomon, K. O. Hodgson), American Chemical Society, Washington DC, **1998**, pp. 262–271.
[65] P. K. Pal, S. Chowdhury, M. G. B. Drew, D. Datta, *New J. Chem.* **2002**, *26*, 367–371.
[66] D. P. Kessissoglou, X. Li, W. M. Butler, V. L. Pecoraro, *Inorg. Chem.* **1987**, *26*, 2487–2492 and references cited therein.

 © 2005 Wiley-VCH Verlag GmbH & Co. KGaA, Weinheim

[67] S. K. Chandra, P. Basu, D. Ray, S. Pal, A. Chakravorty, *Inorg. Chem.* **1990**, *29*, 2423–2428.
[68] In addition, a multiline signal of small intensity is detected between 300 and 380 mT. This signal is attributed to the presence of a small quantity of solvated Mn^{II} in solution.
[69] D. T. Richens, D. T. Sawyer, *J. Am. Chem. Soc.* **1979**, *101*, 3681–3683.
[70] S. M. Saadeh, M. S. Lah, V. L. Pecoraro, *Inorg. Chem.* **1991**, *30*, 8–15.
[71] O. Schlager, K. Wieghardt, B. Nuber, *Inorg. Chem.* **1995**, *34*, 6456–6462.
[72] T. M. Rajendiran, J. W. Kampf, V. L. Pecoraro, *Inorg. Chim. Acta* **2002**, *339*, 497–502.
[73] T. K. Paine, T. Weyhermüller, E. Bothe, K. Wieghardt, P. Chaudhuri, *Dalton Trans.* **2003**, 3136–3144.
[74] W. Adam, C. Mock-Knoblauch, C. R. Saha-Möller, M. Herderich, *J. Am. Chem. Soc.* **2000**, *122*, 9685–9691.
[75] S. Pal, P. Ghosh, A. Chakravorty, *Inorg. Chem.* **1985**, *24*, 3704–3706.
[76] K. L. Brown, R. M. Golding, P. C. Healy, J. K. Jessop, W. C. Tennant, *Aust. J. Chem.* **1974**, *27*, 2075–2081.
[77] B. H. Huynh, T. A. Kent, in *Advances in Mössbauer Spectroscopy. Applications to Physics, Chemistry and Biology* (Eds.: B. V. Thosar, P. K. Iyengar, J. K. Srivastava, S. C. Bhargava), Elsevier Science Publishers B. V., Amsterdam, **1983**, pp. 490–560.
[78] Detection of the molecular peak of the trinuclear complex **1** was always thwarted, whatever the experimental conditions.
[79] M. T. Caudle, P. J. Riggs-Gelasco, A. K. Gelasco, J. E. Penner-Hahn, V. L. Pecoraro, *Inorg. Chem.* **1996**, *35*, 3577–3584.
[80] K. Izutsu, *Acid-Base Dissociation Constants in Dipolar Aprotic Solvents, Vol. 35*, Blackwell Scientific Publications, Brookline Village, M. A., **1990**.
[81] G. M. Sheldrick, *Acta Crystallogr., Sect. A* **1990**, *46*, 467.
[82] G. M. Sheldrick, *SHELXTL: Program for the Refinement of Crystal Structures*, University of Göttingen, Germany, **1993**.
[83] G. M. Sheldrick, *SHELXTL*, Version 5.1, University of Göttingen, Germany, **1999**, distributed by Bruker AXS, Madison, WI, USA.

Received: June 3, 2005
Published Online: October 20, 2005

 © 2005 Wiley-VCH Verlag GmbH & Co. KGaA, Weinheim

DOI: 10.1002/ejic.200500526

A Terephthalato-Bridged Ni^{II} Complex Capped with a Nonchelating Ligand Displays a Three-Dimensional Supramolecular Network Constructed by Coordination and Multi-Intermolecular Forces

Chang Seop Hong,*[a] Jung Hee Yoon,[a] Jeong Hak Lim,[a] and Hyun Hee Ko[a]

Keywords: Magnetic properties / Nickel / Noncovalent interactions / O ligands / Supramolecular chemistry

A new tp-bridged complex $[Ni(pyrazole)_4(tp)]_n$ (**1**; tp = terephthalate) coordinated with a nonchelating pyrazole ligand has been synthesized and characterized using X-ray structure determination and magnetic studies. The crystal structure reveals that the capping ligand functions as a source of hydrogen bonding and intermolecular contacts, such as π–π and CH–π interactions, that result in a three-dimensional supramolecular assembly. Weak antiferromagnetic couplings are transmitted between Ni^{II} centers through the tp linkage.
(© Wiley-VCH Verlag GmbH & Co. KGaA, 69451 Weinheim, Germany, 2005)

Introduction

Coordination polymers have been one of the active research areas applicable to molecular magnets and functional metal–organic frameworks for storage, exchange, and separations.[1,2] The tp ligand is frequently employed in the construction of such complexes due to its diverse binding modes as a linker which allow it to form a variety of structures from discrete molecules to one- (1D), two- (2D), or three-dimensional (3D) networks.[3–7] Interestingly, the molecular dimensionality of coordination polymers bridged by tp can be raised by hydrogen bonding and other intermolecular contacts, such as face-to-face π–π and edge-to-face CH–π interactions.[8,9] The former are realized when lattice water molecules that act as hydrogen donors and acceptors are present in the crystal structures.[10] The use of aromatic bidentate moieties such as 2,2′-bypridine and 1,10-phenanthroline, which fill up coordination spaces around the metal ions, as capping ligands promotes the supramolecular contacts between the aromatic pyridyl groups, which in turn leads to increased dimensionality.[8] It is highly desirable to fabricate dehydrated supramolecular self-assemblies with all these intermolecular interactions (hydrogen bonding, π–π, and CH–π interactions) at the same time as lattice water molecules, which are sources of hydrogen bonds, are easily removed and the crystal lattice could consequently collapse. In this respect, we have selected pyrazole as a capping ligand as it possesses an N–H group for hydrogen bonding and a planar aromatic ring for the other intermolecular interactions.

Here we present the synthesis and detailed structural and magnetic characterization of a new tp-linked dehydrated Ni^{II} compound $[Ni(pyrazole)_4(tp)]_n$ (**1**), which, to the best of our knowledge, is the first example capped by a nonchelating pyrazole ligand among coordinative 1D Ni^{II} systems bridged by tp. The capping ligand plays a crucial role in the formation of the unique 3D supramolecular framework of **1** as it is connected by the combined forces of coordination as well as noncovalent hydrogen bonds and face-to-face π–π and edge-to-face CH–π interactions. Weak antiferromagnetic interactions are operative between the magnetic centers through the long tp bridge.

Results and Discussion

The reaction of Ni^{2+}, pyrazole and dipotassium terephthalate in a ratio of 1:4:1 in water led to the formation of **1**. The strong bands in the IR spectrum centered at 3370 and 3350 cm^{-1} are assigned to the characteristic N–H stretching vibrations of pyrazole, and the presence of the broad bands in the range 2900–2400 cm^{-1} are indicative of hydrogen bonds between the N–H groups of pyrazole and the carboxylate oxygens of tp. The differences (Δ) between the antisymmetric $\nu_a(CO_2^-)$ and symmetric $\nu_s(CO_2^-)$ stretching frequencies in the IR spectrum of **1** are 178 and 203 cm^{-1}. The calculated Δ values, when compared with the reference value (170 cm^{-1}) of dipotassium terephthalate, suggest that the binding mode of tp appears to be monodentate,[11] which was confirmed by X-ray analysis.

A perspective view of **1** together with the atom-labeling scheme is presented in Figure 1. Selected distances and angles are tabulated in Table 1. The specific feature is that two crystallographically different chains exist in the unit cell. Each nickel atom lies on an inversion center and exhib-

[a] Department of Chemistry and Center for Electro- and Photoresponsive Molecules, Korea University,
Seoul 136-701, Korea
E-mail: cshong@korea.ac.kr

 WILEY InterScience DISCOVER SOMETHING GREAT © 2005 Wiley-VCH Verlag GmbH & Co. KGaA, Weinheim

its a distorted octahedral geometry consisting of four equatorial nitrogen atoms of pyrazole ligands, with an average Ni–N distance of 2.097(7) Å, and two axial oxygen atoms of the tp bridge, with an average Ni–O distance of 2.109(1) Å. For a chain including Ni1 atoms (Ni1 chain), the dihedral angle (a) between the carboxylate group and the benzene ring of the tp ligand is 21.41(28)°, whereas the other chain with Ni2 atoms (Ni2 chain) has a dihedral angle of 10.25(32)°. The benzene rings of the two chains are tilted with a dihedral angle of 77.20(13)°, and the shortest intrachain Ni···Ni distance is 11.446(2) Å for both chains.

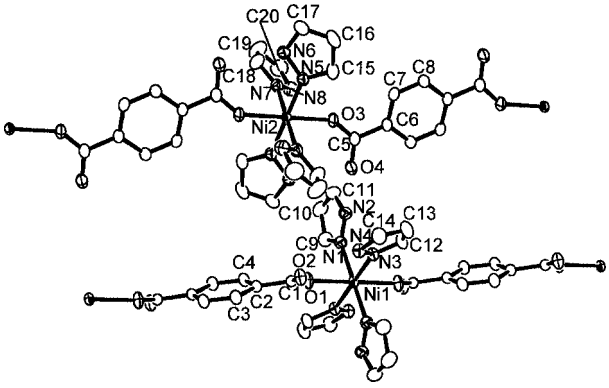

Figure 1. ORTEP diagram of **1** with the atom numbering scheme.

Table 1. Bond lengths [Å] and angles [°] for **1**.

Ni(1)–N(3)	2.0895(15)	Ni(1)–N(1)	2.1017(16)
Ni(1)–O(1)	2.1100(12)	Ni(2)–N(7)	2.0938(16)
Ni(2)–N(5)	2.1061(16)	Ni(2)–O(3)	2.1076(12)
N(3)–Ni(1)–N(1)	90.95(6)	N(3)–Ni(1)–O(1)	94.12(6)
N(1)–Ni(1)–O(1)	85.89(6)	C(1)–O(1)–Ni(1)	146.59(13)
C(9)–N(1)–Ni(1)	131.87(14)	N(2)–N(1)–Ni(1)	123.42(12)
C(12)–N(3)–Ni(1)	131.59(13)	N(4)–N(3)–Ni(1)	122.05(11)
N(7)–Ni(2)–N(5)	91.69(6)	N(7)–Ni(2)–O(3)	87.45(6)
N(5)–Ni(2)–O(3)	87.29(6)	C(5)–O(3)–Ni(2)	144.46(13)
C(15)–N(5)–Ni(2)	131.13(13)	N(6)–N(5)–Ni(2)	122.84(12)
C(18)–N(7)–Ni(2)	132.81(14)	N(8)–N(7)–Ni(2)	122.63(13)

The chains form an extended 3D network structure in which, interestingly, three types of noncovalent forces, namely hydrogen bonds, face-to-face π–π interactions, and edge-to-face CH–π interactions, are involved. As displayed in Figure 2 (a), the 3D molecular view in the *ac* plane can be described as a combination of two sheets that are slanted with respect to each other. Sheet A comprises Ni1 chains and Ni2 chains, with a shortest interchain Ni1···Ni2 distance of 8.060(1) Å (Figure 2, b). There is intrachain hydrogen bonding between unbound carboxylate oxygens and N–H groups of pyrazole in an Ni2 chain. Simultaneously, the free carboxylate oxygen atoms participate in interchain hydrogen bonds to N–H groups in other Ni1 chains, eventually generating a 3D network structure. It is worthwhile to note that interchain edge-to-face CH–π interactions become established between C14–H14 from the pyrazoles and C6-containing benzene rings (2.826 Å), as well as between C3–H3 from the benzene rings and the N5-containing pyrazole rings (3.019 Å). In sheet B, shown in Figure 2 (c), symmetry-related free carboxylate oxygen atoms in an Ni2 chain undergo intrachain and interchain hydrogen bonding to the N–H groups of the pyrazole rings in the same chain and adjacent Ni1 chains, respectively. In comparison with sheet A, sheet B consists of CH–π interactions between pyrazole rings: interchain contacts between C17–H17 from N5-containing pyrazoles and N1-containing pyrazoles (3.007 Å). The C9–H9 moiety from the N1-containing pyrazoles undergoes intrachain contacts with N3-containing pyrazole planes (2.852 Å). For sheets A and B, the distances of the hydrogen bonds are d(D···A) = 2.931(2) Å and ∠(D–H···A) = 134° for N2–H2···O4, d(D···A) = 2.711(2) Å and ∠(D–H···A) = 158° for N6–H6···O4a (–x – 1, –y + 3, –z + 1), d(D···A) = 2.720(2) Å and ∠(D–H···A) = 168° for

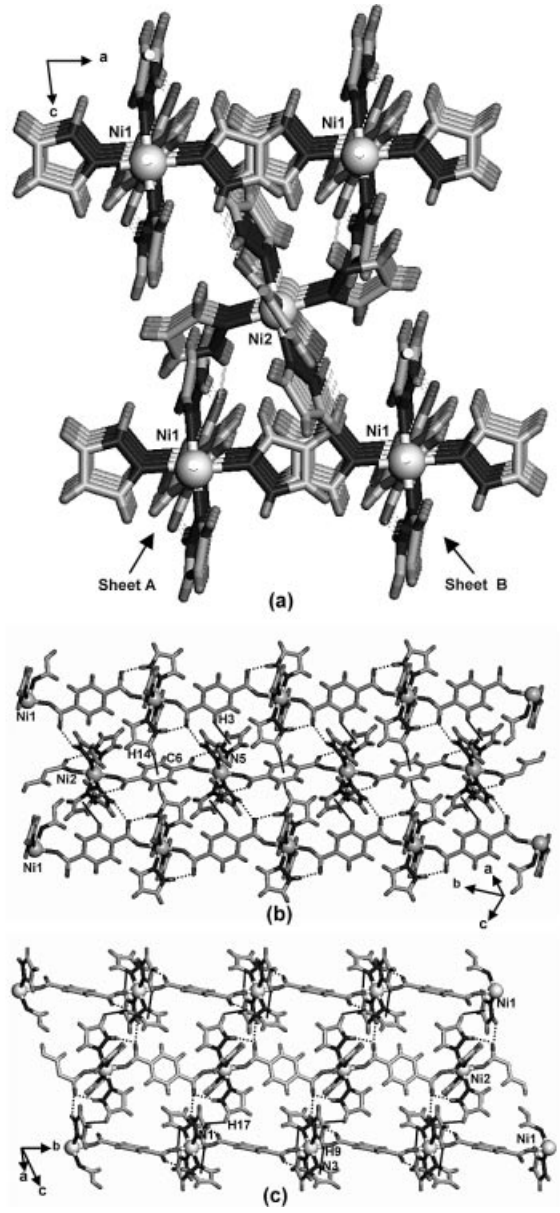

Figure 2. Extended view of **1** showing (a) a 3D network in the *ac* plane, (b) sheet A, and (c) sheet B. Progressively darker shades of grey represent Ni, C, H, N, and O, respectively. The dotted lines indicate hydrogen bonds and the solid lines denote CH–π interactions.

 © 2005 Wiley-VCH Verlag GmbH & Co. KGaA, Weinheim

N4–H4A···O2, and d(D···A) = 2.976(2) Å and ∠(D–H···A) = 137° for N8–H8A···O2b (x – 1, y, z). As seen in Figure 3, additional noncovalent interactions correspond to face-to-face π–π stacking between aromatic pyrazole rings residing on the same type of nearest neighbor chains residing in sheets A and B, respectively, where the shortest interchain distance of Ni1(Ni2)···Ni1(Ni2) is equal to 8.467(1) Å. The pyrazole groups associated with π–π interactions are separated by 3.410–3.507 Å, which is consistent with those between 2,2′-bipyridine or 1,10-phenanthroline ligands in tp-bridged Ni^{II} chain compounds.[8] Thus, it should be noted that the capping pyrazole ligand plays a key role in the construction of the 3D supramolecular network structure by allowing multi-intermolecular interactions concurrently.

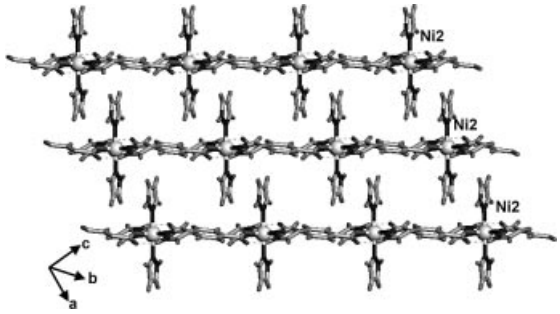

Figure 3. Extended molecular view exhibiting π–π stacking. Progressively darker shades of grey represent Ni, C, H, N, and O, respectively.

The magnetic behavior of **1** is shown in Figure 4 in the form of the temperature dependence of χ_m and $\chi_m T$ at 2000 G in the temperature range 1.8–300 K. At 300 K, the $\chi_m T$ value is 1.24 $cm^3 K mol^{-1}$, which is in the usual range for a noninteracting Ni^{II} ion. The $\chi_m T$ value decreases slowly upon cooling, then drops abruptly below 20 K, finally reaching a value of 0.45 $cm^3 K mol^{-1}$ at 1.8 K, thus indicating the existence of an antiferromagnetic interaction between the magnetic centers. The inverse magnetic susceptibility data obey the Curie–Weiss equation [$\chi_m = C/(T - \theta)$] in the linear region, giving C = 1.24 $cm^3 K mol^{-1}$ and θ = –0.46 K. This definitely demonstrates that adjacent magnetic spins are coupled antiferromagnetically.

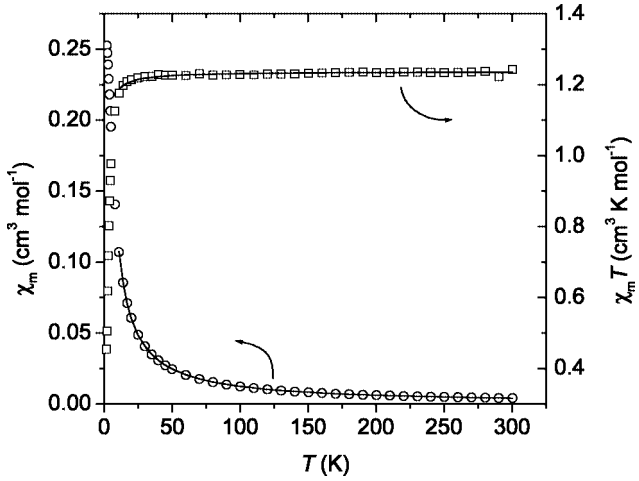

Figure 4. Plots of χ_m and $\chi_m T$ vs. T for **1**. The solid lines show the best theoretical fits.

The magnetic data were fitted to the analytical expression derived by Weng on the basis of the spin Hamiltonian $H = -J \cdot \sum_i S_i \cdot S_{i+1}$, where the local anisotropy is neglected [Equation (1)].[12]

$$\chi_m = \{Ng^2\beta^2/kT\}[2.0 + 0.0194x + 0.777x^2]/ [3.0 + 4.346x + 3.232x^2 + 5.834x^3] \quad (1)$$

in which $x = |J|/kT$. Because this equation does not take into account the zero-field splitting or the Haldane gap, fitting was performed above 10 K. With consideration of a molecular field approximation (zJ'), the magnetic fitting given by the solid line in Figure 4 yields parameters of g = 2.224(1), J = –0.22(1) cm^{-1}, and $zJ' \approx 0$. The use of the infinite chain model derived by Fisher[13] produces similar results of g = 2.224(1), J = –0.24(1) cm^{-1}, and $zJ' \approx 0$ in the same temperature range. Thus, it is evident that a weak antiferromagnetic interaction is operative between the Ni^{II} centers. It is reasonable to assume that the antiferromagnetic behavior occurs via the long tp bridge because, with the given distances, intrachain interactions through covalent linkages are stronger than interchain couplings via the intermolecular contacts, which is consistent with the results reported previously for tp-linked Ni^{II} systems.[3,10,14,15] In comparison with the 1D Ni^{II} macrocyclic complex (J = –1.37 cm^{-1}), where the intrachain Ni–Ni separation is virtually the same (11.5 Å) and a is significantly smaller (5.6°), the weaker antiferromagnetic interaction ($J \approx$ –0.2 cm^{-1}) in **1** arises from the sizeable difference in a (21.41° and 10.25° for **1**).[14]

In summary, we have prepared a tp-bridged Ni^{II} compound with a 3D network structure built by covalent and noncovalent bonds. In particular, the nonchelating capping pyrazole ligand, which contains an N–H group and a planar aromatic ring, behaves as a unique and efficient synthon for noncovalent contacts of hydrogen bonding, face-to-face π–π interactions, and edge-to-face CH–π interactions, thus opening-up an opportunity to create a new class of supramolecular assemblies.

Experimental Section

Physical Measurements: Elemental analyses for C, H, and N were performed at the Elemental Analysis Service Center of Sogang University. Infrared spectra were obtained from KBr pellets with a Bomen MB-104 spectrometer. Magnetic susceptibilities for **1** were carried out using a Quantum Design MPMS-7 SQUID susceptometer. Diamagnetic corrections of **1** were estimated from Pascal's tables.

[Ni(pyrazole)$_4$(tp)]$_n$ (1): Pyrazole (2.0 mmol), dissolved in 5 mL of water, was added, with stirring, to a 10 mL aqueous solution of nickel(II) nitrate hexahydrate (0.50 mmol). The resultant pale-green

 © 2005 Wiley-VCH Verlag GmbH & Co. KGaA, Weinheim

solution was treated with a solution of potassium terephthalate (0.50 mmol) in 5 mL of water. The filtrate of the resulting solution was allowed to stand for several days to give blue crystals of **1** in 70% yield based on Ni in the presence of four equivalents of pyrazole. $C_{20}H_{20}N_8NiO_4$: calcd. C 48.5, H 4.07, N 22.6; found C 48.2, H 4.09, N 22.5. Selected IR data (KBr pellet): $\tilde{\nu}$ = 3379 cm^{-1} (m), 3350 (m), 3138 (w), 3126 (w), 3061 (w), 2595 (m, broad), 1920 (w), 1561 [s, tp $\nu_a(CO_2^-)$], 1523 (m), 1498 (w), 1452 (m), 1383, 1358 [s, tp $\nu_s(CO_2^-)$], 1279 (w), 1166 (w), 1150 (w), 1123 (m), 1059 (s), 1015 (w), 933 (m), 910 (m), 882 (m), 851 (w), 810 (s), 764 (s), 750 (s), 726 (m), 662 (w), 621 (w), 604 (m), 515 (m).

X-ray Structural Analysis: $C_{20}H_{20}N_8NiO_4$, M = 495.15, triclinic, $P\bar{1}$, a = 8.4673(14), b = 11.4460(16), c = 11.920(2) Å, α = 77.663(15)°, β = 80.088(15)°, γ = 71.529(12)°, V = 1063.6(3) $Å^3$, Z = 2, D_c = 1.546 $g\,cm^{-3}$, $F(000)$ = 512. Final R indices were R_1 = 0.0258, wR_2 = 0.0669 [$I > 2\sigma(I)$]. The crystal data for **1** are summarized in Table 2.

Table 2. Crystal data and structure refinement for **1**.

Empirical formula	$C_{20}H_{20}N_8NiO_4$
Formula mass	495.15
Crystal system	triclinic
Space group	$P\bar{1}$
a [Å]	8.4673(14)
b [Å]	11.4460(16)
c [Å]	11.920(2)
α [°]	77.663(15)
β [°]	80.088(15)
γ [°]	71.529(12)
V [$Å^3$]	1063.6(3)
Z	2
μ [mm^{-1}]	0.959
ρ [$g\,cm^{-3}$]	1.546
$F(000)$	512
Goodness-of-fit	1.051
R_1 [$I > 2\sigma(I)$]	0.0258
wR_2 [$I > 2\sigma(I)$]	0.0669

CCDC-274883 contains the supplementary crystallographic data for this paper. These data can be obtained free of charge from The Cambridge Crystallographic Data Centre via www.ccdc.cam.ac.uk/data_request/cif.

Acknowledgments

We would like to thank an Operation Program on Shared Research Equipment of KBSI and MOST. This work was financially supported by the CRM-KOSEF.

[1] O. Kahn, *Magnetism: A Supramolecular Function*, Kluwer, Dordrecht, The Netherlands, **1996**.
[2] S. Kitagawa, R. Kitaura, S.-i. Noro, *Angew. Chem. Int. Ed.* **2004**, *43*, 2334–2375.
[3] J. Cano, G. D. Munno, J. L. Sanz, R. Ruiz, J. Faus, F. Lloret, M. Julve, A. Caneschi, *J. Chem. Soc., Dalton Trans.* **1997**, 1915–1923.
[4] C. S. Hong, Y. S. You, *Polyhedron* **2004**, *23*, 3043–3050.
[5] L. Li, Z. Liu, S. S. Turner, D. Liao, Z. Jiang, S. Yan, *Eur. J. Inorg. Chem.* **2003**, 62–65.
[6] X. Shi, G. Zhu, Q. Fang, G. Wu, G. Tian, R. Wang, D. Zhang, M. Xue, S. Qiu, *Eur. J. Inorg. Chem.* **2004**, 185–191.
[7] C. S. Hong, Y. Do, *Inorg. Chem.* **1997**, *36*, 5684–5685.
[8] Y. Go, X. Wang, E. V. Anokhina, A. J. Jacobson, *Inorg. Chem.* **2004**, *43*, 5360–5367.
[9] C. Ma, Y. Han, R. Zhang, D. Wang, *Eur. J. Inorg. Chem.* **2005**, 1649–1652.
[10] C. S. Hong, Y. S. You, *Polyhedron* **2004**, *23*, 1379–1384.
[11] K. Nakamoto, *Infrared and Raman Spectra of Inorganic and Coordination Compounds: Part B: Applications*, in *Coordination, Organometallic, and Bioinorganic Chemistry*, 5th ed, John Wiley & Sons, Inc: New York, **1997**.
[12] A. Meyer, A. Gleizes, J.-J. Girerd, M. Verdaguer, O. Kahn, *Inorg. Chem.* **1982**, *21*, 1729–1739.
[13] M. E. Fisher, *Am. J. Phys.* **1964**, *32*, 343–346.
[14] K.-Y. Choi, K. M. Chun, I.-H. Suh, *Polyhedron* **2001**, *20*, 57–65.
[15] K.-Y. Choi, K. M. Chun, K.-C. Lee, J. Kim, *Polyhedron* **2002**, *21*, 1913–1920.

Received: June 13, 2005
Published Online: October 20, 2005

 © 2005 Wiley-VCH Verlag GmbH & Co. KGaA, Weinheim

DOI: 10.1002/ejic.200500541

Crystal Structures, EPR Spectra, and Magnetic Properties of a Series of Ionic Multi-Component Complexes $[(TBPDA)_2{\cdot}(C_{60}^{\cdot-}){\cdot}(D^+)]$ (D = Cp^*_2Cr, Cp^*_2Co, TDAE)

Dmitri V. Konarev,*[a,b] Andrey Yu. Kovalevsky,[c] Salavat S. Khasanov,[a,d] Gunzi Saito,*[a] Akihiro Otsuka,[a,e] and Rimma N. Lyubovskaya[b]

Keywords: Crystal engineering / EPR spectroscopy / Fullerenes / IR spectroscopy / Magnetic properties / Metallocenes

New ionic multi-component complexes $[(TBPDA)_2{\cdot}(C_{60}^{\cdot-}){\cdot}(D^+)]$ [TBPDA = *N*,*N*,*N*′,*N*′-tetrabenzyl-*p*-phenylenediamine; D = decamethylchromocene (Cp^*_2Cr, **1**) and decamethylcobaltocene (Cp^*_2Co, **2**)] were obtained additionally to previously characterized $[(TBPDA)_2{\cdot}(C_{60}^{\cdot-}){\cdot}(TDAE^{\cdot+})]$ [TDAE = tetrakis(dimethylamino)ethylene, **3**]. The presence of D^+, $C_{60}^{\cdot-}$, and neutral TBPDA in **1**–**3** was proved by the IR and UV/Visible/NIR spectra. D^+ and $C_{60}^{\cdot-}$ form loose layers in **1** and **3** and are spatially separated by bulky TBPDA molecules. The $C_{60}^{\cdot-}$ radical anions alternate in the layer with the phenylene groups of TBPDA to form π-π stacking, whereas disordered $Cp^*_2Cr^+$ cations are isolated in the voids formed by eight benzyl groups of TBPDA. The EPR spectra of the complexes show single Lorentzian lines with g = 2.2526 and ΔH = 215 mT (**1**), g = 1.9999 and ΔH = 6.7 mT (**2**), and g = 2.0009 and ΔH = 2.93 mT (**3**) at room temperature. The EPR signal of **2** was attributed to $C_{60}^{\cdot-}$ ($Cp^*_2Co^+$ is diamagnetic) and those in **1** and **3** to resonating signals between $C_{60}^{\cdot-}$ (g = 1.9996–2.0000) and $Cp^*_2Cr^+$ [an asymmetric EPR signal with $g_\perp$ = 4.02(1) and $g_\parallel$ = 2.001(1)] (**1**) or $TDAE^{\cdot+}$ (g = 2.0035; **3**) due to indirect coupling. The EPR signals from **2** and **3** are split into two components below 50 and 60 K, respectively, which shift in the opposite directions (to lower and higher fields) with decreasing temperature. The magnetic moments of **1**–**3** decrease below 50–100 K. Both effects are associated with the formation of field-induced short-range antiferromagnetically ordered clusters. It is shown that the D^+ cations do not noticeably affect this interaction. Most probably, it is realized mainly between $C_{60}^{\cdot-}$ spins within the layer and is mediated by the phenylene groups of TBPDA.
(© Wiley-VCH Verlag GmbH & Co. KGaA, 69451 Weinheim, Germany, 2005)

Introduction

Fullerenes, as acceptors, form molecular and ionic complexes with different donor molecules.[1–3] Ionic complexes are interesting due to their magnetic properties,[4] the reversible formation of diamagnetic single-bonded $(C_{60}^-)_2$ dimers,[5–8] and other types of negatively charged σ-bonded structures.[9] However, only a limited number of organic and organometallic donors can ionize fullerenes in the solid state. These include metallocenes [decamethylnickelocene, Cp^*_2Ni;[10] decamethylchromocene, Cp^*_2Cr;[6,7] decamethylcobaltocene, Cp^*_2Co;[11,12] cobaltocene, Cp_2Co;[7,13] bis(benzene)chromium, $Cr(C_6H_6)_2$,[7,14] and its substituted analogs;[8,15,16] $Fe^ICp(C_6Me_6)$[17]], unsaturated amines [tetrakis(dimethylamino)ethylene, TDAE, and related compounds[4,18]], and some metalloporphyrins.[19,20] We have developed a multi-component approach to modify ionic complexes of fullerenes, in which a neutral D_1 molecule is introduced into an ionic complex to produce a new compound with two donor counterparts: $(D_1){\cdot}(D_2^{\cdot+}){\cdot}(\text{fullerene}^{\cdot-})$.[21–24] In such a complex, D_1 forms a supramolecular packing pattern, whereas D_2 is a strong donor of a small size relative to D_1 that is potentially able to ionize the fullerene moiety. D_1 defines not only the complex structure but in some cases affects the electronic state of the fullerenes. In the series of complexes $[Co^{II}TPP{\cdot}(D_2^+){\cdot}(C_{60}^-){\cdot}\text{solvent}]$ [$Co^{II}TPP$ = cobalt(II) tetraphenylporphyrin; D_2 = $Cr(C_6H_6)_2$[21] or TDAE[22]] $Co^{II}TPP$ forms unusual diamagnetic σ-bonded ($Co^{II}TPP{\cdot}\text{fullerene}^-$) anions, whereas in $[CTV{\cdot}(Cs^+)_2{\cdot}(C_{60(70)}^-)_2{\cdot}(DMF)_x]$ (CTV = cyclotriveratrylene; DMF = *N*,*N*′-dimethylformamide; x = 5–7) we observed the formation of single-bonded $(C_{60}^-)_2$ and $(C_{70}^-)_2$

[a] Division of Chemistry, Graduate School of Science, Kyoto University,
Sakyo-ku, Kyoto 606-8502, Japan
Fax: +81-75-753-4035
E-mail: saito@kuchem.kyoto-u.ac.jp
[b] Institute of Problems of Chemical Physics RAS,
Chernogolovka, Moscow region 142432, Russia
Fax: +7-096-5155420
E-mail: konarev@icp.ac.ru
[c] State University of New York at Buffalo,
Buffalo, New York, 14260, USA
E-mail: bioayk@langate.gsu.edu
[d] Institute of Solid State Physics RAS,
Chernogolovka, Moscow region, 142432, Russia
E-mail: khasanov@issp.ac.ru
[e] Research Center for Low Temperature and Materials Sciences, Kyoto University,
Sakyo-ku, Kyoto 606-8502, Japan
Supporting information for this article is available on the WWW under http://www.eurjic.org or from the author.

 © 2005 Wiley-VCH Verlag GmbH & Co. KGaA, Weinheim

dimers[23,24] and in [(TBPDA)$_2$·($C_{60}^{\cdot-}$)·($TDAE^{\cdot+}$)] (Figure 1) a short-range antiferromagnetic interaction of the spins was found.[22] In the present work we have studied the incorporation of cations other than $TDAE^{\cdot+}$ into the (TBPDA)$_2$·C_{60} framework. We used two strong donors − Cp^*_2Cr and Cp^*_2Co (Figure 1) − that ionize C_{60} in the solid state[6,7,11,12] and whose cations are comparable in size to the $TDAE^{\cdot+}$ ones but have different spin states ($Cp^*_2Cr^+$: S = 3/2; $Cp^*_2Co^+$: S = 0) relative to that of $TDAE^{\cdot+}$ (S = 1/2). Thus, we can study how cations with different spin states and shapes ($Cp^*_2Cr^+$, $Cp^*_2Co^+$, and $TDAE^{\cdot+}$) can affect the EPR spectra and the magnetic and structural properties of a series of multi-component complexes [(TBPDA)$_2$·($C_{60}^{\cdot-}$)·(D^+)].

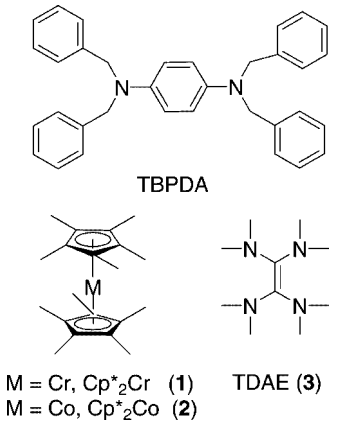

Figure 1. Molecular structures of the components used to prepare **1**–**3**.

The crystal structure of [(TBPDA)$_2$·($C_{60}^{\cdot-}$)·(Cp^*Cr^+)] (**1**) is studied for the first time; the IR and UV/Visible/NIR spectra and the EPR and magnetic susceptibility data down to liquid helium temperatures are presented for **1** and [(TBPDA)$_2$·($C_{60}^{\cdot-}$)·(Cp^*Co^+)] (**2**). These data are compared with those for previously described [(TBPDA)$_2$·($C_{60}^{\cdot-}$)·($TDAE^+$)] (**3**).[22]

Results and Discussion

Synthesis

Complexes **1** and **2** were obtained by a diffusion method in which C_{60}, Cp^*_2M, and an excess of TBPDA dissolved in a mixture of C_6H_6 and C_6H_5CN were precipitated with hexane. Previously, [(TBPDA)$_2$·C_{60}·TDAE] (**3**) was synthesized by the same procedure.[22] The use of smaller Cp_2Co or $Cr(C_6H_6)_2$ molecules under similar conditions did not afford multi-component complexes. Therefore, the size of the D_2 component is important for the stabilization of the [(TBPDA)$_2$·($C_{60}^{\cdot-}$)·(D_2^+)] complexes.

IR and UV/Visible/NIR Spectra

The IR spectra of **1** and **2** in a KBr matrix are a superposition of the spectra of C_{60}, Cp^*_2M, and TBPDA (see Supporting Information). Neutral C_{60} has absorption bands at 527, 577, 1182, and 1429 cm^{-1} [F_{1u}(1–4) modes, respectively]. The F_{1u}(1) and -(2) modes retain their positions (at 526–527 and 575 cm^{-1}), whereas the F_{1u}(4) mode, which is the most sensitive to charge transfer to the C_{60} molecule,[25] is shifted to 1388 cm^{-1} in the spectra of **1** and **2**. The integral intensity of the F_{1u}(2) mode also essentially increases relative to that of the F_{1u}(1) mode. Such changes are characteristic of $C_{60}^{\cdot-}$.[25] The formation of $C_{60}^{\cdot-}$ is justified by the appearance of additional bands in the UV/Visible/NIR spectra of **1** and **2** at 10.75–10.77 × 10^3 and 9.20 × 10^3 cm^{-1}.

Cp^*_2Cr has one band in the IR spectrum that is sensitive to charge transfer and is shifted from 418 to 437 cm^{-1} due to the transition from a neutral to a cationic form in **1** as well as in ($Cp^*_2Cr^+$)·(PF_6^-)[26] and ($Cp^*_2Cr^+$)·($C_{60}^{\cdot-}$)·($C_6H_4Cl_2$)$_2$.[6,7] Similarly, the band of Cp^*_2Co in the IR spectrum is shifted from 429 to 442, 448, and 445 cm^{-1} in **2**, ($Cp^*_2Co^+$)·(PF_6^-),[26] and [($Cp^*_2Co^+$)$_2$·(C_{60}^{2-})·($C_6H_4Cl_2$, C_6H_5CN)$_2$],[12] respectively. The absorption bands of TBPDA in the IR spectrum are shifted by up to 10 cm^{-1} in **1** and **2** relative to those in the spectrum of neutral TBPDA·(C_{60})$_2$.[27] This is probably associated with the different geometry of TBPDA in **1**, **2**, and TBPDA·(C_{60})$_2$. The absence of additional absorption bands in the IR and UV/Visible/NIR spectra of **1** and **2**, which must accompany the dimerization or polymerization of $C_{60}^{\cdot-}$,[28] indicates their monomeric nature at room temperature (room temp.). Complex **3**[22] has IR and UV/Visible/NIR spectra similar to those of **1** and **2**.

Crystal Structures

Complex **1** crystallizes in a tetragonal system in the $I\bar{4}$ space group and has a structure similar to that of [(TBPDA)$_2$·C_{60}·TDAE] (**3**)[22] (see Figures 2 and 3). $C_{60}^{\cdot-}$ and $Cp^*_2Cr^+$ (**1**) or $TDAE^{\cdot+}$ (**3**) occupy positions with $\bar{4}$ or 4/m symmetry and are statistically disordered in both structures as they lie on a symmetry position higher than their own symmetry. Complex **1** has a more complicated disorder pattern than **3**. A fourfold inversion axis passes through the midpoints of oppositely located 6-6 bonds of $C_{60}^{\cdot-}$ and the central C=C bond of $TDAE^{\cdot+}$ in **3** and coincides with the twofold symmetry axes of these ions. The rotation of both ions by 90° about a fourfold axis generates two orientations with equal occupancies.[22] In contrast to **3**, the fourfold inversion axis in **1** passes through the midpoints of oppositely located 6–5 bonds of C_{60} and the Cr atom of $Cp^*_2Cr^+$ to form an angle of about 85° with a fivefold symmetry axis of $Cp^*_2Cr^+$ (as shown in Figure 4). In this case, the symmetry operation generates four orientations of the $C_{60}^{\cdot-}$ and $Cp^*_2Cr^+$ ions with equal occupancies. The ordered TBPDA molecules occupy positions with 2/m symmetry.

The unit-cell parameters a and b (see Experimental Section) are larger by 0.35 Å in **1** than in **3**, whereas the parameter c is smaller by 0.32 Å. The unit-cell volume of **1** is increased by about 180 Å^3 relative to that of **3**, thus indicat-

 © 2005 Wiley-VCH Verlag GmbH & Co. KGaA, Weinheim

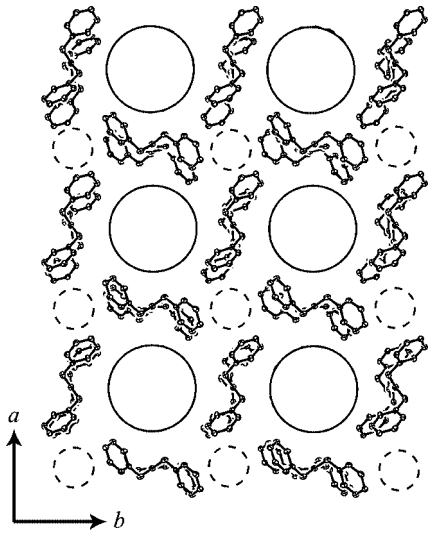

Figure 2. General view of the crystal structures of **1** and **3** on the *ab* plane. The positions of disordered $C_{60}^{\cdot-}$ radical anions are shown by large circles and those of the cations ($Cp^*_2Cr^+$ and $TDAE^{\cdot+}$) are shown by smaller dashed circles.

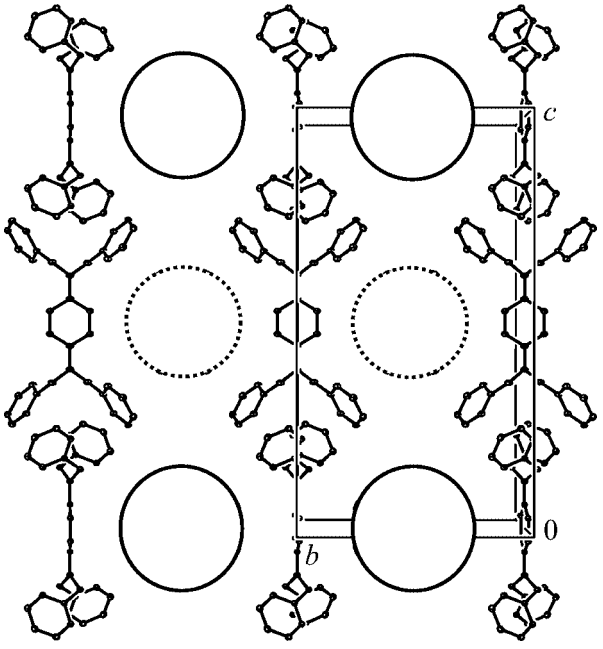

Figure 3. General view of the crystal structures of **1** and **3** on the *bc* plane. The positions of disordered $C_{60}^{\cdot-}$ radical anions are shown by large circles and those of the cations ($Cp^*_2Cr^+$ and $TDAE^{\cdot+}$) are shown by smaller dashed circles.

ing that $Cp^*_2Cr^+$ is slightly larger than $TDAE^{\cdot+}$. $C_{60}^{\cdot-}$, $Cp^*_2Cr^+$ ($TDAE^{\cdot+}$), and TBPDA form square loose layers in **1** and **3** parallel to the *ab* plane (Figure 2). The $C_{60}^{\cdot-}$ radical anions are separated from each other [the shortest center-to-center distance between adjacent fullerenes in the layer is 13.973(2) Å in **1** and 13.626(2) in **3**] and alternate with the central phenylene (-C_6H_4-) groups of TBPDA along the *a* and *b* directions (Figure 2). Consequently, each $C_{60}^{\cdot-}$ forms van der Waals contacts with four phenylene groups of the adjacent TBPDA molecules. The hexagons of

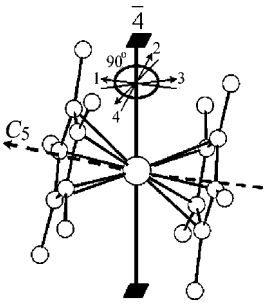

Figure 4. Disorder of the $Cp^*_2Cr^+$ cations. A fourfold inversion axis (solid line) and a fivefold symmetry axis of $Cp^*_2Cr^+$ (dashed line) are shown. Both axes form an angle of ca. 85°. Four positions of $Cp^*_2Cr^+$ with equal occupancies obtained by its rotation by 90° about a fourfold axis are marked by the numbers from 1 to 4.

$C_{60}^{\cdot-}$ and the phenylene groups of TBPDA are nearly parallel in **3** (the corresponding dihedral angle is only 5°), thus indicating the presence of π-π interactions. The C(TBPDA)···$C(C_{60}^{\cdot-})$ contacts lie in the range 3.43–3.68 Å (the sum of the van der Waals radii of two sp^2 carbon atoms is 3.42 Å[29]). Large disorder in **1** does not allow the estimation of the C···C contacts and angles. Nevertheless, the C···C contacts should be slightly larger than those in **3** due to the larger unit-cell parameters *a* and *b*.

Each $Cp^*_2Cr^+$ moiety is located within the layer in the cavities formed by eight benzyl groups of TBPDA (Figure 2). All C(TBPDA)···C($Cp^*_2Cr^+$ or $TDAE^{\cdot+}$) contacts are large (>3.70 Å) to prevent π-π interactions between the Cp* rings and TBPDA fragments. Therefore, the $Cp^*_2Cr^+$ cations are separated from each other. The interlayer space is filled with the benzyl groups of TBPDA (Figure 3). The ordered TBPDA molecules retain pristine geometry, thus showing their neutral state in the complex. Only the torsion angles of the benzyl groups of the TBPDA molecule in **1** are smaller (73°) than those in neutral TBPDA (85–87°).[30] Such changes are probably caused by packing forces.

A schematic view of the crystal structures of **1** and **3** along the *a* direction is shown in Figure 3. The chains of alternating $C_{60}^{\cdot-}$ and D^+ ions can be seen along the *c* direction. These chains are separated from the neighboring ones by bulky TBPDA molecules. The distances between the $C_{60}^{\cdot-}$ and D^+ ions in the chains are rather large [all intermolecular C(C_{60})···C(D^+) contacts are longer than 5 Å]. Thus, **1** and **3** are dilute systems in which the $C_{60}^{\cdot-}$ and D^+ ions are separated in three directions by the TBPDA molecules. Nevertheless, the $C_{60}^{\cdot-}$ radical anions alternate and form π-π interactions with the phenylene groups of TBPDA, which can mediate magnetic coupling between $C_{60}^{\cdot-}$ spins within the layer. The TBPDA molecules can probably also mediate weak coupling between spins localized on $C_{60}^{\cdot-}$ and D^+.

Magnetic Properties

The magnetic properties of polycrystalline **1**, **2**, and **3**[33] sealed in quartz tubes under 10^{-5} Torr vacuum were studied by EPR (Table 1, Figures 5 and 6) and SQUID (Figure 7)

 © 2005 Wiley-VCH Verlag GmbH & Co. KGaA, Weinheim

techniques from room temp. down to liquid helium temperatures.

Table 1. EPR parameters of **1**–**3**.

Complex	290 K		4 K	
	g factor	ΔH [mT]	*g* factor	ΔH [mT]
$[(TBPDA)_2{\cdot}C_{60}{\cdot}Cp^*_2Cr]$ (**1**)	1.9999	6.7	1.9985	0.42
			1.9950	0.51
$[(TBPDA)_2{\cdot}C_{60}{\cdot}Cp^*_2Co]$ (**2**)	2.2526	215	2.7563	168
$[(TBPDA)_2{\cdot}C_{60}{\cdot}TDAE]$ (**3**)[22]	2.0009	2.93	2.0063	0.76
			1.9966	0.21

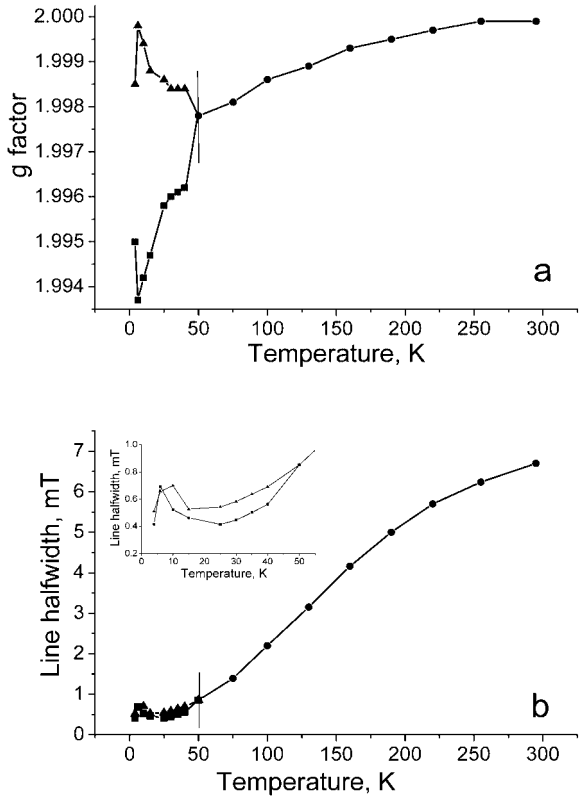

Figure 5. Temperature dependence of the *g*-factor (a) and line halfwidth (b) for $[(TBPDA)_2{\cdot}C_{60}{\cdot}Cp^*_2Co]$ (**2**) in the 4–295 K range.

Complex **2** shows a broad Lorentzian line with g = 1.9999 and line halfwidth (ΔH) of 6.7 mT (Figure 5). This signal is characteristic of $C_{60}^{\cdot-}$, which has a *g*-factor in the range 1.9996–2.0000 and ΔH of 3–5 mT at room temp.[2,3] Diamagnetic and EPR silent $Cp^*_2Co^+$ makes no contribution to the EPR spectrum of **2**.

The EPR signal of **3** has a larger *g*-factor of 2.0009 and a narrower line (ΔH = 2.93 mT).[22] $TDAE{\cdot}C_{60}$ has a similar EPR signal (g = 2.0003 and ΔH = 2.2 mT at room temp.[31]). Both signals can be attributed to resonating ones between $C_{60}^{\cdot-}$ and $TDAE^{\cdot+}$ ion-radicals due to an intermediate *g*-factor value ($C_{60}^{\cdot-}$ has a *g*-factor of 1.9996–2.0000 and $TDAE^{\cdot+}$ of 2.0035[32]). The resonating signal is characteristic of exchange coupling between $TDAE^{\cdot+}$ and $C_{60}^{\cdot-}$ ion-radicals. This coupling in $TDAE{\cdot}C_{60}$ can be realized directly between both ion-radicals due to short C···C contacts (3.401–3.482 Å[33]) and the overlapping of their π-orbitals.

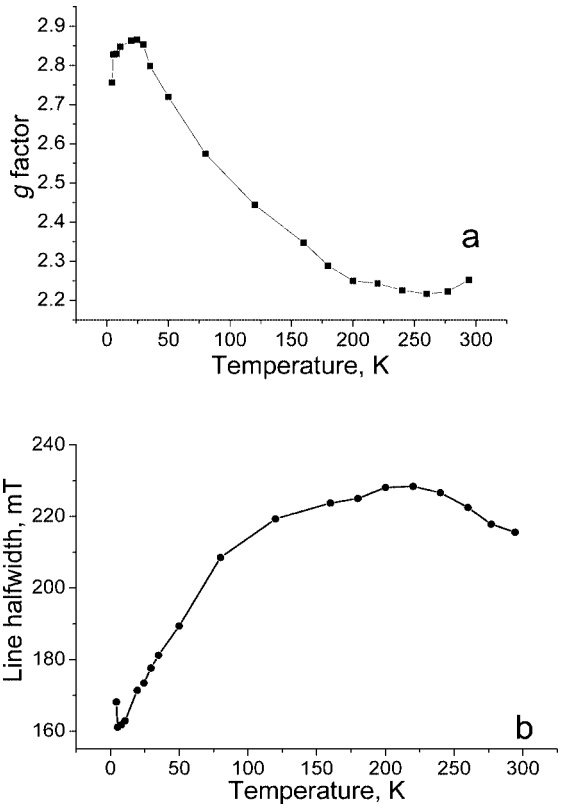

Figure 6. Temperature dependence of the *g*-factor (a) and line halfwidth (b) for $[(TBPDA)_2{\cdot}C_{60}{\cdot}Cp^*_2Cr]$ (**1**) in the 4–295 K range.

The distances between ion-radicals in **3** are large and in this case we can suppose only indirect coupling (for example, through the TBPDA molecules). Indirect coupling through nonmagnetic ligands has previously been observed even in clusters.[34]

The EPR spectrum of **1** contains a single Lorentzian line with g = 2.2526 and ΔH = 215.6 mT at room temp. (Figure 6). A similar EPR signal has been observed for a high-temperature monomeric phase of $[Cp^*_2Cr{\cdot}C_{60}{\cdot}(C_6H_4Cl_2)_2]$ (g = 2.2210 and $\Delta H \approx$ 100 mT at 320 K[24]). The observed *g*-factors are intermediate between those of $C_{60}^{\cdot-}$ and Cp^*_2Cr {an asymmetric EPR signal with $g_\perp$ = 4.02(1) and $g_\parallel$ = 2.001(1)[26]}, thus implying a resonating signal between these ions. Exchange coupling between the $Cp^*_2Cr^+$ and $C_{60}^{\cdot-}$ ions can be realized directly in $[Cp^*_2Cr{\cdot}C_{60}{\cdot}(C_6H_4Cl_2)_2]$ as the shortest C···C distance is 3.049(6) Å[6] and only indirectly in **1** due to the large distances between the ions, similar to **3**.

The EPR signal of **2** essentially narrows with decreasing temperature and the *g*-factor shifts monotonically to 1.9978 at 50 K (Figure 5). A similar behavior of ΔH has been observed for **3** and other solid ionic complexes of C_{60}.[2] The EPR signal becomes asymmetric below 50 K and splits into two components (see Supporting Information). These components shift in the opposite directions (to higher and lower magnetic fields) with decreasing temperature (g = 1.9985 and 1.9950 at 4 K, Figure 5a). The shifts are accompanied by a small broadening of both components (Figure 5b). The

 © 2005 Wiley-VCH Verlag GmbH & Co. KGaA, Weinheim

magnetic moment of **2** (μ_{eff} = 1.65 μ_B at 300 K) is nearly temperature independent down to around 100 K and begins to decrease below this temperature (Figure 7b). Both effects in SQUID and EPR originate from the antiferromagnetic interaction of spins. Such a behavior can be attributed to the formation of a field-induced short-range antiferromagnetically ordered cluster.[35,36] The behavior of **3** is very similar. The temperatures of the splitting of the EPR signal and the decrease of the magnetic moment are 60 and about 80 K, respectively (Figure 7c).[22]

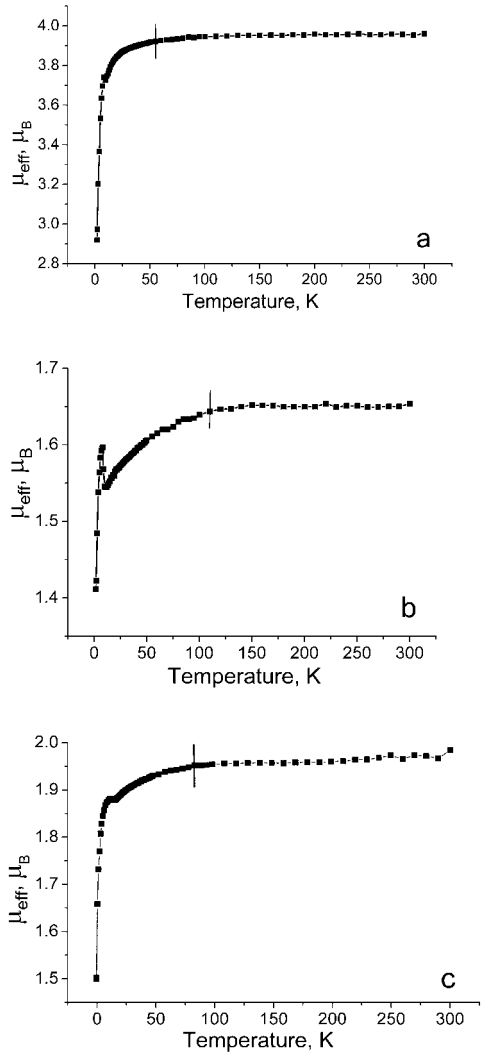

Figure 7. Temperature dependence of the magnetic moments of **1** (a), **2** (b), and **3** (c) in the 1.9–300 K range. Vertical bars show the temperature for a decrease of the magnetic moment.

The EPR signal of **1** shifts to larger *g*-factors with decreasing temperature (g = 2.7563 at 4 K, Figure 6a), whereas ΔH remains very broad in the whole temperature range (approx. 160–230 mT; Figure 6, b). The magnetic moment of **1** (μ_{eff} = 3.96 μ_B at 300 K) indicates a contribution from $Cp^*_2Cr^+$ (S = 3/2) and $C_{60}^{\cdot-}$ (S = 1/2) (μ_{eff} = 4.27 μ_B for a system of noninteracting S = 3/2 and 1/2 spins). Ionic $[Cp^*_2Cr{\cdot}C_{60}{\cdot}(C_6H_4Cl_2)_2]$[7] and $[Cr^{III}TPP{\cdot}C_{60}{\cdot}(THF)_3]$ [Cr^{III}TPP = tetraphenylporphyrinatochromium(III)][20] have similar magnetic moments equal to 4.20 μ_B. The magnetic moment of **1** is temperature independent down to around 50 K and decreases below this temperature due to the antiferromagnetic interaction of spins (Figure 7, a). However, the EPR signal of **1** is unsplit down to 4 K, probably due to a very large ΔH value.

An antiferromagnetic character of interaction of spins in **1**–**3** was justified by SQUID measurements. The complexes show small negative Weiss constants of –0.7 K for **1**, –1.8 K for **2**, and –2.3 K for **3**.

Conclusion

Two new ionic multi-component complexes $[(TBPDA)_2{\cdot}(C_{60}^{\cdot-}){\cdot}(D^+)]$ containing decamethylchromocene (Cp^*_2Cr, **1**) and decamethylcobaltocene (Cp^*_2Co, **2**) have been obtained. Together with previously characterized $[(TBPDA)_2{\cdot}(C_{60}^{\cdot-}){\cdot}(TDAE^{\cdot+})]$ (**3**), they form a series of multi-component complexes with cations of different shape and spin state. The optical absorption spectra of **1**–**3** in the IR and UV/Visible/NIR ranges prove the presence of D^+, $C_{60}^{\cdot-}$, and neutral TBPDA. The D^+ and $C_{60}^{\cdot-}$ ions in the crystal structures of **1** and **3** form loose layers that are spatially separated by the bulky TBPDA molecules. As this takes place, the $C_{60}^{\cdot-}$ radical anions alternate with the phenylene groups of TBPDA to form π-π stacking interactions with them, whereas the D^+ cations are spatially and magnetically isolated in the voids formed by eight benzyl groups of TBPDA. The complexes show single Lorentzian EPR lines with g = 1.9999 and ΔH = 6.7 mT (**2**), g = 2.0009 and ΔH = 2.93 mT (**3**), and g = 2.2526 and ΔH = 215 mT (**1**) at room temp. Two-component ionic complexes of C_{60}, namely $TDAE{\cdot}C_{60}$[31] and $[Cp^*_2Cr{\cdot}C_{60}{\cdot}(C_6H_4Cl_2)_2]$[24] have EPR signals similar to those of **3** and **1**. The EPR signal in **2** was attributed to $C_{60}^{\cdot-}$ as $Cp^*_2Co^+$ is diamagnetic and therefore EPR silent. The EPR signals in **1** and **3** and in corresponding two-component complexes were assigned to resonating signals between $C_{60}^{\cdot-}$ and D^+ ($Cp^*_2Cr^+$ or $TDAE^{\cdot+}$). In two-component complexes this is a result of direct exchange coupling between $C_{60}^{\cdot-}$ and D^+, which is possible due to short intermolecular contacts between them and the overlapping of their π-orbitals. Complexes **1** and **3** are dilute systems with large spatial separation between the $C_{60}^{\cdot-}$ and D^+ ions. In this case only indirect coupling can be supposed through the TBPDA molecules. Below 60 K (**3**) and 50 K (**2**), the EPR signals are split into two components that shift in opposite directions to lower and higher fields. The magnetic moments of **1**–**3** also decrease below 50–100 K. These phenomena can be explained by the formation of field-induced short-range antiferromagnetically ordered clusters. The substitution of paramagnetic $Cp^*_2Cr^+$ and $TDAE^{\cdot+}$ by diamagnetic $Cp^*_2Co^+$ does not noticeably affect the antiferromagnetic interaction of the spins in **1**–**3**. In accordance with X-ray diffraction data, this interaction is realized mainly between $C_{60}^{\cdot-}$ spins within the layer through the phenylene groups of TBPDA as the D^+ cations are surrounded by benzyl groups of TBPDA and are not involved in this interaction. Nevertheless, the TBPDA mole-

 © 2005 Wiley-VCH Verlag GmbH & Co. KGaA, Weinheim

cules probably mediate weak exchange coupling between the $C_{60}^{\cdot-}$ and D^+ spins seen by EPR. The large distances between $C_{60}^{\cdot-}$ and D^+ in **1**–**3** and the mediation of magnetic coupling through the diamagnetic TBPDA molecules are reasons for the relatively weak magnetic interaction of spins with Weiss constants from –0.7 to –2.3 K.

Experimental Section

General: Decamethylchromocene (Cp^*_2Cr) and decamethylcobaltocene (Cp^*_2Co) were purchased from Strem Chemicals, *N*,*N*,*N*′,*N*′-Tetrabenzyl-*p*-phenylenediamine (TBPDA) was purchased from Lancaster and C_{60} of 99.98% purity from MTR Ltd. Solvents were purified under argon. Benzonitrile (C_6H_5CN) was distilled from Na under reduced pressure; benzene and hexane were distilled from Na/benzophenone. The solvents were degassed and stored in a glove box. Synthesis of the complexes was carried out in an MBraun 150B-G glove box with controlled atmosphere (content of H_2O and O_2 less than 1 ppm). The crystals were stored in the glove box and were sealed in 2 mm quartz tubes for EPR and SQUID measurements at 10^{-5} Torr. KBr pellets for IR and UV/Visible/NIR measurements were prepared in the glove box.

UV/Visible/NIR spectra were measured on a Shimadzu-3100 spectrometer in the 240–2600 nm range. FT-IR spectra were measured as KBr pellets with a Perkin–Elmer 1000 Series spectrometer (400–7800 cm^{-1}). A Quantum Design MPMS-XL SQUID magnetometer was used to measure static susceptibilities of **1** and **2** between 300 and 1.9 K in a 0.1 T static magnetic field. A sample holder contribution and core temperature independent diamagnetic susceptibility (χ_0) were subtracted from the experimental values. The values of Θ and χ_0 were calculated from the high-temperature range using the formula $\chi_M = C/(T - \Theta) + \chi_0$. EPR spectra were recorded from room temp. down to 4 K with a JEOL JES-TE 200 X-band ESR spectrometer equipped with a JEOL ES-CT470 cryostat.

Synthesis: Crystals of [(TBPDA)$_2$·C_{60}·Cp^*_2Cr] (**1**) and [(TBPDA)$_2$·C_{60}·Cp^*_2Co] (**2**) were obtained by slow diffusion of hexane (20 mL) into 20 mL of a C_6H_6/C_6H_5CN mixture (4:1) containing C_{60} (25 mg, 0.035 mmol), Cp^*_2M (0.037 mmol), and TBPDA (120 mg, 0.255 mmol). The starting solution was prepared by dissolving C_{60} and Cp^*_2M in 4 mL of C_6H_5CN by stirring at 60 °C for 4 h. After this 16 mL of benzene was added and TBPDA was dissolved by stirring overnight at 60 °C. The obtained solution was cooled down to room temperature and filtered. Diffusion was carried out in a glass tube of 1.8 cm diameter and 50 mL volume with a ground glass plug during one month. The solvent was decanted and the crystals were washed with hexane and dried to yield black square thick plates of complexes **1** and **2** in 60–80% yield.

[(TBPDA)$_2$·C_{60}·Cp^*_2Cr] (1980.3): calcd. C 89.80, H 4.75, Cr 2.62, N 2.83; found C 89.41, H 4.86, N 2.69.

[(TBPDA)$_2$·C_{60}·Cp^*_2Co] (1987.2): calcd. C 89.48, H 4.73; Co 2.97, N 2.82; found C 89.00, H 4.65, N 2.64.

The composition of **1** and **2** was determined from the elemental analysis, and was justified for **1** by X-ray diffraction on a single crystal. The synthesis of crystals of **3** has been described elsewhere.[22]

X-ray Crystallographic Study of 1: $C_{148}H_{94}CrN_4$, M_r = 1980.27, black square plates, tetragonal, space group $I\bar{4}$. Unit cell parameters $a = b$ = 13.9732(3), c = 24.3682(11) Å, V = 4757.9(3) Å^3, Z = 2, D_c = 1.382 g cm^{-3}, μ = 0.186 mm^{-1}, and $F(000)$ = 2068. X-ray diffraction data for **1** were collected at 90(1) K using a Bruker SMART1000 CCD diffractometer installed at a rotating anode source (Mo-K_α radiation, λ = 0.71073 Å), and equipped with an Oxford Cryosystems nitrogen gas-flow apparatus. The data were collected by the rotation method with a 0.3° frame-width (ω scan) and 10 s exposure time per frame. Four sets of data (600 frames in each set) were collected, nominally covering half of the reciprocal space. The data were integrated, scaled, sorted, and averaged using the SMART software package.[37] In total, 42648 reflections were measured up to $2\Theta_{max}$ = 59.98°, 6879 of which were independent. The structure was solved by direct methods using SHELXTL NT Version 5.10.[38] The structure was refined by full-matrix least-squares against F^2. Non-hydrogen atoms were refined in the anisotropic approximation. Positions of hydrogen atoms were calculated geometrically. Subsequently, the positions of H atoms were refined by the "riding" model with U_{iso} = 1.2 U_{eq} of the connected non-hydrogen atom or as ideal CH_3 groups with U_{iso} = 1.5 U_{eq}. The least-squares refinement on F^2 was done to $R_1[I > 2\sigma(F)]$ = 0.0885 for 5626 observed reflections with $F > 2\sigma(F)$, wR_2 = 0.2358 and R_1 = 0.1053 for all 6879 observed reflections with 482 parameters and 7956 restraints; final GoF = 1.078.

CCDC-275769 contains the supplementary crystallographic data for compound **1**. These data can be obtained free of charge from The Cambridge Crystallographic Data Center via www.ccdc.cam.ac.uk/data_request/cif.

Supporting Information (for details see the footnote on the first page of this article): IR, UV/Visible/NIR, and EPR spectroscopic data of complexes **1**–**3** (Tables S1 and S2 and Figures S1–S4).

Acknowledgments

The work was partly supported by a Grant-in-Aid for Scientific Research from the Ministry of Education, Culture, Sports, Science and Technology, Japan (152005019, 21st Century COE, and Elements Science 12CE2005) and the RFBR grant no. 03-03-32699a.

[1] A. L. Balch, M. M. Olmstead, *Chem. Rev.* **1998**, *98*, 2123–2165.
[2] C. A. Reed, R. D. Bolskar, *Chem. Rev.* **2000**, *100*, 1075–1120.
[3] D. V. Konarev, R. N. Lyubovskaya, *Russ. Chem. Rev.* **1999**, *68*, 19–38.
[4] B. Gotschy, *Fullerene Sci. Technol.* **1996**, *4*, 677–698.
[5] A. Hönnerscheid, L. van Wüllen, M. Jansen, J. Rahmer, M. Mehring, *J. Chem. Phys.* **2001**, *115*, 7161–7165.
[6] D. V. Konarev, S. S. Khasanov, A. Otsuka, G. Saito, *J. Am. Chem. Soc.* **2002**, *124*, 8520–8521.
[7] D. V. Konarev, S. S. Khasanov, G. Saito, A. Otsuka, Y. Yoshida, R. N. Lyubovskaya, *J. Am. Chem. Soc.* **2003**, *125*, 10074–10083.
[8] S. Yu. Ketkov, G. A. Domrachev, A. M. Ob'edkov, A. Yu. Vasil'kov, L. P. Yur'eva, C. P. Mehner, *Russ. Chem. Bull.* **2004**, *53*, 2056–2059.
[9] K. Prassides, in *The Physics of Fullerene-Based and Fullerene-Related Materials* (Ed.: W. Andreoni), Kluwer Academic Publishers, The Netherlands, **2000**, pp. 175–202.
[10] W. C. Wan, X. Liu, G. M. Sweeney, W. E. Broderick, *J. Am. Chem. Soc.* **1995**, *117*, 9580–9581.
[11] P. D. W. Boyd, P. Bhyrappa, P. Paul, J. Stinchcombe, R. D. Bolskar, Y. Sun, C. A. Reed, *J. Am. Chem. Soc.* **1995**, *117*, 2907–2914.
[12] D. V. Konarev, S. S. Khasanov, G. Saito, I. I. Vorontsov, A. Otsuka, R. N. Lyubovskaya, Yu. M. Antipin, *Inorg. Chem.* **2003**, *42*, 3706–3708.
[13] A. L. Balch, J. W. Lee, B. C. Noll, M. M. Olmstead, *Recent Advances in the Chemistry and Physics of Fullerenes and Related Materials* (Eds.: K. M. Kadish, R. S. Ruoff), **1994**, vol. 24, 1231–1243.

 © 2005 Wiley-VCH Verlag GmbH & Co. KGaA, Weinheim

[14] Y. Yoshida, A. Otsuka, O. O. Drozdova, K. Yakushi, G. Saito, *J. Mater. Chem.* **2003**, *13*, 252–258.
[15] W. E. Broderick, K. W. Choi, W. C. Wan, *Electrochem. Soc. Proc.* **1997**, *14*, 1102–1113.
[16] A. Hönnerscheid, L. van Wüllen, R. Dinnebier, M. Jansen, J. Rahmer, M. Mehring, *Phys. Chem. Chem. Phys.* **2004**, *6*, 2454–2460.
[17] C. Bossard, S. Rigaut, D. Astruc, M.-H. Delvill, G. Felix, A. Fevrier-Bouvier, J. Amiell, S. Fladroids, P. Delhaes, *J. Chem. Soc., Chem. Commun.* **1993**, 333–334.
[18] P.-M. Allemand, K. C. Khemani, A. Koch, F. Wudl, K. Holczer, S. Donovan, G. Grüner, J. D. Thompson, *Science* **1991**, *253*, 301–303.
[19] A. Pénicaud, J. Hsu, C. A. Reed, A. Koch, K. Khemani, P.-M. Allemand, F. Wudl, *J. Am. Chem. Soc.* **1991**, *113*, 6698–6700.
[20] J. Stinchcombe, A. Pénicaud, P. Bhyrappa, P. D. W. Boyd, C. A. Reed, *J. Am. Chem. Soc.* **1993**, *115*, 5212–5217.
[21] D. V. Konarev, S. S. Khasanov, A. Otsuka, Y. Yoshida, R. N. Lyubovskaya, G. Saito, *Chem. Eur. J.* **2003**, *9*, 3837–3848.
[22] D. V. Konarev, I. S. Neretin, G. Saito, Yu. L. Slovokhotov, A. Otsuka, R. N. Lyubovskaya, *Dalton Trans.* **2003**, 3886–3891.
[23] D. V. Konarev, S. S. Khasanov, I. I. Vorontsov, G. Saito, Yu. A. Antipin, A. Otsuka, R. N. Lyubovskaya, *Chem. Commun.* **2002**, 2548–2549.
[24] D. V. Konarev, S. S. Khasanov, G. Saito, R. N. Lyubovskaya, *Recent Research Developments in Chemistry*, vol. 2, Research Signpost, Trivandrum, Kerala, India, **2004**, 105–140.
[25] T. Picher, R. Winkler, H. Kuzmany, *Phys. Rev. B* **1994**, *49*, 15879–15889.
[26] J. L. Robbins, N. Edelstein, B. Spencer, J. C. Smart, *J. Am. Chem. Soc.* **1982**, *104*, 1882–1893.
[27] D. V. Konarev, A. Yu. Kovalevsky, A. L. Litvinov, N. V. Drichko, B. P. Tarasov, P. Coppens, R. N. Lyubovskaya, *J. Solid State Chem.* **2002**, *168*, 474–485.
[28] M. S. Dresselhaus, G. Dresselhaus, in *Fullerene Polymers and Fullerene Polymer Composites* (Eds.: P. C. Eklund, A. M. Rao), Springer-Verlag, Berlin, **1999**, pp. 1–57.
[29] R. S. Rowland, R. Taylor, *J. Phys. Chem.* **1996**, *100*, 7384–7391.
[30] C. Richert, M. Pirotta, T. Muller, *Acta Crystallogr., Sect. C* **1992**, *48*, 2233–2235.
[31] K. Tanaka, A. A. Zakhidov, K. Yoshizawa, K. Okahara, T. Yamabe, K. Yakushi, K. Kikuchi, S. Suzuku, L. Ikemoto, Y. Achiba, *Phys. Rev. B* **1993**, *47*, 7554–7559.
[32] K. Kuwata, D. H. Geske, *J. Am. Chem. Soc.* **1964**, *86*, 2101–2105.
[33] B. Narymbetov, H. Kobayashi, M. Tokumoto, A. Omerzu, D. Mihailovic, *Chem. Commun.* **1999**, 1511–1512.
[34] P. W. Anderson, *Magnetism*, N. Y. Academic, **1963**, vol. 1, p. 25.
[35] D. Arčon, R. Blinc, P. Cevk, G. Chouteau, A.-L. Barra, *Phys. Rev. B* **1997**, *56*, 10786–10788.
[36] A. L. Maneiro, L. Pasimeni, L. C. Brunel, L. A. Pardi, G. Cao, R. P. Guertin, *Solid State Commun.* **1998**, *106*, 727–732.
[37] SMART and SAINT, Area detector control and integration software, Ver. 6.01. Bruker Analytical X-ray Systems, Madison, Wisconsin, U.S.A., **1999**.
[38] SHELXTL, An integrated system for solving, refining and displaying crystal structures from diffraction data, Ver. 5.10. Bruker Analytical X-ray Systems, Madison, Wisconsin, U.S.A, **1997**.

Received: June 21, 2005
Published Online: October 12, 2005

 © 2005 Wiley-VCH Verlag GmbH & Co. KGaA, Weinheim

DOI: 10.1002/ejic.200500579

Kinetic Inertness and Electrochemical Behavior of Copper(II) Tetraazamacrocyclic Complexes: Possible Implications for in Vivo Stability

Katrina S. Woodin,[a] Katie J. Heroux,[a] C. Andrew Boswell,[b] Edward H. Wong,*[a] Gary R. Weisman,*[a] Weijun Niu,[a] Sterling A. Tomellini,[a] Carolyn J. Anderson,[b] Lev N. Zakharov,[c] and Arnold L. Rheingold[c]

Keywords: Macrocyclic ligands / N ligands / Copper

The kinetic inertness of copper(II) complexes of several carboxymethyl-armed cyclams and cyclens in 5 M HCl have been determined confirming that the complex derived from cross-bridged cyclam (Cu-CB-TE2A) is by far the most resistant to acid decomplexation. FT-IR studies in D_2O solution revealed its unique resistance to full carboxylate protonation and its retention of coordination by both pendant arms even in 1 M DCl. The X-ray structure of its monoprotonated form, [Cu-CB-TE2AH]$^+$, also established full coordination by both COO^- and COOH pendant arms in the solid state. Cyclic voltammograms of four carboxymethyl pendant-armed cyclam and cyclen complexes in aqueous solution were obtained with only Cu-CB-TE2A displaying a quasi-reversible Cu^{II}/Cu^{I} reduction wave. These indicators correlate with the superior in vivo behavior of this complex and its bifunctional conjugate.
(© Wiley-VCH Verlag GmbH & Co. KGaA, 69451 Weinheim, Germany, 2005)

Introduction

Carboxymethyl pendant-armed derivatives of tetraazamacrocycles are promising chelators for copper(II)-based radiopharmaceuticals.[1,2] The 14-membered macrocycle (cyclam) derivative TETA (Figure 1) has been evaluated as a ^{64}Cu-carrier by in vivo studies.[1] Despite its high in vitro thermodynamic stability, significant in vivo loss of radio-metal from both ^{64}Cu-TETA and its bifunctional conjugates was observed.[2] In addition to Cu^{II} dissociation from the chelator, its reduction and subsequent complex destabilization prior to Cu^{I} loss may also be a pathway for loss of radio-copper. The latter demetallation mode has been implicated in the selective trapping of ^{64}Cu from its bis(thiosemicarbazone) complexes in hypoxic cells.[3,4] We therefore hypothesize that *both* kinetic inertness to Cu^{II} dissociation in aqueous solution as well as resistance towards Cu^{II}/Cu^{I} reduction and subsequent Cu^{I} loss are useful indicators of desirable in vivo performance of a potential copper-based radiopharmaceutical.

[a] Department of Chemistry, University of New Hampshire, Durham, New Hampshire 03824, USA
E-mail: ehw@hypatia.unh.edu
gary.weisman@unh.edu
[b] Mallinckrodt Institute of Radiology, Washington University School of Medicine,
St. Louis, Missouri 63110, USA
[c] Department of Chemistry and Biochemistry, University of California,
San Diego, La Jolla, California 92093, USA

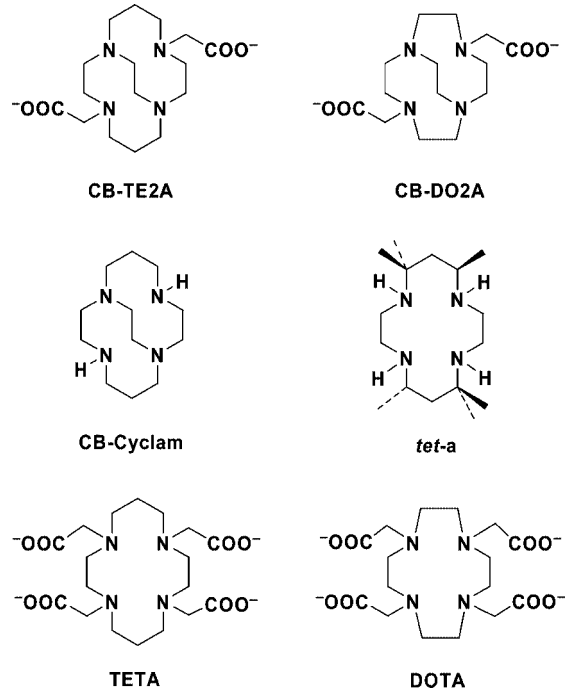

Figure 1. The cross-bridged ligands CB-TE2A, CB-DO2A, and CB-Cyclam with TETA, DOTA, and *tet*-a.

Recently we reported the superior in vivo behavior of a ^{64}Cu-labeled chelator CB-TE2A (Figure 1) and a bioconjugate compared to TETA, DOTA, as well as CB-DO2A analogues.[5–7] Briefly, the respective ligands were labeled

 © 2005 Wiley-VCH Verlag GmbH & Co. KgaA, Weinheim

with ^{64}Cu and injected into rats, the animals were sacrificed at appropriate time points, and the biodistribution and metabolism of the labeled complexes assayed out to 20 h post-injection. It was found that ^{64}Cu-CB-TE2A and its bioconjugate showed a marked improvement in both clearance and resistance to demetallation. Presence in the chelator of both a cross-bridged cyclam backbone and at least one carboxymethyl pendant arm appears to be essential for this enhanced performance. To gain insight into these observations and to develop convenient indicators for bio-stability, we have initiated kinetic inertness as well as electrochemical studies of this and related copper complexes in aqueous media. We report herein the extraordinary kinetic inertness of Cu-CB-TE2A to acid decomplexation as well as its unique electrochemical behavior compared to Cu-TETA and their related cyclen analogues, Cu-CB-DO2A and Cu-DOTA (Figure 1).

Table 1. Half-lives of copper(II) complexes.

Complex	Half-life
5 M HCl, 90 °C	
Cu-CB-TE2A	154(6) h
Cu-TETA	4.5(5) min
Cu-DOTA	< 1 min
Cu-CB-cyclam	11.8(2) min
Cu-*tet*-a	1.1(1) h
5 M HCl, 50 °C	
Cu-TETA	3.2(1) h
Cu-*tet*-a	83.7(6) h
5 M HCl, 30 °C	
Cu-TETA	3.5(2) days
Cu-CB-cyclam	18.5(7) days
Cu-CB-DO2A	< 2 min
Cu-cyclam	2.7(1) days
1 M HCl, 30 °C	
Cu-CB-DO2A	4.0(1) h

Results and Discussion

The primary aim of this work is to develop a convenient and practical, albeit qualitative, assay of in vitro inertness for predicting the suitability of each new copper chelator in follow-up biological studies. Since aqueous acid-assisted decomplexation of polyazamacrocyclic copper complexes is a convenient and useful indicator of their kinetic inertness,[8,9] we chose to compare the decomplexation half-lives of Cu-CB-TE2A and analogues under pseudo first-order conditions in 5 M HCl (Table 1). As the detailed decomplexation mechanisms have not yet been elucidated, the data must be interpreted with caution. Nonetheless, we can readily conclude that Cu-CB-TE2A is by far the most kinetically inert amongst the carboxymethyl pendant-armed tetraazamacrocyclic complexes studied, with the relative order: Cu-CB-TE2A >> Cu-DOTA ≈ Cu-TETA > Cu-CB-DO2A. It is noteworthy that even the extremely robust red isomer of Cu-*tet*-a (Figure 1) decomposed more rapidly under these strongly acidic conditions.[8,10] Neither Cu-CB-Cyclam nor Cu-CB-DO2A showed comparable inertness to Cu-CB-TE2A, suggesting that both the carboxymethyl pendant arms and the bicyclo[6.6.2] cross-bridged cyclam backbone are essential for Cu-CB-TE2A's exceptional robustness. Sargeson and co-workers have reported encapsulated Cu^{II} complexes of hexaaza cage ligands which are also extremely inert to acid decomplexation,[11,12] although direct comparisons with Cu-CB-TE2A have not yet been made.

To gain insight into the speciation of these complexes in acidic aqueous media, FT-IR spectra of Cu-CB-TE2A, Cu-CB-DO2A, Cu-TETA, and Cu-DOTA in DCl/D_2O solutions were examined in the 1550–1800 cm^{-1} region. In 0.1 M DCl, all complexes revealed prominent ν_{asym}(COO) bands due to coordinated carboxylate (1598–1620 cm^{-1}) as well as protonated carboxylic acid (1688–1724 cm^{-1}) bands (Figure 2, a and Figure 3). While Cu-CB-DO2A decomposed in 1.0 M DCl within hours, both the Cu-TETA and Cu-DOTA spectra showed carboxylic acid bands (1685–1727 cm^{-1}) as the only major features (Figure 3). The splitting of these carboxylic acid bands is due to the presence of both coordinated as well as uncoordinated pendant arms. By contrast, the Cu-CB-TE2A complex exhibited both carboxylate (1611 cm^{-1}) and carboxylic acid (1702 cm^{-1}) bands (Figure 2, b). Since the free ligand CB-TE2A displayed distinct carboxylate (at pD 12, not shown) and carboxylic acid (1.0 M DCl, Figure 2, b) bands at 1574 and 1718 cm^{-1}, respectively, we can infer retention of *both* carboxylate and carboxylic acid pendant arm coordination at the copper center of Cu-CB-TE2A.

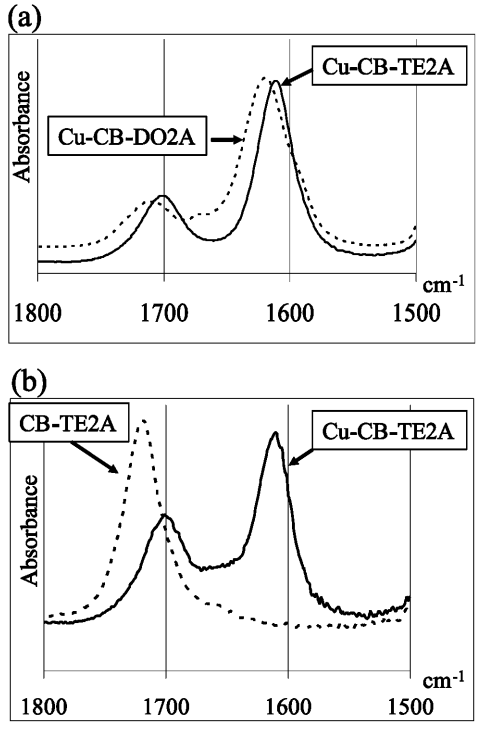

Figure 2. FT-IR spectra of: (a) Cu-CB-TE2A and Cu-CB-DO2A in 0.1 M DCl /D_2O, (b) Cu-CB-TE2A and CB-TE2A in 1.0 M DCl/D_2O.

Slow evaporation of a 0.1 M perchloric acid solution of Cu-CB-TE2A yielded dark-blue crystals of the monopro-

 © 2005 Wiley-VCH Verlag GmbH & Co. KGaA, Weinheim

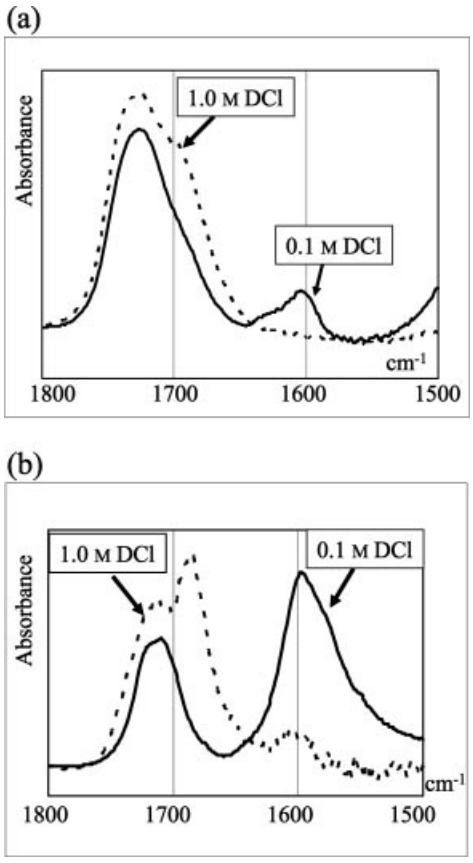

Figure 3. FT-IR spectra in DCl/D_2O solutions of: (a) Cu-DOTA, and (b) Cu-TETA.

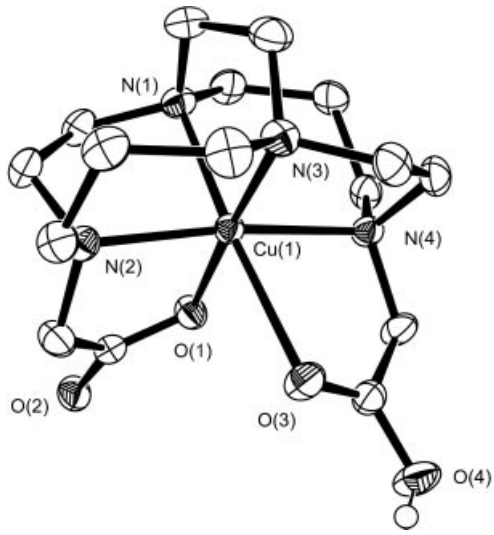

Figure 4. X-ray structure of $[Cu\text{-}CB\text{-}TE2AH]ClO_4$. All non-carboxylic acid protons and perchlorate anion omitted for clarity.

Table 2. Relevant bond lengths [Å] and angles [°] for $[Cu\text{-}CB\text{-}TE2AH]ClO_4$.

Cu(1)–O(1)	1.966(2)	Cu(1)–N(2)	2.057(2)
Cu(1)–O(3)	2.525(2)	Cu(1)–N(3)	2.016(2)
Cu(1)–N(1)	2.216(2)	Cu(1)–N(4)	2.046(2)
O(1)–Cu(1)–N(3)	177.03(8)	O(1)–Cu(1)–N(4)	90.07(4)
O(1)–Cu(1)–N(1)	95.32(7)	O(1)–Cu(1)–N(2)	84.03(7)
N(1)–Cu(1)–N(3)	86.36(8)	N(1)–Cu(1)–N(2)	85.02(8)
N(1)–Cu(1)–N(4)	99.43(7)	N(2)–Cu(1)–N(3)	98.58(8)
N(2)–Cu(1)–N(4)	172.92(8)	N(3)–Cu(1)–N(4)	87.26(8)

tonated complex $[Cu\text{-}CB\text{-}TE2AH]ClO_4$. Its X-ray structure (Figure 4) confirmed the weak coordination of the carboxylic acid pendant arm with a Jahn–Teller elongated Cu(1)–O(3) bond length of 2.525(2) Å as well as strong coordination of the remaining carboxylate arm with a much shorter Cu(1)–O(1) bond at 1.966(2) Å. The C(16)–O(3) distance of 1.219(3) Å relative to C(16)–O(4) of 1.306(3) Å confirmed carbonyl coordination of the COOH group. For comparison, the parent Cu-CB-TE2A complex has less pronounced Jahn–Teller elongated copper-carboxylate bond lengths of 2.30–2.33 Å and undistorted bonds of 2.00–2.01 Å.[13] In both structures, the metal cation fits snugly inside the cross-bridged cyclam ligand's cleft as indicated by nearly linear *trans*-N–Cu–N angles (173–182°). Additional structural data for the $[Cu\text{-}CB\text{-}TE2AH]^+$ cationic complex are listed in Table 2.

The solid-state IR spectrum of the monoprotonated complex displayed both coordinated carboxylate and carboxylic acid COO stretches at 1616 and 1694 cm^{-1}, respectively, reasonably close to the 1.0 M DCl solution values of 1611 and 1702 cm^{-1}. This further supports retention of both carboxylate and carboxylic acid pendant arm coordination of Cu-CB-TE2A in DCl solution. As acid-assisted decomplexation of carboxylate and phosphonate pendant-armed cyclam and cyclen metal complexes typically involves *O*-protonation pre-equilibria,[8,9,14–18] dissociation of protonated arms likely precedes rupture of Cu–N bonds. The 10-membered rings of the ligand adopt [2233] conformations rather than the distorted diamond-lattice [2323] conformation found in the unprotonated analogue. We propose that for protonated Cu-CB-TE2A, at least one coordinated carboxylic acid arm must dissociate from the metal before any Cu–N bond cleavage can occur. Even then, such bond breaking is discouraged by the cross-bridged cyclam's low-energy [2233] or [2323] solution conformation. Indeed, such a ruptured Cu–N bond is predisposed to reform the original complex. Consistent with this rationale, Cu-CB-Cyclam is almost an order of magnitude more kinetically inert than Cu-Cyclam (Table 1).

Since Cu^I has significantly different coordination preferences than Cu^{II}, in vivo reduction of stable Cu^{II} complexes to form Cu^I products can lead to demetallation or disproportionation in an alternative decomplexation pathway. We carried out cyclic voltammetry experiments on Cu-CB-TE2A, Cu-TETA, Cu-DOTA, and Cu-CB-DO2A in 0.1 M aqueous sodium acetate solution adjusted to pH 7 (Figure 5).

Both Cu-TETA and Cu-CB-DO2A yielded irreversible reduction voltammograms. Cu-DOTA gave both a broad reduction peak at –1.00 V (vs. Ag/AgCl) and an attenuated oxidation wave at –0.39 V in the return scan. By contrast, a quasi-reversible reduction was observed for Cu-CB-TE2A at –1.08 V with a peak separation of 120 mV. This voltammogram was reproducible upon repeated cycling between

 © 2005 Wiley-VCH Verlag GmbH & Co. KGaA, Weinheim

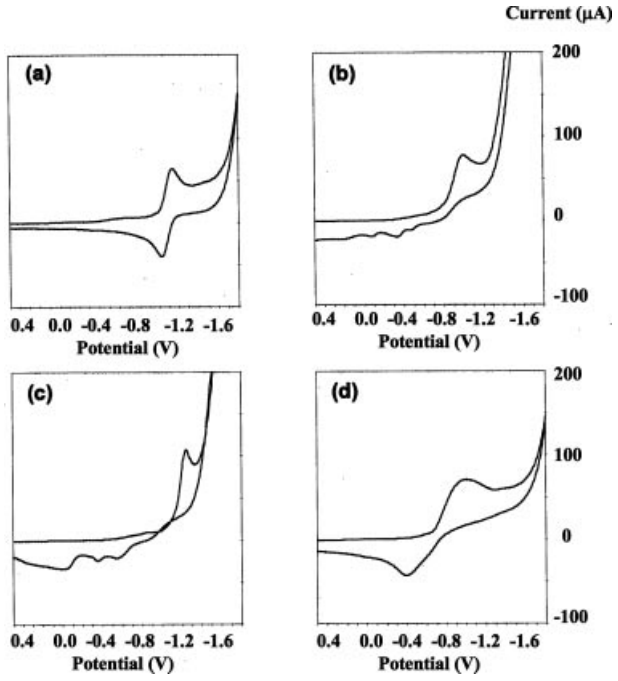

Figure 5. Cyclic voltammograms of (a) Cu-CB-TE2A, (b) Cu-CB-DO2A, (c) Cu-TETA, and (d) Cu-DOTA in 0.1 M sodium acetate, pH 7.0.

+0.8 V and –1.4 V. An increase of the scan rate (ν) resulted in an increased peak separation. A differential pulse voltammogram (0.0 V to –1.4 V at v = 20 mV/s) further confirmed a well-defined reduction peak at –1.06 V. We were also able to observe a similar quasi-reversible reduction of this complex in DMSO ($E_{1/2}$ = –1.23 V, ΔE = 162 mV). The higher chemical reversibility ($i_{pa}/i_{pc} \approx 0.8$) of this redox couple suggests that the reduction product, Cu^{I}-CB-TE2A, must be longer-lived compared to its analogues. Thus none of the related ligands DOTA, TETA, or CB-DO2A appear to be able to adapt to the coordination requirements of Cu^{I} and stabilize it. In contrast, the ability of a dibenzyl derivative of cross-bridged cyclam to accommodate the disparate coordination preferences of both a cuprous as well as a cupric cation has already been demonstrated.[19] Efforts to isolate and characterize the Cu^{I} complex of CB-TE2A are in progress.

Conclusions

Taken together, the relative kinetic inertness, FT-IR and electrochemical data single out the unique properties of Cu-CB-TE2A compared to its closely-related Cu-TETA, Cu-DOTA, and Cu-CB-DO2A analogues. This particular combination of a cross-bridged cyclam backbone together with carboxymethyl pendant arms stabilizes the complex towards *both* acid-assisted and reductive decomplexation and correlate well with the improved in vivo performance of ^{64}Cu-CB-TE2A. Further investigations to confirm these correlations in parallel with biological studies to gain insight into the in vivo mechanism of metal dissociation from ^{64}Cu-labeled tetraazamacrocyclic complexes are underway.

Experimental Section

Caution! Although we encountered no problems, perchlorate salts of organic ligands are potentially explosive and should be handled with care and only in small quantities. All copper(II) complexes of carboxymethyl pendant-armed tetraazamacrocyclic ligands were prepared according to published literature procedures: Cu-TETA,[20] Cu-DOTA,[20] Cu-CB-TE2A,[13] and Cu-CB-DO2A.[6]

Acid-Decomplexation Studies: Sample concentrations of copper complexes studied were between 1–3 mM. Each complex's visible electronic spectrum in 5.0 M HCl at 90 °C was recorded at specific time points using a Cary 50 Bio UV/Vis spectrophotometer. In each case, isosbestic spectra were obtained indicative of a single decomplexation product. The decreasing absorbance at the λ_{max} of each spectrum (Cu-CB-TE2A 529 nm, Cu-CB-DO2A 606 nm, Cu-TETA 615 nm, Cu-DOTA 725 nm, Cu-*tet-a* 516 nm, Cu-cyclam 510 nm, and Cu-CB-cyclam 587 nm) was used to monitor the progress of the decomplexation reaction. Half-lives were calculated from the slopes of the linear *ln*(absorbance) vs. time plots.

Solution FT-IR Spectra: FT-IR absorbance spectra in D_2O solutions were obtained in a barium fluoride cell (0.01 cm pathlength) with a Nicolet 520 FT-IR spectrophotometer. Absorbance spectra were produced by ratioing the single beam spectra of the samples to the corresponding solvents. All spectra were acquired at a nominal 2 cm^{-1} resolution (using a liquid nitrogen-cooled MCT detector).

Synthesis of [Cu-CB-TE2AH]ClO_4: A sample of Cu-CB-TE2A was dissolved in 0.1 M $HClO_4$ and the solvent was evaporated from a beaker to yield dark-blue crystals suitable for X-ray studies. Analytical data for [Cu-CB-HTE2A]ClO_4 $C_{16}H_{29}ClCuN_4O_8(H_2O)_{0.5}$ (513.44): calcd. C 37.43, H 5.89, N 10.91, Cl 6.91; found C 37.47, H 5.78, N 10.82, Cl 6.69. IR (KBr, cm^{-1}): $\tilde{\nu}$ = 3500, 3000–2800,

Table 3. Crystal and refinement data for [Cu-CB-TE2AH]ClO_4.

Formula	$C_{16}H_{29}ClCuN_4O_8$
Mol. mass	504.42
T (K)	213(2)
Crystal system	monoclinic
Space group	$P2_1/n$
a [Å]	7.9631(4)
b [Å]	25.4584(11)
c [Å]	10.0100(5)
α [°]	90.00
β [°]	93.0010(10)
γ [°]	90.00
V [Å^3]	202.52(17)
Z	4
F(000)	1052
$D_{calcd.}$ [g/cm^3]	1.653
Scan type	phi and omega scans
λ [Å]	0.71073
μ [mm^{-1}]	1.263
Crystal size [mm^3]	0.35×0.26×0.21
Index ranges	h: –10; 10
	k: –32; 32
	l: –12; 13
Absorption correction	SADABS
RC = reflections collected	14593
IRC = independent RC	4749
IRCGT = IRC and $I > 2\sigma(I)$	4386
Refinement method	full-matrix least-squares on F^2
Data/parameters	4749/387
R for IRCGT	R_1 = 0.0459, wR_2 = 0.1062
R for IRC	R_1 = 0.0419, wR_2 = 0.1038
Goodness-of-fit	1.096

 © 2005 Wiley-VCH Verlag GmbH & Co. KGaA, Weinheim

1694 (ν_{COOH}), 1616 (ν_{COO}), 1123, 1099, 1088, 623. UV/Vis (H_2O): λ_{max} = 621 nm (44 $M^{-1} cm^{-1}$).

X-ray Structural Determination of [Cu-CB-TE2AH]ClO_4: A blue block crystal was found to produce the crystal and refinement data listed in Table 3. All non-hydrogen atoms were refined anisotropically and all hydrogen atoms were treated as idealized contributions. All software used is contained in libraries maintained by Bruker-AXS (Madison, WI).

CCDC-262407 contains the supplementary crystallographic data for this paper. These data can be obtained free of charge from The Cambridge Crystallographic Data Centre via www.ccdc.cam.ac.uk/data_request/cif.

Electrochemical Studies: Cyclic voltammograms were obtained with an EG&G PAR Model 263A scanning potentiostat with PowerCV data collection and analysis software. A three-electrode cell under argon was used with a glassy carbon disk working electrode, platinum auxiliary electrode, and silver/silver chloride reference electrode. Samples (1 mM) were run in 0.1 M aqueous sodium acetate adjusted to pH 7.0 with glacial acetic acid at scan rates of v = 100 mV/s. Samples in DMSO solution were run using 0.1 M tetra-*n*-butylammonium hexafluorophosphate electrolyte. Differential pulse voltammograms were run with a BAS Model 100B electrochemical system equipped with a PC utilizing BAS software. A similar three-electrode system was used and the scan rate was 20 mV/s.

Acknowledgments

We acknowledge financial support for this research from NIH CA93375 (E. H. W., G. R. W., and C. J. A.), UNH-UROP (K. S. W. and K. J. H.), an NIH-sponsored Chemistry-Biology Interface Training Grant (GM08785-01; C. A. B.), and a U.S. DOE Nuclear Medicine Education Training Grant (DE F0101 NE23051; C. A. B.). We also acknowledge Mr. Evan Southwick's contributions to part of the acid-decomplexation data.

[1] C. J. Anderson, M. J. Welch, *Chem. Rev.* **1999**, *99*, 2219–2234.
[2] L. A. Bass, M. Wang, M. J. Welch, C. J. Anderson, *Bioconjugate Chem.* **2000**, *11*, 527–532.
[3] J. L. J. Dearling, J. S. Lewis, D. W. McCarthy, M. J. Welch, P. J. Blower, *Chem. Commun.* **1998**, 2531.
[4] P. J. Blower, T. C. Castle, A. R. Cowley, J. R. Dilworth, P. S. Donnelly, E. Labisbal, F. E. Sowrey, S. J. Teat, M. J. Went, *Dalton Trans.* **2003**, 4416–4425.
[5] X. Sun, M. Wuest, G. R. Weisman, E. H. Wong, D. P. Reed, C. A. Boswell, R. J. Motekaitis, A. E. Martell, M. J. Welch, C. J. Anderson, *J. Med. Chem.* **2002**, *45*, 469.
[6] C. A. Boswell, X. Sun, W. Niu, G. R. Weisman, E. H. Wong, A. L. Rheingold, C. J. Anderson, *J. Med. Chem.* **2004**, *47*, 1465–1474.
[7] J. E. Sprague, Y. Peng, X. Sun, G. R. Weisman, E. H. Wong, S. Achilefu, C. J. Anderson, *Clin. Cancer Res.* **2004**, *10*, 8674–8682.
[8] J. Kotek, P. Lubal, P. Hermann, I. Cisarova, I. Lukes, T. Godula, I. Svobodova, P. Taborsky, J. Havel, *Chem. Eur. J.* **2003**, *9*, 233–248.
[9] I. Lukes, J. Kotek, J. Vojtisek, P. Hermann, *Coord. Chem. Rev.* **2001**, *216–217*, 287–312.
[10] R. Clay, J. Murray-Rust, P. Murray-Rust, *J. Chem. Soc., Dalton Trans.* **1979**, 1135–1139.
[11] A. M. Sargeson, *Pure Appl. Chem.* **1986**, *58*, 1511–1522.
[12] G. A. Bottomley, I. J. Clark, I. I. Creaser, L. M. Engelhardt, R. J. Geue, K. S. Hagen, J. M. Harrowfield, G. A. Lawrance, P. A. Lay, A. M. Sargeson, A. J. See, B. W. Skelton, A. H. White, F. R. Wilner, *Aust. J. Chem.* **1994**, *47*, 143–179.
[13] E. H. Wong, G. R. Weisman, D. C. Hill, D. P. Reed, M. E. Rogers, J. P. Condon, M. A. Fagan, J. C. Calabrese, K.-C. Lam, I. A. Guzei, A. L. Rheingold, *J. Am. Chem. Soc.* **2000**, *122*, 10561–10572.
[14] L. Burai, R. Kiraly, I. Lazar, E. Brucher, *Eur. J. Inorg. Chem.* **2001**, *3*, 813–820.
[15] E. Toth, E. Brucher, I. Lazar, I. Toth, *Inorg. Chem.* **1994**, *33*, 4070–4076.
[16] H. Z. Cai, T. A. Kaden, *Helv. Chim. Acta* **1994**, *77*, 383–398.
[17] K. Kumar, C. A. Chang, M. F. Tweedle, *Inorg. Chem.* **1993**, *32*, 587–593.
[18] K. Kumar, T. Jin, X. Wang, J. F. Desreux, M. F. Tweedle, *Inorg. Chem.* **1994**, *33*, 3823–3829.
[19] T. J. Hubin, N. W. Alcock, D. H. Busch, *Acta Crystallogr., Sect. C: Cryst. Struct. Comm.* **2000**, *56*, 37–39.
[20] A. Riesen, M. Zehnder, T. A. Kaden, *Helv. Chim. Acta* **1986**, *69*, 2067–2073.

Received: June 29, 2005
Published Online: October 12, 2005

 © 2005 Wiley-VCH Verlag GmbH & Co. KGaA, Weinheim

DOI: 10.1002/ejic.200500499

A Fluxional $Cu^{I}N_2O_2$ Core: Binding of a Keto Oxygen Atom to Cu^{I} and Ag^{I}

Michael G. B. Drew,[a] Jnan P. Naskar,[b] Shubhamoy Chowdhury,[b] and Dipankar Datta*[b]

Keywords: Copper / Fluxional compounds / N ligands / O ligands / Silver

$[Cu(2\text{-acetylpyridine})_2]ClO_4$ (**1**), characterised here, has a novel $Cu^{I}N_2O_2$ core in the solid state. Variable-temperature ^1H NMR studies show that the two chelate rings open up in solution at room temperature and the keto oxygen atoms dangle freely. As the temperature is lowered, the O atoms tend to bind to the metal atom. The corresponding silver(I) complex, $[Ag(2\text{-acetylpyridine})_2]ClO_4$ (**4**), characterised by single-crystal X-ray crystallography, has an $Ag^{I}N_2$ core in the solid state as well as in solution. Thus, while **1** is fluxional, **4** is not. In cyclic voltammetry, complex **1** displays a quasireversible $Cu^{II/I}$ couple with a half-wave potential of 0.40 V vs. SCE. Complex **1** is easily oxidised by air and H_2O_2 in methanol to give rise to a dinuclear copper(II) complex where the ligand framework is not simple acetylpyridine.
(© Wiley-VCH Verlag GmbH & Co. KGaA, 69451 Weinheim, Germany, 2005)

Introduction

The bonding between copper(I) and an aldehyde/ketone oxygen atom has received little attention. While simple Cu^+ ion disproportionates into Cu^{2+} and metallic copper in most O-donor solvents like water, methanol etc., it is considerably more stable towards disproportionation in acetone.[1] Consequently, a copper(I)–keto oxygen bond may not be thermodynamically unfeasible. However, to date, there is only one example of a copper(I) complex where the metal atom has a discrete bond with a keto oxygen atom; the oxygen atom belongs to an acetone molecule.[2] This copper(I) complex was not synthesised deliberately. There is a report by Lin et al.,[3] where the authors have claimed to observe bonds between Cu^{I} and the keto oxygen atoms in bis(triphenylphosphane)bis(phenalenone)copper tetrafluoroborate. In reality, however, they have observed bonds between Cu^{I} and the O^- ends of the zwitterionic phenalenone fragments. However, in the oxidation of benzyl alcohol catalysed by a copper(II) complex, a copper(I) species having a bond between the metal atom and the O atom of benzaldehyde was proposed by Kitajima et al. as a possible intermediate.[4] On the other hand, several structurally characterised examples of copper(II) complexes containing bonds between Cu^{II} and the carbonyl O atom of some aldehydes/ketones are known.[5–8] For example, in azurin − a blue copper-containing protein − there is a peptide carbonyl O atom in close proximity to the metal ion [mean Cu^{I}–O distance = 3.22 Å; mean Cu^{II}–O distance = 3.13 Å],[9] although it is doubtful whether this O atom is bonded to the copper atom in azurin.[10] Thus, the possibility of a copper(I)–keto oxygen bond is of biological relevance as well. Recently, we have undertaken a project to study the chemistry of this bond, and here we make the first report of our efforts by describing some properties of a homoleptic copper(I) complex of 2-acetylpyridine (ACPY) containing copper(I)–keto oxygen bonds. For comparison, we have also studied the homoleptic silver(I) complex of ACPY.

Results and Discussion

Reaction of ACPY with $[Cu(CH_3CN)_4]ClO_4$ in anhydrous methanol under N_2 in a 2:1 molar ratio yields reddish brown $[Cu(ACPY)_2]ClO_4$ (**1**). This complex is stable in air for more than a week in the solid state, although in solution it is not at all stable towards aerial oxidation: the reddish colour of the solution first changes to green and then to pink.

Luo et al.[8] have reported the synthesis and X-ray crystal structure of a mixed-ligand copper(II) complex containing ACPY as one of the ligands. Prior to them, El-Hilaly and El-Zaby reported that reaction of 2-pyridinecarboxaldehyde (PYCA) with hydrated $Cu(NO_3)_2$ in aqueous medium at pH = 8.0 yielded a pink complex which analysed as Cu(pyridin-2-ylmethanediolate monoanion)$_2$, thus indicating aquation of PYCA.[11] However, when we followed the procedure of El-Hilaly and El-Zaby with ACPY, metallic copper was precipitated. Further, reaction of $Cu(ClO_4)_2{\cdot}6H_2O$ with ACPY in methanol in a 1:2 molar proportion yields a blue copper(II) complex which seems to contain pyridin-2-ylmethanediolate monoanion as one of the ligands. Thus, we have not yet been able to characterise any pure homoleptic copper(II) complex of ACPY.

That the keto oxygen atoms of the two ACPY moieties in **1** are bonded to copper(I) is unequivocally revealed in

[a] School of Chemistry, University of Reading, Whiteknights, Reading RG6 6AD, UK
[b] Department of Inorganic Chemistry, Indian Association for the Cultivation of Science, Calcutta 700032, India
E-mail: icdd@mahendra.iacs.res.in

 © 2005 Wiley-VCH Verlag GmbH & Co. KGaA, Weinheim

the FTIR spectra. The ν(C=O) absorption of the free ligand appears at 1697 cm^{-1} as a very strong band, whereas in the complex two ν(C=O) bands are observed at 1689 and 1672 cm^{-1} as moderately strong with unequal intensities. The lowering of the ν(C=O) absorption in the complexes compared to that of free ACPY suggests that π back-bonding between copper(I) and the keto fragments is possible. Since two C=O stretching frequencies are observed in the complex, we can say that there are two types of keto groups in the complex which may be due to the difference in the two Cu^I–O bond lengths [a shorter Cu^I–O bond being associated with the ν(C=O) of 1672 cm^{-1}]. The ν(C=N) absorption of pyridine in ACPY (1583 cm^{-1}) moves to higher energy (1591 cm^{-1}) upon binding to copper(I), therefore it is reasonable to assume that there is a distorted tetrahedral $Cu^IN_2O_2$ chromophore in **1**.

A variable-temperature ^1H NMR study of **1** in CD_2Cl_2 (Figure 1) shows that **1** undergoes a dynamic equilibrium according to Equation (1) in solution leading to broadening of the proton signals at room temperature.

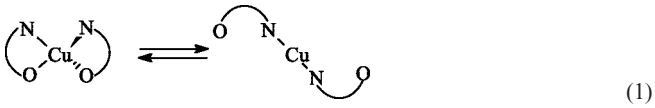

(1)

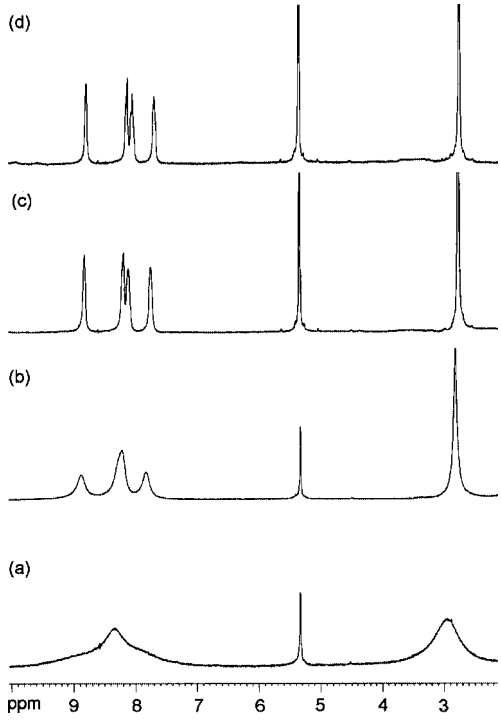

Figure 1. Variable-temperature 300 MHz ^1H NMR spectra of [Cu(ACPY)$_2$]ClO_4 (**1**) in CD_2Cl_2: (a) 298, (b) 253, (c) 213 and (d) 193 K. Assignments: δ [ppm] = 2.2–3.7 (methyl protons), 5.3 (residual protons of the solvent), 7–10 (pyridyl protons).

Since only one type of methyl signal is observed in the temperature range 298–193 K, equilibrium processes involving dissociated and undissociated ligands can be ruled out. We can therefore speculate that **1** is two-coordinate in solution at room temperature, with the ligands bound to the metal atom through the pyridine nitrogen atoms, and at low temperature it is four-coordinate with the keto oxygen atoms also participating in the bonding. This implies that Cu^I–keto oxygen bonds are very weak. Equilibrium (1) indicates that our copper(I) complex **1** is stereochemically nonrigid in solution, i.e. fluxional. Incidentally, the methyl protons in the free ligand ACPY resonate as a singlet at δ = 2.72 ppm and the pyridyl protons at δ = 7.35–7.70 (m), 7.80–8.10 (m) and 8.65–8.72 (d) ppm in $CDCl_3$.[12]

In an attempt to grow single crystals of **1**, we allowed direct diffusion of diethyl ether into its dilute methanolic solution (reddish). After two weeks, there was deposition of shiny, dark-green single crystals of **2**. This green compound is paramagnetic. X-ray crystallography revealed that it is a diperchlorate salt of a dinuclear copper(II) complex where the original ligand, ACPY, has been chemically changed to a monoanionic form of **3**. The formulation of compound **2** is [Cu_2(**3**-H^+)$_2$]$(ClO_4)_2$ (Figure 2). It has a crystallographic centre of symmetry with a Cu···Cu distance of 3.002(3) Å. It is an alkoxo-bridged dinuclear copper(II) complex where each copper atom is five-coordinate; the bridging angle is 101.6(2)°. The coordination sphere of each metal ion is an approximate square pyramid with the alcoholic oxygen atom O(30) in an axial site at a distance of 2.249(6) Å. The atoms in the equatorial plane form shorter bonds [Cu–O(1) = 1.956(5), Cu–O(1) (2 – *x*, –*y*, 2 – *z*) = 1.918(5), Cu(1)–N(11) = 1.982(6) and Cu(1)–N(24) = 1.999(6) Å]. While reports of coordination of an alcoholic oxygen atom to copper(II) are rare,[13,14] many examples of alkoxo-bridged dinuclear copper(II) complexes are known.[15,16]

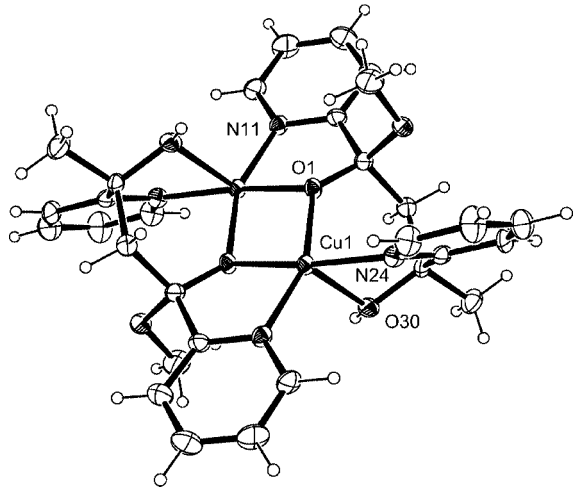

Figure 2. Centrosymmetric structure of the cation in **2** with ellipsoids at 25% probability. Selected bond lengths [Å] and angles [°]: Cu1–O1 1.956(5), Cu1–O30 2.249(6), Cu1–N11 1.983(6), Cu1–N24 2.000(7); O1–Cu1–O30 86.1(2), O1–Cu1–N24 93.6(2), O30–Cu1–N24 76.0(2).

Oxidation of copper(I) to copper(II) is a prerequisite for the conversion of **1** into **2**. In our above experiment, aerial oxygen brings about the required oxidation; the conversion **1** → **2** does not occur under N_2. Later, we found that [Cu_2(**3**-H^+)$_2$]$(ClO_4)_2$ can be easily generated by oxidising **1**

 © 2005 Wiley-VCH Verlag GmbH & Co. KGaA, Weinheim

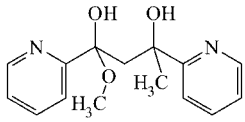

3

with dilute H_2O_2 in methanolic medium. However, our attempts to isolate the free ligand **3** from $[Cu_2(\mathbf{3}\text{-}H^+)_2](ClO_4)_2$ always led to the isolation of ACPY only. A tentative mechanism for the conversion of **1** into **2** is proposed in Scheme 1. The mechanism is shown explicitly for one half of **2**; it is the same for the other half. Oxidation of the metal atom from copper(I) to copper(II) facilitates the enolisation and subsequent formation of the carbanion in Scheme 1.

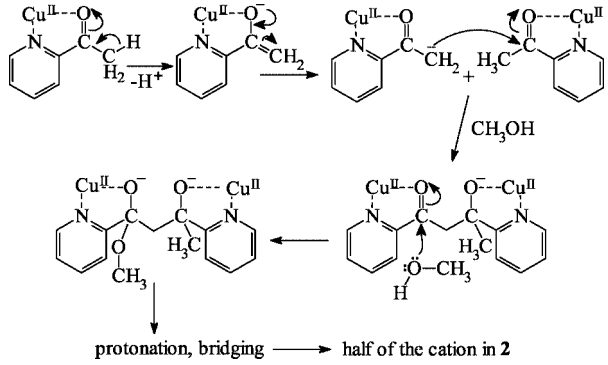

Scheme 1. Proposed mechanism for the conversion of complex **1** into **2** in methanol followed by oxidation of the metal centre from copper(I) to copper(II).

Having failed to obtain single crystals of **1**, we decided to synthesise its silver(I) analogue, as the structure of the Ag^I complex is found to be similar[17] to that of the Cu^I variety for many ligands. Stirring of $AgClO_4{\cdot}xH_2O$ with ACPY in tetrahydrofuran (THF) in the required proportion yielded $[Ag(ACPY)_2]ClO_4$ (**4**). Its X-ray crystal structure is given in Figure 3. There are two pyridyl nitrogen atoms and two keto oxygen atoms in close proximity to the silver atom. The Ag^I–N distances are 2.213(6) and 2.214(5) Å and the Ag^I–O distances 2.544(6) and 2.554(6) Å. The two pyridine rings intersect at 71.2(1)°.

The Ag^I–O bonds in **4** are rather long. In order to find out whether the two keto O atoms are at all bonded to the silver atom, we decided to use the bond valence sum (BVS) model,[18,19] which relates the bond lengths around a metal ion with its oxidation state. Our BVS calculations with a bond valence parameter, r_0, for the Ag^I–N bond of 1.859 Å[20] show that the valency of the silver(I) atom in **4** is well satisfied by the two N atoms; inclusion of the two keto oxygen atoms in the coordination sphere of the silver atom in **4** is unnecessary. This conclusion is also supported by the FTIR spectrum of **4**, where ν(C=O) appears at 1700 cm^{-1}, thus indicating no bonding between the metal atom and the keto oxygen atoms. No silver(I) complex with an Ag^I–keto oxygen bond is known in the literature. In 1997, Lin et al.[21] reported the crystal structure of bis(triphenylphosphane)bis(diphenylcyclopropenone)silver(I) tetrafluoroborate, where there is a bond between Ag^I and the O atom of the diphenylcyclopropenone moiety. However, because of the possible resonance structures of this complex, the O atom behaves more as O^- of the zwitterionic diphenylcyclopropenone fragment. In our case, since the keto oxygen atoms do not bind Ag^I in **4**, no fluxional behaviour is observed in its variable-temperature ^1H NMR spectra in CD_2Cl_2 (Figure 4), in contrast to the copper(I) complex **1**.

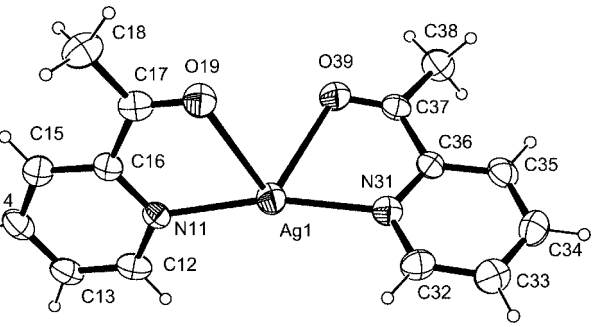

Figure 3. Structure of the cation in **4** with ellipsoids at 25% probability. Selected bond lengths [Å] and angles [°]: Ag1–N11 2.214(5), Ag1–N31 2.213(6), Ag1–O19 2.554(6), Ag1–O39 2.544(6); N31–Ag1–N11 165.8(2), O39–Ag1–O19 84.0(2), N31–Ag1–O39 69.6(2), N11–Ag1–O19 68.83(19).

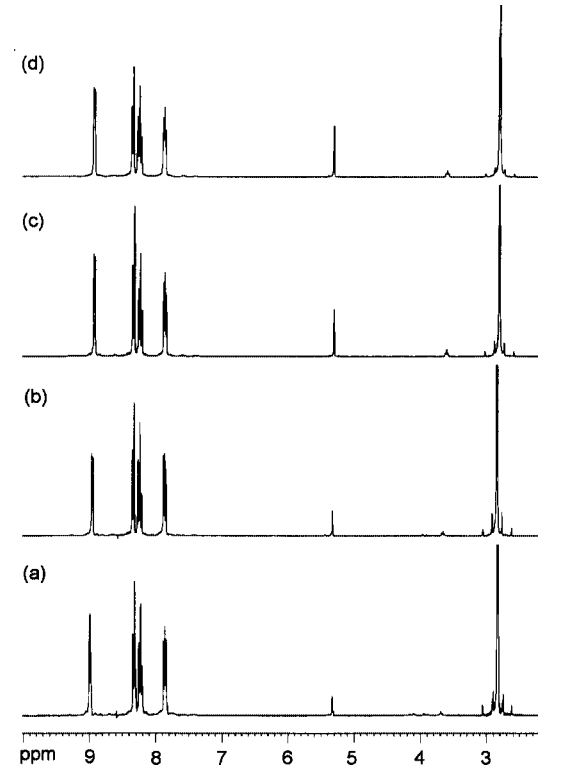

Figure 4. Variable-temperature 300 MHz ^1H NMR spectra of $[Ag(ACPY)_2]ClO_4$ (**4**) in CD_2Cl_2: (a) 298, (b) 253, (c) 213 and (d) 193 K. Assignments: δ [ppm] = 2.83 (methyl protons), 5.3 (residual protons of the solvent), 7.75–9.25 (pyridyl protons).

The keto groups in **1** are capable of forming Schiff bases. This is evidenced by the fact that reaction of ethylenediamine (en) with **1** in an equimolar proportion in anhydrous

 © 2005 Wiley-VCH Verlag GmbH & Co. KGaA, Weinheim

methanol results in $[CuL]^+$ (**5**), where L is the 2:1 condensate of ACPY and en [Equation (2)]. Previously, we have shown by means of X-ray crystallography that the 2:1 condensate of PYCA and en yields a homotopic dicopper(I) cationic double helicate when treated with $[Cu(CH_3CN)_4]ClO_4$ in a 1:1 molar proportion.[22] We believe that **5** has a similar structure.

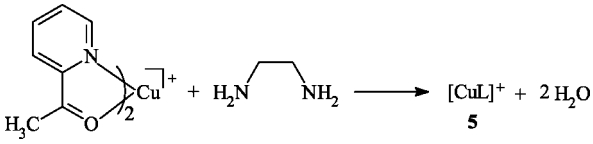

(2)

We have examined the electrochemical behaviour of **1** by cyclic voltammetry and coulometry in purified dichloromethane under dry N_2. At a glassy carbon electrode in cyclic voltammetry, it displays a quasi-reversible oxidative electrode process (Figure 5) with an average half-wave potential, $E_{1/2}$, of 0.40 V vs. SCE (saturated calomel electrode). The involvement of one electron in the electrode process was confirmed by coulometry at a platinum wire gauge electrode (4.35 mg of **1** was electrolysed at 0.65 V vs. SCE in CH_2Cl_2; 1.069 coulomb was collected, against the theoretical count of 1.036. The oxidised solution was almost colourless.). Thus, the couple observed in Figure 5 is a $Cu^{II/I}$ one.

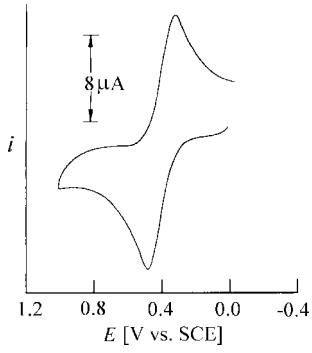

Figure 5. Cyclic voltammogram of $[Cu(ACPY)_2]ClO_4$ (**1**) in dichloromethane (concentration 1.20 mM) containing 0.1 M tetrabutylammonium perchlorate at a glassy carbon electrode at a scan rate of 50 mV s^{-1}. Under the same experimental conditions, the ferrocene–ferrocenium couple appears at 0.47 V vs. SCE with a peak-to-peak separation of 80 mV.

As revealed by the ^1H NMR spectra, our copper(I) complex is two-coordinate in solution at room temperature. The metallophore in **1** in solution can be represented as $[Cu^IN_2]$-O_2, thus indicating that the O atoms of the two ACPY fragments are not bound to the metal atom. The oxidative electrode process observed for **1** can then be described by Equation (3), where the corresponding Cu^{II} species is four-coordinate with the two keto oxygen atoms ligated to the metal atom.

$$Cu^{II}N_2O_2 + e^- \rightleftharpoons [Cu^IN_2]O_2 \quad (3)$$

Since the coordination number of the metal ion changes so much with the change in the oxidation state, the peak-to-peak separation in Figure 5 is quite large (0.17 V). The reasons for assuming that the Cu^{II} species in Equation (3) is four-coordinate are as follows:

(i) While a number of structurally characterised copper(I) complexes having a Cu^IN_2 core are known,[10] no one has ever observed a quasi-reversible cyclic voltammogram for such a core (an irreversible voltammogram with possible characteristics of adsorption is expected for a Cu^IN_2 core).

(ii) No example of a two-coordinate copper(II) complex is known in the literature; hence, the copper(II) species in Equation (3) cannot have a $Cu^{II}N_2$ core.

(iii) The keto oxygen atom of ACPY is known to bind Cu^{II}.[8]

The $Cu^{II/I}$ potential indicates that complex **1** can be oxidised by aerial oxygen, as the potential of the couple according to Equation (4) at pH = 7 is 0.57 V vs. SCE.[23a]

$$\tfrac{1}{2}O_2 + 2H^+ + 2e^- \rightleftharpoons H_2O \quad (4)$$

Concluding Remarks

We have characterised a copper(I) complex, $[Cu(ACPY)_2]$-ClO_4 (**1**), with a novel $Cu^IN_2O_2$ core and having two Cu^I–keto oxygen bonds. These Cu^I–keto oxygen bonds exist in the solid state, where complex **1** provides the first example of a $Cu^IN_2O_2$ core. However, the Cu^I–keto oxygen bonds in **1** are so weak that, even in a non-coordinating solvent like dichloromethane, the two chelate rings open up and the keto ends dangle freely in solution. However, with the lowering of temperature, the keto oxygen atoms tend to bind the metal atom. Thus, the $Cu^IN_2O_2$ core is stereochemically non-rigid in solution. Accordingly, our copper(I) complex **1** is "fluxional". We wish to point out that, so far, to the best of our knowledge, no other fluxional copper(I) complex is known in inorganic chemistry. We have also demonstrated that the silver(I) counterpart of **1** is not fluxional. This is because the keto oxygen atoms do not bind Ag^I even in the solid state. Incidentally, Ag^I shows a pronounced tendency to exhibit linear twofold coordination.[23b] In **4**, the N–Ag–N angle is 165.8(2)°.

Complex **1** has a low-potential $Cu^{II/I}$ couple and is easily oxidised by air in solution. Oxidation by air or H_2O_2 in methanol results in a dinuclear copper(II) complex, although the organic moiety in this dinuclear compound no longer remains as simple ACPY: it undergoes a chemical transformation, which is facilitated by the oxidation of the metal centre, to yield a novel dinucleating ligand.

Experimental Section

General: $[Cu(CH_3CN)_4]ClO_4$ was prepared by a reported procedure.[24] Copper was estimated gravimetrically as CuSCN. Microanalyses were performed with a Perkin–Elmer 2400II elemental analyser. FTIR spectra (KBr disc) were recorded with a Nicolet Magna-IR spectrophotometer (Series II), UV/Vis spectra with a

 © 2005 Wiley-VCH Verlag GmbH & Co. KGaA, Weinheim

Shimadzu UV-160A spectrophotometer and NMR spectra (in CD_2Cl_2) with a Bruker DPX300 spectrometer. Cyclic voltammetry and coulometry were performed using an EG&G PARC electrochemical analysis system (model 250/5/0) in purified dichloromethane, under dry nitrogen, in a conventional three-electrode configuration. A planar EG&G PARC G0229 glassy carbon milli electrode was used as the working electrode in cyclic voltammetry and a platinum wire gauge electrode in coulometry. Magnetic susceptibility was determined at room temperature with a PAR 155 vibrating sample magnetometer. The magnetometer was calibrated with [Hg{Co(SCN)$_4$}] and the susceptibility data were corrected for diamagnetism using Pascal's constants.

Synthesis of [Cu(ACPY)$_2$]ClO$_4$ (1): ACPY (0.6 mL, 5.36 mmol) was dissolved in anhydrous, degassed methanol (15 mL) to which freshly prepared [Cu(CH$_3$CN)$_4$]ClO$_4$ (0.88 g, 2.68 mmol) was added under dry N_2 and stirred for 30 min. The reddish-brown compound precipitated was filtered, washed thoroughly with diethyl ether (50 mL) and stored in vacuo over fused $CaCl_2$. Yield: 0.65 g (60%). $C_{14}H_{14}ClCuN_2O_6$ (405.2): calcd. C 41.46, H 3.48, Cu 15.68, N 6.91; found C 41.43, H 3.60, Cu 15.61, N 7.08. FTIR (KBr): $\tilde{\nu}$ [cm^{-1}] = 1689 (s), 1672 (s) [ν(C=O)], 1591 (m) [ν(C=N)], 1568 (m) [ν(C=C)], 1088 (vs), 625 (s) [ν(ClO$_4$)]. UV/Vis (CH_2Cl_2): λ_{max} [nm] (ε_{max} [M^{-1}cm^{-1}]) = 233 (1.5×10^4), 267 (1.0×10^4), 321 (2.1×10^3); (nujol mull): 260, 350, 465 sh.

Synthesis of [Cu$_2$(3-H$^+$)$_2$](ClO$_4$)$_2$ (2): Solid **1** (0.405 g, 1 mmol) was suspended in 10 mL of methanol to obtain a reddish-brown suspension. 30% (w/v) hydrogen peroxide solution (0.11 mL, 1 mmol) was then added with stirring. A green colour appeared immediately and, after 5 min of stirring, a green solution was obtained from which a dark-green compound started to separate. The reaction mixture was left in the air undisturbed for another 30 min. The precipitated green compound was then filtered, washed thoroughly with 15 mL of methanol cautiously and dried in vacuo over fused $CaCl_2$. Yield: 0.156 g (36%). $C_{30}H_{34}Cl_2Cu_2N_4O_{14}$ (872.61): calcd. C 41.27, H 3.93, Cu 14.57, N 6.42; found C 40.79, H 4.20, Cu 14.55, N 5.98. FTIR (KBr): $\tilde{\nu}$ [cm^{-1}] = 3383 (vs) [ν(OH)], 1609 (sh) [ν(C=N)], 1570 (m) [ν(C=C)], 1146–1053 (vs), 625 (s) [ν(ClO$_4$)]. μ [μ_B] = 1.05 (per Cu; at 298 K). UV/Vis (DMF): λ_{max} [nm] (ε_{max} [M^{-1}cm^{-1}]) = 268 (1.5×10^4), 324 (2.5×10^3), 674 (9.9×10); (nujol mull): 267, 311, 677 sh. Single crystals were grown by direct diffusion of diethyl ether into a methanol solution of the complex.

Attempted Isolation of 3 from [Cu$_2$(3-H$^+$)$_2$](ClO$_4$)$_2$: 30 mL of 25% ammonia was added to a suspension of [Cu$_2$(**3**-H$^+$)$_2$](ClO$_4$)$_2$ (3.2 g, 3.67 mmol) in 75 mL of chloroform with stirring. The stirring was continued for 3 h. The aqueous layer was then discarded and the organic layer was washed thoroughly with 2×25 mL of water and then dried with anhydrous Na_2SO_4. The brown ligand solution thus obtained was concentrated in a rotary evaporator to obtain a dense liquid. The FTIR spectrum of the isolated ligand matched that of ACPY.

Synthesis of [Ag(ACPY)$_2$]ClO$_4$ (4): Solid $AgClO_4{\cdot}xH_2O$ (1.04 g) was added to ACPY (1.12 mL, 10 mmol) in THF (15 mL) and stirred for 30 min. The white compound precipitated was filtered, washed with diethyl ether (10 mL) and dried in vacuo over fused $CaCl_2$. Yield: 1.48 g (66%). $C_{14}H_{14}AgClN_2O_6$ (449.6): calcd. C 37.38, H 3.14, N 6.23; found C 37.49, H 3.05, N 6.20. FTIR (KBr): $\tilde{\nu}$ [cm^{-1}] = 1700 (vs) [ν(C=O)], 1583 (m) [ν(C=N)], 1099 (vs), 630 (s) [ν(ClO$_4$)]. UV/Vis (CH_2Cl_2): λ_{max} [nm] (ε_{max} [M^{-1}cm^{-1}]) = 232 (1.2×10^4), 270 (1.0×10^4). Single crystals suitable for X-ray crystallography were grown by direct diffusion of *n*-hexane into a dilute CH_2Cl_2 solution of **4**.

Reaction 2: Freshly distilled en (0.06 mL, 0.89 mmol) was added to **1** (0.36 g, 0.89 mmol), dissolved in anhydrous methanol (20 mL). The resulting red solution was refluxed for 4 h and then kept in the refrigerator overnight. The red compound, [**5**]ClO$_4{\cdot}0.5H_2O$, precipitated was filtered, washed with diethyl ether (5 mL) and stored in vacuo over fused $CaCl_2$. Yield: 0.30 g (67%). $C_{16}H_{19}ClCuO_{4.5}N_2$ (410.2): calcd. C 43.82, H 4.37, Cu 14.50, N 12.78; found C 43.85, H 4.42, Cu 14.45, N 12.70. FTIR (KBr): $\tilde{\nu}$ [cm^{-1}] = 1589 (s) [ν(C=N)], 1088 (vs), 627 (s) [ν(ClO$_4$)]. UV/Vis (CH_2Cl_2): λ_{max} [nm] (ε_{max} [M^{-1}cm^{-1}]) = 229 (1.9×10^4), 258 (2.2×10^4), 277 (1.3×10^4), 382 (3.5×10^3), 471 (8.3×10^3). ^{1}H NMR (300 MHz, CD_2Cl_2, TMS): δ [ppm] = 3.41–3.82 (alkyl protons), 7.67–8.58 (pyridyl protons).

Caution! *Although we have not met with any incident during our studies, care should be taken in handling these compounds as perchlorate salts are potentially explosive. They should not be prepared and stored in large amounts.*

X-ray Crystallography: Data were measured with Mo-K_α radiation with an MARresearch Image Plate System at 293(2) K. The crystals were positioned at 70 mm from the image plate; 100 frames were measured at 2° intervals with a counting time of 2 min. Data analysis was carried out with the XDS program[25] to provide 3352 independent reflections for **2** and 2951 for **4**. The structures were solved by direct methods with the Shelx86 program.[26] Non-hydrogen atoms were refined with anisotropic thermal parameters. The hydrogen atoms bonded to carbon atoms were included in geometric positions and given thermal parameters equivalent to 1.2-times those of the atom to which they are attached. The hydrogen atom on O30 in **2** was located in the difference Fourier map and refined with a distance constraint. The perchlorate anion in **4** was disordered with two sets of oxygen tetrahedra being refined with half occupancy. An empirical absorption correction was applied using DIFABS.[27] The structures were refined on F^2 using Shelxl.[28] Selected crystallographic data for complexes **2** and **4** are given in

Table 1. Crystallographic data for complexes **2** and **4**.

	2	**4**
Empirical formula	$C_{30}H_{34}Cl_2Cu_2N_4O_{14}$	$C_{14}H_{14}AgClN_2O_6$
Formula mass	872.61	449.6
Crystal system	monoclinic	triclinic
Space group	$P2_1/n$	$P\bar{1}$
a [Å]	10.412(14)	7.342(9)
b [Å]	12.500(14)	9.884(11)
c [Å]	13.877(16)	11.922(13)
α [°]	90	85.60(1)
β [°]	97.096(10)	81.39(1)
γ [°]	90	75.02(1)
Volume [Å^3]	1792(4)	825.7(2)
Z	2	2
Calculated density [g cm^{-3}]	1.617	1.808
Absorption coefficient [mm^{-1}]	1.408	1.415
F(000)	892	448
Θ range [°]	2.2–25.8	2.90–26.01
Index ranges	–12/12	0/8
	–15/15	–11/12
	–16/16	–14/14
Unique reflections	3352	2951
Observed reflections [$I > 2\sigma(I)$]	2649	2951
Parameters	257	269
R indices (observed data)	*R*1 = 0.0837	*R*1 = 0.0601
	*wR*2 = 0.1699	*wR*2 = 0.1619
R indices (all data)	*R*1 = 0.1155	*R*1 = 0.1018
	*wR*2 = 0.2104	*wR*2 = 0.1805
Largest difference peak/hole [e Å^{-3}]	0.48/–0.69	0.74/–0.83

 © 2005 Wiley-VCH Verlag GmbH & Co. KGaA, Weinheim

Table 1. CCDC-267815 (**2**) and -249100 (**4**) contain the supplementary crystallographic data for this paper. These data can be obtained free of charge from The Cambridge Crystallographic Data Centre via www.ccdc.cam.ac.uk/data_request/cif.

Acknowledgments

D. D. thanks the Department of Science and Technology, New Delhi, India, for financial support. M. G. B. D. thanks EPSRC and the University of Reading for funds for the Image Plate system.

[1] D. Datta, *Indian J. Chem., Sect. A* **1987**, *26*, 605–606.
[2] M. Munakata, T. Kuroda-Sowa, M. Maekawa, M. Nakamura, S. Akiyama, S. Kitagawa, *Inorg. Chem.* **1994**, *33*, 1284–1291.
[3] S. Lin, C. J. Lin, S. T. Cheng, Y. S. Wen, L. K. Liu, *Inorg. Chim. Acta* **1997**, *256*, 35–40.
[4] N. Kitajima, K. Whang, Y. Moro-oka, A. Uchida, Y. Sasada, *J. Chem. Soc., Chem. Commun.* **1986**, 1504–1505.
[5] B. Barszcz, T. Glowia, J. Jezierska, *Polyhedron* **1999**, *18*, 3713–3721.
[6] R. López-Garzón, M. N. Moreno-Carretero, M. A. Salas-Peregrin, J. M. Salas-Peregrin, *Transition Met. Chem.* **1993**, *18*, 481–484.
[7] J. M. Domínguez-Vera, A. Rodríguez, R. Cuesta, R. Kivekäs, E. Colacio, *J. Chem. Soc., Dalton Trans.* **2002**, 561–565.
[8] Q. Luo, L. Kong, C. Shen, S. Yu, Q. Lu, L. Huang, *Transition Met. Chem.* **1993**, *18*, 583–584.
[9] W. E. B. Shepard, B. F. Anderson, D. A. Lewandoski, G. E. Norris, E. N. Baker, *J. Am. Chem. Soc.* **1990**, *112*, 7817–7819.
[10] J. P. Naskar, S. Hati, D. Datta, *Acta Crystallogr., Sect. B* **1997**, *53*, 887–894 and references cited therein.
[11] A. E. El-Hilaly, M. S. El-Zaby, *J. Inorg. Nucl. Chem.* **1976**, *38*, 1533–1539.
[12] C. J. Pouchart, *The Aldrich Library of NMR Spectra*, Aldrich Chemical Co., Inc., Milwaukee, WI, 2nd ed., **1983**, vol. 2, p. 659.
[13] G. L. Abbati, A. Cornia, A. Caneschi, A. C. Fabretti, C. Mortalo, *Inorg. Chem.* **2004**, *43*, 4540–4542.
[14] A. K. Sah, M. Kato, T. Tanase, *Chem. Commun.* **2005**, 675–677.
[15] M. Murugesu, C. E. Anson, A. K. Powell, *Chem. Commun.* **2002**, 1054–1055 and references cited therein.
[16] M. Fondo, A. M. Garcia-Deibe, M. Corbella, J. Ribas, A. LIamas-Saiz, M. R. Bermejo, J. Sanmartin, *Dalton Trans.* **2004**, 3503–3507 and references cited therein.
[17] G. Baum, E. C. Constable, D. Fenske, C. E. Housecroft, T. Kulke, M. Neuburger, M. Zehnder, *J. Chem. Soc., Dalton Trans.* **2000**, 945–959 and references cited therein.
[18] I. D. Brown, D. Altermatt, *Acta Crystallogr., Sect. B* **1985**, *41*, 244–247.
[19] S. Hati, D. Datta, *J. Chem. Soc., Dalton Trans.* **1995**, 1177–1182 and references cited therein.
[20] S. Chowdhury, M. G. B. Drew, D. Datta, *New J. Chem.* **2003**, *27*, 831–835.
[21] C. J. Lin, S. Lin, G. H. Lee, Y. Wang, *J. Organomet. Chem.* **1997**, *535*, 149–156.
[22] P. K. Pal, S. Chowdhury, P. Purakayasta, D. A. Tocher, D. Datta, *Inorg. Chem. Commun.* **2000**, *3*, 585–589.
[23] F. A. Cotton, G. Wilkinson, C. A. Murillo, M. Bochmann, *Advanced Inorganic Chemistry*, 6th ed., Wiley, New York, **1999**; a) p. 450; b) pp. 1084–1094.
[24] P. Hemmerich, C. Sigwart, *Experientia* **1963**, *19*, 488–489.
[25] W. Kabsch, *J. Appl. Crystallogr.* **1988**, *21*, 916–921.
[26] SHELX86: G. M. Sheldrick, *Acta Crystallogr., Sect A* **1990**, *46*, 467–473.
[27] DIFABS: N. Walker, D. Stuart, *Acta Crystallogr., Sect A* **1983**, *39*, 158–166.
[28] G. M. Sheldrick, *SHELXL, a Program for Crystal Structure Refinement*, University of Göttingen, **1993**.

Received: June 3, 2005
Published Online: October 18, 2005

 © 2005 Wiley-VCH Verlag GmbH & Co. KGaA, Weinheim

DOI: 10.1002/ejic.200500528

(η^5-Pentamethylcyclopentadienyl)iridium(III) Complexes with η^2-N,O and η^2-P,S Ligands

Michael Gorol,[a] Herbert W. Roesky,*[a] Mathias Noltemeyer,[a] and Hans-Georg Schmidt[a]

Keywords: Cyclopentadienyl ligands / Iridium / N,O ligands / P,S ligands

Chloro(η^5-pentamethylcyclopentadienyl)(η^2-pyridine-2-carboxylato)iridium(III) [Ir(η^5-C_5Me_5)(η^2-C_5H_4N-2-CO_2)Cl] (**2**) and chloro(η^5-pentamethylcyclopentadienyl)[η^2-2-(diphenylphosphanyl)thiophenolato]iridium(III) [Ir(η^5-C_5Me_5)(η^2-2-$Ph_2PC_6H_4S$)Cl] (**3**) were prepared and their structures determined by single-crystal X-ray diffraction analysis. Complex **2** crystallizes in the orthorhombic space group *Pbca*. The number of molecules per unit cell is eight, whereas **3** crystallizes in the orthorhombic space group $Pna2_1$ and the number of molecules per unit cell is four. The coordination of the η^2-bound ligands in **2** and **3** leads to chelate bite angles N–Ir–O(2) and P–Ir–S of 77.0(2)° and 82.42(7)°, respectively. The iridium atoms in **2** and **3** are chiral and both enantiomers are present in the unit cell. The substitution of the chloro ligand in **3** affords hydrido(η^5-pentamethylcyclopentadienyl)-[η^2-2-(diphenylphosphanyl)thiophenolato]iridium(III) [Ir($\eta^5$$C_5Me_5$)($\eta^2$-2-$Ph_2PC_6H_4S$)H] (**4**) and methyl($\eta^5$-pentamethylcyclopentadienyl)[η^2-2-(diphenylphosphanyl)thiophenolato]iridium(III) [Ir(η^5-C_5Me_5)(η^2-2-$Ph_2PC_6H_4S$)Me] (**5**), respectively, in good yields. The $^{31}P\{^1H\}$ NMR resonances of **4** (δ = 33.9 ppm) and **5** (δ = 35.8 ppm) prove unambiguously that the 2-(diphenylphosphanyl)thiophenolato ligand still remains η^2-coordinated.

(© Wiley-VCH Verlag GmbH & Co. KGaA, 69451 Weinheim, Germany, 2005)

Introduction

The chemistry of (η^5-pentamethylcyclopentadienyl)iridium(III) complexes has been extensively investigated during the last few decades.[1] However, there are only a few compounds that contain anionic η^2-coordinated ligands (η^2-A,B), of which α-amino acid complexes are the best-known examples.[2,3] The main aspect of research in this field is focused on the chiral-at-metal behavior of the isolated complexes. However, in general, the diastereoselectivity is low and, due to the configurational instability at the metal center, epimerization reactions occur in solution.[4] Pyridine-2-carboxylic acid is an analog to amino acids and is commercially available. Examples of η^2-coordinated pyridine-2-carboxylato ligands (η^2-N,O) applied in organoiridium chemistry are [Ir(η^5-C_5Me_5)(η^2-N,O)(OH_2)]$^+$ and [Ir(η^5-C_5Me_5)(η^2-N,O)]$_3$(ClO_4)$_3$, although they were structurally not characterized.[5]

Stable thiolato complexes have for some time also been of special interest. Dimeric iridium(I) complexes with bridging thiolato ligands, for example, have been intensely examined for their catalytic activity in hydroformylation reactions.[6] However, the elimination of the free thiol by reaction with dihydrogen has proved problematic. Chelating phosphanyl-thiolate ligands, like the 2-(diphenylphosphanyl)thiophenolato ligand (η^2-P,S), have been introduced to ensure retention of the thiolate. Accordingly, the two compounds [Ir(η^2-P,S)$(Cl)_2$($PMePh_2$)$_2$] and [Ir(η^2-P,S)$_3$]·0.75CH_2Cl_2 have been observed.[7] In addition, an increased stability due to the chelate effect has been observed for the iridium(I) complex [Ir(η^2-P,S)(CO)(PPh_3)].[8]

A particular objective of our research in organoiridium chemistry is the synthesis of stable monomeric complexes with a defined reaction center that allows further reactions. Thus, these compounds are useful as starting materials in the search for new applications in preparative chemistry as well as in catalysis. We present here the syntheses, characterizations, and crystal-structure analyses of the thus far unknown chloro(η^5-pentamethylcyclopentadienyl)iridium(III) complexes [Ir(η^5-C_5Me_5)(η^2-C_5H_4N-2-CO_2)Cl] (**2**) and [Ir(η^5-C_5Me_5)(η^2-2-$Ph_2PC_6H_4S$)Cl] (**3**), which contain η^2-coordinated pyridine-2-carboxylato (η^2-N,O) and 2-(diphenylphosphanyl)thiophenolato (η^2-P,S) ligands, respectively. The substitution of the chloro ligand in **3** by a hydride ion and a methyl group are described too, and the analytical data are given.

Results and Discussion

The reaction of di-μ-chlorobis[chloro(η^5-pentamethylcyclopentadienyl)iridium(III)] [Ir_2(η^5-C_5Me_5)$_2$(μ-Cl)$_2$$Cl_2$] (**1**) with sodium pyridine-2-carboxylate in methanol or sodium 2-(diphenylphosphanyl)thiophenolate in tetrahydrofuran gives the orange crystalline compounds chloro(η^5-pentamethylcyclopentadienyl)(η^2-pyridine-2-carboxylato)iri-

[a] Institut für Anorganische Chemie der Universität Göttingen, Tammannstr. 4, 37077 Göttingen, Germany
Fax: + 49-551-393373
E-mail: hroesky@gwdg.de

 WILEY InterScience DISCOVER SOMETHING GREAT © 2005 Wiley-VCH Verlag GmbH & Co. KGaA, Weinheim

dium(III) [Ir(η^5-C_5Me_5)(η^2-C_5H_4N-2-CO_2)Cl] (**2**) in 89% yield and chloro(η^5-pentamethylcyclopentadienyl)[η^2-2-(diphenylphosphanyl)thiophenolato]iridium(III) [Ir(η^5-C_5Me_5)(η^2-2-$Ph_2PC_6H_4S$)Cl] (**3**) in 72% yield, respectively (Scheme 1).

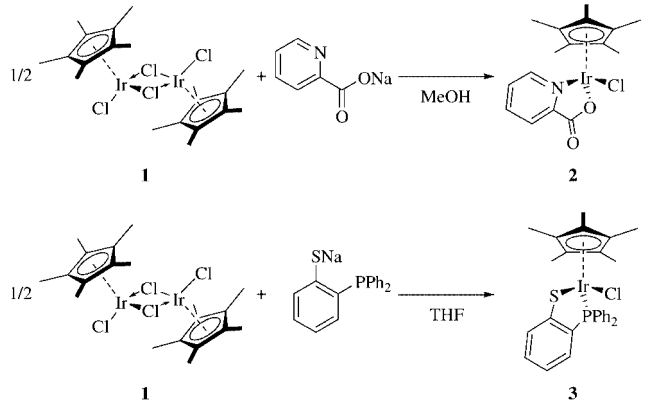

Scheme 1.

The resonances of the protons of the η^5-C_5Me_5 groups appear in the ^{1}H NMR spectrum of **2** as a singlet (δ = 1.63 ppm, 15 H) and that of **3** as a doublet (δ = 1.56 ppm, $J_{H,P}$ = 2.2 Hz, 15 H). In the ^{13}C NMR spectrum of **2**, the resonances of the η^5-C_5Me_5 ring carbon atoms are found at δ = 84.9 ppm and those of the methyl groups at δ = 8.3 ppm. The corresponding resonances of compound **3** are observed at δ = 92.9 ppm (d, $J_{C,P}$ = 3 Hz) and δ = 8.2 ppm (d, $J_{C,P}$ = 1 Hz). The ^{31}P{^{1}H} NMR spectrum of **3** shows a resonance at δ = 30.4 ppm, which is strongly shifted downfield ($\Delta\delta$ = 43.5 ppm) in comparison to the free phosphane (δ = –13.1 ppm).[9]. This is in agreement with the coordination shift typical for the ^{31}P NMR resonances of five-membered rings.[10]

The bands at $\tilde{\nu}$ = 253 and 267 cm^{-1} in the IR spectra of **2** and **3** can be assigned to the absorptions of the Ir–Cl stretching modes.

Single crystals suitable for X-ray diffraction analysis were obtained by slow diffusion of diethyl ether into a saturated solution of **2** in dichloromethane. Compound **2** crystallizes in the orthorhombic space group *Pbca*. Figure 1 shows the molecular structure of [Ir(η^5-C_5Me_5)(η^2-C_5H_4N-2-CO_2)Cl] (**2**) together with selected bond lengths and angles. The Ir–Cl [239.97(15) pm] and Ir–N [208.8(7) pm] bonds are shorter than in the L-prolinato complex [Ir(η^5-C_5Me_5)(L-ProO)Cl] [Ir(1)–Cl(1) = 241.7(2), Ir(2)–Cl(2) = 240.6(3), Ir(1)–N(1) = 212.8(7), and Ir(2)–N(2) = 213.1(7) pm],[2] which is probably due to the π-acceptor properties of the pyridine ring in **2**. The coordination of the η^2-bound pyridine-2-carboxylate leads to an N–Ir–O(2) bond angle of 77.0(2)°, which is similar to that of 77.7(1)° in the corre-

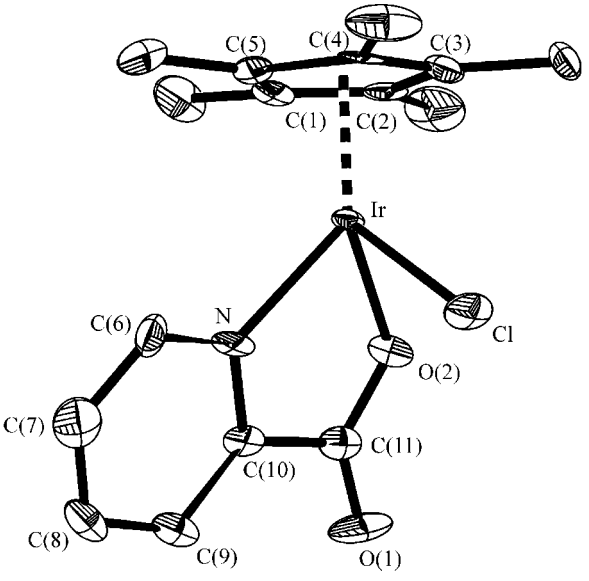

Figure 1. Molecular structure of [Ir(η^5-C_5Me_5)(η^2-C_5H_4N-2-CO_2)Cl] (**2**) with 50% probability ellipsoids and the labelling scheme; selected bond lengths [pm] and angles [°]: Ir–Cl 239.97(15), Ir–N 208.8(7), Ir–O(2) 210.1(5), O(1)–C(11) 122.5(9), O(2)–C(11) 127.9(10); C(1)–Ir–C(2) 37.2(3), C(1)–Ir–C(3) 64.8(3), C(1)–Ir–Cl 160.8(3), C(2)–Ir–C(3) 39.2(3), C(2)–Ir–Cl 129.8(2), C(3)–Ir–Cl 96.92(19), C(4)–Ir–C(1) 66.2(3), C(4)–Ir–C(2) 65.5(3), C(4)–Ir–C(3) 39.1(3), C(4)–Ir–C(5) 39.2(3), C(4)–Ir–Cl 96.16(17), C(5)–Ir–C(1) 40.8(3), C(5)–Ir–C(2) 65.5(2), C(5)–Ir–C(3) 65.7(3), C(5)–Ir–Cl 128.03(18), C(11)–O(2)–Ir 117.7(4), N–Ir–C(1) 111.7(3), N–Ir–C(2) 144.5(3), N–Ir–C(3) 166.1(3), N–Ir–C(4) 127.0(3), N–Ir–C(5) 102.5(3), N–Ir–Cl 84.55(15), N–Ir–O(2) 77.0(2), O(1)–C(11)–O(2) 125.2(7), O(2)–Ir–C(1) 107.9(3), O(2)–Ir–C(2) 95.4(2), O(2)–Ir–C(3) 116.9(2), O(2)–Ir–C(4) 156.0(2), O(2)–Ir–C(5) 146.9(2), O(2)–Ir–Cl 85.02(14).

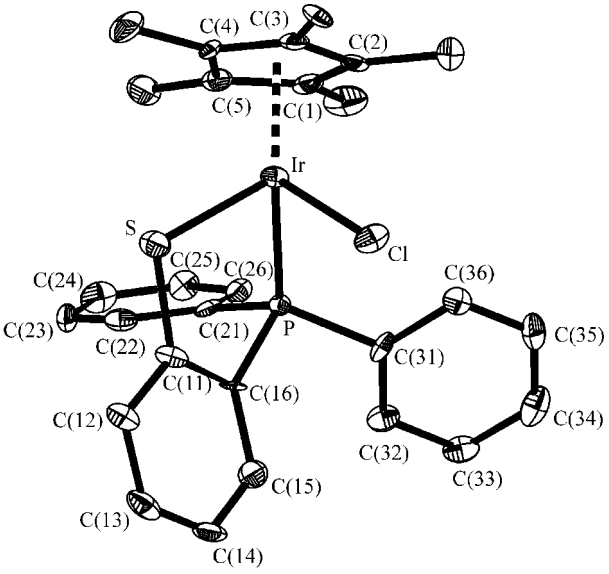

Figure 2. Molecular structure of [Ir(η^5-C_5Me_5)(η^2-2-$Ph_2PC_6H_4S$)Cl] (**3**) with 50% probability ellipsoids and the labelling scheme; selected bond lengths [pm] and angles [°]: Ir–Cl 241.93(18), Ir–P 227.32(18), Ir–S 238.0(2); C(1)–Ir–C(3) 63.7(3), C(1)–Ir–C(4) 64.0(3), C(1)–Ir–Cl 126.9(2), C(1)–Ir–P 103.2(2), C(1)–Ir–S 143.0(2), C(2)–Ir–C(1) 37.6(3), C(2)–Ir–C(3) 38.2(3), C(2)–Ir–C(4) 63.0(3), C(2)–Ir–Cl 95.1(2), C(2)–Ir–P 127.0(2), C(2)–Ir–S 150.3(2), C(3)–Ir–Cl 94.5(2), C(3)–Ir–P 165.1(2), C(3)–Ir–S 112.3(2), C(4)–Ir–C(3) 37.1(3), C(4)–Ir–Cl 125.7(2), C(4)–Ir–P 145.7(2), C(4)–Ir–S 90.67(18), C(5)–Ir–C(1) 38.9(3), C(5)–Ir–C(2) 64.3(3), C(5)–Ir–C(3) 64.5(3), C(5)–Ir–C(4) 39.2(3), C(5)–Ir–Cl 157.9(2), C(5)–Ir–P 110.4(2), C(5)–Ir–S 104.5(2), P–Ir–Cl 88.02(6), P–Ir–S 82.42(7), S–Ir–Cl 89.45(8).

 © 2005 Wiley-VCH Verlag GmbH & Co. KGaA, Weinheim

sponding rhodium(III) complex [Rh(η^5-C_5Me_5)(η^2-C_5H_4N-2-CO_2)Cl].[11]

Slow cooling of a hot solution of **3** in toluene gave single crystals suitable for X-ray diffraction analysis. Compound **3** crystallizes in the orthorhombic space group *Pna*2_1. Figure 2 shows the molecular structure of [Ir(η^5-C_5Me_5)(η^2-2-$Ph_2PC_6H_4S$)Cl] (**3**) together with selected bond lengths and angles. In comparison with [Ir(Cl)$_2$(η^2-2-$Ph_2PC_6H_4S$)(PMePh_2)$_2$] [Ir–P(1) = 236.1(1), Ir–S = 240.1(1), Ir–Cl(1) = 238.42(9), Ir–Cl(2) = 237.36(9) pm; P–Ir–S = 81.06(3)°][7] the Ir–P [227.32(18) pm] and Ir–S [238.0(2) pm] bonds are shorter and the Ir–Cl bond [241.93(18) pm] is longer. The deviation from 90°, with a P–Ir–S bond angle of 82.42(7)°, is of the same order of magnitude and is not as clear as that in **2**. The geometry in both **2** and **3** can be described as pseudo-octahedral coordination of the iridium atom in which the η^5-C_5Me_5 group occupies three *fac* coordination sides. The metal coordination sphere is completed by an η^2-coordinated ligand and a chlorine atom (the bond angles at the iridium atom are listed in the captions of Figures 1 and 2). In each case, the iridium atom is chiral and both enantiomers are present in the unit cell.

Substitution Reactions

Substitution of the chloro ligand by a hydride ion or a methyl group was achieved successfully only for **3**. Thus, the reaction of [Ir(η^5-C_5Me_5)(η^2-2-$Ph_2PC_6H_4S$)Cl] (**3**) with $LiAlH_4$ or MeLi in tetrahydrofuran results, after removal of the solvent and subsequent extraction with hexane, in the corresponding hydrido complex hydrido(η^5-pentamethylcyclopentadienyl)[η^2-2-(diphenylphosphanyl)thiophenolato]iridium(III) [Ir(η^5-C_5Me_5)(η^2-2-$Ph_2PC_6H_4S$)H] (**4**) in 91% yield and the methyl compound methyl(η^5-pentamethylcyclopentadienyl)[η^2-2-(diphenylphosphanyl)-thiophenolato]iridium(III) [Ir(η^5-C_5Me_5)(η^2-2-$Ph_2PC_6H_4S$)-Me] (**5**) in 87% yield, respectively (Scheme 2).

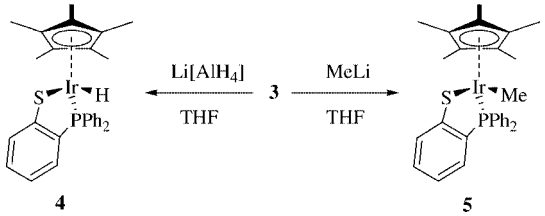

4 5

Scheme 2.

The resonances of the protons of the η^5-C_5Me_5 groups in the ^{1}H NMR spectrum of **4** appear, due to the coupling to the iridium-bound hydrido ligand, as a doublet of doublets (δ = 1.62 ppm, $^4J_{H,P}$ = 2.0, $^4J_{H,H}$ = 0.8 Hz, 15 H) and those of **5** as a doublet (δ = 1.57 ppm, $^4J_{H,P}$ = 1.9 Hz, 15 H). The resonances of the hydrido ligand in **4** and of the methyl group in **5** are observed as doublets at high field at δ = –15.37 (d, $^2J_{H,P}$ = 36.0 Hz, 1 H) and –0.22 ppm (d, $^3J_{H,P}$ = 6.1 Hz, 3 H), respectively. In the ^{13}C NMR spectrum of **4**, the resonance of the η^5-C_5Me_5 ring carbon atoms is found at δ = 93.2 ppm (d, $J_{C,P}$ = 3.1 Hz) and that of the methyl groups at δ = 9.1 ppm (d, $J_{C,P}$ = 0.8 Hz). The corresponding resonances of compound **5** appear at δ = 92.8 (d, $J_{C,P}$ = 3.3 Hz) and 8.20 ppm (d, $J_{C,P}$ = 1.0 Hz). The resonance of the methyl group bound to the iridium atom is observed at δ = –17.4 ppm (d, $J_{C,P}$ = 8.4 Hz). The ^{31}P{^{1}H} NMR spectrum of **4** shows a resonance at δ = 33.9 ppm whereas that of **5** appears at δ = 35.8 ppm. In comparison to the free ligand (δ = –13.1 ppm),[9] this strong downfield shift is good evidence that the 2-(diphenylphosphanyl)thiophenolato ligand still remains η^2-coordinated.

In the IR spectrum of **4**, the band at $\tilde{\nu}$ = 2102 cm^{-1} is characteristic of absorptions of the Ir–H stretching modes.[12]

Conclusions

The cleavage of the chloro bridges in [Ir$_2$(η^5-C_5Me_5)$_2$(μ-Cl)$_2$Cl$_2$] (**1**) by η^2-A,B ligands affords stable monomeric chelate complexes. Thus, the reactions of **1** with pyridine-2-carboxylate and 2-(diphenylphosphanyl)thiophenolate yield [Ir(η^5-C_5Me_5)(η^2-C_5H_4N-2-CO_2)Cl] (**2**) and [Ir(η^5-C_5Me_5)(η^2-2-$Ph_2PC_6H_4S$)Cl] (**3**), respectively. The X-ray diffraction analyses show that the geometry of both complexes can be described as pseudo-octahedral coordination of the iridium atom in which the η^5-C_5Me_5 group occupies three *fac* coordination sides. In each case the complex is chiral at the iridium atom and both enantiomers are present in the unit cell. The complexes [Ir(η^5-C_5Me_5)(η^2-2-$Ph_2PC_6H_4S$)H] (**4**) and [Ir(η^5-C_5Me_5)(η^2-2-$Ph_2PC_6H_4S$)Me] (**5**) are easily accessible by substitution of the chloro ligand in **3**. According to the ^{31}P NMR spectra, the 2-(diphenylphosphanyl)thiophenolato ligand remains η^2-coordinated in both compounds. The hydrido complex **4** and the methyl compound **5** are useful derivatives for further investigations.

Experimental Section

General Remarks: Solvents were dried and distilled under nitrogen prior to use. All reactions were carried out under dry nitrogen, using standard Schlenk techniques. NMR spectra were recorded using a Bruker Avance 200, a Bruker MSL 400, or a Bruker Avance 500 spectrometer and referenced to the resonances of the residual protons in [D_6]DMSO, $CDCl_3$, or C_6D_6. ^{1}H NMR: external standard TMS. ^{13}C NMR: external standard TMS. ^{31}P NMR: external standard 85% H_3PO_4. Infrared spectra were recorded with a BIO-RAD Digilab FTS 7 spectrometer. [Ir$_2$(η^5-C_5Me_5)$_2$(μ-Cl)$_2$Cl$_2$] (**1**) [13] and 2-$Ph_2PC_6H_4SH$[9] were prepared by literature methods. All other materials used in the syntheses were reagent grade chemicals and used without further purification.

[Ir(η^5-C_5Me_5)(η^2-C_5H_4N-2-CO_2)Cl] (2): A mixture of **1** (0.80 g, 1.00 mmol), C_5H_4N-2-CO_2H (0.26 g, 2.12 mmol), and NaOEt (0.12 g, 2.22 mmol) in methanol (70 mL) was heated under reflux for 3 h and finally filtered hot through Celite. The solution was concentrated under reduced pressure to 20 mL. The resulting orange crystalline solid was filtered off, washed with diethyl ether (2 × 10 mL), and dried in vacuo (0.85 g, 89%). M.p. 270 °C (decomp.). $C_{16}H_{19}ClIrNO_2$ (485.00): calcd. C 39.62, H 3.95, Cl 7.31, N 2.89; found C 39.59, H 4.01, Cl 7.39, N 2.96. IR (CsI): $\tilde{\nu}$ = 253

 © 2005 Wiley-VCH Verlag GmbH & Co. KGaA, Weinheim

(Ir–Cl) cm^{-1}. ^1H NMR (500.13 MHz, [D$_6$]DMSO): δ = 8.77 (d, J = 6.0 Hz, 1 H, $C_5H_4NCO_2$), 8.12 (t, J = 5.0 Hz, 1 H, $C_5H_4NCO_2$), 7.90 (d, J = 8.0 Hz, 1 H, $C_5H_4NCO_2$), 7.75 (t, J = 7.0 Hz, 1 H, $C_5H_4NCO_2$), 1.63 (s, 15 H, C_5Me_5) ppm. ^{13}C NMR (125.77 MHz, [D$_6$]DMSO): δ = 171.7 ($C_5H_4NCO_2$), 150.5 ($C_5H_4NCO_2$), 150.3 ($C_5H_4NCO_2$), 139.6 ($C_5H_4NCO_2$), 129.1 ($C_5H_4NCO_2$), 126.2 ($C_5H_4NCO_2$), 84.9 (C_5Me_5), 8.3 (C_5Me_5) ppm. EIMS (70 eV): *m*/*z* (%) = 485 (40) [M], 449 (60) [M – H – Cl], 362 (100) [M – C_5H_4N-2-CO_2 – H].

[Ir(η⁵-C_5Me_5)(η²-2-$Ph_2PC_6H_4S$)Cl] (3): A solution of 2-$Ph_2PC_6H_4SH$ (0.59 g, 2.00 mmol) in THF (30 mL) together with surplus sodium (approx. 200 mg) was stirred at room temperature until the evolution of hydrogen ceased. After filtration, the filtrate was added dropwise to a solution of **1** (0.80 g, 1.00 mmol) in THF (30 mL). The reaction mixture was stirred for an additional 3 h and, subsequently, the solvent was removed under reduced pressure. The residue was crystallized from dichloromethane/diethyl ether (1:4). The reddish crystals obtained accordingly were filtered off and dried in vacuo (0.95 g, 72%). M.p. 325 °C. $C_{28}H_{29}ClIrPS$ (656.24): calcd. C 51.25, H 4.45, P 4.72; found C 50.64, H 4.47, P 4.31.[14] IR (CsI): $\tilde{\nu}$ = 267 (Ir–Cl) cm^{-1}. ^1H NMR (500.13 MHz, $CDCl_3$): δ = 7.97 (m, 2 H, $Ph_2PC_6H_4S$), 7.62 (dd, ^1J = 7.9, ^2J = 3.4 Hz, 1 H, $Ph_2PC_6H_4S$), 7.49 (m, 3 H, $Ph_2PC_6H_4S$), 7.28 (m, 5 H, $Ph_2PC_6H_4S$), 7.13 (t, ^1J = 8.2 Hz, 1 H, $Ph_2PC_6H_4S$), 6.99 (t, ^1J = 7.4 Hz, 1 H, $Ph_2PC_6H_4S$), 6.72 (t, ^1J = 7.4 Hz, 1 H, $Ph_2PC_6H_4S$), 1.56 (d, $^4J_{H,P}$ = 2.2 Hz, 15 H, C_5Me_5) ppm. ^{13}C NMR (125.77 MHz, $CDCl_3$): δ = 155.5 (d, $J_{C,P}$ = 23.4 Hz, $Ph_2PC_6H_4S$), 136.2 (d, $J_{C,P}$ = 52.9 Hz, $Ph_2PC_6H_4S$), 135.8 (d, $J_{C,P}$ = 10.6 Hz, $Ph_2PC_6H_4S$), 134.8 (d, $J_{C,P}$ = 70.6 Hz, $Ph_2PC_6H_4S$), 132.0 (d, $J_{C,P}$ = 3.7 Hz, $Ph_2PC_6H_4S$), 131.7 (d, $J_{C,P}$ = 9.5 Hz, $Ph_2PC_6H_4S$), 131.2 (d, $J_{C,P}$ = 2.7 Hz, $Ph_2PC_6H_4S$), 130.7 (d, $J_{C,P}$ = 2.6 Hz, $Ph_2PC_6H_4S$), 130.0 (d, $J_{C,P}$ = 2.6 Hz, $Ph_2PC_6H_4S$), 128.8 (d, $J_{C,P}$ = 10.4 Hz, $Ph_2PC_6H_4S$), 128.1 (d, $J_{C,P}$ = 10.9 Hz, $Ph_2PC_6H_4S$), 128.0 (d, $J_{C,P}$ = 10.2 Hz, $Ph_2PC_6H_4S$), 126.1 (d, $J_{C,P}$ = 58.5 Hz, $Ph_2PC_6H_4S$), 122.1 (d, $J_{C,P}$ = 7.6 Hz, $Ph_2PC_6H_4S$), 92.9 (d, $^2J_{C,P}$ = 3 Hz, C_5Me_5), 8.2 (d, $^3J_{C,P}$ = 1.0 Hz, C_5Me_5) ppm. ^{31}P NMR (202.46 MHz, $CDCl_3$): δ = 30.4 (s, Ir*P*) ppm. EIMS (70 eV): *m*/*z* (%) = 656 (8) [M], 621 (100) [M – Cl].

[Ir(η⁵-C_5Me_5)(η²-2-$Ph_2PC_6H_4S$)H] (4): A solution of **3** (0.66 g, 1.01 mmol) in THF (20 mL) was treated with $LiAlH_4$ (0.04 g, 1.05 mmol), stirred at room temperature for 12 h, and subsequently filtered through Celite. The solvent was removed from the filtrate under reduced pressure and the resulting residue was extracted with hexane (2 × 60 mL). The removal of the solvent from the combined extracts in vacuo afforded the title compound as a yellow powder (0.57 g, 91%). M.p. 240 °C (decomp.). $C_{28}H_{30}IrPS$ (621.79): calcd. C 54.09, H 4.86; found C 53.71, H 4.80. IR (CsI): $\tilde{\nu}$ = 2102 (Ir–H) cm^{-1}. ^1H NMR (500.13 MHz, C_6D_6): δ = 7.99 (dd, ^1J = 11.5, ^1J = 8.1 Hz, 2 H, $Ph_2PC_6H_4S$), 7.91 (dd, ^1J = 8.1, ^2J = 3.5 Hz, 1 H, $Ph_2PC_6H_4S$), 7.21 (m, 3 H, $Ph_2PC_6H_4S$), 7.11 (m, 3 H, $Ph_2PC_6H_4S$), 6.93 (m, 3 H, $Ph_2PC_6H_4S$), 6.76 (t, ^1J = 7.0 Hz, 1 H, $Ph_2PC_6H_4S$), 6.57 (t, ^1J = 7.0 Hz, 1 H, $Ph_2PC_6H_4S$), 1.62 (dd, $^4J_{H,P}$ = 2.0, $^4J_{H,H}$ = 0.8 Hz, 15 H, C_5Me_5), –15.37 (d, $^2J_{H,P}$ = 36.0 Hz, 1 H, Ir*H*) ppm. ^{13}C NMR (125.77 MHz, C_6D_6): δ = 160.8 (d, $J_{C,P}$ = 26.9 Hz, $Ph_2PC_6H_4S$), 138.0 (d, $J_{C,P}$ = 46.9 Hz, $Ph_2PC_6H_4S$), 135.4 (d, $J_{C,P}$ = 62.7 Hz, $Ph_2PC_6H_4S$), 135.3 (d, $J_{C,P}$ = 69.5 Hz, $Ph_2PC_6H_4S$), 134.6 (d, $J_{C,P}$ = 11.2 Hz, $Ph_2PC_6H_4S$), 132.2 (d, $J_{C,P}$ = 3.7 Hz, $Ph_2PC_6H_4S$), 131.6 (d, $J_{C,P}$ = 10.5 Hz, $Ph_2PC_6H_4S$), 129.9 (d, $J_{C,P}$ = 2.5 Hz, $Ph_2PC_6H_4S$), 129.3 (d, $J_{C,P}$ = 2.4 Hz, $Ph_2PC_6H_4S$), 128.7 (d, $J_{C,P}$ = 2.4 Hz, $Ph_2PC_6H_4S$), (127.8, 127.7, 127.5 overlaps from C_6D_6), 120.4 (d, $J_{C,P}$ = 7.2 Hz, $Ph_2PC_6H_4S$), 93.2 (d, $^2J_{C,P}$ = 3.1 Hz, C_5Me_5), 9.1 (d, $^3J_{C,P}$ = 0.8 Hz, C_5Me_5) ppm. ^{31}P NMR (202.46 MHz, C_6D_6): δ = 33.9 (s, Ir*P*) ppm. EIMS (70 eV): *m*/*z* (%) = 622 (100) [M], 607 (50) [M – H – CH_2].

[Ir(η⁵-C_5Me_5)(η²-2-$Ph_2PC_6H_4S$)Me] (5): A solution of **3** (0.26 g, 0.40 mmol) in THF (10 mL) was treated with MeLi (0.30 mL, 0.48 mmol, 1.6 M in hexane), stirred at room temperature for 12 h, and subsequently filtered through Celite. The solvent was removed from the filtrate under reduced pressure and the resulting residue was extracted with hexane (2 × 40 mL). The removal of the solvent from the combined extracts in vacuo resulted in the title compound as a yellow powder (0.22 g, 87%). M.p. 240 °C (decomp.). $C_{29}H_{32}IrPS$ (635.82): calcd. C 54.78, H 5.07; found C 54.71, H 5.02. ^1H NMR (200.13 MHz, $CDCl_3$): δ = 7.64 (m, 1 H, $Ph_2PC_6H_4S$), 7.46 (m, 5 H, $Ph_2PC_6H_4S$), 7.24 (m, 5 H, $Ph_2PC_6H_4S$), 6.95 (m, 2 H, $Ph_2PC_6H_4S$), 6.70 (m, 1 H, $Ph_2PC_6H_4S$), 1.57 (d, $^4J_{H,P}$ = 1.9 Hz, 15 H, C_5Me_5), –0.22 (d, $^3J_{H,P}$ = 6.1 Hz, 3 H, Ir*Me*) ppm. ^{13}C NMR (125.77 MHz, $CDCl_3$): δ = 157.6 (d, $J_{C,P}$ = 26.2 Hz, $Ph_2PC_6H_4S$), 137.7 (d, $J_{C,P}$ = 50.1 Hz, $Ph_2PC_6H_4S$), 133.9 (d, $J_{C,P}$ = 3.2 Hz, $Ph_2PC_6H_4S$), 133.0 (d, $J_{C,P}$ = 9.7 Hz, $Ph_2PC_6H_4S$), 131.8 (d, $J_{C,P}$ = 10.7 Hz, $Ph_2PC_6H_4S$), 128.3 (d, $J_{C,P}$ = 10.7 Hz, $Ph_2PC_6H_4S$), 120.7 (d, $J_{C,P}$ = 6.9 Hz, $Ph_2PC_6H_4S$), 92.8 (d, $^2J_{C,P}$ = 3.3 Hz, C_5Me_5), 8.2 (d, $^3J_{C,P}$ = 1.0 Hz, C_5Me_5), –17.4 (d, $J_{C,P}$ = 8.4 Hz, IrMe) ppm. ^{31}P NMR (202.46 MHz, $CDCl_3$): δ = 35.8 (s, Ir*P*) ppm. EIMS (70 eV): *m*/*z* (%) = 636 (10) [M], 621 (100) [M – CH_3], 607 (5) [M – CH_3–CH_2].

X-ray Crystallographic Study: The single crystals were mounted on a glass fiber in a frozen drop of paraffin. Diffraction data were collected with a STOE AED2 four-circle diffractometer with graphite-monochromated Mo-K_α radiation (λ = 71.073 pm). The crystal structures were solved by direct methods using SHELXS-97[15] and refined with SHELXL-97[16] against F^2 on all data by full-matrix least squares. All non-hydrogen atoms were refined anisotropically. Hydrogen atoms were included in the model at fixed positions (Table 1). CCDC-272324 (**2**) and -272325 (**3**) contain the supplementary crystallographic data for this paper. These data can be obtained free of charge from The Cambridge Crystallographic Data Centre via www.ccdc.cam.ac.uk/data_request/cif.

Table 1. Crystallographic data for **2** and **3**.

	2	**3**
Empirical formula	$C_{16}H_{19}ClIrNO_2$	$C_{28}H_{29}ClIrPS$
Formula mass [g mol^{-1}]	484.97	656.19
Temperature [K]	203(2)	133(2)
Wavelength λ [pm]	71.073	71.073
Crystal system	orthorhombic	orthorhombic
Space group	*Pbca*	$Pna2_1$
a [pm]	1429.4(3)	1655.0(3)
b [pm]	1457.9(4)	1019.6(2)
c [pm]	1468.1(5)	1456.3(3)
Volume [nm^3]	3.0595(14)	2.4574(8)
Z	8	4
Absorption coefficient [mm^{-1}]	8.906	5.707
F(000)	1856	1288
Reflections collected	5382	31373
Independent reflections	2691 (R_{int} = 0.1867)	7149 (R_{int} = 0.1654)
Data/restraints/parameters	2691/339/189	5681/1/296
Goodness-of-fit on F^2	1.065	1.081
Final *R* indices [$I > 2\sigma(I)$]	0.0462, 0.1169	0.0399, 0.0924
Largest diff. peak/hole [e Å^{-3}]	2.130/–3.595	7.323/–1.967

 © 2005 Wiley-VCH Verlag GmbH & Co. KGaA, Weinheim

Acknowledgments

This work was supported by the Degussa–Hüls AG, the Fonds der Chemischen Industrie, and the Göttinger Akademie der Wissenschaften.

[1] J. K. O'Connor, *Sci. Synth.***2002**, *1*, 617–744.
[2] R. Krämer, K. Polborn, H. Wanjek, I. Zahn, W. Beck, *Chem. Ber.* **1990**, *123*, 767–778.
[3] K. Severin, R. Bergs, W. Beck, *Angew. Chem.* **1998**, *110*, 1722–1743; *Angew. Chem. Int. Ed.* **1998**, *37*, 1634–1654.
[4] H. Brunner, A. Köllnberger, T. Burgmeister, M. Zabel, *Polyhedron* **2000**, *19*, 1519–1526.
[5] T. Poth, H. Paulus, H. Elias, C. Dücker-Benfer, R. van Eldik, *Eur. J. Inorg. Chem.* **2001**, 1361–1369.
[6] M. T. Pinillos, A. Elduque, L. A. Oro, *Inorg. Chim. Acta* **1990**, *178*, 179–183.
[7] J. R. Dilworth, C. Lu, J. R. Miller, Y. Zheng, *J. Chem. Soc., Dalton Trans.* **1995**, 1957–1964.
[8] L. Dahlenburg, K. Herbst, M. Kühnlein, *Z. Anorg. Allg. Chem.* **1997**, *623*, 250–258.
[9] E. Block, G. Ofori-Okai, J. Zubieta, *J. Am. Chem. Soc.* **1989**, *111*, 2327–2329.
[10] P. E. Garrou, *Chem. Rev.* **1981**, *81*, 229–266.
[11] A. P. Abbott, G. Capper, D. L. Davies, J. Fawcett, D. R. Russell, *J. Chem. Soc., Dalton Trans.* **1995**, 3709–3713.
[12] C. B. Cooper, D. F. Shriver, S. Onaka, *Adv. Chem. Ser.* **1978**, *167*, 232–247.
[13] J. W. Kang, K. Moseley, P. M. Maitlis, *J. Am. Chem. Soc.* **1969**, *91*, 5970–5977.
[14] The slight deviations from the calculated values are attributable to traces of the used solvents, which were found in the ^{1}H NMR spectrum.
[15] G. M. Sheldrick, *Acta Crystallogr., Sect. A* **1990**, *46*, 467–473.
[16] G. M. Sheldrick, *SHELX-97, Program for Crystal Structure Analysis*, Institut für Anorganische Chemie der Universität Göttingen, **1998**.

Received: June 14, 2005
Published Online: October 18, 2005

 © 2005 Wiley-VCH Verlag GmbH & Co. KGaA, Weinheim

EurJIC
European Journal of Inorganic Chemistry

Issue 24/2005

Pages 4849–5056

Papers available ahead of print in Early View at www.interscience.wiley.com

The editorial staff and the publishers thank all readers, authors, referees, and advertisers for their interest and support over the past year and wish them all a happy new year.

COVER PICTURE

The cover picture shows three heterobimetallic sodium-bismuth-oxo silanolates: $[Bi_{10}Na_5O_7(OH)_6(OSiMe_3)_{15}]$ (**2**), $[Bi_{15}\text{-}Na_3O_{18}(OSiMe_3)_{12}]$ (**3**) and $[Bi_{14}Na_8O_{18}(OSiMe_3)_{14}(thf)_4]$ (**4**). These novel polynuclear metal-oxo clusters were obtained in addition to the hexanuclear oxygen-centred complex $[Bi_2Na_4O(OSiMe_3)_8]$ (**1**), which represents a well-known structural motif found in several heterometallic group 15/group 1 compounds. As result of the similar ionic radii of sodium and bismuth and the flexible coordination chemistry of these main group metals, the formation of a large variety of heterobimetallic molecular structures is conceivable. Structural relationships between the metal-oxo silanolates are described and a comparison with other polynuclear bismuth-oxo compounds is given in order to identify basic building blocks. The approach is envisaged to develop rational design strategies towards molecular bismuth-containing precursors for heterometallic materials. Details are discussed in the article by M. Mehring et al. on p. 4891ff.

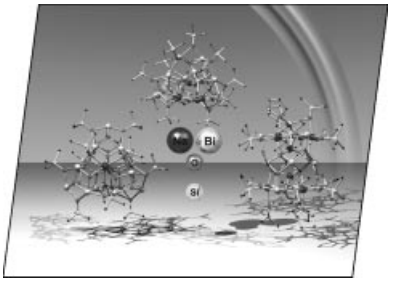

MICROREVIEW

Contents

4863 **A. Chakravorty***

Variable-Valent Rhenium Chemistry of Conjugated Nitrogenous Ligands: Structure and Reactivity

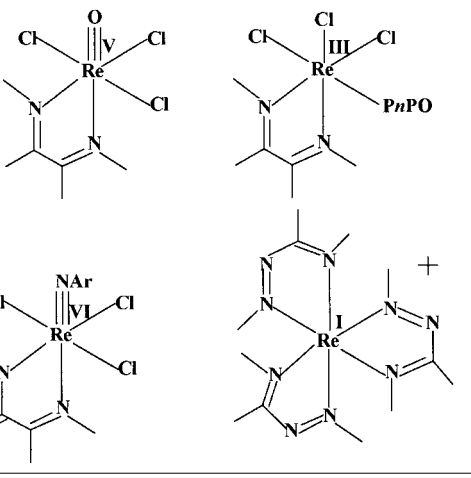

Keywords: Rhenium / Variable valence / Conjugated nitrogen ligands / Oxygen atom transfer / Isomer specificity / Twin isomerization

 © 2005 Wiley-VCH Verlag GmbH & Co. KGaA, Weinheim

SHORT COMMUNICATIONS

4875 **A. Zharkouskaya, A. Buchholz, W. Plass***

A New Coordination Polymer Architecture with (10,3)-a Network Containing Chiral Hydrophilic 3-D Channels

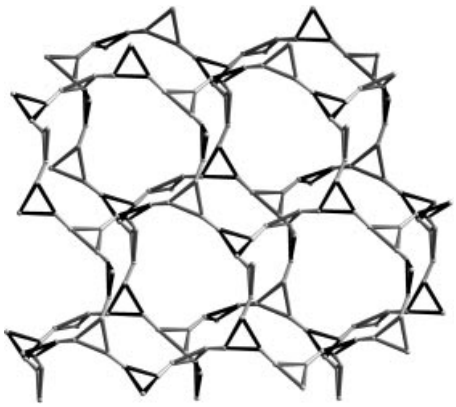

Keywords: Coordination polymer / Copper / Magnetic properties / N,O ligands

4880 **S. K. Ghosh, P. K. Bharadwaj***

Infinite Chains of Quasi-Planar Hexameric Water Clusters Stabilized in a Metal-Organic Framework Built from Co^{II} and Pyrazine-2,3,5,6-tetracarboxylic Acid

Keywords: Water cluster / Supramolecular chemistry / Self assembly / Organic-inorganic hybrid composite

4886 **S. K. Ghosh, P. K. Bharadwaj***

Octameric Water Clusters of Staircase Structure Present in a Metal-Organic Framework Built from Helical Lanthanide Coordination Polymers

Keywords: Water chemistry / Supramolecular chemistry / Self assembly / Metal-organic framework / Helical structure

FULL PAPERS

4891 **M. Mehring,* S. Paalasmaa, M. Schürmann**

Structural Relationships in High-Nuclearity Heterobimetallic Bismuth-Oxo Clusters

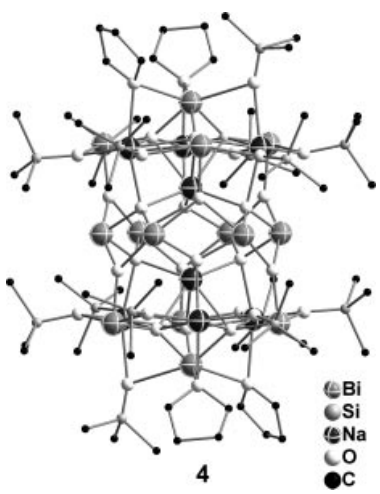

4

Keywords: Bismuth / Sodium / Silanolate / Metal-oxo cluster / Structure elucidation

 © 2005 Wiley-VCH Verlag GmbH & Co. KGaA, Weinheim

4902 **A. Merkoulov, K. Harms, J. Sundermeyer***

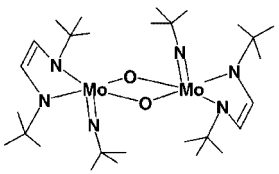

Synthesis and Investigations of the Crystal Structure of a Dinuclear Diazadiene Molybdenum Oxo-Imido Complex with a Unique $N_3Mo(\mu\text{-}O)_2MoN_3$ Core

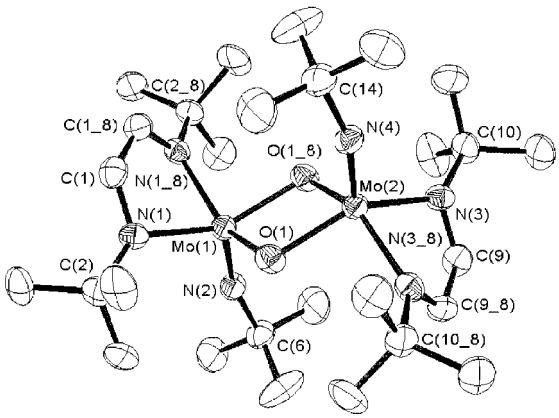

Keywords: Molybdenum / Oxo ligands / Imido ligands / Metathesis / Crystal structure

4907 **A. N. Kuznetsov, B. A. Popovkin, K. Ståhl, M. Lindsjö, L. Kloo***

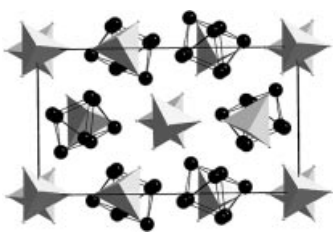

Synthesis of Main Group Polycations in Molten and Pseudo-Molten $GaBr_3$ Media

Keywords: Antimony / Bismuth / Tellurium / Cluster compounds

4914 **C. Jocher, T. Pape, W. W. Seidel, P. Gamez, J. Reedijk, F. E. Hahn***

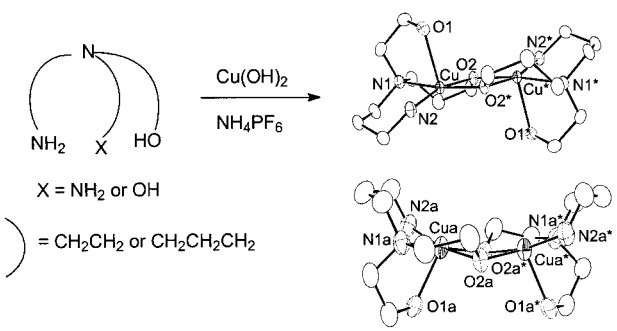

Catechol Oxidation with Dinuclear Copper Complexes of Aliphatic Tripodal Amino Alcohols

Keywords: Tripodal ligands / Amino alcohols / Copper / Catechol oxidase

4924 **G. E. Herberich,* U. Englert, T. Wirth**

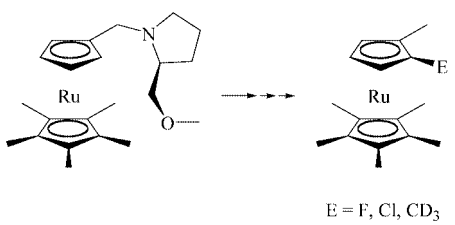

Enantiopure Ruthenocenes $Cp^*Ru(1,2\text{-}C_5H_3\text{-}R^1R^2)$ with a Planar Chiral Cyclopentadienyl Ligand and a Pentamethylcyclopentadienyl Spectator Ligand

Keywords: Ruthenium / Ruthenocene / Sandwich complexes / Planar chirality / (*S*)-2-(methoxymethyl)pyrrolidine

 © 2005 Wiley-VCH Verlag GmbH & Co. KGaA, Weinheim

4936 **K. P. Rao, K. Vidyasagar***

Syntheses, Structure and Intercalation Properties of Low-Dimensional Phenylphosphonates, $A(HO_3PC_6H_5)(H_2O_3PC_6H_5)$ (A = Alkali Metal, NH_4 and Tl)

Keywords: Phenylphosphonates / Organic-inorganic hybrid composites / X-ray diffraction / Layered compounds / Intercalation

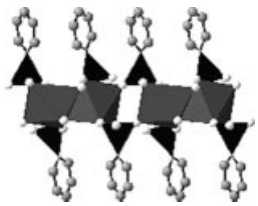

4944 **Y. Jin, M. S. Lah***

Polymorphism Driven by π−π Stacking and van der Waals Interactions: Preparation and Characterization of Polymorphic Vanadium Crystals of $[V^{V}O(Hacshz)(OEt)]$ and $[V^{IV}(Hacshz)_2]$

Keywords: Crystal engineering / Pi interactions / Polymorphism / Supramolecular chemistry / Vanadium

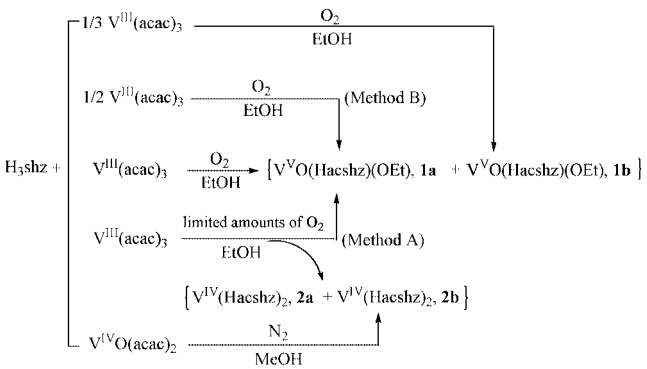

4953 **E. Garribba,* G. Micera,* E. Lodyga-Chruscinska, D. Sanna, G. Sanna**

Binding of Oxovanadium(IV) to Tripeptides Containing Histidine and Cysteine Residues and Its Biological Implication in the Transport of Vanadium and Insulin-Mimetic Compounds

Keywords: Bioinorganic chemistry / Coordination modes / EPR spectroscopy / Peptides / Vanadium

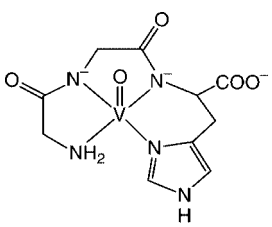

$[VO(GlyGlyHisH_{-2})]^{-}$

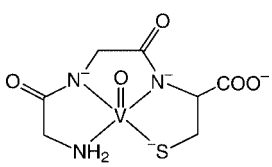

$[VO(GlyGlyCysH_{-2})]^{2-}$

4964 **W. K. Rybak,* A. Skarżyńska, L. Szterenberg, Z. Ciunik, T. Głowiak**

Oxo-Entity-Controlled Diastereomer Peculiarity of Rhenium(V) Complexes $ReOX_2(P{\sim}O)py$ [X = Cl, Br, I; P~O = $(OCMe_2CMe_2O)POCMe_2CMe_2O(1-)$; py = pyridine]: Synthesis and Molecular and Crystal Structural Characterization

Keywords: Noncovalent interactions / Crystal engineering / Rhenium complexes / P,O ligand / Density functional calculations

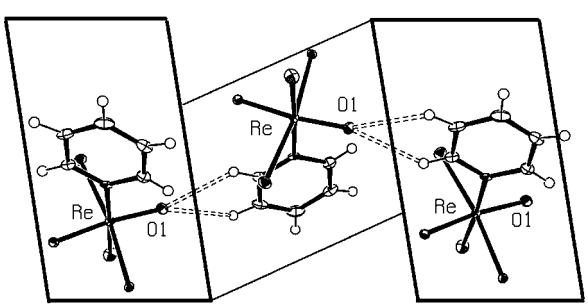

P-{*C*-*cis*-$[ReOCl_2(P{\sim}O)py]\}_n$

 © 2005 Wiley-VCH Verlag GmbH & Co. KGaA, Weinheim

4976 **H.-P. Zhou, Y.-P. Tian,* J.-Y. Wu, J.-Z. Zhang, D.-M. Li, Y.-M. Zhu, Z.-J. Hu, X.-T. Tao, M.-H. Jiang, Y. Xie***

Synthesis, Crystal Structures and Photoluminescence of Mercury(II) Complexes with Two Homologous Novel Functional Rigid Ligands

Keywords: Mercury / Functional rigid ligands / X-ray diffraction / Luminescence

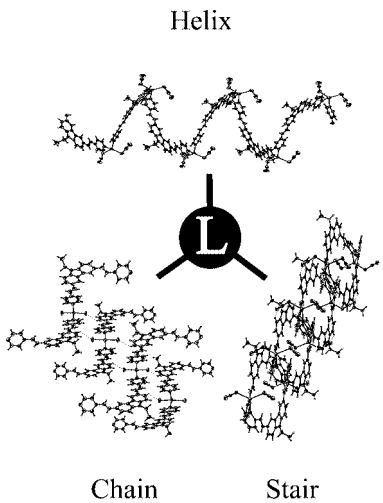

4985 **N. V. Izarova, M. N. Sokolov, D. G. Samsonenko, A. Rothenberger, D. Y. Naumov, D. Fenske, V. P. Fedin***

One-, Two-, and Three-Dimensional Coordination Polymers Built from Large Mo_{36}-Polyoxometalate Anionic Units and Lanthanide Cations

Keywords: Coordination polymers / Lanthanides / Molybdenum / Polyoxometalates

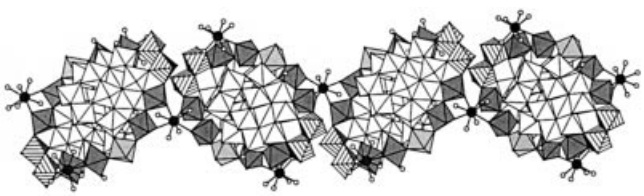

4997 **E. Maimon,* I. Zilbermann, H. Cohen, D. Kost, R. van Eldik, D. Meyerstein***

Mechanism of Isomerization of Ni(cyclam) in Aqueous Solutions

Keywords: Isomerization / Cyclam / Nickel complexes / Oxidation states

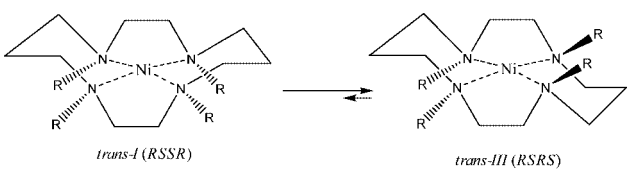

5005 **S. Khatua, S. Dasgupta, K. Biradha,* M. Bhattacharjee***

Self-Assembly of an Alkali Metal Cluster Stabilized by a New Flexidentate Metalloligand: Formation and Structure of Heterobimetallic Na−Mo and Cs−Mo 2D Networks

Keywords: Alkali metals / Heterometallic complexes / Metalloligands / Molybdenum / Self-assembly

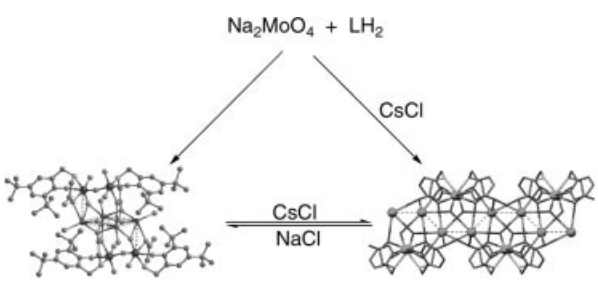

 © 2005 Wiley-VCH Verlag GmbH & Co. KGaA, Weinheim

5011 **J.-C. Lee, M.-G. Wang, F.-E. Hong***

Palladium-Catalysed Amination Reactions Using Cobalt-Containing Bulky Phosphane Ligands

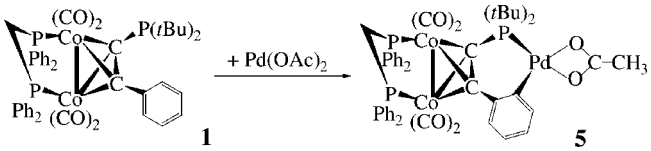

Keywords: Amination / Palladium / Cobalt complexes / Phosphane ligands / Orthometallation

5018 **C. L. M. Pereira, A. C. Doriguetto, C. Konzen, L. C. Meira-Belo, U. A. Leitão, N. G. Fernandes, Y. P. Mascarenhas, J. Ellena, A. L. Brandl, M. Knobel, H. O. Stumpf***

A Crystalline Phase Transition and Optical Properties in a $Co^{II}Cu^{II}$ Oxamato-Bridged Ferrimagnetic Chain

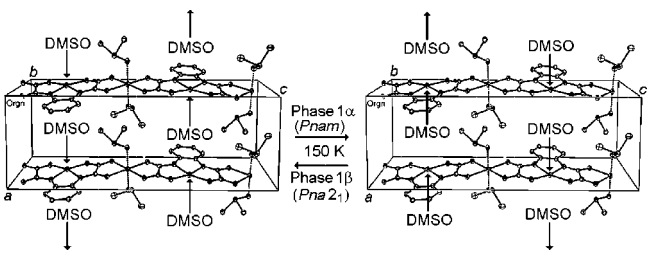

Keywords: Birefringence / Chain structures / Molecular magnetism / Phase transitions / Transition metals

5026 **G. M. Lombardo, G. C. Pappalardo,* F. Punzo, F. Costantino, U. Costantino, M. Sisani**

A Novel Integrated X-ray Powder Diffraction (XRPD) and Molecular Dynamics (MD) Approach for Modelling Mixed-Metal (Zn, Al) Layered Double Hydroxides (LDHs)

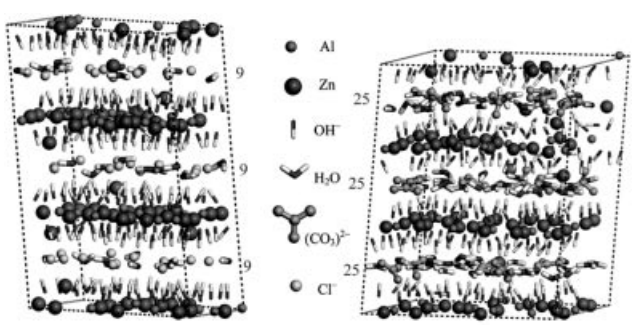

Keywords: Layered double hydroxides / Molecular dynamics / X-ray diffraction / Structure elucidation

CORRECTION

5035 **H. Yin,* M. Hong, H. Xu, Z. Gao, G. Li, D. Wang**

Self-Assembly of Organotin(IV) Moieties with the Schiff-Base Ligands Pyruvic Acid Isonicotinyl Hydrazone and Pyruvic Acid Salicylhydrazone: Synthesis, Characterization, and Crystal Structures of Monomeric or Polymeric Complexes

Keywords: N,O ligands / Self-assembly / Schiff bases / Tin

5037 **Index 2005**

 © 2005 Wiley-VCH Verlag GmbH & Co. KGaA, Weinheim

DOI: 10.1002/ejic.200500615

Variable-Valent Rhenium Chemistry of Conjugated Nitrogenous Ligands: Structure and Reactivity

Animesh Chakravorty*[a,b]

Keywords: Rhenium / Variable valence / Conjugated nitrogen ligands / Oxygen atom transfer / Isomer specificity / Twin isomerization

The valence states of particular concern in this review are VI–I and the ligand types are diimine, azoimine, imineamide and azooxime all bidentate and *N*,*N*-coordinating. Metal reduction potentials and stability of oxidation states are subject to control via variation of the nature and extent of *N*,*N*-chelation and coligation. Back-bonding plays a major role in determining stability and isomer specificity, particularly in the valence domain III–I. Three types of mediated oxygen atom transfer processes have been scrutinized and modeled: from $Re^{V}O$ to tertiary phosphanes and variable-spacer diphosphanes, from water to diimine and from oxime to metal/coligand. Other reactivity topics include isomerizations associated with ligand substitution, stable azo anion radical generation and azo cleavage.
(© Wiley-VCH Verlag GmbH & Co. KGaA, 69451 Weinheim, Germany, 2005)

1. Introduction

Named after the river Rhine, rhenium ($6s^25d^5$) occurs in very low abundance (0.7 ppb) in earth's crust. It was indeed the last of the naturally occurring chemical elements to be discovered (1925).[1] Progress in the chemistry of rhenium which spans the oxidation states –1 to +7 has been comprehensively reviewed from time to time.[2–4] But for a short earlier involvement,[5] our sustained activity in rhenium chemistry dates from the early nineties when we were attracted by the prevalence of the $Re^{V}O$ motif[2,3] and its documented ability to transfer oxygen atoms.[6–9] Since then the chemistry of $Re^{V}O$-promoted transfer reactions has been enriched in several laboratories[4,10–16] including ours (vide infra).

Conjugated nitrogen donor organic molecules constitute a large family of chelating ligands that have been widely used for binding transition metal ions. However, reactive $Re^{V}O$ species incorporating such ligands have been relatively rare[2,3] and this provided the initial lead for us. Our endeavour in this area would eventually lead us to a rich arena of variable-valent rhenium chemistry encompassing interesting reactions, structures and bonding situations. The salient features of this chemistry will be outlined in this article.

[a] Department of Inorganic Chemistry, Indian Association for the Cultivation of Science,
Kolkata 700032, India
E-mail: icac@mahendra.iacs.res.in
animeshc31@yahoo.co.in
[b] Jawaharlal Nehru Centre for Advanced Scientific Research, Bangalore 560064, India

2. Ligands, Coligands and Coordination Types

Three bidentate chelating moieties widely used in our work and generally represented as (NN) are diimine, **1**, azo-

Animesh Chakravorty was born in Mymensingh, Bangladesh, in 1935. He received his PhD degree from Calcutta University and did postdoctoral work at M.I.T. and Harvard University. He was Professor and Head of the Department of Chemistry at I.I.T. Kanpur and subsequently of the Department of Inorganic Chemistry at Indian Association for the Cultivation of Science, Kolkata, where he is now an Emeritus Professor. He is also a Chair Professor of the Jawaharlal Nehru Centre for Advanced Scientific Research, Bangalore. His research interest lies in design and structure of reactive d-block complexes and organometallics, variable valence phenomena and redox transformations. Recent highlights include carbohydrate ligation, crystalline anion radical complexes, metal promoted oxygen atom transfer and insertion into small metallacycles. He has authored 300 papers with his students, sixty of whom have graduated. He has been on the Editoriall Advisory Boards of Inorganic Chemistry, Dalton Transactions, Inorganica Chimica Acta, Comprehensive Coordination Chemistry II and Indian Journal of Chemistry. He is the current President of the Chemical Research Society of India and had been a Golden Jubilee Research Professor of the Indian National Science Academy.

MICROREVIEWS: This feature introduces the readers to the authors' research through a concise overview of the selected topic. Reference to important work from others in the field is included.

 © 2005 Wiley-VCH Verlag GmbH & Co. KgaA, Weinheim

imine, **2** and anionic imineamide, **3** which is derived from **1**. All of these are excellent σ-donors (nitrogen lone pairs); **1** and **2** are also potentially good π-acceptors, **2** being superior in this respect [low-lying π*(azo) orbital].[17,18]

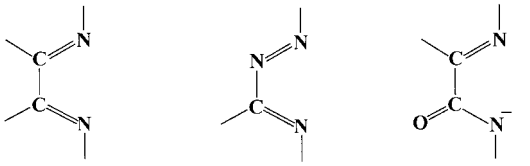

diimine **1** azoimine **2** imineamide **3**

By regulating this duality of bonding with the help of coligands multiple oxidation states of rhenium have been realized. The majority of ligand systems of types **1**–**3** used by us are listed in Table 1 along with abbreviations. Other ligands such as azooximes will be considered in due course.

The majority of coordination types encountered are set out in Table 2. These are uniformly hexacoordinate and generally belong to the (NN)-monochelated [ReQ(NN)] class [chloride ligand(s) omitted] wherein the coligand Q is a good handle for modulation of metal reduction potential and valence. Thus O^{2-} and NAr^{2-} (strong σ-and π-donor)

Table 2. Coordination types.

Complex	Q[a]	(NN)
$[Re^{VI}QCl_3(NN)]$	NAr	**3**
$[Re^{V}QCl_3(NN)]$	O, NAr	**1**, **2**
$[Re^{IV}QCl_3(NN)]^{z+}$	z = 1: OP, OP*n*P	**1**
	z = 0: OP, P	**3**
$[Re^{III}QCl_3(NN)]$	OP, OP*n*P, OP*n*PO, P, P*n*PO	**1**, **2**
$[Re^{II}Cl_2(NN)_2]$	–	**1**, **2**
$[Re^{I}(NN)_3]^{+}$	–	**2**
$[Re^{I}QCl(NN)]$	$(CO)_3$	**2**
$[Re^{I}Q(MeCN)(N^{\cdot-})]$[b]	$(CO)_3$	**2**

[a] P is tertiary phosphorus and *n* is a spacer between two P atoms. [b] ($NN^{\cdot-}$) is the azoimine anion radical.

Table 1. Ligands, functions and their abbreviations.

Ligand	Function	Abbreviation
Diimines		
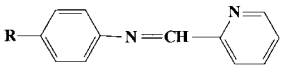	pyridinealdimine	Rpyal
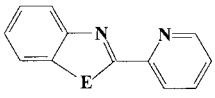	E = O, pyridyloxazole	pyox
	E = S, pyridylthiazole	pyth
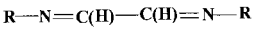	diazabutadiene	Rdabd
Azoimines		
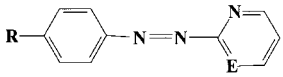	E = CH, azopyridine	Razpy
	E = N, azopyrimidine	Razpm
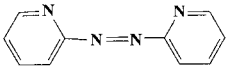	azobipyridine	azbp
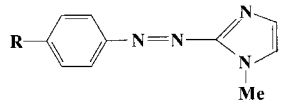	azoimidazole	Razim
Iminoamides		
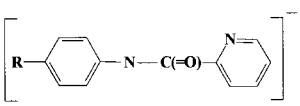	picolinamide	Rpiam
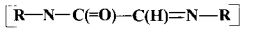	iminoacetamide	Riaam

 © 2005 Wiley-VCH Verlag GmbH & Co. KGaA, Weinheim

are suited for Re^{VI}/Re^{V}; OP (σ-donor) and P (σ-donor and π-acceptor) for Re^{IV}/Re^{III}; $(CO)_3$ (strong σ-donor and π-acceptor) for Re^{I} and azo anion radicals. Bis- and tris-chelation of azoimines (strong σ-donor and π-acceptor) respectively support Re^{II} and Re^{I} without assistance from any special coligand. These can also be formally looked upon as [ReQ(NN)] species where Q stands for (NN) and $(NN)_2$ in bis- and tris-chelates, respectively.

3. The Parent $Re^{V}O$ Systems and $Re^{V}(NAr)$ and $Re^{III}(OPPh_3)$ Derivatives

3.1 Synthetic Methods

The diimine ligands Rpyal, pyox and pyth react with $[Re^{V}OCl_3(PPh_3)_2]$ in nonpolar solvents under mild conditions (to avoid phosphane oxide formation) furnishing oxo species of type **4**.[19,20] In the case of Rdabd phosphane oxide formation is fast even under mild conditions and $[Re^{V}OCl_3(AsPh_3)_2]$ is the convenient (weaker oxygen affinity of $AsPh_3$) starting material.[21]

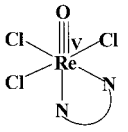

4

On the other hand azoimine ligands react with $KReO_4$ in hot concentrated hydrochloric acid (reducing agent and source of chloride ligand) furnishing **4**.[22–24] Spontaneous aryl chlorination may, however, occur[22,23] as in the formation of $[Re^{V}OCl_3(Clazpy)]$ from Hazpy and $KReO_4$.[22]

The phosphane oxide system **5** can be generally prepared by the reaction of **4** with PPh_3 (other tertiary phosphanes behave similarly) or of the (NN) ligand with $[Re^{V}OCl_3(PPh_3)_2]$ in a polar solvent.[19–27] The imido system **6** is formed via oxide (water) elimination from **4** in presence of $ArNH_2$ which also reacts with **5** in air to furnish **6**.[20–24,29–31]

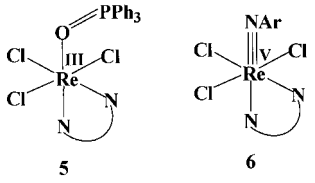

5 **6**

Two observations, both relating to Razpy are noteworthy. First, is the otherwise rare[32] metal-promoted splitting of the azo function, see Equation (1), leading to an imido complex, where the PhN fragment of Hazpy binds to the metal and the pyridyl fragment dimerizes to 2,2′-azobispyridine(azbp).[22] Second, is the synthesis of the first binuclear oxo-imido dimer **7** by the reaction of $[Re^{V}OCl_3(Clazpy)]$ with *p*-toluidine.[22,33]

$$[Re^{III}(OPPh_3)Cl_3(Hazpy)] + Hazpy \rightarrow [Re^{V}(NPh)Cl_3(Hazpy)] + azbp + OPPh_3 \quad (1)$$

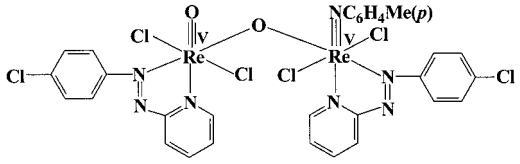

7

3.2 Structural Features

The structures (for a selection see Table 3 and Table 4) of a number of systems of type **4**,[19–24] **5**[22–25,28] and **6**[5,20–24,29–31] are known. All of these have meridional geometry. It is convenient to discuss **4** and **6** together (Table 3). Here the metal atom is systematically shifted from the equatorial plane (Cl_3N) towards the oxo oxygen atom by 0.30–0.35 Å in **4** and towards the imido nitrogen by 0.27–030 Å in **6**. In **4** the Re–O distances generally lie in the range 1.65–1.67 Å representing approximate triple bonding. Idealized $Re^{V}{\equiv}O$, $Re^{V}{=}O$ and Re^{V}–O distances

Table 3. Bond lengths [Å] in $Re^{V}O$ and $Re^{V}(NAr)$ complexes.

Compound	Re–O/[N][a]	Re–N[b]	Re–N[c]	Re–Cl[d]	Ref.
$[Re^{V}OCl_3(Mepyal)]$	1.668	2.295	2.072	2.343	[19]
$[Re^{V}OCl_3(pyth)]$	1.607	2.270	2.118	2.311	[20]
$[Re^{V}OCl_3(NN)]$[e]	1.646	2.171	2.070	2.298	[21]
$[Re^{V}OCl_3(Clazpy)]$	1.663	2.247	2.071	2.341	[22]
$[Re^{V}OCl_3(Hazim)]$	1.660	2.174	2.086	2.339	[24]
$[Re^{V}OCl_3(NN)]$[f]	1.666	2.218	2.072	2.330	[23]
$[Re^{V}OCl(PPh_3)_2(NN)]^{+}$[g]	1.616	2.384	2.002	2.375	[52]
$[Re^{V}(NC_6H_4Cl)Cl_3(Mepyal)]$	1.679	2.224	2.033	2.369	[30]
$[Re^{V}(NC_6H_5)Cl_3(pyox)]$	1.698	2.266	2.075	2.338	[20]
$[Re^{V}(NC_6H_5)Cl_3(Phdabd)]$	1.704	2.194	2.032	2.356	[21]
$[Re^{V}(NC_6H_4Cl)Cl_3(Clazpy)]$	1.719	2.173	2.017	2.371	[22]
$[Re^{V}(NC_6H_4Me)Cl_3(Meazim)]$	1.723	2.140	2.024	2.363	[24]
$[Re^{V}(NC_6H_4Cl)Cl_3(Clazpm)]$	1.719	2.173	2.003	2.358	[23]
$[Re^{V}(NC_6H_5)Cl_3(NN)]$[h]	1.691	2.117	1.998	2.356	[52]
$[Re^{V}(NC_6H_4Me)Cl_2(PPh_3)(NN)]$[i]	1.725	2.191	2.099	2.392	[52]

[a] Oxo O/imido N. [b] N *trans* to O/N. [c] N *cis* to O/N. [d] Average value. [e] (NN) ligand is Schiff base of diacetyl and aniline. [f] (NN) ligand is 2-(*o*,*p*-dichlorophenylazo)pyrimidine. [g] Complex **22** (R = H). [h] Complex **23** (R = Cl). [i] Complex **24**.

 © 2005 Wiley-VCH Verlag GmbH & Co. KGaA, Weinheim

Table 4. Bond lengths [Å] in Re^{III}(phosphane oxide) complexes.

Compound	Re–O	Re–N[a]	Re–N[b]	Re–Cl[c]	Ref.
$[Re^{III}(OPPh_3)Cl_3(Mepyal)]$	2.080	2.030	2.033	2.367	[25]
$[Re^{III}(OPPh_3)Cl_3(Clazpy)]$	2.033	2.032	1.987	2.352	[22]
$[Re^{III}(OPPh_3)Cl_3(Clazim)]$	2.039	1.999	1.978	2.356	[24]
$[Re^{III}(OPPh_3)Cl_3(Hazpm)]$	2.021	2.022	1.957	2.334	[23]
$[Re^{III}(OP2P)Cl_3(Clazim)]$	2.048	2.000	2.002	2.367	[43]
$[Re^{III}(OP1PO)Cl_3(Clazpy)]$	2.030	2.026	1.966	2.369	[27]
$[Re^{III}(OP1PO)Cl_3(Clazim)]$	2.033	1.993	1.985	2.368	[43]
$[(Mepyal)Cl_3Re^{III}(OP2PO)Re^{III}Cl_3(Mepyal)]$[d]	2.068	2.032	2.020	2.368	[27]

[a] Heterocyclic N *trans* to O. [b] Azo/imine N *cis* to O. [c] Average value. [d] Re···Re distance is 8.222(1) Å.

have been estimated to be 1.60, 1.76 and 2.05 Å respectively.[22,34,35] In **6** the Re–N(imido) distance, 1.68–1.72 Å, again corresponds to triple bonding (estimated Re≡NAr, Re=NAr and Re–NAr lengths are 1.69, 1.84 and 2.14 Å respectively).[5,22,36,37] The Re–N bond lying *trans* to Re≡O or Re≡NAr is uniformly longer by 0.1–0.2 Å compared to the other Re–N bond.

In the unique oxo-imido dimer **7**[22] the Re–N(imido) [1.735(10) Å] and Re–O(oxo) [1.685(8) Å] distances are slightly longer than those in **6** and **4**. The oxygen bridge, highlighted in **8**, is unsymmetrical: Re(1)–O(2), 1.849(7) Å and Re(2)–O(2), 1.945(7) Å. Thus the Re(1)–O(2) bond has a large double bond character and this diminishes the bond order of Re(1)–O(1), as depicted by dotted lines in **8**.

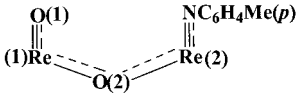

8

The same applies to the O(2)Re(2)N fragment but to a smaller degree. In simple terms, **7** can be described as a complex in which the rare *cis*-$Re^{V}O_2$ moiety acts as a monodentate oxygen donor ligand forming a coordinate bond with the Re^{V}(NAr) moiety.

In the $[Re^{III}(OPPh_3)Cl_3(NN)]$ species, (Table 4) Re–O (2.02–2.08 Å) is a single bond and the metal is no longer shifted towards the oxygen atom. Significant Re(NN) back-bonding is present particularly in the azoimine system. The Re–N(azo) bond is generally shorter than the Re–N(heterocyclic) bond (Table 4) implying involvement of π*(azo) orbitals. Indeed, the N–N(azo) distance in the complexes span the range 1.32–1.35 Å[22–24,27,43] as compared to 1.25 Å in free azo ligands. In the $Re^{V}O$ and Re^{V}(NAr) complexes of azoimines back-bonding is expected to be unimportant but the N–N(azo) distance (1.25–1.31 Å) is still somewhat long possibly due to azo←Re←NAr type interactions.[5,22–24,31]

3.3 Metal Redox

The Re^{VI}/Re^{V} reduction potentials in $[Re^{V}OCl_3(NN)]$[19–24] and $[Re^{V}(NAr)Cl_3(NN)]$[5,20–24,29–31] span the ranges 1.5–2.2 and 0.8–1.5 V, respectively. The Re^{IV}/Re^{III} couple in $[Re^{III}(OPPh_3)Cl_3(NN)]$[19–25] occur in the domain 0.2–1.2 V. Representative data are collected in Table 5. The azo group is electron-withdrawing and in general azoimine complexes have higher $E_{1/2}$ values than diimine complexes. For a given (NN) ligand the Re^{VI}/Re^{V} reduction potential of an Re^{V}(NAr) complex is 0.6–0.8 V lower than that in the $Re^{V}O$ congener reflecting the superior donor ability of NAr^{2-}. Although the $Re^{VI}O$ species are too unstable for chemical/electrochemical generation in solution in bulk quantities, it has been possible to obtain certain Re^{VI}(NAr) species such as $[Re^{VI}\{NC_6H_4Me(p)\}Cl_3(Meazpy)]^{+}$ in solution. It displays a six-line EPR spectrum (see Section 5.3) with g = 1.96 and A = 540 G.[5]

3.4 Bond Lengths Trends in a $Re^{III}(OPPh_3)/Re^{IV}(OPPh_3)$ Pair

The $[Re^{IV}(OPPh_3)Cl_3(NN)]^{+}$ system **9** can be generated by coulometric or dilute nitric acid oxidation of **5**.

Table 5. Reduction potential data [V vs. SCE] for $[Re^{V}OCl_3(NN)]$, $[Re^{V}(NAr)Cl_3(NN)]$, $[Re^{III}(OPPh_3)Cl_3(NN)]$, and $[Re^{III}(PPh_3)Cl_3(NN)]$ in acetonitrile solution at 298 [K].

(NN) ligand	Re^{VI}/Re^{V} [ReO][a]	Re^{VI}/Re^{V} [Re(NAr)][a],[b]	Re^{IV}/Re^{III} [Re(OPPh$_3$)][a]	Re^{IV}/Re^{III} [Re(PPh$_3$)][a]	Ref.
Mepyal	1.72[c]	0.96	0.30	0.62	[19,30,61]
C_6H_{11}dabd	1.72[c]	1.08[d]	0.69	–	[21]
Pyox	1.64	0.85	0.26[e]	0.59	[20,28]
Pyth	1.54	0.81	0.23[e]	0.57	[20,28]
Clazpy	1.91	1.38	0.98	1.20	[22,27]
Clazim	1.88[c]	1.21	0.82	1.08	[24]

[a] Chloride and (NN) ligand not shown. [b] Unless otherwise stated Ar = Ph. [c] Anodic peak potential. [d] Ar = $C_6H_4Cl(p)$. [e] Unpublished results.

 © 2005 Wiley-VCH Verlag GmbH & Co. KGaA, Weinheim

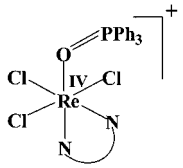

9

The complex $[Re^{IV}(OPPh_3)Cl_3(pyth)]^+$ has been isolated and characterized as the nitrate salt.[28] Its metal–ligand distances are compared with those of $[Re(OPMe_2Ph)Cl_3(pyth)]$ in Table 6. The lengths of the Re–O and Re–Cl bonds decrease by 0.06 Å due to radial contraction upon metal oxidation. On the other hand oxidation increases the average Re–N distance by 0.06 Å, reflecting considerable weakening of back-bonding in the $Re^{IV}(OPPh_3)$ system.

Table 6. Bond lengths [Å] in a pair of rhenium(IV)-rhenium(III) phosphane oxide complexes.[28]

	$[Re^{IV}(OPPh_3)Cl_3(pyth)]^{+}$[a]	$[Re^{III}(OPMe_2Ph)Cl_3(pyth)]$
Re–O	2.018	2.078
Re–N(py)	2.119	2.054
Re–N(azole)	2.123	2.063
Re–Cl[b]	2.310	2.376

[a] The asymmetric unit consists of two molecules and the lengths are average values. [b] Average value.

4. Oxygen Atom Transfer from $Re^{V}O$ to Tertiary Phosphanes

4.1 Monophosphanes: Reactivity Trends and Reaction Model

Oxygen atom transfer reactions involving iron, molybdenum and tungsten sites are important in the chemistry of life.[38,39] Rhenium is not a biometal, but as an element in an adjacent periodic group transfer processes of $Re^{V}O$ are of potential interest as reaction models. The reaction of interest here is stated in Equation (2). In dichloromethane solution the reaction follows second-order kinetics.

$$Re^{V}{\equiv}O + PPh_3 \rightarrow Re^{III}{-}O{=}PPh_3 \quad (2)$$

Selected rate data[19,20] are set out in Table 7. An increase in phosphane basicity makes the transfer reaction more facile, and PPh_2Me reacts nearly six times faster than PPh_3. Electron withdrawal from the $Re^{V}O$ moiety via ligand modification hastens the transfer process. Thus, for $[ReOCl_3(Rpyal)]$ log k increases linearly with the Hammett constant of R (Me<H<Cl).[19] Finally, the $[ReOCl_3(pyox)]$ complex reacts nearly twice as fast as $[ReOCl_3(pyth)]$ which is qualitatively consistent with the heteroatom electronegetivity order O>S.[20]

Table 7. Rates of reactions of $[Re^{V}OCl_3(NN)]$ with phosphanes in dichloromethane solution.

(NN) Ligand	Phosphane	T [K]	$10^3\ k$ [$M^{-1}s^{-1}$][a]	Ref.
Mepyal	PPh_3	299	7.96	[19]
Hpyal	PPh_3	299	12.26	[19]
Clpyal	PPh_3	299	24.02	[19]
Pyox	PPh_3	302	4.18	[20]
Pyth	PPh_3	302	2.00	[20]
Mepyal	PPh_2Me	295	47.00	[19]
Pyox	PPh_2Me	302	24.80	[20]
Pyth	PPh_2Me	302	10.65	[20]
Pyox	$Ph_2P(CH_2)_4PPh_2$	308	30.67	[28]
Pyth	$Ph_2P(CH_2)_4PPh_2$	308	14.17	[28]

[a] Estimated standard deviation lie in the range 0.02–0.06.

For the ligands Mepyal, pyox and pyth the activation enthalpies (kcal mol^{-1}) are 8.91, 13.49 and 14.31 respectively while the activation entropies (cal K^{-1} mole^{-1}) are –38.69, –24.15 and –23.32 respectively.[19,20] The large and negative $\Delta S^{\neq}$ values imply close association of $[Re^{V}OCl_3(NN)]$ and PPh_3 in the transition state. A model[20] of this association and subsequent events are stylized in **10** which has common features with oxygen atom transfer reactions of $Mo^{VI}O_2$ and $W^{VI}O_2$.[40–42]

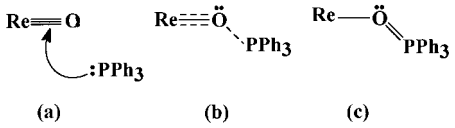

(a) (b) (c)

10

In **10** the full and broken lines, respectively, represent coordinate covalent bonds and weak links. In structurally characterized $[Re^{III}(OPPh_3)Cl_3(NN)]$ complexes the phosphorus atom uniformly lie within 2.8 Å from the centroids of one or both of the triangular OCl_2 faces (see **5**) whereas the distances from the two OClN centroids is greater than 3 Å. It is believed that phosphane attack occurs from the side away from the (NN) chelate ring.

4.2 Diphosphanes: Single and Double Oxygen Atom Transfer

The diphosphanes used are of type **11** abbreviated as P*n*P (n = 1–4). The reaction of $[Re^{V}OCl_3(NN)]$ with excess P*n*P follows second-order kinetics[28] (Table 7) affording **12** which has a dangling phosphane function. The (NN) ligands examined include Mepyal,[27] pyox,[28] pyth,[28] Clazpy[27] and Clazim.[43] Spontaneous solution isomerization is an interesting feature of **12**, vide infra.

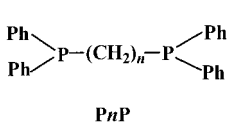

P*n*P

11

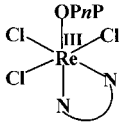

12

The reaction of excess $[Re^{V}OCl_3(NN)]$ with P*n*P leads to successive oxygen atom transfer furnishing binuclear **13**

 © 2005 Wiley-VCH Verlag GmbH & Co. KGaA, Weinheim

when $n > 1$.[27,43] In the case of P1P two atom transfer furnishes only mononuclear $[Re^{III}(OP1PO)Cl_3(NN)]$ (**14**). The dangling phosphane oxide function strongly implicates transient binucleation on the reaction pathway.

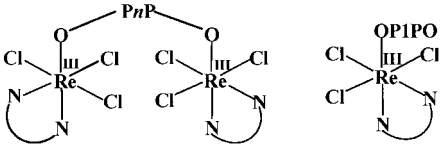

13 **14**

The instability of the binuclear intermediate leading to dissociation of one of the $ReCl_3(NN)$ fragment is due to the excessive steric crowding imposed by the short spacer ($n = 1$).[27]

Metal–ligand bond lengths in the species of type **12**–**14** are very similar to those in $[Re^{III}(OPPh_3)Cl_3(NN)]$ (Table 4). This close similarity extends to other properties including Re^{IV}/Re^{III} reduction potentials.[27,28,43]

5. Oxygen Atom Transfer from Water: Imine→Amide Oxidation

5.1 Re^{IV}(imineamide) Species: Synthesis and Reaction Model

The general reaction is stated in Equation (3) where the imineamide ligand in the product complex is monoanionic (Table 1). This reaction was first encountered in the case of $[Re^{III}(OPPh_3)Cl_3(Rpyal)]$ which afforded $[Re^{IV}(OPPh_3)Cl_3(Rpiam)]$.[19,25,26] The required oxidation equivalents could be provided electrochemically and/or chemically.[19]

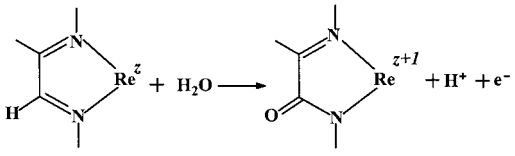

(3)

The quasireversible Re^{IV}/Re^{III} couple in $[Re^{III}(OPPh_3)Cl_3(Rpyal)]$ lie near 0.3 V (Table 5). The rhenium(IV) cation $[Re^{IV}(OPPh_3)Cl_3(Rpyal)]^+$, the actual reactive intermediate, is quantitatively afforded upon coulometry (0.5 V in dry MeCN). Upon regulated addition of H_2O to be the oxidized solution (after completion of coulometry) the spontaneous imine→amide reaction [Equation (3)] occurred and the final solution is found to contain $[Re^{III}(OPPh_3)Cl_3(Rpyal)]$ and $[Re^{IV}(OPPh_3)Cl_3(Rpiam)]$ in the mol ratio 2:1. Of the three electrons of Equation (3), one is accounted by the cathodic process corresponding to the anodic $Re^{III}\rightarrow Re^{IV}$ oxidation. The remaining two electrons are consumed by $[Re^{IV}(OPPh_3)Cl_3(Rpyal)]^+$ regenerating two mol of the precursor.

The imineamide complexes were isolated in excellent yields by oxidizing $[Re^{III}(OPPh_3)Cl_3(Rpyal)]$ with excess of chemical oxidants such as Ce^{IV} or H_2O_2 in wet solutions.[19] Here the aldimine→amide conversion proceed quantitatively since it is no longer necessary for $[Re^{IV}(OPPh_3)Cl_3(Rpyal)]^+$ to act as oxidant. Imineamide complexes of type $[Re^{IV}(OPPh_3)Cl_3(Riaam)]$ have been similarly prepared by oxidising the corresponding $[Re^{III}(OPPh_3)Cl_3(Rdabd)]$ precursors with H_2O_2.[21]

In the case of $[Re^{III}(OPPh_3)Cl_3(Hpyal)]$ the reaction rate was found to be first-order with respect to both $[Re^{IV}(OPPh_3)Cl_3(Hpyal)]^+$ and H_2O.[19] The $\Delta H^{\neq}$ and $\Delta S^{\neq}$ parameters are 13.4 kcal mol^{-1} and –27.3 cal K^{-1} mol^{-1}, respectively.[19] Water attack is believed to occur on the aldimine π*-orbital furnishing the α-hydroxy amine intermediate **15** (Cl^- and $OPPh_3$ ligands not shown).

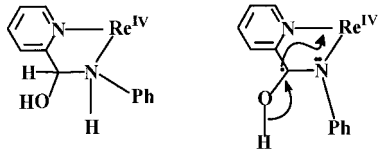

15 **16**

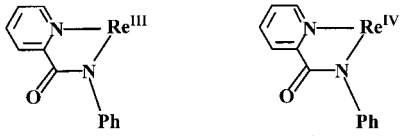

17 **18**

Instances of aqua adduct formation by aldimines have been documented.[44,45] The adduct **15** is however unstable and can undergo rapid transformation via induced transfer of two electrons.[46] The rational steps are: **15**→**16** (oxidative radical formation and proton dissociation), **16**→**17** (internal redox and proton dissociation), and **17**→**18** (metal oxidation). The net result is the imineamide complex **18**.[19]

The crucial requirement for realizing the imine→amide oxidation is the facile accessibility of two oxidation states (here Re^{III} and Re^{IV}) such that the higher state is able to affect sufficient electron withdrawal from the aldimine function to promote nucleophilic water attack. Aldimine→amide oxidation has earlier been documented in ruthenium[47] and iron[48,49] chemistry.

5.2 Re^{VI}(imineamide) Complexes: Regiospecificity and Steric Blockade

The reaction of Equation (3) has provided an elegant way for stabilizing the otherwise rare $Re^{VI}(NAr)$ moiety in the form of $[Re^{VI}(NAr)Cl_3(Rpiam)]$[29,30,50] and $[Re^{VI}(NAr)Cl_3(Riaam)]$[21] which have been isolated via chemical oxidation of $[Re^{V}(NAr)Cl_3(Rpyal)]$ and $[Re^{V}(NAr)Cl_3(Rdabd)]$ in wet solvents.

In the oxidation of the Rdabd complex there are two imine functions to choose from but structure determination of $[Re^{VI}(NC_6H_4Cl)Cl_3(C_7H_{13}iaam)]$ has revealed that the amide nitrogen lie exclusively *trans* to a chloride ligand as in **19** and not to the NAr ligand.[21] This is consistent with the reaction model considered in the previous section of this article. We recall that in $Re^{V}(NAr)$ complexes (see Section 5.1) the Re–N bond lying *trans* to the NAr group is

 © 2005 Wiley-VCH Verlag GmbH & Co. KGaA, Weinheim

elongated (*trans* influence) compared to the other Re–N bond.

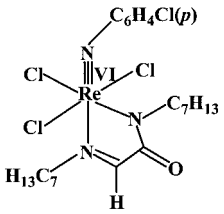

19

The imine function supporting the shorter Re–N bond will thus be more polarized and subject to more facile nucleophilic attack by water. It is indeed this function that is selectively oxidized to amide.

The ketimine analogues, **20**, of Rpyal affords [Re^{V}(NAr)Cl_3(NN)] type systems.[29] The R′ = Me complex was readily converted into the same amide chelate [Re^{VI}(NAr)Cl_3(Rpiam)] obtained from [Re^{V}(NAr)Cl_3(Rpyal)]. But the R′ = Ph system failed to afford any amide complex. Space-filling structural models have revealed that the C=N function in the R′ = Ph system is greatly hindered due to aryl crowding making it inaccessible to nucleophilic water attack. In contrast the function is well exposed in the R′ = H/Me complexes.[29]

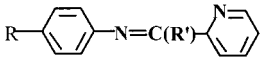

R′ = Me, Ph

20

5.3 Structure and Properties

The structures of one $Re^{IV}(OPPh_3)$ and a few Re^{VI}(NAr) imineamide complexes are known (Table 8). These have meridional geometry as in their precursors and the amide group, C–C(=O)–N is uniformly planar. In going from [$Re^{III}(OPPh_3)Cl_3$(Mepyal)] (Table 4) to [$Re^{IV}(OPPh_3)Cl_3$(Mepiam)] (Table 8) the Re–O and Re–Cl distances decrease while the Re–N distances increase very significantly, reflecting decrease of both radius and extent of back-bonding upon metal oxidation (see also Section 3.3).

In the Re^{VI}(NAr) species[21,30] the metal atom is shifted from the Cl_3N plane towards the imido nitrogen by ca. 0.3 Å and the Re–N bond *trans* to the imide function is lengthened by 0.15 to 0.20 Å (Table 8). The radial changes between rhenium(V) and rhenium(VI) species are relatively small. The Re^{VI}–N(imide) length (1.70–1.72 Å) imply triple bonding as in Re^{V}–N(imide) (see Section 3.2). Outside our work structures of very few Re^{VI}N(imide) complexes are known.[29,51]

In [Re^{V}(NAr)Cl_3(diimine)] species the Re^{VI}/Re^{V} couple occur near 1.0 V (Table 5). In the corresponding imineamide complexes two one-electron couples (Re^{VI}/Re^{V} and Re^{VII}/Re^{VI}) occur near 0.2 and 1.5 V (Table 9).[21,19] The Re^{VI}/Re^{V} reduction potential is thus dramatically lowered upon imine oxidation reflecting stabilization of the hexavalent state by the amide function. A similar relationship applies to the Re^{IV}/Re^{III} and Re^{V}/Re^{IV} couples among diimine and imineamide complexes of Re($OPPh_3$)Cl_3 (Table 5 and Table 9).[19]

Table 9. Reduction potentials [V vs. SCE] of Re(imineamide) species in MeCN at 298 [K].

Compound	$Re^{(z+1)+}/Re^{z+}$	$Re^{(z+2)+}/Re^{(z+1)+}$	Ref.
[$Re^{IV}(OPPh_3)Cl_3$(Mepiam)][a]	–0.46	1.26	[19]
[$Re^{IV}(OPPh_3)Cl_3(C_6H_{11}$iaam)][a]	–0.38[c]	1.66	[21]
[$Re^{IV}(PPh_3)Cl_3$(Mepiam)][a]	–0.15	1.19	[61]
[$Re^{VI}(NC_6H_4Me)Cl_3$(Mepiam)][b]	0.13	1.50	[29]
[$Re^{VI}(NC_6H_4Cl)Cl_3(C_6H_{11}$iaam)][b]	0.20	1.56	[21]

[a] $z = 3$. [b] $z = 5$. [c] Cathodic peak potential.

The Re^{VI}(NAr) complexes (t_2g^1) display six-line EPR spectra in fluid solution[21,29,30] corresponding to the I = 5/2 nuclei ^{185}Re and ^{187}Re which have nearly equal nuclear moments. The centre-field g value and average hyperfine splitting lie near 1.91 and 440 G, respectively.

6. Oxygen Atom Transfer from Azooximes: Oxime→Imine Reduction

In this third type of transfer reaction a preoxidized imine i.e., an oxime function gives up the oxygen atom either to a metal site or to an oxophilic substrate.[52] The concerned oxime ligands are of type **21**, RazoxH (the terminal H is the dissociable oxime proton). Treatment of [Re^{III}(MeCN)$Cl_3(PPh_3)_2$] with the silver salt of **21** in cold affords the azoimine complex **22** isolated as the PF_6^- salt. On the other hand the reaction of [Re^{V}(NPh)$Cl_3(PPh_3)_2$] with **21** furnished the deprotonated azoimine chelated complex **23**. In contrast to **21** the oxime of 2-acetylpyridine reacts with [Re^{V}(NAr)$Cl_3(PPh_3)_2$] without oxygen atom transfer affording stable oximato complexes such as **24**. Bond parameters of **22**–**24** are listed in Table 3.

Table 8. Bond lengths [Å] in Re^{IV}(imineamide) and Re^{VI}(imineamide) complexes.

Compound	Re–O/N[a]	Re–N[b]	Re–N[c]	Re–Cl[d]	Ref.
[$Re^{IV}(OPPh_3)Cl_3$(Mepiam)]	2.003	2.091	2.070	2.345	[25]
[$Re^{VI}(NC_6H_4Me)Cl_3$(Mepiam)]	1.699	2.231	2.026	2.346	[29]
[$Re^{VI}(NC_6H_4Cl)Cl_3$(Mepiam)]	1.722	2.208	2.058	2.339	[30]
[$Re^{VI}(NC_6H_4Cl)Cl_3(C_7H_{13}$iaam)]	1.717	2.214	2.035	2.342	[21]

[a] Phosphane oxide O/imido N. [b] N atom *trans* to O/N. [c] N atom *cis* to O/N. [d] Average value.

 © 2005 Wiley-VCH Verlag GmbH & Co. KGaA, Weinheim

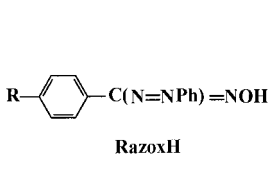

RazoxH

21

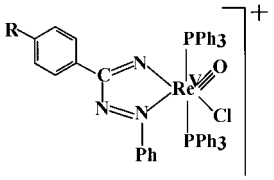

22

The azoimine ligand in **22** and **23** are not known in the free state. There is a report on the chelation of such ligands to bivalent palladium achieved via azooximates reduction.[53] The formation of **22** involves oxidative addition of the oxime function. Instances of such addition are in general rare,[54,55] particularly in rhenium chemistry.[56] Oxime→imine reduction by PPh_3 as in the formation of **23** has been documented in salicylaldoxime chemistry.[57,58] Outside certain dioximates,[59] **24** appears to be the only other structurally characterized oximato complex of rhenium.

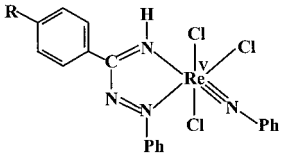

23

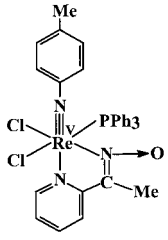

24

The system **25** involving the usual[60] azooxime chelation has been proposed as a possible intermediate in the formation of **22**. The crucial event is activation of oximato oxygen by the electron-withdrawing azo group leading to oxygen atom transfer to the metal site with concomitant displacement of a chloride ligand in *cis* position.[52]

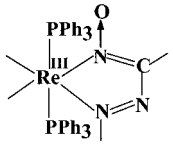

25

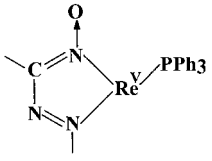

26

In analogy with **24**, the moiety **26** has been proposed to be the possible intermediate in the formation of **23**. Here, rhenium(V) acts as a Lewis acid activator[7] promoting oxygen atom transfer to PPh_3 followed by displacement of $OPPh_3$ by chloride. The relatively weak electron withdrawal by the imine function ensures stability of **24**.

7. Reaction of $[Re^{III}(OPPh_3)Cl_3(NN)]$ with PPh_3

7.1 Geometrical Isomerization

Meridional $[Re^{III}(OPPh_3)Cl_3(NN)]$ (**5**) undergoes facile displacement of coordinated $OPPh_3$ by PPh_3 furnishing facial $[Re^{III}(PPh_3)Cl_3(NN)]$ (**27**).[24,27,28,61] Metal–ligand bond parameters in selected species are listed in Table 10.

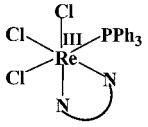

27

Table 10. Bond lengths in Re^{III}(phosphane) complexes.

Compound	Re–N[a]	Re–N[b]	Re–Cl[c]	Re–P	Ref.
$[Re^{III}(PPh_3)Cl_3(Hpyal)]$	2.103	2.083	2.379	2.463	[61]
$[Re^{III}(PPh_2Me)Cl_3(pyox)]$	2.110	2.098	2.383	2.414	[28]
$[Re^{III}(PPhMe_2)Cl_3(pyox)]$	2.089	2.060	2.365	2.373	[28]
$[Re^{III}(PPh_3)Cl_3(Clazpy)]$	2.077	1.994	2.359	2.510	[27]
$[Re^{III}(PPh_3)Cl_3(Clazim)]$	1.997	2.035	2.363	2.476	[24]
$[Re^{III}(P1PO)Cl_3(Clazpy)]$	2.072	2.007	2.363	2.479	[27]
$[Re^{III}(P1PO)Cl_3(Clazim)]$	2.050	2.055	2.375	2.476	[43]

[a] Pyridine/imidazole N. [b] Imine/azo N. [c] Average value.

In **27** two π-acceptor ligands [PPh_3 and (NN)] are present and the net back-bonding is maximized in the facial geometry which ensures minimum competition between the acceptor sites for the same metal orbital. On the other hand in **5** the (NN) ligand can occupy any two *cis* positions and the net geometry is controlled by steric and electrostatic factors. Thus logical stable geometries of **5** and **27** are respectively meridional and facial as observed. Interestingly, the average Re–N distance in a phosphane complex is longer (by upto 0.06 Å) than that in the corresponding $OPPh_3$ complex (see Table 4 and Table 10) where (NN) alone does all the back-bonding. The geometrical selectively is strong and exclusive and in no case isomers have been observed. We recall that $[Re^{V}OCl_3(NN)]$ and $[Re^{V}(NAr)Cl_3(NN)]$ are meridional as expected.

7.2 Metal Redox, Imine→Amide Oxidation and Facial Re^{IV}(imineamide) Species

The Re^{IV}/Re^{III} reduction potential in **27** lie near 0.6 and 1.0 V for diimine and azoimine ligands respectively. These values are higher than those of the corresponding $OPPh_3$ complexes by 0.2–0.3 V (Table 5) reflecting the superior net back-bonding in the PPh_3 complexes.

The complex $[Re^{IV}(PPh_3)Cl_3(Rpyal)]^+$, electrogenerated in solution reacts spontaneously with water affording the corresponding facial imineamide system $[Re^{IV}(PPh_3)Cl_3$-(Rpiam)], **28**. In **28** (R = Cl) the Re–N(py), Re–N(amide), Re–P and Re–Cl(av) distances are 2.123, 2.061, 2.549 and 2.325 Å respectively.[61]

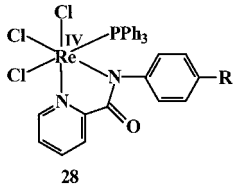

28

The average Re–Cl distance is thus shorter by 0.05 Å and the Re–P distance is longer by 0.1 Å than those in

 © 2005 Wiley-VCH Verlag GmbH & Co. KGaA, Weinheim

$[Re^{III}(PPh_3)Cl_3(Hpyal)]$ (Table 10) consistent with decrease of metal radius and the degree of back-bonding upon oxidation. The Re^{IV}/Re^{III} reduction potential in $[Re^{IV}(PPh_3)Cl_3(Mepiam)]$ is –0.15 V (Table 9)[61] again signifying the dramatic stabilizing influence of imineamide chelation as opposed to diimine chelation on higher oxidation states (see Section 5.3).

8. Twin Isomerization of $[Re^{III}(OPnP)Cl_3(NN)]$

8.1 The Reaction and Its Pathway

The meridional $[Re^{III}(OPnP)Cl_3(NN)]$ species, **12** undergo spontaneous intramolecular twin isomerization (linkage and geometrical), Equation (4), in solution furnishing facial $[Re^{III}(PnPO)Cl_3(NN)]$, **29**.[27,28,43] The metal–ligand bond lengths in type **29** complexes are very similar to those in **27** (Table 10), also **27** and **29** have very similar Re^{IV}/Re^{III} reduction potentials.[27,28,43]

$$[Re^{III}(OPnP)Cl_3(NN)] \rightarrow [Re^{III}(PnPO)Cl_3(NN)] \quad (4)$$

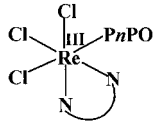

29

The reaction of Equation (4) follows first-order kinetics and is characterized by strongly negative entropy of activation (–20 to –40 cal K^{-1} mol^{-1}). A model for the association of the dangling phosphane function in the transition state (n = 1) is stylized in **30**.

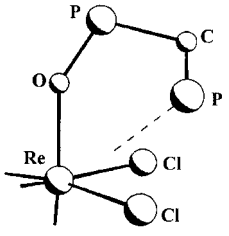

30

Subsequent attack by the P atom on the triangular face with concomitant edge displacement of a chloride ligand and Re–OP bond cleavage affords the facial complex as depicted in **31**.[27]

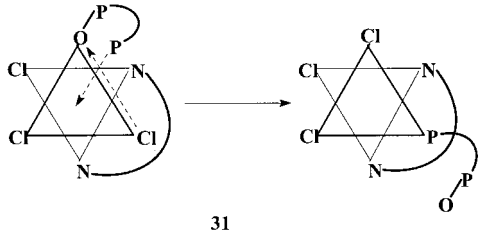

31

8.2 Effect of Spacer Length and Metal Oxidation State

For the $[Re^{III}(OPnP)Cl_3(pyox)]$ and $[Re^{III}(OPnP)Cl_3(pyth)]$ complexes the rate of the twin isomerization reaction has been determined over the domain n = 1–4[28] (Table 11). The rate decreases approximately exponentially as n increases. The number of possible conformations of the dangling $(CH_2)_nPPh_2$ fragment is indeed expected to increase exponentially with increase of n,[62] but only a few of the conformations will be spatially suited (proximal metal and phosphane site) for the reaction to occur.

Table 11. Rate constants for the twin isomerization of $[Re^{III}(OPnP)Cl_3(pyox/pyth)]$ in CH_2Cl_2 at 308 [K].[28]

N	10^5 k $[s^{-1}]$[a]	
	Pyox	pyth
1	8.42	3.62
2	4.07	1.80
3	1.58	0.72
4	0.67	0.25

[a] Estimated standard deviation lie in the range 0.02–0.05.

In the system $[Re^{IV}(OP1P)Cl_3(pyox/pyth)]^+NO_3^-$ prepared by treating the trivalent congener with dilute nitric acid (see also Section 3.4) the isomerization process is completely arrested even though it is n = 1 case which corresponds to maximum reactivity before oxidation. This is consistent with the kinetic inertness of rhenium(IV) ($5d^3$). Other factors also work in the same direction. Thus rhenium(IV) is a harder acceptor than rhenium(III) and oxygen is a harder donor than phosphorus. This as well as the weaker back-bonding ability of rhenium(IV) is expected to disfavor the attack of the metal by the dangling phosphane function.[28]

9. Bis and Tris Chelation: Rhenium(II) and Rhenium(I)

9.1 Ligand Choice, Synthesis, Magnetism and Metal Redox

Metal π-basicity would increase progressively upon reduction: $Re^{III}<Re^{II}<Re^{I}$. In designing (NN)-chelated complexes of the latter two oxidation states it is imperative that good π-acids are chosen. Azoheterocycles are excellent π-acceptors with low-lying π*(azo) orbitals.[17,18,63,64] These have indeed afforded bis and tris chelates of coordination types $[Re^{II}Cl_2(NN)_2]$, **32** and $[Re^{I}(NN)_3]^+$, **33** for the first time in rhenium chemistry.[31,65] In **32** and **33** N^a and N^h are azo and heterocyclic nitrogen atoms respectively. A remarkable feature is the exclusive occurrence of the geometrical forms depicted in **32** and **33**. For synthesis, $[Re^{V}OCl_3(PPh_3)_2]$ and/or $[Re^{V}O(OEt)Cl_2(PPh_3)_2]$ were used as starting materials. For assembling bis and tris chelates the Re:(NN) ratio used was 1:2.5 and 1:6 respectively.[31,65] In most cases the tris chelates were isolated as ReO_4^- salts.

 © 2005 Wiley-VCH Verlag GmbH & Co. KGaA, Weinheim

Table 12. Bond lengths[a] in rhenium(II) and rhenium(I) species and their reduction potentials [V vs. SCE] in MeCN.

Compound	Bond length [Å]			$Re^{(z+1)+}/Re^{z+}$	Ref.
	Re–N[b]	Re–N[c]	N=N		
$[Re^{II}Cl_2(Meazim)_2]$	2.003	2.051	1.34	0.44[d]	[65]
$[Re^{II}Cl_2(Clazpy)_2]$	1.99	2.07	1.33	0.70[d]	[65]
$[Re^{II}Cl_2(azbp)_2]$	2.00	2.06	1.35	0.50[d]	[31]
$[Re^{I}(Hazpy)_3]^+$	1.99	2.10	1.32	0.93[e]	[65]
$[Re^{I}(azbp)_3]^+$	1.98	2.11	1.34	0.60[e]	[31]
$[Re^{I}(CO)_3Cl(Clazpy)]$	2.158	2.153	1.273	1.65[e]	[68]
$[Re^{I}(CO)_3Cl(Hazpm)]$	2.173	2.136	1.271	1.60[e]	[70]
$[Re^{I}(CO)_3Cl(Clazim)]$	2.150	2.166	1.281	1.45[e]	[70]

[a] Average values in bis and tris chelates. [b] Azo N. [c] Heterocyclic N. [d] $z = 2$. [e] $z = 1$.

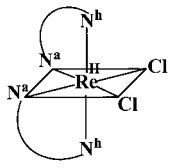

32

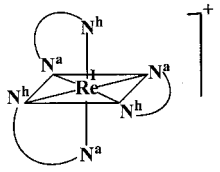

33

The bis-chelates are paramagnetic (t_{2g}^5) and in fluid solution these display well-resolved EPR spectra with six hyperfine lines. The centre-field *g* value and the average hyperfine splitting lie near 2.10 and 280 G, respectively[31,65] [compare with the Re^{VI}(NAr) case, see Section 5.3]. The tris chelates are diamagnetic (t_{2g}^6) and their ^{1}H NMR spectra reveal that the three chelate rings are magnetically equivalent consistent with the facial geometry. The bis and tris chelates display well defined Re^{III}/Re^{II} and Re^{II}/Re^{I} couples respectively (Table 12).

9.2 Structure, Back-Bonding and Isomer Specificity

Selected average bond lengths[31,65] are listed in Table 12. The Re–N^a length is uniformly shorter than Re–N^h length by 0.05–0.1 Å and the average N–N distance is longer by 0.1 Å than that in uncoordinated azo ligands (1.25 Å). Clearly strong d(Re)-π*(azo) back-bonding is present [compare with rhenium(III) species, Section 3.2].

The observed geometrical disposition of the ClCl–N^hN^h–N^aN^a donor sites in $[ReCl_2(NN)_2]$ is uniformly *cis*-*trans*-*cis*, see **32**. Four other isomers are possible but none of these have been observed.[65] Similarly the tris-chelates were isolated exclusively in the facial form (no meridional isomer observed). The *cis* (as opposed to *trans*) disposition of two N^a donor sites as in **32** ensures maximum back-bonding. Further, **32** is sterically more favorable than other possible isomers. In facial **33** the three N^a atoms represent a model situation for back-bonding which more than offsets the steric disadvantage of the facial geometry.

Two comparisons are relevant. First, $[Os(N^aN^h)_3]^{2+}$ which is isoelectronic with $[Re(N^aN^h)_3]^+$ occur in isomeric forms, primarily meridional,[64] reflecting the π-basicity order $Re^{I}>>Os^{II}$. Second, tris chelation of 2,2′-bipyridine stabilizes the rhenium(II)[66] as opposed to rhenium(I) showing that azoheterocycles are superior π-acceptors than bipy.

10. Monochelation of $Re^{I}(CO)_3$ by (NN) and ($NN^{\bullet-}$)

The $[Re^{I}(CO)_3Cl(NN)]$ system, **34**, results from the reaction of $[Re(CO)_5Cl]$ with azoimines.

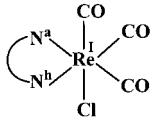

34

The Re–N^a and Re–N^h distances (2.15 ± 0.02 Å) are nearly equal and the azo N–N distance lie close to 1.27 Å (Table 12).[67–70] Thus carbon monoxide does most of the back-bonding and the t_{2g} shell is greatly stabilized as reflected in the high Re^{II}/Re^{I} reduction potential (Table 12). A second one-electron couple (–0.6 to –0.1 V) assignable to azo reduction is also observed and the $[Re^{I}(CO)_3Cl(NN^{\bullet-})]$ species so generated have been spectrally characterized in solution.[71]

The chloride ligand in $[Re^{I}(CO)_3Cl(NN^{\bullet-})]$ is labile furnishing $[Re^{I}(CO)_3(MeCN)(NN^{\bullet-})]$ in acetonitrile solution. These anion radical complexes, as well as $[Re^{I}(CO)_3(PPh_3)(NN^{\bullet-})]$ and $[Re^{I}(CO)_3(imidazole)(NN^{\bullet-})]$ derived from them have been isolated. These are EPR-active in solution with g values lying near 2.003. Six hyperfine lines representing a small metal contribution to the spin-bearing orbital are observed. Thus in $[Re^{I}(CO)_3(D)(Clazim^{\bullet-})]$ coupling constants are 27.25, 28.75 and 39.1 G for D = MeCN, imidazole and PPh_3, respectively.[70]

11. Conclusion

New families of rhenium complexes incorporating chelation of conjugated (NN)-donors have been assembled in a rational manner. Systematic structural and electrochemical studies have revealed interesting trends of bond lengths and reduction potentials. Three types of oxygen atom transfer reactions have been encountered and their pathways scrutinized using rate and structural data. Unusual redox induced oxygen atom transfers from water and from the oximato function have respectively provided access to rare tetra-/hexa-valent imineamide and pentavalent azoimine systems. π-Basicity and back-bonding is a dominant feature of the lower oxidation states ($Re^{III}<Re^{II}<Re^{I}$) as reflected in

 © 2005 Wiley-VCH Verlag GmbH & Co. KGaA, Weinheim

bond parameters. This gets expressed in spontaneous isomerization upon substitution of phosphane oxide by phosphane, in the isomer specificity of bis/tris chelates of di-/mono-valent rhenium and in the stabilization of anion radical species. A concern of ongoing studies is the search for active complexes of new (NN) ligands and unusual atom transfer reactions.

Acknowledgments

No amount of thanking will be sufficient to express my gratitude to the many students who did the work reported and whose names appear in the references cited. Generous funding received from the Department of Science and Technology, New Delhi, and to a certain extent from the Council of Scientific and Industrial Research, New Delhi, is gratefully acknowledged. I am very thankful to S. Sengupta, and S. Das for helping with the preparation of this review.

[1] M. E. Weeks, H. M. Leicester, *Discovery of the Elements*, Paico Publishing House, Cochin, India, **1968**.
[2] G. Rouschias, *Chem. Rev.* **1974**, *74*, 531–566.
[3] K. A. Conner, R. A. Walton, *Comprehensive Coordination Chemistry, Volume 4*, Pergamon Press, Oxford, **1987**.
[4] U. Abram, *Comprehensive Coordination Chemistry II, Volume 5*, (Eds.: J. A. McCleverty, T. J. Mayer), Elsevier, Oxford, **2004**.
[5] G. K. Lahiri, S. Goswami, L. R. Falvello, A. Chakravorty, *Inorg. Chem.* **1987**, *26*, 3365–3370.
[6] J. F. Rowbottom, G. Wilkinson, *J. Chem. Soc., Dalton Trans.* **1972**, 826–830.
[7] J. C. Bryan, R. E. Stenkamp, T. H. Tulip, J. M. Mayer, *Inorg. Chem.* **1987**, *26*, 2283–2288 and references cited therein.
[8] R. R. Conry, J. M. Mayer, *Inorg. Chem.* **1990**, *29*, 4862–4867.
[9] R. H. Holm, *Chem. Rev.* **1987**, *87*, 1401–1449.
[10] G. Lante, J. H. Espenson, *Inorg. Chem.* **2000**, *39*, 4809–4814.
[11] S. B. Symore, S. N. Brown, *Inorg. Chem.* **2000**, *39*, 325–332.
[12] C. Zhang, I. A. Guzei, J. H. Espenson, *Inorg. Chem.* **2001**, *40*, 2437–2438.
[13] Y. Wang, G. Lente, J. H. Espenson, *Inorg. Chem.* **2002**, *41*, 1272–1280.
[14] B. D. Sherry, A. T. Radosevich, F. D. Toste, *J. Am. Chem. Soc.* **2003**, *125*, 6076–6077.
[15] J. J. K. Smith, K. A. Nolin, H. P. Gunterman, F. D. Toste, *J. Am. Chem. Soc.* **2003**, *125*, 4056–4057.
[16] M. M. Abu-Omar, *Chem. Commun.* **2003**, 2102–2111.
[17] C. K. Pal, S. Chattopadhyay, C. Sinha, A. Chakravorty, *Inorg. Chem.* **1994**, *33*, 6140–6147.
[18] M. Shivakumar, K. Pramanik, I. Bhattacharyya, A. Chakravorty, *Inorg. Chem.* **2000**, *39*, 4332–4338 and references cited therein.
[19] B. K. Dirghangi, M. Menon, A. Pramanik, A. Chakravorty, *Inorg. Chem.* **1997**, *36*, 1095–1101.
[20] J. Gangopadhyay, S. Sengupta, S. Bhattacharyya, I. Chakraborty, *Inorg. Chem.* **2002**, *41*, 2616–2622.
[21] S. Das, I. Chakraborty, A. Chakravorty, *Inorg. Chem.* **2003**, *42*, 6545–6555.
[22] S. Banerjee, S. Bhattacharyya, B. K. Dirghangi, M. Menon, A. Chakravorty, *Inorg. Chem.* **2000**, *39*, 6–13.
[23] S. Das, I. Chakraborty, A. Chakraborty, *Polyhedron* **2003**, *22*, 901–907.
[24] I. Chakraborty, S. Bhattacharyya, S. Banerjee, B. K. Dirghangi, A. Chakravorty, *J. Chem. Soc., Dalton Trans.* **1999**, 3747–3753.
[25] M. Menon, A. Pramanik, N. Bag, A. Chakravorty, *Inorg. Chem.* **1994**, *33*, 403–404.
[26] M. Menon, S. Choudhury, A. Pramanik, A. K. Deb, S. K. Chandra, N. Bag, S. Goswami, A. Chakravorty, *J. Chem. Soc., Chem. Commun.* **1994**, 57–58.
[27] S. Bhattacharyya, I. Chakraborty, B. K. Dirghangi, A. Chakravorty, *Inorg. Chem.* **2001**, *40*, 286–293.
[28] S. Sengupta, J. Gangopadhyay, A. Chakravorty, *Dalton Trans.* **2003**, 4635–4643.
[29] B. K. Dirghangi, M. Menon, S. Banerjee, A. Chakravorty, *Inorg. Chem.* **1997**, *36*, 3595–3601.
[30] S. Banerjee, B. K. Dirghangi, M. Menon, A. Pramanik, A. Chakravorty, *J. Chem. Soc., Dalton Trans.* **1997**, 2149–2153.
[31] S. Sengupta, I. Chakraborty, A. Chakravorty, *Eur. J. Inorg. Chem.* **2003**, 1157–1160.
[32] F. A. Cotton, S. A. Duraj, W. J. Roth, *J. Am. Chem. Soc.* **1984**, *106*, 4749–4751.
[33] S. Banerjee, S. Bhattacharyya, I. Chakravorty, B. K. Dirghangi, A. Chakravorty, *Indian J. Chem. Sec A.* **1999**, *38A*, 857–858.
[34] J. M. Mayer, *Inorg. Chem.* **1988**, *27*, 3899–3903.
[35] C. F. Edwards, W. P. Griffith, A. J. P. White, D. J. Williams, *J. Chem. Soc., Dalton Trans.* **1992**, 957–962.
[36] W. A. Nugent, B. L. Haymore, *Coord. Chem. Rev.* **1980**, *31*, 123–175.
[37] G. V. Goeden, B. L. Haymore, *Inorg. Chem.* **1983**, *22*, 157–167.
[38] R. Hille, *Chem. Rev.* **1996**, *96*, 2757–2816.
[39] R. H. Holm, P. Kennepohl, E. I. Solomon, *Chem. Rev.* **1996**, *96*, 2239–2314.
[40] J. H. Enemark, C. G. Young, *Adv. Inorg. Chem.* **1993**, *43*, 1.
[41] M. A. Pietsch, M. B. Hall, *Inorg. Chem.* **1996**, *35*, 1273–1278.
[42] G. C. Tucci, J. P. Donahue, R. H. Holm, *Inorg. Chem.* **1998**, *37*, 1602–1608 and references cited therein.
[43] S. Bhattacharyya, I. Chakraborty, B. K. Dirghangi, A. Chakravorty, *Chem. Commun.* **2000**, 1813–1814.
[44] V. Katovic, S. C. Vergez, D. H. Busch, *Inorg. Chem.* **1977**, *16*, 1716–1720.
[45] G. Bandoli, T. I. A. Gerber, R. Jacobs, J. G. H. du Preez, *Inorg. Chem.* **1994**, *33*, 178–179.
[46] H. Taube, Electron-Transfer Reactions of Complex Ions, in: Solution, Academic Press, New York, **1973**, p73.
[47] M. Menon, A. Pramanik, A. Chakravorty, *Inorg. Chem.* **1995**, *34*, 3310–3316.
[48] H. L. Chum, P. Krumholz, *Inorg. Chem.* **1974**, *13*, 519–524.
[49] H. L. Chum, M. E. M. Helene, *Inorg. Chem.* **1980**, *19*, 876–880 and references cited therein.
[50] B. K. Dirghangi, S. Banerjee, M. Menon, A. Chakravorty, *Indian J. Chem.* **1997**, *36A*, 249–251.
[51] A. A. Danopoulos, G. Wilkinson, T. K. N. Sweet, M. B. Hursthouse, *J. Chem. Soc., Dalton Trans.* **1996**, 2995–3000.
[52] I. Chakraborty, B. K. Panda, J. Gangopadhyay, A. Chakravorty, *Inorg. Chem.* **2005**, *44*, 1054–1060.
[53] C. K. Pal, S. Chattopadhyay, C. Sinha, A. Chakravorty, *Inorg. Chem.* **1996**, *35*, 2442–2447.
[54] A. Tillack, P. Arndt, A. Spannenberg, R. Kempe, V. Rosenthal, *Z. Anorg. Allg. Chem.* **1998**, *624*, 737–740.
[55] A. J. Deeming, D. W. Owen, N. I. Powell, *J. Organomet. Chem.* **1990**, *398*, 299–310.
[56] V. Yu. Kukushkin, A. J. L. Pombeiro, *Coord. Chem. Rev.* **1999**, *181*, 147–175.
[57] X. Chen, F. J. Femia, J. W. Babaich, J. Zubieta, *Inorg. Chim. Acta* **2000**, *306*, 112–115.
[58] A. K. Das, S.-M. Peng, S. Bhattacharyya, *J. Chem. Soc., Dalton Trans.* **2000**, 181–184.
[59] S. Jurrisson, M. M. Halihan, J. D. Lydon, C. L. Barnes, D. P. Nowotnik, A. D. Nunn, *Inorg. Chem.* **1998**, *37*, 1922–1928.
[60] V. Manivannan, B. K. Dirghangi, C. K. Pal, A. Chakravorty, *Inorg. Chem.* **1997**, *36*, 1526–1528.
[61] S. Bhattacharyya, S. Banerjee, B. K. Dirghangi, M. Menon, A. Chakravorty, *J. Chem. Soc., Dalton Trans.* **1999**, 155–159.
[62] P. J. Flory, *Principles of polymer chemistry*, Cornell University Press, Ithaca and London, 4th edn., **1990**, p. 399.

 © 2005 Wiley-VCH Verlag GmbH & Co. KGaA, Weinheim

[63] K. Pramanik, M. Shivakumar, P. Ghosh, A. Chakravorty, *Inorg. Chem.* **2000**, *39*, 195–199.
[64] B. K. Ghosh, A. Mukhopadhyay, S. Goswami, S. Ray, A. Chakravorty, *Inorg. Chem.* **1984**, *23*, 4633–4639.
[65] I. Chakraborty, S. Sengupta, S. Das, S. Banerjee, A. Chakravorty, *Dalton Trans.* **2003**, 134–140, and references cited therein.
[66] M. Stebler, A. Gutierrez, A. Ludi, H. B. Buergi, *Inorg. Chem.* **1987**, *26*, 1449–1451.
[67] R. Samanta, P. Munshi, B. K. Santra, N. K. Lokanath, M. A. Sridhar, J. S. Prasad, G. K. Lahiri, *J. Organomet. Chem.* **1999**, *579*, 311–320.
[68] S. Sengupta, B. K. Panda, *Transition Met. Chem. (Dordrecht, Netherlands)* **2005**, *30*, 426–432.
[69] H. Hartmann, T. Scheiring, J. Fiedler, W. Kaim, *J. Organomet. Chem.* **2000**, *604*, 267–272.
[70] B. K. Panda, S. Sengupta, A. Chakravorty, *J. Organomet. Chem.* **2004**, *689*, 1780–1787.
[71] S. Frantz, H. Hartmann, N. Doslik, M. Wanner, W. Kaim, H. J. Kümmer, G. Denninger, A. L. Barra, C. D. Toia, J. Fiedler, I. Ciofini, C. Urban, M. Kaupp, *J. Am. Chem. Soc.* **2002**, *124*, 10563–10571.

Received: July 12, 2005
Published Online: November 3, 2005

 © 2005 Wiley-VCH Verlag GmbH & Co. KGaA, Weinheim

DOI: 10.1002/ejic.200500652

A New Coordination Polymer Architecture with (10,3)-a Network Containing Chiral Hydrophilic 3-D Channels

Aksana Zharkouskaya,[a] Axel Buchholz,[a] and Winfried Plass*[a]

Keywords: Coordination polymer / Copper / Magnetic properties / N,O ligands

The triaminoguanidine-based Schiff-base ligand H_5L^{OH} reacts with copper(II) ions to afford a three-dimensional coordination polymer with (10,3)-a topology which is solely assembled by a single trigonal molecular building block $\{Cu_3L^{OH}\}^+$. The unusual bridging mode of the phenolate oxygen atoms between the trigonal building blocks leads to a dihedral angle between the interlinked $\{Cu_3L^{OH}\}^+$ units of 71°. The (10,3)-a topology of the singular network results in a rather large void space of about 56 % that is established by interpenetrated chiral channels with a diameter limited by pseudo-tetrahedral cavities defined by non-coordinating phenolate hydroxy groups of the ligand. Additional information to establish the composition is derived from elemental analysis and TGA measurements. For the coordination polymer an overall antiferromagnetic behavior is observed. The spin-frustrated trinuclear building blocks $\{Cu_3L^{OH}\}^+$ are antiferromagnetically coupled via the bis(phenoxide)-bridged dinuclear copper(II) moieties for which a dihedral angle of 132° is observed.

(© Wiley-VCH Verlag GmbH & Co. KGaA, 69451 Weinheim, Germany, 2005)

Over the last decade the design of porous coordination polymers has become one of the most rapidly developing areas because of their potential applications as rationally designed functional solids with interesting optical, electrical and magnetic properties.[1,2] Of great interest is the architecture and the topological variety of frameworks.[3] Particularly challenging is the design of crystalline material combining different properties like porosity and chirality.[4] Because of specific pore size, type and function of cavities such materials can be applied in ion exchange, catalysis, enantioselective sorption, and gas separation.[1,5] Coordination polymers with (10,3)-a topology are particularly interesting, since they are known to form homochiral porous frameworks which at the same time can show considerable structural stability towards the exchange of guest molecules. These properties make such materials important subjects of research for the development of enantioselective sorption and chiral catalysis.[6]

The interaction of transition metal ions with multifunctional ligands by self-assembly processes is a basic strategy to afford a broad variety of coordination polymers.[1] In particular, the assembly of (10,3)-a nets is generally based on trigonal molecular building blocks that are linked by additional connecting units; both can be either appropriate ligands or metal fragments.[3] Triaminoguanidine-based ligand systems have recently been employed by Robson and Müller et al. in the synthesis of a variety of interesting discrete cage molecules with different topologies.[7]

Here, we report a novel three-dimensional coordination polymer with (10,3)-a topology assembled from a single trigonal molecular building block leading to a homochiral three-dimensional channel system. The utilized trigonal building block is derived from tris[(2,5-dihydroxybenzylidene)amino]guanidine (H_5L^{OH}) chelating copper(II) ions as depicted in Scheme 1. Dark brown cube-shaped single crystals of $[Cu_6(L^{OH})_2(HCOO)_2(H_2O)_{0.5}(DMF)_{0.5}]\cdot xH_2O\cdot y$DMF (**1**) were obtained by slow diffusion of a solution of Bu_4NOH in methanol into a DMF solution containing $(H_6L^{OH})Cl$ and $Cu(BF_4)_2\cdot 6H_2O$ in a 1:3 molar ratio at room temperature.

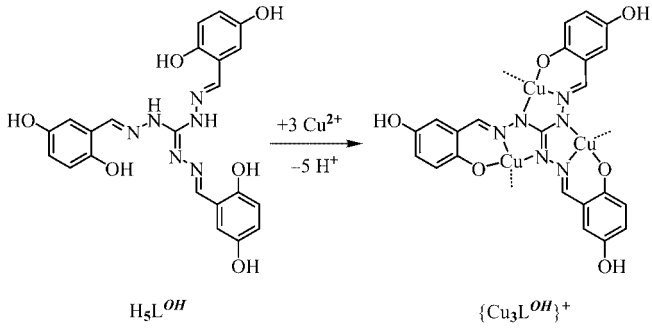

Scheme 1.

Single-crystal X-ray diffraction reveals a three-dimensional porous framework that is composed of trigonal $\{Cu_3L^{OH}\}^+$ units which are interlocked by the formation of bis(phenoxide)-bridged dinuclear copper(II) moieties as

[a] Institut für Anorganische und Analytische Chemie, Friedrich-Schiller-Universität Jena,
Carl-Zeiss-Promenade 10, 07745 Jena, Germany
Fax: +49-3641-948132
E-mail: Sekr.Plass@uni-jena.de

 © 2005 Wiley-VCH Verlag GmbH & Co. KgaA, Weinheim

depicted in Figure 1. In contrast to the generally observed planar coordination motif for the bis(phenoxide)-bridged dinuclear copper(II) moieties a dihedral angle of 132° is observed for compound **1**. The typically observed symmetric planar bridging mode is prevented by the steric requirements of the given ligand. As a consequence, an asymmetric bridging moiety is obtained, with the bridging oxygen atoms O11 and O21 in an equatorial position at Cu1, whereas for Cu2 they occupy axial and equatorial positions, respectively. As a result, the copper ions of the two crystallographically distinct $\{Cu_3L^{OH}\}^+$ units exhibit different coordination environments, which are tetracoordinate square-planar for Cu1 and pentacoordinate square-pyramidal for Cu2. In the latter case the bridging oxygen atom O11 is in the apical position at a distance of 232.5 pm and the fourth equatorial position, not occupied by the ligand L^{OH}, is filled by an oxygen atom from the formate counterion or a solvent molecule (see Exp. Sect.). This leads to distinct conformational variations of the two crystallographically independent $\{Cu_3L^{OH}\}^+$ units as depicted in Figure 2. Within the two trinuclear units the distance between the copper ions is about 475 pm, whereas a distance of 290 pm is found along the bridging dinuclear moiety. The resulting dihedral angle between the interlinked $\{Cu_3L^{OH}\}^+$ units is about 71°.

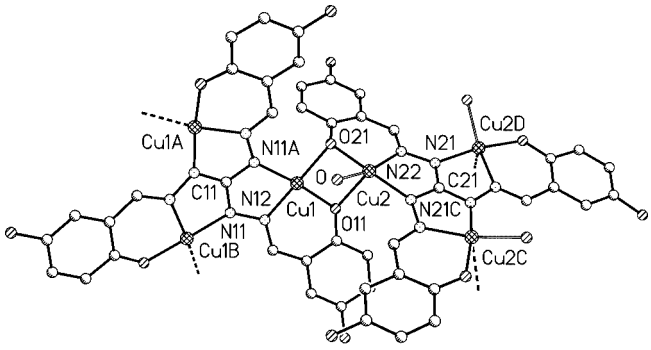

Figure 1. Molecular structure of the $\{Cu_6(L^{OH})_2\}$ building unit of the 3-D coordination polymer **1**. Hydrogen atoms are omitted for clarity; formate anion and solvent molecules are represented by the coordinating oxygen atom; symmetry-equivalent atoms are denoted by A–D. Selected bond lengths [pm] and angles [°]: Cu1–O11 188.9(6), Cu1–O21 200.6(5), Cu1–N12 192.9(6), Cu1–N11A 194.8(6), N11–N12 138.4(9), Cu2–O11 232.5(6), Cu2–O21 195.1(5), Cu2–N22 194.8(6), Cu2–N21C 1.952(6), N21–N22 139.3(9); O11–Cu1–O21 82.9(2), N12–Cu1–N11A 80.5(3), O21–Cu2–O11 73.6(2), N22–Cu2–N21C 80.7(3), Cu1–O11–Cu2 86.4(2), Cu2–O21–Cu1 94.3(2).

The three-dimensional coordination polymer **1** possesses a (10,3)-a network as shown using a simplified view in Figure 3. The fact that two different $\{Cu_3L^{OH}\}^+$ trigonal building blocks assemble the framework leads to a considerable distortion of the archetype (10,3)-a network. The distortion arises from the intercentroid vectors no longer being coplanar, with the angles between the vectors centered at the trigonal building blocks $\{Cu1_3L^{OH}\}^+$ and $\{Cu2_3L^{OH}\}^+$ changing from 120° in an ideal (10,3)-a net to 114.9 and 118.7°, respectively. The chirality of the present (10,3)-a network arises form the [100] pseudo-fourfold and [111] pseudo-

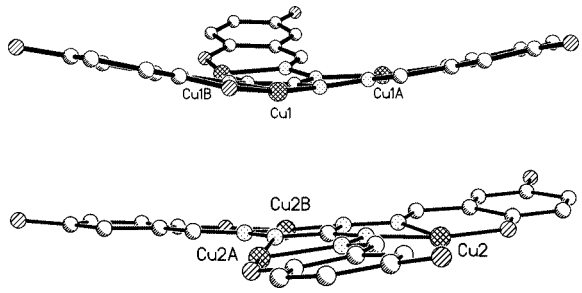

Figure 2. Molecular conformations of the trinuclear building units of **1**: Bowl-shaped $\{Cu1_3L^{OH}\}^+$ (top) and propeller-shaped $\{Cu2_3L^{OH}\}^+$ (bottom).

threefold coordination helices running along the crystallographic 2_1 and 3_2 axes which are of the same handedness propagating in all crystallographic equivalent directions. The packing diagram of compound **1** depicted in Figure 4 shows pseudotetragonal channels along the [100] direction. The size-limiting feature of these channels are the pseudotetrahedral cavities centered at 0,0,1/4 which are defined by the noncoordinating phenol hydroxy groups of the ligand with a diameter of 800 pm for an inscribed sphere. Along the [111] direction this leads to pseudohexagonal zigzag channels passing through these cavities (see Figure 4). The noncoordinating hydroxy groups lead to a hydrophilic character of the solvent-accessible free volume of compound **1**. As a consequence, the resulting void space of **1** is occupied by disordered DMF and H_2O guest molecules.[8] The effective free volume of **1** was calculated with PLATON[9] as 56.4% of the crystal volume (6327 nm^3 out of the 11220 nm^3 unit cell volume). A representation of the void space of **1**, based on the pseudotetragonal channels, is given in Figure 5.

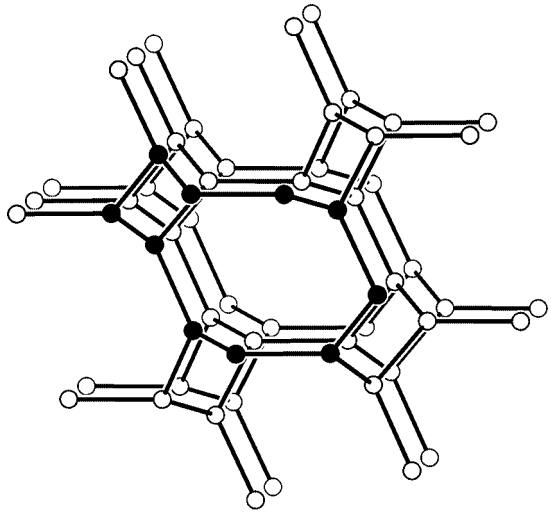

Figure 3. Topology of the 3-D porous framework of **1** shown along [010] with one of the 10-membered rings of the (10,3)-a network highlighted; the nodes represent the central carbon atoms C11 and C21 of the building units.

The thermal behavior of **1** was studied in the range 298–573 K under a flow of nitrogen. The TGA analysis indicates, that the guest molecules can be removed over the tem-

 © 2005 Wiley-VCH Verlag GmbH & Co. KGaA, Weinheim

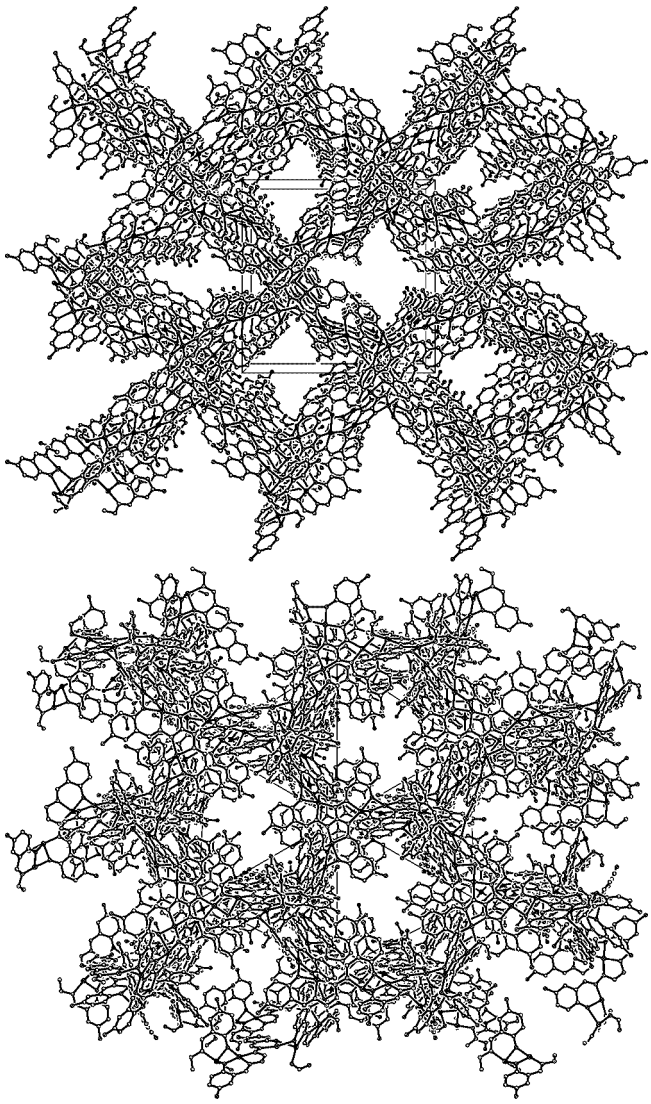

Figure 4. Representation of the network structure of **1** showing the channels along [100] (top) and [111] (bottom).

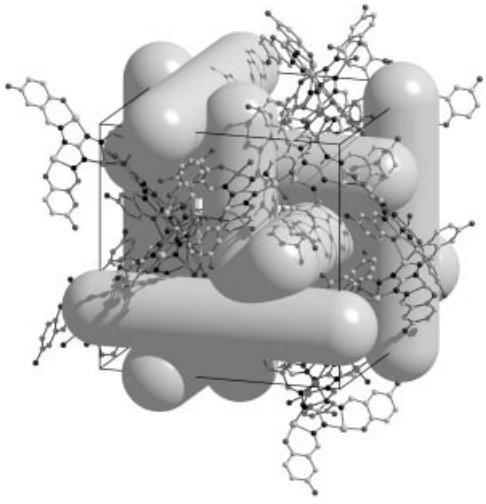

Figure 5. Unit cell of **1** with the pseudo-tetragonal channels represented by cylinders with a diameter of 0.8 nm; all building units originating within the cell are generated.

perature range 313–453 K with an observed weight loss of about 25%. Together with the data from the elemental analyses for samples after prolonged storage under ambient conditions (temperature and atmosphere) this gives a number of three DMF and six H_2O guest molecules per formula unit of **1** filled in the void space.[10] X-ray powder diffraction studies of samples heated to 453 K indicate that the long-range order of the framework structure of **1** is retained upon removal of the guest molecules. If samples of **1** are evacuated at room temperature, a weight loss of about 9% is observed within the first 5.5 h. After 36 h in vacuo, the final weight was constant with an observed loss of about 12%.

The magnetic susceptibility of **1** was measured with a SQUID susceptometer for polycrystalline samples in the temperature range of 2–300 K at a field of 1000 Oe. The temperature dependence of the susceptibility χ and the product χT is shown in Figure 6. For practical reasons the mass susceptibility χ_g was used here, as the actual solvent content can vary considerably.[10] Within the measured range the high-temperature limit expected for a spin-only value of independent copper(II) centers is not reached. In fact, the room-temperature value of χT, based on a molecular mass as derived form TGA and elemental analysis, corresponds to less than 80% of the expected spin-only value. Together with the observed decrease of χT upon cooling, this is indicative for rather strong antiferromagnetic interactions within the system. Nevertheless, within the low-temperature limit of the measurement at 2 K the χT product does not vanish completely with a value that corresponds approximately to the spin-only value of one copper(II) center. The X-band ESR spectrum of **1** recorded on a powdered sample at 77 K exhibits one unstructured broad band at g = 2.072 with a peak-to-peak separation of 29 mT.

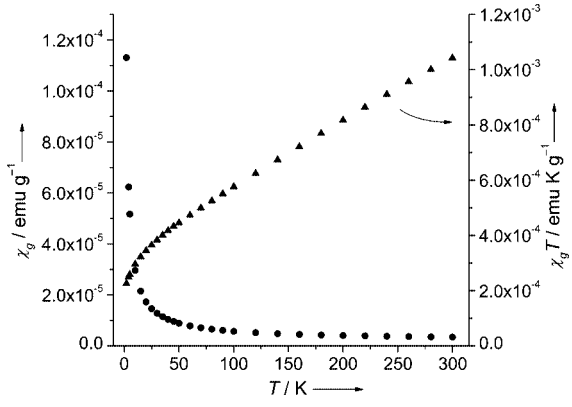

Figure 6. Temperature dependence of χ_g (•) and $\chi_g T$ (▲) for **1**.

Given the structural topology, two basic exchange pathways between the copper(II) centers are possible. One across the trinuclear $\{Cu_3L^{OH}\}^+$ units and the other within the bis(phenoxide)-bridged dinuclear copper(II) moieties. Consequently, two simplified exchange models could be anticipated if either of the two coupling constants prevails the

 © 2005 Wiley-VCH Verlag GmbH & Co. KGaA, Weinheim

overall system. Attempts to fit the experimental data with either isotropic spin Hamiltonian model did not yield satisfactory results, suggesting that both exchange pathways are important. For the interaction of the two bis(phenoxide)-bridged dinuclear copper(II) centers Thompson's linear relationship between the Cu–O(Ph)–Cu angle and the coupling constant J (J = 2462 – 31.95a)[11] gives an estimate of about –400 cm^{-1}, based on an average angle of 90°. Nevertheless, this value probably overestimates the actual exchange coupling constant, since for compound **1** with a dihedral angle of 71° a considerable distortion from the coplanarity of the two square planes is observed (cf. Figure 1). On the other hand for isolated trinuclear $\{Cu_3L^{OH}\}^+$ units as part of complexes with appropriate capping ligands at the copper(II) centers a spin-frustrated system with antiferromagnetic coupling parameters in the order of –320 cm^{-1} is observed.[12] The fact that no plateau in the χT diagram corresponding to the spin-frustrated triangular units is evident, indicates the equal importance of the exchange coupling along the dinuclear copper(II) interlocking moieties.

In summary, a novel magnetic 3-D coordination polymer with distorted (10,3)-a network has been synthesized. The size limit and character of the void space of the polymer is defined by the *para* substituent on the coordinating phenolate moiety of the ligand. Both the variation of the ligand substitution and the metal ion are expected to yield materials with interesting new properties.

Experimental Section

General: $Cu(BF_4)_2{\cdot}6H_2O$ and Bu_4NOH were purchased from commercial sources and used as received. (H_6L^{OH})Cl was prepared analogous to procedures reported in the literature.[13] Yield: 79%. (H_6L^{OH})Cl·3H$_2$O ($C_{22}H_{27}ClN_6O_9$, 554.9): calcd. C 47.62, H 4.90, N 15.14; found C 48.01, H 4.79, N 15.38. ^{1}H NMR (200 MHz, CD_3OD, 298 K): δ = 8.80 (s, 3 H, N=CH), 7.39 (d, J = 2.72 Hz, 3 H, C6-H), 6.73–6.85 (m, 6 H, aromatic CH) ppm. ^{13}C NMR (50 MHz, CD_3OD, 298 K): δ = 114.0, 118.0, 120.9, 121.4, 150.2, 150.5, 151.4, 152.2 ppm.

[$Cu_6(L^{OH})_2(HCOO)_2(H_2O)_{0.5}(DMF)_{0.5}$]·$xH_2$O·$y$DMF (1): A solution of ($H_6L^{OH}$)Cl·3H$_2$O (278 mg, 0.5 mmol) in DMF (5 mL) was added to a solution of $Cu(BF_4)_2{\cdot}6H_2O$ (518 mg, 1.5 mmol) in DMF (5 mL). The resulting dark green-brown solution was carefully layered in a glass tube with DMF (3 mL) and with a 1 M methanolic solution of Bu_4NOH (2.5 mL). The glass tube was sealed and left at room temperature. Slow diffusion afforded dark brown crystals of **1** within 3 weeks. The crystals were isolated, washed with MeOH and dried in air. Yield: 30 mg. **1** with x = 6 and y = 3 (prolonged storage at room temperature, $C_{56.5}H_{69.5}Cu_6N_{15.5}O_{26}$, 1763.0): calcd. C 38.49, H 3.97, N 12.31; found C 38.56, H 3.77, N 12.66. Elemental analyses for freshly prepared samples shown higher C and H values due to a higher content of disordered solvent molecules.

Crystal Data for 1: $C_{47.5}H_{36.5}Cu_6N_{12.5}O_{17}$·guests, M = 1435.7, 0.03 × 0.03 × 0.02 mm, cubic, space group $P2_13$, a = 2238.69(5) pm, V = 11.2197(4) nm^3, Z = 4, $\rho_{calcd.}$ = 0.917 g cm^{-3}, T = 183 K, λ = 71.073 pm, μ(Mo-K_α) = 1.164 mm^{-1}, Θ range 3.28–27.46°, 7530 measured and 5231 independent reflections (R_{int} = 0.0415), 285 parameters with no restraints, R_1 = 0.0746, wR_2 = 0.1799 for 5231 reflections with $I > 2\sigma(I)$, GOF = 1.089, Flack parameter = –0.02(4). The data were collected with a Nonius KappaCCD diffractometer. The structure was solved by direct methods (SHELXS) and subsequent full-matrix least-squares refinement against F^2 (SHELXL). The fourth equatorial position at Cu2 (not occupied by the ligand L^{OH}) is occupied by an oxygen atom from either a formate counterion or a solvent molecule of DMF or H_2O, leading to a partial occupation of the corresponding positions in the ratio of 2:3, 1:6 and 1:6, respectively. CCDC-268709 (**1**) contains the supplementary crystallographic data for this paper. These data can be obtained free of charge from The Cambridge Crystallographic Data Centre via www.ccdc.cam.ac.uk/data_request/cif.

Acknowledgments

This work was supported by the Deutsche Forschungsgemeinschaft and the Fonds der Chemischen Industrie.

[1] S. Kitagawa, R. Kitaura, S. Noro, *Angew. Chem.* **2004**, *116*, 2388–2430; *Angew. Chem. Int. Ed.* **2004**, *43*, 2334–2475.

[2] a) D. Maspoch, D. Ruiz-Molina, J. Veciana, in: *Magnetism: Molecules to Materials, V* (Eds.: J. S. Miller, M. Drillon), Wiley-VCH, Weinheim, **2005**, pp. 261–282; b) B. Kesanli, W. Lin, *Coord. Chem. Rev.* **2003**, *246*, 305–326; c) O. R. Evans, W. Lin, *Acc. Chem. Res.* **2002**, *35*, 511–522; d) G. Ferey, *Science* **2001**, *291*, 994–995; e) M. Eddaoudi, D. B. Moler, H. Li, B. Chen, T. M. Reineke, M. O'Keeffe, O. M. Yaghi, *Acc. Chem. Res.* **2001**, *34*, 319–330; f) B. Moulton, M. J. Zawarotko, *Chem. Rev.* **2001**, *101*, 1629–1658; g) S. R. Batten, R. Robson, *Angew. Chem.* **1998**, *110*, 1558–1595; *Angew. Chem. Int. Ed.* **1998**, *37*, 1460–1494.

[3] a) L. Öhrström, K. Larsson, *Dalton Trans.* **2004**, 347–353; b) A. F. Wells, *Three-Dimensional Nets and Polyhedra*, Wiley, New York **1977**.

[4] M. E. Davis, *Nature* **2002**, *417*, 813–821.

[5] a) B. Kesanli, Y. Cui, M. R. Smith, E. W. Bittner, B. C. Bockrath, W. Lin, *Angew. Chem.* **2005**, *117*, 74–77; *Angew. Chem. Int. Ed.* **2005**, *44*, 72–75; b) Y. Kubota, M. Takata, R. Matsuda, R. Kitaura, S. Kitagawa, K. Kato, M. Sakata, T. C. Kobayashi, *Angew. Chem.* **2005**, *117*, 942–945; *Angew. Chem. Int. Ed.* **2005**, *44*, 920–923; c) P. M. Forster, A. K. Cheetham, *Top. Catal.* **2003**, *24*, 79–86; d) A. Vishnyakov, P. I. Ravikovitch, A. V. Neimark, M. Bülow, Q. M. Wang, *Nano Lett.* **2003**, *3*, 713–718; e) L. Pan, M. B. Sander, X. Huang, J. Li, M. Smith, E. Bittner, B. Bockrath, J. K. Johnson, *J. Am. Chem. Soc.* **2004**, *126*, 1308–1309.

[6] a) D. Bradshaw, T. J. Prior, E. J. Cussen, J. B. Claridge, M. J. Rosseinsky, *J. Am. Chem. Soc.* **2004**, *126*, 6106–6114; b) E. Tynan, P. Jensen, N. R. Kelly, P. E. Kruger, A. C. Lees, B. Moubaraki, K. S. Murray, *Dalton Trans.* **2004**, 3440–3447; c) C. J. Kepert, T. J. Prior, M. J. Rosseinsky, *J. Am. Chem. Soc.* **2000**, *122*, 5158–5168; d) B. F. Abrahams, P. A. Jackson, R. Robson, *Angew. Chem.* **1998**, *110*, 2801–2804; *Angew. Chem. Int. Ed.* **1998**, *37*, 2656–2659; e) O. M. Yaghi, C. E. Davis, G. Li, H. Li, *J. Am. Chem. Soc.* **1997**, *119*, 2861–2868; f) O. M. Yaghi, H. Li, *J. Am. Chem. Soc.* **1995**, *117*, 10401–10402.

[7] a) I. M. Müller, D. Möller, *Angew. Chem.* **2005**, *117*, 3029–3033; *Angew. Chem. Int. Ed.* **2005**, *44*, 2969–2973; b) I. M. Müller, D. Möller, C. A. Schalley, *Angew. Chem.* **2005**, *117*, 485–488; *Angew. Chem. Int. Ed.* **2005**, *44*, 480–484; c) I. M. Müller, S. Spillmann, H. Franck, R. Pietschnig, *Chem. Eur. J.* **2004**, *10*, 2207–2213; d) I. M. Müller, R. Robson, F. Separovic, *Angew. Chem.* **2001**, *113*, 4519–4520; *Angew. Chem. Int. Ed.* **2001**, *40*, 4385–4386; e) I. M. Müller, R. Robson, *Angew. Chem.* **2000**, *112*, 4527–4530; *Angew. Chem. Int. Ed.* **2000**, *39*, 4357–4359.

[8] Although the exact location of the included solvent molecules cannot be unambiguously determined from the single-crystal X-ray diffraction studies due to their high disorder, the formu-

 © 2005 Wiley-VCH Verlag GmbH & Co. KGaA, Weinheim

lation of **1** has been established based on TGA and elemental analyses.
[9] A. L. Spek, *Acta Crystallogr., Sect. A* **1990**, *46*, C34.
[10] Repeated elemental analyses for different samples indicate a considerable variation in the actual solvent content with an estimated range of ±1 for *x* and *y*. Analyses performed on freshly prepared samples gave considerably higher values for carbon and hydrogen, which decrease upon storage or drying in vacuo.
[11] L. K. Thompson, S. K. Mandal, S. S. Tandon, J. N. Bridson, M. K. Park, *Inorg. Chem.* **1996**, *35*, 3117–3125.
[12] A. Zharkouskaya, W. Plass, unpublished results.
[13] a) I. M. Müller, D. Möller, *Eur. J. Inorg. Chem.* **2005**, 257–263; b) E. Winkelmann, W. Raether (Farbwerke Hoechst AG, Deutschland), DE-B 2104346, **1972**; *Chem. Abstr.* **1972**, *77*, 126264.

Received: July 22, 2005
Published Online: November 7, 2005

 © 2005 Wiley-VCH Verlag GmbH & Co. KGaA, Weinheim

DOI: 10.1002/ejic.200500670

Infinite Chains of Quasi-Planar Hexameric Water Clusters Stabilized in a Metal-Organic Framework Built from Co^{II} and Pyrazine-2,3,5,6-tetracarboxylic Acid

Sujit K. Ghosh[a] and Parimal K. Bharadwaj*[a]

Keywords: Water cluster / Supramolecular chemistry / Self assembly / Organic-inorganic hybrid composite

Pyrazine-2,3,5,6-tetracarboxylic acid ($ptcH_4$) reacts with $Co(NO_3)_2 \cdot 6H_2O$ in 1:2 molar ratio in aqueous pyridine (py) at room temperature to form a coordination polymer with the empirical formula, $\{[Co_2(ptc)\cdot(py)_2\cdot 4H_2O]\cdot 4H_2O\}_n$, (**1**). The structure consists of 2D sheets of metal-organic frameworks and infinite chains of cyclic water hexamers that join these sheets to form an overall 3D structure. Thermogravimetry, X-ray powder diffraction and X-ray structural analysis have been used in addition to infrared spectroscopy and elemental analysis to characterize **1**. Crystal data for **1**: monoclinic space group $P2_1$, a = 7.153(4), b = 17.003(2), c = 11.060(5) Å, β = 107.207(5)°, V = 1284.9(11) Å^3, Z = 2, $R1$ = 0.0340, $wR2$ = 0.0875, S = 1.028. This structure demonstrates a new mode of association of water molecules.
(© Wiley-VCH Verlag GmbH & Co. KGaA, 69451 Weinheim, Germany, 2005)

Introduction

Identification of small water clusters[1a–1g] in diverse environments continue to be a subject of considerable interest as it provides the key to test and calibrate theoretical studies to understand this liquid. In spite of characterization of a number of clusters of different nuclearity coupled with advances in computational capabilities, some of the properties of liquid water still cannot be accurately described over a significant range of conditions.[2] The advantage of water clusters/networks having different structures is the possibility to correctly describe the many-body interactions among a group of molecules. It also affords to simply vary the size and to investigate the development of properties of the condensed phase in a step-by-step manner.

Supramolecular association of water molecules in the form of chains constitute an important form of water that is poorly understood.[3] However, water chains are generally accepted to play important roles in several biological processes. In membrane-spanning protein gramicidine *A*, the conduction of protons is believed[4] to take place through a chain of hydrogen-bonded water molecules embedded in the protein. Water chains appear to be important[4] in the control of proton fluxes in a variety of biomolecules such as cytochrome b6f, mitochondral ATPase, carbonic anhydrase II, cytochrome c oxidase, bacteriorhodopsin, etc. The highly dynamic water molecules present in membrane channel protein aquaporin I adopt a chain structure for efficient and selective permeation of water across membranes.[5] Although identification of water chains in crystal hydrates is growing, the structural constraints of the host lattice required to stabilize chain structure or the influence of the chain on the host structure remain incomplete.

Water chains can be built either from zig-zag connections of water molecules or through connections of one or more types of cyclic rings. Of particular interest here is the water chains made from hexameric rings. The hexamer has been subjected to a number of experimental[6] and theoretical[7] studies as it is the building block of ice and also exhibits some of the properties of bulk water.[8] Clusters up to pentamers generally have cyclic and quasi-planar structures and the larger clusters have 3D structures. The hexamer behaves as the transitional point from 2D to 3D structures.[9] Theoretical calculations[7] on the $(H_2O)_6$ cluster show five minima in the potential energy surface that correspond to five almost iso-energetic conformers – "cage", "prism", "book", "boat" and "cyclic". The "cage" conformer is the most stable at low temperature and has been observed[10] by vibration-rotation tunneling spectroscopy while a quasi-planar cyclic hexamer was detected[11] in a helium droplet. The lattice of a crystal host offers an environment where a higher energy conformer can be stabilized and this way, chair,[6b,6c,6f] boat[6a,6d] and planar[6e] forms have been characterized in inorganic as well as in organic crystal hosts.

We report here, the X-ray structure of infinite chains of hexameric quasi-planar water molecules present in a metal-organic framework (MOF) built from Co^{II}, pyridine and pyrazine-2,3,5,6-tetracarboxylic acid.[12] Our recent efforts[1d,e,6a,c,13] are directed towards the synthesis of MOFs with voids of different shapes and sizes that can include

[a] Department of Chemistry, Indian Institute of Technology Kanpur 208016, India
E-mail: pkb@iitk.ac.in
Supporting information for this article is available on the WWW under http://www.eurjic.org or from the author.

 © 2005 Wiley-VCH Verlag GmbH & Co. KGaA, Weinheim

water clusters of different nuclearity. The degree of structuring of water clusters that can be imposed by its environment and vice versa are important in the design of new MOF structures with the ultimate aim(s) of having materials with potentially useful applications.

Results and Discussion

Compound **1** crystallizes in a non-centrosymmetric space group presumably due to unsymmetrical distribution of lattice water molecules. The structure consists of two types of hexacoordinate Co^{II} ions that are bonded to the ligands as shown in Scheme 1. For the ligand, ptc^{4-}, only the carboxylate group at the 2-position is not bonded to a metal. Here, Co2 is equatorially bonded to two pyrazine tetracarboxylate ligands through ring N and one carboxylate O atoms (N_2O_2 donor) and the axial positions on the metal are occupied by a pyridine and a water molecules. Thus, Co2 and ptc^{4-} ligands form a linear coordination polymer extending along the crystallographic *a* axis. The Co1 ion is axially bonded to two carboxylate O atoms belonging to two different polymeric chains thus connecting them to form a 2D coordination polymer in the crystallographic *ac* plane (Figure 1). The equatorial sites of Co1 are occupied by three H_2O and one pyridine molecules. The bond lengths and bond angles involving each Co^{II} center are comparable[13b] with reported values for octahedral Co^{II} complexes. Atoms Ow1 bound to Co1 and Ow4 bound to Co2 are hydrogen-bonded to four other water molecules forming a cyclic hexameric water cluster. The atoms Ow7 and Ow8 are not connected to the cluster. These clusters further assemble the 2D networks along the crystallographic *b* axis into an overall 3D MOF (Figure 2 and Figure 3).

Atom Ow3 of the hexamer is H-bonded to Ow5′′ belonging to another hexamer forming a chain of cyclic hexamers parallel to the *ab* plane and extending along the crystallographic *a* axis (Figure 4). Due to a long distance (3.955 Å) between Ow2′ and Ow6, they are not considered as H-bonded even though one of the H atoms of Ow2 is pointed toward Ow6′. However, the less number of H-bonding interactions among the water molecules are compensated by H-bonding interactions these molecules have with the surroundings (Table 1). Chains of hexameric water clusters with different modes of connectivity present in different crystal hosts are collected[17] in two recent articles. Interconnected hexameric boat conformers are present[18] in hexagonal ice (I_h) and also identified[6g] between the layers of an inorganic polymer constructed from $CdNi(CN)_4$ units. Water molecules forming a hexameric chair conformation and self-assembly of these units into a 1D tape had been found[6f] in an organic host constructed from 5-amino-2,4-dimethylbenzo[*b*]-1,8-naphthyridine. Very recently, 1D chains consisting of cyclic hexameric chair conformers connected by Zn^{II} or Co^{II} have been found[6b] in the complexes, $[M(H_2biim)_2(OH_2)_2](ina)_2{\cdot}4H_2O$ [M = Zn^{II} or Co^{II}, H_2biim = 2,2′-biimidazole, *ina* = isoniconate]. Following the nomenclature suggested by Infantes and Motherwell,[17] the water chain in **1** may be designated as T6(0)A0. Although a structure with the same designation is reported[17] by these authors, the chain is propagated through Ow1 and Ow4 atoms whereas in this case, it is through Ow3′ and Ow5 atoms (Figure 4).

While theoretical calculations[7a] predicts the "cage", "prism", "book", "boat" and "cyclic" conformations that are almost isoenergetic, the lattice of a crystal host may offer an environment for stabilizing a higher energy conformer. In the present structure, the six O atoms of the

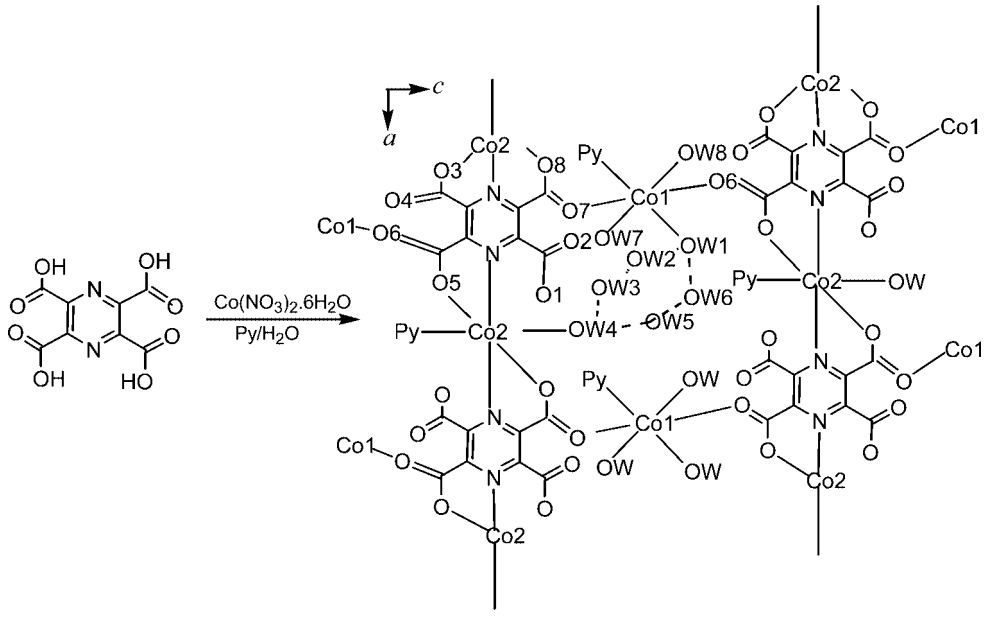

Scheme 1. Schematic diagram showing the bonding modes of the ligand with Co^{II}.

 © 2005 Wiley-VCH Verlag GmbH & Co. KGaA, Weinheim

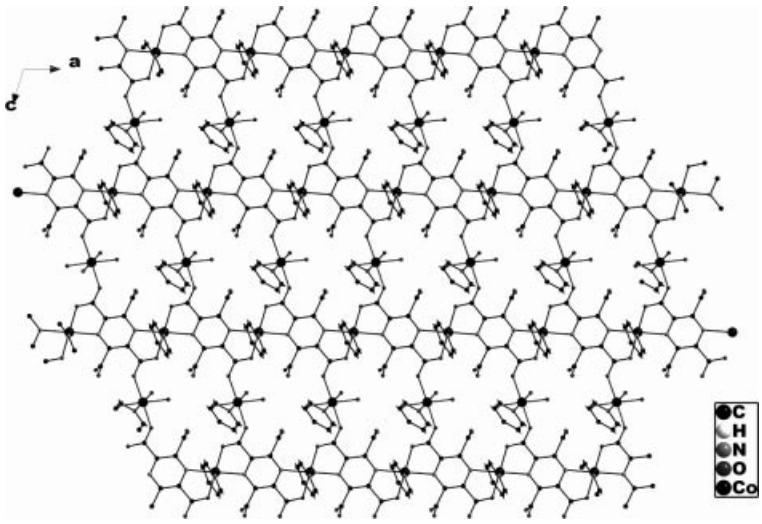

Figure 1. A perspective view of the planar sheet structure of **1** viewed down the *b* axis. Hydrogen atoms are omitted for clarity.

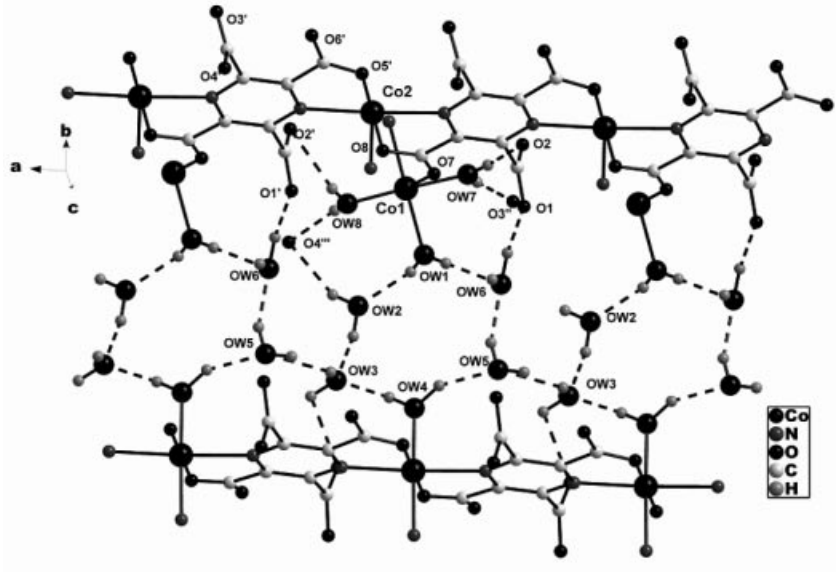

Figure 2. A view showing how water molecules are bound to the MOF. The lone blue spheres are pyridine N atoms. The entire pyridine molecule is not shown for clarity.

hexameric unit assume a slightly puckered conformation and this mode of association results from two factors: (1) the Ow atoms are H-bonded to the carboxylate O atoms which are fixed as almost coplanar in space and (2) the metal-bound pyridine molecules (Figure 3) would obstruct if the conformation is deviated significantly from planarity. Cyclic planar water hexamer is the basic structural motif found[19] in ice II structure under high pressure. This is also a prominent structural unit present[20] in liquid water based on computer simulation while Nauta and Miller detected the "quasi-planar" hexamer within a helium droplet.[11]

The nonbonding Ow···Ow distances (Table 1) show a wide variation commensurate with the MOF structure. The average O···O distance of 2.795 Å is smaller than that of liquid water which shows a value of 2.85 Å from the X-ray diffraction radial distribution curve while for the gas phase, this value is ca. 0.1 Å longer.[18] The water molecules present in clefts of biological/abiological molecules are very different from the gas phase or bulk liquid water. Here, the principle of maximizing H-bonding interactions is followed where the environment plays a major role. Consistent with this principle, the O···O distances in the cluster vary widely for optimized interactions between the water molecules and between a water molecule and its surrounding. For a discrete quasi-planar hexamer[6e] trapped in an organic supramolecular complex with bimesityl dicarboxylic acid, the average O···O distance (2.775 Å) is shorter while in case of a dodecameric[21] water cluster built around a planar cyclic hexamer in a supramolecular complex of a cryptand, the O···O distance (2.801 Å) is similar to the present structure. The nonbonding O···O···O angles (Table 1) in **1** span a wide range [104.8 (3)–132.7(2)°] deviating considerably from an ideal benzene-like structure. In the chain, Ow1 and Ow4 act as double donors, Ow6 as double acceptors while the rest

 © 2005 Wiley-VCH Verlag GmbH & Co. KGaA, Weinheim

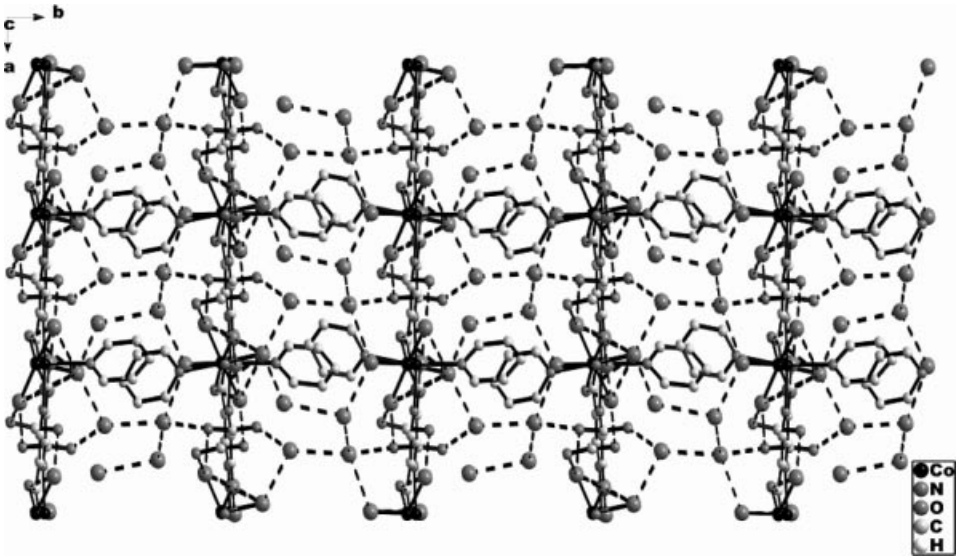

Figure 3. The MOF structure of **1** viewed in the *ab* plane. The chains of quasi-planar water molecules extending along the crystallographic *a* axis.

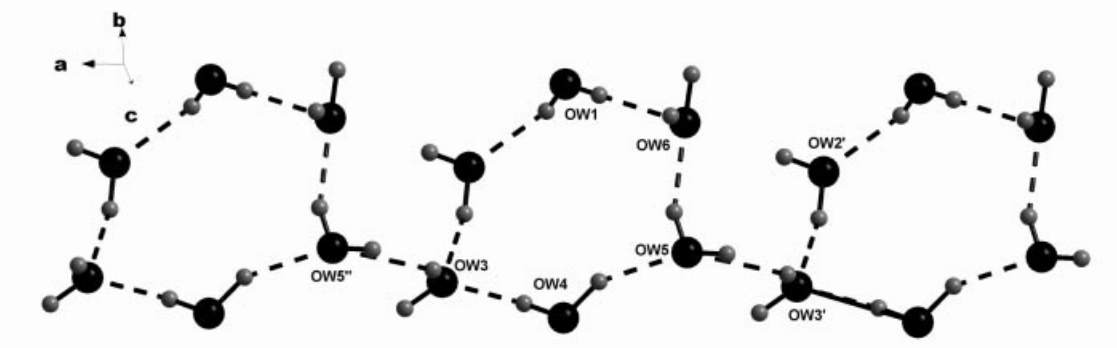

Figure 4. A perspective view of the chain of planar hexamaric water cluster showing the H-bonding Scheme.

Table 1. Non-bonded distances [Å] and angles [°] involving the hexameric water cluster.[a]

Ow1···Ow2	2.691(6)	Ow2···H1–Ow1	175.3(1)
Ow2···Ow3	2.824(3)	Ow3···H1–Ow2	169.2(2)
Ow3···Ow4	2.758(5)	Ow3···H2–Ow4	171.6(2)
Ow4···Ow5	2.808(6)	Ow5···H1–Ow4	162.7(1)
Ow5···Ow6	2.748(2)	Ow6···H1–Ow5	152.4(1)
Ow6···Ow1	2.724(4)	Ow6···H2–Ow1	162.8(1)
Ow3···Ow5′′	3.014(4)	Ow5···H2–Ow3′	129.7(1)
		Ow6···Ow1···Ow2	125.2(2)
		Ow1···Ow2···Ow3	118.2(1)
		Ow2···Ow3···Ow4	104.8(3)
		Ow3···Ow4···Ow5	132.8(2)
		Ow4···Ow5···Ow6	114.3(1)
		Ow5···Ow6···Ow1	113.9(2)
		Ow6···Ow5···Ow3′	91.4(1)
Ow2···O4	2.890(2)	Ow7···O2	2.739(2)
Ow3···O3	2.899(4)	Ow7···O3	2.811(3)
Ow6···O1	2.717(4)	Ow8···O1	2.887(2)
		Ow8···O4	2.759(4)

[a] One H atom in each of Ow4 and Ow5 could not be located in the difference Fourier maps. Their positions were calculated (H2W4 and H2W5) and added to the atom list. Atoms Ow3′ and Ow5′′ are related by 2 – *x*, 1/2 + *y*, 2 – *z* and 2 – *x*, –1/2 + *y*, 2 – *z* respectively.

act both as donors and acceptors of H-bonding. So, every O atom in the unit does not show four coordination. Such hydrogen-bond deficient water molecules are present[22] at the surface of ice while recent X-ray absorption spectroscopy and Raman scattering studies of liquid water also point to the fact that significant number of O atoms show less than tetracoordination in liquid water.[23]

Thermal analysis of the compound shows that onset of water loss starts at ca. 30 °C and complete loss of water takes place within 100 °C without showing any plateau in the thermogram.[24] The FTIR spectrum[24] of **1** shows a broad band centered around 3415 cm^{-1} attributable to the O–H stretching frequency of the water cluster. This broad band vanishes on heating the compound under vacuum (0.1 mm) at 140 °C for 2 h suggesting escape of the water molecules from the lattice. The IR spectrum of ice[18a] shows the O–H stretching at 3220 cm^{-1} while this stretching vibration in liquid water[18a] appears at 3490 and 3280 cm^{-1}. This suggests that the water cluster in **1** shows O–H stretching vibration similar to that of liquid water. Deliberate ex-

 © 2005 Wiley-VCH Verlag GmbH & Co. KGaA, Weinheim

posure to water vapor for 3 days does not lead to re-absorption of water into the lattice as monitored by FTIR spectroscopy. The spectrum below 2000 cm^{-1} does not change appreciably on heating **1** at 140 °C for 2 h that suggests coordination of ptc^{4-} to Co^{II} is still maintained. However, powder X-ray diffraction[24] patterns of **1** before and after water expulsion show major changes with respect to peak positions and intensities suggesting breakdown of the host lattice once the water molecules are expelled.

Conclusion

In conclusion, we have identified infinite chains of quasi-planar hexameric water clusters in an MOF built from Co^{II} and pyrazine-2,3,5,6-tetracarboxylic acid. Each chain assembles two planar 2D coordination polymeric networks where the structure of the water chain is commensurate with the MOF.

Experimental Section

Materials: The metal salt and phenazene were acquired from Aldrich and used as received.

Physical Measurements: Spectroscopic data were collected as follows: IR (KBr disk, 400–4000 cm^{-1}) Perkin–Elmer Model 1320; X-ray powder pattern (Cu-K_α radiation at a scan rate of 3°/min, 293 K) Siefert ISODEBYEFLEX-2002 X-ray generator; thermogravimetric analysis (heating rate of 5 °C/min) Mettler Toledo Star System. Microanalysis data for the compound were obtained from CDRI, Lucknow.

Synthesis of $\{[Co_2(ptc)\cdot(py)_2\cdot 4H_2O]\cdot 4H_2O\}_n$ (1): $Co(NO_3)_2\cdot 6H_2O$ (0.64 g; 2 mmol) was added to a solution of pyrazine-2,3,5,6-tetracarboxylic acid ($ptcH_4$) (0.26 g; 1 mmol) in 25 mL of aqueous pyridine (1:1, v/v). A dark reddish solution was obtained. After filtering the solution, the solvent was allowed to evaporate slowly at room temperature whereupon (after 10 days) red rectangular parallelopiped crystals of **1** appeared (0.302 g, 45% yield). $C_{18}H_{26}Co_2N_4O_{16}$ (672.29): C 32.16, H 3.89, N 8.33; found C 32.67, H 4.02, N 8.14.

X-ray Structural Studies: Single-crystal X-ray data on **1** were collected at 100 K on a Bruker SMART APEX CCD diffractometer using graphite-monochromated Mo-K_α radiation (λ = 0.71069 Å). The linear absorption coefficients, scattering factors for the atoms, and the anomalous dispersion corrections were taken from International Tables for X-ray Crystallography. The data integration and reduction were processed with SAINT[14] software. The structure was solved by the direct method using SHELXTL[15] and was refined on F^2 by full-matrix least-squares technique using the SHELXL-97[16] program package. All non-hydrogen atoms present were anisotropically refined. All hydrogen atoms except two could be easily located in successive difference Fourier maps and they were treated as riding atoms using SHELXL default parameters. The remaining two H atoms were calculated theoretically and added to the list. Crystal data of **1**: M = 672.29 g mol^{-1}, monoclinic, space group $P2_1$, a = 7.153(5), b = 17.003(5), c = 11.060(5) Å, β = 107.207(5)°, U = 1284.9(11) $Å^3$, Z = 2, $R1$ = 0.0340, $wR2$ = 0.0875, S = 1.028. T = 100 K, D_c = 1.738 g cm^{-3}, μ = 1.376 mm^{-1}, $F(000)$ = 688, crystal size = 0.17 × 0.14 × 0.10 mm^3. A total of 8112 reflections up to θ = 28.30 were collected of which 4482 unique reflections were used.

CCDC-236954 contains the supplementary crystallographic data for this paper. These data can be obtained from The Cambridge Crystallographic Data Centre via www.ccdc.cam.ac.uk/data_request/cif.

Acknowledgments

We gratefully acknowledge the financial support received from the Department of Science and Technology, New Delhi, India (grant No. SR/S5/NM-38/2003 to P. K. B.) and an SRF from the CSIR to S. G.

[1] a) M. Yoshizawa, T. Kusukawa, M. Kawano, T. Ohhara, I. Tanaka, K. Kurihara, N. Nimura, M. Fujita, *J. Am. Chem. Soc.* **2005**, *127*, 2798–2799; b) Q.-Y. Liu, L. Xu, *CrystEngComm* **2005**, *7*, 87–89; c) M. T. Ng, T. C. Deivaraj, W. T. Klooster, G. J. McIntyre, J. J. Vittal, *Chem. Eur. J.* **2004**, *10*, 5853–5859; d) S. K. Ghosh, P. K. Bharadwaj, *Inorg. Chem.* **2004**, *43*, 6887–6889; e) S. Neogi, G. Savitha, P. K. Bharadwaj, *Inorg. Chem.* **2004**, *43*, 3771–3773; f) A. Michaelides, S. Skoulika, E. G. Bakalbassis, J. Mrozinski, *Cryst. Growth Des.* **2003**, *3*, 487–492; g) J. L. Atwood, L. J. Barbour, T. J. Ness, C. L. Raston, P. L. Raston, *J. Am. Chem. Soc.* **2001**, *123*, 7192–7193.
[2] a) F. N. Keutsch, R. J. Sykally, *Proc. Natl. Acad. Sci. USA* **2001**, *98*, 2001; b) B. Chen, J. Xing, J. I. Siepmann, *J. Phys. Chem.* **2000**, 2391–2401.
[3] G. Hummer, J. C. Rasaiah, J. P. Noworyta, *Nature* **2001**, *414*, 188–190.
[4] a) R. Pomès, B. Roux, *Biophys. J.* **2002**, *82*, 2304–2307; b) S. Cukierman, *Biophys. J.* **2000**, *78*, 1825–1828; c) G. Sainz, C. J. Carrell, M. V. Ponamerev, G. M. Soriano, W. A. Cramer, J. L. Smith, *Biochemistry* **2000**, *39*, 9164–9169; d) K. M. Jude, S. K. Wright, C. Tu, D. N. Silverman, R. E. Viola, D. W. Christianson, *Biochemistry* **2002**, *41*, 2485–2491.
[5] a) K. Mitsuoka, K. Murata, T. Walz, T. Hirai, P. Agre, J. B. Heymann, A. Engel, Y. Fujiyoshi, *J. Struct. Biol.* **1999**, *128*, 34–43; b) E. Tajkhorshid, P. Nollert, M. Ø. Jensen, L. J. W. Miercke, J. O'Connell, R. M. Stroud, K. Schulten, *Science* **2002**, *296*, 525–526.
[6] a) S. K. Ghosh, P. K. Bharadwaj, *Inorg. Chem.* **2004**, *43*, 5180–5182; b) B.-H. Ye, B.-B. Ding, Y.-Q. Weng, X.-M. Chen, *Inorg. Chem.* **2004**, *43*, 6866–6868; c) S. K. Ghosh, P. K. Bharadwaj, *Inorg. Chem.* **2003**, *42*, 8250–8254; d) Y.-P. Ren, L.-S. Long, B.-W. Mao, Y.-Z. Yuan, R.-B. Huang, L.-S. Zheng, *Angew. Chem. Int. Ed.* **2003**, *42*, 532–535; e) J. N. Moorthy, R. Natarajan, P. Venugopalan, *Angew. Chem. Int. Ed.* **2002**, *41*, 3417–3420; f) R. Custecean, C. Afloroaei, M. Vlassa, M. Polverejan, *Angew. Chem. Int. Ed.* **2000**, *39*, 3094–3096; g) K. M. Park, R. Kuroda, T. Iwamoto, *Angew. Chem. Int. Ed. Engl.* **1993**, *32*, 884–886.
[7] a) J. Kim, K. S. Kim, *J. Chem. Phys.* **1998**, *109*, 5886; b) C. J. Tsai, K. D. Jordan, *Chem. Phys. Lett.* **1993**, *213*, 181–188; c) K. Kim, K. D. Jordan, T. S. Zwier, *J. Am. Chem. Soc.* **1994**, *116*, 11568–11569.
[8] J. K. Gregory, D. C. Clary, K. Liu, M. G. Brown, R. J. Saykally, *Science* **1997**,*275*, 814–817.
[9] R. Ludwig, *Angew. Chem. Int. Ed.* **2000**, *39*, 1808–1827.
[10] K. Liu, M. G. Brown, C. Carter, R. J. Saykally, J. K. Gregory, D. C. Clary, *Nature* **1996**, *381*, 501.
[11] K. Nauta, R. E. Miller, *Science* **2000**, *287*, 293–295.
[12] L. Wolff, *Chem. Ber.* **1987**, *20*, 425.
[13] a) S. Neogi, P. K. Bharadwaj, *Inorg. Chem.* **2005**, *44*, 816–818; b) S. K. Ghosh, J. Ribas, P. K. Bharadwaj, *Cryst. Growth Des.* **2005**, *5*, 623–629; c) S. K. Ghosh, P. K. Bharadwaj, *Inorg. Chem.* **2004**, *43*, 2293–2298; d) S. K. Ghosh, G. Savita, P. K. Bharadwaj, *Inorg. Chem.* **2004**, *43*, 5495–5497; e) S. K. Ghosh, J. Ribas, P. K. Bharadwaj, *CrystEngComm* **2004**, *45*, 250–256.
[14] SAINT+, 6.02 ed.; Bruker AXS, Madison, WI, **1999**.
[15] G. M. Sheldrick, SHELXTL™ *Reference Manual*: version 5.1, Bruker AXS, Madison, WI, **1997**.

 © 2005 Wiley-VCH Verlag GmbH & Co. KGaA, Weinheim

[16] G. M. Sheldrick, SHELXL-97: *Program for Crystal Structure Refinement*: University of Göttingen, Göttingen, Germany, **1997**.
[17] a) L. Infantes, S. Motherwell, *CrystEngComm* **2002**, *4*, 454–461; b) L. Infantes, J. Chisholm, S. Motherwell, *CrystEngComm* **2003**, *5*, 480–486.
[18] a) D. Eisenberg, W. Kauzmann, *The Structure and Properties of Water*, Oxford University Press, Oxford, **1969**; b) N. H. Fletcher, *The Chemical Physics of Ice*, Cambridge University Press, Cambridge, **1970**.
[19] B. Kamb, *Acta Crystallogr.* **1964**, *17*, 1437–1449.
[20] A. Rahaman, F. H. Stillinger, *J. Am. Chem. Soc.* **1973**, *95*, 7943–7948.
[21] S. K. Ghosh, P. K. Bharadwaj, *Angew. Chem. Int. Ed.* **2004**, *43*, 3577–3580.
[22] C. J. Gruenloh, J. R. Carney, C. A. Arrington, T. S. Zwier, S. Y. Fredericks, K. D. Jordan, *Science* **1997**, *276*, 1678–1681.
[23] P. Warnet, D. Nordlund, U. Bergmann, M. Cavalleri, M. Odelius, H. Ogasawara, L. A. Näslund, T. K. Hirsch, L. Ojamäe, P. Glatzel, L. G. M. Pettersson, A. Nilsson, *Science* **2004**, *304*, 995–999.
[24] Supporting Information (for details see footnote on the first page of the contribution): TGA curve, X-ray powder diffraction patterns for **1** before and after exclusion of water and FTIR spectra of **1** before water removal and after water removal.

Received: July 26, 2005
Published Online: November 2, 2005

 © 2005 Wiley-VCH Verlag GmbH & Co. KGaA, Weinheim

DOI: 10.1002/ejic.200500735

Octameric Water Clusters of Staircase Structure Present in a Metal-Organic Framework Built from Helical Lanthanide Coordination Polymers

Sujit K. Ghosh[a] and Parimal K. Bharadwaj*[a]

Keywords: Water chemistry / Supramolecular chemistry / Self assembly / Metal-organic framework / Helical structure

Two lanthanide-carboxylate polymeric complexes containing nine-coordinate lanthanide metal centers, {[Pr(*ptc*$^{-3}$)·2H_2O]·2H_2O} (**1**), {[Nd(*ptc*$^{-3}$)·2H_2O]·2H_2O} (**2**) have been prepared by hydrothermal synthesis of $Pr(NO_3)_3$·6H_2O or $Nd(NO_3)_3$·6H_2O with pyridine-2,4,6-tricarboxylic acid (*ptc*H_3). These network structures are characterized by X-ray crystallography, powder X-ray diffraction, infrared and thermal gravimetric analyses. Both **1** and **2** form infinite single helical chains with large widths and pitches containing six metal ions per turn. The overall structure consists of two helices connected via discrete octameric water clusters.

(© Wiley-VCH Verlag GmbH & Co. KGaA, 69451 Weinheim, Germany, 2005)

Introduction

Water clusters of different nuclearity and structure in both inorganic and organic hydrates continue to attract a lot of attention because such studies facilitate our understanding of the liquid by allowing better description of the many-body interactions in a step by step manner.[1] Of particular interest here is the structure of the $(H_2O)_8$ cluster. Theory predicts[2] two closely related iso-energetic cubane structures with S_4 and D_{2d} symmetries where O atoms occupy the corners and hydrogen bonds along the edges which are supported by experimental proofs in the molecular beam[3] and in gas-phase $C_6H_6(H_2O)_8$ clusters.[4] In crystal hosts, cubane,[5] opened-cubane,[6] cyclic octamer[7] resembling ice I_h and cyclic octamer consisting of a hexamer and two dangling water molecules[8] have been identified. We present here a discrete octamer whose structure is very different from any of these.

The water clusters are present in the voids of 3D metal-organic frameworks built by connecting single helical coordination polymers through carboxylate bridging. Helicate chemistry is not only important in the development and understanding of self-assembly processes, but also to search for new supramolecular architectures endowed with functional properties. The accepted model for helication requires a long multidentate ligand as a molecular thread containing a number of discrete metal-binding sites separated by spacer units. Such a molecular thread can twist around several metal ions controlled by their coordination behavior. Synthesis of only discrete helicates of both transition metals[9] and lanthanides[10] can be achieved following this strategy. We report here formation of open framework structures by connecting infinite single-strand helices[11] made from pyridine-2,4,6-tricarboxylic acid (*ptc*H_3) and either Nd^{III} or Pr^{III} ions.

Results and Discussion

Compounds {[Pr(*ptc*$^{3-}$)·2H_2O]·2H_2O} (**1**) and {[Nd(*ptc*$^{3-}$)·2H_2O]·2H_2O} (**2**) were synthesized hydrothermally in ca. 55% yield, by treating the ligand pyridine-2,4,6-tricarboxylic acid[12] (*ptc*H_3) with $Pr(NO_3)_3$·6H_2O or $Nd(NO_3)_3$·6H_2O, respectively. As both **1** and **2** have an identical structure, only the structure of **1** is discussed.

The asymmetric unit of **1** consists of one *ptc*$^{3-}$ unit, one Pr^{III}, two metal-bound water and two free water molecules. Each metal ion exhibits 9-coordination (Scheme 1) with bonding from six carboxylates of five different ligand units, one ring N atom of one the ligands and two water molecules. All carboxylate groups are bridged to complete the 3D structure. The Pr^{III} ions are arranged in infinite single helices extending along the crystallographic *b* axis (Figure 1) with intervening *ptc*$^{3-}$ ligands. The helical structure is a result of metal–ligand interactions coupled with stereoelectronic characteristics of the ligand and the conditions prevailing during the synthesis. The width of the helix is calculated to be 16.70 Å and the pitch is 11.95 Å and there are six Pr^{III} ions present per turn. Both the width and the pitch are large as a result of the topology of the *ptc*$^{3-}$ ligand and the electrostatic repulsive interactions among the metal ions. The stability of the final helical structure relies on the coordinate bonds that each metal makes with the ligand. Known structures of lanthanide helicates[10] are double- or triple-stranded with long polydentate ligands which are able

[a] Chemistry Department, Indian Institute of Technology, Kanpur, 208016, India
E-mail: pkb@iitk.ac.in

Supporting information for this article is available on the WWW under http://www.eurjic.org or from the author.

 InterScience © 2005 Wiley-VCH Verlag GmbH & Co. KGaA, Weinheim

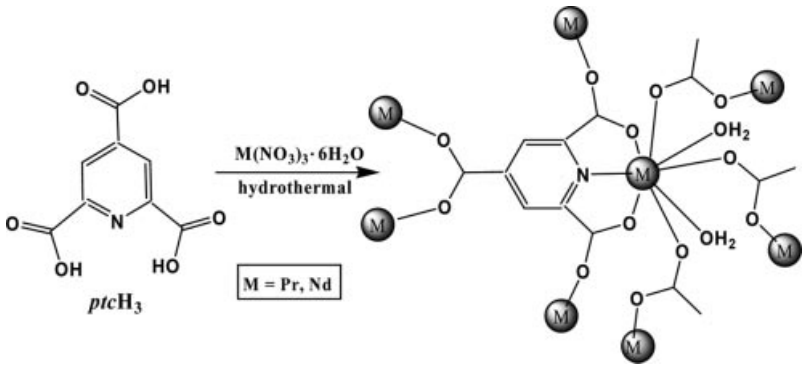

Scheme 1. An illustration showing the binding mode of the ligand.

to wrap around lanthanide ions forming compact helical structures with lower pitch and narrower width. The helices in **1** are further organized into metal-organic framework structures through inter-helix bridging of the carboxylates (Figure 2) with voids occupied by water molecules. Four metal-bound water molecules catch hold of four other water molecules forming an overall discrete octamer. The cluster takes the shape of a staircase-like structure (Figure 3) where only Ow3 and centrosymmetrically related Ow3′ show tetra-coordination while all other water O atoms are tri-coordinated. Such hydrogen-bond deficient water molecules are present[3] at the surface of ice as well as in liquid water.[13] An important feature of this cluster is a very short distance between Ow3 and Ow4′ (2.231 Å). In **2**, this distance is only 1.977 Å although H atoms belong to the water oxygens could not be located in the difference map. Locating these hydrogens by neutron diffraction and probing the nature of Ow···Ow distances in **2** will be another study. Generally, short H bonds are encountered with charged H

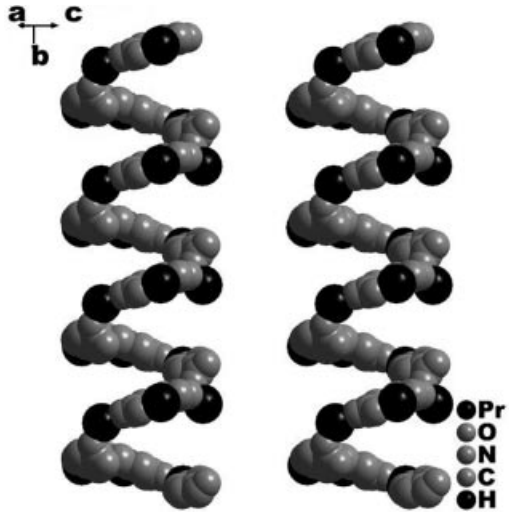

Figure 1. Single helical stereoview of **1**. Other atoms have been omitted for clarity.

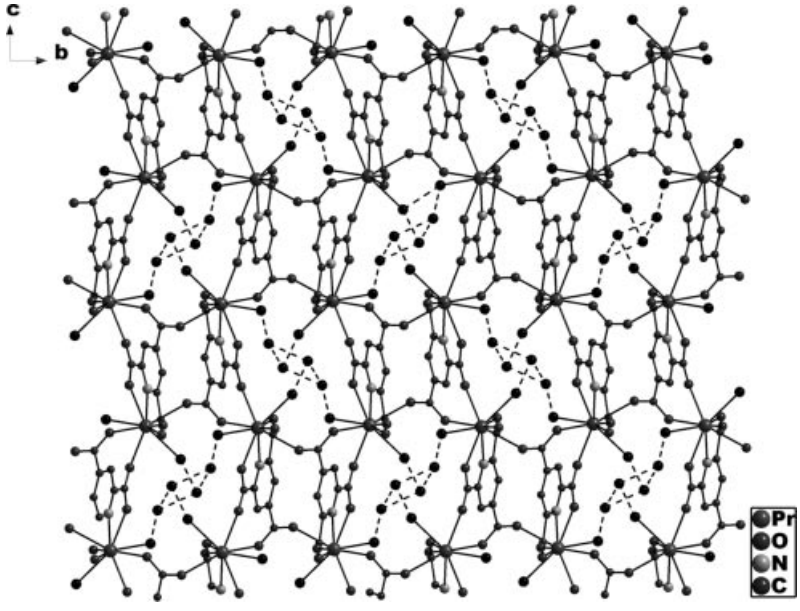

Figure 2. The MOF structure of **1** viewed approximately down the *a* axis. H atoms are omitted for clarity.

 © 2005 Wiley-VCH Verlag GmbH & Co. KGaA, Weinheim

bond donors (O^+–H···O) or acceptors (O–H···O^-) such as the Speakman salts[14] with RCOOH···$^-$OOCR hydrogen bonding. In the present case, the metal organic framework pushes the Ow3 and Ow4 atoms closer together. Values of other Ow···Ow distances (range: 2.668–2.903 Å) and O···H–O angles (range: 140.35–175.38°) (Table 1) suggest strong H-bonding interactions among the water molecules. In comparison, bulk water exhibits a short-range O···O order of 2.85 Å in the X-ray diffraction radial distribution curve while for the gas phase, this value is ca. 0.1 Å longer.[15] Hydrogen atoms of Ow2, Ow2′, Ow3 and Ow3′ are also bonded to the nearby carboxylate O atoms cementing the structure further with the MOF and the ultimate symmetry of the octamer results from interactions between the water molecules and between the water molecules and the MOF.

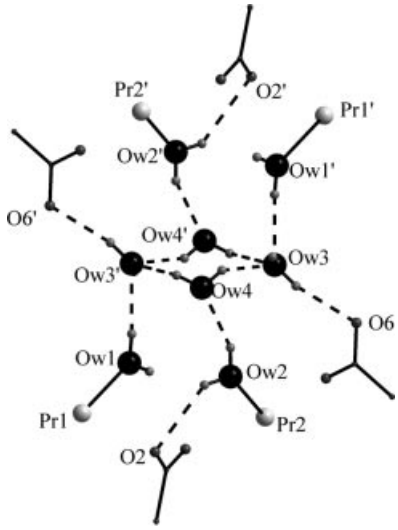

Figure 3. A close view of the water cluster and its surrounding atoms.

Table 1. Geometrical parameters of hydrogen bonds (Å, deg) of the octamer in **1**.

Ow1···Ow4	2.748(2)
Ow2···Ow3	2.868(4)
Ow3···Ow4	2.668(2)
Ow3···Ow4′	2.231(3)
Ow3···O6	2.903(5)
Ow2···O2	2.981(4)
Ow1–H2···Ow4	153.30(5)
Ow2–H1···Ow3	175.38(6)
Ow4–H2···Ow3	145.86(8)
Ow4′–H1···Ow3	140.35(6)
Ow3–H1···O6	165.59(4)
Ow2–H2···O2	155.68(4)
Ow1···Ow4···Ow3	87.29
Ow1···Ow4···Ow3′	109.99
Ow2···Ow3···Ow4	73.21
Ow2···Ow3···Ow4′	109.15
Ow3···Ow4···Ow3′	121.47
Ow4···Ow3···Ow4′	58.53

Thermal gravimetric analyses[16] further corroborate the strong water–MOF interactions. For **1**, with 23.39 mg sample in air shows the loss of first 3 water molecules occur at 145 °C beginning at ca. 100 °C and the loss of all of the water is achieved only above 250 °C and the compound decomposes soon after. Compound **2** shows an almost identical thermogram. The FTIR spectra[16] of **1** and **2** exhibit a broad band centered around 3405 cm^{-1} attributable to the O–H stretching frequency pertaining to the water cluster. All water could be removed by heating either compound at 200 °C for 2 h under 10 mm pressure. However, water expulsion leads to complete breakdown of the 3D lattice as the powder X-ray diffraction patterns[16] of the compounds before and after water expulsion are completely different.

Conclusions

In conclusion, we describe here two open-framework structures formed via carboxylate bridging of infinite single helical coordination polymeric chains. The driving force for helication is the metal–ligand interaction coupled with stereoelectronic characteristics of the ligand and the reaction conditions. Discrete octameric water clusters of hitherto unknown staircase structure occupy the voids in the MOFs.

Experimental Section

Materials and Measurements: The metal salts and 2,4,6-trimethylpyridine were acquired from Aldrich and used as received. Spectroscopic data were collected as follows: IR (KBr disk, 400–4000 cm^{-1}) Perkin–Elmer Model 1320; X-ray powder pattern (Cu-K_α radiation at a scan rate of 3°/min, 293 K) Siefert ISODEBYEFLEX-2002 X-ray generator; thermogravimetric analysis (heating rate of 5 °C/min) Perkin–Elmer Pyris 6. Microanalyses for the compounds were obtained from the Central Drug Research Institute, Lucknow, India. Synthesis of pyridine-2,4,6-tricarboxylic acid (*ptc*H_3): This compound was synthesized in 50% yield by oxidation of 2,4,6-trimethylpyridine with aqueous $KMnO_4$ following a literature method.[12]

Synthesis of {[Pr(*ptc*$^{3-}$)2H_2O]2H_2O}$_n$ (1): This compound is synthesized by mixing 1 mmol of $Pr(NO_3)_3{\cdot}6H_2O$ and 1 mmol of pyridine-2,4,6-tricarboxylic acid (*ptc*H_3) in 5 mL of water in a Teflon-lined autoclave. The autoclave is heated under autogenous pressure to 180 °C for 2 days and then kept at 90 °C for a further 12 h period. Upon cooling to room temp. the desired product appeared as long pale green rectangular parallelopipeds in ca. 55% yield. $C_8H_{10}NO_{10}Pr$ (421.08): calcd. C 22.82, H 2.39, N 3.32; found C 22.16, H 2.47, N 3.21.

Synthesis of [Nd(*ptc*$^{3-}$)2H_2O]2H_2O (2): This was prepared in ca. 54% yield as light purple rectangular parallelopipeds crystals on hydrothermal reaction of 1 mmol of $Nd(NO_3)_3{\cdot}6H_2O$ with 1 mmol of the ligand in 5 mL H_2O and under identical experimental conditions as above. $C_8H_{10}NO_{10}Nd$ (424.41): calcd. C 22.64, H 2.37, N 3.30; found C 22.31, H 2.46, N 3.23.

X-ray Crystallography. Crystal Data for 1: $C_8H_{10}NO_{10}Pr$, M = 421.08, rectangular parallelopiped, light green crystals, 0.17 × 0.14 × 0.11 mm, monoclinic, space group $P2_1c$, a = 6.754(5) Å, b = 11.937(2) Å, c = 13.456(5) Å, β = 100.381(5)°, U = 1067.1(10) $Å^3$, T = 100 K, Z = 4. μ(Mo-K_α) = 4.627 mm^{-1}, 6998 reflections measured, 2454 [$I \geq 2\sigma(I)$] unique reflections were used in all calculations. The final R_1 = 0.0312, wR_2 = 0.0773, S = 1.066. **Crystal Data for 2:** $C_8H_{10}NO_{10}Nd$, M = 424.41, rectangular parallelopiped, light purple crystals, 0.18 × 0.14 × 0.11 mm, monoclinic,

 © 2005 Wiley-VCH Verlag GmbH & Co. KGaA, Weinheim

space group $P2_1c$, a = 6.751(5) Å, b = 11.916(3) Å, c = 13.457(5) Å, β = 103.105(5)°, U = 100.427(5) Å^3, T = 100 K, Z = 4. μ(Mo-K_α) = 4.938 mm^{-1}, 6963 reflections measured, 2426 unique [$I \geq 2\sigma(I)$] reflections were used in all calculations. The final R_1 = 0.0413, wR_2 = 0.0941, S = 1.093.

CCDC-281538 (for **1**) and -281539 (for **2**) contain the supplementary crystallographic data for this paper. These data can be obtained free of charge from The Cambridge Crystallographic Data Centre via www.ccdc.cam.ac.uk/data_request/cif.

Supporting Information (for details see footnote on the first page of this article): TGA curve, X-ray powder diffraction patterns for **1** before and after exclusion of water and FTIR spectra of **1** before water removal and after water removal.

Acknowledgments

We gratefully acknowledge the financial support received from the Council of Scientific and Industrial Research, New Delhi, India (grant No.1638/EMR II) and a SRF to S.G.

[1] F. N. Keutsch, R. J. Saykally, *Proc. Natl. Acad. Sci. U.S.A.* **2001**, *98*, 10533–10540.
[2] a) C. J. Tsai, K. D. Jordon, *J. Chem. Phys.* **1999**, *95*, 3850–3858; b) C. J. Tsai, K. D. Jordon, *J. Chem. Phys.* **1993**, *99*, 6957–6965.
[3] C. J. Gruenloh, J. R. Carney, C. A. Arrington, T. S. Zwier, S. Y. Fredericks, K. D. Jordon, *Science* **1997**, *276*, 1678–1681.
[4] U. Buck, I. Ettisher, M. Melzer, V. Buch, J. Sadlej, *Phys. Rev. Lett.* **1998**, *80*, 2578–2581.
[5] W. B. Blanton, S. Gordon-Wylie, G. R. Clark, K. D. Jordon, T. J. Wood, U. Geiser, T. J. Collins, *J. Am. Chem. Soc.* **1999**, *121*, 3551–3552.
[6] R. J. Doedens, E. Yohannes, M. I. Khan, *Chem. Commun.* **2002**, 62–63.
[7] J. L. Atwood, L. J. Barbour, T. J. Ness, C. L. Raston, P. L. Raston, *J. Am. Chem. Soc.* **2001**, *123*, 7192–7193.
[8] B. Q. Ma, H. L. Sun, S. Gao, *Chem. Commun.* **2005**, 2336–2338.
[9] a) S. J. Coles, J. G. Frey, P. A. Gale, M. B. Hursthouse, M. E. Light, K. Navakhun, G. L. Thomas, *Chem. Commun.* **2003**, 568–569; b) R. Pravaharan, N. C. Fletcher, M. Nieuwenhuyzen, *J. Chem. Soc., Dalton Trans.* **2002**, 602–607; c) L. J. Childs, N. W. Alcock, M. J. Hannon, *Angew. Chem. Int. Ed.* **2001**, *40*, 1079–1081; d) A. J. Blake, N. R. Champness, A. N. Khlobystov, S. Parsons, M. Schröder, *Angew. Chem. Int. Ed.* **2000**, *39*, 2317–2320; e) A. P. Maggard, L. C. Stern, K. R. Poeppelmeier, *J. Am. Chem. Soc.* **2001**, *123*, 7742–7743; f) T. A. Okamura, T. Iwamura, S. Seno, H. Yamoto, N. J. Ueyama, *J. Am. Chem. Soc.* **2004**, *126*, 15972–15973; g) L. D. Sara, R. Halper, S. M. Cohen, *Chem. Commun.* **2004**, 2662–2663; h) Y. Cui, H. L. Ngo, W. Lin, *Chem. Commun.* **2003**, 1388–1389.
[10] a) D.-L. Long, A. J. Blake, N. R. Champness, C. Wilson, M. Schröder, *Angew. Chem. Int. Ed.* **2001**, *40*, 2444–2447; b) J.-C. G. Bünzli, C. Piguet, *Chem. Rev.* **2002**, *102*, 1897–1928.
[11] S. K. Ghosh, P. K. Bharadwaj, *Inorg. Chem.* **2004**, *43*, 2293–2298.
[12] L. Syper, K. Kloc, J. Mlochowski, *Tetrahedron* **1980**, *36*, 123–129.
[13] P. Warnet, D. Nordlund, U. Bergmann, M. Cavalleri, M. Odelius, H. Ogasawara, L. A. Näslund, T. K. Hirsch, L. Ojamäe, P. Glatzel, L. G. M. Pettersson, A. Nilsson, *Science* **2004**, *304*, 995–999.
[14] J. C. Speakman, *Struct. Bonding* **1972**, *12*, 141–199.
[15] A. G. Jeffrey, *An Introduction to Hydrogen Bonding*, Oxford University Press, Oxford, **1997**.
[16] See Supporting Information.

Received: August 18, 2005
Published Online: November 2, 2005

 © 2005 Wiley-VCH Verlag GmbH & Co. KGaA, Weinheim

DOI: 10.1002/ejic.200500636

Structural Relationships in High-Nuclearity Heterobimetallic Bismuth-Oxo Clusters

Michael Mehring,*[a] Sanna Paalasmaa,[a] and Markus Schürmann[a]

Keywords: Bismuth / Sodium / Silanolate / Metal-oxo cluster / Structure elucidation

The novel heterobimetallic sodium-bismuth-oxo clusters $[Bi_2Na_4O(OSiMe_3)_8]$ (**1**), $[Bi_{10}Na_5O_7(OH)_6(OSiMe_3)_{15}]\cdot 1.5C_7H_8$ (**2**·1.5C_7H_8), $[Bi_{15}Na_3O_{18}(OSiMe_3)_{12}]\cdot C_7H_8$ (**3**·C_7H_8) and $[Bi_{14}Na_8O_{18}(OSiMe_3)_{14}(THF)_4]\cdot C_6H_6$ (**4**·C_6H_6) were prepared starting from $BiCl_3$ and $NaOSiMe_3$. Compound **1** crystallises in the trigonal space group $R\bar{3}c$ with the lattice constants a = 12.8844(3) Å and c = 54.6565(3) Å, compound **2**·1.5C_7H_8 crystallises in the triclinic space group $P\bar{1}$ with the lattice constants a = 15.0377(2) Å, b = 16.0373(2) Å, c = 27.8967(5) Å, α = 87.1321(6)°, β = 86.6530(7)° and γ = 63.6617(6)°, compound **3**·C_7H_8 crystallises in the monoclinic space group $C2/c$ with the lattice constants a = 54.311(11), b = 19.846(4), c = 22.885(5) Å and β = 112.32(3)°, and compound **4**·C_6H_6 crystallises in the trigonal space group $R\bar{3}$ with the lattice constants a = 15.9786(4) Å and c = 46.8329(17) Å. The formation of M–O–M bonds results from both partial hydrolysis followed by condensation as well as from elimination of $Me_3SiOSiMe_3$ from M–$OSiMe_3$ groups. The hexanuclear metal-oxo silanolate **1** is more conveniently synthesised by the addition of $NaOSiMe_3$ to a toluene solution of in situ-prepared $[Bi(OSiMe_3)_3]$. The metal-oxo(hydroxo) silanolates differ significantly in composition, but show similar building units. Thermal decomposition of the metal-oxo silanolates in the solid state gave heterogeneous decomposition products containing bismuth silicates.

(© Wiley-VCH Verlag GmbH & Co. KGaA, 69451 Weinheim, Germany, 2005)

Introduction

Bismuth alkoxides are valuable precursors for the synthesis of bismuth oxide-based materials prepared via chemical vapour deposition[1] or via the sol-gel process.[2,3] Their potential application for the synthesis of materials such as high-temperature superconductors or non-volatile random-access memories has prompted several research groups to investigate the reactivity and the structural chemistry of homo- and heterometallic bismuth alkoxides in order to control composition and morphology of the final material on a molecular level.[3–6] Alternatively, bismuth silanolates might serve as molecular precursors to bismuth-containing materials. However, the chemistry of bismuth silanolates was only scarcely explored so far.[7–11] In contrast to bismuth, metallasiloxanes of the heavier group 14 metals tin and lead have received considerable interest.[7,8,12,13] It was noticed that homoleptic heavy metal silanolates of the type $[M(OSiR_3)_2]$ (M = Sn, Pb) readily decompose at moderate temperatures with elimination of $R_3SiOSiR_3$ to give the parent metal oxide or metal-oxo clusters.[7,13] It is promising to exploit this non-hydrolytic strategy for the synthesis of tailor-made bismuth-oxo clusters and bismuth oxide-based nanoparticles. Recently, the potential of metal silanolates as molecular precursors for a variety of mixed metal oxide materials[8,14] as well as for nanoparticles of zinc oxide[15] and zinc silicate[16] was demonstrated.

Among the homoleptic bismuth silanolates the trimethylsilyl derivative $[Bi(OSiMe_3)_3]$ is one of the most promising candidates with respect to materials synthesis. The reaction of $BiCl_3$ with $NaOSiMe_3$ was previously reported to give $[Bi(OSiMe_3)_3]$,[7] but the material obtained gave analytical data which disagreed with the expected values. We have revisited this reaction and report here our findings including the molecular structures of $[Bi_2Na_4O(OSiMe_3)_8]$ (**1**), $[Bi_{10}Na_5O_7(OH)_6(OSiMe_3)_{15}]\cdot 1.5C_7H_8$ (**2**·1.5C_7H_8), $[Bi_{15}Na_3O_{18}(OSiMe_3)_{12}]\cdot C_7H_8$ (**3**·C_7H_8), and $[Bi_{14}Na_8O_{18}(OSiMe_3)_{14}(THF)_4]\cdot C_6H_6$ (**4**·C_6H_6).

Results and Discussion

Reaction of $NaOSiMe_3$ with $BiCl_3$ in a 3:1 stoichiometry using THF as solvent gave a solid material the EDX analysis of which accounted for the presence of both bismuth and sodium. Crystallisation from hot toluene gave single crystals of the heterometallic bismuth-oxo silanolate $[Bi_2Na_4O(OSiMe_3)_8]$ (**1**). The low yield was only slightly improved to approximately 10% when the reaction was carried out in toluene and the stoichiometry was modified to a bismuth-to-sodium ratio of 1:5 (Scheme 1).

Oxygen incorporation into compound **1** does not result from hydrolysis, but from the reaction of M–$OSiMe_3$ groups to give $Me_3SiOSiMe_3$ and the corresponding metal-

[a] Universität Dortmund, Anorganische Chemie II,
44221 Dortmund, Germany
Fax: +49-231-755-5048
E-mail: michael.mehring@uni-dortmund.de

 © 2005 Wiley-VCH Verlag GmbH & Co. KgaA, Weinheim

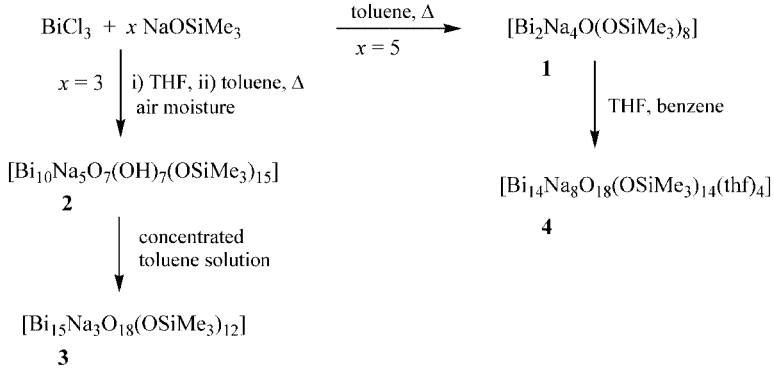

Scheme 1.

oxo fragment. The ^{29}Si NMR spectrum of a crude reaction mixture according to Scheme 1 (x = 5) showed a signal at δ = 7.2 ppm assigned to $Me_3SiOSiMe_3$ and a broad signal at δ = –2.9 ppm assigned to unreacted $NaOSiMe_3$. Due to its poor solubility, no ^{29}Si NMR signal was observed for [$Bi_2Na_4O(OSiMe_3)_8$] (**1**). Compound **1** was obtained with a significantly higher yield when in situ-prepared [$Bi(OSiMe_3)_3$] (^{29}Si NMR δ = 10.9 ppm) and $NaOSiMe_3$ were used as starting materials [Equation (1)]. The synthesis and molecular structure of [$Bi(OSiMe_3)_3$] was reported recently.[11b]

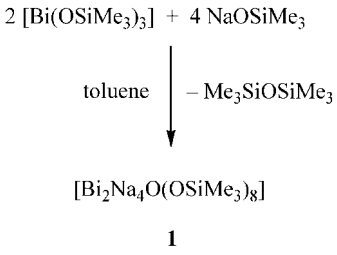

(1)

The molecular structure of compound **1** is best described to be composed of an octahedron with two bismuth atoms and four sodium atoms occupying the corners and a μ_6-oxygen atom being enclosed within the octahedron (Figure 1). Eight silanolate groups cap the trigonal faces. The compound crystallises in the space group $R\bar{3}c$ and only one crystallographic independent position for the metal atoms is found. Each position is occupied by both sodium and bismuth atoms with occupancies of 2/3 and 1/3, respectively. The analogous problem of disorder was reported for the closely related molecular structures of [$Sb_2Na_4O(OSiMe_3)_8$],[17] [$Bi_2Na_4O(O\mathit{t}Bu)_8$],[18] [$Sb_2M_4O(O\mathit{t}Bu)_8(thf)_n$] (M = Na, n = 0; M = K, n = 0, 4),[18] and [$Bi_2Na_4O(OC_6F_5)_8(thf)_4$].[19] For these compounds it was shown by means of solid state NMR, variable-temperature NMR in solution and crystallography that both in the solid state and in solution the group 15 atoms are located in *cis*-position of the octahedron. We have carried out a theoretical study of *cis*- and *trans*-[$Bi_2Na_4O(OSiMe_3)_8$] (**1**) at the RHF/LANL2DZ level of theory which confirms that a *cis*-arrangement is favoured ($\Delta E_{cis/trans}$ = 3.92 kcal mol^{-1}). At room temperature only one ^{1}H NMR signal is observed for the methyl protons, which is indicative of a fast exchange process involving the trimethylsilanolate groups. Further NMR studies in solution, such as variable temperature NMR, were hampered by the low solubility of compound **1**.

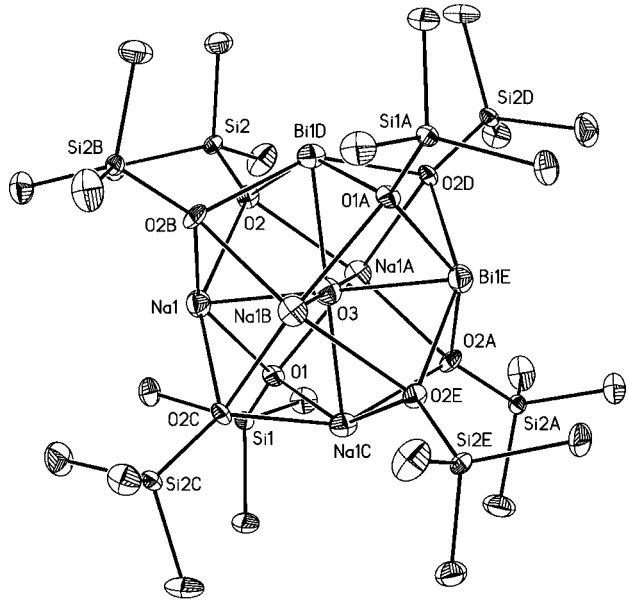

Figure 1. ORTEP diagram of [$Bi_2Na_4O(OSiMe_3)_8$] (**1**) showing 30% displacement ellipsoids and the atom numbering scheme. Hydrogen atoms are omitted. The positions of the metal atoms are occupied by both sodium and bismuth atoms with occupancies of 2/3 and 1/3, respectively. Selected bond lengths [Å] and bond angles [°] (M = Na, Bi): M(1)–O(3) 2.289(1), M(1)–O(2) 2.361(2), M(1)–O(2B) 2.422(2), M(1)–O(2C) 2.405(2), M(1)–O(1) 2.361(2); M(1)–O(3)–M(1E) 180.00(1), M(1)–O(3)–M(1B) 89.55(1), M(1)–O(3)–M(1C) 90.45(1), M(1)–O(2)–M(1A) 84.88(5), M(1)–O(2B)–M(1D) 84.61(5), M(1)–O(1)–M(1C) 86.11(8), O(1)–M(1)–O(2) 86.39(4), O(1)–M(1)–O(3) 73.56(5), O(2)–M(1)–O(3) 74.51(4), O(2)–M(1)–O(2B) 86.09(4), O(2)–M(1)–O(2C) 147.06(7). Symmetry operations used to generate equivalent atoms: A = –y, x – y, z; B = y, –x + y, –z; C = –x + y, –x, z; D = x – y, x, –z; E = –x, –y, –z.

The reaction of $BiCl_3$ with $NaOSiMe_3$ in 1:3 stoichiometry according to Scheme 1 gave a solid material containing sodium, bismuth and silicon as was shown by EDX analysis. The ^{29}Si NMR spectrum of the supernatant solution showed only one signal assigned to $Me_3SiOSiMe_3$. Crystallisation from toluene gave a crop of single crystals of the novel heterobimetallic compound of the formula [Bi_{10}-

 © 2005 Wiley-VCH Verlag GmbH & Co. KGaA, Weinheim

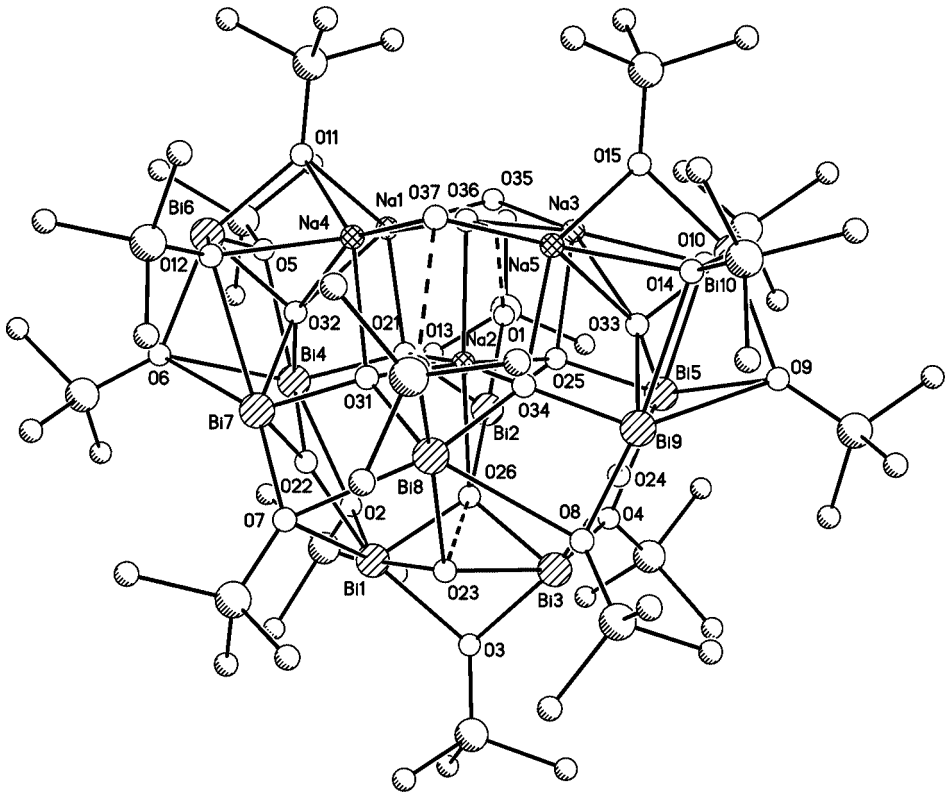

Figure 2. Molecular structure of $[Bi_{10}Na_5O_7(OH)_6(OSiMe_3)_{15}]$ (**2**); hydrogen atoms are omitted; typical bond lengths [Å] and bond angles [°] are found in the ranges: Bi–O 2.056(4)–2.728(5), Na–O 2.369(4)–2.710(5); O–Bi–O 64.5(2)–98.8(2) and 128.0(2)–166.5(2), O–Na–O 62.0(2)–99.2(2) and 122.1(2)–156.7(2), O–Na(2)–O 65.4(2)–106.3(2) and 112.6(2)–175.9(2), Bi–O–Bi 84.9(2)–137.1(2), Bi–O–Na 79.4(2)–158.7(2), Na–O–Na 79.9(2)–168.3(2). Additionally, weak secondary bonds between bismuth and oxygen with distances of 3.0 Å are observed for Bi(7) and Bi(9).

$Na_5O_7(OH)_6(OSiMe_3)_{15}]\cdot 1.5C_7H_8$ (**2**·$1.5C_7H_8$) (Figure 2). Apparently, partial hydrolysis of initially formed compounds took place as a result of contact with air moisture. Noteworthy, formation of single crystals of the metal oxo cluster **2** were also observed when a C_6D_6 solution of "$[Bi(OSiMe_3)_3]$", prepared from $NaOSiMe_3$ and $BiCl_3$, was kept for approximately two weeks under atmospheric conditions. We recently noticed, that reaction of $BiCl_3$ with $NaOSiMe_3$ (ratio 1:3) at room temperature under rigorous exclusion of air moisture again produced compound **1** as major product, but additionally single crystals of the bismuth-oxo silanolates $[Bi_{18}Na_4O_{20}(OSiMe_3)_{18}]$ and $[Bi_{33}NaO_{38}(OSiMe_3)_{24}]$ were obtained from toluene/benzene. A detailed comparison of the molecular structures of these bismuth-rich compounds with polynuclear homometallic bismuth-oxo silanolates is reported elsewhere.[11c] In conclusion, $[Bi_2Na_4O(OSiMe_3)_8]$ (**1**) is always obtained as the major product by the metathesis route and subtle changes regarding temperature, moisture and choice of the solvent lead to various heterobimetallic oxo(hydroxy)silanolates as byproducts.

The molecular structure of $[Bi_{10}Na_5O_7(OH)_6(OSiMe_3)_{15}]$ (**2**) is shown in Figure 2 and selected bond lengths and bond angles are given in the Figure caption. Compound **2** is composed of a metal-oxo core comprising 15 metal atoms and 15 trimethylsilyl groups. The metal-oxo core is best described to be composed of the different subunits **A**, **A′** and **B**, which are connected via Na(2) placed in the centre of the metal-oxo core (Figure 3). At the periphery of the molecule a total of fifteen μ_2- and μ_3-silanolate groups is found.

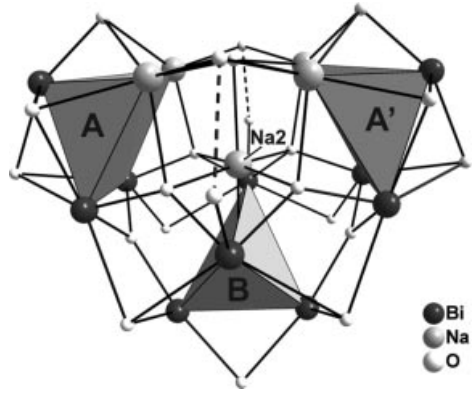

Figure 3. View of the $[Bi_{10}Na_5O_{28}]$ core structure of compound **2** (Me_3Si groups and H atoms are omitted; six oxygen atoms are covered by polyhedra). The sodium atom Na(2) connects the fragments **A**, **A′** and **B**.

Both pentanuclear fragments **A** and **A′** are composed of three bismuth atoms, two sodium atoms and thirteen oxygen atoms. The five metal atoms occupy the corners of a square pyramid with four μ_3-silanolate groups capping each

 © 2005 Wiley-VCH Verlag GmbH & Co. KGaA, Weinheim

trigonal face (Figure 4). A μ_5-oxygen atom occupies approximately the centre of the basal plane. In addition, four oxygen atoms are coordinated terminal to the metal atoms of the basal plane of **A** and four oxo ligands are bidentate bridging. The subunits **A** and **A′** are not related by symmetry, but show similar bond lengths and bond angles. The basic structural motif of the $[Bi_3Na_2O_{13}]$ fragment **A** is closely related to the metal-oxo core of $[Bi_2Na_4O(OSiMe_3)_8]$ (**1**) as is shown in Figure 4. Other examples with related molecular structures were reported among pentanuclear metal μ_5-oxo alkoxides,[20,21] several hexanuclear compounds with μ_6-oxo ligands[17–19,21,22] and hexanuclear bismuth-oxo-hydroxo cations with a $[Bi_6O_8]$ fragment (Figure 4).[23]

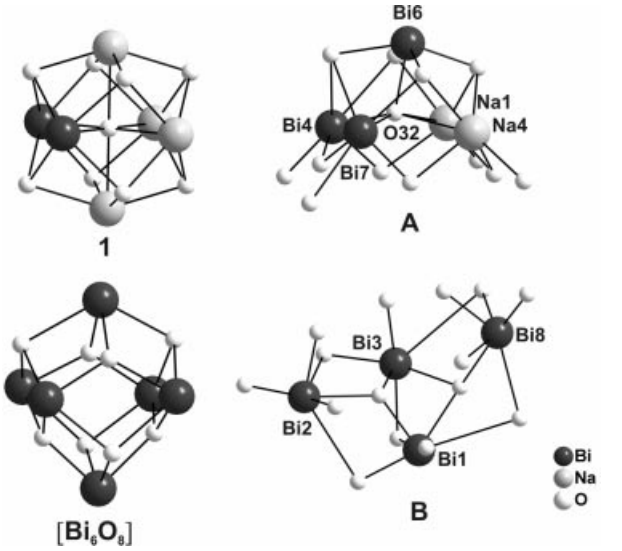

Figure 4. View of the structural fragments, which constitute the metal-oxo clusters **1**, **2** (**A** and **B**) and the $[Bi_6O_8]$ fragment of previously described hexanuclear bismuth-oxo-hydroxo cations.[23]

In compound **1** the oxygen atom is located in the centre of the cluster and thus all M–O (M = Na, Bi) bond lengths equally amount to 2.289(1) Å. This is a result of the disorder model suggested for the symmetric cluster **1**. In contrast, fragment **A** shows two short Bi–μ_5-O distances [Bi(4)–O(32) 2.192(4) Å, Bi(6)–O(32) 2.086(4) Å], a longer Bi–μ_5-O bond length [Bi(7)–O(32) 2.425(4) Å] and two similar Na–μ_5-O distances [Na(1)–O(32) 2.559(5) Å, Na(4)–O(32) 2.588(5) Å]. However, the average M–μ_5-O distance in **A** (av. M–O 2.365 Å) is close to the M–O distance in compound **1**. Comparison of the metal-oxo core structure of **1** with that of **A** sheds some light on the disorder problem reported above for compound **1**. The higher oxophilicity of the bismuth atom compared with the sodium atom should favour the formation of short Bi–O distances to give a *cis*-arrangement in compound **1** as it was observed for subunit **A**. This result is in agreement with our theoretical model. A *cis*-arrangement gives a structure of lower symmetry. Thus, we suggest the disorder observed in compound **1** to be a result of disordered molecules in the crystal lattice rather than disordered metal atoms. Noteworthy, another example, namely $[(Cp^*Zr)_6(\mu_4\text{-}O)(\mu_2\text{-}O)_4(\mu_2\text{-}OH)_8]$, was reported recently, in which an asymmetric structure with an μ_4-oxo ligand in the centre of an octahedron is favoured over the more symmetric structure which requires an ideal μ_6-oxo ligand.[24]

The structural fragment **B** consists of four bismuth atoms and fifteen oxygen atoms (Figure 4). The $[Bi_4O_{15}]$ fragment resembles the Bi_4O_6-ladder-type arrangement (**C**) which was described as a central structural motif in other bismuth-oxo compounds.[6,25] However, in contrast to the ladder-type arrangement **C** fragment **B** is strongly distorted and an additional μ_2-oxo ligand connects the two central bismuth atoms to give an structural arrangement, which is better assigned to type **C′**. Molecular structures based on this motif have been reported for the bismuth-oxo alkoxides $[Bi_6O_3(OR)_{12}]$ (R = C_6F_5,[6] 2,6-$C_6H_3Cl_2$[26]). Both structural arrangements **C** and **C′** can formally be reduced to the trinuclear fragment **D**, which might be expected to be the most stable building unit of bismuth-oxo clusters. However, so far discrete trinuclear units similar to type **D** were solely observed for hydrolysis products of bismuth trifluoroacetate, such as $[Bi_3(OH)(OOCCF_3)_8]$.[23k,27]

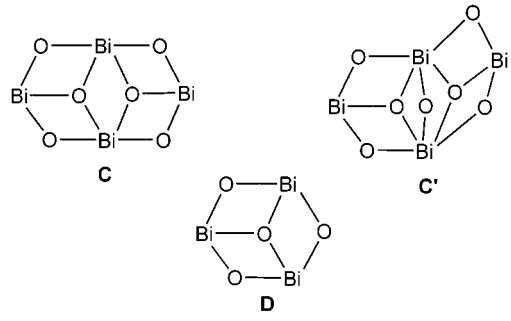

The more symmetric ladder-type arrangement **C** is observed for the central metal-oxo core composed of Bi(7)–Bi(9) and Na(2) (Figure 5). Each bismuth atom belongs to a different subunit [Bi(7) in **A**, Bi(9) in **A′** and Bi(8) in **B**; see Figure 3 and Figure 4] which are connected by Na(2).

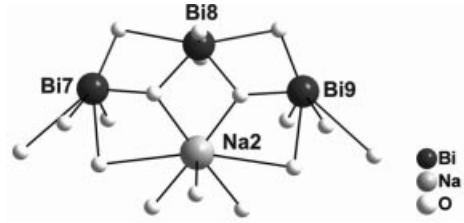

Figure 5. View of the central metal-oxo core of compound **2**, which connects the three subunits **A**, **A′** and **C**.

The heavy metal bismuth in $[Bi_{10}Na_5O_7(OH)_6(OSiMe_3)_{15}]\cdot 1.5C_7H_8$ (**2**·$1.5C_7H_8$) does not unambiguously allow the location of OH hydrogen atoms. However, different O···O distances make an assignment of hydroxy groups possible. Thus, O(35) [O(35)···O(1) 2.618(7) Å], O(37) [O(37)···O(13) 2.680(7) Å], O(23) [O(23)···O(26) 2.564(6) Å], O(22) [O(22)···O(2) 2.766(7) Å], and O(24) [O(24)···O(4) 2.783(7) Å] are assigned to hydroxo ligands. In addition, we suggest O(36), which is located at the periphery of the metal-oxo silanolate, to be a hydroxo ligand.

 © 2005 Wiley-VCH Verlag GmbH & Co. KGaA, Weinheim

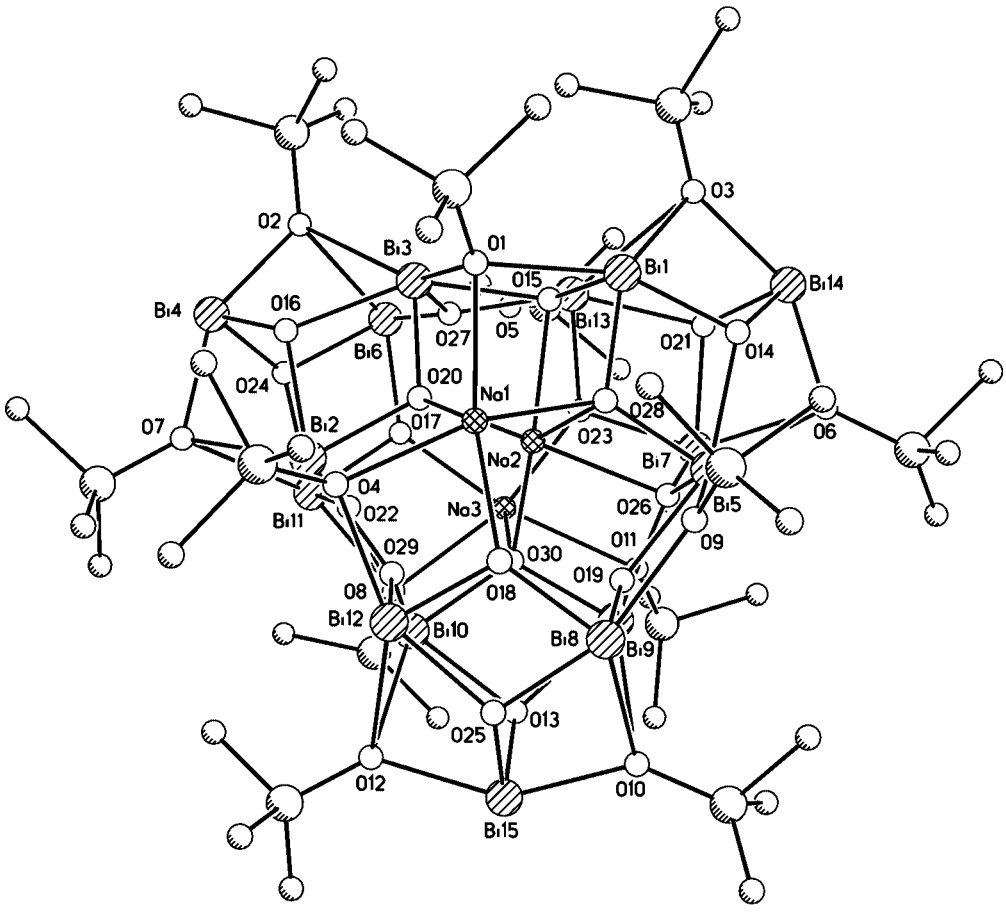

Figure 6. Molecular structure of $[Bi_{15}Na_3O_{18}(OSiMe_3)_{12}]$ (**3**); hydrogen atoms are omitted; typical bond lengths [Å] and bond angles [°] are found in the following ranges: Bi–O 2.033(9)–2.737(9), Na–O 2.264(10)–2.606(12); O–Bi–O 64.9(3)–160.1(3), O–Na–O 70.1(3)–165.1(4), Bi–O–Bi 93.9(3)–134.3(4), Bi–O–Na 84.6(3)–138.0(4). Additionally, weak secondary bonds between bismuth and oxygen with distances in the range of 3.2–3.5 Å are observed for Bi(2), Bi(5), Bi(9) and Bi(11)–Bi(13).

After the batch of single crystals of **2**·1.5C_7H_8 had been separated by filtration, a second crystal fraction, hereafter referred to as **3**·C_7H_8 (Figure 6), was obtained. The molecular structure of $[Bi_{15}Na_3O_{18}(OSiMe_3)_{12}]$·$C_7H_8$ (**3**·C_7H_8) is closely related to that of compound **2** although both compounds differ significantly in composition. The metal-oxo core of compound **3** is best described to be composed of three $[Bi_5O_{12}]$ subunits of type **E**, which are connected via three sodium atoms (Figure 7). Each subunit **E**, **E**′ and **E**′′ shares four oxygen atoms with a neighbouring subunit. The $[Bi_5O_{12}]$ subunits **E**, **E**′ and **E**′′ show similar structural parameters and thus only **E** is discussed in more detail (Figure 8).

The $[Bi_5O_{12}]$ subunit **E** is composed of five bismuth atoms, which occupy the corners of a square pyramid (Figure 8). Two μ_3-silanolate groups and two μ_3-oxygen atoms cap the trigonal faces. Each bismuth atom of the basal plane is connected to two bismuth atoms of the same plane by two oxo ligands. These oxo ligands further link each subunit to another subunit and/or a sodium atom to give six μ_3- and six μ_4-oxo ligands. In addition, six silanolate groups bridge adjacent corners of two subunits. Four of these ligands additionally coordinate to a sodium atom, which results in four μ_3- and two μ_2-$OSiMe_3$ ligands. Noteworthy,

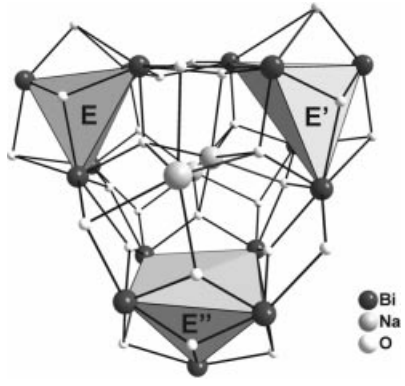

Figure 7. View of the $[Bi_{15}Na_3O_{30}]$ core structure of **3** (Me_3Si groups are omitted). Three sodium atoms connect the subunits **E**, **E**′ and **E**′′.

the molecular structures of the recently reported nonanuclear bismuth-oxo cations $[Bi_9(\mu_3\text{-}O)_8(\mu_3\text{-}OR)_6]^{5+}$ (R = H, Et)[25d] show a remarkable structural relationship with compound **3**. The cations might be described to be composed of a $[Bi_5O_6(OR)_6]$ subunit of type **E** and two edge-sharing trigonal $[Bi_3(\mu_3\text{-}O)]$ subunits.

 © 2005 Wiley-VCH Verlag GmbH & Co. KGaA, Weinheim

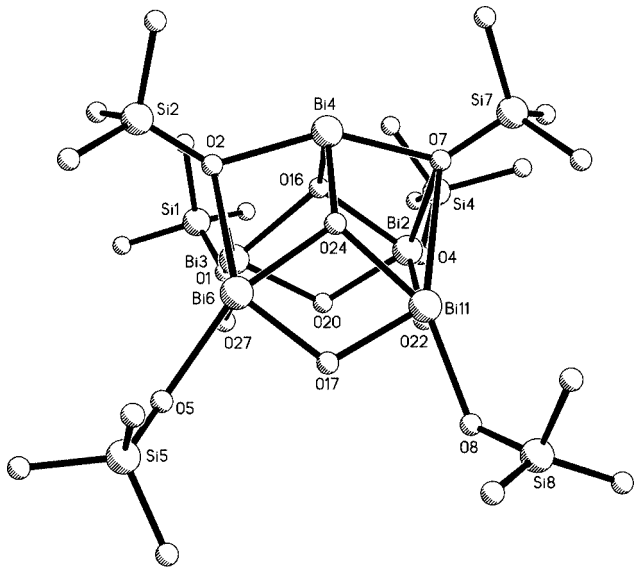

Figure 8. View of the $[Bi_5O_{12}]$ subunit **E** including Me_3Si groups. Two additional Bi–O bonds of Bi(2) and Bi(3) to O(29) and O(15), which are part of **E**′ and **E**′′, are omitted. Selected bond lengths [Å] and angles [°]: Bi(3)–O(1) 2.532(11), Bi(3)–O(2) 3.196(11), Bi(3)–O(16) 2.310(9), Bi(3)–O(20) 2.066(9), Bi(3)–O(27) 2.254(10), Bi(4)–O(2) 2.260(9), Bi(4)–O(7) 2.243(9), Bi(4)–O(16) 2.033(9), Bi(4)–O(24) 2.079(9), Bi(6)–O(2) 2.737(9), Bi(6)–O(5) 2.378(9), Bi(6)–O(17) 2.084(10), Bi(6)–O(24) 2.214(9), Bi(6)–O(27) 2.115(8); Bi(4)–O(2)–Bi(3) 89.7(3), Bi(4)–O(2)–Bi(6) 96.0(3), Bi(3)–O(2)–Bi(6) 83.7(3), Bi(3)–O(16)–Bi(4) 127.8(4), Bi(3)–O(27)–Bi(6) 130.6(4), Bi(4)–O(24)–Bi(6) 120.5(4), O(2)–Bi(6)–O(5) 128.8(3), O(2)–Bi(6)–O(17) 135.6(3), O(2)–Bi(6)–O(24) 65.7(3), O(2)–Bi(6)–O(27) 76.7(3), O(5)–Bi(6)–O(17) 87.3(3), O(5)–Bi(6)–O(24) 158.4(4), O(5)–Bi(6)–O(27) 74.6(3), O(17)–Bi(6)–O(24) 73.2(4), O(17)–Bi(6)–O(27) 93.0(4), O(24)–Bi(6)–O(27) 96.8(4).

In addition, the metal-oxo core of the $[Bi_5O_{12}]$ subunit **E** shows some structural relationship to the $[Bi_3Na_2O_{13}]$ subunit **A** (Figure 4). The basic structural motif of both **A** and **E** is a square pyramid with the metal atoms occupying the corners (Figure 8). An additional oxygen atom in **A** occupies a position within the oxo cage. However, both subunits **E** and **A** can be deduced from the metal-oxo core of bismuth-oxo-hydroxo complexes[23] of the type $[Bi_6O_{4+x}(OH)_{4-x}]^{[6-x]+}$ by removal of one bismuth atom (Figure 4). It might be assumed that only in octahedral structures of the type $[Bi_xNa_yO_z]$ ($x + y = 6$) and $[Bi_xNa_y\square O_z]$ ($x + y = 5$, $\square$ = metal vacancy) with at least two sodium atoms the octahedral void might be occupied by an oxygen atom. Noteworthy, the additional oxygen atom in **A** results in a smaller instead of the expected larger volume of subunit **A** compared with that of **E**. This is best demonstrated by the metal–metal distances along the edges of the pyramid. In structure fragment **A** these distances are in the range 3.290(2)–3.460(2) Å whereas those in fragment **E** are in the range 3.430(1)–3.958(1) Å. In subunit **E** the Bi–O distances are in a large range between 2.033(9) Å and 3.196(12) Å, which is attributed to the combination of strong primary bonds and weak secondary interactions. As a result large distortions of the coordination polyhedra are observed. For example, Bi(6) shows four Bi–O bond lengths in the range 2.084(10)–2.378(9) Å, a significantly longer Bi–O bond length of 2.737(9) Å and O–Bi(6)–O angles in the range 65.7(3)–158.4(4)° (Figure 8). The coordination geometry in the first-coordination shell might be described as distorted *pseudo*-trigonal bipyramid (BiO_4X) built from O(5), O(17), O(24), O(27) and a stereochemically active lone pair. An additional secondary Bi–O bond to O(2) completes the coordination sphere to give a [4+1] coordination. Similarly, all bismuth atoms in compound **3** show irregular coordination geometries which are best described as 4-, [4+1] and [4+2] coordination, respectively.

The metal-oxo silanolate $[Bi_2Na_4O(OSiMe_3)_8]$ (**1**) can be recrystallised from benzene or toluene, but attempts to recrystallise it from THF failed. Instead, the novel heterobimetallic compound $[Bi_{14}Na_8O_{18}(OSiMe_3)_{14}(thf)_4]\cdot C_6H_6$ (**4**·C_6H_6) was obtained. Its molecular structure is shown in Figure 9.

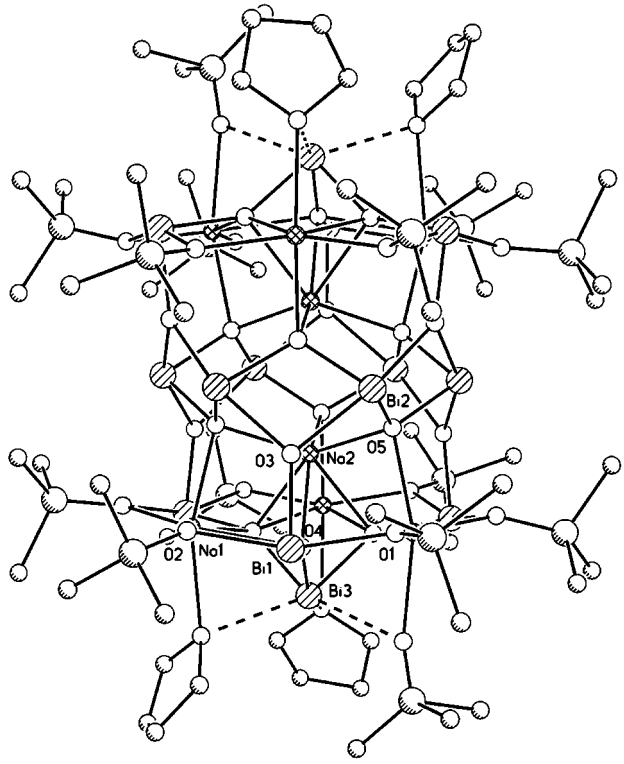

Figure 9. Molecular structure of $[Bi_{14}Na_8O_{18}(OSiMe_3)_{14}(thf)_4]$ (**4**); hydrogen atoms are omitted.

The molecular structure of compound **4** is best described to be composed of a symmetric $[(BiO_2)_6]^{6-}$ unit [Bi(2), O(3) and O(5)] which is sandwiched between two $[Bi_4Na_4O_3(OSiMe_3)_7(thf)_2]^{3+}$ subunits (Figure 10). The $[(BiO_2)_6]^{6-}$ unit resembles a small cylinder which is closed from both sides by Na(2) and Na(2D), respectively [Na(2)–Na(2D) 3.515(5) Å, Bi(2)–Bi(2A) 5.965(1) Å, Bi(2)–Bi(2D) 6.888(1) Å]. The bismuth atoms within the $[(BiO_2)_6]^{6-}$ ring show a *pseudo*-trigonal bipyramidal coordination geometry with Bi(2)–O distances of 2.103(3) Å and 2.268(3) Å. The *cis*-O–Bi–O angles amount to 74.70(9)° and 97.13(5)°, and

 © 2005 Wiley-VCH Verlag GmbH & Co. KGaA, Weinheim

the *trans*-O–Bi–O angle is 156.39(12)°. A similar cyclic structural arrangement of eight such $[BiO_2]$ moieties was recently reported for the ethanol solvate of $[Bi(OEt)_3]_8$.[28] The subunit $[Bi_4Na_4O_3(OSiMe_3)_7(thf)_2]^{3+}$ is composed of a symmetric layer, which consists of three bismuth and three sodium atoms [Bi(1) and Na(1)], three μ_5-oxygen atoms [O(4)] and six μ_2-$OSiMe_3$ ligands [O(1) and O(2)]. The sodium atom Na(2) is placed above the layer and the bismuth atom Bi(3), two thf ligands as well as a silanolate ligand are placed below the layer. Within the layer the bond lengths between the metal atoms and the oxygen atoms of the silanolate ligands are found to be similar for sodium and bismuth with values in the range 2.270(3)–2.319(3) Å. In contrast Bi(1)–O(4) amounts to 2.057(3) Å and Na(1)–O(4) to 2.583(3) Å. The μ_5-oxygen atom O(4) is further coordinated to Na(1A), Na(2) [Na(2)–O(4) 2.540(3) Å] and Bi(3) [Bi(3)–O(4) 2.138(3) Å]. The coordination geometry of Bi(3) is best described as trigonal pyramidal [O(4)–Bi(3)–O(4A) 83.69(5)°]. Additionally, secondary bonds of Bi(3) to the three oxygen-donor ligands thf and $OSiMe_3$ are observed [Bi(3)–O(6) 2.776(5) Å]. A similar coordination of the bismuth atom was reported for $[Bi(OSiPh_3)_3(thf)_3]$,[9] but in contrast to the terminal coordination of the thf ligands in the bismuth triphenylsilanolate those in compound **4** are bridging between Bi(3) and Na(1) [Na(1)–O(6) 2.513(4) Å].

The two subunits $[(BiO_2)_6]^{6-}$ and $[Bi_4Na_4O_3(OSiMe_3)_7(thf)_2]^{3+}$ are linked via O(3), O(5) and their symmetry related counterparts. Thus, μ_4-O(5) is connected to Na(1A), Na(2), Bi(2) and Bi(2B), and μ_3-O(3) to Bi(1), Bi(2) and Bi(2C) [O(5)–Na(1A)/Na(2)/Bi(2)/Bi(2B) 2.388(5)/2.446(3)/2.103(2)/2.103(2) Å; O(3)–Bi(1)/Bi(2)/Bi(2C) 2.045(3)/2.268(3)/2.268(3) Å]. The coordination geometry of Bi(1) is best described as *pseudo*-trigonal bipyramidal assigned to BiO_4X (X = lone pair). The *cis*-O–Bi–O angles are in the range 80.91(11)–91.66(10)° and the *trans*-O–Bi–O angle amounts to 161.65(11)°. Two short bonds between the bismuth atom and the *cis*-positioned oxygen atoms O(3) and O(4) [Bi(1)–O(3) 2.045(3) Å, Bi(1)–O(4) 2.057(3) Å] as well as two elongated bonds to the *trans*-located oxygen atoms O(1) and O(2) [Bi(1)–O(1) 2.319(3) Å, Bi(1)–O(2) 2.295(3) Å] are observed. Noteworthy, the sodium-rich bismuth-oxo cluster **4** is neither composed of the above-mentioned $[M_5O_{12}]$ subunits nor of ladder type arrangements of type **C**. The structural relationship is restricted to the formation of trinuclear $[Bi_3O]$ subunits, planar four-membered $[Bi_2O_2]$ and $[NaBiO_2]$ rings and strongly distorted bismuth-oxygen polyhedra.

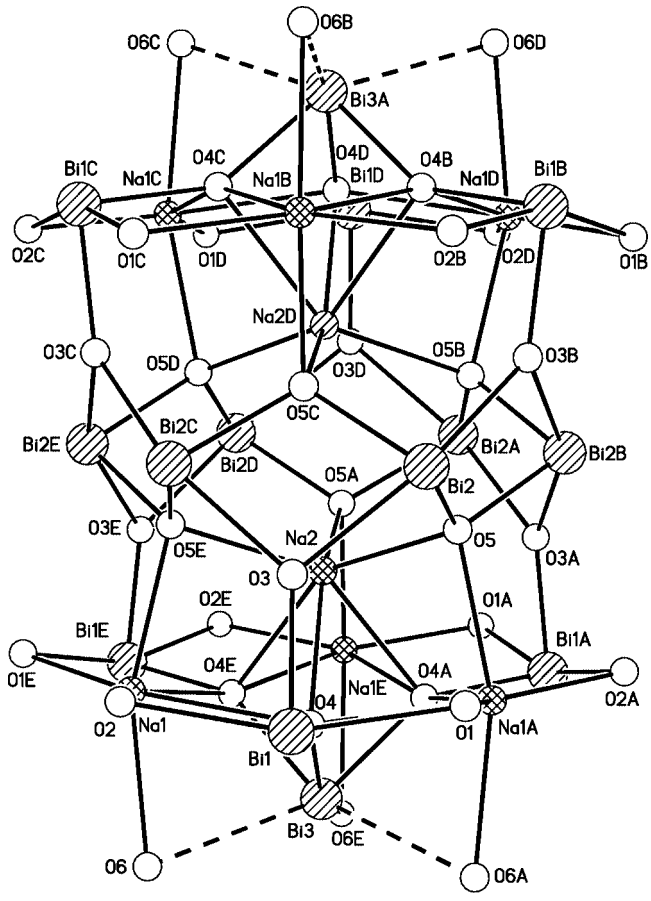

Figure 10. View of the metal-oxo core structure of **4** (Me_3Si groups, C and H atoms are omitted) showing the atom numbering scheme. Selected bond lengths [Å] and angles [°]: Bi(1)–O(1) 2.319(3), Bi(1)–O(2) 2.295(3), Bi(1)–O(3) 2.045(3), Bi(1)–O(4) 2.057(3), Bi(2)–O(3) 2.268(3), Bi(2)–O(3B) 2.263(3), Bi(2)–O(5) 2.103(2), Bi(2)–O(5C) 2.097(3), Bi(3)–O(4) 2.138(3), Bi(3)–O(6) 2.776(5), Na(1)–O(2) 2.270(3), Na(1)–O(1E) 2.277(3), Na(1)–O(5E) 2.388(3), Na(1)–O(6) 2.513(4), Na(1)–O(4) 2.583(3), Na(1)–O(4E) 2.535(3), Na(2)–O(5) 2.446(3), Na(2)–O(4) 2.540(3); O(1)–Bi(1)–O(2) 161.7(1), O(1)–Bi(1)–O(3) 81.0(1), O(1)–Bi(1)–O(4) 91.7(1), O(2)–Bi(1)–O(3) 80.9(1), O(2)–Bi(1)–O(4) 91.6(1), O(3)–Bi(1)–O(4) 90.6(1), O(5C)–Bi(2)–O(5) 94.3(1), O(5C)–Bi(2)–O(3B) 89.5(1), O(5)–Bi(2)–O(3B) 74.7(1), O(5C)–Bi(2)–O(3) 74.7(1), O(3)–Bi(2)–O(5) 88.9(1), O(3)–Bi(2)–O(3B) 156.4(1), O–Na(1)–O 67.6(1)–160.1(1), O–Na(2)–O 68.2(1)–148.2(1), Bi(1)–O(3)–Bi(2) 129.1(1), Bi(2)–O(5)–Bi(2B) 110.2(1), Bi(2)–O(3)–Bi(2C) 99.0(1). Symmetry operations used to generate equivalent atoms: A = $-x + y + 1$, $-x$, z; B = $y + 2/3$, $-x + y + 1/3$, $-z + 1/3$; C = $x - y - 1/3$, $x - 2/3$; $-z + 1/3$; D = $-x + 2/3$; $-y - 2/3$; $-z + 1/3$; E = $x - y - 1$; $x - 1$, $-z$.

Studies on the thermal behaviour of compounds **1**–**3** were carried out. The thermal stability of the clusters **2** and **3** is rather low as was shown by DTA-TG measurements. The onset of decomposition starts below 120 °C and is attributed to the loss of solvate molecules. The major weight loss for compounds **1**–**3** is observed between 150 °C and 250 °C. The observed weight loss (**1** 39.8%; **2** 27.6%; **3** 18.8%) is lower than calculated for the formation of pure Na/Bi/O phases and indicates formation of silicates. The observed values correspond to mixtures with general formulas such as $Bi_2Na_4Si_{2.5}O_{10}$ (calcd. 40.3%, **1b**), $Bi_{10}Na_5Si_{2.5}O_{10}$ (calcd. 26.6%, **2b**) and $Bi_{15}Na_4Si_3O_{30}$ (calcd. 19.0%, **3b**). It should be noted that the sillenite-type bismuth silicate $Bi_{12}SiO_{20}$ was observed upon thermal decomposition of $[Bi_{22}O_{16}(OSiMe_2tBu)_{22}]$.[10] Similarly, the powder X-ray data of the decomposition products **2b** and **3b** were also indicative of $Bi_{12}SiO_{20}$ (JCPDS No. 76–726) as major crystalline material. In case of compound **2** Na_2SiO_3 (JCPDS No. 82–0604) was observed as an additional minor product. The latter was the only crystalline material in the mainly amorphous decomposition product **1b**.

 © 2005 Wiley-VCH Verlag GmbH & Co. KGaA, Weinheim

Conclusions

Both partial hydrolysis and elimination of $Me_3SiOSiMe_3$ from $[Bi(OSiMe_3)_3]$ contribute to the formation of heterobimetallic bismuth-oxo silanolates. We assume that $[Bi(OSiMe_3)_3]$ is formed in situ by reaction of $BiCl_3$ with $NaOSiMe_3$, but the reaction of the bismuth silanolate with additional $NaOSiMe_3$ to give $Me_3SiOSiMe_3$ is faster than the metathesis reaction. The favoured product is $[Bi_2Na_4O(OSiMe_3)_8]$ (**1**). Several different heterobimetallic byproducts are observed, the amounts of which depend on subtle changes in the reaction conditions. The use of THF as solvent favours the elimination of $Me_3SiOSiMe_3$, but its formation is also observed in non-polar solvents. It is noteworthy that in contrast to $[Bi(OSiMe_3)_3]$, the corresponding alkoxide $[Bi(OtBu)_3]$ is accessible via salt elimination. Despite of the ready M–O–M bond formation by elimination of $Me_3SiOSiMe_3$, thermolysis of heterometallic bismuth-oxo silanolates in the solid state results in silicate materials instead of heterobimetallic oxides. The $Bi–OSiMe_3$ moiety is very sensitive towards hydrolysis, and trace amounts of water induce hydrolysis/condensation processes to take place until the reactivity of the metal-oxo silanolate is significantly reduced. The resulting heterobimetallic compounds are covered by Me_3SiO ligands which are still moisture-sensitive but prevent further aggregation.

The peculiarity of sodium and bismuth to assemble into diverse heterobimetallic complexes is explained by their similar ionic radii, and their rich and variable coordination chemistry. As a consequence, heterobimetallic metal-oxo subunits such as the ladder-type $[Bi_{3-x}Na_xO_y]$ and square pyramidal $[Bi_{5-x}Na_xO_y]$ fragments constitute basic building blocks. Thermolysis of bismuth-oxo silanolates gives compounds of the Sillenite-type family, which are extensively studied because of their interesting optical properties such as photorefractivity and photoconductivity.[29] It might be anticipated that novel heterometallic bismuth compounds are accessible starting from heterobimetallic bismuth-oxo silanolate derivatives. Such bismuth-rich metal-oxo silanolates might serve as molecular precursors for doped materials of the Sillenite-type family.

Experimental Section

General Remarks: All manipulations were performed with exclusion of oxygen and moisture by using Schlenk-type techniques and argon atmosphere. Solvents were distilled from appropriate drying agents prior to use. Elemental analyses were performed on a LECO-CHNS-932 analyser. No satisfactory elemental analyses were obtained for compound **1** which is assigned to partial substitution of $OSiMe_3$ by $OtBu$ – isostructural $[Bi_2Na_4O(OtBu)_8]$ was reported previously[18] – and for compound **2** which is assigned to its high moisture sensitivity. The DTA-TG measurements were performed at a heating rate of 6 °C min^{-1} to a maximum temperature of 700 °C in an atmosphere of flowing argon using Al_2O_3 as reference material. The residues were examined by powder X-ray diffraction using a Phillips PW1050/25 diffractometer. ^1H and ^{29}Si NMR spectra were recorded at 400.13 MHz and 59.6 MHz, respectively. Chemical shifts (δ values given in ppm) were referenced against Me_4Si. The IR spectra were run as Nujol mulls and absorption bands assigned to the compounds in the range 400–1400 cm^{-1} are listed. Celite® (FLUKA) and sodium silanolate (Aldrich) were dried in vacuo at 120 °C prior to use. Bismuth trichloride (Lancaster) was heated at reflux in thionyl chloride, washed with pentane and dried in vacuo. $[Bi(OtBu)_3]$[5] and Me_3SiOH[30] were prepared according to literature procedures.

Synthesis of $[Bi_2Na_4O(OSiMe_3)_8]$ (1) (Method a): To a solution of $NaOSiMe_3$ (12.70 g, 113.2 mmol) in toluene (100 mL) was added anhydrous $BiCl_3$ (7.00 g, 22.2 mmol) in small portions at room temperature. The beige suspension was stirred at room temperature for one hour and heated at reflux for two hours. The solid material was filtered off through Celite® and the clear solution was concentrated to approximately 50 mL. Crystallisation at 4 °C gave colourless crystals of compound **1**. The first crop of crystals isolated was not analytically pure and an EDX analysis revealed the presence of chloride in addition to bismuth, sodium and silicon. The second crop of crystals (1.20 g, 9%) was analytically pure **1**, which decomposes upon heating above 150 °C. A small quantity of compound **1** was suspended in THF/benzene and after stirring overnight a clear yellow solution was obtained. From this solution moisture-sensitive single crystals of $[Bi_{14}Na_8O_{18}(OSiMe_3)_{14}(thf)_4]\cdot C_6H_6$ (**4**·C_6H_6) were obtained and dried in vacuo.

Synthesis of 1 (Method b): A solution of Me_3SiOH (1.64 g, 18.2 mmol) in toluene (10 mL) was added dropwise to a solution of $[Bi(OtBu)_3]$ (2.61 g, 6.1 mmol) in toluene. All volatile components were removed in vacuo and the residue was dissolved in toluene. To this solution $NaOSiMe_3$ (1.36 g, 12.1 mmol) was added portionwise and the resulting suspension was heated at reflux for 1.5 h. The solid material was isolated by filtration and dried in vacuo to give compound **1** (2.86 g, 76%).

1: $C_{24}H_{72}Bi_2Na_4O_9Si_8$ (1239.4): C 23.3, H 5.9; found C 24.0, H 6.4. IR (Nujol) $\tilde{\nu}$ = 1298 w, 1258 m, 1246 m, 1021 m, 996 w, 980 w, 967 w, 925 m, 894 s, 829 s, 742 m, 724 sh, 675 w, 660 w, 620 vw, 584 w, 537 w, 462 w, 414 cm^{-1} w.

4: $C_{42}H_{126}Bi_{14}Na_8O_{32}Si_{14}$ (4646.3): C 10.9, H 2.7; found C 11.4, H 2.9. IR (Nujol) $\tilde{\nu}$ = 1257 m, 1241 m, 1051 w, 941 m, 910 m, 826 m, 740 m, 725 m, 668 w, 593 cm^{-1} m.

Synthesis of $[Bi_{10}Na_5O_7(OH)_6(OSiMe_3)_{15}]$ (2) and $[Bi_{15}Na_3O_{18}(OSiMe_3)_{12}]$ (3): To a solution of $BiCl_3$ (11.88 g, 37.4 mmol) in THF (180 mL) was added $NaOSiMe_3$ (12.70 g, 113.2 mmol) in small portions at room temperature to give a beige suspension. The solvent was evaporated, the residue extracted with hot toluene (150 mL) and the solid material filtered through Celite®. Evaporation of the solvent gave a solid containing Na, Bi and Si according to an EDX analysis. The residue was dissolved in toluene and the solution stored at 4 °C for several weeks. Single crystals of **2** were isolated by filtration and dried in vacuo to give 410 mg **2**. The filtrate was collected, the amount of the solvent was reduced to approximately 20 mL, and the solution was kept at 4 °C for several months to give single crystals of **3**. The colourless crystals were isolated by filtration and the solvent was removed from the crystals in vacuo to give 550 mg of **3**. Both compounds show a poor solubility, are moisture sensitive and decompose upon heating above 120 °C.

2: $C_{45}H_{141}Bi_{10}Na_5O_{28}Si_{15}$ (3756.6): C 14.4, H 3.8; found: C 13.4, H 3.0. IR (Nujol) $\tilde{\nu}$ = 3450 br, 1257 m, 1244 m, 1021 w, 925 s, 830 s, 741 m, 669 w, 632 w, 584 w, 536 w, 501 w, 410 cm^{-1} br.

3: $C_{43}H_{116}Bi_{15}Na_3O_{30}Si_{12}$ (4654.1): C 11.1, H 2.5; found: C 10.9, H 2.5. IR (Nujol) $\tilde{\nu}$ = 1258 m, 1244 m, 934 s, 921 s, 907 s, 828 s, 742 m, 674 w, 652 w, 632 m, 600 s, 543 w, 496 m, 442 w, 414 cm^{-1} w.

 © 2005 Wiley-VCH Verlag GmbH & Co. KGaA, Weinheim

Table 1. Crystallographic data for $[Bi_2Na_4(O)(OSiMe_3)_8]$ (**1**), $[Bi_{10}Na_5O_7(OH)_6(OSiMe_3)_{15}]\cdot 1.5C_7H_8$ (**2**·1.5C_7H_8), $[Bi_{15}Na_3O_{18}(OSiMe_3)_{12}]\cdot C_7H_8$ (**3**·C_7H_8) and $[Bi_{14}Na_8O_{18}(OSiMe_3)_{14}(thf)_4]$ (**4**·C_6H_6).

Compound	**1**	**2**·1.5C_7H_8	**3**·C_7H_8	**4**·C_6H_6
Empirical formula	$C_{24}H_{72}Bi_2Na_4O_9Si_8$	$C_{45}H_{141}Bi_{10}Na_5O_{28}Si_{15}\cdot 1.5C_7H_8$	$C_{36}H_{108}Bi_{15}Na_3O_{30}Si_{12}\cdot C_7H_8$	$C_{42}H_{126}Bi_{14}Na_8O_{32}Si_{14}\cdot 4thf\cdot C_6H_6$
Formula weight	1239.46	3894.88	4654.11	5012.85
Crystal system	trigonal	triclinic	monoclinic	trigonal
Space group	$R\bar{3}c$	$P\bar{1}$	$C2/c$	$R\bar{3}$
Cell constants [Å, °]	a = 12.8844(3)	a = 15.0377(2)	a = 54.311(11)	a = 15.9786(4)
		b = 16.0373(2)	b = 19.846(4)	
	c = 54.6565(3)	c = 27.8967(5)	c = 22.885(5)	c = 46.8329(17)
		α = 87.1321(6)		
		β = 86.6530(7)	β = 112.32(3)	
		γ = 63.6617(6)		
Volume [Å^3]	7857.8(3)	6016.8(2)	22819(8)	10355.2(5)
Z	6	2	8	3
$d_{calcd.}$ [g·cm^{-3}]	1.572	2.150	2.709	2.412
Absorption coefficient [mm^{-1}]	6.961	14.788	23.230	17.976
Crystal size [mm]	0.23×0.15×0.10	0.15×0.15×0.05	0.15×0.08×0.03	0.20×0.18×0.05
θ range for data collection [°]	3.16 to 27.46	2.93 to 27.52	2.94 to 25.41	2.98 to 27.49
No. of reflections collected	16688	70719	174201	62724
No. of unique reflections	2006 [R_{int} = 0.039]	27464 [R_{int} = 0.059]	20955 [R_{int} = 0.133]	5276 [R_{int} = 0.073]
R [$I > 2\sigma(I)$]	0.0285	0.0371	0.0445	0.0217
wR_2 (all data)	0.0381	0.0627	0.0809	0.0386
Largest diff. peak/hole [e·Å^{-3}]	0.318/–0.479	1.559/–1.526	3.240/–1.579	1.832/–1.956

Structure Determination: See Table 1. Intensity data for the colourless crystals were collected on a Nonius KappaCCD diffractometer with graphite-monochromated Mo-$K\alpha$ radiation at 173 K. The data collection covered almost the whole sphere of reciprocal space with two (**1**), four (**2**·1.5C_7H_8) and seven sets (**3**·C_7H_8, **4**·C_6H_6) at different κ-angles and 202 (**1**), 510 (**2**·1.5C_7H_8), 652 (**3**·C_7H_8) and 592 (**4**·C_6H_6) frames via ω-rotation (Δ/ω = 1°) at two times 30 s (**1**), 60 s (**2**·1.5C_7H_8), 157 s (**3**·C_7H_8) and 60 s (**4**·C_6H_6) per frame. The crystal–detector distance was 3.4 cm (**1**, **4**·C_6H_6), 4.4 cm (**2**) and 3.8 cm (**3**·C_7H_8). Crystal decay was monitored by repeating the initial frames at the end of data collection. Analysing the duplicate reflections there was no indication for any decay. The structures were solved by direct methods SHELXS97[31] and successive difference Fourier syntheses. Refinement applied full-matrix least-squares methods SHELXL97.[32] The H atoms were placed in geometrically calculated positions using a riding model with U_{iso} constrained at 1.2 times U_{eq} of the carrier C atom for non-methyl and 1.5 times U_{eq} of the carrier C atom for methyl groups. Atomic scattering factors for neutral atoms and real and imaginary dispersion terms were taken from the *International Tables for X-ray Crystallography*. Absorption correction was carried out with multi-scan using SCALEPACK[33] [T_{min} = 0.310, T_{max} = 0.543 (**1**); T_{min} = 0.245, T_{max} = 0.525 (**2**·1.5C_7H_8); T_{min} = 0.085, T_{max} = 0.543 (**3**·C_7H_8); T_{min} = 0.119, T_{max} = 0.467 (**4**·C_6H_6)]. In **1** disorder of the metal atoms was found. Bi1 and Na1 were refined with equal position and occupancies of 0.33 and 0.66, respectively. In **2**·1.5C_7H_8 disorder over two positions was found for C6C, C6C′, C8A, C8A′, C8B, C8B′ with occupancies of 0.5. All solvent molecules toluene (C51–C57, C61–C67) and disordered atoms were refined isotropically. One solvent molecule toluene (C61–C67) was refined with occupancies of 0.5. In **3**·C_7H_8 disorder over two positions was found for C5A–C5′, C6A–C6′, C8A, C8′, C8B, C8′′, C9A–C9′, C10A–C10′, C11A–C11′ with occupancies of 0.5, for C12A, C12B with occupancies of 0.7 and for C12′, C12′′ with occupancies of 0.3. All solvent molecules toluene (C21–C27, C31–C37) and disordered atoms were refined isotropically. The solvent molecules toluene were refined with occupancies of 0.5. In **4**·C_6H_6 a trimethylsilanolate ligand and a solvent molecule THF share the oxygen atom O6. The $SiMe_3$ group (Si3, C11–C13) was refined with occupancies of 0.33 and the C atoms of the solvent molecule THF (C7–C10) were refined with occupancies of 0.66. Si3, C7–C10 were refined anisotropically and C11–C13 were refined isotropically. The figures were created by SHELXTL[34] and DIAMOND (release 2.1e, 2001).

CCDC-276495 (for **1**), -276497 (for **2**·1.5C_7H_8), -276496 (for **3**·C_7H_8) and -276498 (for **4**·C_6H_6) contain the supplementary crystallographic data for this paper. These data can be obtained free of charge from The Cambridge Crystallographic Data Centre via www.ccdc.cam.ac.uk/data_request/cif.

Acknowledgments

We acknowledge the Deutsche Forschungsgemeinschaft, the Fonds der Chemischen Industrie, the Fachbereich Chemie of Dortmund University (support of young scientists) and Professor Dr. K. Jurkschat for support of this work. S. P. is grateful to the department of chemistry at the University of Joensuu (Finland) and the foundation of Heikki and Hilma Honkanen for financial support as well as for receipt of an ERASMUS grant.

[1] a) P. A. Williams, A. C. Jones, M. J. Crosbie, P. J. Wright, J. F. Bickley, A. Steiner, H. O. Davies, T. J. Leedham, G. W. Critchlow, *Chem. Vap. Deposition* **2001**, *7*, 205–209; b) R. Potter, P. A. Marshall, J. L. Roberts, A. C. Jones, P. R. Chalker, M. Vehkamaeki, M. Ritala, M. Leskelä, P. A. Williams, H. O. Davies, N. L. Tobin, L. M. Smith, *Mater. Res. Soc. Symp. Proc.* **2004**, *784*, 97–108; c) H. Kadokura, Y. Okuhara, M. Hijido, *JP 2005–060358*, Kojundo Chemicals Laboratory Co., Ltd., Japan, **2005**; d) F. S. Hintermaier, P. C. Van Buskirk, J. F. Roeder, B. C. Hendrix, T. H. Baum, D. A. Desrochers, *WO 2000–034549*, Infineon Technologies AG, Germany, **2000**.

[2] a) F. Soares-Carvalho, P. Thomas, J. P. Mercurio, B. Frit, S. Parola, *J. Sol-Gel Sci. Technol.* **1997**, *8*, 759–763; b) E. P. Turevskaya, V. B. Bergo, M. I. Yanovskaya, N. Y. Turova, *Zh. Neorg. Khim.* **1996**, *41*, 721–725; c) K. A. Vorotilov, M. I. Yanovskaya, E. P. Turevskaya, A. S. Sigov, *J. Sol-Gel Sci. Technol.* **1999**, *16*, 109–118; d) E. P. Turevskaya, V. B. Bergo, K. A. Vorotilov, A. S. Sigov, D. Benlian, *J. Sol-Gel Sci. Technol.* **1998**, *13*, 889–

 © 2005 Wiley-VCH Verlag GmbH & Co. KGaA, Weinheim

893; e) S. Parola, R. Papiernik, L. G. Hubert-Pfalzgraf, S. Jagner, M. Hakansson, *J. Chem. Soc., Dalton Trans.* **1997**, 4631–4635; f) Y. T. Kim, C. Hwang, H. K. Chae, Y. K. Lee, W. I. Lee, Y. W. Dong, H. Yun, *J. Sol-Gel Sci. Technol.* **2000**, *19*, 301–304; g) Y. Kim, H. K. Chae, K. S. Lee, W. I. Lee, *J. Mater. Chem.* **1998**, *8*, 2317–2319; h) W. F. Su, Y. T. Lu, *Mater. Chem. Phys.* **2003**, *80*, 632–637; i) Y. Kageyama, T. Yoshida, Y. Mitsushima, K. Suzuki, K. Kato, *Integr. Ferroelectr.* **2001**, *36*, 173–181; j) K. Kato, C. Zheng, J. M. Finder, S. K. Dey, Y. Torii, *J. Am. Ceram. Soc.* **1998**, *81*, 1869–1875.

[3] J. H. Thurston, K. H. Whitmire, *Inorg. Chem.* **2003**, *42*, 2014–2023.

[4] a) K. H. Whitmire, *Chemtracts, Inorg. Chem.* **1995**, *7*, 167–181; b) J. H. Thurston, D. Trahan, T. Ould-Ely, K. H. Whitmire, *Inorg. Chem.* **2004**, *43*, 3299–3305; c) J. H. Thurston, A. Kumar, C. Hofmann, K. H. Whitmire, *Inorg. Chem.* **2004**, *43*, 8427–8436; d) R. E. Bachman, K. H. Whitmire, J. H. Thurston, A. Gulea, O. Stavila, V. Stavila, *Inorg. Chim. Acta* **2003**, *346*, 249–255; e) J. H. Thurston, K. H. Whitmire, *Inorg. Chem.* **2002**, *41*, 4194–4205; f) C. M. Jones, M. D. Burkart, R. E. Bachman, D. L. Serra, S. J. Hwu, K. H. Whitmire, *Inorg. Chem.* **1993**, *32*, 5136–5144; g) C. M. Jones, M. D. Burkart, K. H. Whitmire, *J. Chem. Soc., Chem. Commun.* **1992**, 1638–1639; h) S. Parola, R. Papiernik, L. G. Hubert-Pfalzgraf, C. Bois, *J. Chem. Soc., Dalton Trans.* **1998**, 737–739; i) T. J. Boyle, D. M. Pedrotty, B. Scott, J. W. Ziller, *Polyhedron* **1998**, *17*, 1959–1974; j) M. Hunger, C. Limberg, P. Kircher, *Angew. Chem.* **1999**, *111*, 1171–1174; *Angew. Chem. Int. Ed.* **1999**, *38*, 1105–1108; k) M. Hunger, C. Limberg, P. Kircher, *Organometallics* **2000**, *19*, 1044–1050; l) C. Limberg, M. Hunger, W. Habicht, E. Kaifer, *Inorg. Chem.* **2002**, *41*, 3359–3365; m) M. A. Matchett, M. Y. Chiang, W. E. Buhro, *Inorg. Chem.* **1990**, *29*, 358–360; n) C. M. Jones, M. D. Burkart, K. H. Whitmire, *Angew. Chem.* **1992**, *104*, 466–467; *Angew. Chem. Int. Ed. Engl.* **1992**, *31*, 451–452; o) T. A. Hanna, G. Keitany, C. Ibarra, R. D. Sommer, A. L. Rheingold, *Polyhedron* **2001**, *20*, 2451–2455; p) V. G. Kessler, N. Y. Tiurova, E. P. Turevskaya, *Inorg. Chem. Commun.* **2002**, *5*, 549–551; q) J. W. Pell, W. C. Davis, H. C. zur Loye, *Inorg. Chem.* **1996**, *35*, 5754–5755.

[5] W. J. Evans, J. J. H. Hain, J. W. Ziller, *J. Chem. Soc., Chem. Commun.* **1989**, 1628–1629.

[6] K. H. Whitmire, S. Hoppe, O. Sydora, J. L. Jolas, C. M. Jones, *Inorg. Chem.* **2000**, *39*, 85–97.

[7] H. Schmidbaur, M. Bergfeld, *Z. Anorg. Allg. Chem.* **1968**, *363*, 84–88.

[8] K. W. Terry, K. Su, T. D. Tilley, A. L. Rheingold, *Polyhedron* **1998**, *17*, 891–897.

[9] M.-C. Massiani, R. Papiernik, L. G. Hubert-Pfalzgraf, J.-C. Daran, *Polyhedron* **1991**, *10*, 437–445.

[10] D. Mansfeld, M. Mehring, M. Schürmann, *Angew. Chem.* **2005**, *116*, 250–254; *Angew. Chem. Int. Ed.* **2005**, *44*, 245–246.

[11] a) D. Mansfeld, M. Mehring, M. Schürmann, *Z. Anorg. Allg. Chem.* **2004**, *630*, 1795–1796; b) S. Paalasmaa, D. Mansfeld, M. Schürmann, M. Mehring, *Z. Anorg. Allg. Chem.* **2005**, *631*, 2433–2438; c) M. Mehring, D. Mansfeld, S. Paalasmaa, M. Schürmann, *Chem. Eur. J.*, *in press.*

[12] a) W. Patnode, F. C. Schmidt, *J. Am. Chem. Soc.* **1945**, *67*, 2272–2273; b) H. Schmidbaur, *Angew. Chem.* **1965**, *77*, 206–216; *Angew. Chem. Int. Ed. Engl.* **1965**, *4*, 201–211; c) R. Murugavel, A. Voigt, M. G. Walawalkar, H. W. Roesky, *Chem. Rev.* **1996**, *96*, 2205–2236; d) L. King, A. C. Sullivan, *Coord. Chem. Rev.* **1999**, *189*, 19–57; e) J. Beckmann, K. Jurkschat, *Coord. Chem. Rev.* **2001**, *215*, 267–300; f) W.-W. Du Mont, M. Grenz, *Chem. Ber.* **1981**, *114*, 1180–1181; g) M. J. McGeary, R. H. Cayton, K. Folting, J. C. Huffman, K. G. Caulton, *Polyhedron* **1992**, *11*, 1369–1382; h) L. R. Sita, J. R. Babcock, R. Xi, *J. Am. Chem. Soc.* **1996**, *118*, 10912–10913; i) M. Veith, C. Mathur, V. Huch, *J. Chem. Soc., Dalton Trans.* **1997**, 995–999; j) L. H. Kras, A. Euvrard, Y. N. Grassl, S. M. Ronda, J. L. Stewart, *Main Group Met. Chem.* **1994**, *17*, 409–412; k) J. Caruso, C. Roger, F. Schwertfeger, M. J. Hampden-Smith, A. L. Rheingold, G. Yap, *Inorg. Chem.* **1995**, *34*, 449–453; l) J. Caruso, T. M. Alam, M. J. Hampden-Smith, A. L. Rheingold, G. A. P. Yap, *J. Chem. Soc., Dalton Trans.* **1996**, 2659–2664; m) S. D. Kinrade, R. T. Syvitski, K. Marat, C. T. G. Knight, *J. Am. Chem. Soc.* **1996**, *118*, 4196–4197.

[13] a) W.-W. Du Mont, M. Grenz, *Z. Naturforsch., Teil B: Chem. Sci.* **1983**, *38*, 113–114; b) L. R. Sita, R. Xi, G. P. A. Yap, L. M. Liable-Sands, A. L. Rheingold, *J. Am. Chem. Soc.* **1997**, *119*, 756–760; c) C. S. Weinert, I. A. Guzei, A. L. Rheingold, L. R. Sita, *Organometallics* **1998**, *17*, 498–500.

[14] a) R. L. Brutchey, J. E. Goldberger, T. S. Koffas, T. D. Tilley, *Chem. Mater.* **2003**, *15*, 1040–1046; b) M. P. Coles, C. G. Lugmair, K. W. Terry, T. D. Tilley, *Chem. Mater.* **2000**, *12*, 122–131; c) K. L. Fujdala, T. D. Tilley, *Chem. Mater.* **2001**, *13*, 1817–1827; d) K. L. Fujdala, T. D. Tilley, *Chem. Mater.* **2002**, *14*, 1376–1384; e) K. L. Fujdala, T. D. Tilley, *Chem. Mater.* **2004**, *16*, 1035–1047; f) J. Jarupatrakorn, M. P. Coles, T. D. Tilley, *Chem. Mater.* **2005**, *17*, 1818–1828; g) R. Rulkens, J. L. Male, K. W. Terry, B. Olthof, A. Khodakov, A. T. Bell, E. Iglesia, T. D. Tilley, *Chem. Mater.* **1999**, *11*, 2966–2973; h) C. G. Lugmair, K. L. Fujdala, T. D. Tilley, *Chem. Mater.* **2002**, *14*, 888–898.

[15] J. Hambrock, S. Rabe, K. Merz, A. Birkner, A. Wohlfart, R. A. Fischer, M. Driess, *J. Mater. Chem.* **2003**, *13*, 1731–1736.

[16] A. Roy, S. Polarz, S. Rabe, B. Rellinghaus, H. Zahres, F. E. Kruis, M. Driess, *Chem. Eur. J.* **2004**, *10*, 1565–1575.

[17] M. Baier, P. Bissinger, J. Blümel, H. Schmidbaur, *Chem. Ber.* **1993**, *126*, 947–950.

[18] M. Veith, E.-C. Yu, V. Huch, *Chem. Eur. J.* **1995**, *1*, 26–32.

[19] J. L. Jolas, S. Hoppe, K. H. Whitmire, *Inorg. Chem.* **1997**, *36*, 3335–3340.

[20] a) M. Moustiakimov, M. Kritikos, G. Westin, *Inorg. Chem.* **2005**, *44*, 1499–1504; b) M. Kritikos, M. Moustiakimov, M. Wijk, G. Westin, *J. Chem. Soc., Dalton Trans.* **2001**, 1931–1938; c) S. Chitsaz, B. Neumüller, *Z. Anorg. Allg. Chem.* **2001**, *627*, 2451–2459; d) J. Gromada, A. Mortreux, T. Chenal, J. W. Ziller, F. Leising, J. F. Carpentier, *Chem. Eur. J.* **2002**, *8*, 3773–3788; e) W. J. Evans, M. S. Sollberger, *J. Am. Chem. Soc.* **1986**, *108*, 6095–6096; f) L. G. Hubert-Pfalzgraf, S. Daniele, A. Bennaceur, J. C. Daran, J. Vaissermann, *Polyhedron* **1997**, *16*, 1223–1234; g) D. C. Bradley, H. Chudzynska, D. M. Frigo, M. E. Hammond, M. B. Hursthouse, M. A. Mazid, *Polyhedron* **1990**, *9*, 719–726; h) G. Westin, M. Kritikos, M. Wijk, *J. Solid State Chem.* **1998**, *141*, 168–176; i) K. G. Caulton, M. H. Chisholm, S. R. Drake, K. Folting, *J. Chem. Soc., Chem. Commun.* **1990**, 1349–1351.

[21] H. Schumann, G. Kociokkohn, J. Loebel, *Z. Anorg. Allg. Chem.* **1990**, *581*, 69–81.

[22] a) L. G. Hubert-Pfalzgraf, C. Sirio, C. Bois, *Polyhedron* **1998**, *17*, 821–830; b) T. Kräuter, B. Neumüller, *Chem. Eur. J.* **1997**, *3*, 568–572; c) B. A. Vaartstra, W. E. Streib, K. G. Caulton, *J. Am. Chem. Soc.* **1990**, *112*, 8593–8595; d) P. Miele, J. D. Foulon, N. Hovnanian, L. Cot, *J. Chem. Soc., Chem. Commun.* **1993**, 29–31.

[23] a) F. Lazarini, *Cryst. Struct. Commun.* **1979**, *8*, 69–74; b) B. Sundvall, *Acta Chem. Scand. A* **1979**, *33*, 219–224; c) F. Lazarini, *Acta Crystallogr. Sect. B* **1979**, *35*, 448–450; d) F. Lazarini, *Acta Crystallogr., Sect. B* **1978**, *34*, 3169–3173; e) A. N. Christensen, M. A. Chevallier, J. Skibsted, B. B. Iversen, *J. Chem. Soc., Dalton Trans.* **2000**, 265–270; f) B. Sundvall, *Inorg. Chem.* **1983**, *22*, 1906–1912; g) B. Sundvall, *Acta Chem. Scand. A* **1980**, *34*, 93–98; h) B. Sundvall, *Acta Chem. Scand. A* **1974**, *A28*, 1036–1037; i) E. Asato, K. Katsura, M. Mikuriya, U. Turpeinen, I. Mutikainen, J. Reedijk, *Inorg. Chem.* **1995**, *34*, 2447–2454; j) E. Asato, K. Katsura, M. Mikuriya, T. Fujii, J. Reedijk, *Chem. Lett.* **1992**, 1967–1970; k) B. Kugel, W. Frank, *Z. Anorg. Allg. Chem.* **2002**, *628*, 2178.

[24] G. C. Bai, H. W. Roesky, J. Y. Li, T. Labahn, F. Cimpoesu, J. Magull, *Organometallics* **2003**, *22*, 3034–3038.

 © 2005 Wiley-VCH Verlag GmbH & Co. KGaA, Weinheim

[25] a) N. N. Sauer, E. Garcia, R. Ryan, *Mater. Res. Soc. Symp. Proc.* **1990**, *180*, 921–924; b) Y. Uchiyama, N. Kano, T. Kawashima, *Organometallics* **2001**, *20*, 2440–2442; c) M. Mehring, M. Schürmann, *Chem. Commun.* **2001**, 2354–2355; d) J. H. Thurston, D. C. Swenson, L. Messerle, *Chem. Commun.* **2005**, 4228–4230.
[26] S. C. James, N. C. Norman, A. G. Orpen, M. J. Quayle, U. Weckenmann, *J. Chem. Soc., Dalton Trans.* **1996**, 4159–4161.
[27] W. Frank, personal communication.
[28] V. G. Kessler, N. Y. Turova, E. P. Turevskaya, *Inorg. Chem. Commun.* **2002**, *5*, 549–551.
[29] a) P. Gunter, J. Huignard (Ed.), *Photorefractive Materials and Their Applications, I and II*, vol. 61, Springer-Verlag, Berlin, **1988**; b) H. Vogt, K. Buse, H. Hesse, E. Kratzig, R. R. Garcia, *J. Appl. Phys.* **2001**, *90*, 3167–3173; c) D. Dirksen, G. von Ball, *J. Opt. Soc. Am. B* **1994**, *11*, 1858–1863; d) M. Valant, A. Meden, D. Suvorov, *J. Am. Ceram. Soc.* **2004**, *87*, 677–682.
[30] L. H. Sommer, E. W. Pietrusza, F. C. Whitmore, *J. Am. Chem. Soc.* **1946**, *68*, 2282–2284.
[31] G. M. Sheldrick, *Acta Crystallogr., Sect. A* **1990**, *46*, 467–473.
[32] G. M. Sheldrick, *University of Göttingen*, Göttingen, Germany, **1997**.
[33] Z. Otwinowski, W. Minor, in: *Macromolecular Crystallography*, part A, vol. 276 (Eds.: C. W. Carter Jr., R. M. Sweet), Academic Press, New York, **1997**, 307–326.
[34] G. M. Sheldrick, Release 5.1 Reference Manual, Bruker AXS, Inc., Madison, Wisconsin, USA, **1997**.

Received: July 18, 2005
Published Online: November 2, 2005

 © 2005 Wiley-VCH Verlag GmbH & Co. KGaA, Weinheim

DOI: 10.1002/ejic.200400909

Synthesis and Investigations of the Crystal Structure of a Dinuclear Diazadiene Molybdenum Oxo-Imido Complex with a Unique $N_3Mo(\mu\text{-}O)_2MoN_3$ Core

Alexei Merkoulov,[a] Klaus Harms,[a] and Jörg Sundermeyer*[a]

Keywords: Molybdenum / Oxo ligands / Imido ligands / Metathesis / Crystal structure

Ligand metathesis of the diimido and dioxo precursor complexes $[Mo(X)_2Cl_2(DME)]$ (X = O, N*t*Bu) leads to the mixed oxo-imido derivative $[Mo(N\textit{t}Bu)(O)Cl_2(DME)]$ (**1**). By treatment with Li_2DAD (DAD = 1,4-di-*tert*-butyl-1,4-diazabuta-1,3-diene), **1** is converted into the complex $[Mo(N\textit{t}Bu)(O)(DAD)]_2$ (**2**). The crystal structure determination on a non-merohedral twin of **2** reveals a dinuclear molecular structure with nearly symmetrical bridging oxygen atoms. The smaller oxo ligand tends to be a better bridging functionality than the imido ligand; the unprecedented $N_3Mo(\mu\text{-}O)_2MoN_3$ configuration is favored over a $ON_2Mo(\mu\text{-}N)_2MoN_2O$ core. Compared to other known molybdenum DAD complexes, **2** reveals some degree of pyramidalization at the nitrogen atoms of the DAD ligand. In accord with the Mo–N, N–C, and C–C bond lengths, complex **2** is best described as an ene-diamido complex of formally six-valent molybdenum.
(© Wiley-VCH Verlag GmbH & Co. KGaA, 69451 Weinheim, Germany, 2005)

Introduction

Complexes based on the 1,4-diazabuta-1,3-diene DAD ligand backbone have been the focus of attention for many years. Due to several possible coordination modes and their redox activity, DAD ligands can stabilize metals with a wide range of formal oxidation states.[1] While DAD is a strong π-acceptor ligand that stabilizes low-valent metal centers, the two-electron-reduced DAD ligand, which is best described as an ene-diamido functionality, can be envisaged as a strong π-donor ligand that stabilizes high-valent metal centers. The diversity of substituents at the nitrogen and carbon atoms offers a perfect handle for the fine-tuning of electronic and steric ligand features that may be relevant in catalytic applications. For example, complexes of the late transition metals and diazadiene ligands with bulky electron-withdrawing aryl substituents at the nitrogen atom are extensively used in olefin oligomerization and polymerization.[2]

Following our previous investigations[3] on high-valent N-organoimido complexes of group 6 metals with other strong π-donor ligands, such as cyclopentadienyl, oxo, alkylidene or metallated phosphorus ylide ligands, we set out to explore the unknown chemistry of ene-diamido ligands with imido and oxo complexes. We now report the synthesis of a key oxo-imido complex, $[Mo(N\textit{t}Bu)(O)Cl_2(DME)]$ (**1**), and the conversion into its DAD derivative $[Mo(N\textit{t}Bu)(O)(DAD)]_2$ (**2**) (DAD = 1,4-di-*tert*-butyl-1,4-diazabuta-1,3-diene). Complexes with the functional and structural building block $[CpM(DAD)L_n]$ have been investigated for many years. This is the first report of a group 6 complex with a related σ,2π-donor and π-acceptor ligand regime $[(RN)M(DAD)L_n]$.

[a] Fachbereich Chemie, Philipps-Universität Marburg,
Hans-Meerwein-Straße, 35032 Marburg, Germany
Fax: +49-6421-28-28917
E-mail: jsu@chemie.uni-marburg.de

Results and Discussion

The oxo-imido complex **1** is formed in good yield by ligand metathesis between the known dioxo $[Mo(O)_2Cl_2(DME)]$[4] and diimido $[Mo(N\textit{t}Bu)_2Cl_2(DME)]$[5a] complexes in DME (Scheme 1). In agreement with the spectroscopic data and with related structurally characterized d^0 oxo-imido complexes,[5b] **1** probably has an octahedral structure with *trans* chloro ligands and the strong π-donor ligands O^{2-} and NR^{2-} in *cis* configuration. Reduction of DAD by lithium in THF affords the ene-diamide Li_2DAD.[6] The latter reacts with **1** to form the ene-diamido title complex **2** in a fair yield of 59%. Complex **2** is a hexane-soluble, dark purple, diamagnetic compound. ^1H and ^{13}C NMR spectra reveal equivalent *tert*-butyl groups at the DAD and imido N atoms, as well as equivalent methine protons at the C_2 bridge of DAD. These data are consistent with either a mononuclear tetrahedral structure or a binuclear species with either a mirror plane or a center of inversion. The EI mass spectra show mononuclear molecular ions $[Mo(N\textit{t}Bu)(O)(DAD)]$ as the highest peaks. To gain further insight into the nature of the title complex, single crystals for X-ray crystal structure determination were grown from a hexane solution.

 © 2005 Wiley-VCH Verlag GmbH & Co. KGaA, Weinheim

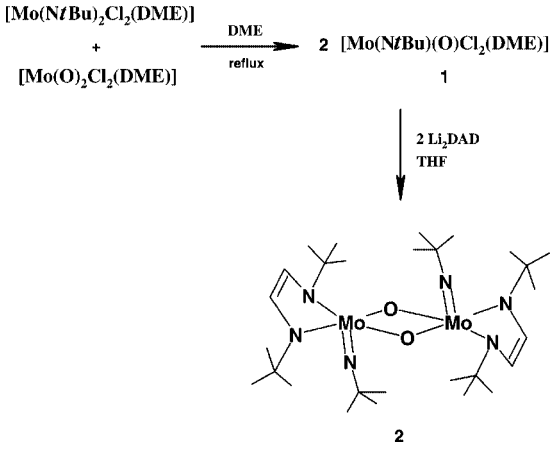

Scheme 1. Preparation of oxo-imido complex **2** using key compound **1**.

Data Collection and Structure Refinement

A crystal with the dimensions $0.35 \times 0.15 \times 0.15$ mm was mounted on a glass fiber by using the "oil drop method". Data were collected at $T = 193$ K with a STOE IPDS area detector system using graphite monochromated Mo-K_α radiation. The crystal is orthorhombic with $a = 19.913(2)$, $b = 18.437(2)$, $c = 9.547(2)$ Å and happens to be a nonmerohedral twin with only minor overlap of the reflections. Only one orientation matrix was used during the integration of the intensities. Overlapping reflections were ignored. This procedure led to 13576 integrated intensities, with 2877 independent ($R_{int} = 12.26\%$) and the completeness was 90% for $\Theta_{max} = 25°$. No absorption correction was applied ($C_{28}H_{58}Mo_2N_6O_2$: $M = 702.68$, $\mu = 7.46$ cm^{-1} for $Z = 4$). Structure solution (direct methods) and refinement in the space group *Pnma* were performed by using the SHELX-97 programs,[7] with all non-hydrogen atoms anisotropic, and hydrogen atoms with fixed isotropic temperature factors determined with a riding model. In the final stage of the refinement, two residual peaks in the difference Fourier map (distance 3.09 Å) were interpreted as disorder positions of atoms Mo(1) and Mo(2) (noncrystallographic transformation close to x, y, $5 - z$). The ratio of the occupancies [all atoms of the main part versus atoms Mo(3) and Mo(4)] were refined to 0.907:0.093. No disordered positions of the light atoms were located, final residuals: $wR_2 = 11.28\%$ (for all unique reflections), conventional $R_1 = 4.86\%$ [for 1346 reflections with $I > 2\sigma(I)$], and 205 refined parameters.

Molecular Structure of 2

The molecular structure of **2** in the crystal is shown by Figure 1, with selected bond lengths and angles in Table 1. Figure 2 displays the disorder and inner coordination spheres. The title complex **2** is binuclear in the solid state. Both molybdenum atoms are tetragonal pyramidal and coordinated by five atoms: an axial imido nitrogen atom, two basal nitrogen atoms of the DAD ligand, and two oxygen atoms of the central planar $Mo_2(\mu\text{-}O)_2$ core. All six basal atoms $N_2O_2N_2$ lie in the same plane. Both imido ligands adopt an *anti* collinear orientation. There is a crystallographic mirror plane defined by the two metal centers and the two Mo–N(imido) vectors. Although there is no inversion symmetry unit, the $Mo_2(\mu\text{-}O)_2$ core can be considered to be symmetrical on the basis of the bond lengths and their standard deviations; the Mo–O bond lengths are 1.959(5) and 1.952(5) Å. These bond lengths correlate with the value for Mo–O single bonds, e.g. in **A**,[8] they are approximately 1.95 Å (Scheme 2).

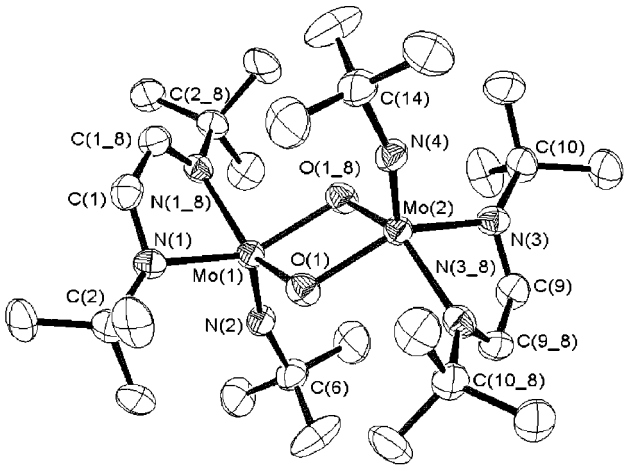

Figure 1. Molecular structure of **2**.

To date, no other structurally characterized example of an $N_3Mo(\mu\text{-}O)_2MoN_3$ coordination polyhedron is known, therefore a direct comparison cannot be made (CCSD search, September 2005). However, a similar framework has been found in a dinuclear thiolato(oxo) complex of the type $S_2(O)Mo(\mu\text{-}O)_2Mo(O)S_2$ (**A**). In contrast to **2**, the two square pyramids with their apical Mo–O vectors are in a *syn* configuration to each other in **A**.

Several molybdenum DAD complexes have been described in the literature, with examples given by **B**–**E**.[9–12] Type **B**[9] represents a four-electron Lewis base adduct of the diazadiene ligand that is coordinated to a formally six-valent molybdenum center, which is characterized by perfectly planar N atoms and long Mo–N distances of ca. 2.40 Å, short N–C distances of ca. 1.27 Å, and long C–C distances of ca. 1.48 Å. It is anticipated, for a metal of d^0 electron configuration that there is no M→L back-bonding in **B**. This is demonstrated by negligible differences between the discussed bond lengths in free DAD[13] and those in **B** (Table 2). However, due to its low-lying π* orbitals, neutral DAD can easily be reduced by more electron-rich metal centers to form the coordinated radical anion $[DAD]^{-}$[14] and the ene-diamido $[DAD]^{2-}$ ligands.[1,6,10,11,15,16] Examples of molybdenum complexes with a fully reduced DAD moiety are **C**[10] and **D**.[11] The structural parameters of their MN_2C_2 units are similar to that of the phenylene-1,2-diamido system **E**[12] (Table 2). Typically, flat[15] and folded[16] ene-diamido units (MN_2C_2) are known. In folded conformations, the metal is located out of the N_2C_2 plane (E^{NCCN}), as indicated by the distance $d(M\text{–}E^{NCCN})$, which

 © 2005 Wiley-VCH Verlag GmbH & Co. KGaA, Weinheim

Table 1. Selected inner core bond lengths [Å] and angles [°] of **2**.

C(1)–N(1)	1.333(11)	N(1)–Mo(1)–N(1_8)	80.4(5)
C(1)–C(1_8)	1.420(20)	N(2)–Mo(1)–Mo(2)	111.0(3)
C(2)–N(1)	1.493(13)	O(1_8)-Mo(1)–Mo(2)	38.4(2)
C(6)–N(2)	1.464(13)	O(1)–Mo(1)–Mo(2)	38.4(2)
C(9)–N(3)	1.345(11)	N(1)–Mo(1)–Mo(2)	119.7(2)
C(9)–C(9_8)	1.389(17)	N(1_8)-Mo(1)–Mo(2)	119.7(2)
C(10)–N(3)	1.501(13)	N(4)–Mo(2)–O(1)	106.2(3)
C14–N(4)	1.471(14)	N(4)–Mo(2)–O(1_8)	106.2(3)
Mo(1)–N(2)	1.716(8)	O(1)–Mo(2)–O(1_8)	77.1(3)
Mo(1)–O(1_8)	1.959(5)	N(4)–Mo(2)–N(3)	110.4(3)
Mo(1)–O(1)	1.959(5)	O(1)–Mo(2)–N(3)	143.3(3)
Mo(1)–N(1)	2.036(8)	O(1_8)–Mo(2)–N(3)	90.0(3)
Mo(1)–N(1_8)	2.036(8)	N(4)–Mo(2)–N(3_8)	110.4(3)
Mo(1)–Mo(2)	3.062(1)	O(1)–Mo(2)–N(3_8)	90.0(3)
Mo(2)–N(4)	1.718(8)	O(1_8)–Mo(2)–N(3_8)	143.3(3)
Mo(2)–O(1)	1.952(5)	N(3)–Mo(2)–N(3_8)	80.1(4)
Mo(2)–O(1_8)	1.952(5)	N(4)–Mo(2)–Mo(1)	110.8(3)
Mo(2)–N(3)	2.017(8)	O(1)–Mo(2)–Mo(1)	38.6(1)
Mo(2)–N(3_8)	2.017(8)	O(1_8)-Mo(2)–Mo(1)	38.6(1)
Mo(3)–Mo(4)	3.085(16)	N(3)–Mo(2)–Mo(1)	120.9(2)
		N(3_8)-Mo(2)–Mo(1)	120.9(2)
N(2)–Mo(1)–O(1_8)	106.2(3)	C(1)–N(1)–C(2)	118.4(7)
N(2)–Mo(1)–O(1)	106.2(3)	C(1)–N(1)–Mo(1)	104.3(6)
O(1_8)–Mo(1)–O(1)	76.8(3)	C(2)–N(1)–Mo(1)	134.5(5)
N(2)–Mo(1)–N(1)	111.4(3)	C(6)–N(2)–Mo(1)	161.5(8)
O(1_8)–Mo(1)–N(1)	142.2(3)	C(9)–N(3)–C10	117.1(7)
O(1)–Mo(1)–N(1)	89.4(3)	C(9)–N(3)–Mo(2)	103.6(6)
N(2)–Mo(1)–N(1_8)	111.4(3)	C(10)–N(3)–Mo(2)	134.8(5)
O(1_8)–Mo(1)–N(1_8)	89.4(3)	C(14)–N(4)–Mo(2)	161.1(8)
O(1)–Mo(1)–N(1_8)	142.2(3)	Mo(2)–O(1)–Mo(1)	103.1(2)

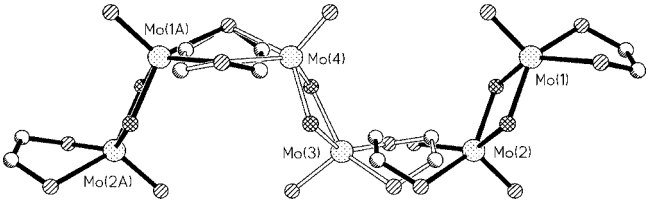

Figure 2. Coordination polyhedra and disorder in the crystal structure of **2**. Open bonds: minor part of disorder, positions of light atoms calculated.

is listed in Table 2. In almost flat conformations, as found in **C** and **D**, the Mo atom is only ca. 0.3 Å out of the plane. Perfectly flat conformations are present in DAD adducts such as **B**. Similarly to those in **B**, the nitrogen atoms of **C** and **D** are close to planar (the sum of angles at the N atoms Σ°N ca. 360°). By comparing the M–N, N–C, and C–C bond lengths, complex **2** is best described as an ene-diamide of d^0-Mo^{VI} and not as a neutral diazadiene adduct of d^2-Mo^{IV}. In contrast to those of **C** and **D**, the Mo atom of **2**

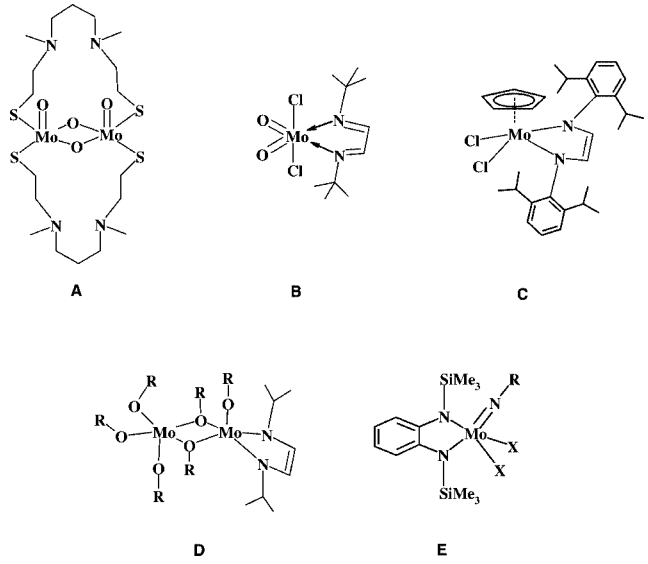

Scheme 2. Related complexes and reference compounds.

Table 2. Comparison of selected bond lengths [Å] and angles [°] in reference compounds.

	Mo–N	N–C	C–C	d(M–E^{NCCN})	Σ°N
*t*Bu-DAD	–	1.264–1.267	1.468(2)	–	–
B	2.388–2.399	1.267–1.271	1.476(3)	0	360.0(5)
C	2.081–2.092	1.353(4)	1.363(2)	0.329	360.0(3)
D	1.957–2.075	1.354–1.392	1.344(8)	0.329	359(1)
E	1.996–2.078	1.373–1.407	1.409–1.452	0.085–1.148	356.3–360.0
2	2.017–2.036	1.333–1.345	1.389–1.420	0.951(1)	355.5–357.2

 © 2005 Wiley-VCH Verlag GmbH & Co. KGaA, Weinheim

is located 0.951(1) Å out of the N_2C_2 plane, and the sum of angles at the nitrogen atoms, Σ°N = 355.5° and 357.2°, respectively, indicates a trend for pyramidalization, which is analogous to that of phenylene-diamido complexes of type **E**. Table 2 shows that the shortening of the Mo–N and C–C bonds is accompanied by a lengthening of the N–C bonds and a higher degree of pyramidalization at the N atoms. Currently we are investigating the scope of this statement by exploring other diazadiene imido complexes of the early transition metals. Preliminary results reveal that the liaison of both DAD and NR ligands at one metal offers access to a growing new class of covalent functional compounds.

Experimental Section

General: All reactions and manipulations were carried out under argon using standard Schlenk techniques. Solvents were refluxed in the presence of an appropriate drying agent and distilled: C_6D_6 and hexane (Na/K alloy), THF and DME (Na/benzophenone), and toluene (Na). Literature methods were employed for the synthesis of starting materials $[Mo(O)_2Cl_2(DME)]$,[4] $[Mo(N\textit{t}Bu)_2Cl_2(DME)]$,[5] 1,4-di-*tert*-butyl-1,4-diazabuta-1,3-diene (DAD),[17] and Li_2DAD.[6] Melting points (uncorrected) were measured with a Büchi MP B-540 apparatus. C, H, and N analyses were carried out with a Heraeus CHN-Rapid analyzer. Mass spectra were recorded with a Varian MAT CH-7a (EI, 70 eV) instrument. ^1H and $^{13}C\{^1H\}$ NMR spectra were recorded with Bruker AMX300 and DRX500 spectrometers; chemical shifts were referenced to the ^1H (δ = 7.15 ppm) and ^{13}C (δ = 128.0 ppm) residual signals of C_6D_6. Infrared spectra were recorded with a Bruker IFS 88 FT instrument, and samples were Nujol mulls between KBr plates.

Preparation of [Mo(N*t*Bu)(O)Cl$_2$(DME)] (1): Under argon, $[Mo(N\textit{t}Bu)_2Cl_2(DME)]$ (400 mg, 1.00 mmol) and $[Mo(O)_2Cl_2(DME)]$ (290 mg, 1.00 mmol) were dissolved in DME (10 mL) and heated to reflux for 3 days. The volatiles were removed in vacuo, and the yellow-green product was extracted into toluene (30 mL) and crystallized at –40 °C. Yield 500 mg (73%). M.p. 71 °C. $C_8H_{19}NCl_2O_3Mo$ (M = 344.09 g mol^{-1}): calcd. C 27.93, H 5.57, N 4.07; found C 27.49, H 5.44, N 3.97. ^1H NMR (C_6D_6, 300 MHz, 300 K): δ = 3.41 (s, 6 H, Me), 3.02 (s, 4 H, CH_2), 1.41 (s, 9 H, N*t*Bu) ppm. $^{13}C\{^1H\}$NMR (C_6D_6, 75 MHz, 300 K): δ = 70.6 (s, CH_2), 63.2 (br s, Me), 27.8 (s, N*t*Bu) ppm. IR (KBr): 3160 (m, vbr), 1587 (m), 1405 (w), 1362 (s), 1276 (w), 1259 (w), 1228 (s, br), 1188 (w), 1162 (w), 1137 (w), 1108 (w), 1086 (s), 1044 (s, b), 1005 (vw), 961 (m), 910 (s), 861 (s), 826 (m), 799 (m), 725 (w), 627 (w), 592 (w), 572 (m), 515 (w) cm^{-1}.

Preparation of [Mo(N*t*Bu)(DAD)(μ-O)]$_2$ (2): A solution of Li_2DAD (265 mg, 1.45 mmol) in THF (20 mL) was added dropwise to a solution of **1** (500 mg, 1.45 mmol) in THF (20 mL) at –80 °C. After 10 min at –80 °C, the reaction mixture reached room temperature within 30 min. After 8 h at room temperature, THF was removed at reduced pressure, and the product was extracted with two portions of hexane (30 mL). The analytically pure dark violet compound was obtained by crystallization from hexane at –80 °C. Yield: 300 mg (59%). M.p. 190 °C (dec.). $C_{28}H_{58}N_6O_2Mo_2$ (M = 702.69 g mol^{-1}): calcd. C 47.86, H 8.32, N 11.96; found C 47.44, H 8.02, N 11.55. EI-MS: *m*/*z* (%) = 353 (1) [M/2$^+$], 338 (2) [M/2$^+$ – Me], 57 (100). ^1H NMR (C_6D_6, 500 MHz, 300 K): δ = 6.75 (s, 2 H, CH–DAD), 1.51 (s, 18 H, *t*Bu-DAD), 1.38 (s, 9 H, N*t*Bu) ppm. $^{13}C\{^1H\}$NMR (C_6D_6, 125 MHz, 300 K): δ = 119.9 (CH–DAD), 69.9 ($NCMe_3$), 57.6 (CMe_3–DAD), 30.5 (DAD–CMe_3), 30.4 ($NCMe_3$) ppm. IR (KBr): 3038 (w), 1605 (w), 1420 (w), 1358 (m), 1262 (s), 1235 (s), 1219 (s), 1148 (w), 1098 (m, br), 1022 (m, br), 936 (w), 864 (w), 804 (s), 766 (m), 723 (w), 644 (m, br), 567 (m), 525 (w), 492 (w) cm^{-1}.

Acknowledgments

Financial support by DFG and H. C. Starck GmbH is gratefully acknowledged.

[1] G. van Koten, K. Vrieze, *Adv. Organomet. Chem.* **1982**, *21*, 151–239.
[2] a) S. D. Ittel, L. K. Johnson, M. Brookhart, *Chem. Rev.* **2000**, *100*, 1169–1203; b) M. D. Leatherman, S. A. Svejda, L. K. Johnson, M. Brookhart, *J. Am. Chem. Soc.* **2003**, *125*, 3068–3081.
[3] Representative examples: a) J. Sundermeyer, D. Runge, J. S. Field, *Angew. Chem.* **1994**, *106*, 679–682; *Angew. Chem. Int. Ed. Engl.* **1994**, *33*, 678–681; b) J. Sundermeyer, D. Runge, *Angew. Chem.* **1994**, *106*, 1328–1331; *Angew. Chem. Int. Ed. Engl.* **1994**, *33*, 1255–1257; c) J. Sundermeyer, U. Radius, C. Burschka, *Chem. Ber.* **1992**, *125*, 2379–2384; d) E. A. Kretzschmar, J. Kipke, J. Sundermeyer, *Chem. Commun.* **1999**, 2381–2382; e) U. Radius, J. Sundermeyer, K. Peters, H.-G. von Schnering, *Eur. J. Inorg. Chem.* **2001**, 1617–1623; f) U. Radius, A. Schorm, D. Kairies, S. Schmidt, F. Möller, H. Pritzkow, J. Sundermeyer, *J. Organomet. Chem.* **2002**, *655*, 96–104; g) X. Li, M. Schopf, J. Stephan, K. Harms, J. Sundermeyer, *Organometallics* **2002**, *21*, 2356–2358; h) X. Li, M. Schopf, J. Stephan, J. Kipke, K. Harms, J. Sundermeyer, *J. Am. Chem. Soc.* **2004**, *126*, 8660–8661.
[4] K. A. Rufanov, D. N. Zarubin, N. A. Ustynyuk, D. N. Goureviteh, J. Sundermeyer, A. V. Churakov, J. A. K. Howard, *Polyhedron* **2001**, *20*, 379–385.
[5] a) H. H. Fox, K. B. Yap, J. Robbins, S. Cai, R. R. Schrock, *Inorg. Chem.* **1992**, *31*, 2287–2289; b) R. C. P. Copley, P. W. Dyer, V. C. Gibson, J. A. K. Howard, E. L. Marshall, W. Wang, B. Whittle, *Polyhedron* **1996**, *15*, 3001–3008.
[6] H. Kawaguchi, Y. Yamamoto, K. Asaoka, K. Tatsumi, *Organometallics* **1998**, *17*, 4380–4386.
[7] G. M. Sheldrick, *SHELX-97, Programs for the solution and the refinement of crystal structures*, University of Göttingen, **1997**.
[8] P. L. Dahlstrom, J. R. Hyde, P. A. Vella, J. Zubieta, *Inorg. Chem.* **1982**, *21*, 927–932.
[9] K. Dreisch, C. Andersson, C. Stålhandske, *Polyhedron* **1993**, *12*, 303–311.
[10] F. Stoffelbach, R. Poli, P. Richard, *J. Organomet. Chem.* **2002**, *663*, 269–276.
[11] M. H. Chisholm, K. Folting, J. C. Huffman, J. J. Koh, *Polyhedron* **1989**, *8*, 123–125.
[12] a) T. M. Cameron, I. Ghiviriga, K. A. Abboud, J. M. Boncella, *Organometallics* **2001**, *20*, 4378–4383; b) C. G. Ortiz, K. A. Abboud, T. M. Cameron, J. M. Boncella, *Chem. Commun.* **2001**, 247–248; c) T. M. Cameron, C. G. Ortiz, K. A. Abboud, J. M. Boncella, R. T. Baker, B. L. Scott, *Chem. Commun.* **2000**, 573–574; d) T. M. Cameron, C. G. Ortiz, I. Ghiviriga, K. A. Abboud, J. M. Boncella, *Organometallics* **2001**, *20*, 2032–2039; e) C. G. Ortiz, K. A. Abboud, J. M. Boncella, *Organometallics* **1999**, *18*, 4253–4260; f) T. M. Cameron, K. A. Abboud, J. M. Boncella, *Chem. Commun.* **2001**, 1224–1225.
[13] C. J. M. Huige, A. L. Spek, J. L. de Boer, *Acta Crystallogr., Sect. C: Cryst. Struct. Commun.* **1985**, *41*, 113.
[14] a) P. J. Daff, M. Etienne, B. Donnadieu, S. Z. Knottenbelt, J. E. McGrady, *J. Am. Chem. Soc.* **2002**, *124*, 3818–3819; b) K. H. Thiele, B. Richter, B. Neumueller, *Z. Anorg. Allg. Chem.* **1994**, *620*, 1627–1630; c) M. G. Gardiner, G. R. Hanson, M. J. Hen-

 © 2005 Wiley-VCH Verlag GmbH & Co. KGaA, Weinheim

derson, F. C. Lee, C. L. Raston, *Inorg. Chem.* **1994**, *33*, 2456–2461.
[15] See for example: a) T. Spaniel, H. Gorls, J. Scholz, *Angew. Chem.* **1998**, *110*, 1962–1966; *Angew. Chem. Int. Ed. Engl.* **1998**, *37*, 1862–1865; b) M. J. Scott, S. J. Lippard, *Organometallics* **1997**, *16*, 5857–5868.
[16] a) L. R. Chamberlain, L. D. Durfee, P. E. Fanwick, L. M. Kobriger, S. L. Latesky, A. K. McMullen, B. D. Steffey, I. P. Rothwell, K. Folting, J. C. Huffman, *J. Am. Chem. Soc.* **1987**, *109*, 6068–6076; b) W. A. Herrmann, M. Denk, W. Scherer, F. R. Klingan, *J. Organomet. Chem.* **1993**, *444*, C21–C24; c) H. Dieck, H. J. Rieger, G. Fendesak, *Inorg. Chim. Acta* **1990**, *177*, 191–197; d) T. G. Ong, D. Wood, G. P. A. Yap, D. S. Richeson, *Organometallics* **2002**, *21*, 1–3; e) J. Scholz, M. Dlikan, D. Strohl, A. Dietrich, H. Schumann, K. H. Thiele, *Chem. Ber.* **1990**, *123*, 2279–2285; f) J. Wunderle, J. Scholz, U. Baumeister, H. Hartung, *Z. Kristallogr.* **1996**, *211*, 423–424; g) F. J. Berg, J. L. Petersen, *Organometallics* **1991**, *10*, 1599–1607; h) G. Hadi, J. Wunderle, K. Thiele, R. Froehlich, *Z. Kristallogr.* **1994**, *209*, 372; i) J. Sánchez-Nieves, P. Royo, M. A. Pellinghelli, A. Tiripicchio, *Organometallics* **2000**, *19*, 3161–3169; j) B. Richter, J. Scholz, J. Sieler, K. H. Thiele, *Angew. Chem.* **1995**, *107*, 2865–2867; *Angew. Chem. Int. Ed. Engl.* **1995**, *34*, 2649–2651; k) A. Galindo, M. Gómez, D. del Rio, F. Sánchez, *Eur. J. Inorg. Chem.* **2002**, 1326–1335.
[17] J. M. Kliegman, R. K. Barners, *Tetrahedron* **1970**, *26*, 2555–2560.

Received: October 27, 2004
Published Online: November 2, 2005

 © 2005 Wiley-VCH Verlag GmbH & Co. KGaA, Weinheim

DOI: 10.1002/ejic.200500161

Synthesis of Main Group Polycations in Molten and Pseudo-Molten $GaBr_3$ Media

Alexei N. Kuznetsov,[a] Boris A. Popovkin,[a] Kenny Ståhl,[b] Martin Lindsjö,[c] and Lars Kloo*[c]

Keywords: Antimony / Bismuth / Tellurium / Cluster compounds

The prospects of synthesizing polycationic species using $GaBr_3$ in benzene solution at room temperature have been investigated. The salts $Bi_8[GaBr_4]_2$, $Sb_8[GaBr_4]_2$ and $Te_4[Ga_2Br_7]_2$ have been isolated and characterized. The first two compounds are isotypic with $Sb_8[GaCl_4]_2$, crystallize in the space group $Pna2_1$, and feature square *anti*-prismatic E_8^{2+} polycations (E = Sb, Bi). Unit-cell parameters for $Bi_8[GaBr_4]_2$ are a = 18.3014(10) Å, b = 10.3391(6) Å and c = 13.5763(7) Å, and for $Sb_8[GaBr_4]_2$; a = 18.096(2) Å, b = 10.1572(9) Å and c = 13.2168(10) Å. $Te_4[Ga_2Br_7]_2$ crystallizes in the space group $P2_1/c$ with a = 10.1600(9) Å, b = 10.8314(9) Å, c = 13.8922(10) Å and β = 99.182(7)°, and features a square-planar Te_4^{2+} polycation. The compound $Bi_5[GaBr_4]_3$ has been synthesized from molten $GaBr_3$ and characterized by using powder diffractometry in space group Fm-3c; a = 17.6263(8) Å. The structure model for this compound suggests the included Bi_5^{3+} cations to be practically freely oriented within its cavities in the solid phase.
(© Wiley-VCH Verlag GmbH & Co. KGaA, 69451 Weinheim, Germany, 2005)

Introduction

Homopolyatomic ions of the main-group elements have for a long time been an area of many studies and discussions, resulting in a large number of publications.[1] Species such as Cd_2^{2+}, Bi_8^{2+}, Bi_9^{5+}, Se_8^{2+}, Te_4^{2+}, I_3^+ etc. have been synthesized employing several different routes, for instance using molten salts or superacidic media.[2] Recently, in a series of papers we have illustrated the possibility to obtain polycations from $GaCl_3$–benzene solutions.[3–6] This method is based on the extraordinarily high solubility of $GaCl_3$ in benzene, which renders a pseudo-melt behavior to the saturated solution.[7] Thus, it has been possible to repeat, at room temperature, several of the reactions previously performed in molten $AlCl_3$. The major advantage of performing reactions at low temperatures is that it allows easier study of reactants and products in solution, using for instance spectroscopy. The method also offers some possibility to influence processes like crystal growth, as recently demonstrated by the successful isolation of the previously unknown $Sb_8[GaCl_4]_2$.[5]

Unfortunately, there are only very few other Lewis acids known with a propensity comparable to $GaCl_3$ for dissolution in benzene or other non-polar solvents. However, there is one obvious alternative – $GaBr_3$. The properties of $GaBr_3$ are similar to those of $GaCl_3$; the same structure in the solid phase and also a very high solubility in arenes, albeit not as high as its chloride congener. It can be noted that only very few *bromo*-aluminate/gallate/indate salts containing main-group polycations have been reported in literature – $Te_4[AlBr_4]_2$[8] and $Bi_8[InBr_4]_2$.[9] It is not known to us if the brevity of this list, in comparison to the record of chloroaluminate structures, is due to unforeseen complications in their syntheses or if it just reflects the small number of synthetic attempts made. The main goal of this investigation is to extend the knowledge on main-group polycation chemistry, employing a $GaBr_3$–benzene system as reaction medium because; (i) it is chemically closely related to the $GaCl_3$–benzene system, known to be successful; (ii) only a few reports have been made about the isolation of crystalline compounds from ternary M–Al/Ga/In–Br systems, and; (iii) it allows the possibility to affect polycation chemistry and thereby a possibility to isolate new polycations in the liquid or solid state.

The following sections describe observations made regarding the synthesis of a selection of main-group polycations in $GaBr_3$–benzene media. Some experiments have also been performed in molten Bi–$BiBr_3$–$GaBr_3$ systems.

Results and Discussion

The syntheses performed in this work followed the general procedures developed for the analogous $GaCl_3$–benzene system, which have been well described in earlier papers.[3–6] The solubility of gallium tribromide in benzene at ambient

[a] Department of Chemistry, Moscow State University, Moscow, Russia
[b] Department of Chemistry, Technical University of Denmark, Lyngby, Denmark
[c] Inorganic Chemistry, Royal Institute of Technology, Stockholm, Sweden
Supporting information for this article is available on the WWW under http://www.eurjic.org or from the author.

 © 2005 Wiley-VCH Verlag GmbH & Co. KgaA, Weinheim

conditions is somewhat lower than that of gallium trichloride, estimated within this work to be ca. 8–9 mol%. In order to confirm the nature of $GaBr_3$ when dissolved in benzene, Raman spectra were recorded, see Figure 1, and compared with known spectra of Ga_2Br_6.[10] This evaluation verifies that gallium tribromide predominantly exists as dimeric units in benzene solution.

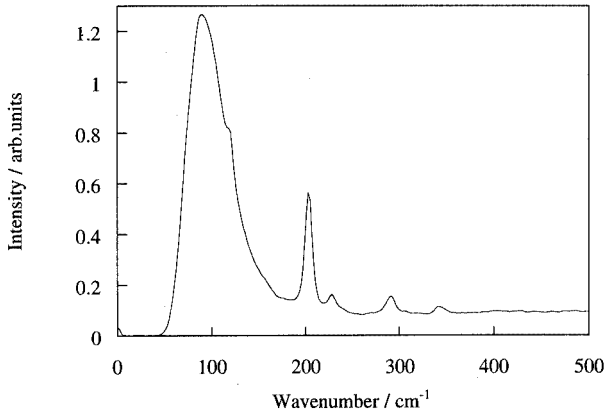

Figure 1. The Raman spectrum of $GaBr_3$ in benzene solution.

Bi–$GaBr_3$–Benzene Systems

Most of our work considering $GaBr_3$–benzene systems has been devoted to attempts to isolate bismuth polycations. First, the oxidation of bismuth metal by $GaBr_3$ in benzene solution was analyzed. In contrast to the reaction between bismuth and $GaCl_3$ in benzene, for which a red color can be noticed after a few hours, no coloration or other visible changes are observed in the Bi–$GaBr_3$–benzene case. However, after a few days it was noticed that the bismuth metal surface had lost it luster due to the formation of a black substance. By repeatedly exposing the crude product to fresh $GaBr_3$-benzene solutions, a sufficient amount of this black phase was obtained.

The final product was characterized by using powder X-ray diffraction. Although bismuth metal constituted a major impurity, it was possible to obtain the unit cell parameters for the black phase from the indexed reflections. The compound crystallizes in space group $Pna2_1$, a = 18.3014(10), b = 10.3391(6), c = 13.5763 Å. It was noted that this cell is very similar to the cells of $Sb_8[GaCl_4]_2$ and $Sb_8[GaBr_4]_2$ (see below), and the black phase was assumed to be $Bi_8[GaBr_4]_2$ (**1**). The coordinates of $Sb_8[GaBr_4]_2$ were used as starting coordinates in the Rietveld refinement of **1**. From the difference pattern it was concluded that the sample contained a third phase, the positions of the unassigned reflections matched known positions of $GaBr_3$, and this phase was added to the refinement.

The structure of **1** features a distorted square-antiprismatic Bi_8^{2+} cation and two tetrahedral $GaBr_4^-$ anions. The distortion of the cation is illustrated by the fact that the two Bi_4 squares are not parallel, see Figure 2. As a consequence, the variation in Bi–Bi distances is large, 2.88(2)–3.23(3) Å, see Table 1. In the discussion on $Sb_8[GaCl_4]_2$,[5] it was observed that for the antimony cluster the inter-square Sb–Sb distances are 3.3% longer than the intra-square distances, while the inter-square metal–metal distances in the case of $Bi_8[GaCl_4]_2$ are only 0.4% longer than the intra-square ones. The mean values for inter-square and intra-square Bi–Bi distances in **1** are 3.07(9) and 3.00(6) Å, respectively, giving a ratio of 1.023. This ratio is close to the one found for the Sb_8^{2+} cation, however, the distortion of the cation in **1** invites to some care in the interpretation.

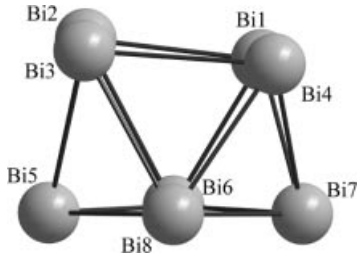

Figure 2. The Bi_8^{2+} cation of **1**. The two Bi_4 squares are not parallel to each other, consequently a large variation in Bi–Bi distances is observed.

Table 1. Bond lengths of **1**. Bismuth atom labels are given in Figure 2.

Atoms	Distance [Å]	Atoms	Distance [Å]
Intra-square bonds		*Inter-square bonds*	
Bi(1)–Bi(2)	2.95(2)	Bi(1)–Bi(6)	2.92(2)
Bi(1)–Bi(4)	3.03(3)	Bi(1)–Bi(7)	3.06(2)
Bi(2)–Bi(3)	2.97(3)	Bi(2)–Bi(5)	3.18(3)
Bi(3)–Bi(4)	3.14(4)	Bi(2)–Bi(6)	3.15(3)
Bi(5)–Bi(6)	2.95(3)	Bi(3)–Bi(5)	3.15(2)
Bi(5)–Bi(8)	2.94(3)	Bi(3)–Bi(8)	3.10(3)
Bi(6)–Bi(7)	3.04(3)	Bi(4)–Bi(7)	2.98(3)
Bi(7)–Bi(8)	2.98(3)	Bi(4)–Bi(8)	3.01(3)
Anion 1		*Anion 2*	
Ga(1)–Br(1)	2.35(4)	Ga(2)–Br(5)	2.33(4)
Ga(1)–Br(2)	2.37(4)	Ga(2)–Br(6)	2.33(5)
Ga(1)–Br(3)	2.32(4)	Ga(2)–Br(7)	2.35(4)
Ga(1)–Br(4)	2.36(4)	Ga(2)–Br(8)	2.36(4)

In our studies, it has been generally observed that the recording of Raman spectra is problematic for solid compounds containing bismuth polycations, probably due to heavy absorption. Therefore, no reliable Raman spectrum for **1** has been obtained.

If instead the reduction of $BiBr_3$ by Ga metal in $GaBr_3$–benzene is considered, the outcome is likewise problematic and different from the analogous reaction in the chloride system. The mixing of a solution containing $BiBr_3$ with one containing Ga^+ ions causes an immediate formation of a black precipitate, while the solution remains colorless. No subvalent bismuth species can be registered in the liquid phase by use of Raman spectroscopy. The black substance can be inspected by means of X-ray powder diffraction and has been found to be amorphous, most likely due to the instantaneous precipitation.

 © 2005 Wiley-VCH Verlag GmbH & Co. KGaA, Weinheim

Obviously, the speed of precipitation has to be reduced in order to obtain proper crystals. By using a special set-up, allowing for a very slow speed of mixing, a small amount of tiny, black, bar-shaped crystals could be isolated. A unit cell determination for one of these crystals shows that they belong to the orthorhombic system with the unit cell parameters: a = 23.854(6) Å, b = 15.634(5) Å, c = 9.128(5) Å; hence in very good agreement with the unit cell parameters of Bi_6Br_7.[11] This is quite remarkable, as it is the first salt, isolated from this synthetic method, that not includes halidogallate anions. Furthermore, this implies that Bi_9^{5+} cations are likely to be present in the solution at very low concentrations, undetectable by spectroscopy. The reasons why bromogallate(III) anions are not incorporated into the crystallization product are not yet clear. One possible explanation may lie in the expected thermodynamic stability of Bi_6Br_7 in combination with weaker Lewis acidity of $GaBr_3$ with respect to $GaCl_3$.

The main conclusion drawn from the synthesis of bismuth polycations in $GaBr_3$–benzene media is that compounds containing polycations form; $Bi_8[GaBr_4]_2$ and Bi_6Br_7 have been isolated. However, although the reaction principles work, the solubility of the formed polycations in media containing bromogallates ions is very low, and the crystal growth is severely hampered with reduced crystal size as consequence.

Molten Bi–$GaBr_3$ and Bi–$GaBr_3$–$BiBr_3$ Systems

In order to obtain crystals of **1** of better quality, an attempt on the direct high-temperature oxidation of bismuth by gallium tribromide was made. However, no interaction between the components was observed even after a week of annealing at 350 °C. This clearly demonstrates the vital role of benzene in coordinating Ga^+ cations formed on the reduction of Ga^{III} in $GaBr_3$–benzene media.

Instead, symproportionation was employed; from a solid state synthesis, the starting materials having the ratio 4Bi:$BiBr_3$:4$GaBr_3$, a red-brown microcrystalline material could be obtained. The recorded powder X-ray diffractogram of this product shows strong similarities to that of the previously characterized cubic modification of $Bi_5[GaCl_4]_3$.[3] In analogy to that structure, the diffraction pattern was indexed as F-centered cubic with a = 17.6263(8) Å. The atomic coordinates for the chloride structure were taken as the initial model for full-profile Rietveld refinement. The atomic coordinates for this phase, cubic $Bi_5[GaBr_4]_3$ (**2**), are given in Table 2.

Both **2** and cubic $Bi_5[GaCl_4]_3$ are related to the rhombohedral form of $Bi_5[GaCl_4]_3$.[6,12] All these three compounds contain trigonal bipyramidal Bi_5^{3+} polycations and tetrahedral GaX_4^- anions as the structural units (see Figure 3). However, the difference for the cubic phases is that their description within the given crystal system implies a substantial degree of disorder. Eight Bi_5^{3+} units, occupying centers of octants in the cubic cell, may in the cubic $Bi_5[GaCl_4]_3$ have 4 different orientations parallel to the body diagonals of the cube. In **2**, the positions of Bi(2) are slightly off the body diagonals, resulting in 8 possible positions. In practice, it is hardly meaningful to discuss the polycations in terms of atomic positions, the number of possible positions, together with the relatively large displacement parameter, suggest that the Bi_5^{3+} polycations can be assumed to rotate freely in all direction within its cavities, defined by the positions of the tetrabromogallate anions. Therefore, it has also not been relevant to analyze any Bi–Bi distances of this cation. In contrast, the anions are found to be almost ordered, although a second bromine site, occupied by 6% of the bromine atoms, has been refined. The Ga–Br(1) distance is found to be 2.338(4) Å, in good agreement with the reported distance of the tetrabromogallate anion.

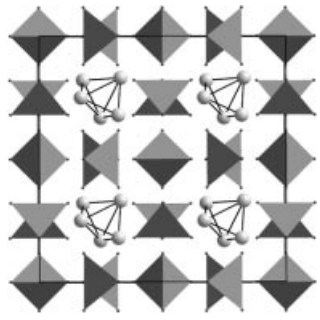

Figure 3. An idealized two-dimensional projection of the unit cell content of **2**. The Bi_5^{3+} polycations are displayed in one of all possible orientations and the Br(2) atoms have been omitted.

In the case of cubic $Bi_5[GaCl_4]_3$ it has already been concluded that no further information is added to the structure solution through the generation of single crystals.[6] One possible explanation may be that the cubic phase is a microtwinned modification of the rhombohedral one (still to be isolated in the case of $Bi_5[GaBr_4]_3$).

It can be noted that all the attempts to produce more bismuth-rich compounds from molten Bi–$BiBr_3$–$GaBr_3$ (e.g. $Bi_8[GaBr_4]_2$) resulted in the formation of **2** and some unreacted bismuth metal in the reaction container, i.e. no

Table 2. Refined fractional coordinates, isotropic temperature coefficients and occupancy factors for **2**.

Atom	Position	SOF	x/a	y/b	z/c	B_{iso} [Å]^2
Bi1	192j	0.070(3)	0.3068(10)	0.1591(10)	0.2609(12)	5.0(4)
Bi2	192j	0.123(3)	0.1632(7)	0.1777(10)	0.2005(6)	5.0(4)
Ga	24*c*	1	0	0	1/4	2.0(2)
Br1	96*i*	0.942(3)	0.3876(2)	0.3204(2)	0	2.8(1)
Br2	96*i*	0.058(3)	0.256(3)	0.162(4)	0	2.8(1)

 © 2005 Wiley-VCH Verlag GmbH & Co. KGaA, Weinheim

other ternary cluster compound was obtained in this system through the molten salt route of synthesis.

Synthesis and Crystal Structure of $Sb_8[GaBr_4]_2$

Also the reactions of antimony in $GaBr_3$–benzene have been studied. In the case of antimony it has previously been noted that elemental antimony is not oxidized in $GaCl_3$–benzene, probably due to low solubility.[5,13] It is assumed that the same is true for the bromide case, hence only the reduction of $SbBr_3$ by Ga metal has been empolyed. From this route, a large amount of a black amorphous phase together with a few small orange crystals have been isolated. Single-crystal X-ray diffraction and Raman spectroscopy experiments have confirmed the orange crystals to be $Sb_8[GaBr_4]_2$ (**3**).

The structure of **3** is isotypic to the structure of **1**, described above, as well as the chloride analogue, $Sb_8[GaCl_4]_2$,[5] with an increase in unit cell volume of 8.6%. The structure features a Sb_8^{2+} polycation, the geometry being very close to square-antiprismatic (although the true molecular symmetry is C_1), and two crystallographically independent tetrabromogallate tetrahedra, see Figure 4. The Sb–Sb distances vary between 2.854(2) and 2.890(2) Å [mean: 2.871(11) Å] within the squares, while the inter-square distances vary between 2.940(2) and 2.987(2) Å [mean: 2.97(2) Å], see Table 3. Thus, the inter-square/intra-square distance ratio is found to be 1.035 (see discussion on the structure of **1**). This is in very good agreement with the distances of the cation found in the tetrachlorogallate structure. The Ga–Br distances are in the interval 2.299(3)–2.327(3) Å. Just as in the case of the chloride structure, there are some rather short cation–anion distances, the shortest being 3.552(2) Å.

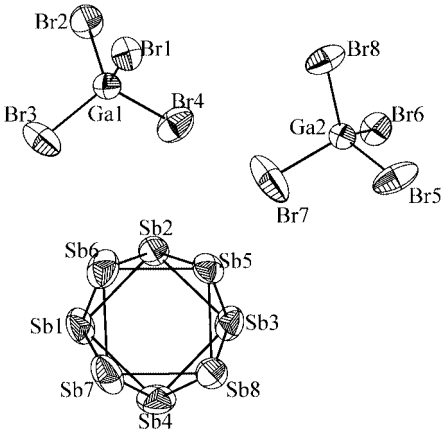

Figure 4. The atoms of the asymmetric unit of **3**. Thermal ellipsoids are drawn at the 70% probability level.

Raman spectroscopy on selected single crystals of **3** reveals signals at $\tilde{\nu}$ = 177 (s) and 209 (m) cm^{-1}. The first one corresponds to the strongest Raman peak of the Sb_8^{2+} polycation, shifted a few wavenumbers down with respect to the chloride structure, while the latter peak corresponds to the strong symmetrical stretch vibration mode of the $[GaBr_4]^-$ ion.[14]

Table 3. Bond lengths of **3**. Atom labels are given in Figure 4.

Atoms	Distance [Å]	Atoms	Distance [Å]
Intra-square bonds		*Inter-square bonds*	
Sb(1)–Sb(2)	2.864(2)	Sb(1)–Sb(6)	2.958(2)
Sb(1)–Sb(4)	2.880(2)	Sb(1)–Sb(7)	2.984(2)
Sb(2)–Sb(3)	2.861(2)	Sb(2)–Sb(5)	2.974(2)
Sb(3)–Sb(4)	2.890(2)	Sb(2)–Sb(6)	2.962(2)
Sb(5)–Sb(6)	2.878(2)	Sb(3)–Sb(5)	2.954(2)
Sb(5)–Sb(8)	2.861(2)	Sb(3)–Sb(8)	2.973(2)
Sb(6)–Sb(7)	2.880(2)	Sb(4)–Sb(7)	2.940(2)
Sb(7)–Sb(8)	2.854(2)	Sb(4)–Sb(8)	2.987(2)
Anion 1		*Anion 2*	
Ga(1)–Br(1)	2.327(3)	Ga(2)–Br(5)	2.303(2)
Ga(1)–Br(2)	2.318(3)	Ga(2)–Br(6)	2.312(2)
Ga(1)–Br(3)	2.301(3)	Ga(2)–Br(7)	2.296(3)
Ga(1)–Br(4)	2.320(3)	Ga(2)–Br(8)	2.310(2)

Neither X-ray diffractometry nor Raman spectroscopy proved to be useful in the characterization of the black precipitate, which is the major product of the reaction above. Energy-dispersive X-ray analysis (EDX) was performed on this compound in order to obtain some information of its contents. Unfortunately, the results of these measurments are ambiguous. The observed Ga:Br ratio (1:2) is unexpectedly low; not an uncomon result of elemental analyses in gallate systems. On the other hand, the observed Sb content tend to match the expected theoretical values. Based on the assumption that the Sb content is in good agreement also for this black product obtained from the reduction of $SbBr_3$, it can be conluded that the phase contains an antimony polycation and that it is likely to be a another polycation than Sb_8^{2+} (theoretical Sb content; 44%). Plausible compounds, based on the antimony content (ca. 24%), include $Sb_5[GaBr_4]_3$ (25%), $Sb_6[GaBr_4]_4$ (23%), $Sb_7[GaBr_4]_5$ (22%) and $Sb_8[GaBr_4]_4$ (29%).

Te–$GaBr_3$–Benzene

It has also proved feasible to synthesize polycations of elements from other groups than group 15 by using the benzene route. Recently, $Te_4[Ga_2Cl_7]_2$ was isolated from $GaCl_3$–benzene media,[15] and other ions may be attainable in the analogous bromide system. Therefore, a series of experiments were pursued, attempting to oxidize different elements to polycations in $GaBr_3$–benzene solution.

No reaction was detected in the case of cadmium, arsenic or selenium. However, in the case of tellurium, the solution becomes slightly green in color within a couple of hours after the addition of elemental tellurium. After a few days this color disappears, and instead small, black, block-shaped crystals are formed. Unfortunately, the crystals are too small to allow for even a unit cell determination and the Raman spectrum is ambiguous, showing only one band at 210 cm^{-1}, which could be attributed to different expected ions such as Te_4^{2+} or $GaBr_4^-$.[14,16]

Instead, reduction of $TeBr_4$ with Ga metal in $GaBr_3$–benzene is successful, and violet, plate-shaped crystals were

 © 2005 Wiley-VCH Verlag GmbH & Co. KGaA, Weinheim

obtained. Single-crystal diffraction confirms these crystals to contain $Te_4[Ga_2Br_7]_2$ (**4**), the formula analogue of the compound previously found in the chlorogallate case.[15] **4** is found to crystallize in the space group $P2_1/c$, just like the previously reported chlorogallate structure, however the unit cell parameters are different, with a much larger β-angle [99.182(7)°] in the case of **4**.

The structure of **4** features a square-planar Te_4^{2+} cation and staggered $[Ga_2Br_7]^-$ anions, see Figure 5. Selected bond lengths for **4** are given in Table 4. The Te–Te distances are 2.6702(14)–2.6720(14) Å, which compares well with other structures containing this cation.[1c] The distances between the gallium atoms and the terminal bromine atoms, 2.266(2)–2.331(2) Å, are in the normal range for Ga–Br bonds. Just as in $Te_4[Ga_2Cl_7]_2$ and $Te_4[Al_2Cl_7]_2$,[17] there are some rather short Te–X distances (X = Cl, Br), of which the shortest are found for bromides positioned in the plane of the cation, capping the edges of the square-planar cation. In this particular structure, the shortest Te–Br distance is 3.412(2) Å.

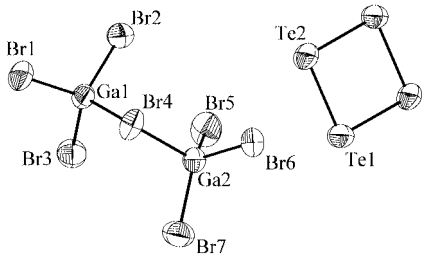

Figure 5. The atoms of the asymmetric unit of **4**. Thermal ellipsoids are drawn at the 70% probability level. Unlabelled Te atoms are related to Te(1) and Te(2) by the inversion operator $(1 - x, 1 - y, -z)$.

Table 4. Bond lengths of **4**. Atom labels are given in Figure 5.

Atoms	Distance [Å]
Te(1)–Te(2)	2.6702(14)
Te(2)–Te(1)^i	2.6720(14)
Ga(1)–Br(1)	2.290(2)
Ga(1)–Br(2)	2.311(2)
Ga(1)–Br(3)	2.275(2)
Ga(1)–Br(4)	2.432(2)
Ga(2)–Br(4)	2.445(2)
Ga(2)–Br(5)	2.274(2)
Ga(2)–Br(6)	2.331(2)
Ga(2)–Br(7)	2.266(2)

In the Raman spectrum recorded from a single crystal of **4**, bands are observed at 419 (*m*), 314 (w), 250 (br) and 210 (s) cm^{-1}. The lowest band is attributable to the cation,[16] and the bands at 250 and 314 cm^{-1} to the anion.[18] The origin of the peak at 419 cm^{-1} is unknown, but a similar band was observed for $Te_4[Ga_2Cl_7]_2$, which in the report of that compound, was suggested to be attributed to the chlorogallate anion.[15] However, this may possibly be a common band of both structures, originating either from the cation or an impurity.

It can be concluded that the Te_4^{2+} cation has the highest solubility of the polycations formed in $GaBr_3$–benzene; a colored solution is retained at least for a couple of minutes when reducing $TeBr_4$ with Ga metal, instead of immediate precipitation as in the cases of $BiBr_3$/$SbBr_3$. Furthermore, a slight coloration of the solution can be observed also when elemental tellurium is put in $GaBr_3$–benzene, and small crystallites are formed spatially separated from the solid reactants, hence, transport via solution must occur.

Conclusions

Experimental attempts to synthesize polycations of different elements in $GaBr_3$–benzene solutions have been performed. For all experiments in such media, the problem of low solubility of the products formed represents a serious complication, lowering the quality of the crystalline materials obtained. Nevertheless, the compounds $Bi_8[GaBr_4]_2$, $Sb_8[GaBr_4]_2$ and $Te_4[Ga_2Br_7]_2$ have been isolated and their structures characterized, illustrating the similarity in chemistry between $GaCl_3$ and $GaBr_3$ in benzene media. Additionally, $Bi_5[GaBr_4]_3$ has been isolated from molten $GaBr_3$ and its structure has been partly characterized.

Experimental Section

Chemicals: Commercial Bi (Aldrich, 99.999%), Ga and In metals (both ALFA Chemicals, 99.9999%), bromine, $BiBr_3$ (Aldrich, 99.9%), $SbBr_3$ (Aldrich, 99.99%), $TeBr_4$ (Aldrich, anhydrous, 99.995%) and $GaBr_3$ (Aldrich, anhydrous, 99.999%) were used as purchased. For certain experiments $GaBr_3$ was synthesized from the elements according to a literature procedure.[19] Benzene (Merck, pro analysi grade) was distilled and stored over molecular sieves in a glovebox under a dry nitrogen atmosphere. Because of the high moisture sensitivity of the anhydrous metal halides used in this work, all operations were performed in a glovebox under dry nitrogen with less than 0.5 ppm H_2O.

Synthesis of 1: Bi metal powder (0.2 g, 1 mmol) was added to 0.7 g of a saturated $GaBr_3$/benzene solution in a standard NMR tube. No obvious signs of reaction, such as change of solution color, were observed, but after a few days it could be noticed that a black substance had formed on the surface of the metal. From X-ray powder diffraction the crude product was found to a mixture of bismuth metal and an unknown compound. In order to improve the purity of the unknown phase, the product was washed with pure benzene, dried, re-ground and added to a fresh $GaBr_3$/benzene solution. These steps were repeated several times until a satisfactory purity of the product was obtained.

Synthesis of Bi_6Br_7: Two solutions, In–$GaBr_3$–benzene and $BiBr_3$–$GaBr_3$–benzene, were prepared and added to two vessels connected by a bridge, an overturned U-shaped tube, filled with pure benzene.[20] The reactor was then sealed to prevent solvent evaporation. After a month, some crystallization was observed in the form of black bars at the bend of the bridge.

Synthesis of 2: A mixture with the ratio of $4Bi:BiBr_3:4GaBr_3$ was heated to 350 °C in a evacuated and sealed standard 5 mm NMR tube for several days and then slowly cooled to room temperature. The excess of gallium tribromide was removed by sublimation at 150 °C under dynamic vacuum. The obtained product is a dark brown microcrystalline mass, brick red when powdered.

 © 2005 Wiley-VCH Verlag GmbH & Co. KGaA, Weinheim

Synthesis of 3: $GaBr_3$ (0.30 g, 1.0 mmol) was dissolved in benzene (1.0 mL) and the solution was separated into two parts. $SbBr_3$ (0.035 g, 0.1 mmol) was added to one of the solutions and Ga metal (0.02 g, 0.3 mmol) to the other. After 24 hours, the two solutions were mixed. A black precipitate formed immediately while the solution remained colorless. When the product was studied under microscope, it was noticed that small crystals of **3** had formed as orange cylinders together with the amorphous, black, main product.

Synthesis of 4: $GaBr_3$ (0.30 g, 1.0 mmol) was dissolved in benzene (1.0 mL) and the solution was separated in two parts. $TeBr_4$ (0.05 g, 0.1 mmol) was added to one solution and Ga metal (0.02 g, 0.3 mmol) to the other. After 24 hours, the two solutions were mixed, and a very darkly green solution formed. After a few minutes a dark precipitate formed and the solution became clear. Crystals of **4** were found as violet plates.

Raman Spectroscopy: Raman spectra from solutions were recorded using Bruker IFS-66/FRA-106 and Bio-Rad FT-Raman spectrometers equipped with a low power Nd:YAG laser (1064 nm) and solid state Ge detector cooled by liquid nitrogen. A resolution of 4 cm^{-1} was used in all measurements. Spectra from single crystals, mounted in standard melting point tubes, were recorded using a Renishaw System 1000 spectrometer, equipped with a DMLM Leica microscope and a 25-mW He-Ne laser (633 nm).

Elemental Analysis: Energy dispersive X-ray Analysis was performed on the amorphous black product formed contemporarily with the formation of **3**, using a JEOL JSM-820 scanning electron microscope. Totally 16 points at three different areas of a sample of the amorphous compound was measured. The observed average contents were (standard deviation in parenthesis): Sb, 24 (3) atom-%; Ga, 26 (3) atom-%; Br, 50 (1) atom-%.

Powder X-ray Diffraction: The powder diffraction data were collected using an INEL powder diffractometer, equipped with CPS-120 position-sensitive detector. The detector was calibrated with a $Pb[NO_3]_2$ standard and the diffraction pattern re-calculated into an equal-step pattern using a cubic-spline function. Standard 0.3 or 0.5 mm Lindemann capillaries were used as sample containers. The samples were kept spinning during the data collection. The Rietveld analyses of the powder diffraction data of **1** and **2** were performed using a local version of the LHPM1 program,[21] and employed pseudo-Voight profile functions, limited to 18 half-widths, with five-peak asymmetry correction, a Lorentzian component $\gamma = \gamma_1 + \gamma_2 (2\theta)$ and FWHM defined as $(U\tan^2\theta + V\tan\theta + W)^{1/2}$. The refinements also included 2θ zero-point correction and Chebyshev background parameters.

1 ($Bi_8[GaBr_4]_2$): An orthorhombic unit cell was indicated from the indexing of the reflections. Certain peaks could be attributed to bismuth metal impurities. On the basis of the similarities in the unit cell parameters of **1** with those of **3**, the compound was believed to be $Bi_8[GaBr_4]_2$. The Rietveld refinement was started with the structural parameters of **3**, including bismuth metal as a second phase. From the difference pattern it was observed that a third phase was present in the sample. The positions of the peaks for this phase matched the known positions of $GaBr_3$, which was included as a third phase in the refinement.[22] The final results suggested the ratio of the different phases in the sample to be Bi metal, 11.3(2)%; $GaBr_3$, 15.9(6)%; $Bi_8[GaBr_4]_2$, 72.8(1.1)%. The structural model of $Bi_8[GaBr_4]_2$ was refined using free coordinates for Bi_8 and restrained for $GaBr_4$ [Ga–Br = 2.35(1) Å]. Individiual isotropic thermal parameters were refined for Bi8 and one each for $GaBr_4$.

Further details of the crystal structure investigation can be obtained from the Fachinformationszentrum Karlsruhe, 76344 Eggenstein-Leopoldshafen, Germany (Fax: +49-7247-808-666; E-mail: crysdata@fiz-karlsruhe.de) on quoting the depository number CSD-415130.

2 ($Bi_5[GaBr_4]_3$): The powder diffraction pattern was collected by using the MAXII synchrotron radiation source at Lund University (beamline I711, λ = 1.3700 Å), also equipped with an INEL CPS-120 detector. The wavelength was calibrated with a Si standard. The Rietveld refinement was started with parameters from cubic $Bi_5[GaCl_4]_3$. A different disorder pattern was found for the Bi_5^{3+} polycation, and the Bi positions were refined in general positions. The structural model was refined using free coordinates, coupled occupancies for Br sites, free for Bi. The thermal parameters were coupled for the Bi and Br sites respectively, and free for Ga (Table 5).

Table 5. Unit cell parameters and experimental crystal data of **1** and **2**.

Compound	$Bi_8[GaBr_4]_2$ (**1**)	$Bi_5[GaBr_4]_3$ (**2**)
Molecular mass ($g\,mol^{-1}$)	2450.51	2212.91
Crystal system	orthorhombic	cubic
Space group	*Pna*2$_1$ (no. 33)	*Fm*-3*c* (no. 226)
a [Å]	18.3014(10)	17.6263(8)
b [Å]	10.3391(6)	
c [Å]	13.5763(7)	
V [Å^3]	2568.9(4)	5476.2(2)
Z	4	8
$D_{calcd.}$ ($g\,cm^{-3}$)	6.335	5.368
μ, [mm^{-1}]	112.54	71.79
Diffractometer	INEL CPS-120	INEL CPS-120
Radiation source	Cu-$K_{\alpha 1}$	MAX II Synchrotron
Wavelength [Å]	1.540598	1.3700
Temperature, [K]	293	293
Scan range, 2θ [°]	8.0–108.0	11.0–100.0
Observations	3282	3039
Bragg reflections	1633	189
No. parameters refined	100	30
R_p	0.109	0.22
R_{wp}	0.114	0.26
R_b	0.069	0.099

Single-Crystal X-ray Diffraction: The crystal structure determinations of **3** and **4** were performed on a Bruker-Nonius KappaCCD diffractometer. Unit cell parameters and crystal data for **3** and **4**, respectively, are found in Table 6. **3** ($Sb_8[GaBr_4]_2$) crystallizes in the orthorhombic system, Laue group *mmm*. The systematic abscences led to the possible space groups *Pna*2$_1$ or *Pnma*, of which the former, non-centrosymmetric, space group was confirmed during the structure determination. **4** ($Te_4[Ga_2Br_7]_2$) crystallizes in the monoclinic system, Laue group 2/*m*. The space group $P2_1/c$ was indicated by the systematic absences. Because of the very weak intensities observed for reflections at high angles, the scan range was limited to $2\theta = 50°$ for the data collection in the case of **4**.

All atoms were refined using anisotropic temperature parameters for both structures. Numerical absorption corrections were applied.[23] Both structures were solved and refined using direct methods and difference Fourier techniques using the SHELXS97/SHELXL97.[24,25]

Further details of the crystal structure investigation can be obtained from the Fachinformationszentrum Karlsruhe, 76344 Eggenstein-Leopoldshafen, Germany (Fax: +49-7247-808-666; E-mail: crysdata@fiz-karlsruhe.de) on quoting the depository numbers CSD-415089 (for $Sb_8[GaBr_4]_2$) and CSD-415090 (for $Te_4[Ga_2Br_7]_2$), respectively.

 © 2005 Wiley-VCH Verlag GmbH & Co. KGaA, Weinheim

Table 6. Unit cell parameters and experimental crystal data of **3** and **4**.

Compound	$Sb_8[GaBr_4]_2$ (**3**)	$Te_4[Ga_2Br_7]_2$ (**4**)
Molecular mass ($g mol^{-1}$)	1752.7	1907.9
Crystal system	orthorhombic	monoclinic
Space group	$Pna2_1$ (no. 33)	$P2_1/c$ (no. 14)
a [Å]	18.096(2)	10.1600(9)
b [Å]	10.1572(9)	10.8314(9)
c [Å]	13.2168(10)	13.8922(10)
β [°]		99.182(7)
V [Å^3]	2429.3(4)	1509.2(2)
Z	4	2
$D_{calcd.}$ ($g cm^{-3}$)	4.792	4.199
Crystal size [mm]	$0.08 \times 0.08 \times 0.15$	$0.04 \times 0.15 \times 0.25$
Temperature [K]	296	296
Radiation, λ [Å]	Mo-K_α, 0.71073	Mo-K_α, 0.71073
Monochromator	graphite	graphite
Data collection method	φ and ω scans	φ and ω scans
Scan range, 2θ [°]	9.02–55.00	9.26–50.04
Range in hkl	$-23 \le h \le 23$, $-11 \le k \le 13$, $-15 \le l \le 17$	$-13 \le h \le 11$, $-11 \le k \le 14$, $-17 \le l \le 18$
μ [mm^{-1}]	24.07	25.85
No. measured reflections	22945	15537
No. unique reflections	5077	2644
No. reflections, $I > 2\sigma(I)$	3411	2142
No. parameters refined	163	100
Max./min. Fourier peak [e·Å^{-3}]	1.25/–1.20	1.17/–1.40
$R(\|F\|)$, all	0.103	0.068
$R(\|F\|)$, $I > 2\sigma(I)$	0.050	0.052
$wR(F^2)$, all	0.075	0.138
GOF	1.132	1.232
Flack parameter	0.00(2)	

The unit cell determination of Bi_6Br_7 was performed on a Siemens SMART P4 diffractometer.

Supporting Information (for details see the footnote on the first page of this article): Powder diffractograms, including final difference pattern, of **1** and **2**, Figures S1 and S2, respectively.

Acknowledgments

We wish to thank Dr. Christer Svensson (Materials Chemistry, Lund University) for performing the unit cell determination of Bi_6Br_7 and Ms. Zuzana Mayerová (Inorganic Chemistry, Stockholm University) for help with the EDX measurements. MAX-Lab, Lund University, is gratefully acknowledged for the allocation of synchrotron beamtime. This work has in part been supported by the Swedish Science Council and the Göran Gustafsson Foundation.

[1] a) *Molecular Clusters of the Main group Elements* (Eds.: M. Driess, H. Nöth), Wiley-VCH, Weinheim, Germany, **2004**; b) S. Ulvenlund, L. Bengtsson-Kloo, in: *Metal Clusters in Chemistry*, vol. 1 (Eds.: P. Braunstein, L. A. Oro, P. R. Raithby), Wiley-VCH, Weinheim, Germany, **1999**, 561–602; c) S. Brownridge, I. Krossing, J. Passmore, H. D. B. Jenkins, H. K. Roobottom, *Coord. Chem. Rev.* **2000**, *197*, 397–481.

[2] a) J. D. Corbett, *Prog. Inorg. Chem.* **1976**, *21*, 129–159; b) R. J. Gillespie, J. Passmore, *Adv. Inorg. Chem. Radiochem.* **1975**, *17*, 49–87.

[3] S. Ulvenlund, L. Bengtsson-Kloo, K. Ståhl, *J. Chem. Soc., Faraday Trans.* **1995**, *91*, 4223–4234.

[4] A. N. Kuznetsov, B. A. Popovkin, W. Henderson, M. J. Taylor, L. Bengtsson-Kloo, *J. Chem. Soc., Dalton Trans.* **2000**, 1777–1781.

[5] M. Lindsjö, A. Fischer, L. Kloo, *Angew. Chem.* **2004**, *116*, 2594–2597; *Angew. Chem. Int. Ed.* **2004**, *43*, 2540–2543.

[6] M. Lindsjö, A. Fischer, L. Kloo, *Eur. J. Inorg. Chem.* **2005**, 670–675.

[7] S. Ulvenlund, A. Wheatley, L. A. Bengtsson, *J. Chem. Soc., Dalton Trans.* **1995**, 245–254.

[8] J. Beck, *Coord. Chem. Rev.* **1997**, *163*, 55–70.

[9] A. N. Kuznetsov, B. A. Popovkin, *Z. Anorg. Allg. Chem.* **2002**, *628*, 2179.

[10] a) A. Balls, A. J. Downs, N. N. Greenwood, B. P. Straughan, *Trans. Faraday Soc.* **1966**, *62*, 521–529; b) E. Kinsella, J. Chadwick, J. Coward, *J. Chem. Soc. (A)* **1968**, 969–972; c) I. R. Beattie, T. Gilson, G. A. Ozin, *J. Chem. Soc. (A)* **1968**, 813–815; d) D. M. Adams, R. G. Churchill, *J. Chem. Soc. (A)* **1969**, 697–703; e) E. Chemouni, *J. Inorg. Nucl. Chem.* **1971**, *33*, 2333–2342.

[11] H. von Benda, A. Simon, W. Bauhofer, *Z. Anorg. Allg. Chem.* **1978**, *438*, 53–67.

[12] S. Ulvenlund, K. Ståhl, L. Bengtsson-Kloo, *Inorg. Chem.* **1996**, *35*, 223–230.

[13] S. Ulvenlund, *PhD. Thesis*, Lund University, Sweden, **1995**.

[14] L. A. Woodward, A. A. Nord, *J. Chem. Soc.* **1955**, 2655–2656.

[15] M. Lindsjö, L. Kloo, *Acta Crystallogr. Sect. E* **2005**, *61*, i18–i19.

[16] R. C. Burns, R. J. Gillespie, *Inorg. Chem.* **1982**, *21*, 3877–3886.

[17] T. W. Couch, D. A. Lokken, J. D. Corbett, *Inorg. Chem.* **1972**, *11*, 357–362.

[18] A. Grodzicki, A. Potier, *J. Inorg. Nucl. Chem.* **1973**, *35*, 61–66.

[19] G. Brauer, *Handbuch der präparativen Anorganischen Chemie*, 3rd ed., Ferdinand Enke Verlag, Stuttgart, Germany, **1981**.

[20] In this particular experiment indium metal, instead of gallium, was used as reducing agent. It has earlier been shown that this choice of reducing agent is irrelevant for the realization of the reaction.[4].

[21] C. J. Howard, R. J. Hill, *A computer program for Rietveld analysis of fixed wavelength X-ray and neutron powder diffraction patterns*, Australian Atomic Energy Commission Report M112, Lucas Heigths Research Laboratory, New South Wales, Australia, **1986**.

[22] S. I. Troyanov, T. Krahl, E. Kemnitz, *Z. Kristallogr.* **2004**, *219*, 88–92.

[23] W. Herrendorf, H. Bärnighausen, *HABITUS, a program for numerical absorption correction*, Universities of Karlsruhe and Giessen, Germany, **1997**.

[24] G. Sheldrick, *SHELXS97, a program for crystal structure solution*, University of Göttingen, Germany, **1997**.

[25] G. Sheldrick, *SHELXL97, a program for crystal structure refinement*, University of Göttingen, **1997**.

Received: February 23, 2005
Published Online: November 7, 2005

 © 2005 Wiley-VCH Verlag GmbH & Co. KGaA, Weinheim

DOI: 10.1002/ejic.200500554

Catechol Oxidation with Dinuclear Copper Complexes of Aliphatic Tripodal Amino Alcohols

Christoph Jocher,[a] Tania Pape,[a] Wolfram W. Seidel,[a] Patrick Gamez,[b] Jan Reedijk,[b] and F. Ekkehardt Hahn*[a]

Keywords: Tripodal ligands / Amino alcohols / Copper / Catechol oxidase

A set of unsymmetrical tripodal (aminoalkyl)bis(hydoxyalkyl)-amine ligands H_4-**2** to H_4-**6** with either ethyl or propyl ligand arms has been prepared and characterized. These ligands react with copper hydroxide and ammonium hexafluorophosphate, copper(II) bromide or tris(triphenylphosphane)copper(I) bromide to give di- and polynuclear complexes. The dinuclear copper complexes **9a–f** catalyze the oxidation of 3,5-di-*tert*-butylcatechol (DTBC). The coordination geometry at the copper center is influenced by the length of the side arms resulting in a different reactivity of complexes **9a–f** in the DTBC oxidation. Alternative preparation procedures lead in selected cases to the formation of coordination polymers **10a** and **10b**. The reversible formation of the poly(dinuclear) cations in **10a** illustrates that the apical alcohol groups are labile. The solid-state structures are neither necessarily identical with solution structure nor do they represent the catalytically active species. Electronic spectra, however, agree with a dinuclear structures in solution as indicated by the characteristics of the oxygen–copper-CT. The observation of comparable catalytic activities for complexes **9a–9d** renders the bridging coordination of the catechol by both copper ions of a dinuclear complex moiety unlikely.
(© Wiley-VCH Verlag GmbH & Co. KGaA, 69451 Weinheim, Germany, 2005)

Introduction

The diverse applications of tripodal tetraamine ligands in coordination chemistry have been reviewed recently.[1] Several transition metal complexes of triethanolamine illustrate the application of aliphatic tripodal ligands in supramolecular chemistry.[2] Furthermore, unsymmetrical tripodal ligands are used in modeling active metal sites in enzymes. For example, a variety of aromatic tripodal NN_2O and NNO_2 ligands have been prepared to model the metal site in the copper enzyme galactose oxidase.[3] The field of aliphatic tripodal ligands with unsymmetrical donor functions developed more recently. Some complexes of the unsymmetrical aliphatic tripodal ligands NN_2O-222 (H_5-**A**),[4] NN_2O-332 (H_5-**1**), NN_2O-333 (H_5-**B**),[5] NNO_2-222 (H_4-**2**),[4c] NNO_2-233 (H_4-**4**),[3i] NNO_2-223 (H_4-**3**),[6] and NNO_2-322 (H_4-**5**)[7] have been prepared (Figure 1). Complexes of sulfur containing unsymmetrical tripodal ligands have also been reported.[8]

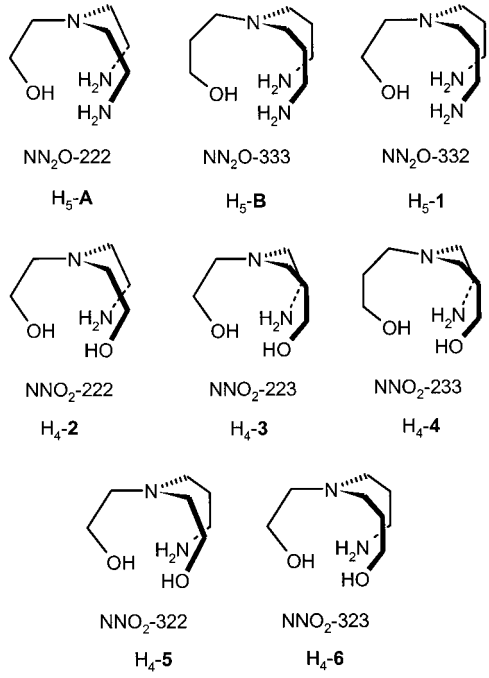

Figure 1. Aliphatic tripodal amino alcohols.

Others and we have studied the correlation between the topology of tripodal ligands and the reactivity of their complexes. A remarkable example for the influence of ligand topology on complex reactivity is the phosphate ester cleavage promoted by tris(3-aminopropyl)amine (trpn) com-

[a] Institut für Anorganische und Analytische Chemie and NRW Graduate School of Chemistry, Westfälische Wilhelms-Universität Münster,
Wilhelm Klemm Straße 8, 48149 Münster, Germany
Fax: +49-251-8333108
E-mail: fehahn@uni-muenster.de
[b] Leiden Institute of Chemistry, Universiteit Leiden,
P. O. Box 9502, 2300 RA Leiden, The Netherlands
E-mail: reedijk@chem.leidenuniv.nl

 © 2005 Wiley-VCH Verlag GmbH & Co. KGaA, Weinheim

plexes of cobalt while the tris(2-aminoethyl)amine (tren) complexes are 300 times less active.[9] Other studies found interrelations between the ligand topology and complex properties for copper(II)[10] and nickel(II)[11] complexes of the tetraamine ligands tren, (3-aminopropyl)bis(2-aminoethyl)amine (baep), (2-aminoethyl)bis(3-aminopropyl)amine (abap), and trpn.

In this contribution, we present a study on copper complexes of a set of NNO_2 ligands and extend the relation between ligand shape and complex properties to catalysis. To allow for a fine-tuning of the geometric strain the flexible aliphatic ligands H_4-**2** to H_4-**6** (Figure 1) and their copper(II) complexes were studied. The copper complexes of ligands H_5-**1** to H_4-**6** (**9a**–**f**) may serve as models of the metal site in type 3 copper proteins. One member of this group is the ubiquitous plant enzyme catechol oxidase (CO, E.C.1.10.3.1) that converts catechols under consumption of molecular oxygen into *o*-quinones, which auto-polymerize to protect the plant from damage.[12] Many models for the active center in CO have been prepared,[13] but so far conversion rates of the model compounds are lower by four orders of magnitude compared to the enzyme.[14] In our study 3,5-di-*tert*-butylcatechol (DTBC) was chosen as model substrate (Figure 2). To date different mechanisms for the oxidation of this substrate are discussed controversially based on measurements on model compounds.[15]

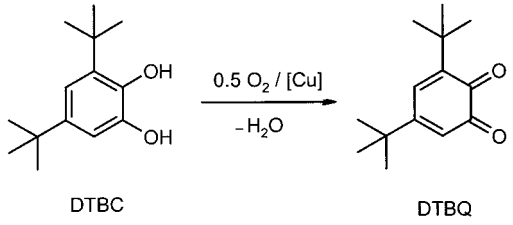

Figure 2. Oxidation of DTBC to 3,5-di-*tert*-butylquinone (DTBQ).

Results and Discussion

Ligand Synthesis

Ethanolamine, propanolamine and diethanolamine, respectively are employed as starting materials for the synthesis of ligands H_5-**1** to H_4-**6**. A Strecker synthesis[16] or Michael addition of acrylic acid derivatives[17] is applied to assemble the tripodal backbone. The ester or nitrile functions of the protected ligands are reduced with aluminum hydride prepared in situ.[18] Alternative synthetic procedures described for the preparation of ligands NNO_2-222 (H_4-**2**),[19] NN_2O-222 (H_5-**A**),[20] NN_2O-332 (H_5-**1**)[21] were found to be less efficient in our hands.

The preparation of the diamino-dihydroxy ligand NNO_2-323 (H_4-**6**) (Scheme 1) starts with the Michael addition of one equivalent ethyl acrylate to ethanolamine.[8a] A small amount of methanol and excess acrylonitrile were added to the wax-like solid **7**. The mixture was heated to 60 °C for 24 h. After removal of volatiles compound **8** was isolated and the ester and nitrile group were reduced with aluminum hydride at temperatures increasing from 0 °C to ambient temperature. The reaction mixture was carefully hydrolyzed after eight hours and H_4-**6** was obtained by Soxhlet extraction with methanol for 24 h. The extract was dried with sodium sulfate, filtered through celite® and volatiles were removed. Bulb to bulb distillation affords ligand NNO_2-323 (H_4-**6**) as colorless viscous oil.

Solid State Structure of Dinuclear Copper Complexes

Copper complexes of the tripodal amino alcohols were prepared as described for complex $[Cu(H_3\text{-}\mathbf{4})]_2(PF_6)_2 \cdot 2MeOH$ **9c**·2MeOH.[2e,3i] For the preparation of the copper complexes, one equivalent of ligand was added to an equimolar suspension of copper(II) hydroxide in deionized water. After stirring for one hour two equivalents NH_4PF_6 were added. The solutions were concentrated to approximately 1 mol/L by warming to 40 °C. Blue solids precipitated upon cooling of these solutions to 5 °C. Diffusion of diethyl ether into an ethanol (**9a**), acetonitrile (**9b**, **9e**, **9f**), or methanol (**9d**) solutions of these residues gave crystals of $[Cu(H_3\text{-}\mathbf{2})_2]_2(PF_6)_4 \cdot 0.5EtOH \cdot 0.5H_2O$ (**9a**·0.5EtOH·0.5H_2O), $[Cu(H_3\text{-}\mathbf{3})]_2(PF_6)_2 \cdot 2H_2O$ (**9b**·2H_2O), $[Cu(H_3\text{-}\mathbf{5})]_2(PF_6)_2 \cdot CH_3OH$ (**9d**·CH_3OH), $[Cu(H_3\text{-}\mathbf{6})]_2(PF_6)_2$ (**9e**), and $[Cu(H_4\text{-}\mathbf{1})]_2(PF_6)_2$ (**9f**). The molecular structures of these complexes were determined by X-ray diffraction (Figure 2 and Figure 3). The dinuclear complexes of type **9** were the dominant species under the reaction conditions selected. All attempts to isolate and characterize mononuclear complexes by adding more NH_4PF_6 or $NaPF_6$ failed.

The structure determinations on **9a**, **9b**, **9d**, **9e**, and **9f** in the solid state show dinuclear dicationic complexes $[Cu_2L_2]^{2+}$ as were previously observed for **9c**, in which one deprotonated alcohol group of each ligand serves as bridging donor to the second copper ion in a μ^3-fashion (Figure 3 and Figure 4). The second hydroxyl arm of each ligand remains protonated as indicated by much longer copper–oxygen distances relative to the bridging alkoxide (com-

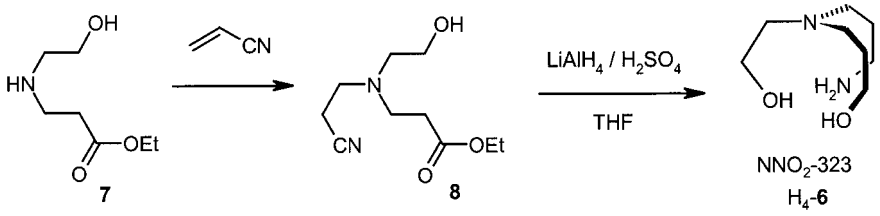

Scheme 1. Synthesis of the ligand NNO_2-323 (H_4-**6**).

 © 2005 Wiley-VCH Verlag GmbH & Co. KGaA, Weinheim

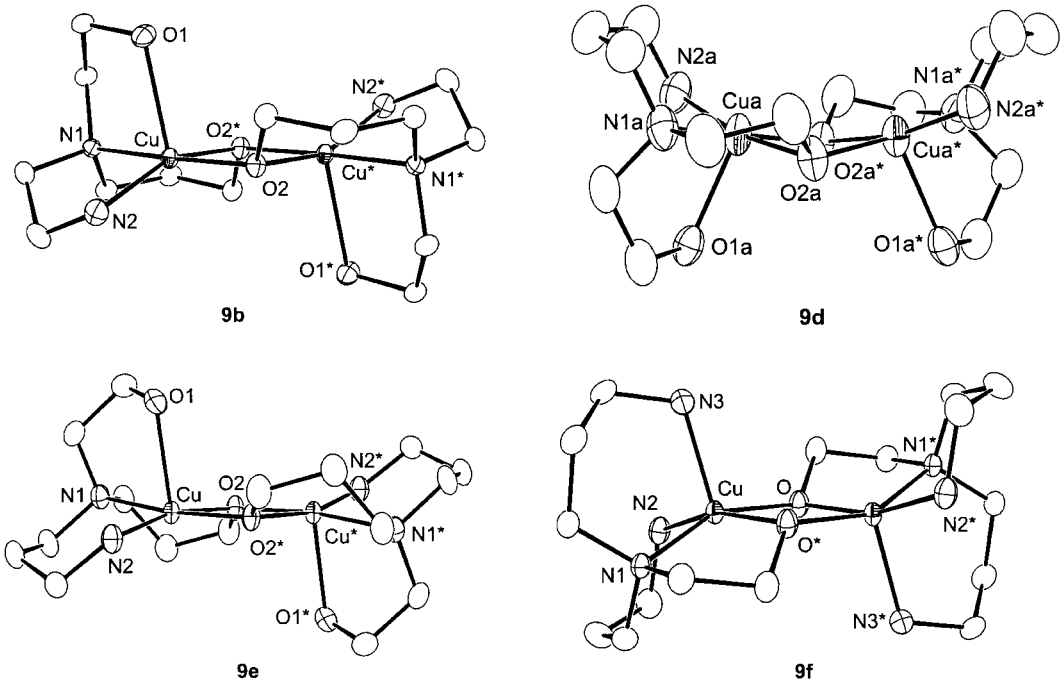

Figure 3. Molecular structures of the dinuclear cations of **9b** and **9d**–**f**.

pare Cu–O1 and Cu–O2 in Table 1). Comparison of the various structures reveals that propylalkoxide ligand arms, if available, preferably act as bridging donors. Complexes **9b**, **9e**, and **9f** form centrosymmetric complex ions with a planar $[Cu_2(OR)_2]^{2+}$ moiety and with *trans*-arrangement of the apical alcohol functions.

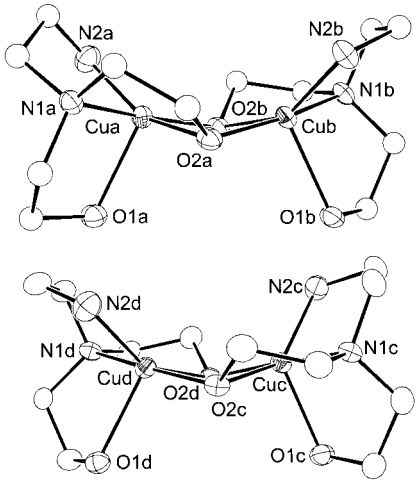

Figure 4. Molecular structure of the two dinuclear isomeric dications in **9a**.

Complexes **9a** and **9d** with ligands H_4-**2** and H_4-**5**, respectively, adopt a rather bowl-shaped geometry with a butterfly-like distorted $[Cu_2(OR)_2]^{2+}$ core and *cis*-constitution of the coordinated alcohol groups. The short ligand arms of the ethyl alcohol lead to geometric strain and a distortion of the angles at the copper atom (Table 1). Hence, metal ions with a different coordination environment are found in the crystal structures of **9a** and **9d**. The unit cell of **9d** contains two not related halves of the dinuclear complex ion $[\mathbf{9d}]^{2+}$. Complex **9a** crystallizes in a polar space group ($P2_1$) and the unit cell contains four different copper atoms of two dinuclear complex dications $[\mathbf{9a}]^{2+}$. The observation of the polar space group $P2_1$ for **9a** can be rationalized by the helicity of the dinuclear units and by the fact that the diamino chelate rings adopt different configurations in the two dinuclear complexes (λλ and λδ, respectively) (Figure 4).

Bond lengths and angles differ between the two dinuclear units in crystals of **9a**. Consequently, four different τ-values[22] (0.21, 0.32, 0.51, 0.36) were observed for the four copper atoms in the asymmetric unit, indicating a distorted tetragonal-pyramidal coordination environment for the metal ions. The Cu–O distances range from 2.177(4) Å to 2.265 Å for the alcohol functions in the apical position. Within the $Cu(\mu\text{-}O)_2Cu$ core the Cu–O2 distances in *trans*-position to the tertiary nitrogen donor are distinctively shorter [1.939(3) Å to 1.956(4) Å] than the Cu–O2 bond lengths *trans* to the primary nitrogen donor [1.998(4) Å to 2.075(4) Å, Table 1].

While **9d** exhibits an almost ideal tetragonal-pyramidal copper environment (τ = 0.03), **9e** and **9f** are also close to such a coordination geometry (τ = 0.10 and τ = 0.12, respectively). The highest τ-value is observed for **9a** and **9b** (τ = 0.3) which can be attributed to the shorter ethyl ligand arms leading to a distortion towards a trigonal-bipyramidal coordination geometry.

An interesting structural feature of these dinuclear complexes is the angle at the bridging oxygen atoms. Often, the magnetic coupling between two paramagnetic Cu^{II} centers is antiferromagnetic for angles larger than 96° while a ferromagnetic interaction is observed for smaller angles.[23a,23b]

 © 2005 Wiley-VCH Verlag GmbH & Co. KGaA, Weinheim

Table 1. Selected bond lengths [Å] and angles [°] for **9a**·0.5EtOH·0.5H_2O, **9b**·2H_2O, **9d**·2CH_3OH, **9e**, **9f**, and **10a**.

	9a[a]	**9b**	**9c**[b]	**9d**[c]	**9e**	**9f**	**10a**
Cu–O1	2.220(4), 2.255(4) 2.177(4), 2.265(4)	2.337(2)	2.338(4)	2.279(5) 2.283(4)	2.358(2)	–	2.500(1)
Cu–O2	1.998(4), 2.005(3) 2.075(4), 2.019(4)	1.9423(15)	1.919(3)	1.957(3) 1.955(3)	1.9231(12)	1.965(2)	1.927(3)
Cu–O2*	1.956(4), 1.947(4) 1.939(3), 1.945(3)	1.9357(14)	1.941(3)	1.966(3) 1.960(3)	1.9525(12)	1.952(2)	1.940(3)
Cu–N1	2.009(5), 2.028(5) 2.000(5), 2.018(4)	2.018(2)	2.030(4)	2.036(4) 2.026(4)	2.0410(14)	2.058(2)	2.024(4)
Cu–N2	1.996(4), 1.994(5) 2.025(4), 2.005(5)	1.997(2)	1.990(4)	1.971(5) 1.978(4)	1.9859(15)	2.009(2)	1.987(4)
Cu–N3	–	–	–	–	–	2.171(3)	–
Cu–Cu	2.8929(9) 2.9060(9)	2.9368(5)	3.0009(11)	2.9278(10) 2.9364(11)	3.0129(4)	2.9692(7)	2.9821(12)
Largest angle	O2*–Cu–N1 166.7(2), 168.3(2) 168.3(2), 169.5(2)	O2*–Cu–N1 175.38(6)	O2*–Cu–N1 172.77(14)	O2–Cu–N2 168.0(2) 168.6(2)	O2*–Cu–N1 171.21(5)	O—Cu—N2 161.84(10)	O2–Cu–N2 174.9(2)
2nd largest angle	O2–Cu–N2 154.0(2) 149.3(2) 137.7(2), 147.9(2)	O2–Cu–N2 157.15(8)	O2–Cu–N2 162.0(2)	O2*–Cu–N1 166.2(2) 166.57(14)	O2–Cu–N2 164.93(7)	O*–Cu—N1 154.85(8)	O2*–Cu–N1 169.93(15)
Cu–O2–Cu*	94.30(15), 93.80(15) 94.45(15), 92.55(14)	98.45(6)	102.01(13)	96.91(13) 96.83(13)	102.05(5)	98.57(8)	100.91(15)

[a] The asymmetric unit contains for copper atoms in two dinuclear complexes **9a**. [b] Published data.[3i] [c] Atoms labeled with an asterisk denote atoms from different ligands not necessarily related by a symmetry element.

The bridging alkoxide groups lead to angles below this value for complex **9a**, while the Cu–O–Cu angles fall in the range 98° and 102° (Table 1) for the other complexes. However, temperature dependent measurements of the magnetic susceptibility for **9b**–**f** indicate that the coupling between the copper centers is antiferromagnetic in all cases.

Electronic Spectra

The electronic spectra of the dinuclear copper complexes **9a**–**f** show three transitions (Table 2, Figure 5 for **9f**). The most intense absorption is observed between 36 500 cm^{-1} (**9a**) and 39 400 (**9e**) cm^{-1} with extinction coefficients between 4900 L/mol·cm (**9c**) to 15700 L/mol·cm (**9f**). This absorption is assigned to a nitrogen-centered ligand-to-metal charge transfer (LMCT) by comparison with a variety of copper amine complexes.[23c] Hence, a distinct difference in intensity appears between the complex with the triamine NN_2O ligand (**9f**) and the complexes with the diamine NNO_2 ligands (**9a**–**9e**).

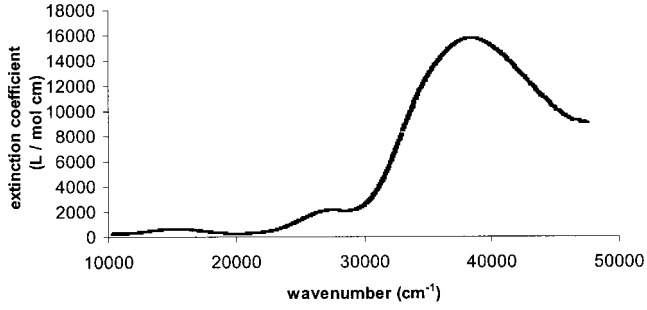

Figure 5. Electronic spectrum of **9f** in acetonitrile solution.

The second absorption is observed between 27300 cm^{-1} (**9c**, **9e**, **9f**) and 27800 cm^{-1} (**9a**) with extinction coefficients around 2000 L/mol·cm (Table 2). As the intensity of this band is similar in all complexes and as the common feature of complexes of type **9** is the dialkoxy bridge, this band is associated with a charge transfer from the alkoxy oxygen atoms to the copper centers.[24] This assignment is sup-

Table 2. Listing of τ-values, parameters of the electronic spectra, redox potentials, DTBQ yields and turnover numbers upon catalytic oxidation with complexes **9a**–**f**.

	9a	**9b**	**9c**	**9d**	**9e**	**9f**
τ-value[22]	0.21, 0.32, 0.51, 0.36	0.30	0.18	0.03	0.10	0.12
UV/Vis [cm^{-1}]	36500	37300	37000	38800	39400	38230
(ε [L/mol cm])	(6700)	(7900)	(4900)	(7100)	(8700)	(15700)
	27800	27400	27300	27500	27300	27300
	(540)	(1800)	(2000)	(1000)	(2300)	(2080)
	15250	16580	17090	16100	16500	15150
	(170)	(160)	(120)	(150)	(180)	(580)
Oxidation vs. Fc/Fc^+ [V]	1.15/1.27	1.01	0.90	1.05	1.42	0.87/1.50
Reduction vs. Fc/Fc^+ [V]	–1.43/–1.31 –1.10/–1.00	–1.42	–1.16	–1.07	–1.33	–1.78
Yield DTBC [%]	15	83	99	80	50	36
TON [h^{-1}]	180	216	227	94	140	504

 © 2005 Wiley-VCH Verlag GmbH & Co. KGaA, Weinheim

ported by the intensity decrease observed for complexes **9a** and **9d**. Within these two complexes the $Cu(\mu\text{-}O)_2Cu$ rings are distorted, because five-membered chelate rings are involved in the formation of the bridging four-membered ring (Figure 4). Apparently, the planarity of this four-membered ring is responsible for an optimum absorption. The observed difference of the extinction coefficient for the band around 27000 cm^{-1} between the *cis* structures **9a** and **9d** and the *trans* structures **9b**, **9c**, and **9e** support retention of the dinuclear structures in solution.

The absorptions with the lowest intensity and energy result from d→d transitions. They fall in the range between 15150 cm^{-1} (**9f**) and 17090 (**9c**) cm^{-1} with extinction coefficients from 120 L/mol·cm (**9c**) to 580 L/mol·cm (**9f**). The increased extinction coefficient in **9f** is most likely associated with the extra nitrogen atom present which causes a stronger mixing of ligand orbitals and metal d-orbitals in **9f**.

The energy of the d→d bands is consistent with either a trigonal-bipyramidal or a square-pyramidal geometry around the copper atoms. The coordination geometry at the copper center has been derived from the energy of the d→d absorption band for CuN_4,[10b] CuN_5 and CuN_6 complex fragments or complexes.[25] However, with compounds **9a**–**9e** no significant correlation was observed between τ-value and energy of the low energy transition. A comparison of different methods to determine the distortion of the trigonal-bipyramidal towards the tetragonal-pyramidal geometry showed the τ-value to be a sufficient criteria to distinguish between the two geometries for CuN_5 chromophores.[26] In general, the d→d transitions of complexes of type **9** shift hypsochromic with an increasing number of six-membered chelate rings as well as for a change in the donor set from NNO_2 to NN_2O ligands (Table 2).

Cyclic Voltammetry

Cyclic voltammetry experiments show one irreversible reduction and one irreversible oxidation peak for the copper complexes **9b**–**9e** in acetonitrile solution (Table 2). The CV′s of complex **9e** are shown as an example in Figure 6. The presence of four reduction peaks for **9a** can be attributed to four different copper centers displaying different τ-values as found in the solid-state structure. For the oxidation process two peaks are observed for compounds **9a** (1.15 V and 1.27 V) and **9f** (0.87 V and 1.50 V). In general, reduction of complexes of type **9** occurs between –1.78 V and –1.07 V while oxidations are observed between 0.87 and 1.50 V vs. Fc/Fc^+.

Compound **9f** with an NN_2O ligand exhibits the strongest ligand field, which is reflected by the lowest reduction potential (–1.78 V) in the series of complexes of type **9**. The precipitation of copper metal during this reduction suggests that Cu^{II} is reduced to Cu^{I}, whose complexes are unstable. The irreversibility of the reduction process with complexes of type **9** is thus explained with the instability of Cu^{I} within a strong ligand field generated by the alkoxide and amine

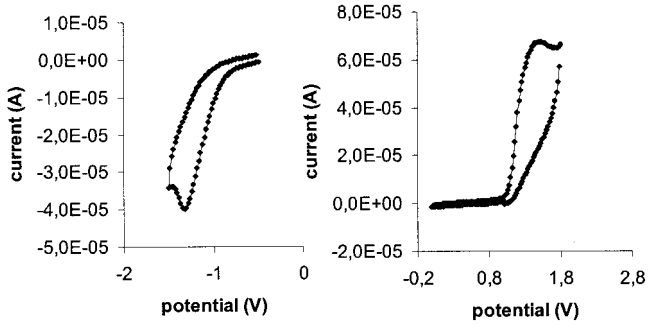

Figure 6. Irreversible reduction and oxidation peaks for **9e**. CV data were recorded in a 0.1 M solution of Bu_4NPF_6 in acetonitrile against Fc/Fc^+.

functions. A sharp reoxidation peak is observed around –0.4 V resulting from the oxidation of metallic copper to Cu^{II} in the presence of ligand. A limited number of stable Cu^{I}–OR species is known.[27] While the Cu^{I} alkoxide can be stabilized in the absence of air or water either sterically or by conjugated π–systems in phenolates or enolates, Cu^{I}–OMe species decomposes vigorously into copper metal, formaldehyde and methanol.

The irreversible nature of the oxidation process suggests that hypothetical Cu^{III} species are highly reactive and might lead to ligand degradation. Within the functional groups present, the bridging alkoxide functions are most susceptible for oxidation, which can produce aldehydes, carboxylic acid derivatives or CC coupled products.

DTBC Oxidation

Acetonitrile solutions of complexes of type **9** and DTBC (30 equiv.) were mixed in a shaking device under an oxygen atmosphere. The amount of oxygen consumed was monitored by an experimental set up described by one of us previously for similar experiments.[28] Typically, green solutions were obtained upon mixing of the catalyst and the DTBC solution. The addition of one equivalent sodium methoxide initiated oxygen consumption, otherwise complexes of type **9** were found catalytically inactive. The order of mixing of the solutions influenced the yield of the oxidation product DTBQ. For example, mixing of **9b** and DTBC followed by addition of base gave lower yields (25%–30%) than mixing **9b** and base followed by DTBC addition (83% yield, Table 2). In general, complexes **9a**–**f** show a variation in catalytic activity giving yields from 15 to 99% with a TON from 90 to 500 h^{-1} (Table 2). A plot of the oxygen consumption during the oxidation of DTBC with complex **9f** as the catalyst is depicted in Figure 7. The experimental data confirm our assumption that a nitrogen (amine) rich coordination environment improves the catalytic activity of the copper center for the DTBC oxidation. Unfortunately, compound **9f** is less stable than **9a**–**e** under the required basic conditions. The coordination geometry described by the τ-value and catalytic activity do not correlate. Reaction rates and yields are best in the presence of six-membered chelate

 © 2005 Wiley-VCH Verlag GmbH & Co. KGaA, Weinheim

rings for the alcohol functions and five-membered chelate rings for the terminal amine functions.

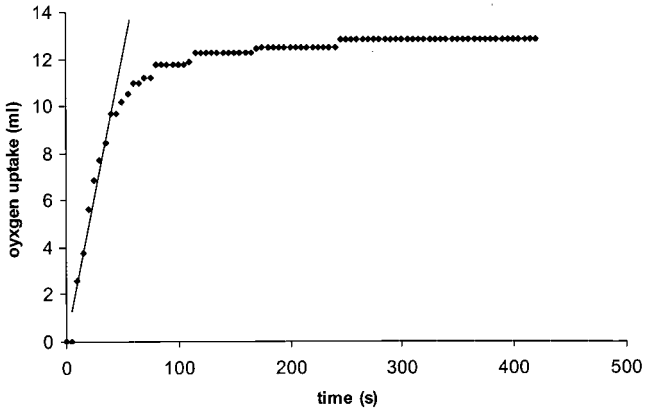

Figure 7. Consumption of O_2 (mL) vs. time (s) for the catalytic oxidation of DTBC (3 mmol) with **9f** in acetonitrile (maximum oxygen uptake: 33.6 mL).

Additional Copper Complexes

The stability of the copper(II) complexes of type **9** was corroborated by the formation of a purple Cu^{II} species upon reaction of $[Cu^{I}(PPh_3)_3Br]$ with ligand NNO_2-233 (H_4-**4**). Equimolar amounts of the copper(I) compound and the ligand were mixed at air in a dichloromethane solution. The initially colorless solution turned blue rapidly and a purple solid **10a** precipitated. The elemental analysis suggested a ratio of Cu/Br/ligand of 1:1:1. The purple color of **10a** differs from the blue color of the dinuclear hexafluorophosphate salts **9a**–**9e**. Compound **10a** can be obtained directly by reaction of anhydrous copper(II) bromide and H_4-**4** in methanol. The X-ray structure analysis revealed that a polymer chain consisting of dinuclear dicationic units, which are bridged by alkoxy functions of the singly deprotonated ligand had formed (Figure 8). The remaining alcohol function of the ligand binds to a copper atom of an adjacent dinuclear unit in the apical position. The coordination geometry around the copper atoms is square-pyramidal with $\tau = 0$ (Table 1).

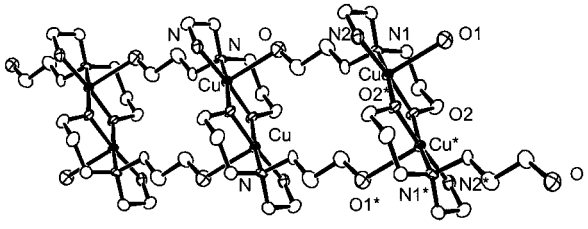

Figure 8. Fraction of the poly(dinuclear) coordination polymer built from $[Cu_2(H_3\text{-}\mathbf{4})_2]^{2+}$ cations of complex **10a**.

In an attempt to exchange the apical protonated alcohol function in the dinuclear complex $[Cu(H_3\text{-}\mathbf{4})]_2(PF_6)_2$ (**9c**) against 2,4,6-trimethylphenol (TMP), purple $[Cu(H_3\text{-}\mathbf{4})(TMP)]_2(PF_6)_2$ (**10b**) precipitated from a green solution. We assume that the TMP ligand substituted the protonated (apical) alcohol function at the copper center. Apparently, this apical alcohol function is the most labile in the complex and can be substituted for other ligands. Furthermore, **10b** can be reconverted to **9c** in the absence of competing ligands such as methanol or TMP. Dissolving the purple complex $[Cu(H_3\text{-}\mathbf{4})(TMP)]_2(PF_6)_2$ (**10b**) in acetonitrile gives a blue solution. Addition of diethyl ether to this solution leads to precipitation of the dark blue dinuclear complex **9c**.

In conclusion, the energy difference between the two solid-state structures of type **9** and type **10** is small enough to allow interconversion. Apparently, the apical alcohol ligands in the dinuclear copper complexes of type **9** are labile and can be substituted for the catechol substrate without breaking up the dinuclear units immediately. The Cu–Cu distances in complexes of type **9** fall in the range between 2.89 Å (**9a**) and 3.01 Å (**9e**). However, the observation of comparable catalytic activity for both the *cis* complexes **9a** and **9d** and the *trans* complexes **9b** and **9c** renders the bridging coordination of the catechol by both copper ions of a dinuclear complex moiety unlikely. We therefore assume that during the catalytic cycle catechol substitutes one of the apical alcohol groups in the dinuclear copper complexes and eventually η^1-coordinated catechol replaces one of the bridging alkoxide arms with the second oxygen donor atom.[29] This process is aided by addition of a base which deprotonates the catechol ligand thereby enhancing its basicity. The addition of bases to the dinuclear complexes of type **9** in the absence of catechol leads to decomposition of the dinuclear complexes to a brown insoluble substance.

Conclusions

The rates of catalytic DTBC oxidation by the model compounds **9a**–**f** are far from modeling the enzyme catechol oxidase. However, **9f** shows an activity which is comparable to some other model compounds.[13b,13d] The aim of this study was to probe the relation between the particular ligand design of basically similar ligands and the catalytic activity of its Cu^{II} complexes. Complexes **9a** to **9e** show indeed a different catalytic activity manifested in a variation of the yield in DTBC oxidation (15% to 99%) and different TON (94 to 227 h^{-1}). Since complexes **9a** to **9e** contain identical donor sets all differences in the activity can be attributed to different arm length at the tripodal ligands. However, the derivation of linear correlations between structural factors and catalytic activity turns out to be difficult.

Experimental Section

Materials and Methods: All manipulations were carried out in air unless noted otherwise. Solvents were purified by standard methods and freshly distilled prior use. Infrared spectra were recorded in KBr (pellets or thin films) with a Bruker Vector 22 FT spectrometer. ^1H and ^{13}C NMR spectra were recorded on Bruker AC 200 or Bruker ARX 300 spectrometers. Elemantal analyses (C,H,N) were

 © 2005 Wiley-VCH Verlag GmbH & Co. KGaA, Weinheim

performed with a Vario EL III Elemental Analyzer at the Institut für Anorganische und Analytische Chemie, University of Münster. MALDI, ESI and EI mass spectra were measured with Bruker Reflex IV, Micromass Quattro LC and Varian MAT 212 instruments, respectively. UV/Vis spectra were recorded in acetonitrile with a Varian Cary 50 spectrophotometer. Cyclic voltammetry experiments were carried out with a Eco-Chemie PGSTAT 30 potentiostat using a three-electrode cell configuration (working electrode: glassy carbon, auxiliary electrode: platinum, reference electrode: Ag/AgCl/3 M KCl). The experiments were performed in 0.1 M acetonitrile solutions of Bu_4NPF_6 as supporting electrolyte with scan rates of 100 mV/s. A computer-controlled apparatus[28] was used for oxygen uptake measurements in oxidation experiments with DTBC (Aldrich). Solutions of DTBC were freshly prepared. 30 equivalents of DTBC were mixed with one equivalent catalyst and one equivalent sodium methoxide in acetonitrile at 25 °C.

Ligand Syntheses: Ligands NNO_2-222 (H_4-**2**),[4c] NNO_2-223 (H_4-**3**),[6b] NNO_2-233 (H_4-**4**),[3i] NNO_2-322 (H_4-**5**),[7] and NN_2O-332 (H_5-**1**)[5] were prepared according to previously published procedures.

Ethyl 3-[(2-Cyanoethyl)(2-hydroxyethyl)amino]propanoate (8): 2.0 equivalents of acrylonitrile (5.46 g, 0.10 mol) were added to a solution of ethyl 3-[(2-hydroxyethyl)amino]propanoate (**7**)[8a] (8.29 g, 0.0514 mol) in methanol (5 mL). The reaction mixture was heated to 60 °C for 48 h. Excess acrylonitrile and methanol were removed under reduced pressure and **8** remained as a colorless liquid. Yield: 10.6 g (0.049 mol, 96%). ^{1}H NMR (200 MHz, $CDCl_3$): δ = 4.07 (q, 2 H, OCH_2CH_3), 3.52 (t, 2 H, CH_3CH_2OH), 2.85–2.70 (m, 4 H, NCH_2), 2.59 (t, 2 H, NCH_2CH_2OH), 2.47–2.33 (m, 4 H, NCH_2CH_2), 1.18 (t, 3 H, OCH_2CH_3). ^{13}C NMR (50.3 MHz, $CDCl_3$): δ = 172.4 [*C*(O)OEt], 118.7 (CN), 60.6 (CH_2O), 59.4 (CH_2O), 55.6 (NCH_2CH_2OH), 49.6 (NCH_2), 48.8 (NCH_2), 32.7 ($NCH_2CH_2CO_2Et$), 16.6 (NCH_2CH_2CN), 13.9 (OCH_2CH_3).

N*-(2-Hydroxyethyl)-*N*-(3-hydroxypropyl)propylene-1,3-diamine NNO_2-323 (H_4-6):** Dry lithium aluminum hydride (8.36 g, 0.209 mol) was suspended in THF (200 mL). After stirring for 60 minutes and cooling to –5 °C concentrated sulfuric acid (4.80 g, 0.047 mol) was added carefully dropwise (Caution:*** this reaction is extremely exothermic, hydrogen is evolved). The suspension was stirred for 60 min and ethyl 3-[(2-cyanoethyl)(2-hydroxyethyl) amino]propanoate (**8**) (15.0 g, 0.020 mol) dissolved in THF (30 mL) was slowly added. The reaction mixture should not be allowed to boil during the addition of **8**. The suspension was stirred at room temperature for 8 h and then quenched by slow addition of degassed water (15.1 g, 0.84 mol) at 0 °C. The reaction mixture was filtered under an argon atmosphere. The filtrate contained H_4-**6** and side products, but most of the ligand was found in the solid residue. It was isolated by continuous extraction with methanol for one day. An immediate work-up after hydrolysis increased the yield of ligand H_4-**6** because otherwise aluminum complexes form. The extract and the filtrate were united and dried with sodium sulfate. Removal of the solvent gave a colorless to yellow residue, which was suspended in dichloromethane (200 mL) and dried with sodium sulfate. The drying agent and precipitated lithium salts were separated by filtration through Celite®. Distillation under reduced pressure (180 °C, 0.05 mbar) afforded H_4-**6** as colorless oil. Yield: 3.37 g (19.1 mmol, 27%). $C_8H_{20}N_2O_2$ (176.26): calcd. C 54.52, H 11.44, N 15.89; found C 53.32, H 11.43, N 15.12. ^{1}H NMR (200.1 MHz, $CDCl_3$): δ = 3.62 (t, 2 H, $NCH_2CH_2CH_2OH$), 3.54 (t, 2 H, NCH_2CH_2OH), 3.29 (s br, 4 H, OH + NH_2), 2.68 (t, 2 H, $NCH_2CH_2CH_2NH_2$), 2.54 (t, 2 H, $NCH_2CH_2CH_2OH$), 2.48 (t, 2 H, NCH_2CH_2OH), 2.46 (t, 2 H, $NCH_2CH_2CH_2NH_2$), 1.63 (qi, 2 H, $NCH_2CH_2CH_2OH$), 1.55 (qi, 2 H, $NCH_2CH_2CH_2NH_2$). ^{13}C NMR (50.3 MHz, $CDCl_3$): δ = 62.2 ($NCH_2CH_2CH_2OH$), 59.4 (NCH_2CH_2OH), 55.6 (NCH_2CH_2OH), 53.3 ($NCH_2CH_2CH_2OH$), 51.8 ($NCH_2CH_2CH_2NH_2$), 39.8 ($NCH_2CH_2CH_2NH_2$), 29.6 ($NCH_2CH_2CH_2NH_2$), 28.7 ($NCH_2CH_2CH_2OH$). IR (KBr film): ν = 3358 (s, NH), 3285 (s, NH), 2949 (s, CH), 2871 (s, CH), 2829 (s, CH), 1662 (w), 1602 (w, NH), 1464 (m, CH), 1375 (w, CH), 1299 (w), 1060 (s, CO), 910 (m), 870 (w), 750 (w). MALDI-MS (337.0 nm, 3 ns) *m*/*z*: 177.0 $[MH]^+$.

Synthesis of Copper Complexes. General Procedure: Copper hydroxide was prepared from copper chloride and sodium hydroxide in the presence of a small amount of polyethylene glycol ether at 0 °C. The turquoise solid can be stored at –30 °C for several months without darkening. The preparation of copper complexes of type **9** was carried out according to a published procedure described for the preparation of complex **9c**.[3i] Copper hydroxide was suspended in deionized water (10–20 mL) and the ligand dissolved in water (10 to 20 mL) was added. The reaction mixture was stirred at 40 °C for 2 h. Solid NH_4PF_6 was added and the volume of the solutions was reduced to reach a concentration of approximately 1 M. Crystalline material precipitated upon storage at 5 °C. For further purification, the raw material was recrystallized from ethanol (**9a**·0.5EtOH·0.5H_2O), methanol (**9d**·MeOH), acetonitrile (**9b**·2H_2O, **9e**, **9f**) or dichloromethane (**10a**). Yields and selected analytical data for complexes **9a**·0.5EtOH·0.5H_2O, **9b**·2H_2O, **9d**·MeOH, **9e**, **9f** and **10a** are given below.

$[Cu_2(H_3\text{-}2)_2](PF_6)_4$·0.5EtOH·0.5$H_2O$ (9a·0.5EtOH·0.5H_2O): $Cu(OH)_2$ (425 mg), 4.36 mmol, ligand H_4-**2** (647 mg, 4.36 mmol) and NH_4PF_6 (711 mg, 4.36 mmol) were used in the procedure described for the preparation of **9c**.[3i] Yield: 340 mg (0.457 mmol, 21%). IR (KBr): $\tilde{\nu}$ = 3364 cm^{-1} (s), 3312 (s), 3208 (s, br), 2990 (s), 2927 (s), 2870 (s), 1597 (m), 1473 (m), 1371 (w), 1269 (w), 1134 (m). MALDI-MS (337.0 nm, 3 ns) *m*/*z*: 482 (45, $[Cu_3(H_3\text{-}2)_2]^+$), 416 (75, $[Cu_2(H_3\text{-}2)_2(CH_3CN)]^+$), 419 (100, $[Cu_2(H_3\text{-}2)_2]^+$).

$[Cu_2(H_3\text{-}3)_2](PF_6)_2$·2$H_2O$ (9b·2H_2O): $Cu(OH)_2$ (195 mg, 2.00 mmol), ligand H_4-**3** (330 mg, 2.00 mmol) and NH_4PF_6 (530 mg, 4.00 mmol) were used. Yield: 308 mg (0.397 mmol, 40%). **9b**·2H_2O $C_{14}H_{38}N_4Cu_2F_{12}O_6P_2$ (775.52): calcd. C 21.68, H 4.94, N 7.22; found C 21.59, H 4.35, N 6.91. ^{19}F NMR (188.3 MHz, CD_3CN): δ = –66.8 ($^1J_{FP}$ = 710 Hz). IR (KBr): $\tilde{\nu}$ = 3627 cm^{-1} (m), 3327 (s), 3128 (m), 2919 (m), 2861 (m), 2821 (m), 1594 (m), 1472 (m), 1320 (m), 1120 (s), 1084 (s), 1062 (s), 830 (s, PF_6). MALDI-MS (337.0 nm, 3 ns) *m*/*z*: 447 (100, $[Cu_2(H_3\text{-}3)_2]^+$), 592.9 (30, $[\{Cu_2(H_3\text{-}3)_2\}PF_6]^+$).

$[Cu_2(H_3\text{-}5)_2](PF_6)_2$·$CH_3OH$ (9d·CH_3OH): $Cu(OH)_2$ (292 mg, 3.00 mmol), ligand H_4-**5** (487 mg, 3.00 mmol) and NH_4PF_6 (980 mg, 6.00 mmol) were used. Yield: 550 mg (0.713 mmol, 48%). IR (KBr): $\tilde{\nu}$ = 3666 cm^{-1} (s), 3448 (s), 3343 (s), 3297 (s), 3131 (s), 2951 (m), 2921 (m), 2880 (m), 2765 (m), 1604 (s), 1463 (m), 1333 (m), 1286 (m), 1265 (m), 1161 (s), 1072 (s), 1044 (s), 1015 (s), 833 (s, PF_6).

$[Cu_2(H_3\text{-}6)_2](PF_6)_2$ (9e): $Cu(OH)_2$ (211 mg, 2.18 mmol), ligand H_4-**6** (383 mg, 2.18 mmol) and NH_4PF_6 (711 mg, 4.36 mmol) were used. Yield: 350 mg (0.456 mmol, 42%). IR (KBr): $\tilde{\nu}$ = 3591 cm^{-1} (s), 3358 (s), 3305 (s), 2951 (m), 2871 (m), 2803 (w), 2712 (w), 1602 (m), 1463 (m), 1311 (w), 1089 (s), 1048 (s), 839 (s, PF_6). MALDI-MS (337.0 nm, 3 ns) *m*/*z*: 475 (100, $[Cu_2(H_3\text{-}6)_2]^+$), 659 (10, $[\{Cu_2(H_3\text{-}6)_2\}PF_6\ CH_3CN]^+$), negative ions *m*/*z*: 910 ($[\{Cu_2(H_3\text{-}6)_2\}(PF_6)_3]^-$).

$[Cu_2(H_4\text{-}1)_2](PF_6)_2$ (9f): $Cu(OH)_2$ (390 mg, 4.00 mmol), ligand H_5-**1** (701 mg, 4.00 mmol) and NH_4PF_6 (1.30 g, 8.00 mmol) were used.

 © 2005 Wiley-VCH Verlag GmbH & Co. KGaA, Weinheim

Yield: 330 mg (0.431 mmol, 22%). IR (KBr): $\tilde{\nu}$ = 3373 cm^{-1} (m), 3355 (m), 3324 (m), 3304 (m), 2974 (m), 2946 (m), 2933 (m), 2892 (m), 2857 (m), 1603 (m), 1487 (w), 1457 (w), 1244 (w), 1150 (m), 1056 (m), 1022 (m), 835 (s, PF_6). MALDI-MS (337.0 nm, 3 ns) *m*/*z*: 238 (24, $[Cu(H_5\text{-}\mathbf{1})]^+$), 422 (24, $[Cu(H_5\text{-}\mathbf{1})(PF_6)(CH_3CN)]^+$), 606 (100, $[Cu(H_5\text{-}\mathbf{1})(PF_6)_2(CH_3CN)_2]^+$).

$[Cu_2(H_3\text{-}4)_2]Br_2$ (10a): Preparation starting from Cu^I: A solution of H_4-**4** (162 mg, 1.0 mmol) in dichloromethane (10 mL) was added to a colorless solution of $[Cu^I(PPh_3)_3Br]$ (930 mg, 1.0 mmol) in dichloromethane (20 mL). Within several minutes the solution turned blue upon stirring under air. Purple crystals precipitated, which were suitable for X-ray diffraction analysis. Yield: 65 mg (0.10 mmol, 20%). $[Cu_2(H_3\text{-}4)_2]Br_2$ **10a** $C_7H_{18}BrCuN_2O_2$ (318.66): calcd. C 30.15, H 6.01, N 8.79; found C 30.78, H 6.04, N 8.90%.

Preparation Starting from Cu^{II}: A solution of H_4-**4** (353 mg, 2.0 mmol) in methanol (10 mL) was added to a brown solution of copper bromide (447 mg, 2.0 mmol) in methanol (10 mL). Immediately upon mixing the color of the solution changed to blue. Purple crystals formed upon standing in air. More crystals were precipitated by diffusion of diethyl ether into this solution. Yield: 227 mg (0.356 mmol, 36%). $C_7H_{18}Br_2CuN_2O_2$ (318.66): calcd. C 30.15, H 6.01, N 8.79; found C 30.19, H 6.01, N 8.72%.

Crystal Structure Analyses: Blue crystals of **9a**·0.5EtOH·0.5H_2O, **9b**·2H_2O, **9d**·MeOH, **9e** and **9f** and purple crystals of **10a** were obtained by recrystallization from ethanol (**9a**·0.5EtOH·0.5H_2O), methanol (**9d**·MeOH), acetonitrile (**9b**·2H_2O, **9e**, **9f**) or dichloromethane (**10a**) at 5 °C. Diffraction data were measured at low temperature (Table 3 and Table 4) on a Bruker APEX diffractometer

Table 3. Summary of crystallographic data for **9a**·0.5EtOH·0.5H_2O, **9b**·2H_2O, and**9d**·2CH_3OH.

	9a·0.5EtOH·0.5H_2O	**9b**·2H_2O	**9d**·MeOH
Crystal size [mm]	0.18 × 0.05 × 0.4	0.26 × 0.21 × 0.18	0.21 × 0.13 × 0.10
Formula	$C_{13}H_{34}Cu_2F_{12}N_4O_5P_2$	$C_{14}H_{38}Cu_2F_{12}N_4O_6P_2$	$C_{15}H_{38}Cu_2F_{12}N_4O_5P_2$
fw, amu	743.36	775.50	771.51
a [Å]	12.9766(13)	7.4536(7)	11.6574(5)
b [Å]	15.2839(15)	10.6827(10)	19.2777(8)
c [Å]	13.5796(14)	17.0136(16)	26.3811(11)
α [deg]	90	90	90
β [deg]	96.874(2)	91.398(1)	90
γ [deg]	90	90	90
V [$Å^3$]	2673.9(5)	1354.3(2)	5928.6(4)
Space group	$P2_1$	$P2_1/c$	Pccn
Z	4	2	8
$d_{calcd.}$ [g cm^{-3}]	1.847	1.902	1.729
μ [mm^{-1}]	1.826	1.810	1.651
T [K]	173(2)	153(2)	173(2)
Unique data	9414	2375	5233
Observed data [$I \geq 2\sigma(I)$]	8217	2254	4247
R (observed data)	0.0420	0.0246	0.0553
w*R* (observed data)	0.0933	0.0596	0.1386
GOF	1.004	1.048	1.043
2θ-range [deg]	3.0–50.1	4.5–50.0	3.7–50.1
Residiual electron density [e/$Å^3$]	0.751/–0.308	0.774/–0.241	1.395/–1.042

Table 4. Summary of crystallographic data for **9e**, **9f**, and **10a**.

	9e	**9f**	**10a**
Crystal size [mm]	0.10 × 0.08 × 0.02	0.20 × 0.07 × 0.02	0.07 × 0.04 × 0.03
Formula	$C_{16}H_{38}Cu_2F_{12}N_4O_4P_2$	$C_{16}H_{40}Cu_2F_{12}N_6O_2P_2$	$C_{16}H_{38}Br_2Cu_2N_4O_4$
fw, amu	767.52	765.56	637.40
a [Å]	7.9889(5)	7.7147(8)	8.316(2)
b [Å]	8.3591(5)	9.6178(10)	16.212(3)
c [Å]	11.0443(7)	9.6401(10)	8.671(2)
α [deg]	76.1580(10)	77.686(2)	90
β [deg]	76.2270(10)	85.577(2)	91.179(4)
γ [deg]	79.0790(10)	89.414(2)	90
V [$Å^3$]	688.63(7)	696.73(13)	1168.7(4)
Space group	$P\bar{1}$	$P\bar{1}$	$P2_1/n$
Z	1	1	2
$d_{calcd.}$ [g cm^{-3}]	1.851	1.825	1.811
μ [mm^{-1}]	1.774	1.750	5.267
T [K]	153(2)	173(2)	123(2)
Unique data	3139	4002	2675
Observed data [$I \geq 2\sigma(I)$]	2859	3087	2159
R (observed data)	0.0265	0.0477	0.0573
w*R* (observed data)	0.0685	0.0886	0.1108
GOF	1.019	0.969	1.107
2θ-range [deg]	3.9–55.0	4.3–60.2	5.0–50.0
Residiual electron density [e/$Å^3$]	0.350/–0.336	0.605/–0.501	1.265/–0.907

 © 2005 Wiley-VCH Verlag GmbH & Co. KGaA, Weinheim

equipped with a rotating molybdenum anode (λ = 0.71073 Å) and a CCD area detector. Empirical absorption corrections were applied to all data sets. The structures were solved and refined by standard Patterson- and Fourier-techniques.[30] All non-hydrogen atoms were refined with anisotropic displacement parameters, and hydrogen atoms were added to the structure model on calculated positions. Selected crystal, data collection and refinement details are listed in Table 3 and Table 4.

Supplementary Material: CCDC-276044 (for **9a**·0.5EtOH·0.5H_2O), -276045 (for **9b**·2H_2O), -276046 (for **9d**·MeOH), -276047 (for **9e**), -276048 (for **9f**), and -276049 (for **10a**) contain the supplementary crystallographic data for this paper. These data can be obtained free of charge from The Cambridge Crystallographic Data Centre via www.ccdc.cam.ac.uk/data_request/cif.

Acknowledgments

The authors thank Dr. R.-D. Hoffmann for temperature dependent measurements of magnetic susceptibilities for complexes **9b**–**9f**. C. J. thanks the NRW Graduate School of Chemistry, Münster (Germany), for a 3-year predoctoral scholarship. Additional financial support was provided by the International Graduate College "Template Directed Chemical Synthesis" (DFG IGK 673).

[1] A. G. Blackman, *Polyhedron* **2005**, 24, 1–39.
[2] a) R. W. Saalfrank, I. Bernt, E. Uller, F. Hampel, *Angew. Chem.* **1997**, *109*, 2596–2599; *Angew. Chem. Int. Ed. Engl.* **1997**, *I36*, 2482–2485; b) O. Waldmann, R. Koch, S. Schromm, J. Schülein, P. Müller, I. Bernt, R. W. Saalfrank, F. Hampel, E. Balthes, *Inorg. Chem.* **2001**, *40*, 2986–2995; c) O. Waldmann, J. Schülein, R. Koch, I. Bernt, R. W. Saalfrank, H. P. Andres, H. U. Güdel, P. Allenspach, *Inorg. Chem.* **1999**, *38*, 5879–5886; d) Y. Chen, Q. Liu, Y. Deng, H. Zhu, C. Chen, H. Fan, D. Liao, E. Gao, *Inorg. Chem.* **2001**, *40*, 3725–3733; e) K. H. Whitmire, J. C. Hutchinson, A. Gardberg, C. Edwards, *Inorg. Chim. Acta* **1999**, *294*, 153–162.
[3] a) S. Itoh, M. Taki, S. Takayama, S. Nagatomo, T. Kitagawa, N. Sakurada, R. Arakawa, S. Fukuzumi, *Angew. Chem.* **1999**, *111*, 2944–2946; *Angew. Chem. Int. Ed.* **1999**, *I38*, 2774–2776; b) R. Uma, R. Viswanathan, M. Palaniandavar, M. Lakshminarayanan, *J. Chem. Soc., Dalton Trans.* **1994**, 1219–1226; c) M. Vaidyanathan, R. Viswanathan, M. Palaniandavar, T. Balasubramanian, P. Prabhaharan, T. P. Mutiah, *Inorg. Chem.* **1998**, *37*, 6418–6427; d) D. Zurita, C. Scheer, J.-L. Pierre, E. Saint-Aman, *J. Chem. Soc., Dalton Trans.* **1996**, 4331–4336; e) M. M. Whittaker, W. R. Duncan, J. M. Whittaker, *Inorg. Chem.* **1996**, *35*, 382–386; f) H. Adams, N. A. Bailey, I. K. Campbell, D. E. Fenton, Q. Y. He, *J. Chem. Soc., Dalton Trans.* **1996**, 2233–2237; g) M. Ruf, C. G. Pierpont, *Angew. Chem.* **1998**, *110*, 1830–1832; *Angew. Chem. Int. Ed.* **1998**, *I37*, 1736–1739; h) Y. Shimazaki, S. Huth, A. Odani, O. Yamauchi, *Angew. Chem.* **2000**, *112*, 1732–1735; *Angew. Chem. Int. Ed.* **2000**, *I39*, 1666–1669; i) C. Ochs, F. E. Hahn, R. Fröhlich, *Eur. J. Inorg. Chem.* **2001**, *9*, 2427–2436.
[4] a) J. Xia, S. Li, Y. Shi, K. Yu, W. Tang, *J. Chem. Soc., Dalton Trans.* **2001**, 2109–2115; b) J. Xia, Y. Xu, S. Li, W. Sun, K. Yu, W. Tang, *Inorg. Chem.* **2001**, *40*, 2394–2401; c) B. Song, J. Reuber, C. Ochs, F. E. Hahn, T. Lügger, C. Orvig, *Inorg. Chem.* **2001**, *40*, 1527–1535.
[5] F. E. Hahn, C. Jocher, T. Lügger, T. Pape, *Z. Anorg. Allg. Chem.* **2003**, *629*, 2341–2437.
[6] a) F. E. Hahn, C. Jocher, T. Lügger, *Z. Naturforsch., Teil B* **2004**, *59*, 855–858; b) F. E. Hahn, C. Jocher, T. Lügger, T. Pape, *Z. Anorg. Allg. Chem.* **2004**, *630*, 2558–2561.
[7] a) C. Jocher, T. Pape, F. E. Hahn, *Z. Naturforsch., Teil B* **2005**, *60*, 667–672.
[8] a) C. Ochs, F. E. Hahn, R. Fröhlich, *Chem. Eur. J.* **2000**, *6*, 2193–2199; b) F. E. Hahn, C. Ochs, T. Lügger, R. Fröhlich, *Inorg. Chem.* **2004**, *43*, 6101–6107.
[9] a) J. A. Connolly, J. H. Kim, M. Banaszczyk, M. Drouin, J. Chin, *Inorg. Chem.* **1995**, *34*, 1094–1099; b) J. A. Connolly, M. Banaszczyk, R. C. Hynes, J. Chin, *Inorg. Chem.* **1994**, *33*, 665–669; c) J. Chin, M. Banaszczyk, *J. Am. Chem. Soc.* **1989**, *111*, 4103–4105; d) J. Chin, M. Banaszczyk, V. Jubian, X. Zou, *J. Am. Chem. Soc.* **1989**, *111*, 186–190.
[10] a) A. M. Dittler-Klingemann, F. E. Hahn, *Inorg. Chem.* **1996**, *35*, 1996–1999; b) A. M. Dittler-Klingemann, C. Orvig, F. E. Hahn, F. Thaler, C. D. Hubbard, R. van Eldik, S. Schindler, I. Fabian, *Inorg. Chem.* **1996**, *35*, 7798–7803.
[11] C. Ochs, F. E. Hahn, T. Lügger, *Eur. J. Inorg. Chem.* **2001**, 1279–1285.
[12] T. Klabunde, C. Eicken, J. C. Sacchettini, B. Krebs, *Nature Struct. Biol.* **1998**, *5*, 1084–1090.
[13] a) J. Mukherjee, R. Mukherjee, *Inorg. Chim. Acta* **2002**, *337*, 429–438; b) J. Reim, B. Krebs, *J. Chem. Soc., Dalton Trans.* **1997**, 3793–3804; c) L. Casella, E. Monzani, M. Gullotti, D. Cavagnino, G. Cerina, L. Santagostini, R. Ugo, *Inorg. Chem.* **1996**, *35*, 7516–7525; d) A. Neves, L. M. Rossi, A. J. Bortoluzzi, B. Szpoganicz, C. Wiezbiecki, E. Schwingel, W. Haase, S. Ostrovsky, *Inorg. Chem.* **2002**, *41*, 1788–1794; e) R. Wegener, M. Gottschaldt, H. Görls, E.-G. Jäger, D. Klemm, *Chem. Eur. J.* **2001**, *7*, 2143–2157; f) C.-T. Yang, M. Vetrichelvan, X. Yang, B. Moubaraki, K. S. Murray, J. J. Vittal, *Dalton Trans.* **2004**, 113–121.
[14] C. Gerdemann, C. Eicken, B. Krebs, *Acc. Chem. Res.* **2002**, *35*, 183–191.
[15] a) L. M. Berreau, S. Mahapatra, J. A. Halfen, R. P. Houser, V. G. Young, Jr., W. B. Tolman, *Angew. Chem.* **1999**, *111*, 180–183; *Angew. Chem. Int. Ed.* **1999**, *I38*, 207–210; b) G. Battaini, E. Monzani, L. Casella, L. Santagostini, R. Pagliarin, *J. Biol. Inorg. Chem.* **2000**, *5*, 262–268; c) K. D. Karlin, Y. Gultneh, T. Nicholson, J. Zubieta, *Inorg. Chem.* **1985**, *24*, 3725–3727.
[16] G. Schwarzenbach, D. Anderegg, W. Schneider, H. Senn, *Helv. Chim. Acta* **1955**, *132*, 1147–1170.
[17] J. Cologne, G. Descortes, G. Frenay, *Bull. Soc. Chim. Fr.* **1963**, 2264–2270.
[18] N. M. Yoon, H. C. Brown, *J. Am. Chem. Soc.* **1968**, *90*, 2927–2938.
[19] R. M. Peck, R. K. Preston, H. J. Creech, *J. Am. Chem. Soc.* **1959**, *81*, 3984–3989.
[20] a) V. F. Vasil'eva, O. Y. Lavrona, N. M. Dyatlova, V. G. Yashunskii, *J. Gen. Chem. USSR* **1968**, *38*, 468–471; b) V. A. Bobylev, V. O. Chechnik, *Zh. Obshch. Khim.* **1990**, *60*, 2721–2725.
[21] a) T. J. Lotz, T. A. Kaden, *Helv. Chim. Acta* **1978**, *61*, 1376–1387; b) A. Farkas, F. Miller (Air Products and Chemicals, Inc.), **1968**, Method for the preparation of *N*,*N*-bis(3-aminopropyl)ethanolamine, patent US 3377383.
[22] A. W. Addison, T. N. Rao, J. Reedijk, J. van Rijn, G. C. Verschoor, *J. Chem. Soc., Dalton Trans.* **1984**, 1349–1356.
[23] a) V. H. Crawford, H. W. Richardson, J. R. Wasson, D. J. Hodgson, W. E. Hatfield, *Inorg. Chem.* **1976**, *15*, 2107–2110; b) H. Muhonen, W. E. Hatfield, J. H. Helms, *Inorg. Chem.* **1986**, *25*, 800–805; c) B. P. Kennedy, A. B. P. Lever, *J. Am. Chem. Soc.* **1973**, *95*, 6907–6913.
[24] a) P. Gamez, I. A. Koval, J. Reedijk, *Dalton Trans.* **2004**, 4079–4088; b) L. Casella, O. Carugo, M. Gullotti, S. Garofani, P. Zanello, *Inorg. Chem.* **1993**, *32*, 2056–2067.
[25] B. J. Hathaway, *J. Chem. Soc., Dalton Trans.* **1972**, 1196–1199.
[26] I. Potocnak, M. Dunaj-Jurco, D. Mikols, L. Jäger, *Monatsh. Chem.* **2001**, *132*, 315–327.
[27] a) G. M. Whitesides, J. S. Sadowski, J. Lilburn, *J. Am. Chem. Soc.* **1974**, *96*, 2829–2835; b) R. Ahlrichs, C. E. Anson, D. Fenske, O. Hampe, A. Rothenberger, M. Sierka, *Angew. Chem.* **2003**, *115*, 4169–4172; *Angew. Chem. Int. Ed.* **2003**, *42*, 4036–4039.

 © 2005 Wiley-VCH Verlag GmbH & Co. KGaA, Weinheim

[28] A. H. J. Tullemans, E. Bouwman, R. A. G. d. Graaf, W. L. Driessen, J. Reedijk, *Recl. Trav. Chim. Pays-Bas* **1990**, *109*, 70–76.
[29] T. Plenge, R. Dillinger, L. Santagostini, L. Casella, F. Tuczek, *Z. Anorg. Allg. Chem.* **2003**, *629*, 2258–2265.
[30] Structure solution: G. M. Sheldrick, SHELXS-97, *Acta Crystallogr., Sect. A* **1990**, *46*, 467–473; structure refinement: G. M. Sheldrick, *SHELXL-97*, University of Göttingen, **1997**.
Received: June 23, 2005
Published Online: November 3, 2005

 © 2005 Wiley-VCH Verlag GmbH & Co. KGaA, Weinheim

DOI: 10.1002/ejic.200500686

Enantiopure Ruthenocenes Cp*Ru(1,2-$C_5H_3R^1R^2$) with a Planar Chiral Cyclopentadienyl Ligand and a Pentamethylcyclopentadienyl Spectator Ligand[‡]

Gerhard E. Herberich,*[a] Ulli Englert,[a] and Tobias Wirth[a][‡‡]

Keywords: Ruthenium / Ruthenocene / Sandwich complexes / Planar chirality / (*S*)-2-(methoxymethyl)pyrrolidine

Kreutzberger's synthesis was used to produce 6-(morpholino)-fulvene (**7a**) from 1,3,5-triazine, cyclopentadiene and morpholine (94 %). Likewise with (*S*)-2-(methoxymethyl)pyrrolidine (HSMP) the 6-[(*S*)-2-(methoxymethyl)pyrrolidino] analogue **7b** was obtained (62 %). Hydride addition from $NaBHEt_3$ in toluene afforded the cyclopentadienides $Na[C_5H_4CH_2–N(C_2H_4)_2O]$ (**8a**) (83 %) and $Na(C_5H_4CH_2–SMP)$ (**8b**) (90 %). Cp*Ru($C_5H_4CH_2$–SMP) (**5**) was synthesized from $[Cp^*RuCl]_4$ and **8b** (84 % yield). The related methyleneiminium salt $[Cp^*Ru(C_5H_4CH{=}SMP)]PF_6$ (**9**) was made from $[Cp^*Ru(MeCN)_3]PF_6$ and **7b** and could be transformed into **5** by hydride addition from $LiAlH_4$ in THF. Diastereoselective lithiation of **5** with Li*s*Bu in Et_2O/cyclohexane and subsequent quenching with electrophiles E–X gave enantiomerically pure (*de* > 98 %), 1,2-disubstituted complexes Cp*Ru(E–$C_5H_3CH_2$–SMP) **10a–i** with E = F, Cl, Br, I, Me, CD_3, $SiMe_3$, PPh_2, $Au(PPh_3)$ as oils. The chiral auxiliary was removed from **10a**, **b**, and **f** by quaternization with MeI and subsequent reductive cleavage with $LiAlH_4$ in THF to afford the exclusively planar chiral complexes Cp*Ru(1-E-2-MeC_5H_3) **14a** (E = F), **14b** (E = Cl), and **14f** (E = CD_3). The complexes **14a**,**b**,**f** no longer possess central chirality. The crystal structure of **12**, a LiI adduct of **10f**, gave the absolute configuration via internal reference to the (*S*)-stereochemistry of the SMP group. The absolute configuration of the planar chiral complex **14b** was determined from the anomalous X-ray dispersion of the crystals of **14b**.

(© Wiley-VCH Verlag GmbH & Co. KGaA, 69451 Weinheim, Germany, 2005)

Introduction

In this paper we describe a synthetic route to ruthenocenes Cp*Ru(1,2-$C_5H_3R^1R^2$) (**1**) that have a planar chiral cyclopentadienyl ligand and a pentamethylcyclopentadienyl (Cp*) spectator ligand, but do not possess any further element of chirality in the substituents R^1 and R^2.

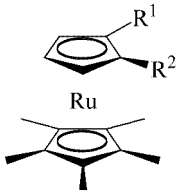

1

Planar chiral ferrocenes[2,3] have found application as excellent chiral ligands in homogeneous asymmetric catalysis. For instance, the industrial production of (+)-biotine makes use of the chiral ferrocene-based ligand **2**,[4,5] and the herbicide (*S*)-metolachlor® is produced with the help of the closely related ligand **3**.[5,6] The quest for chiral ligands which are optimized for specific catalytic processes has led to the development of a large family of chiral pentamethylferrocenes[5b] and a group of similar chiral pentamethylruthenocenes;[7] the complexes Cp*Ru[1,2-C_5H_3(PPh_2)-(CHXMe)] (**4**) (X = e.g. NMe_2, PCy_2) may serve as examples.[7b] All these complexes are deceptively similar to ruthenocenes of type **1**; however, they possess a center of chirality in one of the sidechains as the distinguishing feature.

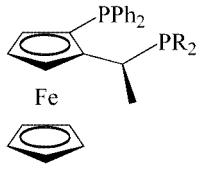

2, R = *t*Bu

3, R = 3,5-$Me_2C_6H_3$

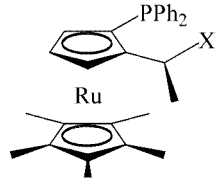

4, X = NMe_2, PCy_2

Although the chemistry of the ruthenocenes is much less developed than that of the ferrocenes a number of planar chiral and enantiopure ruthenocenes are known. There are essentially three methods to produce such complexes. i) The first planar chiral, more or less enantiopure ruthenocenes

[‡] This work is part of a dissertation.[1]

[a] Institut für Anorganische Chemie
Rheinisch-Westfälische Technische Hochschule Aachen,
52056 Aachen, Germany
Fax: +49-241-809-22 88
E-mail: gerhard.herberich@ac.rwth-aachen.de
[‡‡] Present address: Ciba Speciality Chemicals Inc. Switzerland, K-352.P.05
P. O. Box, 4002 Basel, Switzerland

© 2005 Wiley-VCH Verlag GmbH & Co. KGaA, Weinheim

were made by the group of K. Schlögl using the classical method of resolution of racemates.[8] Chiral HPLC has also been used as a modern and efficient resolution method.[9] ii) The second method is the diastereoselective *ortho*-metalation, discovered by I. Ugi et al. as highly stereoselective derivatization reactions of the two [(1-dimethylamino)ethyl]-ferrocene – or (1-ferrocenylethyl)dimethylamine – enantiomers.[10] In this way T. Hayashi et al. synthesized the ruthenocene derivatives $Ru(C_5H_4PPh_2)[C_5H_4(PPh_2)\{CHR(NMe_2)\}]$ (R = Me, Et),[11] and A. Togni et al. synthesized the pentamethylruthenocenes **4**.[7b] iii) Finally, as U. Koelle et al. demonstrated more recently, enantioselective reaction of planar chiral cyclopentadienides with suitable chiral sources of the Cp^*Ru^+ fragment may also give chiral, enantiomerically enriched pentamethylruthenocene derivatives.[12]

We now return to the goal of this work, the development of a synthetic route to complexes of type **1**. We decided to use the method of diastereoselective *ortho*-metalation with the (*S*)-2-(methoxymethyl)pyrrolidino (≡ SMP) group as *ortho*-directing chiral auxiliary. Ruthenium was preferred to iron because ruthenocenes are more robust than ferrocenes. Thus, the synthesis of complex **5** assumes a central role in this work. It seemed reasonable and most promising, to introduce the Cp*Ru group as late as possible, for instance by treating $[Cp^*RuCl]_4$[13] with a salt of the (as yet unknown) chiral cyclopentadienide $\mathbf{6}^-$. Once complex **5** was available, we studied the *ortho*-metalation of **5** and the subsequent quenching with electrophiles, and finally the removal of the chiral auxiliary.

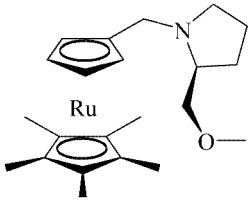

5

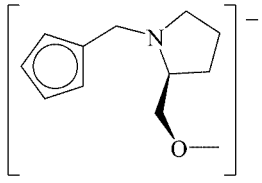

$\mathbf{6}^-$

Results and Discussion

Ligand Precursors

From a retrosynthetic point of view [(dialkylamino)-methyl]cyclopentadienides **A** (such as $\mathbf{6}^-$) are related to [(dialkylamino)methyl]cyclopentadienes **B** (via formal proton addition) and alternatively to 6-(dialkylamino)fulvenes **C** (via formal hydride abstraction)[14] (Scheme 1). The constitution of the cyclopentadienes **B** is reminiscent of products of Mannich condensation reactions. Experimentally, Mannich condensations with cyclopentadienes are stricken with low chemoselectivity. In favorable situations fulvenes are obtained,[15] and under some more special conditions Diels–Alder products are formed.[16] The alternative to use 6-(dialkylamino)fulvenes **C** seemed more promising. Especially the 6-(dimethylamino) derivative $C_5H_4{=}CH(NMe_2)$ is a well known compound which may undergo hydride addition from $LiAlH_4$ to form the corresponding cyclopentadienide.[17]

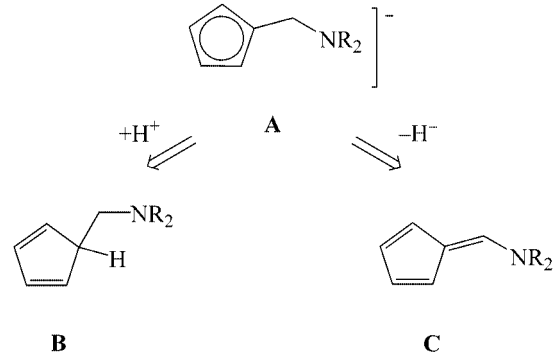

Scheme 1.

We first consider the syntheses of 6-(dialkylamino)fulvenes **C**. The 6-morpholino compound **7a** served as a testing ground. There are essentially three fulvene syntheses: the historical Thiele synthesis,[18] Hafner's synthesis of 6-(dimethylamino)fulvene,[19] and Kreutzberger's synthesis.[20] An attempt to apply Thiele's synthesis, i.e. the direct base-catalyzed condensation of cyclopentadiene with a carbonyl compound,[18a] to formylmorpholide, using an improved procedure,[18b] failed altogether; the dominating process was the dimerization of cyclopentadiene. Hafner's more forcing synthesis (Scheme 2) produced the desired 6-(morpholino) derivative **7a**, but the yield dropped from the 74% obtained for the 6-(dimethylamino)fulvene[19] to unsatisfactory 16% for **7a**. Kreutzberger's method[20] (Scheme 3) uses 1,3,5-triazine[21] as a synthon for formamide and presumably produces 6-aminofulvene as the primary product; this then undergoes nucleophilic substitution[22] of the amino group with morpholine and gave 6-(morpholino)fulvene **7a** as golden-brownish, analytically pure microcrystals in near quantitative isolated yield (94%). Compound **7a** has been mentioned in the literature, but has not been described in any detail.[23]

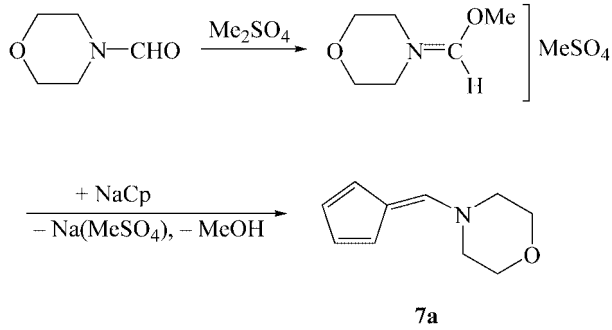

7a

Scheme 2.

Our observations suggest that Kreutzberger's synthesis should be the best option for the preparation of the (*S*)-2-(methoxymethyl)pyrrolidino analogue **7b**. When it was applied to (*S*)-2-(methoxymethyl)pyrrolidine (HSMP),[24] **7b**

 © 2005 Wiley-VCH Verlag GmbH & Co. KGaA, Weinheim

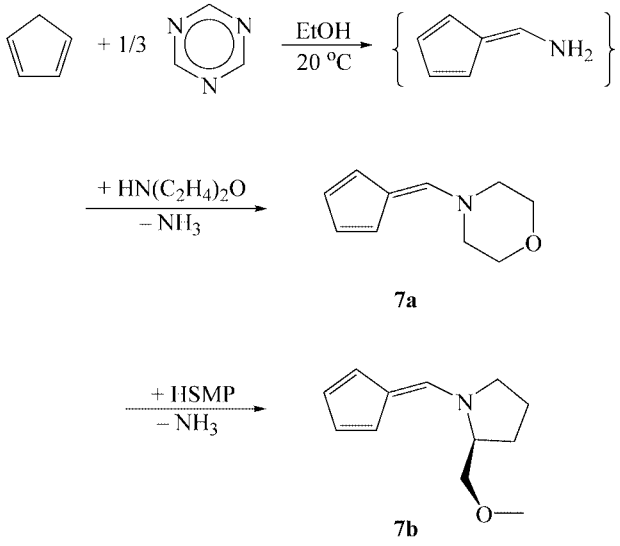

Scheme 3.

was obtained as a yellow to red, analytically pure oil in good yield (62%).

The second task was the hydride addition to the 6-aminofulvenes **7a**,**b** which turned out to be more difficult than in the case of 6-(dimethylamino)fulvene.[17] The reaction of **7b** with $LiAlH_4$ in THF mainly produced LiC_5H_4Me, indicating an undesired substitution of the amide group with a hydride. We found, however, that the milder reagent $NaBHEt_3$ in toluene effected a smooth addition of hydride (Scheme 4). In the case of **7a** the reaction was fast at 0 °C and markedly exothermic. The triethylborane also formed was in part bonded to the nitrogen of the morpholine ring; it was removed by washing the raw product with diethyl ether to give the salt $Na[C_5H_4CH_2–N(C_2H_4)_2O]$ (**8a**) in high yield (83%), but still contaminated with small amounts of BEt_3 (^1H and ^{11}B NMR). The analogous reaction in the SMP series gave $Na(C_5H_4CH_2–SMP)$ (**8b**), again in high yield (90%), but at a much lower rate at ambient temperature. Both salts are highly air-sensitive.

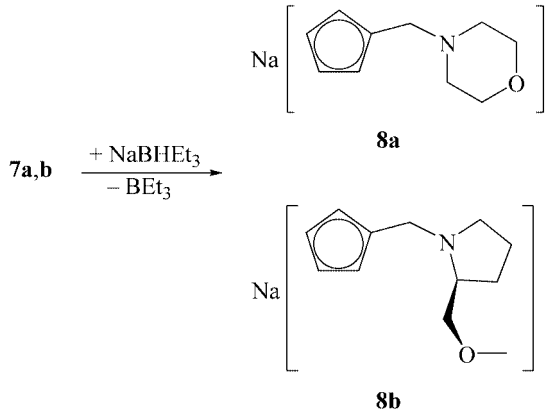

Scheme 4.

The cyclopentadienides **8a**,**b** show surprisingly low solubilities, and only strong donor solvents such as DMF and DMSO give moderately concentrated solutions which tend to decompose at ambient temperature within hours to days. Only solutions in liquid ammonia did not show decomposition, even after several days. Functionalized cyclopentadienides with N- and/or O-donor centers often have the structure of a coordination polymer.[25] This could well be the cause of the observed low solubilities of **8a**,**b**.

Pentamethylruthenocenes with a SMP-Methyl Side Chain

The Starting Material 5

Complex **5** was synthesized from $[Cp^*RuCl]_4$[13] and the sodium cyclopentadienide **8b** in THF (Scheme 5). It is a golden yellow, chemically and thermally robust oil which could not be crystallized. Complex **5** can also be made by a two-step procedure. In the first step a slight excess of the fulvene **7b** is treated with $[Cp^*Ru(MeCN)_3]PF_6$[26] to produce the (ruthenocenylmethylene)iminium salt **9** (Scheme 5). An excess of **7b** can be removed by recrystallization of the material **9** from acetone/ether or from THF/ether. In the second step hydride addition from $LiAlH_4$ in THF smoothly transforms complex **9** into the desired complex **5**. This alternative has not been optimized.

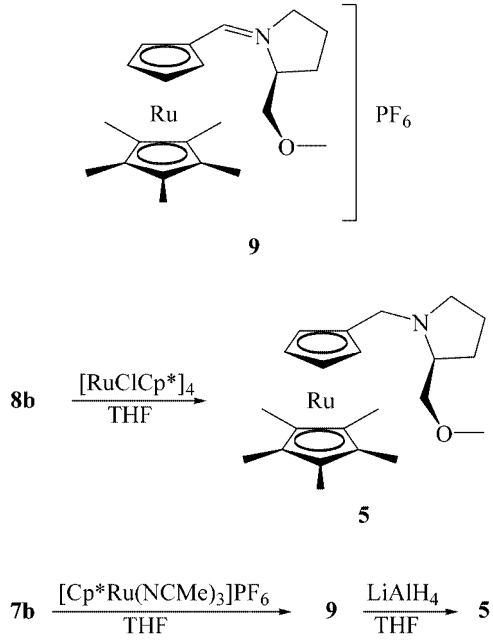

Scheme 5.

Lithiation and Derivatization of 5

We now turn to the diastereoselective lithiation of **5**. Lithiations of ruthenocenes are known to be faster and less selective than those of ferrocenes and may give rise to homo- and heteroannular di- and even trilithiations.[8a,27] In the case of **5** the presence of the Cp* ligand greatly reduces the resulting problems.

All lithiation reactions were conducted under standardized conditions. Complex **5** was used as 0.1 M solution in diethyl ether at –78 °C and the lithiations were performed with titrated[28] ca. 1.5 M Li*s*Bu solutions in cyclohexane

 © 2005 Wiley-VCH Verlag GmbH & Co. KGaA, Weinheim

at –78 °C, usually in a 1:1.7 ratio. After mixing the reagents the reaction mixture was stirred at –78 °C for 3.5 h. A quenching reagent E–X was then added at –78 °C and the mixture was warmed to ambient temperature (Scheme 6). All products Cp*Ru[1-E-2-(SMP–CH_2)C_5H_3] **10a**–**i** are very pale yellow, almost colorless oils. They were analyzed mainly with the help of ^{1}H NMR spectroscopy (500 MHz). In no case could we detect a second diastereomer; hence the diastereomeric excess should be better than 98%. In all cases an admixture of starting material was present as impurity; for more details see below and Experimental Section.

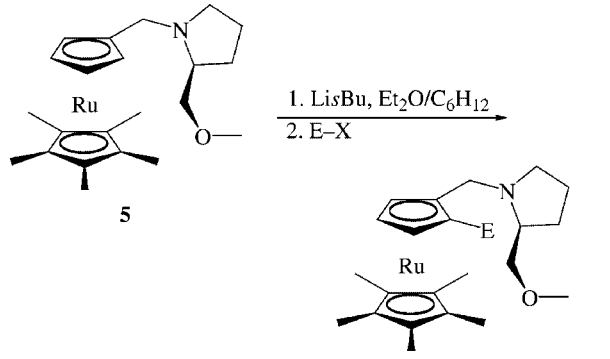

	a	b	c	d	e	f	g	h	i
E =	F	Cl	Br	I	Me	CD_3	SiMe3	PPh2	Au(PPh3)

Scheme 6.

The stereochemistry of complexes **1** may be specified in one of two ways:[29] either by specifying the *planar* chirality of the $C_5H_3R^1R^2$ ring as originally proposed by Schlögl,[30] or by specifying the *central* chirality of the ring carbon bearing the highest ranking substituent with the help of the CIP rules.[31] As we shall prove below, the SMP–CH_2 group of the complexes **10a**–**i** has the role of R^1 in the illustration of complex **1**, and E occupies the position of R^2. For most substituents E we have therefore (S_P)-stereochemistry for the planar chirality;[32] only the low-ranking groups Me and CD_3 of **10e**,**f** leave the higher priority to the SMP–CH_2 group thus implying (R_P)-stereochemistry.

A few details concerning specific cases should be mentioned here. The fluororuthenocene **10a** was obtained by electrophilic fluorination[33] with *N*-fluoro-*N*,*N*-bis(benzenesulfonyl)imide.[34] The higher homologues **10b**, **10c**, and **10d** were obtained with C_2Cl_6, 1,2-$C_2H_4Br_2$, and 1,2-$C_2H_4I_2$, respectively, as source of the halogen. The iodo compound **10d** seems to form an adduct with LiI (cf. below compound **12**), but an aqueous workup step smoothly removed the coordinated LiI. Iodomethane was used to synthesize **10e** and likewise CD_3I gave **10f**, using again an aqueous workup procedure. In the case of **10b** the metalation conditions were varied with the aim to find out the optimum procedure. It was found that temperatures below –78 °C (without change of other parameters) resulted in incomplete lithiation and a higher admixture of starting material **5** in the product. On the other hand, when the lithiation mixture was warmed up to 40 °C and then was cooled again to –78 °C before the addition of the quenching reagent, the admixture of **5** in the product was no longer seen.

The remaining examples are more complex. Quenching with $SiClMe_3$ under the usual conditions gave **10g** and in addition a doubly silylated product **11** in a 3:1 ratio. This by-product could largely be suppressed if the temperature of the quenching mixture was increased more slowly (for instance in 14 h vs. the usual 1.5 h) from –78 °C to ambient temperature. This observation suggests that a transmetalation step is coming into play in this system. In the cases **10h**,**i** byproducts (inter alia P*s*BuPh$_2$[35] in the case of **10h** and *s*BuAu(PPh$_3$)[36] in the case of **10i**) formed from the excess of Li*s*Bu, which were difficult to remove; their formation can be suppressed if the lithiation reagent is used in near equivalent quantity, but then the metalation remains incomplete and the product becomes contaminated by larger admixtures (up to 25%) of starting material **5**. These difficulties were aggravated by the fact that none of the products **10a**–**i** could be crystallized.

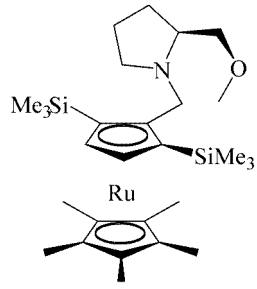

11

First Proof of the Product Stereochemistry: the Structure of the LiI Adduct [10f(LiI)]$_2$

Quite serendipitously we obtained crystals of a lithium iodide adduct [**10f**(LiI)]$_2$ (≡ **12**), when we intended to synthesize **10f** and used a non-aqueous workup procedure. This

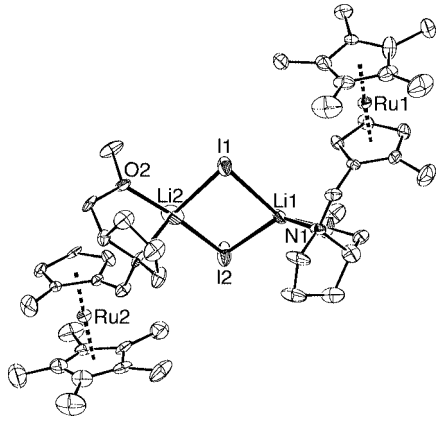

Figure 1. Molecular structure of the LiI adduct **12** (PLATON plot[38] at the 30% probability level). Selected distances [Å]: Ru1–Cp 2.147(13), Ru2–Cp 2.167(12), Ru1–Cp* 2.157(14), Ru2–Cp* 2.138(15).

 © 2005 Wiley-VCH Verlag GmbH & Co. KGaA, Weinheim

allowed us to determine the stereochemistry of the directed *ortho*-lithiation of **5** via *internal reference* to the (*S*)-stereochemistry of the chiral auxiliary group SMP. Compound **12** crystallizes in the monoclinic, noncentrosymmetric space group $P2_1$. The crystal consists of dinuclear molecules. Inspection of Figure 1 shows that the planar chiral cyclopentadienyl rings in **12** are coordinated to the Ru atom with (R_P)-stereochemistry.[37]

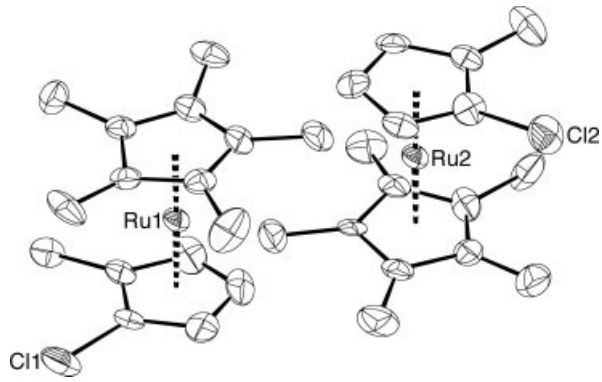

Figure 2. Structure of (S_P)-Cp*Ru(1-Cl-2-MeC_5H_3) (**14b**) (PLATON plot[38] at the 50% probability level). Selected distances [Å]: Ru1–Cp 2.184(12), Ru2–Cp 2.174(12), Ru1–Cp* 2.180(11), Ru2–Cp* 2.165(11), Cl1–C11 1.767(12), Cl2–C31 1.748(11).

Planar Chiral Pentamethylruthenocenes

The removal of the chiral auxiliary group SMP is the next step in our strategy. We give three examples, the replacement of the SMP group in **10a**, **b** and **f** with hydride (Scheme 7). This replacement is achieved in a two-step reaction sequence. In the first step iodomethane was added to give ammonium iodides **13a**,**b**,**f** which were mixtures of diastereomers. As these compounds are of no interest by themselves we give only a minimal description in the Experimental Section. Early in ferrocene chemistry it was found that the NMe_3 group of [CpFe($C_5H_4CH_2NMe_3$)]I is readily amenable to nucleophilic substitution reactions, for instance with CN^- ion.[39] In this vein the tertiary amine moiety *N*-Me–SMP in **13a**,**b**,**f** could readily be substituted with hydride from $LiAlH_4$ in THF. Thus we obtained the planar chiral ruthenocenes Cp*Ru(1-E-2-MeC_5H_3) **14a** (E = F), **14b** (E = Cl), and **14f** (E = CD_3) as enantiomerically pure, crystalline compounds in high yields. It should be emphasized that these complexes possess the planar chirality of the 1,2-disubstituted cyclopentadienyl ring as the sole element of chirality.

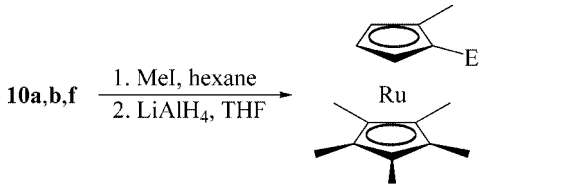

14a, E = F; **14b**, E = Cl; **14f**, E = CD_3

Scheme 7.

Second Proof of the Product Stereochemistry: the Structure of the 1-Cl-2-Me Derivative 14b

The structure of **14b** was determined with the aim to confirm the assigned absolute configuration of the planar chiral ruthenocenes **14a**,**b**,**f** by measuring the anomalous dispersion of the X-ray radiation. Complex **14b** crystallizes in the triclinic space group *P*1 with two independent molecules in the unit cell.[37] The pseudocentrosymmetric arrangement of these molecules (Figure 2) is understandable in view of the roughly similar space filling requirements for a Cl atom and Me substituents.[40] The absolute configuration was found to be the (S_P)-configuration in agreement with the result from the structure determination for **12**.

It could be argued that picking a single crystal from a crystalline sample is unsafe: a crystal of the nonrepresentative stereoisomer might unfortunately be chosen. In the present work this is a most unlikely scenario. In the case of the complexes **10a**–**i** we have never observed any indication for the presence of the alternative stereoisomer. As we have two independent determinations of the configuration the unlikely unfortunate choice would have to have occurred twice. And last not least, in the case of **14b** it would be required that the two enantiomers do form a conglomerate. The very nature of the pseudocentrosymmetric structure of **14b** renders the possibility of conglomerate formation for **14b**/***ent*-14b** unlikely. We would rather expect the formation of racemic crystals or of a solid solution.

Concluding Remarks

In this paper we have established a synthetic route to enantiomerically pure ruthenocenes with a pentamethylcyclopentadienyl spectator ligand and with exclusively planar chirality. The absolute configuration of the metalation product has been determined by two independent methods. As may be seen from the experimental details the choice of the SMP group as a chiral auxiliary was not a very fortunate one, as all complexes **10a**–**i** were oils which did not show any tendency to crystallize. This was a severe disadvantage practically, and might be due to the fact that the SMP group is a five-membered saturated ring. Rings of this type are mechanically soft, and the pending methoxymethyl group adds further conformational flexibility. A six-membered ring as chiral auxiliary might be more recommendable.

It should be noted that complex **5** could also be used to synthesize bidentate chiral ligands which would potentially be useful as chiral ligands in homogeneous catalysis. The first coordinating sidearm could be introduced as in the synthesis of the phosphanyl derivative **10h** which in itself is already a potentially useful, bidentate *N*,*P* ligand. Furthermore, the SMP group can not only be replaced with hydride (as in this work), but also with other nucleophiles such as

 © 2005 Wiley-VCH Verlag GmbH & Co. KGaA, Weinheim

amino or phosphanyl functionalities which would again provide a second coordinating site.

In earlier work we had used achiral (pentamethylcyclopentadienyl)ruthenium sandwich complexes to show that certain ring-ligand transfer reactions take place via triple-decker intermediates.[41] If enantiomerically pure, planar chiral pentamethylruthenocenes were used in such studies, they would give additional, specific and stringent insights into the mechanism and the stereochemistry of ring-ligand transfer reactions. We do, however, not have the means to elaborate these ideas any further.

Experimental Section

General Remarks: All manipulations were carried out under nitrogen or argon using standard Schlenk techniques. 'Vacuum' corresponds to ca. 10^{-6} bar, unless stated otherwise. Solvents were dried by conventional methods,[42] freed from oxygen and stored under nitrogen. Alumina (ICN Alumina N, activity 1), kieselguhr (Merck), silica gel (Merck, Kieselgel 60, 0.063–0.200 mm), molecular sieves (Merck, 4 Å), and seasand were freed from oxygen and water by heating in a vacuum (10^{-6} bar) to 300 °C for 24 h and then stored under nitrogen. Alumina was deactivated before use by controlled addition of water (5%, degassed). IR spectra were recorded on a Nicolet Avatar 360 FT IR spectrometer using NaCl cuvettes with PTFE stoppers. Mass spectra were recorded on a Finnigan MAT 95 (EI, CI, SIMS) or on a Nermag R10/10 spectrometer (DCI). NMR spectra were measured on a Varian VXR 500 Unity (^{1}H, 500.0 MHz; ^{7}Li, 194.2 MHz; ^{11}B, 160.3 MHz; ^{13}C, 125.6 MHz; ^{19}F, 470.1 MHz; ^{29}Si, 99.3 MHz; ^{31}P, 202.3 MHz) in most cases. Chemical shifts are given in ppm; they were referenced to TMS for ^{1}H and ^{13}C. ^{2}H NMR spectra were measured using the deuterated solvent as internal reference; since $\delta(^1H)$ of the natural solvent is equal to $\delta(^2H)$ of the deuterated solvent,[43] the chemical shift of the natural solvent could be taken as reference value. Assignments were based on APT spectra, 2D experiments (COSY, HETCOR, HMQC, HMBC), and on ^{1}H{^{1}H} NOE difference spectra. In the documentation of the NMR spectra the numbering follows the chemical numbering Scheme in most instances; for fulvenes the traditional numbering is used and for the pyrrolidine ring of SMP arbitrary numbers are defined as shown below.

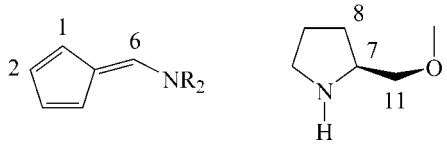

Synthesis of 6-Morpholinofulvene (7a) – Method A: a) (Methoxy)-morpholinocarbenium methyl sulfate: *N*-Formylmorpholide (11.35 g, 98.6 mmol) was placed in a 50 mL three-necked flask equipped with a dropping funnel and a reflux condenser. Dimethyl sulfate (12.44 g, 98.6 mmol) was added dropwise with stirring at 55 °C. Stirring was continued at 75 °C for 2 h, and the reaction mixture turned dark brown and became rather viscous. b) **7a**: A 100-mL three-necked flask equipped with a dropping funnel and a reflux condenser was charged with NaCp (98.6 mmol) in THF (70 mL) and cooled to –10 °C. The carbenium methyl sulfate was then added with stirring at such a rate that the temperature did not rise above –5 °C. The mixture was then warmed up to ambient temperature overnight. Pentane (40 mL) was added. The solid material was filtered off and washed with CH_2Cl_2 and pentane until the filtrate was nearly colorless. The volatiles were removed from the collected filtrates in a vacuum, and the resulting dark residue was crystallized from EtOH/H_2O (1:1) or from hexane to afford **7a** (2.59 g, 16%) as air-stable, orange-yellow platelets; m.p. 75 °C; highly soluble in polar organic solvents, soluble in toluene, moderately soluble in cold hexane, insoluble in water. $C_{10}H_{13}NO$ (163.2): calcd. C 73.59, H 8.03, N 8.58; found C 73.77, H 8.03, N 8.44. MS (EI): *m*/*z* (%) = 163 (100) [M^+, $C_{10}H_{13}NO^+$], 79 (44) [$C_6H_7^+$], 58 (97) [$C_2H_4NO^+$]. ^{1}H NMR (500 MHz, [D$_6$]DMSO, 25 °C): δ = 3.37 (br., $\nu_{1/2}$ = 14 Hz, 2 CH_2N, gives rise to a multiplet at 90 °C), 3.69 (m, 2 CH_2O), 6.03 (m, 2-H), 6.24 (m, 1-H), 6.28 (m, 3-H), 6.44 (dt, 4-H), 7.28 (br. s, 6-H), coupling constants from simulation: $^3J_{12}$ = 4.50, $^4J_{13}$ = 1.88, $^4J_{14}$ = 2.15, $^4J_{16}$ = 0.15, $^3J_{23}$ = 2.51, $^4J_{24}$ = 1.39, $^5J_{26}$ = 0.25, $^3J_{34}$ = 4.77, $^5J_{36}$ = 0.88, $^4J_{46}$ = 0.42 Hz; the line-broadening of the signals for 6-H, CH_2N and CH_2O is caused by hindered rotation around the bond N–C-6. ^{13}C{^{1}H} NMR (125.6 MHz, [D$_6$]DMSO, 25 °C): δ = 147.94 (C-6), 125.40 (C-1), 124.47 (C-3), 118.13 (C-2), 115.50 (C-5), 113.65 (C-4), 65.76 (CH_2O, $\nu_{1/2}$ = 17 Hz; $\nu_{1/2}$ = 0.8 Hz at 90 °C), 49.64 (CH_2N, $\nu_{1/2}$ = 215 Hz; $\nu_{1/2}$ = 4.9 Hz at 90 °C). For NMR spectroscopic data in C_6D_6 and CD_2Cl_2 see ref.[1].

Synthesis of 6-Morpholinofulvene (7a) – Method B: A Schlenk flask equipped with a gas outlet was charged with freshly distilled cyclopentadiene (6.61 g, 100 mmol), morpholine (17.4 g, 200 mmol), and ethanol (absolute, 10 mL). Solid 1,3,5-triazine[21] (3.24 g, 40.0 mmol) was then added with efficient stirring at 0 °C, and stirring was continued at ambient temperature for 24 h. A yellow, glistening suspension formed. Water was added to complete the precipitation of the product. The solid was collected on a frit, washed several times with water (a total of 300 mL), and dried in a high vacuum for 12 h, to give **7a** (15.3 g, 94%) as a golden-brownish, analytically pure [elemental analysis (CHN), NMR] microcrystalline powder; m.p. 77 °C, other data as above.

6-[(*S*)-2-(Methoxymethyl)pyrrolidino]fulvene (7b): As described above for **7a** the reaction of cyclopentadiene (4.29 g, 64.9 mmol), HSMP[24] (14.95 g, 129.8 mmol), ethanol (absolute, 13 mL), and 1,3,5-triazine[21] (2.10 g, 26.0 mmol) produced a dark red oil. Ethanol (5 mL) was added and thereafter water (60 mL). The mixture was vigorously shaken and then kept standing until the phases had separated. The upper turbid, yellow phase was removed with the help of a syringe and the lower, oily, dark red organic phase was washed twice with water. The organic phase was then kept in a high vacuum with occasional shaking to remove the more volatile components. After about 60 h a film of the oil no longer gave off bubbles, and the residue was pure (NMR) **7b** (7.73 g, 62%); could not be crystallized; highly soluble in the common soft and/or polar organic solvents, soluble in Et_2O, moderately soluble in hot hexane. Chromatography on alumina (5% H_2O) with pentane/ether (1:4) gave particularly pure samples, but also resulted in high losses of material. $C_{12}H_{17}NO$ (191.3): calcd. C 75.35, H 8.96, N 7.32; found C 75.49, H 9.01, N 7.19. MS (EI): *m*/*z* (%) = 191 (20) [M^+], 146 (36) [M^+ – CH_2OMe], 70 (100) [$C_4H_8N^+$]. ^{1}H NMR (500 MHz, CD_2Cl_2, 25 °C): δ = 1.81 (br., $\nu_{1/2}$ = 22.0 Hz, 1 H, 8-H), 2.07 (m, 8-H + 2 9-H), 3.36 (s, OMe), 3.44 (m, CH_2O), 3.65 (m, CH_2N), 3.96 (br., $\nu_{1/2}$ = 18.0 Hz, 7-H), 6.22 (m, 2-H), 6.37 (m, 1-H), 6.43 (m, 3-H), 6.48 (m, 4-H), 7.50 (br., $\nu_{1/2}$ = 7.5 Hz, 6-H). ^{13}C{^{1}H} NMR (125.6 MHz, CD_2Cl_2, 25 °C): δ = 24.60 (C-9), 27.86 (C-8), 50.54 (C-10), 59.27 (OMe), 63.94 (C-7), 75.45 (CH_2O), 114.71 (C-4), 118.14 (C-5), 119.46 (C-2), 124.00 (C-1), 124.53 (C-3), 144.92 (C-6).

Sodium (Morpholinomethyl)cyclopentadienide Na[$C_5H_4CH_2$–$N(C_2H_4)_2O$] (8a): A Schlenk tube was charged with toluene

 © 2005 Wiley-VCH Verlag GmbH & Co. KGaA, Weinheim

(30 mL) and **7a** (0.918 g, 5.63 mmol), and cooled to 0 °C. A solution of $NaBHEt_3$ in toluene (1 M, 6.19 mL, 6.19 mmol) was added dropwise with vigorous stirring. The cooling bath was then removed, and stirring was continued at ambient temperature for 20 h. The volatiles were then removed in a vacuum and the solid residue was kept in a high vacuum for 24 h. This raw product contained (inter alia) triethylborane (0.32 equiv.) coordinated to morpholino groups [$\delta(^{11}B)$ = 4 and –2 ppm, two conformers] and borates [$NaBHEt_3$: $\delta(^{11}B)$ = –13 ppm; $NaBEt_4$: $\delta(^{11}B)$ = –16 ppm; in [D_7]-DMF or [D_6]DMSO].[44] The triethylborane could not be removed in a high vacuum at 80 °C. The residue was dispersed in diethyl ether (10 mL) with the help of an ultrasonic bath; when the solid had settled again, the supernatant liquid was removed with a syringe. This procedure was repeated twice with ether and three time with pentane. Drying the solid in a high vacuum overnight left **8a** (0.87 g, 83%, with 0.04 eq BEt_3) as a light brown to ochre colored, extremely air-sensitive solid; soluble in DMF, DMSO and liquid ammonia, and moderately soluble in MeCN, slowly decomposing in solution. ^1H NMR (500 MHz, [D_7]DMF, 25 °C): δ = 2.34 (br., $\nu_{1/2}$ = 21.8 Hz, 2 CH_2N), 3.35 (s, $C_5H_4CH_2$), 3.52 ("t", br, "J" = 4.58 Hz, 2 CH_2O), AA′BB′ system: 5.54 ("t", 3-/4-H), 5.56 ("t", 2-/5-H), $N = J_{12} + J_{13}$ = 2.44 Hz; protons of residual BEt_3: –0.04 (q, BCH_2Me), 0.71 (t, BCH_2), ^3J = 7.94 Hz. $^{13}C\{^1H\}$ NMR (125.6 MHz, [D_7]DMF, 25 °C): δ = 54.38 (NCH_2), 61.65 ($C_5H_4CH_2$), 67.51 (CH_2O), 102.91 (C-3,4), 105.41 (C-2,5), 114.19 (C-1). $^{11}B\{^1H\}$NMR (160.3 MHz, [D_7]DMF, 25 °C, ext. $BF_3{\cdot}OEt_2$): δ = 4.1, –2.0.

Sodium {[(*S*)-2-(Methoxymethyl)pyrrolidino]methyl}cyclopentadienide, Na($C_5H_4CH_2$–SMP) (8b): A Schlenk tube was charged with toluene (3 mL) and **7b** (0.676 g, 3.53 mmol). A solution of $NaBHEt_3$ in toluene (1 M, 3.89 mL, 3.89 mmol) was added dropwise with vigorous stirring, and stirring was continued for 20 h. Further workup as described for **8a** (but with 5 mL volumes of solvent) afforded **8b** (0.684 g, 90%, with 0.018 eq BEt_3) as a light brown to ochre colored, extremely air-sensitive solid; soluble in liquid ammonia, slightly soluble in MeCN and THF, slowly decomposing in solution. There is no improved solubility in DME, TMEDA or in the presence of 15-crown-5. Prolonged washing of **8b** with ether removed the residual triethylborane completely, but also drastically reduced the yield. ^1H NMR (500 MHz, [D_8]THF, 25 °C): δ = 1.47 (m, 1 H, 8-H), 1.56 (m, 2 H, 9-H), 1.78 (m, 1 H, 8-H), 2.37 (m, 1 H, 10-H), 2.74 (m, 7-H), 2.96 (m, 1 H, 10-H), 3.11 (dd, ^2J = 9.46, $^3J_{7,11}$ = 6.10 Hz, 1 H, 11-H), 3.19 (d, ^2J = 9.46 Hz, 1 H, 11-H), 3.25 (s, OMe), AB system $C_5H_4CH_2$: 3.44 (d) and 3.66 (d), ^2J = 12.51 Hz; 5.60 (s, C_5H_4). $^{13}C\{^1H\}$ NMR (125.6 MHz, [D_8]THF, 25 °C): δ = 23.46 (C-9), 28.88 (C-8), 55.19 (C-10), 56.43 ($C_5H_4CH_2$), 58.72 (OMe), 62.62 (C-7), 76.47 (CH_2O), 103.26 (C-3,4), 104.36 (C-2,5), 116.45 (C-1).

Cp*Ru($C_5H_4CH_2$–SMP) (5): A suspension of **8b** (1.615 g, 7.50 mmol) in THF (10 mL) was cooled to –78 °C and [Cp*RuCl]$_4$[13] (2.039 g, 1.876 mmol), also suspended in THF (10 mL), was added. The mixture was stirred and was warmed up to ambient temperature within 4 h and stirring was continued for 2 h. Then the volatiles were removed in a vacuum. The red-brown oily residue was extracted with pentane (15 mL), the solution was separated from solid material by filtration through kieselguhr, which was then washed and extracted with several portions of pentane (a total of 35 mL). Removal of the pentane in a vacuum left a raw product which was contaminated with BEt_3, which had come into the system as a contaminant of **8b**. It was dissolved in diethyl ether (15 mL) and a saturated aqueous solution of NaF (5 mL) was added. After vigorous shaking the two phases were separated, the aqueous phase was extracted several times with diethyl ether (a total of 25 mL); the combined ethereal solutions were dried with Na_2SO_4, filtered and the solvents evaporated to dryness. The yellow-brownish, oily residue was heated in a high vacuum ($5{\cdot}10^{-7}$ bar); above 160 °C a yellow oil was condensed over a short (!) bridge into a small flask. The product **5** (2.70 g. 84%) is a viscous yellow oil, highly soluble in all common organic solvents (except MeOH), insoluble in perfluoropentane and water. $C_{22}H_{33}NORu$ (428.6): calcd. C 61.65, H 7.76, N 3.27; found C 61.79, H 7.95, N 3.34. MS (EI): m/z (%) = 429 (15) [M^+], 315 (100) [M^+ – SMP]. ^1H NMR (500 MHz, CD_2Cl_2, 25 °C): δ = 1.49–1.55 (m, 1 H, 8-H), 1.59–1.66 (m, 2 9-H), 1.77–1.85 (m, 1 H, 8-H), 1.89 (s, Cp*), 2.22 (m, 1 H, 10-H), 2.60 (m, 1 H, 7-H), 2.89 (m, 1 H, 10-H), 2.95 (d, ^2J = 12.97 Hz, 1 H, 6-H), 3.17 (dd, ^2J = 9.33, $^3J_{7,11}$ = 6.52 Hz, 1 H, 11-H), 3.31 (s, OMe), 3.34 (dd, ^2J = 9.33, $^3J_{7,11'}$ = 4.94 Hz, 1 H, 11-H′), 3.36 (d, ^2J = 12.97 Hz, 1 H, 6-H), 4.08 (m, 2-/5-H), 4.10 (m, 3-/4-H). $^{13}C\{^1H\}$ NMR (125.6 MHz, CD_2Cl_2, 25 °C): δ = 12.07 (C_5Me_5), 23.11 (C-9), 29.09 (C-8), 53.43 ($C_5H_4CH_2$), 54.36 (C-10), 59.06 (OMe), 61.96 (C-7), 73.12 and 72.97 (C-3,4), 74.65 and 74.45 (C-2,5), 77.02 (CH_2O), 85.12 (C_5Me_5), 85.48 (C-1).

[Cp*Ru(C_5H_4CH=SMP)]PF_6 (9): To a Schlenk tube charged with [Cp*Ru(MeCN)$_3$]PF_6[26] (0.581 g, 1.151 mmol) was added a solution of **7b** (0.227 g, 1.186 mmol) in THF (15 mL). The resulting reaction mixture was heated to reflux temperature for 24 h. The volatiles were removed in a vacuum. The residue was powdered at liquid nitrogen temperature and was warmed to ambient temperature in a high vacuum. This procedure was repeated several times and left **9** (0.660 g, 100%) as dark red-brown powder; m.p. 155 °C, rather soluble in CH_2Cl_2, THF and acetone, sparingly soluble in ether, decomposes in MeOH. The product may be crystallized as dark yellow needles by layering of acetone solutions with ether. $C_{22}H_{32}F_6NOPRu$ (572.54): calcd. C 46.15, H 5.63, N 2.45; found C 46.19, H 5.62, N 2.56. MS (DCI, NH_3) m/z (%) = 428 (85) [M^+], 116 (100) [H_2SMP^+]. ^1H NMR (500 MHz, CD_2Cl_2, 25 °C): δ = 1.91 (s, Cp*), 1.92–2.00 (m, 1 H, 8-H), 2.19–2. 34 (m, 3 H, 8-H′ + 2 9-H), 3.40 (s, OMe), 3.36–3.48 (m, CH_2N), 3.55 (dd, ^2J = 10.68, $^3J_{7,11}$ = 7.63 Hz, 1 H, 11-H), 3.68 (dd, ^2J = 10.68, $^3J_{7,11}$ = 3.36 Hz, 1 H, 11-H′), 4.26 (m, 7-H), C_5H_4: 4.78 (ddd, 1-H), 4.86 (ddd, 4-H), 4.93 (ddd, 2-H), 4.95 (ddd, 3-H), simulated with $^3J_{12}$ = $^3J_{34}$ = 2.75, $^3J_{23}$ = 2.67, $^4J_{13}$ = $^4J_{14}$ = $^4J_{24}$ = 1.14 Hz; 8.28 (br., $\nu_{1/2}$ = 4.2 Hz, 6-H). $^{13}C\{^1H\}$ NMR (125.6 MHz, CD_2Cl_2, 25 °C): δ = 11.86 (C_5Me_5), 24.52 (C-9), 27.53 (C-8), 53.01 (CH_2N), 59.34 (OMe), 68.08 (C-7), 73.64 (CH_2O), 75.01 (C-5), 76.34 and 76.70 (br., C-1,4), 82.87 and 82.92 (C-2,3), 90.32 (C_5Me_5), 162.95 (C-6).

Synthesis of 5 by Hydride Addition to Complex 9: A solution of **9** in THF (20 mL) was prepared as described above from [Cp*Ru(MeCN)$_3$]PF_6[26] (0.550 g, 1.090 mmol) and **7b** (0.210 g, 1.099 mmol). A solution of $LiAlH_4$ in THF (1 M, 1.090 mL) was added dropwise at –78 °C. The mixture was then warmed to ambient temperature and stirred at that temperature for 7 d. Water (2 mL) was added, then the mixture was evaporated to dryness. The residue was extracted with several portions of pentane (a total 50 mL). The combined, lemon yellow extracts were filtered through kieselguhr. Removal of the pentane left a very pure (NMR) sample of **5** (0.24 g, 50%, yield not optimized).

Lithiation of 5: Complex **5** was used as 0.1 M solution in diethyl ether at –78 °C. A titrated solution of Li*s*Bu in cyclohexane[28] (ca. 1.5 M) was added at –78 °C within 30 s. The ratio **5**/Li*s*Bu was usually 1:1.7 The reaction mixture was kept stirring at –78 °C for 3.5 h. Then the quenching reagent E–X was added, still at –78 °C, and the mixture was warmed to ambient temperature. Stoichiometric quantities are specified below.

(S_P)-Cp*Ru[1-F-2-(SMP–CH_2)C_5H_3] (10a): A solution of **5** in diethyl ether (0.298 g, 0.695 mmol, 1.39 mL) was cooled to –78 °C

 © 2005 Wiley-VCH Verlag GmbH & Co. KGaA, Weinheim

and a solution of Li*s*Bu in cyclohexane (1.58 M, 0.748 mL, 1.181 mmol) (ratio 1:1.70) was added at –78 °C within 20–30 s. The mixture was stirred at –78 °C for 3.5 h. Then a suspension of *N*-fluoro-*N*,*N*-bis(benzenesulfonyl)imide [$(PhSO_2)_2NF$] (0.3835 g, 1.216 mmol) in diethyl ether (a total of 10 mL) was added. The reaction mixture was warmed to ambient temperature within 2.5 h and stirring was then continued for 12 h. The volatiles were removed in a high vacuum and the residue was extracted with several portions of pentane (a total of 25 mL). The combined solutions were passed through kieselguhr and carefully freed of all volatiles to leave **10a** (0.233 g, 75%) as pale yellow oil, de > 98%, 8% admixture of **5** (only the ring protons 1-H – 4-H of **5** are not hidden by signals of **10a**). MS (EI): *m*/*z* (%) = 447 (9) [M^+], 333 (100) [M^+ – SMP]. Further comment: $(PhSO_2)_2NF$ should be colorless. The commercial product (Aldrich) was dissolved in CH_2Cl_2; the solution was passed through kiesel gel (Kieselgel 60, Merck), freed from solvent and carefully dried in a high vacuum. ^1H NMR (500 MHz, CD_2Cl_2, 25 °C): δ = 1.90 (s, Cp*), 3.01 (d, 1 H, 2-CH_2), 3.66 (d, 1 H, 2-CH_2), ^2J(2-CH_2) = 13.42 Hz; 3.846 (dddd, 4-H), 3.897 (dd, 3-H), 4.338 (dddd, 5-H), $^3J(^{19}F,5\text{-H})$ = 3.74, $^3J_{34}$ = 2.52, $^3J_{45}$ = 2.51, $^4J(^{19}F,4\text{-H})$ = 0.61, $^4J(^{19}F,3\text{-H})$ = 0.50, $^4J_{35}$ = 1.29, ^4J(3-H,2-CH_2) = 0.25, ^5J(4-H,2-CH_2) = 0.53, ^5J(5-H,2-CH_2) = 0.57 Hz; SMP fragment: 1.50–1.57 (m, 1 H, 8-H), 1.61–1.68 (m, 2 H, 9-H,H′), 1.78–1.86 (m, 1 H, 8-H′), 2.25 (ddd, br, 1 H, 10-H), 2.67 (br. m, 7-H), 2.95 (ddd, br, 1 H, 10-H′), 3.20 (dd, ^2J = 9.46, $^3J_{7,11}$ = 6.41 Hz, 1 H, 11-H), 3.31 (s, OMe), 3.36 (dd, ^2J = 9.46, $^3J_{7,11'}$ = 5.19 Hz, 1 H, 11-H′). $^{13}C\{^1H\}$ NMR (125.6 MHz, CD_2Cl_2, 25 °C): δ = 11.69 (C_5Me_5), 23.15 (C-9), 29.04 (C-8), 49.42 (d, $^3J_{FC}$ = 3.9 Hz, C-6), 54.31 (C-10), 59.05 (OMe), 61.76 (C-7), 62.32 (d, $^2J_{FC}$ = 15.9 Hz, C-5), 66.26 (d, $^3J_{FC}$ = 3.9 Hz, C-4), 69.68 (d, $^3J_{FC}$ = 2.7 Hz, C-3), 73.72 (small, d, $^2J_{FC}$ = 14.3 Hz, C-2), 77.02 (C-11), 86.29 (C_5Me_5), 133.81 (d, $^1J_{FC}$ = 267.9 Hz, C-1). ^{19}F NMR (470.1 MHz, CD_2Cl_2, 25 °C): δ = –196.8 vs. ext. $CFCl_3$; when measured at 188.1 MHz a doublet was seen with $^3J(^{19}F,5\text{-H})$ = 3.5 Hz.

(S_P)-Cp*Ru[1-Cl-2-(SMP–CH_2)C_5H_3] (10b): The reaction of **5** (59.5 mg, 138.8 μmol), Li*s*Bu (1.65 M, 143 μL, 236 μmol), and C_2Cl_6 (82.2 mg, 347 μmol) gave **10b** (64.0 mg, 100%) as pale yellow oil; de > 98%, ca. 2% admixture of **5** (the signal at δ = 1.893 ppm of the Cp* ligand of **5** was the only impurity signal seen). MS (EI): *m*/*z* (%) = 463 (7) [M^+], 349 (100) [M^+ – SMP], 316 (17) [$RuC_{16}H_{22}^+$]. ^1H NMR (500 MHz, CD_2Cl_2, 25 °C): δ = 1.85 (s, Cp*), 2.91 (d, 1 H, 2-CH_2), 3.59 (d, 1 H, 2-CH_2), ^2J(2-CH_2) = 13.18 Hz; 4.09 (ddd, 4-H), 4.15 (dd, 3-H), 4.34 (ddd, 5-H), $^3J_{34}$ = 2.47, $^3J_{45}$ = 2.38, $^4J_{35}$ = 1.29, ^4J(3-H,2-CH_2) = 0.25, ^5J(4-H,2-CH_2) = 0.40, ^5J(5-H,2-CH_2) = 0.55 Hz; SMP fragment: 1.51–1.57 (m, 1 H, 8-H), 1.60–1.70 (m, 2 H, 9-H,H′), 1.80 –1.90 (m, 1 H, 8-H′), 2.20 (ddd, ^2J = 9.06, $^3J_{9,10} \approx 9.3$ $^3J_{9',10} \approx$Hz, 1 H, 10-H), 2.66 (m, 7-H), 2.99 (ddd, ^2J = 9.06, $^3J_{9,10'}$ = 6.68, $^3J_{9',10'}$ = 2.38 Hz, 1 H, 10-H′), 3.21 (dd, ^2J = 9.33, $^3J_{7,11}$ = 6.40 Hz, 1 H, 11-H), 3.32 (s, OMe), 3.42 (dd, ^2J = 9.33, $^3J_{7,11'}$ = 4.90 Hz, 1 H, 11-H′). $^{13}C\{^1H\}$ NMR (125.6 MHz, CD_2Cl_2, 25 °C): δ = 11.29 (C_5Me_5), 23.12 (C-9), 29.06 (C-8), 50.71 ($C_5H_4CH_2$), 54.57 (C-10), 59.06 (OMe), 62.32 (C-7), 70.98 (C-4), 73.59 (C-3), 73.79 (C-5), 77.15 (CH_2O), 83.57 (C-2), 86.39 (C_5Me_5), 92.11 (C-1).

(S_P)-Cp*Ru[1-Br-2-(SMP–CH_2)C_5H_3] (10c): The reaction of **5** (70.5 mg, 164.5 μmol), Li*s*Bu (1.65 M, 170 μL, 280 μmol), and 1,2-$C_2H_4Br_2$ (54.1 mg, 288 μmol) gave **10c** (83.3 mg, 100%) as pale yellow oil; de > 98%, ca. 5% admixture of **5** (NMR). MS (EI): *m*/*z* (%) = 507/509 (5) [M^+], 393/395 (100) [M^+ – SMP], 315 (22) [$RuC_{16}H_{21}^+$]. ^1H NMR (500 MHz, CD_2Cl_2, 25 °C): δ = 1.84 (s, Cp*), 3.55 (d, 1 H, 2-CH_2), 2.95 (d, 1 H, 2-CH_2), ^2J(2-CH_2) = 13.26 Hz; 4.132 (ddd, 4-H), 4.170 (dd, 3-H), 4.358 (ddd, 5-H), $^3J_{34}$ = 2.29, $^3J_{45}$ = 2.38, $^4J_{35} \approx 1.2$, ^5J(4-H,2-CH_2) = 0.40, ^5J(5-H,2-CH_2) = 0.55 Hz; SMP fragment: 1.554–1.716 (m, 3 H, 8-/9-H,H′), 1.80–1.89 (m, 1 H, 8-H′), 2.22 (ddd, $^2J \approx 9.35$, $^3J_{9,10} \approx 9.40$, $^3J_{9',10} \approx 7.46$ Hz, 1 H, 10-H), 2.68 (m, 7-H), 3.02 (ddd, $^2J \approx 9.2$, $^3J_{9,10'} \approx 7.2$, $^3J_{9',10'} \approx 2.0$ Hz, 1 H, 10-H′), 3.25 (dd, ^2J =.38, $^3J_{7,11}$ = 6.18 Hz, 1 H, 11-H), 3.34 (s, OMe), 3.45 (dd, ^2J = 9.38, $^3J_{7,11'}$ = 4.72 Hz, 1 H, 11-H′). $^{13}C\{^1H\}$ NMR (125.6 MHz, CD_2Cl_2, 25 °C): δ = 11.21 (C_5Me_5), 23.05 (C-9), 28.93 (C-8), 51.49 ($C_5H_4CH_2$), 54.55 (C-10), 59.12 (OMe), 62.31 (C-7), 72.33 (C-4), 73.97 (C-3), 75.99 (C-5), 76.76 (CH_2O), 79.17 (C-1), 84.53 (C-2), 86.54 (C_5Me_5).

(S_P)-Cp*Ru[1-I-2-(SMP–CH_2)C_5H_3] (10d): The reagents were **5** (141.8 mg, 331 μmol), Li*s*Bu (1.65 M, 211 μL, 347 μmol), and 1,2-$C_2H_4I_2$ (93.3 mg, 331 μmol). The reaction mixture was kept at ambient temperature for 50 h. Then the volatiles were removed in a vacuum. the residue was treated with diethyl ether (5 mL) and then with water (5 mL) and vigorously shaken. The aqueous phase was extracted with two portions of ether (5 mL each). The combined ethereal phases were dried with $MgSO_4$ and carefully freed from all volatiles to leave **10d** (99.4 mg, 54%) as a brown oil; de > 98%, ca. 2% admixture of **5** (^1H NMR: δ = 1.893 ppm, Cp* ligand of **5**). MS (EI): *m*/*z* (%) = 555 (7) [M^+], 441 (100) [M^+ – SMP], 315 (21) [$RuC_{16}H_{21}^+$]. ^1H NMR (500 MHz, CD_2Cl_2, 25 °C): δ = 1.81 (s, Cp*), 2.85 (d, 1 H, 2-CH_2), 3.432 (d, 1 H, 2-CH_2), ^2J(2-CH_2) = 13.17 Hz; 4.138 (dd, 3-H), 4.151 (ddd, 4-H), 4.35 (ddd, 5-H), $^3J_{34}$ = 2.42, $^3J_{45}$ = 2.38, $^4J_{35}$ = 1.23, ^5J(4-H,2-CH_2) = 0.55, ^5J(5-H,2-CH_2) = 0.60 Hz; SMP fragment: 1.51–1.57 (m, 1 H, 8-H), 1.61–1.68 (m, 2 H, 9-H,H′), 1.80–1.88 (m, 1 H, 8-H′), 2.16 (ddd, 1 H, 10-H), 2.63 (m, 7-H), 3.00 (ddd, 1 H, 10-H′), 3.22 (dd, ^2J = 9.33, $^3J_{7,11}$ = 6.41 Hz, 1 H, 11-H), 3.33 (s, OMe), 3.52 (dd, ^2J = 9.33, $^3J_{7,11'}$ = 4.94 Hz, 1 H, 11-H′). $^{13}C\{^1H\}$ NMR (125.6 MHz, CD_2Cl_2, 25 °C): δ = 11.04 (C_5Me_5), 23.06 (C-9), 29.09 (C-8), 45.25 (C-1), 53.37 ($C_5H_4CH_2$), 54.77 (C-10), 59.07 (OMe), 62.71 (C-7), 74.13 (C-3), 74.35 (C-4), 77.27 (CH_2O), 80.41 (C-5), 86.41 (C_5Me_5), 87.27 (C-2).

(R_P)-Cp*Ru[1-(SMP–CH_2)-2-MeC_5H_3] (10e): The reagents were **5** (83.2 mg, 194 μmol), Li*s*Bu (1.58 M, 209 μL, 330 μmol), and MeI (48.2 mg, 340 μmol). Workup as described for **10d** (with Na_2SO_4 for drying) gave **10e** as yellow-brown oil; de > 98%, ca. 5% admixture of **5** (^1H NMR: δ = 1.893 ppm, Cp* ligand of **5**). The yield was not determined; cf. however the data for **10f**. MS (EI): *m*/*z* (%) = 443 (15) [M^+], 329 (100) [M^+ – SMP]. ^1H NMR (500 MHz, CD_2Cl_2, 25 °C): δ = 1.84 (s, Cp*), 2.78 (d, 1 H, 2-CH_2), 3.54 (d, 1 H, 2-CH_2), ^2J(2-CH_2) = 12.82 Hz; 4.013 (dd, 4-H), 4.029 (m, 3-H), 4.041 (dd, 5-H), $^3J_{34} \approx 2.4$, $^3J_{45}$ = 2.14, $^4J_{35}$ = 1.22 Hz; SMP fragment: 1.49–1.54 (m, 1 H, 8-H), 1.60–1.64 (m, 2 H, 9-H,H′), 1.75 (s, 2-Me), 1.80 –1.88 (m, 1 H, 8-H′), 2.14 (ddd, 1 H, 10-H), 2.61 (m, 7-H), 2.94 (m, 1 H, 10-H′), 3.22 (dd, ^2J = 9.15, $^3J_{7,11}$ = 6.10 Hz, 1 H, 11-H), 3.32 (s, OMe), 3.39 (dd, ^2J = 9.15, $^3J_{7,11'}$ = 5.19 Hz, 1 H, 11-H′). $^{13}C\{^1H\}$ NMR (125.6 MHz, CD_2Cl_2, 25 °C): δ = 11.66 (2-Me), 11.69 (C_5Me_5), 23.14 (C-9), 29.08 (C-8), 52.03 ($C_5H_4CH_2$), 54.74 (C-10), 59.05 (OMe), 62.50 (C-7), 71.45 (C-4), 74.92 (C-3), 75.29 (C-5), 77.48 (CH_2O), 84.66(C_5Me_5), 84.92(small, C-1), 85.25(small, C-2).

(S_P)-Cp*Ru[1-(SMP–CH_2)-2-$CD_3C_5H_3$] (10f): The reagents were **5** (0.448 g, 1.045 mmol), Li*s*Bu (1.58 M, 0.992 mL, 1.567 mmol), and CD_3I (0.235 g, 1.62 mmol). Workup as described for **10d** (with Na_2SO_4 as drying agent) gave **10f** (0.421 g, 100%) as yellow oil; de > 98%, ca. 3% admixture of **5** (^1H NMR: δ = 1.893 ppm, Cp* ligand of **5**). MS (EI): *m*/*z* (%) = 463 (3) [M^+ – H + CD_3], 446 (14) [M^+], 349 (24) [M^+ – SMP – H + CD_3], 332 (100) [M^+ – SMP]. ^1H NMR (500 MHz, CD_2Cl_2, 25 °C): δ = 1.84 (s, 15 H, Cp*), 2.79 (d, 1 H, 2-CH_2), 3.53 (d, 1 H, 2-CH_2), ^2J(2-CH_2) = 12.90 Hz; 4.009 (ddd, 4-H), 4.023 (ddd, 3-H), 4.038 (dd, 5-H), $^3J_{34}$ = 2.29, $^3J_{45} \approx$

 © 2005 Wiley-VCH Verlag GmbH & Co. KGaA, Weinheim

2.20, $^4J_{35} \approx 1.45$, ^5J(3-H,2-CH_2) = 0.6, ^5J(4-H,2-CH_2) = 0.37 Hz; SMP fragment: 1.48–1.54 (m, 1 H, 8-H), 1.60–1.66 (m, 2 H, 9-H,H′), 1.81–1.87 (m, 1 H, 8-H′), 2.14 (ddd, 1 H, 10-H), 2.62 (m, 7-H), 2.94 (m, 1 H, 10-H′), 3.21 (dd, ^2J = 9.24, $^3J_{7,11}$ = 6.23 Hz, 1 H, 11-H), 3.32 (s, OMe), 3.391 (dd, ^2J = 9.06, $^3J_{7,11'}$ = 5.21 Hz, 1 H, 11-H′). ^{2}H{^{1}H} NMR (61.4 MHz, CD_2Cl_2, 25 °C): δ = 1.74 (CD_3) vs. $\delta(CD_2Cl_2)$ = 5.330. ^{13}C{^{1}H} NMR (125.6 MHz, CD_2Cl_2, 25 °C): δ = 11.66 (C_5Me_5), 23.12 (C-9), 29.06 (C-8), 52.01 ($C_5H_4CH_2$), 54.71 (C-10), 59.03 (OMe), 62.48 (C-7), 71.45 (C-4), 74.91 (C-5), 75.27 (C-3), 77.45 (CH_2O), 84.66 (C_5Me_5), 84.77 (small, C-1), 85.26 (small, C-2); in a ^{13}C NMR spectrum the 2-CD_3 group can be seen as a septet: δ = 10.96 [sept, $^1J(^{13}C–^2H)$ = 19.2 Hz, CD_3].

(S_P)-Cp*Ru[1-(Me_3Si)-2-(SMP–CH_2)C_5H_3] (10g) and Cp*Ru[1,3-(Me_3Si)$_2$-2-(SMP–CH_2)C_5H_2] (11): The reagents were **5** (87.5 mg, 204 μmol), Li*s*Bu (1.65 M, 210 μL, 347 μmol), and $SiClMe_3$ (38.8 mg, 357 μmol). Workup as described for **10d** (with Na_2SO_4 as drying agent) gave a yellow oil (99.4 mg) which consisted of **10g** and **11** in a 3:1 ratio; unconsumed starting material **5** could not be detected. When only a small excess of Li*s*Bu was used, the formation of **11** could be suppressed and some unconsumed **5** was found. MS (EI) *m*/*z* (%): 573 (< 0.5) [**11**$^+$], 501 (12) [**10g**$^+$], 459 (2%) [**11**$^+$ – SMP], 428 (16) [**10g**$^+$ – $SiMe_3$], 387 (100) [**10g**$^+$ – SMP], 316 (27) [$RuC_{16}H_{22}^+$].

Data for 10g: ^{1}H NMR (500 MHz, CD_2Cl_2, 25 °C): δ = 1.87 (s, Cp*), 2.55 (d, 1 H, 2-CH_2), 3.66 (d, 1 H, 2-CH_2), ^2J(2-CH_2) = 12.21 Hz; 4.03 (m, 5-H), 4.08 (dd, 3-H), 4.10 (dd, 4-H), $^3J_{34}$ = $^3J_{45}$ = 2.14, $^4J_{35}$ = 1.22 Hz; 0.17 [s, $^2J(^{29}Si,^1H)$ = 6.41 Hz, $SiMe_3$]; SMP fragment: 1.45–1.61 (m, 3 H, 8-/9-H,H′), 1.83–1.97 (m, 1 H, 8-H′), 2.00 (ddd, 1 H, 10-H), 2.45 (m, 7-H), 2.75 (m, 1 H, 10-H′), 3.21 (dd, ^2J = 9.16, $^3J_{7,11}$ = 6.11 Hz, 1 H, 11-H), 3.300 (s, OMe), 3.47 (dd, ^2J = 9.16, $^3J_{7,11'}$ = 5.50 Hz, 1 H, 11-H′). ^{13}C{^{1}H} NMR (125.6 MHz, CD_2Cl_2, 25 °C): δ = 0.21 [$^1J(^{29}Si–^{13}C)$ = 51.5 Hz, $SiMe_3$], 12.25 (C_5Me_5), 22.73 (C-9), 29.33 (C-8), 54.46 (C-10), 54.69 ($C_5H_4CH_2$), 58.95 (OMe), 63.94 (C-7), 75.01 (C-4), 76.71 (small, C-1), 77.30 (CH_2O), 78.89 (C-5), 79.48 (C-3), 84.96 (C_5Me_5), 91.00 (small, C-2). ^{29}Si{^{1}H} NMR (99.3 MHz, CD_2Cl_2, 25 °C): δ = –5.3 vs. ext. $SiMe_4$, measured as ^{1}H/^{29}Si HMQC NMR spectrum.

Data for 11: ^{1}H NMR (500 MHz, CD_2Cl_2, 25 °C): δ = 1.85 (s, Cp*), 2.75 (d, 1 H, 2-CH_2), 3.51 (d, 1 H, 2-CH_2), ^2J(2-CH_2) = 12.51 Hz; 4.00–4.15 (4-/5-H); 0.197 (s, $SiMe_3$), 0.208 (s, $SiMe_3$); SMP fragment: 1.45–1.61 (m, 3 H, 8-/9-H,H′), 1.83–1.97 (m, 1 H, 8-H′), 2.08 (ddd, 1 H, 10-H), 2.45 (m, 7-H), 2.67 (m, 1 H, 10-H′), 3.17 (dd, ^2J = 9.16, $^3J_{7,11}$ = 6.40 Hz, 1 H, 11-H), 3.27 (s, OMe), 3.41 (dd, ^2J = 9.16, $^3J_{7,11'}$ = 5.49 Hz, 1 H, 11-H′); several signals are hidden by the corresponding signals of the main product **10g**. ^{13}C{^{1}H} NMR (125.6 MHz, CD_2Cl_2, 25 °C): δ = 0.65 and 1.52 *ppm*(1-/3-$SiMe_3$), 12.41 (C_5Me_5), 22.67 (C-9), 29.36 (C-8), 53.97 and 54.39 ($C_5H_4CH_2$ and C-10), 58.86 (OMe), 64.36 (C-7), 76.90 (CH_2O), 80.45 and 81.38 (C-4,5), 81.23 and 81.43 (small, C-1,3), 84.87 (C_5Me_5), 95.20 (small, C-2). ^{29}Si{^{1}H} NMR (99.3 MHz, CD_2Cl_2, 25 °C): δ = –5.7 vs. ext. $SiMe_4$, measured as ^{1}H/^{29}Si HMQC NMR spectrum.

(S_P)-Cp*Ru[1-(Ph_2P)-2-(SMP–CH_2)C_5H_3] (10h): The reagents were **5** (0.272 g, 0.635 mmol), Li*s*Bu (1.41 M, 653 μL, 0.921 mmol), and $PClPh_2$ (0.8974 *M* in hexane, 1.097 mL, 0.984 mmol). After warming the reaction mixture to ambient temperature within 1.5 h, the volatiles were removed in a high vacuum. The yellow oily residue was extracted with several portions of ether. The combined extracts were filtered through kieselguhr and carefully freed of solvent. The residue was heated in a high vacuum (oil diffusion pump, ca. 10^{-9} bar) for several hours; above 80 °C P*s*BuPh_2 was condensed over a short (!) bridge into a small flask. This procedure finally left **10h** (0.327 g, 84%) as a dark yellow, extremely viscous oil; soluble in CH_2Cl_2, THF, and ether, only moderately soluble in pentane; de > 98, ca. 15% admixture of **5** (^{1}H NMR); the P-containing compounds were **10h** (90%), residual P*s*BuPh_2 (ca. 4%), and phosphane oxides (ca. 6%) (^{31}P NMR). MS (EI) *m*/*z* (%): 613 (1) [M$^+$], 499 (3) [M$^+$ – SMP], 429 (15) [**5**$^+$], 315 (100) [$C_{16}H_{21}Ru^+$]. ^{1}H NMR (500 MHz, CD_2Cl_2, 25 °C): δ = 1.80 (s, Cp*), 2.64 (d, 1 H, 2-CH_2), 3.87 [dd, $^4J(^{31}P,2\text{-CH})$ = 2.44 Hz, 1 H, 2-CH_2], ^2J(2-CH_2) = ^2J = 12.21 Hz; 4.01 (ddd, 5-H), 4.217 (dddd, 4-H), 4.235 (ddd, 3-H), $^3J(^{31}P,5\text{-H})$ = 0.54, $^3J_{34}$ = 2.29, $^3J_{45}$ = 2.36, $^4J(^{31}P,3\text{-H})$ = 1.15, $^4J(^{31}P,4\text{-H})$ = 0.68, $^4J_{35}$ = 1.22, ^5J(4-H,2-CH_2) = 0.38 Hz; PPh2 group: 7.17–7.19 (m, 3 H), 7.22 –7.26 (m, 2 H), 7.29–7.31 (m, 3 H), 7.56 –7.59 (m, 2 H); SMP fragment: 0.97–1.16 (m, 2 H, 8-/9-H), 1.34–1.404 (m, 1 H, 9-H′), 1.59–1.67 (m, 1 H, 8-H′), 1.83–1.91 (m, partially overlapped by Cp* signal of **5**, 1 H, 10-H), 2.38 (m, 7-H), 2.61 (dd, ^2J = 9.16, $^3J_{7,11}$ = 7.63 Hz, 1 H, 11-H), 2.69 ("t"m, 1 H, 10-H′′), 3.25 (s, OMe), 3.80 (dd, ^2J = 9.16, $^3J_{7,11'}$ = 4.58 Hz, 1 H, 11-H′). ^{13}C{^{1}H} NMR (125.6 MHz, CD_2Cl_2, 25 °C): δ = 11.85 (C_5Me_5), 22.67 (C-9), 29.32 (C-8), 52.86 (d, $^3J_{PC}$ = 7.1 Hz, $C_5H_4CH_2$), 53.92 (C-10), 58.85 (OMe), 63.06 (C-7), 74.55 (s, C-4), 75.77 (d, $^2J_{PC}$ = 4.9 Hz, C-5), 76.81(d,$^6J_{PC}$= 2.2 Hz, CH_2O), 78.86(d,$^3J_{PC}$ = 3.3 Hz,C-3),78.91 (d,small,$^2J_{PC}$ = 9.3 Hz,C-2), 85.71 (C_5Me_5), 90.74 (d, small, $^1J_{PC}$ = 26.8 Hz, C-1), 8 signals of PPh_2 group 127.4–142.4. ^{31}P{^{1}H} NMR (202.3 MHz, CD_2Cl_2, 25 °C): δ = –24.03 vs. ext. H_3PO_4 (85%).

(S_P)-Cp*Ru[1-{(Ph_3P)Au}-2-(SMP–CH_2)C_5H_3] (10i): The reagents were **5** (72.3 mg, 169 μmol), Li*s*Bu (1.65 M, 107 μL, 177 μmol; only 1.05 equiv. !), and AuCl(PPh_3) (83.5 mg, 169 μmol). The metalation solution was kept at –78 °C for 12 h, was then warmed to ambient temperature within 13 h, and was cooled again to –78 °C. The gold reagent was added as a fine powder. The reaction mixture was warmed to ambient temperature and kept at that temperature for 3 h. Further workup as described for **10a** gave **10i** (0.115 g, 77%) as a yellow oil; de > 98%, ca. 25% admixture of **5** (NMR). MS (EI): *m*/*z* (%) = 887 (0.03) [M$^+$], 429 (8) [**5**$^+$], 315 (49) [$C_{16}H_{21}Ru^+$], 262 (100) [PPh_3^+]. ^{1}H NMR (500 MHz, CD_2Cl_2, 25 °C): δ = 1.92 (s, Cp*), 2.995 (d, overlapping with 10-/11-H, 1 H, 2-CH_2), 3.57 (d, 1 H, 2-CH_2), ^2J(2-CH_2) = 12.51 Hz; 3.97 (m, 5-H), 4.16 (m, 4-H), 4.22 (m, 3-H); PPh3: 7.47–7.541–(m, 9 H), 7.60–7.64 (m, 6 H); SMP fragment: 1.49–1.57 (m, 1 H, 8-H), 1.59–1.67 (m, 2 H, 9-H,H′), 1.74–1.80 (m, 1 H, 8-H′), 2.37 (ddd, 1 H, 10-H), 2.80 (m, 7-H), 2.97 (d, OMe), 2.995 (dd, overlapping with signals of 2-CH_2 and 10-H′, ^2J = 9.16, $^3J_{7,11} \approx 1.2$ Hz, 1 H, 11-H), 3.006 (m, overlapping with signals of 2-CH_2 and 11-H, 1 H, 10-H′), 3.41 (dd, ^2J = 9.15, $^3J_{7,11'}$ = 3.96 Hz, 1 H, 11-H′). ^{13}C{^{1}H} NMR (125.6 MHz, CD_2Cl_2, 25 °C): δ = 12.95 (C_5Me_5), 23.35 (C-9), 29.51 (C-8), 54.92 (C-10), 57.28 (s, $C_5H_4CH_2$), 58.82 (OMe), 61.85 (C-7), 74.23 (d, $^4J_{PC}$ = 6.5 Hz, C-4), 75.26 (d, $^4J_{PC}$ = 6.1 Hz, C-3), 77.14 (CH_2O), 80.96 (d, $^3J_{PC}$ = 5.5 Hz, C-5), 84.55 (C_5Me_5), 92.41 (d, small, $^3J_{PC}$ = 6.1 Hz, C-2), 111.24 (d, small, $^2J_{PC}$ = 121.8 Hz, C-1), 4 signals of PPh_3 group 129.4–134.7. ^{31}P{^{1}H} NMR (202.3 MHz, CD_2Cl_2, 25 °C): δ = 47.46 vs. ext. H_3PO_4 (85%); δ = 44.7 for *s*Bu$Au(PPh_3)$ when present as an impurity.

The Dimer [(R_P)-Cp*Ru{1-(LiI·SMP–CH_2)-2-$CD_3C_5H_3$}]$_2$ (12): Reagents and reaction as described for **10f**. After warming up to ambient temperature the reaction mixture was kept at that temperature for 0.5 h. The volatiles were then removed in a high vacuum. The foamy residue was extracted with 5–10 portions of hexane (5 mL each). The combined solutions were filtered through kieselguhr. Crystallization set in spontaneously and was completed by cooling to –26 °C for 15 h. The mother liquor was removed and the crystals were dried in a vacuum maintaining low temperature during the whole procedure. This gave **12** (0.54–0.60 g, 90–100%)

 © 2005 Wiley-VCH Verlag GmbH & Co. KGaA, Weinheim

as yellowish, almost colorless, rather hygroscopic needles; m.p. 165 °C (dec.); only slightly soluble in hexane. NMR spectra similar to those of **10f**.

(S_P)-Cp*Ru(1-F-2-MeC$_5$H$_3$) (14a): a) A solution of **10a** (0.233 g, 0.522 mmol) and excess MeI (0.50 mL, 8.0 mmol) in hexane (10 mL) was kept at ambient temperature for 10 d. The precipitate was collected, washed with hexane (2 × 3 mL), and dried in a high vacuum to give **13a** (0.251 g, 82%) as ochre-colored powder. The minor stereomer was best seen in the ^{19}F NMR (376.3 MHz, [D$_6$]-DMSO) spectrum which displayed two signals at $\delta(^{19}F)$ = –194.2 and –196.6 ppm vs. ext. $CFCl_3$ in a 8:1 ratio. b) A Schlenk tube was charged with **13a** (0.251 g, 0.427 mmol) and THF (16 mL). A solution of $LiAlH_4$ in THF (1 M, 0.64 mL, 0.64 mmol) was added at ambient temperature, and the mixture was heated to reflux temperature for 50 h. Then the reaction mixture was hydrolyzed with water (2.5 mL) and dried in a vacuum. The residue was extracted with several portions of pentane (a total of 40 mL). The combined extracts were filtered through kieselguhr and dried with $MgSO_4$. The concentrated solution was chromatographed on a column (7 cm long, 1 cm diameter) of alumina (5% H_2O) and eluted with pentane (a total of 20 mL). Careful removal of the solvent left **14a** (80 mg, 56%) as white crystals containing 2% (NMR) of Cp*Ru(C$_5$H$_4$Me);[45] m.p. 43 °C. $C_{16}H_{21}FRu$ (333.4): calcd. C 57.64, H 6.35; found C 57.53, H 6.48. MS (EI): *m/z* (%) = 334(100) [M$^+$],319(47) [M$^+$–Me],316(28) [$C_{16}H_{22}Ru^+$]. ^{1}H NMR (500 MHz, CD_2Cl_2, 25 °C): δ = 1.82 (s, 2-Me), 1.90 (s, Cp*), 3.78 (ddd, $^4J_{FH}$ = 0.76 Hz, 4-H), 3.81 (m, 3-H), 4.28 (ddd, $^3J_{FH}$ = 3.82 Hz, 5-H), $^3J_{34}$ = $^3J_{45}$ = 2.52, $^4J_{35}$ = 1.22 Hz. ^{13}C{^{1}H} NMR (125.6 MHz, CD_2Cl_2, 25 °C): δ = 9.56 (d, $^3J_{FH}$ = 2.8 Hz, 2-Me), 11.58 (C$_5$*Me*$_5$), 61.48 (d, $^2J_{FC}$ = 16.4 Hz, C-5), 65.43 (d, $^3J_{FC}$ = 4.4 Hz, C-4), 69.16 (d, $^3J_{FC}$ = 2.7 Hz, C-3), 73.42 (d, $^2J_{FC}$ = 14.2 Hz, C-2), 85.98 (*C*$_5$Me$_5$), 134.02 (d, $^1J_{FC}$ = 266.5 Hz, C-1). ^{19}F NMR (470.1 MHz, CD_2Cl_2, 25 °C): δ = –198.05 [d, $^3J(^{19}F,5\text{-H})$ = 3.7 Hz] vs. ext. $CFCl_3$.

(S_P)-Cp*Ru(1-Cl-2-MeC$_5$H$_3$) (14b): a) A solution of **10b** (1.890 g, 4.082 mmol) in pentane (60 mL) was treated with excess MeI (2.50 mL, 41 mmol). Workup after 13 d and as described for **13a** gave **13b** (2.47 g; 100%) as colorless solid. In the NMR spectra a second set of signals with ca. 2% relative intensity was seen indicating the presence of a second stereomer in 50:1 ratio. b) A Schlenk tube charged with **13b** (2.47 g, 4.08 mmol), THF (150 mL), and a solution of $LiAlH_4$ in THF (1 M, 6.12 mL, 6.12 mmol) was heated to reflux temperature for 50 h. After hydrolysis with water (20 mL, dropwise addition) all volatiles were removed in a vacuum. The residue was extracted with several portions of Et_2O (a total of 100 mL). The combined ethereal solutions were filtered through kieselguhr and dried with $MgSO_4$. The drying agent was filtered off and washed with diethyl ether (2 × 10 mL). Removal of the solvent left **14b** (1.14 g, 80%) as an off-white solid, contains 4% (NMR) of Cp*Ru(C$_5$H$_4$Me);[45] may be sublimed at 120 °C/10^{-6} bar, m.p. 103 °C. The compound may be recrystallized as needles by cooling pentane solutions to –30 °C. $C_{16}H_{21}ClRu$ (349.9): calcd. C 54.93, H 6.05, Cl 10.13; found C 54.73, H 6.16, Cl 9.98. MS (EI): *m/z* (%) = 350 (77) [M$^+$], 315 (100) [M$^+$ – Cl]. ^{1}H NMR (500 MHz, CD_2Cl_2, 25 °C): δ = 1.78 (s, 2-Me), 1.84 (s, Cp*), 4.02 (dd, 4-H), 4.05 (ddq, 3-H), 4.29 (dd, 5-H), $^3J_{34}$ = 2.47, $^3J_{45}$ = 2.38, $^4J_{35}$ = 1.28, ^4J(3-H,2-Me) = 0.46 Hz. ^{13}C{^{1}H} NMR (125.6 MHz, CD_2Cl_2, 25 °C): δ = 11.04 (2-Me), 11.15 (C$_5$*Me*$_5$), 70.16 (C-5), 72.73 (C-4), 73.01 (C-3), 83.36 (C-2), 86.03 (*C*$_5$Me$_5$), 92.33 (C-1).

(S_P)-Cp*Ru(1-CD$_3$–2-MeC$_5$H$_3$) (14f): a) A solution of **10f** (412 mg, 0.925 mmol) in hexane (10 mL) was treated with MeI (0.30 mL, 4.8 mmol). Workup as described for **13a** gave **13f** (0.503 g, 93%) as a colorless powder. In the NMR spectra a second set of signals with ca. 2% relative intensity was present. This was best seen for the *N*-Me group [$\delta(^1H)$ = 2.78 and 2.99 ppm, $\delta(^{13}C)$ = 41.64 and 48.83 ppm, with the low-field signals assigned to the minor stereomer]. b) The reaction of **10f** (0.503 g, 0.856 mmol) in THF (32 mL) with $LiAlH_4$ in THF (1 M, 1.28 mL, 1.28 mmol) gave, after workup as described for **14b**, the product **14f** (0.231 g, 81%) as a white solid; m.p. 95 °C. The compound may be recrystallized from very concentrated pentane solutions by cooling to –30 °C. $C_{17}H_{21}D_3Ru$ (332.5): calcd. C 61.42, H(D) 7.28 (for, 24 "H" atoms; after combustion D is detected with the same weight as H); found C 61.45, H 7.40. MS (EI): *m/z* (%) = 333 (100) [M$^+$], 318 (40) [M$^+$ – Me]. ^{1}H NMR (500 MHz, CD_2Cl_2, 25 °C): δ = 1.71 (s, 2-Me), 1.83 (s, Cp*), 3.946 (t, 4-H), 3.974 (d, 3-/5-H), $^3J_{34}$ = $^3J_{45}$ = 2.45 Hz. ^{2}H{^{1}H} NMR (61.4 MHz, CD_2Cl_2, 25 °C): δ = 1.69 (CD_3) vs. $\delta(CD_2Cl_2)$ = 5.330. ^{13}C{^{1}H} NMR (125.6 MHz, CD_2Cl_2, 25 °C): δ = 11.49 (2-Me), 11.54 (C$_5$*Me*$_5$), 70.74 (C-4), 74.36 (C-3,5), 84.36 (*C*$_5$Me$_5$), 84.53 (small, C-2), C-1 not observed; in a ^{13}C NMR spectrum (i.e. without proton decoupling) the 1-CD_3 group can be seen as a septet: δ = 10.53 [sept, $^1J(^{13}C,^2H)$ = 19.7 Hz].

Crystal Structure Determinations of 12 and of 14b: Geometry and intensity data were collected with an ENRAF-Nonius CAD4 diffractometer (Mo-*K*α radiation, 0.71073 Å, graphite monochromator). A summary of crystal data, data collection parameters and convergence results is compiled in Table 1. A numerical absorption correction[46] was applied to the intensity data of **12**, and an empirical correction based on azimuthal scans[47] to those of **14b**. The structures were solved by direct methods[48] and subsequent Fourier difference syntheses, and were refined on intensities.[49] Non-hydro-

Table 1. Crystal data, data collection parameters, and convergence results for **12** and **14b**.

	12	**14b**
Empirical formula	$C_{46}H_{70}I_2Li_2N_2O_2Ru_2$	$C_{16}H_{21}ClRu$
Formula weight	1152.86	349.85
Crystal system	monoclinic	triclinic
Space group	$P2_1$ (4)	$P\bar{1}$ (1)
a [Å]	9.0982(13)	7.610(2)
b [Å]	14.319(3)	8.298(2)
c [Å]	19.624(3)	13.361(2)
α [°]		94.21(2)
β [°]	102.888(11)	96.69(2)
γ [°]		114.46(2)
V [Å^3]	2492.2(7)	755.8(3)
Z	2	2
$d_{calcd.}$ [g/cm^3]	1.536	1.537
F(000)	1152	356
μ [mm^{-1}]	1.880	1.195
Absorption correction	Numerical	empirical
Max./min. transmission	0.93/0.49	0.73/0.58
θ range [°]	2–26	3–28
Temperature [K]	223	213
Scan mode	ω–2θ	ω–2θ
Crystal size [mm]	0.45 × 0.18 × 0.04	0.50 × 0.40 × 0.27
Reflections collected	11914	9283
unique	9746	6896
observed $I > 2\sigma(I)$	4318	6298
Variables	519	337
R_1,[a] observed (all data)	0.0779 (0.2021)	0.0562 (0.0641)
wR_2,[b] observed (all data)	0.0945 (0.1072)	0.1493 (0.1543)
GOF[c]	0.966	1.142
Max./min. resid. dens. [e/Å^3]	0.816/–0.712	2.656/–1.480

[a] $R_1 = \Sigma||F_o| - |F_c||/\Sigma|F_o|$. [b] $wR_2 = [\Sigma w(F_o^2 - F_c^2)^2/\Sigma w(F_o^2)^2]^{1/2}$, where $w = 1/[\sigma^2(F_o^2) + (aP)^2]$ and $P = [\max(F_o^2,0) + 2F_c^2]/3$. [c] GOF = $[\Sigma w(F_o^2 - F_c^2)^2/\Sigma(n-p)]^{1/2}$.

 © 2005 Wiley-VCH Verlag GmbH & Co. KGaA, Weinheim

gen atoms were assigned anisotropic displacement parameters and hydrogen atoms were included as riding in standard geometry. The structure of **14b** contains two symmetrically independent molecules of the same planar chirality; pseudo inversion relates the chloro substituent on one molecule to the methyl group of the other moiety and vice versa; all remaining atoms closely match a non-crystallographic inversion. It is therefore no surprise that during refinement of this structure high correlations were encountered, and that similarity and rigid bond restraints were required to ensure physically reasonable molecular geometries and displacement parameters. We note that, despite a clearly acentric intensity distribution in the diffraction pattern, refinement in the centrosymmetric super group $P\bar{1}$ initially proceeds smoothly, but converges at unsatisfactory agreement factors (wR_2 ca. 0.28), and results in apparently disordered substituents in the chloro methyl ring ligand. CCDC-272905 (for **12**) and CCDC-272906 (for **14b**) contain the supplementary crystallographic data for this paper. These data can be obtained free of charge from The Cambridge Crystallographic Data Centre via www.ccdc.cam.ac.uk/data_request/cif.

Acknowledgments

This work was generously supported by the Fonds der Chemischen Industrie.

[1] T. Wirth, *Enantiomerenreine planarchirale 1,2,3,4,5-Pentamethylruthenocene*, Dissertation, Rheinisch-Westfälische Technische Hochschule Aachen, Aachen, Germany, **2002**; *Aachener Beiträge zur Chemie* **2002**, vol. 37, Wissenschaftsverlag Mainz, Aachen, Germany, **2002**, ISBN 3-86073-954-9.
[2] What is meant here, strictly speaking, are ferrocenes with a planar chiral cyclopentadienyl ligand. The shortened expression is very commonly used.
[3] C. J. Richards, A. J. Locke, *Tetrahedron: Asymmetry* **1998**, *9*, 2377–2407.
[4] J. McGarrity, F. Spindler, R. Fuchs, M. Eyer (Lonza AG), EP-A 624 587 A2, **1995**; *Chem. Abstr.* **1995**, *122*, P81369q.
[5] a) A. Togni, R. Dorta, C. Köllner, G. Pioda, *Pure Appl. Chem.* **1998**, *70*, 1477–1485; b) A. Togni, "*New Ferrocenyl Ligands for Asymmetric Catalysis*" in: *Metallocenes*, vol. 2 (Eds.: A. Togni, R. L. Halterman), Wiley-VCH, Weinheim, Germany, **1998**, p. 685–721.
[6] F. Spindler, B. Pugin (Ciba-Geigy AG), EP-A 256 982 A2, **1988**; *Chem. Abstr.* **1990**, *112*, 138725c.
[7] a) H. C. L. Abbenhuis, U. Burckhardt, V. Gramlich, A. Togni, A. Albinati, B. Müller, *Organometallics* **1994**, *13*, 4481–4493; b) H. C. L. Abbenhuis, U. Burckhardt, V. Gramlich, A. Martelletti, J. Spencer, I. Steiner, A. Togni, *Organometallics* **1996**, *15*, 1614–1621.
[8] a) O. Hofer, K. Schlögl, *J. Organomet. Chem.* **1968**, *13*, 443–456; b) O. Hofer, K. Schlögl, *J. Organomet. Chem.* **1968**, *13*, 457–468.
[9] C. E. Garrett, G. C. Fu, *J. Am. Chem. Soc.* **1998**, *120*, 7479–7483.
[10] G. W. Gokel, D. Marquarding, I. Ugi, *J. Org. Chem.* **1972**, *37*, 3052–3058.
[11] T. Hayashi, A. Ohno, S.-j. Lu, Y. Matsumoto, E. Fukuyo, K. Yanagi, *J. Am. Chem. Soc.* **1994**, *116*, 4221–4226.
[12] a) U. Koelle, K. Bücken, U. Englert, *Organometallics* **1996**, *15*, 1376–1383; b) R. Pasch, U. Koelle, B. Ganter, U. Englert, *Organometallics* **1997**, *16*, 3950–3958.
[13] a) P. J. Fagan, M. D. Ward, J. C. Calabrese, *J. Am. Chem. Soc.* **1989**, *111*, 1698–1719; b) P. J. Fagan, W. S. Mahoney, J. C. Calabrese, I. D. Williams, *Organometallics* **1990**, *9*, 1843–1852; c) U. Koelle, J. Kossakowski, *J. Chem. Soc., Chem. Commun.* **1988**, 549–551.
[14] Formal amide abstraction would be an alternative disconnection. However, the properties of the parent fulvene strongly discouraged us from further consideration of this potential route.
[15] a) Cf. refs.[1–9] in: M. L. Peterson, J. T. Strnad, T. P. Markotan, C. A. Morales, D. V. Scaltrito, S. W. Staley, *J. Org. Chem.* **1999**, *64*, 9067–9076; b) M. Neuenschwander: "*Fulvenes*" in: *The Chemistry of Double-bonded Functional Groups* (Ed.: S. Patai), Supplement A, vol. 2, part 2, John Wiley & Sons, Chichester, **1989**, 1131–1268; c) K.-P. Zeller: "*Pentafulvene*" in: *Houben-Weyl, Methoden der organischen Chemie*, vol. 5/2c, Georg Thieme Verlag, Stuttgart, **1985**, 504–684.
[16] a) S. D. Larsen, P. A. Grieco, *J. Am. Chem. Soc.* **1985**, *107*, 1768–1769; b) L. R. Domingo, *J. Org. Chem.* **2001**, *66*, 3211–3214.
[17] E. Sturm, K. Hafner, *Angew. Chem.* **1964**, *76*, 862–863; *Angew. Chem. Int. Ed. Engl.* **1964**, *3*, 749.
[18] a) J. Thiele, *Ber. Dtsch. Chem. Ges.* **1900**, *33*, 666–673; b) K. J. Stone, R. D. Little, *J. Org. Chem.* **1984**, *49*, 1849–1853.
[19] a) K. Hafner, K. H. Vöpel, G. Ploss, C. König, *Justus Liebigs Ann. Chem.* **1963**, *661*, 52–75; b) K. Hafner, K. H. Vöpel, G. Ploss, C. König, *Org. Synthesis Coll. Vol.* **1973**, *5*, 431–433.
[20] A. Kreutzberger, K. Kolter, *Liebigs Ann. Chem.* **1986**, 374–379.
[21] T. Maier, H. Bredereck, W. Kantlehner, *Synthesis* **1979**, 690.
[22] Transamination reactions are known for fulvenes of type **C**. Cf.: K. Hafner, G. Schulz, K. Wagner, *Justus Liebigs Ann. Chem.* **1964**, *678*, 39–53.
[23] a) M. Sato, S. Ebine, J. Tsunetsugu, *Tetrahedron Lett.* **1974**, *15*, 2769–2770; b) S. Stournas, E.-A. I. Heiba, R. M. Dessau (Mobil Oil Corp.), *US Patent* 3706541, **1972**.
[24] a) D. Seebach, H.-O. Kalinowski, B. Bastani, G. Crass, H. Daum, H. Dörr, N. P. DuPreez, V. Ehrig, W. Langer, C. Nüssler, H.-A. Oei, M. Schmidt, *Helv. Chim. Acta* **1977**, *60*, 301–325; b) D. Enders, P. Fey, H. Kipphardt, *Org. Synth.* **1987**, *65*, 173–182; c) D. Enders, M. Klatt, *Synthesis* **1996**, 1403–1418.
[25] a) S. Harder, *Coord. Chem. Rev.* **1998**, *176*, 17–66; b) P. Jutzi, N. Burford, *Chem. Rev.* **1999**, *99*, 969–990.
[26] B. Steinmetz, W. A. Schenk, *Organometallics* **1999**, *18*, 943–946.
[27] a) R. Sanders, U. T. Mueller-Westerhoff, *J. Organomet. Chem.* **1996**, *512*, 219–224; b) L. Bednarik, E. Neuse, *J. Organomet. Chem.* **1979**, *168*, C8–C12; c) M. D. Rausch, E. O. Fischer, H. Grubert, *J. Am. Chem. Soc.* **1960**, *82*, 76–82.
[28] W. G. Kofron, L. M. Baclawski, *J. Org. Chem.* **1976**, *41*, 1879–1880.
[29] For an extensive discussion see: G. Wagner, R. Herrmann, "*Chiral Ferrocene Derivatives. An Introduction*" in: *Ferrocenes* (Eds.: A. Togni, T. Hayashi), VCH Verlagsgesellschaft, Weinheim, Germany, **1995**.
[30] K. Schlögl, *Top. Curr. Stereochem.* **1967**, *1*, 39–91.
[31] a) V. Prelog, G. Helmchen, *Angew. Chem.* **1982**, *94*, 614–631; *Angew. Chem. Int. Ed. Engl.* **1982**, *21*, 567–583; b) R. S. Cahn, C. K. Ingold, V. Prelog, *Angew. Chem.* **1966**, *78*, 413–447; *Angew. Chem. Int. Ed. Engl.* **1966**, *5*, 385–415.
[32] If both planar and central chirality exist in a molecule, the descriptor of the central chirality is conventionally given first. A subscript P is often added to the descriptor of the planar chirality for the sake of clarity.
[33] a) G. S. Lal, G. P. Pez, R. G. Syvret, *Chem. Rev.* **1996**, *96*, 1737–1755; b) T. Umemoto, M. Nagayoshi, K. Adachi, G. Tomizawa, *J. Org. Chem.* **1998**, *63*, 3379–3385; c) R. E. Banks, *J. Fluorine Chem.* **1998**, *87*, 1–17.
[34] E. Differding: "*N-Fluoro-N-(phenylsulfonyl)benzenesulfonamide*" in: *Encyclopedia of Reagents for Organic Synthesis*, vol. 4 (Ed.-in-Chief: L. A. Paquette), John Wiley & Sons, Chichester, **1995**, 2563–2564.
[35] a) S. O. Grim, W. McFarlane, E. F. Davidoff, *J. Org. Chem.* **1967**, *32*, 781–784; b) S. O. Grim, R. P. Molenda, J. D. Mitchell, *J. Org. Chem.* **1980**, *45*, 250–252.

 © 2005 Wiley-VCH Verlag GmbH & Co. KGaA, Weinheim

[36] a) A. Tamaki, J. K. Kochi, *J. Organomet. Chem.* **1973**, *61*, 441–450; b) B. J. Gregory, C. K. Ingold, *J. Chem. Soc. B* **1969**, 276–289.
[37] The geometric data for this complex are of no interest in the given context. See also comments in the Experimental Section and deposition with the Cambridge Crystallographic Data Centre.
[38] A. L. Spek, *Acta Crystallogr., Sect. A* **1990**, *46*, C34.
[39] a) D. Lednicer, J. K. Lindsay, C. R. Hauser, *J. Org. Chem.* **1958**, *23*, 653–655; b) D. Lednicer, C. R. Hauser, *Org. Synth.* **1960**, *40*, 45–46.
[40] Three pertinent observations shall be cited; i) Methyl and chloro derivatives of the same parent compound may be isostructural; e.g.: S. George, A. Nangia, M. Muthuraman, M. Bagieu-Beucher, R. Masse, J.-F. Nicoud, *New J. Chem.* **2001**, *25*, 1520–1527 ii) *p*-chlorotoluene can show orientational disorder as a guest molecule; e.g.: K. Reichenbächer, H. I. Süss, H. Stoeckli-Evans, S. Bracco, P. Sozzani, E. Weber, J. Hulliger, *New J. Chem.* **2004**, *28*, 393–397; iii) The same holds true for *p*-chlorotoluene acting as a ligand: F. Rose-Munch, E. Rose, A. Semra, C. Bois, *J. Organomet. Chem.* **1989**, *363*, 103–121.
[41] a) G. E. Herberich, U. Englert, D. Pubanz, *J. Organomet. Chem.* **1993**, *459*, 1–9; b) G. E. Herberich, U. J. Jansen, *Organometallics* **1995**, *14*, 834–841.
[42] D. D. Perrin, W. L. F. Armarego, *Purification of Laboratory Chemicals*, 3rd ed., Pergamon Press Ltd., Oxford, **1988**.
[43] a) J. W. Akitt: "*Hydrogen and its Isotopes*" in: *Multinuclear NMR* (Ed.: J. Mason), Plenum Press, New York, **1987**, 171–187; b) C. Brevard, J. P. Kintzinger: "*Deuterium and Tritium*" in: *NMR and the Periodic Table* (Eds.: R. K. Harris, B. E Mann), Academic Press, London, **1978**, 107–128.
[44] B. Wrackmeyer, H. Nöth: "*Nuclear Magnetic Resonance Spectroscopy of Boron Compounds*" in: *NMR–Basic Principles and Progress*, vol. 14 (Eds.: P. Diehl, E. Fluck, R. Kosfeld), Springer-Verlag, Berlin, **1978**.
[45] See Supplementary Material for: A. Brettschneider-Hurley, C. H. Winter, *J. Am. Chem. Soc.* **1994**, *116*, 6468–6469.
[46] J. De Meulenaer, H. Tompa, *Acta Crystallogr.* **1965**, *19*, 1014–1018.
[47] A. C. T. North, D. C. Phillips, F. S. Mathews, *Acta Crystallogr., Sect. A* **1968**, *24*, 351–359.
[48] G. M. Sheldrick, *SHELXS-97, Program for Crystal Structure Solution*, University of Göttingen, Göttingen, Germany, **1997**.
[49] G. M. Sheldrick, *SHELXL-97, Program for Crystal Structure Refinement*, University of Göttingen, Göttingen, **1997**.

Received: July 29, 2005
Published Online: November 9, 2005

 © 2005 Wiley-VCH Verlag GmbH & Co. KGaA, Weinheim

DOI: 10.1002/ejic.200500714

Syntheses, Structure and Intercalation Properties of Low-Dimensional Phenylphosphonates, $A(HO_3PC_6H_5)(H_2O_3PC_6H_5)$ (A = Alkali Metal, NH_4 and Tl)

Koya Prabhakara Rao[a] and Kanamaluru Vidyasagar*[a]

Keywords: Phenylphosphonates / Organic-inorganic hybrid composites / X-ray diffraction / Layered compounds / Intercalation

Seven new low-dimensional phenylphosphonates, $A(HO_3PC_6H_5)(H_2O_3PC_6H_5)$ [A = Li (**1**), Na (**2**), K (**3**), Rb (**4**), Cs (**5**), NH_4 (**6**) and Tl (**7**)], have been synthesized and characterized by X-ray diffraction, spectroscopic and thermal studies. They crystallize in triclinic unit cells with two formula units and have approximately planar arrangement of A^+ ions, coordinated to oxygen atoms of phenylphosphonates, on both sides. Compounds **1** and **6** are one-dimensional, whereas others are two-dimensional. All of them undergo room-temperature intercalation reactions with primary *n*-alkylamines and ammonia. Single crystal X-ray structures of compounds **1**, **2** and **6** have been determined.
(© Wiley-VCH Verlag GmbH & Co. KGaA, 69451 Weinheim, Germany, 2005)

Introduction

Metal organophosphonates are a class of organic-inorganic hybrid materials, in which the organophosphonate groups are covalently bonded to the metal inorganic backbone. In the recent past, there has been a renewed interest and activity in the research arena of metal organophosphonates,[1–6] mainly due to their varied compositions, structural diversity and potential applications[7–11] like sorbents, ion-exchangers, sensors, and catalysts. The expansion[1–6,12,13] of metal organophosphonate chemistry includes phosphonates and diphosphonates of *s*-, *p*-, *d*- and *f*-block metals. The structures reported for these compounds could be broadly classified into two categories, namely, zero-dimensional types[14] such as mononuclear and complex molecular clusters and extended framework types[15] of one-, two- and three-dimensional networks. Mostly low-dimensional, namely chain and layered, structures are observed for the compounds of second type, due to the segregation of hydrophobic regions of organic moieties from the rest of the framework.

The solid-state chemistry of phenylphosphonates constitutes a significant portion of this research area. Reported are many investigations about the synthesis, structures and properties of di-, tri-, tetra-, penta-, and hexavalent metal phenylphosphonates[16–21] with extended frameworks, such as $Ca(HO_3PPh)_2$, $Ca(HO_3PPh)_2{\cdot}2H_2O$, $Pb(HO_3PPh)_2$, $Zn(O_3PPh){\cdot}H_2O$, α- and β- forms of $Al(HO_3PPh)(O_3PPh){\cdot}H_2O$, $Al(HO_3PPh)_3{\cdot}H_2O$, $Al_2(O_3PPh)_3{\cdot}2H_2O$, $Mn(HO_3PPh)(O_3PPh)$, $Fe(HO_3PPh)(O_3PPh){\cdot}H_2O$, $HFe(HO_3PPh)_4$, $La(HO_3PPh)(O_3PPh)$, $Zr(O_3PPh)_2$, $Th(O_3PPh)_2$, $[VO(O_3PPh)]{\cdot}2H_2O$, $[MoO_2(O_3PPh)]{\cdot}H_2O$, $[UO_2(O_3PPh)]{\cdot}0.7H_2O$, $[UO_2(HO_3PPh)_2(H_2O)]_2{\cdot}8H_2O$, $[(UO_2)_3(HO_3PPh)_2(O_3PPh)_2]{\cdot}H_2O$. These examples illustrate the structural diversity and the compositional variations with different ratios of metal to phenylphosphonates, mono- and di-anionic forms of phenylphosphonic acid and inclusion of O^{2-} and/or H_2O in the coordination sphere of metals. One noteworthy feature of all reported phenylphosphonates is their insolubility in water that enabled their isolation as precipitates from aqueous solutions. Most of these compounds, especially those with 1:1 and 1:2 ratios of metal to phenylphosphonic acid content, are lamellar phases. They contain layers of metal atoms coordinated to oxygen atoms of phosphonate groups and, in a few cases, additionally to O^{2-} and/or H_2O as well. The hydrophobic phenyl groups of phosphonates protrude into the interlayer region, on both sides of the inorganic metal layer.

Intercalation of metal phenylphosphonates is well studied[16b,17b–17f] and important from the point of view of sensors.[9] For example, the lamellar 1:1 divalent metal phenylphosphonates, such as $Zn(O_3PPh){\cdot}H_2O$, are known to intercalate ammonia and amines, which occupy the interlayer region and coordinate to the metal. This intercalation involves Lewis acid–base reaction that brings a change in the coordination sphere of the metal. The dependence of interlayer distance of intercalates on the chain length of the intercalated *n*-alkyl primary amine, structural elucidation of intercalates and stereo selectivity towards primary amines for intercalation have been reported.[17b–17f]

[a] Department of Chemistry,
Indian Institute of Technology Madras,
Chennai, 600036, India
E-mail: kvsagar@iitm.ac.in

 © 2005 Wiley-VCH Verlag GmbH & Co. KGaA, Weinheim

All 1:2 tri- and divalent metal phenylphosphonates, such as $La(HO_3PPh)(O_3PPh)$[18c] and $Ca(HO_3PPh)_2{\cdot}2H_2O$,[16b] have similar lamellar structure of $Zr(O_3PPh)_2$,[19b] with different coordinations for metals. Lewis acid-base intercalation of primary amines has been reported for only one compound, $Ca(HO_3PPh)_2{\cdot}2H_2O$. These compounds contain mono $(HO_3PPh)^-$ anions and are, therefore, potential solid Brönsted acids. The acid-strength would be higher for lower-valent metal phases, and the potentiality of these compounds as Brönsted-acid hosts, for intercalation of bases such as ammonia and amines, has not been investigated so far. This Brönsted acidity is distinctly different from the one reported[22] as due to functional SO_3H group of the phenyl moiety.

It is in this context that 1:2 phenylphosphonates of monovalent metals, $A(HO_3PPh)(H_2O_3PPh)$ are envisaged to be strong solid Brönsted acids that can undergo intercalation with bases. It is surprising that no structurally characterized monovalent metal phenylphosphonate has been reported so far. $Na_2(O_3PPh)$ and $Na(HO_3PPh)$ are the only two compounds of this family realized by Corbridge and Tromans,[23] who reported the powder X-ray data without any crystallographic information. In view of these observations, we undertook a study of 1:2 phenylphosphonates of alkali and thallium metals and ammonium. We report here the successful synthesis, characterization and intercalation chemistry of seven new phenylphosphonates, $A(HO_3PC_6H_5)(H_2O_3PC_6H_5)$ [A = Li (**1**), Na (**2**), K (**3**), Rb (**4**), Cs (**5**), NH_4 (**6**) and Tl (**7**)].

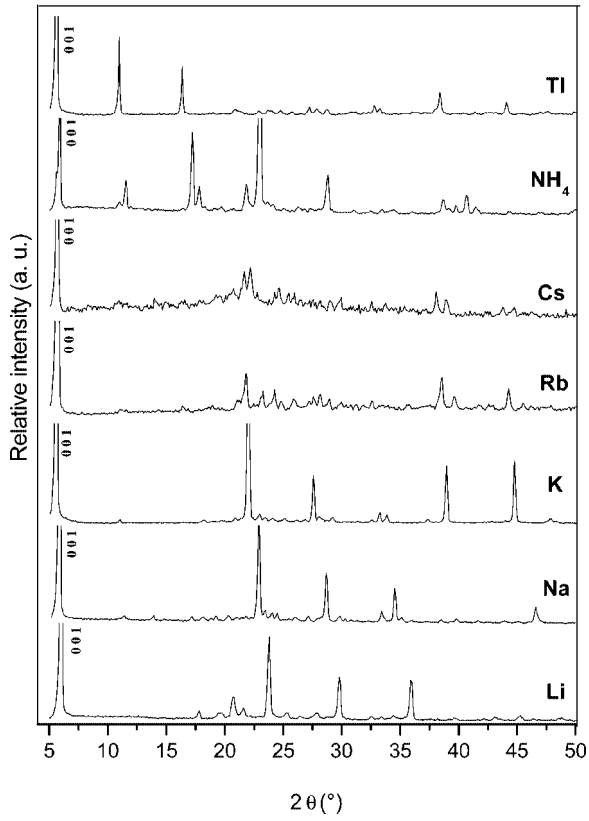

Figure 1. Powder X-ray diffraction patterns of $A(HO_3PC_6H_5)(H_2O_3PC_6H_5)$ [A = Li (**1**), Na (**2**), K (**3**), Rb (**4**), Cs (**5**), NH_4 (**6**) and Tl (**7**)] compounds.

Results and Discussion

X-Ray Diffraction and Crystal Structures: The powder X-ray diffraction (XRD) patterns (Figure 1) of all the seven $A(HO_3PC_6H_5)(H_2O_3PC_6H_5)$ compounds are, in general, similar to one another, corroborating the similarity of the values of their triclinic unit cell parameters. The 001 reflection, with the 2θ value of about 5°, is the most intense and the observed main reflections arise from a family of $\{00l\}$ planes. The values of unit cell volumes of **2**–**7** vary in accordance with the relative sizes of A ions and lithium compound **1**, however, has slightly bigger unit cell volume than sodium compound **2**. For the four structurally characterized compounds **1**, **2**, **5** and **6**, the observed powder XRD patterns agree with those simulated, using the LAZY-PULVERIX program,[24] on the basis of single-crystal X-ray structures. However, the observed relative intensities of some of the $00l$ reflections are more than those calculated, due to the preferential orientation of the crystallites. The XRD powder pattern of **2** is different from those of $Na_2(O_3PPh)$ and $Na(HO_3PPh)$.[23]

The values of the triclinic unit cell parameters of compounds **1**–**7**, though similar, show that they have five types of structures. The single-crystal X-ray data sets of compounds **1**, **2**, **5** and **6** have enabled the identification of the four types, whereas the fifth type, namely the structure of the thallium compound (**7**), could not be ascertained. Compounds **3** and **4** have the structure type of **5**. The structural and crystallographic similarities, as deduced from XRD study, of the seven phosphonates, **1**–**7** are as follows: Two formula units are present in their centrosymmetric triclinic unit cells. A^+ ions are confined approximately to *ab* plane and coordinated to oxygen atoms of phosphonates on both sides. The phenyl groups are oriented, without *interdigitation* and π-π stacking, in approximately perpendicular fashion to the *ab* planes. Thus hydrophobic regions of phenyl groups separate the *inorganic ab* planes. The observed values of bond lengths and angles of these phosphonates compare well with those reported[16–21] in the literature. The labeling Scheme followed is such that P(1) is bonded to O(1)–O(3) oxygen atoms and C(1) carbon atom of phenyl ring C(1)–C(6), whereas P(2) is similarly bonded to O(4)–O(6) and C(7) of phenyl ring C(7)–C(12).

Lithium compound (**1**) is, as shown in Figure 2, one-dimensional in nature. O(3) and O(6) form short P–O bonds of ca. 1.49 Å length. Lithium is tetrahedrally bonded to these two oxygen atoms of four [two $P(1)O_4$ and two $P(2)O_4$] phosphonate moieties. Each LiO_4 tetrahedron is connected to two such tetrahedra, through O(3)–O(6) edges, and also to phosphonate moieties, to form one dimensional chains of $Li(HO_3PC_6H_5)(H_2O_3PC_6H_5)$, along *a*-axis. These chains are apart by 8.50 Å within the *ab* plane and 14.99 Å between such planes. The other four oxygen atoms form longer P–O bonds of 1.53–1.56 Å length and have acidic

 © 2005 Wiley-VCH Verlag GmbH & Co. KGaA, Weinheim

hydrogen atoms.[18d] The hydrogen bonding between these four oxygen atoms hold the chains along *b*-axis.

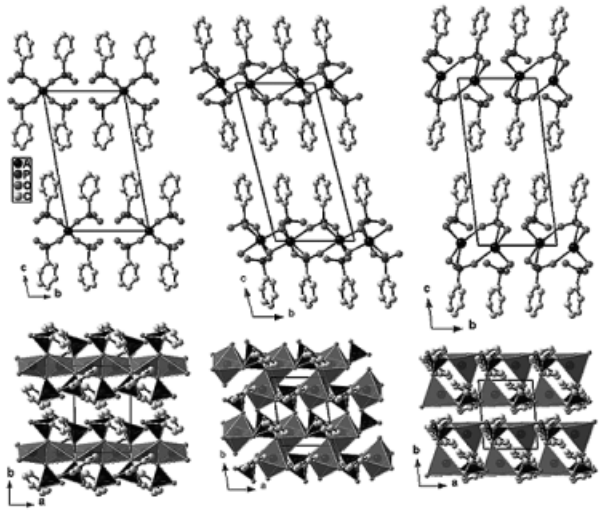

Figure 2. Unit cell of $A(HO_3PC_6H_5)(H_2O_3PC_6H_5)$ [A = Li (**1**) (left), Na (**2**) (middle) and NH_4 (**6**) (right)], viewed along the *a* axis (top: ball-stick representation) and the *c* axis (bottom: polyhedral representation).

Sodium compound (**2**) is a two-dimensional phosphonate (Figure 2). The layered framework could be conceived as being built from centrosymmetric $Na_2O_6(O_3P–C_6H_5)_4$ blocks, each of which consists of an edge-shared bioctahedral Na_2O_{10} unit, corner-connected to four phosphonates. Only five of the crystallographically distinct oxygen atoms, O(1)–O(5), are involved in octahedral coordination of sodium. Two NaO_6 octahedra share an edge, O(5)–O(5)′ to form a Na_2O_{10} unit, which links, at the O(5) and O(3) atoms, to four phosphonate moieties. These building blocks are linked to one another such that the phosphonates of one block are corner-connected to Na_2O_{10} units of another, resulting in the layered framework. Sodium atom is coordinated to oxygen atoms of six phosphonate groups, whereas the phosphonates of P(1) and P(2) are coordinated to three and two sodium atoms respectively. These $Na(HO_3PC_6H_5)$-$(H_2O_3PC_6H_5)$ layers are stacked along *c*-axis, with an interlayer distance of 15.59 Å. The three oxygen atoms, O(1), O(2) and O(4), form longer P–O bonds of 1.54–1.58 Å length and have acidic hydrogen atoms. The hydrogen bonding exists between these oxygen atoms as well as O(6).

$NH_4(HO_3PC_6H_5)(H_2O_3PC_6H_5)$ (**6**) is one-dimensional compound (Figure 2). With the cut-off distance of 3.0 Å for bonding, the nitrogen atom is found to be hydrogen-bonded, in an irregular tetrahedral fashion, to four oxygen atoms, O(1), O(2), O(3) and O(5), of four phenylphosphonate moieties. This arrangement leads to ladder-like chains, parallel to *a*-axis. The layered framework is not feasible, because the nitrogen atoms are not hydrogen-bonded to oxygen atoms of neighbouring chain in the *ab* plane, even with the higher cut-off value of 3.6 Å for bonding. These chains are apart by 7.66 Å within the plane and 16.34 Å between the planes. O(3) and O(6) form longer P–O bonds of ca. 1.56 Å length and have two acidic hydrogen atoms, H(13) and H(14), that are hydrogen-bonded to O(5) and O(2), respectively. Furthermore, O(4)–H(15) is strongly hydrogen-bonded to O(1).

The positional parameters of cesium (**5**) and ammonium (**6**) compounds are similar. However, cesium compound is two-dimensional and cesium is nine-coordinate, with the maximum value of Cs–O bond length being 3.52(2) Å. The layered framework of **5** is due to higher coordination number of cesium, which bonds additionally to oxygen atoms of those corresponding neighbouring chains in one-dimensional **6**. Compounds **3** and **4** are isostructural with the layered **5**, and potassium and rubidium are computed to be eight-coordinate. It could only be inferred that the structure type of thallium compound **7** has a similar arrangement of phosphonate moieties, which bond differently to thallium atoms in the *inorganic ab* plane. Thus the differences between the above five structure types stem from the different types of coordination of A^+ ions.

The reported 1:2 tetra-, tri- and divalent metal phenylphosphonates, with no additional O^{2-}/H_2O, have similar structural features of compounds **1**–**7**. $Zr(O_3PPh)_2$,[19b] $La(HO_3PPh)(O_3PPh)$,[18d] $Mn(HO_3PPh)(O_3PPh)$,[18b] $A(HO_3PPh)_2$ (A = Ca, Sr, Ba, Pb)[16a–16e] and the compounds **1**–**7** are the only 1:2 metal phenylphosphonates, for which the unit cell parameters have been determined from either single-crystal X-ray data or structural elucidation. Similar unit cell lengths of (5.36–6.16) Å × (7.65–10.215) Å are due to analogous planar arrangement of A atoms. The different types of coordination of A atoms and stacking of planes of A atoms are responsible for the variations in the third axis length and unit cell angles.

Spectroscopic and Thermogravimetric Data: Infrared spectra of compounds **2** and **6** are presented in Figure 3. The C–H stretching vibrations of the phenyl ring in the region 3090–3000 cm^{-1}, the aromatic C=C stretching vibrations at 1438 cm^{-1}, the peaks at 692 and 745 cm^{-1} representing the out-of-plane bending of the mono substituted phenyl ring, the peak at 2376 cm^{-1}, characteristic of $PhPO_3H$ group, the peak at 1594 cm^{-1} due to phenyl group stretching, the P–O stretching vibrations in the region 1200–1000 cm^{-1} and the O–P–O bending vibrations in the region 540–410 cm^{-1}, are the common features[18a,21a] observed in the infrared spectra of the seven compounds, **1**–**7**. The infrared spectrum of ammonium compound (**6**), shows two additional peaks at 3240 and 1401 cm^{-1} corresponding to the stretching and bending vibrations of the ammonium ion.[25] All these compounds, as illustrated in the solid-state ^{13}C and ^{31}P spectra (Figure 4) of **2**, show four ^{13}C signals[16b] between 140.0–120.0 ppm, corroborating the presence of aromatic carbon atoms and three ^{31}P signals[18a] between –1.2 and 7.8 ppm. Thermogravimetric analysis revealed, as illustrated with the case of **2** in the Figure 5, that all compounds **1**–**7** are stable up to about 200 °C and then undergo weight losses of 51.5%, 48.5%, 46.0%, 42.0%, 37.0%, 71.1% and 32.50%, respectively, in the temperature range 200–700 °C in four or five steps. These values agree with those calculated for $AP_2O_{5.5}$ as the products of decom-

 © 2005 Wiley-VCH Verlag GmbH & Co. KGaA, Weinheim

position for alkali and thallium metal compounds. All of them undergo further decomposition above 700 °C.

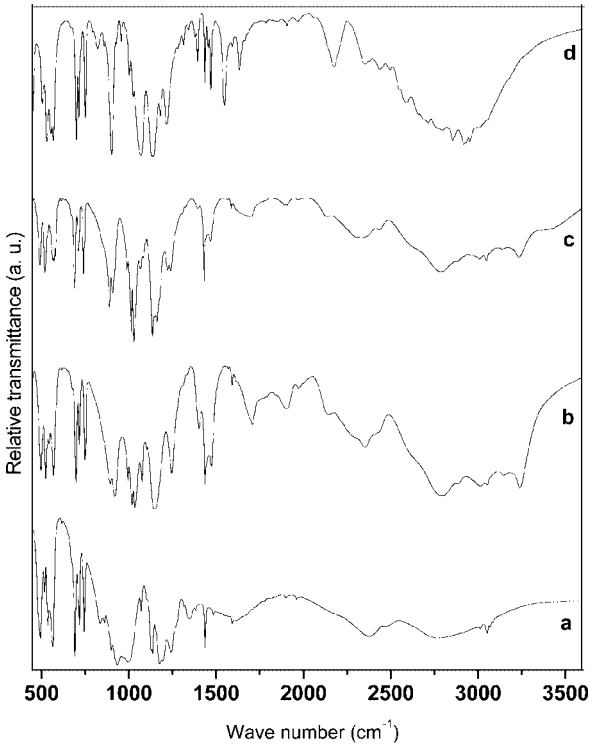

Figure 3. Infrared spectra of (a) sodium (**2**) and (b) ammonium (**6**) compounds and the intercalates of sodium compound, (c) **2**·$(NH_3)_{1.2}$ and (d) **2**·$(C_8H_{17}NH_2)_{1.5}$.

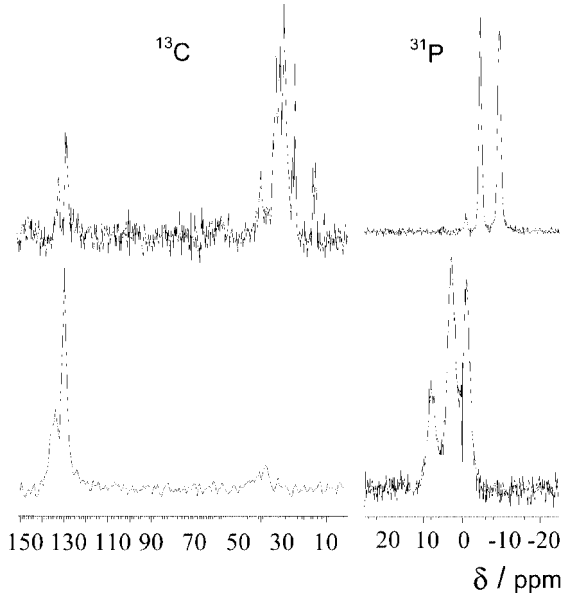

Figure 4. Solid-state ^{13}C (left) and ^{31}P (right) NMR spectra of sodium (**2**) compound (bottom) and it's intercalate **2**·$(C_8H_{17}NH_2)_{1.5}$ (top).

Intercalation Reactions: These seven phosphonates, **1**–**7** are solid Brönsted acids with a porous region between the *inorganic ab* planes. Therefore, they have been investigated from the point of view of Brönsted acid–base intercalation

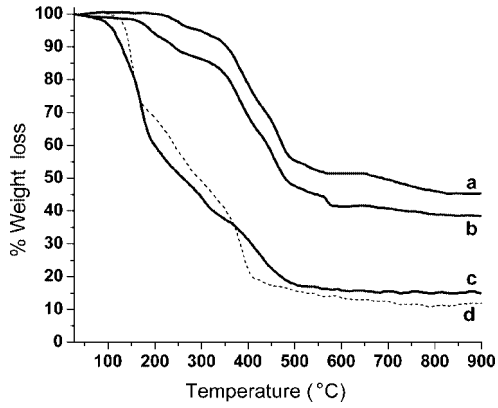

Figure 5. Thermogravimetric curves of (a) sodium (**2**) compound and its intercalates, (b) **2**·$(NH_3)_{1.2}$, (c) **2**·$(C_8H_{17}NH_2)_{1.5}$ and (d) **2**·$(C_8H_{17}NH_2)_{4.1}$.

reactions with ammonia and primary *n*-alkylamines, $CH_3(CH_2)_{n-1}NH_2$ (n = 4–9, 12, 16, 18). These reactions, as determined from chemical analysis and powder XRD, spectroscopic and thermal studies, turned out to be successful.

The optimum conditions, given in experimental section, for the first method of intercalation processes have been realized from the results of several trials, under different conditions, of intercalation reaction of sodium compound with *n*-octylamine. A variation of molar ratio of *n*-octylamine and sodium phosphonate **2**, from 2:1 to 3:1 to 4:1, led to intercalates, **2**·$(C_8H_{17}NH_2)_x$ with the corresponding x values of 0.9, 1.5 and 1.5, showing that the maximum intercalation at room temperature could be achieved with the reactant molar ratio of 4:1. There was no significant increase in the values of x, when similar reactions were carried out under reflux conditions at 70–80 °C. Similar attempts under solvothermal conditions, by heating reactant mixtures with 4 mL of *n*-hexane solvent, at 170 °C over a period of 2 days, resulted in only polycrystalline intercalates without any increase in the values of x. The second method involving neat liquid amines at room temperature is confined to $CH_3(CH_2)_{n-1}NH_2$ (n = 4–9,12) only.

The relevant data of the intercalates, **2**·$[CH_3(CH_2)_{n-1}NH_2]_x$ and **1**–**7**·$(C_8H_{17}NH_2)_x$ obtained by the first method, are presented in Table 1. The values of x range from 0.5 to 4.0 and do not seem to show any systematic trend with either n or A. The powder XRD patterns of **2**·$[CH_3(CH_2)_{n-1}NH_2]_x$ intercalates, as shown for a few selected cases in Figure 6, contain moderate to prominent reflections at low 2θ values of 2–5° and no significant reflections with 2θ of >40°. The first reflection is found to be doubled in a few cases such as **2**·$[CH_3(CH_2)_{11}NH_2]_x$. It is noteworthy that the powder XRD patterns of these intercalates, do not undergo any change, even when the samples were heated in open air at 40–50 °C for 12 h. The d value of the first reflection is considered to be associated with the distance between the *ab* planes. This is found to be higher than that observed for the parent phase **2**, due to incorporation of the amine in the porous region, perpendicularly to the inorganic *ab* planes, with the alkyl chains aligned out of the

 © 2005 Wiley-VCH Verlag GmbH & Co. KGaA, Weinheim

perpendicular. These intercalates, unlike the parent **2**, do not show higher order 00*l* reflections prominently. The *d* value increases with *n* except in the case of nonylamine intercalate. The values of *d* do not show any systematic increase with *n*, probably due to the presence of *gauche* and *trans* conformations of the alkyl chains of the amines in different proportions. In general, these powder XRD patterns confirm the crystalline nature of intercalates and the topotactic intercalation of the amines. The powder XRD patterns of **1**–**7**·$(C_8H_{17}NH_2)_x$ intercalates also contain moderate to prominent reflections at low 2θ values of 2–5° and the values of *d* are higher than those in the parent phases. However, the increase in the *d* values is not systematic with respect to both A and *x*. Structural elucidation of these intercalates would reveal the placement of the intercalated amines and probably explain this lack of systematic variation of *d* with *n*, *x* and A. There are no structurally characterized Brönsted acid–base intercalates of this type reported, for a comparison. However, structurally characterized Lewis acid–base intercalates, $Zn(O_3PPh)(RNH_2)$ (R = C_3H_9, C_4H_{11}, C_5H_{13}), were reported[17b] to exhibit similar nonsystematic behavior, due to coordination of the intercalated amine to the metal.

Table 1. Interplanar distance (*d*), number (*x*) of mol of amine intercalated of the **2**·$[CH_3(CH_2)_{n-1}NH_2]_x$ (top) and **1**–**7**·$(C_8H_{17}NH_2)_x$ (bottom) intercalates.

n	–	4	5	6	7	8	9	12	16	18
x	0.0	0.5	0.9	1.2	1.7	1.5	1.5	2.0	1.7	1.9
d [Å]	15.6	17.7	19.0	19.6	20.9	21.2	20.3	25.8	27.8	28.5
A	Li	Na	K	Rb	Cs	Tl	NH_4			
x	2.7	1.5	2.1	1.6	1.9	2.9	4.0			
d [Å]	18.7	21.2	21.0	21.3	18.8	19.2	19.2			

The infrared spectra (Figure 3) of intercalates contain, in addition to all the features of the infrared spectrum of parent phase **2**, peaks in the region 3100–2700 cm^{-1} attributed to N–H and C–H stretching vibrations[16b] of the amine molecules. The CH_2 bending bands observed around 1437 cm^{-1} and 1470 cm^{-1} are ascribed[26] to *gauche* and *trans* conformations of alkyl chains of amines, respectively. The relative intensities of these two bands indicate that the alkyl chains, in the intercalates containing C_4–C_8 and C_9–C_{18} amines, are predominantly in *gauche* and *trans* conformations, respectively. The shift of N–H stretching vibrations towards lower frequencies suggests that the amine molecules are protonated[25] and electrostatically bonded to oxygen atoms of phosphonate moieties. The solid-state ^{13}C NMR spectra (Figure 4) of the intercalates show signals between 140.0–125.0 ppm and also multiple signals in the region 45.0–15.0 ppm, indicating the presence of both aromatic carbon atoms of the phenyl group and the aliphatic carbon atoms of the amines, respectively. The ^{13}C signals of alkyl carbon atoms, though not fully resolved, are in order of C_1, C_2, C_3,...C_n. The ^{31}P NMR spectra consist of three signals between –0.83 and –9.37 ppm, with up-field shift

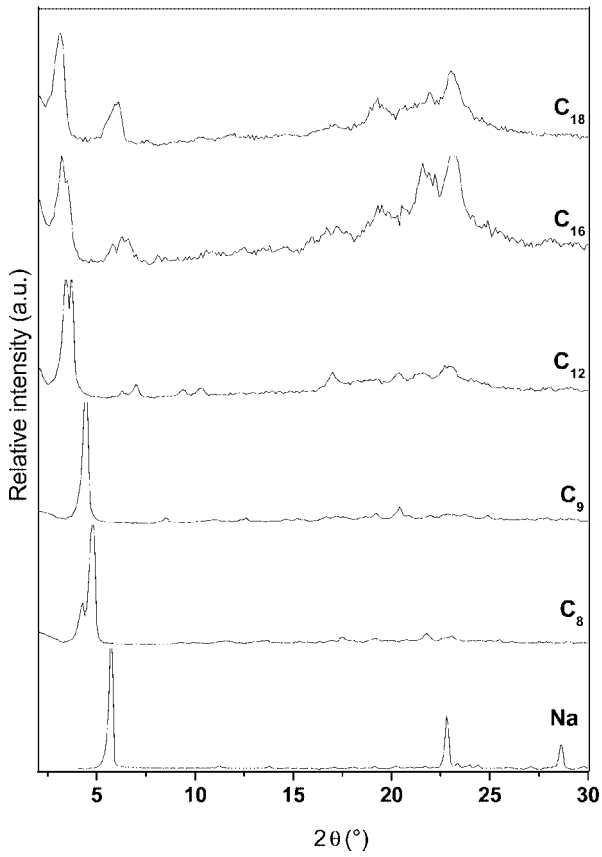

Figure 6. Powder X-ray diffraction patterns of sodium (**2**) compound and its intercalates, **2**·$[CH_3(CH_2)_{n-1}NH_2]_x$ (*n* = 8, 9, 12, 16 and 18).

compared to parent phases. Thermogravimetric analysis of a few selected intercalates revealed that they undergo more percentage of decomposition than the parent phases. For example, the total decomposition of 84% for **2**·$(C_8H_{17}NH_2)_x$ (Figure 5) starts at 70 °C and is completed by 600 °C. The first two stages of weight loss of 36% in the 70–200 °C range are attributable to the loss of intercalated amine, 1.5 mol of $C_8H_{17}NH_2$. The spectral and thermal features of other intercalates are similar to those of the sodium compound.

The second method of intercalation is compared with the first one, in terms of the compositions, the powder XRD patterns and spectral features of the corresponding intercalates. The *x* values of **2**·$[CH_3(CH_2)_{n-1}NH_2]_x$ are 1.5, 2.1, 2.0, 1.4, 4.1, 2.4, 2.5 for *n* = 4–9 and 12, respectively. Similarly the *x* values of **1**–**7**·$(C_8H_{17}NH_2)_x$ are 2.8, 4.1, 2.7, 5.0, 5.0, 3.2, 4.3, respectively. In general, the extent of intercalation, as corroborated by thermogavimetric study (Figure 5), is larger in the second method. The powder XRD patterns revealed no increase in the *d* values with increase in *x* values. There are no significant changes in their infrared and solid-state NMR spectra. The maximum amount of intercalation of primary amines reported is about two molecules per formula unit of $Ca(HO_3PPh)_2{\cdot}2H_2O$[16b] and 1:1 phenylphosphonates.[17b–17f] Contrastingly, the extent of intercalation in the present 1:2 phenylphosphonates **1**–**7** is as high

 © 2005 Wiley-VCH Verlag GmbH & Co. KGaA, Weinheim

as five molecules of amine per formula unit. This could be attributed to the Brönsted acidity of the compounds and thus intercalates with $x > 3$ and $x \leq 3$ values could be represented as $CH_3(CH_2)_{n-1}NH_3]_3[CH_3(CH_2)_{n-1}NH_2]_{x-3}$-$[A(O_3PC_6H_5)_2]$ and $[CH_3(CH_2)_{n-1}NH_3]_x[AH_{3-x}(O_3PC_6H_5)_2]$, respectively. Thus the amine upto the value of $x = 3$ is present as RNH_3^+ ions, whereas the amine in excess of $x = 3$ is present as RNH_2, held together by van der Waals forces in the lattice.

The success and extent of ammonia intercalation in the intercalates, **1**–**7**·$(NH_3)_x$ have been determined from infrared spectra and the analysis of carbon and nitrogen contents. The infrared spectra contain two peaks at 3240 and 1450 cm^{-1} corresponding to the stretching and bending vibrations of the ammonium ion.[17e] The x values of **1**–**7**·$(NH_3)_x$ are 2.0, 1.2, 1.1, 1.5, 1.7, 2.3 and 2.3, respectively, and indicate no systematic variation with A. Thus these intercalates could be represented as $[NH_4]_x[AH_{3-x}$-$(O_3PC_6H_5)_2]$. Some of the reflections in the powder XRD patterns of ammonia intercalates are more intense than those in the parent phases. **2**·$(NH_3)_{1.2}$, unlike the parent phase **2**, decomposes even below 200 °C and shows higher weight loss (Figure 5). The total decomposition of 59% occurs in the 160–700 °C range and the weight loss below 200 °C is probably due to the loss of intercalated ammonia.

The **2**·$(NH_3)_{1.2}$ intercalate undergoes deintercalation, on heating. The success of deintercalation is proved by CHN analysis and absence of vibrational frequencies of NH_4^+ in the infrared spectrum of deintercalate. Moreover, its powder pattern is the same as that of parent phenylphosphonate **2**, showing that the process of intercalation and deintercalation is reversible and topotactic. This process of deintercalation is probably true for other ammonia intercalates of this study.

$Zn(O_3PPh)$ and $[UO_2(HO_3PPh)_2(H_2O)]_2{\cdot}8H_2O$ have been reported[9,21c] to be sensors and proton conductors, due to their intercalation and Brönsted acidic properties, respectively. All the seven title compounds **1**–**7** exhibit both these properties and could be potentially useful as sensors and proton conductors. A similar study of phenylarsonate analogues has revealed interesting structural variations, which we would report elsewhere.

Concluding Remarks

A series of seven, new low-dimensional phenylphosphonates, $A(HO_3PC_6H_5)(H_2O_3PC_6H_5)$ (A = alkali metal, NH_4 and Tl) have been synthesized and characterized by X-ray diffraction and spectroscopic studies. Lithium and ammonium compounds are one-dimensional in nature, whereas others are layered compounds. These compounds are solid Brönsted acids and undergo room-temperature intercalation reactions with primary *n*-alkylamines and ammonia. The deintercalation of ammonia occurs on heating.

Experimental Section

Synthesis: The high-purity chemicals, A_2CO_3 [A = Li, Na, K, NH_4 (SD Fine, India), Rb, Cs and Tl (Aldrich)] carbonates, phenylphosphonic acid, $C_6H_5PO_3H_2$ (Fluka) and primary *n*-alkylamines, $CH_3(CH_2)_{n-1}NH_2$ (n = 4–9,12,16,18) (Fluka) were used, as purchased, for the synthesis.

$A(HO_3PC_6H_5)(H_2O_3PC_6H_5)$ [A = Li (**1**), Na (**2**), K (**3**), Rb (**4**), Cs (**5**), NH_4 (**6**) and Tl (**7**)] compounds were synthesized, on the scale of 1–2 grams, by evaporating aqueous solutions of stoichiometric reactant mixtures of phenylphosphonic acid and appropriate A_2CO_3 carbonate. Slow evaporation, at room temperature, led to the formation of compounds as colourless flaky crystals. However, evaporation on a steam bath yielded products in polycrystalline form. In all the cases, the yields were almost quantitative. These seven compounds were ascertained to be pure from the analysis of their CHN content, using elemental analyzer, Perkin–Elmer series 11 Model. $C_{12}H_{13}LiO_6P_2$ (**1**) (322.10): calcd. C 44.75, H 4.07; found C 44.29, H 4.11. $C_{12}H_{13}NaO_6P_2$ (**2**) (338.15): calcd. C 42.62, H 3.88; found C 42.75, H 4.04. $KP_2O_6C_{12}H_{13}$(**3**) (354.26): calcd. C 40.70, H 3.70; found C 40.59, H 3.77. $C_{12}H_{13}O_6P_2Rb$ (**4**) (400.63): calcd. C 36.00, H 3.27; found C 36.23, H 3.21. $C_{12}H_{13}CsO_6P_2$ (**5**) (448.06): calcd. C 32.17, H 2.90; found C 32.47, H 2.97. $C_{12}H_{17}NO_6P_2$ (**6**) (333.21): calcd. C 43.20, H 5.14, N 4.20; found C 43.70, H 4.89, N 4.50. $C_{12}H_{13}O_6P_2Tl$ (**7**) (519.56): calcd. C 27.74, H 2.52; found C 27.45, H 2.46.

Intercalation Reactions: Intercalation reactions of *n*-alkylamines with the water-soluble phosphonates, **1**–**7** were carried out under nonaqueous conditions by two methods at room temperature. In the first method, a 4:1 molar reactant mixture of *n*-alkylamine and phosphonate (**1**–**7**), along with 15 mL of *n*-hexane, was stirred for 1.5 days. The solid products were in the form of waxy material. In the second method, the phosphonate (**1**–**7**) was added to excess of liquid *n*-alkylamine ($\approx$ 1:10 molar ratio) and the solid immediately swelled, with the evolution of heat. The reaction mixture was left undisturbed for 7 days. The waxy solid products, in both methods of intercalation reactions, turned out to be dry powders after filtration, washing with *n*-hexane and then air drying. Intercalation of ammonia was achieved by passing ammonia gas for 2 h, over solid phosphonates (**1**–**7**). In summary, all these trials pertain to intercalation of nine amines, $CH_3(CH_2)_{n-1}NH_2$ (n = 4–9, 12, 16, 18), into sodium compound (**2**), intercalation of *n*-octylamine into other six phosphonates and intercalation of ammonia into all seven phosphonates. The amount of intercalated amine/ammonia was determined from the analysis of the carbon and nitrogen contents of the solid intercalates, **2**·$[CH_3(CH_2)_{n-1}NH_2]_x$, **1**–**7**·$(C_8H_{17}NH_2)_x$, and **1**–**7**·$(NH_3)_x$.

Ammonia Deintercalation: Ammonia deintercalation of sodium compound intercalate, **2**·$(NH_3)_{1.2}$ was carried out by heating the sample in air-oven at 170 °C over a period of 12 h.

X-Ray Diffraction and Crystal Structure: The powder X-ray diffraction (XRD) patterns of the compounds **1**–**7** and their intercalation products were recorded on XD-D1 X-ray diffractometer, Shimadzu, using Cu-K_α (λ = 1.5406 Å) radiation. Thin plate-like single crystals, suitable for X-ray diffraction, were selected and mounted with glue, on thin glass fibers in the case of compounds **2** and **4** and in glass capillaries along with the mother liquor, for other five compounds. The X-ray data were gathered successfully from the crystals of only four compounds, **1**, **2**, **5** and **6**, at 25 °C, on an ENRAF-NONIUS CAD4 automated four-circle diffractometer, by the standard procedures involving ω-2θ scan techniques. There was no decay of crystals during X-ray data collection. Empirical absorption corrections, based on psi-scans, were applied to the data sets of **1** and **2** only. In the case of **5** and **6**, these corrections were not applied because of abnormal shape and bigger size of the crystals employed. These data sets were reduced by routine computa-

 © 2005 Wiley-VCH Verlag GmbH & Co. KGaA, Weinheim

Table 2. Pertinent crystallographic data for $A(HO_3PC_6H_5)(H_2O_3PC_6H_5)$ [A = Li (**1**), Na (**2**), NH_4 (**6**)] compounds.

Compound	**1**	**2**	**6**
Formula	$C_{12}H_{13}LiO_6P_2$	$C_{12}H_{13}NaO_6P_2$	$C_{12}H_{17}NO_6P_2$
Formula weight	322.10	338.15	333.21
Crystal system	triclinic	triclinic	triclinic
a [Å]	5.4561(8)	5.754(1)	6.036(9)
b [Å]	8.638(1)	7.904(2)	7.732(9)
c [Å]	15.235(3)	16.173(3)	16.61(1)
α [°]	100.26(2)	103.41(1)	96.43(8)
β [°]	91.18(2)	95.848(9)	97.63(8)
γ [°]	89.90(1)	97.03(1)	93.4(1)
V [Å^3]	706.4(2)	703.6(3)	761.3(2)
Space group (no.)	$P\bar{1}$ (2)	$P\bar{1}$ (2)	$P\bar{1}$ (2)
Z	2	2	2
$\rho_{calcd.}$ [g/cm^3]	1.514	1.596	1.454
λ [Å]	1.54180	0.71073	0.71073
μ [mm^{-1}]	3.023	0.363	0.311
Total reflections	2885	2754	2947
Independent reflections	2590	2481	2662
R[a]	0.0446	0.0564	0.0618
R_w[b]	0.1255	0.1378	0.1243

[a] $R = \Sigma||F_o| - |F_c||/\Sigma|F_o|$. [b] $R_w = [\Sigma w(|F_o|^2 - |F_c|^2)^2/\Sigma w(|F_o|^2)^2]^{1/2}$.

tional procedures. The structure solution and refinements were carried out by the program[27] SHELXL-97 and the graphic program[28] DIAMOND was used to draw the structures. The structure solutions were obtained by direct method and all the non-hydrogen atoms were refined anisotropically. The non-hydrogen atom content in the asymmetric unit does not account for charge neutrality and thus indicates the presence of three acidic protons of two phenylphosphonic acid moieties. These acidic hydrogen atoms were located in the difference Fourier maps and refined with riding model restraints. The phenyl hydrogen atoms were introduced in the calculated positions and refined isotropically. The ammonium hydrogen atoms of compound **6** were similarly located in the difference Fourier map and refined with riding model restraints. The structure refinement proceeded smoothly for **1** and **2**. In the case of **6**, the final difference Fourier map showed no residual peak with electron density of > 1 e/Å^3 and the final R value was ca. 12%. Absorption correction, based on the isotropically refined model, was applied to the X-ray data using the program DIFABS[29] and R value had come down to ca. 6.2%. Similar absorption correction was applied to the X-ray data of cesium compound **5**. The ten peaks with electron density of > 1 e/Å^3 found in the final difference Fourier map, were ghosts. The final R value was ca. 8.6% and the crystal structure of **5** is, nevertheless, qualitatively correct. The pertinent crystallographic data of **1**, **2** and **6** are presented in Table 2. CCDC-276185 (for **1**), CCDC-276186 (for **2**) and CCDC-276187 (for **6**) contain the supplementary crystallographic data for this paper. These data can be obtained free of charge from The Cambridge Crystallographic Data Centre via www.ccdc.cam.ac.uk/data_request/cif.

For lithium compound **1**, an alternate triclinic unit cell, with a = 5.4561(8), b = 10.209(2), c = 15.235(3) Å, α = 98.03(2), β = 91.17(2), γ = 122.2(2) ° and V = 706.4(2) Å^3, is possible. However, our choice was based on the least deviation of unit cell angles from the value of 90°. The crystals of the remaining four compounds were good enough for only the determination of their triclinic unit cell parameters, listed below.

3: a = 5.861(3), b = 7.865(3), c = 16.45(1) Å, α = 96.77(4), β = 97.57(9), γ = 94.82(5)°, V = 742.7(8) Å^3.

4: a = 5.9183(5), b = 7.9212(9), c = 16.860(2) Å, α = 96.948(5), β = 93.352(2), γ = 94.519(9)°, V = 771.0(2) Å^3.

5: a = 6.16(1), b = 7.650(7), c = 16.96(2) Å, α = 97.38(7), β = 97.7(1), γ = 93.9(1)°, V = 775.5(6) Å^3.

7: a = 5.946(9), b = 7.999(3), c = 17.11(6) Å, α = 90.1(5), β = 107.6(2), γ = 99.9(2)°, V = 763(4) Å^3.

Spectroscopic Data: The infrared spectra in the range 400 to 4000 cm^{-1}, were measured with a Bruker IFS 66V FT-IR spectrometer. The samples were ground with dry KBr and pressed into transparent discs for infrared spectroscopic study. Solid-state nuclear magnetic resonance (NMR) experiments were performed with magic angle spinning (MAS) with Bruker DSX 300 and Avance 400 series spectrometers with the spinning frequency of 7.0 kHz and recycle delay times of 2 and 5 s for ^{31}P and ^{13}C, respectively. The first instrument operated at resonance frequencies of 121.5 and 75.5 MHz with the pulse lengths of 4.75 and 3.0 μs for ^{31}P and ^{13}C, respectively. Similarly resonance frequencies of 162 and 100.5 MHz with the pulse lengths of 5.0 and 5.0 μs for ^{31}P and ^{13}C, respectively, were employed in the second one. Chemical shifts were referenced to an external standard of 85% H_3PO_4 for ^{31}P and glycine for ^{13}C.

Thermal Analysis: Thermogravimetric analytical data were collected with a Netzsch STA 409C instrument. The samples were heated to 1000 °C at a rate of 10 °C per minute under a stream of nitrogen gas.

Acknowledgments

We gratefully acknowledge the financial support (Project No: 98/37/29/BRNS) received from the Board of Research in Nuclear Sciences, Government of India. We thank the Sophisticated Analytical Instrumentation Facility of our institute for single-crystal X-ray data and Sophisticated Instrument Facility of Indian Institute of Science, Bangalore for solid-state NMR spectroscopic data. We acknowledge the help of Mr. Y. Ram Sai in the isolation and structural characterization of $Na(HO_3PC_6H_5)(H_2O_3PC_6H_5)$.

[1] R. C. Finn, J. Zubieta, R. C. Haushalter, *Prog. Inorg. Chem.* **2003**, *51*, 421–601.
[2] A. Clearfield, Z. Wang, *J. Chem. Soc., Dalton Trans.* **2002**, 2937–2947.
[3] A. Clearfield, *Prog. Inorg. Chem.* **1998**, *47*, 371–510.

 © 2005 Wiley-VCH Verlag GmbH & Co. KGaA, Weinheim

[4] L. A. Vermeulen, *Prog. Inorg. Chem.* **1997**, *44*, 143–166.
[5] A. Clearfield, *Curr. Opin. Solid State Mater. Sci.* **1996**, *1*, 268–278.
[6] M. I. Khan, J. Zubieta, *Prog. Inorg. Chem.* **1995**, *43*, 1–149.
[7] F. Odobel, B. Bujoli, D. Massiot, *Chem. Mater.* **2001**, *13*, 163–173.
[8] a) L. Kullberg, A. Clearfield, *Solv. Extr. Ion Exchange* **1990**, *8*, 187–197; b) C. Y. Ortiz-Avila, C. Bhardwaj, A. Clearfield, *Inorg. Chem.* **1994**, *33*, 2499–2500.
[9] K. Aoki, L. C. Brousseau, T. E. Mallouk, *Sens. Actuators, B* **1993**, *13–14*, 703–704.
[10] a) M. C. C. Costa, R. A. W. Johnstone, D. Whittaker, *J. Mol. Catal. A: Chem.* **1998**, *129*, 79–89; b) K. Segawa, T. Ozawa, *J. Mol. Catal. A: Chem.* **1999**, *141*, 249–255.
[11] a) L. A. Vermeulen, M. E. Thomson, *Nature* **1992**, *358*, 656–658; b) G. Alberti, U. Costantino, M. Casciola, R. Vivani, A. Peraio, *Solid State Ionics* **1991**, *46*, 61–68; c) J. Benavente, F. Carrique, R. Pozas, S. Bruque, L. Moreno, M. Martinez, *Solid State Ionics* **1991**, *46*, 77–82.
[12] a) G. Huan, A. J. Jacobson, V. W. Day, *Angew. Chem. Int. Ed. Engl.* **1991**, *30*, 422–426; b) M. I. Khan, Y.-S. Lee, C. J. O'Connor, R. C. Haushalter, J. Zubieta, *J. Am. Chem. Soc.* **1994**, *116*, 4525–4526; c) S. Drumel, P. Janvier, D. Deniaud, B. Bujoli, *J. Chem. Soc., Chem. Commun.* **1995**, 1051–1052; d) C. B. A. Lima, C. Airoldi, *Int. J. Inorg. Mater.* **2001**, *3*, 907–914.
[13] a) V. Soghomonian, Q. Chen, R. C. Haushalter, J. Zubieta, *Angew. Chem. Int. Ed. Engl.* **1995**, *34*, 223–226; b) G. Alberti, F. Marmottini, S. Murcia-Mascaros, R. Vivani, *Angew. Chem. Int. Ed. Engl.* **1994**, *33*, 1594–1597; c) D. M. Poojary, B. Zhang, P. Bellinghausen, A. Clearfield, *Inorg. Chem.* **1996**, *35*, 4942–4949; d) M. P. Minimol, K. P. Rao, Y. R. Sai, K. Vidyasagar, *Proc. Indian Acad. Sci. (Chem. Sci.)* **2003**, *115*, 419–429; e) K. P. Rao, B. Vidyavathy, M. P. Minimol, K. Vidyasagar, *Inorg. Chem.* **2004**, *43*, 4610–4614.
[14] a) Y.-D. Chang, J. Salta, J. Zubieta, *Angew. Chem. Int. Ed. Engl.* **1994**, *33*, 325–327; b) Y.-D. Chang, J. Zubieta, *Inorg. Chim. Acta* **1996**, *245*, 177–198.
[15] a) K. Maeda, J. Akimato, Y. Kiyozumi, F. Mizukami, *Angew. Chem. Int. Ed. Engl.* **1995**, *34*, 1199–1200; b) W. T. A. Harrison, L. L. Dussack, A. J. Jacobson, *Inorg. Chem.* **1996**, *35*, 1461–1467; c) J. L. Bideau, C. Payen, P. Palvadeau, B. Bujoli, *Inorg. Chem.* **1994**, *33*, 4885–4890.
[16] a) A. H. Mahmoudkhani, V. Langer, *Solid State Sci.* **2001**, *3*, 519–525; b) C. B. A. Lima, C. Airoldi, *Solid State Sci.* **2002**, *4*, 1321–1329; c) A. H. Mahmoudkhani, V. Langer, L. Smrock, *Solid State Sci.* **2002**, *4*, 873–878; d) D. M. Poojary, B. Zhang, A. Cabeza, M. A. G. Aranda, S. Bruque, A. Clearfield, *J. Mater. Chem.* **1996**, *6*, 639–644; e) D. T. Tran, Y.-S. Kam, P. Y. Zavalji, S. R. J. Oliver, *Inorg. Chem.* **2003**, *42*, 2165–2172; f) G. Cao, H. Lee, V. M. Lynch, T. E. Mallouk, *Inorg. Chem.* **1988**, *27*, 2781–2785.
[17] a) J. K. Martin, P. J. Squattrito, A. Clearfield, *Inorg. Chim. Acta* **1989**, *155*, 7–9; b) D. M. Poojary, A. Clearfield, *J. Am. Chem. Soc.* **1995**, *117*, 11278–11284; c) Y. Zhang, A. Clearfield, *Inorg. Chem.* **1992**, *31*, 2821–2826; d) Y. Zhang, K. J. Scott, A. Clearfield, *Chem. Mater.* **1993**, *5*, 495–499; e) K. J. Frink, R. C. Wang, J. L. Colon, A. Clearfield, *Inorg. Chem.* **1991**, *30*, 1438–1441; f) B. Menaa, I. J. Shannon, *Chem. Eur. J.* **2002**, *8*, 4884–4893; g) J. T. Culp, G. E. Fanucci, B. C. Watson, A. N. Morgan, R. Backov, H. Ohnuki, M. W. Meisel, D. R. Talham, *J. Solid State Chem.* **2001**, *159*, 362–370.
[18] a) A. Cabeza, M. A. G. Aranda, S. Bruque, D. M. Poojary, A. Clearfield, J. Sanz, *Inorg. Chem.* **1998**, *37*, 4168–4178; b) A. Cabeza, M. A. G. Aranda, S. Bruque, D. M. Poojary, A. Clearfield, *Mater. Res. Bull.* **1998**, *33*, 1265–1274; c) B. Bujoli, P. Palvadeau, J. Rouxel, *Chem. Mater.* **1990**, *2*, 582–589; d) R.-C. Wang, Y. Zhang, H. Hu, R. R. Frausto, A. Clearfield, *Chem. Mater.* **1992**, *4*, 864–871.
[19] a) G. Alberti, U. Costantino, S. Allulli, N. Tomassini, *J. Inorg. Nucl. Chem.* **1978**, *40*, 1113–1117; b) D. M. Poojary, H.-L. Hu, F. L. Campbell III, A. Clearfield, *Acta Crystallogr., Sect. B* **1993**, *49*, 996–1001; c) M. B. Dines, P. M. Digiacomo, *Inorg. Chem.* **1981**, *20*, 92–97.
[20] J. W. Johnson, A. J. Jacobson, J. F. Brody, J. T. Lewandowski, *Inorg. Chem.* **1984**, *23*, 3842–3844.
[21] a) D. M. Poojary, Y. Zhang, B. Zhang, A. Clearfield, *Chem. Mater.* **1995**, *7*, 822–827; b) D. M. Poojary, D. Grohol, A. Clearfield, *Angew. Chem. Int. Ed. Engl.* **1995**, *34*, 1508–1510; c) D. Grohol, M. A. Subramanian, D. M. Poojary, A. Clearfield, *Inorg. Chem.* **1996**, *35*, 5264–5271; d) D. M. Poojary, A. Cabez, M. A. G. Aranda, S. Bruque, A. Clearfield, *Inorg. Chem.* **1996**, *35*, 1468–1473.
[22] a) C.-Y. Yang, A. Clearfield, *Reactive Polym.* **1987**, *5*, 13–21; b) L. H. Kullberg, A. Clearfield, *Solvent Extr. Ion Exch.* **1989**, *7*, 527–540.
[23] D. E. C. Corbridge, F. R. Tromans, *Anal. Chem.* **1958**, *30*, 1101–1109.
[24] K. Yvon, W. Jeitschko, E. Parthe, *J. Appl. Crystallogr.* **1977**, *10*, 73–74.
[25] R. M. Silverstein, G. C. Bassler, T. C. Morrill, *Spectrometric Identification of Organic Compounds*, John Wiley & Sons, New York, **1963**, p. 128.
[26] L. Basini, A. Raffaelli, G. Zerbi, *Chem. Mater.* **1990**, *2*, 679–684.
[27] G. M. Sheldrick, SHELXL-97, *Program for the Solution of Crystal Structures*, University of Göttingen, Göttingen, Germany, **1985**.
[28] DIAMOND, *Visual Crystal Structure Information System*: W. T. Pennington, *J. Appl. Crystallogr.* **1999**, *32*, 1028–1029.
[29] N. Walker, D. Stuart, *Acta Crystallogr., Sect. A* **1983**, *39*, 158–166.

Received: August 10, 2005
Published Online: November 2, 2005

 © 2005 Wiley-VCH Verlag GmbH & Co. KGaA, Weinheim

DOI: 10.1002/ejic.200500222

Polymorphism Driven by π–π Stacking and van der Waals Interactions: Preparation and Characterization of Polymorphic Vanadium Crystals of $[V^{V}O(Hacshz)(OEt)]$ and $[V^{IV}(Hacshz)_2]$

Yinshi Jin[a] and Myoung Soo Lah*[a]

Keywords: Crystal engineering / Pi interactions / Polymorphism / Supramolecular chemistry / Vanadium

Polymorphic mono-oxo mono-alkoxo square-pyramidal $[V^{V}O(Hacshz)(OEt)]$ (where $Hacshz^{2-}$ is a doubly deprotonated dianionic acetylacetosalicylhydrazone; thick plate-shaped dark-greenish-brown crystals for **1a** and block-shaped dark-reddish-brown crystals for **1b**) and mononuclear trigonal-prismatic $[V^{IV}(Hacshz)_2]$ (block-shaped dark-bluish-brown crystals for **2a** and triangular-shaped dark-violet crystals for **2b**) were synthesized and characterized. The crystals were prepared by simple addition of vanadium(III) acetylacetonate to an ethanol solution of salicylhydrazide (H_3shz). Depending on the ratio of the ligand to the metal ion, the extent of exposure to molecular oxygen, and the filtration of the intermediate, various polymorphs could be obtained as both mixtures and pure forms. A common π–π stacked dimeric species was observed in both polymorphs **1a** and **1b**. The dimeric species behaves as a common repeating motif, but in different interaction modes. A second type of π–π interaction, in addition to van der Waals interactions, was observed in crystals of **1a**, while only van der Waals interactions were observed in crystal **1b**. Another type of π–π-stacked dimeric vanadium(IV) species again behaves as a repeating motif in crystals of **2a** and **2b**, but in different interaction modes. The thermal properties, such as the decomposition behavior and melting points, of the two different polymorphs of the same vanadium complexes are very similar but not identical.

(© Wiley-VCH Verlag GmbH & Co. KGaA, 69451 Weinheim, Germany, 2005)

Introduction

Crystal engineering and supramolecular chemistry are the planning and construction of the structure and properties of materials using relatively weak interactions such as hydrogen bonding,[1] van der Waals interactions,[2] dipole interactions,[3] π–π stacking interactions,[4] and coordination[5] by appropriate design of the molecular building units. Understanding these weak intermolecular interactions is important to comprehend the factors governing crystal engineering and supramolecular chemistry. The building units are arranged into crystalline materials or supramolecular entities as a result of the accumulation of several weak intermolecular interactions. Relatively strong and directional hydrogen-bonding interactions and partly directional π–π stacking interactions are most commonly utilized for rational design in crystal engineering and supramolecular chemistry.[6] Nondirectional van der Waals and dipole interactions are also used to orient molecules in crystals or in solution.[7] It is usually very difficult to utilize these weak intermolecular interactions in rational design because these different types of interactions act together in a concerted rather than in a separate way, so the prediction of the desired structure is often impossible.

Polymorphism − the different packing arrays of the same building units − is frequently found in crystalline materials of some organic and inorganic complexes.[8] This phenomenon is of interest because it utilizes the different intermolecular interactions of the same structural entity for the formation of different polymorphs and, therefore, understanding their role in polymorphism can be utilized for molecular and/or crystal design. There are many examples of polymorphs involving hydrogen-bonding interactions together with other weak interactions.[9] However, only a few examples are known where π–π stacking interactions without hydrogen-bonding interactions play the major role in the formation of different polymorphic crystals.[10] π–π Stacking interactions have been recognized in solid state and supramolecular design, and have been utilized in many research areas such as molecular conductors,[11] molecular machines,[12] and electronics.[13]

Recently, we reported the synthesis and characterization of the mono-oxo mono-alkoxo square-pyramidal vanadium(V) complex $[VO(Hacshz)(OEt)]$.[14] During our investigation of this complex, we identified a polymorphism phenomenon where the building unit is arranged in different packing interaction modes. In addition, we isolated $[V^{IV}(Hacshz)_2]$ as an intermediate or side product, which also appeared in two different packing modes. In both com-

[a] Department of Chemistry and Applied Chemistry, College of Science and Technology, Hanyang University,
1271 Sa-1-dong, Ansan, Kyunggi-do 426-791, Korea
Fax: +82-31-407-3863
E-mail: mslah@hanyang.ac.kr

 InterScience © 2005 Wiley-VCH Verlag GmbH & Co. KGaA, Weinheim

plexes, the intermolecular interactions involved are only π–π stacking and van der Waals interactions, with no hydrogen-bonding interactions. Thus, these complexes could serve as simplified model systems in which the complexity of combined interactions is reduced to only two kinds in polymorphic crystal packing. Here, we report the synthesis and characterization of the polymorphic mono-oxo monoalkoxo square-pyramidal vanadium(v) complex [VO(Hacshz)(OEt)] (**1**) and the mononuclear trigonal-prismatic vanadium(iv) complex [V(Hacshz)$_2$] (**2**). Various π–π stacking interaction modes of the same motif, acetylacetosalicylhydrazone, are presented and discussed.

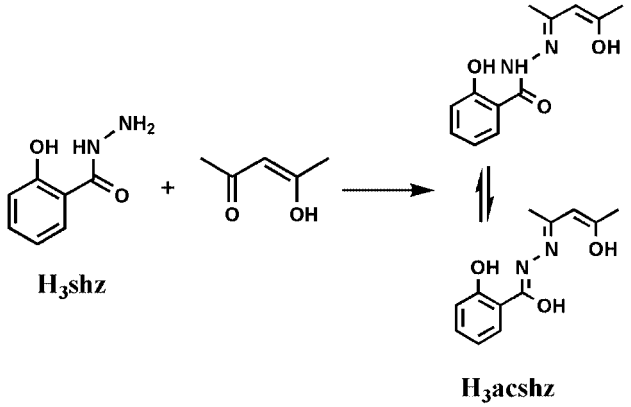

Scheme 1.

Results and Discussion

Preparation and Characterization of Polymorphic Vanadium Crystals

The vanadium(v) complex [V^{V}O(Hacshz)(OEt)] (**1**) was prepared following a reported method.[14] The complex was synthesized by simple addition of one equivalent of vanadium(iii) acetylacetonate to an ethanol solution of H_3shz in a beaker in air; Hacshz^{2-} was formed by the Schiff-base condensation reaction of H_3shz with acetylacetonate in situ (Scheme 1). In repeated experiments under exactly the same conditions, we noticed that the products were a mixture of two slightly different shaped and colored crystals, namely thick, plate-shaped, dark-greenish-brown crystals (**1a**) and block-shaped, dark-reddish-brown crystals (**1b**; Scheme 2). The IR spectrum of **1a** is very similar to that of **1b**, but not identical. The characteristic V=O stretching band is observed at 998 cm^{-1} for **1a** but at 1001 cm^{-1} for **1b**. The crystals also have different physical properties: **1a** melts in the range 115.1–116.9 °C while **1b** melts over a slightly higher temperature range (117.2–118.8 °C). Complexes **1a** and **1b** are indistinguishable in solution, as expected. The ^{1}H NMR spectrum of **1a** in chloroform is identical to that of **1b**.

When the reaction was performed under the same conditions but in a closed 30-mL vial, a crystalline precipitate of **2** formed within a day. Complex **2** was filtered off, and, on standing, the filtrate produced only crystals of **1a**. Complex **2** was confirmed to be [V^{IV}(Hacshz)$_2$], which has no oxo group and two dianionic Hacshz^{2-} ligands per vanadium(iv) ion. In the presence of limited amounts of oxygen, the vanadium(iii) ion is oxidized to the vanadium(iv) complex. Complex **1a** could also be obtained as the sole product with a 2:1 ratio of H_3shz and vanadium(iii) acetylacetonate in ethanol solution in the presence of enough oxygen. Surprisingly, **1b** was obtained as the sole product with a 3:1 ratio of H_3shz and vanadium(iii) acetylacetonate, while a mixture of **1a** and **1b** was obtained with a 1:1 ratio of H_3shz and vanadium(iii) acetylacetonate. It is not clear why different polymorphs are obtained with different amounts of metal ions.

The mononuclear vanadium(iv) complex **2** was obtained when the amount of oxygen was limited. Careful examination of the crystalline precipitate **2** revealed two types of crystalline material, namely block-shaped, dark-bluish-brown crystals (**2a**) as a major species and triangular-

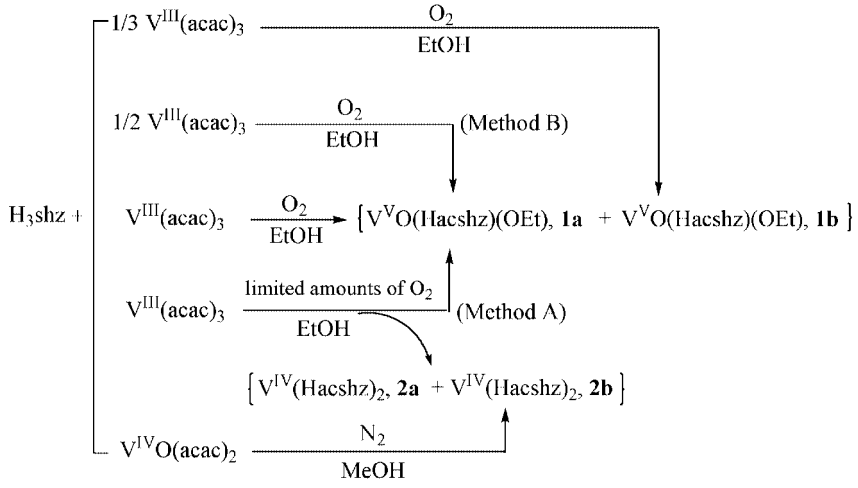

Scheme 2.

 © 2005 Wiley-VCH Verlag GmbH & Co. KGaA, Weinheim

shaped, dark-violet crystals (**2b**) as a very minor species. Complex **2b** is identical to the previously reported crystal structure of $[V^{IV}(Hacshz)_2,]$, which was prepared from H_3shz and vanadyl(IV) acetylacetonate in methanol under nitrogen.[16] Magnetic susceptibility measurements of **2a** (μ_{eff} = 1.80 μ_B after a diamagnetic correction with Pascal's constants) suggest that the complex contains a paramagnetic d^1 vanadium(IV) ion.

Crystal Structure of $[V^{V}O(Hacshz)(OEt)]$ (1)

The molecular structure of **1a** is very similar to that of the previously reported square-pyramidal dialkoxo-bound monooxo-vanadium(V) complex **1b** (Table 1).[14] An ORTEP drawing of **1a** is shown in Figure 1. $Hacshz^{2-}$ serves as a tridentate ligand to form five- and six-membered chelating rings. An ethoxide anion occupies the remaining basal site of the square-pyramidal oxovanadium(V) center.

Table 1. Bond lengths [Å] and bond angles [°] for **1a** and **1b**.

	1a	1b		1a	1b
V1–O1	1.589(1)	1.582(1)	V1–O4	1.863(1)	1.862(1)
V1–O3	1.930(1)	1.939(1)	V1–N2	2.073(1)	2.096(1)
V1–O5	1.766(1)	1.749(1)			
O1–V1–O3	105.67(5)	101.08(6)	O1–V1–O4	103.66(5)	102.90(6)
O1–V1–O5	106.78(6)	106.68(6)	O1–V1–N2	99.92(5)	100.66(6)
O4–V1–O3	146.35(5)	150.10(5)	O5–V1–O3	87.67(5)	90.63(5)
O3–V1–N2	74.97(4)	74.81(5)	O5–V1–O4	99.36(5)	99.28(5)
O4–V1–N2	84.10(5)	83.39(5)	O5–V1–N2	151.30(5)	151.08(6)

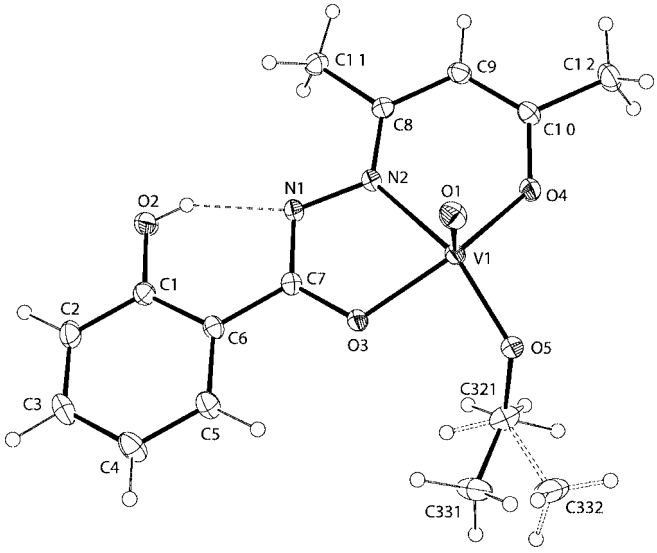

Figure 1. ORTEP drawing of complex **1a**. The minor part of the disordered ethoxide is represented by broken lines.

The packing of **1a** (Figure 2, a) is quite different from that of **1b** (Figure 3, a). In **1b**, the π–π stacked dimeric species (Figure 3, parts a and b) interact only through van der Waals interactions to form a three-dimensional crystal

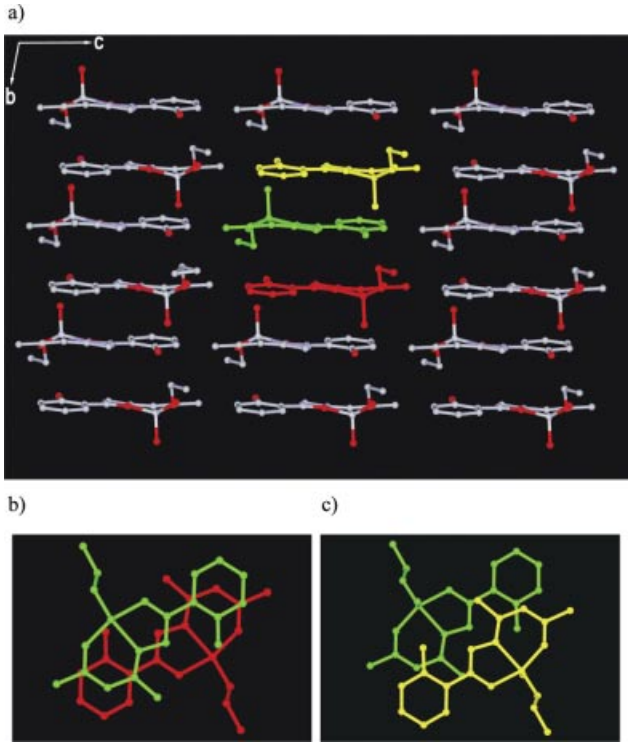

Figure 2. (a) Packing of **la**. The alternation of two types of π–π stacking interactions forms a one-dimensional chain. Only van der Waals interactions are observed between the π–π stacked one-dimensional chains. (b) Type I: the π–π stacking interaction is between the phenoxy and acetylacetohydrazone groups. (c) Type II: the π–π stacking interaction is similar to that of type I but slightly displaced.

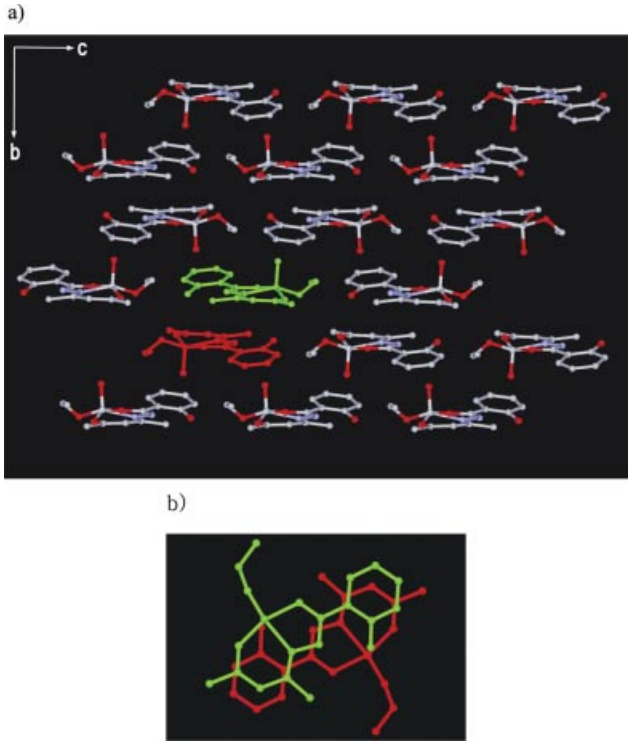

Figure 3. (a) Packing of **lb**. The three-dimensional structure is formed by van der Waals interactions between the π–π stacked dimeric species. (b) Type-I π–π stacking interaction.

 © 2005 Wiley-VCH Verlag GmbH & Co. KGaA, Weinheim

Table 2. π–π stacking interaction distances [Å] for **1a**, **1b**, **2a**, and **2b**.

Type I			Type II			
	1a	**1b**		**1a**		
N1···C7	3.368(2)	3.300(2)	C1···C9	3.442(2)		
C6···C10	3.305(3)	3.315(3)	C7···C11	3.453(2)		
C2···C8	3.421(2)	3.350(2)				
V1···O2	3.418(2)	3.190(2)				
Type III			Type IV		Type V	
	2a	**2b**		**2a**		**2b**
C1b···C7b	3.557(5)	3.655(3)	C2a···C7a	3.478(5)	N1a···C10a	3.303(2)
C2b···C2b	3.511(5)	3.495(3)	C5a···C8a	3.624(5)	C1a···C12a	3.655(3)

structure. A π–π stacking interaction (type I) between the phenoxy group and the conjugated acetylacetohydrazones [N1···C7 = 3.300(2), C6···C10 = 3.315(3), C2···C8 = 3.350(2) Å] is observed in the dimeric species (part b in Figure 3 and Table 2). An additional close contact between the vanadium atom and the symmetry-related O2 atom [3.190(2) Å] is also observed.

In **1a**, two different types of π–π stacking interactions are seen. The first type of π–π stacking interaction (type I) is the same as that found in **1b** (parts b in Figure 2 and Figure 3, and Table 2). The only difference in both dimeric species is in the conformation of the ethoxide groups. The dimeric species in crystal **1a** interacts with two neighboring dimeric species to form a one-dimensional chain through a second type of π–π stacking interaction (type II). The type II interaction is similar to that of type I, but slightly displaced (part c in Figure 2 and Table 2). The type II stacking interaction [C1···C9 = 3.442(2), C7···C11 = 3.453(2) Å] is longer than the type I interaction. In **1a**, the one-dimensional chains connect by alternating the two types of π–π stacking interactions to form a three-dimensional crystal structure containing van der Waals interactions (Figure 2, a).

Crystal Structure of $[V^{IV}(Hacshz)_2]$ (2)

The molecular structure of **2a** is also very similar to that of **2b**. As in **2b**, **2a** has a trigonal-prismatic coordination sphere with pseudo-C_3 symmetry (Figure 4 and Table 3). The bite distances of the prismatic edges formed by the two five-membered chelating bidentate ligands are 2.417(3) Å for O3a···N2a and 2.406(3) Å for O3b···N2b; the bite angles are 75.3(1)° for O3a–V1–N2a and 74.6(1)° for O3b–V1–N2b. The length of the remaining prismatic edge formed by the two alkoxo atoms (O4a···O4b) is 2.505(2) Å, and the O4a–V1–O4b angle is 80.8(1)°. The twist angles[17] determined by the relative orientation of two opposite triangular faces are 4.3° for **2a** and 4.6° for **2b**.

Even though the molecular structure of **2a** is very similar to that of **2b**, the packing of **2a** is quite different to that of **2b**. In **2a**, two different types of π–π stacking interactions (types III & IV) are observed, as in the crystal structure of **1a**. The third type of π–π stacking interaction (type III) is seen between the salicylhydrazones [C2b···C2b = 3.511(5), C1b···C7b = 3.557(5) Å; part b in Figure 5 and Table 2]. As

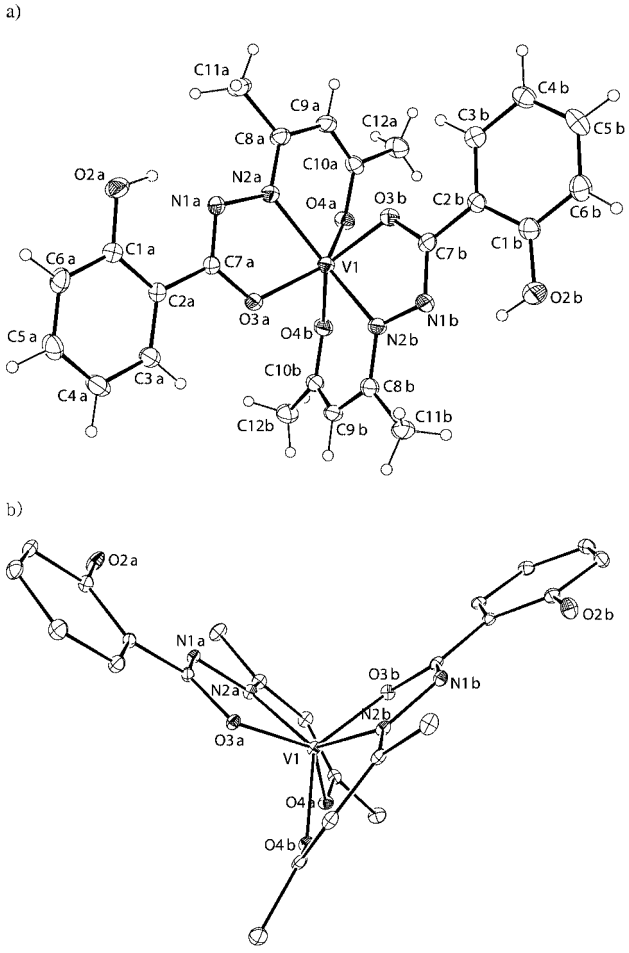

Figure 4. (a) ORTEP drawing of complex **2a** with numbering Scheme. (b) View showing the pseudo-C_3-symmetric trigonal-prismatic coordination geometry of the vanadium center.

in **1a**, the π–π stacked dimeric species formed interacts with two neighboring dimeric species to form a one-dimensional chain through the fourth type of π–π stacking interaction (type IV). The type IV interaction is again longer than the type III interaction [C2a···C7a = 3.478(5), C5a···C8a = 3.624(5) Å; Figure 5 (c) and Table 2]. The one-dimensional chains connect through two types of π–π stacking interactions to form a three-dimensional structure containing van der Waals interactions.

 © 2005 Wiley-VCH Verlag GmbH & Co. KGaA, Weinheim

Table 3. Bond lengths [Å], bond angles [°], bite distances [Å], and bite angles [°] for **2a** and **2b**.

	2a	**2b**		**2a**	**2b**
V1–O3a	1.928(2)	1.931(1)	V1–O3b	1.918(3)	1.912(1)
V1–O4a	1.940(2)	1.933(1)	V1–O4b	1.928(2)	1.920(1)
V1–N2a	2.031(3)	2.032(1)	V1–N2b	2.043(3)	2.044(2)
O3a–V1–O4a	136.3(1)	136.59 (5)	O4a–V1–N2a	83.8(1)	83.73(5)
O3b–V1–O4b	135.5(1)	134.71(5)	O4b–V1–N2b	83.9(1)	83.74(6)
O3a–V1–O4b	86.1(1)	85.10(5)	O3a–V1–N2b	88.1(1)	87.71(5)
O3b–V1–O4a	84.7(1)	83.36(5)	O3b–V1–N2a	86.3(1)	87.81(5)
O4b–V1–N2a	133.0(1)	132.53(6)	N2a–V1–N2b	136.7(1)	136.38(6)
O4a–V1–N2b	131.1(1)	131.43(5)	O3b–V1–O3a	130.6(1)	131.86(5)
O3a···N2a	2.417(3)	2.415(3)	O3b···N2b	2.406(3)	2.395(4)
O4a···O4b	2.505(2)	2.531(2)			
O3a–V1–N2a	75.3(1)	74.92(5)	O3b–V1–N2b	74.6(1)	74.47(5)
O4a–V1–O4b	80.8(1)	82.21(5)			

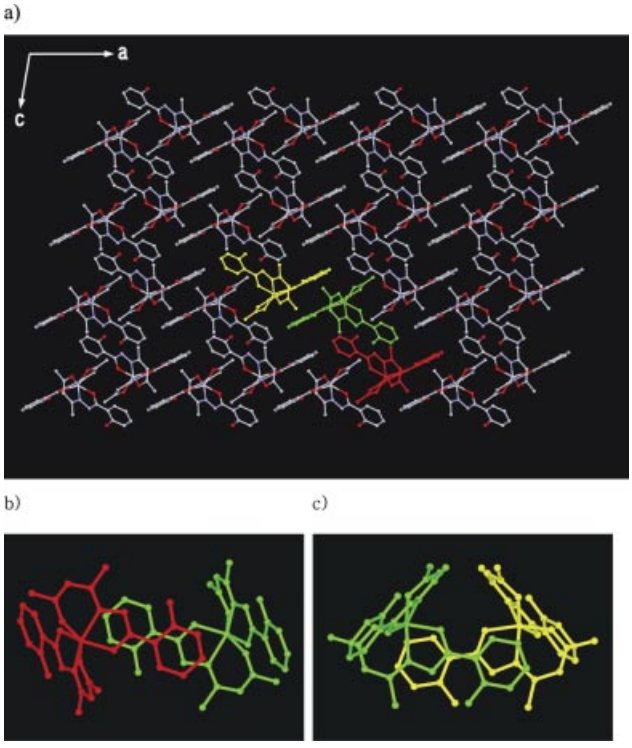

Figure 5. (a) Packing of **2a**. (b) Type-III π–π stacking interaction. (c) Type-IV π–π stacking interaction.

The same type III interaction is also observed in the packing of **2b** (Figure 6, b). However, the same π–π stacked dimeric species formed by the type III interaction is connected by a different type of π–π stacking interaction (type V) with the neighboring dimeric species to form a one-dimensional chain in **2b** (Figure 6, a and c).

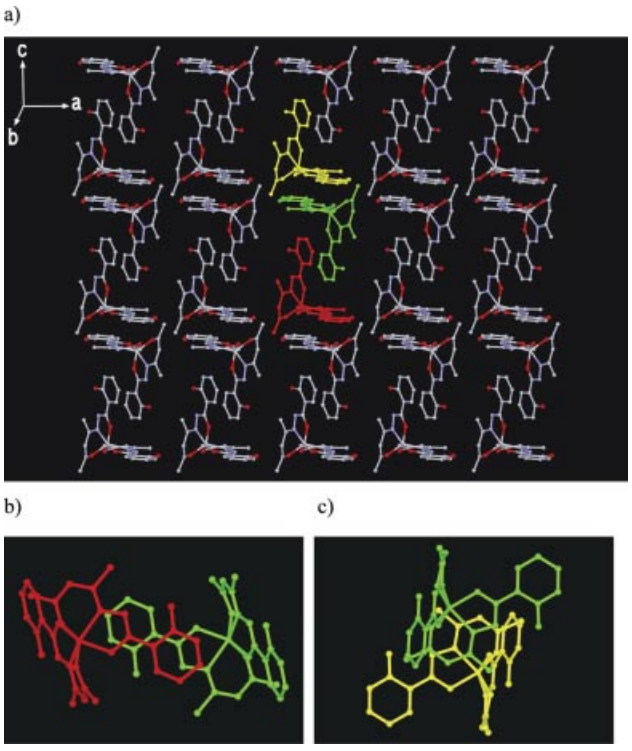

Figure 6. (a) Packing of **2b**. (b) Type-III π–π stacking interaction. (c) Type-V π–π stacking interaction.

Thermal Stability

The TGA and DSC data for polymorphic vanadium crystals **1a**, **1b**, **2a**, and **2b** were obtained in air. The data for **1a** indicate multistage weight loss with the related endotherms and exotherms (Figure 7, a). The first weight loss, related to the first endotherm near 106 °C, can be assigned as the loss of about one equivalent of water (found: 4.97%; calcd.: 4.95%). Even though no water molecules were observed in the crystal structure, water molecules in air are probably physisorbed on the surface of **1a**.[18] The second endotherm near 116 °C, with no weight loss, is assigned to the melting of **1a**. This assignment was also supported by the melting point measurement of a crystal of **1a**. Additional multistage weight loss was observed between 125 and 500 °C. At least four exotherms in the DSC could be related to weight loss in the TGA. However, the decomposition pattern of **1a** could not be followed in detail due to overlapping decomposition steps. The TGA and DSC data for **1b** also indicated multistage weight loss with related endotherms and exotherms (Figure 7, b). The first weight loss occurs near 108 °C and can also be assigned to the loss of about one equivalent of water (found: 5.03%; calcd.: 4.97%). The second endotherm near 118 °C is again assigned to the melting of crystal **1b**. Similar multi-step weight loss and related exotherms are observed to those in crystal **1a**. The thermal properties of the polymorphs are very similar to each other, but not identical. The melting point of crystal **1b** is slightly higher than that of crystal **1a**, even though only one type of π–π stacking interaction is observed in crystal **1b**, while a second type of π–π stacking interaction is also observed in crystal **1a**.

 © 2005 Wiley-VCH Verlag GmbH & Co. KGaA, Weinheim

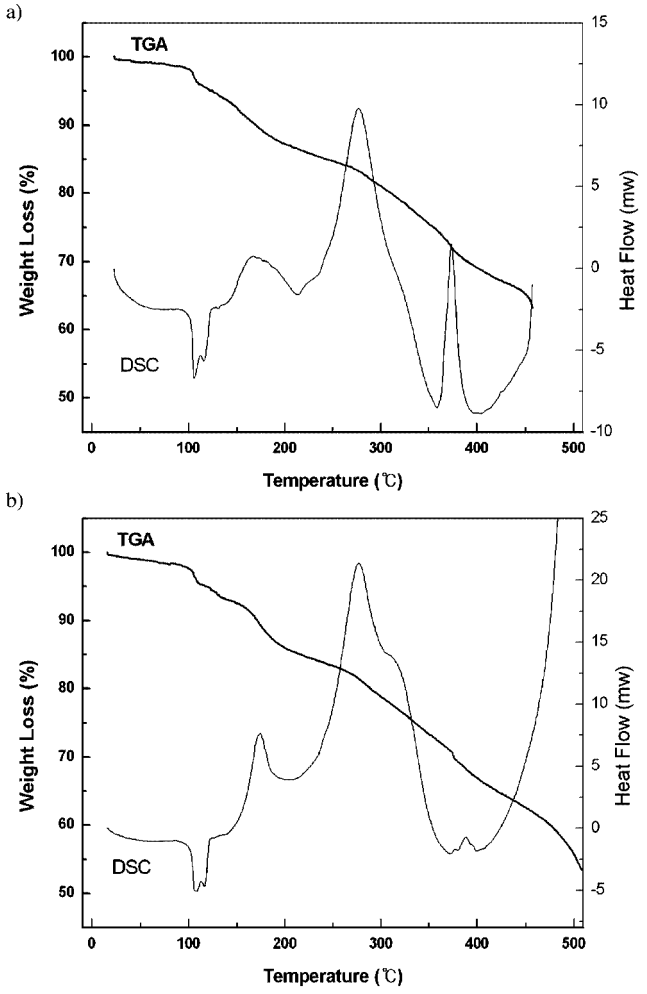

Figure 7. TGA and DSC curves for (a) crystals of **1a** and (b) crystals of **1b**.

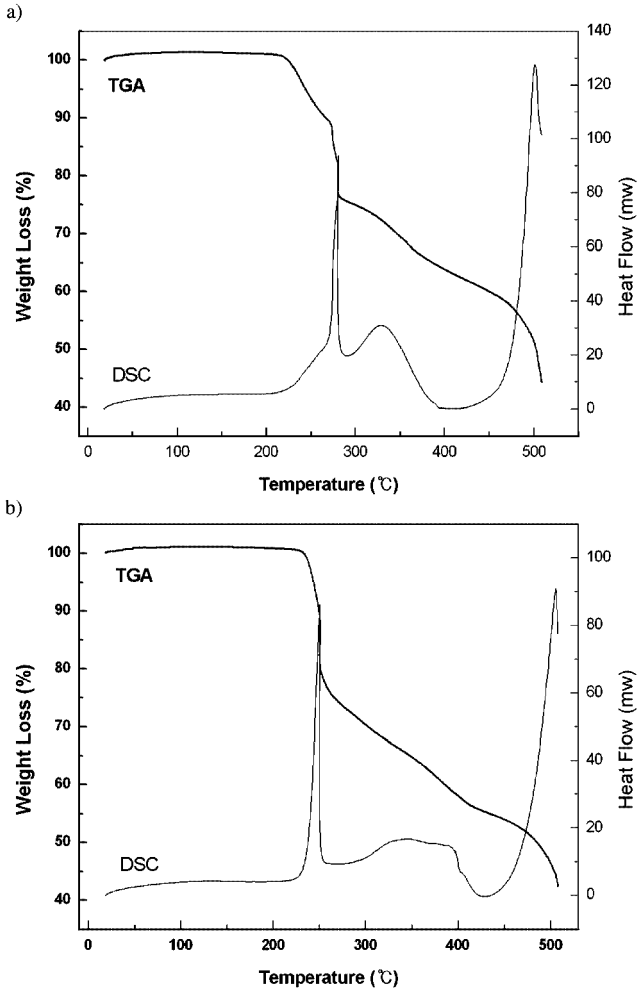

Figure 8. TGA and DSC curves for (a) crystals of **2a** and (b) crystals of **2b**.

The TGA and DSC data for **2a** and **2b** do not show any indication of weight loss or phase transition up to about 200 °C (Figure 8). Crystal **2a** starts an (at least) four-step weight loss around 220 °C (Figure 8, a). The TGA and DSC data for **2b** are also similar to those of crystal **2a**, but not identical (Figure 8, b). Crystal **2b** starts a fast weight loss around 230 °C. The TGA and DSC data for **2a** and **2b** imply that crystals of **2a** and **2b** have slightly different decomposition pathways. The decomposition pattern of crystals **2a** and **2b** could not be followed in detail due to overlapping decomposition steps.

Conclusions

We have prepared two polymorphs of vanadium(IV) and vanadium(V) complexes under slightly different conditions. Depending on the ratio of ligand to metal ion, various polymorphs can be obtained as both mixtures and pure crystal forms. We assume that the extent of exposure to oxygen also affects the formation of polymorphs. The amount of oxygen affects the amount of vanadium(IV) complex in solution, and the precipitation and filtration of the vanadium(IV) intermediate changes the composition of the related species in solution. The mononuclear mono-oxo mono-alkoxo square-pyramidal vanadium(V) complex [$V^{V}O$(Hacshz)(OEt)] (**1**), in two different polymorphs (**1a** and **1b**), was prepared by simple addition of one equivalent of vanadium(III) acetylacetonate to an ethanol solution of H_3shz. The same type of π–π stacking interaction mode (type I) is observed in both polymorphs. This interaction mode results in the very similar dimeric species observed in both polymorphs. While van der Waals interactions between the π–π stacked dimeric species result in polymorph **1b**, a combination of type II interactions and van der Waals interactions between the π–π stacked dimeric species results in polymorph **1a**.

The mononuclear vanadium(IV) complex [V^{IV}(Hacshz)$_2$] (**2**) was obtained as an intermediate or side product in the formation of complex **1** with limited amounts of oxygen, or was alternatively prepared with H_3shz and vanadyl(IV) acetylacetonate in methanol under nitrogen. As in complex **1**, the same (type III) interaction was observed in both polymorphs **2a** and **2b**. This interaction mode again results in the same dimeric species existing in both crystals. Two dif-

 © 2005 Wiley-VCH Verlag GmbH & Co. KGaA, Weinheim

ferent types of π–π stacking interactions (type IV and type V) result in two polymorphs (**2a** and **2b**).

The prenucleation step involves the same dominant π–π stacking in solution, and two subsequent nearly isoenergetic packing modes may be the reason for the formation of the two polymorphs in both complexes **1** and **2**.

The thermal properties, such as the decomposition behavior and melting points, of the two different polymorphs of the same vanadium complexes are very similar, but not identical.

Experimental Section

Materials and Instrumentation: The following were used as received with no further purification: salicylhydrazide (H_3shz), vanadium(III) acetylacetonate, [D_6]dimethyl sulfoxide, and [D]chloroform from Aldrich, Inc.; ethanol (EtOH) from Carlo–Erba. The determination of C, H, and N contents was performed at the Elemental Analysis Laboratory of the Korean Institute of Basic Science, Seoul. Infrared spectra were recorded from KBr pellets in the spectral range 4000–600 cm^{-1} with a Bio-Rad FT-IR spectrophotometer. Absorption spectra were obtained with a Shimadzu UV-2401PC spectrophotometer. ^{1}H-NMR spectra were obtained with a Varian-300 spectrometer. Room-temperature magnetic susceptibilities of well-ground solid samples were measured using the Evans method.[15] Melting points of well-ground solid samples were measured with a Sanyo Gallenkamp PLC melting point apparatus. Thermogravimetric analysis (TGA) and differential scanning calorimetry (DSC) data were obtained simultaneously with a SCINCO STA S-1000.

Synthesis of [V^{V}O(Hacshz)(OEt)] (1): Complex **1** was synthesized following the reported method.[14] H_3shz (0.234 g, 1.53 mmol) was dissolved in 15 mL of ethanol in a 50-mL beaker. One equivalent of vanadium(III) acetylacetonate (0.531 g, 1.52 mmol) was then added to the solution, whereupon the solution changed color to dark brown. After 20 min of stirring, the solution was filtered. Slow evaporation of the filtrate in air over three days produced dark crystals (0.270 g, 51.4%). A mixture of two different colored crystals, with dark greenish-brown crystals as the major component and dark-reddish-brown crystals as the minor component, could be noticed upon careful visual examination. IR data for the mixture: $\tilde{\nu}$ = 1622, 1597, 1543, 1502, 1489, 1432, 1376, 1328, 1305, 1286, 1255, 1158, 1085, 1033, 1000, 954, 916, 825, 791, 761, 717, 696, 662, 600 cm^{-1}.

[V^{V}O(Hacshz)(OEt)] (1a). Method A: H_3shz (0.234 g, 1.53 mmol) was dissolved in 15 mL of ethanol in a 30-mL vial fitted with a cap. One equivalent of vanadium(III) acetylacetonate (0.531 g, 1.52 mmol) was then added to the solution, whereupon the solution changed color to dark brown. The solution was filtered after stirring for 5 min. Dark-bluish-brown crystals of [V^{IV}(Hacshz)$_2$] (**2**) formed from the solution over one day and were filtered off. Allowing the the filtrate to stand for a further three days in a vial gave dark-greenish-brown crystals of **1a**.

Method B: H_3shz (0.234 g, 1.53 mmol) was dissolved in 15 mL of ethanol in a 50-mL beaker. Half an equivalent of vanadium(III) acetylacetonate (0.262 g, 0.752 mmol) was added to the solution, whereupon the solution changed color to dark brown. The solution was filtered after stirring for 5 min. Slow evaporation of the filtrate in air gave dark-greenish-brown crystals of **1a** after three days (0.126 g, 48.6%). [V^{V}O(Hacshz)(OEt)]·H_2O ($C_{14}H_{19}N_2O_6V$; M = 362.26): calcd. C 46.42, H 5.29, N 7.73, V 14.06; found C 46.51, H 5.11, N 8.12, V 14.06. Selected IR bands (KBr): $\tilde{\nu}$ = 1622, 1598, 1545, 1491, 1431, 1385, 1349, 1307, 1288, 1256, 1160, 1086, 1041, 998, 953, 919, 826, 788, 758, 713, 696, 659, 606 cm^{-1}. M.p. 115.1–116.9 °C.

[V^{V}O(Hacshz)(OEt)] (1b): H_3shz (0.234 g, 1.53 mmol) was dissolved in 15 mL of ethanol in a 50-mL beaker. One-third of an equivalent of vanadium(III) acetylacetonate (0.174 g, 0.500 mmol) was then added to the solution, whereupon the solution changed color to dark brown. The solution was filtered after stirring for 5 min. Slow evaporation of the filtrate in air gave dark-reddish-brown crystals of **1b** after four days (0.0554 g, 32.2%). [V^{V}O(Hacshz)(OEt)]·H_2O ($C_{14}H_{19}N_2O_6V$; M = 362.26): calcd. C 46.42, H 5.29, N 7.73, V 14.06; found C 46.74, H 4.98, N 8.14, V 14.50. Selected IR bands (KBr): $\tilde{\nu}$ = 1619, 1599, 1546, 1503, 1490, 1432, 1382, 1346, 1304, 1286, 1254, 1159, 1085, 1035, 1001, 954, 916, 824, 789, 760, 718, 694, 660, 599 cm^{-1}. M.p. 117.2–118.8 °C.

[V^{IV}(Hacshz)$_2$] (2): Two different shaped dark crystals were observed in the precipitate (0.254 g, 32.9%) obtained during the synthesis of **1a** using method A. Most of them were block-shaped, dark-bluish-brown crystals of **2a**, while a few crystals with a different morphology (**2b**) were also noticed. Elemental analysis and spectroscopic analysis were performed with **2a**. V^{IV}(Hacshz)$_2$ ($C_{24}H_{24}N_4O_6V$; M = 515.42): calcd. C 55.93, H 4.69, N 10.87, V 9.88; found C 55.77, H 4.66, N 10.54, V 9.93. Selected IR bands (KBr): $\tilde{\nu}$ = 1623, 1589, 1536, 1485, 1464, 1421, 1375, 1320, 1256, 1159, 1112, 1032, 960, 946, 878, 858, 826, 795, 772, 761, 752, 716, 697, 663, 599 cm^{-1}. Decomposition temperature: 212.6–214.2 °C. μ_{eff} = 1.80 μ_B.

[V^{IV}(Hacshz)$_2$] (2b): Compound **2b** was synthesized following a reported method.[16] H_3shz (0.761 g, 5.0 mmol) was dissolved in 40 mL of anhydrous methanol in a 100-mL round-bottomed flask. Half an equivalent of vanadyl(IV) acetylacetonate (0.663 g, 2.50 mmol) was then added to the solution, whereupon the solution changed color to dark brown. After 40 min of refluxing under nitrogen, the solution was cooled. The deep-purple precipitate formed was filtered off and washed with methanol and hexane (0.661 g, 51.3%). V^{IV}(Hacshz)$_2$ ($C_{24}H_{24}N_4O_6V$; M = 515.42): calcd. C 55.93, H 4.69, N 10.87, V 9.88; found C 55.77, H 4.66, N 10.54, V 11.00. Selected IR bands (KBr): $\tilde{\nu}$ = 1624, 1588, 1536, 1485, 1419, 1376, 1328, 1319, 1256, 1158, 1111, 1091, 1032, 1023, 1013, 961, 945, 878, 858, 825, 794, 772, 762, 752, 717, 705, 696, 663, 599 cm^{-1}. Decomposition temperature: 216.8–217.6 °C.

X-ray Crystallography: Crystals of complexes **1a**, **1b**, **2a**, and **2b** were mounted on a glass fiber. Preliminary examination and data collection were performed using a Bruker SMART CCD Detector single-crystal X-ray diffractometer equipped with a graphite-monochromated Mo-K_α radiation source (λ = 0.71073 Å) equipped with a sealed tube X-ray source operating at –100 °C. Preliminary unit-cell constants were determined from a set of 45 narrow frame scans (0.3° in ω). The data sets collected consisted of 1286 frames of intensity data, collected using a frame width of 0.3° in ω, and a count time of 10 seconds per frame, with a crystal-to-detector distance of 5 cm. The double pass scanning method was used to exclude any noise. The collected frames were integrated using an orientation matrix determined from the narrow frame scans. The SMART and SAINT software packages[19] were used for data collection and integration, respectively. Analysis of the integrated data did not show any decay. The final cell constants were determined using a global refinement of 8192 reflections ($\theta < 25.0°$). Collected data were corrected for absorbance using the SADABS package[20] based upon the Laue symmetry using equivalent reflections. The structural solution and refinement of the structure were carried out

 © 2005 Wiley-VCH Verlag GmbH & Co. KGaA, Weinheim

Table 4. Crystal data and structure refinement for **1**, **1b**, **2a**, and **2b**.

	1a	**1b**	**2a**	**2b**
Formula	$C_{14}H_{17}N_2O_5V$	$C_{14}H_{17}N_2O_5V$	$C_{24}H_{24}N_4O_6V$	$C_{24}H_{24}N_4O_6V$
Formula weight	344.24	344.24	515.41	515.41
Crystal system	monoclinic	triclinic	monoclinic	triclinic
Space group	$P2_1/c$	$P\bar{1}$	$C2/c$	$P\bar{1}$
a [Å]	10.3275(7)	7.0798(6)	27.083(5)	9.7242(9)
b [Å]	14.838(1)	10.3111(9)	9.929(2)	10.1706(9)
c [Å]	10.7251(8)	11.028(1)	18.033(3)	13.547(1)
α [°]	90	80.415(2)	90	100.602(2)
β [°]	113.864(1)	88.745(2)	99.673(3)	94.152(2)
γ [°]	90	71.767(1)	90	112.984 (1)
V [Å^3]	1503.0(2)	753.6(1)	4780(2)	1196.9(2)
Z	4	2	8	2
Crystal size [mm]	0.32×0.25×0.20	0.70×0.45×0.18	0.30×0.13×0.10	0.45×0.35×0.25
θ range [°]	2.16–28.31	2.11–28.26	1.53–28.29	2.24–28.28
GOF on F^2	1.072	1.090	1.021	1.055
Final R [$I > 2\sigma(I)$]	$R1$[a] = 0.0310 $wR2$[b] = 0.0837	$R1$ = 0.0274 $wR2$ = 0.0766	$R1$ = 0.0698 $wR2$ = 0.1199	$R1$ = 0.0357 $wR2$ = 0.0927
R (all data)	$R1$ = 0.0364 $wR2$ = 0.0875	$R1$ = 0.0287 $wR2$ = 0.0775	$R1$ = 0.1393 $wR2$ = 0.1397	$R1$ = 0.0452 $wR2$ = 0.0986
Largest diff. peak and hole [e Å^{-3}]	0.411 & –0.198	0.304 & –0.339	0.614 & –0.311	0.451 & –0.228

[a] $R1 = \Sigma||F_o| - |F_c||/\Sigma|F_o|$. [b] $wR2 = [\Sigma w(F_o^2 - F_c^2)^2/\Sigma wF_o^4]^{1/2}$.

using the SHELXTL v5.1 software package.[21] All non-hydrogen atoms were refined anisotropically. In **1a**, hydrogen atoms were refined isotropically, except for the hydrogen atoms of the disordered ethoxide, which were refined with assigned isotropic displacement coefficients U(H) = 1.2 U(C) or 1.5 $U(C_{methyl})$ on their respective atoms. In **1b** and **2b**, all hydrogen atoms were refined isotropically. In **2a**, hydrogen atoms were refined with assigned isotropic displacement coefficients U(H) = 1.2 U(C) or 1.5 $U(C_{methyl})$ on their respective atoms, except for two phenolic hydrogen atoms, which were refined isotropically. The crystal and intensity data are shown in Table 4.

CCDC-262588 to -262591 contain the supplementary crystallographic data for this paper. These data can be obtained free of charge from The Cambridge Crystallographic Data Centre via www.ccdc.cam.ac.uk/data_request/cif.

Acknowledgments

We thank the Korean Institute of Basic Science for performing the elemental analyses. The authors wish to acknowledge the financial support of the Korea Research Foundation (grant KRF-2002-070-C00053), KISTEP (M1-0213-03-0004), and CBMH.

[1] a) D. Braga, F. Grepioni, G. R. Desiraju, *Chem. Rev.* **1998**, *98*, 1375; b) J. C. M. Rivas, L. Brammer, *Coord. Chem. Rev.* **1999**, *183*, 43; c) D. C. Sherrington, K. A. Taskinen, *Chem. Soc. Rev.* **2001**, *30*, 83; d) M. Yamanaka, A. Shivanyuk, J. Rebek, *J. Am. Chem. Soc.* **2004**, *126*, 2939; e) R. H. Vreekamp, J. P. M. Van Duynhoven, M. Hubert, W. Verboom, D. N. Reinhoudt, *Angew. Chem. Int. Ed. Engl.* **1996**, *35*, 1215.

[2] a) G. Forster, A. Meister, A. Blume, *Phys. Chem. Chem. Phys.* **2000**, *2*, 4503; b) N. Vembu, M. Nallu, S. Durmus, M. Pazner, J. Garrison, W. J. Youngs, *Acta Crystallogr., Sect. C* **2004**, *60*, o65–o68.

[3] a) S. Lee, A. B. Mallik, D. C. Fredrickson, *Cryst. Growth Des.* **2004**, *4*, 279; b) S. P. Anthony, T. P. Radhakrishnan, *Chem. Commun.* **2001**, 931.

[4] a) C. A. Hunter, J. K. M. Sanders, *J. Am. Chem. Soc.* **1990**, *112*, 5525; b) P. J. Nichols, C. L. Raston, J. W. Steed, *Chem. Commun.* **2001**, 1062; c) P. L. Caradoc-Davies, L. R. Hanton, *Chem. Commun.* **2001**, 1098; d) A. Magistrato, P. S. Pregosin, A. Albinati, U. Rothlisberger, *Organometallics* **2001**, *20*, 4178.

[5] a) B. J. Holliday, C. A. Mirkin, *Angew. Chem. Int. Ed.* **2001**, *40*, 2022; b) M. Fujita, *Chem. Soc. Rev.* **1998**, *27*, 417; c) B. Olenyuk, J. A. Whiteford, A. Fechtenkotter, P. J. Stang, *Nature* **1999**, *398*, 796; d) A. B. Mallik, S. Lee, E. B. Lobkovsky, *Cryst. Growth Des.* **2005**, *ASAP*; e) B. Chen, S. Lee, D. Venkataraman, F. J. DiSalvo, E. Lobkovsky, M. Nakayama, *Cryst. Growth Des.* **2002**, *2*, 101; f) O. R. Evans, W. Lin, *Chem. Mater.* **2001**, *13*, 2705.

[6] a) A. Ajayaghosh, S. J. George, *J. Am. Chem. Soc.* **2001**, *123*, 5148; b) P. Gamez, G. A. van Albada, I. Mutikainen, U. Turpeinen, J. Reedijk, *Inorg. Chim. Acta* **2005**, *358*, 1975; c) A. M. Plokhotnichenko, E. D. Radchenko, S. G. Stepanian, L. Adamovicz, *J. Phys. Chem.* **1999**, *103*, 11052; d) D. Braga, L. Maini, L. Prodi, A. Caneschi, R. Sessoli, F. Grepioni, *Chem. Eur. J.* **2000**, *6*, 1310; e) Y. Wang, R. Cao, W. Bi, X. Li, D. Sun, *J. Mol. Struct.* **2005**, *738*, 53; f) D. Braga, L. Maini, M. Polito, M. Rossini, F. Grepioni, *Chem. Eur. J.* **2000**, *6*, 4227; g) Y. Kim, J. G. Verkade, *Inorg. Chem.* **2003**, *42*, 4262; h) A. Y. Ziganshina, Y. H. Ko, W. S. Jeon, K. Kim, *Chem. Commun.* **2004**, 806–807; i) M. Oh, G. B. Carpenter, D. A. Sweigart, *Chem. Commun.* **2002**, 2168; j) W. Lu, M. C. W. Chan, K. Cheung, C. Che, *Organometallics* **2001**, *20*, 2477; k) D. D. Graf, R. G. Duan, J. P. Campbell, L. L. Miller, K. R. Mann, *J. Am. Chem. Soc.* **1997**, *119*, 5888.

[7] a) A. B. Mallik, S. Lee, L. Tran, E. B. Lobkovsky, *Cryst. Growth Des.* **2003**, *3*, 467; b) W. A. Herrebout, T. V. D. Kerkhof, B. J. van der Veken, *Phys. Chem. Chem. Phys.* **2000**, *2*, 4925; c) R. Ricceri, N. V. Romeu, G. Taddei, *Langmuir* **1996**, *12*, 913; d) E. S. Lee, K. Na, Y. H. Bae, *Nano Lett.* **2005**, *ASAP*; e) M. Oishi, Y. Nagasaki, K. Itaka, N. Nishiyama, K. Kataoka, *J. Am. Chem. Soc.* **2005**, *127*, 1624; f) A. Rösler, G. W. M. Vandermeulen, H. Klok, *Adv. Drug Delivery Rev.* **2001**, *53*, 95.

[8] a) F. H. Herbstein, *Cryst. Growth Des.* **2004**, *4*, 1419; b) J. Bernstein, R. J. Davey, J. O. Henck, *Angew. Chem. Int. Ed.* **1999**, *38*, 3440; c) D. Braga, L. Maini, M. Polito, L. Scaccianoce, G. Cojazzi, F. Grepioni, *Coord. Chem. Rev.* **2001**, *216–217*, 225; d) T. Kawamura, Y. Miyazaki, M. Sorai, *Chem. Phys. Lett.* **1997**, *273*, 435; e) A. Kalman, L. Fabian, G. Argay, G. Bernath, Z. Gyarmati, *J. Am. Chem. Soc.* **2003**, *125*, 34.

 © 2005 Wiley-VCH Verlag GmbH & Co. KGaA, Weinheim

[9] a) A. Matsumoto, T. Tanaka, T. Tsubouchi, K. Tashiro, S. Saragai, S. Nakamoto, *J. Am. Chem. Soc.* **2002**, *124*, 8891; b) J. A. McMahon, M. J. Zaworotko, J. F. Remenar, *Chem. Commun.* **2004**, 278; c) V. R. Thalladi, M. Nüsse, R. Boese, *J. Am. Chem. Soc.* **2000**, *122*, 9227; d) J. M. Barendt, E. G. Bent, R. C. Haltiwanger, C. A. Squier, A. D. Norman, *Inorg. Chem.* **1989**, *28*, 4425.
[10] a) D. L. Reger, J. R. Gardinier, M. D. Smith, A. M. Shahin, G. J. Long, L. Rebbouh, F. Grandjean, *Inorg. Chem.* **2005**, *44*, 1852; b) H. Birkedal, H. B. Burgi, K. Komatsu, D. Schwarzenbach, *J. Mol. Struct.* **2003**, *647*, 233; c) S. M. Reed, T. J. R. Weakley, J. E. Hutchison, *Cryst. Eng.* **2000**, *3*, 85; d) L. Ballester, A. M. Gil, A. Gutiérrez, M. F. Perpinan, M. T. Azcondo, A. E. Sanchez, U. Amador, J. Campo, F. Palacio, *Inorg. Chem.* **1997**, *36*, 5291.
[11] a) R. Kato, *Chem. Rev.* **2004**, *104*, 5319; b) R. P. Shibaeva, E. B. Yagubskii, *Chem. Rev.* **2004**, *104*, 5347; c) T. Inabe, H. Tajima, *Chem. Rev.* **2004**, *104*, 5503.
[12] a) H. Tseng, S. A. Vignon, J. F. Stoddart, *Angew. Chem. Int. Ed.* **2003**, *42*, 1491; b) W. S. Jeon, A. Y. Ziganshina, J. W. Lee, Y. H. Ko, J. Kang, C. Lee, K. Kim, *Angew. Chem. Int. Ed.* **2003**, *42*, 4097.
[13] a) C. P. Collier, E. W. Wong, M. Belohradsky, F. M. Raymo, J. F. Stoddart, P. J. Kuekes, R. S. Williams, J. R. Heath, *Science* **1999**, *285*, 391; b) L. Fu, L. Cao, Y. Liu, D. Zhu, *Adv. Colloid Interface Sci.* **2004**, *111*, 133; c) J. R. Reimers, A. Bilic, Z. Cai, M. Dahlbom, N. A. Lambropoulos, G. C. Solomon, M. J. Crossley, N. S. Hush, *Aust. J. Chem.* **2004**, *57*, 1133.
[14] M. Moon, M. Pyo, Y. C. Myoung, C. I. Ahn, M. S. Lah, *Inorg. Chem.* **2001**, *40*, 554–557.
[15] D. F. Evans, *J. Chem. Soc.* **1958**, 2003.
[16] A. A. Dianantis, M. Manikas, M. A. Salam, M. R. Snow, E. R. T. Tiekink, *Aust. J. Chem.* **1988**, *41*, 453–468.
[17] The twist angles were calculated by taking the average of the angles made by the projection of the vertices of the top and bottom faces along the direction of the two centroids of the trigonal faces.
[18] The elemental analysis data are also in conformity with TGA results.
[19] *SMART* and *SAINT*, Area Detector Software Package and SAX Area Detector Integration Program; Bruker Analytical X-ray; Madison, WI, USA, **1997**.
[20] *SADABS*, Area Detector Absorption Correction Program; Bruker Analytical X-ray, Madison, WI, USA, **1997**.
[21] G. M. Sheldrick, *SHELXTL-PLUS*, Crystal Structure Analysis Package; Bruker Analytical X-ray; Madison, WI, USA, **1997**.

Received: March 16, 2005
Published Online: November 2, 2005

 © 2005 Wiley-VCH Verlag GmbH & Co. KGaA, Weinheim

DOI: 10.1002/ejic.200500304

Binding of Oxovanadium(IV) to Tripeptides Containing Histidine and Cysteine Residues and Its Biological Implication in the Transport of Vanadium and Insulin-Mimetic Compounds

Eugenio Garribba,*[a] Giovanni Micera,*[a] Elzbieta Lodyga-Chruscinska,[b] Daniele Sanna,[c] and Gavino Sanna[a]

Keywords: Bioinorganic chemistry / Coordination modes / EPR spectroscopy / Peptides / Vanadium

The complexation of $V^{IV}O$ ion with three tripeptides of biological importance containing L-histidine or L-cysteine (HisGlyGly, GlyGlyHis and GlyGlyCys) has been studied. This study was performed in aqueous solution by the combined application of potentiometric and spectroscopic (electronic absorption and EPR) techniques. The results indicate that these oligopeptides, if a ligand-to-metal molar ratio of 10 or 15 is used, can keep $V^{IV}O$ ion in solution until the deprotonation of the amide group with the donor set (NH_2, CO, $N_{im}{}^{ax}$) for HisGlyGly or (COO^-, CO) for GlyGlyHis and GlyGlyCys. In all the systems, at pH values around neutrality, a $VOLH_{-2}$ species is formed with an (NH_2, N^-, N^-, COO^-) donor set for HisGlyGly, (NH_2, N^-, N^-, N_{im}) for GlyGlyHis and (NH_2, N^-, N^-, S^-) for GlyGlyCys. These species, and those with one deprotonated amide group coordinated to the $V^{IV}O$ ion, can be detected by EPR spectroscopy. The N^-(amide) contribution to the hyperfine coupling constant along the z axis, A_z, depends on the total charge of the donor atoms in the equatorial plane. The participation of albumin in the transport of vanadium and insulin-mimetic $V^{IV}O$ compounds is reconsidered based on these results.

(© Wiley-VCH Verlag GmbH & Co. KGaA, 69451 Weinheim, Germany, 2005)

Introduction

Vanadium plays a number of roles in biological systems.[1] It is present in vanadium-dependent haloperoxidases[2] and nitrogenase enzymes,[3] and many sea squirts accumulate it in very high concentrations, although the reason for this is not completely known.[4] The most recent studies concern the insulin-mimetic activity of vanadium compounds.[5] All these observations suggest interactions between vanadium ions and proteins.

Peptides are the most closely related models for proteins, and in some cases proteins may have specific terminal metal ion binding sites, for example albumin.[6] Among the various residues, histidine and cysteine play a main role: histidine is involved in the active site of vanadium haloperoxidases[2] and in the metal ion binding to albumin,[6] and the cysteine of glutathione takes part in redox processes such as the reduction of V^V to V^{IV} inside the cell. Moreover, peptide sequences containing cysteine mimic the binding sites of thioneins.

The interaction of $V^{IV}O$ with oligopeptides needs the presence of anchoring groups. Those most effective in promoting peptide amide deprotonation and coordination are phenolate-O^- followed by alkoxide-O^- and thiolate-S^-; COO^- and NH_2 are weaker groups.[7] The first examples of amide deprotonation for vanadium involved exclusively V^V,[8] although since then examples have been characterised for $V^{IV}O$ too, both in solution and in the solid state.[9] Recent results[10] have demonstrated that a histidyl residue in the N-terminal position can act as a valid anchor because the coordination of the amino group is assisted by the imidazole nitrogen. In the absence of suitable groups in the N-terminal position, mixed complexes with the (COO^-, CO) donor set can keep vanadium in solution until amide deprotonation occurs. As a consequence, L/M molar ratios of 10 are enough to favour complexation at physiological pH values.

The speciation of $V^{IV}O$ with HisGlyGly, GlyGlyHis and GlyGlyCys is reported in this work. The ligands are displayed in Scheme 1. GlyGlyHis is a model for albumins [e.g., human serum albumin (HSA), bovine serum albumin (BSA) and rat serum albumin (RSA)], neuromedins C and K, human sperm protamine P2a and histatins.[6] This motif binds Cu^{II} and Ni^{II} specifically, although it can release the metal to appropriate ligands, by playing the role of transport site in albumins. For example, 5–10% of serum cop-

[a] Department of Chemistry, University of Sassari
Via Vienna 2, 07100 Sassari, Italy
Fax: +39-079-212-069
E-mail: garribba@uniss.it; micera@uniss.it
[b] Institute of General Food Chemistry, Technical University of Lodz
ul. Stefanowskiego 4/10, 90924 Lodz, Poland
[c] Istituto C.N.R. di Chimica Biomolecolare
Trav. La Crucca 3, 07040 Li Punti, Sassari, Italy

Supporting information for this article is available on the WWW under http://www.eurjic.org or from the author.

 © 2005 Wiley-VCH Verlag GmbH & Co. KgaA, Weinheim

per[11] and 95% of serum nickel is bound to albumin.[12] The Cu^{II} ion can bind albumin in the form of a binary complex or ternary species with amino acids such as histidine.[13]

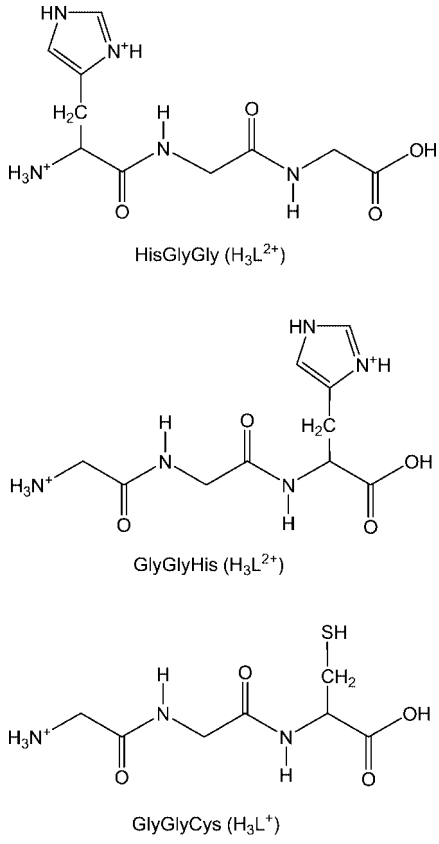

Scheme 1. Fully protonated forms of the ligands.

The form involved in the transport of vanadium in the human body is still unknown. However, the participation of albumin has been proposed for vanadium transport in blood.[14]

As far as $V^{IV}O$ insulin-mimetic compounds are concerned, the form that reaches target organs (bone, liver, kidney, muscles) is unknown. For many years it was suggested that it could be bound by human serum transferrin (hTF) and that the participation of albumin is negligible.[15] However the data for the $V^{IV}O$–transferrin interaction are quite uncertain, and no reliable thermodynamic data exist on the interaction with albumin. Willsky et al.[16] and Liboiron et al.[17] have reported albumin binding to a well-known insulin-mimetic compound [bis(maltolato)oxovanadium(IV)] (BMOV). The results were explained by the formation of adducts like $[VO(maltolato)_2HSA]$.[17] This suggests that adducts or ternary albumin complexes could be the pharmacologically active species or, at least, the main method of vanadium delivery to cells. However, equilibrium studies on the distribution of an insulin-mimetic complex between hTF and HSA are lacking. In particular, it is important to measure the stability constants for the interaction of albumin with $V^{IV}O$ and $V^{IV}O$ chelates to establish its participation in the transport of vanadium and insulin-mimetic vanadium compounds. GlyGlyHis represents a good model of albumin. Albumin can take part in the transport of insulin-mimetic compounds through: i) formation of binary complexes, such as those proposed for Cu^{II} and Ni^{II},[6] and studied in this work for $V^{IV}O$, and ii) formation of ternary complexes or adducts, such as [VO(maltolato)(HSA)] or $[VO(maltolato)_2(HSA)]$, as proposed by Liboiron et al.[17]

Results

L-Histidylglycylglycine (HisGlyGly)

The potentiometric titration of the ligand (H_3L^{2+}, Scheme 1 and Table 1) indicates three deprotonation steps with pK_a values of 3.10 (COOH), 5.39 ($N_{im}H^+$) and 7.34 (NH_3^+). The values are in good agreement with those reported in the literature.[18] The concentration distribution curves of the $V^{IV}O$ complexes as a function of pH are depicted in Figure 1.

Table 1. Protonation constants (log K) and $V^{IV}O$ (log β_{pqr}) stability constants for the studied ligands and complexes at 25.0 ± 0.1 °C and I = 0.1 M (KNO_3).

log K	HisGlyGly	GlyGlyHis	GlyGlyCys
COOH	3.10	3.26	2.98
$N_{im}H^+$	5.39	6.71	–
NH_3^+	7.34	7.93	7.77
SH	–	–	9.59
log β_{pqr}			
$VOLH_2$	14.55(1)	17.44(1)	19.56(2)
VOLH	12.51(2)		
VOL	8.37(2)		
VOL_2H_4		35.01(2)	39.49(1)
VOL_2H_3		30.08(2)	34.99(2)
VOL_2H_2		25.07(1)	29.99(2)
VOL_2H	18.23(1)	18.15(1)	23.50(3)
VOL_2	12.01(1)		15.79(2)
$VOLH_{-1}$	2.22(2)	2.00(2)	
$VOLH_{-2}$	–5.40(2)	–5.01(1)	–4.50(2)

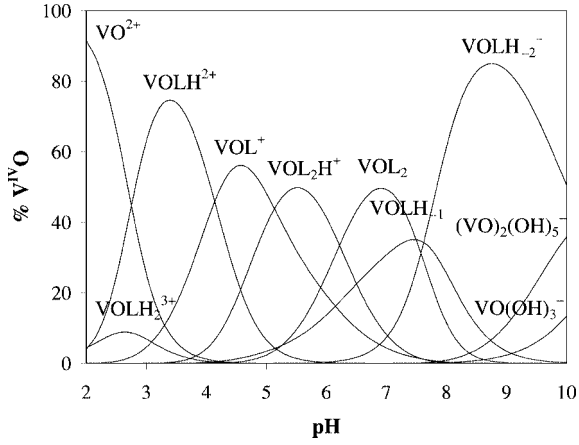

Figure 1. Species distribution for the $V^{IV}O$–HisGlyGly system at a metal-to-ligand molar ratio of 1:10 and a $V^{IV}O$ concentration of 1 mM.

A recent paper of ours[10] demonstrated that a histidyl residue in the N-terminal part of an oligopeptide is a good

 © 2005 Wiley-VCH Verlag GmbH & Co. KGaA, Weinheim

anchoring group due to the binding ability of the imidazole nitrogen. $HisNH_2$, HisGly and HisHis behave as tridentate ligands by coordinating the metal ion through the amino and imidazole nitrogen atoms and the carbonyl oxygen atom.

This speciation process was substantiated by pH-potentiometric titrations (see Experimental Section). Complex formation starts with a $VOLH_2$ species which predominates at pH 3–4 (**I** in Figure 2). To evaluate the "basicity adjusted" stability constant, we assume the following reaction: $VO^{2+} + H_3L^{2+} \rightarrow VOLH_2^{3+} + H^+$. A value of –1.28 is calculated for HisGlyGly, which can be compared with those for GlyGly (–1.43), GlyGlyGly (–1.59),[19] Ala (–1.33),[20] H_2SalGly (–1.29),[9b] H_2sal-RGG (–1.56) and H_2sal-RGGG (–1.51),[9f] for which a pure carboxylate coordination has been substantiated. The EPR parameters (Table 2) support this assignment.

VOLH (**IIa** in Figure 2) is formed upon deprotonation of the amino group, with $g_z = 1.947$ and $A_z = 168 \times 10^{-4}$ cm^{-1}. We compared the EPR spectra with those obtained in the $V^{IV}O$/L-glycine methyl ester (GlyOMe) system at L/M = 500. The stepwise formation of two species was observed, with $g_z = 1.946$, $A_z = 168 \times 10^{-4}$ cm^{-1} and $g_z = 1.951$, $A_z = 163 \times 10^{-4}$ cm^{-1}, respectively.[21] They were identified as VOL and VOL_2, with (NH_2, CO) and [2 × (NH_2, CO)] coordination modes, respectively. The data are also similar to those of mono- and bis-chelated complexes of $V^{IV}O$ with L-histidine methyl ester (HisOMe),[21] $g_z = 1.946$, $A_z = 170 \times 10^{-4}$ cm^{-1} and $g_z = 1.950$, $A_z = 164 \times 10^{-4}$ cm^{-1}. The parameters reported for the mono-chelated complex formed by imidazole-4-acetic acid, with an (N_{im}, COO^-) donor set, are quite different from those observed with HisGlyGly.[22] Therefore, the spectroscopic features of VOLH are typical of an (NH_2, CO) donor set.

The deprotonation of the imidazole N takes place with $pK_a = 4.16$, and VOLH transforms into VOL (**IIb** in Fig-

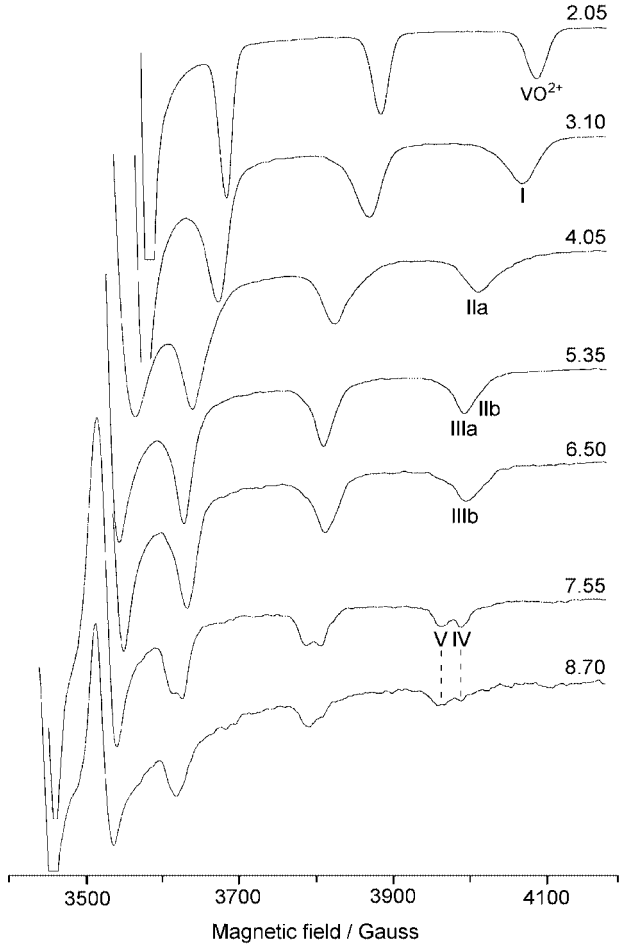

Figure 2. High-field region of the X-Band EPR spectra recorded at 140 K as a function of pH for aqueous solutions of $V^{IV}O$ and HisGlyGly at metal-to-ligand molar ratio of 1:10 and a $V^{IV}O$ concentration of 4 mM. The dotted line indicates the high-field resonance of the complexes with the deprotonated amide group.

Table 2. EPR parameters and donor sets for $V^{IV}O$ complexes.

Ligand	Complex	Symbol[a]	g_z	A_z[b]	Donor set
HisGlyGly	$VOLH_2$	**I**	1.935	177	(COO^-)
	VOLH	**IIa**	1.947	168	(NH_2, CO)
	VOL	**IIb**	1.947	168	(NH_2, CO, N_{im}^{ax})
	VOL_2H	**IIIa**	1.950	164	[(NH_2, CO, N_{im}^{ax}); (NH_2, CO)]
	VOL_2	**IIIb**	1.950	164	[(NH_2, CO, N_{im}^{ax}); (NH_2, CO)]
	$VOLH_{-1}$	**IV**	1.950	161	[(NH_2, N^-, CO, N_{im}^{ax}); H_2O]
	$VOLH_{-2}$	**V**	1.951	159	(NH_2, N^-, N^-, COO^-, N_{im}^{ax})
GlyGlyHis	$VOLH_2$	**I**	1.936	176	(COO^-, CO)
	VOL_2H_4	**II**	1.940	172	[2 × (COO^-, CO)]
	VOL_2H_3	**IIIa**	1.945	169	[(NH_2, CO); (COO^-, CO)]
	VOL_2H_2	**IIIb**	1.945	169	[(NH_2, CO); (COO^-, CO)]
	VOL_2H	**IIIc**	1.945	169	[(NH_2, CO); (COO^-, CO)]
	$VOLH_{-1}$	**IV**	1.950	161	[(NH_2, N^-, CO, N_{im}^{ax}); H_2O]
	$VOLH_{-2}$	**V**	1.960	153	(NH_2, N^-, N^-, N_{im})
GlyGlyCys	$VOLH_2$	**I**	1.935	176	(COO^-, CO)
	VOL_2H_4	**II**	1.940	171	[2 × (COO^-, CO)]
	VOL_2H_3	**III**	1.945	168	[(NH_2, CO); (COO^-, CO)]
	VOL_2H_2	**IV**	1.949	164	[2 × (NH_2, CO)]
	VOL_2H	**V**	1.950	160	[(NH_2, CO); (S^-, COO^-)]
	VOL_2	**VI**	1.960	152	[(NH_2, N^-, CO); (S^-, COO^{-ax})]
	$VOLH_{-2}$	**VII**	1.967	148	(NH_2, N^-, N^-, S^-)

[a] See Figure 2 for HisGlyGly, Figure 4 for GlyGlyHis and Figure 6 for GlyGlyCys. [b] A_z measured in 10^{-4} cm^{-1} units.

 © 2005 Wiley-VCH Verlag GmbH & Co. KGaA, Weinheim

ure 2). The pK_a value is lower, by one order of magnitude, than in the free ligand because of the coordination of the nitrogen atom. The EPR parameters are the same as VOLH and comparable with those of complexes of dipeptides with histidine in N-terminal position, such as HisGly and HisHis.[10] In a previous work,[10] we suggested a tridentate equatorial-axial-equatorial (*eq-ax-eq*) binding mode of the ligand to explain the similar behaviour of $HisNH_2$, HisGly and HisHis. The two external donor groups (NH_2 and CO) are in the equatorial positions and N_{im} is in the axial position. The "basicity adjusted" stability constant for the reaction $VO^{2+} + HL^+ \rightarrow [VOL]^{2+} + H^+$ is –1.03. This means that the involvement of an imidazole nitrogen as the third donor increases the stability of the species with an (NH_2, CO, N_{im}^{ax}) donor set significantly compared with those of (NH_2, CO) or (COO^-, CO).

The imidazole N in the axial position of VOL does not affect the A_z value significantly according to the Chasteen "additivity rule", which assumes that only the equatorial donors contribute to the hyperfine ^{51}V constant along the *z* axis.[23]

The bis-complexes VOL_2H and VOL_2 are the major species at pH 5–7. At ligand-to-metal molar ratios as high as 10 for HisGlyGly and 15 for GlyGlyHis and GlyGlyCys, we believe that weak donor sets like (NH_2, CO) can replace monodentate water molecules in the equatorial plane of $V^{IV}O$. In VOL_2H (**IIIa** in Figure 2), only two positions of the equatorial plane are available for the second ligand, therefore the coordination mode is [(NH_2, CO, N_{im}^{ax}); (NH_2, CO)], with the imidazole nitrogen of the second ligand molecule still protonated.

The transformation of VOL_2H into VOL_2 (**IIIb** in Figure 2) takes place upon deprotonation of the $N_{im}H^+$ group. The pK_a of 5.84 is very close to that of the free ligand, suggesting that the aromatic nitrogen of the second ligand molecule does not participate in the coordination. Since the donor set is the same, the same EPR parameters are observed for VOL_2H and VOL_2 (g_z = 1.950, A_z = 164×10^{-4} cm^{-1}), comparable to those of HisGly (g_z = 1.951, A_z = 165×10^{-4} cm^{-1}) and HisHis (g_z = 1.950, A_z = 164×10^{-4} cm^{-1}).[10]

$VOLH_{-1}$ (**IV** in Figure 2 and **a** in Scheme 2) is detected both by potentiometry and EPR spectroscopy at a pH of around 7.5. Its spectral parameters are g_z = 1.950 and A_z = 161×10^{-4} cm^{-1}, and its pK_a value is 7.55. For this species we propose the deprotonation of the first amide group to give a complex with an [(NH_2, N^-, CO, N_{im}^{ax}); H_2O] coordination mode. The axial binding of an imidazole nitrogen stabilises this coordination mode differently from tripeptides lacking coordinating side-chains.

At higher pH values the formation of $VOLH_{-2}$ (**V** in Figure 2 and **b** in Scheme 2) starts. The EPR parameters (g_z = 1.951 and A_z = 159×10^{-4} cm^{-1}) suggest the deprotonation of the second amide bond and an (NH_2, N^-, N^-, COO^-) donor set with four donor atoms in the equatorial positions, analogously to the Cu^{II} ion;[24] hydrolysis processes occur at pH values above 9.

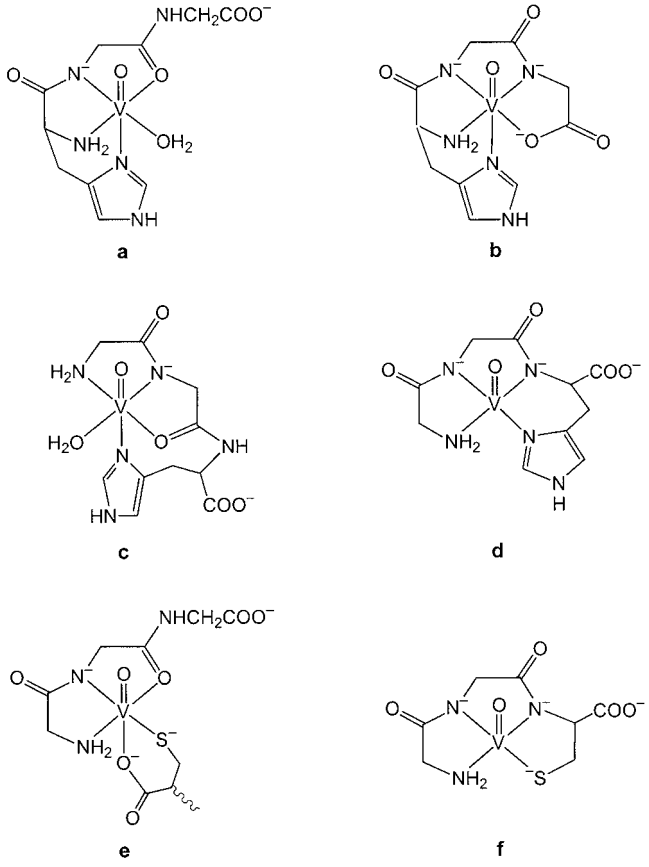

Scheme 2. Structures of $V^{IV}O$ complexes formed by HisGlyGly (a,b), GlyGlyHis (c,d) and GlyGlyCys (e,f) with deprotonated amide groups.

Glycylglycyl-L-histidine (GlyGlyHis)

GlyGlyHis (H_3L^{2+}, Table 1 and Scheme 1) shows three pK_a values in the titrable pH range, 3.26 (COOH), 6.71 ($N_{im}H^+$) and 7.93 (NH_3^+). These values are comparable with those in the literature.[25] Distribution curves are shown in Figure 3 and EPR spectra in Figure 4.

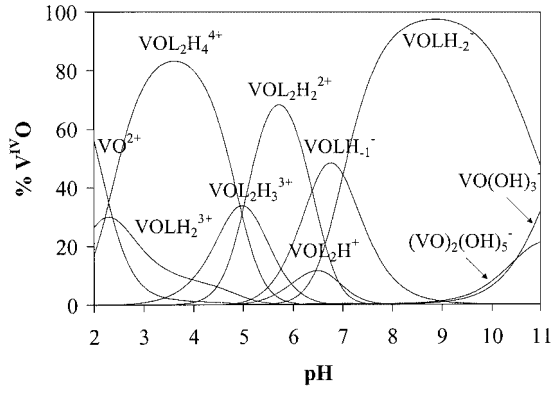

Figure 3. Species distribution for the $V^{IV}O$–GlyGlyHis system at a metal-to-ligand molar ratio of 1:15 and a $V^{IV}O$ concentration of 1 mM.

 © 2005 Wiley-VCH Verlag GmbH & Co. KGaA, Weinheim

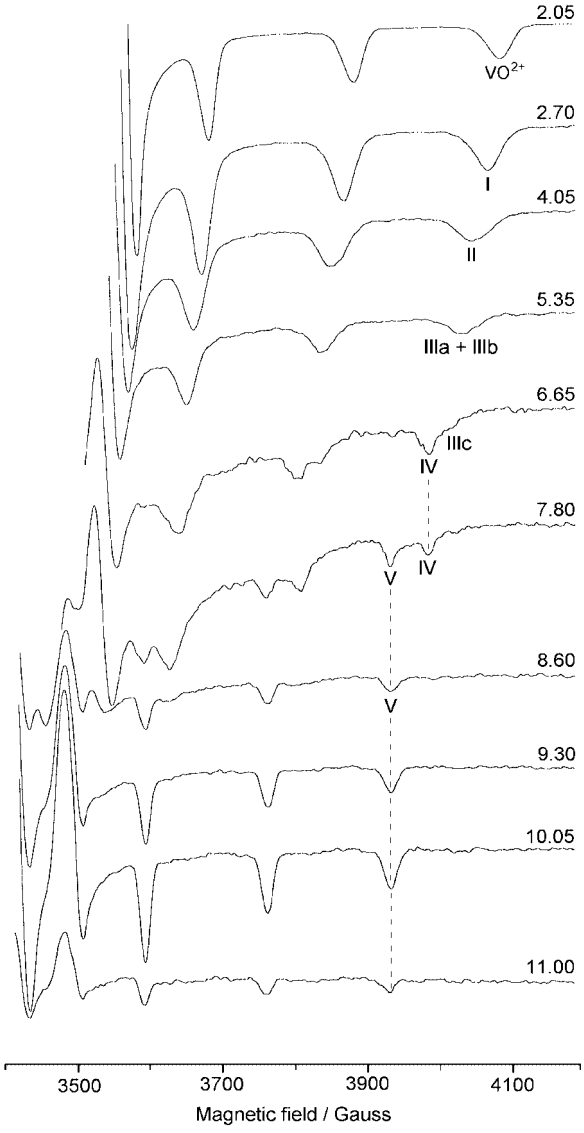

Figure 4. High-field region of the X-Band EPR spectra recorded at 140 K as a function of pH on aqueous solutions of $V^{IV}O$ and GlyGlyHis at a metal-to-ligand molar ratio of 1:15 and a $V^{IV}O$ concentration of 4 mM. The dotted line indicates the high-field resonance of the complexes with the deprotonated amide group.

If the N-terminal residue has no coordinating chain donor, the (NH_2, CO) donor set is not a good anchoring group and the (COO^-, CO) donor set is stronger.[10] This supports the spectroscopic results of previous works.[19] In this system the complexation starts with $VOLH_2$ (**I** in Figure 4), similar to the analogous complexes of GlyHis and GlyCys.[10] The "basicity adjusted" stability constant of this complex (–0.46) is somewhat higher than expected for pure carboxylate coordination[26] and indicates extra donors, presumably the amide carbonyl, which closes a seven-membered chelate ring. The EPR parameters (Table 2) are in agreement with recent reports,[9c,9h,10,27a,27b] which attribute hyperfine coupling constants in the range 175–179×10^{-4} cm^{-1} to mono-chelated species. We believe that the formation of an intramolecular hydrogen bond between the carboxylate oxygen and the NH^+ group of imidazole provides an extra stabilisation of this structure (Scheme 3). In fact, this coordination mode is not observed with dipeptides or tripeptides with glycine in the C-terminal part, for example GlyGly,[19] HisGly,[10] GlyGlyGly[19] or HisGlyGly (this work).

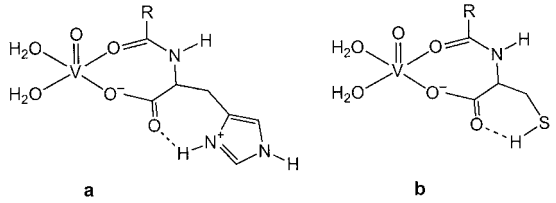

Scheme 3. Structures of $VOLH_2$ complexes formed by GlyGlyHis (a) and GlyGlyCys (b).

Around pH 4 a species of composition VOL_2H_4 (**II** in Figure 4) predominates. It can be described as a bis-chelated complex of the [2×(COO^-, CO)] type (Table 2). The two ligands have their amino and imidazole nitrogens still protonated. The EPR parameters are in agreement with the literature data,[9c,9h,10,27a,27b] which report hyperfine coupling constants in the range $171–174 \times 10^{-4}$ cm^{-1} for bis-chelated species.

In VOL_2H_3 (**IIIa** in Figure 4) one of the two ligands has released a proton from the amino group, and the coordination therefore becomes [(NH_2, CO); (COO^-, CO)], with EPR parameters $g_z = 1.945$ and $A_z = 169 \times 10^{-4}$ cm^{-1}, which are intermediate between those of the [2×(COO^-, CO)] and [2×(NH_2, CO)] donor sets.[10]

VOL_2H_2 and VOL_2H (**IIIb** and **IIIc**, respectively, in Figure 4) form from VOL_2H_3 upon deprotonation of the two imidazole rings (pK_a = 5.03 and 6.02, respectively). The coordination mode can be described as [(NH_2, CO); (CO, COO^-)], since the spectral parameters don't change, although an [(NH_2, CO); (N_{im}, COO^-)] donor set cannot be excluded.

The deprotonation of the first amide group leads to $VOLH_{-1}$, which has an [(NH_2, N^-, CO, $N_{im}{}^{ax}$); H_2O] donor set (**IV** in Figure 4 and **c** in Scheme 2). The weak coordination of the imidazole nitrogen in the axial position could stabilise this species.

The deprotonation of the second amide group gives $VOLH_{-2}$ (**V** in Figure 4 and **d** in Scheme 2), with an (NH_2, N^-, N^-, N_{im}) donor set and g_z = 1.960, A_z = 153×10^{-4} cm^{-1}. The difference between this and the $VOLH_{-2}$ complex formed by HisGlyGly is the presence of an imidazole nitrogen instead of a carboxylate group in the fourth equatorial position, which lowers the hyperfine coupling constant. For an (NH_2, N^-, N^-, COO^-) coordination we expect the same parameters observed for $VOLH_{-2}$ of HisGlyGly.

A special comment must be devoted to the different behaviour of GlyGlyHis and GlyGlyGly. We studied the system with GlyGlyGly up to an L/M molar ratio of 20.[21] The complexation process stops at acid pH values with the formation of species with only COO^- coordination. The higher stability of the (COO^-, CO) donor set for GlyGlyHis is responsible for the stabilisation of the mixed species

 © 2005 Wiley-VCH Verlag GmbH & Co. KGaA, Weinheim

VOL_2H_3, VOL_2H_2 and VOL_2H, which avoids hydroxide precipitation and promotes the amide deprotonation.

Glycylglycyl-L-cysteine (GlyGlyCys)

With oligopeptides containing L-cysteine the complexation of Ni^{II}, Pd^{II}, Co^{II}, Zn^{II} and Cd^{II} depends strongly on the position of the residue in the peptide and on the "hardness" of the metal ion.[28] $V^{IV}O$ follows the same trend: with CysGly a stable cysteine-like (NH_2, S^-) coordination is favoured and mono [VOA] and bis $[VOA_2]^{2-}$ complexes are formed. On the other hand, with a C-terminal cysteine dipeptide like GlyCys, $V^{IV}O$ promotes the coordination of the deprotonated amide group as with Ni^{II} and Pd^{II}.[24a,24b]

GlyGlyCys (H_3L^+, Table 1 and Scheme 1) shows three pK_a values: at 2.98 (COOH), 7.77 (NH_3^+) and 9.59 (SH), in good agreement with those in the literature.[24a] The species distribution for this system as a function of pH is displayed in Figure 5.

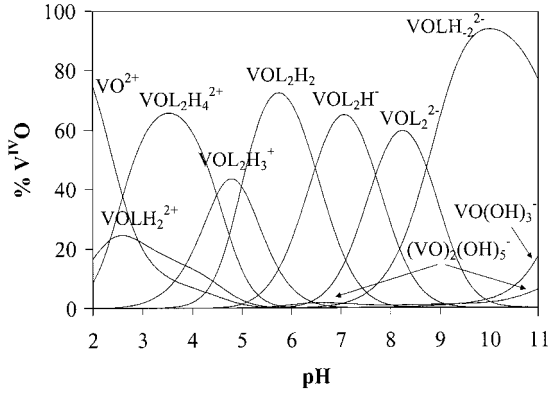

Figure 5. Species distribution for the $V^{IV}O$–GlyGlyCys system at a metal-to-ligand molar ratio of 1:15 and a $V^{IV}O$ concentration of 1 mM.

As with GlyGlyHis, the complexation scheme starts with the formation of $VOLH_2$ (**I** in Figure 6) and VOL_2H_4 (**II** in Figure 6) at pH around 3 and 4, respectively, in strongly overlapping processes. The donor sets are (COO^-, CO) and [2×(COO^-, CO)], respectively, and the EPR parameters (g_z = 1.935, A_z = 176×10^{-4} cm^{-1} and g_z = 1.940, A_z = 171×10^{-4} cm^{-1}) are in good agreement with those of the species formed by 2-mercaptopropionylglycine,[27a] GlyHis and GlyCys,[10] and GlyGlyHis (see above). In both complexes each ligand maintains protonated amino and thiol groups. As for GlyGlyHis, the (COO^-, CO) coordination is stabilised by an intramolecular hydrogen bond between the carboxylate oxygen atom and the SH group of cysteine (Scheme 3).

The consecutive deprotonation of the amino groups gives rise to VOL_2H_3 and VOL_2H_2 (**III** and **IV** in Figure 6) in the pH range 5–7. A mixed [(NH_2, CO); (COO^-, CO)] coordination can be proposed for the first complex and a [2×(NH_2, CO)] coordination for the second. The EPR parameters support this assignment (Table 2). With increasing pH the first SH group undergoes deprotonation and VOL_2H_2 is replaced by VOL_2H (**V** in Figure 6), which is

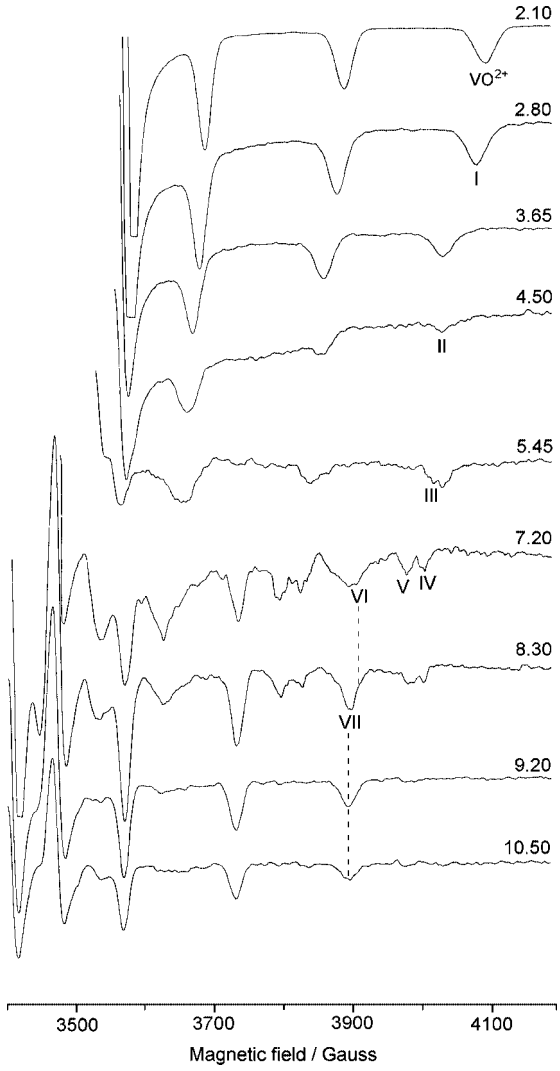

Figure 6. High-field region of the X-Band EPR spectra recorded at 140 K as a function of pH on aqueous solutions of $V^{IV}O$ and GlyGlyCys at a metal-to-ligand molar ratio of 1:15 and a $V^{IV}O$ concentration of 4 mM. The dotted line indicates the high-field resonance of the complexes with the deprotonated amide group.

presumably a complex with a mixed donor set [(S^-, COO^-); (NH_2, CO)]. This conclusion is supported by the EPR parameters (g_z = 1.950, A_z = 160×10^{-4} cm^{-1}), which are intermediate between those of [2×(NH_2, CO)] and [2×(S^-, COO^-)] and similar to those of the analogous species with GlyCys.[10]

Upon deprotonation of the first amide group the coordination of the first ligand molecule switches from (NH_2, CO) to (NH_2, N^-, CO) and VOL_2, with the donor set [(NH_2, N^-, CO); (S^-, COO^{-ax})], is formed (**VI** in Figure 6 and **e** in Scheme 2). Its spectral parameters (Table 2) are consistent with our expectations, as will be discussed later.

At pH values above 8 potentiometry suggests a $VOLH_{-2}$ species, which is explainable by the deprotonation of the second amide group and the coordination of an S^- donor (**VII** in Figure 6 and **f** in Scheme 2). The EPR parameters, g_z = 1.967, A_z = 148×10^{-4} cm^{-1}, are consistent with an

 © 2005 Wiley-VCH Verlag GmbH & Co. KGaA, Weinheim

(NH_2, N^-, N^-, S^-) coordination mode, which is also observed with Ni^{II}.[28a]

Discussion

The Chasteen "additivity rule" is a powerful tool to estimate the ^{51}V hyperfine constant along the z axis of $V^{IV}O$ complexes and is based on the individual contribution to A_z from the four equatorial donors.[23] This rule provides a valid criterion for the identification of the equatorial donor atoms. Data for the contribution of amino and imidazole nitrogen atoms and for thiolate group were taken from Chasteen's publication.[23] For carboxylate, the value of 42.1×10^{-4} cm^{-1} reported by Kiss and Costa-Pessoa was chosen.[27a] The mean value for a neutral oxygen atom belonging to an amide CO group is 43.5×10^{-4} cm^{-1}.[29]

The amide contribution, A_z(amide), is in the range 29–43×10^{-4} cm^{-1},[30] and is sensitive to the charge of the coordination sphere. We have demonstrated previously that this contribution decreases with an increased donation of electron density from the ligands to the $V^{IV}O$ ion.[10] In particular, we found that if the total charge of the donor atoms in the equatorial plane (TEC) is –2, –3 or –4 (including the –1 charge of the deprotonated peptide nitrogen), the mean A_z(amide) values are 35.3, 38.6 and 40.9×10^{-4} cm^{-1}, respectively, in good agreement with those calculated by Kabanos and Deligiannakis.[9d] We were able to extrapolate the contribution of the amide group when TEC is –1 (32.7×10^{-4} cm^{-1}).[10]

Table 3 is based on these contributions to the value of A_z. If we examine the three fully deprotonated $VOLH_{-2}$ species no ambiguity exists in the coordination mode: two amide groups are deprotonated and three of the four equatorial positions are occupied by amino and two deprotonated amide groups. The fourth position is occupied by three different donors: the carboxylate group in HisGlyGly and the side-chain of the C-terminal amino acid in GlyGlyHis and GlyGlyCys (i.e. the imidazole nitrogen of histidine and the thiolate group of cysteine, respectively; Table 3). This is substantiated by the A_z values of 158.6×10^{-4} cm^{-1} for HisGlyGly, 152.9×10^{-4} cm^{-1} for GlyGlyHis and 147.9×10^{-4} cm^{-1} for GlyGlyCys. The experimental values are very close to the calculated ones, with differences of less than 1%.

A substantially good agreement is also found for the other species involving a deprotonated amide group (Table 3), according to our previous analysis.[10] The structures of the complexes formed by deprotonation of the amide groups are displayed in Scheme 2.

We used the thermodynamic data to evaluate in which form the $V^{IV}O$ ion and $V^{IV}O$ insulin-mimetic compounds are transported in the human body. Given the chemical composition of serum,[31] the two h.m.m. (high molecular mass) metal-ion binders in the serum are albumin and transferrin,[16,17] whilst among the l.m.m. (low molecular mass) constituents, oxalic acid, lactic acid, citric acid and phosphate are the most likely.[15] Detailed studies have been reported on the interaction of $V^{IV}O$ ion with transferrin and albumin.[32]

Human serum transferrin (hTF), a bilobal, single-chain protein, is the main Fe^{III} transport protein in serum. It is responsible for tight, reversible binding of two equivalents of Fe^{III} and binds a variety of other metal ions such as $V^{IV}O$.[33] It has two non-equivalent vanadium binding sites, with different binding constants.[32f,34a,34b] This requires a synergistic anion binding.[33] These sites should correspond to the usual N-lobe and C-lobe binding sites of the protein. An approximate value for the two stability constants ($\log K_1^* = 13.2$ and $\log K_2^* = 12.2$) was reported recently by some of us.[15]

Human serum albumin (HSA), bovine serum albumin (BSA) and rat serum albumin (RSA) share the same structural motif in the N-terminal part of the protein, namely two amino acids with non-coordinating or weakly coordinating side-chains in the first two positions and a histidine residue in the third position (AspAlaHis for HSA, AspThrHis for BSA and GluAlaHis for RSA). This results in an identical chemical and spectroscopic behaviour; for instance, Cu^{II} shows the same electronic[35] and EPR parameters.[36] It has been proposed that this is the site preferred by $V^{IV}O$ too, although there are four or five additional weaker binding sites in the side-chain, namely Asp and Glu carboxylates.[14,32c] The substitution in other mammalian species of the histidine residue in the third position, e.g. Tyr in dog serum albumin (DSA) and Glu in chicken serum albumin (CSA), produces a lack of specific binding to metal ions.[37]

These features, as well as the geometry of the ligand array in the native protein and the nature of the donor groups, were considered in the design of the first model of this structural motif, GlyGlyHis-*N*-methylamide. Moreover, theoretical calculations using energy minimisation show similar conformations for AspAlaHis and GlyGlyHis bound to Cu^{II}.[38] For these reasons, we propose that

Table 3. Coordination modes of $V^{IV}O$ complexes with deprotonated amide groups on the basis of the EPR data.

Ligand	Complex	g_z	A_z exp.[a]	A_z calcd.[a]	Donor atoms
HisGlyGly	$VOLH_{-1}$	1.950	161.1	161.9	[(NH_2, N^-, CO, $N_{im}{}^{ax}$); H_2O]
HisGlyGly	$VOLH_{-2}$	1.951	158.6	159.4	(NH_2, N^-, N^-, COO^-, $N_{im}{}^{ax}$)
GlyGlyHis	$VOLH_{-1}$	1.950	161.4	161.9	[(NH_2, N^-, CO, $N_{im}{}^{ax}$); H_2O]
GlyGlyHis	$VOLH_{-2}$	1.960	152.9	151.4	(NH_2, N^-, N^-, N_{im})
GlyGlyCys	VOL_2	1.960	151.9	150.8	[(NH_2, N^-, CO); (S^-, COO^{-ax})]
GlyGlyCys	$VOLH_{-2}$	1.967	147.9	149.3	(NH_2, N^-, N^-, S^-)

[a] A_z measured in 10^{-4} cm^{-1} units.

 © 2005 Wiley-VCH Verlag GmbH & Co. KGaA, Weinheim

GlyGlyHis is also a good model for the interaction between $V^{IV}O$ and albumin. The structure of Cu^{II}-GlyGlyHis-*N*-methylamide has been solved by X-ray crystallography.[39] Cu^{II} ion is chelated by the NH_2-terminal nitrogen, the next two deprotonated amide nitrogens and a histidyl imidazole nitrogen of GlyGlyHis through an (NH_2, N^-, N^-, N_{im}) donor set in a slightly distorted square-planar arrangement similar to that which we propose for $VOLH_{-2}$ (Table 2), the most relevant form under physiological conditions.

An association constant of 2.6×10^6 M^{-1} has been measured for the N-terminal site of BSA at pH 5, although at physiological pH the corresponding value is thought to be several orders of magnitude higher.[14] No data exist for the interaction with a model system like GlyGlyHis.

Chasteen et al.[32b] have found that transferrin binds $V^{IV}O$ about six times more strongly than albumin in vitro. If we accept Chasteen's assumption that albumin is an efficient binder and apply his estimation [K(hTF)/K(alb) ≈ 6], the calculated biodistribution indicates that only the h.m.m. fraction of the serum (80% albumin and 20% transferrin) binds $V^{IV}O$.[15]

By taking into account the data for the association constants for transferrin,[15] the stability constants of the model ligand for albumin (GlyGlyHis), and the binary systems with oxalate,[40] lactate,[41] citrate[42] and phosphate,[43] the complete distribution of $V^{IV}O$ ion can be calculated for the conditions in the serum. The results are reported in Table 4.

Table 4. Species distribution [%] of the $V^{IV}O$ ion between the components of the blood serum at pH 7.4.[a]

$c_{V^{IV}O}$ [μM]	l.m.m. components	Transferrin	GlyGlyHis
1	0.1	99.7	0.2
10	0.1	99.7	0.2
100	22.0	70.8	7.2

[a] Oxalate = 9.20 μM; lactate = 1.51 mM; citrate = 99.0 μM; phosphate = 1.10 mM; transferrin = 37 μM; GlyGlyHis = 630 μM.

Table 4 reveals that at a $V^{IV}O$ concentration of 1 μM and 10 μM the $V^{IV}O$ ion is almost totally bound to transferrin, with less than 1% bound to albumin. However, at a concentration of 100 μM both albumin and l.m.m binders participate in the transport of $V^{IV}O$ ion, with approximately 7% bound to albumin and about 22% bound to l.m.m. ligands, especially citrate.

This discussion can be extended to the transport of insulin-mimetic compounds. We examined the bis-chelate compounds formed by $V^{IV}O$ ion with maltolato (ma),[44] picolinato (pic) and 6-methylpicolinato (6-Mepic),[45] 3-hydroxy-1,2-dimethyl-4(1*H*)-pyridinone (HDP),[46] 5-methoxycarbonylpicolinic acid (5-MeOpic),[47] 2-hydroxypyridine *N*-oxide (HPO) and 2-mercaptopyridine *N*-oxide (MPO).[48] For the calculations we used the association constants for transferrin;[15] the stability constants of the binary complexes with GlyGlyHis, oxalate,[40] lactate,[41] citrate,[42] and phosphate;[43] and the thermodynamic data for the $V^{IV}O$ species formed by the seven carriers[43,47,48b,49] and for the $V^{IV}O$ ternary complexes formed by the carriers and the l.m.m. binders of the serum.[43,47,48b,49b,49c] If a 10 μM level of the insulin-mimetic compounds in the serum is used, $V^{IV}O$ is totally bound to transferrin, with a minor amount bound to albumin, whereas the binding to the l.m.m. components is negligible. Only in the system with HDP, due to the high value of the stability constant of the bis chelated complex, is about 30% of $V^{IV}O$ bound to the carrier.

If the concentration of the $V^{IV}O$ complex is increased to 100 μM, albumin and l.m.m. binders also take part in the metal binding. The results of the biodistribution of insulin mimetics in serum are presented in Table 5.

Table 5. Species distribution [%] of $V^{IV}O$ insulin-mimetic compounds between the components of blood serum at pH 7.4.[a]

Complex[b]	VO^{IV} carrier	l.m.m components		h.m.m. components	
		Binary species	Ternary species	Transferrin	GlyGlyHis
$[VO(ma)_2]$	10.4	4.6	15.4	66.7	2.9
$[VO(pic)_2]$	0.3	2.7	28.8	65.7	2.5
$[VO(6\text{-}Mepic)_2]$	0.1	4.6	24.2	67.7	3.4
$[VO(HDP)_2]$	79.6	0.0	3.4	16.9	0.1
$[VO(5\text{-}MeOpic)_2]$	0.1	2.8	29.3	65.4	2.4
$[VO(HPO)_2]$	30.2	0.1	29.0	40.4	0.3
$[VO(MPO)_2]$	1.5	10.9	13.7	69.2	4.7

[a] $V^{IV}O$ = 100 μM; oxalate = 9.20 μM; lactate = 1.51 mM; citrate = 99.0 μM; phosphate = 1.10 mM; transferrin = 37 μM; GlyGlyHis = 630 μM. [b] ma = maltolato; pic = picolinato; 6-Mepic = 6-methylpicolinato; HDP = 3-hydroxy-1,2-dimethyl-4(1*H*)-pyridinone; 5-MeOpic = 5-(methoxycarbonyl)picolinic acid; HPO = 2-hydroxypyridine *N*-oxide; MPO = 2-mercaptopyridine *N*-oxide.

The amount of $V^{IV}O$ bound to transferrin and albumin depends on the strength of the $V^{IV}O$–carrier interaction. With the two stronger binders (HDP and HPO) a high fraction of $V^{IV}O$ is found in the native form of $[VO(carrier)_2]$, whereas in the other systems most of the $V^{IV}O$ (65–70%) is bound to transferrin and the rest is distributed among the binary and ternary compounds of the l.m.m. binders and the complexes with albumin. In particular, with the five weaker binders about 2–5% is associated with albumin. Of this amount, the highest part is present as $VOLH_{-2}$ and the rest as $VOLH_{-1}$. These data confirm the results of previous studies substantiating that the amount of $V^{IV}O$ bound to albumin is lower than that bound to transferrin.[15] However, it is worth noting that albumin can play a secondary role comparable to that of the l.m.m. components.

The distribution of $V^{IV}O$ between h.m.m. and l.m.m. fractions is very sensitive to the binding constants of $V^{IV}O$–hTF.[15] As a consequence of the relatively high uncertainties in the transferrin binding constants (±0.8 log units),[50] the results could change considerably if the association constants are overestimated. For example, if the values of $\log K_1^*$ and $\log K_2^*$ were 12.4 and 11.4, the amount of $V^{IV}O$ transported by albumin, at a vanadium concentration of 100 μM, rises to 9.1%. In the systems with the insulin-mimetic compounds, the fraction increases to 4.4% with ma, 4.1% with pic, 5.3% with 6-Mepic, 0.2% with HDP, 3.7% with 5-MeOPic, 0.5% with HPO and 6.3% with MPO.

However, in light of the recent results of Liboiron et al.,[17] the equilibrium data concerning the formation of ter-

 © 2005 Wiley-VCH Verlag GmbH & Co. KGaA, Weinheim

nary complexes between the insulin-mimetic $V^{IV}O$ compounds and albumin could be important.

Finally, we would like to note that we have neglected the possibility of reduction and oxidation of $V^{IV}O$ species, although $V^{IV}O$ compounds in aqueous solution at varying pH, ligand-to-metal molar ratios and concentration and in the presence of biogenic ligands are subject to several processes, including redox activity.[51] However, in the conditions of transport (acid pH in the stomach and pH 7.4 in the blood serum), a complex of $V^{IV}O$ is relatively stable. Only after its translocation across the cell membrane into the intracellular medium can reducing agents such as glutathione (GSH), nicotinamide adenine dinucleotide (NADH) or ascorbate reduce $V^{IV}O$ to V^{III} [52a–52c] or potential oxidizing agents such as oxygen, peroxide, superoxide[53] or $OH^{\cdot}$ radicals[54] oxidise $V^{IV}O$ to V^{V}.

Conclusions

Simple HisGlyGly, GlyGlyHis and GlyGlyCys tripeptides coordinate the $V^{IV}O$ ion at acidic pH values and keep it in solution until the deprotonation of the amide group. Two main differences distinguish HisGlyGly, GlyGlyHis and GlyGlyCys. With HisGlyGly, only the weak coordination of carboxylate is observed at very acidic pH values, and this is easily replaced by a stronger (NH_2, CO, N_{im}^{ax}) donor set. With GlyGlyHis and GlyGlyCys an intramolecular hydrogen bond between the carboxylate oxygen and NH or SH bond of GlyGlyHis and GlyGlyCys stabilises the (COO^-, CO) donor set, so that $VOLH_2$ and VOL_2H_4 species with (COO^-, CO) and [2×(COO^-, CO)] coordination are formed. This coordination mode is indicated by a higher value of the "basicity adjusted" stability constant than expected for pure carboxylate coordination and by an accurate measurement of the A_z value, which is around 175–176×10^{-4} cm^{-1} for mono-chelated complexes and 171–172×10^{-4} cm^{-1} for bis-chelated species.

With GlyGlyHis and GlyGlyCys the final complexes (NH_2, N^-, N^-, N_{im}) and (NH_2, N^-, N^-, S^-) are more stable than (NH_2, N^-, N^-, COO^-) because the imidazole nitrogen and thiolate sulfur are more effective donors than carboxylate oxygen. Therefore, at constant L/M molar ratios (15), $VOLH_{-2}$ is the main species in solution until pH 11.6 with GlyGlyCys, pH 11.1 with GlyGlyHis and pH 10.8 with HisGlyGly.

The final species with both the amide groups deprotonated − (NH_2, N^-, N^-, COO^-), (NH_2, N^-, N^-, N_{im}) and (NH_2, N^-, N^-, S^-) − are easily detected by EPR spectroscopy. A contribution of 38.6, 35.3 and 38.6×10^{-4} cm^{-1} to the A_z value is attributed to the N^- donor according to a total charge in the equatorial plane (TEC) of –3, –2 and –3, respectively.[10]

A direct application of these results is of biological interest. In fact, the binding to GlyGlyHis can be considered a good model for the interaction of the $V^{IV}O$ ion with albumin.[6] At physiological pH, GlyGlyHis binds mainly $V^{IV}O$ with an (NH_2, N^-, N^-, N_{im}) donor set, as with Cu^{II} and Ni^{II},[6] to form a very stable $VOLH_{-2}$ species.

Albumin can also take part in the transport of vanadium and insulin-mimetic $V^{IV}O$ compounds such as those formed by maltolato, picolinato, 6-methylpicolinato, 3-hydroxy-1,2-dimethyl-4(1*H*)-pyridinone, 5-methoxycarbonylpicolinato, 2-hydroxypyridine *N*-oxide and 2-mercaptopyridine *N*-oxide. Its contribution is less important than that of transferrin, but cannot be neglected completely as proposed by previous studies.[15,47,48b,49c] Accordingly, the formation of adducts between the insulin-mimetic compounds [VO(maltolato)$_2$] and albumin has been reported.[17] Thus, the role of albumin in these processes must be re-evaluated.

Potentiometric and spectroscopic studies on the biodistribution of $V^{IV}O$ ion between GlyGlyHis and an organic carrier will be useful to establish the importance and role of the ternary complexes in the transport of the insulin-mimetic compounds in vivo.

Experimental Section

Chemicals: The ligands were Aldrich products of puriss. quality. Their purity and concentration were determined by Gran's method.[55] $V^{IV}O$ solutions were prepared following literature methods.[56] The concentration of the metal ion was determined by $KMnO_4$ titration and that of H^+ by a potentiometric titration using the appropriate Gran function. The ionic strength was adjusted to 0.1 M with KNO_3. The temperature was 25.0±0.1 °C.

Potentiometric Measurements: The stability constants of proton and $V^{IV}O$ complexes were determined by pH-potentiometric titrations on 1.2–2 mL of the samples. The ligand-to-metal molar ratio was 1:1, 5:1, 10:1 and 15:1 and $V^{IV}O$ concentration was 0.001–0.004 M. Titrations were performed from pH 2.0 until precipitation or very extensive hydrolysis by adding carbonate-free NaOH of known concentration (ca. 0.1 M NaOH). The pH was measured with a Russel CMAWL/S7 semi-micro combined electrode, calibrated for hydrogen concentration by the method of Irving et al.[57] Measurements were carried out at 25.0±0.1 °C and at a constant ionic strength of 0.1 M KNO_3 with a MOLSPIN pH-meter equipped with a digitally operated syringe (the Molspin DSI 0.250 mL) controlled by a computer. Purified argon was bubbled through the samples to ensure the absence of oxygen. The number of experimental points was 100–150 for each titration curve and the reproducibility of the points included in the evaluation was within 0.005 pH units in the whole pH range examined. As usual, the stability of the complexes is reported as the logarithm of the overall formation constant $\beta_{pqr} = [VO_pL_qH_r]/[VO]^p[L]^q[H]^r$, where L is the deprotonated form of the ligand and H is the proton, calculated with the aid of the SUPERQUAD program.[58] Standard deviations were calculated by assuming random errors. The conventional notation has been used. Negative indices for protons indicate either the dissociation of groups that do not deprotonate in the absence of $V^{IV}O$ coordination, or hydroxo ligands. Hydroxo complexes of $V^{IV}O$ were taken into account. The following species were assumed: $[VO(OH)]^+$ ($\log\beta_{10-1} = -5.94$), $[(VO)_2(OH)_2]^{2+}$ ($\log\beta_{20-2} = -6.95$), with stability constants calculated from the data of Henry et al.[59] and corrected for the different ionic strengths by use of the Davies equation,[60] $[VO(OH)_3]^-$ ($\log\beta_{10-3} = -18.0$) and $[(VO)_2(OH)_5]^-$ ($\log\beta_{20-5} = -22.0$).[61]

Spectroscopic Measurements: Anisotropic EPR spectra were recorded on aqueous solutions with an X-band (9.15 GHz) Varian E-9 spectrometer in the temperature range 120–140 K. As usual for

 © 2005 Wiley-VCH Verlag GmbH & Co. KGaA, Weinheim

low-temperature measurements, a few drops of DMSO were added to the samples to ensure good glass formation. The spectra were simulated with the computer program Bruker WinEPR SimFonia. Electronic spectra were recorded with a Perkin-Elmer Lamda 9 spectrometer. All operations were performed under a purified argon atmosphere in order to avoid oxidation of $V^{IV}O$ ion.

Supporting Information (see footnote on the first page of this article): Figures S1–S3 present the titration curves of the free ligands and of the systems with $V^{IV}O$ ion. Figures S4–S6 show the X-Band EPR spectra of $VOLH_{-2}$ complexes formed by the three ligands.

[1] D. Rehder, in *Metal Ions in Biological Systems* (Eds.: A. Sigel, H. Sigel), Marcel Dekker, New York, **1995**, vol. 31, p. 1–43.

[2] V. L. Pecoraro, C. A. Slebodnick, B. J. Hamstra, in *Vanadium Compounds: Chemistry, Biochemistry and Therapeutic Applications* (Eds.: A. S. Tracey, D. C. Crans), Am. Chem. Soc., Washington, **1998**, p. 157–167.

[3] a) R. L. Robson, R. R. Eady, T. J. Richardson, R. W. Miller, M. Hawkins, J. R. Postgate, *Nature* **1986**, *322*, 388–390; b) R. R. Eady, in *Metal Ions in Biological Systems* (Eds.: A. Sigel, H. Sigel), Marcel Dekker, New York, **1995**, vol. 31, p. 363–405.

[4] M. J. Smith, D. E. Ryan, K. Nakanishi, P. Frank, K. O. Hodgson, in *Metal Ions in Biological Systems* (Eds.: A. Sigel, H. Sigel), Marcel Dekker, New York, **1995**, vol. 31, p. 423–490.

[5] Y. Shechter, I. Goldwaser, M. Mironchik, M. Fridkin, D. Gefel, *Coord. Chem. Rev.* **2003**, *237*, 3–11.

[6] C. Harford, B. Sarkar, *Acc. Chem. Res.* **1997**, *30*, 123–130.

[7] T. Kiss, T. Jakusch, J. Costa Pessoa, I. Tomaz, *Coord. Chem. Rev.* **2003**, *237*, 123–133.

[8] V. M. Fritzsche, V. Vergopoulos, D. Rehder, *Inorg. Chim. Acta* **1993**, *211*, 11–16.

[9] a) A. J. Tasopoulos, A. T. Vlahos, A. D. Keramidas, T. A. Kabanos, Y. G. Deligiannakis, C. P. Raptopoulou, A. Terzis, *Angew. Chem. Int. Ed. Engl.* **1996**, *35*, 2531–2533; b) T. Kiss, K. Petrohan, P. Buglyó, D. Sanna, G. Micera, J. Costa Pessoa, C. Madeira, *Inorg. Chem.* **1998**, *37*, 6389–6391; c) J. Costa Pessoa, T. Gajda, R. D. Gillard, T. Kiss, S. M. Luz, J. J. G. Moura, I. Tomaz, J. P. Telo, I. Török, *J. Chem. Soc., Dalton Trans.* **1998**, 3587–3600; d) A. J. Tasiopoulos, A. N. Troganis, A. Evangelou, C. P. Raptopoulou, A. Terzis, Y. Deligiannakis, T. A. Kabanos, *Chem. Eur. J.* **1999**, *5*, 910–921; e) E. J. Tolis, V. I. Teberekidis, C. P. Raptopoulou, A. Terzis, M. Sigalas, Y. Deligiannakis, T. A. Kabanos, *Chem. Eur. J.* **2001**, *7*, 2698–2710; f) J. Costa Pessoa, I. Correia, T. Kiss, T. Jakusch, M. M. C. A. Castro, C. F. G. C. Geraldes, *J. Chem. Soc., Dalton Trans.* **2002**, 4440–4450; g) A. J. Tasiopoulos, E. J. Tolis, J. M. Tsangaris, A. Evangelou, J. D. Woollins, A. M. Z. Slawin, J. Costa Pessoa, I. Correia, T. A. Kabanos, *J. Biol. Inorg. Chem.* **2002**, *7*, 363–374; h) T. Jakusch, A. Dörnyei, I. Correia, L. M. Rodriguez, G. K. Tóth, T. Kiss, J. Costa Pessoa, S. Marcão, *Eur. J. Inorg. Chem.* **2003**, 2113–2122.

[10] E. Garribba, E. Lodyga-Chruscinska, G. Micera, A. Panzanelli, D. Sanna, *Eur. J. Inorg. Chem.* **2005**, 1369–1382.

[11] B. Sarkar, T. P. A, Kruck, in *Biochemistry of Copper* (Eds.: J. Peisach, P. Aisen, W. Blumberg), Academic Press, New York, **1966**, p. 183–196.

[12] a) B. Sarkar, *Life Chem. Rep.* **1983**, *1*, 165–209; b) M. Lucassen, B. Sarkar, *J. Toxicol. Environ. Health* **1979**, *5*, 897–905.

[13] B. Sarkar, Y. Wigfield, *Can. J. Biochem.* **1968**, *46*, 601–607.

[14] N. D. Chasteen, in *Metal Ions in Biological Systems* (Eds.: A. Sigel, H. Sigel), Marcel Dekker, New York, **1995**, vol. 31, p. 231–247.

[15] T. Kiss, E. Kiss, E. Garribba, H. Sakurai, *J. Inorg. Biochem.* **2000**, *80*, 65–73.

[16] G. R. Willsky, A. B. Goldfine, P. J. Kostyniak, J. H. McNeill, L. Q. Yang, H. R. Khan, D. C. Crans, *J. Inorg. Biochem.* **2001**, *85*, 33–42.

[17] B. D. Liboiron, K. H. Thompson, G. R. Hanson, E. Lam, N. Aebischer, C. Orvig, *J. Am. Chem. Soc.* **2005**, *127*, 5104–5115.

[18] I. Sóvágó, E. Farkas, A. Gergely, *J. Chem. Soc., Dalton Trans.* **1982**, 2159–2163.

[19] a) J. Costa Pessoa, S. M. Luz, R. Duarte, J. J. G. Moura, R. D. Gillard, *Polyhedron* **1993**, *12*, 2857–2867; b) J. Costa Pessoa, S. M. Luz, R. D. Gillard, *J. Chem. Soc., Dalton Trans.* **1997**, 569–576.

[20] J. Costa Pessoa, L. F. Vilas Boas, R. D. Gillard, R. J. Lancashire, *Polyhedron* **1988**, *7*, 1245–1262.

[21] E. Garribba, G. Micera, D. Sanna, unpublished results.

[22] D. Sanna, G. Micera, P. Buglyó, T. Kiss, T. Gajda, P. Surdy, *Inorg. Chim. Acta* **1998**, *268*, 297–305.

[23] N. D. Chasteen, in *Biological Magnetic Resonance* (Eds.:L. J. Berliner, J. Reuben), Plenum Press, New York, **1981**, vol. 3, p. 53–119.

[24] I. Sóvágó, in *Biocoordination Chemistry* (Ed.: K. Burger.), Ellis Horwood, New York, **1990**, ch. 4, p. 135–184.

[25] E. Farkas, I. Sóvágó, T. Kiss, A. Gergely, *J. Chem. Soc., Dalton Trans.* **1984**, 611–614.

[26] A. Lorenzotti, D. Leonesi, A. Cingolani, P. Di Bernardo, *Inorg. Chim. Acta* **1981**, *52*, 149–152.

[27] a) T. Jakusch, P. Buglyó, A. I. Tomaz, J. Costa Pessoa, T. Kiss, *Inorg. Chim. Acta* **2002**, *339*, 119–128; b) J. Costa Pessoa, I. Tomaz, T. Kiss, P. Buglyó, *J. Inorg. Biochem.* **2001**, *84*, 259–270.

[28] a) H. Kozlowski, B. Decock-Le Révérend, D. Ficheux, C. Loucheux, I. Sóvágó, *J. Inorg. Biochem.* **1987**, *29*, 187–197; b) K. Cherifi, B. Decock-Le Révérend, K. Várnagy, T. Kiss, I. Sóvágó, H. Kozlowski, *J. Inorg. Biochem.* **1990**, *38*, 69–80; c) I. Sóvágó, T. Kiss, K. Várnagy, B. Decock-Le Révérend, *Polyhedron* **1988**, *7*, 1089–1093; d) H. Kozlowski, I. Sóvágó, J. Spychala, J. Urbanska, K. Várnagy, A. Kiss, K. Cherifi, *Polyhedron* **1990**, *9*, 831–837.

[29] B. J. Hamstra, A. P. L. Houseman, G. J. Colpas, J. W. Kampf, R. LoBrutto, W. D. Frasch, V. L. Pecoraro, *Inorg. Chem.* **1997**, *36*, 4866–4874.

[30] C. R. Cornman, E. P. Zovinka, Y. D. Boyajina, K. M. Geisre-Bush, P. D. Boyle, P. Singh, *Inorg. Chem.* **1995**, *34*, 4213–4219.

[31] W. R. Harris, *Clin. Chem.* **1992**, *38*, 1809–1818.

[32] a) N. D. Chasteen, E. M. Lord, H. J. Thompson, J. K. Grady, *Biochim. Biophys. Acta* **1986**, *884*, 84–92; b) N. D. Chasteen, J. K. Grady, C. E. Holloway, *Inorg. Chem.* **1986**, *25*, 2754–2760; c) N. D. Chasteen, J. Francavilla, *J. Phys. Chem.* **1976**, *80*, 867–871; d) H. Sakurai, M. Nishida, M. Koyama, J. Takada, *Biochim. Biophys. Acta* **1987**, *924*, 562–563; e) N. D. Chasteen, L. K. White, R. F. Campbell, *Biochemistry* **1977**, *16*, 363–365; f) J. C. Cannon, N. D. Chasteen, *Biochemistry* **1975**, *14*, 4573–4577.

[33] R. Campbell, N. D. Chasteen, *J. Biol. Chem.* **1977**, *252*, 5996–6001.

[34] a) D. M. Taylor, in *Perspectives on Bioinorganic Chemistry* (Eds.: R. W. Hay, J. R. Dilworth, K. B. Nolan), JAI Press, London, **1993**, vol. 2, p. 139–159; b) L. K. White, N. D. Chasteen, *J. Phys. Chem.* **1979**, *83*, 279–284.

[35] K. S. N. Iyer, S. Lau, S. H. Laurie, B. Sarkar, *Biochem. J.* **1978**, *169*, 61–69.

[36] a) G. Rakhit, B. Sarkar, *J. Inorg. Biochem.* **1981**, *15*, 233–241; b) G. Rakhit, W. E. Antholine, W. Froncisz, J. S. Hyde, J. R. Pilbrow, G. R. Sinclair, B. Sarkar, *J. Inorg. Biochem.* **1985**, *25*, 217–224.

[37] a) D. W. Appleton, B. Sarkar, *J. Biol. Chem.* **1971**, *246*, 5040–5046; b) J. W. Dixon, B. Sarkar, *J. Biol. Chem.* **1974**, *249*, 5872–5877.

[38] a) B. Sarkar, V. Renugopalakrishnan, T. P. A. Kruck, S. Lau, in *Environmental Effects on Molecular Structure and Properties* (Ed.: B. Pullman), D. Reidel Publishing Co., Dordrecht, Holland, **1976**, p. 165–178; b) B. Sarkar, in *Metal–Ligand Interactions in Organic Chemistry and Biochemistry* (Eds.: B. Pullman, N. Goldblum), Kluwer Academic Publishers, Dordrecht, Holland, **1977**, p. 193–228.

 © 2005 Wiley-VCH Verlag GmbH & Co. KGaA, Weinheim

[39] N. Camerman, A. Camerman, B. Sarkar, *Can. J. Chem.* **1976**, *54*, 1309–1316.
[40] P. Buglyó, E. Kiss, I. Fabian, T. Kiss, D. Sanna, E. Garribba, G. Micera, *Inorg. Chim. Acta* **2000**, *306*, 174–183.
[41] G. Micera, D. Sanna, A. Dessi, T. Kiss, P. Buglyó, *Gazz. Chim. Ital.* **1993**, *123*, 573–577.
[42] T. Kiss, P. Buglyó, D. Sanna, G. Micera, P. Decock, D. Dewaele, *Inorg. Chim. Acta* **1995**, *239*, 145–153.
[43] T. Kiss, E. Kiss, G. Micera, D. Sanna, *Inorg. Chim. Acta* **1998**, *283*, 202–210.
[44] P. Caravan, L. Gelmini, N. Glover, F. G. Herring, J. H. McNeill, J. Rettig, I. A. Setyawati, E. Shutter, Y. Sun, A. S. Tracey, V. G. Yuen, C. Orvig, *J. Am. Chem. Soc.* **1995**, *117*, 12759–12770.
[45] a) H. Sakurai, K. Fujii, H. Watanabe, H. Tamura, *Biochem. Biophys. Res. Commun.* **1995**, *214*, 1095–1101; b) Y. Fujisawa, S. Fujimoto, H. Sakurai, *J. Inorg. Biochem.* **1997**, *67*, 396.
[46] M. Rangel, A. Tamura, C. Fukushima, H. Sakurai, *J. Biol. Inorg. Chem.* **2001**, *6*, 128–132.
[47] J. Gätjens, B. Maier, T. Kiss, E. M. Nagy, P. Buglyó, H. Sakurai, K. Kawabe, D. Rehder, *Chem. Eur. J.* **2003**, *9*, 4924–4935.
[48] a) H. Sakurai, H. Sano, T. Takino, H. Yasui, *J. Inorg. Biochem.* **2000**, *80*, 99–105; b) E. Kiss, K. Kawabe, A. Tamura, T. Jakusch, H. Sakurai, T. Kiss, *J. Inorg. Biochem.* **2003**, *95*, 69–76.
[49] a) E. Kiss, K. Petrohan, D. Sanna, E. Garribba, G. Micera, T. Kiss, *Polyhedron* **2000**, *19*, 55–61; b) E. Kiss, E. Garribba, G. Micera, T. Kiss, H. Sakurai, *J. Inorg. Biochem.* **2000**, *78*, 97–108; c) P. Buglyó, T. Kiss, D. Sanna, E. Garribba, G. Micera, *J. Chem. Soc., Dalton Trans.* **2002**, 2275–2282.
[50] T. Kiss, Abstracts of the 6th European Conference of Bioinorganic Chemistry, Lund and Copenhagen, **2002**, p. 48.
[51] D. Rehder, J. Costa Pessoa, C. F. G. C. Geraldes, M. M. C. A. Castro, T. Kabanos, T. Kiss, B. Meier, G. Micera, L. Pettersson, M. Rangel, A. Salifoglou, I. Turel, D. Wang, *J. Biol. Inorg. Chem.* **2002**, *7*, 384–396.
[52] a) K. H. Thompson, C. Orvig, *J. Chem. Soc., Dalton Trans.* **2000**, 2885–2892; b) A. Stern, A. J. Davison, Q. Wu, J. Moon, *Arch. Biochem. Biophys.* **1992**, *299*, 125–128; c) K. Kanamori, Y. Kinebuchi, H. Michibata, *Chem. Lett.* **1997**, 423–424.
[53] S. Liochev, I. Fridovich, *Arch. Biochem. Biophys.* **1987**, *255*, 274–278.
[54] a) X. Shi, X. N. S. Dalal, *Arch. Biochem. Biophys.* **1993**, *307*, 336–345; b) A. S. Carmichael, *FEBS Lett.* **1990**, *261*, 165–170.
[55] . Gran, *Acta Chem. Scand.* **1950**, *4*, 559–577.
[56] I. Nagypál, I. Fábián, *Inorg. Chim. Acta* **1982**, *61*, 109–113.
[57] H. Irving, M. G. Miles, L. D. Pettit, *Anal. Chim. Acta* **1967**, *38*, 475–481.
[58] P. Gans, A. Vacca, A. Sabatini, *J. Chem. Soc., Dalton Trans.* **1985**, 1195–1200.
[59] R. P. Henry, P. C. H. Mitchell, J. E. Prue, *J. Chem. Soc., Dalton Trans.* **1973**, 1156–1159.
[60] C. W. Davies, *J. Chem. Soc.* **1938**, 2093–2098.
[61] a) A. Komura, M. Hayashi, H. Imanaga, *Bull. Chem. Soc. Jpn.* **1977**, *50*, 2927–2931; b) L. F. Vilas Boas, J. Costa Pessoa, in *Comprehensive Coordination Chemistry* (Eds.: G. Wilkinson, R. D. Gillard, J. A. McCleverty), Pergamon Press, Oxford, **1987**, vol. 3, p. 453–583.

Received: April 13, 2005
Published Online: October 27, 2005

 © 2005 Wiley-VCH Verlag GmbH & Co. KGaA, Weinheim

DOI: 10.1002/ejic.200500434

Oxo-Entity-Controlled Diastereomer Peculiarity of Rhenium(V) Complexes $ReOX_2(P{\sim}O)py$ [X = Cl, Br, I; P~O = $(OCMe_2CMe_2O)POCMe_2CMe_2O$(1–); py = pyridine]: Synthesis and Molecular and Crystal Structural Characterization

Witold K. Rybak,*[a] Anna Skarżyńska,[a] Ludmiła Szterenberg,[a] Zbigniew Ciunik,[a] and Tadeusz Głowiak[a][†]

Dedicated to Professor Józef J. Ziółkowski on the occasion of his 70th birthday

Keywords: Noncovalent interactions / Crystal engineering / Rhenium complexes / P,O ligand / Density functional calculations

The stability of diastereomers of $ReOX_2(P{\sim}O)py$ complexes determined by the arrangement of the oxo-entity O=Re(–O~P) is manifested in molecular recognition and crystallization behavior [X = Cl, Br, I; P~O = $(OCMe_2CMe_2O)PO$-CMe_2CMe_2O(1–); py = pyridine]. With X = Cl and Br both chiral *cis* [*OC*-6–52] and achiral *trans* [*OC*-6–15] complexes can be obtained concomitantly, while for X = I only a *trans* complex can be afforded. Molecular structures were characterized using NMR IR and UV/Vis spectroscopic methods with the aid of DFT computational analysis and were ultimately corroborated by the single-crystal X-ray diffraction method. These analyses revealed that the most stable diastereomers involve an O=Re(–O~P) oxo arrangement in an axial disposition reinforced with a phosphorus ligating atom mutually *cis* due to extensive π-bonding both for chiral *cis* and achiral *trans* complexes, regardless of whether X = Cl, Br, or I. However, the disparate intramolecular geometry either *cis* or *trans* in the solid state results in enantiomorphic crystals related to space group $P2_12_12_1$ (X = Cl, Br) or crystals pertinent to the centrosymmetric framework $P2_1/c$ (X = Cl, Br, I), respectively. Thoughtful analysis of crystal structures reveals a supramolecular architecture due to intermolecular forces involving hydrogen bonding and electric dipole–dipole interactions (among other contact interactions). Thus, chiral *cis* complexes (X = Cl, Br) show helical crystal packing that succeeds in spontaneous resolution, while *trans* stereoisomers (X = Cl, Br, I) do not and rather exhibit a zig-zag supramolecular framework.
(© Wiley-VCH Verlag GmbH & Co. KGaA, 69451 Weinheim, Germany, 2005)

Introduction

The recognition that crystal structure, among other self-assembled systems (e.g. liquid crystals, molecular layers, wires etc.), is the result of a subtle balance between a multitude of supramolecular noncovalent weak forces has attracted much attention to the ability to predict crystal structures.[1] Most efforts are still devoted to searches for a correlation between intramolecular arrangements and crystal packing.[2] The great structural diversity characteristic of transition metal complexes can play a special role in this context both from a theoretical point of view and from the point of view of experimental chemistry applications in crystal engineering and material sciences.[3] The various coordination sites available on the metal center allow ligands to adopt a structural array appropriate to their steric demands and electronic properties. Still, for a given set of metal ligands several stable diastereomeric arrangements are possible showing different molecular properties with consequences for their supramolecular arrangements.[4] Occasionally, a similar potential energy for the diastereomers may result in an isomerization reaction and in the separation of the diastereomers.[5] Several interesting instances of both isomerization and the separation of diastereomers of coordination compounds have been reported recently.[6]

Metal oxo complexes, however, exhibit pronounced anisotropy that might be recognized by other ligands in the molecular stage and by molecules at the supramolecular level.[7] This anisotropy is manifested in multiple bonding within the metal oxo moiety, e.g. the total bond orders are close to three for M=O or near to four for mutually *trans* O=M–OR oxo arrangements. During the course of our studies on the chelating ability of the spirophosphorane ligand HP~O [HP~O = $HP(OCMe_2CMe_2O)_2$][8a,8b]

[a] Faculty of Chemistry, University of Wrocław,
50383 Wrocław, Poland
E-mail: rybak@wchuwr.chem.uni.wroc.pl
[†] Deceased.
Supporting information for this article is available on the WWW under http://www.eurjic.org or from the author.

 © 2005 Wiley-VCH Verlag GmbH & Co. KGaA, Weinheim

(Scheme 1) we succeeded in the chirally autocatalytic and highly efficient preparation of one enantiomer (from optically inactive precursors) owing to a subtle interplay between chiral *cis* and achiral *trans* oxo-rhenium complexes $ReOCl_2(P{\sim}O)py$ (py = pyridine).[8c] We reasoned that for a particular set of halide ligands X (X = Cl, Br, I) a specific configuration of the complex should be stabilized. Subsequently, we became interested in the more general question of to what extent one can, by selecting ligands, control the preparation of a certain diastereomer and ultimately its crystal structure including intermolecular recognition and conceivable chiral packing. Breu and co-workers have shown, using the example of trisdiimine-metal chelate complexes, that even a minor intramolecular modification related to metal center ions (Ru or Zn) can drastically alter the packing pattern and crystallization behavior proceeding from racemate to enantiomorph, essentially due to weak intermolecular forces.[9] Known oxo-rhenium complexes of the $ReOX_2(Y{\sim}Z)L$ type, containing an oxo dihalide moiety and a bidentate chelate (Y, Z = O, N, P as ligating atoms) in addition to any other monodentate ligand (L), exhibit either *cis* or *trans* geometry. Chloride complexes mostly adopt the *cis* arrangement,[10] although the *trans* geometry also exists.[11] On the other hand, iodide complexes[12] show a *cis* arrangement, while bromide complexes[13] exhibit *trans* stereochemistry. Thus, no preferential stereochemistry for halide complexes with roughly similar structural frameworks has been observed so far. Obviously, the stereochemistry of those complexes is controlled by much more complex matching of the properties of the ligands and of the metal center. These instances did not allow us to verify our reasoning and consequently gave this work a different focus, especially as we had at our disposal a closely related series of $ReOX_2(P{\sim}O)py$ complexes. In this paper we report on the results of experimental studies, aided computationally by the density functional theory (DFT), on structural characterization of the title diastereomeric complexes, including their syntheses as well as spectroscopic and X-ray single crystal determinations.[14]

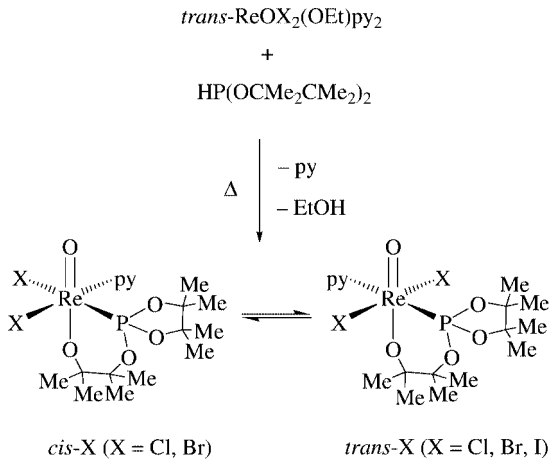

Scheme 1.

Results and Discussion

Synthesis and Spectroscopic Characterization of the $ReOX_2(P{\sim}O)py$ Complexes

The reaction of dihalogeno oxo complexes *trans*-$ReO(OR)X_2py_2$ with an excess of spirophosphorane HP~O, (summarized in Scheme 1) affords corresponding *cis* and/or *trans* $ReOX_2(P{\sim}O)py$ complexes with the new oxo alkoxy entity, O=Re(–O~P), mutually in *trans* disposition. These six-coordinate complexes, besides the monodentate ligands also contain a chelating alkoxy phosphite that derives from a tautomeric deprotonated form of the spirophosphorane $(OCMe_2CMe_2O)POCMe_2CMe_2OH$.[8a,15] Both the chloro and bromo complexes might be isolated in the solid state from the reaction mixture either as the less soluble *cis* or the more soluble *trans* stereoisomer owing to feasible isomerization reactions. Furthermore, certain *cis* or *trans* stereoisomers (X = Cl, Br) can also be obtained from their congeners due to the *cis–trans* equilibration. However, the iodo complex permits only the *trans* isomer. The *cis* and *trans* solubility difference notwithstanding, these complexes are moderately soluble in dichloromethane, acetonitrile, sparingly soluble in toluene, and their solutions are stable at ambient conditions. It is apparent that for the molecular composition of these dihalide $ReOX_2(P{\sim}O)py$ (X = Cl, Br, I) complexes, five chiral *cis* configurations and two achiral *trans* are potentially implicit as depicted in Scheme 2. Configuration indices can been applied to distinguish these diastereomers.[16] Anticipating further discussion of the results, we can for now disclose that *cis*-X-[52] and *trans*-X-[15] are the only synthetically affordable diastereomers.[17]

The relatively distinctive NMR spectra of the obtained complexes are summarized in Table 1. The spectra make it only possible to distinguish between *cis* and *trans* geometry, and no further molecular configuration assignment can be predicted. It is noteworthy that *trans* complexes at room temperature exhibit a C_s ^1H NMR pattern (i.e. four signals related to four enantiotopic pairs of methyl groups) and a long-range coupling $^4J(P,H)$ between ^{31}P and ^1H at the α-position of the py ligand. For *cis* complexes, however, eight resonances related to all the eight methyl groups of the P~O ligand and the absence of a $^{31}P–^1H$ (α-py) coupling corroborate the C_1 symmetry around the metal center and do not reveal much more than this roughly estimated geometry.

IR spectroscopic measurements outlined in the Experimental Section and in the first column of Table 2 are even less distinctive for molecular structure determination. Due to considerable overlapping of the relevant absorption bands, the stretching vibrations attributed to the rhenium-ligating atom set are rather difficult to assign. However, there are exceptions for well-resolved rhenium alkoxo oxygen stretching vibrations ν(Re–O) observed at ca. 621 cm^{-1} both for *cis*-X and *trans*-X complexes. Yet careful examination of the spectral region 1000–900 cm^{-1} by means of mutual comparison of the spectra of all obtained complexes and the spectrum of the free HP~O ligand only makes it possible to tentatively assign the ν(Re=O) vibrations at ca.

 © 2005 Wiley-VCH Verlag GmbH & Co. KGaA, Weinheim

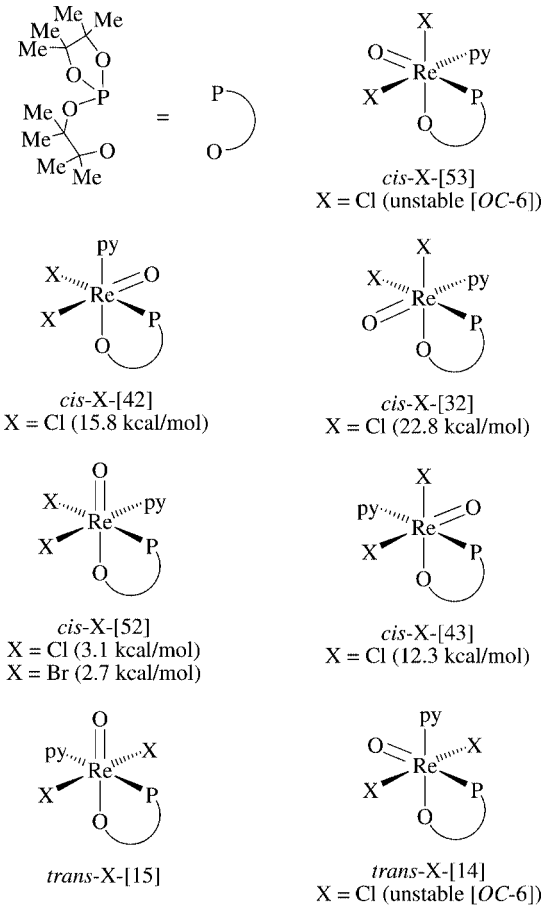

Scheme 2.

956 cm^{-1}, both for *cis* and *trans* complexes. In the low-energy range (FIR), however, ν(Re–X), ν(Re–P), and ν(Re–N) vibrations all occur in a similar region (400–100 cm^{-1}) and straightforward, unambiguous assignment is rather difficult.[18]

Another, fairly indistinctive feature of these complexes is their pink violet color visible in their UV/Vis spectra shown in Table 1. That most likely originates from d–d electronic transitions, which will be discussed later.[19]

To rationalize the above ambiguities in the molecular structure of these complexes and gain insight into their supramolecular arrangements including chirogenesis in the crystal state, more detailed studies were undertaken. The following sections describe molecular electronic structure analyses performed using density functional (DFT) calculations and crystal structure determination supported by single-crystal X-ray analyses.

DFT Computational Analysis of Molecular Structures of $ReOX_2$(P~O)py Diastereomers

This versatile method was used deliberately as it makes it possible to elucidate the experimental uncertainties described above in a reasonable manner and to strike a balance between computational effort and completeness. The primary aim of the computational study was to analyze the relative stability of the seven diastereomers implied above, mainly in the case of the most representative chloride complexes (X = Cl).[20] We expected that general conclusions obtained for the chloride congeners would be largely valid for other halide complexes too. The relative electronic energies for the series *cis*-Cl and *trans*-Cl stereoisomers are shown in Scheme 2. The lowest total electronic energy, and thus the highest stability was found for the *trans*-Cl-[15] configuration located at the bottom left in Scheme 2. Comparison of the calculated relative energy differences reproduces the experimentally observed order of stability of the complexes: achiral *trans*-Cl-[15] > chiral *cis*-Cl-[52] (3.12 kcal mol^{-1}) >> other *cis*- and *trans*-Cl diastereomers (remarkably above 10 kcal mol^{-1}). This low-energy barrier between the Cl-[15] and the Cl-[52] diastereomers supports

Table 1. ^{1}H NMR, ^{31}P NMR, and UV/Vis spectroscopic data of $ReOX_2$(P~O)py complexes.

Complex	^{1}H NMR, δ values [ppm], *J* [Hz]		^{31}P{^{1}H} NMR	UV/Vis
	Methyl	Aryl	δ values [ppm]	λ_{max} [nm] (ε [$M^{-1}cm^{-1}$])
***cis*-Cl**[14]	0.87, 1.31, 1.52, 1.54[a] 1.01, 1.15, 1.40, 1.46[b] (24 H, s)	7.67 (2 H, tm, $^3J_{HH}$ = 7) 7.97 (1 H, tt, $^3J_{HH}$ = 8, $^4J_{HH}$ = 1.6) 8.93 (2 H, dm, $^3J_{HH}$ = 5)	91.03	≈ 650 (30) 499 (147) 314 (4150)
***trans*-Cl**	1.54, 1.57[a] 1.14, 1.41[b] (24 H, s)	7.66 (2 H, tm, $^3J_{HH}$ = 7) 7.98 (1 H, tt, $^3J_{HH}$ = 8, $^4J_{HH}$ = 1.6) 8.83 (2 H, m*, $^4J_{PH}$ ≈ 1)	93.06	≈ 670 (24) 522 (132) 310 (4170)
***cis*-Br**	0.83, 1.27, 1.54, 1.57[a] 1.06, 1.25, 1.44, 1.46[b] (24 H, s)	7.58 (2 H, tm, $^3J_{HH}$ = 7), 7.90 (1 H, tt, $^3J_{HH}$ = 8, $^4J_{HH}$ = 1.6) 8.93 (2 H, dm, $^3J_{HH}$ = 5)	82.73	686 (32) 498 (133) 310 (5720)
***trans*-Br**	1.54, 1.60[a] 1.15, 1.41[b] (24 H, s)	7.67 (2 H, tm, $^3J_{HH}$ = 7), 7.95 (1 H, tt, $^3J_{HH}$ = 8, $^4J_{HH}$ = 1.6), 8.82 (2 H, m*, $^4J_{PH}$ ≈ 1)	95.4	≈ 657 (30) 518 (130) 308 (3850)
***trans*-I**	1.57, 1.62[a] 1.14, 1.40[b] (24 H, s)	7.65 (2 H, tm, $^3J_{HH}$ = 7) 7.96(1 H, tt, $^3J_{HH}$ = 8, $^4J_{HH}$ = 1.6) 8.81(2 H, m*, $^4J_{PH}$ ≈ 1)	103.17	≈ 670 (24) 531 (118) 284 (20800)

[a] Me bound to the five-membered P-containing ring. [b] Me bound to the six-membered rhenium metallacycle ascertained by the 2D NMR experiment. Multiplets consisting of roughly equal intensity signals attributed to the coupling ^{1}H and ^{31}P nucleus based on the 2D NMR experiment are labeled with asterisks *.

 © 2005 Wiley-VCH Verlag GmbH & Co. KGaA, Weinheim

Table 2. Important measured and calculated bands in the IR spectra of the $ReOX_2(P{\sim}O)py$ complexes in selected regions.

	Measured bands		Calculated bands	Assignment
***cis*-Cl**	150.1 w		120.6	ν(Re–P)
	239 m	267 vs	213.4	ν(Re–N)
	284.9 s		305.0	ν_{as}(Re–Cl)
	322.6 s		316.9	ν_{s}(Re–Cl)
	869.7 m	927 s	847	ν(C–O) + ν(P–O)
	891 w	942 vs	874	ν(C–O) + ν(P–O)
	956 vs	976 s	956.0	ν(Re=O)
	1014.2 s		1003.0	ν(Re=O) + ν(C–O)
***trans*-Cl**	154.0 w		119.9	ν(Re–P)
	237.4 m	247 s	214.9	ν(Re–N)
			270.5	ν_{s}(Re–Cl)
	302.6 s		293.4	ν_{as}(Re–Cl)
	863.9 m		844	ν(C–O) + ν(P–O)
	895.1 w	931 s	875	ν(C–O) + ν(P–O)
	956 vs	976 s	965.9	ν(Re=O)
	1024 s			
***cis*-Br**	159.7 w		115.7	ν(Re–P)
	180.7 vs	194 s	183	ν_{as}(Re–Br) + ν(Re–N)
	215.6 s		206.3	ν_{s}(Re–Br) + skelet.
	235 m	247 s, 265 s	223.6	ν(Re–N)
	867.7 m	925.7 vs	839.7	ν(C–O) + ν(P–O)
	891.7 w	939.1 vs	873	ν(C–O) + ν(P–O)
	955.9 vs	975 s	956	ν(Re=O)
	1014.6 s		1003.7	ν(Re=O) + ν(C–O)
***trans*-Br**	150.1 vw		127.0	ν(Re–P)
			167.2	ν_{s}(Re–Br) + skelet.
	205.7 vs	179 s		ν_{as}(Re–Br)
	232.5 s	248 m	217.7	ν(Re–N)
	864.5 m	932 vs	843.0	ν(C–O) + ν(P–O)
	895.9 w		875.0	ν(C–O) + ν(P–O)
	956 vs	977.5 s	965.0	ν(Re=O)
	1023.3 s		1013.4	ν(Re–O) + ν(C–O)
***trans*-I**	hidden			ν(Re–P)
			118.0	ν_{s}(Re–I)
	156.4 s		145.5	ν_{as}(Re–I)
	239.9 vs	228 s	226.4	ν(Re–N)
	868.7 m	929 vs	842.9	ν(C–O) + ν(P–O)
	896.9 m	937 vs	874.8	ν(C–O) + ν(P–O)
	957.2 vs	979 m	965.1	ν_{as}(Re=O) + ν(C–O)
	1022.7 m		1012.2	ν_{s}(Re=O) + ν(C–O)

the above-mentioned *cis–trans* isomerization reaction and the feasible separation of *cis* and *trans* complexes.[21] Furthermore, the resulting diastereomer stability trend is in good agreement with the expected promotion and efficiency of the π-donor-acceptor bonding pattern at the metal center with the arrangement of O and P ligating atoms. Phosphorus ligating atoms with their intrinsic π-acidity show a preference to adopt a *cis* disposition with respect to the inherent *trans* O=M–OR oxo arrangement [R = (CMe_2CMe_2O)-$P(OCMe_2CMe_2O)$].[7]

Consequently, the multiply bonded *trans* oxo arrangement is stabilized to some extent due to accessible π-back-donation from rhenium to phosphorus. Other hypothetical diastereomers with mutually *cis* O=M(–OR) oxo arrangements are evidently less encouraging (Scheme 2). Besides, computational studies indicate the lowest stability for pseudo-octahedral complexes [*OC*-6] comprising mutually *cis* oxo arrangements with phosphorus in the *trans* location to the terminal oxygen atom (*trans* -Cl-[14] and *cis* -Cl-[53]), which tend rather to transform to five coordinating species loosing the phosphorus ligand.

Notably, energy differences calculated only for selected bromide and iodide congeners (*trans* -X-[15] and *cis* -X-[52]), assumed to be the most stable, are again in good agreement with the experimental observations. Thus, for bromides, a low energy difference between *trans* -Br-[15] and *cis* -Br-[52] (2.68 kcal mol^{-1}), again implies facile *cis-trans* isomerization. In the case of iodides, *trans* -I-[15] appears to be the only stable complex. To sum up, computational study at this stage dispelled the configuration ambiguity indicating not only the geometry of the most stable diastereomers, X-[15] and X-[52], but also the feasibility of the *cis-trans* isomerization reaction, excluding X = I congeners. For the sake of clarity, below we simply use the abbreviations *trans*-X and *cis*-X for the affordable complexes of X-[15] and X-[52] configurations, respectively.

Afterwards, with computed structures fully optimized using the B3LYP functional, we also tried to deal with am-

 © 2005 Wiley-VCH Verlag GmbH & Co. KGaA, Weinheim

biguities in the IR spectra using the DFT method. A summary of the spectral characteristics and stretching vibrations for the *trans*-X and *cis*-X complexes in selected relevant regions are presented in Table 2. Tentative assignment of the observed absorption bands to those calculated was based on the order of their appearance and intensity, in experimental and calculated spectra. In the FIR range, the equivocal position of stretching vibrations ν(Re–P), ν(Re–N), and ν(Re–X) can be verified to some extent. Thus, weak absorption at 150–160 cm^{-1} and medium to strong absorption at 230–240 cm^{-1} can be cautiously assigned to ν(Re–P) and ν(Re–N) vibrations, respectively. Meanwhile, ν(Re–X) absorptions occur in the region of ca. 300 cm^{-1} for ν(Re–Cl), 200 cm^{-1} for ν(Re–Br), and 150 cm^{-1} for ν(Re–I) (accurate values in Table 2), usually as strong bands. Apart from these, ν(Re=O) stretching vibrations resolved using DFT appear, interestingly, at almost invariable positions, 956–957 cm^{-1} for all the attainable complexes. This suggests once more a very stable moiety comprised of ligating phosphorus in *cis* disposition to the oxo arrangement O=M–OR, powered by π-backdonation.

Similarly, the near nonpeculiarity of the electronic absorption spectra intrinsic to complexes with a *cis* or *trans* geometry and the observed complexes with different halides (Table 1) might also suggest that the oxo-metal entity has a controlling nature. With the aim of elucidating this observation in more detail, we performed time-dependent density functional (TDDFT) calculations of the spectral properties. Recently, several computational analyses have been performed for rhenium complexes,[22] which improve the rationalization of their electronic absorption spectra including the related oxo complexes *trans*-$ReO(OEt)Cl_2(L)_2$ (L = py, pyrazine, pyrimidine).[23] Computational analysis has been accomplished in the case of the pair of *trans*-Cl and *cis*-Cl complexes, which represent an exceptional term as a precursor in this series. In comparing the experimental and calculated spectra we consider only the first two bands in the visible range mainly involving the d orbitals. A third, very intensive and higher-energy band occurs in the UV region and is not needed for the purpose of this comparison. The calculated orbital excitations and the corresponding electronic transitions are summarized in Table 3. The assignment of the calculated orbital excitations to the observed absorption bands was guided by an overview of the contour plots and relative energy appropriate to the orbitals HOMO and LUMO involved in the electronic transitions depicted in Figure 1.

The lower-energy excitations are attributed to the two HOMO → LUMO and HOMO → LUMO +1 transitions either for *cis*-Cl or for *trans*-Cl complexes (set 1, Table 3). The contour plots corresponding to these MOs comprise mainly rhenium 5d atomic orbitals (Figure 1). Thus, initial HOMOs involve the rhenium d_{xy} (π*) orbital interacting with chlorine 3p (π*). Both LUMO and LUMO +1 also engage the rhenium d_{xz} (π*) orbital but interact with the π* orbitals of the oxo arrangement. Therefore, the low-energy absorption bands, observed at 650 nm (*cis*-Cl) and 670 nm (*trans*-Cl), can be assigned to d–d (π*) transitions with a certain contribution of metal-to-oxo-ligand charge transfer (MLCT). Two higher-energy excitations, however, are attributed to the two HOMO → LUMO +2 and HOMO → LUMO +4 transitions, which involve rhenium d orbitals but with slightly different contributions (for *cis*-Cl and *trans*-Cl complexes, sets 2–3 in Table 3 and Figure 1). While LUMO +2 comprise substantially pyridine molecular orbitals, easily visible in the contour plots, LUMO +4 again involves mainly rhenium atomic orbitals but with a $d_{x^2-y^2}$ (σ*) symmetry. The observed absorptions at 499 nm (*cis*-Cl) and 522 nm (*trans*-Cl) can be related to a metal-to-pyridine ligand charge transfer (MLCT) with a certain contribution of d (π*)–d (σ*) transitions. Consequently, the similar natures of the above transitions seem to be responsible for the nearly identical absorption spectra at least for *cis* and *trans* chloride complexes.

Table 3. The most important electronic transitions calculated with the TDDFT method: wavelength λ, oscillator strength *f*, and measured λ_{exp} (ε) for *cis*- and *trans*-$ReOCl_2$(P~O)py.

Set	Orbital excitations	λ [nm]	*f*	λ_{exp} [nm] (ε [$M^{-1}\,cm^{-1}$])
***cis*-Cl**				
1	H-(d_{xy} + π* Cl) → L-(d_{yz} + π* O) H-(d_{xy} + π* Cl) → L+1-(d_{xz} + π* O)	717.0	0.001	650 (30)
2	H-(d_{xy} + π* Cl) → L+1-(d_{xz} + π* O) H-(d_{xy} + π* Cl) → L+2-(d_{yz} + π* py)	591.8	0.0007	
3	H-(d_{xy} + π* Cl) → L+2-(d_{yz} + π* py) H-(d_{xy} + π* Cl) → L+4-($d_{x^2-y^2}$ + σ* Cl)	443.3	0.007	499 (147)
***trans*-Cl**				
1	H-(d_{xy} + π* Cl) → L-(d_{xz} + π* O) H-(d_{xy} + π* Cl) → L+2-(d_{xz} + π* py)	678.6	0.004	670 (24)
2	H-(d_{xy} + π* Cl) → L+1-(d_{yz} + π* O)	599.3	0.005	522 (132)
3	H-(d_{xy} + π* Cl) → L+4-($d_{x^2-y^2}$)	421.3	0.0001	

 © 2005 Wiley-VCH Verlag GmbH & Co. KGaA, Weinheim

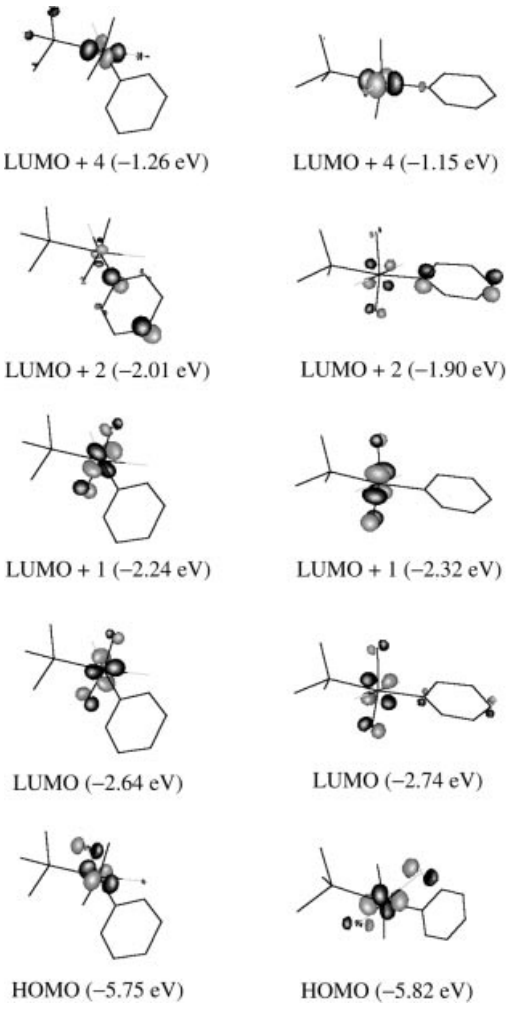

Figure 1. Contour plots relative to selected orbitals HOMO and LUMO active in the electronic transitions in *cis*- (left) and *trans*-$ReOCl_2(P{\sim}O)py$ (right). The orbitals were plotted with the contour values –0.12 (black) and 0.12 au (gray), and referred to the *z*-axis adjacent to the oxygen atoms and the *y*-axis occupied by pyridine and or chlorides. The chlorides are printed in gray.

X-ray Crystal Structure Determination

In general chiral molecules, if they are not pure enantiomers, may form either chiral (conglomerate) or achiral (racemate, racemic solution) crystal structures. Yet, the same might be true for achiral molecules.[24] The question arises what a crystal structure will be if only minor structural changes are applied to a molecule that prior to these changes formed chiral crystals (e.g. Cl^- vs. Br^- ligands or chiral *cis*- vs. achiral *trans*-arrangements) and whether the formation of enantiomorph crystals will still be possible although the molecular structure might now be achiral.

The crystallographic data of $ReOX_2(P{\sim}O)py$ complexes are summarized in Table 5. While two *cis*-X (X = Cl, Br) complexes crystallize in the orthorhombic space group $P2_12_12_1$, as enantiomorphic crystals (conglomerate), three *trans*-X (X = Cl, Br, I) isomers yield monoclinic crystals belonging to the centrosymmetric space group $P2_1/c$. The unit cell of each crystal structure consists of four molecules of $ReOX_2(P{\sim}O)py$ complexes. The packing of the achiral *trans* complexes is slightly less compact (ca. 5% ρ) than that of the chiral *cis* isomers. The Flack parameter, *x*,[25] for selected single chiral crystals of *cis*-Cl [*x* = 0.024(5)] and *cis*-Br [*x* = –0.018(12)] indicates packing with molecules of one enantiomer that accidentally appeared with the opposite absolute configuration of *C* and *A*, respectively. Figure 2 shows the ORTEP drawings with the selected atom numbering schemes for representative *cis*-X (X = Cl) and *trans*-X (X = Cl) complexes. Except for rather insignificant differences related to the coordination of pyridine, the molecular structures do not show extraordinary features in terms of bond lengths and angles. Significant coordination bond lengths and angles for these complexes are submitted in the supporting information in Table S1. All pseudo-octahedral complexes exhibit the characteristic multiply bonded *trans* oxo arrangement, O=Re–O. The rhenium bond lengths with terminal oxo at ca. 1.7 Å and the bridging alkoxo below 1.9 Å are in the usual range, which imply a total bond order of close to four.[7] Furthermore, the coplanarity of the rhenium atom with the plane traced by phosphorus and oxo-moiety donor atoms is a rather meaningful feature of all those complexes. The dihedral angles close to zero between the least-squares planes Re O(1) P and Re O(2) P for *cis*-X [Cl, 4.5(1)°, Br 4.7(2)°] and *trans*-X [Cl, 1.0(1)°, Br 0.0(1)°, I 0.4(2)°], respectively, confirm the approximately coplanar arrangements. This may suggest the remarkable stability of such a four-membered core arrangement, O=Re(–O~P–), due to a versatile π-bonding already anticipated from DFT computational analysis for all the readily affordable diastereomers.

Besides the similarity, there are also some well-pronounced disparities in the intramolecular structures of these stereoisomers between the geometry types, *cis*-X (X = Cl, Br) or *trans*-X (X = Cl, Br, I). Ring puckering analysis[26,27] shows that both fluxional (in solution) five-membered phosphorus and six-membered rhenium cycles in the crystal state adopt conformations relevant for each geometry (i.e. *cis*- or *trans*-), albeit with slight differences between them.[28] Thus, the relevant five-membered phosphorus cycle, -PO4C7C8O5-, embraces the envelope (E) tilted on the enantiotopic carbon atoms, either C7 (*cis*-X) or C8 (*trans*-X). For the relevant six-membered rhenium metallacycles, -RePO2C1C2O3-, tentative inquiries disclose either half-chair (HC) or envelope conformations on C2 for *cis*-X and *trans*-X complexes, respectively.

The molecular peculiarities and similarities discussed above, while subtle, have further consequences in the supramolecular structure and the crystal packing of these stereoisomers. Yet, this might be expected from the molecular self-recognition and self-assembly paradigm[1a,29] for the structure of supramolecular objects and crystals due to weak noncovalent intermolecular forces.[30] These intermolecular interactions might be both directional and nondirectional in nature. To minimize the void volume in 3D structures, molecules tend to pack exploiting weak specific interactions, including directional hydrogen bonds and/or minimal dipole–dipole electrostatic forces. The representative

 © 2005 Wiley-VCH Verlag GmbH & Co. KGaA, Weinheim

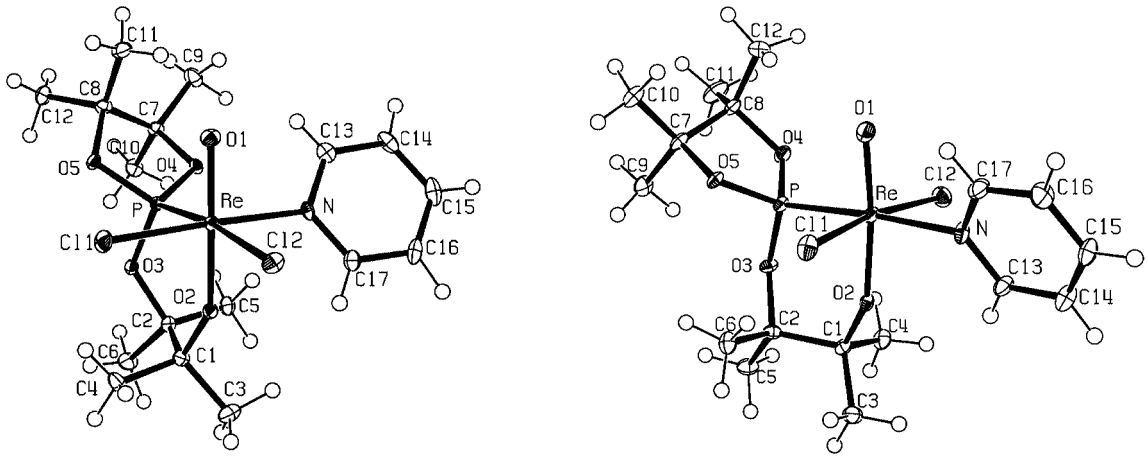

Figure 2. ORTEP molecular diagram (with 30% probability ellipsoids) showing selected atom labeling in *cis*-$ReOCl_2$(P~O)py (left) and *trans*-$ReOCl_2$(P~O)py (right) with hydrogen atoms unlabeled.

modes of crystal packing for *cis*-X (X = Cl) and *trans*-X (X = Cl) complexes are shown in Figures 3 and 4, respectively. Crystals within each stereoisomer type, *cis*-X or *trans*-X (X = Cl, Br), are isomorphous, except for the *trans*-I complex (Table 5). Both *cis*-X and *trans*-X complexes disclose columnar structures in their crystal states. *Cis*-X complexes reveal molecules arranged in cylinders running along the crystallographic axis 2_1, that is parallel to the cell *b* axis (Figure 3), and maintain molecules forming a helical pattern.[31] Meanwhile, *trans*-X complexes exhibit molecules stacked along the *c* axis with stacks mutually related by axis 2_1 parallel to the *b* axis (Figure 4), which sustain them in stacks rather than in any helical structures. The driving noncovalent interactions are obviously responsible for either a cylindrical or stacking disposition of the molecules in the crystals.

Avoiding precarious quantification of the strength of these intermolecular interactions, one can take the opportunity to only roughly classify them. Thoughtful qualitative analysis of the packing shows that molecules might be held together by hydrogen bonds, contact interactions, and dipole–dipole electrostatic interactions.[32] Interactions that are sustained almost twice as often are effected through intermolecular arrangement (11 to 13) rather then by intramolecular arrangement (6 to 7 encounters) for each compound. Notably, in spite of the rather modestly realistic (or very weak) hydrogen bonds involving alkyl hydrogen atoms (H3–H6, H9–H12), the aryl hydrogen atoms (H13–H17) may make an energetically significant contribution to H bonding. This may result in a substantial influence on the type of supramolecular arrangement. With great caution, we can only shed light on the difference in intermolecular

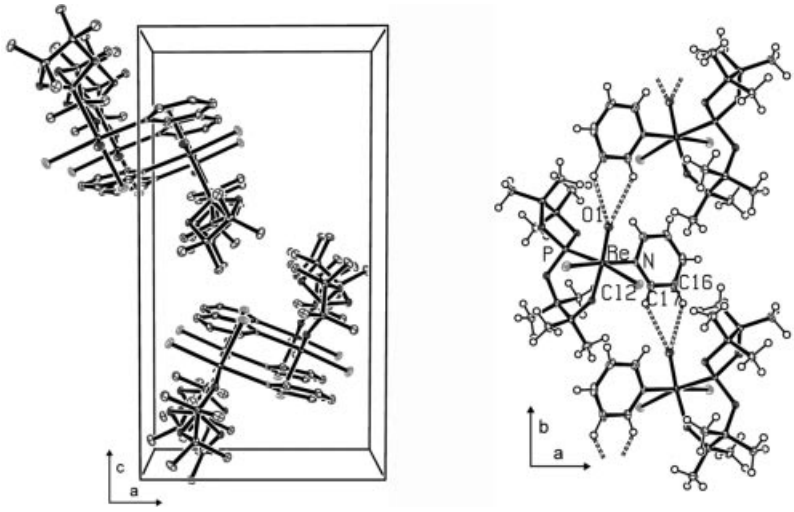

Figure 3. Crystal structure of *cis*-$ReOCl_2$(P~O)py. Perspective view along columns (left), in which molecules are connected by the intracolumn hydrogen bonds (right).

 © 2005 Wiley-VCH Verlag GmbH & Co. KGaA, Weinheim

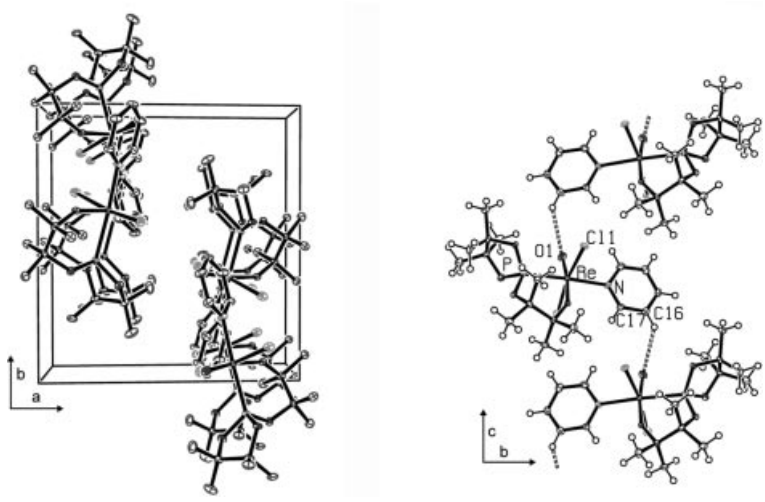

Figure 4. Crystal structure of *trans*-$ReOCl_2(P{\sim}O)py$. Perspective view along columns (left), in which molecules are connected by the intra-column hydrogen bonds (right).

hydrogen bonding acquired by terminal oxygen atoms with both α and β pyridine hydrogen atoms (H17, H16) for *cis*-X (X = Cl, Br, Figure 3, b) and only with β pyridine hydrogen atoms (H16) for *trans*-X (X = Cl, Br, I, Figure 4, b) complexes. Other implied interactions seem to be more concealed and do not allow clear-cut conclusions.[32]

However, on the other hand, the apparent difference in polarity and in the dipole moment[33] between *cis* and *trans* geometry complexes offers an additional possibility of discriminating between intermolecular dipole–dipole electrostatic interactions. In the *cis*-X molecules, a substantial dipole moment (ca. 12.7 D) is pointed out of the most polar bonds and electronegative donor atoms (X1, X2 O1 and O2), whereas in the *trans* stereoisomers a rather moderate dipole moment (ca. 3.15 D) is situated in proximity to the donor atoms, which is depicted in a simplified form in Figure 5. Thus, within each column, the *cis*-X molecules adjust the obtuse angle of the dipole–dipole arrangement, while the *trans* molecules seem not to. We can consider the obtuse angles of dipole arrangements to be a result of the subtle interplay between the tendency towards antiparallel alignment of dipoles and a variety of other weak specific intermolecular forces. This obtuse angle of dipole arrangement (for *cis*-X) allows the bulky part of the molecule to improve accommodation within the column, which manifests itself in a shorter Re–Re distance (e.g. 6.84 Å, X = Cl), as shown in Table 4. In the case of *trans* isomers, substantially smaller dipole moments of molecules are arranged in a parallel way with longer Re–Re distances (e.g. 7.20 Å, X = Cl) within each column. These distances are not too different from inter-column Re–Re distances (e.g. 8.24 Å, X = Cl).

Using this uncomplicated cooperative model, which includes hydrogen bonding and dipole–dipole electrostatic interactions, we can rationalize the supramolecular structure of the title complexes. Both of these specific directional interactions seem to be controlling in the case of *cis*-X complexes. This is manifested in the helical arrangement of the molecules, the shorter Re–Re distance within the column, and the more compact packing. Consequently, this is seen in the greater lattice energies and in the enantiomorphic

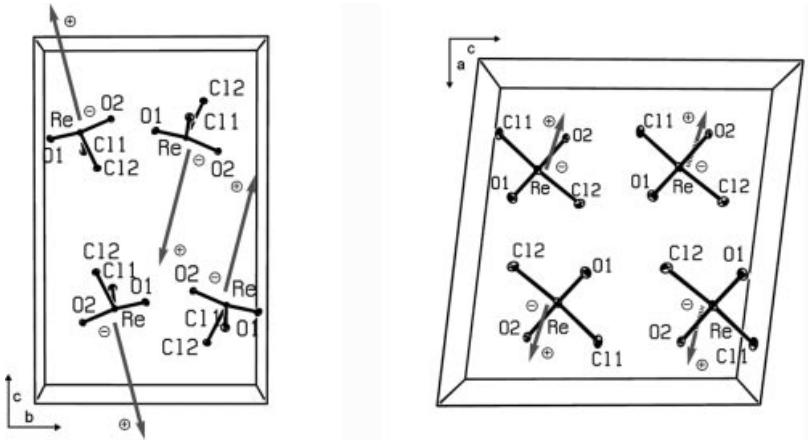

Figure 5. Supramolecular arrangement of molecular dipoles along columns for *cis*-$ReOCl_2(P{\sim}O)py$ (12.65 D, left) and *trans*-$ReOCl_2(P{\sim}O)py$ (3.18 D, right), a schematic overview of the projection of the dipole moments on respective planes.

 © 2005 Wiley-VCH Verlag GmbH & Co. KGaA, Weinheim

Table 4. Adjacent intermolecular distances for $ReOX_2$(P~O)py complexes.

Complex	Re–Re distances [Å] Intra-column	Inter-column
cis-Cl	6.84	10.02
trans-Cl	7.20	8.24
cis-Br	6.87	10.20
trans-Br	7.66	8.67
trans-I	8.40	8.25

crystal structures. In contrast, in the case of *trans* geometry complexes, with no dipole–dipole disposition consequences, hydrogen bonding along with other weak interactions including dispersion forces seems to be the operating driving force. This revealed in a stacking arrangement of molecules longer Re–Re distances within the column (Table 4), and less compact packing with a definitely lower lattice energy.

Conclusions

Systematic studies of the title $ReOX_2$(P~O)py complexes definitely illustrate that the oxo entity O=M–OR inherently in *trans* disposition is a building block determining the stability of these diastereomers. Even with this fixed oxo entity, different arrangements of halide ligands are still available, either *trans* or *cis* (X = Cl, Br), implying nonrigidity of these complexes in terms of configuration and conformation. Further, we can stipulate that due to the self-recognition nature of molecules, the molecular structure of the compound may affect the supramolecular arrangement in the crystal state, the eventual spontaneous resolution (X = Cl, Br vs. I), and ultimately chirogenesis. This points to the involvement of fine-tuning in the form of specific interactions involving molecular recognition, which utilize the electronic and steric properties of the ligands and the metal center. We bear in mind the stimulating accounts of Breu and his associates,[9] which showed that for similar complexes with a rigid molecular shape (e.g. $[M(bpy)_3]^{2+}$), a small difference in molecular composition (M = Ni, Zn, Ru) may have a dramatic influence on the form of crystal packing. In fact, that observation validates one of the alternative clear-cut assumptions that crystal structure cannot be predicted.[34] In our case, however, the described structural intramolecular properties and the related intermolecular arrangements of the molecules do not seem to corroborate the above assumption. Replacements of halides do not dramatically alter the packing pattern. Both chloride and bromide complexes can crystallize in the orthorhombic ($P2_12_12_1$) and monoclinic centrosymmetric ($P2_1/c$) space groups, depending intimately on their intramolecular geometry. Consequently, these observations seem to support the alternative statement of Grepioni, Braga, and co-workers that "objects of similar shape tend to pack in a similar manner."[35] It is noteworthy that in our system, the related molecules exhibit pronounced anisotropy owing to the oxo arrangement and are not rigid. This obviously convenient case makes it possible to utilize intramolecular degrees of freedom and optimize the similar packing for the corresponding halide (X = Cl, Br, I) diastereomers.

Experimental Section

All preparations were performed under dry, oxygen-free nitrogen, using conventional Schlenk techniques. Solvents were carefully dried and deoxygenated by standard methods.[36] *trans*-$ReOX_2$(OEt)py_2 (X = Cl, Br, I),[37] *cis*-$ReOCl_2$(P~O)py[8a], and the ligand $HP(OCMe_2CMe_2O)_2$[8a] were prepared according to literature procedures.

IR and FIR measurements were performed in KBr pellets either with a Nicolet FTIR Impact 400 or in Nujol with a Bruker IFS 113V. ^1H, ^{13}C, ^{31}P NMR spectra were obtained with a Bruker AMX (300 MHz for ^1H NMR). The chemical shifts (δ) are given in ppm towards the TMS (^1H, ^{13}C) and H_3PO_4 (^{31}P) using deuterated solvents as lock and reference (^1H, ^{13}C), respectively. 2D NMR and ^1H-^{31}P COSY experiments made it possible to distinguish and unambiguously assign the chemical shifts of methyl groups attributed to both phosphorocycles and metallacycles (Table 1). UV/Vis spectra in CH_2Cl_2 solution were obtained with a Carry 500. Elemental analyses were performed with a Perkin–Elmer 2400 CHN by the Laboratory of Elemental Analyses in our Department.

***trans*-$ReOCl_2$(P~O)py (*trans*-Cl):** Finely ground crystalline *cis*-[$ReOCl_2${$OCMe_2CMe_2OP(OCMe_2CMe_2O)$}py] (0.025 g, 0.04 mmol) was added to toluene (50 mL). It was vigorously stirred and slowly distilled (over 1 h) to about 25 mL. After cooling to room temperature, the remaining solid, which appeared to be the starting *cis* complex, was filtered (0.0024 g, 9.6%). The mother liquor yielded crystals (0.018 g, 72%) of pure *trans*-[$ReOCl_2${$OCMe_2CMe_2OP(OCMe_2CMe_2O)$}py]. Single crystals suitable for X-ray analysis were obtained by re-crystallization from a dichloromethane/ethyl ether solution as a purple-violet compound. $C_{17}H_{29}Cl_2NO_5PRe$ (615.5): calcd. C 33.17, H 4.75, N 2.28; found C 33.5, H 4.65, N 2.52. IR (KBr): $\tilde{\nu}$ = 623.0 [m, ν(Re–O)], 931.8 (s), 956.3 [vs., ν(Re=O)], 1024.7 [s, ν(C–O–P)], 1608.4 [m, ν(C=N)] cm^{-1}; FIR (nujol): 154.0 (w), 237.4 (m), 247(s), 302.6 [ν(Re–P)], ν(Re–N), ν(Re–Cl) cm^{-1}. The compound was also isolated as a side product from the toluene filtrate remaining after the preparation of the isomer *cis*. The filtrate was evaporated to dryness, the residue washed several times with pentane and ethyl ether, than crystallized from toluene with ca. 8% yield. In addition, when the sample of the pure *trans*-Cl complex (0.066 g) was placed in boiling toluene (10 mL) for 1 h, it again afforded the *cis*-Cl complex (65%) as a solid, which proves the isomerization reaction.

***cis*-$ReOBr_2$(P~O)py (*cis*-Br):** A suspension of the blue complex $ReOBr_2$(OEt)py_2 (0.395 g, 0.699 mmol) and the spirophosphorane ligand $HP(OCMe_2CMe_2O)_2$ (0.341 g, 1.292 mmol) in toluene (25 mL) was stirred and boiled for 6 h until the starting rhenium compound reacted and a light-violet crystalline solid was afforded. The product was filtered, washed with Et_2O, and dried in vacuo (0.368 g, 74.8%). Single crystals suitable for X-ray analysis were obtained by crystallization from a dichloromethane/ethyl ether solution as a purple-violet compound. $C_{17}H_{29}Br_2NO_5PRe$ (704,4): calcd. C 28.99, H 4.15, N 1.99; found C 29.06, H 3.93, N 2.07. IR (KBr): $\tilde{\nu}$ = 618.6 [m, ν(Re–O)], 925.7 (vs), 955.9 [vs., ν(Re=O)], 1014.6 [s, ν(C–O–P)], 1605.3 [m, ν(C=N)] cm^{-1}; FIR (nujol) 159.7 (w), 180.7(s), 215.6(s), 235[m, ν(Re–Br)], ν(Re–N), ν(Re–P) cm^{-1}.

***trans*-$ReOBr_2$(P~O)py (*trans*-Br):** A suspension of the pink-violet compound *cis*-$ReOBr_2$(P~O)py (0,05 g, 0,071 mmol) in toluene

 © 2005 Wiley-VCH Verlag GmbH & Co. KGaA, Weinheim

(50 mL) was stirred and boiled for 1 h. After cooling to room temperature, the remaining *cis*-$ReOBr_2(P{\sim}O)py$ solid was filtered. The remaining solution was evaporated to dryness affording *trans*-$ReOBr_2(P{\sim}O)py$ (0.04 g, 80%). Single crystals suitable for X-ray analysis were obtained by crystallization from a dichloromethane/ethyl ether solution as a purple-violet compound. Besides, this complex was afforded as a side product from the remaining toluene filtrate obtained in the *cis*-Br preparation, by a method similar to that used for *trans*-Cl, with ca. 12% yield. $C_{17}H_{29}Br_2NO_5PRe$ (704.4): calcd. C 28.99, H 4.15, N 1.99; found C 29.0, H 4.09, N 2.02. IR (KBr): $\tilde{\nu}$ = 622.9 [m, ν(Re–O)], 931.9 (vs), 955.9 [vs., ν(Re=O)], 1023.3 [s, ν(C–O–P)], 1609.1 [m, ν(C=N)] cm^{-1}; FIR (nujol) 150.1 (vw), 179 (s), 205.7 (vs), 232 (s), 248 [m, ν(Re–P)], ν(Re–Br), ν(Re–N) cm^{-1}.

***trans*-$ReOI_2(P{\sim}O)py$ (*trans*-I):** A mixture of $ReOI_2(OEt)py_2$ (0.359 g, 0.545 mmol), toluene (25 mL), and the spirophosphorane ligand $HP(OCMe_2CMe_2O)_2$ (0.279 g, 1.059 mmol) was stirred and boiled for 6 h until the starting rhenium compound reacted and new a deep-orange solution appeared. The solution was concentrated in vacuo by half to obtain a red-violet precipitate of $ReOI_2(P{\sim}O)py$. The product was filtered, washed with Et_2O and dried (0.38 g, 87%). Single crystals suitable for X-ray analysis were obtained by crystallization from dichloromethane/ethyl ether solution as a red-violet compound. For $C_{17}H_{29}I_2NO_5PRe$ (798,41): calcd. C 25.57, H 3.66, N 1.75; found C 25.66, H 3.34, N 2.00. IR (KBr): $\tilde{\nu}$ = 622.6 [m, ν(Re–O)], 929.5 (vs), 957.2 [vs., ν(Re=O)], 1022.7 [m, ν(C–O–P)], 1606.6 [m, ν(C=N)] cm^{-1}; FIR (nujol) 156.4 (s), 228 (s), 239.9 (vs), ν(Re–P), ν(Re–I), ν(Re–N) cm^{-1}.

Computational Analysis: The calculations were carried out with the GAUSSIAN 2003 program.[38] All structures were optimized starting from experimental geometries (X-ray) with no symmetry restrictions, using the Kohn–Sham density functional theory (DFT) with Becke's three-parameter[39] exchange functionals and the gradient-corrected functionals of Lee, Yang, and Parr [DFT(B3LYP)] with the SDD basis set. Vibrational frequencies were calculated in order to confirm the nature of the stationary points and to achieve the zero-point energies (ZPEs). Calculations of electronic spectra were performed at the TDDFT level. Molecular structures were visualized using the program MOLDEN.[40] Molecular orbitals were drawn by the program gOpenMol.[41] The programs ORTEP[42] and GSVIEW[43] were used for graphical presentation of crystallographic results. Cartesian coordinates for optimized structures have been deposited with the Supporting Information.

Crystal Structure Determination: Crystal data for *cis*- and *trans*-$ReOX_2(P{\sim}O)py$ complexes are summarized in Table 5. The data collected with the KM4CCD diffractometer were corrected for Lorentz and polarization effects. Data reduction and analysis were carried out using the Oxford Diffraction (Poland) programs. The structure was solved by means of heavy atom methods using SHELXS-97 and refined by the full-matrix least-squares method on F^2 using SHELXL-97 procedures (G. M. Sheldrick, University of Göttingen, Germany, **1997**). Non-hydrogen atoms were refined with anisotropic thermal parameters. Hydrogen atoms were included from the Δρ maps and refined with isotropic thermal parameters. Crystallographic data (excluding structure factors) for the structures reported in this paper have been deposited with the Cambridge Crystallographic Data Center (CCDC) as a supplementary publication. CCDC-167174 (for *cis*-Cl) and -271243 ... -271246 contain the supplementary crystallographic data for this paper. These data can be obtained free of charge from The Cambridge Crystallographic Data Centre via www.ccdc.cam.ac.uk/data_request/cif.

Supporting Information (details see footnote on the first page of this article): A PDF file with supporting information for this article is also available from the authors. It contains tables showing the relevant bond lengths and angles (Table S1), the ring puckering analysis (Table S2), the analysis of possible hydrogen bonding and contacts (Table S3), and color versions of Figures 1, 3, and 4, which ensure better visualization of the 3D structures (Figure S1, S2, and S3, respectively).

Table 5. Crystallographic data for *cis*- and *trans*-$ReOX_2(P{\sim}O)py$ complexes.

	cis-Cl[8c]	*trans*-Cl	*cis*-Br	*trans*-Br	*trans*-I
Empirical formula	$C_{17}H_{29}Cl_2NO_5PRe$	$C_{17}H_{29}Cl_2NO_5PRe$	$C_{17}H_{29}Br_2NO_5PRe$	$C_{17}H_{29}Br_2NO_5PRe$	$C_{17}H_{29}I_2NO_5PRe$
Formula weight	615.48	615.48	704.39	704.39	798.38
Temperature [K]	100(1)	100(2)	293(2)	100(1)	100(2)
Color	pink violet	pink violet	pink violet	pink violet	red violet
Crystal size [mm]	0.15×0.10×0.10	0.15×0.14×0.12	0.20×0.17×0.14	0.15×0.10×0.06	0.23×0.17×0.14
Space group	$P2_12_12_1$ (No.19)	$P2_1/c$ (No.14)	$P2_12_12_1$	$P2_1/c$	$P2_1/c$
a [Å]	9.988(2)	13.2196(12)	10.124(2)	12.579(2)	16.0501(8)
b [Å]	11.655(2)	13.8204(12)	11.756(2)	13.870(1)	10.0633(5)
c [Å]	18.301(4)	12.3231(12)	18.632(4)	13.338(2)	16.8049(11)
α [°]	90.00	90.00	90.00	90.00	90.00
β [°]	90.00	97.077(8)	90.00	95.05(3)	118.313(6)
γ [°]	90.00	90.00	90.00	90.00	90.00
V [Å^3]	2130.4(7)	2234.3(4)	2217.5(7)	2316.50(16)	2389.6(2)
Z	4	4	4	4	4
$\rho_{calcd.}$ ($Mg\,m^{-3}$)	1.919	1.830	2.110	2.020	2.219
λ [Å]	0.71073	0.71073	0.71073	0.71073	0.71073
μ [mm^{-1}]	6.057	5.776	9.182	8.784	7.761
F(000)	1208	1208	1352	1352	1496
θ range [°]	3.49 ≤ 28.64	3.33 ≤ 27.00	3.44 ≤ 27.00	3.07 ≤ 27.00	3.16 ≤ 27.99
Reflections collected	14435	14659	14696	17528	28809
Unique reflections	5031	4809	4819	4971	5750
R_1/wR_2 indices[f]	0.0195/0.0514[a]	0.0311/0.0724[b]	0.0371/0.0700[c]	0.0288/0.0596[d]	0.0226/0.0388[e]

[a] a = 0.0308, b = 0.9807. [b] a = 0.0418, b = 0.0. [c] a = 0.0181, b = 0.0. [d] a = 0.0274, b = 0.0. [e] a = 0.0172, b = 0.0. [f] Calcd. $w = 1/[\sigma 2(F_o^2) + (aP)^2 + bP]$, where $P = (F_o^2 + F_c^2)/3$.

 © 2005 Wiley-VCH Verlag GmbH & Co. KGaA, Weinheim

Acknowledgments

The quantum calculations were carried out at the Poznań Supercomputer Center (Poznań) and Wrocław Supercomputer Center (Wrocław).

[1] a) J. M. Lehn, J. L. Atwood, J. E. D. Davies, D. D. MacNicol, F. Vögtle (Eds.), *Comprehensive Supramolecular Chemistry*, Pergamon, Oxford, **1996**; b) D. Braga, F. Grepioni, *Chem. Commun.* **1996**, 571–578; c) C. B. Aakeröy, *Acta Crystallogr., Sect. B* **1997**, *53*, 569–586.

[2] a) J. A. R. P. Sarma, G. R. Desiraju, *Cryst. Growth Des.* **2002**, *2*, 93–100; b) P. Verwer and F. J. J. Leusen in *Reviews in Computational Chemistry* (Eds.: K. B. Lipkowitz, D. B. Boyd), Wiley-VCH, New York, **1998**, vol. 12, pp. 327–365; c) W. D. S. Motherwell, H. L. Ammon, J. D. Dunitz, A. Dzyabchenko, P. Erk, A. Gavezzotti, D. W. M. Hofmann, F. J. J. Leusen, J. P. M. Lommerse, W. T. M. Mooij, S. L. Price, H. Scheraga, B. Schweizer, M. U. Schmidt, B. P. van Eijck, P. Verwer, D. E. Williams, *Acta Crystallogr., Sect. B* **2002**, *58*, 647–661; d) S. M. Woodley, P. D. Battle, J. D. Gale, C. R. A. Catlow, *Phys. Chem. Chem. Phys.* **2004**, *6*, 1815–1822; e) S. M. Woodley, *Structure Bonding* **2004**, *110*, 95–132.

[3] a) D. Braga, F. Grepioni, *Acc. Chem. Res.* **2000**, *33*, 601–608; b) J. Breu, H. Domel, P. O. Norrby, *Eur. J. Inorg. Chem.* **2000**, 2409–2419; c) V. V. Borovkov, T. Harada, Y. Inoue, R. Kuroda, *Angew. Chem. Int. Ed.* **2002**, *41*, 1378–1381; d) C. Janiak, *Dalton Trans.* **2003**, *14*, 2781–2804; e) S. L. James, *Chem. Soc. Rev.* **2003**, *32*, 276–288; f) G. R. Desiraju, *J. Mol. Struct.* **2003**, *656*, 5–15; g) L. Brammer, *Chem. Soc. Rev.* **2004**, *33*, 476–489; h) D. Huttner, J. Breu, *Z. Anorg. Allg. Chem.* **2004**, *630*, 2527–2531.

[4] A. von Zelewsky, *Stereochemistry of Coordination Compounds*, Wiley, New York, **1996**.

[5] R. G. Wilkins, *Kinetics and Mechanism of Reactions of Transition Metal Complexes*, 2nd ed., VCH, Weinheim, **1991**.

[6] a) Y. Ihara, R. Nakamura, *Thermochim. Acta* **1997**, *302*, 211–214; b) E. H. S. Sousa, C. P. Oliveira, L. C. G. Vasconcellos, L. G. F. Lopez, I. C. N. Diógenes, I. M. M. Carvalho, J. C. V. Miranda, F. A. Dias, I. S. Moreira, *Thermochim. Acta* **2001**, *376*, 141–145; c) Y. Takashima, Y. Nakayama, H. Yasuda, A. Nakamura, A. Harada, *J. Organomet. Chem.* **2002**, *664*, 234–244; d) M. S. Hannu-Kuure, J. Komulainen, R. Oilunkaniemi, R. S. Laitinen, R. Suontamo, M. Ahlgren, *J. Organomet. Chem.* **2003**, *666*, 111–120; e) F. M. Nareetsile, O. P. M. Horwood, D. G. Billing, D. C. Levendis, N. J. Coville, *J. Organomet. Chem.* **2003**, *682*, 2–7.

[7] a) C. J. L. Lock, G. Turner, *Can. J. Chem.* **1977**, *55*, 333–339; b) C. J. L. Lock, G. Turner, *Can. J. Chem.* **1978**, *56*, 179–188; c) J. M. Mayer, *Inorg. Chem.* **1988**, *27*, 3899–3903; d) W. A. Nugent, *Metal Ligand Multiple Bonds*, Wiley, New York, **1988**; e) T. S. Franczyk, K. R. Czerwinski, K. N. Raymond, *J. Am. Chem. Soc.* **1992**, *114*, 8138–8146.

[8] a) T. Głowiak, W. K. Rybak, A. Skarżyńska, *Polyhedron* **2000**, *19*, 2667–2672; b) A. Skarżyńska, W. K. Rybak, T. Głowiak, *Polyhedron* **2001**, *20*, 2667–2674; c) W. K. Rybak, A. Skarżyńska, T. Głowiak, *Angew. Chem. Int. Ed.* **2003**, *42*, 1725–1727.

[9] a) J. Breu, H. Domel, A. Stoll, *Eur. J. Inorg. Chem.* **2000**, 2401–2408; b) J. Breu, W. Seidl, D. Huttner, F. Kraus, *Chem. Eur. J.* **2002**, *8*, 4454–4460.

[10] a) M. B. Hursthouse, S. A. A. Jayaweera, A. Quick, *J. Chem. Soc., Dalton Trans.* **1979**, 279–282; b) T. I. A. Gerber, J. Bruwer, G. Bandoli, J. Perils, J. G. H. du Preez, *J. Chem. Soc., Dalton Trans.* **1995**, 2189–2192; c) F. Tisato, F. Refosco, C. Bolzati, A. Cagnolini, S. Gatto, G. Bandoli, *J. Chem. Soc., Dalton Trans.* **1997**, 1421–1427; d) T. I. A. Gerber, J. Perils, J. G. H. du Preez, G. Bandoli, *Acta Crystallogr., Sect. C* **1997**, *53*, 217–219; e) Xiaoyuan Chen, F. J. Femia, J. W. Babich, J. Zubieta, *Inorg. Chim. Acta* **2000**, *306*, 113–116; f) Xiaoyuan Chen, F. J. Femia, J. W. Babich, J. Zubieta, *Inorg. Chim. Acta* **2000**, *308*, 80–90.

[11] G. Bandoli, S. Gatto, T. I. A. Gerber, J. Perils, J. G. H. du Preez, *J. Coord. Chem.* **1996**, *39*, 299–312.

[12] S. M. O. Quintal, H. I. S. Nogueira, V. Felix, M. G. B. Drew, *New J. Chem.* **2000**, *24*, 511–517.

[13] V. Bertolasi, M. Sacerdoti, G. Gilli, U. Mazzi, *Acta Crystallogr. Sect. B* **1982**, *38*, 426–429.

[14] Although some chemical properties of $ReOCl_2$(P~O)py have been reported previously (see ref.[8a,c]), this work comprises either updated (NMR UV/Vis) or new results. Furthermore, their detailed molecular and crystal structure has not been discussed before.

[15] a) D. Bernard, C. Laurenco, R. Burgada, *J. Organomet. Chem.* **1973**, *47*, 113–123; b) R. Burgada, *Bull. Soc. Chim. Fr.* **1975**, 407–424.

[16] IUPAC, *Nomenclature of Inorganic Chemistry. Recommendations* (Ed.: G. J. Leigh), Blackwell, Oxford, **1992**.

[17] For the sake of brevity we adopt the abbreviated form of configuration indices, for example [52] instead of the long form [*OC*-6-52].

[18] K. Nakamoto, *Infrared Spectra of Inorganic and Coordination Compounds*, 4th ed., Wiley Interscience, New York, **1986**.

[19] a) A. B. P. Lever, *Inorganic Electronic Spectroscopy*, 2nd ed., Elsevier, Toronto, **1984**; b) M. Baluka, J. Hanuza, B. Jezowska-Trzebiatowska, *Bull. Acad. Pol. Sci. Ser. Sci. Chim.* **1972**, *20*, 271–278.

[20] These chloride complexes, and in particular *trans*-Cl and *cis*-Cl appear to be the most effective in terms of enantioselectivity in chirally autocatalytic syntheses; see ref.[8c].

[21] Other details on *cis–trans* equilibration contained in the paper dealing with the mechanism of chiral amplification will be reported elsewhere.

[22] a) J. Bossert, N. B. Amor, A. Strich, C. Daniel, *Chem. Phys. Lett.* **2001**, *342*, 617–624; b) B. Machura, M. Jaworska, R. Kruszynski, *Polyhedron* **2004**, *23*, 1819–1827; c) B. Machura, *Polyhedron* **2004**, *23*, 2363–2371.

[23] a) E. Iengo, E. Zangrando, S. Mestroni, G. Fronzoni, M. Stener, E. Alessio, *J. Chem. Soc., Dalton Trans.* **2001**, 1338–1346.

[24] J. Jacques, A. Collet, S. H. Wilen, *Enantiomers, Racemates and Resolutions*, W. Krieger Publishing, Malabar, FL, USA, **1994**.

[25] a) H. D. Flack, *Acta Crystallogr., Sect. A* **1983**, *39*, 876–881; b) H. D. Flack, G. Bernardinelli, *J. Appl. Crystallogr.* **2000**, *33*, 1143–1148; c) H. D. Flack, *Helv. Chim. Acta* **2003**, *86*, 905–921.

[26] a) D. Cremer, J. A. Pople, *J. Am. Chem. Soc.* **1975**, *97*, 1354–1358; b) D. Cremer, *Acta Crystallogr., Sect. B* **1984**, *40*, 498–500; c) S. T. Rao, E. Westhof, M. Sundaralingam, *Acta Crystallogr. Sect. A* **1981**, *37*, 421–425.

[27] A. L. Spek, *J. Appl. Crystallogr.* **2003**, *36*, 7–13 [A. L. Spek, *PLATON, A Multipurpose Crystallographic Tool*, Utrecht University, The Netherlands, **2002** (http://www.cryst.chem.uu.nl/platon.)].

[28] Electronic Supporting Information: C&P and Sundaralingam ring puckering analysis and its parameters are presented in Table S2.

[29] a) J. M. Lehn, *Pure Appl. Chem.* **1994**, *66*, 1961–1966; b) J. D. Dunitz, *Acta Crystallogr., Sect. B* **1995**, *51*, 619–631; c) L. Perez-Garcia, D. B. Amabilino, *Chem. Soc. Rev.* **2002**, *31*, 342–356.

[30] a) A. I. Kitaigorodskii, *Molecular Crystal and Molecules*, Academic Press, New York, **1973**; b) G. R. Desiraju (Ed.), *Perspectives in Supramolecular Chemistry*, Wiley, Chichester, **1966**, vol. 2.; c) G. R. Desiraju, T. Steiner, *The Weak Hydrogen Bond in Structural Chemistry and Biology*, Oxford University Press, Oxford, **1999**.

[31] The 2_1 screw axis operates either in a clockwise or anti clockwise manner with the same result. Yet, the path of a helix can be traced if intermolecular hydrogen bonds, O1···Hpy, between adjacent molecules in the columns are distinguished (Figure 3).

 © 2005 Wiley-VCH Verlag GmbH & Co. KGaA, Weinheim

[32] Electronic Supporting Information: The geometry of the possible inter- and intramolecular hydrogen bonds, and contact interactions is presented in Table S3.
[33] Total dipole moments, its orientations were calculated with GAUSSIAN for isolated molecules and yielded: *cis*-X-[52] 12.65 D (X = Cl), 12.76 D (X = Br), *trans*-X-[15] 3.18 D (X = Cl), 3.08 D (X = Br), 3.22 D (X = I), respectively.
[34] A. Gavezzotti, *Acc. Chem. Res.* **1994**, *27*, 309–314.
[35] F. Grepioni, G. Cojazzi, S. M. Drapper, N. Scully, D. Bragga, *Organometallics* **1998**, *17*, 296–307.
[36] D. D. Perrin, W. L. F. Armarego, *Purification of Laboratory Chemicals*, 3rd ed., Pergamon Press, Oxford, **1988**.
[37] M. Freni, D. Giusto, P. Romiti, G. Minghetti, *Gazz. Chim. Ital.* **1969**, *99*, 286–299.
[38] M. J. Frisch, G. W. Trucks, H. B. Schlegel, G. E. Scuseria, M. A. Robb, J. R. Cheeseman, J. A. Montgomery, Jr. T. Vreven, K. N. Kudin, J. C. Burant, J. M. Millam, S. S. Iyengar, J. Tomasi, V. Barone, B. Mennuci, M. Cosssi, G. Scalmani, N. Rega, G. A. Petersson, H. Nakatsuji, M. Hada, M. Ehara, K. Toyota, R. Fukuda, J. Hasegawa, M. Ishida, T. Nakajima, Y. Honda, O. Kitao, H. Nakai, M. Klene, X. Li, J. E. Knox, H. P. Hratchian, J. B. Cross, C. Adamo, J. Jaramilo, R. Gomperts, R. E. Stratmann, O. Yazyew, A. J. Austin, R. Cammi, C. Pomelli, J. W. Ochterski, P. Y. Ayal, K. Morokuma, G. A. Voth, P. Salvador, J. J. Dannenberg, V. G. Zakrzewski, S. Dapprich, A. D. Daniels, M. C. Strain, O. Farkas, D. K. Malick, A. D. Rabuck, K. Raghavachari, J. B. Foresman, J. V. Ortiz, Q. Cui, A. G. Baboul, S. Clifford, J. Cioslowski, B. B. Stefanov, G. Liu, A. Liashenko, P. Piskorz, I. Komaromi, R. L. Martin, D. J. Fox, T. Keith, M. A. Al.-Laham, C. Y. Peng, A. Nanayakkara, M. Challacombe, P. M. W. Gill, B. Johnson, W. Chen, M. W. Wong, C. Gonzalez, J. A. Pople, Gaussian, Inc., Pittsburgh, PA, **2003**.
[39] a) A. D. Becke, *Phys. Rev. A* **1988**, *38*, 3098–3100; b) C. Lee, W. Yang, R. G. Parr, *Phys. Rev. B* **1988**, *37*, 785–789; c) B. G. Johnson, P. M. W. Gill, J. A. Pople, *J. Chem. Phys.* **1993**, *98*, 5612–5626; d) A. D. Becke, *J. Chem. Phys.* **1993**, *98*, 5648–5652.
[40] G. Schaftenaar, *Molden*, Release 3.6, CMBI, The Netherlands, **2000**, http://www.caos.kun.nl/schft/molden/molden.html.
[41] L. Laaksonen, *gOpenMol* program for the display and analysis of molecular structures, version 2.00, Center for Scientific Computing, Espoo, Finland, **1997**–**2001**, http://www.csc.fi/gopenmol/index.phthml.
[42] a) L. J. Farrugia, *J. Appl. Crystallogr.* **1999**, *32*, 837–838; b) Program based on *ORTEP III* by C. K. Johnson and N. N. Burnett; L. J. Farrugia, University of Glasgow, **1997**–**2005**.
[43] R. Lang, *GSVIEW 32*, Ghostgum Software Pty Ltd., **2003**, http://www.ghostgum.com.au/.

Received: May 12, 2005
Published Online: November 2, 2005

 © 2005 Wiley-VCH Verlag GmbH & Co. KGaA, Weinheim

DOI: 10.1002/ejic.200500439

Synthesis, Crystal Structures and Photoluminescence of Mercury(II) Complexes with Two Homologous Novel Functional Rigid Ligands

Hong-Ping Zhou,[a,b] Yu-Peng Tian,*[a,c,d] Jie-Ying Wu,[a] Ju-Zhou Zhang,[a] Dong-Mei Li,[a] Yong-Min Zhu,[a] Zhang-Jun Hu,[a] Xu-Tang Tao,[c] Min-Hua Jiang,[c] and Yi Xie*[b]

Keywords: Mercury / Functional rigid ligands / X-ray diffraction / Luminescence

Two novel functional rigid ligands, 2,2′- and 4,4′-bipyridyl-based "building blocks", 9-ethyl-3,6-bis[2-(4-pyridyl)ethenyl]carbazole ($\mathbf{L^1}$) and 9-ethyl-3,6-bis[2-(2-pyridyl)ethenyl]-carbazole ($\mathbf{L^2}$), were synthesized. Treatment of $L^{1,2}$ as "building blocks" with $Hg(SCN)_2$ or HgI_2 afforded helixes, macrocycles, and chains, which can be further self-assembled by a π–π stacking interaction, hydrogen bond, and interatomic force in the solid state to form two-dimensional networks. In complexes **1**–**4**, Hg^{II} centers all adopt four-coordination modes in different coordination environments, but they present different architectures with slightly adjusted structures of the ligands and counteranions, indicating that the nature of the ligand and anion plays an important role in the coordination networks. The luminescent properties of compounds **1**–**4** have been studied.

(© Wiley-VCH Verlag GmbH & Co. KGaA, 69451 Weinheim, Germany, 2005)

Introduction

In the past decade, more and more attention has been focused on the crystal design and engineering of multidimensional arrays and networks containing metal ions as nodes because of the potential application of such molecular materials in catalysis, electronics, molecular sensing, magnetic devices, and porous and nanosize materials.[1,2] The rational design and construction of metal–organic frameworks, with their fascinating structures and potential properties, continues to attract interest in current supramolecular chemistry.[3] Up to now, extensive studies have been carried out to give many novel one- (1D), two- (2D), and three-dimensional (3D) frameworks based on the assembly of metal salts with rigid *N*,*N*′- donor ligands, such as 4,4′-bipyridine or 2,2′-bipyridine and their derivatives. Bridging bis(pyridyl) ligands are often used in the construction of metal-containing macromolecules, and the geometry of the bis(pyridyl) ligand can define the primary structure of the self-assembled macromolecule through metal-coordination, hydrogen bonds and π–π stacking interactions.[4] However, some organic ligands with special functionality for supramolecular architectures and functional compounds, because of synthetic difficulties, have been reported rarely to date.

On the other hand, carbazole compounds, as is well known, exhibit good hole transporting properties and their charge transporting complexes can create free carriers in the visible region through the photocarrier generation process.[5] Recently, carbazole-containing compounds have been extensively studied for the application of an electroluminescent (EL) device and fabrication of light-emitting diodes (LED)[6] because of their sufficient hole/electron transporting and luminescent properties. However, the devices are mostly organic compounds or polymers, and the low melting points or low decomposition temperatures inhibit their applications. Functionalization of the organic molecule (addition of donor atoms, e.g. N or O) to allow incorporation into inorganic/organic coordination complexes can offer the advantages of high thermal stability and solvent resistance compared to all-organic materials. So we have tried to design and synthesize functional ligands 9-ethyl-3,6-bis[2-(4-pyridyl)ethenyl]carbazole ($\mathbf{L^1}$) and 9-ethyl-3,6-bis[2-(2-pyridyl)ethenyl]carbazole ($\mathbf{L^2}$). Interestingly, by the careful design of rigid ligands containing carbazole cores and bipyridyl, we were able to obtain complexes with functionally different structures. Furthermore, mercury(II) complexes have been extensively studied because of their structural diversities and attractive optical properties such as photoluminescence and nonlinear optical effects.[7] In this article, we present a series of mercury(II) complexes containing the new functional rigid ligands $\mathbf{L^1}$ and $\mathbf{L^2}$ (Scheme 1). Slightly adjusting the structure of the

[a] Department of Chemistry, Anhui University,
Hefei 230039, P.R. China
E-mail: yptian@ahu.edu.cn
[b] Department of Chemistry, University of Science and Technology of China,
Hefei 230026, P.R. China
E-mail: yxie@ustc.edu.cn
[c] State Key Laboratory of Crystal Materials, Shandong University,
Jinan 250100, P.R. China
[d] State Key Laboratory of Coordination Chemistry, Nanjing University,
Nanjing 210093, P.R. China

 © 2005 Wiley-VCH Verlag GmbH & Co. KGaA, Weinheim

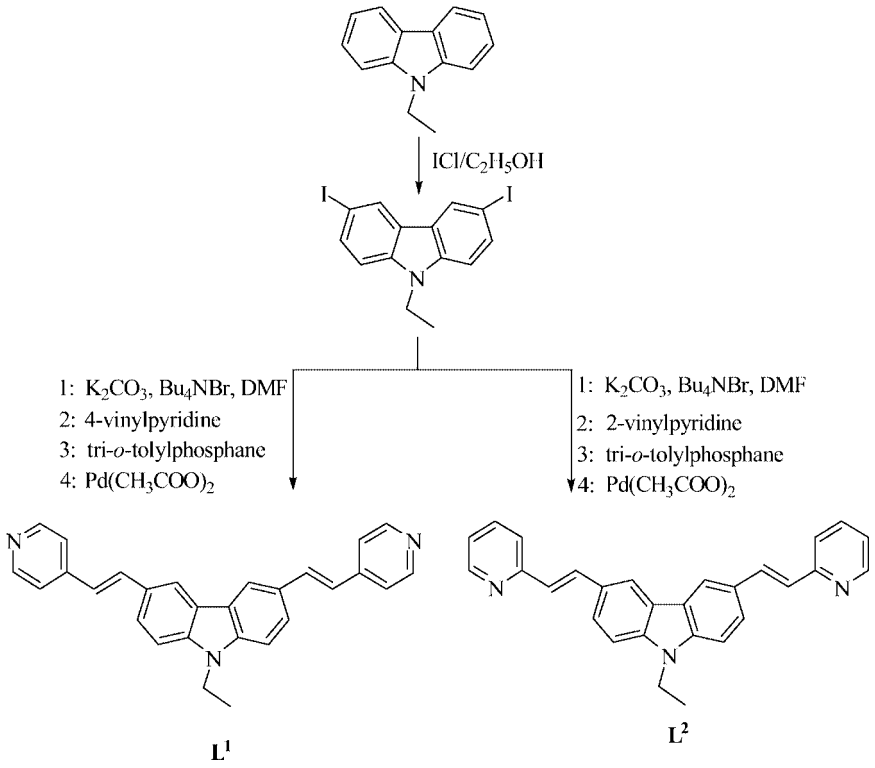

Scheme 1. Synthesis of ligands $\mathbf{L^1}$, $\mathbf{L^2}$.

ligands and counteranions gives potential changes to form different architectures. Here the syntheses, structures, photoluminescence and high thermal stability properties of mercury(II) complexes are reported.

Results and Discussion

All of the compounds are stable in air and insoluble in water or in common organic solvents. High yields of the products indicate that these compounds are thermodynamically stable under the prevailing reaction conditions. IR spectra of the same counteranion compounds are similar, compounds **1** and **3** showing strong absorption bands at about 2065 and 2061 cm^{-1} respectively that are diagnostic of coordinated sulfocyan; middle absorption bands at about 419 and 420 cm^{-1} respectively that are the Hg–N stretching frequencies; and middle absorption bands at about 327 and 328 cm^{-1} respectively that are the Hg–S stretching frequencies. Compounds **2** and **4** show middle absorption bands at about 420 and 419 cm^{-1} respectively that are the Hg–N stretching frequencies and strong absorption bands at about 151 cm^{-1} that are the Hg–I stretching frequencies.

Crystal Structures

In many previous examples, the Hg^{II} cation was found to act as a tetrahedral node with a coordination angle of about 90° to generate 1-D, 2-D, and 3-D structures.[7] It has recently been reported that macrocycles, polymers, or sheets resulted from the reaction of a pyridine spacer with an angle of 120° and a metal node with an angle of 90°.[7] Thus, the reaction of $\mathbf{L^1}$ and $\mathbf{L^2}$ with $Hg(SCN)_2$ and HgI_2 was anticipated to afford 1-D, 2-D, and 3-D structures bearing metallacyclic or metallamacrocyclic analogous structures.

The reaction of equimolar amounts of the bis(pyridine) ligands $\mathbf{L^1}$ and $\mathbf{L^2}$ (Scheme 1) and mercury(II) halide or sulfocyanate gave the corresponding complexes **1**–**4**. These compounds were isolated as analytically pure, air-stable, yellow or red solids that are very sparingly soluble in common organic solvents such as chloroform, dichloromethane, and tetrahydrofuran. Complexes **1**–**4** were characterized by X-ray structure determinations.

Crystal Structure of $[HgL^1(SCN)_2]_n$ (1)

By the slow diffusion of MeOH solution of $Hg(SCN)_2$ into a solution of $\mathbf{L^1}$ in CH_2Cl_2, red crystalline **1** was obtained. Its formulation, $[Hg(\mathbf{L^1})(SCN)_2]_n$, was confirmed by elemental analysis and the use of the single-crystal X-ray diffraction method. The X-ray structural analysis revealed the formation of single-stranded helical chain structures. Each Hg^{II} center exhibits a distorted tetrahedral coordination geometry with two pyridines from $\mathbf{L^1}$ and two sulfur atoms of $Hg(SCN)_2$ as anticipated (Figure 1, a). The bond angles around the mercury atom are in the range 98.67(14)–127.06(6)°, indicating a quite distorted tetrahedral geometry. The coordinated pyridine rings are perpendicularly twisted relative to each other, presumably to minimize the steric hindrance between them.

It is shown in part a of Figure 1 that the ligand takes on the *cis*-conformation in this structure to connect two crystallographically different Hg^{II} ions. Two pyridine rings

 © 2005 Wiley-VCH Verlag GmbH & Co. KGaA, Weinheim

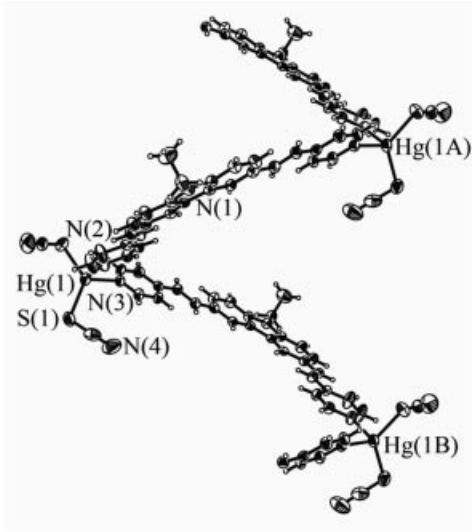

(a)

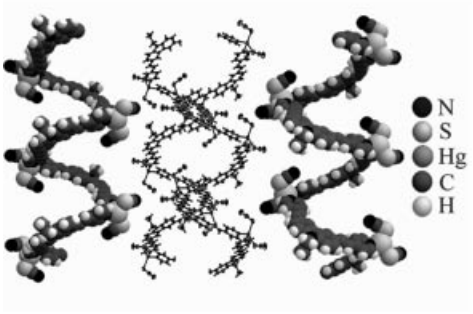

(b)

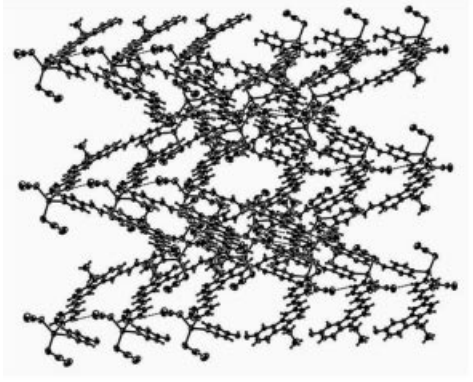

(c)

Figure 1. (a) Molecular structure of **1** showing different coordination environments of the two structurally independent Hg^{II} ions. (b) Space-filling plots of the right-handed chain (left), left-handed chain (right), and the ball-and-stick plot (middle) of the double helix bridged by a π–π stacking interaction in complex **1**. (c) Molecular packing of complex **1**.

are connected by Hg(1) to adopt the same orientation, while those connected by Hg(1A) take on the opposite orientation. This connectivity extends the span of the two ligands and forces a turn in the chain. Such an arrangement endows the chain structure with an intrinsic helical sense. The repeating unit in this single-stranded helix consists of a pair consisting of the $Hg(SCN)_2$ unit and the ligand. As depicted in part b of Figure 1, a fairly flattened, loose helix runs along the *b* axis with a pitch of about 7.99 Å (distance between the two mercury centers at the same phase); at the widest point the diameter of the helix equals 16.03 Å. Left-handed helicates connect through an intermolecular π–π stacking interaction between phenyl and pyridine rings with the short distance of 3.38 Å, and there is some evidence of a weak interaction between each nitrogen atom of $Hg(SCN)_2$ and the pyridyl C–H group of a molecule in an adjacent chain (C–H···N = 3.24 Å);[4] right-handed helicates also connect in this way (Figure 1, c). Unlike most double-helical complexes,[9] the adjacent left-handed and neighboring right-handed helical chains are not entangled together but interact through π–π stacking interactions with the short distance of 3.24 Å as illustrated in Figure 1 (parts b and c), which may contribute to stabilizing the formation of the helical structure. Then a two-dimensional network is formed through the C–H···N hydrogen bond interaction established between ligands and thiocyanate anions of adjacent chains and intermolecular π–π stacking interactions. Because left-handed and right-handed helical chains coexist in the crystal structure, the whole crystal is mesomeric and does not exhibit chirality.

Crystal Structure of $Hg(L^1)_2I_2$ (2)

The crystal contains individual $Hg(\mathbf{L^1})_2I_2$ neutral molecules. A perspective drawing with atom-labeling scheme is shown in Figure 2 (a). Each metal atom is tetracoordinated by two N donors from different ligands and two terminal iodine atoms of HgI_2. The Hg–N distance (Table 1) in the complex is in the range of those found in the other complexes;[7] Hg–I distances are also in the range of those found in other Hg^{II} iodine complexes with terminal Hg–I bonds.[7] The bond angles N(2A)–Hg(1)–N(2), N(2A)–Hg(1)–I(1), N(2)–Hg(1)–I(1) and I(1)–Hg(1)–I(1A) are 76.3(3), 105.10(2), 106.74(2) and 139.18(3)°, respectively. Table 1 shows that the Hg–N and Hg–I distances are almost equal; thus the strong distortion in the tetrahedral environment of the four donor atoms is explained on the basis of strong stereo interactions between the two $\mathbf{L^1}$ ligands in each complex.

However, in crystal complex **2**, the ligand with two potential coordination nitrogen atoms, only one pyridine nitrogen atom of the ligand participates, coordinating to mercury(II). It does not present helices like the reported 2,2′- and 4,4′-bipyridyl-based "building block" compounds before. It is possible that the large volume of two iodine atoms repulses the ligands to form the very small angle of N–Hg–N [76.3(3)°], which produces strong stereo interactions when Hg^{II} ions bridge ligands to form the coordination polymer. The adjacent molecules are stacked to sheets through π–π interaction along the *b* axis with the short distance of 3.44 Å, and opposite sheets interact through pairwise C–H···I contacts [C–H···I = 3.92 Å, H···I = 3.16 Å][4] along the *c* axis, which have 2D sheets propagated as depicted in Figure 2 (b). Taking the van der Waals radii of H and I to be 1.20 and 2.15 Å, respectively, any H···I contact

 © 2005 Wiley-VCH Verlag GmbH & Co. KGaA, Weinheim

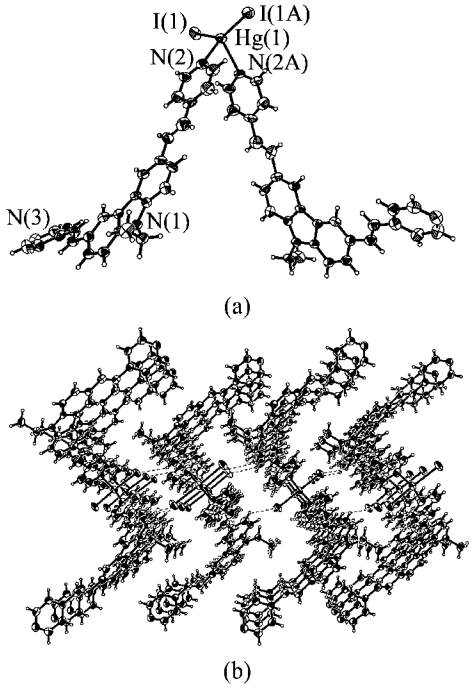

Figure 2. (a) Molecular structure and atom numbering of Hg-$(\mathbf{L^1})_2I_2$. The thermal ellipsoids are drawn at the 50% probability level. (b) Molecular packing of complex **2**.

Table 1. Selected intra- and intermolecular bond lengths [Å] and angles [°] for **1**–**4**.

1			
Hg(1)–N(2)	2.354(4)	N(3)–Hg(1)–N(2)	98.67(2)
Hg(1)–N(3)	2.299(4)	S(2)–Hg(1)–S(1)	127.06(6)
Hg(1)–S(2)	2.4371(2)	N(2)–Hg(1)–S(2)	101.00(1)
Hg(1)–S(1)	2.4493(2)	N(3)–Hg(1)–S(2)	107.89(1)
		N(3)–Hg(1)–S(1)	113.72(1)
		N(2)–Hg(1)–S(1)	103.49(1)
2			
Hg(1)–N(2)	2.425(6)	N(2)–Hg(1)–N(2A)	76.3(3)
		I(1)–Hg(1)–I(1A)	139.18(3)
Hg(1)–I(1)	2.6339(6)	N(2A)–Hg(1)–I(1A)	106.74(2)
		N(2)–Hg(1)–I(1A)	105.10(2)
3			
Hg(1)–N(2)	2.449(3)	N(3)–Hg(1)–N(2)	95.77(1)
Hg(1)–N(3)	2.336(4)	S(1)–Hg(1)–S(2)	126.19(5)
Hg(1)–S(1)	2.4510(2)	N(2)–Hg(1)–S(1)	101.63(1)
Hg(1)–S(2)	2.460(2)	N(3)–Hg(1)–S(1)	117.23(9)
		N(2)–Hg(1)–S(2)	103.30(9)
		N(3)–Hg(1)–S(2)	106.70(9)
4			
Hg(1)–N(2)	2.381(1)	N(3)–Hg(1)–N(2)	99.2(4)
Hg(1)–N(3)	2.447(1)	I(2)–Hg(1)–I(1)	128.51(6)
Hg(1)–I(2)	2.670(3)	N(2)–Hg(1)–I(1)	104.9(3)
Hg(1)–I(1)	2.674(2)	N(3)–Hg(1)–I(2)	103.5(3)
		N(3)–Hg(1)–I(1)	106.9(2)
		N(2)–Hg(1)–I(2)	110.1(2)

less than 3.35 Å and C–H···I angle >130° may therefore potentially be considered significant.[8] In complex **2**, the distance of H···I is 3.16 Å and the C–H···I angle is 152°, which indicate the formation of C–H···I hydrogen bonds. The importance of such C–H···I hydrogen bonds in supramolecular self-assembly has also been reported recently.[8] The overall structure is compact with small cavities.

Crystal Structure of $Hg_2(L^2)_2(SCN)_4$ (3)

The structure of complex **3** is shown in Figure 3 (a). The molecules of **3** exist as a centrosymmetric 30-membered macrometallacyclic ring formed by two $\mathbf{L^2}$ ligands bridging two Hg^{II} ions with pyridine nitrogen in *trans*-form. However, the macrocycle **3** is nonplanar and its cavity is large [N(2)–N(3A) = 12.713 Å, Hg(1)–Hg(1A) = 12.122 Å]; the dihedral angles between the pyridyl and carbazolyl rings, and the neighboring pyridyl ring are 31.6° and 20.2°, respectively. The opposite carbazolyl rings and pyridyl rings are parallel to each other.

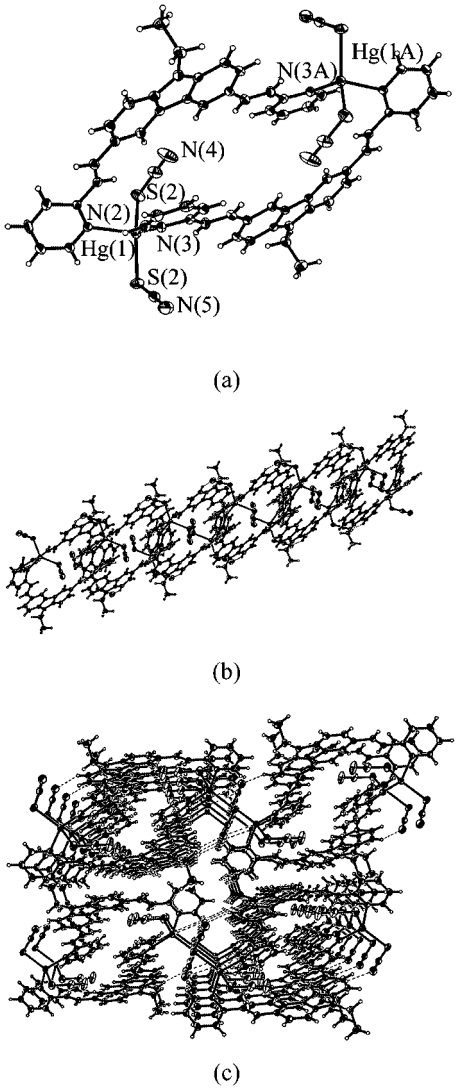

Figure 3. (a) Perspective view of the 30-membered macrometallacyclic ring of complex **3**. (b) The packing diagram of complex **3** showing π–π stacking interaction and the weak C–H···N interactions along the *b* axis. (c) The packing diagram of complex **3** between different chains showing the weak Hg···N interactions along the *c* axis.

 © 2005 Wiley-VCH Verlag GmbH & Co. KGaA, Weinheim

In this complex, the $\mathbf{L^2}$ ligand has bidentate coordination, and each Hg^{II} center is coordinated by two pyridine nitrogen atoms from two different ligands and two sulfur atoms from two thiocyanate anions, showing a distorted tetrahedron geometry with a N–Hg–N bond angle of 95.77(1)°. The bond lengths of Hg–N_{av} of 2.39 Å and Hg–S_{av} of 2.455 Å fall within the expected values (Table 1). The dinuclear structures connect to each other through a π–π stacking interaction (the shortest distance of two macrocycles is 2.85 Å) and weak C–H···N interactions (C–H···N = 3.45 Å)[4] to form an infinite chain of macrocycles like a stair structure along the *b* axis (Figure 3, b). In particular, the difference chains (Figure 3, c) show some weak interaction through single, secondary Hg···N–C–S interactions (Hg···N = 3.59 Å) along the *a* axis. Together, the π–π stacking interaction and hydrogen bond form the overall two-dimensional network.

Crystal Structure of $[HgL^2I_2]_n$ (4)

Helical structures represent a longstanding synthetic target for the supramolecular chemist because of their intrinsic aesthetic appeal and potentially exploitable properties.[9] At this time, our attempts are directed toward the generation of a helical chain through the variation of the anion while maintaining the metal ion and ligand structure. The most striking feature of compound **4** is the interesting arrangement of $\mathbf{L^2}$ molecules and usual coordination of mercury atoms forming a unique helical structure. As described in Figure 4 (a), complex **4** also contains a pair of HgI_2 units and two $\mathbf{L^2}$ ligands in its asymmetric unit cell. However, these components do not connect to another to form a macrocyclic structure like complex **3**, but rather connect to form an infinite polymeric chain structure. A compact single-stranded helical chain is formed by self-assembly of $[HgL^2I_2]$ by coordination of *meta*-related peripheral pyridine-N of this unit to the neighboring Hg^{II} center running along a crystallographic 2_1 axis in the *a* direction with a long pitch of about 11.69 Å; at the widest point the diameter of the helix equals 6.13 Å.

In addition, like complex **1**,[7] the adjacent helical chains in compound **4**, one exhibiting left-handedness and the other right-handedness, are not entangled together but interact through π–π stacking interactions (the shortest distance of pyridyl and benzyl rings is 3.42 Å), which are alternatively offered by two helical chains to generate a compact double-stranded helical chain (Figure 4, b). To illustrate this clearly, the left- and right-handed helical chains are represented in Figure 4, b. Like complex **1**, these double-stranded helical chains are further extended into the two-dimensional architecture by C–H···I hydrogen bond interactions established between ligands and iodine anions of adjacent chains (C–H···I = 4.14 Å, H···I = 3.23 Å)[4] with interactions along the *b* axis in compound **4** (Figure 4, c). In complex **4**, the distance of H···I is 3.23 Å and the C–H···I angle is 142°, which indicate the formation of C–H···I hydrogen bonds. Because left-handed and right-handed helical chains coexist in the crystal structure, the whole crystal is mesomeric and does not exhibit chirality.

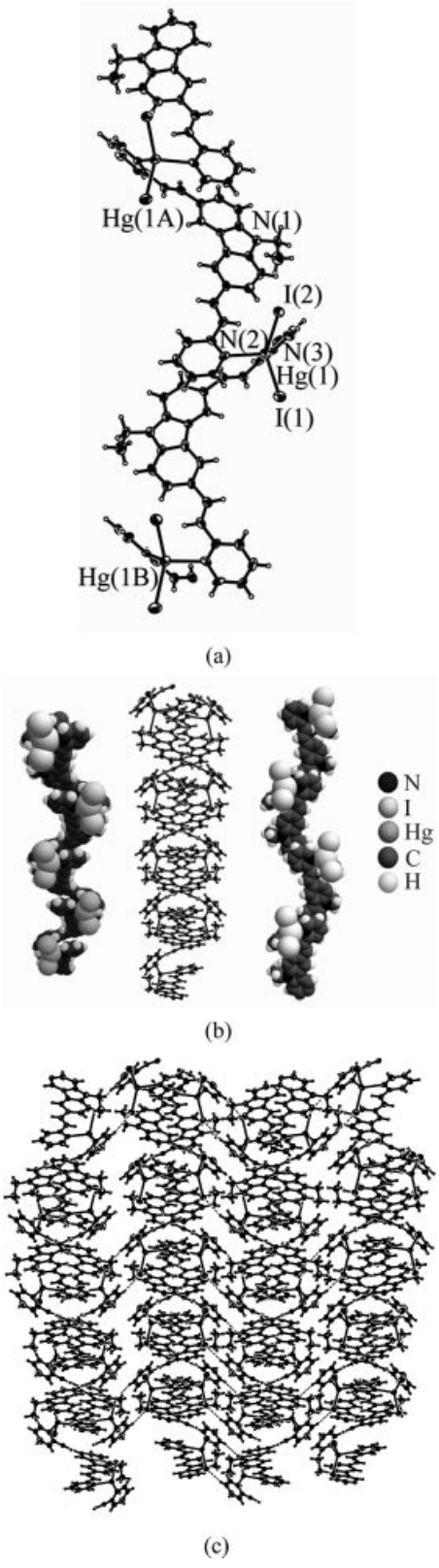

Figure 4. (a) Molecule structure of **4** showing different coordination environments of the two structurally independent Hg^{II} ions. (b) Space-filling plots of the right-handed chain (left), left-handed chain (right), and the ball-and-stick plot (middle) of the double helix bridged by a π–π stacking interaction in complex **4**. (c) Molecular packing of **4** viewed along the *b* axis by intermolecular hydrogen bond C–H···I.

 © 2005 Wiley-VCH Verlag GmbH & Co. KGaA, Weinheim

In the present work, four different Hg^{II} coordination complexes **1**–**4** with bis(pyridyl) ligands (**L**^{1}, **L**^{2}) have been prepared and structurally characterized, giving metal–organic supramolecular architectures. Although compared with rigid bridging ligands, flexible bridging ligands are able to produce some unique frameworks with aesthetics and useful properties because of their flexibility and conformational freedom,[10] we designed and synthesized two novel functional rigid ligands with long conjugated chains that also present flexibility and conformational freedom to a certain extent. In complexes **1**–**4**, Hg^{II} centers all adopt four-coordination modes in different coordination environments. By comparing the structures of the four complexes, it is clear that the conformations of ligands in the complexes are related to the position of the nitrogen atom. Although complexes **1** and **3** have the same mercury(II) cation and thiocyanate counterion, ligand **L**^{1} of 4-N atoms in complex **1** takes on the *cis*-conformation to form helical chains and ligand **L**^{2} of 2-N atoms in complex **3** takes on the *trans*-conformation to form the macrometallacyclic ring; otherwise, ligand **L**^{1} of 4-N atoms in complex **1** and ligand **L**^{2} of 2-N atoms in complex **4** all take on the *cis*-conformation to form similar helical chains with nearly uniform bond lengths and angles (Table 1). Also, it should be noted that although **L**^{1}, with two potential coordination nitrogen atoms but only one pyridine nitrogen atom of the ligand, coordinates to mercury(II) in complex **2**, it is possible that the very small angle of N–Hg–N [76.3(3)°] produces strong stereo repulsion. This indicates that the conformations of ligands in the complexes may play an important role, indicating that the nature of the ligand is a determining factor in controlling the structural topology of these metal–organic supramolecular architectures, which offers the opportunity to control the coordination networks by ligand modifications.

Characterization

Thermogravimetric Analysis

The TG-DSC measurements of complexes **1**–**4** were determined in the range of 20–800 °C under nitrogen. To study the thermal stability of compounds **1**–**4**, thermal gravimetric analyses (TGA) were performed on the single crystal samples. TG data show that **1** is stable up to 235.2 °C, loses weight from 235.2 to 474 °C corresponding to decomposition of ligand **L**^{1}, and finally loses weight from 557 to 764 °C corresponding to the losses of $Hg(SCN)_2$. The TG data of **2** show that it is also stable up to 250 °C and then keeps losing weight from 250 °C to 768 °C, corresponding to decomposition of ligand **L**^{1} and HgI_2. The TG data for **3** show that it begins to decompose at 197 °C, then there are two weight-loss stages in the ranges 197–481 °C and 530–775 °C, corresponding to decomposition of ligand **L**^{2} and the losses of $Hg(SCN)_2$, respectively. The TG data of **4** show that the weight loss from 192 to 292 °C corresponds to the losses of ligand **L**^{2}, and the weight loss from 292 to 520 °C corresponds to decomposition of HgI_2.

Luminescent Properties

Luminescent transition-metal complexes containing multichromophoric ligands with extended conjugation have been extensively studied in recent years, partly because of their potential use as sensors, probes, and photonic devices.[11] Owing to the ability to affect the emission wavelength of organic materials, syntheses of inorganic–organic coordination complexes by the judicious choice of organic spacers and transition-metal centers can be an efficient method for obtaining new types of electroluminescent materials.[12] Free ligands **L**^{1} and **L**^{2}, and their metal complexes **1**–**4** show emission in solid state at room temperature (Figure 5). The nanosecond range of lifetime in the solid state at 298 K reveals that the emission is fluorescent in nature. The solid-state fluorescent analyses show that complexes exhibit different properties. As shown in Figure 5 (a), complex **1** exhibits an intense broad emission band centered at 608 nm, which is completely invariant to the excitation over the range of 300 to 534 nm and complex **2** always displays a weak broad emission band centered at 604 nm upon excitation over the range of 300 to 543 nm. These fluorescent emissions can be tentatively assigned to the ligand-to-metal charge transfer (LMCT), as two emissions at 452 and 522 nm upon excitation over the range of 300–428 nm can be observed for the free **L**^{1}. Complex **3** exhibits a broad

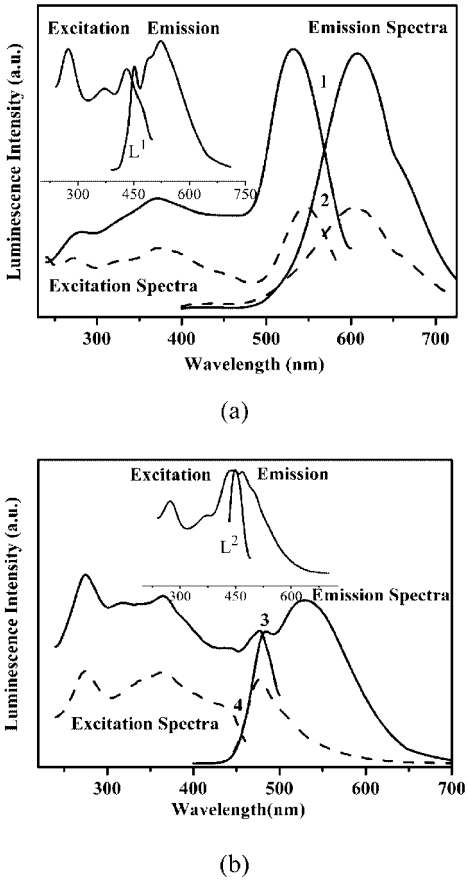

Figure 5. Solid-state emission spectra of complexes at room temperature: (a) **L**^{1}, **1**, and **2**; (b) **L**^{2}, **3** and **4**.

 © 2005 Wiley-VCH Verlag GmbH & Co. KGaA, Weinheim

intense emission band at 528 nm with a shoulder at 484 nm upon excitation over the range of 365–477 nm, which can be tentatively assigned to LMCT and the intraligand fluorescent emission. However, complex **4** presents a sharp weak emission band with the maximum at 477 nm, which is completely invariant to the excitation over the range of 300–429 nm. The emission spectrum in complex **4** is largely characteristic of the intraligand fluorescent emission, as two emissions at 448 and 467 nm upon excitation over the range of 300 to 423 nm can be observed for the free $\mathbf{L^2}$. Thus the difference in the intense emission results from the different coordinated counteranions to Hg^{II} (I^- for **2**, **4** and SCN^- for **1**, **3**), which suggests that the change of counteranions has an important effect on their fluorescent property.[13]

Experimental Section

All chemicals and solvents were dried and purified by the usual methods. Elemental analyses were performed with a Perkin–Elmer 240C elemental analyzer. IR spectra were recorded with a Nicolet FTIR Nexus 870 instrument in the range 4000–400 cm^{-1} by using KBr pellets. The far-IR spectra (600–50 cm^{-1}) were recorded as Nujol mulls between polyethylene sheets. ^1H and ^{13}C NMR spectra were performed on a Bruker av600 MHz Ultrashield spectrometer and are reported as parts per million (ppm) from TMS (δ). The thermal behaviors were recorded with a Perkin–Elmer Pris-1 DMDA-V1 analyzer in N_2 at a heating rate of 5 °C min^{-1}. The luminescent spectra were measured on single crystals at room temperature using a Fluorolog-3-TAU steady-state/lifetime spectrofluorometer. The excitation slit was 2 nm, and the emission slit was 2 nm also.

X-ray Crystallography: Single-crystal X-ray diffraction measurements were carried out on a Bruker Smart 1000 CCD diffractometer equipped with a graphite crystal monochromator situated in the incident beam for data collection at room temperature. The determination of unit cell parameters and data collections were performed with Mo-K_α radiation (λ = 0.71073 Å). Unit cell dimensions were obtained with least-squares refinements, and all structures were solved by direct methods using SHELXL-97.[14] The other non-hydrogen atoms were located in successive difference Fourier syntheses. The final refinement was performed by full-matrix least-squares methods with anisotropic thermal parameters for non-hydrogen atoms on F^2. The hydrogen atoms were added theoretically and riding on the concerned atoms. Crystallographic crystal data and processing parameters for compounds **1**–**4** are shown in Table 2. Selected bond lengths and bond angles are listed in Table 1.

CCDC-245193 (for **1**), -245192 (for **2**), -241585 (for **3**), and -241588 (for **4**) contain the supplementary crystallographic data for this paper. These data can be obtained free of charge from The Cambridge Crystallographic Data Centre via www.ccdc.cam.ac.uk/data_request/cif.

Preparation of 9-Ethyl-3,6-diiodocarbazole: 9-Ethylcarbazole (10 g, 51 mmol) and anhydrous ethanol (150 mL) were added to a three-necked flask equipped with a magnetic stirrer, a reflux condenser, and an isobaric dropping funnel. ICl (20 g, 123 mmol)/ethanol (20 mL) was added to the mixture at 80 °C. The reaction mixture was refluxed for 2 h, cooled to room temperature and filtered. The grey needle crystals (20.52 g, 45.9 mmol) obtained (90%) were washed with ethanol. M.p. 154–155 °C. ^1H NMR (600 MHz, [D_6]-DMSO): δ = 1.27 (t, J = 6.6 Hz, 3 H), 4.41 (q, J = 6.6 Hz, 2 H), 7.50 (d, J = 8.4 Hz, 2 H), 7.74 (d, J = 8.4 Hz, 2 H), 8.61 (s, 2 H).

Preparation of 9-Ethyl-3,6-bis[2-(4-pyridyl)ethenyl]carbazole ($\mathbf{L^1}$): 9-Ethyl-3,6-diiodocarbazole (3.13 g, 7 mmol), potassium carbonate (2.42 g, 17.5 mmol), tetra-*n*-butylammonium bromide (2.26 g, 7 mmol), tri-*o*-tolylphosphane (0.21 g, 0.7 mmol), 4-vinylpyridine (4 mL, 30 mmol), palladium(II) acetate (0.047 g, 0.2 mmol) and redistilled *N*,*N*-dimethylformamide (7 mL) under nitrogen were added to a three-necked flask equipped with a magnetic stirrer, a reflux condenser and a nitrogen input tube. The reaction mixture was refluxed in an oil bath at 100 °C under nitrogen. The resulting solution was refluxed for 48 h and then cooled to room temperature. The residue was extracted with dichloromethane (600 mL), washed three times with distilled water, and dried with anhydrous magnesium sulfate. Then it was filtered and concentrated. The resulting solution was chromatographed over 200 g of silica gel. Elution with ethyl acetate and the recrystallization from ethanol produced light yellow crystals. Yield: 1.99 g (71%). M.p. 247.1–247.4 °C. ^1H NMR (600 MHz, [D_6]DMSO): δ = 1.35 (t, J = 6.9 Hz, 3 H), 4.49 (q, J = 6.9 Hz, 2 H), 7.29 (d, J = 16.3 Hz, 2 H), 7.59 (d, J = 4.8 Hz, 4 H), 7.69 (d, J = 8.4 Hz, 2 H), 7.74 (d, J = 16.3 Hz,

Table 2. Crystallographic data and structure refinement summary for complexes **1**–**4**.

Complex	**1**	**2**	**3**	**4**
Empirical formula	$C_{30}H_{23}HgN_5S_2$	$C_{56}H_{46}HgI_2N_6$	$C_{60}H_{46}Hg_2N_{10}S_4$	$C_{28}H_{23}HgI_2N_3$
Formula mass	718.24	1257.38	1436.49	855.88
Crystal system	monoclinic	monoclinic	monoclinic	monoclinic
Space group	$P2_1/c$	$C2/c$	$P2_1/n$	$P2_1/c$
a [Å]	8.2569(1)	34.732(7)	15.919(1)	8.468(9)
b [Å]	15.978(2)	8.4181(2)	8.119(6)	23.28(3)
c [Å]	21.205(3)	16.785(3)	21.663(2)	13.933(2)
β [°]	91.673(2)	98.698(3)	103.640(1)	98.012(2)
V [Å^3]	2796.4(7)	4851.0(17)	2721(3)	2719(5)
Z	4	4	2	4
D_{calcd} [g cm^{-3}]	1.706	1.996	1.753	2.091
θ range [°]	1.92–25.03	2.37–25.03	1.44–25.03	1.72–25.02
Total no. of data	14504	12284	13838	11579
No. of unique data	4940	4257	4811	4613
No. of parameters refined	343	295	343	307
R_1	0.0332	0.0407	0.0270	0.0574
wR_2	0.0686	0.0917	0.0630	0.1347
Gof	1.006	1.015	1.002	1.002

 © 2005 Wiley-VCH Verlag GmbH & Co. KGaA, Weinheim

2 H), 7.83 (d, J = 8.4 Hz, 2 H), 8.52 (s, 2 H), 8.55 (d, J = 4.8 Hz, 4 H). ^{13}C NMR (600 MHz, [D$_6$]DMSO): δ = 150.43, 145.34, 140.83, 134.51, 128.16, 126.11, 123.63, 123.12, 121.06, 119.97, 110.32, 37.81, 14.31. IR (KBr): $\tilde{\nu}$ = 2927 (m), 2860 (w), 1729 (m), 1627 (m), 1600 (s), 1485 (m), 1413 (w), 1344 (m), 1233 (m), 1155 (w), 1126 (w), 1022 (w), 960 (m), 805 (m), 705 (m), 591 (w), 525 (w) cm^{-1}. $C_{28}H_{23}N_3$ (401.50): calcd. C 83.76, H 5.77, N 10. 47; found C 83.80, H 5.76, N 10.44.

Preparation of 9-Ethyl-3,6-bis[2-(2-pyridyl)ethenyl]carbazole (L^2): 9-Ethyl-3,6-diiodocarbazole (3.13 g, 7 mmol), potassium carbonate (2.42 g, 17.5 mmol), tetra-*n*-butylammonium bromide (2.26 g, 7 mmol), and 2-vinylpyridine (4 mL, 30 mmol) were dissolved in redistilled *N*,*N*-dimethylformamide (7 mL). Palladium(II) acetate (0.047 g, 0.2 mmol) and tri-*o*-tolylphosphane (0.21 g, 0.7 mmol) were added to it. The resulting solution was refluxed for 5 days and then cooled to room temperature. The residue was extracted with dichloromethane (600 mL), washed three times with distilled water, and dried with anhydrous magnesium sulfate. Then it was filtered and concentrated. The resulting solution was chromatographed over silica gel (200 g). Elution with ethyl acetate/petroleum ether (2:1) and the recrystallization from ethyl acetate produced light yellow crystals. Yield: 1.88 g (67%). M.p. 189.3–189.4 °C. ^{1}H NMR (600 MHz, [D$_6$]DMSO): δ = 1.35 (t, J = 7.2 Hz, 3 H), 4.48 (q, J = 7.2 Hz, 2 H), 7.24 (t, J = 6.0 Hz, 2 H), 7.36 (d, J = 16.2 Hz, 2 H), 7.57 (d, J = 7.2 Hz, 2 H), 7.66 (d, J = 7.2 Hz, 2 H), 7.80 (q, 4 H), 7.87 (d, J = 16.2 Hz, 2 H), 8.55 (s, 2 H), 8.59 (d, J = 4.2 Hz, 2 H). ^{13}C NMR (600 MHz, [D$_6$]DMSO): δ = 155.59, 149.50, 140.21, 136.81, 133.11, 127.87, 125.58, 125.44, 122.76, 121.91, 121.87, 119.53, 109.74, 37.31, 13.84. IR (KBr): $\tilde{\nu}$ = 2933 (m), 2866 (w), 1733 (m), 1626 (m), 1590 (s), 1488 (m), 1412 (w), 1385 (m), 1347 (w), 1236 (m), 1193 (w), 1160 (w), 1124 (w), 970 (m), 810 (m), 597 (w), 520 (w) cm^{-1}. $C_{28}H_{23}N_3$ (401.50): calcd. C 83.76, H 5.77, N 10.47; found C 83.72, H 5.78, N 10.50.[15]

Preparation of $[HgL^1(SCN)_2]_n$ (1): L^1 (40.01 mg, 0.1 mmol) in CH_2Cl_2 solution (5 mL) was layered onto a solution of $Hg(SCN)_2$ (31.6 mg, 0.1 mmol) in MeOH (5 mL) and stood for several days to give red single crystals of **1**. Yield 64.64 mg (90%). IR: $\tilde{\nu}$ = 2065 (vs), 419 (m), 327 (m). $C_{30}H_{23}HgN_5S_2$ (718.24): calcd. C 50.17, H 3.23, N 9.75; found C 50.14, H 3.24, N 9.77.

Preparation of $Hg(L^1)_2I_2$ (2): L^1 (40.01 mg, 0.1 mmol) in $CHCl_3$ solution (5 mL) was layered onto a solution of HgI_2 (45.4 mg, 0.1 mmol) in MeOH (10 mL) and stood for a week to give yellow single crystals of **2**. Yield 111.91 mg (89%). IR: $\tilde{\nu}$ = 420 (m), 151 (s). $C_{56}H_{46}HgI_2N_6$ (1257.38): calcd. C 53.49, H 3.69, N 6.68; found C 53.51, H 3.68, N 6.69.

Preparation of $Hg_2(L^2)_2(SCN)_4$ (3): L^2 (40.01 mg, 0.1 mmol) and $Hg(SCN)_2$ (31.6 mg, 0.1 mmol) were dissolved in MeOH (20 mL), refluxed for 2 h at 70 °C, and cooled to give a clear yellow solution. Yellow crystals suitable for X-ray diffraction were obtained after two weeks by slow evaporation of the methanol solution at room temperature. Yield 57.46 mg (80%). IR: $\tilde{\nu}$ = 2061 (vs), 420 (m), 328 (m). $C_{60}H_{46}Hg_2N_{10}S_4$ (1436.49): calcd. C 50.17, H 3.23, N 9.75; found C 50.14, H 3.24, N 9.77.

Preparation of $[HgL^2I_2]_n$ (4): L^2 (40.01 mg, 0.1 mmol) and HgI_2 (31.6 mg, 0.1 mmol) were dissolved in MeOH (20 mL), refluxed for 2 h at 70 °C, and cooled to room temperature giving a clear yellow solution. Pale yellow crystals suitable for X-ray diffraction were obtained after several days by slow evaporation of the methanol solution at room temperature. Yield 77.89 mg (91%). IR: $\tilde{\nu}$ = 419 (m), 151 (s). $C_{28}H_{23}HgI_2N_3$ (855.88): calcd. C 39.29, H 2.71, N 4.91; found C 39.28, H 2.72, N 4.92.

Acknowledgments

We thank the National Natural Science Foundation of China (50272001, 50335050, 50532030), and Person with Ability Foundation of Anhui Province 2002Z021. We also wish to thank Prof. D. Q. Wang of University of Liao Cheng for his assistance with the X-ray structure determinations.

[1] a) J. S. Evans, R. L. Musselman, *Inorg. Chem.* **2004**, *43*, 5613–5629; b) Z. Q. Qin, M. C. Jennings, R. J. Puddephatt, *Inorg. Chem.* **2001**, *40*, 6220–6228; c) B. Moulton, M. J. Zaworotko, *Chem. Rev.* **2001**, *101*, 1629–1658; d) K. Kim, *Chem. Soc. Rev.* **2002**, *31*, 96–107; e) S. Sailaja, M. Rajasekharan, *Inorg. Chem.* **2003**, *42*, 5675–5684.

[2] a) M. L. Tong, X. M. Chen, B. H. Ye, L. N. Ji, *Angew. Chem. Int. Ed.* **1999**, *38*, 2237–2240; b) M. Eddaoudi, H. Li, O. M. Yaghi, *J. Am. Chem. Soc.* **2000**, *122*, 1391–1397; c) K. S. Min, M. P. Suh, *J. Am. Chem. Soc.* **2000**, *122*, 6834–6840; d) J. Y. Lu, A. M. Babb, *Inorg. Chem.* **2001**, *40*, 3261–3262; e) A. Fu, X. Huang, J. Li, T. Yuen, C. L. Lin, *Chem. Eur. J.* **2002**, *8*, 2239–2247; f) M. L. Tong, Y. M. Wu, J. Ru, X. M. Chen, S. Kitagawa, *Inorg. Chem.* **2002**, *41*, 4846–4848; g) D. M. Shin, I. S. Lee, Y. K. Chung, *Inorg. Chem.* **2003**, *42*, 8838–8848; h) X. H. Bu, Y. B. Xie, J. R. Li, R. H. Zhang, *Inorg. Chem.* **2003**, *42*, 7422–7430; i) T. J. Burchell, D. J. Eisler, R. J. Puddephatt, *Inorg. Chem.* **2004**, *43*, 5550–5557; j) S. Mukhopadhyay, P. B. Chatterjee, D. Mandal, G. Mostafa, A. Caneschi, J. V. Slageren, T. J. R. Weakley, M. Chaudhury, *Inorg. Chem.* **2004**, *43*, 3413–3420; k) H. Zheng, H. B. Song, M. Du, Sh. T. Chen, X. H. Bu, *Inorg. Chem.* **2004**, *43*, 931–944.

[3] a) S. K. Ghosh, P. K. Bharadwaj, *Inorg. Chem.* **2004**, *43*, 2293–2298; b) T. P. Losier, M. J. Zaworotko, *Angew. Chem. Int. Ed. Engl.* **1996**, *35*, 2779–2782; c) K. N. Power, L. Hennigar, M. J. Zaworotko, *Chem. Commun.* **1998**, 595–596; d) P. J. Hagrman, D. Hagrman, J. Zubieta, *Angew. Chem. Int. Ed.* **1999**, *38*, 2638–2684; e) Z. Q. Qin, M. C. Jennings, R. J. Puddephatt, *Inorg. Chem.* **2002**, *41*, 5174–5186; f) T. Akutagawa, T. Nakamura, *Coord. Chem. Rev.* **2003**, *226*, 3–81; g) Y. B. Dong, P. Wang, R. Q. Huang, *Inorg. Chem.* **2004**, *43*, 4727–4739.

[4] a) A. M. Beatty, *Coord. Chem. Rev.* **2003**, *246*, 131–143; b) H. W. Roesky, M. Andruh, *Coord. Chem. Rev.* **2003**, *236*, 91–119.

[5] H. J. Hoegl, *Phys. Chem.* **1965**, *69*, 755–759.

[6] a) M. He, R. J. Twieg, U. Gubler, D. Wright, W. E. Moerner, *Chem. Mater.* **2003**, *15*, 1156–1164; b) K. R. Justin Thomas, J. T. Lin, Y. T. Tao, Ch. H. Chuen, *Chem. Mater.* **2002**, *14*, 3852–3859; c) B. Liu, L. W. Yu, Y. H. Lai, W. Huang, *Chem. Mater.* **2001**, *13*, 1984–1991; d) Ch. W. Ko, Y. T. Tao, J. T. Lin, K. R. Justin Thomas, *Chem. Mater.* **2002**, *14*, 357–361; e) H. Chun, I. K. Moon, D. H. Shin, N. Kim, *Chem. Mater.* **2001**, *13*, 2818–2823.

[7] a) Ch. Y. Su, A. M. Goforth, M. D. Smith, H. C. Z. Loye, *Inorg. Chem.* **2003**, *42*, 5685–5692; b) T. J. Burchell, D. J. Eisler, R. J. Puddephatt, *Inorg. Chem.* **2004**, *43*, 5550–5557.

[8] a) C. J. Horn, A. J. Blake, N. R. Champness, A. Garau, V. Lippolis, C. Wilson, M. Schröder, *Chem. Commun.* **2003**, 312–313; b) L. Y. Kong, Zh. H. Zhang, T. A. Okamura, M. J. Fei, W. Y. Sun, N. Ueyama, *Chem. Lett.* **2004**, *12*, 1572–1573.

[9] a) P. A. Maggard, C. L. Stern, K. R. Poeppelmeier, *J. Am. Chem. Soc.* **2001**, *123*, 7742–7743; b) Z. Shi, S. H. Feng, S. Gao, L. R. Zhang, G. Y. Yang, J. Hua, *Angew. Chem. Int. Ed.* **2000**, *39*, 2325–2326; c) C. Z. Lu, C. D. Wu, S. F. Lu, J. C. Liu, Q. J. Wu, Q. J. Hui, H. H. Zhuang, J. S. Huang, *Chem. Commun.* **2002**, 152–153; d) Y. Wang, J. H. Yu, M. Guo, R. R. Xu, *Angew. Chem. Int. Ed.* **2003**, *42*, 4089–4092; e) M. C. Hong, W. P. Su, R. Cao, M. Fujita, J. X. Lu, *Chem. Eur. J.* **2000**, *6*, 427–431; f) X. H. Bu, H. Liu, M. Du, L. Zhang, Y. M. Guo, M. Shionoya, J. Ribas, *Inorg. Chem.* **2002**, *41*, 5634–5634; g) J. Vinje, J. A. Parkinson, P. J. Sadler, T. Brown, E. Sletten, *Chem.*

 © 2005 Wiley-VCH Verlag GmbH & Co. KGaA, Weinheim

Eur. J. **2003**, *9*, 1620–1630; h) Z. Wu, Q. Chen, S. Xiong, B. Xin, Z. Zhao, L. Jiang, J. S. Ma, *Angew. Chem. Int. Ed.* **2003**, *42*, 3271–3274; i) M. Barboiu, G. Vaughan, R. Graff, J. M. Lehn, *J. Am. Chem. Soc.* **2003**, *125*, 10256–10265.

[10] a) M. Du, X. H. Bu, Z. Huang, S. T. Chen, Y. M. Gao, *Inorg. Chem.* **2003**, *42*, 552–559; b) X. H. Bu, W. Chen, S. T. Lu, R. H. Zhamg, D. Z. Liao, W. M. Bu, M. Shionoya, F. Brisse, J. Ribas, *Angew. Chem. Int. Ed.* **2001**, *40*, 3201–3203; c) F. A. Paz, Y. Z. Khimyak, A. D. Bond, J. Rocha, J. Klinowski, *Eur. J. Inorg. Chem.* **2002**, 2823–2828; d) Y. B. Dong, M. D. Smith, R. C. Layland, H. C. zur Loye, *Inorg. Chem.* **1999**, *38*, 5027–5033.

[11] a) Sh.-Sh. Sun, A. J. Lees, *Coord. Chem. Rev.* **2002**, *230*, 170–191; b) V. Balzani, A. Juris, M. Venturi, S. Campagna, S. Serroni, *Chem. Rev.* **1996**, *96*, 759–834.

[12] a) D. M. Ciurtin, N. G. Pschirer, M. D. Smith, U. H. F. Bunz, H. C. zur Loye, *Chem. Mater.* **2001**, *13*, 2743–2745; b) E. Cariati, X. Bu, P. C. Ford, *Chem. Mater.* **2000**, *12*, 3385–3391; c) F. Würthner, A. Sautter, *Chem. Commun.* **2000**, 445–446.

[13] Y. Q. Gong, R. H. Wang, Y. F. Zhou, D. Q. Yuan, M. Ch. Hong, *J. Mol. Struct.* **2005**, *705*, 29–33.

[14] G. M. Sheldrick, *SHELXL-97, Program for Crystal Structures Refinement*, University of Göttingen, Göttingen, Germany, **1997**.

[15] H. P. Zhou, J. Zh. Zhang, D. M. Li, Y. M. Zhu, Zh. J. Hu, J. Y. Wu, Y. Xie, M. H. Jiang, X. T. Tao, Y. P. Tian, *J. Mol. Struct.* **2005**, *743*, 93–97.

Received: May 16, 2005
Published Online: October 27, 2005

 © 2005 Wiley-VCH Verlag GmbH & Co. KGaA, Weinheim

DOI: 10.1002/ejic.200500484

One-, Two-, and Three-Dimensional Coordination Polymers Built from Large Mo_{36}-Polyoxometalate Anionic Units and Lanthanide Cations

Natalia V. Izarova,[a,b] Maxim N. Sokolov,[a] Denis G. Samsonenko,[a] Alexander Rothenberger,[b] Dmitrij Yu. Naumov,[a] Dieter Fenske,[b] and Vladimir P. Fedin*[a]

Keywords: Coordination polymers / Lanthanides / Molybdenum / Polyoxometalates

The Mo_{36}-polyoxometalate $[Mo_{36}O_{108}(NO)_4(H_2O)_{16}]^{12-}$ reacts with Ln^{3+} to give crystalline solids with 1D, 2D, and 3D polymeric frameworks, depending on the size of Ln^{3+} and the reaction conditions. Reaction of $LaCl_3$ with $(NH_4)_{12}$-$[Mo_{36}O_{108}(NO)_4(H_2O)_{16}]$ gives $(H_3O)_2[\{La(H_2O)_5\}_2\{La(H_2O)_6\}$-$\{La(H_2O)_5Cl\}\{Mo_{36}(NO)_4O_{108}(H_2O)_{16}\}]Cl{\cdot}21H_2O$ (**1**), in whose structure the La^{3+} cations and the polyoxometalate anions are united in a 3D framework, whereas $NdCl_3$ and $SmCl_3$ give $[\{Ln(H_2O)_6\}_4\{Ln(H_2O)_4\}\{Mo_{36}(NO)_4O_{108}(H_2O)_{16}\}]$-$Cl_3{\cdot}nH_2O$ [Ln = Nd, n = 24 (**2**); Ln = Sm, n = 21 (**3**)], which have 2D frameworks. Under different conditions, large Ln^{3+} ions (La–Nd) give the one-dimensional coordination polymers $[\{Ln(H_2O)_6\}_2\{Ln(H_2O)_7\}_2\{Mo_{36}(NO)_4O_{108}(H_2O)_{16}\}]{\cdot}nH_2O$ [Ln = La, n = 29 (**4**); Ln = Ce, n = 41 (**5**), Ln = Pr; n = 40 (**6**), Ln = Nd, n = 36 (**7**)], whereas reaction with $Gd(NO_3)_3$ gives $[\{Gd(H_2O)_5\}_4\{Mo_{36}(NO)_4O_{108}(H_2O)_{16}\}]{\cdot}34H_2O$ (**8**), which has a unique 2D layered structure. Smaller Ln^{3+} ions (Tb–Lu) give isostructural 1D chain coordination polymers $(H_3O)_3$-$[\{Ln(H_2O)_6\}_2\{Ln(H_2O)_4\}\{Mo_{36}(NO)_4O_{108}(H_2O)_{16}\}]{\cdot}nH_2O$ [Ln = Tb, n = 42 (**9**); Ln = Dy, n = 43 (**10**), Ln = Ho, n = 46 (**11**), Ln = Er, n = 50 (**12**); Ln = Yb, n = 56 (**13**); Ln = Lu, n = 31 (**14**)]. The first coordination polymer based on $[Mo_{36}O_{112}$-$(H_2O)_{16}]^{8-}$, namely $(H_3O)_2[\{Nd(H_2O)_5\}_2\{Mo_{36}O_{112}(H_2O)_{16}\}]{\cdot}$ $40H_2O$ (**15**), was prepared from MoO_4^{2-}, NH_2OH, and Nd^{3+}. It has a 2D layered structure. All these compounds are obtained in moderate to high yields (35–93 %), and were characterized by elemental analysis, IR spectroscopy, and single-crystal X-ray structural analysis. Direct coordination of Ln^{3+} to the oxygen atoms of terminal *cis*-MoO_2^{2+} groups is responsible for the formation of these polymeric frameworks. The coordination numbers of Ln^{3+} change from 9 (La–Sm) to 8 (Gd–Lu).
(© Wiley-VCH Verlag GmbH & Co. KGaA, 69451 Weinheim, Germany, 2005)

Introduction

Giant polyoxometalates (POMs) are relatively recent but increasingly fascinating objects of study owing to their potential applications in catalysis, photochemistry, sorption, magnetism, medicine, etc.[1–5] Furthermore, they are attractive building blocks for the design of new one-, two-, and three-dimensional frameworks in new functional materials because they possess both well-defined tunable structures and properties and can act as macroligands toward heterometals.[6,7] The heterometal can bring into play its own properties, such as magnetism. The oxophilic and paramagnetic lanthanide ions are especially well suited for these purposes[8,9] as they also may serve as luminescent[10–16] and Lewis acid catalytic centers.[17] Organic linkers between the lanthanide centers can also be inserted, giving rise to new hybrid organic–inorganic polymeric frameworks.[18] Lanthanide complexes of $[SiW_{11}O_{39}]^{8-}$ and $[P_2W_{17}O_{61}]^{10-}$, for example, show antiviral activity against HIV virus,[19] and there are some examples of using Anderson[20] $\{[Al(OH)_6$-$Mo_6O_{18}]^{3-}\}$ and Keggin[21–23] $\{[XM_{12}O_{40}]^{n-}$, $[Mo_8O_{27}]^{6-}$,[24] $[Mo_9O_{30}]^{6-}$,[25] $[V_{18}O_{42}(X)]^{n-}$,[26–30] and $[Mo_{36}O_{108}(NO)_4$-$(H_2O)_{16}]^{12-}\}$ anions[31–32] as building blocks for inorganic polymers.

Herein we report a series of new compounds (**1**–**15**) with one-, two-, and three-dimensional extended structures, which were obtained by linking large Mo_{36}-polyoxometalate anionic units by lanthanide cations.

Results and Discussion

Syntheses

Orange rhombic crystals of **1**–**3** and **5**–**14** were prepared from the ammonium salt of the polyoxomolybdate $[Mo_{36}(NO)_4O_{108}(H_2O)_{16}]^{12-}$ and the corresponding Ln^{3+} salts in a 1:4 molar ratio in moderate to high yields by the synthetic procedures described in the Experimental Section. The reactions generally occur in a straightforward manner, although only in the case of La (**1**), Ce (**5**), Pr (**6**), Nd (**7**, synthesis 2), and Gd (**8**) does the Ln/POM ratio in the product correspond to the reagent ratio. The counterion of the

[a] Nikolaev Institute of Inorganic Chemistry, Siberian Branch of the Russian Academy of Sciences,
Lavrentiev Avenue 3, Novosibirsk 630090, Russia
E-mail: cluster@che.nsk.su
[b] Institut für Anorganische Chemie, Universität Karlsruhe,
Engesserstrasse Geb. 30.45, Karlsruhe 76128, Germany
Supporting information for this article is available on the WWW under http://www.eurjic.org or from the author.

 © 2005 Wiley-VCH Verlag GmbH & Co. KgaA, Weinheim

Ln salts sometimes enters the final product, as in **1**–**3**, but more often does not influence the final composition: chlorides, nitrates, and sulfates were used for the preparation of isostructural compounds **9**–**14** with equal efficiency. Some of the isolated solids could actually be metastable phases and sometimes longer crystallization times led to different products (as in the case of **1** and **4**). The POM building blocks $[Mo_{36}(NO)_4O_{108}(H_2O)_{16}]^{12-}$ or $[Mo_{36}O_{112}(H_2O)_{16}]^{8-}$ can also be generated in situ, and the compounds **4**, **7** (synthesis 1), and **15** were obtained by refluxing the mixture of $Na_2MoO_4{\cdot}2H_2O$ and $NH_2OH{\cdot}HCl$ at pH ≈ 2, followed by addition of $LaCl_3{\cdot}7H_2O$ or $NdCl_3{\cdot}6H_2O$. In the case of Nd, longer refluxing followed by slow cooling and crystallization below room temperature led to NO-free $(H_3O)_2[\{Nd(H_2O)_5\}_2\{Mo_{36}O_{112}(H_2O)_{16}\}]{\cdot}40H_2O$ (**15**). The Gd compound **8**, which was previously obtained by reaction of the ammonium salt of keplerate, $[\{(Mo^{VI})Mo^{VI}_5O_{21}(H_2O)_6\}_{12}\{Mo^{V}_2O_4(CH_3COO)\}_{30}]^{42-}$, with $Gd(NO_3)_3$,[33] was obtained from $[Mo_{36}(NO)_4O_{108}(H_2O)_{16}]^{12-}$ and Gd^{3+} in a more straightforward manner.

The compounds were characterized by elemental analysis and FT-IR spectroscopy. Compounds **1**–**14** and the parent $(NH_4)_{12}[Mo_{36}(NO)_4O_{108}(H_2O)_{16}]{\cdot}36H_2O$ have similar FT-IR spectra, showing only slight shifts in some band positions. All spectra show characteristic absorption bands attributable to H_2O, ν(Mo–O_{term}), ν(Mo–{μ_2-O}), and ν(Mo–{μ_3-O}) groups. The ν(NO) vibrational frequency of 1617 cm^{-1} overlaps with δ(HOH) and is typical for the linear $\{MoNO\}^{3+}$ moiety.[34] There are three types of water in compounds **1**–**15**: water of crystallization, water coordinated to Ln^{3+}, and water attached to the POM anion. Theoretically, it should be possible to follow the water loss by TGA and to discriminate between the types of water leaving the structure. However, our preliminary experiments showed only one nondifferentiated step for water loss over a wide temperature range.

Structures

The structures of compounds **1**–**15** were determined by single-crystal X-ray diffraction. The main bond lengths and angles are given as Supporting Information. The structures show remarkable diversity, being 1D, 2D, or 3D, neutral or anionic frameworks where the discrete POM fragments $\{Mo_{36}(NO)_4O_{108}(H_2O)_{16}\}$ (for **1**–**14**) or $\{Mo_{36}O_{112}(H_2O)_{16}\}$ (for **15**) are united by $\{Ln(H_2O)_n\}$ units depending on the identity of Ln^{3+}. The coordination environment of the lanthanide cations in **1**–**15** is summarized in Table 1.

The polyoxomolybdate anions $[Mo_{36}(NO)_4O_{108}(H_2O)_{16}]^{12-}$ $\{Mo_{36}(NO)_4\}$, and $[Mo_{36}O_{112}(H_2O)_{16}]^{8-}$ $\{Mo_{36}\}$,[34,35] which serve as building blocks, are built of two $\{Mo_{17}\}$ subunits that are joined together by two MoO_2^{2+} groups. There are two MoL^{n+} groups (L = NO, n = 3; or L = O, n = 4) within each subunit with pentagonal-bipyramidal coordination, surrounded by five MoO_6 octahedra: three are derived from MoO^{4+} and two from *cis*-

Table 1. Coordination environment of the lanthanide cations in **1**–**15**.

Compound and type of Ln atom		CN	Polyhedra type	Coordination type
$\{La_4Mo_{36}(NO)_4_3D\}$ (**1**)	La1	9	triply capped trigonal prism	$O^A_2O^C_1O^D_1O^W_5$
	La2	9	triply capped trigonal prism	$O^A_2O^B_1O^W_6$
	La3	9	distorted triply capped trigonal prism	$O^A_2O^B_1O^W_5Cl$
$\{Nd_5Mo_{36}(NO)_4\}$ (**2**)	Nd1	9	triply capped trigonal prism	$O^A_2O^B_1O^W_6$
	Nd2	9	triply capped trigonal prism	$O^C_2O^W_7$
$\{Sm_5Mo_{36}(NO)_4\}$ (**3**)	Sm1	9	triply capped trigonal prism	$O^A_2O^B_1O^W_6$
	Sm2	9	triply capped trigonal prism	$O^C_2O^W_7$
$\{La_4Mo_{36}(NO)_4_1D\}$ (**4**)	La1	9	triply capped trigonal prism	$O^A_2O^C_1O^W_6$
	La2	9	distorted triply capped trigonal prism	$O^A_2O^W_7$
$\{Ce_4Mo_{36}(NO)_4\}$ (**5**)	Ce1	9	triply capped trigonal prism	$O^A_2O^C_1O^W_6$
	Ce2	9	distorted triply capped trigonal prism	$O^A_2O^W_7$
$\{Pr_4Mo_{36}(NO)_4\}$ (**6**)	Pr1	9	triply capped trigonal prism	$O^A_2O^C_1O^W_6$
	Pr2	9	distorted triply capped trigonal prism	$O^A_2O^W_7$
$\{Nd_4Mo_{36}(NO)_4\}$ (**7**)	Nd1	9	triply capped trigonal prism	$O^A_2O^C_1O^W_6$
	Nd2	9	distorted triply capped trigonal prism	$O^A_2O^W_7$
$\{Gd_4Mo_{36}(NO)_4\}$ (**8**)	Gd1	8	doubly capped trigonal prism	$O^A_2O^C_1O^W_5$
	Gd2	8	doubly capped trigonal prism	$O^A_2O^C_1O^W_5$
$\{Tb_3Mo_{36}(NO)_4\}$ (**9**)	Tb1	8	dodecahedron	$O^A_4O^W_4$
	Tb2	8	distorted square antiprism	$O^A_2O^W_6$
$\{Dy_3Mo_{36}(NO)_4\}$ (**10**)	Dy1	8	dodecahedron	$O^A_4O^W_4$
	Dy2	8	distorted square antiprism	$O^A_2O^W_6$
$\{Ho_3Mo_{36}(NO)_4\}$ (**11**)	Ho1	8	dodecahedron	$O^A_4O^W_4$
	Ho2	8	distorted square antiprism	$O^A_2O^W_6$
$\{Er_3Mo_{36}(NO)_4\}$ (**12**)	Er1	8	dodecahedron	$O^A_4O^W_4$
	Er2	8	distorted square antiprism	$O^A_2O^W_6$
$\{Yb_3Mo_{36}(NO)_4\}$ (**13**)	Yb1	8	dodecahedron	$O^A_4O^W_4$
	Yb2	8	distorted square antiprism	$O^A_2O^W_6$
$\{Lu_3Mo_{36}(NO)_4\}$ (**14**)	Lu1	8	dodecahedron	$O^A_4O^W_4$
	Lu2	8	distorted square antiprism	$O^A_2O^W_6$
$\{Nd_2Mo_{36}O_{112}\}$ (**15**)	Nd	9	triply capped trigonal prism	$O^A_4O^W_5$

 © 2005 Wiley-VCH Verlag GmbH & Co. KGaA, Weinheim

MoO_2^{2+}. These six Mo atoms form a five-pointed star. Two such stars are held together by two pairs of edge-sharing octahedra (*cis*-MoO_2^{2+} type), and by one "inner" Mo atom with no terminal oxygen atoms, and are also octahedrally coordinated. Only the terminal MoO_2^{2+} groups coordinate lanthanide cations, and altogether 16 terminal oxygen atoms of $[Mo_{36}(NO)_4O_{108}(H_2O)_{16}]^{12-}$ can participate in this bonding. For the sake of simplicity we will call the two octahedra attached to the $Mo(NO)^{3+}$ unit as "coordinated" (type A), those in the dimer that hold two "stars" together in each subunit as "peripheral" (type B), those holding two $\{Mo_{17}\}$ subunits together as "closing" (type C), and the MoO_2^{2+} units in the dimer that hold two "stars" together in each subunit as "inner" (type D; Figure 1). Two neighboring A-type MoO_2^{2+} groups always behave as a bidentate ligand, while the others are monodentate.

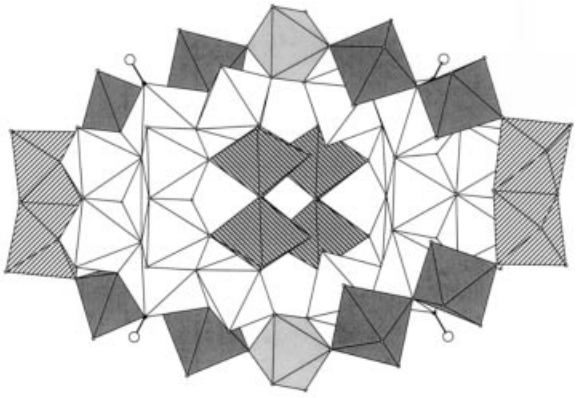

Figure 1. The structure of building block $[Mo_{36}L_4O_{108}(H_2O)_{16}]^{n-}$ (L = NO, n = 12; L = O, n = 8). Representation in polyhedra: dark-grey: type A octahedra; hatched white: type B octahedra; light-grey: type C octahedra; hatched dark-grey: type D octahedra; white: the remaining polyhedra.

The compound $(H_3O)_2[\{La(H_2O)_5\}_2\{La(H_2O)_6\}\{La(H_2O)_5Cl\}\{Mo_{36}(NO)_4O_{108}(H_2O)_{16}\}]Cl\cdot 21H_2O$ (**1**) is the only one in this series with a 3D-framework structure. Each POM anion is coordinated by 10 La^{3+} cations through 14 oxygen atoms. In turn, these 10 La^{3+} cations join each polyoxoanion with another eight POM anions. All possibilities for coordination of the POM anion to La^{3+} are realized in **1**: through oxygen atoms of A-type groups (eight atoms of four "bidentate ligands"), B-type groups (two atoms), C-type (two atoms), and D-type groups (two atoms). In fact, **1** is the only example of a $\{Mo_{36}(NO)_4\}$-based polymer compound where oxygen atoms of D-type groups take part in coordination to the lanthanide cation. There are two types of La^{3+} cations, with two of each type for every POM fragment. Cations of the first type ensure the binding together of POM building blocks along the crystallographic axes *a* and *b*. Each POM is coordinated by six La cations of this type, such that an A-MoO_2^{2+}–La^{3+}–D-MoO_2^{2+} sequence runs along the *a* axis, while in the other direction (along the *b* axis) the pattern of the sequence is C-MoO_2^{2+}–La^{3+}–D-MoO_2^{2+} and C-MoO_2^{2+}–La^{3+}–A-MoO_2^{2+} (Figure 2). Thus, one La^{3+} cation joins together three POM fragments to form pseudo-layers packed along the crystallographic *c* axis. Four oxygen atoms of type A, two of type C, and two of type D take part in this coordination for each POM fragment. Cations of the second type join together the aforementioned "layers" in a 3D framework along the diagonal between the crystallographic *a* and *c* axes in ay A-MoO_2^{2+}–La^{3+}–B-MoO_2^{2+} sequence. Each POM is coordinated by four La^{3+} cations of this type. Four oxygen atoms of an A-type group (as two "bidentate ligands") and two oxygens of two B-type groups, which are joined together in pairs by an inversion center, participate in this bonding. Every two neighboring POM fragments are bound together by two La cations of this type (Figure 3). Lanthanum cations of this type are disordered over two positions in such a way that in the first position La^{3+} additionally coordinates six water molecules and in the other position five water molecules and one Cl^- anion. There are two types of solvent water molecules in **1**. Two water molecules are clathrated in the inner cavity of the POM whereas the others lie in the voids of framework. There is an extended network of hydrogen bonds involving water molecules and oxygen atoms of the cluster.

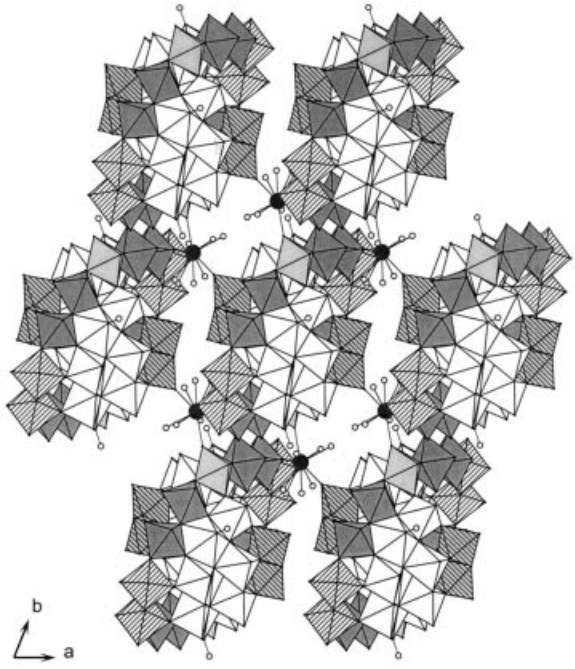

Figure 2. Connectivity pattern in the crystal structure of compound **1** in the *ab* plane. $\{La(H_2O)_5\}$ fragments in ball-and-stick representation (La: dark-grey; O: white); polyoxometalate fragments as polyhedra (for "color" legend see Figure 1).

Compounds $[Nd_5Mo_{36}(NO)_4]$ (**2**), $[Sm_5Mo_{36}(NO)_4]$ (**3**), $[Gd_4Mo_{36}(NO)_4]$ (**8**), and $[Nd_2Mo_{36}]$ (**15**) have different 2D-network structures. The networks in **2** and **3** are isostructural. Each POM anion is coordinated by ten lanthanide cations through fourteen oxygen atoms. In turn, the latter join it to another six POM anions (Figure 4). There are two types of Ln^{3+} in the structure: one is disordered

 © 2005 Wiley-VCH Verlag GmbH & Co. KGaA, Weinheim

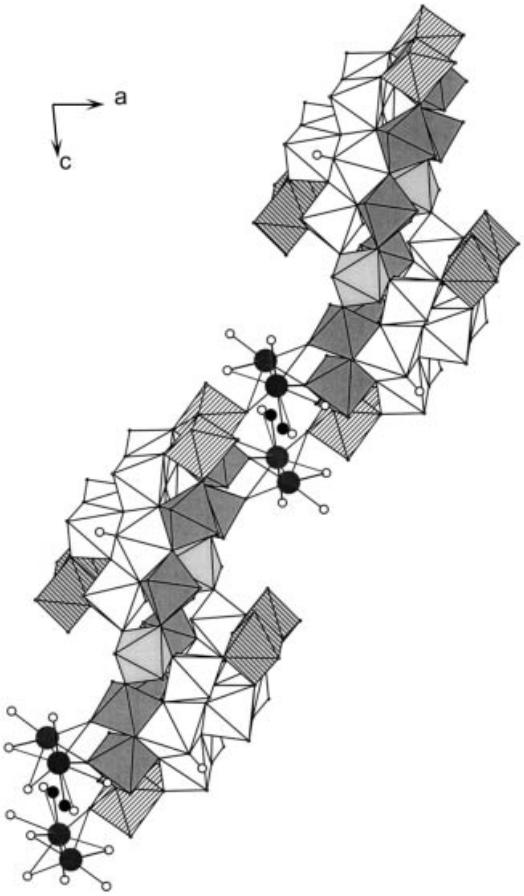

Figure 3. Connectivity pattern in the crystal structure of compound **1** along the diagonal between the crystallographic *a* and *c* axes. Lanthanum cations are disordered over two positions. $\{La(H_2O)_5Cl\}$ and $\{La(H_2O)_6\}$ fragments in ball-and-stick representation (La: dark-grey; O: white; Cl: black); polyoxometalate fragments as polyhedra (for "color" legend see Figure 1).

and coordinates oxygens of C-type groups of two adjacent $\{Mo_{36}(NO)_4\}$ units, whereas the other coordinates oxygen atoms of A-type groups of one POM unit and oxygen atoms of B-type groups of a neighboring POM. Thus, a layered structure forms with a C-MoO_2^{2+}–Ln^{3+}–C-MoO_2^{2+} sequence along the *b* axis and an A-MoO_2^{2+}–Ln^{3+}–B-MoO_2^{2+} sequence along the diagonal between the *b* and *c* axes (Ln = Nd and Sm; Figure 5).

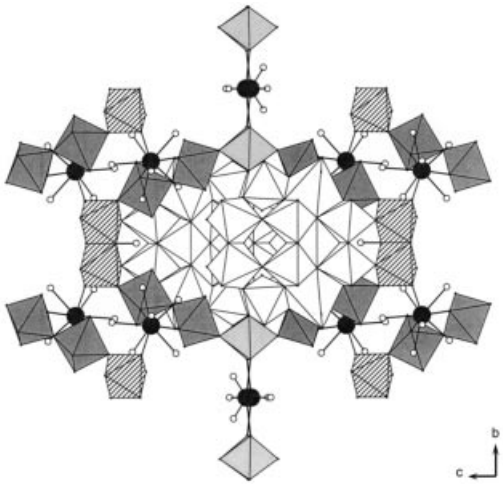

Figure 4. Connectivity pattern in the crystal structure of compounds **2** and **3**. $\{Ln(H_2O)_n\}$ fragments in ball-and-stick representation (Ln: dark-grey; O: white) and $\{Mo_{36}(NO)_4\}$ fragments as polyhedra (for "color" legend see Figure 1).

The structure of $[Gd_4Mo_{36}(NO)_4]$ (**8**) was described in detail in our previous work.[33] This compound was ob-

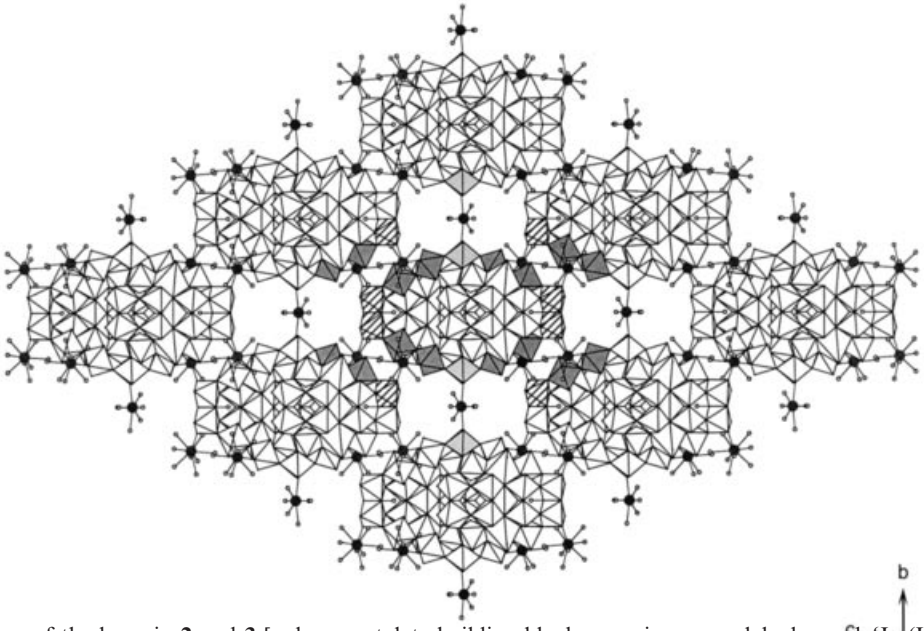

Figure 5. The structure of the layer in **2** and **3** [polyoxometalate building blocks are given as polyhedra and $\{Ln(H_2O)_nCl_m\}$ fragments in ball-and-stick representation]. Crystallization water molecules have been omitted.

 © 2005 Wiley-VCH Verlag GmbH & Co. KGaA, Weinheim

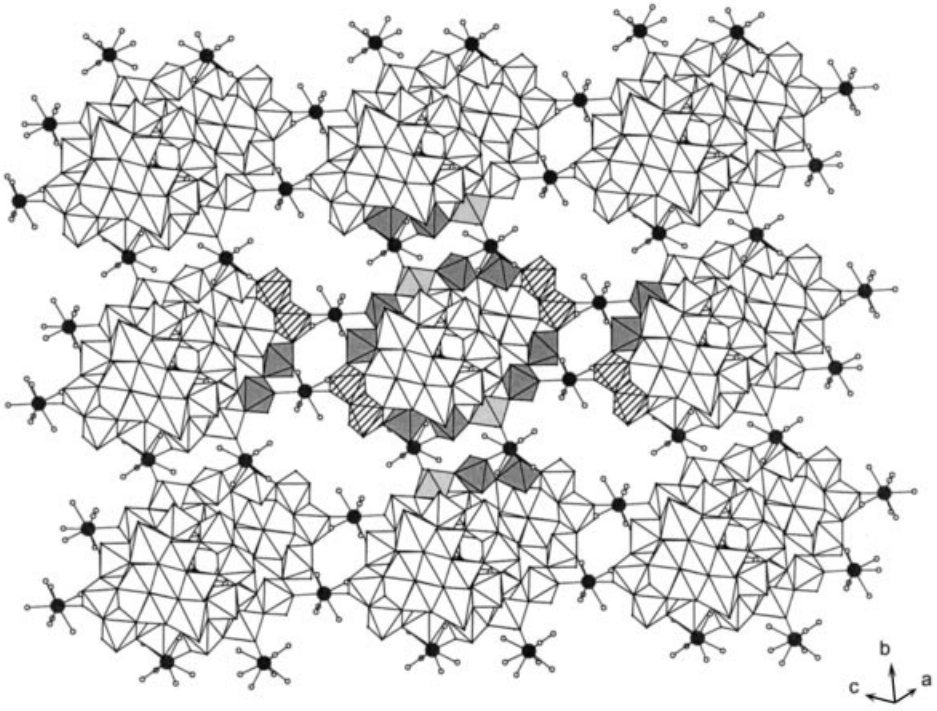

Figure 6. The structure of the layer in **8** [polyoxometalate building blocks are given as polyhedra, $\{Gd(H_2O)_5\}$ fragments in ball-and-stick representation]. Crystallization water molecules have been omitted.

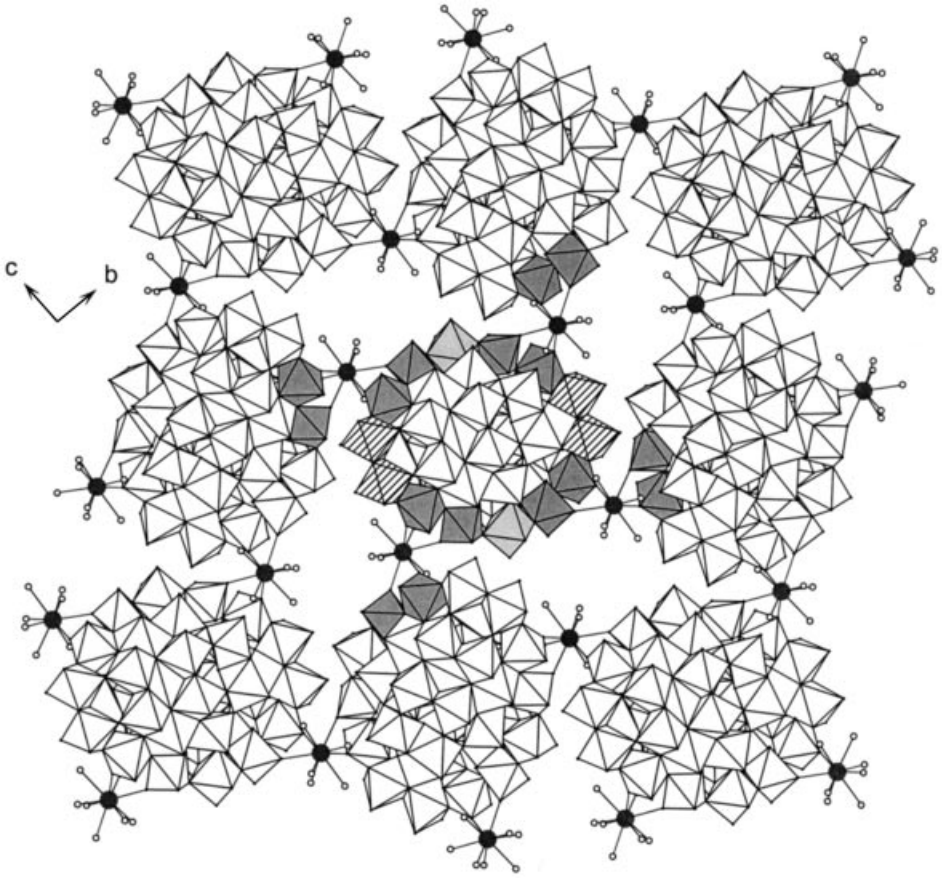

Figure 7. The structure of the layer in **15** [polyoxometalate building blocks as polyhedra, $\{Nd(H_2O)_5\}$ fragments in ball-and-stick representation]. Crystallization water molecules have been omitted.

 © 2005 Wiley-VCH Verlag GmbH & Co. KGaA, Weinheim

tained by decomposition of Keplerate polyoxoanions, $[\{(Mo^{VI})Mo^{VI}_5O_{21}(H_2O)_6\}_{12}\{Mo^{V}_2O_4(CH_3COO)\}_{30}]^{42-}$, in the presence of Gd^{3+} cations. Every POM building block in $[Gd_4Mo_{36}(NO)_4]$ is surrounded by eight Gd^{3+} cations and in that way is joined to four adjacent polyoxoanions. There are two unique gadolinium(III) atoms in the structure of **8**, each of which is octacoordinate. The Gd cations of the first type coordinate terminal oxygen atoms of two MoO_2^{2+} groups of type A and one oxygen atom of an MoO_2^{2+} group of type B, whereas the Gd cations of the second type coordinate two oxygens of neighboring A-type groups and one oxygen atom of an MoO_2^{2+} C-type group. In this way the coordination polyhedron of each Gd is filled with three POM oxygen atoms, the rest being coordinated water. Thus, we have an A-MoO_2^{2+}–Gd^{3+}–C-MoO_2^{2+} regularity along the *b* axis, while in the other direction (along the *c* axis) this pattern is A-MoO_2^{2+}–Gd^{3+}–B-MoO_2^{2+} (Figure 6).

Each POM fragment in $[Nd_2Mo_{36}O_{112}]$ (**15**) is surrounded by four Nd^{3+} cations, all of which are equivalent. Only oxygen atoms of type A take part in coordination to form infinite layers where every polyoxoanion is bonded together with four adjacent POM blocks (Figure 7). These layers are perpendicular to the crystallographic *a* axis. Only one (molecular) complex of this polyoxoanion with a lanthanide $(NH_4)_6[Gd_2Mo_{36}O_{112}(H_2O)_{22}]\cdot 50H_2O$ has been described previously.[36]

The crystal packing of **2**, **3**, **8**, and **15** consists of adjusted neutral, in the cases of **2**, **3**, and **8**, and anionic, in the case of **15**, layers stacked in an ABAB... mode (Figure 8). There are three types of solvent water molecules in these network compounds: two water molecules are clathrated in the inner cavity of the POM, and of the rest, some are placed inside the layers and the others fill the gap between adjacent layers. There is an extended network of hydrogen bonds involving water molecules and oxygen atoms of the cluster.

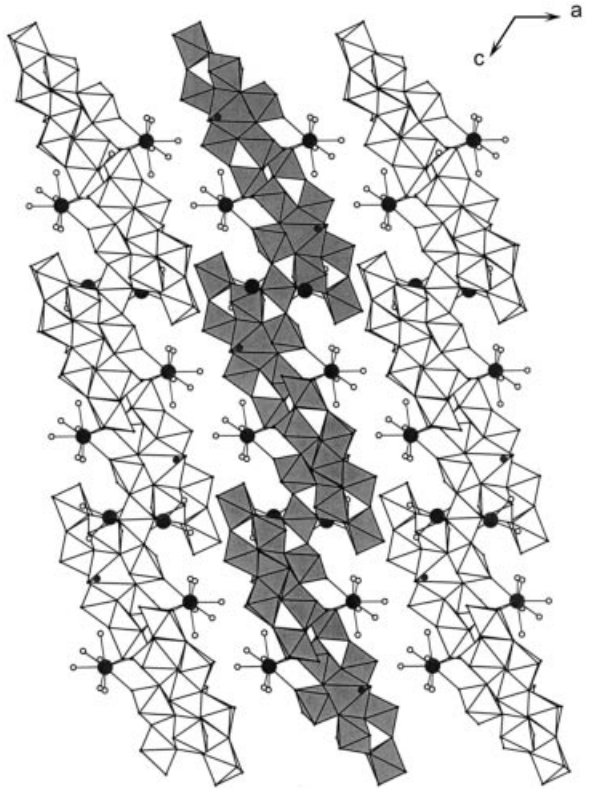

Figure 8. Three neighboring layers (view along the *b* axis) in the crystal structures of **2** and **3**. Polyoxometalate building blocks are given as polyhedra, Ln atoms in ball-and-stick representation. Polyoxometalate fragments of neighboring layers have different "colors" for clarity. Crystallization water molecules have been omitted.

The rest of the coordination polymers in this series have 1D-chain frameworks of different structure. Isostructural compounds with general formula $[\{M(H_2O)_6\}_2\{M(H_2O)_7\}_2\{Mo_{36}(NO)_4O_{108}(H_2O)_{16}\}]\cdot nH_2O$ were obtained for the larger lanthanides La^{3+} (**4**), Ce^{3+} (**5**), Pr^{3+} (**6**), and Nd^{3+} (**7**). There are two types of lanthanide cations in the lattice, and only one type takes part in the formation of infinite chains. It provides connection between POM fragments to give an ...A-MoO_2^{2+}–Ln^{3+}–C–MoO_2^{2+}... sequence along the *a* axis. The cations of the other type are attached to the oxygen atoms of A-type MoO_2^{2+} groups of only one POM anion. These lanthanide cations are disordered over two positions. Every polyoxoanion is coordinated to four cations through eight A-type oxygen atoms (acting as four "bidentate ligands") and to two C-type oxygen atoms (Figure 9). The chains run parallel to each other, forming *ac* pseudolayers which pack up in the ABAB... mode, as observed for **2**, **3**, **8**, and **15** (Figure 10).

We obtained six isostructural compounds with a different 1D chain structure by using the smaller Ln^{3+} ions Tb^{3+}, Dy^{3+}, Ho^{3+}, Er^{3+}, Yb^{3+}, and Lu^{3+} as linkers, namely $(H_3O)_3[\{M(H_2O)_6\}_2\{M(H_2O)_4\}\{Mo_{36}(NO)_4O_{108}(H_2O)_{16}\}]\cdot nH_2O$ (M = Tb, Dy, Ho, Er, Yb and Lu; **9**–**14**) Here, oxygen atoms of all A-type groups of each polyoxoanion $[Mo_{36}(NO)_4O_{108}(H_2O)_{16}]^{8-}$ are coordinated to lanthanide cations. Two lanthanide cations coordinate only one POM fragment and another two Ln^{3+} ions coordinate oxygen atoms of A-type groups of two neighboring POMs (Figure 11). These compounds crystallize in the trigonal system in the space group $R\bar{3}c$. The infinite chains pack to form pseudo-layers perpendicular to the *c* axis. These pseudo-layers are stacked in such a way that chains of each layer are turned relative to the chains of two neighboring layers by 60° (Figure 12). There is an extended network of hydrogen bonds involving water molecules and oxygen atoms of the cluster.

There are two more $\{Mo_{36}(NO)_4\}$-based one-dimensional polymers $(H_3O)_{12}\{[Mo_2O_5(H_2O)_2][Mo_{36}(NO)_4O_{108}(H_2O)_{16}]\}\cdot 44H_2O$ (**16**)[31] and $[La_2(MoO)_2Mo_{36}(NO)_4O_{108}(H_2O)_{28}]\cdot 56H_2O$ (**17**).[32] These were obtained by refluxing $(H_3O)_{12}[Mo_{36}(NO)_4O_{108}(H_2O)_{16}]$ with an excess of $NH_2OH\cdot HCl$ in water for no more than 30 min (in the presence La^{3+} salt in the case **17**). The $\{Mo_{36}(NO)_4O_{108}(H_2O)_{16}\}$ units in **16** are connected by bridging $\{Mo_2O_4(\mu\text{-}O)(H_2O)_2\}$ groups coordinated to A-type MoO_2^{2+} groups only (A-MoO_2^{2+}–{Mo–O–Mo}–A-MoO_2^{2+} connectiv-

 © 2005 Wiley-VCH Verlag GmbH & Co. KGaA, Weinheim

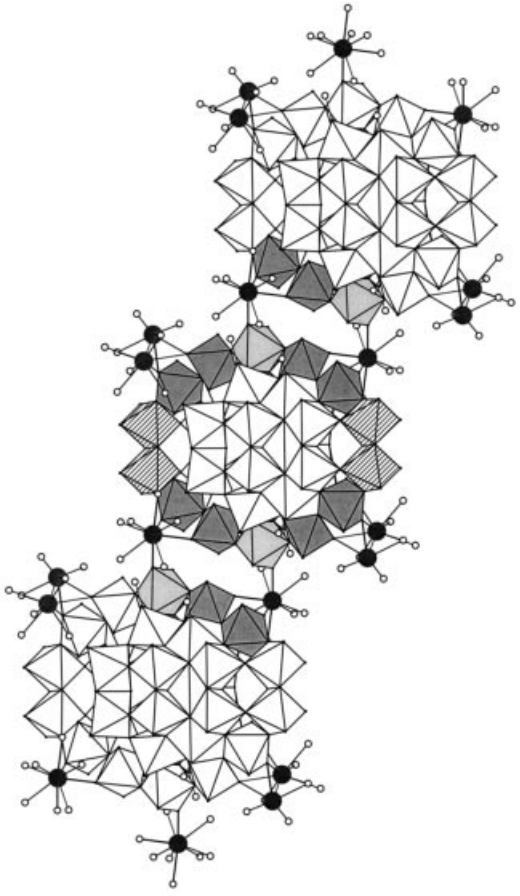

Figure 9. Connectivity pattern in the chains in compounds **4**–**7** distinguishing between the building units or constituents: $\{Ln(H_2O)_n\}$ fragments in ball-and-stick representation and $\{Mo_{36}(NO)_4\}$ fragments as polyhedra (for "color" legend see Figure 1).

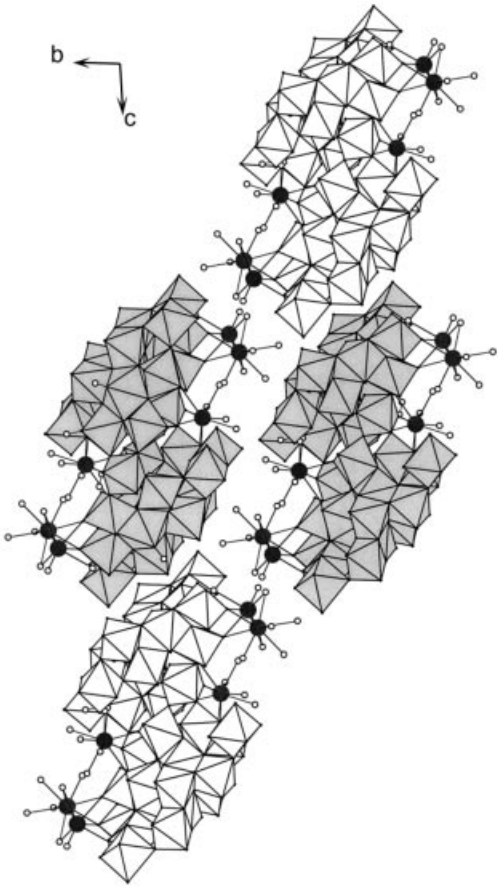

Figure 10. Packing of infinite chains in the crystal structures of **4**–**7** (view along the *a* axis). Polyoxometalate building blocks are given as polyhedra, $\{Ln(H_2O)_n\}$ fragments in ball-and-stick representation. Polyoxometalate fragments of neighboring chains have different "colors" for clarity. Crystallization water molecules have been omitted.

ity),[32] and in **17** two MoO^{3+} groups are coordinated to the A-type *cis*-MoO_2^{2+} units. Chain-building is realized through A-MoO_2^{2+}–La^{3+}–C-MoO_2^{2+} interactions.[31]

Thus, we can see that the nature of Ln^{3+} is decisive with respect to the type of framework adopted. For the same stoichiometry $\{Ln_4Mo_{36}(NO)_4\}$ and without extra ligands (except H_2O) attached to the Ln^{3+}, the larger Ln^{3+} ions (La–Nd, compounds **4**–**7**) adopt a chain structure with nine-coordinate lanthanide, in the middle of the lanthanide series another, layered arrangement appears, exemplified here by the Gd salt **8** (CN Gd^{3+} = 8), and with the smaller Ln^{3+} ions (Tb–Lu, compounds **9**–**14**) a chain-like 1D ar-

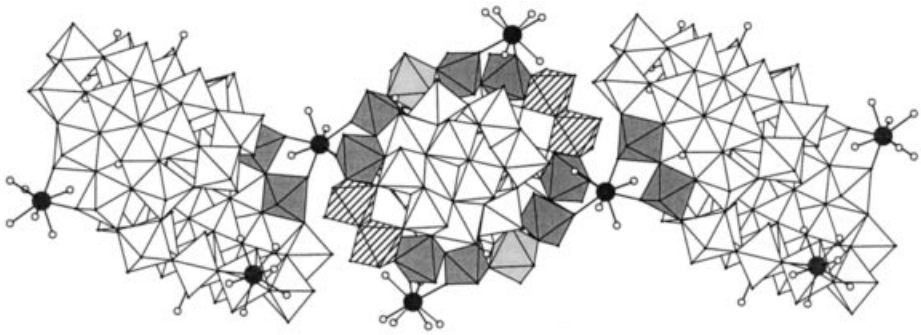

Figure 11. Connectivity pattern in chains in compounds **9**–**14** distinguishing between the building units or constituents: $\{Ln(H_2O)_n\}$ fragments in ball-and-stick representation and $\{Mo_{36}(NO)_4\}$ fragments as polyhedra (for "color" legend see Figure 1).

 © 2005 Wiley-VCH Verlag GmbH & Co. KGaA, Weinheim

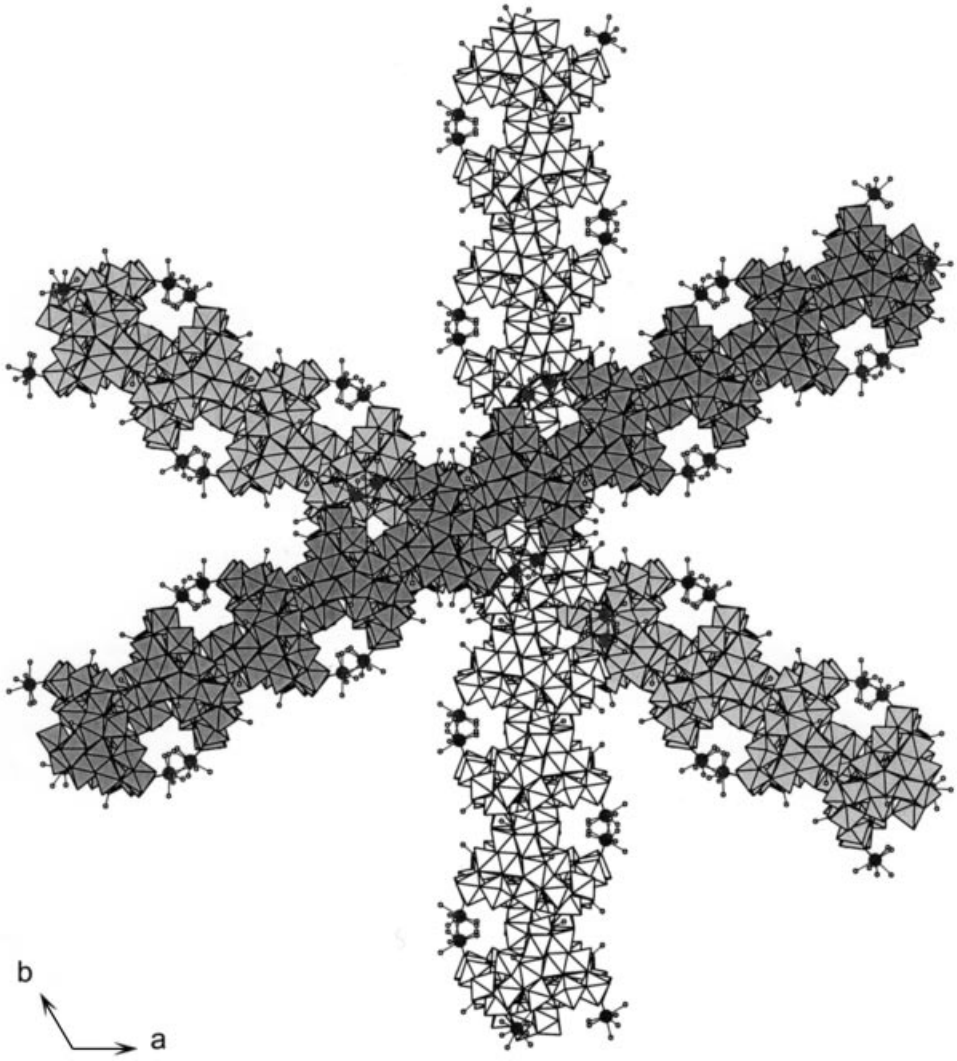

Figure 12. Packing of infinite chains in the crystal structures of **9**–**14** (view along the *c* axis). Polyoxometalate building blocks are given as polyhedra, $\{Ln(H_2O)_n\}$ fragments in ball-and-stick representation. Polyoxometalate fragments of neighboring chains have different "colors" for clarity. Crystallization water molecules have been omitted.

rangement reappears. It is, however, not identical to that found in **4**–**7** as the Ln^{3+} ions are now eight-coordinate and their coordination polyhedra correspond to a dodecahedron and a distorted square antiprism rather than the bicapped trigonal prism of **8**. A similar influence of the Ln^{3+} size can also be found for the series of 1:1 salts formed by Ln^{3+} and monovacant lacunary $[\gamma\text{-}SiW_{11}O_{39}]^{8-}$: the La and Ce salts feature a nine-coordinate lanthanide, the Eu salt is eight-coordinate, and the Yb salt is seven-coordinate. All these compounds are built from 1D chains that change from zig-zag to linear on going from La to Yb.[16]

In conclusion, we have developed a simple synthetic method that allows us to obtain polymeric compounds based on $\{Mo_{36}(NO)_4\}$ building blocks and Ln^{3+} in high yields. Only two compounds were known before our work, both of which are 1D chain polymers. We have synthesized fifteen new polymeric compounds, among which are one with a 3D framework, three with 2D networks of two different types, and eleven with 1D chains, also of two different types. We have also synthesized one 2D network, $[Nd_2Mo_{36}]$, which is the only example of a polymeric compound, based on $\{Mo_{36}O_{112}\}$ building blocks. The influence of the counterion and the reaction conditions (pH crystallization time, and temperature) on the structural type, observed in this work, allows us to expect even more complex architectures to be realized from these nanosized building blocks.

Experimental Section

Materials: $(NH_4)_{12}[Mo_{36}(NO)_4O_{108}(H_2O)_{16}]\cdot 33H_2O$ was prepared according to the previously published procedure.[34] All other reagents were obtained commercially and used as supplied.

X-ray Data Collection and Structural Determination: Single crystals of the complexes were selected and mounted on a Stoe IPDS II

 © 2005 Wiley-VCH Verlag GmbH & Co. KGaA, Weinheim

Table 2. Crystal data, data collection, and structure-refinement parameters for **1**–**5**.

Compound	**1**	**2**	**3**	**4**	**5**
Formula	$H_{122}Cl_2La_4Mo_{36}N_4O_{172}$	$H_{136}Cl_3Mo_{36}N_4Nd_5O_{180}$	$H_{130}Cl_3Mo_{36}N_4O_{177}Sm_5$	$H_{142}La_4Mo_{36}N_4O_{183}$	$H_{166}Ce_4Mo_{36}N_4O_{195}$
Mol. mass	7011.40	7354.52	7331.02	7136.66	7357.69
Crystal system	triclinic	monoclinic	monoclinic	triclinic	triclinic
Space group	$P\bar{1}$	$C2/m$	$C2/m$	$P\bar{1}$	$P\bar{1}$
a [Å]	13.6821(7)	24.8059(8)	26.178(5)	16.415(3)	16.452(3)
b [Å]	16.4159(7)	19.7684(7)	19.389(4)	16.717(3)	16.582(3)
c [Å]	19.1401(11)	20.5187(9)	20.901(4)	19.085(4)	18.990(4)
α [°]	77.722(1)	90.00	90.00	88.29(3)	88.01(3)
β [°]	80.456(1)	121.792(1)	122.97(3)	77.32(3)	77.02(3)
γ [°]	67.389(2)	90.00	90.00	60.60(3)	60.45(3)
V [Å^3]	3860.9(3)	8552.2(6)	8900(3)	4423.4(15)	4374.0(15)
Z	1	2	2	1	1
$D_{calcd.}$ [g cm^{-3}]	3.016	2.856	2.735	2.674	2.793
T [K]	273	273	100	100	100
$2\theta_{max}$ [°]	65.46	72.02	54.16	56.56	59.56
Range h, k, l	$-20 \le h \le 15$	$-19 \le h \le 37$	$-18 \le h \le 33$	$-18 \le h \le 20$	$-13 \le h \le 21$
	$-24 \le k \le 12$	$-29 \le k \le 26$	$-24 \le k \le 24$	$-21 \le k \le 21$	$-10 \le k \le 21$
	$-28 \le l \le 28$	$-33 \le l \le 30$	$-26 \le l \le 25$	$-24 \le l \le 24$	$-20 \le l \le 24$
μ [mm^{-1}]	4.059	4.199	4.223	3.513	3.633
Reflns. measured	37088	40758	17668	25858	13432
Unique reflns.	26640	15945	8787	17053	11481
R_{int}	0.0293	0.0501	0.0567	0.0584	0.0815
Observed [$I > 2\sigma(I)$]	14647	9102	7296	14620	7178
Refined parameters	1025	601	617	1070	1093
Restraints	49	0	42	59	68
R_1[a], wR_2[b]	$R_1 = 0.0572$	$R_1 = 0.0581$	$R_1 = 0.0581$	$R_1 = 0.0823$	$R_1 = 0.0677$
[$I > 2\sigma(I)$]	$wR_2 = 0.1493$	$wR_2 = 0.1603$	$wR_2 = 0.1737$	$wR_2 = 0.2318$	$wR_2 = 0.1623$
R_1[a], wR_2[b]	$R_1 = 0.1189$	$R_1 = 0.1196$	$R_1 = 0.0675$	$R_1 = 0.0907$	$R_1 = 0.1086$
(all data)	$wR_2 = 0.1657$	$wR_2 = 0.1899$	$wR_2 = 0.1821$	$wR_2 = 0.2420$	$wR_2 = 0.1807$
Goodness-of-fit on F^2	0.950	0.949	1.035	1.036	0.939
Largest diff. peak/hole [e Å^{-3}]	5.041/–5.177	3.292/–3.599	3.471/–2.750	2.486/–3.654	1.000/–1.185

[a] $R_1 = \Sigma||F_o| - |F_c||/\Sigma|F_o|$. [b] $wR_2 = \{\Sigma[w(F_o^2 - F_c^2)^2]/\Sigma[w(F_o^2)^2]\}^{1/2}$.

diffractometer equipped with graphite-monochromated Mo-K_α radiation (λ = 0.71073 Å). Absorption corrections were made with SADABS.[37] The structures were solved by direct methods and refined by the full-matrix least-squares method minimization of $[\Sigma w(F_o - F_c)^2]$ with anisotropic thermal parameters for all skeleton non-hydrogen atoms, and for practically all oxygen atoms of the lattice water molecules, using the SHELX 97 program package.[38] The crystallographic and refinement data are listed in Tables 2, 3, and 4. Selected bond lengths and angles of complexes **1**–**15** are given as Supporting Information.

$(H_3O)_2[\{La(H_2O)_5\}_2\{La(H_2O)_6\}\{La(H_2O)_5Cl\}\{Mo_{36}(NO)_4O_{108}(H_2O)_{16}\}]Cl\cdot 21H_2O$ [$La_4Mo_{36}(NO)_4$-3D, 1]: $(NH_4)_{12}[Mo_{36}(NO)_4O_{108}(H_2O)_{16}]\cdot 33H_2O$ (0.300 g, 0.047 mmol) was dissolved in 25 mL of water whilst stirring and heating gently (50 °C). The solution was then allowed to cool down to room temperature and filtered. $LaCl_3\cdot 7H_2O$ (0.070 g, 0.188 mmol) was added to the filtrate with stirring (5 min). Small orange crystals of the product started to appear after one hour. These were filtered off and the filtrate was kept at room temperature for three days to produce a crop of single crystals, which were collected by filtration, washed twice with a minimal amount of ice-cooled water, and dried in air. Yield: 0.236 g [72% based on $\{Mo_{36}(NO)_4\}$]. $H_{122}Cl_2La_4Mo_{36}N_4O_{172}$: calcd. H 1.74, N 0.80; found H 1.96, N 0.83. IR (KBr pellet): $\tilde{\nu}$ = 3431 cm^{-1} (s, br), 1626 (s), 1399 (m), 957 (m), 875 (s), 835 (w), 776 (m), 619 (s), 566 (s), 531 (m), 369 (m).

$[\{Nd(H_2O)_6\}_4\{Nd(H_2O)_4\}\{Mo_{36}(NO)_4O_{108}(H_2O)_{16}\}]Cl_3\cdot 24H_2O$ [$Nd_5Mo_{36}(NO)_4$}, 2]: $(NH_4)_{12}[Mo_{36}(NO)_4O_{108}(H_2O)_{16}]\cdot 33H_2O$ (0.300 g, 0.047 mmol) was dissolved in 25 mL of water whilst stirring and heating gently (50 °C). After the solution had cooled down and been filtered, $NdCl_3\cdot 6H_2O$ (0.066 g, 0.184 mmol) was added to the filtrate whilst stirring (5 min). After one hour small, orange, rhombic crystals of product started to form. After one day they were collected by filtration, washed twice with a small amount of ice-cooled water, and dried in air. X-ray quality single crystals were obtained by reagent diffusion in a U-tube. Yield: 0.250 g [73% based on $\{Mo_{36}(NO)_4\}$, 93% based on $NdCl_3\cdot 6H_2O$]. $H_{136}Cl_3Mo_{36}N_4Nd_5O_{180}$: calcd. H 1.87, N 0.77; found H 2.03, N 0.84. IR (KBr pellet): $\tilde{\nu}$ = 3442 cm^{-1} (s, br), 1622 (s), 1402 (m), 950 (m), 874 (s), 774 (m), 614 (s), 566 (s), 478 (m), 370 (m), 338 (m).

$[\{Sm(H_2O)_6\}_4\{Sm(H_2O)_4\}\{Mo_{36}(NO)_4O_{108}(H_2O)_{16}\}]Cl_3\cdot 21H_2O$ [$Sm_5Mo_{36}(NO)_4$}, 3]: Compound **3** was prepared by exactly the same protocol as **2**, but with $SmCl_3\cdot 6H_2O$ (0.066 g, 0.181 mmol). Dark-orange crystals. Yield: 0.166 g [49% based on $\{Mo_{36}(NO)_4\}$, 63% based on $SmCl_3\cdot 6H_2O$]. X-ray quality single crystals were grown by reagent diffusion in a U-tube. $H_{130}Cl_3Mo_{36}N_4O_{177}Sm_5$: calcd. H 1.79, N 0.77; found H 2.01, N 0.90. IR (KBr pellet): $\tilde{\nu}$ = 3393 cm^{-1} (s, br), 1617 (s), 1410 (w), 952 (m), 870 (s), 776 (m), 616 (s), 568 (m), 537 (m).

$[\{La(H_2O)_6\}_2\{La(H_2O)_7\}_2\{Mo_{36}(NO)_4O_{108}(H_2O)_{16}\}]\cdot 29H_2O$ [$La_4Mo_{36}(NO)_4$-1D}, 4]: A suspension of $Na_2MoO_4\cdot 2H_2O$ (1.500 g, 6.20 mmol), $NH_2OH\cdot HCl$ (0.900 g, 12.95 mmol), and $LaCl_3\cdot 7H_2O$ (1.280 g, 3.44 mmol) in 30 mL of water was acidified with concd. HCl until the pH reached 2. The resulting mixture was refluxed for 1 h and slowly cooled to room temperature. The resulting solution was filtered and the filtrate was kept for a week at room temperature in an open dish. Orange rhombic crystals were collected by filtration, washed twice with a minimal amount of water and dried in air. Yield: 0.846 g (69% based on $Na_2MoO_4\cdot 2H_2O$). $H_{142}La_4$-

 © 2005 Wiley-VCH Verlag GmbH & Co. KGaA, Weinheim

Table 3. Crystal data, data collection and structure refinement parameters for **6**–**10**.

Compound	**6**	**7**	**8**	**9**	**10**
Formula	$H_{164}Mo_{36}N_4O_{194}Pr_4$	$H_{156}Mo_{36}N_4Nd_4O_{190}$	$H_{140}Gd_4Mo_{36}N_4O_{182}$	$H_{157}Mo_{36}N_4O_{189}Tb_3$	$H_{159}Dy_3Mo_{36}N_4O_{190}$
Mol. mass	7342.83	7284.09	7192.00	7168.90	7194.65
Crystal system	triclinic	triclinic	triclinic	trigonal	trigonal
Space group	$P\bar{1}$	$P\bar{1}$	$P\bar{1}$	$R\bar{3}c$	$R\bar{3}c$
a [Å]	16.419(3)	16.292(3)	13.5035(14)	35.955(5)	36.209(5)
b [Å]	16.568(3)	16.604(3)	16.2894(17)	35.955(5)	36.209(5)
c [Å]	19.025(4)	19.003(4)	18.905(2)	83.285(17)	83.795(17)
α [°]	88.47(3)	89.45(3)	77.376(2)	90.00	90.00
β [°]	77.21(3)	77.47(3)	80.336(2)	90.00	90.00
γ [°]	60.30(3)	60.95(3)	76.042(2)	120.00	120.00
V [Å^3]	4362.7(15)	4359.1(15)	3908.8(7)	93241(26)	95145(27)
Z	1	1	1	18	18
$D_{calcd.}$ [g cm^{-3}]	2.795	2.775	3.055	2.298	2.261
T [K]	200(2)	200(2)	120(2)	200(2)	120(2)
$2\theta_{max}$ [°]	63.52	63.86	52.00	50.70	54.36
Range h, k, l	$-11 \le h \le 21$	$-22 \le h \le 12$	$-16 \le h \le 16$	$-39 \le h \le 35$	$-42 \le h \le 46$
	$-14 \le k \le 21$	$-20 \le k \le 12$	$-20 \le k \le 19$	$-43 \le k \le 24$	$-46 \le k \le 46$
	$-27 \le l \le 23$	$-23 \le l \le 24$	$-23 \le l \le 23$	$-100 \le l \le 76$	$-107 \le l \le 107$
μ [mm^{-1}]	3.715	3.789	4.587	3.215	3.208
Reflns. measured	29538	24097	34353	41957	170198
Unique reflns.	18902	17738	15291	17483	23281
R_{int}	0.0571	0.0343	0.0859	0.0538	0.1274
Observed [$I > 2\sigma(I)$]	13029	15253	6856	12725	16795
Refined parameters	1123	1097	987	1090	1097
Restraints	73	35	0	66	0
R_1[a], wR_2[b]	$R_1 = 0.0659$	$R_1 = 0.0637$	$R_1 = 0.0781$	$R_1 = 0.0871$	$R_1 = 0.0792$
[$I > 2\sigma(I)$]	$wR_2 = 0.1773$	$wR_2 = 0.1825$	$wR_2 = 0.1599$	$wR_2 = 0.2372$	$wR_2 = 0.1913$
R_1[a], wR_2[b]	$R_1 = 0.0922$	$R_1 = 0.0728$	$R_1 = 0.1703$	$R_1 = 0.1126$	$R_1 = 0.1001$
(all data)	$wR_2 = 0.2198$	$wR_2 = 0.2002$	$wR_2 = 0.1848$	$wR_2 = 0.3647$	$wR_2 = 0.2048$
Goodness-of-fit on F^2	1.036	1.053	1.012	1.056	1.343
Largest diff. peak/hole [e Å^{-3}]	4.340/–3.314	4.864/–6.864	4.543/–4.027	4.493/–2.887	2.658/–1.802

$Mo_{36}N_4O_{183}$: calcd. H 1.99, N 0.79; found H 2.13, N 0.96. IR (KBr pellet): $\tilde{\nu}$ = 3516 cm^{-1} (m), 3441 (m), 3328 (s, br), 3179 (s, br), 1606 (m), 1402 (w), 953 (m), 879 (s), 777 (m), 624 (m), 566 (m), 538 (m), 367 (m), 334 (w).

[{Ce(H$_2$O)$_6$}$_2${Ce(H$_2$O)$_7$}$_2${Mo$_{36}$(NO)$_4$O$_{108}$(H$_2$O)$_{16}$}]·41H$_2$O [Ce$_4$Mo$_{36}$(NO)$_4$, 5]: $(NH_4)_{12}[Mo_{36}(NO)_4O_{108}(H_2O)_{16}]\cdot 33H_2O$ (0.300 g, 0.047 mmol) were dissolved in 25 mL of water with stirring and slight heating (about 50 °C), then the reaction solution was cooled to room temperature and filtered. $CeCl_3\cdot 7H_2O$ (0.066 g, 0.177 mmol) was then added to the filtrate whilst stirring (5 min). The reaction mixture was kept in a closed flask at 5 °C for 2 d, and the resulting orange rhombic crystals were collected by filtration, washed twice with a little iced water, and dried in air. Crystallization at room temperature gave some white precipitate formed together with orange crystals of the product. Yield: 0.237 g [69% based on {Mo$_{36}$(NO)$_4$}]. $H_{166}Ce_4Mo_{36}N_4O_{195}$: calcd. H 2.26, N 0.76; found H 2.12, N 0.71. IR (KBr pellet): $\tilde{\nu}$ = 3398 cm^{-1} (s, br), 3194 (s, br), 1617 (s), 1410 (w), 952 (m), 874 (s), 776 (m), 616 (s), 568 (m), 542 (m).

[{Pr(H$_2$O)$_6$}$_2${Pr(H$_2$O)$_7$}$_2${Mo$_{36}$(NO)$_4$O$_{108}$(H$_2$O)$_{16}$}]·40H$_2$O [Pr$_4$Mo$_{36}$(NO)$_4$, 6]: The compound was prepared by exactly the same protocol as **5**, but with $PrCl_3\cdot 6H_2O$ (0.066 g, 0.187 mmol), to give dark-orange crystals. Yield: 0.231 g [67% based on {Mo$_{36}$(NO)$_4$}]. $H_{164}Mo_{36}N_4O_{194}Pr_4$: calcd. H 2.23, N 0.76; found H 2.01, N 0.90. IR (KBr pellet): $\tilde{\nu}$ = 3437 cm^{-1} (s, br), 1620 (s), 1405 (m), 957 (m), 875 (s), 776 (m), 619 (s), 566 (m), 531 (m), 369 (m).

[{Nd(H$_2$O)$_6$}$_2${Nd(H$_2$O)$_7$}$_2${Mo$_{36}$(NO)$_4$O$_{108}$(H$_2$O)$_{16}$}]·36H$_2$O [Nd$_4$Mo$_{36}$(NO)$_4$}, 7]. Synthesis 1: A suspension of $Na_2MoO_4\cdot 2H_2O$ (0.500 g, 2.07 mmol) and $NH_2OH\cdot HCl$ (0.300 g, 4.32 mmol) in 30 mL of water was acidified with concd. HCl until pH 2. The resulting mixture was refluxed for 5 min and slowly cooled to room temperature. The deep-orange solution was filtered and then $NdCl_3\cdot 6H_2O$ (0.150 g, 0.418 mmol) was added to the filtrate with vigorous stirring for 5 min. The solution was kept for 2 d at 5 °C. Orange rhombic crystals were collected by filtration, washed twice with a minimum amount of ice-cooled water, and dried in air. Yield: 0.309 g (74% based on $Na_2MoO_4\cdot 2H_2O$).

Synthesis 2: $AgNO_3$ (0.093 g, 0.552 mmol) was added to a solution of $NdCl_3\cdot 6H_2O$ (0.066 g, 0.184 mmol) in 5 mL of water. The resulting mixture was filtered and the filtrate was added to a solution of $(NH_4)_{12}[Mo_{36}(NO)_4O_{108}(H_2O)_{16}]\cdot 33H_2O$ (0.300 g, 0.047 mmol) in 25 mL of water whilst stirring. Small orange crystals of the product started to appear after one hour. After two days orange crystals were collected by filtration, washed twice with a minimal amount of ice-cooled water, and dried in air. Yield: 0.230 g [67% based on {Mo$_{36}$(NO)$_4$}]. X-ray quality single crystals were grown by reagent diffusion in a U-tube. $H_{156}Mo_{36}N_4Nd_4O_{190}$: calcd. H 2.14, N 0.77; found H 2.13, N 1.05. IR (KBr pellet): $\tilde{\nu}$ = 3421 cm^{-1} (s, br), 3174 (s, br), 1617 (m), 1406 (m), 952 (m), 878 (s), 776 (m), 624 (m), 565 (m).

[{Gd(H$_2$O)$_5$}$_4${Mo$_{36}$(NO)$_4$O$_{108}$(H$_2$O)$_{16}$}]·34H$_2$O [Gd$_4$Mo$_{36}$(NO)$_4$, 8]: This compound was prepared by exactly the same protocol as **5**, but with $Gd(NO_3)_3\cdot 5H_2O$ (0.080 g, 0.185 mmol), to give an orange crystalline product. Yield: 0.205 g [{61% based on $Mo_{36}(NO)_4$}]. $H_{140}Gd_4Mo_{36}N_4O_{182}$: calcd. H 1.96, N 0.78; found H 2.09, N 0.85. IR (KBr pellet): $\tilde{\nu}$ = 3414 cm^{-1} (s, br), 1620 (s), 1399 (m), 957 (m), 875 (s), 776 (m), 619 (s), 566 (m), 531 (m), 369 (w), 322 (w).

(H$_3$O)$_3$[{Tb(H$_2$O)$_6$}$_2${Tb(H$_2$O)$_4$}{Mo$_{36}$(NO)$_4$O$_{108}$(H$_2$O)$_{16}$}]·42H$_2$O [Tb$_3$Mo$_{36}$(NO)$_4$, 9]: This compound was prepared by exactly the

 © 2005 Wiley-VCH Verlag GmbH & Co. KGaA, Weinheim

Table 4. Crystal data, data collection and structure refinement parameters for **11**–**15**.

Compound	**11**	**12**	**13**	**14**	**15**
Formula	$H_{165}Ho_3Mo_{36}N_4O_{193}$	$H_{173}Er_3Mo_{36}N_4O_{197}$	$H_{185}Mo_{36}N_4O_{203}Yb_3$	$H_{135}Lu_3Mo_{36}N_4O_{178}$	$H_{138}Mo_{36}Nd_2O_{180}$
Mol. mass	7258.99	7338.04	7463.48	7018.87	6761.42
Crystal system	trigonal	trigonal	trigonal	trigonal	monoclinic
Space group	$R\bar{3}c$	$R\bar{3}c$	$R\bar{3}c$	$R\bar{3}c$	$P2_1/c$
a [Å]	36.006(5)	36.153(5)	35.945(5)	35.991(5)	32.022(6)
b [Å]	36.006(5)	36.153(5)	35.945(5)	35.991(5)	24.209(5)
c [Å]	83.540(17)	83.700(17)	83.550(17)	83.475(17)	21.914(4)
α [°]	90.00	90.00	90.00	90.00	90.00
β [°]	90.00	90.00	90.00	90.00	90.18(3)
γ [°]	120.00	120.00	120.00	120.00	90.00
V [Å^3]	93792(27)	94742(27)	93485(26)	93640(27)	16988(6)
Z	18	18	18	18	4
$D_{calcd.}$ [g cm^{-3}]	2.313	2.315	2.386	2.240	2.644
T [K]	100(2)	100(2)	150(2)	200(2)	293(2)
$2\theta_{max}$ [°]	54.60	49.94	56.56	63.74	41.64
Range h, k, l	$-46 \le h \le 46$	$-27 \le h \le 42$	$-46 \le h \le 35$	$-40 \le h \le 52$	$-32 \le h \le 31$
	$-42 \le k \le 46$	$-37 \le k \le 42$	$-46 \le k \le 45$	$-43 \le k \le 45$	$-24 \le k \le 24$
	$-106 \le l \le 107$	$-91 \le l \le 96$	$-96 \le l \le 52$	$-106 \le l \le 103$	$-10 \le l \le 21$
μ [mm^{-1}]	3.319	3.357	3.545	3.597	3.281
Reflns. measured	178561	37156	73313	91224	47825
Unique reflns.	23019	17547	21807	28866	17427
R_{int}	0.0920	0.0579	0.0867	0.0866	0.0865
Observed [$I > 2\sigma(I)$]	17350	14150	15390	15582	15221
Refined parameters	1116	1100	1196	1156	2098
Restraints	48	54	96	102	546
R_1[a], wR_2[b]	$R_1 = 0.0630$	$R_1 = 0.0674$	$R_1 = 0.1088$	$R_1 = 0.1009$	$R_1 = 0.1044$
[$I > 2\sigma(I)$]	$wR_2 = 0.1832$	$wR_2 = 0.2033$	$wR_2 = 0.2765$	$wR_2 = 0.2662$	$wR_2 = 0.2509$
R_1[a], wR_2[b]	$R_1 = 0.0804$	$R_1 = 0.0815$	$R_1 = 0.1409$	$R_1 = 0.1837$	$R_1 = 0.1142$
(all data)	$wR_2 = 0.1957$	$wR_2 = 0.2179$	$wR_2 = 0.3107$	$wR_2 = 0.3247$	$wR_2 = 0.2659$
Goodness-of-fit on F^2	1.033	1.042	1.049	1.063	1.138
Largest diff. peak/hole [e Å^{-3}]	2.513/–1.525	3.236/–1.803	4.019/–3.374	5.498/–3.404	3.346/–2.204

same protocol as **5**, but with $TbCl_3 \cdot 6H_2O$ (0.069 g, 0.185 mmol), to give an orange crystalline product. Yield: 0.175 g [52% based on $\{Mo_{36}(NO)_4\}$]. $H_{157}Mo_{36}N_4O_{189}Tb_3$: calcd. H 2.19, N 0.78; found H 1.87, N 0.94. IR (KBr pellet): $\tilde{\nu}$ = 3437 cm^{-1} (s, br), 1626 (s), 1397 (m), 1106 (w), 956 (m), 871 (s), 777 (m), 614 (s), 562 (m), 532 (m), 367(w).

$(H_3O)_3[\{Dy(H_2O)_6\}_2\{Dy(H_2O)_4\}\{Mo_{36}(NO)_4O_{108}(H_2O)_{16}\}]\cdot 43H_2O$ [$Dy_3Mo_{36}(NO)_4$, 10]: This compound was prepared by exactly the same protocol as **5**, but with $Dy(NO_3)_3 \cdot 5H_2O$ (0.081 g, 0.185 mmol), to give an orange crystalline product. Yield: 0.143 g [42% based on $\{Mo_{36}(NO)_4\}$]. $H_{159}Dy_3Mo_{36}N_4O_{190}$: calcd. H 2.21, N 0.78; found H 1.99, N 0.87. IR (KBr pellet): $\tilde{\nu}$ = 3414 cm^{-1} (s, br), 1615 (s), 1405 (m), 1247(w); 957 (m), 870 (s), 770 (m), 613 (s), 560 (m), 531 (m), 363(w).

$(H_3O)_3[\{Ho(H_2O)_6\}_2\{Ho(H_2O)_4\}\{Mo_{36}(NO)_4O_{108}(H_2O)_{16}\}]\cdot 46H_2O$ [$Ho_3Mo_{36}(NO)_4$, 11]: This compound was prepared by exactly the same protocol as **5**, but with $Ho(NO_3)_3 \cdot 5H_2O$ (0.081 g, 0.184 mmol), to give an orange crystalline product. Yield: 0.202 g [59% based on $\{Mo_{36}(NO)_4\}$]. $H_{169}Ho_3Mo_{36}N_4O_{193}$: calcd. H 2.32, N 0.77; found H 2.13, N 0.82. IR (KBr pellet): $\tilde{\nu}$ = 3431 cm^{-1} (s, br), 1626 (s), 1400 (m), 957 (m), 872 (s), 780 (m), 617 (s), 564 (m), 532 (m), 357(w).

$(H_3O)_3[\{Er(H_2O)_6\}_2\{Er(H_2O)_4\}\{Mo_{36}(NO)_4O_{108}(H_2O)_{16}\}]\cdot 50H_2O$ [$Er_3Mo_{36}(NO)_4$, 12]: This compound was prepared by exactly the same protocol as **5**, but with (0.082 g, 0.185 mmol) of $Er(NO_3)_3 \cdot 5H_2O$, to give an orange crystalline product. Yield: 0.200 g [58% based on $\{Mo_{36}(NO)_4\}$]. $H_{173}Er_3Mo_{36}N_4O_{197}$: calcd. H 2.36, N 0.76; found H 2.13, N 1.05. IR (KBr pellet): $\tilde{\nu}$ = 3424 cm^{-1} (s, br), 1614 (m), 1406 (w), 958 (m), 868 (s), 774 (m), 611 (s), 562 (m), 534 (m), 366 (m).

$(H_3O)_3[\{Yb(H_2O)_6\}_2\{Yb(H_2O)_4\}\{Mo_{36}(NO)_4O_{108}(H_2O)_{16}\}]\cdot 56H_2O$ [$Yb_3Mo_{36}(NO)_4$, 13]: This compound was prepared by exactly the same protocol as **5**, but with (0.072 g, 0.186 mmol) of $YbCl_3 \cdot 6H_2O$, to give an orange crystalline product. Yield: 0.208 g [59% based on $\{Mo_{36}(NO)_4\}$]. $H_{185}Mo_{36}N_4O_{203}Yb_3$: calcd. H 2.48, N 0.75; found H 1.95, N 0.96. IR (KBr pellet): $\tilde{\nu}$ = 3420 cm^{-1} (s, br), 1620 (m), 1405 (w), 957 (m), 869 (s), 770 (m), 613 (s), 561 (m), 531 (m), 369 (w).

$(H_3O)_3[\{Lu(H_2O)_6\}_2\{Lu(H_2O)_4\}\{Mo_{36}(NO)_4O_{108}(H_2O)_{16}\}]\cdot 31H_2O$ [$Lu_3Mo_{36}(NO)_4$, 14]: This compound was prepared by exactly the same protocol as **5**, but with $Lu(NO_3)_3 \cdot 5H_2O$ (0.066 g, 0.183 mmol), to give an orange crystalline product. Yield: 0.132 g [40% based on $\{Mo_{36}(NO)_4\}$]. $H_{135}Lu_3Mo_{36}N_4O_{178}$: calcd. H 1.92, N 0.80; found H 1.77, N 0.90. IR (KBr pellet): $\tilde{\nu}$ = 3390 cm^{-1} (s, br), 3190 (s, br), 1606 (s), 1406 (w), 1246 (w), 956 (m), 866 (s), 769 (m), 608 (s), 565 (m), 537 (m).

$(H_3O)_2[\{Nd(H_2O)_5\}_2\{Mo_{36}O_{112}(H_2O)_{16}\}]\cdot 40H_2O$ [Nd_2Mo_{36}, 15]: A suspension of $Na_2MoO_4 \cdot 2H_2O$ (0.500 g, 2.07 mmol) and $NH_2OH \cdot HCl$ (0.300 g, 4.32 mmol) in 30 mL of water was acidified with concd. HCl until pH 2. The resulting mixture was refluxed for 30 min and then slowly cooled down to room temperature. The deep-orange solution was filtered and $NdCl_3 \cdot 6H_2O$ (0.150 g, 0.418 mmol) was added to the filtrate with vigorous stirring for five minutes. The reaction solution was kept at room temperature in an open beaker. The amorphous solids that separated were removed by filtration from time to time. After 10 days colorless rhombic crystals of **15** were collected by filtration, washed twice with a minimum amount of ice-cooled water, and dried in air. Yield: 0.136 g (35% based on Mo). $H_{138}Mo_{36}Nd_2O_{180}$: calcd. H 2.04; found H 1.98. IR (KBr pellet): $\tilde{\nu}$ = 3415 cm^{-1} (s, br), 1623 (m), 1384 (w),

 © 2005 Wiley-VCH Verlag GmbH & Co. KGaA, Weinheim

938 (m), 897 (m), 864 (m), 839 (m), 778 (w), 711 (m), 653 (m), 552 (m), 500 (w), 402 (w), 374 (w), 346 (w).

Further crystallographic details may be obtained from the Fachinformationzentrum Karlsruhe, 76344 Eggenstein-Leopoldshafen, Germany, on quoting the depository numbers CSD-415381 (for **1**), -415403 (for **2**), -415441 (for **3**), -415401 (for **4**), -415400 (for **5**), -415404 (for **6**), -415402 (for **7**), -391260 (for **8**), -415398 (for **9**), -415383 (for **10**), -415385 (for **11**), -415384 (for **12**), -415399 (for **13**), -415397 (for **14**), and -415382 (for **15**).

Supporting Information (see footnote on the first page of this article) includes the bond lengths and angles for compounds **1**–**15**.

Acknowledgments

This work was supported by the Russian Foundation for Basic Research (grant no. 05-03-32126) and INTAS (grant no. 01-2346). NVI thanks Haldor Topsoe A/S for a fellowship, and MNS and NVI are thankful to the Russian Science Support Foundation for grants.

[1] M. T. Pope, *Heteropoly and Isopoly Oxometalates*; Springer-Verlag: Berlin, **1983**.
[2] M. T. Pope, A. Müller, *Angew. Chem. Int. Ed. Engl.* **1991**, *30*, 34–48.
[3] A. Müller, S. Roy, *Coord. Chem. Rev.* **2003**, *245*, 153–166.
[4] A. Müller, F. Peters, M. T. Pope, D. Gatteschi, *Chem. Rev.* **1998**, *98*, 239–271.
[5] S. Uchida, M. Hashimoto, M. Mizuno, *Angew. Chem. Int. Ed.* **2002**, *41*, 2814–2817.
[6] A. K. Cheetham, G. Férey, T. Loiseau, *Angew. Chem. Int. Ed.* **1999**, *38*, 3268–3292.
[7] A. Müller, S. K. Das, S. Talismanov, S. Roy, E. Beckmann, H. Bögge, M. Schmidtmann, A. Merca, A. Berkle, L. Allouche, Y. Zhou, L. Zhang, *Angew. Chem. Int. Ed.* **2003**, *42*, 5039–5044.
[8] A. Müller, C. Beugholt, H. Bögge, M. Schmidtmann, *Inorg. Chem.* **2000**, *39*, 3112–3113.
[9] L. Cronin, C. Beugholt, E. Krickemeyer, M. Schmidtmann, H. Bögge, P. Kögerler, T. K. K. Luong, A. Müller, *Angew. Chem. Int. Ed.* **2002**, *41*, 2805–2808.
[10] Q.-M. Wang, B. Yan, *Inorg. Chem. Commun.* **2004**, *7*, 1124–1127.
[11] J.-C. Bünzli, *Luminescent Probes*, in *Lanthanide Probes in Chemistry, Biology and Earth Science*, in *Lanthanide Probes in Life, Chemical and Earth Sciences: Theory and Practice* (Eds.: J.-C. Bünzli, G. Choppin), Elsevier, Amsterdam, **1989**.
[12] J. Kido, Y. Okamoto, *Chem. Rev.* **2002**, *102*, 2357–2368.
[13] V. Shivaiah, N. P. V. Reddy, L. Cronin, S. K. Das, *J. Chem. Soc., Dalton Trans.* **2002**, 3781–3782.
[14] Y. Naruke, T. Ozeki, T. Yamase, *Acta Crystallogr., Sect. C* **1991**, *47*, 489–492.
[15] R. Ballardini, E. Chiorboli, V. Balzani, *Inorg. Chim. Acta* **1984**, *95*, 323.
[16] P. Mialane, L. Lisnard, A. Mallard, J. Marrot, E. Antic-Fidancev, P. Aschehoug, D. Vivien, F. Sécheresse, *Inorg. Chem.* **2003**, *42*, 2102–2108.
[17] H. C. Aspinall, *Chem. Rev.* **2002**, *102*, 1807–1850.
[18] A. Dolbecq, P. Mialane, L. Lisnard, J. Marrot, F. Sécheresse, *Chem. Eur. J.* **2003**, *9*, 2914–2920.
[19] J. Bartis, S. Sukal, E. Davis, R. Kronzon, L. Blumenstein, L. Francesconi, *Preparation, Characterization and anti-HIV Activity of Lanthanide Polyoxoanions*, 210th ACS National Meeting, Chicago, **1995**, 646.
[20] V. Shivaiah, M. Nagaraju, S. K. Das, *Inorg. Chem.* **2003**, *42*, 6604–6606.
[21] M. Sadakane, M. H. Dickman, M. T. Pope, *Angew. Chem. Int. Ed.* **2000**, *39*, 2914–2916.
[22] J. R. Galán-Mascarós, C. Giménez-Saiz, S. Triki, C. J. Gómez-García, E. Coronado, L. Quahab, *Angew. Chem. Int. Ed. Engl.* **1995**, *34*, 1460–1462.
[23] A. Müller, M. Koop, P. Schiffels, H. Bögge, *Chem. Commun.* **1997**, 1715–1716.
[24] T. Yamase, H. Naruke, *J. Chem. Soc., Dalton Trans.* **1991**, 285–292.
[25] L. Hu, C. Qin, X. Wang, Y. Wie, E. Wang, *Inorg. Chem.* **2003**, *42*, 7342–7344.
[26] M. I. Khan, E. Yohannes, R. J. Doedens, *Inorg. Chem.* **2003**, *42*, 3125–3129.
[27] M. I. Khan, E. Yohannes, D. Powell, *Chem. Commun.* **1999**, 23–24.
[28] M. I. Khan, E. Yohannes, D. Powell, *Inorg. Chem.* **1999**, *38*, 212–213.
[29] M. I. Khan, E. Yohannes, R. J. Doedens, *Angew. Chem. Int. Ed.* **1999**, *38*, 1292–1294.
[30] M. I. Khan, E. Yohannes, R. J. Doedens, S. Tabussum, S. Cevik, L. Manno, D. Powell, *Cryst. Eng.* **1999**, *2*, 171–179.
[31] S.-W. Zhang, Y.-G. Wie, Q. Yu, M.-Ch. Shao, Y.-Q. Tang, *J. Am. Chem. Soc.* **1997**, *119*, 6440–6441.
[32] G. Liu, Y.-G. Wie, Q. Yu, Q. Liu, Sh.-W. Zhang, *Inorg. Chem. Commun.* **1999**, *2*, 434–437.
[33] N. V. Izarova, M. N. Sokolov, F. M. Dolgushin, M. Yu. Antipin, D. Fenske, V. P. Fedin, *C. R. Chimie*, in press.
[34] A. Müller, E. Krickemeyer, S. Dillinger, H. Bögge, W. Plass, A. Proust, L. Dloczik, C. Menke, J. Meyer, R. Rohlfing, *Z. Anorg. Allg. Chem.* **1994**, *620*, 599–619.
[35] B. Krebs, I. Paulat-Boeschen, *Acta Crystallogr., Sect. B* **1982**, *38*, 1710–1718.
[36] C.-D. Wu, X. Lin, W.-B. Yang, C.-Z. Lu, H.-H. Zhuang, *Jiegou Huaxue* **2001**, *20*, 358–362; *Chem. Abstr.* **2002**, *136*, 78847.
[37] G. M. Sheldrick, *SADABS. Program for Absorption Corrections for Area Detector Data*, University of Göttingen, Göttingen, Germany, **1997**.
[38] G. M. Sheldrick, *SHELX-97, Release 97-2*, University of Göttingen, Göttingen, Germany, **1998**.

Received: May 30, 2005
Published Online: November 2, 2005

 © 2005 Wiley-VCH Verlag GmbH & Co. KGaA, Weinheim

DOI: 10.1002/ejic.200500523

Mechanism of Isomerization of Ni(cyclam) in Aqueous Solutions

Eric Maimon,*[a,b] Israel Zilbermann,[a,b] Haim Cohen,[a,d] Daniel Kost,[a] Rudi van Eldik,[c] and Dan Meyerstein*[a,d]

Keywords: Isomerization / Cyclam / Nickel complexes / Oxidation states

Nickel complexes of cyclam and cyclam derivatives isomerize in aqueous solutions via two different mechanisms: i. deprotonation of one of the coordinated amino groups followed by inversion and ii. cleavage of the Ni–N bond followed by inversion. While the first mechanism is relevant for the di- and tri-valent nickel complexes, the second one occurs for the mono-valent complexes, and for complexes with tertiary amines as ligands.
(© Wiley-VCH Verlag GmbH & Co. KGaA, 69451 Weinheim, Germany, 2005)

Introduction

Qualitative studies based on molecular models first performed by Bosnich et al.[1,2] described the five possible conformational isomers (*trans-I*-*trans-V*, Figure 1, a) of planar complexes of the "classic" macrocyclic ligand system, cyclam. Of the five possible configurational isomers of [Ni(cyclam)]$^{2+}$, (NiL^1)$^{2+}$, it has long been supposed that the *trans-III* configuration is the most stable one.[1,3]

Molecular mechanics (MM) theoretical studies predicted that when four-coordinate low-spin species are involved, the *trans-I* isomer is favoured over the *trans-III* one, while if six-coordinate species are present, the stabilities are reversed.[4] Later theoretical studies applying MM techniques[5–8] and local density functional theory analysis[9] that compare the calculated data to the already published X-ray structures of *trans-III* and *trans-V*,[5,11–13] indicated that the *trans-I* and *trans-III* isomers of [Ni(cyclam)]$^{2+}$ (Figure 1, c), are energetically most stable, and that the energy difference between them is insignificant.

Solution ^{1}H-NMR studies[10a,10b] indicate that both [Ni(cyclam)]$^{2+}$ *trans-I* and *trans-III* forms coexist in aqueous solutions, the *trans-I* isomer comprising ca. 15% of the total complex at room temperature. The rate of equilibration (1) is rapid at high pH, but extremely slow at acidic pH. On the other hand, the equilibrium is shifted to produce more of the *trans-I* isomer at higher temperatures. Based on the latter and on the fact that *trans-I*-[Ni(cyclam)]$^{2+}$ has an extremely small tendency to add axial ligands, the latter complex could be isolated.[10b]

trans-I-[Ni(cyclam)]$^{2+}$ ⇄ *trans-III*-[Ni(cyclam)]$^{2+}$ (1)

Studies performed on the low-spin *N*-alkylated derivative (tmc)-(NiL^3)$^{2+}$ of [Ni(cyclam)]$^{2+}$ (tmc = *N*,*N*′,*N*′′,*N*′′′-Me$_4$-cyclam) led to the conclusion that the *trans-III* configuration is the lowest energy structure and the *trans-I* configuration is kinetically favored.[12–14] The two isomers are not interconvertable unless strong coordinating solvents are present[12] and then the *trans-I* species is favoured.

Solution ^{13}C-NMR studies[15] showed that the published methods[16] for the preparation of *trans-I*-[Ni(tmc)]$^{2+}$ also produce some amounts of the *trans-II* isomer in the crude product. If triflate is used instead of perchlorate as the precipitation agent, a markedly higher proportion of the *trans-II* isomer is obtained. Recrystallization of these products in CH_3NO_2 converts the *trans-II* isomer almost entirely to the *trans-I* isomer. A strong donor solvent such as DMF enhances the rate of isomerization from *trans-II* to *trans-I*. The authors[15] propose that the isomerization mechanism involves the inversion about a nitrogen, which probably requires the inverting nitrogen to detach from the divalent metal centre rendering the previously tetradentate tmc temporarily to become a tridentate chelate.

A very similar mechanism is proposed for the isomerization of the Ni^{II} complex with an alkylated derivative of diazacyclam,[17] L^9 [see reaction (2) and Figure 1, b].

trans-I-[Ni(L^9)]$^{2+}$ ⇄ *trans-III*-[Ni(L^9)]$^{2+}$ (2)

The authors suggest an inversion of one tertiary and one secondary nitrogen donor in the six-membered chelate ring. The coordination of a water molecule to the metal centre following the detachment of a coordinated nitrogen in the transition state is also proposed. The authors also propose

[a] Department of Chemistry, Ben-Gurion University of the Negev, Beer-Sheva, Israel
E-mail: emymon@bgumail.bgu.ac.il
danmeyer@bgumail.bgu.ac.il
[b] Nuclear Research Centre Negev, Beer-Sheva, Israel
[c] Institute for Inorganic Chemistry, University of Erlangen-Nürnberg, 91058 Erlangen, Germany
[d] Department of Biological Chemistry, The College of Judea and Samaria, Ariel, Israel

 © 2005 Wiley-VCH Verlag GmbH & Co. KgaA, Weinheim

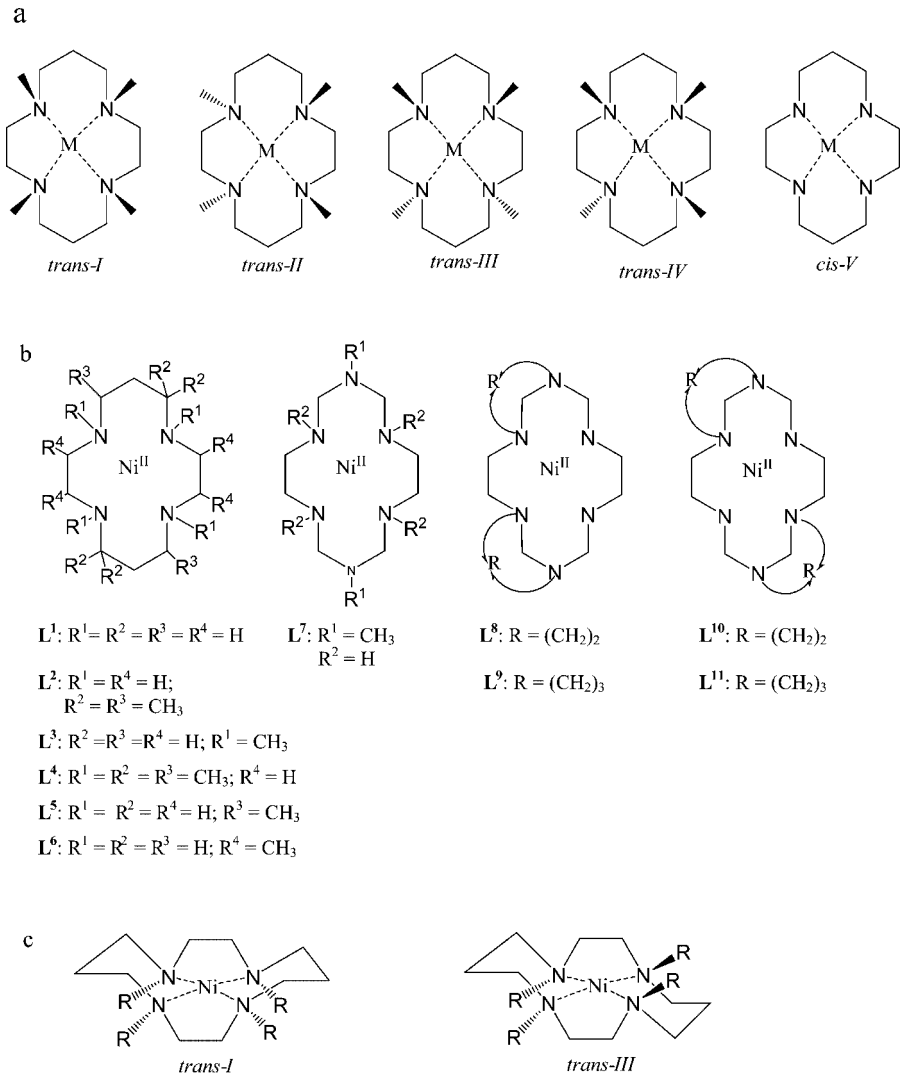

Figure 1. **a**: The five known isomers of metal complexes of cyclam. **b**: The nickel complexes of cyclam and alkylated derivatives. **c**: The most stable isomers of cyclam and derivatives (in this study R = H or CH_3).

the formation of the *trans-II* isomer as one of the intermediates in the mechanistic cycle.

The isomerization of the macrocyclic frame bound to the nickel ion both in the +1 and +3 oxidation states of the metal was also reported. Isomerization according to (3) leads to an equilibrated mixture of a ca. 1:3 ratio, respectively, has been reported to occur in aqueous solutions over a period of several hours.[18a,18b]

$$\textit{trans-I}\text{-}[Ni^{I}(tmc)]^{+} \rightleftarrows \textit{trans-III}\text{-}[Ni^{I}(tmc)]^{+} \quad (3)$$

It is of interest to note that the very fast reduction of $[Ni(cyclam)]^{2+}$ and analogous complexes by e^{-}_{aq} or by $CO_2^{\cdot-}$,[19] is followed by reactions obeying first order kinetics with rate constants in the range $(0.1–2.6)\times10^3\ s^{-1}$, which were attributed to isomerization processes.

Kelly et al.[20] showed that the fast addition of CO to $[Ni^{I}(cyclam)]^{+}$ in aqueous solutions is followed by a slower first-order reaction with a rate constant of 1.8 s^{-1}, which was tentatively attributed to the isomerization process (4).

$$\textit{trans-III}\text{-}[Ni^{I}(cyclam)CO]^{+} \rightleftarrows \textit{trans-I}\text{-}[Ni^{I}(cyclam)CO]^{+} \quad (4)$$

Such a reaction channel was not observed for $[Ni^{I}(L^{6})CO]^{+}$ perhaps due to steric constrains, but it does operate for $[Ni^{I}(L^{5})CO]^{+}$, which is less sterically restrained.[21]

Electrochemical studies[10b] demonstrated the rapid conversion (5) on a time scale of 400 ms.

$$\textit{trans-I}\text{-}[Ni^{III}(cyclam)]^{3+} \rightleftarrows \textit{trans-III}\text{-}[Ni^{III}(cyclam)]^{3+} \quad (5)$$

Isomerization processes of $[Ni^{III}(cyclam)]^{3+}$[22] or cyclam and diazacyclam derivatives were observed following the oxidation of the divalent nickel by strong single electron oxidizing agents.[23–27] Furthermore, the decomposition processes of $[Ni^{III}(cyclam)]^{3+}$ or diazacyclam $(L^{7–11})$[27–29] complexes were shown to obey first order kinetics even though the common decomposition mechanism requires second order kinetics. It was proposed that the rate-determining step in the decomposition process is presumably an isomerization reaction.

 © 2005 Wiley-VCH Verlag GmbH & Co. KGaA, Weinheim

Clearly the suggestion that $[Ni^{III}(L^1)(H_2O)_2]^{3+}$ isomerizes faster than $[Ni^{II}(L^1)]^{2+}$[10b] and the effect of pH on the rate of isomerization of $[Ni^{II}(L^1)]^{2+}$[10b] do not fit a mechanism requiring the detachment of a nitrogen atom from the central nickel ion. The availibility of *trans-I*-$[Ni^{II}(L^1)]^{2+}$ and *trans-III*-$[Ni^{II}(L^1)]^{2+}$ suggested that the homogeneous isomerization of the corresponding $[Ni^{I}(L^1)]^{+}$ and $[Ni^{III}(L^1)(H_2O)_n]^{3+}$ could be studied in order to elucidate the isomerization mechanisms and the factors that affect them.

Results and Discussion

The Case of $[Ni^{III}(L^1)]$

As already mentioned, the *trans-III*-$[Ni^{II}(L^1)]^{2+}$ and *trans-I*-$[Ni^{II}(L^1)]^{2+}$ isomers were separated[10a] and their oxidatively induced interconversion was studied using electrochemical techniques.[10b] Since the time scale of the isomerization process is 400 ms, which is close to the detection limit of the electrochemical techniques used, and as it occurs near the electrode and might therefore be a heterogeneous process, it was decided to study this process in homogeneous solutions using the pulse radiolysis technique.

N_2O saturated aqueous solutions containing 5×10^{-4} M *trans-III*-$[Ni^{II}(L^1)]^{2+}$ or *trans-I*-$[Ni^{II}(L^1)]^{2+}$ at pH 3.4–4.2, were irradiated by fast 5 MeV electrons at a dose rate of 2.5–25 Gy/pulse. Under these experimental conditions over 90% of the primary radicals formed by the radiation, reaction (6), are transformed into $^{\cdot}OH$ radicals via reaction (7).

$$H_2O \xrightarrow{e^-,\,\gamma} e^-_{aq}\ (2.65);\ H^{\cdot}\ (0.60);\ {}^{\cdot}OH\ (2.65);\ H_2\ (0.45);\ H_2O_2\ (0.75);\ H^+\ (2.65) \quad (6)$$

where the values in parentheses give the relative yields of the primary products.[36a]

$$N_2O + e^-_{aq} + H_2O \rightarrow N_2 + {}^{\cdot}OH + OH^-$$
$$k_7 = 8.7\times10^9\ M^{-1}\,s^{-1}\ [31] \quad (7)$$

The $^{\cdot}OH$ radicals then oxidize $[Ni^{II}(L)]^{2+}$ according to equation (8), presumably with conservation of the isomeric composition.

$$^{\cdot}OH + [Ni^{II}(L)]^{2+} \rightarrow OH^- + [Ni^{III}(L)]^{3+}$$
$$k_8 > 2\times10^9\ M^{-1}s^{-1}\ [27] \quad (8)$$

The spectra of *trans-III*-$[Ni^{III}(L^1)_{aq}]^{3+}$ and *trans-I*-$[Ni^{III}(L^1)_{aq}]^{3+}$ thus formed differ considerably, Figure 2. *trans-III*-$[Ni^{III}(L^1)_{aq}]^{3+}$ is long-lived, whereas the spectrum of *trans-I*-$[Ni^{III}(L^1)_{aq}]^{3+}$ changes in a process which obeys first order kinetics, Figure 3, to form a species with a spectrum which is identical to that of *trans-III*-$[Ni^{III}(L^1)_{aq}]^{3+}$. Therefore the observed process is attributed to the isomerization reaction (5).

$$trans\text{-}I\text{-}[Ni^{III}(L^1)_{aq}]^{3+} \rightarrow trans\text{-}III\text{-}[Ni^{III}(L^1)_{aq}]^{3+}$$
$$k_5 = (3.3\pm0.7)\times10^3\ s^{-1}\ \text{at pH 3.2} \quad (5)$$

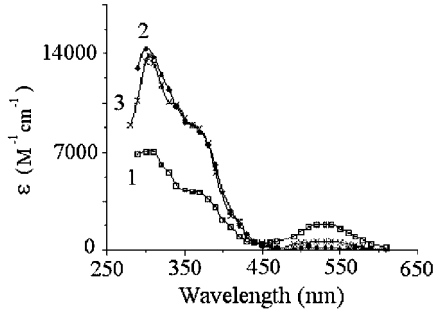

1) 14 μs after the pulse → $5\cdot10^{-4}$ M *trans-I*-($Ni^{II}L$); N_2O saturated; pH 3.2; 8 Gy/pulse

2) 40 ms after the pulse → $5\cdot10^{-4}$ M *trans-I*-($Ni^{II}L$); N_2O saturated; pH 3.2; 8 Gy/pulse

3) 40 ms after the pulse → $5\cdot10^{-4}$ M *trans-III*-($Ni^{II}L$); N_2O saturated; pH 3.2; 8 Gy/pulse

Figure 2. Spectra of the tervalent nickel complexes of the *trans-I* and *trans-III* complexes formed by the oxidation of $[Ni^{II}(L^1)]^{2+}$.

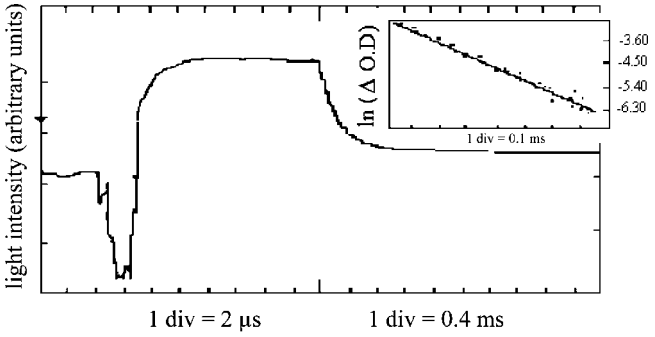

Figure 3. The formation and isomerization of *trans-I*-$[Ni^{III}(L^1)_{aq}]^{3+}$ 5×10^{-4} M *trans-III*-$[Ni^{II}(L^1)]^{2+}$, N_2O-saturated solution, pH 3.2, irradiation at λ = 550 nm, 18 Gy.

The observed rate constant, k_5, decreases by a factor of 10 when the pH of the solutions is raised from 3.2 to 4.2. The experiments could not be performed either at more alkaline pH values since *trans-I*-$[Ni^{II}(cyclam)]^{2+}$ isomerizes fast at higher pH,[10b] or at a more acidic pH since at pH < 3 the production of $^{\cdot}OH$ radicals is not quantitative.[23] The pH effect may be explained by the formation of *trans-I*-$[Ni^{III}(L^1)(OH)]^{2+}$[22] which might slow down the isomerization process by allowing a more energetically appropriate pentacoordinate geometry for the latter and by raising the pK_a of the Ni–N–H group, see below.

The product *trans-III*-$[Ni^{III}(L^1)_{aq}]^{3+}$ is stable on a time scale of hours at pH 3.2. At this point it must be mentioned that the specific rate constant for the isomerization process

 © 2005 Wiley-VCH Verlag GmbH & Co. KGaA, Weinheim

measured here differs by three orders of magnitude from that reported by Billo et al.[10b] for the same pH. This apparent discrepancy might be explained in terms of different conditions in the electrochemical experiments i.e probably the involvement of heterogeneous factors (viz. the electrode surface) in the latter study.

The isomerization process in reaction (5) might in principle proceed via one of the following mechanisms:
a) deprotonation of one of the coordinated amino groups followed by inversion
b) cleavage of the Ni–N bond followed by inversion, though it is difficult to envisage why this should be faster for $[Ni^{III}(L^1)_{aq}]^{3+}$ than for $[Ni^{II}(L^1)_{aq}]^{2+}$.

In order to differentiate between these mechanisms, it was decided to see whether the isomerization is accompanied by proton exchange of the N–H groups with the solvent. For this purpose ^{1}H-NMR experiments were carried out in order to see whether the N–H groups are transformed into N–D groups when the oxidation reaction is carried out in D_2O. The following experiments were performed.

^{1}H-NMR measurements were performed using D_2O solutions of $(2–5)\times10^{-3}$ M of *trans-I*-$[Ni^{II}(L^1)_{aq}]^{2+}$ at pH 2.0 (Figure 4, a). The broad singlet at 3.5 ppm is attributed to N–H. The quartet at 3.1 ppm is interpreted as an overlapped double triplet and is attributed to H–C–H (Figure 4, a, $–H_C$), i.e. it is a result of the splitting of the genuine triplet by coupling to the N–*H* proton. Due to overlaps the detailed signals of H_d, H_e and H_f could not be separated. When solutions containing *trans-I*-$[Ni^{II}(L^1)_{aq}]^{2+}$ were made alkaline by the addition of NaOD, the singlet disappeared and the quartet was transformed into a triplet, indicating that the amine proton exchanged with deuterium (Figure 4, b). The same solution at pH 2.0 was reacted with an equivalent amount of $Na_2S_2O_8$ to oxidize the metal centre and then immediately reduced by an equivalent amount of $NaHSO_3$. The ^{1}H-NMR spectrum of the product was then recorded. The broad known spectrum[11a] of the paramagnetic "blue" *trans-III*-$[Ni^{II}(L^1)(H_2O)_2]^{2+}$ was shifted by raising the temperature to 75 °C, where the "yellow" diamagnetic species is the prevailing one.[10b] Under these conditions the ^{1}H-NMR spectrum could be resolved. The spectrum showed no singlet at 3.5 ppm and a triplet at 3.1 ppm (Figure 4, c), indicating that isomerization proceeds via deprotonation, i.e. via route (a) above.

As sulfate was shown to stabilize $[Ni^{III}(L^i)]^{3+}$ (i = 1, 2, 7),[22,23,27,28] it seemed of interest to investigate the difference in behaviour of the two $[Ni^{III}(cyclam)]^{3+}$ isomers. CV and square-wave experiments showed that the *trans-III*-$[Ni^{III}(cyclam)]^{3+}$ isomer as expected for the relative symmetrical octahedral environment, binds two sulfate anions (Figure 5) with $K = 2\times10^6$ M^{-2}, the CVs are reversible. While the *trans-I*-$[Ni^{III}(cyclam)]^{3+}$ isomer prefers to be pentacoordinate binding only one sulfate anion with $K = 8.2\times10^5$ M^{-1}, in this case the CVs are quasi-reversible. The latter result indicates that the rate of isomerization of *trans-I*-$[Ni^{III}L]_{aq}$ is slowed down at least by several orders of magnitude by the complexation with sulfate.

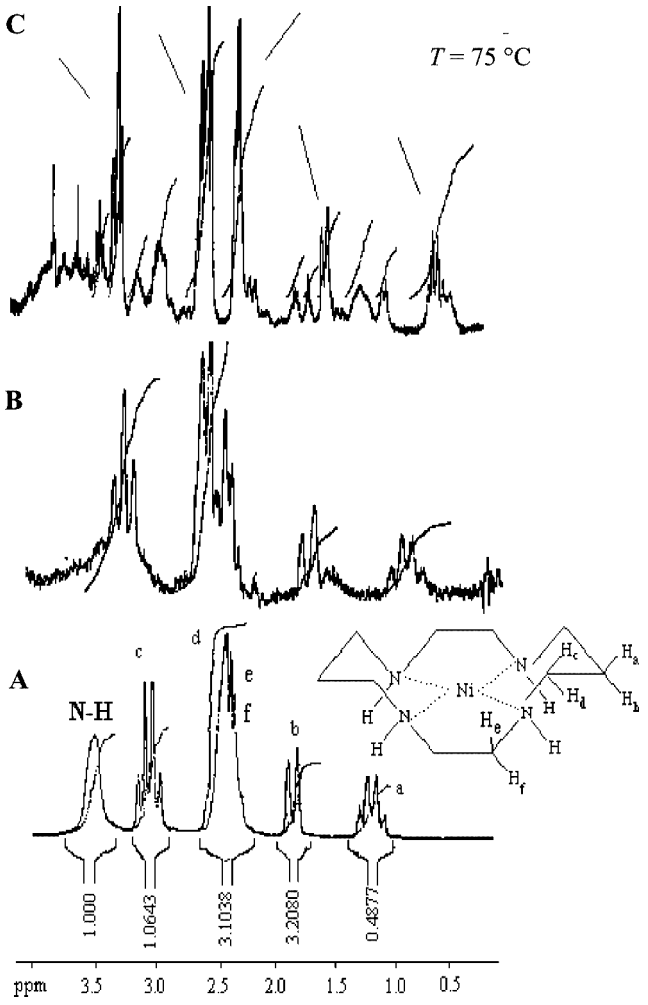

Figure 4. ^{1}H-NMR measurements performed for *trans*-I-$[Ni^{II}(L^1)]^{2+}$. **A**: *trans-I*-$[Ni^{II}(L^1)]$, pH 2.0, D_2O, room temperature. **B**: *trans*-I-$[Ni^{II}(L^1)]$, pH 8.0, D_2O, room temperature. **C**: $[Ni^{II}(L^1)]$, pH 2.0, D_2O, obtained by oxidation of the *trans-I* isomer to give the *trans-III* isomer and then reduction.

The Case of $[Ni^I(L^i)]$

Ni^{II} complexes of saturated tetraazamacrocycles undergo an one-electron reduction to produce Ni^I species, both in organic solvents[30a,30b] and in aqueous solutions.[31] The reduced species react with CO and were studied in water,[32–34] dimethylformamide[32] and in acetonitrile[21,35] as solvents.

As already mentioned, Kelly et al.[20] reported the chemistry of $[Ni^I(L^1)]^+$ in the presence of CO in aqueous solutions. When *trans-III*-$[Ni^{II}(L^1)]^{2+}$ was reduced in the presence of CO, two consecutive reactions were observed.
i. The formation of the complex *trans-III*-$[Ni^I(L^1)(CO)]^+$, in a process approaching the diffusion-controlled limit, which has an absorption band with λ_{max} = 470 nm.
ii. Followed by a unimolecular rearrangement to yield a more stable product with λ_{max} = 350 nm. The $\Delta S^{\#}$ of the latter reaction was determined to be –14.4 cal K^{-1} mol^{-1}. The observed reaction is assumed to proceed according to reaction (9).

trans-III-$[Ni^I(L^1)(CO)]^+ \rightarrow$ *trans-I*-$[Ni^I(L^1)(CO)]^+$ (9)

 © 2005 Wiley-VCH Verlag GmbH & Co. KGaA, Weinheim

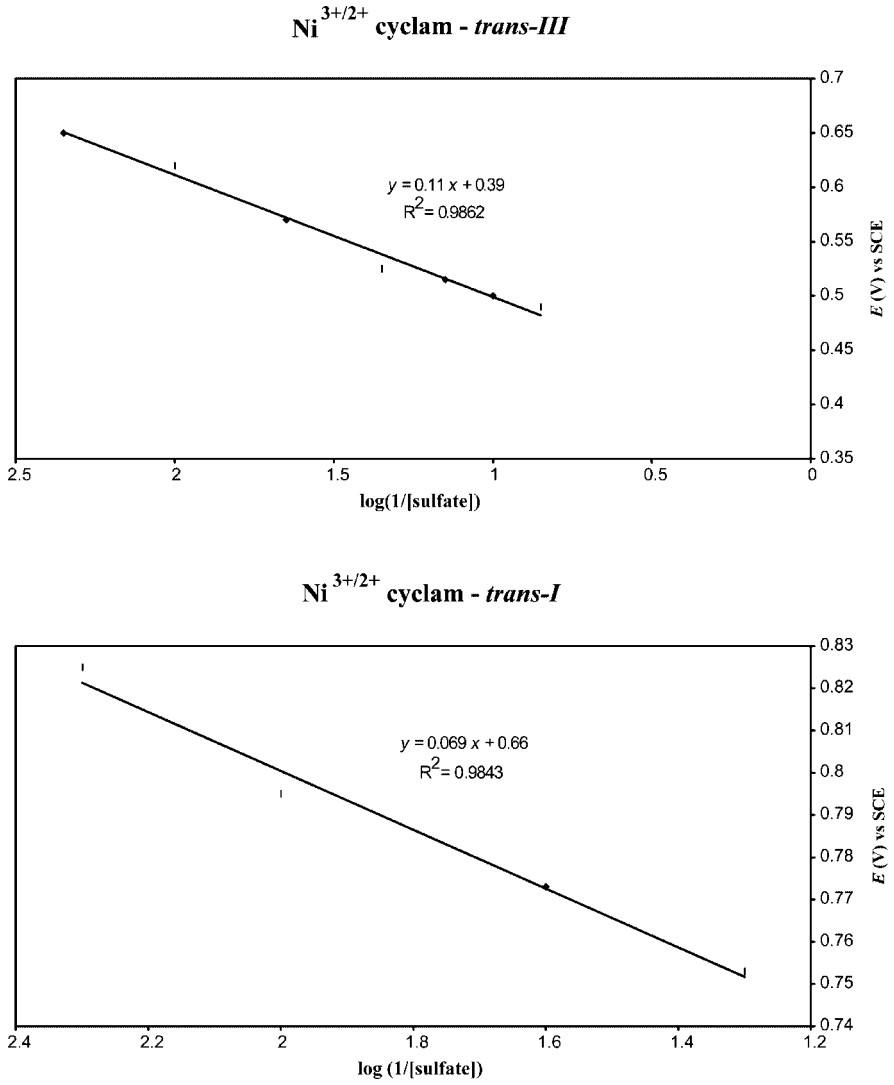

Figure 5. The dependence of $E^{1/2}$ $[Ni(L^1)]^{3+/2+}$ of the two isomers on [sulfate] 5×10^{-4} M $[Ni^{II}(L^1)]^{2+}$, 0.005–0.14 M Na_2SO_4, pH 3.2, ionic strength kept constant by addition of $NaClO_4$, working electrode: glassy carbon, 80 mV/s.

It seemed of interest to verify this assignment and to determine the source of the negative $\Delta S^{\#}$ value. For this purpose *trans-III*-$[Ni^I(L^3)]^+$ (L^3 = 1*R*,4*R*,8*S*,11*S*-1,4,8,11-tetramethyl-1,4,8,11-tetraazacyclotetradecane ≡ *trans-III*-tmc) and *trans-I*-$[Ni^I(L^3)]^+$ (L^3 = 1*R*,4*S*,8*R*,11*S*-1,4,8,11-tetramethyl-1,4,8,11-tetraazacyclotetradecane ≡ *trans-I*-tmc) were prepared in the presence of CO and their reactions with CO were studied. These experiments are of interest as it is known that the interconversion between *trans-I*- and *trans-III*-$[Ni^I(L^3)]^+$ is very slow.[18a,18b] Furthermore, we also determined $\Delta V^{\#}$ for reaction (9).

Indeed the formation of *trans-I*-$[Ni^I(L^3)]^+$ in the presence of CO is followed by a fast reaction. The rate of this process is proportional to [CO] and is attributed to reaction (13).

trans-I-$[Ni^I(L^3)]^+$ + CO ⇄ *trans-I*-$[Ni^I(L^3)(CO)]^+$
$k_{13} = 3.7 \times 10^8$ M^{-1} s^{-1}, $K_{13} = 4.3 \times 10^3$ M^{-1} (13)

The product does not isomerize and decomposes on a time scale of several minutes. The spectra of *trans-I*-$[Ni^I(L^3)]^+$ and *trans-I*-$[Ni^I(L^3)(CO)]^+$ were measured, see Figure 6. The spectrum and the kinetics of decomposition of *trans-I*-$[Ni^I(L^3)(CO)]^+$ at pH 10.5 were also measured, Figure 7, and no isomerization was observed during the decomposition process.

No complexation of *trans-III*-$[Ni^I(L^3)]^+$ by CO was observed at pH 10.5 and a slow isomerization process was observed, which has a life time of several minutes, Figure 8. The *trans-I*-$[Ni^I(L^3)]^+$ formed in the isomerization process naturally forms the *trans-I*-$[Ni^I(L^3)(CO)]^+$ complex. Neither *trans-I*-$[Ni^I(L^3)(CO)]^+$ nor *trans-III*-$[Ni^I(L^3)]^+$ isomerizes in the presence of CO, on the time scale on which $[Ni^I(L^1)(CO)]^+$ isomerizes. This finding is in agreement with expectations due to the known rigidity of complexes of the L^3 ligand. Thus our observations corroborate the sugges-

 © 2005 Wiley-VCH Verlag GmbH & Co. KGaA, Weinheim

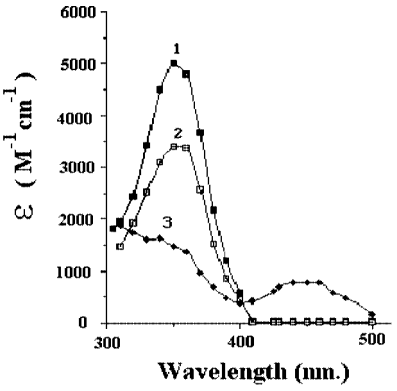

1. Spectrum measured 8 μs after the pulse no CO
2. Spectrum measured 8 μs after the pulse 0.0002 M CO
3. Spectrum measured 36 μs after the pulse 0.0002 M CO

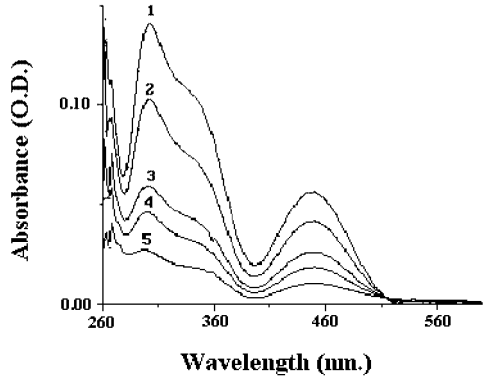

1. 30 s after irradiation
2. 180 s after irradiation
3. 480 s after irradiation
4. 1380 s after irradiation
5. 2670 s after irradiation

Figure 6. UV/Vis spectra of *trans-I*-$[Ni^{I}(L^{3})_{aq}]^{+}$ and *trans-I*-$[Ni^{I}(L^{3})(CO)]^{+}$: 5×10^{-4} M *trans-I*-$[Ni^{II}(L^{3})]^{2+}$, 0.1 M HCOONa, 2×10^{-4} M CO, pH 7.4, He saturated solution. The second plot shows the spectra obtained after the solution was irradiated with 200 Gy in a 1-cm quartz cell (blank: non-irradiated solution).

tion by Kelly et al.[20] that the fast isomerization observed is described by reaction (9).

The volume of activation of reaction (9) was found to be $\Delta V^{\#} = 0\pm1$ cm^3 mol^{-1}. This result points out that the reported $\Delta S^{\#}$ is due to a transition state in which the macrocyclic ligand is less flexible which does not involve a significant volume change during the isomerization process.

Concluding Remarks

The results obtained in this study indicate that two different mechanisms are involved in the isomerization processes of nickel complexes with cyclam and cyclam derivatives as chelates.

i. Detachment of the Ni–N bond and inversion presumably via the *cis-V* isomer. This mechanism is relevant to low valent complexes and seems to occur in general for tmc complexes as was also observed for copper.[37]

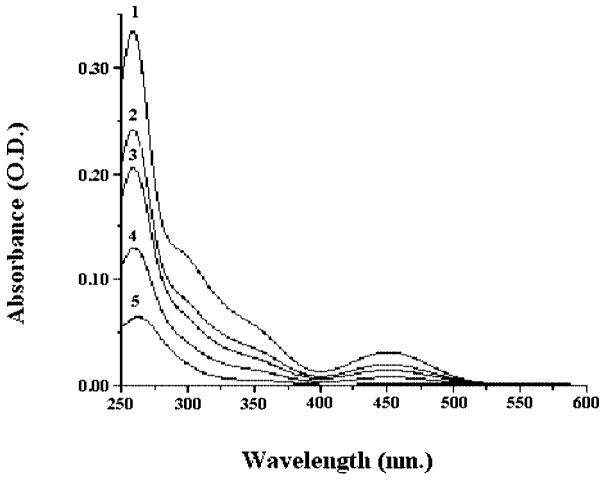

1. 30 s after irradiation
2. 270 s after irradiation
3. 840 s after irradiation
4. 1620 s after irradiation
5. 2550 s after irradiation

Figure 7. UV/Vis spectra of *trans-I*-$[Ni^{I}(L^{3})(CO)]^{+}$ at pH 10.5: 5×10^{-4} M *trans-I*-$[Ni^{II}(L^{3})]^{2+}$, 0.1 M HCOONa, 2×10^{-4} M CO, He saturated solution. The solution was irradiated with 200 Gy in a 1-cm quartz cell (blank: non-irradiated solution).

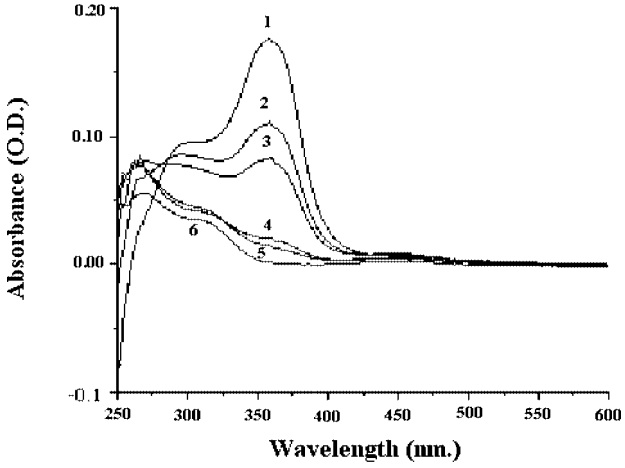

1. 30 s after irradiation
2. 210 s after irradiation
3. 330 s after irradiation
4. 600 s after irradiation
5. 780 s after irradiation
6. 2160 s after irradiation

Figure 8. UV/Vis spectra of *trans-III*-$[Ni^{I}(L^{3})]^{+}$ in the presence of CO. 5×10^{-4} M *trans-III*-$[Ni^{II}(L^{3})]^{2+}$, 0.1 M HCOONa, 2×10^{-4} M CO, pH 10.5, He saturated solution. The solution was irradiated with 200 Gy in a 1-cm quartz cell (blank: non-irradiated solution).

ii. Deprotonation of coordinated N–H and inversion, presumably also via the *cis-V* isomer. This mechanism seems to be relevant to high oxidation state complexes. This mechanism explains the reason for a faster isomerization step in the case of nickel for the tervalent complex vs. the divalent complex. This mechanism corroborates also the

 © 2005 Wiley-VCH Verlag GmbH & Co. KGaA, Weinheim

pH effect in the case of the $[Ni^{II}(L^1)]^{2+}$ complex. A similar effect was observed also for $[Cd^{II}(L^1)]^{2+}$ and $[Zn^{II}(L^1)]^{2+}$.[38a,38b]

Experimental Section

Materials: All the chemicals used were of AR grade and were used without further purification. The solutions were prepared with heat-distilled water that was then passed through a Millipore set-up, the final resistance being greater than 10 MΩ

The complexes $[Ni^{II}(cyclam)](ClO_4)_2$, *trans-III*-$[Ni^{II}(cyclam)](ClO_4)_2$, *trans-I*-$[Ni^{II}(cyclam)](ClO_4)_2$, *trans-III*-$[Ni^{II}(tmc)](ClO_4)_2$, *trans-I*-$[Ni^{II}(tmc)](ClO_4)_2$ were prepared according to literature procedures.[10a,11,39] The complexes were characterized by C,H,N elemental analysis and UV/Vis and IR spectroscopy. The results for all the complexes were in excellent agreement with the expected formula and the literature data.

NMR Measurements: ^{1}H-NMR measurements were run at 200 MHz on a Bruker-WP-200-SY spectrometer using a 5-mm broadband probe. Spectra were acquired in the double precision mode at ambient (20 °C) and at higher (75 °C) temperatures.

A typical sample consisted of 1–2 mg of complex dissolved in 1 mL of D_2O. Homonuclear decoupling experiments were carried out using the lowest decoupling power which saturated the desired resonance. Chemical shifts were referenced by computer to the TMS frequency.

Electrochemical Measurements: A three-electrode cell was used. The working electrode for the CV measurements was a Metrohm teflon-shrouded glassy carbon electrode (0.07 cm^2). The auxiliary electrode was a Pt wire and a SCE was used as the reference electrode. The auxiliary and the reference electrodes were placed in separate compartments of the cell. All potentials are reported vs. SCE CV measurements were performed using a EG&G Princeton Applied Research potentiostat/galvanostat, Model 263, operated by a Research Electrochemistry Software EG&G PARC. Potentials were determined by square wave voltammetry. Measurements were performed at 80 mv/s.

Pulse Radiolysis: The solutions were handled by the syringe technique. Deaeration was performed by bubbling He or N_2O (when oxidizing conditions were required) through the solutions. The experiments were carried out at the linear accelerator facility of the Hebrew University of Jerusalem: 0.5–1.5 μs, 5 MeV and 200-mA pulses were used. The dose per pulse was in the range of 2.5–25 Gy/pulse. The experimental set up and the techniques used for evaluating the results have been described elsewhere in detail.[40] The high-pressure experiments were performed using an instrument which has been described in detail elsewhere.[41,42]

Preparation of *trans-I*- and *trans-III*-$[Ni^IL^3]^+$ Complexes: *trans-I*-$[Ni^I(L^3)(CO)]^+$ was prepared via the reduction of the corresponding Ni^{II} complex in the presence of CO. Aqueous He-saturated solutions containing 5×10^{-4} M *trans-I*-$[Ni^{II}(L^3)]^{2+}$, 0.1 M HCOONa, and $(0.1–1)\times10^{-3}$ M CO at pH 7.4, were irradiated by a pulse of 5 MeV electrons. Under these conditions reactions (10)–(12) have to be considered.

$$HCOO^- + H^{\cdot}/{}^{\cdot}OH \rightarrow COO^{\cdot-} + H_2/H_2O$$
$$k_{10\ H/OH} = 2.1\times10^8/3.2\times10^9\ M^{-1}\ s^{-1}\text{[36b]} \quad (10)$$

$$trans\text{-}I\text{-}[Ni^{II}(L^3)]^{2+} + e^-_{aq} \rightarrow trans\text{-}I\text{-}[Ni^{I}(L^3)]^{+}$$
$$k_{11} > 1\times10^{10}\ M^{-1}\ s^{-1} \quad (11)$$

$$trans\text{-}I\text{-}[Ni^{II}(L^3)]^{2+} + COO^{\cdot-} \rightarrow trans\text{-}I\text{-}[Ni^{I}(L^3)]^{+} + CO_2$$
$$k_{12} \approx 1\times10^9\ M^{-1}s^{-1} \quad (12)$$

trans-III-$[Ni^I(L^3)]^+$ was prepared by using an analogous experimental approach.

Spectrophotometric Measurements and Slow Kinetics: The spectra and the kinetics of the relatively long lived species ($t_{1/2} \geq 20$ s) were recorded using a HP 8452 A diode-array spectrophotometer. The long lived monovalent nickel species were produced by irradiating He-saturated solutions in a 1-cm quartz spectrophotometric cell.

IR Spectra: Were recorded using KBr pellets on a NICOLET 5ZDX FT-IR spectrometer.

Elementary Analyses: Were performed at the micro-analysis laboratory at the Hebrew University in Jerusalem.

Acknowledgments

This study was supported in part by grants from the Israel Academy of Sciences and from the Israel Atomic Energy Committee. D. M. expresses his thanks to Ms Irene Evens for her continuous interest and support.

[1] B. Bosnich, C. K. Poon, M. L. Tobe, *Inorg. Chem.* **1965**, *4*, 1102.
[2] B. Bosnich, C. K. Poon, M. L. Tobe, *Inorg. Chem.* **1965**, *4*, 1109.
[3] P. O. Whimp, M. F. Bailey, N. F. Curtis, *J. Chem. Soc. A* **1970**, 1956.
[4] K. R. Adam, M. Antolovich, L. G. Brigden, A. J. Leong, L. F. Lindoy, P. J. Baillie, D. K. Uppal, M. McParthin, B. Shah, D. Proserpio, L. Fabrizzi, P. A. Tasker, *J. Chem. Soc. Dalton Trans.* **1991**, 2493.
[5] P. J. Connoly, E. J. Billo, *Inorg. Chem.* **1987**, *26*, 3224.
[6] K. R. Adam, M. Antolovich, L. G. Brigden, L. F. Lindoy, *J. Am. Chem. Soc.* **1991**, *113*, 3346.
[7] K. R. Adam, M. Antolovich, I. M. Atkinson, L. G. Brigden, L. F. Lindoy, *J. Mol. Struct.* **1994**, *323*, 223.
[8] V. J. Thon, C. C. Fox, J. C. A. Boeyens, R. D. Hancock, *J. Am. Chem. Soc.* **1984**, *106*, 5947.
[9] K. R. Adam, I. M. Atkinson, L. F. Lindoy, *Inorg. Chem.* **1997**, *36*, 480.
[10] a) E. J. Billo, P. J. Connoly, D. J. Sardella, J. P. Jasinski, R. J. Butcher, *Inorg. Chim. Acta* **1995**, *230*, 19; b) D. T. Pierce, T. L. Hatfield, E. J. Billo, Y. Ping, *Inorg. Chem.* **1997**, *36*, 2950.
[11] M. J. D′Aniello, M. T. Mocella, F. Wagner, E. K. Barefield, I. C. Paul, *J. Am. Chem. Soc.* **1975**, *97*, 192.
[12] P. Moore, J. Sachinidis, G. R. Willey, *J. Chem. Soc. Chem. Commun.* **1983**, 522.
[13] P. Moore, J. Sachinidis, G. R. Willey, *J. Chem. Soc. Dalton Trans.* **1984**, 1323.
[14] T. W. Hambley, *J. Chem. Soc. Dalton Trans.* **1986**, 565.
[15] S. F. Lincoln, J. A. Coates, D. A. Hadi, D. L. Pisaniello, *Inorg. Chim. Acta* **1984**, *81*, L9.
[16] a) E. K. Barefield, F. Wagner, *Inorg. Chem.* **1973**, *12*, 2435; b) E. K. Barefield, F. Wagner, *Inorg. Chem.* **1976**, *15*, 408.
[17] D. Lee, M. P. Suh, J. W. Lee, *J. Chem. Soc. Dalton Trans.* **1997**, 577.
[18] a) A. Bakac, J. H. Espenson, *J. Am. Chem. Soc.* **1986**, *108*, 713; b) M. S. Ram, A. Bakac, J. H. Espenson, *Inorg. Chem.* **1986**, *25*, 3267.
[19] I. Zilbermann, M. Winnik, D. Sagiv, A. Rotman, H. Cohen, D. Meyerstein, *Inorg. Chim. Acta* **1995**, *240*, 503.
[20] C. A. Kelly, Q. G. Mulazzani, E. L. Blinn, M. A. J. Rodgers, *Inorg. Chem.* **1996**, *35*, 5122.
[21] D. J. Szalda, E. Fujita, R. Sanzenbacher, H. Paulus, H. Elias, *Inorg. Chem.* **1994**, *33*, 5855.

 © 2005 Wiley-VCH Verlag GmbH & Co. KGaA, Weinheim

[22] E. Zeigerson, G. Ginzburg, D. Meyerstein, L. J. Kirschenbaum, *J. Chem. Soc. Dalton Trans.* **1980**, 1243.
[23] H. Cohen, L. J. Kirschenbaum, E. Zeigerson, M. Jaacobi, E. Fuchs, G. Ginzburg, D. Meyerstein, *Inorg. Chem.* **1979**, *18*, 2763.
[24] E. Zeigerson, G. Ginzburg, J. Y. Becker, L. J. Kirschenbaum, H. Cohen, D. Meyerstein, *Inorg. Chem.* **1981**, *20*, 3988.
[25] P. V. Bernhardt, G. A. Lawrance, D. F. Sangster, *Inorg. Chem.* **1988**, *27*, 4055.
[26] M. G. Fairbank, A. McAuley, *Inorg. Chem.* **1986**, *25*, 1233.
[27] I. Zilbermann, H. Cohen, D. Meyerstein, results to be published.
[28] I. Zilbermann, A. Meshulam, H. Cohen, D. Meyerstein, *Inorg. Chim. Acta* **1993**, *206*, 127.
[29] J. Taraszewska, G. Roslonek, *ACS Proceedings* **1996**, P A52.
[30] a) J. Lewis, M. Schroeder, *J. Chem. Soc. Dalton Trans.* **1982**, 1085; b) R. R. Gagne, D. M. Ingle, *Inorg. Chem.* **1981**, *20*, 420.
[31] N. Jubran, G. Ginzburg, H. Cohen, Y. Koresh, D. Meyerstein, *Inorg. Chem.* **1985**, *24*, 251.
[32] M. Beley, J. P. Collin, R. Rupert, J. P. Sauvage, *J. Am. Chem. Soc.* **1986**, *108*, 7461–7467.
[33] M. Fujihira, Y. Hirata, K. Suga, *J. Electroanal. Chem.* **1990**, *292*, 199–215.
[34] G. B. Balasz, F. C. Anson, *J. Electroanal. Chem.* **1993**, *361*, 149–157.
[35] L. R. Furenlid, M. W. Renner, D. J. Szalda, E. Fujita, *J. Am. Chem. Soc.* **1991**, *113*, 883–892.
[36] a) MS Matheson, L. M. Dorfman, *Pulse Radiolysis*, **1969**, MIT Press, Cambridge, MA; b) G. V. Buxton, C. L. Greenstock, W. P. Helman, A. B. Ross, *J. Phys. Chem. Ref. Data* **1988**, *17*, 512.
[37] C. Amatore, J. M. Barbe, C. Bucher, E. Duval, R. Guilard, J. N. Verpeaux, *Inorg. Chim. Acta* **2003**, *356*, 267–278.
[38] a) X. Liang, J. A. Parkinson, M. Weishaupl, R. O. Gould, S. J. Paisey, H. S. Park, T. M. Hunter, C. A. Blindauer, S. Parsons, P. J. Sadler, *J. Am. Chem. Soc.* **2002**, *124*, 9105–9112; b) X. Liang, J. A. Parkinson, S. Parsons, M. Weishaupl, P. J. Sadler, *Inorg. Chem.* **2002**, *41*, 4539–4547.
[39] a) F. Wagner, E. K. Barefield, *Inorg. Chem.* **1976**, *15*, 408; b) F. Wagner, M. T. Mocella, M. J. D′Aniello, A. H. J. Wang, E. K. Barefield, *J. Am. Chem. Soc.* **1974**, *96*, 2625; c) E. K. Barefield, A. Bianchi, E. J. Billo, P. J. Connolly, P. Paoletti, J. S. Summers, D. G. Van Derveer, *Inorg. Chem.* **1986**, *25*, 4197.
[40] S. Goldstein, G. Czapski, H. Cohen, D. Meyerstein, *Inorg. Chem.* **1992**, *31*, 2439.
[41] R. van Eldik, A. E. Merbach, *Commun. Inorg. Chem.* **1992**, *12*, 341.
[42] R. van Eldik, H. Cohen, D. Meyerstein, *Inorg. Chem.* **1994**, *33*, 1566.

Received: June 11, 2005
Published Online: November 7, 2005

 © 2005 Wiley-VCH Verlag GmbH & Co. KGaA, Weinheim

DOI: 10.1002/ejic.200500601

Self-Assembly of an Alkali Metal Cluster Stabilized by a New Flexidentate Metalloligand: Formation and Structure of Heterobimetallic Na–Mo and Cs–Mo 2D Networks

Snehadrinarayan Khatua,[a] Sohaham Dasgupta,[a] Kumar Biradha,*[a] and Manish Bhattacharjee*[a]

Keywords: Alkali metals / Heterometallic complexes / Metalloligands / Molybdenum / Self-assembly

A new tridentate ligand, {(3,5-di-*tert*-butyl-2-hydroxybenzyl)amino}acetic acid, has been synthesized. This ligand forms $[\{Na_4(H_2O)_4(\mu\text{-}H_2O)_2\}\subset(Mo_2O_5L_2)_2]$ (**1**), which contains an Na_4^{4+} cluster cation stabilized by $[LMoO_2(\mu\text{-}O)MoO_2L]^{2-}$, upon reaction with Na_2MoO_4 in aqueous methanol. This compound has been characterized by various spectroscopic techniques and crystallizes in the triclinic space group $P\bar{1}$. Furthermore, compound **1** undergoes smooth exchange of Na^+ for Cs^+ to give $[Cs_2(Mo_2O_5L_2)\cdot H_2O]_n$ (**2**) upon treatment with CsCl in aqueous methanol. Similarly, **2** reacts with an excess of NaCl to produce **1**. Complex **2** crystallizes in the monoclinic space group $C2/c$. The crystal structure of this compound reveals that the geometry of the $[LMoO_2(\mu\text{-}O)MoO_2L]^{2-}$ unit stays almost intact but that it stabilizes a polymeric chain of Cs^+ cations, unlike in **1**.

(© Wiley-VCH Verlag GmbH & Co. KGaA, 69451 Weinheim, Germany, 2005)

Introduction

The role of judiciously designed ligands in the synthesis of supramolecular assemblies containing two types of metal ions has been demonstrated.[1,2] In recent years, a large number of metalloligands have been synthesized for the assembly of bimetallic complexes.[3] The main thrust has been on the aggregation of transition metal ions using main group metals as templates.[2] However, alkali metal cluster cations have received scant attention. Molybdates and tungstates have been widely used as ligands for metal ions due to their diverse structural flexibility and their applications in fields such as catalysis, analytical and clinical chemistry, biochemistry, and medicine.[4] Although a lot of attention has been paid to the synthesis of transition metal and rare-earth metal derivatives of polyoxometalates, alkali metal complexes of polyoxometalates have received much less attention.[5–7] We were interested in the synthesis of a flexible metalloligand that can coordinate alkali metal cations, and the effect of their size on the architecture of the structure. Also, we intended to explore the transmetalation of the alkali metal cations.

Herein we report the synthesis of the ligand {(3,5-di-*tert*-butyl-2-hydroxybenzyl)amino}acetic acid, and the synthesis and structure of an unusual polyoxomolybdate, $[\{Na_4(H_2O)_4(\mu\text{-}H_2O)_2\}\subset(Mo_2O_5L_2)_2]$ (**1**), which bears an Na_4^{4+} cluster cation stabilized by the metalloligand $[LMoO_2(\mu\text{-}O)MoO_2L]^{2-}$ ($\mathbf{L^{Mo}}$), and the corresponding cesium compound, a helical 1D infinite chain of $[Cs_2(Mo_2O_5L_2)\cdot H_2O]_n$ (**2**), obtained by transmetalation of the Na^+ ions in **1**. The transmetalation behavior of the compounds has also been investigated.

[a] Department of Chemistry, Indian Institute of Technology Kharagpur,
Kharagpur 721 302, India
Fax: +91-3222-282252
E-mail: mxb@iitkgp.ac.in
kbiradha@chem.iitkgp.ernet.in

Results and Discussion

Synthesis and Characterization of {(3,5-Di-*tert*-butyl-2-hydroxybenzyl)amino}acetic Acid

Our synthetic strategy was to design a tridentate, dibasic ligand (L) containing one carboxylate donor site that is expected to form the metalloligand $[LMoO_2(\mu\text{-}O)MoO_2L]^{2-}$ ($\mathbf{L^{Mo}}$). This ligand has the potential to coordinate alkali-metal cations through bridging carboxylate and self-assemble into various architectures (Scheme 1).

Accordingly, the ligand was synthesized by a one-pot Mannich reaction of glycine, 2,4-di-*tert*-butylphenol, and formaldehyde in aqueous ethanol. Glycine and formaldehyde (40%) were dissolved in water in a 1:10 ratio and an ethanolic solution of the phenol was added. The reaction solution afforded the ligand on standing for about 10 h. The ligand was characterized by elemental analysis, mass spectrometry, and IR, UV/Vis, and ^1H and ^{13}C NMR spectroscopy. The elemental analysis and mass spectral measurements agreed well with the proposed composition. The ^1H and ^{13}C NMR data were also in agreement with the proposed structure (see Experimental Section).

 © 2005 Wiley-VCH Verlag GmbH & Co. KgaA, Weinheim

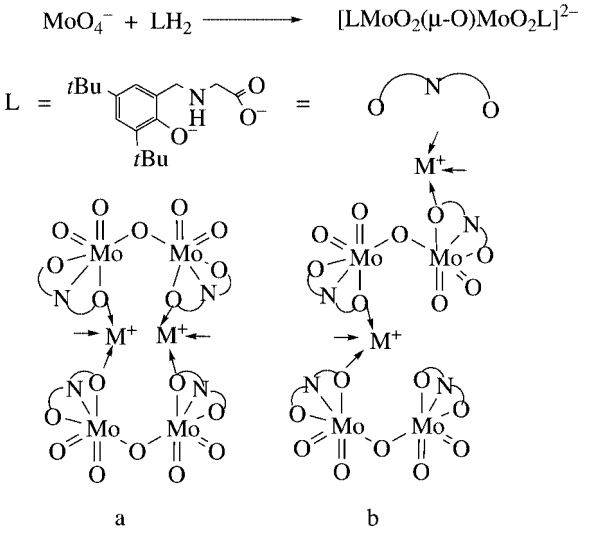

Scheme 1.

Synthesis, Characterization, and Solution Properties of the Molybdenum Complexes 1 and 2

Compound **1** was synthesized by the reaction of LH_2 with $Na_2MoO_4{\cdot}2H_2O$ in aqueous methanol and **2** was obtained by the reaction of CsCl with **1** in aqueous methanol. Compound **2** can also be prepared from an in situ reaction between an excess of CsCl and Na_2MoO_4 and the ligand. It should be noted that Cs^+ ions can be exchanged by Na^+ ions by treating **2** with an excess of NaCl. Thus, it is clear that both compounds show the ability to exchange cations and are interconvertable, which is rare in such molecules.

The elemental analyses agree well with the compositions. The compounds were further characterized by IR, UV/Vis, and ^1H, ^{13}C, ^{95}Mo, and ^{23}Na (compound **1**) NMR spectra and solution conductivity measurements. The IR spectrum of the compounds show two sharp bands at about 920 and 880 cm^{-1} due to symmetric and antisymmetric *cis*-Mo=$(O)_2$ stretches, respectively, and a band at around 780 cm^{-1} due to the Mo–O–Mo stretch; these clearly show the presence of the [MoO_2(μ-O)MoO_2] moiety. The UV/vis spectra of the compounds show strong bands due to a ligand-to-metal charge-transfer transition at about 350 nm along with internal ligand transitions.

The ^1H NMR spectra of **1** in [D_6]DMSO show signals at δ = 1.20 (br. s, 9 H) and 1.30 ppm (br. s, 9 H) due to the methyl protons of the *tert*-butyl groups. The CH_2 proton signals appear at δ = 3.36 (br. m, 2 H) and 4.25 ppm (br. m, 2 H). The signal at δ = 4.80 ppm (br. s, 1 H) can be assigned to the NH proton. We could not observe the signals due to the protons of coordinated water. This may be due to excessive broadening of the signals. The signals for the aromatic protons appear at δ = 6.85 (br. m, 1 H) and 7.10 ppm (br. m, 1 H). The ^{13}C NMR spectrum of **1** in [D_6]-DMSO shows signals at δ = 29.6, 29.9, 30.1, 31.5, 31.7, 33.7, 34.4, and 34.5 ppm due to the CH_3 and tertiary carbons of the *tert*-butyl group. The CH_2 signals appear at δ = 51.3, 51.6, 52.7, and 53.1 ppm, with the aromatic carbon signals at δ = 121.5, 121.9, 122.5, 122.7, 123.0, 124.1, 124.3, 136.7, 136.8, 137.9, 138.3, 159.8, and 159.9 ppm. The carboxylate carbon signals appear at δ = 175.2 and 175.3 ppm. The appearance of two signals for each carbon indicates that the ligands are bonded in a slightly different fashion. Thus, the ^1H and ^{13}C NMR and IR spectral studies clearly indicate the presence of an [$LMoO_2$(μ-O)MoO_2L] moiety in solution and the solid state. The ^{23}Na NMR spectrum of **1** shows a single broad signal at δ = 2.0 ppm (relative to NaCl as an external reference). This clearly shows that the coordinated nature of the sodium is maintained even in solution and that all the sodium ions are in a similar chemical environment. The observed low-field position of the ^{23}Na NMR signal, with respect to the NaCl reference, indicates the existence of an interaction between the sodium ions and between sodium and molybdenum, even in solution. The ^{95}Mo NMR spectra of the compounds show a sharp signal at δ = 0.3 ppm, which indicates that the molybdenum atoms are in a predominantly oxo environment. Similar spectral features were observed in the case of **2**. The observed molar conductance of **1** in methanol (95 $\Omega^{-1}cm^2mol^{-1}$) clearly indicates that the aggregate [{$Na_4(H_2O)_4$(μ-$H_2O)_2$}⊂($Mo_2O_5L_2)_2$] partially disintegrates in solution. The high-resolution ESI mass spectrum (methanol solution) of **1** shows a peak at *m*/*z* = 936.3138, which corresponds to $C_{34}H_{54}Mo_2N_2Na_2O_{13}$ {or [Na_2-($Mo_2O_5L_2$)($H_2O)_2$]}. Similarly, the mass spectrum of compound **2** shows a peak at *m*/*z* = 1138.2913 corresponding to $C_{34}H_{52}Cs_2Mo_2N_2O_{12}$, which can be formulated as [Cs_2($Mo_2O_5L_2$)(H_2O)]. The mass spectral studies clearly show that the coordinated nature of the alkali metals is maintained even in solution and that the clusters undergo partial disintegration in solution.

Crystal Structures of [{$Na_4(H_2O)_4$(μ-$H_2O)_2$}⊂($Mo_2O_5L_2)_2$] (1) and [$Cs_2(Mo_2O_5L_2){\cdot}H_2O]_n$ (2)

X-ray diffraction analysis revealed that the asymmetric unit of **1** contains only half of the cluster as it sits on an inversion center, with one L^{Mo} unit, two Na atoms, and three water molecules being present (Figure 1). The coordination environments of the two Mo atoms are almost similar: both have an octahedral geometry and are bonded to five oxygens and one nitrogen. The ligand L^{Mo} binds the two sodium atoms in two different ways and one of the Mo centers has an interaction with sodium [Mo1···Na2 = 3.553(5) Å]. The distinctive feature of the structure is the formation of a rectangular $(Na_4)^{4+}$ cluster cation (Figure 2, a). The distinctly shorter Na···Na distances of 3.539(5) Å (Na1–Na2) and 3.728(6) Å (Na1–Na1′) compared to that in elemental sodium (3.82 Å) show attractive Na–Na interactions in the cluster. The Na1–Na2′ distance [3.898(5) Å] is longer than that in elemental sodium. Recently, a tetrasodium dication, Na_4^{2+}, stabilized by two silyl(fluorosilyl) phosphonides, with a similar structure but with shorter Na–Na distances has been reported.[8] The $(Na_4)^{4+}$ unit binds six O atoms to form a Na_4O_6 cluster that can be described as a dicubane unit of the type M_6O_6 in which the two ex-

 © 2005 Wiley-VCH Verlag GmbH & Co. KGaA, Weinheim

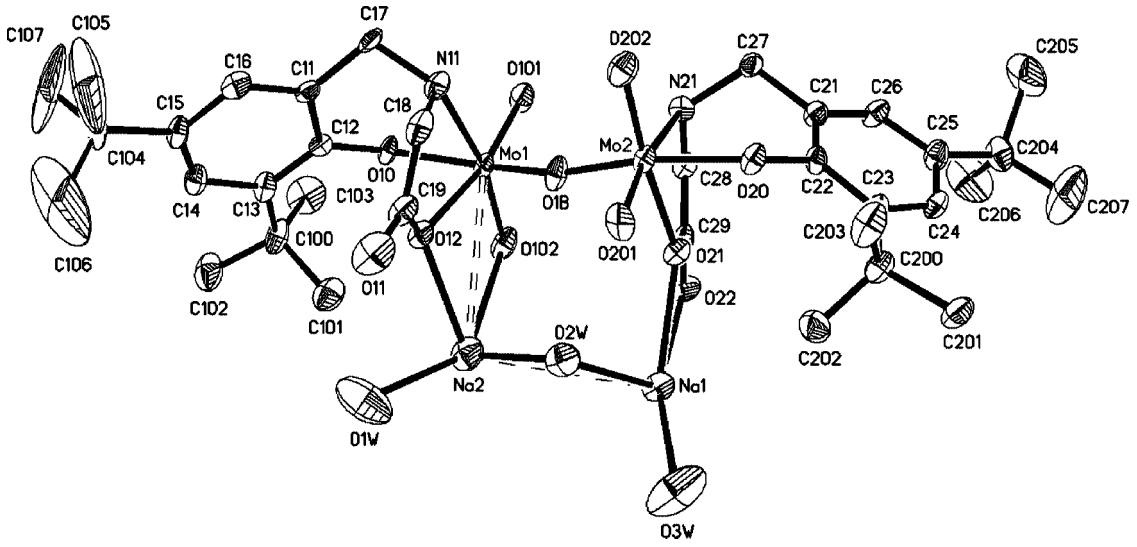

Figure 1. ORTEP drawing of the asymmetric unit of **1** (thermal ellipsoids at 50% probability).

treme and opposite corners have been removed (Figure 2, b). Two of the Na^+ ions (Na1) in the Na_4O_6 cluster are coordinated to five oxygens, and two (Na2) are hexacoordinate. Each of the four Na^+ ions is coordinated to one terminal water molecule [Na1–O3W = 2.277(9) and Na2–O1W = 2.301(11) Å] and are bridged by one water molecule [Na2–O2W = 2.366 (8) and Na1–O2W = 2.512 (7) Å; Na1–O2W–Na2 = 93.0(2)°]. In addition, Na1 and Na2 are also bridged by a Mo–O μ_3 oxygen (O102) [Na2–O102 = 2.727 (7) Å] and one carboxylate oxygen (O22) bridges three sodiums in a μ_3-fashion [Na1–O22 = 2.567(6), Na2–O22 = 2.318 (6) Å; Figure 2, b]. The compound forms a one-dimensional chain through Mo–O···H–N hydrogen bonding, and the 1D chains are joined by –COO···O and Mo–O···O hydrogen bonds to form a 2D network (Figure 3).

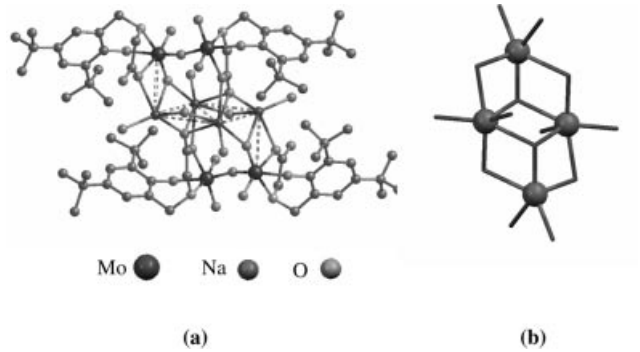

Figure 2. (a) Illustration of the tetramolybdate cluster **1**. The double dashed lines are long-distance interactions; H atoms have been omitted for the sake of clarity. (b) Illustration of the Na_4O_6 cluster with its terminal O atoms on Na; some atoms have been omitted for the sake of clarity.

The crystal structure of **2** reveals that the geometry of L^{Mo} (Figure 4) is almost the same as that of compound **1**. However, unlike in structure **1**, the asymmetric unit in **2** contains half of L^{Mo}, one Cs^+ ion, and one H_2O. The Cs^+ ions are found to form an infinite 1D-helical chain, which is stabilized by coordination of the $–COO^–$ and Mo–O

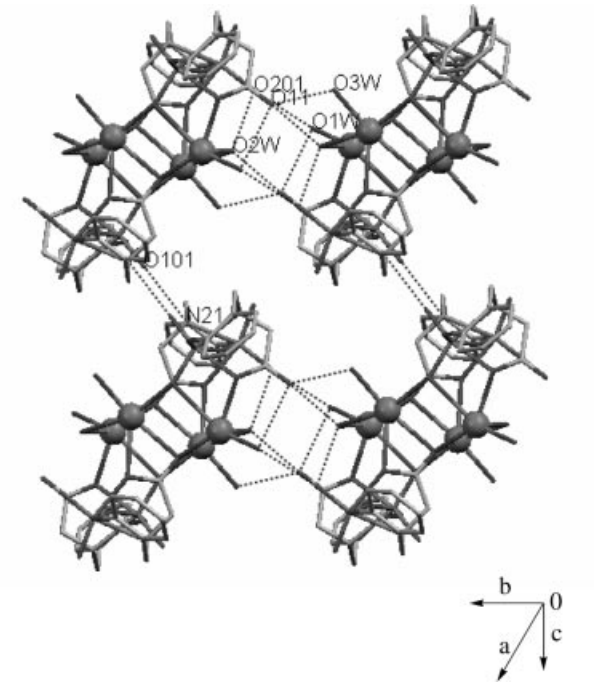

Figure 3. View of the 2D hydrogen-bonding network along the *c* axis (H bonds are shown as dotted lines; *tert*-butyl groups have been omitted for clarity).

groups of L^{Mo}, and are coordinated to six oxygens (Figure 5, a). This polymeric chain is generated by two Cs–Cs distances of 4.093(11) and 4.717(12) Å. The shorter Cs–Cs bond is bridged by two O atoms of two $–COO^–$ groups [Cs–O11 = 3.099(6) and 3.263(7) Å], whereas the longer one is not bridged by O atoms (Figure 5, b). The observed Cs···Cs distance clearly shows that there is substantial interaction between the Cs^+ ions. Similar to the structure **1**, the Mo atom interacts with Cs^+ with a distance of 4.172 Å. Interestingly, unlike **1**, the water molecules do not bind to the alkali metal ion (Cs^+) but join the one-dimensional polymeric chains of [{$(Cs)_2LO_2Mo$-O-MoO_2L}] via hydrogen

 © 2005 Wiley-VCH Verlag GmbH & Co. KGaA, Weinheim

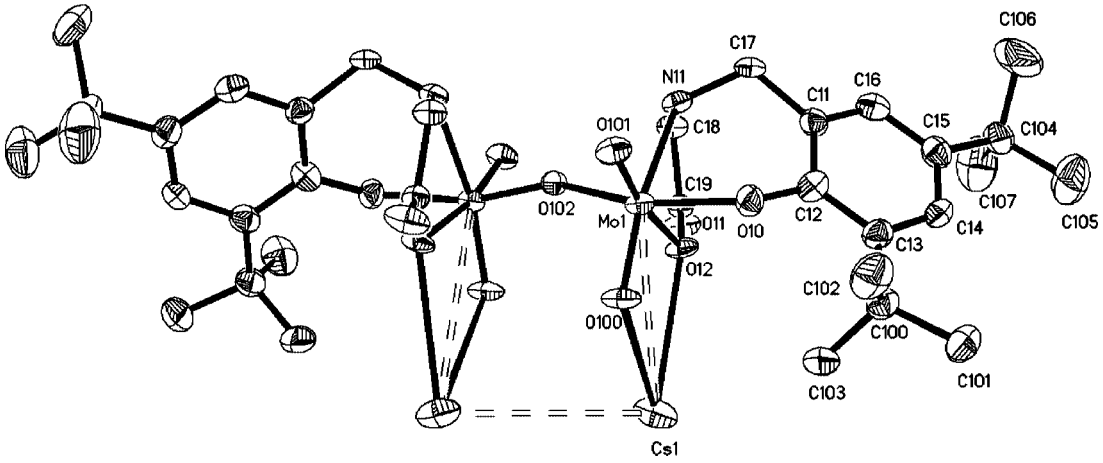

Figure 4. ORTEP drawing of the $[Cs_2(LO_2Mo\text{-}O\text{-}MoO_2L)]$ unit in the crystal structure of **2** (thermal ellipsoids at 50% probability). The double dashed lines represent long-distance interactions.

bonds [N–H···O = 3.006(8) Å (178°); O···O = 2.764(8); Figure 5, c]. In **1**, water is able to bridge two Na^+ ions, whereas, due to the larger size of the cation, water cannot bind the Cs^+ ions in a similar fashion in **2**. Similarly, in **1**, one of the O atoms of $–COO^–$ binds three Na^+ ions, whereas in **2**, due to the larger size of the Cs^+ ion, only two cations are bonded by the $–COO^–$ oxygen to form a 1D chain. Thus, both **1** and **2** form 2D networks but in **1** the network is built by hydrogen bonding only, whereas in **2** a 1D network is generated by Cs–Cs polymeric cluster chains that are joined by hydrogen bonding to form a 2D network.

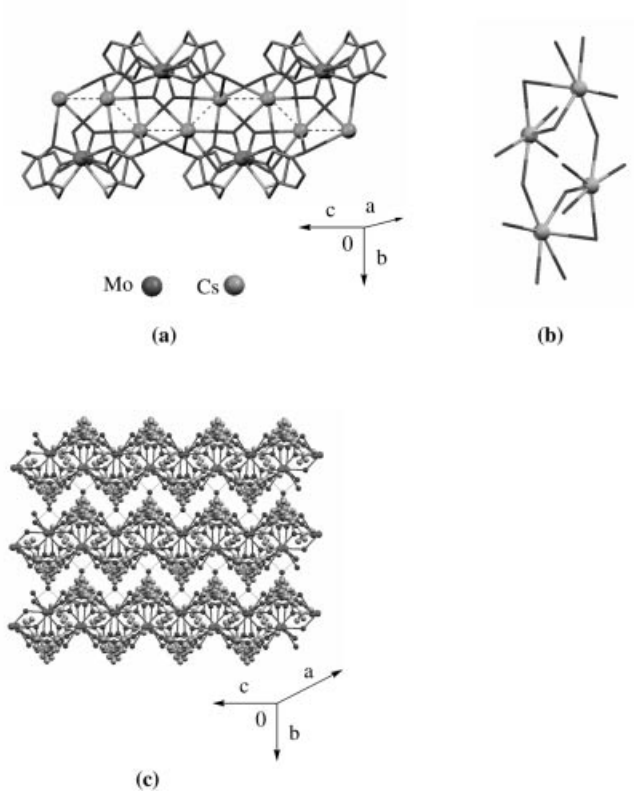

Figure 5. (a) Binding of Cs^+ ions by $[LO_2Mo\text{-}O\text{-}MoO_2L]$ units in the crystal structure of **2**. The *tert*-butyl groups have been omitted for the sake of clarity. The 1D chain is parallel to the crystallographic *c* axis. (b) Illustration of the Cs_4O_6 unit with its terminal O atoms on Cs; some atoms have been omitted for the sake of clarity. (c) 2D arrays of infinite 1D chains of **2** formed by hydrogen bonds.

Conclusions

A tridentate dibasic ligand has been designed which forms a new metalloligand, $[LMoO_2(\mu\text{-}O)MoO_2L]^{2–}$ (L^{Mo}) upon reaction with $MoO_4^{2–}$. This metalloligand binds Na^+ ions to form a heterobimetallic octanuclear compound. It has been shown that the alkali metal cations in **1** and **2** can easily undergo exchange with each other and the resulting compounds are structurally different. It should be noted that such interconvertibility in this type of molecules is rare. The structural differences between **1** and **2** can be attributed to the difference in size of the cations. Thus, L^{Mo} may be treated as a new polydentate flexible metalloligand for assembly of heterobimetallic complexes. These complexes are expected to afford mixed oxides of molybdenum on heating to high temperature, and work in this direction is already in progress. It should be mentioned that such mixed oxides have been shown to be effective catalysts for various coupling and oxidation reactions.[9] It would be interesting to explore the reactions of L^{Mo} with various transition metal ions and study their structural, magnetic, and catalytic properties.

Experimental Section

General Remarks: 2,4-Di-*tert*-butylphenol was purchased from Fluka. Glycine, formaldehyde, $Na_2MoO_4{\cdot}2H_2O$, and all solvents used were reagent-grade products. Elemental analyses were performed with a Perkin–Elmer C,H,N analyzer model 2400. Sodium was estimated by a flame photometric method. Molybdenum was estimated by gravimetric analysis [dioxobis(oxinate)molybdenum;

 © 2005 Wiley-VCH Verlag GmbH & Co. KGaA, Weinheim

$MoO_2(C_9H_9ON)_2$]. ^1H, ^{13}C, ^{23}Na, and ^{95}Mo NMR spectra were recorded in $CDCl_3$, CD_3OD, or [D_6]DMSO on a Bruker AC-200 instrument. The IR spectra were recorded on a Perkin–Elmer model 883 spectrometer. UV/vis spectra were recorded in solution with a Shimadzu model UV-1601 spectrophotometer. For the mass spectral measurements a methanolic solution of the compounds was prepared and the spectra recorded on a Waters LCT mass spectrometer using the electrospray ionization (ES^+ mode) technique.

Synthesis of {(3,5-Di-*tert*-butyl-2-hydroxybenzyl)amino}acetic Acid (L): Glycine (3.00 g, 40 mmol) was dissolved in water (20 mL), a 40% aqueous formaldehyde (30 mL, 400 mmol) solution was added, and the mixture was stirred for 20 min. An ethanolic solution (30 mL) of 2,4-di-*tert*-butylphenol (2.06 g, 10 mmol) was then added dropwise and the reaction mixture was stirred for 30 min and allowed to stand overnight. The precipitated ligand was filtered, washed with water, dried, and finally recrystallized from a mixture of methanol and dichloromethane. Yield: 2.53 g (86.5%). $C_{17}H_{27}NO_3$ (293.4): calcd. C 69.59, H 9.28, N 4.77; found C 69.25, H 9.10, N 4.46. IR (KBr pellet): $\tilde{\nu}$ = 2960 cm^{-1}, 1710, 1630, 1230, 1122. UV/Vis: λ_{max} (ε) = 280 nm (2290), 220 (7470). ^1H NMR ($CDCl_3$): δ = 1.28 (s, 9 H), 1.37 (s, 9 H), 3.62 (s, 2 H), 4.10 (s, 2 H), 4.86 (s, 1 H), 6.79 (d, J = 2.3 Hz, 1 H), 7.19 (d, J = 2.4 Hz, 1 H) ppm. ^{13}C NMR ($CDCl_3$): δ = 29.6, 31.4, 34.2, 34.8, 52.0, 53.3, 116.8, 121.9, 122.8, 137.3, 143.5, 149.4, 172.6 ppm. MS: m/z = 293 [M^+] ($C_{17}H_{27}NO_3$).

Synthesis of [{$Na_4(H_2O)_4(\mu\text{-}H_2O)_2$}⊂$(Mo_2O_5L_2)_2$] (1): An aqueous solution (5 mL) of $Na_2MoO_4{\cdot}2H_2O$ (0.121 g, 0.5 mmol) was added to a methanolic solution (25 mL) of the ligand (0.147 g, 0.5 mmol). The solution immediately turned orange. The solution was stirred for 3 h and was then allowed to stand overnight. The precipitated crystalline compound was filtered, washed 3–4 times with water, dried in vacuo, and finally recrystallized from a mixture of methanol and acetonitrile. Yield: 0.13 g (54%). $C_{68}H_{112}Mo_4N_4Na_4O_{28}$ (1909.3): calcd. C 42.78, H 5.91, Mo 20.10, N 2.93, Na 4.82; found C 43.25, H 6.10, Mo 19.45, N 2.40, Na 4.20 (by flame photometry). IR (KBr pellet): $\tilde{\nu}$ = 3433 cm^{-1}, 2960, 1600, 1470, 1250, 1170, 920, 880, 780. UV/Vis: λ_{max} (ε) = 355 nm (11830), 270 (22950), 230 (24440). ^{95}Mo NMR ([D_6]DMSO) [reference Na_2MoO_4 (δ = 0 ppm)]: δ = 0.3 ppm. ^{23}Na NMR ([D_6]DMSO) [reference NaCl (δ = 0 ppm)]: δ = 2.0 ppm. ^1H NMR ([D_6]DMSO): δ = 1.20 (br. s, 9 H), 1.34 (br. s, 9 H), 3.36 (br. m, 2 H), 4.25 (br. m, 2 H), 4.78 (br. s, 1 H), 6.85 (br. m, 1 H), 7.10 (br. m, 1 H) ppm. ^{13}C NMR ([D_6]DMSO): δ = 29.6, 29.9, 30.1, 31.5, 31.7, 33.7, 34.4, 34.5, 51.3, 51.6, 52.7, 53.1, 121.5, 121.9, 122.5, 122.7, 123.0, 124.1, 124.3, 136.7, 136.8, 137.9, 138.3, 159.8, 159.9, 175.2, 175.3 ppm. ESI HRMS: m/z = 936.3138 [$Na_2(Mo_2O_5L_2)(H_2O)_2$].

Reaction of 1 with CsCl. Synthesis of $[Cs_2(Mo_2O_5L_2){\cdot}H_2O]_n$ (2): Compound **1** (0.048 g, 0.025 mmol) was dissolved in methanol (20 mL), an aqueous solution (5 mL) of CsCl (0.037 g, 0.2 mmol) was added, and the reaction solution was stirred for 5 h. On standing for about 20 days orange crystals of **2** were obtained in 50% yield. $C_{34}H_{52}Cs_2Mo_2N_2O_{12}$ (1138.5): calcd. C 35.87, H 4.60, Mo 16.85, N 2.46; found C 36.05, H 4.34, Mo 17.15, N 2.54. IR (KBr pellet): $\tilde{\nu}$ = 2960 cm^{-1}, 1580, 1475, 1260, 906, 870, 790. UV/Vis: λ_{max} (ε) = 356 nm (6460), 213 (27590). ESI HRMS: m/z = 1138.2913 [$Cs_2(Mo_2O_5L_2)(H_2O)$]. ^1H NMR ([D_6]DMSO): δ = 1.27 (br. s, 9 H), 1.39 (br. s, 9 H), 3.28 (br. m, 2 H), 4.64 (br. s, 1 H), 6.95 (br. m, 1 H), 7.20 (br. m, 1 H) ppm.

Independent Synthesis of $[Cs_2(Mo_2O_5L_2){\bullet}H_2O]_n$ (2): An aqueous solution (5 mL) of $Na_2MoO_4{\cdot}2H_2O$ (0.061 g, 0.25 mmol) was added to a methanolic solution (25 mL) of the ligand (0.073 g, 0.25 mmol). The solution immediately turned orange. The reaction solution was stirred for 6 h and then CsCl (0.2524 g; 1.5 mmol) was added and solution was stirred for a further hour. On standing for 10 days crystals of compound **2** were obtained in 60% yield.

X-ray Crystallographic Study: Suitable crystals of **1** and **2** were grown from dilute acetonitrile/MeOH and MeOH/water solutions, respectively, at room temperature over a period of 5 to 20 days. The single crystal data were collected on Bruker–Nonius Mach3 CAD4 X-ray diffractometer that uses graphite monochromated Mo-K_α radiation (λ = 0.71073 Å) by the ω-scan method. No absorption correction was used. The structure was solved by direct methods and refined by least-squares methods on F^2 using SHELX-97.[10] Non-hydrogen atoms were refined anisotropically and hydrogen atoms on C atoms were fixed at calculated positions and refined using a riding model. The H atoms of the water molecules in **1** and **2** and N atoms in **1** and **2** could not be located. The details of crystal data are given in Table 1; selected bond lengths are summarized in Table 2.

CCDC-269980 (for **1**) and -269981 (for **2**) contain the supplementary crystallographic data for this paper. These data can be ob-

Table 1. Crystal data for [{$Na_4(H_2O)_4(\mu\text{-}H_2O)_2$}⊂$(Mo_2O_5L_2)_2$] (**1**) and $[Cs_2(Mo_2O_5L_2){\cdot}H_2O]_n$ (**2**).

	1	**2**
Empirical formula	$C_{68}H_{112}Mo_4N_4Na_4O_{28}$	$C_{34}H_{52}Cs_2Mo_2N_2O_{12}$
Formula mass	1909.34	1138.47
Temperature [K]	293(2)	293(2)
Wavelength [Å]	0.71073	0.71073
Crystal system	triclinic	monoclinic
Space group	$P\bar{1}$	$C2/c$
a [Å]	10.746(2)	38.280(8)
b [Å]	11.517(2)	10.961(2)
c [Å]	18.427(4)	10.391(2)
α [°]	104.26(3)	
β	94.19(3)	103.41(3)
γ	90.62(3)	
Volume [Å^3]	2203.4(8)	4241.1(15)
Z	1	4
$D_{calcd.}$ [Mg/m^3]	1.439	1.783
Absorption coefficient [mm^{-1}]	0.649	2.340
F(000)	984	2240
Final R indices [$I > 2\sigma(I)$]	R_1 = 0.0751, wR_2 = 0.1834	R_1 = 0.0550; wR_2 = 0.1343

 © 2005 Wiley-VCH Verlag GmbH & Co. KGaA, Weinheim

Table 2. The bond lengths [Å] around the Mo and alkali metal atoms in compounds **1** and **2**.[a]

1		**2**	
Mo(1)–O(1B)	1.887(5)	Mo(1)–O(101)	1.702(5)
Mo(1)–O(10)	1.947(5)	Mo(1)–O(100)	1.729(5)
Mo(1)–O(12)	2.235(5)	Mo(1)–O(102)	1.887(2)
Mo(1)–O(101)	1.707(6)	Mo(1)–O(10)	1.944(5)
Mo(1)–O(102)	1.750(7)	Mo(1)–O(12)	2.248(5)
Mo(1)–N(11)	2.360(7)	Mo(1)–N(11)	2.355(6)
Mo(2)–O(1B)	1.904(5)	Cs(1)–O(12)[a]	3.048(6)
Mo(2)–O(20)	1.931(5)	Cs(1)–O(100)	3.066(5)
Mo(2)–O(21)	2.211(5)	Cs(1)–O(11)[b]	3.263(7)
Mo(2)–O(201)	1.725(6)	Cs(1)–O(100)[c]	2.986(5)
Mo(2)–O(202)	1.706(7)	Cs(1)–O(101)[c]	3.287(5)
Mo(2)–N(21)	2.343(6)	Cs(1)–O(11)[d]	3.099(6)
Na(1)–O(2W)	2.511(7)		
Na(1)–O(3W)	2.277(13)		
Na(1)–O(21)	2.511(7)		
Na(1)–O(22)	2.567(7)		
Na(1)–O(22)[e]	2.476(6)		
Na(1)–O(102)[e]	3.409(7)		
Na(2)–O(1W)	2.300(12)		
Na(2)–O(2W)	2.367(8)		
Na(2)–O(12)	2.395(7)		
Na(2)–O(102)	2.726(8)		
Na(2)–O(22)[e]	2.319(7)		

[a] Symmetry transformations used to generate equivalent atoms: a: 1 – *x*, *y*, 1/2 – *z*; b: 1 – *x*, –*y*, –*z*; c: *x*, –*y*, –1/2 + *z*; d: *x*, –*y*, 1/2 + *z*; e: 2 – *x*, 1 – *y*, –*z*.

tained free of charge from The Cambridge Crystallographic Data Centre via www.ccdc.cam.ac.uk/data_request/cif.

Acknowledgments

This work was funded by DST, Government of India, New Delhi. The single crystal XRD facility was provided by DST under the FIST Program.

[1] a) X. Sun, D. W. Johson, D. L. Caulder, R. E. Powers, K. N. Raymond, E. H. Wong, *Angew. Chem. Int. Ed.* **1999**, *38*, 1303–1307; b) X. Sun, D. W. Johnson, D. L. Caulder, K. N. Raymond, E. H. Wong, *J. Am. Chem. Soc.* **2001**, *123*, 2752–2763; c) X. Sun, D. W. Johnson, K. N. Raymond, E. H. Wong, *Inorg. Chem.* **2001**, *40*, 4504–4506.

[2] K. Fukaya, T. Yamase, *Angew. Chem. Int. Ed.* **2003**, *42*, 654–658.

[3] a) X. Lin, D. M. J. Doble, A. J. Blake, A. Harrison, C. Wilson, M. Schroder, *J. Am. Chem. Soc.* **2003**, *125*, 9476–9483; b) S. M. Contakes, T. B. Rauchfuss, *Chem. Commun.* **2001**, 553–554; c) S. Noro, H. Miyasaka, S. Kitagawa, T. Wada, T. Okubo, M. Yamashita, T. Mitani, *Inorg. Chem.* **2005**, *44*, 133–146; d) K. Yaum, S. Huh, Y. J. Park, S. Park, M. Choi, M. Jun, *Chem. Commun.* **2004**, 2384–2385;

[4] a) *Polyoxometalates: From Platonic Solids to Anti-Retroviral Activity* (Eds.: M. T. Pope, A. Müller), Kluwer Academic Publishers, Dordrecht, The Netherlands, **1994**; b) A. Müller, E. Krickmeyer, H. Bogge, M. Schmidtmann, B. Botar, M. O. Talsimanova, *Angew. Chem. Int. Ed.* **2003**, *42*, 2085–2090; c) Y. Wong, Y. Yan, E. H. Chan, Q. Yang, T. W. Mak, D. P. Ng, *J. Chem. Soc. Dalton Trans.* **1998**, 3057–3064.

[5] a) D. Hergman, P. Hergman, J. Zubieta, *Angew. Chem. Int. Ed.* **1999**, *38*, 3165–3168; b) P. Hagrman, D. Hagrman, J. Zubieta, *Angew. Chem. Int. Ed.* **1999**, *38*, 2638–2684; c) B. J. S. Johnson, S. A. Geers, W. W. Brennessel, V. G. Young Jr., A. Stein, *Dalton Trans.* **2003**, 4678–4681; d) R. S. Rarig Jr., J. Zubieta, *J. Chem. Soc. Dalton Trans.* **2001**, 3446–3452.

[6] Q. Chen, J. Zubieta, *Coord. Chem. Rev.* **1992**, *114*, 107–167.

[7] a) W. Yang, C. Lu, X. Lin, H. Zhung, *Inorg. Chem.* **2002**, *41*, 452–454; b) V. Shivaiah, M. Nagaraju, S. K. Das, *Inorg. Chem.* **2003**, *42*, 6604–6606.

[8] M. Driess, H. Pritzkow, M. Skipinski, U. Winkler, *J. Am. Chem. Soc.* **1998**, *120*, 10774 –10775.

[9] a) S. A. Driscoll, U. S. Ozkan, *J. Phys. Chem.* **1993**, *97*, 11524–11529; b) A. Erdohelyi, K. Fodor, R. Nemeth, A. Hancz, A. Oszko, *J. Catal.* **2001**, *199*, 328–337.

[10] G. M. Sheldrick, *Program for solution and refinement of crystal structures*, University of Göttingen, Germany, **1997**.

Received: July 6, 2005
Published Online: November 2, 2005

 © 2005 Wiley-VCH Verlag GmbH & Co. KGaA, Weinheim

DOI: 10.1002/ejic.200500306

Palladium-Catalysed Amination Reactions Using Cobalt-Containing Bulky Phosphane Ligands

Jian-Cheng Lee,[a] Ming-Gin Wang,[a] and Fung-E. Hong*[a]

Keywords: Amination / Palladium / Cobalt complexes / Phosphane ligands / Orthometallation

Aminations of aryl bromides by morpholine have been investigated using palladium complexes as catalyst precursors modified by the cobalt-containing phosphane ligand [(μ-$PPh_2CH_2PPh_2$)$Co_2(CO)_4$][μ,η-PhC≡CP(*t*Bu)$_2$] (**1**). Reactions were carried out under various conditions with satisfactory results. The components of the optimised reaction conditions consist of 1.0 mmol of aryl bromide, 1.2 equiv. of morpholine, 1.4 equiv. of NaO*t*Bu, 1 mL of toluene and 1 mol-% of a 1:1 mixture of **1** and $Pd(OAc)_2$. In contrast, related aminations using [(μ-$PPh_2CH_2PPh_2$)$Co_2(CO)_4$][μ,η-pyC≡CP(*t*Bu)$_2$] (**2**), [(μ-$PPh_2CH_2PPh_2$)$Co_2(CO)_4$][{μ,η-PhC≡CP(cy)$_2$}] (**3**) and [(μ-$PPh_2CH_2PPh_2$)$Co_2(CO)_4$][μ,η-PhC≡CP(*i*Pr)$_2$] (**4**) as phosphane ligands do not exhibit comparable efficiency. A novel palladium complex **5**, i.e. Pd(OAc) chelated by deprotonated **1** was obtained from the reaction of **1** with $Pd(OAc)_2$. As revealed by the crystal structure, an orthometallation process occurs between the phenyl ring of **1** and the palladium ion. Presumably, the process is accompanied by release of one equivalent of acetic acid. The coordinated acetate ligand binds to the palladium ion in a bidentate chelating mode.
(© Wiley-VCH Verlag GmbH & Co. KGaA, 69451 Weinheim, Germany, 2005)

Introduction

The amination of aryl halides by a phosphane-coordinated palladium catalyst is a much more superior method for the preparation of aromatic amines than the original methods using tin amides.[1] Clearly, it is neither ecologically friendly nor practical to use stoichiometric amounts of tin amides in the amination reaction. Recently, momentous improvements have been achieved by Buchwald[2] and Hartwig[3] in the catalytic amination of aryl bromides using free amines. Based on their extensive investigations into this subject, a well accepted mechanism has now been proposed.[4] Recently, a second-generation of much more efficient catalysts for aminations was introduced by Buchwald[5] and Hartwig.[6] These are palladium complexes chelated by biphosphane ligands such as 1,1′-bis(diphenylphosphanyl)ferrocene (dppf) or BINAP. As is known for transition-metal-complex-assisted catalytic reactions, the rate of the reductive elimination process is normally enhanced by employing a bulky ligand such as dppf. Lately, because of their bulky nature, the use of using metal-containing phosphanes in transition-metal catalysed reactions has received increasing attention.[7] In particular, we were interested in exploiting a new type of metal-containing phosphane ligand which would allow us to gain direct access to a family of phosphanes which would hopefully be electron-rich and bulky in character.[7,8] As a result, a new family of novel cobalt-containing (mono- or bidentate) phosphanes has been prepared and their catalytic efficiencies in phosphane modified, palladium-catalysed reactions have been evaluated.[9] It was also found that in most of the phosphane assisted cases, the catalytic efficiencies are higher when using monodentate rather than bidentate phosphanes. Among the monodentate phosphane ligands possible, a series of organometallic versions of tris(alkylphosphanes), [(μ-$PPh_2CH_2PPh_2$)$Co_2(CO)_4$][μ,η-$R^2C{\equiv}CPR^1{}_2$] (**1**: R^1 = *t*Bu, R^2 = Ph; **2**: R^1 = *t*Bu, R^2 = py; **3**:[9a] R^1 = Cy, R^2 = Ph; **4**: R^1 = *i*Pr, R^2 = Ph), were chosen and used in palladium-catalysed amination reactions (Scheme 1). Results of a careful examination of the amination reactions catalysed by $Pd(OAc)_2$ complexes chelated with **1**, **2**, **3** or **4** are reported in this paper. Following this, the efficiencies of these ligands in the reactions are compared and discussed.

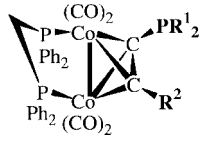

1: R^1 = *t*Bu, R^2 = Ph
2: R^1 = *t*Bu, R^2 = py
3: R^1 = Cy, R^2 = Ph
4: R^1 = *i*Pr, R^2 = Ph

Scheme 1.

Results and Discussion

Amination Reactions Using Palladium Complexes Chelated by the Cobalt-Containing Phosphane Ligands 1, 2, 3 and 4

Amination reactions of bromobenzene by morpholine were carried out using palladium complexes chelated by the

[a] Department of Chemistry, National Chung Hsing University, Taichung 40227, Taiwan
E-mail: fehong@dragon.nchu.edu.tw

 © 2005 Wiley-VCH Verlag GmbH & Co. KgaA, Weinheim

cobalt-containing phosphane ligands **1**, **2**, **3** or **4** as the catalyst precursors (Scheme 2).

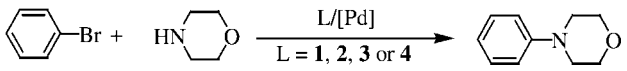

Scheme 2.

The general procedure for the catalytic reactions under investigation is as follows. A suitable Schlenk tube was first charged with 1.0 mmol of bromobenzene, 1.2 equiv. of morpholine, 1.4 equiv. of NaO*t*Bu, 1 mL of toluene and 1 mol-% of **1**/$Pd(OAc)_2$. The reaction mixture was then stirred at either 40 °C or 60 °C for 2 to 24 h depending on the reaction under investigation. The results are shown below (Table 1). Excellent yields (>99%) were obtained when the reaction was carried out at 60 °C for 20 h or more (entries 2 and 3). As shown, the reactions reach a satisfactory yield after about 4 h (entry 7). An induction period is obviously needed before the reaction reaches a reasonable rate (entry 8). Similar reactions were carried out employing **2**/$Pd(OAc)_2$ as the catalyst precursor. However, a reduction in the efficiency of the catalysis was observed using this L/Pd combination.

Table 1. Amination reactions employing **1**/$Pd(OAc)_2$ or **2**/$Pd(OAc)_2$ as the catalyst at various temperatures and reaction times.

Entry	Time (h)	Temp. (°C)	Yield (%) (L = **1**)[a]	Yield (%) (L = **2**)[b]
1	24	40	67	–
2	24	60	>99	80
3	20	60	>99	–
4	16	60	93	–
5	12	60	94	82
6	8	60	95	–
7	4	60	94	72
8	2	60	52	–

[a] Reaction conditions: 1.0 equiv. of bromobenzene, 1.2 equiv. of morpholine, 1.4 equiv. of base, 1 mL of solvent and 1 mol-% **1**/$Pd(OAc)_2$. Average of two runs. Determined by gas chromatography. [b] 1 mol-% **2**/$Pd(OAc)_2$.

Compound **2** was synthesised according to the procedure shown in the Experimental Section. The identity of **2** was established by spectroscopic means as well as by X-ray diffraction methods. Two distinct chemical shifts at δ = 3.04 and 4.26 ppm were observed for the methylenic protons of **2** by ^{1}H NMR spectroscopy. Large differences in the shifts imply that the back-and-forth motion of the bridging dppm group around the dicobalt fragment is rather slow. The ^{31}P NMR spectrum displays two singlets in a ratio of 2:1 at δ = 39.03 ppm (2 P, dppm) and 42.74 ppm (1P), respectively, for three phosphorus atoms. The ORTEP diagram for **2** is depicted in Figure 1. As revealed from the structure, the pyridyl ring and the phosphanyl group of the bridged alkyne point away from the centre of the molecule to prevent severe steric hindrance. This situation is also true for the coordinated dppm ligand and the P(*t*Bu)$_2$ substituent. All four carbonyls are located at the terminal positions.

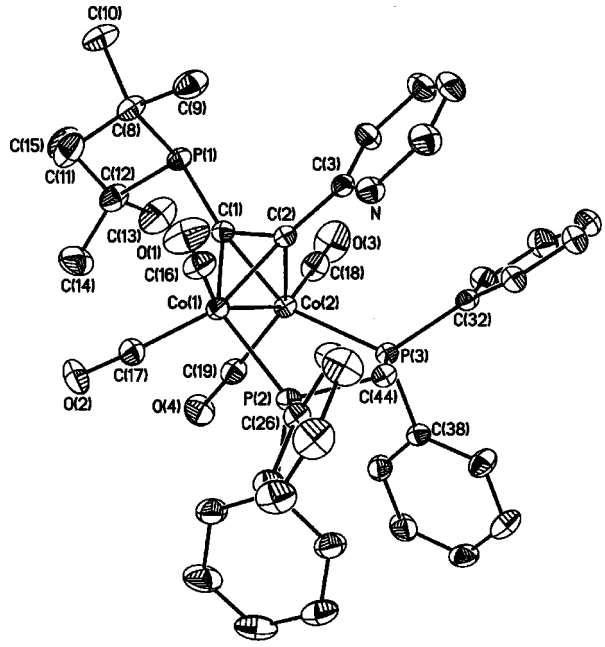

Figure 1. Diagram of **2**. Hydrogen atoms are omitted for clarity. Selected bond lengths [Å] and bond angles [°]: Co(1)–C(2) 1.946(2); Co(1)–C(1) 2.007(2); Co(1)–P(2) 2.2267(8); Co(1)–Co(2) 2.4876(5); Co(2)–C(2) 1.957(2); Co(2)–C(1) 1.998(3); Co(2)–P(3) 2.2415(8); P(1)–C(1) 1.809(3); P(2)–C(44) 1.828(3); P(3)–C(44) 1.828(3); N–C(3) 1.340(3); C(1)–C(2) 1.359(3); C(2)–C(3) 1.470(4); C(2)–Co(1)–C(1) 40.17(10); C(1)–Co(1)–P(2) 138.98(8); C(1)–Co(1)–Co(2) 51.43(7); C(2)–Co(2)–C(1) 40.17(10); C(1)–Co(2)–P(3) 131.70(8); C(1)–Co(2)–Co(1) 51.76(7); C(2)–C(1)–P(1) 132.4(2); Co(2)–C(1)–Co(1) 76.81(9); C(1)–C(2)–C(3) 136.5(2); Co(1)–C(2)–Co(2) 79.18(9); N–C(3)–C(2) 118.2(2); P(3)–C(44)–P(2) 109.79(15).

For comparison, similar reactions were carried out using $Pd(OAc)_2$ complexes chelated with **3** or **4** as catalyst precursors. In these cases, higher reaction temperatures of 80 °C and longer reaction times of 16 h were required for the reactions to be reasonably efficient. Generally speaking, amination reactions carried out employing **3**- or **4**/$Pd(OAc)_2$ as the catalytic systems are not as effective as those based on **1**/$Pd(OAc)_2$ (Table 2). These experimental observations are consistent with the commonly accepted idea that a phosphane ligand with bulky *t*Bu substituents is generally more efficient than that with a less bulky Cy or *i*Pr group.[8a,10]

Table 2. Reactions employing **3**/$Pd(OAc)_2$ or **4**/$Pd(OAc)_2$ as a catalyst at various reaction temperatures and times.

Entry	Time (h)	Temp. (°C)	Yield (%) (L = **3**)[a]	Yield (%) (L = **4**)[b]
1	4	60	20	–
2	6	60	21	–
3	6	80	52	25
4	8	80	53	31
5	10	80	62	47
6	14	80	74	62
7	16	80	85	82

[a] Reaction conditions: 1.0 equiv. of bromobenzene, 1.2 equiv. of morpholine, 1.4 equiv. of base, 1 mL of solvent and 1 mol-% **3**/$Pd(OAc)_2$. Average of two runs. Determined by gas chromatography. [b] 1 mol-% **4**/$Pd(OAc)_2$.

 © 2005 Wiley-VCH Verlag GmbH & Co. KGaA, Weinheim

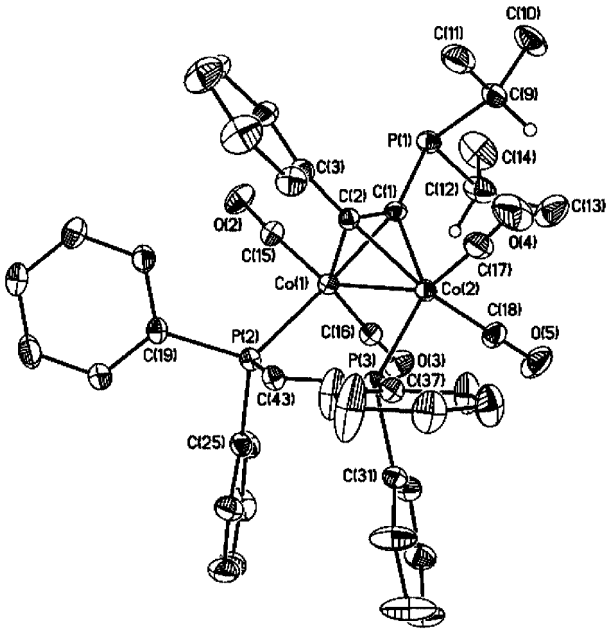

Figure 2. Diagram of **4**. Hydrogen atoms are omitted for clarity. Selected bond lengths [Å] and bond angles [°]: Co(1)–C(1) 1.959(4), Co(1)–C(2) 1.978(4), Co(1)–P(2) 2.2427(10), Co(1)–Co(2) 2.4896(7), Co(2)–C(2) 1.951(3), Co(2)–C(1) 1.984(3), Co(2)–P(3) 2.2253(10), P(1)–C(1) 1.795(3), P(2)–C(43) 1.841(3), P(3)–C(43) 1.840(4), C(1)–C(2) 1.351(5), C(2)–C(3) 1.478(5), C(1)–Co(1)–C(2) 40.13(14), C(1)–Co(1)–P(2) 139.80(11), C(2)–Co(1)–P(2) 101.18(10), C(1)–Co(1)–Co(2) 51.30(10), C(2)–Co(1)–Co(2) 50.21(10), P(2)–Co(1)–Co(2) 99.21(3), C(2)–Co(2)–C(1) 40.15(14), C(1)–Co(2)–P(3) 138.94(11), C(2)–Co(2)–Co(1) 51.17(10), C(1)–Co(2)–Co(1) 50.41(11), C(43)–P(2)–Co(1) 108.62(12), C(43)–P(3)–Co(2) 110.70(11), C(2)–C(1)–P(1) 137.7(3), C(2)–C(1)–Co(1) 70.7(2), C(2)–C(1)–Co(2) 68.6(2), P(1)–C(1)–Co(2) 142.8(2), Co(1)–C(1)–Co(2) 78.29(12), C(1)–C(2)–C(3) 137.1(3), C(1)–C(2)–Co(2) 71.2(2), C(1)–C(2)–Co(1) 69.2(2), Co(2)–C(2)–Co(1) 78.62(13), O(2)–C(15)–Co(1) 176.0(4), P(2)–C(43)–P(3) 110.73(18).

Compound **4** was prepared and characterised by spectroscopic means. Its crystal structure was also determined by X-ray diffraction methods (see below). In the ^{1}H NMR spectrum of **4**, two distinct chemical shifts at δ = 3.27 and 3.42 ppm were observed for the methylenic protons. In addition, the ^{31}P NMR spectrum displays two singlets in the ratio of 2:1 at δ = 37.89 ppm (2 P, dppm) and 23.48 ppm (1 P) for three phosphorus atoms. The ORTEP diagram for complex **4** is depicted in Figure 2. The structural features observed in **4** were similar to those observed for **2** except that the *i*Pr groups are not as bulky.

Amination reactions were carried out with various ratios of **1**/Pd(OAc)$_2$ or **3**/Pd(OAc)$_2$ under the reaction conditions shown below (Table 3). The optimum yield was achieved when the reaction was conducted with an NaO*t*Bu / toluent solvent system and a L/Pd(OAc)$_2$ ratio of 1:1 (Table 3, entry 3). The positive role played by the phosphane ligand in the reaction can be clearly seen. No conversion was observed without the presence of phosphane (Table 3, entry 6). Again, better efficiency was obtained by employing **1**/Pd(OAc)$_2$.

Table 3. Reactions employing various ratios of Pd(OAc)$_2$/L.

Entry	L/Pd(OAc)$_2$	Yield (%) (L = **1**)[a]	Yield (%) (L = **3**)[b]
1	2:1	36	54
2	1.5:1	73	62
3	1:1	94	85
4	0.5:1	88	71
5	0.1:1	57	23
6	0:1	0	0

[a] Reaction conditions: 1.0 equiv. of bromobenzene, 1.2 equiv. of morpholine, 1.4 equiv. of NaO*t*Bu, 1 mL of toluene and **1**/Pd(OAc)$_2$ at 60 °C for 4 h. Average of two runs. Determined by gas chromatography. [b] **3**/Pd(OAc)$_2$ at 80 °C for 16 h.

As has been established, a well chosen base/solvent system is essential for the success of an efficient palladium-catalysed coupling reaction. As a consequence, amination reactions of bromobenzene by morpholine employing **1**- or **3**/Pd(OAc)$_2$ as the catalyst precursor with various base/solvent systems were carried out at 60 °C for 4 h (Table 4). As shown, the best base/solvent composition is NaO*t*Bu/toluene (entry 1). This may be partially due to the reductive capacity of NaO*t*Bu in toluene.[11]

Amination reactions of bromobenzene by morpholine employing **1** with various Pd sources in a NaO*t*Bu/toluene system were carried out at 60 °C for 4 h (Table 5). As shown, excellent yields were obtained using Pd(OAc)$_2$ or [(η^3-C$_3$H$_5$)PdCl]$_2$ as palladium sources (entries 1 and 6) and this was true using **1** or **3** as the ligand. However, while the [(η^3-C$_3$H$_5$)PdCl]$_2$ system exhibits good catalytic efficiency, the complex is not suitable for use because of its air-sensitivity. Interestingly, no product was detectable when using PdCl$_2$ as the palladium source (entry 2).

Table 4. Reactions employing Pd(OAc)$_2$/L with various bases and solvents.

Entry	Pd/Ligand	Base	L = **1**[a]		L = **3**[b]	
			Solvent	Yield (%)	Solvent	Yield (%)
1	1:1	NaO*t*Bu	toluene	94	toluene	85
2	1:1	NaO*t*Bu	THF	67	–	–
3	1:1	NaO*t*Bu	DME	30	DME	37
4	1:1	NaO*t*Bu	–	–	DMF	23
5	1:1	KO*t*Bu	toluene	3	toluene	24
6	1:1	KOH	toluene	≈ 1	toluene	0
7	1:1	NaOH	toluene	4	toluene	13
8	1:1	Cs$_2$(CO)$_3$	toluene	0	toluene	8
9	1:1	K$_3$PO$_4$	toluene	0	toluene	0

[a] Reaction conditions: 1.0 equiv. of bromobenzene, 1.2 equiv. of morpholine, 1.4 equiv. of base, 1 mL of solvent and 1 mol-% **1**/Pd(OAc)$_2$ at 60 °C for 4 h. Average of two runs. Determined by gas chromatography. [b] 1 mol-% **3**/Pd(OAc)$_2$ at 80 °C for 16 h.

 © 2005 Wiley-VCH Verlag GmbH & Co. KGaA, Weinheim

Table 5. Reactions employing various Pd sources.

Entry	Pd source	Yield (%) (L = **1**)[a]	Yield (%) (L = **3**)[b]
1	$Pd(OAc)_2$	94	85
2	$PdCl_2$	0	0
3	$Pd(COD)Cl_2$	19	75
4	$PdCl_2(CH_3CN)_2$	59	68
5	$Pd_2(dba)_3$	2	28
6	$[(\eta^3\text{-}C_3H_5)PdCl]_2$	94	90

[a] Reaction conditions: 1.0 equiv. of bromobenzene, 1.2 equiv. of morpholine, 1.4 equiv. of NaO*t*Bu, 1 mL toluene and 1 mol-% **1**/$Pd(OAc)_2$ at 60 °C for 4 h. Average of two runs. Determined by gas chromatography. [b] 1 mol-% **3**/$Pd(OAc)_2$ at 80 °C for 16 h.

It has been commonly observed that a better conversion may be reached for an aryl halide with an electron-withdrawing rather than an electron-donating substituent in a palladium-catalysed coupling reaction.[8c] Amination reactions employing **1**/$Pd(OAc)_2$ and aryl bromides, with various electron-withdrawing/donating capacities in a NaO*t*Bu /toluene system were carried out at 60 °C for 4 h (Table 6). The best yield was obtained for aryl halides with an electron-withdrawing group which is in agreement with the common observation for palladium-catalysed coupling reactions (entry 6). Similar trends were observed when employing **3**/$Pd(OAc)_2$ or **4**/$Pd(OAc)_2$ as the catalyst precursor (Table 6). Interestingly, in our previous work using **4**/$Pd(OAc)_2$ as a catalyst precursor in Suzuki reactions, the catalytic efficiency was rather poor. Nevertheless, the efficiency was comparable with that using **1**- or **2**/$Pd(OAc)_2$ as a precursor in amination reactions.

Table 6. Reactions of various aryl bromides employing L/$Pd(OAc)_2$.

Entry	Substrate	Yield (%) (L = 1)[a]	Yield (%) (L = 3)[b]	Yield (%) (L = 4)[c]
1	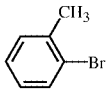	27	28	17
2	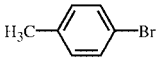	68	66	67
3	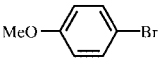	95	62	68
4	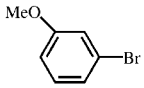	80	70	42
5	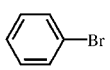	94	85	82
6	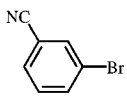	99	80	81

[a] Reaction conditions: 1.0 equiv. of bromobenzene, 1.2 equiv. of morpholine, 1.4 equiv. of NaO*t*Bu, 1 mL of toluene and 1 mol-% **1**/$Pd(OAc)_2$ at 60 °C for 4 h. Average of two runs. Isolated yield. [b] 1 mol-% **3**/$Pd(OAc)_2$ at 80 °C for 16 h. [c] 1 mol-% **4**/$Pd(OAc)_2$ at 80 °C for 16 h.

Characterisation of a Novel Deprotonated Palladium Complex Chelated with 1

Interestingly, a novel palladium complex **5**, namely Pd(OAc) chelated by deprotonated **1**, was obtained from the reaction of **1** with $Pd(OAc)_2$ in toluene at 25 °C for 1 h (Scheme 3). Compound **5** was characterised by spectroscopic means and its crystal structure was determined by X-ray diffraction (Table 7). As revealed by its crystal structure, a process of orthometallation must have occurred which was presumably accompanied by the release of one equiv. of acetic acid (Figure 3). The acetate ligand is coordinated to the palladium through a bidentate chelating mode.[12] The palladium metal centre is in a square planar environment. Two bulky units, $P(t\text{Bu})_2$ and dppm, are in *anti* positions. There is one diethyl ether molecule in each asymmetric unit. As has been established, most acetate palladium complexes are dimeric with two acetates bridging two palladium ions. We believe that the formation of this exceptional monomeric structure of **5** is due to the unique bulkiness and bonding mode of ligand **1**. A rather downfield ^{31}P NMR shift at δ = 91.6 ppm was observed which we assigned to the corresponding palladium attached phosphorus site. A triplet signal was observed in the ^1H NMR spectrum corresponding to the two methylenic protons of the coordinated dppm. This implies that the coordinated dppm is in a rapid back-and-forth thermal motion. All these spectroscopic data are consistent with the data obtained from the solid-state structure. The crystal structure of **5** also demonstrates that only one molar equivalent of phosphane ligand is needed for effective coordination to a palladium ion. For a conventional PR_3 (R: alkyl or aryl), two or even three ligands are required to sustain a stable palladium complex.

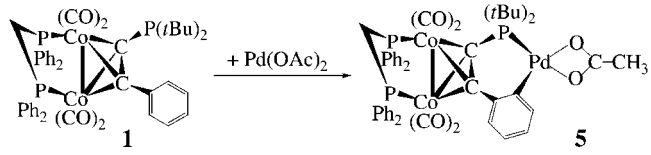

Scheme 3.

Table 7. Amination reactions employing **5** as catalyst.[a]

Entry	**5**/Substrate (mol-%)	Yield (%)
1	0.5	40
2	1	78
3	1.5	>99

[a] Reaction conditions: 1.0 equiv. of aryl halide, 1.2 equiv. of morpholine, 1.4 equiv. of NaO*t*Bu, 1 mL of toluene at 60 °C for 4 h. Average of two runs. Determined by gas chromatography.

Buchwald has proposed a phosphane ligand coordinated palladium complex **6** as an active species in one of the palladium-catalysed amination reactions.[13] However, nothing further was stated about the bonding mode of the acetate ligand in **6** probably because its crystal structure was not established. By comparing **5** and **6**, the structural similarities for these two compounds are clear (Scheme 4). The

 © 2005 Wiley-VCH Verlag GmbH & Co. KGaA, Weinheim

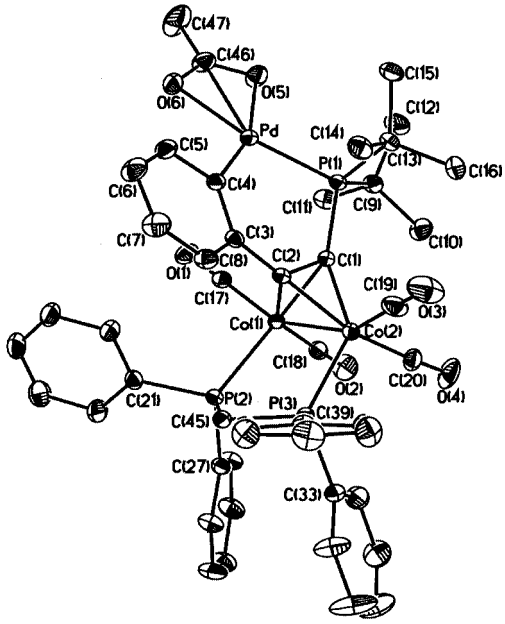

Figure 3. Diagram of **5**. Hydrogen atoms are omitted for clarity. Selected bond lengths [Å] and angles [°]: Pd–C(4) 2.001(4), Pd–O(5) 2.163(3), Pd–O(6) 2.171(3), Pd–P(1) 2.2182(11), Pd–C(46) 2.509(5), Co(2)–C(1) 1.970(4), Co(2)–P(3) 2.2241(11), Co(2)–Co(1) 2.4764(8), Co(1)–C(2) 1.969(4), Co(1)–C(1) 1.968(4), P(1)–C(1) 1.778(3), O(6)–C(46) 1.240(6), O(5)–C(46) 1.266(7), C(46)–C(47) 1.495(8), C(3)–C(4) 1.405(6), C(3)–C(2) 1.460(5), C(5)–C(4) 1.396(6), C(1)–C(2) 1.362(5), C(4)–Pd–O(5) 161.12(15), C(4)–Pd–O(6) 101.56(15), O(5)–Pd–O(6) 59.92(14), C(4)–Pd–P(1) 92.04(12), O(5)–Pd–P(1) 106.48(11), O(6)–Pd–P(1) 166.39(10), C(2)–Co(2)–C(1) 40.76(15), C(2)–Co(1)–C(1) 40.48(15), C(1)–P(1)–Pd 108.10(13), C(46)–O(6)–Pd 90.5(3), C(46)–O(5)–Pd 90.2(3), O(5)–C(46)–O(6) 119.4(4), C(47)–C(46)–Pd 177.4(6), C(4)–C(3)–C(2) 119.5(3), C(2)–C(1)–P(1) 121.8(3), C(1)–C(2)–C(3) 130.6(3), C(5)–C(4)–C(3) 117.8(4), C(5)–C(4)–Pd 111.1(3), C(3)–C(4)–Pd 131.1(3).

newly characterised compound **5** can be regarded as a more complicated, metal-containing version of **6**.

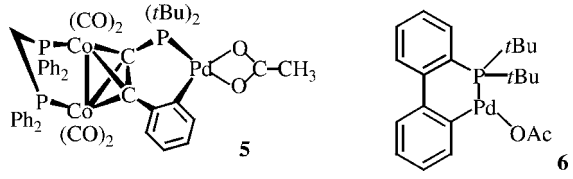

Scheme 4.

Complex **5** was employed as the Pd source for the aminations of bromobenzene by morpholine. Reactions were carried out in an NaO*t*Bu/toluene phase at 60 °C for 4 h (Table 7). The catalytic efficiency of the reaction employing complex **5** is clearly not as good as that carried out in situ (Table 1, entry 7 vs. Table 7, entry 2). It indicates that complex **5** is not a genuinely catalytically active species. Rather, complex **5** could be regarded as the precursor to a genuine catalytically active Pd^0 species. It still requires a reduction process to convert the Pd^{II} to the more active Pd^0 species.[14] Furthermore, the catalytic efficiency could be greatly improved by increasing the molar ratio of **5** (Table 7, entry 3).

For comparison, amination reactions of aryl bromides bearing various electron-withdrawing/electron-donating substituents, with morpholine, employing **5** in a NaO*t*Bu/toluene system, were carried out at 60 °C for 4 h (Table 8). Generally speaking, the efficiencies are lower for **5** than for **1**/$Pd(OAc)_2$ (Table 6 vs. Table 8). The best yield was found in the case of the aryl bromide with an electron-withdrawing group (entry 6).

Table 8. Reactions of various aryl bromides employing **5**.[a]

Entry	Substrate	Yield (%)
1	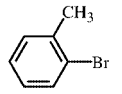	23
2	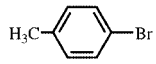	64
3	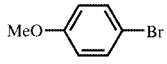	77
4	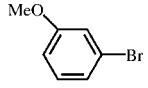	78
5	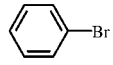	80
6	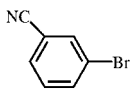	94

[a] Reaction conditions: 1.0 equiv. of aryl halide, 1.2 equiv. of morpholine, 1.4 equiv. of base and 1 mL of solvent. Average of two runs. Isolated yield.

Concluding Remarks

We have demonstrated that the amination reactions of aryl bromides by morpholine can be carried out catalytically with palladium complexes modified with a novel cobalt-containing phosphane ligand **1**. The catalytic performance is best with a **1**/$Pd(OAc)_2$ ratio of 1:1. The same reactions may also be carried out using palladium complexes modified with **2**, **3** or **4** but with reduced efficiency.

A novel palladium complex **5** was obtained from the reaction of **1** with $Pd(OAc)_2$. As revealed by the crystal structure, a process of orthometallation occurs presumably accompanied by the release of one equiv. of acetic acid. We propose that **5** could be the precursor to the true catalytically active Pd^0 species.

Experimental Section

Synthesis of (μ-$PPh_2CH_2PPh_2$)$Co_2(CO)_4$[μ,η-PyC≡CP(*t*Bu)$_2$] (2): Dicobalt octacarbonyl $Co_2(CO)_8$ (1.00 mmol, 0.34 g), dppm (1.00 mmol, 0.38 g) and toluene (10 mL) were placed in a 100 mL capacity round flask charged with a magnetic stirrer. The solution was stirred at 65 °C for 6 h and a yellow coloured compound, $Co_2(CO)_6$(μ-P,P-dppm), was produced. Without further separation, the reaction flask was then charged with one equiv. of

 © 2005 Wiley-VCH Verlag GmbH & Co. KGaA, Weinheim

PyC≡CP(tBu)$_2$ (0.25 g) in toluene (5 mL). Subsequently, the solution was stirred at 80 °C for 16 h before the solvent was removed under reduced pressure. The residue was further separated by CTLC. A dark green coloured band was eluted using a mixed solvent mobile phase (CH_2Cl_2/hexane, 1:3) and was identified as **2**. The yield was 72% (0.62 g, 0.72 mmol). ^{1}H NMR ($CDCl_3$): δ = 6.90–8.50 (m, 24 H, arene), 3.04 (q, 1 H, dppm), 4.26 (q, 1 H, dppm), 1.23 ppm [d, 18 H, P(tBu)$_2$]. ^{31}P NMR ($CDCl_3$): δ = 39.03 (s, 2 P, dppm), 42.74 ppm [s, 1 P, P(tBu)$_2$]. ^{13}C NMR ($CDCl_3$): δ = 127.86–133.07 (29 C, arene), 30.43 ppm (1 C, dppm). $C_{44}H_{44}Co_2NO_4P_3$: calcd. C 60.91, H 5.11; found C 61.34, H 5.15. MS (EI): m/z = 862 [M]$^+$

Synthesis of (μ-PPh$_2$CH$_2$PPh$_2$)Co$_2$(CO)$_4$[μ,η-PyC≡CP(iPr)$_2$] 4: Dicobalt octacarbonyl, $Co_2(CO)_8$ (1.00 mmol, 0.34 g), dppm (1.00 mmol, 0.39 g) and toluene (10 mL) were placed in a 100 mL capacity round flask containing a magnetic stirrer. The solution was stirred at 65 °C for 6 h during which time a yellow coloured compound, $Co_2(CO)_6$(μ-P,P-dppm), was formed. Without further separation, the reaction flask was charged with one equiv. of PyC≡CP(iPr)$_2$ (0.22 g) in toluene (5 mL) and the solution was then stirred at 80 °C for 16 h. The solvent was removed under reduced pressure and the resultant dark red coloured residue was separated by CTLC. A dark red band was eluted out using mixed solvent mobile phase (CH_2Cl_2: hexane = 1:3) and the compound was identified as **4**. The yield was 82.0% (0.69 g, 0.82 mmol). ^{1}H NMR ($CDCl_3$): δ = 7.77–7.00 (m, 25 H, arene), 3.27–3.42 (d, 2 H, CH_2), 2.23–2.25 (m, 2 H), 1.23–1.43 ppm [m,12 H, P(iPr)$_2$]. ^{31}P NMR ($CDCl_3$): δ = 37.89 (s, 2 P, dppm), 23.48 ppm [s, 1 P, P(iPr)$_2$]. $C_{43}H_{41}Co_2O_4P_3$: calcd. C 61.95, H 4.90; found: C 62.03, H 4.96.

Synthesis of [(μ-PPh$_2$CH$_2$PPh$_2$)Co$_2$(CO)$_4${μ,η-PhC≡CP(tBu)$_2$}]-PdOAc (5): The two reactants, Pd(OAc)$_2$ (1.00 mmol, 0.22 g) and [(μ-PPh$_2$CH$_2$PPh$_2$)Co$_2$(CO)$_4${μ,η-PhC≡CP(tBu)$_2$}] **1** (1.00 mmol, 0.86 g) were placed in a 100-mL round-bottomed flask charged with a magnetic stirrer and toluene (5 mL). The solution was stirred at 25 °C for 1 h before the solvent was removed in vacuo. The crude material was further purified by CTLC. A red-brown band was eluted with CH_2Cl_2 and was identified as **5**. The yield was 80% (0.82 g, 0.80 mmol). ^{1}H NMR ($CDCl_3$): δ = 7.54–6.92 (24 H, arene), 3.30 (t, J_{PH} = 10.2 Hz, 2 H, CH_2), 1.53 ppm (d, J_{PH} = 7 Hz, 18 H, tBu). ^{13}C NMR ($CDCl_3$): δ = 137.16–124.92 (30 C, arene), 41.32 (t, 1 C, CH_2), 38.93 [d, 2 C, -C(CH$_3$)$_3$], 30.55 [d, 6 C, -C(CH$_3$)$_3$], 67.97 ppm [s, 1 C, PhC≡CP(tBu)$_2$]. ^{31}P NMR ($CDCl_3$): δ = 38.8 (s, 2 P, dppm), 91.6 ppm [s, 1 P, P(tBu)$_2$]. MS (ESI): m/z = 1024 [M]$^+$. $C_{51}H_{57}Co_2O_7P_3Pd$: calcd. C 55.07, H 4.62; found: C 53.85, H 4.63.

Amination of Aryl Bromides

Method: An oven-dried Schlenk tube was charged with **1** (8.60 mg, 0.01 mmol), Pd(OAc)$_2$ (2.24 mg, 0.01 mmol) and base (1.4 mmol). The tube was evacuated, filled with nitrogen and then the aryl bromide (1.00 mmol), toluene (1 mL) and morpholine (1.20 mmol) were added. The tube was sealed with a Teflon screw cap and the mixture was stirred at 60 °C for 4 h. After all the starting materials had been consumed, the mixture was cooled to room temperature and was then diluted with diethyl ether (40 mL). The resultant suspension was transferred to a separating funnel and washed with water (10 mL). The organic layer was separated, dried with anhydrous $MgSO_4$ and concentrated in vacuo. The crude residue was purified by CTLC with a mixture of hexane/ethyl acetate as the mobile phase.

The couplings of morpholine with bromobenzene, 4-bromotoluene, 3-bromoanisole or 3-chloronitrobenzene were examined using the method. The isolated yields of the corresponding products, *N*-phenylmorpholine, *N*-(4-methyl)phenylmorpholine, *N*-(3-methoxyphenyl)morpholine and *N*-(3-nitrophenyl)morpholine were 94% (0.153 g), 68% (0.120 g), 80% (0.155 g) and 99% (0.206 g), respectively.

***N*-Phenylmorpholine:** ^{1}H NMR ($CDCl_3$): δ = 6.88–6.93, 7.25–7.30 (m, 5 H), 3.87 (t, 4 H, J = 2.4 Hz), 3.16 ppm (t, 4 H, J = 2.6 Hz).

***N*-(4-Methylphenyl)morpholine:** ^{1}H NMR ($CDCl_3$): δ = 3.10 (t, 4 H, J = 5 Hz), 3.86 (t, 4 H, J = 4.6 Hz), 6.83 (d, 2 H, J = 8.6 Hz), 7.10 ppm (d, 2 H, J = 8.4 Hz).

Table 9. Crystal data for **2**, **4** and **5**.

Compound	**2**	**4**	**5**
Formula	$C_{44}H_{44}Co_2NO_4P_3$	$C_{43}H_{41}Co_2O_4P_3$	$C_{51}H_{57}Co_2O_7P_3Pd$
Formula weight	861.57	832.53	1099.14
Crystal system	monoclinic	monoclinic	monoclinic
Space group	$P2_1/c$	$P2_1/c$	$P2_1/c$
a (Å)	13.8627(12)	16.0552(12)	13.6654(17)
b (Å)	14.1883(12)	11.6582(9)	17.291(2)
c (Å)	21.8278(19)	23.1912(18)	22.379(3)
α (°)	90	90	90
β (°)	96.748(2)	109.574(2)	102.903(2)
γ (°)	90	90	90
V (Å^3)	4263.5(6)	4089.9(5)	4858.2(14)
Z	4	4	4
D_c (Mg m^{-3})	1.342	1.352	1.416
λ (Mo-K_α) [Å]	0.71073	0.71073	0.71073
μ (mm^{-1})	0.932	0.968	1.122
θ range [°]	2.06 to 26.01	1.86 to 26.02	1.87 to 26.11
Observed reflections [$F > 4\sigma(F)$]	8354	8001	10219
No. of refined parameters	495	469	577
R_1 for significant reflections[a]	0.0373	0.0469	0.0429
wR_2 for significant reflections[b]	0.0852	0.1649	0.1494
GoF[c]	0.947	1.618	1.035

[a] $R_1 = |\Sigma(|F_o| - |F_c|)/|\Sigma F_o||$. [b] $wR_2 = \{\Sigma[w(F_o^2 - F_c^2)]^2/\Sigma[w(F_o^2)^2]\}^{1/2}$; w = 0.0497, 0.0731 and 0.1277 for **2**, **4** and **5**, respectively. [c] GoF = $[\Sigma w(F_o^2 - F_c^2)^2/(\text{number of reflections} - \text{number of parameters})]^{1/2}$.

 © 2005 Wiley-VCH Verlag GmbH & Co. KGaA, Weinheim

***N*-(3-Methoxyphenyl)morpholine:** ^{1}H NMR ($CDCl_3$): δ = 3.15 (t, 4 H, J = 2.4 Hz), 3.85 (t, 4 H, J = 2.4 Hz), 6.45 (d, 1 H, J = 3.6 Hz), 6.54 (d, 1 H, J = 4.0 Hz), 7.20 ppm (t, 2 H, J = 4.0 Hz).

***N*-(3-Nitrophenyl)morpholine:** ^{1}H NMR ($CDCl_3$): δ = 3.18 (t, 4 H, J = 2.4 Hz), 3.87 (t, 4 H, J = 2.4 Hz), 7.10–7.14 (m, 3 H), 7.34 ppm (t, 1 H, J = 3.8 Hz).

4-Methoxyphenylmorpholine: ^{1}H NMR ($CDCl_3$): δ = 6.84–6.91 (m, 4 H), 3.76 (s, 3 H), 3.78–3.87 (m, 4 H), 3.05–3.07 ppm (m, 4 H).

X-ray Crystallographic Studies: Suitable crystals of **2**, **4** and **5** were sealed in thin-walled glass capillaries under nitrogen and mounted on a Bruker AXS SMART 1000 diffractometer. Intensity data were collected from 1350 frames with increasing ω (width of 0.3° per frame). The absorption correction was based on the symmetry equivalent reflections using the SADABS program. The space group determination was based on a check of the Laue symmetry and systematic absences and was confirmed using the structure solution. The structure was solved by direct methods using the SHELXTL package.[15] All non-hydrogen atoms were located from successive Fourier maps and the hydrogen atoms were refined using a riding model. Anisotropic thermal parameters were used for all non-hydrogen atoms and fixed isotropic parameters were used for H atoms.[16] The crystallographic data of **2**, **4** and **5** are summarised in Table 9.

Crystallographic data for the structural analyses have been deposited with the Cambridge Crystallographic Data Centre. CCDC-261777, -261778 and -261779 for compounds **2**, **4** and **5**, respectively, contain the supplementary crystallographic data for this paper. These data can be obtained free of charge from The Cambridge Crystallographic Data Centre via www.ccdc.cam.ac.uk/data_request/cif.

Acknowledgments

We are grateful to the National Science Council of the R. O. C. (Grant NSC 93-2113-M-005-020) for financially supporting.

[1] M. Josugi, M. Kameyama, T. Migita, *Chem. Lett.* **1983**, 927–928.
[2] a) A. S. Guram, R. A. Rennels, S. L. Buchwald, *Angew. Chem. Int. Ed. Engl.* **1995**, *34*, 1348–1350; b) J. P. Wolfe, S. L. Buchwald, *J. Org. Chem.* **1996**, *61*, 1133–1135.
[3] J. Louie, J. F. Hartwig, *Tetrahedron Lett.* **1995**, *36*, 3609–3612.
[4] a) J. F. Hartwig, in: *Modern Amination Methods* (Ed.: A. Ricci), Wiley-VCH: Weinheim, Germany, **2000**.; b) R. A. Wiedenhoefer, H. A. Zhong, S. L. Buchwald, *Organometallics* **1996**, *15*, 2745–2754; c) J. Louie, F. Paul, J. F. Hartwig, *Organometallics* **1996**, *15*, 2794–2805; d) L. M. Aleazar-Roman, J. F. Hartwig, *J. Am. Chem. Soc.* **2001**, *123*, 12905–12906; e) U. Christmann, R. Vilar, *Angew. Chem. Int. Ed.* **2005**, *44*, 366–374.
[5] J. P. Wolfe, S. Wagaw, S. L. Buchwald, *J. Am. Chem. Soc.* **1996**, *118*, 7215–7216.
[6] M. S. Driver, J. F. Hartwig, *J. Am. Chem. Soc.* **1996**, *118*, 7217–7218.
[7] General reviews, see: a) O. Delacroix, J. A. Gladysz, *Chem. Commun.* **2003**, 665–675; b) A. Salzer, *Coord. Chem. Rev.* **2003**, *242*, 59–72.
[8] a) A. F. Littke, C. Dai, G. C. Fu, *J. Am. Chem. Soc.* **2000**, *122*, 4020–4028; b) G. Mann, J. F. Hartwig, *J. Am. Chem. Soc.* **1996**, *118*, 13109–13110; c) N. Kataoka, Q. Shelby, J. P. Stambuli, J. F. Hartwig, *J. Org. Chem.* **2002**, *67*, 5553–5566; d) J. G. Planas, J. A. Gladysz, *Inorg. Chem.* **2002**, *41*, 6947–6949; e) Q.-S. Hu, Y. Lu, Z.-Y. Tang, H.-B. Yu, *J. Am. Chem. Soc.* **2003**, *125*, 2856–2857; f) T. E. Pickett, F. X. Roca, C. J. Richards, *J. Org. Chem.* **2003**, *68*, 2592–2599; g) Z.-Y. Tang, Y. Lu, Q.-S. Hu, *Org. Lett.* **2003**, *5*, 297–300.
[9] a) F.-E. Hong, Y.-J. Ho, Y.-C. Chang, Y.-C. Lai, *Tetrahedron* **2004**, *60*, 2639–2645; b) F.-E. Hong, Y.-C. Chang, C.-P. Chang, Y.-L. Huang, *Dalton Trans.* **2004**, 157–165; c) F.-E. Hong, Y.-C. Lai, Y.-J. Ho, Y.-C. Chang, *J. Organomet. Chem.* **2003**, *688*, 161–167; d) F.-E. Hong, C.-P. Chang, Y.-C. Chang, *Dalton Trans.* **2003**, 3892–3897; e) F.-E. Hong, Y.-C. Chang, R.-E. Chang, S.-C. Chen, B.-T. Ko, *Organometallics* **2002**, *21*, 961–967.
[10] J. P. Wolfe, R. A. Singer, B. H. Yang, S. L. Buchwald, *J. Am. Chem. Soc.* **1999**, *121*, 9550–9561.
[11] L. M. Aleazar-Roman, J. F. Hartwig, A. L. Rheingold, L. M. Liable-Sands, I. A. Guzei, *J. Am. Chem. Soc.* **2000**, *122*, 4618–4630.
[12] S.-J. Lin, T.-N. Hong, J.-Y. Tung, J.-H. Chen, *Inorg. Chem.* **1997**, *36*, 3886–3891.
[13] D. Zim, S. L. Buchwald, *Org. Lett.* **2003**, *5*, 2413–2415.
[14] R. B. Bedford, C. S. J. Cazin, *Chem. Commun.* **2001**, 1540–1541.
[15] G. M. Sheldrick, *SHELXTL PLUS User's Manual*. Revision 4.1 Nicolet XRD Corporation, Madison, Wisconsin, USA, **1991**.
[16] The hydrogen atoms were allowed to ride on carbon atoms or oxygen atoms in their idealised positions and were held fixed with C–H distances of 0.96 Å.

Received: April 14, 2005
Published Online: November 2, 2005

 © 2005 Wiley-VCH Verlag GmbH & Co. KGaA, Weinheim

DOI: 10.1002/ejic.200500474

A Crystalline Phase Transition and Optical Properties in a $Co^{II}Cu^{II}$ Oxamato-Bridged Ferrimagnetic Chain

Cynthia L. M. Pereira,[a] Antonio C. Doriguetto,[b] Cibele Konzen,[c] Luiz C. Meira-Belo,[c] Ulisses A. Leitão,[d] Nelson G. Fernandes,[a] Yvonne P. Mascarenhas,[b] Javier Ellena,[b] Ana L. Brandl,[e] Marcelo Knobel,[e] and Humberto O. Stumpf*[a]

Keywords: Birefringence / Chain structures / Molecular magnetism / Phase transitions / Transition metals

The compound [CoCu(opba)$(DMSO)_3$] (**1**) [opba = *ortho*-phenylenebis(oxamato)] has been synthesized and characterized. Its crystal structure has been analyzed by X-ray diffraction techniques at 100 and 298 K. A structural phase-transition has been detected at around 150 K. An orthorhombic crystalline system is found at both temperatures, with very similar unit-cell dimensions. At room temperature **1** crystallizes in the *Pnam* space group (**α-1** phase), with a = 7.6712(2), b = 14.8003(3), c = 21.0028(5) Å, and Z = 4, whereas at low temperature it crystallizes in the $Pna2_1$ space group (**β-1** phase), with a = 7.3530(2), b = 14.5928(4), c = 21.0510(7) Å, and Z = 4. Both crystalline phases consist of linearly ordered bimetallic chains with the $[Cu(opba)]^{2-}$ units tied by Co^{II} ions to form a one-dimensional system. The DMSO molecules in **α-1**, which are coordinated to either Cu^{II} or Co^{II}, are disordered. At low temperature, a small reorganization of the Cu^{II} and Co^{II} environments is observed. The origin of this phase transition, which is completely reversible, is the modification of the crystalline packing with the temperature. Linear birefringence measurements were done on single crystals in the 100–300 K temperature range. Around 150 K, the linear birefringence curve shows an inflexion that is interpreted as being related to the conversion of **α-1** into **β-1**. Both dc and ac magnetic measurements were performed on the polycrystalline sample. The results reveal a one-dimensional ferrimagnetic behavior. Single crystal optical characterization at room temperature shows that **1** presents a very strong dichroism superposed on the linear birefringence.
(© Wiley-VCH Verlag GmbH & Co. KGaA, 69451 Weinheim, Germany, 2005)

Introduction

The first molecule-based magnets described were the organometallic compound $[Fe(Me_5Cp)_2][TCNE]$ (Me_5Cp = pentamethylcyclopentadienyl; TCNE = tetracyanoethylene)[1] and the chain $[MnCu(pbaOH)(H_2O)_3]$ [pbaOH = 2-hydroxy-1,3-propylenebis(oxamato)].[2] Since then, there has been a rapid development of this field of research, with special focus on the design of materials with predictable magnetic properties and potential technological applications.[3–5] In the last two decades, the chemistry of molecular magnetic materials has been widely exploited in two branches. In the first one, the key goal is to optimize the magnetic properties by increasing the Curie temperature, coercivity, spin transition, blocking temperature, or tunneling effects,[6–11] whereas in the second branch the focus is on aggregating other characteristics to the magnetic materials, such as optical properties or conductivity.[12–14] What these two branches have in common is the employment of molecular chemistry in a bottom-up strategy. Let us illustrate this using the oxamato-bridged system as an example. One of the first steps of this approach consists in synthesizing a building block like $[Cu(opba)]^{2-}$ [Figure 1; opba = *ortho*-phenylenebis(oxamato)].[15] This precursor possesses two lone pairs on either side of the peripheral oxygen atoms and therefore it may behave as a bis-bidentate ligand. The next stage is the choice of a metal ion whose characteristics must induce the production of a material with desirable properties. Supramolecular aspects can become very impor-

[a] Departamento de Química, ICEx, Universidade Federal de Minas Gerais,
Av. Antônio Carlos 6627, Pampulha, Belo Horizonte, MG, 31270-901, Brazil
Fax: +55-31-3499-5700
E-mail: stumpf@ufmg.br
[b] Instituto de Física de São Carlos, Universidade de São Paulo, C. P. 369, São Carlos, SP, 13560-970, Brazil
Fax: +55-16-273-9881
E-mail: dorigue@if.sc.usp.br
[c] Laboratório de Física Aplicada, Centro de Desenvolvimento da Tecnologia Nuclear,
C. P. 941, BH, MG, 30932-970, Brazil
Fax: +55-31-3499-3390
E-mail: lcmb@cdtn.br
[d] Departamento de Física, ICEx, Universidade Federal de Minas Gerais,
Av. Antônio Carlos 6627, Pampulha, BH, MG, 31270-901, Brazil
Fax: +55-31-3499-5700
E-mail: uli@fisica.ufmg.br
[e] Instituto de Física Gleb Wataghin, Universidade Estadual de Campinas,
C. P. 6165, 13083-970, Campinas, SP, Brazil
Fax: +55-19-3788-5480
E-mail: knobel@ifi.unicamp.br
Supporting information for this article is available on the WWW under http://www.eurjic.org or from the author.

 InterScience © 2005 Wiley-VCH Verlag GmbH & Co. KGaA, Weinheim

tant in this step. Besides the stoichiometric ratios, concentration, and counterion nature, the solvent can play a key role. Indeed, the first chain to be synthesized using this precursor was [MnCu(opba)$(DMSO)_3$], which was obtained in DMSO.[15] This compound has an unexpected zigzag chain structure with two DMSO molecules bound to the manganese atom in a *cis* fashion. [MnCu(opba)$(DMSO)_3$] is an almost perfect one-dimensional ferrimagnet where the chains are isolated by DMSO molecules in the crystalline packing. When the reaction is performed in a DMSO/H_2O mixture, the octahedral environment of the Mn^{II} is completed by two water molecules in *trans* positions and the product obtained, [MnCu(opba)$(H_2O)_2$]·DMSO, consists of linear chains.[16] In this latter compound, the chains interact weakly within the crystal lattice and the compound shows an antiferromagnetic transition with T_N = 5 K and metamagnetic behavior. By making some changes we can prepare 2D, graphite-like compounds with the general formula $[cat]_2[M_2\{Cu(opba)\}_3]$[15,17] or interlocked systems[6,18,19] where the counterion cat^+ is a nitronyl-nitroxide radical cation. Very recently, a new class of bidimensional metallacyclophane-based compounds $[Co_2Cu_2(mpba)_2(H_2O)_6]\cdot 6H_2O$ [mpba = *meta*-phenylenebis(oxamato)], which present a corrugated brick-wall structure, have been obtained.[20]

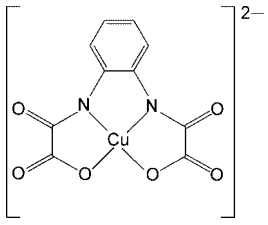

Figure 1. Building block $[Cu(opba)]^{2-}$.

The aim in preparing these 2D and 3D molecule-based systems was to increase the critical temperatures of the magnetic ordering. With the report of the [$Co(hfac)_2$NITPhOMe] nanowire, which shows slow relaxation of the magnetization and hysteretic effects, by Gatteschi et al.,[21] a renewed interest in linear systems has emerged. In this paper, we will describe the synthesis, structure, and magnetic and optical properties of the chain [CoCu(opba)$(DMSO)_3$] (**1**). Furthermore, a study of the linear birefringence measurements and single-crystal X-ray crystallography in order to confirm a temperature-induced crystalline phase-transition for **1** will be presented.

Results and Discussion

Crystal Structures of [CoCu(opba)$(DMSO)_3$] Phases

X-ray diffraction experiments were carried out at two different temperatures (298 and 100 K). The structures of **α-1** and **β-1** are shown in Figure 2. In both cases the structure consists of ordered infinite linear chains running along the *c* axis with adjacent Co^{II} and Cu^{II} ions bridged by oxamato groups. This compound does not have the zigzag structure of [MnCu(opba)$(DMSO)_3$];[15] it is more similar to the linear chain of [MnCu(opba)$(H_2O)_2$]·DMSO.[16] However, in contrast to this latter chain, the aromatic rings of **1** are alternately on one and the other side of the chain axis.

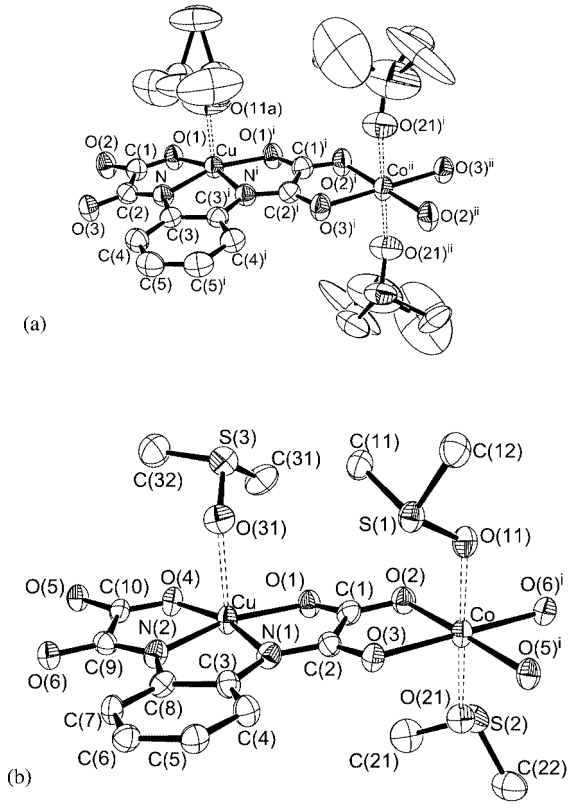

Figure 2. ORTEP3 drawing of the phases **α-1** (a) and **β-1** (b) of the chain [CoCu(opba)$(DMSO)_3$] (**1**) showing some atom designation. The thermal ellipsoids are drawn at the 50% probability level.

The main geometric parameters for phases **α-1** and **β-1** are given in Table 1. It is important to emphasize that **α-1** has half as many independent atoms as **β-1** due to its extra inversion center.

The geometry around the copper atom is approximately square pyramidal with two nitrogen atoms and two oxygen atoms from the opba group in the basal plane and one DMSO oxygen atom in the apical position. The DMSO molecules bonded to the Cu ions are disordered in **α-1**. This disorder disappears at low temperature, and a subsequent phase transition occurs to give **β-1**. In the phase **α-1**, the two N–Cu–O fragments present identical geometry due to their mirror symmetry. The $[Cu(opba)]^{2-}$ unit geometry is not analogous to those previously found for $Mn^{II}Cu^{II}$ bimetallic compounds either for **α-1** or **β-1**.[15,16]

The cobalt atom is coordinated to six oxygen atoms in a distorted octahedral surrounding. Two of these oxygen atoms, arising from the DMSO molecules, are in *trans* positions; the other four belong to oxamido groups of two different opba ligands. Similar to the Cu coordination sphere, the DMSO molecules coordinated to the Co atoms are disordered in **α-1**, whereas no disorder is observed in the **β-1** phase. In **α-1**, the Co ions are located on the inversion center. Therefore, only two of four opba oxygen atoms and one

 © 2005 Wiley-VCH Verlag GmbH & Co. KGaA, Weinheim

Table 1. Main geometric parameters (Å, °) for **1**.[a]

Phase **α-1**		Phase **β-1**	
Cu–N	1.921(3)	Cu–N(2)	1.908(5)
		Cu–N(1)	1.937(5)
Cu–O(1)	1.994(2)	Cu–O(1)	2.002(4)
		Cu–O(4)	2.005(4)
Cu–O(11A)	2.19(3)	Cu–O(31)	2.333(5)
Co^{i}–$O(2)^{i}$	2.083(2)	Co–O(2)	2.120(4)
Co^{i}–$O(3)^{i}$	2.074(2)	Co–O(3)	2.052(4)
		Co–$O(5)^{i}$	2.105(4)
		Co–$O(6)^{i}$	2.044(4)
Co^{i}–$O(21)^{i}$	2.123(3)	Co–O(11)	2.103(4)
		Co–O(21)	2.141(4)
$N–C_{(mean)}$	1.36(7)	$N–C_{(mean)}$	1.36(6)
$O–C_{(mean)}$	1.25(1)	$O–C_{(mean)}$	1.26(1)
C(1)–C(2)	1.549(5)	C(1)–C(2)	1.539(8)
		C(9)–C(10)	1.540(8)
$C–C_{Ar(mean)}$	1.39(1)	$C–C_{Ar(mean)}$	1.39(2)
		$S–O_{(mean)}$	1.52(1)
		$S–C_{(mean)}$	1.77(2)
N(1)–Cu–O(1)	83.7(1)	N(1)–Cu–O(1)	83.6(2)
		N(2)–Cu–O(4)	83.4(2)
N–Cu–N^{i}	82.5(2)	N(1)–Cu–N(2)	82.5(2)
N–Cu–O(11a)	101.1(6)	N(1)–Cu–O(31)	98.3(2)
		N(2)–Cu–O(31)	99.5(2)
O(1)–Cu–O(11a)	92.8(5)	O(1)–Cu–O(31)	89.8(2)
		O(4)–Cu–O(31)	89.5(2)
$O(2)^{i}$–Co^{ii}–$O(21)^{i}$	90.5(1)	O(2)–Co–O(11)	92.5(2)
$O(3)^{i}$–Co^{ii}–$O(21)^{i}$	88.8(1)	O(3)–Co–O(11)	93.1(2)
$O(2)^{i}$–Co^{ii}–$O(21)^{ii}$	89.5(1)	$O(5)^{i}$–Co–O(11)	90.3(2)
$O(3)^{i}$–Co^{ii}–$O(21)^{ii}$	91.2(1)	$O(6)^{i}$–Co–O(11)	88.5(2)
		O(2)–Co–O(21)	86.7(2)
		O(3)–Co–O(21)	88.8(2)
		$O(5)^{i}$–Co–O(21)	90.5(2)
		$O(6)^{i}$–Co–O(21)	89.6(2)
$O(2)^{i}$–Co^{ii}–$O(3)^{i}$	81.43(9)	O(2)–Co–O(3)	80.8(2)
		O(2)–Co–$O(6)^{i}$	97.3(2)
$O(3)^{i}$–Co^{ii}–$O(2)^{ii}$	98.57(9)	O(3)–Co–$O(5)^{i}$	100.3(2)
		$O(5)^{i}$–Co–$O(6)^{i}$	81.6(2)
		$C–S–C_{(mean)}$	97(1)
		$O–S–C_{(mean)}$	106(1)
$C(2)–N–Cu_{(mean)}$	115.3(7)	$C–N–Cu_{(mean)}$	115.4(5)
C(1) –O(1) –Cu	111.2(2)	C(1)–O(1)–Cu	110.4(4)
		C(10)–O(4)–Cu	110.9(4)
$C–O–Co_{(mean)}$	111.4(9)	$C–O–Co_{(mean)}$	111.7(4)
		S(1)–O(11)–Co	122.8(2)
		S(2)–O(21)–Co	122.1(2)
		S(3)–O(31)–Cu	133.9(2)
$O–C–C_{(mean)}$	117.8(9)	$O–C–C_{(mean)}$	117.6(9)
$N–C–C_{(mean)}$	112(2)	$N–C–C_{(mean)}$	112(1)
$C–C–C_{Ar(mean)}$	120(1)	$C–C–C_{Ar(mean)}$	120.0(6)

[a] Symmetry codes: phase **α-1**: [i] *x*, *y*, –*z* + 1/2; [ii] *x*, –*y* + 1, *z* + 1/2; phase **β-1**: [i] –*x*, –*y* + 1, *z* + 1/2.

of the two DMSO oxygen atoms are independent. In spite of this, the geometric parameters of the Co octahedron do not exhibit significant differences when the two phases are compared (see Table 2).

Both phases have very similar packing in which each chain is surrounded by six others (see Figure 3).[22] The shortest metal–metal distances (approx. 5.3 Å) occur between intrachain nearest neighbor Cu^{II} and Co^{II} ions. In **α-1** there is just one independent Cu···Co intrachain separation [5.303(1) Å], whereas in **β-1** there are two symmetrically independent intrachain Cu···Co contacts with distances equal to 5.336(1) (Cu···Co) and 5.305(1) Å (Cu···Co^{ii}; *ii* = –*x*, –*y* + 1, *z* – 1/2). The separation between adjacent chains along the *a* axis is exactly equal to the length of the cell parameter in this direction. This means that interchain Co···Co^{i} and Cu···Cu^{i} (*i* = *x* + 1, *y*, *z*) distances along the *a* axis are equivalent and decrease by about 0.3 Å from **α-1** to **β-1**. The interchain metal–metal separations considering transverse adjacent chains show significant differences between the **α-1** and **β-1** phases, mainly with respect to the Co···Co distances. For **α-1** there is just one independent transversal Co···Co distance [8.335(1) Å] since the Co atom is in the special position (0, 0, 1/2). For **β-1** the Co atom is shifted from the unit-cell edges mainly for the *z* coordinate. Therefore, the Co···Co distance is split in two: [Co···Co^{vi} = 7.818(1) Å (*vi* = *x* + 1/2,–*y* + 1/2, *z*) and Co···Co^{vii} = 8.526(1) Å (*vii* = *x* + 1/2,–*y* + 3/2, *z*)]. Due to the waving of the chain along the *c* axis, the structure presents two very different interchain Cu···Cu separations among transverse adjacent chains. One of them is the shortest metal–metal interchain separation [Cu···Cu^{v} = 7.108(1) Å for **α-1** (*v* = *x* + 1/2, –*y* + 3/2, –*z* + 1/2) and Cu···Cu^{vii} = 6.965(1) Å for **β-1** (*vii* = *x* + 1/2, –*y* + 3/2, *z*)], and the other one is the longest metal–metal first-neighbor separation [Cu···Cu^{iv} = 9.614(1) Å (*iv* = *x* + 1/2, –*y* + 1/2, –*z* + 1/2) for **α-1** and Cu···Cu^{vi} = 9.424(1) Å for **β-1** (*vi* = *x* + 1/2, –*y* + 1/2, *z*)]. The Cu···Co interchain distances range

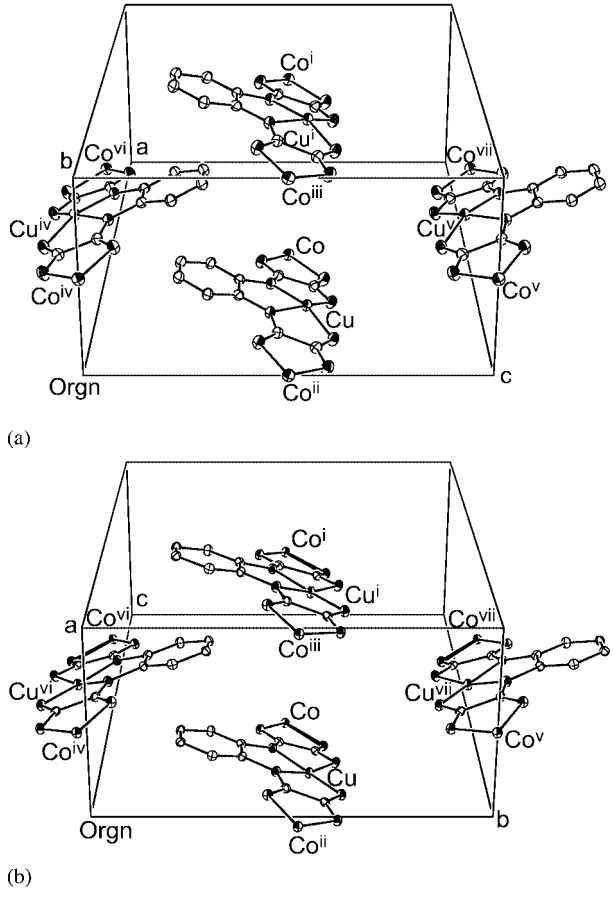

Figure 3. Packing diagram showing the unit cell and the chain neighborhood of the phases **α-1** (a) and **β-1** (b).

 © 2005 Wiley-VCH Verlag GmbH & Co. KGaA, Weinheim

Table 2. Crystal data, data collection, and structure-refinement parameters for **1**.

	Phase **α-1** (298 K)	Phase **β-1** (100 K)
Formula	$C_{16}H_{22}N_2O_9S_3CoCu$	
Fw [g mol^{-1}]	605.01	
Crystal system	orthorhombic	
λ (Mo-K_α)	0.71073	
Z	4	
Crystal size [mm]	0.03 × 0.08 × 0.09	
Space group	*Pnma*	*Pna*2$_1$
a [Å]	7.6712(2)	7.3530(2)
b [Å]	14.8003(3)	14.5928(4)
c [Å]	21.0028(5)	21.0510(7)
Volume [Å^3]	2384.6(1)	2258.8(1)
$D_{calcd.}$ [g cm^{-1}]	1.685	1.779
Absorption coefficient [mm^{-1}]	1.898	2.004
F(000)	1232	1232
θ range for data collection [°]	$2 \le \theta \le 50$	$2 \le \theta \le 50$
Index ranges	$-9 \le h \le 9$	$-8 \le h \le 8$
	$-17 \le k \le 17$	$-17 \le k \le 17$
	$-24 \le l \le 24$	$-24 \le l \le 24$
Reflections collected	23067	19898
Independent reflections	3934 [R_{int} = 0.043]	3702 [R_{int} = 0.064]
Data / parameters	2152 / 208	3702 / 290
Max. / min. transmission	0.9111 / 0.8786	0.9064 / 0.8725
Goodness-of-fit on F^2	1.171	1.111
Final *R* indices [$I > 2\sigma(I)$]	R_1 = 0.039, wR_2 = 0.099	R_1 = 0.042, wR_2 = 0.102
R indices (all data)	R_1 = 0.049, wR_2 = 0.105	R_1 = 0.049, wR_2 = 0.107
Largest diff. peak and hole	0.624 & –0.343 e Å^{-3}	0.455 & –0.678 e Å^{-3}

from 9.134(1) to 10.481(1) Å for **α-1** and from 8.752(1) to 10.546(1) Å for **β-1**. For both phases, the shortest contact takes place between parallel chains stacking along the *a* axis. Comparing the two phases, the biggest split due to the inversion symmetry break occurs for the Cu···Co^{i} and Cu···Co^{iii} distances, which are equal to 9.513(1) Å for **α-1** and decrease to 9.256(1) and 8.752(1) Å, respectively, for **β-1**.

Since *Pnam* (**α-1**) differs from *Pna*2$_1$ (**β-1**) only in the extra inversion symmetry in the former, there is no additional peak in the low-temperature diffraction pattern. Due to the reversibility, the phase transition involves only small changes in the atomic positions. This is true for the $[Cu(opba)]^{2-}$ unit and the Co atom. In spite of the fact that the Co ions leave the inversion center on going from phase **α-1** to phase **β-1**, the chains are very similar in both phases. On the other hand, the orientations of the DMSO molecules change significantly between the two phases. With

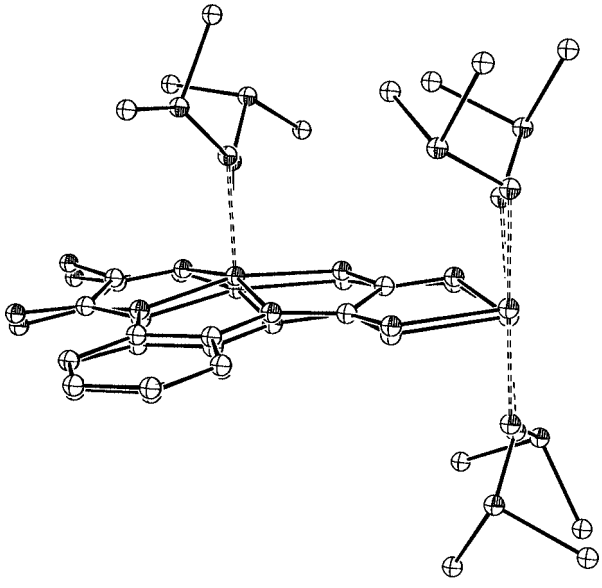

Figure 4. ORTEP3 representation showing a superposition of the molecular structures of **α-1** and **β-1** phases (mechanism 1).

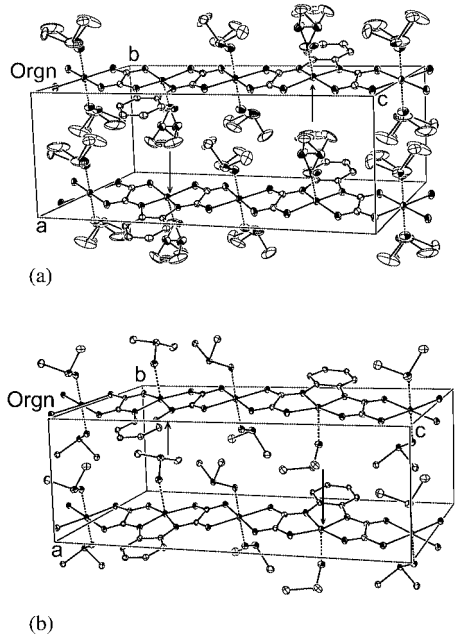

Figure 5. Packing diagram showing two parallel chains along the *b* axis. Arrows indicate the Cooper's DMSO path during the phase transition. Phase **α-1** (top) and phase **β-1** (bottom).

 © 2005 Wiley-VCH Verlag GmbH & Co. KGaA, Weinheim

these results in mind, two DMSO ordering mechanisms have been proposed to explain the structural transition. Initially, it was considered that all DMSO molecules could suffer a rotation of 180° around its O–S bond, as depicted in Figure 4 (mechanism 1), where both **α-1** and **β-1** crystalline phases are superposed. However, comparing the packing of the two phases (Figure 5), it is possible to conclude that mechanism 1 should not be the most plausible due to the steric hindrance effects. The most probable is that the DMSO molecule coordinated to the Cu^{II} ion migrates from a chain to another parallel one whilst maintaining almost the same orientation (Figure 5; mechanism 2). Therefore, the DMSO molecule ordering from 298 to 100 K occurs concomitantly with the displacement of DMSO molecules bonded to the Cu ions, with the DMSO groups bonded to the Co ions remaining in almost the same place.

Optical Properties

In order to verify optical anisotropy effects, namely linear birefringence (LB) and linear dichroism (LD), the sample was placed between crossed polarizers. Upon rotating the sample relative to the polarizers, points of extinction were noticed at 90°. Both effects, LB and LD, could be responsible for the observed optical behavior. Upon removing one polarizer we noted extinction points at 180°, thus revealing the LD effect in the sample. The photographic records of these results are available as Supporting Information.

The temperature dependence of the LB is dominated by small differences in the thermal expansion coefficients of the lattice parameters, as shown in Figure 6. This gives rise to an almost linear temperature-dependence behavior, except for the anomalies in the LB. This kind of anomaly is typical of a first-order structural phase transition. A large thermal hysteresis of about 70 K was observed.

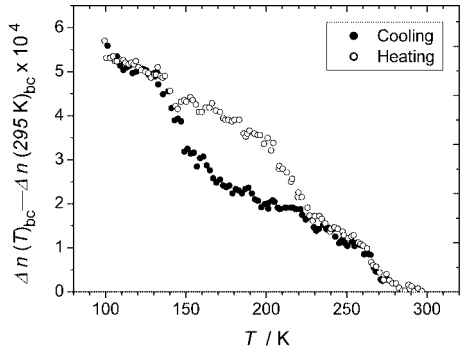

Figure 6. Cooling (solid circles) and heating (open circles) runs of the linear birefringence thermal dependence for **1**.

The optical properties assigned to the structural symmetry of transparent crystals can be described by their characteristic indicatrix, an ellipsoid on phase space of the refraction indices.[23] Orthorhombic crystals have three different values for the axes of its indicatrix, with two circular central sections characterizing a biaxial system, i.e., the crystal has two optical axes. Although both symmetry point groups for **α-1** and **β-1** are orthorhombic, their tensorial properties are different, which became evident by the changes in the birefringence curve on both runs.

The temperature dependence of the LD for **1** was obtained by using a lock-in detector technique analogous to the LB experiment, except for the removal of the analyzer polarizer.[24] The data were collected in the 20–295 K temperature range and the sample was oriented at 45° in order to maximize the LD signal. No significant variation of the lock-in amplifier signal was detected upon maintaining the LD approximately constant during the whole experiment.

Magnetic Studies

The temperature dependence of the magnetic susceptibility for **1** is shown in Figure 7 in the form of a $\chi_M T$ vs. T plot, with χ_M being the molar magnetic susceptibility and T the temperature. At 300 K, $\chi_M T$ (2.87 emu K mol^{-1}) corresponds to what is expected for uncoupled Co^{II} and Cu^{II} ions.[25] At high temperatures, a spin S, of 3/2 can be assigned for Co^{II} ions. As T is lowered, $\chi_M T$ decreases smoothly and reaches a rounded minimum around 90 K with $\chi_M T$ = 2.31 emu K mol^{-1}, and then increases as T is lowered further. Such behavior is characteristic of one-dimensional ferrimagnetism. This decrease of $\chi_M T$ could be due to the spin-orbit coupling effect of octahedral Co^{II} ion,[26] but it is strong enough to confirm the presence of antiferromagnetic coupling between near neighbors, as expected for oxamato-bridged compounds.[27] As T is lowered further below the minimum of $\chi_M T$, the correlation length within the chain increases rapidly. At very low temperatures, the Co^{II} ion behaves as an effective spin of 1/2, but the different g value with respect to the Cu^{II} centers ensures that the ground state will be magnetic.[28]

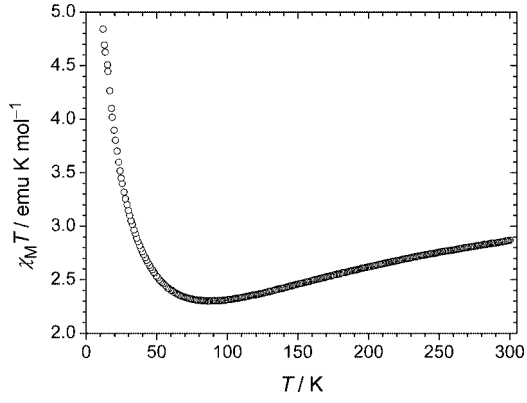

Figure 7. Temperature dependence of $\chi_M T$ for **1** at 1 kOe.

The temperature dependence of the magnetization for **1** is shown in Figure 8. The field-cooled magnetization (FCM), recorded by cooling the sample under a field of 100 Oe, shows a continuous increase, and reaches a value of 600 emu Oe mol^{-1} at 2 K. The zero-field cooled magnetization (ZFCM, not shown) was measured by cooling the sample without an applied field, then warming up under

 © 2005 Wiley-VCH Verlag GmbH & Co. KGaA, Weinheim

a 100 Oe field. ZFCM and FCM are coincident, thereby revealing the absence of remnant magnetization.

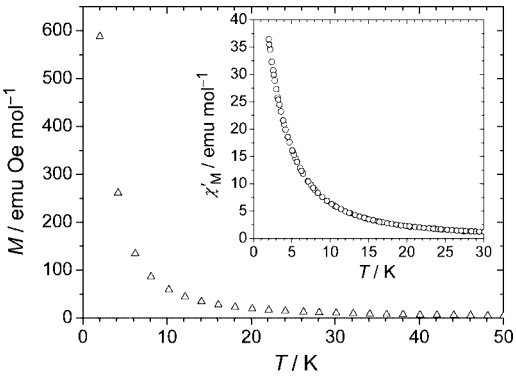

Figure 8. Field-cooled magnetization (FCM) in an applied field of 100 Oe. Inset: Real (χ_M') component of the ac magnetic susceptibility at a frequency of 1 kHz.

The thermal dependence of the in-phase (χ_M') and out-of-phase (χ_M'') components of the ac magnetic susceptibility were also investigated. The χ_M' results at an ac field of 10 Oe measured at 1 kHz and no dc field applied (inset of Figure 8) are very similar to the FCM curve with a rapid increase below 4 K. The χ_M'' curves are close to zero in the investigated temperature range.

Figure 9 shows the field dependence of the magnetization at 2 K for the chain **1**. As the applied field increases, M increases, and does not saturate even for fields as high as 65 kOe, where it reaches a value of 1.4 μ_B mol^{-1} (Nβ). The saturation magnetization is expected to be higher than 2 Nβ, a value related to all S_{Co} local spins aligned along the field direction and all the S_{Cu} local spins aligned along the opposite direction.[25,27] The difference between these values indicates that the local magnetic moments do not reach a perfect alignment with the field direction. This is probably due to the anisotropy of the spin carriers, which prevents the magnetic moments from rotating freely when applying the field. Such behavior is typical for oxamato-based magnets containing Co^{II} ions. No magnetic hysteresis is observed for this compound, even at 2 K (inset of Figure 9).

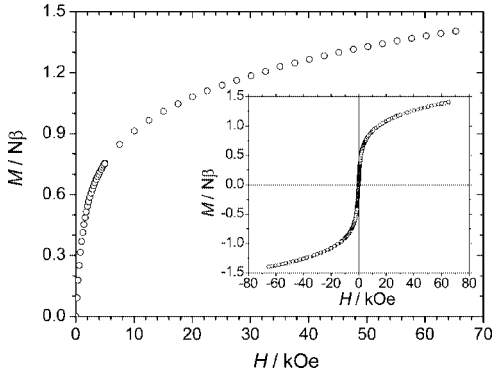

Figure 9. Molar magnetization vs. applied magnetic field for **1** at 2 K. Inset: Hysteresis loop at 2 K.

Let us now briefly discuss the relationship between structure and magnetic properties for **1**. The high-temperature behavior of the magnetic properties is widely dominated by the intrachain couplings along the c axis (J_c or J_{CoCu}). The mechanism of these M^{II}–Cu^{II} interactions (M being a transition metal ion) through the oxamato bridge is rather well understood. These interactions are due to the overlap of the $d_{x^2-y^2}$ magnetic orbitals centered on adjacent spin carriers. The strong covalent bonds and electron delocalization in molecule-based magnets with ligands like opba have, as a consequence, J_{MCu} values of about –30 cm^{-1}. This is a strong coupling and we can expect a similar value for **1**. In contrast, the interchain couplings are not very effective at high temperatures since kT is considerably larger than J_a and J_b. It is well established that a purely one-dimensional system is not able to exhibit spontaneous magnetization, except at absolute zero; a magnetic transition is generally a three-dimensional phenomenon.[28] For **1**, the structural changes in the crystalline phase transition are small and not sufficient to increase the interactions along the a or b axes to lead to a magnetic transition.

Conclusions

The ferrimagnetic chain [CoCu(opba)$(DMSO)_3$] (**1**) has been synthesized and characterized. It presents two crystalline phases – *Pnam* at room temperature and $Pna2_1$ at 100 K – whose structures consist of ordered infinite linear chains running along the c axis with adjacent Co^{II} and Cu^{II} ions bridged by oxamato groups. In the **α-1** phase, the DMSO molecules are disordered over the Co^{II} and Cu^{II} coordination sphere, whereas at low temperatures this structural disorder vanishes. The crystalline phase transition has been confirmed by a study using linear birefringence in a small single crystal with no polished surfaces. In addition, the LB results show a large thermal hysteresis associated to the structural changes in **1**, thereby revealing that the structural phase transition is a first-order process.

Magnetic studies (dc and ac) have been performed for **1** in a polycrystalline sample. At high temperatures, the stronger interactions along the c direction are responsible for the ferrimagnetic behavior. Since the changes that occur in the structural phase transitions do not affect this coupling significantly, anomalies in the magnetic data at the same temperatures observed by X-ray diffraction and LB measurements were not detected. The bimetallic chains in **1** are almost isolated from each other. The intrachain interaction between nearest neighbor ions is rather large but the interchain interactions are negligibly small. It is possible that **1** presents only a ferrimagnetic behavior, with correlation length increasing with a decrease of temperature without divergence of these values until the magnetometer temperature limit. In view of the crystalline arrangement, interactions along the packing direction (a axis) probably take place while the interactions along the b axis must be very weak. Therefore, the magnetic behavior for **1** below 2 K, where the effective spin of Co^{II} ions is 1/2, needs to be better investigated.

 © 2005 Wiley-VCH Verlag GmbH & Co. KGaA, Weinheim

Compound **1** exhibits some interesting features with respect to magnetic nanowires. Indeed, good candidates to present slow relaxation of the magnetization and hysteretic effects require strong anisotropy, ferromagnetic intrachain coupling or ferrimagnetic behavior, and the chains must be rather isolated. Therefore, the control of the chemistry, including supramolecular aspects, of compound **1** and related systems gives rise to a challenge: the preparation of oxamato-based nanowires, and also 2D systems, with higher blocking temperatures. We are presently focusing ours efforts in this direction.

Experimental Section

Preparation of [CoCu(opba)(DMSO)$_3$] (1): Compound **1** was prepared by adding $Co(NO_3)_2 \cdot 6H_2O$ (15 mg, 0.05 mmol), previously dissolved in DMSO (3 mL), to a solution of $Na_2[Cu(opba)] \cdot 3H_2O$[15] (170 mg, 0.41 mmol) in DMSO (22 mL) whilst stirring. The crystals obtained after three months under controlled temperature (35 °C) were separated by filtration, washed with DMSO, and dried in a desiccator. Yield: 105 mg (29%). $C_{16}H_{22}CoCuN_2O_9S_3$ (605.01): calcd. C 31.76, H 3.64, Co 9.74, Cu 10.50, N 4.63, S 15.91; found C 30.80, H 3.46, Co 9.64, Cu 9.90, N 4.93, S 15.52. IR (KBr): $\tilde{\nu}$ = 3450 cm^{-1} (vs), 1610 (vs), 1575 (s, br), 1475 (m), 1400 (m), 1350 (m), 1025 (s), 940 (m), 750 (m), 575 (w), 550 (w), 450 (m).

X-ray Crystallographic Study: A blue prismatic crystal of dimensions $0.03 \times 0.08 \times 0.09$ mm^3 was used for data collection. The X-ray diffraction data were collected at 298 and 100 K on an Enraf–Nonius Kappa-CCD diffractometer with graphite-monochromated Mo-K_α radiation (λ = 0.71073 Å) up to 50° in 2θ, with a redundancy of 4. The final unit-cell parameters were based on all reflections. The temperature was controlled with an Oxford Cryosystem low temperature device. Absorption corrections were carried out using the multi-scan method.[29] The structures were solved by direct methods with SHELXS-97.[30] The models were refined by full-matrix least-squares procedures on F^2 using SHELXL-97.[31] The H atoms of the phenyl and methyl groups were positioned stereochemically and they were refined with fixed individual displacement parameters [U_{iso}(H) = 1.2 U_{eq}(C_{phenyl}) or 1.5 U_{eq}(C_{methyl})] using the SHELXL riding model. Crystal data, data collection procedures, structure determination methods and refinement results are summarized in Table 2.

CCDC-272758 (for **α-1**) and -231896 (for **β-1**) contain the supplementary crystallographic data for this paper. These data can be obtained free of charge from The Cambridge Crystallographic Data Centre via www.ccdc.cam.ac.uk/data_request/cif.

Optical Measurements: The single crystal optical characterization, namely linear birefringence (LB) and linear dichroism (LD), was done at room temperature, under incoherent light, using an Olympus model BX50 optical microscope equipped with an Olympus SC35 camera. The temperature dependence of the birefringence was investigated using a lock-in null detector technique applied for LB.[32] The equipment consists of a photoelastic modulator working at 50 kHz and a computer-controlled Soleil–Babinet compensator, with resolution of $\delta(\Delta n) \leq 3 \times 10^{-8}$, corresponding to a phase difference of about 0.01°. The system has a built-in microscope to allow the study of small samples.[33] The typical dimensions of the samples studied in this paper were a thickness of 0.1 mm and 0.25×0.50 mm^2 transverse dimensions. Due to the reduced dimensions of the crystals, no polishing procedure was possible. A pinhole inserted into the microscope allows it to choose the best regions on the surface of the sample. Measurements were made at the 488-nm line of an argon ion laser. The sample containing a drop of the mother solution where the crystal was grown was placed on a thin glass plate. Thermally conducting glue was used to connect the glass plate to the sample holder, which was inserted into an evacuated cryostat, horizontally positioned, and cooled by helium flux. When the mother solution had evaporated, the crystals were fixed to the glass plate by surface tension. The sample was oriented in the crystallographic *ac* plane. The data were collected from 295 to 20 K. The cooling and heating rates were kept to be approximately 1 K min^{-1}. The chosen orientation of 45° maximizes the birefringence.[23]

Magnetic Measurements: The dc magnetic properties of **1** were studied in a Quantum Design SQUID MPMS XL7 in the 2–300 K temperature range using polycrystalline samples. The ac magnetic properties were studied in a commercial Quantum Design PPMS system. The diamagnetic corrections were estimated from Pascal's tables.

Supporting Information (see footnote on the first page of this article): Single-crystal photographs showing LB and LD properties at room temperature.

Acknowledgments

This work was supported by CNPq, CAPES, FAPEMIG, and FAPESP. The authors thank Dr. L. Ghivelder for ac measurements. We also thank the Instituto de Nanociências CNPq/MCT and FAPESP for a postdoctoral fellowship to one of us (ACD).

[1] J. S. Miller, J. C. Calabrese, A. J. Epstein, R. W. Bigelow, J. H. Zang, W. M. Reiff, *J. Chem. Soc., Chem. Commun.* **1986**, 1026–1028.
[2] Y. Pei, M. Verdaguer, O. Kahn, J. Sletten, J. P. Renard, *J. Am. Chem. Soc.* **1986**, *108*, 7428–7430.
[3] J. S. Miller, A. J. Epstein, *Angew. Chem. Int. Ed. Engl.* **1994**, *33*, 385–415.
[4] J. M. Manriquez, G. T. Yee, R. S. McLean, A. J. Epstein, J. S. Miller, *Science* **1991**, *252*, 1415–1417.
[5] S. Ferlay, T. Mallah, R. Ouahès, P. Veillet, M. Verdaguer, *Nature* **1995**, *378*, 701–703.
[6] H. O. Stumpf, L. Ouahab, Y. Pei, D. Grandjean, O. Kahn, *Science* **1993**, *261*, 447–449.
[7] G. De Munno, M. Julve, F. Nicolò, F. Lloret, J. Faus, R. Ruiz, E. Sinn, *Angew. Chem. Int. Ed. Engl.* **1993**, *32*, 613–615.
[8] J. A. Real, A. B. Gaspar, V. Niel, M. C. Muñoz, *Coord. Chem. Rev.* **2003**, *236*, 121–141.
[9] R. Clérac, S. O'Kane, J. Cowen, X. Ouyang, R. Heintz, H. H. Zhao, M. J. Bazile, K. R. Dunbar, *Chem. Mater.* **2003**, *15*, 1840–1850.
[10] G. Christou, D. Gatteschi, D. N. Hendrickson, R. Sessoli, *MRS Bull.* **2000**, *25*, 66–71.
[11] D. Gatteschi, R. Sessoli, *J. Magn. Magn. Mater.* **2004**, *272–276*, 1030–1036.
[12] E. Coronado, J. R. Galán-Mascarós, C. J. Gómes-García, V. Laukhin, *Nature* **2000**, *408*, 447–449.
[13] S. S. Turner, D. Pevelen, P. Day, *Synth. Met.* **2003**, *133*, 497–500.
[14] A. Dei, D. Gatteschi, C. Sangregorio, L. Sorace, *Acc. Chem. Res.* **2004**, *37*, 827–835.
[15] H. O. Stumpf, Y. Pei, O. Kahn, J. Sletten, J. P. Renard, *J. Am. Chem. Soc.* **1993**, *115*, 6738–6745.
[16] H. O. Stumpf, Y. Pei, L. Ouahab, F. L. Berre, E. Codjovi, O. Kahn, *Inorg. Chem.* **1993**, *32*, 5687–5691.
[17] C. L. M. Pereira, E. F. Pedroso, M. A. Novak, A. L. Brandl, M. Knobel, H. O. Stumpf, *Polyhedron* **2003**, *22*, 2387–2390.

 © 2005 Wiley-VCH Verlag GmbH & Co. KGaA, Weinheim

[18] M. G. F. Vaz, L. M. M. Pinheiro, H. O. Stumpf, A. F. C. Alcântara, S. Golhen, L. Ouahab, O. Cador, C. Mathonière, O. Kahn, *Chem. Eur. J.* **1999**, *5*, 1486–1495.
[19] M. G. F. Vaz, M. Knobel, N. L. Speziali, A. M. Moreira, A. F. C. Alcantara, H. O. Stumpf, *J. Braz. Chem. Soc.* **2002**, *13*, 183–189.
[20] C. L. M. Pereira, E. F. Pedroso, H. O. Stumpf, M. A. Novak, L. Ricard, R. Ruiz-Garcia, E. Rivière, Y. Journaux, *Angew. Chem. Int. Ed.* **2004**, *43*, 955–958.
[21] A. Caneschi, D. Gatteschi, N. Lalioti, C. Sangregorio, R. Sessoli, G. Venturi, A. Vindigni, A. Rettori, M. G. Pini, M. A. Novak, *Angew. Chem. Int. Ed.* **2001**, *40*, 1760–1763.
[22] Symmetry codes for phase **α-1**: [i] $x + 1, y, z$; [ii] $-x, -y + 1, z - 1/2$; [iii] $-x + 1, -y + 1, z - 1/2$; [iv] $x + 1/2, -y + 1/2, -z + 1/2$; [v] $x + 1/2, -y + 3/2, -z + 1/2$; [vi] $-x + 1/2, y - 1/2, -z + 1$; [vii] $-x + 1/2, y + 3/2, -z + 1$. Symmetry codes for phase **β-1**: [i] $x + 1, y, z$; [ii] $-x, -y + 1, z - 1/2$; [iii] $-x + 1, -y + 1, z - 1/2$; [iv] $-x + 1/2, y - 1/2, z - 1/2$; [v] $-x + 1/2, y + 1/2, z - 1/2$; [vi] $x + 1/2, -y + 1/2, z$; [vii] $x + 1/2, -y + 3/2, z$.
[23] J. F. Nye, *Physical Properties of Crystals; Their Representation by Tensors and Matrices*, Oxford University Press, **1985**.
[24] T. Oakberg, *PEM-90TM Photoelastic Modulator User Manual*, Hinds Instruments, Hillsboro, **1994**.
[25] O. Kahn, *Molecular Magnetism*, VCH, New York, **1993**.
[26] P. J. van Koningsbruggen, O. Kahn, K. Nakatani, Y. Pei, J. P. Renard, M. Drillon, P. Legoll, *Inorg. Chem.* **1990**, *29*, 3325–3331.
[27] S. Turner, O. Kahn, L. Rombardel, *J. Am. Chem. Soc.* **1996**, *118*, 6428–6432.
[28] R. L. Carlin, *Magnetochemistry*, Springer-Verlag, Berlin, **1986**.
[29] R. H. Blessing, *Acta Crystallogr., Sect. A* **1995**, *51*, 33–38.
[30] G. M. Sheldrick, SHELXS-97. *Program for Crystal Structure Resolution*, University of Göttingen, Germany, **1997**.
[31] G. M. Sheldrick, SHELXL-97. *Program for Crystal Structures Analysis*, University of Göttingen, Germany, **1997**.
[32] High Frequency Polarization Modulation Method for Measuring Birefringence: F. A. Modine, R. W. Major, E. Sonder, *Appl. Optics* **1975**, *14*, 757–760.
[33] M. A. S. Oliveira, J. Y. Gesland, L. C. Meira-Belo, U. A. Leitão, R. L. Moreira, *Phys. Rev. B* **2000**, *62*, 215–222.

Received: May 25, 2005
Published Online: November 2, 2005

 © 2005 Wiley-VCH Verlag GmbH & Co. KGaA, Weinheim

DOI: 10.1002/ejic.200500666

A Novel Integrated X-ray Powder Diffraction (XRPD) and Molecular Dynamics (MD) Approach for Modelling Mixed-Metal (Zn, Al) Layered Double Hydroxides (LDHs)

Giuseppe M. Lombardo,[a] Giuseppe C. Pappalardo,*[a] Francesco Punzo,[a] Ferdinando Costantino,[b] Umberto Costantino,[b] and Michele Sisani[b]

Keywords: Layered double hydroxides / Molecular dynamics / X-ray diffraction / Structure elucidation

A combination of experimental (XRPD) and computational (MD-simulation) techniques was used for a detailed study of the structural, dynamic and hydration properties of the ZnAl layered double hydroxides (LDHs) of formula $[Zn_{0.65}Al_{0.35}(OH)_2]Cl_{0.35}\cdot yH_2O$ (**I**) and $[Zn_{0.65}Al_{0.35}(OH)_2](CO_3)_{0.175}\cdot yH_2O$ (**II**), with y = 0.35 and 0.69, respectively. Our approach was based on a direct comparison made, for the first time, between the observed XRPD diffraction pattern and the MD-simulated pattern of each model that was considered. The XRPD curve is affected (reflection angles and line shapes) by dynamic and structural factors, and the interlayer distribution of the water content. Accordingly, its reproduction through MD modelling is the most suitable means of monitoring these properties of the material. Molecular modelling was performed by MD simulations of models of **I** and **II** built up through appropriate modifications of their interlayer total water contents and related distribution. The validated models, namely those that provided the best MD-simulated pattern of **I** and **II**, were then used to determine structures and features which have not been previously determined by conventional diffraction techniques. The calculated XRPD curves were corrected to take into account the "size" broadening effect. The approach provided structural data that matched well those obtained by Rietveld analyses for the usual parameters. Furthermore, the study was original in its capability to detect and thus to discriminate between the different interatomic distances Zn–O, Al–O, Al···Al, Zn···Zn, Zn···Al in the slabs. The MD-simulated models of **I** and **II** provided the best reproduction of the XRPD curves for total water of hydration contents of y = 0.25 and y = 0.69, respectively. In the case of **II**, a domain with a homogeneous distribution of total water contents predominated. Conversely, in the case of **I**, a nonhomogeneous distribution featured by two (or multiple) shared crystalline domains having different interlayer water contents was evidenced.

(© Wiley-VCH Verlag GmbH & Co. KGaA, 69451 Weinheim, Germany, 2006)

Introduction

Layered double hydroxides (LDHs), also known as anionic clays or hydrotalcite-like compounds (HTlc), are solid compounds having positively charged layers and intercalated exchangeable interlayer anions to maintain charge neutrality.[1–11] Their general formula is $[M^{II}_{1-x}M^{III}_{x}(OH)_2]^{x+}(A^{n-}_{x/n})^{x-}\cdot yH_2O$ in which M^{II} = Mg, Zn, Co, Ni, Mn, etc., M^{III} = Cr, Fe, V, Co, etc., A^{n-} = an inorganic or organic anion of charge *n*.

The great technological relevance of LDHs stems from their use as precursors in catalysis.[7,10,12–16] In particular, ternary LDHs of type $[Cu_yZn_{1-x-y}Al_x(OH)_2](CO_3)_{x/2}\cdot(1–3x/2)H_2O$, after thermal decomposition and successive reduction of the copper oxide to the metal with hydrogen, attain a tight mixture of oxides with copper particles (Cu/ZnO/Al_2O_3) that is active as a catalyst for hydrogen production from oxidative steam reforming of methanol (OSRM). This is useful for developing a clean power source for vehicles.[17–19]

Understanding the structural and dynamic properties of this important class of materials is a central issue in studies focusing on the design of second-generation LDH precursors and derived catalysts with enhanced or new performances.

The arrangement of the interlayer species is not well understood and is difficult to probe experimentally. It frequently happens that anions and water molecules associate strongly with particle surfaces, and some adsorbed water molecules are indistinguishable from interlayer water in thermal analyses.

[a] Dipartimento di Scienze Chimiche, Facoltà di Farmacia, Cattedra di Chimica Generale ed Inorganica, Università di Catania, Viale A. Doria 8, 95125 Catania, Italy
E-mail: gcpappalardo@dipchi.unict.it
[b] CEMIN Centro di Eccellenza Materiali Innovativi Nanostrutturati, Dipartimento di Chimica, Università di Perugia, Via Elce di Sotto 8, 06123 Perugia, Italy

 © 2005 Wiley-VCH Verlag GmbH & Co. KGaA, Weinheim

Unfortunately, these materials are obtained only as powders, often with a low degree of crystallinity, thus making structural determinations by single-crystal X-ray analysis impossible. Further, even in cases where the powdered solids initially exhibit a high degree of crystallinity, large overlapping bands from relatively poor diffraction patterns are often observed when these solids are modified by heating, ion-exchange, intercalation, pillaring or topotactic functionalisation by ligand substitution. Therefore, detailed structural information on these systems from X-ray powder diffraction (XRPD) data is difficult to obtain or otherwise inaccessible.

We have recently used molecular dynamics (MD), combined with large angle X-ray scattering (LAXS)[20–24] or XRPD experiments,[25,26] for determining structural parameters (molecular assembly, interatomic and intermolecular distances).

Application of MD for simulating these materials provides the following: (i) an ability to monitor the internal molecular fluctuations, thus revealing, by implementing high-temperature MD runs, processes leading to metal segregation and to the breakdown of the structure of the precursor; (ii) the ability to generate microscopic-level structural information that can be correlated directly with the experimentally detectable activity and selectivity of catalysts for OSRM; (iii) the capacity to refine molecular structures by using experimental data, especially from X-ray diffraction experiments for microcrystalline and amorphous solid phases.

The ability to predict macroscopic properties of HTlc on the basis of microscopic structures derived from MD simulations has a fundamental impact on the design of new materials with improved technological requisites. To accomplish this, not only should the molecular simulations be carried out on a long enough time scale to sample a significant volume of phase space, but also: (i) a suitable unit or fragment of the material should be selected to serve as the model of the real system; and (ii) the force field (FF) used by the MD program should feature a high-quality parameterisation developed ad hoc for the system that is being dealt with.

Previous computer modelling focused on interlayer distance dynamics in binary LDH systems[27–32] by using generic force fields. Quite recently, a force field (CLAYFF) designed for simulations of clay phases was optimised on the basis of known mineral structures for the Si, Al, Mg, Ca, Fe and Li species.[33] In order to model binary Zn-containing LDHs by using MD simulations for the first time, we relied on a modified version of the CLAYFF into which suitable ad hoc developed Zn parameters were inserted.

The models used for the simulations (Figure 1) of $[Zn_{0.65}Al_{0.35}(OH)_2]Cl_{0.35}\cdot 0.35H_2O$ (**I**) and $[Zn_{0.65}Al_{0.35}(OH)_2](CO_3)_{0.175}\cdot 0.69H_2O$ (**II**) were preliminarily validated on the basis of a direct agreement between the experimental XRPD patterns and those calculated from MD. The calculated XRPD patterns were obtained by averaging patterns calculated from snapshots collected along the entire evolution time of the MD simulation for each of the models considered. By this procedure, the positions of the observed diffraction lines could be reproduced by taking the thermal, dynamic and structural factors, as well as the water content of the material into account.

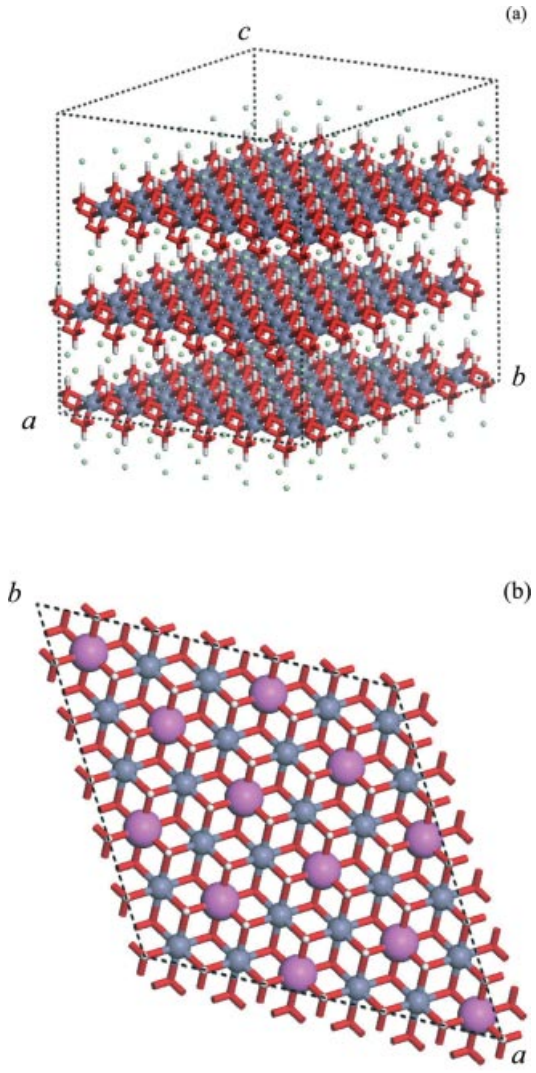

Figure 1. (a) The 3-layered model supercell with independent variables a, b, c, α, β, γ used for the MD simulations of both the LDHs **I** and **II**. The green balls represent the positions available for accommodation of interlayer water molecules with chloride (**I**) or carbonate (**II**) anions. (b) View of the preferred planar arrangement of metallic ions in the Zn/Al slab in the ratio 2:1 (element colours: Zn blue-grey; Al pink; O red, H white).

In the present study the combined approach, validated as stated above, was used for featuring the LDHs **I** and **II** in terms of structure, dynamics and arrangement of their interlayer water molecules and anionic species.

Results and Discussion

Analysis of XRPD Patterns

The Rietveld plots and crystallographic data obtained from the XRPD patterns of the well-crystallised samples of **I** and **II** are given in Figure 2 and Table 1, respectively.

 © 2005 Wiley-VCH Verlag GmbH & Co. KGaA, Weinheim

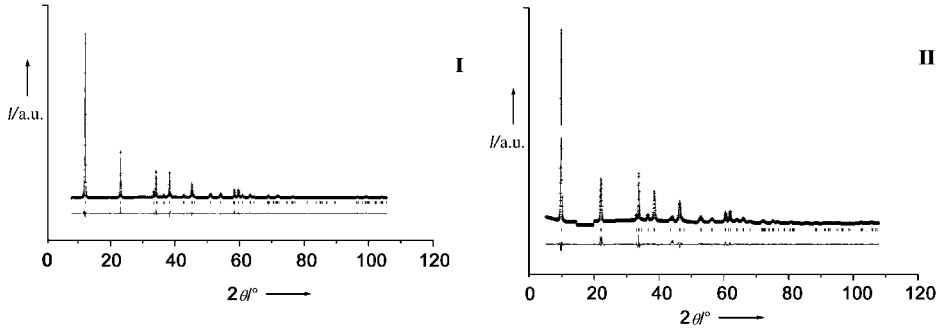

Figure 2. Rietveld plots for **I** and **II**; experimental (+), calculated (–) and difference (lower) profiles.

Table 2 contains the atomic parameters and main geometrical data of compounds **I** and **II**. These results show a good general agreement with those already known in the literature for analogous HTlc.[9,10] The relative positions of the atoms inside the unit cells, as attained by the fractional coordinates given in Table 1 and Table 2, and their relative images due to the *R*3*m* symmetry are depicted in Figure 3.

Table 1. Crystallographic data for $[Zn_{0.65}Al_{0.35}(OH)_2](Cl)_{0.35}\cdot 0.35H_2O$ (**I**) and $[Zn_{0.65}Al_{0.35}(OH)_2](CO_3)_{0.175}\cdot 0.69H_2O$ (**II**) from Rietveld analysis.

	I	**II**
Space group	*R*3*m*	*R*3*m*
a [Å]	3.07497(6)	3.0758(1)
c [Å]	23.1524(5)	22.8089(8)
Cell volume [Å^3]	189.588(6)	186.87(1)
Z	3	3
Calculated density [g cm^{-3}]	2.759	2.904
Unit cell formula weight	315.0	326.7
R_{wp}[a]	0.119	0.104
R_p[b]	0.088	0.071
R_F[c]	0.076	0.086
χ[d]	4.7	7.9

[a] $R_p = \Sigma|I_o - I_c| / \Sigma I_o$. [b] $R_{wp} = \{\Sigma[w(I_o - I_c)^2] / \Sigma[wI_o^2]\}^{1/2}$. [c] $R_{F^2} = \Sigma|F_o^2 - F_c^2| / \Sigma|F_o^2|$. [d] $\chi = \{\Sigma[w(I_o - I_c)^2] / (N_o - N_{var})\}^{1/2}$.

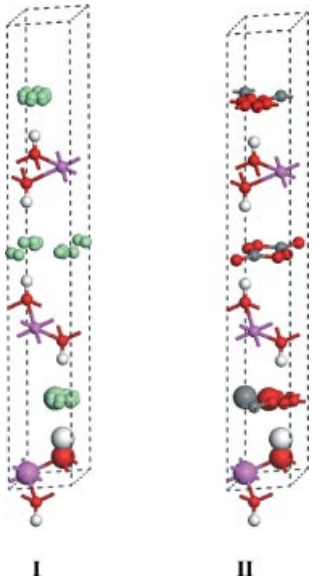

Figure 3. Spatial distributions of atoms in the cells of **I** and **II** obtained from Rietveld analyses. The atoms whose positional parameters were achieved using the Rietveld analyses are evidenced by larger spheres; the atomic positions generated by *R*3*m* symmetry are denoted by smaller spheres. Zn, Al pink; O, red; Cl, green; C, grey; H, white.

Table 2. Positional and thermal parameters for **I** and **II**.

Atom	*x*/*a*	*y*/*b*	*z*/*c*	$100U_{iso}$ [Å^2][a]	Wyckoff notation	Occupancy	Number of atoms per cell
I $[Zn_{0.65}Al_{0.35}(OH)_2](Cl)_{0.35}\cdot 0.35H_2O$							
Zn	0.0	0.0	0.0	2.21(4)	3a	0.65	2
Al	0.0	0.0	0.0	2.21(4)	3a	0.35	1
O(1)	0.0	0.0	0.3745(1)	3.3(1)	6c	1	6
O(2)	0.1586(12)	–0.3172(23)	0.1676(7)	8.8(5)	18h	0.056	1
Cl	0.1586(12)	–0.3172(23)	0.1676(7)	8.8(5)	18h	0.056	1
H	0.0	0.0	0.4135(5)	3.3(1)	6c	1	6
II $[Zn_{0.65}Al_{0.35}(OH)_2](CO_3)_{0.175}\cdot 0.69H_2O$							
Zn	0.0	0.0	0.0	2.15(9)	3a	0.65	2
Al	0.0	0.0	0.0	2.15(9)	3a	0.35	1
O(1)	0.0	0.0	0.3740(2)	3.4(2)	6c	1	6
O(2)	0.1137(15)	–0.1137(15)	0.5004(14)	3.4(2)	18h	1/6	3
C	1/3	2/3	0.5004(14)	3.4(2)	6c	1/12	0.5
H	0.0	0.0	0.4142(6)	3.4(2)	6c	1	6

[a] U_{iso} = mean square displacement, $B_{iso} = 8\pi^2 U_{iso}$.

 © 2005 Wiley-VCH Verlag GmbH & Co. KGaA, Weinheim

In both samples the hydroxy groups are coordinated to the metal (octahedral) pointing alternatively upwards and downwards from the layer, giving rise to three cavities in the interlayer region around each metal on both sides of the layer. The chloride anions occupy a single site in the unit cell of **I**, whereas the carbonate anions are arranged parallel to the layer and occupy three sites with the oxygen atoms in the unit cell of **II**. This determines, assuming that ionic exchange is the same, a greater number of positions available for the water of hydration in the chloride phase.

MD Simulations of XRPD Patterns

The examination of the whole series of simulations was performed in terms of comparisons between the calculated and experimental XRPD patterns. The best MD simulations of the XRPD patterns of compounds **I** and **II** were achieved for models containing 27 (y = 0.25) and 75 (y = 0.69) water molecules, respectively. Measures of similarity (R_{wp}) between experimental and MD-simulated patterns as a function of the total water contents y are quoted in Figure 4. All the experimental peak positions were located well by MD, whereas, as expected, the peak heights and line shapes did not exactly reproduce the experimental curves of either **I** or **II**. The heights of the calculated peaks are lower than the experimental ones. This is typical in the case of the occurrence of very thin microcrystals (exfoliation along the c axis) for which: (i) the intensity of the first peak (003) decreases significantly, and (ii) the normalisation with respect to this small angle peak determines the higher intensities at the large angle portion of the pattern. Further, the MD simulations of the crystal (see forthcoming section Structural Data) reveal the skidding of the c planes and the important concerted fluctuations, which affects the entire set of cell parameters. A further contribution to such a discrepancy comes from the restricted spanning of the phase space resulting from the small size of the simulated models. In fact, the interlayer species of the models cannot attain all the reticular positions made available by the Rietveld analysis in the $R3m$ symmetry (Figure 3). Figure 5 shows the XRPD patterns of **I** and **II** compared with the simulated ones after corrections have been made for crystallite size broadening (see Computational Details).

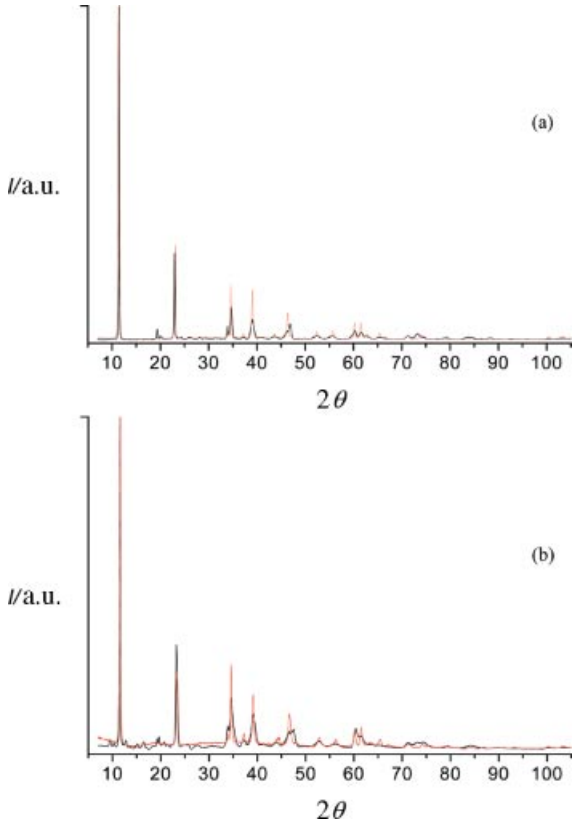

Figure 5. Comparison of experimental (red) and MD-simulated (black) XRPD patterns of **I** (a) and **II** (b).

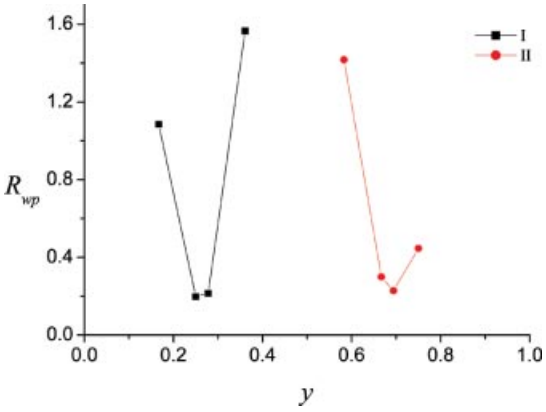

Figure 4. A measure of the similarity (R_{wp}) between experimental and MD-simulated patterns as a function of the total water content y. The minima show that the models which best reproduce the XRPD patterns of **I** and **II** have formula coefficients y = 0.25 and y = 0.69, respectively.

Hydration Properties

The MD runs showed that the simulated models of **I** and **II** having total water of hydration contents of 27 (y = 0.25) and 75 (y = 0.69), respectively, were the best at reproducing the experimental XRPD curves. In the case of the carbonate compound **II**, the MD simulation attained a value of the averaged empirical formula coefficient y = 0.69 for reproducing the experimental data of the sample as determined by using TG analysis. This corresponds to the model in which the water molecules (N_w = 75) are distributed in a homogeneous fashion, i.e. as three sets of 25 water molecules per interlayer.

In the case of the chloride compound **I** the theoretical model having a total N_w of 27 (y = 0.25) distributed as nine

 © 2005 Wiley-VCH Verlag GmbH & Co. KGaA, Weinheim

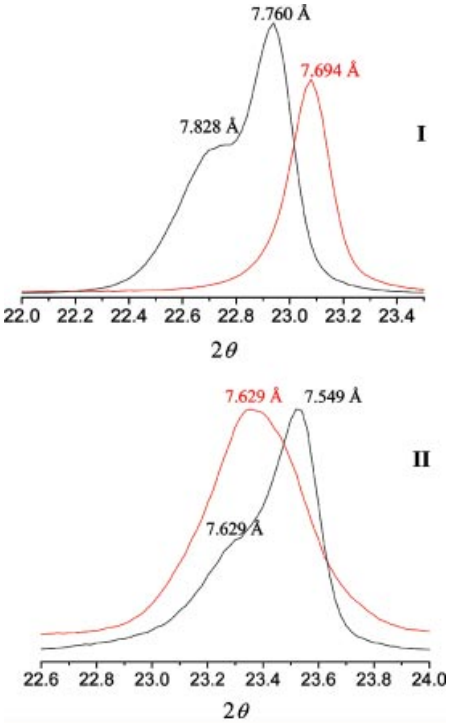

Figure 6. Detailed view of the (006) peaks of the treated (red) and nontreated (black) samples of **I** and **II**. The interlayer distances [Å] are indicated on the corresponding peaks and shoulders of the curves. This multiplicity collapsed into a well-resolved single peak shifted to a higher (2θ = 23.1°) and lower angle (2θ = 23.3°) in the case of the treated samples **I** and **II**, respectively. In **I** the treated sample gave rise to a single peak due to water loss; in **II** the treated sample took on a single peak shape due to the decreased size of the microcrystals and a shift towards increasing water content in the interlayer. In fact, the raised baseline and the broader peak denote the formation of amorphous material due to disaggregation resulting from the exfoliation process of the layers after the treatment.

water molecules per interlayer does not coincide with the average formula index value y = 0.35 measured for the synthesized sample. By keeping in mind that all the simulated models featured a regular interlayer distribution of the total number of water molecules, N_w, and that the MD simulation of the model N_w = 27 corresponds well with the experimental pattern, the observed discrepancy in the water contents between the experimental formula index value measured by TGA (y = 0.35) and the theoretical value (y = 0.25) can be accounted for in terms of a predominantly heterogeneous distribution of the water content in the interlayer of the material. Further evidence for this was provided by the (006) peaks observed in the XRPD patterns at ca. 2θ = 23.0° of the freshly prepared samples of **I** and **II**, both showing a marked shoulder (Figure 6). This multiplicity is consistent with two (or multiple) shared crystalline domains that have different water contents in the interlayer. The above findings are consistent with the results provided by the averaged total energies calculated from MD trajectories of the models of **I** and **II** at the various arrangements (Table 3; Figure 7). These results confirmed on an energy basis that: (i) the approach is sensitive to the more or less homogeneous distribution of the total water content in the interlayer; (ii) in the case of **I** the most heterogeneous interlayer water arrangement is the predominant motif; (iii) in the case of **II** the homogeneous motif predominates at the values of total water content measured by thermogravimetric techniques (y = 0.69); and (iv) in the case of both **I** and **II**, for total water contents higher than the measured ones, a more heterogeneous interlayer distribution of the water contents is predicted on the basis of the force field that was used. The theoretical relationship between interlayer distance and total water content is shown in Figure 8.

Table 3. MD-calculated total average energies (E, kcal mol^{-1}) assuming different interlayer distributions of the water molecules (N_w) for models of **I** and **II**.

I				**II**			
$[Zn_{0.65}Al_{0.35}(OH)_2](Cl)_{0.35}\cdot\leqslant y>H_2O$				$[Zn_{0.65}Al_{0.35}(OH)_2](CO_3)_{0.175}\cdot\leqslant y>H_2O$			
$<y>$ = 0.361				$<y>$ = 0.694			
Layer	N_w	y	E	Layer	N_w	y	E
1	13	0.361		1	25	0.694	
2	13	0.361	–31943.086	2	25	0.694	–35522.575
3	13	0.361		3	25	0.694	
1	10	0.278		1	22	0.611	
2	19	0.528	–31945.351	2	31	0.861	–35520.586
3	10	0.278		3	22	0.611	
1	7	0.194		1	19	0.528	
2	25	0.694	–31970.793	2	37	1.028	–35517.807
3	7	0.194		3	19	0.528	
$<y>$ = 0.500				$<y>$ = 0.861			
Layer	N_w	y	E	Layer	N_w	y	E
1	18	0.500		1	31	0.861	
2	18	0.500	–32058.498	2	31	0.861	–35574.264
3	18	0.500		3	31	0.861	
1	15	0.417		1	28	0.777	
2	24	0.666	–32077.331	2	37	1.028	–35584.367
3	15	0.417		3	28	0.777	
1	12	0.333		1	25	0.694	
2	30	0.833	–32076.940	2	43	1.194	–35646.050
3	12	0.333		3	25	0.694	

 © 2005 Wiley-VCH Verlag GmbH & Co. KGaA, Weinheim

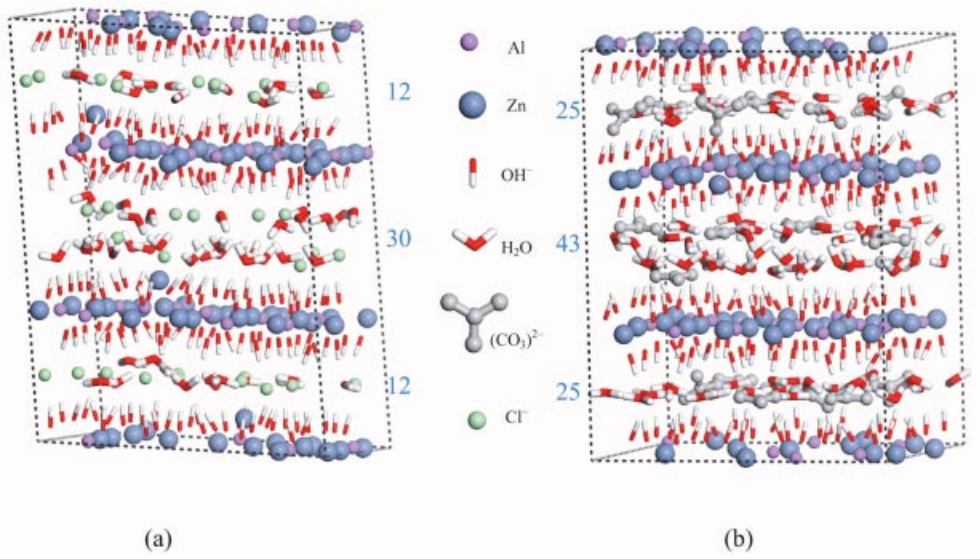

Figure 7. Example of models of **I** (a) and **II** (b) with $y = 0.500$ and $y = 0.861$, respectively (snapshot after the 200-ps simulation). The nonhomogeneous distribution of water molecules between the layers (see Table 3) is shown here by the blue numbers along the *c* axis. The notation used for atoms and interlayer species (water and anions) is given in colours.

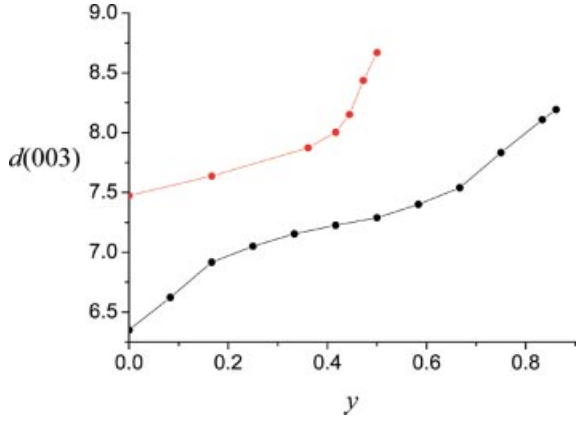

Figure 8. MD-calculated (averaged collection of 200-ps trajectories) interlayer distances [*d*(003)] in **I** (red) and **II** (black) as a function of the total interlayer water content.

Structural Data

The acceptable agreement of the interatomic distances calculated from MD with those provided by Rietveld analyses is shown in Table 4. This constitutes a further validation of the good quality of the FF used and consequently of the whole combined approach. The MD analyses of both **I** and **II** provide a complete set of layer interatomic distances (Zn–O, Zn···Zn, Zn···Al) that agree with those available from EXAFS experiments on the nitrate analogues (Table 4). Furthermore, the analysis of the trajectories of the models of **I** and **II** bearing $y = 0.25$ and $y = 0.69$ water molecules, respectively, which produced the best MD reproduction of the experimental XRPD pattern, provided (Figure 9a and b) microscopic information concerning: (i) the fluctuating orientation (from parallel to perpendicular) of the interlayer planar moieties of the CO_3^{2-} anions, (ii) the effective ten-

Table 4. MD-calculated average interatomic distances [Å] compared with those obtained from Rietveld analyses for models of **I** and **II**. EXAFS[41] data available for the analogous LDHs $(Zn_xAl_{1-x})(OH)_2(NO_3)\cdot(1-x)H_2O$ are quoted for the purpose of comparison.

	MD		Rietveld		EXAFS[41]
	I	**II**	**I**	**II**	
Zn–O(1)	2.080	2.059	2.015	2.003	2.07
Al–O(1)	1.970	1.963	2.015	2.003	
Zn–Zn	3.078	3.090	3.074	3.076	3.10
	5.321	5.335	5.328	5.327	
Al–Al	5.316	5.317	5.326	5.327	
Zn–Al	3.067	3.075	3.076	3.076	3.06
O(1)–Cl,C	3.207	3.148	3.030	3.386	
O(2)–Cl,C	3.191	3.161			
O(1)–O(1)	2.750	2.756	2.622	2.568	
O(1)–O(2)	2.785	2.766	2.879	2.937	
Zn–Cl,C	2.196	2.225			
	4.060	4.179	4.004	3.790/4.204	
Al–Cl,C	4.792	4.215	4.004	3.790/4.204	
		4.927			
Cl–Cl, C–C	4.312	4.179			

 © 2005 Wiley-VCH Verlag GmbH & Co. KGaA, Weinheim

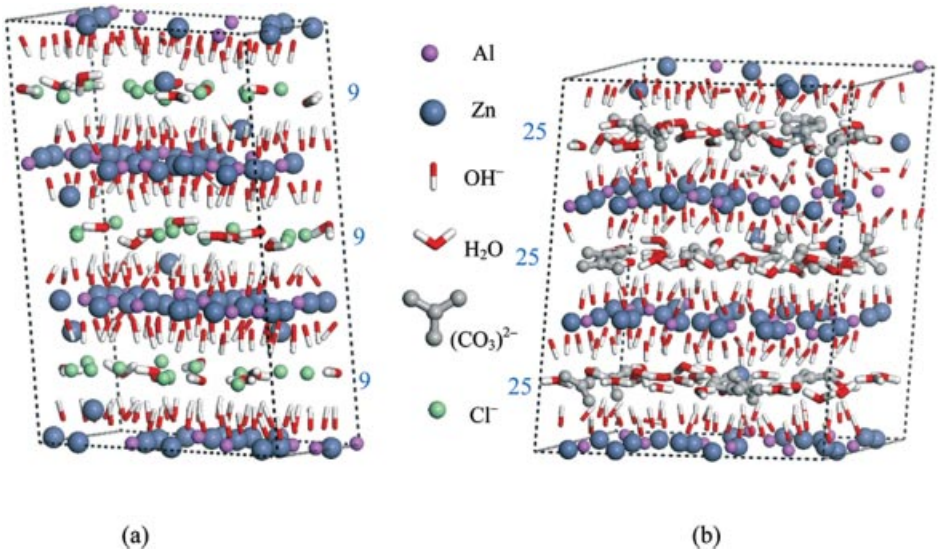

Figure 9. Perspective view of the supercells of **I** (a) and **II** (b) with $y = 0.25$ and $y = 0.69$, respectively, (snapshot after the 1-ns simulation) which best reproduce the experimental patterns. The homogeneous distribution of water molecules between the layers is indicated here by the blue numbers along the *c* axis. The notation used for the atoms and interlayer species (water and anions) is given in colours.

dency of the Zn atoms to segregate in the samples of both compounds **I** and **II**, (iii) the interlayer H_2O molecules of **I** and **II** that fluctuate about the coplanar arrangement with respect to the layer; and (iv) the dynamics of the layer as determined by the concerted sliding of the slabs about the equilibrium position.

Conclusions

The structural features, dynamics and arrangement of the interlayer species (total water content and anions) for the ZnAl hydrotalcite-like compounds in the chloride (**I**) and carbonate (**II**) forms were studied by using experimental (XRPD, TGA) and computational (MD) techniques in a complementary fashion. To this purpose we first implemented, for the systems in which Me(II) = Zn, a set of parameters from the recent CLAYFF force field[34] that included suitable parameters for LDH species. The structural data coming from the XRPD Rietveld analyses were in agreement with the MD results, thus providing a first validation of the FF parameters that were used.

The main findings of the present work revealed: (i) the general ability of this approach to monitor microscopic-level properties such as the guest orientations, their fluctuations and the interlayer arrangement in the studied LDHs; (ii) the ability to detect and thus to discriminate between the different interatomic distances (Zn–O, Al–O, Al···Al, Zn···Zn, Zn···Al) of the slab, in a manner independent from other X-ray diffraction techniques such as EXAFS; (iii) the tendency of the zinc atoms to segregate, which occurs in both compounds **I** and **II**; (iv) the tendency of compound **I** to adopt a heterogeneous interlayer distribution of water. This heterogeneous distribution, although it includes domains having $y = 0.25$, leads to a higher average formula index value (y) in compound **I**; (v) that the crystal size of **I** remained unaffected by dehydration (even down to $y = 0$) of the material; (vi) that material **II** preferred the homogeneous distribution (25 per interlayer) of the experimental total water content ($y = 0.69$); (vii) the fact that, for the same reason as in (iv), the crystal was likely to disaggregate through exfoliation of the *c* layers, leading to water loss and consequently a smaller size of the microcrystals; and (viii) the capability of the computational approach to indicate with good accuracy the interlayer water distribution of the material.

In conclusion, the following general issues were achieved: first, a nonexpensive approach, which shows the tendency of LDHs to attain structures bearing heterogeneous or homogeneous interlayer distribution of their total water contents, and second, the symbiosis between experiment and theory that played a role in validating MD-simulated structure models of LDHs through direct matching of the experimental XRPD patterns. The direct reproduction of the diffraction pattern made possible a model that accounts for microscopic thermal, dynamic and structural factors, in addition to water-content distribution of the material being studied.

Experimental Section

Preparation of the Samples: A large batch of Zn–Al hydrotalcite-like compound, with the formula $[Zn_{0.65}Al_{0.35}(OH)_2](CO_3)_{0.175}\cdot 0.69H_2O$ (**II**), was prepared by the urea method[9] according to the following procedure: a clear solution, obtained by mixing $AlCl_3$ (100 mL, 0.50 M), $ZnCl_2$ (200 mL, 0.50 M) and urea (30 g), was maintained at reflux temperature for 3 d. The precipitate obtained was filtered, washed with deionised water and equilibrated, whilst stirring, with Na_2CO_3 (100 mL, 0.1 M) for 1 d in order to exchange the chloride ions (sometimes incorporated during the synthetic procedure) with carbonate ions. After equilibration, the solid was recovered, washed with deionised water, and finally dried and stored over P_4O_{10} in the presence of soda lime.

 © 2005 Wiley-VCH Verlag GmbH & Co. KGaA, Weinheim

The Zn–Al hydrotalcite-like compound in the chloride form, $[Zn_{0.65}Al_{0.35}(OH)_2]Cl_{0.35}\cdot 0.35H_2O$ (**I**), was obtained by titrating the carbonate form, previously dispersed in NaCl (0.1 M, mass/volume ratio 1 g 50 mL^{-1}), with HCl (0.1 M) by means of a Radiometer automatic titrator operating in the pH stat mode and at pH 5. The solid was washed with CO_2-free deionized water and stored over P_4O_{10} in the presence of soda lime.

Analytical Procedures: The metal ion content of HTlc was determined by ion chromatography, after dissolution of about 100 mg of sample in concentrated HCl. The metal ion concentration in the resulting solution was measured by the following procedures: (i) Zn content: column Dionex CS5a, eluent PDCA, flow 1.0 mL min^{-1}, spectrophotometric detection after Post Column Reaction (PCR) with PAR; (ii) Al content: column Dionex CS5a, eluent HCl (0.75 M), flow 1 mL min^{-1}, spectrophotometric detection after PCR with Tiron. The chloride content was determined by ion chromatography for the solution obtained by soaking the solid samples in Na_2CO_3 (1 M) at 80 °C for 4 h. C and H elemental analysis was performed with a Carlo Erba 1106 analyser. Carbonate and water contents were also evaluated from TGA.

Characterisation: X-ray powder patterns were collected in the 7–110° and 0.02° step size (2θ range) according to the step scanning procedure using Cu-K_α radiation with a Philips X'Pert APD diffractometer, PW3020 goniometer equipped with a bent graphite monochromator on the diffracted beam. Divergence and scatter slits of 0.5° and a receiving slit of 0.1 mm were used. The LFF ceramic tube operated at 40 kV and 30 mA. To minimise preferred orientations, the sample was carefully side loaded onto an aluminium sample holder with an oriented quartz monocrystal underneath. The counting time was 20 sec step^{-1} for all the diffraction patterns. The TG/DTG/DTA analyses were performed in air with a Netzsch STA449C thermal analyser at a heating rate of 5 °C min^{-1} under an air flow.

Rietveld Refinement: Rietveld refinements for **I** and **II** were performed using the GSAS program.[34] Sample displacement, cell parameters and background were first refined. Fractional coordinates and isotropic thermal factors for all the atoms, and profile shape were also refined. The profile was modelled using a pseudo Voigt profile function (six terms) with two terms for the modelling of asymmetry at low 2θ angle. The interatomic distances and bond lengths were refined freely, except for the O–H distance that was restrained to 0.9(3) Å. Isotropic thermal factors were refined by constraining the program to apply the same shift to the metal atoms and another shift to the light atoms. The metal atom occupancies were set at fixed values (according to the stoichometry) and were not refined. At the end of the refinement the shifts on all parameters were less than their standard deviations.

Computational Details

FF Parameters: The Materials Studio package (Accelrys Inc., San Diego) was used to perform all MD simulations through the Discover module. In the present work, the recently developed CLAYFF force field[34] was included. This FF features suitable parameters for LDHs containing the Si, Al, Mg, Ca, Fe and Li species. Accordingly, to overcome the lack of parameters for systems in which Me(II) = Zn, the Zn parameters were derived by using the following minerals, for which structural data are available, as model compounds: ε-$Zn(OH)_2$[35,36] γ-$Zn(OH)_2$,[37] $Zn_5(OH)_8Cl_2\cdot H_2O$.[38] For the VDW function, the following parameters were obtained: $D_0 = 1.0\times10^{-6}$ kcal mol^{-1}, $R_0 = 5.0$ Å, charge = 1.05 *e*. The orders of magnitude of these calculated Zn nonbonding parameters were in agreement with those of the species Si, Al, Mg, Ca, Fe, Li as quoted in Table 1 of ref.[34]. The parameter values of the electrostatic terms reported in this table were readjusted as follows: hydroxy oxygen (OH) = –0.875 *e*; aqueous chloride ion (Cl^-) = –0.975 *e*, on the basis of the hydrotalcite-type structure used for modelling. This was done in order to achieve total electroneutrality through the redistribution of the charge on Al among the surrounding hydroxy groups.

Protocols: The MD simulations started from the energy-minimised structures. The periodic boundary conditions (PBC) with an NPT ensemble were used for all the runs. Transients of 200 ps and 1 ns were collected for the models at various hydration degrees and for the models selected for the validation procedure of the simulations, respectively. In both cases the integration time step was 0.001 ps, and the sampling interval was 1000 time steps. The energy-optimised structures were obtained with the smart minimiser of the Discover module, satisfying a gradient of 0.1 kJ mol^{-1}. The nonbonding (NB) settings were those provided by default in this module for VDW interaction: atom-based summation method with cutoff = 9.5 Å, spline width = 1.0, buffer width = 0.50, and long-range energy correction = 9.5. For the Coulomb interaction, an Ewald summation method was used with accuracy = 0.01, update width = 1.0, dielectric constant $\varepsilon = 1$.

Modelling: The structural models of the samples **I** and **II**, which were submitted to all the simulations, were generated on the basis of the X-ray crystal structures (unit cells and atomic fractional coordinates) provided by refinement of their XRPD data by Rietveld analysis (Table 1, Table 2). All structures were 3-layered periodic supercells built up by setting *R*3*m* symmetry conditions and the factors 6, 6 and 1 for the unit-cell parameters *a*, *b* and *c*, respectively. Each layer included 36 atoms of the two metals in the ratio Zn/Al = 2:1 (Figure 1) for 108 formula units. The supercell parameters *a*, *b*, *c*, *α*, *β*, *γ*, were independent variables in the MD simulations. The interlayer water molecules and chloride (**I**) or carbonate (**II**) anions from the Rietveld analyses (Figure 2) were regularly distributed in the lattice positions denoted by green balls in Figure 1. Preliminary molecular modelling energy calculations showed that the energy-preferred position of the metallic atoms in the slab was the most regularly ordered one, i.e., that in which six Zn atoms were the nearest neighbours of each Al atom, and three Al atoms and three Zn atoms were the nearest neighbours of each Zn atom (Figure 1b). The simulated models of **I** and **II** were obtained by determining the amount of the regularly distributed interlayer water molecules for each compound by varying the sequence of the total number of water molecules (N_w) from 54, 51, 48 down to 0, and from 93, 90, 81, 72 down to 0, respectively. This corresponded to the formula coefficients (y) which varied from $y = 0.5$, 0.47, 0.44 down to 0 for **I**, and from $y = 0.86$, 0.83, 0.75 down to 0, for **II**. In the search for the best model, the interval over which N_w was varied was adequately restricted.

Calculation of XRPD Pattern from MD Trajectory (MD-XRPD): The cell and atomic positional parameters were calculated from the MD trajectory and stored. The angles θ and Miller indices (h, k, l) for which a diffraction peak should appear were determined for each of these snapshots by using the Bragg equation, $n\lambda = 2d\times\sin\theta_{(hkl)}$.

The intensity of these diffraction peaks is $I_{hkl} = |F_{hkl}|^2$, in which $F_{hkl} = \Sigma f_n e^{2\pi i(hu_n + kv_n + lw_n)}$, where u, v, w are atomic fractional parameters and f_n X-ray scattering factors.

The intensity obtained in this way was then stored in an array of bin size $\delta(2\theta)$ at the position corresponding to $2\theta(N) = 2\theta_{(hkl)} \pm \frac{1}{2}\delta(2\theta)$. Averaging all of the snapshots of the MD simulation

 © 2005 Wiley-VCH Verlag GmbH & Co. KGaA, Weinheim

completed the above MD-XPRD procedure. The diffraction intensity $I(2\theta)$, obtained in this way, was then scaled[39] for the Lorentz [$L = 1/(\sin\theta \times \sin 2\theta)$] and polarization [$p$] corrections (Lp).

Crystallite Size Broadening: The above procedure led to an MD-determined XRPD pattern for a perfect crystal of infinite dimension, whose atomic and cell parameters fluctuated due to thermal motions. When crystallites are less than approximately 1000 Å in size, appreciable broadening in the XRPD lines will occur. The shape of the peaks take on a predominantly Lorentzian profile[40] centred at $\theta_{(hkl)}$, with a full width at the half maximum (FWHM) that depends on the crystallite size. The relation that quantitatively describes the FWHM [$\Delta(2\theta_{hkl})$] as a function of the dimensions of the crystal and the order of the diffraction peak (hkl) is[40]

$$\Delta(2\theta_{hkl}) = \frac{\lambda}{\cos\theta_{hkl}} \frac{1}{d_{hkl}} \left[h^2 \left(\frac{L_a}{a} \right)^2 + k^2 \left(\frac{L_b}{b} \right)^2 + l^2 \left(\frac{L_c}{c} \right)^2 \right]^{\frac{1}{2}}$$

in which h, k and l are the Miller indices, and L_a, L_b, L_c are the crystallite dimensions along a, b and c, respectively. The procedure for calculating the size-broadened MD-XRPD pattern, given the dimensions L_a, L_b and L_c of the crystallite, was the same as that for a perfect crystal, whereas the values of the intensity profile of the broadened peaks were stored in the array along the bins centred around $2\theta(K) = 2\theta_{(hkl)}$ for a width of $\pm 10\,\Delta(2\theta_{hkl})$.

Modelling the XRPD Pattern: The experimental XRPD pattern (line shape and peak heights) was modelled by calculating a set of XRPD patterns from the MD trajectory that corresponded to different crystallite sizes (N patterns for N crystal sizes). Subsequently the calculated pattern was compared with the experimental XRPD curve by using the equation having the best fit for the coefficients w_i.

$$I(\theta)_{calcd} = w_1 I_1(\theta) + w_2 I_2(\theta) + \cdots + w_N I_N(\theta) = \sum_{i=1}^{N} w_i I_i(\theta)$$

Acknowledgments

This work was supported by the MIUR (Italy) within the PRIN Program (prot. 2004031878_002). Thanks also go to Prof. Kenny B. Lipkowitz for useful suggestions and discussions.

[1] H. F. W. Taylor, *Miner. Mag.* **1969**, *37*, 338–342.
[2] R. Allmann, *Chimia* **1970**, *24*, 99–342.
[3] G. Mascolo, O. Marino, *Miner. Mag.* **1980**, *43*, 619–621.
[4] W. T. Reichle, *Solid State Ionics* **1986**, *22*, 135–141.
[5] K. J. Martin, T. J. Pinnavaia, *J. Am. Chem. Soc.* **1986**, *108*, 541–542.
[6] M. Meyn, K. Beneke, G. Lagaly, *Inorg. Chem.* **1990**, *29*, 5201–5207.
[7] F. Cavani, F. Trifirò, A. Vaccari, *Catalysis Today* **1991**, *11*, 173–301.
[8] S. P. Newman, W. Jones, *New J. Chem.* **1998**, *22*, 105–115.
[9] U. Costantino, F. Marmottini, M. Nocchetti, R. Vivani, *Eur. J. Inorg. Chem.* **1998**, 1439–1446.
[10] *Layered Double Hydroxides: Present and Future* (Ed.: V. Rives), Nova Science Publishers Inc., New York, **2001**, p. 439 .
[11] A. I. Khan, D. O'Hare, *J. Mater. Chem.* **2002**, *12*, 3191–3198.
[12] V. R. L. Constantino, T. J. Pinnavaia, *Inorg. Chem.* **1995**, *34*, 883–892.
[13] W. Kagunya, Z. Hassan, W. Jones, *Inorg. Chem.* **1996**, *35*, 5970–5974.
[14] A. Vaccari, *Appl. Clay Sci.* **1999**, *14*, 161–198.
[15] B. F. Sels, D. E. De Vos, P. A. Jacobs, *Catalysis Reviews* **2001**, *43*, 443–488.
[16] D. Tichit, B. Coq, *CATTECH* **2003**, *7*, 206–217.
[17] S. Velu, K. Suzuki, M. Okazaki, M. P. Kapoor, T. Osaki, F. Ohashi, *J. Catal.* **2000**, *194*, 373–384.
[18] S. Murcia-Mascaros, R. M. Navarro, L. Gomez-Sainero, U. Costantino, M. Nocchetti, J. L. G. Fierro, *J. Catal.* **2001**, *198*, 338–347.
[19] M. Turco, G. Bagnasco, U. Costantino, F. Marmottini, T. Montanari, G. Ramis, G. Busca, *J. Catal.* **2004**, *228*, 43–55.
[20] R. Caminiti, M. Gleria, K. B. Lipkowitz, G. M. Lombardo, G. C. Pappalardo, *J. Am. Chem. Soc.* **1997**, *119*, 2196–2204.
[21] R. Caminiti, M. Gleria, K. B. Lipkowitz, G. M. Lombardo, G. C. Pappalardo, *Chem. Mater.* **1999**, *11*, 1492–1497.
[22] M. E. Amato, R. Caminiti, G. A. Carriedo, F. J. García-Alonso, J. L. García-Alvarez, G. M. Lombardo, G. C. Pappalardo, *Chem. Eur. J.* **2001**, *7*, 1486–1494.
[23] M. E. Amato, G. A. Carriedo, F. J. García-Alonso, J. L. García-Alvarez, G. M. Lombardo, G. C. Pappalardo, *J. Chem. Soc. Dalton Trans.* **2002**, 3047–3053.
[24] G. A. Carriedo, F. J. García-Alonso, J. L. García-Alvarez, G. M. Lombardo, G. C. Pappalardo, F. Punzo, *Chem. Eur. J.* **2004**, *10*, 3775–3782.
[25] G. Alberti, A. Grassi, G. M. Lombardo, G. C. Pappalardo, R. Vivani, *Inorg. Chem.* **1999**, *38*, 4249–4255.
[26] G. Alberti, G. M. Lombardo, G. C. Pappalardo, R. Vivani, *Chem. Mater.* **2002**, *14*, 295–303.
[27] S. P. Newman, H. C. Greenwell, P. V. Coveney, W. Jones, in: *Layered Double Hydroxides: Present and Future* (Ed.: V. Rives), Nova Science Publishers, Inc. New York, **2001**, Chapter 2, p. 93 and references cited therein.
[28] A. G. Kalinichev, R. J. Kirkpatrick, R. T. Cygan, *Am. Mineralogist* **2000**, *85*, 1046–1052.
[29] A. M. Fogg, A. L. Rohl, G. M. Parkinson, D. O'Hare, *Chem. Mater.* **1999**, *11*, 1194–1200.
[30] A. G. Kalinichev, J. Wang, R. J. Kirkpatrick, R. T. Cygan, in: *Foundations of Molecular Modeling and Simulations* (Ed.: P. T. Cummings), AIChE Symposium Series No. 325, **2001**, v. 97, 251 pp.
[31] A. G. Kalinichev, J. Wang, R. J. Kirkpatrick, X. Hou, *Chem. Mater.* **2001**, *13*, 145–150.
[32] J. Wang, A. G. Kalinichev, J. E. Amonette, R. J. Kirkpatrick, *Am. Mineralogist* **2003**, *88*, 398–409.
[33] R. T. Cygan, J. J. Liang, A. G. Kalinicev, *J. Phys. Chem. B* **2004**, *108*, 1255–1266.
[34] A. Larson, R. B. Von Dreele, *GSAS, Generalized Structure Analysis System*, Los Alamos National Laboratory, **1988**.
[35] R. Stahl, C. Jung, H. D. Lutz, W. Kockelmann, H. Jacobs, *Z. Anorg. Allg. Chem.* **1998**, *624*, 1130–1136.
[36] A. Noerlund Christensen, *Acta Chem. Scandinavica* **1969**, *23*, 2016–2020.
[37] W. Nowacki, J. N. Silverman, *Z. Kristallogr.* **1962**, *117*, 238–240.
[38] W. Nowacki, J. N. Silverman, *Z. Kristallogr.* **1961**, *115*, 21–51.
[39] Accelrys Inc., *MS Modeling Theory in Reflex*, San Diego: Accelrys Inc., **2003**.
[40] *The Rietveld Method* (Ed.: R. A. Young), IUCr Monograph on Crystallography, 5, Oxford University Press, **1993**.
[41] D. R. Roberts, R. G. Ford, L. Sparks, *J. Colloid. Interface Sci.* **2003**, *263*, 364–376.

Received: July 26, 2005
Published Online: November 23, 2005

 © 2005 Wiley-VCH Verlag GmbH & Co. KGaA, Weinheim

DOI: 10.1002/ejic.200501034

Self-Assembly of Organotin(IV) Moieties with the Schiff-Base Ligands Pyruvic Acid Isonicotinyl Hydrazone and Pyruvic Acid Salicylhydrazone: Synthesis, Characterization, and Crystal Structures of Monomeric or Polymeric Complexes

Handong Yin,*[a] Min Hong,[a] Haolong Xu,[a] Zhongjun Gao,[a] Gang Li,[a] and Daqi Wang[a]

Keywords: N,O ligands / Self-assembly / Schiff bases / Tin

Scheme 4 on page 4578 of the original article[1] inadvertently represents a copy of Scheme 3; the correct Scheme 4 is shown below.

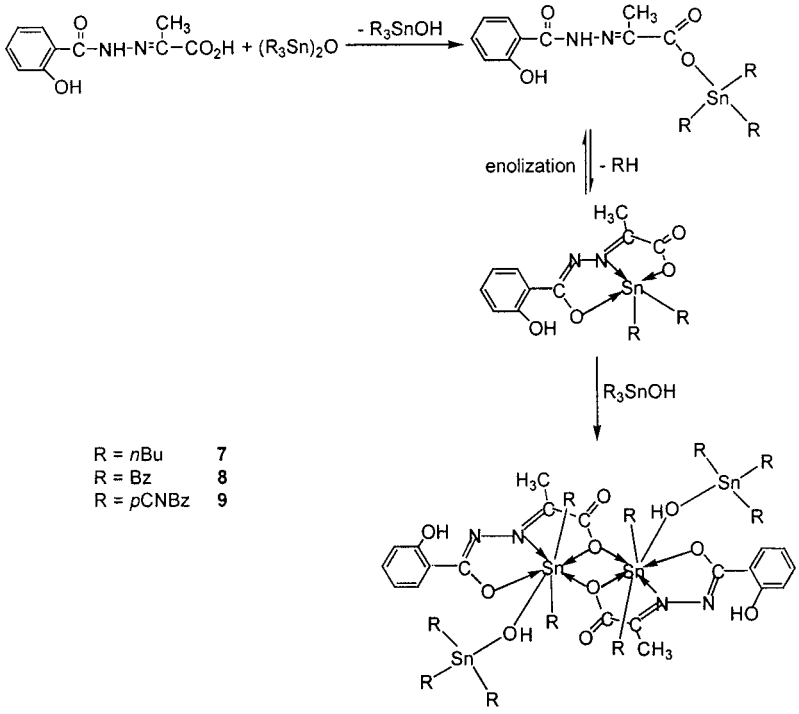

Scheme 4.

[1] H.-D. Yin, M. Hong, H.-L. Xu, Z.-J. Gao, G. Li, D.-Q. Wang, *Eur. J. Inorg. Chem.* **2005**, 4572–4581.

Received: November 18, 2005
The Editors

[a] Department of Chemistry, Liaocheng University, Liaocheng 252059, China
E-mail: handongyin@lctu.edu.cn

 © 2005 Wiley-VCH Verlag GmbH & Co. KgaA, Weinheim